Proceedings of the 11th European Review Meeting on Severe Accidents Research (ERMSAR2024)

KTH Royal Institute of Technology, Stockholm, Sweden

May 13-16, 2024

Funded by the European Union

ERMSAR 2024 was organized under the frame of the SEAKNOT project. This project has received funding from the Euratom Research and Training Programme 2021-2023 under grant agreement No 101060327.
The content of the papers reflects only the authors' views and do not necessarily reflect those of the European Union or EURATOM. Neither the European Union nor EURATOM can be held responsible for them.

FOREWORD

The 11th edition of the ERMSAR Conference was held from 13 to 16 May 2024 in Stockholm, hosted and locally organized by KTH, after 2 years from the previous 10th edition in Karlsruhe. For the first time it has been organized in the frame of the EURATOM SEAKNOT project and the Technical Area 2 of the Nuclear Generation II & III Alliance (NUGENIA TA2) of the Sustainable Nuclear Energy Technology Platform SNETP, together with IAEA and OECD/NEA.

The Technical Programme Committee involved 19 researchers and engineers from diverse organizations (BT, CEA, CIEMAT, ENEA, Framatome GmbH, GRS, IAEA, INRN, IRSN, JSI, KIT, KTH, LGI, NEA and University of Pisa).

ERMSAR 2024 gathered 157 participants from 77 organizations settled in 26 countries worldwide. A total of 73 papers were orally presented, and 33 more were exhibited in the posters stand. These numbers highlight ERMSAR as the reference international conference on Severe Accidents. The conference was focused on the latest progress of international knowledge on severe accidents and has been mainly an opportunity for researchers to discuss about the most recent achievements and future R&D priorities in this field. The Conference topics are highlighted in the following technical tracks:

1. In-vessel corium and debris coolability
2. Ex-vessel corium interactions and coolability
3. Containment behavior incl. Explosion risk
4. Source term
5. Analysis, Management, and Consequences of Severe Accidents for Gen I-III reactors
6. Severe accidents in innovative reactors such as Gen IV and Small Modular Reactors
7. Other applications (fusion reactors, interim SNF storage, Accident Tolerant Fuels, etc.)

In addition, the technical programme included three plenary sessions:

- Singular careers in the severe accident research;
- Regulatory perspective and approaches for severe accidents in SMRs;
- Looking ahead in severe accident research;

As top-level conclusions from ERMSAR 2024, one may highlight:

- A good part of R&D is and will continue investigating on SA mitigation, in particular on feasibility/development of “new” mitigation measures;
- An emerging substantial amount of work is being devoted to very near-term deployment systems, like WC-SMRs (Water-Cooled Small Modular Reactor), with a major take on “safety demonstration”. At the same time, current analytical tools are being adapted to more innovative systems (i.e., non-water-cooled systems and Gen. IV technologies) by including new phenomena and/or extended ranges of known phenomena that might be necessary to overcome some of their present drawbacks to model those advanced systems;
- An important shift has been observed in severe accident analyses, which to a good extent is moving from a best estimate (BE) approach to include uncertainty quantification and sensitivity analysis (BEPU). However, there is still significant constraints for a systematic application of BEPU, and further research is planned to consolidate a soundly supported methodology.

Next conference edition, ERMSAR 2026, will be again organized in the frame of the SEAKNOT project by CIEMAT in Madrid on the week from 18 to 22 May 2026.

Editors: Fabrizio Gabrielli, Luis E. Herranz and Sandro Paci

Funded by
the European Union

ORGANIZATION

Technical Program Committee

- Luis E. Herranz (Centro de Investigaciones Energéticas, Medioambientales y Tecnológicas, CIEMAT, Spain)
- Fabrizio Gabrielli (Karlsruhe Institute of Technology, KIT, Germany)
- Pascal Piluso (Commissariat à l'énergie atomique et aux énergies alternatives, CEA, France)
- Sami Strola (LGI Sustainable Innovation, France)
- Ivo Kljenak (Jozef Stefan Institute, IJS, Slovenia)
- Sanjeev Gupta (Becker Technologies, Germany)
- Federico Rocchi (Agenzia nazionale per le nuove tecnologie, l'energia e lo sviluppo economico sostenibile, ENEA, Italy)
- Sandro Paci (University of Pisa, Italy)
- Ahmed Bentaib (Institut de Radioprotection et de Sûreté Nucléaire, IRSN, France)
- Sevostian Bechta (Royal Institute of Technology, KTH, Sweden)
- Victor H. Sanchez Espinoza (Karlsruhe Institute of Technology, KIT, Germany)
- Walter Tromm (Karlsruhe Institute of Technology, KIT, Germany)
- Thorsten Hollands (Gesellschaft für Anlagen- und Reaktorsicherheit, GRS, Germany)
- Pavlin Groudev (Institute for Nuclear Research and Nuclear Energy, Bulgaria)
- Markus. Hupp (Framatome GmbH, Germany)
- Alexei. Miassoedov (IAEA, Austria)
- Stephan. Brumm (European Commission's Joint Research Centre, Netherlands)
- Martina Adorni (Nuclear Energy Agency, France)
- Didier Jacquemain (Nuclear Energy Agency, France)

Organizing committee

- Patrick Isaksson (Swedish Radiation Safety Authority, SSM, Sweden)
- Nils Sandberg (Swedish Radiation Safety Authority, SSM, Sweden)
- Sean Roshan (Royal Institute of Technology, KTH, Sweden)
- Marta Marko-Tisch (Royal Institute of Technology, KTH, Sweden)

LIST OF THE PARTICIPANTS

Name	Institution	Country
Addad, Y.	Khalifa University of science and technology	UAE
Agrell, M.	SSM	Sweden
Ahn, K.	KAERI	Republic of Korea
Angelucci, M.	University of Pisa	Italy
Anschuetz, L.	Framatome GmbH	Germany
Arfinengo del Carpio, S.	UPM	Spain
At Khen, K.	EDF R&D	France
Auvinen, A.	TVO	Finland
Bachrata Kubic, A.	CEA Cadarache	France
Bakouta, N.	EDF	France
Basnet, S.	University of Eastern Finland	Finland
Batek, D.	ÚJV Řež	Czechia
Bechta, S.	KTH	Sweden
Beck, S.	GRS	Germany
Bentaib, A.	IRSN	France
Bittan, J.	Électricité de France	France
Bläsius, C.	GRS	Germany
Bligny, M.	Framatome	France
Börjesson Sandén, F.	Chalmers University of Technology	Sweden
Bouyer, V.	CEA	France
Brumm, S.	EC JRC	Netherlands
Busbach, R.	MVM Paks NPP Ltd.	Hungary
Cantrel, L.	IRSN	France
Carenini, L.	IRSN	France
Cazado, M. E.	Karlsruhe Institute of Technology	Germany
Chao, W.	Nuclear and Radiation Safety Center of Ministry of Ecology and Environment	China
Chen, E.	China Nuclear Power Engineering Co., LTD	China
Chen, L.	KTH	Sweden
Clain, C.	TechnicAtome	Lithuania
Coindreau, O.	IRSN	France
Concilio Hansson, R.	Forsmark	Sweden
Cormack, M.	NNL	United Kingdom
D'Alessandro, C.	Paul Scherrer Institute	Switzerland
De Malmazet, E.	EDF	France
Deng, Y.	KTH	Sweden
Denoix, A.	CEA	France
Di Giuli, M.	Tractebel (ENGIE)	Belgium
Dieter, K.	Becker Technologies GmbH	Germany
Dittmer, S.	Ringhals NPP, Vattenfall	Sweden
Domínguez-Bugarín, A.	UPM	Spain

Dougall, A.	EDF Energy	United Kingdom
Dukaj, F.	GRS	Germany
Engström, B.	KTH	Sweden
Fang, D.	KTH	Sweden
Farkas, R.	HUN-REN Centre for Energy Research	Hungary
Fichot, F.	IRSN	France
Fowles, J.	Rolls-Royce SMR	United Kingdom
Gabicagogeascoa, C.	UPM	Spain
Gabrielli, F.	Karlsruhe Institute of Technology	Germany
Gal, P.	ÚJV Řež	Czechia
Galushin, S.	Vysus Sweden AB	Sweden
Garcia, M.	CIEMAT	Spain
García-Herranz, A.	UPM	Spain
Gauntt, R.	Gauntt Technical Safety Associates	USA
Girault, N.	IRSN	France
Glänneskog, H.	Vattenfall AB	Sweden
Glover, J.	Office for Nuclear Regulation	United Kingdom
Grippo, G.	University of Bologna	Italy
Gupta, S.	Becker Technologies GmbH	Germany
Gyepi-Garbrah, S.	Canadian Nuclear Safety Commission	Canada
Hage, M.	GRS	Germany
Hammouch, Z.	Framatome	France
Harti, M.	Fortum	Finland
Herranz, L. E.	CIEMAT	Spain
Himi, M.	CRIEPI	Japan
Hollands, T.	GRS	Germany
Hrbek, J.	ÚJV Řež	Czechia
Hudson, R.	EDF Energy	United Kingdom
Hupp, M.	Framatome	Germany
Isaksson, P.	SSM	Sweden
Ishida, S.	Japan Atomic Energy Agency	Japan
Jacquemain, D.	OECD/NEA	France
Jimenez, G.	UPM	Spain
Journeau, C.	CEA	France
Kaliatka, T.	Lithuania Energy Institute	Lithuania
Kaneko, J.	Nuclear Regulation Authority	Japan
Kärkelä, T.	VTT	Finland
Keim, T.	Framatome	Germany
Kelm, S.	Forschungszentrum Jülich GmbH	Germany
Klauck, M.	Forschungszentrum Jülich GmbH	Germany
Kljenak, I.	Jozef Stefan Institute	Slovenia
Kojima, Y.	Waseda University	Japan
Komlev, A.	KTH	Sweden
Komrska, J.	UJV Rez	Czechia

Kotouc, M.	UJV Rez	Czechia
Kumagai, Y.	OECD/NEA	France
Kuznetsov, M.	Karlsruhe Institute of Technology	Germany
Laborde, L.	IRSN	France
Langrock, G.	Framatome GmbH	Germany
Le Tellier, R.	CEA	France
Lecoanet, A.	CEA	France
Li, X.	Japan Atomic Energy Agency	Japan
Li, X.	KTH	Sweden
Liljequist , K.	Swedish Radiation Safety Authority	Sweden
Lind, T.	Paul Scherrer Institut	Switzerland
Luxat, D.	Sandia National Laboratories	USA
Ma, E.	KTH	Sweden
Ma, W.	KTH	Sweden
Maaouia, M.	SSM	Sweden
Malicki, M.	Paul Scherrer Institut	Switzerland
Mann, S.	EDF-Energy	United Kingdom
Marquie, C.	IRSN	France
Mårtensson, O.	SSM	Sweden
Mascari, F.	ENEA	Italy
Mathe, E.	TechnicAtome	France
Mathé, G.	TechnicAtome	France
Matsumoto, T.	Japan Atomic Energy Agency	Japan
Matsuoka, K.	Waseda University	Japan
McMinn, P.	Fauske and Associates	USA
Mészáros, B.	Research centre Řež s.r.o.	Czechia
Miassoedov, A.	IAEA	IAEA
Monestier, M.	IRSN	France
Morreale, A.	CNL	Canada
Müer, M.	Ruhr-Universität Bochum	Germany
Murat, O.	Karlsruhe Institute of Technology	Germany
Nakamura, H.	Japan Atomic Energy Agency	Japan
Nakamura, K.	Japan Atomic Energy Agency	Japan
Nasselahsen, M.	CEA	France
Nudi, M.	EPRI	USA
Olofsson, J.	Ringhals AB	Sweden
Paci, S.	University of Pisa	Italy
Pandazis, P.	GRS	Germany
Park, R.	KAERI	Korea, Republic of
Patterson, G.	CNL	Canada
Peng, C.	Shanghai University of Electric Power	China
Piluso, P.	CEA	France
Pontillon, Y.	CEA	France
Poubeau, B.	IRSN	France

Principato, M.	Sapienza University of Rome	Italy
Ramos Perez, A.	Paul Scherrer Institut	Switzerland
Rehrmann, J.	Ruhr-Universität Bochum	Germany
Reinecke, E.	Forschungszentrum Jülich GmbH	Germany
Rempe, J.	Rempe and Associates, LLC	USA
Rickard, J.	Rolls-Royce SMR Ltd	United Kingdom
Riglet-Martial, C.	CEA	France
Rimbert, N.	Université de Lorraine	France
Rizaal, M.	Japan Atomic Energy Agency	Japan
Rocchi, F.	ENEA	Italy
Rochedy, M.	CEA	France
Rodrigues, A.	Office for Nuclear Regulation	United Kingdom
Roshan, S.	KTH	Sweden
Rydl, A.	INSET s.r.o.	Czechia
Ryman, A.	SSM	Sweden
Sagan, M.	Framatome	France
Sartoris, C.	IRSN	France
Seiler, N.	CEA	France
Serra Lopez, L.	UPM	Spain
Sevón, T.	VTT Technical Research Centre of Finland	Finland
Shewitah, M.	Alexanderia University	Egypt
Shimomura, K.	Japan Atomic Energy Agency	Japan
Smieszek, H.	Framatome Oy	Finland
Spengler, C.	GRS	Germany
Stahlberg, G.	Ruhr-Universität Bochum	Germany
Stakhanova, A.	Karlsruhe Institute of Technology	Germany
Steinbrück, M.	Karlsruhe Institute of Technology	Germany
Tagami, H.	Japan Atomic Energy Agency	Japan
Tatidis, A.	KTH	Sweden
Tehrani, A.	Office for Nuclear Regulation	United Kingdom
Tóthné Laki, E.	MVM Paks NPP LTD.	Hungary
Tourneix, A.	CEA	France
Trundle, G.	KTH	Sweden
Turner, M.	Jacobs	United Kingdom
Ursic, M.	Jozef Stefan Institute	Slovenia
Vacha, P.	UJV Rez	Czechia
Vazquez-Rodriguez, C.	Forschungszentrum Jülich GmbH	Germany
Venzhego, G.	SSM	Sweden
Xiang, Y.	KTH	Sweden
Yamada, H.	MHI NS Engineering Co.,Ltd.	Japan
Yamashita, T.	Japan Atomic Energy Agency	Japan
Yepes Ramirez, H.	ATG Europe / Fusion for Energy (F4E)	Spain
Zhang, L.	CNPE	China
Zhao, L.	KTH	Sweden



The 11th European Review Meeting on Severe Accidents Research

May 13-16, 2024, Royal Institute of Technology, Stockholm, Sweden

Conference Program

MONDAY, MAY 13th, 2024

PLENARY SESSION: WELCOME AND INTRODUCTORY

Chairs: S. Bechta (KTH), F. Gabrielli (KIT)

Welcoming Addresses
S. Östlund, Vice President of the KTH
M. Knochenhauer, Director General, Swedish Radiation Safety Authority (SSM)
Opening of the ERMSAR2024 Conference
L.E. Herranz (CIEMAT), Coordinator of the SEAKNOT project

PLENARY SESSION: SINGULAR CAREERS IN THE SEVERE ACCIDENT RESEARCH

Chairs: L. E. Herranz (CIEMAT), T. Lind (PSI)

Reflections on a career in reactor safety: Severe Accident Code Development
Dr Randall Gauntt (MELCOR Code Development Manager, Retired Sandia National Laboratories)
Progress in Predicting Reactor Pressure Vessel Failure
J. Rempe (Rempe and Associates, LLC)
Your Research Maps: Needs and challenges with scaling consideration
H. Nakamura (JAEA)

Technical Session 2.1: Severe Accident Scenarios

Chairs: S. Gupta (Becker Tech. GmbH), D. Jacquemain (OECD/NEA)

ID76	**SEAKNOT: Looking Ahead of Severe Accident Research** L. E. Herranz (CIEMAT)	**Paper** **Presentation**
ID16	**ASTEC core degradation calculations in support of Level-2 Probabilistic Safety assessment for 1300MWe French reactors: methodology and preliminary results** M. Monestier (IRSN)	**Paper** **Presentation**
ID12	**MELCOR Analyses for Investigation on Hydrogen Management during BWR Severe Accidents with the Filtered Containment Venting System** Y. Kojima (Waseda University)	**Paper** **Presentation**

ID27	**On the progress made in safety assessment and severe accident management as part of the French Fukushima post-accident research programme** A. Bentaib (IRSN)	**Paper** **Presentation**

Technical Session 1.1: In-vessel Corium and debris coolability

Chairs: F. Gabrielli (KIT), A. Miassoedov (IAEA)

ID73	**IVMR Modelling with Transient Effects during Molten Pool Formation and Stabilization – Outcomes from Models' Comparison Performed in the IAEA CRP J46002** L. Carénini (IRSN)	**Paper** **Presentation**
ID24	**Numerical Analysis of Melt Penetration Behavior in the Control Rod Drive Housing of Fukushima Daiichi Nuclear Power Station Unit-2** X. Li (JAEA)	**Paper**
ID66	**Reactor pressure vessel integrity during severe accident with core meltdown: characterization of material parameters, structure integrity assessment and thermal-hydraulic assessment** P. Gal (UJV)	**Paper** **Presentation**
ID58	**Improvement of thermochemical corium stratification accounting for uranium and zirconium composition difference in metallic and oxide phases** A. Lecoanet (CEA)	**Paper** **Presentation**

Technical Session 2.2: Severe Accident Scenarios

Chairs: A. Bentaib (IRSN), L. E. Herranz (CIEMAT)

ID05	**Horizon Euratom ASSAS project: Can machine-learning make fast and accurate severe accident simulators a reality?** B. Poubeau (IRSN)	**Paper** **Presentation**
ID26	**Preliminary Strategies for Training Dataset Generation and Surrogate Modeling of SBO Management Measures in PWR** C. D'Alessandro (PSI)	**Paper** **Presentation**
ID86	**Analysis of accident progression behavior and simulation of FP release into the environment using MELCOR code for the Fukushima Daiichi Nuclear Power Station Units 1 to 3** M. Himi (CRIEPI)	**Paper** **Presentation**
ID63	**Long-term severe accident management at Loviisa NPP** M. Harti (Fortum Power and Heat Oy)	**Paper** **Presentation**

Technical Session 1.2: In-vessel Corium and debris coolability

Chairs: L. Carénini (IRSN), T. Hollands (GRS)

ID21	**Stainless Steel Oxidation at both Solid and Liquid State Under Ar-H_2O Gas Mixture in Severe Accident Conditions** M. Nasselahsen (CEA)	**Paper** **Presentation**
ID25	**A Thermodynamic Study of Molten Pool Stratification Morphology** E. Chen (China Nuclear Power Eng. Co.)	**Paper** **Presentation**
ID78	**In-Vessel Corium Thermochemistry Benchmark based on MASCA Experimental Data** R. Le Tellier (CEA)	**Paper** **Presentation**
ID07	**Coolability of a Corium Pool in a Debris Bed – Calculation of Critical Heat Flux (CHF) Tests with the ASTEC Code** C. Sartoris (IRSN)	**Paper** **Presentation**

Technical Session 2.3: Severe Accident Scenarios - U&S analysis

Chairs: O. Coindreau (IRSN), S. Paci (University of Pisa)

ID75	**Major Achievements of the EC MUSA Project** L. E. Herranz (CIEMAT)	**Paper** **Presentation**
ID101	**Source Term Uncertainty Analysis of Filtered Containment Venting Scenarios in Nordic BWR** S. Galushin (Vysus Group)	**Paper** **Presentation**
ID01	**Uncertainty and Sensitivity Analysis of the ASTEC Source Term Results of a MBLOCA Scenario with the Activation of Severe Accident Management Actions in a Generic KONVOI Plant** A. Stakhanova (KIT)	**Paper** **Presentation**
ID72	**Source Term Uncertainties in unmitigated SBO sequences in a PWR-1000: Insights from the EU-MUSA project** R. Iglesias (CIEMAT)	**Paper** **Presentation**

Technical Session 4.1: Severe Accident Scenarios - Small Modular Reactors

Chairs: F. Gabrielli (KIT), D. Jacquemain (OECD/NEA)

ID75	**SASPAM-SA: Assessment of the relevance and applicability of existing experimental databases to iPWR** T. Lind (PSI)	**Paper** **Presentation**
ID101	**Numerical Investigation of Natural Circulation Inside a Scaled-Down Prismatic Modular Reactor By RHYS** M. Shewitah (Minia University)	**Paper** **Presentation**
ID01	**Development of a LW-SMR dry containment model with containmentFOAM** C. Vázquez-Rodríguez (FZJ)	**Paper** **Presentation**
ID72	**Comparison of a DBA sequence in a generic iPWR between MELCOR and ASTEC codes** G. Grippo (ENEA)	**Paper** **Presentation**

TUESDAY, MAY 14th, 2024

Technical Session 2.4: Severe Accident Scenarios - U&S analysis

Chairs: M. Angelucci (University of Pisa), L. E. Herranz (CIEMAT)

ID98	**Synthesis of Source Term Assessments for a Loss-Of-Cooling Accident in a Spent Fuel Pool: Uncertainty and Sensitivity Analyses and Potential Benefit of Water Injection by Spray System** O. Coindreau (IRSN)	**Paper Presentation**
ID03	**Uncertainties on Fission Product Release for a Loss-Of-Cooling Scenario in a Spent Fuel Pool with MELCOR2.2** M. Garcia (CIEMAT)	**Paper Presentation**
ID10	**Uncertainty and Sensitivity Analyses of Severe Accident Codes Using the ACE Algorithm-based Surrogate Model** Kwang-Il Ahn (KAERI)	**Paper Presentation**
ID42	**System Identification and Ranking Table (SIRT) for chemical thermodynamics of severe accidents** C. Journeau (CEA)	**Paper Presentation**

Technical Session 4.2: Severe Accident Scenarios - Small Modular Reactors

Chairs: T. Lind (PSI), A. Bentaib (IRSN)

ID77	**Analysis of Postulated Severe Accidents in Generic Integral PWR Small Modular Reactors in the frame of the Horizon Euratom SASPAM-SA Project** F. Gabrielli (KIT)	**Paper Presentation**
ID116	**Update on Severe Accident Analysis Research at CNL for Small Modular and Advanced Reactor Designs** A. Morreale (CNL)	**Paper Presentation**
ID127	**Application of the Probabilistic Method to Propagate Input Uncertainty on a DBA Sequence in a Generic iPWR** G. Grippo (ENEA)	**Paper Presentation**
ID04	**Comparison between EDF MAAP5.04 and ASTECv3 codes on an hypothetical Severe Accident on the ELSMOR project NUWARD-Like SMR Design** J. Bittan (EdF)	**Paper Presentation**

Technical Session 3.1: Ex-vessel corium interactions and coolability

Chairs: L. Carénini (IRSN), M. Hupp (Framatome GmbH)

ID06	**Results of the SSM-SICOPS melt tests in the frame of the EU-SAFEST project** G. Langrock (Framatome GmbH)	**Paper Presentation**

ID90	**Ex-Vessel stabilization of corium: An analysis of corium-concrete interaction with top flooding for siliceous concrete** F. Fichot (IRSN)	**Paper**
ID123	**Fluids Mixing Modelling with Phase Change for Molten Corium-Concrete Interaction** I. Khurshid (Khalifa University)	**Paper** **Presentation**
ID45	**Characterisation of prototypic ex-vessel fuel debris simulating MCCI at Fukushima Daiichi** C. Journeau (CEA)	**Paper** **Presentation**

Technical Session 6.1: Hydrogen risk and Containment behavior

Chairs: I. Kljenak (IJS), S. Gupta (Becker Tech. GmbH)

ID94	**AMHYCO Project Overview and First Outcomes** G. Jiménez (UPM)	**Paper** **Presentation**
ID103	**Outcomes of the experimental and numerical work on the operational behavior of passive autocatalytic recombiners in the late phase of a severe accident in the framework of the AMHYCO project** E.-A. Reinecke (FZJ)	**Paper** **Presentation**
ID82	**Assessment of Unmitigated Combustion Risk in Late Phase Within the AMHYCO Project** S. Kelm (FZJ)	**Paper** **Presentation**
ID18	**Heat Removal to Large Water Pools – Macroscopic Modelling of Microscopic Phenomena in the Simulation Code AC^2/COCOSYS** C. Spengler (GRS)	**Paper** **Presentation**

PLENARY SESSION: REGULATORY PERSPECTIVE AND APPROACHES FOR SEVERE ACCIDENTS IN SMALL MODULAR REACTOR

Chairs: D. Jacquemain (OECD/NEA), A. Miassoedov (IAEA)

U.S. NRC Regulatory Perspective and Approaches for Severe Accidents in Small Modular Reactors
Jason Schaperow, (USNRC Office of Nuclear Reactor Regulation)

The Canadian Nuclear Regulatory Role, Approaches and Challenges for Severe Accidents in Small Modular Reactors
Samuel Gyepi-Garbrah (Canadian Nuclear Safety Commission)

Beyond Design Basis Analysis: Regulatory Perspective on New Reactor Designs
Ali Tehrani (Office for Nuclear Regulation, UK)

Applicability of new Swedish regulations to Small Modular Reactors – Opportunities and challenges of a performance based approach
A. O. Mowitz (Swedish Radiation Safety Authority, SSM)

Poster Session

ID04	**MELCOR 2.2 analyses of passive systems modeling based on the PANDA facility experiments** M. Malicki (PSI)	Abstract Poster
ID48	**Model Development for the Simulation of Fission Product Release from Molten Pools** F. Krist (PSS-RUB)	Abstract Poster
ID14	**Severe Accident Sequence of LOCA for APR1400 using CINEMA Computer Code** Rae-Joon Park (KAERI)	Abstract Poster
ID20	**Comparative Study of the Hydrogen Distribution Among Different PWR-W Lumped-Parameter and 3D Containment Models with GOTHIC 8.3 (QA)** A. García-Herranz (UPM)	Paper Poster
ID22	**Thermophysical property measurement of oxide melts using aerodynamic levitation** Y. Gong (CNPE)	Paper Poster
ID23	**PLINIUS – experimental platform for nuclear excellence** A. Bachrata (CEA)	Abstract Poster
ID31	**Thermodynamic Evaluation of Liquid-Gas Surface Tension for U-O-Zr Mixtures Using the Butler Equation** A. Tourneix (CEA)	Paper
ID32	**Analysis of combustible gases distribution with accident management action in a generic PWR-W containment** J. Fontanet (CIEMAT)	Paper Poster
ID34	**Development of 3D view application debrisEye for decommissioning of Fukushima Daiichi Nuclear Power Plant** T. Yamashita (JAEA)	Paper Poster
ID36	**Thermal shock resistant geopolymers as refractory material for core catcher** B. Mészáros (UJV)	Abstract Poster
ID38	**Investigation of New Inorganic Materials for Nuclear Industry under Severe Accident Conditions** J. Hrbek (UJV)	Abstract Poster
ID41	**Modeling of pool scrubbing and sensitivity analysis using GOTHIC** X. Wang (KTH)	Abstract
ID49	**MELCOR analyses of Severe Accident sequences in an integral PWR with passive systems** F. Giannetti (Sapienza University of Rome)	Abstract
ID52	**Development of severe accident simulation code for sodium-cooled fast reactors: SIMMER-V (2) Development and verification of detailed fuel pin model** S. Ishida (JAEA)	Paper Poster

ID61	**Analysis of the combustion risk mitigation inside the containment during a postulated severe accident in a PWR using the code package AC2** M. Müer (PSS-RUB)	**Paper** **Poster**
ID65	**Uncertainty quantification analysis with radiological consequences for a loss of cooling accident in a spent fuel pool** M. D'Onorio (Sapienza University of Rome)	**Abstract**
ID67	**THS-15 Experimental Facility: Effect of Surface Roughness on CHF Values** D. Batek (UJV)	**Paper** **Poster**
ID81	**Cooperative Nuclear Safety Research Activities at the Nuclear Energy Agency in Response to the Fukushima-Daiichi Accident** Y. Kumagai (OECD/NEA)	**Abstract** **Poster**
ID87	**Filtration efficiency of electrostatic precipitator for iodine particles in different gas atmospheres simulating the severe accident scenarios** S. Basnet (University of Eastern Finland)	**Abstract** **Poster**
ID91	**Study on AP1000 accident diagnosis and treatment for loss of monitoring and control** Y. Yu (China Nuclear Power Engineering Co.)	**Abstract**
ID92	**Failure modes of the reactor coolant pressure boundary in high-pressure core melt accident scenarios** C. Bläsius (GRS)	**Abstract** **Poster**
ID95	**Parametric sensitivity studies for RELAP/SCDAPSIM model of QUECH-20 test** N. Elsalamouny (LEI)	**Abstract** **Poster**
ID102	**Assessment of how Zr-clad oxidation affects the speciation and release of FPs under accidental conditions** C. Riglet-Martial (CEA)	**Paper**
ID105	**LPM vs. 3D Analysis of an In-Vessel LBLOCA Sequence using the ALMARAZ NPP GOTHIC Containment Model** C. Gabicagogeascoa-Cuesta (UPM)	**Paper** **Poster**
ID109	**Some results of the AMICO project** G. Langrock (Framatome GmbH)	**Paper** **Poster**
ID110	**Effect of the Stages of the Accumulators on the Hydrogen Production During LOCA+SBO in BNPP VVER-1000** A. Hosseini (Shahid Beheshti University)	**Abstract**
ID112	**Comparative Study of Two Experimental Configurations with an Internal Compartment in the PANDA Facility** S. Arfinengo-del-Carpio (UPM)	**Paper** **Poster**
ID113	**Numerical Simulation of LIVE2D Two-Layer Melt Pool Experiment** P. Guo (Tsinghua University)	**Paper** **Poster**
ID114	**Severe Accident R&D in UJV Group** P. Vácha (UJV)	**Paper**
ID117	**Investigation of IVMR Strategy for BNPP-1 VVER 1000**	**Abstract**

A. Najafi (Sharif University of Technology)

ID121	**Assessment of RELAP5-3D condensation models for small modular reactor passive safety** P. K. Bhowmik (INL)	**Abstract**
ID122	**V&V of nuclear fuel oxidation behavior in sleeveless SiC-matrix during air ingress accident** Y. Nishimura (University of Tokyo)	**Abstract**
ID125	**Numerical Analyses on Melt Water Interactions with Super Absorbing Polymers Added to the Cooling Water** M. Buck (University of Stuttgart)	**Abstract**
ID130	**Study on the influence of the Core support structure on the migration process of molten material** C. Wei (Nuclear and Radiation Safety Center)	**Poster**

Technical Session 3.2: Ex-vessel corium interactions and coolability

Chairs: S. Bechta (KTH), P. Piluso (CEA)

ID62	**Production of prototypic corium in the VULCANO facility using uranothermite and induction heating** A. Denoix (CEA)	**Paper** **Presentation**
ID68	**Overview of Ex-Vessel Severe Accident Scenarios Simulations at UJV Rez** J. Komrska (UJV)	**Paper** **Presentation**
ID120	**Simulations of FLOAT debris quenching experiments** M. Uršič (JSI)	**Paper** **Presentation**

Technical Session 5.1: Severe accident scenarios - Model development and validation

Chairs: M. Angelucci (University of Pisa), F. Gabrielli (KIT)

ID53	**Formulation of material property formula for calculation of damage in reactor pressure vessel during accident evaluation** K. Shimomura (JAEA)	**Paper** **Presentation**
ID60	**Correlation Development for the Determination of Aerosol Particle Retention in Liquid Pools** J. Rehrmann (PSS-RUB)	**Paper** **Presentation**
ID43	**In Vessel Melt Retention 0D model for integral Pressurized Water Reactors** M. Principato (Sapienza University of Rome)	**Paper** **Presentation**

WEDNESDAY, MAY 15th, 2024

PLENARY SESSION: LOOKING AHEAD IN SA RESEARCH

Chairs: L. Carénini (IRSN), S. Gupta (Becker Technologies GmbH)

Incoming Euratom Research funded Projects on Severe Accident and Nuclear Safety
A. Iorizzo (European Commission)
Recent IAEA Activities Related to Severe Accidents
A. Miassoedov (IAEA)
Status and Perspectives in NEA Joint Nuclear Safety Research Projects in the Severe Accident Area
D. Jacquemain (OECD/NEA)

Technical Session 7.1: Source term

Chairs: I. Kljenak (IJS), S. Gupta (Becker Tech. GmbH)

ID119	**The Reduction of Radiological Consequences of design basis and extension Accidents: re-assessment of calculation results and main outcomes of the R2CA project** N. Girault (IRSN)	**Paper Presentation**
ID124	**Progress in understanding fission products remobilization behaviour and hydrogen risk in water cooled reactors under severe accident conditions: OECD/NEA THAI-3 project** S. Gupta (Becker Technologies GmbH)	**Paper Presentation**
ID88	**Source Term Assessment for a VVER-1000 Reactor Equipped with Filtered Venting: Sensitivity Study of the Impact of Different Forms of Iodine in the Containment** M. Kotouc (UJV)	**Paper Presentation**
ID97	**Source Term Dispersion Analysis and Construction of the Risk Map around the Peach Bottom Unit-2 Plant Using the ASTEC and JRODOS codes** O. Murat (KIT)	**Paper Presentation**

Technical Session 5.2: Severe accident scenarios - Model development and validation

Chairs: A. Stakhanova (KIT), T. Hollands (GRS)

ID126	**Assessment of pH-values in water pools during severe accidents in PWR using the lumped parameter code COCOSYS** L. Anschuetz (Framatome GmbH)	**Paper Presentation**
ID99	**Modeling of oxidation behavior of Accident Tolerant Fuel by using AC²** G. Stahlberg (PSS-RUB)	**Paper Presentation**

ID40 **ASTEC validation of SFP Dewatering using Results from the DENOPI project** — Paper Presentation
L. Laborde (IRSN)

ID39 **A review of correlations of stainless steel oxidation in steam, and modeling the reaction with MELCOR** — Paper Presentation
T. Sevón (VTT)

Technical Session 7.2: Source Term

Chairs: L. E. Herranz (CIEMAT), S. Gupta (Becker Tech. GmbH)

ID80 **Effect of Boric Acid on Fission Product Tellurium and Iodine in Severe Accident-Like Conditions: Analysis with X-Ray Photoelectron Spectroscopy** — Paper Presentation
F. Börjesson Sandén (Chalmers University of Technology)

ID15 **Local measurements on particle mass transfer in gas-liquid flows** — Paper Presentation
A. Ramos Perez (PSI)

ID29 **New Experimental Devices for Severe Accident Study: a Laser Based Approach** — Paper Presentation
Y. Pontillon (CEA)

ID33 **On the progress made in source terms evaluation and possible open issues relative to advanced technologies** — Paper Presentation
L. Cantrel (IRSN)

Technical Session 6.2: Hydrogen risk and Containment behavior

Chairs: I. Kljenak (IJS), S. Kelm (FZJ)

ID17 **Validation of REKO-DIREKT and ContainmentFOAM-9 Code Coupling Using THAI-HR Experiments** — Paper Presentation
L. Serra Lopez (UPM)

ID11 **THAI Experiment on Iodine Absorption Capacity of Pre-Stressed Paint Coatings on Different Surfaces** — Paper Presentation
K. Dieter (Becker Techn. GmbH)

ID37 **Validation of the PARUPM and GOTHIC 8.3 Code Coupling using THAI Hydrogen Recombination Tests** — Paper Presentation
A. Domínguez-Bugarín (UPM)

Technical Session 7.3: Source Term

Chairs: T. Lind (PSI), F. Rocchi (ENEA)

ID35 **Gaseous and aerosol formations in the pseudo-binary CsI-MoO3 reaction system** — Paper Presentation
M. Rizaal (JAEA)

ID69	**Experimental study on removal effect of radioactive materials in the course of the leakage through the equipment hatch** K. Nakamura (CRIEPI)	**Paper** **Presentation**

Technical Session 6.3: Hydrogen risk and Containment behavior

Chairs: I. Kljenak (IJS), S. Kelm (FZJ)

ID56	**Evaluation of hydrogen risk and its mitigation strategies adopted in isotope manufacturing building** C. Peng (Shanghai University)	**Paper** **Presentation**
ID85	**The Scaling of Turbulent Flame Acceleration and Detonation Transition for Hydrogen-Air mixtures in the RUT Facility** M. Kuznetsov (KIT)	**Paper**

THURSDAY, MAY 16th, 2024

Technical Session 9.1: Severe Accident Scenarios - Accident Tolerant Fuels

Chairs: S. Gupta (Becker Tech. GmbH), M. E. Cazado (KIT)

ID74	**Overview of KIT activities on ATF cladding materials** M. Steinbrück (KIT)	**Paper** **Presentation**
ID118	**Application of AC²/ATHLET-CD and ASTEC for ATF Experiments in the Frame of OECD QUENCH-ATF and IAEA CRP ATF-TS** T. Hollands (GRS)	**Paper** **Presentation**
ID51	**The CODEX-ATF experiment** R. Farkas (EK-CER)	**Paper** **Presentation**

Technical Session 8.1: Severe Accident Scenarios - Fast Reactors

Chairs: A. Stakhanova (KIT), F. Gabrielli (KIT)

ID13	**Preliminary Evaluation of Reactivity Insertion during BDBA-LOCA of Super Fast Reactor** K. Matsuoka (Waseda University)	**Paper** **Presentation**
ID54	**Development of severe accident simulation code for sodium-cooled fast reactors: SIMMER-V (1) Overview of the SIMMER-V code development** H. Tagami (JAEA)	**Paper** **Presentation**
ID08	**Experimentation & simulation of ablated surface by jet impingement for core-catcher safety issue** N. Seiler (CEA)	**Paper** **Presentation**

PLENARY SESSION: CLOSING

Chairs: L.E. Herranz (CIEMAT), F. Gabrielli (KIT)

Summary and conclusions of the plenary sessions
L.E. Herranz (CIEMAT), Coordinator of the SEAKNOT project
Summary and conclusions of the technical sessions
NUGENIA TA2 Leaders
Concluding Remarks
L.E. Herranz (CIEMAT), Coordinator of the SEAKNOT project
F. Gabrielli (KIT)
Introduction of ERMSAR2026
L.E. Herranz (CIEMAT), Coordinator of the SEAKNOT project

The 11th European Review Meeting on Severe Accidents Research

May 13-16, 2024, Royal Institute of Technology, Stockholm, Sweden

PLENARY SESSION: WELCOME AND INTRODUCTORY

Chairs: S. Bechta (KTH), F. Gabrielli (KIT)

Welcoming Addresses

S. Östlund, Vice President of the KTH

M. Knochenhauer, Director General, Swedish Radiation Safety Authority (SSM)

Opening of the ERMSAR2024 Conference

L.E. Herranz (CIEMAT), Coordinator of the SEAKNOT project

SEAKNOT

SEvere Accident Research and KNOwledge ManagementT for LWRs

ERMSAR Conference Series

ERMSAR 2024
Stockholm, May 13th–16th, 2024

Funded by the European Union

SEAKNOT

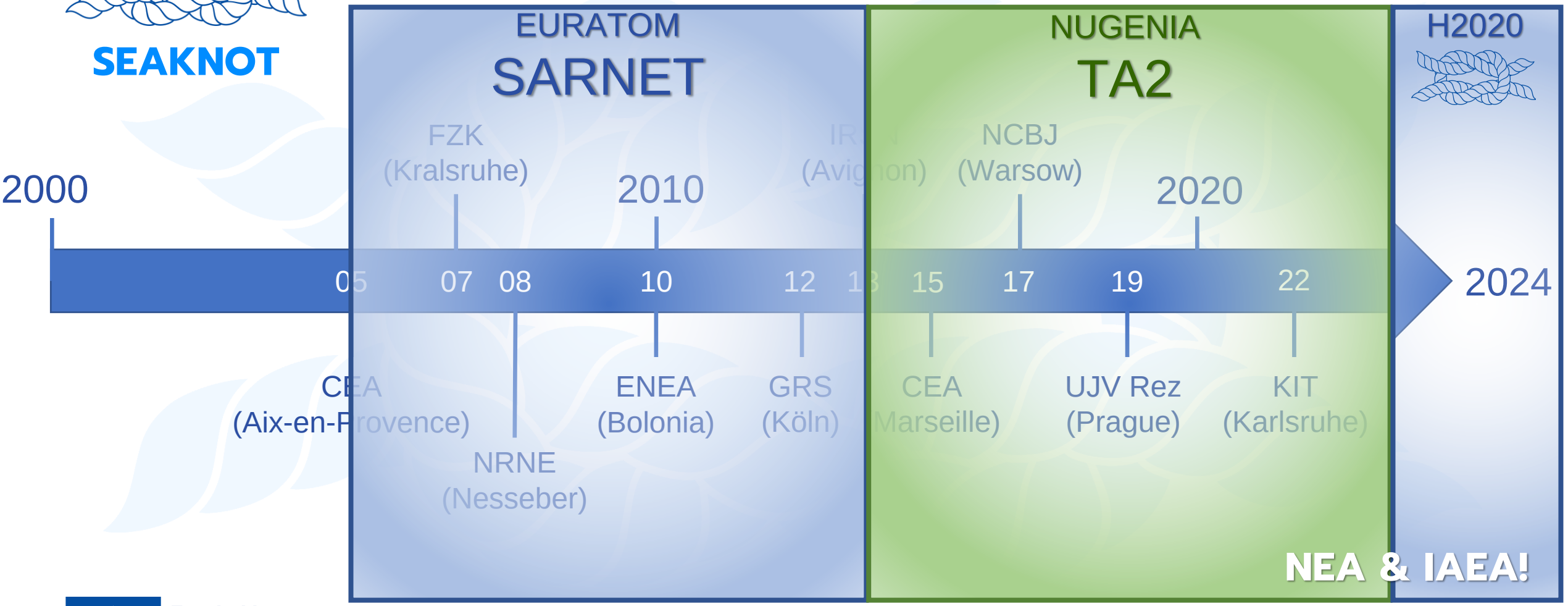

Funded by
the European Union

From Meeting

A meeting formally gathers **individuals within an organization**, focusing on structured discussions, decision-making, and agenda-driven interactions. **It is internal**, involving team, board, or departmental meetings.

Meetings facilitate effective communication and coordination among team members and stakeholders.

They are typically **smaller, shorter in duration, and more focused on internal matters**.

to Conference

A conference is a gathering of people, **spanning for multiple days,** who come together to participate in:

- **Presentations & Discussions.**
- **Breakout sessions/workshops.**
- **Networking.**

The primary purpose of a conference is to **facilitate the dissemination of information, promote collaboration, and advance knowledge** within a specific field or industry.

Funded by the European Union

GLOBAL CONFERENCE ALLIANCE INC.

SEAKNOT

SEAKNOT

Enjoy ERMSAR-2024!



Funded by
the European Union



SEAKNOT

www.seaknot-project.eu

THE SEAKNOT WEBSITE

The aim of the four-year project is two-fold: to shape up a roadmap for severe accident research in the coming 10 years by means of which to achieve both a substantial reduction of remaining uncertainties and a measurable progress in the practical elimination of radiological consequences; and, no less important, to efficiently manage the knowledge and knowhow transfer to the young generation of nuclear scientists and engineers who will be involved in its implementation.

Coordinated by CIEMAT (Spain), SEAKNOT is constituted by seventeen well-known organizations from ten countries.

Funded by
the European Union

THANK YOU!

Get in touch for more information

All of the reports of the project will be available for download on the SEAKNOT website: **www.seaknot-project.eu**

Project coordinator: Luis Enrique Herranz, CIEMAT
Contact us: **contact@seaknot-project.eu**

Follow us on LinkedIn!
@seaknot-eu

Funded by the European Union

SEAKNOT

The 11th European Review Meeting on Severe Accidents Research

May 13-16, 2024, Royal Institute of Technology, Stockholm, Sweden

PLENARY SESSION: SINGULAR CAREERS IN THE SEVERE ACCIDENT RESEARCH

Chairs: L. E. Herranz (CIEMAT), T. Lind (PSI)

Reflections on a career in reactor safety: Severe Accident Code Development

Dr Randall Gauntt (MELCOR Code Development Manager, Retired Sandia National Laboratories)

Progress in Predicting Reactor Pressure Vessel Failure

J. Rempe (Rempe and Associates, LLC)

Your Research Maps: Needs and challenges with scaling consideration

H. Nakamura (JAEA)

Reflections on a career in reactor safety: Severe Accident Code Development

Dr Randall Gauntt
(MELCOR Code Development Manager, Retired Sandia National Laboratories)

The 11th European Review Meeting on Severe Accidents Research May 13-16, 2024 KTH Royal Institute of Technology, Stockholm, Sweden

A Brief Bio

- 1972 Left home to begin Veterinary school at Texas A&M University in the Fall
- I found that the veterinary college was on a trimester schedule – *not possible to register for Vet school then*
  - I was handed a regular session curriculum book, and I started to explore career choices
  - Nuclear Engineering looked cool! I kind of moved on from Vet school because the math and physics looked so interesting
- BS degree in NE: large cohorts went to nuclear navy, others to industry, I had 20 hours of graduate level courses and thought I needed to get a few more hours for MS. Same story with PhD in 1982
- Aerosol mechanics research topic – handy in later code development days
- McFarland story about TMI and that “nuclear was dead” and I shouldn’t go to SNL (weapons lab)
- Began career Sandia in 1982 and joined the in-pile experimental division doing fuel damage experiments in the ACRR
- At about this same time the MELCOR code development project was getting started
- Joined the MELCOR as project lead around 1995
- Basic code architecture established – brilliant in my view
- MELCOR was just beginning to enjoy broad usage in experiment analysis, model assessments, and safety evaluations
- Analysis of Phebus and many other experiments led to core degradation and fission product release modeling refinements
- Code development and model additions continued to today

A Few Notable Accidents along the way

- SRE (Sodium Reactor Experiments - Santa Susanna)
- SL-1 Accident
- Fermi 1
- Browns Ferry 1 Fire
- Chernobyl
- TMI 2



Perspectives on Reactor Safety

NUREG/CR-6042, Rev. 2
SAND 93-0971

Timeline of Nuclear Safety Technology Evolution



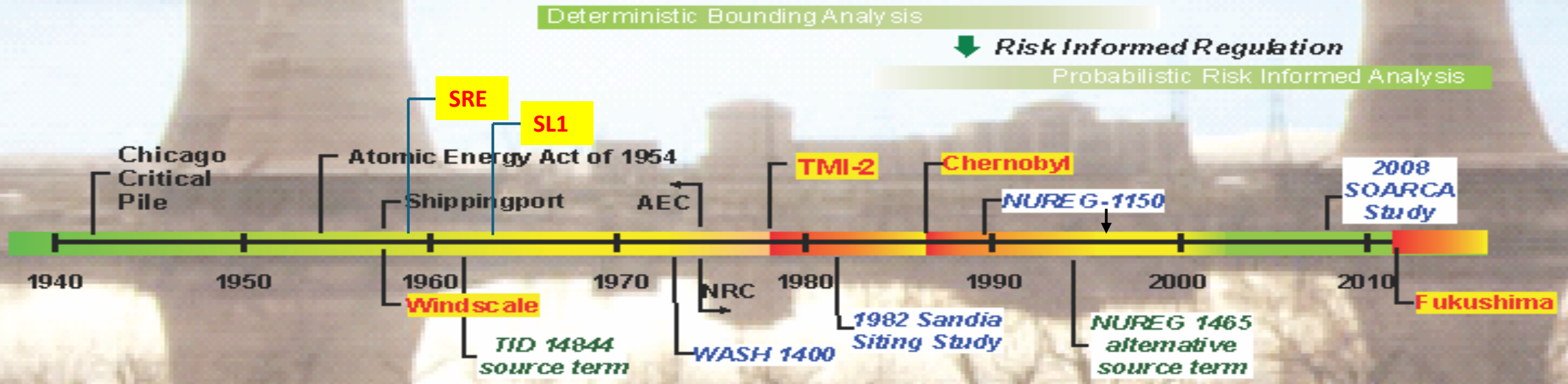

Nuclear Power Outlook

- Optimistic
- Guarded
- Pessimistic

Emerging Issues.....

Post Fukushima reactions

Non-LWR reactors
Small reactors & "Functional" containments
Reduced Exclusion Areas
Accident Management
Consequence Mitigation

Early Accidents: Sodium Reactor Experiment July 1959

- July 1959
- Reactor built to test sodium cooled fuel and provide power to grid
- Organic coolant in pumps leaked into sodium coolant
- Degraded coolant blocked coolant flow
- Operators noticed something unusual but continued to operate reactor
- Next day, took reactor to higher power!
- Damage only discovered months later
- Radionuclide release to the environment
- Movement in AEC for procedures and conservative ops.

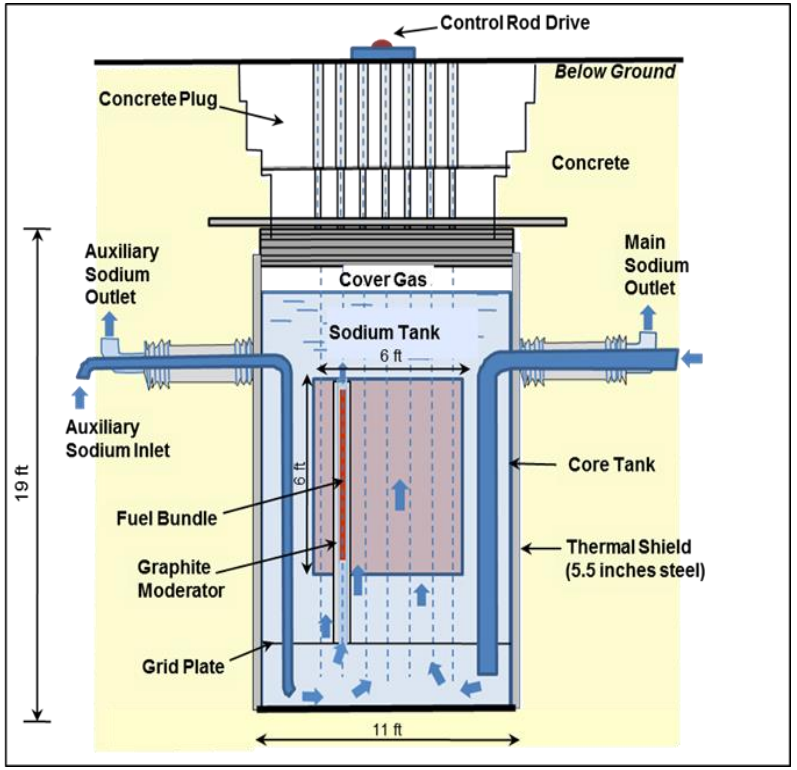



Damaged fuel from SRE

Early Accidents: Stationary Low Power Reactor 1: SL-1

- Jan. 3, 1961
- US Army BWR
- Re-attaching control rod drive after outage
  - Long known to stick
- Sudden excessive movement on manually pulling on stuck rods added reactivity
- 3 killed
  - Buried in lead caskets
  - Building dose ~1000 R/hr
- Huge emphasis on maintenance and conduct of operations in aftermath
- Over reliance on administrative controls?
- Lack of knowledge about consequences of large reactivity insertion ?

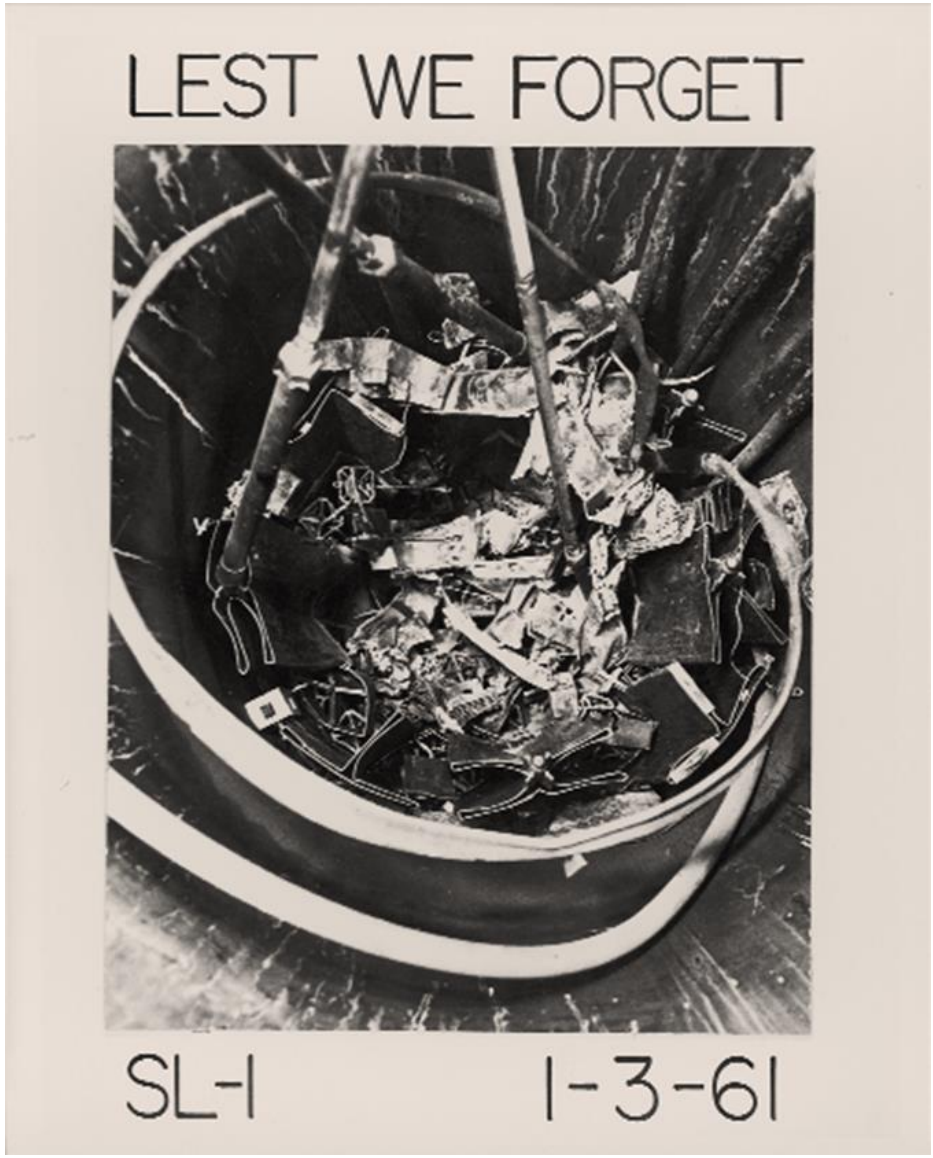

Early Accidents: Fermi-I

- Oct. 5, 1966 partial core melt
- Sodium-cooled fast breeder reactor
- 6 zirconium sheets in lower reactor vessel to avoid criticality in event of core meltdown
- One sheet came detached and blocked flow
- Two assemblies melted together
- ~30 miles from downtown Detroit
  - "We Almost Lost Detroit"
- Aware of flow blockage as something to be designed against – but failed anyway

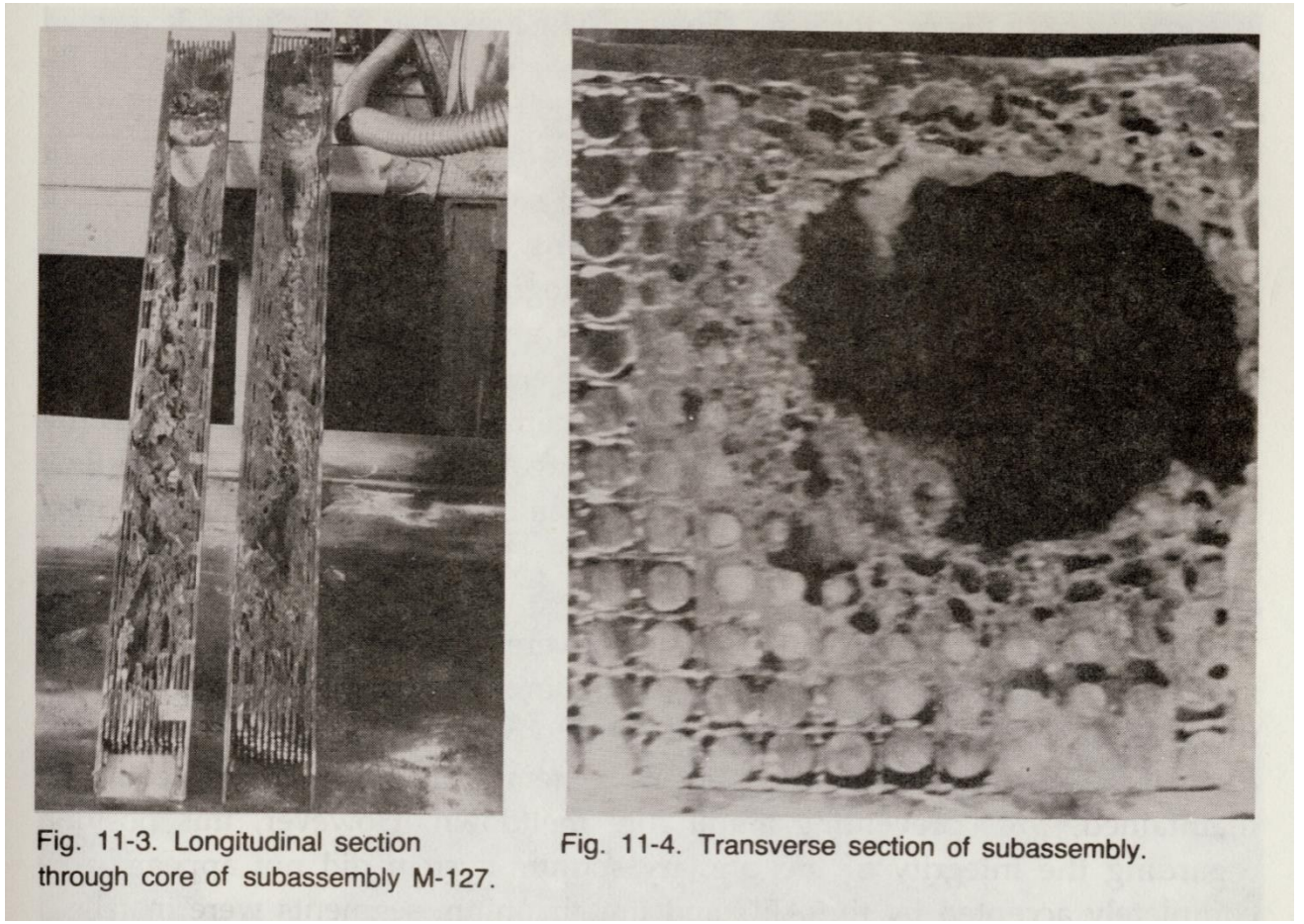

Fig. 11-3. Longitudinal section through core of subassembly M-127.

Fig. 11-4. Transverse section of subassembly.

E.P. Alexanderson , H.A. Wagner, editors, "FERMI-I New Age for Nuclear Power"

Browns Ferry Fire

- Reactor building maintained at negative pressure
- Cable tray penetration sealed
  - Polyurethane foam
  - Flameproof coating
- Candle used for testing
  - Common practice
  - Good visual indicator of sealing
- Foam caught fire during leak testing
  - Pressure differential drew flame into reactor building
  - Delay in decision to use water to extinguish fire
  - Cable spreading room fire out after 4 hours
  - Reactor building fire out after 3 additional hours
    - Water used in last half-hour

- Estimated CDF for Browns Ferry was 50% in probabilistic evaluation

- A candle – really?

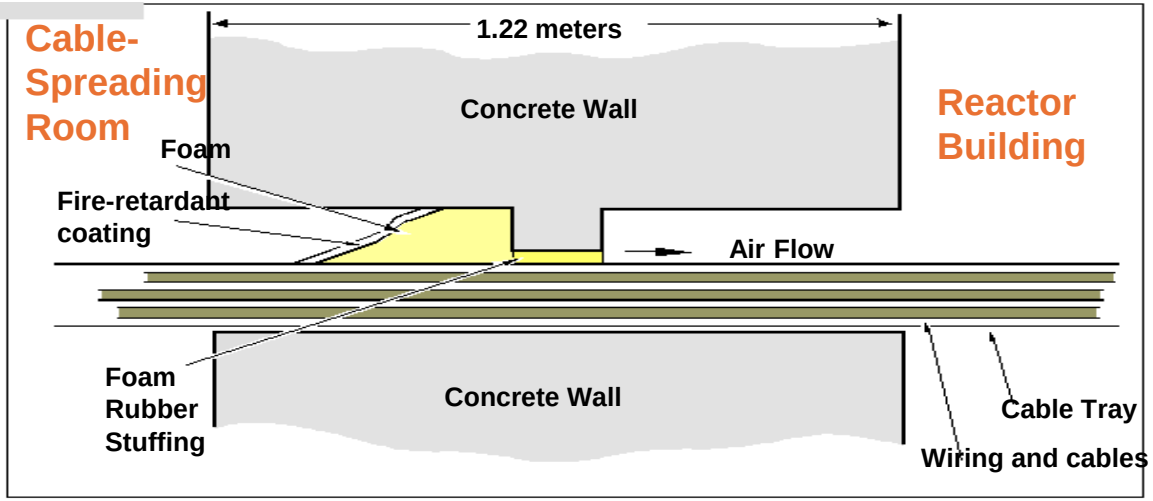

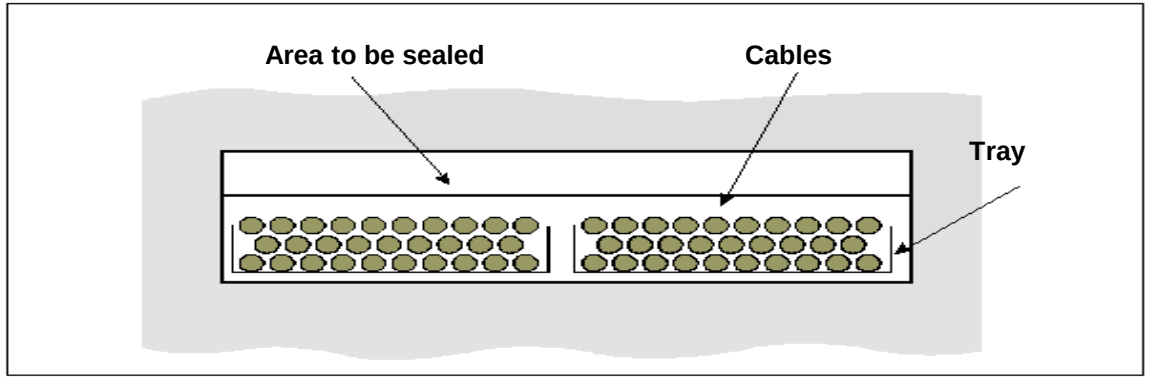

Early Safety Studies

- WASH 740 (1957)
  - One of the first studies on public consequences of hypothetical severe accidents in LWRs
  - Bounding estimates of severe accidents
  - Concluded such accidents were rare
  - Stressed importance of containments and remote siting
- WASH-1400 (1975)
  - A first systematic evaluation of consequences and probabilities of select severe accidents
  - FP release categories were established for making consequence estimates
- 1982 Sandia Siting Study
  - Study focused on siting characteristic and included weather effect on source term transport
  - Troubling results for certain extreme weather conditions suggested mass casualties could happen (Appendix material)
  - The SOARCA project was initiated in part to re-baseline the 1982 the believed-over conservative study

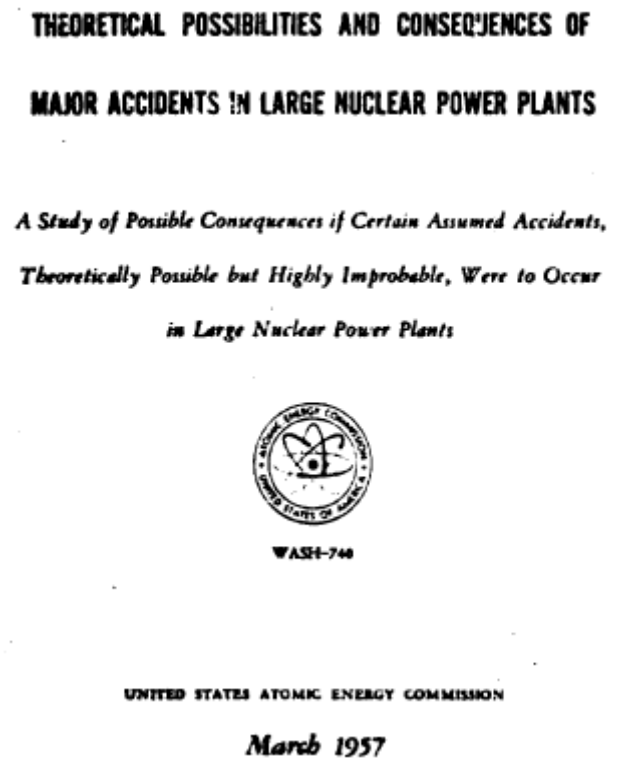
THEORETICAL POSSIBILITIES AND CONSEQUENCES OF

MAJOR ACCIDENTS IN LARGE NUCLEAR POWER PLANTS

A Study of Possible Consequences if Certain Assumed Accidents, Theoretically Possible but Highly Improbable, Were to Occur in Large Nuclear Power Plants

WASH-740

UNITED STATES ATOMIC ENERGY COMMISSION

March 1957



Timeline of Nuclear Safety Technology Evolution



Deterministic Bounding Analysis

Risk Informed Regulation

Probabilistic Risk Informed Analysis

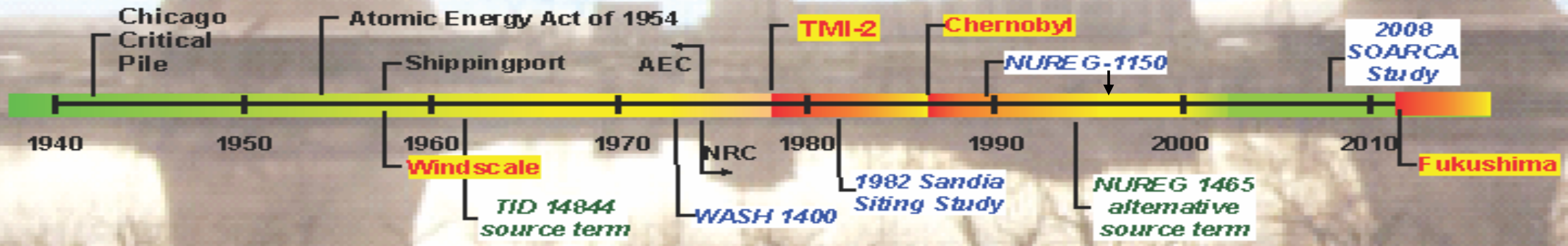

Nuclear Power Outlook

- Optimistic
- Guarded
- Pessimistic

Emerging Issues.....

Post Fukushima reactions

Non-LWR reactors
Small reactors & "Functional" containments
Reduced Exclusion Areas
Accident Management
Consequence Mitigation

Regulatory Support and Contributions

- Revision of Regulatory Source Term: NUREG-1465
  - Phebus, Vercors and Verdon data captured in MELCOR models used to update original NUREG1465 regulatory source term prescription for “gap” and early in-vessel release phases for high burnup and MOX LWR fuel
    - It was incidentally found that the original low burnup prescription needed revision as well to factor in extended early in-vessel duration implied by MELCOR
- Main Steam Isolation Valves
  - Industry request for regulatory relief on MSIV leak rate on valve closure
    - Large seating area very hard to recondition and seal with worker dose implications
    - Key to the analysis was how to model aerosol transport in extensive piping
    - Aerosol size distribution was a major aspect of source term retention in MS piping
    - Topic still under discussion (I think?)
- SGTR Issue
  - Steam generator tube rupture in severe accident falls into “Containment Bypass” (early containment failure) class of accidents
    - Issue: counter current natural circulation transports heat from RPV to hot leg nozzle and steam generator tubes: would the hot leg nozzle fail before the steam generator tube(s) rupture
    - SGTR failure open pathway via SG secondary to environment
    - Hot leg nozzle failure releases
    - After much study using W 1/7 Scale data, CFD and MELCOR it was concluded that Hot Leg nozzle failure was significantly more likely than SGTR – good news, early containment failure likelihood low
    - Issue involved a decade of work within industry and regulatory research organizations

SOARCA Study

- Initiated to assess knowledge gained since TMI-2
- Focus on realism
  - Remove PRA-style conservatisms
  - Best Estimate with Uncertainty Quantification
- Intended to re-baseline the prior 1982 Sandia Siting Study
- Peach Bottom GE BWR Mark-1 plant
  - Same design as Fukushima Daiichi plants
- Surry 3-loop Westinghouse PWR plant
- PRA-informed sequence selection
  - “the usual suspects” - SBO, ISLOCA, SGTR
- Considered unmitigated and mitigated sequences

SOARCA Emphasized Realism

- Deterministic licensing applications often use biased or conservative modeling
  - Ensure margins of safety – defense in depth concept
  - But, conservative for one metric may not be conservative for a different metric
- PRA applications often “throw in the towel” and accept worst-case result because branch frequency is very low
  - Easy to justify as being conservative and less work
- Such approaches skew results and are not realistic
- SOARCA made use of “best estimate” principles to produce as realistic analyses as possible
- Uncertainty propagation was also conducted, yielding subtle yet crucially important insights

Severe Accident Modeling Insights from SOARCA

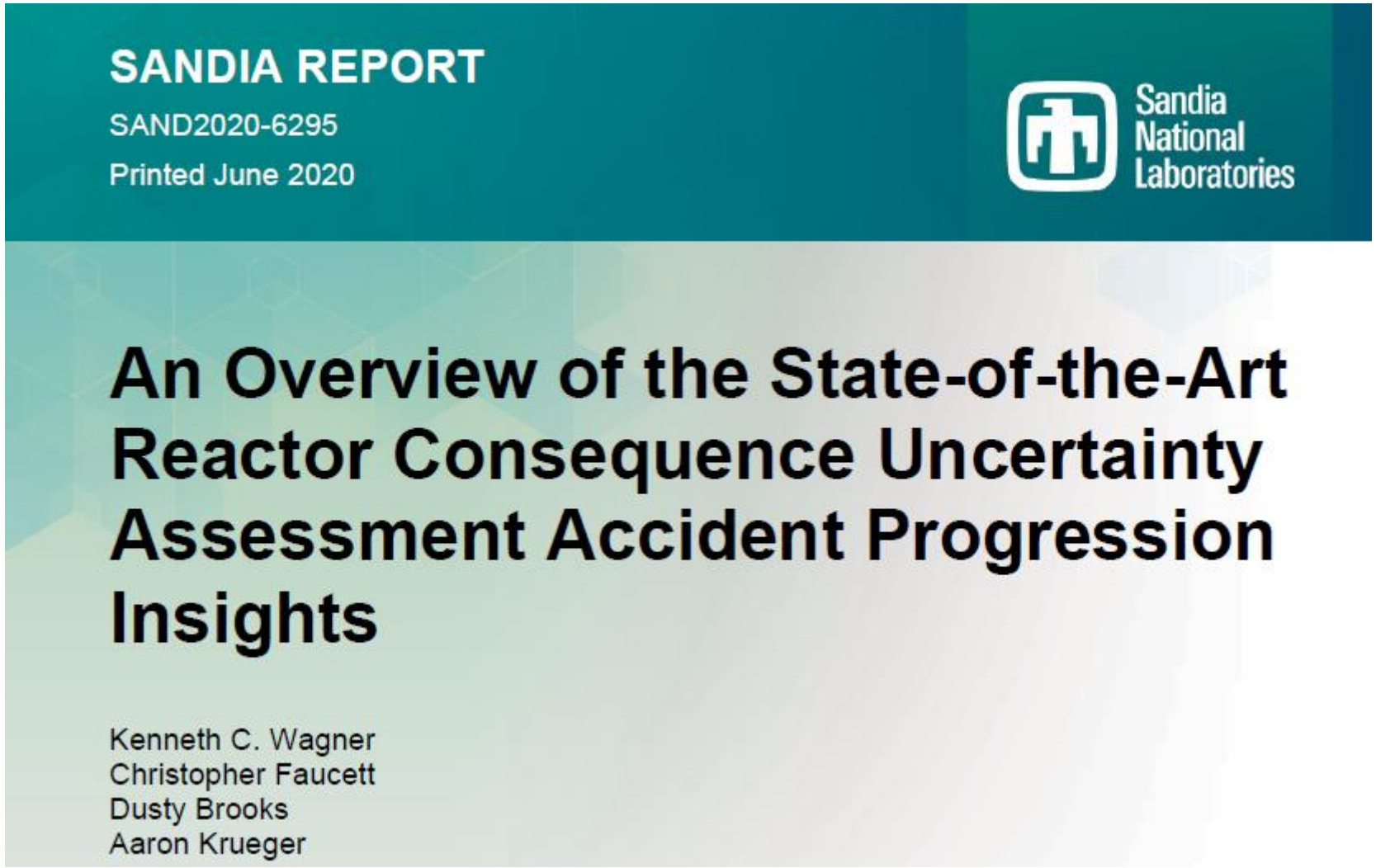

Sequoyah Containment Failure Outcomes from SOARCA Uncertainty Propagation Analyses

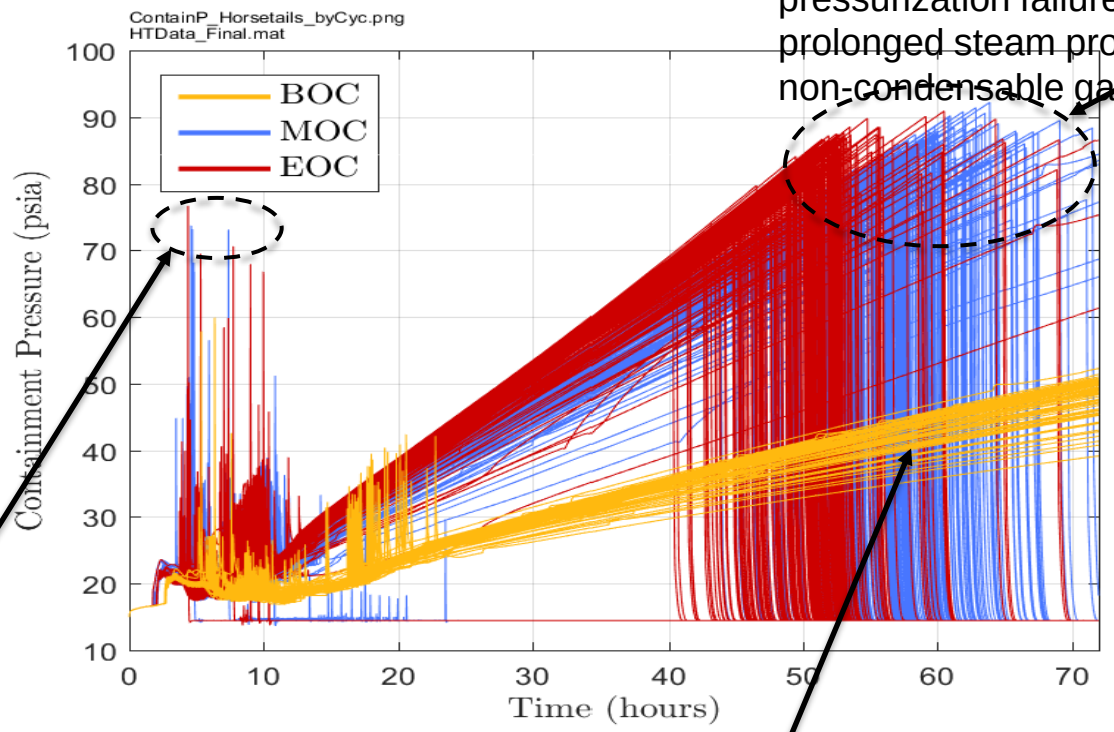

Long-tem containment over-pressurization failure due to prolonged steam production and non-condensable gas generation

Early containment overpressure failures due to sufficiently large burns in containment

No BOC cases exhibit long-term overpressure failure before 72 hours

Main Take-aways

- Hydrogen burns in Ice Condenser containments a long-standing concern
  - Low failure pressure and potential de-inerting of hydrogen in ice beds and dome
- Detailed compartmented MELCOR containment model used in Sequoyah UA
- Deep-dive interrogation of MELCOR UA realizations showed:
  - Uncertainty in ultimate pressure important (*obviously*)
  - In spite of low failure pressure, hydrogen burns only rarely failed the containment (4 out of 567 realizations), and
  - Containment over-pressure was only observed on the ***first*** hydrogen burn (of many subsequent burns)
  - Subsequent H2 burns were too small to fail the containment owing to hydrogen and oxygen depletion

Real World MELCOR Application to Fukushima Accidents

- Shortly after the accidents the DOE sent SA Experts (Gauntt and LaChance) to Tokyo for a month to support DOE and NRC at their field Emergency Response center at the US Embassy
- SOARCA Peach Bottom station blackout analyses had been recently completed and provisional results were available for comparison to the Fukushima SBO's
  - We took them with us to Japan
-
-
- After accidents in Japan in 2011 MELCOR Accident Reconstruction studies were commissioned by DOE and NRC for 1F1, 1F2, 1F3 and the Unit 4 spent fuel pool
- BSAF Forensics project continued Fukushima research by global participating community

- Initial comparisons of SOARCA and Fukushima showed the SOARCA SBO analyses to be prescient – *with some notable unresolved issues*
  - Vessel lower failure predicted by MELCOR was a bit hard to accept by some stakeholders
  - Fukushima specific MELCOR analyses predict SRV valve seizure or Main Steam Line rupture via Larson-Miller as mode of RPV depressurization in 1F1 and 1F3
  - Competing opinions are that MSL rupture did not occur and SRV gasket blowout being a preferred suspected mode of depressurization
  - LM failure modeling for Fukushima is the same as earlier modeling applied to SGTR issue analyses – decommissioning examinations may reveal dispositively if MSL rupture happened
  - MELCOR analyses (and virtually all codes) predicted persistent MCCI following lower head failure and ongoing non-condensable gas generation (H2 and CO) however decommissioning examination do not support the extensive MCCI predicted up to now: implications for the "Mark-1 liner failure issue"

Comparison of SOARCA PB-STSBO with 1F1

Peach Bottom STSBO

NUREG/CR-7110, Vol. 1

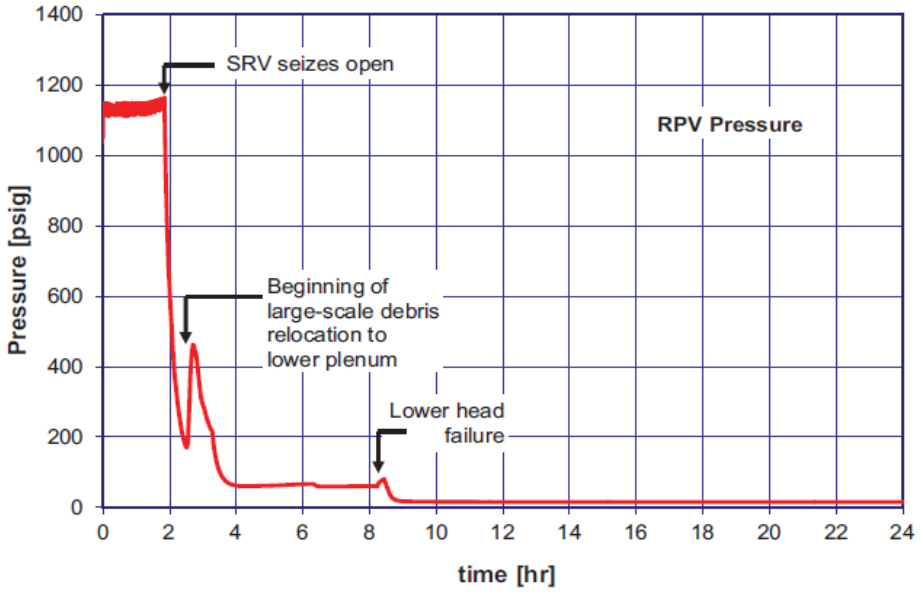

- SBO at start of accident
- Core damage by 1 hour
- SRV seizure just before 2 hours
- Core slumping by ~2.5 hours
- Lower head failure ~8.5 hours
- MCCI and Dry well liner failure ~8.5 hours+

1F1 STSBO

SAND2012-6173

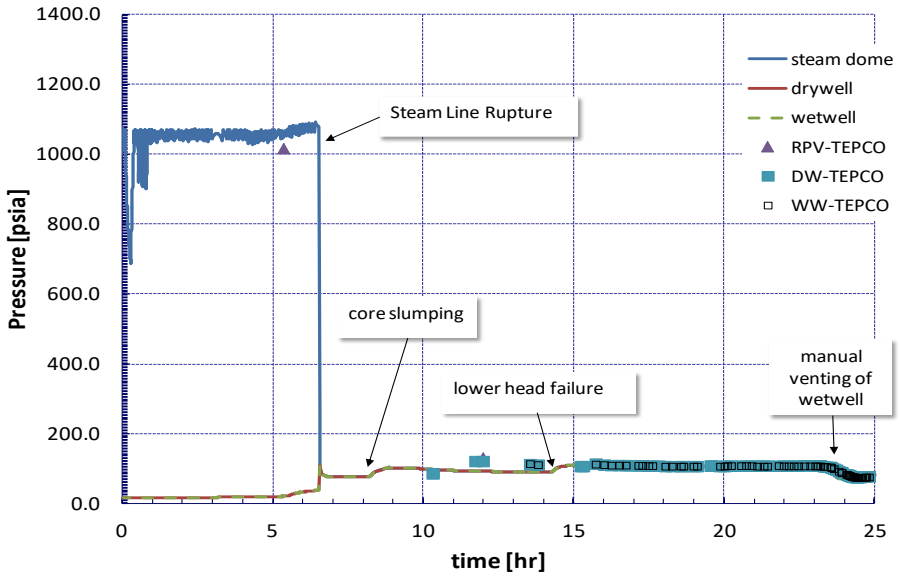

- SBO at ~1 hour due to tsunami
- Core damage at ~4 hours
- MSL rupture at ~ 6.5 hours
- Core slumping by ~8 hours
- Lower head failure ~14.5 hours (12.5 hr est.)
- MCCI and DW head flange leak ~14.5 hours+
- No liner failure evidence in DW pressure trend but possible liner failure below basemat

SOARCA PB LTSBO vs 1F3

Peach Bottom LTSBO
NUREG/CR-7110, Vol. 1

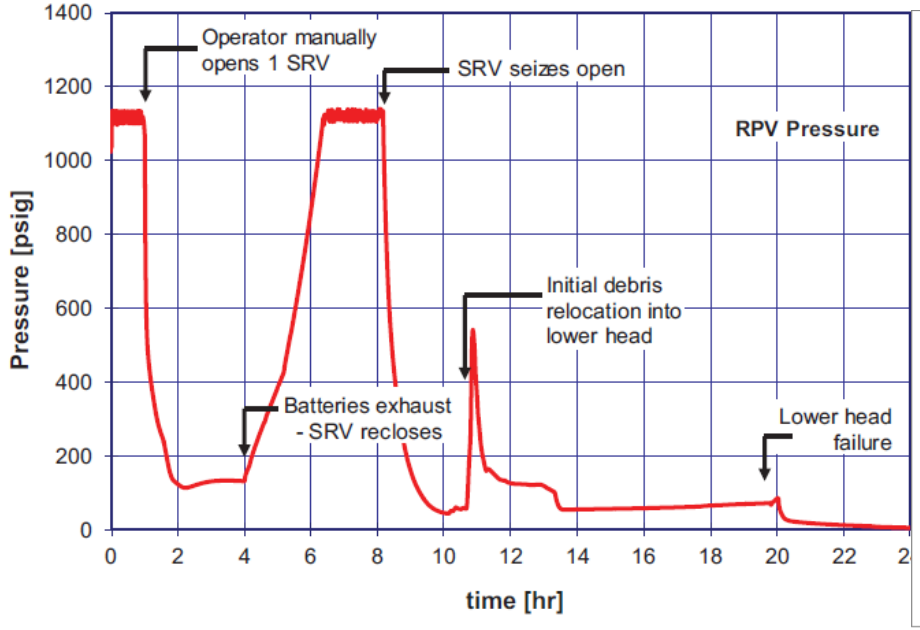

- RCIC starts level control
- Operator SRV control on pressure
  - RCIC controlling level
- Battery depletion @4 hours
  - SRV closes and RCIC runs full on
  - MSL floods and RCIC fails
- Water level loss and core damage
- Time to core slump – 7 hrs after RCIC fails

1F3 LTSBO
SAND2012-6173

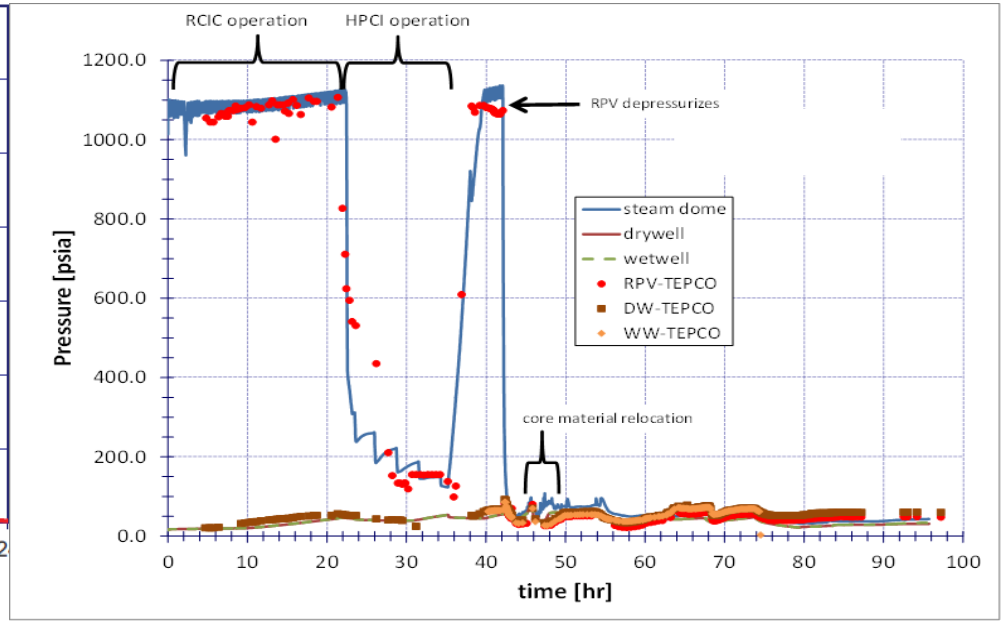

- RCIC starts level control – runs 21 hours
- Operators keep RPV pressure high
  - RCIC controlling level
- HPCI run continuously using bypass mode until failure @ ~35 hours
- Water level loss, manual SRV open
- Time to core slump – 10 hrs after HPCI fails

Severe Accident Code “Crosswalk”

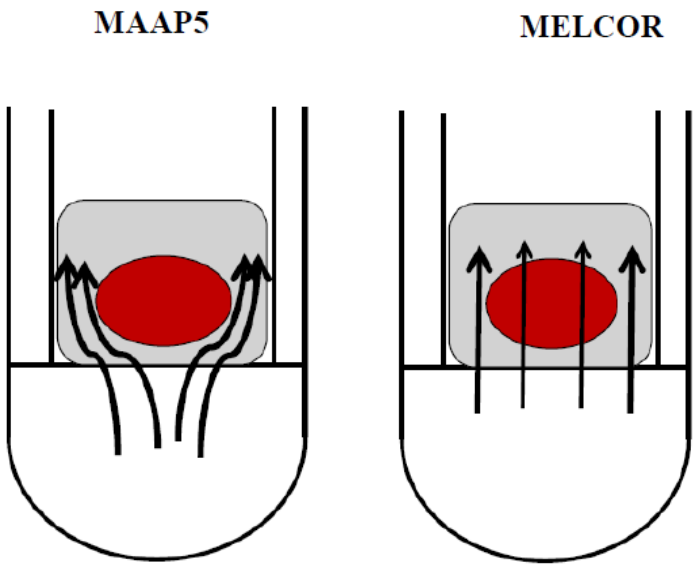

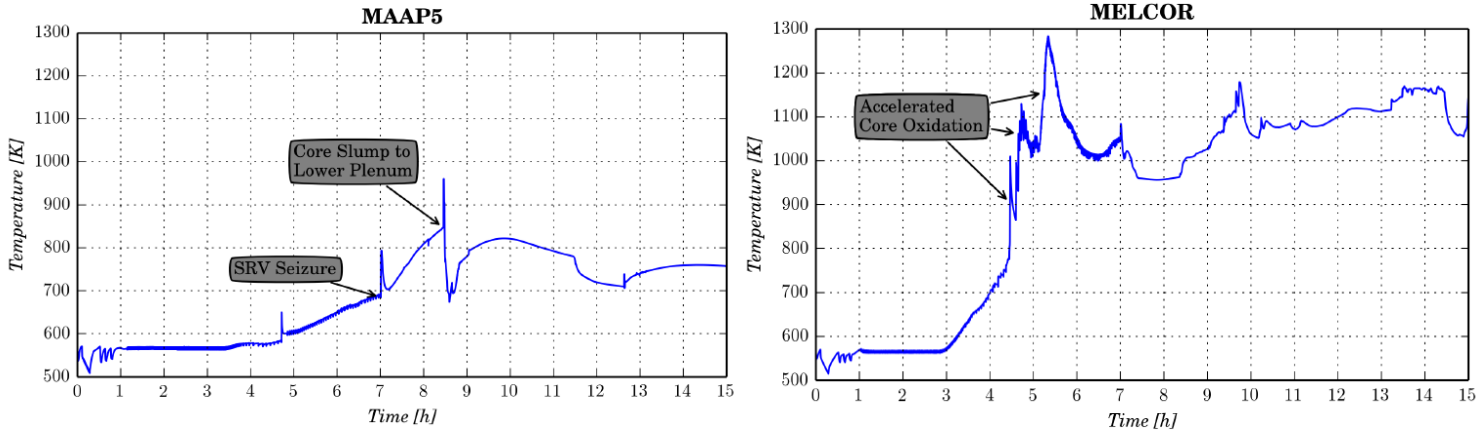

Modular Accident Analysis Program (MAAP) – MELCOR Crosswalk

Phase 1 Study

3002004449

- DOE and EPRI sponsored “crosswalk” study of MELCOR and MAAP using 1F1 as basis for comparison
- MELCOR compared to MAAP
  - Allows greater steam penetration into degraded core
  - Higher hydrogen generation
  - Higher core exit gas temperatures
- MAAP compared to MELCOR
  - Higher fuel debris/melt temperatures
  - More fluid-like material exiting failed lower head
  - Greater melt spreading ex-vessel
- In-core degradationmodeling differences impact subsequent phenomena
  - Hydrogen production
  - Hot leg or MSL rupture
  - Core concrete interaction
  - MK-1 liner failure

Dunning-Kruger Effect

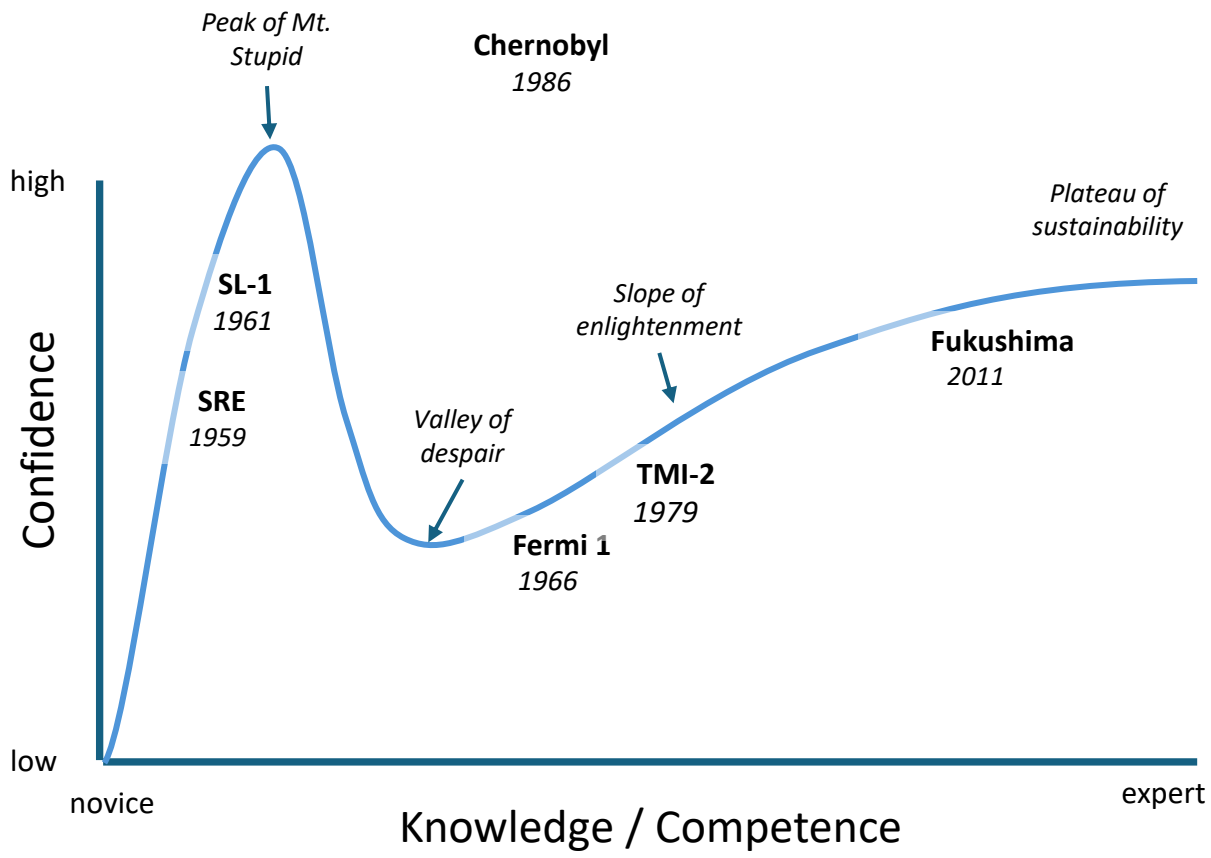

- *Don't take this too seriously*
- SRE - reactor built as a fueled sodium experiment that powered the grid in California - melted fuel and didn't know it for a long time
- SL-1: ability to go critical my manual rod withdrawal – shocking lack of hazards or consequences
- Fermi 1: Quite a bit more knowledge brought to bear, and recognized need to design against flow blockage; it happened anyway
- TMI-2: Five years after the accident many were surprised that the core was missing. Accident was largely misdiagnosed, other issues at play as well
- Fukushima accidents: Aside from totally overwhelming tsunami and key safety equipment below grade, pretty well understood accidents and meeting expectations
- Going forward, perhaps continue guarding against technological hubris, and watch for the unknown unknowns
- Uncertainty Propagation is an essential methodology fro severe accident analysis

---

Unskilled and Unaware of It: How Difficulties in Recognizing One's Own Incompetence Lead to Inflated Self-Assessments

Justin Kruger and David Dunning
Cornell University

Journal of Personality and Social Psychology
1999, Vol. 77, No. 6, 1121–1134

Progress in Predicting Reactor Pressure Vessel Failure

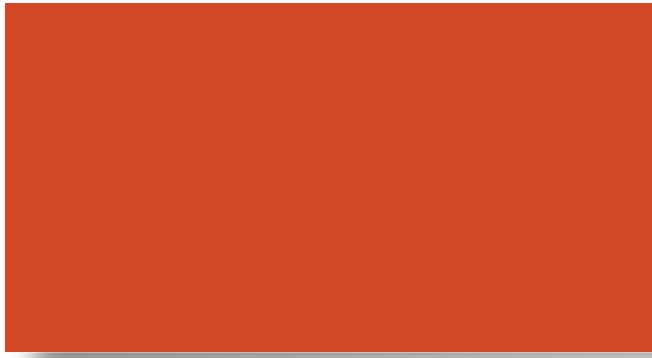

11th European Review Meeting on Severe Accident Research (EMSAR 2024)
Stockholm, Sweden
May 13-16, 2024

Joy Rempe, Rempe and Associates, LLC

Why is predicting reactor pressure vessel (RPV) failure mode and timing important?

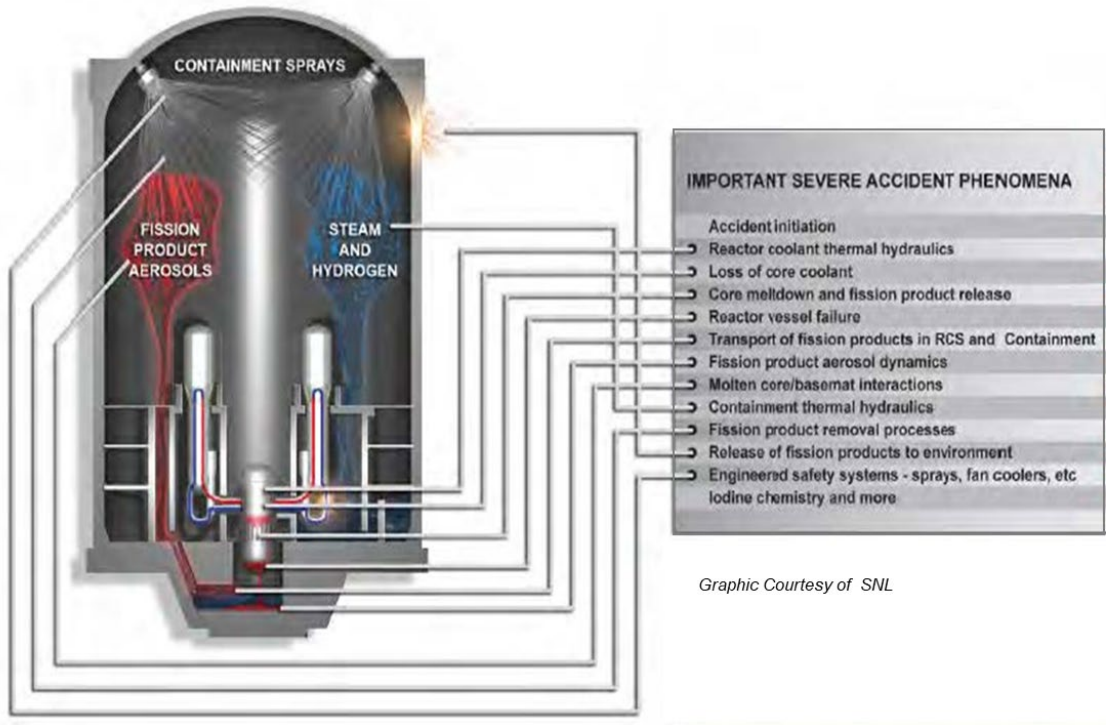

Graphic Courtesy of SNL

- **Key point in severe accident progression**
  - Degradation of important barrier to fission product release
  - Defines initial conditions for ex-vessel phenomena
  - Provides basis for developing accident prevention and mitigation strategies
- **Consideration for many types of reactors**

Approach to Reduce Uncertainties Associated with Vessel Failure Modeling

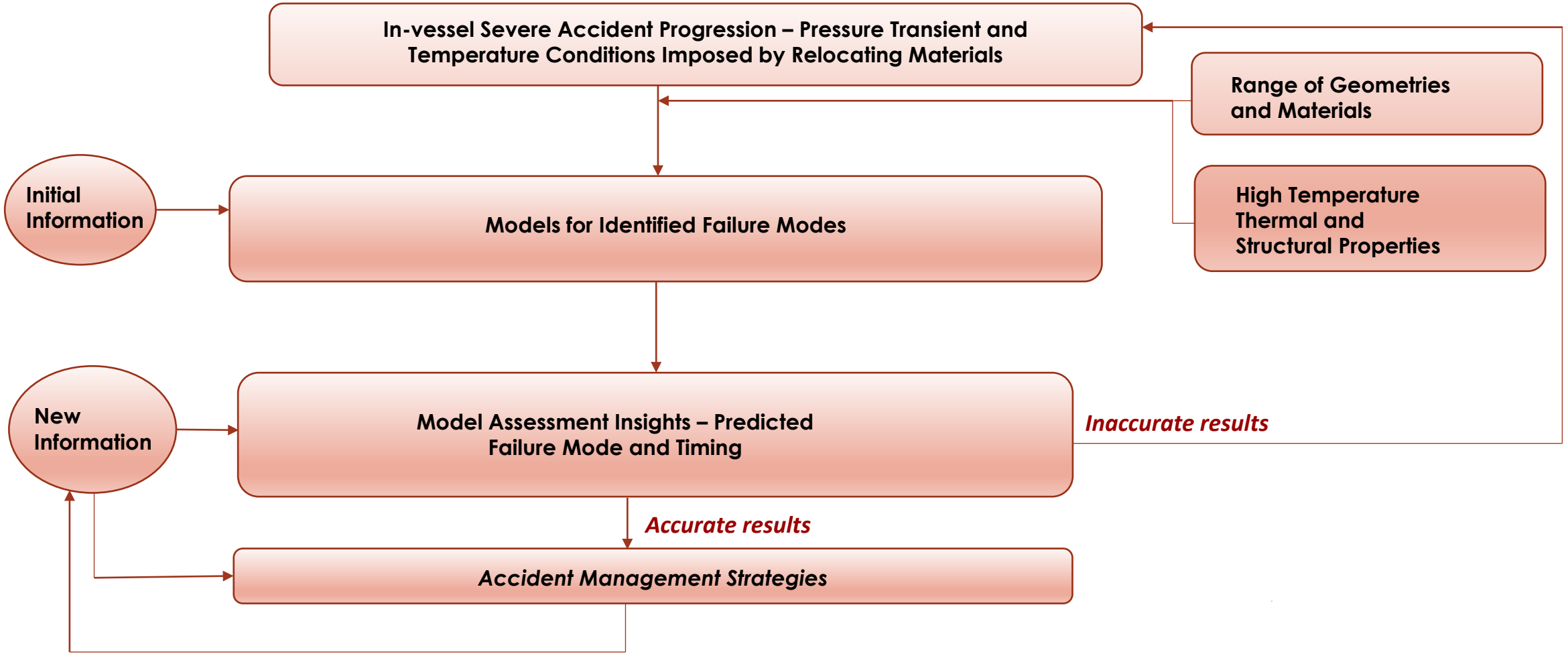

TMI-2 Information Motivated Efforts to Reduce Uncertainties in Predicting Vessel Failure

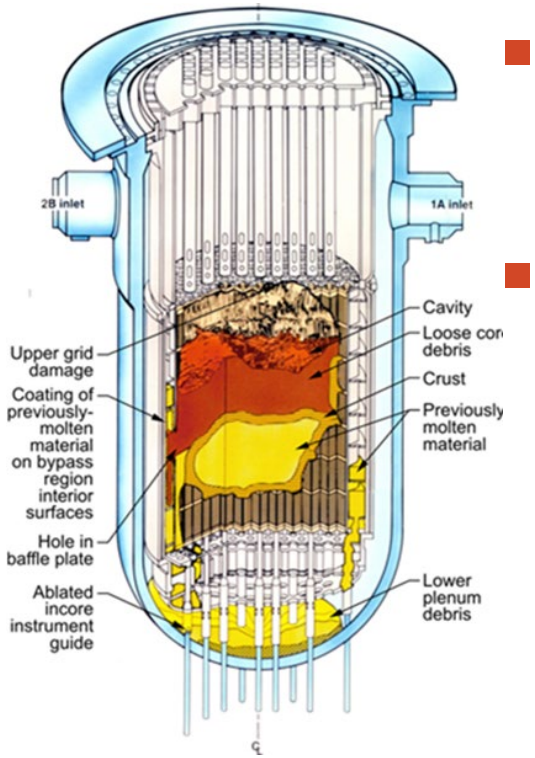

- **Codes typically assumed early penetration failure or global vessel failure based on temperature criterion**
- **NUREG-1150 RPV failure distributions derived using *expert opinion* based on initial TMI-2 data, severe fuel damage test data, and a range of available code calculation results**
  - Distributions suggested penetration failure followed by high pressure melt ejection more likely
  - Wide variation in expert opinion



Graphics Courtesy of INL and FirstEnergy

TMI-2 Information Motivated Efforts to Reduce Uncertainties in Predicting Vessel Failure (Continued)

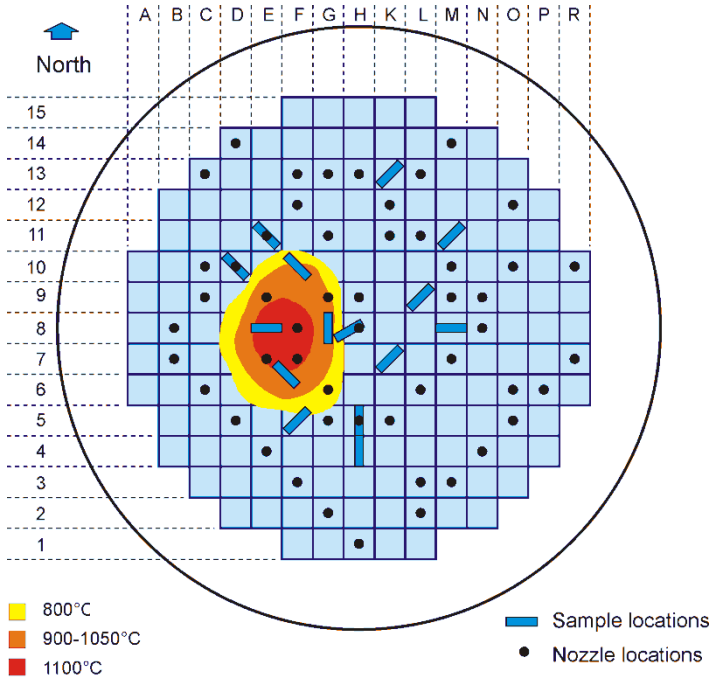

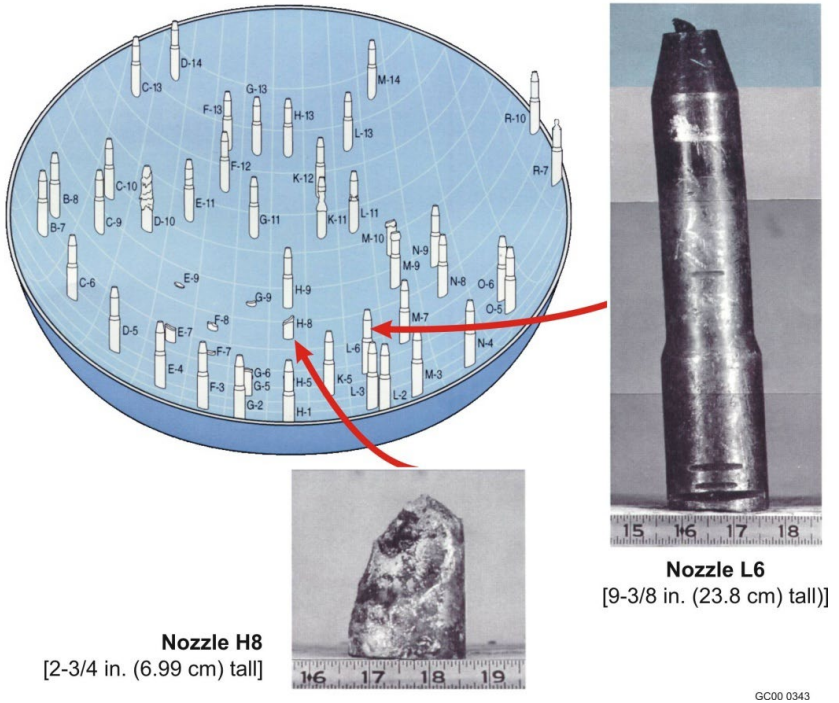

Graphics Courtesy of INL

TMI-2 information limitations:

- One reactor design
- One accident scenario (essentially a small break LOCA with throttled makeup and no safety injection)
- Scenario uncertainties – not a well-instrumented experiment
- Uncertainties increase when extrapolating to other reactors and scenarios

***General Insight*: Identify initial information limitations**

Approach to Reduce Uncertainties Associated with Vessel Failure Modeling

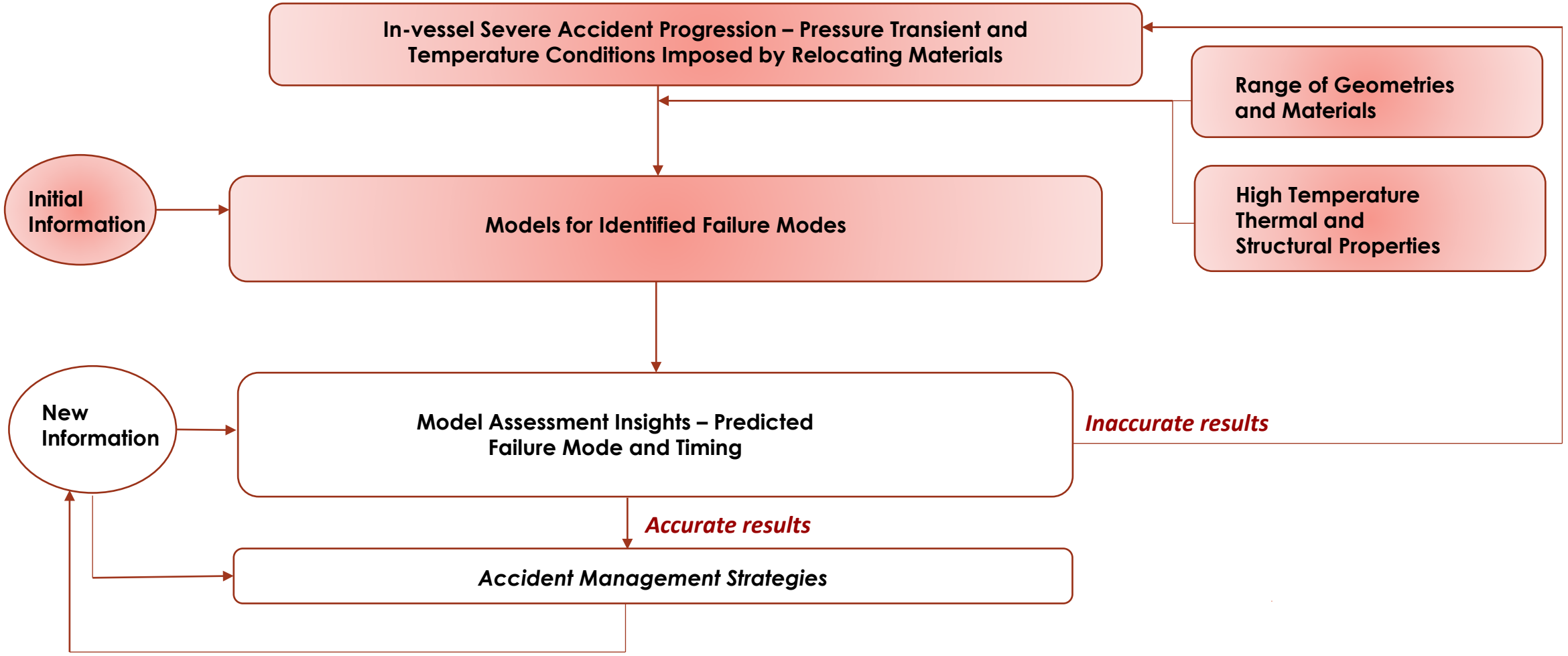

Range of LWR Lower Head and Penetration Designs and Materials

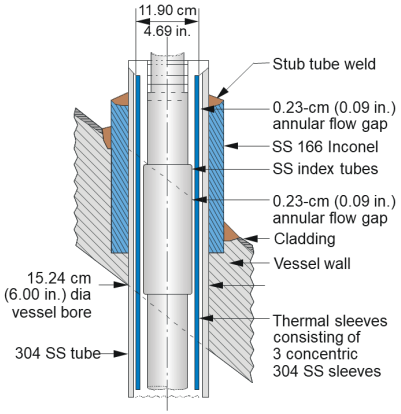

Typical GE CRD Assembly Penetration

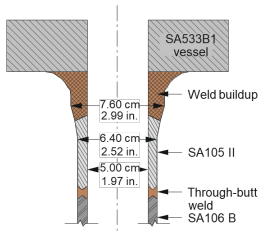

Typical GE Drain Line Nozzle Penetration

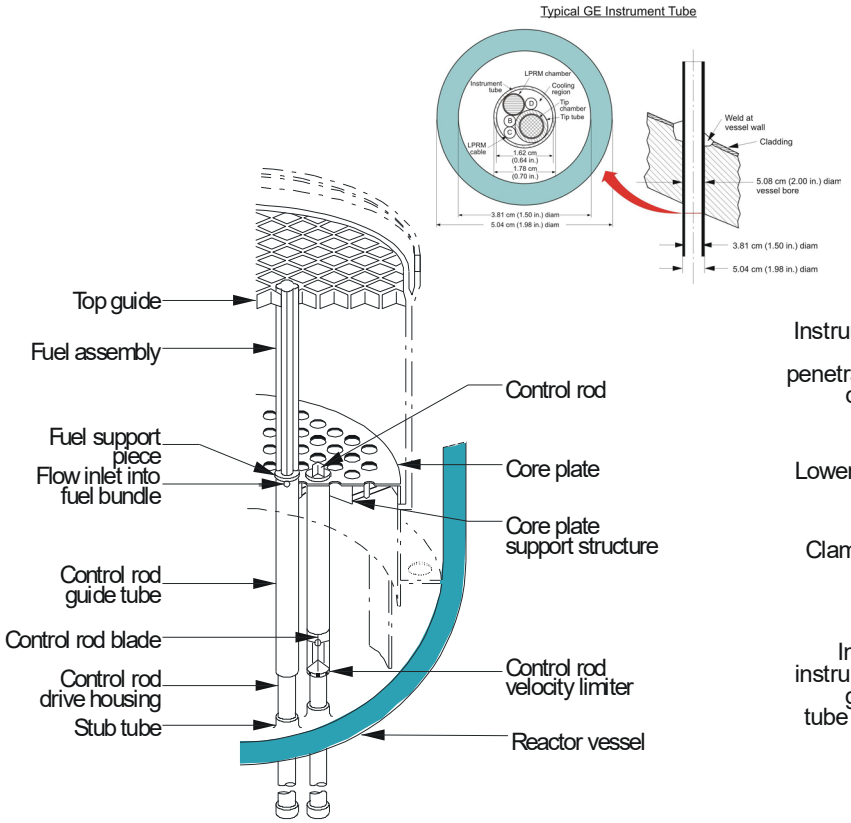

BWR

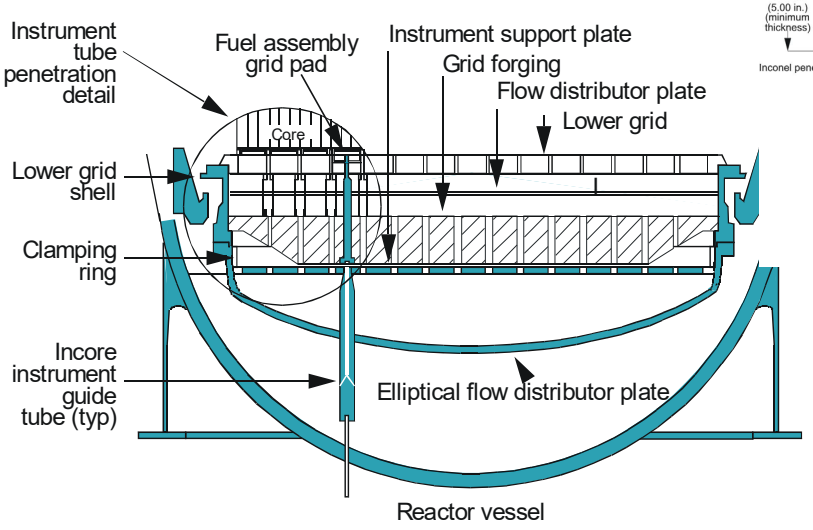

PWR

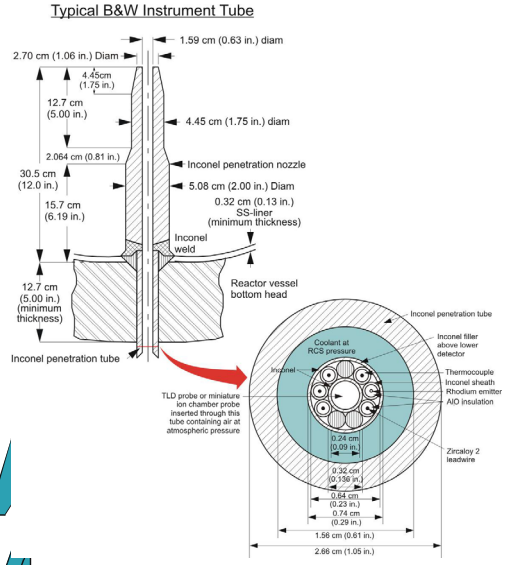

High-temperature Tensile and Creep Data Obtained for Vessel and Penetration Materials

- **Data for vessel (SA533B1) and penetration materials (SS304, Inconel 600 and SA105/106) obtained**
- **For SA533B1 vessel material:**
  - Significantly reduced SA533B1 yield strength at temperatures above 1000 K
  - Stress versus time to rupture only moderately sensitive to phase transition
  - Compared to published values, high-temperature thermal diffusivity data higher and thermal expansion data smaller

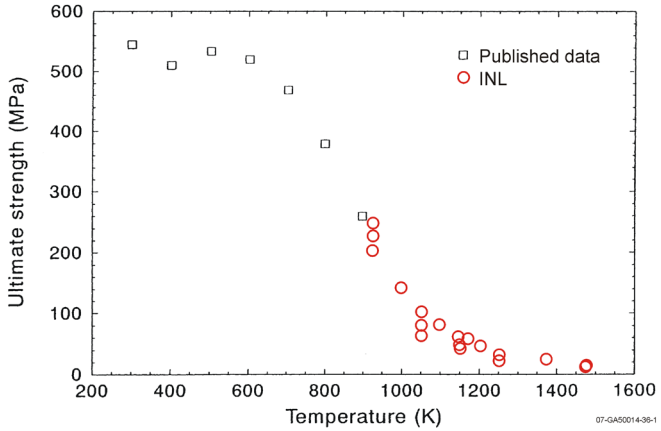

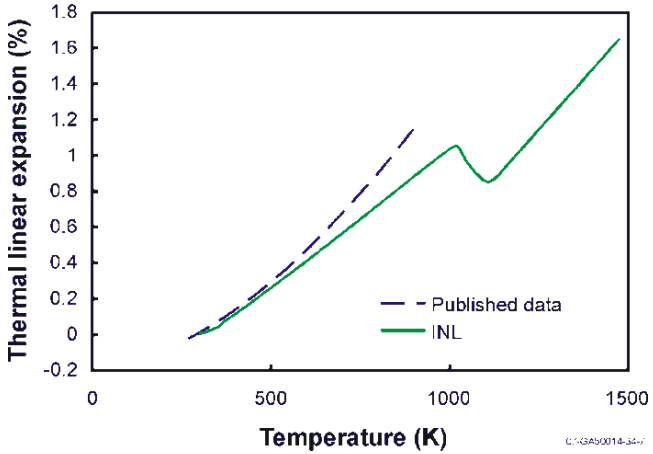

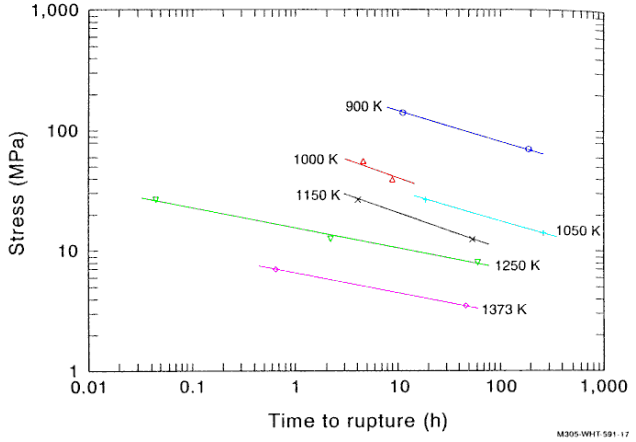

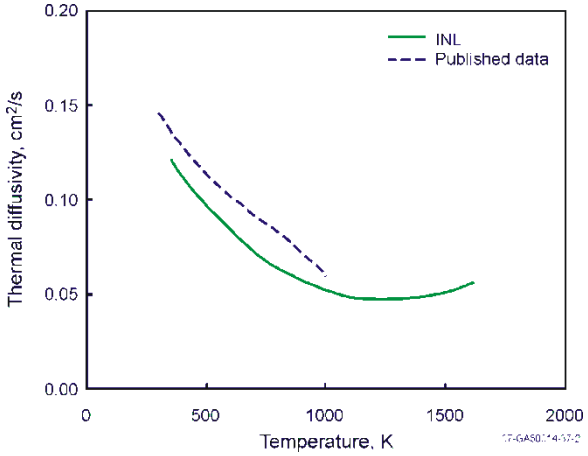

Graphics Courtesy of INL

General Insight: Don't extrapolate

Vessel Failure Modes Identified and Models Developed

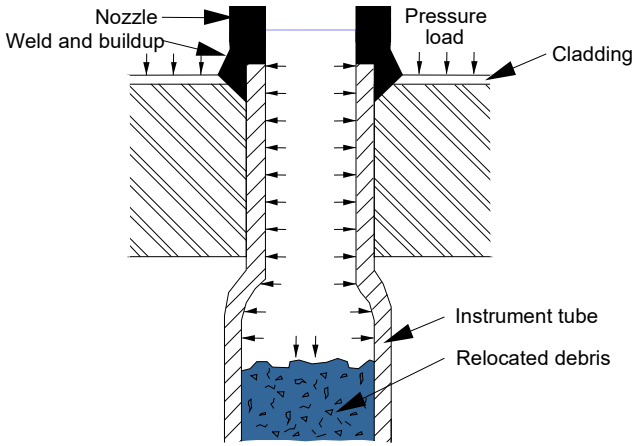

Tube rupture

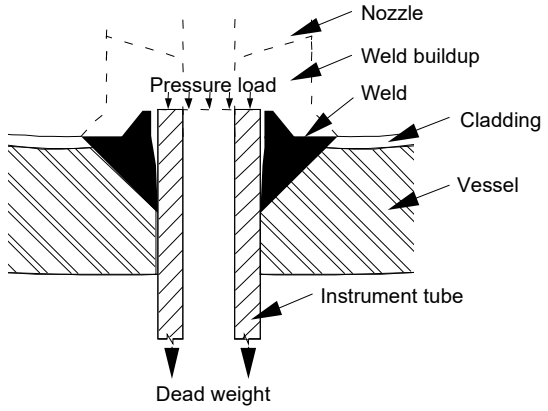

Weld failure/tube ejection

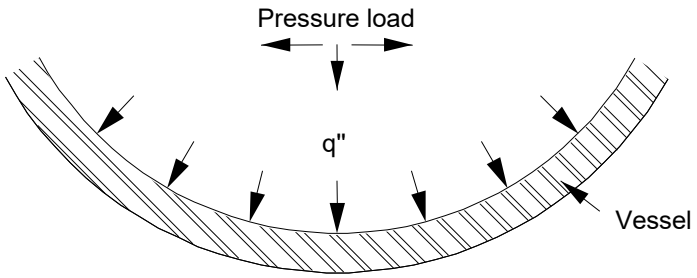

Global vessel failure

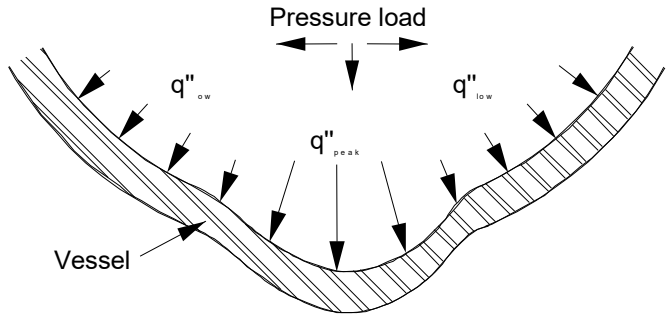

Localized vessel failure

Closed-form models developed for each identified failure mode

Graphics Courtesy of INL

General Insight: ***Start simple (consider model input uncertainties)***

Approach to Reduce Uncertainties Associated with Vessel Failure Modeling

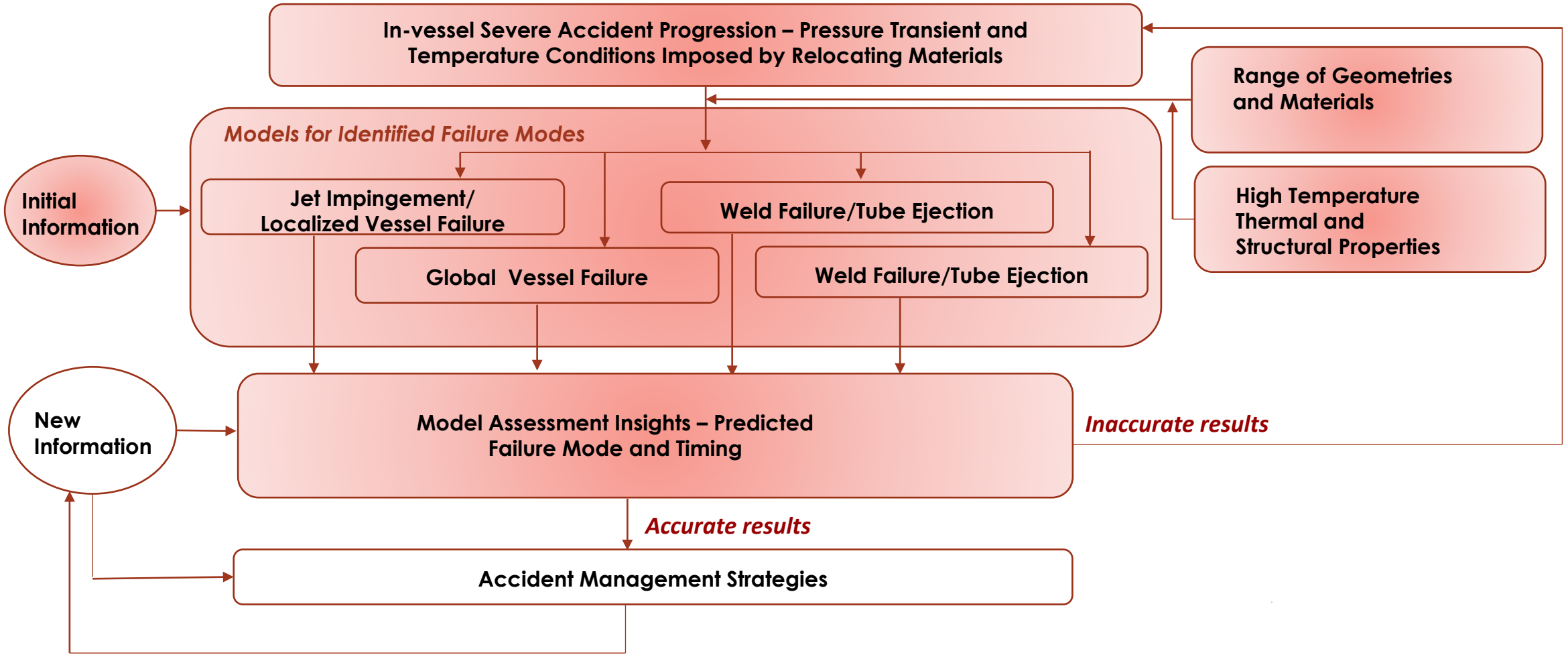

OECD TMI-2 Vessel Investigation Program Analysis Provided Important Insights

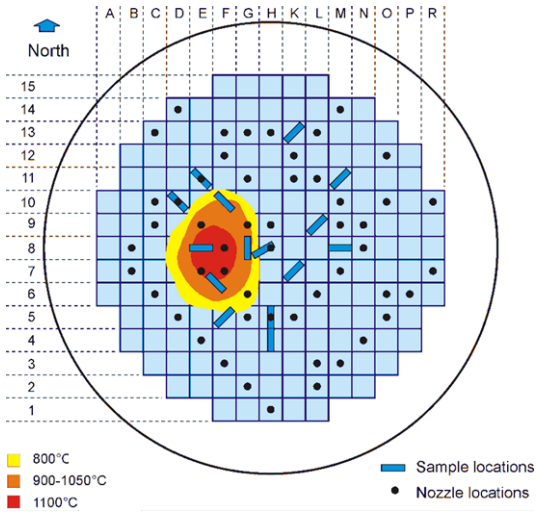

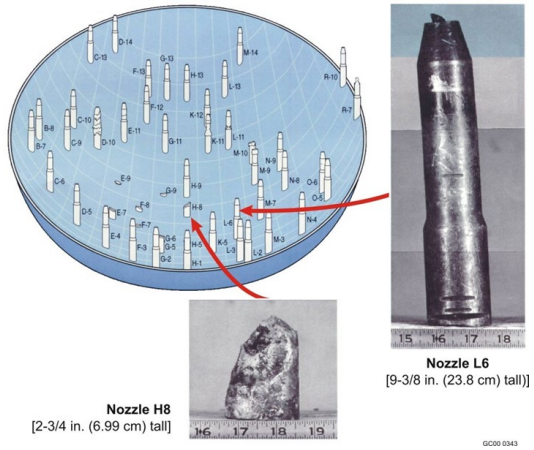

- **Large margin-to-failure estimated for tube rupture and tube ejection failure modes**
  - melt traveling below lower head insufficient to heat tube
  - thermal and pressure loads insufficient to fail weld
- **Localized "hot spot" not due to jet impingement**
- **Global or localized creep rupture estimated as failure modes with least margin**
- **Additional margin, not considered in severe accident analyses codes, existed**

Best Estimate Models Erroneously Predict TMI-2 Vessel Failure

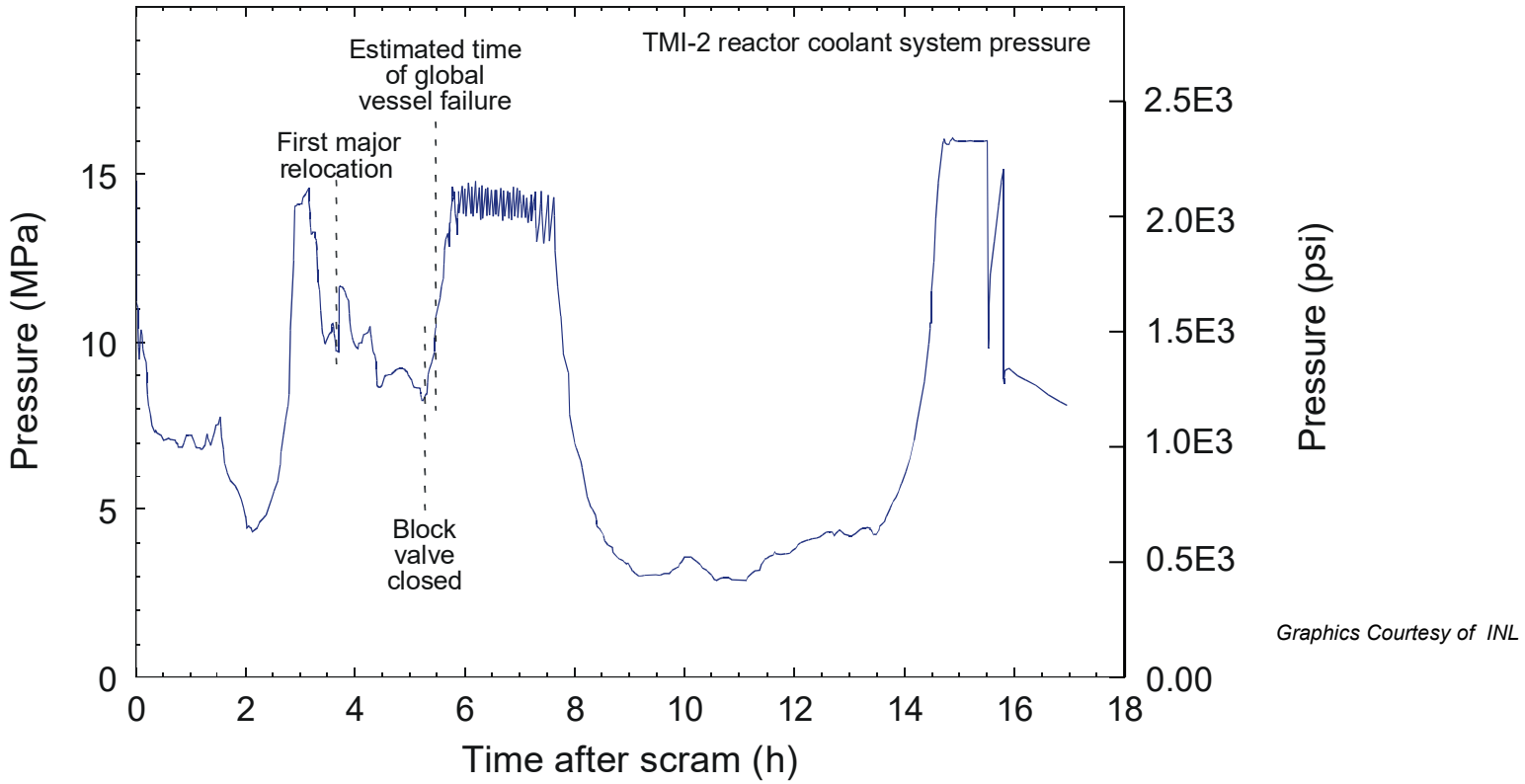

Graphics Courtesy of INL

General Insight: ***Assess models early and often***

Approach to Reduce Uncertainties Associated with Vessel Failure Modeling

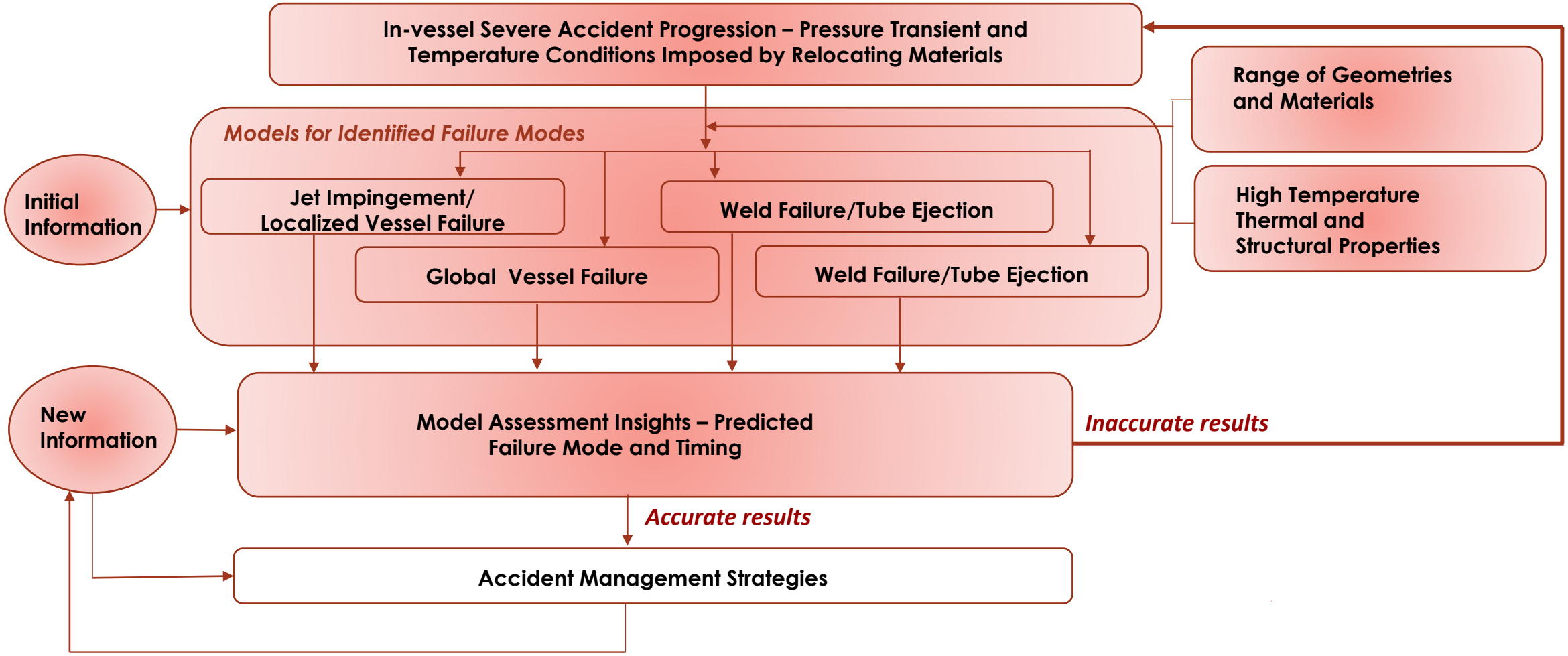

Debris Heat Loads Complicated

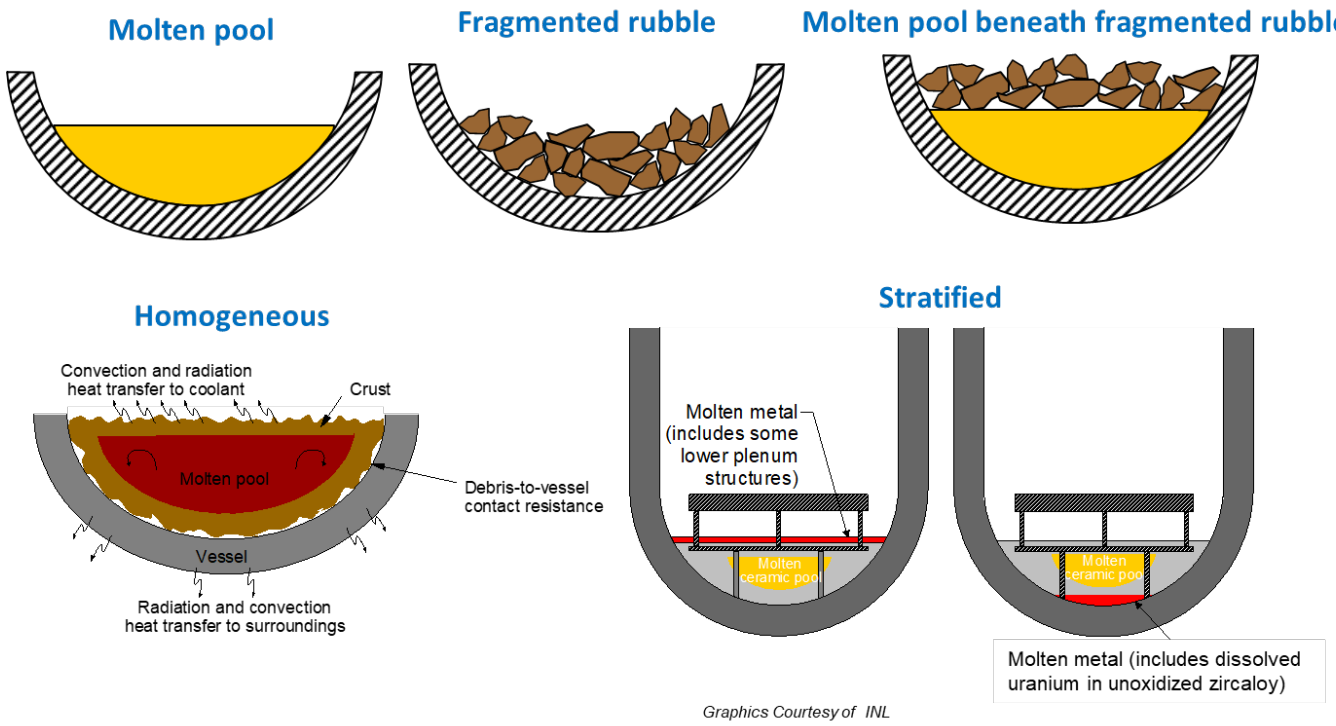

Graphics Courtesy of INL

- **Information needed to address questions, such as:**
  - what debris endstates may occur?
  - what phenomena affect debris coolability?
- **NUREG-1150 developed relocated debris heat load distributions derived from *expert opinion***
- **Wide variation in expert opinion (due to limited data)**

Enhanced Debris Cooling Complicated

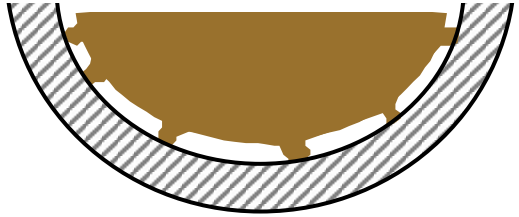

Intermittent debris-to-vessel gaps

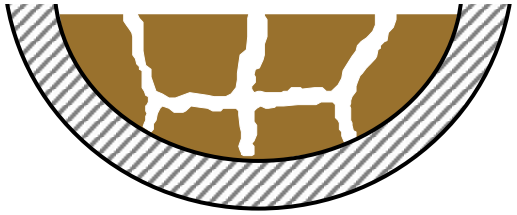

Interconnected debris cracks

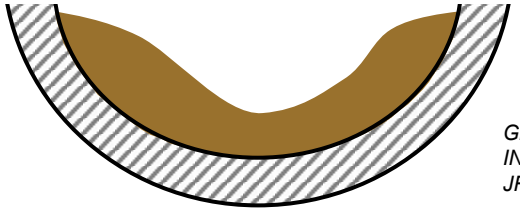

Concave upper debris surface area

Graphics Courtesy of INL, FirstEnergy, JRC, and OECD



TMI-2 Investigations

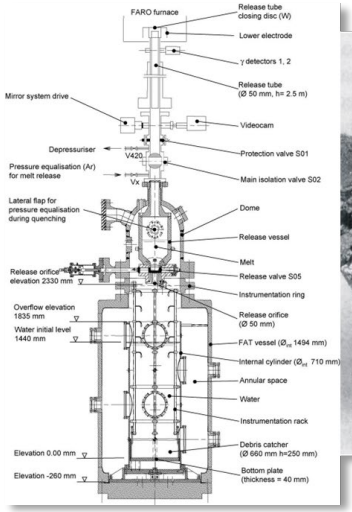

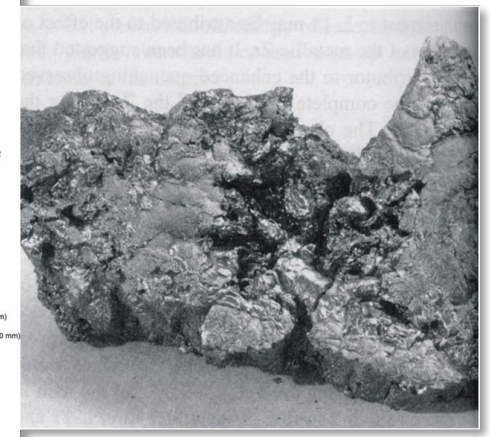

JRC FARO Tests

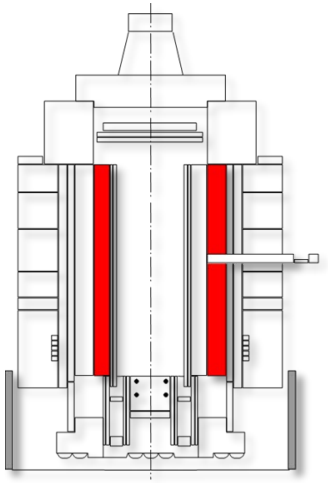

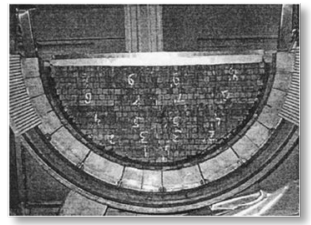

Before

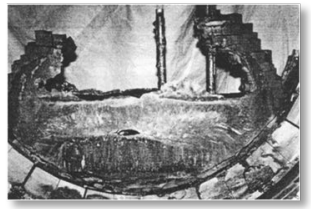

After

OECD RASPLAV Tests

Vessel Failure Complicated

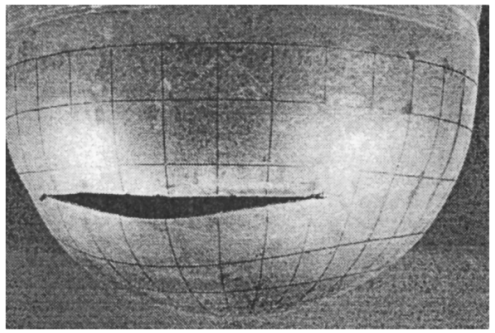

LHF-3



LHF-5

Graphics Courtesy of NRC and OECD

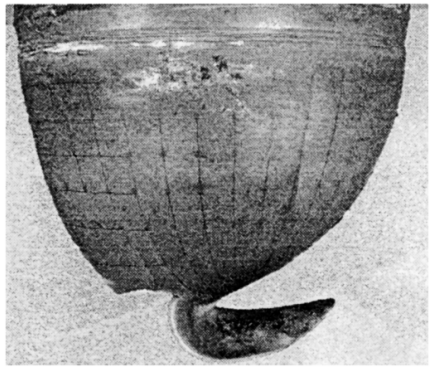

LHF-1

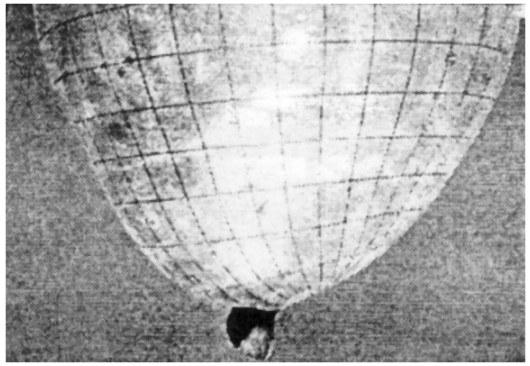

LHF-6

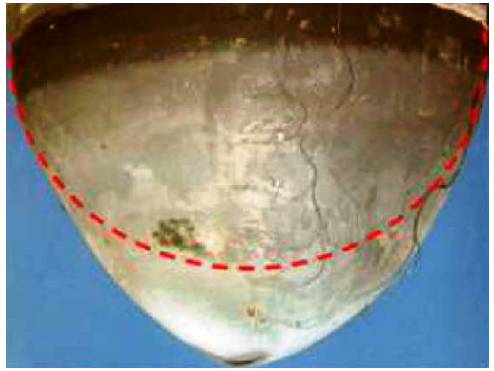

OECD LHF Test OLHF-1

- **NRC and OECD SNL Lower Head Failure (LHF) tests emphasize variations in:**
  - heat load
  - pressure load
  - vessel thickness
  - vessel material composition

***General Insight:* Consider information limitations**

Approach to Reduce Uncertainties Associated with Vessel Failure Modeling

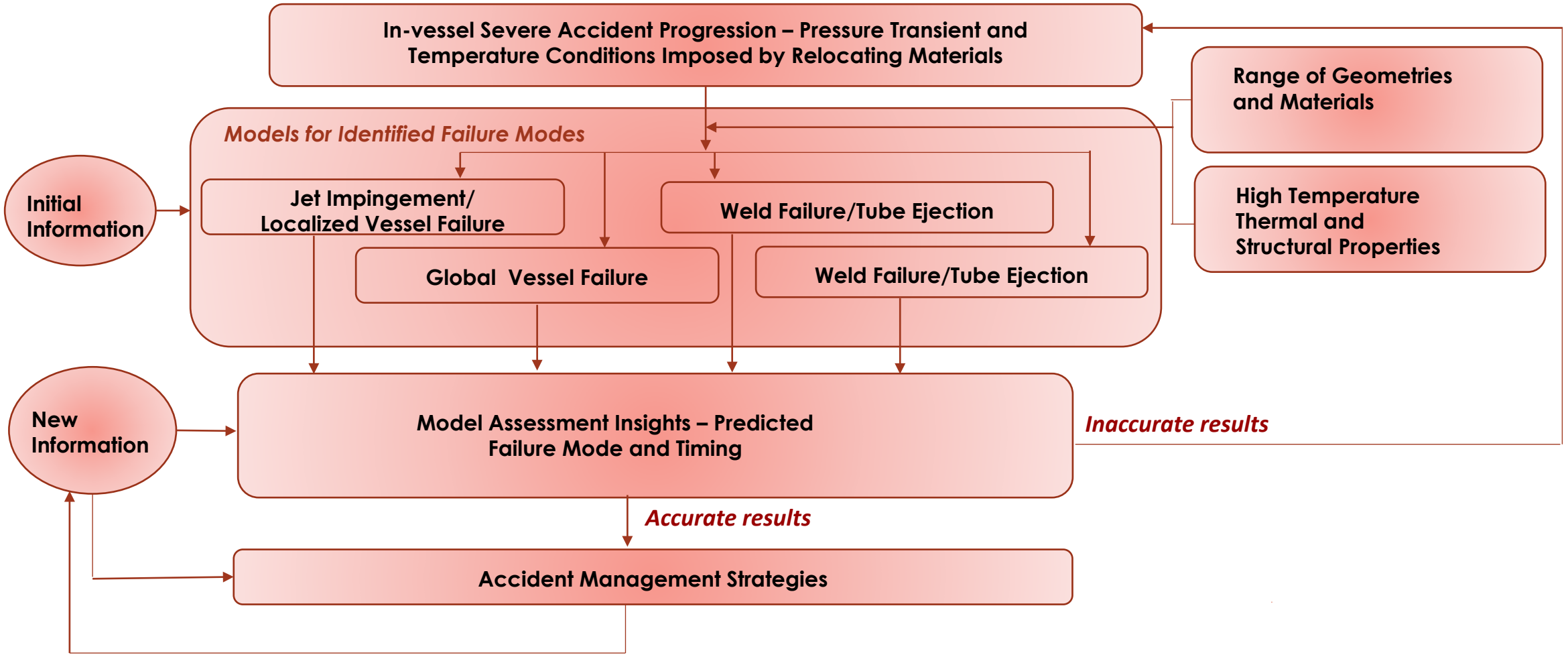

Accident Management Strategies to Preclude Vessel Failure in Existing and Future Reactors

EPR Depressurization

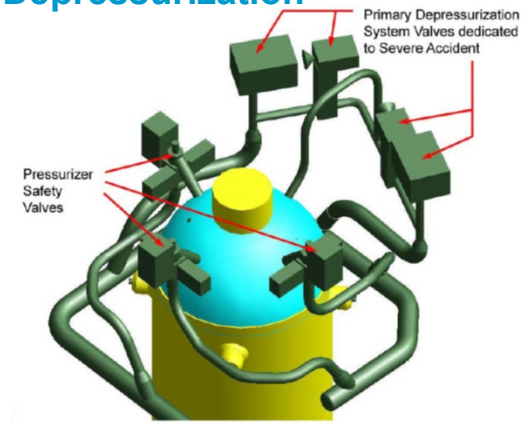

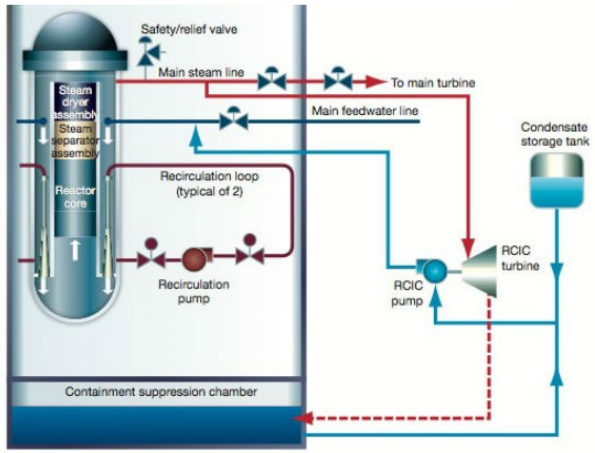

BWROG Water Addition

- **RCS depressurization strategies (intentional and unintentional):**
  - Reactor coolant pump seal leakage
  - Induced primary system piping failures
  - Safety valve(s) failing open
  - Intentional relief valve depressurization
- **Water addition strategies (in-vessel and ex-vessel)**
- **In-Vessel Retention (IVR) strategies requiring:**
  - Heat flux to vessel (from relocated debris) less than heat removed from the vessel
  - Ex-vessel flooding prior to melt relocation
  - Sufficient areas for coolant ingress and steam egress
  - Vessel must withstand thermal shock
  - Vessel insulation/shield/supports must withstand forces associated with external reactor vessel cooling

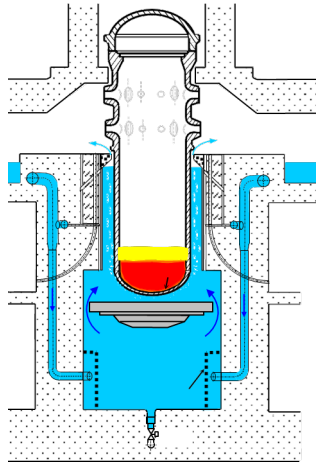

Loviisa VVER IVR

Graphics Courtesy of Framatome, IVS, Nuclear Engineering International, and NuScale

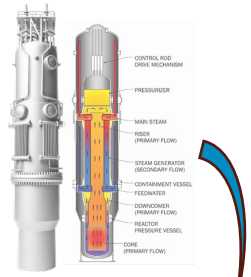

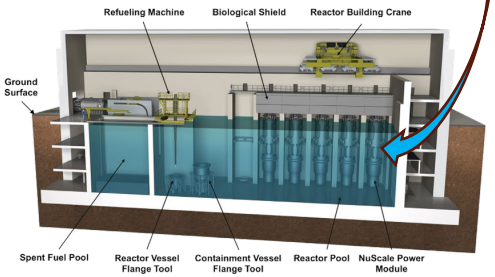

NuScale SMLWR IVR

***General Insights:* Implement research insights (when appropriate)**

Concluding Remarks – General Insights

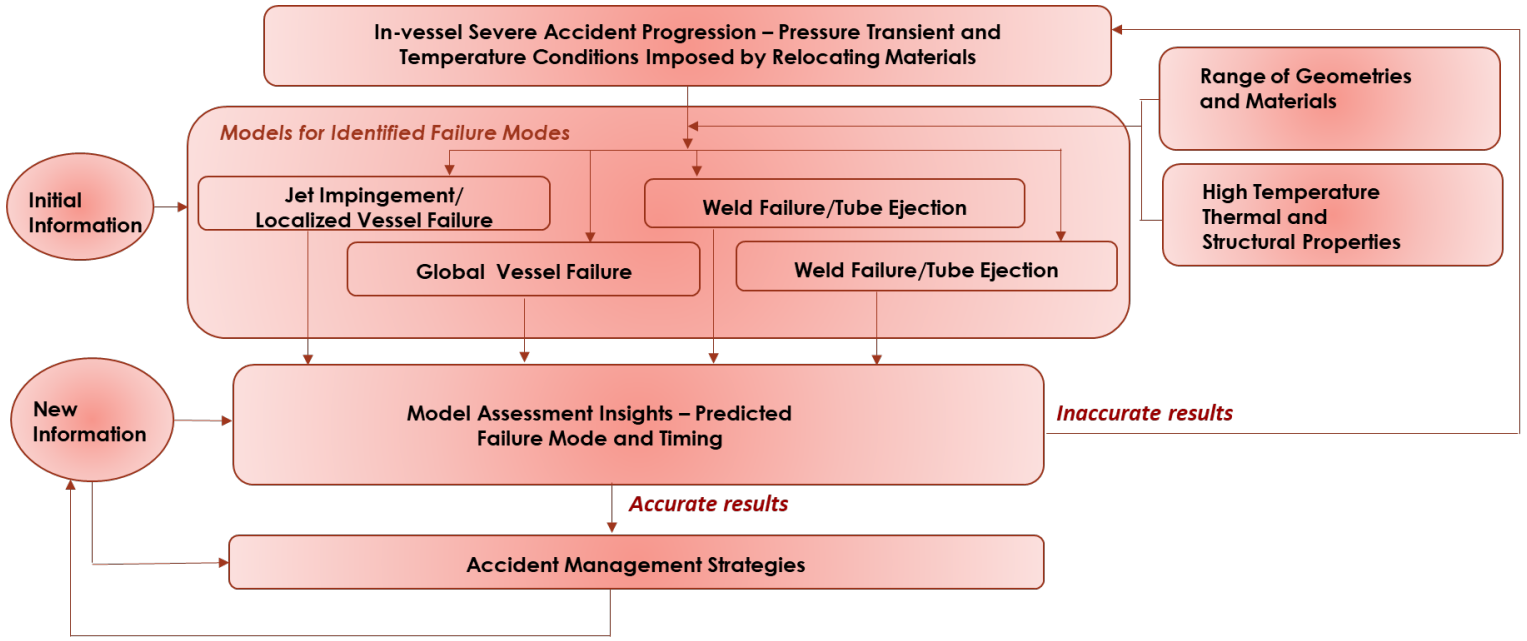

- Identify initial information limitations
- Don't extrapolate
- Start simple (consider model input uncertainties)
- Assess models early and often
- Evaluate new information limitations
- Implement research insights (when appropriate)
- *Continue to assess adequacy of models and research insights*

Fukushima Daiichi Another "Game-Changer"?

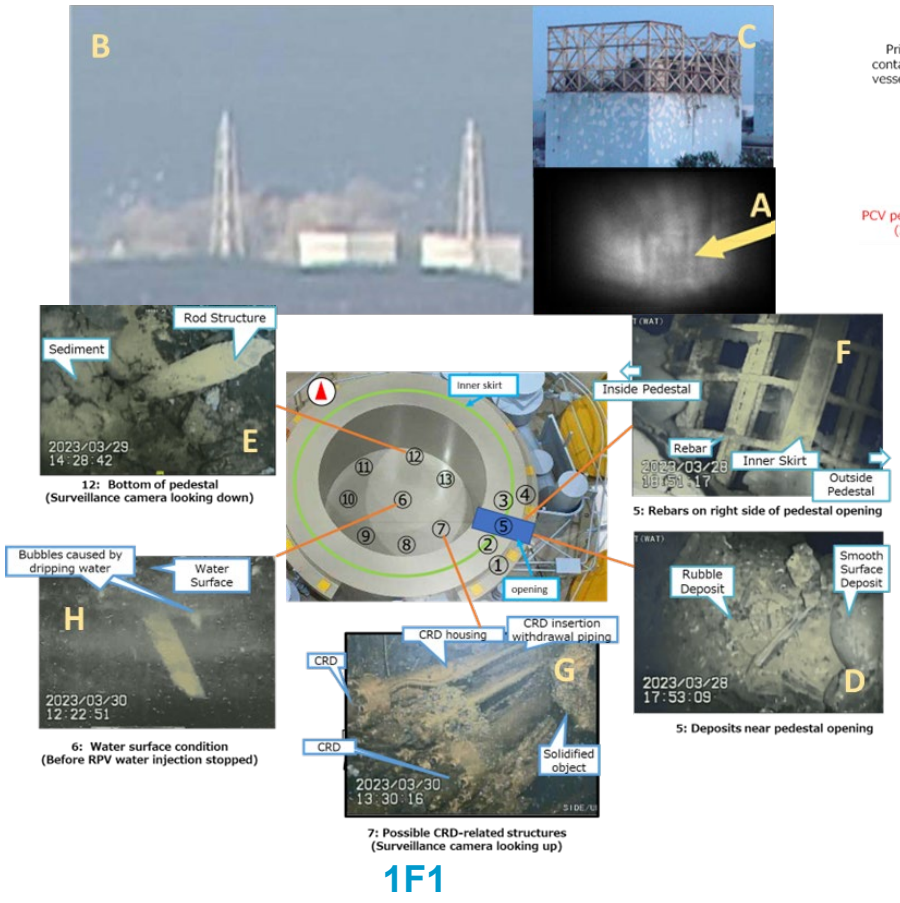

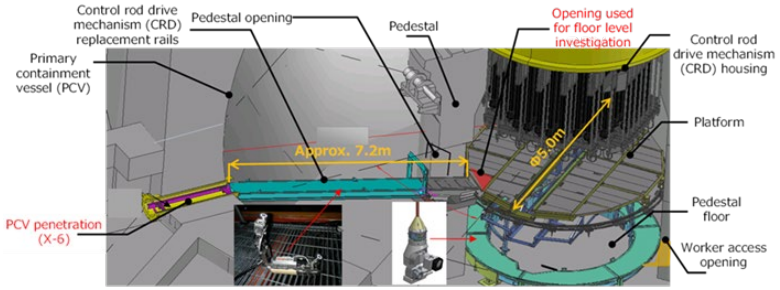

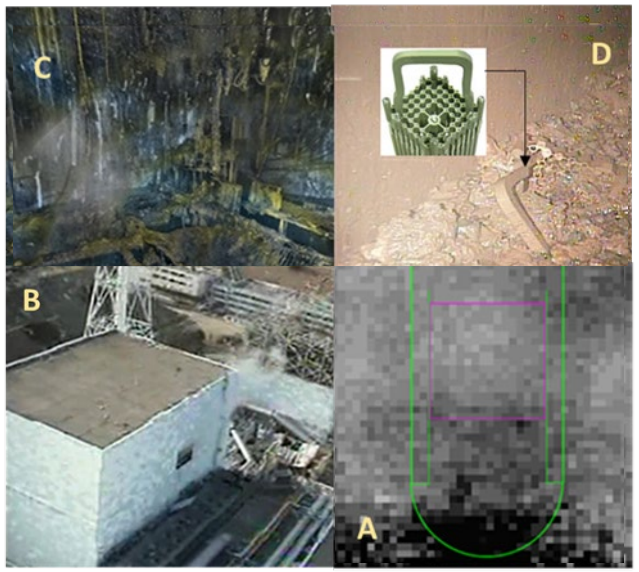

1F2

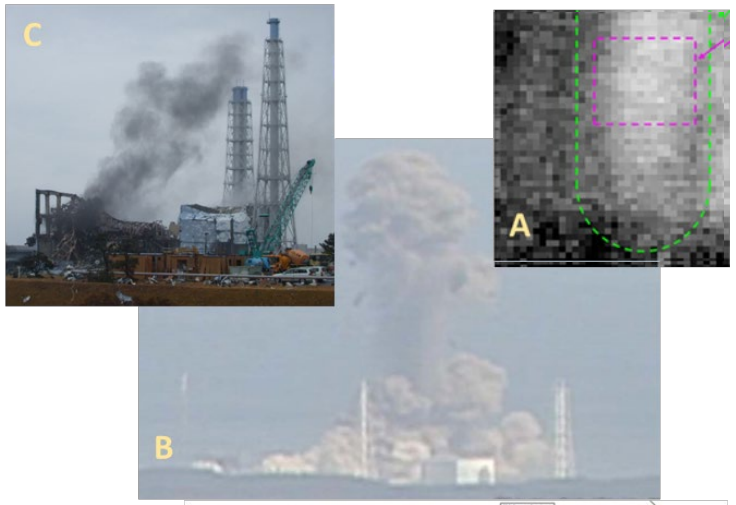

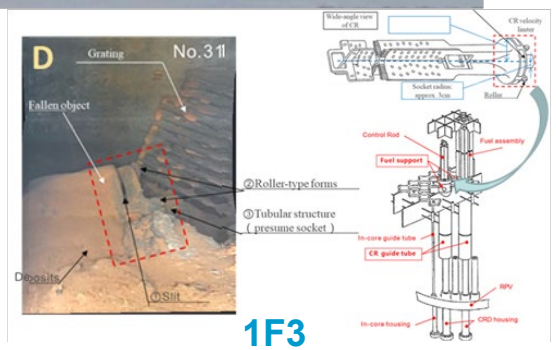

Graphics Courtesy of TEPCO, IRID, and FCT

1F3

General Insight: ***Continue to assess adequacy of models and research insights***

PLENARY SESSION (Room: Nya Matsalen)
Singular Careers in the Severe Accident Research
Chairs: **L. E. Herranz** (CIEMAT), **T. Lind** (PSI)

Your-own Research Roadmap with Scaling Consideration

through the ***Kitchen Door***

Hideo NAKAMURA
Japan Atomic Energy Agency (JAEA)

ERMSAR 2024
Stockholm, Sweden, May 13, 2024

This represents my personal opinions, and not of **JAEA** nor **AESJ T/H Div.**

Contents

- **Examples of Roadmap (RM)**
  - RMs for SA Research
  - RM in Japan ***before*** 1F accident
  - RM in Japan ***after*** 1F accident
  - Rolling (Revision) for RM in Japan
- **Your-own Roadmap ?**
  - What is the **challenge** ..
- **Concluding Remarks**

Examples of Roadmap (RM)

Examples of Roadmap (1/2)

Severe Accident R&D Trend

SARNET
1: 2004 - 2008
2: 2009 - 2013

- **2008** Ranking of severe accident research **priorities**.
  (*B. Schwinges et al., ERMSAR2008, Nesseber*)

Fukushima-Daichi Accident

- **2013** NUGENIA Roadmap, 2013
- **2014** Conclusions on severe accident research **priorities**
  (*W. Klein-Heßling et al., Annals of Nuclear Energy 74 (2014) 4–11 on SARNET2 FP7*)
- **2015** NUGENIA Global Vision (*Ver. April 2015, Revision 1.1*)
  NEA Nuclear Innovation 2050 (NI2050) + International Workshop (*July*)
- **2016** ETSON views on R&D **priorities** for implementation of the 2014 Euratom Directive on safety of nuclear installations
  (*J. P. Van Dorsselaere et al., KERNTECHNIK 81 (2016) 5*)

  United States Department of Energy (USDOE)
  Severe Accident Research Following the Fukushima Daiichi Accidents
  (*M. T. Farmer et al., Nucl. Technol. 196 (2016) 141*)
- **2019** Severe Accident Research **Priority Ranking**:
  A New Assessment Eight Years after the Fukushima Daiichi Accident
  (*D. Manara et al., ERMSAR2019 098, Prague*)
- **2021** NUGENIA VISION (*June*)

Examples of (2/2)

Nuclear Global (whole) Perspectives

- **2023 NEA for New Nuclear**
  Government and industry representatives (*September*)



Ministerial communiqué
Energy ministers and heads of delegations of 20 countries issued a call to action and guiding principles in support of roadmaps for nuclear energy. The communiqué outlines guiding principles for:

- Nuclear financing
- Policy and regulation
- Research and development (R&D)
- Supply chains
- Fuel supply
- Skills
- Public engagement
- Energy systems innovation
- International collaborations

Industry communiqué
Associations representing the nuclear industry in OECD countries signed a joint communiqué highlighting the essential role of nuclear energy and calling on deepening the co-operation with governments, international organisations and across the industry.

- **2024 NEA for New Nuclear (*September*)**



- **2024 NEA Initiative for SMR**



by AESJ* T/H Roadmap *before* 1F Accident (1/3)

* AESJ: Atomic Energy Society of Japan)

- **Former T/H Roadmap (RM)**

Request from Government

- **The first RMs** via **AESJ*** (**2006**) for **Advanced Utilization of Current LWR** concerning (a) **high-burnup fuel**, (b) **aging management,** (c) **power uprate**

similar to **"Sustainability"** by **US DOE**

- **A Project** by Government & Utilities (**2007**) : "**Development of Next-Generation Light Water Reactor capable of winning a world standard**" to start **operation on 2030**

- **T/H field** was, at first, expected to play a major role in development & verification of fundamental technology to support **stable, economic & safe high-performance LWRs** (**PWR** & **BWR**).

- **A special committee** established in **AESJ*** (2007) provided **The thermal-hydraulic and safety roadmap** (**2009**) under collaboration of **industries**, **government** & **academia**

by AESJ T/H Roadmap *before* 1F Accident (2/3)

- **Member of AESJ Special Committee for Former T/H Roadmap (RM)**

Industries	TEPCO (BWR), KEPCO (PWR), JAPC (B & P) out of 9 utilities who operate LWRs
	Hitachi-GE NE, Toshiba, MHI, CRIEPI, TEPSYS, INSS, GNF-J, JANSI
Governmental	JNES*, **JAEA**, IAE, **Observers** (NSC*, NISA*/METI, ANRE/METI)
Academia	Tokyo U., TiTech, Kyoto U., Osaka U., Kyushu U., Nagoya U,. Hokkaido U., Tsukuba U., Tokyo-City U., Kogakuin U.

* Former Name

- **T/H division of AESJ contributed to development & revision**
- **The same members continue the activity**

by AESJ T/H Roadmap *before* 1F Accident (3/3)

Scope

- To **develop common understanding among stakeholders:**
  - ✓ **Safety improvement**
  - ✓ **Advanced utilization of current LWRs**
    including high burn-up fuel and aging management – *Long-term*
  - ✓ **Development of new LWRs** with new safety features
- To **overview role of** and **requirements for**
  development & safety regulation by **considering world R&D trend**

● Stakeholder Requirements for RM

- ✓ **3 Major Subjects – *Working Group*** *established for each*
  Severe Accident, ***Plant Improvement Technology***, ***Scaling*** ***(safety analysis)***
- ✓ **Consistency** with fundamental research, and development
- ✓ **Cross-cutting issues** among different domain of subject
  such as material, structure, fuel etc. (not including natural hazard)
- ✓ **Human resource** (***Researchers***) development

in Japan

Next Generation LWRs

High-Performance LWRs (Planned)

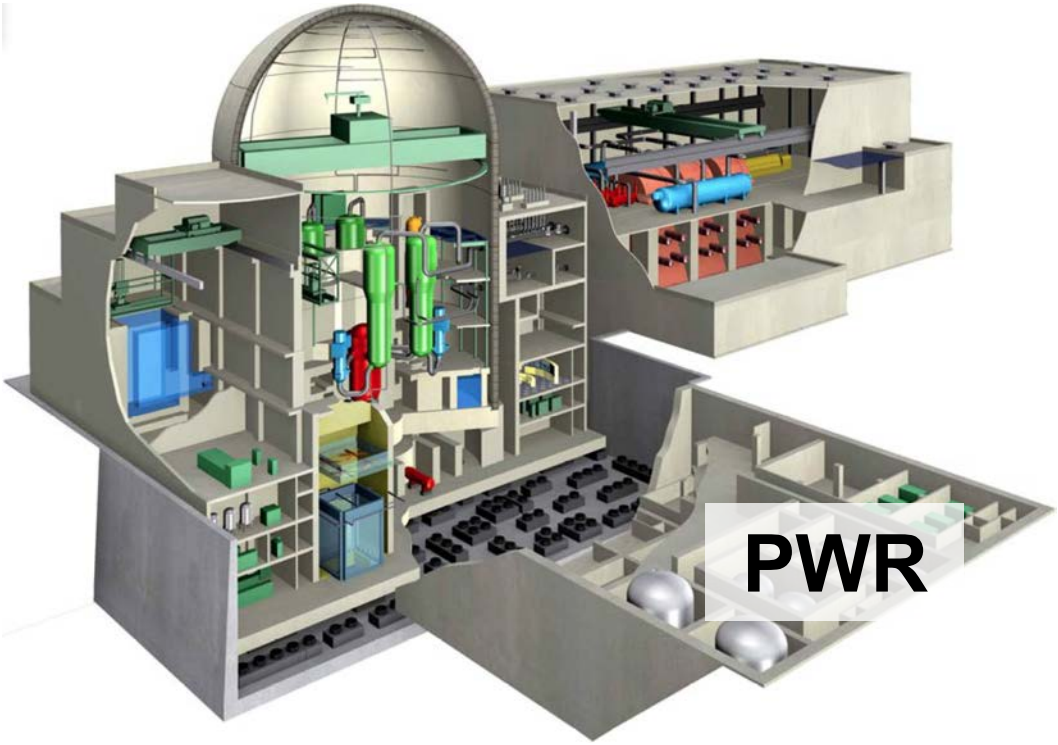

PWR

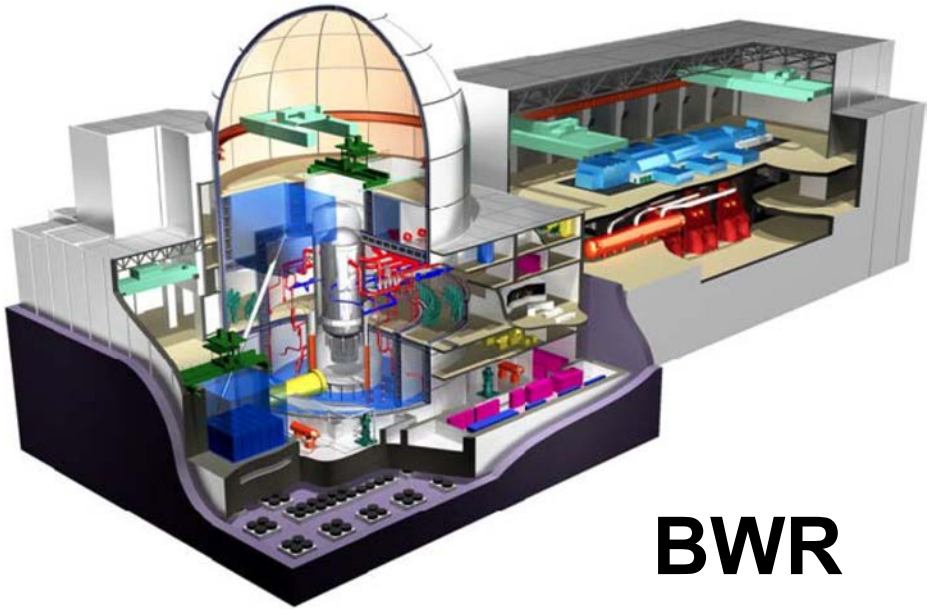

BWR

IAE The Institute of Applied Energy

August, 2010

Conceptual Design

- **Large LWRs (1.76 GWe + half-power option)**
- **Mostly with *Proven Technologies***
  - ***R&D not much* in T/H and SA**

What's New ??

by AESJ Structure of RM (Technology Strategy Map)

● 3 General Steps/Components for RM Development

1. **Technology Adoption Scenario** ***Whole View***
   to explain the background, objectives and measure(s) to perform research and/or developments utilized to give the LWR-relevant technology of interest (**description document**)

2. **Technology Map**
   to collect & summarize major & latest information relevant to the technical subject, to identify necessary R&Ds to achieve the intended development by solving relevant issues
   (**Table of Info. & classification**)

3. **Roadmap**
   to indicate method(s) and progress of each subject on time axis common to all the subjects (**Time table**)

by AESJ

Whole View of Former T/H RM

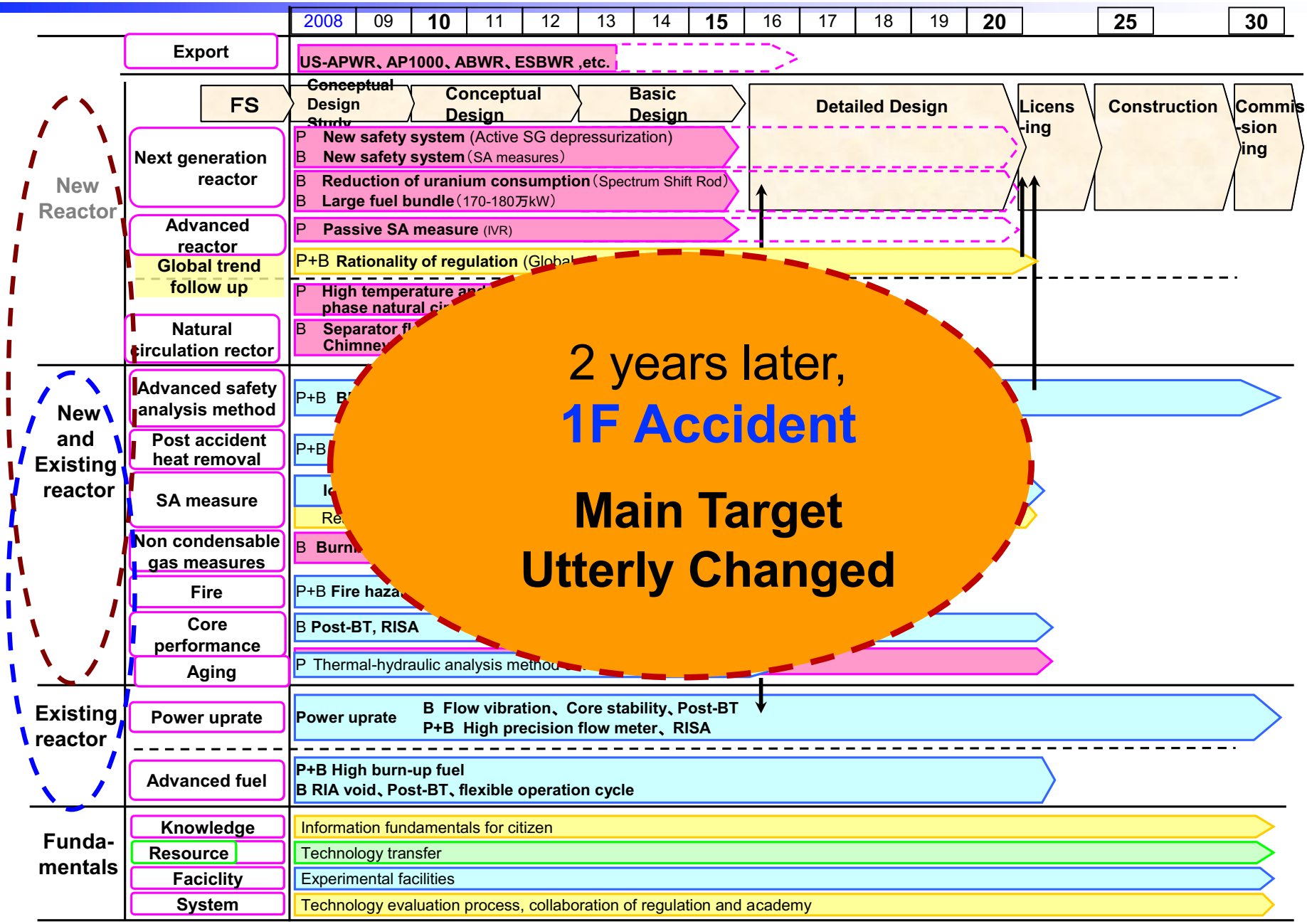

by AESJ

T/H RM *after* 1F Accident

Scope

- **Revise the target utterly**
  based on **Lessons-learned from 1F Accident**
- **Implement** rigorous, fundamental yet profound
  counter-measures into **current LWRs** via **RM subjects**
  to never cause the disastrous accident again
- **Development of Human Resources**
  prominent issue *than* ***before***

- ***Practical Issues***
  - ***Newly create Whole View & Technology Maps for each major area***
  - ***Define Key Subjects (under post-1F confusions)***
- ***AESJ T/H Div. Working Group: Development of Strategy Map to Advance Base Technologies for Thermal-Hydraulic Safety Assessment***

by AESJ

T/H RM *after* 1F Accident

General Role of RM (newly defined)

- RM provides a platform for widely sharing the significance and relevance of the technical challenges to be addressed, as well as the appropriateness of the implementation details with the public, ensuring transparency in the process
- RM explicitly outlines the milestones, importance assessment, R&D activities, necessary technological foundations, utilization of outcomes, involved stakeholders (implementers, budget providers), and evaluation methods for planning and results, facilitating communication and shared understanding among stakeholders, including interfaces with other fields
- RM serves as a tool for planning and managing progress, evaluating and confirming the utilization of achievements, and considering revisions.
- RM functions as a library and guidebook that supports researchers in exploring themes etc., facilitating ***the matching of needs and seeds***
- RM serves as ***a reference material good for human resource development*** in organizations involved in R&D activities

Key Issues and T/H R&D Subjects

Three Sub-WGs

- Fundamental Technology
- Severe Accident
- Safety Assessment

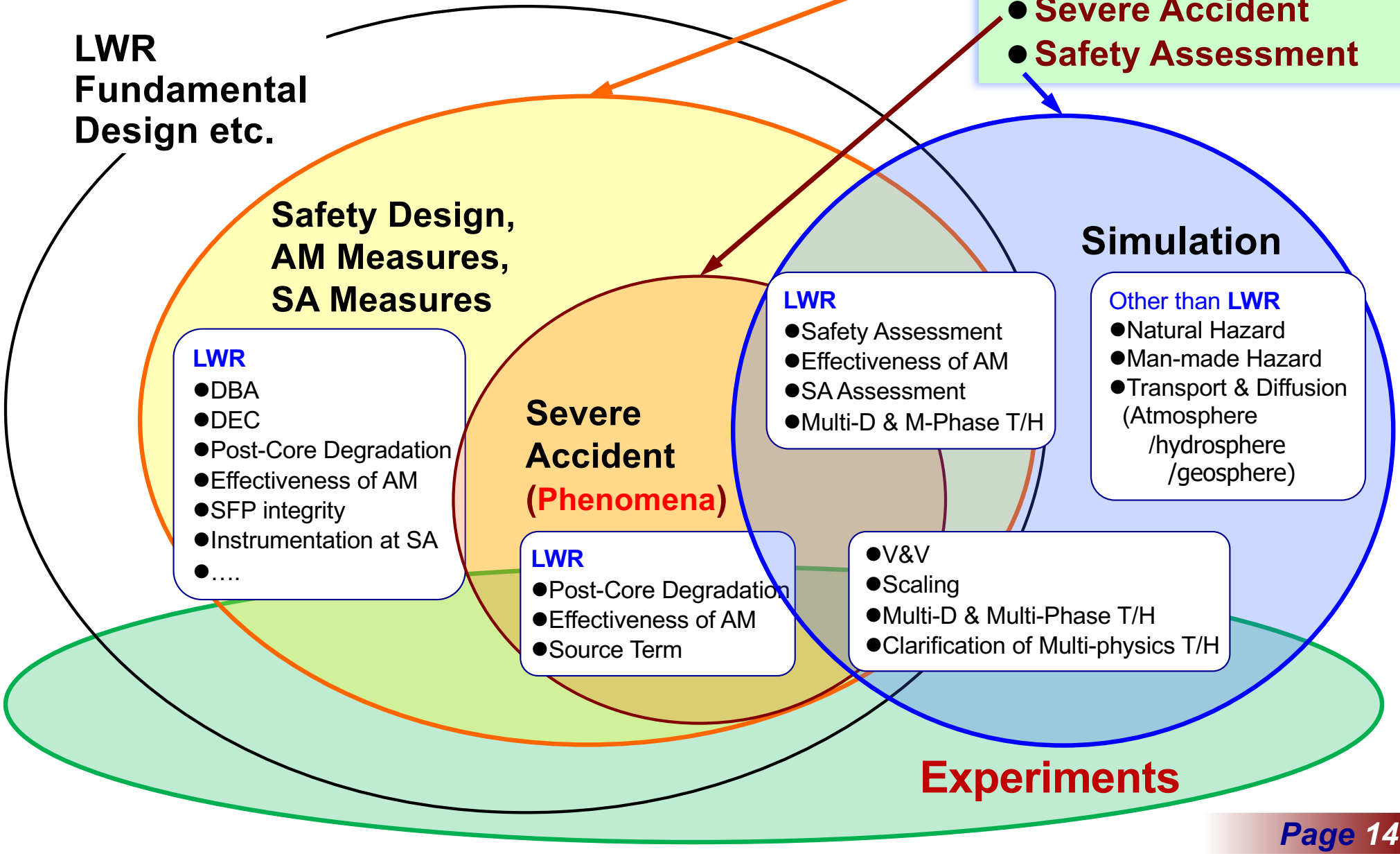

Severe Accident SWG

completed development of
Technology Map (Phenomena-Basis)
by 2013

Severe Accident (SA) SWG (1/3)

Technology Map (*developed by 2013*)

- **Provide Phenomena Identification (PI) Table by means of break-down of various SA phenomena, AM measures and their responses into fundamental (elementary) process**
  - ❖ to achieve "**Matching of Needs & Seeds**"

    ☞ **common to other Sub-WGs**

- **Re-evaluate and complement SA phenomena and AM measures, in the light of 1F Accident**
- **Prioritize each of fundamental subjects by reviewing status and degree of sufficiency of state-of-the-art knowledge as well as data base**

➢ ***Chronological Road Map****, however, was* ***not*** ***prepared****..*

Severe Accident (SA) SWG (2/3)

Before 1F Accident

- **Major SA Phenomena and Technologies**

1. **Core degradation + IVR**
2. **Hydrogen behavior**
3. **FCI** (steam explosion)
4. **HPME & DCH**
5. **MCCI**
6. **Source term**
7. **Air-tightness of CV**
8. **Debris cooling in CV**
9. **Re-criticality of melt/debris**
10. **Instrumentation**

After 1F Accident

- **Re-evaluated Subjects**

1. **Core melting progression**
2. **Re-criticality** & **Source-term** (influences of pool-scrubbing during depressurization boiling etc.)
3. **Influences of Sea-water Injection**

- **Complemented Subjects**

1. **Countermeasures to suppress leakage by maintaining CV airtightness**
2. **Methods to minimize Environmental Impact**
3. **Instrumentation during SA**

Severe Accident (SA) SWG (3/3)

Example

Technology Map — *Portion of* Hydrogen Behavior

Technical Subject	State-of-Art of Subject	Database and/or Knowledge Base	Extent of Influences	Evaluation Method		Uncertainty		R&D Priority
				Integral Code	Detailed Code	Pheno-mena	Code Maturity	
Mixing	• Many experiments • CFD prediction of stratification, mixing, wall condensation is premature (ISP-47 etc.) • In sufficient counter-measure for H2 accumulation in RB	• Refs. on experiments and CFD analysis on H2 distribution in CV • Code analysis by former JNES • OECD/**THAI** Projects	Small influences onto CV failure frequency However, risk of large release may exist in case of DDT in CV	Lumped-parameter code such as **MELCOR** and **MAAP** may be possible	**CFD** prediction may perform detailed multi-D analysis	**Small:** Prototypal-size experiment done	**High:** Many codes and experiences	**Low:** Many experiments and code analyses done
Combus-tion	• combustion limit, combustion form, frame propagation, DDT have experiments respectively • Model developments done • Small knowledge on combustion during spray, OECD-NEA/THAI2 may provide data	• Experiments on deflagration such as NUPEC, NTS, BMC and LSVCTF • Experiments on detonation such as SNL, BNL and RUT • Analysis on detonation by JNES			Several codes such as **SODIV**	**Medium:** Prototypal-size experiment done Uncertainty in DDT analysis	**Medium:** Code developed for deflagration and detonation	**Low:** Experiments on combustion and model developmen ts done
• • •								

● **Continuous investigation necessary to *update* info. & priority**

Fundamental Technology SWG
("Generic Safety")

started development in 2013

Fundamental Technology SWG (1/6)

started in 2013

Target and Approach to Revise T/H RM

- **Establish a R&D Technology RM to enhance LWR Safety in the light of 1F Accident**
  1. **Identify AM relevance to T/H Phenomena during DBE + SA (considering DiD)**
  2. **Consider External Events related to SA**
  3. **Make Prioritization from viewpoints of Risk Reduction**
  4. **Create Work Description Sheet (WDS) for Key R&D Subjects (R&D Status, Development Issues, Expected R&D, etc.)**
  5. **Chronological RM for Major Relevant Technologies**

Defence -in-Depth

- **Technology Map by SA-SWG was referred**

Fundamental Technology SWG (2/6)

started in 2013

Prioritization of R&D Subjects

1. Level of Risk Reduction (High /Mid /Low)

- ✓ Risk Reduction (Operational Safety, Level-1/2/3 PRA)
- ✓ Robustness Enhancement (Stress Test)

2. Uncertainty in Phenomena and AM Performance (H /M /L)

- ✓ Experiential Data Range, Accuracy (Phenomena)
- ✓ Dependence on operator action and environmental condition (AM)

3. Level of Knowledge *Maturity of Evaluation Method* (H /M /L)

- ✓ Phenomenological /Experimental knowledge
- ✓ Theoretical Model (Empirical or Mechanistic)
- ✓ Evaluation Methods
  (System Performance Evaluation or Phenomena-specific models)

12 R&D Subjects *selected*

Fun.-Tech (3/6) SWG

Safety Enhancement

Prevention of Core Damage/ In-Vessel Retention

Enhancement of Accident Tolerance
- Development of New Reactor Material (ex. SiC Cladding/ Material with High Temperature Stability and Low H2 Generation) (4)

Reliability for Reactor Depressurization
- Improvement of predictability for transient two-phase level behavior (ex. Multi-dimensional void fraction) (1)

Enhancement of Reactor Cooling and Make-up Capability
- Cooling with PWR 2ndary System (2) (ex. Cooling performance with less inventory of PWR primary system)
- Alternative Cooling System (ex. Effect of contained substance in cooling water on heat transfer) (3)

Maintaining Containment Integrity (Prevention of Excessive FP release)

Enhancement of Containment Leak-Sealing Capability
- Coolant injection to Reactor well cavity for containment top-head flange cooling/ Development of sealing material with high heat-resistance (8)

Debris Cooling / MCCI prevention
- Lower drywell coolant injection (ex. Verification of cooling performance)
- Core catcher development (5) (ex. Material data base of refractory material/ Performance evaluation and verification)

Diversification of Containment Cooling
- Verification of drywell air cooling system performance under SA condition (6) (ex. Non-condensable gas effect)
- Passive Containment Cooling System (7)

Maintaining Integrity of Spent Fuel Pool (SFP)

SFP Cooling Reliability Improvement
- Spray cooling/ Natural convection (ex. Heat transfer test)

Prevention of Hydrogen Combustion/ Hydrogen Removal
- Autocatalytic recombiner (9)
- Hydrogen removal system for SA convergence termination (10) (ex. Catalysis for H2 removal in SA late-phase condition)

Effective Operation of Containment Vent
- Pool scrubbing (ex. Transient FP removal performance)
- Filtered venting system (11) (+ Experimental data for FP transport, Iodine behavior, deposit, vaporization)

Common Fundamental Technology

Enhancement to monitoring capability for SA status and progression
- Development of instrumentation and measurement devices for severe accidents (12)

Fundamental Technology SWG (4/6)

started in 2013

Selected R&D Subjects

1. **Improvement of Predictability for Transient Two-phase Level Behavior**
   (ex. Multi-dimensional void fraction)
2. **Cooling with PWR 2ndary System**
   (ex. Cooling performance with less-inventory of PWR primary system)
3. **Alternative Cooling System**
   (ex. Effect of solutes in cooling water on heat transfer)
4. **Development of New Reactor Material**
   (ex. SiC Cladding/ Material with High-T stability and low H_2 generation)
5. **Development of Core Catcher**
   (ex. Data base of refractory material/ Performance evaluation and verification)
6. **Verification of Drywell Air Cooling System Performance under SA condition**
   (ex. Non-condensable gas effect)
7. **Passive Containment Cooling System (PCCS)**
8. **Coolant injection to Reactor Well Cavity** for Containment Top-head Flange Cooling + Development of **Sealing Material with High Heat-Resistance**
9. **Autocatalytic Recombiner (PAR)**
10. **Hydrogen Removal System** for SA Convergence Termination
    (ex. Catalysis for H_2 removal in SA late-phase condition)
11. **Filtered Venting System**
    (+ Experimental data for FP transport, Iodine behavior, deposit, vaporization)
12. **Development of Instrumentation and Measurement Devices for SA Conditions**

Fundamental Technology SWG (5/6)

started in 2013

Subjects Details

- **Work Description Sheet (WDS)** *for each of 12 R&D Subjects*

Major AM Countermeasure

e.g.) **Core Catcher**

Reason(s) & Objective(s) for R&D

e.g.) Effective to prevent MCCI. Further R&D is needed for ablation behavior due to jet impinging fro its detailed design

Current Knowledge Level

e.g.) Up-to-date knowledge & technologies + List of existing **Literatures**

Expected R&D

e.g.) Ablation behavior of refractory materials, Debris property at very High-T, Heat transfer characteristics in cooling channel, etc.

Expected Achievements & Applications,
R&D Priority (extent of risk reduction, maturity of knowledge etc.)
Role & Responsibility of Stakeholders (Budget)

Fundamental Technology SWG (6/6)

Chronological Roadmap *Example:* Cooling of Molten Fuel (Core)

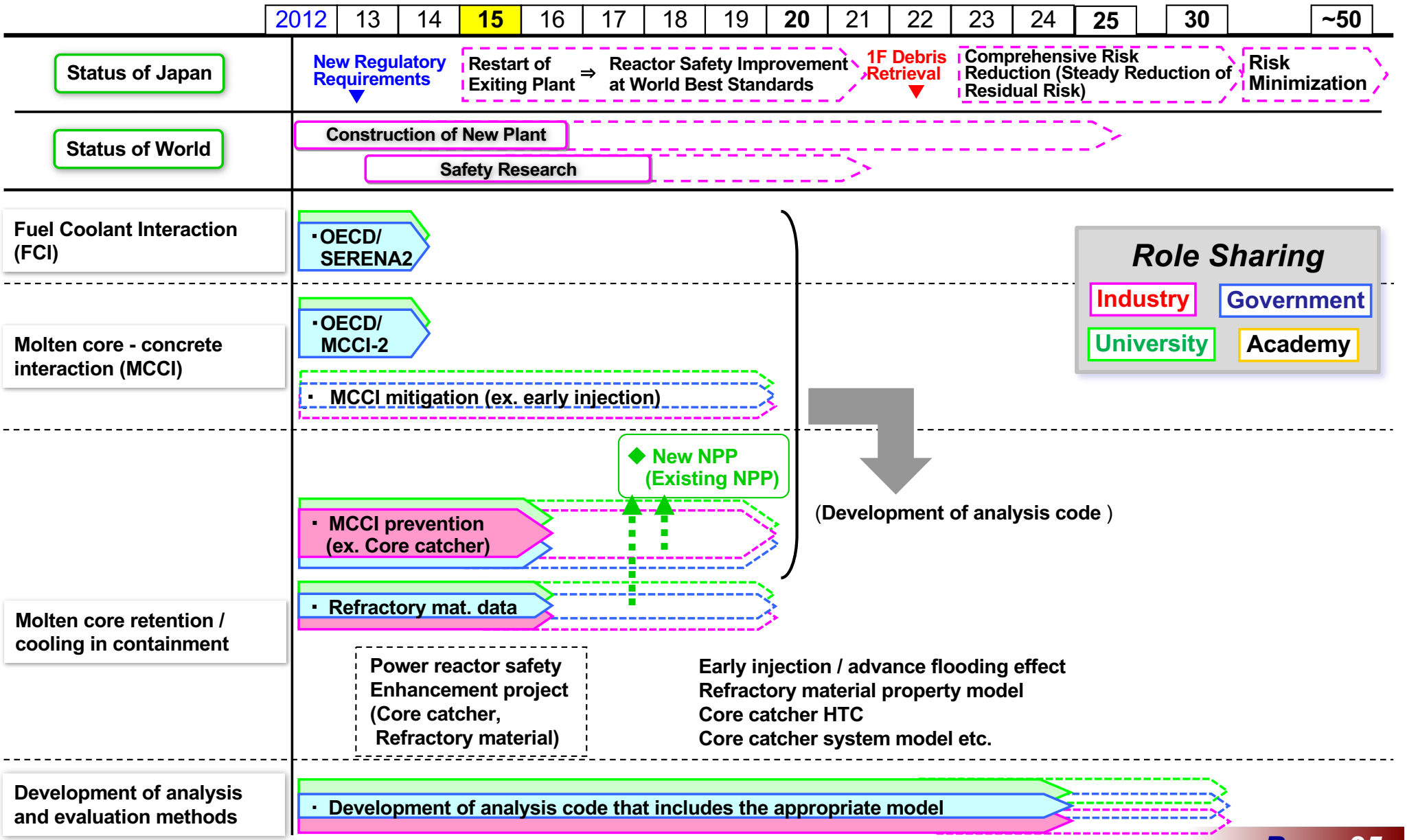

Safety Assessment SWG

started development in 2013

Safety Assessment SWG (1/6)

started in 2013

Target

- **Develop computer codes** >> They did "**AMAGI**"
  reactor design, safety assessment, CFD (local phenomena)
  with discussions on ***model V&V + scaling***

Approach to Revise RM

i. Identify 3 Technical Subjects in the light of 1F Accident

ii. Arrangement Table (= Technology Map by SA-SWG)
to understand maturity of simulation methods etc.

iii. Organized Information Tables (= WDS by Fund.-Tech SWG)
for 4 Objectives *re-organized* + 5 External Events

- Point-out desirable features for future computer codes
  (e.g. 3D-multifield model, coupling of micro- & macroscopic models)

iv. Chronological Roadmap to incorporate outputs from
12 R&D subjects *selected by* ***Fund.-Tech SWG***

Safety Assessment SWG (2/6)

started in 2013

3 Technical Subjects (A, B, C) on T/H Simulation identified in the light of 1F Accident

A. Phenomena in RV, CV and Containment Building

1. **Phenomena during DBA and SA**
   (DBA: ECCS, Natural circulation, Neutronics-T/H coupling under ATWSs,
   SA: fuel degradation & melt progression, IVR, DCH, FCI, MCCI etc.**)**
2. **Transfer and/or diffusion of radioactive materials**
   (faster calculation /prediction**,** with chemical reaction, pool scrubbing, FCVS, etc. **)**
3. **Hydrogen Behavior**
   (Generation, Transfer, Ignition/Deflagration/Detonation & DTT,
   effectiveness and safe function of PAR, FCVS, etc.**)**
4. **Structure Integrity against core melt and debris**
   (T-H boundary condition to structures, in case of IVR, Core Catcher, etc.**)**
5. **T/H behaviors in spent fuel storage pool (SFP),**
   including effects of **corrosion, oxidation, re-criticality, etc.**
6. **Fluid-structure interaction (**sloshing, explosion impact, etc.**)**

Safety Assessment SWG (3/6)

started in 2013

3 Technical Subjects (A, B, C) on T/H Simulation identified in the light of 1F Accident (Cont'd)

B. Decommissioning Technology for 1F NPP

1. **Decommissioning-related Technology**
   (Estimation of fuel debris situations in damaged CV)

C. External Events (*to study*)

1. **External natural phenomena**
   (tsunami, volcano, tornado/high wind, fire, internal flooding, overflow stream, cold wave, severe heat wave, etc.)
2. **Tsunami** (including evaluations of the effect of **floating object**)
3. **Counter-terrorism measures** (**Fire** caused by **aircraft crash**)

Safety Assessment SWG (4/6)

started in 2013

An Arrangement Table

To overview current status & needs for code development/ improvement for Technical Subject A

column

- **Phenomena (= 4 Objectives *re-organized*):**
  1. within RV before Core Damage,
  2. after Core Damage/Melting
  3. within CV,
  4. within SFP (RB)
- **Subjects to consider:**
  - ✓ Major physical phenomena + System responses + Countermeasures

row

- **Codes under utilization & development: status**
  - ✓ Entities: Vendors (B & P), Res. Institutes (Gov. & Util.), Univs.
  - ✓ Conservative + BE, Lumped-P + Advanced + CFD, T/H (system) + SA
- **Development subjects: output**
  - ✓ Applications + Scopes on Code Technology

Safety Assessment SWG (5/6)

started in 2013

Organized Information Table

= WDS for Fund.-Tech SWG

Provide detailed compilation of relevant information,
to indicate objectives & applications, and to evaluate priority for

- **4 Objectives *re-organized***
  as classified in the Arrangement Table
  1. within RV *before* Core Damage,
  2. *after* Core Damage/Melting,
  3. within CV,
  4. within SFP (RB)

To investigate subjects on

- **5 External Events (low probability + high consequences),**
  based mostly on new regulatory requirements by NRA
  1. Tsunami,
  2. Volcano,
  3. Tornado/high wind,
  4. Fire,
  5. Internal flooding

NRA: Nuclear Regulatory Authority in Japan

- to perform domestic & international cooperation with certain Academic Societies, and development of human resources

Safety Assessment SWG (6/6)

started in 2013

Organized Information Table (Cont'd)

Example: Phenomena within RPV *after* Core Damage

- **Field and Phenomena to Simulate**
  - ✓ To assess effectiveness of AMs and to support continuous safety enhancement
  - ✓ To predict event propagation and/or chronology related to reactor core cooling & RI confinement by thrashing out all of important event sequences
- **State-of-the-Art Simulation Technology**
  - ✓ Lumped parameter + mechanistic or phenomenological models + many empirical formulations（MAAP, MELCOR)
  - ✓ Multi-D + mechanistic or phenomenological models（RELAP/SCDAP, SAMPSON)
  - ✓ Coupling of SA system code with CFD code
- **Model V&V and Expansion of Experiment Database**
  - ✓ Multi-phase & multi-component experiments including material behavior (molten fuel spreading, MCCI, FCI)
- **Priority / Division of Roles / Stakeholders**
  - ✓ High / Industry, Gov. & Academia / Industry & Gov. (International Coop.)

Whole View and Rolling of RM

Whole View of Revised RM

Introduction Scenario of T/H Technological Strategy RM

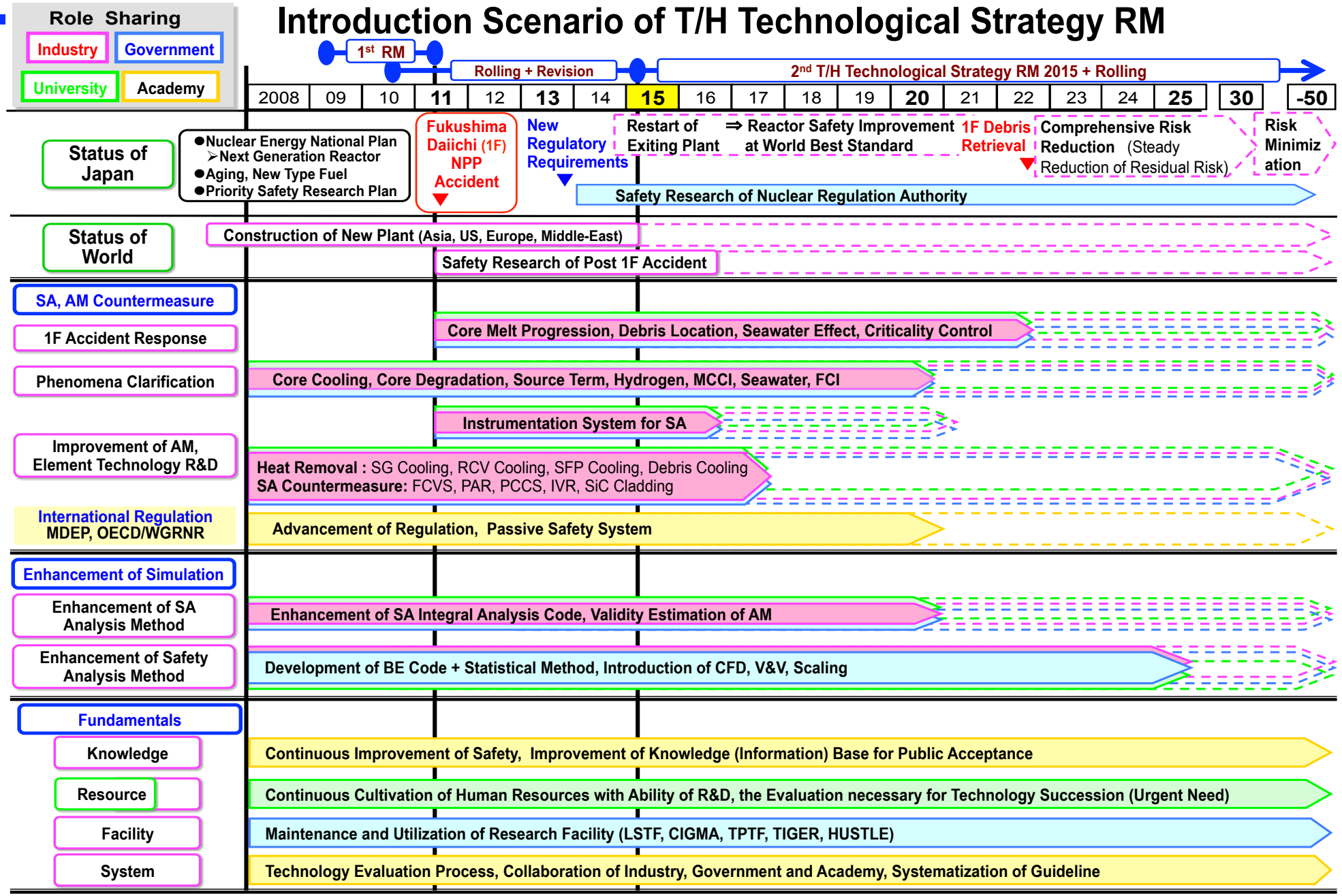

Rolling: Utilization and Revision of T/H RM

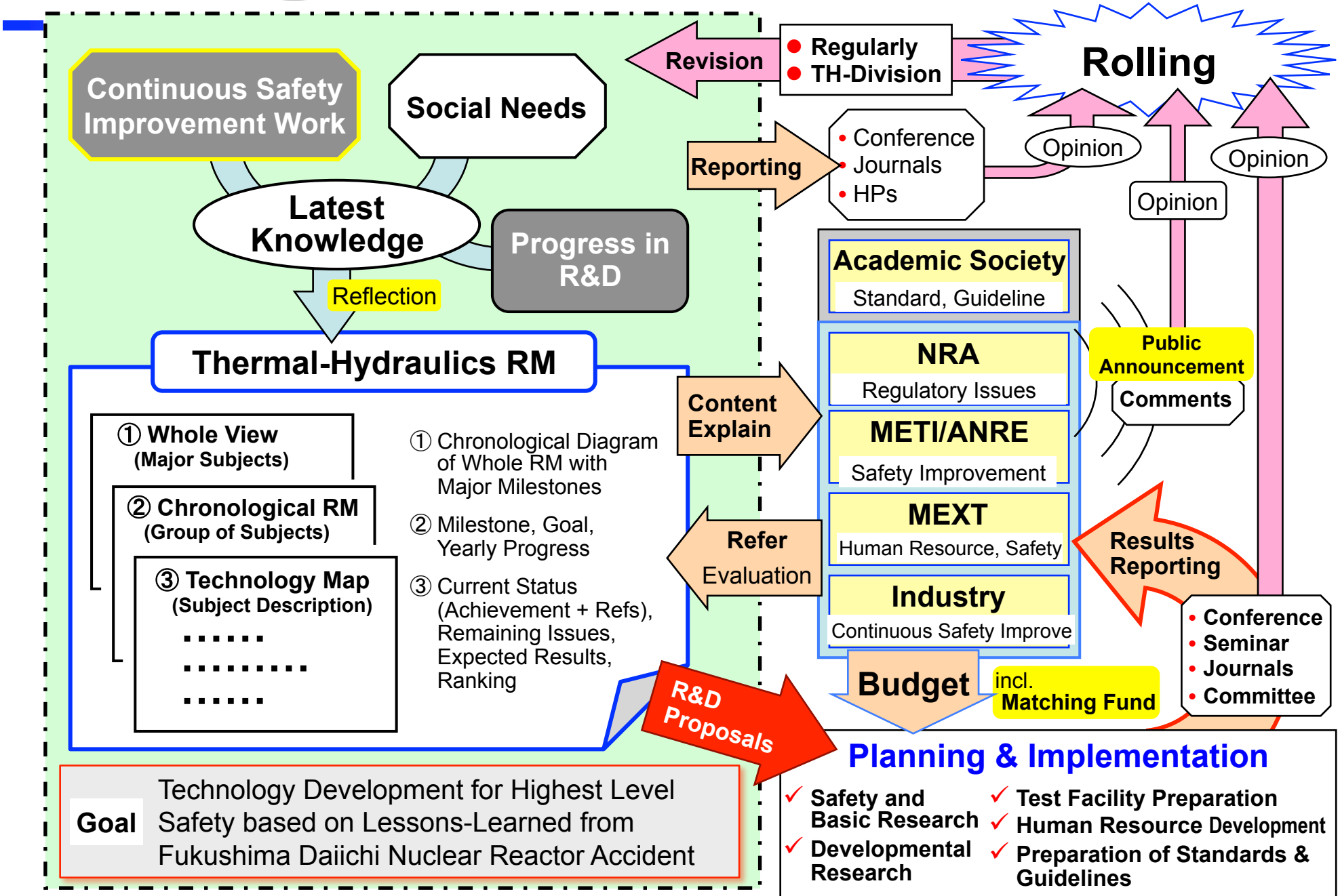

1st Revision (2017)

Progress through Rolling

- **AESJ Thermal Hydraulics (T/H) Division [*Continuous Management*]** with **Working Group: Development of Strategy Map to Advance Base Technologies for Thermal-Hydraulic Safety Assessment**

- **Contents revisions:**
  - ✓ **Newly include External Hazard: Natural Hazard (Tsunami, Fire, Volcano, Tornado, Flooding/Internal Spillage) and Man-made Hazard**
  - ✓ **Update Fundamental Technology R&D Subjects: e.g., Passive safety effectiveness**
  - ✓ **Achievement descriptions for each of R&D Subjects**

- **Collaboration with AESJ Computational Science and Engineering Division in Natural Hazard descriptions**

- **Visualize R&D subject relationships with "Roadmap on R&D and Human Resource for LWR Safety" (2015) from AESJ and METI - ANRE**

AESJ: Atomic Energy Society of Japan
METI: Ministry of Economy, Trade and Industry
ANRE : Agency for Natural Resources and Energy

2nd Revision (2020)

Progress through Rolling

- **AESJ Thermal Hydraulics (T/H) Division [*Continuous Management*]**
  with **Working Group: Development of Strategy Map to Advance Base Technologies for Thermal-Hydraulic Safety Assessment**

- **Technology Map (TM) Restructuring:**
  - ✓ **Fundamental Technology (sequence-based) TM and Severe Accident (phenomena-based) TM**

    Corresponds → **Consolidate two TMs into Base R&D Technology TM, which follows an accident sequence *from before core degradation to after RCV failure* with SFP response, to address all accident responses in detail**
  - ✓ **Safety Assessment TM**

    Corresponds → **Develop detailed Matrix Description of computer code models by using Excel Spread Sheet, by considering the Safety Assessment Process to assure the reactor safety is the prominent goal of all R&D effort**

- **RM utilization: >> All Files downloadable from AESJ webpage**
  - ✓ **Refer 2017 version for Whole View RM and Chronological Description of each subjects**

2nd Revision (2020)

***Demonstration* :**

Safety Assessment Technology Map

in Excel Spread Sheet

extend & collapse of rows & columns

You can manipulate/customize the table by yourself for your own purpose !

Your-own Roadmap ?

- **Role of Roadmap**
  - Promote your R&Ds in a **back-casting manner**, thus efficiently and effectively
  - Visualize the processes **how to reach your-own R&D objectives** with some detailed description of the status of relevant subjects in a chronological diagram
- **Required Method**
  - **Scaling Consideration** necessary to reach the **true destination** = **Prototype Phenomena**

WGAMA Scaling SOAR

  - **Absolutely Challenging !!**

You may not know what is the prototype phenomena

  - **Some Experiences:**

Facility Size = CCFL (PWR LB-LOCA), **MCCI**
Simulant = FCI (Steam Explosion)

Budget and Time are limited

- **Question**
  - ***How do you build and use Your-own Roadmap to realize your-own R&D objectives (for what ?)***

Where is The Peak of Mt. Fuji ??

- **Total View (bird-eye)**

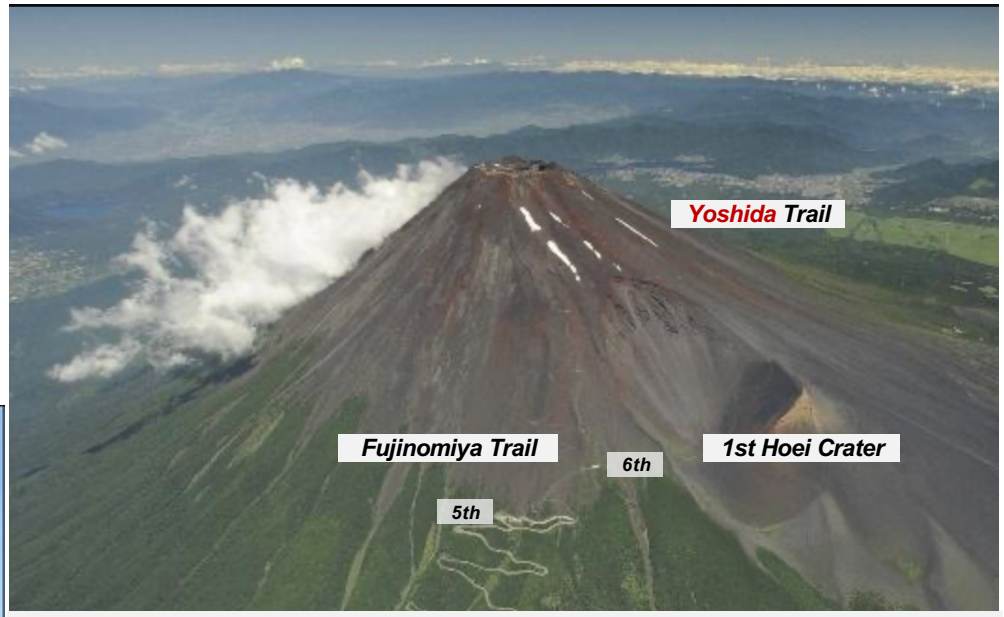

Source: The Shizuoka Shimbun and Shizuoka Broadcasting System (SBS)

https://www.at-s.com/news/photo_collection/detail.html?ft=7&no=71

- **View at 6th Station**
  Yoshida-Guchi

  - ***Hey Guide,***
    Where is our final destination ?



Source: Fujiyoshida Tourism Promotion Service

https://fujiyoshida.net/spot/260

What is The Elephant ??

- **Blind People and Elephant**
  - How do you recognize What is the reality ?
  - It is difficult to tell What we do not know.

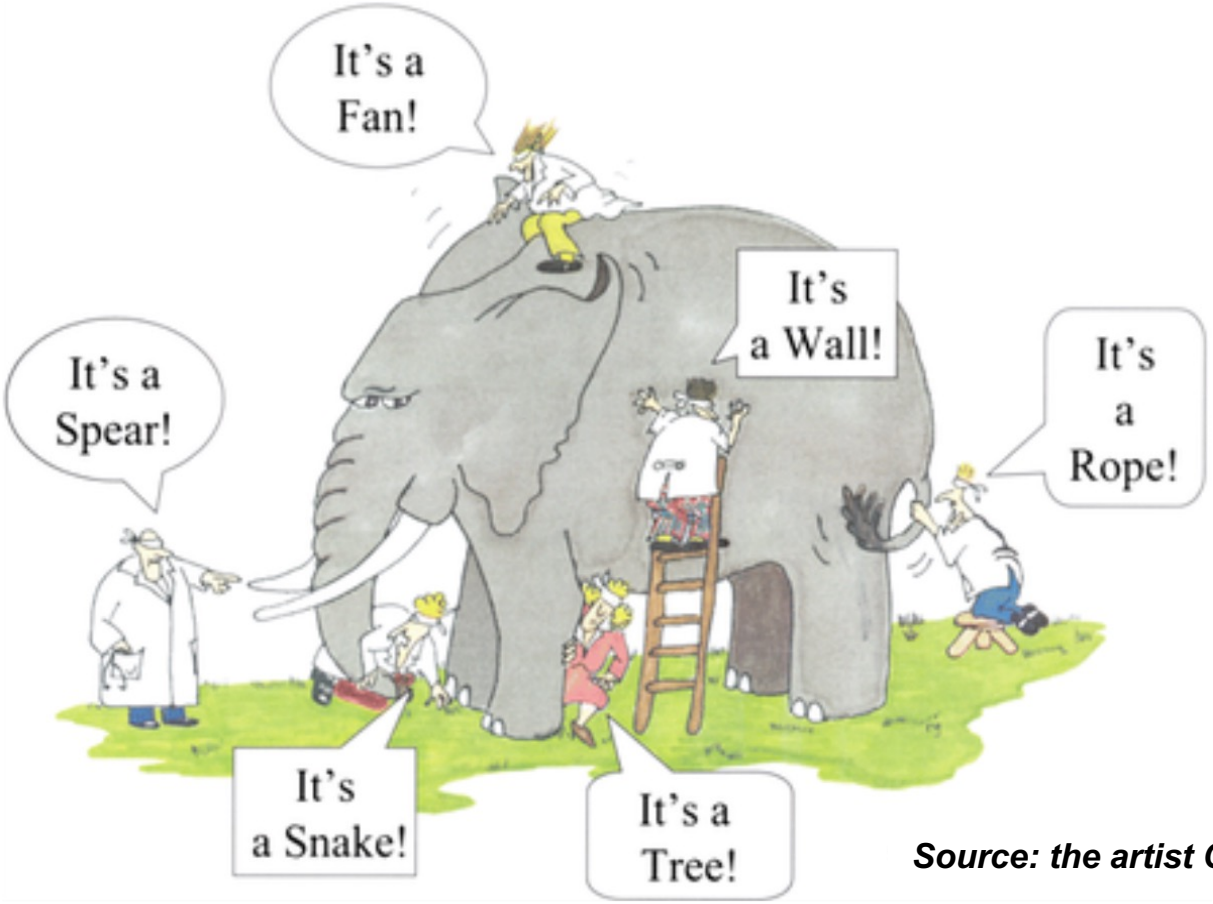

Source: the artist G. Renee Guzlas

- It is important (to try) to understand What is the total, under possible *Cognitive Bias.*
- *Maybe* under influences of mutual relationship of relevant subjects.
- What is your answer to this?

Concluding Remarks

- **AESJ T/H Roadmap**
  - Complete different **backbone subjects** between
    1st version (2009) New LWR Development
    2nd version (2015) Fukushima Daiichi (1F) Accident Relevant
    - To never cause disastrous accident again
    - Continuous updating via **Rolling** (*Twice to date*)
      by a Working Group under AESJ Thermal Hydraulics (T/H) Division
  - All R&Ds in **T/Hs, SA, Safety Assessment**, with consideration on **External Hazard**, and **Human Resource Development** – *RM shows mutual relevance*
- **How do we go?**
  - Backbone definition (= **Whole View**) controls your mind to go
  - Collaboration [**International** & **Domestic**] is important to overcome difficulties in R&Ds regarding Reactor Design update including SMRs
  - Scaling on SA phenomena is necessary for uncertainty evaluation
  - Yet, important to seek R&Ds **for continuous improvements** in LWR safety, including influences from **External Hazards**

Thank you for your attention!

Questions, and Your Opinions ?

through the ***Kitchen Door***

AESJ URLs to download RMs

Thermal Hydraulics Division

all in Japanese

https://thd.aesj.net/index.php/committees/archive

2nd revision of version 2020

https://thd.aesj.net/index.php/download_file/354/0
https://thd.aesj.net/index.php/download_file/355/0
https://thd.aesj.net/index.php/download_file/356/0
https://thd.aesj.net/index.php/download_file/357/0

Version 2017

https://thd.aesj.net/application/files/6616/4844/9955/TH-RM_r.pdf

Range of R&D Roadmaps for LWR Safety and Development

METI Ministry of Economy, Trade and Industry
ANRE Agency for Natural Resources and Energy
NRA Nuclear Regulation Authority
MEXT Ministry of Education, Culture, Sports, Science and Technology, Japan
AESJ Atomic Energy Society of Japan

METI / ANRE + AESJ

Roadmap on R&D and Human Resource for LWR Safety

2015

Ref. (1)

AESJ Special Committee on Nuclear Safety Research Roadmap
- 8 Categories of Challenges
- 6 Sub-committees

ANRE WG on Voluntary Improvement of Safety, Technology and Human Resource

AESJ / TH-D

Thermal-Hydraulics

2015

Safety Analysis Code Development

Severe Accident Countermeasures

NRA

Safety Research in NRA

2013

Ref. (1 - 3)

- Research to obtain technical knowledge necessary to develop regulatory requirements and application, and technical basis for decision making
- former JNES merged into NRA
- Support from JAEA/NSRC & NIRS

Refs.
(1): N. Sekimura, IAEA CN-235 IEM8, Session 3 Vienna (2015)
(2): NRA, FY2013 Annual Report, p.p. 65
(3): M. Hirano, RIC 2014, Washington (2014)

The 11th European Review Meeting on Severe Accidents Research

May 13-16, 2024, Royal Institute of Technology, Stockholm, Sweden

TECHNICAL SESSION 2.1: SEVERE ACCIDENT SCENARIOS

Chairs: S. Gupta (Becker Tech. GmbH), D. Jacquemain (OECD/NEA)

ID76	**SEAKNOT: Looking Ahead of Severe Accident Research** L. E. Herranz (CIEMAT)	**Paper** **Presentation**
ID16	**ASTEC core degradation calculations in support of Level-2 Probabilistic Safety assessment for 1300MWe French reactors: methodology and preliminary results** M. Monestier (IRSN)	**Paper** **Presentation**
ID12	**MELCOR Analyses for Investigation on Hydrogen Management during BWR Severe Accidents with the Filtered Containment Venting System** Y. Kojima (Waseda University)	**Paper** **Presentation**
ID27	**On the progress made in safety assessment and severe accident management as part of the French Fukushima post-accident research programme** A. Bentaib (IRSN)	**Paper** **Presentation**

SEAKNOT: LOOKING AHEAD OF SEVERE ACCIDENT RESEARCH

L.E. Herranz[1]
[1]CIEMAT, Unit of Nuclear Safety Research, Av. Complutense 40, 28040 Madrid, Spain.
luisen.herranz@ciemat.es

S. Gupta[2]
[2]BT, Becker Technologies GmbH, Rahmannstrasse 11, 65760 Eschborn, Germany.
gupta@becker-technologies.com

S. Paci[3]
[3]UNIPI, Dipartimento di Ingegneria Civile e Industriale, via Diotisalvi 2, 56122 Pisa, Italy
sandro.paci@unipi.it

P. Piluso[4]
[4]CEA/IRESNE, Centre de Cadarache – Bât.219-D – 13108 St Paul Lez Durance cedex, France.
pascal.piluso@cea.fr

ABSTRACT

Severe Accidents (SAs) dominate the risk associated to the commercial production of nuclear energy. Despite the major achievements made in their research, still existing gaps, upcoming new technologies as Accident Tolerant Fuels (ATFs) and Small Modular Reactors (SMRs), more stringent safety requirements, optimization of SA management, and other factors, point the need for an efficient use of research resources in the years to come. Three major elements should integrate any SA roadmap to be proposed: preservation of knowledge and know-how; identification of key issues which research would result in the best accident management (AM) feasible; and, no less important, strengthening the workforce who will be responsible for such research. The SEAKNOT project (SEvere Accident research and KNOwledge managemenT for LWRs) was born to address this need in all and every aspect. The present article outlines the major pillars of SEAKNOT and synthesizes the progress made since its onset at the end of 2022. The methodologies adopted to develop a SA PIRT (Phenomena Identification and Ranking Table) and to build a Validation Database Directory (VADD) are described along with the ongoing phenomena listing and ranking. Besides, the first steps towards an experimental infrastructure capable of dealing with present and future needs (SAINET) are included. No less relevant the actions already made and the novelties coming on the side of knowledge and know-how transfer are also discussed.

KEYWORDS
Severe Accident PIRT, knowledge and knowhow transfer, data and infrastructures

1. INTRODUCTION

Severe accidents are known to dominate the risk associated to the commercial production of nuclear power. A vast amount of research has been done in this field after the TMI2 accident in 1979. Preservation of knowledge and know-how gathered, though, might be at stake at present because of the retirement of senior scientists and engineers and the loss of access to old archives. At the same time, innovation in nuclear technologies (i.e., SMRs and ATFs) and in severe accident analysis, i.e., Uncertainty and Sensitivity Analysis (UaSA) and Artificial Intelligence (AI), might mean a change in the SA paradigm. These factors, along with the progressive reduction of resources in SA, stand out timeliness of critically review the

knowledge acquired to project a SA research roadmap that result in an efficient reduction and understanding of accident unfolding and, consequently, an optimization of AM. A key element to achieve the goal is to involve and enable young scientists and engineers by conducting a proper transfer of both knowledge and knowhow. These are the major drivers underneath the EURATOM SEAKNOT project (GA 101060327 [1]), which is coordinated by CIEMAT and participated by a total of 16 European organizations plus 1 associated partner (PSI) (Figure 1).

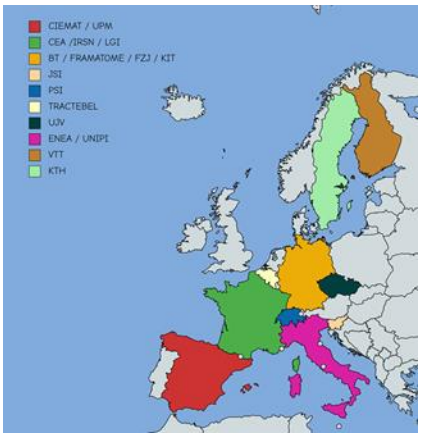

Figure 1. European countries and organizations participating in SEAKNOT

Accordingly, SEAKNOT pursues three major objectives: carrying out a sound and critical analysis of the current knowledge on SAs, including both existing (Gen II and Gen III) and forthcoming nuclear technologies (SM LWRs & ATFs); identifying experimental research needs required to support any further research resulting from the critical analysis; and strengthening the background and skills of young generations in the field.

The next sections describe SEAKNOT methodology, partnership and structure. Likewise, an overview of the current status of the project, one almost half-way to the end, will be given, including all what has been done and is planned concerning the K2T (Knowledge and Knowhow Transfer).

2. METHODOLOGY

The SEAKNOT methodology heavily relies on senior expertise. Bringing together senior experts with diverse perspectives (i.e., researchers, regulators, industry, academia …) and mind-sets is an essential element to achieve a sound critical assessment that are not biased by the lack of sufficient background or the "research inertia" of keeping "business-as-usual". This relevance is also fundamental when transferring the best knowledge and know-how to young researchers.

The backbone of SEAKNOT is the Phenomena Identification and Ranking Table (PIRT) that will be produced together with consolidated information on the experimental database and critical SA experimental infrastructure. It is worth highlighting that the PIRT will be grounded on State Of the Art (SOAR) reports recently issued, previous global and partial PIRT exercises, and the outcomes of open research projects since practically the beginning of this century. All sources of information will be considered, particularly those stemming from activities conducted in the frame of SNETP/NUGENIA Technical Area 2 [2-5].

Figure 2 shows the conceptual methodology of SEAKNOT. The PIRT development is the central activity. Once the fundamental SA library, which will consist of a list of the references used for the individual PIRT in each SA domain (i.e., in-vessel, ex-vessel, containment and source term) is gathered, the main sources of relevant data will be identified and employed to characterize the existing knowledge on the matter under

study. Through the expertise that will be available within the project, both the safety significance as well as the existing modelling capabilities of the phenomena under study will be assessed according to the PIRT methodology [6-8].

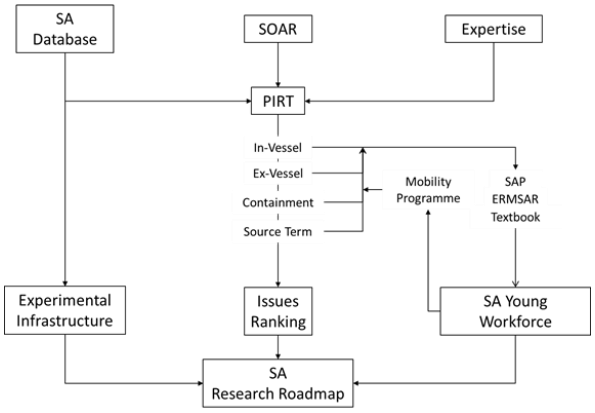

Figure 2. Sketch of SEAKNOT conceptual methodology

The SEAKNOT methodology results in a work-package (WP) structure (Figure 2), which is briefly described next. Four WPs were set plus the WP5 PROC on Project coordination. The PIRTSA WP (WP1) aims at developing the PIRT, with a specific sub-WP (WP1.1) devoted to set a methodology and the other sub-WPs (WP1.2-WP1.5) to its application in the in-vessel, ex-vessel, containment, and source term domains. The VADD WP (WP2) structure is practically identical to WP1 but its focus is the SA database (DB) to finally provide a sort of DB directory for SA codes validation. Note the strong interaction of VADD (Validation Database Directory) and PIRTSA, as input on available representative data is one of the pillars of the PIRT. WP3 SAINET (Severe Accident experimental Infrastructure NETwork) plans to build a map of experimental infrastructures in Europe with potential to be used in the coming years, as well as to identify what sort of facility should be set up to address some of the primary PIRT issues, if none of the existing ones can do it. Finally, WP4 KNOS responds to the SEAKNOT need of a powerful WP for dissemination, communication, and exploitation of the project results, also in the view of an effective K2T to young generations of researchers and technicians.

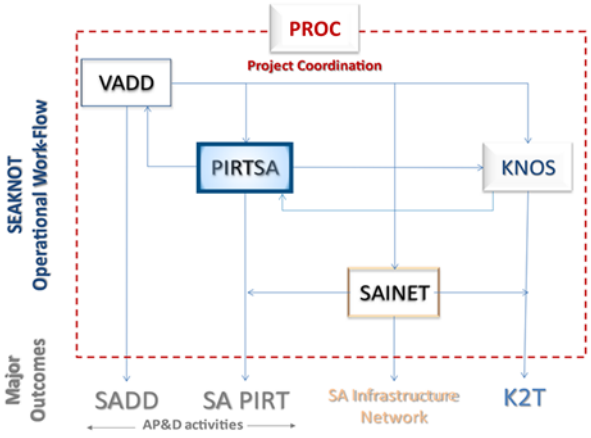

Figure 3. SEAKNOT work-packages, work flow and major outcomes

This work structure in Fig. 3 gets embedded in the project governance, in which the project Executive Board (ExB), which is integrated by the project and WPs coordinators, interact with two project supporting bodies:

Advisory Body (AB), consisting mostly of regulators and TSO experts; and, End User Group (EUG), where external Agencies (NEA, IAEA, and ENEN) involved in SA research and education and training are involved. Both of them will follow closely the project. The former will specifically bring in substantiated assessment on phenomena safety relevance. The latter might be instrumental in two major aspects: orchestrating ongoing activities and projects under their frames with SEAKNOT activities, and helping to make the SEAKNOT resulting research roadmap a reality through their upcoming projects portfolio.

3. MAJOR PROGRESS

Since its inception in October 2022, SEAKNOT has made a substantial progress in all the areas addressed. Here below an update of the most meaningful ones is synthesized.

3.1. PIRTSA: Phenomena Identification and Ranking Table on Severe Accidents

As stated above, the SA PIRT is the core of SEAKNOT. The main purpose is to identify those SA areas/phenomena which should be given most attention when launching new R&D activities, either because they dominate the remaining uncertainties or because they have got a substantial potential to mitigate SA consequences. The PIRT scope is extended to the SA entire domain, including in-vessel, ex-vessel, containment, and source term areas. Likewise, WC-SMRs and near-term ATFs are being also considered.

Nearly 20 years ago, the EURSAFE project [2] set a historic milestone by building a soundly grounded PIRT on SA by reducing more than one thousand identified phenomena to about one hundred of them deserving further investigation, as they were both important for safety and still lacking sufficient knowledge. About ten years later, driven by the Fukushima-Daiichi accident in Japan in 2011, two independent studies were conducted by Japanese organizations and USA ones. The former addressed specifically source term issues resulting from the accident aftermath [10], whereas the latter was closer to a technology gap analysis [11]. In the European land, SNETP/NUGENIA-TA2 periodically published SA research priorities, mostly of a qualitative nature though [12]. This short list of works provide orientation in PIRTSA, which will be fed additionally by technical and State-Of-the-Art (SOAR) reports as well as by major outcomes from research projects conducted under different frames. References [13-19] are just some examples of them.

The first step when facing a PIRT on SA is to adapt the work initially proposed in the field of thermal-hydraulics and Design Basis Accidents (DBA) [6] to the SA specific domain. In addition to [10], a few applications in the SA domain have been reported [17, 20] recently, but they were restricted to specific systems and scenarios, i.e., in-vessel melt retention and spent fuel pools (SFPs), respectively.

The specific problem the PIRT addresses is the identification of the SA issues which research would lead to better characterize and, if possible, reduce uncertainties, as well as to efficiently enhance mitigation of SA consequences. The focus is on the potential issues effect on source term, i.e., radiological releases from the Nuclear Power Plant (NPP), specifically on onset time, rates and composition of the releases to the environment of a selection of radionuclides: I131; I132; Cs137; Ru106; Te132; Kr88; Xe133; Xe135. The drastic difference expected in source term between the in-vessel and the ex-vessel phases recommends to split accident sequences accordingly.

Ranking consists in assessing the relative importance of processes and phenomena with respect to the evaluation criteria selected as parameters of interest. The research priority is being assessed based on existing knowledge and safety significance of each phenomenon; each of these concepts split in three levels (i.e., low, L; medium, M; high, H). Knowledge is weighed on data availability and representativeness, and modeling maturity; as in the case of priority, three levels are given to both data and models. Figure 4 shows how knowledge and safety significance combine to define priority. It is high priority (H) whenever knowledge is poor (L) and safety significance is high. Low priority is attributed whenever safety

significance is low and/or existing knowledge is high. The rest of cases (3), is given a medium ranking level but ordered by priority: the maximum (M1) given to high safety significance and the minimum (M3) to mid-impacting phenomena on which there is some knowledge.

		Safety Significance		
		Low	Medium	High
Knowledge	Low	L (Poor understanding; irrelevant)	M2 (Poor understanding; mild effect)	H (Poor understanding; impacting)
	Medium	L (Some understanding; irrelevant)	M3 (Some understanding; mild effect)	M1 (Some understanding; impacting)
	High	L (Sound understanding; irrelevant)	L (Sound understanding; mild effect)	L (Sound understanding; impacting)

Figure 4. PIRT ranking

In Figure 5 the structure of the table used to list and rank phenomena is displayed.

					Knowledge		Safety Significance	Priority		
Ref. Number	**Phenomenon**	**Short Description**	**Comp/ Sub-system**	**Accident Phase**	**Data**	**Model**			**Refs.**	
C-1	Homogeneous steam condensation	Phase change of steam in a gas atmosphere driven by a local oversaturation	N.A.	In-v	H	M	L	L	D M	[1], [2] [3]
ST-1									D M	

C-Containment; ST- Source Term; In-v – In-vessel; Ex-v – Ex-vessel; N.A. – Not Applicable

Figure 5. Basic PIRT template

At present phenomena has been listed in the in-vessel, ex-vessel, containment and source term domains and have been orchestrated in the two accident phases mentioned above. The criteria set to bring a phenomenon in the list have been: 1) playing a role in an accident scenario of interest and, 2) potential effect on the Figures Of Merit (FOMs) chosen. It is considered that evaluation of some phenomena might require conducting *ad-hoc* sensitivity studies.

3.2. VADD: Validation Database Directory

The use of validation databases plays a pivotal role in enhancing the accuracy and reliability of the computer codes employed for nuclear safety analysis by validating the underlying physics and mathematical models incorporated into these codes. Verification and validation efforts are extensively taken over by the code developers and code users for specific modeling implemented in their codes [21;22]. Moreover, joint activities with a focus on a specific subject have been organized by international agencies, such as OECD/NEA containment code validation matrix [23] or SNETP/NUGENIA CoreSOAR [18], to provide a "common" validation database.

However, as SA involve various sub-domains, including in-vessel, ex-vessel, containment, and source term, the available validation database matrices do not comprehensively cover all these sub-domains with the same level of detail, leaving gaps in the understanding and validation of codes across the entire spectrum of SA phenomena. Another challenge with the current validation database is the lack of a standard methodology for evaluating the quality and applicability of experimental data for code validation. Standardized criteria are essential for ensuring a systematic and consistent approach towards assessing the

suitability of data for different SA phenomena [24; 25]. Inconsistent data quality may pose challenges in accurately assessing the performance of SA analysis codes, leading to uncertainties in their predictions.

Addressing the above-mentioned shortcomings requires concerted efforts from the nuclear community, including researchers, regulatory bodies, and industry stakeholders, to enhance the quality, diversity, and relevance of the validation database for SA analysis codes. The SEAKNOT work package WP2 which follows a similar structure as WP1 has been tailored to answer the aforesaid needs of the validation database. For this purpose, the sub-work packages within WP2 focus on different SA sub-domains, namely in-vessel, ex-vessel, containment, and source term. The main outcome will be an up-to-date Validation Database Directory (VADD) of "relational data" prepared by conducting critical analyses of the existing SAdatabase, with a clear definition of data suitability for modeling assessment and SA mitigation. While keeping the main focus on existing LWRs, the overall work scope also includes collecting relevant databases on advanced technologies, e.g., LW-SMRs and near-term ATFs.

As an outcome of the work done during the first year, a comprehensive literature review was performed based on a Template to collect SA database information as per pre-defined SA research sub-domains. In parallel, database information has also been collected on verification & validation matrices implemented in a number of the existing safety analysis codes, such as MELCOR, ASTEC, AC^2, GASFLOW. Indeed, the information on new/complementary validation data providing additional insights on a specific phenomenon modelled in these codes will also be of added value providing a possibility to update current V&Vs implemented in the aforesaid SA analyses codes. As the work is still in progress, any supplementary work done as part of WP1 related to sensitivity and uncertainty analyses to understand the impact of input parameters on the code predictions will further help in identifying the most influential parameters and their uncertainties, contributing to a more realistic representation of the code's predictive capabilities – further providing insights to look for a specific database.

The following elements have been considered during the review phase of experimental data:

- Relevance of experimental data; experimental data used for validation closely represents the physical phenomena occurring during severe accidents in light water reactors. The data should cover a wide range of accident conditions and scenarios.
- Applicability to various reactor designs; the validation database includes a diverse set of experimental data applicable to different light water reactor designs, such as pressurized water reactors (PWRs), boiling water reactors (BWRs) designs covering both large LWRs and WC-SMRs. This broadens the applicability of the severe accident analysis codes across various reactor types.
- Validation at different scales; validation at different spatial and temporal scales, from the molecular scale to the plant scale, ensures the accuracy of the code predictions in capturing the progression of complex events throughout the reactor system.
- Data used in code benchmarks; experiments that simulate severe accident scenarios and provide data for benchmarks. This encompasses datasets ranging from SET (Separate Effect Test) data for validation of a specific model, to IT (Integral Test) data for validation of an integral code. CET (Combined Effect Test) data have also been included for strongly linked phenomena for code module validation.
- Documentation; technical reports and any kind of scientific publications supports the credibility of the validation efforts and facilitates readily available information for use in the validation process by potential users of the proposed validation database.

The type and amount of experimental data collected so far are highlighted below in Fig. 6 by using an example of a database collected as part of the source term sub-WP. The collected database belongs to a broad spectrum of experimental facilities in Europe involved in source-term experimental research. A wide range of test characteristics, e.g. chemistry, fission product distribution, and material have been covered in

the experimental investigations conducted in these test facilities. To support in extrapolation of experimental results to the reactor scale, different facility scales and boundary conditions without any doubt are beneficial. Moreover, the application of instrumentation to provide measured data at different tempo-spatial resolutions is suitable for codes based on different modeling approaches, from empirical to mechanistic.

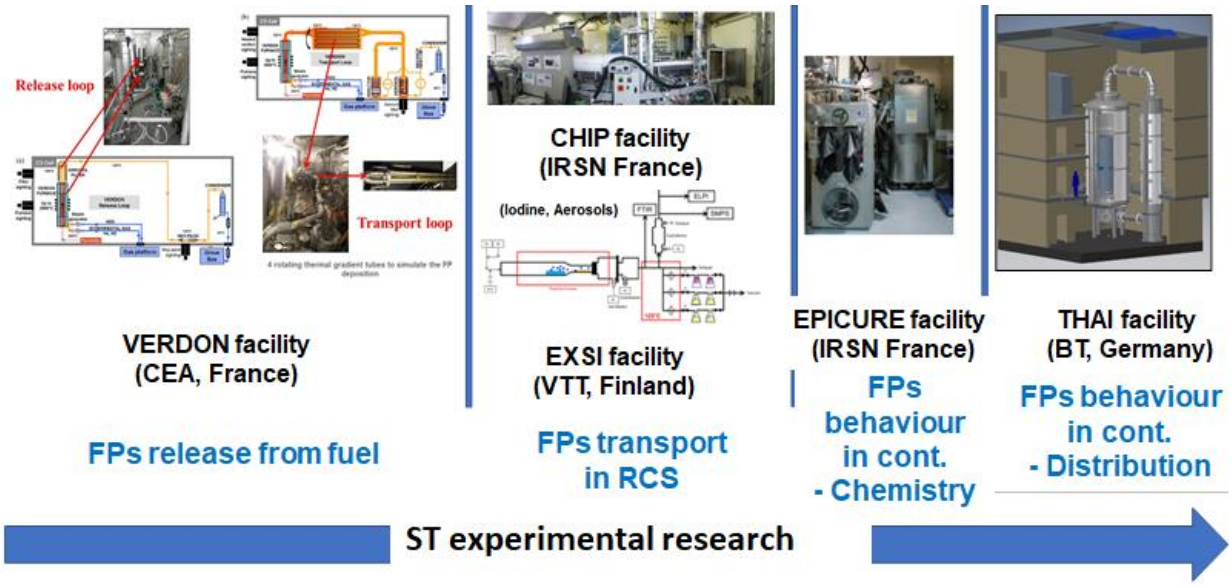

Fig.6. Test facilities contributing to the database on source term research

In parallel to the ongoing literature review activity to collect the experimental database information, the development of a methodology to assess and consolidate SA database to finally select data as part of VADD is also ongoing. Leveraging the consolidated SA expertise within SEAKNOT, the methodology aims to establish guidelines for assessing the quality and applicability of these databases, a crucial step in validating SA codes for specific phenomena. Lessons learned from the related database collection and evaluation activities, such as SAPIUM [24] and SNETP-NUGENIA IPRESCA [25] are being considered as a good basis to develop a larger scope methodology suitable for the assessment of the entire SA domain. The guidelines evolved as part of the methodology will not only identify missing information regarding a specific phenomenon of high interest as per current state-of-the-art but also facilitate the identification of complementary databases. Continuous updates will be informed by close interaction with WP1, ensuring responsiveness to knowledge gaps or newly recognized phenomena of safety significance. The main elements of the database assessment methodology are shown in Fig. 7. This check involves assessing the quality, representativity, and applicability of data, covering factors, such as spatial and temporal scales, boundary conditions, and relevant phenomena. The finalized database methodology is aimed to provide two main outcomes. First, an index for assessing the adequacy of experimental data based on available information on measured data and available documentation providing information on test protocol and other details as necessary for employing the data for validation purposes. Secondly, the establishment of criteria for classifying experimental databases as per their suitability for code validation purposes.

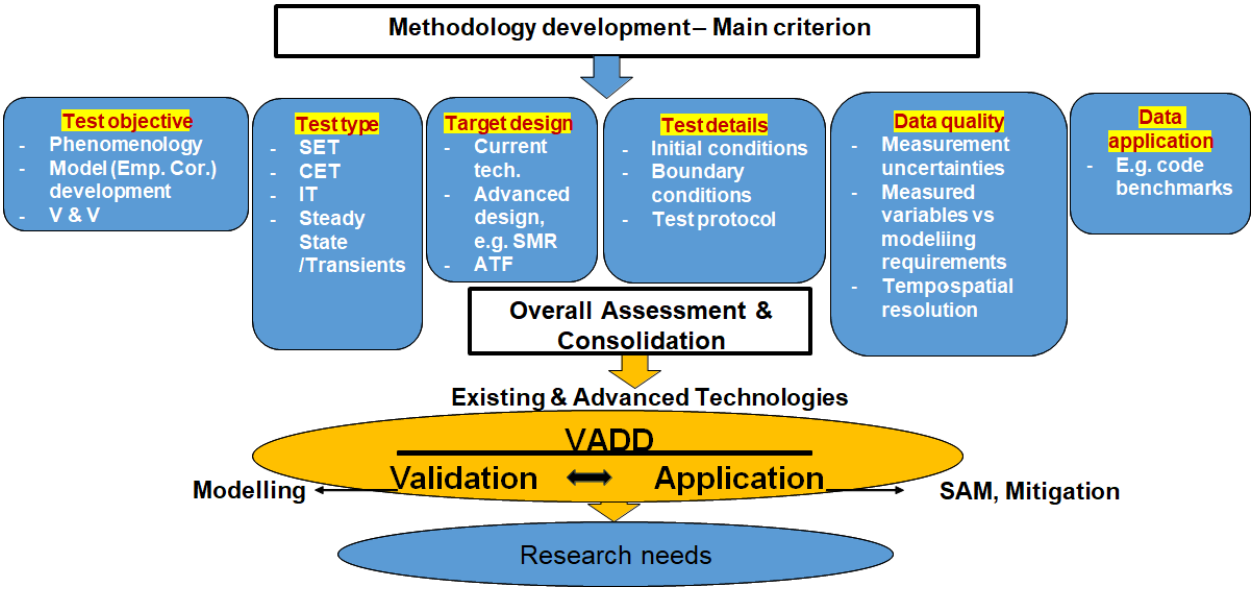

Figure 7. Elements of the database assessment methodology

Finally, to facilitate broader outreach of "database" findings beyond SEAKNOT, the development of an analytical tool "website" is foreseen to be launched at a later time within WP2. This relational database, inspired by existing thermal-hydraulic tools, e.g. OECD/NEA THIESYS, will not store experimental data online but will serve as a valuable resource for code validation and mitigation strategy assessments.

3.3. SAINET: SA infrastructure NETwork

The SA roadmap coming out from SEAKNOT intends not just to highlight what the purpose of upcoming research should be, but also what conditions still need to be addressed and provide recommendations on how to do it. This holistic approach requires settling a broad view of infrastructures that would be necessary to do it. Some of which might already exist such as they are or need some adaptation, but some specific issues might need facilities and infrastructures currently not available. This is the main purpose of SAINET (SA Infrastructure NETwork).

SAINET will cover all SA sub-domains: in-vessel, ex-vessel, containment response including hydrogen combustion risk, and source term. A special focus will be devoted on existing experimental facilities to evaluate the behavior of instrumentation under SA conditions, the performance of mitigation devices and their qualification, and new technologies upcoming in the near future, like WC-SMRs and ATFs.

To start with, a mapping of the current European experimental facilities investigating SA has been built. By surveying the entire European SA community, information has been collected on facilities (characteristics and materials), running teams (expertise and professional situation), data provided for SA codes validation, current and planned activities in the coming years, and open references including their contribution in recent years. As an illustration of the outcome from this activity, Figure 8 gives an overview of the phenomena that have been experimentally investigated in the recent past: source term & fission products, ex-vessel, in-vessel, pool scrubbing, and containment and H_2-risk.

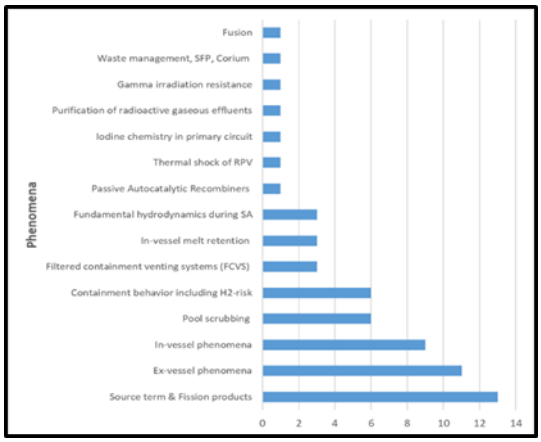

Figure 8. Number of facilities involved in a severe accident topic

Beyond the statistical map of facilities and issues, there are a number of insights from this study that are worth highlighting: more than 20 European facilities do not have any planned activity ahead in the coming years; "critical competences" are threatened to get lost with no chance to transfer them in about 10 of them; and, currently few facilities are being used for WC-SMRs and ATFs research under SA conditions.

3.4. KNOS: KNOwledge Spreading

At present time, when some of the knowledge acquired in the SA field is at risk of being lost (as many specialists are retiring) and new approaches for the SA assessment (as UaSA) are being explored, it is an appropriate timing to articulate the most efficient ways possible to bring young generation on board to face the new research challenges in this field and, at the same time, preserving the high level of European expertise. Therefore, it is of utmost relevance to pass the current State-of-the-Art on SA - deriving from the technical WP1-WP3 - onto the generations who are inheriting such legacy. Consequently, the main expected outcomes from this WP4 KNOS are:

- A strengthening of background and skills of young generations in the SA field, by a range of dissemination and communication activities in which an internal mobility programme is the backbone of an efficient K2T from expert senior scientists and engineers together with the Severe Accident Phenomenology (SAP) Course and the new Severe Accident Summer Camp (SASCAMP).
- A vast and diverse Communication & Dissemination (C&D) plan, with particular emphasis on the transfer of the SEAKNOT technical outcomes beyond the partnership boundaries to broadly reach the international SA community through the ERMSAR (European Review Meeting on Severe Accident Research) Conferences but also through AB and EUG organizations, which might significantly increase the range of stakeholders reached out.

Activities in WP4 are carried out in 4 sub-WPs and will be performed for the whole duration of the project.

Under the general NUGENIA TA2 framework, two editions of the SAP short course (one week) have been planned in SEAKNOT (WP4.1). This SAP course, from its first edition in 2006, represents the only international course offered to train or to complete the training of persons recently involved in the SA field, focusing on the dissemination of the knowledge gained on SA in the last two decades with a program covering the SA phenomenology, progression and mitigation in current water-cooled reactors of Gen. II and III, but also the different design solutions in Gen. III NPPs and recently in SMRs. Lectures for these Courses are given by international experts from major nuclear institutes, industries and universities, with a strong involvement of the SEAKNOT partners. A special focus is always on the Fukushima-Daiichi Severe

Accident, but the course also includes background lectures on NPP safety and SA codes and their uncertainties.

The first SEAKNOT SAP course was held in Madrid on June 19-23, 2023, jointly co-organized by UPM Universidad Politécnica de Madrid, CEA - IRESNE, CIEMAT, University of Pisa and Jožef Stefan Institute. The technical programme is displayed in Figure 9.

Monday, June 19	Tuesday, June 20	Wednesday, June 21	Thursday, June 22	Friday, June 23
8:00-8:30 Registration				
8:30-9:00 Introd. Welcome (X Y,UPM Director)				
9:00-10:00 1. Severe Accidents in NPP Safety	9:00-10:00 6. Late In-Vessel Phase	9:00-10:00 10. Ex-Vessel Phase - Part 2	9:00-10:00 14. SAMG	9:00-10:00 17. Decommisionning
10:00-11:00 2. TMI-2 Accident	10:00-11:00 7. Early Containment Failure	10:00-11:00 11 Source Term - Part 1	10:00-11:00 15. Nuclear Energy in Spain	10:00-11:00 18. New design Feature-Gen 3
11:00-11:30 Coffee Break	11:00-11:30 Coffee Break	11:00-11:30 Coffee Break	11:00-11:30 Coffee Break	11:00-11:30 Coffee Break
11:30-12:30 3. Chernobyl accident	11:30-12:30 8. Hydrogen Risk-Part 1	11:30-12:30 11 Source Term - Part 2	11:30-12:30 16. Radiological impact	11:30-12:30 19. SMRs
12:30-13h30 Lunch	12:30-13h30 Lunch	12:30-13h30 Lunch	12:30-13h30 Lunch	12:30-13h30 Lunch
13:30-14:30 4. Fukushima Accident-Part 1	13:30-14:30 8. Hydrogen Risk-Part 2	13:30-14:30 12. SA code & uncertainties-Part 1	Visit of SA facilities	13:30-14:30 Feedback and Conclusions
14:30-15:30 4. Fukushima Accident-Part 2	14:30-15:30 9. Steam Explosions -Part 1	14:30-15:30 12. SA code & uncertainties-Part 2		
15:30-16:00 Coffee Break	15:30-16:00 Coffee Break	15:30-16:00 Coffee Break		
16:00-17:00 5. Early In-Vessel Phase-Part 1	16:00-17:00 9. Steam Explosions -Part 2	16:00-17:30 13.Safety Assessment (PSA)		
17:00-18:00 5. Early In-Vessel Phase -Part 2	17:00-18:00 10. Ex-Vessel Phase - Part 1			

Figure 9. SAP 2023 technical programme

The attendance to this Course (Figure 10), the first in presence after the 2021 virtual edition forced by COVID-19 emergency, were the following: 27 professional and 33 students participants (13 were lecturers and 2 were UPM staff). In big numbers, organizations from 14 countries and people with about 20 nationalities attended.



Figure 10. SAP 2023 participants.

Next SAP 2025 edition will be organized from 23 to 27 June 2025 at Forschungszentrum Jülich (FZJ) and will be followed by the first edition of the SASCAMP initiative, also at FZJ. The SAP 2025 organization and the technical contents will be similar to the SAP 2023 ones, with further new/updated lectures (ATFs, SMRs and new methodology on UASA, etc.), while SASCAMP will be intended to be a residential K2T experience where "instructors" will pose a SA-related assignment (one single topic per day , i.e., in-vessel; ex-vessel; containment; source term; uncertainties) to participants and will support small groups of participants while "solving" the assignment by any means they might come up with (i.e., codes; models; data; "expert judgement"; …).

Other traditional flagship of SNETP/NUGENIA TA2 that the SEAKNOT project has taken over is the organization of ERMSAR 2024 and 2026 conferences (WP4.2). ERMSAR generic objective is to provide an open forum to foster deep and practical exchanges in the SA area across the entire community. This conference, traditionally open to both NUGENIA and non-NUGENIA members, has become the only international event fully focused on SA, with room to discuss recent research results, new and innovative methodologies, and needs to better manage these potential events in case they happen again. From the last 10th ERMSAR edition in May 2022 organized by KIT in SNETP/NUGENIA/TA2 framework and gathering 118 participants from nearly 50 organizations settled in 21 countries worldwide, the scope of the conference also includes innovative nuclear technologies, such as ATFs, SMRs, fusion, etc. The first ERMSAR Conference in the SEAKNOT framework is the current 11th edition, hosted by KTH Stockholm, while the next one will be organized by CIEMAT Madrid in 2026.

The textbook "Nuclear Safety in Light Water Reactors - Severe Accident Phenomenology", edited in 2011 by Bal Raj Sehgal [9], under the frame of the SARNET FP6 project, is foreseen to be extended (WP4.3). At the moment, this book is the only one-stop resource on how to assess, prevent, and manage SAs in LWRs. Nonetheless, the progress made by all the investigations conducted after the Fukushima-Daiichi accident and some innovative aspects brought in by nuclear technology (i.e., installation of new engineering safety systems, new insights into accident management, ATFs, and WC-SMRs, among others) recommend updating and extending it. The textbook nature as a walk-through knowledge and understanding SA complexity will be preserved, though, and by no means it is intended to end up in a

SEAKNOT C&D activities are giving emphasis on the transfer of the SEAKNOT technical outcomes beyond the project's partners (WP4.4). Three major axis for these activities have been set: public communication; external dissemination; and mobility of young researchers. A short description of each is given next:

- Public communication: A detailed C&D strategy plan has been developed with specific communication actions, key messages to get across and target audiences. To assess the impact of the plan, key performance indicators have been set. Additionally, a series of communication tools and actions have been already implemented, as the project logo (Figure 9) and the visual identity, including presentation and document templates, a roll-up and a flyer. Among them, a public project website (www.seaknot.com), yearly newsletters and a Linkedin account to promote and advertise SEAKNOT outcomes and activities.



Fig. 9: SEAKNOT logo.

The main C&D activity in the first part of the project has been the participation to relevant public events, presenting and promoting SEAKNOT at international conferences and meetings (as ERMSAR 2022 at KIT Karlsruhe, SNETP Coordinators' Hub Day in Brussels, MUSA Final Open Workshop in Madrid and ICONE 30 Conference in Kyoto) as well as in fora (FISA 2022, NUGENIA TA2 General Meeting and SNETP 2023 Forum) and this activity will continue for the entire project duration.

- External Dissemination. The dissemination of SEAKNOT results should use any means available, particularly scientific joint and individual publications in peer-reviewed journals, and presentations in international conferences, workshops, seminars, working groups, etc. The first edition of an electronic newsletter has been released in October 2023 and will be issued at the end of each year of the project to inform stakeholders of the project's progress by using the foreseen SEAKNOT dissemination channels (public website, mailing list, LinkedIn account), and those of SNETP and ENEN too.

- Mobility of young researchers. A mobility program aims at training young researchers and PhD/Master students from consortium organizations through delegations in partners' laboratories to enhance the exchanges and the dissemination of knowledge. Additionally, the presence of these young students or researchers in international conferences, workshops, and seminars to present some SEAKNOT results, is also supported. During this initial period 7 actions have been just supported, including one long mobility, and 4 further actions are under approval of the ExB.

4. FINAL REMARKS

The SEAKNOT project was born to respond to the current circumstances and the forthcoming needs in the domain of SA. Awarded by the Euratom Research and Training Programme 2021-2023 (GA#101060327), SEAKNOT is aimed at and orchestrated to outline a SA research roadmap based on technical grounds and oriented to efficiently address issues that might significantly contribute to enhancing the safety of actual and next generation NPPs. This encompasses consideration of multiple aspects, among which special attention is being given to identifying the critical experimental infrastructure as part of the SEAKNOT roadmap together with knowledge transfer efforts for the strengthening of the workforce who will run SA in vestigation in decades to come. It is foreseen that a suitable implementation of the roadmap will allow Europe to keep leading the area of SA research in Gen. II and III in the world in the coming decades, extending the scope to innovative technologies, like WC-SMRs and ATFs.

Since its inception in October 2022, SEAKNOT has achieved major progress. Having been described in the preceding sections, they are here summarized:

- A PIRT methodology has been proposed to address the challenge of a holistic approximation to the SA domain, which has required a proper adaptation of the original formulation. Oriented towards source term, both in-depth knowledge of significant phenomena and mitigation, the issue ranking process is to be conducted according to the SA phases (in-vessel and ex-vessel).
- An evaluation of the SA database for validation purposes has been drafted. The collected data are to be assessed in terms of representativeness and completeness based on a specifically developed methodology.
- A mapping of current European experimental facilities devoted to severe accident studies has been gathered. It is still too early to know if the existing infrastructure will be adequate for the forthcoming R&D demand, as this will depend on the PIRT outcome and the data base validation. Nonetheless, concerns about continuation of some facilities and preservation of skills in some running teams have been identified.

- An ambitious K2T plan has been articulated, with a well-supported mobility programme and a range of communication activities ongoing. The first SAP edition within SEAKNOT (SAP 2023) was held in Marid and met the expectations in terms of the technical programme, quality of lectures (material and delivery), attendance, venue and organization. The next edition of SAP course in SEAKNOT framework is scheduled in 2025 at FZJ (D), together with the first edition of SASCAMP initiative. As for ERMSAR 2024, the number of submissions has doubled the previous edition.

No matter how much has been already accomplished, SEAKNOT does have a path to go and it is foreseen a major direct impact in the domain of SA research in the coming decade.

ACKNOWLEDGMENTS

The work presented in this communication was done under the frame of the SEAKNOT project. This project has received funding from the Euratom Research and Training Programme 2021-2023 under grant agreement No 101060327. The content of this paper reflects only the authors' view. The European Commission is not responsible for any use that may be made of the information it contains.



REFERENCES

[1] https://cordis.europa.eu/project/id/101060327

[2] Magallon, D., Mailliat, A., Seiler, J.-M., Atkhen, K., Sjövall, H., Dickinson, S., Jakab, J., Meyer, L., Buerger, M., Trambauer, K., Fickert, L., Sehgal, B.R., Hozer, Z., Bagues, J., Martin-Fuentes, F., Zeyen, R., Annunziato, A., El-Shanawany, M., Guentay, S., Tinkler, C., Turland, B., Puebla, L.E.H., 2005. European expert network for the reduction of uncertainties in severe accident safety issues (EURSAFE). Nuclear Engineering and Design 235, 309–346. https://doi.org/10.1016/j.nucengdes.2004.08.042.

[3] Van Dorsselaere, J.-P., Auvinen, A., Beraha, D., Chatelard, P., Herranz, L.E., Journeau, C., Klein-Hessling, W., Kljenak, I., Miassoedov, A., Paci, S., Zeyen, R., 2015. Recent severe accident research synthesis of the major outcomes from the SARNET network. Nuclear Engineering and Design 291, 19–34. https://doi.org/10.1016/j.nucengdes.2015.03.022.

[4] Van Dorsselaere, J.-P., Bréchignac, F., Rosa, F., Herranz, L.E., Kljenak, I., Miassoedov, A., Paci, S., Piluso, P., 2017. Trends in severe accident research in Europe: SARNET network from Euratom to NUGENIA. EPJ Nuclear Sciences & Technologies 3, 28. https://doi.org/10.1051/epjn/2017021.

[5] NUGENIA/TA2 Achievements in Severe Accidents Research (2015-2020), 2020. Revista Nuclear España. https://www.revistanuclear.es/seguridad/nugenia-TA2-achievements-in-severe-accidents-research-2015-2020/.

[6] Wilson, G.E. and B.E. Boyack.¡, 1998. The role of the PIRT process in experiments, code development and code applications associated with reactor safety analysis. Nuclear Engineering and Design, 1998. 186: pp.23-27.

[7] Shaw, R.A. et al., 1988. Development of a phenomena identification and ranking table (PIRT) for thermal-hydraulics phenomena during a PWR large-break LOCA. NUREG/CR-5074, U.S. Nuclear Regulatory Commission, Washington, DC, USA.

[8] Kang, K.H., et al., 2015. Development of a phenomena identification ranking table for simulating a station blackout transient of a pressurized water reactor with a thermal-hydraulic integral effect test facility. Annals of Nuclear Energy, 2015. 75: pp. 72-78.

[9] Sehgal, B.R. (Ed.), 2012. Nuclear Safety in Light Water Reactors, in: Nuclear Safety in Light Water Reactors. Academic Press, Boston. https://doi.org/10.1016/B978-0-12-388446-6.01001-7.

[10] Suehiro S., Sugimoto J., Hidaka A., Okada H., Mizokami S., Okamoto K., 2015. Development of the source term PIRT based on findings during Fukushima Daiichi NPPs accident, Nuc. Eng. And Des. 286, 163-174, ISSN 0029-5493, https://doi.org/10.1016/j.nucengdes.2015.02.005.

[11] Farmer M.T., Corradini M., Rempe J., Reister R. & Peko D., 2016. United States Department of Energy Severe Accident Research Following the Fukushima Daiichi Accidents, Nuclear Technology, 196:2, 141-148, DOI: 10.13182/NT16-42.

[12] Manara D, Jacquemain D, Van Dorsselaere JP, Bottomley PD, Adorni M, Journeau C, Pontillon Y, Lind T, Herranz LE, Rocchi F, Schaffrath A, de la Rosa Blul JC, Bechta S, Duspiva J, Kljenak I & Dejardin P, 2019. Severe accident research priority ranking: a new assessment eight years after the Fukushima Daiichi accident. Proceedings of the 9th European Review Meeting on Severe Accident Research (ERMSAR 2019), Prague, Czech Republic, March 18-20, 2019.

[13] NEA, 2018. Status Report on Ex-Vessel Steam Explosion: EVSE. URL https://www.oecd-nea.org/jcms/pl_19814/status-report-on-ex-vessel-steam-explosion-evse?details=true

[14] NEA, 2017. State-of-the-Art Report on Molten Corium Concrete Interaction and Ex-Vessel Molten Core Coolability [Internet]. Nuclear Energy Agency (NEA). URL https://www.oecd-nea.org/jcms/pl_15070/state-of-the-art-report-on-molten-corium-concrete-interaction-and-ex-vessel-molten-core-coolability?details=true

[15] IAEA Report on Severe Accident Management in the Light of the Accident at the Fukushima Daiichi Nuclear Power Plant [WWW Document], 2017. URL https://www.iaea.org/publications/10949/iaea-report-on-severe-accident-management-in-the-light-of-the-accident-at-the-fukushima-daiichi-nuclear-power-plant.

[16] A. Miassoedov, et al., 2015. Severe accident facilities for European safety targets. The safest project. NURETH-16, Chicago (IL-USA), August 30-September 4, 2015.

[17] F. Fichot et al., 2020. Elaboration of a Phenomena Identification Ranking Table (PIRT) for the modelling of In-Vessel Retention. Annals of Nuclear Energy 146, 107617.

[18] T. Haste et al., 2018 "In-Vessel Core Degradation in Water-Cooled Reactor Severe Accidents: State-of-the-Art Report Update (CoreSOAR), 1996-2018", SARNET-CoreSOAR-D3, IRSN PSNRES/SAG/2018-00239, ISBN 978-2-919313-13-6.

[19] OECD/NEA. 2016. Benchmark Study of the Accident at the Fukushima Daiichi Nuclear Power Plant (BSAF Project). NEA/CSNI/R(2015).

[20] Martin J. Trégourès N., 2023. OECD/NEA R&D priorities for loss-of-cooling and loss-of-coolant accidents in Spent-Fuel-Pools. Nuclear Engineering and Design 410, 112380, https://doi.org/10.1016/j.nucengdes.2023.112380.

[21] H.-J. Allelein, S. Arndt, W. Klein-Heßling, S. Schwarz, C. Spengler, G. Weber, "COCOSYS: Status of development and validation of the German containment code system", Nuclear Engineering and Design, Vol 238, Issue 4, pp 872-889 (2008).

[22] P. Chatelard and L. Laborde, "Synthesis of the ASTEC V2.2 code validation against experimental data", The 10th European Review Meeting on Severe Accident Research (ERMSAR2022) Akademiehotel, Karlsruhe, Germany, May 16-19 (2022).

[23] OECD/NEA, "Containment Code Validation Matrix", Nuclear Safety NEA/CSNI/R(2014)3 May (2014).

[24] OECD/NEA, "SAPIUM: Development of a Systematic Approach for Input Uncertainty Quantification of the Physical Models in Thermal-Hydraulic Codes", Nuclear Safety NEA/CSNI/R(2020)16 May 2023.

[25] Herranz, L. E., Sánchez, F., Gupta, S., 2022. Validation Matrix for Pool Scrubbing Models, Nuclear Technology, 2022.

SEAKNOT

SEvere Accident Research and KNOwledge ManagemenT for LWRs

First steps towards a SA roadmap

Luis E. Herranz – CIEMAT, Spain
S. Gupta – BT, Germany
P. Piluso – CEA, France
S. Paci – UNIPI, Italy

ERMSAR 2024

Stockholm, May 13th-16th, 2024

Funded by the European Union

SEAKNOT

OUTLINE

- Introduction
- Structure
- WP Description
- Final Outcomes

Funded by
the European Union

SEAKNOT

INTRODUCTION

Funded by
the European Union

Why SEAKNOT

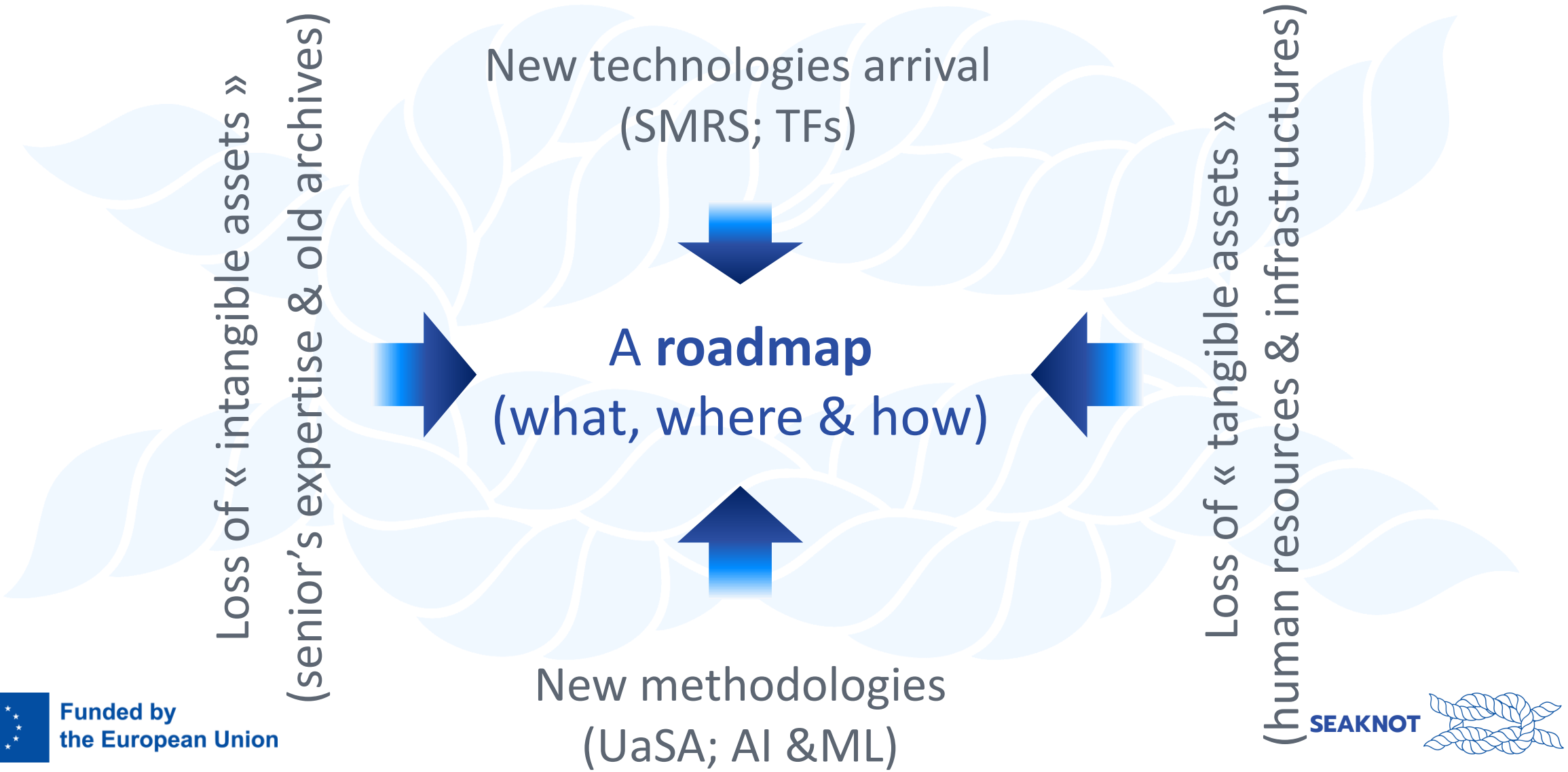

Funded by
the European Union

SEAKNOT

Objectives

- To carry out a **sound and critical analysis** of the current knowledge.
- To identify **forthcoming research needs**.
- To strengthen the background and skills of **young generations**.

Efficiently mitigate and practically eliminate SA consequences

Funded by
the European Union

SEAKNOT


SEVERE
ACCIDENTS
PRESENT
SOUND
EXPERTISE
FUTURE
WORKFORCE
POWER

SEAKNOT in Numbers

- Oct., 2022 – Sept., 2026.
- Total cost: 2.725 M€ (79% EURATOM).
- Human resources: 260 person-month.

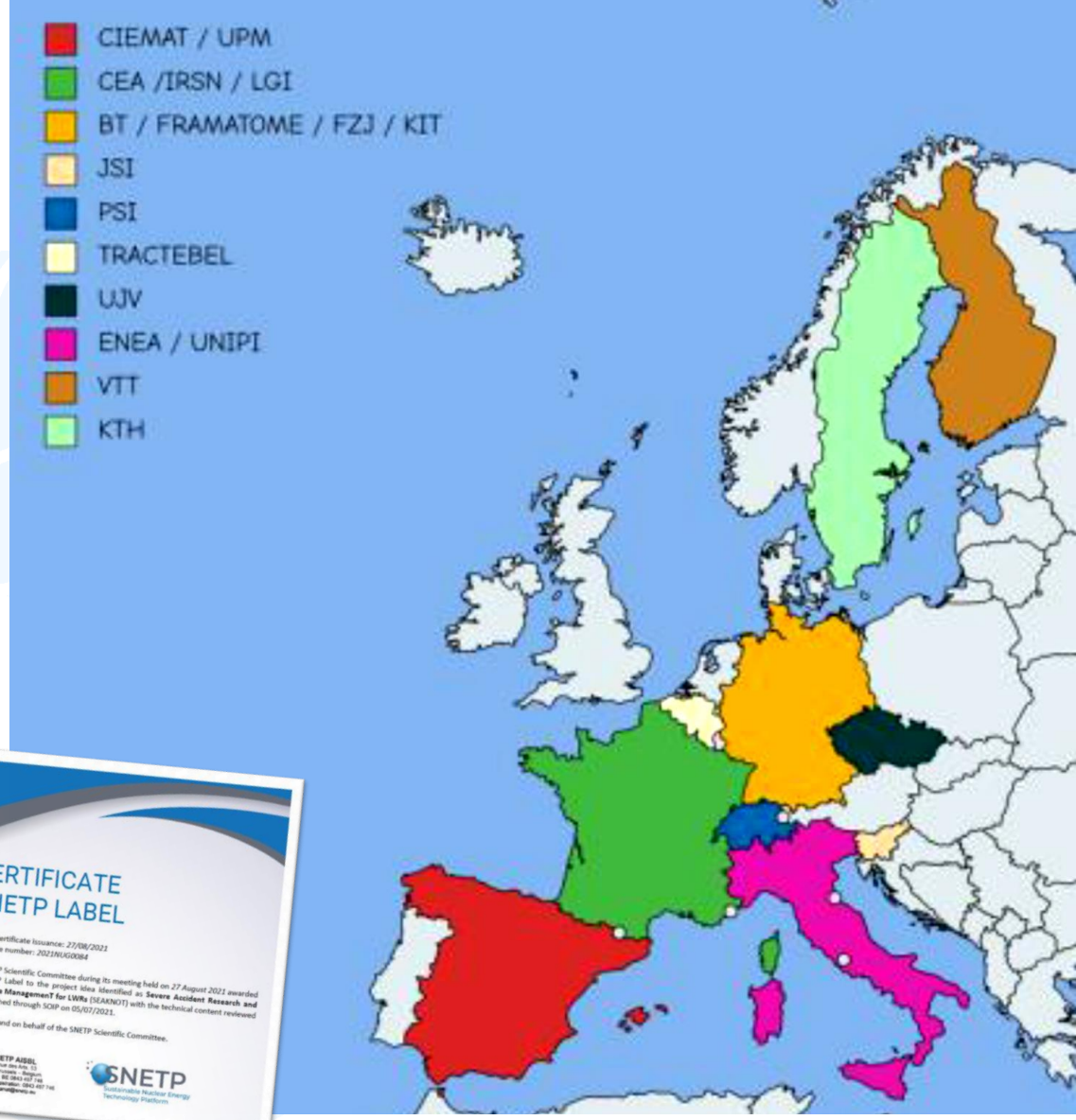



Funded by the European Union

Expertise complemented with **AB** and **EUG!**

SEAKNOT

SEAKNOT

STRUCTURE

Funded by
the European Union

Organic Structure

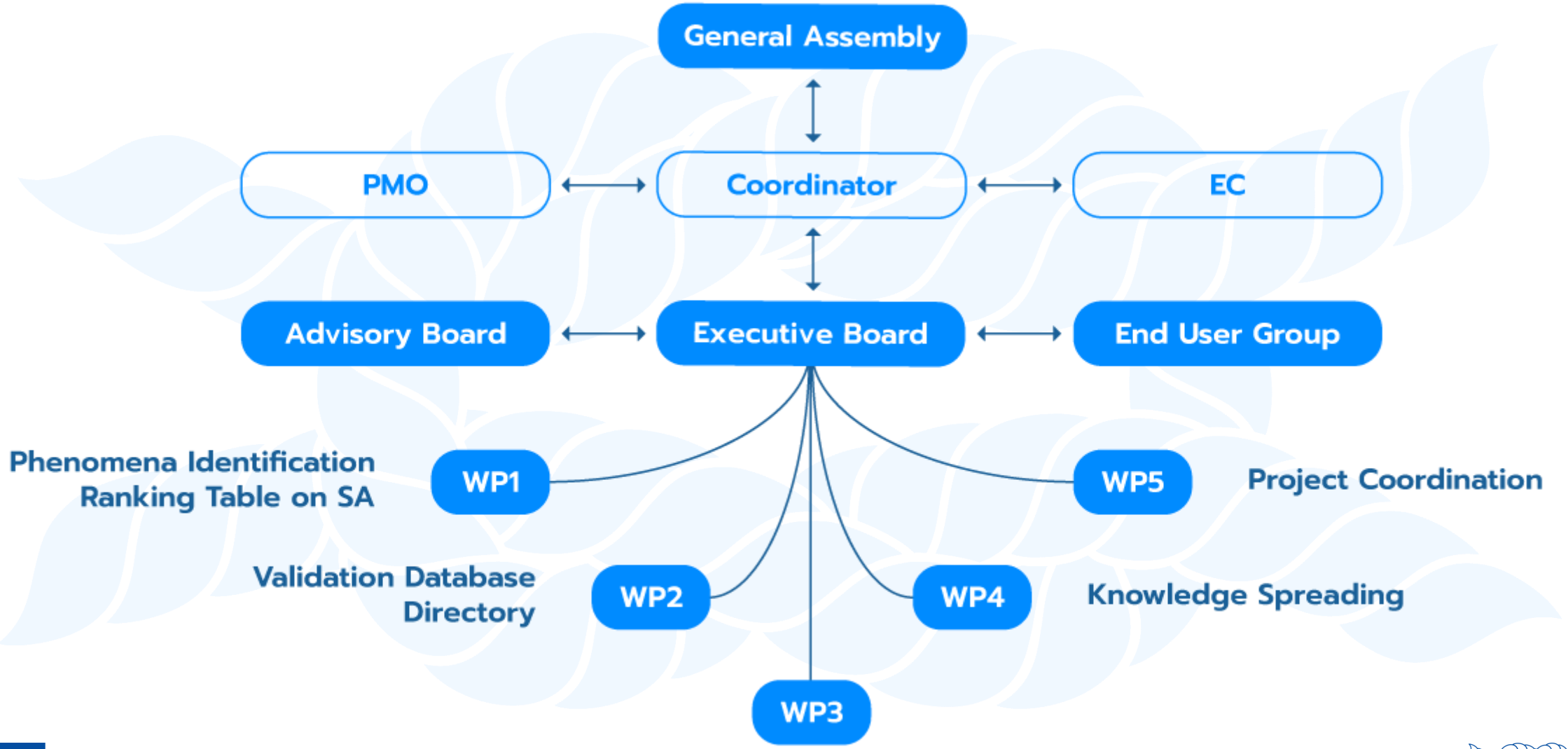

Funded by
the European Union

Severe Accident experimental
Infrastructure NETwork

SEAKNOT

Organic Structure

- H. Esmaili (NRC; USA)
- D. Luxat (SNL; USA)
- S. Gyepi-Garbrah (CNSC)
- P. Isaksson (SSM)
- F. Robledo (CSN)
- T. Hollands (GRS)
- A. Tehrani (ONR)
- J. Kaneko (NRA)

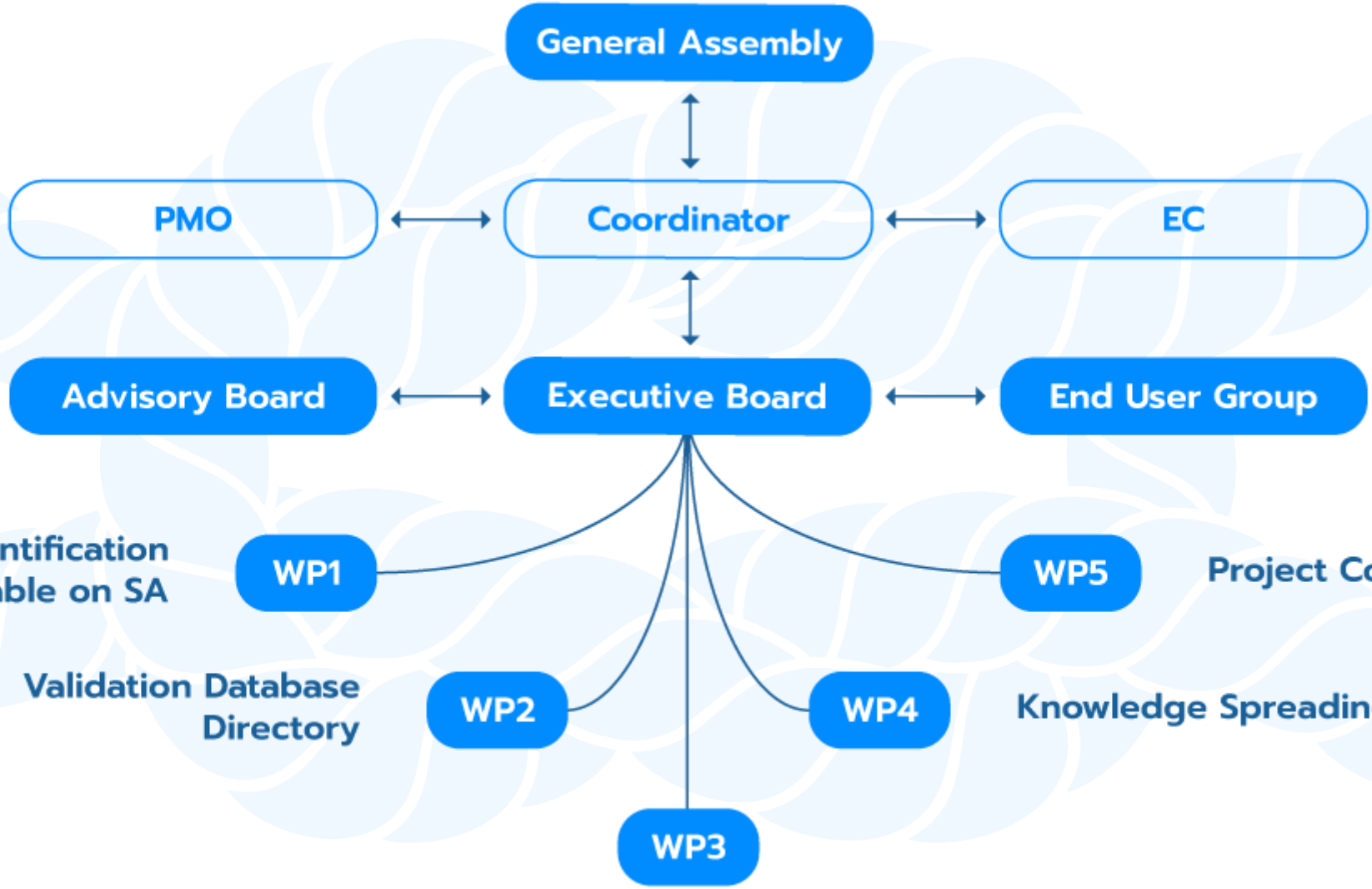

- D. Jacquemain (NEA)
- A. Miasseidov (IAEA)
- J. Starflinger (ENEN+)
- A. Al-Mazouz (SNETP)
- S. Petoukhov (CNL)

Funded by the European Union

Severe Accident experimental Infrastructure NETwork

SEAKNOT

Working Structure

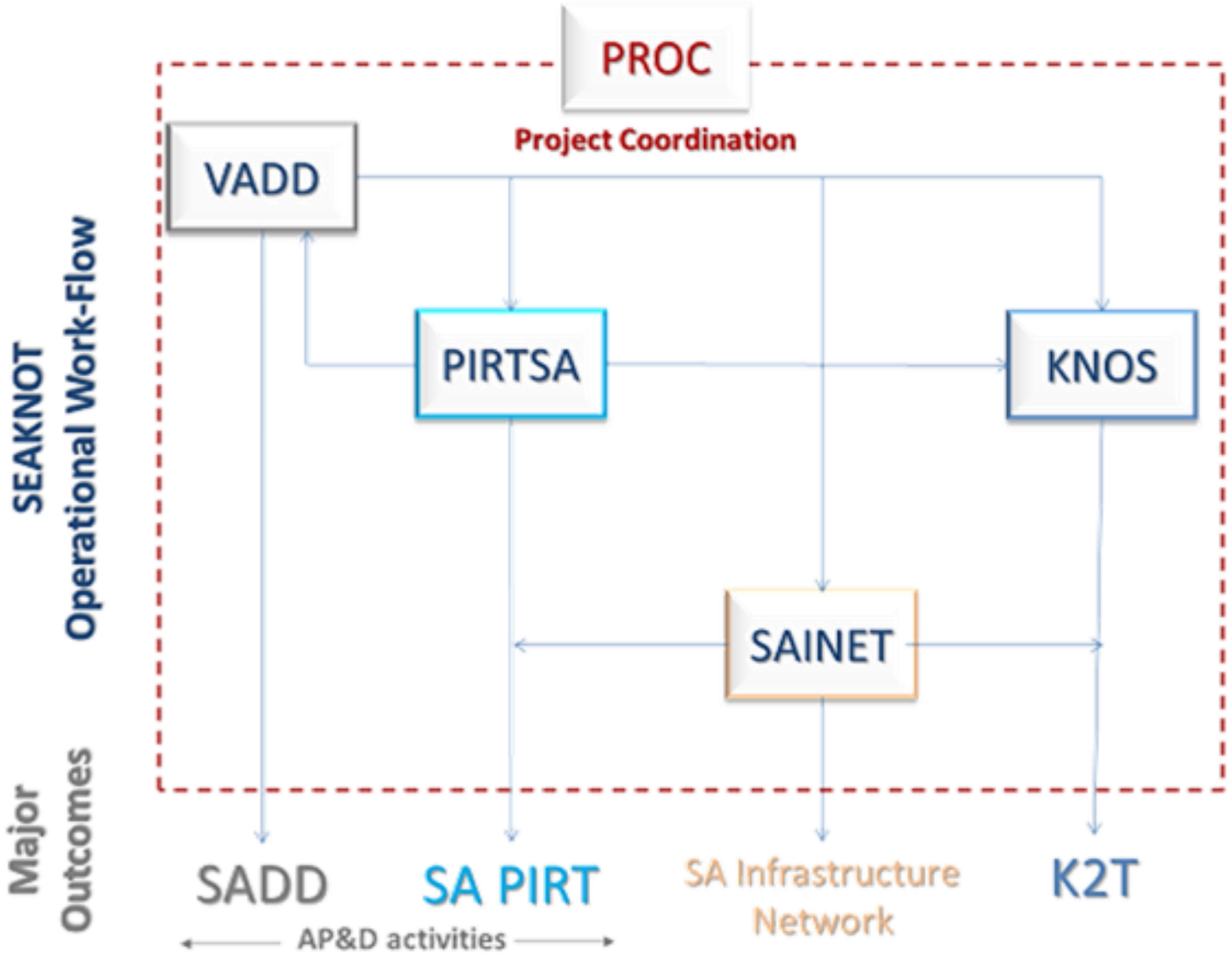

VP1 PIRTSA Phenomena Ident. & Rank. Table

VP2 VADD Validation Database Directory

VP3 SAINET Severe Accident Infrastructure NETw

VP4 KNOS Knowledge Spreading

VP5 PROC Project Coordination

SEAKNOT

SEAKNOT

WP DESCRIPTION

Funded by
the European Union

WP1 PIRTSA Objective

Identify the major SA issues worth new R&D activities

- Developed by a critical assessment of existing SA knowledge
- Assess the knowledge gaps (data & models)
- Evaluate the safety significance

PIRT focus on LWRs but including WC-SMRs & ATFs related aspects

- In-Vessel
- Ex-Vessel
- Containment
- Source Term

Funded by the European Union

WP1 Background

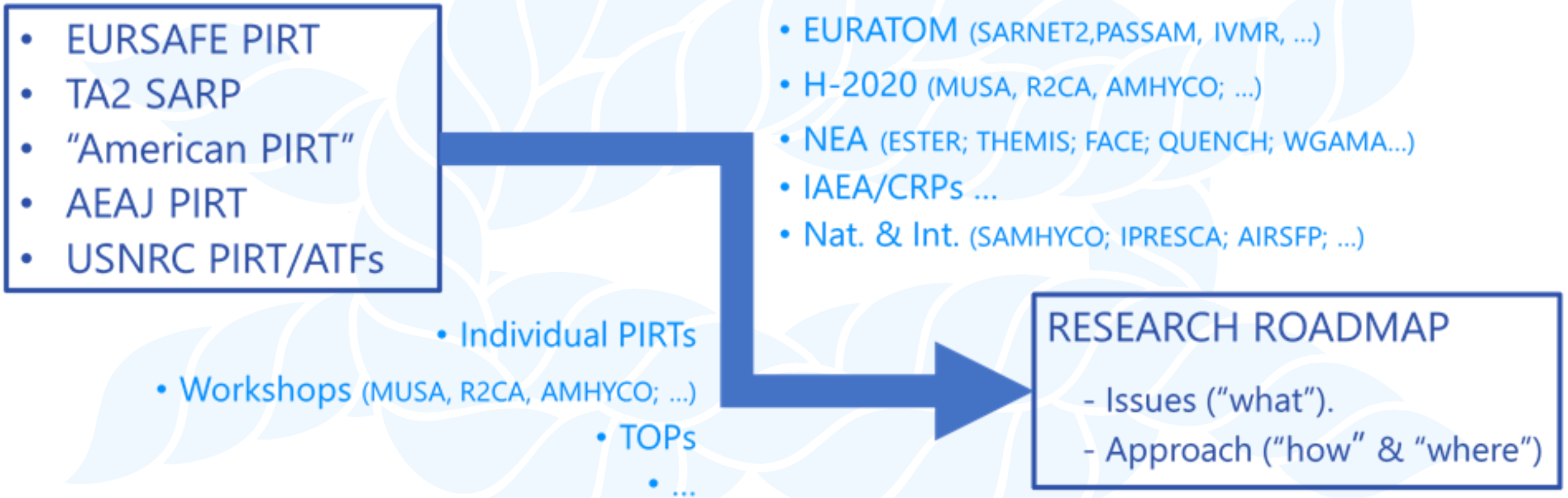

Funded by
the European Union

SEAKNOT

WP1 Challenges

- To adopt a sound **methodology** (in the right time frame).
- To achieve **a uniform application of the methodology** in WP1.x.
- To **integrate** the input from WP1.2-5.
- To **stretch the boundaries** to WC-SMRs and ATFs (WP1.2-.5) .
- To keep the **safety-focus** throughout the work.
- To articulate a neutral procedure to **accommodate AB insights**.

Funded by
the European Union

SEAKNOT

WP1.1 PIRT Methodology

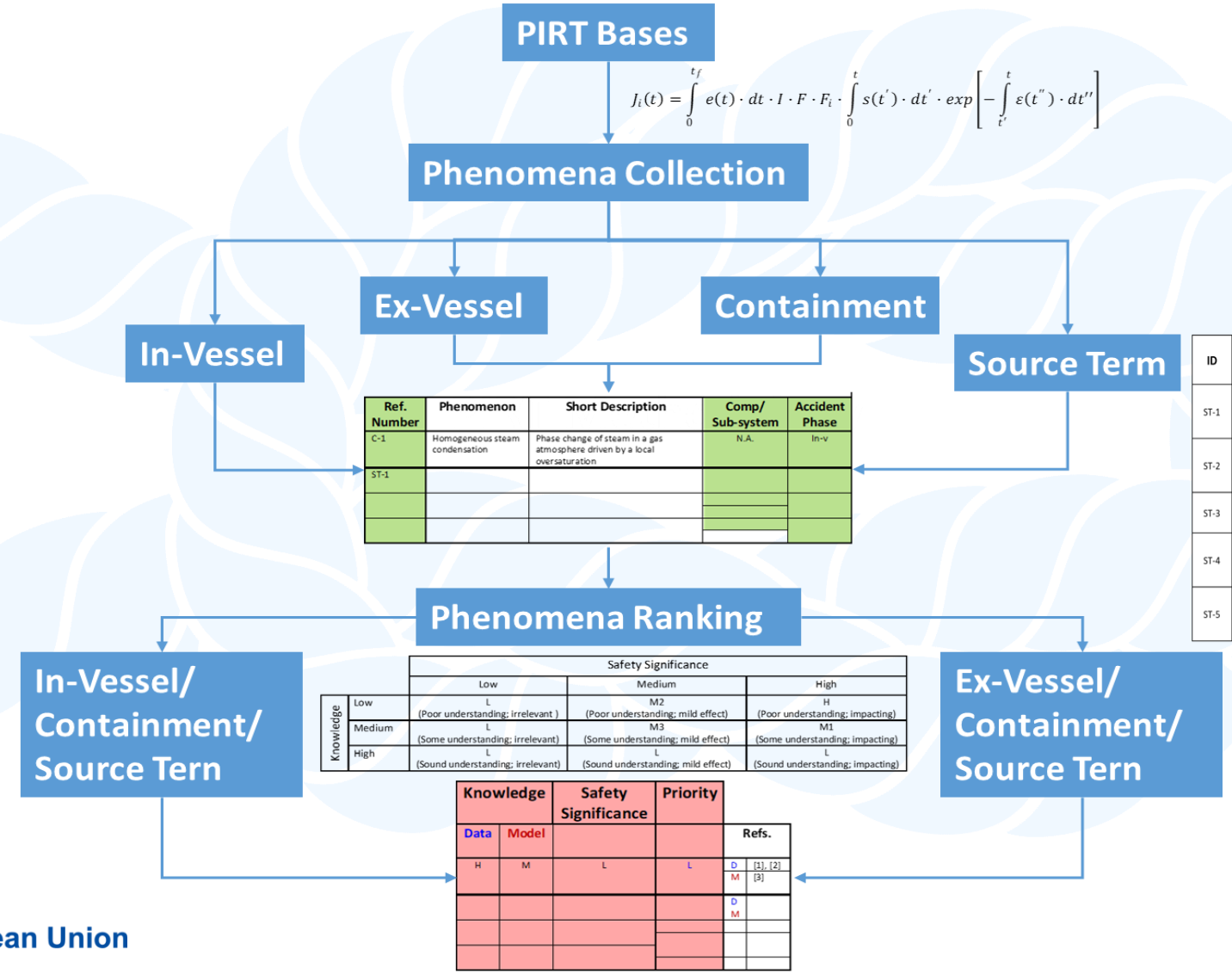

ID	Phenomena	Short description	Accident Phase (In-V, Ex-V)
ST-1	**High temperature iodine chemistry**	The chemical speciation of iodine can be strongly influenced under high-temperature conditions while interacting with atmospheres, surfaces, and water pools under SA conditions. The gas composition (oxidizing or reducing) conditions may further impact the iodine source term.	In-V
ST-2	**Aerosols transport within containment**	Influenced by diffusion, convection, and advection mechanisms, which are affected by factors like temperature and pressure. The state of mixing (homogenous or stratified) can further affect the transport processes essential for evaluating aerosol deposition on surfaces like walls and pools → **also relevant for LW-SMRs**	In-V, Ex-V
ST-3	**Aerosols and gaseous RN interaction with FCVS (also Spray and PARs)**	FCVS operation can influence in-containment source term, e.g. due to aerosols or gaseous RN remobilization from water pools. → *Also relevant to assess reliability of Active and Passive safety systems*	In-V, Ex-V
ST-4	**Fission product release from fuel**	Factors such as fuel composition, temperature, and burn-up can influence the extent and rate of fission product migration from the fuel matrix, affecting the severity and duration of radioactive releases into the environment, e.g. E.g. UO2 or MOX, low or high burn-up → **also relevant for ATF**	In-V, Ex-V
ST-5	**Fission products release through containment cracks/penetrations**	The condition of vents, seals, and other potential release pathways in the containment structure becomes crucial once the reactor vessel is breached. The behavior of these components under accident conditions can significantly influence the extent and composition of the radiological release.	Ex-V

Funded by the European Union

SEAKNOT

WP1.1 PIRT-Step 11: Ranking

MODEL	DATA: L	DATA: M	DATA: H
L	L (Unknown)	L (Qualitative understaning)	M (Bases for "known" set)
M	L (Uncertain approximation)	M (Qualitatively assessed app.)	M (Soundly assessed app.)
H	L (Uncertain model)	M (Qualitatively assessed model)	H

KNOWLEDGE	SAFETY: L	SAFETY: M	SAFETY: H
L	L	M_2	H
M	L	M_3	M_1
H	L	L	L

Funded by the European Union

SEAKNOT

WP2 VADD Objectives

BECKER TECHNOLOGIES

Review of SA experimental data used to develop and validate codes presently used to model SAs and support SAMGs

- Critical analyses of database (incl. OECD, EU reports, etc.)

Creation of a SA Database Directory (SADD)

- SADD will be a website analytical tool
- Future share outside the project (i.e., SNETP, IAEA or NEA)
- Target: future expansions to new experimental data sources

Funded by the European Union

VADD focus on LWRs but including WC-LWRs & ATFs related aspects

SEAKNOT

WP2 Current Status

BECKER TECHNOLOGIES

- A draft **methodology for database assessment** prepared
  - Literature review & IPRESCA experience
- **Literature review** (validation database matrix)
  - "Focus areas": In- and Ex-vessel, Containment, Source Term
  - Template based collection of information on tests ("relational data")
  - Assessment on test objective, BC, procedure, measurements, refs. etc
  - Collection from past to present and allocation for future
- **Collection of validation tests** of SA tools (MELCOR, MAAP, ASTEC, AC2)

Funded by the European Union

SEAKNOT

WP3 SAINET Objectives

Assessment of EU experimental SA Facilities activities 2022-2030

- Mapping of EU experimental facilities in operation
- Identification of EU key experimental infrastructures to shoot key needs
- Identify forthcoming infrastructures needs

Creation of SAINET (Severe Accident Infrastructure NETwork **)**

- Outline means, recommendations and framework for a network

Funded by the European Union

SEAKNOT

WP 3 Current status

Institution	Name	Start	Topics	Team					Critical Situation	
				Technician	Researcher	PostDOc	PhD	Staff	yes	no
CEA	MERARG	2000	LWR, SMR	3	3		1	6		x
CEA	VERDON	2011	LWR, SMR, ATF	2	2		1	4		x
CEA	CRACOUCASS	2023	LWR	2	2			4		x
CEA	ATALANTE	2001	other: waste management	5	15		3	20		x
CEA	VITI	2000	Gen II, 3 and 4, ATF, SMR, instrumentation	1	2	1	3	7		x
CEA	ATTILHA	2016	LWR, SMR, ATF		2+1		1	4	x	
CEA	MISTRA	2001	LWR, SMR, ATF	1	1		1	3		x
CEA	MERELAVA	1997	LWR, mitigation, instrumentation	2	8	1				x
CEA	VULCANO	1997	Mitigation, instrumentation	2	8	1				x
CEA	KROTOS	2003	LWR, SA, FCI, steam explosion, debris bed	5	10	1	3			x
CEA	SAFeTy Platform	2028	LWR Gen2 to 4 large scale tests for prototype corium		13+6	2	3			x
PSI	PANDA	1991	LWR, SMR, Mitigation, Instrumentation	2	3			5		x
PSI	HERZSAN	2022	Source term mitigation	2	1	1		3	x	
PSI	VEFITA	2014	Mitigation of source term for LWRs by wet	2	2			4	x	
PSI	TRISTAN	2008	Mitigation of source term for LWR's, Pool	2	1	1		4	x	
PSI	ISOLDE	2016	Mitigation of source term for LWR's, Pool	2	1			3	x	
CIEMAT	LASS	1991	LWR, Mitigatin, instrumentation	1		1			x	
FRAMG	JAVA	1989	LWR, CANDU, VVER	8	2					x
KIT	QUENCH	1998	LWR, ATF					7	x	
KIT	HYKA	1999	LWR, SMR, ATF, mitigation	6	5		2			x
IRSN	TYFON	2022	LWR				3	15		x
IRSN	EPICUR Gamma, LEAR hot cell	2000	LWR, ATF, source term							x
IRSN	DOFIN	2000	LWR, source term							x
IRSN	START	2000	LWR, source term							x
IRSN	COPIN	2000	LWR							x
IRSN	MASSE COMPACTE	2019	LWR			0	0	2		x
IRSN	TOSCAN	2000	LWR, H2/aerosol in containment, decommisioning	1	2			3		x
IRSN	FAAMUS	2020	Study of Flash Atomisation Aerosols Mobilization under vacUum System, fusion							x
IRSN	PERSEE	2017	Platform to study purification of radioactive effluents		3+1					x
IRSN	IRMA	1969	Co-60 Gamma irradiation cell		2+1					x
KTH	CoSMUS	2022	LWR		2+1			3		x
KTH	DEFOR	2000	LWR		3		1	3		x
KTH	MISTEE	2005	LWR		2		1			x
KTH	MRSPOD	2019	LWR, in-/ex-vessel		2		1			x
KTH	SIMECO-2	2021	LWR		3+1			4		x
KTH	SPaYCOR	2018	LWR			1	1	1		x
UJV	BESTH-2	2013	LWR, SMR		2+6			8	x	
UJV	THS-15	2018	VVER-1000		5+6			11	x	
UJV	KRNEC	2022	LWR, instrumentation		2+6					x
VTT	VTT-FP transport	2000	LWR, SMR, HTGR		3+1		1	4		x
VTT	EXSI-PC	2010	LWR, SMR		3+1			4		x
VTT	VTT-POOL	2018	LWR, SMR, mitigation		3+1			4		x

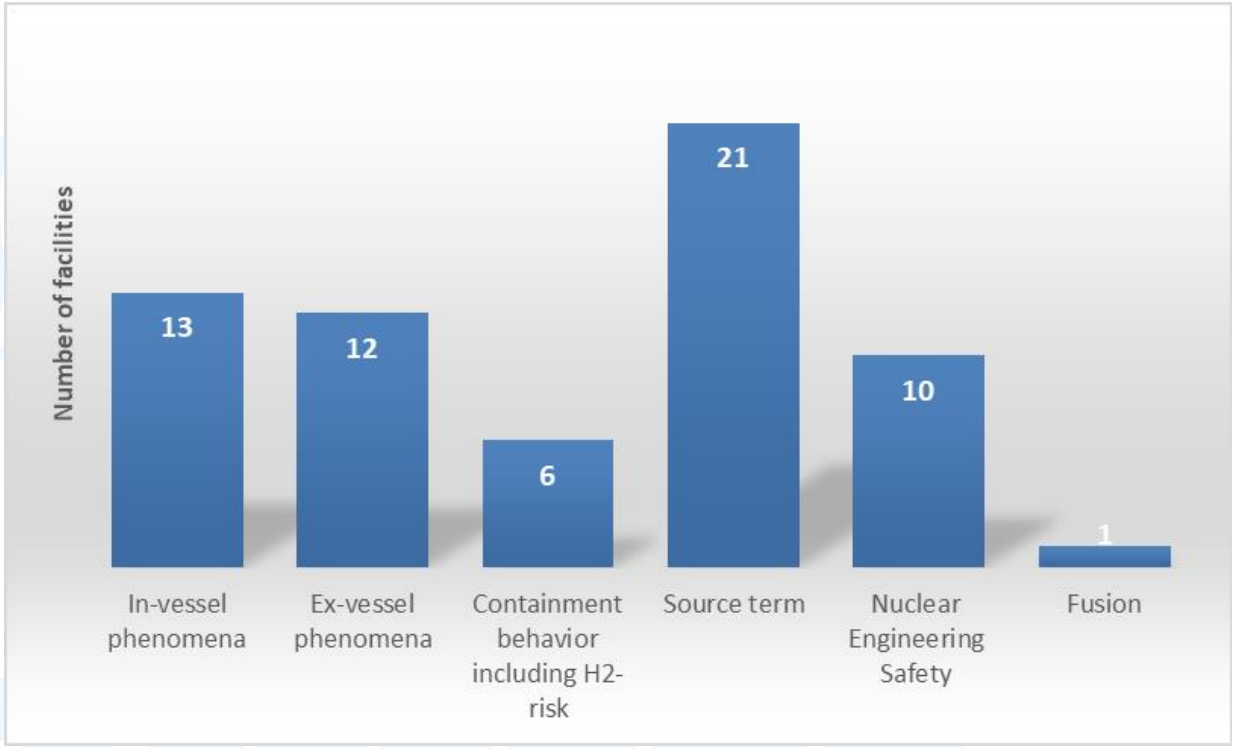

- 59 SA facilities identified in Europe (quest).
- More than 20 with no exptl. plans.
- Some planning "to test" SMR & ATFs.
- Threat to critical competences in ~ 10.
- Eight facilities in "critical situation".

SEAKNOT

WP4 KNOS Objectives

- **Strengthen EU leadership on SA E&T**
- **Efficiently foster C&D activities of the whole project**
  - Two consolidated NUGENIA TA2 events:
    - **Severe Accident Phenomenology (SAP) Course**
    - **European Review Meeting on Severe Accident Research (ERMSAR)**
  - New extended edition of SARNET **SA Textbook** (WP1 - WP3 activities)
  - **Internal mobility program** for young researchers & students
- **Articulate means to update SA R&D agenda according to SEAKNOT outcomes**

Funded by the European Union

SAP 2023 / SAP & SASCamp 2025



POLITÉCNICA

UNIVERSIDAD POLITÉCNICA DE MADRID

Severe Accident Phenomenology (SAP) Course 2023

11th edition June 19-23, 2023 at UPM Madrid
13 Lecturers, 27 professional and 33 students (20 natlts.)



TIME	Monday, June 19	Tuesday, June 20	Wednesday, June 21	Thursday, June 22	Friday, June 23
8:30	8:30-9:30 Registration				
9:00	9:30-10:00 Welcome from UPM & SEAKNOT	9:00-10:00 5. Early In-Vessel Phase (part 1) Florian Fichot	9:00-10:00 9. Steam Explosions (part 2) Pascal Piluso	9:00-10:00 13. SAMG Matthias Braun	9:00-10:00 18. Decommissioning of SA da reactors Christophe Journeau
9:30					
10:00	10:00-11:00 1. Severe Accidents in NPP Safety Luis E. Herranz	10:00-11:00 5. Early In-Vessel Phase (part 2) Florian Fichot	10:00-11:00 10. Ex-Vessel Phase (part 1) Christophe Journeau	10:00-11:00 14. Safety Assessment (PSA) Juan M. Martín-Valdepeñas	10:00-11:00 19. New design Feature-Gen 3 (Manfred Fischer
10:30					
11:00	11:00-11:30 Coffee Break	11:00-11:30 Coffee Break	11:00-11:30 Coffee Break	11:00-11:30 Coffee Break	11:00-11:30 Coffee Break
11:30	11:30-12:30 2. TMI-2 Accident Florian Fichot	11:30-12:30 6. Late In-Vessel Phase Florian Fichot	11:30-12:30 10. Ex-Vessel Phase (part 2) Christophe Journeau	11:30-12:30 15. Post-Fukushima improvements in Spanish NPPs. Impact in SA Phenomenology César Queral & José R. Alonso	11:30-12:30 19. New design Feature-Gen 3 (p Manfred Fischer
12:00					
12:30	12:30-13h30 Lunch	12:30-13h30 Lunch	12:30-13:30 Lunch	12:30-13:30 Lunch	12:30-13:30 Lunch
13:00					
13:30	13:30-14:30 3. Chernobyl accident Pascal Piluso	13:30-14:30 7. Early Containment Failure Pascal Piluso	13:30-14:30 11 Source Term (part 1) Luis E. Herranz	13:30-14:30 16. Radiological impact Federico Rocchi	13:30-14:30 20. Severe accidents in Advance reactors and SMRs Philippe Dejardin
14:00					
14:30	14:30-15:30 4. Fukushima Accident (part 1) Luis E. Herranz	14:30-15:30 8. Hydrogen Risk (part 1) Ivo Kljenak	14:30-15:30 11 Source Term (part 2) Luis E. Herranz	14:30-15:30 17. Long Term Accident Management Ahmed Bentaib	14:30-15:30 21. Status of SA Research Luis Herranz
15:00					15:00-15:30 Feedback and Conclusion
15:30	15:30-16:00 Co	15:30-16:00 Coffee Break	15:30-16:00 Coffee Break	15:30-16:00 Coffee Break	
16:00		16:00-17:00 Risk (part 2)	16:00-17:00 12. SA code & uncertainties (part 1) Fulvio Mascari	16:00-17:00 Transfer to CIEMAT	
16:30	4. Fukush				
17:00			17:00-18:00 ties (part 2)	17:00-18:00 Visit of CIEMAT fusion facilities (Stellarator TJ-II)	
17:30					

SAP & Severe Accident Summer Camp 2025

12th SAP Course (23-27 June 2025) at FZJ Jülich, followed by the **1st edition of SASCamp** (June 30 – July 4)

SASCAMP: A residential camp where participants will address specific assignments (in-V; ex-V; CONT; STerm; UQ) with the guidance of qualified instructors.

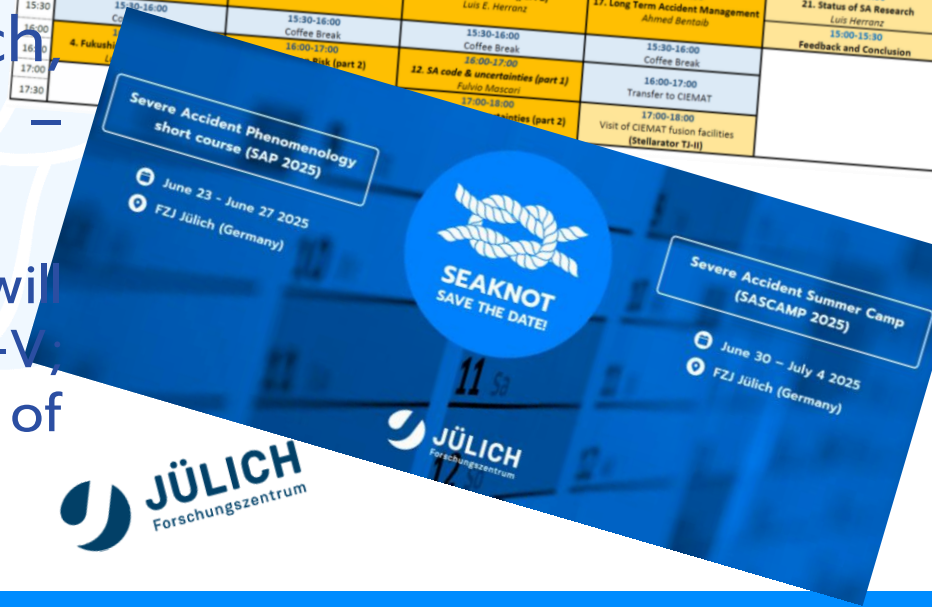

Funded by the European Union

ERMSAR European Review Meeting on Severe Accident Research

11th ERMSAR edition, after 2 years from the previous edition in Karlsruhe

- **124 abstracts submited by 623 authors, 77 institutions from 26 countries**
- 74 papers for oral presentation + 33 poster

Topic	Presentations
In-vessel corium and debris coolability	**13**
Ex-vessel corium interactions and coolability	**13**
Containment behaviour incl. Explosion risk	**19**
Source term	**19**
Analysis, Management, and Consequences of SAs for Gen I-III reactors	**26**
Severe accidents in innovative reactors such as Gen IV and SMRs	**15**
Other applications (fusion, interim SNF storage, ATFs, …)	**9**



12th ERMSAR edition will be in Madrid from 18 to 21 May 2026

Funded by the European Union

SA Textbook

Jožef Stefan Institute

New edition of the **SARNET textbook**

"Nuclear Safety in LWRs – Severe Accident Phenomenology"

- **Updates needed after more than 10 years**
- **New extended edition,** including WP1 - WP3 activities
- A **TEXTBOOK**, not a research compilation.

- Workplan ongoing:
  - ✓ Review of the book contents
  - ✓ Identification of missing aspects

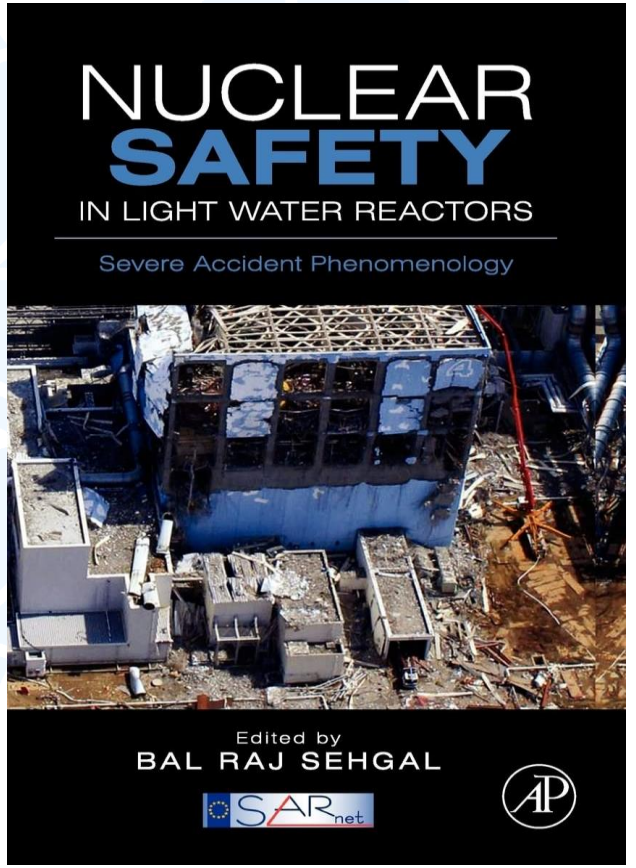

Funded by the European Union

SEAKNOT

Internal Mobility

Internal mobility program - young researchers & MSc/PhD students

- **Grants for SAP 2023 participation**
  6 mob grants plus
  15 students have attended the Course at no cost

- **Two long mobilities (MSc students):**
  - ✓ Application of inverse uncertainty quantification in the severe accident domain (6 months at CIEMAT)
  - ✓ Analysis of hypothetical severe accidents in a generic VVER-1000 nuclear power plant (5 months at KIT)

- **Six open positions on SEAKNOT website** (CIEMAT, KIT, PSI)

Funded by the European Union

SEAKNOT

EXPECTED OUTCOMES

Funded by
the European Union

SEAKNOT

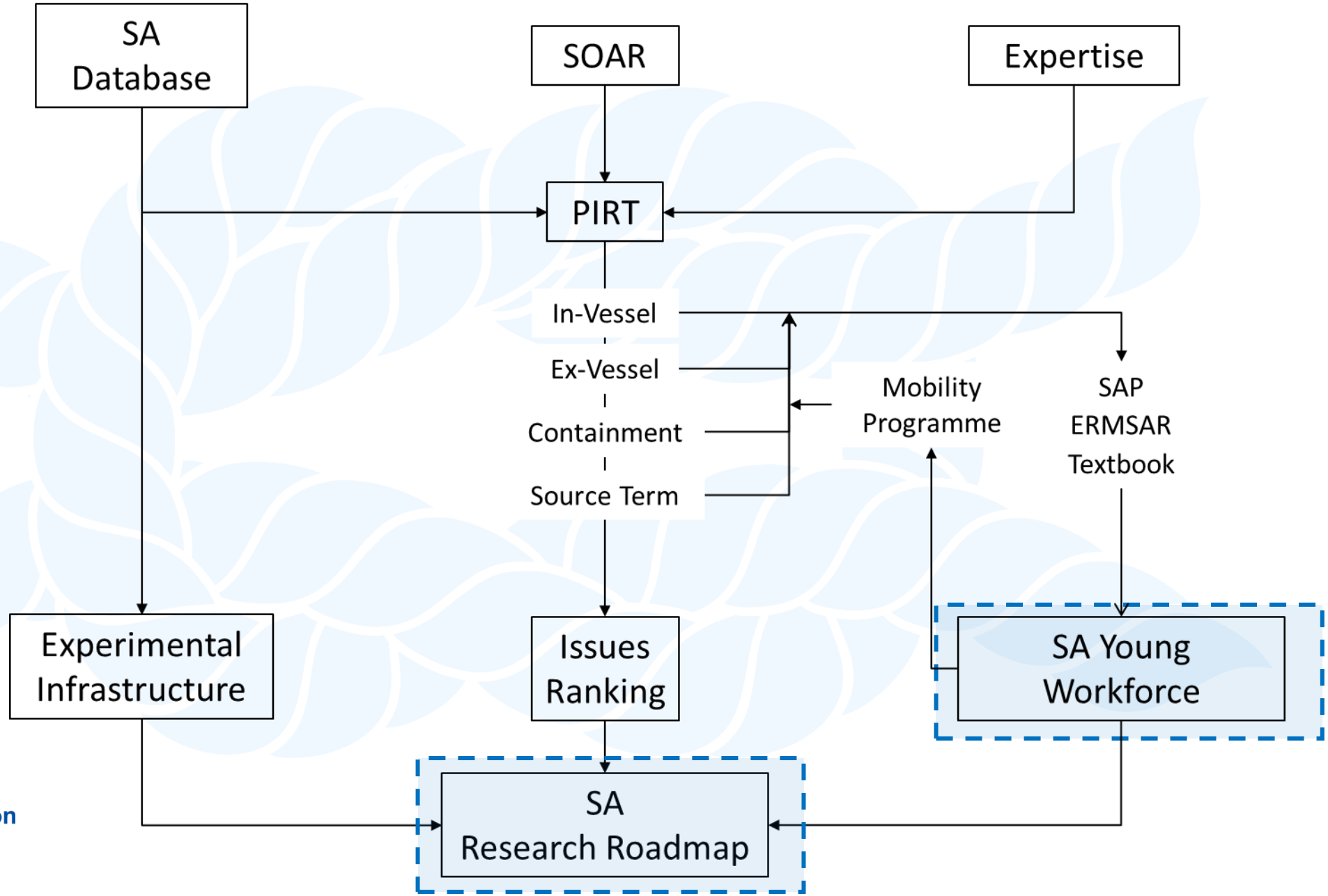

Funded by the European Union



SEAKNOT

www.seaknot-project.eu

THE SEAKNOT WEBSITE

The aim of the four-year project is two-fold: to shape up a roadmap for severe accident research in the coming 10 years by means of which to achieve both a substantial reduction of remaining uncertainties and a measurable progress in the practical elimination of radiological consequences; and, no less important, to efficiently manage the knowledge and knowhow transfer to the young generation of nuclear scientists and engineers who will be involved in its implementation.

Coordinated by CIEMAT (Spain), SEAKNOT is constituted by seventeen well-known organizations from ten countries.

Funded by
the European Union

THANK YOU!

Get in touch for more information

All of the reports of the project will be available for download on the SEAKNOT website: **www.seaknot-project.eu**

Project coordinator: Luis Enrique Herranz, CIEMAT
Contact us: **contact@seaknot-project.eu**

Follow us on LinkedIn!
@seaknot-eu

Funded by the European Union

SEAKNOT

ASTEC core degradation calculations in support of Level-2 Probabilistic Safety Assessment for 1300MWe French reactors: methodology and preliminary results

M. Monestier, L. Bellenfant, G. Kioseyian, L. Foucher and L. Laborde
Institut de Radioprotection de Sûreté Nucléaire (IRSN)
31, avenue de la Division Leclerc – 92260 – Fontenay-aux-Roses – France
Corresponding Address
mathieu.monestier@irsn.fr;

ABSTRACT

The Institute for Radiation Protection and Nuclear Safety (IRSN) in France has updated its Level-2 Probabilistic Safety Assessment (L2 PSA) for the French 1300MWe Pressurized Water Reactors (PWRs) as part of the decennial safety reevaluation for these specific reactor units. This study was particularly underpinned by computations performed using the IRSN ASTEC V2.2 code. ASTEC, which stands for Accident Source Term Evaluation Code, is the reference integral code employed by IRSN for modeling and predicting the progression of severe accidental sequences. Within this framework, IRSN has conducted a total of 554 simulations of accidental sequences, for both conditions of 100% Nominal Power and of reactor shutdown. These accidental sequences have been defined based on the IRSN results of Level-1 PSA. They encompass the entire spectrum of events starting from initiating event to the point of vessel rupture. Furthermore, these simulations implement state-oriented Emergency Operating Procedures (EOPs) and Severe Accident Management Guidelines (SAMGs). This paper presents the different calculations carried out, outlines the methodology used to define them and the primary outcomes derived.

KEYWORDS
Severe Accident, L2 PSA, PWR, ASTEC, SAMG

1. INTRODUCTION

The IRSN has completed a comprehensive update of its Level-2 Probabilistic Safety Assessment (L2 PSA) for the 1300 MWe Pressurized Water Reactors. This update is part of the ten-year safety review of these reactors, aiming to incorporate the latest advances in safety methodology.

The goal of this Level-2 Probabilistic Safety Assessment is to provide, for the accident sequences identified by the Level-1 PSA, the failure modes of the containment during the progression of a severe accident, the magnitude of the releases into the environment, and the associated probabilities.

A key step in this L2 PSA was to perform thermohydraulic and core degradation calculations for as many representative sequences as possible of those identified by the Level-1 PSA. To this end, IRSN used its ASTEC V2.2 code, which serves as the integral reference code for modeling and predicting the progression of severe accident sequences. In this context, a series of 554 simulations of accidental sequences from initiating events to reactor vessel failure were conducted.

This paper presents the tools and the methodology used for these calculations, as well as the different simulation hypotheses. It also provides an overview of the results, thus offering a basis for more in-depth analysis and perspectives that can contribute to the improvement of the safety of French PWRs.

2. FRENCH PWR 1300 MODELING WITH ASTEC

2.1. ASTEC code

ASTEC (Accident Source Term Evaluation Code) [1] is the IRSN reference integral code to model and predict the progression of severe accidental sequences and associated environmental source term. Developed for many years by IRSN, its models reflect the state-of-the-art knowledge on severe accidents and are continuously updated and validated against experimental results and benefit from the experience of international collaborations around ASTEC developed in the European Framework Programs. Its modular structure facilitates its validation by comparing simulation results to experimental outcomes. The different ASTEC modules are shown in the Figure 1.

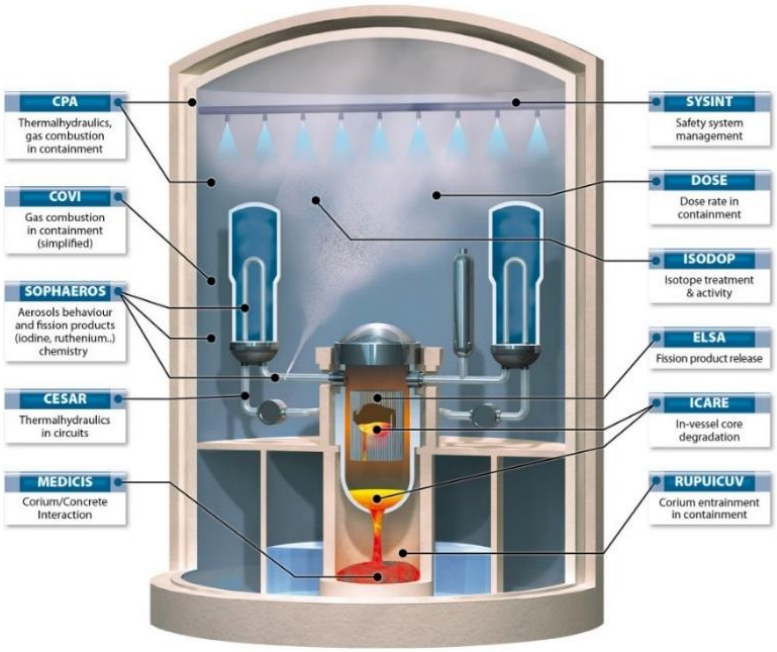

Figure 1. ASTEC modules

2.2. Models and main assumptions

2.2.1. Primary and secondary circuits

The two-phase thermohydraulic of the primary and secondary circuits of the reactor is performed by the CESAR module. The thermohydraulic modeling of the primary and secondary circuits is based on one-dimensional discretization (except in the core where it is two-dimensional) with a numerical approach involving 6 equations. The six-equation two-phase model and the interface temperature model are essential for 'Shutdown States' sequences characterized by low speeds and pressures, separated phases, and non-condensable, as well as for reflooding sequences. Moreover, with the intention of unifying the models used, the six-equation model is also employed for 'Power States' sequences. This model has been validated through experimental tests and is presented in documents [2], [3] and [4].

The primary circuit of the 1300 MWe PWR dataset is discretized into 12 volumes, while the secondary circuit is discretized into 5 volumes.
For initial shutdown states, the Reactor Shutdown Cooling System (RRA) and the Intermediate Cooling System (RRI) have been modeled with the CESAR module. The RRA system consists of 2 identical paths, each mainly comprising an aspiration line on 2 hot legs, 1 circulation pump, 1 heat exchanger (with the RRI), an RRA valve, and a discharge line on 2 cold legs.

The mass, residual power, and activity of fission products and actinides in the degraded core, primary circuit, containment enclosure, as well as in the environment are calculated by the ISODOP module. It particularly assesses the transmutation and natural decay of several thousand isotopes.

The transport and chemical behavior, in the primary and secondary circuits and in the containment, of vapors and aerosols formed by the condensation of fission products released during core degradation is calculated with SOPHAEROS. It specifically calculates the retention of radionuclides in the primary circuit as well as the size of aerosols and their chemical speciations in the containment and at the level of primary breaches, which could lead to a modification of their behaviors.

2.2.2. Containment enclosure

The containment of the French 1300 MWe reactors is ensured by an internal enclosure and an external enclosure, both made of concrete, separated by a space between enclosures maintained under negative pressure, allowing the collection and filtration of any potential releases.
The conditions within the containment enclosure (thermohydraulics, hydrogen risk, etc.) is evaluated by the CPA module. It includes modeling of passive hydrogen recombiners. Furthermore, the CPA module simulates leaks from the Inner Containment to the Space Between Containments, the environment, and the surrounding buildings.
In the dataset, the containment enclosure of the 1300 MWe PWR is discretized into 19 compartments (18 compartments for the inner containment and 1 for the space between containment). Surrounding buildings and the environment are represented by an additional 5 compartments.

The CPA module is coupled with the COVI module. If the ignition criteria are met in at least one area of the containment, the COVI module provides the value of the peak pressure generated by the adiabatic and isochoric combustion of all the hydrogen present in the containment. The peak pressure value calculated by COVI is an enveloping value in the case of a slow deflagration only.
The results of COVI do not impact the thermohydraulic calculation of the CPA module (no feedback): the calculation of the accidental sequence continues beyond the virtual combustion without considering this potential combustion.

To estimate the dose rate in each compartment constituting the containment enclosure the DOSE module is used. It also calculates the dose rate on the internal walls of each area of the containment enclosure. Both β and γ emitters are considered in the dose rate calculation.

2.2.3. Core Degradation

The ICARE module models the core degradation in a severe accident situation. This module invokes the ELSA module, which calculates the release of fission products and materials from the core structure. Numerous models are utilized from the onset of degradation, covering aspects like cladding burst, oxidation of components, flows of molten materials, etc., up to advanced degradation: potential formation of a corium pool, corium flow to the bottom of the vessel, and vessel rupture.
Due to insufficient cooling, the core and vessel components degrade and transform into magma and debris. The bottom-of-the-vessel model in ASTEC V2.2, depending on the simulated transient, considers up to 5

distinct layers of corium: 1 to 3 dense layers of magma surrounded by two layers of debris beds. As the vessel, internal structures, and debris bed particles melt, their components are transferred into the dense magma layers in contact. Regarding mass transfers between corium layers at the bottom of the vessel, a detailed phase separation model is used.

The Corium-Concrete Interactions (CCI) in the reactor vessel pit (and potentially other areas) is calculated by the MEDICIS module.

2.2.4. Induced break model

During a core meltdown accident, part of the power in the uncovered core areas is dissipated by natural convection. The hot gases exiting the core move towards the cooler areas of the primary circuit, thus forming natural convection circulation loops.

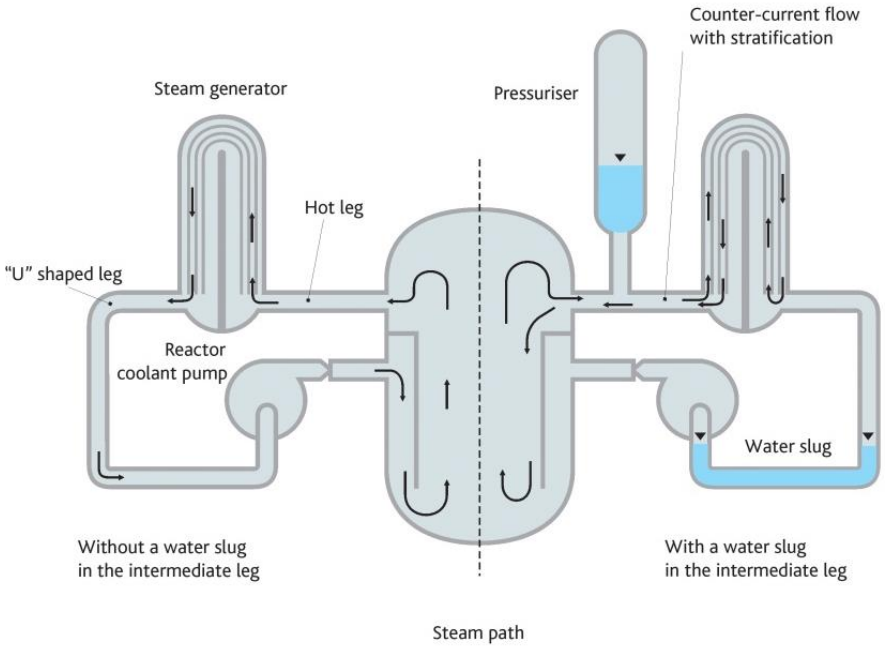

Figure 2. Modes of steam circulation in the RCS

As show at the Figure 2, there are two modes of steam circulation in the primary circuit:

- Without a water plug in the U-tube, the gases exit the core pass through the Hot Leg (HL), then through the Steam Generator (SG) tubes, then through the intermediate branch, and then through the Cold Leg (CL) before being reinjected into the lower part of the core.
- With a water plug in the U-tube, the steam circulation is blocked: the gases exit the core pass through the HL and some of the SG tubes (direct tubes) where the gases were cooled down. Once cooled, the gases use the other SG tubes (indirect tubes) to go back. Thus, in the HL, there are two directions of gas flow (the hot gases flowing from the reactor vessel to the SG in the upper part of the HL and the cooled gases flowing from the SG to the reactor vessel in the lower part of the HL)

The current version of the code and dataset do not allow modeling the two-way flow when there is a water plug in the U-tube. As these situations can be encountered for pressurized core melt scenarios, the modeled flow is therefore incomplete and could underestimate the heating of the hot legs and SG tubes in these situations, where the risk of induced breach opening (in the hot leg or on an SG tube) is important. The possible occurrence of induced breaks is therefore delayed.

Because of these limitations, the PSA uses an additional specific model, based on previous studies, to assess the risk of induced breach opening and their location. Thus, in the ASTEC calculation, even if induced breaches model is activated their opening section is set to zero, in order to continue the calculation as long as possible, to have the primary conditions data for the dedicated induced break model.

The locations of the induced breaks correspond to the "weak" points identified in the primary circuit: on the primary hot legs, on the SG tubes and on the pressurizer surge line.

2.2.5. Primary pumps seals leak

Based on recent technological advancements in primary pump seals and new loop tests (Karlstein tests from 2014 to 2020), a new and more representative model for leak rates at primary pump seals has been implemented in ASTEC. This model, known as the "Karlstein model," considers the evolution of the leak rate at primary pump seals during the accidental transient, depending on the thermohydraulic conditions of the primary circuit.
This model is applied in scenarios where the primary pump seals are not cooled, specifically in sequences of small primary breaches and in sequences with SG tube ruptures.

2.2.6. Safety Injection system failure for high sump temperature

The primary purpose of the Containment Spray System (CSS) is to mitigate the consequences of a severe accident by reducing the pressure and temperature within the containment building, and by scrubbing and washing out radioactive particles from the containment.
For sequences in which the CSS is unavailable, due to the increasing temperature inside the containment, it is considered in this study that the Safety Injection System also fails from the following instants:

- when a temperature of 120°C is reached for the medium pressure injection system (ISMP) and 140°C for the low-pressure injection system (ISBP) in the sumps,
- 24 hours of Safety Injection System (SIS) recirculation operation after the CSS loss.

2.2.7. Ultimate Backup Diesel (DUS) and Combustion Turbine (TAC)

After the Fukushima-Daiichi accident, an additional power source, the Ultimate Backup Diesel (DUS),was installed in the French nuclear reactors to supply backup systems in the event of a loss of internal power supplies,. Additionally, each power plant is equipped with a common internal ultimate backup power source for all its reactors, the Combustion Turbine (TAC).
In the ASTEC dataset, and for some sequences with a total loss of electrical power, for the L2 PSA purpose, it was assumed that the DUS and TAC allow the recovery of certain systems, previously unavailable, 4 hours after the start of the accident.

2.2.8. Stop criterion for ASTEC calculations

In this study, 3 types of scenarios have been considered: scenarios with core degradation and no induced breaks, scenarios with core degradation and induced breaks, and scenarios without core degradation.
For scenarios with core degradation and no induced break, ASTEC calculation is stopped when 200 tons or more of corium is released from the reactor vessel, or 24 hours after the vessel failure (to study the secondary flows of corium out of the vessel).
For scenarios without core degradation after 7 days, ASTEC calculation is stopped. It is considered that beyond this delay, the restorations and repairs are sufficient to prevent core meltdown.

For sequences meeting the criteria for induced breach opening, the calculation is stopped at the vessel rupture. Indeed, due to the non-opening of the induced breaks in the calculation, the end of the degradation is not considered realistic, and anything simulated after the vessel rupture would not be relevant.

2.3. Operating procedures

Due to the significant number of calculations required for this support study (554 accidental scenarios), it was necessary to automatize the drive actions of EOPs (Emergency Operating Procedures) and SAMGs (Severe Accident Management Guidelines) into the ASTEC data set.
The correct application of theses operating procedures was then subject to a comprehensive validation, as well as a verification on several in-power and shutdown state scenarios.

2.3.1. Emergency Operating procedures (EOPs)

The state-based approach involves applying procedures that are developed based on the identified physical state of the reactor, regardless of the events that led to that state.
All EOPs documents are composed of modules and tests that define the steps to be taken to safeguard the reactor. To adapt theses operating procedures to the modeling capabilities of the reactor by ASTEC, several hypotheses have been developed and serve as the basis for simplifying the EOPs (for example some systems are partially or not modeled).
The coding of the operation is based on the SENSOR objects of the ASTEC code. These SENSORS are used to define real variables that are used for the management of systems, alarms, automatisms, and operating procedures.
In this study, EOPs operation are halted upon reaching the first criterion between the very high dose rate in the containment (dome or upper annular space) and the exit temperature from the core (TRIC) exceeding 1100°C.

2.3.2. Severe Accident Management Guidelines (SAMGs)

When the operators conclude the EOP operations, they implement the SAMGs procedures. This SAMG is a post-accident management approach for scenarios with core meltdown, defining recommended actions. The purpose of SAMG is to minimize real-time expert debates and to promote quick and effective decision-making.
Thus, the objectives of SAMG are:

- to prevent or minimize radioactive releases outside of the containment,
- to allow sufficient time before potential loss of containment for implementing population protection measures under emergency plans,
- to bring the unit back to a controllable situation (residual heat removal, submerged corium).

For this study, as for EOPs actions, SAMGs actions were coded based on operators' documents.
Implementation timelines, depending on the plant's situation and system availability (action execution locally or in the control room), were estimated and implemented in the ASTEC input deck. Finally, in situations with total loss of electrical power, field agents and their availability are modelized in the input deck for executing actions locally.
The main immediate actions include stopping the primary pumps and heaters, opening the pressurizer discharge line valves, deisolating the accumulators, managing water make-up operations, isolating the cooling circuit, etc. The main deferred actions concern the management of water supply operations and containment spray system, replenishing the Auxiliary Feed Water (AFW) tank, and managing ventilation of peripheral buildings.

3. Connection with Level-2 Probability Safety Analysis

3.1. Methodology to select scenarios

The ASTEC simulations in support of the L2 PSA are defined with the Plant Damage State (PDS) list, that is the result of the interface between L1 and L2 PSA. Each PDS is defined by a large set of interface variables attributes, some of them containing useless information for ASTEC simulation. For example, the status of the containment isolation system is only considered in the Accident Progression Event Tree (APET) and is not useful for ASTEC. Therefore, different PDS may be associated to the same ASTEC simulation. Thus, it appears necessary to have a strong and efficient bridge between PDS and definition of ASTEC simulated sequences. To facilitate this task, the IRSN L2 PSA team has specifically developed a graphical interface, presented in [5].

3.2. Selected scenarios

A total of 345 scenarios (261 power states and 84 shutdown states) were defined from around 10,000 PDS. These scenarios are grouped into families of accidents and differ from each other based on the initiating events leading to the accident (breaches, system availability, human errors, etc.). These scenarios are presented in the Tables I and II.

Table I. Power states scenarios selected for the PSA-2 Studies

Scenario type	Number of scenarios	Sub-scenario type	Description
Loss of Coolant accident (LOCA)	120	Intermediate breach	Break from 2.55” to 4.123”
		Small breach	Break from 0,6173” to 0,8344” (on HL or on primary pumps seal)
		Steam breach	1 PZR valve blocked open
		Large breach	10.512” break (on CL or HL)
		Very Large breach	Guillotine break (on CL or HL)
		Very small breach	0.265” break on CL
		Leak at the seals of the primary pumps	0.6173” or 0.8344” break for each primary pump
Primary circuit intact	99	SG Auxiliar Feed Water is unavailable	With possible leaks at the seals
		SG Auxiliar Feed Water is available	With possible leaks at the seals
		Refilling auxiliar feed water tank is unavailable	With possible leaks at the seals
Steam generator tube rupture	25	Steam generator tube rupture	Rupture of 1 or 2 steam generator tubes
		Steam generator tube rupture and steam pipe rupture	Rupture of 1 steam generator tube cumulated with steam pipe rupture
Secondary pipe rupture	14	-	Break inside or outside the confinement enclosure
Loss of Coolant accident outside confinement enclosure	3	-	A small primary break located at the thermal barrier of the primary pump motor group in loop 2 leading to the rupture of the RRI circuit and a breach extending outside the containment

Table II. Shutdown states scenarios selected for the PSA-2 Studies

Shutdown states	Number of scenarios	Scenario type	Description
AN/RRA1	4	Break on the cooling circuit	3.021" to 10.512" break
		Steam break	One PZR valves blocked open
AN/RRA3	13	Primary circuit intact	-
		Break on the primary circuit	1.093" break
		Break on the cooling circuit	1.093" break
API2/3/4 (Shutdown for maintenance)	67	Primary circuit intact	-
		Break on the primary circuit	2.121" break
		Break on the cooling circuit	2.121" break

Among the 345 scenarios calculated for this study, not all lead to an accident with core melt. For each sequence leading to core melt, two calculations are performed: one without applying the SAMGs procedure and one applying the SAMGs procedure. In total, this study includes 554 accidental scenarios calculated with ASTEC V2.2.

4. RESULTS OVERVIEW

4.1. Core meltdown scenarios

For all the scenarios selected for this support study to the PSA-2 for 1300 MWe reactors of the French fleet, ASTEC V2.2 calculations were carried out until one of the predefined stop criteria was reached.
For the 261 scenarios where the initial state of the reactor is at power, ASTEC V2.2 calculations lead to core degradation in 136 scenarios, representing 92% of the total Core Damage Frequency (CDF) for power states, while 125 scenarios are stopped 7 days after the initiating events, without core meltdown, representing only 8% of the total CDF for power states.
For the 84 scenarios where the initial state of the reactor is in shutdown, ASTEC V2.2 calculations lead to core degradation in 73 scenarios, representing 94% of the total CDF for shutdown states, while 11 scenarios are stopped 7 days after the initiating events, without core meltdown, representing only 6% of the total CDF for shutdown states.

4.2. Induced breaks and water plugs

As previously mentioned, in this study it was decided to keep the induced breach model activated in the ASTEC V2.2 code despite the underestimation of steel temperature due to the double flow caused by the presence of water plugs. However, a zero section was systematically imposed. This was done to detect the achievement of criteria at the 9 identified weak points on the primary circuit (primary hot branches, steam generator tubes, and pressurizer expansion line). Therefore, there is no actual opening of the induced breaches. In case these criteria are met, the presence of potential water plugs in the primary circuit is indicated, and the calculations are stopped at the vessel's failure.

For all 136 power state scenarios leading to core melt, 48 scenarios meet the criteria for an induced breach occurrence. These sequences represent 29.7% of the total CDF for power states.
According to ASTEC v2.2 calculations, the most likely scenario families to present induced breaches are the followings:

- Intact primary circuit with possible leaks at the primary pump seals.
- LOCA with very small breaks in the primary circuit.
- Steam Generator Tube Rupture.

- Secondary piping rupture, with a small break in the containment.

Among the 48 scenarios showing criteria for the occurrence of an induced breach, there are 22 scenarios where induced breaches appear on the pressurizer surge line (representing 14% of the total power states CDF), 26 scenarios present induced breaches on hot leg (representing 15% of the total power states CDF).

The Figure 3 indicates the value of the primary pressure when the criteria for opening an induced breach are met for the 'Power States' sequences, depending on the location of the induced break.

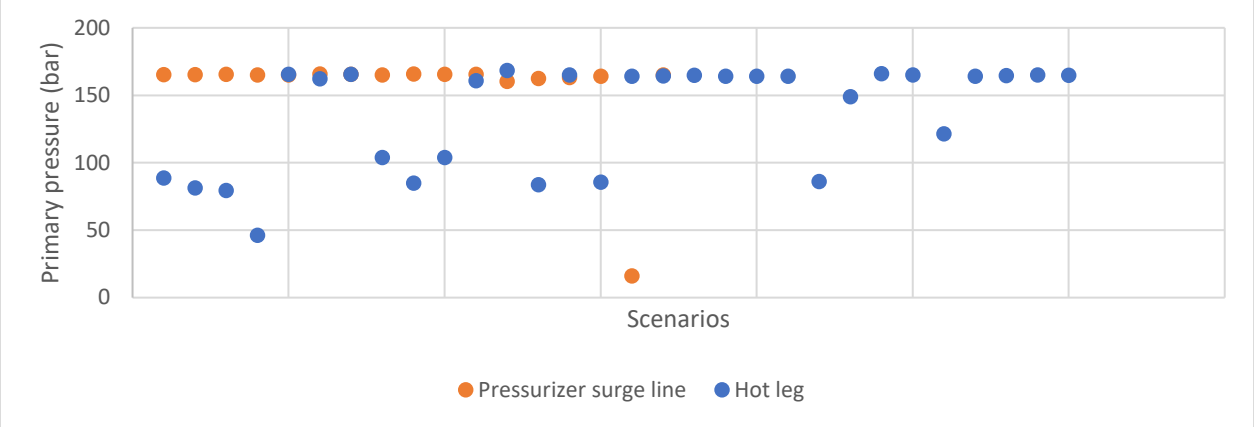

Figure 3. Primary pressure at the opening an induced break for the 'Power States' scenarios

Almost all scenarios that meet the criterion for opening an induced break on the pressurizer surge line exhibit very high primary pressure, exceeding 160 bar. Meanwhile, those with the criterion for opening an induced break on the hot leg present primary pressures between 80 and 160 bar.

4.3. SBO scenarios and recovery of water injection systems during SAMGs

For reference cases, meaning without considering Severe Accident Management Guidelines (SAMGs) actions, 136 'power state' scenarios and 73 'shutdown state' scenarios lead to core meltdown. These sequences have been subject to additional calculations with ASTEC V2.2, considering the application of the (SAMGs).
Only a limited number of the foreseen SAMGs actions have a significant influence on the degradation phases of the sequences calculated with the ASTEC V2.2 code:

- the opening of pressurizer surge line valves,
- initiating maximum cooling through the still available SGs,
- the discharge of accumulators,
- the management of water injection systems such as the Chemical and Volume Control System (CVCS), SIS, and CSS.

These actions can change the characteristic moments of the accident scenario (for example, by delaying the moment of vessel rupture) and modify numerous physical parameters (primary pressure at vessel rupture, H_2 production and hydrogen risk, corium mass at the bottom of the vessel, etc.).
In this study, the Ultimate Diesel Generators (DUS) and/or the Emergency Power Supply (TAC) are recovered 4 hours after the initiating events (L2 PSA assumption) in 12 “Power State” scenarios. In these scenarios, the end criteria for the EOPs operation are met before this 4-hours limit (high-level dose rate or TRIC temperature exciding 1100°C). Therefore, in these calculations, after the end of EOPs operation and without the SAMGs operation, systems that could be recovered using the DUS and TAC, such as the CVCS,

are never recovered. On the other hand, in calculations that consider SAMGs operation, the CVCS can be recovered and can delay the progression of the degradation phase.
Table III presents the main results of 3 scenarios among the 12 discussed previously.

Table III. Impact of recovering water injection systems during SAMGs on the timing of vessel rupture for 3 scenarios

Scenario name	Scenario type	Time of end of EOP application	Time of vessel rupture (without SAMGs)	Time of vessel rupture (with SAMGs)	Accumulator volume of injected water (m^3)	CVCS volume of water injected (m^3)
LOCA_PP_14	LOCA with break at primary pumps seals + SBO	2h 44min	4h 28min	8h 57min	Full accumulators discharge	236
PCint_2_4	Primary circuit intact with leaks at primary pumps leaks + SBO	2h 52min	4h 23min	5h 48min	Full accumulators discharge	40
PCint_1_7	Primary circuit intact with leaks at primary pumps leaks + SBO	1h 41min	7h 18min	3days 12h	109	2844

For LOCA_PP_14 and PCint_2_4 scenarios, the primary pressures at the exit of the EOPs procedure are respectively 120 and 160 bar. The opening of the PZR surge line valves allows to reduce primary pressure and thus allows the full discharge of water accumulators. The CVCS is put into operation with a maximum injection flow rate. All these actions will not be sufficient to prevent the rupture of the vessel, which occurs before the complete emptying of the RWST (Refueling Water Storage Tank).
However, these actions have significantly delayed the moment of the reactor vessel rupture, by approximately 1 hour and 30 minutes for the PCint_2_4 scenario, and by 4 hours and 30 minutes for the LOCA_PP_14 scenario.

In the PCint_1_7 scenario, the primary pressure at the exit of the EOPs procedure is around 35 bar. The PZR surge line valves are already open, and about 100 m^3 of water are still present in the accumulators and will be injected in the primary during the SAMGs procedure. Moreover, the injection of water by the CVCS system at a maximum flow rate delays by more than 3 days the rupture of the vessel, which occurs after the complete emptying of the RWST (2850 m^3). An additional calculation has shown that by limiting the flow rate of the CVCS charge, this sequence could be stabilized in 5 days. However, the injection of water via the accumulators and the CVCS during the degradation phase while applying the SAMGs has no significant impact on hydrogen production in the vessel or the amount of corium at the bottom of the vessel, as shown in the Table IV.

Table IV. Impact of recovering water injection systems during SAMGs on the H_2 mass production and the mass of corium in the vessel

Scenario name	H_2 mass produced (kg)		Mass of corium at the bottom of the vessel (metric ton)	
	Without SAMGs	With SAMGs	Without SAMGs	With SAMGs
LOCA_PP_14	590	600	130	130
PCint_2_4	600	510	60	60
PCint_1_7	690	730	130	110

4.4. Main conclusions about SAMGs application for power state scenarios

The Table V presents the effects of the main SAMG actions on several key parameters that are characteristic

of accidental scenarios. It is particularly noticeable that the deisolation and complete discharge of the accumulators are always beneficial. This action significantly delays the vessel rupture moment without significantly increasing the hydrogen risk. Moreover, opening the pressurizer surge valves is always a favorable action. It delays the vessel rupture while depressurizing the primary circuit. However, it should be noted that the late opening of the pressurizer valves can have a negative impact on the hydrogen risk. Furthermore, opening these valves in conjunction with water injection via accumulator discharge can delay vessel rupture, but may have a negative effect on the hydrogen risk.

Table V. Main conclusions about SAMGs actions

SAMGs actions	Time between the end of EOPs and vessel rupture	Primary pressure at vessel rupture time	Hydrogen risk before vessel rupture
Deisolate and complete discharge of accumulators before vessel rupture (13 scenarios)	Significant increase (>10%), especially with high accumulator water mass for 10 scenarios	Pressure remains < 10 bar No impact clearly identified	Maximum PAICC remains < 4 bar PAICC decreases by more than 10% for 8 scenarios
Maximum cooling with SGs (3 scenarios)	Significant increase for 1 scenario (Low residual power at the end of EOPs)	Pressure < 20 bars with SAMGs actions	Maximum PAICC < 4.5 bar Small impact on PAICC
Enabling CVCS after DUS/TAC starting (1 scenario)	Vessel rupture is delayed by 2 days (possibly 5 days if CVCS is not set at max flow rate)	Decrease from 12 to 7 bar	No more hydrogen risk (without SAMGs action, max PAICC was 5.2 bar)
Opening PZR valves without water injection (6 scenarios)	Increase (>10%) for 3 scenarios	Significant decrease, Pressure <20 bar for 5 scenarios, 40 bar Pressure for one scenario (PZR valve open just before vessel rupture)	No impact for 5 scenarios, 15% PAICC increase for 1 scenario
Opening PZR valves combined with accumulators' discharge (11 scenarios)	Increase (>10%) for 9 scenarios	Significant decrease	No more hydrogen risk for 2 scenarios, Increase of hydrogen risk for 8 scenarios, Max PAICC > 5 bars for 7 scenarios

4.5. Description of the PSA-2 prevailing scenario

The scenario discussed in this section is of particular interest, as it was by far the most probable accidental sequence, representing 43% of the total core melt frequency of this PWR 1300MWe PSA 2.

This is a sequence of loss of electrical power with 4 leaks at the primary pump seals of 5 t/h (0.0803 inches per breach, or 0.13 cm^2). No safety system is operational. The SGs are unavailable and thus the impossibility to cool the primary circuit. The 3 pressurizer relief valves operate on battery power. Therefore, in this sequence, only the pressurizer relief valves can potentially open before the battery discharge, and only the passive accumulators can inject water. The table VI presents the main characteristics times of this scenario.

Table VI. Main characteristics times

Instant	Event
23min	Application of EOPs
42min	The 4 GVs are isolated
52min	PZR valves are opened
1hr	PZR valves 1 is out of battery and will remain opened
1hr11min	PZR valves 2 and 3 in neutral position
1hr17min	Start of core uncovering
1hr25min	Opening PZR valves 2 and 3
1hr36min	Accumulators discharge
1hr42min	Reach of criteria TRIC>1100 and stop of EOPs application
2hr	PZR valves 2 and 3out of batterie and will remain opened
6hr22min	End of accumulator's discharge
6hr45min	First corium pour into the vessel's lower cavity (at least 10 tons)
6hr46min	60 tons of corium into the vessel's lower cavity
6hr53min	Vessel failure

With the SG levels assumed to be unavailable, the reactor operator is quickly directed to the appropriate procedure, asking for the PZR valves opening, and the steam operator must isolate the SGs that have become unavailable. With no cooling from the SGs and no water injection to compensate for the water lost through leaks at the seals and PZR valves, the primary circuit level dropped, and the core was uncovered about 1hour after the initiating event.

At 1 hour and half, the accumulators start to discharge their water and the end criterion for the EOP is reached about 10 minutes after. The first pour of corium (more than 10 tons) into the bottom of the vessel occurs at 6 hours 45 minutes. The rupture of the vessel occurs few minutes later, the primary pressure is around 20 bar and about 80 tons of corium are ejected from the vessel, with 50 tons going towards the vessel pit, the rest being sprayed by DCH (Direct Containment Heating) into the inner containment. Two additional pours of about 15 and 65 tons occur into the vessel pit subsequently around 7 hours and 12 hours after the initiating event. The collapse of the vessel happens at 12 hours and 45 minutes. Finally, 175 tons of corium pours have exited the vessel 24 hours after its rupture, and about 500 tons of corium stay in the vessel bottom.
The Figure 4 presents the evolution of the primary pressure and corium mass in the vessel's lower plenum.

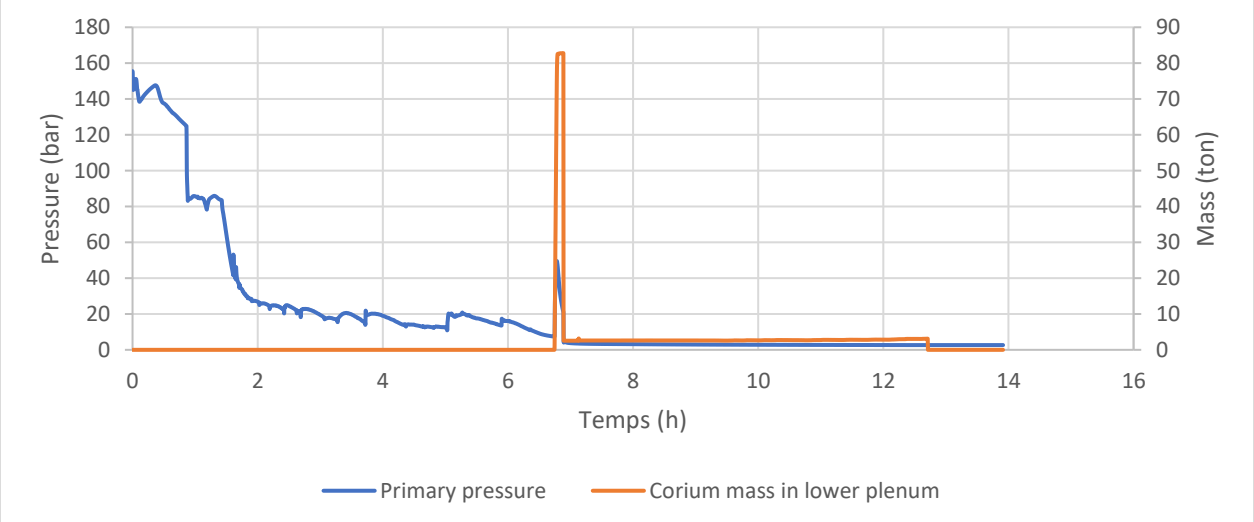

Figure 4. Evolution of the primary pressure and corium mass at the bottom of the vessel

During the degradation phase, the PZR relief valves are open, but the primary pressure remains high, around 20 bar. When reaching the TRIC 1100 criterion, the primary pressure is around 40 bar. Before the corium pours into the bottom of the vessel at 6 hours 45 minutes, the primary pressure is around 8 bar, and it abruptly increases when the corium pours into the bottom of the vessel (80 tons) up to 50 bar. It then decreases following the opening of the PZR valves, but, at such pressure with the current mechanical models of the vessel, the rupture of the vessel occurs rapidly. Subsequently, the primary pressure is still at 20 bar at the time of the vessel rupture implying a risk of DCH (Direct Containment Heating), which could potentially lead to the destruction of the containment.
The Figure 5 presents an ASTEC visualization of the core degradation.

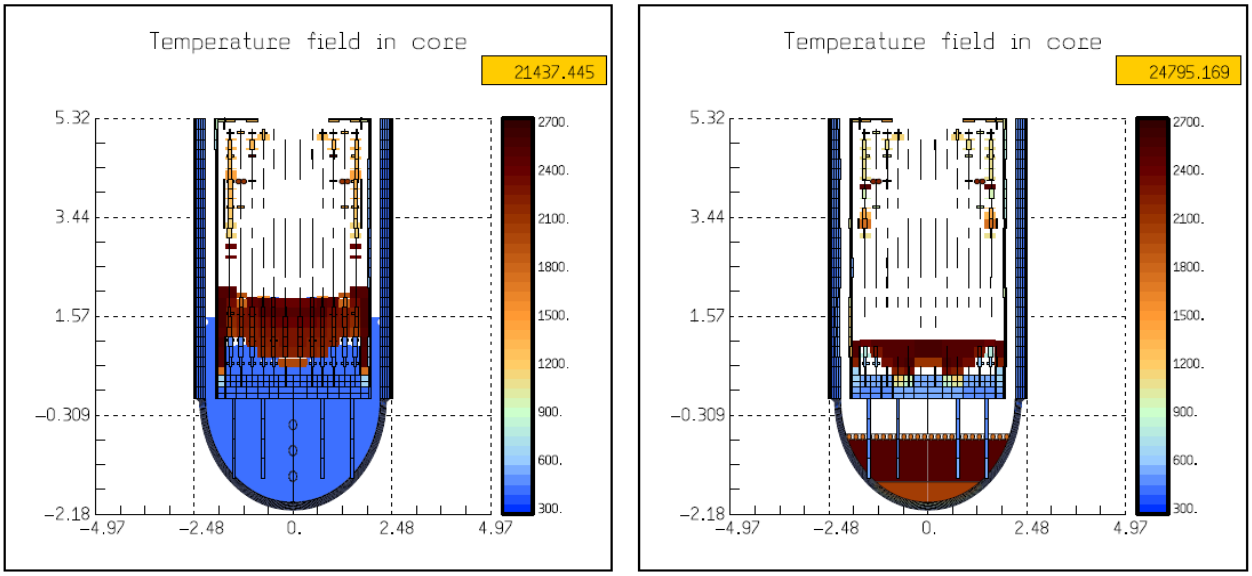

Figure 5. Core degradation at 5h57 (left) and at 6h53 (right)

One of the main reasons for this risk of DCH is the rapid rupture of the vessel following the relocation of corium to the bottom of the vessel (only 8 minutes between the two events). This delay, estimated by the ASTEC V2.2, is quite penalizing, and there are many uncertainties regarding whether the vessel will hold or not. With a slightly longer delay between these two events, the primary circuit would have had time to continue depressurizing via the PZR valves, and the risk of DCH would have been reduced.
Besides, a significant hardware modification on the PZR valves have been deployed in the framework of the post-Fukushima upgrade for the 1300 MWe reactors and are not fully modeled in this ASTEC input deck. These modifications allow for a faster depressurization of the primary circuit. For example, considering these modifications in the specific scenarios studied previously enables to reduce the primary pressure at the vessel failure and thus allow excluding the DCH risk.
Furthermore, an earlier start of the DUS and TAC prevents core meltdown.

5. CONCLUSION

This study has provided a comprehensive overview of accidental scenarios related to the 1300MWe reactors in the French nuclear power plant, employing the methodology of Level-2 Probabilistic Safety Assessment (PSA-2).
The 554 simulations conducted with the ASTEC V2.2 code allow quantifying various physical phenomena impacting the primary circuit, reactor vessel, secondary circuit, and containment structure. Among these 554 simulations, many scenarios identified as potentially leading to core meltdown by the Level-1 PSA do not lead into a core meltdown situation according to the ASTEC V2.2 calculations.

EOPs and SAMGs driving procedures were coded and implemented into the ASTEC input decks to simulate all operational actions. They have been subjected to validation and verification across many scenarios, both for power and shutdown states. The impact of the main actions carried out within the framework of the SAMGs application have been evaluated on a significant number of accident scenarios.

The results highlight the significance of ongoing material modifications as part of the post-Fukushima and the 4th decade inspection of the 1300MWe reactors allowing reducing the likelihood of a severe accident occurring and to lessen the consequences of a severe accident for both populations and the environment.

Ultimately, these findings provide crucial insights for the updating of the Probabilistic Safety Assessment for the 1300MWe reactors, contributing to the enhancement of nuclear safety and informing future decisions regarding reactor design and operation.

NOMENCLATURE

AFW	Auxiliar Feed Water
ASTEC	Accident Source Term Evaluation Code
CDF	Core degradation frequency
CL	Cold Leg
CSS	Containment Spray System
DUS	Diesel Ultime de Secours (in French)
EOP	Emergency Operating Procedures
HL	Hot Leg
IRSN	Institut de Radioprotection et de Sûreté Nucléaire
PAICC	Adiabatic isochoric complete combustion pressure
PSA	Probabilistic Safety Assessment
SAMG	Severe Accident Management Guidelines
SBO	Station Black Out
SG	Steam generator
SIS	Safety Injection System
TAC	Turbine à Combustion interne (in French)

REFERENCES

1. P. Chatelard, L. Laborde, “ASTEC V2.2 code validation : illustrative results and main outcomes”, *ERMSAR 2022*, Karlsruhe, May 16-19, 2022
2. I. Gómez-García-Torano and L. Laborde, « Validation of Selected Cesar Friction Models of the ASTECV21 Code Based on Moby Dick Experiments », *Journal of Nuclear Engineering and Radiation Science*, Vol. 5 / 020908-9, 2019
3. I. Gómez-García-Torano and L. Laborde, « Modelling reflooding of intact core geometries in ASTEC V2.1: Improvements and validation on PERICLES experiments », *Nuclear Engineering and Design*, 378 (2021) 111157, 2021
4. I. Gómez-García-Torano, L. Laborde, F. Fichot, and H. Mutelle, « Reflooding of degraded cores in ASTEC V2.1: Modelling and validation on pearl experiments », *Nuclear Engineering and Design*, 393 (2022) 111768, 2022
5. Y. Guigueno *et al.*, « Severe accident risk assessment for NPPs – Software tools and methodologies for level 2 PSA development available at IRSN”, PSAM 13, 2016

RÉPUBLIQUE FRANÇAISE
Liberté
Égalité
Fraternité

IRSN
INSTITUT DE RADIOPROTECTION ET DE SÛRETÉ NUCLÉAIRE

ASTEC core degradation calculations in support of level-2 PSA for 1300MWE French reactors: methodology and preliminary results

Mathieu Monestier
Severe Accident Department

IRSN/FRM-296 ind. 07

MEMBRE DE ETSON

Introduction

- IRSN performed an update of its Level-2 Probabilistic Safety Assessment (L2 PSA) for the 1300 MWe French PWRs

- The goal of L2 PSA is to provide :
  - the failure modes of the containment during the progression of a severe accident,
  - the magnitude of the releases into the environment,
  - the associated probabilities.

- Need to perform thermohydraulic and core degradation calculations
  - Use of ASTEC V2.2 reference code developed by IRSN
  - 554 simulations of accidental sequences from initiating events to reactor vessel failure

Presentation plan

- French 1300 MWe Model with ASTEC and L2 PSA hypothesis
- Connection of this study with L2 PSA
- Selected scenarios
- Results Overview
  - Core Meltdown scenarios
  - Main conclusion about SAMGs application
  - Description of the L2 PSA prevailing scenario
- Conclusion

French PWR 1300 modelling with ASTEC

- ASTEC (Accident Source Term Evaluation Code)
- State-of-art code, validated on 300+ experiments (separate effects, coupled effects, integral tests)
- Modelling the whole reactor :
  - at nominal power (power states)
  - for shutdown states
- Using different ASTEC modules : CESAR, ICARE, CPA, ISODOP, DOSE, COVI, SOPHAEROS, RCSMESH, MEDICIS, RUPUICUV and CORIUM

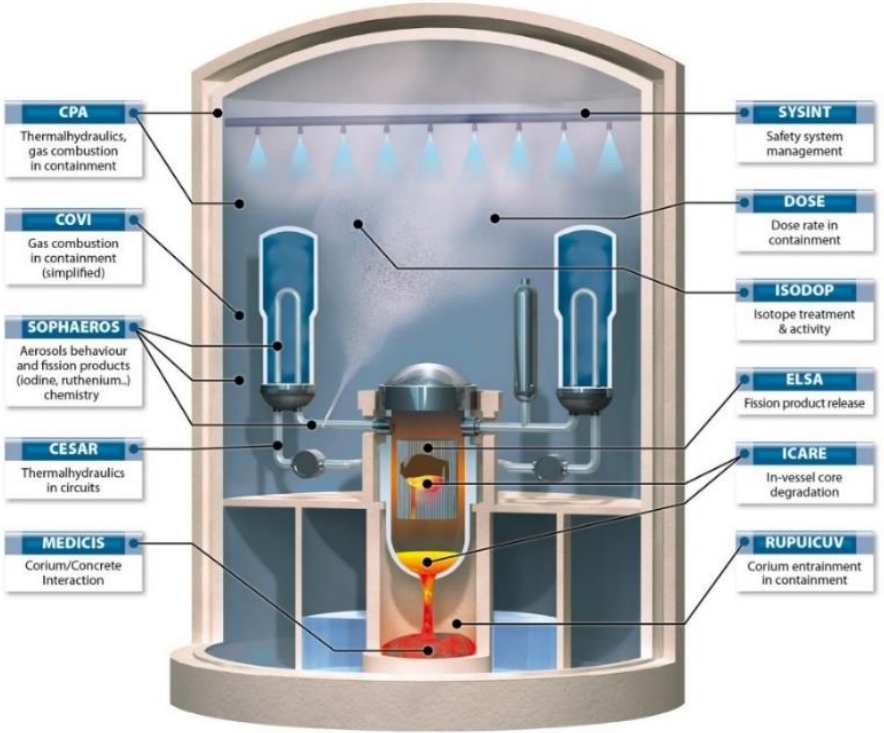

French PWR 1300 modelling with ASTEC

OPERATING PROCEDURES

- 554 accidental scenarios calculations required for the study,

- Need an automation of Emergency Operating Procedures (EOPs) and Severe Accident Management Guidelines (SAMGs) to be implemented in the ASTEC dataset.

- **EOPs :**
  - State-based approach utilized, focusing on reactor's physical state regardless of preceding events.
  - EOPs structured into modules and tests outlining steps to safeguard the reactor.
  - Adaptation of procedures to ASTEC's modeling capabilities involved development of hypotheses and simplifications, considering partially or unmodeled systems.
  - Operation coded based on SENSOR objects in ASTEC, defining real variables for system management, alarms, automatisms, and procedures.
  - In this study, EOPs operations cease upon meeting criteria such as high dose rate in containment or core exit temperature (TRIC) exceeding 1100°C.

French PWR 1300 modelling with ASTEC

OPERATING PROCEDURES

SAMGs :

- Activated by operators after EOP operations to manage scenarios involving core meltdown.
- SAMGs facilitate rapid decision-making, aiming to minimize radioactive releases outside containment and restore control.
- Objectives include containment integrity maintenance, implementation of population protection measures, and restoration of controllability.
- Coding of SAMG actions based on operators' documents, with implementation timelines estimated based on plant's situation and system availability.
- In situations of total electrical power loss, field agents' availability modeled for local action execution.

SAMGs Immediate and Deferred Actions:

- Immediate actions include stopping primary pumps and heaters, opening pressurizer discharge line valves, managing water supplies, and isolating cooling circuits.
- Deferred actions involve water supply management, containment spray system operation, Auxiliary Feed Water (AFW) tank replenishment, and peripheral building ventilation

French PWR 1300 modelling with ASTEC

Starting from the **initiating event** until **200 tons of corium relocated in the cavity** :

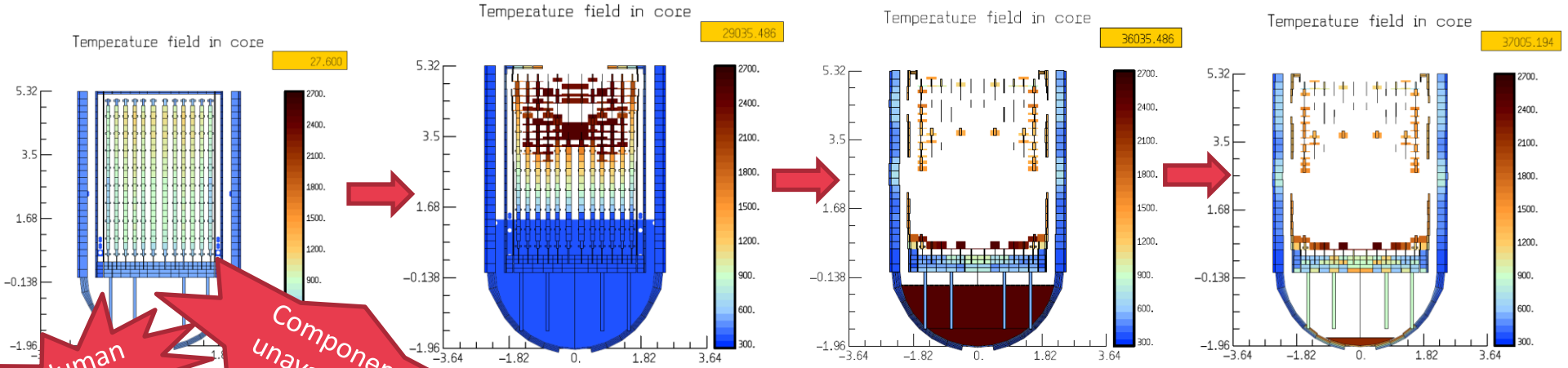

Human Error

Components unavailability

Automatisms / systems
+
Emergency Operating Procedures (EOPs)
With credible delays

Severe Accident Management Guideline (SAMG)

Immediate actions
With credible delays

Delayed actions
With credible delays

Without SAMG actions

L2 PSA assumptions

ULTIMATE BACKUP DIESEL (DUS) AND COMBUSTION TURBINE (TAC)

Following the Fukushima-Daiichi accident, additional power sources were implemented in French nuclear reactors :

- Ultimate Backup Diesel (DUS) installed to supply backup systems in case of internal power loss.
- Each power plant equipped with a common internal ultimate backup power source, the Combustion Turbine (TAC).

DUS and TAC enable recovery of specific systems, previously unavailable, 4 hours after the accident initiation.

SAFETY INJECTION SYSTEM FAILURE DUE TO HIGH SUMP TEMPERATURE

For scenarios in which the Containment Spray System (CSS) is unavailable :

- Increase of temperature and pressure in the containment building
- Can lead to a failure of the safety injection system

Integration into ASTEC Dataset, SIS fails when:

- 120°C is reached for the medium pressure injection system (ISMP)
- 140°C for the low-pressure injection system (ISBP) in the sumps,
- 24 hours of Safety Injection System (SIS) recirculation operation after the CSS loss.

L2 PSA assumptions

INDUCED BREAK MODEL

Modes of Steam Circulation during a core meltdown accident:

- **Without Water Plug in U-Tube:** Gases exit core, pass through Hot Leg (HL), Steam Generator (SG) tubes, intermediate branch, and Cold Leg (CL), then reinjected into lower part of core,

- **With Water Plug in U-Tube:**
  - Steam circulation is blocked.
  - Gases exit core through HL and some SG tubes (direct tubes), cooled down.
  - Cooled gases use other SG tubes (indirect tubes) to return.
  - In HL, two directions of gas flow: hot gases from reactor vessel to SG (upper part), cooled gases from SG to reactor vessel (lower part).

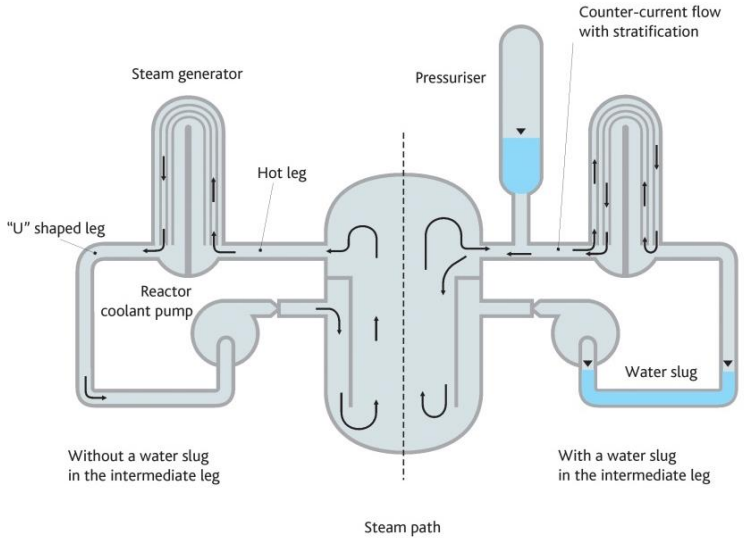

French PWR 1300 modelling with ASTEC

INDUCED BREAK MODEL

Limitations in modeling :

- ASTEC does not currently allow to simulate two-way flow with water plug in U-tube.
- Modeled flow incomplete, may underestimate heating of hot legs and SG tubes, increasing risk of induced breach opening.

Approach used in this study :

- L2-PSA uses additional specific model based on previous studies to assess risk of induced breach opening and location.
- In ASTEC calculations, induced breaches model is activated, but opening section set to zero to continue calculation for primary conditions data.

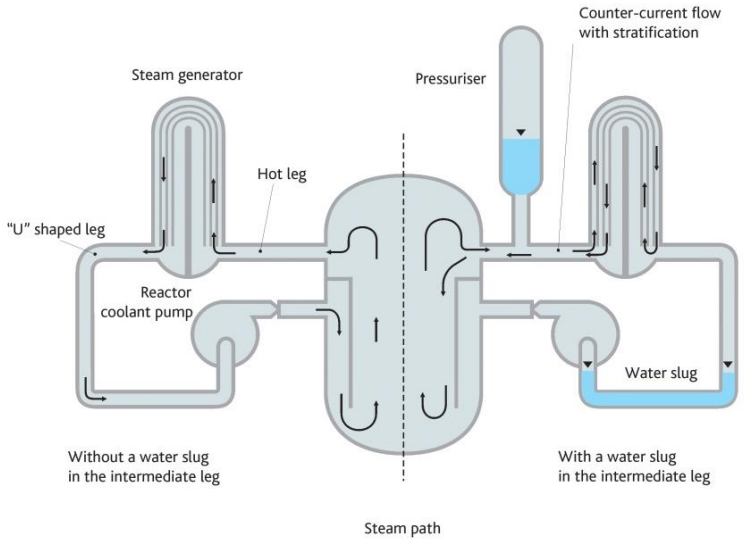

Connection with the L2-PSA

ASTEC simulation and L2 PSA

- ASTEC simulations conducted to support Level 2 Probabilistic Safety Assessment (L2 PSA).
- Plant Damage State (PDS) list defines scenarios resulting from interface between Level 1 (L1) and Level 2 (L2) PSA.

Characteristics of Plant Damage State (PDS)

- Each PDS defined by extensive set of interface variables attributes.
- Some attributes contain information irrelevant for ASTEC simulations, such as containment isolation system status, mainly relevant for Accident Progression Event Tree (APET).
- IRSN L2 PSA team developed a graphical interface to facilitate mapping between PDS and ASTEC simulated sequences.
- Interface designed to enhance efficiency and accuracy in defining ASTEC simulations based on PDS characteristics.

Scenarios selected

[POWER STATE SCENARIOS

- 261 power states were defined from around 10,000 PDS
- Scenarios are grouped into families of accidents
- For every scenario leading to core meltdown, 2 versions of the calculation are made :
  - One without SAMGs application
  - One with SAMGs application

Scenario type	Number of scenarios	Sub-scenario type	Description
Loss of Coolant accident (LOCA)	120	Intermediate breach	Break from 2.55" to 4.123"
		Small breach	Break from 0,6173" to 0,8344" (on HL or on primary pumps seal)
		Steam breach	1 PZR valve blocked open
		Large breach	10.512" break (on CL or HL)
		Very Large breach	Guillotine break (on CL or HL)
		Very small breach	0.265" break on CL
		Leak at the seals of the primary pumps	0.6173" or 0.8344" break for each primary pump
Primary circuit intact	99	SG Auxiliar Feed Water is unavailable	With possible leaks at the seals
		SG Auxiliar Feed Water is available	With possible leaks at the seals
		Refilling auxiliar feed water tank is unavailable	With possible leaks at the seals
Steam generator tube rupture	25	Steam generator tube rupture	Rupture of 1 or 2 steam generator tubes
		Steam generator tube rupture and steam pipe rupture	Rupture of 1 steam generator tube cumulated with steam pipe rupture
Secondary pipe rupture	14	-	Break inside or outside the confinement enclosure
Loss of Coolant accident outside confinement enclosure	3	-	A small primary break located at the thermal barrier of the primary pump motor group in loop 2 leading to the rupture of the RRI circuit and a breach extending outside the containment

Scenarios selected

SHUTDOWN STATE SCENARIOS

Shutdown states	Number of scenarios	Scenario type	Description
AN/RRA1	4	Break on the cooling circuit	3.021" to 10.512" break
		Steam break	One PZR valves blocked open
AN/RRA3	13	Primary circuit intact	-
		Break on the primary circuit	1.093" break
		Break on the cooling circuit	1.093" break
API2/3/4 (Shutdown for maintenance)	67	Primary circuit intact	-
		Break on the primary circuit	2.121" break
		Break on the cooling circuit	2.121" break

- 84 shutdown states were defined
- Scenarios are grouped by shutdown states and scenario type
- For every scenario leading to core meltdown, 2 versions of the calculation are made :
  - One without SAMGs application
  - One with SAMGs application

RESULTS OVERVIEW

CORE MELTDOWN SCENARIOS (POWER STATES)

For the 261 power state scenarios :

- ASTEC V2.2 calculations lead to core degradation in 136 scenarios, representing 92% of the total Core Damage Frequency (CDF) for power states,
- while 125 scenarios are stopped 7 days after the initiating events, without core meltdown, representing only 8% of the total CDF for power states.

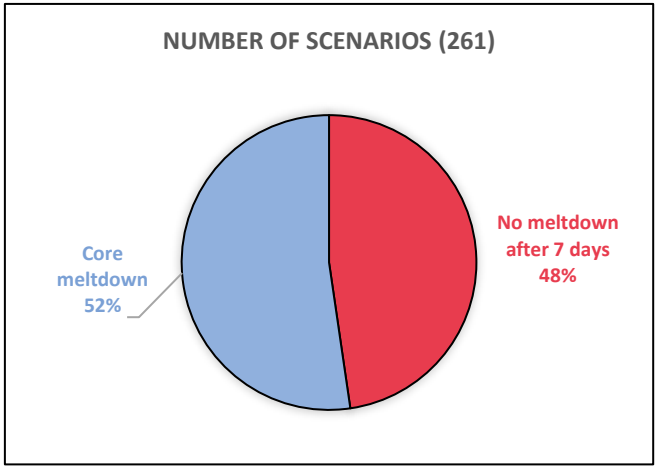

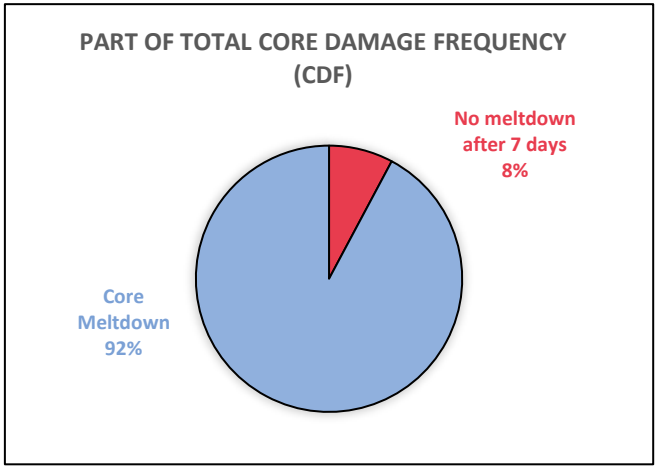

Main conclusions about SAMGs application for power state scenarios

SAMGs actions	Time between the end of EOPs and vessel rupture	Primary pressure at vessel rupture time	Hydrogen risk before vessel rupture
Deisolate and complete discharge of accumulators before vessel rupture (13 scenarios)	Significant increase (>10%), especially with high accumulator water mass for 10 scenarios	Pressure remains < 10 bar No impact clearly identified	Maximum PAICC remains < 4 bar PAICC decreases by more than 10% for 8 scenarios
Maximum cooling with SGs (3 scenarios)	Significant increase for 1 scenario (Low residual power at the end of EOPs)	Pressure < 20 bars with SAMGs actions	Maximum PAICC < 4.5 bar Small impact on PAICC
Enabling CVCS after DUS/TAC starting (1 scenario)	Vessel rupture is delayed by 2 days (possibly 5 days if CVCS is not set at max flow rate)	Decrease from 12 to 7 bar	No more hydrogen risk (without SAMGs action, max PAICC was 5.2 bar)
Opening PZR valves without water injection (6 scenarios)	Increase (>10%) for 3 scenarios	Significant decrease, Pressure <20 bar for 5 scenarios, 40 bar Pressure for one scenario (PZR valve open just before vessel rupture)	No impact for 5 scenarios, 15% PAICC increase for 1 scenario
Opening PZR valves combined with accumulators' discharge (11 scenarios)	Increase (>10%) for 9 scenarios	Significant decrease	No more hydrogen risk for 2 scenarios, Increase of hydrogen risk for 8 scenarios, Max PAICC > 5 bars for 7 scenarios

Description of the PSA-2 prevailing scenario

- The most probable accidental sequence, representing 43% of the total core melt frequency of this PWR 1300MWe PSA 2
- Loss of electrical power with 4 leaks at the primary pump seals of 5 t/h (0.0803 inches per breach, or 0.13 cm2).
- No safety system is operational.
- The SGs are unavailable and thus the impossibility to cool the primary circuit.
- The 3 pressurizer relief valves operate on battery power.

Instant	Event
23min	Application of EOPs
42min	The 4 GVs are isolated
52min	PZR valves are opened
1hr	PZR valves 1 is out of battery and will remain opened
1hr11min	PZR valves 2 and 3 in neutral position
1hr17min	Start of core uncovering
1hr25min	Opening PZR valves 2 and 3
1hr36min	Accumulators discharge
1hr42min	Reach of criteria TRIC>1100 and stop of EOPs application
2hr	PZR valves 2 and 3out of batterie and will remain opened
6hr22min	End of accumulator's discharge
6hr45min	First corium pour into the vessel's lower cavity (at least 10 tons)
6hr46min	60 tons of corium into the vessel's lower cavity
6hr53min	Vessel failure

Description of the PSA-2 prevailing scenario

- Primary pressure abruptly increases when corium pours into the bottom of the vessel (80 tons) : 50 bars
- Rupture of the vessel occurs quickly after corium relocation (7 min)
- PZR valves reducing pressure, but it remains around 20 bar during the vessel failure -> High risk of DCH (Direct Containment Heating)

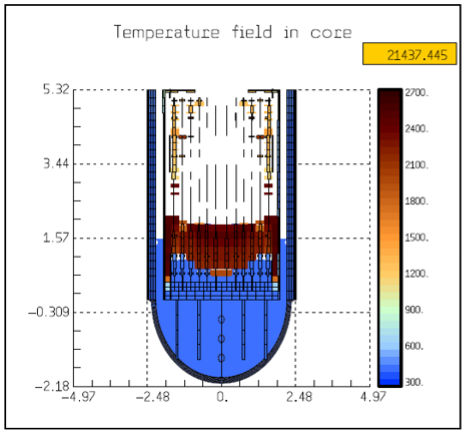

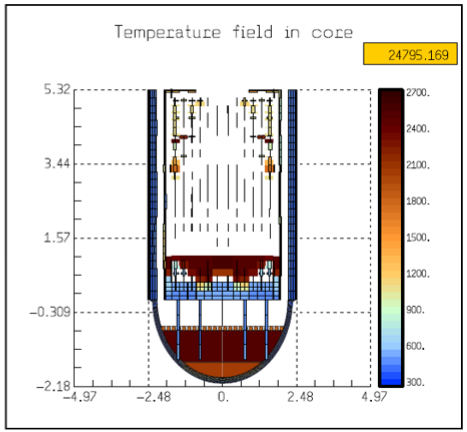

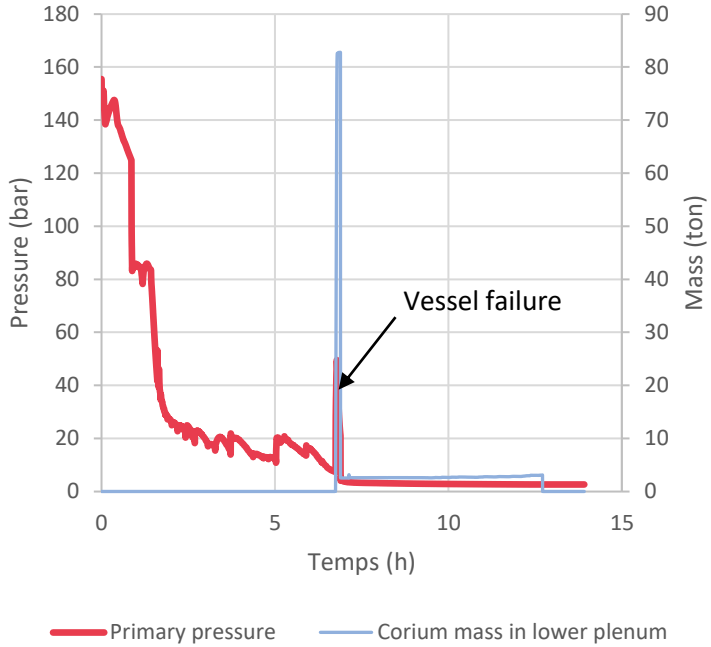

Description of the PSA-2 prevailing scenario

POST-FUKUSHIMA UPDATES

- Significant hardware modification on the PZR valves have been deployed in the framework of the post-Fukushima upgrade for the 1300 MWe reactors
- These Post-Fukushima valves are not modeled in the L2 PSA ASTEC input deck
- New PZR valves allow for a faster depressurization of the primary circuit
- New ASTEC calculation shows that DCH risk is excluded for this scenario with these new valves (Pprim = 3,7 bar at vessel failure)
- In the context of the fourth decade inspection (VD4), the DUS and TAC may allow for the recovery of some electrical supplies more quickly than in the third decade inspection state (VD3)
  - An ASTEC calculation confirms that an earlier start of DUS and TAC prevent core meltdown for this scenario

Conclusion

- 554 simulations using ASTEC V2.2 code provided insights into various physical phenomena affecting primary circuit, reactor vessel, secondary circuit, and containment structure.
- Despite identification of potential core meltdown scenarios by Level-1 PSA, ASTEC V2.2 calculations show that many of these scenarios do not result in core meltdown situations (but they represent only 8% of the total CDF)
- Emergency Operating Procedures (EOPs) and Severe Accident Management Guidelines (SAMGs) driving procedures were integrated into ASTEC input decks for operational action simulation.
- Validation and verification conducted across numerous scenarios, including power and shutdown states, to ensure accurate representation
- Ongoing material modifications performed for the 4th decade inspection and the post-Fukushima material modifications play a crucial role in reducing the likelihood and consequences of severe accidents.

The 11th European Review Meeting on Severe Accident Research (ERMSAR2024)
KTH, Stockholm, Sweden, May 13-16, 2024

MELCOR ANALYSES FOR INVESTIGATION ON HYDROGEN MANAGEMENT DURING BWR SEVERE ACCIDENTS WITH THE FILTERED CONTAINMENT VENTING SYSTEM

Yuga Kojima, Akifumi Yamaji
Cooperative Major in Nuclear Energy, Graduate School of Advanced Science and Engineering,
Waseda University,3-4-1, Okubo, Shinjuku-ku, Tokyo 169-8555, Japan
yugakojima@akane.waseda.jp; akifumi.yamaji@waseda.jp

ABSTRACT

In the unlikely event of a severe accident, the basic hydrogen gas (H_2) management of a BWR differs from that of a Pressurized Water Reactor (PWR) as it cannot be condensed by the Suppression Chamber (S/C) water pool and directly contributes to pressurization of the small PCV. Moreover, unlike the PWR, the risk of H_2 explosion does not exist inside the PCV but outside as H_2 leaks out from the N_2 filled containment to the O_2 rich atmosphere of the Reactor Building (R/B). In particular, the risk of H_2 explosion in the Reactor Well (R/W) may be of worth investigating as it is a closed small volume and is not suited for installing the Passive Autocatalytic Recombiner (PAR) to keep H_2 concentration low. Normally, such risk is mitigated by injecting water into the R/W so that gas leakage from the PCV top head flange is prevented. Nevertheless, as anything may happen during the severe accident, this study focuses on the scenario that the planned R/W water injection fails and significant H_2 leaks out of the PCV to the R/W. In particular, this study investigates the possible side effect of the filter containment venting system (FCVS), which may in principle, further enhance possibility of such H_2 leak from the PCV in post-containment venting phase.

MELCOR-2.2 was utilized to identify a possible accident scenario with the standard “intact PCV gas leakage model”, which is commonly assumed for evaluation of a BWR. By numerous parametric scenario studies with different venting combinations at different venting timings, the analysis results could identify a scenario, in which the PCV venting accompanied with high pressure loss (i.e., venting through S/C and FCVS) led to continuous hydrogen leakage from PCV to R/W after the venting due to the residual pressure (slightly higher than the atmospheric pressure) in the PCV and led to ex-containment H_2 explosion.

KEYWORDS

Severe accident management (SAM), boiling water reactor (BWR), filtered containment venting system (FCVS), MELCOR

1. INTRODUCTION

In the unlikely event of a severe accident, the basic hydrogen gas (H_2) management of a BWR differs from that of a Pressurized Water Reactor (PWR) as it cannot be condensed by the Suppression Chamber (S/C) water pool and directly contributes to pressurization of the small PCV. Moreover, unlike the PWR, the risk of H_2 explosion does not exist inside the PCV but outside as H_2 leaks out from the N_2 filled containment to the O_2 rich atmosphere of the Reactor Building (R/B) as experienced in Fukushima Daiichi (1F) Unit-1 and Unit-3.

Following the 1F accidents, various measures have been taken to the Japanese BWRs to prevent ex-containment H_2 explosion including installation of the Passive Autocatalytic Recombiner (PAR) to keep H_2 concentration low in the Reactor Building (R/B). However, the residual risk of H_2 explosion in the Reactor Well (R/W) may be of worth investigating as it is a closed small volume and is not suited for installing PAR. According to the latest measures, such risk is mitigated by injecting water into the R/W so that gas leakage from the PCV top head flange is prevented. Nevertheless, as anything may happen during a severe accident, this study focuses on the scenario that the planned R/W water injection fails and significant H_2 leaks out of the PCV to the R/W. In particular, this study investigates the possible side effect of the filter containment venting system (FCVS), which may in principle, further enhance possibility of such H_2 leak from the PCV in post-containment venting phase.

The Filtered Containment Venting System (FCVS) is designed to remove radioactive materials from the venting gas so that radioactive release can be minimized when the PCV venting is operated. There are different types of FCVS with different filters, such as water scrubbers, metal fiber filters, and sand bed filters [1]. Since severe accident involves complex phenomena and the accident management may also be diverse, studies have been focusing on evaluation of the decontamination factor (DF) performance of FCVS under various conditions. For example, experiments have been carried out to measure and evaluate the DFs of aerosol, elemental iodine (I_2) and organic iodine (CH_3I) under various temperature, pressure and flow rate conditions [2]. In the meantime, analytical works have also been carried out to evaluate DF under various accidental conditions. For example, a study indicated boiling of scrubbing water for long term severe accidents [3]. Another MELCOR analysis study evaluated the DF performance of FCVS for Advanced BWR (ABWR) for different severe accident scenarios [4]. Some analytical work has indicated possibility of excess buildup and combustion of hydrogen in the FCVS vessel as the venting gas compositions change through the system [5].

Thus, performance of FCVS have been studied under various conditions. However, there seems to be lack of studies regarding possible side effect of FCVS with respect to prevention of the ex-containment H_2 explosion in the BWR R/B (especially, R/W). In severe accident analyses of a BWR, the PCV is

assumed to allow some gas leakage depending on the pressure [6]. Then, it may be worth considering possible impact of FCVS on the PCV gas leakage and the risk of subsequent H_2 explosion in the R/B. More specifically, PCV venting with FCVS may be compared with a hypothetical venting case when FCVS is bypassed. Since FCVS is a filtering system, the venting through FCVS has additional pressure loss compared with the case when FCVS is bypassed and the post venting PCV pressure with FCVS is expected to be higher than the case when FCVS is bypassed. Consequently, if the PCV is not depressurized sufficiently, the gas leakage from the PCV may continue even after the PCV venting and increase the risk of hydrogen explosion in the R/B. In particular, the PCV top head flange is considered to be one of the likely locations of the gas leakage [7], which may lead to H_2 explosion in the R/W if the accident management fails to inject water to the R/W. This study aims to investigate whether such accident scenarios exist, where excess H_2 may be accumulated in the R/W of BWR during severe accidents.

In short, this study intends to highlight that although severe accident management is well established, the management may involve complex side effects, which may not be welcomed. One of such examples may be found in use of FCVS, which is certainly necessary to reduce radioactive release, but may have some side effects regarding H_2 explosion in the R/B (in particular, the R/W) of BWR, which is ex-containment event and may not directly threaten radioactive release but is certainly not welcomed.

2. MELCOR MODELS AND ANALYSES CONDITIONS

2.1 Plant Design Specifications

In this study, the MELCOR-2.2 input models were developed based on the BWR-4 / Mark-I models of the preceding studies [8] [9] and the set of parameters recommended in the best practices of MELCOR [10]. The design specifications of the plant system and FCVS are summarized in Table 1. The FCVS was assumed to consist of a scrubber filter section (a volume with water pool of 40 m^3), a metal fiber filter section, and an iodine filter section.

Table I Assumed plant design specifications [8][9]

	BWR4 / Mark-1
Operating pressure (MPa)	6.23
Core thermal power (MWth)	2381
Core power density (MW/m^3)	41.8
Active core height (m) / equivalent diameter (m)	3.71 / 4.42
Fuel mass (kg)	106600
Core structure material / mass (kg)	Zircaloy (Zry) / 47682
	Stainless-steel / 26713
D/W volume / W/W volume (m^3)	3842 / 6140
W/W water pool mass (kg)	2959
FCVS scrubber water volume (m^3)	40

2.2 Control Volume Divisions and Flow Path Connections

The control volumes (CVs) and the flow paths (FLs) connecting the CVs of the RPV, PCV, R/B and FCVS are shown in Fig. 1. The PCV was composed by the CVs, which represented the pedestal, the annular volume around the RPV, the upper D/W, the lower D/W, the vent line and the wet well (W/W). The FCVS was connected from both the D/W and W/W to activate the system through either path by opening the corresponding valve.

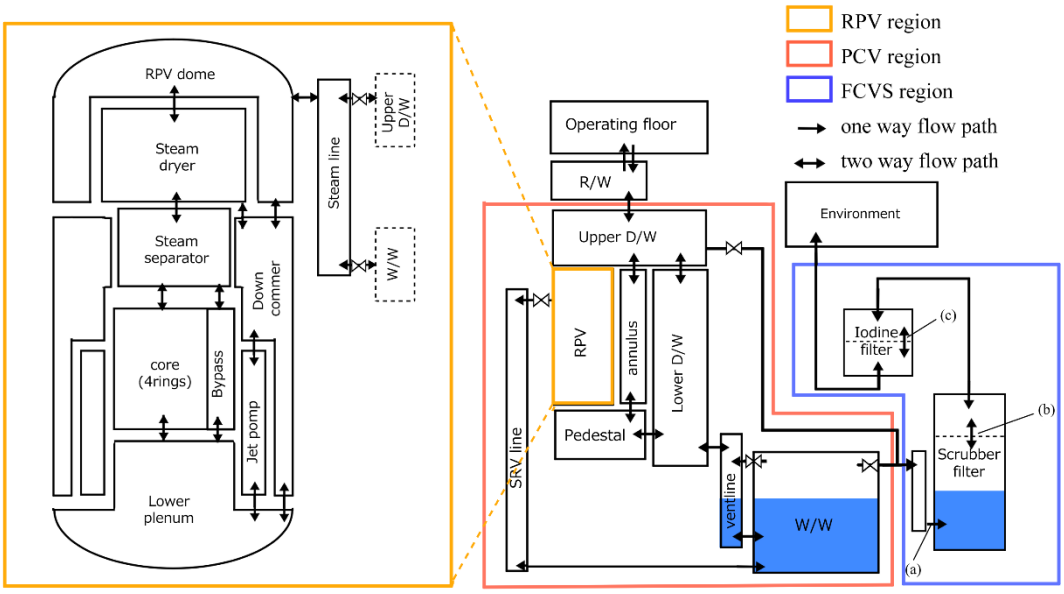

Figure 1. Control volumes and flow paths (RPV, PCV, R/B, FCVS)

The leakage from the upper D/W to the R/W was assumed to represent one of the likely scenarios of the PCV top head flange gasket leakage. The leakage area was adjusted with few test analysis cases so that the leakage rates at different D/W pressures agreed with the estimates given by the AEC's formula [5]:

$$L = L_0 \sqrt{\frac{(P_t - P_a) \cdot R_t \cdot T_t}{(P_b - P_a) \cdot R_b \cdot T_b}} \quad (1)$$

where, L: leakage rate, L_0: design leakage rate (0.5%/day), P_t: D/W pressure, P_b: D/W design pressure (411kPa[abs]), P_a: atmospheric pressure (101 kPa[abs]), T_t: D/W gas temperature, T_b: D/W design temperature (444 K), R_t: Gas constant during accident, R_b: atmospheric gas constant (287.1 J/K·kg).

The flow path between the R/W and the operating floor was represented by a pair of one-way flow paths of opposite directions to consider the gas exchange induced by the small pressure difference. The one-way flow path with the valve that opens when the pressure difference exceeds 14 kPa from the W/W cavity to the vent line represented the vacuum breaker. All the other flow paths were two-way flow paths.

For the R/W, the hydrogen combustion package was activated, which assumed the combustion of the gas mixture of H_2 and CO when the Le Chatelier's condition as shown in Equation 2 were satisfied regardless of presence of igniters [11].

$$\begin{aligned} X_{H2} + \frac{0.1}{0.167} X_{CO} &\geq 0.1 \\ X_{O2} &\geq 0.05 \\ X_{H2O} &\leq 0.5 \end{aligned} \quad (2)$$

where, X_{H2}: mole fraction of hydrogen, X_{CO}: mole fraction of carbon monoxide, X_{H2O}: mole fraction of steam, X_{O2}: mole fraction of oxygen

Table II summarizes the DF evaluations adopted in this study for the purpose of estimating decay heat generated in the FCVS water pool and the subsequent water evaporation, which affects the FCVS pressure loss and the corresponding post-venting PCV pressure. In MELCOR, the decontamination factor (DF) is either evaluated or assumed for a given FL when defined. In this study, the DFs for the scrubbing water, the metal fiber filter, and the iodine filter were defined for the flow paths (a), (b), and (c) shown in Fig. 1, respectively. In MELCOR, the DFs of the scrubbing water for fission product

aerosols and vapor are evaluated with the SPARC-90 model [12]. Furthermore, in this study, the DF of the metal fiber filter and the iodine filter for fission product was taken from some experiments [13][14].

Table II. DF evaluation adopted in this study

	Flow path (See Fig.1)	Decontamination factor (DF)	Decontaminated species
Scrubbing water	(a)	SPARC-90 model [12]	Fission product aerosols and vapor
Metal fiber filter	(b)	1000 [13]	Fission product aerosol
Iodine filter	(c)	50[14]	Fission product vapor

3. MELCOR ANALYSIS RESULTS

3.1 Reactor Depressurization with Loss of Water Injection and Ultimate Heat Sink (TQUV)

To highlight the side effect of FCVS, a scenario that promotes PCV to R/W gas leakage by sustaining the PCV pressure high for long duration is desired. Hence, the reactor depressurization with loss of water injection and ultimate heat sink (TQUV) scenario was analyzed as one of such scenarios. Following the reactor scram, all water injection systems were assumed to fail, except the D/W spray with S/C water pool as the water source, so that the PCV pressure could be maintained high for long duration with relatively large amount of H_2 generation by in-vessel water-Zr reaction. The major events and the D/W pressure history (together with the partial pressures of steam and hydrogen) are shown in Fig. 2 until the PCV venting. The venting timing was tuned so that the H_2 concentration in the R/W was just below the combustion threshold.

The RPV was depressurized by actuation of the Automatic Depressurization System (ADS operation), which opened the safety relief valves (SRVs) when the core water level declined to 10% of the active core height from the bottom of the active core (BAF+10%), (about 2.1 h after the reactor scram). By this time, the peak core temperature had reached about 1900 K and the core degradation with release of some fission products had started. During the reactor depressurization, the core heat up was accelerated due to the exothermic oxidation reaction of Zr with steam at elevated temperature. Then, the core degradation further proceeded involving core slumping to the lower plenum of the RPV, which resulted in total boil-off of the plenum water at about 3.9 h. The RPV lower head failed at about 7.6 h and the molten core-concrete interaction (MCCI) started while the D/W spray was activated with a flow rate of 120 m^3/h from the W/W water supply to suppress the D/W pressure increase. At 16.7h, the PCV was vented, because the H_2 concentration in the R/W reached almost the combustion threshold as will be shown later in this section.

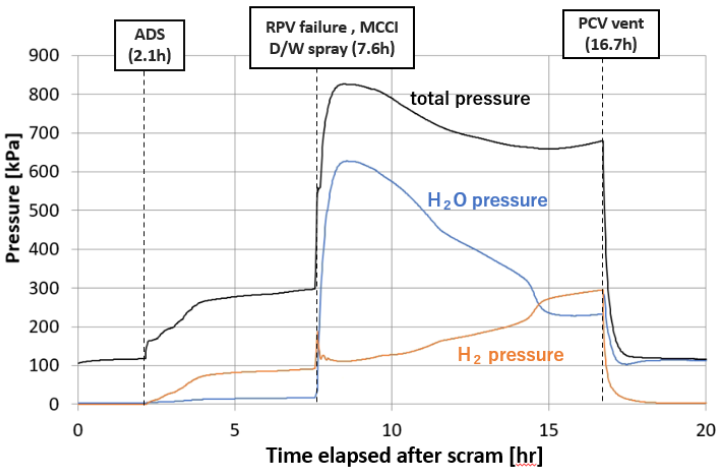

Figure 2. D/W Pressure Until PCV venting (TQUV)

Fig. 3 shows the post venting D/W pressure histories for the following four cases: (1) D/W venting; (2) W/W venting; (3) D/W venting + FCVS; (4) W/W venting + FCVS. The differences among the four cases can be understood in terms of the pressure losses during venting. In all the cases, the D/W pressure rapidly decreased immediately after the venting. However, the rate of reductions slowed down as the difference between the D/W pressure and the environment decreased. While the D/W venting case decreased to almost the atmospheric pressure after about 25 h, the W/W venting case remained at higher pressure. The pressure difference was equivalent to the head pressure of the W/W water pool. When FCVS was used, the post-venting D/W pressures were raised from those without FCVS and the difference was equivalent to the additional head pressure of the FCVS water pool. The gradual decreases of the D/W pressures with FCVS reflected gradual boil-off of the FCVS water pool as it continuously received heat from the gas passing through the system (in the actual management, water injection to FCVS to makeup the water loss is expected).

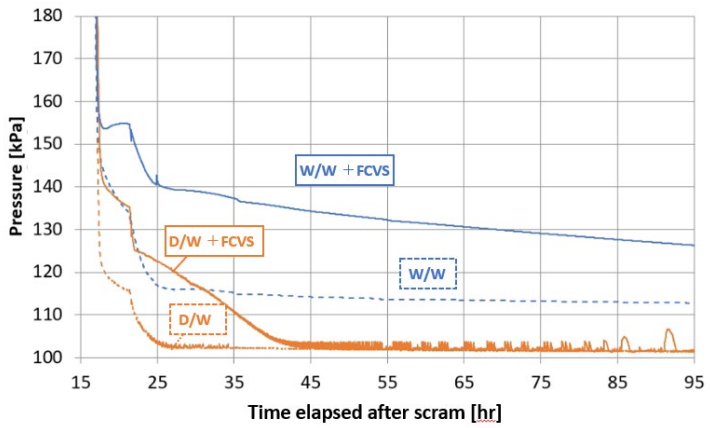

Figure 3. D/W Pressure Histories after the PCV Venting (TQUV)

Fig. 4 shows the R/W hydrogen concentration histories of the analyzed four cases. The PCV venting timing was deliberately chosen, so that the R/W hydrogen concentration was close to the point of hydrogen combustion, but still slightly lower than the threshold. Then, for all the four cases, the R/W hydrogen concentrations decreased by the PCV venting, However, the concentration started to increase again for the W/W venting + FCVS case, because the post venting D/W pressure was high enough to allow continuous PCV gas leakage to the R/W even after the venting. As the result, the R/W hydrogen concentration reached the combustion point, while such hydrogen concentration increases were not evident with the other three cases as the post-venting PCV pressures were low enough. Hence, the results demonstrated that in the scenario when the planned R/W water injection failed and by choosing a very specific timing just before H_2 explosion in the R/W, there exists a case (in principle), where venting with FCVS could lead to undesired consequence of post-venting ex-containment (R/W) H_2 explosion, which could be avoided if FCVS was bypassed. Otherwise, the results show that PCV venting with FCVS is an effective way to prevent ex-containment H_2 explosions as is originally intended.

It may be worth mentioning that if the venting timing was earlier than the tuned timing, then none of the cases resulted in H_2 explosions and if the venting timing was delayed, then all the cases showed H_2 explosions before venting. A very specific moment was chosen for this study to find different post-venting PCV to R/B gas leakages with different venting methods. It should also be stressed that although ex-containment H_2 explosion is not desirable, it may not be the nature of management that is directly compared with the merit of FCVS, which substantially reduces radioactive release with venting.

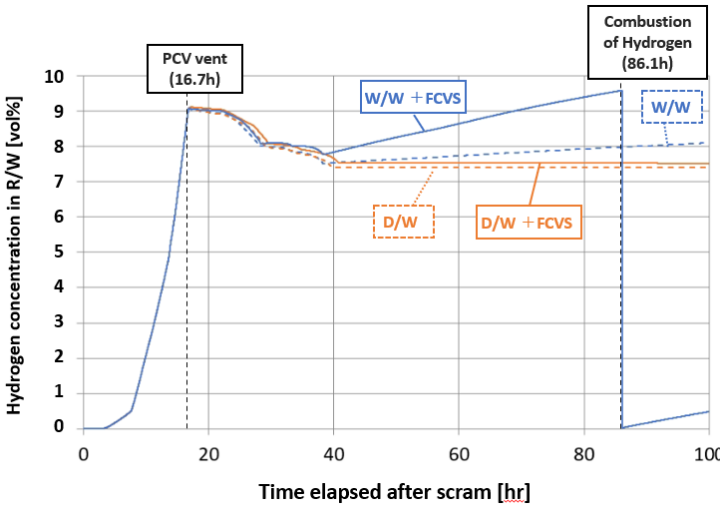

Figure 4. Hydrogen Concentration in R/W (TQUV)

3.2 Loss-Of-Coolant Accident (LOCA) with Loss of Water Injection and Ultimate Heat Sink (AE)

As TQUV may be understood as a late-vessel failure scenario, the Loss-Of-Coolant Accident with loss of water injection and ultimate heat sink (AE) scenario was analyzed as an example of the early vessel failure. As for the LOCA, the 100% main steam line break was assumed. The major events and the D/W pressure history (together with the partial pressures of steam and hydrogen) are shown in Fig. 5 until the PCV venting.

In this scenario, the reactor was initially scrammed and the RPV was also depressurized at the same time due to the main steam line break. The D/W spray was activated earlier than the TQUV scenario (which was after the RPV failure) at about 1.4 h to suppress the rapid D/W pressure increase due to the main steam line break. The core degradation and collapse progressed fast and the RPV lower head failed and MCCI was initiated at about 4.8 h.

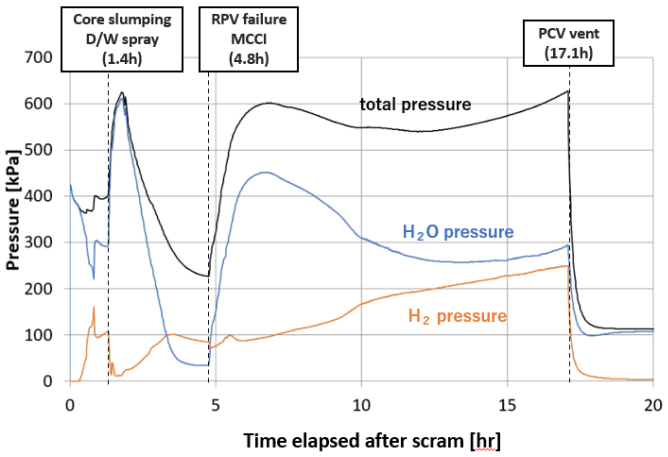

Figure 5. D/W Pressure Until PCV Venting (AE)

The PCV venting timing was deliberately chosen in the same way as was the case for the TQUV scenario at 17.1 h. In the same way as for the TQUV scenario, Fig. 6 shows the post venting D/W pressure histories for the following four cases: (1) D/W venting; (2) W/W venting; (3) D/W venting + FCVS; (4) W/W venting + FCVS. The pressure histories were similar to those of the TQUV scenario, but the long-term pressure tended to be slightly higher than those of the TQUV scenario, probably because larger energy was dissipated to D/W in AE compared to TQUV.

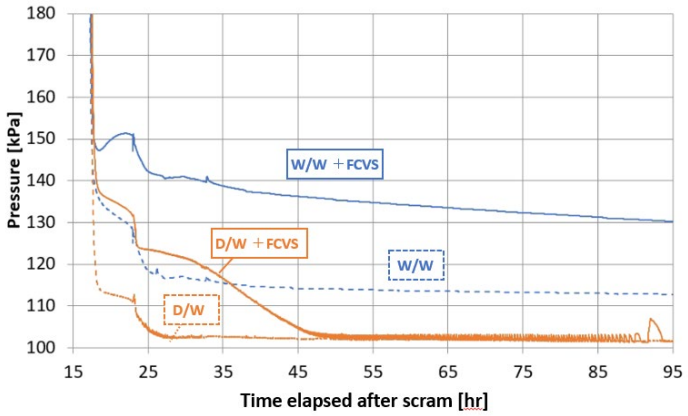

Figure 6. D/W Pressure Histories after the PCV Venting (AE)

Finally, the hydrogen gas concentration histories of the four cases are compared in Fig. 7. As was the case of TQUV, the PCV venting timing was deliberately chosen, so that the R/W hydrogen concentration was close to the point of hydrogen combustion, but still slightly lower than the threshold. The overall histories were similar to those of TQUV. The combustion timing of the W/W venting + FCVS case was slightly delayed from that of TQUV, probably because the D/W hydrogen concentration was slightly less, as the steam was directly released to the D/W from the line break of LOCA.

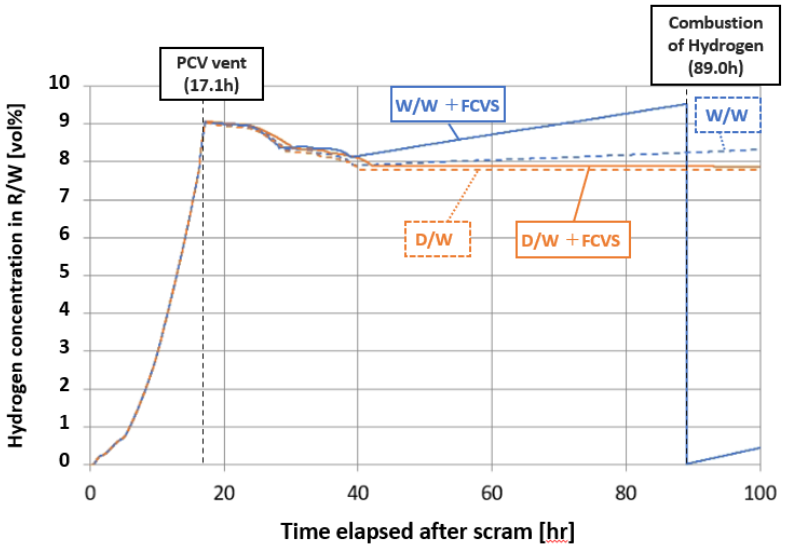

Figure 7. Hydrogen Concentration in R/W (AE)

4. CONCLUSIONS

Although severe accident management is well established, the management may involve complex side effects / influences, which may not be welcomed. One of such examples may be the influence of the additional pressure loss associated with use of FCVS compared with the PCV venting without using FCVS in BWRs. The influence is not evident when water injection to the R/W is successful and PCV venting (depressurization of the PCV) with FCVS is an effective way to prevent H_2 leakage from the PCV and to prevent ex-containment H_2 explosions as is originally intended. However, when the R/W water injection fails and the venting timing happened to be just at the specific moment (just before the moment of H_2 explosion in the R/B (in particular, the R/W)), the additional pressure loss would become evident. Namely, the H_2 leakage could continue even after the venting to result in ex-containment H_2 explosion in the R/W. It should be noted that if the venting timing was earlier, none of the analyzed cases resulted in H_2 explosions and if the venting timing was later, then all the cases resulted in H_2 explosions. The current study showed (after numerous trial and errors) that a very specific venting timing could exist.

NOMENCLATURE (IF NEEDED)

PCV : primary containment vessel
RPV : reactor pressure vessel
R/B : reactor building
FCVS : filtered containment venting system
D/W: drywell
W/W : wetwell
R/W : reactor-well
SRV : safety relief valve
ADS : automatic depressurization system
FP : fission products
PAR : passive autocatalytic recombiner
MCCI : molten core concrete interaction
TQUV : reactor depressurization with loss of water injection and ultimate heat sink
LOCA : Loss-Of-Coolant Accident
AE : large break LOCA with loss of water injection and ultimate heat sink

ACKNOWLEDGEMENTS

A part of this study is the result of “Understanding Mechanisms of Severe Accidents and Improving Safety of Nuclear Reactors by Computer Science” of Waseda Research Institute for Science and Engineering and the authors acknowledge support of the Institute for Advanced Theoretical and Experimental Physics, Waseda University.

References

[1] OECD/NEA/CSNI, “Status Report on Filtered Containment Venting”, NEA/CSNI/R(2014), 2014.
[2] T. Kanai, M. Furuya,T. Arai, et al. “Decontamination Process of Elemental Iodine With Filtered Containment Venting System”, Proc.ICONE23, Chiba, Japan, May 17-21, 2015.
[3] Y. S. NA et al.," Thermal Hydraulic Issues of Containment Filtered Venting System for a Long Operating Time" Nuclear Engineering and Technology, Vol 46, 2014.
[4] Ui. A, Furuya. M, Kanai. T, et al. “Accident progression analyses of a BWR with filtered containment venting system during long term severe accident conditions”, Proc. NURETH2017, Xi'an, China, September 3-8, 2017.
[5] G. Choi et al. “Analyses of hydrogen risk in containment filtered venting system using MELCOR”, Nuclear Engineering and Technology, Vol 54, 2022
[6] United States Atomic Energy Commission report,"reactor containment leakage testing and surveillance requirements", USAEC technical safety guide,1966.
[7] Tokyo Electric Power Company Holdings ,”The 6th Progress Report on the Investigation and Examination of Unconfirmed and Unsolved Issues on the Development Mechanism of the Fukushima Daiichi Nuclear Accident” ,November 10, 2022.
[8] T. Sevón, “MELCOR modeling of Fukushima Daiichi 2 Accident”, Proc.NENE2013, Bled, Slovenia, September 9-12, 2013
[9] A. Takashima, A. Yamaji, “Analyses of wet and dry cavity strategies for BWR severe accident management with MELCOR-2.2”, ICONE2021, August 4-6, 2021, Online.
[10] U.S. Nuclear Regulatory Commission, “MELCOR Best Practices as Applied in the State-of-the-Art Reactor Consequence Analyses (SOARCA) Project”, NUREG/CR-7008 ,2014.
[11] Sandia National Laboratories, “MELCOR Computer Code Manuals Vol. 2: Reference Manual Version 2.2.14959”, 2019.
[12] P C. Owczarski, K W. Burk, “SPARC-90: A Code for Calculating Fission Product Capture in Suppression Pools”, NUREG/CR-5765 ,1991.
[13] S. Kawamura, T. Kimura, S. Omori, T. Narabayashi, “Development of a Filtered Containment Venting System for Nuclear Power Plants”, J. Nucl. Sci. Technol. 15(1), pp.12-20, 2016.
[14] S. Kawamura, T. Kimura, et al..“Development of an organic iodine filter for filtered containment venting systems of nuclear power plants”, Transactions of the Atomic Energy Society of Japan 15(4), pp. 192-209,2016.

MELCOR Analyses for Investigation on Hydrogen Management during BWR Severe Accident with The Filtered Containment Venting System

ERMSAR 2024

2024/05/13

Yuga Kojima, Akifumi Yamaji

Waseda University, Tokyo, Japan

Outline

- **Background and Objective**
  Features and Issue of Ex-Containment H2 management in BWRs

- **Method**
  PCV and R/B model
  FCVS model
  Analysis scenario

- **Result**
  TQUV sequence
  AE sequence

- **Conclusions and Future Work**

Outline

- **Background and Objective**
  Features and Issue of Ex-Containment H2 management in BWRs

- **Method**
  PCV and R/B model
  FCVS model
  Analysis scenario

- **Result**
  TQUV sequence
  AE sequence

- **Conclusions and Future Work**

Features of H_2 management in BWRs

H_2 generation during SA

Oxidation of the core

Molten Core-Concrete Interaction (MCCI)

Pressure management by S/C

H_2 is non-condensable and accumulates in the primary containment vessel (PCV)

The PCV is a N_2 atmosphere

The risk of H_2 explosion inside is extremely low

The risk of H_2 explosion is in the R/B

H_2 leakage from the PCV to the R/B must be assumed in safety evaluations.

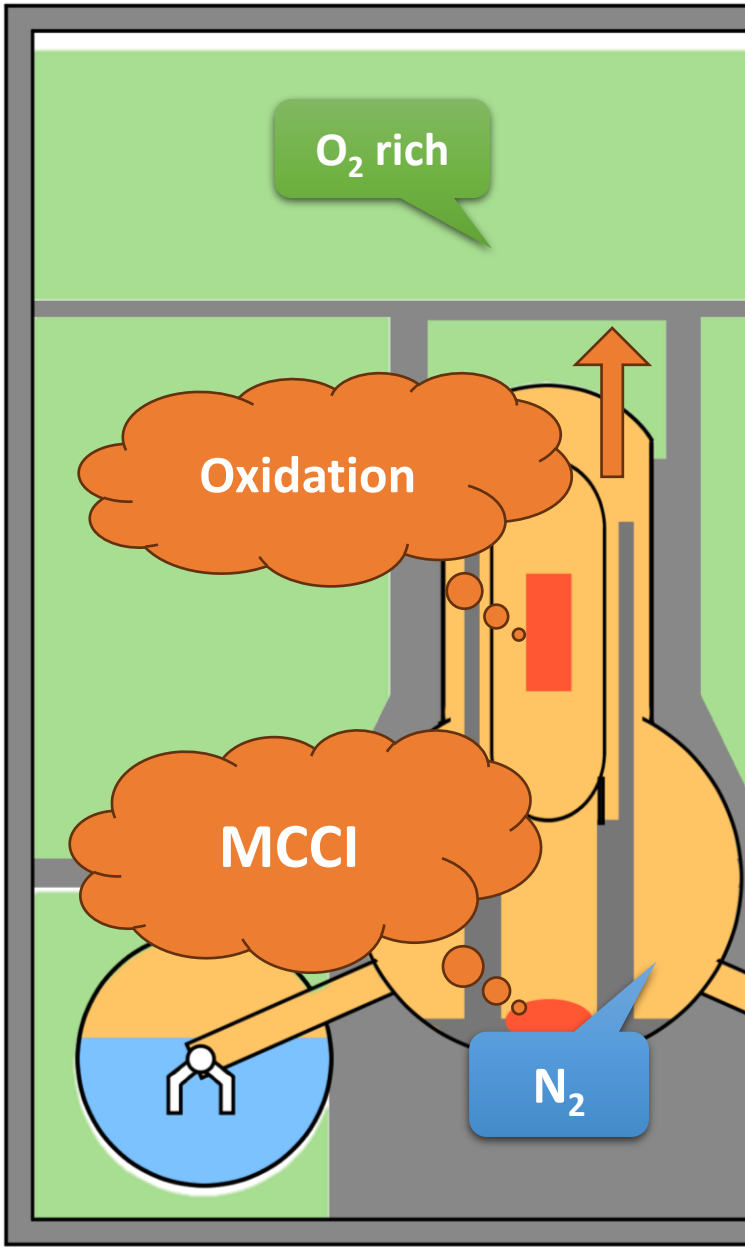

Ex-Containment H_2 Management in BWRs

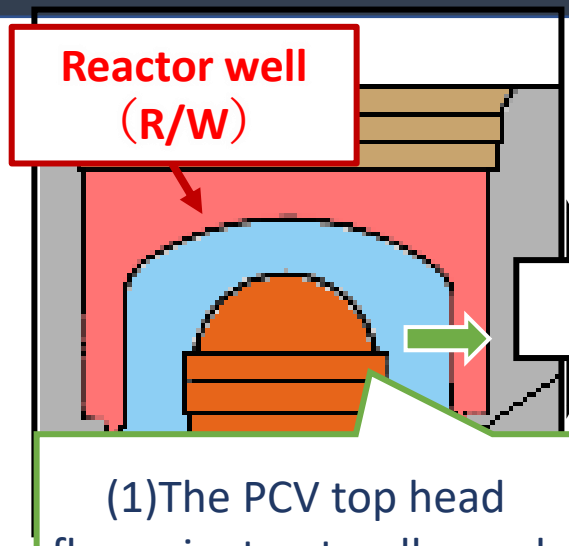

(1)The PCV top head flange is structurally weak.

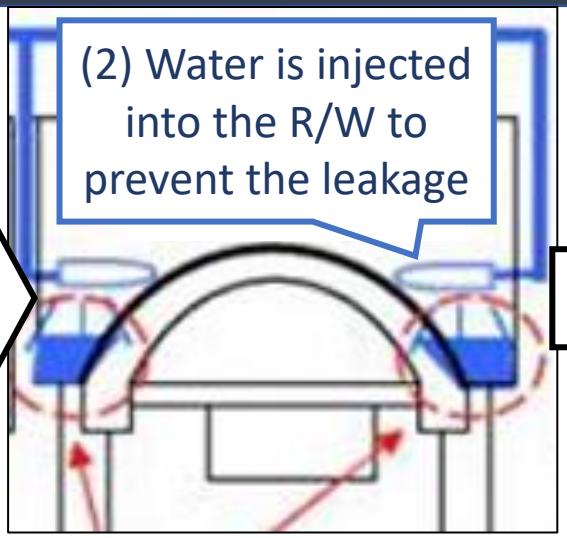

(2) Water is injected into the R/W to prevent the leakage

(3) H_2 concentration in the R/B is monitored and suppressed by PAR, and the PCV is vented when necessary.

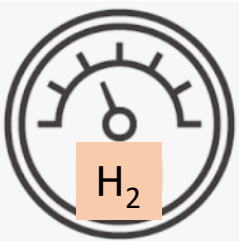



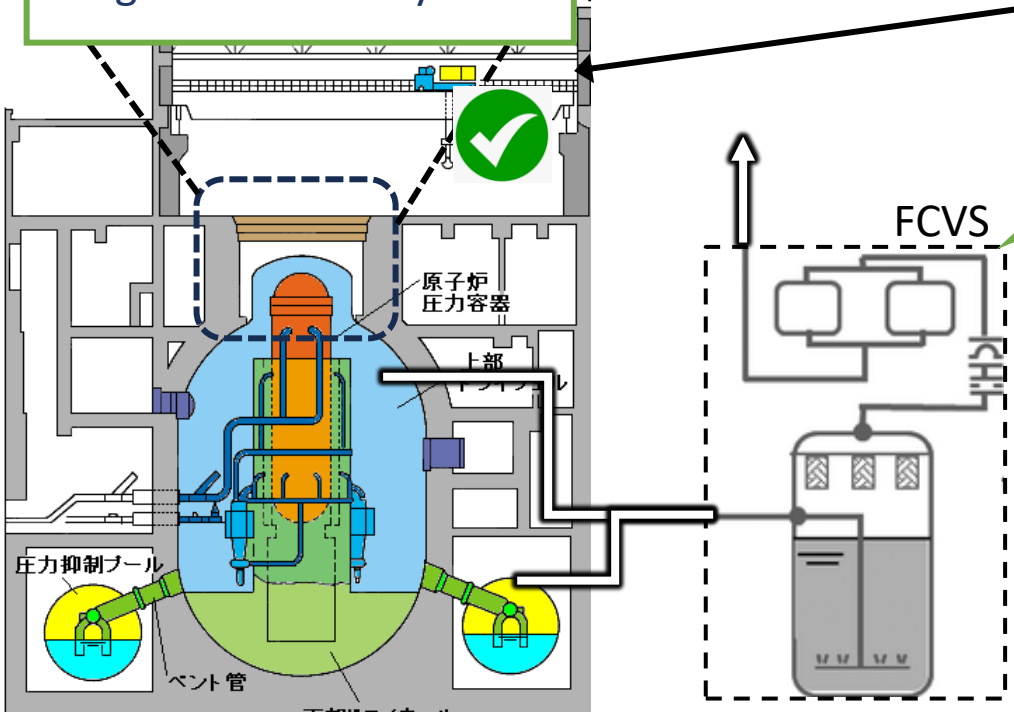

(4) RN release to the environment is minimized by FCVS.

Ex-containment H_2 well managed by PAR, H_2 monitor and PCV venting though FCVS.

- Issues to consider for ex-containment H_2 explosion:
  - Any management may fail.
  - Variety of different accident

Issue of Ex-Containment H_2 Explosion and the Management

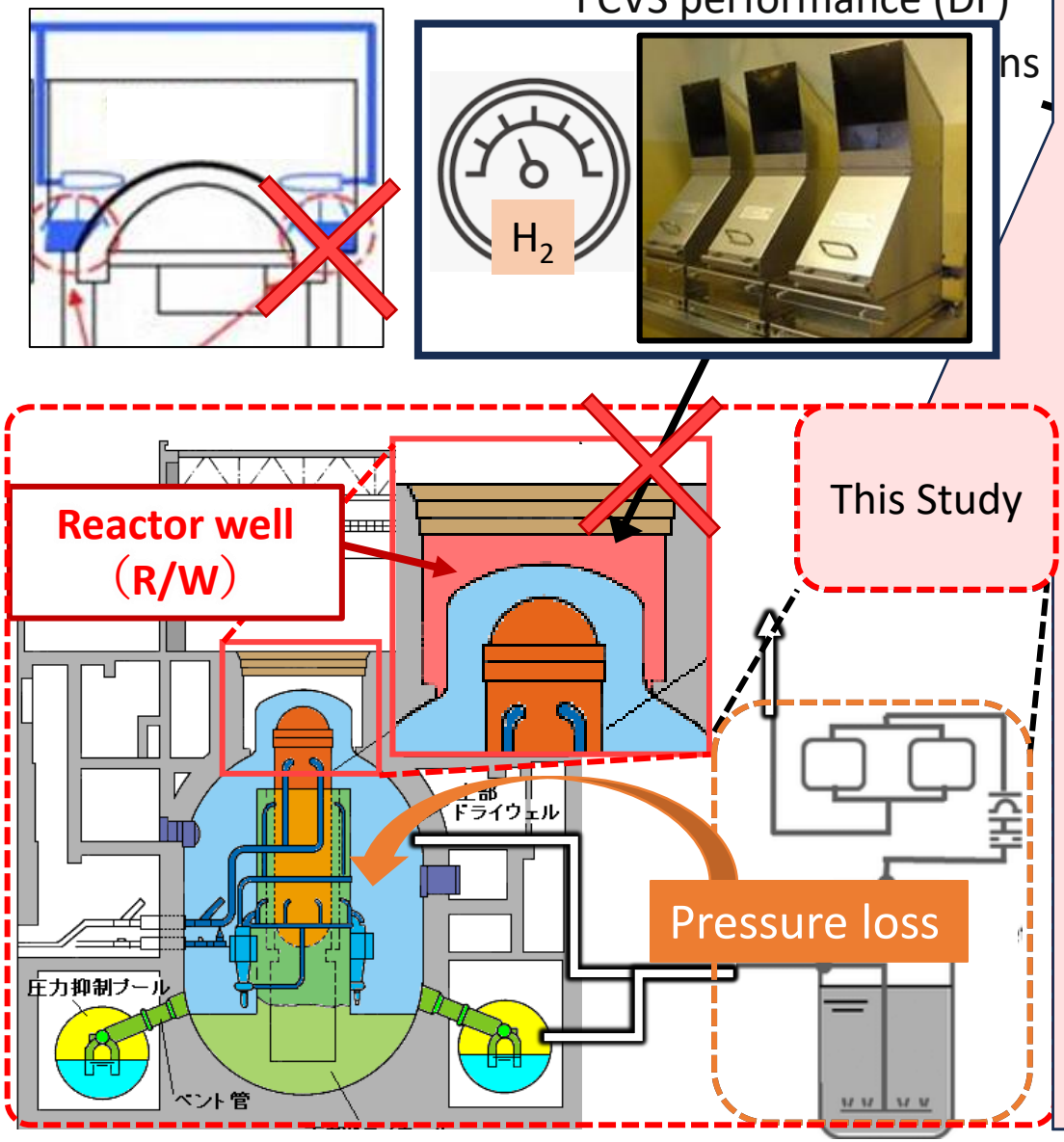

This study focuses on:

- Ex-containment (R/W)
- Post-venting

・In case of loss of R/W injection and leakage to R/W …

▹ R/W is not suitable for the installation of PAR.

▹ Post-FCVS venting residual pressure may lead to additional H_2 leakage to the R/W.

Is there a possibility of H_2 explosion in R/W after venting?

Purpose of This Study

To reveal potential issues of **ex-containment** H_2 management in **post-venting** phase of BWR severe accident management through accident progression analyses.

Outline

- **Background and Objective**
  Features and Issue of Ex-Containment H2 management in BWRs
- **Method**
  PCV and R/B model
  FCVS model
  Analysis scenario
- **Result**
  TQUV sequence
  AE sequence
- **Conclusions and Future Work**

Assumed Scenario in This Study

(1) the reactor core and RPV failure and the loss of R/W water injection

(2) SAM (e.g., D/W spray) control the PCV pressure

(3) H_2 continues to accumulate in the R/W over long time

(4) FCVS venting starts to prevent further leakage. (when R/W is close to combustion)

Is there a possibility of H_2 explosion in R/W after venting?

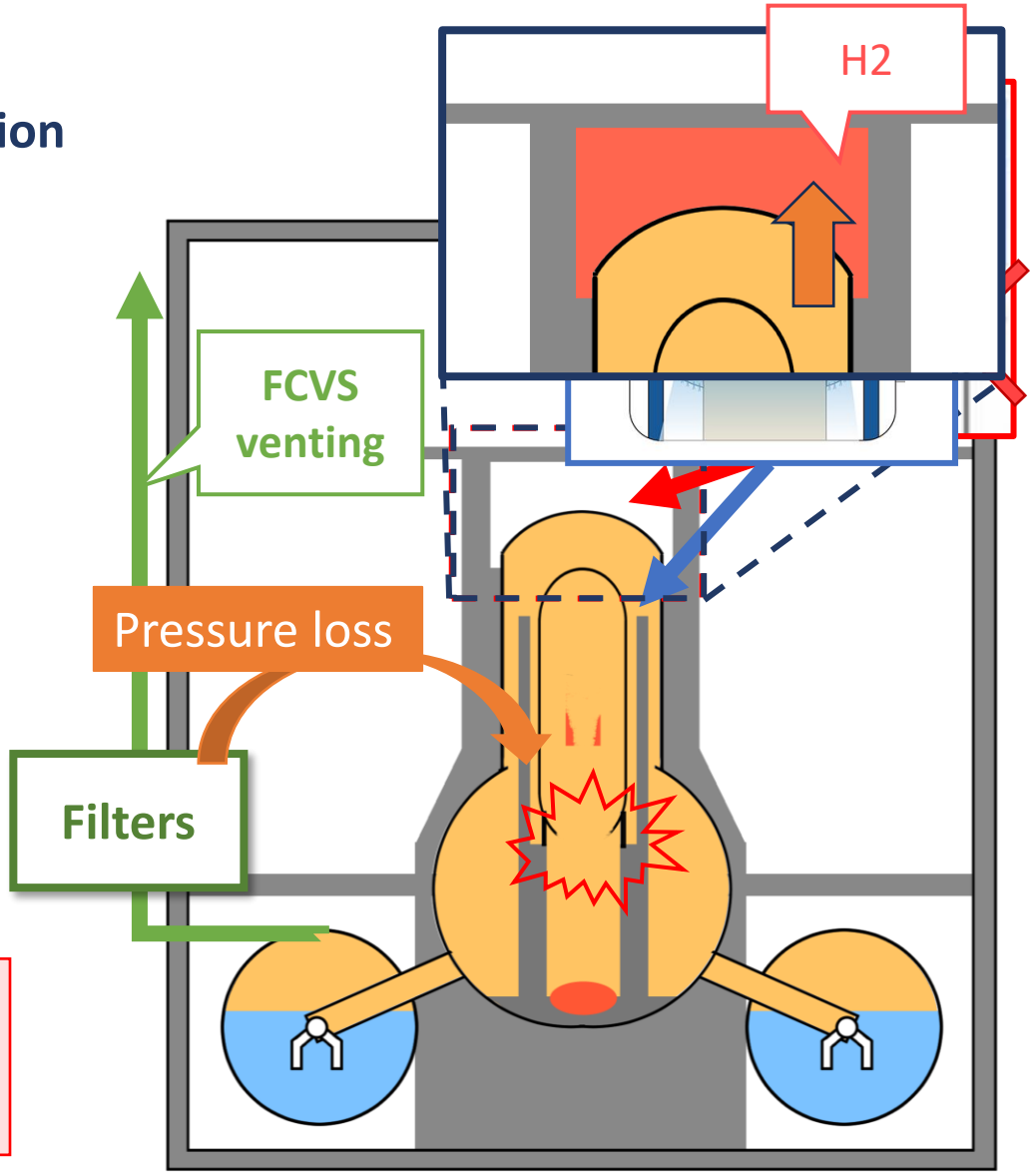

PCV and R/B model (MELCOR)

D/W Spray model

PCV Leakage Model [2]

Turned according to the AEC formula

$$L = L_0 \cdot \sqrt{\frac{(P_t - P_a)\cdot R_t \cdot T_t}{(P_b - P_a)\cdot R_b \cdot T_b}}$$

0.5%/day in design pressure assumed

Burn Model

simulate consumption of H_2, O_2, and CO

・condition

$$X_{H_2} + 0.6X_{CO} \geq 0.1$$

$$X_{O_2} \geq 0.05$$

$$X_{H_2O} \leq 0.5$$

(X_m:mole fracton)

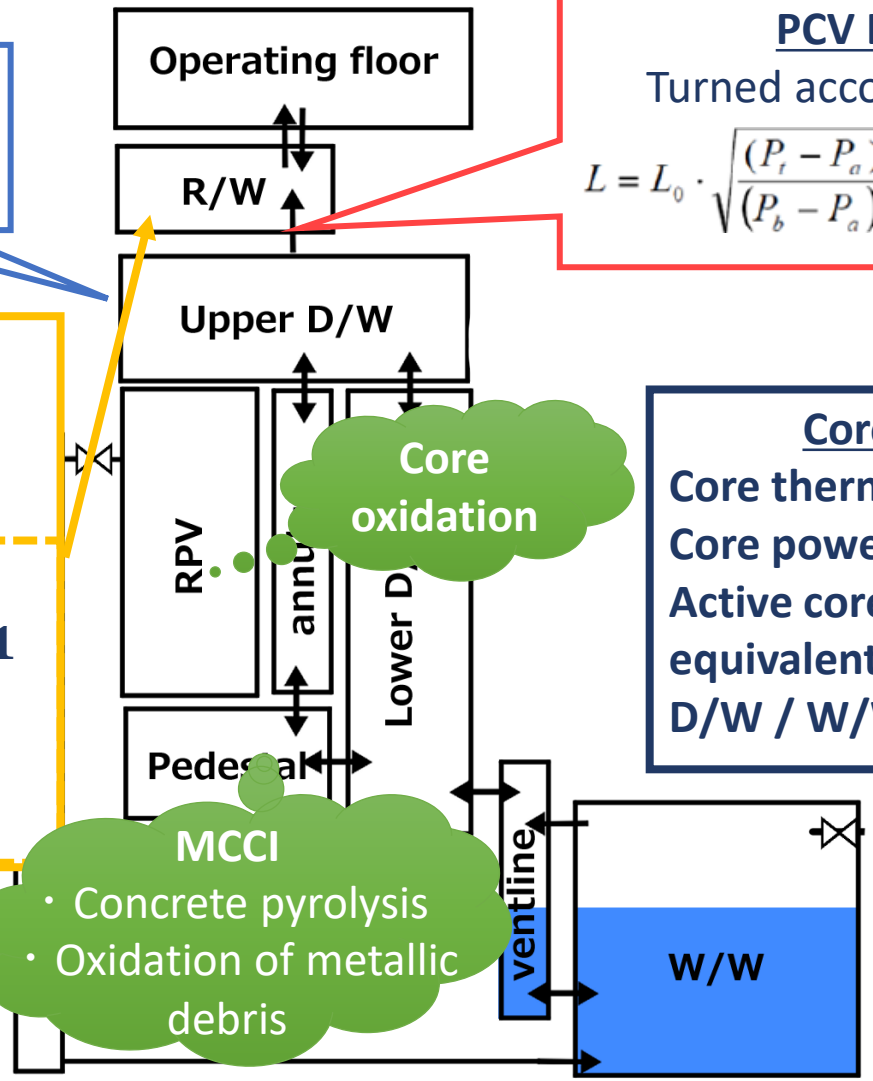

Core and PCV Design [1]

Core thermal power 2381 MWth
Core power density 41.8 MW/m^3
Active core height 3.71 m
equivalent diameter 4.42 m
D/W / W/W volume 3842 / 6140 m^3

↔ **Single path**

⇄ **Countercorrent**

[1] T. Sevón, "MELCOR modeling of Fukushima Daiichi 2 Accident", Proc.NENE2013, Bled, Slovenia, September 9-12, 2013
[2] United States Atomic Energy Commission report,"reactor containment leakage testing and surveillance requirements", USAEC technical safety guide,1966.

FCVS model (MELCOR)

- The decontamination factor (DF) of each filter is set to consider the impact of RN decay heat on the water level.
- The release routes are W/W vent and D/W vent.

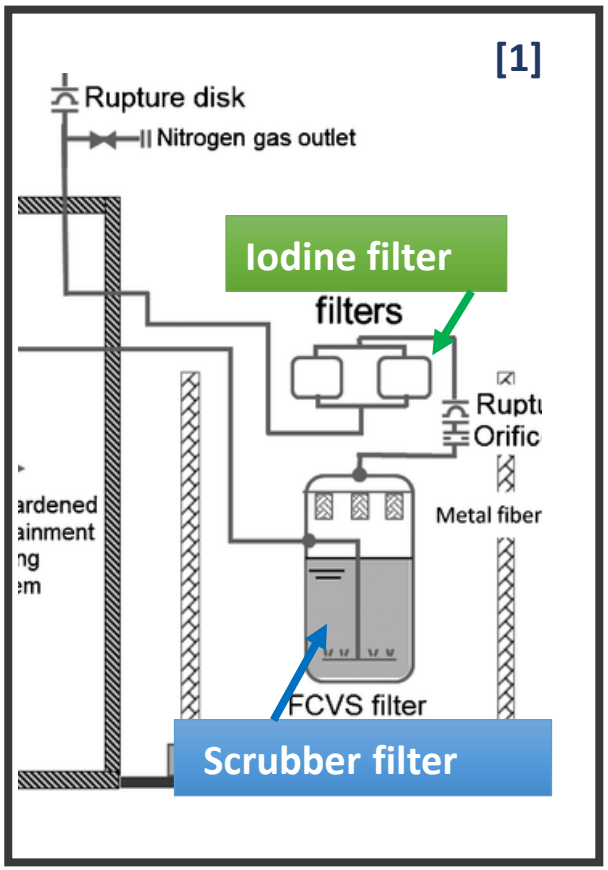

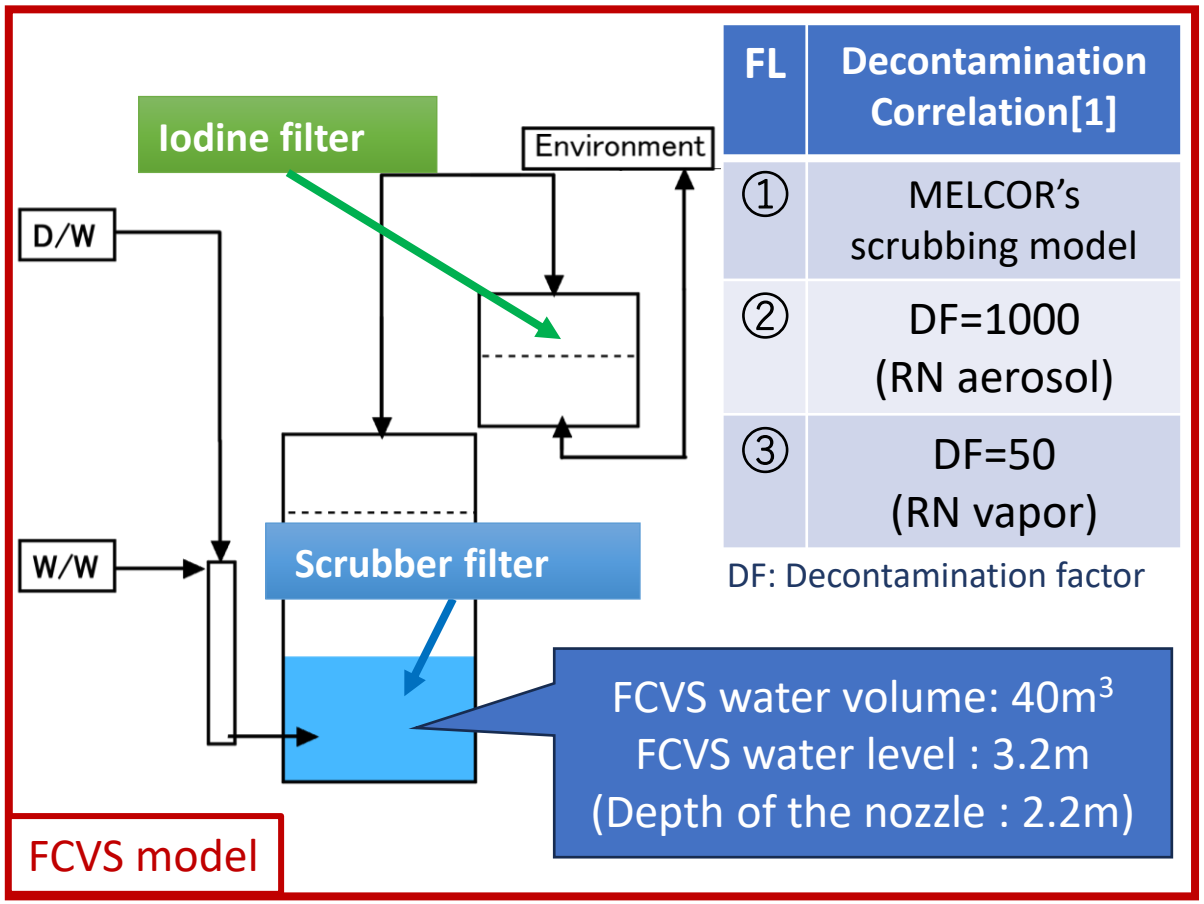

FL	Decontamination Correlation[1]
①	MELCOR's scrubbing model
②	DF=1000 (RN aerosol)
③	DF=50 (RN vapor)

DF: Decontamination factor

[1]Kawamura S, Ohmori, S, Kimura T, Umeda Y, Hashimoto K., Hirao K. Sasa D. 'Development of an organic iodine filter design and performance improvement of filtered containment venting system.'

Analysis scenario

Analyze 2 sequence - TQUV and **AE**

TQUV Scenario of failing to cool the core with the high-pressure injection system, succeeding in depressurizing the RPV, but failing to cool the core with the low-pressure injection system.

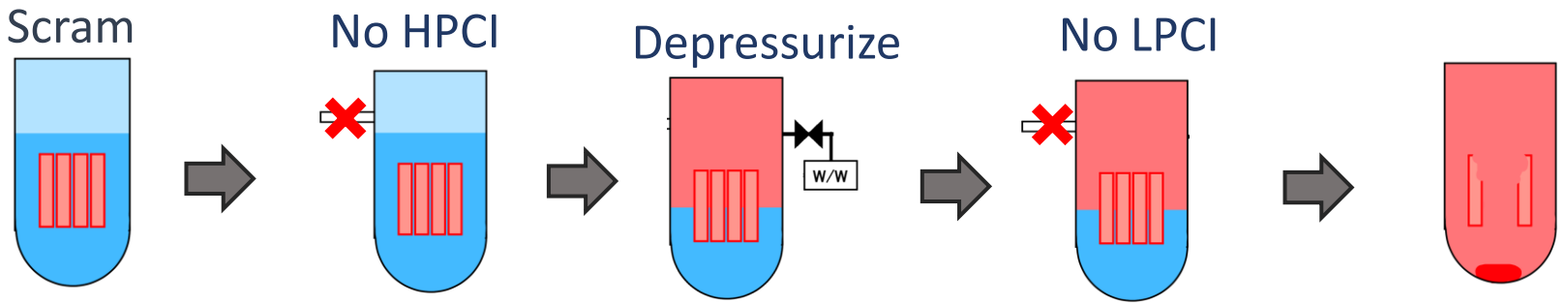

AE Scenario of failing to cool the core with high-pressure and low-pressure injection systems after 100% hot-leg break LOCA.

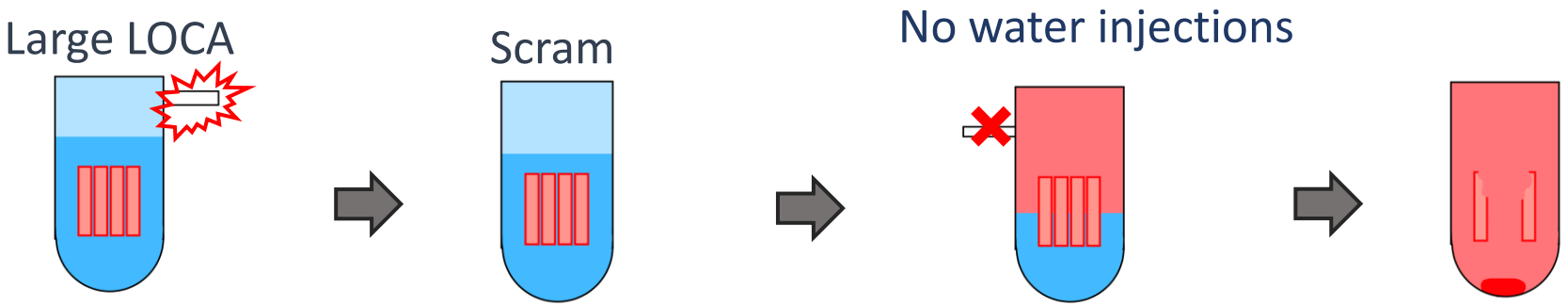

Analysis scenario

Analyze 4 cases - W/W-FCVS , D/W-FCVS , W/W , D/W

Core damage

D/W spray

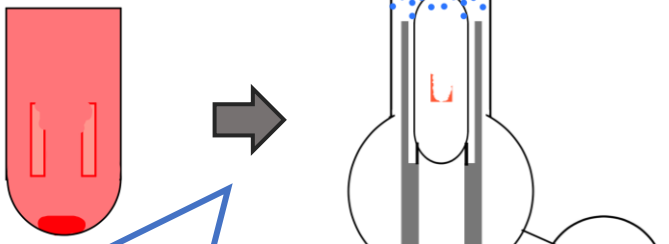

Spray conditions

120m³/h ,W/W source

ON D/W pressure > 565kPa

(1.5 × design pressure)

OFF start of PCV vent

Vent conditions

R/W H_2 mole fraction

> 0.09

combustion condition:

$X_{H2} + 0.6X_{CO} \geq 0.1$

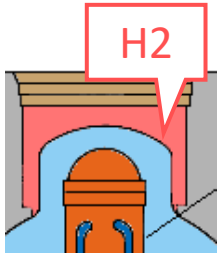

W/W vent

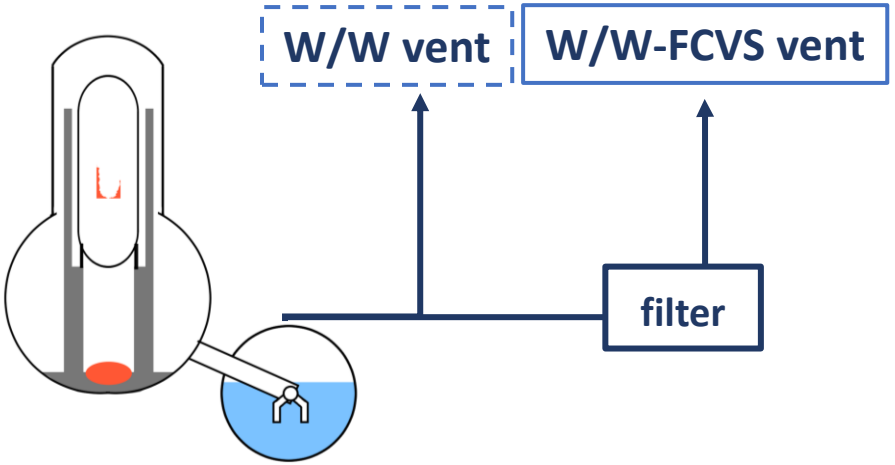

D/W vent

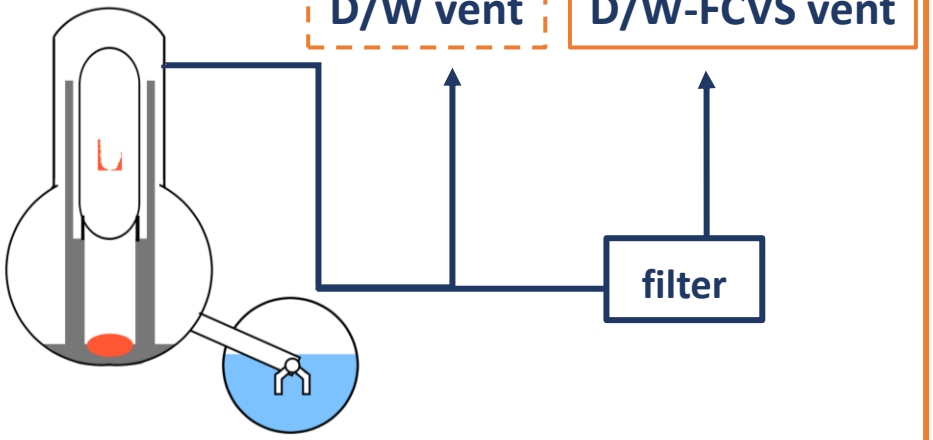

Outline

- **Background and Objective**
  Features and Issue of Ex-Containment H2 management in BWRs

- **Method**
  PCV and R/B model
  FCVS model
  Analysis scenario

- **Result**
  TQUV sequence
  AE sequence

- **Conclusions and Future Work**

TQUV：Until the PCV Venting

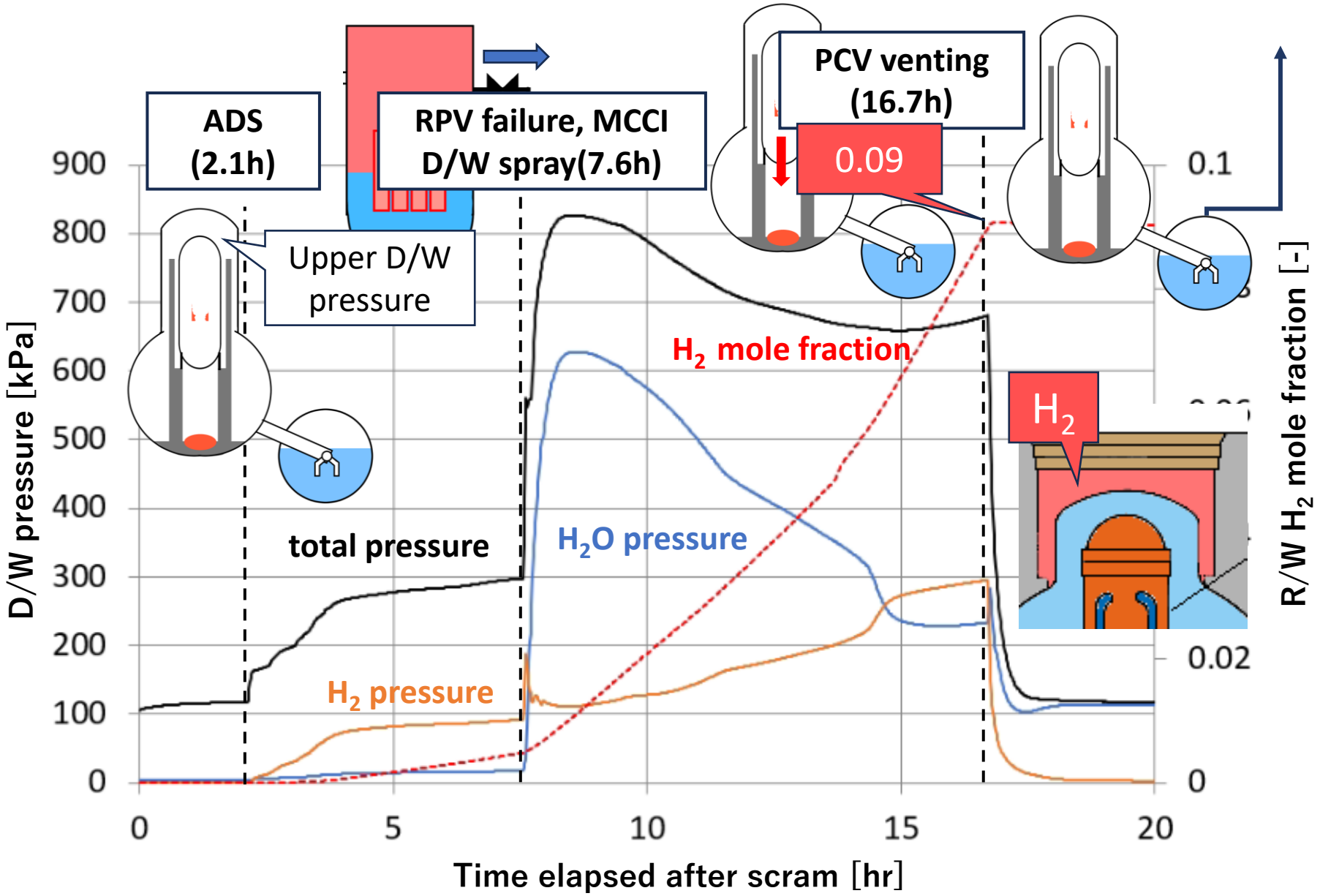

TQUV：Post Venting Phase

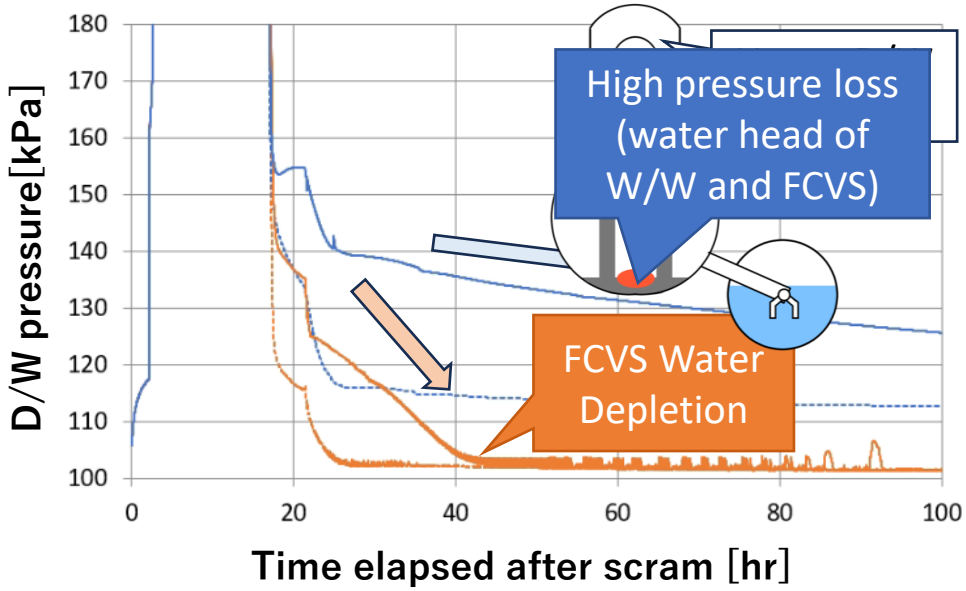

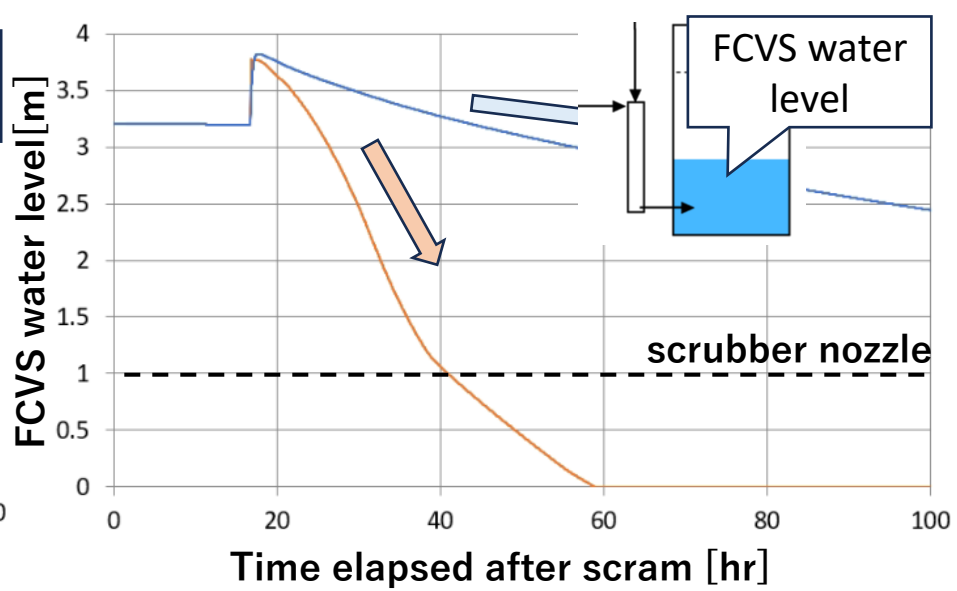

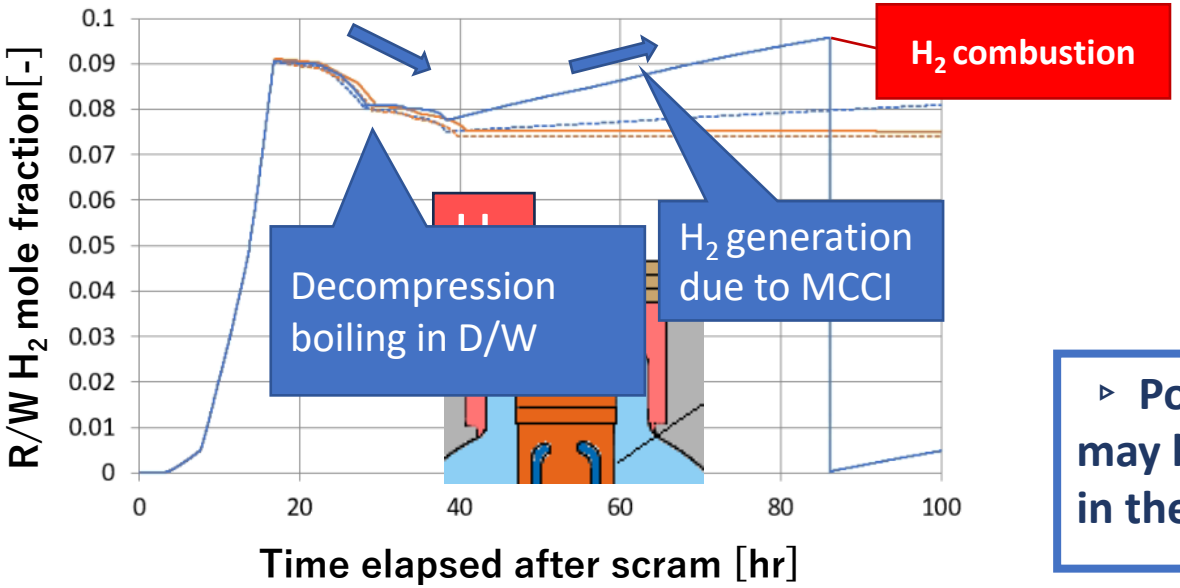



▹ **Post-venting residual pressure may lead to re-accumulation of H2 in the R/W.**

AE：Until the PCV Venting

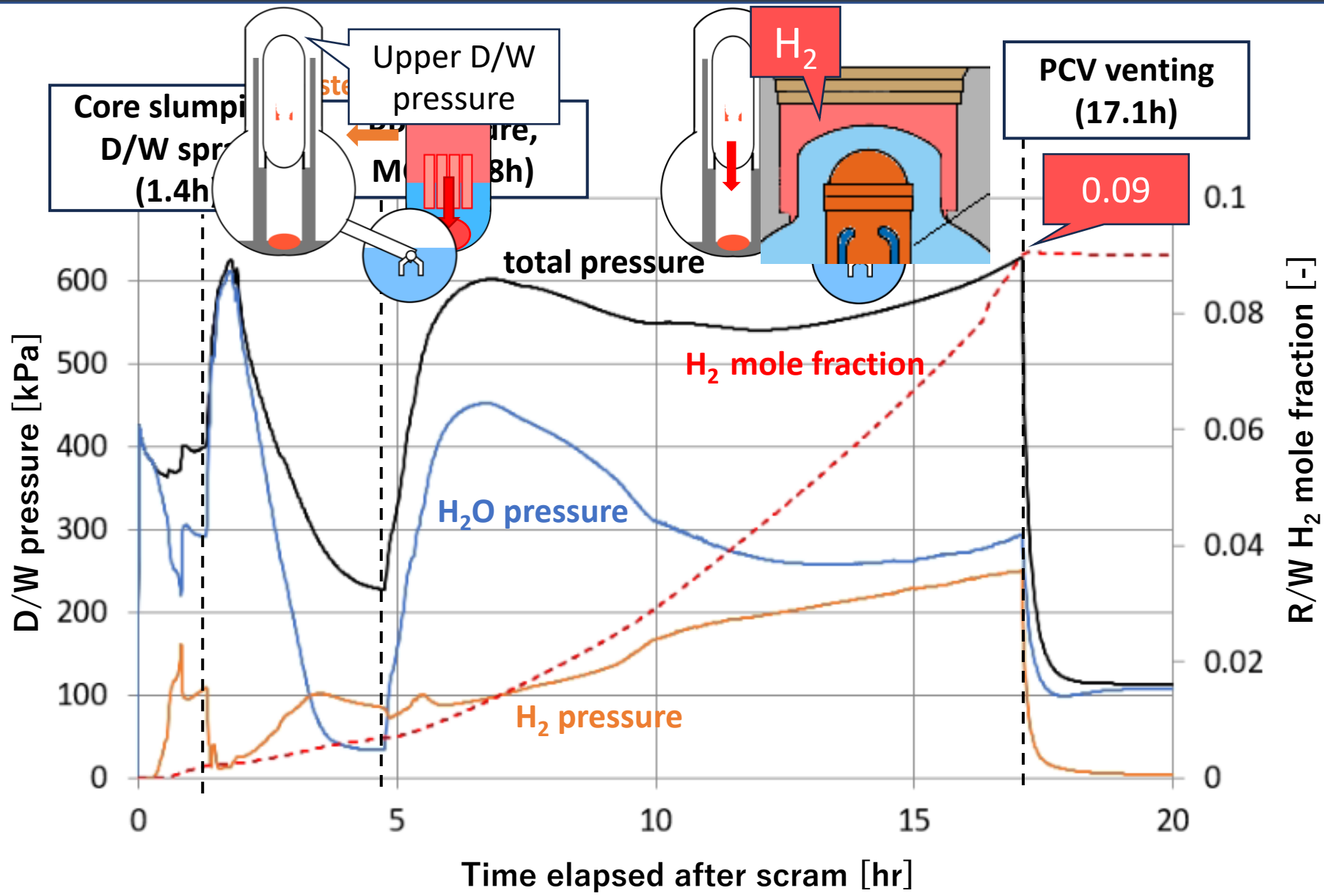

AE：Post Venting Phase

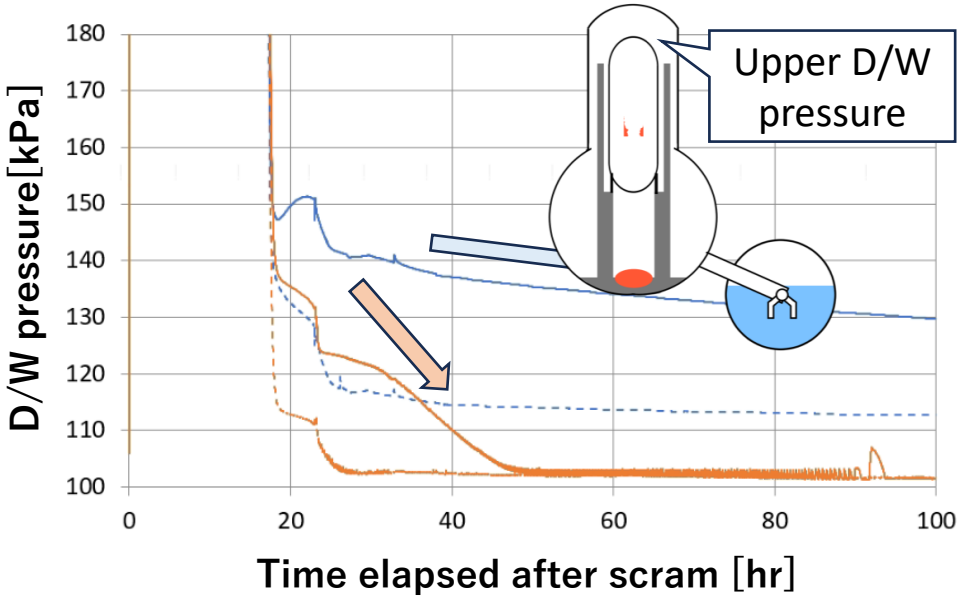

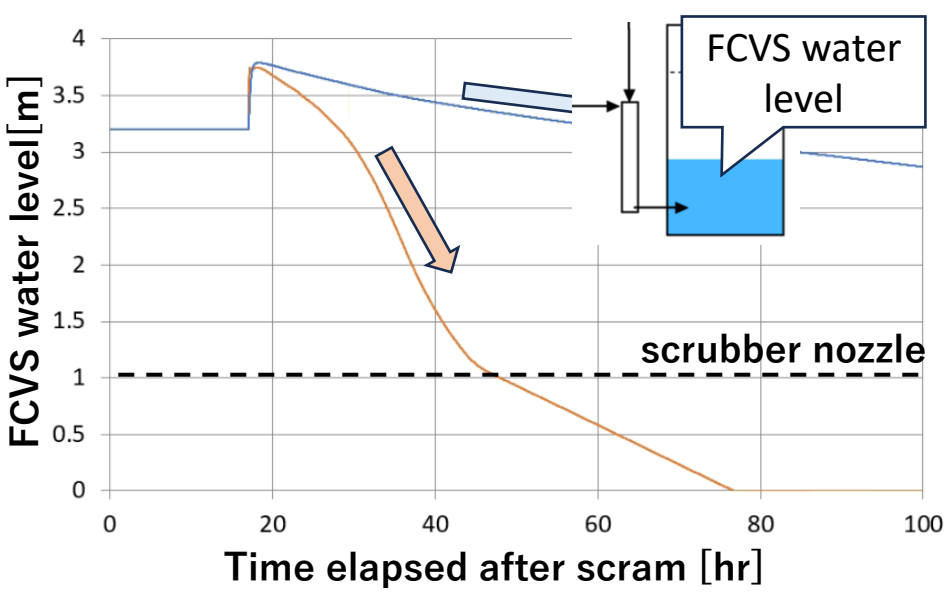

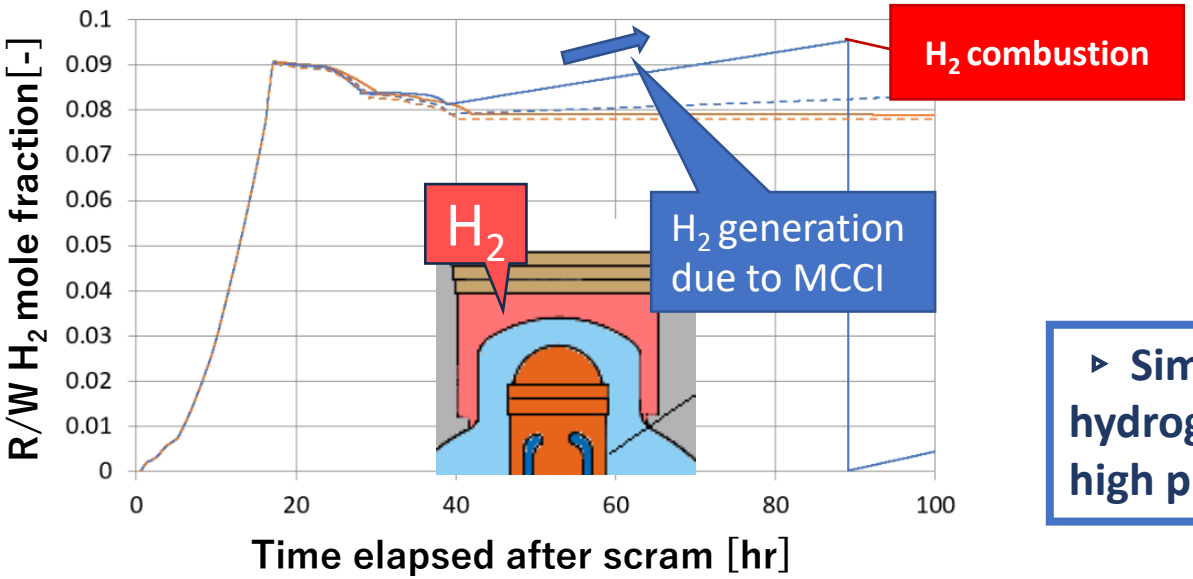

- W/W-FCVS vent
- W/W vent
- D/W-FCVS vent
- D/W vent

▸ Similar to the analysis of TQUV, hydrogen burned in a scenario with high pressure loss.

Outline

- **Background and Objective**
  Features and Issue of Ex-Containment H2 management in BWRs

- **Method**
  PCV and R/B model
  FCVS model
  Analysis scenario

- **Result**
  TQUV sequence
  AE sequence

- **Conclusions and Future Work**

Conclusions and Future Work

Conclusions

- When the R/W water injection fails and the venting timing happened to be just before the moment of H2 explosion in the R/W, the pressure loss of FCVS would lead post-venting H2 leakage and ex-containment H_2 explosion.

- The current study showed (after numerous trial and errors) that a very specific venting timing could exist.

Future work

- More analyses are necessary regarding accident scenarios that significantly affect the thermal state of the D/W after venting.

Thanks for your attention.

ON THE PROGRESS MADE IN SAFETY ASSESSMENT AND SEVERE ACCIDENT MANAGEMENT AS PART OF THE FRENCH FUKUSHIMA POST-ACCIDENT RESEARCH PROGRAMME

A. Bentaib[(a)], R. Meignen[(b)], L. Cantrel[(b)], S. Morin[(b)], G. Repetto[(b)]

[(a)]Institut de Radioprotection et de Sûreté Nucléaire
31, avenue de la Division Leclerc 92260 Fontenay-aux-Roses, France
ahmed.bentaib@irsn.fr
[(b)]Institut de Radioprotection et de Sûreté Nucléaire
BP 3 13115 Saint-Paul-Lez-Durance Cedex, France
renaud.meignen@irsn.fr; laurent.cantrel@irsn.fr; sandrine.morin@irsn.fr;
georges.repetto@irsn.fr

ABSTRACT

The Fukushima-Daiichi accidents in 2011 underlined the importance of severe accident management (SAM), including external events, in nuclear power plants (NPP) and the need of deepen safety research implementing efficient mitigation strategies. For these reasons, the French General Commissariat for Investment has released significant additional resources to strengthen research in this area. Within this framework, several projects have been launched on the highest priority issues, in order to fill the knowledge gap and reduce the uncertainties still hanging over the main phenomena governing severe accidents and their management.

Among them, the PERFROI, DENOPI, ICE, MITHYGENE and MIRE projects, led by IRSN, addressed remaining issues related respectively to fuel degradation and reflooding, spent fuel loss of cooling, fuel-coolant interaction, hydrogen risk and source term mitigation. For each of the projects mentioned, experimental and analytical activities were carried out to help understand possible accident scenarios and related phenomena, and to contribute to improving the safety of existing and future reactors.

This article gives an overview of the main results of these projects. The achievements in terms of modelling severe accidents and improving severe accident management are presented and their applicability to innovative reactors, including SMRs, is discussed.

KEYWORDS
Reflooding, spent fuel, ICE, hydrogen, source term

1. INTRODUCTION

Despite accident prevention measures, including design modification and operating procedures, used in the nuclear power plants (NPP) under operation, some accidents, within very low probability, may evolve into severe accidents with core melting and plant damage and lead to release and dispersion of radioactive materials into the environment, thus constituting a danger for the public health and for the environment. This risk was unfortunately evidenced by the Fukushima Daiichi accidents in Japan in March 2011, which

underlined the importance of severe accident management and the need to implement and to improve the corresponding mitigation strategies and systems. Moreover, the ENSREG (European Nuclear Safety Regulators Group) stress tests [1] and the French complementary safety assessment reports [2] have highlighted the need to further improve the safety of nuclear power plants. To this end, the French General Commissariat for Investment has released, in 2012, significant additional resources to strengthen research in this area. Within this framework, the PERFROI, DENOPI, ICE, MITHYGENE and MIRE projects, led by IRSN, were carried out with the objective to address remaining issues related respectively to fuel degradation and reflooding, spent fuel loss of cooling, fuel-coolant interaction, hydrogen risk and source term mitigation.
For each of the projects mentioned, experimental and analytical activities have been carried out, leading to a better understanding of the phenomena addressed and improvements to the corresponding models. These projects have also led to the development of new instruments, reliable under severe accident conditions, and the development of a coherent experimental database for the validation of LP (Lumped Parameter) and CFD (Computational Fluid Dynamic) codes.
In the following, each of the mentioned projects is briefly described and main achievements presented. The last section discusses the relevance of the obtained results to the advanced reactors as water cooled SMRs.

2. PERFROI project

During a loss of coolant accident (LOCA), the fuel assemblies may dry out partially or even completely. Under these conditions, the rise in fuel temperature and drop in coolant pressure in the reactor core can lead to significant deformation and breakage of the fuel rod cladding. Fuel fragmentation can occur, causing the fuel to move within the ballooned zone. Depending on the size and distribution of the ballooned areas in the fuel bundle, the cooling flow can be disrupted, which can compromise the cooling capacity of the fuel assembly and, by extension, the cooling capacity of the reactor core. The PERFROI [2] general objective is to study the coolability of a partially deformed core in the event of a loss of coolant accident (LOCA) and thus provide relevant data to improve accident management before a severe accident. To this end, the following two objectives were achieved:

Objective 1. concerns the study of the thermomechanical deformation mechanism and fuel rods burst under LOCA conditions. To this end, separate effects and integral were carried out respectively in the ELFE[1] and the COCAGNE[2] facilities (Figure **1**. Illustration of the COCAGNE facility.Figure **1**)

Objective 2. aims to characterize the thermal hydraulics behavior in the ballooned area, during cooling phase by water injection considering the effect of pressure and the water flow rate. To this end, dedicated experimental campaign was carried in the COAL facility (Figure **3**).

In the ELFE facility, several creep tests were carried out over a wide temperature range from 700 to 1030°C. The samples used were manufactured either in Zircaloy or in M5 alloy. The tests carried out enabled new strain rate values to be obtained for intact, pre-oxidized and pre-hydrated Zircaloy samples. The results obtained are in line with those reported in the literature [4]. The tests carried out showed that the creep rate decreases with the presence of a pre-oxide layer for low stresses, and it increases slightly with the hydrogen content [5]. However, the effect remains weak for stresses that are representative of the LOCA conditions. Tests were also carried out in a frame of a PhD [6] to get additional information on thermal mechanical properties on cladding including Hydrogen.

In the COCAGNE facility, the aim of the test campaign was to study the behavior of sections of Zircaloy-4 rods during ballooning of the cladding, considering contacts between rods. To this end, various conditions

[1] (Etablissement des Lois de FluagE) device on IRSN's MAESTRO experimental platform at Cadarache

[2] (COmportement d'un Crayon en APRP soumis à un GradieNt de températurE) device on IRSN's MAESTRO experimental platform at Cadarache

were considered: internal pressure varying from 20 to 100 bar; temperature increase ramp of 1 to 5°C/s or state of the sample: single or double-sided oxidation.
The main outcomes of these experimental campaigns [7] can be summarized as follow:

- Increasing the internal pressure increases the deformation at rupture, as well as the temperature at the moment of bursting. On the other hand, double-sided oxidation leads to less deformation of the rod;
- The observed opening formed on the burst balloons have the shape of an "elongated fish mouth" for tests performed at 20 and 50 bar and a rectangular shape for tests performed at 100 bar;
- There is a linear dependence between the size of the fishmouth-shaped openings formed in the test carried out at 5 and 10°C/s.
- The axial deformation profiles of the rods revealed balloon lengths with radial deformations (example in Figure **2**) greater than 41%, corresponding to a clogging rate of the passage section of 80%, and deformation peaks of up to 65 and 80%. A radial deformation of 50% corresponds to a clogging rate of 90%.

These COCAGNE thermomechanical tests therefore validate the choices of clogging rates and cluster rod balloon lengths for the COAL experimental campaign.

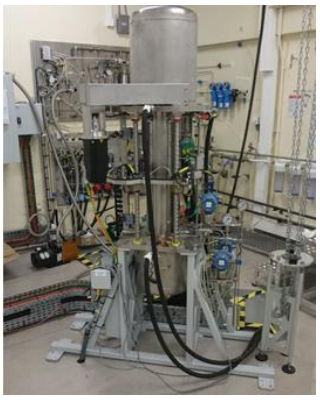

Figure 1. Illustration of the COCAGNE facility.

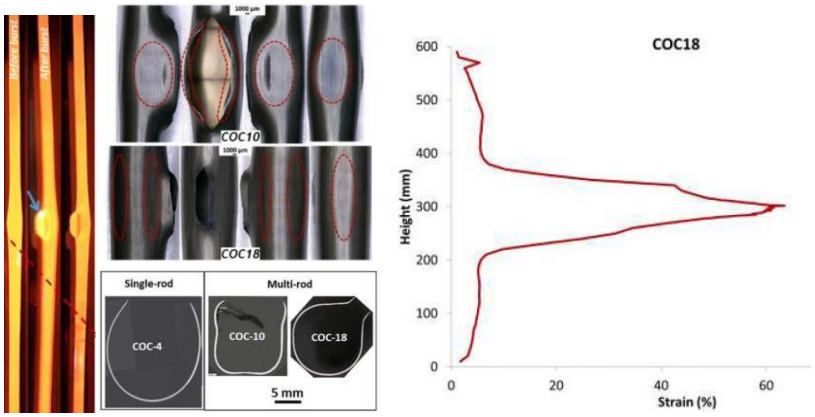

Figure 2. typical results of rod deformation during COCAGNE experiments.

In the COAL facility (Figure **3**), the objective followed was to investigate the antagonistic influences that may have the presence of a blockage induced by the rods ballooning on the flow. On one hand, the reduction of the section between the deformed fuel rods will increase the flow velocity [8]. On the other hand, the flow bypass [9] from the deformed fuel rods (Figure **4**) in the blocked region to the peripheral intact rods (crossflow phenomena), will lead to a reduction of mass flowrate.
82 experiments were performed (28 tests for B0 reference campaign in 2020, 26 tests for B1 campaign in 2021 and 28 tests for B2 campaign in 2022) to investigate the different physical main inlet parameters considering a wide range of parameter pressure (2, 3, 5, 10, 15, 20 and 30 bar), water injection speed (17, 20, 25, 30, 36, 50 and 80 kg/m2/s) and rod power (1.5, 2, 2.4 and 3.3 kW per rod). B1 and B2 campaigns were performed with bundles including a partially blocked by ballooned rods at a blockage ratio respectively 80% and 90% (length of 100 mm and 300 mm), including a local power in the balloons of factor 1.5 with respect to the normal cosine profile in order to take into account the fuel relocation in the balloons, more representative to irradiated fuel rods with fragmented pellets.
These COAL experiments [10] highlighted very important results concerning the duration of reflooding and the impact on the local cladding temperature peak due to the presence of a plug in a fuel assembly (see Figure **4** a). The maximum temperature (1105°C) was obtained during the test (Figure **4**b) from [11] performed at low pressure (0.3 MPa – 3 bar) with the maximum power per rod (3.3 kW) and a medium water flow rate (25 kg/m^2/s, i.e 2.5 cm/ s) for the B1 configuration.

We succeed to perform high pressure tests from 1 up to 3 MPa which was one of the major objectives of the COAL experiments to investigate the coolability for Medium Break size LOCA conditions.



a)



b)

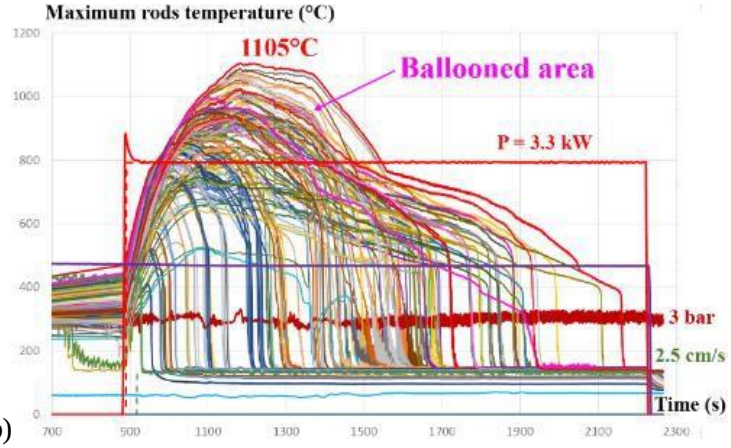

Figure 3. Illustration of the COAL facility.	Figure 4. Ballooned rods and typical thermal results of reflooding experiments.

These COAL experiments outlined very important results regarding the duration of the reflooding and the impact on the PCT (increase of peak cladding temperature) due to the presence of a blockage inside the fuel assembly. These experiments will provide thermal hydraulic information needed to improve the codes modelling during the reflooding under LOCA sequence, with the thermal behavior of the rods in a well define boundary conditions (heated shroud at well controlled temperature) and all the hydraulic parameters such as the water (as droplets) and the steam flow at the outlet of the test section. Once the simulation tools validated in such complex configuration, there may be used for safety study in real nuclear reactor conditions.

3. DENOPI project

Following the Fukushima-Daiichi accident, the international community identified R&D needs regarding loss of cooling or coolant accident in Spent Fuel Pool (SFP) [12]. To enhance knowledge on accidental SFP conditions and to better evaluate the safety margins, the DENOPI project was launched aiming at improving the knowledge of thermal hydraulics phenomena involved in SFP accident prior to the severe accident phase, to evaluate the efficiency of water spray system as mitigation means[3] and to analyze the fuel clad oxidation. For these purposes, experimental campaigns had been conducted considering different time frames of the LOCA accident and different scales of interest providing then valuable data for model development and code validation. Thus, several facilities with different scales were used at clad scale using standard laboratory equipment, at the fuel assembly scale, in ASPIC facility (see Figure **9**), and at integral scale with pool, in the MIDI facility (see Figure **5**).

3.1. Thermal hydraulics in a large basin: MIDI

The MIDI facility is dedicated to the study of thermal-hydraulic phenomena on the full scale of a SFP in the event of a loss-of-coolant accident by contributing to better understanding of natural convection flows and closely coupled vaporization regimes. Three main modes of water vaporization are likely to occur in a pool with a heater located at its lower end, such as spent fuel pools: evaporation at the free surface, pool flutter

[3] Fuel degradation and fission products release are not addressed in the framework of the DENOPI project

and nucleate boiling inside the fuel assemblies. Their appearance and potential predominance are closely linked to large-scale natural circulation in the pool.

The MIDI facility is designed as a scale model of a typical French SFP, with a ratio of 1:6 for the free surface and 1:3 for the height of the pool [14] (see Figure **5**) and is well instrumented to measure heat and mass transfer. The MIDI's characteristics are given Table 1, it is scale by homothety of SFP and maximum stored residual power. The height and total heating power of the facility were both distorted to allow studying, in a parametric way, the contributions of the three different vaporization modes, to the pool energy bdget (free surface evaporation), the nucleate boiling of water along the spent fuels and the gravity –driven flashing of superheated water. The last step was to check that the main hydrodynamic and thermal regimes which might be reached during a SFP loss-of-cooling accident may be well reproduced using MIDI. For those purposes, a set of selected dimensionless numbers resulting from a similarity analysis introduced in [13], was computed for both MIDI and the prototypical SFP scales. This facility can be operated at different stages of the accident by varying parameters such as the initial pool level (from 0.5 to 4.5 meters above the simulated 3X7 cell storage rack, see Figure **6**), the loading pattern into the storage rack or the overall power (from 0 to 50 kW per cell depending on the residual power distribution in an SFP) and the maximum overall heating of 300 kW.

Table 1: Geometrical parameters of the MIDI facility and scaling factors.

Parameters	MIDI facility	Prototypical SFP	Scale ratio
Maximum water level (m)	4.0	12.0	1/3
Bundle active length (m)	0.7	~ 4.0	~ 1/3
Basin width (m)	1.35	8.50	1/6
Basin length (m)	2.10	12.60	1/6
Rack flow section (m²)	0.65	22.86	~ 1/35
Free surface area (m²)	2.835	107.1	~ 1/36
Bundle width (m)	0.225	0.225	1/1
Bundle porosity (-)	0.61	0.57	~ 1/1
Number of cells (-)	21 (7X3)	792	~ 1/37
Power range (kW)	[50;300]	10 000	-
Max. power per bundle (kW)	50	58	~ 6/7
Volumetric power (kW/m³)	[4.2;25.1]	7.8	-

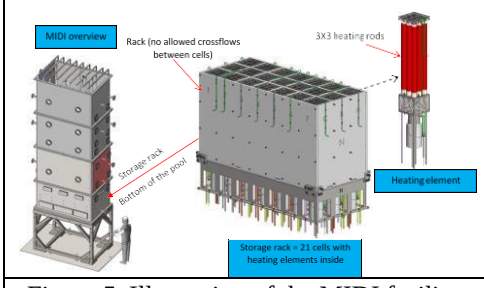

Figure 5. Illustration of the MIDI facility.

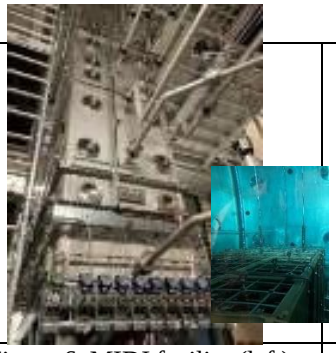

Figure 6. MIDI facility (left) and the 189 heating elements simulating the spent fuels

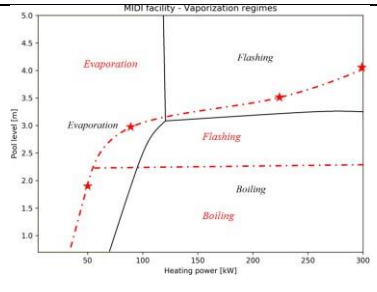

Figure 7 Vaporization regimes map

	assemblies in 3X7 cells inside the pool (right).	

The performed experiments confirmed the anticipated phenomenology with the competition during the transient of three modes of vaporization: evaporation at the free surface, boiling in the fuel bundle and "flashing" of superheated water above the racks. The “flashing” vaporization mode is highlighted in a 3D geometry such as a parallelepiped pool. Under MIDI test conditions, in addition to the evaporation that exists throughout the transient, "flashing" is the vaporization mode which participates the longest time to mass loss. Indeed, boiling begins to contribute to the loss of mass only at the end of the transient when the water level is approximately one meter above the rack. The existence of a gravity flow of superheated water in a pool heated from below was demonstrated in the DENOPI experiment. The phenomenon would preferably occur on unheated immersed surfaces such as the side walls, which would develop in the mass of liquid. Secondly, it was pointed out that the degassing process is generally completed before the liquid flashes/boils-off, and that it is maintained for a short time at that point. The tests highlighted the important role of certain parameters in the onset of flashing, in particular dissolved gases when the liquid begins to overheat. or the above free surface conditions.
Based on the obtained experimental data, analytical modelling of the vapor diffusion process was proposed as well as the free surface evaporation, degassing of dissolved non-condensable species and bubbles escape processes. A vaporization regimes map as a function of the residual power and water level was also dressed (see Figure **7**).

3.2. Thermal hydraulics in a spent fuel assembly: ASPIC

The second topic addressed in the framework of the DENOPI project concerns the coolability of an assembly during or after dewatering but before fuel clad degradation. The ASPIC facility is designed to study, at the assembly scale, different SFP accidents scenarios during partial or total fuel assembly uncovery. The ASPIC is a full height electrically heated 17x17 rod bundle (4 meters) in a cell (equivalent to a cell of a storage rack in SFP), see Figure **8** and Figure **9**. The assembly has the full geometrical characteristics of a standard PWR 900MWe assembly with prototypical top nozzle, spacer grids, and mixing grids [14]. Experimentation on the scale of the assembly makes it possible to study the thermal-hydraulics parametrically and to carry out different scenarios.

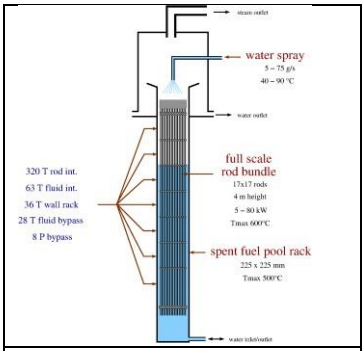

Figure 8. Main characteristics of the ASPIC facility.



Figure 9. ASPIC facility (left) and the 17x17 electrically heated and instrumented fuel assembly inserted inside the ASPIC test section (right)

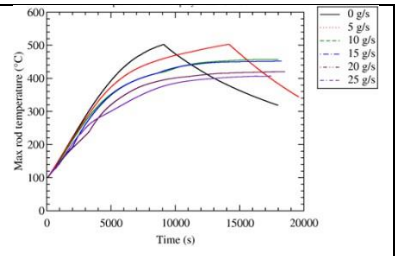

Figure 10. Impact of the spray mass flow rate on the mean rod temperature at the upper part of the assembly

To assess the cooling efficiency of the spray, experimental campaign was carried out by varying the following parameters: the residual power of the assembly (10, 40 and 60 kW - 60 kW corresponding to a hot assembly according to the safety reports of the French PWR900), the height dewatered (1 m or 2 m), the mass flow rate of the sprinkler (10, 15, 20 and 25 g/s – 25 g/s to compensate for the steam production

generated by a assembly of 60 kW), the sprinkling temperature (80 °C) and the criterion of spraying trigger it the water temperature (200, 300°C and 400°C). The obtained results show that on one hand the spray temperature does not have a significant impact on the temperature evolution in the assembly and on the other hand, the spray flow rate significantly modifies the kinetics of the temperature of the assembly (see Figure **10**). Moreover, the test campaign outlined that for 20kW of residual power and one meter of dewatering, the spray flow rate of 10g/s maintained the temperature of the assembly below 500°C. Within, DENOPI projects provides first answers on the aspersion efficiency to cool of an assembly, further investigations are needed to determine the assembly coolability limit considering spray as mitigation means.

3.3. Oxidation of the clad in accidental condition

After assembly uncovering, the exothermic oxidation of the zirconium alloy cladding material becomes significant and contributes noticeably to the overall heating power and lead to hydrogen production. In the framework of DENOPI, Zircaloy 4 oxidation kinetics laws under mixed air-steam atmosphere had been studied with the objective to understand the protective effect (or its absence) of the pre-existent oxide layer formed during in-reactor irradiation (called pre-oxide hereafter). Particular attention was paid to the effect of a low temperature pre-oxidation scale that as far as possible simulates the corrosion scale formed in reactor during in-service operation.

The performed experiments highlighted the effect of defects or singularities of the pre-oxide [15], see Figure 11 & 12. Actually, it was observed that oxidation begins from the edges. To discard experiment artefact, tests were performed with Zy-4 spherical beads to eliminate edges. The protective effect is then linked to the presence of pre-existing defects. It is expected that in real fuel rods, such defects might be preexisting or created by clad swelling due to heat-up. Finally, a kinetic model considering the influence of the partial pressure of oxygen and steam has been developed for implementation in the ASTEC code developed by IRSN.

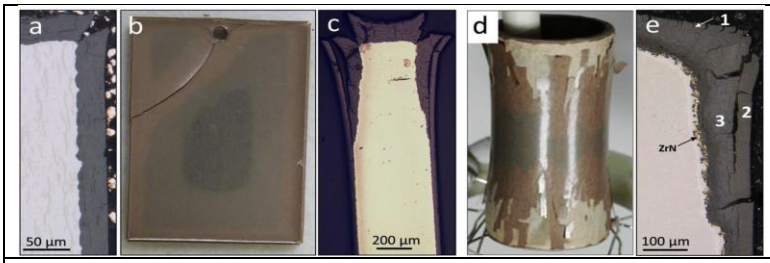

Figure 11 a) Cross section showing the defect of the pre-oxidation scale at the edge of a pre-oxidized Zy4 plate. b) and c) Zy-4 plate, pre-oxidized then oxidized at 850 °C in 40% air +5% steam +55% He during 125 min, ECR= 7.1%. d) Zy-4 tube, pre-oxidized, cut to a 20 mm length, then oxidized at 850 °C in air +30% H_2O during 163 min, ECR_{HT} = 8.5%. e) Cross section at one of the edges of specimen presented in d); 1= dense oxide first formed on the initially bare end surface, 2= pre-oxide scale, 3= porous oxide.

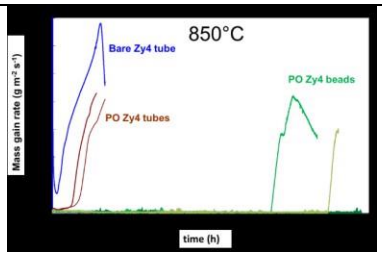

Figure 12: Isothermal oxidation tests in dry air with bare and pre-oxidized Zy-4 tubes and beads, at850°C. Different green colors are used for the different tests on beads. More details in [15]

4. ICE project

The goal of the ICE project is to improve the knowledge and modeling the interaction between the fuel and the coolant during a melt relocation phase in the event of a nuclear reactor core meltdown accident. Pressure build-up, hydrogen generation though oxidation and debris bed constitution are the foreseen outputs of the models. But the associated major risk is that of the occurrence of a destructive explosive interaction. The understanding of such phenomena is crucial to identify ways to enhance the mitigation of this risk. The

project main objectives follow closely the conclusions of the OECD SERENA-2 program [16], with an orientation of research towards 3 areas:

- the melt fragmentation and mixing in the coolant, being the leading phenomenon, still needing improvements in understanding and thus in modeling;
- the so-called material effect, including oxidation and solidification, being the area with most important uncertainties;
- the mechanisms of pressurization during the steam explosion; the existence of 2 general types of models with antagonist fundamental hypotheses, e.g. Micro-Interaction versus Non-Equilibrium heat transfer, highlights clearly the lack of understanding.

To achieve this goal, the strategy adopted several interconnected steps as indicated in Figure 13. The performed experiments and simulations provide then unique database to improve the FCI models the MC3D software, a digital simulation tool developed by the IRSN with the support of EDF.
Additional tasks regarding MC3D were related to the modeling of the behavior of the coolant (flow patterns) and to numerical issues.
Indeed, it was decided to extend the project with the decision to build a totally revisited version of MC3D, said version 4, with a new architecture to improve versatility and allow parallel computing (MPI process), preserving most the physical description principles and models but enhancing/clarifying where necessary.

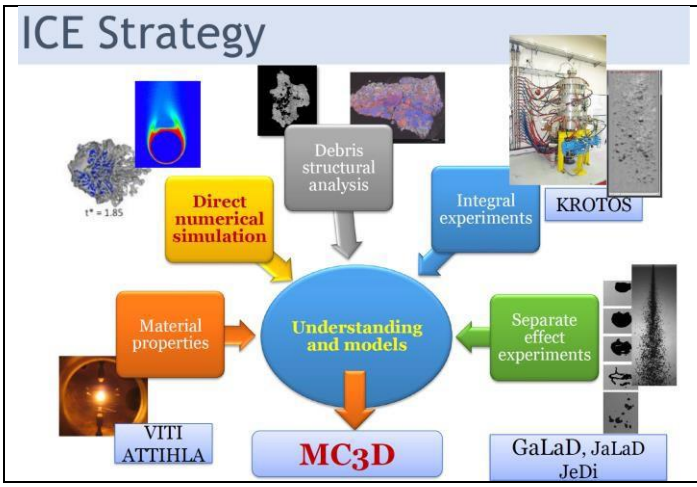

Figure 13. General strategy of the ICE project**.** Analyses - based on integral experiments in the KROTOS installation (CEA), material properties measurements and debris structural analysis (CEA), separate effect experiments on metal drops and jets fragmentation in water (LEMTA/CNRS) and Direct Numerical Simulations on phenomena related to the explosion phase (IRSN) - are gathered to improve understanding and modeling in the multiphase flow code MC3D.

4.1. Some results of the KROTOS experiments

KROTOS is a mid-scale facility built at JRC-Ispra to explore the energetics and propagation characteristics of steam explosion [17]. It has been transferred to CEA-Cadarache in 2000 to continue investigating the pending FCI issues using prototypical corium melts. Apart from the numerous sensors installed along the test section, the facility comes with a high energy X-ray system to enable a detailed visualization of the flow evolution: melt progression and fragmentation, production and dynamics of the void in the mixing zone. 4 tests were performed, one of which, KA-1, was devoted to get more information about fragmentation processes and debris bed formation, using UO_2-ZrO_2 corium, Figure 14. The test KA-4 was devoted to explosion, using a corium composition expected to be more realistic, including some fission product simulant oxides, which strongly expands the interval liquidus-solidus [17].

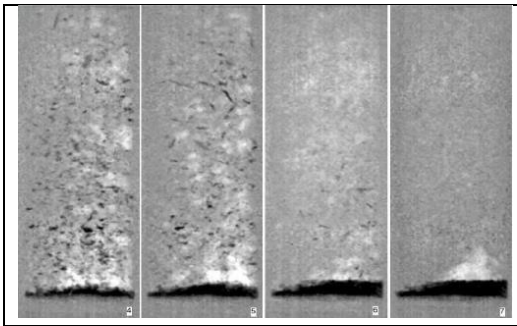

Figure 14. Observation of debris bed formation in the KROTOS KA-1 test

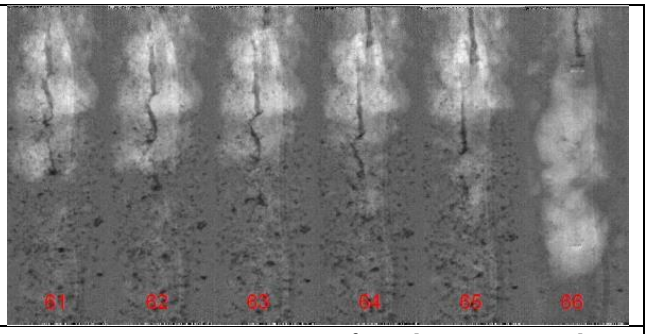

Figure 15. Raw X-ray images from the KA-4 test. The last image is after the explosion trigger.

The debris of the tests were collected and examined with different other CEA installations to analyze the composition, the thermos-physical properties and the internal structure. Of particular interest was the extent and role of oxidation of a stoichiometric or sub-stoichiometric $(UZr)O_{2-x}$ composition.

4.2. Fragmentation studies

The largest part of the research ICE program was devoted to study fragmentation. Small-scale to mid-scale experiments have been built by LEMTA/CNRS to investigate the fragmentation of a liquid metal in water, without considering boiling aspects, thanks to advanced visualization and post-treatment methods. One particular issue was to get information on drop fragmentation in water, a configuration for which very limited information is available in the literature, in contrast with drop/gas case. The GaLaD experiments [19] provided important information on drop fragmentation in liquids, highlighting important differences compared to the fragmentation in gas. These data were complemented by Direct Numerical Simulations performed with the Gerris and Basilik softwares [20-21]. A particularly important finding is that the fragmentation occurs without dispersion of the fragments (as in gas), these ones being trapped in the wake (see Figure **17**). This gives strength of the so-called "Micro-interaction" process during the explosion, a concept popularized by Theofanous.

JaLaD is an upgrade of GaLaD to allow small jet studies. However, a larger-scale facility called JeDi has also been built. Information on the fragmentation process could be obtained from post-processing methods, (see e.g. Figure **16**) An important conclusion is that the fragmentation occurs through a 2-step cascading mechanism, with an integral scale mechanism driven by tangential Kelvin-Helmholtz like destabilization process followed by a local-scale fragmentation mechanism. This hypothesis has been translated to a model for MC3D involving both primary large-scale and secondary small-scale mechanisms.

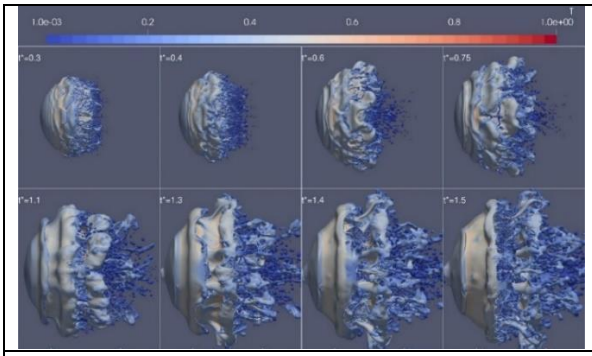

Figure 16. Simulation with Basilisk software of the fragmentation of a metal drop submitted of a velocity jump of the ambient liquid fluid [21].

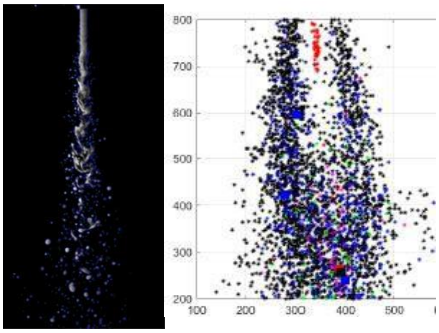

Figure 17. Laser sheet visualization and post-treatment of a test with Cargille as jet fluid. The right figure shows the fragmentation event. [22]

4.3. Outcomes of studies related to oxidation.

Despite the expected scenario related to ex-vessel FCI, where the melt is expected to be fist a metallic mixture (SS-Zr mainly), oxidation is incorporated only in few FCI codes, with poor verification, very parametrically. Although the general mechanisms are well-known, the very high temperatures involved, and the liquid nature of the fuel leads to strong uncertainties. The theoretical works were focus on the elaboration of a modeling for MC3D, based on a scarce and quite old experimental database, although recent studies could also be considered [23]. In principle, oxidation is limited by external diffusion processes in the gas boundary layer (in the film in the situation of film boiling) and internal ones in the melt. Attention has been focused first on the external processes. No data has been found for the drop in gas configuration and numerical simulations allowed to build and verify a proposed correlation. As for the oxidation in water, though film boiling, the new model (not published yet) allows to retrieve the dynamics and strength of oxidation in most cases without the need for a precise modeling of the internal diffusion. This conclusion needs to be strengthened but it would be quite fortunate as internal diffusion is a pure matter of material properties, which represents a particular difficulty.

4.4. On the pressurization process during explosion

This issue was tackled though direct numerical situations. As already mentioned, fragmentation process could be largely clarified [21]. Note that these simulations did not account for the boiling. It is believed that this is not a too strong hypothesis for a large part of the process, which occurs at very high pressure mostly before the expansion process with large void production [24]. Meanwhile, other DNS studies related to the boiling process, made with a specific application of MC3D code, concluded on the existence of a film even at very highly supercritical conditions, so that film boiling correlations are still usable during this process. Although there is not real interface, a film composed of hot light water (quasi-vapor) separates the melt fragment and the cold heavy liquid with a strong thermal disequilibrium. The overall conclusion is that the principles of the two “opposite” general models of ‘Micro-Interaction’ and ‘Non-Equilibrium heat transfer’ should be joined to a ‘Non-Equilibrium Micro-Interaction model’. Non equilibrium transfers occur very locally, and micro-interaction occurs dynamically at the scale of the fragmenting drop.

4.5. Status of MC3-V4

The analyses made during the project led to numerous improvements of the MC3D code in the latest version 3.10. However, some of the foreseen improvements were found difficult to implement and subject to instability. Also, discussion with partners led to the need to launch the development of a totally revisited version of the code, with a new application for FCI as a first goal. The version is based on several innovative features:

- New architecture allowing a step-by-step construction of an model through the deployment of intermediate but possibility autonomous applications (see Figure 18);
- Multi-Domain structure to allow fast building of data sets with complex geometries.
- Parallel computing based the multi-Domain capabilities (MPI);
- Simplified interface for the user with a new notion of “meta-models”, collections of coherent models and parameter setting with different levels of complexity.

The complete version of the FCI application is expected end of 2024.

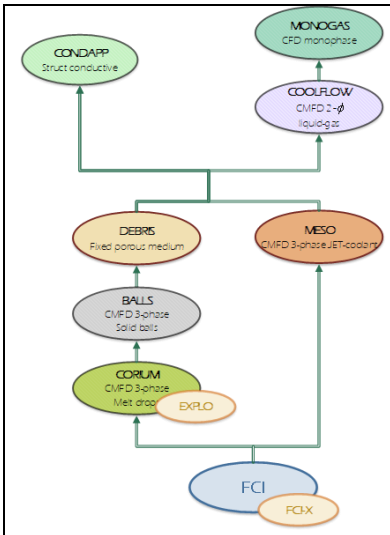

Figure 18: Scheme of application architecture for the build-up of a new FCI application.

CONDAPP application does not involve fluid movement but introduces multi-material capabilities of the melt in a simple conduction model. MONOGAS is for pure gas flow. COOFLOW is new two-phase flow application. DEBRIS is a new feature of the model, introducing the management of debris bed through the agglomeration of solid material. CORIUM adds a multi-field model to describe the melt drops (MUSIG method), whereas MESO introduces the JET field of version 3 to describe continuous melt. MESO will also be used for DNS-like studies at the scale of the drops to further investigate mechanisms of boiling, solidification and oxidation.

FCI is the ultimate application, built from double heritage of CORIUM and MESO. The Jet in MESO will be allowed to fragment into the Drops of the CORIUM app. EXPLO and FCI-X will be used for steam explosion calculations. These are in fact only mostly model modifications from respectively the CORIUM and FCI applications.

5. MITHYGENE project

After the Fukushima Daichi accidents, the European stress tests highlighted the need for further research to practically eliminate containment failures due to hydrogen combustion. To this end, the MITHYGENE project explored ways of strengthening the capacity of safety tools and the management of hydrogen-related risks in nuclear power plants [27]. Fundamental and applied research activities were carried out on the remaining safety issues related to hydrogen distribution and combustion, as well as flame-structure interaction. In addition, in situ gas monitoring prototype, reliable with severe accidents have been developed, with the objective to provide information on containment atmosphere flammability in emergency conditions. The updated models and codes were then used to analyze the hydrogen explosion occurred in the Fukushima Daïchi NPP. In the following and for each of the mentioned area, selected achievements are presented and discussed.

5.1. Hydrogen distribution: effect of passive autocatalytic recombiners location

To prevent the risk of hydrogen explosions and limit their consequences, most mitigation strategies adopted in Western countries are based on the use of passive autocatalytic recombiners (PARs). PAR operation converts hydrogen to steam in an exothermic chemical reaction that activates the natural convection flow which brings hydrogen to the PAR inlet ensuring then its passive operation. This convection flow affects the distribution of hydrogen in the surrounding area and, consequently, the efficiency of recombination. As the PAR implementation design was mainly carried out using LP codes, the effect of the convection flow on PARs efficiency is not explicitly addressed. To answer the question of PAR location effect on its efficiency and consequently derive recommendation for optimal PARs implementation design, experimental campaigns were carried out in the MISTRA facility.

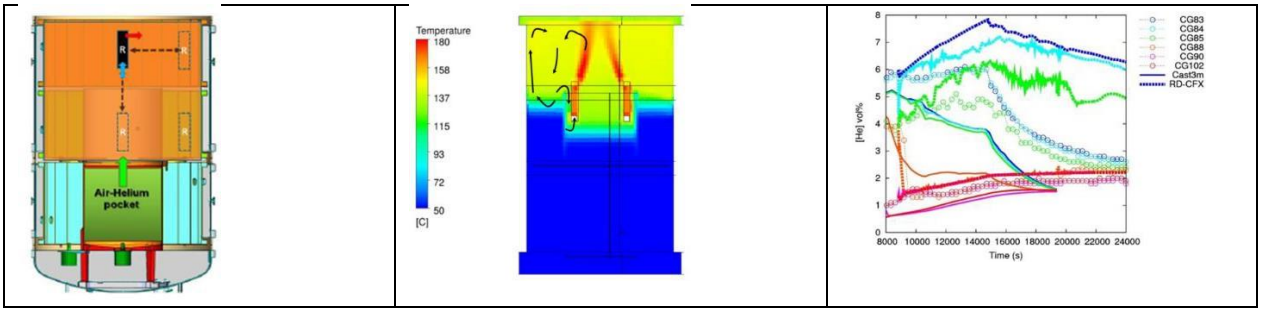

Figure 19: MISTRA facility scheme	Figure 20: illustration of convection loop induced by PARs	Figure 21: example of CFD analysis results of PARs experiments

The obtained experimental data were used validate the CFD models [28]. The analysis of the experimental and numerical results help deducing recommendations on the PAR optimal locations that allow atmosphere mixing and high recombination rate.

5.2. Hydrogen combustion

For combustion, experience feedback and lessons learned from the various benchmarks (HYCOM, SARNET, SARNET2 and ISP49) [25][26] show that the calculation codes can predict reasonably well the combustion pressure peaks. Hower, most of the combustion models were not able to predict the flame regimes observed experimentally in particular the transition to detonation, as was a priori the case for the explosion that occurred in reactor 3 at the Fukushima Daïchi NPP. In the framework of the MITHYGENE project, the new highly instrumented ENACCEF2 facility had been constructed with the objective to provide relevant data to fill the knowledge gap regarding: 1) water vapor effect on hydrogen flame propagation, 2) initial temperature effect on hydrogen flame propagation, 3) initial mixture heterogeneities on hydrogen flame regimes and 4) water spray actuation on hydrogen flame propagation regimes. To this end, several experimental campaigns were performed providing then unique data for combustion modelling improvement [29].

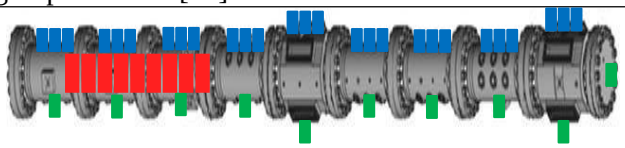

Figure 22: ENACCEF 2 facility

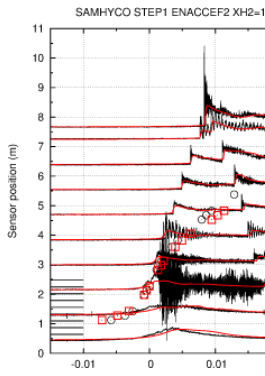

Figure 23: example of pres
along the ENACCEF 2 hei

The experiments thus carried out contribute to filling the lack of data on the hydrogen flames propagation in wet medium and to the combustion modeling improvement. Moreover, the obtained results highlight the promotional effect of the initial temperature on flame acceleration and permit the flame acceleration criteria extension to representative gaseous containment atmosphere temperature. This revised acceleration criterion allows a better identification of potentially dangerous mixtures and improves consequently, the relevance of the risk assessment.

5.3. Flame structure interaction

As pointed out previously, in case of severe accident, the containment of a nuclear reactor is the last barrier to avoid radioactive materials release into the environment. Therefore, excessive loads should not jeopardize its integrity. Moreover, the availability of different safety components important for accident management and mitigation should be ensured over the entire duration of the accident. The hydrodynamic force acting on a freestanding object depends not only on the pressure field but also on the flow velocity via the drag force and inertia. Hence, the importance of a fine characterization of flame and shock wave propagation in confined geometries. To this end, experimental campaign was carried out at the SSEXHY facility to build up a database on the deformations of simple structures following an internal hydrogen explosion [30].

Different explosion propagation regimes were studied, ranging from slow deflagration to detonation. Different targets were tested, such as cylinders and plates of varying thickness and diameter. Detailed instrumentation was used to obtain data to validate the coupled CFD models of combustion and structural dynamics. These improvements are an asset for predicting the response of the equipment needed to manage the accident to loads induced by hydrogen combustion.

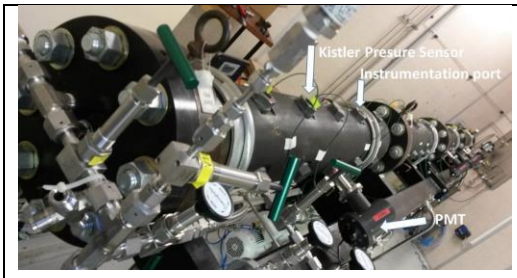

Figure 24. SSEXHY tube and associated instrumentation.

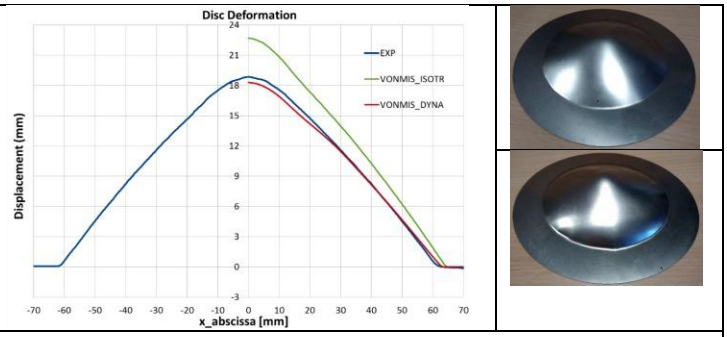

Figure 25: Comparison between the experimentally measured disc deformation (blue curve) and the numerical data obtained using Von Mises isotropic model (green curve) and Von Mises dynamic model (red curve).

5.4. In situ gas monitoring system reliable with severe accidental conditions

As part of the MITHYGENE project, a prototypical device was developed based on Raman spectrometry measurement technology for in situ gas monitoring [31]. Several qualification campaigns were carried out to check the effect of conditions representative of a severe accident, including radiation, on the response of the device. To this end, qualification tests were carried out in the IRSN-IRMA facility, for resistance to irradiation, and in ENACCEF2, for the simultaneous measurement of 6 gases (H_2, O_2, CO, CO_2, H_2O, N_2) and the impact of initial temperature. The technological maturity level (TRL) of the Raman probe is estimated at 6 (demonstration of a prototype in a representative environment), while that of the measurement unit (qualifiable) is estimated at 3 (proof-of-concept analytical functions). A patent has been filed for this development.

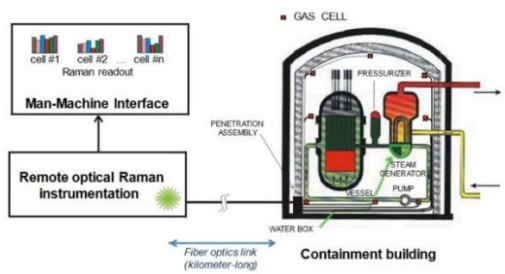

Figure 26: sketch of gas monitoring system implementation in reactor containment

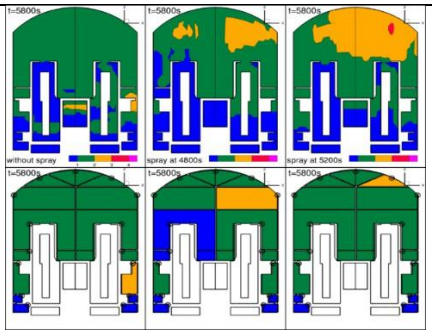

Figure 27: Hydrogen distribution, CFD simulation (upper section) vs reconstituted distribution (lower section) based on measurements taken using 15 gas sensors.

At the same time, a study of the optimal location of the probes in the containment vessel was carried out. This study identified the minimum number of probes and determined their locations. Secondly, a simple algorithm was developed to use point measurements to reproduce the distribution of gases in the containment and thus provide information on the risks of ignition and flame acceleration.

6. MIRE project

The MIRE (Mitigation of Releases to the Environment in the event of a nuclear accident) project aimed to study and improve the mitigation of gaseous radioactive releases during a core melt accident on a nuclear reactor (referred to as a severe accident). When a core melt accident occurs in a nuclear reactor, the radioactive elements contained in the fuel rods can be released to the containment in the form of particles (aerosols) or gases. To mitigate outside releases in the event of an excessive increase in pressure in the containment, filtering containment venting system (FCVS) [32] are commonly used. In France, the FCVS used is made up of metallic prefilters and sand filters arranged inside and outside of the containment, respectively. This system, which is relatively effective for the filtration of aerosols, cannot retain gaseous forms. Among gaseous fission products, iodine and ruthenium may form volatile species with potential high radiological consequences. The main objective of the MIRE project is to improve mitigation means in case of the containment venting by increasing trapping capacity of gaseous fission products (I_2, CH_3I and RuO_4). To achieve this objective, the following three main topics were addressed by performing both experimentation and modelling activities.

6.1. Topic 1: Source term studies

This topic aimed to improve existing knowledge concerning the resuspension or revolatilization of radioactive elements that could occur during venting or subsequently, over the longer term (delayed releases). Two main issues were then addressed:

- The remobilization of radioactive elements deposited on, or adsorbed by, wall and equipment surface inside the containment. These processes were analyzed using tests involving revolatilization (caesium, iodine and ruthenium) from surfaces of the reactor coolant system. The main parameters studied were the type of carrier gas and thermal conditions. It was shown that in some oxidizing conditions, deposits can be remobilized with the formation of gases and aerosols. This issue is linked to experimental observations during the Fukushima-Daiichi accident corresponding to releases that occurred few days/weeks after the accident starts.
- The characterization of iodine oxides particles issued from the oxidation of volatile iodine by air radiolysis products (ozone formed under radiation, for example). Although these particles can in certain cases represent a large portion of the iodine particles suspended in the containment. Only few data is available on their features (size, composition, stability, etc.). To fill the gap of knowledge, experiments were conducted to obtain qualitative and quantitative information (size, mass, distribution, composition, etc.) on the interactions between iodine oxides and air radiolysis products, as well as on the chemical stability of these oxides in the medium term [33-34]. These studies concluded that iodine oxides are formed by (UV and radiolytic) oxidation of volatile iodine species, and are found in the form of small particles (several hundreds of nanometres) whose chemical composition can vary as a function of temperature and humidity. These particles are also unstable and can be partially redecomposed into gaseous iodine (I_2), depending on the chemical form of the oxides.

6.2. Evaluation of the effectiveness of existing filtration systems

The studies performed aimed to evaluate and compare the effectiveness of filtration systems currently available worldwide [32]. Research conducted in this area focused on determining experimentally the effectiveness of trapping molecular iodine and organic iodide, as well as ruthenium in gaseous form but in lesser extent. The filters tested were those already installed in nuclear facilities in France and elsewhere in the world: sand filters, liquid filters (sparge filters), metal filters. Adsorption tests for the gaseous species considered were performed on at lab scale (SAFERI experimental device) for each type of filter. The parameters studied included adsorption rate, maximum trapping capacity, temperature and humidity effect

in some cases. The irreversibility of this capture under radiation conditions has also been checked. These tests were complemented by tests on a new IRSN facility, the PERSEE test bench, designed for studying filtration and purification systems with potentially the use of labeled iodine. The data acquired confirmed that for volatile iodine species, metallic, sand-bed or liquid filters do not effectively trap organic iodides, and CH_3I in particular [35].

6.3. Research and development of new filtration systems based on the use of dedicated porous materials

Some porous materials have the advantage to be quite selective and can be implemented in passive systems. The potential of "innovative" porous materials for trapping volatile iodine (I_2 and CH_3I) and gaseous ruthenium as ruthenium tetroxide (RuO_4) had been investigated. Two types of porous materials were examined: zeolites and MOFs (Metal Organic Framework). Zeolites are aluminosilicate species with high porosity and thermally resistant. MOFs are porous and crystalline materials created by combining metal ions and organic linkers, they are very tunable due to this hybrid configuration. After synthesis and complete characterizations of the studied porous materials, trapping of different iodine species was studied along with associated mechanisms (modelling at molecular scale by DFT and/or *ab initio* methods and experimental studies). Analytical tests in conditions as close as possible to severe accident conditions (radiation, temperature, steam, presence of gaseous inhibitors, etc.) were performed using the SAFARI (measuring the filtration efficiency of materials on ruthenium and iodine) test bench and PERSEE test bench (cf. **Figure 29**). The most promising materials are silver exchanged zeolites for trapping methyl iodide [36] with some difference in performance linked to their structure and silver mass content (see Figure 28). For ruthenium tetroxide, MOF appears to be more suitable due to their higher tunability than zeolite type [33].

To help interpretation/understanding experiments, theoretical simulations were performed to study impact of metal exchanged zeolites, gas contaminants (H_2, Chlorine, organic compounds, H_2O …) [37]. For gaseous iodine, density functional theory (DFT) molecular dynamic calculations confirmed that silver dispersed in zeolite is the best candidate for trapping iodine. For gaseous pollutants, carbon monoxide (CO) may have an inhibiting effect on the adsorption of iodine species, even at low concentrations. This point has been checked by co-adsorption tests of CO/ CH_3I mixtures in steam/air carrier gas and not confirmed experimentally. There was high water content in the gas, which can also have a significant effect. From an experimental perspective, of the zeolites tested, adsorbents prepared by ion exchange with silver in Y-faujasite (particularly with around 20% of silver by mass) showed the highest performance for CH_3I and I_2 trapping. A commercial Ag-X zeolite with 35% silver by mass also showed good trapping capacities. For MOFs, some materials offer good radiation resistance, but at this stage, we have not been able to find a structure that can efficiently trap iodomethane. For gaseous ruthenium, the results obtained show variable trapping capacities depending on the porous materials studied. The series of tests performed provides an initial ranking of existing porous solid materials. MOFs and organically modified silica had the highest trapping capacities of the compounds tested. Additional tests are required to explore their performance in conditions that are as representative as possible of severe accidents. To sump-up, the most advanced materials/capable of trapping volatile iodine and in particular methyl iodide are zeolites "exchanged" with silver to promote chemical adsorption and form silver iodide (AgI), compound with very low volatility and thermodynamic stability. Two suitable zeolites studied are, an AgY type faujasite with 25% in mass of Ag and a natural zeolite, with approximately 9%$_{/w}$ of Ag. Depending of the design of the filter implemented on the venting line of the containment, such able can efficiently trap volatile iodine and thus should reduce the radiological consequences in the event of containment venting. The knowledge developed within the

framework of the MiRE program has been translated into different criteria to guide the choice of the filtering material and possibly improve the efficiency of trapping volatile iodine in the French U5 line.

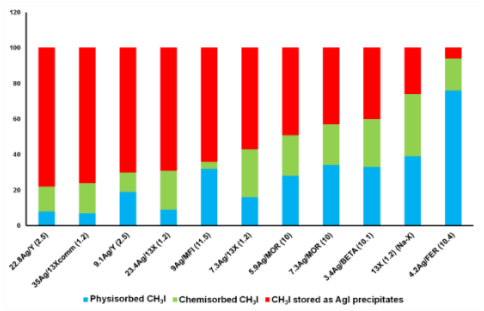

Figure 28. Relative stability of methyl iodide trapping for different silver zeolites (T = 100°C) [**38**].



Figure 29. PERSEE facility dedicated to iodine filtering tests.

7. Conclusion

The Fukushima Daiichi accidents claimed the crucial need to improve the safety equipment and the mitigation strategies for severe accident. To achieve this ambitious goal, several projects were launched in the severe accidents field of endeavor to address the topics considered of highest priority and reduce the still pending uncertainties on several selected main phenomena. The PERFROI, DENOPI, ICE, MITHYGENE and MIRE projects, led by IRSN, addressed remaining issues related respectively to fuel degradation and reflooding, spent fuel loss of cooling, fuel-coolant interaction, hydrogen risk and source term mitigation.

The achievements of these projects allow getting a better understanding of the above phenomena and providing unique data base for LP and CFD codes validation. Moreover, the lessons learned from the projects supported the development of gas monitoring systems and criteria to guide the choice of the filtering material and the improvement of the efficiency of trapping volatile iodine in the French U5 line.

The lessons learned also allow recommendations to be made for improving the SAMG model for water-cooled reactors and constitute an asset for assessing the safety of water-cooled SMR reactors. These recommendations include delaying spray activation if severe accident conditions are met. These projects have also led to the launch of new projects within the European framework, the AMHYCO project, and within the OECD framework, the POLCA project, which will respectively extend the results obtained to the late phases of severe accidents and study cooling by natural convection, which is of interest for the passive systems planned for installation in SMRs.

ACKNOWLEDGMENTS

The authors acknowledge the support of the French government within the program "Investissement d'Avenir" – PERFROI Grant agreement n° ANR 11-RSNR-0017, DENOPI Grant agreement n° ANR 11-RSNR-0006, ICE Grant agreement n° ANR 11-RSNR-0010, MITHYGENE Grant agreement n° ANR 11-RSNR-0015 and MIRE Grant agreement n° ANR 11-RSNR-0013.

REFERENCES

1. Post Fukushima accident, peer review report Stress tests performed on European nuclear power plants, ENSREG report v12i – 2012 04 25
2. Behaviour of French nuclear facilities in the event of extreme situations and relevance of the proposed improvements (irsn.fr)
3. G. Repetto et. al, “Core coolability in loss of coolant accident: the PERFROI project”, WRFPM conference - *Top Fuel*14, Sendai, Japan, September 14-17 (2014)

4. C. Dominguez, Effect of pre-oxide and hydrogen on creep of Zircaloy-4 at 1123K - Journal of Nuclear Materials, 511, pp 446-458, 2018
5. G. Repetto , C. Dominguez, T. Taurines - The PERFROI project investigating the thermal behaviour of a fuel rod assembly during a Loss of coolant accident, Water Reactor Fuel Performance Meeting TOP FUEL 2017, Jeju Island, Korea, September 10 - 14, 2017
6. D. Campello, N. Tardif, A. Maynadier, M.C. Baietto, M. Coret, J. Desquines - Identification of the steady-state creep behavior of Zry-4 claddings under Loss-Of-Coolant Accident conditions based on a coupled experimental – International Journal of Solids and Structures, 2016
7. C. Dominguez, P. Lacote, A. Viretto , S. Charbaut, G. Repetto - Experimental study of the effect of neighboring rods in fuel cladding deformation under LOCA conditions – TOPFUEL 2022, Raleigh, USA, Oct 9-13, 2022
8. Pena Carrillo, J.D., Oliveira, A.V.S., Labergue, A., Glantz, T., Gradeck, M., Experimental thermal hydraulics study of the blockage ratio effect during the cooling of a vertical tube with an internal steam-droplets flow. International Journal of Heat Mass Transfer. 140, 648–659, 2019
9. A.V.S. Oliveira, D. Stemmelen, S. Leclerc, T. Glantz, A. Labergue, G. Repetto, Parametric effects on the flow redistribution in ballooned bundles evaluated by magnetic resonance velocimetry, Experimental Thermal and Fluid Science, 125, 110383, 2021
10. G. Repetto et all, "COAL experiments investigating the reflooding of a 7 x 7 rod bundle during a loos of cooling accident – thermal hydraulics results," *Proceedings of 2019 International Topical Meeting on Nuclear Reactor Thermal Hydraulics (NURETH-19)*, Brussels, Belgium, march 6–11 (2022).
11. G. Repetto, Q. Grando, B. Bruyère,S. Eymery, R.Van Lochen, R. Fortman -COAL experiments investigating the reflooding of a 7 X 7 rods bundle during a LOCA – Thermalhydraulics results, 19th Int. Topical Meeting on Nuclear Reactor ThermalHydraulics (NURETH20) August 19-25, 2023, Washington, USA
12. OECD Nuclear Energy Agency, "*Phenomena Identification and Ranking Table. R&D Priorities for Loss-Of-Cooling and Loss-Of-Coolant Accident in Spent Nuclear Fuel Pools"*, Report NEA n°7443 (2018)
13. J. Martin (2023). "*The gravity-driven flashing of metastable water in a pool heated from below – An experimental study",* PhD thesis, Université Catholique de Louvain, Institute of Mechanics, Materials and Civil Engineering, Louvain-la-Neuve, Belgium
14. B. Migot, G. Brillant, J. Martin and S. Morin. "*DENOPI project devoted to spent fuel pool accidents: overview on the thermal hydraulics experimental facilities",* In 19th International Topical Meeting on Nuclear Reactor Thermal Hydraulics (NURETH), 364126-11 mars, 2022.
15. C. Duriez, O. Coindreau, M. Gestin, A. Kasperki, V. Peres, M. Pijolat, H. Buscail, C. Issartel,R. Rolland, M. Mermoux, *"Zircaloy-4 high temperature oxidation in atmospheres representative of SFP-LOCA: Investigation of the influence of a low temperature peroxidation scale",* Journal of Nuclear Materials 513 (2019) 152-174
16. OECD/SERENA Project Report, NEA/CSNI/R(2014)1, February 2015, https://www.oecd-nea.org/upload/docs/application/pdf/2021-02/csni-r2014-15.pdf
17. I. Huhtiniemi, D. Magallon and H. Hohmann, "Results of recent KROTOS FCI tests: alumina versus corium melts", *Nuclear Engineering and Design*, **Volume 204**, Issues 1-3, pp. 391-400 (2001)
18. V. Bouyer, N. Cassiaut-Louis, P. Fouquart, P. Piluso, 'Plinius prototypic corium experimental platform: major results and future works', *NURETH 16*, Aug 2017, Chicago, United States.
19. M. Hadj-Achour, N. Rimbert, M. Gradeck, and R. Meignen Fragmentation of a Liquid Metal Droplet Falling in a Water Pool, Physics of Fluids 33 (10), 103315 (2021)
20. S. Castrillon-Escobar Instabilité et dispersion de jets de Corium liquide, modélisation numérique Thèse de l'université de Lorraine (2016)
21. L. Wei Développement d'un nouveau modèle d'explosion de vapeur pour le logiciel MC3D Thèse de l'université de Lorraine (2023)
22. G. Kewalramani, B. Ji, Y. Dossman, M. Gradeck, N. Rimbert Experimental analysis of Lagrangian paths of drops generated by liquid/liquid sprays Experiments in Fluids 63(9) (2022)
23. V. Loisel, J.-A. Zambaux, M. Hadj-Achour, S. Picchi, O. Coindreau, R. Meignen, 'Oxidation during fuel-coolant interaction: Advances and modeling', *Nuclear Engineering and Design* **346** (2019) 200–208
24. L. Wei, R. Meignen, S Picchi, N. Rimbert, 'Analysis and sensitivity study of steam explosion loads', *Annals of Nuclear Energy* **194** (2023) 110064
25. ISP-49 on Hydrogen Combustion, rapport OCDE/AEN; NEA/CSNI/R(2011)9.
26. Bentaib, A. Bleyer, N. Meynet, N. Chaumeix, B. Schramm, M. Höhne, P. Kostka, M. Movahed, S. Worapittayaporn, T. Brähler, H. Seok-Kang, M. Povilaitis, I. Kljenak, P. Sathiah, SARNET hydrogen deflagration

benchmarks: Main outcomes and conclusions, Annals of Nuclear Energy, Volume 74, December 2014, Pages 143-152, ISSN 0306-4549.

27. Bentaib, E. Studer, N. Chaumeix, S. Magne, E. Reinecke, D. Pinet, MITHYGENE project Towards the improvement of hydrogen risk assessment models and safety management procedures, Int. Workshop on Nuclear Safety and Severe Accident (NUSSA-2014) Sept. 3-5, 2014, Chiba, Japan
28. E. Studer, J. Alengry, D. Abdo, F. Dabbene, J. Baggemann, S. Kelm, E. Reinecke, H.-J. Allelein, Hydrogen mobilization by Passive Autocatalytic Recombiners, NUTHOS-11 Conference, Gyeongli Korea, October 9-13 2016,
29. R. Grosseuvres , A. Chakraborty , J. Goulier , A. Bentaib , A. Bleyer , E. Reinecke , N. Chaumeix, The flame "curriculum vitae" in the framework of safety analysis with mitigation assessment, NURETH-17, Xian, Chine
30. R. Scarpa, E. Studer, B. Cariteau, S. Kudriakov, and N. Chaumeix, "Infrared Absorption Measurements of the Velocity of a Premixed Hydrogen/Air Flame Propagating in an Obstacle-Laden Tube," *Combust. Sci. Technol.*, pp. 1–15, Jul. 2018.
31. S. Magne, S. Nehr, X. Buet, A. Bentaib, E. Porcheron, R. Grosseuvres, E. Studer, R. Scarpa, D. Abdo, J-L. Widloecher, O. Norvez, N. Chaumeix, J. Dhote, M. Freyssinier, A. Ruffien-Ciszak, In situ gas monitoring by Fiber-Coupled Raman Spectrometry for H2-risk management in nuclear containment during a severe nuclear accident, IEEE Trans. Nucl. Sci. 67 (4), 2020, pp. 617-624
32. D. Jacquemain, S. Guentay, S. Basu, M. Sonnenkalb, L. Lebel, H.-J. Allelein, B. Liebana, B. Eckardt, L. Ammirabile, Status Report on Filtered Containment Venting, OECD/NEA/CSNI, Report NEA/CSNI/R(2014)7.
33. R'Mili B.; Strekowski R.S.; Temime-Roussel B.; Wortham H.; Monod A. " Important effects of relative humidity on the formation processes of iodine oxide particles from CH3I photo-oxidation", *Journal of Hazardous Materials* 4335, Article number 128729 (2022).
34. Leroy O., Bosland L.; " Study of the stability of iodine oxides (IxOy) aerosols in severe accident conditions", *ANE* 181, Article number 109526 (2023).
35. Nerisson P. Hu H.; Paul J.F.; Cantrel L.; Vesin C. "Filtration tests of gaseous ruthenium tetroxide by sand bed and metallic filters", *Journal of Radioanalytical and Nuclear chemistry* 321, Pages 591-598 (2019).
36. Ayadi, T.; Badawi M.; Cantrel L.; Lebègue S. "Rational approach for an optimized formulation of silver-exchanged zeolites for iodine capture from first-principles calculations", *Molecular Systems Design and Engineering* 7(5), Pages 422 - 433 (2022)
37. Chebbi M., Chibani S. Paul J-F.; Cantrel L.; Badawi M."Evaluation of volatile iodine trapping in presence of contaminants: A periodic DFT study on cation exchanged-faujasite"**,** *Microporous and Mesoporous Materials*
38. B. Azambre, M. Chebbi, *ACS Applied Materials and Interfaces* 9 (30), p. 25194-25203, 2017.

RÉPUBLIQUE FRANÇAISE
Liberté
Égalité
Fraternité

IRSN
INSTITUT DE RADIOPROTECTION ET DE SÛRETÉ NUCLÉAIRE

ON THE PROGRESS MADE IN SAFETY ASSESSMENT AND SEVERE ACCIDENT MANAGEMENT AS PART OF THE FRENCH FUKUSHIMA POST-ACCIDENT RESEARCH PROGRAMME

A. Bentaib, R. Meignen, L. Cantrel, S. Morin, G. Repetto
Institut de Radioprotection et de Sûreté Nucléaire, France

IRSN/FRM-256 ind. 06

MEMBRE DE ETSON

MOTIVATION







Need of further investigation to improve the Severe Accident Management strategies including external hazards

PERFROI, DENOPI and ICE projects

filling the gap of knowledge and reduce the uncertainties on phenomena participating in severe accidents

MITHYGENE and MIRE projects

developing new mitigation systems and strategies to reduce the source term release

improving code suitability to address severe accident phenomena and severe accident management for a large number of reactor design including PWR, BWR, VVER and CANDU.

PERFROI Project : PERte de reFROIdissement (Loss of coolant)

Safety objective: preserving the long-term core coolability to avoid a Severe Accident on a Nuclear Power Plant

Adressed topics:

- ✓ Study of the thermomechanical deformation mechanism and fuel rods burst under LOCA conditions
- ✓ Characterization of the thermal hydraulics behavior in the ballooned area, during cooling phase by water injection considering the effect of pressure and the water flow rate

Main outcomes: improvement of code modeling and validation

Period : October 2013-June 2023
Contact person: Georges Repetto (georges.repetto@irsn.fr)

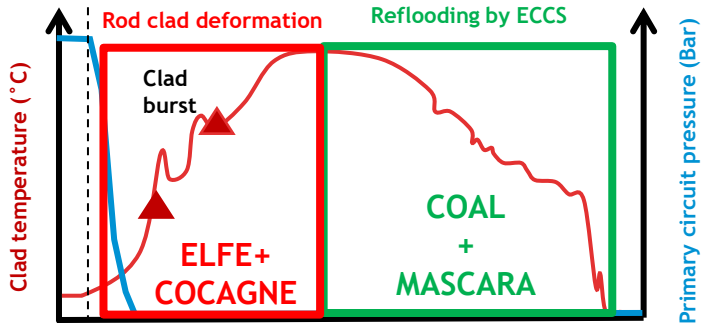

Beginning of the accident



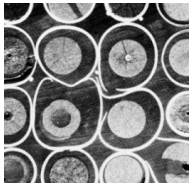

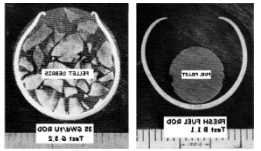

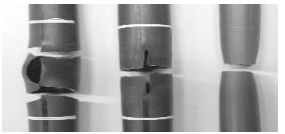

PERFROI Project : Achievements and Key findings

ELFE+PhD

Experiments for Creep Law determination on small sample (range 700 to 900°C)



Furnace





Two thermomechanical facility at Cadarache and one in Lyon (France)

Topic 1: thermal mechanical

COCAGNE

Experiments for 3D modeling/Validation of clad deformation with contact between fuel rods (guard)

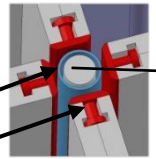



Topic 2: thermal hydraulics

COAL

Experiments for Modeling/validation Reflooding process in deformed fuel assembly

(COolability of a fuel Assembly under LOCA)

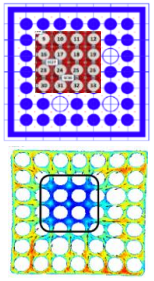

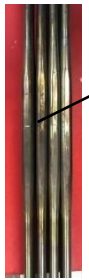



COAL Facility in Canada

COLIBRI+MASCARA

Heat transfers in small-scale experiments and flow redistribution

PERFROI Project : PERte de reFROIdissement (Loss of coolant)

Safety objective: preserving the long-term core coolability to avoid a Severe Accident on a Nuclear Power Plant

Adressed topics:

- ✓ Study of the thermomechanical deformation mechanism and fuel rods burst under LOCA conditions
- ✓ Characterization of the thermal hydraulics behavior in the ballooned area, during cooling phase by water injection considering the effect of pressure and the water flow rate

Main outcomes: improvement of code modeling and validation

Period : October 2013-June 2023
Contact person: Georges Repetto (georges.repetto@irsn.fr)

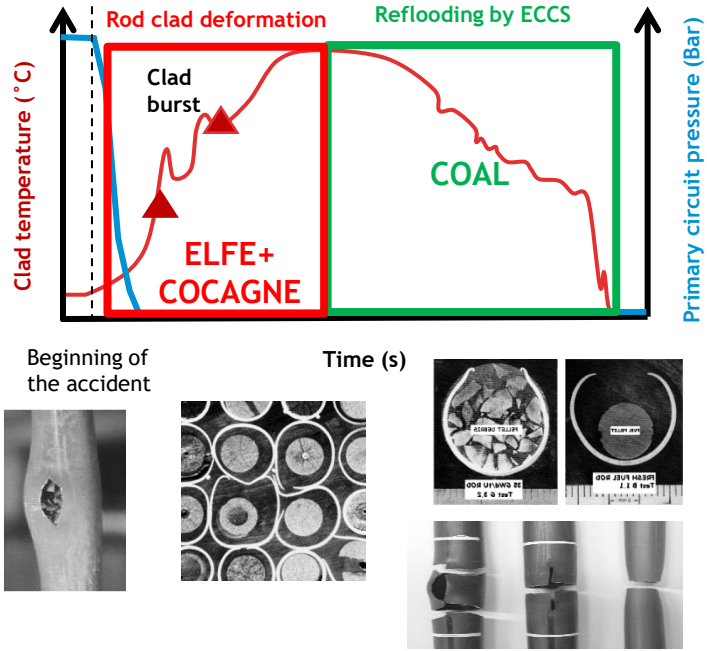

PERFROI Project : Achievements and Key findings

ELFE

Experiments for Creep Law determination on small sample (range 700 to 900°C)







Two thermomechanical facility at Cadarache (France)

Furnace

Topic 1: thermal mechanical

COCAGNE

Experiments for 3D modeling/Validation of clad deformation with contact between fuel rods (guard)

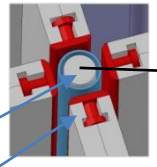



Topic 2: thermal hydraulics

COAL

Experiments for Modeling/validation Reflooding process in deformed fuel assembly

(**CO**olability of a fuel **A**ssembly under **L**OCA)

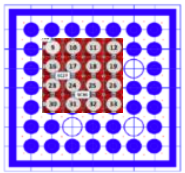

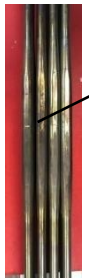



COAL Facility

PERFROI Project : Achievements and Key findings

24 COCAGNE tests (2018-19-20)

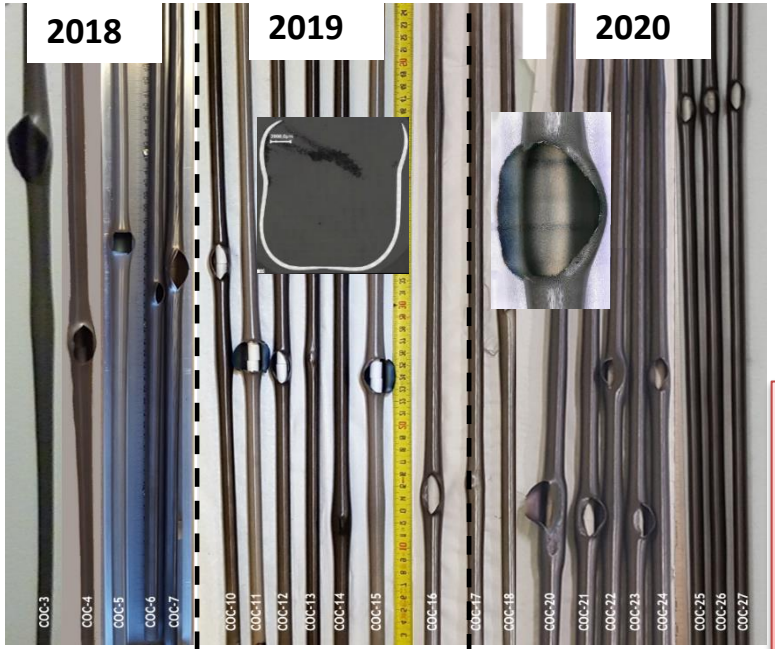

C1 campaign without guard | **C2 campaign with guards** | **C3 campaign with guards**

→ Rods deformation in agreement to that observed in a bundle geometry (In-pile Phebus experiments)

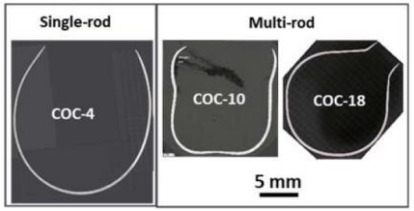

Radial rod deformation

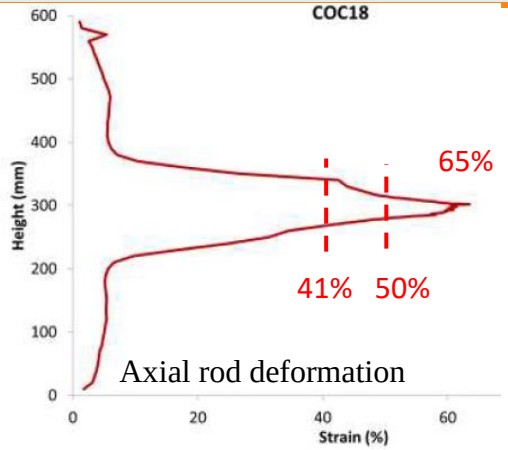

Axial rod deformation

- Increasing the internal pressure (20 to 100 bar) increases the deformation at rupture, as well as the temperature at the moment of bursting.
- There is a linear dependence between the size of the fish mouth-shaped openings formed in the test carried out at 5 and 10°C/s.
- The axial deformation profiles of the rods revealed balloon lengths with radial deformations greater than 41%, corresponding to a clogging ratio of the passage section of 80%, and deformation peaks of up to 65 and 80% A radial deformation of 50% corresponds to a clogging ratio of 90%.

→ These results justified the blockage ratio used in the reflooding COAL experiments

PERFROI Project : Achievements and Key findings

Reflooding experiments performed on a 7x7 full length (3m) electrically heated fuel-rod assembly with 4x4 deformed fuel rods with simulation of fuel relocation (local overpower increase in the balloons x 1.5)

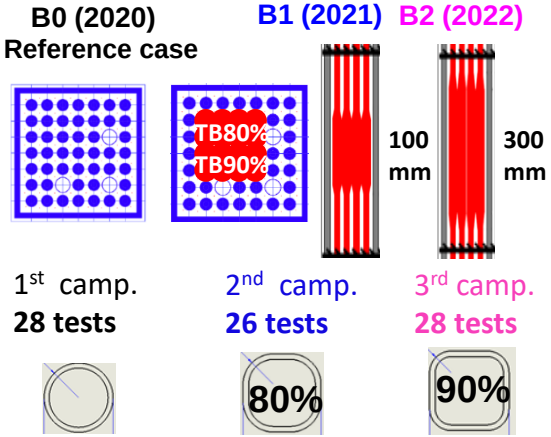

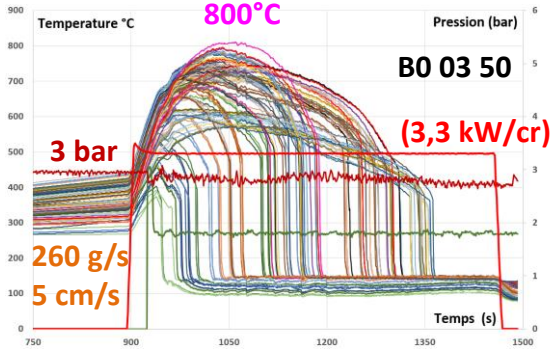

1st B0 COAL test (6 October 2020)

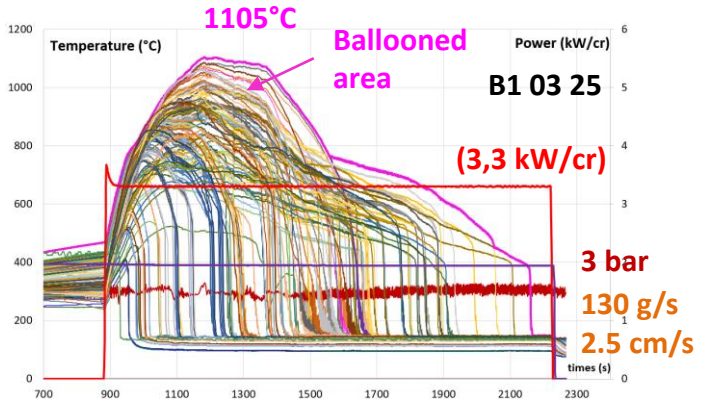

B1 COAL test (with the highest PCT)

82 COAL tests (2020-21-22)

Fixed parameters : geometries and axial power profiles
Thermal hydraulic parameters

System pressure (2 b up to 30 bar)
Water Flow velocity (1.5 to 8 cm/s)
Water inlet temperature
Power per rod (2, 2.4 , 3.3 kW/rod)

These COAL experiments outlined very important results regarding the duration of the reflooding and the impact on the PCT (increase of peak cladding temperature) due to the presence of a blockage inside the fuel assembly.

DENOPI Project : DENoyge Piscine (SFP dewatering)

Safety objective: To enhance knowledge on accidental SFP conditions and to better evaluate the safety margins

Adressed topics:

- ✓ Study of thermal hydraulics phenomena involved in SFP accident prior to the severe accident phase,
- ✓ Evaluation of water spray efficiency of as mitigation means
- ✓ Study of Zircaloy 4 oxidation kinetics laws under mixed air-steam atmosphere to understand the protective effect of the pre-existent oxide layer formed during in-reactor irradiation

Main outcomes: improvement of code modeling and validation

Period : 2014-2021

Contact person: Sandrine Morin (sandrine.morin@irsn.fr)





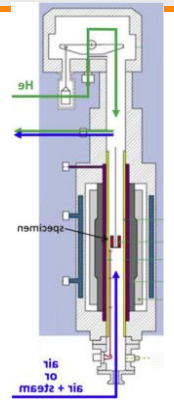

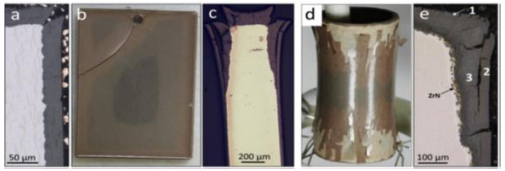



MINES Saint-Étienne
Une école de l'IMT

UNIVERSITÉ Clermont Auvergne

EDF

U.S.NRC

BELV Belgian TSO

Convection Phenomena at pool scale (MIDI facility)

- Analytical modelling of the vapor diffusion process was proposed as well as the free surface evaporation, degassing of dissolved non-condensable species and bubbles escape processes.

- A vaporization regimes map as a function of the residual power and water level was also dressed





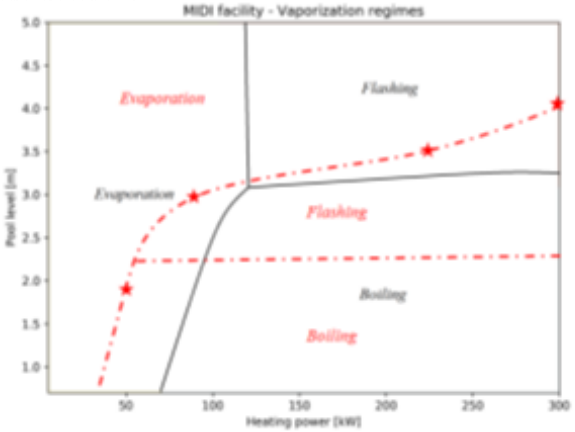

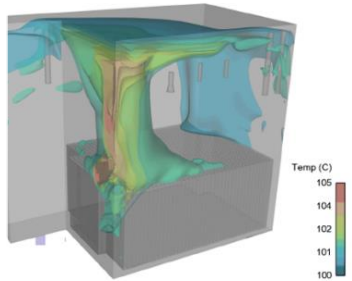

Assembly scale phenomena

(Aspic facility)

- Spray temperature does not have a significant impact on the temperature evolution in the assembly
- Spray flow rate significantly modifies the kinetics of the temperature of the assembly
- 20kW of residual power and one meter of dewatering, the spray flow rate of 10g/s maintained the temperature of the assembly below 500°C.
- Further investigations are planned in the framework of the OECD/POLCA project

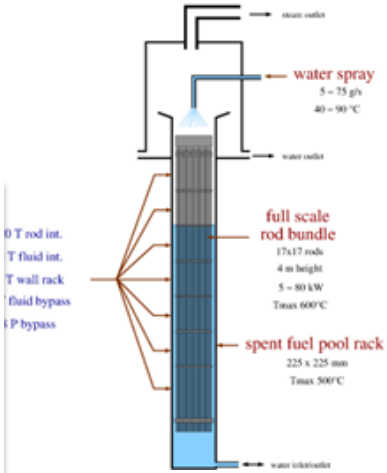





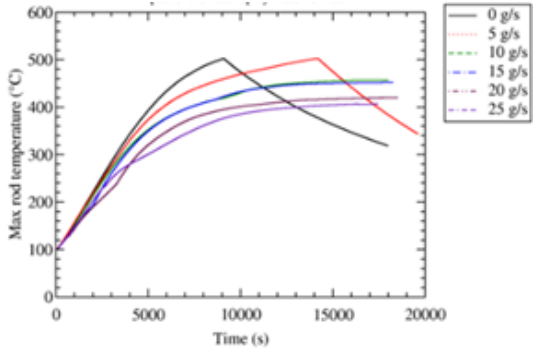

DENOPI Project : Achievements and Key findings

Fuel clad scale phenomena : zircalloy oxidation under steam/air mixture and mechanical behavior of oxidized cladding

- Effect of defects or singularities of the pre-oxide.
The protective effect is then linked to the presence of pre-existing defects. It is expected that in real fuel rods, such defects might be preexisting or created by clad swelling due to heat-up.
-kinetic model considering the influence of the partial pressure of oxygen and steam has been developed for implementation in the ASTEC code developed by IRSN
.

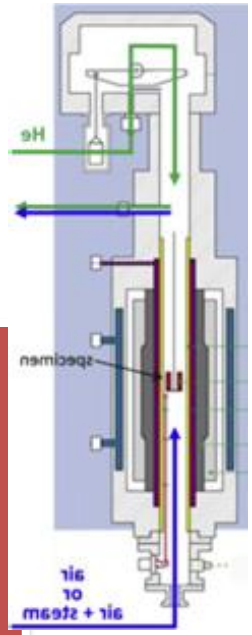

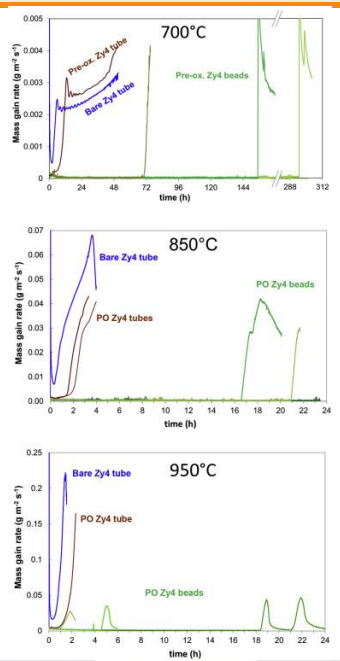

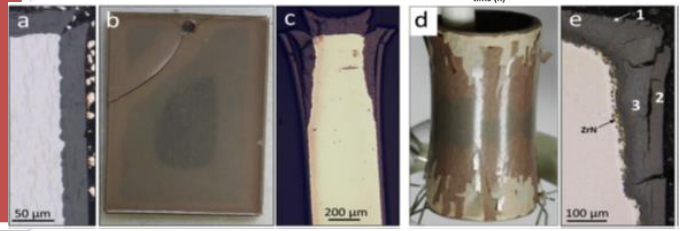

ICE Project : Interaction Combustible Eau (fuel coolant interaction)

Safety objective:

- Enhance knowledge and understanding
- Improve modeling in MC3D
- Better characterize the risk for reactor safety

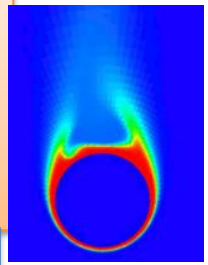





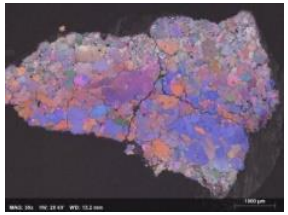

Adressed topics:

- Melt fragmentation
  - Jet fragmentation
  - Secondary liquid/liquid drop fragmentation
- Mechanisms of explosion (heat & mass transfer)
- Oxidation – solidification
- Coolant flow configuration (premixing)

Main outcomes: improvement of code modeling and validation

Period : 2014-2023

Contact person: Renaud Meignen(Renaud.meignen@irsn.fr)

ICE Project : Achievements and Key findings

Melt fragmentation

- The conjunction of integral and separate effect experiments, complemented with the DNS, led to important clarification regarding melt fragmentation mechanisms and characteristic drop sizes
- An important conclusion is that the fragmentation occurs through a 2-step cascading mechanism, with an integral scale mechanism driven by tangential Kelvin-Helmholtz like destabilization process followed by a local-scale fragmentation mechanism.

Small scale experiments of drop fragmentation at low Weber number (GaLaD)

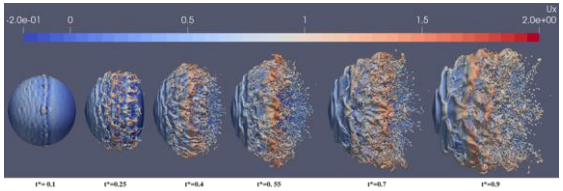

At large We, appearance of Kelvin-Helmholtz instabilities.



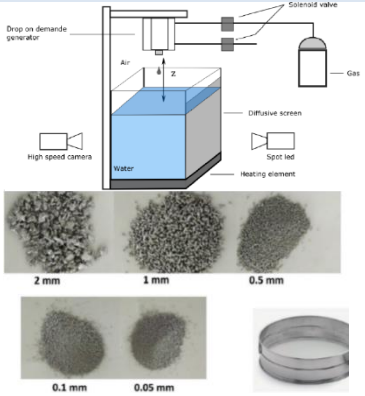

The PREMIXING KROTOS KA-1 test

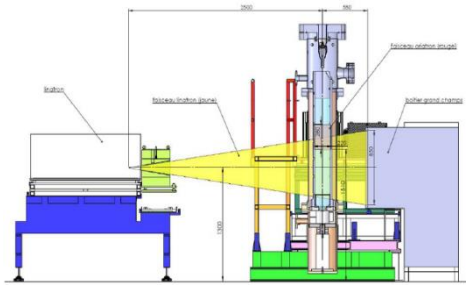

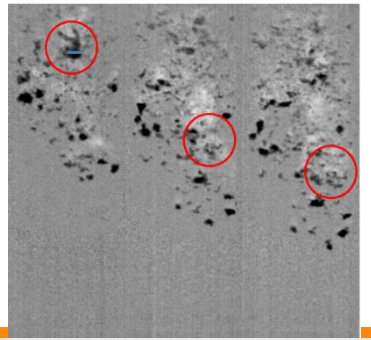



Explosion: reminder on the issue

- Due to the lack of experimental observation and obvious limits in analytical modeling, there is a strong uncertainty on the process of pressurization
- Two types of models :
  - The **Micro-Interaction** (Theofanous) : fragments, vapor and a fraction of the water are in thermal and dynamical equilibrium
  - **Direct Non-Equilibrium boiling** description : fragment heat transfers are estimated and boiling is deduced **=> MC3D**
  - ➢ **Both models need rational and may be joined in one**.
- Use of direct simulation models
  - MC3D=> MESO application for film boiling heat transfer at high pressure
  - GERRIS/Basilisk for the fragmentation and heat transfer without boiling (already discussed)

Example:
Density field
D=250 µm, Tw=2150 K;
U=1,1 m/s et Tl=600 K)
P = 240 bars

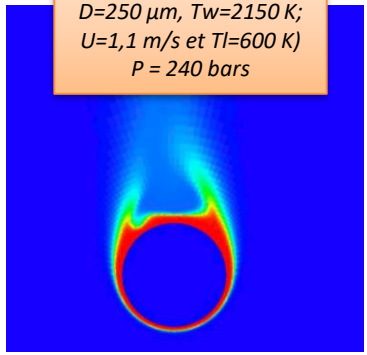

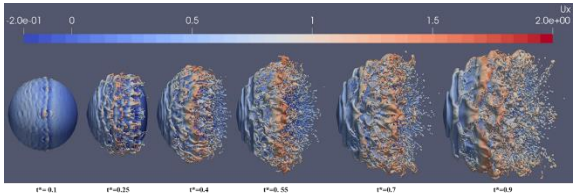

ICE Project : Achievements and Key findings

MC3D V4

- Project involving IRSN and EDF
- Much more than a new version : full refactoring of the code to allow
  - *More flexibility thanks to a new architecture and revision of the concept of application*
    - *Each application is build on top of other ones and autonomous*
      - *E.g. the COOLFLOW app. manages liquid-gas <é-phase flow for all following app.*
  - *Improved interface with users*
  - *Revision of available physical models*
  - *« Multi-Domain » capabilities and parallelized computation (MPI)*

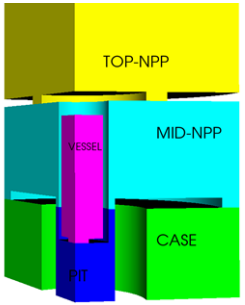

Example of possible (rough) decomposition of a reactor building in sub-domains

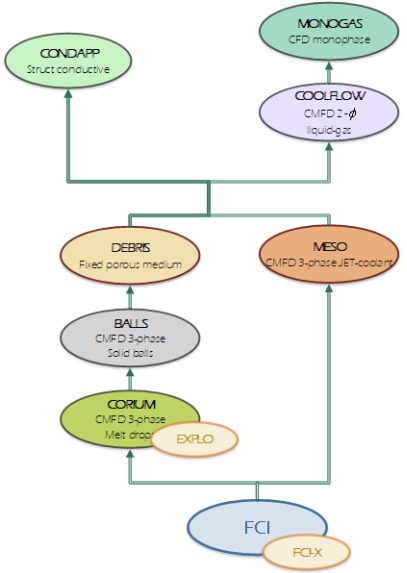

V4 new architecture of application dependencies

MITHYGENE Project : MITigation du risque HYdroGENE

Safety objective: Enhance the knowledge (PAR-atmosphere interaction, hydrogen-air-steam combustion, flame structure interaction)

- Develop gas monitoring system reliable with Severe Accident conditions
- Provide guidelines to improve the Severe Accident Management Guidelines
- Perform Fukushima Daïchi accident analysis

Adressed topics:

- ✓ Gas distribution
- ✓ H2-AIR-Steam combustion
- ✓ Flame Structure interaction
- ✓ Optical gas monitoring system reliable with SA

Main outcomes:

- ✓ Improvement of code modeling and validation
- ✓ SAMG recommandations

Period : 2013-2022

Contact person: ahmed.bentaib(ahmed.bentaib@irsn.fr)

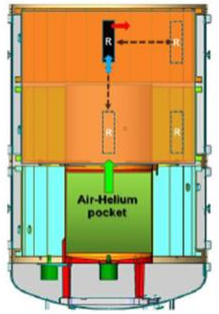





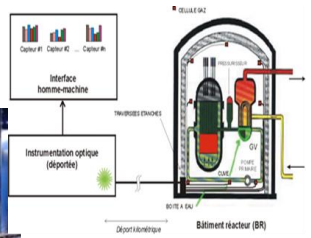

PAR- atmosphere interaction

Objectives:
- Optimal PARs locations – ability to mobilize hydrogen located in the lower part of the containment
- Jet impingement effect on Hydrogen stratification homogenisation

Achievements:
- 2 test series performed on MISTRA facility (CEA)
- CFD analysis of the performed tests
- Organization of benchmark exercise to experiments analysis

Main outcomes: Important data base for codes validation
- ➢PAR-atmosphere interaction
- ➢Hydrogen Stratification in the presence of free convection induced by wall condensation

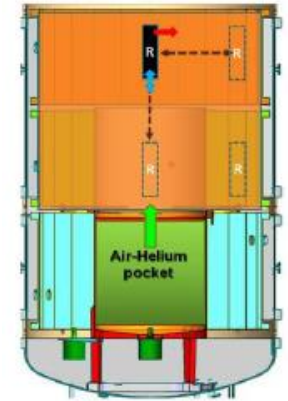

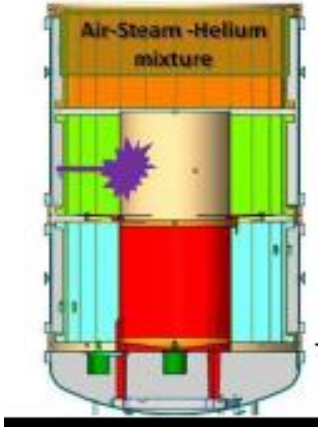

H_2-Air-Steam Combustion

Objectives:
- Effect of steam, initial temperature and initial pressure on flame propagation in homogenous and stratified gas mixtures
- Effect of spray actuation on flame acceleration

Achievements:
- Test series performed on ENACCEF2 facility (ICARE) (designed and constructed in the framework of the project)
- LP & CFD experiments analysis(2 international benchmarks supported by ETSON)

Outcomes and lessons learned
- Unique Data base for code validation
- Flame acceleration criteria update
- Flame-spray interaction



Flame structure interaction

Objectives

- Quantification of metallic structures deformation induced by hydrogen deflagration and hydrogen detonation
- Effect of structure deformation on flame propagation

Tools:

- Test series performed on SSEXHY facility (CEA)(founded by the project)
- Tests analysis using CFD codes

Outcomes and lessons learned

- Unique Data base for code validation



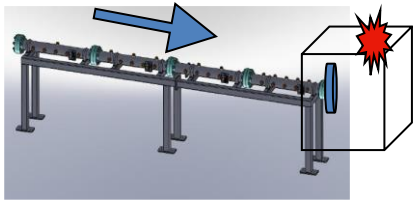

Gas monitoring reliable with SA conditions

Objectives:
- Development of in situ monitoring with remote Raman instrumentation
- Recommendation for sensors implementation inside the containment

Achievements:
- Measurement of six gas (H_2, O_2, N_2, H_2O, CO_2, CO) to cover In and Ex vessel phases
- Qualification to SA conditions (Radiation, T, P, Vibration, Chocs..)

Outcomes and lessons learned
- Development of proof of concept (TRL 5 to 6)
- Recommendation for TRL upgrade towards industrial applications
- Patent (ongoing)

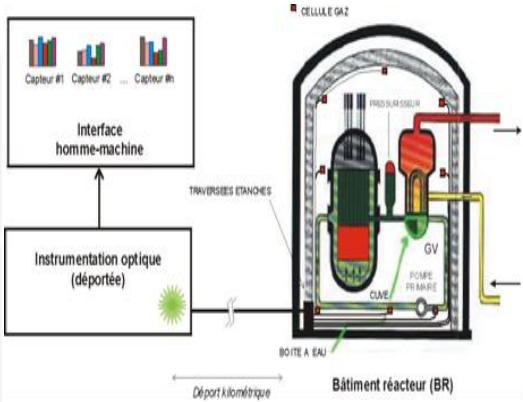



MIRE Project : MITigation des Rejets à l'Environnement en cas d'accident nucléaire

Safety objective:

to improve mitigation means in case of the containment venting by increasing trapping capacity of gaseous fission products (I_2, CH3I and RuO_4)

Addressed topics:

- ✓ Revolatilization of radioactive elements during venting
- ✓ Evaluation of the effectiveness of existing FCVS
- ✓ Development of new filtration systems (porous materials)

Main outcomes:

- ✓ Design, synthesis and validation of new materials able to trap gaseous fission products in severe accident conditions
- ✓ SAMG recommendations

Period : 2013-2022

Contact person: Laurent Cantrel (laurent.cantrel@irsn.fr)



Aix*Marseille université Socialement engagée

SOMEZ

Université de Lille

MINES ParisTech ARMINES

framatome

UNIVERSITÉ DE LORRAINE

EDF

IMT Atlantique

cnrs

Source term characterization

Remobilization of radioactive elements during venting:

- ✓ Processes were analyzed using tests involving revolatilization (caesium, iodine and ruthenium) from surfaces of the reactor coolant system shown that in some oxidizing conditions, deposits can be remobilized with the formation of gases and aerosols (Fukushima-Daiichi accident with delayed release)

- ✓ Characterization of iodine oxides particles issued from the oxidation of volatile iodine by air radiolysis products → formation of small particles (several hundreds of nanometers) whose chemical composition can vary as a function of temperature and humidity.

→ Data useful to assess performance of current FCVS as well as design of new porous materials for future filters

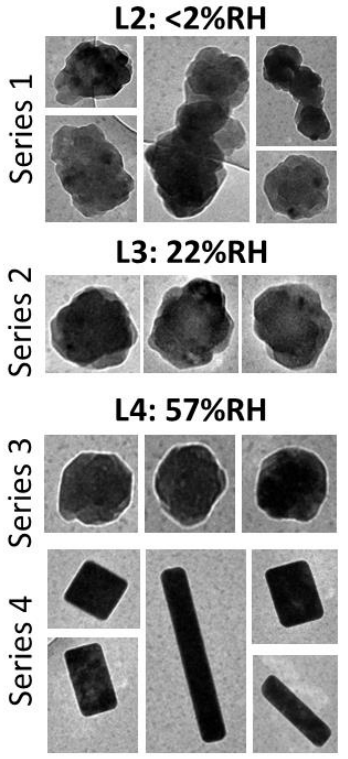

morphological characterization of IOx

Evaluation of the existing filtration systems effectivness

Research conducted in this area focused on determining experimentally the effectiveness of trapping molecular iodine and organic iodide, as well as ruthenium in gaseous form but in lesser extent. The filters tested were those already installed in nuclear facilities in France and elsewhere in the world: sand filters, liquid filters (pool-scrubbing filters), metallic filters. Adsorption tests for the gaseous species considered were performed on at lab scale (SAFARI experimental device) for each type of filter.

The parameters studied included adsorption rate, maximum trapping capacity, temperature and humidity effect in some cases. The irreversibility of this capture under radiation conditions has also been checked.

Sand bed filter on a French 900 MWe PWR







→ Org-I not trapped without specific adsorbents



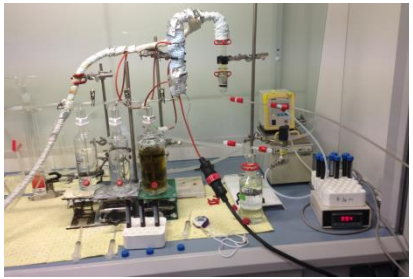

Development of new porous materials

The potential of “innovative” porous materials for trapping volatile iodine (I_2 and CH_3I) and gaseous ruthenium as ruthenium tetroxide (RuO_4) had been investigated. Two types of porous materials were examined: **zeolites and MOFs (Metal Organic Framework**).

Synthesis and complete characterizations of the studied porous materials, trapping of different iodine species was studied along with associated mechanisms (modelling at molecular scale by DFT and/or ab initio methods and experimental studies).

Analytical tests in conditions as close as possible to severe accident conditions (radiation, temperature, steam, presence of gaseous inhibitors, etc.) were performed using the SAFARI (measuring the filtration efficiency of materials on ruthenium and iodine) test bench and PERSEE test bench.

The most promising materials are silver exchanged zeolites for trapping methyl iodide with some difference in performance linked to their structure and silver mass content. For ruthenium tetroxide, MOF appears to be more suitable due to their higher tunability than zeolite type

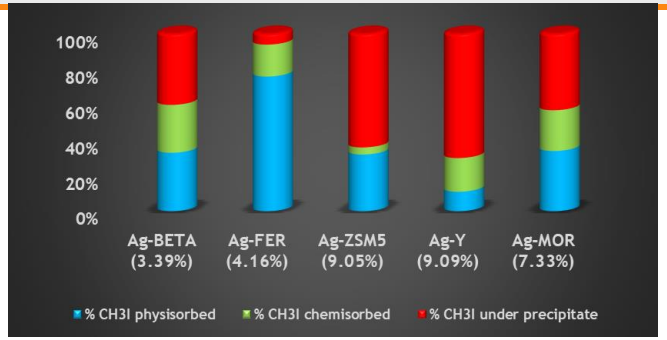

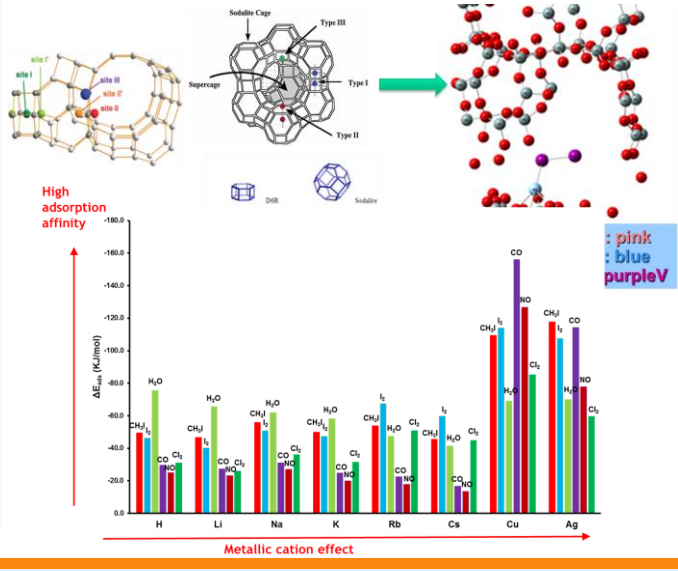

SUMMARY

Main achievements

- ❑ better understanding of the severe accident phenomena, such as the fuel degradation and reflooding, spent fuel loss of cooling, fuel-coolant interaction, hydrogen risk and source term mitigation and contribute significantly to reduce the related uncertainties,
- ❑ development of novel gas monitoring systems,
- ❑ improvement of innovative strategies in support of the source term reduction and recommendations for specific Org-I filter
- ❑ improvement of both LP and CFD codes abilities to address severe accident phenomena and severe accident management for a large number of reactor designs including PWR, BWR, VVER and CANDU.

Knowledge dissemination and education

- ❑ involvement of PhDs student,
- ❑ numerous peer review publications,
- ❑ organization of open workshop
- ❑ participation to IAEA and OECD (SOAR, CRPs, ..)

- ❑ New projects as OECD/COAL benchmark, OECD/POLCA and EU-AMHYCO Projects
- ❑ Asset for assessing the safety of WC SMR reactors

SASPAM-SA

FIRST OPEN WORKSHOP

1st Call for Papers

International Workshop on SMR Safety for a Sustainable Short-term Deployment

IRSN Headquarters, 31 av. De la Division Leclerc, Fontenay-aux-Roses, France
October 17th – 18th, 2024



The SASPAM-SA open workshop will promote international exchange of information and practices related to light water SMR safety considering the outcomes from the current ongoing Horizon Euratom SASPAM-SA project, other EU-Projects and other international initiatives (e.g. European SMR Pre-partnership, IAEA, OECD/NEA, ETSON, etc.). The workshop's objective is to share the advancements of the current major research activities on light water SMR safety and give the opportunity to discuss the main results. This allows to identify the needed knowledge development, in the view of additional short-term research actions, to support the SMR European licensing process.

SCOPE AND TECHNICAL CONTENT OF THE WORKSHOP

The scope considers the safety demonstration of LW-SMRs and the related aspects. Therefore, the focus of the Workshop is to discuss and review the state-of-art and the needed knowledge development on:

- Accident scenarios in LW-SMRs and related phenomenology;
- Capabilities of safety computer codes to predict LW-SMR phenomenology in transient conditions;
- Applicability of existing experimental database to characterize LW-SMR phenomenology in steady-operational and transient conditions;
- Analyses of the current severe accident mitigation strategies and features (e.g. IVMR, hydrogen management) and related modeling aspects;
- Computer code guidelines and best practices for the simulation of LW-SMR;
- Applicability of tools and methods to determine the emergency planning zone (EPZ) for LW-SMR;
- Applicability of high-fidelity tools for the safety analysis of LW-SMRs;
- Safety of LW-SMR integrated into a hybrid energy systems;
- Safety research in standardization and nuclear safety.

OUTCOMES OF THE WORKSHOP

SASPAM-SA open workshop aims to create a platform to specifically discuss about the safety of LW-SMRs in the view of a sustainable short-term deployment. The workshop will be a thematic platform to share with the participants the current advancements on SMR safety. In addition, the applicability of the operating large-LWR reactor knowledge and know-how to the near-term deployment of LW-SMR will be presented, in the view of licensing analysis needs in Europe regarding severe accident and EPZ. Key outcomes of the workshop will be:

- Provide an overview of the progress made in the SASPAM-SA project;
- Bring together EU-projects dealing with the safety of light water cooled SMR;
- Bring together the main activities related to the safety of the light water cooled SMR at international level;
- Discuss safety issues inherent to LW-SMRs, including coupling with industrial facilities, and how to address them;
- Identify potential remaining safety issues to be investigated;
- Foster coordination among international activities.



ACKNOWLEDGMENTS

- The authors acknowledge the support of the French government within the program "Investissement d'Avenir" – PERFROI Grant agreement n° ANR 11-RSNR-0017, DENOPI Grant agreement n° ANR 11-RSNR-0006, ICE Grant agreement n° ANR 11-RSNR-0010, MITHYGENE Grant agreement n° ANR 11-RSNR-0015 and MIRE Grant agreement n° ANR 11-RSNR-0013.



The 11th European Review Meeting on Severe Accidents Research

May 13-16, 2024, Royal Institute of Technology, Stockholm, Sweden

TECHNICAL SESSION 1.1: IN-VESSEL CORIUM AND DEBRIS COOLABILITY

Chairs: F. Gabrielli (KIT), A. Miassoedov (IAEA)

ID73	**IVMR Modelling with Transient Effects during Molten Pool Formation and Stabilization – Outcomes from Models' Comparison Performed in the IAEA CRP J46002** L. Carénini (IRSN)	**Paper** **Presentation**
ID24	**Numerical Analysis of Melt Penetration Behavior in the Control Rod Drive Housing of Fukushima Daiichi Nuclear Power Station Unit-2** X. Li (JAEA)	**Paper**
ID66	**Reactor pressure vessel integrity during severe accident with core meltdown: characterization of material parameters, structure integrity assessment and thermal-hydraulic assessment** P. Gal (UJV)	**Paper** **Presentation**
ID73	**Improvement of thermochemical corium stratification accounting for uranium and zirconium composition difference in metallic and oxide phases** R. Le Tellier (CEA)	**Paper** **Presentation**

IVMR MODELLING WITH TRANSIENT EFFECTS DURING MOLTEN POOL FORMATION AND STABILIZATION – OUTCOMES FROM MODELS' COMPARISON PERFORMED IN THE IAEA CRP J46002

Laure Carénini
Institut de Radioprotection et de Sûreté Nucléaire (IRSN)
Cadarache B.P. 3 13115 St-Paul-lez-Durance, France
laure.carenini@irsn.fr

Muhammad Abu Bakar
Pakistan Atomic Energy Commission (PAEC),
P.O. Box 3140 Islamabad, Pakistan
ab4abubakar@gmail.com

Aleksandr Filippov
Nuclear Safety Institute, Russian Academy of Sciences (IBRAE)
52 B. Tulskaya St. RU-115191 Moscow, Russia
phil@ibrae.ac.ru

Romain Le Tellier
Commissariat à l'Energie Atomique et aux Energies Alternatives (CEA, DES, IRESNE, DTN)
Cadarache F-13108 Saint Paul-lez-Durance, France
romain.le-tellier@cea.fr

Ivan Melnikov
National Research Center "Kurchatov Institute" (NRC-KI)
1, Akademika Kurchatova Pl., RU-123182 Moscow, Russia
Melnikov_IA@nrcki.ru

Peter Pandazis
Gesellschaft für Anlagen-und Reaktorsicherheit (GRS)
Boltzmannstraße 14, 85748, Garching, Germany
peter.pandazis@grs.de

Mindaugas Valincius
Lithuanian Energy Institute (LEI)
Breslaujos str. 3, LT-44403 Kaunas, Lithuania
Mindaugas.Valincius@lei.lt

Zijie Wu
China Nuclear Power Technology Research Institute (CNPRI)
China Nuclear Power Technology Research Institute, Shenzhen, China
wuzijie@cgnpc.com.cn

Yapei Zhang
Xian Jiaotong University (XJTU)
Xi'an Jiaotong University, Shaanxi, China
zhangyapei@xjtu.edu.cn

ABSTRACT

In 2020 the International Atomic Energy Agency (IAEA) has started the 4-year Coordinated Research Project (CRP) on In-Vessel Melt Retention (IVMR) with the main objective to harmonize the international understanding of the scientific and technological bases underpinning crucial parts of the safety demonstration of this Severe Accident (SA) management strategy. IVMR is already implemented in several nuclear power plants of generation II and III (VVER440, AP1000, HPR1000…) and under consideration for implementation in existing VVER-1000 reactors and future Small Modular Reactor (SMR) for examples. This strategy consists in maintaining the degraded reactor core (corium) within the vessel by ensuring its cooling thanks to cavity flooding and power extraction through the vessel wall.
In the scope of this CRP, several analytical benchmarks were performed focusing on different reactor designs: a generic 1000 MWe PWR design, the Russian VVER-1000 design, the Chinese CAP1400 design and the Canadian CANDU design. This paper focuses on work done and achievements obtained within the generic 1000 MWe PWR design benchmark. This benchmark is a follow up and an extension of the one developed in the scope of the European H2020 IVMR project. Compared to the other benchmarks dedicated to a specific reactor design, this benchmark is called "generic" because its objective is not to simulate expected corium configuration for a given scenario and reactor but to allow detailed comparison of models between codes based on prescribed and simplified configurations. It intends to cover generic models to be implemented in capable codes (either integral SA code or dedicated code) which may be used for IVMR simulations. Several cases are defined with increasing complexity to allow step by step comparison of the code models. Such an approach is useful for code developers but also for code users in order to better understand results and code capabilities or limitations. Specific attention is paid to molten pool formation and transient effects until reaching steady state configuration. Eight different benchmarks have been developed covering molten pool formation from solid particles, progressive corium relocation to the lower plenum, progressive molten steel incorporation, vessel wall ablation and possible stratification inversion. State of codes performance and remaining issues are discussed in this paper, focusing on configurations involving progressive molten material arrival in the lower plenum.

KEYWORDS

Severe accident, In-Vessel Retention, code benchmark, transient phase, BEPU

1. INTRODUCTION

In 2020 the International Atomic Energy Agency (IAEA) has started the 4-year Coordinated Research Project (CRP) on In-Vessel Melt Retention (IVMR) with the main objective to harmonize the international understanding of the scientific and technological bases underpinning crucial parts of the safety demonstration of this Severe Accident (SA) management strategy [1]. IVMR strategy relies on external cooling of the Reactor Pressure Vessel (RPV) wall to stabilize the degraded reactor core (corium) and maintain the vessel integrity. This would significantly reduce the threats to the containment (last barrier) and therefore the risk of large release of low-volatile radioactive products to the environment. IVMR strategy is already implemented in several nuclear power plants of generation II and III (VVER440 [2] [3], AP1000 [4], HPR1000 [5]…) and under consideration for implementation in existing VVER-1000 reactors [6] [7] and future Small Modular Reactor (SMR) for examples [8] [9].
One of the main issues associated with this strategy lies in the evaluation of the corium behavior in the lower plenum and associated heat fluxes to be extracted through the vessel wall. If first evaluations were performed 30 years ago [10] [11], recently the importance of considering transient effects was highlighted with identification of possible higher heat fluxes [12]. Such transient effects may be associated with the progressive melting of the metallic structures but also to the thermochemistry effects in the corium pool leading to species transfers between oxide and metallic phases [13]. Therefore, dedicated models and codes have been improved to quantify those effects. Studying capabilities of codes used for IVMR strategy evaluation can be seen as an important step towards the international harmonization of understanding of associated phenomena. This work began during the European H2020 IVMR project [14], with in particular a code benchmark performed on a generic PWR design of 1000 MWe [15]. This benchmark was elaborated

to be used as a reference. Considering this basis, new activities were performed during the IAEA CRP in order to update and extend this benchmark, notably including the following points: (i) New codes; (ii) Extension to non-developers code users (only developers were involved in the first benchmark), allowing significant benefit for users training but also a confirmation of the limited extent of the so-called "user effect"; (iii) New benchmark configurations.
This paper presents an overview of the work done on this generic 1000 MWe PWR design benchmark in the scope of the IAEA CRP. A synthesis of the different configurations studied during the project is first proposed. Then, the focus is made on the configurations involving progressive material arrival in the corium pool, with presentation of the different results and discussion of outcomes. To consolidate the results and further analyze the discrepancies, uncertainty analyses are also proposed based on the identification of main uncertainties from the benchmark outputs.

2. DESCRIPTION OF THE BENCHMARK CONFIGURATIONS AND STEADY STATE RESULTS

It is worth noting that this benchmark is not dedicated to a specific reactor design but focuses on a generic 1000 MWe PWR reactor. Indeed, its objective is not to simulate expected corium configuration for a given scenario and reactor but to allow detailed comparison of models between codes based on prescribed and simplified configurations. It intends to cover generic models to be implemented in capable codes (either integral SA code or dedicated code) which may be used for IVMR simulations and thus rather independently from the reactor design. Such an approach appears necessary to better understand codes results and identify their capabilities or limits. In this benchmark, the focus is made on the corium behavior, so that the efficiency of the external cooling is not evaluated, as well as the mechanical resistance of the ablated vessel wall.
In total, nine different organizations participated in this benchmark: IRSN and CNPRI with ASTEC code [16], GRS and LEI with AIDA module of AC² code [17], NRC-KI with HEFEST_ULR – stand-alone version of corresponding module of the SOCRAT code [18], IBRAE with HEFEST_URAN code [19], CEA with PROCOR code [20], PAEC with in-house DCMR code and XJTU with MIDAC code [21]. Both integral severe accident codes (ASTEC, AC², SOCRAT) and codes dedicated to lower plenum (PROCOR, DCMR, MIDAC) are used.
In the first benchmark cases defined during the H2020 IVMR project, the attention is paid to transient effects during vessel wall ablation, progressive molten steel incorporation and possible stratification inversion, considering the corium as already molten in the lower plenum. Two steady-state cases were defined plus three transient configurations. The second part of the benchmark, defined during this CRP focuses on models dealing with the molten pool formation. Indeed, directly considering significant part of the core relocated as molten pool in the lower plenum is often used when studying IVMR and considered as conservative. However, in integral codes, when core relocates to the lower plenum, significant mass of solid debris may be formed initially either due to molten corium jet fragmentation in the water or to the collapse of the core support plate leading to relocation of solid debris directly from the core part of the vessel. In addition, this relocation process may occur in several steps. This transient phase during which the molten corium pool forms in the lower plenum may have a significant impact on the mass of molten steel and thus directly impact the maximum heat flux applied to the vessel wall due to the focusing effect. Therefore, it appears necessary to evaluate and benchmark also the models implemented in the codes for this phase.
Three new cases were defined to study models associated with these phenomena. Overall, this benchmark is thus composed of eight different cases as illustrated in Figure 1 and detailed in Table I.
Depending on code capabilities and manpower resources, some participants were not able to calculate all cases. However, all partners calculated steady state configurations and transient case 3. Then, three main limitations were identified in the codes:

- Lack of thermochemistry model.
- Lack of heavy metal layer model.
- Lack of debris melting model.

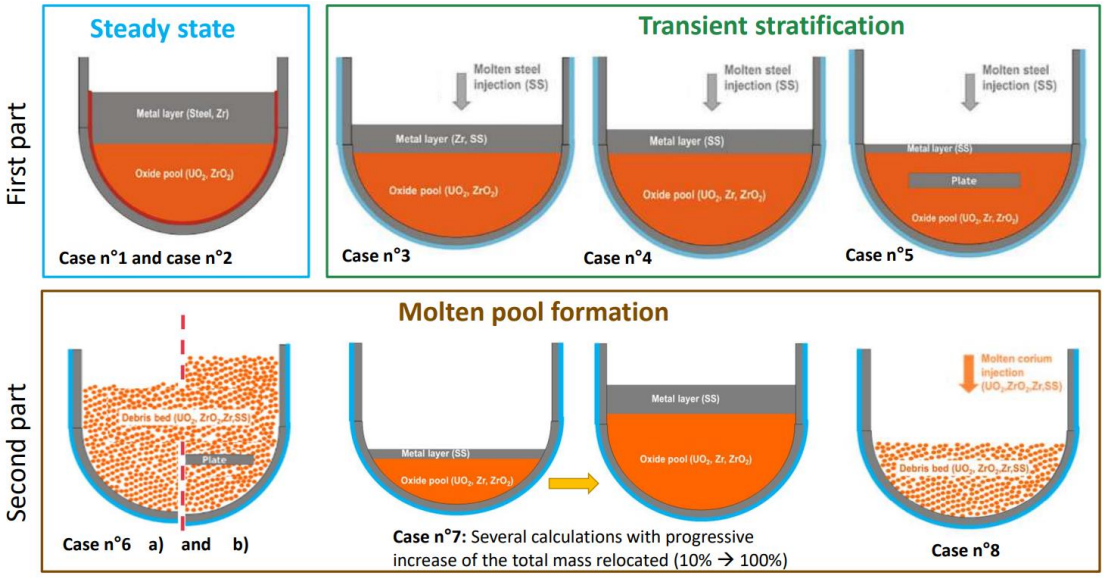

Figure 1. Illustration of the 8 benchmark cases.

Table I. Specifications of the 8 benchmark cases

Cases	**1**	**2**	**3**	**4**	**5**	**6**	**7**	**8**
Initial corium configuration	Liquid oxide at melting temperature Top liquid metal at melting temperature					Solid debris at 450K Particles size 4mm Porosity 0.4	Same as case 4	Same as case 6
Initial oxide composition (mass fraction)								
UO_2	0.8			0.735	0.75	Same as case 4		
ZrO_2	0.2			0.184	0.1			
Zr	-			0.081	0.15			
Cox[i]	-			0.63	0.3			
Oxide height or mass (total core fraction)	1.5 m or about 85t (70%)			92.5t (70%)	90t (70%)	Same as case 4	13.2t-132.1t (10-100%)	66.1t (50%)
Residual power[ii]	206 W/kg of UO_2 corresponding to 14 MW						206 W/kg of UO_2	
Initial metal masses								
Zr	7.5t			-				
Steel	60t		30t		10t	Same as case 4	4.3t-42.9t	21.4t
Initial mass of steel at 450K[iii]	-				20t	6a: - 6b: 20t	-	
Top relocation of material								
Composition	-		Steel			-		Same as debris
Flow rate			6kg/s					875kg/s
Overheat[iv]			0					100
Time frame			from 9000s to 14000s					7200 to 7300s
Boundary conditions								
Top	Adiabatic		Radiative heat transfer towards surrounding structures at 950K					
Along the vessel wall	Melting temperature of steel on inner surface		Saturation temperature of water and boiling heat transfer coefficient on the outer surface to simulate efficient ERVC (no CHF limitation)					

i Cox being the Zr oxidation degree (mole number of oxidized Zr divided by the mole number of total Zr).
ii This corresponds to about 5 hours after the reactor shutdown.
iii Cylindrical plate with a diameter of 3.15m and a thickness of 33.5cm located in the oxide pool (downward surface located 1.2m above the bottom of the lower head).
iv Above melting temperature.

For the steady state configurations, results of heat fluxes profiles obtained by the different participants are presented in Figure 2. They are also compared with analytical results since for such simple configurations, heat fluxes can also be evaluated analytically as detailed in [15] for the adiabatic case or following approach presented in [22] for the radiative case. Globally, the results follow the same general trend, and the accuracy is good, especially for the adiabatic case. However, some discrepancies in power partitioning are identified in the oxide in AC² and MIDAC simulations. This is mainly associated with the heat transfer correlations used in the oxide layer, as discussed in [15]. LEI results obtained with AC² code with different choice of heat transfer correlations (Bonnet-Seiler [23] instead of Kelkar [24] and Asfia-Dhir [25]) confirmed this analysis.
For the radiative case, higher heat flux is evaluated in ASTEC_CNPRI simulation and directly associated with the modelling of the radiative heat transfer: Firstly, conservative model considering only radiation to a top plate is used (thus neglecting radiative heat transfer to the vessel wall) and secondly, a low value is taken for the metal emissivity (equal to 0.2 by default in the code and modified to 0.38 in IRSN evaluations). In IRSN evaluation, simple model for radiative heat transfer to a fictitious boundary condition is used in ASTEC code, for the sake of comparison in the scope of this benchmark. New results obtained for these simple steady-state cases confirm the conclusions of the analysis performed in the H2020 IVMR benchmark: impact of uncertainties on the top radiative heat transfer and especially the metal layer properties (mainly emissivity and melting temperature) are still observed. However, new results also highlight the impact of the modelling of the radiative heat transfer from the top of the pool, which may be expected as significant in integral calculations. Here, due to simplification of the top boundary conditions, simplified models are sufficient but in reactor case a more complex model may be used to consider the real geometry and temperature of the structures above the pool. It could be noted that due to the chosen configuration (significant metal layer thickness), the correlations used for the heat transfer in the top metal layer and the way the correlations are implemented in the codes (assumption for axial temperature gradient for example) play a limited role, as well as variation of other metal properties.

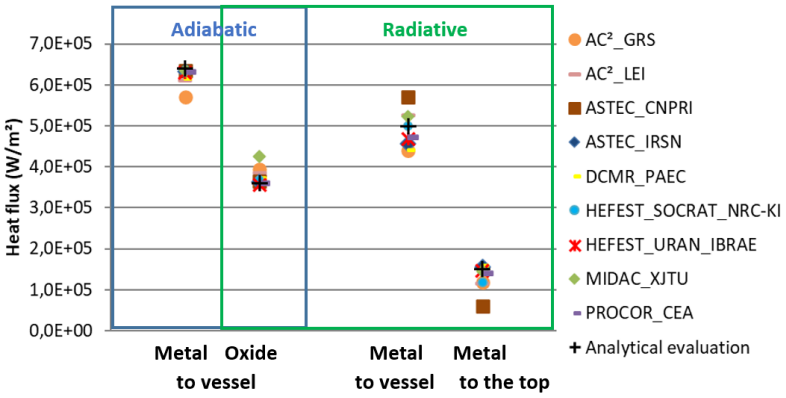

Figure 2. Average heat fluxes: case 1 (adiabatic top boundary condition) on the left; case 2 (radiative top boundary condition) on the right.

The following part focuses on cases 3, 4 and 7 dealing with transient configurations with progressive arrival of molten steel and molten corium. Due to length limitations of this paper, configurations involving stratification inversion and molten pool formation from solid debris will not be discussed. Priority is given to cases were most of the partners were able to participate with their codes.

3. FOCUS ON TRANSIENT CONFIGURATIONS WITH PROGRESSIVE ARRIVAL OF MATERIAL

3.1. Configurations with progressive molten steel arrival

As defined in the previous benchmark [15], in addition to steady-state calculations, two additional cases are proposed, in which the mass of molten steel incorporated increases progressively according to a given

kinetics to simulate the progressive melting of the metallic structures in the reactor vessel. Besides, the molten steel addition due to the vessel wall melting is also simulated, up to steady state. Firstly, the thermo-chemical equilibrium in the U-O-Zr-Fe quaternary system is not simulated as it is the case in simplified steady state configurations described before. In a second test, it is proposed to activate this evaluation in the codes, when available, to identify the impact on the corium stratification.

Results obtained by the participants for the heat flux profile at the outer surface of the vessel wall when maximum heat flux is reached are presented in Figure 3. Here again, conclusions from previous benchmark [15] remain applicable, with: (i) In all codes the increase of the focusing effect during the transient evolution of the metal layer thickness is evaluated; (ii) Discrepancies between maximum heat flux results increase compared to steady-state configurations; (iii) Transfer of species due to thermochemistry evaluation in the pool leads to increase the maximum heat flux, due to modification of phases composition and consideration of part of the residual power in the metal phase (modelling of the transfer of metallic uranium and fission products having affinity with the metal phase). The particular case of IBRAE results with HEFEST_URAN code, whose maximum heat flux does not increase from case 3 to case 4, is directly associated with the consideration of part of the residual power in the metal already in case 3 and independently from the consideration of the species transfer between oxide and metal phase as illustrated in Figure 6. Despite the addition of DCMR and MIDAC codes and the involvement of code users, the increase of the dispersion of the maximum heat flux in case 3 is very limited: ±25% versus 21% in previous benchmark [15].

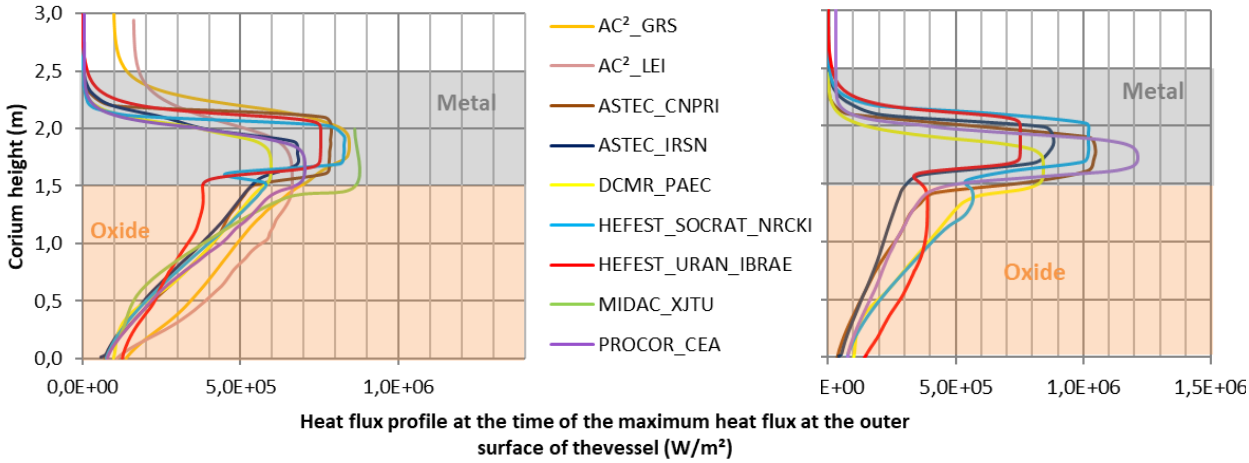

Figure 3. Heat fluxes profiles in case of transient molten steel incorporation: without thermochemistry (case 3) on the left and with thermochemistry (case 4) on the right.

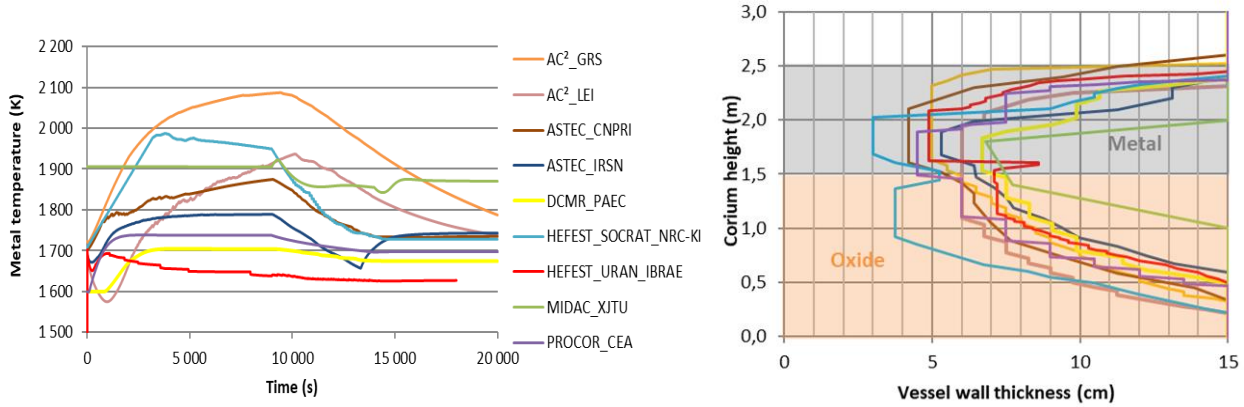

Figure 4. Transient molten steel incorporation without thermochemistry (case 3): Average metal temperature evolution on the left and ablated vessel profile at steady state on the right.

In Figure 4, a significant discrepancy on the metal temperature is identified (difference up to 450K), which cannot be explained only by the variation of the melting temperature considered for the metal layer (1600-1740K). It was identified that this discrepancy is obtained during the ablation of the vessel wall and directly associated with insufficient meshing of the vessel wall for participants with the highest metal temperature. In general, considering a too coarse meshing of the vessel wall may lead not only to underestimate the heat flux (if there are not sufficient meshes in the residual part of the vessel wall after ablation) but also to an increase of the metal layer temperature during the ablation process, which has an impact on the power dissipated due to radiative heat transfer at the top of the pool. This effect is illustrated in Figure 5.
The ablated profiles of the vessel wall at steady state exhibit some discrepancies and especially no coherence between high outer heat flux values and low residual thickness. Here again, the issue of insufficient meshing of the vessel wall may play a major role, as for example visible on the simplified profile evaluated by MIDAC code.

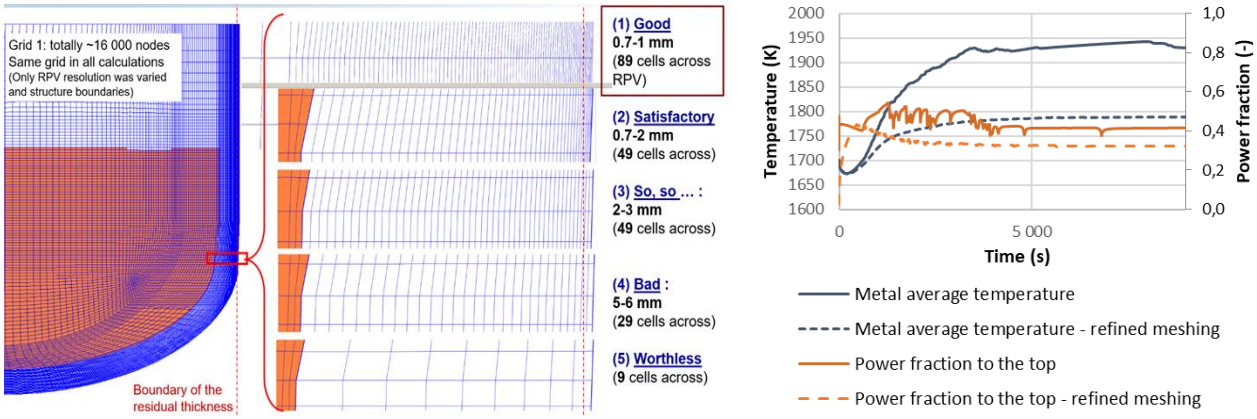

Figure 5. Synthesis of meshing effect studies with HEFEST_URAN code (left) and identification of impact of refined radial meshing (66 regular radial meshes versus 13) on metal temperature during transient phase (right).

Regarding case 4, the underpinning reasons of discrepancies in maximum heat flux evaluated by the six participants (cf. Figure 3) are identified as being the following:

- The correlations of heat transfer in the oxide pool influence the power transferred from the oxide to the metal: Power partitioning from the oxide pool to the top was identified as being between 0.4 and 0.55 among the participants in the steady-state configurations analysis.
- Then, the issue of the metal layer emissivity varying between 0.2 and 0.4 depending on the participants was identified. It should be noted that in this transient case, the maximum heat flux is reached when the metal layer thickness is reduced and close to 50cm (against 90cm in the steady-state configurations), this may also increase the impact of the differences associated with the heat transfers in the metal layer (radiative boundary and correlations), since for thinner metal layer the relative importance of the radiative top boundary condition is increased. This point is further discussed in § 3.3.
- Regarding other material properties, the main discrepancy lies in the value of the thermal conductivity of the metal phase ranging from 20 to 40 W/m/K. Variation of melting temperature of the metal and oxide phase may also play a role (1600-1740K for the metal and 2750-2950K for the oxide phase).
- Finally, a discrepancy is identified for the species transfer between oxide and metal. Especially for the fraction of the total residual power evaluated to be present in the metal phase, it ranges from 10 to 20% and has a direct impact on the maximum heat flux value. Figure 6 presents the results and the associated kinetics of transfer which is also subject to significant variation. Difference of modelling option for the kinetics between the two ASTEC calculations are visible: IRSN evaluation considered reduced kinetics compared to default value in the code used by CNPRI, based on recent validation work performed on MASCA-RCW and CORDEB2 tests [26].

Uncertainties associated with the behavior of the oxide crust during metal and oxide phases interaction were highlighted in [15], with high heat flux evaluated by PROCOR code when considering that, during chemical interaction, the metal layer is progressively transferred below the oxide crust. This point is not further discussed in this work, but potential transient impact of the significant uncertainties associated with the oxide crust behavior during material interaction and at reactor scale should be kept in mind.

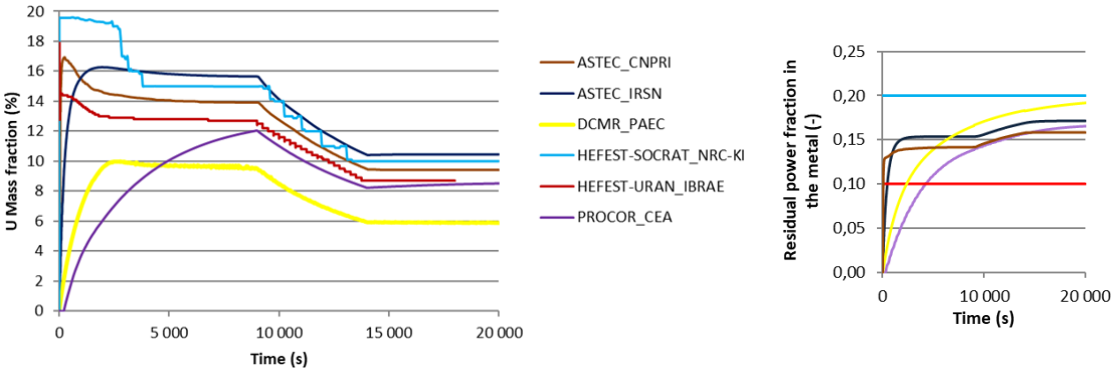

Figure 6. Transfer of metallic uranium and residual power in the metal phase: transient molten steel incorporation with thermochemistry effects (case 4).

3.2. Uncertainties propagation based on case 4 benchmark configuration

To consolidate analysis performed with codes comparison and better assess the uncertainties associated with transient evolution of the corium pool in the lower plenum in IVMR configuration in case of standard corium stratification (i.e. metal layer on the top), Best Estimate Plus Uncertainty (BEPU) evaluations were performed based on case 4 benchmark configuration and uncertain parameters previously identified: Power partitioning in the oxide layer: fraction to the top, $P_{ox} \in$ [0.4-0.55]; Conductivity of the metal layer: $\lambda_m \in$ [20-40] W/m/K; Liquidus temperature of the oxide layer: $Tliq_{ox} \in$ [2750-2950] K; Liquidus temperature of the metal layer: $Tliq_{met} \in$ [1600-1740] K; Emissivity of the metal layer: $\varepsilon_m \in$ [0.2-0.4]; Residual power fraction in the metal layer: CPres $\in$ [0.1-0.2].

IRSN with ASTEC code and IBRAE with HEFEST-URAN code participated in this BEPU analysis[1], considering for each parameter uniform distribution over its variation range. Results are summarized in Figure 7 and Figure 8. BEPU studies realized with ASTEC and HEFEST-URAN show comparable results and conclusions. The most probable values for the maximum heat flux range between 0.7 and 0.9MW/m², with maximum below 1.1MW/m². In addition, negligible impact of metal conductivity and liquidus temperature of the oxide phase is observed, as well as major impact of power partitioning in the oxide phase. When correlation coefficients are small (typically below 0.2), such values are not meaningful due to very weak correlation, hence the differences should not be interpreted.

In order to understand the maximum heat flux evaluated in PROCOR code (1.2MW/m²), which is above the maximum identified in BEPU studies, a specific analysis was performed by CEA at the time of this maximum heat flux. It was identified that about 2MW, associated with the thermal inertia of species coming from the oxide pool at a higher temperature, are dissipated in the metal layer. This difference compared to other codes may be related to the slower kinetics for species transfer from the oxide pool (cf. Figure 6), leading to still have effect of this additional power when the vessel has been ablated in front of the top metal layer and the maximum heat flux is reached at the outer surface of the vessel. This outcome illustrates the complementary between benchmark of different codes on one hand and BEPU analysis on the other. The two enrich each other leading to a better understanding of the results and of the complex coupling of the different physical phenomena modelled in SA codes.

[1] Since heat transfers in the metal layer are fixed by the user in this simplified configuration for HEFEST-URAN simulation, variation of upper and lateral Nusselt numbers was also proposed, in accordance with the results of ASTEC code evaluation: Nu_up [50-100], Nu_lat [300-600].

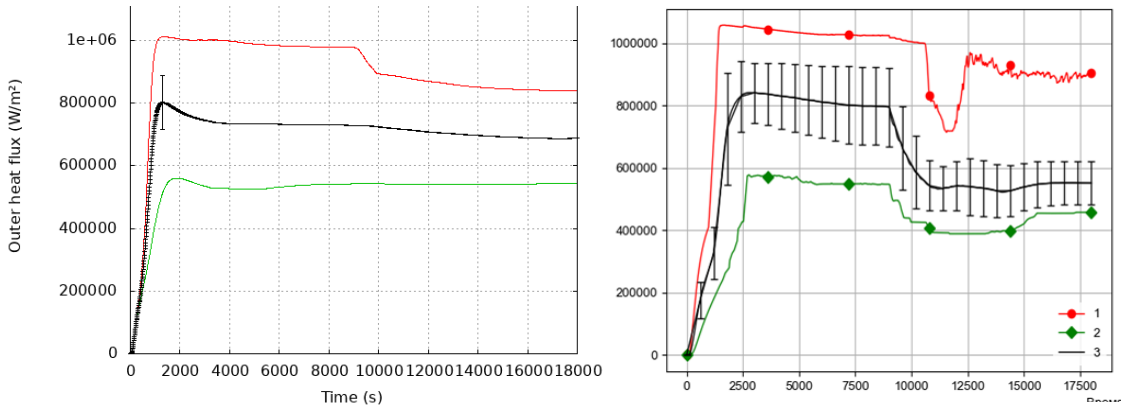

Figure 7. Maximum heat flux evolution considering propagation of uncertainties on material properties and models: 200 ASTEC calculations on the left and 96 HEFEST-URAN calculations on the right; red: maximum, green: minimum, black: average.

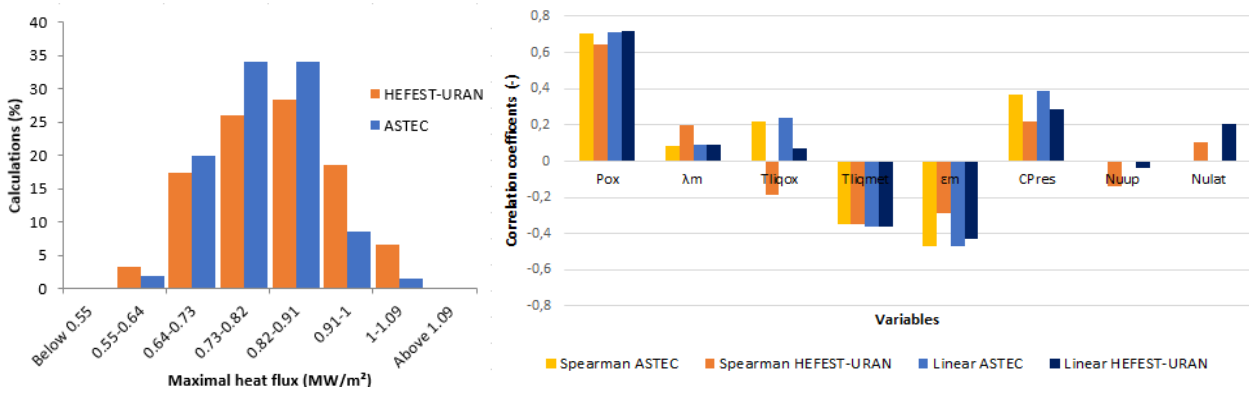

Figure 8. Maximum outer heat flux distribution (left) and correlation coefficients of uncertain parameters (right) considering propagation of uncertainties on material properties and models.

3.3. Configurations with progressive corium arrival

In this case, the impact of considering the relocation of a reduced part of the core is studied. Case n°7 is proposed as a series of calculations with various masses in the lower plenum but keeping the same composition and ratio between species. It is proposed to vary from 10 to 100% of the core mass, so that the case with 70% of core relocated will correspond to case 4 (before the relocation of the molten steel, and thus when maximum outer heat flux is reached). The mass of molten steel initially incorporated in the slumping corium is thus assumed to be proportional to the mass of the slump, keeping the ratio considered for the case n°4, i.e. 24.5% (30t out of 122,5t). Since the power decreases with the reduction of the mass, the focusing effect is expected to be eliminated for the low values of corium mass relocation: 10% (resp. 100%) of core relocated corresponds to about 10cm (resp. 47.5cm) for the initial metal thickness and 2MW (resp. 20MW) of total residual power.

Six different partners take part to this benchmark case. However, it should be noted that for AC² results, no material interaction is modelled, and residual power fraction in the metal layer is assumed constant (10% in LEI calculations and 5% in GRS calculations). Results of maximum outer heat flux and minimum vessel thickness are summarized in Figure 9, where each point corresponds to a simulation.

Significant discrepancies are identified between the two ASTEC simulations, directly associated with the difference in the metal emissivity and assumption for radiative heat transfer as highlighted in § 3.1. The comparison of the radiative heat transfer considered at the top of the pool in the different codes (cf. left of Figure 10) illustrates this impact. The higher heat fluxes evaluated by PROCOR code, despite the significant fraction of power dissipated in the top metal layer by radiation can be explained thanks to the analysis

performed for the case 4 (cf. 3.2), which identify additional power in the metal layer associated with species transfers from the oxide pool with significant thermal inertia.

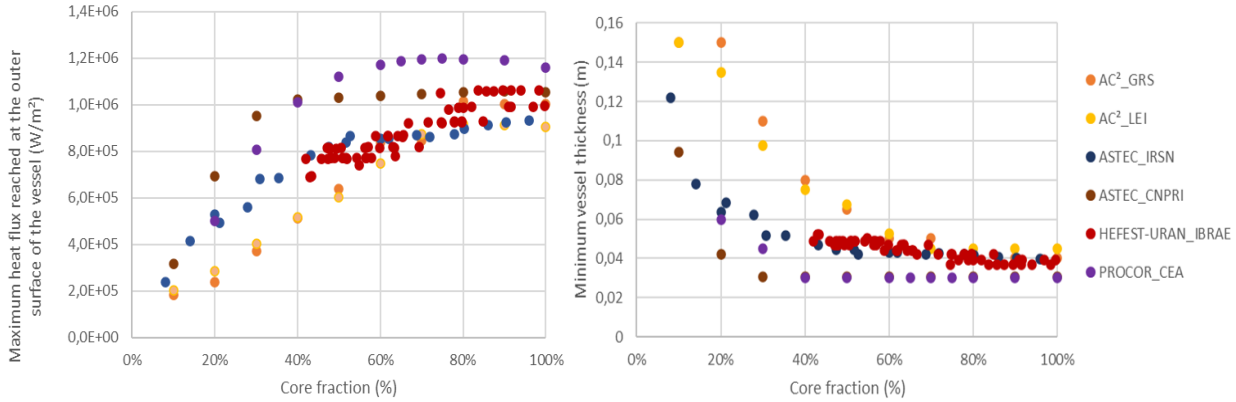

Figure 9. Case 7 (progressive corium relocation): Maximum heat fluxes at the outer surface of the vessel (left) and minimum vessel thickness (right) function of the core fraction relocated in the lower plenum.

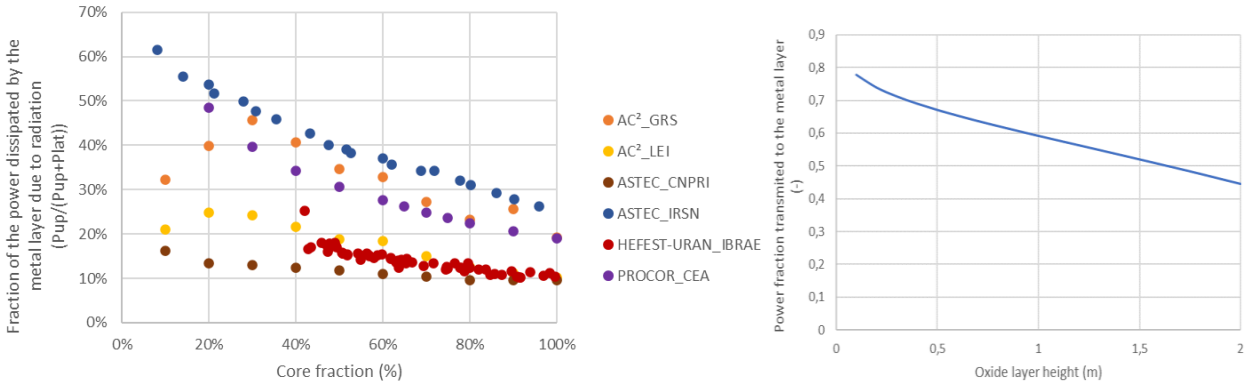

Figure 10. Case 7 (progressive corium relocation): Power fraction dissipated in the top metal layer due to radiative heat transfer, function of the core fraction relocated in the lower plenum (left) and power fraction transfer to the top metal layer from the oxide pool depending on its height – use of BALI correlations [23] (right).

All codes evaluate almost no decrease of the maximum heat flux between 80 and 90%. This is associated with the geometry of the vessel and the fact that in this zone the metal layer is in the cylindrical part. Regarding the minimum vessel thickness, for core fraction above 60%, the discrepancies are limited, and the minimum thickness is almost constant. On the opposite, for lower core fraction, the decrease of the maximum heat flux is not the same depending on the codes. Significant ablation of the vessel is evaluated in ASTEC and PROCOR codes even for limited core fraction relocation (about 20%), due to limited mass of steel and associated focusing effect. These differences may be associated with the correlations used for the heat transfer in the layers. In the oxide pool, the power transmitted to the top metal layer may depend to the height to radius ratio as in BALI correlations [23], with an increase when the thickness of the oxide pool decreases, as illustrated in right side of Figure 10. In the metal, the use of Mayinger [27] and BALI correlations [23] for respectively axial and lateral heat transfer in AC² leads to lower heat flux when the metal layer height decreases. Compared to standard approach for the heat transfer evaluation in the metal layer [22] based on the temperature difference between the bottom and the top of the layer (i.e. considering that convective heat transfer is driven by bottom heating of the metal layer from the oxide), the use of correlations based on the residual power underestimates the focusing effect.

4. CONCLUSIONS

In the scope of the IAEA CRP J46002, nine different code developers and users have participated with seven different codes in a benchmark exercise based on the generic 1000 MWe PWR benchmark developed during the H2020 IVMR project [15]. The main objective was to extend the work done previously, whose benefits for harmonization of understanding of main phenomena associated with IVMR were recognized. New transient configurations dedicated to study formation of the corium molten pool in the lower plenum were also defined.

Main code limitations were identified with, depending on the code used, lacks in models regarding thermochemistry of the quaternary system U-O-Zr-Fe, possibility of transient 3-layers configurations and debris melting. Requirements regarding vessel wall meshing were also formulated.

Results obtained confirmed conclusions drawn with code developers in the first benchmark and limited impact of modelling choices, which may vary between different users of the same code. Moreover, new results also highlight the impact of the modelling of the radiative heat transfer from the top of the pool, which may be expected as significant in integral calculations. The overheat in the metal layer associated with species transfer from the oxide pool during thermochemical interactions before reaching equilibrium composition in oxide and metal phases was also identified. BEPU analyses were performed and show complementarity with benchmark comparison of the different codes for better identification of uncertainties and understanding of the complex coupling of physical phenomena involved.

In addition, results obtained for a new case defined to study the progressive corium relocation in the lower plenum were presented. Series of calculations were performed by the participants considering from 10% to 100% of the total fuel mass relocated in the lower plenum, keeping steel to UO_2 ratio constant. If comparable trends are observed, it shows that higher discrepancies are associated with small layer thicknesses mainly due to the larger impact of the correlations used for the heat transfer in the metal, as well as the larger influence of radiative heat transfer associated with the increase of the metal temperature. A maximum variation of +/-45% on the maximum heat flux value is obtained for corresponding metal layer of about 20cm (30% of core relocated). However, in this case the resulting side heat flux lies below the safety margin for all calculations (maximum of 1.2MW/m²).

In this paper, the focus was made on transient configurations with progressive arrival of molten steel and molten corium but configurations involving stratification inversion and molten pool formation from solid debris were also studied in this benchmark, although with reduced number of participants. Associated results will be available in the TECDOC report dedicated to this CRP.

ACKNOWLEDGMENTS

Authors would like to acknowledge the IAEA for the coordination of this CRP and in particular Mr Alexei Miassoedov from the Division of Nuclear Power and Mr Simone Massara and Ms Tania Veneau from the Division of Nuclear Installation Safety.

REFERENCES

1. L. Carénini, W. Ma, P. Matejovic, P. Pandazis, S. Massara, A. Miassoedov, “The IAEA coordinated research project on developing a phenomena identification and ranking table and a validation matrix and performing a benchmark for in-vessel melt retention”, *Proceedings of 2022 European Review Meeting on Severe Accident Research (ERMSAR2022)* Karlsruhe, Germany, May 16-19, 2022 (2022).
2. O. Kymälainen, H. Tuomisto and T.G. Theofanous, “In-vessel retention of corium at the Loviisa plant”, *Nuclear Engineering and Design*, **169** (1997).
3. P. Matejovic, M. Barnak, M. Bachraty, L. Vranka, R. Berky, “Adoption of IVR concept for VVER-440/V213 reactors in Central European Countries”, *Nuclear Engineering and Design*, **314**, (2017).
4. H. Esmaili, M. Khatib-Rhabar, “Analysis of in-vessel retention and ex-vessel fuel coolant interaction for AP-1000”, NUREG/CR-6849, ERI/NRC 04-201 (2004).
5. Y.B. Li, L.L. Tong, X.W. Cao, D.Q. Guo, “In-vessel retention coolability evaluation for Chinese improved 1000 MWe PWR”, *Ann Nucl Energy*, **76** pp. 343-349 (2015).

6. M. Kotouk, P. Matejovic, M. Barnak, I. Melnikov, "VVER-1000 IVMR benchmark", *Proc. of the Int. Seminar "In-vessel retention: outcomes of IVMR project"* Juan-les-Pins, France, Jan 21-22 (2020).
7. R. Gencheva, A. Stefanova, P. Groudev, B. Chatterjee, D. Mukhopadhyay, "Study of in-vessel melt retention for VVER-1000/v320 reactor", *Nuclear Engineering and Design*, **298**, pp. 208-217 (2016).
8. H. Esmaili S. Campbell J. Schaperow, "Independent Assessment of In-Vessel Retention and Steam Explosion for the NuScale Small Modular Reactor" USNRC RES/FSCB 2018-02 (2018).
9. R.J. Park, D. Son, H.S. Kang, S.M. An, K.S. Ha, "Development of IVR-ERVC evaluation method and its application to the SMART", *Annals of Nuclear Energy*, **161** (2021).
10. R.E. Henry, H.K. Fauske, "External cooling of a reactor vessel under severe accident conditions", *Nuclear Engineering and Design*, **139**, pp. 31-43 (1993).
11. H. Tuomisto, T.G. Theofanous, "A consistent approach to severe accident management", *Nuclear Engineering and Design*, **148** (1994).
12. M. Sangiorgi et al., "Justification of best-estimate transient calculations in comparison to the steady-state bounding-case approach", *Pro. of the Int. Seminar "In-vessel retention: outcomes of IVMR project"* Juan-les-Pins, France, January 21-22, 2020 (2020).
13. R. Le Tellier, L. Viot, L. Carénini, F. Fichot, N. Bakouta, A. Filippov, "Transient stratified corium pool modelling for In-Vessel Retention analysis", *Proc. of the International Seminar "In-vessel retention: outcomes of IVMR project"* Juan-les-Pins, France, January 21-22 (2020).
14. F. Fichot, L. Carénini, S. Brumm, M. Sangiorgi, "Methodology of safety evaluation of In-Vessel Retention", *Proc. of the Int. Seminar "In-vessel retention: outcomes of IVMR project"* Juan-les-Pins, France, January 21-22 (2020).
15. L. Carénini et al., "Main outcomes from the IVR code benchmark performed in the European IVMR project", *Annals of Nuclear Energy*, **146** (2020).
16. L. Carénini, F. Fichot, "The Impact of Transient Behavior of Corium in the Lower Head of a Reactor Vessel for In-Vessel Melt Retention Strategies", *Proc. of ICONE24 Conference*, Charlotte, USA, (2016).
17. P. Pandazis, S. Weber, "Investigation of a severe accident late phase scenario in a PWR with ATHLET-CD", *Proceedings of the 27th Nuclear Energy for New Europe Conference*, Portoroz, Slovenia, (2018).
18. A.S. Filippov et al., "SOCRAT/HEFEST code: models of VVER core melt interaction with reactor structures under severe accident conditions", *Bull. Russ. Acad. Sci., Energetics*, **3**, (2010) (in Russian).
19. A.S. Filippov, N.I. Drobyshevsky, D.D. Kamenskay, A.E. Kisselev, E.V. Moiseenko, "End-to-end technology of modeling a melt-structure interaction during IVMR in VVER with HEFEST-URAN toolkit". *Proc. of 22nd Int. Conf. Nucl. Eng., ICONE22*, Prague, Czech Republic, July 7-11 (2014).
20. R. Le Tellier, L. Saas, S. Bajard, "Transient stratification modelling of a corium pool in a LWR vessel lower head", *Nuclear Engineering and Design* **287**, pp. 68-77, (2015).
21. J. Wang, W.X. Tian, Y.P. Zhang, L. Chen, L.Z. Li, L.T. Zhang, Y.K. Zhou, G.H. Su, S.Z. Qiu. The development of Module In-vessel degraded severe accident Analysis Code MIDAC and the relevant research for CPR1000 during the station blackout scenario, Progress in Nuclear Energy 76 (2014).
22. T.G. Theofanous, C. Liu, S. Additon, S. Angelini, O. Kymalainen, T. Salmassi, "In-vessel coolability and retention of a core melt", DOE/ID-10460 VOLUME 1 October 1996, (1996).
23. J.M. Bonnet, J.M. Seiler, "Thermal hydraulic phenomena in corium pool: the BALI experiment", *Proceedings of ICONE7 Conference*, Tokyo, Japan, (1999).
24. K.M. Kelkar, K.K. Khankari, S.V. Patankar, "Computational modelling of turbulent natural convection in flows simulating reactor core melt", Sandia National Laboratories, Albuquerque, December (1993).
25. F.J. Asfia, V.K. Dhir, "An experimental study of natural convection in a volumetrically heated spherical pool bounded on top with a rigid wall", *Nuclear Engineering and Design,* **163**, pp. 333-348, (1996).
26. R. Le Tellier, L. Carénini, F. Fichot, R. Gencheva, P. Groudev, I. Melnikov, A. Filippov, "In-vessel corium thermochemistry benchmark based on MASCA-CORDEB2 experimental data", *Proc. of 2024 European Review Meeting on Severe Accident Research (ERMSAR2024,* Stockholm, Sweden, May 13-16, 2024 (2024).
27. F. Mayinger, M. Jahn, H. Reineke, V. Steinbrenner, "Examination of thermohydraulic processes and heat transfer in a core melt" BMFT RS 48/1, Institute für Verfahrenstechnic der TU, Germany (1976).

RÉPUBLIQUE FRANÇAISE
Liberté
Égalité
Fraternité

IRSN
INSTITUT DE RADIOPROTECTION ET DE SÛRETÉ NUCLÉAIRE

IVMR MODELLING WITH TRANSIENT EFFECTS DURING MOLTEN POOL FORMATION AND STABILIZATION: OUTCOMES FROM MODELS' COMPARISON PERFORMED IN THE IAEA CRP J46002

L. Carénini, IRSN, M. Abu Bakar, PAEC, A. Filippov, IBRAE, R. Le Tellier, CEA, I. Melnikov, NRC-KI, P. Pandazis, GRS, M. Valincius, LEI, Z. Wu, CNPRI, Y. Zhang, XJTU

The 11th European Review Meeting on Severe Accident Research (ERMSAR2024) KTH, Stockholm, Sweden, May 13-16, 2024

IRSN/FRM-296 ind. 06

MEMBRE DE ETSON

The IAEA Coordinated Research Program (CRP) J46002 Developing a Phenomena Identification and Ranking Table and a Validation Matrix, and Performing a Benchmark for In-Vessel Melt Retention

- The general objective of the CRP is to **harmonize the international understanding of scientific and technological bases underpinning crucial parts of the safety demonstration of IVMR**, including for (but not limited to) high-power reactors

- The CRP aims at providing a platform facilitating interactions among IAEA Member States

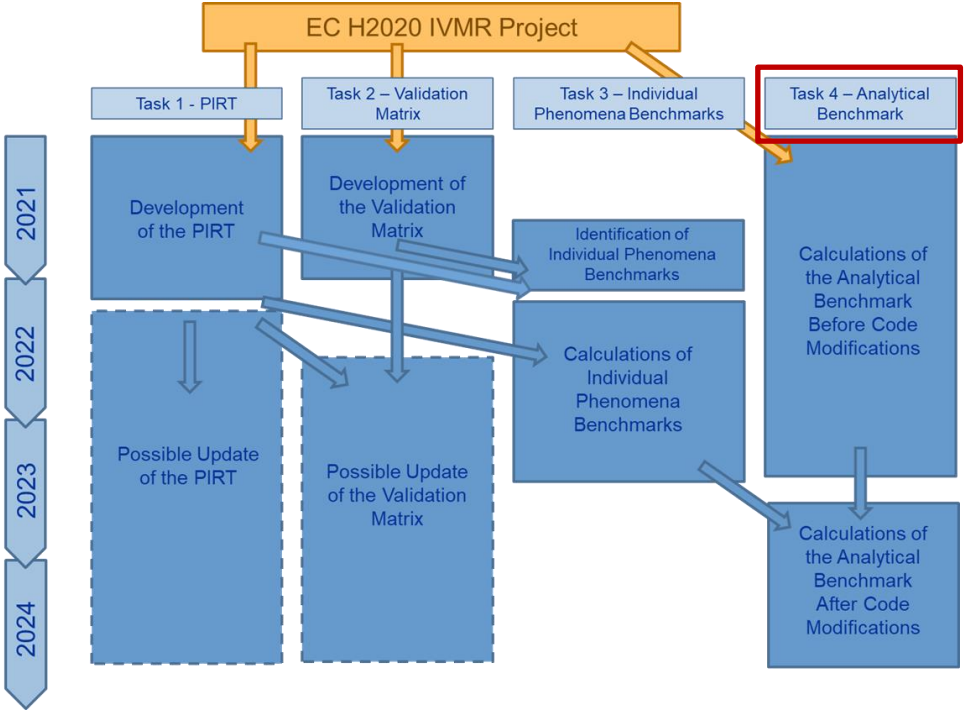

IVMR generic PWR benchmark

- Main objective: **benchmark of the different models** used in the codes for IVMR simulation
- Based on the H2020 European IVMR benchmark
- Generic configuration: 1000MWe PWR

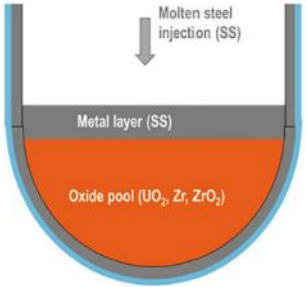

Lower head geometry	Hemispherical
Fuel mass	70% of the total
U/Zr atomic ratio	1.14
Oxidation degree of the Zr	60%
Residual power	14MW ~5 hours after SCRAM
Initial molten steel mass	30t
Kinetics of molten steel incorporation	30t after 2h30

- 3 parts in the benchmark:
  - Part1: H2020 IVMR benchmark → step by step approach with increasing complexity
  - Part 2: New configurations to study model dedicated to molten pool formation
  - Part 3: Best Estimate Plus Uncertainties (BEPU) analyses

Generic PWR benchmark: 8 different configurations

Part 1

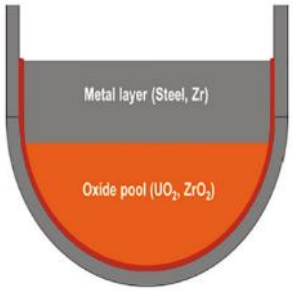

Steady state

Cases n°1 and 2

Transient stratification

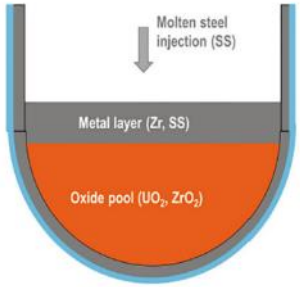

Case n°3

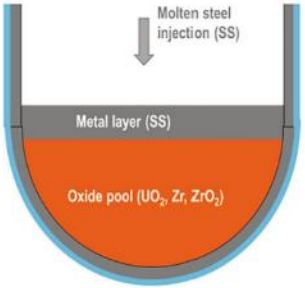

Case n°4

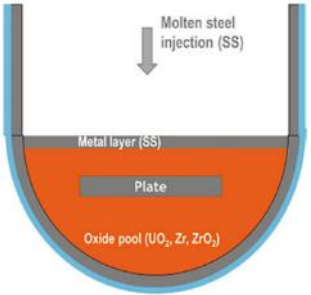

Case n°5

Part 2

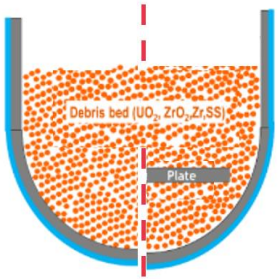

Case n°6 a) and b)



Several calculations with progressive increase of the total mass relocated (10% → 100%)

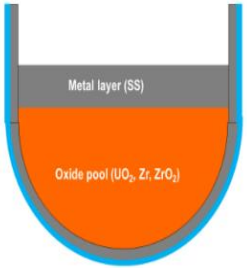

Case n°7

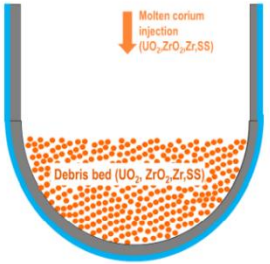

Case n°8

Molten pool formation

Participation to the different benchmark cases

- 9 participants with 7 codes

X: new results compared to H2020 IVMR benchmark
X: updated results compared to H2020 IVMR benchmark

Organization	Code	Part 1				Part 2			BEPU
		Cases 1 & 2	Case 3	Case 4	Case 5	Case 6	Case 7	Case 8	Case 4
CEA	PROCOR	X	X	X	X		X		
CNPRI	ASTEC	X	X	X	X	X	X	X	
GRS	AC^2	X	X				X		
IBRAE	HEFEST_URAN	X	X	X	X	X	X	X	X
IRSN	ASTEC	X	X	X	X	X	X	X	X
LEI	AC^2	X	X				X		
NRC-KI	HEFEST-ULR	X	X	X					
PAEC	DCMR (2.0)	X	X	X					
XJTU	MIDAC	X	X						

Increased number of codes and inclusion of code users

New configurations

Focus on results obtained for liquid corium pool configuration with top metal layer

BEPU

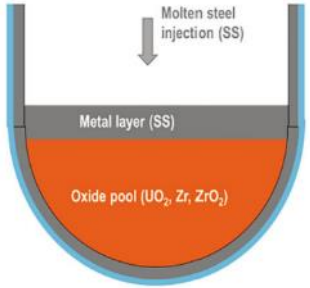

Case n°4

Transient stratification:
Progressive molten steel incorporation (including wall ablation)

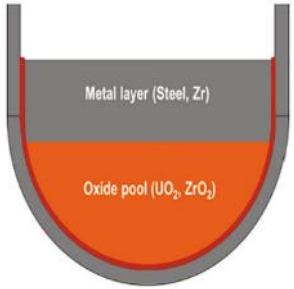

Cases n°1 and 2

Steady state

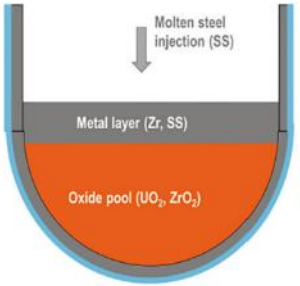

Case n°3

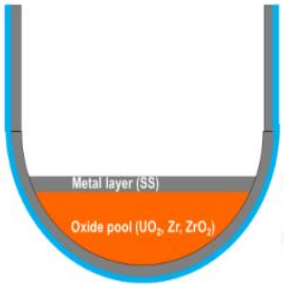

Several calculations with progressive increase of the total mass relocated (10% → 100%)

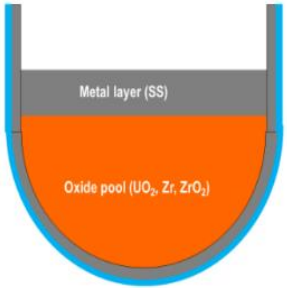

Case n°7

Molten pool formation

Steady-state configurations

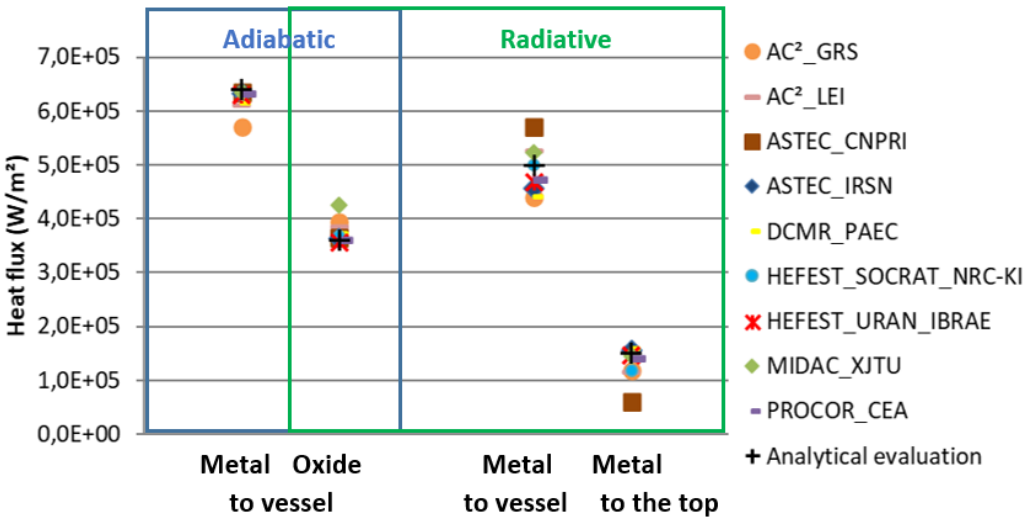

- Results are comparable → higher dispersion in radiative case +/-13%
- Impact of radiative heat transfer modelling: directly quantified between the two ASTEC results (low metal emissivity by default in the code used in ASTEC_CNPRI)
- Impact of heat transfer correlations in oxide pool

Transient configuration case 3: Kinetics of molten steel incorporation - Vessel wall ablation – No thermochemistry

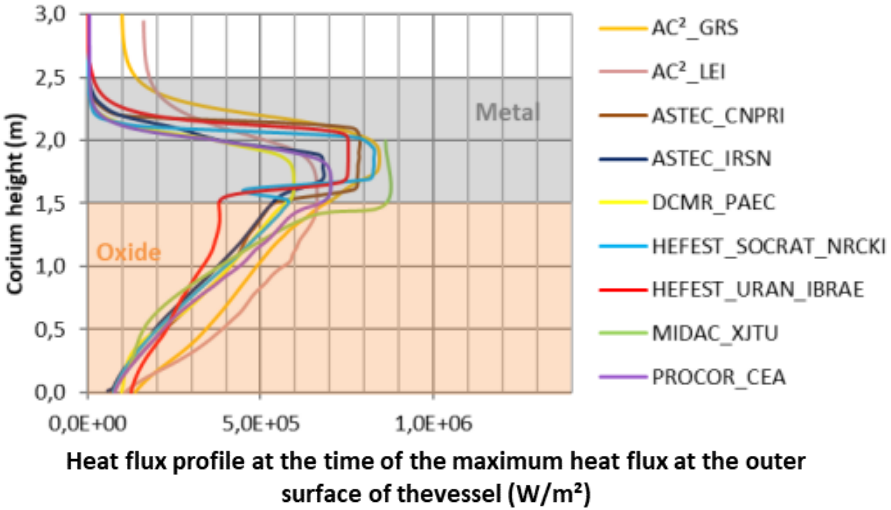

Heat flux profile at the time of the maximum heat flux at the outer surface of thevessel (W/m²)

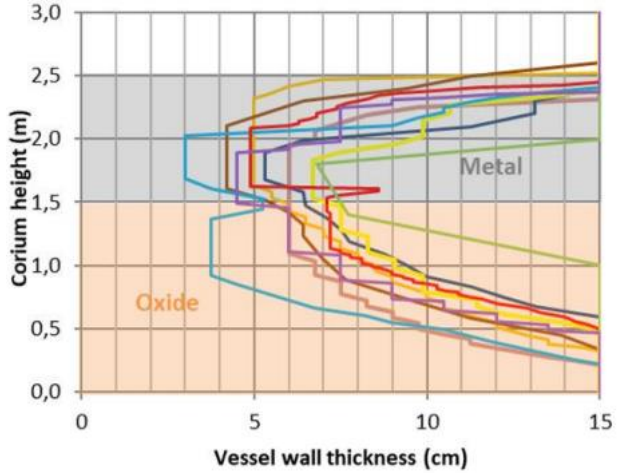

- Maximum heat flux reached during transient phase when top metal layer thickness is reduced
- Discrepancy on maximum heat flux +/-20%
- Impact of vessel wall meshing depending on codes and steel conductivity

Transient configuration case 4: Kinetics of molten steel and species partitionning between layers

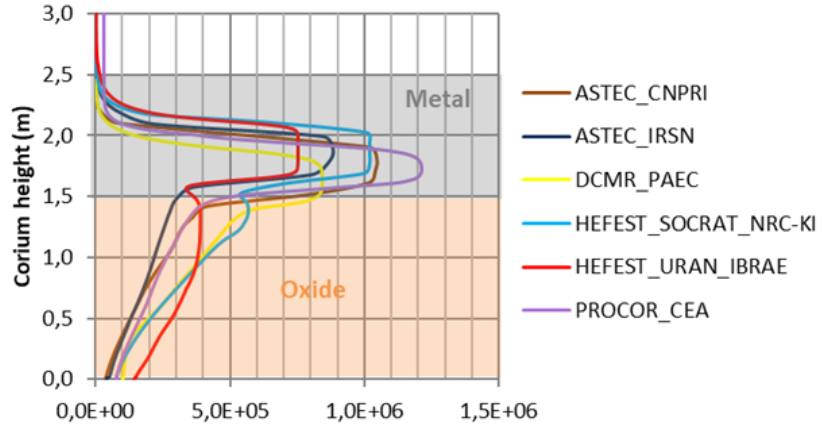

Heat flux profile at the time of the maximum heat flux at the outer surface of thevessel (W/m²)

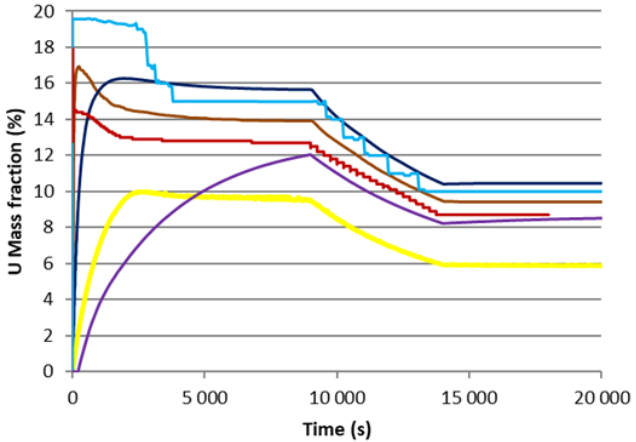

- Increase of the maximum outer heat flux [0.75-1.2]MW/m² (versus [0.5-0.9]MW/m² in case 3)
- Discrepancy on maximum heat flux +/-23%
- Effect of thermochemical equilibrium models (limitation for AC² and MIDAC codes)
- Uncertainties on kinetics of species partitioning → *R. Le Tellier et al., In-Vessel Corium Thermochemistry Benchmark based on MASCA experimental data, ERMSAR2024 Conference*

Transient configuration case 4: Kinetics of molten steel and species partitionning between layers – BEPU Analysis

- Code benchmarks allowed identification of the main differences in models and material properties:
  - Power partitioning in the oxide layer: fraction to the top, Pox ϵ [0.4-0.55];
  - Conductivity of the metal layer: λm ϵ [20-40] W/m/K;
  - Liquidus temperature of the oxide layer: Tliqox ϵ [2750-2950] K;
  - Liquidus temperature of the metal layer: Tliqmet ϵ [1600-1740] K;
  - Emissivity of the metal layer: εm ϵ [0.2-0.4];
  - Residual power fraction in the metal layer: CPres ϵ [0.1-0.2].

- Best Estimate Plus Uncertainty (BEPU) calculations considering the uncertain parameters identified in the code-to-code benchmark
  - Comparable results with ASTEC and HEFEST-URAN (resp. 200 and 96 calculations)

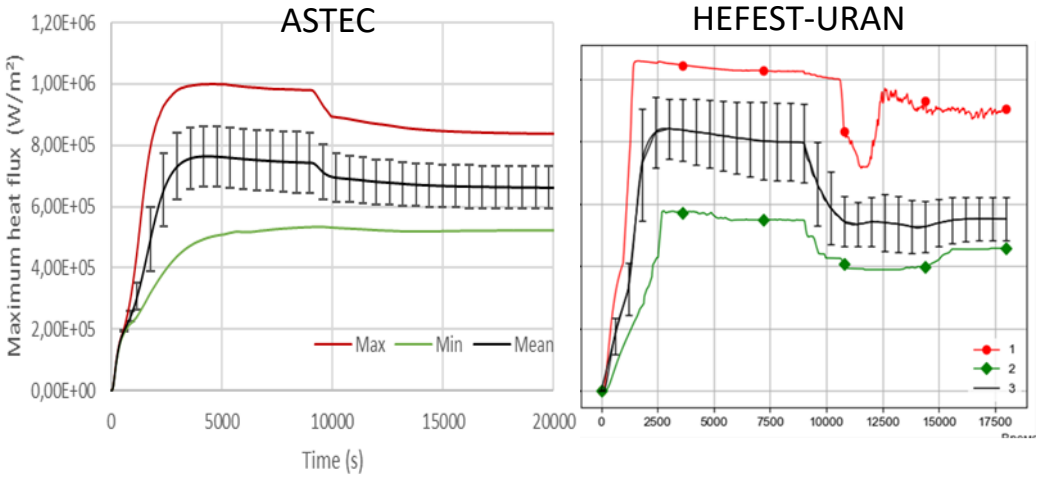

Transient configuration case 4: Kinetics of molten steel and species partitionning between layers – BEPU Analysis

- For this configuration, looking at maximum outer heat flux:
  - Major impact of power in the metal layer (partitioning in this oxide and residual power)
  - Significant impact of radiative properties (metal temperature and emissivity)
  - Negligible impact of metal conductivity and oxide liquidus temperature

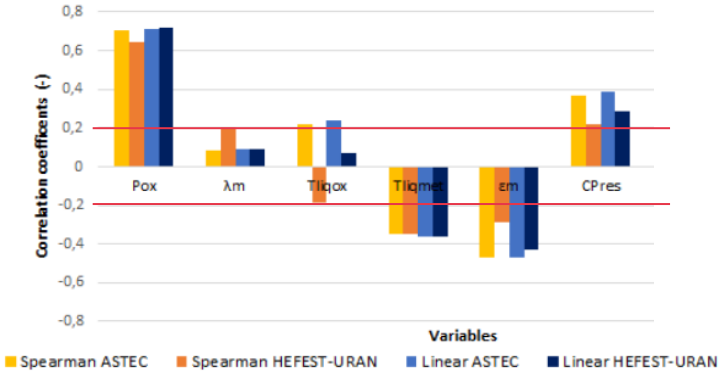

- Distribution of outer maximum heat flux
  - Benchmark codes results are included in BEPU results, except PROCOR.
  - Additional power (~2MW) in the metal when max. heat flux is reached in PROCOR code: thermal inertia of species coming from the oxide pool at a higher temperature combined with slower kinetics for species transfer

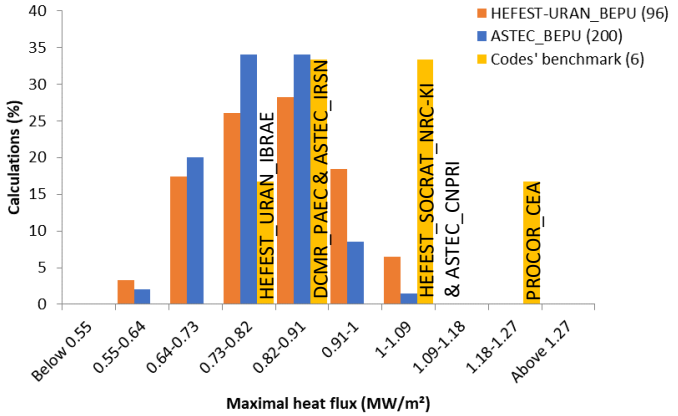

Molten pool formation case 7 – Series of calculations dedicated to 2 layers configurations and focusing effect

- All models activated (vessel ablation, thermochemistry)

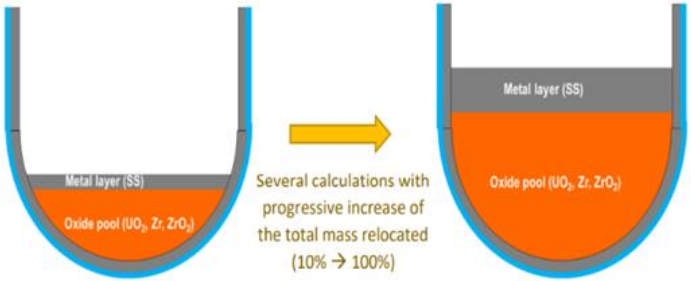

Table 8 – Inputs for the benchmarking calculation n°7

Parameter	Value									
Mass fraction of the core	10%	20%	30%	40%	50%	60%	70%	80%	90%	100%
Oxide pool										
UO_2	74% (mass fraction in the oxide pool)									
ZrO_2	18% (mass fraction in the oxide pool)									
Zr	8% (mass fraction in the oxide pool)									
Oxide mass	13.2t	26.4t	39.6t	52.9t	66t	79.3t	92.5t	115.6t	102.8t	132.1t
Residual power	206 W/kg of UO_2									
Metallic pool										
Steel mass	4.3t	8.6t	12.9t	17.1t	21.4t	25.7t	30t	37.5t	33.3t	42.9t

Case 4 configuration before 2nd molten steel relocation from the top

Molten pool formation case 7 – Series of calculations dedicated to 2 layers configurations and focusing effect

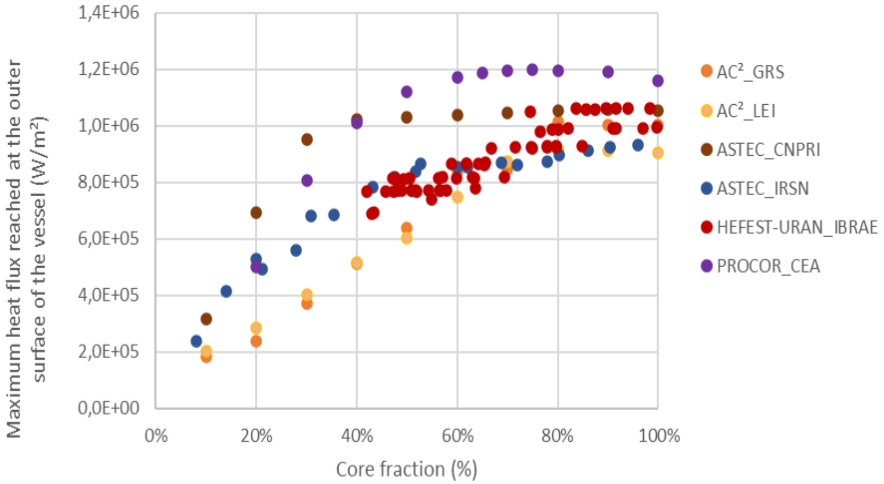

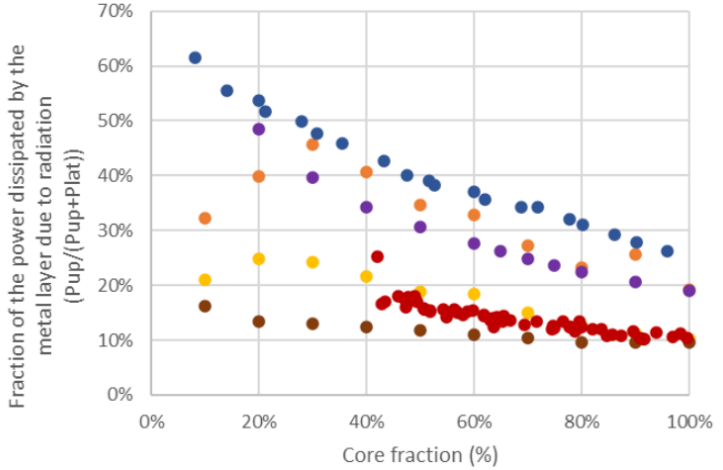

- No thermochemistry effects in AC², residual power imposed in the metal (10% in LEI calculations and 15% in GRS calculations)
- Higher values in PROCOR explained by species transfer from oxide pool and associated thermal inertia

- Impact of top radiative heat transfer: increase with thin metal layer → Increase of discrepancies

Molten pool formation case 7 – Series of calculations dedicated to 2 layers configurations and focusing effect

- Minimum vessel thickness

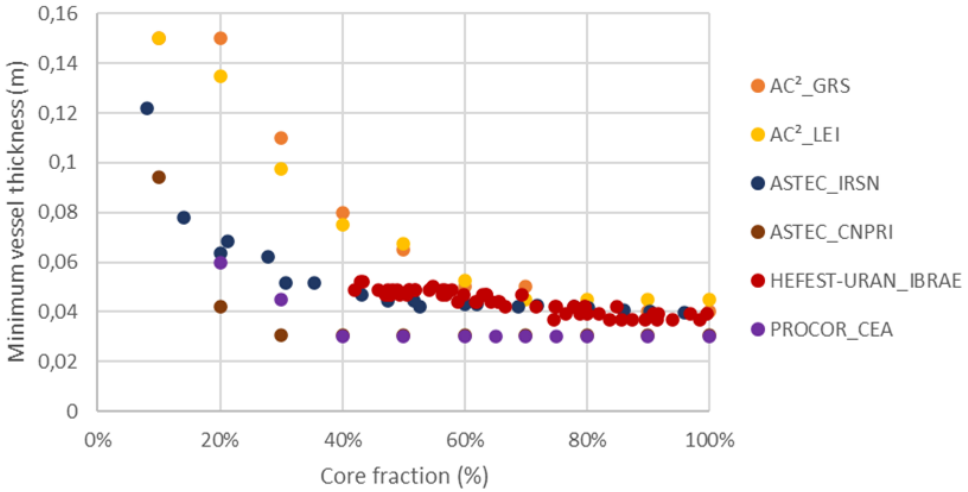

- Comparable results above 60% of core relocation
- Significantly reduced vessel thickness even at 30% of core relocation

Conclusions

- Approach developed in the H2020 IVMR benchmark was followed and extended
  - Several steps in this benchmark with different levels of complexity
  - Models dealing with molten pool formation (used in integral SA simulation)
  - BEPU calculations
- Complementarity between benchmark of different codes and BEPU analyses
- Benefits for:
  - Harmonization of understanding of main phenomena associated with IVMR
  - Modelling improvement in codes
  - Users training
  - Definition of uncertainties to be considered in safety assessment

Conclusions

- Towards a “Meta-benchmark” for IVMR
- All results to be published in the TECDOC report

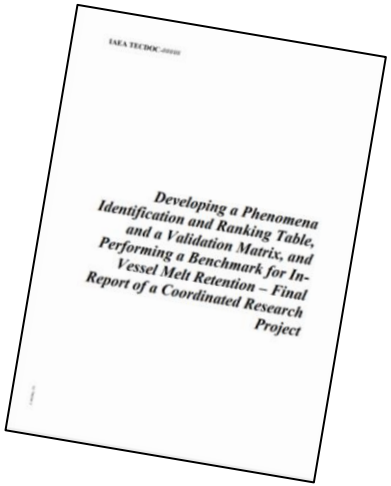

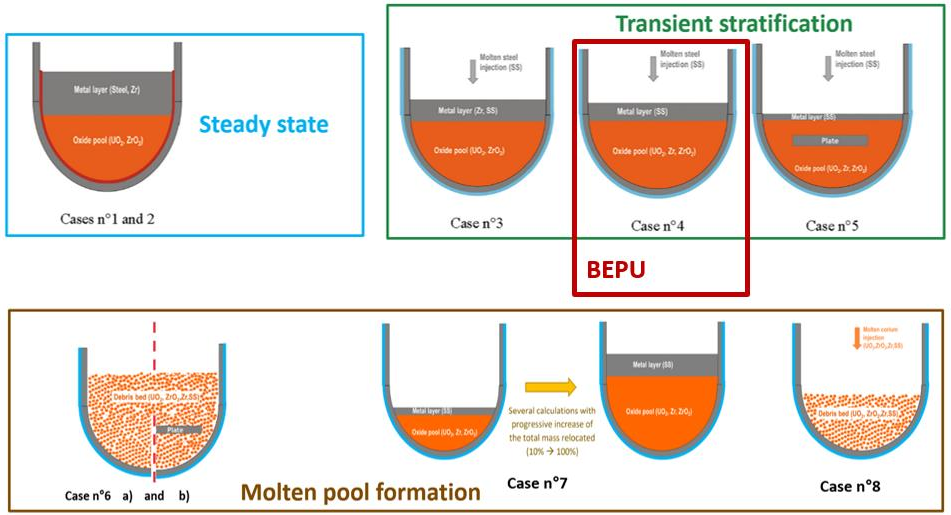

Many thanks to all contributors

M. Abu Bakar, PAEC, L. Carénini, IRSN,
A. Filippov, IBRAE, R. Le Tellier, CEA,
I. Melnikov, NRC-KI, P. Pandazis, GRS,
M. Valincius, LEI, Z. Wu, CNPRI,
Y. Zhang, XJTU

A. Miassoedov, T. Veneau, IAEA

NUMERICAL ANALYSIS OF MELT PENETRATION BEHAVIOR IN THE CONTROL ROD DRIVE HOUSING OF FUKUSHIMA DAIICHI NUCLEAR POWER STATION UNIT-2

Xin Li[1], Akifumi Yamaji[2], Ikken Sato[3]
[1] Japan Atomic Energy Agency
4002 Narita-cho, Oarai, Higashi-ibaraki, Ibaraki 311-1393, Japan
li.xin@jaea.go.jp

[2] Graduate School of Advanced Science and Engineering
Waseda University
3-4-1 Okubo, Shinjuku-Ku, Tokyo 169-8555, Japan
akifumi.yamaji@waseda.jp

[3] Waseda Research Institute for Science and Engineering
Waseda University
3-4-1 Okubo, Shinjuku-Ku, Tokyo 169-8555, Japan
kenichivich@aoni.waseda.jp

Takuya Yamashita[4], Yuji Nagae[5]
[4] Japan Atomic Energy Agency
4002 Narita-cho, Oarai, Higashi-ibaraki, Ibaraki 311-1393, Japan
yamashita.takuya38@jaea.go.jp

[5] Japan Atomic Energy Agency
790-1 Otsuka, Motooka, Tomioka-machi, Futaba-gun, Fukushima 979-1151, Japan
nagae.yuji@jaea.go.jp

ABSTRACT

The decommissioning of Fukushima Daiichi Nuclear Power Station (1F) Unit-1 to 3 requires information regarding the statuses of the damages of the reactors and distribution of the fuel debris for the purpose of debris removal. For Unit-2, the muon radiography and the Primary Containment Vessel (PCV) internal investigation results indicate that the fuel debris are largely retained inside the Reactor Pressure Vessel (RPV), although multiple breaches are expected at the RPV lower head, some of which must be large enough to let the upper tie plate of the fuel assembly to relocate down to the pedestal floor. Hence, numerical analyses are necessary to deduce comprehensive scenario candidates, which can explain the current observations.

The previous accident scenario analysis suggested that in the 1F Unit-2 the dryout (disappearance of liquid water) of debris bed formed in the lower plenum of RPV following core slumping (relocation to lower plenum) and quenching probably took place at ca. 4:00 on March 15th, 2011. Subsequently, the debris bed in the lower plenum was estimated to gradually heat up due to decay power, and metallic melt could have first formed and caused damages to the Control Rod Drive (CRD) housings made of Stainless Steel (SS). Such damages could occur below the melting point of SS as suggested in the experiment ELSA-1 which

revealed the possibility of CRD housing breach by eutectic melting. Once such CRD housing breach occurs, the metallic eutectic melt could penetrate inside the CRD housing followed by fuel pellets which can heat up from the inside of the CRD housing inducing its further potential failure. To investigate such possibility, the current study focuses on the analysis of such metallic melt penetration behavior in the CRD housing. To well capture the melt flow and its interactions with the CRD housing, including the heat transfer and melting / solidification, it is beneficial to apply the Moving Particle Semi-implicit (MPS) method, which is a Lagragian method that excels in capturing the free surface and melt/solid interface. A three-dimensional CRD housing model with simplified inner structures was established. The injection of SS-Zircaloy eutectic melt into the CRD housing was simulated and its downstream penetration and freezing behavior under vertically varying temperature boundary conditions was analyzed. It is found that the melt would start to freeze and form channel blockages soon after it enters the region with a relatively cold boundary in the downstream.

KEYWORDS
Fukushima Daiichi (1F), BWR penetration, severe accident, MPS method

1. INTRODUCTION

In light of the ongoing demanding decommissioning work of Fukushima Daiichi Nuclear Power Station (1F) Unit-1 to 3, it is important to gain the information regarding the statuses of the damages of the reactors and distribution of the fuel debris for the purpose of debris removal. For Unit-2, the investigation with cosmic muon radiography, aiming at locating the fuel debris inside the reactor, was carried out in 2016 [1][2]. The evaluations of the results reported that dense materials were located in the lower part of Reactor Pressure Vessel (RPV) with estimated mass of about 160 tons (although with large uncertainty of about ±50 tons), which indicated that most of the fuel debris were retained at the bottom of the Reactor Pressure Vessel (RPV). On the other hand, the Primary Containment Vessel (PCV) internal investigation results of Unit-2 carried out in 2017 showed that the entire pedestal floor was covered with clay-like and rubble deposits and a top tie-plate of a fuel assembly has been identified to have fallen to the bottom of the pedestal [3]. Moreover, the investigation video showed that water kept falling onto the pedestal floor like raindrops from above across wide area [4]. These indicated that there should be multiple breaches at the RPV lower head, some of which must be large enough to let the upper tie plate of the fuel assembly to relocate down to the pedestal floor. Therefore, it is necessary to conduct numerical analyses in order to deduce the comprehensive scenario candidates, which can explain the current observations in Unit-2, especially the possible flow path of melt/fuel debris from in-vessel to ex-vessel regions considering the accident progression with the specific BWR penetration and structures.

According to the previous accident scenario analyses with plant data and severe accident codes such as MELCOR and RELAP/SCAPSIM, it is suggested that the fuel collapse and core slumping (relocation to lower plenum) in the Unit-2 possibly started around 23:00 on March 14th, 2011 [5][6]. Due to insufficient effective cooling that could reach the RPV lower plenum, the dryout (disappearance of liquid water) of debris bed probably occurred at ca. 4:00 on March 15th, 2011 [7]. Subsequently, the debris bed in the lower plenum was estimated to gradually heat up due to decay power, and metallic melt could have first formed and caused damages to the CRD housings made of Stainless Steel (SS). As suggested in the ELSA-1 experiment to investigate the failure mechanism of the CRD housing in BWR, such damages could occur below the melting point of SS due to formation of the Zircoloy and SS (Zr-SS) eutectic between the metallic molten pool and the CRD housing [8]. Once such CRD housing breach occurs, the metallic eutectic melt could penetrate inside the CRD housing followed by fuel pellets which can heat up from the inside of the CRD housing inducing its further potential failure. To investigate such possibility, the current study focuses on the analysis of such metallic melt penetration behavior in the CRD housing, under the expected conditions of Unit-2.

To well capture the melt flow and its interaction with the CRD housing, including the heat transfer and melting / solidification, it is beneficial to apply the Moving Particle Semi-implicit (MPS) method, which is a Lagragian method that excels in capturing the free surface and melt/solid interface as demonstrated in several previous studies involving melt and structure interactions [9][10][11][12]. In the current study, a three-dimensional CRD housing model with simplified inner structures was established. The injection of SS-Zircaloy eutectic melt into the CRD housing was simulated and its downstream penetration and freezing behavior under vertically varying temperature boundary conditions was analyzed.

2. MPS METHOD FOR THE MELT PENETRATION AND FREEZING ANALYSIS

2.1. Governing Equations of MPS Method

In MPS method, the basic governing equations for incompressible multi-phase flows are described as conservation of mass, momentum, and energy as follows:

$$\frac{D\rho}{Dt} = -\rho\nabla.\mathbf{u} = 0 \tag{1}$$

$$\frac{D\mathbf{u}}{Dt} = -\frac{1}{\rho}\nabla P + \frac{1}{\rho}\nabla.(\mu\nabla\mathbf{u}) + \mathbf{g} + \frac{\mathbf{F_s}}{\rho} \tag{2}$$

$$\frac{DT}{Dt} = \frac{k}{\rho C_P}\nabla^2 T \tag{3}$$

where ρ is the density, $\mathbf{u}$ is the velocity, P is the pressure, μ is the dynamic viscosity, $\mathbf{g}$ is the gravitational acceleration, $\mathbf{F_s}$ is the interface tension, T is the temperature, k is the thermal conductivity and C_P is the specific heat capacity.

2.2. Second-Order Corrective Matrix and Particle Shifting

In order to reduce the discretization error and improve the numerical accuracy, the original particle interaction models have been modified using the second-order corrective matrix developed by Duan [13] [14]. The discretization models for the gradient, divergence Laplacian operators are shown in Eqs (6) – (8):

$$\langle\nabla\phi\rangle_i = \frac{1}{n_0}\sum_{j\neq i}\left\{w_{ij}\frac{\phi_j-\phi_i}{r_{ij}}\left(\begin{bmatrix}\mathbf{C}_1\\ \mathbf{C}_2\\ \mathbf{C}_3\end{bmatrix}P\right)\right\} \tag{4}$$

$$\langle\nabla\cdot\mathbf{u}\rangle_i = \frac{1}{n_0}\sum_{j\neq i}\left\{w_{ij}\frac{\mathbf{u}_j-\mathbf{u}_i}{r_{ij}}\left(\begin{bmatrix}\mathbf{C}_1\\ \mathbf{C}_2\\ \mathbf{C}_3\end{bmatrix}P\right)\right\} \tag{5}$$

$$\langle\nabla^2\phi\rangle_i = \frac{1}{n_0}\sum_{j\neq i}\left\{w_{ij}(\phi_j-\phi_i)\frac{[\mathbf{C}_4+\mathbf{C}_5+\mathbf{C}_6]P}{l_0 r_{ij}}\right\} \tag{6}$$

where ϕ is a scalar variable; $\mathbf{C}_1$ to $\mathbf{C}_6$ the first to sixth rows of the corrective matrix $\mathbf{C}$ defined in [14], respectively; r_{ij} is the distance between particle i and particle j; l_0 is the constant initial particle size.

The weight function (between the reference particle i and its neighbor particle j) w_{ij} and particle number density n_i are defined as:

$$w(r) = \begin{cases}\dfrac{r_e}{r_{ij}} - 1, & 0 \le r_{ij} < r_e \\ 0, & r_e \le r_{ij}\end{cases} \tag{7}$$

$$n_i = \sum_{j \neq i} w(|\mathbf{r_i} - \mathbf{r}_j|) \tag{8}$$

The particle shifting technique is implemented by relocating the particles from the particle-dense region to the particle-dilute region. The particles in a particle-dense region are moved by the position vector as:

$$\delta \mathbf{r_i} = -\frac{l_0 \Delta r_i}{n_0} \sum_{j \neq i} \frac{w_{ij}}{r_{ij}^2} \mathbf{r_{ij}} \tag{9}$$

More details on the particle shifting technique for the internal and surface particles can be found in [15].

2.3. Phase Change and Viscosity Models

To model the melting and solidification of the debris, the phase change of a particle is evaluated based on its solid fraction γ (the volume fraction of the solid in fluid) and enthalpy as follows:

$$\gamma(T) = \begin{cases} 1, & T < T_s \\ \dfrac{T_l - T}{T_l - T_s}, & T_s \leq T \leq T_l \\ 0, & T_l < T \end{cases} \tag{10}$$

where T_l and T_s are the particle's liquidus and solidus temperature, respectively.

It is known that the viscosity of a melt between solidus and liquidus temperature (the so-called mushy zone) can increase dramatically compared to the viscosity at liquidus temperature. Such viscosity change can be estimated from the solid fraction by using correlations, such as the Ramacciotti viscosity model for the corium [16]. Moreover, as previously discussed in VULCANO spreading experiments [17], the melt flow is deemed as effectively terminated in the spreading experiments, when it reaches the so-called immobilization solid (volume) fraction, which is normally between 0.6-1.0. In the current study, the following refined viscosity model based on the Ramacciotti viscosity model for corium is applied to the solidifying and solidified particles to describe the highly viscous behavior of the debris with a large solid fraction.

$$\mu(T) = \begin{cases} \mu_l e^{(2.5\gamma(T)c)}, & \gamma(T) < \gamma_{critical} \\ 10\mu_l e^{(2.5\gamma(T)c)}, & \gamma(T) \geq \gamma_{critical} \end{cases} \tag{11}$$

where μ_l is the viscosity of the material at liquidus temperature, c is an empirical parameter normally ranging from 4.0 to 8.0 and 6.0 is used in the current study; $\gamma_{critical}$ is the immobilization solid (volume) fraction and is chosen as 0.5.

2.4. Convective Boundary Condition

The heat flux q due to the convective vapor cooling effect from the CRD housing outer surface is described with Newton's law of cooling in the following manner:

$$q = h_c A_i (T_i - T_\infty) \tag{12}$$

where h_c is the heat transfer coefficient of vapor cooling from the CRD housing outer surface and is chosen as 5 W/m^2/K in the current study. T_i is the temperature of particle i, T_∞ is the environment temperature, and A_i is the area of the surface particle i and is calculated with the particle size as l_0^2.

3. SIMULATION GEOMETRY AND CONDITIONS

The MPS simulation geometry of CRD housing with simplified inner structures is depicted in Figure 1 (a). The particle size used in the current study is 2.33 x 10^{-3} m. The CRD housing is represented with a 1.5 m long cylindrical tube with an outer diameter of 0.149 m and a wall thickness of 0.0115 m. The inner structures in the CRD housing such as tubes and piston for hydraulic pressure drive were simplified and represented with two cylindrical tubes and a cylinder concentric to the outermost CRD housing. As a result, three flow channels were formed with a hydraulic diameter of 0.028 m, 0.032 m, and 0.023 m from the periphery to the center, respectively. It should be noted that since the actual CRD housing is considered to have more complex structures within than assumed in this study, the actual internal flow paths are believed to be smaller than the assumed paths. These assumptions imply that the current MPS analysis results tend to indicate greater amount of melt to penetrate deeper into the downstream interior of CRD housing, resulting in a more significant decay heat load on the CRD housing structure than what may be expected in Unit-2.

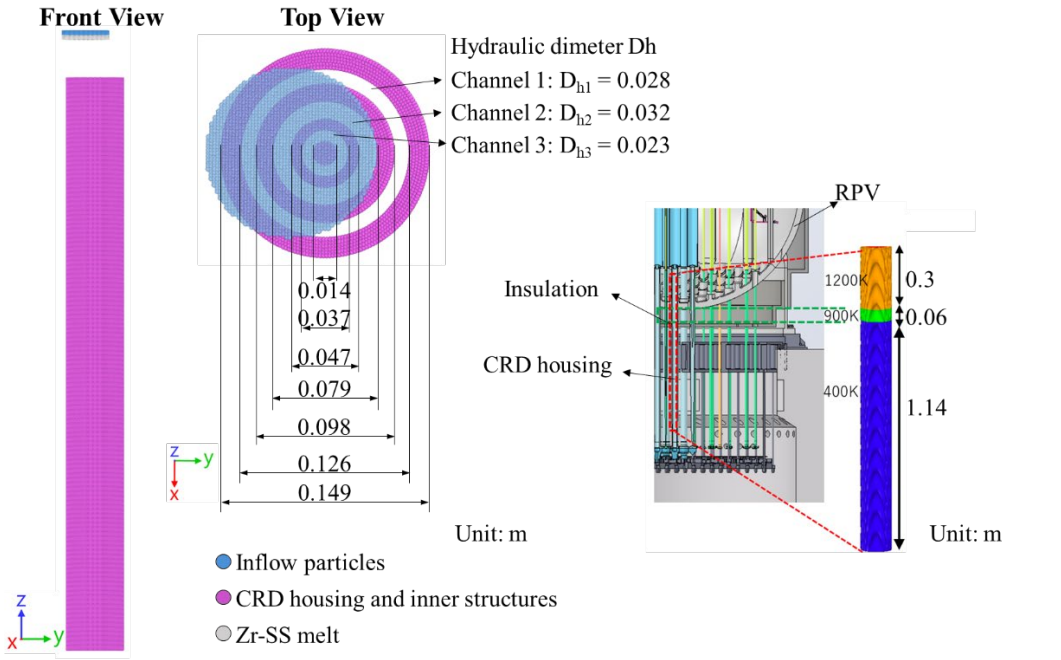

(a) Front and top views of CRD housing

(b) Vertical temperature boundary division on the CRD housing outer surface

Figure 1. MPS simulation geometry and boundary conditions [18]

Using such simulation geometry, an inflow boundary condition was applied 0.1 m from the top of the CRD housing with melt being injected at a constant velocity of 0.1 m/s. Since the CRD housing is installed inside RPV and extends all the way down to the pedestal region, it is reasonable to consider that the outer surface of CRD housing could face an environment with large vertical temperature gradient during the accident scenario. As shown in Figure 1 (b), vertically downwards, the convective boundary condition with atmosphere temperature of 1200 K, 900 K, and 400 K is set on the CRD housing outer surface, respectively. Such divisions are assumed to represent the parts of the CRD housing that is above the insulation layers (0.3

m), between the insulation layers (0.06 m), and below the insulation layers (namely in the pedestal region of PCV, 1.14 m).

The thermos-physical properties of the metallic melt (Zr-SS eutectic) and CRD housing (SS) are summarized in Table I. The composition of 80%Zr-20%SS and 85%SS-15%Zr eutectics are chosen because they have the lowest and second lowest liquidus temperature according to the quasi-binary phase diagram of stainless steel (74%Fe-18%Cr-8%Ni) – zirconium based on thermodynamic analysis [8]. Two simulation cases with the initial Zr-SS melt temperature being 1353 K (80%Zr-20%-SS) and 1523 K (85%SS-15%Zr) are performed in a conservative sense to represent the lowest and second lowest eutectic melting temperature that can form to cause CRD housing breach at relatively low temperature. In another word, for both cases, the initial melt temperatures were set to be the liquidus temperature of the melt. The thermos-physical properties of Zr-SS eutectic are estimated with weighted average based on mass fraction of Zr and SS using the thermos-physical properties of zircaloy and SS.

Table I. Thermo-physical properties of the materials used in the current study [6] [7]

Thermo-physical properties	Stainless Steel	80%Zr-20%SS	85%SS-15%Zr
Density (kg/m^3)	7800.0	6475.0	7075.0
Specific heat (J/kg/K)	500.0	644.0	410.4
Heat conductivity (W/m/K)	25.0	26.8	33.0
Viscosity at liquidus temperature (Pa·s)	5.0 x10^{-3}	2.7 x10^{-3}	5.0 x10^{-3}
Solidus temperature (K)	1718[8], [19]	1223	1223
Liquidus temperature (K)	1728	1353	1523
Fusion heat (kJ/kg)	280.0	167.0	272.0
Surface tension (N/m)	1.79	1.79	1.4

4. MELT PENETRATION AND FREEZING ANALYSIS RESULTS

The history of the solid fraction of the Zr-SS melt in the CRD housing (the cross-section view is normal to x=0 plane) is shown in Figure 2. Time t=0 s represents the start of injection of the melt. A solid fraction of 0 represents a purely liquid state, while a solid fraction of 1.0 represents a completely solidified state. In this study, it is assumed that the flowability of the Zr-SS melt is lost at an immobilization solid fraction of 0.5 or higher.

In the 1353 K case, approximately 2 seconds after the start of metallic melt injection (hereafter t=2 s), the solid fraction of the Zr-SS melt increased downstream (lower region) from around 0.3 m below the top of the CRD housing. This indicates that some melt particles in the flow channels began to solidify as soon as entered the relatively cold temperature boundary at 900 K. The solidified particles were transported downward along with the flow of surrounding bulk fluid particles. When they came into contact with the walls of the flow channels in the CRD housing, the strong viscous interaction between the solidified particles and the walls causes the solidified particles to adhere to the flow channel walls. Subsequently, as more solidified particles adhere, the flow channels were gradually blocked. Similar phenomena can be seen for the 1523 K case. However, due to the higher initial melt temperature and consequent slower viscosity increase downstream, the solid fraction increase was delayed causing the onset position of the blockage formation to shift slightly downstream compared to that in 1353 K case.

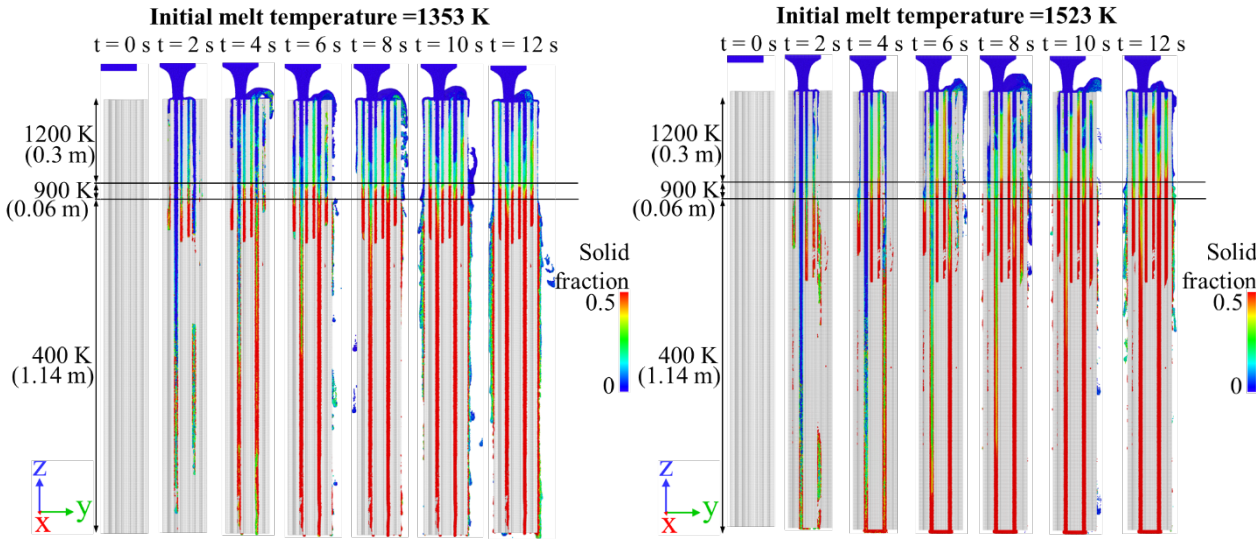

(a) 80%Zr-20%SS melt, with initial temperature being 1353 K (b) 85%SS-15%Zr melt, with initial temperature being 1523 K

Figure 2. Solid fraction distribution of Zr-SS melt in the CRD housing

Due to partial blockage of flow channels in the CRD housing, it is observed that some of the injected melt started to overflow from the top of the CRD housing near the inflow boundary at t=4 s for 1353 K case. For 1523 K case, such overflow occurred later at t=6 s because onset position of the blockage shifted further downstream causing the blockage of flow channels to happen later. The flow blockage behavior in Channel 1 to 3 unfolds as follows (see also the bottom view of CRD housing in Figure 3):

As shown in the bottom views in Figure 3, the complete blockage of Channel 3 first occurred around t=4 s in both cases, with the solid fraction distribution of particles in the channel all above 0.5, namely only solidified particles can be observed in the bottom view in Channel 3. Following the blockage of Channel 3, the blockage of Channel 2 can be observed to occur at t=6 s in both cases. For 1353 K case, after t=8 s, almost all the particles in Channel 1 to 3 in the bottom view showed a solid fraction above 0.5, while for 1523 K case it is after 10 s that such distribution can also be observed.

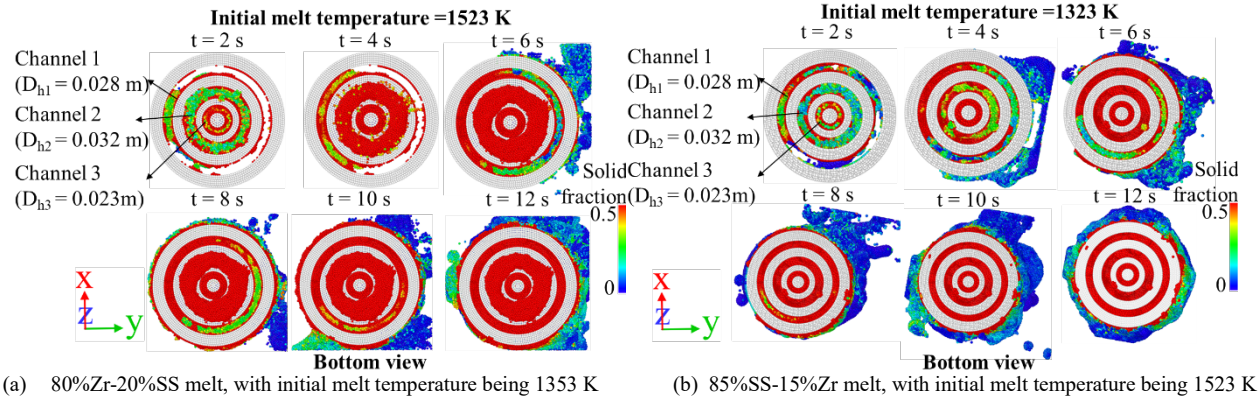

(a) 80%Zr-20%SS melt, with initial melt temperature being 1353 K (b) 85%SS-15%Zr melt, with initial melt temperature being 1523 K

Figure 3. Solid fraction distribution of Zr-SS melt (bottom view)

The melt penetration depths from the top of CRD housing in all the flow channels for 1323 K and 1523 K cases were summarized in Table II. In both cases, Channel 2 is the most-penetrated as it has the largest

hydraulic diameter among the three channels and Channel 3 is least penetrated as it has the smallest hydraulic diameter.

Besides the influence of hydraulic diameter, initial melt temperature also plays a part as the melt penetration depths in all the channels were shorter in the 1353 K case compared to those in the 1523 K case. It may be worth referring to the phase diagram of Zr-SS, that while liquidus temperature varies greatly depending on the Zr-SS composition, the solidus temperature remains the same at 1253 K. This indicates that if the Zr-SS melt at a relatively low temperature manages to penetrate into the CRD housing, it is likely that such melt can be solidified and cause early blockage of the flow paths inside the CRD housing, without occupying all the flow paths downstream. Once formed, such blockage can make it difficult for subsequent melt/debris to penetrate down in the CRD housing, since it is unlikely that the remelting of solidified melt forming the blockage would take place unless the relatively cold temperature boundary (i.e., 900 K and 400 K) is challenged, i.e. the 900 K and 400 K boundary cannot be maintained and increase to much higher temperature.

Table II. Maximum Melt Penetration Depth in Flow Channels 1 to 3 for 1323 K and 1523 K cases

Cases	Channel 1 [m]	Channel 2 [m]	Channel 3 [m]
80%Zr-20%SS, 1323 K	0.6	≈ 1.5	0.5
85%SS-15%Zr, 1523 K	0.72	> 1.5	0.65

The maximum velocity magnitude in each channel that is 0.42 m or more below the top of CRD housing, which is sufficiently in the downstream for the blockage to form, is depicted in Figure 4. In both cases, the maximum velocity magnitude decreased to 0 first in Channel 3, then followed by Channel 2 and Channel 1. Among the three channels, the maximum velocity magnitude in Channel 2 reached the highest value and maintained at it for the longest period, indicating that the melt penetration in Channel 2 was the most significant in both cases. Overall, the maximum velocity magnitude in all the channels decreased to 0 roughly 6 seconds and 10 seconds after the initiation of the injection of melt in 1353 K and 1523 K cases, respectively. This again shows that 1) flow blockage occurred in all the flow channels of CRD housing relatively fast, and 2) the location where the flow blockage started was near where the relatively cold temperature boundary was set at 900 K.

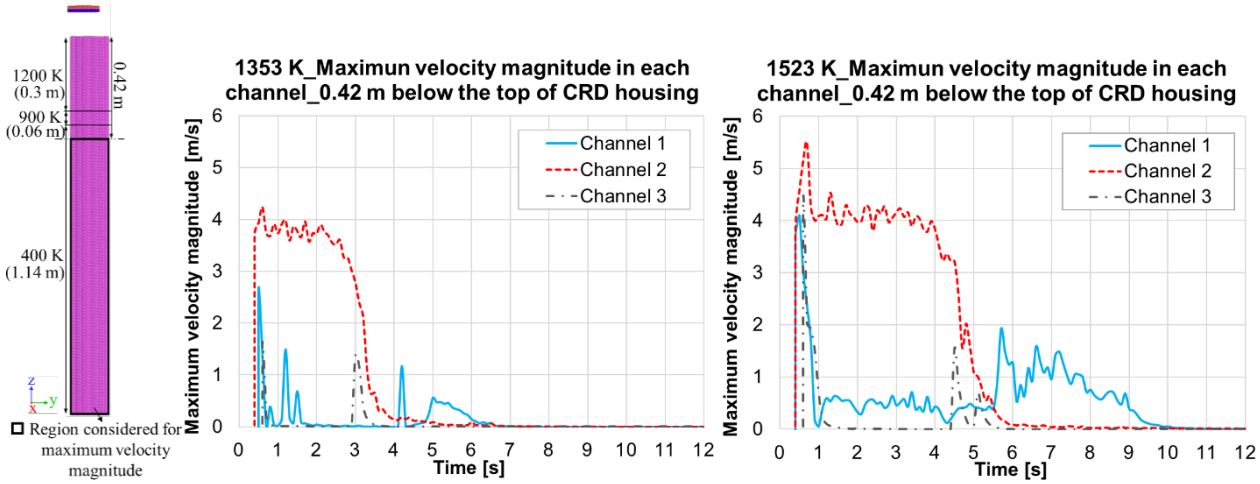

(a) 80%Zr-20%SS melt, with initial temperature being 1353 K (b) 85%SS-15%Zr melt, with initial temperature being 1523 K

Figure 4. Maximum velocity magnitude in each channel at 0.42 m below the top of CRD housing

The history of the total mass of Zr-SS held in the CRD housing during the simulation is depicted in Figure 5 (a). At t=12 s, the total mass of Zr-SS held in the CRD housing is 38 kg and 54 kg for 1353 K and 1523 K cases, respectively. About 50% more Zr-SS mass is held in CRD housing in 1523 K case compared to that of the 1353 K case, which is due to the later melt blockage occurred in 1523 K case. This can also be interpreted by the time at which the total Zr-SS mass started to plateau in Figure 5 (a), which is approximately from t = 7 s and t = 10 s for 1353 K and 1523 K cases, respectively.

The history of the total solidified mass of Zr-SS during the simulation for the 1353 K and 1523 K cases is depicted in Figure 5 (b). At t = 12.0 s, the solidified Zr-SS held within the CRD housing in the 1523 K case is roughly 36 kg (accounts for 66% of the total mass of Zr-SS held in the CRD housing), which is about 64% more than the 22 kg (accounts for 58% of the total mass of Zr-SS held in the CRD housing) that was achieved in the 1353 K case. This is consistent with the observation that melt with relatively high temperature can cause more significant melt penetration while low temperature melt tends to cause early blockage.

The final mass fraction distribution in the Channels 1 to 3 for both cases are shown in Figure 5 (b). The solidified melt mass in Channel 2 accounts for roughly 70% to 80% of the total solidified melt. The solidified melt held in the Channel 3 is merely a few percent at 4%-6%, indicating that the amount of the solidified melt can vary largely depending on the hydraulic diameter of the flow path formed inside the CRD housing, besides the influence of the initial temperature and viscosity change of the melt.

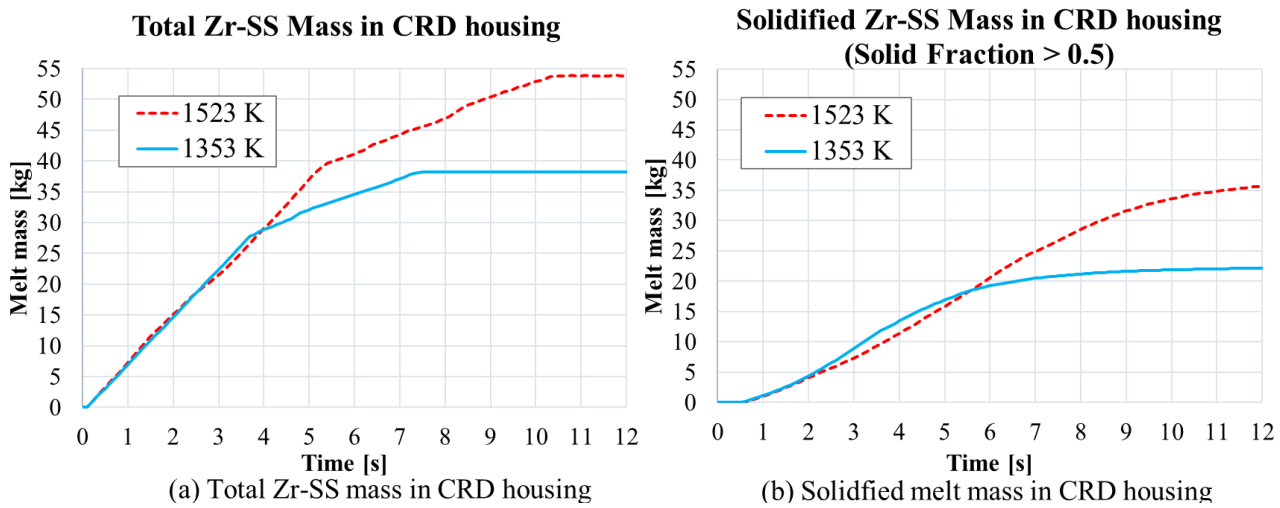

(a) Total Zr-SS mass in CRD housing (b) Solidfied melt mass in CRD housing

Figure 5. Toal and solidified Zr-SS melt mass in CRD housing in 1353 K and 1523 K cases

The final mass fraction distribution in the Channels 1 to 3 for both cases are shown in Figure 6. The solidified melt mass in Channel 2 accounts for roughly 70% to 80% of the total solidified melt. The solidified melt held in the Channel 3 is merely a few percent at 4%-6%, indicating that the amount of the solidified melt can vary largely depending on the hydraulic diameter of the flow path formed inside the CRD housing, besides the influence of the initial temperature and viscosity change of the melt.

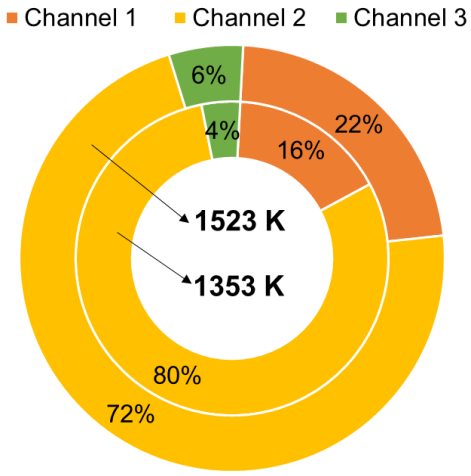

Figure 6 Final solidified Zr-SS melt mass fraction distribution in Channel 1 to 3

5. EXTRAPOLATION TO THE FUKUSHIMA SCENARIO

Extrapolating the understandings from the current study to the Fukushima scenario, the following scenario development can be expected:

(1) Expectations from the preceding works on the accident progression of 1F Unit-2: Upon core slumping, the collapsed fuel relocated to the water pool in the lower plenum and was once fully quenched to the temperature of saturated vapor at RPV pressure, forming a debris bed in the lower plenum [6][7]. As sufficient cooling to the debris bed was not ensured during the accident progression of Unit-2, the dryout of debris bed occurred and the debris gradually heated up due to decay power. Assuming that the decay power distribution in the debris bed is rather uniform and homogeneous, it is reasonable to consider that the hottest region would always occur in the central part of the solid debris bed, before melting of the materials in the debris bed occurred to form a convective molten pool that could help reduce the temperature gradient in the lower plenum.

(2) Expectation from the ELSA-1 experiment: With such debris bed configuration, the CRD housings in the central region of RPV would first be challenged by the hot region of the debris bed. When the temperature of the hot region of debris bed reached around 1500 K, it is likely that the CRD housings breached by eutectic melting due to formation of Zr-SS melt [8]. The Zr-SS melt then penetrated into the CRD housings and relocated down along the flow paths free from inner structures within the CRD housings.

(3) Assumptions from the 1F Unit-2 configuration and accident scenario: At this stage, it can be considered that the large vertical temperature gradient was still maintained outside the CRD housings. The inner surface of RPV vessel can reach ~1200 K, the part of the CRD housings above top of insulation layer can reach ~900 K, while beyond insulation layers the outer surface of the CRD housings still remained 400 K.

(4) Expectation from the MPS analysis results of the current study: With such vertical temperature gradient, it can be considered that the 1500 K melt that was penetrated into the CRD housings would start to solidify near the height of the insulation layers. For the part of CRD housings inserted above the insulation layers, it is very likely to be fully filled with solidified melt. Meanwhile, it cannot be ruled out that the melt could penetrate down within the CRD housings rather far away, i.e., more than 1 meter, although it is highly dependent on the initial melt velocity, viscosity change with temperature, and the hydraulic diameter of the flow path in the CRD housings.

6. CONCLUSIONS AND FUTURE WORK

Numerical simulations of the melt penetration and freezing behavior of Zr-SS eutectic melt at different initial temperatures into the CRD housing with simplified internal structures were carried out with MPS method, with a vertical temperature boundary considering the 1F Unit-2 accident scenario. The following conclusions can be drawn from the current study.

(1) The melt would start to freeze and form channel blockages soon after it enters the region with a relatively cold boundary downstream. The influence of the initial temperature on where the blockage starts to form seems minimal.

(2) The melt penetration depth in the flow channels in the CRD housing can vary largely depending on the hydraulic diameter of the flow path formed inside the CRD housing, the initial temperature, and the immobilization solid fraction of the melt.

(3) Considering the 1F Unit-2 accident scenario, it is likely that solidified metallic melt can be found filled inside the CRD housing.

Finally, it is worth noting that since the simulation geometry in the current study only considered one CRD housing in the central part of the RPV, the melt overflowed from the top of CRD housing upon filling up the internal flow channels after blockage due to melt solidification. In the actual condition, the overflow melt could have been retained in the RPV continuing to heat the RPV-internal structures and the RPV lower head. Such more comprehensive simulation geometry addressing both CRD housing and the RPV lower head will be considered in the future study to elucidate the mechanism of RPV lower head boundary failure.

ACKNOWLEDGMENTS

The authors gratefully appreciate the help from Mr. Ryotaro Sasaki in providing test simulation results, which helped development of the setup for the 1F Unit-2 cases. This study has been performed by the funds from Japanese Ministry of Economy, Trade and Industry as The Subsidy Program “Project of Decommissioning, Contaminated Water and Treated Water Management (Development of Analysis and Estimation Technologies for Characterization of Fuel Debris)”.

REFERENCES

[1] H. Fujii *et al.*, “Investigation of the status of Unit 2 nuclear reactor of the Fukushima Daiichi by Cosmic Muon Radiography,” *Prog. Theor. Exp. Phys.*, **2021** (2), pp. 023C01, doi: 10.1093/ptep/ptaa137 (2021).

[2] TEPCO, “Locating Fuel Debris inside the Unit 2 Reactor Using a Muon Measurement Technology at Fukushima Daiichi Nuclear Power Station,” 2016. https://www.tepco.co.jp/en/nu/fukushima-np/handouts/2016/images/handouts_160728_01-e.pdf (accessed Feb. 14, 2023).

[3] I. Tokyo Electric Power Company Holdings, “Fukushima Daiichi Nuclear Power Station Unit 2 Primary Containment Vessel Internal Investigation,” 2018. https://www.tepco.co.jp/en/nu/fukushima-np/handouts/2018/images/handouts_180426_02-e.pdf (accessed Jun. 20, 2023).

[4] TEPCO, “2019/02/28 Fukushima Daiichi Nuclear Power Station Unit 2_Panorama image visualization of the Primary Containment Vessel internal investigation,” 2019. https://www4.tepco.co.jp/en/news/library/archive-e.html?video_uuid=h788k82q&catid=61785 (accessed Feb. 14, 2023).

[5] G. Li, J. Zhang, B. Qiu, M. Liu, and J. Yan, "MELCOR modeling and sensitivity analysis of Fukushima Daiichi unit 2 accident considering the latest TEPCO investigations," *Ann. Nucl. Energy*, **112**, pp. 364–373, doi: https://doi.org/10.1016/j.anucene.2017.10.029 (2018).

[6] H. Madokoro and I. Sato, "Estimation of the core degradation and relocation at the Fukushima Daiichi Nuclear Power Station Unit 2 based on RELAP/SCDAPSIM analysis," *Nucl. Eng. Des.*, **376**, pp. 111123, 2021, doi: https://doi.org/10.1016/j.nucengdes.2021.111123 (2021).

[7] I. Sato, S. Yoshikawa, T. Yamashita, M. Cibula, and S. Mizokami, "MAAP code analysis focusing on the fuel debris condition in the lower head of the pressure vessel in Fukushima-Daiichi Nuclear Power Station Unit 2," *Nucl. Eng. Des.*, **404**, pp. 112205, doi: https://doi.org/10.1016/j.nucengdes.2023.112205 (2023).

[8] T. Yamashita, T. Sato, H. Madokoro, and Y. Nagae, "BWR lower head penetration failure test focusing on eutectic melting," *Ann. Nucl. Energy*, **173**, pp. 109129, doi: https://doi.org/10.1016/j.anucene.2022.109129 (2022).

[9] X. Li *et al.*, "Estimation of debris relocation and structure interaction in the pedestal of Fukushima Daiichi Nuclear Power Plant Unit-3 with Moving Particle Semi-implicit (MPS) method," *Ann. Nucl. Energy*, pp. 108923, doi: https://doi.org/10.1016/j.anucene.2021.108923 (2021).

[10] N. Takahashi, G. Duan, A. Yamaji, X. Li, and I. Sato, "Development of MPS method and analytical approach for investigating RPV debris bed and lower head interaction in 1F Units-2 and 3," *Nucl. Eng. Des.*, **379**, pp. 111244, (2021).

[11] R. Kawakami, X. Li, G. Duan, A. Yamaji, I. Sato, and T. Suzuki, "Improvement of solidification model and analysis of 3D channel blockage with MPS method," *Front. Energy*, pp. 1–13, (2021).

[12] X. Li, A. Yamaji, M. Furuya, I. Sato, H. Madokoro, and Y. Ohishi, "Preliminary Evaluation on the Relocation Phase of Ex-Vessel Debris of Fukushima Daiichi Nuclear Power Plant Unit-3." Aug. 04, 2021. doi: 10.1115/ICONE28-64540 (2021).

[13] G. Duan, S. Koshizuka, A. Yamaji, B. Chen, X. Li, and T. Tamai, "An accurate and stable multiphase moving particle semi-implicit method based on a corrective matrix for all particle interaction models," *Int. J. Numer. Methods Eng.*, **115** (10), doi: 10.1002/nme.5844 (2018).

[14] G. Duan, A. Yamaji, and S. Koshizuka, "A novel multiphase MPS algorithm for modeling crust formation by highly viscous fluid for simulating corium spreading," *Nucl. Eng. Des.*, **343**, pp. 218–231, doi: https://doi.org/10.1016/j.nucengdes.2019.01.005 (2019).

[15] Z. Sun, K. Djidjeli, J. T. Xing, and F. cheng, "Modified MPS method for the 2D fluid structure interaction problem with free surface," *Comput. Fluids.*, **122**, pp. 47–65, 2015, doi: https://doi.org/10.1016/j.compfluid.2015.08.017 (2015).

[16] M. Ramacciotti, C. Journeau, F. Sudreau, and G. Cognet, "Viscosity models for corium melts," *Nucl. Eng. Des.*, **204** (1), pp. 377–389, 2001, doi: https://doi.org/10.1016/S0029-5493(00)00328-9 (2001).

[17] C. Journeau *et al.*, "Ex-vessel corium spreading: results from the VULCANO spreading tests," *Nucl. Eng. Des.*, **223** (1), pp. 75–102, doi: https://doi.org/10.1016/S0029-5493(02)00397-7 (2003).

[18] JAEA, "JAEA's summary results of subsidy program (the First solicitation) for the" Project of Decommissioning, Contaminated Water and Treated Water Management (Development of Analysis and Estimation Technologies for Characterization of Fuel Debris (Development o," 2022. https://en.dccc-program.jp/wp-content/uploads/20231019_JAEA.pdf (accessed Jan. 26, 2024).

[19] P. Hofmann, "Current knowledge on core degradation phenomena, a review," *J. Nucl. Mater.*, vol. **270**(1), pp. 194–211, doi: https://doi.org/10.1016/S0022-3115(98)00899-X (1999).

REACTOR PRESSURE VESSEL INTEGRITY DURING SEVERE ACCIDENT WITH CORE MELTDOWN: CHARACTERIZATION OF MATERIAL PARAMETERS, STRUCTURE INTEGRITY ASSESSMENT AND THERMAL-HYDRAULIC ASSESSMENT

Petr Gal, Miroslav Kotouc,
UJV Rez, a. s.
Hlavni 130, Husinec
petr.gal@ujv.cz; miroslav.kotouc@ujv.cz;

Petr Dymacek
Institute of Physics of Materials CAS
Žižkova 22, 616 00 Brno
pdymacek@ipm.cz

Dusan Gabriel, Jan Masak
Institute of Thermomechanics CAS
Dolejškova 1402/5, 182 00 Praha 8
gabriel@it.cas.cz; masak@it.cas.cz;

ABSTRACT

For high power reactors, such as VVER 1000, is the assessment of reactor pressure vessel (RPV) during several accident (SA) with application of In-Vessel Melt Retention (IVMR) still an open issue. There is no international consensus or document that defines the exact procedure how to assess the RPV during SA as in “conventional” assessment such as fatigue. This paper is focused on the basic steps of structural and thermal RPV assessment and how to compute deformations on RPV wall. This paper describes material inputs, severe accident progression calculations to obtain thermal boundary conditions and finally the structural assessment of RPV for the reference plant being Czech Temelin nuclear power plant (NPP), equipped with 2 VVER-1000/320 units.

KEYWORDS
IVMR, FEM, RPV integrity, TH calculations, Creep, Ablation

1. INTRODUCTION

The work is focused on the thermal and structural assessment of VVER 1000 reactor pressure vessel (RPV) during the hypothetical severe accident (SA), which assumes that due to insufficient cooling of the reactor core, the RPV internals, including the fuel elements, melt down. The objective is to assess the integrity of RPV from structural point of view, taking into account the inelastic material behavior, such as creep and plasticity at high temperatures, and, on this basis, to propose a general methodology for evaluating the integrity of RPV under emergency conditions.
The VVER 1000 material characterization at high temperatures is a key task, because this data were not available from the design phase of the power plant and serve as an input properties for integrity evaluation.

The key properties that need to be obtained are the density, thermal expansion coefficient, thermal conductivity, specific heat capacity and specific heat of fusion, modulus of elasticity (Young modulus), shear modulus, Poisson's ratio, tensile properties represented by loading curves from which ultimate tensile strength (UTS), yield strength (YS) and ductility can be obtained, creep properties represented by creep curves at various elevated temperatures from which time to rupture and minimum creep rate can be obtained. In order to acquired the thermal (and geometrical, in terms of wall ablation and the volume and density of the in-vessel molten corium) boundary conditions for structural analysis, the integral code for SA analyses ASTEC was used (see Section 3). From the ASTEC calculations, the heat fluxes (HF), and other loading conditions (such as primary pressure) serve as mechanical-load boundary conditions for detailed mechanistic assessment of RPV integrity using analyses by Finite Element Method (FEM).
The FEM part of the analysis was treated in a simplified way as an axisymmetric task which enables a detailed modeling of RPV wall melting (ablation on focusing area) and determination of local deformations at critical area of RPV. Analysis was solved as a coupled thermal – displacement problem. The non-stationary temperature analysis was solved when the heat flux from ASTEC analysis was adopted as a loading condition. The integrity analysis was solved with large deflection definition, and creep and plasticity were taken into account. Another fact that influences the analysis is the wall melting – ablation which was incorporated into analysis. The behavior of RPV material during SA is expected to be significantly influenced by high stress and deformation values which will be reached during short time period. For this purpose it seems appropriate to use a creep model which is able to describe the secondary and tertiary creep stage.

2. MATERIAL CHARACTERIZATION OF VVER RPV STEEL

The material characterization of the RPV steel is one of the main inputs to the thermo-mechanical analysis and to prove the success of the IVMR strategy. Thermo-physical and mechanical properties may vary between steel types. The RPV steel 15Ch2NMFA-A of representative batch applied in Czech VVER 1000 nuclear power plant (NPP) was used for the investigation. This steel is characterized as a ferritic-pearlitic and steel chemical composition is listed at the Tab. I.

Table I. Chemical composition of 15Ch2NMFA-A steel.

Elements (%)													
C	**Mn**	**Si**	**S**	**P**	**Cr**	**Ni**	**Mo**	**V**	**As**	**Cu**	**Co**	**Sn**	**Sb**
0.17	0.41	0.25	0.009	0.005	2.33	1.22	0.58	0.1	0.005	0.05	0.006	0.002	0.001

2.1. Thermo-physical measurements of VVER steel

For a proper thermal analysis of RPV during SA it is necessary to know the heat capacity (c_p), thermal conductivity (λ) and density (ρ) and information about the temperature of solidus and liquidus of the studied material. The density of tested material was determined by the double weighting method at room temperature. The resulting value was determined as a ρ = 7,8191 g·cm^{-3}. For higher temperatures, the density was calculated using the relation

$$\rho = \rho_0 \cdot (1 - \beta \cdot \Delta t), \quad (1)$$

where ρ_0 is reference density, β is coefficient of thermal volume expansion which can be replaced by $\beta=3\cdot\alpha$, where α is the thermal expansion coefficient and Δt is the difference between the given and reference temperature.

Specific heat capacity (c_p) of the tested material is graphically shown in Fig. 1. From this result, the initial melting temperature is 1456°C (solid state temperature) and the melting of material is terminated by the liquid temperature which is 1515°C. During the experimental measurement, the latent heat of melting was found.

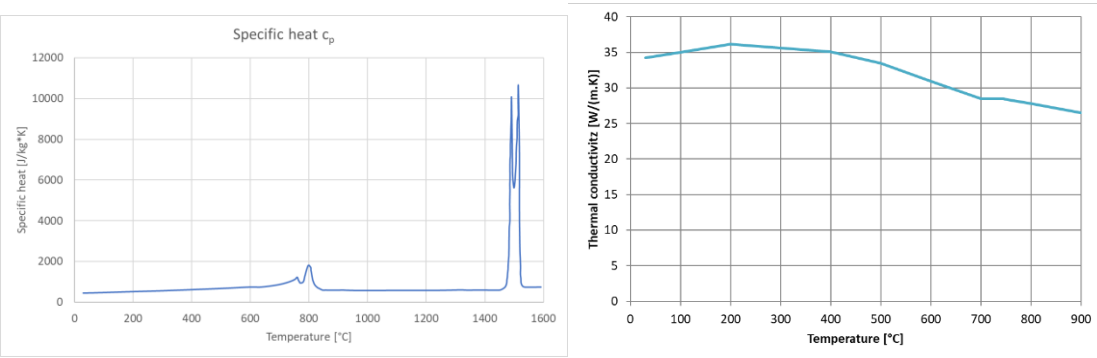

Figure 1. Specific heat and Thermal conductivity of material.

Interesting fact that affects mechanical properties of this steel is phase transition temperature. The temperature of 759 °C corresponds to the Currie temperature (TC), when steel with ferromagnetic properties becomes paramagnetic (loses its magnetic properties); for pure Fe it corresponds to TC = 769 °C. A phase transition from BCC to FCC (transformation of α ferrite to γ austenite) has been observed in the temperature range between 774 and 859 °C.

2.2. Mechanical properties of VVER steel

Mechanical properties, not only the yield stress etc., but the overall mechanical behavior serves as an input for deformations and mechanical resistance of RPV during SA. For this reason, measurements were taken for tensile tests at {20, 100, 200, 300, 500, 700, 900, 1000, 1100}°C and also short term creep tests at {500, 700, 800, 900, 1000, 1100}°C (in tension and also in compression). Creep loads have been determined for several load levels lower than yield stress for a given temperature. The tests were performed in air up to 300 °C while from 500 °C up in vacuum (tensile tests) and in argon (AR 5.0 with purity 99,999%) atmosphere (creep tests) to prevent the specimen oxidation. The comparison of UTS obtained by testing and published by V. Loktionov on different batch of the 15Ch2NMFA-A steel [1] is shown in Fig. 2. It is visible there is a good agreement between three sets of data with small differences given by the batch and possibly also by the strain rate.
The partial creep results are listed in Fig. 3 for 700°C and 900°C, mainly the time to rupture for different loading levels. Measured results are compared with published data in [2]. The comparison shows for 700°C similar trend of the time-stress relationship with comparable stress exponents and a bit more different at 900°C.

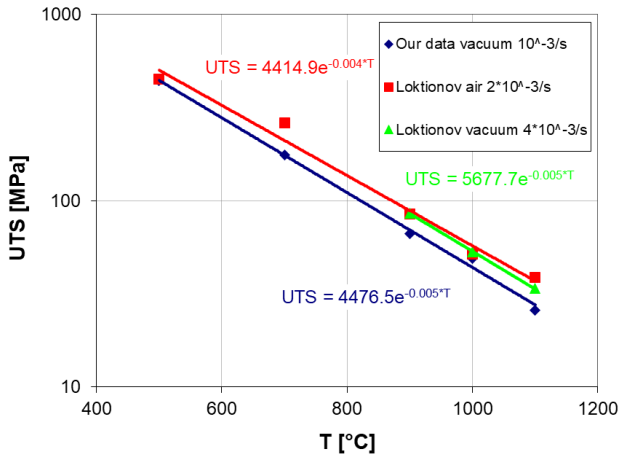

Figure 2. Comparison of the ultimate tensile strength for different conditions. Source: (own) and [1].

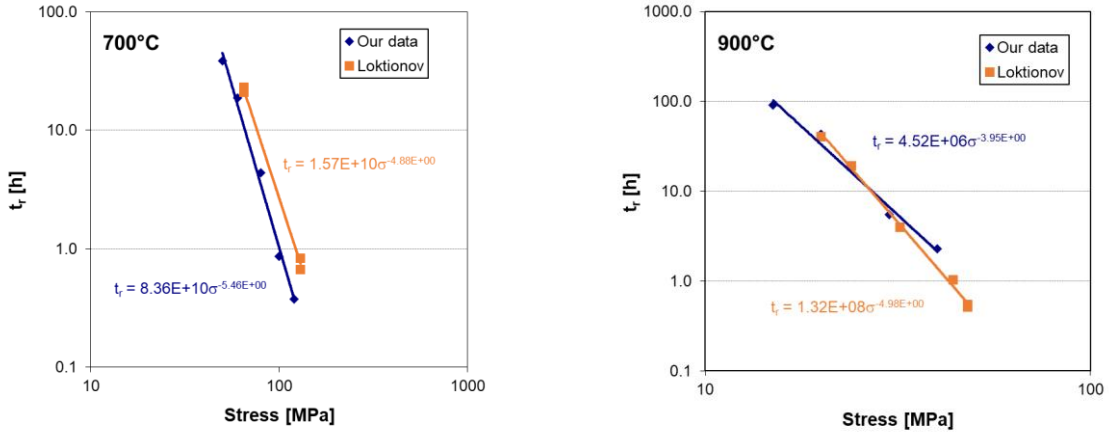

(a) (b)

Figure 3. Comparison of times to rupture vs. stress at (a) 700 °C and (b) 900 °C Source: (own) and [2].

Another measured data were the Young modulus (E), shear modulus (G) and the Poisson's ratio (μ). These data were measured at temperatures range between 20°C to 800°C by a non-destructive test performed by the resonance method.

3. THERMAL ANALYSIS USING ASTEC CODE

In order to obtain boundary conditions for consequent structural analyses, the integral code for SA analyses ASTEC (developed by IRSN, France) was used. The ASTEC code is of type "lumped parameter" (LP), which means that the spatial discretization of the computational domain is rather rough - large nodes are used to represent parts of the core and RPV internals, of the primary/secondary circuit and of the containment. Thanks to this relatively coarse plant representation, the ASTEC code is able of simulating a SA evolution since an initiating event up to a hypothetical radioactive release into the environment. Nodalization of the core and the lower plenum into 6 thermal-hydraulic channels and 46 axial levels,

together with the representation of the so-called macro-components, representing core part and RPV internals, is shown in Fig. 4.
Two SA scenarios, initiated, respectively, with large break loss of coolant (LOCA) and with station blackout (SBO), were analyzed with the ASTEC code. Both SA sequences were launched with and without consideration of the IVMR strategy. Thus, in total, 4 qualitatively different SA sequences were evaluated.

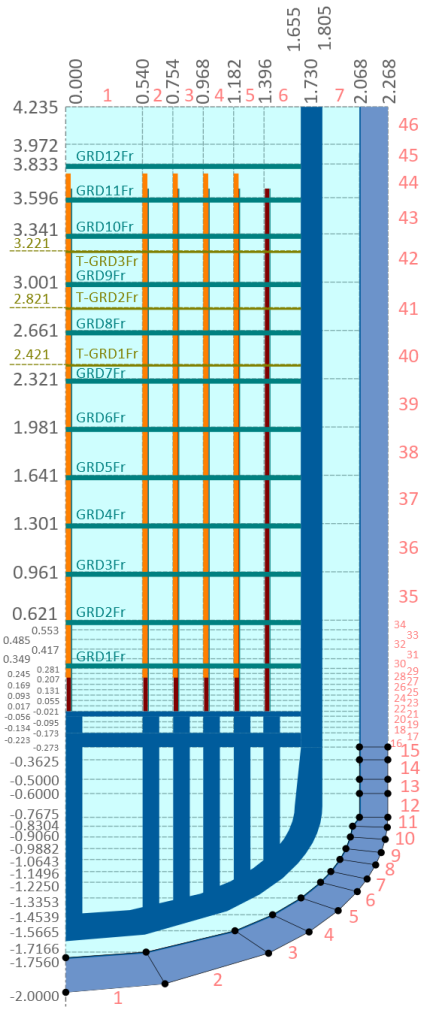

Figure 4. Nodalization of the core and lower plenum as prepared for the ASTEC code.

Example of characteristic results, obtained from the ASTEC analysis of the LOCA-initiated SA scenario with the IVMR strategy applied, is shown in Fig. 5. The picture shows a late-phase of the accident progression, with most of the reactor core being relocated into the lower plenum where it forms a 2-layer molten pool, consisting of an oxidic and a metallic layer. The heavily ablated RPV wall and temperature profile through the RPV is also visible in the figure.
The results from ASTEC, as a time-dependent heat flux in each node of RPV, pressure inside the RPV and on containment and the weight of corium serves as boundary condition for the consequent detailed mechanistic assessment of RPV integrity, carried out with the aid of structural analysis method - the FEM for the case of this study.

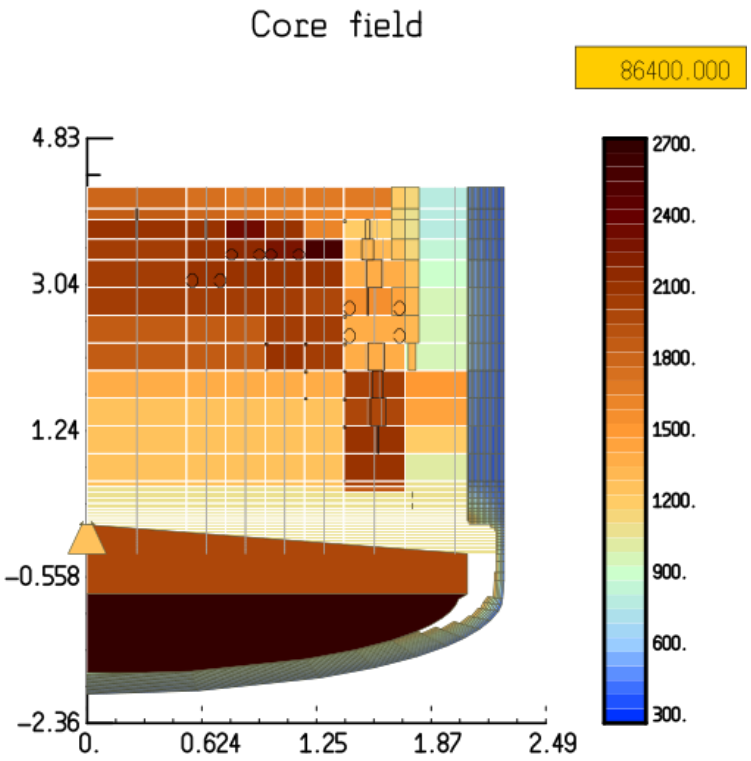

Figure 5. State of the core and RPV wall at time t=86 400 s. Outcomes of an ASTEC code analysis.

4. FINITE ELEMENT ANALYSIS OF RPV INCLUDING NON-LINEAR MATERIAL BEHAVIOUR

The detailed mechanistic assessment of RPV during SA was performed using FEM program Abaqus. The problem was treated in simplified way as an axisymmetric one which enables more detailed modeling of RPV on lower bottom and area of focusation where is expected the wall melting (ablation process). The analysis was solved as a coupled temperature-displacement problem while the boundary conditions were transported from ASTEC calculation, so one-way coupling was used. The key is to predict local inelastic deformation as accurately as possible at the interesting locations. The behavior of RPV material during SA is expected to be significantly influenced by the fact that high temperatures and stresses will be reached in a relatively short time instant. Thus, it seems appropriate to use a combined material model that considers plastic and creep deformations.

For this purpose a combined creep model which considers mainly the secondary and tertiary creep phase of material was used. This is fulfilled by a well-established complex creep probabilistic model developed by Bína and Hakl [3]. The governing equation furnishing the dependence of the total strain ε_c on initial strain ε_0, limit strain ε_m and damage $\pi(t) = t/t_r$ at time t is

$$\varepsilon_c(\sigma_e, T, t) = \varepsilon_0 \left(\frac{\varepsilon_m}{\varepsilon_0}\right)^{g(\pi(t))} \tag{2}$$

where σ_e is the effective stress in [MPa], T is the thermodynamic temperature in [K], t the time in [hours]. The initial strain ε_0 can be calculated from the elastic solution

$$\varepsilon_0(\sigma, T) = \frac{\sigma}{E(T)} 10^2 \tag{3}$$

where the dependence of the Young modulus on temperature is supposed to have the form

$$E(T) = E_1 + E_2 exp\left(-\frac{E_3}{T}\right) \tag{4}$$

The limit strain ε_m can be expressed by

$$\varepsilon_m(T,\sigma) = exp\left(M_1 + M_2 \tanh\left(\frac{ln(t_r(T,\sigma)) - M_3 - M_4 T}{M_5}\right)\right) + \varepsilon_0 \tag{5}$$

The time elapsed at rupture t_r [hours] is estimated by the empiric formula

$$\log t_r = A_1 + A_2 \log\left|\frac{1}{T} - \frac{1}{A_5}\right| + A_3 \log\left|\frac{1}{T} - \frac{1}{A_5}\right| \log[\sinh(A_6 \sigma T)] \tag{6}$$
$$+\log[\sinh(A_6 \sigma T)].$$

The hardening function $g[\pi(t)]$ can be expressed as

$$g(\pi(t)) = [\pi(t)]^N \left[\frac{1+exp[-2\pi^{K(T)}(t)]}{1+exp(-2)}\right]^M \tag{7}$$

Material data are given by parameters for the initial strain E_1–E_3, rupture strain M_1–M_5, creep strength A_1–A_6 and hardening function N, M, K. A careful calibration of parameters of complex model was performed based on measurement of creep properties of RPV steel 15Ch2NMFA-A, which was described in section 2.2. Fig. 6 shows the comparison between experimental data (measured creep curves) and analytical curves for a selected temperature T = 900°C and stresses $\sigma = \{10, 15, 20, 30\}$ MPa. This material model was implemented into Abaqus software through the subroutine “Creep”.

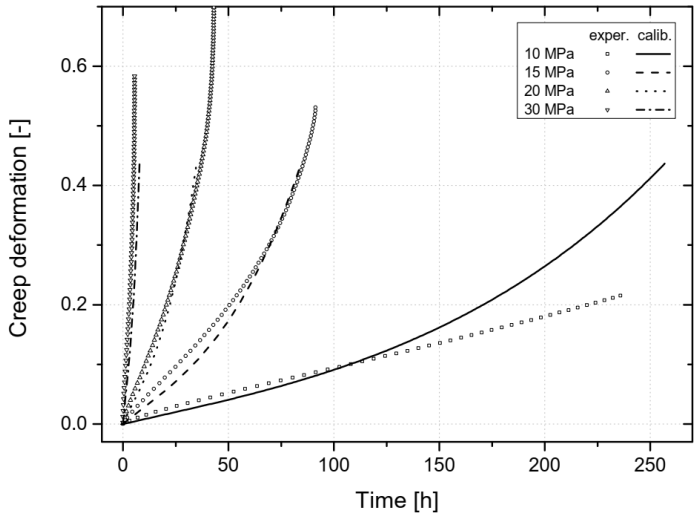

Figure 6. Comparison of the calibrated creep curves with experimental data for a selected temperature and stresses.

Further, in computation is included the linear isotropic rule, which defines the plastic deformation. The rule is expressed as

$$dR = \sigma_y dp, \quad (8)$$

where σ_y is the yield stress of material, dp is the increment of plastic deformation and dR is increment of plastic surface.

4.1. Ablation on FEM simulation

One of the main challenges in solving SA using FEA is a reliable description of the RPV wall ablation process. Since this is not a common task, it was necessary to find an approach to include it in the analysis. Since the heat fluxes on focusation area are high, and the ablation is strong, is important to include ablation process. There are several ways to do this, but for these analyses the "ALE adaptive meshing" method was used with combination of the "MESH to MESH" mapping process. This means, that once the melting temperature is reached, the FEM mesh, mainly the nodes of elements, are moved to a new location. This procedure was implemented in the analysis via "UMESHMOTION" subroutine. The advantage of the used approach is that it is not necessary to find new boundaries to apply boundary conditions as in the case of removing elements from the analysis. The disadvantage of the used approach is the requirement to remesh the model and readjust the calculation from time to time.

4.2. Results of computation

Fig. 7 shows an example of characteristic result using the complex creep model at time 37 083 s. Figure shows a strong ablation in the focusing area and temperature profile, where the temperature is close to the melting temperature in some regions (Fig. 7a). The creep deformation is localized on the inner surface of ablated area and the maximal creep deformation is 8% (Fig. 7b). At this time (37 083 s) the heat fluxes start to decrease, so the ablation process has been stopped.

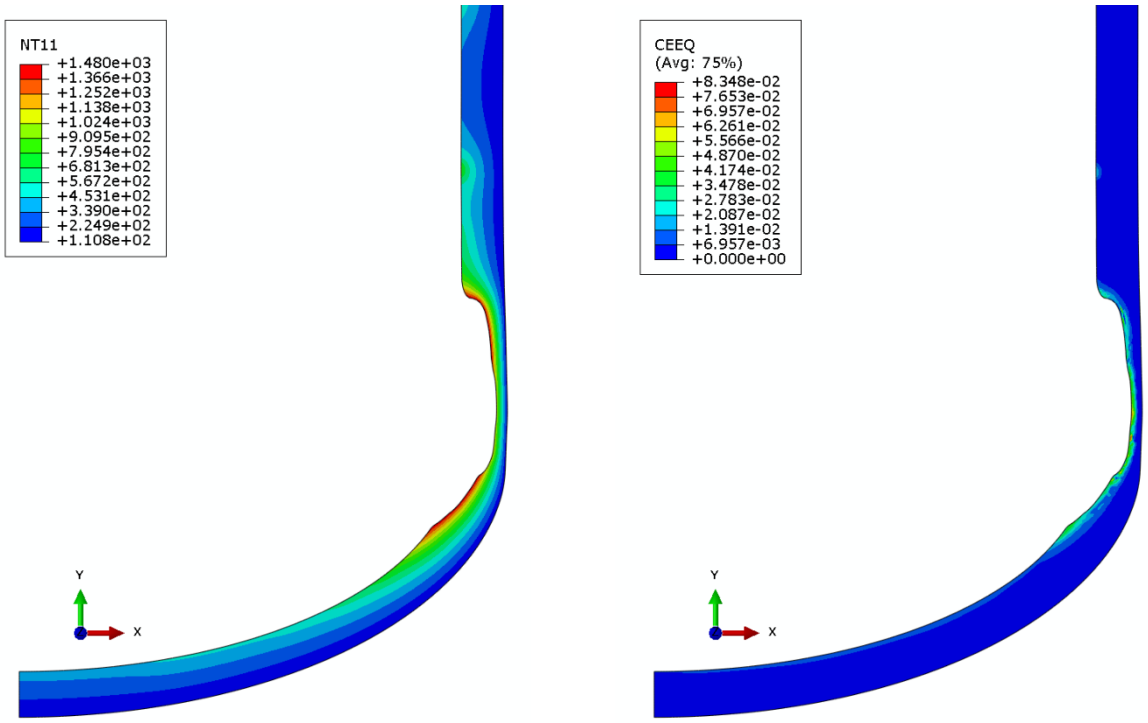

(a) (b)

Figure 7. Outcomes from FEM analysis of SBO with IVMR at time 37 083 s, (a) temperature distribution, (b) creep deformation.

5. CONCLUSIONS

The assessment of the RPV during SA is a challenging computational task because the temperature field at the RPV is non-stationary, furthermore, due to high temperatures (near the melting temperature) ablation of material is applied. High temperatures and stresses are reached in a relatively short time, so that inelastic deformation such as a creep and plastic deformation occur. For this purpose, a combined creep model, which mainly describes the secondary and tertiary phases of creep, and linear isotropic rule describing plastic deformation were used.

Prior the FEM simulation and detailed RPV assessment, thermal analysis was performed using the LP code ASTEC. The results from the ASTEC program serve as boundary conditions, especially the heat fluxes from corium to the RPV. Thus, the assessment was made as a one-way coupling approach.

For a detailed structural assessment of the RPV accurate material data including thermo-physical and mechanical material behavior was required. Experimental measurement were performed on the VVER 1000 15Ch2NMFA-A material because the properties available so far were only available for the assumed operating temperatures of the reactor and, in addition, it was not expected that creep deformation would occur during operation.

There is still much work to be done in this area, for example to develop failure criteria that will be internationally acceptable and accepted. Some outstanding issues are being discussed in the framework of the OECD “Integrity assessment for In-vessel retention”, which is still ongoing.

ACKNOWLEDGMENTS

This work was supported by Technology Agency of the Czech Republic under grant No. TITSSUJB938 "Methodology for evaluation the integrity of VVER-1000 RPV at high temperatures due to fuel melting during severe accident".

REFERENCES

1. LOKTIONOV, V., LYUBASHEVSKAYA, I., SOSNIN, I., TERENTYEV, O. E.: "Short-term strength properties and features of high-temperature deformation of VVER reactor pressure vessel steel 15Kh2NMFA-A within the temperature range 20–1200 °C", *Nuclear Engineering and Design,* **352**, 2019, 110188. Available from: doi:10.1016/j.nucengdes.2019.110188.
2. LOKTIONOV, V., LYUBASHEVSKAYA, I., TERENTYEV, O. E.: "The regularities of creep deformation and failure of the VVER's pressure vessel steel 15Kh2NMFA-A in air and argon at temperature range 500-900°C", *Nuclear Materials and Energy,* **28**, 2021, Available from: doi: 101019. 10.1016/j.nme.2021.101019.
3. BÍNA, V. HAKL, J.: "Probabilistic approach to description of the creep strain characteristic and prediction for long life-time," *Proc. Conf. Materials for Advanced Power Engineering,* Coustouradis, Kluwer Academic Publishers, Dordrecht (Boston), pp 601-610 (1994).

NUCLEAR RESEARCH INSTITUTE

REACTOR PRESSURE VESSEL INTEGRITY DURING SEVERE ACCIDENT WITH CORE MELTDOWN: CHARACTERIZATION OF MATERIAL PARAMETERS, STRUCTURE INTEGRITY ASSESSMENT AND THERMAL-HYDRAULIC ASSESSMENT

13-16.5.2024, Stockholm/Sweden

P. Gal, M. Kotouc, P. Dymacek, D. Gabriel, J. Masak

UJV Group
PEOPLE | INNOVATION | TECHNOLOGY

OUTLINE

- Introduction + Motivation
  - Relationship between each part of analysis
- Material characterization
- Integral analysis using LP (lumped parameter) code ASTEC
- FEM (Finite Element Method) analysis of RPV (Reactor Pressure Vessel)
  - FEM model + boundary conditions
  - Constitutive creep material model
- Results
- Conclusion and Outlook

INTRODUCTION AND MOTIVATION (1)

- Thermal and structural assessment of the VVER-1000 RPV during a hypothetical severe accident (SA),
- Due to insufficient cooling of the reactor core, the RPV internals, including the fuel elements, melt down,
- RPV structural integrity assessment, *taking into account the inelastic material behavior*, such as creep and plasticity at high temperatures,
- Including the ablation effect – melting and thinning of RPV walls

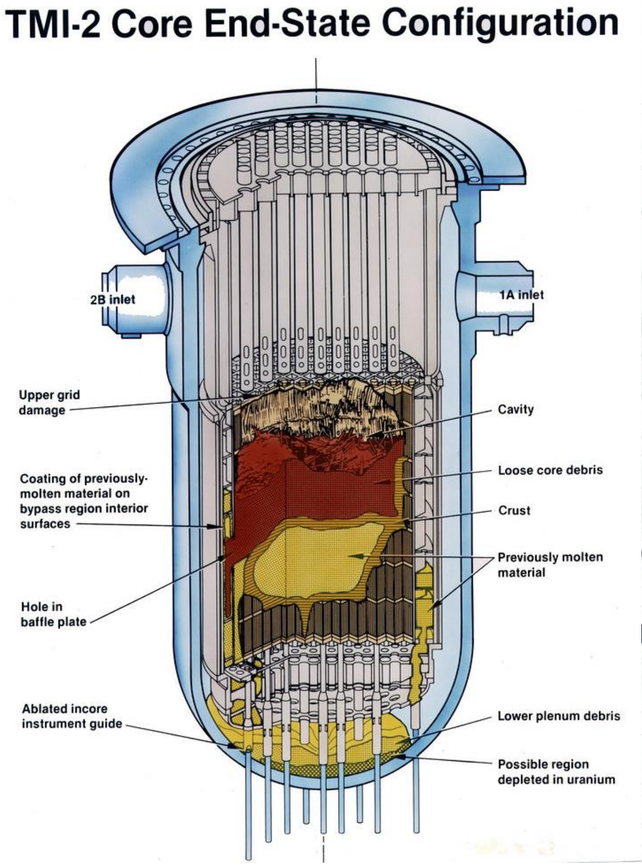

Picture from: Rempe, Joy & Knudson, D.. (2013). *TMI-2 - A Case Study for PWR Instrumentation Performance during a Severe Accident*.

INTRODUCTION AND MOTIVATION (2)

- Material parameters affect results of integral calculations → temperature of RPV wall, heat flux (HF) from corium to RPV …
- And also affect structural assessment of RPV → temperature of RPV, elastic, creep and plastic deformations,
- Hence, a general methodology for the assessment of the integrity of RPVs under emergency conditions was proposed and conducted,
- The VVER-1000 RPV steel 15Ch2NMFA-A was used for the investigation

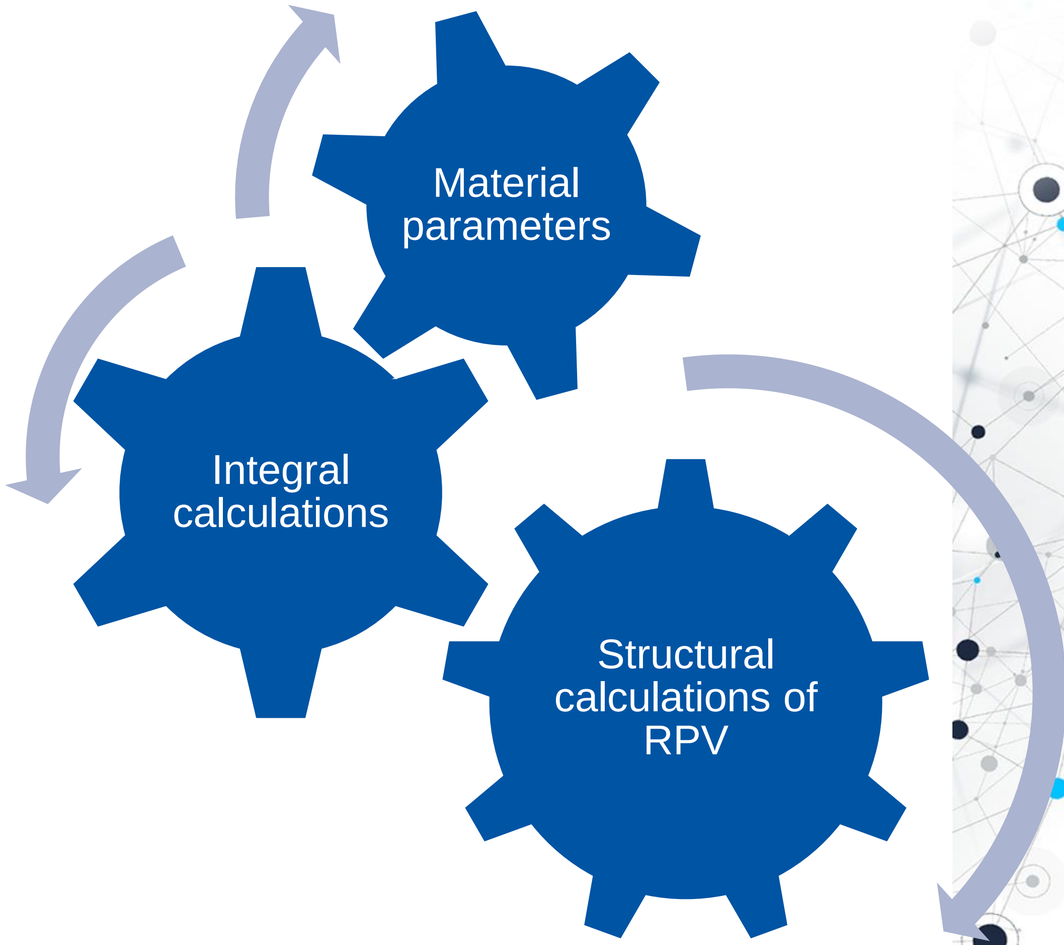

This work was supported by Technology Agency of the Czech Republic under grant No. TITSSUJB938 “Methodology for evaluation the integrity of VVER-1000 RPV at high temperatures due to fuel melting during severe accident”.

MATERIAL CHARACTERIZATION (1)

- Crucial thermo-physical material properties are the density **ρ**, thermal expansion coefficient **α**, thermal conductivity **λ**, specific heat capacity c_p and specific heat of fusion,
- The density at room temperature was determined to be **ρ = 7,8191 g·cm^{-3}**,
- The temperature dependence was calculated using the relation: $\rho = \rho_0 \cdot (1 - \beta \cdot \Delta t)$,
- Melting material was found to begin at 1456 °C (solidus temperature) and end at 1515 °C (liquidus temperature).

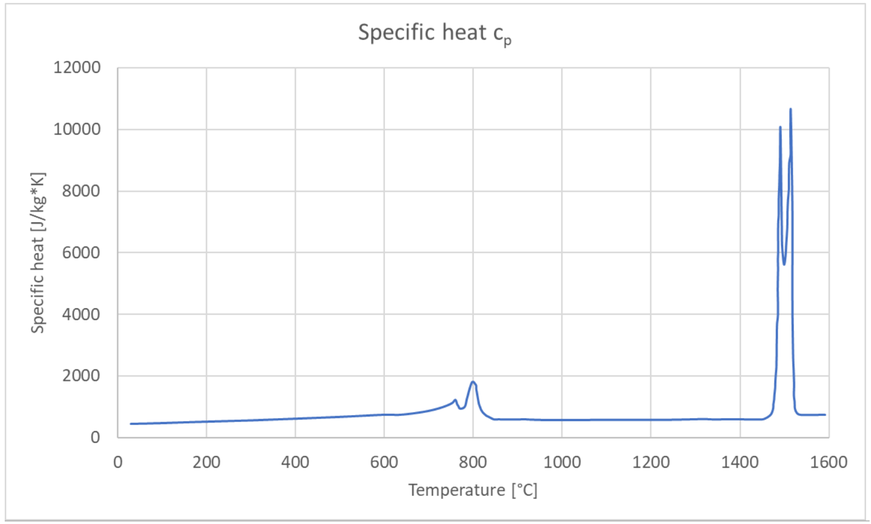

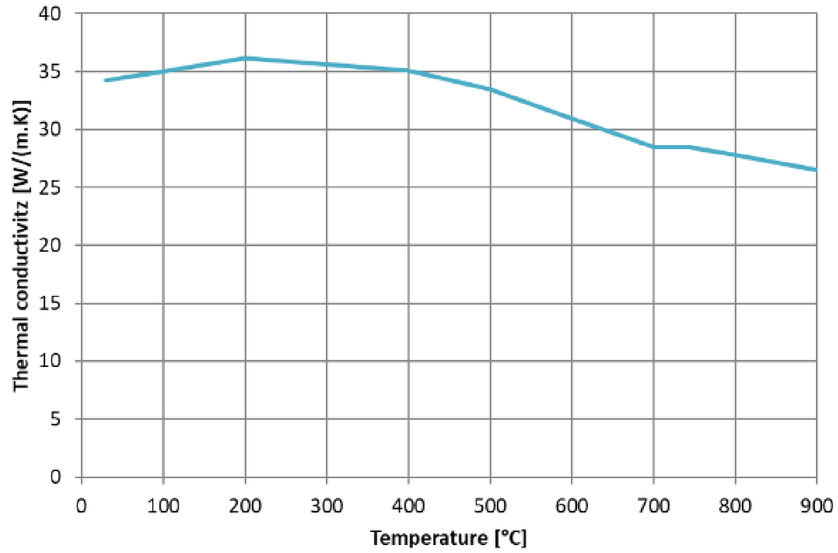

MATERIAL CHARACTERIZATION (2)

- Essential mechanical properties are modulus of elasticity (Young modulus) ***E***, shear modulus ***G***, Poisson's ratio ***v***, ultimate tensile strength (UTS), yield strength (YS) and ductility ***A*** and flow curves – stress strain curves to account for plastic deformation.
- Creep properties are represented by creep curves at various elevated temperatures and loads from which time to rupture and minimum creep rate can be obtained.
- Creep curves were also used to calibrate the parameters of the complex creep model (Bina model).

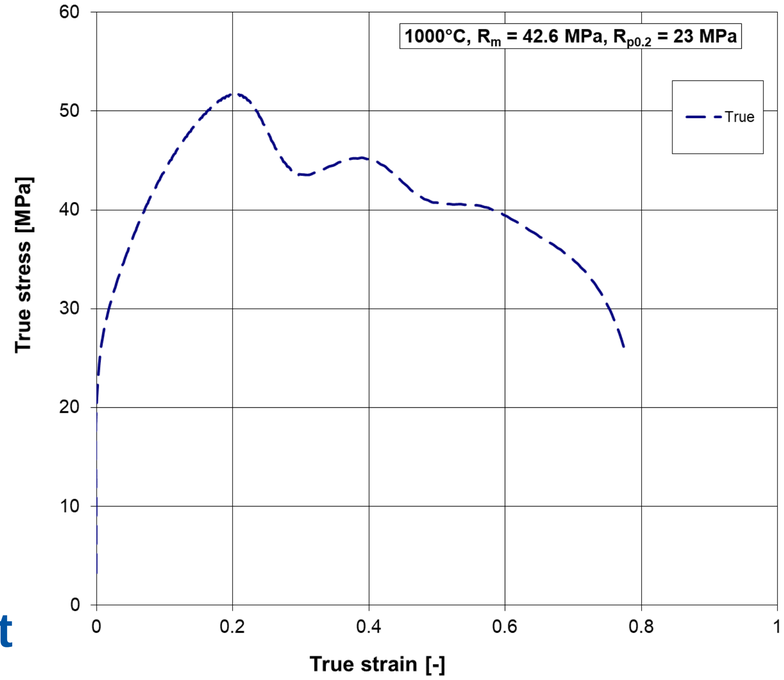

1000°C, 15 MPa

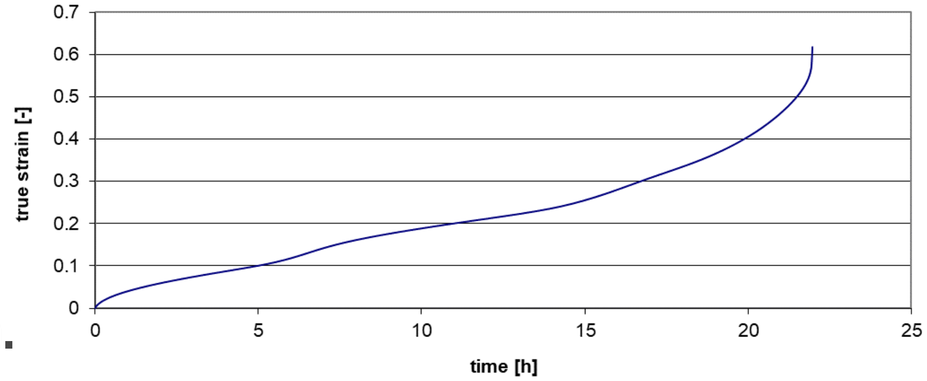

INTEGRAL ANALYSIS USING THE ASTEC CODE (1)

ASTEC

- Integral analyses were performed to obtain boundary conditions for subsequent structural analyses,
- LP code ASTEC was used to perform the integral analysis,
  - Its advantage is a detailed modelling of corium thermo-chemical behavior in the 0-D lower plenum (LP) model, where the molten material – based on the U-Zr-O-Fe quaternary diagram – can adopt a 3-layer configuration:
    - 1. heavy metals (U), 2. oxides (UO2, ZrO2), 3. light metals (Zr, Fe)
- Two SA scenarios were analyzed :

1. Large break loss of coolant accident (LB LOCA) and
2. Station blackout (SBO)

- Both were calculated with & without the assumptions of In-Vessel Melt Retention (IVMR).

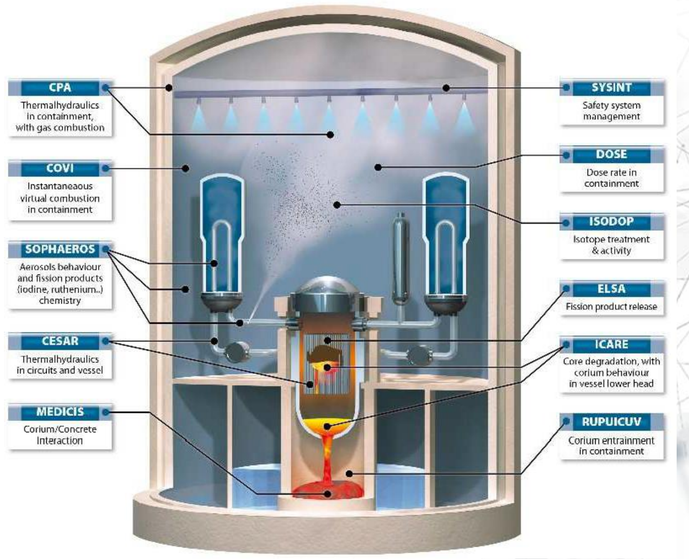

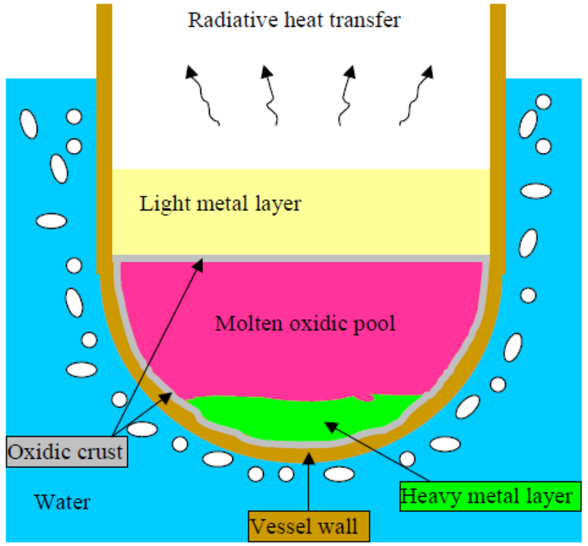

INTEGRAL ANALYSIS USING THE ASTEC CODE (2)

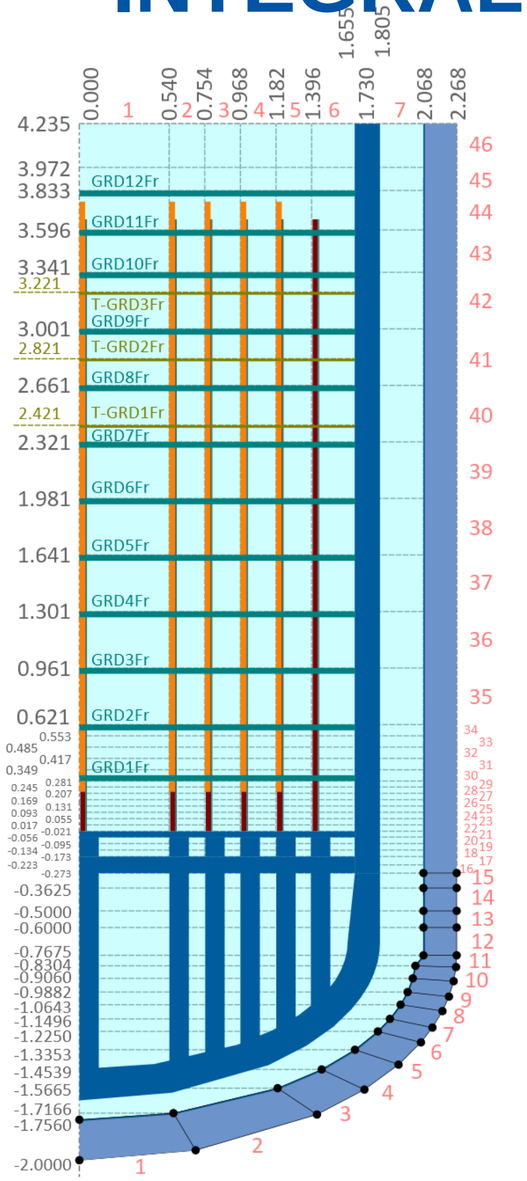

- **RPV & core**
  - detailed representation of VVER-1000 components

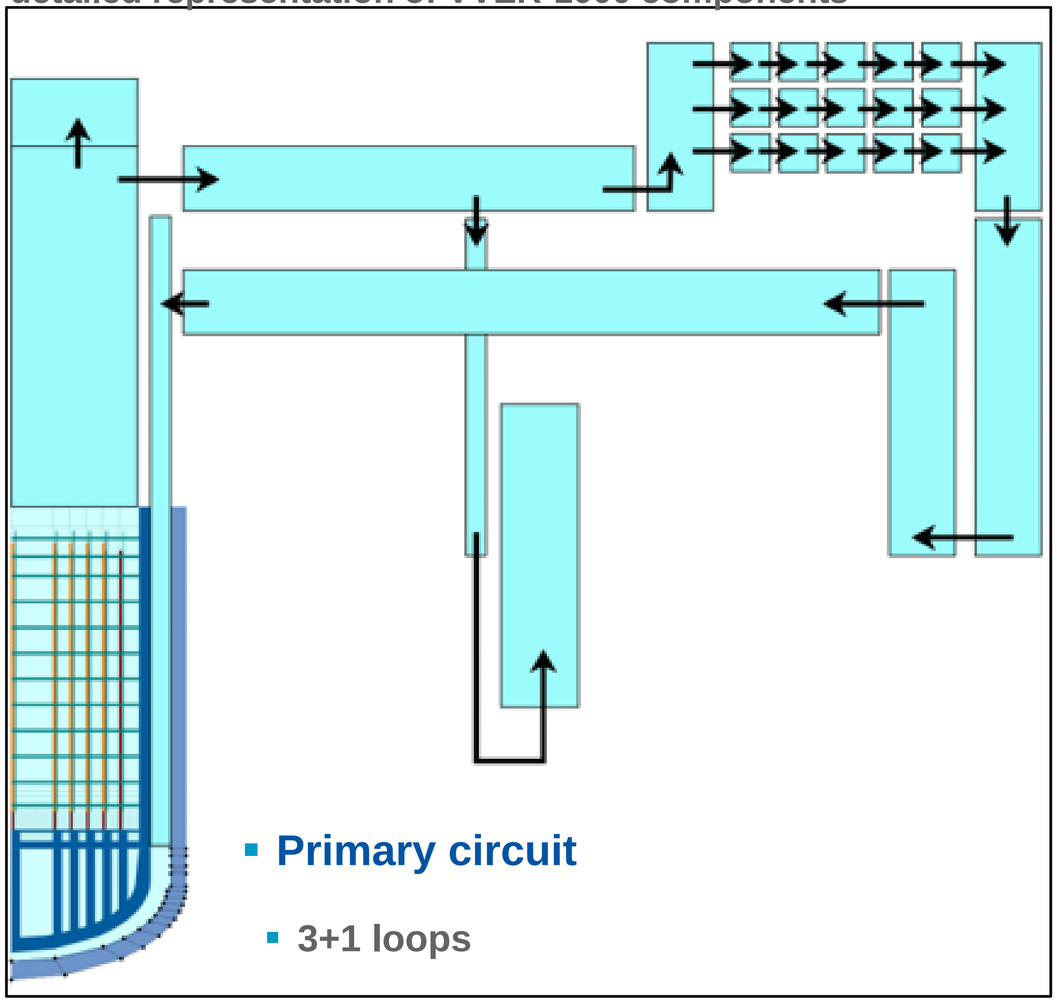

- **Primary circuit**
  - 3+1 loops

- **Containment**
  - simplified

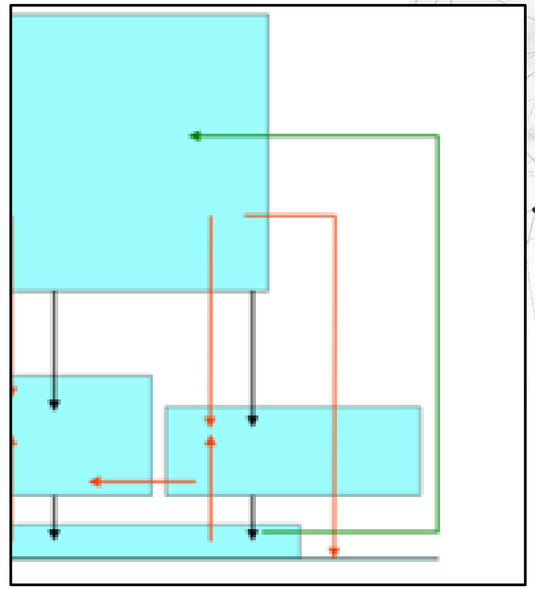

INTEGRAL ANALYSIS USING THE ASTEC CODE (3)

- Example of characteristic results, obtained from the ASTEC analysis of the LOCA-initiated SA scenario without the IVMR strategy applied,
- The picture shows a late-phase state of the „in-vessel“ phase of the accident (right before RPV failure),
- Most of the reactor core is relocated into the LP where it forms a 3-layer molten pool, consisting of an oxidic and a heavy/light metallic layers,
- The heavily ablated RPV wall is clearly visible,

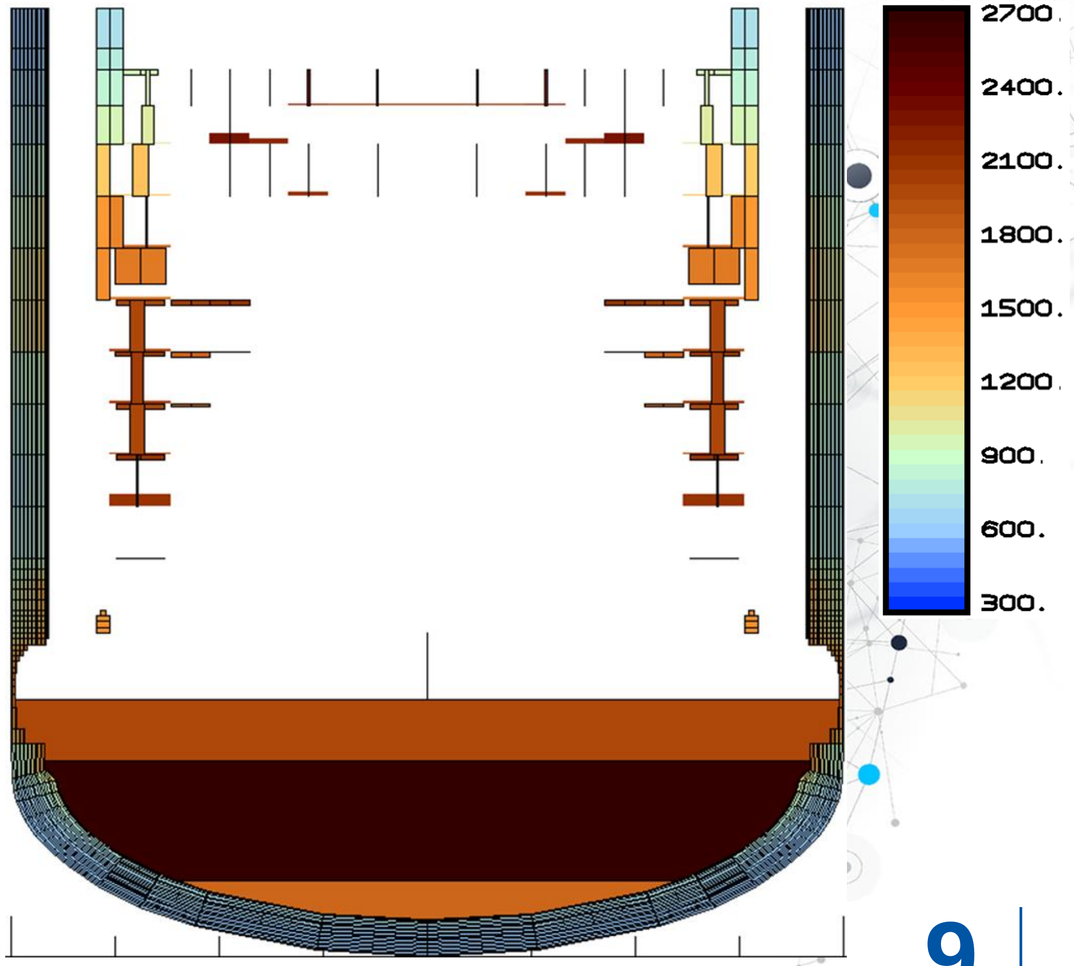

State of the core and RPV wall at time t=12 100 s

INTEGRAL ANALYSIS USING THE ASTEC CODE (4)

- **Heat flux in each axial layer as a function of time (for the case with the IVMR strategy applied)**

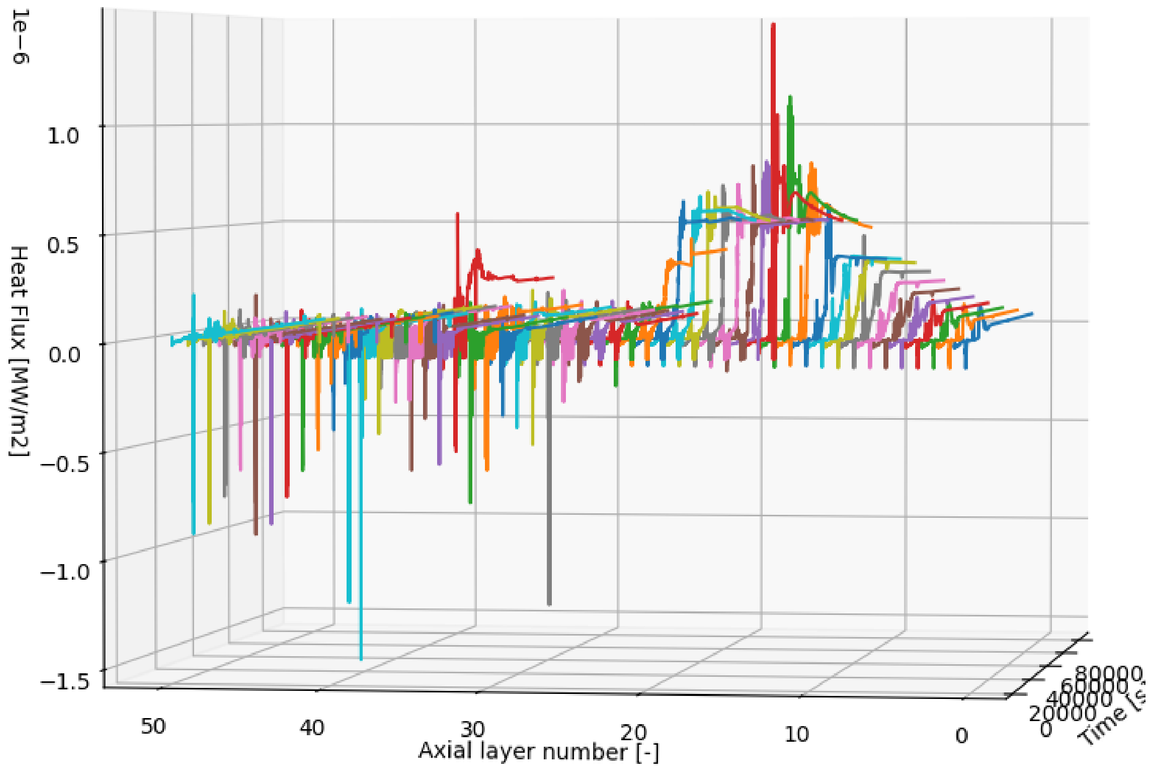

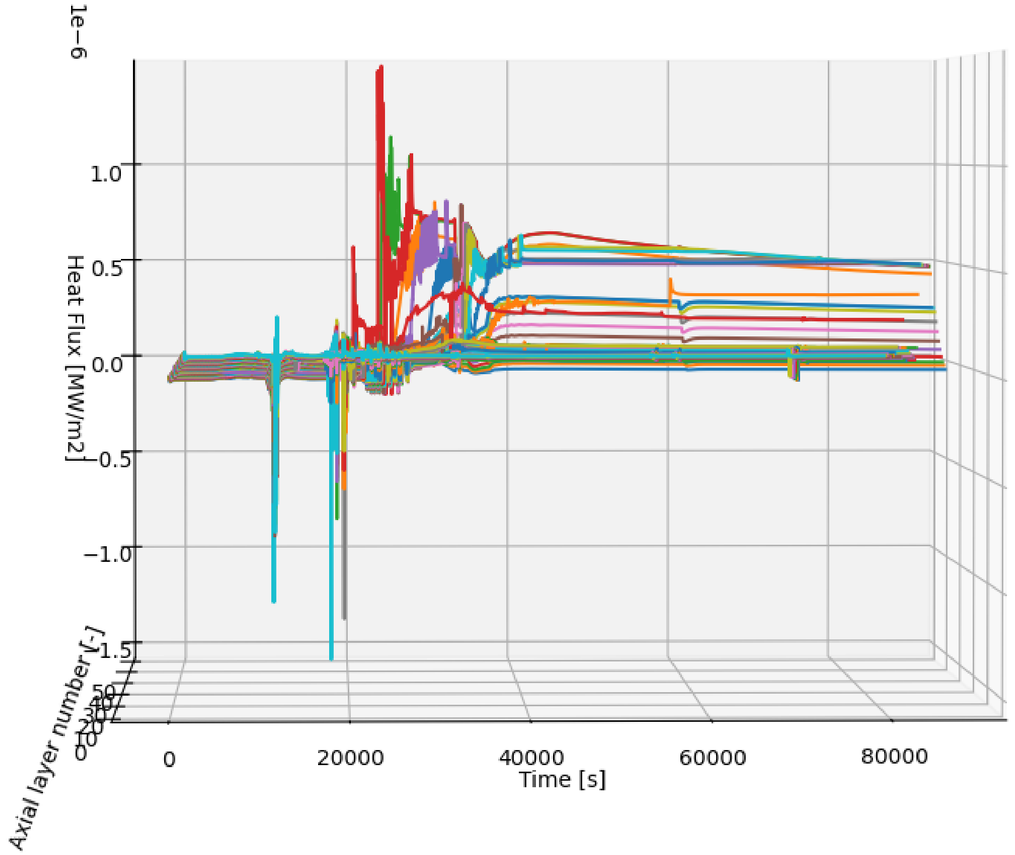

FEM ANALYSIS OF RPV (1)

- The detailed structural analysis was solved as an axisymmetric problem → enables more detailed modeling of the areas of interest:
  - Lower bottom,
  - area of focusation – expected the wall melting and thinning,
- Boundary conditions were transported from ASTEC calculation, so one-way coupling was used.
- The key is to predict local inelastic deformation as accurately as possible at the interesting locations.
- The creep behavior of RPV material is significantly influenced by the fact that high temperatures and stresses will be reached in a relatively short time instant.
- Thus, it seems appropriate to use a combined material model that considers plastic and creep deformations.

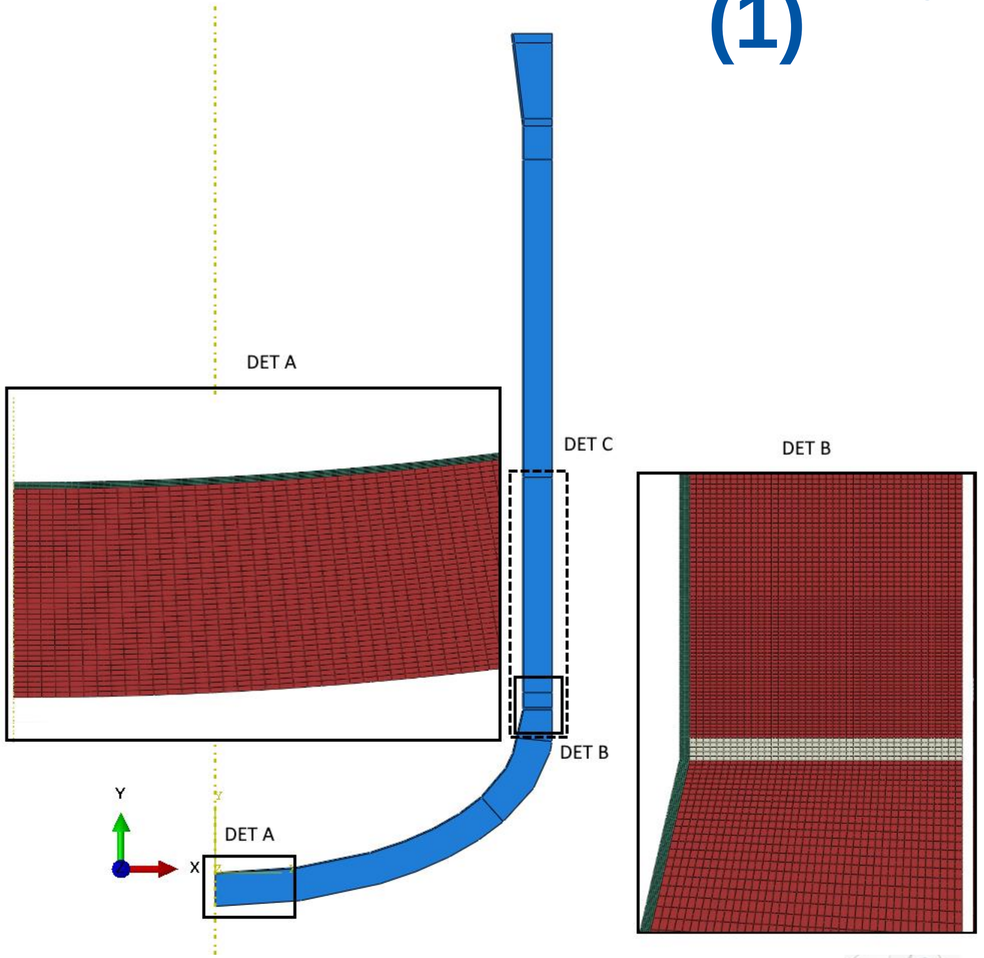

FEM ANALYSIS OF RPV (2)

- The complex model proposed by Bina and Hakl* was chosen to describe the creep deformation,
- Model describes mainly secondary and tertiary creep phase of material,
- Governing equation furnishing the dependence of the total strain:

$$\varepsilon_c(\sigma_e, T, t) = \varepsilon_0 \left(\frac{\varepsilon_m}{\varepsilon_0}\right)^{g(\pi(t))}$$

- The limit strain ε_m can be expressed by:

$$\varepsilon_m(T, \sigma) = exp\left(M_1 + M_2 \tanh\left(\frac{ln\left(t_r(T, \sigma)\right) - M_3 - M_4 T}{M_5}\right)\right) + \varepsilon_0$$

- The hardening function g[π(t)] can be expressed as:

$$g(\pi(t)) = [\pi(t)]^N \left[\frac{1+exp\left[-2\pi^{K(T)}(t)\right]}{1+exp(-2)}\right]^M$$

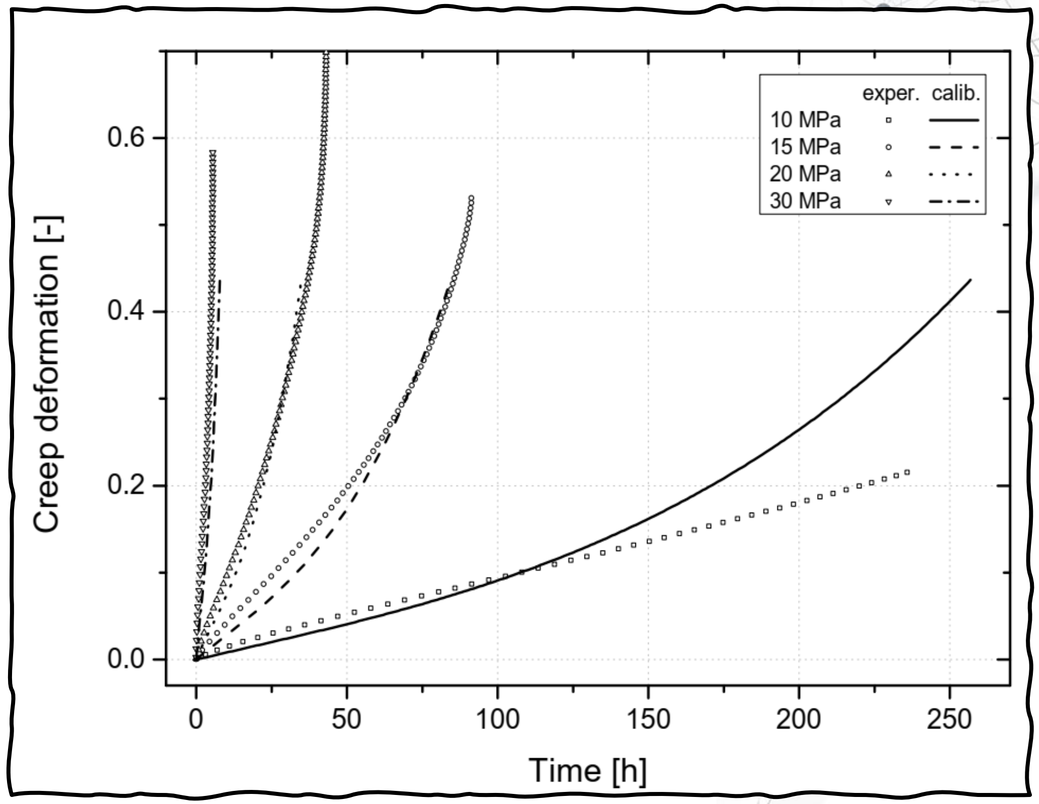

* BÍNA, V. HAKL, J.: "Probabilistic approach to description of the creep strain characteristic and prediction for long life-time," *Proc. Conf. Materials for Advanced Power Engineering*, Coustouradis, Kluwer Academic Publishers, Dordrecht (Boston), pp 601-610 (1994).

FEM ANALYSIS OF RPV (3)

- Input data for calibration the creep model were creep curves for all temperatures in the test range,
- For calibrating process was used the least square method,
- Creep model is defined by a total of **17 material parameters**,
- This creep material model was implemented into FEM software Abaqus through UMAT subroutine,
- Plastic deformation is included in the calculation using the linear isotropic rule $dR = \sigma_y dp$
- Ablation process in simulation:
  - Ablation is accounted for in the simulation by the ALE adaptive process with combination of „Mesh to Mesh mapping“ process,
  - Melting rate is drive by a simple equation

$$v_a = \frac{q_a}{\rho \cdot H_s}$$

Heat flux

Specific heat of sublimation

Material density

FEM ANALYSIS OF RPV - RESULTS (1)

- **Example of results: SBO with application of IVMR strategy – Temperature field**

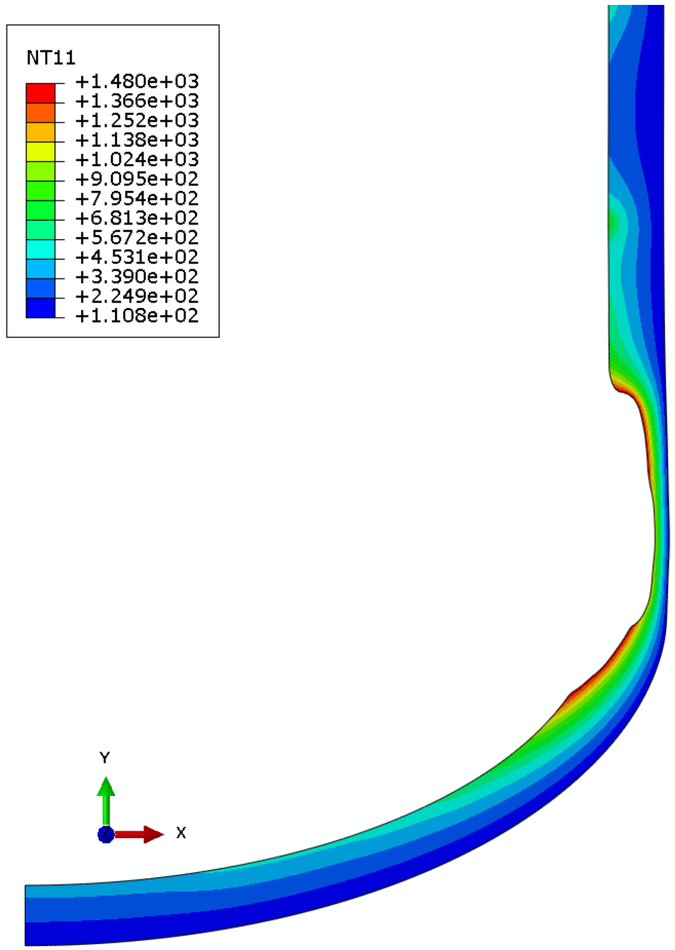

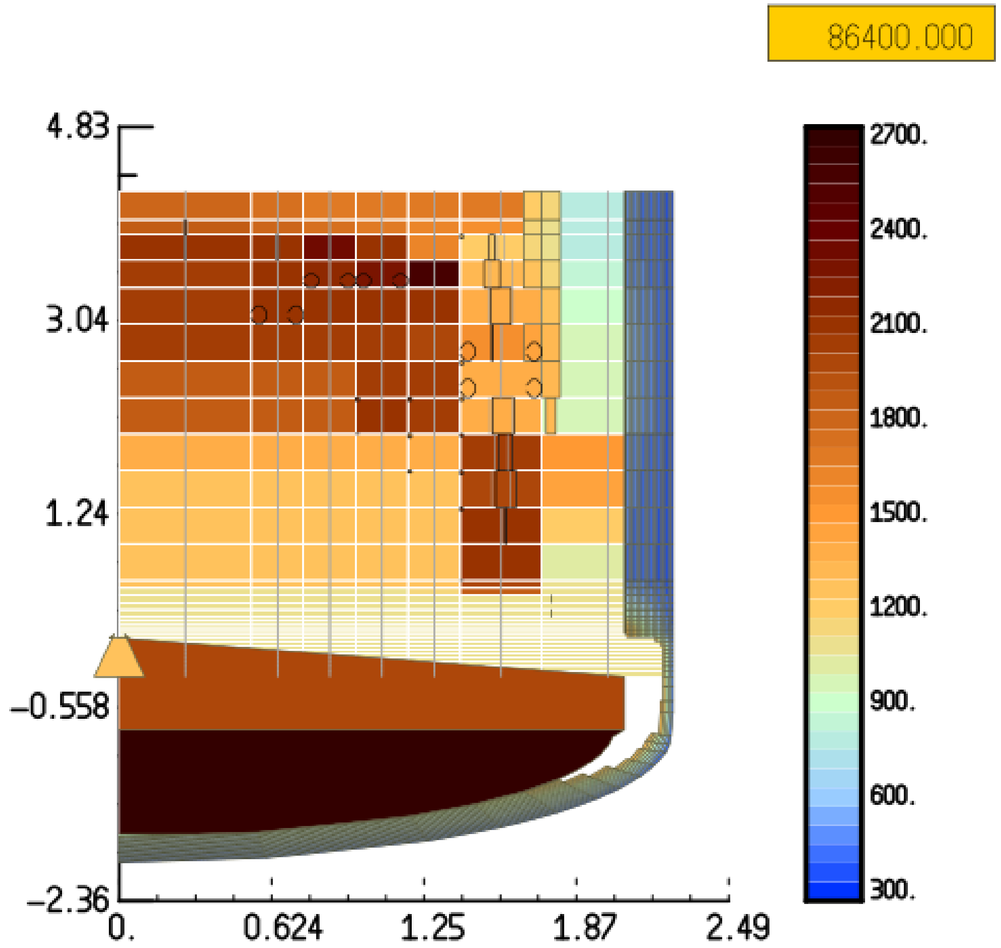

FEM ANALYSIS OF RPV - RESULTS (2)

- **Example of results: SBO with application of IVMR strategy – Creep and plastic deformation**

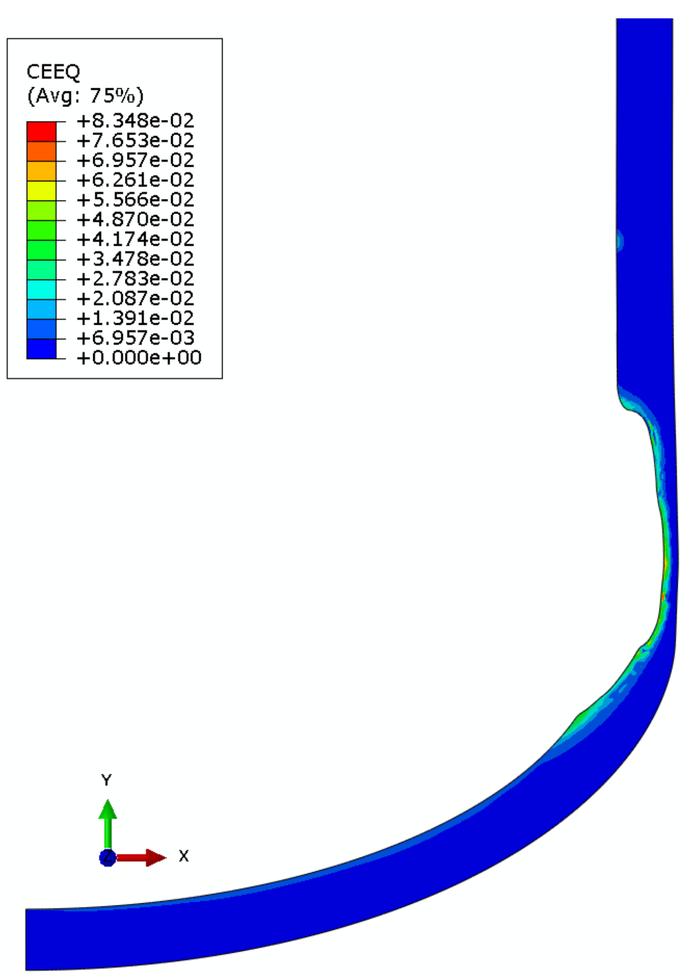

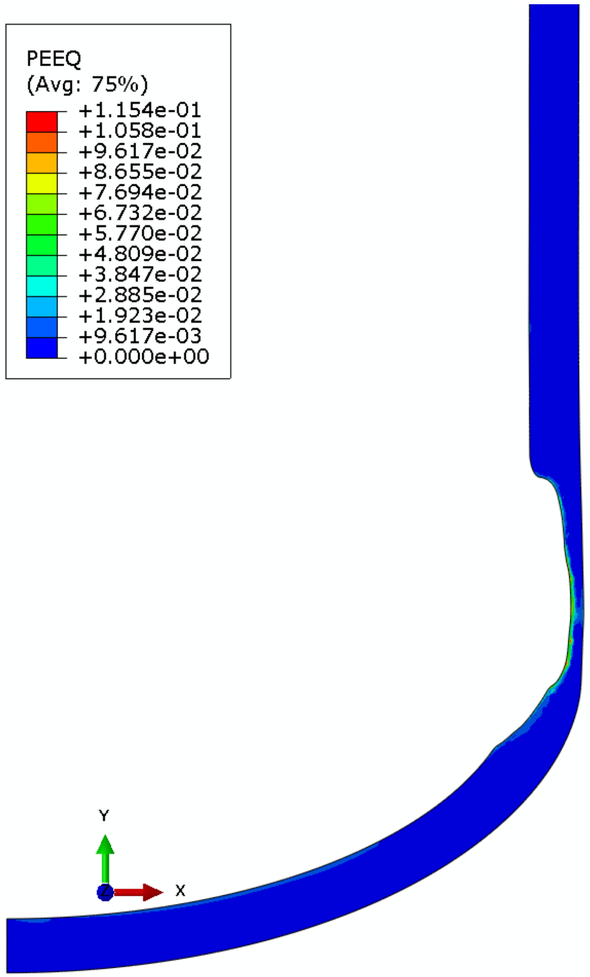

SUMARY (1)

- **Assessment of RPV during SA is a challenging task! – during the course of our national project has been achieved:**
  - **RPV evaluation procedure including the ablation process (melting of RPV wall),**
  - **Implementation of the complex creep model + calibration of material parameters,**
  - **Development of criteria for RPV failure,**
  - **Identification and removal of errors detected in the ASTEC code:**
    - **Errors reported during the project and corrected within a short time period,**
    - **Unrealistic RPV melting process → affects the HF to the RPV,**

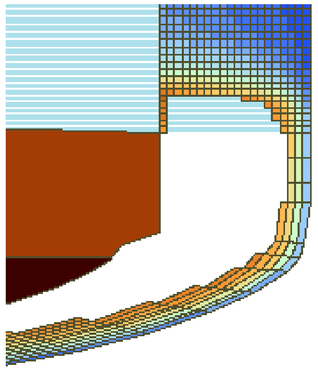

This work was supported by Technology Agency of the Czech Republic under grant No. TITSSUJB938 "Methodology for evaluation the integrity of VVER-1000 RPV at high temperatures due to fuel melting during severe accident".

SUMARY - GAPS (2)

- There is still much work to do as:
  - Proposal for internationally accepted failure criteria,
  - Transformation of boundary conditions from Integral analysis to the FEM analysis,
  - Outer boundary condition on outer surface of RPV,
  - etc…

This work was supported by Technology Agency of the Czech Republic under grant No. TITSSUJB938 “Methodology for evaluation the integrity of VVER-1000 RPV at high temperatures due to fuel melting during severe accident”.

Thank you for your attention

NUCLEAR
RESEARCH
INSTITUTE

ÚJV Řež, a. s.
Hlavní 130, Řež
250 68 Husinec, Czech Republic

e-mail: sales@ujv.cz
www.ujv.cz

UJV Group
PEOPLE I INNOVATION I TECHNOLOGY

Improvement of thermochemical corium stratification accounting for uranium and zirconium composition difference in metallic and oxide phases

Mativet J., Le Tellier R., and Lecoanet A.
CEA, DES, IRESNE, DTN, Cadarache
F-13108 Saint Paul-lez-Durance, France
Jules.mativet@cea.fr; romain.le-tellier@cea.fr; alexandre.lecoanet@cea.fr

ABSTRACT

The in-vessel melt retention (IVR) is a mitigation strategy aiming at keeping the corium pool inside the reactor pressure vessel (RPV). The success of this mitigation strategy requires that the RPV keeps its integrity. It must withstand the heat transfers delivered by the corium pool, *i.e.* it shall not be ablated beyond its rupture point. To ascertain this last point, the heat fluxes coming from the corium pool must be calculated as precisely as possible. The main threats for RPV integrity are, the focusing effect and the rising of an overheated heavy metal layer to the upper part of the corium bath, due to the large heat fluxes these events impose on the RPV. The kinetics of the focusing effect layer height, as well as the heavy metal layer rising, are dictated by the inter-layer thermochemical transfers at play. These are often modelled as 0D integral models in severe accident codes where only inter-layer mass transfers are explicitly taken into account *i.e.* the transitory relocation of metal droplets through the oxide phase is considered as infinitely fast. While this dispersed phase relocation kinetics is fast in comparison with the inter-layer mass transfer, it can have a significant impact, as droplets keep on exchanging mass as they pass through the oxide layer. This was shown in a previous model prototyping work in which the impact of the steel relocation either on top of the pool or as droplets in the oxide was studied. However, this last work is limited by the assumption that the Uranium over Zirconium ratio ($R_{U/Zr}$) is kept uniform among the phases (which is contrary to thermodynamic equilibrium data) and constant in time (preventing the analysis of scenarios with multiple corium relocations from the core). It is important to lift the latter hypothesis as $R_{U/Zr}$ may change with the course of the accident and thermodynamic predictions show that a difference of 33 % between the $R_{U/Zr}$ in the oxide phase and in the metallic phase. It is also typically greater than 1 in the oxide and lower than 1 in the metal phase. In this paper, a model taking into account this difference in $R_{U/Zr}$ between the oxide phase and the metallic phase is derived and tested. It is shown, through numerical simulations, that this difference in $R_{U/Zr}$ can change the stratification transient duration.

KEYWORDS
In-vessel melt Retention, Corium pool Stratification, Multicomponent diffusion, Lumped parameter model, Droplets

1. INTRODUCTION

During the course of a hypothetical severe accident in Pressurized Water Reactors (PWR) a corium may form and relocation in the lower plenum where it interacts with the Reactor Pressure Vessel (RPV). To prevent release of radioactive material outside of the nuclear plant several strategies may be applied. The In-Vessel Retention (IVR) strategy is one of those and aims at maintain the corium inside the RPV [1,2].The main phenomenon jeopardizing the RPV integrity is its ablation by the corium. Therefore, the study of the heat fluxes imposed by the corium to the RPV is of paramount importance in IVR studies. These heat fluxes depend on the corium composition not only due to the residual power density provided by the radioactive element, but also due to the phases that may form based on the corium composition.

The corium is initially composed of a mixture of molten nuclear fuel, molten zircalloy coming from the fuel rod cladding, and steel coming from other structural elements. Based on its actual composition the mixture, may separate into a metallic phase and an oxide phase, as shown by past experimental program on suboxidized corium, namely OECD MASCA 1 and 2 [3]. The heat fluxes imposed by the oxide phase and the metallic phase are different due to the difference in thermal properties. The oxide phase in which the heat releasing elements mostly are, heats up the metallic phase which transfers the heat toward the RPV. The phenomenon called Focusing Effect (FE) induces a heat flux concentration and poses a threat to the RPV integrity. The lower the height of the metallic layer the higher the heat flux concentration up to a certain height. The global composition of the corium evolves during the severe accident due to the adjunction of molten material coming from the core and also due to the incorporation of material coming from the melting of the RPV and internal steel structures. In addition, as there is a residual power inside the corium, its temperature evolves with time. Therefore, the thermodynamic equilibrium evolves over time and so do the corium phases in composition, mass and temperature. When multiple phases are present the composition evolution of each phases occurs via mass transfers which are not instantaneous.

An example of such transfers is provided by MASCA-RCW experiment in which a metallic phase is poured over an oxide layer. A post-mortem cut of MASCA-RCW experiment is available in **Figure 1**. Analyses of MASCA-RCW experiment [4,5,6] demonstrated that a transient relocation of metal droplet was frozen in place and that it provided a valuable insight on the relocation transient.

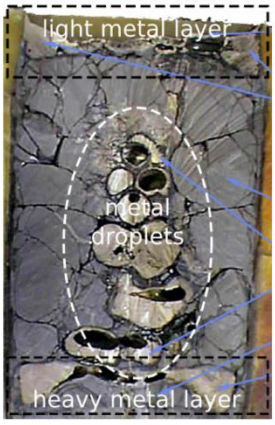

Figure 1. Post mortem cut of MASCA-RCW experiment.

In MASCA-RCW, the metal layer, which was initially over the oxide phase, got enriched in U and Zr elements up to a state in which near the interface, it was heavier than the oxide phase (a typical evolution of the metallic and oxide phase equilibrium densities with the ratio of the steel mass to the oxide mass is given in **Figure 2**), then forming droplets plunging into the oxide phase and creating a heavy-metal phase. It was

shown that mass transfers between the metal droplets and the oxide can change the composition of the droplets and consequently the composition of the metallic layer been formed [7, 8].

As the system evolves and more steel is added to the corium, by means of ablation or material relocation from the core, the equilibrium state of the global corium may change to a metallic phase lighter than the oxide phase.

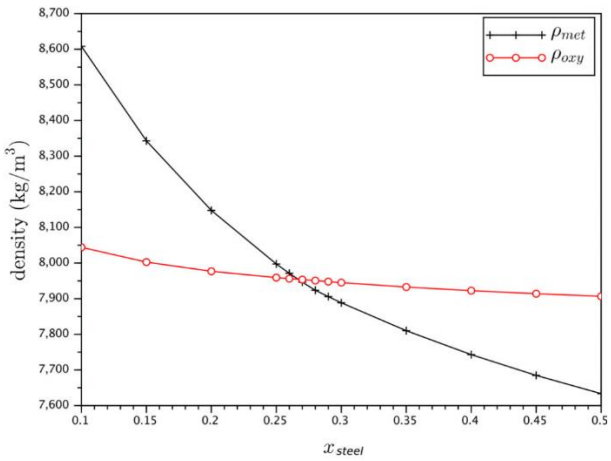

Figure 2. Evolution of the metallic and oxide phase equilibrium densities with x_{steel} the overall ratio of the steel mass to the oxide mass.($T = 3\,000\ K$, $R_{U/Zr}$, and $C_{Zr} = 32\%$)

This transient evolution of the corium pool must be taken into account in the Severe Accidents Codes like PROCOR [9], or ASTEC [10]. Oftentimes the models that are built to take the thermochemical evolution of the corium pool are based on simplifying assumptions, and the dispersed phase that forms during the relocation phase is not explicitly modeled see [5] for PROCOR and [11] for ASTEC. Recently an attempt was made to overcome this limitation. Integral models, which took the dispersed phase into account, were put forward for an isolated droplet [7] then for a full corium pool stratification [8]. The latter model [8] was based on the following set of assumptions:

- **H1.** The metallic dispersed phase is considered as monodispersed and interactions between droplets are neglected, i.e. droplets are considered as isolated;
- **H2.** Convection in the continuous oxide pool bears no effect on the droplets' dynamic;
- **H3.** The two phase, namely Ω_{met} and Ω_{oxy}, are in thermal equilibrium;
- **H4.** The interface between the two phases is considered to be at chemical equilibrium;
- **H5.** The molar ratio U/Zr is uniform between both phases, i.e. $R_{U/Zr} = R^{oxi}_{U/Zr} = R^{met}_{U/Zr}$;
- **H6.** There is no steel elements in the oxide phase, and there no oxygen in the metallic phase.

In previous study [8], it was reported that hypothesis H5 may affect the quantitative results. In the present work, it is proposed to adapt the model to lift hypothesis H5. So first the previous model noted here HOM is described before introducing the modification made which lead to model here noted VAR. This model is then applied to an isolated droplet evolving into an infinite oxide layer as shown in **Figure 3**a. Finally, this model is used to compute the thermochemical evolution of the phases in presence during the stratification of a corium pool, which evolves from an initial oxide pool on top of which metal is added to a corium pool composed of a heavy metal layer beneath an oxide layer, as shown in **Figure 3**b.

The final goal of the present study to improve the accuracy of the codes, like PROCOR [9], simulating the evolution of the corium in the lower head of a PWR RPV, for which the modelling of the transient relocation of the metallic phase first beneath the oxide phase then above the oxide phase, must be improved.

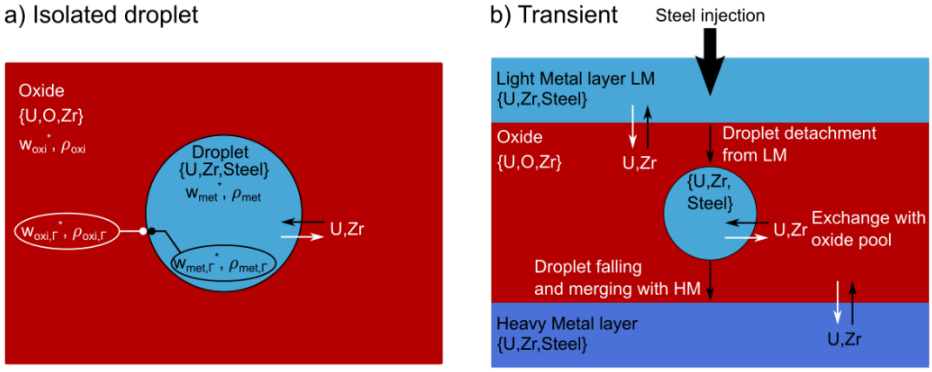

Figure 3: Schematic representation of a) the system considered to establish the model and b) the full transient stratification considered.

2. MODEL DESCRIPTION

As stated before the present model is an improvement of the one presented in [8]. Throughout the present paper the model presented here is referred to as VAR while the previous one is referred to as HOM. Here the model VAR as well as the necessary parts of model HOM needed to understand the present model VAR are presented. This model aims at predicting the thermochemical evolution of a metal droplet passing through an oxide phase of a corium pool while allowing a non-uniform value of $R_{U/Zr}$ across all the phases. The first step taken here is to describe the fundamentals of the previous model before introducing the modifications made. The system considered here is the one shown in **Figure 3a**.

According to hypotheses H5 and H6 of model HOM the initial quaternary system $\{U, Zr, O, Steel\}$ is described in it miscibility gap by two pseudo binary systems $\{(U, Zr), O\}$ and $\{(U, Zr), Steel\}$ in which (U, Zr) is considered as a pseudo component as the relative composition of the Uranium (U) and the Zirconium (Zr) are given by the value of $R_{U/Zr}$.
Applying hypotheses H1 to H6 leads to the following equation system Eq. (1):

$$\begin{cases} \dfrac{d}{dt}\left(w_{oxi}^{O} m_{oxi}\right) = 0 & (a) \\ \dfrac{d}{dt}\left(w_{met}^{Steel} m_{met}\right) = 0 & (b) \\ w_{oxi,\Gamma}^{O}\dot{m}_{\Gamma} + J_{oxi,\Gamma}^{O} S_{\Gamma} = 0 & (c) \\ -w_{met,\Gamma}^{Steel}\dot{m}_{\Gamma} + J_{met,\Gamma}^{Steel} S_{\Gamma} = 0 & (d) \end{cases} \quad (1)$$

In a binary system only two equations sets must be written for each considered element, one to describe the evolution of the element mass conservation within the phase (Eqs. (1a) & (1b)) and one for the transfer from one phase to the other (Eqs. (1c) & (1d)). In both models HOM and VAR (U, Zr) is transferred across Γ, while oxygen stays in the oxide phase, and Steel stays in the metallic phase.

The mass fluxes $J_{*,\Gamma}^{j}$ can be expressed using effective mass transfer coefficient $h_{*,eff}^{j}$ by means of the following equations (Eq. (2)).

$$\begin{cases} J^{O}_{oxi,\Gamma} = -\rho_{oxi,\Gamma} h^{O}_{oxi,eff}\left(w^{O}_{oxi,\Gamma} - w^{O}_{oxi}\right) \\ J^{steel}_{met,\Gamma} = -\rho_{met,\Gamma} h^{Steel}_{met,eff}\left(w^{Steel}_{met,\Gamma} - w^{Steel}_{met}\right) \end{cases} \quad (2)$$

Eqs. (1c), (1d) and (2) give Eq. (3).

$$\rho_{oxi,\Gamma} h^{O}_{oxi,eff}\left(w^{O}_{oxi,\Gamma} - w^{O}_{oxi}\right) w^{Steel}_{met,\Gamma} + \rho_{met,\Gamma} h^{Steel}_{met,eff}\left(w^{Steel}_{met,\Gamma} - w^{Steel}_{met}\right) w^{O}_{oxi,\Gamma} = 0 \quad (3)$$

Following Hypothesis H4, $w^{O}_{oxi,\Gamma}$ and $w^{Steel}_{met,\Gamma}$ are linked by the fact that they are located on the same tie-line meaning that there exists a thermodynamic function, here noted f_1, so that $f_1 : w^{O}_{oxi,\mathrm{eq}} \mapsto w^{Steel}_{met,eq} = w^{O}_{oxi,\mathrm{eq}}$. f_1 is called a thermodynamic closure. Then solving Eq. (3) is equivalent to solving Eq. (4).

$$\rho_{oxi,\Gamma} h^{O}_{oxi,eff}\left(w^{O}_{oxi,\Gamma} - w^{O}_{oxi}\right) f_1\left(w^{O}_{oxi,\Gamma}\right) + \rho_{met,\Gamma} h^{Steel}_{met,eff}\left(f_1\left(w^{O}_{oxi,\Gamma}\right) - w^{Steel}_{met}\right) w^{O}_{oxi,\Gamma} = 0 \quad (4)$$

f_1 is obtained using thermodynamic equilibria computed using OpenCalphad (OC) [12,13], and the thermodynamic database NUCLEA 17 [14]. H5 hypothesis is not consistent with the thermodynamic For instance in **Figure 4**, $R^{oxi}_{U/Zr}$ and $R^{met}_{U/Zr}$ are plotted for $R_{U/Zr} = 1.2$, $\mathrm{C_{Zr}} \in [0.3,0.9]$ and $\mathrm{x_{steel}} \in [5.10^{-3}, 1]$. A difference of 20 % to 30 % between $R^{oxi}_{U/Zr}$ and $R^{met}_{U/Zr}$ is observed. This entails a preferential transfer of zirconium for the oxide phase to the metallic phase. Lifting hypothesis H5 is the basis for model VAR.

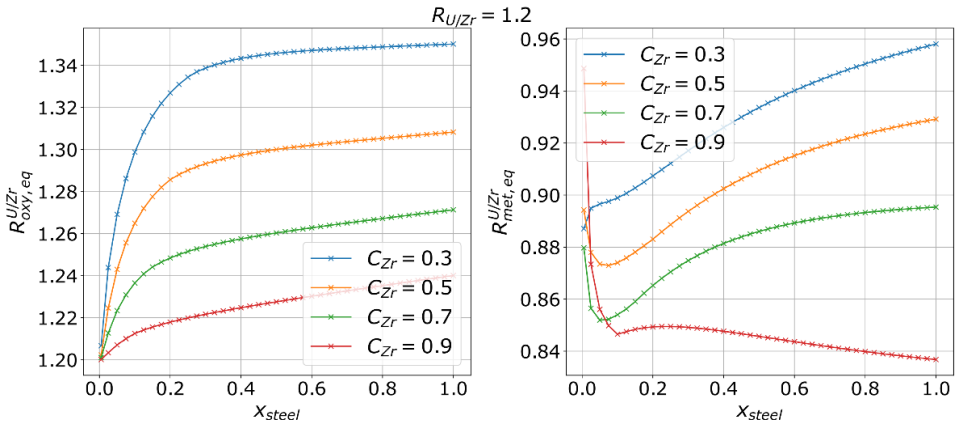

Figure 4. $R^{oxi}_{U/Zr}$ & $R^{met}_{U/Zr}$ at equilibrium for an overall $R_{U/Zr} = 1.2$, $C_{Zr} \in \{0.3, 0.5, 0.7, 0.9\}$, $x_{Steel} \in [5.10^{-3}, 1]$.

Lifting H5 means removing a constitutive equation and adding a degree of freedom. The phases are modeled in model VAR as two ternary systems: $\{U, Zr, O\}$ for the oxide phase and $\{U, Zr, Steel\}$ for the metallic phase. To close the system it was chosen to follow the Zr concentration[1]. Mass conservation leads to the following Eq. (5).

$$\frac{d}{dt}\left(w^{Zr}_{*} m_{*}\right) + J^{Zr}_{*,\Gamma} S_{\Gamma} + w^{Zr}_{*} \dot{m}_{\Gamma} = 0 \quad (5)$$

The same equation should be written for the Uranium and the surface mass fluxes of Zr and U should be written as follows Eq. (6).

$$\begin{cases} J^{U}_{*,\Gamma} = -\rho_{*,\Gamma} h^{U}_{*,eff}\left(w^{U}_{*,\Gamma} - w^{U}_{*}\right) \\ J^{Zr}_{*,\Gamma} = -\rho_{*,\Gamma} h^{Zr}_{*,eff}\left(w^{Zr}_{*,\Gamma} - w^{Zr}_{*}\right) \end{cases} \quad (6)$$

[1] U mass concentration could have been chosen.

However, following a step by step strategy it was chosen to introduce a new hypothesis to prevent the introduction of new unknown parameters. This hypothesis is the following:

H7. The mass transfer coefficients are equals in all the phases, *i.e.* $h^{U}_{*,eff} = h^{Zr}_{*,eff}$. Due to the Sherwood number definition (*i.e.* for $j \in \{U, Zr\}, Sh_j = \frac{h_j d}{D_j}$) H7 implies that the mass diffusion coefficients of both the Uranium and the Zirconium are equal, $D^{U}_{*} = D^{Zr}_{*}$.

Hypothesis H7 links $J^{U}_{*,\Gamma}$ and $J^{Zr}_{*,\Gamma}$ according to Eq. (7).

$$J^{U}_{*,\Gamma} = \beta_* J^{Zr}_{*,\Gamma} \text{ with } \beta_* = \frac{w^{U}_{*,\Gamma} - w^{U}_{*}}{w^{Zr}_{*,\Gamma} - w^{Zr}_{*}} = \frac{\Delta w^{U}_{*}}{\Delta w^{Zr}_{*}} \tag{7}$$

This hypothesis expresses the fact that the more $|\Delta w^{U}_{*}| > |\Delta w^{Zr}_{*}|$, the more uranium diffuses. This means that among the two main phenomena concurring during mass transfer that are the resistance to transfer, represented by $h^{U}_{*,eff}$ & $h^{Zr}_{*,eff}$, and the driving force, represented by $|\Delta w^{U}_{*}|$ & $|\Delta w^{Zr}_{*}|$, the one that impacts the mass transfers evolution the most is the driving force evolution. This is a first step to dissociate U and Zr mass transfers.

The conservation of mass written as: $\Sigma_j J^{j}_{*,\Gamma} = 0$ used in conjunction to Eq. (2) leads to the following Eq. (8) which is valid in both phases.

$$J^{O}_{*,\Gamma} = (1 + \beta_*) J^{Zr}_{*,\Gamma} \tag{8}$$

Eqs. (1) still holds as they stem from H6 which is maintained. Therefore, using Eqs. (1c) & (1d) leads to Eq. (9).

$$J^{Zr}_{oxi,\Gamma} S_\Gamma = -\frac{\dot{m}_\Gamma w^{O}_{oxy,\Gamma}}{1+\beta_{oxi}} \text{ and } J^{Zr}_{met,\Gamma} S_\Gamma = -\frac{\dot{m}_\Gamma w^{Steel}_{met,\Gamma}}{1+\beta_{met}} \tag{9}$$

Together Eqs. (5) & (9) yield the following system of equation Eq. (10).

$$\begin{cases} \frac{d}{dt}\left(w^{Zr}_{oxi} m_{oxi}\right) = -\dot{m}_\Gamma \left[\frac{w^{O}_{oxi,\Gamma}}{1+\beta_{oxi}} + w^{Zr}_{oxi,\Gamma}\right] = -\dot{m}_\Gamma w^{Zr}_{oxi,\mathrm{MT}} \quad (a) \\ \frac{d}{dt}\left(w^{Zr}_{met} m_{met}\right) = -\dot{m}_\Gamma \left[\frac{w^{Steel}_{met,\Gamma}}{1+\beta_{met}} + w^{Zr}_{met,\Gamma}\right] = +\dot{m}_\Gamma w^{Zr}_{met,\mathrm{MT}} \quad (b) \end{cases}$$
$$\text{with} \begin{cases} w^{Zr}_{oxi,\mathrm{MT}} = \frac{w^{O}_{oxi,\Gamma}}{1+\beta_{oxi}} + w^{Zr}_{oxi,\Gamma} \\ w^{Zr}_{met,\mathrm{MT}} = \frac{w^{Steel}_{met,\Gamma}}{1+\beta_{met}} + w^{Zr}_{met,\Gamma} \end{cases} \tag{10}$$

Mass is conserved in the global system. Therefore, the two equations of the preceding system Eq. (10) convey the same information as $\frac{d}{dt}\left(w^{Zr}_{oxi} m_{oxi}\right) = -\frac{d}{dt}\left(w^{Zr}_{met} m_{met}\right)$. Practically this means that only one of the two equations needs to be solved, Eq. (10a) was chosen.

While Eq. (4) and the first thermodynamic closure (*i.e.* f_1) still hold as they stem from hypothesis H6, lifting hypothesis H5 prompts the need of two knew thermodynamic closures f_2 and f_3, *cf.* Eq. (11). f_2 is used for Eq. (10a) while f_3 is required to compute $\rho_{oxi,\Gamma}$ and $\rho_{met,\Gamma}$ is Eq. (4).

$$\begin{cases} w^{Zr}_{oxi,\Gamma} = f_2\left(w^{O}_{oxi,\Gamma}\right) \quad (a) \\ w^{Zr}_{met,\Gamma} = f_3\left(w^{O}_{oxi,\Gamma}\right) \quad (b) \end{cases} \tag{11}$$

For model HOM f_1 was the only thermodynamic closure that was required. However, as previous hypothesis H5 is replaced by H7, mass concentrations of both zirconium and uranium evolve independently. Therefore at equilibrium (*i.e.* at the interface) both $w_{oxi,eq}^{Zr}$ and $w_{met,eq}^{Zr}$ must be linked to $w_{oxi,eq}^{O}$. In the end, three thermodynamic closures are required.

$$\begin{cases} f_1 : w_{oxi,\mathrm{eq}}^{O} \mapsto w_{met,eq}^{Steel} = f_1\left(w_{oxi,\mathrm{eq}}^{O}\right) \\ f_2 : w_{oxi,\mathrm{eq}}^{O} \mapsto w_{oxi,eq}^{Zr} = f_2\left(w_{oxi,eq}^{O}\right) \\ f_3 : w_{oxi,\mathrm{eq}}^{O} \mapsto w_{met,\mathrm{eq}}^{Zr} = f_3\left(w_{oxi,eq}^{O}\right) \end{cases} \tag{12}$$

As for the HOM model, the starting point for constructing these closures are thermodynamic equilibrium calculations (made with OpenCalphad [12,13] and the NUCLEA database [14]) to determine the tie-lines in the range of composition of the liquid miscibility gap. Two important points should be made regarding this construction. First, for the sake of simplicity, it is assumed that f_1 to f_3 are associated with the tie-lines determined by $R_{U/Zr}, C_{Zr}$ values of the overall composition of the corium pool. Second, it should be noted that the thermodynamic equilibrium calculations made with OpenCalphad and the NUCLEA database do not take the hypotheses of the model into account. Accordingly, the mass of oxygen (resp. steel) in the metallic (resp. oxide) phase is not strictly zero and hypothesis H6 is not strictly enforced. For the model consistency, closures obtained directly from the thermodynamic calculations have to be modified to take hypothesis H6 into account. To do so, the overall equilibrium is computed using mass conservation Eq. (13):

$$m_{tot} = m_{oxi} + m_{met} = \frac{m_{oxi}^{O}}{w_{oxi}^{O}} + \frac{m_{met}^{Steel}}{w_{met}^{Steel}} \tag{13}$$

Then Hypothesis H6 is applied to Eq. (13) leading to the following Eq. (14), as under H6 $m_{oxi}^{O} = m^{O}$ & $m_{met}^{Steel} = m^{Steel}$.

$$m_{tot} = m_{oxi} + m_{met} = \frac{m^{O}}{w_{oxi}^{O}} + \frac{m^{Steel}}{w_{met}^{Steel}} \Leftrightarrow w_{met}^{Steel} m^{O} + w_{oxi}^{O} m^{Steel} - w_{met}^{Steel} w_{oxi}^{O} m_{tot} = 0 \tag{14}$$

The latter equation is always valid even at equilibrium, and at equilibrium all the phases are homogeneous and their composition equal to the equilibrium one. From there it is possible to obtain a value of w_{oxi}^{O} consistent with Hypothesis H6 by solving Eq. (14) while considering f_1 closure, which is equivalent to solve Eq. (15). This value of w_{oxi}^{O} is noted $\widetilde{w}_{oxi,\mathrm{eq}}^{O}$.

$$f_1\left(w_{oxi,\mathrm{eq}}^{O}\right) m^{O} + w_{oxi}^{O} m^{Steel} - f_1\left(w_{oxi,\mathrm{eq}}^{O}\right) w_{oxi}^{O} m_{tot} = 0 \tag{15}$$

Likewise, the equilibrium mass fraction of steel in the metal phase consistent with H6 ($\widetilde{w}_{met,\mathrm{eq}}^{Steel}$) is determined by using f_1, namely $\widetilde{w}_{met,\mathrm{eq}}^{Steel} = f_1\left(\widetilde{w}_{oxi,\mathrm{eq}}^{O}\right)$. These are used in Eq. (13) to determine $\widetilde{m}_{*,eq}$. f_2 is used to determined $\widetilde{w}_{oxi,\mathrm{eq}}^{Zr} = f_2\left(\widetilde{w}_{oxi,\mathrm{eq}}^{O}\right)$. To maintain the consistency $\widetilde{w}_{met,\mathrm{eq}}^{Zr}$ is determined purely from mass conservation and not from thermodynamic equilibrium[2], Eq. (16).

$$m_{met,eq}^{Zr} = m_{Zr} - m_{oxi,eq}^{Zr}$$

$$\Leftrightarrow \widetilde{w}_{met,\mathrm{eq}}^{Zr} = \frac{m_{Zr} - \widetilde{w}_{oxi,\mathrm{eq}}^{Zr} m_{oxi,eq}}{m_{met,eq}} = \frac{m_{Zr} - f_2\left(\widetilde{w}_{oxi,\mathrm{eq}}^{O}\right) m_{oxi,eq}}{\dfrac{m^{Steel}}{f_1\left(\widetilde{w}_{oxi,\mathrm{eq}}^{O}\right)}} = f_3\left(\widetilde{w}_{oxi,\mathrm{eq}}^{O}\right) \tag{16}$$

The value of the mass transfer coefficients required for the calculations (*cf.* Eqs. (2)-(4)) is obtained from a heat-mass transfer analogy. To use it a Sherwood number must be computed. The same correlations are considered here as in [8], namely Juncu2010 [15] and Wegener2014 [16]. These correlations require a

[2] Meaning that *stricto sensus* only f_1 and f_2 are thermodynamic closures.

vertical velocity for the droplets. The vertical velocity is determined the same way for both models, using a 1D vertical momentum, for more details see [8].

3. COMPARISON BETWEEN MODELS HOM AND VAR

3.1. Thermodynamic Accuracy

First, to assess the impact of hypothesis H6 on equilibrium variables of the two phases, a calculation was performed with the parameters values summed up in Table I in the configuration described in **Figure 3**a. The relative deviations of the phases' mass densities at steady-state are reported in Table II, while the relative deviation of Zr & U equilibrium mass fractions for the two phases are reported in Table II. Tables II & III show that model VAR outperform the previous model HOM in terms of accuracy with respect to the thermodynamic values. Model VAR is at the same time accurate and consistent. The deviations are deemed acceptable compared to other models, see [17].

Table I. Values of important parameters used for the calculations performed to compare the present model to the previous one.

$R_{U/Zr}$	C_{Zr}	x_{Steel}	r_0	D_{oxi}	Sh_{oxi}	D_{met}	Sh_{met}
1.2	0.5	0.1	$10^{-2}\ m$	$5.10^{-9}\ m^2.s^{-1}$	2.10^3	$5.10^{-9}\ m^2.s^{-1}$	$Juncu2010$

Table II. Relative deviation of the mass density (between the one obtained with the model and the one obtained considering the thermodynamic equilibrium computed with OpenCalphad and NUCLEA 17) for the two phases.

	$\varepsilon(\rho_{oxi,eq})[\%]$	$\varepsilon(\rho_{met,eq})[\%]$
HOM	-1.144	1.952
VAR	-0.583	-1.215

Table III. Relative deviation of the mass fraction of both Zr and U (between the one obtained with the model and the one obtained considering the thermodynamic equilibrium computed with OpenCalphad and NUCLEA 17) for the two phases.

	$\lvert\varepsilon(w^{Zr}_{oxi,eq})\rvert[\%]$	$\lvert\varepsilon(w^{Zr}_{met,eq})\rvert[\%]$	$\lvert\varepsilon(w^{U}_{oxi,eq})\rvert[\%]$	$\lvert\varepsilon(w^{U}_{met,eq})\rvert[\%]$
HOM	4.89	25	0.54	2.93
VAR	$8.27\ 10^{-6}$	0.29	0.94	7.91

3.2. Parametric study w.r.t. x_{Steel}, C_{Zr} and r_0

The parametrized study presented here aims at analyzing the effect of lifting the hypothesis of a homogeneous value of $R_{U/Zr}$ across all phases for an isolated droplet. The parameters which impact are studied here are, x_{Steel}, C_{Zr} and $r_0 = d/2$ [7]. The system considered is the one represented in **Figure 3**a.

The basis values of the parameters are the ones gathered in Table I. The variation of C_{Zr} did not show any significant variation. Therefore, the focus is here on the effect of x_{Steel} and r_0.

Figure 5 gives the time evolution of mass fractions of Zr and U among the two phases for model HOM assuming an homogeneous value of $R_{U/Zr}$, figured as plain lines, and the model VAR, figured by dashed lines. **Figure 5** shows that the evolution of the model does not affect the tendencies on mass transfer kinetics. The lower the x_{Steel} the longer the transient (the same tendency is observed

for C_{Zr}).This can be understood considering that the lower the x_{Steel} the lower the mass fractions of transferring elements (Zr & U) the lower the transfer driving force. Moreover, in the metal phase model VAR predicts a higher Zr mass fraction and a lower U mass fraction. In **Figure 4**[3], for all values of x_{Steel}, $R_{U/Zr}^{met} < R_{U/Zr}^{oxi}$, $R_{U/Zr}^{met} < 1$, $R_{U/Zr}^{oxi} > 1$. Therefore, these results are coherent with thermodynamic equilibrium computed using OC, which prompted for improvement of model HOM.

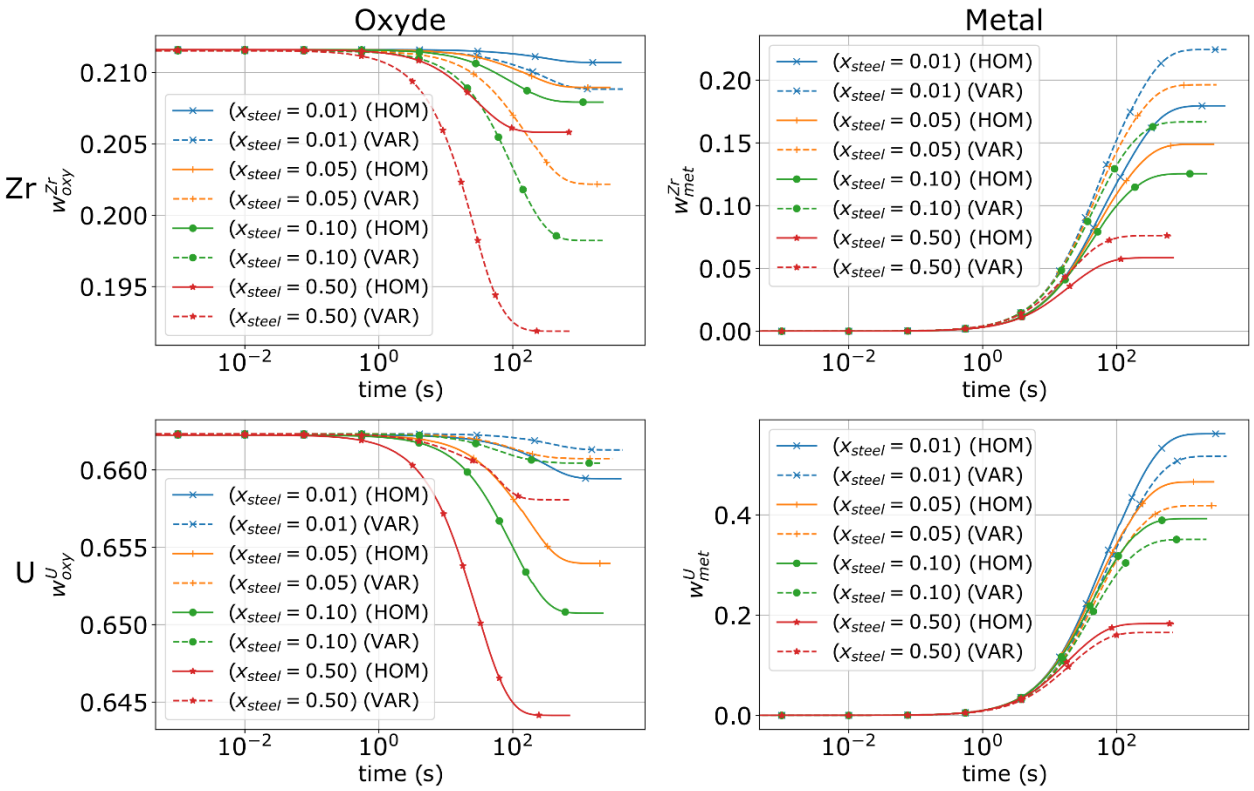

Figure 5. Time evolution of the mass fraction of Zr and U, in both the oxide and the metal phase with both models HOM and VAR for the mass transfers and considering $x_{Steel} \in \{0.01, 0.05, 0.10, 0.50\}$.

3.3. Application to a stratification transient

To assess the effect of change of model from HOM to VAR on a more realistic case a stratification transient was computed. The system considered and its evolution are represented in **Figure 3**b. For this case in addition to the thermochemical evolution of a metal droplet passing through an oxide pool the evolutions of a light metal layer on top of the pool and a heavy metal layer beneath the pool are also considered. The droplets detachment and coalescence with a metal layer are also modelled. To do so, the same procedure as in [8] was used, *i.e.* it considered that the droplets were generated by Rayleigh-Taylor instability.
A density threshold was considered for the onset of the instability, which is noted $\Delta\rho$. Droplets were created when the interface density of a metal phase was either higher than the oxide for the light metal phase, or lower for the heavy metal one. To determine the total mass of created droplets $\tilde{m}_i$ from metallic phase i, a

[3] Error! Reference source not found. illustrates the thermodynamic equilibrium by showing the evolution of $R_{U/Zr}^{*}$ with x_{Steel} and $R_{U/Zr} = 1.2$ and multiple values of C_{Zr}, coherent with Table I.

concentration profile constant by part was assumed in the considered metallic phase. This leads to the following Eq. (17):

$$\widetilde{m}_i = \frac{w_i^{Steel} - w_{i,\infty}^{Steel}}{w_{i,\Gamma_i}^{Steel} - w_{i,\infty}^{Steel}} m_i \tag{17}$$

The time discretization of the coupled equations is the same here as described in [8] except for a specific treatment associated with Eq. (17) in order to avoid any negative mass. Indeed, as the evolutions of the U and Zr mass fraction are now distinct, the model could compute a mass of Zr pull out of a metallic layer greater than the actual Zr mass of the metallic phase. To avoid this, $\widetilde{m}_i$ is limited so that the quantity of Zr entrained is not greater than the available mass in the metallic phase. From t_n and on a time step Δt, the detached mass of Zr must be lower than the mass of Zr at Δt minus the mass transferred between the oxide phase and the metallic phase $\left(\dot{m}_\Gamma w_{oxi,MT}^{Zr} \Delta t\right)$. This is given by Eq. (18).

$$\widetilde{m}_i < \frac{w_i^{Zr} m_i(t_n) - \dot{m}_\Gamma w_{oxy,MT}^{Zr} \Delta t}{w_{i,\Gamma_i}^{Zr}} \tag{18}$$

A calculation was performed using the parameters given in Table IV. It was considered that $D_{oxi} = D_{met} = 5.10^{-9}\, m^2.s^{-1}$ to stay coherent with study [8], on which the present study is based, as no new information are available on this subject. Initially the corium pool was composed of only an oxide pool. Then steel is added on top, as showed in **Figure 6**. These parameters were chosen to achieve the formation of an heavy metal layer as [8] reports that this stratification transient leads more regular droplets detachments contrary to the stratification inversion for which the entire heavy metal layer tends to rise at once through the oxide layer to reach the light metal layer.

Table IV. Values of important parameters used for the calculations performed to compare models HOM and VAR on a full transient calculation.

$R_{U/Zr}$	C_{Zr}	x_{Steel}	r_0	D_{oxi}	Sh_{oxi}	D_{met}	Sh_{met}	$\Delta\rho$
1.2	0.3	0.1	$10^{-2}\, m$	$5.10^{-9}\, m^2.s^{-1}$	4.10^4	$5.10^{-9}\, m^2.s^{-1}$	$Wegener2014$	$10 kg.m^{-3}$

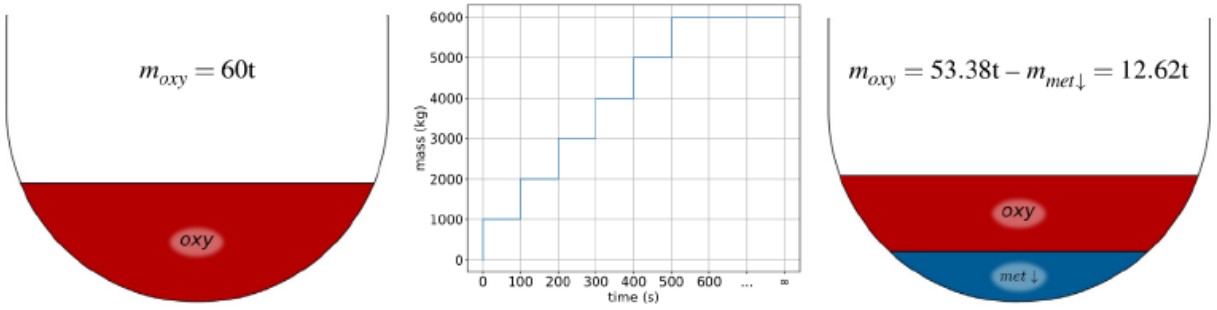

(a) Initial state. (b) Accumulated mass of molten steel added to the pool as a function of time. (c) Expected steady-state.

Figure 6. Description of the calculation of the transient formation of a heavy metal layer carried out to test and both models HOM and VAR. $R_{U/Zr} = 1.2$, $C_{Zr} = 0.3$, $T = 3\,000\, K$.

The temporal evolution of mass of the metallic phases and the population of droplets are shown in **Figure 7** for model HOM (in plain lines) and model VAR (in dashed lines). Likewise the temporal evolution of the metallic phases mass fractions are available in **Figure 8**.

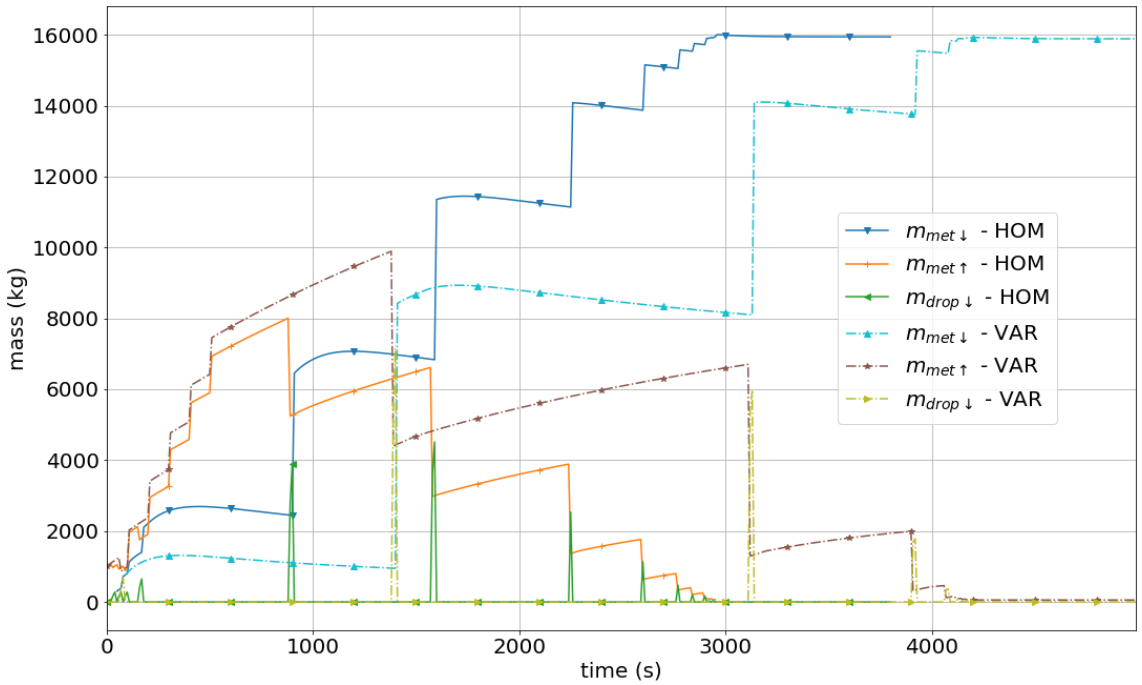

Figure 7. Time evolution of the masses of, the light metal layer $(m_{met\downarrow})$, the heavy metal layer $(m_{met\uparrow})$, the droplets relocating downward $(m_{drop\downarrow})$, for model HOM and model VAR.

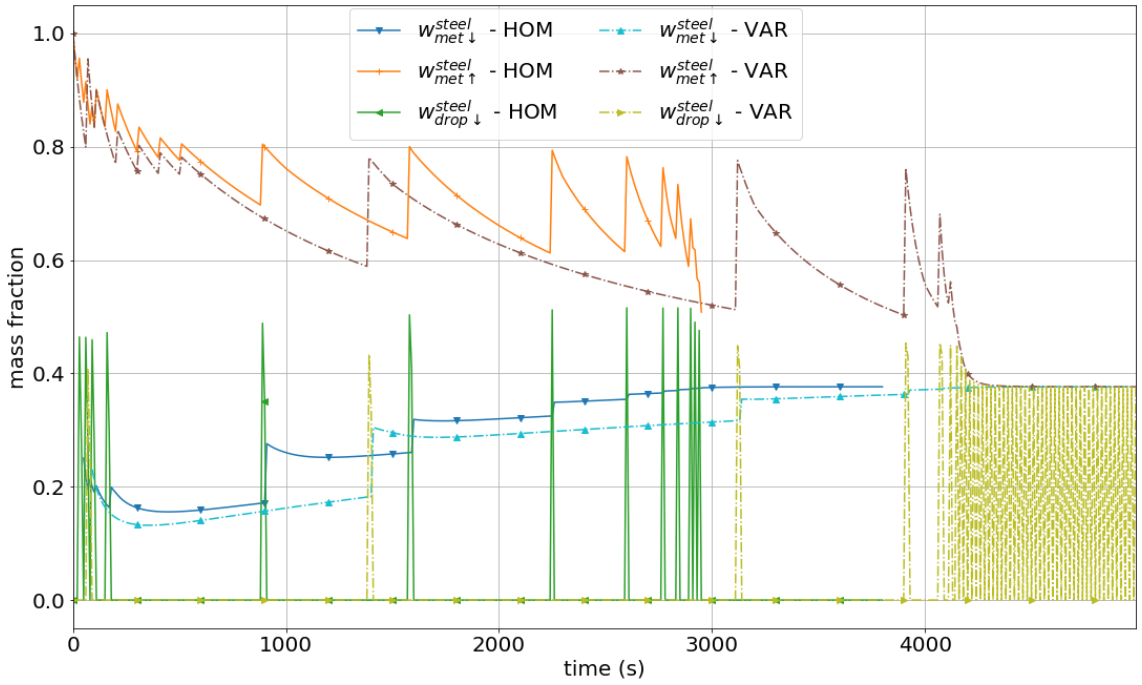

Figure 8. Time evolution of steel mass fraction, the light metal layer $(m_{met\downarrow})$, the heavy metal layer $(m_{met\uparrow})$, the droplets relocating downward $(m_{drop\downarrow})$ for model HOM and model VAR.

For both models HOM and VAR the same global tendencies are witnessed. The formation of the heavy metal layer is discontinuous as it is due to the droplets forming via Rayleigh-Taylor instability. With model VAR the transient is longer. This is explained by the fact that Zr transfer is increased with respect to U transfer and as $\rho_{Zr} < \rho_U$ it takes more time for the light metal layer to reach Rayleigh-Taylor onset threshold. Before 3 000 s model VAR predicts less relocation events than model HOM. This leads to bigger changes in light

metal layer mass. For both models, $w_{met\downarrow}^{Steel}$ is the same at the end of the transient. This is coherent with the fact that the equations dictating the evolution of w_{met}^{Steel} are the same for both models.

The model presented here was further used in a benchmark based on MASCA experimental data [17] and compared well with the other participants. It showed to be real improvement on PROCOR results.

4. CONCLUSIONS

In this research project an incremental strategy is pursued. Therefore, from observation on MASCA-RCW experiment a simpler approach was proposed, then a more detailed one was put forward for a single droplet, then for a full stratification transient, and finally in the present paper a limiting hypothesis was lifted. The next step is to integrate this model with the other models of the PROCOR application.

A new thermochemical model was derived to compute the thermochemical evolution of a corium pool in the miscibility gap. Its main feature is to lift the previously made hypothesis of a homogeneous value for $R_{U/Zr}$. This hypothesis was deemed limiting, as it was not coherent with thermodynamic calculations. This model relies on thermodynamic closure, which had to be reworked to comply with the assumptions of the model. For a single droplet evolving inside an infinite oxide layer, it was shown that this model (VAR) gives results both coherent with the thermodynamic and the previous model (HOM). The new model (VAR) which is closer to the thermodynamic results, induces a modification of the layers composition of up to 30 % (*cf.* **Figure 5** w_{met}^{Zr}, $x_{Steel} = 0.01$).

To assess the effect of the new model (VAR) on a more realistic transient, a calculation was performed to simulate the creation of a heavy metal layer from an oxide layer on top of which steel is poured. The results show that the new model (VAR) is coherent with the thermodynamic as well as with the previous model (HOM). The results also show that the use of this new model (VAR) can induce substantial changes in the light metal layer mass evolution as well as in the transient duration.
The next step is to interface this model in the frame of the PROCOR application dedicated to lower head corium simulations and to use it for comprehensive computations taking into account actual inputs from degradation codes as well as the melting of the vessel.

NOMENCLATURE

Latin letters		
C_{Zr}	Zr molar oxidation index	-
D	Mass diffusion coefficient	$m^2.s^{-1}$
d	Droplet diameter	m
f_i	Thermodynamic closure i	-
$h_{*,\Gamma}^{c}$	Effective mass transfer coefficient relative to component c at interface Γ for phase $*$	$m.s^{-1}$
J^j	Mass flux of component j	$kg.m^{-2}.s^{-1}$
m_*	Mass of Ω_*	kg
$\dot{m}_{*,\Gamma}$	Total mass flowrate through Γ (positive when leaving Ω_*)	$kg.s^{-1}$
$\widetilde{m}_i$	Mass of metallic phase i detached as droplets	kg
$R_{U/Zr}^{*}$	U/Zr molar ratio, $R_{U/Zr}$ refer to the overall ratio	-
S_Γ	Surface of Γ	m^2
Sh_j	Sherwood number	-
U	Uranium	-
v	Velocity (considered axial)	$m.s^{-1}$

V	Volume	m^3
w_*^j	Mass fraction of component j in phase $*$	-
x_{Steel}	Global mass ratio between steel and oxide	-
Zr	Zirconium	-

Greek letters		
Γ	Interface between the phases	-
$\Delta\rho$	Density threshold for Rayleigh-Taylor onset	$kg.m^{-3}$
Ω_*	Spatial domain corresponding to phase $*$	-
ρ	Density	$kg.m^{-3}$

Subscripts & superscripts	
$drop$	Refers to the droplets
met	Metal phase (↓: heavy layer; ↑: light metal)
oxi	Oxide phase

Glossary	
FE	Focusing Effect
HOM	Model presented in [8]
PWR	Pressurized Water Reactor
RPV	Reactor Pressure Vessel
VAR	Refers to the presented model as opposed to HOM

ACKNOWLEDGMENTS

This work was funded in the framework of the PROCOR platform development by CEA, EDF and Framatome.

REFERENCES

1. R. E. Henry, H. K. Fauske, "External cooling of a reactor vessel under severe accident conditions," *Nuclear Engineering and Design*, **139** (1), pp.31 – 43 (1993).
2. H. Tuomisto and T. Theofanous, "A consistent approach to severe accident management," *Nuclear Engineering and Design*, **148** (2), pp.171-183 (1994).
3. D. F. Tsurikov, V. F. Strizhov, S. V. Bechta, V. N. Zagriazkin and N. P. Kiselev, "Main results of MASCA1 and 2 projects", *Tech. rep., RRC*, **425** Kurchatov Institute (2007).
4. G. Ratel, F. Deffort, K. Froment, B. Tourniaire and J. M. Seiler, "Considerations on mass transfer kinetics for layer inversion and layer oxidation: from MASCA program to the reactor situation," *Proc. of MASCA-2 Seminar,* Cadarache, France (2007).
5. R. Le Tellier, L. Saas and S. Bajard, "Transient Stratification Modelling of a Corium Pool in a LWR Vessel Lower Head," *Nuclear Engineering and Design*, **287**, pp.68–77 (2015).
6. R. Le Tellier, "Mass Transfer Induced Rayleigh-Taylor Instabilities between Two Immiscible Liquids: The Unique Case of Corium," *Proceedings. of 9th International Conference on Fluid Flow, Heat and Mass Transfer (FFHMT'22),* june (2022), doi: https://doi.org/10.11159/ffhmt22.148
7. R. Le Tellier, "Mass transfer between a continuous oxide phase (U-O-Zr) and a steel droplet at liquid state: Potential impact on corium pool behaviour during in-vessel melt retention," *Nuclear Engineering and Design*, **385**, 111525 (2021).

8. R. Le Tellier, "A lumped parameter model of continuous/dispersed phases mass transfer for simulating in-vessel corium stratification transients," *Annals of Nuclear Energy*, **181**, 109539. (2023), doi: https://doi.org/10.1016/j.anucene.2022.109539
9. R. Le Tellier, L. Saas and F. Payot, "Phenomenological analyses of corium propagation in LWRs: The PROCOR software platform," *Proceedings of the 7th European Review Meeting on Severe Accident Research ERMSAR-2015*, (2015).
10. P. Chatelard, N. Reinke, S. Arndt, S. Belon, L. Cantrel, L. Carénini, K. Chevalier-Jabet, F. Cousin, J. Eckel, F. Jacq, C. Marchetto, C. Mun, L. Piar, "ASTEC V2 severe accident integral code main features, current V2.0 modelling status, perspectives", *Nuclear Engineering and Design*, **272**, p.119-135 (2014).
11. L. Carénini and F. Fichot, "Evaluation of the kinetics of molten pool stratification in case of In-Vessel Melt Retention Strategy," *Proceedings of 26th International Conference on Nuclear Engineering ICONE 26*, London, England, (2018).
12. B. Sundman, U. R. Kattner, M. Palumbo and S. G. Fries, "OpenCalphad—A free thermodynamic software," *Integrating Materials and Manufacturing Innovation*, **4**(1), (2015).
13. B. Sundman, U. R. Kattner, C. Sigli, M. Stratmann, R. Le Tellier, M. Palumbo and S. G. Fries, "The OpenCalphad thermodynamic software interface," *Computational Materials Science*, **125**, pp.188–196, (2016).
14. S. Bakardjieva, M. Barrachin, S. Bechta, D. Bottomley, L. Brissoneau, B. Cheynet, E. Fischer, C. Journeau, M. Kiselova, L. Mezentseva, P. Piluso and T. Wiss, "Improvement of the European thermodynamic database NUCLEA," *Progress in Nuclear Energy*, **52**(1), pp.84–96, (2010).
15. G. Juncu, "A numerical study of the unsteady heat/mass transfer inside a circulating sphere," *International Journal of Heat and Mass Transfer*, **53**, pp. 3006–3012 (2010).
16. M. Wegener, N. Paul and M. Kraume, "Fluid dynamics and mass transfer at single droplet in liquid/liquid systems," *International Journal of Heat and Mass Transfer*, **71**, pp.475–495, (2014).
17. R. Le Tellier, L. Carénini, F. Fichot, R. Gencheva, P. Groudev, I. Melnikov, M. Golubev and A. Filippov, "In-vessel corium thermochemistry benchmark based on masca experimental data," *Proceedings of the 11th European Review Meeting on Severe Accident Research Conference ERMSAR 2024*, KTH, Stockholm, Sweden, May 13-16, (2024).

Improvement of thermochemical corium stratification accounting for uranium and zirconium composition difference in metallic and oxide phases

J. Mativet, R. Le Tellier, and A. Lecoanet

CEA, DES, IRESNE, DTN, Cadarache

F-13108 Saint Paul-lez-Durance, France

Context

Nuclear Severe Accident with melt relocation in the lower head

- **In-Vessel Melt Retention → corium pool time evolution**
  - 1st order effect on thermal flux to the vessel
- General observations (equilibrium):
  - A miscibility gap exists in the U-O-Zr-Steel phase diagram (Salay 2005) & (Nandan 2020)
  - Corium pool stratification into a metallic and an oxide phase
  - Phases density evolve with composition (Le Tellier 2015)
  - Stratification order can change with time due to overall corium pool changes due to:
    - Incorporation of material ariving from the core
    - Incorporation of steel from the vessel, melted by the corium pool
  - Stratification kinetics are influenced by :
    - **The mass transfers among the pool phases**
    - The refractory crust behavior (Stable or not ?→ **put aside**)

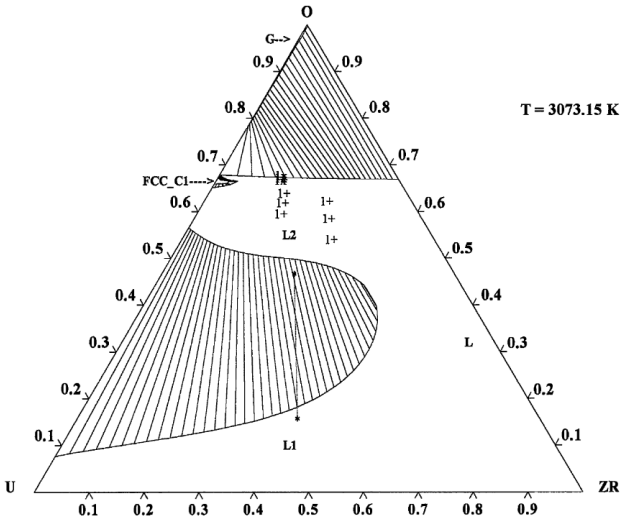

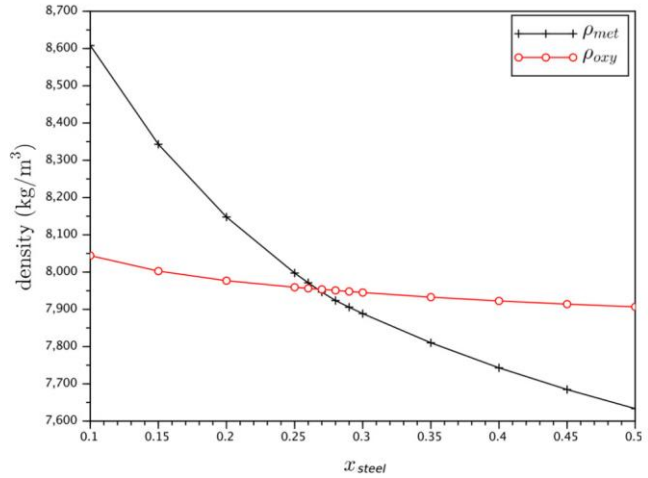

Context transient stratification

Observation during stratification transient:

- Types of transients :
  - Light Metal → Heavy Metal (1)
  - Heavy Metal → Light Metal (2)

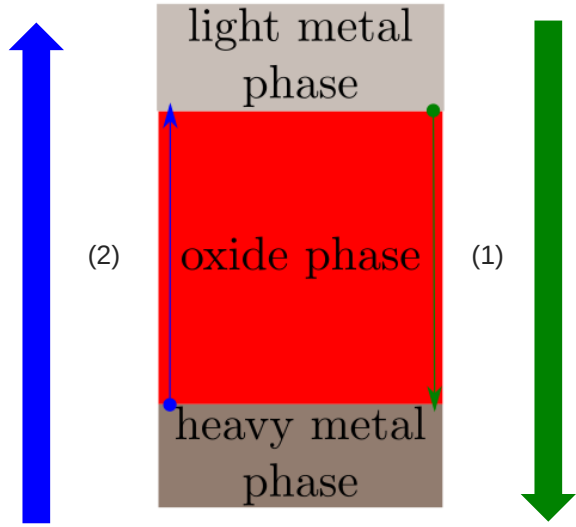

- How does the metallic phase moves during transient stratification ?
  - In bulk for smaller geometry (MASCA (Tsurikov 2007))
  - As separated droplets from MASCA-RCW (Asmolov 2003)
    - Rayleigh Taylor instability
      - Actual geometry larger → **Relocation as droplets is more likely**

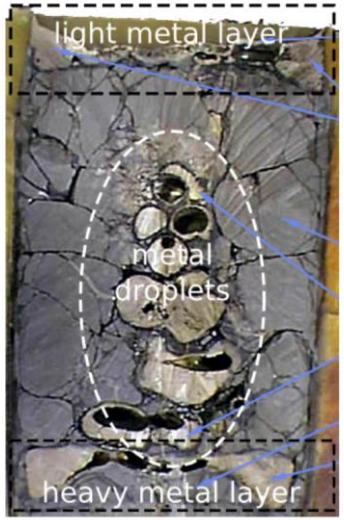

Context – modelling in SA codes

From MASCA—RCW (Asmolov 2003):

- Continuous modelling (Le Tellier 2015):
  - A basic model is implemented in PROCOR, MAAP, ASTEC (for which equilibrium is computed 2by2):
    - Based on Salay Fichot model (Salay 2005)
    - Mass fraction of U given by

$$f_U^{oxy}(t) = f_{U,eq}^{oxy} - \left(f_{U,eq}^{oxy} - f_U^{oxy}(0)\right) e^{-\frac{t}{\tau}} \; with \; \tau = \frac{V^{oxy}}{h_m S^{int}}$$

    - h_m determined by heat/mass transfer analogy

$$\Delta f_U^{oxy}(t) = f_U^{oxy}(t+\Delta t) - f_U^{oxy} \rightarrow \Delta M_U^{oxy} \rightarrow \Delta M_e^{oxy} = \frac{\Delta M_U^{oxy}}{\Delta M_{U,eq}^{oxy}} \Delta M_{e,eq}^{oxy}$$

    - All transfers proportional to U transfer
  - Disregards the discontinuous phenomenology
- ➔ Need for a more detailed model for :
  - **The isolated droplets**
  - **The full transient with these droplets**

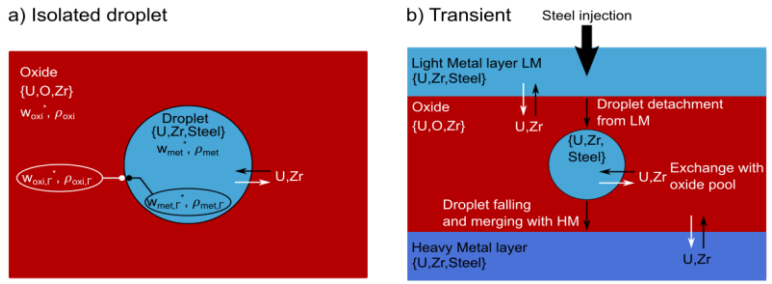

Context – modelling – one step further
Isolated droplet

Isolated droplet

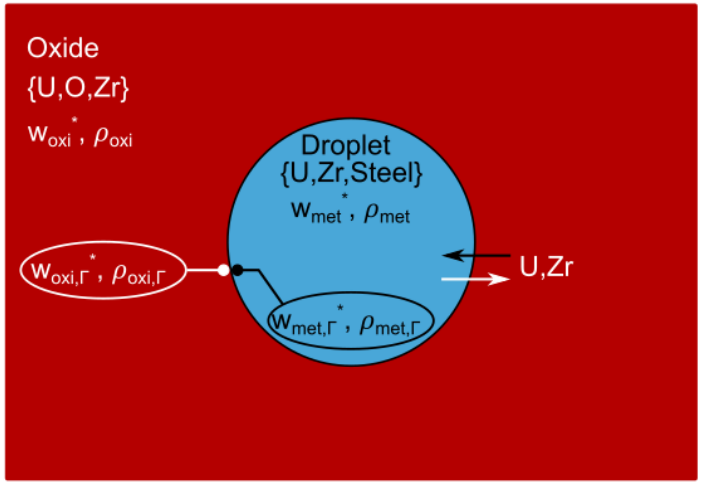

Taking the dispersed phase into account:

- Modelling an isolated droplet (Le Tellier 2021):
  - Main hypotheses:
    - **H1.** The metallic dispersed phase is considered as monodispersed and interactions between droplets are neglected, i.e. droplets are considered as isolated;
    - **H2.** Convection in the continuous oxide pool bears no effect on the droplets' dynamic;
    - **H3.** The two phase, namely Ω_met and Ω_oxy, are in thermal equilibrium;
    - **H4.** The interface between the two phases is considered to be at chemical equilibrium;
    - **H5.** The molar ratio U/Zr is uniform between both phases, i.e. $R_{U/Zr} = R^{oxi}_{U/Zr} = R^{met}_{U/Zr}$;
    - **H6.** There is no steel elements in the oxide phase, and there no oxygen in the metallic phase.

Context – modelling – one step further
Isolated droplet

Isolated droplet

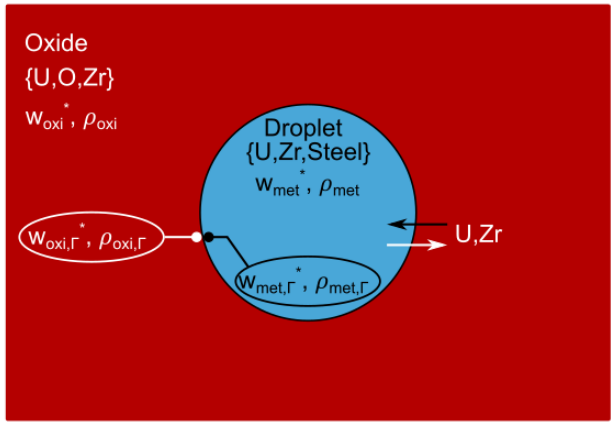

Taking the dispersed phase into account:

- Modelling an isolated droplet (Le Tellier 2021):
  - Equations :

$$\begin{cases} \frac{d}{dt}\left(w_{oxi}^{O} m_{oxi}\right) = 0 \quad (a) \\ \frac{d}{dt}\left(w_{met}^{Steel} m_{met}\right) = 0 \quad (b) \\ w_{oxi,\Gamma}^{O}\dot{m}_{\Gamma} + J_{oxi,\Gamma}^{O} S_{\Gamma} = 0 \quad (c) \\ -w_{met,\Gamma}^{Steel}\dot{m}_{\Gamma} + J_{met,\Gamma}^{Steel} S_{\Gamma} = 0 \quad (d) \end{cases} \quad + \quad \begin{cases} J_{oxi,\Gamma}^{O} = -\rho_{oxi,\Gamma} h_{oxi,eff}^{O}\left(w_{oxi,\Gamma}^{O} - w_{oxi}^{O}\right) \\ J_{met,\Gamma}^{steel} = -\rho_{met,\Gamma} h_{met,eff}^{Steel}\left(w_{met,\Gamma}^{Steel} - w_{met}^{Steel}\right) \end{cases}$$

$$\rho_{oxi,\Gamma} h_{oxi,eff}^{O}\left(w_{oxi,\Gamma}^{O} - w_{oxi}^{O}\right) w_{met,\Gamma}^{Steel} + \rho_{met,\Gamma} h_{met,eff}^{Steel}\left(w_{met,\Gamma}^{Steel} - w_{met}^{Steel}\right) w_{oxi,\Gamma}^{O} = 0$$

  - $h_{oxi,eff}^{O}$ fixed value via Sherwood ($Sh_j = \frac{h_j d}{D_j}$) & $h_{met,eff}^{Steel}$ determined via Sh correlation for a droplet
  - Only one closure required (H5. Homogeneous $R_{U/Zr}$):

$$f_1 : w_{oxi,\mathrm{eq}}^{O} \mapsto w_{met,eq}^{Steel} = w_{oxi,\mathrm{eq}}^{O}$$

  - Solving the following equation gives $w_{oxi,\Gamma}^{O}$ → $w_{met,\Gamma}^{Steel}$ → $J_{oxi,\Gamma}^{O}$ & $J_{met,\Gamma}^{steel}$ → $\dot{m}_{\Gamma}$

$$\rho_{oxi,\Gamma} h_{oxi,eff}^{O}\left(w_{oxi,\Gamma}^{O} - w_{oxi}^{O}\right) f_1\left(w_{oxi,\Gamma}^{O}\right) + \rho_{met,\Gamma} h_{met,eff}^{Steel}\left(f_1\left(w_{oxi,\Gamma}^{O}\right) - w_{met}^{Steel}\right) w_{oxi,\Gamma}^{O} = 0$$

Context – modelling – one step further transient stratification

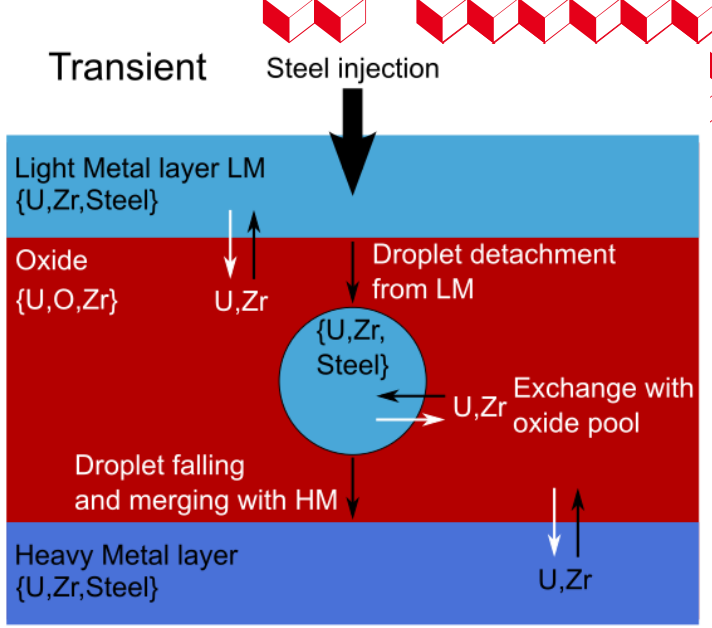

- Full transient (Le Tellier 2023):
  - Same equations used for thermochemical equilibrium & mass transfers
  - $h^{O}_{oxi,eff}$ & $h^{Steel}_{met,eff}$ determined by heat / mass transfer analogy
  - **Droplets creation:**
    - Rayleigh Taylor instability
      - Onset for a given $\Delta\rho$
      - Mass of droplets detached $\widetilde{m}_i$
        - Constant by part composition profile
        - w_i^{Steel} : bulk mass fraction
        - w_{i,Γ_i}^{Steel} : interface = equilibrium mass fraction
        - $w_{i,\infty}^{Steel}$: bulk mass fraction before mass transfer (reseted at each droplet detatchment)

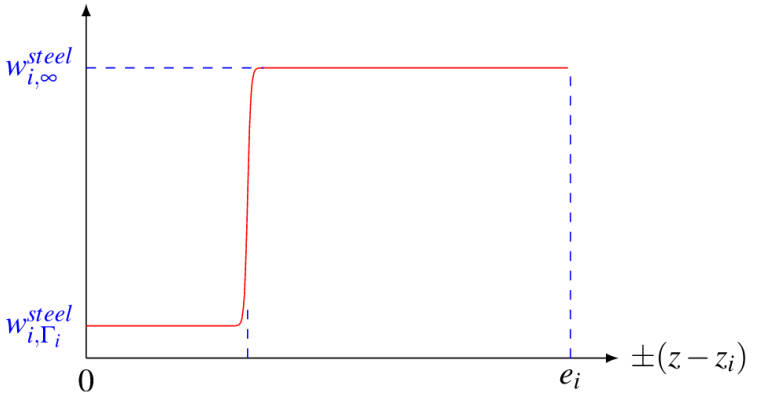

$$\widetilde{m}_i = \frac{w_i^{Steel} - w_{i,\infty}^{Steel}}{w_{i,\Gamma_i}^{Steel} - w_{i,\infty}^{Steel}} m_i$$

Present work aim and goal

- Previous modelling shortcoming
  - Homogeneous $R_{U/Zr}$ is not coherent with thermodynamic results
  - Constant $R_{U/Zr}$ is not realistic as it may vary during the transient due to material origin in the core
  - For $R_{U/Zr} = 1.2$:
    - $R_{oxy,eq}^{U/Zr} > 1$; $R_{met,eq}^{U/Zr} < 1$

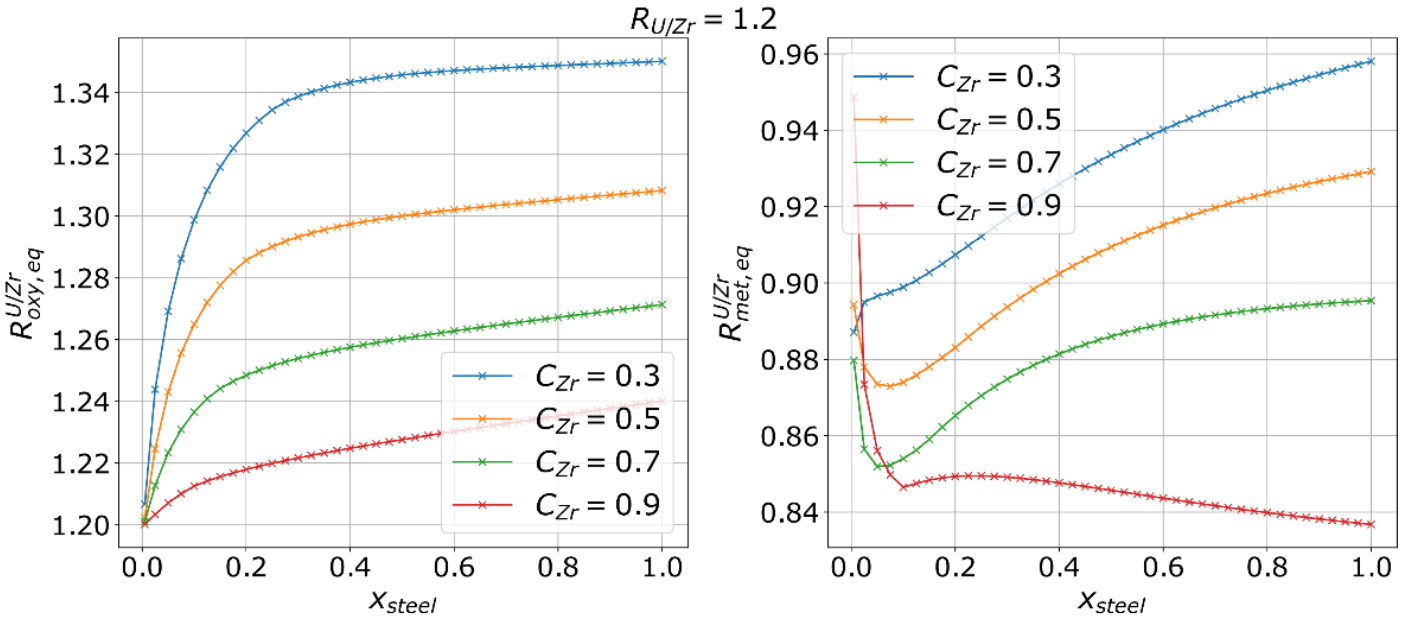

- Present work aim
  - Lifting hypothesis of a Uniform and homogeneous $R_{U/Zr}$
  - To make the model usable for realistic full transient calculations
    - Realistic material arrival
    - Realistic interaction with the vessel
    - …

Model evolutions

Previous model (HOM)

- **Thermochemical system:**
  - 2 Pseudo-binary systems:
    - Oxide phase → {{U,Zr},O}
    - Metal phase → {{U,Zr},Steel}

- **Assumptions:**
  - H5. The molar ratio U/Zr is uniform between both phases, i.e. $R_{U/Zr} = R_{U/Zr}^{oxi} = R_{U/Zr}^{met}$;

Present Model (VAR)

- **Thermochemical system:**
  - 2 Pseudo-ternary systems:
    - Oxide phase → {U,Zr,O}
    - Metal phase → {U,Zr,Steel}
  - **1 new degree of freedom** → another equation
    - Zr evolution chosen

- **Assumptions:**
  - H7. U and Zr diffusion coefficients are equals $D_U = D_{Zr}$ (*i.e.* $h_{*,eff}^{U} = h_{*,eff}^{Zr}$. Due to the Sherwood number definition (*i.e.* for $j \in \{U, Zr\}, Sh_j = \frac{h_j d}{D_j}$)

Present model – new equations

1 new degree of freedom in each phase

- Zr mass fraction evolution:

$$\frac{d}{dt}\left(w_*^{Zr} m_*\right) + J_{*,\Gamma}^{Zr} S_\Gamma + \boldsymbol{w_*^{Zr} \dot{m}_\Gamma} = 0 \quad \& \begin{cases} J_{*,\Gamma}^{U} = -\rho_{*,\Gamma} h_{*,eff}^{U}\left(w_{*,\Gamma}^{U} - w_*^{U}\right) \\ J_{*,\Gamma}^{Zr} = -\rho_{*,\Gamma} h_{*,eff}^{Zr}\left(w_{*,\Gamma}^{Zr} - w_*^{Zr}\right) \end{cases}$$

- To avoid introduction of new unknown, a new assumption:
  - H7. The mass diffusion coefficients of both the Uranium and the Zirconium are equal, $D_*^U = D_*^{Zr}$.

$$J_{*,\Gamma}^{U} = \beta_* J_{*,\Gamma}^{Zr} \text{ with } \beta_* = \frac{w_{*,\Gamma}^{U} - w_*^{U}}{w_{*,\Gamma}^{Zr} - w_*^{Zr}} = \frac{\Delta w_*^{U}}{\Delta w_*^{Zr}}$$

  - Conservation of mass → $J_{*,\Gamma}^{O} = (1 + \beta_*) J_{*,\Gamma}^{Zr}$

$$\begin{cases} \frac{d}{dt}\left(w_{oxi}^{Zr} m_{oxi}\right) = -\dot{m}_\Gamma \left[\frac{w_{oxi,\Gamma}^{O}}{1+\beta_{oxi}} + w_{oxi,\Gamma}^{Zr}\right] = -\dot{m}_\Gamma w_{oxi,\mathrm{MT}}^{Zr} \\ \frac{d}{dt}\left(w_{met}^{Zr} m_{met}\right) = -\dot{m}_\Gamma \left[\frac{w_{met,\Gamma}^{Steel}}{1+\beta_{met}} + w_{met,\Gamma}^{Zr}\right] = +\dot{m}_\Gamma w_{met,\mathrm{MT}}^{Zr} \end{cases} \quad \text{with} \quad \begin{cases} w_{oxi,\mathrm{MT}}^{Zr} = \frac{w_{oxi,\Gamma}^{O}}{1+\beta_{oxi}} + w_{oxi,\Gamma}^{Zr} \\ w_{met,\mathrm{MT}}^{Zr} = \frac{w_{met,\Gamma}^{Steel}}{1+\beta_{met}} + w_{met,\Gamma}^{Zr} \end{cases}$$

Thermodynamic closures

1 new degree of freedom on both the oxide and the metal

- Need for 2 new thermodynamic closures

$$\begin{cases} f_1 : w^O_{oxi,\mathrm{eq}} \mapsto w^{Steel}_{met,eq} = f_1\left(w^O_{oxi,\mathrm{eq}}\right) \\ f_2 : w^O_{oxi,\mathrm{eq}} \mapsto w^{Zr}_{oxi,eq} = f_2\left(w^O_{oxi,eq}\right) \\ f_3 : w^O_{oxi,\mathrm{eq}} \mapsto w^{Zr}_{met,\mathrm{eq}} = f_3\left(w^O_{oxi,eq}\right) \end{cases}$$

$At\ given\ T,\ R_{U/Zr}\ and\ C_{Zr}$

- For thermodynamic equilibria:
  - For given T, global $R_{U/Zr}$ and C_{Zr}
  - OpenCalphad (Sundman 2015)
  - NUCLEA (thermodynamic database) (Barkardjieva 2010)

- Closures must take all asumptions into account:
  - Especially H6 (no O in metal phase & no Steel in oxide)
  - Construction:
    - f_1 from thermodynamic equilibrium
    - f_2 from mass conservation and f_1
    - f_3 from mass conservation alone

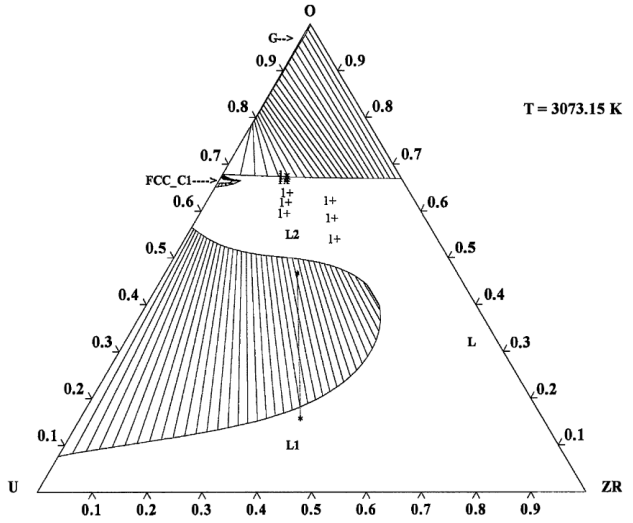

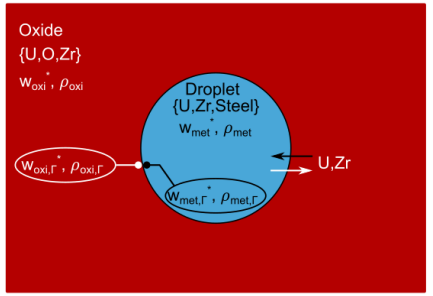

Model comparison on isolated droplet Thermodynamic accuracy

First question : Is the present model really closer to the thermodynamic predictions ?

- Comparisons on a synthetic case of an isolated droplet evolving in an infinite oxide phase
  - With the following parameters:

$R_{U/Zr}$	C_{Zr}	x_{Steel}	r_0	D_{oxi}	Sh_{oxi}	D_{met}	Sh_{met}
1.2	0.5	0.1	$10^{-2}\ m$	$5.10^{-9}\ m^2.s^{-1}$	2.10^3	$5.10^{-9}\ m^2.s^{-1}$	$Juncu2010$

- Equilibrium mass density
  - Pivotal for Rayleigh Taylor instability

	$\varepsilon(\rho_{oxi,eq})[\%]$	$\varepsilon(\rho_{met,eq})[\%]$
HOM	-1.144	1.952
VAR	-0.583	-1.215

Cf. presentation by R. Le Tellier: **In-Vessel Corium Thermochemistry Benchmark based on MASCACORDEB2 Experimental Data** Gröten → 13/05 → 15h20

- Mass fractions

	$\lvert\varepsilon(w^{Zr}_{oxi,eq})\rvert[\%]$	$\lvert\varepsilon(w^{Zr}_{met,eq})\rvert[\%]$	$\lvert\varepsilon(w^{U}_{oxi,eq})\rvert[\%]$	$\lvert\varepsilon(w^{U}_{met,eq})\rvert[\%]$
HOM	4.89	25	0.54	2.93
VAR	$8.27\ 10^{-6}$	0.29	0.94	7.91

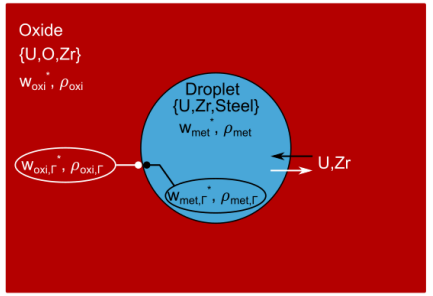

Model comparison on isolated droplet
Mass fractions transient evolution

- Tendencies remain the same
- Difference is blattant on the final (equilibrium value)
  - Coherent with:
    - $R^{U/Zr}_{oxy,eq} > 1$; $R^{U/Zr}_{met,eq} < 1$
      For $R_{U/Zr} = 1.2$

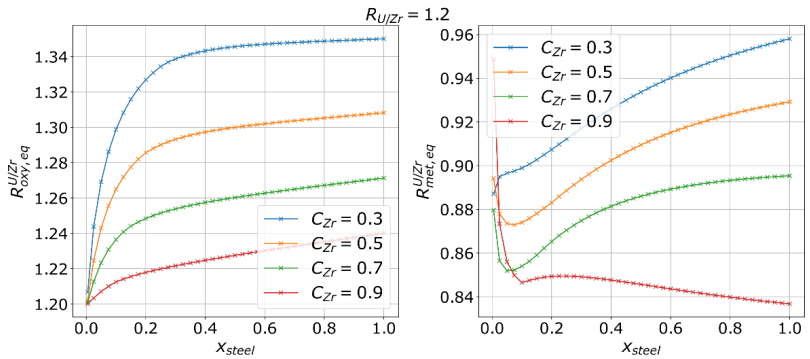

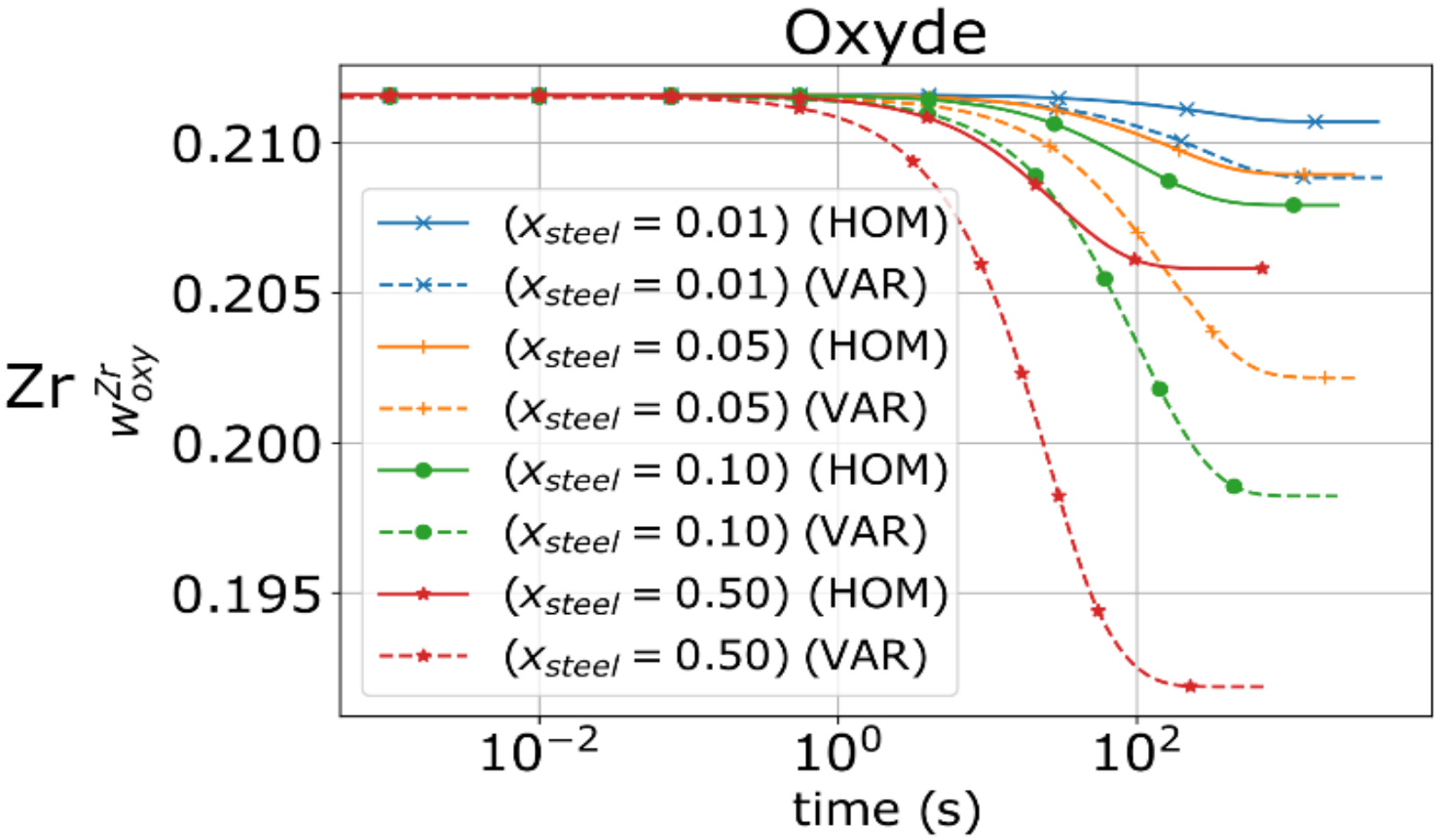

Application to a stratification transient

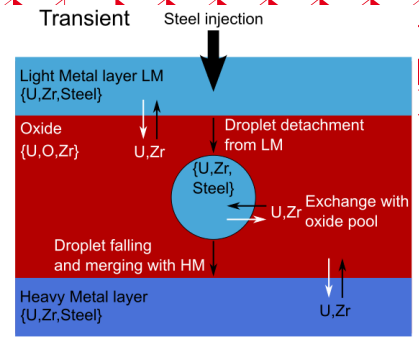

Isolated droplet → **stratification transient**

- Reminder on the model
  - Same equation for thermochemical equilibrium
  - Heat / Mass transfer analogy → Sh closure at interface
  - Droplet formation → Rayleigh Taylor modelling (step wise mass fractions)
- Transient considered: **Heavy metal formation**

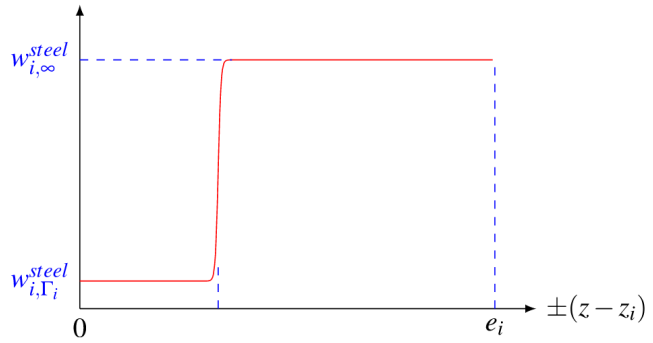

$R_{U/Zr}$	C_{Zr}	x_{Steel}	r_0	D_{oxi}	Sh_{oxi}	D_{met}	Sh_{met}	$\Delta\rho$
1.2	0.3	0.1	$10^{-2}\ m$	$5.10^{-9}\ m^2.s^{-1}$	4.10^4	$5.10^{-9}\ m^2.s^{-1}$	$Wegener2014$	$10kg.$

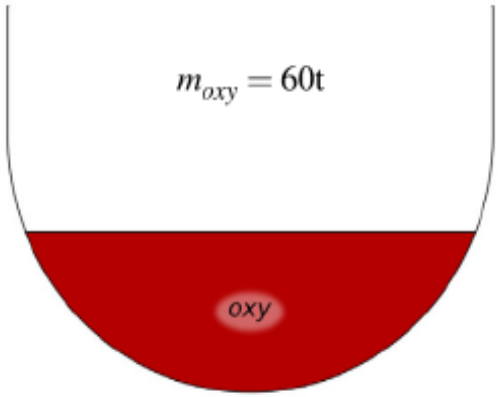

(a) Initial state.

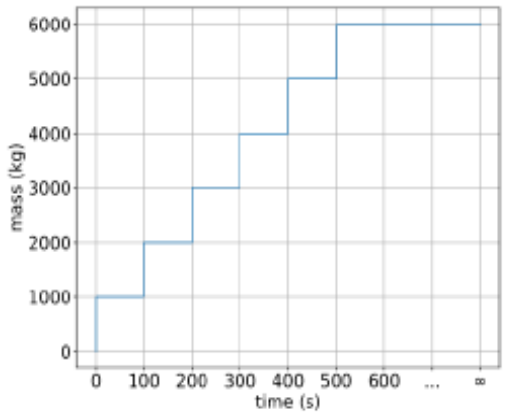

(b) Accumulated mass of molten steel added to the pool as a function of time.

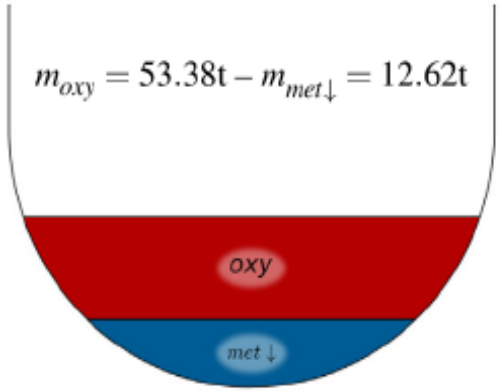

(c) Expected steady-state.

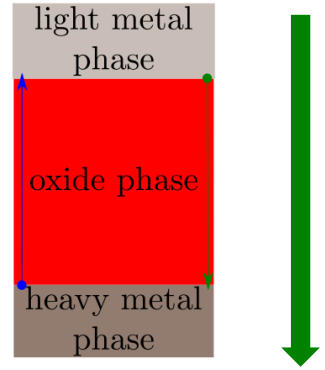

Application to a stratification transient Analysis - Masses

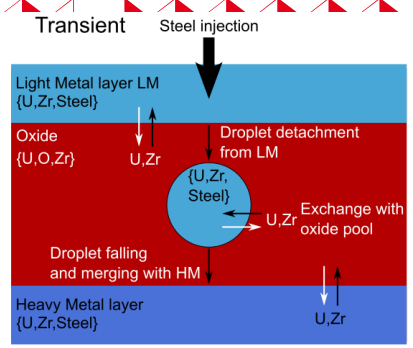

Phases masse evolution:

- For both models:
  - Discreet relocation events
  - Similar final state
    - Composition are different (U-Zr)

- For model VAR compared to HOM:
  - Longer transient
  - Less big relocation events
  - Preferential Zr enrichment of metal phase & $\rho_{Zr} < \rho_U$

HOM = Previous Model & VAR = Present model

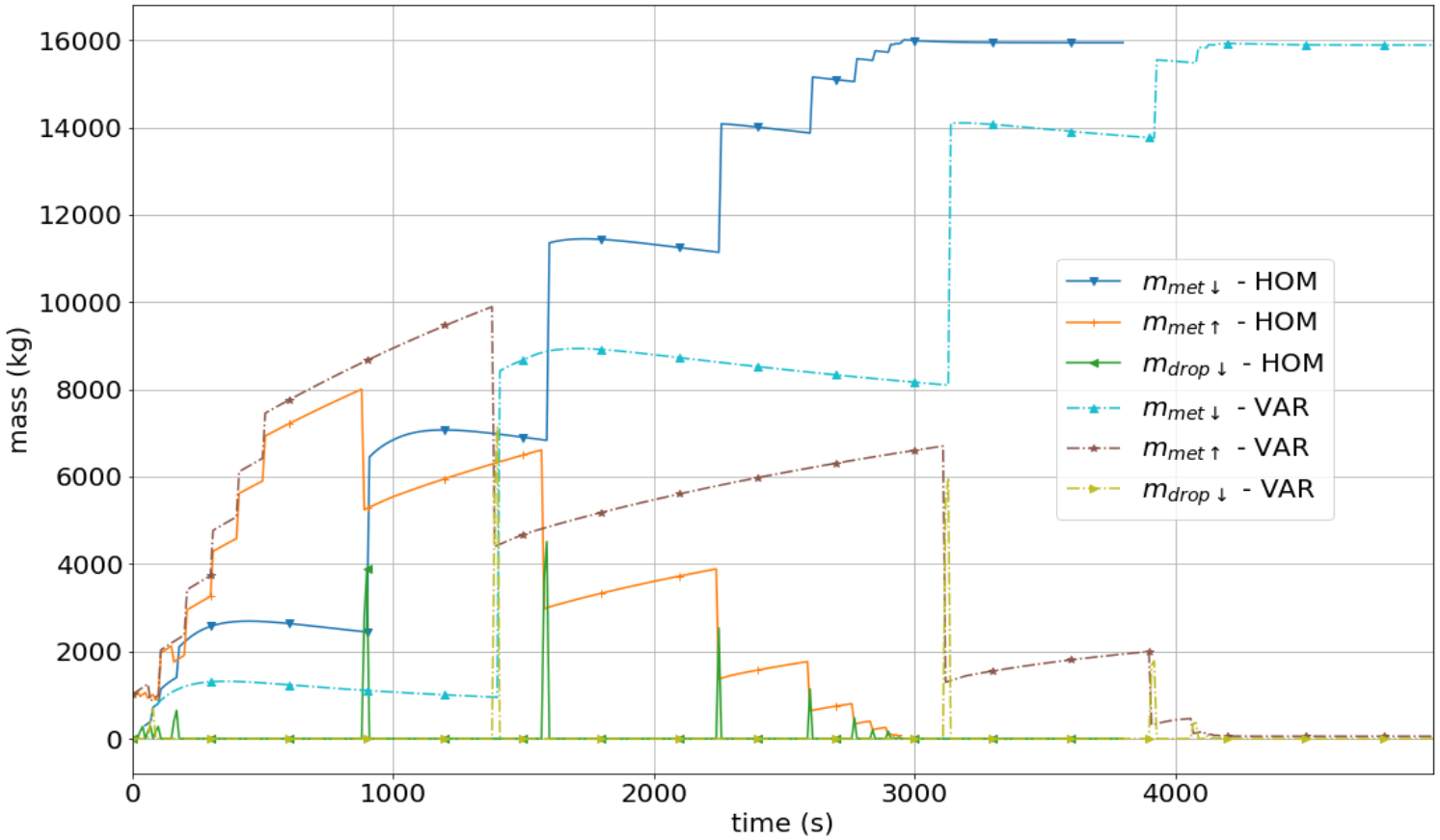

Application to a stratification transient Analysis – Mass fractions

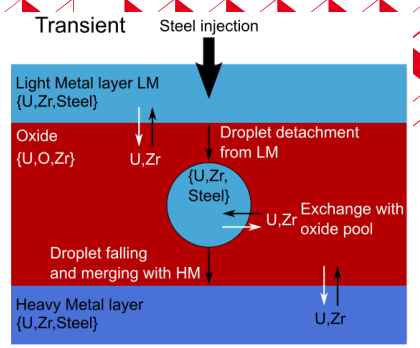

Mass fractions evolutions:

- For both models:
  - Same global tendencies
  - Converge to almost the same final state for steel mass fraction
  - Influence on Zr + U composition
- For model VAR compared to HOM:
  - Quasi-steady state reached at the end of the transient with low mass detatchments

HOM = Previous Model & VAR = Present model

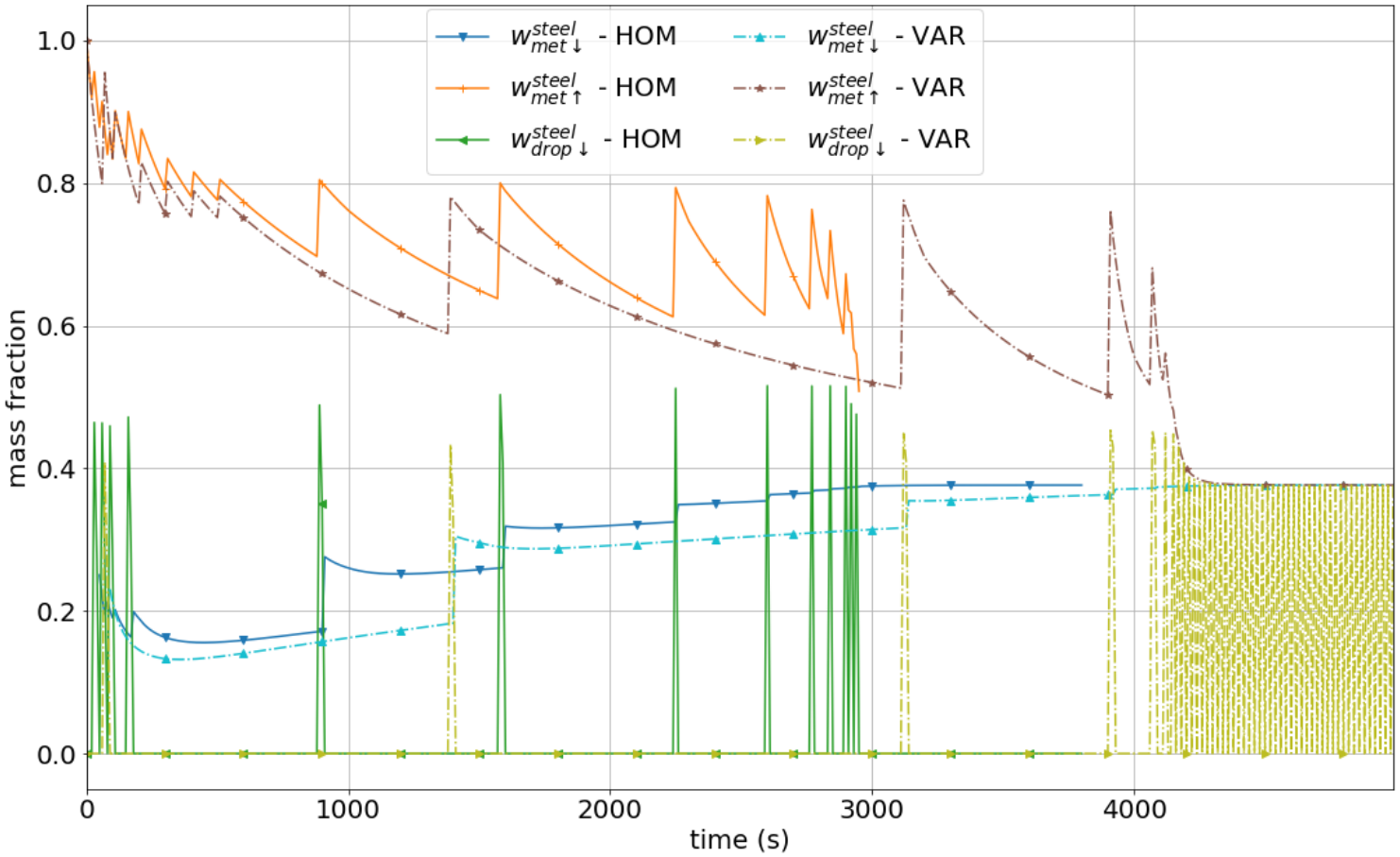

Conclusion

- A step further was taken to consider the relocation of the metallic phase as droplets
  - The limiting assumption of an Uniform and constant value of $R_{U/Zr} = R_{U/Zr}^{oxi} = R_{U/Zr}^{met}$ was replaced by less limiting one $h_{*,eff}^{U} = h_{*,eff}^{Zr}$
    - The thermochemical evolution of two pseudo ternary was taken into account

- The effect of the present model was assessed on a transient stratification with heavy metal formation
  - The transient is longer
  - The behavior is coherent with the physical phenomenology

- To take things further:
  - Now that the limiting assumption of an Uniform $R_{U/Zr}$ has been lifted this model should be used in PROCOR on a more realistic transient with realistic inputs from the core and interactions with the vessel and the results should be compared to the basic model in place in PROCOR.

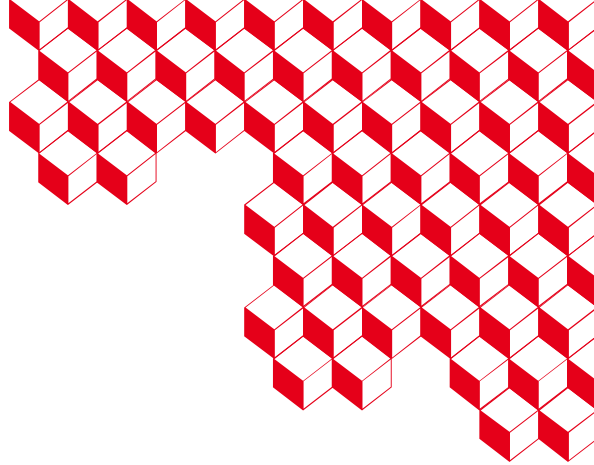

Thank you for your attention !

This work was funded in the framework of the PROCOR platform development by CEA, France, EDF, France and Framatome, France.

CEA, DES, IRESNE, DTN, Cadarache
F-13108 Saint Paul-lez-Durance, France
Alexandre.lecoanet@cea.fr

Bibliography

(Asmolov 2003) V.G. Asmolov, S.S. Abalin, Yu.A. Veselkin, V.Yu. Vishnevsky, V.V. Vlasov, B.L.Gershman, Yu.G. Degaltsev, Ye.K. Dyakov, J.F. Isaev, A.N. Kiselev, N.P. Kiselev, A.M.Kovalev, A.G. Ol'khovsky, K.V. Pechalin, LM. Semenov, V.F. Strizhov, T.V.Trushkina, V.S. Uglov, Yu.M. Utkin, V.V.Chudanov, A.E.Aksenova, V.A.Pervichko and L.M. Khazanivich, RCW Post-Test Analysis Results, Technical Report MP-TR-11, Russian Research Centre Kurchatov Institute, 2003.

(Barkardjieva 2010) S. Bakardjieva, M. Barrachin, S. Bechta, D. Bottomley, L. Brissoneau, B. Cheynet, E. Fischer, C. Journeau, M. Kiselova, L. Mezentseva, P. Piluso and T. Wiss, “Improvement of the European thermodynamic database NUCLEA,” *Progress in Nuclear Energy*, **52**(1), pp.84–96, (2010).

(Fichot 2022) F. Fichot, B. Michel, V. Almjashev, C. Le Guennic, N. Bakouta, R. Le Tellier, P. Piluso, T. Keim, “Chemical Interactions of Molten Steel with (U-Zr-O) Corium: Main Outcomes of the CORDEB Program”, Nuclear Engineering and Design 388 (2022).

(Le Tellier 2015) R. Le Tellier, L. Saas and S. Bajard, Transient Stratification Modelling of a Corium Pool in a LWR Vessel Lower Head, Nuclear Engineering and Design, 287, 68-77, 2015.

(Le Tellier 2021) R. Le Tellier, “Mass transfer between a continuous oxide phase (U-O-Zr) and a steel droplet at liquid state: Potential impact on corium pool behaviour during in-vessel melt retention,” Nuclear Engineering and Design, 385, 111525, 2021.

(Le Tellier 2023) R. Le Tellier, “A lumped parameter model of continuous/dispersed phases mass transfer for simulating in-vessel corium stratification transients,” Annals of Nuclear Energy, 181, 109539, 2023.

(Nandan 2020) S. Nandan, F. Fichot, and B. Piar, “A simplified model for the quaternary U-Zr-Fe-O system in the miscibility gap,” Nuclear Engineering and Design, 364, 110608, Aug. 2020.

(Salay 2005) M. Salay and F. Fichot, “Modelling of Metal-Oxide Corium Stratification in the Lower Plenum of a Reactor Vessel,” in Proc. of Int. Topical Meeting on Nuclear Thermal-Hydraulics (NURETH-11), Avignon, France, 2005.

(Sundman 2015) B. Sundman, U. R. Kattner, M. Palumbo and S. G. Fries, “OpenCalphad—A free thermodynamic software,” *Integrating Materials and Manufacturing Innovation*, **4**(1), (2015).

(Tsurikov 2007) D. F. Tsurikov, V. F. Strizhov, S. V. Bechta, V. N. Zagriazkin and N. P. Kiselev, Main Results of MASCA1 and 2 Projects, Technical Report, RRC Kurchatov Institute, 2007.

(Juncu 2010) G. Juncu, “A numerical study of the unsteady heat/mass transfer inside a circulating sphere,” *International Journal of Heat and Mass Transfer*, **53**, pp. 3006–3012 (2010).

(Wegener 2014) M. Wegener, N. Paul and M. Kraume, “Fluid dynamics and mass transfer at single droplet in liquid/liquid systems,” *International Journal of Heat and Mass Transfer*, **71**, pp.475–495, (2014).

The 11th European Review Meeting on Severe Accidents Research

May 13-16, 2024, Royal Institute of Technology, Stockholm, Sweden

TECHNICAL SESSION 2.2: SEVERE ACCIDENT SCENARIOS

Chairs: A. Bentaib (IRSN), L. E. Herranz (CIEMAT)

ID05	**Horizon Euratom ASSAS project: Can machine-learning make fast and accurate severe accident simulators a reality?** B. Poubeau (IRSN)	**Paper** **Presentation**
ID26	**Preliminary Strategies for Training Dataset Generation and Surrogate Modeling of SBO Management Measures in PWR** C. D'Alessandro (PSI)	**Paper** **Presentation**
ID86	**Analysis of accident progression behavior and simulation of FP release into the environment using MELCOR code for the Fukushima Daiichi Nuclear Power Station Units 1 to 3** M. Himi (CRIEPI)	**Paper** **Presentation**
ID63	**Long-term severe accident management at Loviisa NPP** M. Harti (Fortum Power and Heat Oy)	**Paper** **Presentation**

HORIZON EURATOM ASSAS PROJECT: CAN MACHINE-LEARNING MAKE FAST AND ACCURATE SEVERE ACCIDENT SIMULATORS A REALITY?

Bastien POUBEAU, Yann RICHET
Institut de Radioprotection et de Sûreté Nucléaire (IRSN), PSN-RES, PSE-ENV/SCAN
F-92262, Fontenay-aux-Roses, France
bastien.poubeau@irsn.fr, yann.richet@irsn.fr

Lionel CHAILAN
Institut de Radioprotection et de Sûreté Nucléaire (IRSN), PSN-RES/SAM
F-13115, Saint-Paul-lez-Durance, France
lionel.chailan@irsn.fr

Fulvio MASCARI, Mattia MASSONE, Simone GIANFELICI
Agenzia Nazionale per le Nuove Tecnologie, l'Energia e lo Sviluppo Economico Sostenibile (ENEA)
Via Martiri di Monte Sole 4 - 40129 Bologna Italy
fulvio.mascari@enea.it, mattia.massone@enea.it, simone.gianfelici@enea.it

Luis Enrique HERRANZ, Joan FONTANET
Centro de Investigaciones Energeticas, Medioambientales y Tecnologicas (CIEMAT)
Avenida Complutense 40 - 28040 Madrid Spain
luisen.herranz@ciemat.es, joan.fontanet@ciemat.es

Terttaliisa LIND, Christophe D'ALESSANDRO
Paul Scherrer Institut (PSI)
Forschungstrasse 111 - 5232 Villingen PSI Switzerland
terttaliisa.lind@psi.ch, christophe.dalessandro@psi.ch

Jure BRENCE, Ivo KLJENAK, Saso DZEROSKI
Institut Jozef Stefan (JSI)
Jamova 39 - 1000 Ljubljana Slovenia
jure.brence@ijs.si, ivo.kljenak@ijs.si, saso.dzeroski@ijs.si

Fabrizio GABRIELLI, Anastasia STAKHANOVA, Jonas DRESSNER
Karlsruher Institut für Technologie (KIT)
Kaiserstrasse 12 - 76131 Karlsruhe Germany
fabrizio.gabrielli@kit.edu, anastasia.stakhanova@kit.edu, jonas.dressner@kit.edu

Isabel PARRADO RODRIGUEZ
Westinghouse Spain (formerly Tecnatom)
Avenida Montes de Oca 1 - 28703 San Sebastian de los Reyes - Madrid Spain
isabel.parradorodriguez@westinghouse.com

ABSTRACT

Interfacing reference severe accident (SA) codes with commercial nuclear simulators can help spread SA knowledge to a larger audience and build more accurate plant models. However, this requires improving the performance of calculation codes. The Horizon Euratom ASSAS project (Artificial intelligence for the Simulation of Severe AccidentS) addresses this issue and evaluates, among other strategies, the possible added-value of machine-learning (ML) to speed-up calculations.

Efficient programming will be applied to ASTEC (Accident Source Term Evaluation Code, developed by IRSN) [1], with negligible impact on accuracy. This might be sufficient to achieve a real time execution of ASTEC if combined with simplifications of some physical models and of the nodalization used in the input decks. Nevertheless, such modifications are hard to implement, and high acceleration factors are out of reach for complex legacy multiphysics codes like ASTEC.

ML could be a game-changer to reach significantly higher acceleration factors. The first step is the definition of the parts of the SA code that can be replaced by a data-driven surrogate model. Global models, replacing the code integrally, can be more efficient and do not require access to the source code. They will be tested on ASTEC for the ex-vessel phase of the accident. On the other hand, they are expected to be data-greedy since they need to capture a large diversity of physical phenomena. Therefore, ASSAS also explores hybrid approaches, for which surrogate models will replace only selected functions of ASTEC and will be interfaced with other modules.

The specifications of the basic-principles simulator to be developed during ASSAS must be selected at the beginning of the project, to ensure the consistency between the plant model and the training data for ML models. Exercise scenarios have been chosen to determine the systems to be modelled, their scope and the data to be displayed on the Human-Machine Interface.

The present paper aims at providing a description of the ASSAS project and its goals. The adopted strategy and the related challenges will be discussed.

KEYWORDS
Simulator, hybrid machine-learning, ASTEC, nuclear energy, severe accident, training, efficient programming

1. INTRODUCTION

1.1. General objectives of the ASSAS project

Severe accident (SA) calculation codes usually require computer programming skills to launch calculations and visualise the results. The properties of the reactor, of its safety systems, and of its Instrumentation and Control (I&C) must be implemented manually in the input decks. Interfacing SA codes with commercial simulation environments can overcome those limitations. An ergonomic human-machine interface (HMI) makes it possible to interact with the simulation and visualise the results easily, even during the calculation. Simulators usually include computer aided design tools for safety systems and I&C, which generate data for the input deck from graphical representations. Those features can improve the learning curve and efficiency of SA engineers and researchers and limit the risk of errors. Simulators are also powerful tools for education and training, making SA phenomenology more accessible. The use of realistic simulators for accident management training has been recommended for a long time [2], especially since the Fukushima-

Daiichi accidents [3]. Finally, nuclear simulators tend to become a central asset for data centric approaches in the nuclear industry. It can be anticipated that utilities would not develop simulators dedicated to SA modelling, but they would rather extend the capacities of their existing simulators to SA, benefiting from the already existing detailed description of the power plant.

The main objective of the Horizon Euratom Artificial intelligence for the Simulation of Severe AccidentS (ASSAS) project, coordinated by IRSN (France), is to make substantial progress in the deployment of SA simulators. Only few such simulators exist in the world, and they often have limitations [4]. ASSAS plans to develop a proof-of-concept for a SA simulator based on ASTEC, with a level of accuracy close to best estimate models. The prototype will feature a generic basic-principles simulator for a 4-loop Western-type pressurized water reactor (PWR). The HMI will be developed by Westinghouse Spain benefiting from its simulation environment TEAM_SUITE®. It will prove the feasibility to interface ASTEC with industrial simulators. Actions are also planned in the project to prepare the design of VVER (Water-Water Energetic Reactor) simulators in the future. ASSAS focuses on the main scientific and technological challenges, while keeping a simplified description of systems. It is hoped that the prototype will give confidence to industrials to develop more complex simulators, as described in [5].

1.2. Specifications of the simulator

The simulator developed in ASSAS is meant to support educational activities about SAs. Specifications have been defined by project partners to show the different phenomena happening during a SA and the effect of the main mitigation actions. Two sequences have been selected to be implemented in the simulator:

- A 6-inch cold-leg Loss-of-Coolant Accident (LOCA) with Safety Injection (SI) failure and Containment Spray System (CSS) temporary failure,
- A Station Black-Out (SBO) with Steam Generator (SG) Auxiliary FeedWater (AFW) failure.

In both sequences, Portable Equipment Systems (PES) can be used after some delay to inject water into the SGs and the Reactor Coolant System (RCS). The instructor, who manages the failure and recovery of the different systems, will also have the possibility to trigger malfunctions like an induced Steam Generator tube rupture (SGTR).

The systems connected to the reactor will be simplified to focus on the most critical equipment to manage the SA. The Residual Heat Removal System (RHRS), the Chemical and Volume Control System (CVCS), and the balance-of-plant will not be considered for the accident management. Boundary conditions will be used to calculate the steady-state conditions of the reactor before the postulated initiating event. Containment isolation is also assumed to be successful. The most energetic phenomena of a SA, like steam explosion or direct containment heating, are out of the scope of the simulator. The simulation will end at the failure of the containment, caused by overpressure or basement erosion.

Different screens will be accessible from the HMI, for example the SA dashboard partially reproduced in Figure 1. The main sensors and alarms of the Main Control Room (MCR) will be displayed. Additional information will be provided to show the evolution of the SA, including the degradation of the core, the corium-concrete interaction, the pressurization of the containment (including combustible gases), and the release of fission products. It is also planned to develop a Virtual Reality (VR) display with an interactive three-dimensional representation of the plant. The trainee and the instructor will be able to manage the operator actions and interact with the simulation (freezing the simulation, loading new initial conditions, plotting variables, *etc*.) directly from the HMI. A plug-in has also been developed to interact with the simulator directly from a spreadsheet.

The coupling of ASTEC with TEAM_SUITE® is well advanced. The development of the simulator interface and the corresponding physical description in ASTEC and TEAM_SUITE® should be completed before the end of 2024.

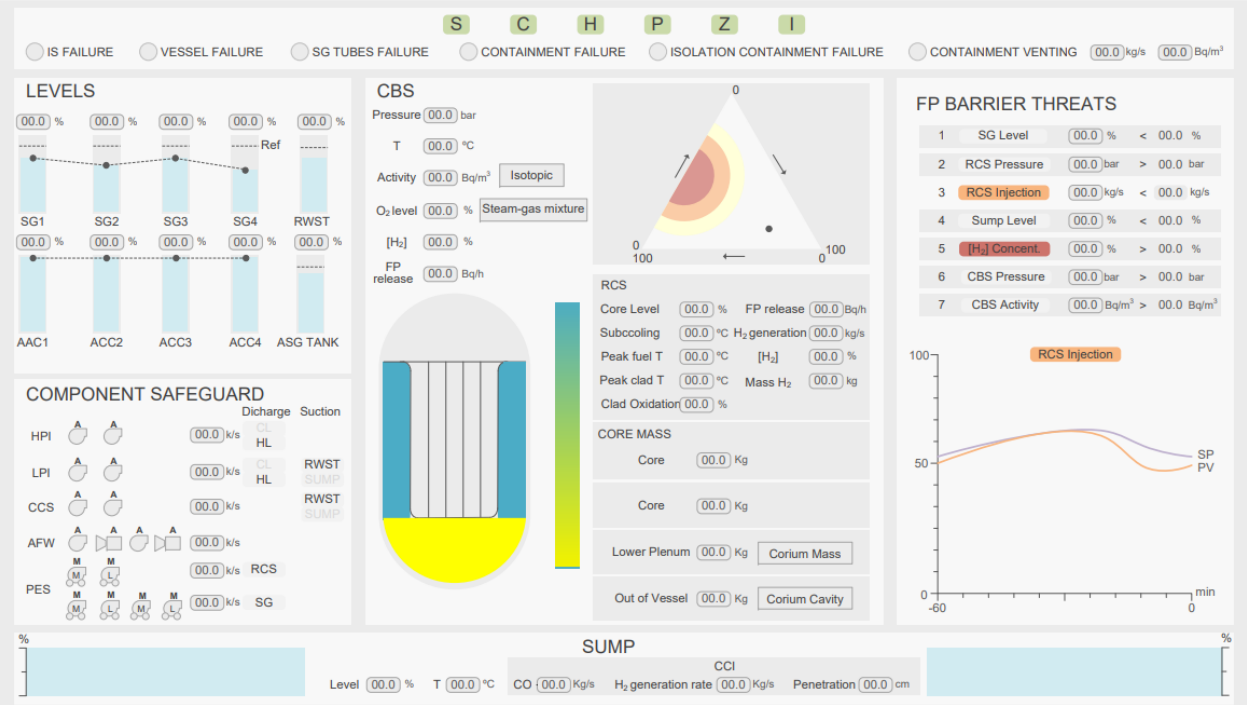

Figure 1: Draft SA screen of the basic-principles simulator (partial view of the SA display)

2. CLASSICAL COMPUTATIONAL OPTIMISATION OF ASTEC

In its current implementation, ASTEC is composed of several modules that are called sequentially and exchange data at a meeting point in time called the macro timestep. The main modules are:

- CESAR, which computes thermal-hydraulics in the vessel, primary and secondary circuits;
- ICARE, which calculates the core degradation in the vessel and the release of fission products;
- SOPHAEROS, which models the transport and speciation of fission products in the primary circuit and the containment;
- MEDICIS, which models the corium-concrete interaction in the reactor cavity;
- CPA, which computes thermal-hydraulics in the containment.

The different modules read and write data in a central database managed by the ODESSA tool. Most physical models need several internal timesteps to calculate the updated values of variables at the end of the macro timestep. In addition, algorithmic considerations impose CESAR's timestep to be a fraction of ICARE's timestep, which is in turn a fraction of the macro timestep. Therefore, three levels of timesteps exist in ASTEC. They are managed dynamically, which means that they will automatically be decreased or increased depending on the convergence rate of the solver.

2.1. Identification of the most time-consuming operations in ASTEC

Identifying the most computationally demanding functions in ASTEC is a prerequisite to launch any action to reduce the execution time of the code, either with classical optimisation, or with ML models. Profiling tools have been used to measure the CPU (central processor unit) time consumed by the different modules, routines, and subroutines of ASTEC, for the different phases of the accident. New data are generated periodically to measure the effects of source code or input deck modifications.

The most time-consuming module of ASTEC is CESAR, followed by ICARE and SOPHAEROS. The relative contribution of the different modules depends on the sequence and the nodalization of the plant. For example, SOPHAEROS becomes the first contributor to the CPU time for a SBO sequence calculation with a simplified input deck (see sub-section 2.3 for more details). CESAR solves a large system of non-linear partial differential equations, which accounts for most of its computation time. On the contrary, ICARE is composed of several different models that have a more balanced time consumption. Hence, optimising or replacing only one of those models cannot speed-up the code drastically.

2.2. Efficient programming

The objective of efficient programming is to improve the performance of ASTEC with a negligible impact on the results accuracy.

Different optimisations have been implemented in ASTEC, enabling a significant reduction in CPU time. Low-level optimisations have been carried out to accelerate memory access and variable search functions. Different post-treatment operations and database savings have been removed because there are not relevant for the simulator. The MEDICIS module has been fully reengineered to reduce its execution time significantly. Besides, several functions of the code have been parallelised thanks to OpenMP [6]. It has been checked that calculation results are not affected by parallelisation.

Additional actions are planned during the ASSAS project. New optimised linear algebra solvers will be considered. Moreover, the adaptive timestep management in CESAR may be improved. New strategies will also be explored for the initialisation of the Newton-Raphson solver in CESAR, to limit the number of necessary iterations to converge to the solution. Code parallelisation will also be tested more extensively, especially for SOPHAEROS and ICARE.

Moreover, a study has been carried out to identify variables in CESAR that require more iterations of the Newton-Raphson solver to reach convergence criteria. It appears that a few variables are responsible for most of the solver iterations. In some cases, these variables face an undesired behaviour of the governing equations: strong non-linearity, non-derivability, non-monotonousness, coexistence of different solutions, absence of solutions, *etc*. If the maximum number of iterations is reached, ASTEC will restart the calculation of the timestep with a shorter time horizon. Different strategies must be explored to limit the occurrence of such situations, for example thanks to smoothing functions.

If the above-mentioned actions are not sufficient, other strategies will be explored. For example, different modules could be executed in parallel, or the thermal-hydraulics equations may be solved separately in the vessel and the circuits. Optimisations offered by the compiler and currently deactivated may improve performances as well. These approaches may have drawbacks on the accuracy or the reproducibility of results and on its numerical stability, so they must be evaluated carefully.

2.3. Reactor model optimisation

Another option to improve the performances of ASTEC is to simplify the reactor model, while checking that the effects on the calculation results are acceptable.

The first simplifications that have been carried out concern the physical models used by the simulator. A simplified criterion will be used for the vessel failure, which is supposed to occur at the bottom of the lower plenum. It is assumed that the corium will be integrally poured into the reactor pit, leading to a clear transition between the in-vessel and the ex-vessel phases of the accident. Therefore, all calculations in the vessel and the circuits will be stopped after the vessel failure, switching off CESAR and ICARE completely. CO_2 and BHO_2 have also been removed from the list of non-condensable gases in CESAR, because of their

low influence on SA phenomenology. Hence, the boron oxidation model of ICARE, BCOX, has been disabled, with limited impact on accuracy. Other possible improvements include the identification and removal from the model of less significant elements and chemical species released during the degradation.

The other actions concern the simplification of the nodalization used for the reactor design featured by the simulator. The input decks have been evaluated on large-break LOCA (hot leg and cold leg breaches) and SBO sequences, which are representative of the sequences used in the simulator.

The description of the reactor core in ASTEC is two-dimensional and axisymmetric. It is divided into several concentric cylinders, piled up in the vertical axis. The best-estimate input deck is composed of 6 concentric rings and 24 axial nodes vertically. Different nodalizations have been investigated, reducing the number of rings down to 3, and the number of axial nodes down to 12. The study has been combined with two descriptions of the primary and secondary circuits: a best-estimate one with 276 control volumes, and a simplified one with 158 control volumes. Introducing both simplifications increases ASTEC's performances substantially while preserving an acceptable accuracy for a basic principles simulator.

The simplification of the containment has been evaluated in parallel. The number of control volumes has been decreased from 28 to 18, the number of walls from 107 to 62, and the number of junctions between control volumes from 79 to 54, without significant impact on the results.

The final step was to evaluate the performances and accuracy of the input deck combining the simplified circuit and containment descriptions, compared to the best estimate nodalization. The increase of performance is larger than a factor of two for all sequences. However, dispersion in results led to investigate the numerical sensitivity of ASTEC. It has been chosen to evaluate the input decks on 50 runs with non-significant modifications of the volume of the sumps and to compare the dispersion of results. The relative variation of the input parameters was small enough to ensure that variations had no physical meaning and could be attributed to numerical sensitivity. Several conclusions can be drawn from this study. First, results are more dispersed for long-lasting sequences, especially the SBO. Second, the simplified input deck usually yields to a higher dispersion of results: the standard deviation of results can be up to a few times higher. Third, for most figures of merit (e.g. time of vessel rupture or activity released to the environment), the mean value obtained with the simplified description differs from the mean value calculated with the best estimate description by less than a few standard deviations. One noticeable exception concerns the time of vessel rupture: it occurs in average after 10 hours with the reference input deck but is delayed by 40 minutes with the simplified one. The long-term efforts spent to reduce the numerical sensitivity of ASTEC need to be pursued. It must also be considered for the development of ML models.

Thanks to the above-mentioned improvements and simplifications, ASTEC is an order of magnitude faster than real time for the ex-vessel phase of the accident. It is in average close to a real-time execution for the in-vessel phase, despite a few strong local slowdowns. Figure 2 depicts the calculation time versus simulated time for the LOCA scenario included in the simulator and compares it to the real time (X=Y curve).

The discrepancies caused by the simplified nodalization have been considered acceptable as regards to the objectives of the project. The simplifications will not only make the simulator faster, but also make the generation of the training database for ML applications easier. However, a general use of simplified input decks requires further investigations.

3. MACHINE-LEARNING APPROACHES

The employment of ML surrogate models aims at reproducing the behaviour of a calculation tool based on a database of pre-computed cases [7]. Instead of solving first principles equations, a direct relationship is established between the inputs and outputs of the code, which can be seen as a high-dimensional regression

task. This can lead to a reduction in calculation time by orders of magnitude, enabling for instance uncertainty propagation [8]. However, the complexity of the problem increases exponentially with the number of degrees of freedom of the calculation tool, a phenomenon called the “curse of dimensionality”. Complex regression functions and large training databases (sets of inputs and outputs) are then required. The use of state-of-the-art deep neural network architectures with large data infrastructures has made it possible to develop advanced surrogate models in physics. One of the most remarkable achievements is related to the development of data-driven weather forecasting models [9], that can outperform classical approaches both in terms of accuracy and calculation time, thanks to the combination of real and simulated data. Deep learning methods proved they could tackle the high dimensionality of the physical description of the atmosphere and the chaotic behaviour of the underlying equations.

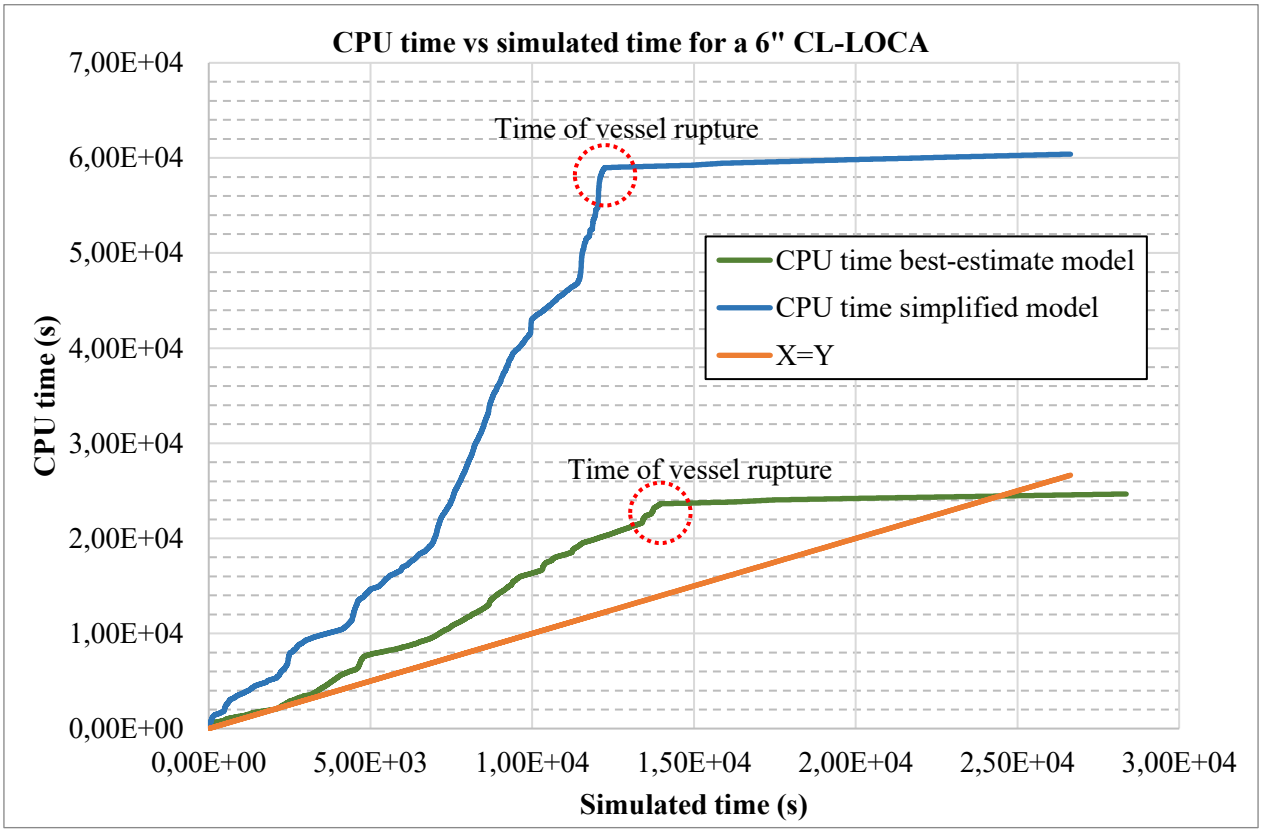

Figure 2: ASTEC CPU time versus simulated time for a 6-inch cold leg LOCA sequence with the best-estimate and simplified input decks

Anticipating the complexity of a ML task is almost impossible without a preliminary analysis on small data samples. This is necessary to evaluate the regularity of the functions to be modelled and their so-called intrinsic dimensionality, which corresponds to the minimal number of dimensions that must be considered to achieve a given accuracy [10]. It has been chosen in ASSAS to explore different surrogate modelling strategies to assess their respective advantages and drawbacks. Physics-informed models will be investigated to ensure that the most important conservation laws (mass and energy balance) are respected, improving the trustworthiness of the models.

To limit the complexity of the surrogate models developed in ASSAS, it has been decided to reduce the number of degrees of freedom of the simulator as much as possible, while preserving its representativeness

and pedagogical function. Hence, only full power initial conditions have been considered. Only a few operator actions will be possible and only best-estimate physical parameters will be considered. Such assumptions are in line with the objectives of a basic-principles simulator, that features a simplified reactor and gives a deterministic result to the trainee.

In addition to the already mentioned numerical noise propagation, numerical and physical oscillations of results can be encountered with ASTEC. This is a challenge for the training of the models. On the other hand, ML models may be able to solve those numerical issues and smooth calculation results.

3.1. Data generation

Quality of the generated data is decisive for the development of surrogate models. Using ML models in a region of the parameter space not sufficiently covered by training data is highly risky and not recommended. Data sampling must be all the denser as the phenomena to model are complex. It must also be representative of the diversity of situations in which the model will be called. Surrogate models will only be trained for a specific SA code and a specific reactor design.

Efforts to build-up the training database will be pooled up: several ASSAS partners will generate training data with ASTEC and upload it to a central database hosted by the Large-Scale Data Facility (LSDF) of KIT. Each partner will be able to retrieve the data it needs for the type of surrogate model it plans to develop. The database will consist of time-dependent raw data for different scenarios, with all ASTEC modules activated. The strategy for time sampling is still an open question. Keeping data for all timesteps is safer to avoid discarding data they may be valuable later in the project. However, data storage costs may be prohibitive if a large variety of scenarios is necessary to ensure training data representativity. In this case, only short series of timesteps will be saved at given time intervals.

In the context of a simulator, the inputs that influence the simulation are the malfunctions and operator actions defined in the training scenarios. The timing of these events will be sampled to generate the training data. A statistical analysis will be performed to evaluate if this approach leads to a balanced sampling of the physical conditions encountered by the reactor. If it is not the case, adaptative sampling methods will be used to generate more data in the under-sampled regions of the parameter space. Additional refinement of the database may be necessary to increase the precision of models for hard-to-predict conditions [11].

3.2. Global models

A first approach consists in replacing ASTEC by a surrogate model completely, at least for some phases of the accident. This black-box approach is the most common in the ML community, since it does not require access to the source code of the calculation tool to be replaced. In the context of ASSAS, it would mean that the simulator would interact directly with the surrogate model, while ASTEC would be switched off. This would make integration easier. In addition, a global model would be faster to execute. On the other hand, this approach is expected to be more data-greedy, because of the possibly higher dimensionality of the problem.

JSI will test the possibility to replace ASTEC by a global surrogate model for the ex-vessel phase of the accident. Two models will be developed respectively for the reactor design featured by the simulator and for a generic VVER-1000 design. The state of the plant at the time of the vessel rupture will constitute the initial conditions of the model. The outputs of the surrogate models must include at least the variables displayed to the user by the simulator. In the context of a simulator, operator and instructor actions may change the boundary conditions dynamically during the progress of the accident. So, two main approaches can be employed in this context, as described for example in [12].

The first method is time-stepping. The objective is to learn the mathematical operator that computes the next timestep(s) from the previous one(s). The timestep is imposed by the refreshment rate of the simulator. Such approaches usually require less simulations, because each timestep of the training database can be considered as a learning point. However, they are subject to error accumulation and, consequently, instability. Using several timesteps in the past and predicting several timesteps in the future, as well as advanced training strategies, may limit such undesired behaviour.

The second methodology is based on time-series prediction. In this case, the complete transient is calculated in advance based on the initial conditions. Such approaches are usually more stable and accurate, but they require more data. Indeed, each sequence is only one training point. The possibility for the operator and the instructor to make an action at any time during the simulation is another challenge. Different approaches can be investigated to address the bifurcations of the simulation at such events. The limited number of possible actions during the ex-vessel phase of the accident is an advantage for this strategy.

3.3. Hybrid approaches

ASSAS will take advantage of the modular structure of ASTEC to explore hybrid ML approaches, for which surrogate models will replace only a part of the code. Different criteria must be considered to choose their appropriate boundaries:

- The contribution of the corresponding function to the CPU time, which gives an upper limit of the achievable speed-up factor;
- The complexity of the surrogate model, depending primarily on the intrinsic dimensionality of the problem;
- The complexity of data generation;
- The complexity of the integration of the surrogate model into ASTEC.

One additional complexity to consider is the coexistence of three levels of timesteps in ASTEC. Until the version 3.1 of ASTEC, data could only be extracted at each macro timestep, making it impossible to develop surrogate models interacting with a module at each of its internal timestep. An additional feature has been added in version 3.1.1, which gives access to the variables generated by CESAR at every internal timesteps, broadening the possibilities for ML approaches.

Three strategies have been selected for the development of surrogate models. Contrary to the global approach mentioned in subsection 3.2, they address the in-vessel phase of the accident only. They are described in the next sub-subsections. In each case, the identification of the inputs and outputs of the models has been a complex task, requiring a deep understanding of ASTEC. It is strongly connected to the functional specifications of the simulator as well because the surrogate models must at least predict the data displayed by the HMI.

3.3.1. CESAR solver initialisation

The most time-consuming operation of the thermal-hydraulics module CESAR is to solve a non-linear system of partial differential equations, thanks to a Newton-Raphson iterative method. Such methods are efficient if they are initialised close to the solution. In the current version of ASTEC, the solver is initialised with the converged solution of the previous timestep. The idea is to use a ML algorithm to initialise the solver with a first guess of the solution, as it has been tested in [13]. This strategy could decrease the number of necessary iterations to find the converged solution, even allowing the use of longer timesteps. One major advantage is that the level of accuracy of calculations is not impacted since the convergence criteria of the solver are not modified. It is also relatively easy to integrate this approach into ASTEC's source code. On the other hand, the execution of the surrogate model must be efficient, as it will be called at each internal timestep of CESAR, so very frequently.

As mentioned in subsection 2.2, specific variables need more iterations of the solver to converge, depending on the phase of the accident. Efforts should focus on them, while keeping simpler models (linear extrapolation or initialisation with the solution of the previous timestep) for other variables. Since the problematic variables change during the accident progression, it could be convenient to develop an ensemble of surrogate models, governed by a classifier that choose which one to apply, depending on the state of the reactor.

3.3.2. Modelling thermal-hydraulics in a portion of the circuits

An alternative strategy to accelerate thermal-hydraulic calculations consists in replacing CESAR completely in a specific zone of the circuits, to be selected cautiously.

Developing a surrogate model for thermal-hydraulics within the vessel has been excluded for computational and physical reasons. First, thermal-hydraulics and core degradation are tightly coupled phenomena. The runaway core oxidation at high temperature is an instable phenomenon because the chemical reaction is accelerated by the heat it releases. It has been anticipated that small prediction errors of the surrogate model would lead to inacceptable discrepancies in results. Second, practical reasons linked to the management of different levels of timesteps made data retrieval and integration of the surrogate model more complex, requiring several adaptations of the source code. It has been estimated that a global surrogate model for the vessel coupling thermal-hydraulics and core degradation was more promising, as described in subsection 3.3.3.

Therefore, it has been decided to concentrate efforts on thermal-hydraulics in the primary and secondary circuits. Contrary to the approach described in sub-subsection 3.3.1, the surrogate model will predict the thermal-hydraulic conditions in the concerned systems only at each macro timestep. A first attempt has been carried out to replace the SGs by a surrogate model, taking advantage of their four-fold symmetry [14]. A data pipeline has been built to integrate the new model in ASTEC:

- First, CESAR calculates thermal-hydraulic conditions in all circuits except the SG,
- Then, the surrogate model calculates variables in the SG,
- Finally, data is combined to reconstruct the flow in all circuits.

The last step is necessary for SOPHAEROS to access the flow conditions in the circuits, which determine the transport of fission products.

The scope of the surrogate models will be progressively complexified, starting with a limited region of the RCS, possibly stretching up to the complete primary and secondary circuits. Autoencoder neural networks have so far proved to be the most appropriate dimension reduction methods, that scale up with the large number of variables in the system and their non-linear behaviour.

3.3.3. Primary vessel modelling

The last surrogate modelling option explored by ASSAS focuses on the global phenomenology in the primary vessel, computing thermal-hydraulics and core degradation simultaneously, to account for their strong coupling. It is hoped that this approach will reduce the dimensionality of the problem. In fact, the vessel (as defined numerically in the ASTEC input decks) is connected to other control volumes only by the 4 cold legs of the primary circuits and the upper plenum. The variables exchanged at these junctions include only thermal-hydraulic conditions and the mass of the different chemical elements released by the core degradation. In ASTEC, the speciation of the fission products is re-calculated by SOPHAEROS at the outlet of the core. Finally, the data displayed by the simulator to represent the core degradation is quite synthetic.

3.4. Validation of machine-learning models

Since they do not compute calculation results from first-principles equations, the validation of ML models requires a different methodology than for physical models. The training data must be split into a training set (to train the models), a validation set (to tune the hyperparameters of the models, like the number of layers for a neural network) and a test set (to evaluate the generalisation capabilities of the models). For hybrid approaches, the interactions between the native physical models of ASTEC and the machine-learning models must be assessed.

The ML community generally relies on simple metrics to train and validate models, like the root-mean-squared (RMS) error. Such error functions may not be suited for SA simulations, which are subject to large uncertainties due to the complexity of the phenomenology and the lack of experimental validation data. It has been decided to complement the RMS metric with expert judgement and the Fast Fourier Transform Based Method (FFT-BM) metric, which has already been used to assess the agreement between experimental results and severe accident code results [15]. Other relevant metrics may be explored as a benchmark. Particular attention will be paid to the good timing of the transitions between the different phases of the SA: core uncovery, start of fission product release, start of molten material relocation, vessel rupture, containment failure, *etc*. The discrepancies between the results provided by the best-estimate calculations and the calculations performed with the simulator (which will include simplified physical models and possibly ML models) will be compared to the usual dispersion of results between different users and calculation codes, as well as the effect of numerical sensitivity.

4. CONCLUSIONS

ASSAS is a 4-year Horizon Euratom project focused on the development of a proof-of-concept SA simulator, which require to increase the performances of ASTEC. Several approaches will be explored during the project to reach a real-time execution of the simulator at any phase of the SA simulation. Improving the algorithmics of the code is appealing because it almost does not affect the physical models. However, the corresponding modifications of the source code are time-consuming. Simplifying the physical models and the plant nodalization is simple and effective but it degrades the accuracy of results and increases numerical sensitivity. Machine-learning may be a game-changer to develop fast surrogate models, replacing SA codes partially or totally. Preliminary tests must be performed to evaluate the complexity of the various options envisaged in ASSAS. The project will help to determine if such approaches can scale-up to industrial simulators, which are used for much more diverse situations than the prototype developed in ASSAS. The efforts associated with data generation and ML models training should not be prohibitive.

Beside the prototype simulator, ASSAS will produce various results for the SA community, like a faster version of ASTEC, more detailed recommendations for the nodalization of reactors, or a higher modularity of the code. The training database generated during the project will be a central asset to explore new data-driven methodologies, like the design of expert systems supporting emergency response, pursuing the work of [16]. It may also interest data scientists to test new neural network architectures on real data.

ACKNOWLEDGMENTS

The authors acknowledge the support provided by the partners and stakeholders of the ASSAS project, in particular Alexei Miassoedov (International Atomic Energy Agency, Vienna, Austria), Alban Martinez-Delcayrou (Framatome, Courbevoie, France), and Francisco Chinesta (Ecole Nationale Supérieure d'Arts et Métiers, Paris, France).

Funded by the European Union

Funded by the European Union under the grant agreement no. 101059682. Views and opinions expressed are however those of the author(s) only and do not necessarily reflect those of the European Union or the European Commission-Euratom. Neither the European Union nor the granting authority can be held responsible for them.

REFERENCES

1. Lionel Chailan, Loic Bosland, Laure Carénini, Julien Chambarel, Frederic Cousin, *et al.*, "Overview of ASTEC integral code status and perspectives," 9th European Review Meeting on Severe Accident Research (ERMSAR2019), Prague, Czech Republic, March 2019, doi: ⟨irsn-04106726⟩
2. *Application of simulation techniques for accident management training in nuclear power plants*, IAEA TECDOC SERIES, IAEA-TECDOC-1352 (May 2003).
3. European Nuclear Safety Regulators Group, *Compilation of recommendations and suggestions – Peer review of stress tests performed on European nuclear power plants* (26th July 2012).
4. Nuclear Energy Agency Committee on the Safety of Nuclear Installations, *Informing Severe Accident Management Guidance and Actions for Nuclear Power Plants through Analytical Simulation*, NEA/CSNI/R (2017)16 (2nd July 2018).
5. *Classification, Selection and Use of Nuclear Power Plant Simulators for Education and Training*, IAEA TECDOC SERIES, IAEA-TECDOC-1887 (2019).
6. OpenMP Application Programming Interface, Version 5.1 November 2020, www.openmp.org
7. S. Girard, V. Mallet, I. Korsakissok, and A. Mathieu, "Emulation and Sobol' sensitivity analysis of an atmospheric dispersion model applied to the Fukushima nuclear accident", *Journal of Geophysical Research: Atmospheres*, **121** (7), pp. 3484– 3496 (2016), doi:10.1002/2015JD023993.
8. Sergey Galushin, Dmitry Grishchenko, Pavel Kudinov, "Implementation of framework for assessment of severe accident management effectiveness in Nordic BWR", *Reliability Engineering & System Safety* **203** (107049) (2020), doi: 10.1016/j.ress.2020.107049
9. Espeholt, L., Agrawal, S., Sønderby, C. *et al.* "Deep learning for twelve-hour precipitation forecasts", *Nat Commun* **13** (2022) https://doi.org/10.1038/s41467-022-32483-x.
10. Bac J, Mirkes EM, Gorban AN, Tyukin I, Zinovyev, A., "Scikit-Dimension: A Python Package for Intrinsic Dimension Estimation," *Entropy*, 19th October 2021, **23** (10), pp. 1368, doi: 10.3390/e23101368
11. Fahad Alsayyari, Zoltán Perkó, Danny Lathouwers, Jan Leen Kloosterman, "A nonintrusive reduced order modelling approach using Proper Orthogonal Decomposition and locally adaptive sparse grids", *Journal of Computational Physics* **399** (2019), https://doi.org/10.1016/j.jcp.2019.108912.
12. Lucas Meyer, Louen Pottier, Alejandro Ribes, Bruno Raffin, "Deep Surrogate for Direct Time Fluid Dynamics", *Proceedings of meeting NeurIPS 2021 - Thirty-fifth Workshop on Machine Learning and the Physical Sciences*, Vancouver, Canada, Dec 2021, pp.1-7 ⟨hal-03451432v1⟩.
13. Antoine Lechevallier, Sylvain Desroziers, Thibault Faney, Eric Flauraud, Frédéric Nataf. "Hybrid Newton method for the acceleration of well event handling in the simulation of CO2 storage using supervised learning", preprint (2023), ffhal-04085358v3f.
14. Louis Proffit, "Internship report – ASSAS project" (25th July 2023), https://assas-horizon-euratom.eu/documents-and-data/
15. Pietro Maccari, Andrea Bersano, Stefano Ederli, Fabrizio Gabrielli, Fulvio Mascari, "Validation and uncertainty analysis of ASTEC in early degradation phase against QUENCH-06 experiment", *Nuclear Engineering and Design* **414** (2023), https://doi.org/10.1016/j.nucengdes.2023.112600
16. F. Mascari, F. Rocchi, P. Carny, L. Liptak, M. Adorni, J. Fontanet, L.E. Herranz, M. Shawkat, W. Raskob, F. Cousin, J. C. de la Rosa Blul, E. Urbonavicius, F. Di Dedda, T. Augustsson, M. Constantin, G. Arbaev, P. Isaksson, J. Kubicek, "FASTNET Scenarios Database Development and Status". *Proceedings of the 9th European Review Meeting on Severe Accident Research (ERMSAR2019)*, Praga (Czech Republic), 18-20 March 2019.

Artificial intelligence for
Simulation of Severe Accidents
http://assas-horizon-euratom.eu
info@assas-horizon-euratom.eu

ERMSAR 2024

CAN MACHINE-LEARNING MAKE FAST AND ACCURATE SEVERE ACCIDENT SIMULATORS A REALITY?

INSTITUT DE RADIOPROTECTION
ET DE SÛRETÉ NUCLÉAIRE

Version 1 – 13/05/2024

Funded by the European Union. Views and opinions expressed are however those of the author(s) only and do not necessarily reflect those of the European Union or the European Commission-Euratom. Neither the European Union nor the granting authority can be held responsible for them.

Summary

1. General objectives of ASSAS
2. Specifications of the simulator
3. Optimisation of ASTEC
4. Machine-learning approaches

Summary

1. General objectives of ASSAS
2. Specifications of the simulator
3. Optimisation of ASTEC
4. Machine-learning approaches

A basic-principles SA simulator



Desktop simulator (Westinghouse)

Need for severe accident (SA) simulators

- Education & training
- Accelerating the learning curve for SA codes
- Importing plant data from existing simulators: data-centric approach

A prototype simulator for a Western-type PWR

- Close to best-estimate accuracy
- Interfacing ASTEC and TEAM_SUITE®
- Prepare the path for more realistic simulators & other designs & other SA codes

Summary

1. General objectives of ASSAS
2. Specifications of the simulator
3. Optimisation of ASTEC
4. Machine-learning approaches

Specifications of the simulator

Showing SA phenomenology

- 2 scenarios:
  - LB-LOCA with SI failure
  - SBO with AFW failure
- Synthetic screen + virtual reality display
- Deterministic answer (no uncertainty)

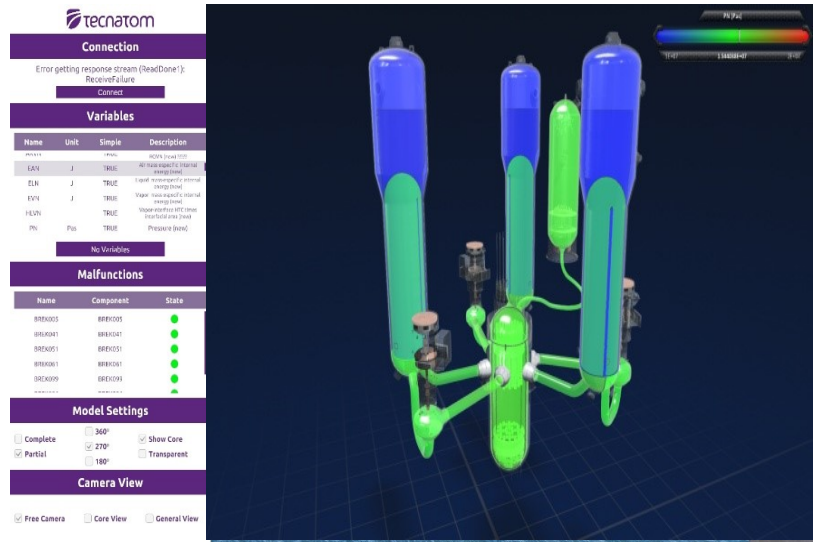

Example of virtual reality display (Westinghouse)

Running in real time or faster

- A challenge for SA codes… an opportunity to use machine-learning!
- Perspectives for fast running tools after the end of the project: uncertainty propagation, emergency response, PSA…

Specifications of the simulator

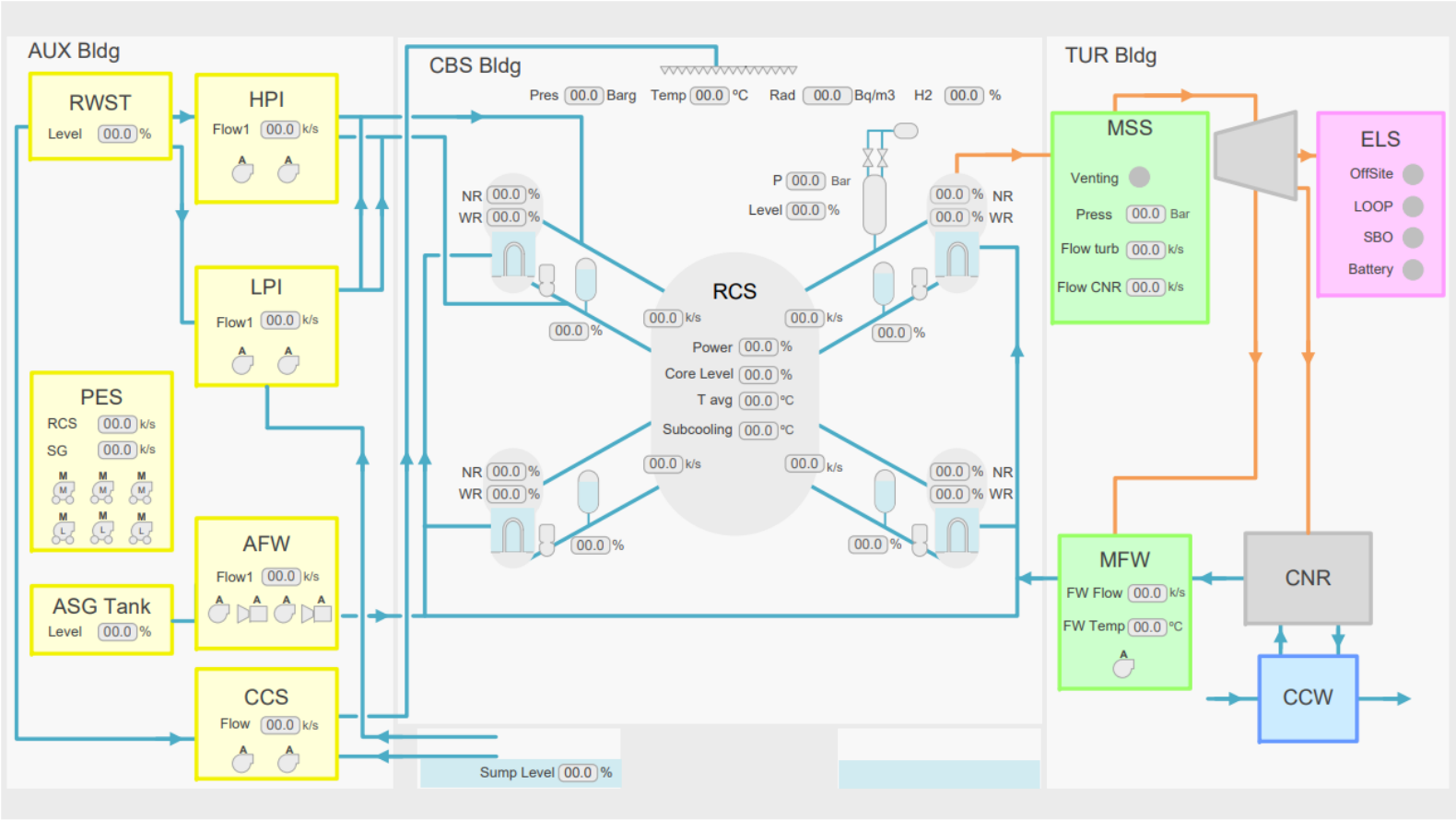

Simulator overview *SA screen* *Alarm display*

All phases of a SA:

- From initiating event to SA
- Core degradation
- Release and transport of FPs
- Vessel rupture and MCCI
- Containment pressurisation up to the filtered release of FPs
- Some phenomena are excluded: steam explosion, direct containment heating...

Ergonomic interface:

- Simulation control (speed-up factor, freeze, load...)
- Main control room sensors + pedagogical information
- Plot variables & extract data

Summary

1. General objectives of ASSAS
2. Specifications of the simulator
3. Optimisation of ASTEC
4. Machine-learning approaches

ASTEC structure

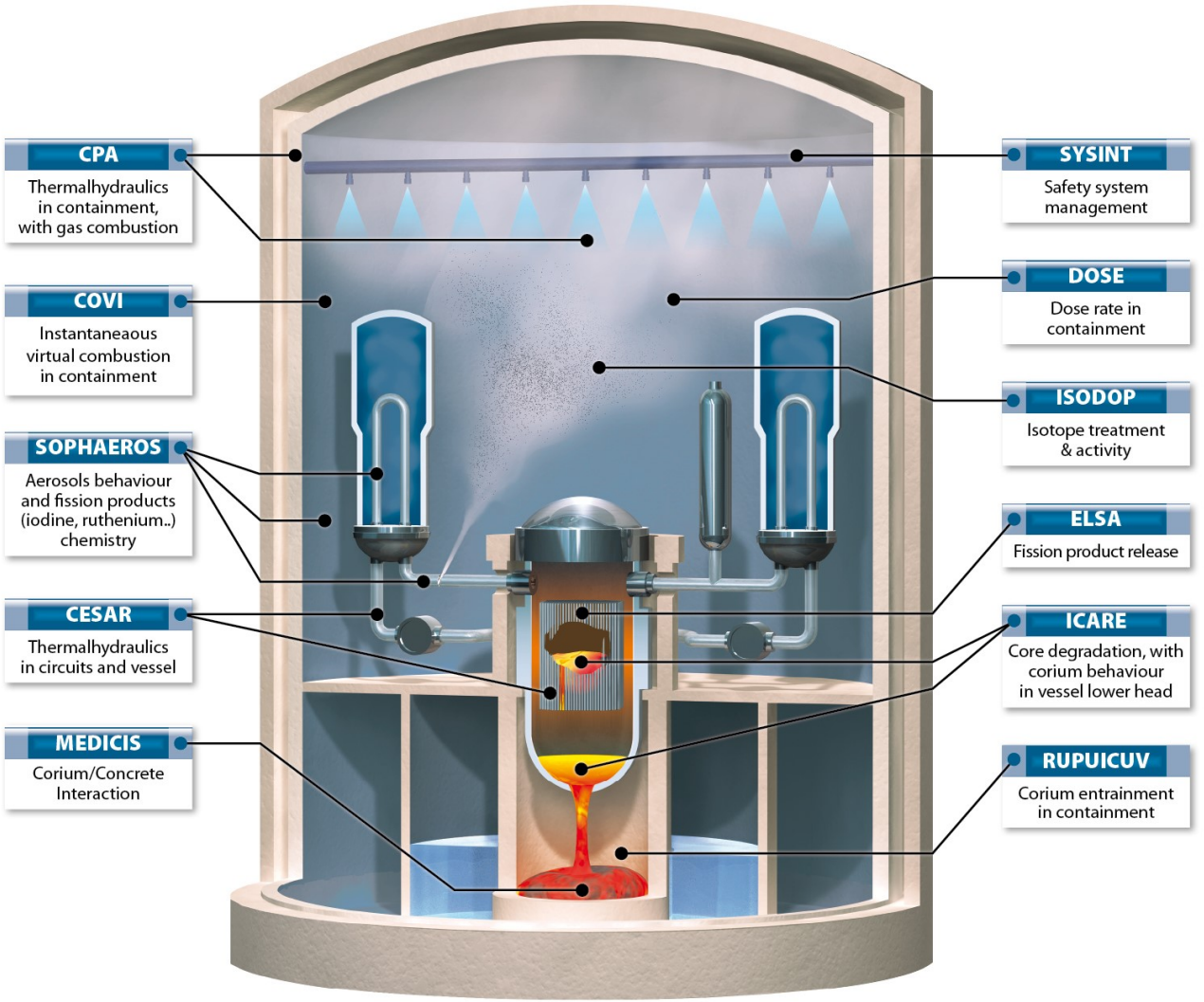

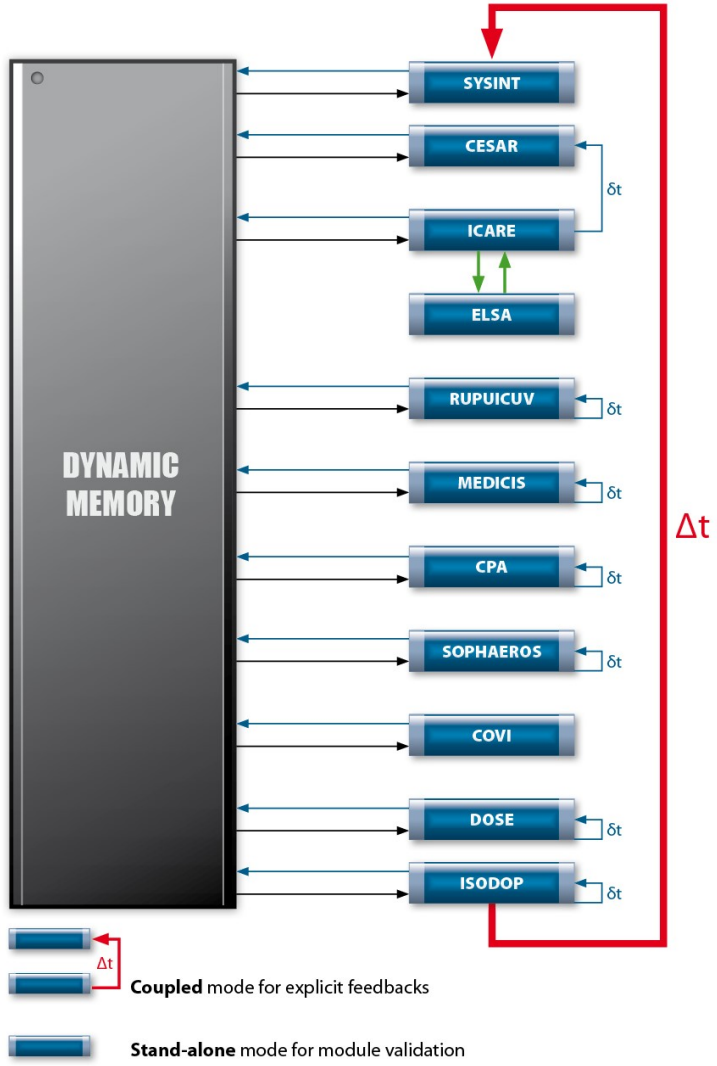

Efficient programming

Improving performances without impacting accuracy

Algorithmic improvements:

- Low-level optimisations (memory access, data management...)
- New solvers to be tested

Parallelisation:

- Sequential structure of ASTEC optimised for batch calculations (more sequences than processors) → Run only one sequence but faster
- Results obtained with OpenMP will be delivered to users in 2024



Simplification of the input deck

Simplified models

- ICARE+CESAR stop at vessel rupture
- Limited list of incondensable gases in the RCS

Simplified discretization

- Circuits + containment
- Acceptable results
- Higher numerical sensitivity

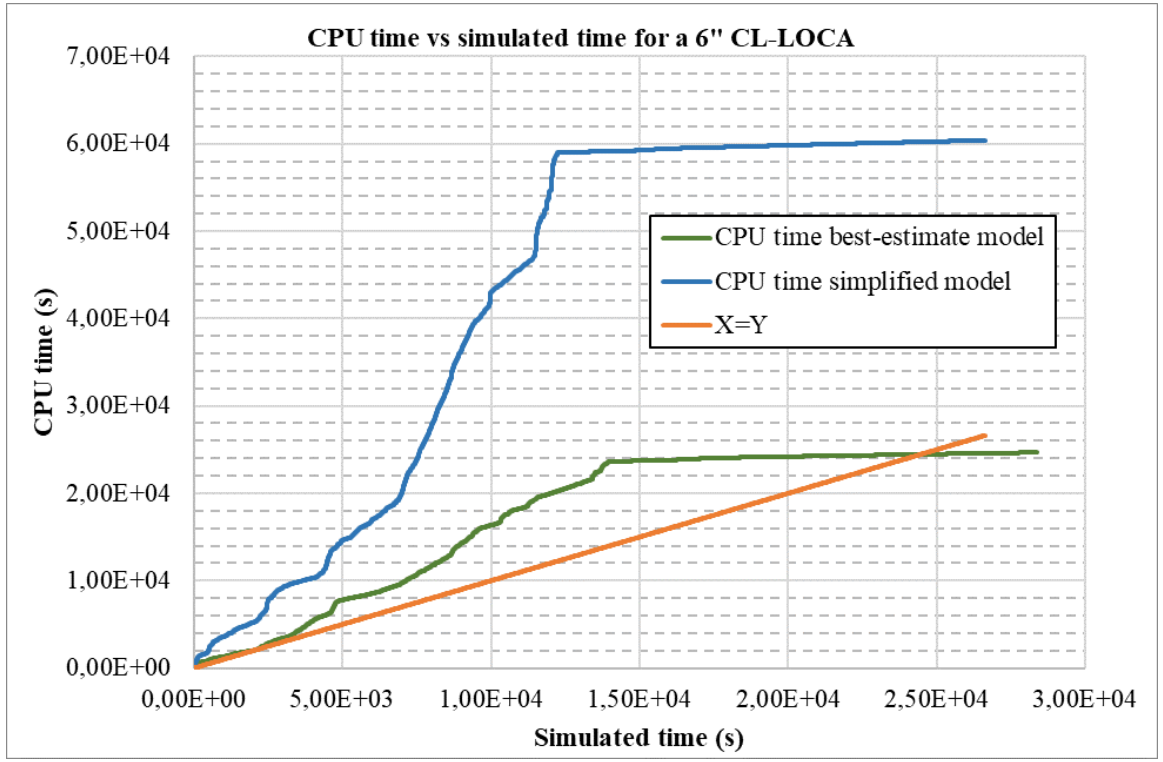

Numerical sensitivity

Numerical noise propagation with the best-estimate (blue) and simplified (red) input decks for a SBO sequence (higher sensitivity)

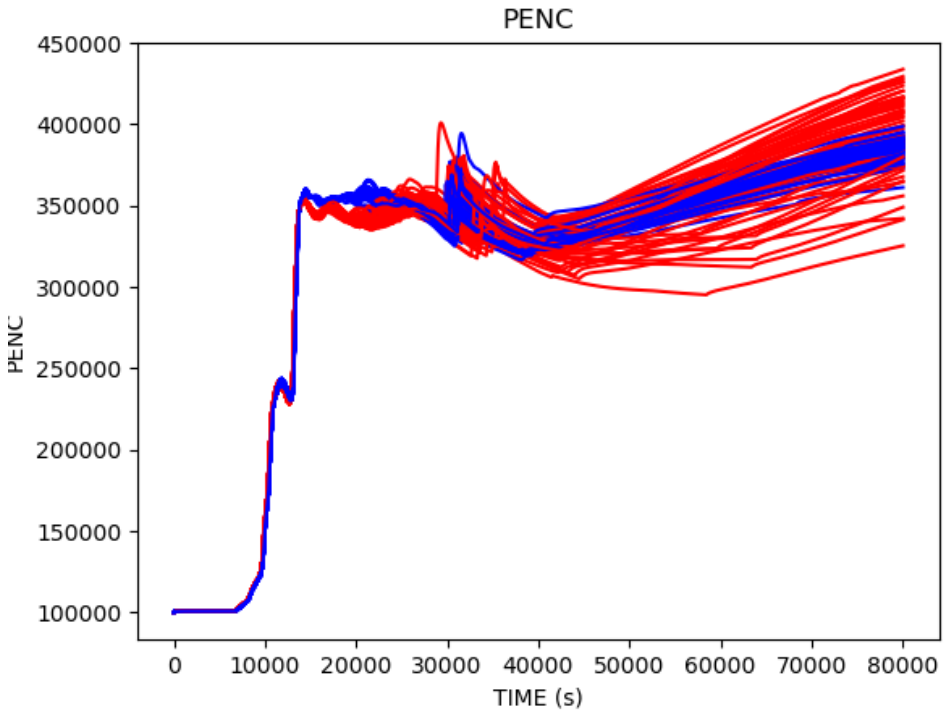

Containment pressure (Pa) versus time

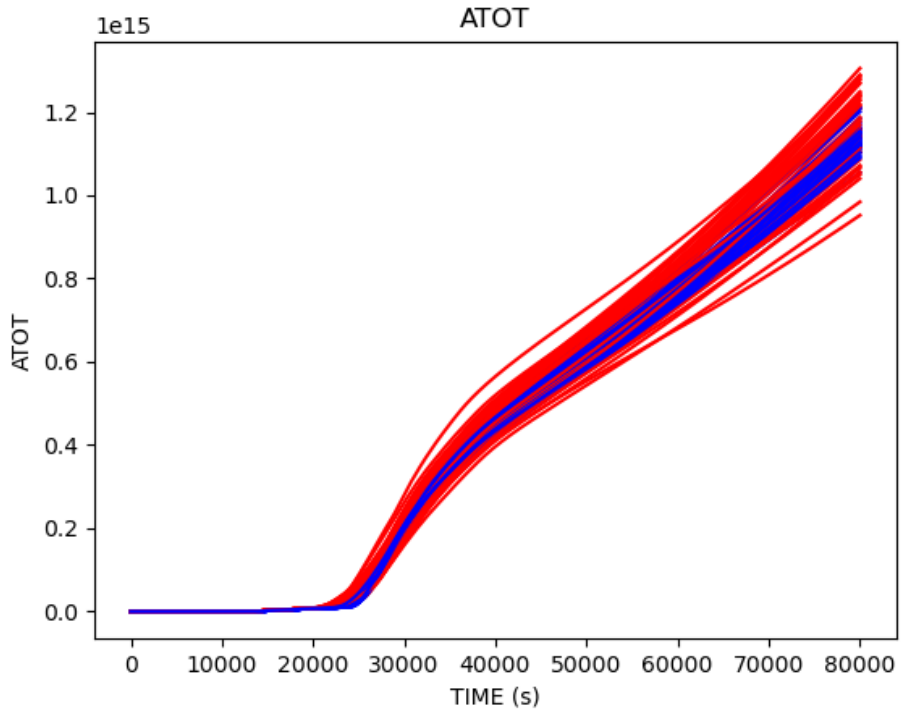

Total activity (Bq) released to the environment versus time

Summary

1. General objectives of ASSAS
2. Specifications of the simulator
3. Optimisation of ASTEC
4. Machine-learning approaches



Data-driven surrogate models

Machine-learning (ML) for scientific calculation

- ML can emulate complex models, like weather models
- ML learns from data: in our case, precalculated sequences
- Neural networks calculate fast, especially with GPUs

Requirements

- Computational resources to train the models
- Representative data: the amount increases with the complexity of functions and number of degrees of freedom
  - → Necessary to have trustworthy results
  - → Models will be specific to the considered design & scenarios

Global models

Replacing the SA code completely:

- Faster but more complex

Global containment model after the vessel rupture

- Few actions are possible during the MCCI phase
- Large variety of initial conditions after the vessel rupture
- Preferred option: time-series prediction with bifurcations at operator actions
- JSI & Energorisk for PWR-1300 and VVER-1000 designs

Melcor surrogate model: explored by KTH (BWR)

Hybrid models

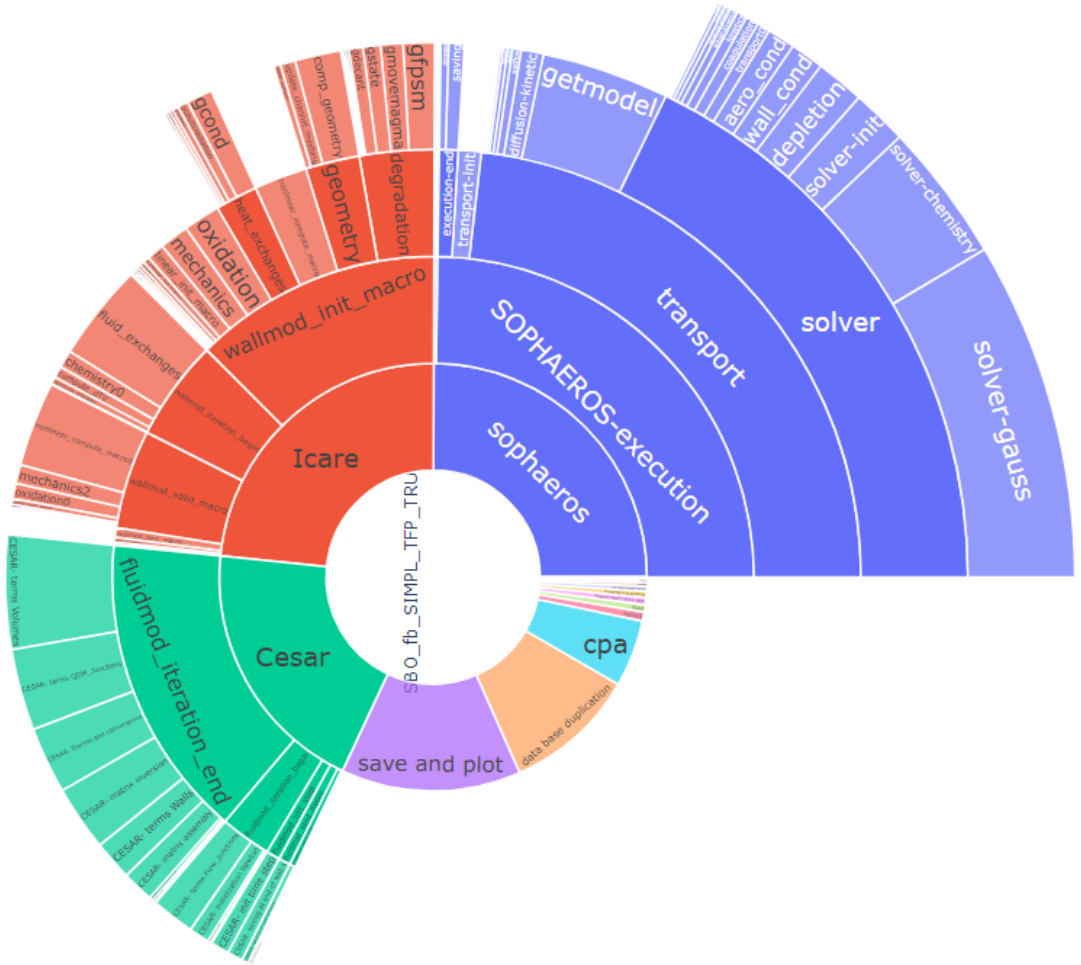

Share of the CPU time required by different models of ASTEC during the degradation phase (SBO, simplified input deck)

Replacing only a part of the code

- Data exchange with physical models at each ASTEC macro time-step

→ time-stepping methods are required: error accumulation must be controlled

- Interface with the native code to be developed
- Speed-up factor limited to the share of the replaced model to the global CPU time

→ Worth-case scenario illustrated by the chart: 3 modules have the same computational cost

3 options illustrated in the next slides

Local thermal-hydraulic models

CESAR discretization

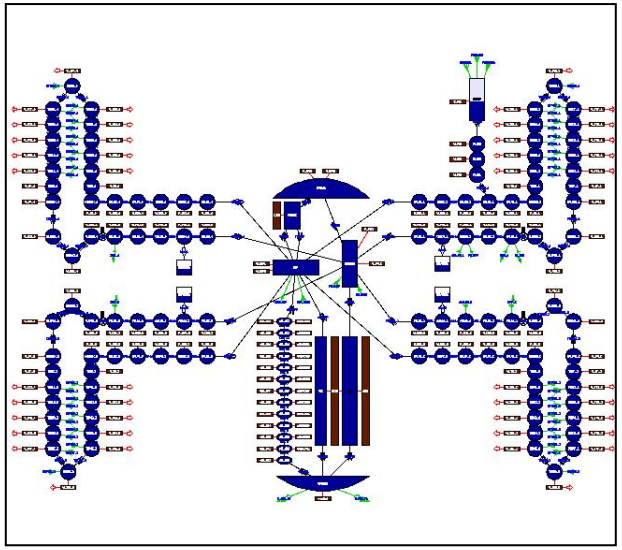

Objective:

- replace (part(s) of) the primary and secondary circuits by a surrogate model

Advantages

- Thermal-hydraulics is computationally intensive
- Relatively few variables to predict (flow conditions + wall temperature)

Challenges

- Smaller time resolution than the native model (macro time-step vs. CESAR micro time-step)
- Numerous combinations of operator actions on safety systems

CESAR solver initialisation

Accelerate the Newton-Raphson algorithm of the solver

- A gradient descent is used to solve the non-linear system of equations.
- The algorithm is initialised with the converged solution of the previous timestep.
- The ML model should predict a first guess of the solution, to reduce the number of iterations to reach convergence.

Advantages:

- Same accuracy as physical models
- Easy implementation

Challenges:

- Few examples in literature using ML
- Impact on the computational time to be evaluated

Primary vessel model

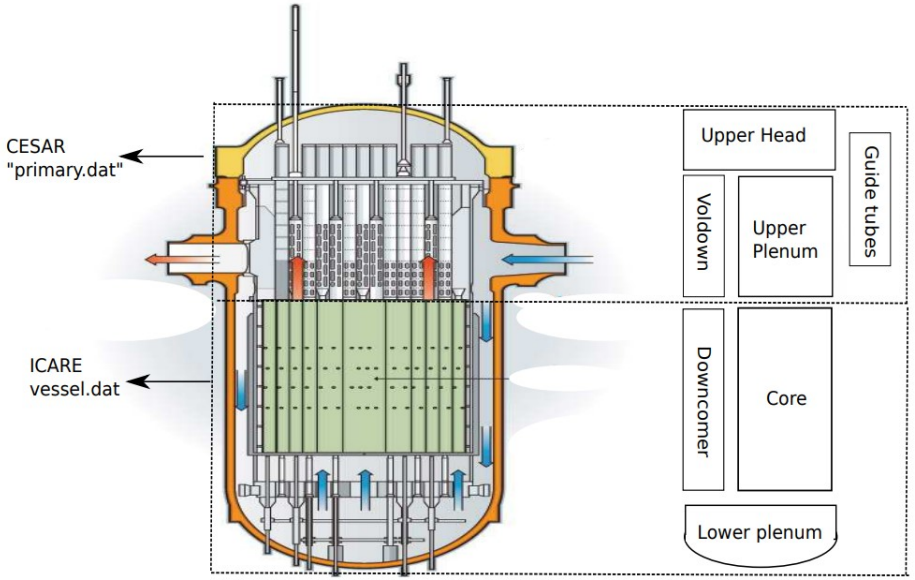

ASTEC Vessel model

Replacing ICARE + CESAR in the vessel

Advantages

- Modelling thermal-hydraulics and core degradation together to account for their strong coupling
- Possibly a higher generalisation capacity since no safety system is directly connected to the vessel

Challenges

- Number of variables and number of meshes to consider: high dimensionality
- Complexity of physical models

Conclusion

A simulator to make SA knowledge more accessible

Improving ASTEC’s performances for a real time execution

Explore different ML strategies (possibly in combination) to reach higher acceleration factors

Share a high-quality database for future collaborative work

- The ASSAS training database will be openly accessible for reuse:

→ International nuclear ML benchmark

→ Applications for emergency response

List of authors

B. Poubeau, Y. Richet, L. Chailan, F. Mascari, M. Massone,
S. Gianfelici, L.-E. Herranz, J. Fontanet, T. Lind,
C. d'Alessandro, J. Brence, I. Kljenak, S. Dzeroski,
F. Gabrielli, A. Stakhanova, J. Dressner,
I. Parrado-Rodriguez







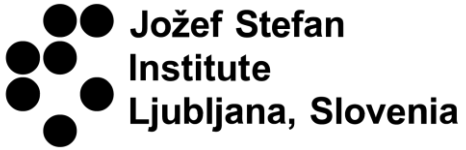







assas

Artificial intelligence for
Simulation of Severe Accidents
http://assas-horizon-euratom.eu
info@assas-horizon-euratom.eu

ERMSAR 2024

CAN MACHINE-LEARNING MAKE FAST AND ACCURATE SEVERE ACCIDENT SIMULATORS A REALITY?

IRSN
INSTITUT DE RADIOPROTECTION
ET DE SÛRETÉ NUCLÉAIRE

Version 1 – 13/05/2024

Funded by the European Union. Views and opinions expressed are however those of the author(s) only and do not necessarily reflect those of the European Union or the European Commission-Euratom. Neither the European Union nor the granting authority can be held responsible for them.

Primary vessel model (alternative slide)

Physical description of the reactor

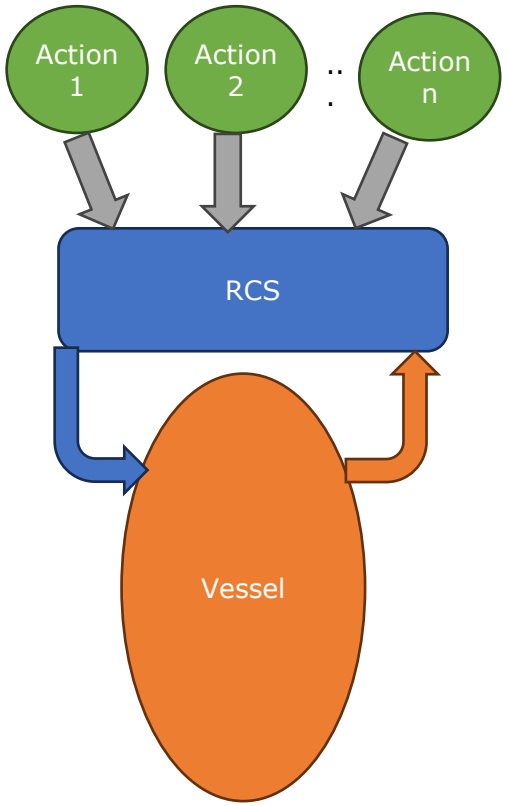

Modelling used for the development of a surrogate model

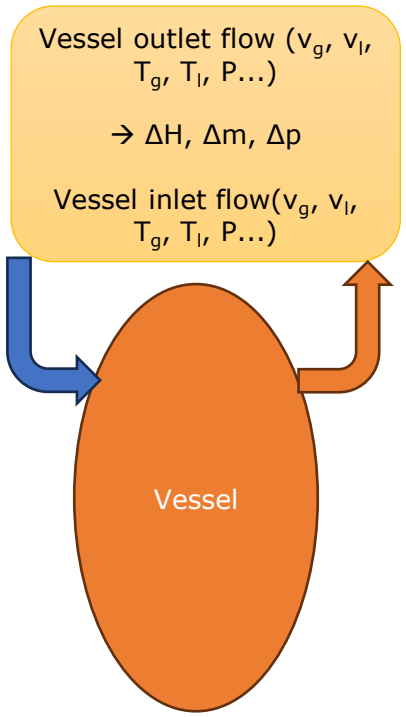

Schematic description of the modelling strategy: The RCS is considered as a black-box modifying mass, momentum and enthalpy of the fluid, whatever the operator actions are.

Replacing ICARE + CESAR in the vessel

Advantages

- Consider the coupling between thermal-hydraulics and core degradation
- Possibly a higher generalisation capacity

Challenges

- Number of variables and number of meshes to consider: high dimensionality
- Complexity of physical models

PRELIMINARY STRATEGIES FOR TRAINING DATASET GENERATION AND SURROGATE MODELLING OF STATION BLACKOUT MANAGEMENT MEASURES IN PWR

Christophe D'Alessandro* and Terttaliisa Lind
Paul Scherrer Institut (PSI)
Forschungsstrasse 111, 5232 Villigen, Switzerland
christophe.dalessandro@psi.ch; terttaliisa.lind@psi.ch

Raphaël Périllat and Gaëtan Blondet
PHIMECA Engineering
34 Rue de Sarlième, 63800 Cournon-d'Auvergne, France
perillat@phimeca.com; blondet@phimeca.com

ABSTRACT

This study is conducted in the frame of the EU-funded project ASSAS (Artificial intelligence for Simulation of Severe AccidentS), which aims at developing a basic-principles severe accident simulator for a generic PWR-1300 MW and at evaluating the possibility to replace some ASTEC models with machine-learning surrogate models. This paper presents the preliminary stage of the surrogate model development, focusing mostly on the generation of training datasets necessary for the machine learning process, and addresses essentially the CESAR module, which handles thermal-hydraulics in the primary and secondary circuits.
To achieve this, a base case scenario involving a Station Blackout (SBO) without any safety measures until Reactor Pressure Vessel (RPV) failure is considered. From this base case, various calculations are performed by introducing safety measures (e.g. low-pressure injections) at different times. This safety measures sampling is applied within the time range between the onset of the primary pressure drop (enabling low-pressure injections) and the RPV failure initially predicted in the base case.

Two approaches are employed. The first involves conducting a batch of 22 runs, varying one or two criteria in each run, and saving most relevant ASTEC variables at each time step (especially state variables from CESAR cells, but also system signals such as pump actuation). This should generate a suitable dataset for the development of time-stepping surrogate models, that are expected to compute each time-step, like ASTEC does, and also account for user's decisions during the accident calculation interactively.

Alternatively, another approach would consist of developing a meta-model that predicts key outcomes of the SBO - such as the delayed RPV failure time or final hydrogen production - with respect to one criteria (to simplify the problem): the safety injection time. However, due to the intricate mechanisms leading to RPV failure, training the neural network requires a dataset with a larger amount of samples, i.e. a finer variation of the injection time; here, a batch of 110 runs. Unlike the previous approach, preserving results at every time step is not as necessary. This last strategy is quite independent of the ASSAS project, as this global approach cannot suit the requirements of an online simulator; the purpose here is more exploratory. The last part of the paper proposes machine-learning strategies and discusses the optimal utilization of the generated training datasets.

KEYWORDS
ASTEC, SBO, machine-learning, training

1. INTRODUCTION

1.1. ASSAS Project

ASSAS (Artificial intelligence for the Simulation of Severe Accidents) [1] is an EU-funded project, led by IRSN in France (Institut de Radioprotection de Sûreté Nucléaire) and involving 14 partners in Europe. This project aims at developing a prototype for a PWR-1300MW basic principles severe accident simulator. Accident simulations will be based on the European reference code ASTEC [2], with which operators will be able to interactively apply safety actions and observe the impact of decisions on the evolution of the accident. To be realistic, simulations must run at least as fast as real-time. This is a major issue, because transient calculations, due to all the thermal-hydraulic and the in-vessel degradation phenomena, as well as fission product transport, are time-consuming and tend to use a small timestep (<< 1 s) in the early phase. That is why it is appealing to replace parts of the code with simpler and faster models developed by Machine Learning (ML) approach. This project wants to explore different ML methods and different approaches for replacing models with meta-models, and thus, enhancing the calculation performance. In that sense, the end-product will be a "proof-of-concept" simulator, which will also gather the gained experience on feasibility and know-hows for future severe accident code applications.
This paper addresses the thermal-hydraulic part of the Reactor Coolant Systems (RCS) only; that is, the CESAR module of ASTEC. The ultimate goal is to provide a new version of CESAR that speeds up the transient calculation of the thermal-hydraulics in the primary and secondary circuits, from an initiating event (station blackout, loss of coolant accident, steam generator tube rupture etc.) until reactor pressure vessel (RPV) failure. However, CESAR is also coupled to other ASTEC modules, and in particular to the one called ICARE, which computes the core degradation and has strong influence on the thermal-hydraulics.
This paper focuses on the first step of meta-models development, which is one of the most essential: the dataset generation. The datasets are the bricks of ML, with which the meta-models are going to be built. ML methods and treatment of the data (data analysis, selection of inputs and outputs) are discussed in the section 3.

1.2. Beyond the Project

Regarding the project, one would rely first and foremost on time-stepping approaches, as the simulator will reproduce time-sequences in real-time, and operator must be able to influence the thermal-hydraulic behavior during the simulation. For exploratory purposes, it is also of particular interest to investigate other kinds of methods that are more global and predict accident outcomes (end results), such as RPV failure time, total hydrogen generation, molten corium mass etc. Such investigations might provide some deeper insights on ML feasibility and give some ideas for possible applications in the future.

2. GENERATING TRAINING DATASETS

2.1. PWR-1300MW Model

The simulator will simulate pre-defined accident sequences in a generic PWR-1300MW including selected operator actions for accident management. The considered simplified PWR input deck is described by IRSN in [3]. The cooling system of this PWR is composed of four cooling loops (four hot legs, four cold legs, four steam generators, one pressurizer), that are discretized as follows (see Figure 1):

- for the primary circuits: 147 volumes and 155 junctions
- for the secondary circuits: 129 volumes and 132 junctions

The reactor domain is discretized into 3 inner concentric rings representing channels between fuel rods, as well as 2 outer channels for bypass and downcomer. The thermal-hydraulics of the vessel is also computed by CESAR. The lower plenum is initially represented by one control volume only, the upper head is split into 2 control volumes that are both part of the primary domain. Connections between primary and vessel domains are located at the downcomer and between the upper plenum and the core domain.

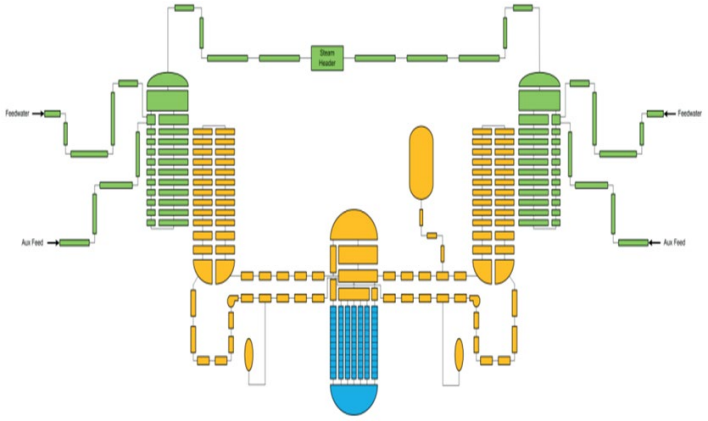

Figure 1. Nodalisation of CESAR (yellow: primary circuits; green: secondary circuits; blue: vessel channels) – (illustration from [4])

2.2. Station-Blackout Scenario

The scenario considered is a station-blackout (SBO) in the PWR-1300MW. All active systems get suddenly lost: main coolant pump, safety injection system, steam generator feedwater, auxiliary feedwater etc. Only passive systems are operational, such as valves (secondary steam generator valves, Pressure Operated Relief Valves of pressurizer, turbine valves) and hydro-accumulators. The decay heat is steadily removed through the steam generators, until the water inventory in the secondary circuits is fully depleted. Because of the insufficient heat removal, primary pressure increases after approx. 6000 s (Figure 2), reaching the pressure threshold of the Pressure Operated Relief Valves (PORV). One observes a cycling opening of the valves (between 6000 s and 12400 s), during which steam is released from the primary circuits to the containment. Primary water inventory decreases leading to a gradual core uncovering.
Opening of the PORV is remotely forced to reduce the primary pressure more quickly, and thus, to enable the discharge of the hydro-accumulators when dropping below the hydro-accumulator pressure (initially, 41 bar). Then, it results in a passive supply from the accumulators from around 14000 s, increasing the water level in reactor. Figure 3 presents captions of the reactor state at different times of the ASTEC calculation, from 13000 s (10 min after PORV forced opening) until 23893 s (1 second before RPV failure), where colors refer to temperatures in [K]. The core reflooding by the hydro-accumulators is observable on the captions at 15000 and 16000 s. Accumulators stop discharging before getting completely depleted (stop when pressure lays under 15 bar) in order to prevent any nitrogen ingression into the primary system. Subsequently, the water level sinks again. The core is getting uncovered, and thus, undergoes degradation such as swelling, melting, rupture etc. (see caption at 19000 s).

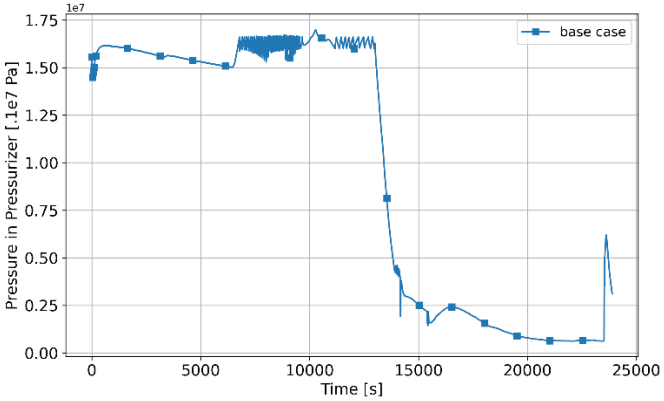

Figure 2. Primary pressure during the SBO scenario (base case)

A molten pool forms above the support plate (see captions after 21000 s), which thereafter slumps in the lower head. RPV fails after 23893 s, i.e. after approx. 6 h 40 min. This calculation took a CPU time of around 24345 s (i.e. approx. 6 h 45 min), as one can also see on Figure 4. One could conclude that this SBO scenario was eventually calculated as fast as reality, since the global acceleration factor is approx. of 1. But the local acceleration factor was not 1 all the time; the start of the transient was very unstable. Besides, the effect of water injection on a degraded core may require more computation time.

2.3. Severe Accident Management Measures

This SBO scenario with no safety measures to prevent or delay the vessel rupture must be considered as base case scenario (or reference scenario) for the samplings described in the next sub-section. Regarding SBO management, the first measure to take is to depressurize the primary system to enable the hydro-accumulator discharge. Consequently, the time of depressurization may play a role. However, in the base case above, it was assumed that the remote opening is always actioned once the Core Exit Temperature (CET) has reached 800°C. This input setting is subject to discussion though and might change in a near future. Once the hydro-accumulators have stopped, no injection source is available. The only hope is to recover some safety injection (SI) systems. In the present study, low-pressure injections may be re-activated; which is here an academic assumption (it is foreseen that the simulator eventually relies on a portable equipment system to mitigate the accident). As a matter of fact, the evolution of the accident will strongly depend on the time of injection. Reflooding a reactor that is not fully uncovered yet and quasi-intact, or reflooding a reactor that has already melted are two different things in terms of phenomenology. In the latter case, the coolant channels within the reactor present a totally different geometry and may be totally or partly obstructed. Besides, intact rods are easier to cool than molten pool, due to the larger heat exchange area to evacuate the decay heat. It is not possible for water to ingress a molten pool. Furthermore, it is assumed that the recirculation system also fails, so that the safety injection stops once its water tank is empty.

2.4. Sampling

In order to capture the impact of safety measures during the accident, batches of simulations were run, in which parameters of safety measures were varied. As it was assumed in the first place that the forced opening of the PORVs is conditioned by the CET, only the safety injection can be played with once the pressure is low enough. From the base case, one observes that the primary pressure drops due to PORV remote opening around 13000 s, and the RPV fails eventually at 23893 s. Therefore, safety injection must be varied within the time range [13000 – 23893 s].

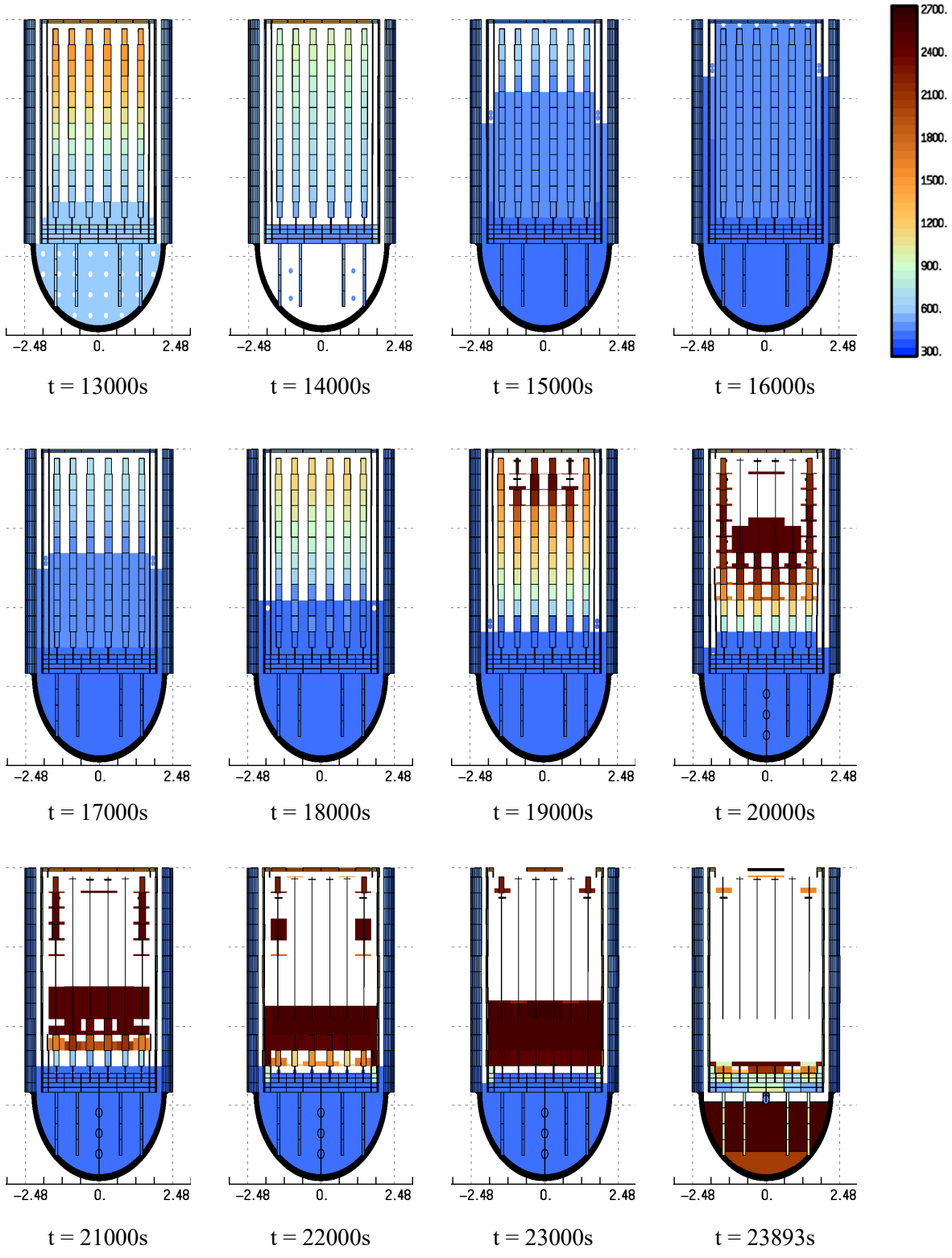

Figure 3. Evolution of core degradation from 13000 s until RPV failure (just after 23893s) in the base case scenario

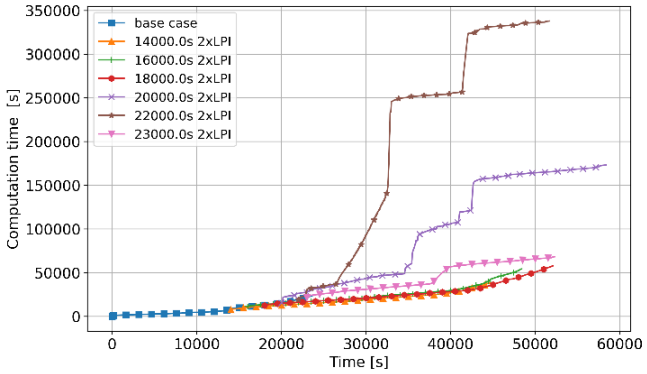

Figure 4. Calculation time for different runs

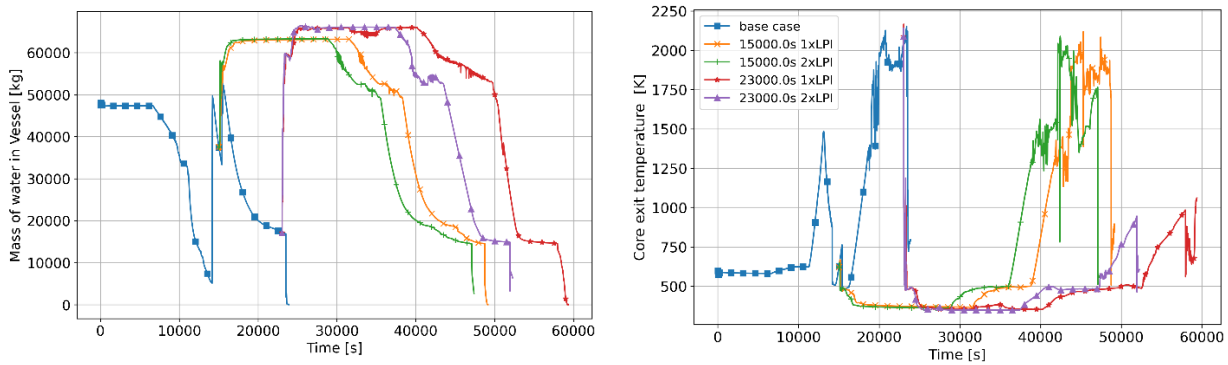

Figure 5. Samples of SBO with recovery of 1 or 2 LPIs in cold legs after 15000 s or 23000 s

2.4.1. Batch of 22 runs

A first batch of calculations was launched, in which the recovery time of Low Pressure Injection (LPI) in cold legs was varied between 13000 and 23000 s, with a 1000 s variation step, as well as the number of available LPIs (1 or 2); in overall, 22 runs. Lest some important information for time-series get lost, results were saved at each ASTEC timestep. The standard timesteps in ASTEC are adaptive. In the present calculations, Δt lays in the quite wide range of [0.01 – 10.0 s]. Depending on the injection time, calculations can take several hours to several days, as depicted on Figure 4 showing the computation time for different recovery times. Indeed, the topology of the core can change drastically during an accident sequence (see again the different stages on Figure 3). Injecting water at a late stage of core degradation may lead to more complex mechanisms, such as two-phase flow in porous media (debris bed), thermal interaction with hot molten material, additional oxidation, corium ablation, cladding rupture by mechanical stress etc. [5]; this all may result in stronger calculation instabilities. As one can see from Figure 3 and Figure 4, injecting water until 18000 s, while the core is still intact, doesn't impact the calculation time; but injecting after 20000 s, as the core presents more complex channel geometries or even molten pool, slows down the calculation. Furthermore, by looking at the evolution of CET, as well as the water inventory in the vessel, for different recovery times (Figure 5), one notices different patterns whether the water was injected at an earlier or a late stage of degradation (with presence of molten pool). When injecting at an earlier stage, as the core is still intact, the accident evolution will follow the one of the base case once the water level is depleted again. When injecting at late stage, the evolution depends strongly on the state of the channels that can be more or less obstructed.

As each calculation yields a significant amount of data, a filter is applied to save only the essential variables. The application of the filter should cause no information loss when restarting a calculation at any time point (see [6]). The generated dataset of 22 calculations should be sufficient to explore some preliminary approaches to create first surrogate models. This will be described in more detail in section 3.

2.4.2. Batch of 110 runs

A wider batch of simulations with a finer parameter variation was run in order to produce a dataset dedicated to more global machine learning approaches. The recovery time of LPI was varied between 13000 and 23900 s with a 100 s variation step, yielding 110 runs. Here, only the recovery time of LPI was varied; the number of available pumps was set to 2. The timestep is still adaptive, like in the previous calculations, but instead of saving the database at each timestep, it is now saved at a certain frequency; every 200 s. This considerably reduces the size and the amount of data, which is a crucial point considering the high number of simulations and large amount of data generated by every simulation.
For this approach, less variables are needed, as the purpose of this dataset is to investigate the impact of operator actions on the final outcomes rather than reproducing the whole sequence for each point of time.

Focusing on general variables can already give much valuable information on the global behavior of the accident progression. Figure 6 shows the RPV failure time as a function of the LPI activation time. Three phases can be distinguished:

1. An early phase before 18000 s: the failure time seems to slowly increase with increasing LPI activation time.
2. After 23500 s, the RPV failure happens at the same time as in base case scenario, meaning that injection plays no role anymore; it is too late. In the base case scenario, this time corresponds to the molten pool relocation into the lower head.
3. The zone between 18000 and 23500 s must be investigated much deeper as it shows large variations, presumably due to the different state of the core during LPI injection.

From this, one can notice the benefit of using a finer variation of the injection recovery time. Indeed, the variation range after 23500 s wasn't covered by the previous batch of 22 runs, which then missed the cliff-edge effect after that time.

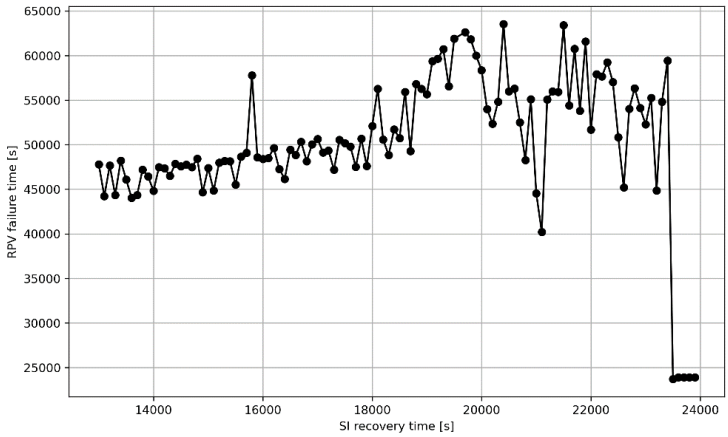

Figure 6. RPV failure time vs injection time

3. SURROGATE MODEL FOR CESAR

The main goal of this work is to design a surrogate model for the CESAR module outside the vessel, i.e., build a meta-model that reproduces the thermal-hydraulic evolution of fluid variables within the RCS. Using the batch of 22 calculations, in which each timestep was saved, a preliminary surrogate modelling approach was developed, that encompasses the whole primary circuit by focusing on vessel inlets and outlets; more precisely, in the volumes directly connected to vessel channels (see Figure 7 below).

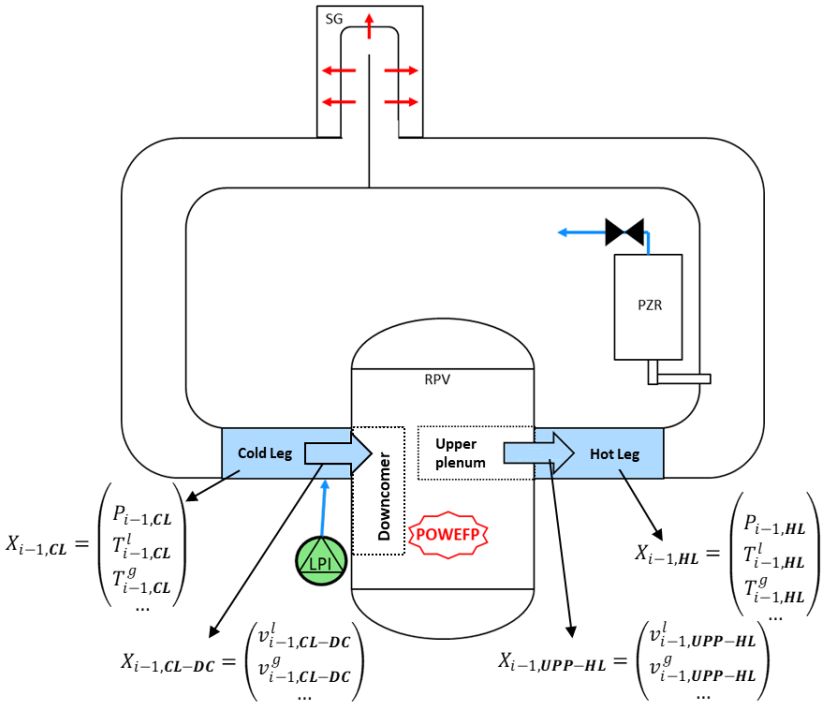

Figure 7. Illustration of the preliminary surrogate-modelling strategy for CESAR

First step addressed the selection of input and output variables. As the aim is to simulate whole sequences until RPV failure, outputs will essentially be state variables at timestep $t+\Delta t$, given these same state variables at the current timestep t as inputs. The vessel itself is not included but features such as decay heat must be considered as input. Other aspects such as the inventory loss through the valves, heat loss in the steam generator, and mass and enthalpic flows from/into the vessel must be considered also as inputs and outputs. Regarding the secondary circuits, only the water inventory is considered as input, since it has a strong influence on the heat transfer in the steam generators, but nothing happens on this side anymore once the water inventory is fully depleted. In the future, some other parameters will be eventually also predicted with respect to the requirements for the simulator; mostly, parameters that are usually displayed to operators in the control room.

Operator's actions must be also accounted for as an input. In the SBO scenario presented in this work, recovery of LPI is the only considered operator's action. This input can be represented in the surrogate model by a binary value (ON/OFF) or by the LPI mass flow. The latter variable makes maybe more sense, as the mass flow is dependent on the system pressure. Therefore, probably both (status and mass flow) should be accounted as inputs for the calculation, while only LPI status might be "playable" by the operator. But, in this preliminary study and for simplification, only the LPI mass flow is taken as input.

After extracting the wanted variables from the batch of 22 simulations and from the base case calculation, covering an already filtered database of 153 physical variables for between 2000 and 10000 timesteps for

each run, it seemed necessary to work on dimension reduction. As a first attempt to lower the number of variables, redundant variables were identified by Pearson's linear correlation measurements. The Pearson's correlation was calculated for each pair of variables (Figure 8). From it, it was namely observed that the symmetry of the modelling between the legs of the four loops resulted in almost identical evolutions of the state variables; thus, it was possible to reduce the dataset to 89 variables. Then, these 89 quantities were normalized so that they varied between 0 and 1, in order to facilitate the work of the surrogate models by avoiding them having to manage several different orders of magnitude for the different variables.

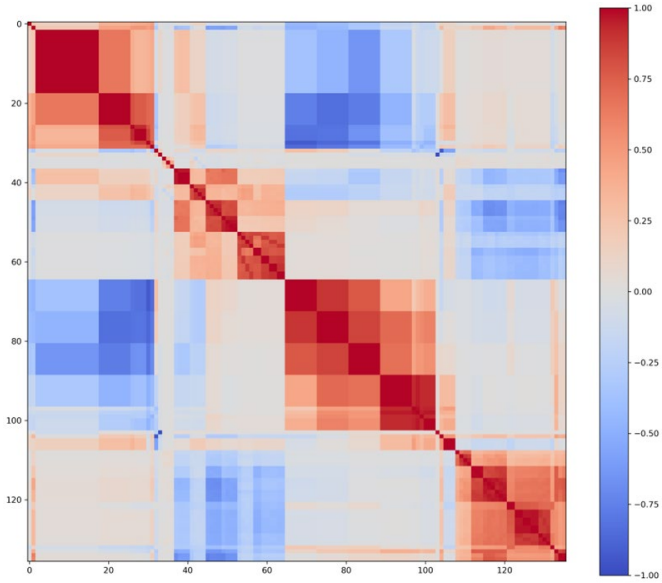

Figure 8. Correlation matrix of the 153 physical variables in the dataset

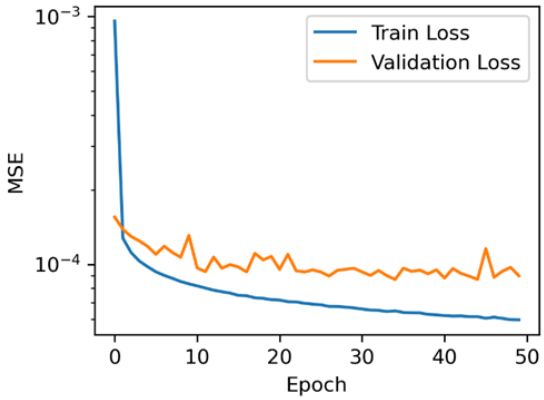

Figure 9. Training and validation loss (Mean Square Error) curves for the LSTM network

Analogously to [6], each simulation was divided into sub-sequences of 10 consecutive timesteps. A meta-model was trained to predict the 11th timestep of each sub-sequence, given the previous 10 timesteps as input. As the timestep is adaptive during the ASTEC calculation, and therefore not constant, the data were first interpolated to re-create a database with a uniform timestep of 1 second throughout the calculations. 80% of the sub-sequences were used for the training (randomly chosen), while the remaining 20% were used as test samples to evaluate the model.

This first attempt consists of a Long-Short Term Memory networks (LSTMs), which is a particular type of Recurrent Neural Network (RNN) widely used to predict time-series [7]. The preliminary network settings in this first attempt are as follows: 2 LSTMs layers at 100 units each, and a dense layer. Figure 9 shows that training loss (i.e., error between the predicted value and the target value during the training) decreases rapidly at the start of training, then continues to decrease more gradually through epochs. This suggests that the model is learning well from the training data. Validation loss (i.e., error of the model on the validation dataset, which is not used for the training) also decreases, but more slowly than training loss, tending to indicate that the model is generalizing and learning from relevant patterns and not simply memorizing the training data. On Figure 10, one can observe how far the predictions (i.e., meta-model's predictions for the 11th timestep) deviate from the values of the ASTEC simulations. The points on this graph are generally gathered around the '$y=x$' line. The error is unbiased but also presents a significant variance (Figure 11); far too large to be able to predict a complete time-series without an error that would accumulate over timesteps.

Several ways were identified to improve these results:

1. Clean up the data by removing certain outliers (for instance, variables linked to the PORV, such as the steam outflow, which create peaks in the data, and thus, greatly disrupt the learning process).
2. Adapt the number of layers in the LSTM, and/or the number of units in the LSTM layers, or also the number of timesteps in input. This may require more simulations to work.
3. Improve dimension reduction, since linear correlation are limited. Considering more physical knowledge, or applying more advanced dimension reduction method, may lead to more relevant variables.
4. Consider the operator action as a binary variable would add valuable information in the LSTM training.
5. Train the model on more data.

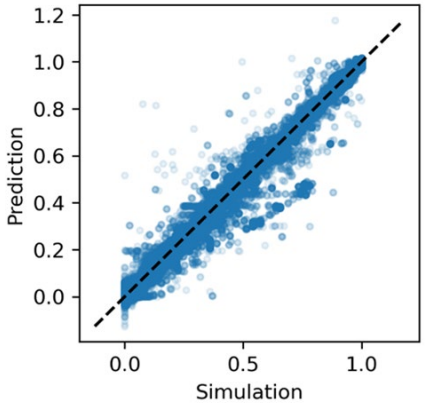

Figure 10. Compare predicted normalized values with ASTEC simulations

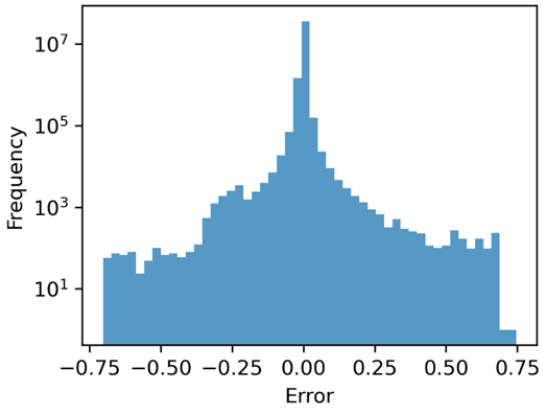

Figure 11. Error frequency

4. GLOBAL MODEL

4.1. Predictions of Accident Outcomes

As already observed when discussing the data presented in Figure 6, there is no linear correlation between the RPV failure time and the time of LPI injection. This is due to the complex phenomena occurring in the core during the degradation. Injecting water at certain times may delay or accelerate the RPV rupture, depending on the interaction of the cold water with the core, which is either quasi-intact, or partly degraded or destroyed, as a debris bed or a molten pool.

Interesting would be to find key-parameters that can be representative of the actual state of the core, or also detect the decisive events that may drastically change the outcomes, like for example at approximately 23500 s, after which point it seems that nothing can be done anymore to save or delay the rupture of the RPV due to so-called ductile failure (equivalent Von Mises stress exceeding the maximal material stress along the meridional curve of the lower head).

Many methods could be tested such as clustering methods, which could split the problem into categories, or more trendy approaches such as attention [8], which can capture key-events that are decisive for the outcomes of each time-sequence. However, the variations observed in Figure 6 suggest that numerical sensitivity must also be taken into account, which is also a real challenge for the project.

4.2. Beyond the Scope of ASSAS Project?

Thinking back to the time-stepping approach discussed in section 3, developing a single time-stepping meta-model for the thermal-hydraulics outside the vessel, that is able to deal with all possible changes from the vessel, is a real challenge: predicting the evolutions of state variables when the core is quasi-intact, then later on, taking into account the generation of hydrogen from cladding oxidation, and even later, the presence of some other materials in the systems from chemical interaction, gas release such as namely CO_2, or molten mixture. Global methods may be very useful by capturing the decisive event, in order to classify the different configurations. An idea would be to develop several time-stepping meta-models for the different topologies. The simulator could switch from a meta-model to another when meeting some criteria based on the thermal-hydraulics or the state of the core. These criteria are key-parameters that should be first identified by using global methods. Figure 12 shows the evolution of CET, as this parameter is one of the only thermal-hydraulic quantities displayable to the operator, that is directly impacted by the processes taking place in the reactor and may give some insights on these phenomena. Intuitively, this kind of parameters could help classifying the different topologies. All these peaks and drops that one can observe for example for the base case or even the 14000s- and 19000s-injection cases, are most probably yielded by some sudden movements of materials occurring in the core during the degradation: relocation of structures, molten pool formation, slump of material in residual water of the lower head, small or massive slump of corium into the lower head. Interesting to see that in some cases, like the 21000s- or 22000s-injection cases for example, the RPV fails before giving the CET a chance to increase. It is hard to investigate the phenomena occurring in each case separately though, because only essential variables were saved during the calculations, in order to save some storage space. But the goal is to find a few variables directly related to the vessel that may provide some more context for the CESAR-meta-model outside of the vessel, and that can capture cliff-edge events. It is worth mentioning that, concerning the in-vessel domain, it is planned within the project to design a meta-model that groups CESAR and ICARE, but this topic is beyond the scope of this paper.

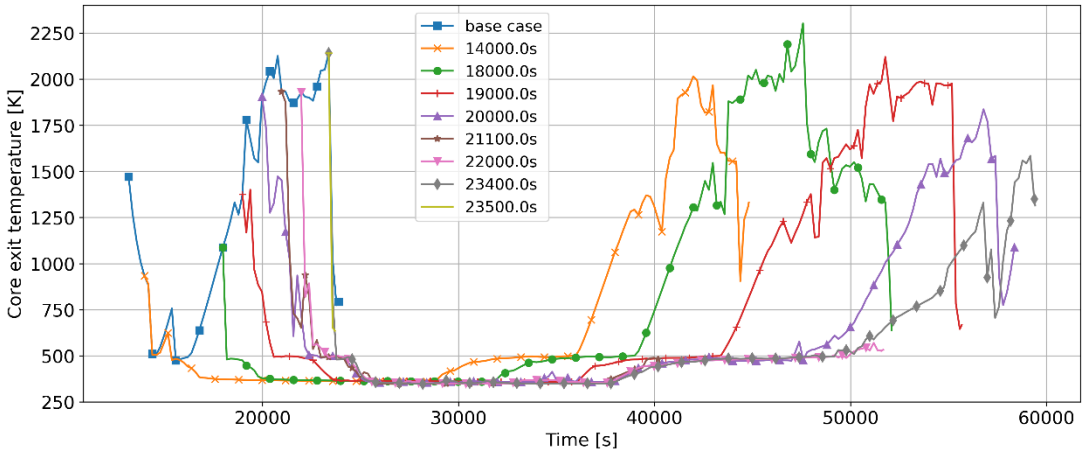

Figure 12. Evolution of CET for different injection recovery times

5. CONCLUSIONS

To develop ML models for a severe accident simulator, a batch of 22 ASTEC simulations was run to generate a preliminary database for primary system thermal-hydraulics. A SBO was selected as the base case accident scenario. As operators should be able to activate safety systems interactively during the calculation, it was

decided to focus first on time-stepping approaches for the meta-model. Building such a model requires a dataset in which ASTEC results are saved at each timestep. The simulation consists of a SBO scenario in which one or two LPIs were recovered after different times. The first attempt to generate a meta-model from this dataset is satisfactory, but still needs improvement, since the final meta-model should be eventually able to encompass the effects of the different phenomena occurring in the core during the accident, as well as to deal with materials and gases appearing during the simulation. Besides, the present model is still subject to error accumulation, which is a major issue if the meta-model is supposed to work over timesteps. This task is still in progress.

Investigating in parallel more global methods that would predict accident outcomes instead of each timestep may provide some insights regarding the general behavior of the systems. Some methods such as clustering approaches or attention mechanism may help finding out some general patterns during the accident sequence or some decisive parameters that could be used to classify our time-series. A dataset has been generated for this purpose, consisting in 110 runs of SBO, with finer variations of LPI recovery time, which already highlights three different time ranges for injection by presenting three distinguishable patterns of RPV failure time for example. This reveals at least three different behaviors of the thermal-hydraulics due to the different topologies of the core within these time ranges. The time-stepping approach developed for the simulator could probably benefit from global method insights, for instance by designing not one but several time-stepping meta-models that would be selected with respect to some key-parameters. Or switching from one meta-model to another when meeting a cliff-edge event during the calculation.

ACKNOWLEDGMENTS

Project funded by

Schweizerische Eidgenossenschaft
Confédération suisse
Confederazione Svizzera
Confederaziun svizra

Swiss Confederation

Federal Department of Economic Affairs, Education and Research EAER
State Secretariat for Education, Research and Innovation SERI

This work has received funding from the Swiss State Secretariat for Education, Research and Innovation (SERI)

Funded by the European Union

Funded by the European Union under grant agreement No 101059682. Views and opinions expressed are however those of the author(s) only and do not necessarily reflect those of the European Union or European Commission-Euratom. Neither the European Union nor the granting authority can be held responsible for them.

REFERENCES

1. "ASSAS project", https://assas-horizon-euratom.eu/ (2023).
2. "ASTEC", https://www.irsn.fr/recherche/systeme-logiciels-astec (in French).
3. S. Bertusi,"ASTEC V2.2 PWR1300-like Input Deck", IRSN (2022).
4. S. Šadek et al,"Severe Accident Analysis in the NPP Krško with the ASTEC Code", *22nd International Conference Nuclear Energy for New Europe (NENE)*, Bled, Slovenia (2013).
5. B.R. Sehgal, *Nuclear Safety in Light Water Reactors: Severe Accident Phenomenology*, chap 2.2.4, pp. 104-107, Elsevier, (2012).
6. L. Proffit,"Internship report – ASSAS project" (2023), (https://assas-horizon-euratom.eu/documents-and-data/).
7. F. Chollet, *Deep Learning with Python*, chap 6.2, Manning Publications Co., USA (2018).
8. A.Vaswani et al,"Attention Is All You Need", *31st Conference on Neural Information Processing Systems (NIPS 2017)*, Long Beach, CA, USA (2017).

PAUL SCHERRER INSTITUT

PSI

PHIMECA

The responsible engineering



C. D'Alessandro, T. Lind *(PSI)*

R. Périllat, G. Blondet *(PHIMECA)*

Preliminary Strategies for Training Dataset Generation and Surrogate Modelling of SBO Management Measures in PWR

ERMSAR 2024 – May 13th-16th , 2024, KTH, Stockholm, Sweden

ASSAS project

Artificial intelligence for the **S**imulation of **S**evere **A**ccident**S**

- EU-funded project
- 14 partners in Europe
- Goal:
  - Developing a prototype of severe accident simulator based on **ASTEC** for training of NPP operators
  - Trainees must be able to interactively apply safety measures during the SA simulation

- PSI's task in this project:
  - Replace the TH models of the reactor coolant systems with surrogate models capable of computing the accident sequence at least as fast as real-time

PWR-1300MW input deck

- Thermal hydraulic module: CESAR

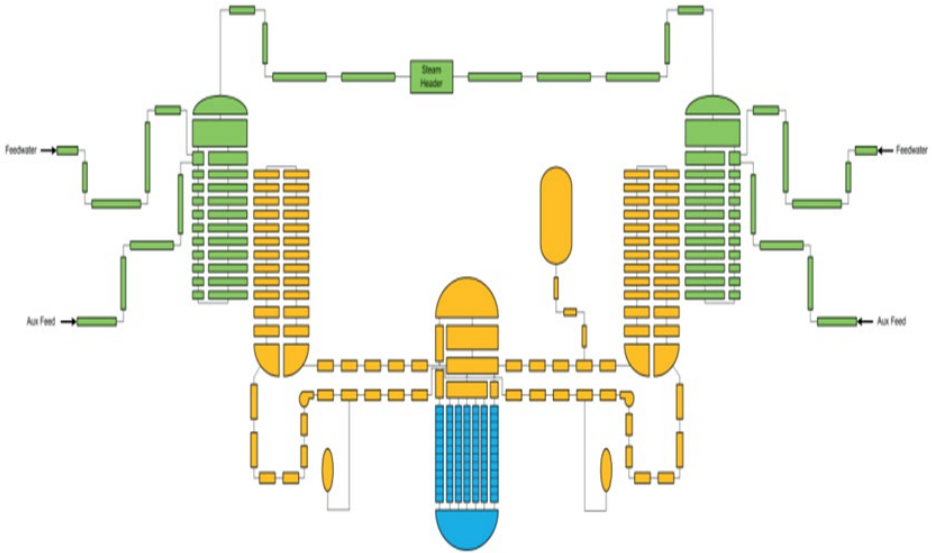

Source: Šadek et al.

- 4 loops
- Primary:
  - 147 volumes
  - 155 junctions
- Secondary:
  - 129 volumes
  - 132 junctions
- Reactor domain:
  - Core channels: 3 concentric rings
  - Bypass
  - Downcomer
  - Lower head
- CESAR runs until RPV failure

SBO scenario

Base case

- Failure of all active systems:
  - main coolant pump,
  - Safety injection systems etc.
- Only passive system available:
  - safety valves,
  - hydro-accumulator injection
- Assumption:
  - When CET > 800°C

  →(forced) remote opening of pressurizer PORV

  →pressure drops in PRIMARY

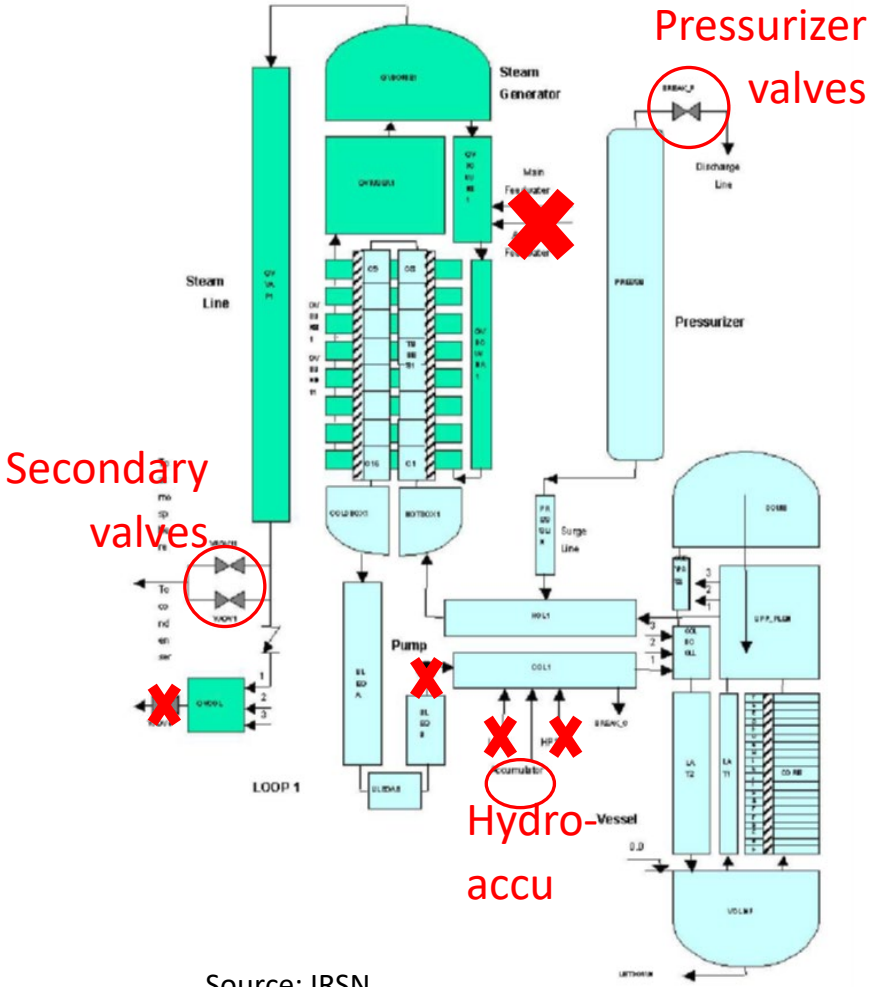

Source: IRSN

SBO scenario

Base case

- Failure of all active systems:
  - main coolant pump,
  - Safety injection systems etc.
- Only passive system available:
  - safety valves,
  - hydro-accumulator injection
- Assumption:
  - When CET > 800°C

  →(forced) remote opening of pressurizer PORV

  →pressure drops in PRIMARY

ASTEC calculation

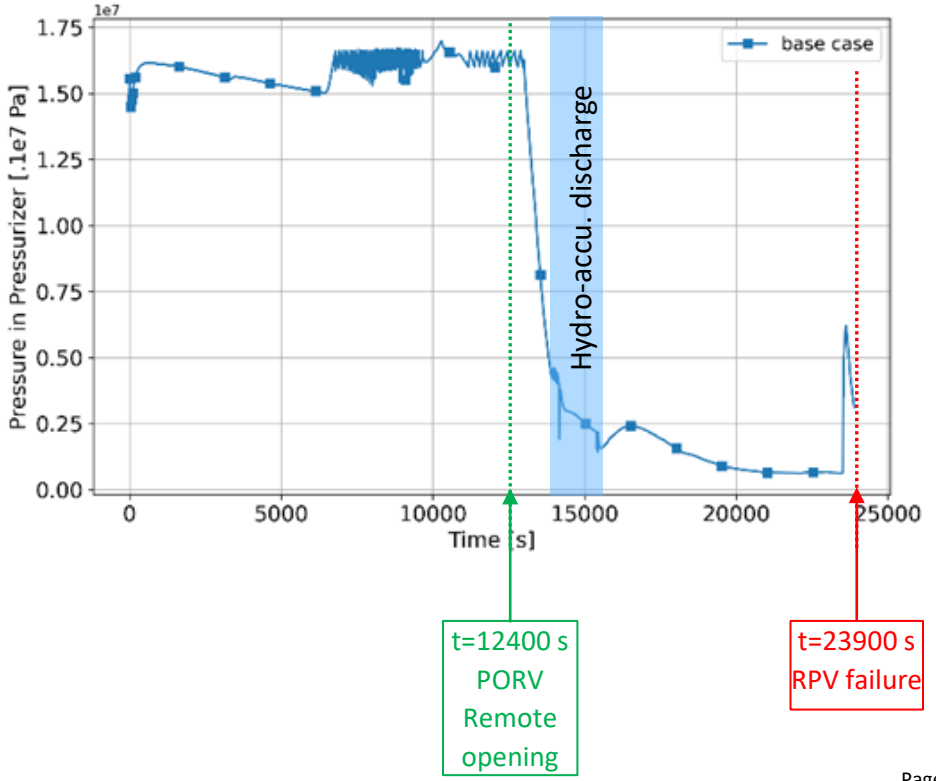

SBO scenario

State of the reactor

From 18000 s (after hydro-accumulator discharge) until 23893 s (RPV failure)

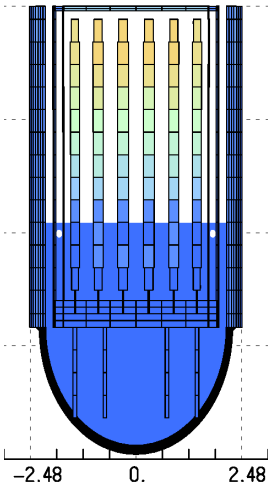

18000 s

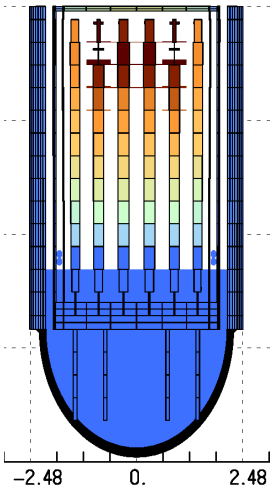

19000 s

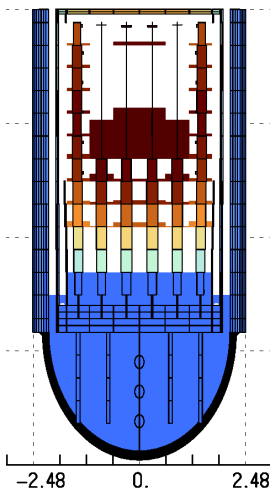

20000 s

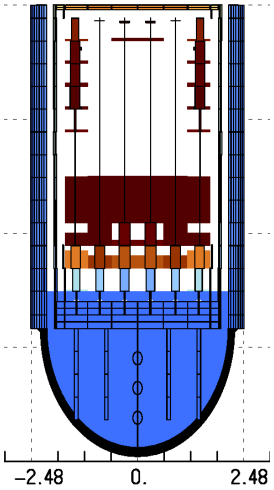

21000 s

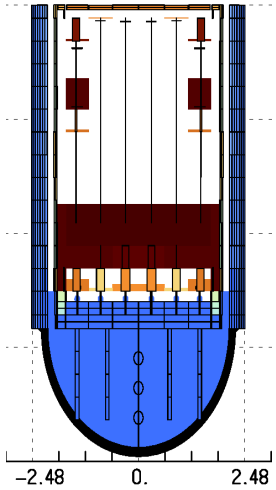

22000 s

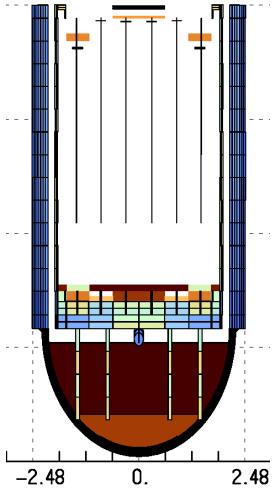

23893 s

Generation of training datasets

Sampling:

- **Recovery time of LPI in Cold Legs**:
  - First after PORV remote opening
  - Before «base case» RPV failure
  - Variation step: 1000 s

  →Time range: [13000 – 23000 s]
- **Number of available LPIs**: 1 or 2
- In overall 22 runs
- Saving of database at each time step
- Δt = [0.01 – 10.0 s]

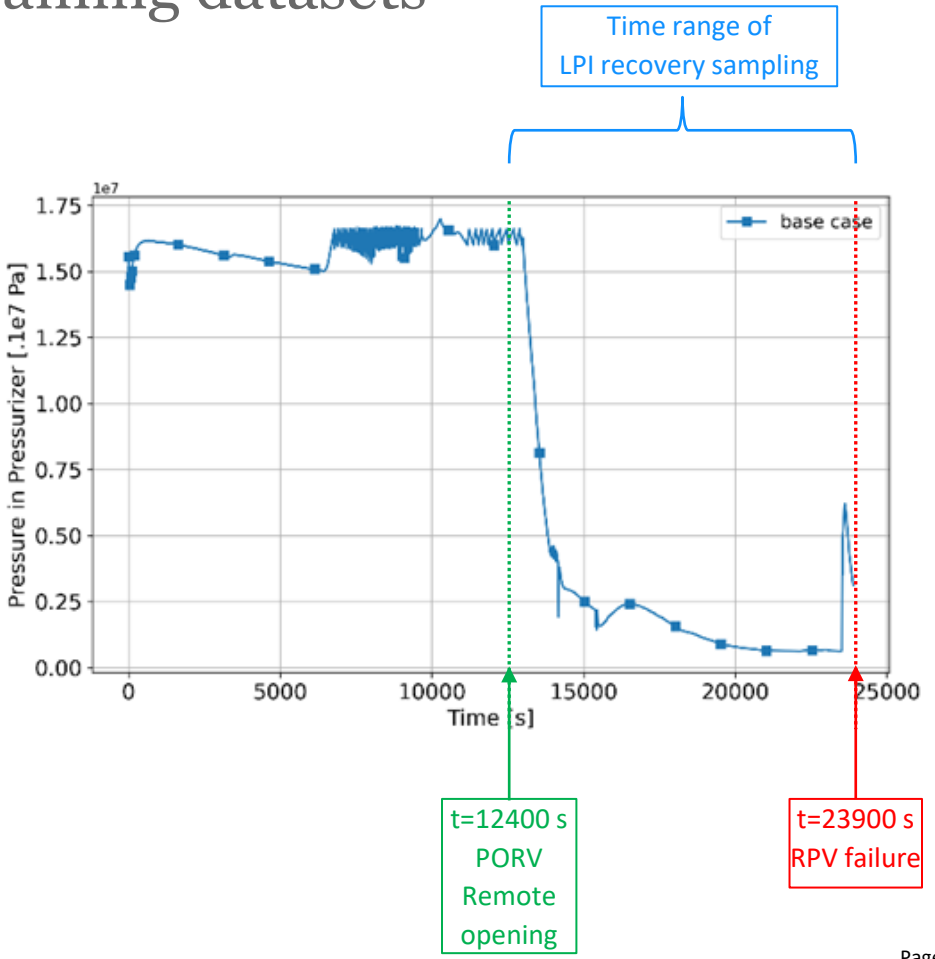

Observations of training datasets

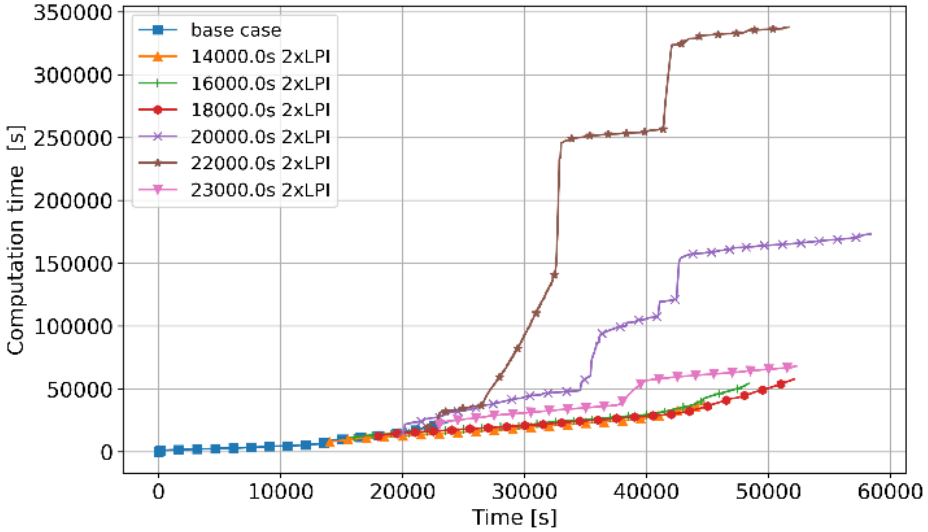

Until 18000 s: core still intact

→Injection has no noticeable impact on the CPU time compared to base case

After 20000 s: different geometries (quasi-intact, swollen rods, obstructed, partly molten, molten pool, …)

→Injection leads to more complexe mechanisms

→CPU time increases

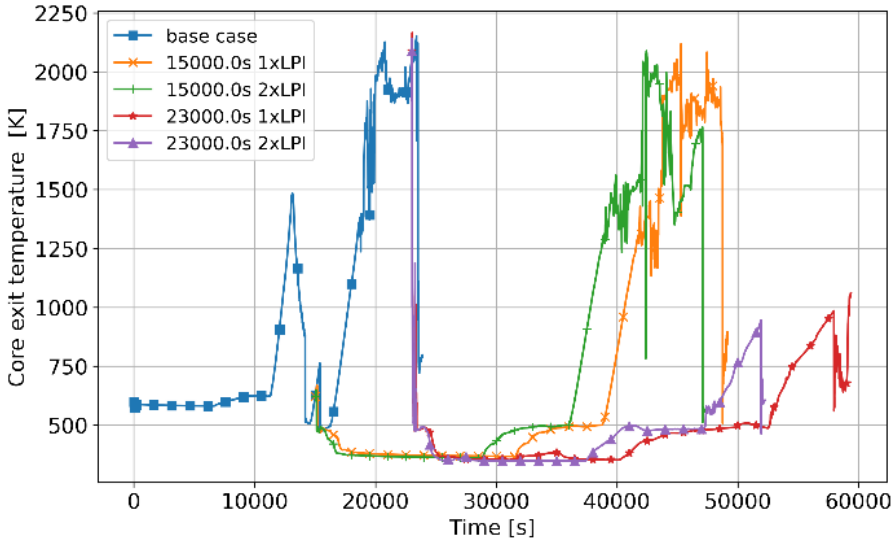

CET evolution:

When injecting at an early stage, similar pattern to base case

Surrogate modelling

Preliminary approach

Prediction of the evolution of fluid state variables at the inlet and outlet of the RPV
→ Prediction at each timestep (time-stepper)

- TH variables in:
  - Cold leg
  - Hot leg
  - Junction Cold leg - Downcomer
  - Junction Upper plenum - Hot leg
- Variables describing loss/gain of mass and energy in PRIMARY must be taken into account
- Besides, some variables giving more context about what is happening

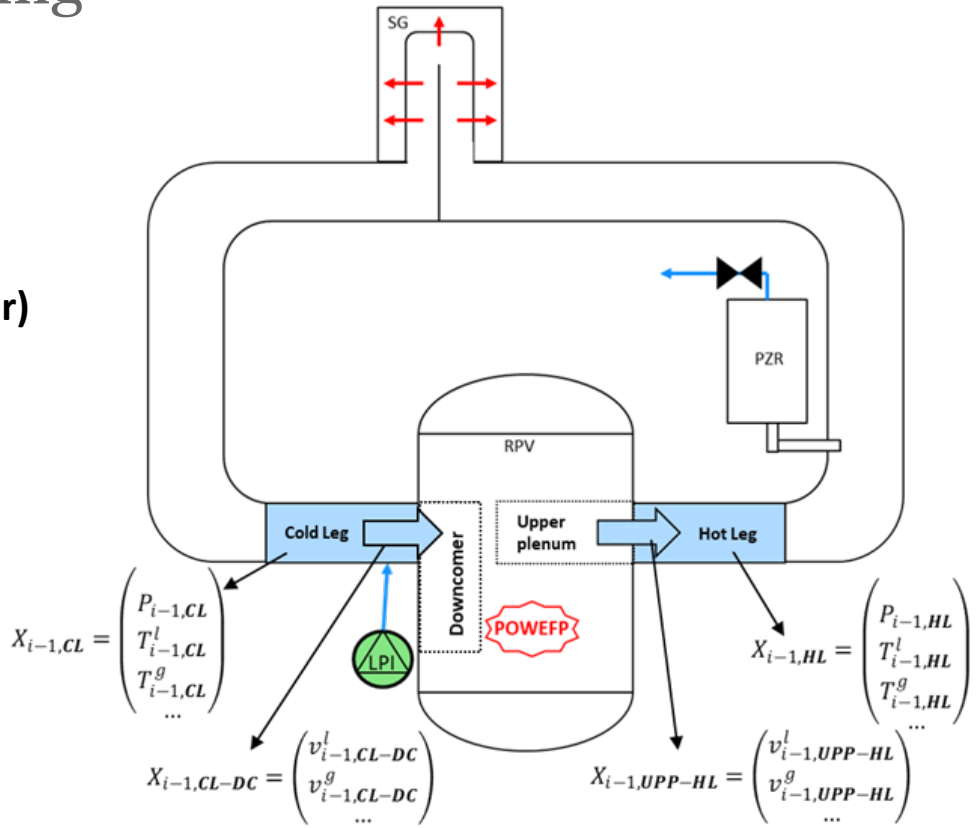

Data analysis

Dimension reduction

- High-dimensional problem :
  - 23 simulations
  - ~10^4 timesteps
  - 153 physical variables.
- Reduced to 89 variables by removing redundant variables.

Normalization

- These 89 variables were normalized between 0 and 1.

Pearson correlation matrix

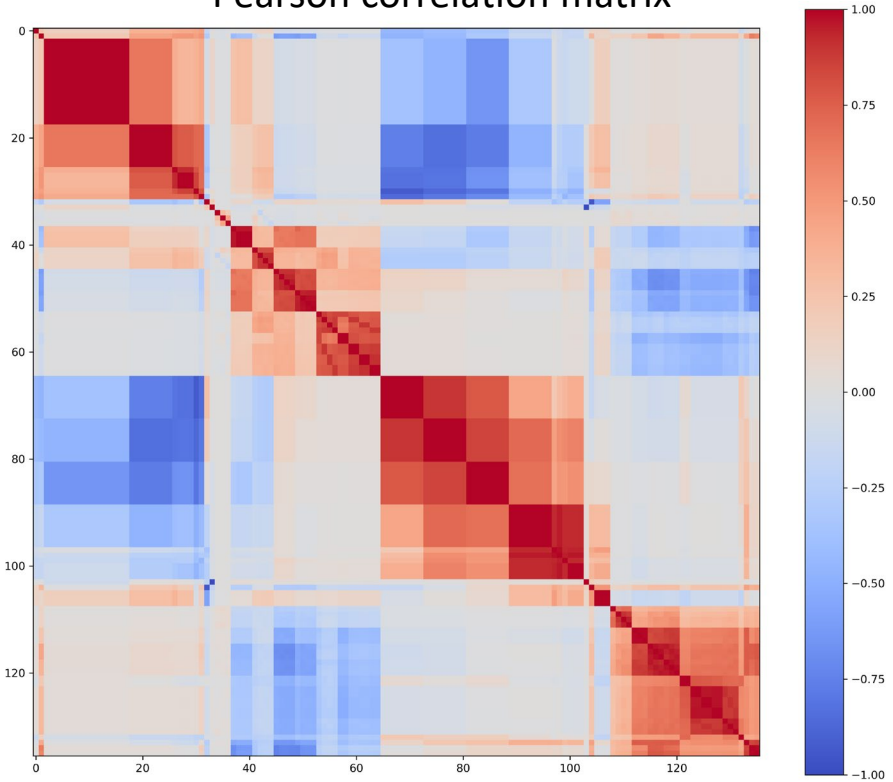

Preliminary metamodel

Learning strategy

- Train on sequences of 10 timesteps
- Prediction on the 11th timestep.

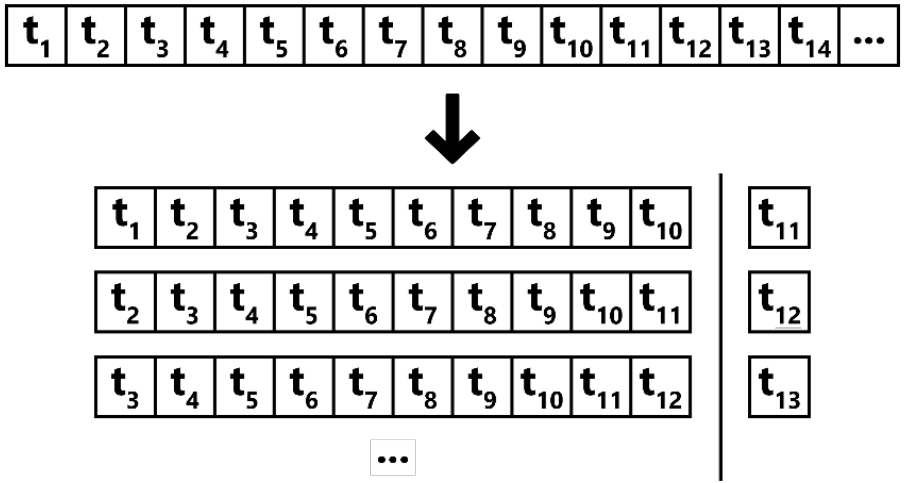

ML method

- 2 LSTMs layers
  at 100 units each
- + 1 dense layer

Timestep regularization

- Timestep interpolated to maintain a constant timestep (1 sec).

Train & test datasets

- 80 % randomly chosen as training data

Preliminary metamodel

Learning process

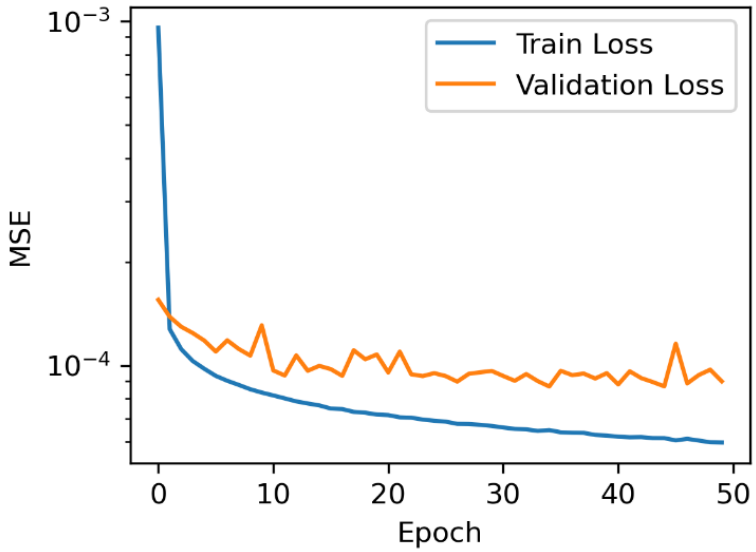

Results

- Small bias,
- but large variance.

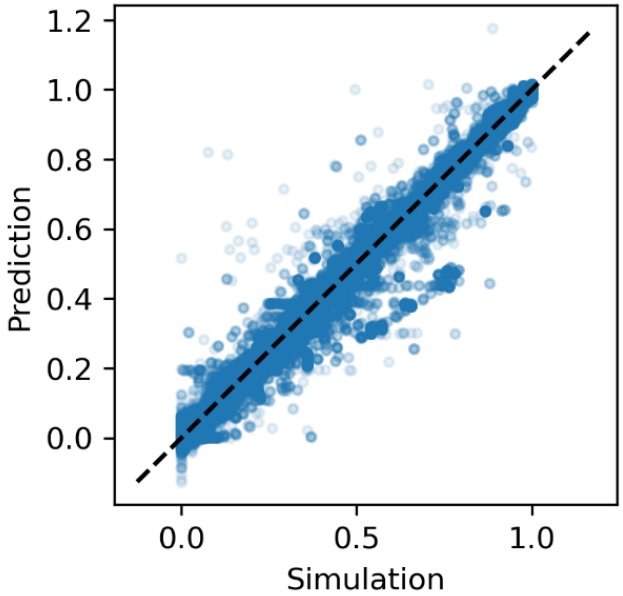

Metamodel improvement and outlook

Improvement ideas

- Cleaning up the data by removing certain outliers
- Adapting:
  - the number of layers in the LSTM,
  - and/or the number of units in the LSTM layers,
  - or also the number of timesteps in input.
- Improving dimension reduction:
  - considering more physical knowledge,
  - or applying more advanced dimension reduction methods
- Training the model on more data.
- … Or testing other approaches than LSTM

Further steps

- Redefining inputs and outputs according to project specifications
- Developping surrogate models for Hot Legs and Cold Legs…
- … but also for the others parts of the RCS
- Calculating time-sequences with the surrogates models

Exploring more global approaches

- For exploratory purposes

- Prediction of accident outcomes or global behaviour of the accident progression
- For example:
  - RPV failure time
  - Total hydrogen generation
  - Total mass of molten material
  - Etc.

- Could provide deeper insights on ML feasibility

Exploring more global approaches

Generation of a training dataset

- To observe the general impact of injection time on accident evolution outcomes

Sampling:

- Recovery time of LPI in Cold Legs:
  - First after PORV remote opening
  - Before «base case» RPV failure
  - Finer variation step: 100 s

  →Time range: [13000 – 23900 s]
- Fixed number of available LPIs: 2
- In overall 110 runs

- Saving of database each 200 s

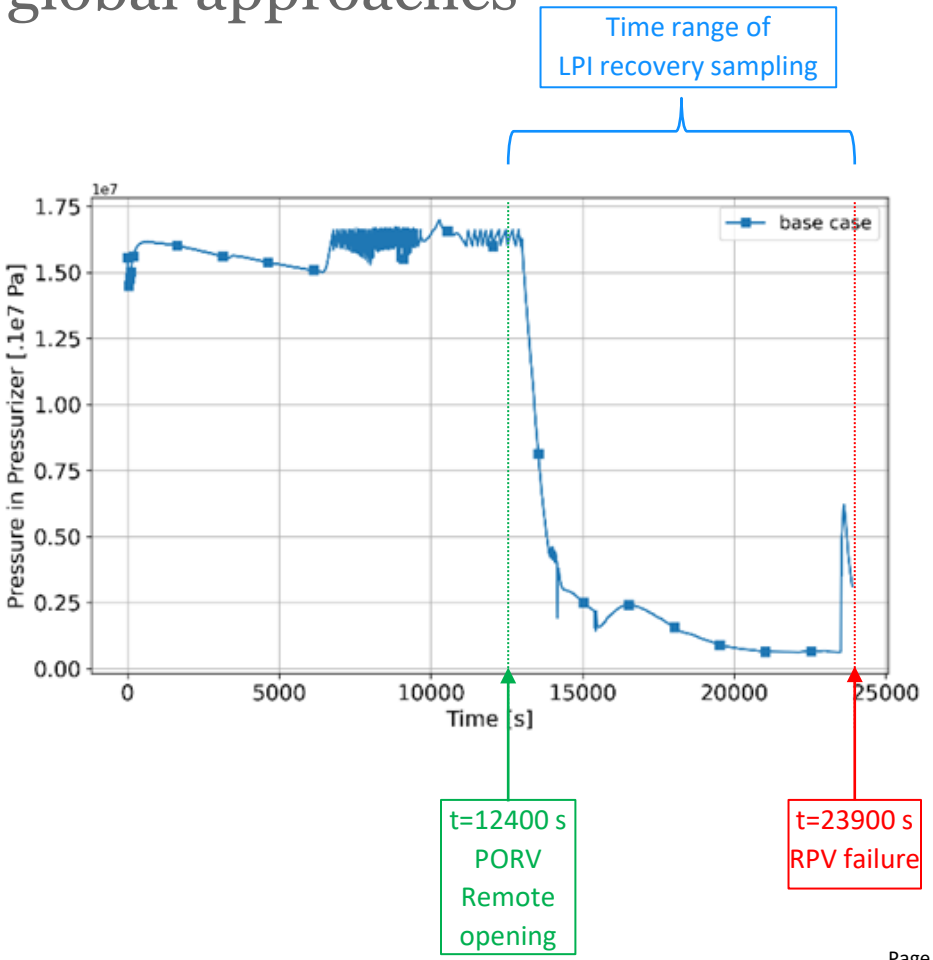

Exploring more global approaches

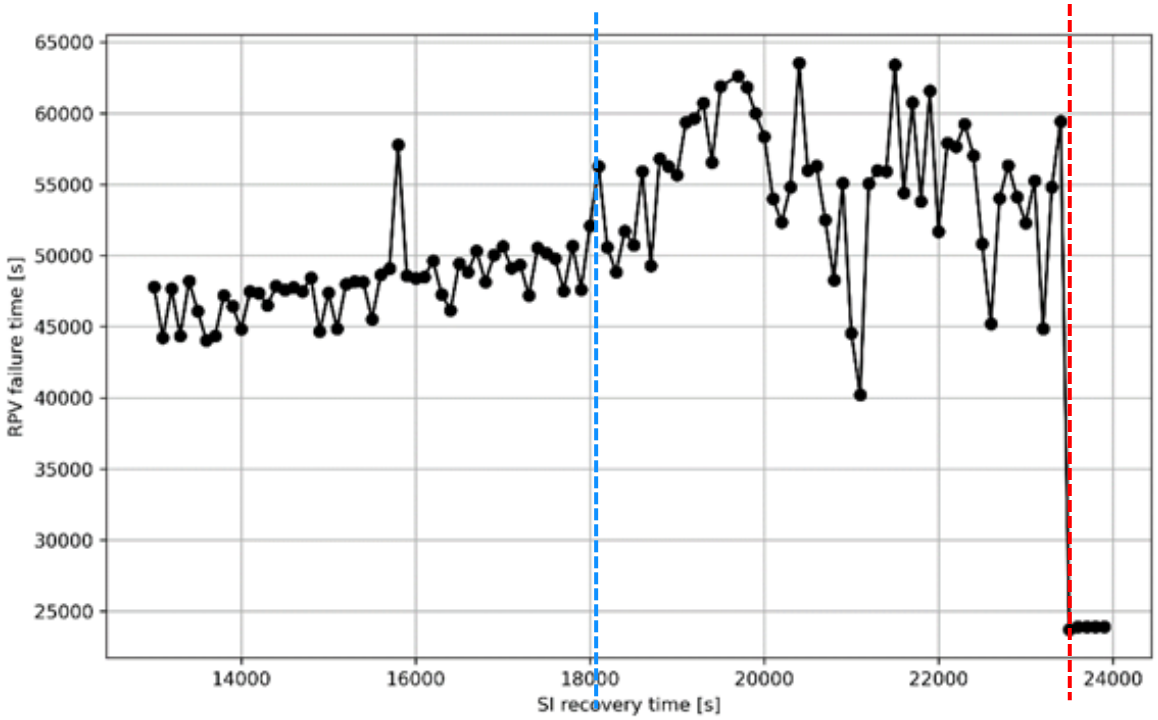

RPV failure time slowly increases with injection time

(must be further investigated)

Injection no longer plays any role

Outlook

- Global approaches could be investigated to determine:
  - Key-parameters of the accident progression, FoM
  - Decisive events

- This could give more insights on the state of the core

- Such insights could be beneficial to time-stepping methods (providing more context)
  - For example, in order to categorize metamodels with respect to the state of the core

Wir schaffen Wissen – heute für morgen

Thank you for your Attention!

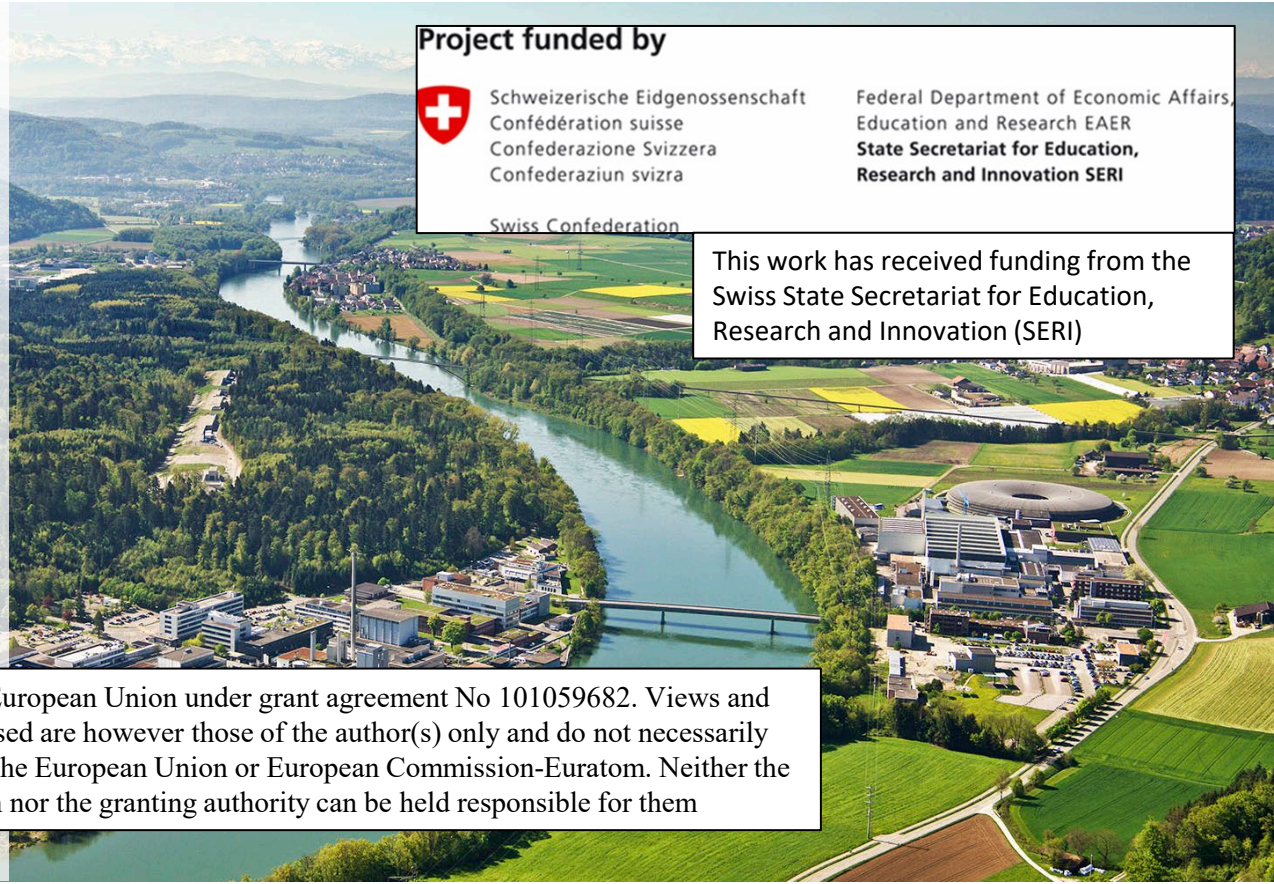

Project funded by

Schweizerische Eidgenossenschaft
Confédération suisse
Confederazione Svizzera
Confederaziun svizra

Swiss Confederation

Federal Department of Economic Affairs, Education and Research EAER
State Secretariat for Education, Research and Innovation SERI

This work has received funding from the Swiss State Secretariat for Education, Research and Innovation (SERI)

Funded by the European Union

Funded by the European Union under grant agreement No 101059682. Views and opinions expressed are however those of the author(s) only and do not necessarily reflect those of the European Union or European Commission-Euratom. Neither the European Union nor the granting authority can be held responsible for them

Analyses of accident progression behavior and simulation of FP release into the environment using MELCOR code for the Fukushima Daiichi Nuclear Power Station Units 1 to 3

Masashi Himi, Koichi Nakamura, and Satoshi Nishimura *
Central Research Institute of Electric Power Industry, Nuclear Risk Research Center
2-6-1, Nagasaka, Yokosuka-shi, Kanagawa 240-0196, Japan
yohimi@criepi.denken.or.jp; k-naka@criepi.denken.or.jp; satoshi@criepi.denken.or.jp

Hideo Nagasaka
Laboratory for Zero-Carbon Energy, Inst. of Innovative Research, Tokyo Institute of Technology
N1-7, 2-12-1, Ookayama, Meguro-ku, Tokyo 152-8550, Japan
nagasaka.h.ab@m.titech.ac.jp

ABSTRACT

Plant data from the accident at Fukushima Daiichi Nuclear Power Station Units 1 to 3 are not enough to understand the overall picture of the accident. It was identified which unit's each event was responsible for the peak of the dose rate measurements at the on-site monitoring post. Although it was not possible to confirm the time of core meltdown from the measured pressures of the reactor pressure vessel (RPV) and the primary containment vessel (PCV), it was possible to estimate the time of the RPV failure. For the purpose of assisting the detailed explication of the accident, we conducted MELCOR2.2 code analysis applying plant data from Units 1 to 3 and safety function operating conditions during the accident to reproduce the time of the RPV failure and the hydrogen explosion, and also to predict the stabilization of the accident. It was predicted that the accident had not stabilized at any of the units by 24:00 on 3/31 2011 as the end of calculations, which was consistent with the measured plant data.
The amount of leakage from the PCV that can be read from plant data at the accident was estimated on condition that the decay heat might be reduced by the amount of water injected to cool the reactor core, its amount of evaporation and the amount of leakage. Also, the amount of leakage was estimated so that the measured pressure of the PCV could be simulated. Inside the RPV, the fuel debris collapsed into fragments with the temperature not rising to its melting point, and the control rod drive mechanism remained in its original shape to some extent due to the injection of cooling water. The other side, MELCOR2.2/CORCON handles the debris like molten material and hastens the molten core-concrete interaction after it falls onto the pedestal, so that MELCOR analysis results in a conservative assessment. The temperature of the debris was below the melting point of iron as around 1500 K after falling onto the pedestal and dissipating heat, so that it was considered the debris eroded not the steel wall but the concrete floor. Therefore, we conducted the evaluation that only caused erosion to the floor. The most plausible analyses cases for the Units 1 to 3 accident were prepared based on the above idea. The analyses results of FP release timings into the environment agreed well with the measured plant data.

KEYWORDS
Fukushima Daiichi Nuclear Power Station accident, MELCOR, severe accident, source term, on-site dose rate, environmental FP release

1. INTRODUCTION

The accident progressions in the BWR Mark I type Fukushima Daiichi Nuclear Power Station (FDNPS) Units 1 to 3 were studied from the analysis of the relationship between pressure changes in the plants [1]. Based on those [1], we perform severe accident (SA) analyses using MELCOR code [2],[3] for the purpose of supplementing plant data [4] having the few measured values during the accident, so that the accident will be investigated by the obtained information.
It is not possible to confirm the time of core meltdown from the measured values during the accident [4]. When the reactor pressure vessel (RPV) pressure decreased to the primary containment vessel (PCV) pressure along the core degradation process, we regard that the RPV was failed and debris fell into the pedestal. One of the challenges of SA analyses is simulating the fuel debris behavior. In the FDNPS accident, the hydrogen explosion occurred largely enough to blow away the reactor building (R/B), which was a visually shocking event, but it is unlikely affected the damage of the fuel debris progressing in the PCV. If the time of the RPV failure will be able to be simulated accurately through numerical analysis, it may be possible to reproduce the accident progression mainly determined by the debris behavior. Also, we try to simulate it because it will serve as a guide to the hydrogen explosion time. Furthermore, we judge the stabilization of the accident, evaluate FP release into the environment and compare it with the measured value.
Many studies [5] have been carried out until now. The plant data and several phenomena anticipated in the FDNPS accident have been investigated and discussed in [4]. They summarized remained problems as the unsolved issues [4]. We will intend to perform MELCOR analyses used by improved boundary conditions for the future study based on the unsolved issues [4].

2. DOSE RATE MEASUREMENTS AT ON-SITE MONITORING POST AND ITS CORRESPONDING EVENTS

It was investigated what event caused the behaviors of the RPV pressure, the drywell (D/W) pressure, and the suppression chamber (S/C) pressure for Units 1 to 3 in the accident [1]. Based on this evaluation, as shown in Figure 1, it is inferred that the peak of the dose rate measured at the on-site MP corresponds to FP release conjectured from the pressure measurements of each unit as follows.
(1) according to Unit 1: FP was released due to the RPV failure and the PCV upper part failure before 2:45 on 3/12. (2) according to Unit 1: FP was released due to wetwell (W/W) vent at 10:17 on 3/12. (3) according to Unit 1: the PCV lower part failed at 14:00 on 3/12 and FP was released due to the W/W vent at 14:30 on 3/12. (4) according to Unit 1: FP was released due to the hydrogen explosion at 15:36 on 3/12. (5) according to Unit 1: FP was released due to steam generation associated with seawater injection at 19:04 on 3/12. (6) according to Unit 3: the RPV failed at 9:00 on 3/13 and FP was released due to the W/W vent at 9:20 on 3/13. (7) according to Unit 3: seawater was injected at 13:12 on 3/13 and FP was released due to the W/W vent at 12:30 on 3/13. (8) according to Unit 3: FP was released due to steam generation associated with seawater injection at 3:20 on 3/14. (9) according to Unit 3: FP was released due to the PCV pressure changed after seawater injection from3:20-11:01 on 3/14. (10) according to Unit 2: FP was released due to the safety relief valve (SRV) open at 21:20 on 3/14. (11) according to Unit 2: FP was released due to the RPV failure at 2:00 on 3/15. (12) according to Unit 2: FP was released due to the damaged lower D/W at 7:20 on 3/15. (13) according to Unit 3: FP was released due to the W/W vent at 21:30 on 3/15. (14) according to Unit 3: FP was released due to liquid phase leakage from the lower D/W at 9:00 on 3/16 and sequentially pedestal water flashing under reduced pressure. (15) according to Unit 3: water injection into the spent fuel pool (SFP) began at 0:30 on 3/19; some water accumulated from the shield plug into the reactor well (R/W) and flowed into the D/W from the damaged flange, which caused steam generation, increased pressure and released FP. (16) according to Unit 3: FP was released due to the D/W temperature rising caused by the decrease in water injection amount from 3/21. [17] according to Unit 1: FP was released due to the change in the RPV pressure caused by the fuel debris falling into the

lower plenum at 6:00 on 3/22 during the water injection rate decrease between 3/21 and 3/23. [18] according to Unit 1: FP was released due to the change in the RPV pressure caused by the fuel debris falling into the lower plenum at 11:00 on 3/23 when the water injection was increased on 3/23. [19] according to Unit 2: FP was released due to the D/W pressure changed caused by the fuel debris falling into the pedestal when the amount of water injection increased on 3/25. [20] according to Unit 1: FP was released due to the fuel debris falling into the lower plenum and the pedestal at 0:00 on 3/29 caused by the change in the RPV and the D/W pressure.
Here, the events numbered with () can be simulated using the boundary conditions and event prediction of MELCOR analysis. On the other hand, the events numbered with [] are caused by sudden debris behavior, so it seems difficult to simulate them using analysis code.
Note that the early dose rate plateau before FP release (1) is thought to be due to radiation from the R/B, not due to FP release.

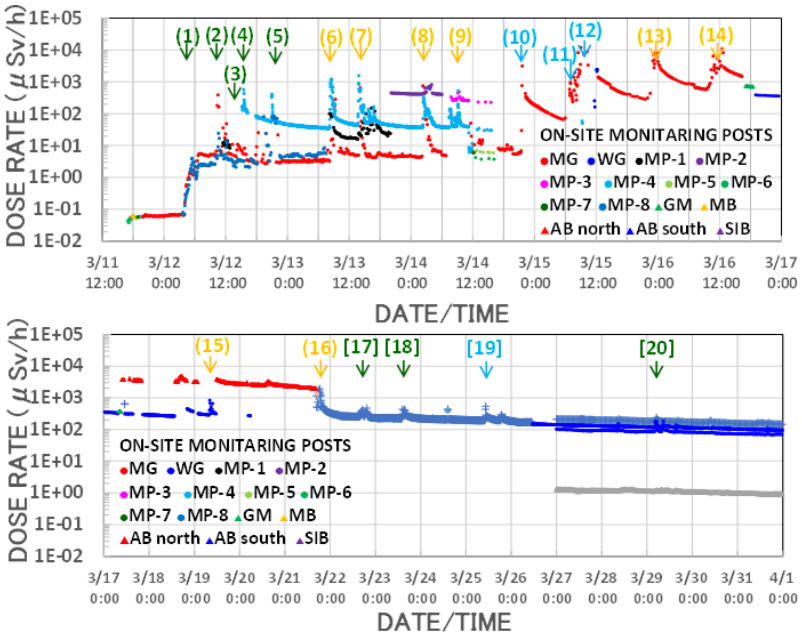

Figure 1. Dose Rate Measurements at the On-site MP of the FDNPS [4].

3. ANALYSIS PROCEDURE, BOUNDARY CONDITIONS AND PARAMETER SURVEYS OF LEAK AREA USING MELCOR CODE

In this chapter, we will conduct an accident progression analysis using MELCOR code, for the purpose of assisting the detailed explication of the accident to supplement the small number of measured values [4] in the accident.
It was thought that a leak had occurred in the PCV based on changes in the PCV pressure measurements. If the amount of leak from the PCV is not large, the decay heat can be removed by injecting water into the reactor core, and the accident will be stabilized. A parameter survey of the leak area is conducted to estim ate the leak area under which the accident will be stabilized. The analysis procedure and reproduction goal s are shown in Section 3.1. Boundary conditions and alternative water injection flow rates are shown in Se ction 3.2. The leak area will be estimated by performing parameter survey as shown in Sections 3.3 to 3.5. It will be predicted the end of the accident by conducting a parameter survey of the leak area.

3.1. Analysis Procedure

The accident progressions of the FDNPS Units 1 to 3 are analyzed using MELCOR 2.2.9541[2],[3]. Figure 2 shows the measured values [4] of changes in the RPV pressure, the D/W pressure, the S/C pressure and changes in water injection flow rate along the accident progression. After the accident occurs, the time of the RPV failure is estimated to when the RPV pressure decreases and equals to the D/W pressure along the core degradation process. The analysis targets to reproduce the RPV failure. Also, it is aimed to reproduce the hydrogen explosion and to predict the stabilization of the accident. The analysis time is from 2011/3/11 14:47 of the reactor scram 1 minute after the earthquake occurs to 3/31 24:00. The time of the RPV failure was before 2:45 on 3/12 for Unit 1, at 2:00 on 3/15 for Unit 2, and at 9:00 on 3/13 for Unit 3. The hydrogen explosion occurred at 15:36 on 3/12 in the R/B of Unit 1, did not occur in Unit 2, and occurred at 11:01 on 3/14 in the R/B of Unit 3. The stabilization of the accident was after the end of April 2011 in Unit 1, until the end of August 2011 in Unit 2, and after the end of August 2011 in Unit 3. Calculation results are shown as Table II in Chapter 4.

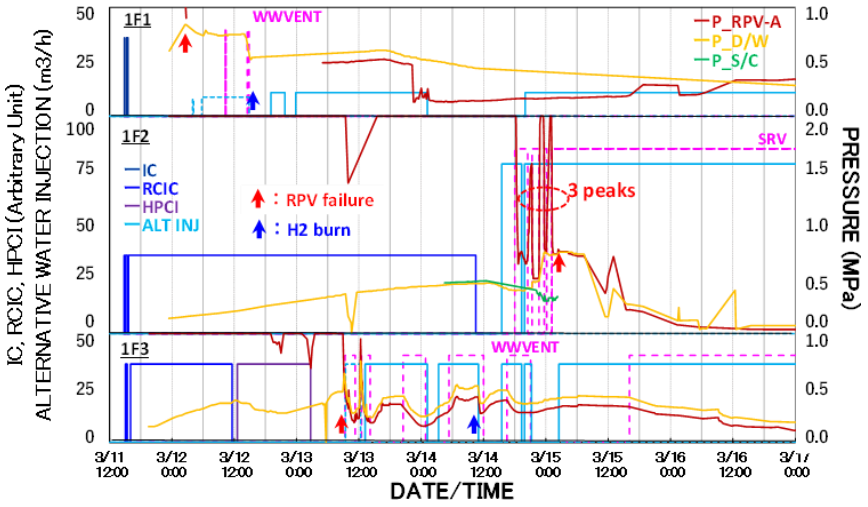

Figure 2. Water injection into the Core of the FDNPS Units 1 to 3, RPV, D/W and S/C Pressures [4].

3.2. Boundary Conditions

The FDNPS Units 1 to 3 are divided into a diagram of nodes for thermal-hydraulics and FP behaviors by using MELCOR as shown in Figure 3. The core degradation, hydrogen explosion and MCCI models will be described later. Plant data for Units 1 to 3 and safety function operating conditions at the accident [4] are applied to boundary conditions shown in Table I. For Unit 1, the isolation condenser (IC) flow rate will be adjusted to reproduce the estimated time of the RPV failure. Since the RPV failure occurred before the start of alternative water injection, the officially announced alternative water injection flow rate [4] was used. For Unit 2, the tsunami water flooded into the torus room, the reactor core isolation cooling system (RCIC) flow rate, the alternative water injection flow rate and the liquid phase leak from the damaged W/W at 12:00 on 3/14 will be adjusted for the purpose of reproducing the estimated time of the RPV failure and the 3 peaks of the RPV pressure caused by the SRV open and close during the core degradation process. Since the RPV failure occurred after the start of alternative water injection, the officially announced alternative water injection flow rate [4] will be modified to reproduce the 3 peaks of the RPV pressure and the RPV failure. It would be assumed that the automatic depressurization system (ADS) opened at 18:00 on 3/14 led to reduce the pressure in the core, to generate steam by flashing and to cool down the fuel temperature. The process would suppress the oxidation reaction of Zr by steam cooling. The officially announced alternative water injection flow rate [4] will be adjusted so as not to cause excessive Zr oxidation reaction. The area of the liquid phase leak to the torus room from the damaged W/W at 12:00 on 3/14 was set on 1E-2 m^2. Choosing these four adjusted parameters would not

be necessarily optimal to reproduce the phenomena. It might be required more precise choice. For Unit 3, the RCIC flow rate and the high-pressure cooling injection system (HPCI) flow rate will be adjusted to reproduce the estimated time of the RPV failure. Since the RPV failure occurred before the start of alternative water injection, the officially announced alternative water injection flow rate [4] will be used.

Table I. Boundary conditions extracted from the data during the accident of the FDNPS Units 1 to 3 [4]

	Unit 1	Unit 2	Unit 3
gas phase leak from damaged lower D/W		3/15 7:20	3/16 9:00
liquid phase leak from damaged lower D/W	3/12 14:00		3/16 9:00
liquid phase leak from damaged W/W		3/14 12:00	
W/W vent	3/12 10:17 3/12 10:23 3/12 10:24 3/12 14:30-14:49		3/13 9:20-11:17, 12:30-14:10, 3/15 21:30- 3/13 20:30-3/14 0:50, 3/14 16:30-21:04, 3/15 16:05-
ADS open and close		3/14 18:00-20:30	
SRV open and close		3/14 21:20-22:40 3/14 23:40-3/15 0:10 3/15 0:10-	

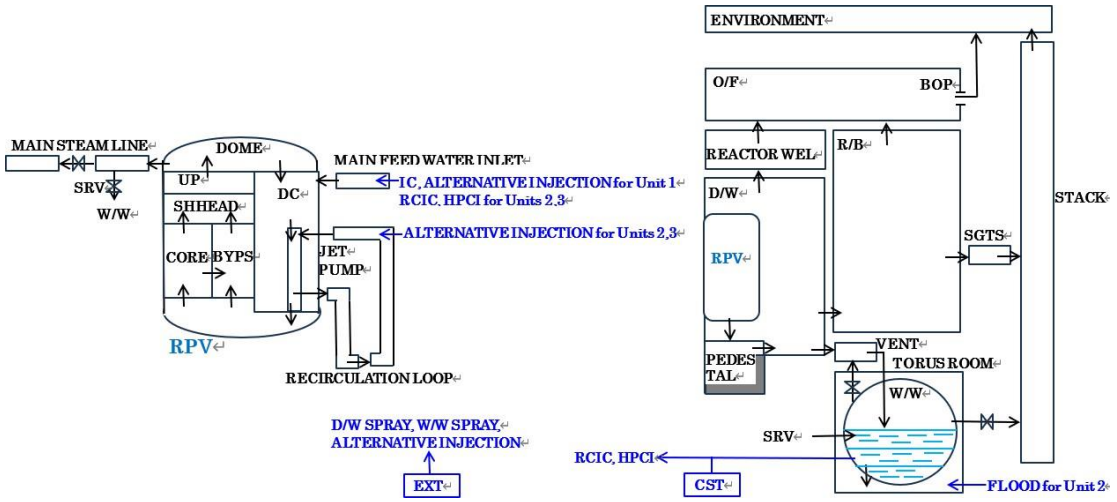

Figure 3. MELCOR Nodalization of the FDNPS Units 1 to 3.

3.3. Parameter Survey of Leak Area of Unit 1

As it is aimed to predict the PCV pressure and appropriate leakage, a parameter survey was conducted on the area of the liquid phase leak to the R/B from the damaged lower D/W at 14:00 on 3/12. The results for the RPV pressure were almost the same not dependent on the leak area, and the measured values could be reproduced. The PCV pressure increased as the leak area became smaller. If the leak area is 1E-4 m^2 or less, subtracting the evaporation amount and leak amount from the total water injection amount will still be positive, so the decay heat could be removed, and the leak area of 1E-4 m^2 was judged to be appropriate to predict the stabilization of the accident and to reproduce the PCV pressure. The analysis results are shown in Figure 4.

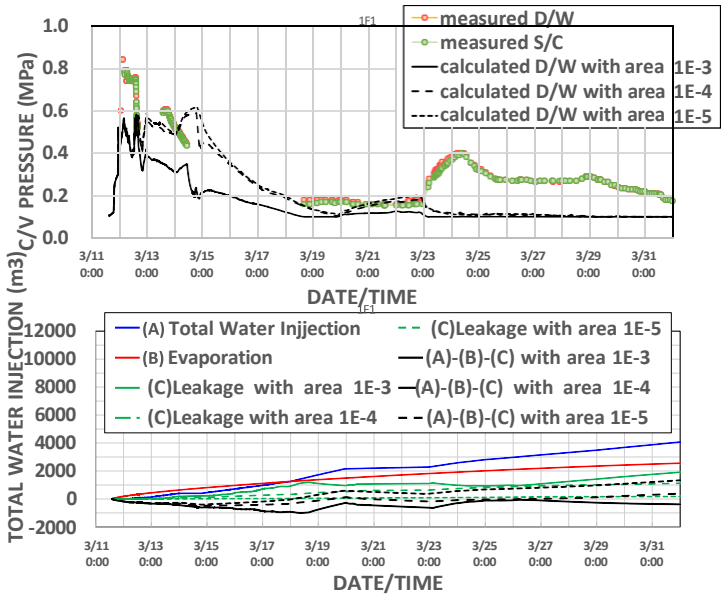

Figure 4. Analysis Results of PCV pressure and Net Water Injection Amount at the FDNPS Unit 1.

3.4. Parameter Survey of Leakage Area of Unit 2

A parameter survey was conducted on the area of the gas phase leak to the R/B from the lower D/W damaged at 7:20 on 3/15. The results for the RPV pressure were almost the same, and the 3 peaks of the measured RPV pressure and the time of the RPV failure were reproduced. The PCV pressure was almost the same before the gas phase leak to the R/B from the damaged lower D/W at 7:20 on 3/15. After the gas phase leak to the R/B from the damaged lower D/W at 7:20 on 3/15, the decay heat could be removed irrespective of the leak area once the core degradation process had passed. Additionally, since we were able to reproduce the changes in the D/W pressure reduction after the start of the leakage, we determined that the leak area of 1E-2 m^2 was appropriate to reproduce the PCV pressure. The analysis results are shown in Figure 5.

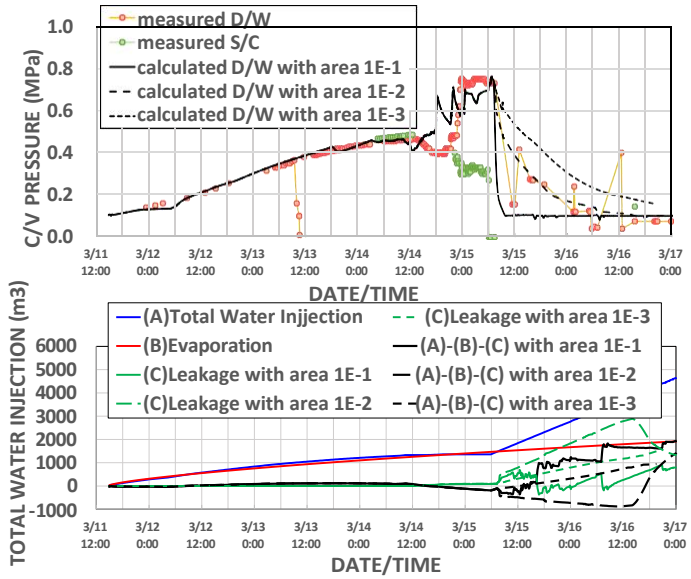

Figure 5. Analysis Results of PCV Pressure and Net Water Injection Amount at the FDNPS Unit 2.

3.5. Parameter Survey of Leakage Area of Unit 3

As it is aimed to predict the PCV pressure and appropriate leakage, a parameter survey was conducted on the area of the gas phase and the liquid phase leak to the R/B from the damaged lower D/W at 9:00 on 3/16. The results for the RPV pressure were almost the same, and the measured values could be reproduced. The PCV pressure was almost the same before the liquid phase leak to the R/B from the lower damaged D/W at 9:00 on 3/16. If the leak area is 1E-4 m^2 or less, subtracting the evaporation amount and leak amount from the total water injection amount will still be positive, so the decay heat could be removed, and the leak area of 1E-4 m^2 was judged to be appropriate to predict the stabilization of the accident and to reproduce the PCV pressure. The analysis results are shown in Figure 6.

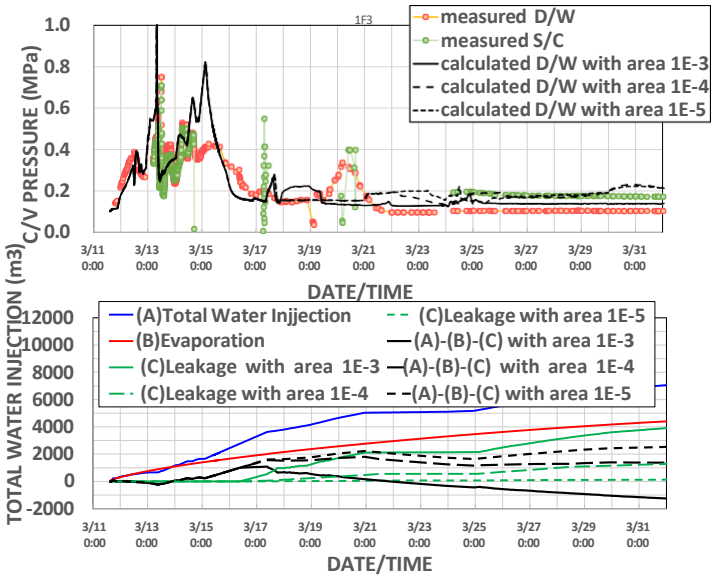

Figure 6. Analysis Results of PCV Pressure and Net Water Injection Amount at the FDNPS Unit 3.

4. MELCOR MOST PLAUSIBLE ANALYSIS

The most plausible analysis will be performed to simulate the accident progression as much as possible based on the parameter surveys shown in Chapter 3. The analysis results of the RPV pressure, the D/W pressure, the S/C pressure, the hydrogen explosion, the core degradation process, the molten core-concrete interaction (MCCI), and FP release to the environment are shown below.

4.1. Analysis Results of Core Degradation Process

Figure 7 shows the analysis results of the core degradation process. The core and lower plenum are treated as an axisymmetric two-dimensional model. The initial state shows the core and lower plenum region divided into radial rings and axial levels for MELCOR. During the core degradation process, the fuel was heated up to 2500 K. The fuel debris did not heat up enough to melt and collapsed into fragments as the particulate debris, and the control rod drive remained in its original shape to some extent due to the injection of cooling water into the lower plenum and fell onto the pedestal. Depending on the temperature rise of the fuel, a large amount of FP is released during this period. On the other hand, the oxidation rate of Zr in the core structure during this period was 29.2 % in Unit 1, 20.6 % in Unit 2, and 29.1 % in Unit 3. Whether the oxidation rate of the core structure affected FP release will be investigated in the future.

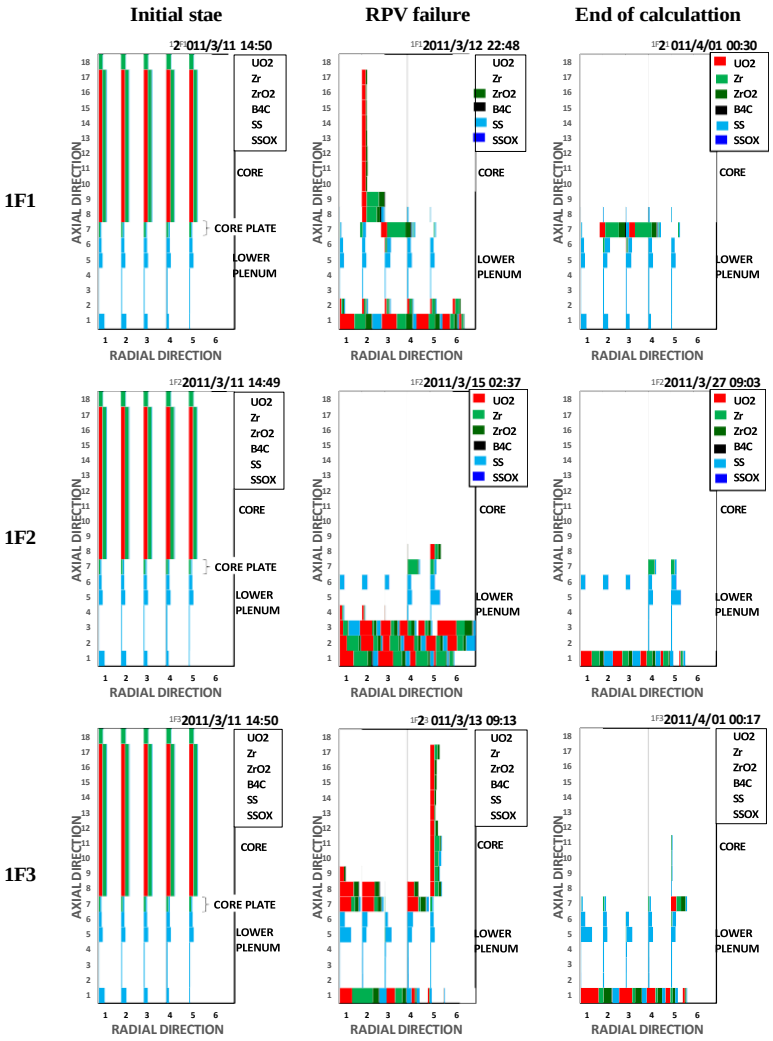

Figure 7. Analysis Results of Core Degradation Behavior of the FDNPS Units 1 to 3.

4.2. Analysis Results of RPV Pressure and PCV Pressure

Figure 8 shows the analysis results for the RPV pressure and the PCV pressure. Table II shows the observed and calculated times of the RPV failure. The calculated values almost agreed with the observed values. In Unit 2, we reproduced the 3 peaks of the measured RPV pressure and the time of the RPV failure.

Table II. Analysis results of the FDNPS Units 1 to 3

Event	Unit 1		Unit 2		Unit 3	
	Observed	Calculated	Observed	Calculated	Observed	Calculated
RPV failure	before 3/12 2:45	3/11 22:48	3/15 2:00	3/15 3:21	3/13 9:00	3/13 7:54
Hydrogen burn	O/F on 3/12 15:36	O/F on 3/12 14:45	-	No occurrence	R/B on 3/14 11:01	STACK on 3/13 9:20
Stabilization of accident	After the end of April 2011	Not attainable by April 1st	Until the end of August 2011	Not attainable by April 1st	After the end of August 2011	Not attainable by April 1st

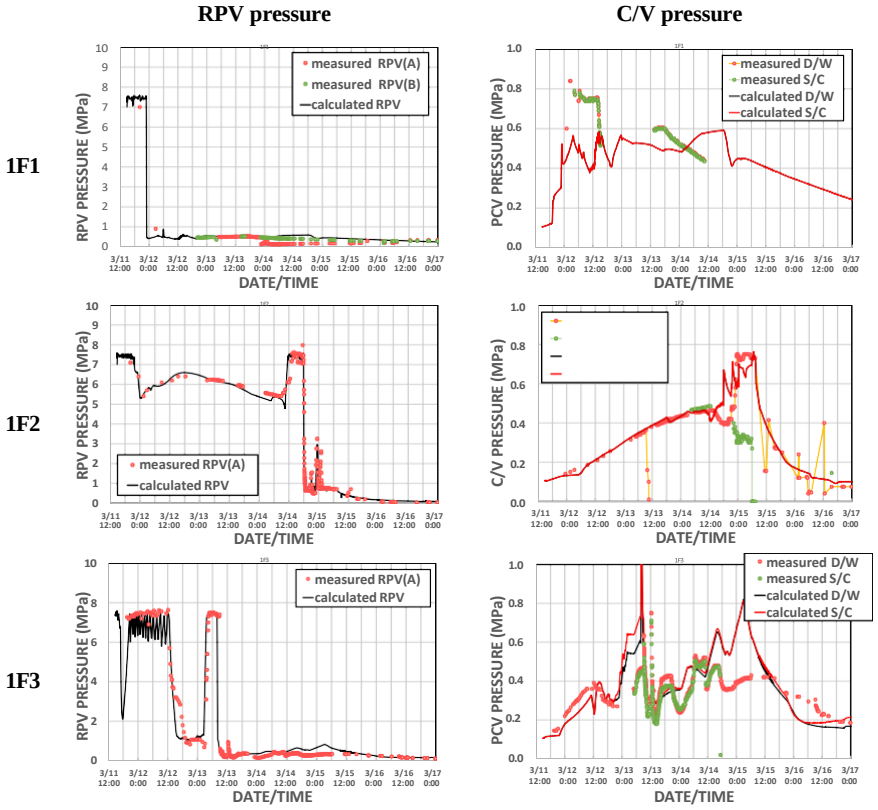

Figure 8. Analysis Results of RPV Pressure, D/W, S/C Pressures of the FDNPS Units 1 to 3.

4.3. Analysis Results of Hydrogen Explosion

In the hydrogen combustion model MELCOR/HECTR1.5, hydrogen combustion occurs frequently. Since the hydrogen explosion that occurred in the FDNPS accident was enough to blow away the R/B, it was assumed that a detonation had occurred in the accident. We modified the detonation model to simulate hydrogen explosion [6].
Table II shows the observed and calculated time and location of the hydrogen explosion occurrence. The calculated hydrogen explosion time for Unit 1 almost agreed with the observed value. At the time of the hydrogen explosion at Unit 1, damage to the O/F blowout panel (BOP) at Unit 2 was set as an input condition, so no hydrogen explosion occurred, similar to the observation. In Unit 3, there is a path to the W/W vent exhaust stack (STACK), so hydrogen leaks to STACK. According to the analysis, STACK is directly connected to the environment, but because it is divided as one compartment, hydrogen leaks to STACK and a hydrogen explosion occurred. However, no hydrogen explosion occurred at the R/B.

4.4. Analysis Results of MCCI

When the fuel debris formed inside the RPV falls onto the pedestal, it is handled as layers of HOX (high density oxide) consisting of UO2, ZrO2, SSOX, MET (high density metal) consisting of Zr and HMX (high density mixture) consisting of a mixture of these in the MCCI model MELCOR/CORCON-Mod3. The concrete of the pedestal is handled as layers of LOX (low density oxide) and LMX (low density mixture). Each layer is a collection of microparticles. While the fuel debris erodes concrete, high-density particles sink and low-density particles float in the debris layers and spread to the surrounding area. A layer mixing model, a coking reaction, and an ablation enthalpy of basaltic concrete of 2.3E+6 J/kg [7]

were applied for use in analysis, because MELCOR default value of ablation enthalpy 0.0 J/kg is considered inappropriate.
The temperature of the fuel debris falling from the RPV onto the pedestal did not rise to its melting point, and as shown in Figure 7, the control rod drive remained in its original shape to some extent due to the injection of cooling water. However, once it falls onto the pedestal, CORCON handles the fuel debris and the concrete as a collection of microparticles like molten material and hastens the MCCI, so that MELCOR analysis results in a conservative assessment. The temperature of the debris lowered below the melting point of iron as around 1500 K after falling onto the pedestal and dissipating heat, so that it was considered the debris eroded not the steel wall but the concrete floor. This corresponds to the situation at Unit 1, where the steel of the pedestal remained, and the concrete floor was eroded. Therefore, we conducted an evaluation that would only cause erosion to the floor. But CORCON needs to have the pedestal with a volume surrounded by concrete that can accommodate the falling debris onto the pedestal for erosion calculations. Erosion calculations were performed for not only concrete floor but also concrete wall. Figure 9 shows the analysis results for the MCCI calculations. The debris temperature had not lowered largely by the end of the calculations at 24:00 on 3/31 2011 in any analyses, so that the accident was not stabilized. The analysis of Unit 2 stopped on the way to the end of the calculation because debris volume on the pedestal exceeded the preset pedestal volume with the wall height as low as possible.

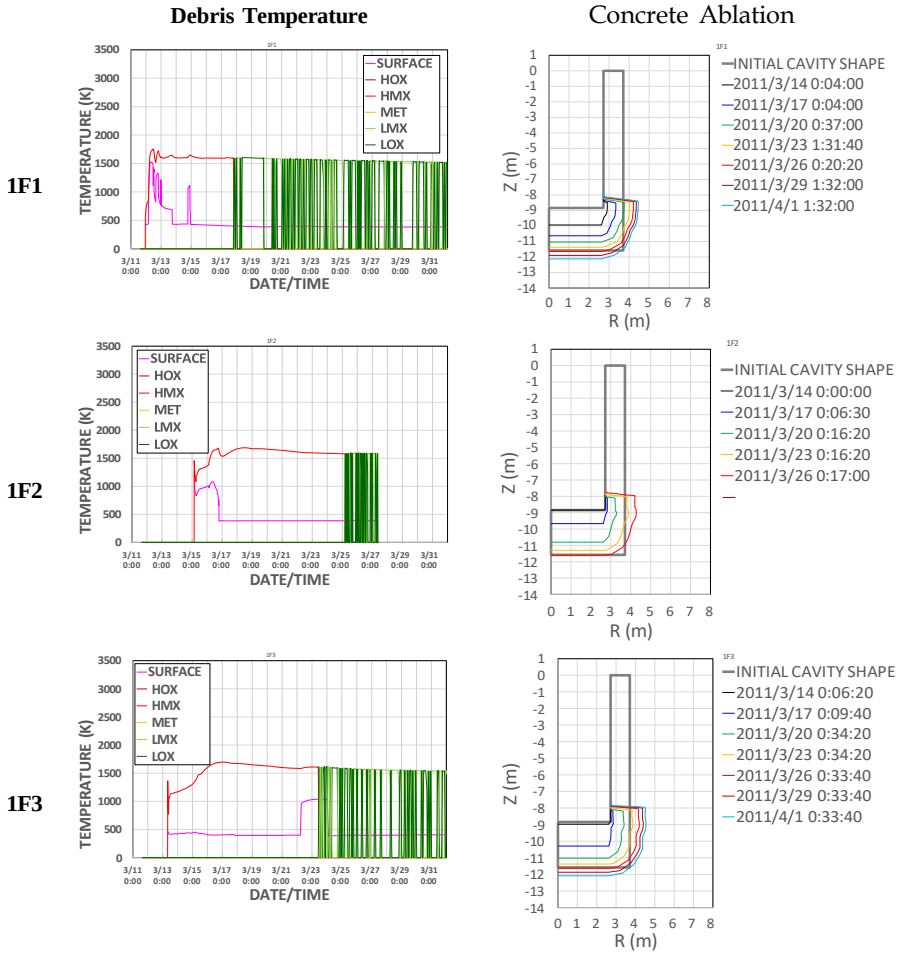

Figure 9. Analysis Results of Debris Behavior at the Pedestal of the FDNPS Unit 3.

4.5. FP release to the Environment

FP was released into the environment due to the events associated with the accident progression described in Chapter 2. Figure 10 shows the environmental release of cesium as a major FP. The effects of FP deposition at the RPV, the PCV, and the R/B were considered appropriately in the analysis. The analysis results well reproduced the peak timings of the dose rate measured at the on-site MP shown in Figure 1 for the events numbered with () that occurred due to the boundary conditions and the accident progression. However, the events numbered with [] are thought to be caused by sudden debris behavior change and could not be predicted using MELCOR code. In addition, it was not implemented the boundary conditions to simulate FP releases (14) and (15). Here, FP release (14) was inferred that FP was released due to liquid phase leakage from the lower part of the D/W at 9:00 on 3/16 and sequentially pedestal water flashing under reduced pressure in Unit 3, and FP release (15) was inferred that water injection into the spent fuel pool (SFP) began at 0:30 on 3/19 and some water accumulated in the R/B floor and flowed into the D/W from the flange, generating water vapor and releasing FP in Unit 3.
FP release (10) was assumed to be caused by the SRV open at 21:20 on 3/14 in Unit 2. But it might be possible to happen that the FP release was caused by the W/W vent in Unit 3 at 16:30-21:04 on 3/14. It would be considered how this FP release happened considering other knowledge in the future.

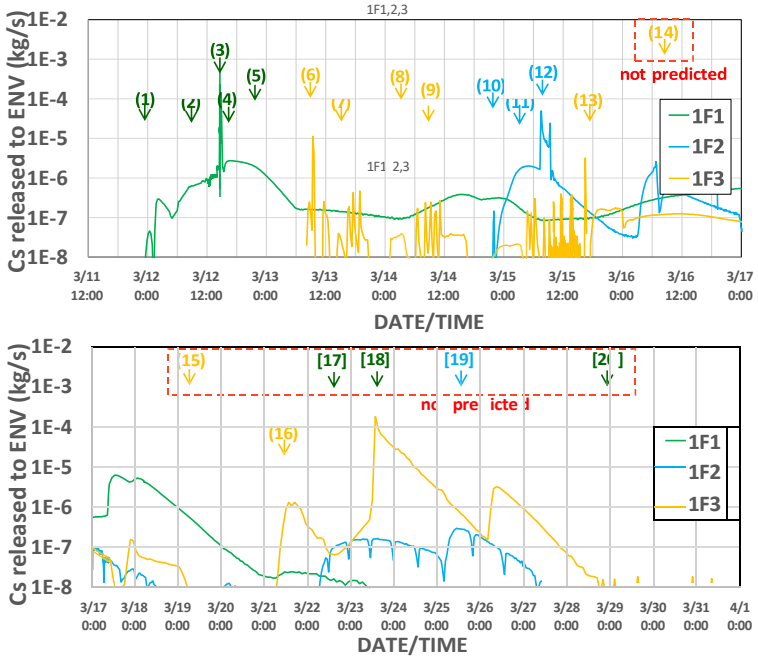

Figure 10. Analysis Results of Cesium Release Behavior into the Environment.

5. CONCLUSIONS

The conclusions are as follows.
- Plant data in the accident [4] alone is not sufficient to understand the overall picture of the accident. Accident progression analyses were performed using MELCOR code [2],[3] to complement the plant data. Information that could not be observed in the accident, such as erosion of pedestal concrete due to interaction between fuel debris and concrete after falling to the pedestal, release of FP inside and outside the reactor, and water accumulation in the containment vessel, will contribute to predicting accident progression hereafter.
- It was thought that a leak had occurred in the PCV based on pressure measurements. Parameter surveys using the leak area as a parameter was conducted to estimate a reasonable leak area that would allow

water injection into the core to remove the decay heat and stabilize the accident, which was reflected in the most plausible analysis.
- By applying the plant data of Units 1 to 3 and safety function operating conditions in the accident, the time of the RPV failure and the time of hydrogen explosion occurrence could be almost reproduced the observed values along the accident progression.
- The temperature of the fuel debris falling from the RPV onto the pedestal did not rise to its melting point, and the control rod drive remained in its original shape to some extent due to the injection of cooling water. However, once it falls onto the pedestal, CORCON handles the fuel debris and the concrete as a collection of microparticles like molten material and hastens the MCCI, so that MELCOR analysis results in a conservative assessment. The temperature of the debris lowered below the melting point of iron as around 1500 K after falling onto the pedestal and dissipating heat, so that it was considered the debris eroded not the steel wall but the concrete floor. Therefore, we conducted an evaluation that would only cause erosion to the floor. But CORCON needs to have the pedestal with a volume surrounded by concrete that can accommodate the falling debris onto the pedestal for erosion calculations. Erosion calculations were performed for not only concrete floor but also concrete wall. Figure 9 showed the analysis results for the MCCI calculations. The debris temperature had not lowered largely by the end of the calculations at 24:00 on 3/31 2011 in any analyses, so that the accident was not stabilized. The analysis of Unit 2 stopped on the way to the end of the calculation because debris volume on the pedestal exceeded the preset pedestal volume with the wall height as low as possible.
- The analysis results of FP release into the environment reflecting boundary conditions and events occurring along the accident progression well reproduced the peak timing of the dose rate measured at the on-site MP. It was found that if the accident progression could be accurately simulated, it would be possible to reproduce the release of FP into the environment.
It was difficult to simulate sudden debris behavior change such as falling from the core to the lower plenum and from the lower plenum to the pedestal, though it might have affected FP release.
FP release (10) was assumed to be caused by the SRV open at 21:20 on 3/14 in Unit 2, but it might be possible to happen that the FP release was caused by the W/W vent in Unit 3 at 16:30-21:04 on 3/14. It would be considered how FP release (10) happened considering other knowledge in the future.

ACKNOWLEDGMENTS

We would like to express our deep gratitude to Ryoichi Hamasaki for his helpful comments.

REFERENCES

1. Report of Japanese Government to the IAEA Ministerial Conference on Nuclear Safety - The Accident at TEPCO's Fukushima Nuclear Power Stations -, June 2011.
2. MELCOR Computer Code Manuals, Vol. 1: Primer and Users' Guide, Version 2.2.9541 2017," SAND2017-0455 O R, Sandia National Laboratories, January 2017.
3. MELCOR Computer Code Manuals, Vol. 2: Reference Manual, Version 2.2.9541 2017," SAND2017-0876 O R, Sandia National Laboratories, January 2017..
4. Tokyo Electric Power Company, Inc. Evaluation of the situation of cores and containment vessels of Fukushima Daiichi Nuclear Power Station Units1 to 3 and examination into unsolved issues in the accident progression – Progress; 2022. (Report No. 6) in Japanese.
5. For example, NEA/CSNI/R(2015)18; Benchmark Study of the Accident at the Fukushima Daiichi Nuclear Power Plant (BSAF Project) March 2015.
6. NUREG/CR-2726, A. L. Camp, J. C. Cummings, M. P. Sherman et al.; "Light Water Reactor Hydrogen Manual," U.S.NRC, June 1983.
7. NUREG/IA-0129, V. Strizhov, V. Kanukova et al.; "International Report: An Assessment of the CORCON-MOD3 Code, Part I: Thermal-Hydraulic Calculations," U.S.NRC, September 1996.

Analyses of accident progression behavior and simulation of FP release into the environment using MELCOR code for the Fukushima Daiichi Nuclear Power Station Units 1 to 3

Masashi Himi, Koichi Nakamura, and Satoshi Nishimura
Central Research Institute of Electric Power Industry,
Nuclear Risk Research Center

Hideo Nagasaka
Laboratory for Zero-Carbon Energy,
Inst. of Innovative Research, Tokyo Institute of Technology

The 11th European Review Meeting on Severe Accident Research (ERMSAR2024)
KTH, Stockholm, Sweden, May 13-16, 2024

© CRIEPI

CRIEPI Central Research Institute of Electric Power Industry

Outline

The accident progression was investigated in [1].

[1] Report of Japanese Government to the IAEA, June 2011.

Their study indicated that each accidental event corresponded to a peak of dose rate measured at the on-site monitoring post (MP) as shown later.

In this paper, we performed MELCOR [2],[3] analysis for the Fukushima accident and aimed to complement plant data [4]. Because plant data during the accident were not sufficient to understand the overall picture of the accident.

[2] MELCOR 2.2.9541 Primer and Users' Guide, January 2017.
[3] MELCOR 2.2.9541 Reference Manual, January 2017.
[4] TEPCO Report No. 6, November 10 2022 in Japanese.

The several studies for the Fukushima accident have been performed and discussed in [4], [5].

[5] BSAF Project, March 2015 et al.

TEPCO summarized remained problems as the unsolved issues [4].
We will intend to perform MELCOR analysis for the future study with the boundary conditions reflected on the latest TEPCO information.

Objectives

The measured plant data do not tell us when the core melted.
When the RPV failure occurred, the RPV pressure decreases to the D/W pressure.
The hydrogen explosion occurred largely enough to blow away the reactor building (R/B).
It was a visually shocking event, but it is unlikely affected the fuel debris behavior.
The RPV failure is the most important event for debris behavior to influence the accident progression.
One of the objectives is to predict the RPV failure accurately.

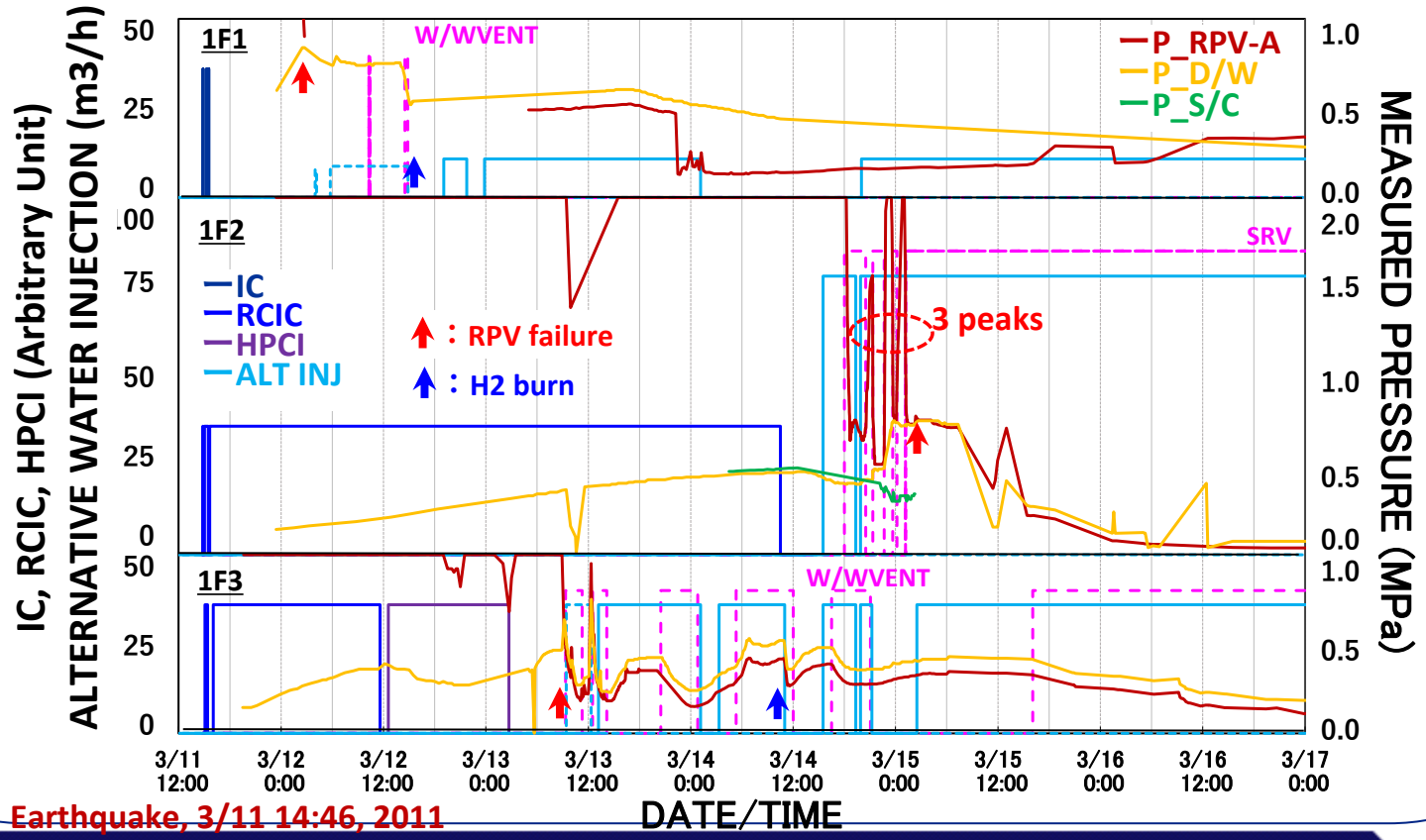

Events inferred from measured data of RPV, D/W and S/C pressures in Unit 1

It might be thought that W/W vent at 10:17, 10:23 and 10:24 on 3/12 was not sufficient, because D/W and S/C pressures did not lower at the time.
It was supposed that the W/W vent did not operate effectively.

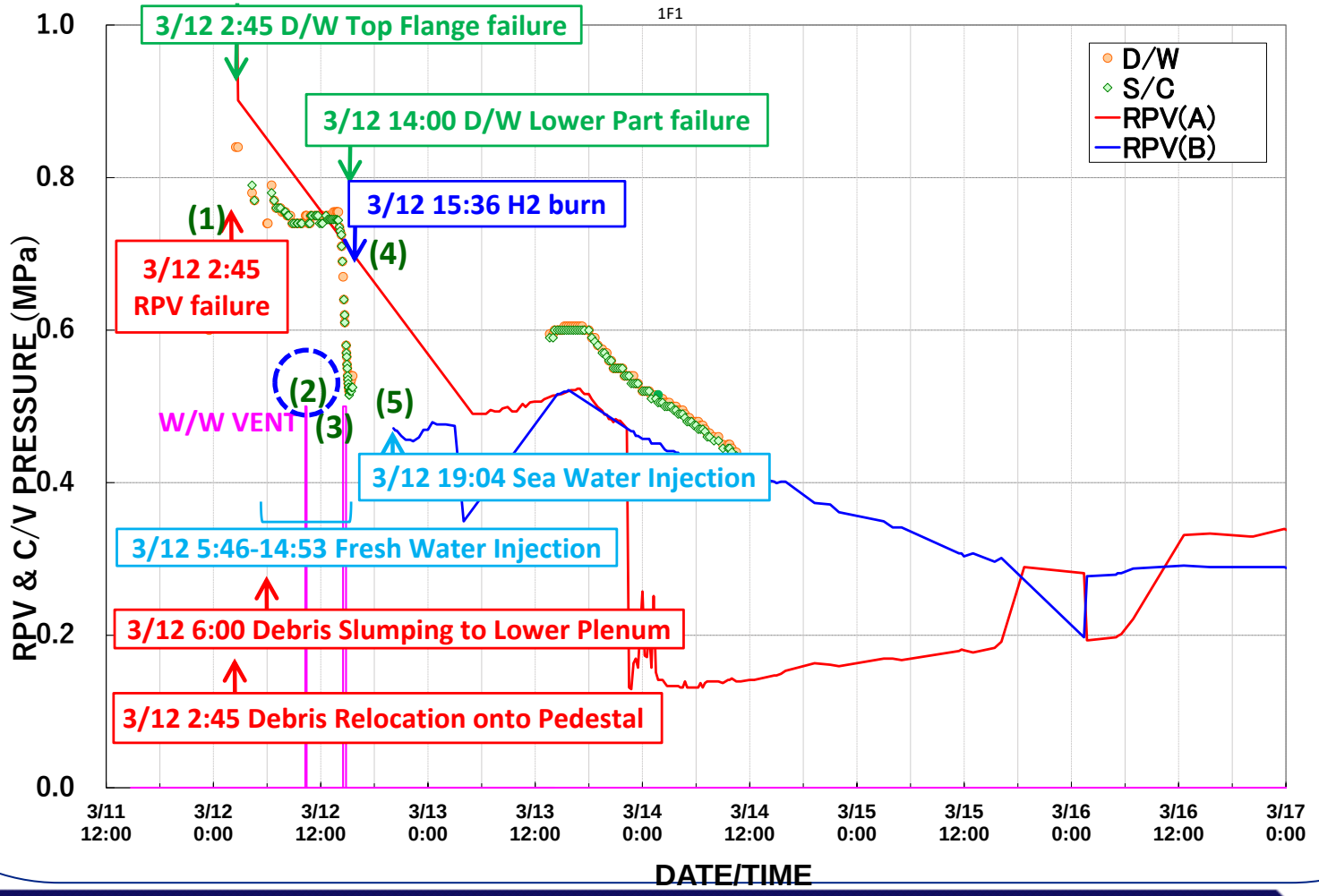

Events inferred from measured data of RPV, D/W and S/C pressures in Unit 1 (Continued)

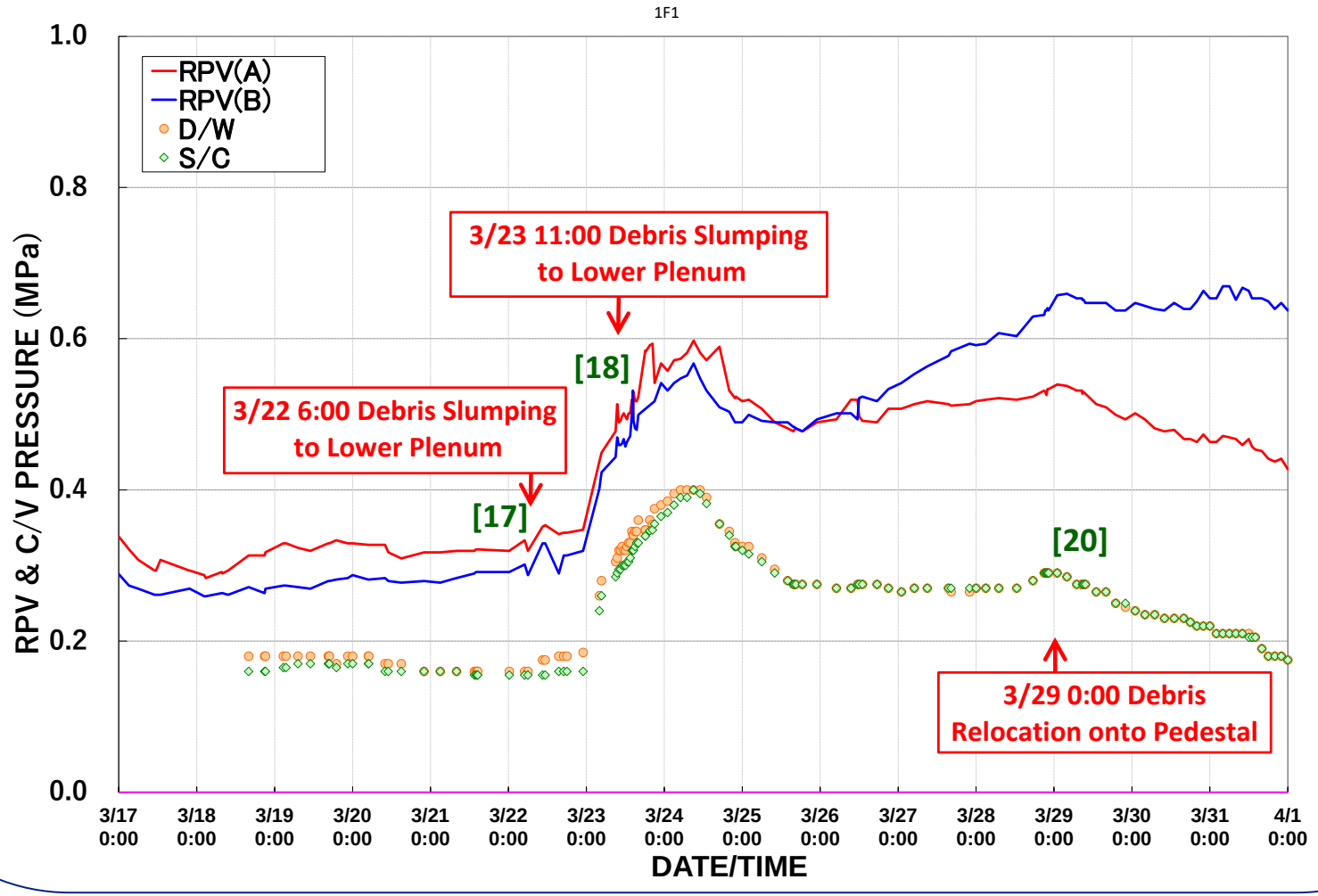

© CRIEPI

CRIEPI Central Research Institute of Electric Power Industry

Events inferred from measured data of RPV, D/W and S/C pressures in Unit 2

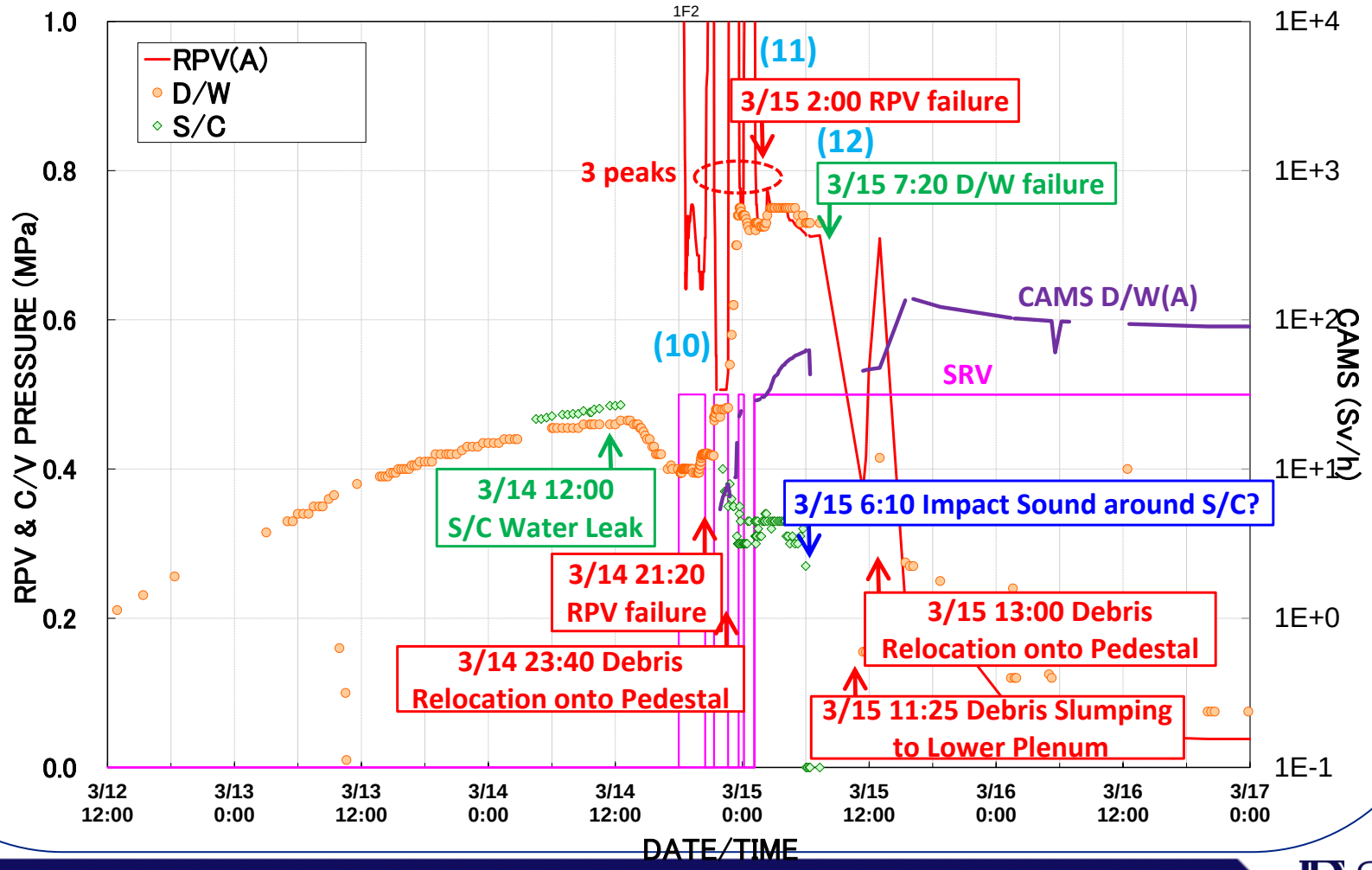

Events inferred from measured data of RPV, D/W and S/C pressures in Unit 2 (Continued)

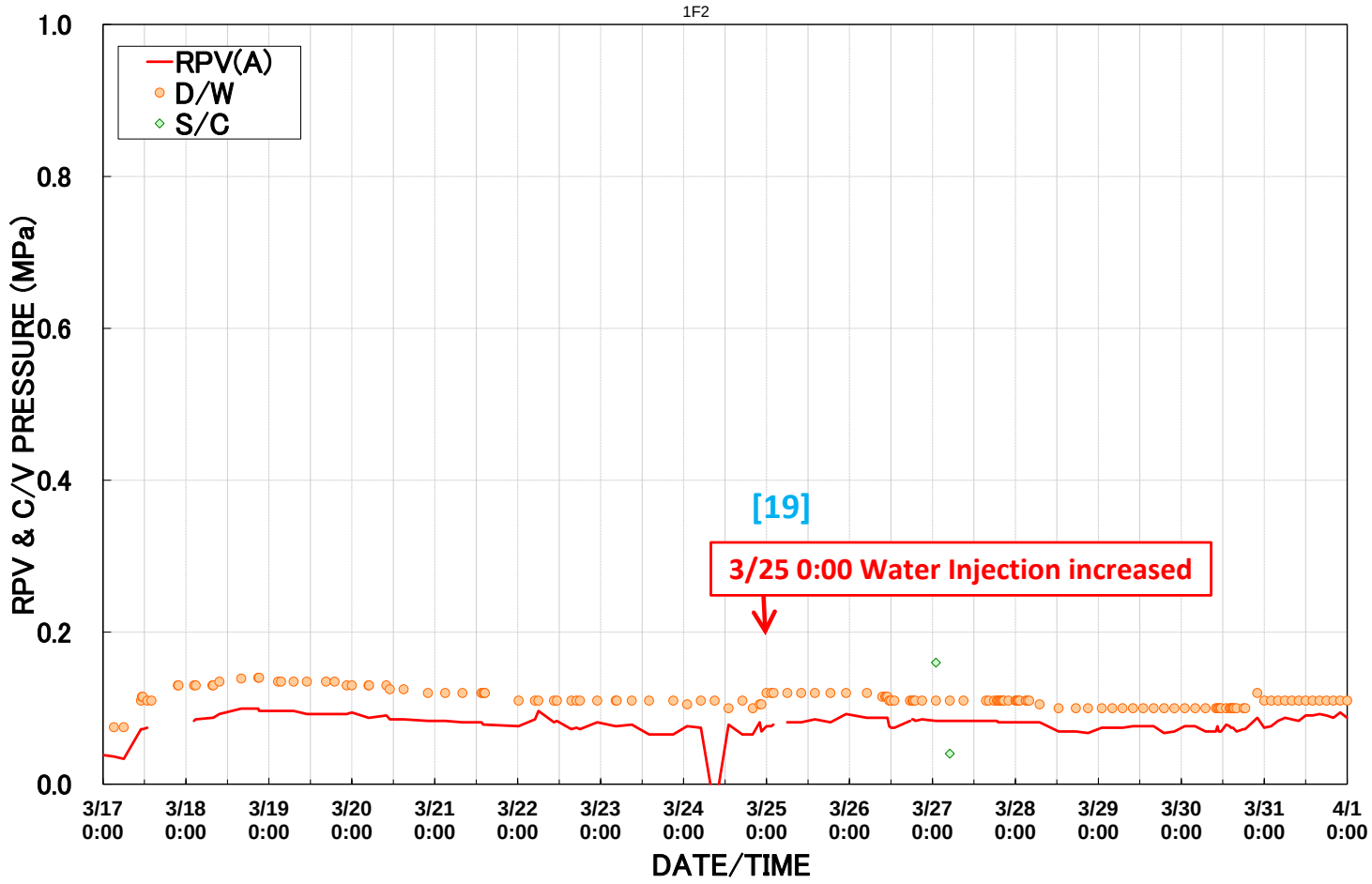

Events inferred from measured data of RPV, D/W and S/C pressures in Unit 3

It is thought that W/W vent at 5:20-12:00 on 3/14 did not operated.
It was supposed that the C/V pressure increased due to the change in alternative water injection from 3:20 to 11:01 on 3/14.

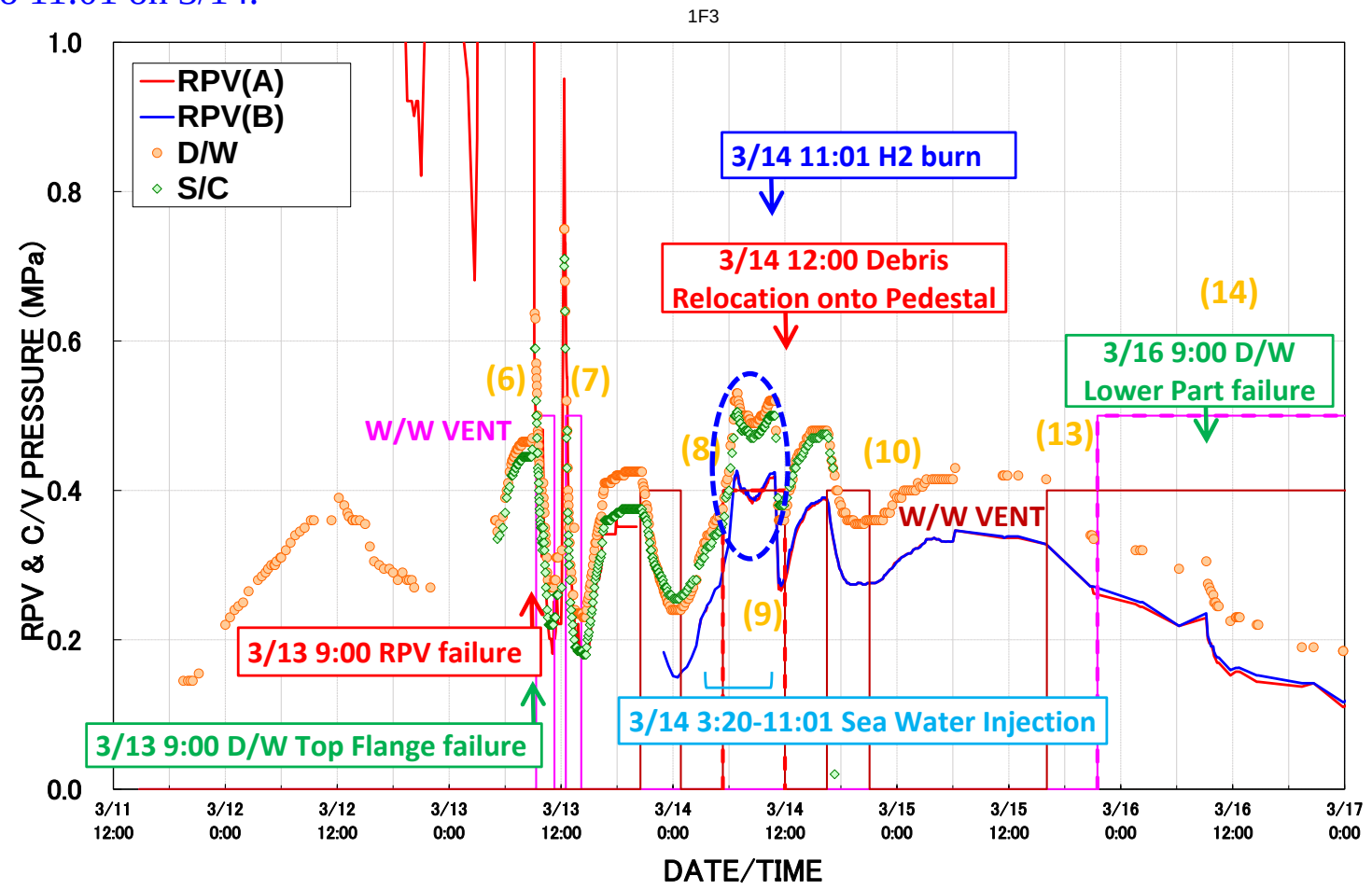

Events inferred from measured data of RPV, D/W and S/C pressures in Unit 3 (Continued)

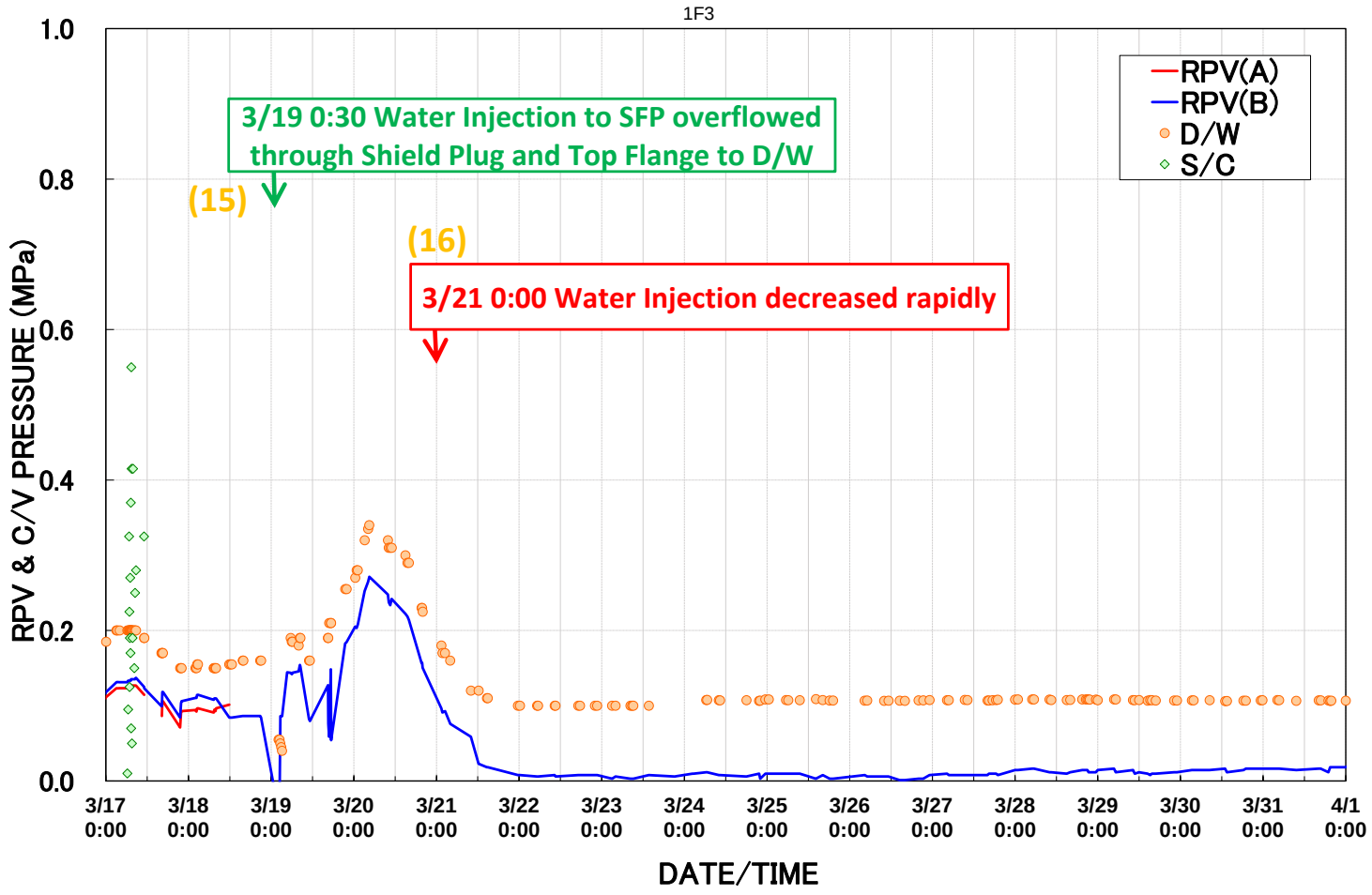

Dose Rate Measurements at on-site Monitoring Post (MP) and Corresponding Events

FP release, that is, each peak of dose rate measured at the on-site MP was originated from each event occurred in the accident. The events were inferred from measured RPV, D/W and S/C pressures in Units 1 to 3.

The events with parenthesized number (#) will be simulated by MELCOR analysis with boundary conditions referred the plant data.

The events with bracketed number [#] is supposed to have been caused by sudden debris behavior, so it seems difficult to simulate them using analysis code.

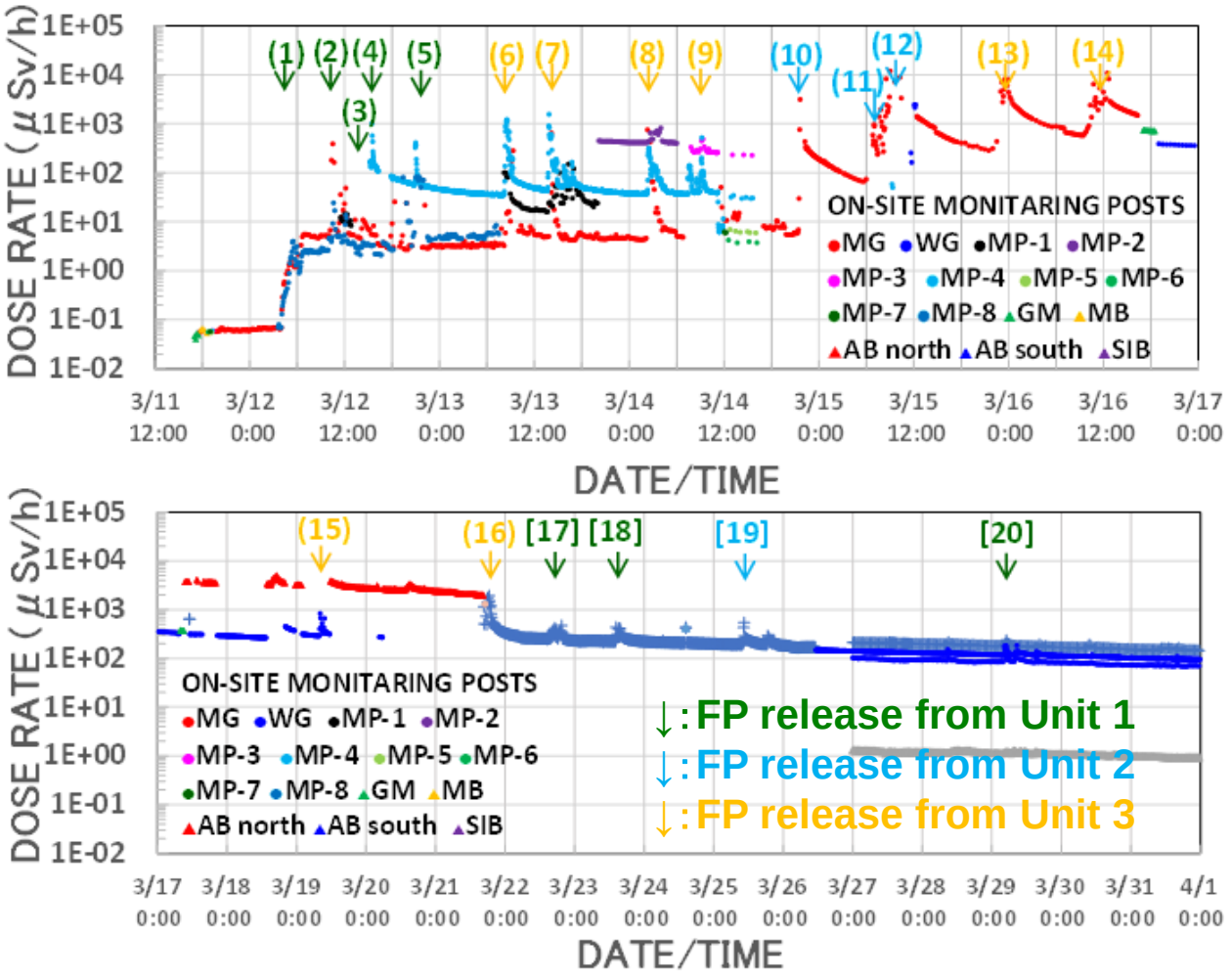

Dose Rate Measurements at on-site Monitoring Post (MP) and Corresponding Events

(1) according to Unit 1: FP was released due to the RPV failure and the PCV upper part failure before 2:45 on 3/12.
(2) according to Unit 1: FP was released due to W/W vent at 10:17 on 3/12.
(3) according to Unit 1: the PCV lower part failed at 14:00 on 3/12 and FP was released due to the W/W vent at 14:30 on 3/12.
(4) according to Unit 1: FP was released due to the hydrogen explosion at 15:36 on 3/12.
(5) according to Unit 1: FP was released due to steam generation associated with seawater injection at 19:04 on 3/12.
(6) according to Unit 3: the RPV failed at 9:00 on 3/13 and FP was released due to the W/W vent at 9:20 on 3/13.
(7) according to Unit 3: seawater was injected at 13:12 on 3/13 and FP was released due to the W/W vent at 12:30 on 3/13.
(8) according to Unit 3: FP was released due to steam generation associated with seawater injection at 3:20 on 3/14.
(9) according to Unit 3: FP was released due to the PCV pressure changed after seawater injection from3:20-11:01 on 3/14.
(10) according to Unit 2: FP was released due to the safety relief valve (SRV) open at 21:20 on 3/14.
(11) according to Unit 2: FP was released due to the RPV failure at 2:00 on 3/15.
(12) according to Unit 2: FP was released due to the damaged lower D/W at 7:20 on 3/15.
(13) according to Unit 3: FP was released due to the W/W vent at 21:30 on 3/15.
(14) according to Unit 3: FP was released due to liquid phase leakage from the lower D/W at 9:00 on 3/16 and sequentially pedestal wate r flashing under reduced pressure.
(15) according to Unit 3: water injection into the spent fuel pool (SFP) began at 0:30 on 3/19; some water accumulated from the shield p lug into the reactor well (R/W) and flowed into the D/W from the damaged flange, which caused steam generation, increased pressure an d released FP.
(16) according to Unit 3: FP was released due to the D/W temperature rising caused by the decrease in water injection amount from 3/21
[17] according to Unit 1: FP was released due to the change in the RPV pressure caused by the fuel debris falling into the lower plenum at 6:00 on 3/22 during the water injection rate decrease between 3/21 and 3/23.
[18] according to Unit 1: FP was released due to the change in the RPV pressure caused by the fuel debris falling into the lower plenum at 11:00 on 3/23 when the water injection was increased on 3/23.
[19] according to Unit 2: FP was released due to the D/W pressure changed caused by the fuel debris falling into the pedestal when the a mount of water injection increased on 3/25.
[20] according to Unit 1: FP was released due to the fuel debris falling into the lower plenum and the pedestal at 0:00 on 3/29 caused by the change in the RPV and the D/W pressure.

Note that the early dose rate plateau before FP release (1) is thought to be due to radiation from the R/B, not due to FP release.

© CRIEPI

Boundary Conditions

The plant is divided into a diagram of nodes used for thermal-hydraulics and FP dynamics in MELCOR.

Core degradation, hydrogen explosion and MCCI models will be described later.

As shown in next page, boundary conditions are referred plant data like safety function operations at the accident, and leakages are supposed.

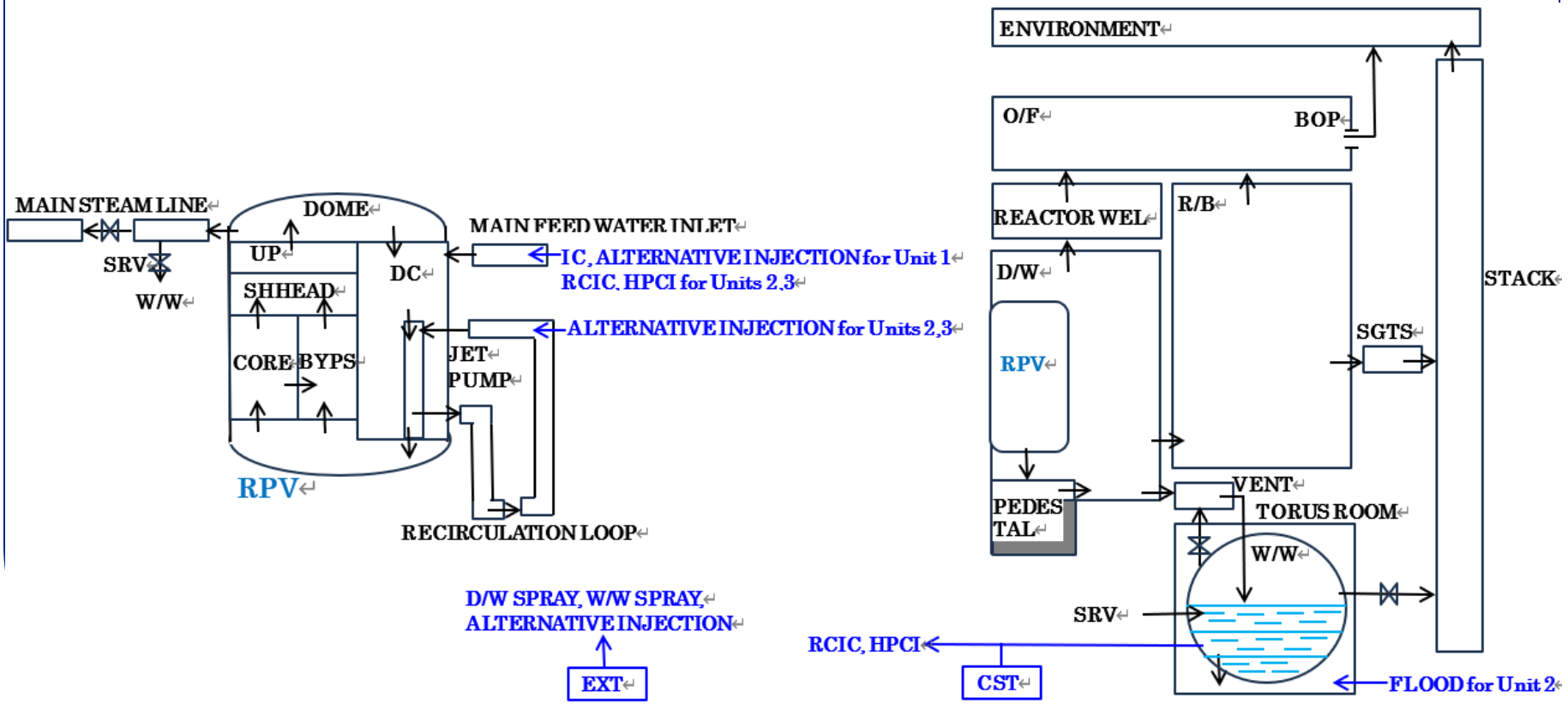

Boundary Conditions (Continued)

Supposition of Leakage is as follows.

Water is injected into the RPV for cooling the core.
A part of water is evaporated to steam by decay heat and transfers from the SRV to the S/C.
But amount of water remained exceeds the RPV volume significantly.
It is supposed that leakage occurred from the PCV at an early stage but near the time of the RPV failure.
It might be found in change of the measured PCV pressure.

	Unit 1	Unit 2	Unit 3
gas phase leak from damaged lower D/W		**3/15 7:20**	**3/16 9:00**
liquid phase leak from damaged lower D/W	**3/12 14:00**		**3/16 9:00**
liquid phase leak from damaged W/W		**3/14 12:00**	
W/W vent	**3/12 10:17 3/12 10:23 3/12 10:24 3/12 14:30-14:49**		**3/13 9:20-11:17, 12:30-14:10, 3/15 21:30- 3/13 20:30-3/14 0:50, 3/14 16:30-21:04, 3/15 16:05-**
ADS open and close		**3/14 18:00-20:30**	
SRV open and close		**3/14 21:20-22:40 3/14 23:40-3/15 0:10 3/15 0:10-**	

© CRIEPI

Boundary Conditions (Unit 1) (Continued)

The isolation condenser (IC) flow rate was adjusted to reproduce the time of the RPV failure.
The RPV failure occurred before the start of alternative water injection, the officially announced alternative water injection flow rate was used.
A parameter survey was conducted on the area of the liquid phase leak to the R/B from the damaged lower D/W at 14:00 on 3/12 to predict the PCV pressure and appropriate leakage.

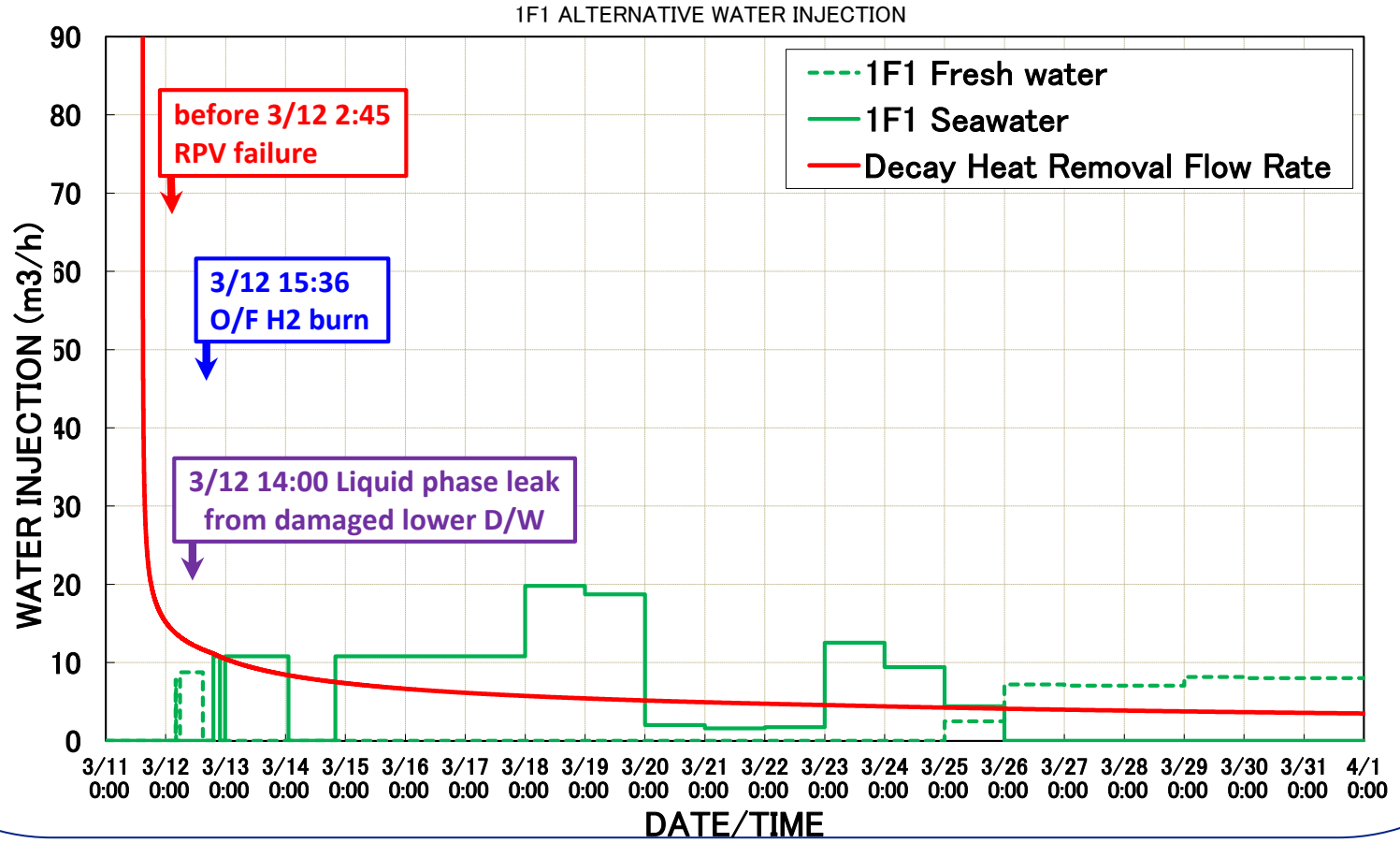

Boundary Conditions (Unit 2) (Continued)

It was supposed that the automatic depressurization system (ADS) opened at 18:00 on 3/14, led to reduce the pressure in the core, steam by flashing was generated, the fuel temperature was cooled down and Zr oxidation reaction by steam was suppressed. The officially announced alternative water injection flow rate was adjusted so as not to cause excessive Zr oxidation reaction.
So, the officially announced alternative water injection flow rate was be modified.

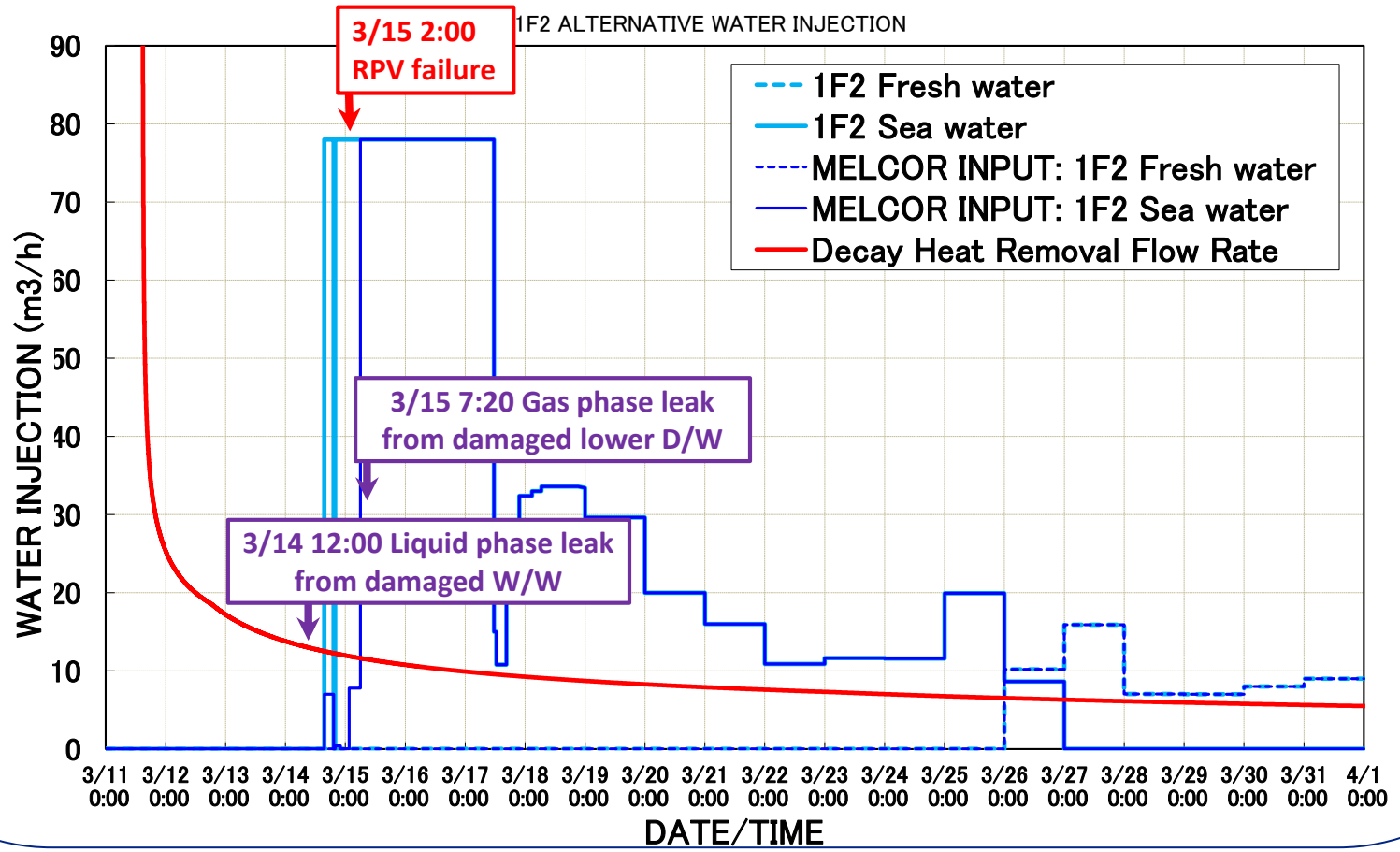

Boundary Conditions (Unit 2) (Continued)

The RPV failure was reproduced due to adjustment of the tsunami water flooded into the torus room, the reactor core isolation cooling system (RCIC) flow rate, the liquid phase leak from the damaged W/W and the alternative water injection flow rate.
The 3 peaks of the RPV pressure caused by the SRV open and close was also reproduced.

The leak area was selected to 1E-2 m2. Choosing these four adjusted parameters would not be necessarily optimal to reproduce the phenomena. It might be required more precise choice.

A parameter survey was conducted on the area of the gas phase leak to the R/B from the lower D/W damaged at 7:20 on 3/15.

© CRIEPI

Boundary Conditions (Unit 3) (Continued)

The reactor core isolation cooling system (RCIC) flow rate and the high-pressure cooling injection system (HPCI) flow rate was adjusted to reproduce the time of the RPV failure.
The RPV failure occurred before the start of alternative water injection, the officially announced alternative water injection flow rate was used.
A parameter survey was conducted on the area of the gas phase and the liquid phase leak to the R/B from the damaged lower D/W at 9:00 on 3/16 to predict the PCV pressure and appropriate leakage.

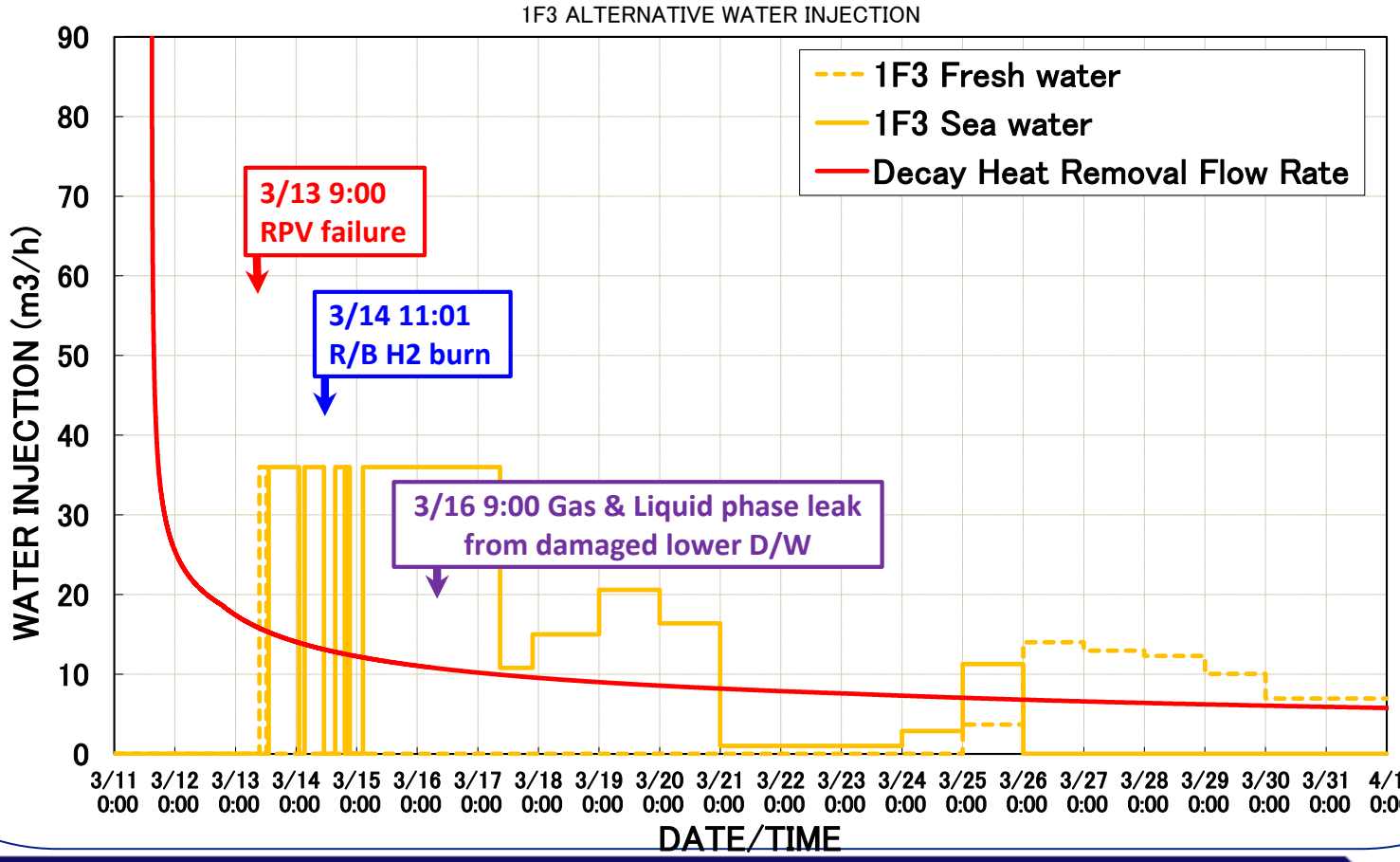

Parameter Survey of Leak Area of Unit 1

A parameter survey was conducted on the leak area of the liquid phase leak from the damaged lower D/W at 14:00 on 3/12.

If amount of leak from the D/W is not large, decay heat can be removed by injecting water into the reactor core, and the accident will be stabilized.
The PCV pressure increased as the leak area became smaller.
If the leak area is 1E-4 m2 or less, subtracting the evaporation amount and leak amount from the total water injection amount will still be positive.

(injection) - (evaporation) - (leak) > 0

So, the decay heat could be removed.
The leak area of 1E-4 m2 is applied to the most plausible analysis later.

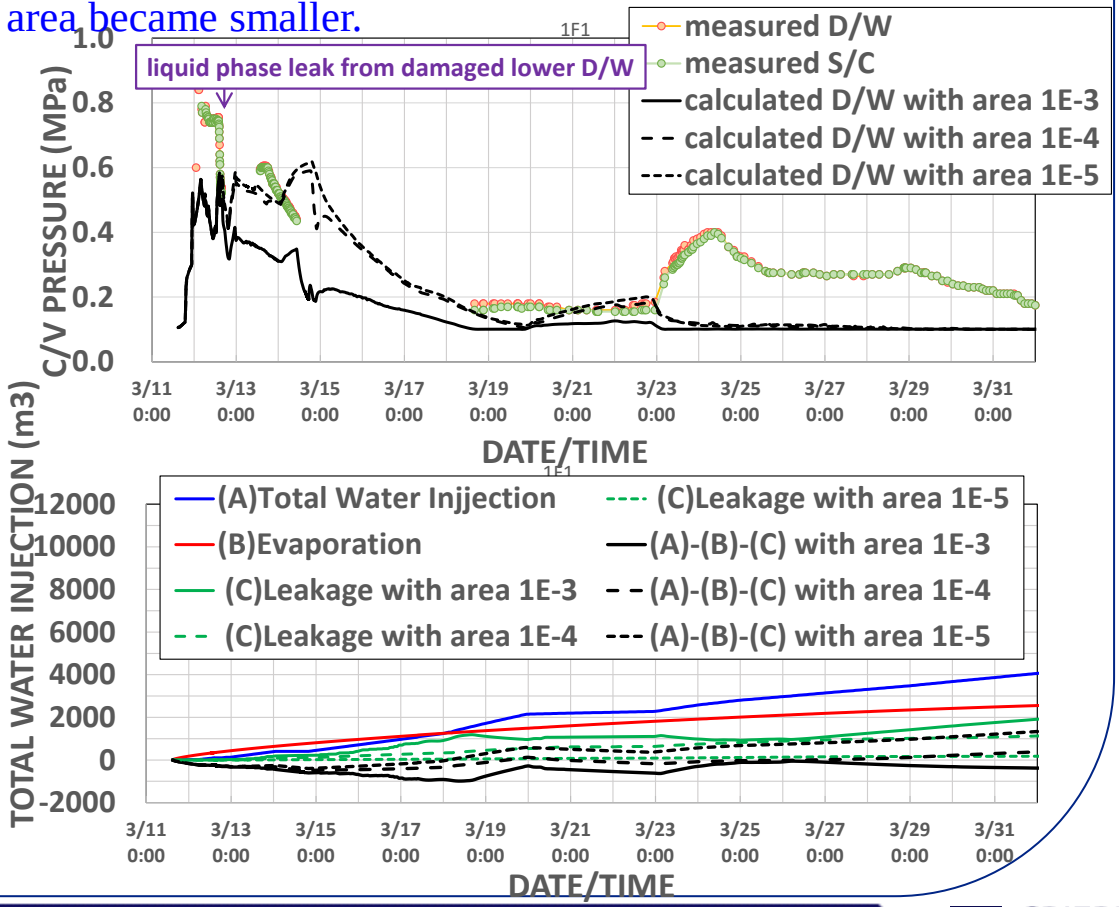

Parameter Survey of Leak Area of Unit 2

A parameter survey was conducted on the leak area of the gas phase leak from the damaged lower D/W at 7:20 on 3/15.

As described later, the result of the RPV pressure before 7:20 on 3/15 was adjusted to reproduce the time of the RPV failure and the 3 peaks in the RPV pressure.

The decay heat could be removed irrespective of the leak area of the gas phase leak from the damaged lower D/W at 7:20 on 3/15 after the core degradation process had passed. Additionally, we were able to reproduce the reduction of the D/W pressure after the start of the leakage.
The leak area of 1E-2 m2 was judged to appropriate to reproduce the D/W pressure.

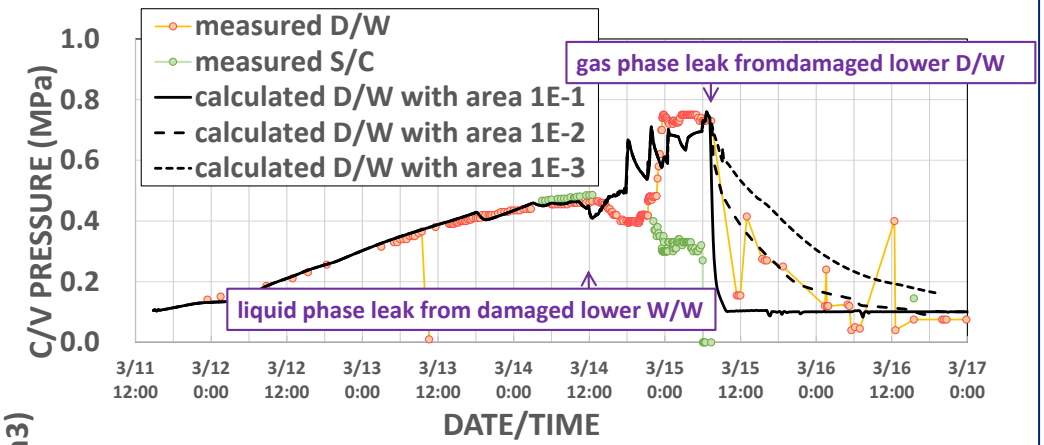

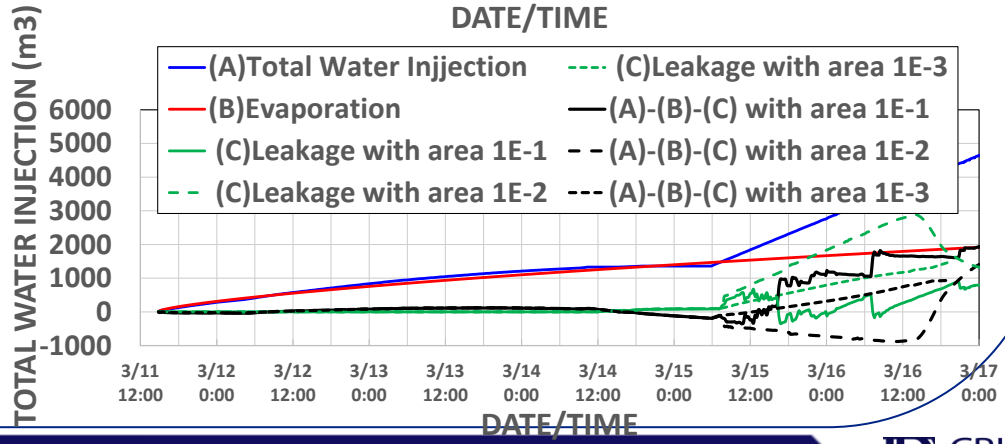

Parameter Survey of Leak Area of Unit 3

A parameter survey was conducted on the leak area of the gas and the sequential liquid phase leak from the damaged lower D/W at 9:00 on 3/16.

If the leak area is 1E-4 m2 or less, subtracting the evaporation amount and leak amount from the total water injection amount will still be positive.

(injection) - (evaporation) - (leak) > 0

So, the decay heat could be removed.
The leak area of 1E-4 m2 is applied to the most plausible analysis later.

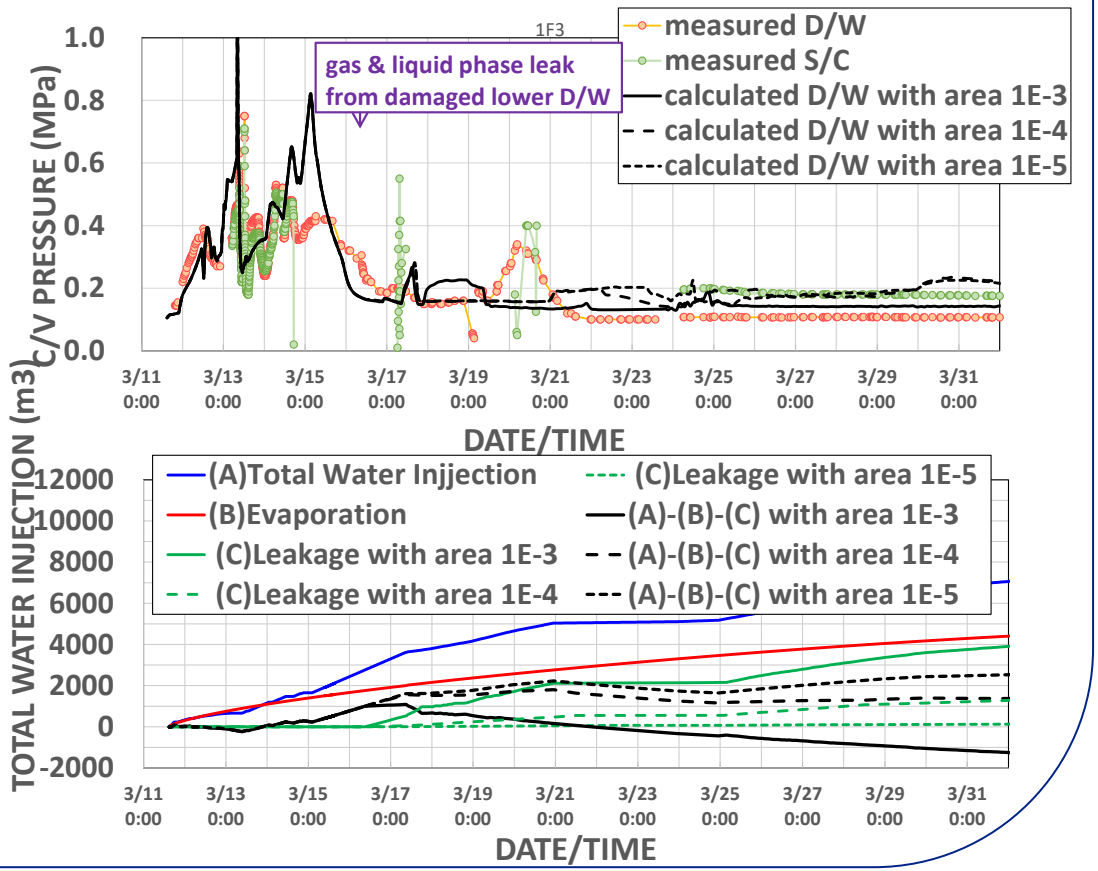

MELCOR Most Plausible Analysis (Core Degradation Process)

Figure shows the core degradation process.
The core and lower plenum are treated as an axisymmetric two-dimensional model.
The initial state shows the core and lower plenum region divided into radial rings and axial levels for MELCOR.

During the core degradation process, the fuel was heated up to 2500 K.
The fuel debris did not heat up enough to melt and collapsed into fragments as the particulate debris.
The control rod drive remained in its original shape to some extent due to the injection of cooling water into the lower plenum.
The fuel debris and the control rod drive fell onto the pedestal.

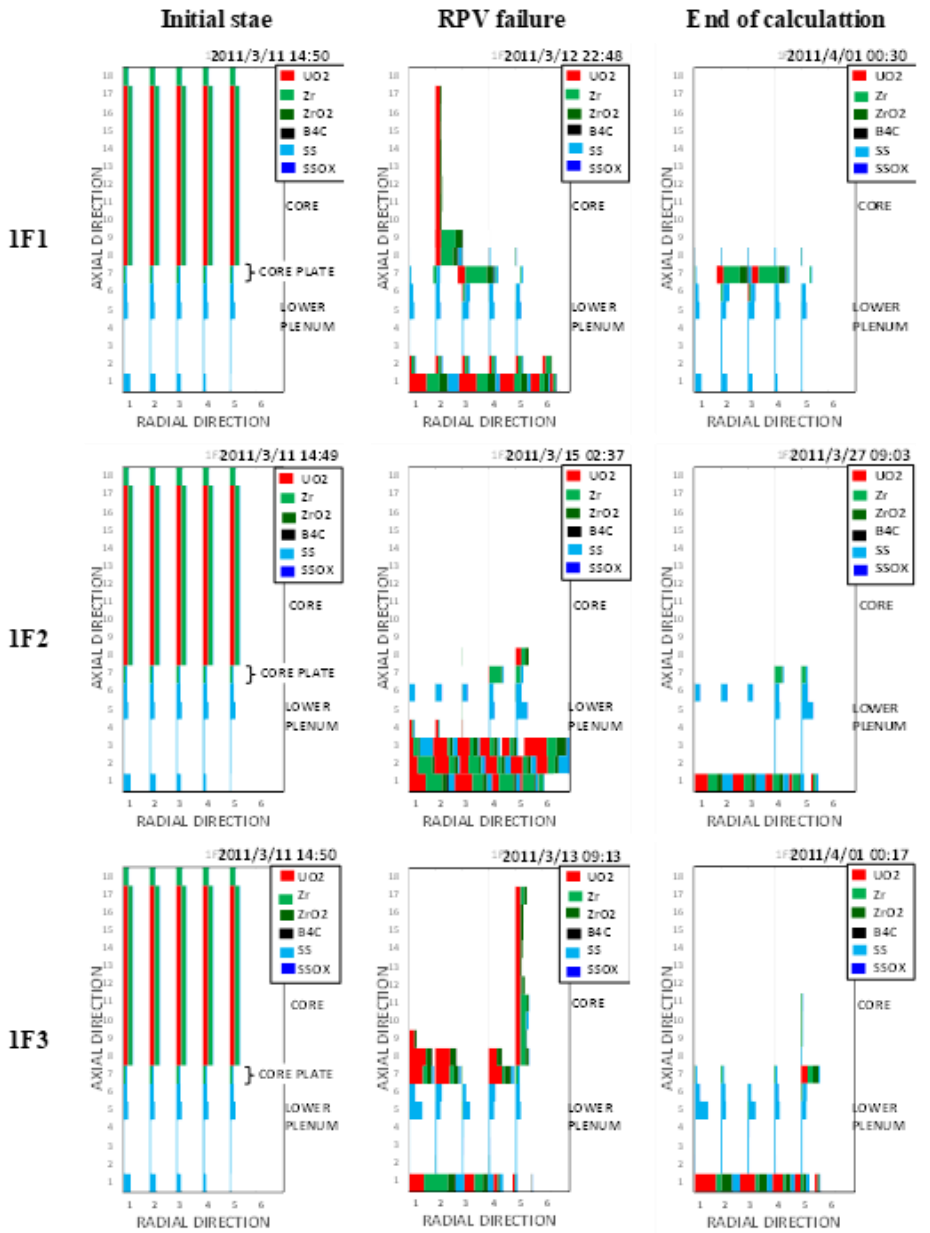

MELCOR Most Plausible Analysis (Core Degradation Process)

Depending on the temperature rise of the fuel, a large amount of FP is released during this period.
The oxidation rate of Zr in the core structure during this period was 29.2 % in Unit 1, 20.6 % in Unit 2, and 29.1 % in Unit 3.
Whether the oxidation rate of the core structure affected FP release will be investigated in the future.

	Relocation	Fuel Temperaturs	Non Condensable Gas
1F1	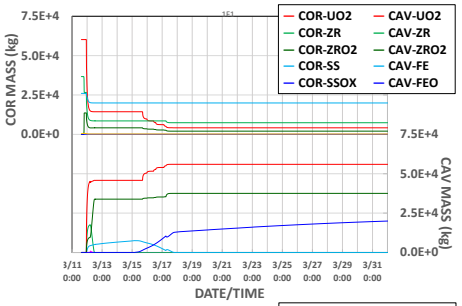	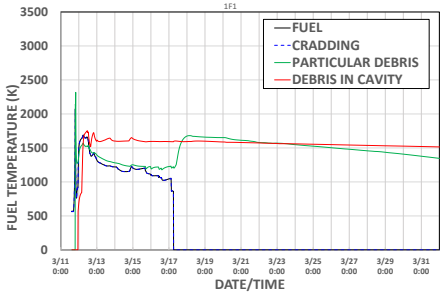	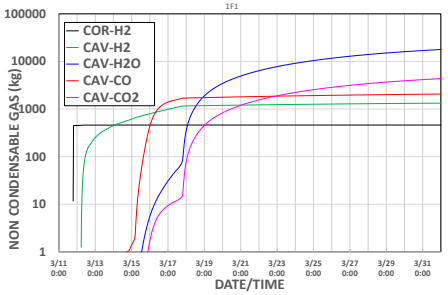
1F2	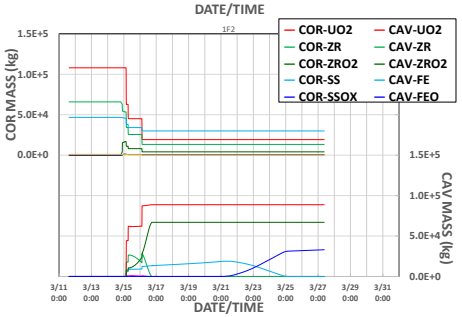	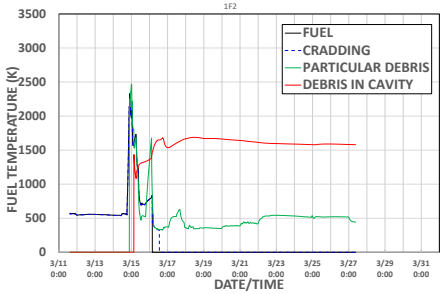	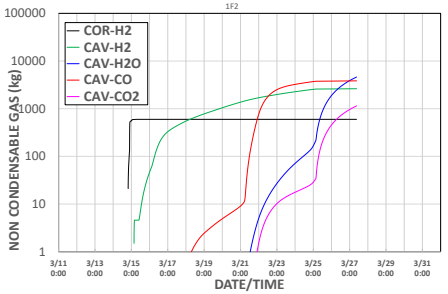
1F3	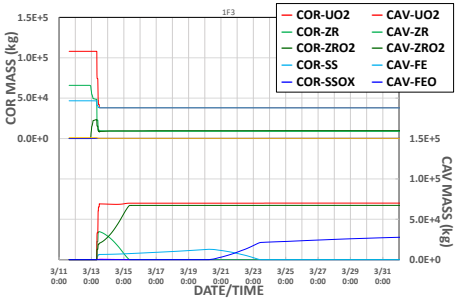	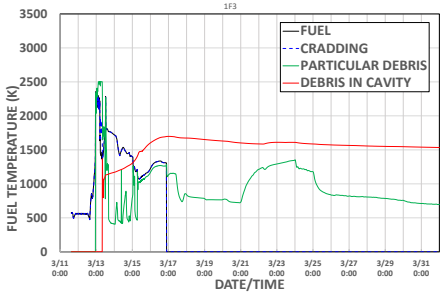	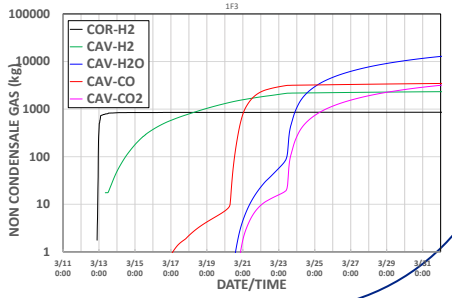

MELCOR/CORCON-Mod3 (MCCI Model)

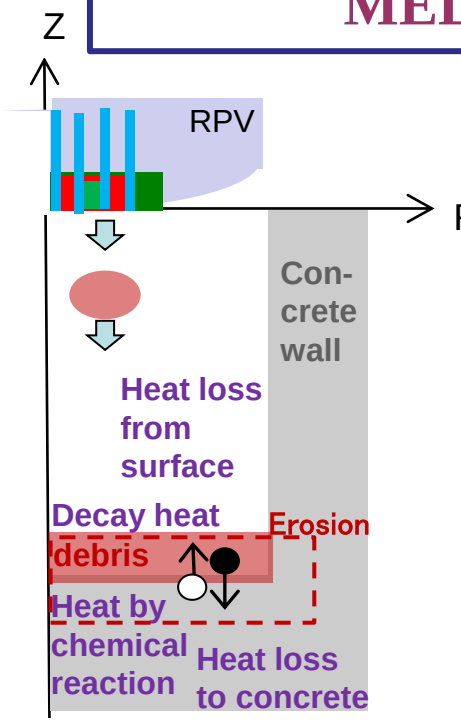

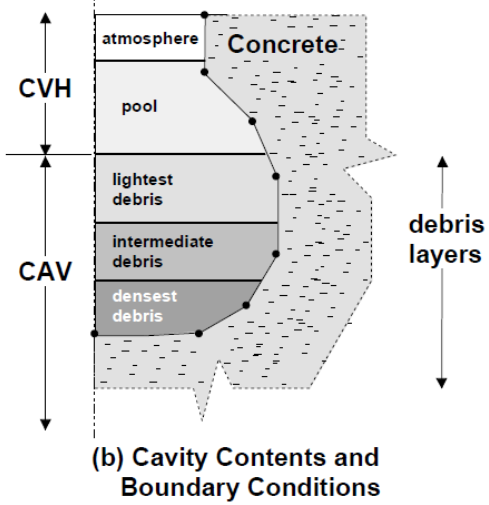

Figure 3.1 Cavity System Components [3] MELCOR RM

Even if the fuel debris and the control rod drive are not melted on the pedestal, CORCON handles them a collection of microparticles like fluid and hastens the MCCI.
So, MELCOR analysis results in a conservative assessment.

The fuel debris on the pedestal is handled as layers of HOX (high density oxide) consisting of UO2, ZrO2, SSOX, MET (high density metal) consisting of Zr and HMX (high density mixture) consisting of a mixture of these.
The concrete of the pedestal is handled as layers of LOX (low density oxide) and LMX (low density mixture). Each layer is regarded as a collection of microparticles..

While the fuel debris erodes concrete, high-density particles ● sink and low-density particles ○ float in the debris layers and spread to the surrounding area.

A layer mixing model, a coking reaction, and an ablation enthalpy of basaltic concrete of 2.3E+6 J/kg [7] were applied for use in analysis.
[7] NUREG/IA-0129, 1996, p.49.
MELCOR default value of ablation enthalpy 0.0 J/kg is considered inappropriate.

MELCOR Most Plausible Analysis (MCCI)

Debris Temperature | **Concrete Ablation**

1F1

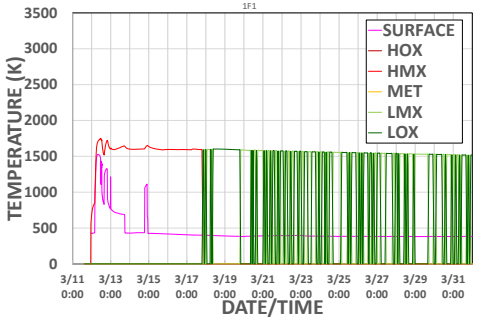

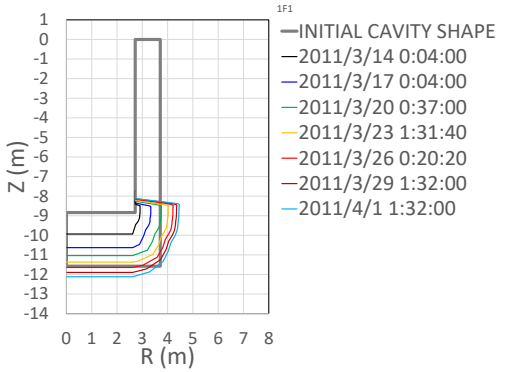

1F2

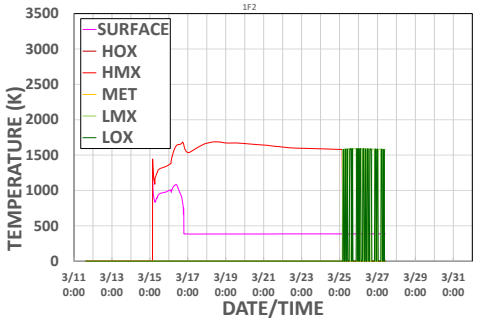

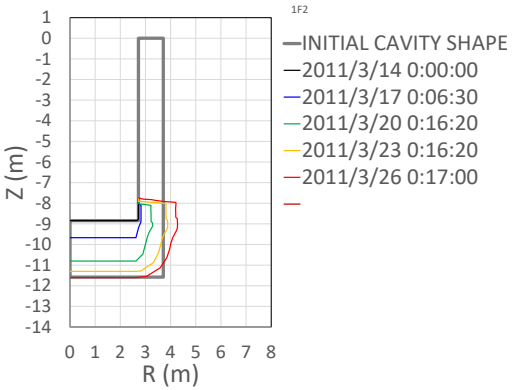

1F3

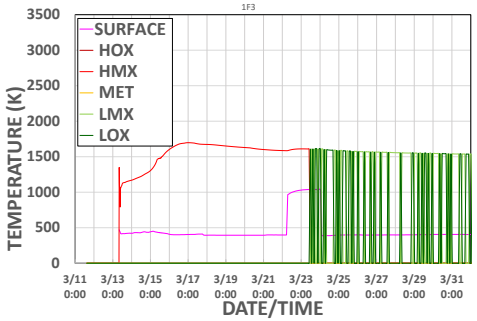

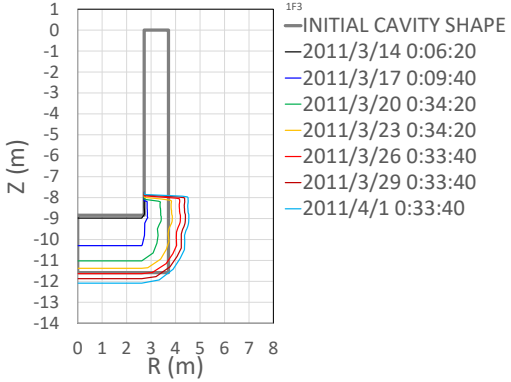

Figure shows the analysis results for the MCCI calculations.

After the debris falling onto the pedestal, the debris temperature lowered to dissipate heat but suppressed by exothermic reaction in MCCI and it kept around 1500 K, below the melting point of iron.

The debris eroded concrete floor and wall.

On the recent observation in Unit 1, the steel of the pedestal was not melted, and the concrete floor was eroded.

It might be observed in Unit 2 and 3 whose pedestal had a double cylindrical steel wall filled with concrete.

The debris temperature did not lower by the end of the calculations in any analyses, so that the accident was not stabilized.

MELCOR Most Plausible Analysis (RPV and PCV Pressures)

Figure shows the RPV pressure and the PCV pressure.

For Unit 1, the RPV failure occurred before the start of the alternative water injection. It was reproduced due to adjustment of the IC.

For Unit 2, the RPV failure occurred after the start of the alternative water injection.
It was reproduced due to adjustment of
the tsunami water flooded into the torus room,
the RCIC flow rate,
the liquid phase leak from the damaged W/W
and the alternative water injection flow rate.
The 3 peaks in the RPV pressure caused by the SRV open and close was also reproduced.
Choosing these four adjusted parameters would not be necessarily optimal to reproduce the phenomena.
It might be required more precise choice.

For Unit 3, the RPV failure occurred before the start of the alternative water injection.
It was reproduced
due to adjustment of the RCIC flow rate and the HPCI flow rate.

RPV pressure | **C/V pressure**

1F1

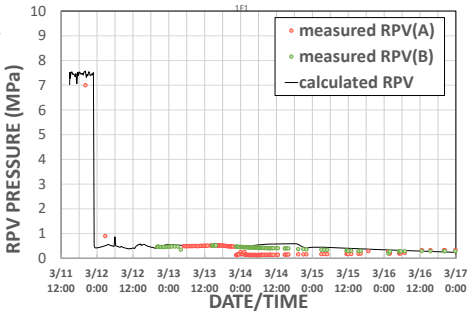

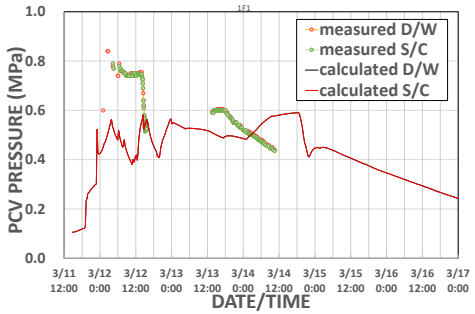

1F2

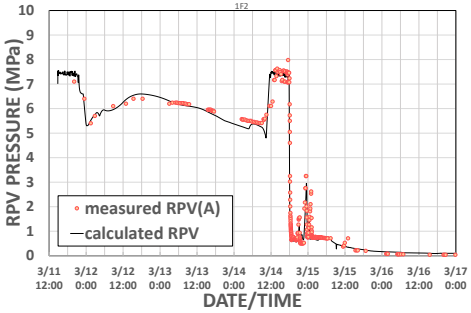

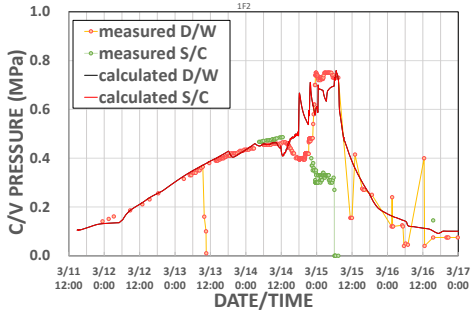

1F3

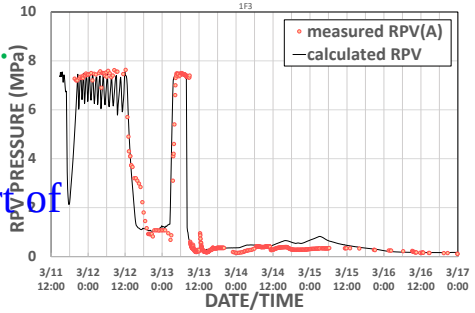

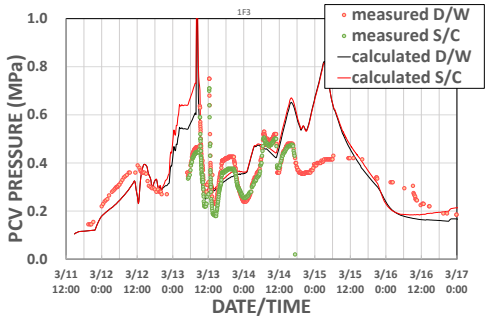

MELCOR /HECTR1.5 (Hydrogen Explosion Model)

Expected major migration routes for gas
Additional routes for Unit 2

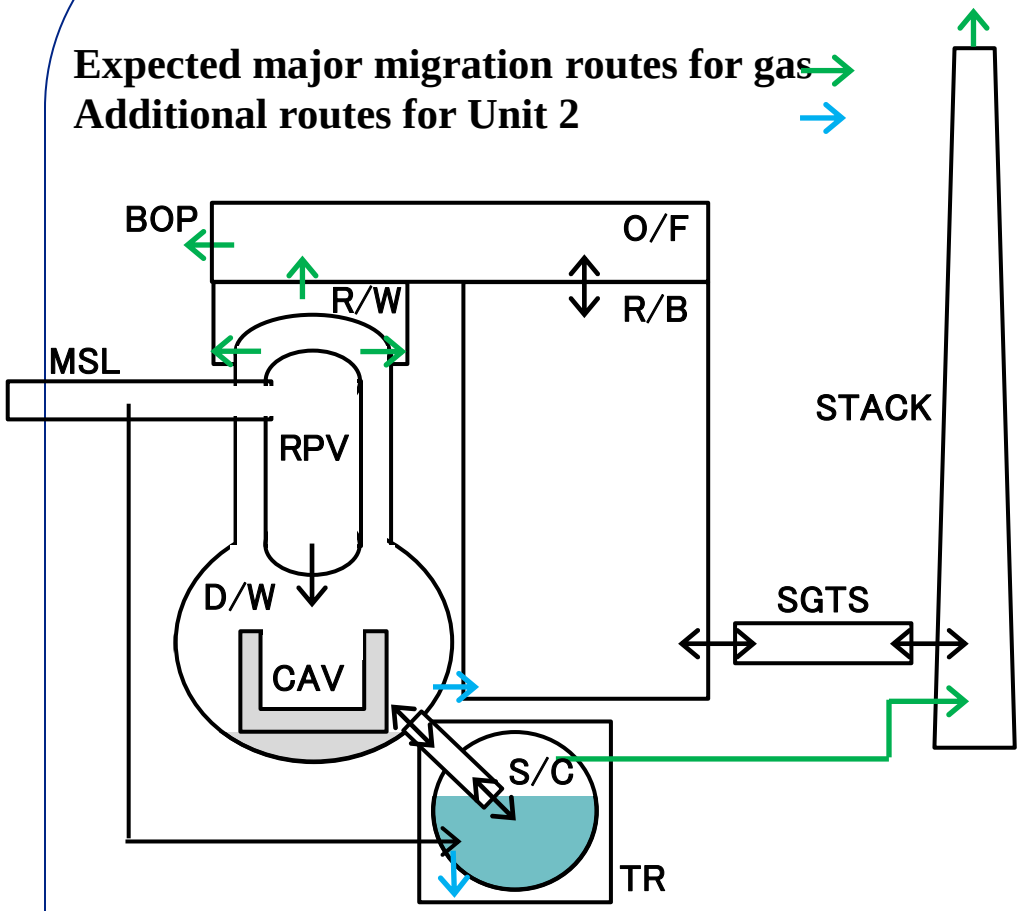

The default model of hydrogen explosion in MELCOR/HECTR1.5 is deflagration.
Since the hydrogen explosion that occurred in the Fukushima accident was enough to blow away the R/B, we suppose that detonation had occurred in the accident.
We modified the model to detonation [6].

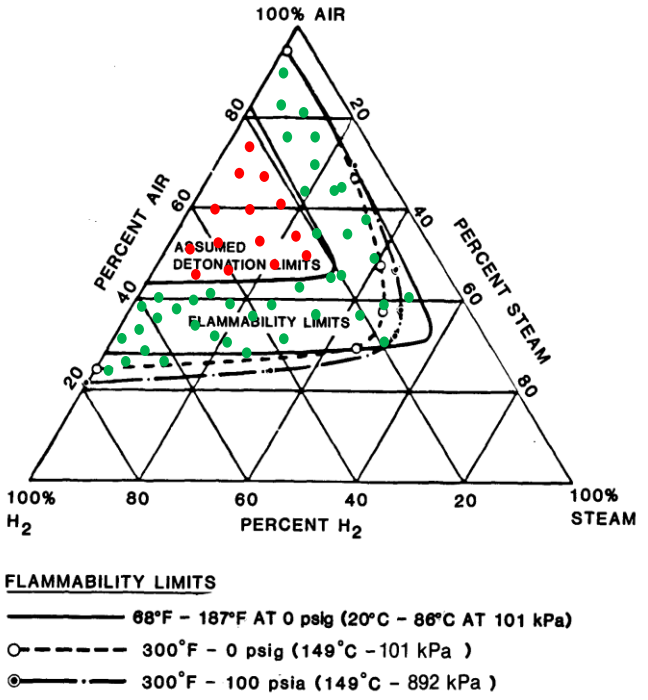

Figure 2-16. Flammability and Detonation Limits of Hydrogen:Air:Stem Mixtures

It is replaced deflagration model with
$X_{H2} \geq 0.1$, $X_{O2} \geq 0.05$, $X_{H2O} < 0.55$ to detonation model
with $X_{H2} \geq 0.1507$, $X_{O2} \geq 0.09$, $X_{H2O} < 0.30$.

[6] NREG/CR-2726, 1983.

MELCOR Most Plausible Analysis (Summary)

	Unit 1		Unit 2		Unit 3	
Event	Observed	Calculated	Observed	Calculated	Observed	Calculated
RPV failure	before 3/12 2:45	3/11 22:48	3/15 2:00	3/15 3:21	3/13 9:00	3/13 7:54
Hydrogen burn	O/F on 3/12 15:36	O/F on 3/12 14:45	—	No occurrence	R/B on 3/14 11:01	STACK on 3/13 9:20
Stabilization of accident	After the end of April 2011	Not attainable by April 1st	Until the end of August 2011	Not attainable by April 1st	After the end of August 2011	Not attainable by April 1st

We aimed to predict the time of the RPV failure.

An impact sound at 6:10 on 3/15 coming from Unit 4 was misunderstood as a hydrogen explosion in the torus room of Unit 2 in those days.
The torus room was flooded by the tsunami following the earthquake. Water leaked from the S/C to the torus room at 12:00 on 3/14 and hydrogen gas also leaked to the torus room. MELCOR analysis showed that the mole fraction of water vapor was high in the torus room, so hydrogen explosion did not occur.

In Unit 3, there was a leakage of hydrogen to the exhaust stack (STACK) due to the W/W vent. It led that a hydrogen explosion occurred at the STACK. We should investigate more detail analysis.

FP release to the Environment

The figure shows the calculation result of cesium as a major FP released to the environment.
FP release with parenthesized number (#) corresponds to the event that MELCOR predicted according to the boundary conditions.
On the other hand, FP release with bracketed number [#] corresponds to the event that occurred from sudden debris behavior like the fuel debris falling onto the pedestal and so on, and that could not be reproduced by MELCOR.

FP release (1) from Unit 1 due to the RPV failure before 2:45 on 3/12
FP release (6) from Unit 3 due to the W/W vent at 9:20 on 3/13
FP release (11) from Unit 2 due to the RPV failure at 2:00 on 3/15

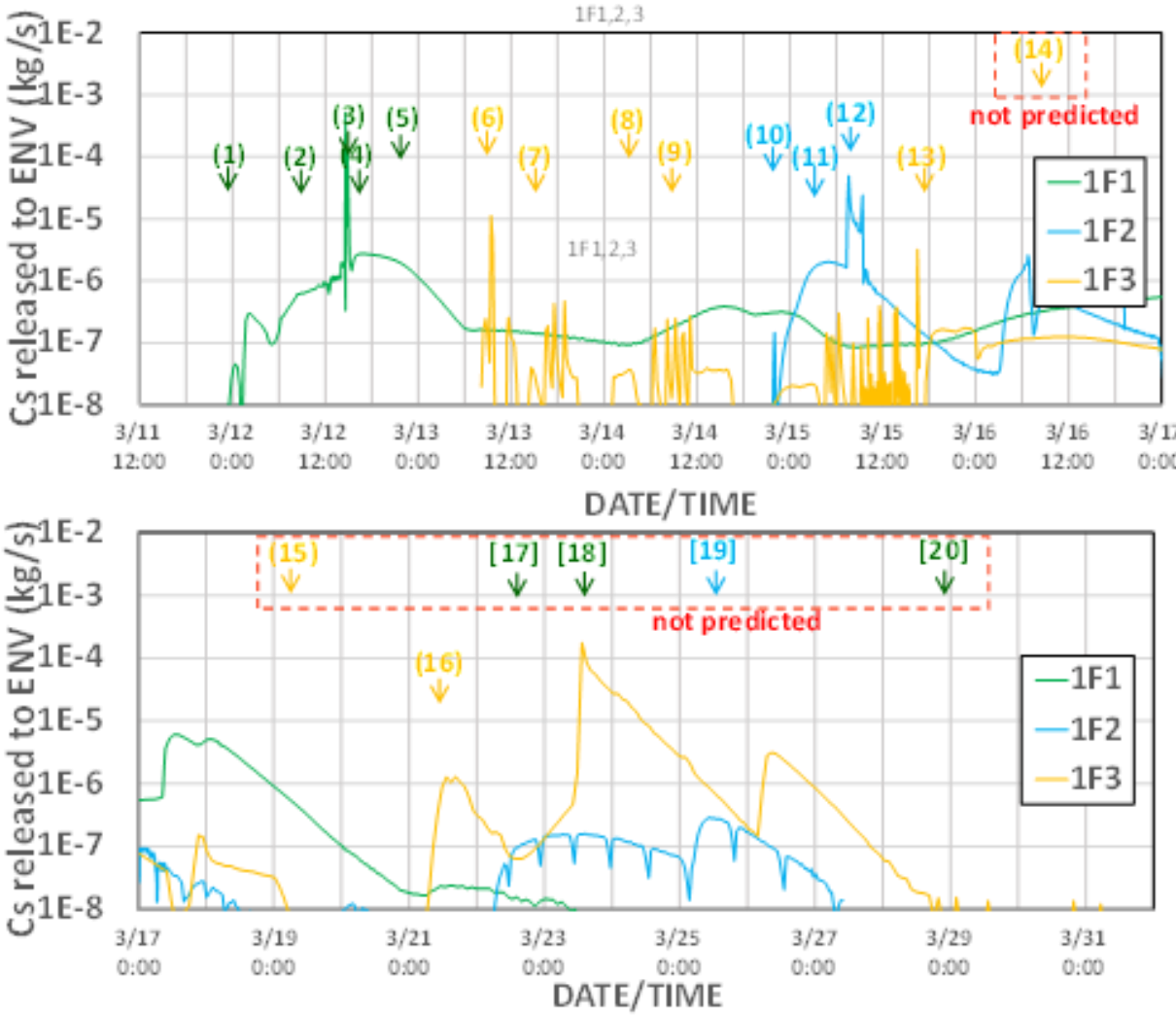

FP release to the Environment (Continued)

We did not implement the complicated boundary conditions to simulate FP releases (14) and (15).

FP release (14) was inferred that FP was released due to liquid phase leakage from the lower part of the D/W at 9:00 on 3/16 and sequentially pedestal water flashing under reduced pressure in Unit 3.

FP release (15) was inferred that water injection into the spent fuel pool (SFP) began at 0:30 on 3/19 and some water accumulated in the R/B floor and flowed into the D/W from the flange, generating water vapor and releasing FP in Unit 3.

FP release (10) was assumed to be caused by the SRV open at 21:20 on 3/14 in Unit 2.
But it might be possible to happen that the FP release was caused by the W/W vent in Unit 3 at 16:30-21:04 on 3/14.
It would be considered how this FP release happened considering other knowledge in the future.

Conclusions

We investigated the following items.

- Plant data during the accident not sufficient to understand the overall picture of the accident

Accident progression analyses using MELCOR code were performed to complement plant data predicted information not able to be observed in the accident such as MCCI, in and ex-vessel FP release, and water accumulation in the containment vessel.

- Leak thought to have occurred in the PCV based on pressure measurements

Parameter surveys using the leak area as a parameter were conducted to estimate the reasonable leak area to remove the decay heat.

- The most plausible analyses

We reproduced the time of the RPV failure, the time of hydrogen explosion occurrence and the accident not to be stabilized by the end of the calculations.

- Concrete erosion in MCCI analysis

MELCOR/CORCON to handle the fuel debris and the concrete as a collection of microparticles like fluid even though the temperature of the fuel debris below the melting point of iron as around 1500 K. The debris temperature did not lower, and the accident was not stabilized by the end of the calculations in any analyses.

- FP release into the environment corresponding to boundary conditions and events in the accident

It is imagined that if the accident progression could be simulated accurately, it would be possible to reproduce the release of FP into the environment.

References

1. Report of Japanese Government to the IAEA Ministerial Conference on Nuclear Safety - The Accident at TEPCO's Fukushima Nuclear Power Stations -, June 2011
2. MELCOR Computer Code Manuals, Vol. 1: Primer and Users' Guide, Version 2.2.9541 2017," S AND2017-0455 O R, Sandia National Laboratories, January 2017.
3. MELCOR Computer Code Manuals, Vol. 2: Reference Manual, Version 2.2.9541 2017," SAND2 017-0876 O R, Sandia National Laboratories, January 2017..
4. Tokyo Electric Power Company, Inc. Evaluation of the situation of cores and containment vessels of Fukushima Daiichi Nuclear Power Station Units1 to 3 and examination into unsolved issues in the accident progression – Progress; 2022. (Report No. 6) in Japanese.
5. For example, NEA/CSNI/R(2015)18; Benchmark Study of the Accident at the Fukushima Daiichi Nuclear Power Plant (BSAF Project) March 2015.
6. NUREG/CR-2726, A. L. Camp, J. C. Cummings, M. P. Sherman et al.; "Light Water Reactor Hydr ogen Manual," U.S.NRC, June 1983.
7. NUREG/IA-0129, V. Strizhov, V. Kanukova et al.; "International Report: An Assessment of the C ORCON-MOD3 Code, Part I: Thermal-Hydraulic Calculations," U.S.NRC, September 1996.

© CRIEPI

LONG-TERM SEVERE ACCIDENT MANAGEMENT AT LOVIISA NPP

Mika Harti
Fortum Power and Heat Oy
P.O.Box 100, FI-00048 FORTUM
mika.harti@fortum.com

ABSTRACT

Loviisa nuclear power plant is located in Finland and has two VVER-440 units. The implementation of severe accident management systems was finalized in 2003, but the accident management strategy did not consider fully long-term issues. For long-term severe accident management it is essential that core melt can be solidified and pressure and temperature inside containment can be brought down. In Finland new regulations to achieve these objectives have been presented in 2019.

Equipment survivability in high radiation conditions is a fundamental issue in long term severe accident management. For Loviisa nuclear power plant a long term severe accident management strategy has been developed and justified by a set of analyses. Source term and containment pressure were key parameters to evaluate the acceptability of the strategy as the goal of the new regulations is that the radioactive releases are low even if containment building loses its leak tightness at some point.

The strategy is to use low pressure emergency core cooling system, that will be taken in service after the early phase of an accident. At this stage the core has already melted and radioactive material has spread into the containment thus the pumped water will be highly radioactive. Equipment survivability will be assessed based on the need to operate the components, dose estimates and materials used in the components. This work is still ongoing and possible actions are considered based on the results.

KEYWORDS
MELCOR, Apros, MCNP, SAMG, dose

1. INTRODUCTION

Fortum is an energy company with core operations are located in the Nordics and consist of CO2-free power generation. Loviisa nuclear power plant is fully owned and operated by Fortum. The power plant is located at southeastern coast of Finland and has two VVER-440 units. Severe accident management strategy and systems to reach and maintain a controlled state following a severe reactor accident were implemented in 1990–2003. The strategy did not consider fully issues to reach and maintain a safe state following a severe reactor accident and survivability of equipment in high radiation conditions for an extended period.

For long term severe accident management it is essential that core melt can be solidified and pressure and temperature inside containment can be brought down. In Finland new regulations to achieve these objectives have been presented in regulation Y/1/2018 [1] section 11 in 2018 and regulatory guide YVL B.6 [2] req. 339 in 2019.

In Finland an operating license is needed for operation of a nuclear power plant. In 2023 a new operating license for Loviisa NPP until the end of 2050 was granted by the Finnish government [3]. Positive safety assessment from Radiation and Nuclear Safety Authority (STUK) was needed for that decision. At that time the work was already ongoing and STUK mentioned this work in chapter 3.9 of their safety assessment [4].

For Loviisa NPP a long term severe accident management strategy has been recently developed and justified by a set of analyses done using Apros [5] and MELCOR [6] and separate assessments. Source term and containment pressure were key parameters to evaluate the acceptability of the strategy. According to the regulations, the radioactive release needs to be low even if containment building loses its leak tightness at some point and therefore dose analyses for public population were performed with Tuulet software. This software was develop by Fortum for dispersion and dose analyses. Analyses for radiation levels and absorbed doses inside the plant were performed using MCNP [7] and equipment survivability for 1 year period was partially already assessed and partially the work is still ongoing. Based on the work presented in this paper some actions are possibly needed and they are to be agreed later with STUK.

2. CURRENT SEVERE ACCIDENT MANAGEMENT STATEGY AT LOVIISA NPP

Implementation of severe accident management systems at Loviisa NPP was finalized in 2003. After Fukushima there were additional modification related to water injection into fuel pools and monitoring the state of the fuel pools. The mitigation part of the SAM approach is built around the following SAM safety functions [8]:

- Successful containment isolation
- Primary circuit depressurization: Additional large capacity depressurization lines presented in Figure 2 were implemented.
- Absence of energetic events: Mitigation of hydrogen combustion by mixing the containment atmosphere and hydrogen removal with passive autocatalytic recombiners and glow-plug type igniters were implemented. Successful in-vessel retention of molten corium excludes other energetic events. Mixing is achieved by opening the doors in ice condenser marked with number 9 in Figure 1 with specific pressurized nitrogen operated system. Recombiners are located all over the containment and are marked with number 17 Figure 1. Igniters are located in steam generator rooms and are marked with number 18 in Figure 1.
- Cooling of reactor core or core debris in the reactor pressure vessel lower head by in-vessel melt retention was implemented. Arrangements for in-vessel melt retention are presented in Figure 2.
- Mitigation of slow containment over pressurization by containment external spray system was implemented. This system is marked with number 16 in Figure 1.

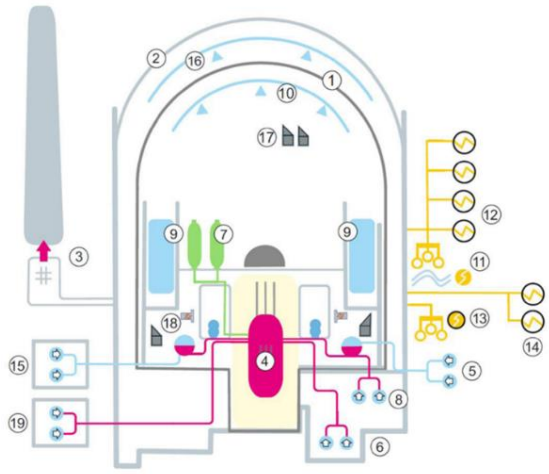

1. Containment
2. Reactor building
3. Filters for ventilation exhaust
4. Reactor and control rods
5. Emergency feedwater system
6. Low-pressure safety injection system
7. Pressurised hydro accumulators
8. High-pressure safety injection system
9. Ice condenser
10. Containment spray system
11. Power supply from hydro power station
12. Emergency diesel generators
13. Diesel generators plant
14. Severe accident diesel generators
15. Auxiliary emergency feedwater pumps
16. Containment external spray system
17. Hydrogen removal (passive autocatalytic recombiners)
18. Hydrogen removal (igniters)
19. Boron supply system

Figure 1. Reactor building and the most important safety systems at Loviisa NPP [9].

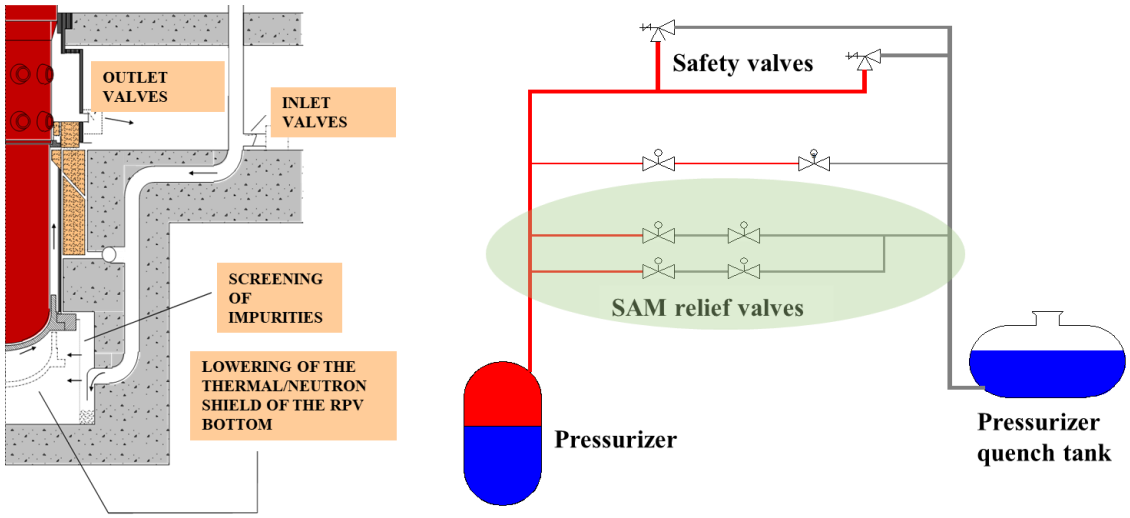

Figure 2. Arrangements for in vessel melt retention (left) and additional lines circled with green color for primary circuit depressurization (right).

3. DEVELOPMENT OF STRATEGY FOR LONG TERM SEVERE ACCIDENT MANAGEMENT

In a long term melt solidification and decay heat removal from containment are relevant. Melt solidification is a preferable solution as it limits the subsequent release of radioactivity from the corium. Heat is removed from the melt by in-vessel melt retention and heat removal can enhanced by injecting water into the primary circuit.

Containment external spray system marked with number 16 in Figure 1 is not able to lower the containment pressure down to atmospheric pressure. Only 1.3 to 1.4 bar_{abs} can be achieved in a long term. Heat transfer from the containment can be enhanced by containment (internal) spray system marked with number 10 in Figure 1 or cooling the water injected into the primary circuit.

There are two systems at Loviisa NPP able to inject water into the primary circuit in recirculation mode. High pressure safety injection can inject to operating pressure of primary circuit and is marked with number 8 in Figure 1. Low pressure safety injection marked with number 6 in Figure 1 is able inject only in low pressure and primary circuit depressurization either as a result of initiating event or by dedicated depressurization lines is needed for operating this system. Only the low pressure safety injection system has heat exchanger and is able to cool the injected water. In recirculation mode water is taken from the containment and using injection in this way means that excessive amount of water in the containment can be avoided. Injection and cooling using low pressure safety injection was expected to have also significant impact on containment pressure and as a result it was assumed that the containment spray system was not needed.

Original design for in-vessel melt retention presented in reference [10] was done using 2-layer corium configuration for heat transfer analyses. The results show more than enough thickness of RPV wall and therefore significant tolerance to high primary circuit pressure. Heat transfer analyses done in 2013 [11] with possible 3-layer corium configuration show higher heat fluxes and consequently thinner reactor pressure vessel wall. The limit for pressure in this case is ~70 bar_{abs}, which is significantly below normal operating pressure. The goal in severe accident management guideline is conservatively to have primary pressure below 20 bar_{abs} and this is assumed to cover the epistemic uncertainties.

At the start-up of water injection the primary pressure depends on depressurization capacity and coolant boiling rate on top of the melt that is impacted by injection capacity and pump head. Despite of dedicated severe accident depressurization lines the pressure could exceed ~70 bar_{abs} if high pressure safety injection would be used. Low pressure safety injection is not capable to injecting into 20 bar_{abs} and this together with primary circuit depressurization effectively limits the primary circuit pressure.

Due to abovementioned reasons the low pressure safety injection was chosen as best candidate for long term severe accident management.

4. VALIDATION OF STRATEGY FOR LONG TERM SEVERE ACCIDENT MANAGEMENT

In a short term, due to in-vessel melt retention, significant boiling is expected in the reactor cavity as heat from the corium is transferred through the vessel wall into the reactor cavity water. The water is assumed to be in saturated condition at the reactor cavity inlet as heat is not removed from the water. In a long term, when the injected water is cooled, the water discharged from the primary circuit into the containment is cool and the containment sump is not anymore in a saturated condition. The reactor cavity model in MELCOR-model was described with one node and this is too simple modelling approach for evaluations of possible water boiling in the reactor cavity in these kind of conditions. Boiling would have significant impact on containment pressure and therefore realistic modelling has high importance.

Fortum uses mainly Apros code [5] for safety analyses. The plant model including among others containment and low pressure safety injection system was connected to a separate detailed reactor cavity model originally developed for pressurized thermal shock analyses. For long term severe accident management scoping analyses were done with different boundary conditions for heat flows into the reactor cavity and into the coolant inside the vessel. The analyses showed that no boiling was to be expected in the reactor cavity and the containment pressure would be close to the atmospheric pressure. The results were promising and it was decided, that more detailed analyses will be performed.

Severe accident analyses were renewed using MELCOR code [6] in 2018 for power operation and 2020 for shutdown states. The reason was that the analyses done in 1990s did not systematically follow current analysis rules of applying single failure criterion and best-estimate methodology. Also several codes were

used and there were no up to date integral analyses. The existing MELCOR analysis model was modified for long term calculations. New reactor cavity nodalization was created and models for low pressure safety injection system and its cooling system were refined.

The objective for the analyses was to define containment pressure in the long term and to evaluate the radioactive releases and amount of radioactive material in water for radiation level calculations. Different initiating events, assumptions for containment leakage and heat removal were applied as listed in Table 1. Injection into the primary circuit in the early state of accident is achieved by pressurized hydro accumulators, but no pumped injection was assumed and this eventually leads to core dry out and melting. Possible containment leakage was defined in regulatory requirement and therefore it was important to analyze the impact of the leak and if efficient heat transfer was even needed to avoid significant doses of population in the environment. Comprehensive understanding helps to develop procedures for severe accident management. The assumed leak is quite small as it is not credible to have energetic events causing large holes in the containment in a late stage of an accident. Instead the leak may be caused for example by failure of containment penetration. A very small (0,07 cm^2) leakage is allowed from the containment as in reality the containment is not fully leak tight and this so called allowable leakage is always assumed in the analysis. This allowable leakage corresponds to 0.2%/day leak rate from the containment in design pressure.

Table I. Analysis cases. Containment allowable leakage is assumed from the start of initiating event

Initiating event	Leak [cm^2]	Injection to primary circuit	Containment heat removal	Containment leak
SBO	-	LP safety injection starts at 72 h	External spray started at 1,7 bar (~60 h)	Allowable leakage (0,07 cm^2)
SBO	-	-	External spray started at 1,7 bar (~60 h)	Allowable leakage (0,07 cm^2) + 20 cm^2 leak at 120 h
XSLOCA	1	LP safety injection starts at 72 h	External spray started at 1,7 bar (~60 h)	Allowable leakage (0,07 cm^2)
XSLOCA	1	LP safety injection starts at 72 h	External spray started at 1,7 bar (~60 h)	Allowable leakage (0,07 cm^2) + 20 cm^2 leak at 120 h
XSLOCA	1	LP safety injection starts at 72 h	External spray started at 1,7 bar (~60 h), fails at 100 h	Allowable leakage (0,07 cm^2) + 20 cm^2 leak at 120 h
XSLOCA	1	LP safety injection starts at 72 h (different injection location)	External spray started at 1,7 bar (~60 h)	Allowable leakage (0,07 cm^2)
XSLOCA	1	-	External spray started at 1,7 bar (~60 h)	Allowable leakage (0,07 cm^2) + 20 cm^2 leak at 120 h
XSLOCA	1	-	External spray started at 1,7 bar (~120 h)	Allowable leakage (0,07 cm^2) + 20 cm^2 leak from the beginning
MLOCA	22	LP safety injection starts at 72 h	External spray started at 1,7 bar (~50 h)	Allowable leakage (0,07 cm^2)

The containment pressure in selected initiating events are presented in Figure 3. The containment pressure increases slowly due to large ice volume in ice condenser and significant heat sinks in the containment. At about 2-2.5 days, depending on initiating event the pressure has reached containment design pressure and containment external spray system is started. The containment pressure starts to decrease until injection on

top of the melt at 3 days starts to increase the pressure. The injection is started at low capacity and after 4 hours of injection the injection mass flow is increased. Injection causes significant evaporation as there is a lot of accumulated energy in the melt and reactor internals, and this evaporation increases the containment pressure. Eventually there will be less or no evaporation at all inside the pressure vessel due to increase of injection rate and cooling of the injected water. As this cool water reaches the containment, the water temperature in the reactor cavity also starts to decrease as presented in Figure 4. Evaporation is not anymore possible in the reactor cavity despite significant amount heat is transferred through the reactor pressure vessel into the reactor cavity. Lack of steam source and cooling of the containment gas leads to decrease in containment pressure.

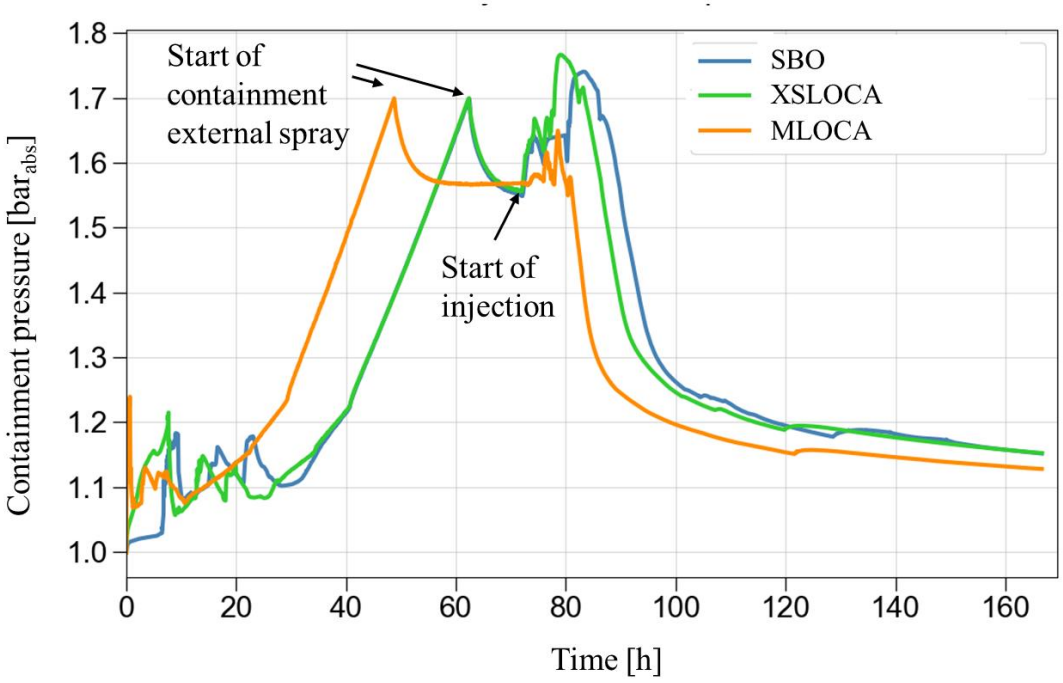

Figure 3. Containment pressure in different initiating events assuming only containment design leakage, low pressure safety injection is started at 72 h and containment external spray system is started at 1.7 bar$_{abs}$.

As can be seen in Figure 3 using the low pressure safety injection system and external spray system it was possible to reach containment pressure of ~1.15 bar$_{abs}$ in 7 days (167 h) from initiating event. The different initiating events are very similar in a long term. MLOCA analysis was continued to 13.5 days (325 h) and the final containment pressure was 1.1 bar$_{abs}$. Pressure decrease is very slow and is partially caused by the assumption of allowable leakage.

Larger containment leakage (20 cm^2) in addition to allowable leakage is able to lower the containment pressure to practically atmospheric pressure during the analyses (7 days from initiating event). Naturally the radioactive releases to the environment are significantly higher than just assuming allowable leakage.

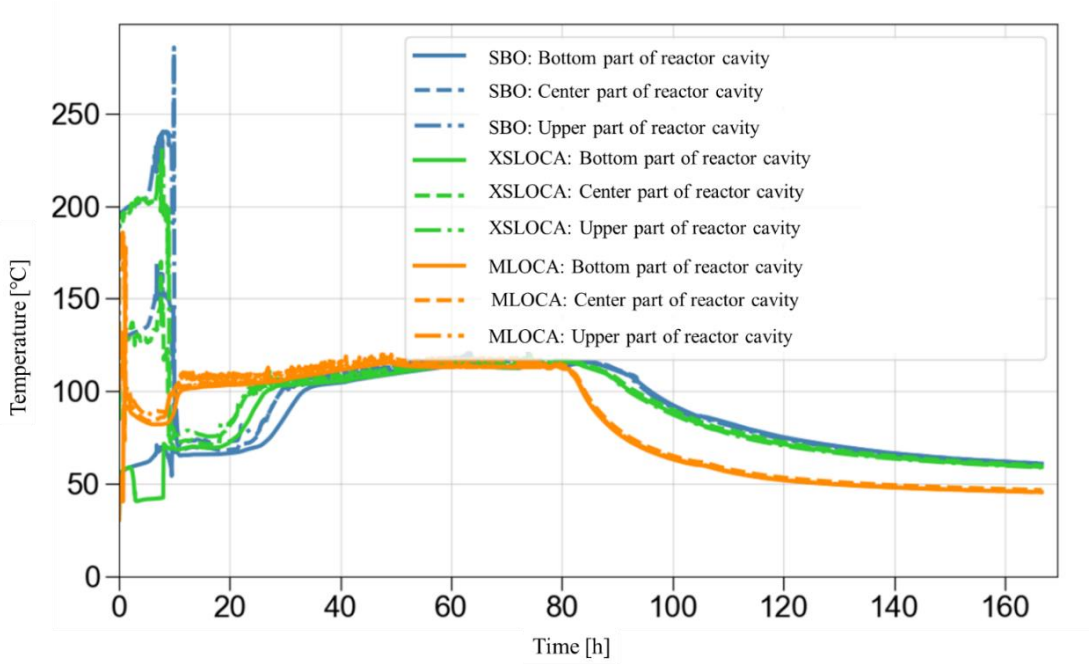

Figure 4. Water temperature in the reactor cavity.

Doses for population in the environment for each analyzed case were calculated by Tuulet software developed by Fortum for dispersion and dose analyses. Tuulet considers all exposure pathways like direct radiation, exposure from fallout, inhalation and food. No countermeasures like seeking shelter and evacuation are assumed.

Release of radioactive material in analyses depends mainly on containment leak size, timing of leak and containment pressure at the time of leak (that depends on cooling by low pressure safety injection and containment external spray). In cases with allowed leakage the doses in the environment with 0.5 % exceedance probability and 1 year integration time were significantly below 1 mSv and with late (120 h from initiating event) containment leak below 4 mSv (with injection) and ~15 mSv (without injection). The largest dose using same exceedance probability and integration time is ~150 mSv in XSLOCA without injection into the primary circuit and early containment leak (allowable leakage + 20 cm^2 from the beginning of the analysis). In all cases the doses were highest at 1 km distance from the affected plant unit, that is the closest analyzed point for population exposure. The doses are rather small as long as the containment stays intact. If there is leak in the late stage of the accident the releases and doses depend a lot on containment pressure. Using low pressure safety injection means the containment pressure is low and releases in analyzed cases are low leading to doses below 4 mSv. The highest doses (~15 and ~150 mSv) are in cases without low pressure safety injection.

In all cases the releases, even with containment leak, are below acceptance limit for severe accident. The acceptance limit is mentioned in Nuclear Energy Decree section 22b [12] and is 100 TBq Cs-137. Despite of this the requirement in regulatory Y/1/2018 [1] and regulatory guide YVL B.6 [2] state, that the low pressure inside the containment pressure needs to be achieved. The results give confidence, that there is no rush to achieve low containment pressure and in this situation injection into the primary circuit may be considered beneficial only if there is very low risk of failing the containment due to potential energetic events.

5. ANALYSES OF DOSES INSIDE THE PLANT

MELCOR data was used to define the properties of containment water. In Loviisa MELCOR model 12 fission product groups are used. As low pressure safety injection takes water from containment in recirculation mode, the pipes in low and high pressure safety injection systems (the systems are connected with each other) are filled with radioactive water from the containment. Containment (internal) spray system is located in the same room and use of this system during the accident would increase the radiation levels further. As a conservative assumption the pipes in all these systems were assumed to contain radioactive water.

Dose rates and cumulative doses were calculated with MCNP [7] in various locations in the pump room, where majority of components are located. Same results can be applied for other rooms as well as there are no other significant radiation sources. Detailed model for real piping configuration was created and the pipes were assumed contain highly radioactive water. The doses were calculated for 1 year use and are presented in Figure 5. Largest doses are observed in the water and in parts of components that are in contact with water. Outside piping the radiation levels are lower but still very high. Significantly lower radiation levels are observed in locations further away from piping. The results can be divided in three different groups depending on their location and the analyzed doses for 1 year for these groups are:

- Water and components in contact with water: 1300 - 1800 kGy.
- Components close to piping: 140 - 200 kGy.
- Other components: 44 - 100 kGy.

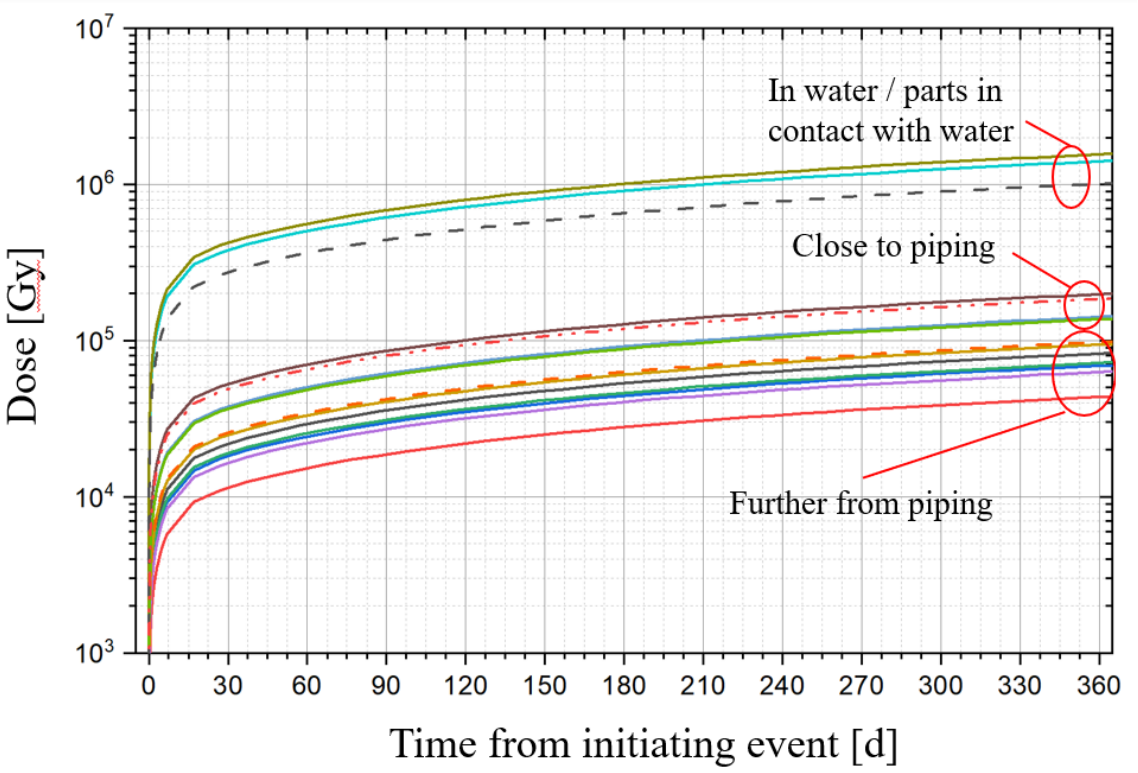

Figure 5. Cumulative doses in different parts of low pressure safety injection pump room.

6. ANALYSES FOR EQUIPMENT SURVIVABILITY

The objective of the work is to assess radiation tolerance and not to aim of full scope qualification usually done when new components are purchased. This work is currently ongoing for Loviisa NPP.

Radiation doses calculated by MCNP were compared to known radiation tolerance of components or materials used in the components. Typically the components in low and high pressure safety injection systems and their support systems located in same room are not qualified for long term high radiation conditions. In some cases same or similar components (same manufacturer and very similar component) have been used inside the containment and are qualified for condition in loss of coolant accident and steam line break including also high radiation dose. Used materials can be compared and conclusion related to radiation tolerance can be made. In many cases radiation tolerance of materials are compared to values found in the literature.

Sometimes the materials are not defined in such details that their radiation tolerance can be assessed or information of radiation tolerance is not available. Often radiation tolerance for example found in the literature is not sufficient as higher radiation doses are expected. Generally speaking valves and actuators are designed in a way that this type of equipment tolerates well high radiation doses. Some sealing material found in valves and measurements and some electrical and I&C cables are made using materials, which are assumed to have low radiation tolerance. In these cases one possibility is to test the material and in this way have better understanding of the radiation tolerance. In some cases changing the material could be preferable solution. It should be pointed out, that these possible actions have not yet been decided.

7. RELATION OF ACCIDENT MANAGEMENT AND RADIATION DOSES

The purpose of severe accident management guidelines (SAMG) and other procedures is to instruct the operators and emergency response organization on use of severe accident management system and also other systems that might be available. At Loviisa NPP the risks caused by the actions are considered in SAMG, emergency response organization guides and other material like severe accident management handbook.

Use of high or low pressure safety injection systems or containment spray system are possibilities in SAMG. Using these systems in severe accident in recirculation mode contaminates the piping and makes the rooms inaccessible for humans and radiation tolerance of certain materials can be exceeded quite fast. Before starting injection or spray certain actions, like closing selected valves, are beneficial. In this way challenges to operate the equipment can be minimized and requirements for components can be relaxed.

Different classes have been defined for components:

- Full operability is required: This class is applied to pumps, containment isolation valves and selected valves that allow operation of low pressure safety injection.
- Leak tightness is required: Low and high pressure safety injection systems are connected to each, there are measurements connected to pipe, and there are connections to other system like special sewerage system and drain and venting system. The connecting lines are often equipped with hand operated valves or valve operations can be made before the pipelines are contaminated and rooms become inaccessible. Therefore it is not necessary to operate these valves in high radiation conditions, but they and all other connections shall remain leak tight.

Different philosophy of operation can be included in SAMG.

8. SUMMARY

Fortum owns and operates Loviisa NPP that has two VVER-440 reactors. Severe accident management systems were implemented at Loviisa NPP 1990 – 2003, but did not fully consider long term issues. Regulatory requirements have changed in 2018 and state that the nuclear power plant shall be designed so that it can be reliably brought into a safe state after a severe reactor accident. In a safe state containment pressure needs to be low and component survivability needs to justified. Complying with new regulation is an important issue as the lifetime was extended up to 2050.

Fortum has done extensive analyses how this kind of long term safe state can be achieved, what kind radiation doses are expected to population in the environment and components inside the plant, and to assess if the components can tolerate high radiation doses.
Solidification of core melt in a severe accident is possible using high or low pressure safety injection systems, but only low pressure system is able to cool the injected water. Cooling was expected to have also significant impact on containment pressure and as a result the containment spray system would not be needed. For these reasons low pressure safety injection was chosen as best candidate for long term severe accident management.

Analyses of plant behavior were performed with Apros code developed in Finland and MELCOR. Containment pressure of 1.15 bar_{abs} was achieved in 7 days and 1.1 bar_{abs} in 13.5 days from initiating event and this fulfills the regulatory requirements.

Releases fulfill regulatory requirement that is 100 TBq of Cs-137. Doses for population in the environment were calculated by Tuulet software developed by Fortum for dispersion and dose analyses. Doses remain low when containment stays intact in the early stage of an accident or containment pressure can be lowered using low pressure safety injection system. Detailed model of low and high pressure safety injection for radiation dose analyses was developed and analyses were performed with MCNP code.

At this stage the work is ongoing for assessment of radiation tolerance of components. Based on the assessment results possible actions are defined and agreed with Radiation and Nuclear Safety Authority.

REFERENCES

1. "Radiation and Nuclear Safety Authority Regulation on the Safety of a Nuclear Power Plant. STUK Y/1/2018,". https://www.stuklex.fi/en/maarays/stuk-y-1-2018 (2018).
2. "Regulatory guide YVL B.6. Containment of a nuclear power plant," https://www.stuklex.fi/en/ohje/YVLB-6 (2019).
3. "Government decision on Fortum Power and Heat Oy's application for a licence referred to in section 20 of the Nuclear Energy Act to operate the nuclear power plant units Loviisa 1 and Loviisa 2 and the buildings and storage facilities belonging to them that are necessary for the management of spent nuclear fuel and nuclear waste," https://tem.fi/en/loviisa-power-plant (2023).
4. "Säteilyturvakeskuksen arvio Loviisan ydinvoimalaitoksen käytön jatkamisesta vuosista 2027 (LO1) ja 2030 (LO2) eteenpäin," https://tem.fi/loviisan-voimalaitos file STUK_voimalaitos_liite1_turvallisuusarvio (2023).
5. https://www.apros.fi/.
6. https://www.sandia.gov/MELCOR/.
7. https://mcnp.lanl.gov/index.html.
8. Petra Lundström, Olli Kymäläinen and Harri Tuomisto, "Implementation of Severe Accident Management Strategy at the Loviisa NPP". *Implementation of Severe Accident Management Measures. Workshop Proceedings PSI-Villigen*, Switzerland, 10-13 September, 2001. NEA/CSNI/R(2001)20, (2001). https://inis.iaea.org/collection/NCLCollectionStore/_Public/39/057/39057220.pdf?r=1 (2001).

9. "Loviisa nuclear power plant, Environmental impact assessment report", https://tem.fi/en/loviisa-eia-report (2021).
10. O. Kymäläinen, H. Tuomisto, T.G. Theofanous, "In-vessel retention of corium at the Loviisa plant," *Nuclear Engineering and Design.* **169,** pp. 109–130 (1997).
11. T. Laato, "In-vessel Melt Retention at Loviisa NPP: Past and Present Activities," *IAEA Technical Meeting on Phenomenology and Technologies Relevant to In-Vessel Melt Retention and Ex-Vessel Corium Cooling*, Shanghai, October 17-21, (2016), https://inis.iaea.org/collection/NCLCollectionStore/_Public/51/089/51089922.pdf.
12. "Nuclear Energy Decree, 161/1988," https://www.finlex.fi/en/laki/kaannokset/1988/en19880161_20201039.pdf (2020).

Long-term severe accident management at Loviisa NPP

The 11th European Review Meeting on Severe Accident Research Conference (ERMSAR 2024). May 13-16, 2024 Stockholm, Sweden.

Mika Harti

Leading Senior Expert in Nuclear Safety

fortum
Powering a thriving world

Loviisa NPP

- Loviisa NPP commercial operation started in 1977 (Unit 1) and 1981 (Unit 2).
- VVER-440 type 213 pressurized water reactor.
- Heavily modified in the design phase and significant differences to standard design.
  - Steel containment with Westinghouse ice condenser.
  - Different layout.
  - Western I&C.
  - And lots of other modifications.
- Lifetime extension:
  - Several large modernisation projects were finalised ~2018.
  - New operating license until the end of 2050 was granted by the Finnish government in 2023.
    - Previous licenses until 2027 (Loviisa 1) and 2030 (Loviisa 2).
  - Investment planning ongoing, some projects already started.



Severe accident management

- In 1991 new regulation for considering severe accident led to large modification project, that was finalised in 2003.
- New systems for severe accident management:
  - Successful containment isolation.
  - Primary circuit depressurization: Additional large capacity depressurization lines.
  - Mitigation of hydrogen combustion by mixing the containment atmosphere and hydrogen removal with passive autocatalytic recombiners and glow-plug type igniters were implemented.
  - Cooling of reactor core or core debris in the reactor pressure vessel lower head by in-vessel melt retention was implemented.
  - Mitigation of slow containment over pressurization by containment external spray system.
  - Dedicated SA electrical systems and I&C systems and SAM control room.
- Long term issues were not fully considered when severe accident systems were implemented.

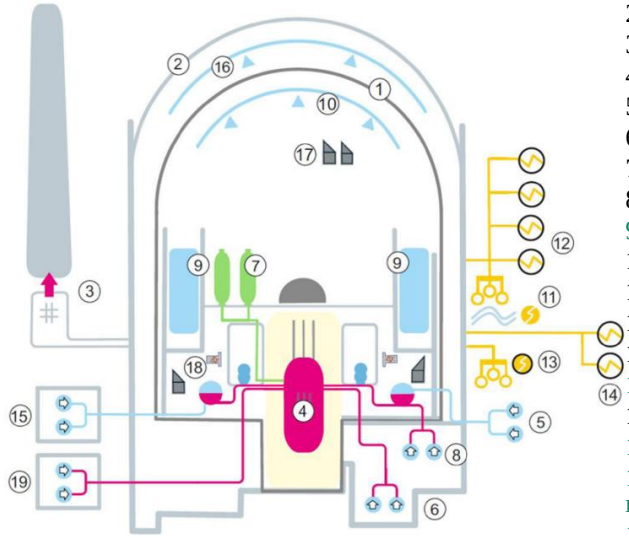

1. Containment
2. Reactor building
3. Filters for ventilation exhaust
4. Reactor and control rods
5. Emergency feedwater system
6. Low-pressure safety injection system
7. Pressurised hydro accumulators
8. High-pressure safety injection system
9. Ice condenser
10. Containment spray system
11. Power supply from hydro power station
12. Emergency diesel generators
13. Diesel generators plant
14. Severe accident diesel generators
15. Auxiliary emergency feedwater pumps
16. Containment external spray system
17. Hydrogen removal (passive autocatalytic recombiners)
18. Hydrogen removal (igniters)
19. Boron supply system

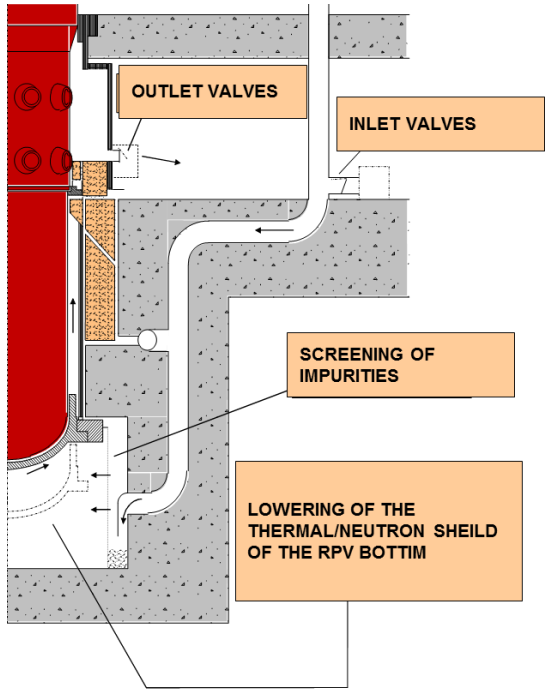

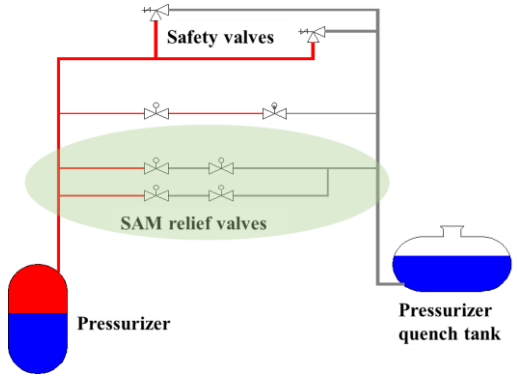

fortum
Powering a thriving world

Requirements

- New requirements presented in 2019 (YVL guide B.6)
  - Safe state following a severe reactor accident shall refer to a state where the conditions for the controlled state of a severe reactor accident are met and, in addition, the pressure inside the containment is low enough that leak from the containment is minor, even if the containment is not leak-tight.
  - Systems used in bringing the plant to a safe state following a severe reactor accident are not required to be independent from the systems designed for normal operation, anticipated operational occurrences and postulated accidents. When using systems that do not fulfil this independence in order to bring the plant to a safe state or to maintain it following a severe reactor accident, the operability of the systems shall be demonstrated in conditions following a severe reactor accident.
- Just staying below 100 TBq Cs-137 as stated in Nuclear Energy degree from 2020 is not enough
  - The release of radioactive material as a result of a severe accident at a nuclear power plant may not necessitate large-scale protective measures for the population or any long-term restrictions on the use of extensive areas of land and water.
  - In order to limit the long-term effects, the limit for atmospheric releases of caesium-137 shall be 100 terabecquerels. The possibility of exceeding the limit shall be extremely small

fortum
Powering a thriving world

Long term accident management

- In a long term melt solidification and decay heat removal from containment are relevant.
- Containment external spray is not enough to achieve close atmospheric pressure as required. Only 1.3..1.4 bar_{abs} is achievable in very long term..
- Possibilities: Low pressure safety injection or containment (internal) spray system.
  - Both systems can lower the containment pressure as they can effectively remove heat into the environment. They take water from the containment or separate tank and are able to cool the water.
  - LP safety injection solidifies the melt inside the RPV, containment spray doesn't.

  → LP safety injection was chosen.
- Scoping analyses were done using Apros code.
- Final analyses were done using MELCOR.
  - Time delays and plant parameters (especially containment pressure).
  - Fission product distribution for equipment dose analyses.
  - MELCOR data used for dispersion analyses (doses in the environment).
- Doses in the environment are actually quite low due to long time delay. Doses without LP ECCS are ~15 mSv and with LP ECCS below 4 mSv with late containment leak (leak at 120 h).
  - Doses were calculated using Tuulet software developed by Fortum.

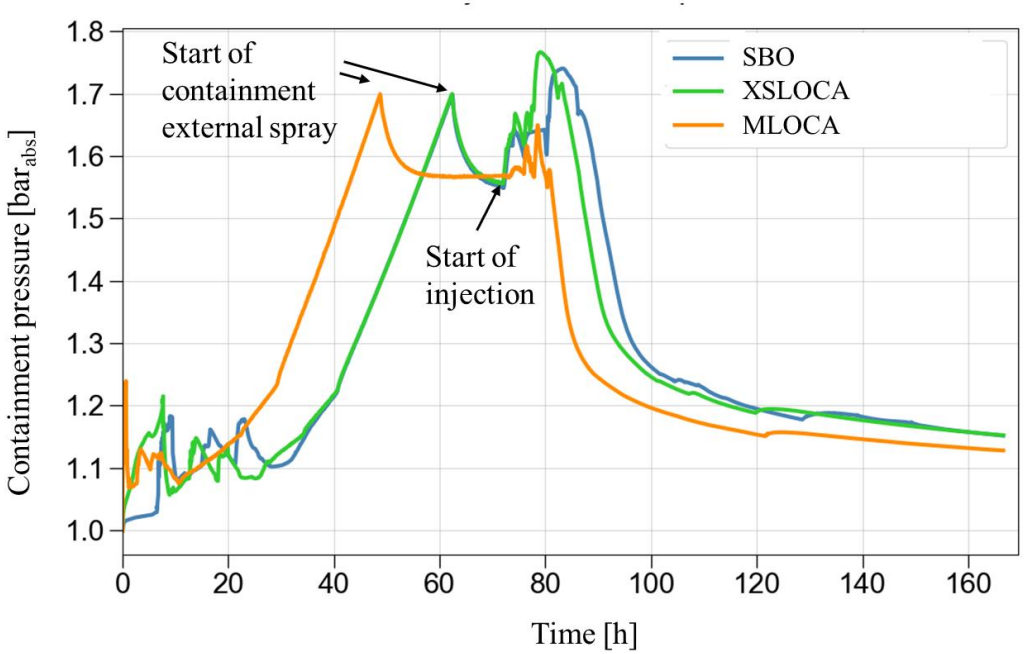

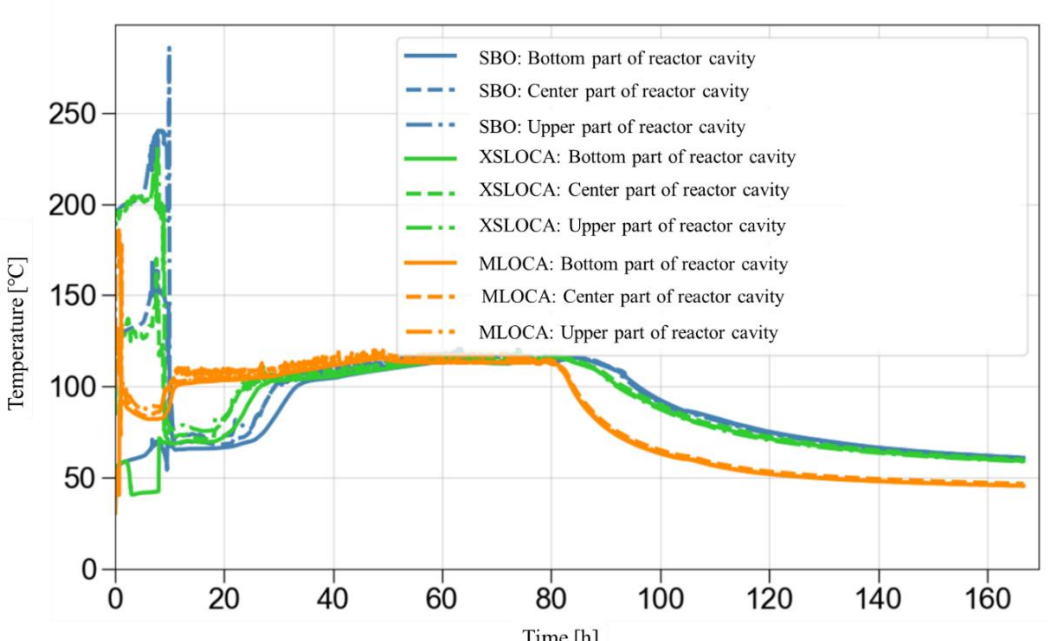

Radiation doses

- No need to operate components inside the containment.
- Radiation is basically the only challenging condition outside the containment.
  - The LP safety injection components are designed for elevated fluid temperature and those ones, that need to operated, are located outside the containment.
- Radiation tolerance needs to justified.
- Detailed MCNP model of LP safety injection systems and other systems in the same room was made considering main piping. Doses for 1 year use are:
  - Water and components in contact with water: 1300 - 1800 kGy.
  - Components close to piping: 140 - 200 kGy.
    - During plant walkdowns done in 4-5/2024 it was noticed that some cables and actuators are located very near or in contact to (insulated) piping or radiation doses are caused by several pipes closeby. In these cases we need to apply higher dose of about 500 – 600 kGy.
  - Other components: 44 - 100 kGy

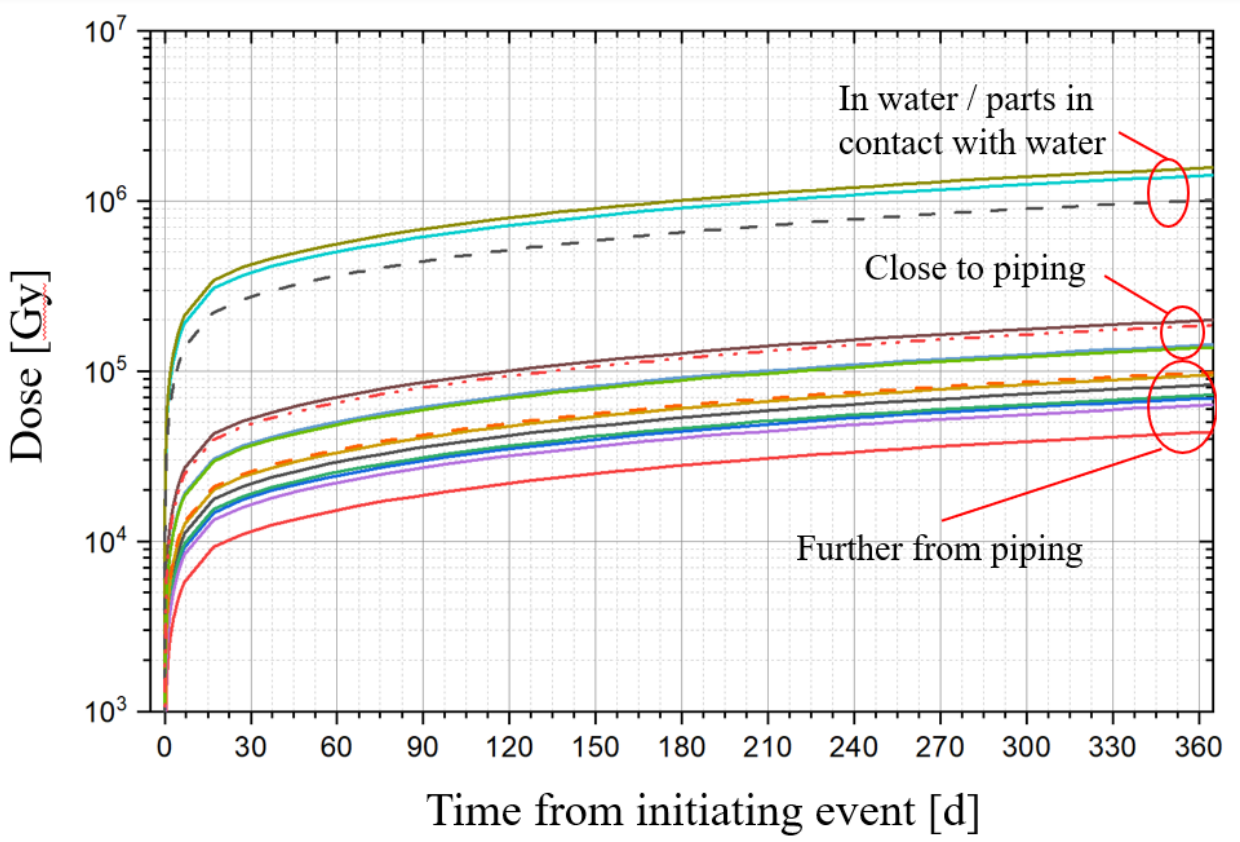

fortum
Powering a thriving world

Radiation tolerance

- Typically the components in low and high pressure safety injection systems and their support systems located in same room are not designed or qualified for long term high radiation conditions.
- The two injection systems are interconnected meaning both will be contaminated.
- In many cases radiation tolerance of materials are compared to values found in the literature. Full scale qualification is not the objective but finding weak points.
- Results
  - Valves tolerate radiation well.
  - Actuators tolerate some radiation and are often located a little bit further away from piping lowering the doses. Radiation tolerance was considered sufficient, but this impression is changing based on the results of plant walkdowns and observed nearby piping.
- Electrical and I&C cables are mainly made using materials, which are assumed to have low radiation tolerance. Cables are often routed close to piping and the doses are high.





fortum
Powering a thriving world

Operability requirements and guidance

- Different classes have been defined for components:
  - Full operability is required for pumps and selected valves, like containment isolation valves.
  - Leak tightness is required, especially relevant they are for:
    - Hand operated valves,
    - valves connected to other systems and
    - valves operated before the piping is contaminated.
- There is no rush
  - Before starting injection or internal spray certain actions are beneficial, like closing selected valves and checking valve postitions. In this way challenges to operate the equipment can be minimized and requirements for components (at least for current ones) can be relaxed.
  - Injection into the primary circuit may be considered beneficial only if there is very low risk of failing the containment due to potential energetic events like steam explosion.

fortum
Powering a thriving world

Summary and next steps

- Extensive analysis work has been performed how to achieve low containment pressure in a long term.
- Analyses and plant walkdowns were carried to evaluate doses to equipment.
- The situation currently is good. Even if there is a small containment leak, doses in the environment are low.
- In the future
  - Guidance adjustments how to use the systems in such a way that potential problems in equipment radiation tolerance are minimised.
  - Decision if testing of materials (like cables) is to be done or not and scope. By testing we could have better understanding of the radiation tolerance.
  - Decision if replacements is to be done (cable, seal, whole equipment like actuator).
  - Or something else…

fortum
Powering a thriving world

The 11th European Review Meeting on Severe Accidents Research

May 13-16, 2024, Royal Institute of Technology, Stockholm, Sweden

TECHNICAL SESSION 1.2: IN-VESSEL CORIUM AND DEBRIS COOLABILITY

Chairs: L. Carénini (IRSN), T. Hollands (GRS)

ID21	**Stainless Steel Oxidation at both Solid and Liquid State Under Ar-H_2O Gas Mixture in Severe Accident Conditions** M. Nasselahsen (CEA)	**Paper** **Presentation**
ID25	**A Thermodynamic Study of Molten Pool Stratification Morphology** E. Chen (China Nuclear Power Eng. Co.)	**Paper** **Presentation**
ID78	**In-Vessel Corium Thermochemistry Benchmark based on MASCA Experimental Data** R. Le Tellier (CEA)	**Paper** **Presentation**
ID07	**Coolability of a Corium Pool in a Debris Bed – Calculation of Critical Heat Flux (CHF) Tests with the ASTEC Code** C. Sartoris (IRSN)	**Paper** **Presentation**

STAINLESS STEEL OXIDATION AT BOTH SOLID AND LIQUID STATE UNDER AR-H_2O GAS MIXTURE IN SEVERE ACCIDENT CONDITIONS

Mehdi Nasselahsen, Pascal Piluso, and Jules Delacroix*
CEA, DES, IRESNE, DTN, SMTA, LEAG.
Cadarache F-13108 Saint-Paul-Lez-Durance, France.
mehdi.nasselahsen@cea.fr; pascal.piluso@cea.fr; jules.delacroix@cea.fr

Emmanuel de Bilbao and Sawsen Youssef
CNRS, CEMHTI UPR3079
Univ. Orléans
F-45071 Orléans, France
emmanuel.debilbao@univ-orleans.fr; sawsen.youssef@univ-orleans.fr

ABSTRACT

Extensive failures in nuclear reactor cooling system could lead to different severe accident scenarios. At high temperature, highly corrosive magma called corium is formed as a mixture of molten materials constituting the nuclear fuel, the cladding and the vessel. Consequently, corium is likely to interact with the oxidizing gaseous atmosphere of water steam. This phenomenon is responsible for oxidation process, heat release and hydrogen production, which may result to explosion. The available literature on corium oxidation kinetics and mechanisms appears to be lacking and questionable, as it often relies on integral experiments assuming a specific configuration of corium pool layout that could occur during a severe nuclear accident. The multiphasic aspect inherent to this kind of experiment limits access to knowledge on the kinetics of corium oxidation, as well as on the evolution of its chemical composition when the temperature increases. In order to contribute to fill the lack of information in this area, several high temperature oxidation tests have been conducted recently on VITI facility of the PLINIUS Severe Accident Platform at CEA Cadarache. The VITI separate-effect set-up allows testing at high temperatures using induction heating, up to 3000 K. It also enables to measure hydrogen production in-situ using online gas analysis during sample oxidation. For this matter, a new optical gas analyzer, calibrated to the hydrogen absorption wavelength has been used and qualified, providing reliable quantitative data on in-situ hydrogen measurement. The oxidation of the vessel's 304L stainless steel was studied, under an oxidizing atmosphere of steam by a two-gas mixture: 90% mol. Ar - 10% mol. H_2O. The focus will first be on the mechanisms and kinetics of oxidation just below the solidus point, as appropriate, in the solid state. Subsequently, attention shifts to higher temperature levels, studying oxidation in the liquid state. Finally, a new dihydrogen production law for 304L stainless steel is proposed.

KEYWORDS
stainless steel, steam oxidation, hydrogen in-situ, solid state, liquid state

1. INTRODUCTION

The sequence of a severe nuclear accident is marked by the formation of liquid corium at high temperature, composed of elements of the core such as the nuclear fuel UO_2 and the zircaloy claddings along with the stainless steel of the vessel [1, 2]. During this sequence, corium can interact with an oxidizing atmosphere of steam and dioxygen. This sequence can occur during a Fuel Coolant Interaction (FCI) or throughout the cooling of a liquid corium pool by water injection in the reactor vessel (in-vessel configuration) or in the containment (ex-vessel configuration). A crucial aspect of Severe Accident Management (SAM) strategies for Light Water Reactors (LWRs) of Generations 2, 3, 3+, and SMRs is to prevent the release of fission products into the environment. The main approach to mitigating the progression of severe accidents involves the ability to cool the corium throughout direct water injection or indirect cooling. This hence implies various configurations of interaction between hot materials and steam.

The interaction between metallic alloys at liquid state and steam [3] lasts from minutes to several tens of minutes for the In-Vessel Melt Retention (IVMR) strategies, which include possible stratification and the formation of a multi-layer configuration [4]. Once hot liquid corium starts its re-localization, the interaction between the hot melt and the steam would be shortened, lasting for few seconds. This accident scenario could occur within the vessel or the reactor pit in case of Fuel Coolant Interaction (FCI) and Steam Explosion (SE) [5]. Hot metallic phases could consequently interact with steam coming from concrete during the so-called Ex-Vessel Melt Retention (EVMR), leading to Corium Concrete Interaction (MCCI) [6]. The interaction between the free surface of liquid metals and steam at high temperature involves crucial mechanisms and reaction kinetics, which are critical for fission products mitigation. Moreover, hydrogen production resulting from fuel coolant interaction is essential to be assessed, as it plays a major role in quantifying any risk of further possible explosion.

This article aims to formulate the oxidation kinetics of both solid and liquid states of 304L stainless steel, first at 1623 K and then at 1823 K. A law describing the mass production of hydrogen as a function of the exposure time to steam is then formulated. The investigation is progressively supported by a comparative study to previous literature results.

2. THE ART OF HIGH TEMPERATURE OXIDATION

Bittel et al. [7] investigated the oxidation of stainless steel 304L under steam between 1273 and 1623 K. Table I. summarizes the chemical composition of 304L stainless steel, that is a low carbon content steel with 18 wt.% of Cr and about 11 wt.% of Ni. Samples were placed within a resistive heating furnace, and a Pt/Pt-10Rh thermocouple was used to control temperature variations, with an uncertainty of ±8 K. The entire apparatus was purged with argon while the sample was brought to the working temperature. Steam was then injected with a flow of 100 std ml/min as soon as the working temperature was stabilized. The mass of the samples was continuously recorded during the one-hour oxidation trials at both 1573 and 1623 K. The authors noted that the weight gain, measured in mg/cm², followed a predominantly linear trend until 28 minutes of oxidation and then transitioned to a parabolic pattern until the end of each trial between 1573 and 1623 K.

Table I. Chemical composition of 304L stainless steel

Species	C	Cr	Ni	Mn	Si	Cu	Mo	Co	P	S
Wt.%	0.02	18.0	10.95	1.69	0.70	0.280	0.160	0.050	0.024	0.011

X-ray diffraction technique was used to identify the oxide phases formed during the stainless steel oxidation. Bittel et al. [7] mentioned that the oxide scale of the sample heated at 1573 K exhibited an outer layer consisting of spinel, magnetite Fe_3O_4, along with 35 wt% iron plus 80 wt% nickel. At the metal interface, iron and chromium oxide were formed with a weight fraction of 40% each. Small grains and voids were observed at the inner surface, while larger oxide grains and voids were depicted at the outer surface of the oxide scale. Chromium was concentrated in the inner layer and absent from the outer layer, while the outer spinel layer contained 2 wt% of Mn. The authors suggested that the protective layer $(Cr,Fe)_2O_3$ was more likely to form during oxidation in air than under steam due to the higher partial pressure of oxygen, which was approximately 10^{-2} atm in the air for an alloy composition of 18%Cr-69%Fe. This level of partial pressure was sufficiently high to stabilize the protective layer. Furthermore, the authors pointed out that the oxygen activity in steam, starting from 1273 K, was insufficient to stabilize ferric oxide. Ferric oxide, (Fe_2O_3) was absent in the phases formed under steam, although it was present in Ishida's study at 1573 K.

On the other hand, Ishida et al. [8] investigated the oxidation kinetics of 304 stainless steel at high temperatures under steam atmosphere. The oxidation behaviour was studied within a temperature range of 1173 to 1623 K. Surface roughness was measured prior to each test to evaluate its effect on oxidation mechanisms. The authors mentioned a surface roughness of 2.2 microns at the inner surface and 2.6 microns at the outer surface. The samples were centered within an electric radiative furnace once the working temperature was established, given that the oxidation tests lasted from 2 minutes to 1 hour. At the end of each test, samples of 304 stainless steel were cooled to room temperature. The authors did not mention the cooling rate nor the uncertainty of temperature measurement.

Ishida et al. [8] results showed that the oxidation kinetics followed a parabolic law during the whole period of oxidation. After a first 8-minute stage, the parabolic reaction rate constant, measured in cm^2/s, decreased, especially at temperatures between 1373 and 1523 K. After six minutes of oxidation, the oxide scale had a two-layered structure, with the first layer consisting of a large oxide grains at the outer surface and the second layer consisting of small oxide grains and metallic particles, at the inner surface. This microstructure was observed at both 1573 and 1623 K. The second layer was yet thicker than the first layer at 1473 K after 15 minutes of oxidation. The authors mentioned that chromium was rich in the inner surface at 1573 K, while iron remained predominantly high at the first oxide layer. On the other hand, it was found that chromium was rather localized at the non-oxidized metal boundary at 1523 K after 60 minutes of oxidation, while iron remained higher in the metal. Chromium was then predominantly present at 1523 K but its area of high concentration was lower than at 1573 and 1623 K, evidently within the inner oxide scale.

The weight gain was therefore measured in mg/cm^2 and supposedly calculated solely from the thickness of three oxide phases : wustite FeO , magnetite Fe_3O_4 and ferric oxide Fe_2O_3 [8]. After 28 minutes of oxidation, the time required to reach the parabolic kinetic state, Bittel et al. [7] observed parabolic kinetics at 1573 K, which corroborates with the results reported by Ishida et al. [8] at the same temperature. The similarity between both results [7] [8] suggested that the controlling process was governed by diffusion through the Fe-Ni-Cr spinel layer, which was sustained by the parabolic rate law. However, the calculation method described by the evaluation from oxide thickness has not been assessed. Even though a fraction of chromium oxide was expected to evaporate during 304L oxidation, no regime variation was observed at 1623 K after 8 minutes. Furthermore, no correlation was established regarding the formation of chromium oxides, assuming that it remained present within the inner oxide scale for at least 8 minutes of oxidation at 1623 K. Instead, the chromium fraction within the inner oxide scale decreased from 1523 to 1623 K, and the difference in chromium fraction between these two temperatures was not mentioned. The authors then outlined a significant shift in the parabolic rate at 1523 K, which was attributed to the initial surface treatment. Yet, the same authors attributed the reduction in kinetics at 1523 K to chromium presence within the inner oxide scale, after about 10 minutes of oxidation.

The determination of kinetic laws based on thickness measurements could be questionable. Ishida et al. [8] considered oxidation kinetics to be deduced only from magnetite Fe_3O_4, without accounting for the interface effects, nor for the void density at the oxide interfaces. Although the limited duration of the 1623 K-oxidation test stands understandable, it would be interesting to extend this duration to determine the effect of chromium oxides, present in the inner part of the oxide scale, on the reaction kinetics. On the other hand, oxide thickness was measured in order to determine the weight gain at 1573 K after 4 minutes of oxidation. Both magnetite (Fe_3O_4) and ferric oxide (Fe_2O_3) corroborated with the weight gain calculated from the thickness data, while wustite (FeO) weight gain underestimated the weight gain measured at 2, 4, and 8 minutes of oxidation. The authors [8] mentioned then that this result confirmed the assumption that oxygen was consumed to form magnetite (Fe_3O_4) mainly, which thickness described the oxidation kinetics.

Oxidation under steam proves to be quite challenging, given the various difficulties associated with the supply of oxidizing gas, temperature, and surface condition. The literature describes two papers focusing on the oxidation of stainless steel at approximately 1623 K, given the temperature uncertainties under steam atmosphere. The oxidation kinetics between the two papers do not align from the initial moments of oxidation, hence the need for additional experimental data in the literature. The uncertainty regarding the temperature can be problematic, as the kinetic constant depends on an exponential of the inverse of the temperature.

In this respect, and in addition to the aforementioned elements, the article is going to propose a kinetic law for the evolution of hydrogen at the test temperatures for stainless steel in both states: solid at 1623 K and liquid at 1823 K. Since literature does not provide any data on the liquid state oxidation, it is possible to emphasize the elementary mechanisms of the oxidation process of a liquid metal by steam as stated by Delacroix et al. [9], e.g., Fig. 1. The authors studied the oxidation of liquid (over)stoichiometric corium under steam atmosphere, along with oxygen adsorption at the interface with oxidant gas, and its diffusion within the metallic bulk. Oxidation mechanisms of liquid corium have been evaluated as steam is initially transported to the initial non-oxidized reactive surface where it is adsorbed, creating a thin layer of hydrogen, oxygen, and steam at the outer surface of the sample. With an infinite supply of steam, thermal cracking of steam continues to occur at the external interface, as shown in Fig 1, increasing oxygen and hydrogen concentration within the boundary layer. The liquid metal is oxidized, forming a first oxide layer, hence a second internal interface. Metallic cations and oxygen anions diffuse through the oxide layer which boosting the oxidation reaction until the total consumption of the liquid metal. The different aspects of liquid-state oxidation can be addressed as follows [9]:

① : Transport of steam to the free external interface with “infinite” source of oxidation condition
② : Adsorption of steam on the free external interface followed by steam cracking, as follows:

$$H_2O \rightarrow H_2 + O^{\bullet}$$

③ : Hydrogen release
④ : Oxidation reaction at the external interface:

$$xMe + y\ H_2O \rightarrow Me_xO_y + yH_2$$
$$xMe + y\ O_2 \rightarrow Me_xO_y$$

⑤ : Oxidation reaction at the internal Interface:

$$xMe + y\ O_2 \rightarrow Me_xO_y$$

⑥ : Diffusion of O^{2-} or Me^{z+} through the oxide layer

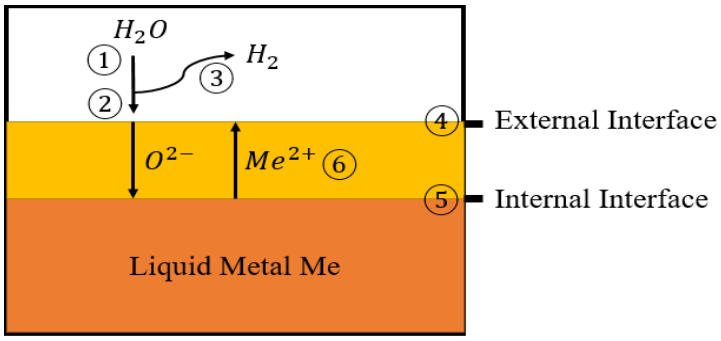

Figure 1. Oxidation mechanism of liquid metal alloys

3. EXPERIMENTAL PROCEDURE

3.1. VITOX Experimental facility:

The VITI (Viscometer Temperature Installation) facility located on the experimental severe accident platform PLINIUS at CEA Cadarache is used to conduct experiments at high temperatures, up to 3000 K. In this study, the VITOX (VITI-Oxidation) configuration was designed to carry out separate effects experiments on 304L stainless steel samples at both solid and liquid state. The crucible, the support, the crucible lid, and the separating tube are all made of yttria stabilized zirconia. The sample is initially centred within the confinement vessel after setting up the internal pressure at 0.3 bar. The inductor is then electromagnetically coupled with a tungsten susceptor whose temperature increases by Joule effect then radiates towards the high temperature cell, heating the sample up to the target temperature. With this heating system, the use of Calcarb® as thermal shield is necessary to limit heat losses and protect the equipment around the VITOX set up.

The VITOX facility is equipped with a steam supply system composed of two mass flowmeters provided by Bronkhorst®. The manufacturer specifies an accuracy of ± 0.5% of the reading for both instruments. A second argon flow of 2 L/min is simultaneously injected between the separating tube and the susceptor in order to flush the residual gas out of the chamber. During steam oxidation, the release of hydrogen gas stands for an indicator of the oxidation reaction and can be quantified throughout a VITOX oxidation test using a hydrogen detector. This device measures the partial pressure of gaseous species in a mixture and determines the volumetric concentration of each gaseous species. In fact, gas measurement is conducted through spectrophotometry technique. The hydrogen detector quantifies the spectrum of hydrogen absorption by evaluating the amount of light entering the device, which is absorbed at the wavelength corresponding to hydrogen absorption. In practice, the gas circulates in the device's chamber equipped with highly reflective mirrors. The light is then trapped and travels several kilometers within the chamber, allowing for the rapid detection of hydrogen traces through its absorption wavelength. The volumetric concentration of hydrogen is determined with a response time of approximately 10 seconds, and monitored over time to measure the real-time hydrogen production during steam oxidation tests.

A bi-chromatic video pyrometer from Keller is used for temperature measurement, remaining consistently focused on the sample surface. The operational wavelengths are set at λ_1 = 0.95 µm and λ_2 = 1.05 µm. A second bi-chromatic video pyrometer with identical working wavelengths is utilized to follow the susceptor temperature. The uncertainty on the temperature is about ±2 %. Fig. 2 shows a sectional view of the VITOX configuration.

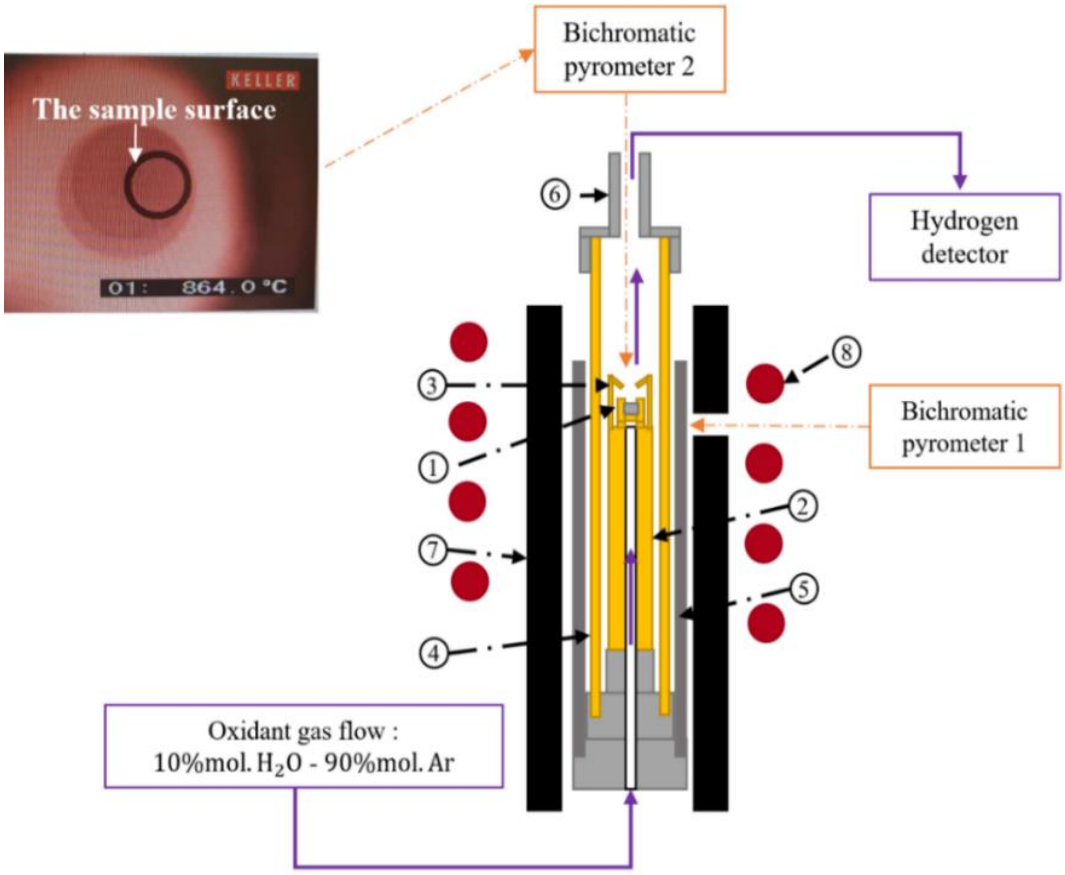

Figure 2. VITOX set-up: ① crucible and sample ② support ③ crucible lid ④ separating tube ⑤ susceptor ⑥ tube lid ⑦ thermal shield ⑧ inductor.

3.2. Experimental protocol:

The confinement vessel was placed under primary vacuum by pumping. After that, gaseous argon was injected into the furnace until the pressure reaches 0.5 bar (absolute), with 2 L/min as flow rate. This preliminary step was cycled until the initial oxygen concentration is reduced to 3×10^{-3} vol.% to limit initial oxidation during the heating process. Cylindrical samples of stainless steel, 0.5 cm in diameter and 0.2 cm in length, were first purged into ethanol then centered within the confinement vessel. Heating was then initiated under a static argon atmosphere at a rate of approximately 20 K/min. Upon reaching and stabilizing the desired working temperature, steam was introduced into the confinement vessel at a temperature of 423 K, along with a flow rate of 2 std L/min of argon. This creates a two-phase oxidant gas with a molar concentration of 90% mol. Ar - 10% mol. H_2O. After a specified oxidation duration, the supply of oxidant gas was stopped, and the heating system is turned off to quench the oxidized sample with a cooling rate of 50 K/min. Each sample was weighed before and after oxidation, with a balance uncertainty of 0.01%, to quantify oxygen uptake relative to the duration of exposure to steam flow. The online measurement of hydrogen production, using the hydrogen detector, allowed for dynamic measurement and final weight verification.

The tracking of oxygen up-take, standardized to the reactive surface and measured in g/cm², was established as a function of an adjustment factor, set to align the in-situ mass reading at time "t_f" with the actual mass, determined after a "t_f" duration test. The hydrogen concentration revealed by the detector indicates the volumetric concentration produced by the sample, which is a punctual measurement at a "t" instant. It does

not however indicate the total amount of hydrogen from the beginning of the reaction, hence the use of the integral formula, expressed as follows:

$$W(t) = \frac{k}{S} \times \int_0^t [H_2](u).du \quad ; \quad k = \frac{m_{t_f} - m_i}{\int_0^{t_f} [H_2](u).du} \tag{1}$$

- $W(t)$: oxygen up-take during oxidation at "t" seconds, (g/cm²)
- k : adjustment factor for conversion, (g/vol.%)
- $[H_2]$: relative volumetric concentration of in-situ hydrogen released at a "t" instant, (vol.%)
- S : reactive surface determined as the interface with the gas for liquid state test, to that is added the circumferential surface for solid-state tests, (cm²)
- m_i : initial mass of the sample, (g)
- m_{t_f} : final mass of the sample, weighed after a "t_f" duration test, (g)

Dihydrogen mass production per reactive surface unit (g/cm²) is calculated as the following relationship assuming that one mole of dihydrogen released corresponds to one mole of oxygen adsorbed at the reactive surface:

$$H_2(t) = \frac{W(t) \times M_{H_2}}{M_O} \tag{2}$$

- $W(t)$: oxygen up-take during oxidation at "t" seconds, (g/cm²)
- M_O : molar mass of oxygen, (g/mol)
- M_{H_2} : molar mass of dihydrogen, (g/mol)

Table II summarizes oxidation tests that were conducted, indicating the temperature and the initial mass of the samples.

Table II. Experimental grid for 304L stainless steel oxidation tests with steam.

Temperature (K)	Initial mass (g)	Test duration (s)
1623	0.4064	2000
1623	0.4054	4050
1823	0.6130	5100

4. RESULTS AND DISCUSSION

4.1. Solid state:

Two oxidation tests were conducted at 1623 K. The first oxidation test lasted 2000 seconds while the second test lasted 4050 seconds, with a plateau formed at the end of the oxidation. Fig 3 shows the evolution of the oxygen up-take, measured in g/cm², as function of time, as well as hydrogen mass release after 2000 and 4000 seconds of oxidation. For clarity purposes, one experimental point is outlined for every 700 points.

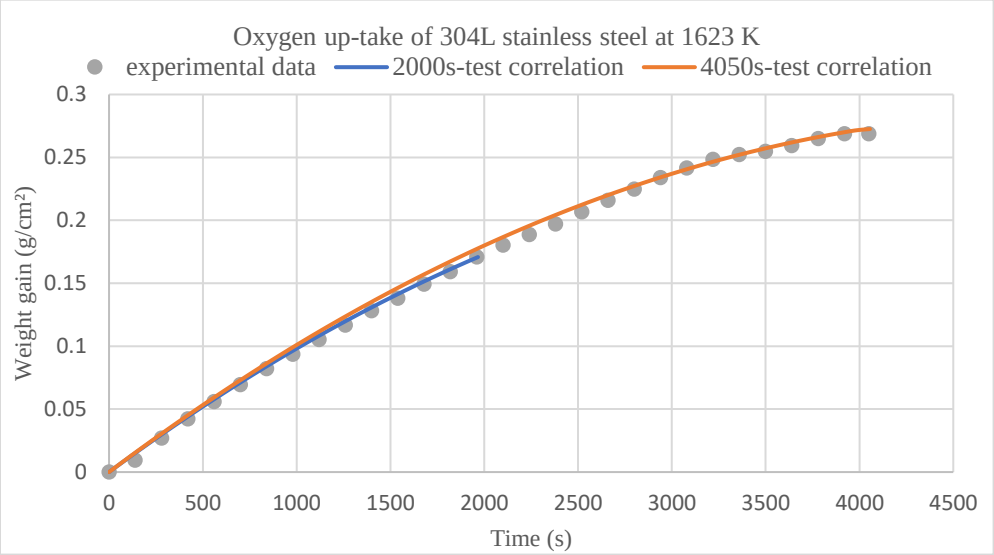

Figure 3. Oxygen up-take of 304L stainless steel at 1623 K

The oxidation kinetics followed a two-stage evolution. In the initial stage, rapid oxidation was observed until 4000 seconds, after which the kinetics tended to stabilize, eventually reaching for an oxidation plateau. In fact, the 2000s-test aligned with the 4050s-test, with a maximum variation of about 4%, confirming the repeatability of the experimental apparatus. The general oxidation law of stainless steel at 1623 K can be described as follows, with a correlation coefficient R^2=0.996:

$$W(t) = 1.12 \times 10^{-4}\, t - 1.10 \times 10^{-8}\, t^2 \quad (3)$$

In order to relate to the literature results, the oxygen up-take formulated in this work was characterized in order to illustrate the classical kinetic laws (linear/parabolic/cubic). The oxidation kinetics exhibited an initial linear regime within the first 2000 seconds of reaction, followed by an accelerated parabolic regime. This preceded the establishment of an oxidation plateau, which began at 4000 seconds of oxidation. A second correlation was established to describe the general evolution of oxygen up-take, established from linear and parabolic constants assessed by Bittel et al. [7], which can be expressed as follows:

$$W_B(t) = 1.05 \times 10^{-3} + 1.26 \times 10^{-4}\, t - 1.97 \times 10^{-8}\, t^2 \quad (4)$$

According to Fig 4, the linear regime described in the first 2000 s of oxidation aligned with the work of Bittel et al. [7]. It is important to mention that the authors described linear kinetics only in the first 1680 seconds of reaction. The parabolic regime formulated by both curves corroborated until 2100 seconds of reaction, followed by a last reactional regime of an oxidation plateau. While the curve described in this work tended toward its asymptote with a maximum oxygen up-take of 0.27 g/cm², Bittel et al. [7] illustrated an oxidation plateau 1000 seconds earlier, with an ultimate oxygen up-take of 0.20 g/cm². A maximum deviation between the two curves was set to be up to 35%, mostly once the last reactional regime was established. This discrepancy could be attributed to several factors, including uncertainties in steam flow rate and temperature. These uncertainties were addressed as ±2% in the VITOX set-up, and as ±8 K in the work of Bittel et al. [7]. Oxide thickness measurements by Ishida et al. [8] formulated parabolic kinetics from extrapolating three thickness sets during 500 seconds of oxidation. Extrapolating data could introduce unmanageable uncertainties, hence complicating the comparison of kinetics. Therefore, calculating the mass through the density of the supposedly major oxide formed, Fe_3O_4, required knowing the oxide area, whose

values were not determined [8]. It was hence assumed that the external surface in contact with the oxidant medium was entirely and uniformly oxidized. This step was significant in order to align with previous results of oxygen up-take, measured in g/cm². In this respect, Fig 4 shows that the curve of the same authors corroborated with both this work and Bittel et al. [7], with an ultimate oxygen up-take of approximately 0.05 g/cm².

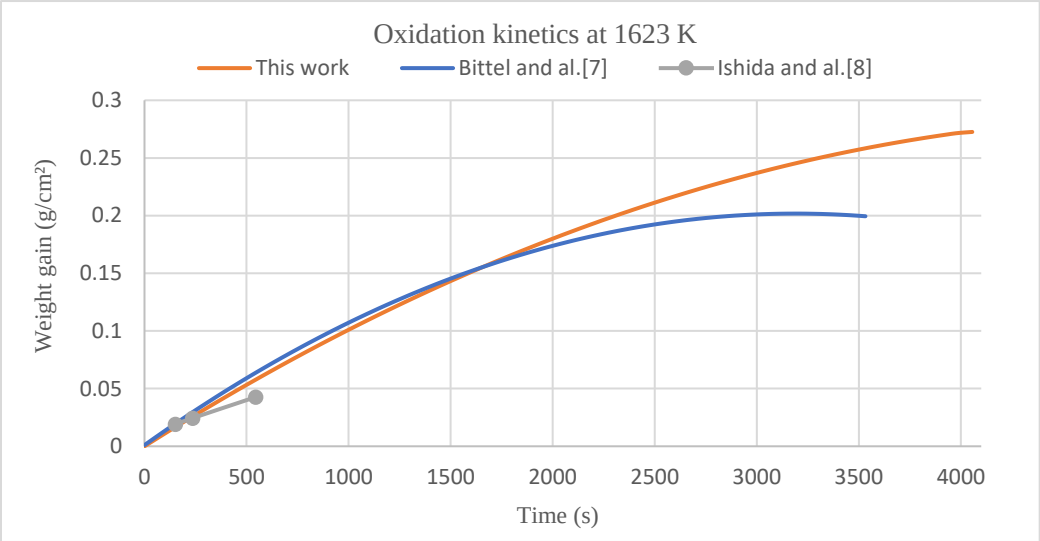

Figure 4. Oxidation kinetics of 304L stainless steel oxidation at 1623 K

This similarity in oxidation kinetic regimes between the three data suggests that the oxidation of 304L stainless steel was governed by diffusion through the Fe-Ni-Cr spinel layer, formed with a molar quantity of 3.26×10^{-2} mol, as stated by Bittel et al. [7]. Alongside this oxide phase, a second solid oxide was supposedly formed with a molar quantity of 4.04×10^{-4} mol. Both molar compositions were calculated, based on the sample initial mass and the molar composition of the oxidant gas, stated at the experimental protocol, with TafiD database on ThermoCalc software [10]. Linear and parabolic kinetics laws can be formulated as follows:

$$W_l(t) = 9.49 \times 10^{-5}\, t\,, \quad t < 2000s \tag{5}$$

$$W_p(t) = 5.24 \times 10^{-3}\sqrt{t} - 5.54 \times 10^{-2}\,, \quad t > 2000s \tag{6}$$

- $W_l(t)$: linear weight gain, (g/cm²)
- $W_p(t)$: parabolic weight gain, validating the function continuity, (g/cm²)

Fig 5 depicts the dihydrogen mass production at 1623 K continuously determined and modelled according to equation 7, with a correlation coefficient R^2=0.996. Again, and for clarity purposes, one experimental point was displayed for every 700 points.

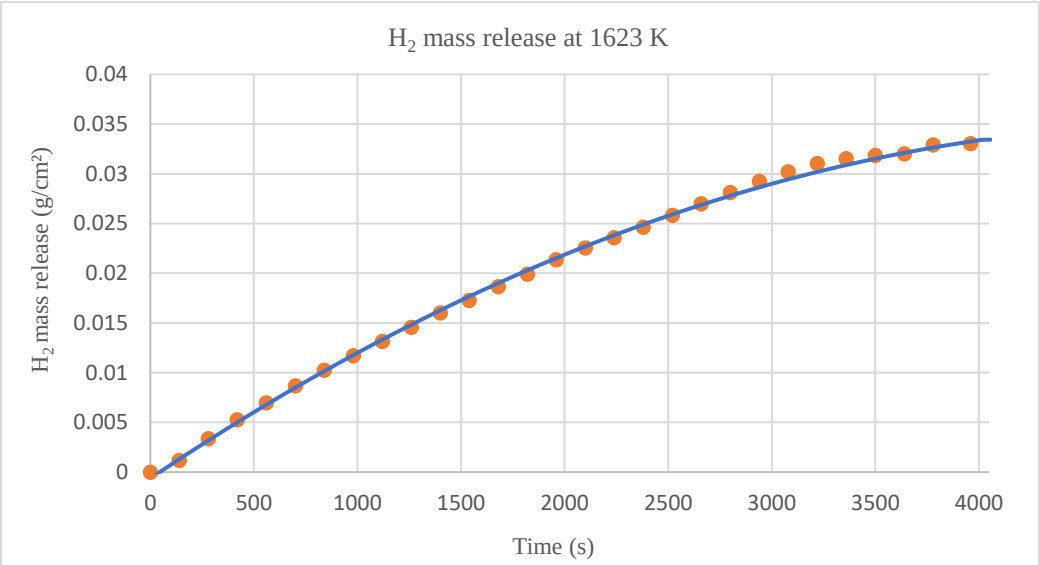

Figure 5. H_2 mass release for 304L stainless steel oxidation at 1623 K

$$H_{2,1623K}(t) = -6.33 \times 10^{-4} + 1.40 \times 10^{-5}\, t - 1.38 \times 10^{-9}\, t^2 \quad (7)$$

4.2. Liquid state:

Oxidation tests were conducted on liquid 304L stainless steel at 1823 K. Fig 6 shows the oxygen up-take evolution of solid and liquid state trials, measured in g/cm². For more clarity purposes, one experimental point was displayed for every 900 points, with a correlation coefficient R^2=0.996.

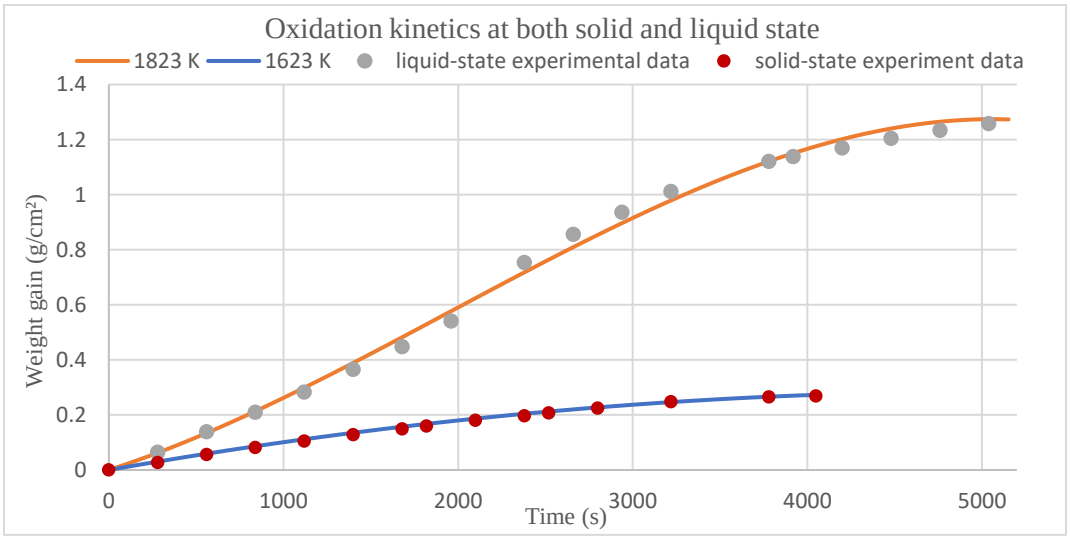

Figure 6. Oxidation kinetics of 304L stainless steel at solid and liquid state

Both curves showed similar behaviour. At 1623 K, the first stage was rapid and lasted about 4000 seconds, then reached for an oxidation plateau with a maximum weight gain of about 0.27 g/cm². At 1823 K, the

initial stage appeared to be faster, lasting approximately 4700 seconds, and then gradually decreased, reaching for an oxidation plateau, at about 4900 s of oxidation, with an ultimate oxygen up-take of about 1.27 g/cm². After 4000 seconds of oxidation, an oxygen up-take of about 1.16 g/cm² was measured, which was about 4.5 times higher that solid-state oxygen up-take after the same oxidation duration. General time evolution of liquid oxygen up-take can be expressed as follows:

$$W_{1823K}(t) = 2.05 \times 10^{-4}\, t + 6.82 \times 10^{-8}\, t^2 - 1.17 \times 10^{-11}\, t^3 \quad (8)$$

The initial conditions of liquid state experiments (mass, molar composition, and temperature) revealed, according to TafiD database [10], the formation of 1.73×10^{-2} mol of solid spinel along with 1.42×10^{-2} mol of first (Fe,Cr,Ni) liquid oxide and 2.46×10^{-4} mol of second (Fe,Cr,Ni) liquid oxide, at 1823 K,. It was hence important to take into account the gradient of surface tension at each interface; *solid/liquid* and *liquid/liquid*, which might govern the liquid state oxidation mechanisms. Liquid evolution was set to describe parabolic kinetics as of 300 s of reaction, while solid state depicted parabolic regime as of 2000 seconds of reaction. This could be primarily attributed to the nature of oxide interface, alongside with the oxide formed itself. This therefore implied the necessity of conducting EDS analysis in order to identify different oxide phases, formed at both working temperatures. Parabolic law at liquid state can be assessed as follows:

$$W_{p,1823K}(t) = 2.38 \times 10^{-2}\sqrt{t} - 0.40\,, \quad t > 300s \quad (9)$$

Moreover, dihydrogen mass release was determined as function of time at 1823 K, as shown in Fig 7:

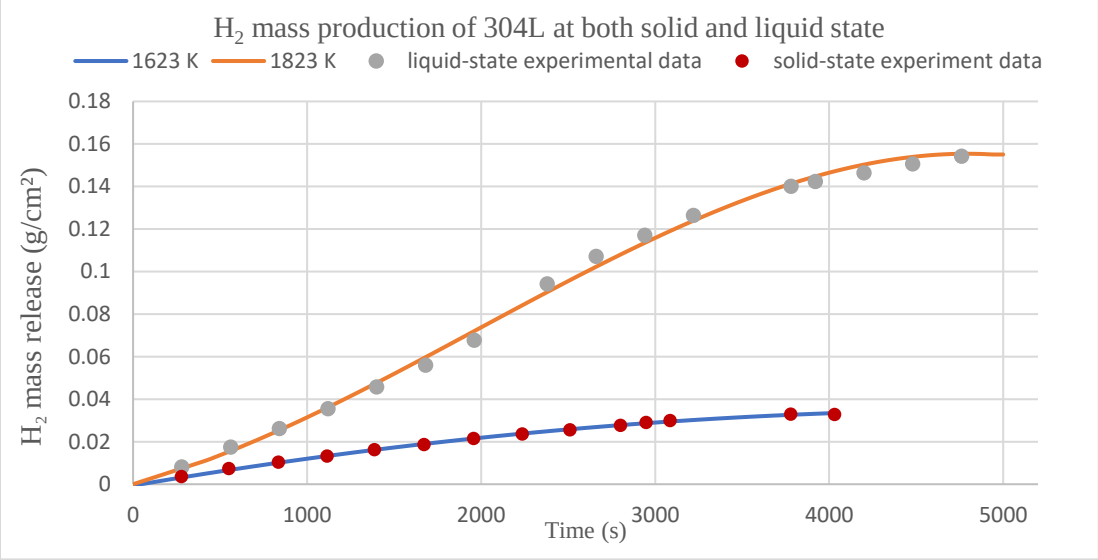

Figure 7. H_2 mass release for 304L stainless steel oxidation at liquid and solid state

The dihydrogen mass release during the oxidation of liquid 304L stainless can be addressed as follows:

$$H_{2_{1823K}}(t) = 2.23 \times 10^{-5}\, t + 1.10 \times 10^{-8}\, t^2 - 1.85 \times 10^{-12}\, t^3 \quad (10)$$

For instance, 1 m² of 304L stainless steel, after a 4000s-oxidation test at 1823 K would release 1468 g of dihydrogen, while at 1623 K, it would release 333 g of dihydrogen, indicating about a 4.5 time-higher release at liquid state oxidation.

5. CONCLUSIONS

The aim of this study was to describe the oxidation kinetics of the main element of the reactor vessel stainless steel, at both solid and liquid state. The experimental results, conducted at the VITOX facility at CEA CADARACHE, were first established at solid state and then compared to the literature, in order to show both concordance and potential divergence. Regarding the complexities involved in the measuring apparatus, a H_2 detector was configured to continuously monitor dihydrogen production and, consequently, oxygen consumption at various oxidation temperatures. In this respect, the oxidation kinetics revealed a linear regime at first, followed by a parabolic evolution at 1623 K, while parabolic kinetics govern liquid oxidation at 1823 K as of 300 seconds of reaction. Dihydrogen production for melted alloys oxidation at high temperature was 4.5 times higher than that for solid state. As perspectives, scanning electronic microscope and energy dispersive spectrometer out micrographic analyses will be performed to identify the the oxide phases, which would also serve as validation data for the theoretical molar fractions provided in this work.

REFERENCES

1. A. Bentaïb, H. Bonneville, G. Cénérino, B. Clément, F. Corenwinder, M. Cranga, G. Ducros, F. Fichot, D. Jacquemain, C. Journeau et others, *Les accidents de fusion du cœur des réacteurs nucléaires de puissance,* EDP sciences, 2013.
2. B. R. Sehgal et others, *Nuclear safety in light water reactors: severe accident phenomenology, Academic Press,* 2011.
3. F. Fichot, L. Carénini, M. Sangiorgi, S. Hermsmeyer, A. Miassoedov, S. Bechta, J. Zdarek et D. Guenadou, “Some considerations to improve the methodology to assess In-Vessel Retention strategy for high-power reactors, ” *Annals of Nuclear Energy,* vol. 119, p. 36–45, 2018.
4. V. I. Almjashev, V. S. Granovsky, V. B. Khabensky, S. Y. Kotova, E. V. Krushinov, A. A. Sulatsky, S. A. Vitol, V. V. Gusarov, F. Fichot, B. Michel et others, "Experimental study of transient phenomena in the three-liquid oxidic-metallic corium pool, “*Nuclear Engineering and Design*”, vol. 332, p. 31–37, 2018.
5. P. Piluso, W. Zhou, N. Cassiaut-Louis, C. Journeau, Shein et Y. Liao, "Corium behavior and steam explosion risks: A review of experiments, “*Annals of Nuclear Energy*”, vol. 121, p. 162–176, 2018.
6. M. Sanchez-Brusset, “*Mécanismes d'oxydation de l'acier liquide lors de l'Interaction Corium-Béton à haute température en cas d'accident grave de réacteur nucléaire,* ”, Ph-D thesis, Université de Perpignan Via Domitia, France, (2015).
7. J. T. Bittel, L. H. Sjodahl et J. F. White, “Oxidation of 304L stainless steel by steam and by air, ” *Corrosion,* vol. 25, p. 7–14, 1969.
8. T. Ishida, Y. Harayama et S. Yaguchi, “Oxidation of 304 stainless steel in high-temperature steam, ” *Journal of Nuclear Materials,* vol. 140, p. 74–84, 1986.
9. J. Delacroix, R. Le Tellier et P. Piluso, “Oxygen diffusion in liquid (over) stoichiometric corium, ” *Nuclear Engineering and Design,* vol. 337, p. 148–160, 2018.
10. C. Guéneau, N. Dupin, L. Kjellqvist, E. Geiger, M. Kurata, S. Gossé, E. Corcoran, A. Quaini, R. Hania, A. Smith, M. Piro, T. Besmann, P. Turchi, J. Dumas, M. Welland, T. Ogata, B. Lee, J. Kennedy, C. Adkins, M. Bankhead and D. Costa, “*TAF-ID: An international thermodynamic database for nuclear fuels applications*,” Calphad, vol. 72, 2021.

STAINLESS STEEL OXIDATION AT BOTH SOLID AND LIQUID STATE UNDER AR-H_2O IN SEVERE ACCIDENT CONDITIONS

PhD candidate: Mehdi NASSELAHSEN (CEA)

Thesis directors: Emmanuel DE BILBAO (CNRS/CEMHTI)
Pascal PILUSO (CEA)

Thesis supervisors: Jules DELACROIX (CEA)
Sawsen YOUSSEF (CNRS/CEMHTI)

Communication: **021**

Contents

01 Context and objectives

02 State of the art

03 Experimental apparatus

04 Experimental results at solid & liquid state

05 Conclusions and perspectives

Context and objectives

Formation of **corium** melt ⟷ **Oxidation** kinetics ⟷ **Dihydrogen** Production

Corium melt **pouring** into **water:**

(TMI-2 , USA, 1979, Chernobyl 1986)

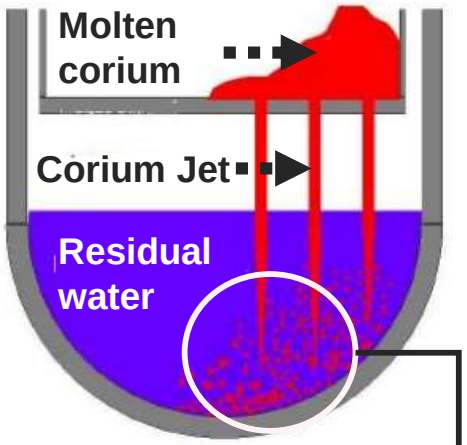

- **Oxidation** of corium droplets
- **Oxidation** of the **stainless steel** coming from the vessel

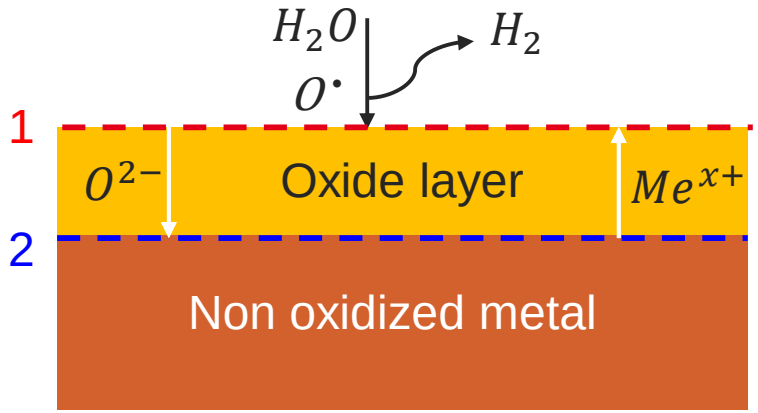

Oxidation reaction for **dihydrogen** release:

$$(\boldsymbol{Fe, Ni, Cr})_x + y\ H_2O = (\boldsymbol{Fe, Ni, Cr})_xO_y + \boldsymbol{yH_2}$$

Linear kinetics :

- **Limitating** factor: Reaction at **interface 1**
- **Porous** oxide layer at the **interface 1**

Parabolic kinetics:

- **Limitating** factor: **Diffusion** of chemical species at **interface 2**
- **Non porous** oxide layer at **interface 1**

Objectives

- Oxidation **kinetics of 304L-SS** at **solid** and **liquid** states under steam
- **Dihydrogen** production rates at **solid** and **liquid** states under steam

State of the art: steam oxidation of SS modelling for SA codes

Solid-state conditions: **T = 1 350°C**

Oxidation **kinetics**

Bittel *et al.*[1] (1969):

- Temperature uncertainty: ±**8 °C**
- Evaluated entity: **weight gain** in mg/cm²

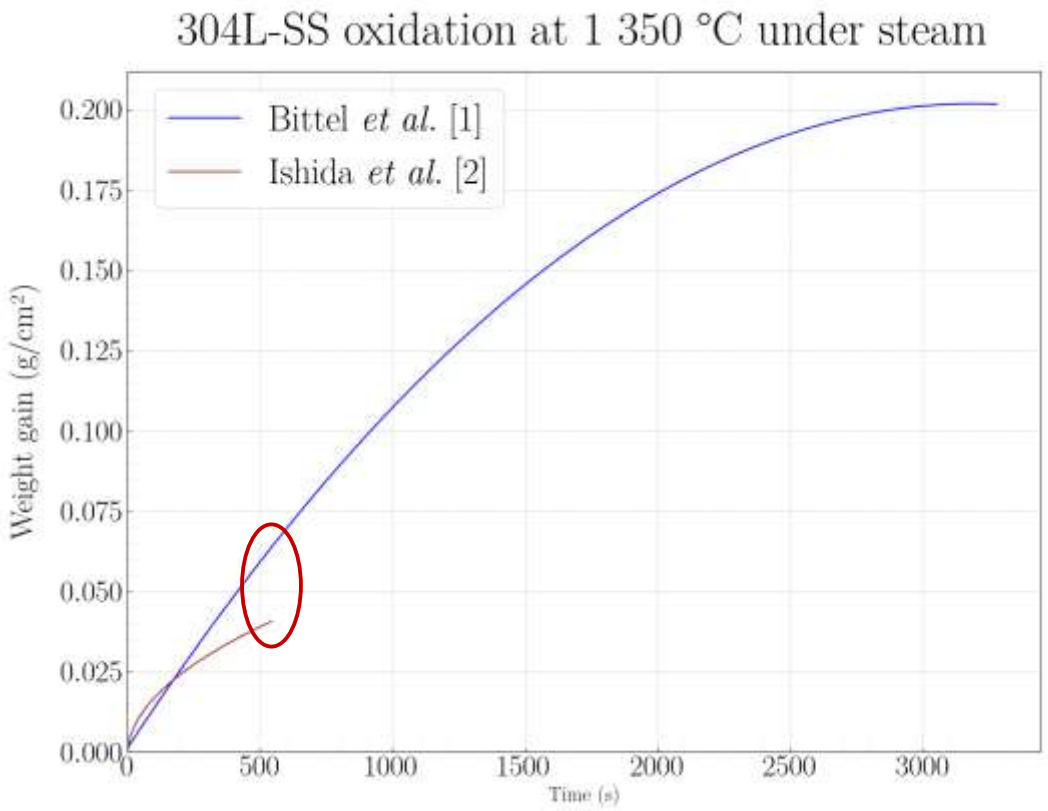

Bittel *et al.*[1] (1969):

- **Linear kinetics** until 1 800 seconds
- **Parabolic trend** then till 3 000 seconds

Ishida *et al.*[2] (1986):

- Temperature uncertainty: **not mentionned**
- Evaluated entity: **thickness gain** in µm

Ishida *et al.*[2] (1986):

Parabolic kinetics until 500 seconds

Comparative synthesis:

- Unit **uniformisation -> (g/cm²)**
- Maximum **difference** of **50% at 500 seconds**

[1] J. T. Bittel, L. H. Sjodahl et J. F. White, "Oxidation of 304L stainless steel by steam and by air, " Corrosion, vol. 25, p. 7–14, 1969.
[2] T. Ishida, Y. Harayama et S. Yaguchi, "Oxidation of 304 stainless steel in high-temperature steam, " Journal of Nuclear Materials, vol. 140, p. 74–84, 1986.

VITOX : Experimental apparatus

VITOX apparatus

Crucible-Sample cell

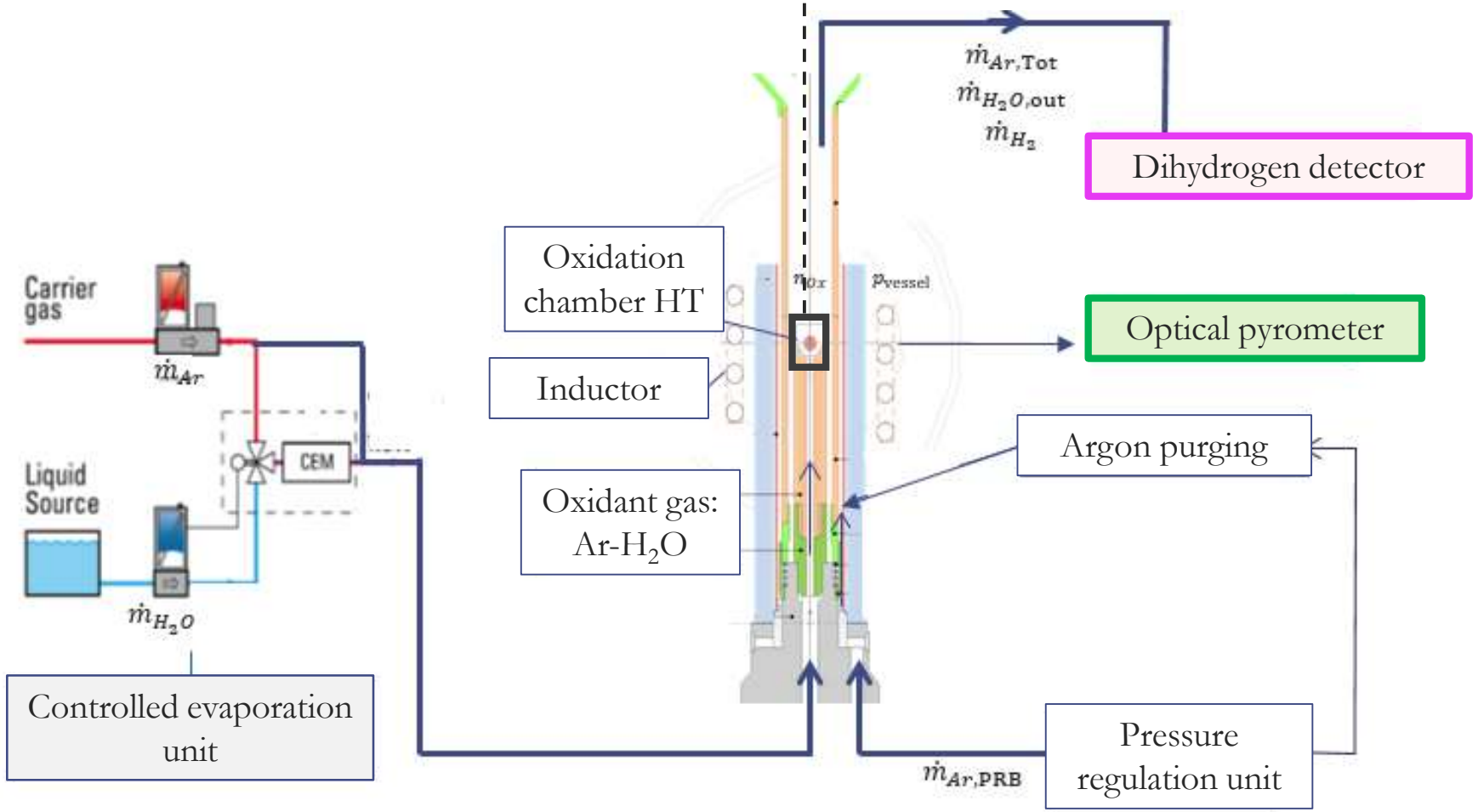

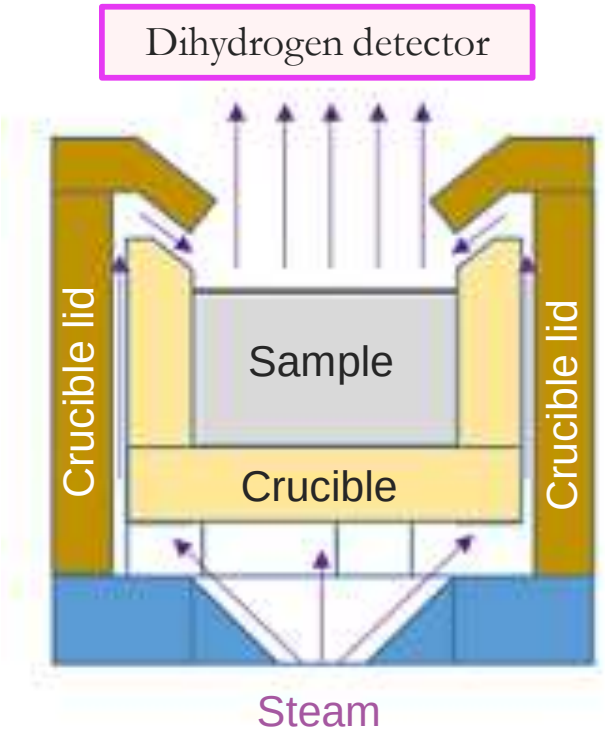

Improvements for temperature and dihydrogen measurements

Temperature measurement: **Optical Pyrometry**

- Measurement range: **[850 - 3 000] °C**
- Precision: **2%**
- **Correcting** the temperature T_p against a verified **thermocouple** measure T_{TC}

Dihydrogen concentration: **dihydrogen detector**

- Measurement range: **[0 - 100] vol.%**
- Precision: **1%**

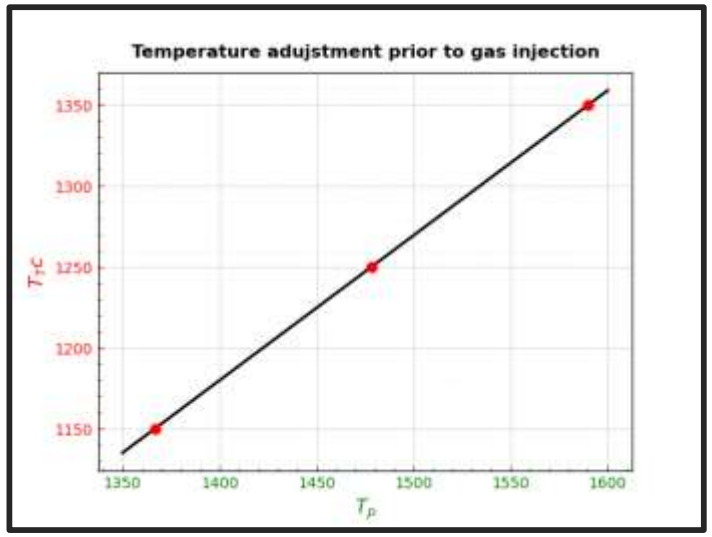

$$T_{TC} = 0{,}897 \times T_p - 75{,}856\ (\pm\ \mathbf{2}\%)$$

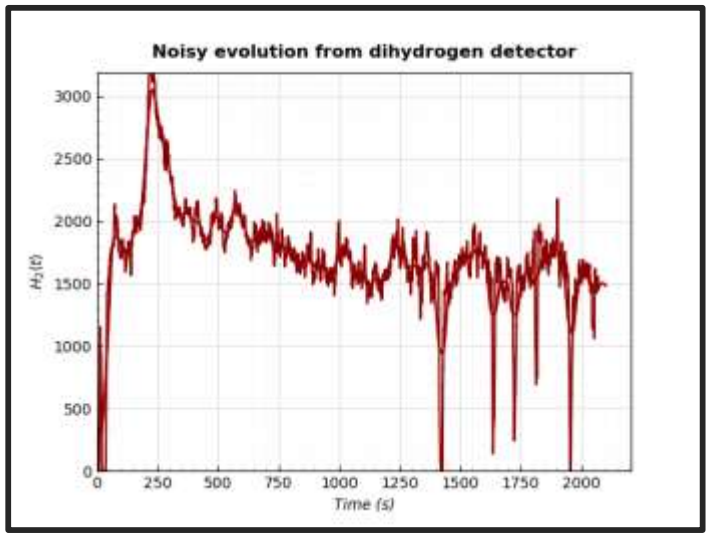

Noisy distribution

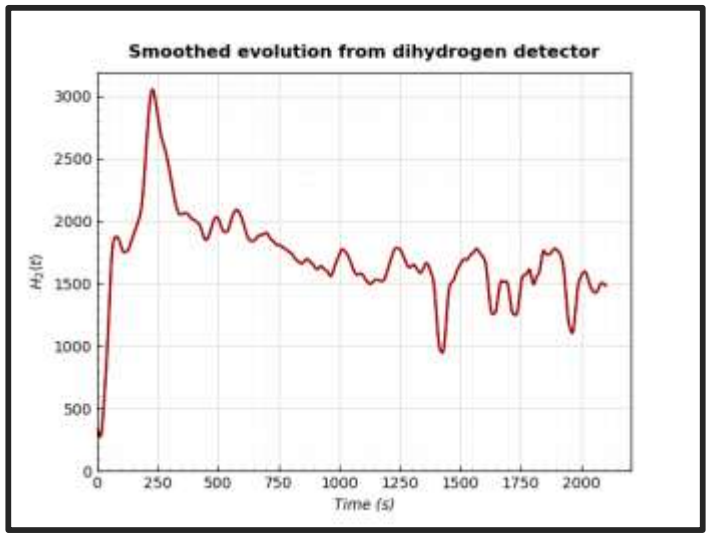

Smoothed distribution

Experimental and analytical procedure

Experimental protocol

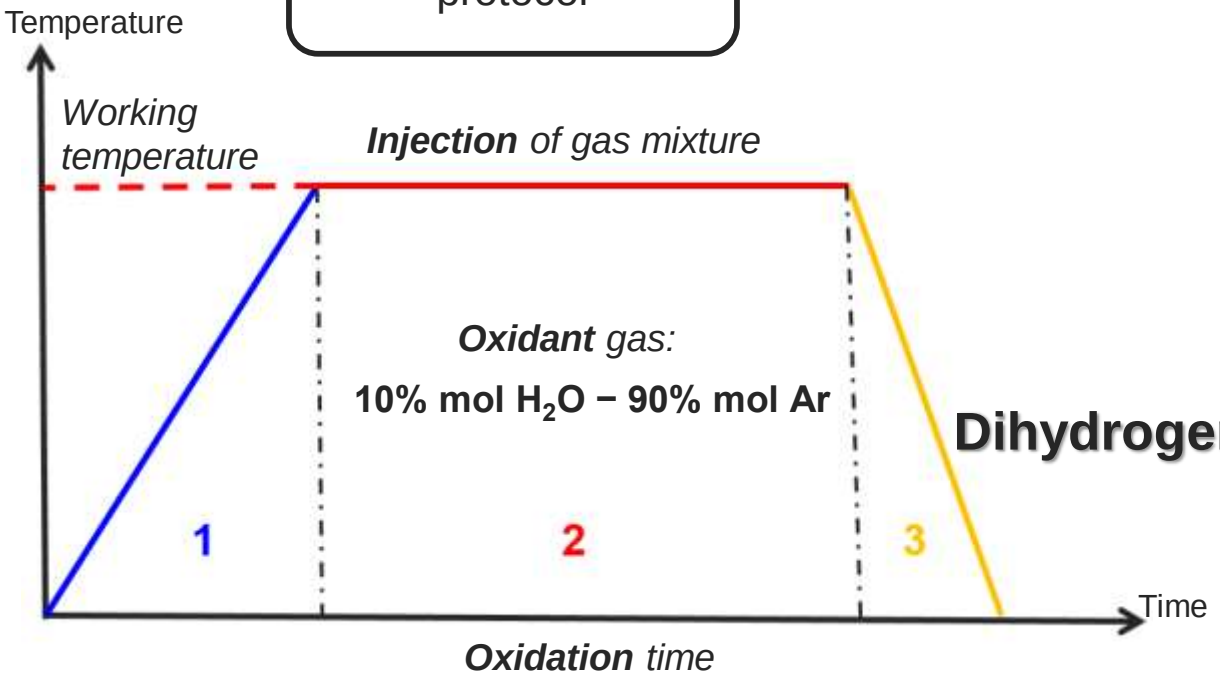

1 : Temperature **rise of 20 °C/min** under static **argon**

2 : Isothermal plateau under **argon and steam**

3 : Generator **shutdown** and **cooling rate of 250 °C**

Dihydrogen data analysis

Analytical protocol

$$W(t) = \frac{k}{S} \times \int_0^t [H_2](u).du \quad ; \quad k = \frac{m_{t_f} - m_i}{\int_0^{t_f} [H_2](u).du}$$

- W(t): weight gain (g/cm²)
- **k: Adjustment coefficient (g/vol.%)**
- $[H_2]$: instantaneous volumetric concentration (vol.%)
- **S: Reactive surface (cm²)**
- m_i: initial mass of the sample (g)
- m_{t_f}: final mass of the sample (g)

$$m_{H_2}(t) = \frac{W(t) \times M_{H_2}}{M_O}$$

- m_{H_2}: dihydrogen mass release, (g/cm²)
- M_O: molar mass of oxygen, (g/mol)
- M_{H_2}: molar mass of dihydrogen, (g/mol)

Oxidation at solid state

Solid-state conditions:
T = 1 350°C

VITOX (2024)

- Oxidation time: 4 050 s

Bittel *et al.*[1] (1969):

- Oxidation time: 3 500 s

Ishida *et al.*[2] (1986):

- Oxidation time: 500 s

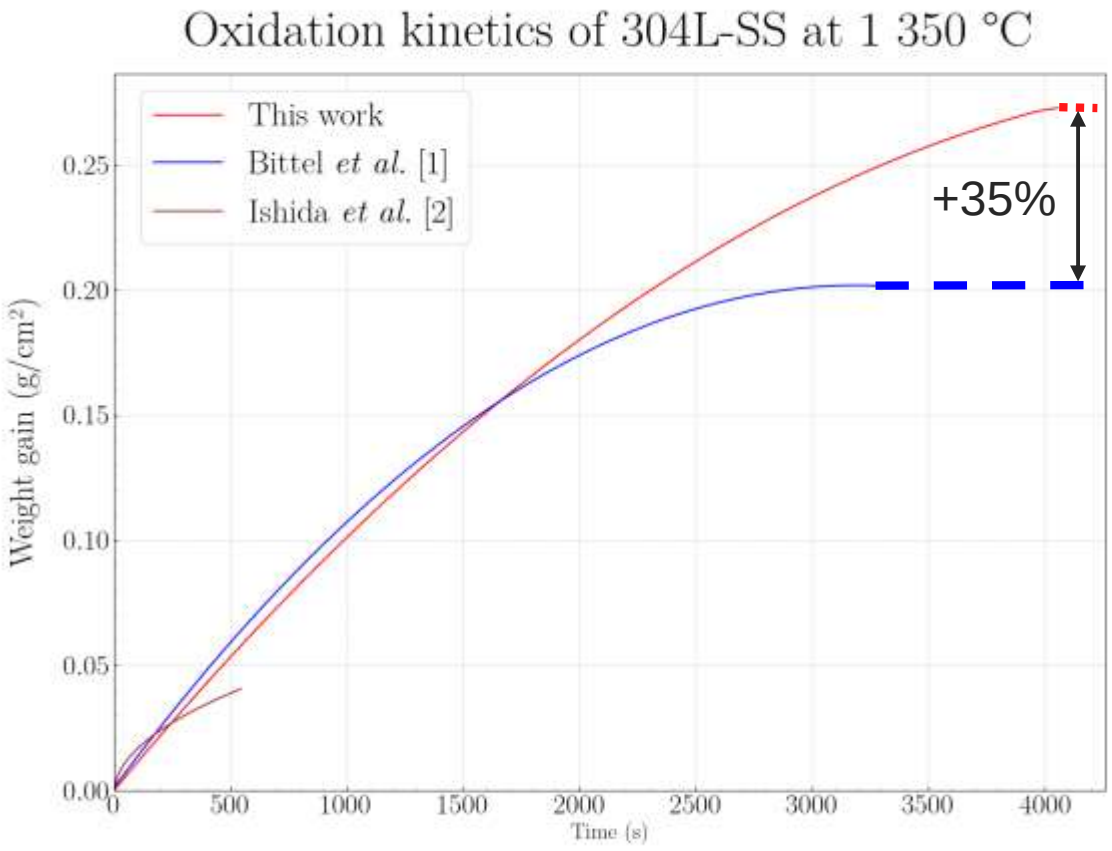

- **Good agreement** between **VITOX** and **Bittel *et al.*[1]** curve until 1893 seconds.
- First-time **deviation** at **1893 seconds**, then reaching **+35 % at 4 000 s** of oxidation

Oxidation **Kinetics**

VITOX: **Linear** till **2 000 s** then **parabolic**

Bittel *et al.*[1]: **Linear** till **1 800 s** then **parabolic**

Ishida *et al.*[2]: **Parabolic** until **500 s**

Oxidation **Plateau**

VITOX: 0,27 g/cm²

Bittel *et al.*[1]: **0,20 g/cm²**

Ishida *et al.*[2]: Short-time oxidation **no plateau observed**

Oxidation at liquid state

Liquid-state conditions:
T = 1 550°C

State of the art:

Liquid-state oxidation: **no data** mentionned in the litterature

VITOX (2024):

- Oxidation time: 5 060 s
- Oxidation temperature: **1 550°C**
- **Same** gas mixture and flow rate as **solid state**

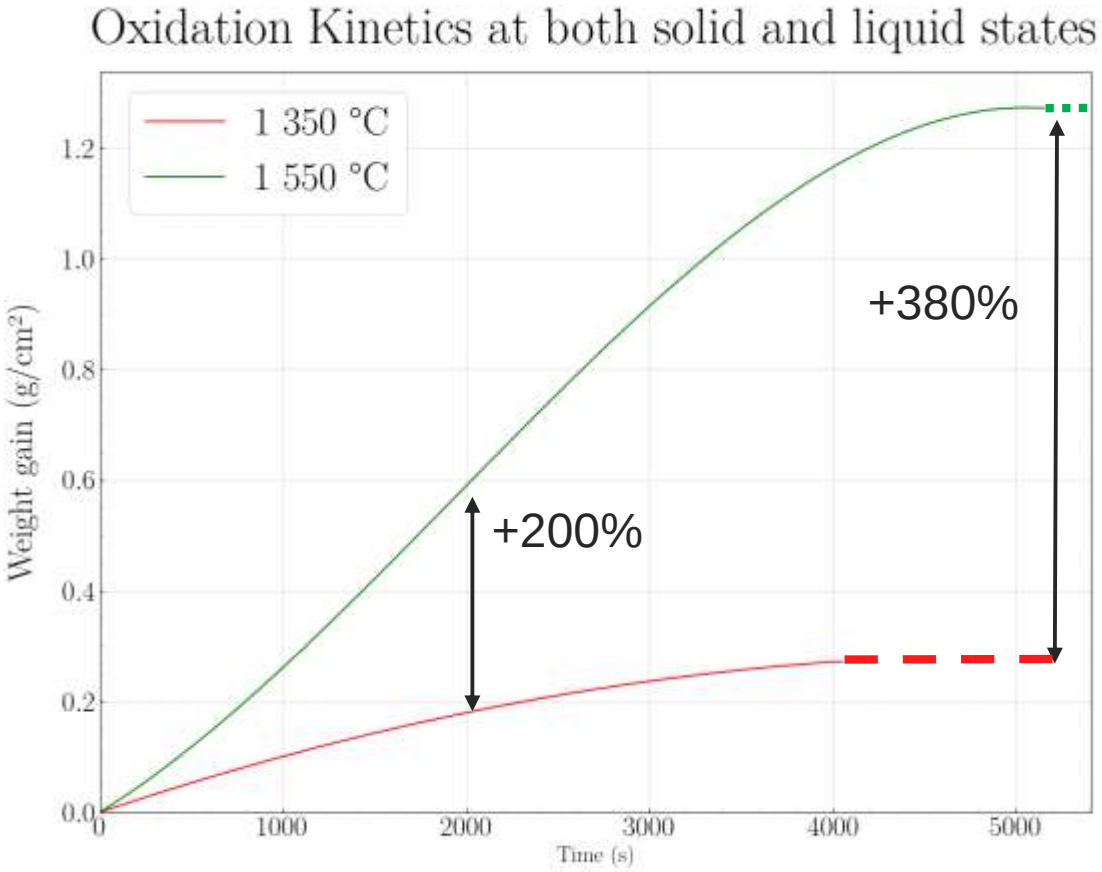

Area of the reactive surface: 1 m²
Oxidation **time**: 4 000 s
Oxidation **temperatures**: 1 350 °C / 1 550 °C

× 4, 5 → Solid: **0,27 g/cm²** at **4 000 s**
Liquid: **1,16 g/cm²** at **4 000 s**

Oxidation **Kinetics**

Solid-state:

- **Linear** till **2 000 s**
- **Parabolic** till **4 000 s**

Liquid state:

Parabolic as of **300 s**

Oxidation **Plateau**

Solid: 0,27 g/cm² → **+380%**
Liquid: 1,27 g/cm²

Dihydrogen release

$$m_{H_2}(t) = \frac{W(t) \times M_{H_2}}{M_O}$$

m_{H_2}: dihydrogen mass release, (g/cm²)

M_O: molar mass of oxygen, (g/mol)

M_{H_2}: molar mass of dihydrogen, (g/mol)

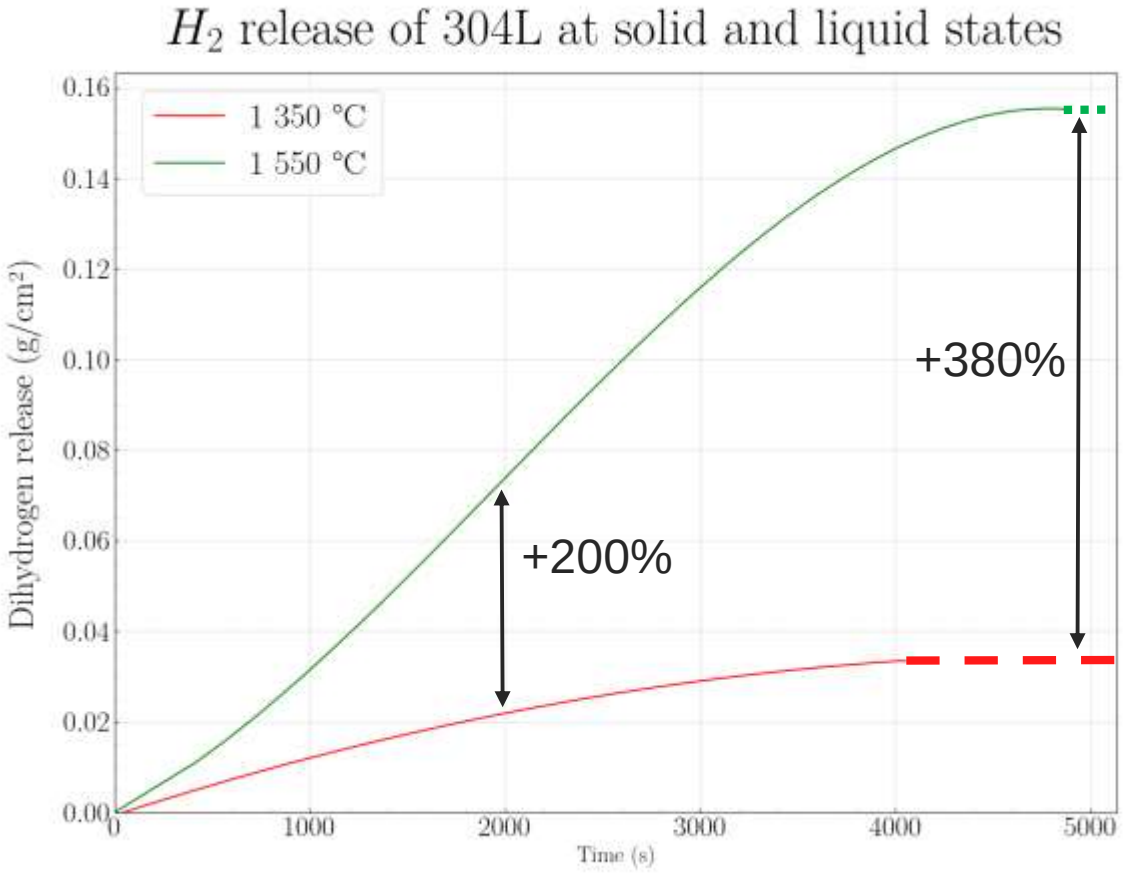

Plateau of **mass release**

Solid: 0,03 g/cm²

Liquid: 0,15 g/cm²

+380%

Area of the reactive surface: 1 m²
Oxidation **time**: 4 000 s
Oxidation **temperatures**: 1 350 °C / 1 550 °C

$\times 4,5$ Solid: **333 g** at **4 000 s**
Liquid: **1486 g** at **4 000 s**

Conclusions

1- Oxidation Kinetics of 304L-SS

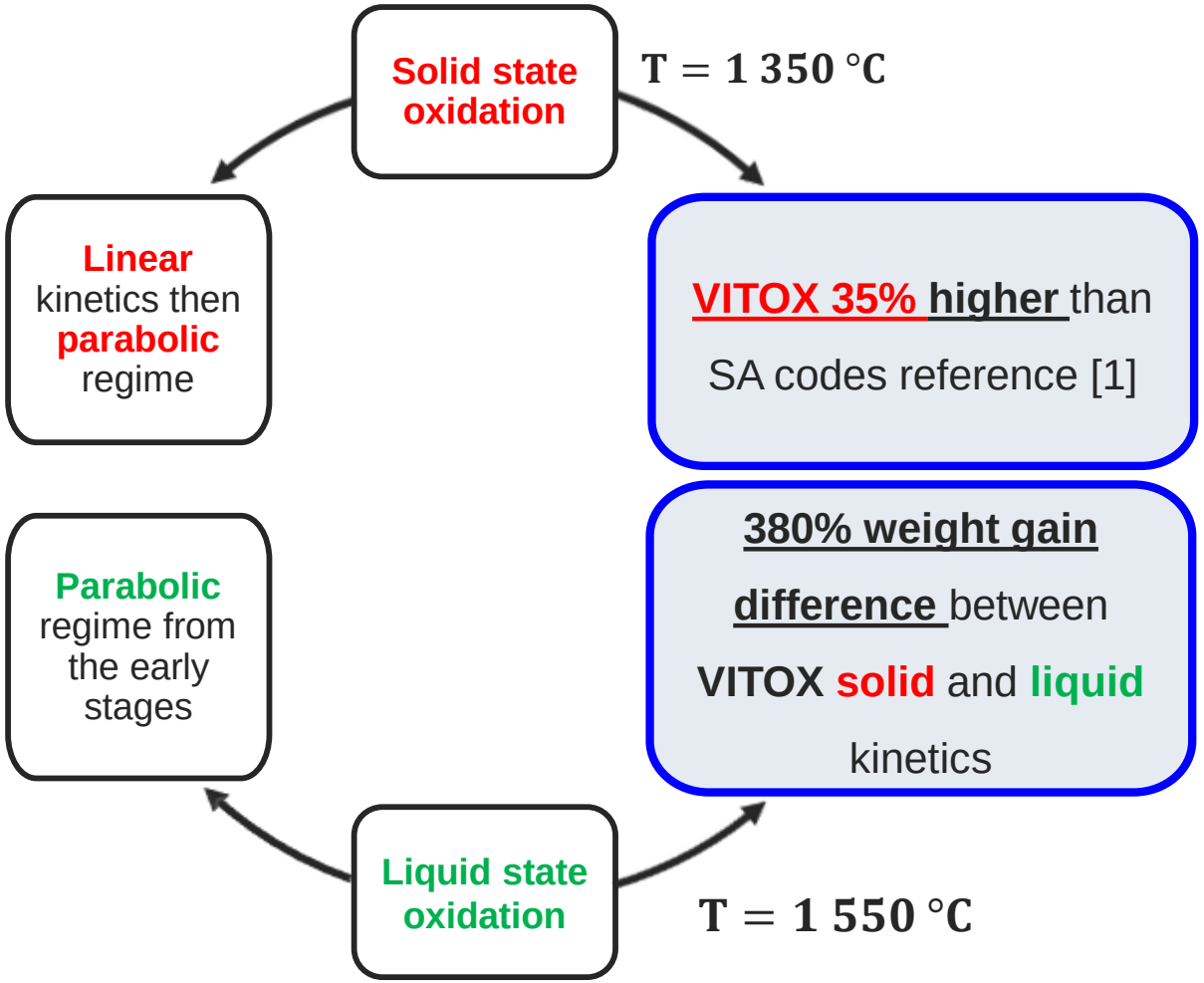

2- Hydrogen mass release of 304L-SS

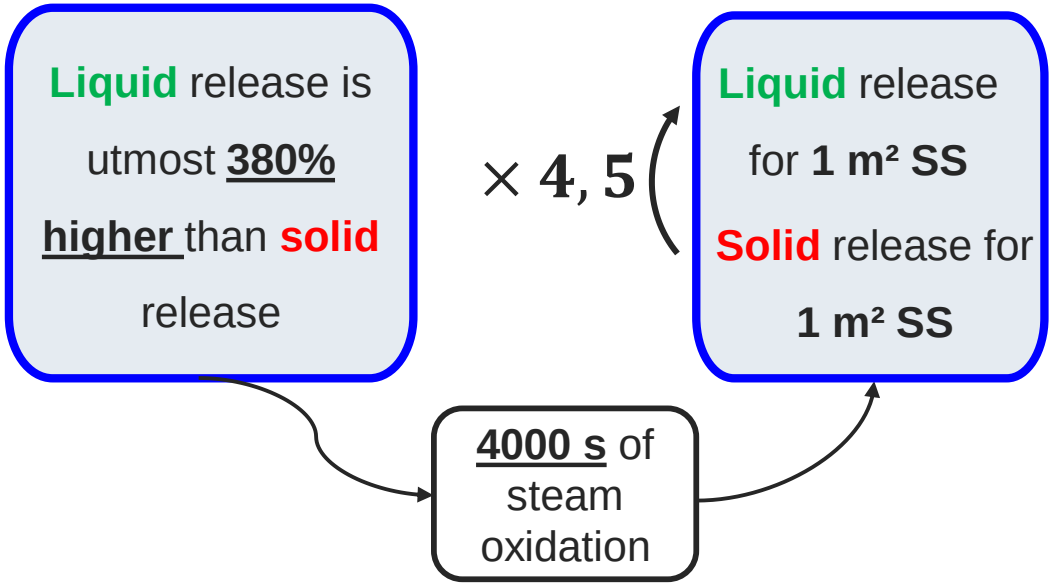

Perspectives

- **SEM/EDS** analysis for **oxide phase** identification
- **Liquid** state **oxidation** of **Zry** under **steam**
- **Liquid** state **oxidation** of **(Fe, Zr, U)** under **steam**
- **Hydrogen** kinetics of oxidized **Zry and (Fe, Zr, U)** under **steam**

Thank you for your time and attention

VITOX : Experimental apparatus

Graphical depiction
VITOX apparatus

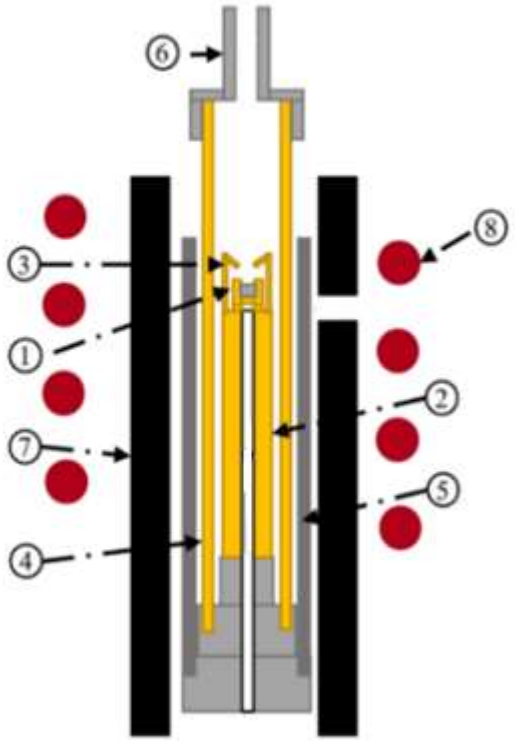

Actual depiction
VITOX apparatus



Oxidation chamber
V=70l



VITOX components	
1	Crucible
2	Support
3	Crucible lid
4	Separating tube
5	Susceptor
6	Tube lid
7	Calcarb
8	Inductor

VITOX : Experimental apparatus

Graphical depiction
VITOX apparatus

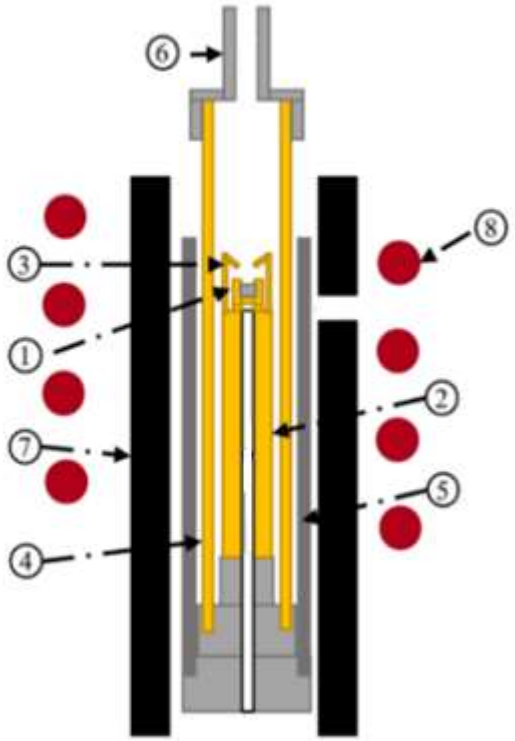

Actual Top-View of
VITOX apparatus

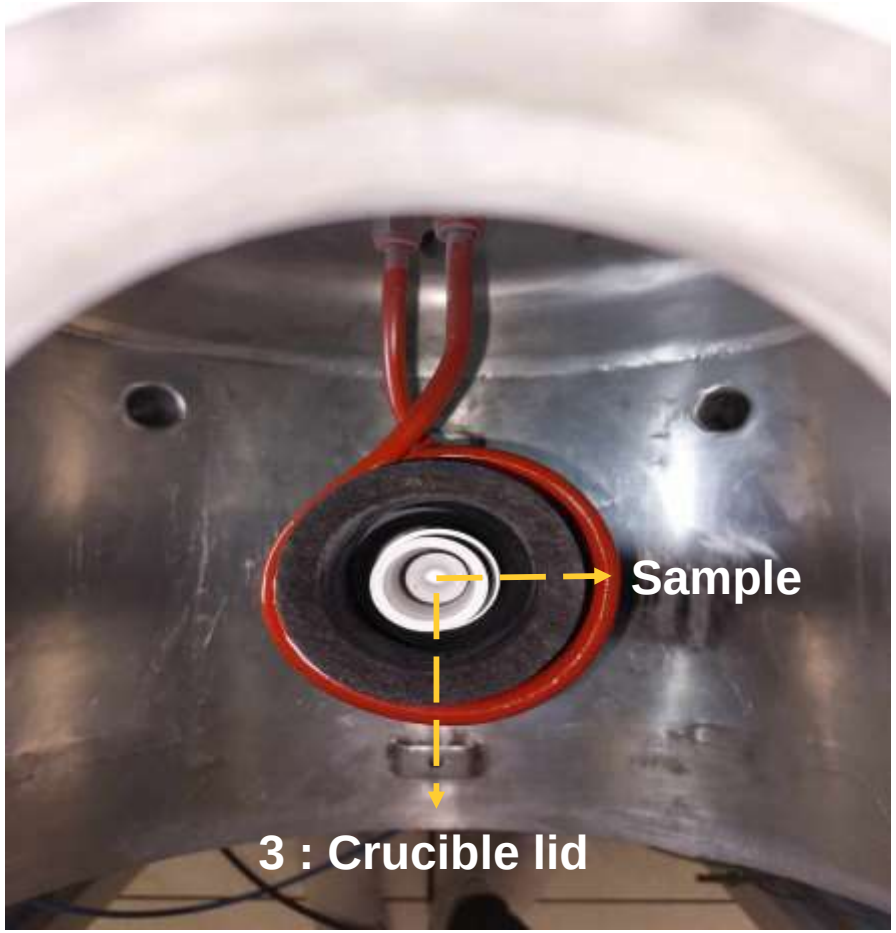



VITOX components	
1	Crucible
2	Support
3	Crucible lid
4	Separating tube
5	Susceptor
6	Tube lid
7	Calcarb
8	Inductor

VITOX : Experimental apparatus

Graphical depiction
VITOX apparatus

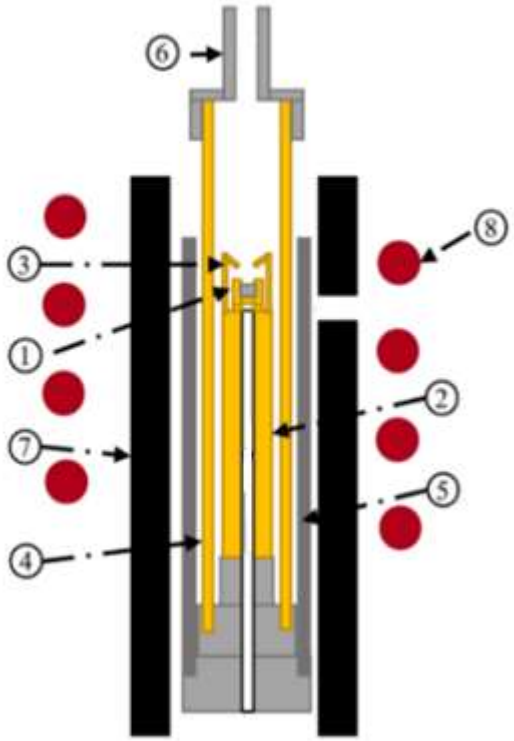

Actual depiction
VITOX apparatus

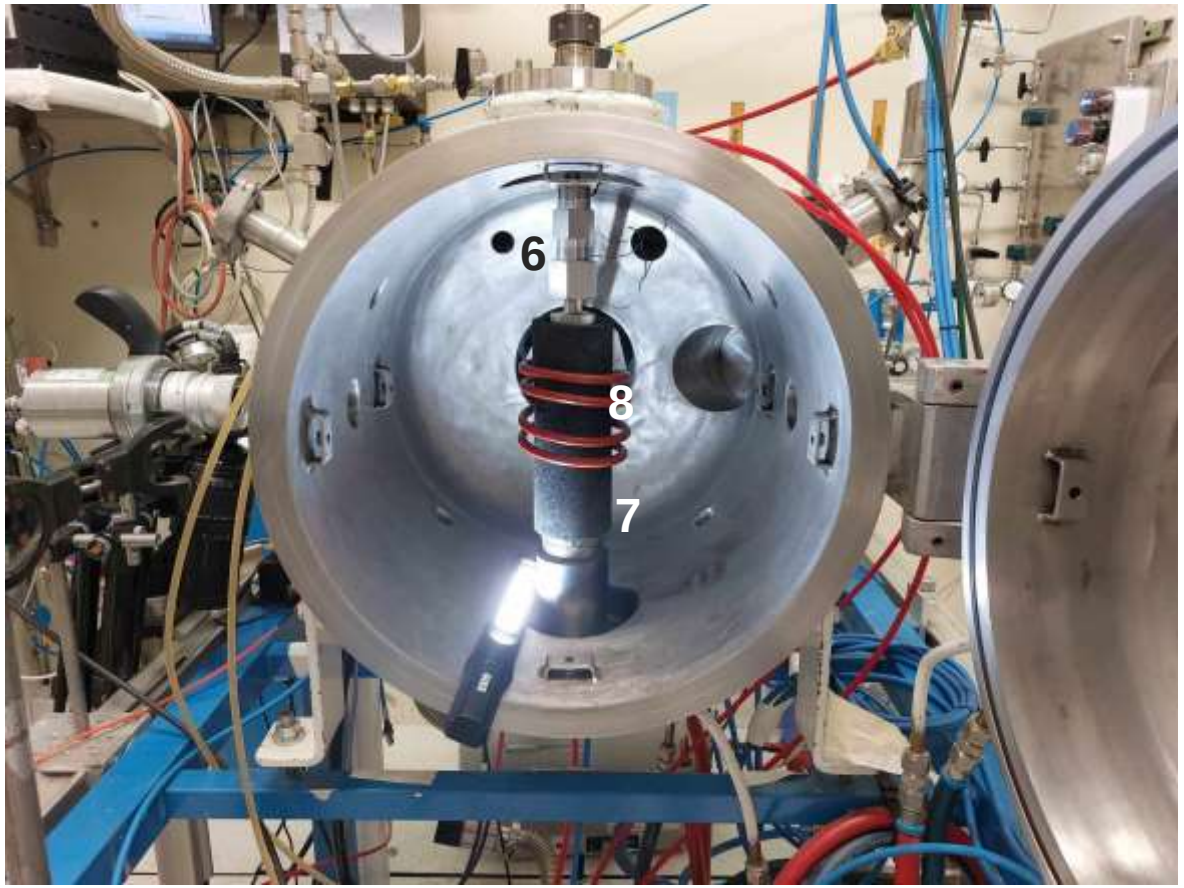



VITOX components	
1	Crucible
2	Support
3	Crucible lid
4	Separating tube
5	Susceptor
6	Tube lid
7	Calcarb
8	Inductor

Hydrogen detector

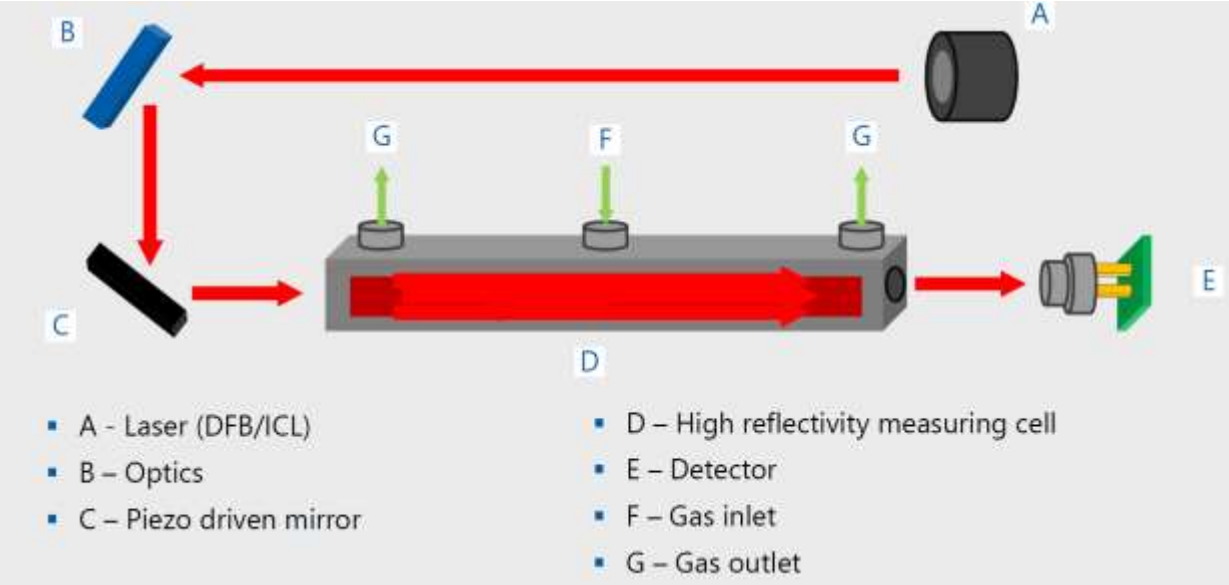



Measurement range: **[0;5] %vol**.
Manufacturer's precision: **1% of reading.**
Verified against standard bottle

The measurement of light intensity before and after passing through the gas sample allows for the determination of absorbance A -1-

$$A_\lambda = \log_{10} \frac{I_{incident}}{I_{transmitted}} \ (1)$$

Absorbance is related to the concentration of the species of interest and the optical path length probed by the Beer-Lambert -2-

$$A_\lambda = \varepsilon_{0,\lambda} \times L \times C \ (2)$$

A_λ **: absorbance at a given wavelength**
L **: length of the optical path**
C **: Volumetric concentration of hydrogen continuously detected**

VITOX Analytical protocol

- Hydrogen production monitored by the hydrogen detector

⟺

- Oxygen kinetics as a key parameter to describing the evolution of hydrogen release

⟺

- Oxygen up-take by the oxidizing sample, calibrated to actual initial and final mass of the sample

$$W(t) = \frac{k}{S} \times \int_0^t [H_2](u).du \quad ; \quad k = \frac{m_{t_f} - m_i}{\int_0^{t_f} [H_2](u).du}$$

- $W(t)$: *Oxygen up-take (g/cm²)*
- k : *Adjustment coefficient for conversion (g/vol.%)*
- $[H_2]$: *instantaneous volumetric concentration (vol.%)*
- S : *Reactive surface (cm²)*
- m_i : *initial mass of the sample (g)*
- m_{t_f} : *final mass of the sample (g)*

$$m_{H_2}(t) = \frac{W(t) \times M_{H_2}}{M_O}$$

- m_{H_2}: *hydrogen mass release, (g/cm²)*
- M_O : *molar mass of oxygen, (g/mol)*
- M_{H_2} : *molar mass of dihydrogen, (g/mol)*

Why the integral formula ?

The hydrogen concentration is a punctual measurement at a "t" instant. It does not indicate the total amount of hydrogen from the beginning of the reaction

Important assumption

Why the « k » coefficient ?

Align the in-situ mass reading at final time with the actual mass, determined after a "t_f" duration test.

A mole of released dihydrogen is equivalent to one mole of adsorbed oxygen.

$$H_2O \rightarrow H_2 + O^{\bullet}$$

A THERMODYNAMIC STUDY OF MOLTEN POOL STRATIFICATION MORPHOLOGY

Erhui Chen, Li Zhang, Nan Li, Yidan Yuan*
CNNC Key Laboratory for Severe Accident Research in Nuclear Power Safety, China Nuclear Power Engineering Co.,LTD.
117 Xisanhuan North Road, Haidian District, Beijing
chenerhui97@163.com; zhanglif@cnpe.cc; linanb@cnpe.cc; yuanyd@cnpe.cc

ABSTRACT

In the event of severe accident in nuclear power plant, the stratification morphology of the molten pool within the pressure vessel's lower head has a profound impact on the effectiveness of In-Vessel Retention strategies. The analysis of the melt pool stratification requires liquid density data of nuclear materials, which are rarely included in general thermodynamic databases. This study presents a novel thermodynamic analysis method by integrating a dedicated volumetric database with NUCLEA15 to calculate densities of stratified liquid phase at high temperatures, using the Thermo-Calc software. Various stratification patterns under changing conditions of U/Zr ratios, Zr oxidation, and steel content are investigated to explore their influence on element distribution and layer density. It is found that a decrease in Zr oxidation or steel content leads to an increase in metal phase density, making it more likely to be situated beneath the oxide layer. The calculation results agree with data from MASCA-1 and CESEF experiments, confirming its effectiveness and reliability.

KEYWORDS
stratification morphology; thermodynamics; liquid density; severe accident

1. INTRODUCTION

In the event of severe accident in nuclear power plant, the molten core may fall into the lower head of the pressure vessel, forming a high-temperature molten pool with different stratification patterns. In Vessel Retention (IVR) aims to cool and retain the corium by submerging the lower head with external cooling water. The effectiveness of IVR is significantly influenced by the heat flux density of the vessel, which is determined by the molten pool's structure, including the thickness and components of layered phases. Therefore, the stratification morphology of the molten pool under various conditions is crucial for optimizing the IVR strategy and enhancing safety measures during severe accidents.

In recent decades, many prototype experiments have been conducted to investigate the influence of chemical reactions and composition of corium mixture on molten pool stratification, such as the RASPLAV[1,2] and MASCA[3,4] project funded by OECD/NEA, the COSMOS[5] project in South Korea, and the CESEF[6] experiment in China. In addition to experimental research, various thermodynamic models[7,8] based on different theories have been employed to explore and predict the behavior of corium. The prediction of the melt pool stratification requires density data of core materials at high temperatures. However, existing models and databases often rely on a weighted average of the single material densities, leading to relatively imprecise outcomes. NUCLEA15[9,10] is a nuclear material database developed by IRSN, when combined with thermodynamic calculation software Thermo-Calc, it can be used for thermodynamic calculation of

any equilibrium state in severe accidents. But volume data is not contained in the database either, making it impossible to analyze the molten pool stratification.

This work presents a novel thermodynamic analysis method by integrating a dedicated volumetric database to NUCLEA15 to calculate densities of stratified liquid phases at high temperatures. Various stratification patterns under changing conditions of U/Zr atomic ratios, Zr oxidation degree, and steel content are investigated. To validate this method and the database, the calculation results are compared with the experimental data from MASCA-1 and CESEF.

2. HIGH-TEMPERATURE VOLUME DATABASE

The CALPHAD[11,12] (CALcalculation of PHAse Diagram) method is the fundamental principle behind Thermo-Calc and the establishment of thermodynamic databases for multi-component and multi-phase systems. The methodology relies on the minimization of Gibbs free energy, ensuring that the Gibbs free energy of an equilibrium system, at a constant temperature and pressure, attains its minimum value. The model contains the expression of Gibbs free energy, typically a function of temperature and composition, obtained through the fitting of experimental data. The phase behavior for materials under varying temperature and composition conditions can be obtained by solving these models.

A volume database can be integrated into the thermodynamic database NULCEA15 using the same method. The process initiates by establishing reasonable volume models for both pure substances and solution phases. This study compiles experimental data for the required pure substances to fit the corresponding volume model. Subsequently, the pure component model is extended to the solution phase model.

2.1. Pure substances

Volume, considered an extensive property, is often analyzed in a system containing one mole of atoms or molecules, referred to as molar volume. For non-magnetic materials, the molar volume at atmospheric pressure, V_m , can be expressed as[13]

$$\begin{aligned} V_m(T) &= V_0 e^{\int_{T_0}^{T} 3\alpha \, dT} \\ &= V_0 e^{V_a} \end{aligned} \tag{1}$$

where V_0 is the molar volume at the reference temperature T_0, and α represents the coefficient of linear thermal expansion (CLE) of a phase. For non-cubic crystal structures, α donates the average CLE of polycrystalline materials. 3α represents the volume expansion coefficient, with its integral term regarding temperature is denoted as V_a. Given the scarcity of high-temperature volume data at present, the volume database established in this work ignores the relationship between α and temperature. Consequently, $V_m(T)$ can be expressed as equation (2). Using the least squares method to fit experimental data to obtain V_0 and α.

$$V_m(T) = V_0 e^{3\alpha(T-T_0)} \tag{2}$$

2.2. Solution phases

The molar volume of solution phase requires interaction parameters and mole fraction of all constitutes. For a binary system, V_0 and V_a can be expressed as[13]

$$\begin{aligned} V_0 &= (1-x){V_0}_A^{\beta} + x{V_0}_B^{\beta} + V_0^E \\ &= (1-x){V_0}_A^{\beta} + x{V_0}_B^{\beta} + x(1-x)L_0 \end{aligned} \tag{3}$$

$$V_a = (1-x)V_{a_A}^{\beta} + xV_{a_B}^{\beta} + V_a^E$$
$$= (1-x)V_{a_A}^{\beta} + xV_{a_B}^{\beta} + x(1-x)L_a \quad (4)$$

where the superscripts and subscripts represent that A and B exists with the structure of phase β. x is the mole fraction of B. V_0^E and V_a^E are the excess molar volume, which represent the volume change caused by solution mixing. L represents the interaction parameter with a function of temperature. High order interaction parameter should be considered for more complicated system, which needs more experiments data or first-principles calculations, especially for metastable and non-stable phase. In the absence of sufficient experimental data, it is acceptable to ignore interaction parameters. For instance, in a mixed liquid phase containing two substances, A and B, with the mole fractions x and y respectively, the molar volume of the solution phase at a certain temperature T is

$$V_m^{Liq}(T) = \left(xV_0^A + yV_0^B\right)e^{(xV_a^A + yV_a^B)} \quad (5)$$

The volume database currently contains 27 metals and oxides composed of 11 elements (U, Zr, O, Fe, Cr, Ni, Al, Mg, Ca, Si, Sr). Figure 1 displays the liquid phase densities of several typical metals and oxides, including U[14], Zr[15], Fe[16], Al[17], UO_2[18], SiO_2[19], etc., obtained from both the volume model and various literature sources. The comparative results of multi-component density are presented in section 3.2 and 4.1.

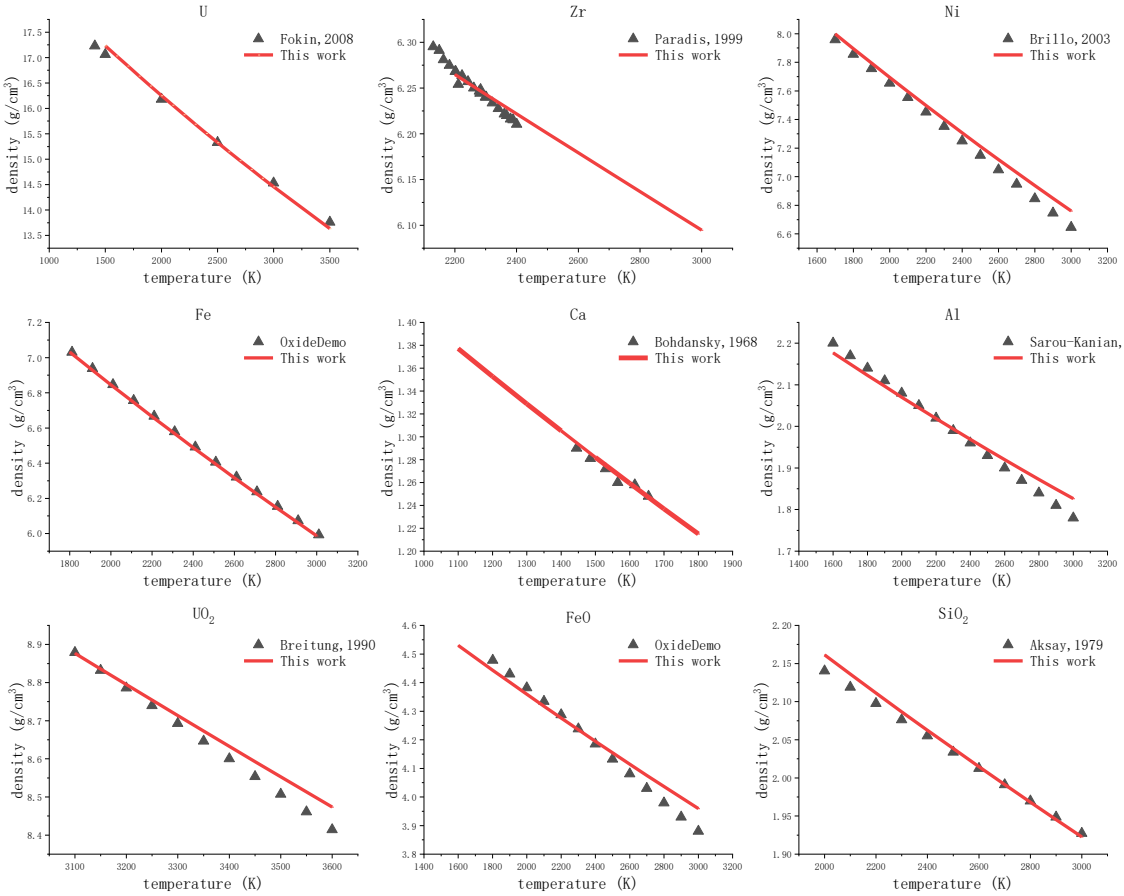

Figure 1. Comparison of Liquid Densities of Typical Metals and Oxides

3. COMPARATIVE ANALYSIS OF MASCA TEST

The MASCA project involved a series of corium tests at different scales and various prototypic composition experiments to investigate the interaction between corium and the vessel steel. The experiments observed and summarized the molten pool stratification, along with the distribution of the main basic corium components under different initial conditions. Table I presents the experimental conditions for corium interacting with iron. In this table, $R_{U/Zr}$ represents the atom ratio of U and Zr, C_n(%) indicates the oxidation degree of Zr and X_{Fe} (%) is the mass percent of iron. The reactants in Table II are corium and stainless-steel, with X_{ss} (%) representing the mass percent of stainless-steel.

Table I. Corium-iron tests in MASCA-1[3,4]

Test	m_total(g)	$R_{U/Zr}$	C_n(%)	X_{Fe}(%)	Temperature(℃)
Fe-2	281.24	1.15	32.6	1.84	2500
Fe-3	306.31	1.15	32.6	1.59	2500
Fe-4	329.52	1.16	33.4	4.36	2500
Fe-5	327.59	1.15	32.6	1.29	2500
Fe-6	303.71	1.2	54.6	1.57	2550
Fe-7	314.7	1.19	69.2	1.52	2600
Fe-8	291.07	1.6	100	1.86	2650
Fe-9	302.4	1.14	35.6	9.52	2500
Fe-10	304.42	1.19	69.2	4.3	2600
Fe-14	313.5	1.14	35.6	15.22	2500

Table II. Corium-stainless steel tests in MASCA-1[3,4]

Test	m_total(g)	$R_{U/Zr}$	C_n(%)	X_{ss}(%)	Temperature(℃)
Fe-15	333.25	1.14	35.6	11.26	2500
Ma-1	1608.11	1.45	33.1	11.42	2500
Ma-2	1750.41	1.28	74.5	10.8	2500

The distribution of elements and the density of layers can be determined through thermal equilibrium calculations using Thermo-Calc. The mass fractions of each element in every test can be computed from Table I and Table II, serving as input conditions for the thermal equilibrium calculations, as depicted in Table III and Table IV. In the corium-stainless steel tests conducted in MASCA-1, the detailed components of stainless steel were not provided in the report. Therefore, the commonly used composition of 304 stainless steel (71wt%Fe-19wt%Cr-10wt%Ni) is employed for subsequent calculations. Notably that the temperatures listed in the Table I and Table II represent experimental conditions. Calculations found that at these temperatures, some corium did not fully form a liquid phase. Thus, the temperatures used in the calculations (Table III and Table IV) may slightly exceed the experimental temperatures. Some subsequent validations indicate that once a melt pool is formed, temperature increases have no impact on the distribution of elements.

Table III. Calculation input condition of corium-iron tests in MASCA-1

Test	m_total(g)	U(wt%)	Zr(wt%)	O(wt%)	Fe(wt%)	Temperature(K)
Fe-2	281.24	65.19	21.72	11.25	1.84	2750
Fe-3	306.31	65.35	21.78	11.28	1.59	2750
Fe-4	329.52	63.61	21.02	11.01	4.36	2800
Fe-5	327.59	65.55	21.85	11.31	1.29	2750
Fe-6	303.71	64.97	20.75	12.71	1.57	2800
Fe-7	314.7	64.17	20.67	13.64	1.52	2850
Fe-8	291.07	67.31	16.12	14.70	1.86	2900
Fe-9	302.4	59.82	20.11	10.55	9.52	2850
Fe-10	304.42	62.36	20.08	13.26	4.30	2850
Fe-14	313.5	56.05	18.84	9.89	15.22	2850

Table IV. Calculation input condition of corium-stainless steel tests in MASCA-1

Test	m_total (g)	U (wt%)	Zr (wt%)	O (wt%)	Fe (wt%)	Cr (wt%)	Ni (wt%)	Temperature(K)
Fe-15	333.25	58.67	19.72	10.35	7.99	2.14	1.13	2850
Ma-1	1608.11	61.97	16.38	10.23	8.11	2.17	1.14	2850
Ma-2	1750.41	58.99	17.66	12.55	7.67	2.05	1.08	2850

3.1. Elements Distribution

Figure 2 illustrates the comparison of element distribution between the calculated results and the MASCA experimental results. On the x-axis, different experiments are represented, while the y-axis denotes the mass fraction of different elements in the oxide or metal layer. It is observed that the mass fractions of each element in both layers are essentially consistent with the experimental values, which validates the accuracy of the thermodynamic database.

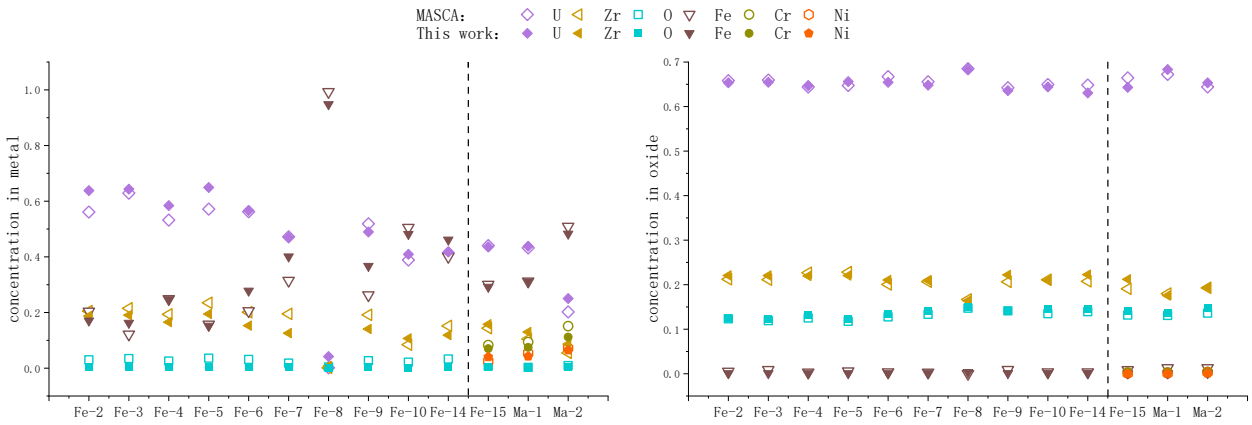

Figure 2. Comparison of Element Distribution with MASCA-1 (Left: metal. Right: oxide)

The relative positioning of the metal and oxide layers is influenced by their density. Higher concentrations of heavier metal elements within the metal layer result in increased density, facilitating the location of the metal layer beneath the oxide layer. The correlation between the stainless-steel or zirconium content and changes in the metal layer's elemental composition is depicted in Figure 3. Analysis reveals that, with a greater stainless-steel interaction with corium, the concentration of Fe in the metal layer increases, while the concentrations of U and Zr decrease. This migration contributes to a reduced density in the metal phase. Additionally, a decrease in Zr oxidation leads to an increase in the concentrations of U and Zr in the metal phase, making it more likely for the metal layer to be situated beneath the oxide layer. Further analysis about layer densities is presented in section 3.2.

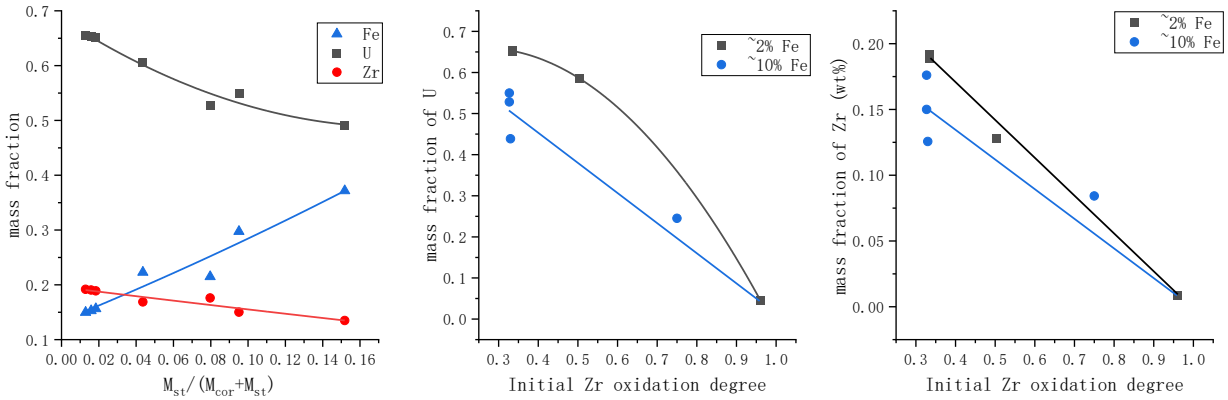

Figure 3. Elements Concentration in Metal Phase with SS Content and Zr Oxidation Degree

3.2. Density

3.2.1. Solid density

The densities of oxide and metal ingots were measured after the MASCA tests, as shown in Figure 4. The calculated densities are also presented in the same figure. Note that the database densities, representing the liquid state at high temperatures, which are lower than the solid densities but follow the same changing trends. The density of metals is influenced by the atomic ratio of U and Fe, where a larger U/Fe ratio corresponds to a heavier metal layer. Oxide density correlates with oxygen content—increased oxygen content leads to lower oxide density.

Notably, the liquid phase density of metals is approximately 10-20% lower than its solid density, while oxide phase density is about 13-14% lower than its solid density. Results from [20] and [21] indicated that the particular liquid oxides have a density 10-15% lower than their solid state, further confirming the accuracy of the volume database.

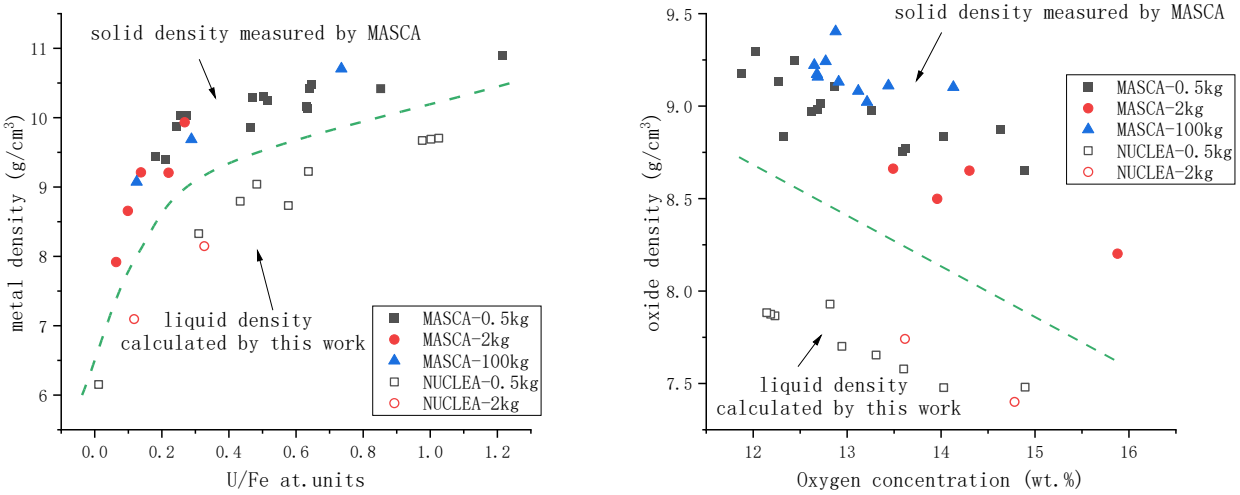

Figure 4. Densities Comparison with MASCA (left: metal, right: oxide)

3.2.2. Liquid density

The primary researcher of the MASCA project conducted experiments[22] and developed models[18] to measure and calculate the densities of molten materials at high temperatures. The results available for comparison are presented in Table V, with corresponding figures listed in Figure 5. In Figure 5 (a), a comparison is made with the measured liquid density of a UO_2-ZrO_2 system, demonstrating a close agreement with calculated and experimental results. Figure 5 (b) presents results for a UO_2-ZrO_2-Zr system, calculated from a theoretical model, showing consistency with our database. For the UO_2-ZrO_2-Zr-Fe systems (Figure 5 (c)), which represent materials from the corium and iron test in MASCA, the oxide density calculated by both models is similar. The maximum relative error of the metal density is only 3.78%.

Table V. Liquid Densities from Experiment or Model

Figure	System	Condition	Exp. or Model
(a)	UO_2-ZrO_2	U/Zr=1.528	experimental data[22]
(b)	UO_2-ZrO_2-Zr	U/Zr=0.9/1.2/1.6 C_n=0-100%	model[18]
(c)	UO_2-ZrO_2-Zr-Fe	MASCA Fe-2/3/4/5/6/9/14	model[18]

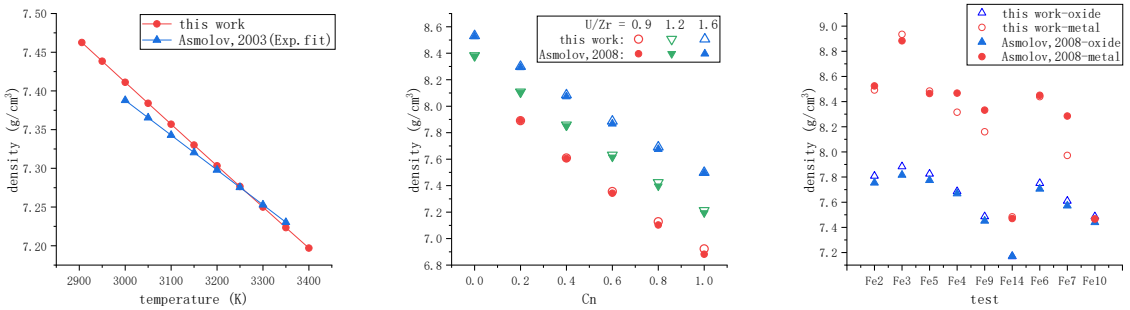

(a) (b) (c)

Figure 5. Densities Comparison with Experiment or Model

4. COMPARATIVE ANALYSIS OF CESEF TEST

The Corium Evolution and Stratification Experimental Facility (CESEF) test, conducted by the Nuclear Power Institute of China, aims to investigate the stratification of the molten pool at the lower head of the pressure vessel under severe accidents. This test specifically analyzed the influence of Zr oxidation degree on stratification morphology and element distribution. The experimental conditions are detailed in Table VI. Table VII shows the input parameters for thermal equilibrium calculations performed with Thermo-Calc, which are computed from Table VI. The composition of 304 stainless steel (71wt%Fe-19wt%Cr-10wt%Ni) is employed.

Table VI. Corium-stainless steel tests in CESEF [6]

Test	m_total(g)	$R_{U/Zr}$	C_n(%)	X_{ss}(%)
1	5000	1.5	100	10
2	5000	1.5	80	10
3	5000	1.5	40	10

Table VII. Calculation input condition of corium-stainless steel tests in CESEF

Test	m_total (g)	U (wt%)	Zr (wt%)	O (wt%)	Fe (wt%)	Cr (wt%)	Ni (wt%)	Temperature(K)
Fe-15	5000	60.90	13.62	15.48	7.1	1.9	1.0	3000
Ma-1	5000	61.65	12.68	15.67	7.1	1.9	1.0	3000
Ma-2	5000	63.20	10.75	16.05	7.1	1.9	1.0	3000

4.1. Stratification Morphology

The longitudinal sectional diagram of the CESEF corium ingot is presented in Figure 6. The darkened section represents the oxide layer, while the brighter region denotes the metal layer. In test 1, no significant stratification was observed, and the metal formed at the top of the molten pool, taking the shape of a ball with a diameter of approximately 10mm. Stratification became noticeable in test 2 with a decrease in Zr oxidation degree. In this case, the metal layer was located in the upper part of the molten pool, while the oxide layer settled in the lower part. Test 3 exhibited a distinctive observation, where the oxide layer enveloped the metal layer, which means the density of the metal layer is similar to that of oxide layer.

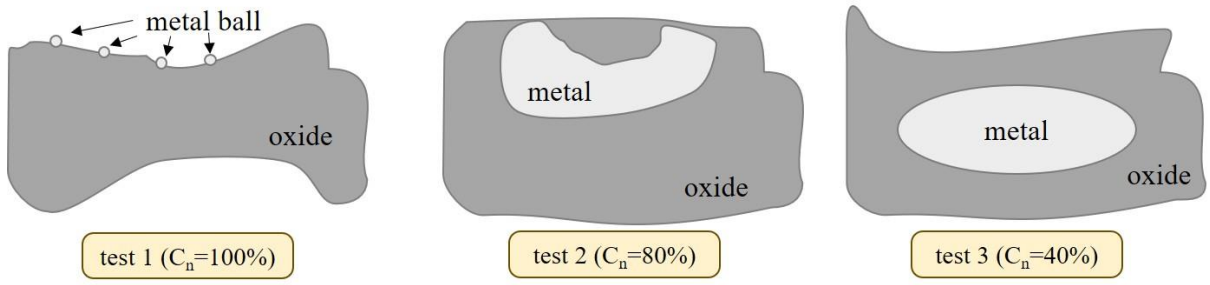

Figure 6. Longitudinal Sectional Diagram of the Corium Ingot in CESEF[6]

The calculation results from the database are presented in Table VIII. In the first test, the density of the metal is significantly smaller than that of the oxide, and the mass of the metal layer is only about 1/10 of that of the oxide layer. It can be approximated that a small amount of metal floats above the oxide in this test. The density of the metal gradually increased in tests 2 and 3. In test 3, the density of the metal slightly exceeded that of the oxide, potentially resulting in the metal layer sinking or the inversion of the molten pool. It is evident that the calculated results agree with the experimental findings.

Table VIII. Calculation Results with Tests in CESEF

Test	Density(g/cm^3)		Mass(g)		Stratification
	metal	oxide	metal	oxide	
1	6.27	7.36	488	4512	upper: metal lower: oxide
2	6.90	7.47	659	4341	upper: metal lower: oxide
3	7.91	7.66	1075	3925	upper: oxide lower: metal

In the CESEF report, it is asserted that a decrease in the oxidation degree of Zr leads to an increase in the content of U and Zr in the metal layer, resulting in higher metal layer density and a layered flipping of the molten pool. This conclusion is further supported by the element migration process obtained through Thermo-Calc in this work. As depicted in Figure 7, a reduction in Zr oxidation leads to a gradual decrease in the concentrations of Fe, Cr, and Ni in the metal layer, and a simultaneous increase in the concentrations of U and Zr. This explains the observed increase in metal layer density, consistent with the findings from MASCA. Additionally, Figure 7 indicates a relatively stable distribution of elements in the oxide layer.

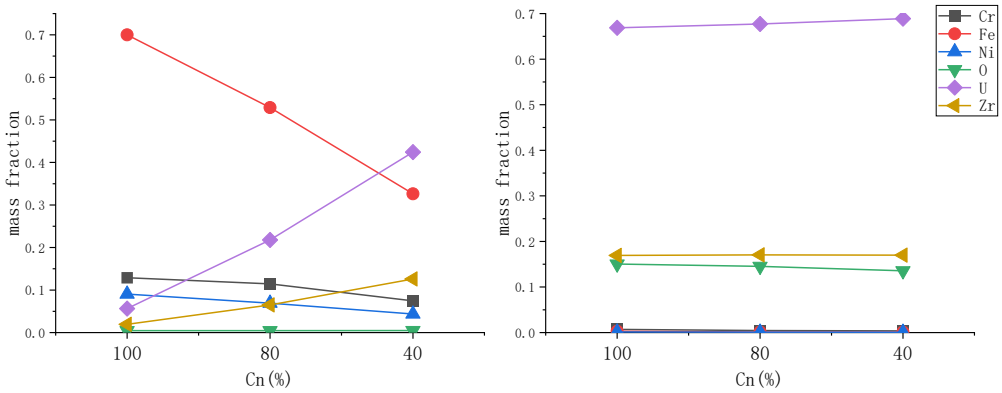

Figure 7 Elements distribution with Zr Oxidation Degree (Left: metal, Right: oxide)

4.2. Elements Distribution

Figure 8 displays the element distribution of test 1 to 3. The element distribution in the oxide layer is consistent with the experimental results, but the metal layer shows a maximum deviation of 16% (absolute value) from the calculations. This deviation may be attributed to variations in measurement points. The

report offers 7-12 measurement points for the oxide sample, in contrast to only one measurement point for the metal sample, resulting in significant deviations in the analysis.

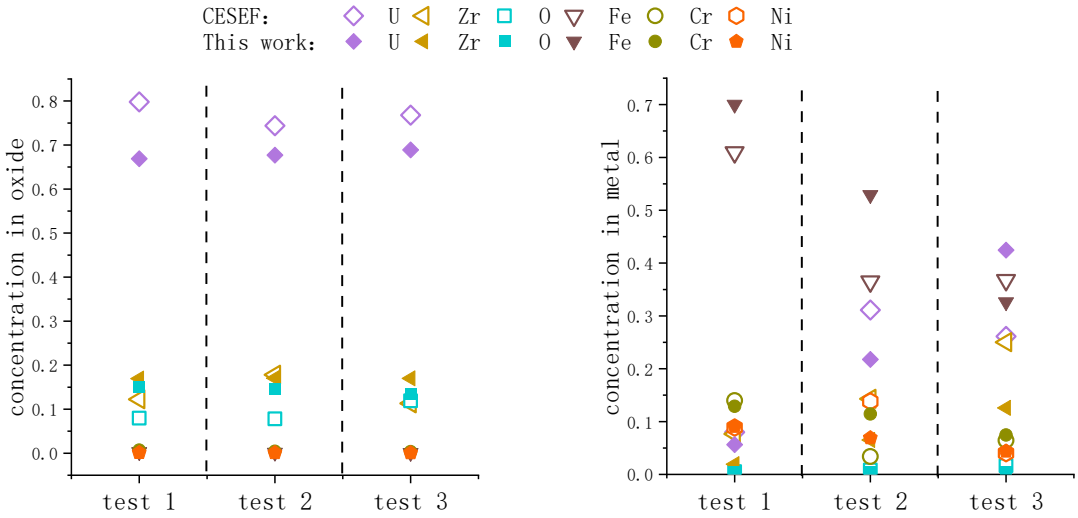

Figure 8 Comparison of Element Distribution with CESEF

5. CONCLUSIONS

This paper uses Thermo-Calc combined with NUCLEA15 and a volume database to calculate the stratification behavior of a high-temperature molten pool. Upon comparison with the MASCA-1 experiment and CESEF experiment, the following findings can be drawn:

1) The calculated results about stratification morphology of the molten pool, representing the relative positioning of the metal layer and the oxide layer, are consistent with all experimental observations.
2) The calculated densities of the molten pool agree with experiments and models.
3) The calculated element distribution results in each layer are consistent well with the MASCA-1 test. There is a certain deviation in the elements distribution of CESEF. This discrepancy may arise because the element distribution results in MASCA are axial average values, while CESEF provides local measurement values.
4) The element migration process and density changes of metal and oxide layers are consistent with the experimental results. Specifically:
   a) As the initial oxidation degree of Zr decreases, the relative content of U and Zr in the metal layer of the molten pool increases, while the relative content of steel decreases. This results in a higher density of the metal layer.
   b) When more stainless-steel/iron reacts with the corium, the relative content of U and Zr in the metal layer of the molten pool decreases, while the relative content of steel increases. This results in a lower density of the metal layer.

It is concluded that the thermodynamic calculation method proposed and the volume database built in this article is applicable for analyzing the stratification morphology of molten pool following the reaction between corium and steel. This includes determining the equilibrium melt pool layering, illustrating the distribution of melt pool elements, and calculating the density of the melt pool. Except for the utility in calculating the stratification of corium in IVR, this method and database can also be employed for analyzing the equilibrium molten pool formed during Molten Core Concrete Interaction (MCCI) and Ex-Vessel Retention (EVR) processes.

REFERENCES

1. Almjashev, V. I., Granovsky, V. S., Khabensky, V. B., Kotova, S. Y., Krushinov, E. V., Sulatsky, A. A., Vitol, S. A., Gusarov, V. V., Fichot, F., and Michel, B., "Experimental study of transient phenomena in the three-liquid oxidic-metallic corium pool", *Nucl. Eng. Des.*, **332**, pp. 31–37 (2018).
2. Bechta, S. V., Khabensky, V. B., Vitol, S. A., Krushinov, E. V., Lopukh, D. B., Petrov, Yu. B., Petchenkov, A. Y., Kulagin, I. V., Granovsky, V. S., Kovtunova, S. V., Martinov, V. V., and Gusarov, V. V., "Experimental studies of oxidic molten corium–vessel steel interaction", *Nucl. Eng. Des.*, **210**(1–3), pp. 193–224 (2001).
3. Asmolov, V. G., Bechta, S. V., and Strizhov, V. F., *Main Results of the First Phase of MASCA Project*, RRC Kurchatov Institute, Paris, France (2004).
4. Tsurikov, D. F., Strizhov, V. F., Bechta, S. V., Zagriazkin, V. N., and Kiselev, N. P., *Main Results of the MASCA1 and 2 Projects*, RRC Kurchatov Institute, Paris, France (2007).
5. Kang, K.-H., Park, R.-J., Hong, S.-H., Hong, S.-W., and Ha, K. S., "An experimental study on layer inversion in the corium pool during a severe accident", *Nucl. Eng. Des.*, **278**, pp. 163–170 (2014).
6. Li, Y., Gong, H., Hu, Y., Yang, S., Li, Y., and Zan, Y., "Experimental Study on Stratification Morphology of the Molten Pool During Severe Accident", *Front. Energy Res.*, **9**, p. 813298 (2021).
7. FUKASAWA, M. and TAMURA, S., "Thermodynamic Analysis for Molten Corium Stratification Test MASCA with Ionic Liquid U-Zr-Fe-O-B-C-FPs Database", *J. Nucl. Sci. Technol.*, **44**(9), pp. 1210–1219 (2007).
8. Jiang, Y., He, Y., Zheng, W., Zhang, J., Zhang, D., and Lu, X., "Thermodynamic analysis for molten corium stratification with U-Zr-O-Fe database", *J. Nucl. Mater.*, **574**, p. 154180 (2023).
9. Bakardjieva, S., Barrachin, M., Bechta, S., Bottomley, D., Brissoneau, L., Cheynet, B., Fischer, E., Journeau, C., Kiselova, M., and Mezentseva, L., "Improvement of the European thermodynamic database NUCLEA", *Prog. Nucl. Energy*, **52**(1), pp. 84–96 (2010).
10. Bechta, S., Khabensky, V. B., Granovsky, V. S., Krushinov, E. V., Vitol, S. A., Gusarov, V. V., Almjashev, V. I., Mezentseva, L. P., Petrov, Y. B., and Lopukh, D. B., "CORPHAD and METCOR ISTC projects", *First Eur. Rev. Meet. Sev. Accid. Res. ERMSAR-2005 Aix-En-Provence Fr. 14-16 Novemb. 2005* (2005).
11. Kaufman, L. and Bernstein, H., "Computer Calculation of Phase Diagrams Academic Press", *N. Y.* (1970).
12. Sundman, B., Lukas, H. L., and Fries, S. G., *Computational Thermodynamics: The Calphad Method*, Cambridge university press, Cambridge (2007).
13. He, Y., Lu, X., Zhu, N., and Sundman, B., "CALPHAD modeling of molar volume", *Chin. Sci. Bull.*, **59**(15), pp. 1646–1651 (2014).
14. Belashchenko, D. K., Smirnova, D. E., and Ostrovski, O. I., "Molecular-dynamic simulation of the thermophysical properties of liquid uranium", *High Temp.*, **48**(3), pp. 363–375 (2010).
15. Paradis, P.-F. and Rhim, W.-K., "Thermophysical properties of zirconium at high temperature", *J. Mater. Res.*, **14**(9), pp. 3713–3719 (1999).
16. Plevachuk, Y., Egry, I., Brillo, J., Holland-Moritz, D., and Kaban, I., "Density and atomic volume in liquid Al–Fe and Al–Ni binary alloys", *Int. J. Mater. Res.*, **98**, pp. 107–111 (2007).
17. Sarou-Kanian, V., Millot, F., and Rifflet, J. C., "Surface Tension and Density of Oxygen-Free Liquid Aluminum at High Temperature", *Int. J. Thermophys.*, **24**(1), pp. 277–286 (2003).
18. Asmolov, V. G., Zagryazkin, V. N., and Tsurikov, D. F., "Estimation of the density of U-Zr-Fe-O melts", *High Temp.*, **46**(4), pp. 579–582 (2008).
19. Aksay, I. A., Pask, J. A., and Davis, R. F., "Densities of SiO2-Al2O3Melts", *J. Am. Ceram. Soc.* (1979).
20. Rempe, J. L., Chavez, S. A., and Thinnes, G. L., *Light Water Reactor Lower Head Failure Analysis*, Nuclear Regulatory Commission, Washington, D.C., United States (1993).

21. Siefken, L. J., Coryell, E. W., and Harvego, E. A., *SCDAP/RELAP5/MOD 3.3 Code Manual: MATPRO - A Library of Materials Properties for Light-Water-Reactor*, Nuclear Regulatory Commission, Washington, D.C., United States (2001).
22. Asmolov, V., Zagryazkin, V., Astakhova, E., Vishnevskii, V., D'Yakov, E., Kotov, A., and Repnikov, V., "The density of UO2-ZrO2 alloys", *High Temp.*, **41**(5), pp. 714–719 (2003).

A Thermodynamic Study of Molten Pool Stratification Morphology

Erhui Chen, Li Zhang, Nan Li, Yidan Yuan*

CNNC Key Laboratory for Severe Accident Research in Nuclear Power Safety (*SARLab*)
China Nuclear Power Engineering Co.,LTD. (*CNPE*)

ERMSAR 2024, May13-16, 2024, Stockholm, Sweden

Outline

1. Research Objective
2. High-temperature Volume Database
3. Comparative Analysis of MASCA Test
4. Comparative Analysis of CESEF Test
5. Conclusions

Research Objective

- Molten pool stratification morphology

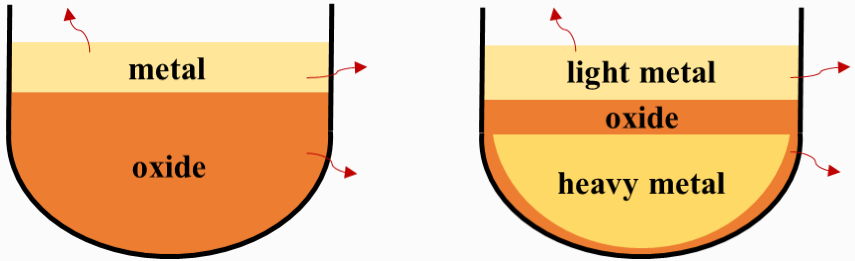

IVR effectiveness
↓
heat flux of RPV
↓
stratification morphology

- Method: thermodynamic equilibrium calculation

Initial molten core

UO_2 : mass
ZrO_2 : mass
Zr : mass
Fe : mass
……

At a certain temperature → thermodynamic equilibrium

Results

a) Phase: metal/oxide
b) Each phase:
- mass
- element distribution
- **density**

Tools need

Software: Thermo-Calc 2023
Database: NUCLEA15
Volume database

CALPHAD and NUCLEA

- CALPHAD (CALculation of PHAse Diagram):
  - the fundamental principle behind Thermo-Calc and the establishment of thermodynamic databases
  - **minimization of Gibbs free energy**
    - the Gibbs free energy of an equilibrium system, at a constant temperature and pressure attains its minimum value
    - $\triangle G(c,T)$——c: composition $c=(c_i)_{i=1,2,\ldots,N}$ T: temperature

- NUCLEA (Nuclear Alloys-Oxides Database)
  - A thermodynamic database for nuclear database owned by IRSN
  - Elements(18+2): U-O-Zr-Fe-Ni-Cr-B-C-Ag-In-La-Ru-Sr-Ba-Mg-Al-Si-Ca-(Ar-H)
  - **Lack of density(volume) property**

High-temperature Volume Database

- Pure substances
  - molar volume at atmospheric pressure(for non-magnetic material) [1]

$$V_m(T) = V_0 e^{\int_{T_0}^{T} 3\alpha \, dT} = V_0 e^{V_a}$$

    - V_m: molar volume
    - V_0: molar volume at the reference temperature T_0
    - α: coefficient of linear thermal expansion (CLE) of a phase
    - V_a: integral term of 3α
  - ignore the relationship between α and temperature, then $V_m(T) = V_0 e^{3\alpha(T-T_0)}$

- Solution phases
  - For a binary system

$$V_0 = (1-x){V_0}_A^{\beta} + x{V_0}_B^{\beta} + V_0^E = (1-x){V_0}_A^{\beta} + x{V_0}_B^{\beta} + x(1-x)L_0$$

$$V_a = (1-x){V_a}_A^{\beta} + x{V_a}_B^{\beta} + V_a^E = (1-x){V_a}_A^{\beta} + x{V_a}_B^{\beta} + x(1-x)L_a$$

[1] X. G. Lu, M. Selleby, and S. Bo, "Theoretical modeling of molar volume and thermal expansion," Acta Materialia, 53, no. 8, pp. 2259-2272, (2005).

High-temperature Volume Database

- Solution phases
  - For a binary system

$$V_0 = (1-x)V_{0_A}^{\beta} + xV_{0_B}^{\beta} + V_0^E = (1-x)V_{0_A}^{\beta} + xV_{0_B}^{\beta} + x(1-x)L_0$$

$$V_a = (1-x)V_{a_A}^{\beta} + xV_{a_B}^{\beta} + V_a^E = (1-x)V_{a_A}^{\beta} + xV_{a_B}^{\beta} + x(1-x)L_a$$

    - A,B,β: substances A and B exist with structure of phase β
    - x: mole fraction of B
    - V_0^E, V_a^E: excess molar volume, represent the volume change caused by solution mixing
    - L: interaction parameter (a function of temperature)

  - Ignore interaction parameter for the absence of sufficient experiment data
  - For a binary system:

$$V_m^{Liq}(T) = \left(xV_0^A + yV_0^B\right)e^{(xV_a^A + yV_a^B)}$$

    - x,y: mole fraction of substance A and B

High-temperature Volume Database

- 27 metals and oxides composed of 11 elements (U-Zr-O-Fe-Cr-Ni-Al-Mg-Ca-Si-Sr)

U	UO_2	Zr	ZrO_2	O	Fe	FeO	Fe_2O_3	Cr
CrO_2	Cr_2O_3	Ni	NiO	Al	Al_2O_3	Ca	CaO	Mg
MgO	Sr	SrO	Si	SiO_2	$CaSiO_3$	Ca_2SiO_4	Mg_2SiO_4	$AlCa_{0.5}SiO_4$

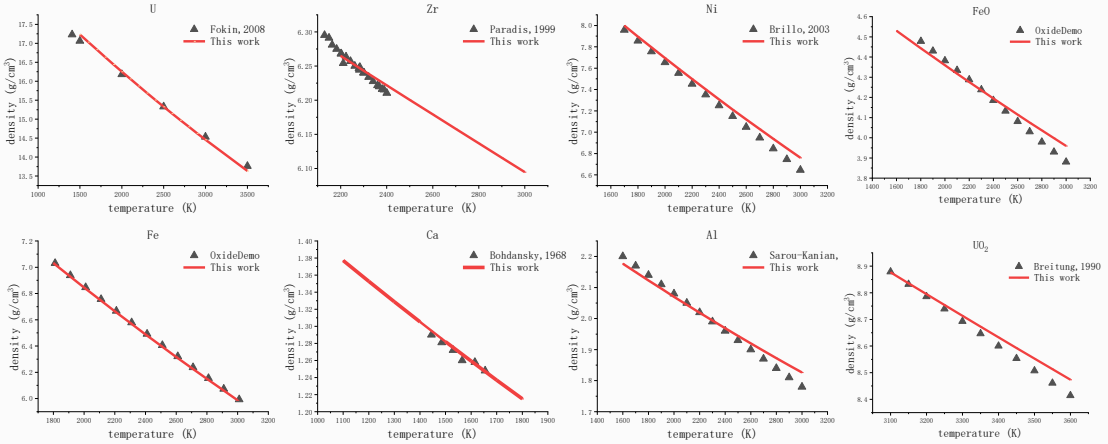

U	[2] Belashchenko D K, Smirnova D E, Ostrovski O I.Molecular-dynamic simulation of the thermophysical properties of liquid uranium[J].High Temperature,2010, 48 (3): 363-375.
Zr	[3] Paradis P-F, Rhim W-K.Thermophysical properties of zirconium at high temperature[J].Journal of Materials Research,1999, 14 (9): 3713-3719.
Ni	[4] Brillo J, Egry I.Density Determination of Liquid Copper, Nickel, and Their Alloys[J].International Journal of Thermophysics,2003, 24 (4): 1155-1170.
Ca	[5] Bohdansky J, Schins H E J.Surface tension and density of the liquid earth alkaline metals Mg, Ca, Sr, Ba[J].Journal of Inorganic and Nuclear Chemistry,1968, 30 (9): 2331-2337.
Al	[6] Sarou-Kanian V, Millot F, Rifflet J C.Surface Tension and Density of Oxygen-Free Liquid Aluminum at High Temperature[J].International Journal of Thermophysics,2003, 24 (1): 277-286.
UO_2	[7] Asmolov V G E, Zagryazkin V N, Tsurikov D.Estimation of the density of U-Zr-Fe-O melts[J].High Temperature,2008, 46: 579-582.
Fe FeO	[8] Thermo-Calc 2022a OxideDemo Database

Outline

1. Research Objective
2. High-temperature Volume Database
3. Comparative Analysis of **MASCA** Test
4. Comparative Analysis of CESEF Test
5. Conclusions

Comparative Analysis of MASCA Test

- **Corium-iron** tests in MASCA-1 [9,10]

Test	m_total(g)	$R_{U/Zr}$	C_n(%)	X_{Fe}(%)	Temperature(℃)
Fe-2	281.24	1.15	32.6	1.84	2500
Fe-3	306.31	1.15	32.6	1.59	2500
Fe-4	329.52	1.16	33.4	4.36	2500
Fe-5	327.59	1.15	32.6	1.29	2500
Fe-6	303.71	1.2	54.6	1.57	2550
Fe-7	314.7	1.19	69.2	1.52	2600
Fe-8	291.07	1.6	100	1.86	2650
Fe-9	302.4	1.14	35.6	9.52	2500
Fe-10	304.42	1.19	69.2	4.3	2600
Fe-14	313.5	1.14	35.6	15.22	2500

- **Corium-stainless-steel** tests in MASCA-1 [9,10]

Test	m_total(g)	$R_{U/Zr}$	C_n(%)	X_{ss}(%)	Temperature(℃)
Fe-15	333.25	1.14	35.6	11.26	2500
Ma-1	1608.11	1.45	33.1	11.42	2500
Ma-2	1750.41	1.28	74.5	10.8	2500

- MASCA project involved a series of **prototypic** corium tests at different scales to investigate the interaction between **corium and the vessel steel**

- m_total: total mass
- $R_{U/Zr}$: atom ratio of U and Zr
- C_n(%): oxidation degree of Zr
- X_{Fe} (%): mass percent of iron
- X_{ss} (%): mass percent of steel (71wt%Fe-19wt%Cr-10wt%Ni)

[9] Asmolov, V. G., Bechta, S. V., and Strizhov, V. F., Main Results of the First Phase of MASCA Project, RRC Kurchatov Institute, Paris, France (2004).
[10] Tsurikov, D. F., Strizhov, V. F., Bechta, S. V., Zagriazkin, V. N., and Kiselev, N. P., Main Results of the MASCA1 and 2 Projects, RRC Kurchatov Institute, Paris, France (2007).

Comparative Analysis of MASCA Test

- Calculation input condition of **corium-iron** tests

Test	m_total(g)	U(wt%)	Zr(wt%)	O(wt%)	Fe(wt%)	Temperature(K)
Fe-2	281.24	65.19	21.72	11.25	1.84	2750
Fe-3	306.31	65.35	21.78	11.28	1.59	2750
Fe-4	329.52	63.61	21.02	11.01	4.36	2800
Fe-5	327.59	65.55	21.85	11.31	1.29	2750
Fe-6	303.71	64.97	20.75	12.71	1.57	2800
Fe-7	314.7	64.17	20.67	13.64	1.52	2850
Fe-8	291.07	67.31	16.12	14.70	1.86	2900
Fe-9	302.4	59.82	20.11	10.55	9.52	2850
Fe-10	304.42	62.36	20.08	13.26	4.30	2850
Fe-14	313.5	56.05	18.84	9.89	15.22	2850

- Calculation input condition of **corium-stainless-steel** tests

Test	m_total(g)	U(wt%)	Zr(wt%)	O(wt%)	Fe(wt%)	Cr(wt%)	Ni(wt%)	Temperature(K)
Fe-15	333.25	58.67	19.72	10.35	7.99	2.14	1.13	2850
Ma-1	1608.11	61.97	16.38	10.23	8.11	2.17	1.14	2850
Ma-2	1750.41	58.99	17.66	12.55	7.67	2.05	1.08	2850

Comparative Analysis of MASCA Test

- Element distribution
  (upper: oxide, lower: metal)

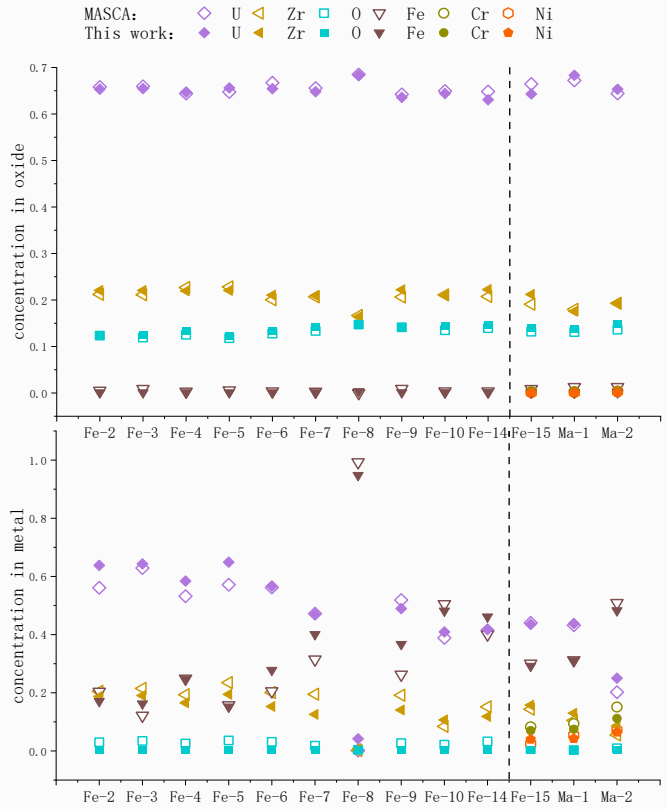

mass fractions of each element are **consistent** with the experimental values, which validates the accuracy of the thermodynamic database

- Element concentration in metal phase

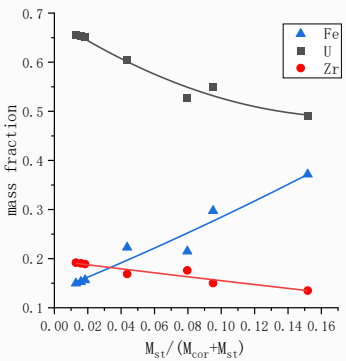

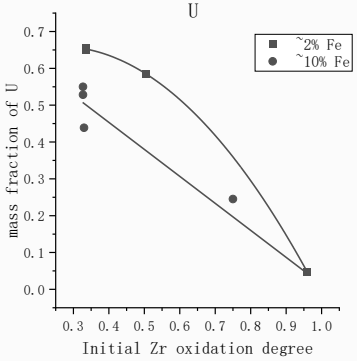

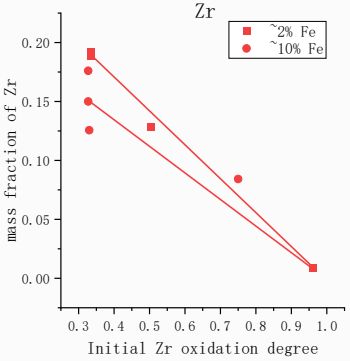

	U,Zr	Fe	metal density	result
steel content ↑	↓	↑	↓	
Zr oxidation ↑	↓	↑	↓	

Comparative Analysis of MASCA Test

- Solid density
  - MASCA: measured the densities of oxide and metal ingots after tests
  - This work: calculated the densities of oxide and metal liquid using volume database

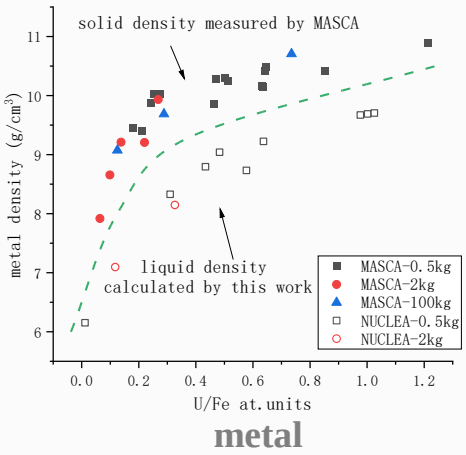

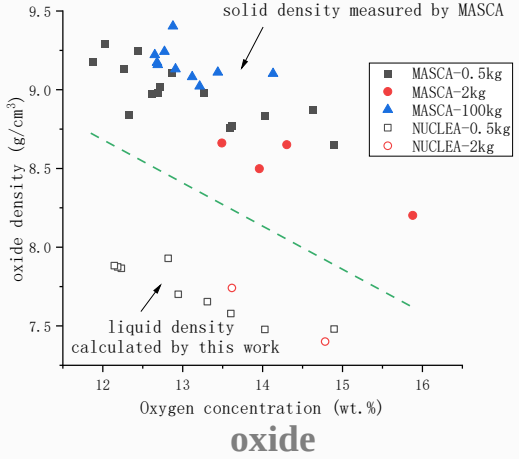

- metal phase density is 10-20% lower than its solid density
- oxide phase density is 13-14% lower than its solid density

  - The liquid densities and the experiment values follow the **same trends**
    - U/Fe ratio↑ → metal density↑
    - oxygen content↑ → oxide density↓

Comparative Analysis of MASCA Test

- Liquid density
  - The primary researcher of the MASCA project conducted experiments[11] and developed models[12] to get the densities of molten materials at high temperatures.

Figure	System	Condition	Exp. or Model
(a)	UO_2-ZrO_2	U/Zr=1.528	experiment[11]
(b)	UO_2-ZrO_2-Zr	U/Zr=0.9/1.2/1.6 C_n=0-100%	model[12]
(c)	UO_2-ZrO_2-Zr-Fe	MASCA Fe-2/3/4/5/6/9/14	model[12]

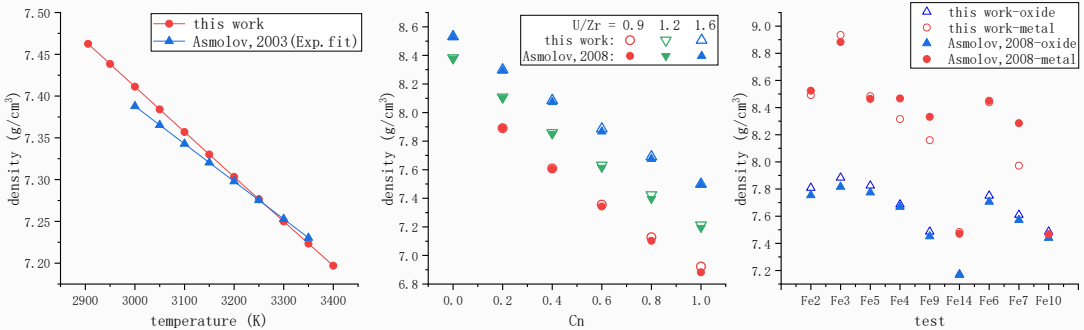

(a) (b) (c)

Maximum relative error: **3.78%**

Validates the **accuracy of volume database**

[11] Asmolov, V., Zagryazkin, V., Astakhova, E., Vishnevskii, V., D'Yakov, E., Kotov, A., and Repnikov, V., "The density of UO2-ZrO2 alloys", High Temp., 41(5), pp. 714–719 (2003).
[12] Asmolov, V. G., Zagryazkin, V. N., and Tsurikov, D. F., "Estimation of the density of U-Zr-Fe-O melts", High Temp., 46(4), pp. 579–582 (2008).

Outline

1 Research Objective

2 High-temperature Volume Database

3 Comparative Analysis of MASCA Test

4 Comparative Analysis of **CESEF** Test

5 Conclusions

Comparative Analysis of CESEF Test

- **Corium-stainless-steel** tests in CESEF[13] by Nuclear Power Institute of China

Test	m_total(g)	$R_{U/Zr}$	C_n(%)	X_{ss}(%)
1	5000	1.5	100	10
2	5000	1.5	80	10
3	5000	1.5	40	10



CESEF facility

- Calculation input condition

71wt%Fe-19wt%Cr-10wt%Ni

Test	m_total(g)	U(wt%)	Zr(wt%)	O(wt%)	Fe(wt%)	Cr(wt%)	Ni(wt%)	Temperature(K)
1	5000	60.90	13.62	15.48	7.1	1.9	1.0	3000
2	5000	61.65	12.68	15.67	7.1	1.9	1.0	3000
3	5000	63.20	10.75	16.05	7.1	1.9	1.0	3000

[13] Li, Y., Gong, H., Hu, Y., Yang, S., Li, Y., and Zan, Y., "Experimental Study on Stratification Morphology of the Molten Pool During Severe Accident", Front. Energy Res., 9, p. 813298 (2021).

Comparative Analysis of CESEF Test

- Experiment results

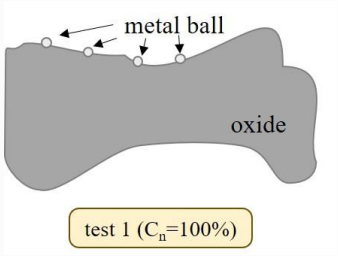

- test 1: no obvious stratification, metal ball(about ϕ10mm)at the top

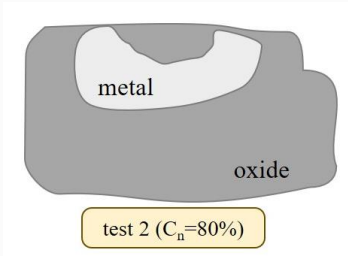

- test 2: metal layer was in the upper

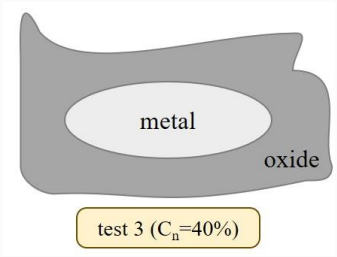

- test 3: oxide enveloped the metal layer

- Calculation results

Test	Density(g/cm^3)		Mass(g)		Stratification
	metal	oxide	metal	oxide	
1	6.27	7.36	488	4512	upper: metal lower: oxide
2	6.90	7.47	659	4341	upper: metal lower: oxide
3	7.91	7.66	1075	3925	upper: oxide lower: metal

- The density and mass of the metal are significantly smaller than that of oxide metal
- Metal density gradually increased in tests 2 and 3
- In test 3, the metal density slightly exceeded oxide

calculated results agree with the experiments
Validates the **accuracy of volume database**

Comparative Analysis of CESEF Test

- Elements distribution (left: oxide, right: metal)

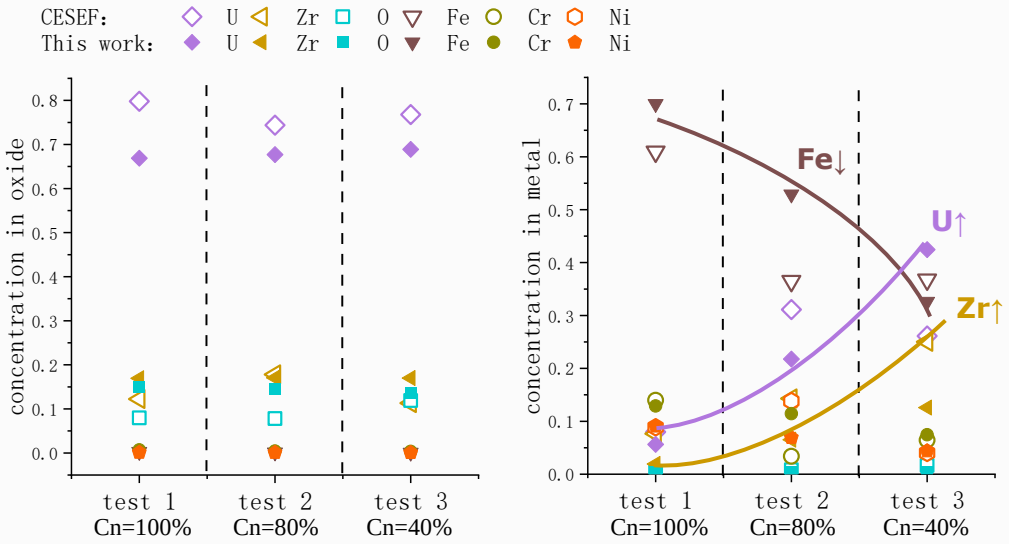

- The metal layer shows a maximum deviation of 16% (absolute value)
  - oxide sample: 7-12 measurement points
  - metal sample: 1 measurement point
- CESEF: local points measurement
- MASCA: axial average values

Zr oxidation degree ↓ ➡ U/Zr concentration ↑ Fe concentration ↓ In metal layer ➡ metal layer density ↑

The calculated results **consistent** with the experimental findings

Conclusions

- This paper uses **Thermo-Calc** combined with **NUCLEA15** and a **volume database** to calculate the stratification behavior of a high-temperature molten pool.
  Upon comparison with the MASCA-1 and CESEF experiment, we found:
  - The calculated stratification morphology of the molten pool are consistent with MASCA-1 and CESEF.
  - The calculated densities agree with experiments and models.
  - The calculated element distribution in each layer are consistent well with the MASCA-1 test.
    The deviation in the elements distribution of CESEF may because CESEF provides local points measurement of samples.
  - The element migration process and density changes of metal and oxide layers are consistent with the experimental results.

The **thermodynamic calculation method** and the **volume database** is applicable for:

- determining the **equilibrium molten pool stratification**
- illustrating the **elements distribution** of molten pool
- calculating the **density** of the metal/oxide phase in the molten pool

Q&A

Erhui Chen, Li Zhang, Nan Li, Yidan Yuan*

CNNC Key Laboratory for Severe Accident Research in Nuclear Power Safety (*SARLab*)
China Nuclear Power Engineering Co.,LTD. (*CNPE*)

ERMSAR 2024, May13-16, 2024, Stockholm, Sweden

IN-VESSEL CORIUM THERMOCHEMISTRY BENCHMARK BASED ON MASCA EXPERIMENTAL DATA

R. Le Tellier
CEA, DES, IRESNE, DTN, Cadarache
F-13108 Saint Paul-lez-Durance, France
romain.le-tellier@cea.fr

L. Carénini, F. Fichot
IRSN, Cadarache
F-13108 Saint Paul-lez-Durance, France
laure.carenini@irsn.fr, florian.fichot@irsn.fr

R. Gencheva, P. Groudev
Institute for Nuclear Research and Nuclear Energy – Bulgarian Academy of Sciences, INRNE-BAS
72 Tsarigradsko shosse Blvd. BG-1784 Sofia, Bulgaria
r.gencheva@inrne.bas.bg, pavlinpg@inrne.bas.bg

I. Melnikov, M. Golubev
NRC "Kurchatov Institute"
1 Akademika Kurchatova Pl., RU-123182 Moscow, Russia
Melnikov_IA@nrcki.ru

A. Filippov
IBRAE
52 B. Tulskaya St. RU-115191 Moscow, Russia
phil@ibrae.ac.ru

ABSTRACT

This paper presents the first two steps of a benchmark on in-vessel corium thermochemistry, which is part of the IAEA Coordinated Research Project on In-Vessel Melt Retention. The benchmark focuses on the stratification of corium in the lower plenum of a reactor vessel during a severe accident. The experimental data from the MASCA test facilities are used to validate/calibrate the models of the different codes used by the participants. The paper gives an overview of the different models, including their underlying assumptions. The results show that the models are generally in good agreement with the experimental data, but further experimental data is needed for model validation. Besides the need for further work, this paper highlights the fact that integral models (published in the open literature for most of them) are available to account for the first-order phenomena associated with in-vessel corium. Accordingly, this paper may be useful for code developers that would like to upgrade their models in order to take into account transient stratification kinetics, a prerequisite for a state-of-the-art analysis of in-vessel melt retention.

KEYWORDS
corium, thermochemistry, stratification, benchmark

1. INTRODUCTION

In the framework of the IAEA Coordinated Research Project (CRP) on In-Vessel Melt Retention*, a code-to-experiment benchmark devoted to in-vessel corium thermochemistry was proposed by CEA and IRSN with participation from IRNRE-BAS, NRC "Kurchatov Institute" and IBRAE. Based on results of prototypic corium experiments from the open literature, it is devoted to oxide/metal pool thermochemistry phenomena of first-order importance when assessing in-vessel corium behavior [1]. Indeed, as clearly demonstrated by the H2020 IVMR European project, taking into account the transient multilayer corium configuration in the vessel lower head is mandatory for assessing In-Vessel Retention (IVR) for high power reactors.
It is a three-step benchmark involving both severe accident codes (ASTEC, HEFEST-URAN, HEFEST) and thermodynamic equilibrium solvers (TSAR, OpenCalphad) with associated databases (NUCLEA).
The first step considers two-layer stationary (under chemical equilibrium conditions) pool configurations using oxide/metal phases' composition and relative position information taken from the MASCA-MA tests series [2]. It is used for comparison and validation of the modelling of the liquid miscibility gap of the U-O-Zr-steel thermodynamic system and the liquid phase density laws. The second step is focused on the heavy metal layer formation kinetics considering the last phase of the MASCA-RCW experiment and associated post-mortem ingot information [3]. Here, a semi-quantitative comparison with experimental results (in terms of metal phase spatial distribution and composition) is performed in order to assess intra-layer mass transfer models that simulate corium stratification transients in severe accident codes. In this second step, the light metal layer and the oxide phase are not separated by a solid crust contrarily to the reactor case. In the third step, it is the transient evolution of a three-layer stratified corium pool in presence of a solid crust at the top oxide surface that is studied considering the results of CORDEB2 CP7-02 test on the stratification kinetics [4]. In this experiment, the thermal gradient expected in reactor configuration leading to crust formation between the oxide and the top metal layer is considered, albeit in a small geometry for which the crust is mechanically stable.
This paper presents the specifications of the first two steps of this benchmark along with an analysis of the results obtained by the participants.

2. STEP 1: MASCA MA

2.1. Brief summary of the experiments

The OECD-MASCA experimental program (see [2]) has studied the thermochemical interactions between an oxide phase and a metallic phase. Among other achievements, it has helped characterizing the (U, Zr) mass transfer to the metal phase that can lead to a significant increase in its density so that, in some conditions, the metal phase can be relocated at the bottom of the pool because of gravity.
In particular, some experiments of the MA series (MA-1 to MA-6), under inert atmosphere in the RASPLAV-3 facility (NITI), have shown, both through direct observation of the free surface during the experiment and by post-mortem analyses of the solidified ingots, the possibility of two stratified configurations at steady-state. These experiments were conducted using the cold-crucible technique to melt about 2kg of oxidic corium by inductive heating in a 7cm-diameter crucible. Steady state was reached in any case in less that 30min.
The MA series partial test matrix is given at Table I in terms of the melt temperature T^{exp}, the exposure time, the suboxidized corium initial composition (defined by its U-over-Zr molar ratio $R_{U/Zr}$ and the Zr

* https://www.iaea.org/projects/crp/j46002

molar oxidation degree C_{Zr}) and the ratio between the steel mass and the initial corium mass (denoted x_{steel}^{exp}).
Note that Table I give the specified test conditions; actual molten masses at play in the corium-steel interactions slightly differ.†
The post-mortem ingots analysis gives information about the phases stratification as illustrated in Figure 1. For the MA-1, MA-3, MA-4, MA-5, MA-5b tests, a clear stratification with a metal phase heavier than the oxide has been observed while the metal phase is lighter and on top of the oxide in the MA-6 test.
■ ***Nota Bene*** The MA-2 test with a highly oxidized corium ($C_{Zr}^{exp} = 74.5\%$) is the only test that does not exhibits a clear phase stratification. In this case, the metal phase is inhomogeneous and has a "diabolo" shape with a top (resp. bottom) part that is lighter (resp. heavier) with a density of 7930 kg/m^3 (resp. 8890 kg/m^3) than the oxide phase (8610 kg/m^3). Obviously, an equilibrium calculation cannot reproduce or explain such a configuration. Different supplementary explanations (magneto-hydrodynamic effects associated with the inductive heating, helicoidal shrinkage during solidification, complicated phase segregation during solidification - possibly largely impacted by oxygen redistribution) have been proposed in the literature; they are out of the scope of this benchmark. ■

Table I. MA series partial test matrix.

Test	T^{exp} (°C)	Exposure time (min)	$R_{U/Zr}^{exp}$	C_{Zr}^{exp} (%)	$\frac{x_{steel}^{exp}}{x_{steel}^{exp}+1}$ (%)
MA-1	2500	30	1.45	33.1	11.42
MA-2			1.28	74.5	10.80
MA-3			1.14	36.5	10.78
MA-4			1.17	39.7	19.09
MA-5			0.89	31.5	9.89
MA-5b		120	0.90	30.5	7.05
MA-6	2600	30	1.14	29.1	29.71

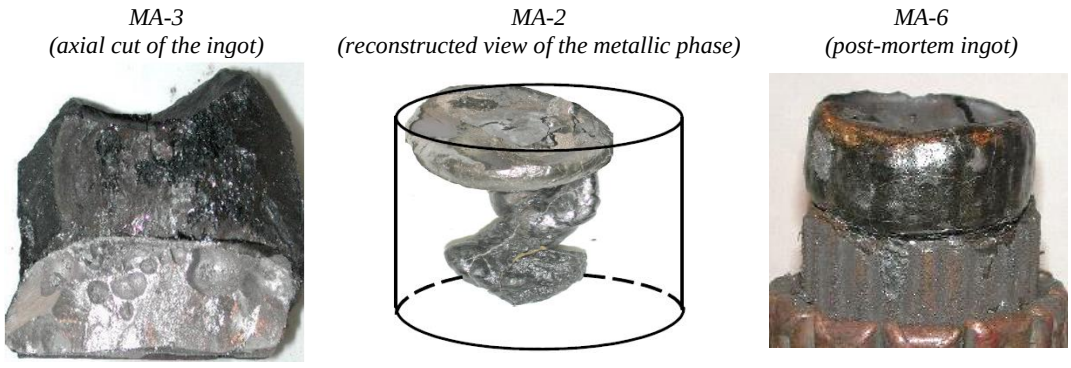

Figure 1. Different views associated with the post-mortem ingots of MA-3, MA-2 and MA-6 tests (adapted from [2]).

† Moreover, in MA-3 and MA-4 tests, the corium load contained fission products (FP) simulant elements with a mass fraction of about 3%. The goal was to characterize the FP partitioning between the metal and oxide phases. These elements are not considered in the first step of this benchmark.

2.2. Benchmark definition

The objective is to compare both the experimental results (associated with the post-mortem ingots analyses) and numerical results obtained by different models that predict the two-phase thermodynamic equilibria in the liquid miscibility gap of the U-O-Zr-steel system. These calculations are performed from the element inventories deciphered from the actual molten masses as evaluated from post-mortem test analyses in [5].‡ They are given in Table II.

Table II. Inventory considered in the different MA tests.

Test	Mass (kg)	Element mass fractions					
		U	Zr	O	Fe	Ni	Cr
MA-1	1.620500	0.6180692	0.1631392	0.1062624	0.0774678	0.0124510	0.0226104
MA-2	1.749200	0.5898773	0.1760788	0.1266666	0.0743082	0.0113718	0.0216974
MA-3	1.648984	0.5871907	0.1967083	0.1063043	0.0846189	0.0098253	0.0153524
MA-4	1.828151	0.5393137	0.1757293	0.0910485	0.1390972	0.0196035	0.0352079
MA-5	1.913298	0.5592548	0.2417220	0.1010353	0.0705727	0.0107234	0.0166917
MA-5b	1.914332	0.5780783	0.2470213	0.1052485	0.0521638	0.0099463	0.0075419
MA-6	1.836680	0.4693826	0.1572136	0.0780316	0.2104556	0.0321988	0.0527179

For each experiment, two different calculations are performed:

C1. A first one at the composition given in Table II that is used for direct comparison with the experimental results in terms of element phases partitioning;

C2. A second one where, the composition given in Table II is varied in terms of steel amount near x_{steel}^{exp} ($R_{U/Zr} = R_{U/Zr}^{exp}$ and $C_{Zr} = C_{Zr}^{exp}$ are kept); more precisely, five calculations with $x_{steel} \in \{0.75, 0.875, 1.0, 1.125, 1.25\} \times x_{steel}^{exp}$ are performed in order to characterize the evolution of the mass densities.

Regarding the temperature, while the different species phase partitioning models are or not temperature dependent, the mixture density laws are in any case temperature dependent. For calculation C1, the temperature is set to $T_{calc} = \max\left(T^{exp}, T_{liquidus}\right)$, where $T_{liquidus}$ is the liquidus temperature (calculated by the model if available) at which the fluorite refractory phase $\left(\mathrm{U_y, Zr_{1-y}}\right)\mathrm{O_{2-x}}$ is formed when the melt is cooled down (assuming thermodynamic equilibrium). For calculations C2, a temperature of $T^{exp} + 100°$ is used in order to ensure that, for all compositions when varying x_{steel}, the system remains into the liquid miscibility gap.§

2.3. Codes and models involved

Different thermodynamic equilibrium models for the liquid miscibility gap of the U-O-Zr-Steel system are used by the participants through different codes as described in Table III. These different models provide the phase mass fractions along with their composition. From there, the phase densities are calculated from:

- a non-ideal mixture law based on element density laws and an excess volume term function of the temperature (see [6]) in NRC "Kurchatov Institute" and IBRAE calculations;

‡ Inventories reported in [5] differs from those in [2] because of more accurate measurements of the oxygen content in the metallic layers.

§ Then, one should keep in mind that the densities will be lower than in C1 calculations.

- an ideal mixture law based on species density laws function of the temperature $\rho_i(T)$ (see [7]) in case of IRSN, INRNE-BAS and CEA calculations.

The parameters of these laws are code/model dependent and are based on different experimental results compilated in different databases. In the case of CEA calculations, the laws proposed in [7] were used (even if there are not the default ones considered in PROCOR) considering two treatments when, for a given species i, the mixture temperature T is below the species liquidus temperature $T_i^{liquidus}$: either $\rho_i\left(T < T_i^{liquidus}\right)$ is set to $\rho_i\left(T_i^{liquidus}\right)$ (M1 hypothesis) or it is extrapolated (M2 hypothesis).

Table III. The different codes and models for the liquid miscibility gap of the U-O-Zr-Steel system involved in step-1.

Institution	N°	Code / model	Description/comments	Ref.
NRC "Kurchatov Institute"	1	TSAR / GIBBS	Thermodynamic approach based on Gibbs energy minimization using regular solution model (CALPHAD-like technique)	[8]
IRSN	2	ASTEC / Salay-Fichot model	Analytical model calibrated on experimental results from MASCA MA-1, 2, 3, STFM-Fe-2, 3, 4, 5, 6, 7, 8, 9, 14, 15	[9]
INRNE-BAS	3			
IBRAE	4	HEFEST_URAN	Interpolation scheme based on MASCA MA and STFM-Fe test experimental results	[10]
CEA	5	PROCOR interface with OpenCalphad / Gibbs energy minimizer with NUCLEA'19 database	CALPHAD method with a non-ideal associate model for the Gibbs energy of the liquid phase	[11] [12]
	6	PROCOR / Salay-Fichot model	See ASTEC above	[9]
	7	PROCOR / Nandan-Fichot model	Analytical model calibrated on OpenCalphad calculations with NUCLEA'19 database	[13]
	8	PROCOR / thermodynamic closures associated with the stratification kinetics model proposed in [14]	Interpolation scheme based on OpenCalphad calculations with NUCLEA'19 database	[14]

2.4. Results comparison and analysis

Results for the C1 calculations are presented in Table VI as a comparison with the experimental values in terms of the oxide phase mass fraction (w^{oxy}), the uranium (resp. zirconium) mass fraction in the metal phase w_U^{met} (resp. w_{Zr}^{met}). It can be observed that, in most cases, the relative discrepancy associated with the phase partitioning (in terms of oxide phase mass fraction) is less than 10%. For calculations based on the NUCLEA database (n°5 and, through fitting/interpolation, n°7 and 8), results are deteriorated in MA-6 conditions *i.e.* with a higher x_{steel}^{exp} value. The same comment applies to Salay-Fichot models based results n°6, 2 and 3[**] along with IBRAE result n°4. Regarding the metal phase enrichment in Zr, it is underestimated in most calculations in MA-3, 4, 5, 5b, 6 conditions. Note that it is worst in results n°2, 3, 6 and 7 because of the underlying hypothesis of the Salay-Fichot and Nandan-Fichot models that considers the $R_{U/Zr}$ ratio as uniform between the two phases while actually, it significantly decreases in the metal phase at equilibrium

[**] Note that ASTEC results obtained independently by IRSN and INRNE are almost the same while, apparently, the Salay-Fichot model implemented in PROCOR differs significantly from the one in ASTEC code.

(*i.e.* Zr is preferentially extracted in the metal phase). Only result n°1 shows a limited Zr underestimation in these five tests. In MA-1 (higher $R_{U/Zr}$ w.r.t. MA-3) and MA-2 (higher C_{Zr} w.r.t. MA-3) conditions, calculations 1 and 5 are consistent with a significant overestimation of the Zr content (a compensation effect can be observed for results n°2, 3, 6 and 7 because of the previously mentioned hypothesis). Regarding result n°8, because of the way the interpolation scheme is constructed (see [14]), it gives consistent results w.r.t. result n°1 in terms of w^{oxy} and w_{Zr}^{met} and about 10% difference in w_U^{met} in all cases.
On the overall, considering the fact that these tests are not strictly at thermodynamic equilibrium and the underlying experimental uncertainty, it is worth noting that the results based on a thermodynamic database with a Gibbs energy minimizer (n°1 and 5) are in fairly good agreement.
Regarding C2 calculations, the oxide (resp. metal) phase density ρ^{oxy} (resp. ρ^{met}) as a function of x_{steel} is depicted in the MA-1 (heavier metal) and MA-6 (lighter metal) cases in Figure 4 (resp. Figure 5) while the phase density differences $\rho^{met} - \rho^{oxy}$ [kg.m^{-3}] for $x_{steel} = x_{steel}^{exp}$ are given for all the cases in Table VII. For this second set of calculations, PROCOR results are only shown with the Salay-Fichot equilibrium model (n°6) with the two different hypotheses (denoted M1 and M2) regarding the density calculation introduced in §2.3. It can be observed that, as expected, these hypotheses have only an impact on the oxide phase density. Moreover, using M1 (resp. M2), the oxide mass density calculated by PROCOR is rather consistent with result n°1 by NRC KI (resp. n°2 by IRSN). In all cases, result n°4 by IBRAE exhibits a significantly higher oxide density. In the case of INRNE result (n°3), they were performed at a lower temperature in such a way that, compared with result n°2 (that uses the same ASTEC code), a higher oxide density is obtained. Regarding the metal density, result n°4 gives lower density than results n°2 and 6 while calculation n°1 gives a higher (resp. lower) density for a low (resp. high) x_{steel} value as in MA-1 (resp. MA-6) conditions. On the overall, when looking at the phase density differences, PROCOR results with M2 hypothesis, ASTEC results produced by IRSN and NRC-KI results are rather close with a difference in magnitude that is comparable with the temperature effect that can be quantified when comparing ASTEC results between IRSN and INRNE. The calculations that give difference that is more significant are the ones produced by IBRAE with HEFEST_URAN.
These density differences would need further analysis going back to the density laws implemented in the different codes that may not be at the state-of-the-art (this comment applies to PROCOR based on TOLBIAC-ICB physical properties laws for instance) taking into account recent experimental data.

3. STEP 2: MASCA RCW-100

3.1. Brief summary of the experiment

In the OECD-MASCA experimental program [2], one prototypical experiment of larger scale than the previous MA tests has been conducted and is of interest for characterizing the stratification transient. It is the MASCA-RCW test [3] where 45.3kg of suboxidized corium has been put in interaction with about 4.6kg of steel (in such a way that the global system is, in terms of thermodynamic equilibrium, below the stratification inversion threshold). This experiment was carried out in a cold crucible of about 18cm-diameter. It was interrupted after 22min of interaction between molten corium and molten steel poured on top and the analysis of the post-mortem ingot clearly shows that the system has not reached a stationary state with two stratified layers. The vertical cross-section of the ingot is shown in Figure 2. The interpretation proposed in [15] consists in considering this post-mortem ingot as the solidified state of the system during the transient relocation of steel below the oxide; the metal phases are spatially distributed as follows:

- a continuous light metal phase (7) above the oxide pool (5);
- a dispersed metallic phase enriched in U and Zr that can be viewed as centimetric droplets[††] (4) relocating downward through oxide (5);

[††] In the post-mortem state, internal porosities can be observed in these droplets. The SEM/EDX composition analysis reveals that they were probably filled by CO gas (traces of $Zr(O_{0.14}C_{0.85})$ are found at the interface). Accordingly, as

- a continuous heavy metal phase (2) below the oxide (5).

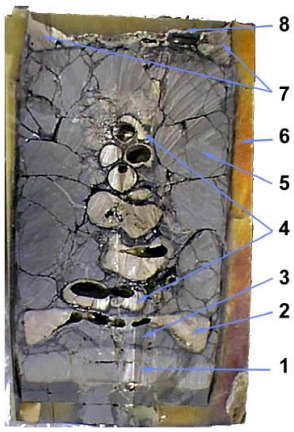

1. The corium lower non-melted briquettes;
2. The lower metallic part;
3. Zone of a partially melted corium;
4. Roundish metallic parts in the central zone;
5. The ingot oxidic part;
6. Epoxy;
7. The upper metallic part;
8. The ingot surface;

Figure 2. Vertical cross-section of the MASCA-RCW post-mortem ingot (adapted from [2]) – diameter ~18cm and height ~26cm – without (1).

From there, two mechanisms are at play, as discussed in [15]. First, there is a transfer of U and Zr from the oxide to the steel (associated with modification of the redox equilibrium $U + ZrO_2 \leftrightarrow UO_2 + Zr$) that induces local changes in mass density. Then, when the metal in the boundary region becomes "sufficiently" heavier than the oxide, the triggering and growth of Rayleigh-Taylor instabilities at the interface between the light metal layer and the oxide lead to the formation and detachment of heavy metal droplets that sink through the oxide (and form a continuous heavy metal phase at the bottom). These hydrodynamic phenomena appear to be periodic in nature and are much faster than the bulk transport of components within the light metal layer. Indeed, as shown in Figure 3, the U, Zr components in the light metal phase are concentrated in a boundary region near the interface.
This interpretation was used in the construction of the legacy PROCOR stratification model [17] (originating from the modelling hypotheses proposed in [15]) where the overall kinetics is supposed to be controlled by the interlayer mass transfer (the hydrodynamic phenomena are not modelled).

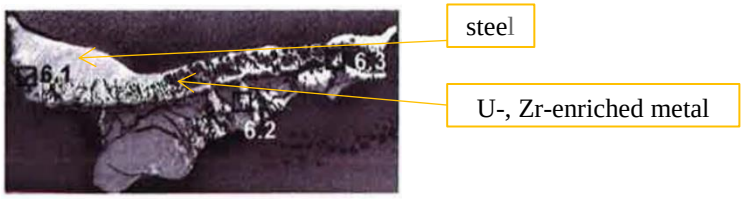

Figure 3. Microscopic structure of the solidified light metal phase of the MASCA-RCW post-mortem ingot (adapted from [2]) – dimensions ~9x4cm.

3.2. Benchmark definition

The objective is to compare both the experimental results (associated with the post-mortem ingots analyses) and numerical results obtained by different models that simulate such a stratification transient where, from a two-layer pool with steel on the top, a heavy metal phase is formed.

---

mentioned in [3], it is considered that this gas formation is associated with the decrease of the oxygen solubility in metal when solidification took place and CO was formed by the interaction between this oxygen and carbon coming from the steel. Accordingly, at liquid state, no gas is expected.

Because of the complexity of such an experiment and the fact that, from the point of view of phases stratification, only indirect post-mortem data are available, the considered simulation set-up is actually an idealized two-layer configuration representative of the system state after the corium has been melted and the molten steel has been poured on top.
Accordingly, the code-to-experiment comparison can only be semi-quantitative but, considering the level of uncertainty of this stratification issue, it is the authors' point of view that such a comparison (and the associated code-to-code comparison) is still very valuable.
The initial state of the two-layer system given in Table IV is considered in a geometry consisting in a 9-cm cylinder. From there, the time-dependent spatial distribution of the phases is simulated until steady-state has been reached.
This initial inventory was constructed back from the inventory of the different phases in the post-mortem that is used for comparison with simulation results at time t=22min.
During these 22min of interaction between molten steel and molten corium, the thermal power deposited into the melt was about 25kW while the liquidus temperature of the overall system is about 2500°C.

Table IV. Inventory considered in the RCW-100 test.

Phase α	Mass (kg)	Species mass fraction (%)					
		UO_2	Zr	ZrO_2	Fe	Cr	Ni
Steel	3.989	0.0	0.0	0.0	69.64291	16.22873	14.12836
Oxide	48.781	76.25693	14.24420	0.949887	0.0	0.0	0.0

■ ***Nota Bene*** The first phase of the experiment (corium melting), while not the focus of this benchmark, is also of interest for code validation as demonstrated by supplementary calculations (not shown here) performed by IBRAE with HEFEST_URAN in the frame of this collaborative work. ■

3.3. Codes and models involved, main parameters selection

The different stratification kinetics models used by the participants through different codes are described in Table V.

Note that in most of these models, the detachment of U-/Zr- enriched metal from the upper metal phase under the form of droplets (that relocate downwards to form the heavy metal phase formation) is based on a simple density difference criterion between the interfacial enriched metal and the oxide. In addition, it should be noted that only the model associated with result n°5 explicitly takes into account the metal droplets and their relocation; in other models, the time for relocation is neglected.
In all these models, the main important parameters (either effective diffusion coefficients or mass transfer coefficients) are related to the inter-layer mass transfer kinetics and they have been approximately calibrated so that the mass of the heavy metal phase at t=22min is in good agreement with the experiment. In addition, for result n°5, the model parameters were selected so that the first droplet detachment occurs slightly before t=22min in accordance with the measurements during the experiment that show a rapid increase in the temperature at the bottom of the crucible slightly before the power was shutdown, indicating a change in the melt phase topology. This model calibration is not further discussed for the sake of conciseness.

Table V. The different codes and models for the stratification kinetics involved in step-2.

Institution	N°	Code / model	Description/comments	Ref.
IRSN	1	ASTEC / inter-layer mass transfer model	Mass transfer considered simultaneously at the two interfaces upper metal/oxide, oxide/lower metal; local interface equilibrium approximated by the thermochemical equilibrium (Salay-Fichot model, see n°2/3 in Table III) of the two phases at this interface	[16]
INRNE-BAS	2			
IBRAE	3	HEFEST_URAN / MultiMelt module	1D finite element diffusion model for uranium in the upper metal phase	-
CEA	4	PROCOR / legacy inter-layer mass transfer model	Evolution equation for the uranium mass fraction in the oxide phase considering the exchange with the upper metal phase; degree of advancement towards global thermochemical equilibrium (Salay-Fichot model, see n°6 in Table III)	[17]
	5	PROCOR / "new" integral mass transfer model that takes into account the dispersed metal phase (mass transfer and dynamics)	Mass and element mass conservation for all phases; interface jump conditions associated with local equilibrium simplified under the hypothesis that there is no oxygen (resp. steel) in the metal (resp oxide) phases; thermodynamic closures: see n°8 in Table III; 1D droplet momentum conservation equation	[18] [19] [14]

3.4. Results comparison and analysis

The results for the different codes are given in Figure 6 in terms of the oxide (m^{oxy}) and heavy metal phase ($m^{met\downarrow}$) masses as a function of time along with the evolution of the U ($w_U^{met\downarrow}$) and Zr ($w_{Zr}^{met\downarrow}$) mass fractions in the heavy metal phase. Values associated with post-mortem analyses of the experiment ingot (metal phases) are also depicted at t=22min for comparison purpose. More precisely, three values are depicted for $m^{met\downarrow}$, $w_U^{met\downarrow}$ and $w_{Zr}^{met\downarrow}$ considering:

- the actual heavy metal phase below the oxide ($met\downarrow$) ;
- the actual heavy metal phase ($met\downarrow$) plus the droplets inside the oxide ($drop\downarrow$);
- the actual heavy metal phase ($met\downarrow$) plus the droplets ($drop\downarrow$) plus the U-, Zr-enriched boundary region of the light metal layer ($\widetilde{met}\uparrow$).

The following general trends can be observed on the phase masses evolution. In results n°1, 2, and 4, the formation of the heavy metal phase is described continuously (as the underlying models do not intend to capture the discontinuous nature of the process associated with the Rayleigh-Taylor instabilities) and starts from t=0s. In result n°3, the heavy metal formation starts around 800s and then steadily increases by further continuous relocation from the light metal layer. In result n°5, a first droplets detachment occurs just around 1310s to form the heavy metal layer which mass then slowly increases by mass transfer through its interface with the oxide phase until the next droplet detachment (not shown in Figure 6, that occurs around 2750s). As expected, the different models having been approximately calibrated, their prediction of the heavy metal mass at 22min is fairly good.

When looking at the evolution of the U and Zr mass fractions in the heavy metal layer in Figure 6, further remarks can be made. First, in PROCOR legacy model, because of the underlying modelling hypotheses, the heavy metal phase composition is constant in time, set to its value at global thermochemical equilibrium. With ASTEC model (in both IRSN and INRNE calculations that are almost undistinguishable), this composition in U and Zr exhibits a rapid increase starting after 200s and then a slow decrease towards its global equilibrium value. At the experiment exposure time, for both models, the U mass fraction is approximately reproduced while the Zr mass fraction is underestimated; this is consistent with the trends observed with the Salay-Fichot equilibrium model in both codes in Table VI for MA-3 conditions (close to

RCW global inventory). Second, in PROCOR "new" model, looking at the heavy metal phase composition when it is formed around 1310s, the opposite trend is observed consistently with the observations made in Table VI in MA-3 conditions for result n°8. After its formation, the U and Zr content of the heavy metal phase increases by mass transfer through its interface with the oxide phase. Third, in IBRAE calculation, the heavy metal formed around 650s exhibits a high U and Zr content that rapidly decreases (by further addition of metal relocated from the light metal layer) ; at the experiment exposure time, the U mass fraction is approximately reproduced while the Zr mass fraction is underestimated.
While this experiment offers a unique qualitative comparison for stratification kinetics and can be used for calibration purpose, it appears clearly that additional experimental results are needed to go further in the model validation as already stated in [20].

4. CONCLUSIONS AND PERSPECTIVES

In this paper, the first two steps of a benchmark devoted to in-vessel corium thermochemistry have been presented both in terms of test specifications and results obtained so far by the participants involved in the frame of the IAEA CRP on In-Vessel Melt Retention. The first step, based on the MASCA MA experiment series, has highlighted the overall good capability of either simple models published in the open literature or thermodynamic equilibrium calculations (based on a thermodynamic database and a Gibbs energy minimizer) to evaluate the mass and species partitioning of the two-layer pool at steady-state. It has also shown discrepancies among codes regarding the phase density evaluation that would require further analysis and comparison with state-of-the-art experimental measurements of such mixture densities. Considering the MASCA RCW-100 experiment, the second step was devoted to the stratification transient associated to an heavy metal formation at the bottom of the pool. Four different models were approximately calibrated and compared based on the experimental post-mortem analyses highlighting the needs for further work on the transient model validation.
In the near future, by the end of the CRP in mid-2024, this benchmark will be completed by a last step considering the transient evolution of a three-layer stratified corium pool in presence of a solid crust at the top oxide surface based the CORDEB2 CP7-02 experimental results.

ACKNOWLEDGMENTS

Authors would like to acknowledge the IAEA for the coordination of this CRP and in particular Mr Miassoedov from the Division of Nuclear Power and Mr Massara and Ms Veneau from the Division of Nuclear Installation Safety.

REFERENCES

[1] F. Fichot, L. Carénini, N. Bakouta, H. Esmaili, L. Humphries, T. Laato, R. Le Tellier, L. Saas, I. Melnikov, P. Pandazis, S. Weber, R. J. Park, A. Philippov, and V. Strizhov, "Elaboration of a Phenomena Identification Ranking Table (PIRT) for the modelling of In-Vessel Retention," Annals of Nuclear Energy, 146, 107617, 2020.

[2] D. F. Tsurikov, V. F. Strizhov, S. V. Bechta, V. N. Zagriazkin and N. P. Kiselev, Main Results of MASCA1 and 2 Projects, Technical Report, RRC Kurchatov Institute, 2007.

[3] V.G. Asmolov, S.S. Abalin, Yu.A. Veselkin, V.Yu. Vishnevsky, V.V. Vlasov, B.L.Gershman, Yu.G. Degaltsev, Ye.K. Dyakov, J.F. Isaev, A.N. Kiselev, N.P. Kiselev, A.M.Kovalev, A.G. Ol'khovsky, K.V. Pechalin, LM. Semenov, V.F. Strizhov, T.V.Trushkina, V.S. Uglov, Yu.M. Utkin, V.V.Chudanov, A.E.Aksenova, V.A.Pervichko and L.M. Khazanivich, RCW Post-Test Analysis Results, Technical Report MP-TR-11, Russian Research Centre Kurchatov Institute, 2003.

[4] F. Fichot, B. Michel, L. Carénini and V. Almjashev, "Final report on stratified corium pool behaviour – CORDEB-2 tests", Delivrable D3.2 of H2020 IVMR project, December 2019.

[5] S. V. Bechta, V. S. Granovsky, K. V. B, V. V. Gusarov, V. I. Almiashev, L. P. Mezentseva, E. V. Krushinov, S. Yu. Kotova, R. A. Kosarevsky, M. Barrachin, D. Bottomley, F. Fichot, and M. Fischer, "Corium Phase Equilibria based on MASCA, METCOR and CORPHAD Results," Nuclear Engineering and Design, vol. 238, pp. 2761–2771, 2008.
[6] V. G. Asmolov, V. N. Zagryazkin, and D. F. Tsurikov, "Estimation of the density of U-Zr-Fe-O melts," High Temp, vol. 46, no. 4, pp. 579–582, Aug. 2008.
[7] M. Barrachin and F. Defoort, Thermophysical Properties of In-Vessel Corium: MASCA Programme Related Results, Proc. Of MASCA Seminar, Aix-en-Provence, France, 2004.
[8] M. A. Golubev, I. A. Melnikov, G. B. Shmelkov, A. V. Velikanov, "Thermodynamic model of the corium for NPP with VVER" in Proc. of XXIII Int. Conf. of Nuclear Power Plants, National Research Center "Kurchatov Institute", Moscow, Russia, 2023 (in russian).
[9] M. Salay and F. Fichot, "Modelling of Metal-Oxide Corium Stratification in the Lower Plenum of a Reactor Vessel," in Proc. of Int. Topical Meeting on Nuclear Thermal-Hydraulics (NURETH-11), Avignon, France, 2005.
[10] V. D. Ozrin, O. V. Tarasov, V. F. Strizhov, and A. S. Filippov, "A model for calculating composition and density of the core melt in the water-moderated water-cooled reactor in case of severe accident," Therm. Eng., 57, 13, 1099–1111, 2010.
[11] B. Sundman, U. R. Kattner, C. Sigli, M. Stratmann, R. Le Tellier, M. Palumbo, and S. G. Fries, "The OpenCalphad thermodynamic software interface," Computational Materials Science, 125, 188–196, 2016.
[12] S. Bakardjieva, M. Barrachin, S. Bechta, D. Bottomley, L. Brissoneau, B. Cheynet, E. Fischer, C. Journeau, M. Kiselova, L. Mezentseva, P. Piluso, and T. Wiss, "Improvement of the European thermodynamic database NUCLEA," Progress in Nuclear Energy, 52, 1, 84–96, 2010.
[13] S. Nandan, F. Fichot, and B. Piar, "A simplified model for the quaternary U-Zr-Fe-O system in the miscibility gap," Nuclear Engineering and Design, 364, 110608, Aug. 2020.
[14] J. Mativet, R. Le Tellier, and A. Lecoanet, Improvement of thermochemical corium stratification modelling accounting for uranium and zirconium composition difference in metallic and oxide phases, in Proc. of the 11th European Review Meeting on Severe Accident Research Conference (ERMSAR 2024), KTH, Stockholm, Sweden, May 13-16, 2024.
[15] G. Ratel, F. Deffort, K. Froment, B. Tourniaire and J. M. Seiler, Considerations on mass transfer kinetics for layer inversion and layer oxidation: from MASCA program to the reactor situation. Proc. of MASCA-2 Seminar, Cadarache, France 2007.
[16] L. Carénini and F. Fichot, "Evaluation of the kinetics of molten pool stratification in case of In-Vessel Melt Retention Strategy," in Proc. of 26th International Conference on Nuclear Engineering ICONE 26, London, England, 2018.
[17] R. Le Tellier, L. Saas and S. Bajard, Transient Stratification Modelling of a Corium Pool in a LWR Vessel Lower Head, Nuclear Engineering and Design, 287, 68-77, 2015.
[18] R. Le Tellier, "Mass transfer between a continuous oxide phase (U-O-Zr) and a steel droplet at liquid state: Potential impact on corium pool behaviour during in-vessel melt retention," Nuclear Engineering and Design, 385, 111525, 2021.
[19] R. Le Tellier, "A lumped parameter model of continuous/dispersed phases mass transfer for simulating in-vessel corium stratification transients," Annals of Nuclear Energy, 181, 109539, 2023.
[20] F. Fichot, L. Carénini, R. Le Tellier, L. Viot, N. and Bakouta, and A. Filippov, "Identification and evaluation of the remaining uncertainties for transient situations," in Proc. of International Seminar "In-vessel retention: outcomes of IVMR project," Juan-les-Pins, France, Jan. 2020.

APPENDIX A: Results

Table VI. Step-1, C1 calculations: experimental values for the oxide phase mass fraction w^{oxy}, the U (resp. Zr) mass fraction in the metal phase w_U^{met} (resp. w_{Zr}^{met}) and relative difference (%) for the different codes and models. Cell colors correspond to the error range (green ≤ 5% ≤ yellow ≤ 10% ≤ orange ≤ 15% ≤ red).

		Experimental value	5 CEA - PROCOR - NUCLEA	6 CEA - PROCOR - S&F	7 CEA - PROCOR - N&F	8 CEA - PROCOR - closures	2 IRSN - ASTEC	3 INRNE - ASTEC	1 NRC KI - TSAR	4 IBRAE - HEFEST_ URAN
MA-1	w^{oxy}	0.781	-2.4%	-1.6%	-3.1%	-1.0%	1.0%	1.0%	4.2%	-2.7%
	w_U^{met}	0.425	-5.9%	-1.9%	0.1%	-14.2%	-8.3%	-8.1%	-2.9%	-10.7%
	w_{Zr}^{met}	0.103	34.0%	6.5%	8.7%	35.3%	-0.5%	-0.3%	36.3%	24.5%
MA-2	w^{oxy}	0.878	-3.4%	-2.5%	-3.7%	-3.0%	-1.3%	-1.4%	1.6%	-1.9%
	w_U^{met}	0.201	16.2%	10.5%	17.0%	-6.5%	-2.8%	-1.6%	-4.9%	-14.4%
	w_{Zr}^{met}	0.055	66.2%	21.0%	28.1%	66.4%	6.4%	7.8%	69.9%	-15.0%
MA-3	w^{oxy}	0.726	1.9%	3.1%	1.6%	4.0%	5.3%	5.2%	8.0%	4.5%
	w_U^{met}	0.430	-3.5%	-0.0%	1.5%	-12.5%	-3.7%	-3.6%	-5.5%	-10.1%
	w_{Zr}^{met}	0.173	-1.5%	-16.9%	-15.6%	1.3%	-19.9%	-19.9%	4.0%	-21.8%
MA-4	w^{oxy}	0.639	-3.2%	-3.3%	-2.9%	-0.3%	-0.2%	-0.2%	6.3%	-2.2%
	w_U^{met}	0.322	9.8%	15.9%	14.8%	0.3%	11.1%	11.1%	5.9%	-0.7%
	w_{Zr}^{met}	0.158	-9.9%	-23.0%	-23.7%	-9.0%	-26.2%	-26.1%	-3.1%	-10.7%
MA-5	w^{oxy}	0.754	-7.6%	-6.6%	-7.1%	-4.7%	-3.7%	-3.7%	-0.5%	-3.1%
	w_U^{met}	0.374	21.9%	26.2%	26.0%	12.4%	22.9%	23.0%	16.4%	18.6%
	w_{Zr}^{met}	0.256	-11.7%	-20.3%	-20.5%	-9.3%	-22.4%	-22.3%	-0.4%	-35.9%
MA-5b	w^{oxy}	0.799	-7.0%	-5.3%	-6.6%	-4.2%	-2.8%	-2.9%	-1.4%	-3.9%
	w_U^{met}	0.428	15.3%	18.7%	19.3%	6.5%	16.1%	16.2%	10.4%	16.3%
	w_{Zr}^{met}	0.274	-12.7%	-20.9%	-20.5%	-9.7%	-22.6%	-22.5%	-1.5%	-37.7%
MA-6	w^{oxy}	0.565	-9.6%	-11.3%	-8.1%	-13.6%	-7.9%	-7.2%	2.4%	-7.7%
	w_U^{met}	0.215	30.7%	41.3%	35.0%	41.2%	35.1%	35.2%	21.0%	16.7%
	w_{Zr}^{met}	0.142	-18.1%	-28.6%	-31.8%	-15.7%	-31.8%	-31.7%	-12.2%	-19.9%

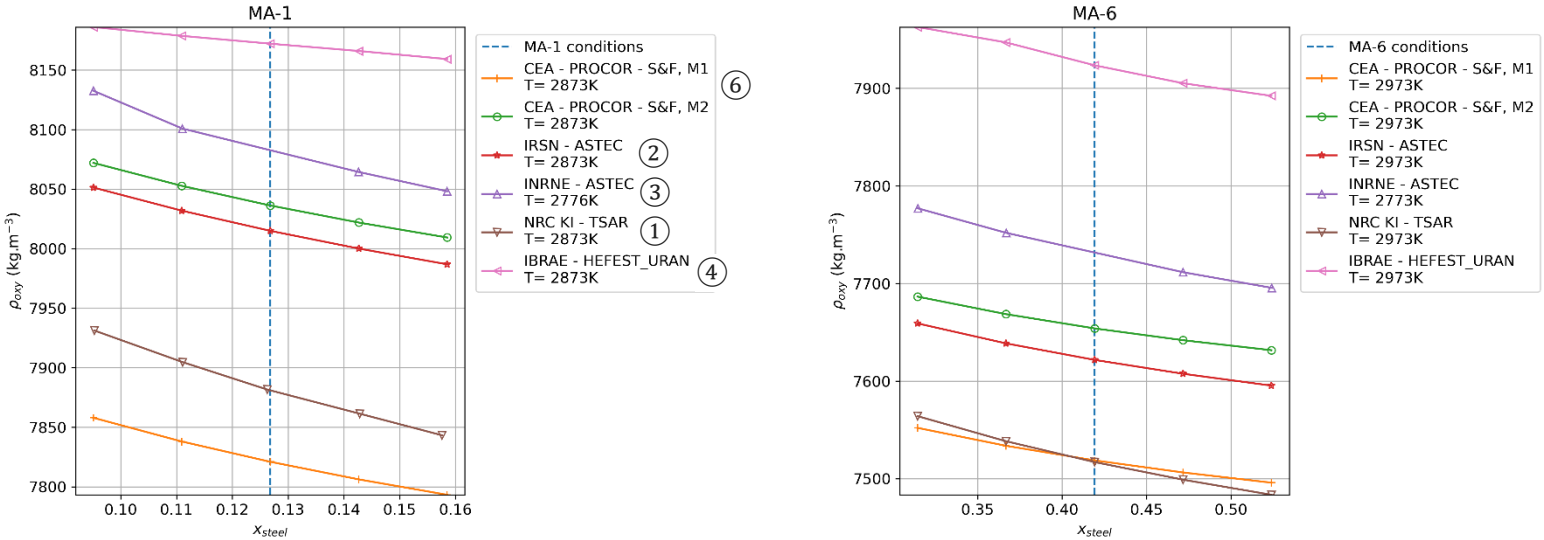

Figure 4. Step -1, C2 calculations: oxide phase density ρ^{oxy} as a function of x_{steel} in MA-1 (left) and MA-6 cases – circled numbers in the legend refer to the code/model numbering of Table III.

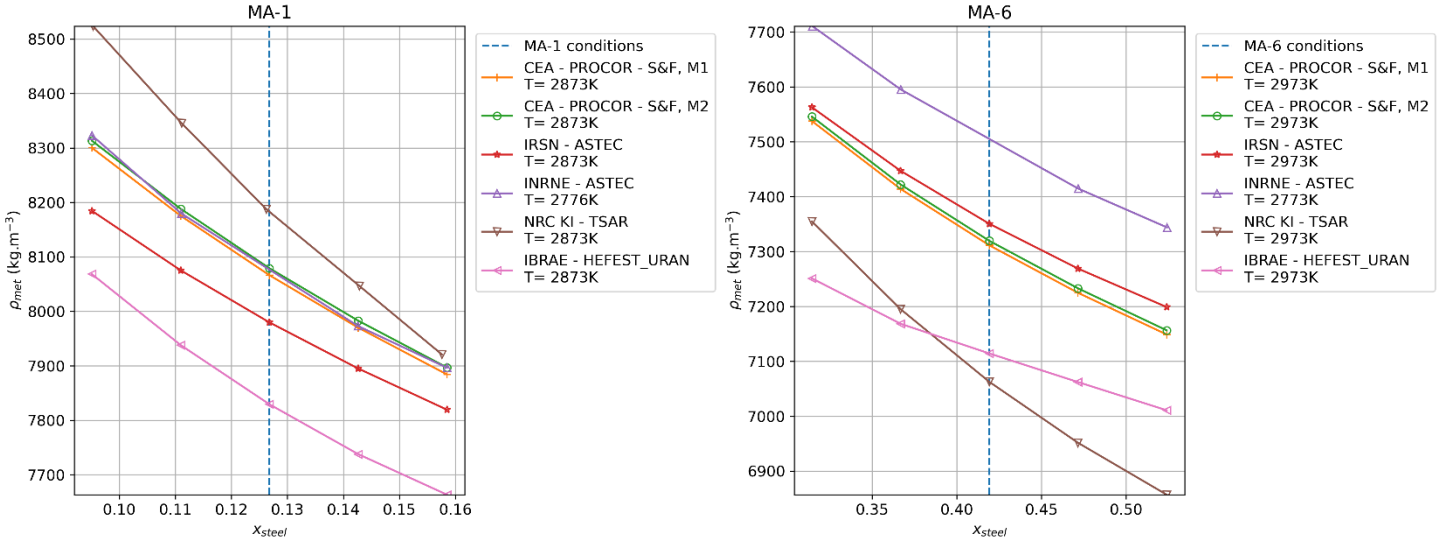

Figure 5. Step -1, C2 calculations: metal phase density ρ^{met} as a function of x_{steel} in MA-1 (left) and MA-6 cases.

Table VII. Step-1, C2 calculations: phase density difference $\rho^{met} - \rho^{oxy}$ [kg.m^{-3}] for $x_{steel} = x_{steel}^{exp}$.

	6	6	2	3	1	4
	CEA - PROCOR - S&F, M1	CEA - PROCOR - S&F, M2	IRSN - ASTEC	INRNE - ASTEC	NRC KI - TSAR	IBRAE - HEFEST_URAN
MA-1	245.3	42.8	-35.3	-91.4	305.6	-342.9
MA-2	-559.3	-763.2	-771.1	-785.6	-717.3	-1075.9
MA-3	503.3	316.1	315.4	316.1	543.6	-68.3
MA-4	183.6	-7.6	-4.5	-50.5	64.8	-489.1
MA-5	907.3	740.9	712.7	721.0	794.0	542.4
MA-5b	1100.8	937.7	927.0	936.2	955.1	984.1
MA-6	-207.4	-334.4	-271.1	-296.8	-454.4	-809.3

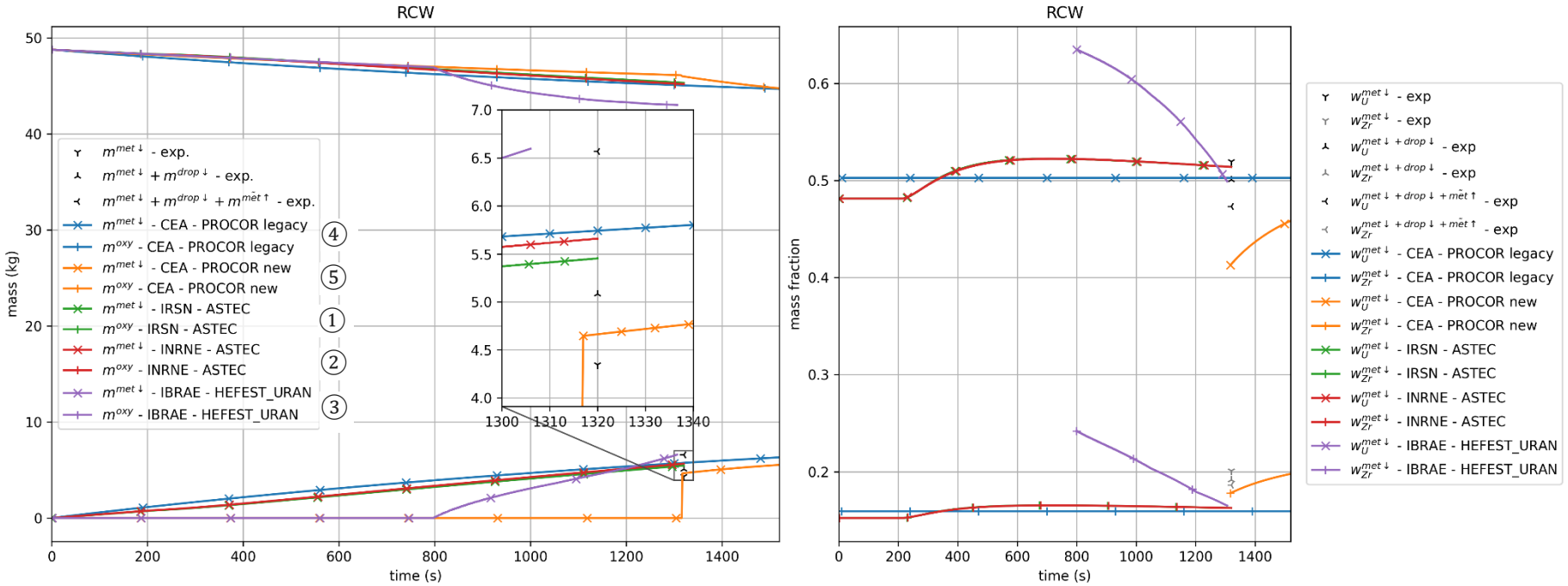

(a) oxide (m^{oxy}) and heavy metal phase ($m^{met\downarrow}$) masses (b) U ($w_U^{met\downarrow}$) and Zr ($w_{Zr}^{met\downarrow}$) mass fractions in the heavy metal phase

Figure 6. Step-2: phase masses and heavy metal phase composition evolution for the different simulations and comparison with experimental values – circled numbers in the legend refer to the code/model numbering of Table V.

IN-VESSEL CORIUM THERMOCHEMISTRY BENCHMARK BASED ON MASCA EXPERIMENTAL DATA

R. Le Tellier (CEA), L. Carénini, F. Fichot (IRSN), R. Gencheva, P. Groudev (INRNE-BAS), I. Melnikov, M. Golubev (NRC “Kurchatov Institute”), A. Filippov (IBRAE)

The 11th European Review Meeting on Severe Accident Research (ERMSAR2024), KTH, Stockholm, Sweden, May 13-16, 2024

Context
In-Vessel Melt Retention

- In the frame of the IAEA-CRP “Developing a phenomena identification and ranking table (PIRT) and a validation matrix, and performing a benchmark for In-Vessel Melt Retention”

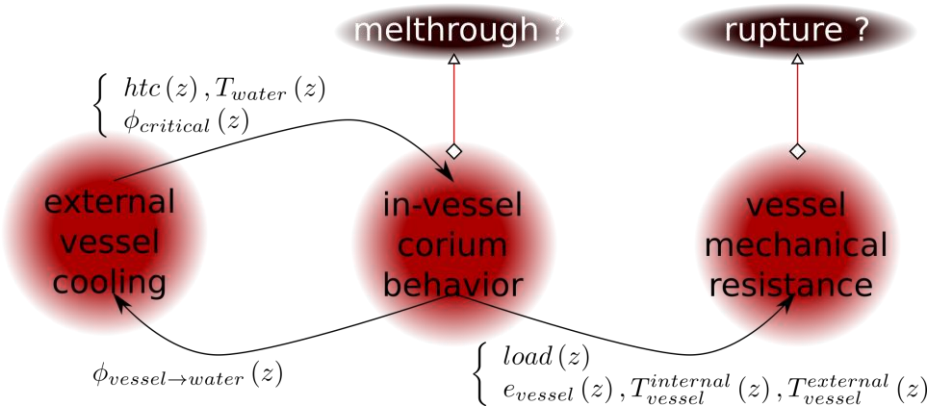

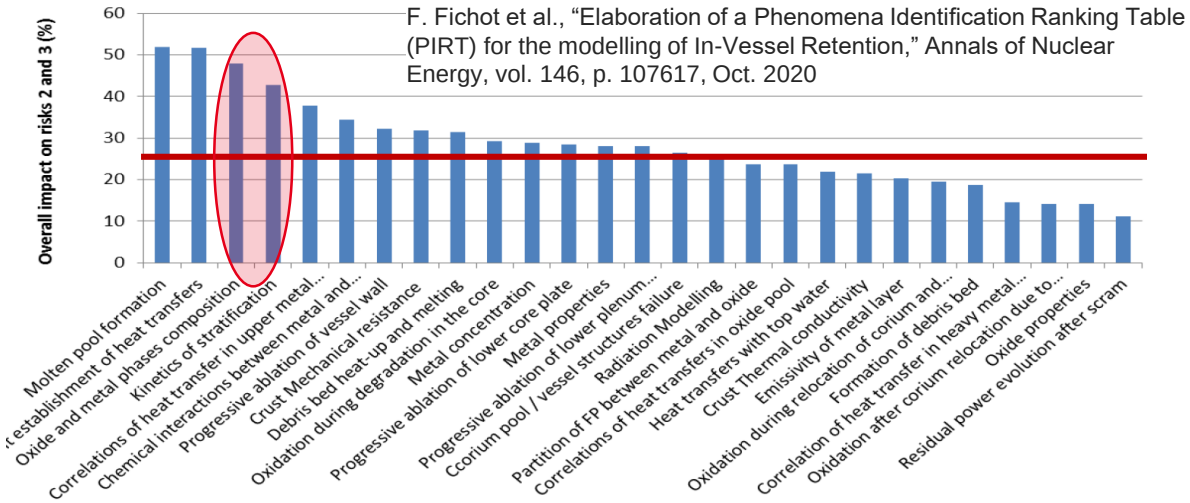

F. Fichot et al., “Elaboration of a Phenomena Identification Ranking Table (PIRT) for the modelling of In-Vessel Retention,” Annals of Nuclear Energy, vol. 146, p. 107617, Oct. 2020

- Corium pool transient behavior → an important topic exhibiting high sensitivities to some uncertain “parameters/phenomena” with a high impact on the vessel melthrough risk
- In particular, oxide/metal corium pool thermochemistry and stratification
- Paradoxical situation: a prerequisite for a state-of-the-art analysis of in-vessel melt retention… that is not always taken into account in SA codes (few models in need for validation/calibration)

Context
MASCA-CORDEB2 benchmark

- IAEA-CRP Task 3 (Code-code and code-exp. data comparison) → a dedicated benchmark
- A three-step benchmark constructed by “merging” initial CEA proposal (MASCA) and IRSN proposal (CORDEB2) – joint CEA/IRSN coordination
- Based on prototypical experiments - cold crucible technique with inductive heating
- Benchmark participants: NRC KI, INRNE, IBRAE, IRSN, CEA
- Addressing in a progressive manner, a high-uncertainty, high-impact “phenomenon”
- Establishing a common basis for further R&D, model development and validation
- Maybe useful for code developers that would like to upgrade their models

Context
MASCA-CORDEB2 benchmark

This presentation

- Step 1: Code-to-experiment comparisons using small scale prototypic experiments of the MASCA projects: MA 6-test series
  - Species partitioning in a two-layer pool under chemical equilibrium conditions
  - Benchmark suitable for comparing different approaches (e.g. surface response, tabulation/ interpolation from CALPHAD thermodynamic database) for modelling the liquid miscibility gap of the U-O-Zr-steel thermodynamic system
- Step 2: Code-to-experiment comparisons using medium scale prototypic experiment MASCA RCW-100 test
  - kinetics of interfacial mass transfer (without crust) + Rayleigh-Taylor instabilities + droplet relocation
  - Benchmark suitable for comparing stratification models in SA codes (inter-layer mass transfer model + liquid miscibility gap model)
- Step 3: Code-to-experiment comparisons using small scale prototypic experiment CORDEB2 CP7-02 test
  - Stratification kinetics in presence of a mechanically stable crust at the top oxide surface
  - Benchmark suitable for comparing stratification models in SA codes (inter-layer mass transfer model + liquid miscibility gap model)





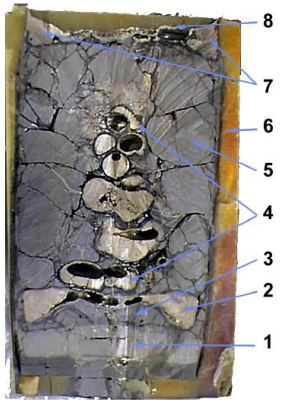



Step-1: MASCA-MA
Description

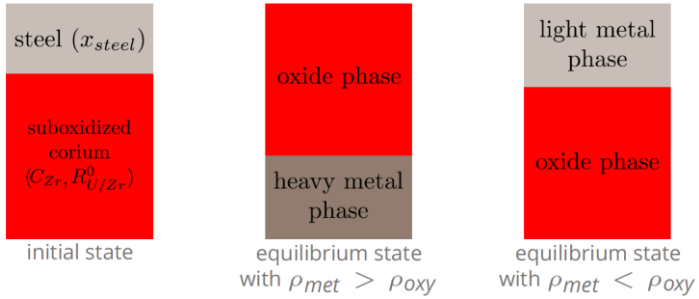

- Seven tests (about 2kg of suboxidized corium + steel / Ø7cm crucible)

Test	T^{exp} (°C)	Exposure time (min)	$R^{exp}_{U/Zr}$	C^{exp}_{Zr} (%)	$\frac{x^{exp}_{steel}}{x^{exp}_{steel}+1}$ (%)
MA-1	2500	30	1.45	33.1	11.42
MA-2			1.28	74.5	10.80
MA-3			1.14	36.5	10.78
MA-4			1.17	39.7	19.09
MA-5			0.89	31.5	9.89
MA-5b		120	0.90	30.5	7.05
MA-6	2600	30	1.14	29.1	29.71

MA-3
(axial cut of the ingot)



MA-2
(reconstructed view of the metallic phase)



MA-6
(post-mortem ingot)



- For each experiment, two different calculations:
  - A first one at the actual experiment composition (deciphered from post-mortem analyses) and $T_{calc} = \max(T^{exp}, T_{liquidus})$ → code-to-experiment comparison (species partitioning)
  - A second one at $T^{exp} + 100°$ where the composition is varied in terms of steel amount near x^{exp}_{steel} ($R_{U/Zr} = R^{exp}_{U/Zr}$ and $C_{Zr} = C^{exp}_{Zr}$ are kept) → code-to-code comparison (phase densities)

Step-1: MASCA-MA
Codes/Models

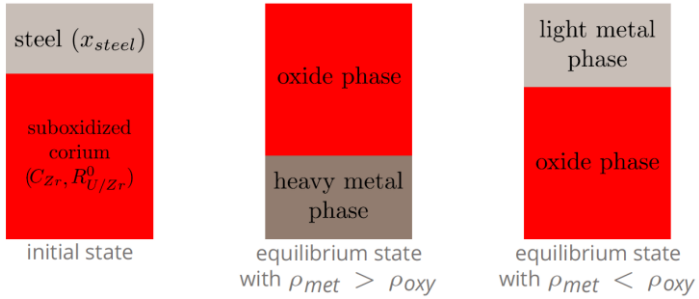

- Five participants
- Different liquid miscibility gap models

Institution	N°	Code / model	Description/comments
NRC "Kurchatov Institute"	1	TSAR / GIBBS	Thermodynamic approach based on Gibbs energy minimization using regular solution model (CALPHAD-like technique)
IRSN	2	ASTEC / Salay-Fichot model	Analytical model calibrated on experimental results from MASCA MA-1, 2, 3, STFM-Fe-2, 3, 4, 5, 6, 7, 8, 9, 14, 15
INRNE-BAS	3		
IBRAE	4	HEFEST_URAN	Interpolation scheme based on MASCA MA and STFM-Fe test experimental results
CEA	5	PROCOR interface with OpenCalphad / Gibbs energy minimizer with NUCLEA'19 database	CALPHAD method with a non-ideal associate model for the Gibbs energy of the liquid phase
	6	PROCOR / Salay-Fichot model	See ASTEC above
	7	PROCOR / Nandan-Fichot model	Analytical model calibrated on OpenCalphad calculations with NUCLEA'19 database
	8	PROCOR / thermodynamic closures associated with "new" stratification kinetics model (*cf.* A. Lecoanet's presentation)	Interpolation scheme based on OpenCalphad calculations with NUCLEA'19 database

- Phase densities calculated from:
  - a non-ideal mixture law (element density laws + excess volume term): NRC KI, IBRAE
  - an ideal mixture law (species density laws): IRSN, INRNE-BAS, CEA

Step-1: MASCA-MA
Results

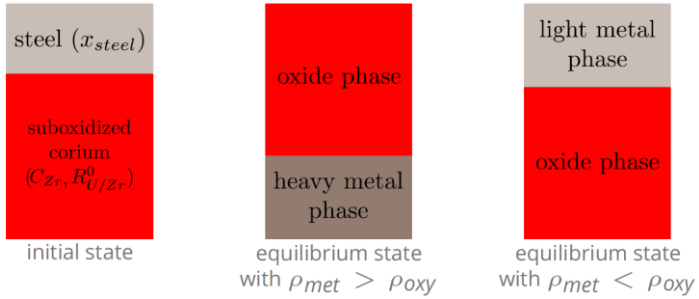

- Phase partitioning (in terms of the oxide phase wt fraction)
  - Overall good agreement
  - Salay-Fichot model: not the same in PROCOR and ASTEC
  - Except for NRC-KI (n°1), results deterioration in MA-6 case (higher x^{exp}_{steel})

	$R^{exp}_{U/Zr}$	$\frac{x^{exp}_{steel}}{x^{exp}_{steel}+1}$ (%)	**Oxide phase amount (wt)**	5 CEA - PROCOR - NUCLEA	6 CEA - PROCOR - S&F	7 CEA - PROCOR - N&F	8 CEA - PROCOR - closures	2 IRSN - ASTEC	3 INRNE - ASTEC	1 NRC KI - TSAR	4 IBRAE - HEFEST_URAN
MA-1	1.45	11.42	**0.781**	-2.4%	-1.6%	-3.1%	-1.0%	1.0%	1.0%	4.2%	-2.7%
MA-2	1.28	10.80	**0.878**	-3.4%	-2.5%	-3.7%	-3.0%	-1.3%	-1.4%	1.6%	-1.9%
MA-3	1.14	10.78	**0.726**	1.9%	3.1%	1.6%	4.0%	5.3%	5.2%	8.0%	4.5%
MA-4	1.17	19.09	**0.639**	-3.2%	-3.3%	-2.9%	-0.3%	-0.2%	-0.2%	6.3%	-2.2%
MA-5	0.89	9.89	**0.754**	-7.6%	-6.6%	-7.1%	-4.7%	-3.7%	-3.7%	-0.5%	-3.1%
MA-5b	0.90	7.05	**0.799**	-7.0%	-5.3%	-6.6%	-4.2%	-2.8%	-2.9%	-1.4%	-3.9%
MA-6	1.14	29.71	**0.565**	-9.6%	-11.3%	-8.1%	-13.6%	-7.9%	-7.2%	2.4%	-7.7%

Step-1: MASCA-MA
Results

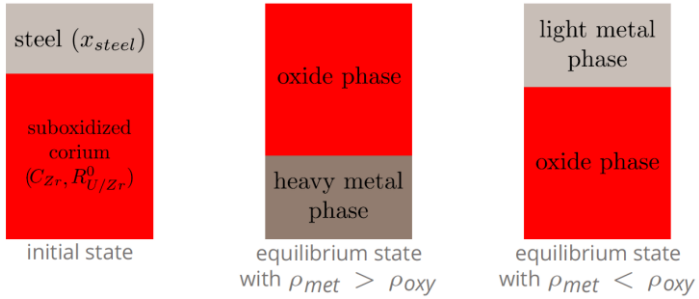

- Species phase partitioning (in terms of the Zr mass fraction in the metal phase w_{Zr}^{met})
  - MA-3, 4, 5, 5b, 6 conditions:
    - underestimation in most cases
    - worsened for Salay&Fichot, Nandan&Fichot models (n°2, 3, 6, 7) because of the models hypothesis of uniform $R_{U/Zr}$ ratio
  - MA-1 (higher $R_{U/Zr}$ w.r.t. MA-3), MA-2 (higher C_{Zr} w.r.t. MA-3) conditions:
    - thermodynamic database + Gibbs energy minimizer (n°1, 5): (consistent) significant overestimation of the Zr content
    - Salay&Fichot, Nandan&Fichot models (n°2, 3, 6, 7): compensation with previous trend

	$R_{U/Zr}^{exp}$	C_{Zr}^{exp} (%)	w_{Zr}^{met}	5 CEA - PROCOR - NUCLEA	6 CEA - PROCOR - S&F	7 CEA - PROCOR - N&F	8 CEA - PROCOR - closures	2 IRSN - ASTEC	3 INRNE - ASTEC	1 NRC KI - TSAR	4 IBRAE - HEFEST_URAN
MA-1	1.45	33.1	**0.781**	34.0%	6.5%	8.7%	35.3%	-0.5%	-0.3%	36.3%	24.5%
MA-2	1.28	74.5	**0.878**	66.2%	21.0%	28.1%	66.4%	6.4%	7.8%	69.9%	-15.0%
MA-3	1.14	36.5	**0.726**	-1.5%	-16.9%	-15.6%	1.3%	-19.9%	-19.9%	4.0%	-21.8%
MA-4	1.17	39.7	**0.639**	-9.9%	-23.0%	-23.7%	-9.0%	-26.2%	-26.1%	-3.1%	-10.7%
MA-5	0.89	31.5	**0.754**	-11.7%	-20.3%	-20.5%	-9.3%	-22.4%	-22.3%	-0.4%	-35.9%
MA-5b	0.90	30.5	**0.799**	-12.7%	-20.9%	-20.5%	-9.7%	-22.6%	-22.5%	-1.5%	-37.7%
MA-6	1.14	29.1	**0.565**	-18.1%	-28.6%	-31.8%	-15.7%	-31.8%	-31.7%	-12.2%	-19.9%

⚠ experiments not strictly at thermodynamic equilibrium + uncertainty
→ good agreement between results (n°1 and 5) through Gibbs energy minimization with different thermodynamic databases

Step-1: MASCA-MA
Results

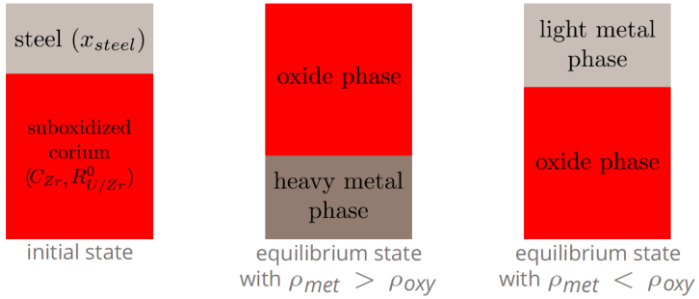

- Phase densities (in terms of phase density difference $\rho^{met} - \rho^{oxy}$ [kg.m-3] for $x_{steel} = x_{steel}^{exp}$):
  - In PROCOR, sensitivity to species law extrapolation (oxide phase):
    - M1 (n°6a) : $\rho_i\left(T < T_i^{liquidus}\right) = \rho_i\left(T_i^{liquidus}\right)$ M2 (n°6b) : $\rho_i\left(T < T_i^{liquidus}\right)$ extrapolated
    - M1 (n°6a) → NRC KI (n°1) while M2 (n°6b) → IRSN - ASTEC (n°2)
  - CEA - PROCOR with M2 hypothesis, IRSN - ASTEC and NRC KI → fairly consistent
  - INRNE - ASTEC (n°3) : T^{exp} instead of $T^{exp} + 100°$ → limited impact
  - Further analysis → critical review of the density laws implemented in the different codes that may not be at the state-of-the-art taking into account recent experimental data

	6a	6b	2	3	1	4
	CEA - PROCOR - S&F, M1	CEA - PROCOR - S&F, M2	IRSN - ASTEC	INRNE - ASTEC	NRC KI - TSAR	IBRAE - HEFEST_URAN
MA-1	245.3	42.8	-35.3	-91.4	305.6	-342.9
MA-2	-559.3	-763.2	-771.1	-785.6	-717.3	-1075.9
MA-3	503.3	316.1	315.4	316.1	543.6	-68.3
MA-4	183.6	-7.6	-4.5	-50.5	64.8	-489.1
MA-5	907.3	740.9	712.7	721.0	794.0	542.4
MA-5b	1100.8	937.7	927.0	936.2	955.1	984.1
MA-6	-207.4	-334.4	-271.1	-296.8	-454.4	-809.3

Step-2: MASCA-RCW 100
Description

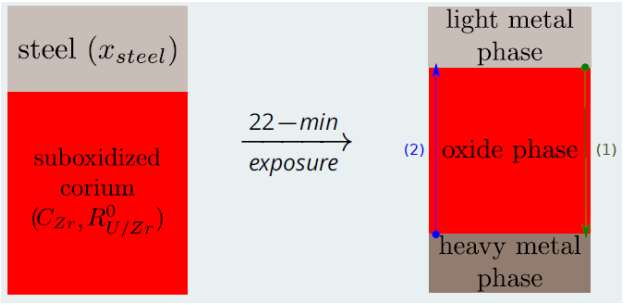

- A single test
  - 45.3kg of suboxidized corium + 4.6kg of steel (close to MASCA MA-3 conditions × 20)
  - Ø18cm crucible
  - 22-min exposure

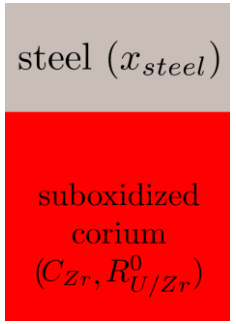

Phase α	Mass (kg)	Species mass fraction (%)					
		UO_2	Zr	ZrO_2	Fe	Cr	Ni
Steel	3.989	0.0	0.0	0.0	69.64291	16.22873	14.12836
Oxide	48.781	76.25693	14.24420	0.949887	0.0	0.0	0.0

- Post-mortem ingot as the solidified state of the system during the transient relocation of steel below the oxide:
  - a continuous light metal phase (7) above the oxide pool (5)
  - a dispersed metallic phase enriched in U and Zr that can be viewed as centimetric droplets (4) relocating downward through oxide (5)
  - a continuous heavy metal phase (2) below the oxide (5)

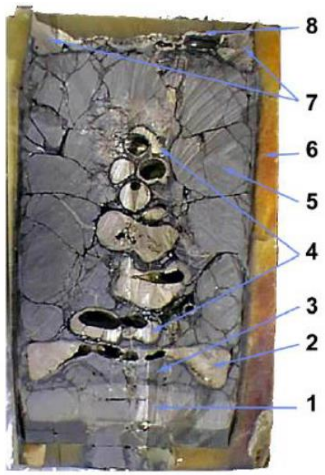

1. non-molten oxide briquette
2. continuous heavy metal phase at the bottom
3. partially molten oxide zone
4. metallic droplets of the central region
5. continuous oxide phase
6. epoxy resin
7. continuous light metal phase at the top, see details below

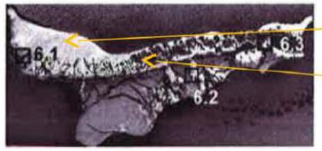

8. ingot surface

Step-2: MASCA-RCW 100
Codes/Models

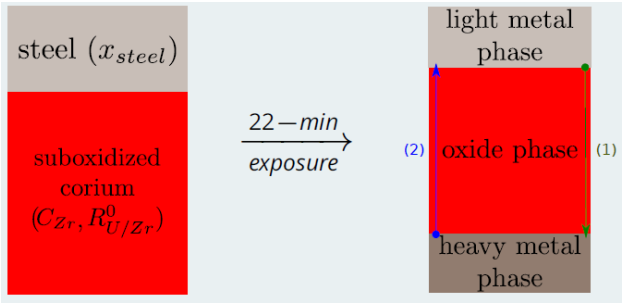

- Four participants
- Different transient stratification models based on different liquid miscibility gap models (see step-1)

Institution	N°	Code / model	Description/comments	Liquid miscibility gap model
IRSN	1	ASTEC / inter-layer mass transfer model	Mass transfer considered simultaneously at the two interfaces upper metal/oxide, oxide/lower metal; local interface equilibrium approximated by the thermochemical equilibrium of the two phases at this interface	Salay-Fichot model: see n°2/3 in step-1
INRNE-BAS	2			
IBRAE	3	HEFEST_URAN / MultiMelt module	1D finite element diffusion model for uranium in the upper metal phase	
CEA	4	PROCOR / legacy inter-layer mass transfer model	Evolution equation for the uranium mass fraction in the oxide phase considering the exchange with the upper metal phase; degree of advancement towards global thermochemical equilibrium	Salay-Fichot model: see n°6 in step-1
	5	PROCOR / "new" integral mass transfer model that takes into account the dispersed metal phase (mass transfer and dynamics)	Mass and element mass conservation for all phases; interface jump conditions associated with local equilibrium simplified under the hypothesis that there is no oxygen (resp. steel) in the metal (resp oxide) phases; 1D droplet momentum conservation equation	thermodynamic closures: see n°8 in step-1

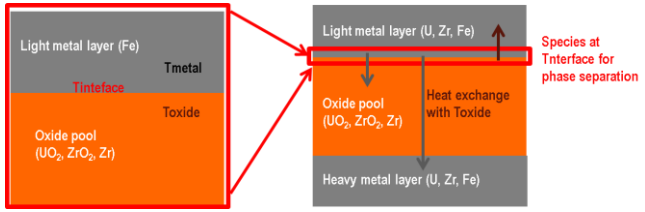

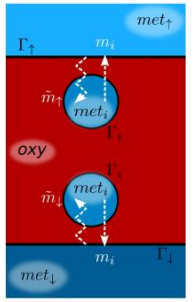

(see A. Lecoanet's presentation)

- In all cases, a (limited) parametric analysis for parameter calibration (not shown)

e.g. effective diffusion coefficient in n°1, 2 and 4

Step-2: MASCA-RCW 100
Results

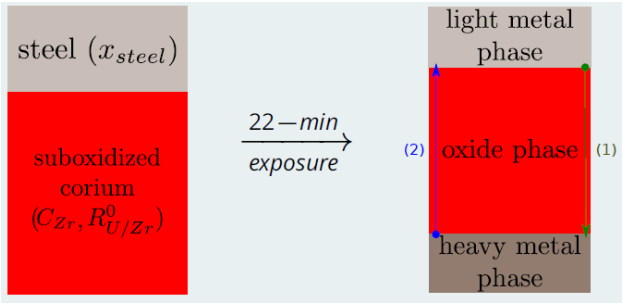

- Phase partitioning (in terms of oxide m^{oxy} and heavy metal $m^{met\downarrow}$ masses):
  - Qualitative differences between models:
    - Continuous heavy metal formation from t=0s in ASTEC, PROCOR legacy models (n°1, 2, 4)
    - Continuous heavy metal formation starting at t=800s in HEFEST_URAN (n°3)
    - First droplets detachment at t=1310s with PROCOR "new" model → heavy metal layer formation; then slow increase of $m^{met\downarrow}$ (mass transfer through interface) until next droplet detachment (not shown, occurs around 2750s)
  - By calibration, fairly good agreement on $m^{met\downarrow}$ at 22min

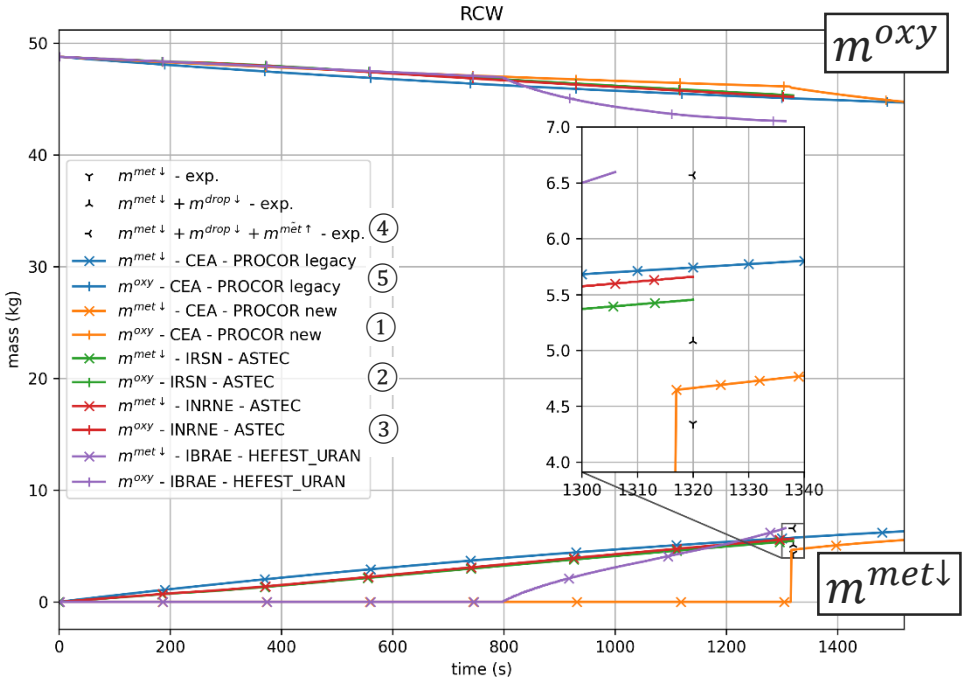

Three exp. values for $m^{met\downarrow}$, $w_U^{met\downarrow}$ and $w_{Zr}^{met\downarrow}$ for comparison:
- actual heavy metal phase ($met\downarrow$)
- actual heavy metal phase ($met\downarrow$) + droplets ($drop\downarrow$)
- actual heavy metal phase ($met\downarrow$) + droplets ($drop\downarrow$)

+ U-, Zr-enriched boundary region of light metal layer ($\widetilde{met}\uparrow$)

Step-2: MASCA-RCW 100
Results

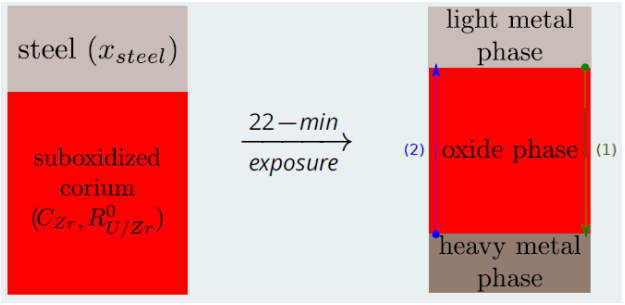

- Species partitioning (in terms of U ($w_U^{met\downarrow}$) and Zr ($w_{Zr}^{met\downarrow}$) mass fractions in the heavy metal phase):
  - PROCOR legacy model (n°4): constant heavy metal composition (at global thermochemical equilibrium)
  - ASTEC (n°1, 2): limited departure from PROCOR legacy constant values

  At 22min, $w_U^{met\downarrow}$ fairly well reproduced; underestimation of $w_{Zr}^{met\downarrow}$
  → consistent with Salay-Fichot model trends in MA3 conditions
  - HEFEST_URAN (n°3): very high U, Zr content at heavy metal formation with rapid decrease toward consistent values with previous models
  - PROCOR "new" (n°5): at heavy metal formation, underestimation of $w_U^{met\downarrow}$ → consistent with trends in MA3 conditions with associated thermodynamic closures

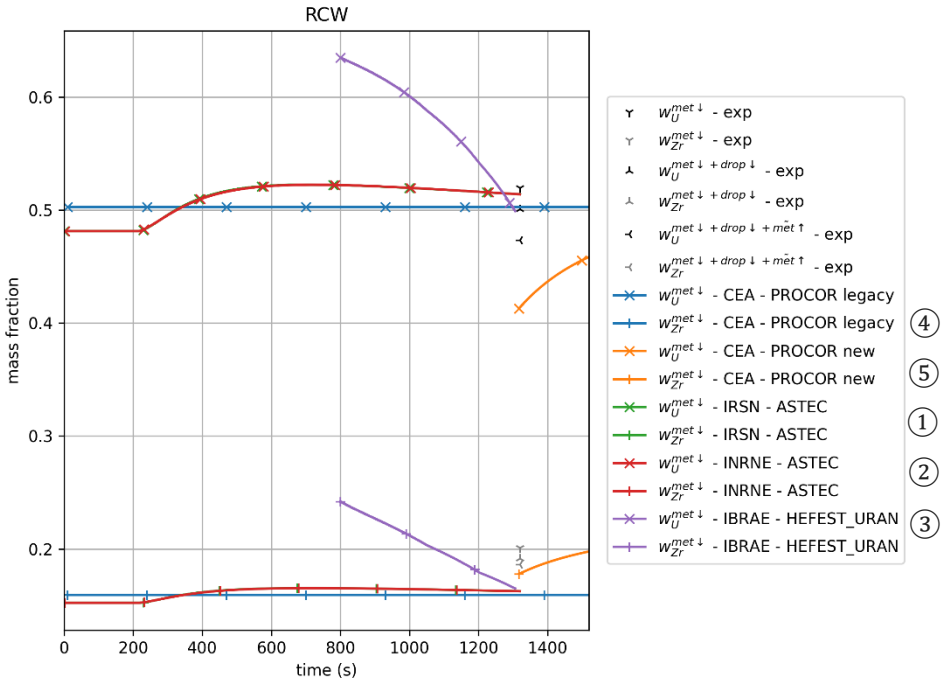

- RCW-100: a unique qualitative comparison for stratification kinetics… with limited information
  → additional experimental results are needed to go further in models validation

Conclusions and perspectives
MASCA-CORDEB2 benchmark

- A three-step benchmark based on prototypical experiments - cold crucible technique with inductive heating
- Addressing in a progressive manner, a high-uncertainty, high-impact “phenomenon”: oxide/metal corium pool thermochemistry and stratification
- Results of the two first steps: a valuable exercise for validation/calibration of existing models… highlighting the need for further analysis and comparison / R&D

- All results to be published in TECDOC including third step (stratification kinetics in presence of a mechanically stable crust at the top oxide surface – CORDEB2 - CP7-02 test)
- A common basis for further R&D, model development and validation

Thank you for your attention

romain.le-tellier@cea.fr
laure.carenini@irsn.fr
florian.fichot@irsn.fr
r.gencheva@inrne.bas.bg
pavlinpg@inrne.bas.bg
Melnikov_IA@nrcki.ru
phil@ibrae.ac.ru

Authors would like to acknowledge the IAEA for the coordination of this CRP and in particular Mr Miassoedov from the Division of Nuclear Power and Mr Massara and Ms Veneau from the Division of Nuclear Installation Safety.

COOLABILITY OF A CORIUM POOL IN A DEBRIS BED – CALCULATION OF CRITICAL HEAT FLUX (CHF) TESTS WITH THE ASTEC CODE

Zambaux J-A. and Sartoris C.
Institut de Radioprotection et de Sureté Nucléaire
Cadarache, 13115, BP3, Saint Paul lez Durance
julie-anne.zambaux@irsn.fr; christine.sartoris@irsn.fr

ABSTRACT

In case of severe accident in a light water reactor, a debris bed may form in the core and possibly melt, as it happened in TMI-2. Knowledge about the coolability of such molten pool surrounded by debris is crucial to investigate the possibility of stabilizing a part of the fuel inside the vessel. Based on experimental tests conducted at IRSN investigating the effect of debris size, steam and liquid flowrate, inclination and pressure, some numerical simulations have been conducted with the severe accident system code ASTEC. Some global conclusions could be drawn: the surface temperature evolution is well reproduced and the pool boiling CHF value is correctly calculated except in presence of debris. Pressure and liquid flowrate are satisfactorily evaluated but differences are shown as concerns the debris diameter impact, the inclination impact and the gas flowrate impact. The observed discrepancies are analyzed here and prospects for improvements of CHF and void fraction modelling are provided.

KEYWORDS
Severe accident, Corium coolability, Critical Heat Flux, ASTEC code

1. INTRODUCTION

In case of a severe accident in a nuclear reactor, a large debris bed may be created in the core. If, in some part of this debris bed, the temperature keeps on rising up to the melting point, it may form a molten pool of corium, as it happened in TMI-2 [1]). The molten pool is expected to become less and less coolable as it grows larger because the heat flux at the periphery of the pool increases linearly with the pool diameter. Therefore, it is of primary interest to determine the maximum size of a molten pool surrounded by debris which may be stabilized under water after reflooding the vessel (as in TMI-2) or in case of a debris bed formed in a flooded reactor pit where the presence of denser zones may limit the coolability ([2], [3]). The maximum heat flux that may be extracted, or Critical Heat Flux (CHF), is a key parameter for that issue.
Severe accident codes are a needed tool for safety analysis and should be able to correctly assess this degraded core cooling capability in case of reflooding scenarios. The ASTEC v3.1.1 code is a severe accident system code developed by IRSN [4], used for safety analysis and source term evaluation studies. ASTEC is organized in different coupled independent modules, each for a different type of physics, therefore allowing dedicated studies and validation (see [5] for the main validation elements). In the frame of this paper, the ASTEC code has been used for CHF evaluation validation. Only the system thermal-hydraulic module CESAR (based on 1D two-fluid model approach [6]) and the core degradation module ICARE (evaluating the heat transfer and mechanical state of the core) were activated.
In most of studies for thermal-hydraulic system codes, CHF evaluation experiments have been performed in small diameters and high length vertical tube geometries in order to represent the fuel assembly

configuration. Among the different experimental data available, the Groeneveld look-up table [7] is widely used in thermal-hydraulic system codes, for example in the CATHARE code [8] or the TRACE and the RELAP 5 codes [9]. Severe accident system codes follow the same approach. However, core configuration can be strongly modified during the degradation process, as stated in [10]. The use of CHF correlation established for intact core geometries is often extended for partially degraded core geometries, as it is the case in the ASTEC code. The global evolution for degraded core reflooding can be reasonably reproduced (see [11] for an assessment of the ASTEC code ability to calculate the TMI-2 accident for example). Nevertheless, these global validation studies involve important uncertainties and potential compensating effects. Therefore, specific validation of each phenomenon such as the boiling crisis is still needed to improve code reliability.

Experiments such as PEARL and PRELUDE [12] have given important insight about the reflooding process in a heated debris bed. They have given validation elements for the porous media approach in ASTEC [13]. More recently, other experiments were performed, in order to evaluate the CHF in a geometry representative of a degraded core [14,15]. These experiments have explored the influence of several geometrical and flow parameters on the CHF. They provide an important addition to the very limited available data for CHF evaluation in those porous media geometries.

The current paper aims at assessing the validation status of the current version of the ASTEC v3.1.1 code using these new CHF evaluation experiments [14,15]. A brief reminder of the experimental facility and performed tests for CHF evaluation in degraded core configuration is first given. Then the ASTEC code modelling proposed, and results analysis is presented. As in the experimental work, different simulations have been performed, varying different parameters that are expected to influence the CHF in porous media configuration. The influence of each parameter is specifically studied in the last section of the paper.

2. EXPERIMENTAL DEVICE

The CHF tests are performed in a test section (see Figure 1, left) mainly composed of a tank filled with steel balls and deionized water at saturation temperature. A 50 mm diameter copper cylinder is positioned, one of its ends abutting this debris bed and its other end heated by electrical cartridges. The 90° orientation corresponds to a horizontal cylinder and thus to a vertical heated plate. The test section is possibly equipped with another electrically heated copper block used as a steam generator and can be connected to a deionized water loop to inject liquid water at the debris bed bottom. A connection is also possible to a water tank situated above the test section to achieve higher pressure in the test section thanks to the water column weight (connections not shown here). All the external surfaces are thermally insulated.

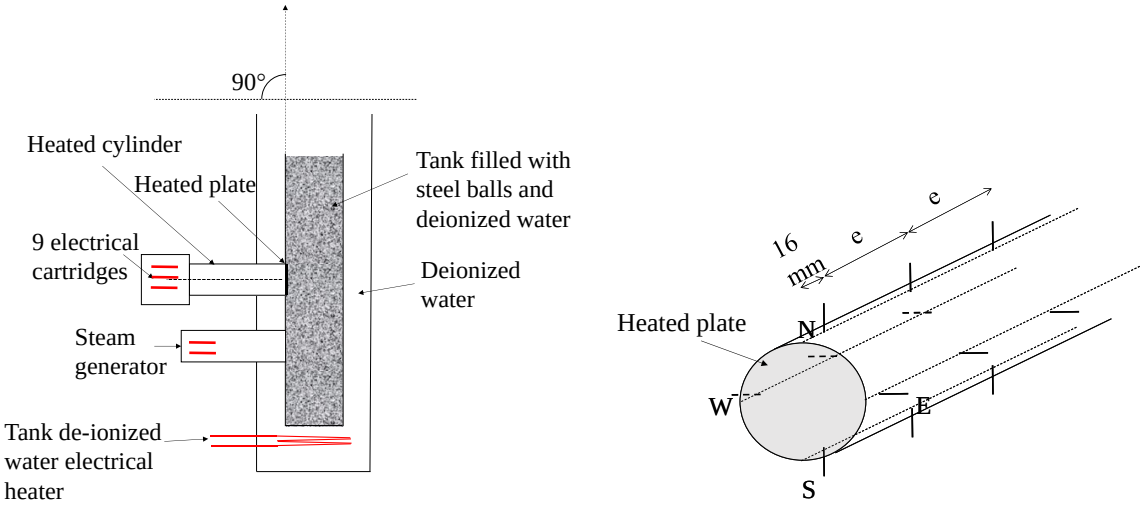

Figure 1. Test Section (left) and Thermocouples Implantation inside the Heated Cylinder (right).

The thermal heat flux is calculated by Fourier's law thanks to measurements of thermocouples inserted in the heated copper cylinder (see Figure 1, right). The copper cylinder is slowly heated until the CHF achievement signaled by a dramatic increase of the cylinder temperature. Then the power is shut down. Detailed descriptions of devices, instrumentation, uncertainties calculations, heated plate surface preparation and detailed heating procedure are given in [14] and [15].
The following parameters impacts are experimentally investigated and compared to numerical simulations in the next paragraphs:

- Ball size of 2, 3 and 4 mm,
- Different inclinable test sections are used to study inclinations from 0° (horizontal plate) up to 150° (nearly downward facing plate) to simulate different local zones of a corium mass,
- Pressure from atmospheric pressure up to 2.5 absolute bar.

3. CALCULATIONS PRESENTATION

3.1. ASTEC v3.1.1 Modelling

The ASTEC code can be used in 2D for axi-symmetrical domains. In the 2D modelling, internal reactor structures can be considered and impact the flow and the heat transfer. These structures can be used to represent an intact core but also a degraded core with highly viscous liquid magma or debris. Debris are considered as spherical monodisperse and are assimilated to a porous media. This approach in the ASTEC code has been validated for flow in a porous media with the results of the PEARL experiments [12].
The heat transfer between core elements and the fluid phase is evaluated depending on local flow conditions in the considered mesh. The heat transfer is distributed into three contributions, one to the liquid phase, one to the gas phase and one to the interface, directly used for the mass transfer (by vaporization/condensation). This last contribution depends mainly on the water subcooling. At saturation conditions, all the heat flux is directed to the interface.
Depending on the value of the void fraction in the considered mesh, the heat transfer happens preferentially with the liquid phase or with the gas phase (the dry-out condition is set in the code for a void fraction above 0.999). In the case of a heated wall or object in presence of liquid, the heat transfer regime depends on the wall temperature:

- If the wall temperature is below the fluid saturation temperature: this is the liquid convection regime, the wall exchanges energy with the liquid phase.
- When wall temperature becomes higher than saturation conditions: this is the boiling regime. Nucleate boiling is first observed. Depending on the water subcooling, most of the heat flux is directly used for mass change in this regime. It is assumed that the regime remains nucleate boiling as long as the calculated heat transfer due to nucleate boiling remains below the calculated CHF value and the void fraction does not exceed 0,999.
- When nucleate boiling is left, a transition regime is assumed during which the heat flux remains at the CHF value. As in the nucleate boiling regime, this heat flux is distributed between the interface and the liquid phase. Film boiling regime is entered when the wall temperature reaches minimum temperature for a stable film condition.

In ASTEC v3.1.1, the CHF is assessed by the code with the Zuber correlation for pool flow [16], using the correcting coefficient proposed by Lienhard and Dhir [17] with additional correction factors. The complete expression is given by:

$$\phi_{CHF} = F_l C_{sub} 0.149 \left(\frac{g\gamma(\rho_L - \rho_G)}{\rho_G^2}\right)^{\frac{1}{4}} \rho_G h_{LG} \qquad (1)$$

with $C_{sub} = 1 + 0.1\frac{1}{h_{LG}} Cp_L(T_{sat} - T_L)\left(\frac{\rho_L}{\rho_G}\right)^{\frac{3}{4}}$ (2) and $F_l = \begin{cases} 1.259 & if\ L_c < 4\ mm \\ \left(\frac{8}{L_c(mm)}\right)^{\frac{1}{3}} & if\ 4\ mm < L_c < 16\ mm \\ 0.79 & otherwise \end{cases}$ (3)

In this expression (1), h_{LG} is the latent heat needed to vaporize water, ρ_L and ρ_G are respectively the steam and the liquid water density, γ is the surface tension and g is the gravity. The first coefficient correction factor $C_{sub}$is a correction coefficient proposed by Ivey and Morris [18] for subcooled flow. The second correction factor F_l has been introduced for degraded core configuration, where a porous media is assumed with small characteristic length. It is based on the correction advised by Groeneveld et al. [7] to take into account variation in flow characteristic length L_c is here applied.

3.2. ASTEC v3.1.1 Dataset and Meshing

The ASTEC code cannot simulate the real parallelepipedal test section geometry because as it can only consider 2D axi-symmetrical meshing. Therefore, the calculations only represent a cross-section of the whole experimental device as shown on Figure 2, left. Due to the axi-symmetrical nature of the mesh, this 2D plan is in fact cylindrical with its axis opposite to the domain wall. The heated surface is then modelled as part of the wall, as a crown whose height corresponds to the experimental heated surface diameter and whose internal radius corresponds to the total fluid domain width (see Figure 2, left). In the calculation, a domain width of 50 cm is considered (the domain width should not impact the results as only the flow close to the heated wall should impact the CHF evaluation). After verification, that it is not too narrow to impact the steam flow around the heated surface. In the experiments, the heated device is a long full copper cylinder whereas in the calculations, its thickness corresponds to the thickness of the rest of the wall. The height of the domain is kept the same as in the experiments, to have the same hydrostatic pressure.

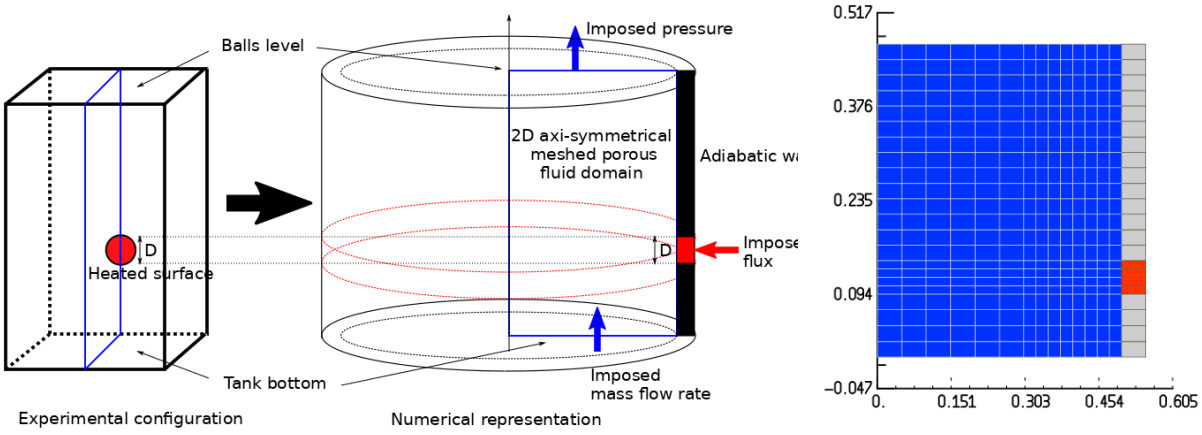

Figure 2. Numerical representation of the experimental set-up (left) and domain discretization considered for the study

ASTEC is a system code using correlations and transitions between regime parameters based on mean values in control volumes (for example, dry-out condition is based on the void fraction value in the considered mesh which is directly dependent on the mesh volume). After a preliminary meshing dependency study, the discretization presented on Figure 2, right is retained. On this figure, the fluid domain is in blue while the solid wall is in grey. The red part on the wall indicates the location of the heating condition. The meshing

is refined in the heated zone levels and in the vicinity of the wall to give a better insight on the flow close to the wall and on the radial void fraction evolution in the domain. In the fluid domain, the porosity is imposed to 0.34, from the experimental data measurement [14]. At the top of the domain, an imposed pressure boundary condition is set with water being allowed to flow back. A mass source inlet condition can be set at the bottom of the domain for both water and steam. A heat flux is imposed on the red part of the wall while an adiabatic condition is considered on the rest.

3.3. Reference Case

This reference calculation considers no inlet liquid nor gas mass flow rate at the bottom, the imposed pressure is set at 1.08 bar at the top of the domain, the test section is vertical (90° angle) and the balls have a 4 mm diameter. In the experiments, an increasing heat flux was applied on the heated copper mass with an increase slope of 0.09 W/s. The numerical imposed slope takes into account the 30% heat losses estimated in the experiments on the copper cylinder length. Moreover, in order to keep the same heat flux density as in the experiment, the imposed numerical heat flux also considers the geometry modification and heat surface modification. Figure 3 presents the detail of the calculated temperature of each heated wall element along with the void fraction in the cells facing each element.

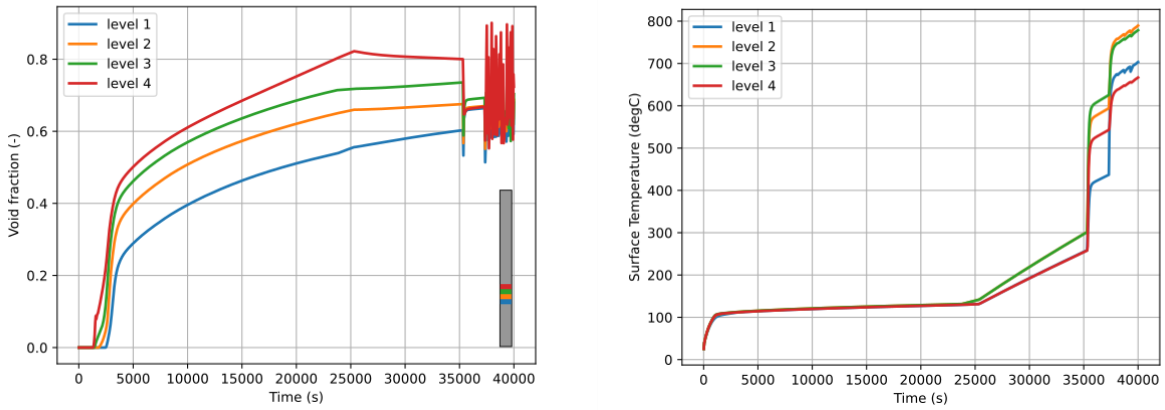

Figure 3. Detailed evolution of the void fraction close to the heated surface (left) And wall temperature (right) (level 1 height=0.101 m ; level 2 height=0.114 m ; level 3 height=0.126 m and level 4 height=0.139 m)

As expected, the void fraction increases with height but always remains in this case lower than the dry-out condition set in the code (void fraction of 0.999) and thus does not impact the heat transfer evaluation. Surface temperature behaviour is interesting to note here as it increases faster for cells located in the middle of the heated surface compared with the bottom and top elements. This is in fact due to conduction to the rest of the cold wall on the sides of the heated part of the wall. This conduction in the experiments was limited due to insulation but it was not taken into account in the calculations. During the nucleate boiling regime, when the cooling by the fluid is very efficient, this conduction heat flux is very limited (amounting around 5% of the total imposed heat flux). In the transition regime, when the heat flux extracted by the fluid is limited, this conductive heat transfer increases up to 20% of the total imposed heat flux and limits the temperature increase of the heated part of the surface. This conductive heat transfer introduces a small bias in the calculations compared with the experimental set-up.

For the nucleate boiling process to be sustained, vapour needs to get away from the heating wall so liquid water can access it. When this process is no longer possible and vapour accumulates in the vicinity of the heated wall, efficient cooling is no longer possible and CHF condition is reached.
The cooling process in the nucleate boiling regime in the porous media is illustrated on Figure 4. This figure presents the fields of liquid superficial velocity j_L and the gas superficial velocity j_G close to the heated part of the wall at 15 060 s, when the nucleate boiling regime is established. Arrows indicate the direction and magnitude of the flow. It shows that the vapor flow remains contained on a thin layer close to the wall (up to two radial meshes, i. e. 5 cm). The strong vapor flow seems to drive the liquid flow: the water is accessing the heated part of the wall from below and not radially. Direct radial liquid flow to the heated surface is prevented by the vapour layer and a loop develops, fed by water coming from the lower part of the fluid domain.

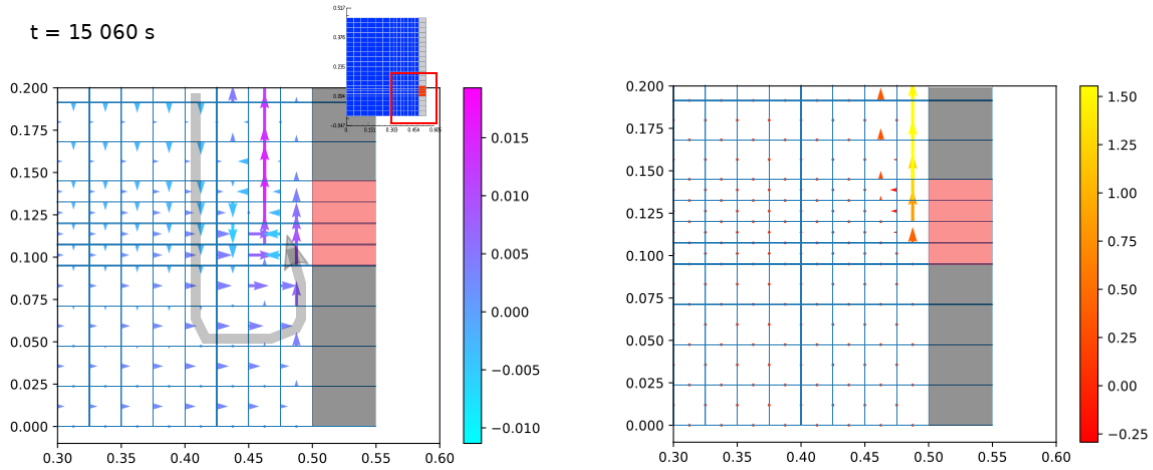

Figure 4. Liquid (left) and vapor (right) superficial velocity map (m/s) close to the heated wall during the nucleate boiling regime

The numerical results can be compared with the experimental data. On Figure 5 (left), it is interesting to note that at the beginning, the time needed by the surface to reach nucleate boiling conditions (fluid saturation temperature) is well reproduced by the calculation, validating the imposed numerical heat flux. During the nucleate boiling phase, both calculated wall temperature and estimated heat flux increases are comparable to experimental ones. However, the calculated departure from the nucleate boiling regime and subsequent temperature increase happens significantly later than the experimental ones (Figure 5 right). Moreover, after CHF, the experimental flux drops drastically while the numerical simulation keeps a nearly constant heat flux (in consistency with the transition regime modelling limiting the heat flux by the CHF estimated by correlation). A drastic drop in the exchanged flux is observed in the numerical simulation only when the minimum stable film temperature is reached.
In all experiments performed in the same conditions as the reference case, the CHF was evaluated around 200 kW/m² (+-24 kW/m^2). This uncertainty does not take into account strong scattering of the experimental results, partially due to the difficulty to control the surface state as stated in [15]. However, this would not explain the difference with the calculated CHF of 756 kW/m^2. This shows that the current evaluation of the CHF with the correlations defined in the code in not satisfactorily in this configuration. A verification has been made in pool boiling configuration (no porous media, free volume), the other parameters being kept the same. The calculated CHF is then 1346 kW/m² whereas experiments performed in these conditions give a CHF around 1275 kW/m² (+-166 kW/m^2). So, in pool boiling conditions, the agreement between the code

and the experiments is rather good. Consequently, it is the evaluation of the CHF for porous media with small porosity and small particle size that is not adequately predicted.

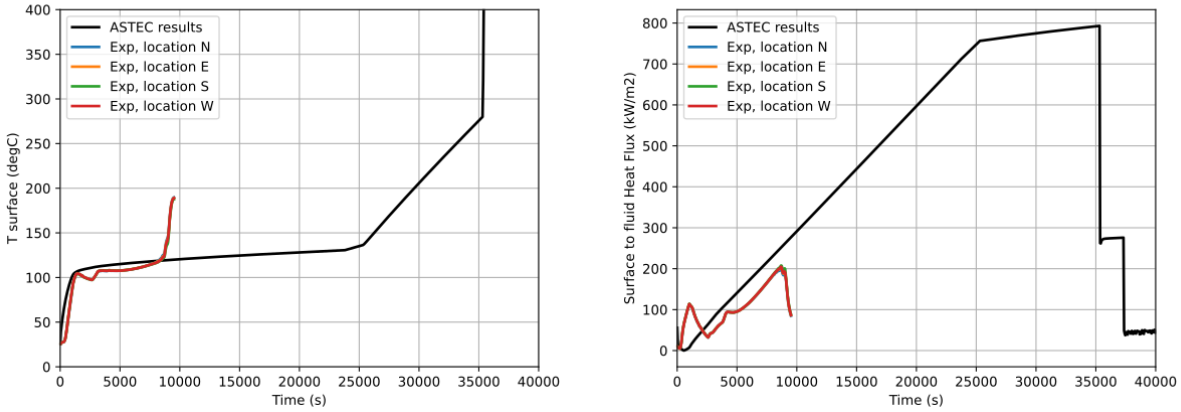

Figure 5. Comparison between the experimental and the numerical results

4. INFLUENCE OF THE MAIN PARAMETERS

Vapor and liquid flowrate impacts are not presented here. Study has shown that influence of liquid flowrate was satisfactorily calculated in the narrow experimental liquid flowrate range. The strong impact of steam flowrate was not observed on the calculations results. More complete numerical calculations will be considered in future work to better understand this discrepancy.

4.1. Pressure Effect

Experimentally, several operating pressures have been studied by varying the height of the water column on top of the test section. In the calculation, the pressure is imposed at the top of the domain (corresponding to the top of the section filled with steel balls). Four calculations are performed at 1.08 bar (reference case), 1.51 bar, 1.85 bar and 2.49 bar. All the other initial and boundary conditions are kept the same as in the reference calculation presented in the above section. Figure 6 presents the CHF ratio between the pressured case CHF and the reference one for the numerical and experimental results. A dependence around $P^{0.5}$ has been found in the experiments (in agreement with literature) while it is slightly lower, closer to $P^{0.4}$ in the calculations. Nevertheless, the current evolution given in the code does seem rather reasonable.

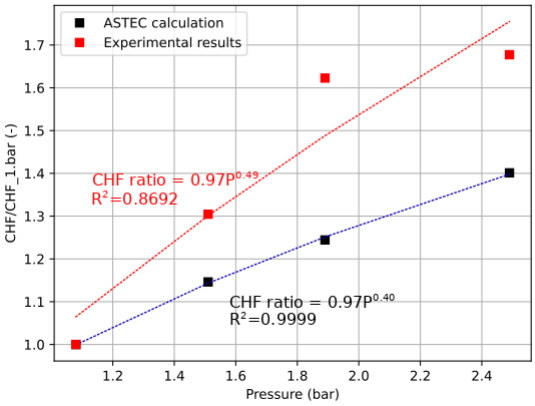

Figure 6. CHF ratio evolution with pressure (coefficient R=$\frac{\sum(x-\overline{x})(y-\overline{y})}{\sqrt{\sum(x-\overline{x})^2(y-\overline{y})^2}}$)

4.2. Steel Ball Diameter

The experiments involved 2 mm, 3 mm and 4 mm balls (reference case). The porosity remains the same. Table 1 presents experimental and numerical CHF ratios (CHF/CHF_4 mm). As it is shown in paragraph 3.3, the calculated CHF values are far from experimental results. Thus, only the CHF ratio is compared here with the experimental results in order to assess the relative impact of the studied parameter.

Table I. CHF evolution with steel balls diameter D_p

Ball diameter Dp (mm)	Numerical CHF (kW/m^2)	Numerical CHF ratio	Experimental CHF ratio
2	614	0.810	0.630
3	760	1.005	0.740
4	756	1.000	1.000

Although experimental results show an increasing CHF with ball diameter, the numerical results do not follow a regular trend. For the 3 mm ball diameter, the CHF ratio is slightly increased compared with the 4 mm reference case. This is due to the Groeneveld correction [7] for flows with small characteristic length – ball diameter – currently used in CHF ASTEC modelling (see equation (3)). This correction, established for flows in pipes, predicts an increase for the CHF when the characteristic length decreases (with a $D_p^{-1/3}$ dependency) for diameters greater than 4 mm. It is kept constant for lower diameters. Therefore, a very slight increase in the CHF correlation for the 3 mm case is expected compared with the 4 mm case (the low CHF value calculated for 2 mm balls is explained below). To verify the trend of the numerical results, an additional calculation was performed with 11 mm balls and lead to a CHF of 410 kW/m², confirming that the ASTEC code CHF correlation predicts a decreasing CHF trend with diameter increase. This evolution is opposite to the experimental findings, where a $D_p^{0.5}$-$D_p^{0.7}$ dependency of the CHF was observed, in accordance with other literature findings [14]. It shows that the current correlation used in ASTEC is not fit to represent flow effects on the CHF correlation in here. In particular, the use of the Groeneveld correction, established for flow in small diameter pipe, cannot be extended to flow in porous media with a very small porosity.

For 2 mm balls, a lower numerical CHF was reached, as in the experiments (see Figure 7). This can be explained by a local drying observed on the top of the surface: due to the small characteristic length and

capillarity effect, it is more difficult for vapor to leave the heated surface vicinity and void accumulates until reaching the dry-out condition (void fraction of 0.999). Then the top of the surface starts heating a lot and makes the rest of the surface also heat-up. Figure 8 presents the evolutions of the void fraction and the surface temperature for each heated wall element and the adjacent fluid meshes (to compare to Figure 3).

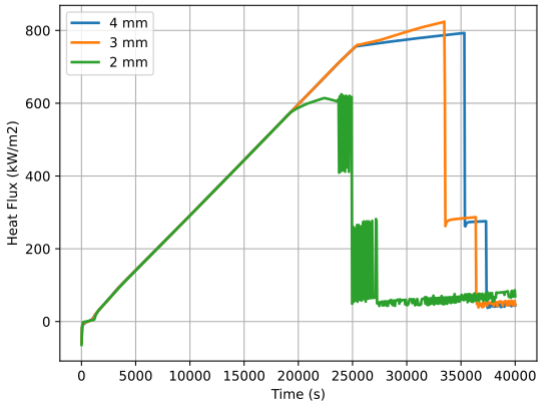

Figure 7. Evolution of the total heat flux from the heated wall to the ball bed for different ball diameters

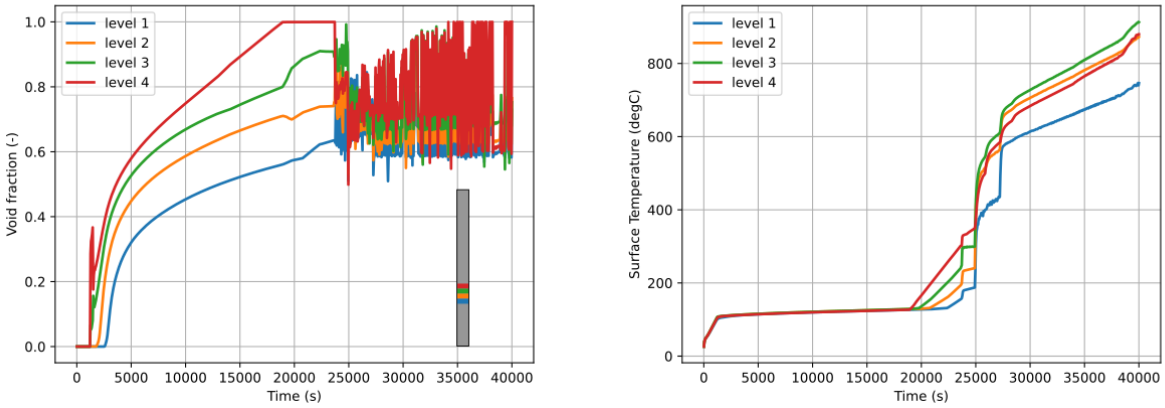

Figure 8. Local void fraction and surface temperature evolution for 2 mm balls diameter case (level 1 height=0.101 m ; level 2 height=0.114 m ; level 3 height=0.126 m and level 4 height=0.139 m)

Numerical results show that, with a fine enough nodalization, the flow in the porous media takes into account capillarity effect and can reproduce the experimentally results by reaching local dry-out conditions. However, this type of behavior is highly mesh dependent (as dry-out conditions is based on global void fraction value in a given mesh) and is not taken into account in the global CHF correlation. This one should be changed to involve this local void fraction effect.

4.3. Tilting Angle

The next effect that has been studied is the tilting angle of the heated surface and wall. In the experiments, the facility was inclined with different angles. In ASTEC v3.1.1, it is possible to tilt the 2D axi-symmetrical calculation domain by specifying a rotation angle that modifies the gravity term projection on the domain

two axis. In the present ASTEC v3.1.1 release, only angles between 90° (vertical default configuration) and 180° (horizontal up facing configuration) can be considered. Boundary condition is also modified to take into account hydrostatic pressure variation on the domain outlet.
Three calculations with an inclination angle of 90° (reference), 120° and 150° are performed and compared with the experimental results. Evaluated numerical and experimental CHF ratios (CHF/CHF_90°) to the reference case are given in Table 2.

Table II. CHF evolution for different tilting angles

Tilting angle (°)	Numerical CHF (kW/m^2)	Numerical CHF ratio	Experimental CHF ratio
90	756	1.000	1.000
120	757	1.003	0.850
150	497	0.650	0.65

As for the ball diameter effect, there is a difference in behavior between the 120° case, where no effect of the tilting angle is observed, compared with the 150° tilting angle case. Due to inclination, it is more difficult for the vapor to leave the domain as gravity effect is decreased and dry-out conditions are favored. As for 2 mm diameter case, this behavior would not be observed with a coarser meshing.
Figure 9 presents the axial profile of the gas superficial velocity and void fraction close to the domain wall during the nucleate boiling regime for the three studied tilting angle (profile along an axis parallel to the wall). The profile is plotted at 10 060 s. In the three cases, at this time, the nucleate boiling regime is established while the CHF is not yet reached. Calculations do indicate that vapor accumulation is enhanced with tilting angle. For the 150° tilting angle, there is only vapor close to the wall above the heated surface.

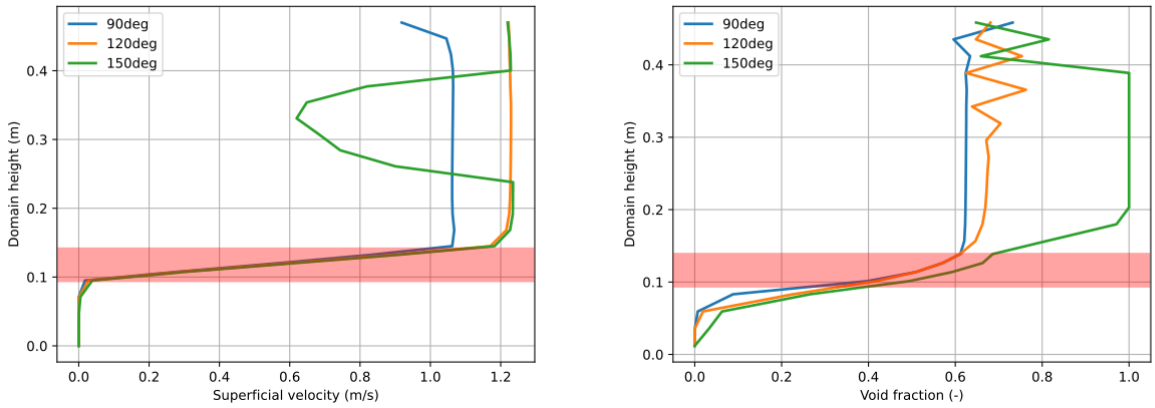

Figure 9. Axial gas superficial velocity (left) and void fraction profile close to the wall (right) during nucleate boiling regime (t=10 060 s) for three tilting angles

5. CONCLUSION

The severe accident system code ASTEC capacity to evaluate the CHF in degraded core configuration has been assessed using experimental data specifically designed for this type of configuration. The CHF achievement rests on two main mechanisms. The first one relies on the CHF correlation that is currently implemented in ASTEC v3.1.1 and stands as a maximum for the exchanged heat flux by nucleate boiling.

Although the current correlation used was shown to give good results for CHF evaluation in free water configuration, the calculations performed in the frame of this study in porous media show that the code highly over-estimate the CHF in those cases. This study highlights the need to propose a more adequate correlation for heat transfer in porous media configuration. The relative effect of different parameters on the CHF was also investigated, giving important insight on missing elements in the current CHF correlation. Pressure and inlet liquid mass flow rate impacts are in a relatively good agreement with the experimental data, at least in the range of their experimental variation. Other parameters impact such as balls diameter, tilting angle or the inlet gas mass fraction were less well reproduced by the code. New correlations taking into account the void fraction and capillarity length effect as well as the gas mass flow rate effect are needed. Future work will use this assessment study as a validation basis.
For inclined cases and small balls, the vapor retention is well reproduced, proving the code ability to predict heat flux reduction due to flow modification. DNB was reached due to local void fraction high level. As dry-out condition is given by a void fraction threshold value, this behavior is strongly dependent on meshing size. Improving dry-out condition is thus another important part for future work, especially for a system code such as ASTEC that relies on very large meshing for reactor scale applications.

ACKNOWLEDGMENTS

The authors acknowledge Electricité De France (EDF) for their financial support, Thierry Garcin for his involvement in experimental work, Florian Fichot for scientific discussions and Abdelmalek Ourabah (internship) for his participation in the numerical modelling.

REFERENCES

1. Broughton, J. M., Kuan, P., Petti, D. A., & Tolman, E. L., "A scenario of the Three Mile Island unit 2 accident", Nuclear Technology, 87, pp. 34-53 (1989) - https://doi.org/10.13182/NT89-A27637
2. Kudinov, P., Karbojian, A., Tran, C.T., Villanueva, W. 'Agglomeration and size distribution of debris in DEFOR-A experiments with Bi2O3-WO3 corium simulant melt', Nuclear Engineering and Design, 263, pp. 284-295. doi: 10.1016/j.nucengdes.2013.06.011.
3. Hwang, B., Moriyama, K., Hwang G., Kaviany, M., Lee, M., Kim, E., Park, H.-S., 'Sensitivity and uncertainty analyses of ex-vessel molten core cooling in a flooded cavity during a severe accident', Nuclear Engineering and Design, 328 (2017), pp. 121-133. doi: 10.1016/j.nucengdes.2017.12.031.
4. L. Chailan, A. Bentaïb, P. Chatelard, Overview of ASTEC code and models for Evaluation of Severe Accidents in Water Cooled Reactors, Proceedings of IAEA Technical Meeting on Status and Evaluation of Severe Accident Simulation Codes for Water Cooled Reactors, Vienna (Austria), October 9-12, 2017
5. P. Chatelard, L. Laborde, ASTEC v2.2 code validation: Illustrative results and main outcomes, Nuclear Engineering and Design, Vol. 413, 2023, 112547
6. T. Glantz, T. Taurines, O. de Luze, S. Belon, G. Guillard, F. Jacq, DRACCAR: A multi-physics code for computational analysis of multi-rod ballooning, coolability and fuel relocation during LOCA transients Part one: General modelling description, Nuclear Engineering and Design, Vol. 339, 2018, pp. 269-285.
7. D.C. Groeneveld, L.K.H. Leung, P.L. Kirillov, V.P. Bobkov, I.P. Smogalev, V.N. Vinogradov, X.C. Huang, E. Royer, The 1995 look-up table for critical heat flux in tubes, Nuclear Engineering and Design, Vol. 163, 1996, pp. 1-23
8. D. Bestion, The physical closure laws in the CATHARE code, Nuclear Engineering and Design, Vol. 124, 1990, pp. 229-245.
9. S. G. Shin, J. I. Lee, Comparative study of constitutive relations implemented in RELAP5 and TRACE - Part II: Wall boiling heat transfer, Nuclear Engineering and Technology, Vol. 54, 2022, pp. 1860-1873.
10. O. Coindreau, F. Fichot, J. Fleurot, " Nuclear fuel rod fragmentation under accidental conditions" Nuclear Engineering and Design, 255, pp. 68-76 (2013) https://doi.org/10.1016/j.nucengdes.2012.09.021

11. G. Bandini, F. De Rosa, ASTEC validation on TMI-2 and LOFT LP-FP-2, Nuclear Engineering and Design, Vol. 272, 2014, pp. 163-172.
12. G. Repetto, T. Garcin, S. Eymery, F. Fichot, Experimental program on debris reflooding (PEARL) - Results on PRELUDE facility, Nuclear Engineering and Design, Vol. 264, 2013, pp. 176-176.
13. I. Gomez-Garcia-Torano, L. Laborde, F. Fichot and H. Mutelle, "Reflooding of degraded core in ASTEC v2.1: Modelling and validation on PEARL experiments", Nuclear Engineering and Design, Vol. 393, 2022, 111768
14. C. Sartoris, T. Garcin, F. Fichot, "Coolability of a Corium Pool in a Debris Bed - Critical Heat Flux (CHF) Dependency with Tilting Angle, Debris Size and Steam Flowrate", Nuclear Engineering and Design, 403 (2022) - https://doi.org/10.1016/j.nucengdes.2022.112146
15. C. Sartoris, T. Garcin, F. Fichot , "Coolability of a Corium Pool in a Debris Bed - Impact of Debris Size, Steam and Liquid Flowrate, Tilting Angle and Pressure on Critical Heat Flux (CHF)", Proceedings of the 20th International Topical Meeting on Nuclear Reactor Thermal Hydraulics (NURETH-20) - August 20-25, 2023 - Washington, D.C.
16. N. Zuber, Hydrodynamic aspect of boiling heat transfer (Thesis), 1959
17. J.H. Lienhard, V.K. Dhir, Hydrodynamic prediction of peak pool-boiling heat fluxes from finite bodies, J. Heat Transfer 95 (1973), pp. 152-158
18. H.J. Ivey, D.J. Morris, Critical heat flux of saturation and subcooled pool boiling in water at atmospheric pressure (2nd Edn.), 3rd Int. Heat Transfer Conference, 3, 1966, pp. 129-142

RÉPUBLIQUE FRANÇAISE
Liberté
Égalité
Fraternité

IRSN
INSTITUT DE RADIOPROTECTION ET DE SÛRETÉ NUCLÉAIRE

COOLABILITY OF A CORIUM POOL IN A DEBRIS BED

CALCULATION OF CRITICAL HEAT FLUX (CHF) TESTS WITH THE ASTEC CODE

Julie-Anne ZAMBAUX
Christine SARTORIS

Institut de Radioprotection et de Sûreté Nucléaire

ERMSAR 05/13/2024

IRSN/ERM-296 ind. 06

MEMBRE DE ETSON

Content

- Context
- Testing device
- ASTEC code and CHF calculation
- Modelling and meshing
- Results for the reference case and impact of pressure, debris size and inclination
- Conclusions and perspectives

Context

- In case of a severe accident in a nuclear reactor, possible presence of a debris bed in the core. If temperature exceeds melting point, formation/extension of a molten pool of corium. More and more difficult to cool down as it grows.

- Thermal exchanges (Critical Heat Flux) between corium pool and its surrouding debris bed when reflooded by water (in-vessel conditions) or in a flooded reactor pit (ex-vessel conditions)

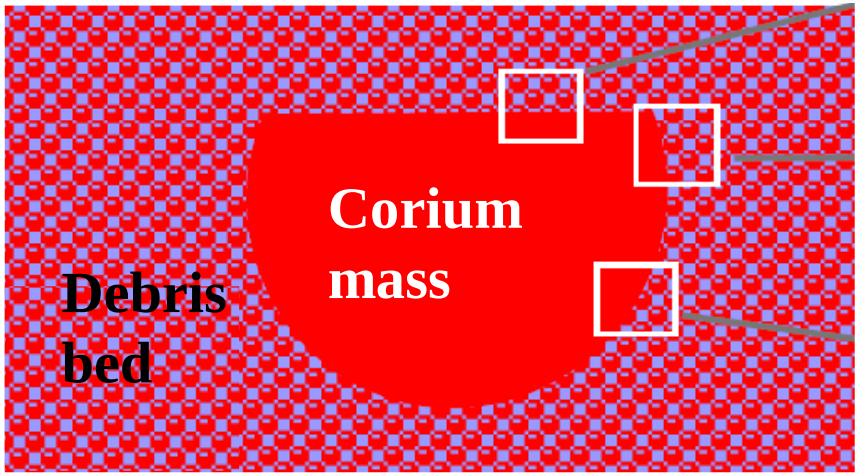

Testing device

- Corium mass -> copper cylinder
  Debris bed and water -> Steel ball bed and deionized water

- Several insulated test sections

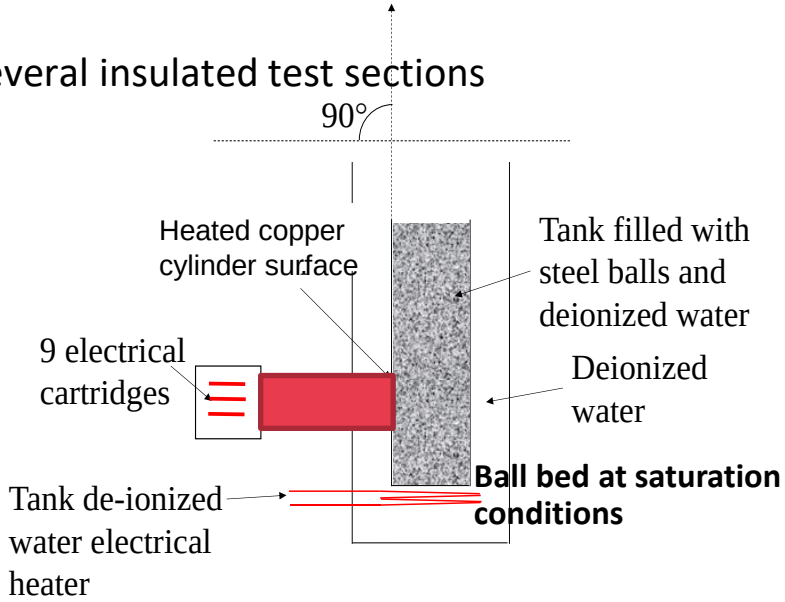

Inclinable test section
Can be relied to a water loop for liquid flowrate and to a water column for pressure impact

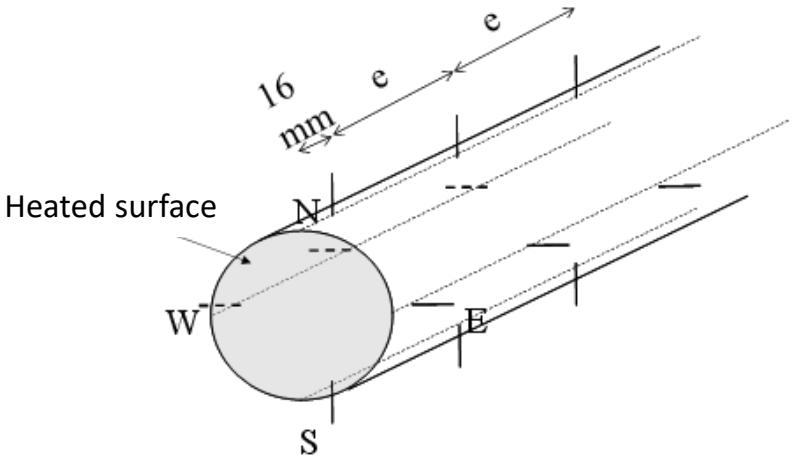

Thermocouples implantation in the heated cylinder

ASTEC v3.1.1 code

- Severe accident system code developed by IRSN
  Different coupled independent modules. Here : thermal-hydraulic module CESAR and core degradation module ICARE (heat transfer and core mechanical state)

- CHF correlation built for an intact core. Often extended to a degraded core.
  Global evolution for degraded core reflooding proved to be reasonably reproduced, but important uncertainties and potential compensating effects remain.

- **=> specific validation of each phenomenon such as the boiling crisis**

CHF calculation in ASTEC code

$$\phi_{CHF} = F_l C_{sub} 0.149 \left(\frac{g\gamma(\rho_L - \rho_G)}{\rho_G^2} \right)^{\frac{1}{4}} \rho_G h_{LG}$$

C_{sub} correction for subcooled flows (Ivey and Morris*)

F_l Groeneveld correction factor for degraded core configuration, porous media with small characteristic length

$$F_l = \begin{cases} 1.259 & if\ L_c < 4\ mm \\ \left(\frac{8}{L_c(mm)}\right)^{\frac{1}{3}} & if\ 4\ mm < L_c < 16\ mm \\ 0.79 & otherwise \end{cases}$$

- Dry out condition achieved if heat flux reaches CHF OR void fraction reaches 0.999

* H.J. Ivey, D.J. Morris, Critical heat flux of saturation and subcooled pool boiling in water at atmospheric pressure (2nd Edn.), 3rd Int. Heat Transfer Conference, 3, 1966, pp. 129-142

Modelling and meshing

- 2D axi-symmetrical => heated surface -> heated crown

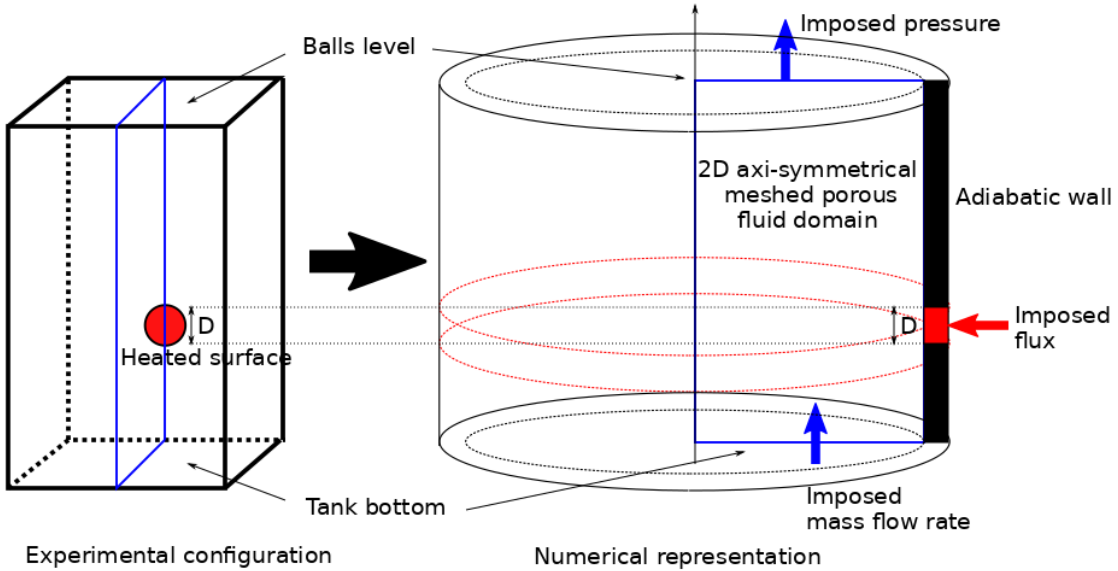

- H crown = D heated surface
- Internal radius = fluid domain width
- Porous media height conserved => hydrostatic pressure kept
- Imposed heat flux considers
  - geometry modification
  - experimental power ramp
  - experimental heat losses

Modelling and meshing

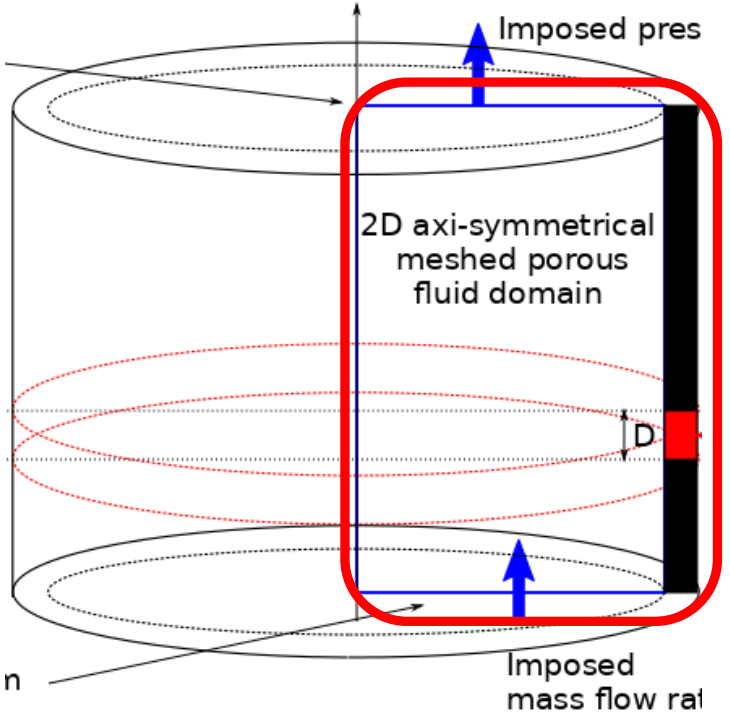

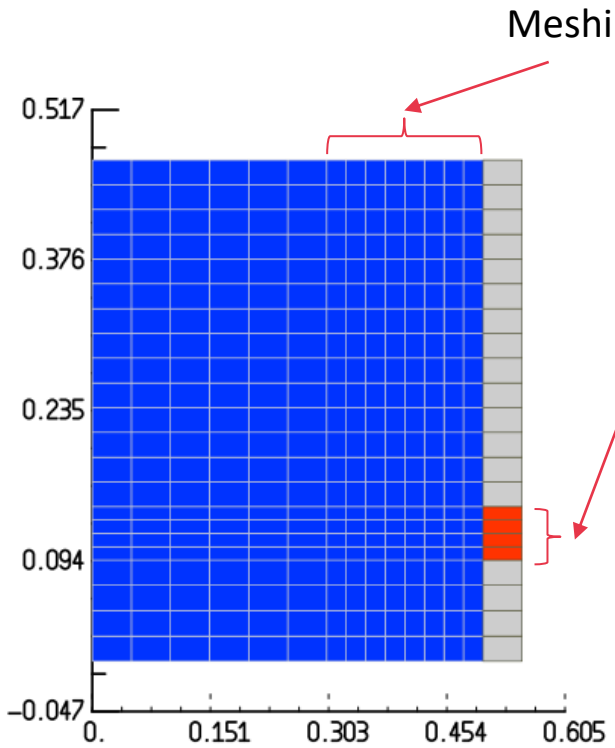

Good insight of the flow close to the wall and of the void fraction in the domain

Reference case (90°, P=1.08 bar, 4 mm diameter balls)

Surface temperature (°C)

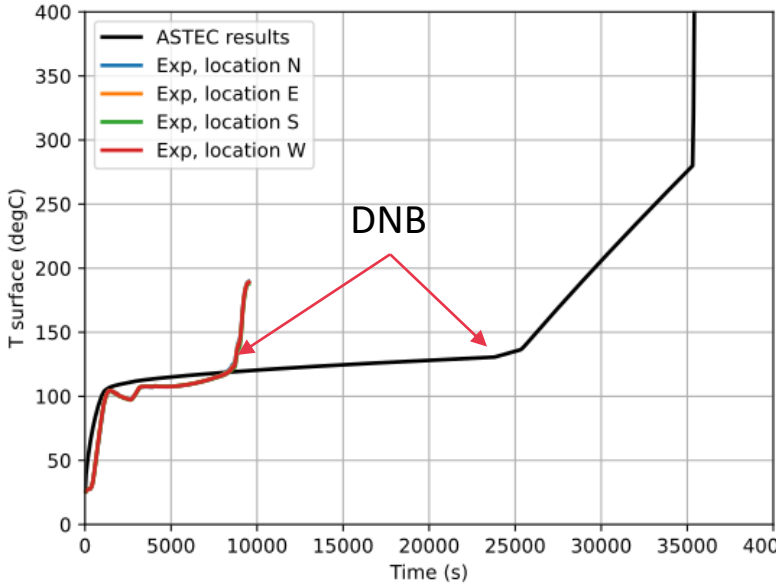

Surface to fluid heat flux (kW/m²)

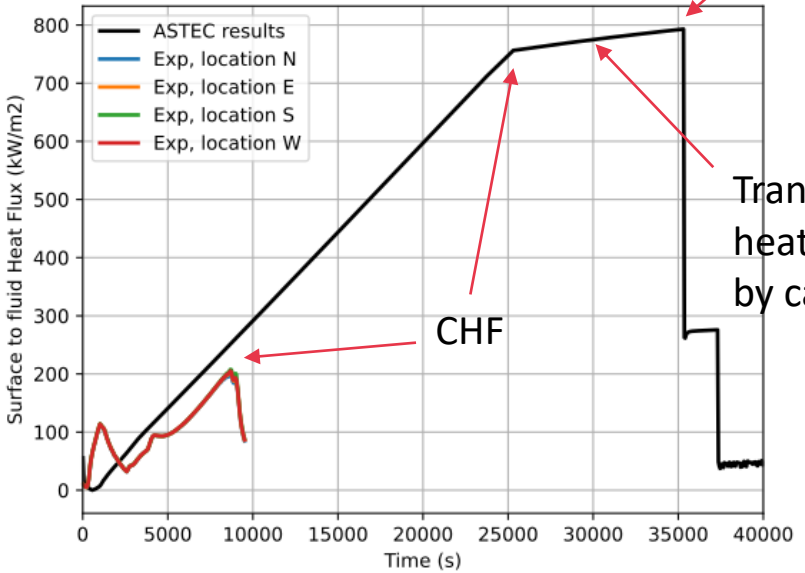

Minimum stable film reached

Transition regime, heat flux limited by calculated CHF

Good agreement in pool boiling conditions : calc CHF (1346 kW/m2) ~ exp CHF (1275 kW/m² ±166 kW/m2)

CHF for porous media with small porosity and small particle size is not adequately predicted

Pressure effect

- 1.08 bar (reference case), 1.51 bar, 1.85 bar and 2.49 bar

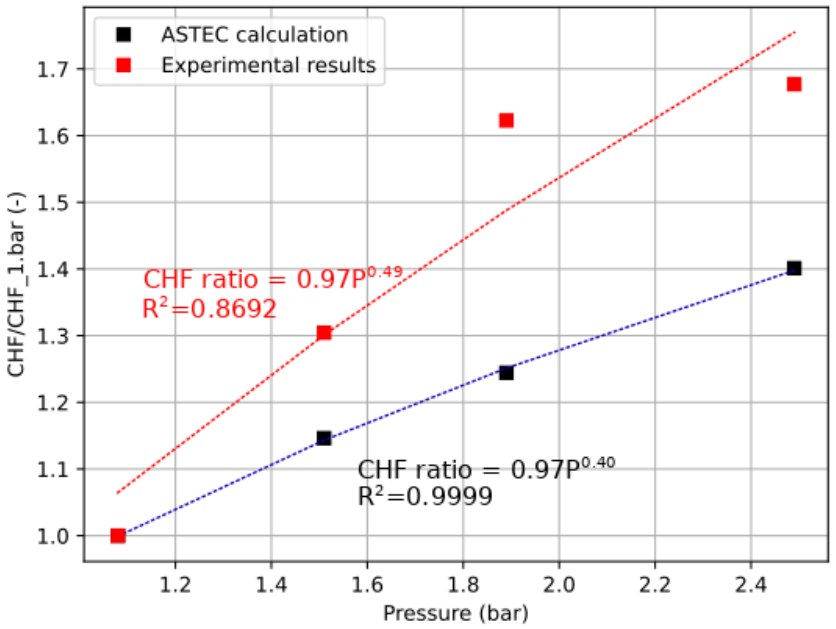

$P^{0.5}$

$P^{0.4}$

The present numerical tendency is rather correct

Debris size effect

Ball diameter Dp (mm)	Numerical CHF (kW/m^2)	Numerical CHF ratio	Experimental CHF rati
2	614	0.810	0.630
3	760	1.005	0.740
4 (ref. case)	756	1.000	1.000

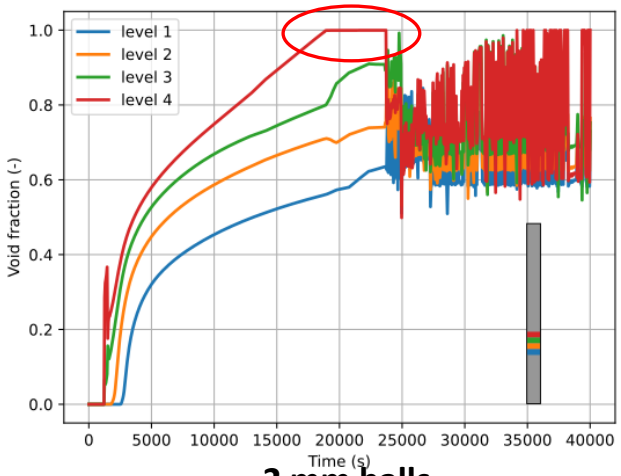

2 mm balls

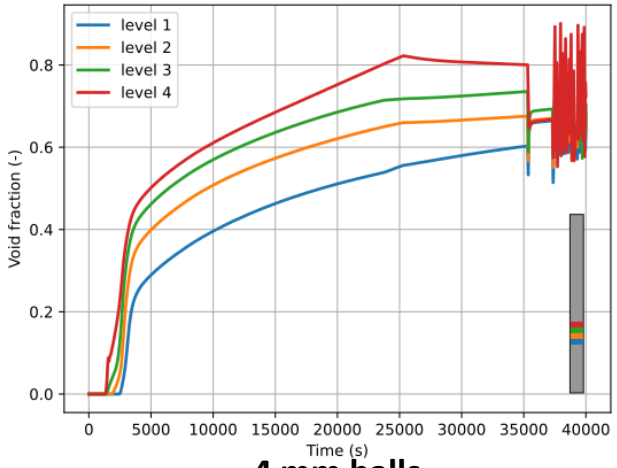

4 mm balls

- For 2 mm balls : capillarity effect, vapor accumulates near the heated surface, void fraction reaches dry-out condition (void fraction = 0.999) (≠4 mm balls, CHF limit achieved)

Debris size effect

Ball diameter Dp (mm)	Numerical CHF (kW/m^2)	Numerical CHF ratio	Experimental CHF rati
2	614	0.810	0.630
3	760	1.005	0.740
4 (ref. case)	756	1.000	1.000
11	**410**		

- Decreasing tendency due to Groeneveld correction factor for small characteristic length
  - **CHF decreases when characteristic length increases (lc > 4 mm, -1/3 exponent dependency),**
  - correction constant for lower diameters

  - ASTEC recalculates lc : 4.02 => very slight decrease of CHF between 3 mm and 4 mm ball cases.

- **The Groeneveld correction currently used in ASTEC is not adapted to porous media**

Inclination impact

Tilting angle (°)	Numerical CHF (kW/m^2)	Numerical CHF ratio	Experimental CHF rati
90 (ref. case)	756	1.000	1.000
120	757	1.003	0.850
150	497	0.650	0.650

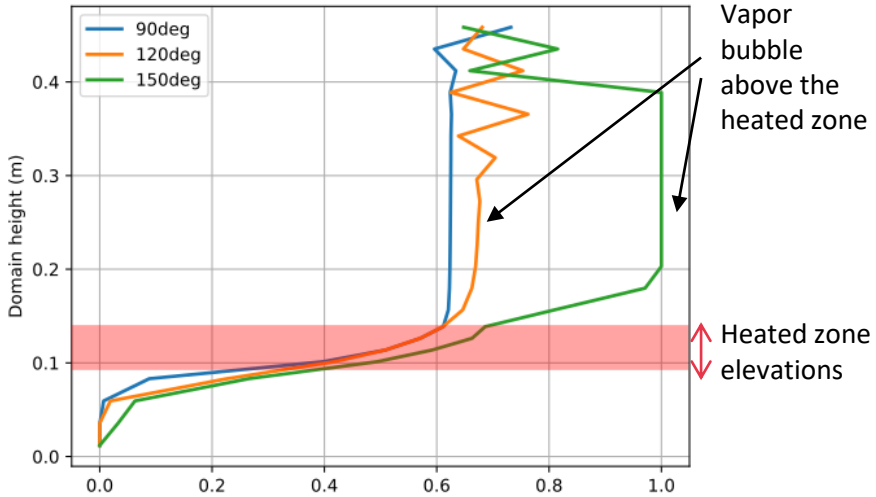

Void fraction profile close to the wall during nucleate boiling regime

- With time, the vapor bubble extends downwards. When it hits the heated zone, the DNB is reached.
- The inclinaison is taken into account in the fluid flow calculation **but not in the CHF correlation**

Conclusions

- Good CHF evaluation in pool-boiling configuration
  but a more adequate correlation for CHF in porous media configuration must be proposed

- Well reproduced : impact of pressure and liquid mass flowrate (not shown here) on CHF

- To be improved :
  - impacts of debris diameter, inclination and steam mass flowrate (not shown here : experimental strong impact of steam flowrate not numerically reproduced).
    New correlations taking into account void fraction, capillarity length and steam mass flowrate effects are needed.

  - dry-out condition based on a void fraction threshold value depending on meshing size.

THANK YOU FOR YOUR ATTENTION

Results - Ball diameter and tilting angle : CHF ratio

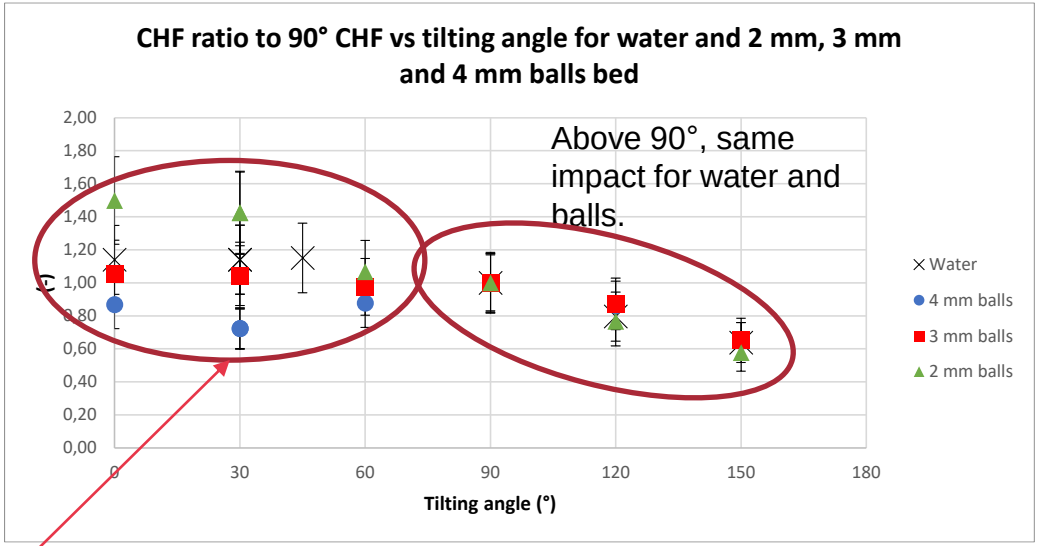

CHF ratio to 90° reference for each ball diameter

For near horizontal upwarding surfaces (below 90°), the tilting angle impact depends on the balls presence and diameter

=> coupling of angle and diameter. For small angles, gravity enhances the properties of small balls to retain the liquid close to the surface by capillarity.

Heating transient

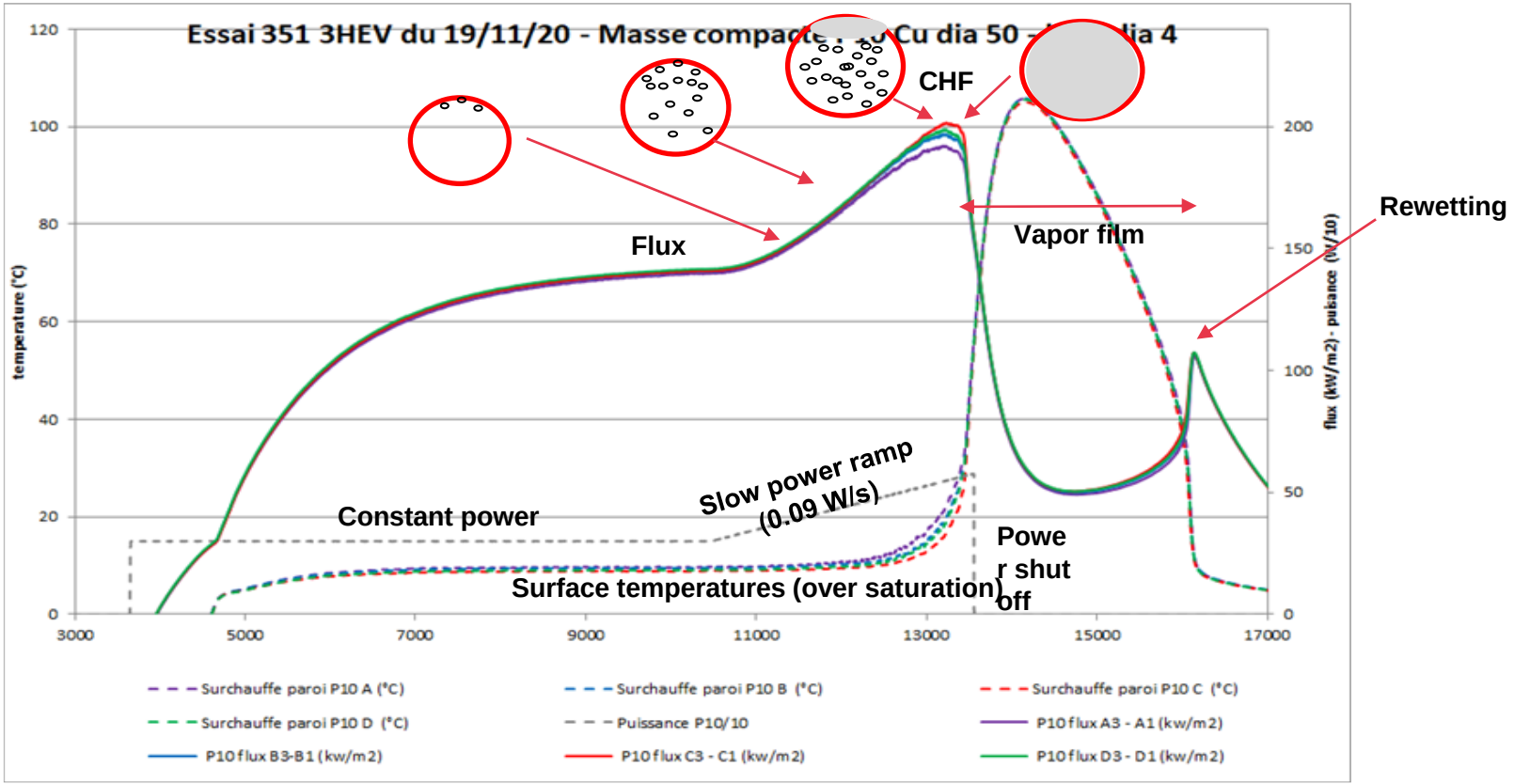

Characteristic length calculation

$$Dh = 4 \times Vfluid / Sfric$$

With :

Dh : hydraulic diameter = characteristic length

V fluid = free volume of the fluid in the mesh

S fric = solid éléments total surface in the mesh

The 11th European Review Meeting on Severe Accidents Research

May 13-16, 2024, Royal Institute of Technology, Stockholm, Sweden

TECHNICAL SESSION 2.3: SEVERE ACCIDENT SCENARIOS - U&S ANALYSIS

Chairs: O. Coindreau (IRSN), S. Paci (University of Pisa)

ID75	**Major Achievements of the EC MUSA Project** L. E. Herranz (CIEMAT)	**Paper** **Presentation**
ID101	**Source Term Uncertainty Analysis of Filtered Containment Venting Scenarios in Nordic BWR** S. Galushin (Vysus Group)	**Paper** **Presentation**
ID01	**Uncertainty and Sensitivity Analysis of the ASTEC Source Term Results of a MBLOCA Scenario with the Activation of Severe Accident Management Actions in a Generic KONVOI Plant** A. Stakhanova (KIT)	**Paper** **Presentation**
ID72	**Source Term Uncertainties in unmitigated SBO sequences in a PWR-1000: Insights from the EU-MUSA project** R. Iglesias (CIEMAT)	**Paper** **Presentation**

MAJOR ACHIEVEMENTS OF THE EC MUSA PROJECT

L. E. Herranz[1*], S. Beck[2], V. H. Sánchez-Espinoza[3], F. Mascari[4], S. Brumm[5], O. Coindreau[6], S. Paci[7]

[1]Centro de Investigaciones Energéticas, Medioambientales y Tecnológicas (CIEMAT), 28040 Madrid, Spain
[2]Gesellschaft für Anlagen- und Reaktorsicherheit (GRS), 50667 Köln, Germany
[3]Karlsruhe Institute of Technology (KIT), 76131 Karlsruhe, Germany
[4]Agenzia Nazionale per le Nuove Tecnologie, L'energia e lo Sviluppo Economico Sostenibile (ENEA), Italy
[5]Joint Research Centre (Petten), European Commission, 1755LE Petten, The Netherlands
[6]Institut de Radioprotection et de Sûreté Nucléaire (IRSN), CEDEX, 13115 Saint-Paul-Lez-Durance, France
[7]Department of Civil and Industrial Engineering, University of Pisa (UNIPI), 56122 Pisa, Italy

luisen.herranz@ciemat.es; sara.beck@grs.de; victor.sanchez@kit.edu; fulvio.mascari@enea.it; stephan.brumm@ec.europa.eu; olivia.coindreau@irsn.fr; sandro.paci@unipi.it

*Corresponding author

ABSTRACT

Maturity of severe accident (SA) codes, progress in the computational methods, and computer infrastructures were considered a sound platform to conduct, for the first time in SA modelling, a systematic and broad application of Uncertainty and Sensitivity Analysis (UaSA) in this domain. The overall objective of the HORIZON-2020 project on "Management and Uncertainties of Severe Accidents (MUSA)" was to quantify the uncertainties of SA integral codes when modelling reactor and spent fuel pool (SFP) accident scenarios of Gen II and Gen III reactor designs for the prediction of the radiological source term. This paper presents the major achievements accomplished by MUSA. To name a few: a database on input parameter uncertainties has been assembled; SA codes and statistical tools, either in-house built or existing ones, have been properly coupled by scripting or interfaces; major specific challenges have been identified and different solutions have been worked out; and, applications to several reactor types and SFP scenarios have shown interesting insights of this simulation approach, particularly when dealing with Source Term variables as figures of merit. No less important, major challenges were found and are here discussed as needs to be addressed before achieving an effective implementation of UaSA in the SA domain.

KEYWORDS
Severe accident analysis; Uncertainty and Sensitivity Analysis, UaSA; Source Term

1. INTRODUCTION

Numerical simulation of severe accidents (SA) is a central element of the safety demonstration of any Nuclear Power Plant (NPP). Along decades, results from SA research have been capitalized in SA integral codes built on validated models and correlations [1]. They are fully integrated, engineering analytical tools developed to describe the progression of accidents in light water reactors. This aim requires addressing multiple phenomena of a different nature: thermal-hydraulics of the reactor coolant systems, containment, reactor cavity; core heat-up, oxidation, degradation, melting and relocation; core-concrete interaction; fission product and aerosol release, transport and deposition of fission products (FPs); hydrogen production, distribution and combustion; and engineering safety features performance. This broad scope pictures the complexity of the dynamic system targeted in SA simulations. Despite the wide range of models implemented, the extensive validation, and the enhanced numerical methods, their estimates are associated with uncertainties. Their identification and understanding would provide meaningful insights for a better assessment of nuclear safety, such as time and failure mode of safety barriers (cladding, boundary of reactor

coolant system, and containment), effectiveness of accident management (AM) action, and prediction of the radiological Source Term (ST) released to the environment. Examples of widely used SA codes are AC^2 [2], ASTEC [3], MELCOR [4] and MAAP [5].

Uncertainty quantification (UQ) was proposed in the area of thermal-hydraulic modelling as part of the Best Estimate Plus Uncertainty (BEPU) methodology to analyze Design Basis Accidents (DBA) and, more specifically, to the licensing of the Emergency Core Cooling System (ECCS) [6]. After about 10 years (1974-1986), USNRC brought the matter to the attention of the Committee on the Safety of Nuclear Installations (CSNI) of OECD (Organization for the Economic Cooperation and Development) and since early 90's, a significant progress has been made in further developing the initial methodology and applying it in a massive way. The Working Group of Analysis and Management of Accidents (WGAMA) has launched several activities in the last two decades: BEMUSE (2004-2010), PREMIUM (2012-2015), SAPIUM (2017-2019) and ATRIUM (2021-present). A synthesis of the progress made until ATRIUM, still ongoing, can be read in [7].

Much of the progress made in BEPU has fed some attempts of application in the SA field but, given the intrinsic and major differences between both domains, BEPU application in SA modelling has been proved far more complicated. "Pioneering" studies were carried out, though, in the SA domain. More than 30 years ago, by using the Source Term Code Package (STCP) [8], a reduced number of input uncertainties were propagated through the different modules, and they concluded that source term uncertainties depended on core meltdown parameters, FP release rate coefficients, chemical activity coefficients during molten core-concrete interaction and containment performance. More than ten years later, practically the same methodology was employed with MELCOR 1.8.5 [9]. Two scenarios were addressed this time: a Station Black-Out (SBO) in an Ice-Condenser NPP, with the focus on hydrogen production; and an MBLOCA in an AP1000 with the focus on in-containment aerosol depletion. As in the previous study, the intended analyses had a limited scope (in analysis time and uncertainties propagated), although meaningful insights were gained.

In 2010, USNRC launched an Uncertainty and Sensitivity Analysis (UaSA) focused on unmitigated SBO scenarios in 3 US NPPs (Peach Bottom, Surry, and Sequoyah), within the project called "State Of the Art Reactor Consequences Analyses (SOARCA)" [10]. This study encompassed both the accident progression (MELCOR) and the environmental consequences (MAACS) and uncertainties were propagated by applying the Monte Carlo (MC) method to generate samples populated with over 1100 cases in one of the studies. A Latin Hypercube Sampling (LHS) was used to sample the uncertainty parameters selected (between 15 and 20, depending on the study). Despite the relevant insights gained, the scope of the UaSA was again limited and expert judgement was noted as an essential tool.

In addition to the above studies, UQ has been used in SA to support model's validation [11] and to characterize specific model uncertainties in scenarios of interest [12]. These type of "reduced-scope" analyses, though, are out of the scope of the present paper.

In 2019, the EURATOM HORIZON-2020 project on Management and Uncertainties of Severe Accidents (MUSA) project started (2019-2023) coordinated by CIEMAT (Spain). MUSA lasted for 4-year aimed to orchestrate a broad application of the UaSA methodology in SA scenarios by combining SA codes and uncertainty propagation analytical tools. The focus of the project was put on Source Term of Gen. II and Gen. III reactors and encompassed both reactor and Spent Fuel Pool (SFP) accident sequences; in both cases, AM measures were considered.

This paper summarizes the major achievements accomplished and the lessons learned in the next sections. Under the frame of IAEA, a Coordinated Research Project (CRP), which is still running, was launched with a similar purpose (https://www.iaea.org/projects/crp/i31033).

2. MAJOR ACTIVITIES and FEATURES

The organization and structure of MUSA was reported in [13].

Quantification of ST uncertainty in SA codes' estimates when modelling accident scenarios of Gen II and Gen III designs was the top level objective of MUSA. Two important activities were considered in MUSA:

- Activities to provide essential elements for the application of BEPU such as uncertainties of model parameters in SA codes' decks, and analytical tools assembled in computational frames enabling propagation of uncertainties and analysis of the results of the calculation campaigns.
- Activities aimed at applying the BEPU methodologies. It includes the set-up of a diversity of accident scenarios, both in reactor and SFP. It was initiated with a "hands-on-training" simulation exercise based on the simplified scenario of PHEBUS-FPT1 [14].

Some features of MUSA with genuine character addressing UaSA in SA are the following:

- The broad range of competences and experience on SA phenomena from all over the world that was involved, merging different perspectives (i.e., Technical Support Organizations (TSO), utilities, research centers, and academia). MUSA partnership consisted of 30 organizations. This large community also made a difference when coming to dissemination of MUSA outcomes.
- The ST focus stemmed naturally from the ultimate goal of SA codes and was inspired by the uncertainties around ST in Fukushima Daiichi accidents [15].
- The integrating nature that encompassed both in-reactor and SFP scenarios, with a substantial diversity in water-cooled reactor designs (Gen. II and Gen. III).
- The strong link with the communities dealing with Probabilistic Safety Assessment (PSA) level 2, emergency response, environmental consequence analysis, and AM, through the project Advisory Board and the End-Users Group.

Quantification of ST uncertainty in SA codes' estimates when modelling accident scenarios of GEN II, GEN III designs was the top level objective of MUSA. In addition, important project objectives were the following:

- Identification of key SA processes/phenomena affecting the ST and quantification of their associated uncertainties.
- Identification and quantification of key parameters of AM measures implemented in the SA affecting the ST, and their associated uncertainties.
- Preparation and assessment of UQ methods (sensitivity analyses included) applicable to the SA field and recommendations on how to use them.
- Trial of UaSA methodologies against risk-dominant reactor and SFP SA sequences.
- Pinpointing steps in the UaSA application that might require further investigation before proposing a systematic methodology.
- Potential recommendations for an effective reduction of remaining code uncertainties associated with ST estimates and their interaction with AM measures.

3. OUTSTANDING OUTCOMES

MUSA achievements may be classified in two categories: "intangible" and "tangible". Before giving a technical description of the latter ones in the coming sub-sections, it is fair to explain what meant by "intangible".

At the onset of MUSA, partners expertise on dealing with UaSA in SA was quite different. There were partners intending for the first time the BEPU approach in SA modelling, whereas others had sound experience. At the end, all the partners had gained good BEPU "hands-on-training" and insights, learning from their own work and from exchanging with most experienced ones. At the same time, the ones holding an initial standing position, benefited from accessing to a large and broad diversity of others' results across the project. Some of the tasks that need to be done when applying UaSA in SA simulation are very resource demanding and teamwork has been proved a sound path; this is, for example, the case of building up a database of input parameter uncertainties. At the end of MUSA 30 organizations around the world did have access to all the assets built within MUSA and, no less important, are aware of the challenges that UaSA in SA simulation entails and the major constrains to be overcome. In short, the MUSA major "intangible" achievement is a community technically enabled to bring UaSA into SA analysis in a systematic way.

3.1. Uncertainty database of system code input parameters

A matrix containing the selected variables, parameters and models together with its uncertainty ranges has been built. Based on MUSA ST focus, the first step was to propose a consistent set of Figures Of Merit (FOM). The criteria adopted concerned mostly the radiological relevance of RadioNuclides (RN), which drew attention to Iodine, Cesium, Noble Gases and Ruthenium releases, particularly during the in-vessel phase (although it was extended to other RN, like Strontium and Barium, in the SFP scenario). Timing of the releases to the environment was considered of utmost interest and, when available, gas and/or particulate nature of some RNs was also a matter of attention. Both liquid and gas paths were considered.

Figure 1 shows the logics under the final identification of input variables whose uncertainties should be characterized. Once the FOMs are set, the phenomena affecting them were scrutinized all the way upstream to core degradation and RN release through code models. This process required considering multiple aspects, like reactor type, scenarios (particularly, in SFP ones), AM actions, and others. It is worth underlining that uncertain parameter identification is code-dependent. Even though most times SA codes are built on common bases, there are specifics were differences may come out, like the RN chemical modelling. Even further, occasionally, codes might name an input deck parameter the same way and then play a substantial different role in the model they are embedded in. Namely, the identification of uncertain parameters needs to code tracked and the final database customized to include such code dependency.

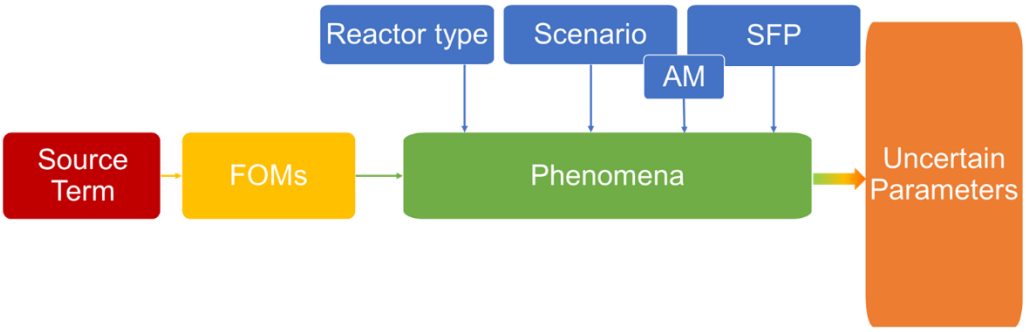

Figure 1. Rationale flowchart to identify uncertain parameters

Once the input deck parameters were identified, a uncertainty database was created. More than 450 uncertain parameters directly related to ST have been characterized through their reference value, lower and upper bounds (uncertainty range) and Probability Density Function (PDF). Additionally, another about 150 parameters, indirectly involved in ST variables, also were characterized. Besides the magnitudes given, the database includes references supporting the specific values. Three criteria were set for each parameter characterization: defensible on scientific grounds, whenever existing; justifiable on physical bases, when no

specific value available in the open literature; and, reasonable on indirect evidences, whenever a physical rationale is not easy to set due to the system complexity. Table I shows a piece of the database concerning particle sedimentation.

Table I. Characterization of input deck parameters involved in sedimentation (MELCOR 2.2)

Phenomena	Uncertain Parameter	Reference value	Lower bound	Upper bound	pdf	References
Sedimentation	Gas viscosity [kg/ms]	1.0 / N/A	-5% / N/A	+5% / N/A	Uniform	Expert Judgment
	Gas temperature [K]	N/A	N/A	N/A	N/A	N/A
	Gas pressure [Pa]	1.55E+07 / N/A	-1.5% / N/A	+1.5% / N/A	Normal	Expert Judgment
	Gas mean free path	N/A	N/A	N/A	N/A	N/A
	Particle diameter Lower Bound [m]	0,000000011	0,00000001	0,0000002	Triangular	1986 Helton et al. "Uncertainty and Sensitivity Analysis of a Model for Multicomponent Aerosol Dynamics"; 2009 NEA/CSNI. "State-of-the-Art Report on Nuclear Aerosols"
	Particle diameter Upper Bound [m]	0,000199	0,000005	0,00002	Triangular	1986 Helton et al. "Uncertainty and Sensitivity Analysis of a Model for Multicomponent Aerosol Dynamics"; 2009 NEA/CSNI. "State-of-the-Art Report on Nuclear Aerosols"
	Slip factor (default = 1.257)	1,257	1,14	1,28	Triangular	1990 D. J. Rader. "Momentum slip correction factor for small particles in nine common gases"; MELCOR Default; Expert judgment (pdf)

As noted in Table I, the database is conditioned by the ST focus of MUSA. Even though the characterization of all the parameters included would be applicable in other UaSA analysis with a different focus, an extension of the database consistent with the objective of the UaSA application would be necessary.

3.2. Methodologies

In the frame of UaSA, "methodologies" essentially refer to three major elements of the calculation environment necessary to propagate uncertainties. First, it is the integral SA code capable of predicting SA progression. A number of them have been already introduced above and are shown in Table II.

Second, it is the statistics behind each realization of an individual campaign. It extends from the sampling in the PDF of uncertain parameters to build an input deck to the final sensitivity analyses, whatever the method used. The own heart of the uncertainty quantification, the size of the realization campaign, usually lands in the approximation of order statistics (usually referred to as the Wilks' theorem [16]) to avoid tremendous computational costs required by thousands of realizations when embracing the Monte Carlo method to propagate uncertainties.

Third is the uncertainty tool There are several statistical tools available that can be coupled with SA codes (i.e., DAKOTA, SUNSET, SUSA, RAVEN or URANIE), but still some UaSA applicants might develop their own tools to tailor the statistical processes and analyses and to gain further flexibility when managing data. In Table II the pairing used in MUSA between SA codes and the statistical tool is displayed; the shadowed boxes are the most popular among partners. This selection was the outcome of a partners' review and assessment of strengths and weaknesses of the existing options.

Table II. Pairing of SA codes and statistical tools in MUSA.

SA Code	UQ Tools

ASTEC 2.2	SUNSET
ASTEC 2.1	URANIE
MELCOR 2.2	DAKOTA
MELCOR 2.2	In-house scripts
MELCOR 2.2	SUSA
MELCOR 2.2	RAVEN
MAAP 5.0	DAKOTA
AC^2	SUSA
RELAP/SCDAP	SUSA

In Figure 2, an example of the coupling between SA code and UQ tools is shown in the flowchart of a UaSA analysis.

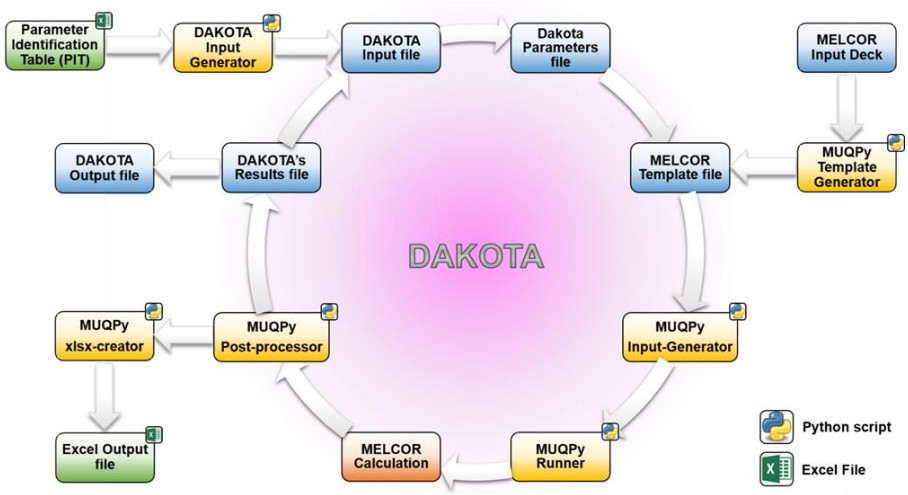

Figure 2. CIEMAT's scheme of UaSA analysis.

Beyond the insights gained applying each methodology to scenarios addressed in MUSA, some generic lessons have been learned:

- The best estimate plant model is the reference case for the follow-up quantification of the uncertainty representing the optimal model regarding the accidental scenario for a specific reactor design characterized by robustness and computational efficiency. Model robustness is fundamental to reduce code crashes and outliers, which is of an exceptional relevance when using the minimum number of realizations according to the order statistics selected.
- The selection of the size and composition of the uncertain parameters set is a crucial step that should be based on a sound background. The complexity, the multi-physics nature and the interconnection of SA phenomena might determine a large number of input uncertainty parameters and certain combination can affect more the FOMs creating also possible outliers that should be investigated. To optimize the analyses based on the chosen FOMs, the parameters with the highest impact on FOMs should be identified. At the same, no essential parameters should be missed in the set. Hence, a balanced choice, between comprehensiveness and potential impact should orient the final selection, for which there is no "magic recipe". To do that, experimental data, analytical data and expert judgement are necessary coupled with existing Phenomena Identification and Ranking Table (PIRT) practices that can support the identification of uncertain input parameters and help reducing their number. Different recommendations on this issue have been raised in the MUSA.

- Expert judgement should be considered during several steps of the entire process. The selection of the input parameters has been already mentioned, but it should be also involved in the post-processing of the realizations campaign. SA code is the crucial element of UASA and can notably affect the UA application (e.g. sampled or even not sampled parameters can affect the stability of the calculations and the consequent failures, models involved may still need some development and validation, more modules/package can be involved and therefore consistency between the parameters need to be investigated). Therefore, the users need to ensure the code is used in its validation domain, the input deck is as robust as possible, and the input parameter values are consistently set based on their involvement in different modules.
- Sensitivity analysis should make use of various techniques. Drawbacks of different techniques have been identified and the "single-bullet" strategy seems not to be the best option. By using different techniques, the existing drawbacks might be partially compensated by a wise use of several of them. This is a field to keep exploring, though.

In addition to those points already highlighted in the list above, there are further issues still open when applying UaSA in SA: the suitability of purely random techniques to sample input parameter PDFs (versus other options like Latin Hypercube Sampling, LHS); or the consideration of failed cases in the realization campaign. These aspects demand further work to explore consequences and to substantiate recommendations.

3.3. Applications to real scale scenarios

The real scale applications during MUSA progress came after an insightful "hands-on-training" exercise based on the PHEBUS-FPT1 experimental scenario. This step was of an exceptional importance, not just because it allowed acquiring experience in applying UaSA in SA, but also because it meant optimizing the methodologies used and identifying critical steps in the process. A thorough recapitulation of this exercise can be read in [14].

As for reactor scenarios, MUSA addressed a large variety of reactor designs (PWR, BWR, VVER, etc.) and scenarios (LB- and MB-LOCAs, SBOs, SGTRs, etc.), with and without AM actions. Table III shows an example of the PWR database. Likewise, the employed methodologies were also quite diverse. Beyond the specific SA codes and UQ tool used, the size of the sets of uncertainty parameters and FOMs were also notably diverse. As for the number of realizations, even if most times the order statistics was adopted and the number of calculations were around 100, occasionally some partners ran hundreds of cases (300, 900). This broad database demonstrates the ability achieved to bring UaSA into SA scenarios, no matter the reactor design, the accident sequence, or the methodology used. Unfortunately, such variety prevents from making specific statements concerning ST, as it would be hard to reach consensus or to find the reasons for the differences found in alike scenarios. Nevertheless, from the studies conducted, it has been observed that implementation of some AM actions can lead to bifurcations in the code predictions, which should be analyzed to make it sure that they respond to the physical dynamics of the system and not to artifacts caused by modelling the specific AM action. The amount of analyses carried out, though, was not enough to propose any specific enhancement of AM actions, but it showed how beneficial BEPU might be when making recommendations in that regard. Constrains linked to the applicability of the order statistics to display uncertainty margins along time in selected FOMs, as initially intended, were discussed, as such application seems not to be supported by the reduced number of cases.

Table III. PWR scenarios database and methodologies used.

NPP	Scenario(s)	SAM	SA Code	U&S Tool	#UPs	#FoM	#Calcs. for UQ
PWR-1000	LBLOCA		MELCOR	URANIE			
PWR (Surry)	SBO		MELCOR	DAKOTA	24	3	93
HPR-1000	LBLOCA		ASTEC	SUNSET	5	8	100
PWR-900	SBO		MELCOR	DAKOTA	8	1	130
PWR 4-Loops	LT-SBO at Low P		RELAP/SCDAP	IUA2.0	19	26	124
PWR (Surry)	ELAP w/o SAM ELAP+SAM	AC restored at RPV failure	MAAP	Python	232	12	500
KONVOI	MBLOCA+SBO		AC2	SUSA	81	10	100
PWR-900	SBO+Loss of aux. FW	Sump flooding, CFVS	ASTEC	SUNSET, Python	43	12	100
APR-1400	C-SGTR by SBO		MELCOR	DAKOTA	6	4	300
KONVOI	MBLOCA w/o SAM MBLOCA+SBO MBLOCA+SAM	CFVS	ASTEC	KATUSA	18	6	900 (300*3)
PWR-1100	SBO+SGTR	SG re-flooding	MELCOR	DAKOTA, Python	17	2	100
CAP-1400	LOCA+SBO		MAAP	DAKOTA			
PWR-1000	SBO	Cavity flooding+CFVS	MELCOR	Python	15	6	111

Figure 3 shows two FOMs examples picked from independent calculations for a similar but not identical scenario. The former shows the aerosol airborne mass in containment, expressed in mass units. The latter shows the cumulative discharge of iodine to the environment. As noted, while in the former scenario uncertainties might range over orders of magnitude at given times, the latter just shows a narrow variation of the uncertainty range (not in the release onset time), which is associated to the nature of this FOM (cumulative) and the unit chosen to express it (fraction of the initial inventory). This illustrates how hard it would be to draw any quantitative conclusion from even similar studies.

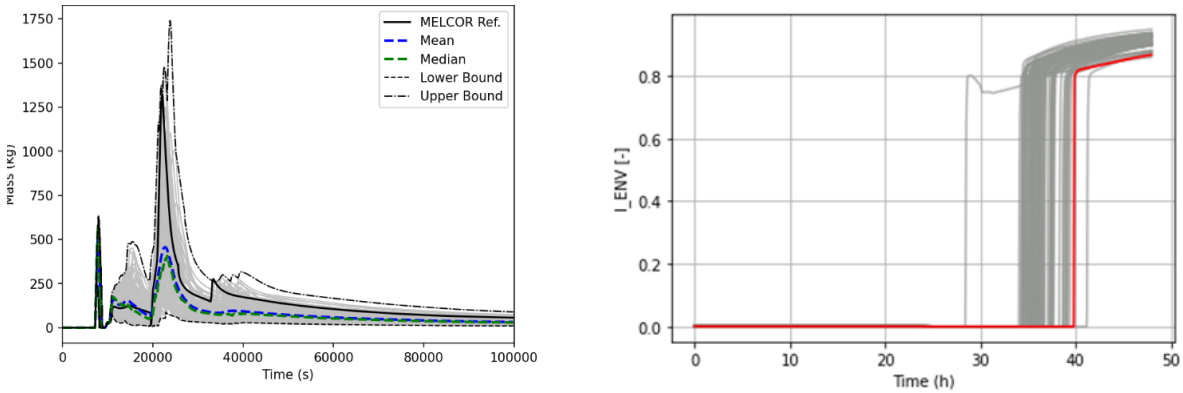

a. Airborne aerosol in containment (PWR-SBO) b. Iodine release to the environment (PWR-SBO)

Figure 3. Example of FOMs for 2 independent PWR-SBO UaSA analysis.

As for UaSA applications in SFP scenarios, they were to a good extent similar to the reactor applications in terms of employed methodologies. In this case, though, a single scenario was addressed: a loss-of-cooling accident in a SFP similar to the one in Unit 4 of Fukushima Daiichi NPP with a limited damage of spent fuel rods. A thorough description was given in [17]. The variability observed in the results of the BEPU application were moderate when compared to discrepancies noted in the best estimate modelling, which stemmed from differences in nodalization, in-code models, modelling of the building surrounding the SFP, and the calculation end time (set at 1-3% of fuel relocated). Table IV illustrates the model variability among the applications, with particular emphasis on the nodalization.

Table IV. Codes, nodalization and building consideration in SFP BEPU

SA code	Modelling of the SFP					Modelling of the building
	Nb of rings	Nb of FA types	By-pass channel*	Nb of axial meshes		
				in the FAs zone	above FAs	
MELCOR	4	3	Yes	12	1	No
ASTEC	3	2	Yes	24	5	Yes, 7 zones
MELCOR	2	2	Yes	10	2	Yes, 3 zones
ASTEC	4	3	Yes	15	10	Yes, 1 zone
ASTEC	3	2	Yes	24	5	Yes, 7 zones
ASTEC	3	2	Yes	10	10	Yes, 7 zones
RELAP/ SCDAP	1	1	No	8	12	No
MELCOR	4	2	Yes	15	0	No
MELCOR	3	3	No	14	1	No
ASTEC	4	3	Yes	15	10	Yes, 1 zone
MELCOR	3	3	No	26	4	Yes, 6 zones

The narrow uncertainty band associated to SFP FOMs came to a good extend from neglecting important uncertainty sources, many of which were of a thermal-hydraulic nature. Based on these shortcomings, this BEPU application to SFP can be seen as a proof of feasibility, but by no means should it be intended to draw quantitative lessons out of it. The conducted sensitivity analyses revealed that release from fuel plays a more dominant role in SFP scenarios than in reactor ones (particularly if no building is modelled), emphasizing some modeling needs of thermal-hydraulic processes, like the oxidation in presence of air or the radiative transfer in SFP topology. Similarly, aerosol modelling in the building becomes quite influential on FOMs, as it is not conditioned by transport in the RCS (as in the case of reactor applications). As expected, when considering the building presence, the fraction of RN released is substantially smaller, but anyway the uncertainty band is narrow in both cases (Figure 4).

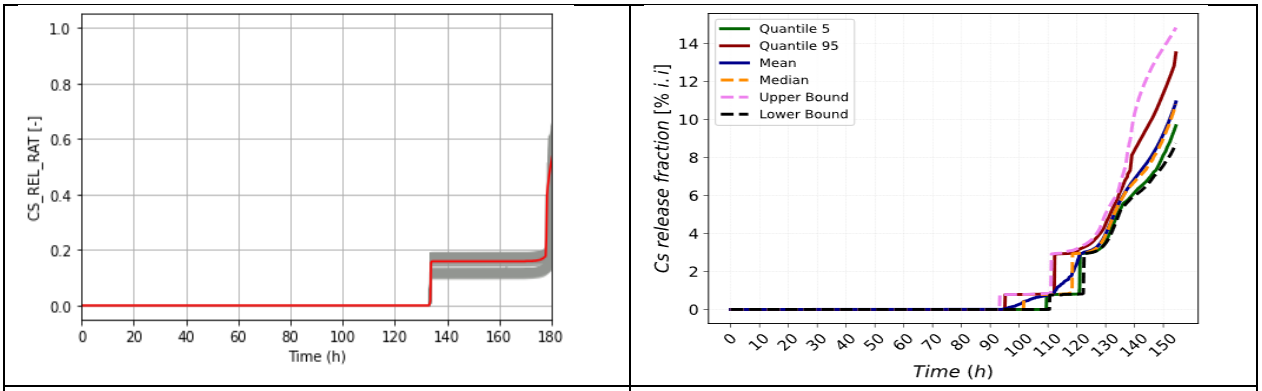

a. SFP building not considered b. SFP building considered

Figure 4. Fraction of Cs (i.i.) released to the environment

Outlining the conclusions of this part of the activities, sensitivity analyses were associated with BEPU (UaSA) both in reactor and SFP applications. Most times FOMs correlations with input parameters were sought through correlation coefficients, which proved to be a too simple approach and provide just a partial view of potential correlations. Occasionally, more advanced techniques were intended (i.e., stepwise regularization, Lasso regularization, Sobol coefficients, etc.). The main insight into the area was that for a complex system like SAs, it is highly likely that the most sound choice is a combination a several sensitivity analysis techniques. Anyway, this is still an open issue for further investigation.

4. FINAL REMARKS & RECOMMENDATIONS

The MUSA project meant a decisive progress towards a systematic application of UaSA in SA analysis. Aside the specific insights discussed in the preceding sections, two top-level conclusions may be drawn:

- Application of UaSA in SA analysis domain has been proved to be doable at a large scale, both in reactor and SFP scenarios. It requires, though, some indispensable elements built within the progress of the MUSA project: a reliable database of uncertain parameters, a computational infrastructure based on SA codes, UQ analytical tools and tailored scripts to analyze the huge database resulting, and sound SA and statistical skills. It is worth emphasizing that engineering judgement becomes an essential tool throughout each of the main stage of the procedure (i.e., selection of uncertain parameters, discussion of FOMs scatter, and sensitivity analysis).
- A systematic application of UaSA, however, still needs to develop a procedure that guide practitioners across the options that should be made in each of the steps along UaSA. This entails to investigate strengths/weaknesses of any assumption/hypothesis needed, and most importantly, the best way to handle the massive information resulting from any UaSA realization campaign. In short, a systematic methodology needs to be consolidated for a sound assessment of uncertainties associated to SA modelling.

The second conclusion points what should be done next in practical terms:

- Completion of the MUSA parameters uncertainty database. This database was mostly focused on in-code physical model parameters and, despite how valuable it is, it requires further work. To start with, the database should be peer reviewed, fed with additional model parameters and extended to components and safety systems parameters. In addition, its structure should be revisited, to make it flexible enough to guarantee its full usefulness no matter the focus of the UaSA analysis.
- Assembly of a systematic procedure to apply UaSA into SA modelling. Several still open issues related to management of aspects like bifurcations, outliers, realizations crashes and many others (i.e., noding, numerics, numerical noise, etc.) need to be worked out. In each of the procedure steps, options need to be explored, and their strengths and weaknesses discussed, so that any potential practitioner becomes aware of them and properly assesses their impact in the results of the analysis.
- Investigation of advanced techniques for data analysis. Instead of using traditional correlation coefficients (i.e., Pearson, Spearman and the like), which were almost exclusively the focus in MUSA, an extension to more advanced techniques and methods (i.e., stepwise regularization; Lasso regularization; multiple regression; etc.) should be conducted, so that analysts might maximize the insight gained when interpreting their results.
- Extensive application of the consolidated methodology. This methodology requires to be proven through extensive application against selected SA scenarios for several Gen. II and Gen. III reactor designs, with specific emphasis on the uncertainties effect on AM measures and vice versa. Additionally, showcases for innovative technology are necessary to show its applicability to forthcoming nuclear technologies, likely to be installed in Europe and elsewhere.

ACKNOWLEDGMENTS

The MUSA project has received funding from the Euratom Research and Training Programme 2014-2018 under grant agreement No 847441. The content of this paper reflects only the authors' view. The European Commission is not responsible for any use that may be made of the information it contains.



REFERENCES

[1] Herranz L.E., Gauntt R., 2018. Severe Accident Analyses: A historical review from the very early days to the near-term future. Nucl. Esp. 2018, 395, 12–18. [Google Scholar]
[2] Weyermann F., et al. 2023. AC^2 2023.0 User Manual. GRS-P-15/Vol. 1 Rev.1.
[3] Chatelard, P., Laborde L., 2023. ASTEC V2.2 code validation: Illustrative results and main outcomes. Nucl. Eng. Des. 413, https://doi.org/10.1016/j.nucengdes.2023.112547.
[4] Wachowiak R., 2013. Use of Modular Accident Analysis Program (MAAP) in support of Post-Fukushima applications. EPRI Report number 3002001785.
[5] Humphreis L.L. et al. 2017. MELCOR Computer Code Manuals Vol. 1: Primer and Users' Guide Version 2.2.9541 2017, SAND2017-0455 O.
[6] Rohatgi U.S., Kaizer J.S., 2020. Historical perspectives of BEPU research in US. Nuclear Engineering and Design 358, ISSN 0029-5493, https://doi.org/10.1016/j.nucengdes.2019.110430.
[7] Herranz L.E. et al., 2020. The working group on the analysis and management of accidents (WGAMA): A historical review of major contributions. Progress in Nuclear Energy 127, ISSN 0149-1970, https://doi.org/10.1016/j.pnucene.2020.103432.
[8] Khatib-Rahbar, M., et al., 1989. A Probabilistic Approach to Quantifying Uncertainties in the Progression of Severe Accidents. Nuclear Science and Engineering 102, 219-259.
[9] Gauntt, R.O, 2007. Uncertainty Analyses Using the MELCOR Severe Accident Analysis Code. OECD Workshop Proceedings, Session-III-Applications-to-Uncertainty-Assessment-on-Severe-Accidents, NEA 6053, Aix-en-Provence, France.
[10] Ghosh S.T. et al., 2022. Summary of the Uncertainty Analyses for the State-of-the-Art Reactor Consequence Analyses Project. NUREG-2254.
[11] López C., Herranz L.E., 2012. ARI3SG: Aerosol retention in the secondary side of a steam generador. Part II: Model validation and uncertainty analysis. Nuclear Engineering and Design 248, 282-292.
[12] Herranz L.E., et al., 2020. Uncertainty quantification of in-pool fission product retention during BWR station BlackOut sequences. Annals of Nuclear Energy 141, ISSN 0306-4549, https://doi.org/10.1016/j.anucene.2019.107290.
[13] Herranz L.E. et al., 2021. The EC MUSA Project on Management and Uncertainty of Severe Accidents: Main Pillars and Status. Energies 2021, 14(15), 4473; https://doi.org/10.3390/en14154473
[14] Mascari F. et al., 2024. Main outcomes of the Phebus FPT1 uncertainty and sensitivity analysis in the EU-MUSA project. Annals of Nuclear Energy 196, ISSN 0306-4549, https://doi.org/10.1016/j.anucene.2023.110205.
[15] Suehiro S. et al., 2015. Development of the source term PIRT based on findings during Fukushima Daiichi NPPs accident. Nuclear Engineering and Design 286, 163-174, ISSN 0029-5493, https://doi.org/10.1016/j.nucengdes.2015.02.005.
[16] Wilks, S.S., 1941. Determination of Sample Sizes for Setting Tolerance Limits. The Annals of Mathematical Statistics 12, 91–96. https://doi.org/10.1214/aoms/1177731788.
[17] Coindreau et al., 2018. Severe accident code-to-code comparison for two accident scenarios in a spent fuel pool. Annals of Nuclear Energy 120, 880-887, ISSN 0306-4549, https://doi.org/10.1016/j.anucene.2018.06.043.

MUSA Insights into Uncertainty Quantification in Severe Accident Analyses

Luis E. Herranz (CIEMAT), Sandro Paci (UNIPI)

Sara Beck (GRS), Victor H. Sánchez (KIT), Fulvio Mascari (ENEA), Stephan Brumm (JRC), Olivia Coindreau (IRSN)

ERMSAR 2024, Stockholm (Sweeden), May 13-16, 2024

MUSA

MUSA has received funding from the Euratom research and training programme 2014-2018 under grant agreement No 847441.



"Dear MUSA Community,

… let me sincerely thank you for each and every piece of work you have done along the last 4 years ..."

GOBIERNO DE ESPAÑA MINISTERIO DE CIENCIA, INNOVACIÓN Y UNIVERSIDADES

Ciemat
Centro de Investigaciones Energéticas, Medioambientales y Tecnológicas

OUTLINE

- Background
- Key Elements
- Outcomes
- Production
- What's Next

MUSA

The Drivers

Severe Accidents are the major contributors to NPP risk!

The “safety case” heavily relies on simulations!

How accurate are SA simulations?

Can uncertainties affect Accident Management?

Can Accident Management affect uncertainties?

Priorities for further research?

Background

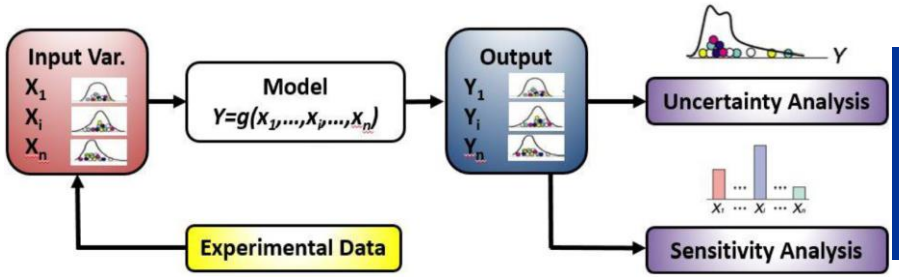

Not the first, BUT ...

- **BEPU** was born in **Thermal-hydraulics** (USNRC: 1974-1986).
- **BEPU** was "passed to & taken forward" by OECD/CSNI.

  (NEA/CSNI/R(1994)20; NEA/CSNI/R(97)35; NEA/CSNI R(97)4; …)
- **BEPU** has since been under development.

  BEMUSE(2004-2010); PREMIUM(2012-2015); SAPIUM (2017-2019); ATRIUM (2021-)

- Pioneering work brought **BEPU into SA** (Khatib-Rahbar et al., 1989).
- And … updated 15 years later (Gauntt et al., 2005).
- Ending up in the SOARCA Study (NUREG-2254; 2022)

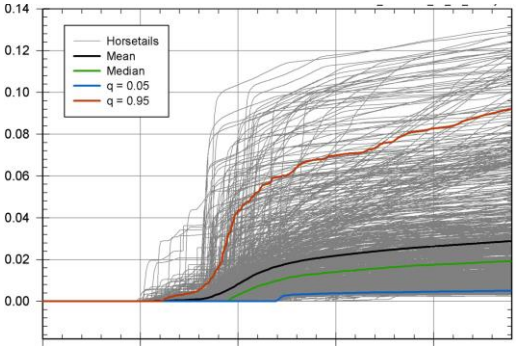

The Right Timing

- **“Maturity”** of SA codes.
- Need to know SA codes **predictability.**
- **Optimization** of SA research (C/B).
- Major **computational resources!**

“The Age of UaSA in SA”

Key Elements

Objectives & Structure

- Management and Uncertainties of Severe Accidents).

  H2020 GA nº 847441 (625 p-m); 2019-2023.

- **Aim:** To quantify uncertainties in SA codes' predictions (AM!) (FOM: Source Term).

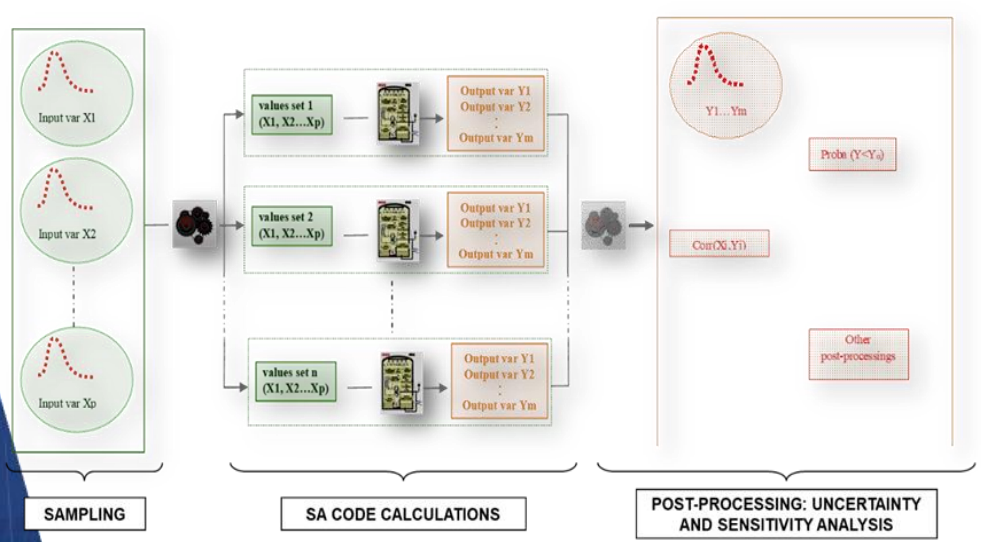

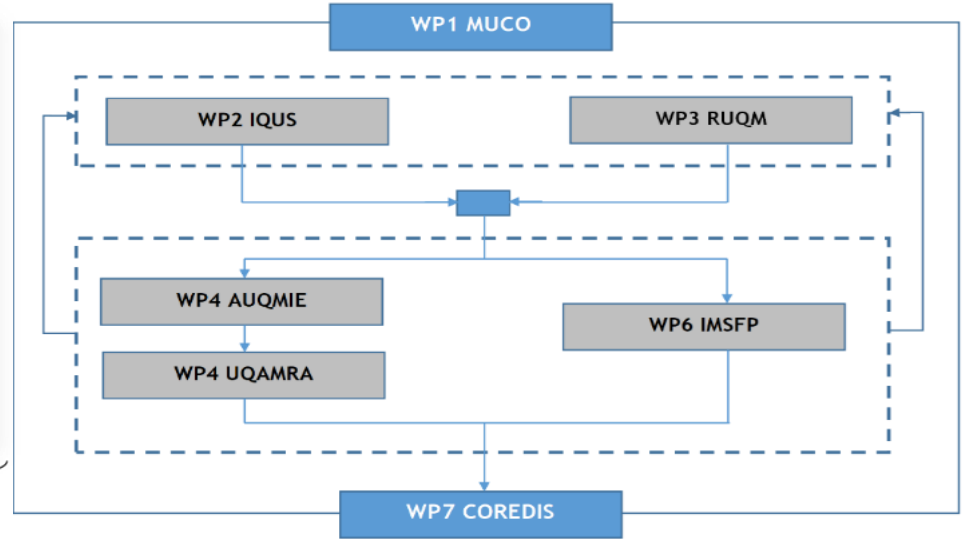

(Gen. II & III; SFPs)

Major «tangible» achievements

- An extensive **UP* database!**
- A vastly diverse & tested range of **methods & tools!**
- A large variety of reactor & scenarios **UQ database!**
- A "first-of-a-kind" **UQ SFP application!**
- A "still growing" dossier of **open references & more!**

* Uncertain Parameter

The UP Database

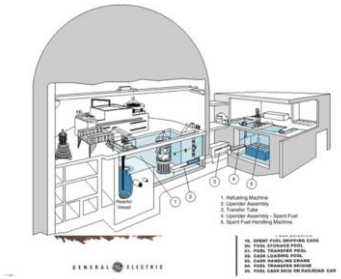

- **400 (+150) UP identified & characterized** (UB; LB; pdf).
- **“Substantiated expert judgement”.**

The UP Database: Characterization

Phenomena	Uncertain Parameter	Reference value	Lower bound	Upper bound	pdf	References
Sedimentation	Gas viscosity [kg/ms]	1.0 / N/A	-5% / N/A	+5% / N/A	Uniform	Expert Judgment
	Gas temperature [K]	N/A	N/A	N/A	N/A	N/A
	Gas pressure [Pa]	1.55E+07 / N/A	-1.5% / N/A	+1.5% / N/A	Normal	Expert Judgment
	Gas mean free path	N/A	N/A	N/A	N/A	N/A
	Particle diameter Lower Bound [m]	0,000000011	0,00000001	0,0000002	Triangular	1986 Helton et al. "Uncertainty and Sensitivity Analysis of a Model for Multicomponent Aerosol Dynamics"; 2009 NEA/CSNI. "State-of-the-Art Report on Nuclear Aerosols"
	Particle diameter Upper Bound [m]			0,00002	Triangular	1986 Helton et al. "Uncertainty and Sensitivity Analysis of a Model for Multicomponent Aerosol Dynamics"; 2009 NEA/CSNI. "State-of-the-Art Report on Nuclear Aerosols"
	Slip factor (default = 1.257)			1,28	Triangular	1990 D. J. Rader. "Momentum slip correction factor for small particles in nine common gases"; MELCOR Default; Expert judgment (pdf)

- **Reasonable**
- **Justifiable**
- **Defensible**

Outcomes

Methods & Tools

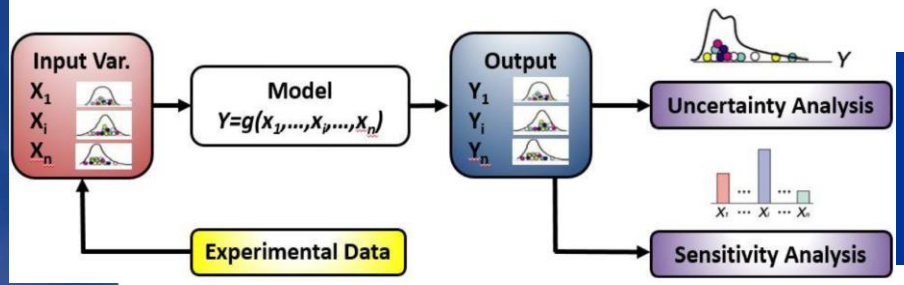

UQ Tool	SA Code
DAKOTA/Python scripts	MELCOR2.2
DAKOTA	MELCOR2.2
DAKOTA /SNAP	MELCOR2.2
DAKOTA/SNAP, MATLAB script	MELCOR2.2
DAKOTA/SNAP	MELCOR2.2
DAKOTA	MELCOR1.8.6
DAKOTA, Python, ass. packages	MAAP5.05

UQ Tool	SA Code
SUNSET	ASTEC2.2b
SUNSET	ASTEC2.2b
SUNSET	ASTEC2.2b

UQ Tool	SA Code
SUSA4.2	AC^2
SUSA4.0	MELCOR2.2
SUSA4.2	RELAP/SCDAP

UQ Tool	SA Code
Python Tools	MELCOR 2.2
Python in-house Tool	MELCOR 2.2
Scripts	MELCOR2.2

UQ Tool	SA Code
RAVEN	MELCOR2.2
URANIE	ASTEC2.1

- **Diversity in codes and tools** (strength/weakness).
- **Convergence in key choices … to come!**

Outcomes

Methods & Tools

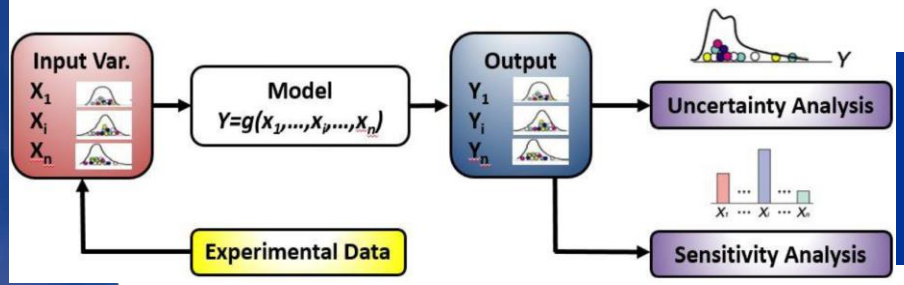

Propagation of Uncertainties

UQ Tool	SA Code
DAKOTA/Python scripts	MELCOR2.2
DAKOTA	MELCOR2.2
DAKOTA /SNAP	MELCOR2.2
DAKOTA/SNAP, MATLAB script	MELCOR2.2
DAKOTA/SNAP	MELCOR2.2
DAKOTA	MELCOR1.8.6
DAKOTA, Python, ass. packages	MAAP5.05

UQ Tool	SA Code
Python Tools	MELCOR 2.2
Python in-house Tool	MELCOR 2.2
Scripts	MELCOR2.2

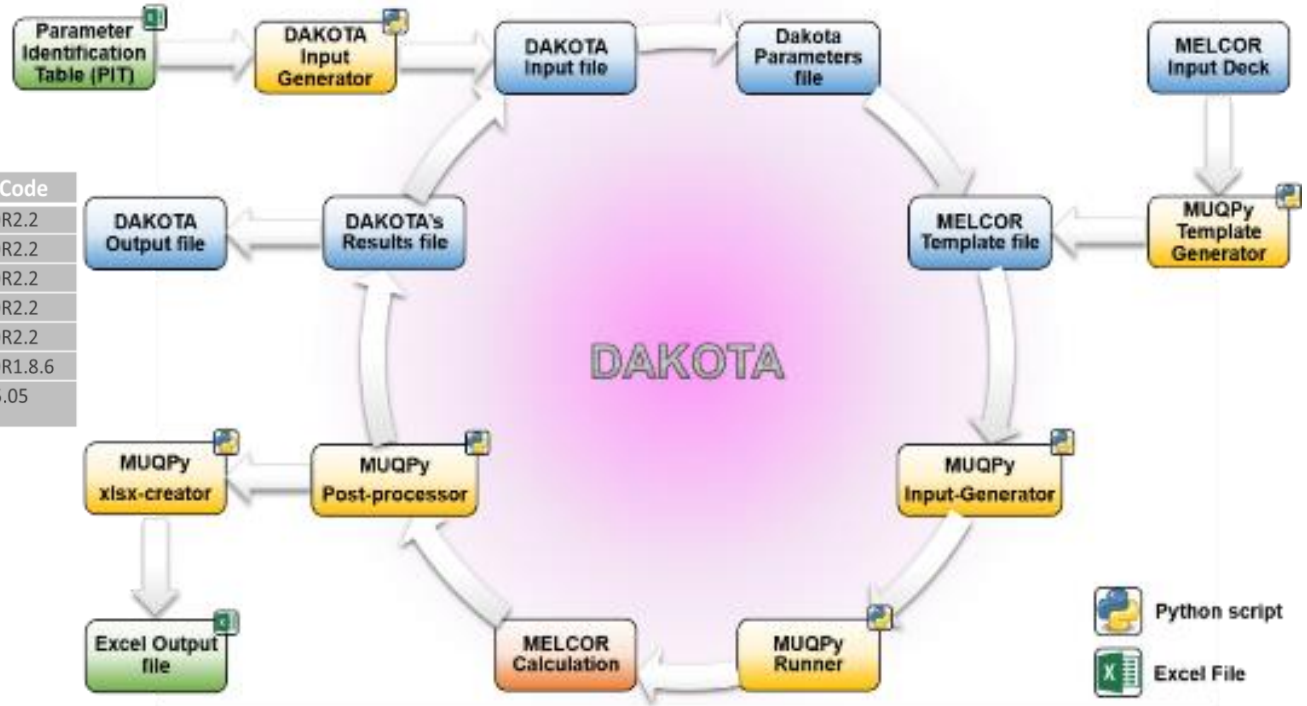

UQ Tool	SA Code
SUNSET	ASTEC2.2b
SUNSET	ASTEC2.2b
SUNSET	ASTEC2.2b

UQ Tool	SA Code
SUSA4.2	AC^2
SUSA4.0	MELCOR2.2
SUSA4.2	RELAP/SCDAP

UQ Tool	SA Code
RAVEN	MELCOR2.2
URANIE	ASTEC2.1

Automatization!

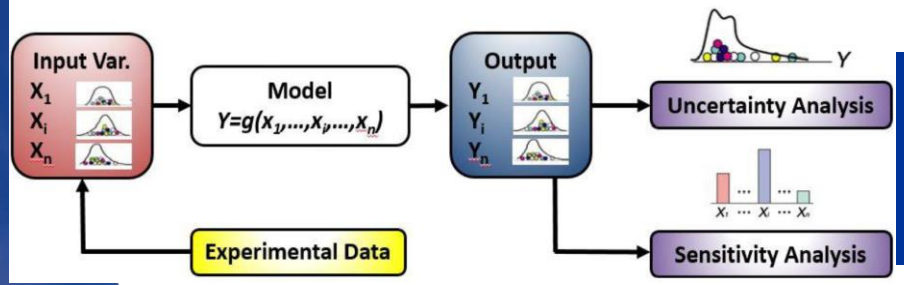

Generation of Samples

- **Monte Carlo** ($n\sim10^3$)
- **Wilks/Wald** ($n\sim10^2$) Order statistics

- **Sampling** SRS (random)
  LH (Latin Hypercube)

Outcomes

The Coupling & Training

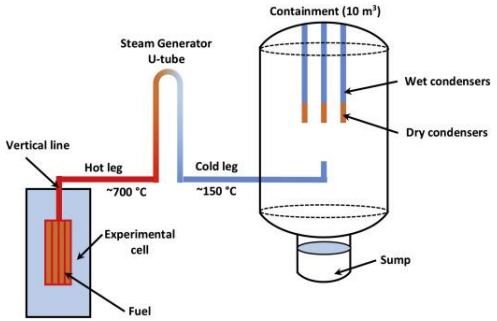

PHEBUS-FPT1 modeling

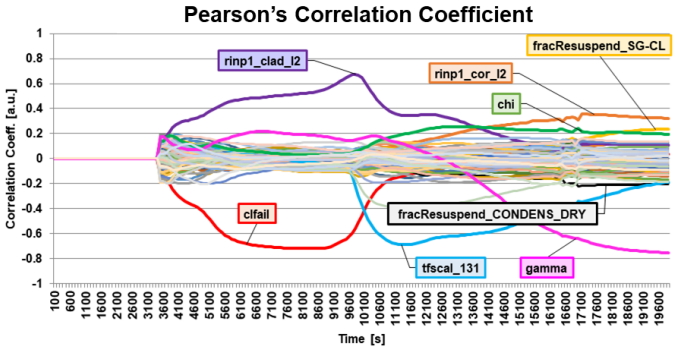

- Initial I_2 mass in gap
- Initial I_2 mass in fuel
- Cladding Failure Temperature
- ZrO_2 Thermal Conductivity
- Aerosol Dynamic Shape Factor
- Aerosol Agglomeration Factor
- Aerosol Resuspension Fraction

Iodine Aerosol in Containment

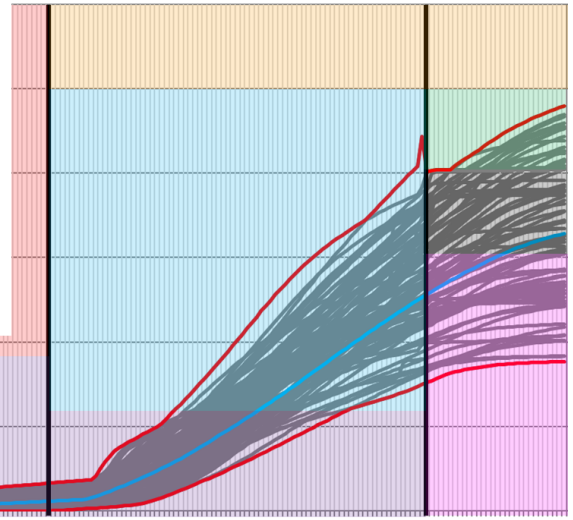

(Bocanegra & Herranz, 2022)

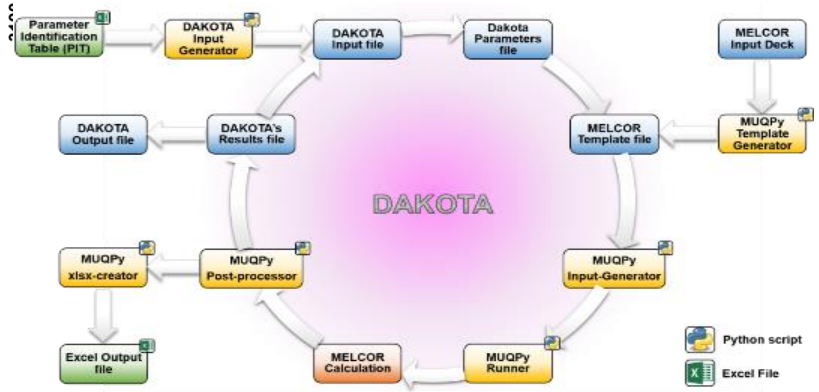

Outcomes

In-Reactor Applications

#	Partner	NPP	Scenario(s)	SAM
1	BelV	**PWR-1000**	**LBLOCA**	
2	CIEMAT/UNIPI	**PWR (Surry)**	**SBO**	
3	CNPRI	**HPR-1000**	**LBLOCA**	
4	ENEA	**PWR-900**	**SBO**	
5	ENSO	**PWR 4-Loops**	**LT-SBO** at Low P	
6	EPRI	**PWR (Surry)**	**ELAP** w/o SAM **ELAP**+SAM	**AC restored at RPV failure**
7	GRS	**KONVOI**	**MBLOCA+SBO**	
8	IRSN	**PWR-900**	**SBO**+Loss of aux. FW	**Sump flooding, CFVS**
9	KAERI	**APR-1400**	C-SGTR by **SBO**	
10	KIT/Framatome	**KONVOI**	**MBLOCA** w/o SAM **MBLOCA+SBO** **MBLOCA**+SAM	**CFVS**
11	PSI	**PWR-1100**	**SBO**+SGTR	**SG re-flooding**
12	SNERDI	**CAP-1400**	**LOCA+SBO**	
13	TRACTEBEL	**PWR-1000**	**SBO**	**Cavity flooding+CFVS**

Outcomes

In-Reactor Applications

#	Partner	NP
1	BelV	PWR-
2	CIEMAT/UNIPI	PWR (
3	CNPRI	HPR-
4	ENEA	PWR
5	ENSO	PWR 4-
6	EPRI	PWR (
7	GRS	KON
8	IRSN	PWR
9	KAERI	APR-
10	KIT/Framatome	KON
11	PSI	PWR-
12	SNERDI	CAP-1400
13	TRACTEBEL	PWR-1000

#	SA Code	U&S Tool	#UPs	#FoM	#Calcs. for UQ
1	MELCOR	URANIE			
2	MELCOR	DAKOTA	24	3	93
3	ASTEC	SUNSET	5	8	100
4	MELCOR	DAKOTA	8	1	130
5	RELAP/SCDAP	IUA2.0	19	26	124
6	MAAP	Python	232	12	500
7	AC2	SUSA	81	10	100
8	ASTEC	SUNSET, Python	43	12	100
9	MELCOR	DAKOTA	6	4	300
10	ASTEC	KATUSA	18	6	900 (300*3)
11	MELCOR	DAKOTA, Python	17	2	100
12	MAAP	DAKOTA			
13	MELCOR	Python	15	6	111

LOCA+SBO		
SBO	Cavity flooding+CFVS	

Outcomes

In-Reactor Applications

#	Partner	NP
1	BelV	PWR-
2	CIEMAT/UNIPI	PWR (
3	CNPRI	HPR-
4	ENEA	PWR
5	ENSO	PWR 4-
10	KIT/Framatome	KON
11	PSI	PWR-
12	SNERDI	CAP-1400
13	TRACTEBEL	PWR-1000

#	SA Code	U&S Tool	#UPs	#FoM	#Calcs. for UQ
1	MELCOR	URANIE			
2	MELCOR	DAKOTA	24	3	93
3	ASTEC	SUNSET	5	8	100
4	MELCOR	DAKOTA	8	1	130
5	RELAP/SCDAP	IUA2.0	19	26	124
6	MAAP	Python	232	12	500
7	AC2	SUSA	81	10	100
11	MELCOR	Python	17	2	100
12	MAAP	DAKOTA			
13	MELCOR	Python	15	6	111

- **DB in technology/scenarios/UQ approaches/ …** (strength/weakness)**.**
- **Preliminary insights into AMgmt.**
- **Cross-comparison might “substantiate” some options!**

12	SNERDI	CAP-1400	LOCA+SBO		
13	TRACTEBEL	PWR-1000	SBO	Cavity flooding+CFVS	

Outcomes

In-SFP Applications

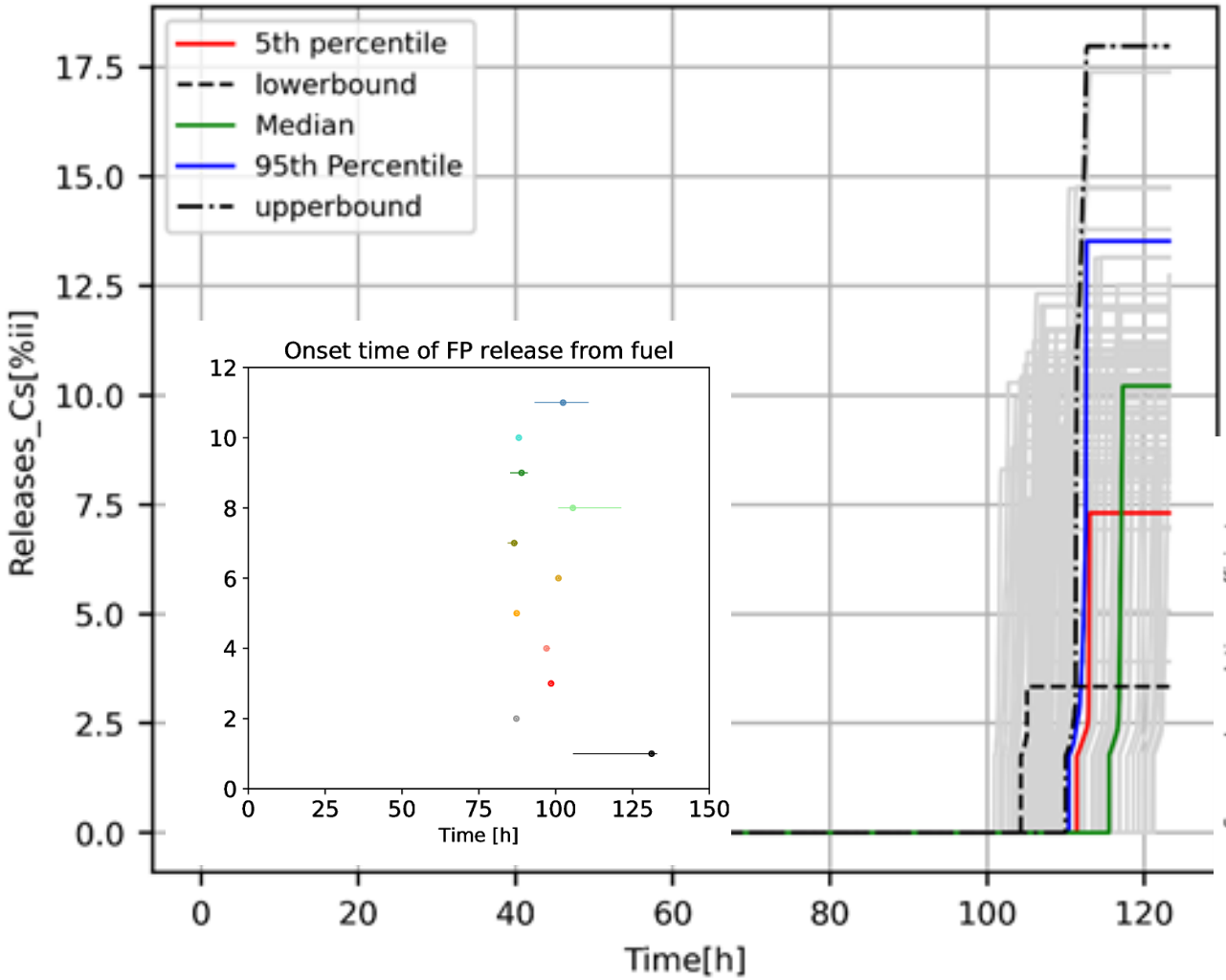

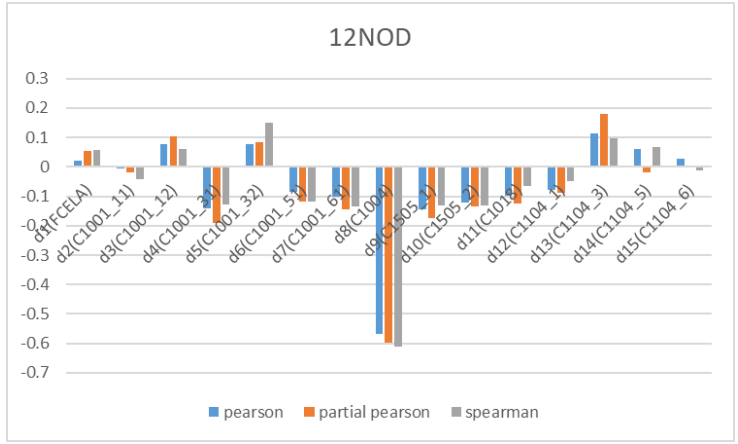

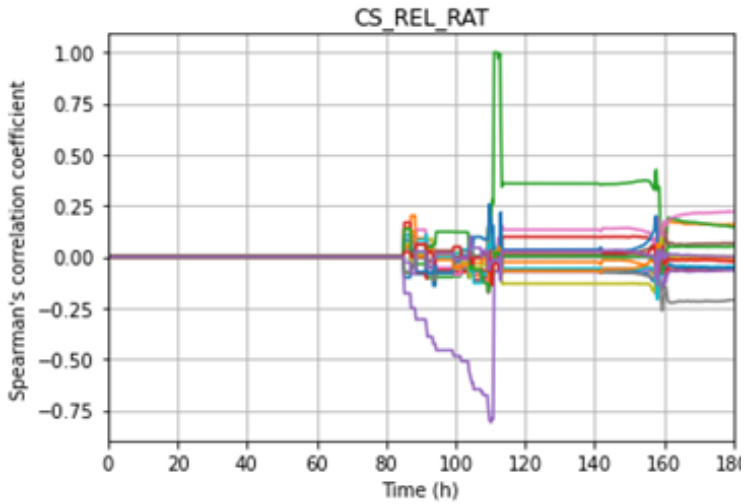

Outcomes

In-SFP Applications

- **Onset of fuel melting (1%)**
- **Specific, highly conditioned** (FOMs; termination; phenomena; BCs; codes; …) scenario.

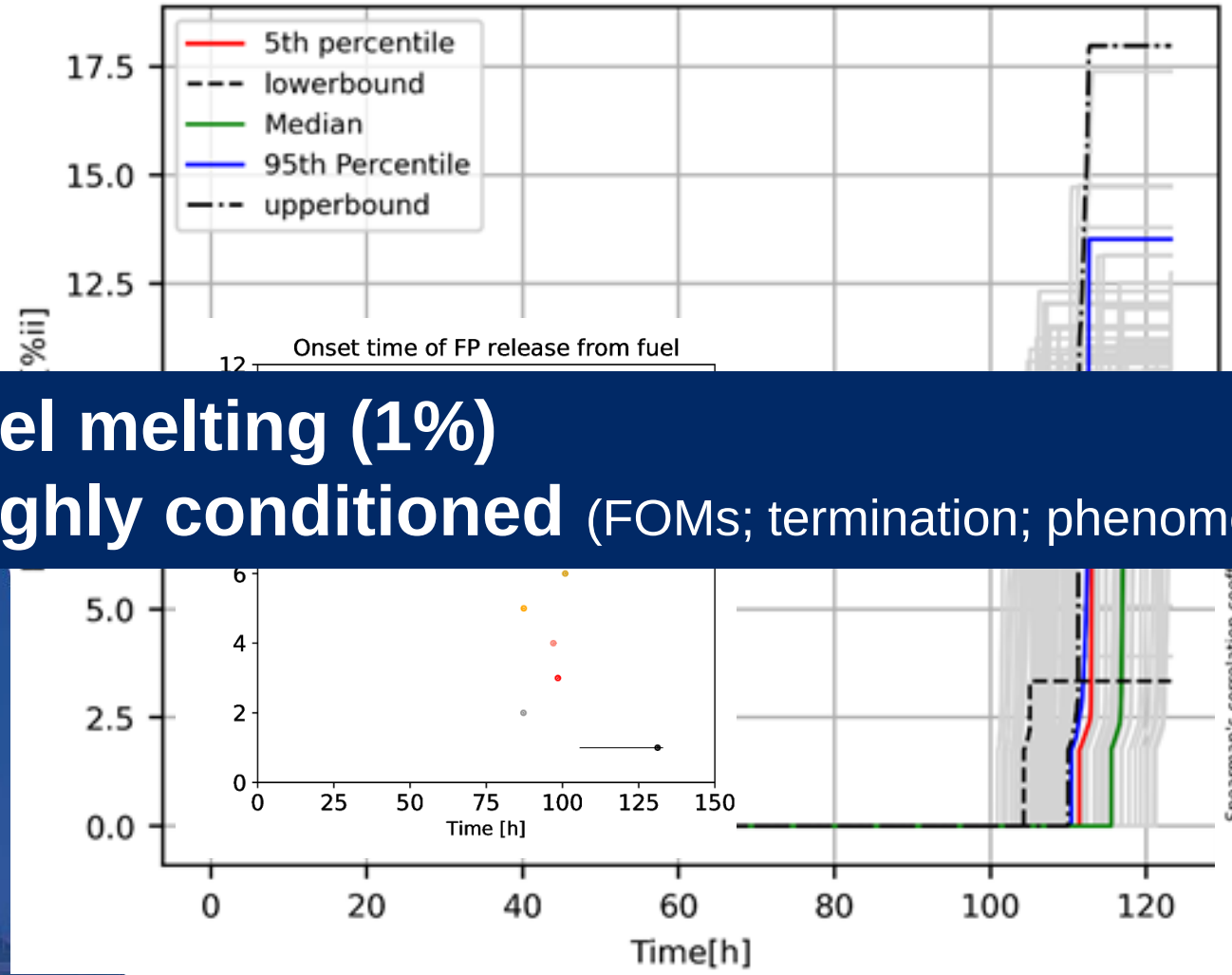



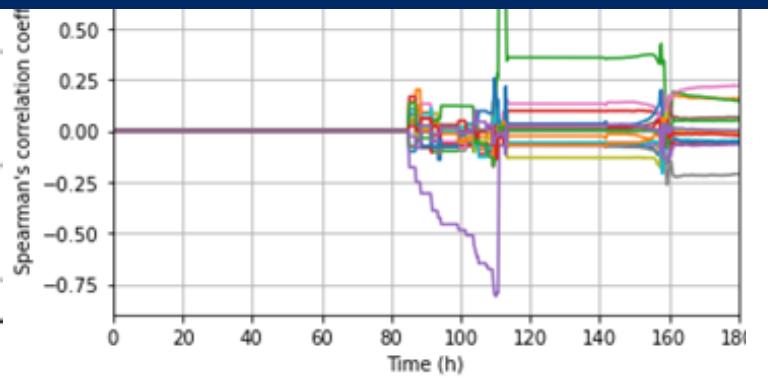

Evaluation of Uncertainties

- **Dispersion plots**

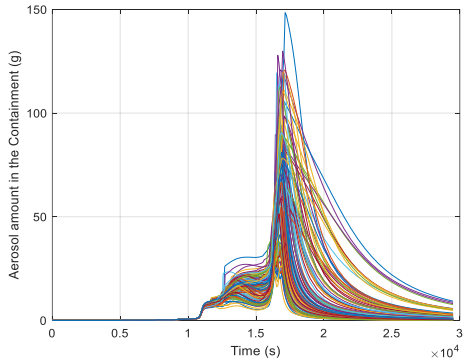

- **CDF; PDF**

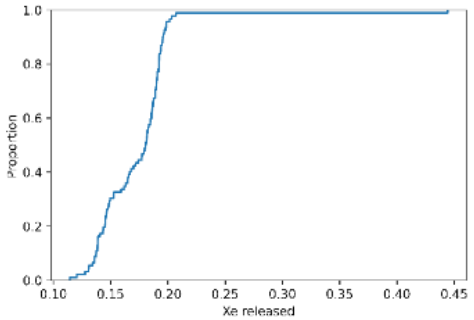

- **Scatter plots**

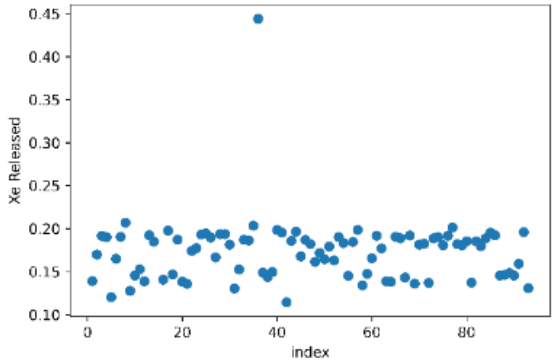

- **Descriptive statistics**

Statistical parameter	Xe
MELCOR reference case (%i.i.)	24.21
Mean (% i.i.)	17.33
Median (% i.i.)	18.07
Lower bound (% i.i.)	11.44
Upper bound (% i.i.)	44.42
Standard deviation (% i.i.)	3.71

...

Analysis of Sensitivity

- **Correlation coefficients** (Pearson; Spearman)

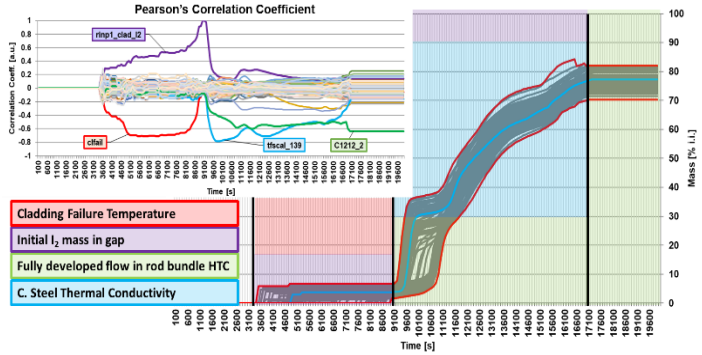

- **Simple regressions**

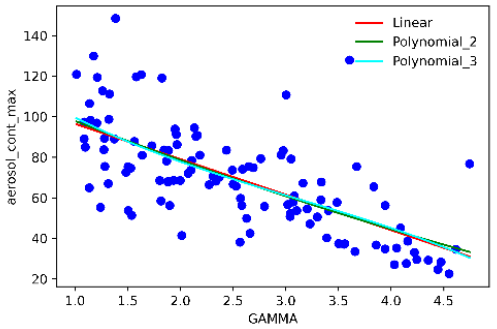

- **More advanced techniques** (stepwise reg.; Lasso reg.; Sobol coefs.)

Outcomes

Major «intangible» achievements

- **A journey from an uneven to an “even” community:**

  “Diffusion driven by expertise & knowledge forward/backward gradients”.

- **A “grown” community in an “unexplored world”**

  “Team work” proved to be resourceful when working out of the comfort zone. (BaU)

- **An “empowered community” ready to give the best**

  Self-criticism, stamina to keep fighting, and an open mind to look ahead.

NUGENIA 2019 Forum
FISA 2019
EUROSAFE 2021 Forum
SNETP 2021 Forum
NESTet Conference 2021
FISA 2022
SNETP Coordinators Hub Day
SNETP 2023 Forum

MUSA C&D Numbers

Production

MUSA presentations at conferences and meetings	30
Main Communication events	10
Technical Presentations at Conferences	> 25 (9, joint)
Articles on scientific journals	12 (6, joint)
Forecasts	> 15 ind. pap.

Production

Education & Training

- **3 learning modules** (MSc students & generic audience):

1. **Analysis of SA from the Early Days to the Next Future** (CIEMAT) – on web
2. **Methodologies for uncertainty assessment in SA** (UNIPI) – on web
3. **ST Uncertainties in Fukushima-like scenarios** (CIEMAT) – on web

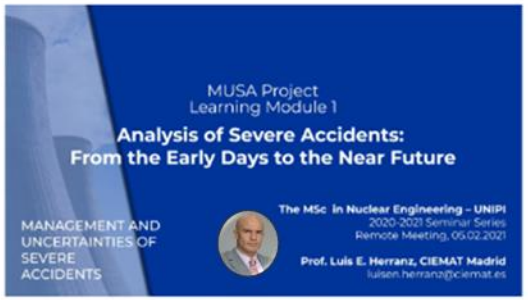

Module 1

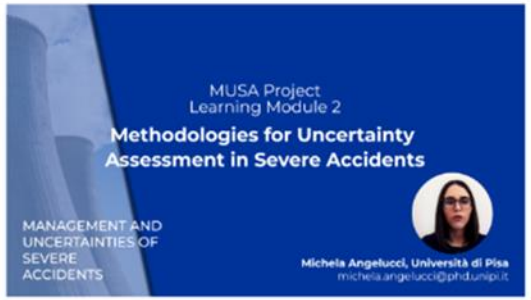

Module 2



Module 3

(https://musa-h2020.eu/educationtraining-modules/)

- **A Specific lecture in the SAP Course Technical Programme**

What's Next

Challenges Ahead

- **The UP database optimization** (filling; extension; restrc.).
- **A systematic consolidation of UaSA application in SA.** (#UP; nodding; FOMs; …) – **Innovation.**
- **A "balanced" use of expert judgement.**
- **Further attention to accident management** (forward/reverse effect).
- **Show-cases for innovative technologies** (ST-ATFs; LW-SMRs)

Remaining Issues

- Id. & charac.
- AM-related
- Equip.-related
- …

- FoM
- Parameters
- Code crashes
- Bifurcations
- Outliers
- Data analysis
- …

- Nodalization
- Noise
- Phasing
- ...

INNOMUSA: General Goals

- **To exploit the achievements made in MUSA.**
- **To consolidate a systematic methodology.**
- **To focus on AM*:** Effect of U on AM & Effect of AM on U.
- **To address innovation Ntech.:** NT-ATFs; LW-SMR

*** Decision making efficiency and effectiveness**

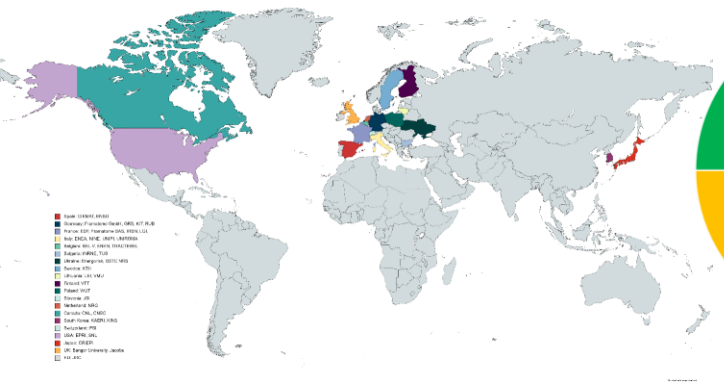

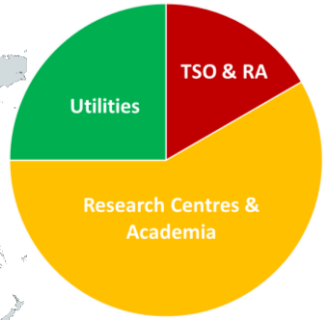

INNOMUSA: Working Structure

& (UNIPI)

Dissemination

METHOD
(KIT; GRS)

- Uncertainty DB
  (approach?; qualification; extensión; …)
- UA Approach
  (MC, Wilks, others, …;
  FOMs; parameters;
  bifurcations; outliers; bias; crashes; …)
- Data analysis (SA)
  (“Best suite”; physical consistency; …)
- Noding/ Phasing / Noise / Nmrcs

EDUCATION & TRAINING
(ENEN)

APPLON
(ENEA; INRNE)

- Water-cooled reactors
  (Gen-II & Gen-III; AMgmt)
- LW-SMRs
  (Av. Designs; SASPAM)
- Short-term ATFs (shc)

Communication

Thank you for your attention!

MUSA has received funding from the Euratom research and training programme 2014-2018 under grant agreement No 847441.

SOURCE TERM UNCERTAINTY ANALYSIS OF FILTERED CONTAINMENT VENTING SCENARIOS IN NORDIC BWR

Sergey Galushin
Vysus Sweden AB
sergey.galushin@vysusgroup.com

Govatsa Acharya, Dmitry Grishchenko, Pavel Kudinov
Department of Nuclear Engineering
Royal Institute of Technology (KTH)
govatsa@kth.se; dmitrygr@kth.se; pkudinov@kth.se

ABSTRACT

Nordic Boiling Water Reactors employ filtered containment venting and ex-vessel debris coolability in the deep pool located under the reactor pressure vessel as a severe accident management strategy.

This paper focuses on the uncertainty analysis of the source term in accident sequences that result in filtered containment venting to the environment using the MELCOR code. The impact of uncertain MELCOR modeling parameters and modeling options on the timing and magnitude of the source term released to the environment has been evaluated in accident sequences initiated by a large break LOCA and SBO.

The performed simulations illustrate the effect of MELCOR modeling parameters and options on the code's predictions of severe accident progression, event timing, and the magnitude of the source term released to the environment in different accident scenarios. Furthermore, the results highlight the importance of various retention mechanisms that limit the release of fission products into the environment.

KEYWORDS
MELCOR Uncertainty MVSS Severe Accident

1. INTRODUCTION

Nordic Boiling Water Reactors employ filtered containment venting and ex-vessel debris coolability in the deep pool beneath the reactor pressure vessel as a severe accident management strategy. In the event of a severe accident involving significant core damage and melting, the molten core is expected to be released from the vessel into a deep pool of water in the lower drywell. The molten core is expected to fragment, quench, and form a debris bed that can be cooled by the natural circulation of water. At the same time the pressure in the containment will gradually increase prompting the opening (either manually or automatically) of the containment depressurization line via the multi-venturi scrubbing system (MVSS).

In Level 2 Probabilistic Safety Assessments (L2 PSA), the primary frequency estimate of interest is the unacceptable release frequency[1]. Evaluating these frequencies involves summing over a large number of possible event sequences. This process implies, among other considerations, that radioactive releases (the source term) must be calculated for a set of representative scenario classes and then compared to a predefined threshold to classify them as acceptable or unacceptable. Typically, these assessments are conducted using integral plant response codes such as ASTEC, MAAP, or MELCOR. The assessments themselves are subject to uncertainty, both in terms of accident scenarios (aleatory uncertainty) and in the modeling of phenomena (epistemic uncertainty).

Aleatory uncertainty arises from the natural variability of stochastic processes and cannot be reduced beyond this level. In contrast, epistemic uncertainty pertains to our knowledge of systems, processes, or parameters and can therefore be reduced by gathering more knowledge.

Typically, source term evaluations are conducted for a limited set of accident scenarios, utilizing point-estimate values for epistemic uncertain parameters in the employed code. The uncertainty associated with the source term poses a challenge for any attempt to develop, use or increase the level of detail in L2 PSA results and merits targeted research solely on the basis of this.

Furthermore, within the field of nuclear emergency preparedness towards severe accidents, the ultimate goal is to perform relevant and efficient actions to protect the public. This is typically based on pre-calculated accident scenarios and their associated source terms. Therefore, the knowledge about source term uncertainty and timing of major release is of paramount importance.

2. APPROACH

The analysis was performed using MELCOR code version 2.2 rev 18019 with the Nordic BWR model, originally developed in [1]. The Nordic-type BWR operates a nominal thermal power of 3900 MW_{th}, and a primary system pressure of 7 MPa. Its core comprises of 700 SVEA-96 Optima 2 fuel assemblies, divided into 5 radial rings and 8 axial levels. For additional details about the core and thermal hydraulic nodalization of the Nordic BWR, refer to [1-3].

In this work, we consider two accident scenarios: (i) an accident initiated by a Loss of Coolant Accident (LOCA) denoted as RC7B – LOCA MVSS, with all active safety systems unavailable, such as Emergency Core Cooling Systems (High and Low pressure ECCS) or containment sprays; (ii) an accident initiated by a Station Blackout (SBO) denoted as RC7A – SBO-MVSS, with successful operation of safety relief valves (SRVs) and the automatic depressurization system (ADS), as discussed in [2]. In both accident scenarios, the lower drywell is flooded with water from the condensation pool (as discussed in [3]), to prevent failure of cable penetrations and ensure ex-vessel debris coolability. Containment filtered venting via MVSS is initiated automatically when the pressure in the drywell exceeds 0.55 MPa (absolute) [2]. According to the grouping of accident scenarios into release categories (RC) in the L2 PSA for Nordic BWR, the accident sequences that belong to the RC7 release category belong to the acceptable release category[1][2].

To conduct uncertainty analysis, discussed in this paper, first a set of MELCOR code modelling parameters, along with their respective ranges, which can influence severe accident progression and the source term released to the environment was identified. This identification was based on a literature review conducted in [2]. Subsequently, a screening analysis was performed to eliminate MELCOR code modeling parameters with a negligible effect on the predictions of severe accident progression and source terms. Additional details on parameter selection and the screening analysis can be found in [2].

[1] Releases over 0.1 % of the inventory of the cesium isotopes Cs-134 and Cs-137 in a core of 1800 MW_{Th}, excluding noble gases, which corresponds to a release of 160 TBq of Cs-134 and of 103 TBq of Cs-137 [16].

Typically, the sources of uncertainty in a Level 2 PSA are numerous and it is impractical to address all of them quantitatively. Experience in performing uncertainty studies for limited aspects of severe accident phenomena suggests that the effects of uncertainties from some sources are larger and more dominant than the effects of uncertainties from other sources. In an integral sense, then, the aggregate uncertainty in Level 2 PSA results can be estimated by selecting the dominant sources of uncertainty and treating them in detail. To identify the dominant sources of uncertainty, the Morris method for sensitivity analysis was employed. The detailed results of the sensitivity analysis are presented and discussed in [3]. The most influential parameters identified by the Morris method are summarized in APPENDIX A and will be utilized in the uncertainty analysis presented in this paper.

2.1. Uncertainty analysis

According to the sensitivity analysis results in [3], a total of four sets of the most influential MELCOR modelling parameters have been identified for the RC7A and RC7B scenarios These sets also include combinations of the mode of debris ejection from the vessel (IDEJ), considered as a phenomenological splinter[2] for every accident scenario considered in the analysis. The parameters and associated uncertainty distributions are summarized in [3].

The MELCOR code has two options for core debris ejection from the vessel, determined by a solid debris ejection switch (IDEJ). In the default option (ON, IDEJ = 0), the masses of each material available for ejection are the total debris and molten pool material masses, regardless of whether or how much they are molten [11]. In the second option (OFF, IDEJ = 1), the masses of steel, Zircaloy, and UO2 available for ejection are simply the masses of these materials that are molten; the masses of steel oxide and control poison materials available for ejection are the masses of each of these materials multiplied by the steel melt fraction, based on an assumption of proportional mixing; the mass of ZrO_2 available for ejection is the ZrO_2 mass multiplied by the Zircaloy melt fraction. Additionally, the mass of solid UO_2 available for ejection is the Zircaloy melt fraction times the mass of UO_2 that could be relocated with the Zircaloy as calculated in the candling model using the secondary material transport model [11]. Furthermore, the MELCOR code puts additional constraints on the mass that can be ejected at vessel failure: (i) to initiate melt ejection, the mass of molten materials should be greater than SC1610(2) (5000 kg – default value), or a melt fraction should be larger than SC1610(1) (0.1 – default value). Here, the values of sensitivity coefficients SC1610(1,2) were set to zero, so any amount of melt available for ejection would be ejected [12,13]. In the event of a gross failure of the vessel lower head (e.g. due to creep-rupture), it is assumed that all debris in the bottom axial level of the corresponding ring, regardless its state, is discharged linearly over a 1-second time step without taking into account the failure opening diameter [11].

The uncertainty distributions are based on a literature review [4-9] and, in many cases, on expert judgment, due to a lack of publicly available information.

Furthermore, the results of the bounding analysis show that the mode of debris ejection from the vessel (IDEJ) has a dominant effect on the code predictions of the fractions of Cs and I2 released to the environment in case of an accident initiated by a LOCA. As it is not feasible to treat this parameter probabilistically due to a lack of knowledge, it will be considered as a phenomenological splinter[2]. Consequently, both sensitivity and uncertainty analyses will be conducted for the two aforementioned accident scenarios and two IDEJ parameter combinations, resulting in four sets of calculations:

- RC7A-IDEJ1 – SBO-MVSS-IDEJ1 (solid debris ejection off).
- RC7A-IDEJ0 – SBO-MVSS-IDEJ0 (solid debris ejection on).

[2]In ROAAM formulation a splinter scenario is a phenomenological scenario where relevant epistemic uncertainties are *beyond the reach of any reasonably verifiable quantification*.

- RC7B-IDEJ1 – LOCA-MVSS-IDEJ1 (solid debris ejection off).
- RC7B-IDEJ0 – LOCA-MVSS-IDEJ0 (solid debris ejection on).

According to the sensitivity analysis results in [3], the MVSS filter decontamination factor for radioactive vapors stands out as one of the most influential parameters for the RC7B scenario (LOCA-MVSS), particularly in the case of IDEJ1 (solid debris ejection off). Standalone calculations using the SPARC-90 model for the MVSS filter indicate the possibility of achieving decontamination factors (DFs) for gaseous forms of Cs in the order of 10-100. Moreover, given that the current MELCOR model of the Nordic BWR lacks the necessary level of detail regarding the MVSS structures (multi-venturi assembly, moist separator, etc., and associated heat structures), the actual decontamination factor could be even higher.

For the purpose of uncertainty analysis, presented in this paper, the decontamination factor for radioactive aerosols (MVSSDFA) will follow a normal distribution with parameters (mean and standard deviation, μ=500, σ=250), truncated within the range [100,1000] [17]. Meanwhile, the decontamination factor for radioactive vapors (excluding RN class 1 – noble gases, MVSSDFV) will be modeled with a log-normal distribution (mean and standard deviation on the log scale [10], λ=4.6, ζ=0.91), truncated within the range [10,1000]. Both parameters are assumed to be correlated. It is important to note that the uncertainty distribution for MVSSDFV used in this study may not be conservative and requires further investigation, which will be addressed in the future work.

For the uncertainty analysis, a sample size of 500 MELCOR code calculations was chosen for each accident scenario and IDEJ parameter combination. This sample size is expected to yield adequate results based on the 99% tolerance/confidence levels for upper bounds (one sided), as discussed in section 4.1.2.2 of [3]. The sampling will be performed using the Latin Hypercube Sampling (LHS) method, using the Dakota software package [10]. The sampling process and MELCOR code simulations will be managed by the pyMELCOR and pyDakota tools, as detailed in [3].

3. RESULTS

The summary of uncertainty analysis results is presented in Table I.

Table I. Summary of uncertainty analysis results (mean/median values and [range])

Scenario\FOM	MVSS Time (h)	Vessel lower head failure (h)	Cs release fraction[3] (-)	I release fraction[3] (-)
LOCA-MVSS-IDEJ1	6.61/6.69 [2.23, 15.56]	2.18/1.73 [0.95, 7.59]	9.70E-4/6.62E-4 [1.33E-4, 1.91E-2]	1.26E-3/8.8E-4 [1.70E-4, 2.46E-2]
LOCA-MVSS-IDEJ0	3.69/3.76 [1.76, 6.78]	2.09/1.75 [0.87, 6.52]	1.67E-4/1.05E-4 [2.74E-5, 1.78E-3]	1.79E-4/1.09E-4 [2.62E-5, 2.05E-3]
SBO-MVSS-IDEJ1	7.67/7.36 [5.00, 15.2]	3.21/2.97 [1.71, 8.06]	5.44E-6/4.46E-6 [9.30E-7, 3.69E-5]	4.23E-5/3.37E-5 [1.25E-6, 3.83E-4]
SBO-MVSS-IDEJ0	5.62/5.65 [2.64, 10.06]	2.80/2.71 [1.61, 8.19]	3.60E-6/2.98E-6 [5.73E-7, 1.48E-5]	1.64E-5/1.30E-5 [6.88E-7, 1.04E-4]

The results presented in Figure 1 show the timing of activation of the MVSS system and the beginning of filtered containment venting (filtered containment venting is initiated automatically when the pressure in the containment exceeds 0.55 MPa). The results show that, on average, the MVSS release starts at approximately 4 h after the initiating event in the case of LOCA-MVSS-IDEJ0 and 7 h in the case of LOCA-

[3] Fraction of the initial core inventory released to the environment.

MVSS-IDEJ1. In the case of SBO-MVSS-IDEJ1 the MVSS release starts at approximately 6 h after the initiating event, and approximately 7 h after the initiating event in the case of SBO-MVSS-IDEJ1.

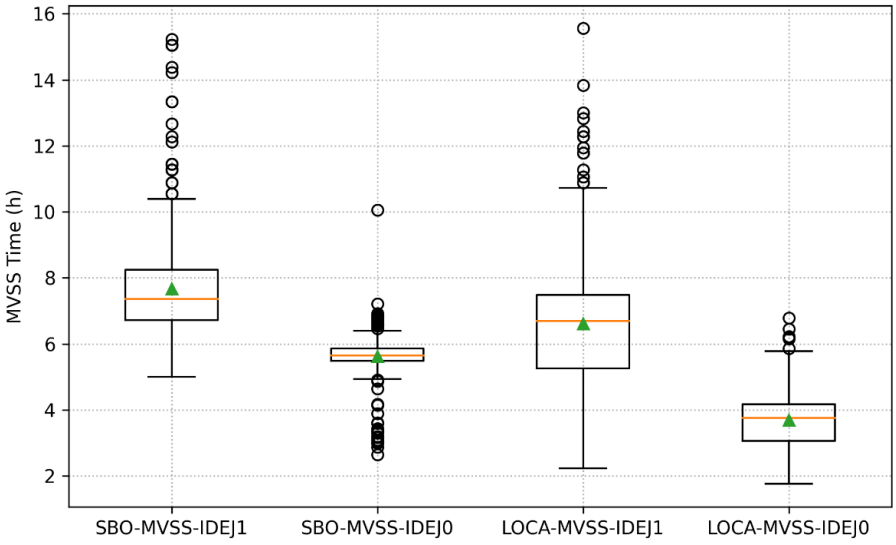

Figure 1. Box and whisker plot of the timing of MVSS opening[4]

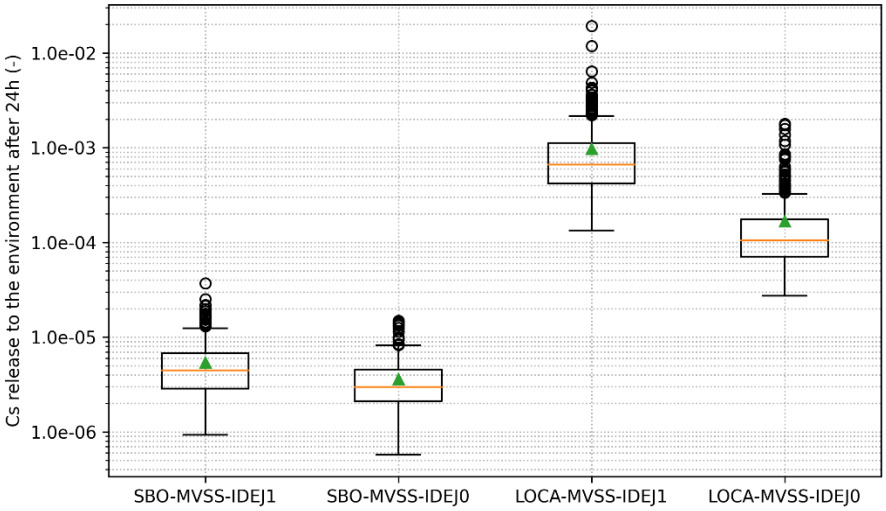

Figure 2. Box and whisker plot of the fraction of Cs [-] released to the environment after 24h after the initiating event.

These results show that the mode of debris ejection from the vessel has the highest contribution to the uncertainty in the results. For instance, in the case of IDEJ1, the uncertainty range for LOCA is between 2 hours up to almost 16 hours after the initiating event, while in the case of IDEJ0, the uncertainty range is between 2 and 7 hours after the initiating event. Similar results can be observed in the case of SBO.
The fraction of Cs released to the environment strongly depends on the accident scenario, i.e., transient (SBO) or LOCA, and the mode of debris ejection from the vessel (IDEJ).

[4] Whiskers' lengths are defined by IQR - the interquartile range (Q3-Q1), and the first and the third quartiles. The upper whisker will extend to last data point less than (Q3 + 1.5*IQR). Similarly, the lower whisker will extend to the first datum greater than (Q1 – 1.5*IQR). Beyond the whiskers, data points are considered as outliers and are plotted as individual points.

The fraction of Cs released to the environment in the case of a transient (SBO) is in the range of ~1.0E-6 to 4.0E-6, and the mode of debris ejection from the vessel does not significantly affect the results. According to the results presented in Figures 3-6, the most influential parameters are MVSSDFA (MVSS decontamination factor for aerosols) and GAMMA (agglomeration shape factor for aerosols). Larger values of the MVSS decontamination factor lead to a higher fraction of radioactive aerosols being trapped in the MVSS filter, and thus, a smaller release to the environment, as illustrated in Figure 3.

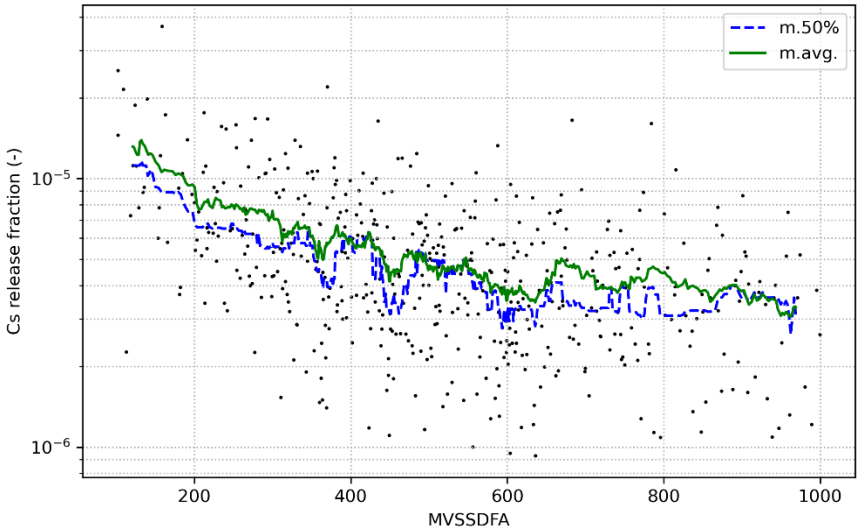

Figure 3. RC7A-IDEJ1 - Scatter plot and moving average (green)/median(dashed blue) of the fraction of Cs released to the environment as a function of MVSSDFA [-]

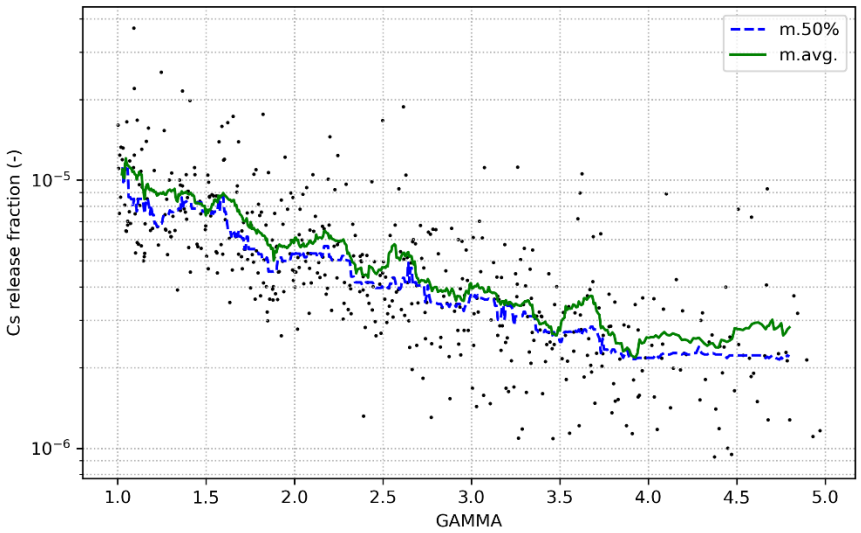

Figure 4. RC7A-IDEJ1 - Scatter plot and moving average (green)/median(dashed blue) of the fraction of Cs released to the environment as a function of GAMMA [-]

Larger values of GAMMA lead to higher deposition of suspended aerosols in the containment atmosphere and, thus, a smaller release to the environment, as illustrated in Figure 4 and 5.

In the SOARCA study, presented in [14], it has been assumed that agglomeration and dynamic shape factors are equal to 1 (which represents a perfectly spherical aerosol particle). The assumption is based on hygroscopic effects during the accident sequence, which induce some condensation of moisture on the aerosol particles causing the particles to tend towards being spherical and limit the degree of non-spherical

shapes. The findings presented in [15] suggest that dynamic shape factors can range from 1 (for water filled voids) to 4 (dry voids), depending on accident conditions.

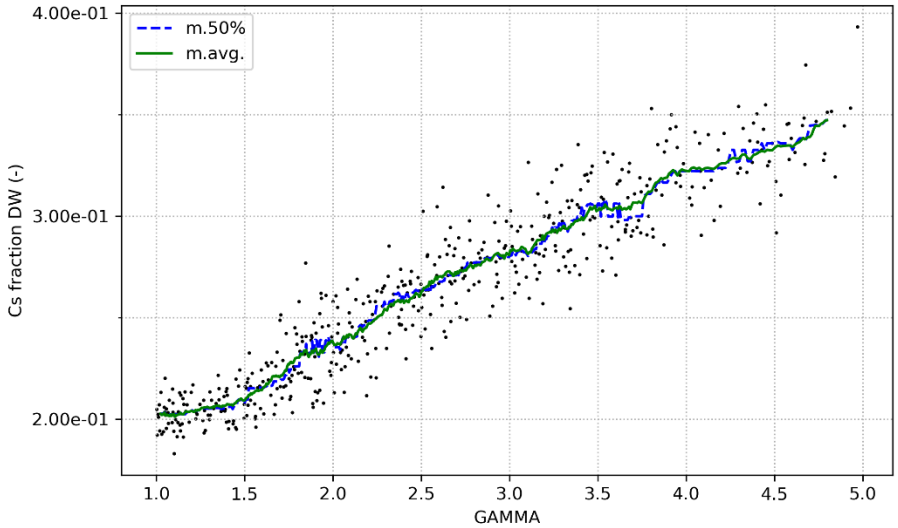

Figure 5. RC7A-IDEJ1 - Scatter plot and moving average (green)/median (dashed blue) of the fraction of Cs deposited in the drywell as a function of GAMMA [-]

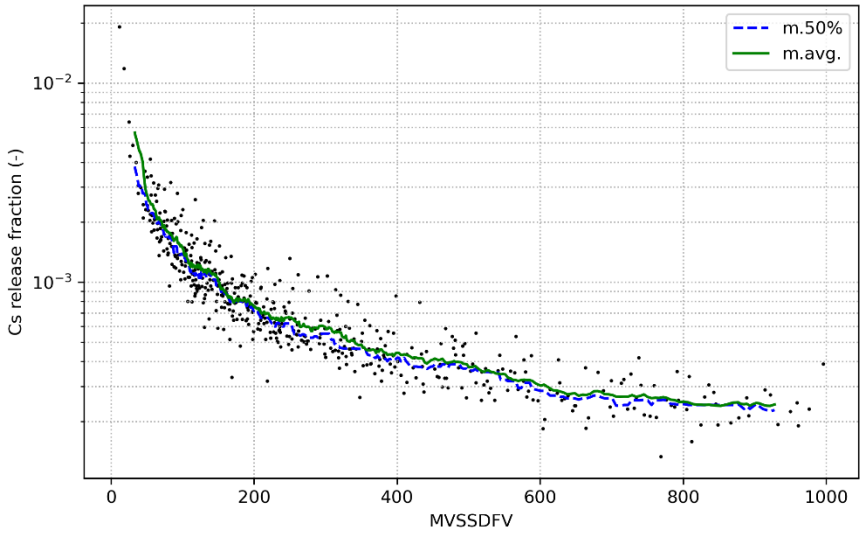

Figure 6. RC7B-IDEJ1 Scatter plot and moving average (green)/median (dashed blue) of the fraction of Cs released to the environment as a function of MVSSDFV [-]

The fraction of Cs released to the environment in the case of a LOCA strongly depends on the mode of debris ejection from the vessel (IDEJ). In the case of IDEJ1 (solid debris ejection OFF), the fraction of Cs released to the environment is almost one order of magnitude larger than in the case of IDEJ0 (solid debris ejection ON). In the case of LOCA-MVSS-IDEJ1 it ranges from ~1.7E-4 to 2.5E-2, while in the case of LOCA-MVSS-IDEJ0 the fraction of Cs released to the environment ranges from ~2.6E-5 to 2.E-3.

The scatter plots and moving averages/medians presented in Figure 6-8 show that the uncertainty in the results is dominated by the MVSSDFV (MVSS decontamination factor for radioactive vapors) for both LOCA-MVSS-IDEJ1 and IDEJ0; and MVSSDFA (MVSS decontamination factor for radioactive aerosols) in the case of LOCA-MVSS-IDEJ0.

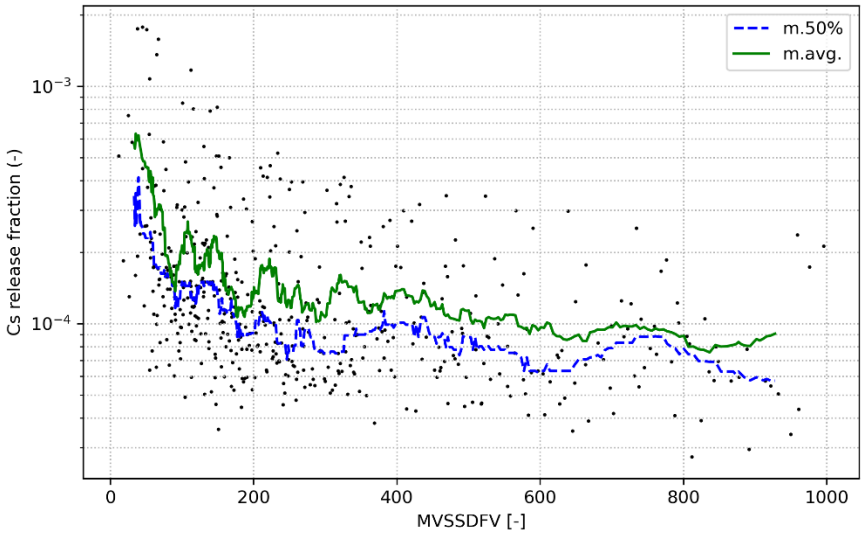

Figure 7. RC7B-IDEJ0 Scatter plot and moving average (green)/median (dashed blue) of the fraction of Cs released to the environment as a function of MVSSDFV [-]

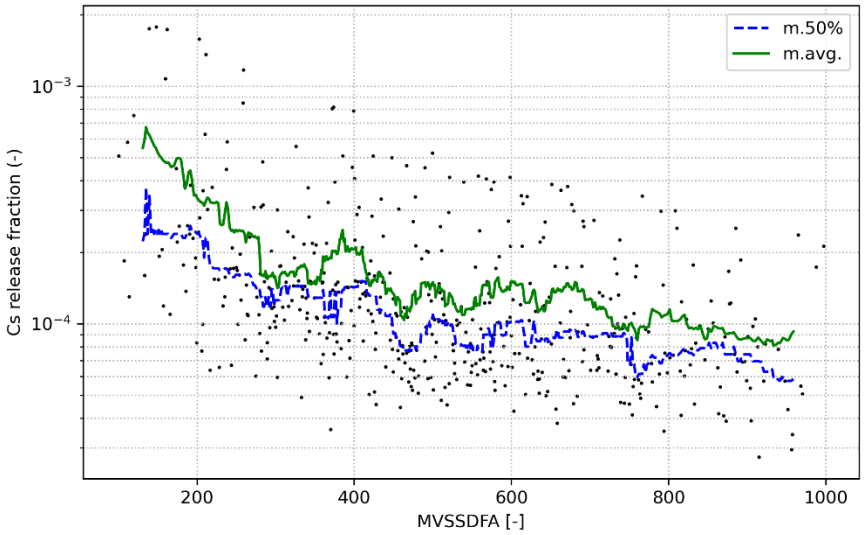

Figure 8. RC7B-IDEJ0 Scatter plot and moving average (green)/median (dashed blue) of the fraction of Cs released to the environment as a function of MVSSDFA [-]

The overall results show that in the case of SBO scenario the expected fraction of Cs released to the environment is almost 2 orders magnitude lower than the acceptable release boundary (0.1% of a 1800 MWth reactor yields ~0.046% for a 3900 MWth reactor), and both uncertainty distributions are well below the acceptability criterion.

On the other hand, in the case of LOCA the fraction of scenarios that exceed the acceptability criterion is 65.4% for LOCA-MVSS-IDEJ1 and 15.6% for LOCA-MVSS-IDEJ0. The magnitude of the release strongly depends on the value of the MVSS decontamination factor for radioactive vapors and the mode of debris ejection from the vessel (IDEJ) which was considered as a phenomenological splinter[2] in this study.

4. CONCLUSIONS

The uncertainty analysis results for the RC7 release category show that the pressure in the containment reaches the MVSS rupture disk setpoint (5.5 Bar(abs)) on average at approximately 4-7 hours after the initiating event. The mode of debris ejection from the vessel (IDEJ) has one of the major contributions to the uncertainty in the timing of MVSS release.

The results indicate that the fraction of Cs released to the environment is significantly larger in the case of RC7B (LOCA) compared to the RC7A (SBO) scenario. This difference can be explained by the effect of condensation pool scrubbing, since in the case of a transient, up until the vessel lower head failure, the fission products released from the fuel will be transported and scrubbed in the wetwell, before entering the drywell and being released to the environment.

In the case of RC7A (SBO), the release fraction of Cs released to the environment is well below the MVSS acceptance criterion for acceptable release[1], and the average value is equal to 5.44E-6/3.60E-6 for IDEJ1/0. In the case of RC7B (LOCA) the fraction of Cs released to the environment exceeds the MVSS acceptance criterion[1] for some parameter combinations, with the average value equal to 9.7E-4/1.67E-4 for IDEJ1/0. The uncertainty for the RC7B (LOCA) scenario is dominated by the mode of debris ejection from the vessel (IDEJ) and MVSS decontamination factor for radioactive vapors.

The mode of debris ejection from the vessel in the MELCOR code is the major source of uncertainty and controlled by the user-defined switch (IDEJ). In reality this process involve several interacting phenomena such as the formation and accumulation of melt, gravity driven drainage of molten materials through the porous debris bed, resolidification of molten materials and formation of crusts in colder regions of the debris bed, that prevent further material drainage, which can result in either the slow melt dripping from the vessel or the accumulation of significant amounts of superheated metallic melt above the crust, which will be released upon crust remelting/failure. Crust formation can facilitate the interaction of significant amounts of debris at high temperatures with the vessel lower head wall, and significant mechanical load on the structure. This can lead to creep-rupture failure of the vessel lower head and rapid ejection of debris from the vessel. The reduction of uncertainty in the mode of ejection of a multi-component mixture of solid and liquid debris, melt filtration through the porous debris, and crust formation is a necessary step for modelling of severe accident progression and fission products behavior in the reactor and the containment.

Furthermore, is important to note that the current MELCOR model of Nordic BWR lacks the necessary level of detail regarding the MVSS filter and employs this system as a simple filter with constant decontamination factors for radioactive aerosols and vapors. The values and uncertainty ranges for the MVSS decontamination factor for aerosols are established through both experimental and analytical work and are well-discussed in the literature. However, information regarding the MVSS decontamination factor for vapors is lacking, making it difficult to assess the performance of the MVSS filter in all accident conditions. To address this issue, it is proposed to perform a more detailed modeling of the MVSS filter, such as modeling injection paths with associated heat structures and scrubbing in the pool using the SPARC-90 model implemented in the MELCOR code [11]. This will be addressed in future work.

ACKNOWLEDGMENTS

The authors would like to express gratitude to Patrick Isaksson, Elisabeth Tengborn, Sara Ojalehto, Tuomo Sevón, Ilona Lindholm, Naeem Ul-Syed and Anders Riber Marklund for very useful discussions, insights and contributions to the NKS-STATUS project.

The work is supported by the Nordic Nuclear Safety Research (NKS), under the NKS-R STATUS activity (Contract: AFT/NKS-R(21)133/5 and AFT/NKS-R(22)133/5) and by the Swedish Radiation Safety Authority (SSM).

REFERENCES

1. L. Nilsson, "Development of an Input Model to MELCOR 1.8.5 for Oskarshamn 3 BWR" SKI Report 2007:05 (2006)
2. Sergey Galushin, Anders Riber Marklund, Dmitry Grishchenko, Pavel Kudinov, Tuomo Sevón, Sara Ojalehto, Ilona Lindholm, Patrick Isaksson, Elisabeth Tengborn, Naeem Ul-Syed, Source Term And Timing Uncertainty in Severe Accidents (NKS-STATUS), NKS-461, 978-87-7893-554-0, (2022)
3. Sergey Galushin, Govatsa Acharya, Dmitry Grishchenko, Pavel Kudinov, Tuomo Sevón, Sara Ojalehto, Ilona Lindholm, Patrick Isaksson, Naeem Ul-Syed, Source Term And Timing Uncertainty in Severe Accidents (NKS-STATUS), NKS-475, 978-87-7893-570-0, (2023)
4. Rafael Bocanegra, Luis E. Herranz, CIEMAT's outcomes from the PHEBUS-FPT1 uncertainty analysis in the framework of the EU-MUSA project, The 10th European Review Meeting on Severe Accident Research (ERMSAR2022), Karlsruhe, Germany, May 16-19, (2022)
5. Darnowski, P.; Mazgaj, P.; Włostowski, M. Uncertainty and Sensitivity Analysis of the In-Vessel Hydrogen Generation for Gen-III PWR and Phebus FPT-1 with MELCOR 2.2. Energies 2021, 14, 4884, (2021)
6. Rafael Bocanegra, Luis Enrique Herranz, The importance of characterizing input uncertainties in severe accident analyses. The effect on pool scrubbing modeling in a Fukushima Unit 1 sequence, Sociedad Nuclear Española, Reunion Virtual, (2020)
7. Fukushima Daiichi Unit 1 Accident Progression Uncertainty Analysis and Implications for Decommissioning of Fukushima Reactors – Volume I, SAND2016-0232, Sandia National Laboratories (2016)
8. Lucas I. Albright, Nathan Andrews, Larry L. Humphries, David L. Luxat, Tatjana Jevremovic, Material Interactions in Severe Accidents – Benchmarking the MELCOR V2.2 Eutectics Model for a BWR-3 Mark-I Station, Nuclear Engineering and Design Volume 383 (2021)
9. F. Mascari, M. Massone, G. Agnello, M. Angelucci, S. Paci, M. D'Onorio, F. Giannetti, Comparison of PHEBUS FPT1 uncertainty applications using MELCOR 2.2 with three different methodologies The 13th Meeting of the "European MELCOR and MACCS User Group" 27th –29th (2022).
10. Adams, B.M., et al., Dakota, A Multilevel Parallel Object-Oriented Framework for Design Optimization, Parameter Estimation, Uncertainty Quantification, and Sensitivity Analysis: Version 6.0 Reference Manual. 2014, Sandia National Laboratories. (2014).
11. L.L. Humphries, B.A. Beeny, F. Gelbard, T. Haskin, D.L. Louie, J. Phillips, R.C. Schmidt, MELCOR Computer Code Manuals Vol. 2: Reference Manual Version 2.2.18019, SAND2021-0241 O, (2021)
12. S. Galushin, P Kudinov "Uncertainty Analysis of Vessel Failure Mode and Melt Release in Station Blackout Scenario in Nordic BWR Using MELCOR Code." 18th International Topical Meeting on Nuclear Reactor Thermal Hydraulics (NURETH-18), Portland, OR, USA, August 18-22, (2019)
13. S. Galushin, P. Kudinov, "Comparison of Vessel Failure Mode and Melt Release Conditions in Unmitigated and Mitigated Station Blackout Scenarios in Nordic BWR using MELCOR code", ICONE-27, 27th International Conference on Nuclear Engineering, Tsukuba, Ibaraki, Japan, May 19-24, (2019)
14. P. Mattie, R. Gauntt, K. Ross, N. Bixler, D. Osborn, C. Sallaberry, and J. Jones, State-of-the-Art Reactor Consequence Analyses Project Uncertainty Analysis of the Unmitigated Long-Term Station Blackout of the Peach Bottom Atomic Power Station, NUREG/CR-7155, SAND2012-10702P. (2012)
15. Nuclear Energy Agency (NEA), State-of-the-Art Report on Nuclear Aerosols, NEA/CSNI/R(2009)
16. J-E. Holmberg, M. Knochenhauer, Probabilistic Safety Goals, Phase 1 – Status and Experiences in Sweden and Finland, NKS-153, ISBN 978-87-7893-216-7, (2007)
17. OECD/NEA/CSNI Status Report on Filtered Containment Venting, NEA/CSNI/R(2014)7, (2014)

APPENDIX A

Table II. MELCOR code parameters selection for uncertainty analysis.

Parameter ID	Parameter description and proposed distribution	Accident scenario
STICK [-]	Particle sticking probability. Scaled beta (2.5, 1.0), scaled on [0.5, 1.0] [9]	All
FCELRA [-]	Radiative exchange factors. Truncated normal (0.1, 0.035) truncated on [0.020, 0.30] [5]	LOCA-MVSS, SBO-MVSS-IDEJ0
SC71521 [m]	Initial bubble diameter correlation coefficient in SPARC-90 model. Triangular M = 7.E-3, range [5.E-3, 8.E-3] [EJ][5]	LOCA-MVSS IDEJ0
SC1020 [-]	Multiplication factor for time constant for radial solid and molten debris relocation. Scaled beta (1.33, 1.67) scaled on range [1.0, 4.0] [7]	LOCA-MVSS IDEJ0 SBO-MVSS IDEJ1
CORNSBLD [K]	NS failure temperature threshold. Uniform [1520-1700] [8]	LOCA-MVSS, SBO-MVSS-IDEJ1
VFALL [m/s]	Velocity of falling debris. Scaled beta (0.85, 1.14), scaled on range [0.01, 1.0] [7]	All
TZRSSINC [K]	Solidus temperatures for ZR/SS and ZR/INC eutectic pairs. Scaled beta (2.0, 1.0), scaled on range [1210, 1700] [EJ]	All
SC715010 [-]	Scaling factor for SPARC-90 model vent exit condensation decontamination factor. Triangular M = 2, range [1.0, 3.0] [EJ]	LOCA-MVSS
CHI [-]	Aerosol dynamic shape factor. Scaled beta (1.0, 1.5) scaled on [1.0, 5.0] [9]	All
MVSSDFV [-]	MVSS decontamination factor for radioactive vapors. Lognormal (λ, ζ - 4.6, 0.916) truncated on [10,1000], 0.99 – correlation with MVSSDFA [EJ]	All
SC71568 [-]	Multiplicative constant in a temperature correction correlation in the SPARC-90 model. Triangular M = -0.00232, [-2.6691e-03, -1.9728e-03] [EJ]	LOCA-MVSS, SBO-MVSS-IDEJ0
TPFAIL [K]	Penetration failure temperature. Scaled beta (2.0, 2.0) scaled on [1273, 1600] [EJ]	LOCA-MVSS
HFRZZR [W/m^{2}K]	Refreezing heat transfer coefficient for Zr. Lognormal (8.9227, 0.55962) truncate on [2000, 22000] [5]	All
SC7170CSM [kg/kgH_2O]	Saturation solubility at high and low temperature reference for CsM. Triangular M = 0.67, range [0.5695, 0.7705] [EJ]	SBO-MVSS, LOCA-MVSS IDEJ0
SC71555 [-]	SPARC-90 model multiplication constants in the DF factor correlations for and large Stokes numbers. Triangular M = 1.13893, range [0.9681, 1.3098] [EJ]	LOCA-MVSS, SBO-MVSS-IDEJ1
RHONOM [kg/m^3]	Aerosol density. Triangular M = 2000, range [870,4500] [4]	All

[5] EJ – expert judgement.

Parameter ID	Parameter description and proposed distribution	Accident scenario
SC7111CS2 [K]	Characteristic energy of interaction between the molecules divided by the Boltzmann constant for CsI/CsM. Triangular M = 97, range [82.450,111.550] [EJ]	LOCA-MVSS IDEJ0
SC7170CS [kg/kgH_2O]	Saturation solubility at low/high temperature reference for Cs. Triangular M = 3.95, range [3.3575, 4.5425] [EJ]	LOCA-MVSS IDEJ1
SC7111CS1 [Å]	Characteristic diameter of the molecule for Cs. Triangular M = 3.617, range [3.0745,4.1595] [EJ]	LOCA-MVSS IDEJ1 SBO-MVSS IDEJ0
TURBDS [m^2/s^3]	Turbulence dissipation rate. Uniform [7.5E-4, 1.25E-3] [6][EJ]	LOCA-MVSS IDEJ1
SC7111I1 [Å]	Characteristic diameter of the molecule for I. Triangular M = 4.982, range [4.2347, 5.7293] [EJ]	SBO-MVSS LOCA-MVSS IDEJ1
NUMSEC [-]	Number of sections. Uniform [10, 20] [EJ]	SBO-MVSS IDEJ0
SC71551 [-]	SPARC-90 model multiplication constants in the DF factor correlations for small Stokes numbers. Triangular M = 1.79182, range [1.5230, 2.0606] [EJ]	SBO-MVSS
SC7170CSI3 [kg/kgH_2O]	Saturation solubility at low temperature reference for CsI. Triangular M = 0.44, range [0.374, 0.5060] [EJ]	SBO-MVSS IDEJ0
GAMMA [-]	Aerosol agglomeration shape factor. Scaled beta (1.0,1.5) scaled on range [1.0, 5.0] [9]	All
MVSSDFA [-]	MVSS decontamination factor for radioactive aerosols. Truncated normal (500, 250) truncated on [100,1000], 0.99 – correlation with MVSSDFV [EJ][17]	All
SC11321 [K]	Oxidized fuel rod collapse temperature. Scaled beta (2, 5) scaled on range [2500-2800] [EJ]	SBO-MVSS
HDBPN [W/m^2K]	Heat transfer coefficient between particulate debris and LH penetration. Uniform [100, 1000] [EJ]	SBO-MVSS IDEJ0
PDPor [-]	Particulate debris porosity. Truncated normal (0.38, 0.1) truncated on [0.25, 0.50] [5][EJ]	All
HFRZSS [W/m^2K]	Refreezing heat transfer coefficient for SS. Lognormal (7.824, 0.40547), truncated on [1000, 5000] [5]	All
DHYPDLP [m]	Lower plenum particulate debris equivalent diameter. Truncated normal (0.0035, 0.001) truncated on [0.002, 0.005] [EJ]	SBO-MVSS IDEJ1
SC11312 [K]	Critical temperature at which molten materials are released from an oxide shell or local blockage. Triangular M = 2400, range [2100, 2500] [5]	SBO-MVSS IDEJ1
SC7111I2 [K]	Characteristic energy of interaction between the molecules divided by the Boltzmann constant for I2. Triangular M = 550, range [467.50, 632.50] [EJ]	SBO-MVSS IDEJ1

Vysus Group

Source Term Uncertainty Analysis

of Filtered Containment Venting Scenarios in Nordic BWR

Sergey Galushin
PhD, Principal consultant

Ingenuity.
Imagination.
Insight.

Introduction

- This work was performed as a part of the NKS-STATUS project (Phase 1&2)*,**
- The work is supported by the Nordic Nuclear Safety Research (NKS), under the NKS-R STATUS activity (Contract: AFT/NKS-R(21)133/5 and AFT/NKS-R(22)133/5) and by the Swedish Radiation Safety Authority (SSM).
- NKS-STATUS – Participating organizations
  - Vysus Sweden AB, Sweden (VG), Project coordinator
  - Technical Research Centre of Finland, Finland (VTT)
  - Swedish Radiation Safety Authority, Sweden (SSM)
  - Royal Institute of Technology, Sweden (KTH)
  - Norwegian Radiation and Nuclear Safety Authority, Norway (DSA)

*Sergey Galushin, Anders Riber Marklund, Dmitry Grishchenko, Pavel Kudinov, Tuomo Sevón, Sara Ojalehto, Ilona Lindholm, Patrick Isaksson, Elisabeth Tengborn, Naeem Ul-Syed, “Source Term And Timing Uncertainty in Severe Accidents”, NKS-461, 01 Jul 2022
https://www.nks.org/en/nks_reports/view_document.htm?id=111010214698139

**Sergey Galushin, Govatsa Acharya, Dmitry Grishchenko, Pavel Kudinov, Sara Ojalehto, Tuomo Sevón, Ilona Lindholm, Patrick Isaksson, Elisabeth Tengborn, Naeem Ul-Syed, “Source Term and Timing Uncertainty in Severe accidents NKS-STATUS Phase 2 report”, NKS-475, 03 Jul 2023
https://www.nks.org/en/nks_reports/view_document.htm?id=111010214698428

Introduction

- Nordic Boiling Water Reactors employ ex-vessel debris coolability in the deep pool beneath the reactor pressure vessel and filtered venting of the containment as a severe accident management strategy.
  - The lower drywell is flooded with water to prevent failure of the containment penetrations and provide ex-vessel debris coolability.
  - Following the vessel lower head failure, the debris is ejected into the water-filled drywell, fragment, quench and form a debris bed coolable by natural circulation of water.
  - Filtered containment venting is initiated either manually (by operators) or automatically (via rupture disk (0.55 MPa)) through the MVSS.
    - > *Supposed to lead to an acceptable release to the environment.*
      - *Release below 0.1 % of the inventory of the cesium isotopes Cs-134 and Cs-137 in a core of 1800 MWTh reactor (~0.046% of the core inventory of Cs of Nordic BWR)*

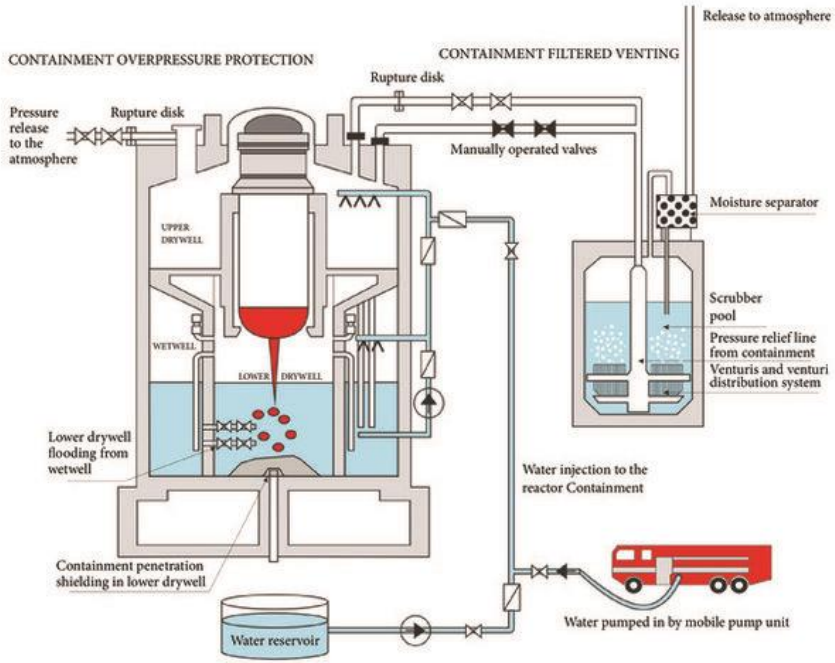

Image source: Strålsäkerhetsmyndigheten (SSM) - Swedish National Action Plan Response to ENSREG's request within the European Stress Tests, revision 1, December 2014.

MELCOR model of Nordic BWR

- Current MELCOR model of Nordic BWR employs simplified modelling of the MVSS:
  - Simple filter with constant decontamination factor (DF)*:
    - > *DF for aerosols design value – 100*
    - > *DF for aerosols best estimate value – 500*
      - UA range [100-1000]
    - > *Previous analyses showed high importance of the MVSS DF for vaporous FPs:*
      - Will be assumed as a separate parameter in UA.
        - UA range [10-1000]
  - SPARC90 model for FL362 switched off.
  - DFs (V&A) do not depend on the MVSS pool properties.

FL362 – Filtered containment venting (MVSS relief)
- Flow path opens when the pressure in the containment exceeds 5.5 Bars
- Constant DF applied.
- SPARC90 model switched off.

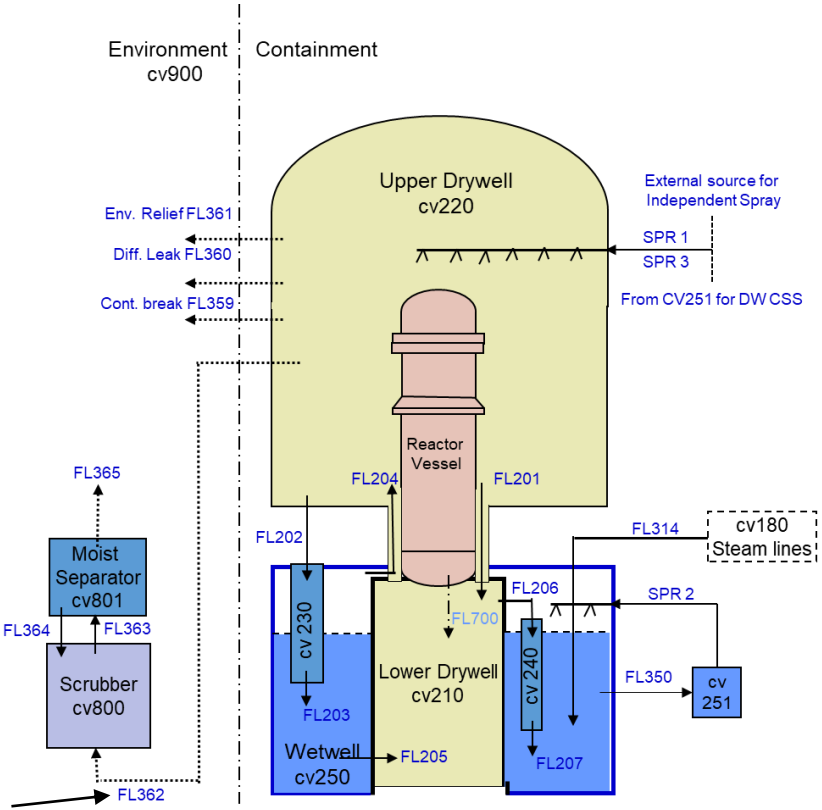

*S. Johst, T. Steinrötter, Optimization of the MELCOR Input Deck of Oskarshamn-3 NPP for Source Term Analyses with MELCOR 2.2, GRS – V – SSM2019 – BWR

Parameter Selection

- Based on the literature review and sensitivity analysis results 34 MELCOR modelling parameters were selected for uncertainty analysis.
- These parameters cover MELCOR modelling of:
  - Core degradation and relocation,
  - RPV lower head failure,
  - FP & Aerosol dynamics,
  - Engineered Safety Features (Spray and Pool scrubbing).

Parameter Selection

Parameter ID	Parameter description and proposed distribution	Accident scenario
STICK [-]	Particle sticking probability. Scaled beta (2.5, 1.0), scaled on [0.5, 1.0] [9]	All
FCELRA [-]	Radiative exchange factors. Truncated normal (0.1, 0.035) truncated on [0.020, 0.30] [5]	LOCA-MVSS, SBO-MVSS-IDEJ0
SC71521 [m]	Initial bubble diameter correlation coefficient in SPARC-90 model. Triangular M = 7.E-3, range [5.E-3, 8.E-3] [EJ]	LOCA-MVSS IDEJ0
SC1020 [-]	Multiplication factor for time constant for radial solid and molten debris relocation. Scaled beta (1.33, 1.67) scaled on range [1.0, 4.0] [7]	LOCA-MVSS IDEJ0 SBO-MVSS IDEJ1
CORNSBLD [K]	NS failure temperature threshold. Uniform [1520-1700] [8]	LOCA-MVSS, SBO-MVSS-IDEJ1
VFALL [m/s]	Velocity of falling debris. Scaled beta (0.85, 1.14), scaled on range [0.01, 1.0] [7]	All
TZRSSINC [K]	Solidus temperatures for ZR/SS and ZR/INC eutectic pairs. Scaled beta (2.0, 1.0), scaled on range [1210, 1700] [EJ]	All
SC715010 [-]	Scaling factor for SPARC-90 model vent exit condensation decontamination factor. Triangular M = 2, range [1.0, 3.0] [EJ]	LOCA-MVSS
CHI [-]	Aerosol dynamic shape factor. Scaled beta (1.0, 1.5) scaled on [1.0, 5.0] [9]	All
MVSSDFV [-]	MVSS decontamination factor for radioactive vapors. Lognormal (λ, ζ - 4.6, 0.916) truncated on [10,1000], 0.99 – correlation with MVSSDFA [EJ]	All
SC71568 [-]	Multiplicative constant in a temperature correction correlation in the SPARC-90 model. Triangular M = -0.00232, [-2.6691e-03, -1.9728e-03] [EJ]	LOCA-MVSS, SBO-MVSS-IDEJ0
TPFAIL [K]	Penetration failure temperature. Scaled beta (2.0, 2.0) scaled on [1273, 1600] [EJ]	LOCA-MVSS
HFRZZR [W/m^{2}K]	Refreezing heat transfer coefficient for Zr. Lognormal (8.9227, 0.55962) truncate on [2000, 22000] [5]	All
SC7170CSM [kg/kgH_2O]	Saturation solubility at high and low temperature reference for CsM. Triangular M = 0.67, range [0.5695, 0.7705] [EJ]	SBO-MVSS, LOCA-MVSS IDEJ0
SC71555 [-]	SPARC-90 model multiplication constants in the DF factor correlations for and large Stokes numbers. Triangular M = 1.13893, range [0.9681, 1.3098] [EJ]	LOCA-MVSS, SBO-MVSS-IDEJ1
RHONOM [kg/m^3]	Aerosol density. Triangular M = 2000, range [870,4500] [4]	All
SC7111CS2 [K]	Characteristic energy of interaction between the molecules divided by the Boltzmann constant for CsI/CsM. Triangular M = 97, range [82.450,111.550] [EJ]	LOCA-MVSS IDEJ0
SC7170CS [kg/kgH_2O]	Saturation solubility at low/high temperature reference for Cs. Triangular M = 3.95, range [3.3575, 4.5425] [EJ]	LOCA-MVSS IDEJ1
SC7111CS1 [Å]	Characteristic diameter of the molecule for Cs. Triangular M = 3.617, range [3.0745,4.1595] [EJ]	LOCA-MVSS IDEJ1 SBO-MVSS IDEJ0

Parameter ID	Parameter description and proposed distribution	Accident scenario
TURBDS [m^2/s^3]	Turbulence dissipation rate. Uniform [7.5E-4, 1.25E-3] [6][EJ]	LOCA-MVSS IDEJ1
SC7111I1 [Å]	Characteristic diameter of the molecule for I. Triangular M = 4.982, range [4.2347, 5.7293] [EJ]	SBO-MVSS LOCA-MVSS IDEJ1
NUMSEC [-]	Number of sections. Uniform [10, 20] [EJ]	SBO-MVSS IDEJ0
SC71551 [-]	SPARC-90 model multiplication constants in the DF factor correlations for small Stokes numbers. Triangular M = 1.79182, range [1.5230, 2.0606] [EJ]	SBO-MVSS
SC7170CSI3 [kg/kgH_2O]	Saturation solubility at low temperature reference for CsI. Triangular M = 0.44, range [0.374, 0.5060] [EJ]	SBO-MVSS IDEJ0
GAMMA [-]	Aerosol agglomeration shape factor. Scaled beta (1.0,1.5) scaled on range [1.0, 5.0] [9]	All
MVSSDFA [-]	MVSS decontamination factor for radioactive aerosols. Truncated normal (500, 250) truncated on [100,1000], 0.99 – correlation with MVSSDFV [EJ][17]	All
SC11321 [K]	Oxidized fuel rod collapse temperature. Scaled beta (2, 5) scaled on range [2500-2800] [EJ]	SBO-MVSS
HDBPN [W/m^{2}K]	Heat transfer coefficient between particulate debris and LH penetration. Uniform [100, 1000] [EJ]	SBO-MVSS IDEJ0
PDPor [-]	Particulate debris porosity. Truncated normal (0.38, 0.1) truncated on [0.25, 0.50] [5][EJ]	All
HFRZSS [W/m^{2}K]	Refreezing heat transfer coefficient for SS. Lognormal (7.824, 0.40547), truncated on [1000, 5000] [5]	All
DHYPDLP [m]	Lower plenum particulate debris equivalent diameter. Truncated normal (0.0035, 0.001) truncated on [0.002, 0.005] [EJ]	SBO-MVSS IDEJ1
SC11312 [K]	Critical temperature at which molten materials are released from an oxide shell or local blockage. Triangular M = 2400, range [2100, 2500] [5]	SBO-MVSS IDEJ1
SC7111I2 [K]	Characteristic energy of interaction between the molecules divided by the Boltzmann constant for I2. Triangular M = 550, range [467.50, 632.50] [EJ]	SBO-MVSS IDEJ1

Parameter Selection

Debris ejection modelling in MELCOR (IDEJ)

- Two options for debris ejection from the vessel in case of penetration failure.
  - IDEJ = 0: Solid debris ejection – ON
    - > *both solid and liquid (molten) debris can be ejected (default).*
  - IDEJ = 1: Solid debris ejection – OFF
    - > *only molten debris can be ejected (plus small fraction of solids)*
    - > *Typically leads to gross failure of the vessel lower head.*
- Gross failure of vessel wall,
  - all debris in the bottom axial level of the corresponding ring is discharged linearly over 1s time step (no regards to IDEJ).
- Different debris ejection modes will be considered as phenomenological splinter scenarios*

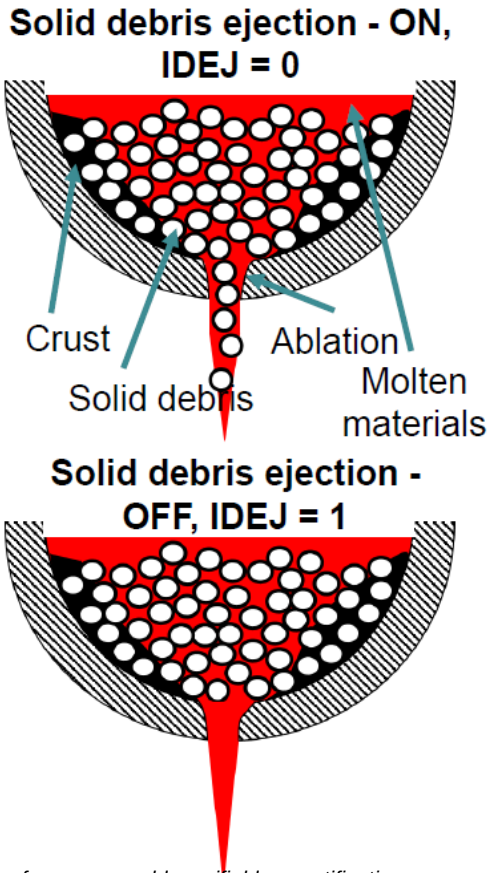

* In ROAAM** formulation a splinter scenario is a phenomenological scenario where relevant epistemic uncertainties are *beyond the reach of any reasonably verifiable quantification*.
** T.G. Theofanous, On the proper formulation of safety goals and assessment of safety margins for rare and high-consequence hazards, Reliability Engineering & System Safety, Volume 54, Issues 2–3, 1996.

Accident scenario

- RC7B – LOCA-MVSS
  - Initiating event: LB-LOCA in the steam line inside the containment.
  - LPSI/HPSI/CSS – unavailable.
  - LDW flooding is initiated according to the standard logic.
  - Containment venting through the MVSS is initiated automatically via rupture disk (0.55 MPa)
- RC7A – SBO-MVSS
  - Initiating event: SBO.
  - LPSI/HPSI/CSS – unavailable.
  - RCS depressurization according to the standard logic.
  - LDW flooding is initiated according to the standard logic.
  - Containment venting through the MVSS is initiated automatically via rupture disk (0.55 MPa).
- Scenarios considered in the analysis (considering phenomenological splinter – IDEJ)
  - RC7A-IDEJ1 – SBO-MVSS-IDEJ1 (solid debris ejection off).
  - RC7A-IDEJ0 – SBO-MVSS-IDEJ0 (solid debris ejection on).
  - RC7B-IDEJ1 – LOCA-MVSS-IDEJ1 (solid debris ejection off).
  - RC7B-IDEJ0 – LOCA-MVSS-IDEJ0 (solid debris ejection on).

Analysis Setup

- Accident scenario:
  - SBO-MVSS-IDEJ1
  - SBO-MVSS-IDEJ0
  - LOCA-MVSS-IDEJ1
  - LOCA-MVSS-IDEJ0
- Uncertainty tool:
  - pyMELCOR/pyDAKOTA
    - > *Python wrapper for MELCOR/DAKOTA*
    - > *Number of runs*
      - 500 runs per accident scenario (2000 in total)
    - > *Sampling*
      - LHS
    - > *Crashed cases restarted with reduced DTMAX*
    - > *MELCOR 2.2 rev18019*
- Simulation time was limited to 24 hours after initiating event.

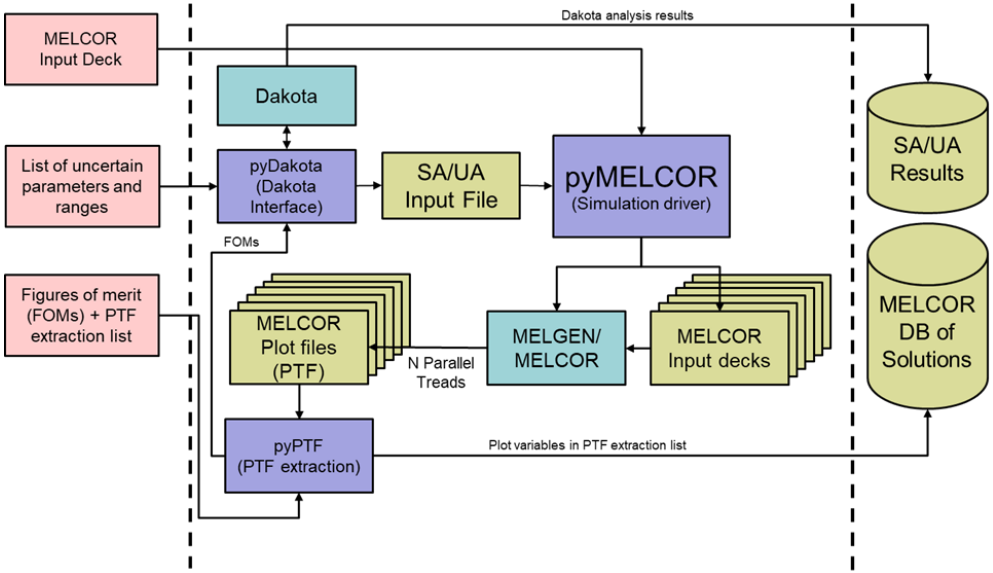

- Main FOMs:
  - Fraction of core inventory of Cs released to the environment.
  - Time of automatic activation of the MVSS (pressure in the containment > 5.5 Bar)

Results

- MVSS activation time (mean\median [range]
  - LOCA-IDEJ1: 6.61\6.69 [2.23,15.56] hours
  - LOCA-IDEJ0: 3.69\3.76 [1.76, 6.78] hours
  - SBO-IDEJ1: 7.67/7.36 [5.00, 15.2] hours
  - SBO-IDEJ0: 5.62/5.65 [2.64, 10.06] hours

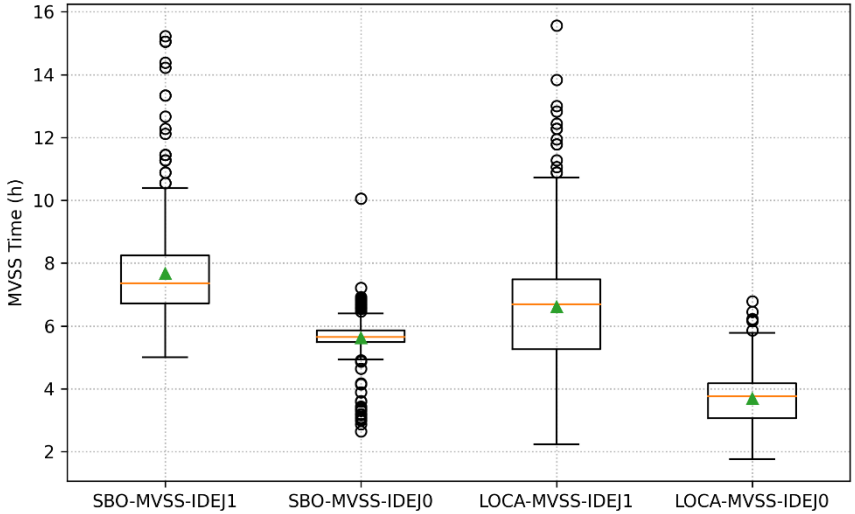

- Time delay between the vessel lower head failure and MVSS activation
  - In all SBO cases MVSS opening occurs after some time delay (~3-5 hours) after RPV failure.
  - In most of the LOCA cases MVSS opening after some time delay after RPV failure (~2-5 hours).

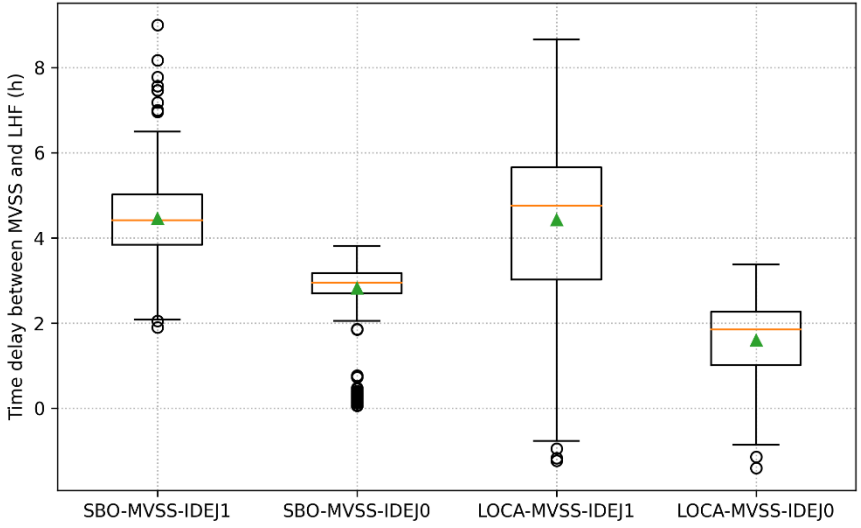

Results

- Cs release fraction [-] to the environment after 24 hours after IE.
  - Well below acceptable release threshold* for the accident scenarios initiated by the SBO (transient).
  - The threshold is exceeded in:
    - *4.6% of LOCA-MVSS-IDEJ0 simulations*
    - *71.0% of LOCA-MVSS-IDEJ1 simulations*
  - The mode of debris ejection from the vessel – IDEJ has the dominant effect on the code predictions of the Cs release.

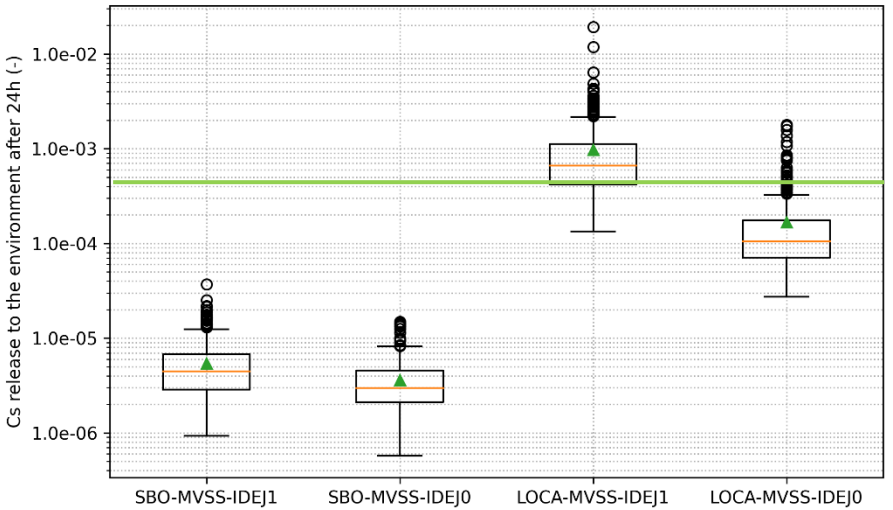

*0.1% of a 1800 MWth reactor yields ~0.046% for a 3900 MWth reactor

Results

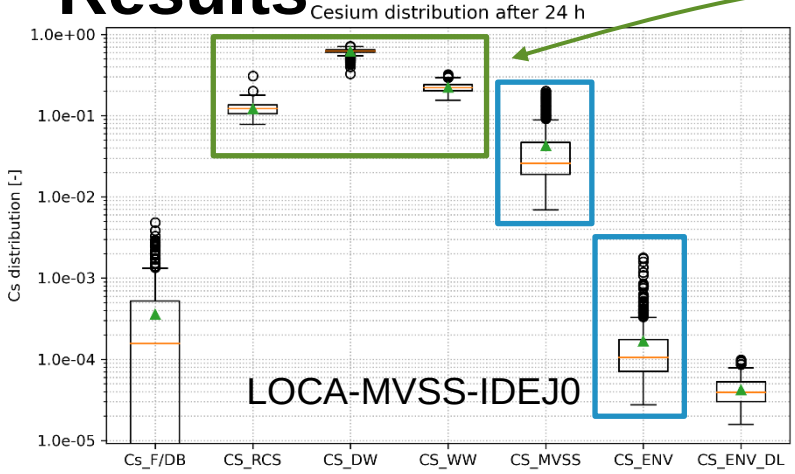

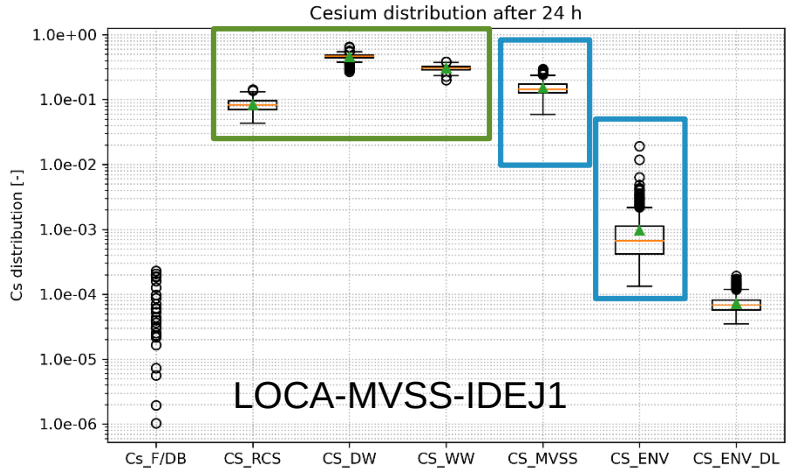

- More Cs is deposited inside the RCS and WW in SBO scenarios compared to LOCA,
- More Cs is deposited inside the DW in LOCA scenarios compared to SBO

- Significant effect of the mode of debris ejection from the vessel (IDEJ) on the fraction of Cs released from the containment to the MVSS and deposited inside the MVSS and Cs released to the environment in LOCA scenarios.
- Significant difference between SBO and LOCA scenarios.

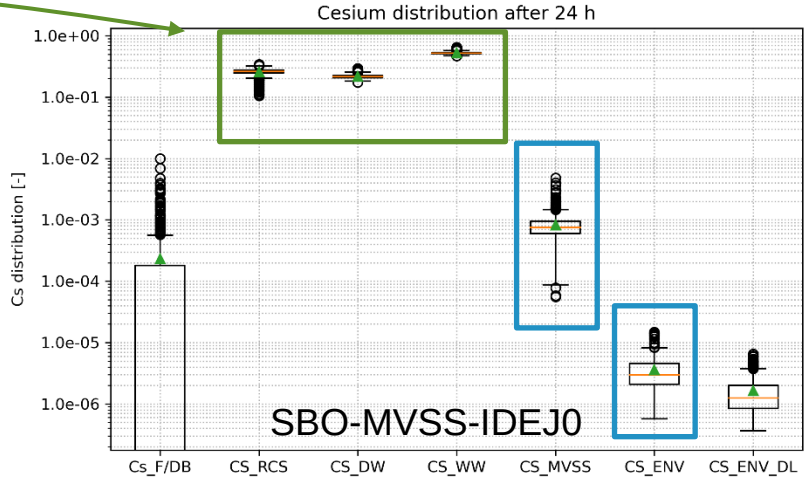

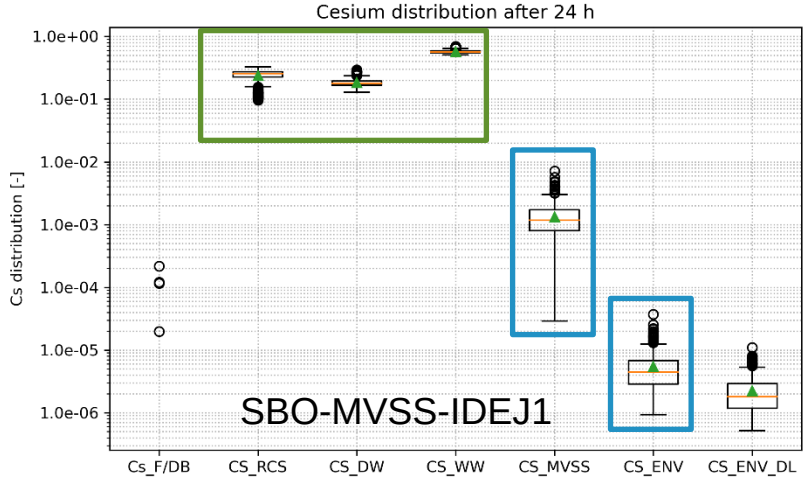

Results

- Decontamination factor for vapor FPs has the dominant effect on the Cs source term in LOCA-MVSS-IDEJ1.
  - Protracted debris ejection from the vessel leads to elevated temperatures inside the vessel/containment, remobilization of the FPs deposited inside the vessel/containment and larger release to the environment, compared to the IDEJ0 scenario.
- For the LOCA-MVSS-IDEJ0 scenario, both vapor and aerosol DFs important for the total Cs release to the environment.

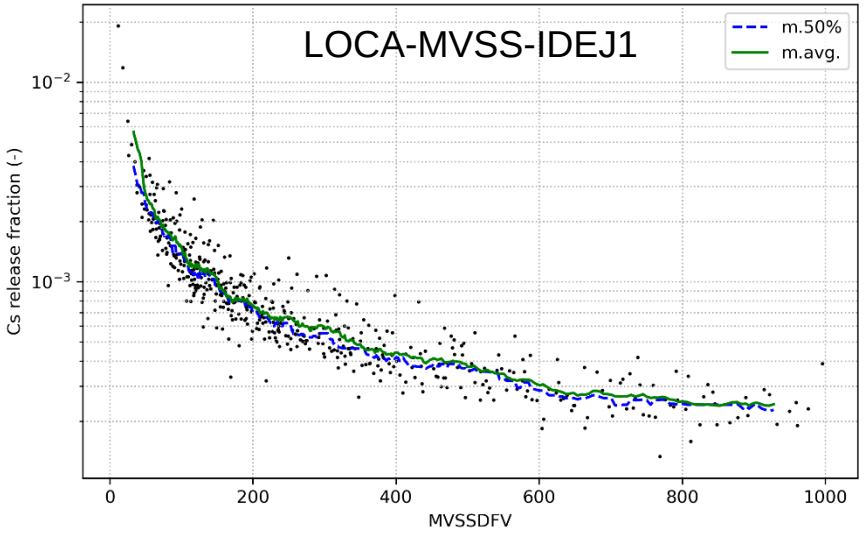

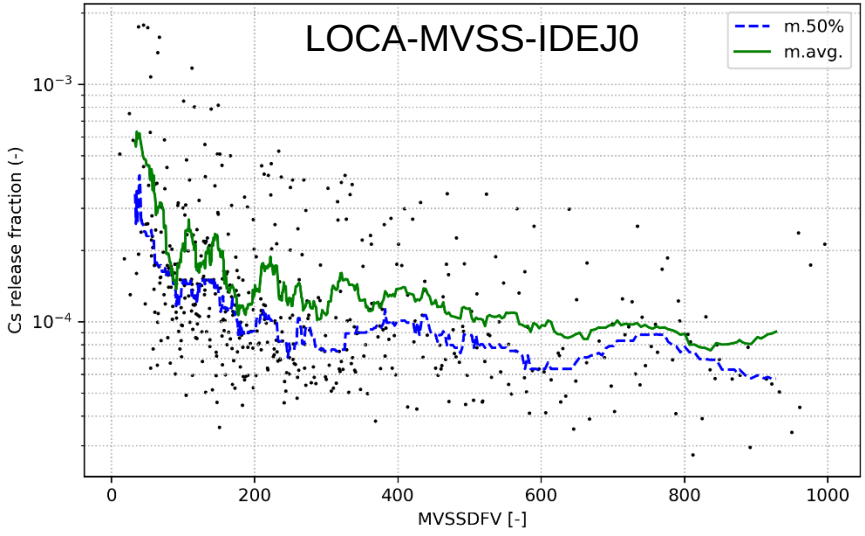

Results

- Debris ejection from the vessel (IDEJ)
  - IDEJ1 – Leads to a more protracted debris ejection from the vessel compared to IDEJ0.

LOCA-MVSS-IDEJ1

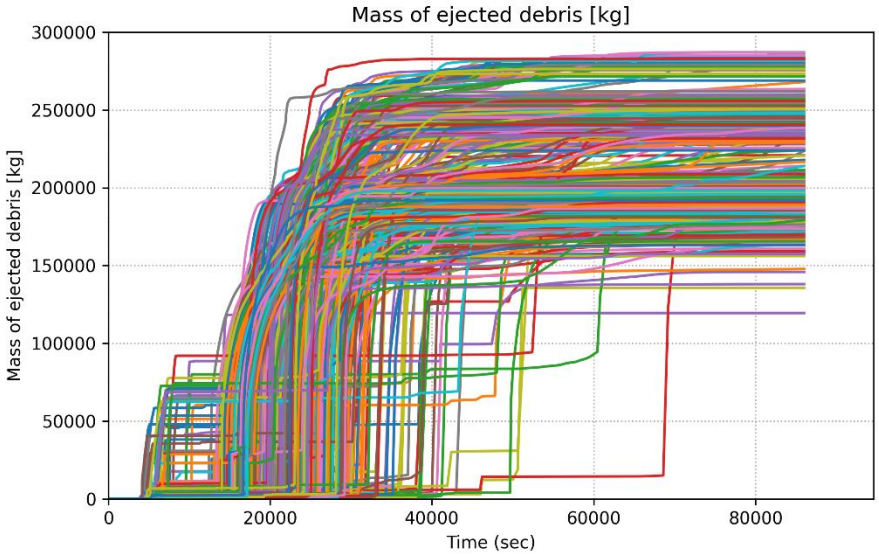

LOCA-MVSS-IDEJ0

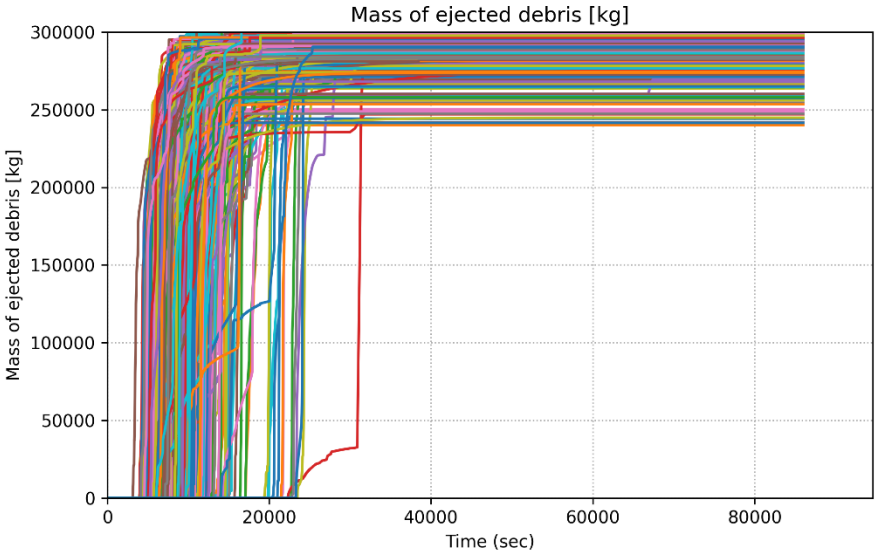

Results

- The difference between IDEJ0 and IDEJ1 is also reflected in the temperature of the drywell atmosphere.
  - Exposed debris inside the RPV (in case of IDEJ1) leads to a significantly higher temperature in the containment.

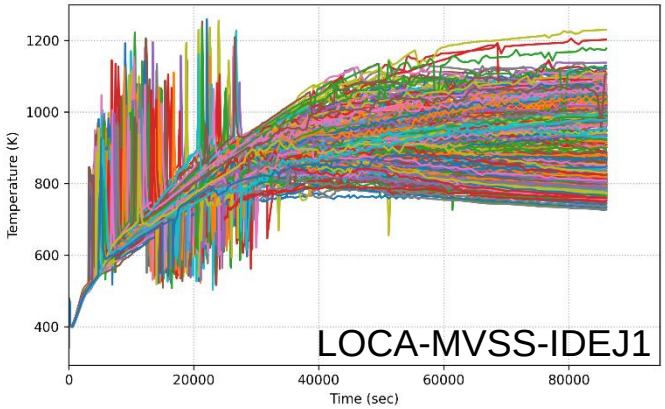

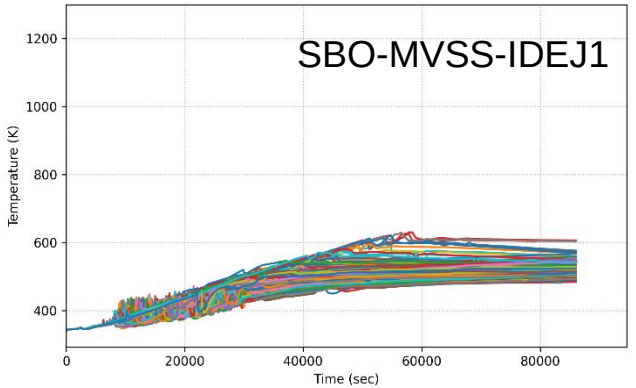

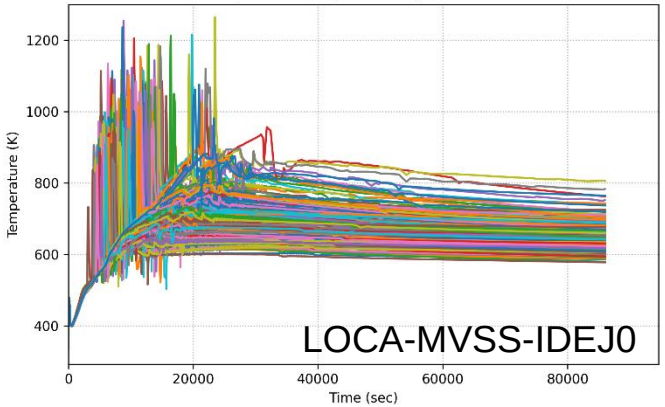

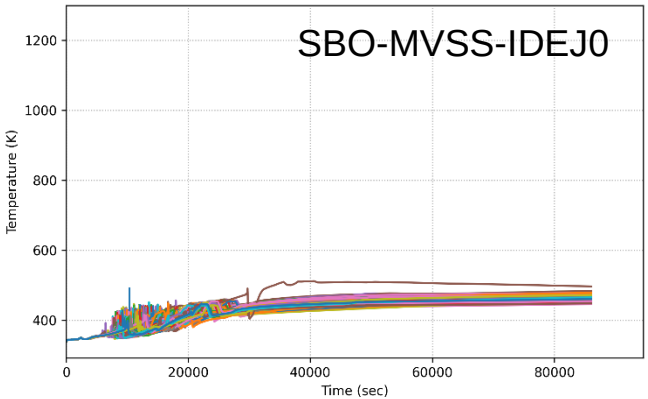

Results

- Protracted debris ejection (IDEJ1) leads to a larger release of Cs to the environment.
  - Most likely due to a larger contribution of vapor-form of CsOH (RN2), due to
    - > *Remobilization of the Cs deposited inside the vessel and the drywell.*

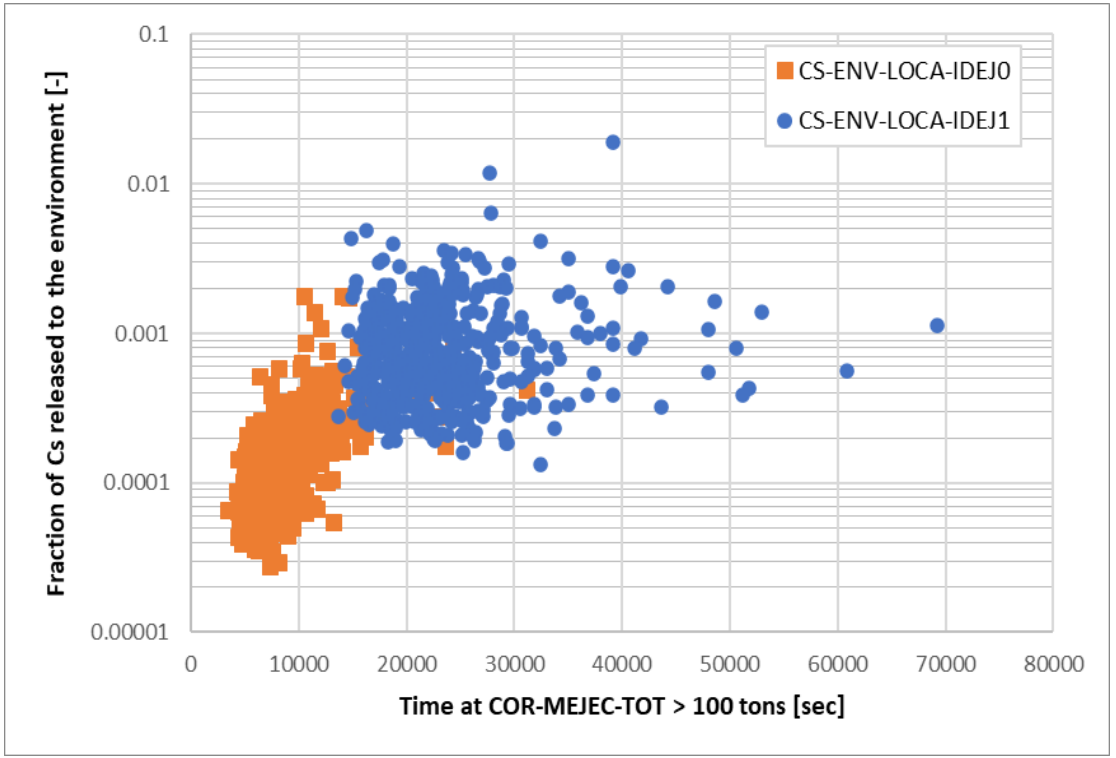

Main conclusions

- Accident scenarios initiated by a transient (SBO) that lead to filtered containment venting via MVSS lead to an acceptable release to the environment.
  - Regardless uncertainty in the MELCOR code uncertain parameters (within the ranges considered in the analysis).

- Accident scenarios initiated by a LOCA that lead to filtered containment venting via MVSS may lead to an unacceptable release to the environment.
  - The uncertainty in the results is majorly driven by:
    - *Decontamination factor for vapor FPs and*
    - *Mode of debris ejection from the vessel (IDEJ).*

Outlook

- Simulations were performed for 24 hours after initiating event
  - the long-term behavior of the FPs deposited inside the containment and MVSS is of interest and will be evaluated.

- More detailed modeling of the MVSS will be conducted to account for factors such as the water pool level, temperature, and deposition inside the pipes and venturi manifold.

- The possible effect of mitigative actions,
  - such as late spraying in the containment with the independent spray system, is of interest and will be investigated.

- PSA evaluation of the results.

Vysus Group

Sergey Galushin
sergey.galushin@vysusgroup.com
PhD, Principal consultant, Vysus Sweden AB

Govatsa Acharya
govatsa@kth.se,
Department of Nuclear Engineering, Royal Institute of Technology (KTH)

Dmitry Grishchenko
dmitrygr@kth.se
Department of Nuclear Engineering, Royal Institute of Technology (KTH)

Pavel Kudinov
pkudinov@kth.se
Department of Nuclear Engineering, Royal Institute of Technology (KTH)

Thank you

UNCERTAINTY AND SENSITIVITY ANALYSIS OF THE ASTEC SOURCE TERM RESULTS OF A MBLOCA SCENARIO WITH THE ACTIVATION OF SEVERE ACCIDENT MANAGEMENT ACTIONS IN A GENERIC KONVOI PLANT

A. Stakhanova, F. Gabrielli, V.H. Sanchez-Espinoza
Karlsruhe Institute of Technology, KIT
Hermann-von-Helmholtz-Platz 1, Eggenstein-Leopoldshafen, Germany
anastasia.stakhanova@kit.edu, fabrizio.gabrielli@kit.edu, victor.sanchez@kit.edu

E.-M. Pauli
Framatome GmbH
Paul Gossen Strasse 100, 91052 Erlangen, Germany
eva-maria.pauli@framatome.com

A. Hoefer
Framatome GmbH
Seligenstädter Strasse 100, 63791 Karlstein am Main, Germany
axel.hoefer@framatome.com

ABSTRACT

The current paper aims at summarizing and describing the results of the joined contribution of KIT/Framatome to the HORIZON 2020 MUSA project relevant to the uncertainty and sensitivity analysis of the ASTEC results for a MBLOCA scenario with the activation of severe accident management actions in a generic KONVOI NPP. The calculation platform assessed for such analyses is based on the ASTEC code, developed by IRSN, for the severe accident simulations, and on the KATUSA tool, developed by KIT in the frame of the KIT/Framatome WAME project. Eighteen uncertain parameters have been selected whose uncertainties have been characterized in terms of probability distribution functions. The Xe, I, Cs, and Ba release to the containment and to the environment have been considered as a figure-of-merit in the study. Results for the simple statistics and for the Spearman correlations are shown and discussed.

KEYWORDS
ASTEC, SAM, KATUSA, MBLOCA, Uncertainty and Sensitivity Analysis

1. INTRODUCTION

The overall objective of the HORIZON 2020 Management and Uncertainties of Severe Accidents (MUSA) project (2019-2023) [1], coordinated by CIEMAT, has been the assessment of the capability of severe accident (SA) codes when modelling reactor and spent fuel pool accident scenarios of Generation II and III nuclear power plants (NPPs). In particular, the project aimed at consolidating a harmonized approach for uncertainty and sensitivity analysis (U&Sa) of the source term (ST) associated with mitigated and unmitigated SA analyses.

In the framework of the joint contribution to the MUSA project of the Karlsruhe Institute of Technology (KIT) and of Framatome GmbH, a calculation platform has been developed at KIT and employed in MUSA to perform the U&Sa of the results of SA simulations by means of an integral code for a generic KONVOI NPP [2]. The European reference Accident Source Term Evaluation Code (ASTEC) [3], developed by the Institut de Radioprotection et de Sûreté Nucléaire (IRSN), is employed for performing the SA analyses. Furthermore, the KArlsruhe Tool for Uncertainty and Sensitivity Analysis (KATUSA) [4], developed by KIT, is used to assess a database of SA simulation results, by propagating the uncertainty of selected input parameters, and to perform the U&Sa.

KIT's and Framatome's contribution have been in particular focused on the application of the KATUSA tool to the ASTEC results of three SA scenarios in a generic KONVOI NPP: a Medium Break Loss of Coolant accident (MBLOCA), a MBLOCA scenario in conjunction with a Station Black Out (SBO), and a MBLOCA scenario with the activation of the Filtered Containment Venting System (FCVS) as Severe Accident Management (SAM) action. In addition to fulfilling the main goals of MUSA, KIT's and Framatome's contribution also aimed at improving the existing approaches of ST calculations in case of SA as well as quantifying the corresponding uncertainty to support the emergency team with making decisions [5, 6].

The current paper is devoted to the U&Sa of the ASTEC results concerning the MBLOCA SA scenario with the activation of the FCVS simulated up to basemat rupture. The paper is organized in the following way:

- Chapter 2 – description of the KATUSA tool;
- Chapter 3 – brief information about the ASTEC model of KONVOI used for the simulations;
- Chapter 4 – list of uncertain input parameters used for multiple ASTEC simulations;
- Chapter 5 – short description of the SA scenario;
- Chapter 6 – results of the U&Sa.

2. THE KARLSRUHE TOOL FOR UNCERTAINTY AND SENSITIVITY ANALYSES

The KArlsruhe Tool for Uncertainty and Sensitivity Analysis (KATUSA) has been developed at KIT in the frame of the KIT/Framatome WAME project. The flowchart of the KATUSA tool is shown in Figure 1

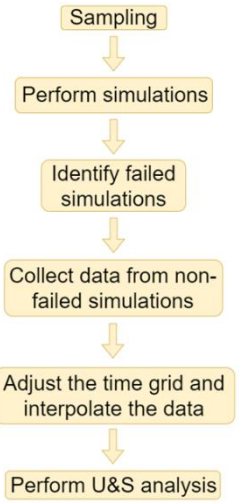

Figure 1. Flowchart of the KATUSA tool.

KATUSA is the U&Sa tool of the more general Fast Source Term Calculation (FSTC) tool [4], which has been developed at KIT in the frame of the WAME project [7]. The FSCT tool combines the functionalities for U&Sa (KATUSA) and an algorithm for the ST prediction based on the mathematical framework of the Monte-Carlo Bayes procedure (MOCABA) [5, 6, 8], developed by Framatome. KATUSA consists of six modules (Figure 1):

- *Sampling*: the uncertain parameters (Ups) and the corresponding probability density functions (PDFs) are provided to the sampling algorithm, which employs either Simple Random Sampling (SRS) or Latin Hypercube Sampling (LHS). The UPs may be pre-correlated. In that case, the sampled values are rearranged according to the correlation matrix calculated by using the Iman-Conover method [9, 10];
- *Perform simulations*: a dedicated interface allows automatically running multiple ASTEC simulations, each simulation has its own input deck with a corresponding set of sampled UP values. Simulations can be run in parallel;

- *Identify failed simulations*: failed runs are identified and excluded from the further analysis. The information (like, when did the simulation stop and why) about these simulations is collected, to allow the user to perform additional investigations of the reasons behind the failures;
- *Collect data from non-failed simulations*: the results for the selected Figure-Of-Merit (FOM) for all non-failed samples are collected and stored in a database. Due to the individual accident progressions of the different simulations, the collected results generally have different time scales. To prepare this data for U&Sa, the collected data are interpolated to a common time grid. The interpolated data is stored again in the database.
- Finally, the U&Sa is performed with the assessed database. For each selected FOM, simple statistics (minimum, mean, maximum, 5th, 50th and 95th percentiles values) and time-dependent correlation coefficients can be computed.

3. ASTEC MODEL OF KONVOI NPP

The core and the containment nodalizations of the ASTEC model are shown in Figure 2. The core is modelled by means of six cylindrical rings plus two additional channels representing the downcomer and the bypass. Fuel rods, control rods, grid spacers and plates are being considered in each core channel. The containment is modelled by means of 26 rooms plus an auxiliary building. In Figure 2, the plant (green, red, gray, and light blue boxes), the operating (white boxes), and the annulus (light yellow boxes) rooms are shown. The containment and the annulus are connected with each other and with the environment by means of fans (light blue arrows). Two filtering systems are modelled. The annulus air extraction system (AAES) connects the annulus to the environment and is always available. The efficiency of the AAES filters is 99.995% for aerosols and 99% for gaseous iodine. The FCVS is located on the connection between the containment to the environment and the efficiency of the filters is 99.9% for aerosols and 99% for gaseous iodine. The FCVS is activated as SAM action when the absolute pressure in the containment reaches 6.3 bar, and it is deactivated when the absolute pressure in the containment is equal to 3.65 bar. The goal is the containment depressurization aiming at avoiding containment rupture.

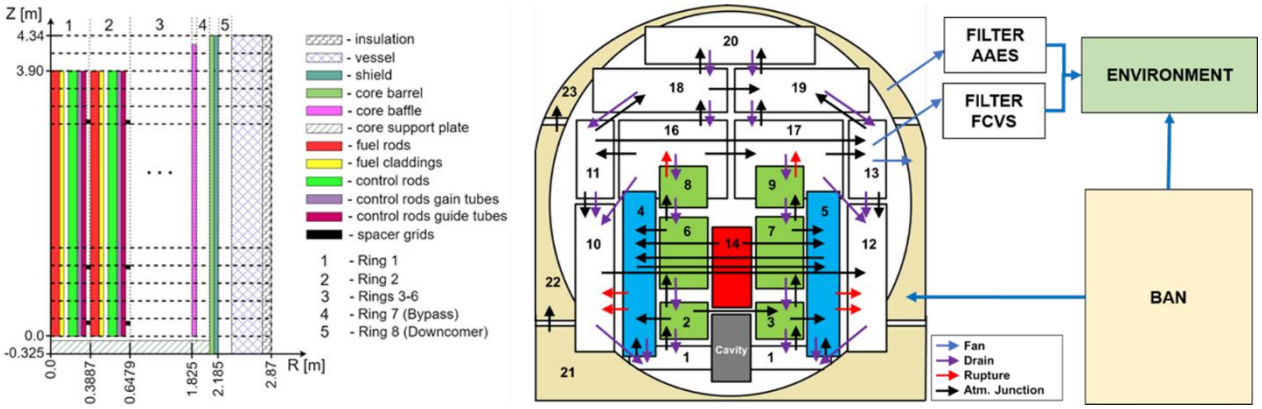

Figure 2. Core (left) and containment (right) nodalization of the ASTEC model of a generic KONVOI NPP (dimensions not in scale) [11, 12].

All the calculation options are activated in the ASTEC model to consider the main in-vessel and ex-vessel phenomena occurring during the severe accident scenario from the initiation up to the fission product (FP) release to the environment.

Efforts have been spent to properly evaluate the fuel inventory for a typical equilibrium cycle [12]. With this goal, the core has been loaded with 193 fuel assemblies (FA) composed of 48 U FA (6 batches), 81 U-Gd FA (6 batches), and 64 MOX FA (4 batches). The ORIGEN depletion code of SCALE 6.2.3 [13] has been employed to evaluate a library of fuel inventories, each 30 effective full power days (efpd), for a total of 328 efpd. The activity (in Ci) of the fuel initially loaded in the core at the beginning of cycle (BOC), at

the middle of cycle (MOC), and at the end of cycle (EOC) is shown in Table I, where the main element-wise contributions are indicated.

Table I. Initial activity of the fuel inventory at the beginning of cycle (BOC), at the middle of cycle (MOC), and end of cycle (EOC)

Volatility	Element	BOC [Ci]	MOC [Ci]	EOC [Ci]
Noble Gases	Xe	4.06E+08	4.59E+08	4.53E+08
	Kr	1.17E+08	1.33E+08	1.24E+08
Very Volatile	I	1.16E+09	1.28E+09	1.28E+09
	Cs	1.00E+09	1.09E+10	2.08E+10
Moderately Volatile	Te	6.10E+08	6.92E+08	6.88E+08
	Sr	2.98E+08	3.56E+08	3.76E+08
	Ba	1.48E+10	1.85E+10	1.87E+10
Less Volatile	Ru	3.50E+08	3.91E+08	4.16E+08
	La	6.04E+08	6.76E+08	6.66E+08
	Ce	4.49E+08	5.09E+08	5.12E+08

4. UNCERTAIN INPUT PARAMETERS

Eighteen UPs have been selected for uncertainty propagation. The UPs, as well as the corresponding PDFs, have been selected based on literature review, parametric analyses, and engineering judgement. The full list of the selected UPs and the corresponding PDFs are shown in Appendix A. The UPs *par1*, *par2*, *par5*, and *par5a* are used to model the fission product release simulated by the ASTEC ELSA model. The UPs *par14*, *par15*, and *par16* are used to model the fuel cladding integrity criteria which affects the degradation process in the reactor core. The Ups *par31 -par37* are related to the modelling of the behavior of the aerosols in the reactor coolant system and in the containment, which is simulated by the ASTEC SOPHAEROS and CPA calculation models. The UP *par41* refers to the uncertainty of the leakage rate from the containment to the annulus. The UP *parBU* refers to the uncertainties of the fuel burn-up, namely the number of effective full power days. Finally, two UPs have been considered for characterizing the performance of the FCVS: *parAE* (filter efficiency for aerosols) and *parI2* (filter efficiency for gaseous iodine).

Correlations between uncertain input parameters have been introduced in the KATUSA sampling module.

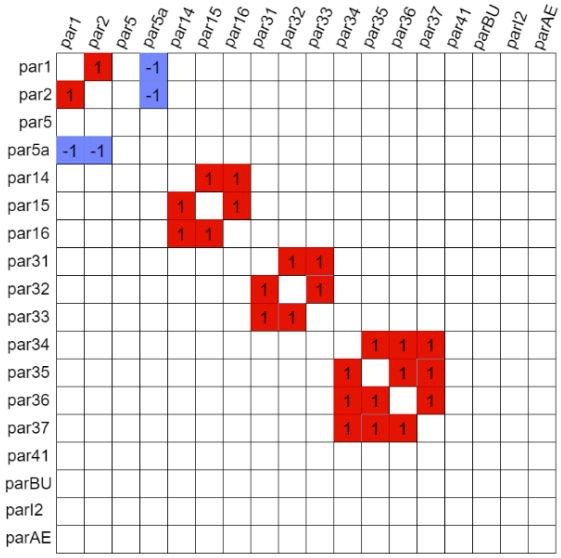

Figure 3. Pre-correlation matrix of the uncertainty parameters used as input for the KATUSA sampling module.

The pre-correlation matrix employed in the current work is shown in Figure 3. The correlation coefficients are based on engineering judgment. The employment of a pre-correlation matrix aims at improving the correctness of the modelling in the sampling process. As an example, *par34*, *par35*, *par36*, and *par37* are directly pre-correlated in Figure 3, since the minimum particle radius (*par34*) is expected to be directly pre-correlated with the maximum particle radius (*par35*). Furthermore, *par34* is directly pre-correlated with the shape factor of the particles (*par36* and *par37*).

5. DESCRIPTION OF THE ACCIDENT SCENARIO

The KONVOI plant is assumed to work at full power before the start of the transient. The MBLOCA SA scenario is initiated by a 12'' break on the cold leg at t=0 s. After the SCRAM signal (t=1 s), the admission to turbine and the main feed water pumps into the steam generator are closed. Then the conditions for the activation of the Emergency Core Cooling System (ECCS) are fulfilled (at 2.8 s and at 6 s) and the Main Coolant Pumps (MCPs) are coasted down and the pressure regulation in the pressurizer is switched off. The Emergency Feed Water System (EFWS) is activated when the liquid level of one steam generator falls below 4.50 m. When the gas temperature in the primary circuit exceeds 650 °C, the High- and Low-Pressure Injection Systems (HPIS/LPIS) are activated. The water injections stop when the tanks are empty leading to the start of core degradation. When the reactor pressure vessel fails, corium is relocated into the cavity, which is flooded by water when the horizontal erosion reaches 0.5 m. As mentioned above, the FCVS is activated when the absolute pressure reaches 6.3 bar and it is deactivated when the absolute pressure in the containment reaches 3.65 bar. The simulation ends when basemat rupture occurs.

6. RESULTS OF THE U&Sa

The results of the U&Sa are discussed in this section. The results are presented for the release into the containment and the environment of FPs with different volatility (Xe, Cs, I, and Ba). 300 ASTEC simulations have been run, the LHS method being used to propagate the uncertainty of the input parameters. 12 ASTEC simulations failed due to convergence problems and other issues and have been excluded from the U&Sa.

6.1. Simple statistics

The results in Figure 4 and Figure 5 provide an overview of the progression of the accident. The instant of the lower head vessel failure ranges from 3,064 s to 29,454 s, while the basemat rupture occurs between 187,242 s to 402,073 s (Figure 4). The activation of the FCVS occurs in 48 out of the 300 considered scenarios. Note that the conditions for the activation of the FCVS depend on the fuel burn-up. As shown in Figure 5 (left), the time of activation of the FCVS is between 200,000 s to 370,000 s. Furthermore, the instants at which the FCVS activation and the basemat rupture occur in each sample are shown in Figure 5 (right).

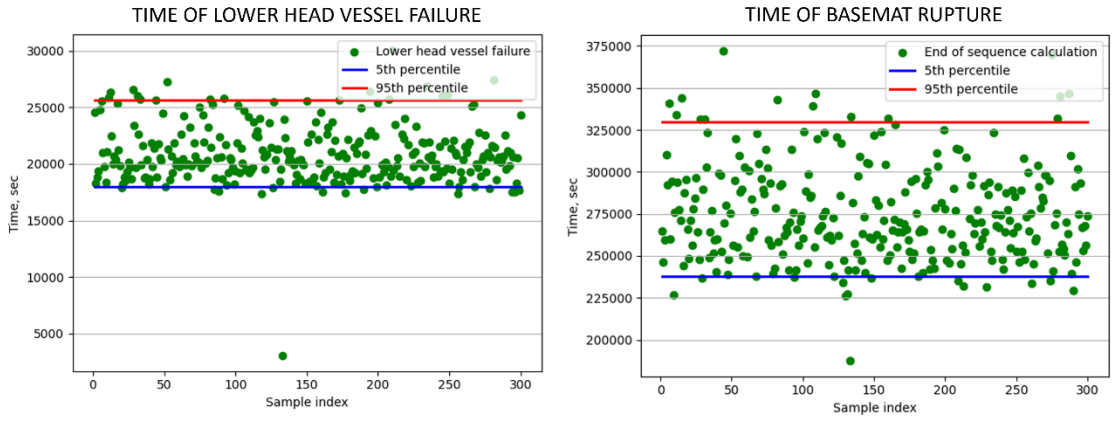

Figure 4. Time of lower head vessel failure and basemat rupture.

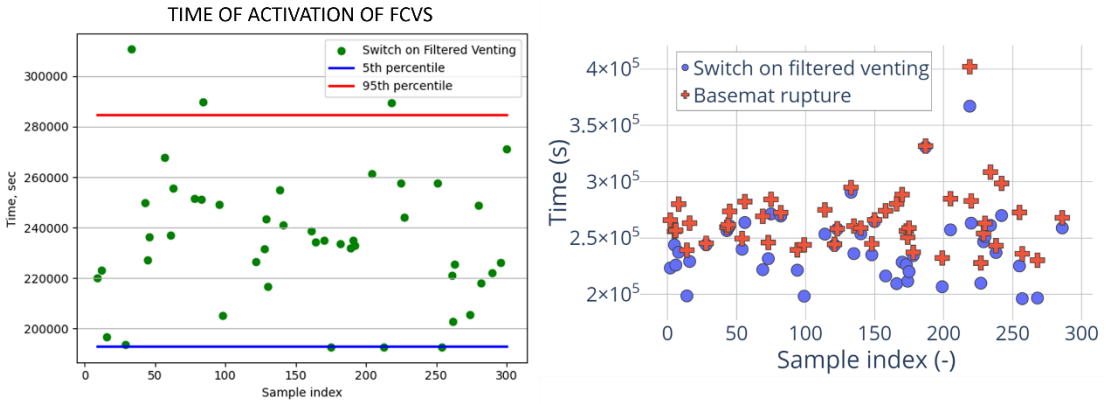

Figure 5. Time of activation of the FCVS (left) and instants of FCVS activation and Basemat rupture (right).

One key issue in the U&Sa of the SA scenarios is the identification of the time window to be analyzed, namely the start and end points of the analysis. The goal is to have a database for U&Sa composed by as many as possible ASTEC results relevant to the key phenomena occurring between SA initiation and basemat rupture. Having this in mind, the time window of the database for the U&Sa covers the time window starting from the minimum time when the FP release from the fuel occurs. About the end time, a compromise has been preliminary employed. As shown in Figure 4, for most of the scenarios basemat rupture occurs later than ~250,000 s. As shown in Figure 5 (right), at this instant the condition for the activation of FCVS has been reached in 38 ASTEC scenarios. Therefore, this end time has been employed for the U&Sa. If the time window was extended to consider all the scenarios with the activation of FCVS (up to 370,000 s), there would be an enormous lack of data to be statistically analyzed since most of the scenarios reach basemat rupture at about 300,000 s. How to improve such 'approximation' is currently a topic under study at KIT.

The simple statistics of the total amount of Xe in the containment and in the environment is shown in Figure 6. Since the conditions for the activation of the FCVS are reached in 48 samples out of 300, the effect of this SAM clearly appears in the results. It should be also reminded that in the MBLOCA+SAM ASTEC dataset, the AAES is also activated from the beginning of the transient. The mean value of the amount of Xe in the containment is about 90% of the initial amount of Xe loaded in the core, since the activation of the FCVS mainly drives the release of a mean amount of about 10% to the environment (Figure 6, right).

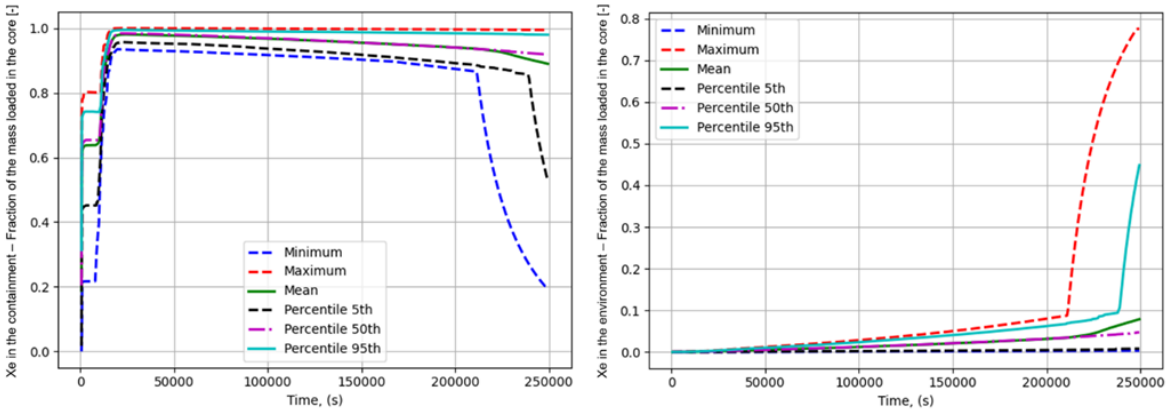

Figure 6. Simple statistics of the mass of Xe in the containment (left) and in the environment (right) as fraction of the total amount in the initial core loading.

The results concerning the total mass of I in the containment and in the environment are shown in Figure 7. The mass fraction in the containment is about 10% for the mean value and about 38% for the 95th percentile.

Concerning the environment, the mean value and the 95th percentile is about $1 \cdot 10^{-3}$ % and $2 \cdot 10^{-2}$ % of the initial loading, respectively.

The results concerning the total mass of Cs in the containment and in the environment are shown in Figure 8. The mass fraction in the containment is about 32% for the mean value and about 47% for the 95th percentile. Concerning the environment, the mean value and the 95th percentile is about $1 \cdot 10^{-4}$ % and $3 \cdot 10^{-4}$ % of the initial loading, respectively.

The results concerning the total mass of Ba in the containment and in the environment are shown in Figure 9. The mass fraction released to the containment is about 0.6% for the mean value and about 0.9% for the 95th percentile. Concerning the environment, the mean value and the 95th percentile is about $2 \cdot 10^{-5}$ % and $5 \cdot 10^{-5}$ % of the initial loading, respectively.

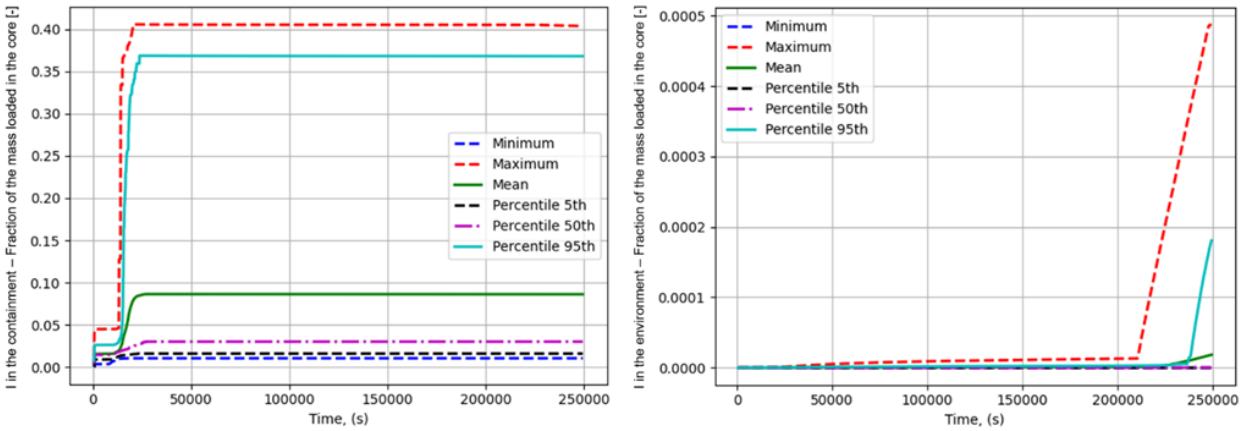

Figure 7. Simple statistics of the mass of I in the containment and in the environment as fraction of the total amount in the initial core loading.

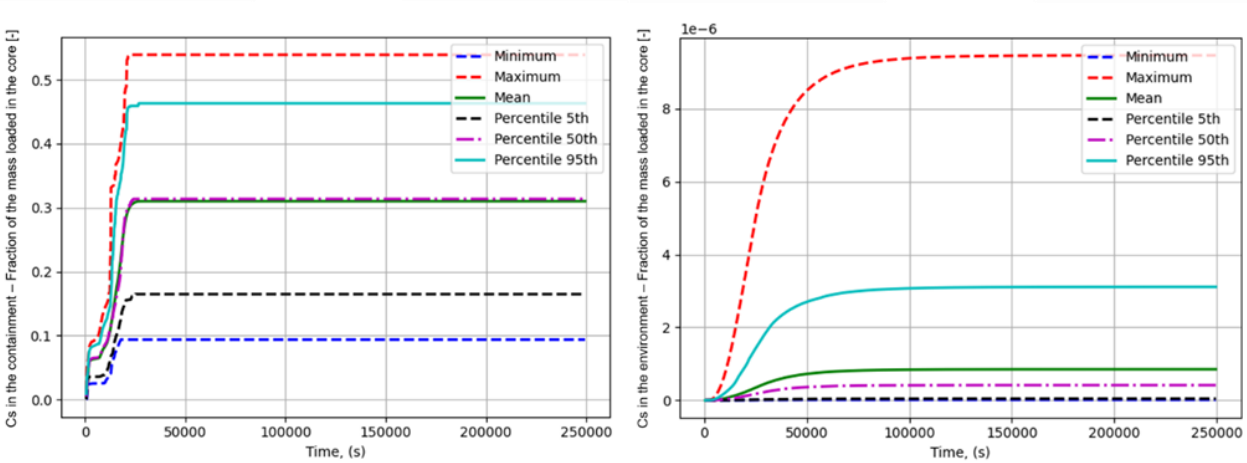

Figure 8. Simple statistics of the mass of Cs in the containment and in the environment as fraction of the total amount in the initial core loading.

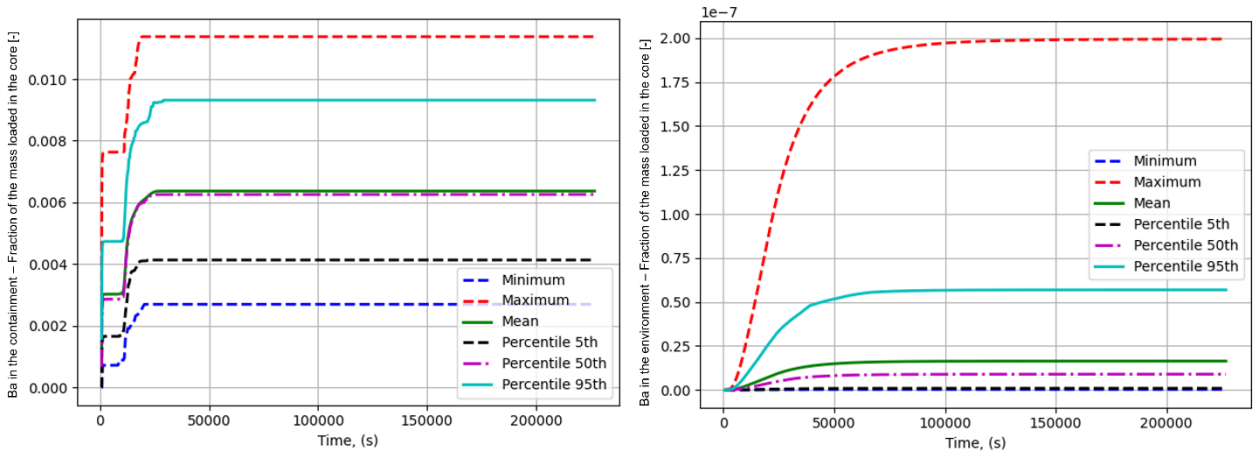

Figure 9. Simple statistics of the mass of Ba in the containment and in the environment as fraction of the total amount in the initial core loading.

2.2. Sensitivity analysis

The Spearman correlations between the UPs and the selected FoMs have been computed by means of KATUSA. In the following, results for correlations larger than 30% are shown.

The Spearman correlation coefficients between the amount of Xe release to the containment and to the environment (as fraction of the initial mass in the core) are shown in Figure 10. The results show that the parameters *parBU* (fuel burn-up) and *par41* (containment leakage) have the major impact on these FoMs. Concerning the release to the containment, *parBU* shows a strong correlation (about 80%) during the in-vessel phase of the scenario, while the correlation of *par41* decreases to up to about -80%, since more Xe is released to the environment for larger the containment leakage. It is important to mention that the correlation of *par41* with the release to the environment tends to decrease when the FCVS is activated at about 200,000 s (Figure 5). This is the result of the sudden massive release because of the activation of the FCVS. Concerning the release to the environment, the correlation of *par41* increases (in absolute value) in time, approaching about 90% at 200000 s from the beginning of the transient.

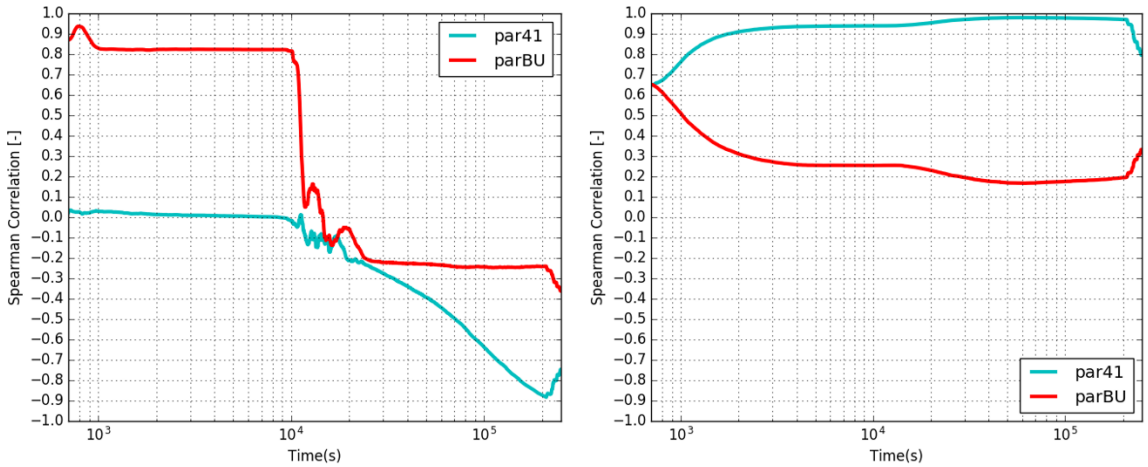

Figure 10. Spearman correlations between the dominant UPs and the mass fraction of the initial loading of Xe in the containment (left) and in the environment (right).

The Spearman correlations for the cesium aerosols into the containment and the cesium release into the environment are shown in Figure 11. Concerning the aerosols in the containment, correlation coefficients

larger than 30% are observed for the UPs related to the fuel burn-up (*parBU*), thermal properties (*par31*, *par32*, and *par33*), geometry (*par34* and *par35*), and aerosol behavior (*par36* and *par37*). These correlations are particularly relevant after the flooding of the cavity (~50000 s). The correlation related to *parBU* is in the 30%-40% range in the in-vessel phase of the scenario and becomes between -30% and -60% after flooding of the cavity. The correlations for the particle mean thermal conductivity (*par31*) and the particle mean density (*par33*) parameters are ~ -30% at about the instant corresponding to the flooding of the cavity. As shown in Figure 11, from this event on, the correlations for *par34* to *par37* become significant, the values reaching 50% at ~75000 s.

Concerning the release to the environment, the results show significant correlations between the UPs related to the containment leakage (*par41*) and the efficiency of the filters for aerosols (*parAE*). In particular, the Spearman correlation for *par41* is ~55%, while the correlation for *parAE* is negative, the value being ~75% (in absolute value) for the transient.

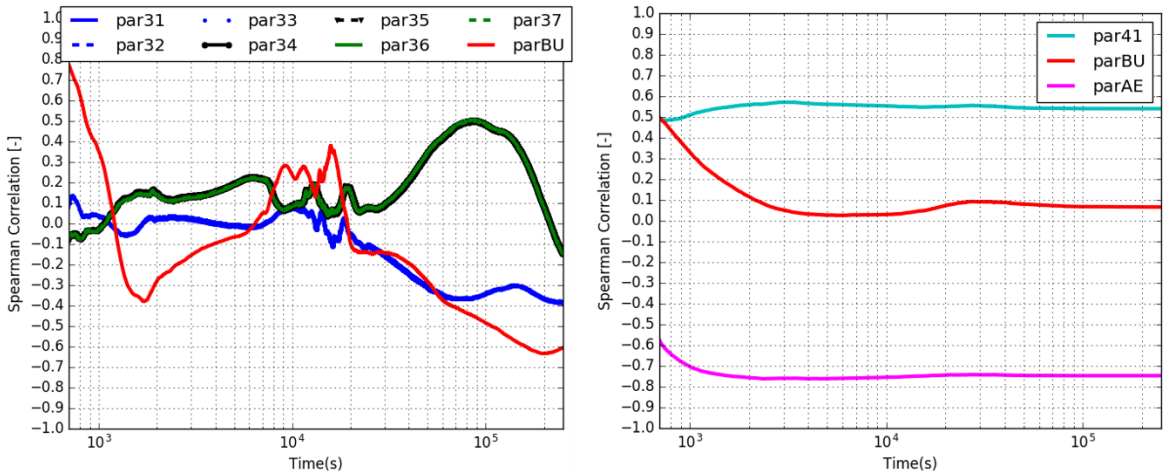

Figure 11. Spearman correlations between the dominant UPs and the mass fraction of the initial loading of Cs aerosols in the containment (left) and of the Cs released to the environment (right).

The time dependent behavior of the Spearman correlations for the iodine aerosols in the containment are shown in Figure 12 (left). The results reveal that the UPs related to the fuel burn-up (*parBU*), the minimum geometrical radius of the particles (*par34*), the maximum geometrical radius of the particles (*par35*), the shape factor relative to particle coagulation (*par36*), and the shape factor relative to Stokes velocity (*par37*) mainly affect the FOM during the transient. The correlation for *parBU* reaches about -30% in correspondence of the occurrence of massive corium relocations in the lower plenum and the vessel rupture (~15000 - 20000 s) and then increases up to 70%. In the same time window, where the highest amount of aerosols in the containment is reached, the correlations of the *par34* to *par37* UPs are ~40%, while the correlations for the *par31-par33* UPs reach about -30%. The results in Figure 12 also show that such the correlations of the *par34* to *par37* UPs increase (in absolute value) up to ~30% from ~200000 s.

The Spearman correlations for the release of iodine to the environment are shown in Figure 12 (right). The results in Figure 12 show that the fuel burn-up (*parBU*) and the containment leakage (*par41*) have a significant effect on the FOM. In particular, the correlation of *parBU* increases to ~30-40% after vessel rupture and the correlation of par41 is always larger than 40% for the full transient. The results highlight the large correlation between the efficiency of the filters for aerosols (*parAE*) and the FOM. For this parameter, the Spearman correlation is ~-75% during the in-vessel phase, due to the employment of the AAES, and remains lower than ~-40% for the whole transient.

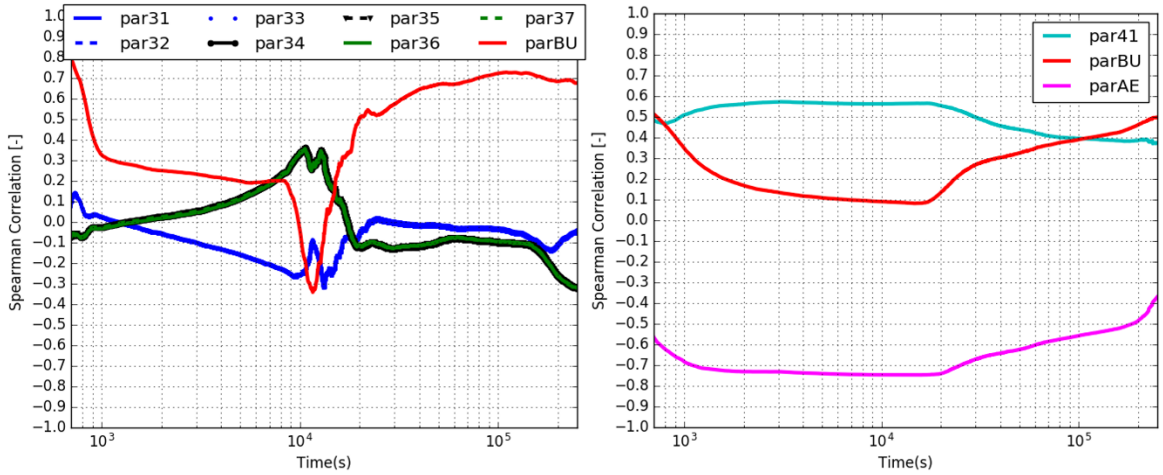

Figure 12. Spearman correlations between the dominant UPs and the mass fraction of the initial loading of I aerosols in the containment (left) and of the I released to the environment (right).

The results of the sensitivity analysis for the release of barium to the containment and to the environment are shown in Figure 13. Because of the lower volatility of barium, the selected UPs related to ASTEC model for the release from the fuel show significative correlations with the release to the containment (Figure 13, left). In fact, this FOM shows a non-negligible positive dependence of the properties of the fuel grains (*par1* and *par2*) during the scenario, the correlations being ~35%. Furthermore, a negative correlation of about 40% is observed between the FOM and the UPs geometrical diameter of the fuel grain (*par5a*). The correlation with the fuel burn-up (*parBU*) is significant immediately after the starting of the FP release from the fuel and then decreases fast to about 20% during the first 1000 s of the transient.

The release of barium to the environment (Figure 13, right) shows a rather strong correlation with the containment leakage (*par41*) and with the efficiency of the filters for aerosols (*parAE*), the maximum corresponding Spearman coefficients being 60% and -80%, respectively.

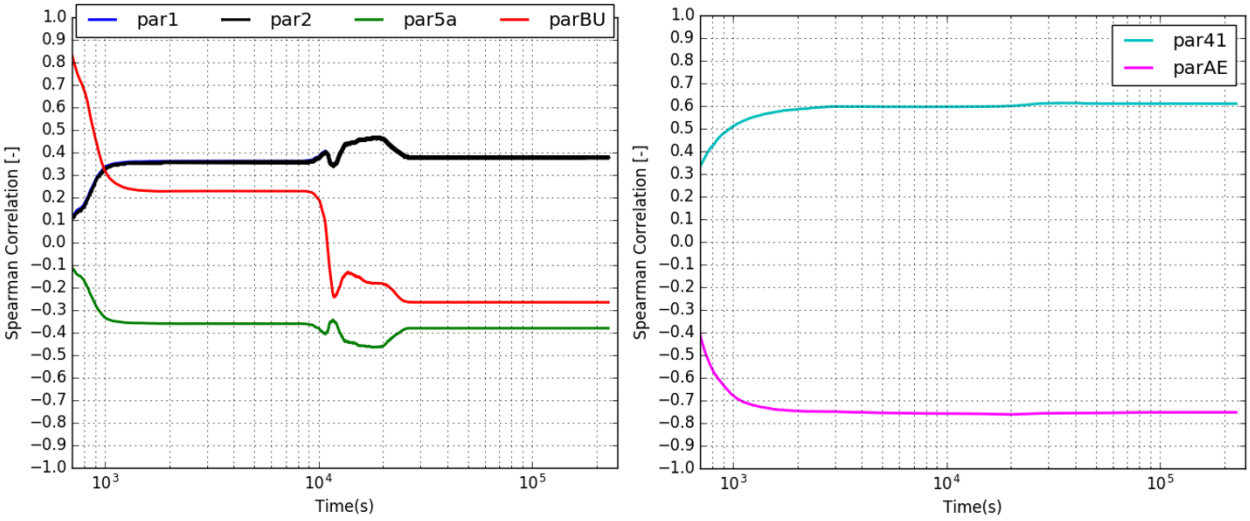

Figure 13. Spearman correlations between the dominant UPs and the mass fraction of the initial loading of Ba released in the containment (left) and in the environment (right).

7. CONCLUSIONS

A database of severe accident simulation results has been assessed for a MBLOCA scenario employing the FCVS SAM action for a generic KONVOI NPP. The work has been performed in the frame of the

KIT/Framatome joint participation to the HORIZON MUSA project, coordinated by CIEMAT. All the simulations have been performed with the ASTEC code, developed by IRSN, and U&Sa have been carried out by means of the KATUSA tool developed at KIT in the framework of the KIT/Framatome WAME project, devoted to the development and application of a fast source term prediction methodology.

The attention has been focused on the effect of the propagation of the uncertainty of eighteen ASTEC input parameters on the source term, and in particular on the Xe, I, Cs, and Ba release to the containment and to the environment. With this goal the uncertainty of each parameter has been characterized in terms of lower and upper limits as well as of PDFs based on open literature and engineering judgment. Simple statistics and Spearman correlation coefficients have been computed. The Xe, I, and Cs release to the containment is mainly affected by the containment leakage (Xe), by the burn-up, and, for I and Cs, also by the parameters related to the properties and the behavior of the aerosols. The release to the environment is mainly affected by containment leakage, the fuel burn-up (Xe, I, and Cs), and the efficiency of the filters of the FCVS system (I, Cs, and Ba). When elements characterized by lower volatility are considered, as Ba, other UPs show significant effects. In particular, the Ba release to the containment is affected by the properties and the geometry of the fuel grains.

Finally, a rather large amount of ASTEC results have been collected by KIT/Framatome in the frame of the MUSA project for scenarios with FCVS activation, and the results of the U&Sa allowed the identification of the main parameters affecting the source term. This provides a solid basis for further analyses of scenarios involving SAM actions.

AKNOWLEDGEMENT

This project has received funding from the Euratom research and training programme 2014-2018 under grant agreement No 847441. This paper reflects only the author's view, and the European Commission is not responsible for any use that may be made of the information it contains.

REFERENCES

1. L. E. Herranz, et al., “The EC MUSA Project on Management and Uncertainty of Severe Accidents: Main Pillars and Status,” *Energies* 14 (4473), pp. 1–11 (2021).
2. A. Stakhanova, F. Gabrielli, V.H. Sanchez-Espinoza, A. Hoefer, E.M. Pauli, “Uncertainty and sensitivity analysis of the ASTEC simulations results of a MBLOCA scenario in a generic KONVOI plant using the FSTC tool,” *Annals of Nuclear Energy* **192** (2023).
3. P. Chatelard, et al., “Main modelling features of the ASTEC V2.1 major version,” *Annals of Nuclear Energy* **93**, pp. 83-93 (2016).
4. A. Stakhanova, F. Gabrielli, V.H. Sanchez-Espinoza, A. Hoefer, E.M. Pauli, “Uncertainty and sensitivity analysis of the QUENCH-08 experiment using the FSTC tool,” *Annals of Nuclear Energy* **169**, 108968 (2022).
5. A. Stakhanova, F. Gabrielli, V.H. Sanchez-Espinoza, A. Hoefer, E.M. Pauli, “Application of the MOCABA algorithm and the FSTC tool for source term predictions during severe accident scenarios,” *Annals of Nuclear Energy* **184** (2023).
6. E. Pauli, A. Hoefer, A. Stakhanova, F. Gabrielli, V.H. Sanchez-Espinoza, “Prediction of the Radiological Consequences of a Severe Accident Scenario in a Generic KONVOI Nuclear Power Plant,” *Proceedings of ERMSAR2022*, Karlsruhe, Germany, 16-19 May, 2022, Paper 311, pp. 338-350 (2022).
7. “Strategy for Competence Building and the Development of Future Talent for Nuclear Safety,” https://www.bmwi.de/Redaktion/EN/Publikationen/Energie/strategyfor competence-building-and-the-development-of-future-talent-for-nuclear-safety.pdf (2020).
8. A. Hoefer, et al., “MOCABA: A general Monte Carlo–Bayes procedure for improved predictions of integral functions of nuclear data,” *Annals of Nuclear Energy* **77**, pp.514-521 (2015).
9. R.L. Iman, W.J. Conover, “A distribution-free approach to inducing rank correlation among input variables,” *Communications in Statistics-simulation and Computation* **11**, pp.311-334 (1982).

10. S.C. Maree, "Correcting non positive definite correlation matrices," Bachelor thesis, Delft University of Technology (TU Delft), Department of Applied Mathematics (2012).
11. I. G. García-Toraño, "Further development of Severe Accident Management Strategies for a German PWR Konvoi Plant based on the European Severe Accident Code ASTEC," Dissertation, Karlsruher Institut für Technologie, Fakultät für Maschinenbau (2017).
12. F. Gabrielli, et al., "Impact of Realistic Fuel Inventories on the Radiological Consequences of a Severe Accident Scenario in a Generic Konvoi Plant by Means of the ASTEC Code," *Proceedings of the KERNTECHNIK*, Leipzig, Germany, 21-22 June, 2022.
13. SCALE: A comprehensive modeling and simulation suite for nuclear safety analysis and design. ORNL/TM-2005/39, Version 6.2.3, 2022.
14. T. Ikeda, et al., "Analysis of core degradation and fission products release in Phebus FPT1 test at IRSN by detailed severe accidents analysis code, IMPACT/SAMPSON," *Nuclear Science and Technology* **40**, no. 8, pp.591-603 (2003).
15. G. Brillant, C. Marchetto, W. Plumecocq, "Fission product release from nuclear fuel I. Physical modelling in the ASTEC code," *Annals of Nuclear Energy* **61**, pp.88-95 (2013).
16. G. Brillant, C. Marchetto, W. Plumecocq, "Fission product release from nuclear fuel II. Validation of ASTEC/ELSA on analytical and large-scale experiments," *Annals of Nuclear Energy* **61**, pp.96-101 (2013).
17. G. Pastore, et al., "Uncertainty and sensitivity analysis of fission gas behavior in engineering-scale fuel modelling," *Journal of Nuclear Materials* **456**, pp.398-408 (2015).
18. K.W. Song, et al., "Sintering of mixed UO2 and U3O8 powder compacts," *Journal of nuclear materials* **277**, pp.123-129 (2000).
19. Y. Pontillon, et al., "Lessons learnt from VERCORS tests: Study of the active role played by UO2–ZrO2–FP interactions on irradiated fuel collapse temperature," *Journal of nuclear materials* **344**, pp.265-273 (2005).
20. Nuclear Regulatory Commission (NRC). "State-of-the-art reactor consequence analyses (SOARCA) project: Sequoyah integrated deterministic and uncertainty analyses". Nuclear Regulatory Commission, NUREG/CR-7245, Technical report (2018).
21. P. Hofmann, P., et al., "ZrO2 dissolution by molten Zircaloy and cladding oxide shell failure. New experimental results and modelling," Forschungszentrum Karlsruhe, FZKA 6383, Technical report (1999).
22. Nuclear Regulatory Commission (NRC). "State-of-the-Art Reactor Consequence Analyses Project: Uncertainty Analysis of the Unmitigated Long-Term Station Blackout of the Peach Bottom Atomic Power Station". Nuclear Regulatory Commission, NUREG/CR-7155, SAND2012-10702P, Technical report (2012).
23. J.C. Helton, et al., "Uncertainty and sensitivity analysis of a model for multicomponent aerosol dynamics," *Nuclear technology* **73**, pp.320-342 (1986).

APPENDIX A

Par.	PDF	PDF parameters	Description	Reference
par1	Normal	$\mu = 5.0$, $\sigma = 30\%$	Correction factor for the ratio S/V of the fuel pellets due to roughness	[14, 15, 16]
par2	Normal	$\mu = 0.03$, $\sigma = 30\%$	Correction factor for the ratio S/V of the fuel pellets for the limited steam access	[14, 15, 16]
par5	Normal	$\mu = 1.2E\text{-}5$, $\sigma = 30\%$	Geometrical diameter of the grain	[17, 18]
par5a	Triangular	mode = 2.0E-6, min = 1.6E-6 max = 3.4E-6	Standard deviation of geometrical diameter of the grain	[17, 18]
par14	Normal	$\mu = 2500.0$, $\sigma = 10\%$	Threshold Temperature of the cladding Dislocation [K]	[19, 20]
par15	Normal	$\mu = 2300.0$, $\sigma = 10\%$	Threshold Temperature of the oxide layer Dislocation [K]	[21]
par16	Normal	$\mu = 250.0E\text{-}4$, $\sigma = 20\%$	Threshold thickness of the oxide layer [mm]	[21]
par31	Uniform	min = 2.975, max = 4.025	Particle mean thermal conductivity (J/m/K)	Engineering judgement
par32	Uniform	min = 714.0, max = 966.0	Average specific heat (J/kg K) of the aerosol	Engineering judgement
par33	Triangular	mode = 3000.0, min = 2610.0, max = 10000.0	Particle mean density (kg/m3)	[22]
par34	Triangular	mode = 1.1E-8, min = 1.0E-8, max = 2.0E-07	Particle minimum geometrical radius (m)	[23]
par35	Triangular	mode = 1.99E-5, min = 5.0E-6, max = 2.0E-5	Particle maximum geometrical radius (m)	[23]
par36	Triangular	mode = 1.0, min = 0.9, max = 1.0	Shape factor relative to particle coagulation	[22]
par37	Beta	$\alpha = 1.0$, $\beta = 5.0$, min = 1.0, max = 3.0	Shape factor relative to Stokes velocity	[20]
par41	Uniform	min = 1.0, max = 30.0	Coefficient for the leakage rate between containment and annulus	Engineering judgement
parBU	Uniform	min = 10.0, max = 328.0	Effective full power days	Engineering judgement
parAE	Truncated Log-normal	min=0.9, max=0.9995	Filter efficiency for Aerosols	Truncated Log-normal
parI2	Truncated Log-normal	min=0.9, max=0.999	Filter efficiency for Gases (I2)	Truncated Log-normal

The 11th European Review Meeting on Severe Accident Research (ERMSAR-2024), KTH, Stockholm, Sweden. May 12-16, 2024

UNCERTAINTY AND SENSITIVITY ANALYSIS OF THE ASTEC SOURCE TERM RESULTS OF A MBLOCA SCENARIO WITH THE ACTIVATION OF SEVERE ACCIDENT MANAGEMENT ACTIONS IN A GENERIC KONVOI PLANT

Stakhanova A, Gabrielli F, Sanchez-Espinoza V. H - Karlsruhe Institute of Technology (KIT)
Pauli E.-M., Hoefer A - Framatome GmbH





Table of content

- Introduction
- KArlsruhe Tool for Uncertainty and Sensitivity Analysis (KATUSA)
- ASTEC model of a generic KONVOI NPP
- MBLOCA SA scenario
- Uncertain input parameters
- Results of U&S analysis
- Conclusions and outlook

Introduction

Karlsruhe Institute of Technology

➢ Joint contribution KIT/Framatome GmbH to the H2020 Management and Uncertainties Of Severe Accidents (MUSA) project (2019-2023) coordinated by CIEMAT

- ✓ SA code: ASTEC (version - 2.2.0.1)
- ✓ Generic KONVOI NPP
- ✓ MBLOCA scenario up to the basemat rupture with activation of SAM (Filtered Containment Venting System and Annulus air extraction system); MBLOCA without SAM, MBLOCA+SBO - not presented here
- ✓ Tool for U&S analysis – in-house KArlsruhe Tool for Uncertainty and Sensitivity Analysis (KATUSA)

Previous work - MBLOCA without SAM - described in:

Stakhanova, A., Gabrielli, F., Sanchez-Espinoza, V.H., Pauli, E., Hoefer, A., Uncertainty and sensitivity analysis of the ASTEC simulations results of a MBLOCA scenario in a generic KONVOI plant using the FSTC tool. In Proceedings of 10th European Review Meeting on Severe Accident Research (ERMSAR-2022), 2022, pp.861-872.

Stakhanova, A., Gabrielli, F., Sanchez-Espinoza, V.H., Pauli, E., Hoefer, A., Uncertainty and sensitivity analysis of the ASTEC simulations results of a MBLOCA scenario in a generic KONVOI plant using the FSTC tool. Annals of Nuclear Energy, 192, (2023), p.109964. DOI: https://doi.org/10.1016/j.anucene.2023.109964

KATUSA tool for U&S analysis

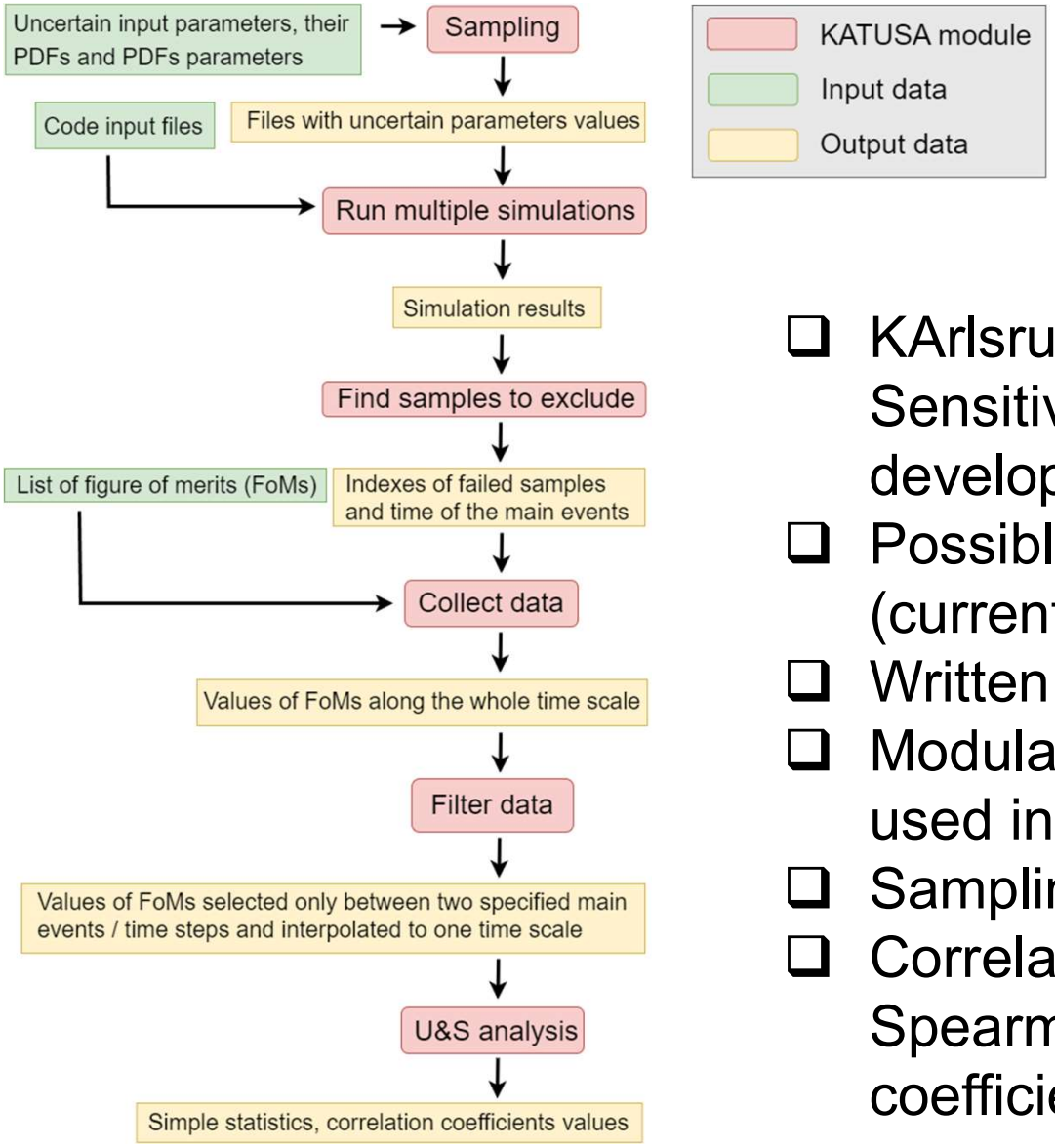

KATUSA tool scheme

- KArlsruhe Tool for Uncertainty and Sensitivity Analysis (KATUSA) tool developed at KIT
- Possible to couple with different codes (currently: ASTEC, TwoPorFlow)
- Written in Python language
- Modular structure. Each module could be used independently
- Sampling algorithms: SRS, LHS
- Correlation coefficients: Pearson, Spearman, distance, Maximal Information coefficient

KONVOI NPP ASTEC model

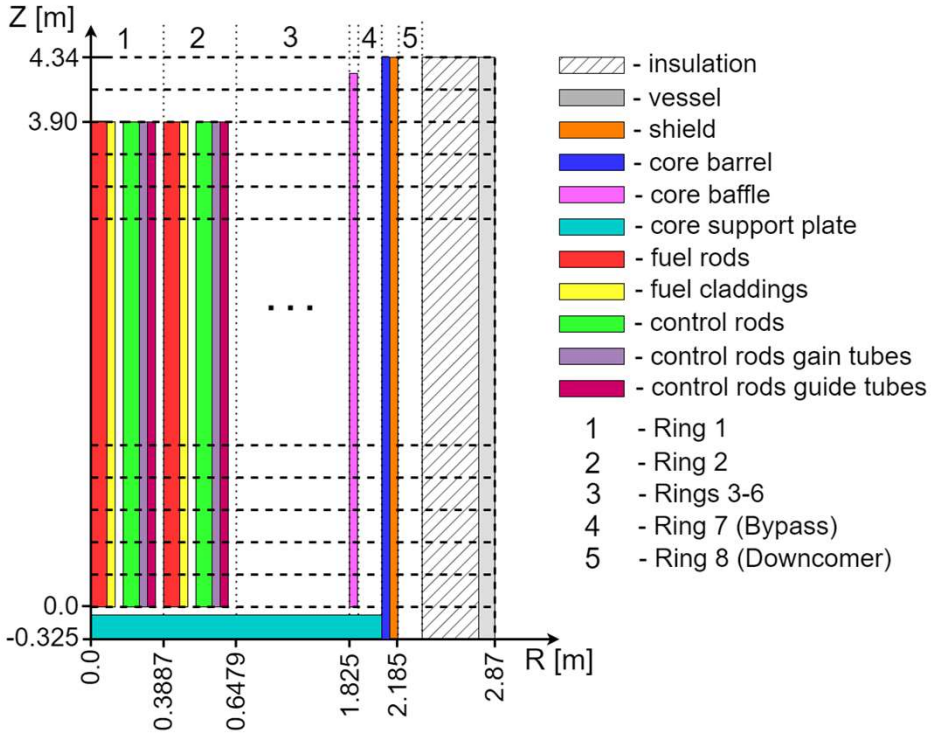

Core nodalization

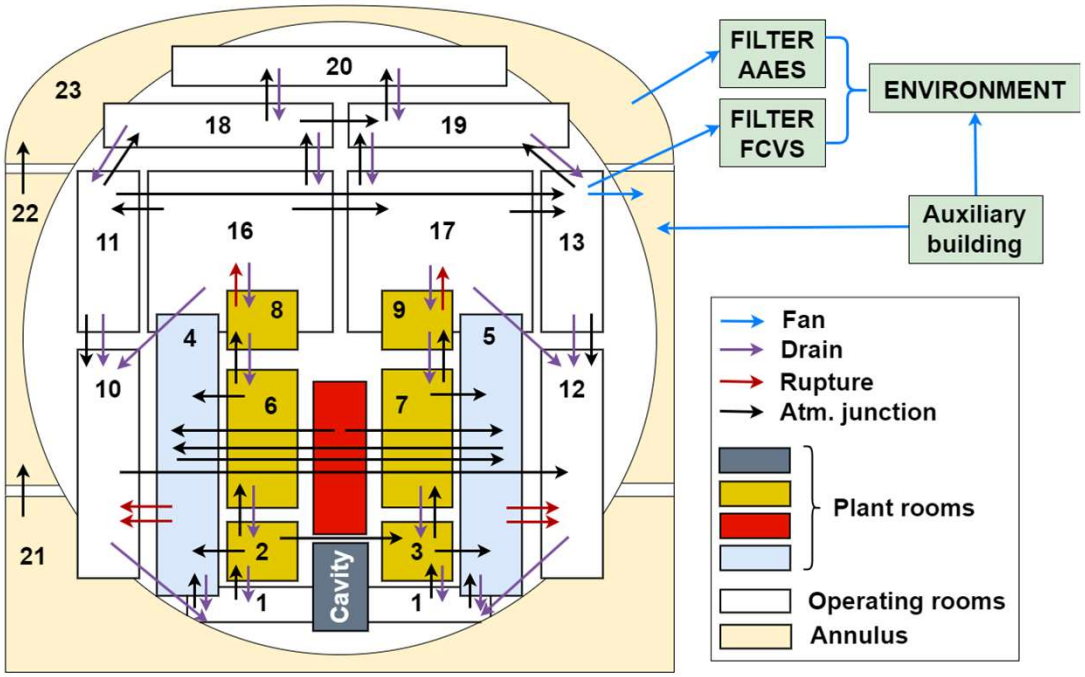

Containment nodalization

- Core: six cylindrical rings plus two channels for the downcomer and the bypass
- Containment: 26 rooms plus an auxiliary building.

- Annulus air extraction system (AAES): always available. Efficiency of the filters: 99.995% for aerosols; 99% for gaseous iodine
- Filtered Containment Venting System (FCVS): activated as SAM action, efficiency of the filters is 99.9% for aerosols and 99% for gaseous iodine

MBLOCA SA scenario

Karlsruhe Institute of Technology

- Plant works at full power before the start of the transient.
- Scenario is initiated by a 12” break on the cold leg (t=0 s).
- SCRAM signal (t=1 s). The admission to turbine and the main feed water pumps into the steam generator are closed (t=1.5 s).
- The Emergency Core Cooling System (ECCS) signal (t=6 s)
- The Main Coolant Pumps (MCPs) are coasted down (t=7 s) and the pressure regulation in the pressurizer is switched off.
- The Emergency Feed Water System (EFWS) is activated when the liquid level of one steam generator falls below 4.50 m.
- The gas temperature in the primary circuit exceeds 650 °C, the High- and Low-Pressure Injection Systems (HPIS/LPIS) are activated.
- The water injections stop when the tanks are empty leading to the start of core degradation (start of fission products release at t=564 s in base case scenario).
- The reactor pressure vessel fails (t=12054 s in base case scenario)
- Corium is relocated into the cavity (end of corium slump t=12071 s in base case scenario)
- Cavity is flooded by water when the horizontal erosion reaches 0.5 m.
- The simulation ends when basemat rupture occurs.

Uncertain input parameters

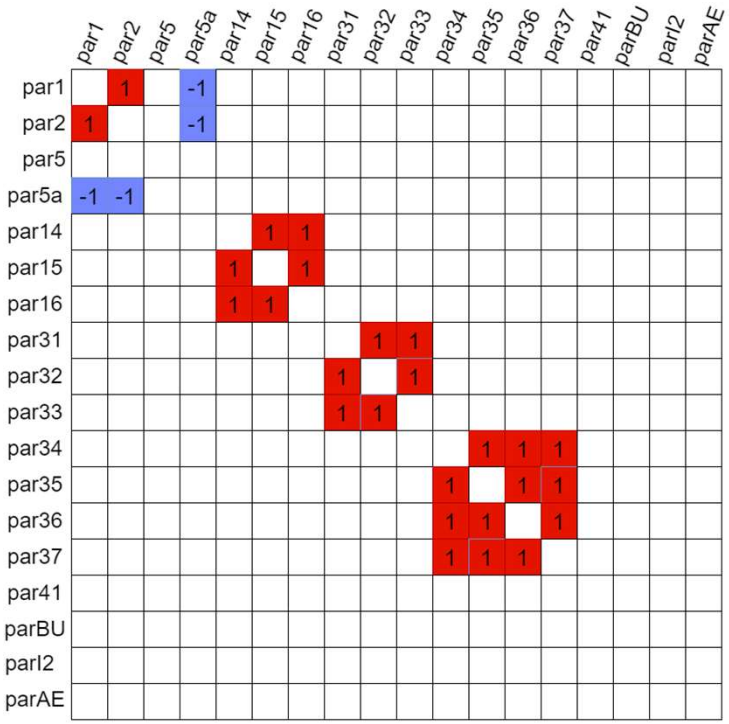

Uncertain input parameters correlation matrix

Two new parameters added comparing to the previous simulations:

parI2 – Filter efficiency for Gases (I2) – Not analyzed yet in the presented results

parAE - Filter efficiency for Aerosols

Par-r	Phenomenon	Meaning
par1	Fission product release from the fuel	Correction factor for the ratio S/V of the fuel pellets due to roughness
par2		Correction factor for the ratio S/V of the fuel pellets for the limited steam access
par5		Geometrical diameter of the grain
par5a		Standard deviation of geometrical diameter of the grain
par14	Cladding integrity criteria	Threshold Temperature of the cladding Dislocation [K]
par15		Threshold Temperature of the oxide layer Dislocation [K]
par16		Threshold thickness of the oxide layer [mm]
par31	Aerosols behavior in the RCS	Particle mean thermal conductivity (J/m/K)
par32		Average specific heat (J/kg K) of the aerosol
par33		Particle mean density (kg/m3)
par34		Particle minimum geometrical radius (m)
par35		Particle maximum geometrical radius (m)
par36		Shape factor relative to particle coagulation
par37		Shape factor relative to Stokes velocity
par41	Containment leakage	Flow rate (m3/s)
parBU	Fuel burn-up	Effective full power days

U&S analysis results

- 300 simulations
- 12 finished incorrectly
- In 48 simualtions FCVS is activated

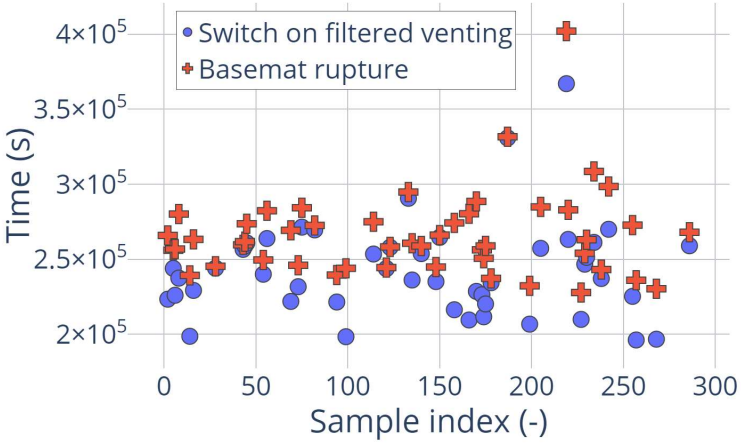

Longer time till basemat rupture due to depressurization

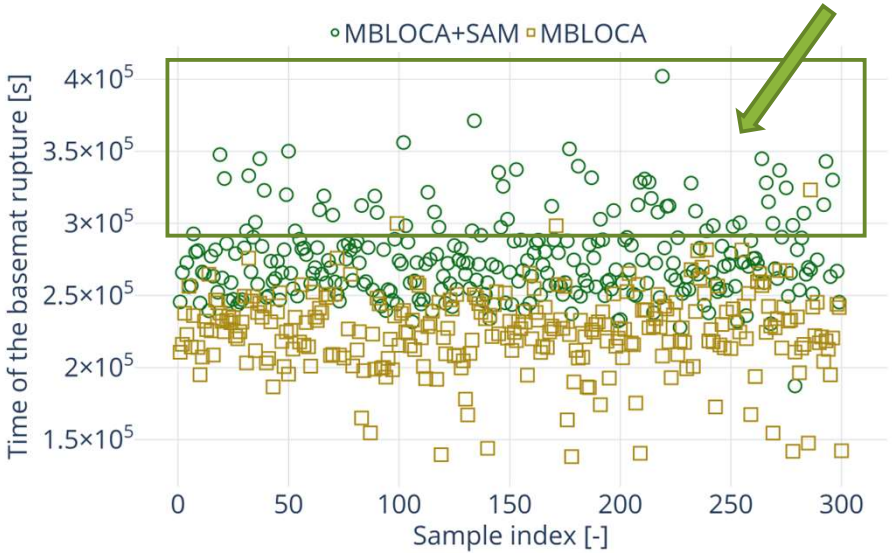

Event	Minimum (s)	Maximum (s)
Start of FPs release	464	684
20. tons of corium relocated to the lower plenum	844	17194
Lower head vessel failure	3064	29454
End of the corium slump to the cavity	3066	29533
Switch on filtered venting	196245	367073
Basemat rupture	187242	402073

U&S analysis results

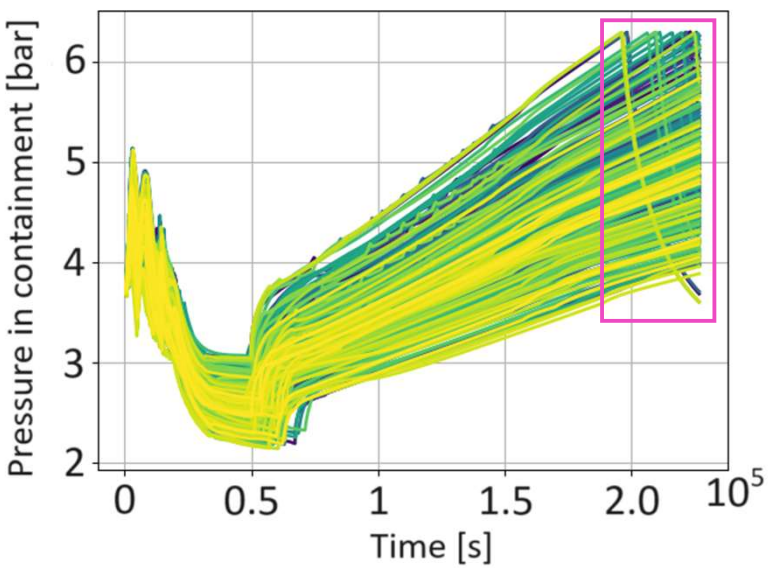

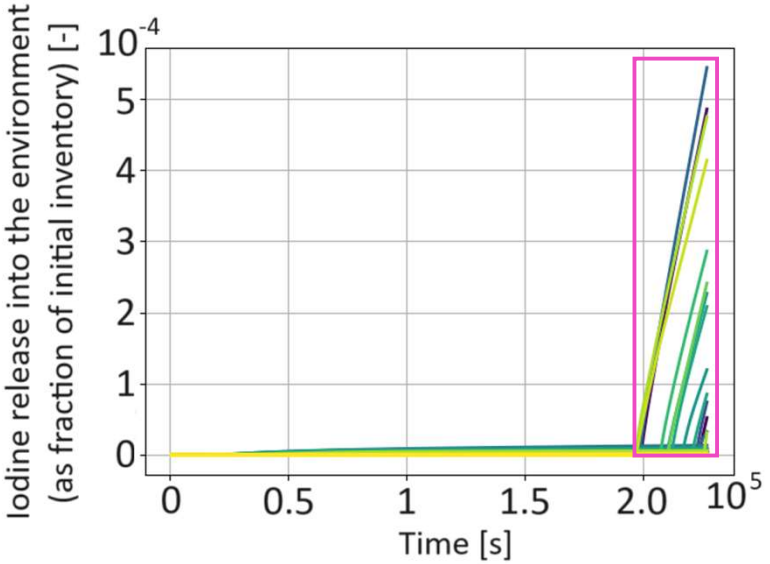

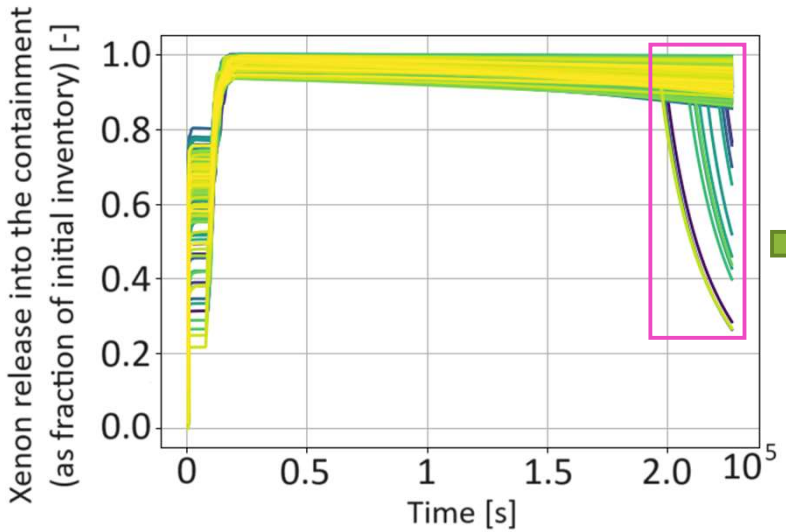

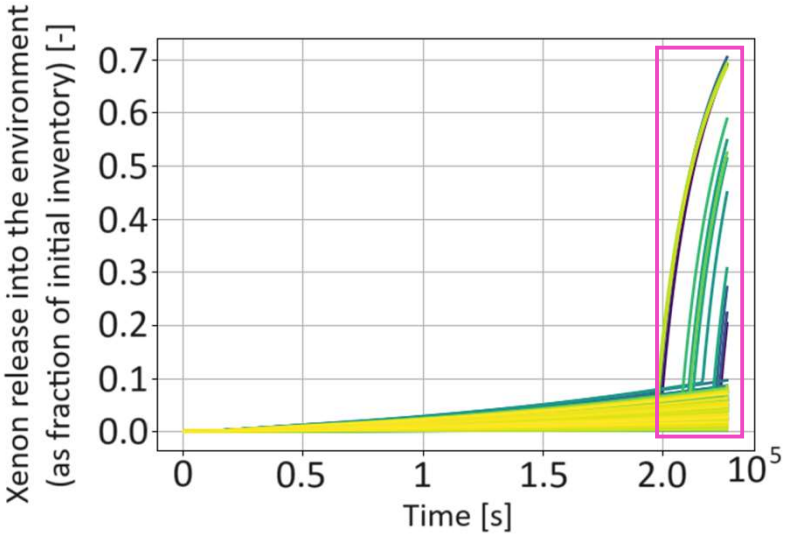

- FCVS activation

U&S analysis results

Karlsruhe Institute of Technology

- FCVS activation

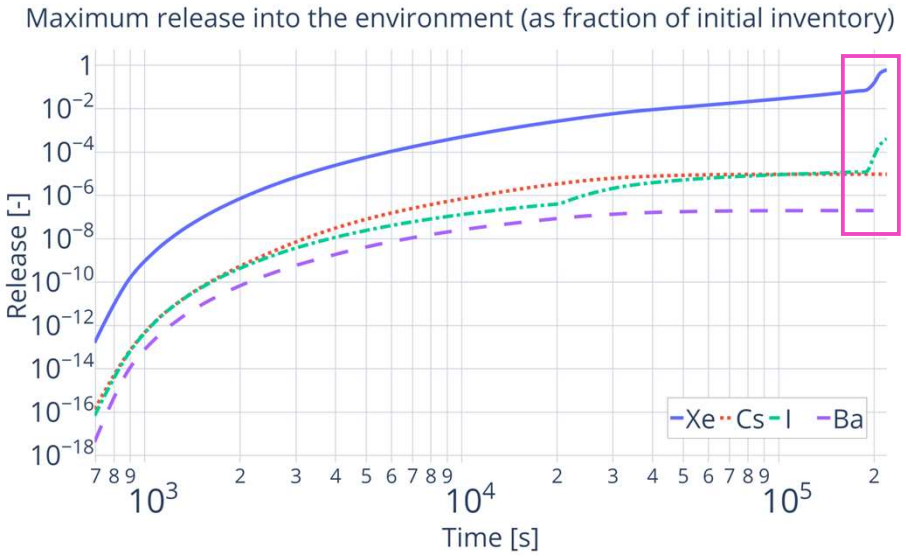

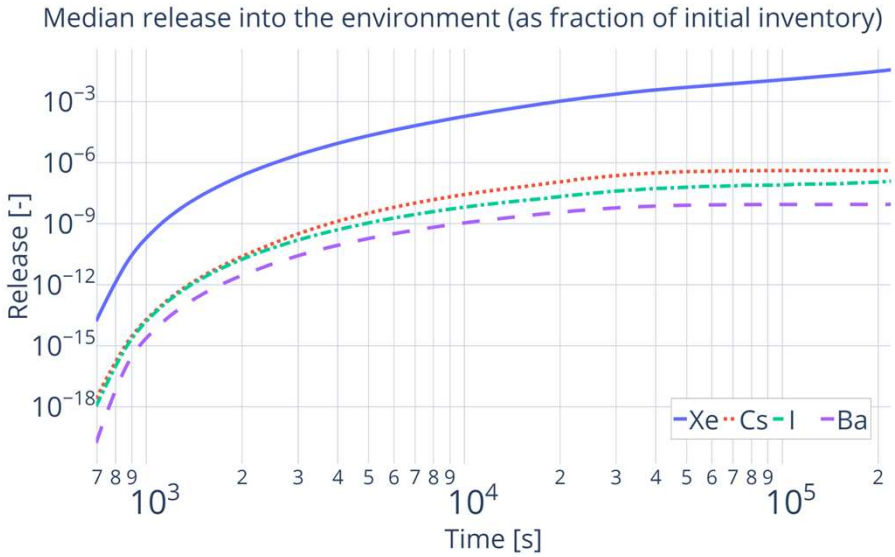

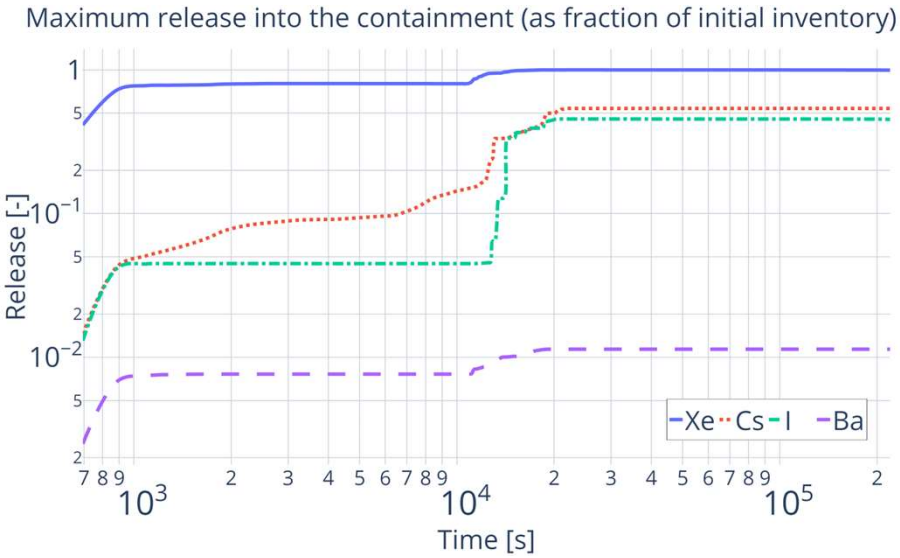

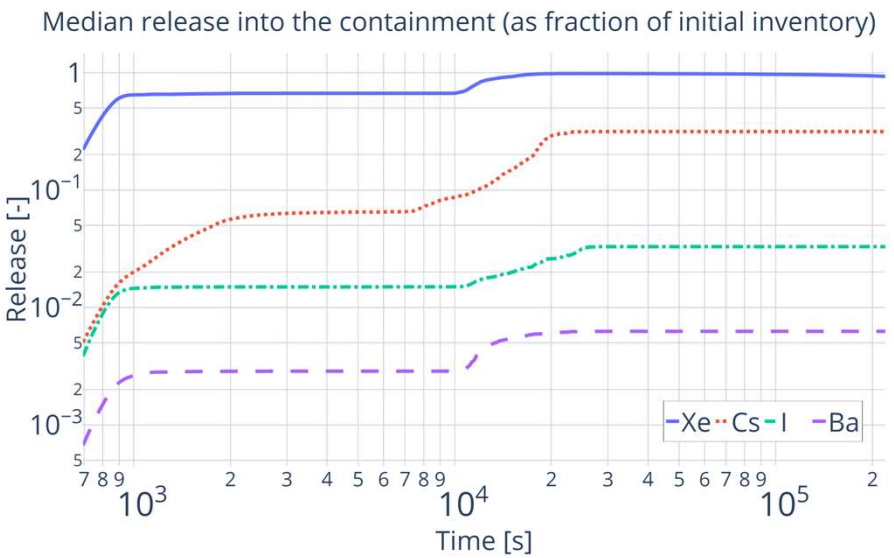

U&S analysis results





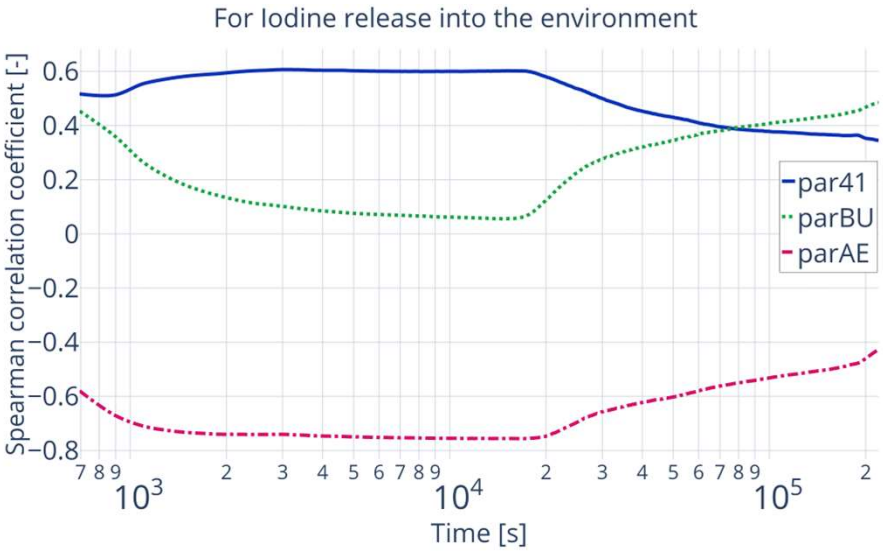

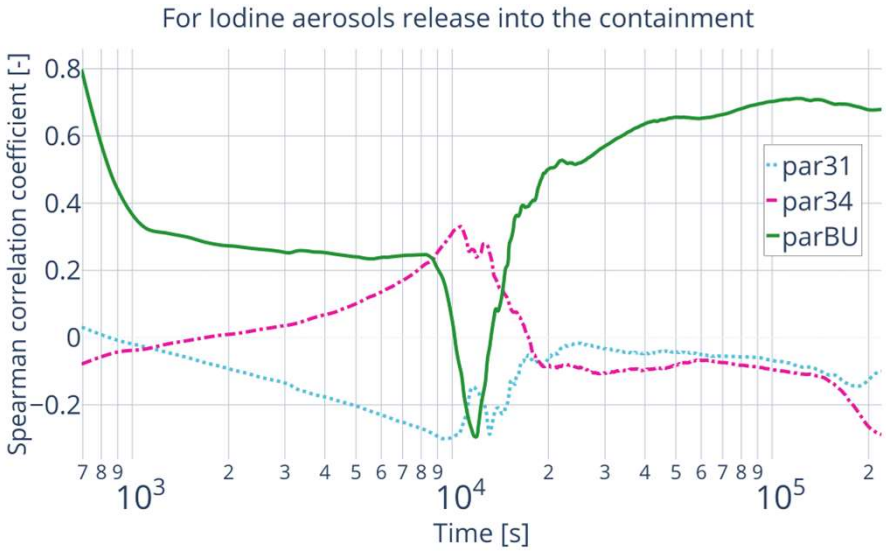

U&S analysis results

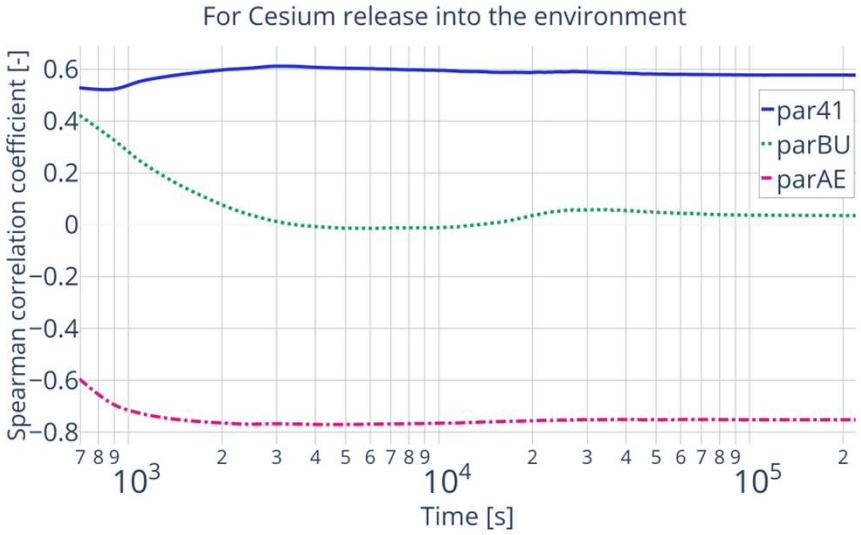

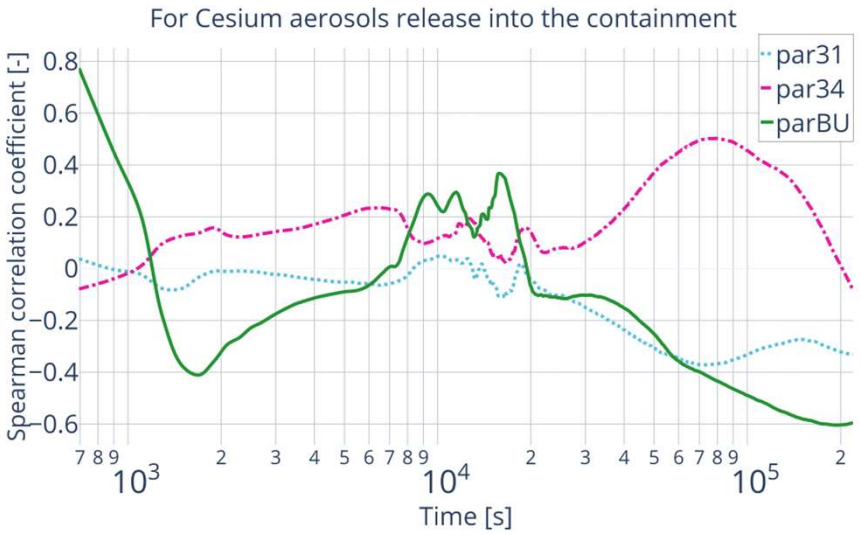

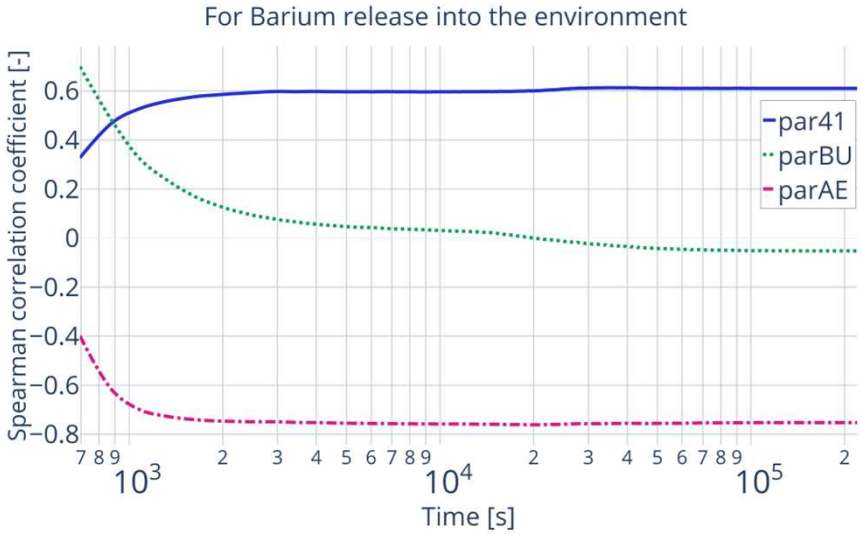

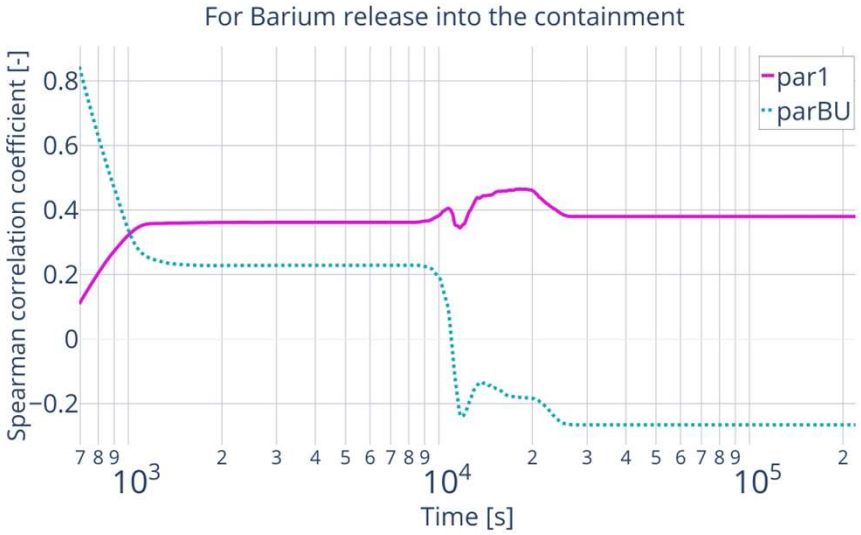

U&S analysis results

- Release into the environment is correlated with par41 (containment leakage) and parBU (burnup) as in previous MBLOCA analysis
- For Iodine, Cesium and Barium release into the environment now is also affected by parAE (Filter efficiency for aerosols)
- Release into the containment for all FPs is affected by parBU. For Xe – now also by par41. For Ba – by par1-par5a; for Cs and I aerosols – by par31-par37 as in previous MBLOCA analysis

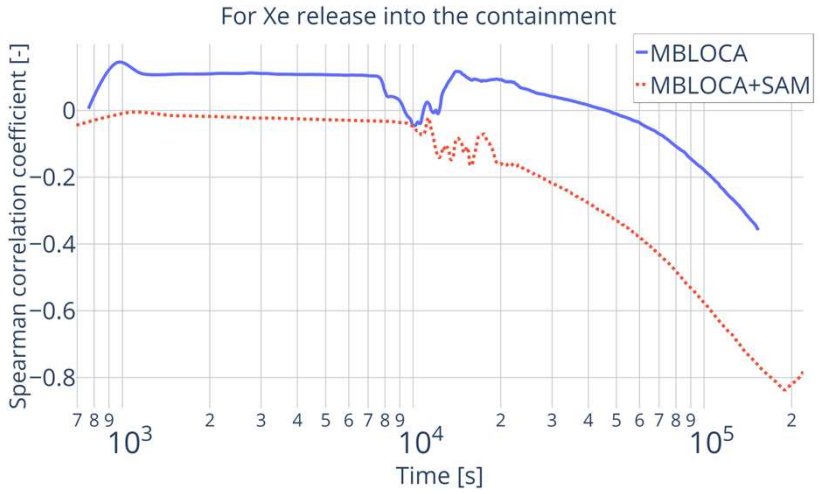

Conclusions and outlook

- ✓ In the frame of the MUSA project performed simulations of MBLOCA scenario with applying SAM (filtered containment venting)
  - In total 900 simulation results were analyzed in the frame of the MUSA project (300 simulations for each of the: MBLOCA, MBLOCA+SBO, MBLOCA+SAM)
- ✓ For simulations ASTEC SA code and KATUSA tool for U&S analysis are used
- ✓ The uncertainty of the FP release to the environment has been evaluated
  - Contribution to the application of U&S analysis to support the emergency and prepardeness strategy in case of severe accidents

Conclusions and outlook

Karlsruhe Institute of Technology

- ✓ Influence on the FPs release of previously used uncertain parameters and new parameter related to the filtered venting is investigated

→ Difference between results of simulations MBLOCA with/without SAM should be investigated more thoroughly

→ Are more calculations required in case of SAM to have a good statistics? (FCVS was activated in 48 simulations from 300)

→ Investigate different statistical methodologies/interpretation of the results?

↪ KIT/Framatome database of SA simulation results could be used for the ST predictions (see application of MOCABA framework and FSTC tool)

↪ U&S analysis importance for a reliable characterization of the source term (see KIT studies with ASTEC-KATUSA-JRODOS for, i.e., BWR, VVER-1000)

Thank you for your attention!

Acknowledgements

This project has received funding from the Euratom research and training programme 2014-2018 under grant agreement No 847441. This paper reflects only the author's view, and the European Commission is not responsible for any use that may be made of the information it contains.

Contacts: KIT, INR; Stakhanova Anastasia, anastasia.stakhanova@kit.edu

References

- *Stakhanova, A.,* Gabrielli, F., Sanchez-Espinoza, V.H., Hoefer, A. and Pauli, E., 2022. Uncertainty and sensitivity analysis of the QUENCH-08 experiment using the FSTC tool. *Annals of Nuclear Energy*, *169*, (2022), p.108968. DOI: https://doi.org/10.1016/j.anucene.2022.108968
- *Stakhanova, A.,* Gabrielli, F., Sanchez-Espinoza, V.H., Pauli, E., Hoefer, A., Uncertainty and sensitivity analysis of the ASTEC simulations results of a MBLOCA scenario in a generic KONVOI plant using the FSTC tool. In *Proceedings of 10th European Review Meeting on Severe Accident Research (ERMSAR-2022),* 2022, pp.861-872.
- *Stakhanova, A.,* Gabrielli, F., Sanchez-Espinoza, V.H., Pauli, E., Hoefer, A., Uncertainty and sensitivity analysis of the ASTEC simulations results of a MBLOCA scenario in a generic KONVOI plant using the FSTC tool. *Annals of Nuclear Energy, 192*, (2023), p.109964. DOI: https://doi.org/10.1016/j.anucene.2023.109964
- Sanchez-Espinoza, V. H., Gabrielli, F., Imke, U., Zhang, K., Mercatali, L., Huaccho, G., et. al., KIT reactor safety research for LWRs: Research lines, numerical tools and prospects. Nuclear engineering and design, 414, (2023), p. 112573. DOI: https://doi.org/10.1016/j.nucengdes.2023.112573
- Brumm, S., Gabrielli, F., Sanchez-Espinoza, V. H., *Stakhanova, A.,* et. al., 2024, Uncertainty Quantification for Severe-Accident reactor modelling: results and conclusions of the MUSA reactor applications work package. *Under review in Annals of Nuclear Energy*

SOURCE TERM UNCERTAINTIES IN UNMITIGATED SBO SEQUENCES IN A PWR-1000: INSIGHTS FROM THE EU-MUSA PROJECT

R. Iglesias[1], M. Angelucci[2], S. Paci[2], L.E. Herranz[1]
[1] CIEMAT, Avenida Complutense 40
28040 Madrid (Spain)
[2] University of Pisa (UNIPI), Largo Lucio Lazzarino
56122 Pisa (Italy)
rafael.iglesias@ciemat.es; michela.angelucci@unipi.it; sandro.paci@unipi.it;
luisen.herranz@ciemat.es

ABSTRACT

The Management and Uncertainties of Severe Accidents (MUSA) project focused on the testing, adapting, and employing Uncertainty Quantification (UQ) and sensitivity methods for Severe Accident (SA) analysis. In collaboration with the University of Pisa, CIEMAT conducted an Uncertainty and Sensitivity Analysis (UaSA) of Source Term (ST) estimates in an unmitigated Station Black-Out (SBO) scenario involving a 3-loop Pressurized Water Reactor with Westinghouse design (PWR-W). The study employed the MELCOR 2.2 code (version 2.2.21402) in conjunction with DAKOTA 6.7 as the UQ tool. To propagate uncertainties, the Wilks' approach was employed, with random sampling of 24 selected uncertain parameters. The Figures Of Merit (FOMs) chosen for the analysis were iodine, cesium, and noble gases releases to the environment. A sensitivity analysis, based on Pearson's and Spearman's Correlation Coefficients (CCs), was also conducted. In relative terms, the magnitude of the ST displayed a narrow uncertainty band. The early containment failure led to most iodine released from fuel to reach the environment, with a narrow variability. Conversely, a visible uncertainty surrounded the onset time of release to the environment (approximately 5 hours), potentially influencing the implementation of Accident Management (AM) measures that might be adopted in the scenario. Although sensitivity analyses did not identify dominant variables, emphasis was placed on the relationship between the release onset time and fuel failure time (temperature controlled), as well as the subsequent diffusional release of radionuclides.

KEYWORDS
Source Term, Severe Accident, UaSA, MELCOR.

1. INTRODUCTION

Given the complexity of the physical-chemical and thermal-hydraulic processes occurring throughout various stages of a Severe Accident (SA) and the inherent characteristics of numerical codes (including numerical methods, discretization, initial and boundary conditions, etc.), it is imperative to quantify the inherent uncertainties embedded in them. This involves considering the latest advancements in methods and algorithms, along with acknowledging the availability and capability of computational resources. Currently, numerous SA codes have achieved a notable level of maturity in terms of their modeling, precision, simulation capacity for safety-critical phenomena, and validation across a diverse range of reactor types. Moreover, these codes are utilized for the development and enhancement of Accident Management (AM) measures, as well as for supplying the Source Term (ST) essential for estimating the radiological impact of an accident in and around the Nuclear Power Plant (NPP) site [1].

The primary goal of Management and Uncertainties of Severe Accidents (MUSA) project [1] is to assess and measure the uncertainty inherent in SA codes during the modeling of both reactor and Spent Fuel Pool (SFP) accident scenarios for Generation II and Generation III reactor designs. This assessment specifically focuses on predicting the radiological ST. To achieve this objective, Uncertainty Quantification (UQ) methodologies and sensitivity methods for Severe Accident (SA) analysis are employed. These methodologies take into account not only the initial, boundary conditions, and model parameters but also incorporate AM measures. The aim is to evaluate how these measures influence the prediction of the ST.

The MUSA project, structured in different Work Packages (WPs), proposed the application of these methods in WP5, specially targeting the evaluation of the ST in selected SA scenarios for different types of Light Water Reactors (LWRs). Within this context, CIEMAT, in collaboration with the University of Pisa, conducted an in-depth Uncertainty and Sensitivity Analysis (UaSA) of ST estimates. The analysis involved a Best Estimate Plus Uncertainty (BEPU) calculation of an unmitigated Station Black-Out (SBO) scenario occurring in a 3-loop PWR-W. The primary objective of this paper is to present the outcomes and insights resulting from this study.

2. SBO SCENARIO: BASE CASE

2.1. Scenario description and main assumptions

The simulated scenario is an unmitigated SBO in a generic generation II 3-loop PWR-W [2]. The reactor is assumed to be operating at full power before the transient event. The modeling considers various factors, including the availability of accumulators, turbo-pumps (2) for the Auxiliary Feed Water (AFW) system, batteries with a 6-hour duration, and the operational status of safety valves (for both steam generators and pressurizer). Additionally, the unavailability of high and low-pressure injection systems is taken into account in the simulation.

The analysis of the sequence included the following failures:

- AFW turbines: when the Main Steam Lines (MSLs) become flooded;
- MSLs fail: when water level reaches half pipe height;
- Hot Leg: due to creep (following the dedicated MELCOR model [3,4]);
- Containment: over-pressure (with p > 8 bar) [5];
- Vessel: due the thermal creep.

The accident sequence spans a duration of 48 hours, with no consideration given to Severe Accident Management (SAM) actions. The analysis of the accident is specifically concentrated on the released activity to the environment following containment failure, commonly referred to as the ST [2].

2.1.1. Plan model

The plant model implemented in the MELCOR 2.2 code [2] is visually depicted in Figure 1. The nodalization of the Nuclear Steam Supply System (NSSS) encompasses both the primary and secondary systems. The Reactor Coolant System (RCS) is modelled as three loops, incorporating components such as pressurizer, Reactor Pressure Vessel (RPV), accumulators, Refuelling Water Storage Tank (RWST), among others. The RPV is discretized into 10 interconnected Control Volumes (CVs): downcomer, lower plenum, core region (5), bypass, upper-plenum and upper head. Compartment connections are represented as Flow Paths (FPs), some of which are controlled through valves. The RPV core barrel, internals and guide tubes structures are modelled using Heat Structures (HSs). The core is divided in 6 radial rings and 13 axial nodes

for core degradation modelling (as required by MELCOR COR package). The first five rings represent the fuel, and the sixth ring represents the core bypass region.

The nodalization of the secondary system includes the Steam Generators (SGs), the model of the feed water system and the pipelines representing the MSLs. The secondary side of every SG is modelled with two CVs, one of which is the SG downcomer. Two CVs represent the ascending and descending SG tubes. The large dry containment nodalization is represented with 30 CVs interconnected through FPs. The input deck contains 94 CVs, 178 FPs and 326 HSs.

The MELCOR RN package is used for modelling the release, transport, and behavior of the Fission Products (FPs). It works on the material classes that group element that share similar chemical properties, in this case 17 RN classes were adopted.

The modeling of radionuclide release utilized an updated version of the CORSOR-Booth model, referred to as the Revised CORSOR-Booth model. This revision incorporates the latest default parameters of CORSOR-Booth, refined through testing against PHEBUS and VERCORS data. Beyond adjusting parameter values through meticulous tuning procedures, a significant modification has been implemented specifically for the release rate of Cs. Notably; the gas-phase mass limitation is no longer calculated for this element. In other terms, Revised CORSOR-Booth assumes that the release rate R_{Cs} only accounts for diffusion. Additionally, the calculation of fission product (FP) transport involving aerosols relies on the MAEROS computer code, which is an integral component of the MELCOR RN package. MAEROS represents a multisectional, multicomponent aerosol dynamics code that assesses the size distribution of each type of aerosol mass or component over time [4].

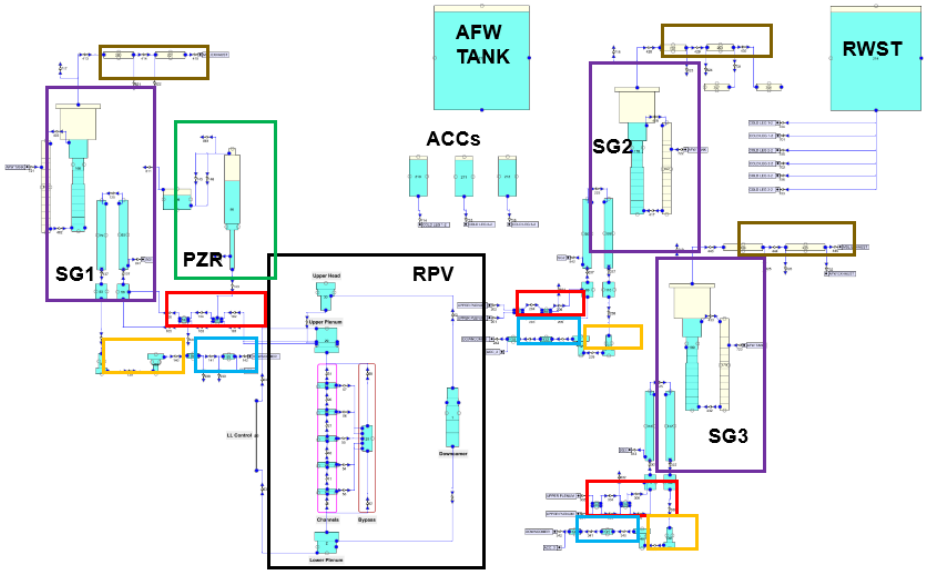

Figure 1. NPP MELCOR nodalization.

2.1.2. BE Transient analysis results

The accident sequence starts with the loss of offsite power and failure of onsite emergency AC (Alternate Current) power (SBO event) followed by the reactor trip and MSIV (Main Stem Isolation Valve) closure. The DC (Direct Current) buses are available for instrumentation, Power Operated Relief Valve (PORV) operation, and Turbine Driven Auxiliary Feed Water (TDAFW) operation.

After the reactor trip and the beginning of the AFW system, the primary pressure decreases (Figure 2) until the pressurizer empties at 22.9 h. At this time of the transient, the decay power is still effectively removed from the core. As a result of the closure of MSIVs, the pressure in the SGs increases leading to the opening of the PORV in the SG1. The initial opening of the PORV of the SG1 causes a rapid decrease of the pressure in the other SGs until the depletion of the AFW flow rate to all the SGs at approximately 1.8 h. After this time the pressure in all SGs begins to increase reaching the PORVs set point.

Due to the AFW system injection, the water level in all SGs increases. When the batteries run out, the AFW pumps run at full capacity without regulation, leading to the filling of all SGs. The filling of the SGs comes first in SG1 causing a MSL break in this SG and the release of the water material to the containment. As a result of the MSL break, at 7.4 h, the SG1 pressure and level decrease until its complete depressurization (Figure 2) and dry out.

After the MSL break, the pressurizer water level begins to increase and therefore the primary pressure and pressure in the SGs (SG2 and SG3). The pressurizer filling causes the increase of the pressure in the pressurizer relief tank until the reaching of the set point pressure for the failure of the relief tank at approximately 21.0 h.

At approximately 27.3 h the creep rupture in the third hot leg occurs. As result of the rupture, high pressure water is released to containment causing the increase of the containment pressure. After the RPV fail at 30.1 h and with the corium debris being relocated, the containment pressure increases reaching the set point for the containment failure at 39.8 h.

The SBO event timeline is presented in Table 1.

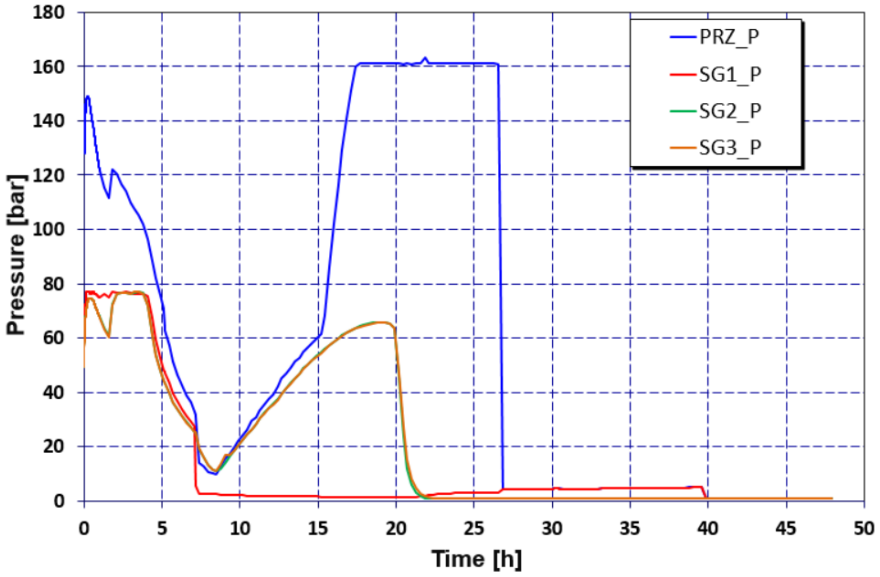

Figure 2. Evolution of the primary and SG pressure.

Figure 3 shows the release from the fuel and to the environment (dotted lines) of Xe, I_2 as a fraction of the i.i. According to the figure, 100 % of Xe and almost 99.8% of I_2 are released from the core.

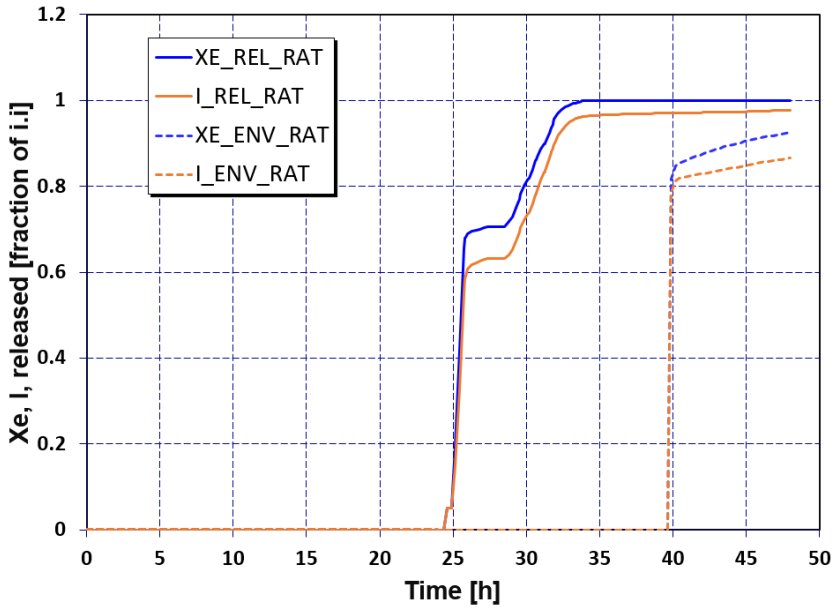

Figure 3. Release of Xe, I2, Cs (fraction of i.i) from the fuel and to the environment.

The release to environment of radioactive materials begins after the containment failure. At the end of the transient approximately 90% of Xe and 86 % of I_2 are released to the environment. In the following Table 1 the chronology of events of the SBO simulation is presented.

Table 1. Timing of the main SBO sequence events.

Key Event	Time
SBO	0.0 s
Reactor SCRAM	0.0 s
All RCPs tripped	< 1.0 s
AFW system start	10.0 s
MSL 1 break (water discharge into the containment)	7.4 h
Hot leg creep rupture	27.3 h
Vessel failure and start of the corium debris relocation in the cavity	30.1 h
Containment failure and beginning of radioactive release	39.8 h

3. UNCERTAINTY AND SENSITIVITY ANALYSIS

For the Uncertainty Analysis (UA), the MELCOR code (version 2.2.21402) was employed in combination with DAKOTA 6.7 [6] as UQ tool through complex Python scripts.

Considering the complex nature of the SA phenomenology, a huge number of input parameters might contribute to uncertainties in the Figures Of Merit (FOMs). Thus, a large set of input parameters should be selected to conduct a comprehensive UA. However, the expertise gained in the MUSA project highlighted the fact that a large number of input parameters makes the analysis hard to manage. In this sense, 24 IPs were selected to conduct the present analysis.

The choice of the input parameters was made based on the adoption of ST-related variables as FOMs. Then, they were grouped as follows:

- Core initial inventory;
- Fission product release model (CORSOR-BOOTH);
- Fuel and cladding failure;
- Aerosol characterization.

Considering that the analysis of the accident was focused on ST, three main FOMs were selected: Iodine, Cesium and Noble Gases releases to the environment. FOMs were analysed in relative terms as fraction of the releases from the fuel. Even though the magnitude at the end of the calculation is the main interest, the time history of the "into-environment" fraction released allows paying attention to the release kinetics.

Due to its involvement in the accident evolution, the containment failure time was selected, as an additional variable to be studied, since it indicates the onset of the radiological emission to the environment.

The uncertainties were propagated using Monte Carlo method, and tolerance intervals were obtained for the main FOMs according to the Wilks' formula [7]. A sensitivity analysis, based on Pearson's and Spearman's Correlation Coefficients (CCs) [8], was also performed to evaluate the most influential parameters over the main FOMs results.

3.1. Uncertainty quantification results

The main UA was carried out at a specific time (48 h). According to Figure 4, in all realizations, releases begin right after containment failure, and they sharply increase initially, to drastically slow down over time. In order to keep the paper length within reasonable limits and given that Cesium behavior mostly follows Noble Gases and Iodine, these are the ones taken to display the work results.

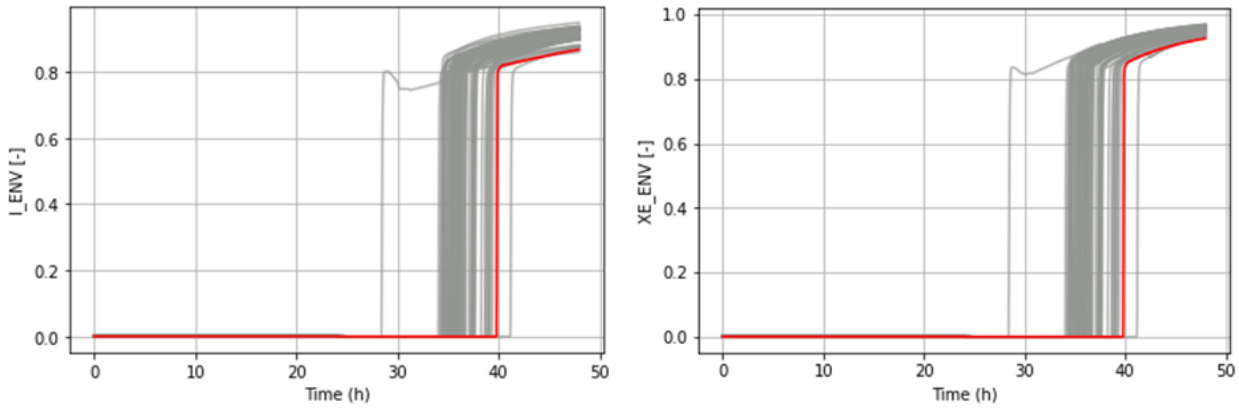

Figure 4. Dispersion plots.

Evolution in time is similar for all the FOMs: even though the release starts at different times, results seem to converge towards the end of the calculation, where the uncertainty band is quite narrow.

Other statistical quantities (such as mean, median, and standard deviation) for the selected FOMs at 48 h are reported in Table 2.

Table 2. Statistical analysis of the FOMs, at the end of the calculation.

Statistical parameter	Iodine release to the environment	Noble Gases release to the environment
MELCOR reference case (%)	86.57	92.47
Mean (%)	90.97	95.25
Median (%)	90.995	95.48
Lower bound (%)	85.88	92.59
Upper bound (%)	94.71	96.89
Standard deviation (%)	1.94	1.11

The scatterplots and the Cumulative Distribution Functions (CDFs) for FOMs on FPs release are presented in Figure 6 at 48 h. Notably, the results demonstrate a relatively uniform distribution across the FOM space for all three parameters. Furthermore, no outliers are discerned in the presented data.

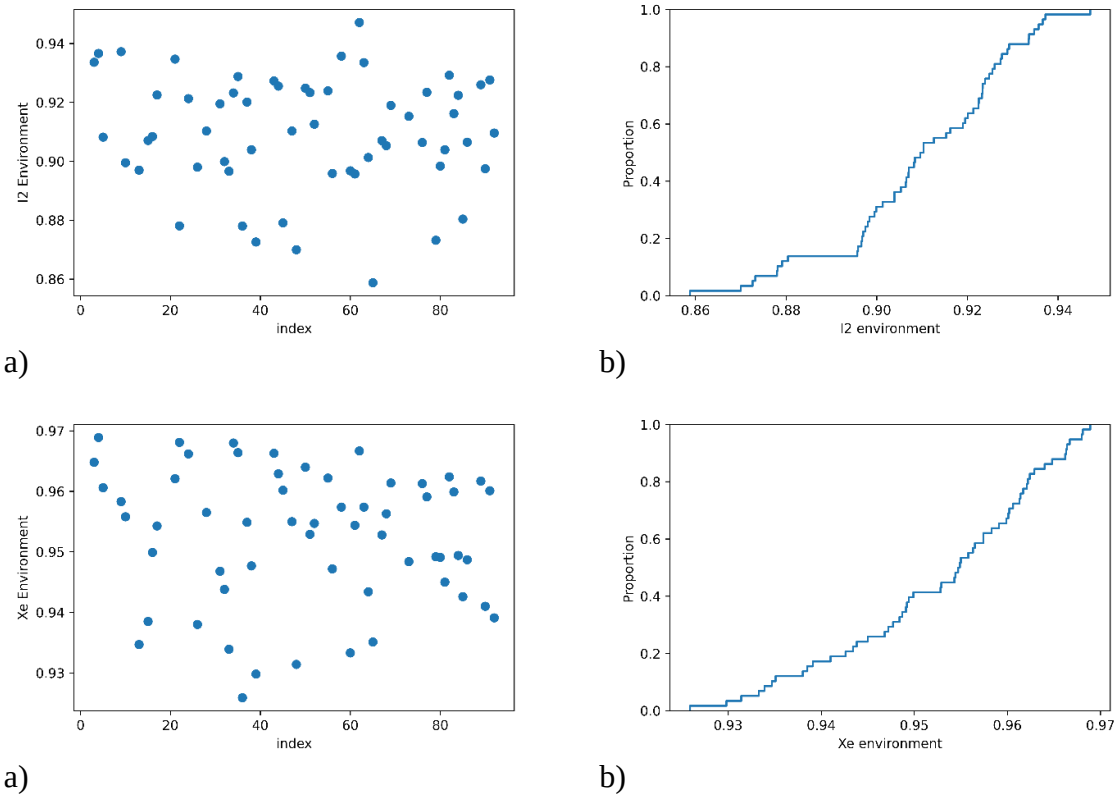

a) b)

a) b)

Figure 5. Scatterplots (a) and CDFs (b) for the selected FOMs.

As expected, Noble Gases present the highest releases, ranging from 92.5% to 97%, aligning with their inherently volatile nature. Iodine also shows substantial releases, albeit slightly below those of Noble Gases. This discrepancy can be attributed to the deposition of Iodine along the transport path between the core and the environment.

Attention was paid to containment failure time prediction due to its major role on the release of FPs into the environment. As shown in the Figure 6, the bulk of the realizations estimate that containment failure time lies within 34 h – 40 h. The plot also reveals the presence of a couple of outliers. Two cases show differences with respect to the rest of the calculations:

- In one case, the containment fails slightly later (at around 41 h).
- In the other case, the containment fails much sooner (at around 28 h).

Table 3 summarizes the statistical analysis related to the containment failure time. It can be observed that the standard deviation is small (only 5% with respect to the mean/median value), thus confirming that most data are located within a narrow distance from the mean. The BE prediction is much closer to the upper bound than to the mean/median values.

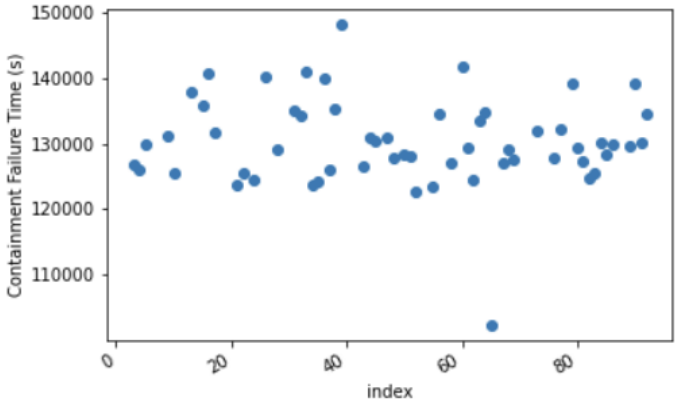

Figure 6. Scatterplot for the selected AV.

Table 3. Statistical analysis of the AV.

Statistical parameter	Time (s)	Time (h)
MELCOR reference case	143362.0	39.8
Mean	130306.5	36.2
Median	129564.5	36.0
Lower bound	102351.0	28.43
Upper bound	148285.0	41.2
Standard deviation	6710.7	1.86

3.2. Sensitivity analysis results

For sensitivity analysis, both Pearson's and Spearman's Correlation Coefficients (CCs) have been employed, as illustrated in Figure 7 and Figure 8. Notably, these coefficients exhibit dynamic changes over time, aligning with the progression of the accident scenario. It is important to highlight that values before the release onset time are deemed insignificant and likely associated with negligible releases.

In the current analysis, emphasis is placed on a specific time point, namely 48 hours, consistent with the UA. Concerning the Iodine release, both Pearson and Spearman coefficients reveal a moderate correlation with the molecular Iodine inventory in the gap of rods in the central ring of the core (rinp1_clad_I2), with is physically consistent. Additional parameters exhibit some correlation, albeit notably weaker, including the scale coefficients of Cs in the CORSOR-BOOTH model (C7103_CS), the particles' shape factor for agglomeration (gamma), and the thermal accommodation coefficient (FTHERM). The sensitivities shown by Pearson and Spearman in the case of Xenon release may be considered misleading and challenging to support from a physical standpoint. The only consistency that can be reasonably understood is with Cs

scaling coefficients (C7103_CS) due to the employed MELCOR model. Sensitivities shown with parameters related to particle behavior, such as fslip, stick, and ftherm, are difficult to justify given that Xenon is a Noble Gas, and no relation with aerosols would be expected.

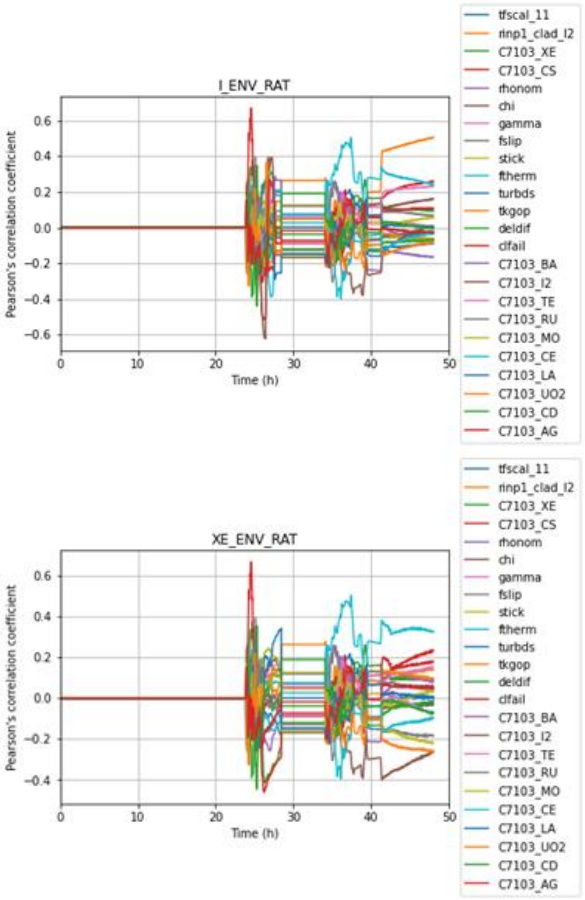

Figure 7. Pearson's coefficients for selected FOMs.

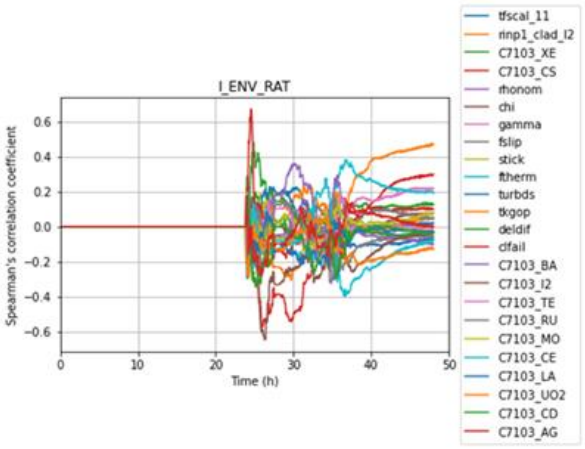

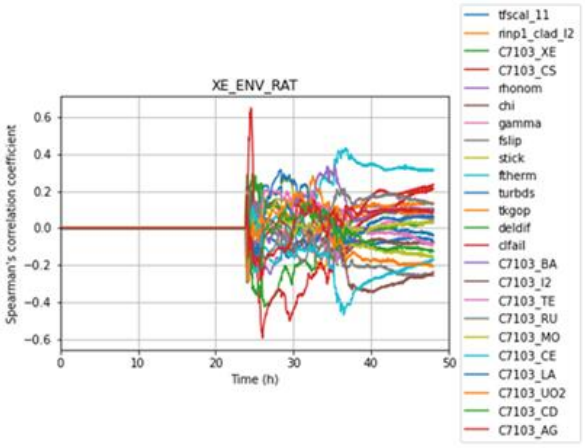

Figure 8. Spearman's coefficients for selected FOMs.

4. CONCLUSIONS

The results of the analysis provided some major insights that are summarized as follows:

- The ST relative magnitude is affected by a small uncertainty band. If Iodine is taken as a reference, most of the radiological load initially in the core reaches the environment as a consequence of the containment failure (at 48 h, release to the environment is higher than 85% of the release from the fuel), and the uncertainty band is just a few percent points;

- The onset time of the release to the environment is significantly uncertain. An approximate five-hour uncertainty band (with an onset time predicted at around 39 h in the base case) might have an effect in the emergency measures to be taken for the AM;

- The sensitivity analysis did not point at any phenomenon of outstanding significance; however, the time of fuel failure (controlled by a temperature setting) and the diffusional release of radionuclide from fuel have been found to affect the ST to the environment.

Nevertheless, these insights should not be taken as definitive for the scenario addressed, since the BEPU application in the SA domain still requires further work concerning multiple aspects, like how to better set the FOMs depending on the final aim of the BEPU, how to choose the uncertain parameters whose uncertainty should be propagated, how to optimize the sensitivity analysis so that it is restricted to linear or monotonous correlation, and many others. Additionally, there are some factors that might affect FOMs uncertainties, like nodalization, which was not included in this study. To address these and more still pending issues, a European project names INNOMUSA (INNOvation in Management and Uncertainties of Severe Accidents) was built and, at the time this articles is written, is being evaluated.

ACKNOWLEDGEMENTS

The authors wish to express gratitude to the partners of the MUSA project. This project has received funding from the Euratom Research and Training Programme 2019-2013 under grant agreement No 847441. The content of this paper reflects only the authors' view. The European Commission is not responsible for any use that may be made of the information it contains

REFERENCES

1. L.E. Herranz, S. Beck, V.H. Sanchez, F. Mascari, S. Brumm, O. Coindreau, S. Paci. The EC MUSA Project on Management and Uncertainty of Severe Accidents: Main Pillars and Status. Energies. (2021).
2. R. Iglesias, M. Angelucci, S. Paci, L.E. Herranz. Contribution of CIEMAT to D5.1 – Uncertainty and sensitivity analyses of Source Term estimates during an unmitigated SBO sequence in a PWR-1000 reactor. MUSA Project, (2023).
3. L.L. Humphries, B.A. Beeny, C. Faucett, F. Gelbard, T. Haskin, D.L. Louie, J. Phillips. MELCOR Computer Code Manuals, Vol.1: Primer and User' Guide Version 2.2.14959, SAND2019-12536 O Sandia National Laboratories, (2019).
4. L.L. Humphries, B.A. Beeny, C. Faucett, F. Gelbard, T. Haskin, D.L. Louie, J. Phillips. MELCOR Computer Code Manuals, Vol.2: Reference Manual Version 2.2.14959, SAND2019-12537 O Sandia National Laboratories, (2019).
5. P. Mattie, R. Gauntt, K. Ross, N. Bixler, D. Osborn, C. Sallaberry, and J. Jones. Uncertainty Analysis of the Unmitigated Long-Term Station Blackout of the Peach Bottom Atomic Power Station (NUREG/CR-7155). U.S.N.R.C. (2016).
6. Adams, B.M., Eldred, M.S., Dalbey, K.R., Bohnhoff, W.J., Swiler, L.P., Hough, P.D., Gay, D.M., Eddy, J.P., Haskell, K.H., 2018. DAKOTA : a multilevel parallel object-oriented framework for design optimization, parameter estimation, uncertainty quantification, and sensitivity analysis. Version 5.0, user's manual. https://doi.org/10.2172/991842.
7. Wilks, S.S., 1941. Determination of Sample Sizes for Setting Tolerance Limits. The Annals of Mathematical Statistics 12, 91–96. https://doi.org/10.1214/aoms/1177731788.
8. M. M. Mukaka, "A guide to appropriate use of Correlation coefficient in medical research," Malawi Med. J., vol. 24, no. 3, p. 69. (2012).

GOBIERNO DE ESPAÑA
MINISTERIO DE CIENCIA, INNOVACIÓN Y UNIVERSIDADES

Ciemat
Centro de Investigaciones Energéticas, Medioambientales y Tecnológicas

SOURCE TERM UNCERTAINTIES IN UNMITIGATED SBO SEQUENCES IN A PWR-1000: INSIGHTS FROM THE EU-MUSA PROJECT

R. Iglesias*, M. Angelucci, S. Paci, L.E. Herranz
Presented by M. Garcia

**rafael.iglesias@ciemat.es*
Unit of Nuclear Safety Research
Department of Nuclear Fission
CIEMAT

11th European Review Meeting on Severe Accident Research (ERMSAR2024)
KTH, Stockholm, Sweden, May 13-16, 2024

Contents:

01 Introduction

02 SBO Scenario: BE Case

03 Uncertainty Quantification

04 Sensitivity Analysis

05 Conclusions & Lessons learned

INTRODUCTION

➢ Objective of the work

- Present the outcomes and insights resulting from the Uncertainty and Sensitivity Analysis (UaSA) of Source Term (ST) estimates in a Best Estimate Plus Uncertainty (BEPU) calculation of an **unmitigated Station Black-Out (SBO) occurring in a 3-loop PWR-W.**

➢ Frame

- **HORIZON 2020 MUSA project**: Towards an harmonized approach for the UaSA application to SAs.
- **WP5**: Uncertainty Quantification in Analysis & Management of Reactor Accidents.

SBO SCENARIO: BE CASE

Scenario & Nodalization

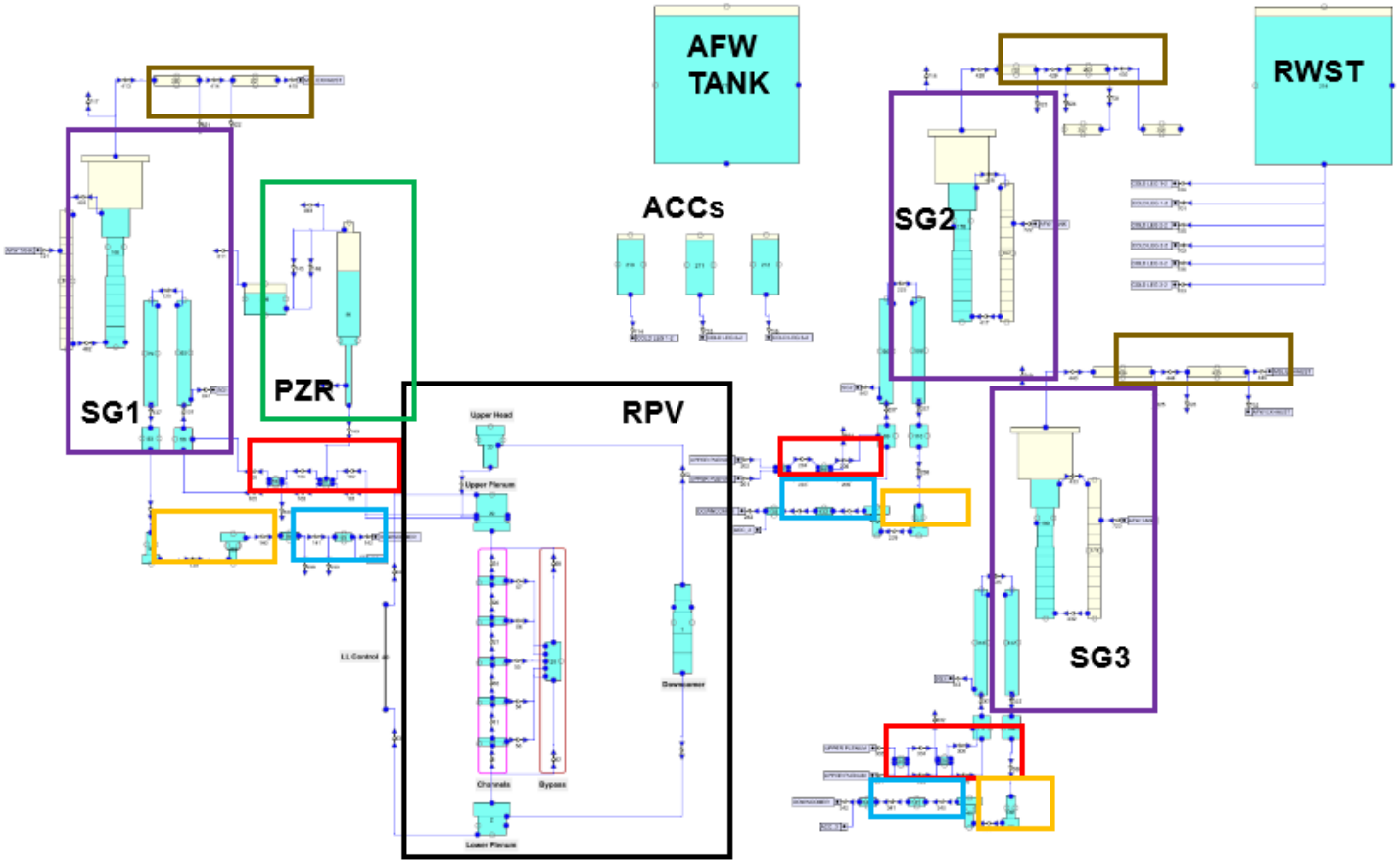

MELCOR nodalization scheme

Scenario

- Unmitigated SBO
- PWR-W 3 loop NPP

Nodalization

- NPP (94 CVs, 178 FLs, 326 HSs)
- RCS (3 loops)
- RPV (10 CVs)
- Core (6 radial rings, 13 axial nodes)
- SSs (HPSI, LPSI, ACCs)
- Containment (30 CVs)

MELCOR 2.2.21402

SBO SCENARIO: BE CASE

Main assumptions

- Reactor was operating at full power before the transient
- **Available safety systems**
  - Accumulators
  - Turbo-pumps (2) for the Auxiliary Feed Water (AFW) system
  - Batteries (6-hour duration)
  - Safety valves (SGs and PZR)
- **Unavailable safety systems**
  - HPSI/LPSI systems
- **Failures included**
  - AFW turbines: when the Main Steam Lines (MSLs) become flooded
  - MSLs fail: when water level reaches half pipe height
  - Hot Leg failure: due to creep (following the dedicated MELCOR model
  - Containment failure: over-pressure
  - Vessel failure: due to the thermal creep
- **No severe accident management action was considered**

SBO SCENARIO: BE CASE

BE results

Key Event	Time
SBO	0.0 s
Reactor SCRAM	0.0 s
All RCPs tripped	< 1.0 s
AFW system start	10.0 s
MSL 1 break (water discharge into the containment)	7.4 h
Hot leg creep rupture	27.3 h
Vessel failure and start of the corium debris relocation in the cavity	30.1 h
Containment failure and beginning of radioactive release	39.8 h

Evolution of the PRZ and SGs pressure

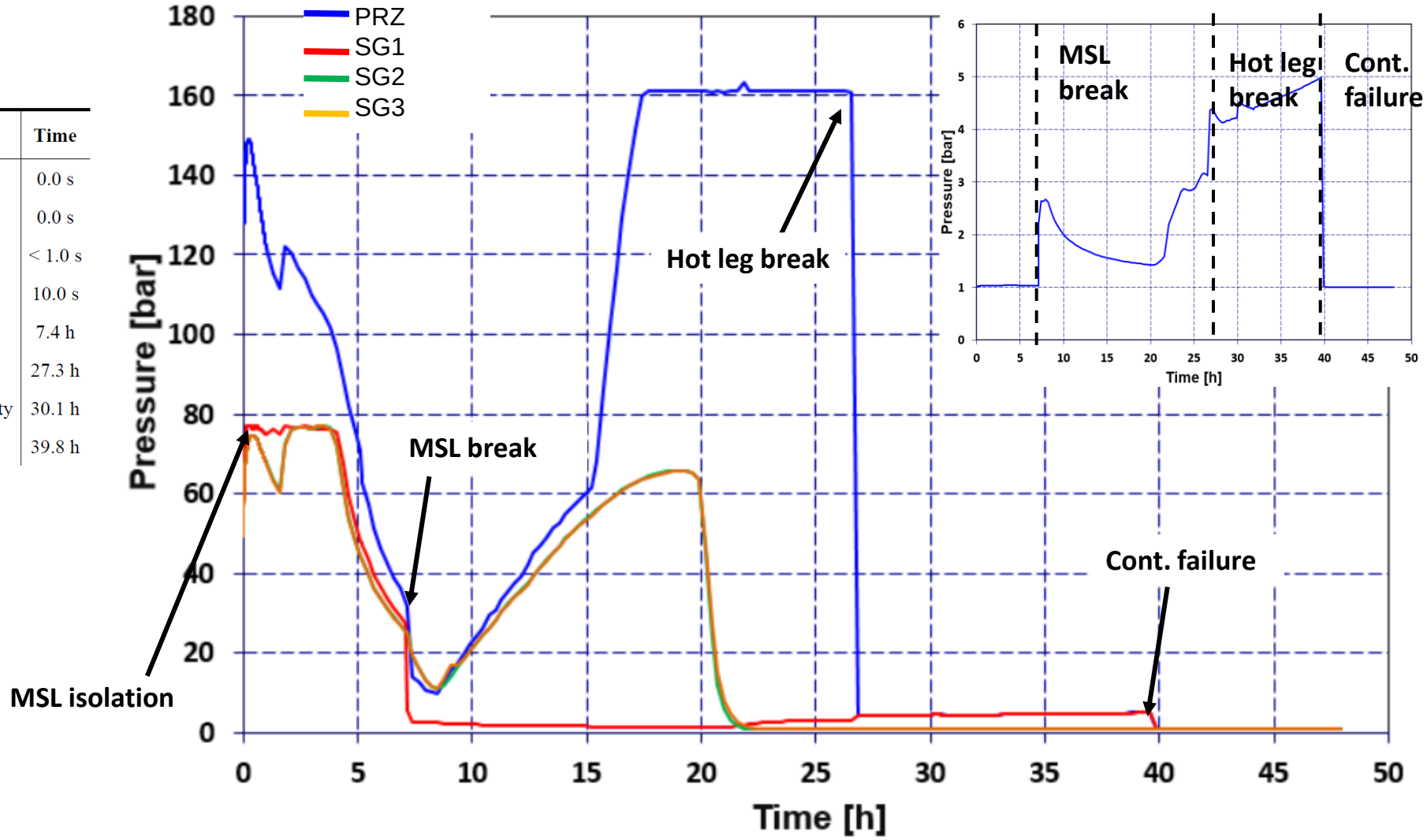

SBO SCENARIO: BE CASE

BE results

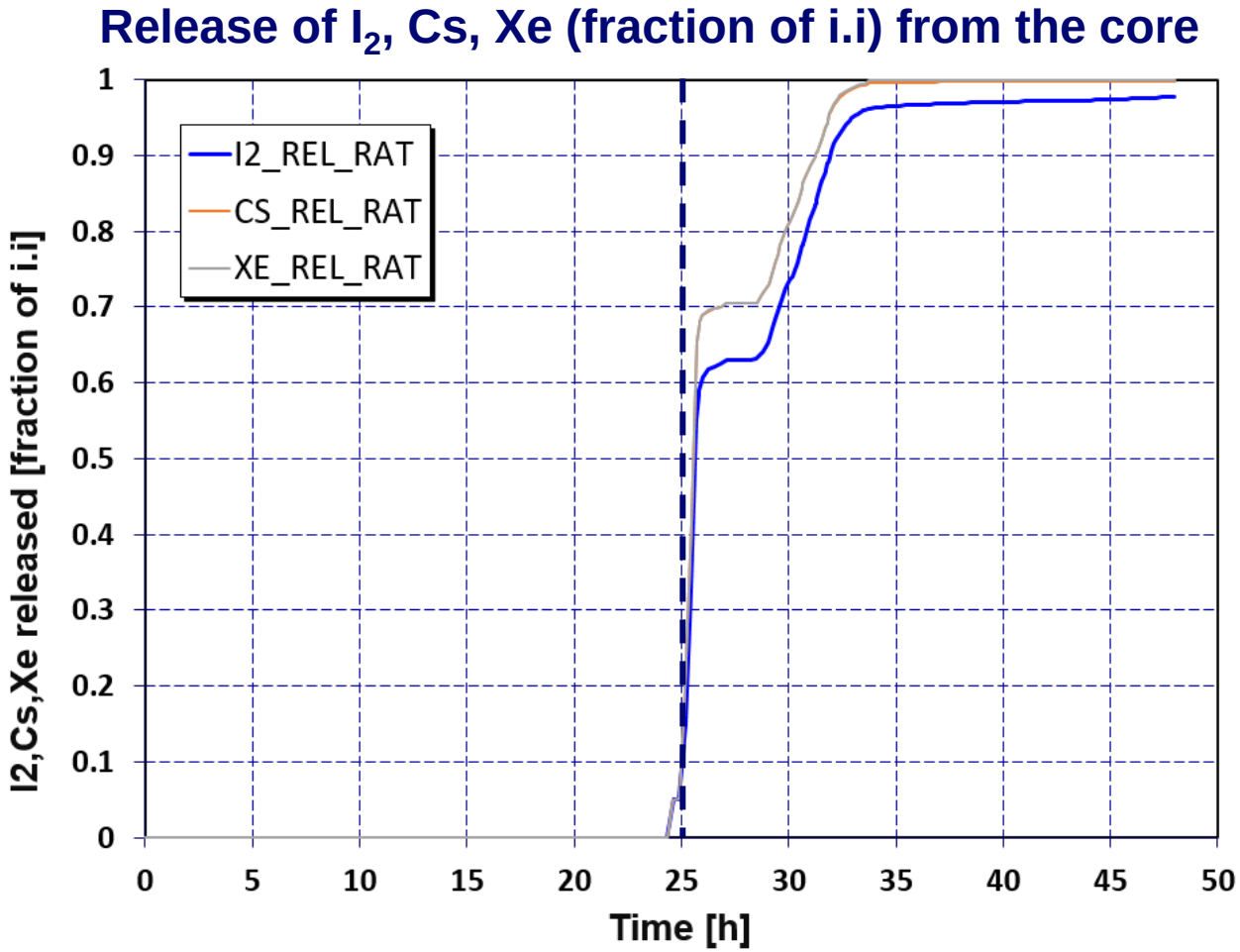

- Onset time of FPs release at 25 h
- Almost 99.8% of iodine is released from the core.
- Similar evolution for Xe and Cs.

UaSAs

Uncertainty Methodology

- MELCOR 2.2.21402/DAKOTA 6.7
- Use of home-made Python scripts.
- Order statistics (Wilks; 93 runs to get 95/95).
- Simple Random Sampling (Input driven methodology).
- Uncertainty propagation - 24 u.p. grouped as follows:
  - Core initial inventory.
  - Fission product release model (CORSOR-BOOTH).
  - Fuel and cladding failure.
  - Aerosol characterization.
- FOMs targeted: Iodine, Cesium and noble gases releases to the environment.
- Containment failure time was selected as an additional variable to be studied.

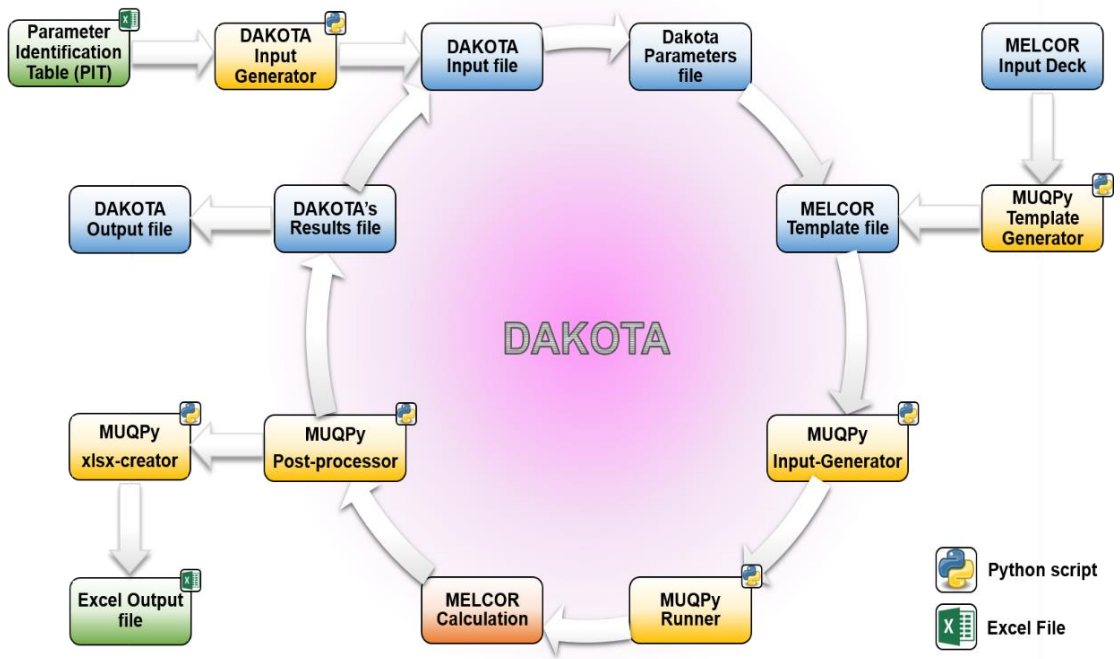

(Bocanegra & Herranz, 2022)

UaSAs

Uncertainty Quantification Results

Dispersion plots
(iodine released to environment as a fraction of i.i.)

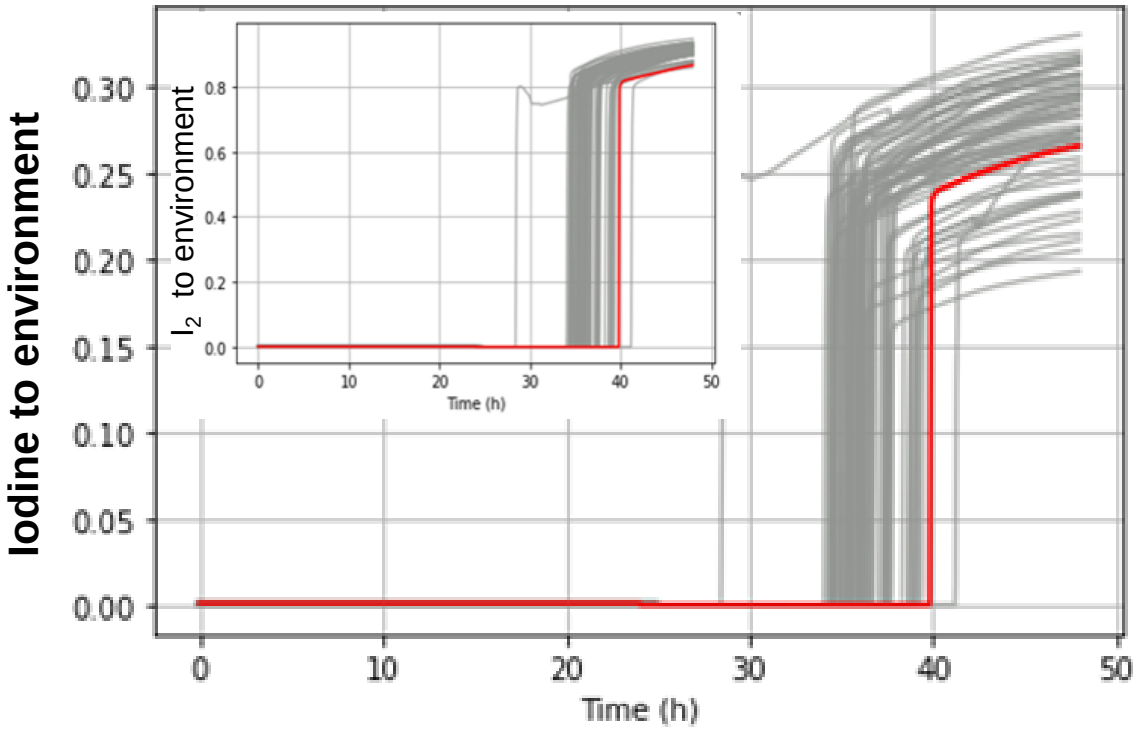

Statistical analysis of the FOMs
(end time)

Statistical parameter	Iodine	Noble gases
MELCOR RC (%)	26.59	92.47
Mean (%)	27.81	95.25
Median (%)	28.42	95.48
Lower bound (%)	19.33	92.59
Upper bound (%)	33.02	96.89
Standard deviation (%)	3.22	1.11

- Releases begin right after containment failure. Evolution in time is similar for all the FOMs.

- Noble gases present less dispersion than other RN (92.5 - 97%).
- Iodine spread, though, is substantial because of the small release fraction (19% - 33%).

Uncertainty Quantification Results

Scatterplot for the selected added variable (Containment failure time)

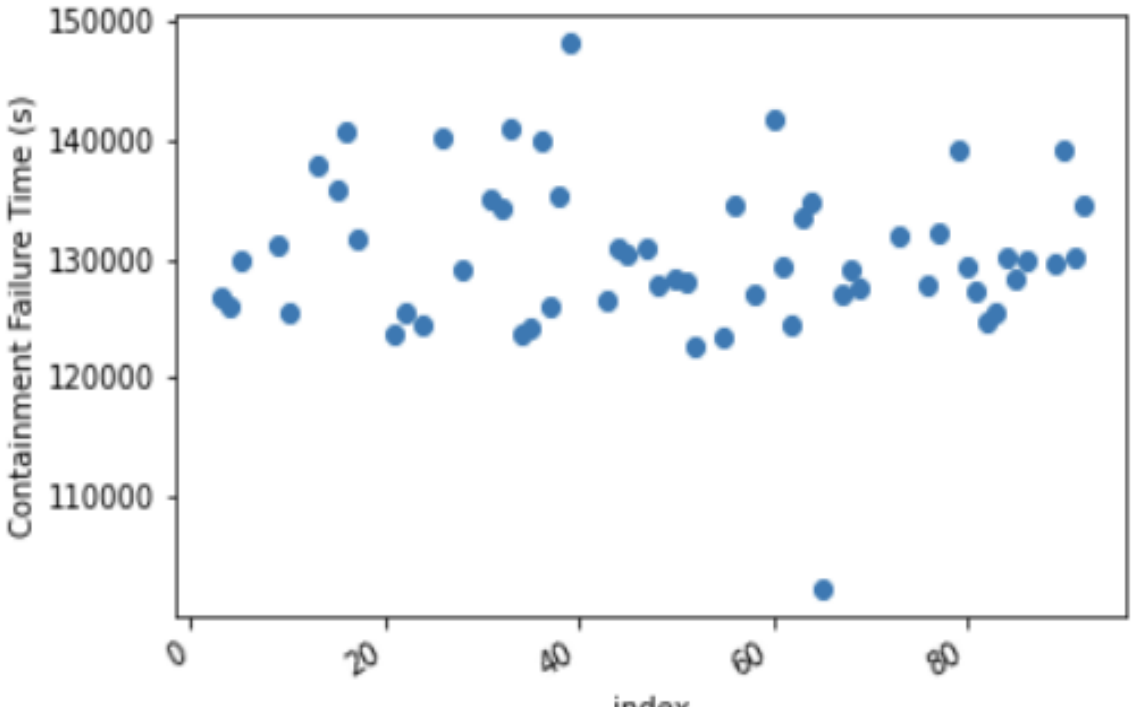

Statistical analysis of the AV (Containment failure time)

Statistical parameter	Time (s)	Time (h)
MELCOR reference case	143362.0	39.8
Mean	130306.5	36.2
Median	129564.5	36.0
Lower bound	102351.0	28.43
Upper bound	148285.0	41.2
Standard deviation	6710.7	1.86

- Containment failure time lies within 34 h – 40 h.
- Two cases show differences with respect to the rest of the calculations:
  Case 1: containment fails at 41 h.
  Case 2: containment fails at 28 h.

- Standard deviation is small (5% with respect to mean/median value).
- Most data are located within a narrow distance from the mean.

Sensitivity analysis

- Sensitivity analysis, based on Pearson's and Spearman's Correlation Coefficients (CCs),
- Objective: to evaluate the most influential parameters over the main FOMs results.

Pearson's coefficient

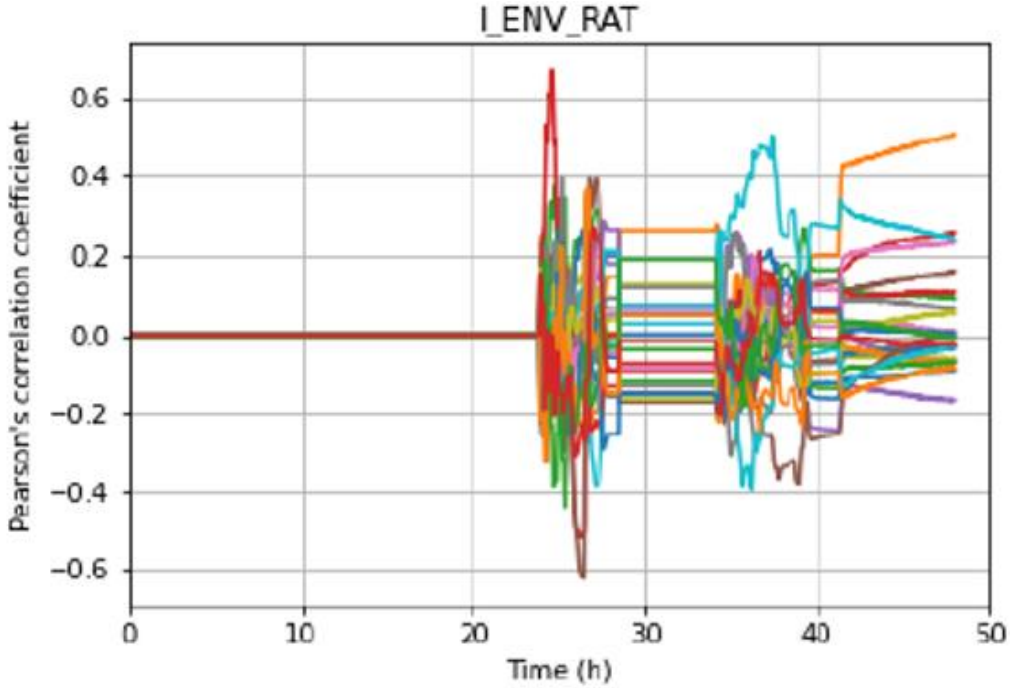

- Moderate correlation with the molecular iodine inventory in the gap of rods in the central ring of the core (rinp1_clad_I2).

Spearman's coefficient

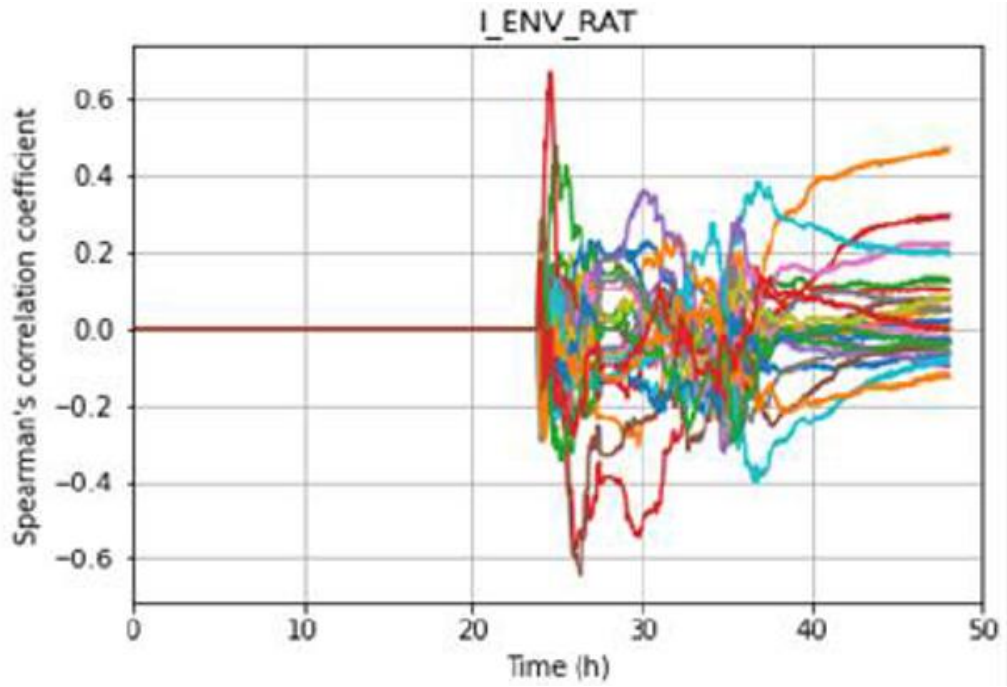

- Additional parameters exhibit some correlation:
  - Scale coefficients in the C-B model.
  - Particle shape factor (gamma).
  - Deposition by thermophoresis (FTHERM).

Conclusions

- A fraction of the radiological load (~30 % I, Cs) reaches the environment.

- Uncertainty in the release fraction affected by the processes involved. A narrow band affect NG estimates, whereas the iodine one spans over ~30 % of the best estimate.

- No conclusive correlations between FOMs and U.P.'s found. However, RN transported mostly as particles show sensitivity to particle characteristic (shape).

- The onset of release to the environment is associated with a substantial uncertainty (~ 5 h) that might affect the emergency measures to be considered.

Lessons learned

BEPU application in the SA domain still requires further work concerning multiple aspects, like:

- How to better set the FOMs depending on the final aim of the BEPU,
- How to choose the uncertain parameters whose uncertainty should be propagated,
- How to optimize the sensitivity analysis so that it is restricted to linear or monotonous correlation, and many others.

Acknowledgement

This MUSA project has received funding from the European Union's **EURATOM Horizon 2020** research and innovation programme **grant number 847441**.

The content of this paper reflects only the authors' view. The European Commission is not responsible for any use that may be made of the information it contains.





Thank you for your attention!

Unit of Nuclear Safety Research
Department of Nuclear Fission
CIEMAT
rafael.iglesias@ciemat.es

The 11th European Review Meeting on Severe Accidents Research

May 13-16, 2024, Royal Institute of Technology, Stockholm, Sweden

TECHNICAL SESSION 4.1: SEVERE ACCIDENT SCENARIOS - SMALL MODULAR REACTORS

Chairs: F. Gabrielli (KIT), D. Jacquemain (OECD/NEA)

ID75	**SASPAM-SA: Assessment of the relevance and applicability of existing experimental databases to iPWR** T. Lind (PSI)	**Paper Presentation**
ID101	**Numerical Investigation of Natural Circulation Inside a Scaled-Down Prismatic Modular Reactor By RHYS** M. Shewitah (Minia University)	**Paper Presentation**
ID01	**Development of a LW-SMR dry containment model with containmentFOAM** C. Vázquez-Rodríguez (FZJ)	**Paper Presentation**
ID72	**Comparison of a DBA sequence in a generic iPWR between MELCOR and ASTEC codes** G. Grippo (ENEA)	**Paper Presentation**

SASPAM-SA: Assessment of the relevance and applicability of existing experimental databases to iPWR

T. Lind
Paul Scherrer Institute
terttaliisa.lind@psi.ch

A. Bersano F. Mascari
ENEA, Italy
fulvio.mascari@enea.it
L.E. Herranz
CIEMAT, Spain
luisen.herranz@ciemat.es
N. Chaumeix
CNRS, France
chaumeix@cnrs-orleans.fr
E. Reinecke
FZJ, Germany
e.-a.reinecke@fz-juelich.de
P. Nerisson
IRSN, France
philippe.nerisson@irsn.fr
P. Kudinov
KTH, Sweden
pkudinov@kth.se
M. Constantin
RATEN, Romania
marin.constantin@nuclear.ro
D. Gumenyuk
SSTC, Ukraine
dv_gumenyuk@sstc.ua
I. Ivanov
TUS, Bulgaria
ivec@tu-sofia.bg
T. Kärkelä
VTT, Finland
teemu.karkela@vtt.fi

ABSTRACT

SASPAM-SA project, funded by Euratom, aims to investigate the applicability and transfer of the operating large light-water reactor knowledge and know-how to the iPWR, taking into account European licensing analysis needs for the severe accidents and Emergency Planning Zone. Project outcomes will help accelerate the licensing and siting process of iPWRs in Europe. One of the objectives of SASPAM-SA, in particular Work Package 3 (Applicability and Transfer of the Existing SA experimental database for iPWR Assessment), is to evaluate the relevance and applicability of the existing experimental database to iPWR.

Based on postulated plant severe accident scenarios, identified and investigated in the Work Package 2 of the SASPAM-SA project, the main boundary conditions and the specific features of iPWR are determined and compared to those of large LWR. Based on this comparison, the applicability of the existing experimental data to iPWR is assessed for in-vessel, containment, source term and ex-vessel coolability (if applicable) phenomena. The specific data to be evaluated include, e.g., natural circulation, debris bed formation, liquid melt spreading, steam explosion, re-flooding of an overheated core, in-vessel melt pool formation, corium cooling under water, hydrogen distribution, combustion and mitigation, aerosol characteristics, transport and hygroscopic growth, iodine speciation and mitigation, as well as pool scrubbing. If needed, different ways to extend the applicability of existing data to iPWRs will be explored. Finally, the potential need for new experiments is determined. In this paper, a summary of the work done during the first project year is given.

KEYWORDS
iPWR, experimental data, SASPAM-SA

1. INTRODUCTION

Small Modular Reactors (SMR) are one of the key options for the near-term deployment of new nuclear reactors. Currently in Europe there is a growing interest towards the deployment of SMRs, and several activities are underway in many countries preparing for possible licensing needs. To address this need, an Horizon Euratom collaboration project SASPAM-SA (Safety Analysis of SMR with PAssive Mitigation strategies - Severe Accident), coordinated by ENEA (Italy), was started in October, 2022, for four years. The key objective of SASPAM-SA is to investigate the applicability and transfer of the operating large Light Water Reactor (LWR) knowledge and know-how to the near-term deployment of integral PWR (iPWR), in the view of the European licensing analyses needs with emphasis on severe accidents and emergency planning zone [1].

Advanced designs, such as iPWRs, are in general characterized by common features with the current operating large-LWR and by other specific features typical of their inherent evolutionary designs, providing safety advantages that reinforce the first three levels of the Defence-in-Depth (DiD) principle. However, even if a plant is designed with advanced inherent features (through the reinforcement of the 1,2,3 DiD levels) allowing a reduction of the Core Damage Frequency (CDF), independent features for preventing and mitigating a severe accident sequence have to be included in its design (DiD level 4) together with the offsite emergency response (DiD level 5). Therefore, some scenarios that could lead to severe accidents need to be postulated and deterministically studied [2]. Though most of the significant severe accident phenomena have been the subject of research efforts in the past, those efforts have focused on large-LWRs. Due to different geometries and configuration (e.g. integral RPV, larger core surface-to-volume and coolant inventory-to-power ratios within RPV), specific phenomena (e.g. closed coupling of the reactor pressure vessel and the containment in accident conditions, low pressure phenomena), the use of specific components (e.g. compact steam generator, passive safety systems), and different operating parameters of iPWRs and large-LWRs (e.g. lower core power), the accident progression can be expected to be different in iPWRs as compared to large LWRs. As a consequence, the conditions in the RPV and in the containment of an iPWR can differ from those in large-LWRs [1,2,3,4]. Thereby, the applicability of the available data developed for large LWRs also to iPWR technology has to be proven.

The main objectives of the Work Package 3 of the SASPAM-SA project: “Applicability and Transfer of the Existing severe accident experimental database for iPWR Assessment” are i) to study the relevance and applicability of the existing experimental database to iPWR, ii) to develop methods to extend the

applicability of existing data, and iii) to identify the need for new experiments. The relevant phenomena will be identified, and the review of the current experimental database will be done considering the following phenomena: a) In-vessel degradation and coolability; b) Containment, including hydrogen ignition and self-sustained combustion; c) ST; d) Ex-vessel coolability, if any ex-vessel phenomenology will be identified in the project. It is worth noting that SASPAM-SA/WP3 will be tightly linked to EU SEAKNOT, supporting the inclusion of specific water-cooled-SMR phenomena in a mid-term severe accident research roadmap.

2. METHODS

2.1. iPWR designs

The applicability of the large LWR data to iPWRs will be assessed for two generic iPWR designs selected based on publicly available information, Figure 1. The two designs are characterized by different evolutionary innovations in comparison to larger operating reactors. Even though the designs are generic, they have common features with iPWR designs which are under development, and thereby available data in the open literature can be used in the work. The two generic designs are:

- Design 1: iPWR characterized by a submerged containment and an electric power of about 60 MWe;
- Design 2: iPWR characterized by the use of several passive systems, a dry containment and an electric power of about 300 MWe.

These two generic reactor concepts include the main iPWR design features considered in some of the promising designs ready to go on the European market allowing a broad assessment of the capability of severe accident and CFD codes to simulate the severe accident phenomena typical of iPWRs.

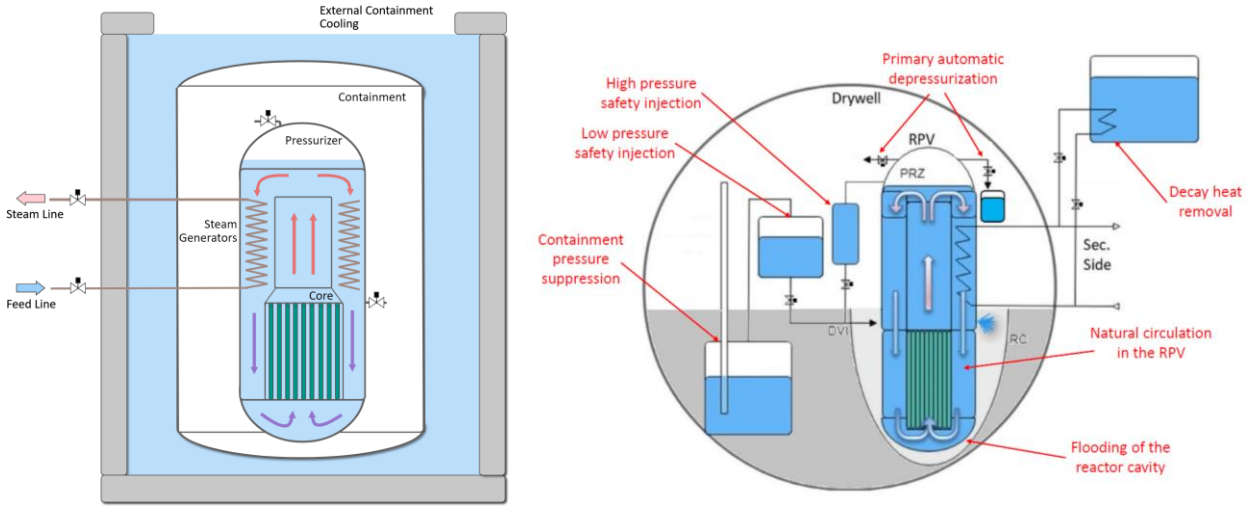

Figure 1. The designs 1 (on the left) and 2 (on the right) used in the SASPAM-SA project (figure from SASPAM-SA).

2.2. Assessment of the Data

The outline of the methodology to be applied to evaluate the applicability of the existing experimental data to iPWRs is depicted in Figure 2. A review of the existing experimental database, relevant to severe accidents, will be done for the following severe accident phenomena:

a) In-vessel degradation and coolability;
b) Containment, including hydrogen risk;
c) Source term; and
d) Ex-vessel coolability, if any, based on the accident analyses of iPWR design 1 and design 2.

Based on the postulated plant severe accident scenarios as identified and investigated for designs 1 and 2 in the Work Package 2 of the SASPAM-SA project, the main boundary conditions and the specific phenomenological features will be determined. The predominant phenomena, i.e., those phenomena having a decisive impact on the accident progression, will be identified, and governing equations determined. The phenomena will be described by the most significant parameters and / or dimensionless numbers. Based on the main phenomena, potential facilities in which these phenomena have been investigated will be explored, and suitable tests in those facilities selected for further assessment. In the next step, the key features of the selected facilities and tests will be listed, including the facility scaling factor and other relevant geometrical and operational features. Comparison with iPWR severe accident conditions for SASPAM-SA designs 1 and 2 can be done, for example, using a table in which all the main parameters and, when deemed useful, dimensionless numbers are presented.

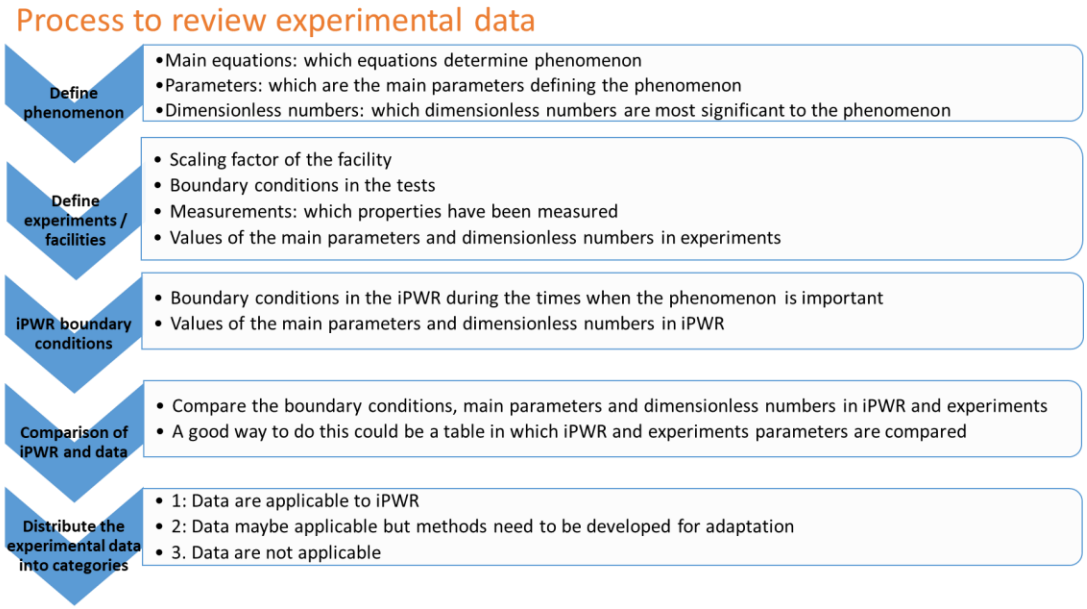

Figure 2. The proposed methodology for evaluation of the applicability of existing experimental data to iPWRs.

Based on the comparison of the experimental data with the iPWR designs, assessment of the applicability of the data to iPWRs will be made. The data will be divided into three categories:

i) data which are directly applicable to iPWR,
ii) data which can be used by developing extrapolation and other methods to extend their applicability to iPWR conditions, and
iii) data which are not applicable to iPWRs.

If the facility scaling is appropriate and the main parameters and dimensionless numbers during iPWR severe accidents fall within the range of parameters in the experiments, the data can be assessed as belonging to category i), applicable to iPWRs. For the category ii), application methods will be proposed and developed in further work.

In the end of the investigation, to be reported later, the phenomena to which no applicable data are available or to which the database is not sufficient will be identified, and the critical experimental data needs to enable credible SA analysis of iPWRs will be determined.

2.3. Investigated Phenomena

To optimize the use of resources, the phenomena to be investigated were distributed between different scientists. The following phenomena are included:

a) Natural circulation: ENEA;
b) In-vessel degradation and coolability by KTH, RATEN, SSTC NRS, and TUS,
c) Containment: CIEMAT, CNRS-ICARE, FZJ, KTH, PSI and IRSN,
d) Source term: VTT, PSI, CIEMAT and IRSN,
e) Ex-vessel coolability: If ex-vessel phenomena are observed in the severe accident scenarios postulated for iPWR designs 1 and 2, these phenomena will be studied by KTH, TUS, RATEN and SSTC NRS.

3. FIRST RESULTS

3.1. Natural Circulation

The passive systems relying on natural circulation are, on one side, advanced solution to increase the inherent safety of the plant (e.g. there is no need of pump), on the other hand a) they required more investigation for assessing the functional failure related to the thermal-hydraulic phenomena driving the operation of the systems and assess the related uncertainties, b) may still need an active initiation, and c) are characterized by less operational experience [5,6]. Considering this, the impact of passive systems operation on postulated severe accident progression needs to be assessed.

iPWR designs rely on natural circulation during accident situations and for some designs also in steady operational condition [e.g.,3]. To assess if the existing experimental data for natural circulation are applicable to iPWRs, ENEA has selected a number of facilities in which experiments for natural circulation have been conducted. The majority of the experiments have been carried out at Design Basis Accident (DBA) conditions but some may be applicable to characterize natural circulation in severe accident conditions. When selecting the data to be assessed, the focus was on thermal-hydraulics of integral RPV, primary/containment coupling, and on passive systems that affect the progression of severe accident scenarios[1]. Both the scaling factors and other features of the potential facilities were listed, and based on those, a series of tests in each facility was selected for further review.

For natural circulation, the main affecting parameters are the geometry, e.g., elevation between the source and sink, and piping diameters; phases: single-phase/two-phase; pressure and temperature fields; pressure losses, both local and continuous; heat provided/removed in the core and heat exchangers; as well as possible presence of non-condensable gases. As non-dimensional numbers, e.g. Richardson and SG heat transport number, are important numbers to be considered. These are the parameters which are compared in the

.

experiments with those of iPWR in DBA and severe accident conditions as computed in the WP2 of the SASPAM-SA project.

The work started with assessment of data from the OSU-MASLWR facility [4]. For natural circulation in the RPV, three relevant tests were identified: DOE OSU-MASLWR-002, DOE OSU-MASLWR-003A, and IAEA ICSP SP-2. Figure 3 shows an example comparison of the Richarson number range [7] for the test OSU-MASLWR-002 and the design 2 DBA data. It is seen that the experimental Richarson number envelop some of the design 2 calculated data. Based on the SASPAM-SA schedule, currently DBA and severe accident calculated data are under collection and the comparison will be carried out based on the results of all the severe accident codes used in SASPAM-SA (AC2, ASTEC, MAAP, MELCOR).

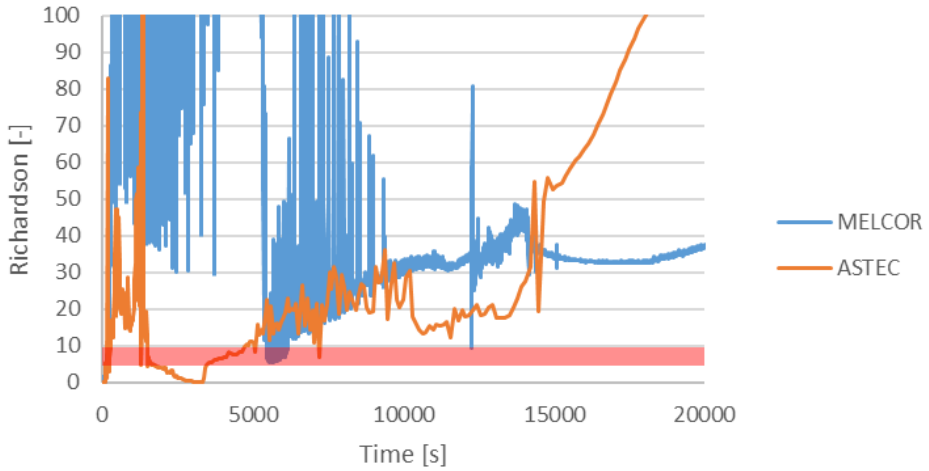

Figure 3. Comparison of the OSU-MASLWR-002 Richardson number range against design 2 data in DBA condition.

3.2. In-Vessel Cooling and Degradation

3.2.1. Re-flooding of rod-like geometry

When an over-heated core is re-flooded, steam will oxidize the Zr in the cladding leading to hydrogen generation and eventually to cladding failure. The QUENCH program carried out at the KIT has investigated phenomena related to reflooding since mid 1990s [8]. For the assessment in this work, QUENCH-06 test (OECD ISP-45) was chosen [9]. The QUENCH facility and SASPAM-SA designs 1 and 2 have been compared, and the main phenomena relevant to reflooding defined. In continuation, scenario analysis data will be used to compare with QUENCH-06 data. Potentially, other QUENCH tests and results from other experimental programs such as OECD/NEA RBHT can be added in the analysis.

3.2.2. Melt jet behaviour and steam explosion

The following melt jet and in-vessel phenomena will be assessed based on experimental data available at Royal Institute of Technology in Stockholm (KTH): Melt jet breakup and debris bed formation (DEFOR-A and DEFOR-S tests), liquid melt spreading under water (PULiMS-E and SES-E tests), lower head failure and breach ablation / plugging during melt release, particulate debris spreading (PDS-C tests), steam explosion in stratified melt-coolant configuration, and melt propagation in a porous debris bed. In addition, lower head failure test data are available from DEFOR-MGF experiments.

3.2.3. In-vessel cooling of a molten core

To assess in-vessel coolability and degradation, the following parameters need to be investigated:

- Reduced core power, less power-to-surface ratio;
- Materials (vessel, vessel internals, core);
- Geometry (incl. vessel internals);
- Containment atmosphere composition.

Data for lower plenum phenomena related to in-vessel cooling of a molten core are available from the test series LIVE (Large-scale Tests on In-vessel Melt Relocation and Retention) conducted in the Karlsruhe Institute of Technology [10]. The LIVE-L1 test was focused on the core melt behavior in the lower plenum of the RPV and the influence of the cooling of the vessel outer surface with water [11,12]. The LIVE3D test facility simulates the lower plenum of a water-cooled reactor pressure vessel and investigates the transient and steady state thermal-hydraulics and heat transfer of solid and liquid corium under various accident scenarios. Experimental data from five tests are assessed in this work, i.e., LIVE-1, -2, -L3A, L4 and L5L. The main data relevant to iPWRs are shown in Table 1. According to preliminary assessment, comparison should use Pr, Ra and Nu numbers.

Table 1. The main parameters of the LIVE experiments to be compared with iPWR conditions of SASPAM-SA designs 1 and 2.

Melt characteristic	LIVE-1	LIVE-2	LIVE-L3A	LIVE-L4	LIVE-L5L
Height [m]	0.31	0.31	0.31	0.435	0.435
Volume [l]	120	120	120	210	210
LH heat flux min/max [W/m^2]	1.5E+03/ 1.0E+04	1.25E+03/ 8.0E+03	1.5E+03/ 1.73E+04	4.91E+02/ 1.94E+04	7.09E+2/ 2.26E+4
$Q_{heating}$ [W]	-	-	-	18064.2	18088
Q_{wall} [W]	-	-	-	14488.7	14661
Q_{wall}/ $Q_{heating}$	-	-	-	0.802	0.81
Average heat density [W/m^3]	-	-	-	87692	87970
v [m^2/s]	-	-	-	1.56E-06	1.56E-06
Pr	-	-	-	9.3	9.3
Nu	-	-	-	-	227
Ra	-	-	-	4.31E+13	4.29E+13

3.3. Containment

3.3.1. Hydrogen distribution

The hydrogen risk may be reduced in iPWR as compared to large PWRs due to inerted or sub-atmospheric containments. However, as the containment and reactor vessel are closely coupled during accidents, the effect of hydrogen is not only the risk of explosion but also its effect on the establishment and continuity of natural circulation needed to cool the core during accidents.

Experimental data for the hydrogen distribution as well as natural circulation are available from various test programs in the PANDA facility at PSI [13]. The available data will be reviewed and evaluated using the methodology presented in section 2.

3.3.2. Hydrogen combustion

As air ingress can not be completely excluded in iPWR containments [14], hydrogen combustion data from a series of tests conducted at CNRS are assessed. Among the tests to be investigated are those in the experimental programs ANR-PIA-MITHYGENE, ANR-PHYSSA and CNRS Projects on H_2 based mixtures (different diluents).

iPWR containments are typically smaller than those in large LWRs with restricted geometries which tend to cause flame acceleration in case hydrogen combustion occurs. In addition, hydrogen release may be rather rapid having also an impact on combustion behaviour. The expected hydrogen combustion conditions in iPWR (SMR) as compared to large PWRs are depicted in Figure 4 showing that data might be missing at conditions relevant to iPWRs. Further work will be conducted to evaluate the conditions in the iPWRs and experimental data, and if deemed needed, selected tests may be carried out to fill the gaps of missing data.

For SMRs, the path towards flammable mixtures is through rich mixtures, unlike for LWR for which it is through the lean branch, Fig. 2. The knowledge on the explosion risk for the relevant mixtures is rather scarce and it will be the goal of this project to derive methods to enhance the knowledge for these mixtures. Moreover, the effect of the initial pressure and temperature on the flammability limits and minimum ignition energy will be derived. Finally, the presence of other gases and/or particles can have an important effect of the flammability/severity domain.

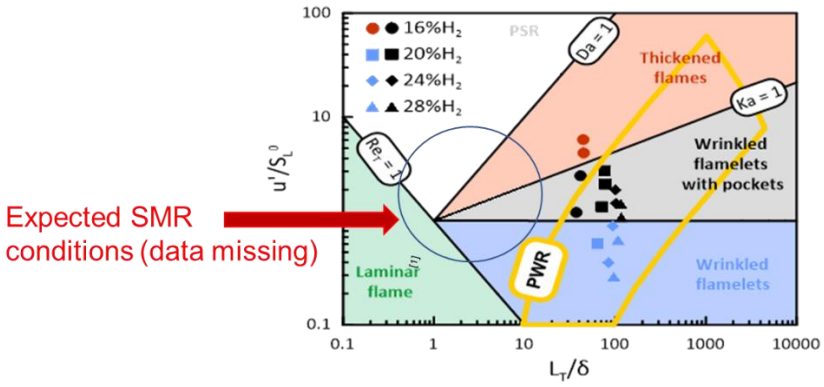

Figure 4. Hydrogen combustion regimes with an indication of the area of iPWR conditions.

3.3.3. Hydrogen mitigation with passive auto-catalytic recombiners (PARs)

PARs are installed in non-inerted LWR containments to reduce the hydrogen concentration in the containment atmosphere. Their performance at different containment conditions has been studied in series of test campaigns, e.g., France: H2PAR, KALI (1995 – 1999); Germany: HGF-NUSAFE (on-going), REKO-I to REKO-III (2005 – 2018), THAI (on-going); Canada: various AECL/CNL programs; European projects: SAMHYCO-NET (2017-2022) and AMHYCO (2020 on-going); and OECD/NEA projects: THAI/THEMIS HR series (2007 on-going). Based on these investigations, the PAR response to different pressures, gas mixtures, humidity, temperature and the presence of inhibitors has been broadly assessed [15].

While PAR operation in the SMR designs under consideration could only be conceivable for air-ingress scenarios, the accident conditions in iPWR containments would be distinctly different from large LWRs. Depending on the time of the air ingress, accident scenarios would follow pathways starting from inert conditions instead of air, Figure 5 [15]. Based on the existing accident analyses, there is lack of data for

PAR performance at pressures higher than 0.5 MPa, start-up at extremely wet conditions, as well as fast H2 injection rates. Furthermore, there is the need to identify for both designs, if and where the installation of PARs could be feasible and meaningful. In addition to the containment, these considerations should also include reactor and auxiliary buildings.

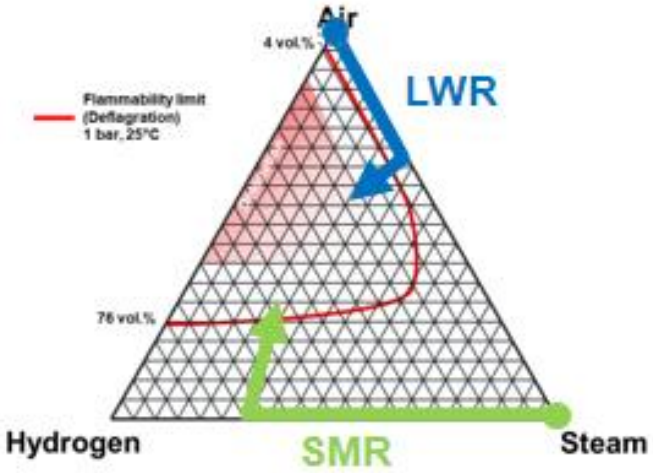

Figure 5. Shapiro diagram for hydrogen flammability indicating the pathways in large PWRs and iPWRs.

3.4. Source Term

3.4.1. Aerosol characteristics

The characteristics of aerosol particles formed during severe accidents would depend, among other things, on the type and stage of the accident, the conditions (temperature, pressure, gas atmosphere) during fission product release, as well as fuel type and burnup. It has not been conclusively shown what would be the main aerosol characteristics. To date, the best summary of aerosol particles formed during severe accidents, partly based on samples from the Phèbus FPT tests, has been given by Kissane [16] showing that " … a particle comprising one-third metal, one-third metal oxide and one-third a mixture of fission-product species would not be out of place in any potential reactor-accident sequence. Particle shapes appear relatively compact without branching chain-like structures. On size and structure, aerosols in the upstream part of the primary circuit would comprise a near-lognormal population with aerosol mass median diameter (AMMD) no more than 2 μm and geometric standard deviation around 2, particles comprising agglomerates of highly-coordinated clusters as small as 0.1 μm". However, as the author points out, the results are based on samples which could have undergone changes before analysis and thereby could have shown different characteristics once air-borne in the reactor coolant system or containment.

In this work, VTT will review experimental data on aerosol characteristics from a series of experiments in VTT FP transport and VTT EXCI-PC facilities, representing conditions in the primary circuit, Figure 6 [17]. It is especially emphasized that particle shape is important in the confined spaces of iPWRs and in filtering devices as it affects particle transport significantly. The aim of this work is to assess the data in relation to the postulated severe accident conditions in both designs 1 and 2.

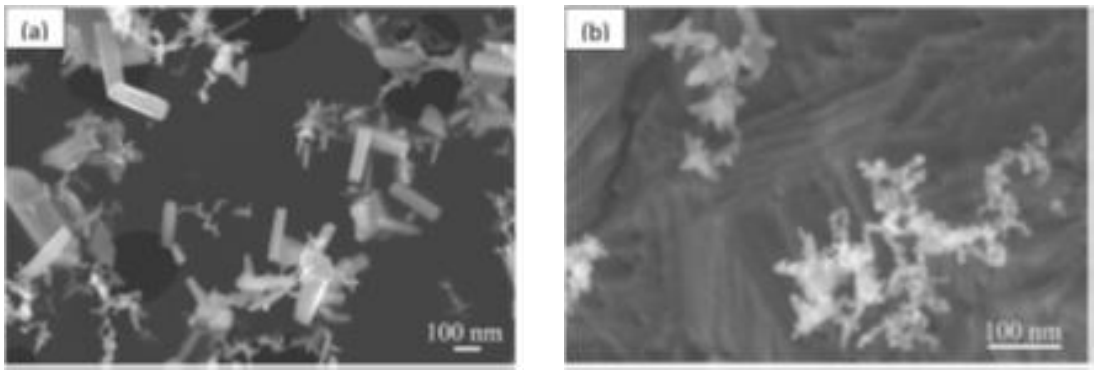

Figure 6. Examples of particle morphology from tests using simulant fission products in the VTT facilities [12].

3.4.2. In-containment source term and hygroscopic aerosol transport

iPWRs rely only on natural circulation and a large amount of water is available to cool the reactor in the case of a malfunction. Thereby it is to be expected that accident conditions are characterized by high steam fractions in the atmosphere. As aerosol particles formed by nucleation and condensation of fission products are often hygroscopic containing, e.g., CsI and/or CsOH, they grow rapidly in the high humidity, condensing atmosphere. The hygroscopic growth can be very fast accelerating the deposition of particles in the containment.

Experiments relevant to transport of hygroscopic aerosols in the condensing atmosphere have been conducted in the AHMED facility at VTT [18]. In the experiments, both hygroscopic and inert Ag aerosols were used, Table 2. It is seen that a shape factor may also have a significant effect on transport of hygroscopic aerosols. It could be noted once the aerosol particle of any shape grows by absorption of water due to hygroscopicity, it is expected that any fractal structures would collapse and they would reach a relatively spherical shape.

Table 2. An example of a comparison of the experimental results with iPWR designs 1 and 2. Data for aerosol transport in the AHMED facility [18].

Parameter	Unit	AHMED	Design 1	Design 2
Relative volume	[-]	1.0	99	2031
Relative diameter	[-]	1.0	2.8	19.7
Relative height	[-]	1.0	16	8.2 + 8.1
Pressure	[MPa]	0.1	> 0.01 – 1.0	0.1 – 1.0
Temperature	[°C]	17-51	15 – 180	15 – tbd
Relative humidity	[%]	7.3-97	Up to 100	Up to 100
D_p	[µm]	2.1-2.7	Sequence analysis	Sequence analysis
GSD	[-]	1.7	Sequence analysis	Sequence analysis
Aerosol material		CsOH, NaOH, CsI, Ag, CsOH+Ag	Mixture	Mixture

Stokes number	[-]	<< 0.1	Sequence analysis	Sequence analysis
Reynolds number	[-]	Not measured	Sequence analysis	Sequence analysis
Shape factor	[-]	1.0	Unknown, could be close to 1	Unknown, could be close to 1

3.4.3. Pool scrubbing of aerosols

With large amounts of water present in the accident situations, it is likely that retention of radioactive compounds by pool scrubbing can be significant in iPWRs for reducing potential release of activity. For example, in design 1, in the case of containment by-pass the radioactive compounds maybe transported to the reactor pool where pool scrubbing would take place.

For assessment of the experimental data for pool scrubbing, synthesis of more than 20 experimental programs on pool scrubbing ranging in time from the 1980's to 2016 has been conducted. Database is built on public access documents including information about the particles, carrier gas, and water pool characteristics [19,20]. Pool scrubbing experimental programs have been qualified in three categories: QfV (Qualified for Validation), UfU (Useful for Understanding), and NU (Not Useful). In the next step, the conditions prevailing in iPWR will be determined, and the comparison between iPWR and large LWR phenomena will be carried out. Applicability of the experimental data to iPWR conditions will then be assessed based on the analysis and comparison, and potential data needs identified.

3.4.4. Iodine chemistry

Iodine being one of the most significant fission products due to its volatility, reactivity and radio-toxicity, it is important to assess its behaviour in iPWRs [21,22,23]. The knowledge of both fission product chemistry, including iodine, and mitigation, e.g., pool scrubbing and porous media filters, will be assessed, and the applicability of the data to iPWRs determined. If new data needs are identified, it is possible to define new experiments to be carried out to generate the missing data.

3.5. Ex-Vessel Cooling and Degradation

iPWRs are designed to be able to cope with any accident conditions without breach of the reactor vessel. However, as it is not yet possible to totally exclude the possibility of a vessel breach, experimental data for ex-vessel phenomena are included in the work in a limited scope. For this, the applicability of the OECD-MCCI and DISCO-L2 experiments will be reviewed and evaluated [24]. Scenario analyses for designs 1 and 2 will be used to determine if ex-vessel phenomena are of significance for iPWRs.

4. SUMMARY

The applicability of existing large LWR severe accident experimental database for two generic iPWR designs is under assessment in SASPAM-SA project. In this work, we have developed a methodology to assess the applicability of the data. Based on DBA and postulated severe accident scenarios for designs 1 and 2, the main boundary conditions and the specific phenomenological features of the two selected iPWR designs are determined. Comparison with experimental data is currently on-going using the main parameters and dimensionless numbers determined based on the governing equations for each phenomenon. Comparison with DBA and severe accident conditions for the iPWR designs 1 and 2 can be done using a table (or plot) in which all the main parameters and, when deemed useful, dimensionless numbers are presented.

The assessment work is divided into four phenomenological areas, namely in-vessel, containment, source term and ex-vessel phenomena. In addition, in this paper natural circulation was presented as its own area due to its importance in the investigated iPWR designs. First results of the assessment work are presented with a description of further work. Classification of the data to applicable, extendable and non-useful will be done to define any further experimental data needs. A close link with the SEAKNOT project will be maintained to include iPWR specific phenomena in the severe accident research roadmap.

ACKNOWLEDGMENTS

Project funded by

Schweizerische Eidgenossenschaft
Confédération suisse
Confederazione Svizzera
Confederaziun svizra

Swiss Confederation

Federal Department of Economic Affairs, Education and Research EAER
State Secretariat for Education, Research and Innovation SERI

This work has received funding from the Swiss State Secretariat for Education, Research and Innovation (SERI)

Funded by the European Union

Funded by the European Union. Views and opinions expressed are however those of the author(s) only and do not necessarily reflect those of the European Union or European Commission-Euratom. Neither the European Union nor the granting authority can be held responsible for them.

REFERENCES

1. https://www.saspam-sa.eu/. Accessed on January 17, 2024.
2. SMR Regulators' Forum Pilot Project Report: Considering the Application of a Graded Approach, Defence-in-Depth and Emergency Planning Zone Size for Small Modular Reactors, January 2018
3. F. Mascari, B.G. Woods, K. Welter, F. D'Auria, A. Bersano, P. Maccari, Small modular reactors and insights on passive mitigation strategy modeling, Nuclear Engineering and Design, Volume 401, January 2023, 112088, doi.org/10.1016/j.nucengdes.2022.112088
4. Longze Li, Tae Woon Kim, Yapei Zhang, Shripad T. Revankar, Wenxi Tian, G.H. Su, Suizheng Qiu, MELCOR severe accident analysis for a natural circulation small modular reactor, Progress in Nuclear Energy, Volume 100, September 2017, Pages 197-208, doi.org/10.1016/j.pnucene.2017.06.003
5. F. Mascari, et al., Scaling-up assessment of natural circulation phenomena in integral Small Modular Reactor by TRACE code, Nuclear Engineering and Design, 420. doi.org/10.1016/j.nucengdes.2024.113018
6. European SMR pre-Partnership Report, Workstream 5 – Research, Development, and Innovation Roadmap, June 2023, (https://snetp.eu/wp-content/uploads/2023/07/European-SMR-pre-Partnership-WS5-report-and-roadmap-30-June-2023.pdf
7. F. Mascari, G. Vella, B. G. Woods, F. D'Auria, Analyses of the OSU-MASLWR Experimental Test Facility. Sci.Techn. of Nuclear Inst., 2012, 528241, doi.org/10.1155/2012/528241.
8. M. Steinbrück, M. Große, L. Sepold, J. Stuckert, Synopsis and outcome of the QUENCH experimental program. Nucl. Eng. Design, 240, pp. 1714-1727, doi.org/10.1016/j.nucengdes.2010.03.021.
9. Sepold, L.; Hering, W.; Homann, C.; Miassoedov, A.; Schanz, G.; Stegmaier, U.; Steinbrück, M.; Steiner, H.; Stuckert, J., Experimental and computational results of the QUENCH-06 test (OECD ISP-45). Forschungszentrum Karlsruhe, Wissenschaftl. Berichte FZKA 6664. doi: 10.5445/IR/270057214.
10. Miassoedov A., Cron T., Gaus-Liu X., Palagin A., Schmidt-Stiefel S., Wenz T., LIVE Experiments on Melt Behaviour in the Reactor Pressure Vessel Lower Head. In Proc. HEFAT2011, 8th International

Conference on Heat Transfer, Fluid Mechanics and Thermodynamics, 11 – 13 July 2011, Pointe Aux Piments, Mauritius.

11. Miassoedov A., T. Cron, J. Foit, S. Schmidt-Stiefel, T. Wenz, I. Ivanov, D. Popov, Results of the LIVE-L1 Experiment on Melt Behaviour in RPV Lower Head performed within the LACOMERA Project at the Forschungszentrum Karlsruhe, 15th International Conference on Nuclear Engineering, Nagoya, Japan, April 22-26, 2007, ICONE 15-10227.
12. Miassoedov A., H. Alsmeyer, L. Meyer, M. Steinbruck, P. Grudev, Ivanov I., G. Sdouz, Results of the QUENCH-L2, DISCO-L2, and COMET-L2 Experiments Performed Within the LACOMERA Project at the Forschungszentrum Karlsruhe, ELSEVIER, Nuclear Engineering and Design, 238, 2008, pp.2017-2026. https://doi.org/10.1016/j.nucengdes.2007.11.015.
13. D. Paladino, R. Kapulla, S. Paranjape, S. Suter, M. Andreani, PANDA experiments within the OECD/NEA HYMERES-2 project on containment hydrogen distribution, thermal radiation and suppression pool phenomena. Nucl. Eng. Design, 392, 111777. doi.org/10.1016/j.nucengdes.2022.111777.
14. S. J. Weber, E. M. Mullin, Severe Accident Phenomena: A Comparison Among the NuScale SMR, Other Advanced LWR Designs, and Operating LWRs. Nucl. Technology, 206, 1351-1360. DOI: doi.org/10.1080/00295450.2020.1756160.
15. 10. Z. Liang, M. Sonnenkalb, A. Bentaïb, M. Sangiorgi, Status Report on Hydrogen Management and Related Computer Codes. NEA/CSNI/R(2014)8.
16. M.P. Kissane, On the nature of aerosols produced during a severe accident of a water-cooled nuclear reactor. Nucl. Eng. Design, 238, 2792-2800 (2008). https://doi.org/10.1016/j.nucengdes.2008.06.003.
17. T. Kärkelä, I. Kajan, U. Tapper, A. Auvinen, C. Ekberg, Ruthenium transport in an RCS with airborne CsI, Progr. Nucl. Energy, 99, 2017, 38-48, https://doi.org/10.1016/j.pnucene.2017.04.019.
18. J.M. Mäkynen, J.K. Jokiniemi, P.P. Ahonen, E.I. Kauppinen, R. Zilliacus, AHMED experiments on hygroscopic and inert aerosol behaviour in LWR containment conditions: experimental results. Nucl. Eng. Design 178, 45-59 (1997). https://doi.org/10.1016/S0029-5493(97)00174-X.
19. L.E. Herranz, F. Sanchez, S. Gupta, Validation Matrix for Pool Scrubbing Models. Nucl. Technology, 209, doi.org/10.1080/00295450.2022.2122679.
20. S. Gupta, L.E. Herranz, L.S. Lebel, M. Sonnenkalb, M. Pellegrini, C. Marchetto, Y. Maruyama, A. Dehbi, D. Suckow, T. Kärkelä, Integration of pool scrubbing research to enhance Source-Term calculations (IPRESCA) project – Overview and first results, Nuclear Engineering and Design 404, 2023, 112189, ISSN 0029-5493, https://doi.org/10.1016/j.nucengdes.2023.112189.
21. S. Dickinson, F. Andreo, T. Karkela, J. Ball, L. Bosland, L. Cantrel, F. Funke, N. Girault, J. Holm, S. Guilbert, L.E. Herranz, C. Housiadas, G. Ducros, C. Mun, J.-C. Sabroux, G. Weber, Recent advances on containment iodine chemistry. Progr. Nucl. Energy, 52, 128-135. doi.org/10.1016/j.pnucene.2009.09.009.
22. Farhat, M et al., Chemical Engineering Research and Design 191, 646-657 (2023). https://doi.org/10.1016/j.cherd.2023.02.004
23. Leloire M et al. J Hazard Mater 416:125890 (2021). https://doi.org/10.1016/j.jhazmat.2021.125890 ; Leloire M et al. Chem Eur J 28(14): e202104437 (2022). https://doi.org/10.1002/chem.202104437.
24. Farmer, M. T., Lomperski, S., Kilsdonk, D. J., Aeschlimann, R. W., Basu, S., OECD MCCI project final report, February 28, 2006. OECD/MCCI-2005-TR06. doi.org/10.2172/1014859.

PAUL SCHERRER INSTITUT

PSI



Terttaliisa Lind :: Paul Scherrer Institute

A. Bersano, F. Mascari, ENEA; L.E. Herranz, CIEMAT; N. Chaumeix, CNRS; E. Reinecke, FZJ; P. Nerisson, IRSN; P. Kudinov, KTH; M. Constantin, RATEN; D. Gumenyuk, SSTC; I. Ivanov, TUS; T. Kärkelä, VTT

SASPAM-SA: Assessment of the relevance and applicability of existing experimental databases to iPWR

ERMSAR2024, KTH, Stockholm, May 13-16, 2024

In this presentation

- **Brief introduction of SASPAM-SA**
- **WP3: Applicability of experimenal data to iPWR**
- **Investigated iPWR designs 1 and 2**
- **Process to review the data**
- **Examples:**
  - Natural circulation
  - Aerosol transport
  - Data review: pool scrubbing
- **Next steps**



SASPAM-SA

- **Key objective of SASPAM-SA:**
  - To investigate **applicability and transfer of the operating large-LWR reactor knowledge** and know-how to the near-term deployment of integral PWR (iPWR), in the view of Severe Accident and Emergency Planning Zone (EPZ) European licensing analyses needs
- **Key outcomes of SASPAM-SA :**
  - To be supportive for the iPWR licensing process by bringing up key elements of the safety demonstration
  - To speed up the licensing and siting process of iPWRs in Europe

More information about SASPAM-SA in session 4.2:

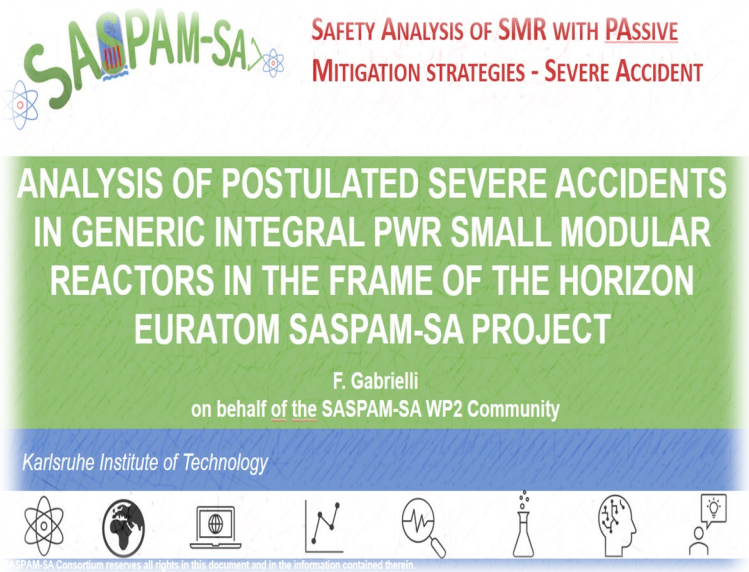

SASPAM-SA

- **Euratom project 2022-26 (4 years)**
- **23 partners from 13 European countries**



SASPAM-SA WP3: Experimental data

- **Applicability and transfer of existing severe accident experimental database for iPWR assessment (EXP)**
- **The main objectives**:
  - To assess the relevance and applicability of existing experimental database to iPWR
  - To develop methods to extend the applicability of data
  - To identify the need for new experiments
- **Needed background:**
  - Boundary conditions and specific iPWR features => WP2
  - Conditions in the RPV and containment during the accident

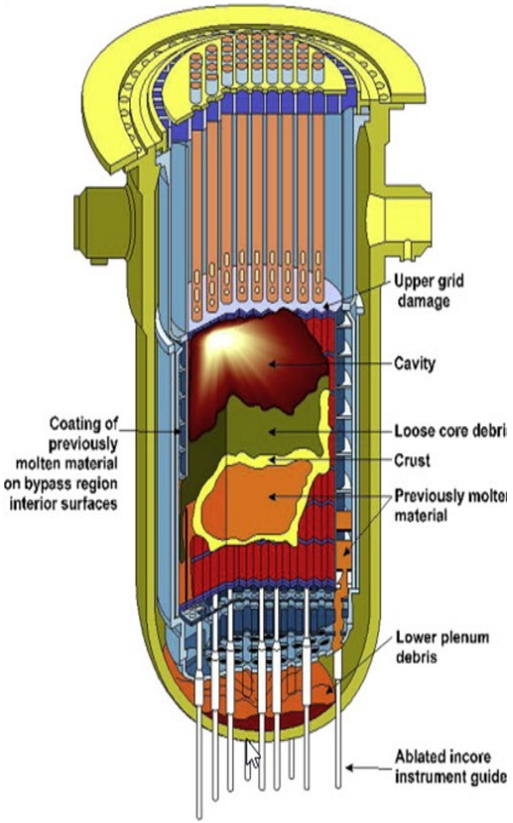

SASPAM-SA WP3: Phenomena to investigate

Partner	In-vessel	Ex-vessel	Containment	Source term
ENEA	Natural circulation			
RATEN	Re-flooding	Corium cooling		
SSTC	Degradation and coolability			
KTH	Debris, liquid melt, FCI		Pool T	
TUS	Melt pool	Coolability		
CIEMAT				Pool scrubbing
IRSN	Natural circulation (passive systems)			Iodine behavior, pool scrubbing
CNRS			Combustion risk	
FZJ			PAR	
PSI				Aerosol transport
VTT				Aerosol properties

iPWR designs 1 and 2

Design 1: iPWR, a submerged containment, about 60 MWe

Design 2: iPWR, several passive systems, a dry containment, about 300 MWe

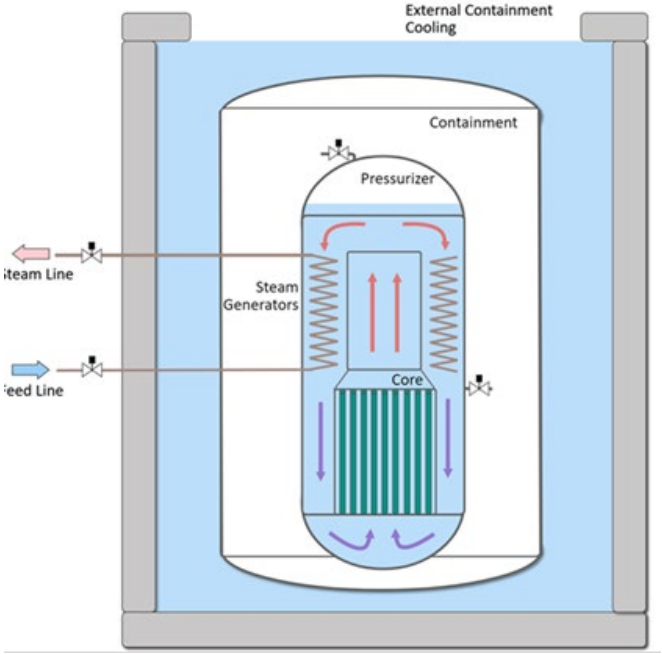

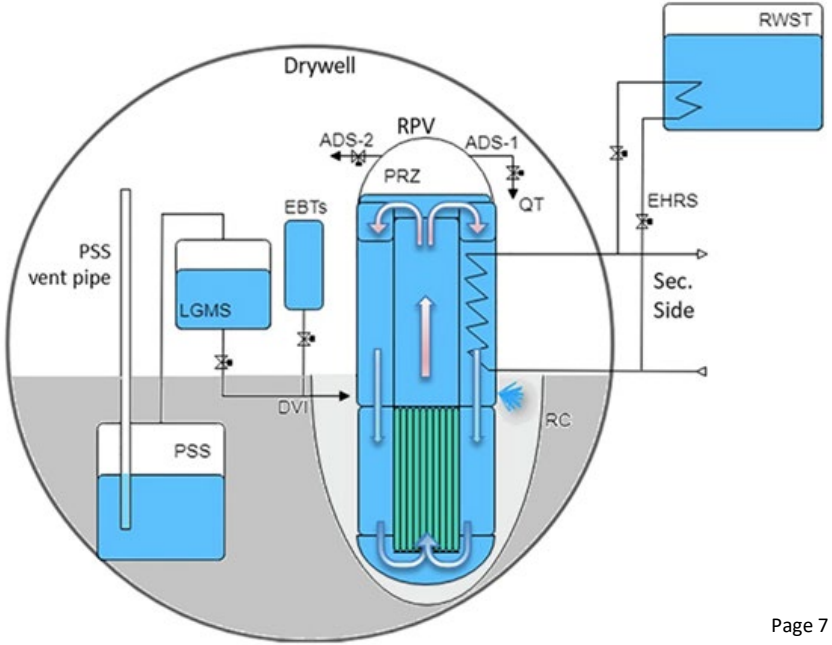

WP3: Process to review experimental data

Define phenomenon

Main equations: which equations determine phenomenon
Parameters: which are the main parameters defining the phenomenon
Dimensionless numbers: which dimensionless numbers are most significant to the phenomenon

Define experiments / facilities

- Scaling factor of the facility
- Boundary conditions in the tests
- Measurements: which properties have been measured
- Values of the main parameters and dimensionless numbers in experiments

iPWR boundary conditions

- Boundary conditions in the iPWR during the times when the phenomenon is important
- Values of the main parameters and dimensionless numbers in iPWR

Comparison of iPWR and data

- Compare the boundary conditions, main parameters and dimensionless numbers in iPWR and experiments
- A good way to do this could be a table in which iPWR and experiments parameters are compared

Distribute the experimental data into categories

- 1: Data are applicable to iPWR
- 2: Data maybe applicable but methods need to be developed for adaptation
- 3. Data are not applicable

Data review: Natural circulation #1

- **Step 1**. Define phenomenon: Natural circulation
- **Step 2**. Define facility: OSU-MASLWR (OSU)
  - It is scaled 1:254.7 with respect to the MASLWR design

	Test	Test Type
DOE	OSU-MASLWR-001	Inadvertent Actuation of 1 Submerged ADS Valve
	OSU-MASLWR-002	Natural Circulation at Core Power up to 210 kW
	OSU-MASLWR-003A	Natural Circulation at Core Power of 210 kW
	OSU-MASLWR-003B	Inadvertent Actuation of 1 High Containment ADS Valve
IAEA	ICSP test SP-2	Loss of Feedwater Transient
	ICSP test SP-3	Power Maneuvering

Data review: Natural circulation #2

- **Step 3**. iPWR boundary conditions
- **Step 4**. Comparison of iPWR and data

DBA

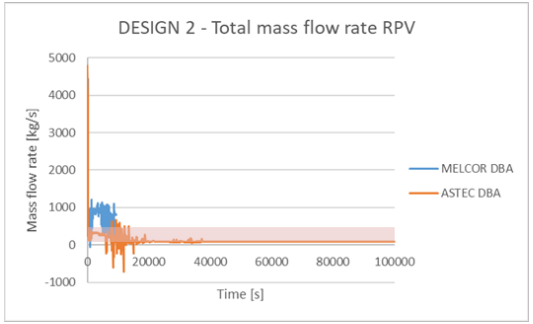

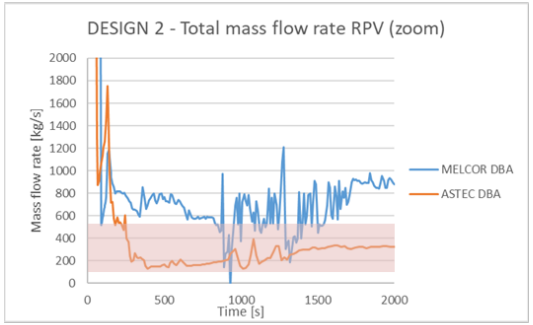

SA

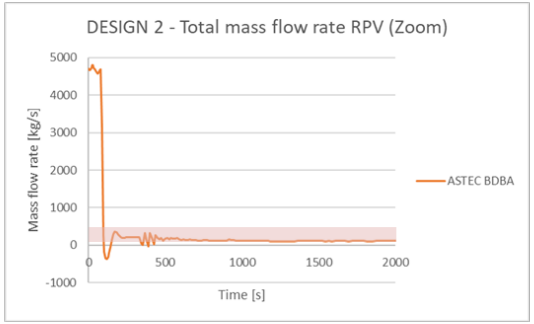

SA2

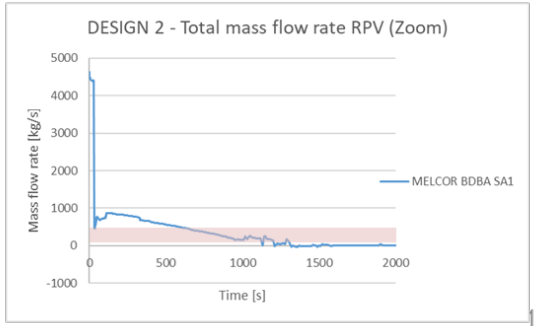

SA1

12

Data review: Natural circulation #3

- **Step 4**. Comparison of iPWR and data
  - Data extrapolation strongly depends on the reference reactor design and the scaling factor of the related experimental facility
  - A more detailed analysis based on the comparison of selected non-dimensional numbers:

Richardson number: represents the ratio of natural convection to the forced convection

$$\prod_{Ri} = \frac{\beta g (T_H - T_c)_o L_{th}}{u_{co}^2}$$

Steam generator heat transport number:

$$\prod_{SG} = \frac{q_{SG}}{q_{core}}$$

Data review: Natural circulation #4

- **Step 4**. Comparison of iPWR and data
  - Richardson number: enveloped the experimental data in narrow windows. In general, higher in Design 2
  - Steam generator heat transport number: enveloped the experimental data after the first phase of the transient

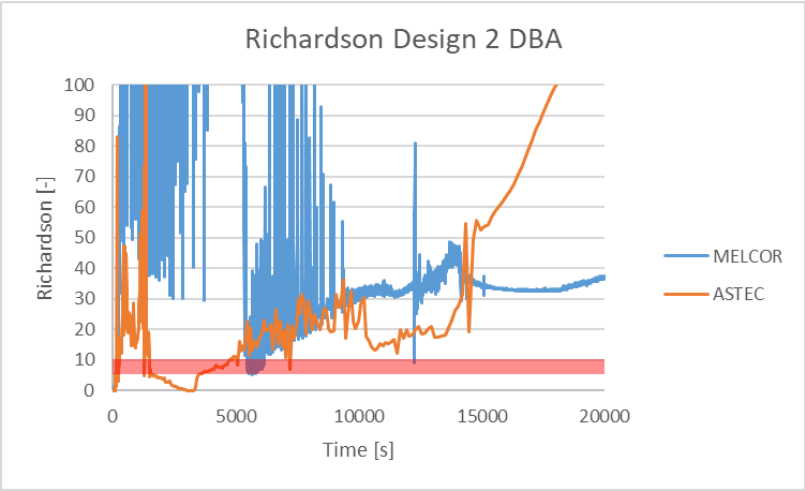

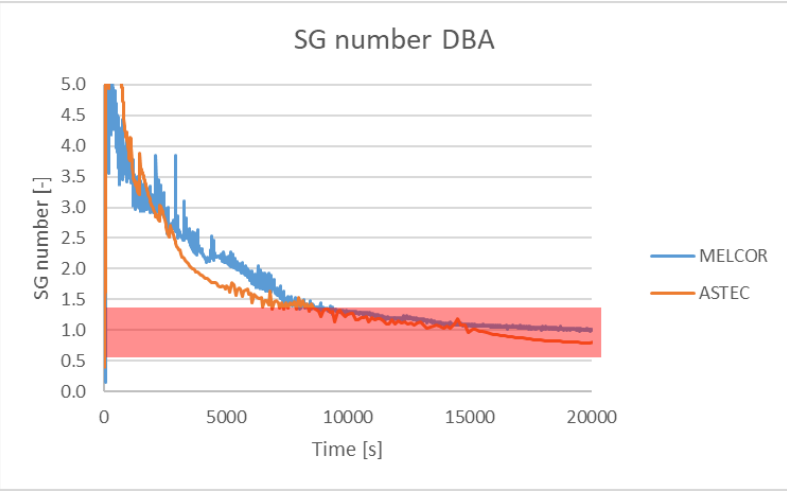

Data review: Aerosol transport #1

- **Step 1**. Define phenomenon: Depletion of hygroscopic aerosols
- **Step 2**. Define facility: AHMED (VTT)
  - Separate effect facility
  - Depletion of inert and hygroscopic aerosols in containment conditions

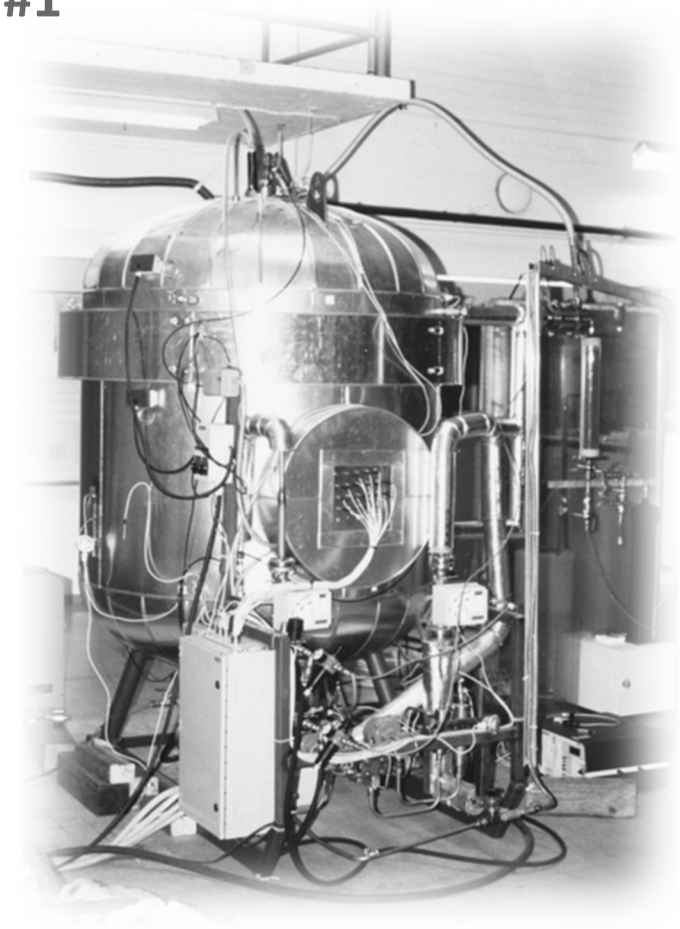

Data review: Aerosol transport #2

- **Step 1**. Define phenomenon: Dimensionless numbers

- Gravitation ⟹ $V_{ts} = \frac{\rho_p d_p^2 g C_c}{18 \mu_g}$

- Inertial effects ⟹ $Stk = \frac{\tau U_0}{d_c}$ $\quad \tau = \frac{\rho_p d_p^2 C_c}{18 \mu_g}$

- Diffusiophoresis; Stefan flow ⟹ $U_0 = -k_D D \nabla \gamma$

- Turbulent deposition, $\tau_+ \rightarrow$ Re, d^2 ⟹ $V_+ = (6 \times 10^{-4}) {\tau_+}^2$

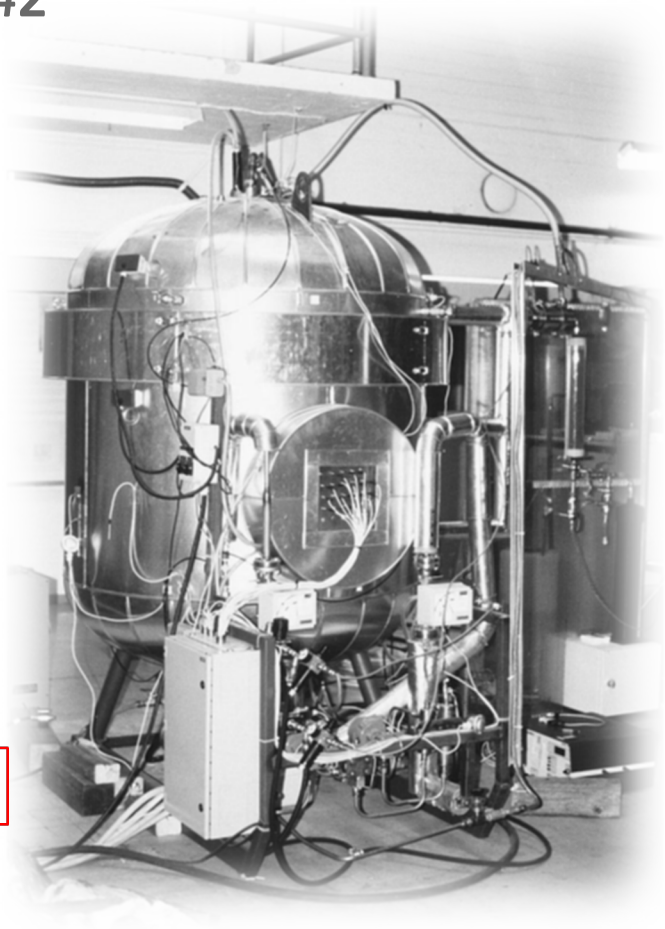

Data review: Aerosol transport #3

- **Step 1**. Define phenomenon: Dimensionless numbers

Particle growth factor:

$$G_f(RH) = \frac{D_w(RH)}{D_p(RH < 10\%)}$$

Relative humidity

$$G_f = \sqrt[3]{1 + K_R \frac{M_w}{\rho_W}\left(\frac{a_w}{1 - a_w}\right)}$$

K_R → number of hygroscopic molecules in the particle

a_w → Relative humidity

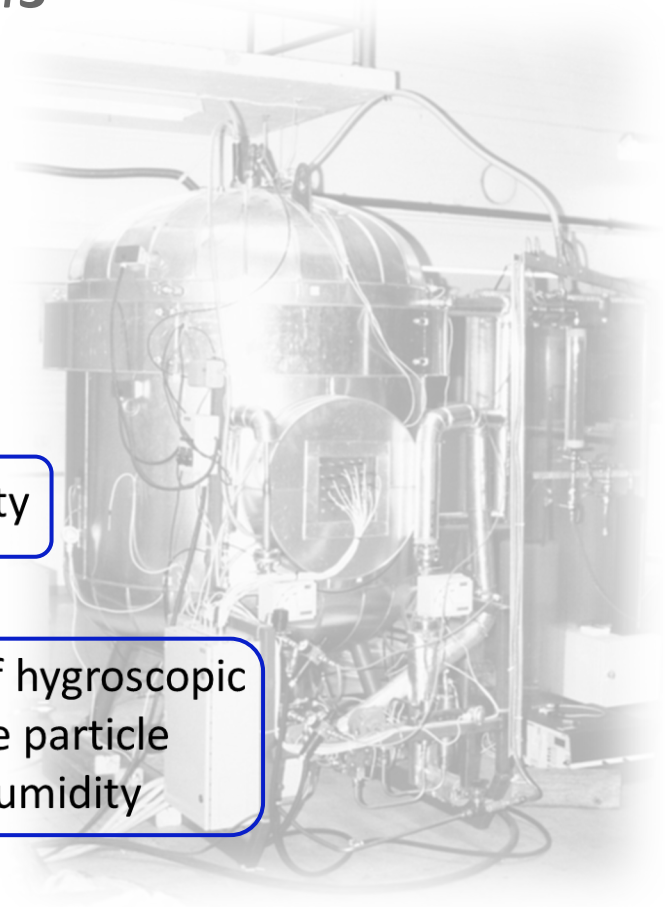

Data review: Aerosol transport #4

Step 3. iPWR boundary conditions; **Step 4**. Comparison of iPWR and data

Parameter	Unit	AHMED	Design 1	Design 2	Comments
Volume	[-]	1.0	99	2031	
Radius	[-]	1.0	2.8	20	
Height	[-]	1.0	16	8.2 + 8.1	
Pressure	[MPa]	0.1	> 0.01 – 1.0	0.1 – 1.0	BDBA
Temperature	[°C]	17-51	15 – 180	15 – 180	
Relative humidity	[%]	7.3-97	Up to 100	Up to 100	
D_p	[µm]	2.1-2.7	tbd	tbd	
GSD		1.7	tbd	tbd	
Aerosol material		CsOH, NaOH, CsI, Ag, CsOH+Ag	Mixture	Mixture	Not prototypical
Reynolds number		Not measured	From containment analysis		Exp. lower

Data review: Pool scrubbing #1

- The database 1960-2017

PROGRAM		THERMALHYDRAULICS				POOL GEOMETRICS			
		Pool temperature (K)	Pool pressure (Pa)	Gas temperature (K)	Injection pressure (Pa)	Injector configuration	Injector orientation	Injector diameter (m)	Submergence (m)
UKAEA		293 - 323	n.a.	n.a.	n.a.	Single lute	Downward	0.003 - 0.050	0.00 - 0.75
		308						0.003	0.06
		308 - 323						0.003 - 0.050	0.06 - 0.50
		323						0.050	0.5
		273 - 333	Atmospheric	n.a.	n.a.	Four lute orifices	Downward	0.1	0.305 - 0.61
		273 - 283							0.61
GE		293 - 333	n.a.	333	n.a.	Single orifice	Upward	7.0E-05 - 2.40E-04	0.343 - 1.677
		293						2.40E-04	1.677
EPRI		293	1.013E+05	n.a.	n.a.	Single orifice	Horizontal	1.27E-02	0.1 - 1.65
		373		410 - 524					1.65
EPSI		546	1.1E+06 - 6.1E+06	n.a.	n.a.	Single nozzle	Upward	1.00E-02	1 - 3
		n.a.	6.0E+05 - 6.1E+06						2
POSEIDON-I		294 - 333	n.a.	n.a.	1.01E+05 - 1.04E+05	Single orifice	Upward	5E-04 - 1.2E-02	1.0 - 4.0
JAERI		Ambient	Atmospheric	n.a.	n.a.	Single orifice	Upward	9.0E-03	1.0 - 2.0
ACE		297 - 356	1.01E+05	411 - 423	1.21E+05 - 1.50E+05	Quencher (51 holes)	Upward	9.525E-03	1.38 - 4.61
		297		n.a.	n.a.				2.6 - 4.5
LACE-España		382.3 - 385.4	2.82E+05 - 3.00E+05	397.1 - 444.3	3.28E+05 - 3.49E+05	Monoorifice / Multiorifice (9 holes)	Horizontal	1.00E-02	2.50
SPARTA		293	Atmospheric	363 - 368	n.a.	Two vents	Horizontal	0.150	1.8
RCA		386.9 - 391.5	2.30E+05 - 2.51E+05	394.9 - 414.1	2.84E+05 - 2.91E+05	Single orifice	Horizontal	1.00E-02	0.25 - 2.50
POSEIDON-II		335.9 - 363.6	Atmospheric	485.9 - 583.8	1.16E+05 - 1.71E+05	Single orifice	Upward	2.00E-02	0.3 - 4.0
AASC-PS		392.4 - 399.5	2.30E+05	377.9 - 393.4	2.7E+05 - 2.8E+05	Single orifice	Horizontal	1.0E-02	1.25
SG-Experiments	EU-SGTR	302.9 - 368.2	1.02E+05 - 1.12E+05	303.7 - 430.1	1.56E+05 - 3.96E+05	Tube break	Horizontal	1.68E-02	0.0 - 3.80
	ARTIST-I	295.0 - 297.0	Atmospheric	297 - 298.9	1.40E+05 - 4.90E+05	Tube break	Horizontal	1.670E-02	2.952 - 3.552
	ARTIST-II	298.8 - 301.3	Atmospheric	326.3 - 364.6	1.12E+05 - 4.93E+05	Tube break	Horizontal	1.67E-02	0.30
PASSAM Experiments	RSE	293 - 300	1.01E+05	Ambient	1.130E+05	Single orifice	Upward	1.00E-02	1.0
	CIEMAT	295.9 - 307.8	91860 - 92530	300.8 - 383.1	96390 - 1698890	Single orifice	Horizontal	6.53E-03 - 8.85E-03	0.3
	AREVA	353 - 404.3	2.2E+05 - 5.8E+05	n.a.	n.a.	Venturi nuzzle	Downward	n.a.	n.a.

Data review: Pool scrubbing #2

- The database 1960-2017

PROGRAM		PARTICLE/GAS CHARACTERISTICS				CARRIER GAS		
		Chemical species	AMMD (μm)	GSD	Concentration (g/m³)	Composition	Mass flow rate (kg/s)	Steam mass fraction
UKAEA		I_2	-	-	n.a.	Air / Air + Steam	Air: 5.33E-07 - 9.50E-06 (m^3/s) Steam: 4.17E-02	n.a.
		HI	-	-		Air + Steam	Air: 5.33E-07 (m^3/s)	
		CH_3I	-	-		Air + Steam	Air: 5.33E-07 (m^3/s) Steam: 4.17E-02	
		Ni / Cr	0.06	n.a.				
		I_2	-	-	n.a.	Air / Steam / Air + Steam	Air: 0.150 - 3.311 Steam: 1.179 - 3.992	0 - 1
		Cr / Ni	0.06	n.a.		Air + Steam	Air: 0.044 - 3.402 Steam: 1.134 - 4.082	0.25 - 0.963
GE		Eu_2O_3	n.a.	n.a.	0.02 - 5.5	Air (N_2)	n.a.	-
		CsI	< 0.3	n.a.	0.76 - 10.17			
EPRI		CsI / TeO_2	0.40	n.a.	n.a.	Air / Air + Steam	Air: 0.0 - 1.5E-02	0.00 - 0.95
		Sn	2.70				Air: 1.83E-03 - 1.251E-02	
		CsI	0.40					
EPSI		CsI	9.0	n.a.	15	Steam	0.03	1
		CsOH	n.a.	n.a.	n.a.		n.a.	
POSEIDON-I		I_2	-	-	n.a.	N_2	5E-05 - 6.7E-05 (m^3/s)	-
JAERI		DOP	0.3 - 10.0	n.a.	1E-03 - 1 (ppm)	Air	7.0E-05 - 2.45E-04 (m^3/s)	-
ACE		CsOH	1.74 - 2.72	1.77 - 2.26	4.70 - 9.51	N_2 + Steam	Gas: 6.37E-02 - 1.09E-01 Steam: 8.50E-04 - 2.92E-02	n.a.
		MnO	1.72 - 2.31	1.90 - 2.22	3.82 - 8.36			
		CsI	1.69 - 2.88	1.90 - 2.36	0.645 - 0.993			
		DOP	0.6	1.53	0.06 - 0.12	N_2	0.042 - 0.134 (m^3/s)	-
LACE-España		CsI	0.55 - 7.2	1.4 - 5.4	Cs: 0.064 - 0.51 I: 0.041 - 0.54	N_2 + Steam	Gas: 1.04E-04 - 7.182E-03 Steam: 7.50E-05 - 7.04E-04	0.10 - 0.90 (molar)
SPARTA		CsI	0.67	0.318	4.7 - 7.0	N_2	0.090	-
RCA		Ni	MMD: 1.11 - 1.30	1.38 - 1.44	n.a.	N_2	7.260E-03 - 7.791E-03	-
POSEIDON-II		SnO_2	0.29 - 0.54	1.36 - 1.73	n.a.	N_2 / N_2 + Steam	0.0242 - 0.0424	0.000 - 0.750
AASC-PS		Ni	2.41 - 2.77	1.46 - 1.77	n.a.	Air	4.392E-04 - 5.409E-04 (m^3/s)	-
SG-Experiments	EU-SGTR	TiO_2	2.92 - 3.70	n.a.	n.a.	N_2 / N_2 + Steam	Total: 1.76E-02 - 9.48E-02	0.0 - 77.0
	ARTIST-I	Nanophase TiO_2	2.9 - 4.6	2 - 3	n.a.	N_2	1.26E-02 - 1.79E-01	-
	ARTIST-II	SiO_2	1.4 - 3.7	n.a.	n.a.	N_2	1.39E-02 - 1.72E-01	-
PASSAM Experiments	RSE	SiO_2	0.4 - 1	1.19 - 1.3	0.035 - 0.136	Air	5.00E-03 - 6.67E-03	-
	CIEMAT	SiO_2	0.72 - 0.96	1.30 - 1.58	0.2453 - 1.243 (g/Nm³)	Air / Air + Steam	Total: 2.62E-03 - 7.63E-03 (m^3/s)	0.0 - 0.0977
	AREVA	CH_3I	-	-	1E-08 - 1E-09 (mol/l)	Air + Steam	Gas: 0.002	n.a.

CIEMAT's progress

Data review: Pool scrubbing #3

- The database 1960-2017

Experimental program	Thermalhydraulics		Carrier gas		Particle/Gas characteristics			Injector		
	Tpool	Tgas	YH2O	Flow rate	Compound	dpart	[parts]	Configuration	Diameter	Submergence
GE	x	x				x	x			x
EPRI			x	x						x
POSEIDON-I									x	x
JAERI				x			x			x
ACE	x		x		x	x				x
LACE-España			x			x		x		
RCA										x
POSEIDON-II	x		x			x				x
AASC-PS										
SG-Experiments			x	x		x				x
PASSAM-RSE				x		x				
PASSAM-CIEMAT			x	x						
PASSAM-AREVA	x									

Next steps

- Complete iPWR conditions with containment data
- Complete data analysis and comparison with iPWR
- Distribute the data into three categories:
  1. Data applicable to iPWR
  2. Data partly applicable but methods need to be developed for adaptation / extrapolation
  3. Data not applicable
- Identify possible experimental data needs / gaps in existing data

PAUL SCHERRER INSTITUT

Thank you to all the SASPAM-SA partners

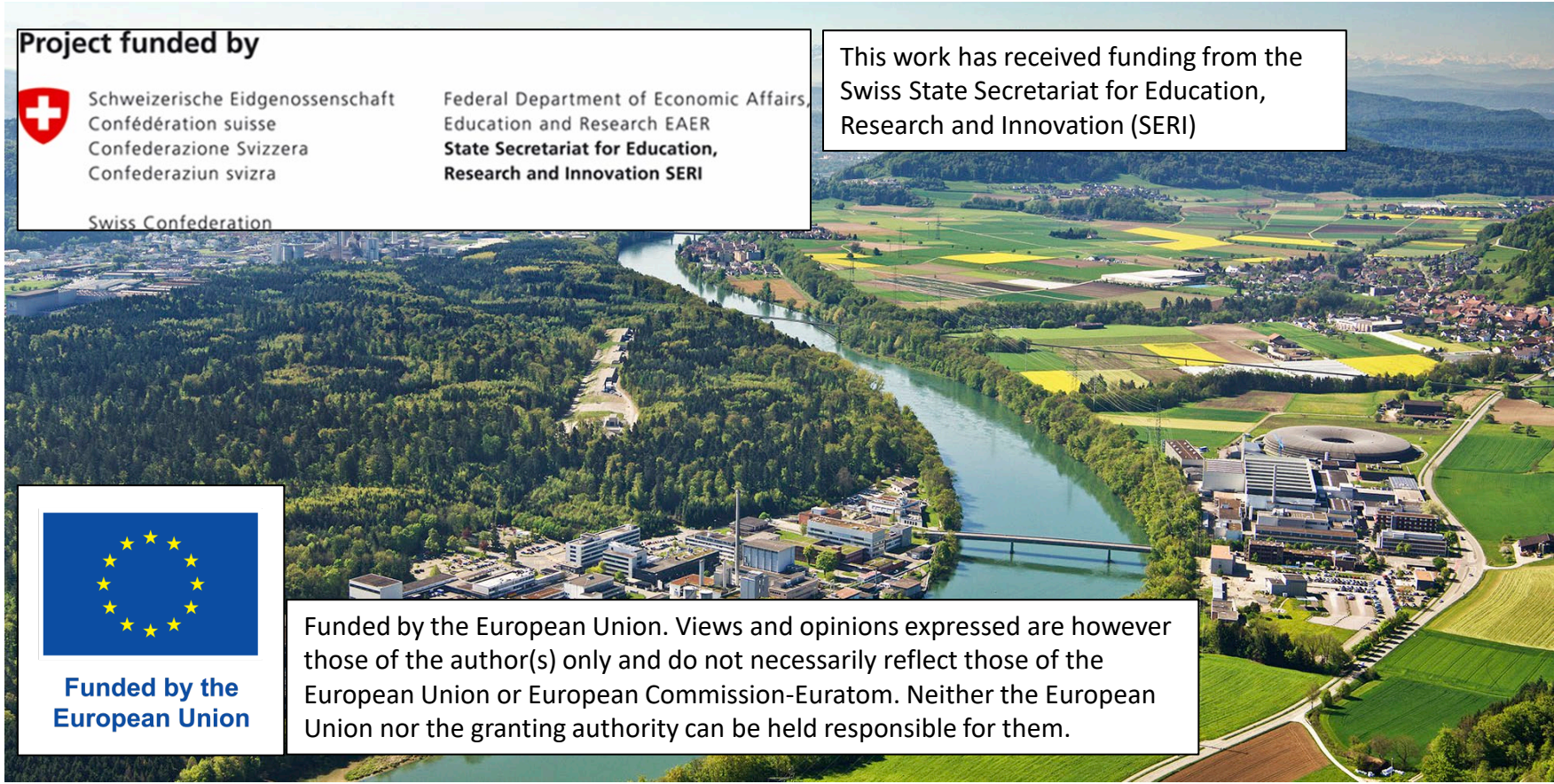

Project funded by

Schweizerische Eidgenossenschaft
Confédération suisse
Confederazione Svizzera
Confederaziun svizra

Swiss Confederation

Federal Department of Economic Affairs, Education and Research EAER
State Secretariat for Education, Research and Innovation SERI

This work has received funding from the Swiss State Secretariat for Education, Research and Innovation (SERI)

Funded by the European Union

Funded by the European Union. Views and opinions expressed are however those of the author(s) only and do not necessarily reflect those of the European Union or European Commission-Euratom. Neither the European Union nor the granting authority can be held responsible for them.

NUMERICAL INVESTIGATION OF NATURAL CIRCULATION INSIDE A SCALED-DOWN PRISMATIC MODULAR REACTOR

Marwa A. Shewitah, C. Allison, Ibrahim Ismail Ibrahim
Chemical Engineering Department, Alexandria University, Alexandria, Egypt.
Innovative System Software Company (ISS), United States.
Chemical Engineering Department, Minia University, Minia, Egypt.
eng-marwa.abozed@alexu.edu.eg, issgml97@gmail.com, Egypt.ebrahiem59@yahoo.com

Moustapha Salem Mansour, Mahmoud M. Taha
Chemical Engineering Department
Alexandria University, Alexandria, Egypt.
mansourms@alexu.edu.eg, mtaha@alexu.edu.eg

Ayah E. Elshahat
Nuclear Engineering Department
Alexandria University, Alexandria, Egypt.
ayah.elshahat@icloud.com

ABSTRACT

This study investigates codes that simulate the dynamic and thermal-hydraulic behavior that are present in the natural circulation processes inside prismatic modular reactors. The RHYS coupling ASYST VER 4 package, a crucial part of the RELAP 5 framework, is deployed to enable this emulation. The setup of the research system is a plenum-to-plenum facility with two vertical pipes that are intended to imitate the radial temperature gradients found in prismatic modular reactors (PMR) cores. By implementing a range of uniform iso-flux (200 to 1400W/m^2) and distinct outer surface temperatures (278 to 308K), axial temperature distributions were analyzed to provide a comprehensive assessment of the heat transfer in the heated and cooled channels. As a result of spontaneous convection, temperature and velocity reversals were seen following maximum spots. The flux of 1400W/m^2 records a temperature increase from the entrance by 63.6 and 51% for the air and the wall, respectively, while the flux of 200W/m^2 gives a smaller increase of 14.6 and 14%. Also, the air and inner wall temperatures were impacted by 85 and 81%, respectively, as the temperature rose 30 degrees from 278 to 308K. There was a small effect of elevating the cooling temperature on the air velocity, although the high temperature of 308K was the highest one. The Nusselt number is calculated using heat transfer coefficients, which are a representation of convective heat transmission. Furthermore, data from additional literature sources shows significant agreement with the RHYS model.

KEYWORDS
RELAP 5; RHY; ASYST; Natural Circulation; Prismatic Modular Reactor

1. INTRODUCTION

The current global interactions force us to search for new energy sources with high productivity, low operating and capital costs, sustainability, and inherent safety features. This is absolutely the IV nuclear generation reactor developed for, such as the Prismatic Modular Reactor (PMR).

Prismatic Modular Reactors have high output temperatures, and a small footprint, and can connect directly to the electric production cycle in the Brayton cycle, decreasing heat loss. The high outlet temperature of the PMR affords high-efficiency electrical generation and the use of nuclear power for potential process heat applications, especially carbon-free hydrogen production, where hydrogen production represents a major potential use for Gen IV systems [1]. Safety has been given top priority since the occurrence of the accident at the Fukushima power plant in 2011 [2]. As a result, Gen IV concentrates on naturally eliminating decay heat in the event of an accident while avoiding the release of significant quantities of radioactive material [3]. During the stoppage of flow owing to loss of power supplies, failures of the initial circulating equipment, or loss of grid loads, natural circulation is the predominant mechanism of transferring heat inside the core, resulting in a reversal in temperature and flow. The natural circulation circumstance is triggered by a complete gas flow loss, which eliminates forced convection through the core. It is hypothesized that when gas inertia reduces, the flow through some core channels will reverse and transition to intra-core recirculation [4]. Many reactors, such as AHWR [5], CHTR [6], CAREM [7], and ESBWR [8], are examples of advanced reactors that rely on passive ideas to remove nominal fission heat without the need for mechanical pumps [9].

Due to the extremely high expense of experiments in the fields of design, operation, licensing, and safety assessment of nuclear power plants, system codes have been employed to imitate the natural circulation within nuclear reactors [9]. The new program RHYS [10, 11] is relevant to RELAP 5 and represents a graphical user interface used in this study to simulate a plenum to plenum dual channel facility representing the outer and inner cooling areas in the Prismatic Modular Reactor (PMR) core with scale-down geometries that were designed and constructed by a scientific team at Missouri University [12-20].

The main objectives of this work are to conduct a validated code to simulate different conditions for the Prismatic Modular Reactor core that happened during the loss of flow (LOFA). This is done by applying several heat fluxes and different outer temperatures to simulate the real situation. The results of utilizing such conditions on the temperature and velocity are studied inside the hot and cold channels. The code in this work is used to build a model for a natural circulation loop based on real dimensions, and the result has been validated with open-literature empirical works.

2. SYSTEM SETUP

The plenum-to-plenum facility was designed and established by the Missouri S&T University Multiphase Reactors Engineering and Applications Laboratory (MReal) research team [12-20]. This developed facility consists of two vertical channels connecting in an analogous way to the PMR's core coolant channels, representing the hot and cold areas in the core. The dimensions of the components of this facility are introduced in Missouri’s drawing in Fig. 1. Meanwhile, a detailed description of the facility can be found elsewhere [12-20].

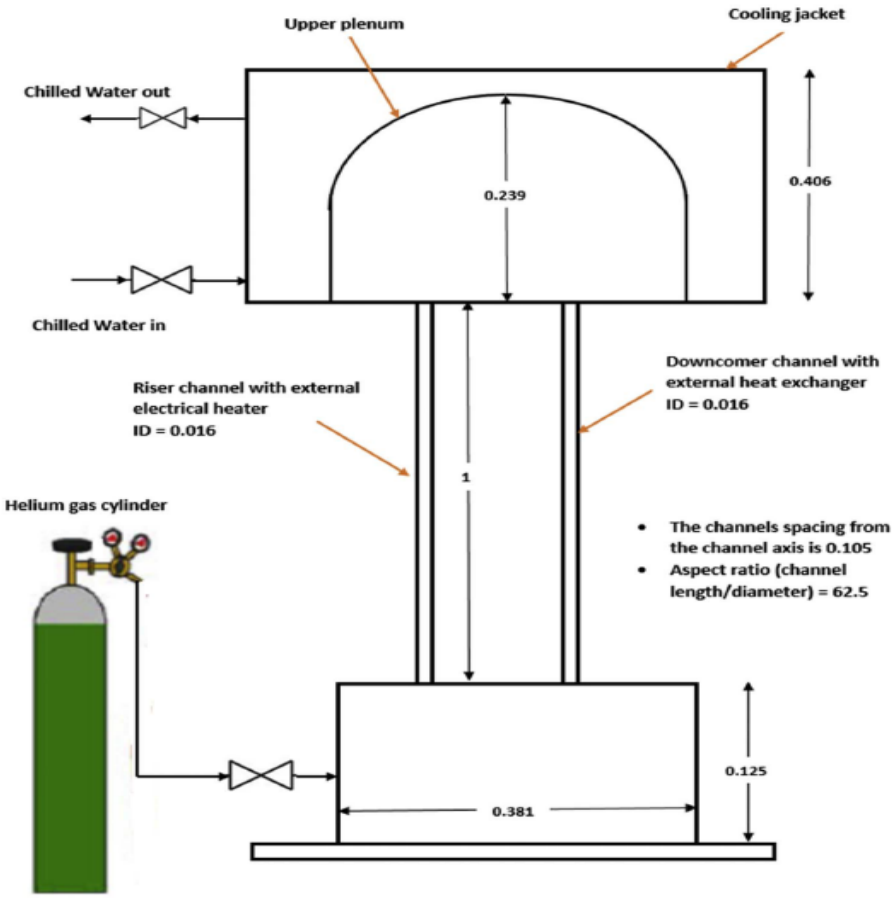

Figure 1. Missouri S&T Plenum-to-Plenum Facility (P2PF) [12-20].

3. NODALIZATION USING RHYS PROGRAM

RHYS program [10, 11] represents a new graphical user interface (GUI) for the ASYST VER 4, supporting users to improve the efficiency of system code modeling, simulation, and post-processing.
To simplify the modeling work, a nodalization flowsheet of the system was built by converting any part into blocks and giving each part a specific number or symbol. An initial nodal was made manually, and then it was transferred to the RHYS program, by choosing a suitable volume or block that matches the specific system. The RHYS's user can give a suitable number and name while also inputting the boundary (dimensional) and initial conditions and connecting the volumes or RHYS's blocks by junctions, as seen in Fig. 2, which represents the nodalization of the current system. The hot pipe has been modeled as an annulus (120) with 50 control volumes and 50 heat structures; also, the cooled pipe is modeled as an annulus (150) and has been divided into 50 control volumes and 50 heat structures; and the surrounding cooling channels were divided into 50 volumes and 50 heat structures. The upper plenum was divided into 5 stacked annulus with different diameters to simulate the hemispherical shape of the upper plenum (140); the outer cooling jacket (145) was divided into 3 annulus volumes; and the lower plena (100) was simulated as a single volume. Table I, represents the numbering details for all the system components and connections. The system dimension (boundary condition) and the initial operating condition were integrated for each volume. The power input for the electrical heater simulation. Therefore, 15000 sec (4.17 hrs.) was adjusted to be the end time for the RHYS operation for every single run, depending on each specific condition of steady state.

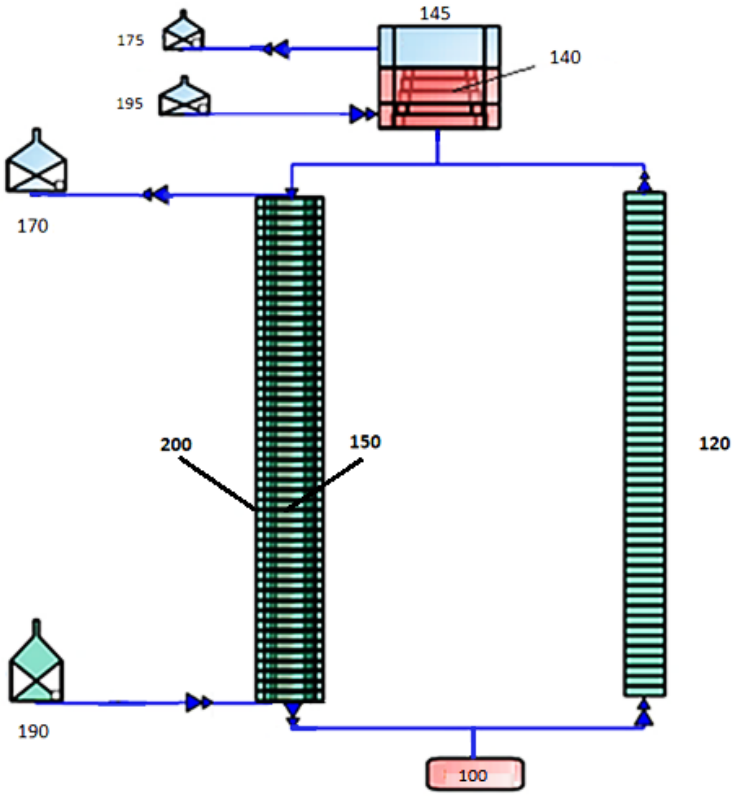

Figure 2. System nodalization by the RHYS program.

Table I. Nodalization Volumes

No.	Type	Description
100	Single Volume	Lower plenum
120 (1:50)	Annulus	Riser channel
140 (1:5)	Annulus	Upper plenum
145 (1:3)	Annulus	Upper plenum water cooling jacket
150 (1:50)	Annulus	Downcomer channel
170	Single Volume	Downcomer cooling water out
175	Single Volume	Upper cooling jacket water out
190	Time-Dependent Volume	Downcomer cooling water in
195	Time-Dependent Volume	Upper cooling jacket water in
200 (1:50)	Annulus	Water jacket

4. RESULTS AND DISCUSSION

4.1. Flux Impact

Several models have been conducted to examine the effects of 200–1400 W/m^2 of iso-flux heating intensity on the P2PF's air temperature and velocity at atmospheric pressure.

4.1.1. Temperatures

Fig. 3, displays the axial distribution of air and inner wall surface temperatures at various heating intensities (200, 600, 1000, and 1400W/m^2). It is demonstrated that the inner wall surface temperature of the heated channel rises for all heating intensity from the leading edge to a certain nondimensional axial point (Z/L) where the maximum temperature is seen. The surface temperature drops after this point in the direction of the channel exit (Z/L =1). This discovery aligns with previous research results [21-25]. According to the references, this inflection of the surface temperature is one of the key indicators of flow instability (i.e., a change in the flow regime or a reversal of the flow), highlighting the unstable character of buoyancy-driven flow [21, 24, 26, 27]. RHYS and the other's experiment [19] showed good agreement, with an average absolute relative error (AARE) of ±0.22% to ±1.14%.
The percentage increase and decrease in temperature from the inlet to the outlet of the hot and cooled pipes for the air and the inner wall are discussed in Fig. 4. The percentage ascending and descending in temperature increases as the heat flux increases, giving the highest increase at 1400W/m^2 with 63.6 and 51% for the air and the wall, respectively, while the flux at 200W/m^2 gives the least with 14.6 and 14% for the air and the wall, respectively. Furthermore, it shows that as the heat flux increases, the difference between the fluid and the surface temperature elevation increases. Also, it is observed that the air is more affected by heat transfer than the inner wall, although the temperature of the wall is higher than that of the air, as illustrated in Fig. 3. This is due to the heat loss from the connections at both ends of the hot pipe to the upper and lower plenum and the big temperature difference. Also, P2PF is fabricated from stainless steel, which causes a high heat dissipation by conduction at the hot pipe ends.
The same observations were found at the cooled pipe, where the air gives a higher temperature decrease (represented by a negative sign) than the wall and the highest percent decrease, as introduced in Fig. 4. This is because the heat conducts from the hot pipe connection to the upper and lower plenum. The flux of 1400W/m^2 gives a 20.4% and 19.11% temperature decrease for the air and the wall, respectively, while the flux of 200W/m^2 gives a decrease of 3.82% and 3.39% for the air and the wall, respectively.

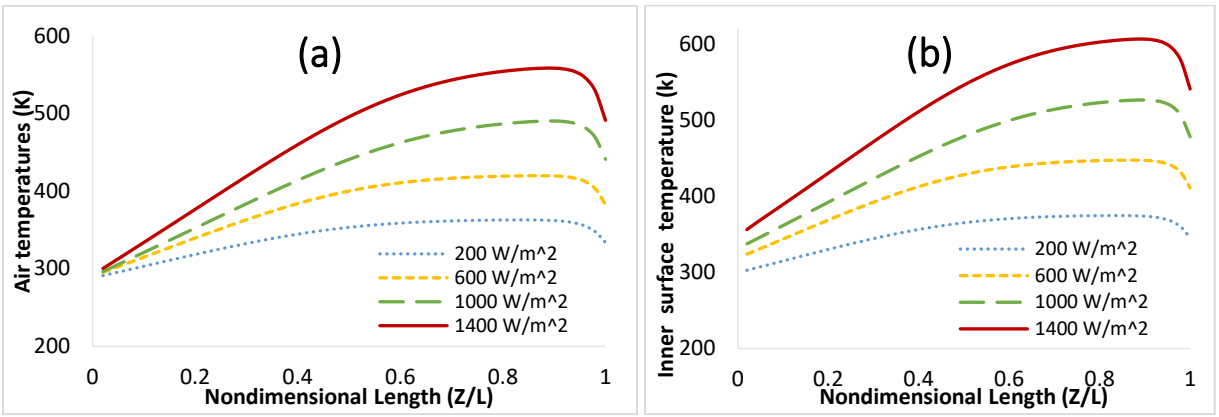

Figure 3. Axial temperature disruptions inside the hot pipe for (a) air temperature and (b) inner wall surface temperature.

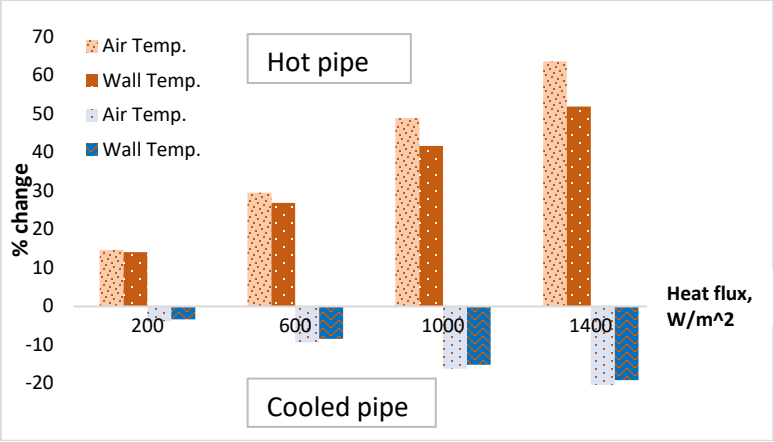

Figure 4. The percentage of air temperature changes inside the hot and cooled pipes.

4.1.2. Velocity

The flow fields in the vertical heated, which resembled the P2PF, were well characterized., Fig. 5, illustrates how velocity along the hot pipe increases from the entry until it reaches a particular point and then starts to drop until it reaches the hot pipe's exit. This pattern aligns with the temperature profiles discussed earlier. Additionally, the curves in Fig. 5, present a comparison between the RHYS code results and the experimental data obtained by Said et al.[14] validating the code. The deviation between the RHYS predicted and experimental results is presented in terms of the average absolute relative error (AARE). The relative errors for fluxes from 200W/m^2 to 1400W/m^2 are between ±2.47% and ±5.46%, which are reasonable.

It is evident that the increase in air velocity during the hot pipe is proportional to the heat flux, as seen in Fig. 6, the flux of 1400W/m^2 gives a 74.17% elevation in air velocity, while the flux of 200W/m^2 gives only 18.24%. In the same manner, the decrease (represented by a negative sign) in the velocity inside the cooled pipe is proportional to the flux, giving 4.04% and 20.98% for fluxes of 200W/m^2 and 1400W/m^2, respectively.

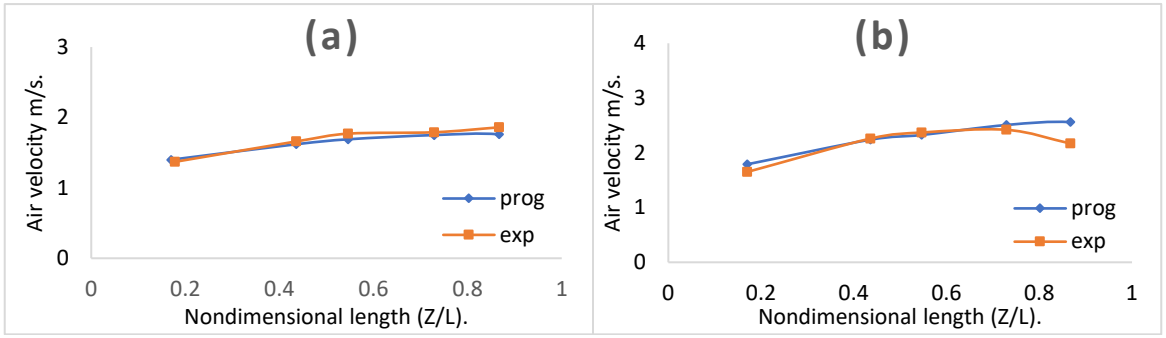

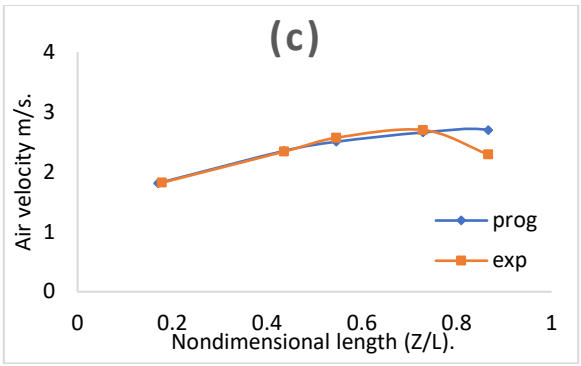

Figure 5. Experimental [14] and RHYS predicted velocity along the pipe nondimensional length (Z/L) for heat flux (a) 600W/m2, (b) 1000W/m2, and (c) 1400W/m2.

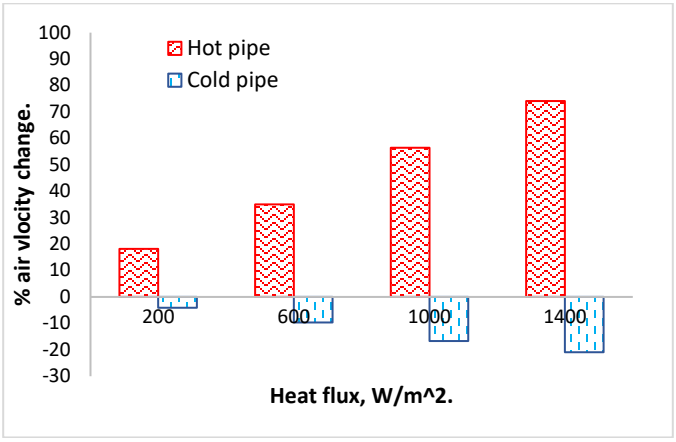

Figure 6. Velocity change in P2PF at different heat fluxes.

4.2. Outer Surface Temperatures Impact

In this section, we investigate the impact of elevating the cooling temperature by 10, 20, and 30 degrees above 278K at the cooled pipe and upper plenum, which represent the outer surface of the modular reactor, on the natural circulation inside the system that is produced during the loss of flow.

4.2.1. Within the hot channel

Different RHYS codes are initiated to study the effect of changing the outer surface temperature or the cooler fluid temperature on the PMR core. Although the PMR reactors are fully insulated, air ingress during the LOFA or any leakage or change in the coolant fluid temperature can cause a continuous change in temperature. Four different temperatures (278, 288, 298, and 308K) for cooling the upper plenum and cooled pipe are chosen to represent the ambient temperature during all the seasons and different regions. Referring to Said et al. [13], who used a heat flux of 2046W/m^2 and an air pressure of 413.685kPa in their empirical works, RHYS codes are developed at different water cooler temperatures. The impact of elevating the cooling water temperatures above 278K is calculated using the equation (1) :

$$\% \text{ Change} = \sum_{0}^{Z/L} \left(100 * \frac{T_{m,i} - T_{278,i}}{n}\right) \quad (1)$$

Where T_m: is the cooling temperatures at 288, 298, and 308K, n: is the degree elevation in temperature over 278K (n = 10, 20, and 30), and i: is the instantons value.

For the air and the inner surface of the hot pipe, the effect of elevating the cooling temperature is introduced in Fig. 7 (a and b). We observed that the biggest impact of increasing the cooling temperature over 278K was recorded at the entrance of the hot pipe, and the 30-degree temperature elevation was the highest one by 88.6% and 87.6% for air and wall, respectively. This effect diminishes by moving up through the hot pipe (Z/L = 0 to 1) to 81.84% and 79.67% for air and wall, respectively. This evidence is correct for the hot pipe inner wall temperature, as shown in Fig. 7(b), but for the air in Fig. 7(a), there is an inversion at the last section in the hot pipe path; this increase in the impact reflects the end effect that happened due to the back-mixing that occurred through the thermal fluid interactions in PMR [13]. Also, the axial conduction along the heated channel decreases the effect of elevating the cooling temperature as the wall temperature decreases near the pipe outlet due to the connections to the upper plenum. In that sense, buoyancy-induced acceleration (laminarization) has a significant influence on the centerline and wall temperatures [28-31].

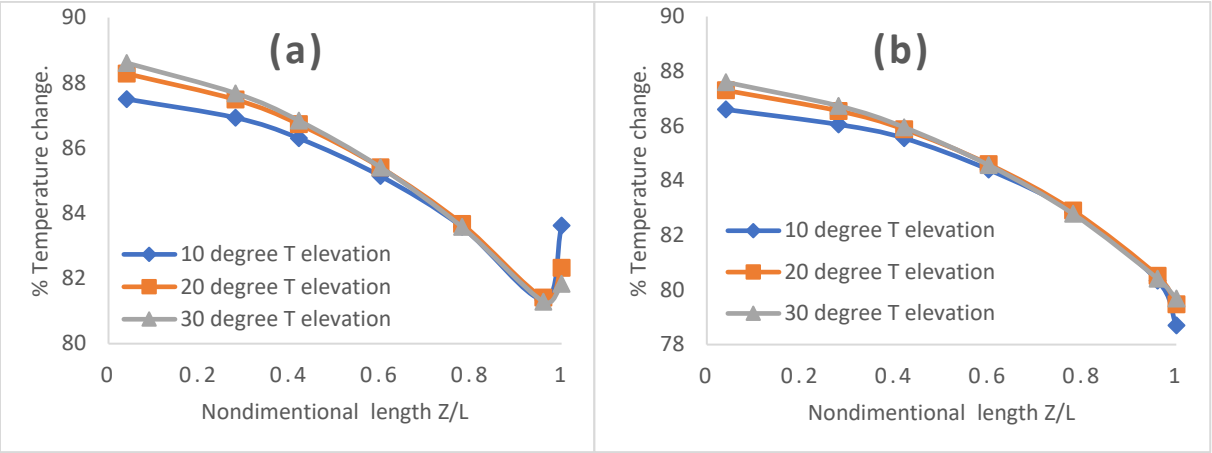

Figure 7. Effect of cooling temperature elevation on the (a) air and (b) inner wall temperatures across the hot pipe.

Fig. 8, represents the effect of elevating the cooling water temperature on the air velocity inside the hot pipe. As noticed, the absolute cooling effect on the velocity is low at the pipe entrance (0.29, 0.56, and 0.86%) for 10, 20, and 30-degree elevation, respectively, then it begins to increase to a certain limit at the mid-section reaches (1.86, 3.47, and 4.96%), then starts to decrease near the hot pipe outlet, and this is the main trend for all the temperature cooling elevations as seen in Fig. 8.

The elevation in cooling temperature affects the air velocity, and the high-temperature elevation gives the high impacted velocity inside the hot pipe, but on the other side, the three cooling temperature elevations have the same percent impact on the velocity at the end, although there is a great difference between them inside the pipe length.

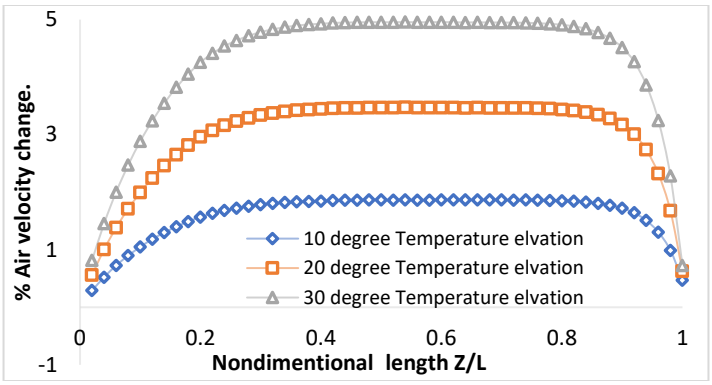

Figure 8. Effect of increasing cooling temperature on the air velocity in the hot pipe

4.2.1. Within the cooled channel

The elevation in cooling temperature above 278K by 10, 20, and 30 degrees influences the cooling rate in the cooled pipe as it affects the hot pipe's inner wall the same as the inside air. As seen in Fig. 9, at the entrance (the top of the cooled pipe) (Z/L=1) the effect was high (85 and 81%) for the air and the inner surface, respectively, with a small difference in the entrance behavior of descending for the air and ascending then descending for the inner wall. After that, a gradual decrease in the effect through the pipe continued with a sharp decrease at the last section near the exit (Z/L=0). This may be due to the end effect and the increase in air temperatures at the pipe outlet. Also, we can see the approach for the three elevation effects at the entrance for the air and the inner wall, but at the exit, the situation is different. For the air in Fig. 9 (a), a small difference of about 0.5% between the three temperature elevations, while in Fig. 9 (b), the cooled pipe inner wall temperature is significantly affected by the elevation in cooling water temperatures, giving 64, 66, and 69.4% for 288, 298, and 308K cooling water temperatures, respectively. The reason for this can be explained as the stainless-steel materials that fabricate the system making direct connections between the lower plena and the hot and cooled channels, which are responsible for the heat transfer through conduction that is causing the increase in temperature close to the cooled channel's wall ends. Added to that, the higher cooling temperature of 308K has a higher effect on the temperature inside the cooled pipe in comparison to the other cooling temperatures.

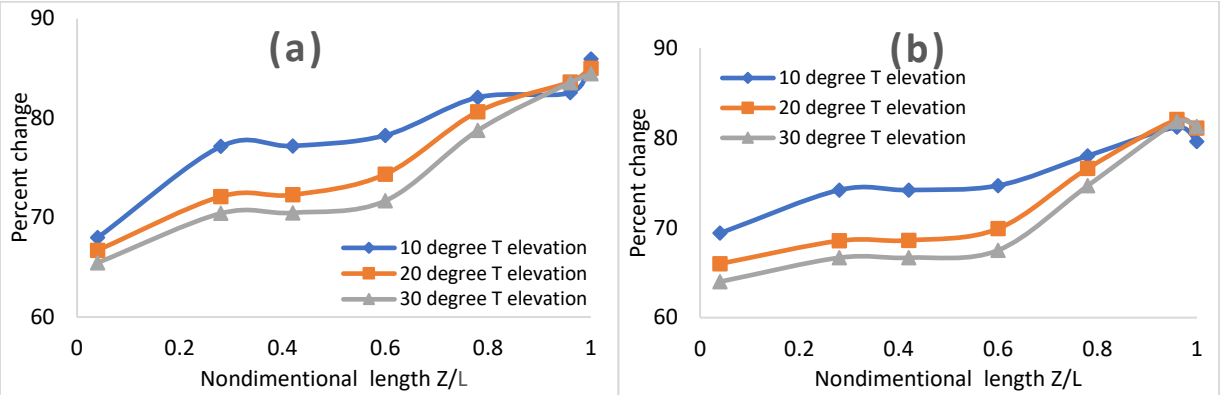

Figure 9. Effect of the outer surface temperature elevation on (a) the air temperature and (b) the inner surface temperature along the cooled channel.

The effect of increasing the cooling temperature above 278K by 10, 20, and 30 on the air velocity through the cooled pipe is introduced in Fig. 10. It is expected that the air velocity will increase as the cooling intensity decreases (the cooling temperature increases), but the effect of the elevation in cooling temperature is not as high as the effect on the temperature in the last section. The mean percent increase in velocity as the temperature increases by 10, 20, and 30 degrees is 0.78, 1.53, and 2.26%, respectively. Starting from a low effect at the entrance (Z/L = 1) with an ascending profile, it then reaches a peak, then descends on different slopes for the three elevations until it reaches a steady state, and the effect is fixed. After that, the effect is diminished at the last section near the pipe outlet (Z/L = 0). A high similarity was well observed between the three-degree temperature elevation shapes in their effect on the velocity inside the cooled channel. The end effect strongly persisted at both ends of the cooled pipe for all the cooling intensities. The high difference in cooling (30 degrees) has a big impact on the velocity, especially at the entrance, making a big peak due to the turbulence at the upper section due to the difference in pipe diameter and the difference in temperature between the air and the cooled pipe.

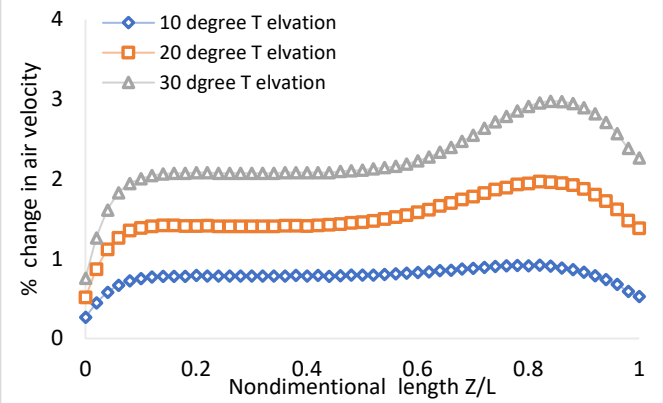

Figure 10. The effect of increasing the cooling temperature on the air velocity in the cooled pipe.

4.3. Variations in the Heat Transfer Coefficient and Nusselt Number Along the Heated Channel

The heat transfer coefficient (h) is directly obtained from RHYS, while the Nusselt number (Nu) is calculated at each axial location using the equation (2):

$$\mathrm{Nu} = \frac{\mathrm{h_{avg}}\,\ell}{\mathrm{k}} \tag{2}$$

where k: is the thermal conductivity of the air and ℓ: is height.
The heat-transfer coefficient and Nusselt number are represented in Table II. According to the operation conditions, it is evident that for the heat fluxes from 200 to 1400W/m^2, the heat transfer coefficient and the Nu are consistent and increase as the flux increases, except for the flux of 1400W/m^2, where the Nu decreased. This may be due to the increase in thermal conductivity that is related to the fluid temperature, which is highly increased in this case. For the cooling temperatures of 278, 288, 298, and 308K, the heat transfer coefficient increases as the cooling temperature increases, but on the other side, Nu decreases as the temperature increases.

Table II. Heat transfer and Nusselt number for different fluxes.

		$(h)_{avg}$	$(Nu)_{avg}$
Heat flux	200W/m^2	7.94	5.64
	600W/m^2	10.4	7.85
	1000W/m^2	13.17	7.9
	1400W/m^2	13.74	7.55
Outer surface temperature	278 K	12.32	8.15
	288 K	12.37	8.02
	298 K	12.41	7.89
	308 K	12.45	7.77

5. CONCLUSIONS

In this work, an RHYS model was established to simulate a scale-down prismatic modular reactor, and this model was validated with others' experimental work. The heat fluxes and the outer surface temperatures are utilized to study their effects on the thermal-hydraulic behavior of the coolant air. The results show that: The temperature was proportional to the heat flux from the entrance to the exit. Also, the increase in air velocity at both the hot and cooled pipes depends on the heat fluxes. The elevation in the outer surface temperature above 278 K has a great effect on the system temperatures, and also, affects the air velocity and the 30-degree elevation gives a high impact inside the hot and cooled pipe.

ACKNOWLEDGMENTS

The authors would like to express profound gratitude to the ISS team and the FUTURE RHYS team, for the license of ASYST VER 4, and RHYS programs. Also, we would like to express our thanks to the computer lab at the Faculty of Engineering, Alexandria University.

REFERENCES

1. Alshehri, S.M., "*Plenum-to-plenum heat transfer characteristics under natural circulation in a scaled-down prismatic modular reactor*"*(* 2019). Google Scholar
2. Acton, J.M. and M. Hibbs, *Why Fukushima was preventable*, page 6, Washington, DC: Carnegie endowment for international peace (2012).
3. Chapin, D., S. Kiffer, and J. Nestell, "The very high temperature reactor: a technical summary," *MPR Associates,* Alexandria, VA (2004).
4. McVay, K.L., et al.,"Preliminary tests of particle image velocimetry for the upper plenum of a scaled model of a very high temperature gas cooled reactor," *Progress in Nuclear Energy*, **83**, p. 305-317(2015).
5. Sinha, R.K. and A. Kakodkar, "Design and development of the AHWR—the Indian thorium fuelled innovative nuclear reactor*," Nuclear Engineering and design*, **236**(7-8), pp. 683-700 (2006).
6. Maheshwari, N., et al.,Passive safety features of Indian innovative nuclear reactors, No. IAEA-TECDOC--1451 (2005).
7. Delmastro, D., "Thermal-hydraulic aspects of CAREM reactor, No. IAEA-TECDOC--1281 (2002).
8. Cheung, Y., "Design evolution of natural circulation in ESBWR," *6th Int. Conf. Nuclear Engineering,* ICONE-6, (1998).

9. Mangal, A., V. Jain, and A. Nayak, "Capability of the RELAP5 code to simulate natural circulation behavior in test facilities," *Progress in Nuclear Energy*, **61**: pp. 1-16(2012).
10. Zheng Fu, S.J., *FUTURE RHYS* 2023. lifewatermaomao@gmail.com
11. (ISS), I.S.S.c., Idaho Falls, United State. http://www.relap.com/
12. Moharam, M.M.T., "Experimental investigations of natural circulation in a separate-and-mixed effects test facility mimicking prismatic modular reactor (PMR) core," Missouri University of Science and Technology (2017). Google Scholar
13. Said, I.A., et al., "Investigation of natural convection heat transfer in a unique scaled-down dual-channel facility," *AIChE Journal*, **63**(1): pp. 387-396(2017).
14. Said, I.A., et al., "Axial dispersion and mixing of coolant gas within a separate-effect prismatic modular reactor," *Nuclear Energy and Technology*, **4**(3): p. 167-178(2018).
15. Said, I.A., et al., "Effect of helium pressure on natural convection heat transfer in a prismatic dual-channel circulation loop," *International Journal of Thermal Sciences*, **124**: pp. 162-173(2018).
16. Said, I.A., et al., "Experimental investigation of the helium natural circulation heat transfer in two channels facility using varying riser channel heat fluxes," *Experimental Thermal and Fluid Science*, **93**: pp. 195-209(2018).
17. Taha, M.M., et al., "Buoyancy-driven air flow within plenum-to-plenum facility down-comer channel," *Experimental Thermal and Fluid Science*, **94**: pp. 205-214(2018).
18. Taha, M.M., et al., "Temperature and velocity instrumentation and measurements within a separate-effects facility representing modular reactor core," *International Journal of Thermal Sciences*, **136**: pp. 148-158(2019).
19. Taha, M.M., et al., "Natural convection inside heated channel of a facility representing prismatic modular reactor core,", *AIChE Journal*, **64**(9): pp. 3467-3478(2018).
20. Taha, M.M., et al., "Effect of non-uniform heating on temperature and velocity profiles of buoyancy driven flow in vertical channel of prismatic modular reactor core," *Applied Thermal Engineering*, pp. 120209 (2023).
21. Lau, G.E., et al., "Numerical and experimental investigation of unsteady natural convection in a vertical open-ended channe," *Computational Thermal Sciences: An International Journal,* **4**(5) (2012).
22. Miyamoto, M., et al., "Turbulent free convection heat transfer from vertical parallel plates" *International Heat Transfer Conference Digital Library*. Begel House Inc.(1986).
23. Fedorov, A.G. and R. Viskanta, "Turbulent natural convection heat transfer in an asymmetrically heated, vertical parallel-plate channel,'' *International Journal of Heat and Mass Transfer*, **40**(16): pp. 3849-3860(1997).
24. Sanvicente, E., et al., "Transitional natural convection flow and heat transfer in an open channel," *International Journal of Thermal Sciences,* **63**: p. 87-104 (2013).
25. Cocheme, F.G., "Assessment of passive decay heat removal in the General Atomics Modular Helium Reactor," Doctoral dissertation, Texas A&M University(2005).
26. Jaluria, Y. and B. Gebhart, "On transition mechanisms in vertical natural convection flow," *Journal of Fluid Mechanics*, **66**(2): pp. 309-337(1974).
27. Muresan, C., et al., "Numerical simulation of a vertical solar collector integrated in a building frame: radiation and turbulent natural convection coupling," *Heat transfer engineering*, **27**(2): pp. 29-42(2006).
28. Ede, A., "Natural convection on free vertical surfaces," East Kilbride, Glasgow: *Mechanical Engineering Research Laboratory Report Heat*, **141(**1956).
29. Kageyama, M. and R. Izumi, "Natural heat convection in a vertical circular tube," *Bulletin of JSME*, **13**(57): pp. 382-394(1970).
30. Davis, L.P. and J.J. Perona, "Development of free convection flow of a gas in a heated vertical open tube," *International Journal of Heat and Mass Transfer*, **14**(7): pp. 889-903(1971).
31. Dyer, J., "The development of laminar natural-convective flow in a vertical uniform heat flux duct," *International Journal of Heat and Mass Transfer*, **18**(12): pp. 1455-1465(1975).

Numerical Investigation Of Natural Circulation Inside A Scaled-down Prismatic Modular Reactor by RHYS

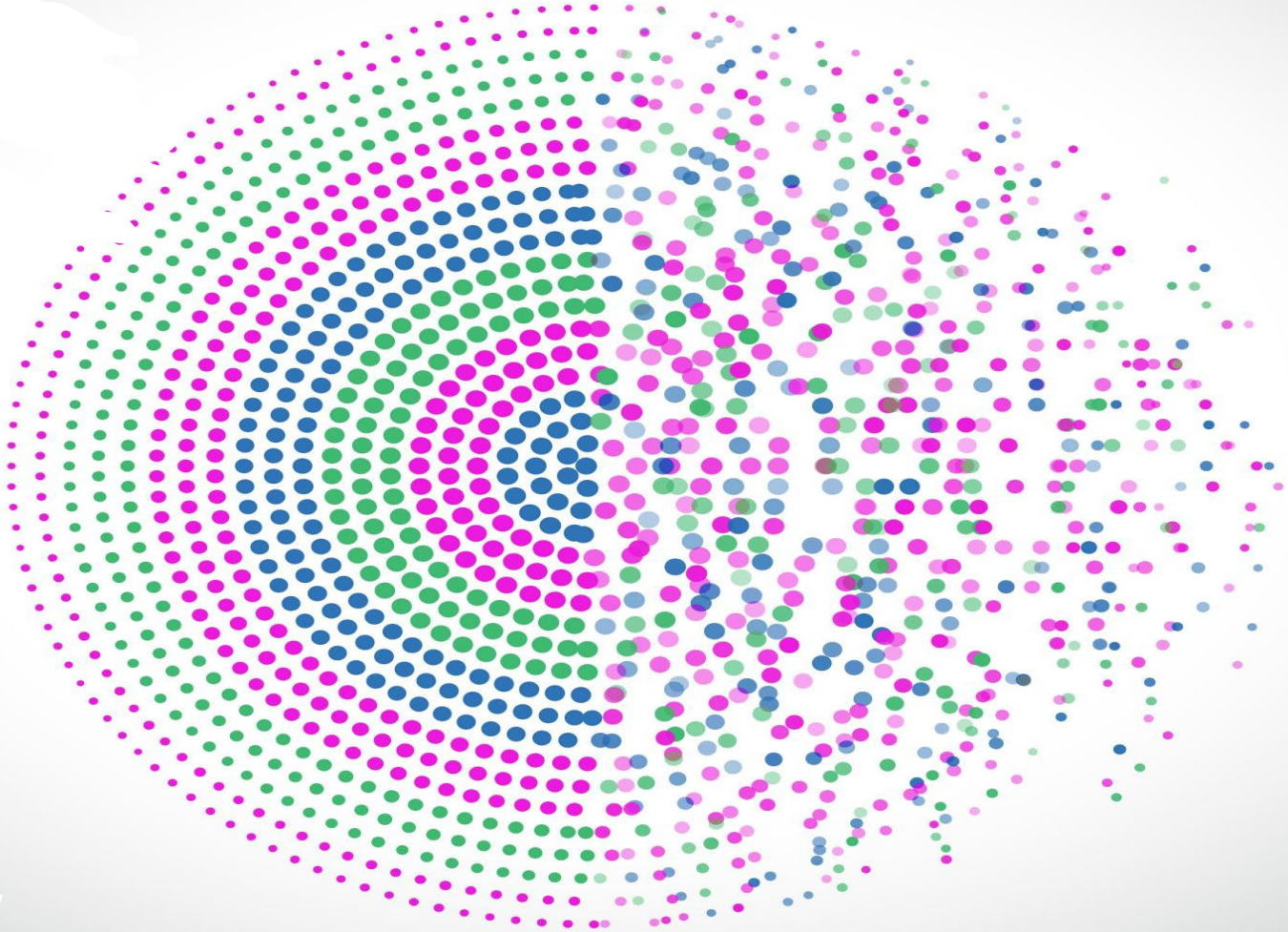

Presented by:

Marwa Abozeid Shewita

Biography



Marwa Abozeid Shewita

- **PhD researcher,** Faculty of Engineering, Minia University, Egypt.
- **Bachelor's** and **Master of Science** degrees in **Chemical Engineering from Alexandria University, Egypt.**
- Participated in training at **Innovative System Software on Relap and ASYST Codes, Idaho, USA.**
- Drilled at **Water and Environmental Technology Center (WET)**, Faculty of Engineering, Temple University, Philadelphia, USA.
- Participated at **Alexandria Desalination Studies and Technology Center (ADST)** on the Design and Operation of Thermal & Membrane Desalination Technology.
- Have More than **8 paper publications**, besides contributing to many conferences and workshops either as a presenter or speaker.
- **Work as a Teaching Assistant** at the Civil & Environmental Specialized Scientific Program, and Gas and Petrochemicals Specialized Scientific Program, Faculty of Engineering, Alexandria University, Egypt.
- **International Trainer** in Regional Technical Support and Training Center for RELAP/SCDAPSIM, Alexandria University, Egypt.
- **Technical Manager for C.O.E Lab**, at the Center of Excellence for Water (C.o.E) at Alexandria University in cooperation with the American University (AUC) in Egypt.

Authors

Eng. / Marwa Abozeid Shewita

Prof. / Chris Allison

Prof. / Ibrahim Ismail Ibrahim

Prof. / Moustapha S. Mansour

Dr. / Mahmoud M. Taha

Dr. / Ayah E. Elshahat



Outline

- ✓ **Introduction**
- ✓ **System Set Up**
- ✓ **RHYS Program**
- ✓ **RHYS Nodalization**
- ✓ **Results And Discussion**
    1. **Flux Impact**
    2. **Outer Surface Temperature Impact**
- ✓ **The Heat Transfer Coefficient and Nusselt Number**

INTRODUCTION

Gen IV systems,

- **Prismatic Modular Reactors (PMR)** have:
- High outlet temperatures,
- Small footprint,
- Connect directly to the electric production cycle,

decreasing heat loss,

- High-efficiency electrical generation,
- Used in carbon-free hydrogen production.

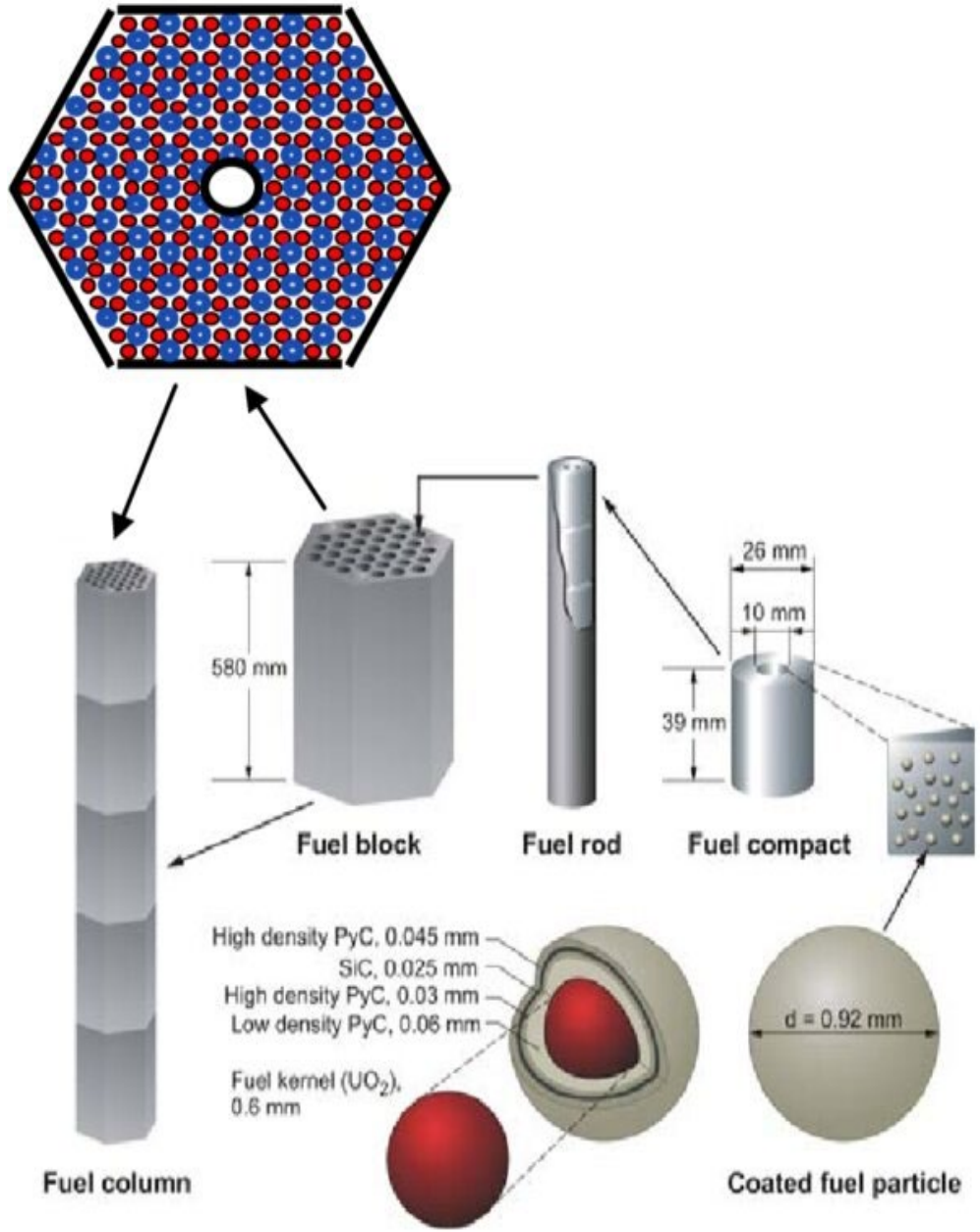

Reference [1]

Gen IV systems,

❑ Safety

- **Accident of Fukushima power plant in 2011.**
- Concentrates on naturally eliminating decay heat in the event of an accident while avoiding the release of significant quantities of radioactive material.



https://hfswitzerland.ch/radiation-protection-the-ppe-needed-for-nuclear-power-plant-work/

Natural Circulation

- During the stoppage of flow owing to
  - Loss of power supplies,
  - Failures of the initial circulating equipment,
  - Loss of grid loads.
- The complete gas flow loss eliminates forced convection through the core.
- Natural circulation is the predominant mechanism of transferring heat inside the core, resulting in a reversal in temperature and flow.
- **Examples** of advanced reactors that rely on passive ideas to remove fission heat without the need for mechanical pumps are **AHWR** [2], **CHTR** [3], **CAREM** [4], and **ESBWR** [5].

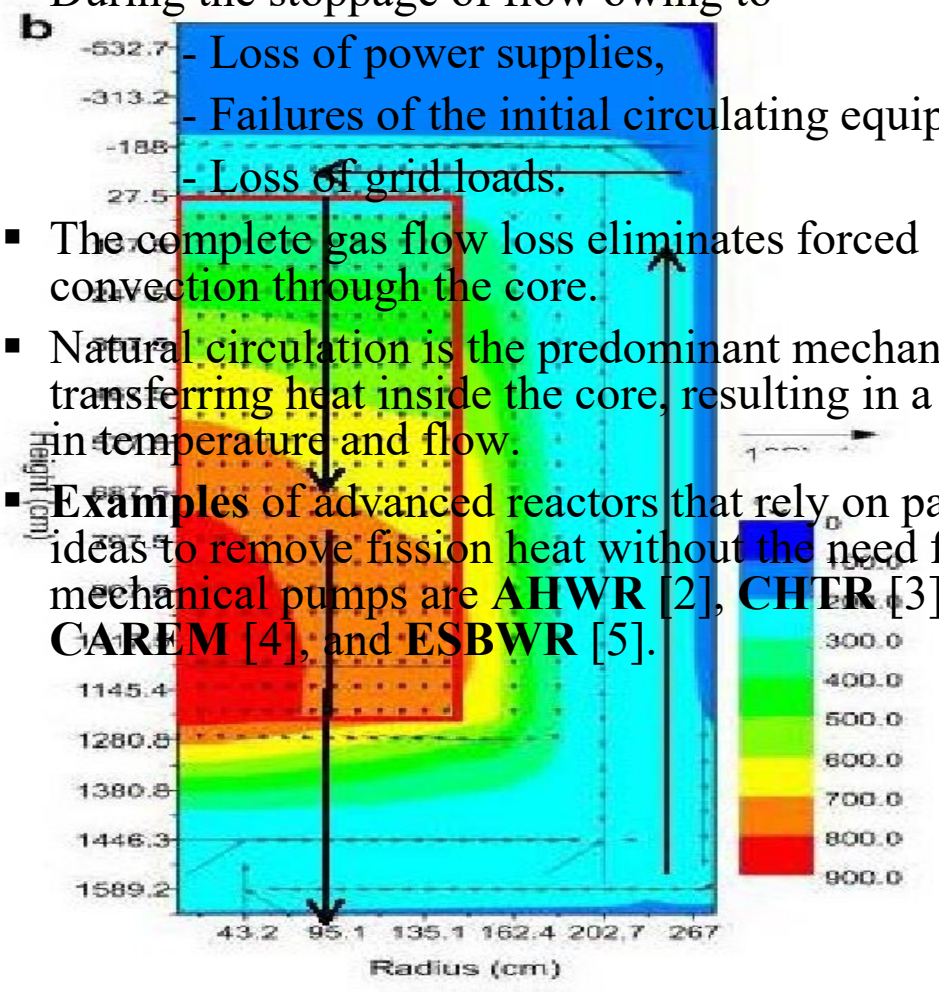

ACCIDENTS:

- Loss of flow
- Loss of pressure

or

Normal shut down

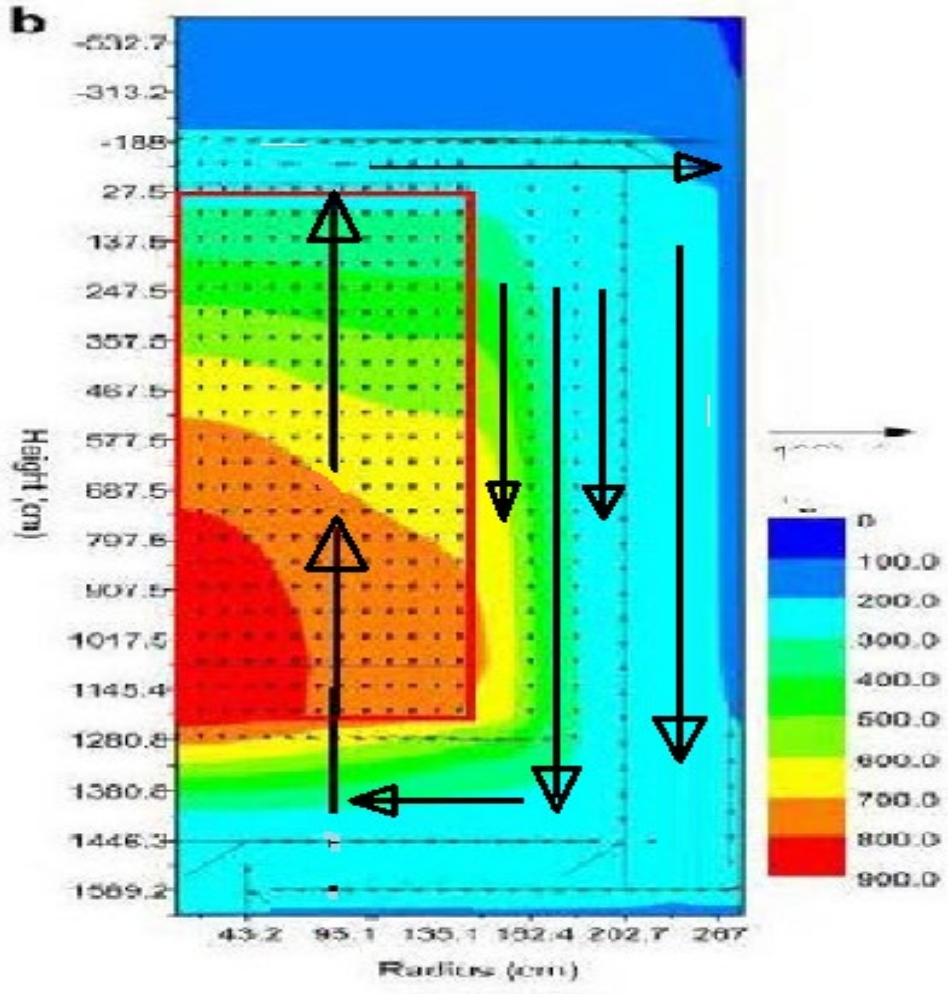

Reference [1]

RHYS Program

Is an innovative UI extension designed to enhance the efficiency of the ISS ASYST and RELAP/SCDAPSIM system code.

- Building input models and simulations to running result analysis
- Makes complex thermal-hydraulic modeling and simulation more accessible.

Try a Free 30-day of RHYS

By contacting:

fuzheng@breitac.com or jiangshuying@breitac.com or

Innovative Systems Software ISS, http://www.relap.com/

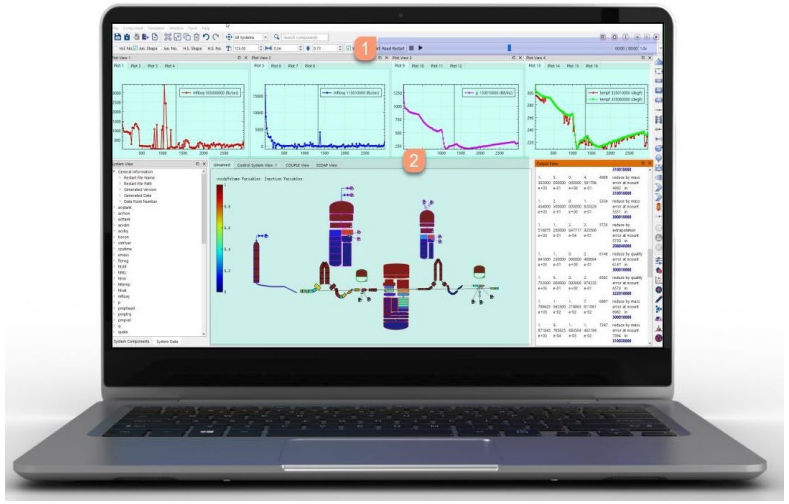

RHYS - Input builder

Visualization

RHYS - Node Viewer

Check input connections

RHYS - Simulation

Real time check simulation results

RHYS - Plot

Run results post processing

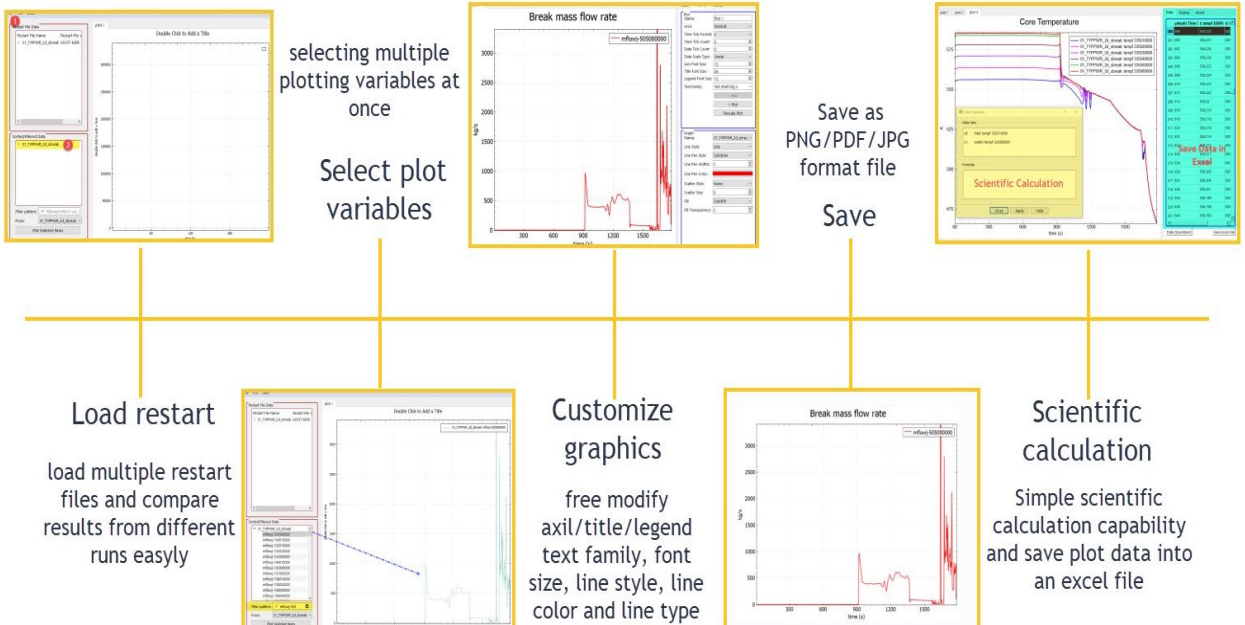

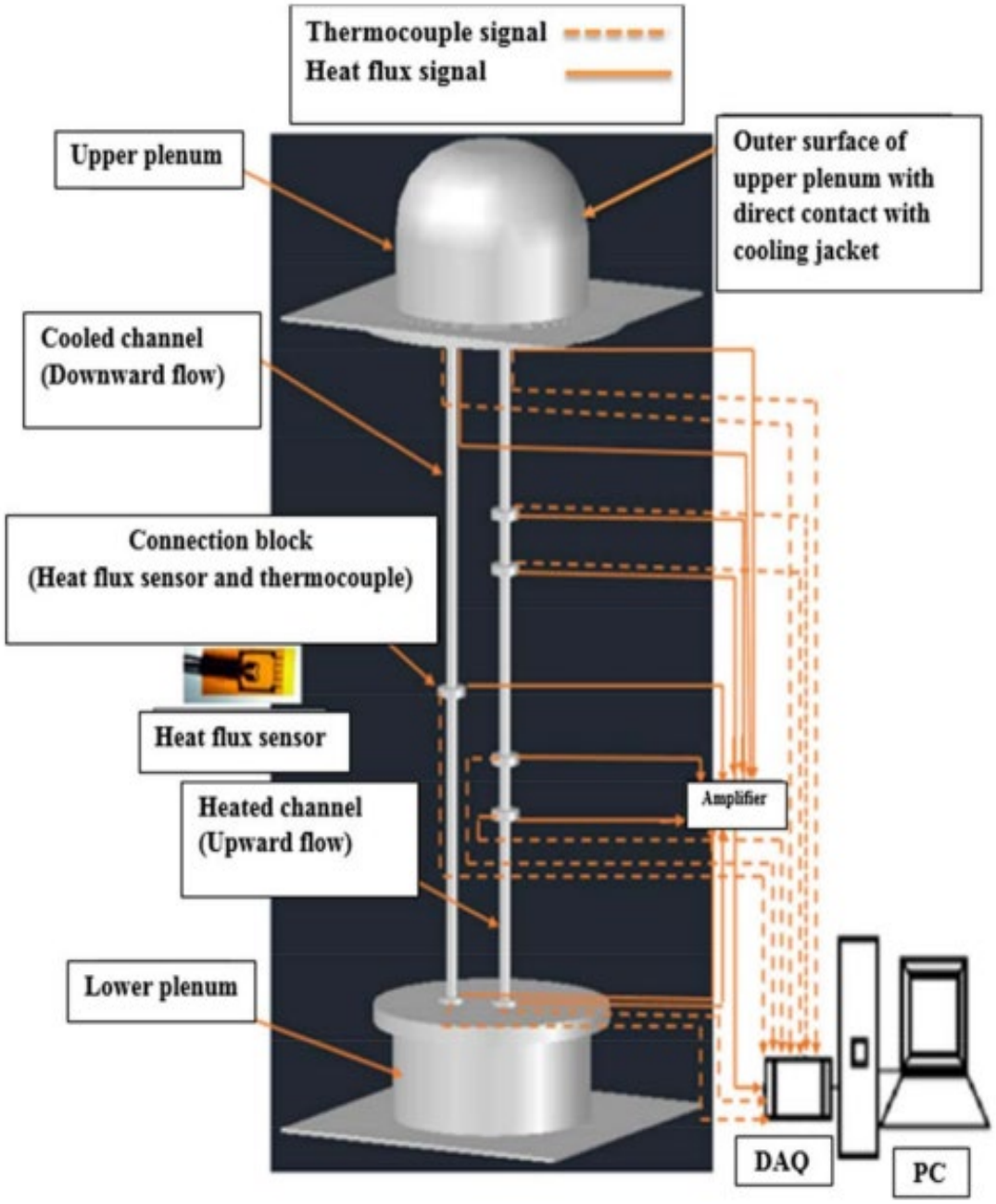

System set up

- Missouri S&T University Multiphase Reactors Engineering and Applications Research Lab (MReal) [6-14].
- This facility consists of two vertical channels connecting in an analogous way to the PMR's core coolant channels, representing the hot and cold areas in the core.
- The system constructed from a stainless steel.
- Air is used as a fluid.
- The applied fluxes are 200,600,1000, and 1400 W/ m^2.
- The cooling water has different cooling temperature of 278, 288, 298, 308 K.

Reference [6-14]

RHYS Nodalization

No.	Type	Description
100	Single Volume	Lower plenum
120 (1:50)	Annulus	Riser channel
140 (1:5)	Annulus	Upper plenum
145 (1:3)	Annulus	Upper plenum water cooling jacket
150 (1:50)	Annulus	Downcomer channel
170	Single Volume	Downcomer cooling water out
175	Single Volume	Upper cooling jacket water out
190	Time-Dependent Volume	Downcomer cooling water in
195	Time-Dependent Volume	Upper cooling jacket water in
200 (1:50)	Annulus	Water jacket

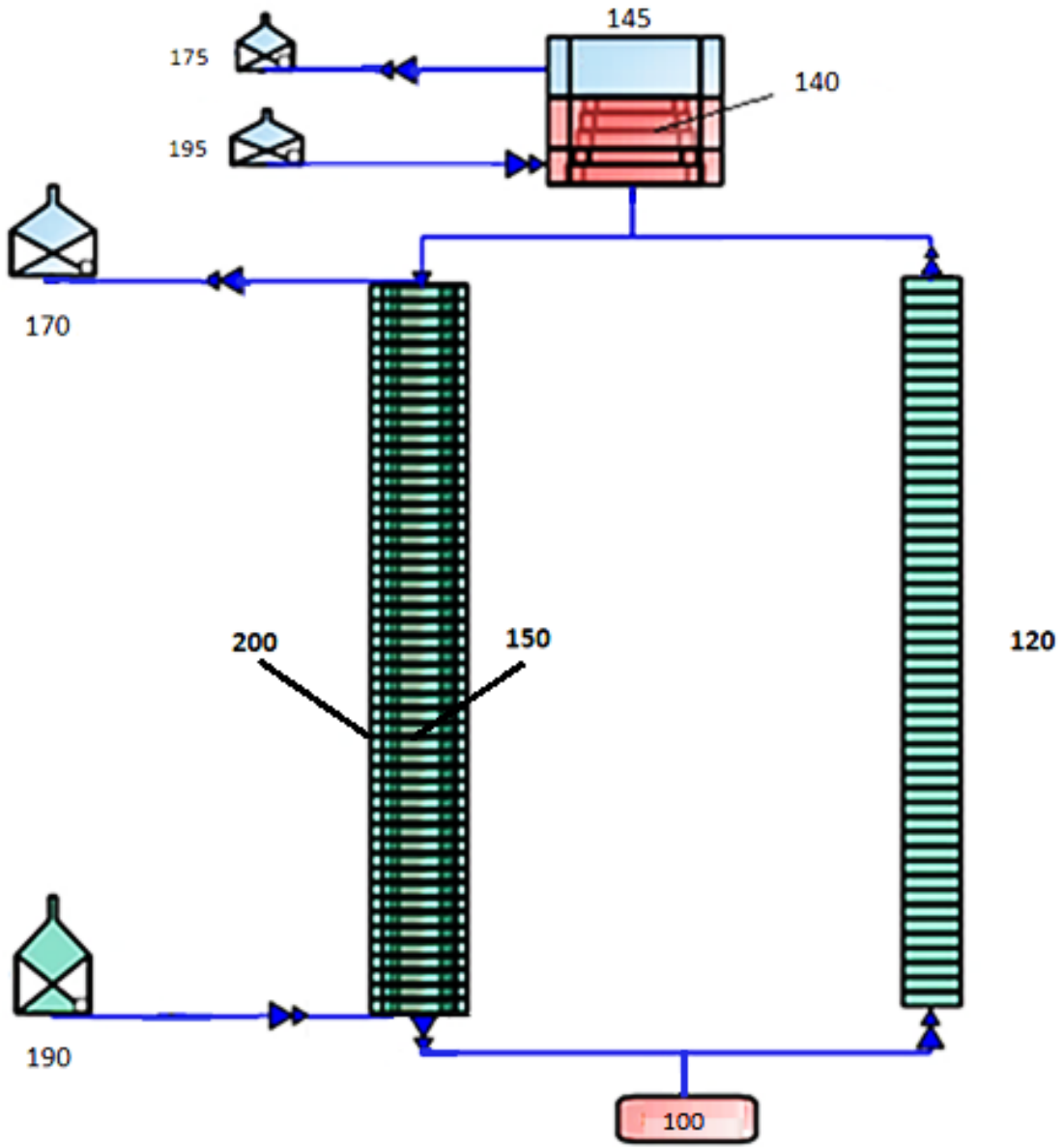

RESULTS

AND

DISCUSSION

1. Flux Impact

1.1 Temperature

Axial temperature disruptions inside the hot pipe for:

(a) Air temperature

(b) Inner wall surface temperature

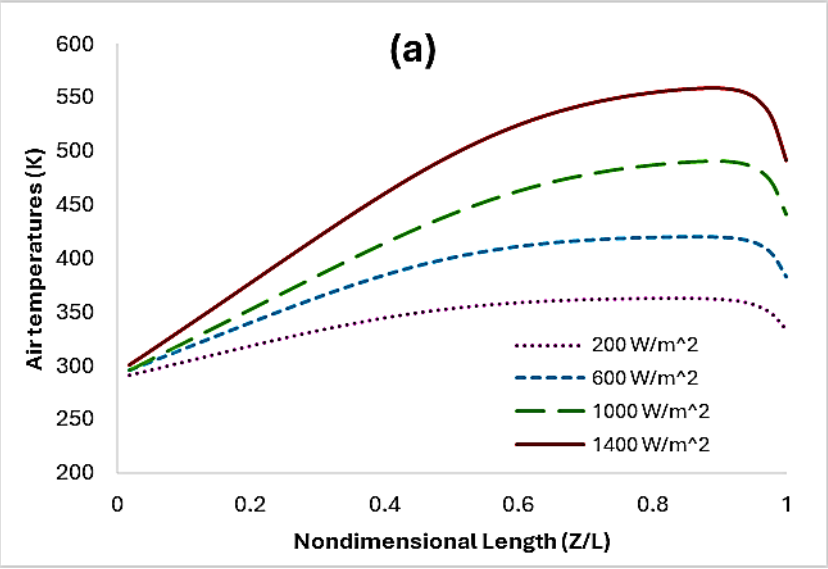

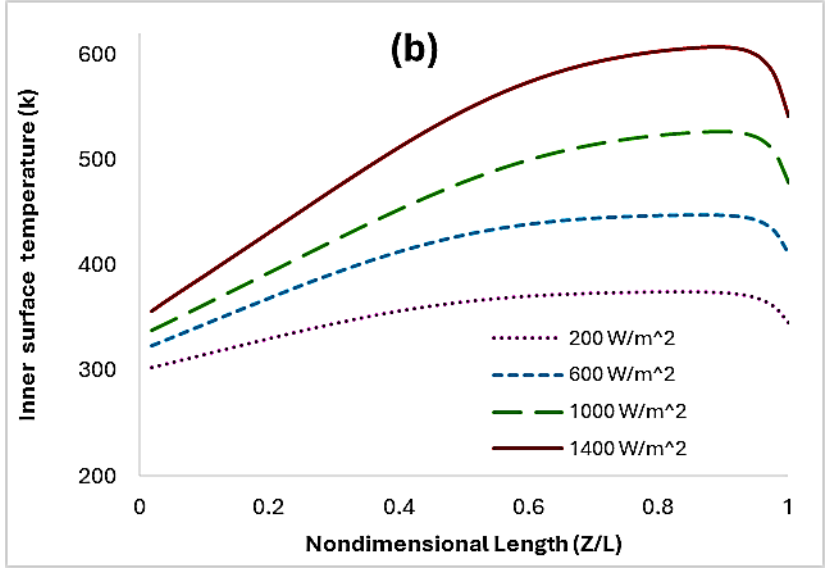

1. Flux Impact

1.1 Temperatures

- The percentage ascending in the hot channel and descending in the cold channel in temperature proportional to the heat flux.
- The air gives a higher response to the change in flux than the wall.

At the hot pipe :

- At the flux of 1400 W/m^2 the air increased by 63.6%, while the wall increase by 51%.
- Flux of 200 W/m^2 gives the least increase with 14.6 and 14% for the air and the wall, respectively.

At the cold pipe:

- The flux of 1400W/m^2 gives a 20.4% and 19.11% temperature decrease for the air and the wall, respectively,
- The temperature decreased by 3.82% and 3.39% for the air and the wall at flux 200W/m^2

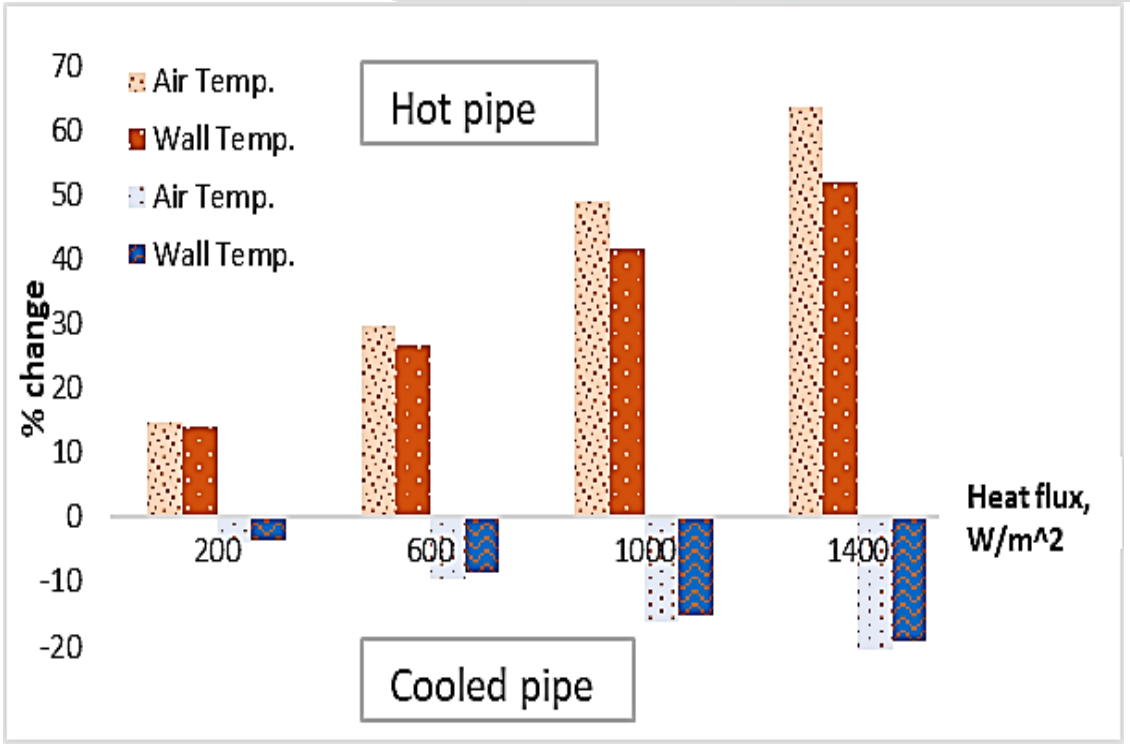

Percentage of air temperature changes inside the hot and cooled pipes

1. Flux Impact

1.2 Velocity

Experimental [14] and RHYS predicted velocity along the pipe nondimensional length (Z/L) for heat flux

(a) 600W/m^2

(b) 1000W/m^2

(c) 1400W/m^2

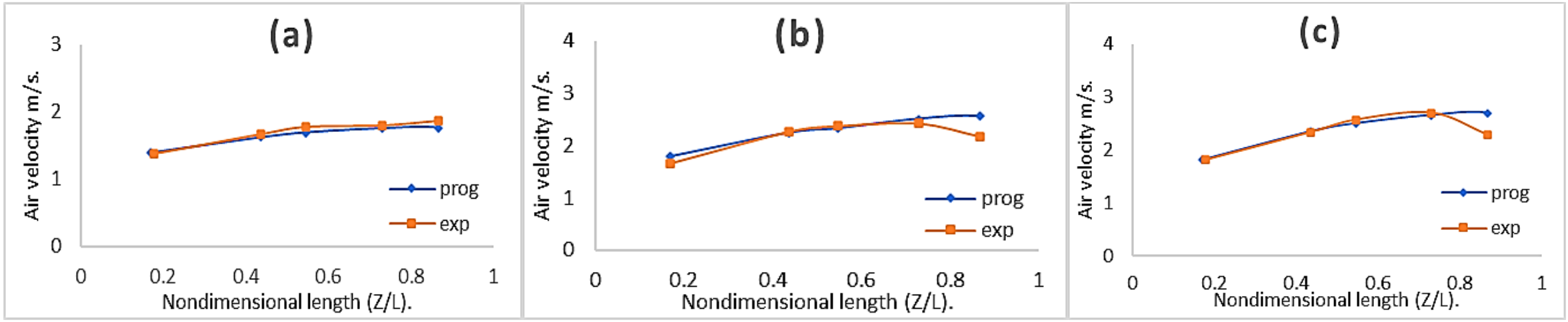

1. Flux Impact

1.2 Velocity

Velocity change at different heat fluxes.

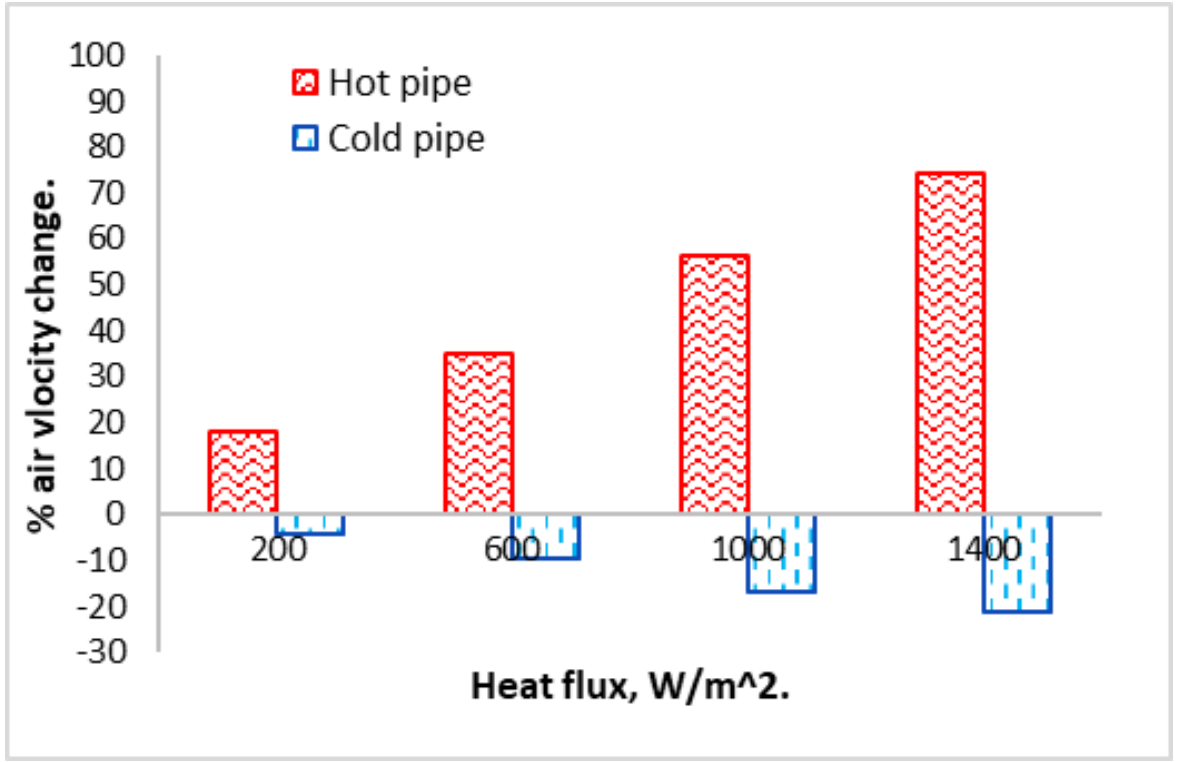

2. Outer Surface Temperatures Impact

2.1 Within the Hot Channel

Effect of cooling temperature elevation on:
(a) Air
(b) Inner wall temperatures across the hot pipe.

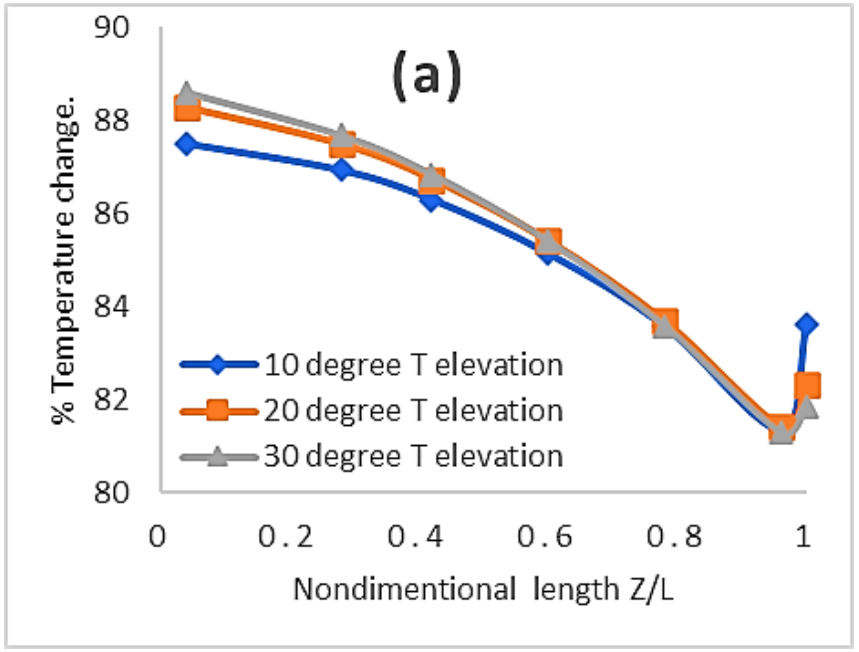

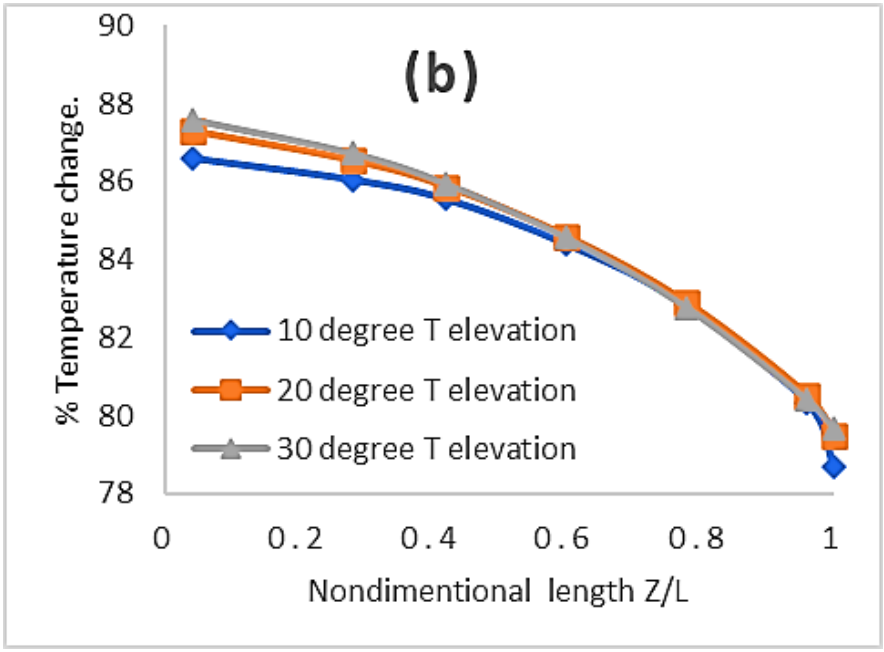

2. Outer Surface Temperature Impact

2.1 Within the Hot Channel

Effect of increasing cooling temperature on the air velocity in the hot pipe

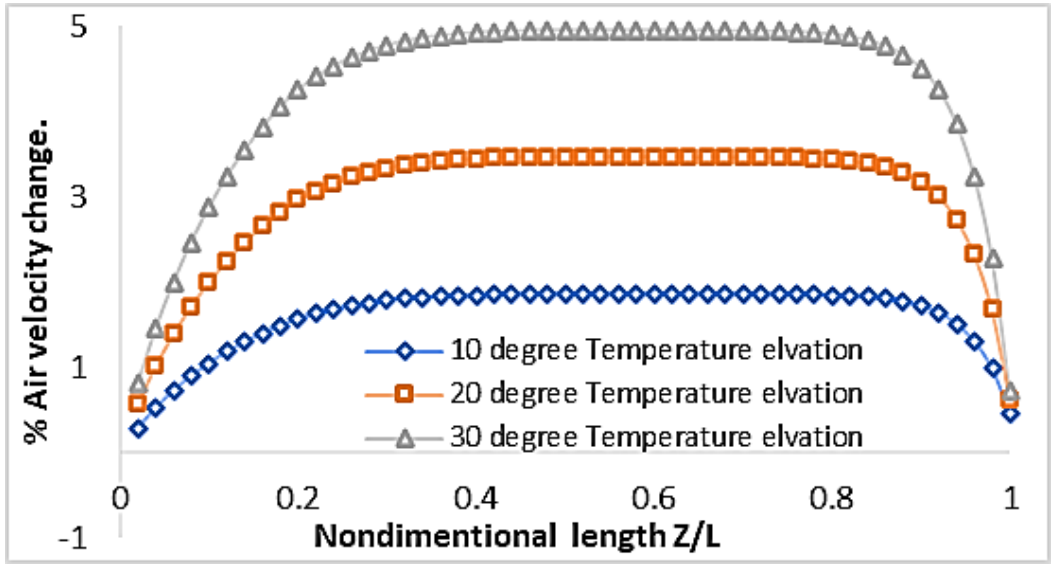

2. Outer Surface Temperature Impact

2.2 Within the Cold Channel

Effect of the outer surface temperature elevation on:

(a) The air temperature

(b) The inner surface temperature along the cooled channel.

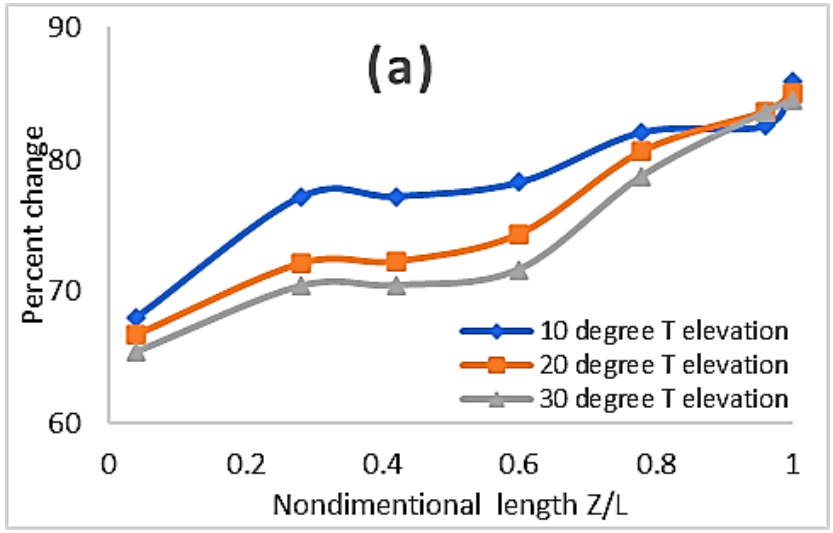

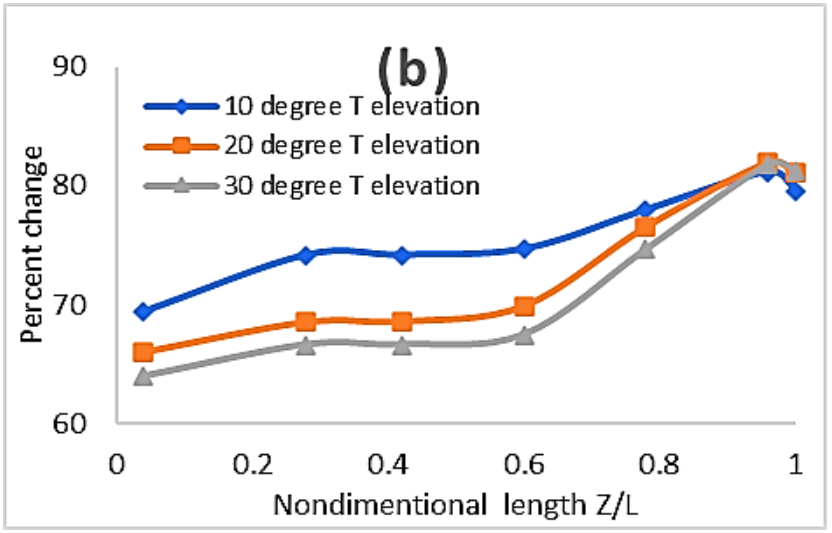

2. Outer Surface Temperature Impact

2.2 Within the Cold Channel

The effect of increasing the cooling temperature on the air velocity in the cooled pipe

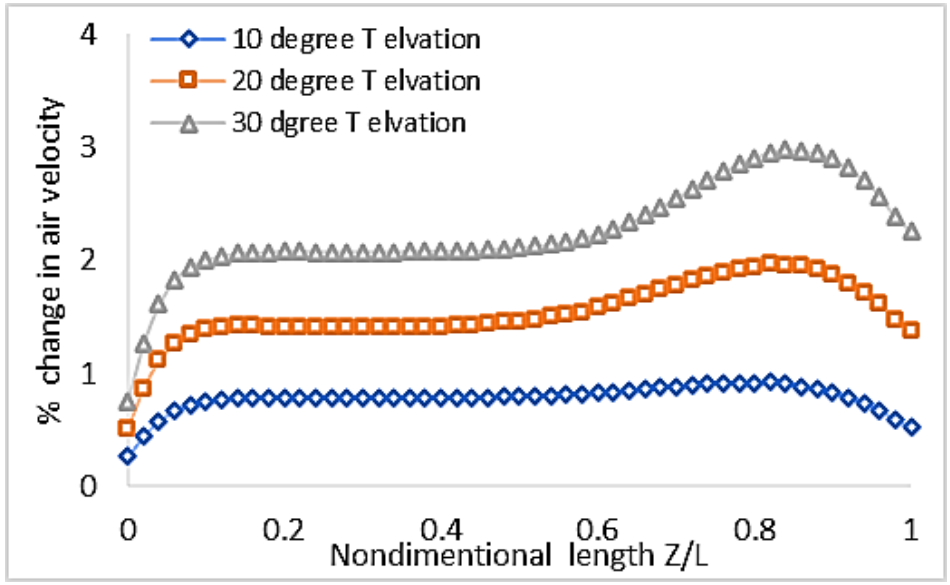

3. The Heat Transfer Coefficient and Nusselt Number Along the Heated Channel

- The heat transfer coefficient (h) is directly obtained from RHYS
- The Nusselt number (Nu) is calculated at each axial location using equation:

$$Nu = \frac{h_{avg}\,\ell}{k}$$

Where k: is the thermal conductivity of the air and ℓ: is height.

3. Variations in the Heat Transfer Coefficient and Nusselt Number Along the Heated Channel

- For the heat fluxes from 200 to 1400 W/m^2, the heat transfer coefficient and the Nu increase as the flux increases, except for the flux of 1400W/m^2, where the Nu decreased.
- For the cooling temperatures of 278, 288, 298, and 308K, the heat transfer coefficient increases as the cooling temperature increases, but Nu decreases as the temperature increases.

		$(h)_{avg}$	$(Nu)_{avg}$
Heat flux	200 W/m^2	7.94	5.64
	600 W/m^2	10.4	7.85
	1000 W/m^2	13.17	7.9
	1400 W/m^2	13.74	7.55
Outer surface temperature	278 K	12.32	8.15
	288 K	12.37	8.02
	298 K	12.41	7.89
	308 K	12.45	7.77

Reference

1) Windes, W., et al., Role of nuclear grade graphite in controlling oxidation in modular HTGRs. 2014, Idaho National Lab.(INL), Idaho Falls, ID (United States).
2) Sinha, R.K. and A. Kakodkar, ''Design and development of the AHWR—the Indian thorium fuelled innovative nuclear reactor,'' Nuclear Engineering and design, 236(7-8), pp. 683-700 (2006).
3) Maheshwari, N., et al., Passive safety features of Indian innovative nuclear reactors, No. IAEA-TECDOC--1451 (2005).
4) Delmastro, D., ''Thermal-hydraulic aspects of CAREM reactor, No. IAEA-TECDOC--1281 (2002).
5) Cheung, Y., ''Design evolution of natural circulation in ESBWR,'' 6th Int. Conf. Nuclear Engineering, ICONE-6, (1998).
6) Moharam, M.M.T., ''Experimental investigations of natural circulation in a separate-and-mixed effects test facility mimicking prismatic modular reactor (PMR) core,'' Missouri University of Science and Technology (2017). Google Scholar
7) Said, I.A., et al., ''Investigation of natural convection heat transfer in a unique scaled-down dual-channel facility,'' AIChE Journal, 63(1): pp. 387-396(2017).
8) Said, I.A., et al., ''Axial dispersion and mixing of coolant gas within a separate-effect prismatic modular reactor,'' Nuclear Energy and Technology, 4(3): p. 167-178(2018).
9) Said, I.A., et al., ''Effect of helium pressure on natural convection heat transfer in a prismatic dual-channel circulation loop,'' International Journal of Thermal Sciences, 124: pp. 162-173(2018).
10) Said, I.A., et al., ''Experimental investigation of the helium natural circulation heat transfer in two channels facility using varying riser channel heat fluxes,'' Experimental Thermal and Fluid Science, 93: pp. 195-209(2018).
11) Taha, M.M., et al., ''Buoyancy-driven air flow within plenum-to-plenum facility down-comer channel,'' Experimental Thermal and Fluid Science, 94: pp. 205-214(2018).
12) Taha, M.M., et al., ''Temperature and velocity instrumentation and measurements within a separate-effects facility representing modular reactor core,'' International Journal of Thermal Sciences, 136: pp. 148-158(2019).
13) Taha, M.M., et al., ''Natural convection inside heated channel of a facility representing prismatic modular reactor core,'', AIChE Journal, 64(9): pp. 3467-3478(2018).
14) Taha, M.M., et al., ''Effect of non-uniform heating on temperature and velocity profiles of buoyancy driven flow in vertical channel of prismatic modular reactor core," Applied Thermal Engineering, pp. 120209 (2023).

Thank you…

Questions?



Development of a LW-SMR dry containment model with containmentFOAM

Carlos Vázquez-Rodríguez, Karl J. X. Sturm, Allen George, Stephan Kelm

Forschungszentrum Jülich (FZJ)
Wilhelm-Johnen-Straße, 52428 Jülich, Germany
c.vazquez-rodriguez@fz-juelich.de; s.kelm@fz-juelich.de

ABSTRACT

In line with the growing interest in Europe for the deployment of Small Modular Reactors (SMRs), the Horizon Euratom SASPAM-SA Project launched in 2022 aims to investigate the applicability of the know-how for large-LWRs to water-cooled SMR (LW-SMR). More specifically, the project investigates postulated Severe Accident (SA) sequences for two different "generic" SMRs, Design-I with a submerged containment and Design-II with a dry containment and several passive safety features, based on information available in the open literature. On this basis, the ability of different codes widely used in Europe to analyse the identified SA sequences are evaluated.

This paper presents the up-to-date status of the 'Design-II' LW-SMR dry containment model development using containmentFOAM, a CFD package tailored for containment safety analyses based on OpenFOAM-9, which is developed at Forschungszentrum Jülich (FZJ). The use of the code in SASPAM-SA aims to complement the calculations performed with lumped parameter codes, such as MELCOR, ASTEC, or AC2. Due to the close coupling of the containment and the reactor cooling phenomena, the additional insights of containmentFOAM for the buoyancy-driven transport processes and the condensation in presence of non-condensable gases are relevant for the system response. However, the new safety concepts that are feasible due to the reduced size of SMR containments come with novel challenges for the code.

The first priority of the modelling process is to ensure a consistent definition of the model geometry, as it is based on a database conceived for lumped parameter models. The evaluation of the thermal-hydraulic conditions predicted by the lumped parameter codes motivates a review of the applicability of the code to the expected higher pressures and steam concentrations (fluid properties, condensation regimes, etc.). Besides, the liquid released from the reactor vessel occupies a significantly larger fraction of the smaller containment volume. Therefore, two-phase models are currently being tested to consider the more prominent role of the liquid for the containment behaviour. Last, an OpenModelica-containmentFOAM coupling scheme is under implementation to represent the specific safety features of Design-II, such as the pressure suppression system.

KEYWORDS
SMR, CFD, containmentFOAM, two-phase flow, system code coupling

1. INTRODUCTION

Ten years after the Fukushima Daiichi accident, the International Atomic Energy Agency (IAEA) foresees for the first time a positive tendency on the potential growth of nuclear power capacity worldwide [1], a tendency consolidated by the most optimistic net-zero scenarios of other institutions such as the International Energy Agency (IEA) [2], and the Nuclear Energy Agency (NEA) [3]. In this last scenario,

the NEA foresees the installation of up to 400 GW of Small Modular Reactors (SMR), which are expected to occupy a central role in the coming years. Among all the concepts being considered, the Light Water SMRs (LW-SMRs) have higher chances of being developed in the short term, which should ease the licensing of these advanced concepts. Indeed, the identification of Severe Accident (SA) sequences[1] is a key step towards the licensing of SMRs, as those are needed to inform level 4 (severe accident management) and level 5 (off-site emergency response) of the defence-in-depth concept [4,5].

The Horizon Euratom SASPAM-SA Project [6,7], coordinated by ENEA (Italy) launched in 2022 goes all the way from the identification of potential postulated SA sequences to the evaluation of the extension of the emergency planning zones. Notably, SASPAM-SA investigates the applicability of the know-how for large-LWRs to LW-SMR, with a focus on identifying potential phenomenological differences of relevance for postulated SA progressions and the ability of the SA codes to replicate the expected phenomena. The project is currently ongoing and the results for the Work Package 2, coordinated by KIT (Germany) and focused on the identification of sequences, are summarised in [8].

The LW-SMR studied in SASPAM-SA are not replicas of any concept being explored for commercial deployment. Instead, the evaluations are performed using generic concepts with representative features for a range of designs[2]. The so-called Design-I in SASPAM-SA features a generic integral Pressure Water Reactor (i-PWR) of about 60 MWe embedded in a metallic containment submerged in a pool. The Design-I does not have a safety injection system and relies on a global natural circulation loop for the long-term removal of the decay heat. The Design-II consists of a generic integral i-PWR of about 300 MWe and a large dry spherical containment. Though also fully relying on passive safety, the design includes a full range of safety systems typically used in advanced LWRs: high- and low-pressure safety injections, a pressure suppression system for the containment pooling, and a pool with a heat exchanger for decay heat removal[3]. Examples of postulated SA sequences applicable for both generic designs are discussed in [4] and [6].

The focus of this paper will be on the large dry containment of Design-II, which will be simulated using containmentFOAM [11]. containmentFOAM is an open-source CFD package based on OpenFOAM [12] that is specifically tailored towards the needs of containment SA analysis for conventional large PWRs. Accordingly, containmentFOAM used a single-phase approach where the liquid phase inside the containment was treated as a passive scalar and simply removed from the simulation domain when it is condensed at the walls. Most of the code developments aimed to obtain a detailed characterisation of the multi-species gas phase heat and mass transport phenomena of the containment. This was accomplished by adding specific models for wall condensation, turbulent buoyancy-driven flows, aerosol deposition, engineering systems, etc. The accidental sequences of LW-SMRs bring scenarios with distinct characteristics, and therefore the general modelling approach of containmentFOAM needs to be re-evaluated for its applicability.

[1] Advanced designs, as iPWRs, are in general characterized by common features with the current operating large-LWR and by other specific features typical of their inherent evolutionary designs, providing safety advantages that reinforce the first three levels of the DiD principle. However, even if a plant is designed with advanced inherent features (through the reinforcement of the 1,2,3 DiD levels) allowing a reduction of the Core Damage Frequency (CDF), independent features for preventing and mitigating a severe accident sequence have to be included in its design (DiD level 4) together with the offsite emergency response (DiD level 5). Therefore, some scenarios that could lead to severe accidents need to be postulated and deterministically studied. More detailed information's in [4].

[2] It is not the project's objective to assess the generic reactor designs selected but, based on the project findings, allow a more general statement on the code's applicability to currently favored designs under postulated SA condition.

[3] Considering the selected passive systems and the generic SMR features, a generic IRIS-SMR type has been considered as reference for this analysis (no proprietary data have been used); therefore, the main geometric information has been determined by scaling the data available from the SPES-3 facility, by engineering evaluation or public general data available from the IRIS reactor [9].

This article is structured into three main sections. First, the containment thermal-hydraulics of the different phases of the available Design-II sequences is described in detail. The evaluation of the scenarios is used as a basis for the identification of containmentFOAM modelling upgrades to tackle the expected phenomenology. Afterwards, chapter 3 presents a preliminary validation of the domain decomposition approach and code coupling scheme used to model the containment and Pressure Suppression System (PSS) of Design-II by coupling containmentFOAM and OpenModelica [13]. Last, a summary of the insights of the work performed so far, and an outlook will be given as a conclusion.

2. TAILORING containmentFOAM FOR LW-SMR SCENARIOS

As briefly introduced above, one of the main objectives of the SASPAM-SA project is to evaluate the applicability of the know-how from large LWRs to LW-SMRs. Specifically, for containmentFOAM, this evaluation is aimed at identifying the features of the code tailoring to simulate conventional large PWRs that may limit its ability to address LW-SMR scenarios. The evaluation is performed before developing a containment model for the Design-II of SASPAM-SA. The anticipated detailed analysis of the foreseen technical-scale application drives the prioritisation of the code development needs. The evaluation has been performed on the basis of previous publications [10,14] and the ongoing work in SASPAM-SA [8]. The description of a generic sequence for Design-II is used to list the principal development needs of containmentFOAM. Therefore, only the most relevant thermal-hydraulic differences for conventional large PWRs and the LW-SMR will be addressed, referring the reader to the original references to have a complete description of the transient. The generic accidental sequence is separated into four phases represented in Figure 1, three for the Design Basis Accident (DBA) consisting of the Direct Vessel Injection (DVI) break and one for a hypothetical postulated SA. Figure 1 separates the containment free volume between the drywell and the Reactor Cavity (RC), also representing the main passive safety systems: Pressure Suppression System (PSS), Automatic Depressurization System (ADS), Long-term Gravity Make-up System (LGMS), Quench Tank (QT), and Emergency Borated Tanks (EBT).

Generally, the accident evolution is driven by the pressure differences of three connected "systems": the Reactor Pressure Vessel (RPV) – P_1, the Drywell – P_2, and the PSS – P_3. The four phases of the transient highlighted in Figure 1 reflect the principal flow transport processes to/from the containment for different pressure differences. A brief description of each phase with its main modelling challenges is given below:

Pressure suppression ($P_1 >> P_2 > P_3$)

The first phase in Figure 1 shows the situation immediately after the DVI line break. The break will produce a rapid release of superheated liquid that will flash in the containment atmosphere. Design-II, as well as Design-I and several other LW-SMRs, has as a design target to equalise the pressure of the RPV (P_1) and the Drywell (P_3) as fast as possible. Therefore, a second flow path from the RPV is open via the ADS-1. The pressure increase in the containment will induce a pressure difference, allowing the flow transport from the Drywell (P_2) to the PSS (P_3), as shown in Figure 1. The steam purged into the PSS will be condensed in the subcooled pool, limiting the pressure increase in the Drywell. The backpressure at the PSS, whose gas space is connected to the LGMS, will determine the flow from the Drywell to the PSS. Since the PSS is dimensioned to condense all the steam while remaining subcooled, the pressure increase in the PSS will be characterised by the accumulation of Non-Condensable Gases (NCGs) in its gas space.

The first challenge for the modelling basis of containmentFOAM, arising from the chain of events described above, is related to the physics of the wall condensation. For the range of pressures expected in conventional large reactors, the presence of NCGs in the boundary layer is the main thermal resistance to delimit the condensation rates [15,16]. However, as Design-II is designed to accelerate the pressure equalisation, the pressure peaks in the containment can be in a range between 9 bar and 14 bar [10,14]. The larger steam concentrations associated with these higher pressures, in other LW/SMRs [5] will induce a film-wise

condensation regime [17] where the main thermal resistance to delimit the condensation rates is the liquid film. This motivates the need for an extension of the wall condensation models and the validation matrix of containmentFOAM, which is currently ongoing.

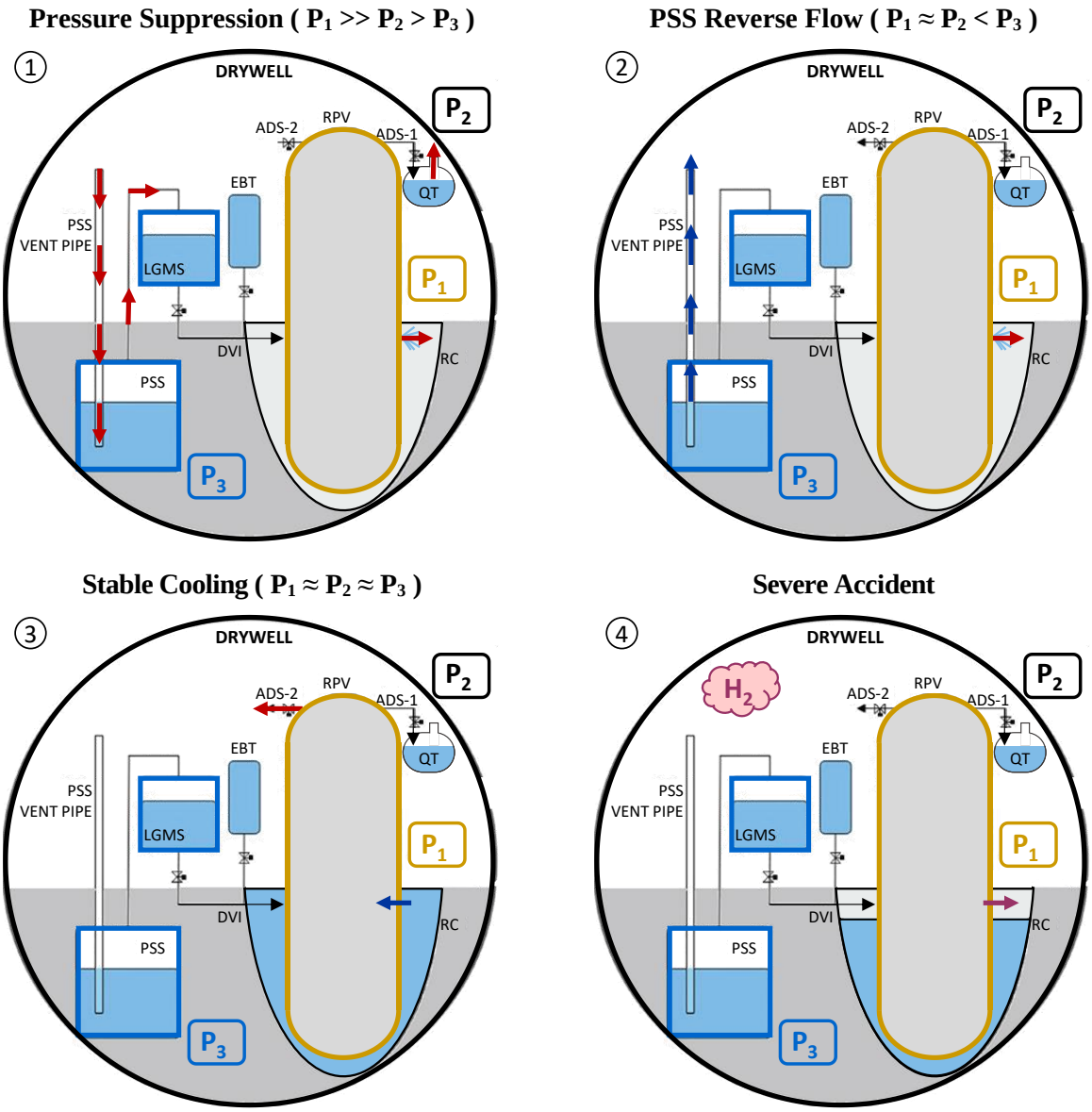

Figure 1. Representation of three phases of a DBA (DVI break) and a SA in the Design-II

PSS reverse flow ($P_1 \approx P_2 < P_3$)

The PSS reverse flow represents the second phase in Figure 1. The maximum pressure reached in the drywell for a DBA happens at the same time as the pressure equalisation with the RPV ($P_1 \approx P_2$). After that, the pressures of RPV and Drywell start decreasing again by the combined effect of the core cooling systems and wall condensation, respectively. However, these cooling processes do not affect the PSS and LGMS (P_3). At a certain point of the transient, the higher pressure at the PSS will be large enough to push back water from the PSS to the drywell.

Similarly to the pressure suppression phase, the pressure differences drive the succession of events foreseen in the Design-II safety concept. Remarkably, the pressures of the three different systems are strongly linked, and the mass and energy transfer processes controlling the evolution of the pressure at each separate system influence the others. Therefore, the simulation of the primary, the containment or the safety system with different codes, a typical approach for conventional PWRs, would have stronger limitations for the LW-SMRs.

While the coupled simulation of RPV, drywell, and PSS has a clear added value for the representativeness of the calculations, it comes with a significant additional bargain in terms of computational cost. Hence, for the technical scale application foreseen in this work, it is not practical to use the same level of detail to simulate all the systems. To have the flexibility for cleverly deciding where to put the detail, i.e. to enable multi-scale calculations, arises as an essential feature for containmentFOAM. Consequently, a coupling scheme to facilitate multi-scale calculations using the Modelica [18] programming language for representing the system domain is under development. The coupling scheme and preliminary validation of the system-code-like modelling of the PSS will be described in the following chapter.

Stable cooling ($P_1 \approx P_2 \approx P_3$)

The third phase in Figure 1 represents the status of the containment after reaching a stable long-term cooling. The water transported from the PSS to the RC is above the break elevation. At this moment, the second phase of the ADS (ADS-2) would ensure the equalisation of the pressure of Drywell and RPV. In a DBA, the water from the RC will enter the RPV by the additional pressure of the water column. The steam produced at the RPV will be released to the Drywell by the ADS-2, condensed at the metallic walls, and injected back into the RPV, closing the cooling loop.

The relevance of considering the presence of liquid phase in the containment is evident in the third phase in Figure 1. Apart from the relevance of confirming that the water is transferred to the cavity and reaches a higher elevation of the break, it occupies more than 10% of the containment free volume, a value that can get close to 50% in other LW-SMR [5]. Therefore, the space occupied by the liquid phase will have a significant impact when calculating the containment pressure. The larger relevance of the liquid phase motivates the upgrade of the current multi-species single-phase solver of containmentFOAM with a two-phase volume of fluid approach [19].

Severe accident

When it is postulated that some of the safety systems briefly mentioned above do not comply with their safety function (through the postulated failure of correspondent valves to open), the core cooling may be compromised. In this case, a hypothetical core degradation may induce the release of up to 480 kg of H2 to the containment [10]. Commonly, the SA may happen when the postulated failure of safety systems does not allow long-term stable cooling. For example, in the fourth phase in Figure 1, the water level at the cavity stays below the break location. The conditions of this scenario, while there is no significant flow transport between PRV, drywell and PSS, would be within the modelling basis of the current version of containmentFOAM (v9). The presence of NCG would limit the condensation, and the presence of water and its mass and energy exchange with the gas phase could be easily modelled.

3. COUPLING Modelica AND containmentFOAM

The technical-scale application of CFD codes to reactor safety analysis has an intrinsic multi-scale nature. The characteristic lengths in the order of μm of relevant phenomena such as turbulence, homogeneous condensation, or the physics at the boundary layer are combined with convection loops or safety systems whose actuation can be represented with larger scales. As discussed in the previous section, the coupling of

the containment thermal-hydraulics and the passive safety system is stronger for LW-SMRs than for conventional large PWRs. Consequently, this chapter describes the ongoing work to support a multi-scale modelling approach by coupling containmentFOAM with simplified models of the safety systems using the Modelica language. The general features of the coupling scheme used in this work, which will be extended to simulate other components (PARs, heat exchangers, etc.), are described in a first subsection to later present the model of the PSS developed for simulating the Design-II. The preliminary validation for the PSS model based on the public information of PPOOLEX experiments in [20] is also described below.

3.1 Characteristics of the Coupling

The central feature of the coupling approach is the use of the Functional Mock-up Interface (FMI) 2.0 standard [21] for defining the exchange of information between containmentFOAM and the system-code-like model of the PSS. The model of the PSS was developed and exported as an executable simulator called Functional Mock-up Unit (FMU) using OpenModelica. The FMI is a standard extensively used in the automotive and aerospace industries that offers a clear and open interface whereby multiple parties can develop FMUs to be coupled with the same integral model. The three main characteristics to highlight for this coupling approach are as follows:

- The FMI standard and Modelica are aligned with the open-source nature of containmentFOAM. The foundational aim of Modelica was to unify the concepts of different languages designed to solve system of differential and algebraic equations with different purposes, designing a new open language to boost the collaboration between different fields [18]. The same applies to the FMI coupling, an open standard for the exchange of information between codes. Every simulation tool adapted to support the FMI standard can be straightforwardly coupled [21].
- Most of the coupling solutions in the nuclear industry are code specific, and usually require access to the source code of proprietary tools [22]. Contrary, as it is defined as a standard for the exchange of information, FMI compatibility is code agnostic.
- The combination of the previous two features gives a total modularity to the proposed coupling scheme. Different institutions can develop individual FMUs for different purposes, and those could be easily coupled to solve an integral problem thanks to the FMI standard.

At its current status, the coupling scheme uses a domain decomposition approach allowing the pressure-velocity coupling of uni-directional fluid flow. The system ("SYS") and CFD models can exchange pressure, temperature, mass composition, and mass flow fields of the gas phase [13]. It uses a semi-implicit scheme with Picard-iterations for the time discretisation and allows: (i) several updates of the serial mapping of field values until reaching convergence (see Figure 2, left), and (ii) for sub-cycling on the FMU side, if only an explicit forward Euler solver is available for the Modelica model. Parallel processing and simulation restart features are also included in the coupling. Its implementation is a "native" extension of the main containmentFOAM solver loop, utilising only the FMI Library [21] and the OpenFOAM-provided parallel MPI-based communication mechanisms.

The descriptions of the previous paragraph define the characteristics of the coupling within the six tiers proposed by [22] for couplings classification. As it is shown in [23], the implemented coupling scheme has been systematically verified to ensure numerical stability and conservativeness, and have not been included here for the sake of brevity.

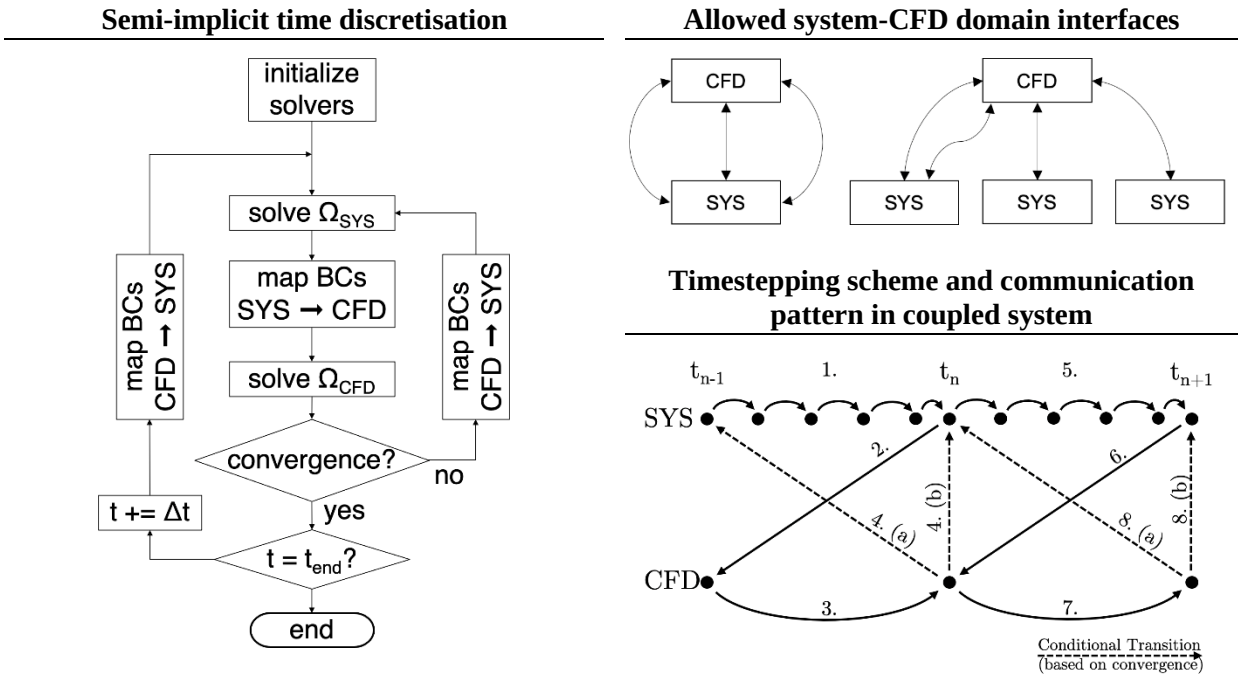

Figure 2. Sketch of the main characteristics of the proposed coupling scheme (Source [18])

3.2 Preliminary validation using the PPOOLEX MIX-04 test

The preliminary validation selected for this paper aims to showcase the performance of the described coupling in a scenario close to the technical scale application foreseen in SASPAM-SA. Specifically, the transport of the gas mixture from the drywell to the PSS during the pressure suppression phase (see Figure 1). To reproduce the pressure-based coupling using the multi-species single phase solver of containmentFOAM, a simple model of the PSS was programmed and exported as an FMU using OpenModelica. The model of the PSS is based on the ThermoPower library [24]. The FMU models the PSS as a single node where the liquid and gas spaces are separated.

The temperature, pressure and mass flow rate flowing through the vent lines are calculated by containmentFOAM and averaged to be compatible with the 0D approach of the FMU. Since the PSS is expected to have tens of degrees of subcooling during the transient, all the steam reaching the PSS is immediately condensed in the liquid phase of the FMU after releasing its latent heat. The non-condensable gases coming from the drywell bypass the pool and accumulate in the gas space.

The preliminary validation for the coupling scheme and the FMU is based on the MIX-04 experiment performed at PPOOLEX, a test facility designed and constructed by the Lappeenranta University of Technology [20]. The facility was conceived to investigate BWR issues, and therefore the PPOOLEX vessel is split into a drywell and a wetwell connected by a pipe, as indicated in Figure 3. The analogy between the PPOOLEX configuration and the Design-II containment is straightforward, being the drywell of PPOOLEX equivalent to the PSS of the Design-II. As it is indicated in the scheme in Figure 3, the drywell of PPOOLEX is modelled with containmentFOAM and the wetwell with the FMU developed to simulate the PSS. The interface of the domain-decomposition coupling is realized at the exit of the pipe connecting drywell and wetwell using the FMI standard.

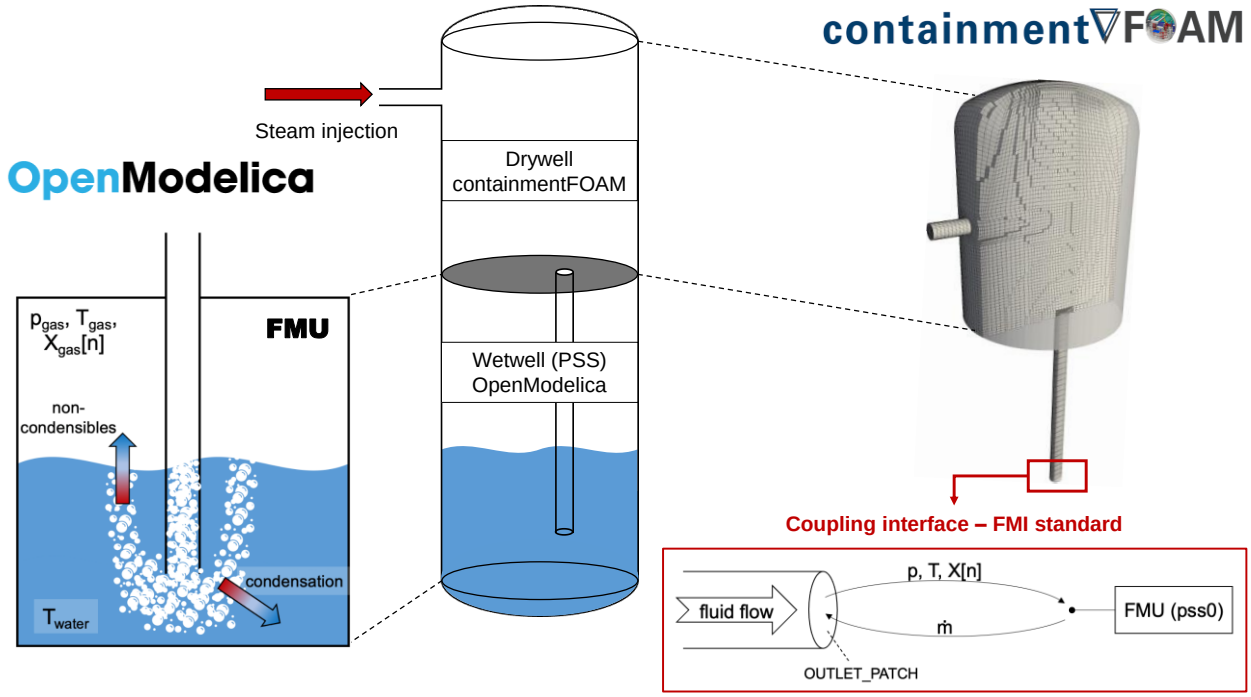

Figure 3. Sketch of the strategy used to model the PPOOLEX facility with OpenModelica & containmentFoam

The MIX-04 test is part of a series of experiments [20] investigating different flow regimes for the direct contact condensation process associated to the injection of steam to a subcooled pool. Specifically, the key parametric change is the steam mass flow rate, which may induce the development of a thermal stratification within the pool. As it is shown in Figure 4, the steam injection in MIX-04 can be split into three phases. At the beginning of the experiment, a relatively large flow rate is used to push the NCGs to the wetwell and to heat up the metallic walls of the vessel until reaching the thermal equilibrium with the injected steam. In the second phase, the steam flow rate is reduced for a period of 4000 seconds to increase later to 350 g/s in the third phase. The analysis of the liquid level and average pool temperature data proved that the actual steam injection rate during the stratification phase ('Flow correction-EXP' in Figure 4) was lower than the nominal value ('Flowmeter-EXP' in Figure 4).

The impact of the different flow rates on the water pool can be understood from the experimental recordings plotted with markers in Figure 5 (experimental data and simulation results showed together due to space limitations). During the first phase, the pool temperature increase was below 5 °C, and the main phenomenon was the pressure increase produced by the accumulation of the NCGs in the wetwell. The second phase is characterised by the pool stratification, which has not been represented in the graphs. The pool average temperature is a better figure of merit for the comparisons with the simulation results, but the difference between the maximum and minimum temperatures recorded in the pool reached 25 °C. The third phase of the experiments is characterised by the faster increase in the pool average temperature driven by the higher steam flow rate. The chugging induced by the larger flow rates homogenised the pool temperature.

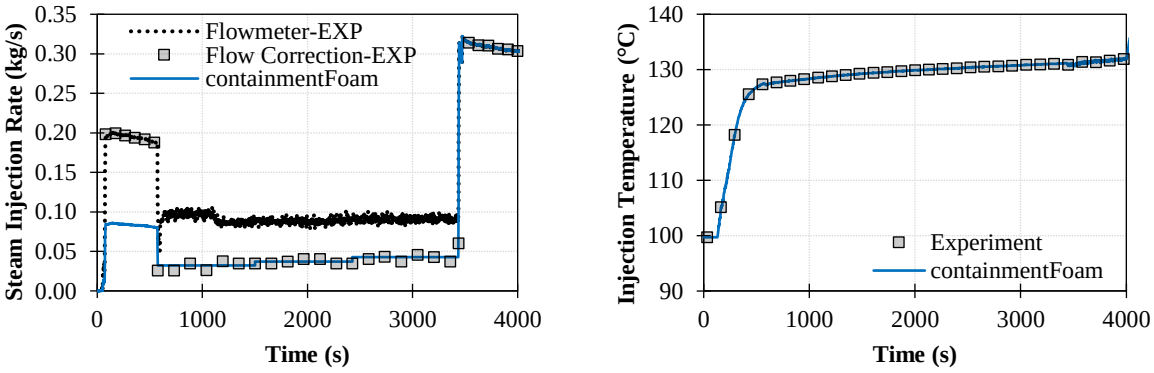

Figure 4. Boundary conditions for steam injection in the drywell.

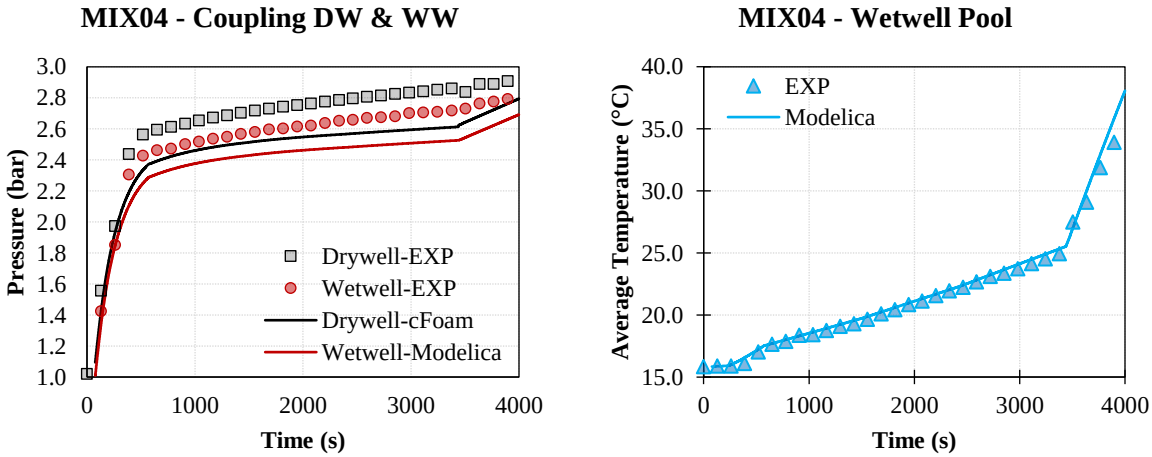

Figure 5. Comparison of experimental data and simulation results.

As indicated from the beginning, the validation exercise is preliminary, and there are several simplifications to consider before describing the simulation results:

- The FMU model uses a 0D approach where the liquid phase is characterised by a single temperature. Therefore, it is not possible to model pool stratification with this approach. This limitation was accepted because the priority of the validation was to demonstrate the stability of the pressure/velocity coupling. Indeed, for the technical scale application of the Design-II SMR, the pressure increase is driven by the transport of NCGs, not by the pool heating.
- The FMU is currently under development, and the version used for this work did not have a complete implementation of all the physics of the problem. The two main limitations to consider are the (i) non-inclusion of the heat transfer between the drywell and the wetwell, (ii) and the lack of an evaporation/condensation model for the liquid/gas interface. Again, it is important to highlight that these limitations affect the simulation of PPOOLEX but not the foreseen technical scale application, where there is no heat transfer from the PSS to the Drywell.
- For the sake of simplicity, the wall condensation process and the heat capacity of the metallic walls were not considered in the containmentFOAM model for the drywell. Therefore, the steam injection rate was reduced during the first phase of the experiment, reducing the energy injected in the simulation domain according to the energy that would be absorbed by the walls. The reduced flow

steam flow rate used in containmentFoam for the first phase of the experiment was shown in Figure 4. The steam flow rate reduction was equivalent to the energy needed to heat the metallic walls of the drywell (calculated by the wall thermocouples measurements)

Figure 5 presents the comparison of the simulations and the experimental results. The graph shows the pressure of the drywell, calculated with containmentFOAM, the gas pressure of the wetwell and an average temperature for the wetwell pool, both taken from the FMU (Modelica). The first thing to highlight on the simulations side is the stability and smooth convergence of the calculation. The simulation ran with a constant Courant number of 5, a time step of 0.012 seconds, and doing between 4 and 5 PIMPLE iterations each time step (approx. 500 s / day on 16 Xeon cores). Adding to the stable performance of the pressure coupling is its capability to qualitatively represent the evolution of PPOOLEX conditions. The fast pressurisation of the facility was driven by the accumulation of NCGs in the drywell, which was observed on both the CFD and FMU sides. The simulation also reproduced the slower pressurisation in the second and third phases of the transient driven by the facility's temperature increase.

The quantitative deviations between the experimental measurements and the simulation results shown in Figure 5 are related to the limitations of the modelling approach listed in the previous bullet points. The predicted pressure was approximately 0.25 bar lower than the experimental recordings, which is explained by the non-inclusion of the heat transfer between the drywell and the wetwell. This heat transfer from the drywell (approximately at 130 °C) to the wetwell (initially at 20 °C) would increase the temperature, and thus the pressure, of the gas space of the wetwell. However, since this heat transfer process does not have a significant impact on the quantity of energy arriving at the pool, the simulations showed a solid quantitative agreement for the increase of the pool's average temperature.

The work to consolidate the results of this preliminary validation is currently ongoing. The coupling scheme allows multiple connections between an FMU and the CFD model. Therefore, the implementation of the heat transfer from the drywell to the wetwell is relatively simple. Furthermore, the FMU will be updated to include the free surface evaporation and the heat losses of the wetwell. Last, the CFD model will be modified to simulate the wall condensation in the Drywell, where the thermal-hydraulic (almost pure steam) has similar characteristics to the blowdown of the i-PWR Design-II SMR that will be simulated in SASPAM-SA. Yet, the stability and qualitative behaviour of the pressure-based coupling scheme have been proven to be a successful proof of concept for these further developments.

4. CONCLUSIONS AND FURTHER WORK

The phenomenological differences between the SA scenarios of LW-SMRs and the conventional large PWR (those used as the reference scenarios for the development of containmentFOAM) motivated a re-evaluation of the traditional modelling approach of containmentFOAM. The knowledge acquired by participating in SASPAM-SA allowed the prioritisation of the code developments needed to use containmentFOAM for LW-SMRs simulations. Essentially, these developments should help to handle the characteristic stronger pressure coupling between containment, primary, and safety systems and to consider the more prominent role of two-phase issues in the unfolding of an accident. Besides, the general validation matrix of the code should be extended to consider other flow regimes, such as the film-wise wall condensation.

The work described in this article focused on the need to represent the stronger pressure coupling between the containment and the passive safety systems. A technical scale application for the SMR Design-II evaluated in SASPAM-SA requires the use of multi-fidelity simulation tools, where the modellers should carefully choose the level of detail to represent each part of the problem. The multi-fidelity modelling frameworks have been enabled by developing a coupling framework for containmentFOAM and OpenModelica using the FMI standard. The solution is open source, transparent, and uses a well-defined framework that is compatible with any other FMI-compatible code.

The coupling scheme is in continuous development and is currently under validation. Yet, it has proved its stability in a demanding domain-decomposition pressure-coupling to model the PPOOLEX MIX-04 experiment. Besides, the simulations reproduced the qualitative behaviour of an experiment with relevant common features with the foreseen technical scale application. Still, advancing the preliminary validation of this article to a solid final validation matrix based on PPOOLEX experiments requires additional work along different lines. So far, the primary phenomena for the foreseen technical scale application, the transport of non-condensable gases and the steam condensation in the PSS, showed a promising quantitative and qualitative agreement with the experimental results.

ACKNOWLEDGMENTS

Funded by the European Union

This work has been partially funded by the European Union through the SASPAM-SA project, HORIZON-EURATOM-2021-NRT-01, under the grant agreement ID: 101059853. Views and opinions expressed are however those of the author(s) only and do not necessarily reflect those of the European Union or European Commission-Euratom. Neither the European Union nor the granting authority can be held responsible for them.

This work is complementary to and partly motivated by the IAEA Open-source Nuclear Codes for Reactor Analysis (ONCORE) initiative, a collaborative framework for the development and application of open-source multiphysics to support research, education, and training in analysis of advanced reactor designs.

The authors want to acknowledge Markku Puustinen and his co-workers at LUT, who operate the PPOOLEX facility, for the simple and straightforward process of providing the experimental data for the validation of the PSS model.

REFERENCES

1. IAEA, *Energy, Electricity and Nuclear Power Estimates for the Period up to 2050* (2021).
2. IEA, *World Energy Outlook 2023* (2023).
3. OECD/NEA, *Meeting Climate Change Targets: The Role of Nuclear Energy* (2022).
4. IAEA, *SMR Regulators' Forum Pilot Project Report: Considering the Application of a Graded Approach, Defence-in-Depth and Emergency Planning Zone Size for Small Modular Reactors* (2018).
5. Morreale, A. C., "Severe Accident Analyis Of A Generic Integral Pressurized Water Reactor with MELCOR", *Fourth International Conference on Generation IV & Small Reactors (G4SR-4)*, Toronto, ON (2022).
6. "Horizon Europe: Safety Analysis of SMR with PAssive Mitigation strategies - Severe Accident", https://cordis.europa.eu/project/id/101059853.
7. "Webpage of the SASPAM-SA Project", https://www.saspam-sa.eu/#.
8. Gabrielli, F., Mascari, F., Bersano, A., Maccari, P., Ederli, S., Cazado, M., Sanchez-Espinoza, V. H., di Giuli, M., Bittan, J., Bakouta, N., Malicki, M., Lind, T., Yesipenko, Y., Zhabin, O., Gumenyuk, D., Kelm, S., Vázquez-Rodríguez, C., Koch, M., Krieger, J., Stahlberg, G., Garcia-Martin, M., Herranz, L. E., Reinke, N., Bentaib, A., Carenini, L., De la Rosa, J. C., Papera-Villacampa, O., Kudinov, P., Grishchenko, D., Kaliatka, A., Valincius, M., Constantin, M., Gianetti, F., Sevon, T., Groudev, P., Makarenko, M., Jankowski, T., and Reinecke, E.-A., "Analysis of Postulated Severe Accidents in Generic Integral Small Modular Reactors in the frame of the Horizon Euratom SASPAM-SA Project", *11th European Review Meeting on Severe Accident Research* (2024).
9. Gianetti, F., Imperatori, I., D'Onorio, M., Garcia, M., Herranz, L. E., Bersano, A., and Mascari, F., "Analyses of the MELCOR Capability to Simulate Integral PWR Using Passive Systems", *NURETH-20* (2023).

10. Maccari, P., Agnello, G., Mascari, F., and Ederli, S., "Analysis of BDBA sequences in a generic IRIS reactor using ASTEC code", *Annals of Nuclear Energy*, **182**, p. 109611 (2023).
11. Kelm, S., Kampili, M., Liu, X., George, A., Schumacher, D., Druska, C., Struth, S., Kuhr, A., Ramacher, L., Allelein, H.-J., Prakash, K. A., Kumar, G. V., Cammiade, L. M. F., and Ji, R., "The Tailored CFD Package 'containmentFOAM' for Analysis of Containment Atmosphere Mixing, H2/CO Mitigation and Aerosol Transport", *Fluids*, **6**(3), p. 100 (2021).
12. Fiorina, C., Clifford, I., Kelm, S., and Lorenzi, S., "On the development of multi-physics tools for nuclear reactor analysis based on OpenFOAM®: state of the art, lessons learned and perspectives", *Nuclear Engineering and Design*, **387**, p. 111604 (2022).
13. Sturm, K. and Kelm, S., "Towards a collaborative open-source platform for accident analysis with containmentFOAM and OpenModelica", *European Nuclear Young Generation Forum ENYGF'23* (2023).
14. Maccari, P., Mascari, F., Ederli, S., Meloni, P., and Manservisi, S., "ASTEC code DBA analysis of a passive mitigation strategy on a generic IRIS SMR", *Annals of Nuclear Energy*, **156**, p. 108194 (2021).
15. Kelm, S., Müller, H., Hundhausen, A., Druska, C., Kuhr, A., and Allelein, H.-J., "Development of a multi-dimensional wall-function approach for wall condensation", *Nuclear Engineering and Design*, **353**, p. 110239 (2019).
16. Vijaya Kumar, G., Cammiade, L. M. F., Kelm, S., Arul Prakash, K., Groß, E. M., Allelein, H.-J., Kneer, R., and Rohlfs, W., "Implementation of a CFD model for wall condensation in the presence of non-condensable gas mixtures", *Applied Thermal Engineering*, **187**, p. 116546 (2021).
17. Bhowmik, P. K., Schlegel, J. P., and Revankar, S., "State-of-the-art and review of condensation heat transfer for small modular reactor passive safety: Experimental studies", *International Journal of Heat and Mass Transfer*, **192**, p. 122936 (2022).
18. Mattsson, S. E., Elmqvist, H., and Otter, M., "Physical system modeling with Modelica", *Control Engineering Practice*, **6**(4), pp. 501–510 (1998).
19. George, A., Kelm, S., and Cheng, X., "CFD Modeling of Wall and Bulk Condensation by Two Phase Volume-of-Fluid Approach for Application to Containment Scale", *NURETH-20* (2023).
20. Laine, J., Puustinen, M., and Räsänen, A., "PPOOLEX experiments on the dynamics of free water surface in the blowdown pipe", *Nordic Nuclear Safety Research*, **NKS-281**, pp. 1–37 (2013).
21. Modelon Community, "FMI Library", https://github.com/modelon-community/fmi-library.
22. Zhang, K., "The multiscale thermal-hydraulic simulation for nuclear reactors: A classification of the coupling approaches and a review of the coupled codes", *Int J Energy Res*, **44**(5), pp. 3295–3315 (2020).
23. Sturm, K., "Development of a coupling scheme for Modelica and OpenFOAM to simulate the pressure suppression system of a small modular reactor (Master Thesis)", RWTH Aachen University (2023).
24. Casella, F. and Leva, A., "Modelica open library for power plant simulation: design and experimental validation", *3rd International Modelica Conference* (2003).

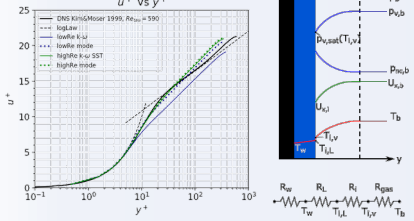

$$\frac{\partial(\rho\vec{U})}{\partial t} + \nabla\cdot(\rho\vec{U}\otimes\vec{U}) = -\nabla p + \nabla\cdot\tau + \rho\vec{g}$$

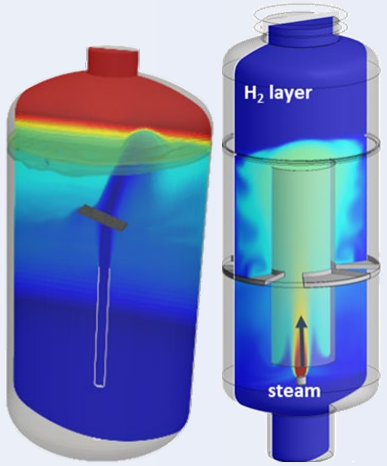

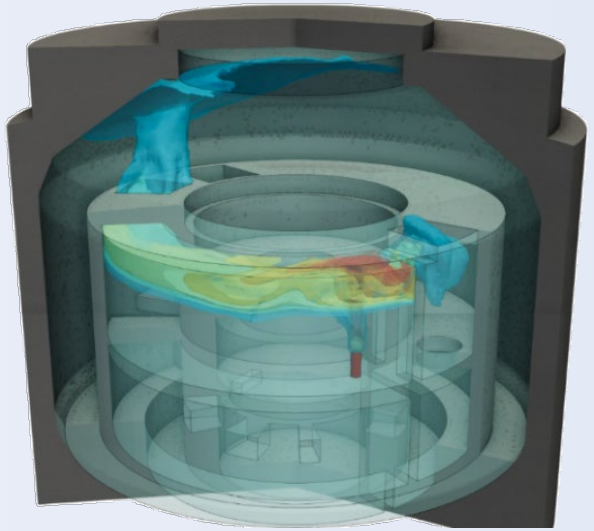

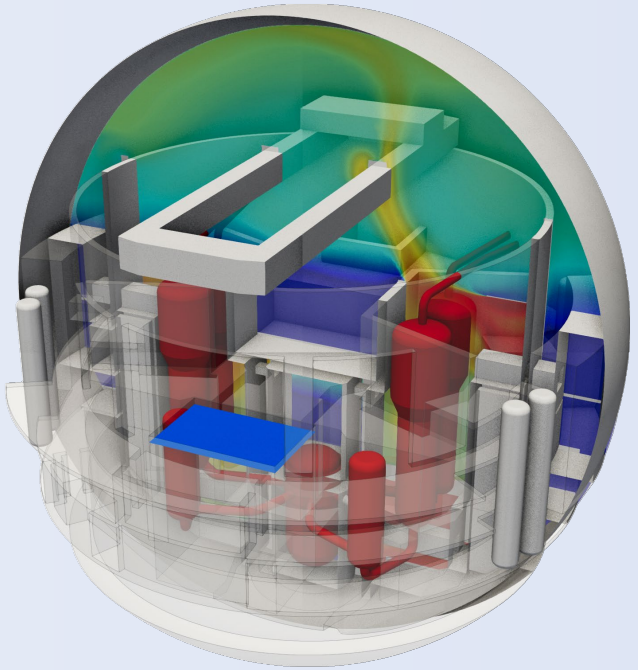

Development of containmentFOAM towards LW-SMR analyses

Carlos Vázquez-Rodríguez, Karl J. X. Sturm, Allen George, Stephan Kelm
Forschungszentrum Jülich (FZJ)

ERMSAR2024 - 11th Conference on Severe Accidents Research, May 13-16th 2024

containmentFOAM

Supported by:
Federal Ministry for the Environment, Nature Conservation, Nuclear Safety and Consumer Protection
based on a decision of the German Bundestag
Project No. 150 1633B

JÜLICH Forschungszentrum
Mitglied der Helmholtz-Gemeinschaft

OUTLINE

1. Background
2. containmentFOAM for LW-SMRs
3. System coupling by FMI
4. Validation with PPOOLEX
5. Conclusions

1. Background

SASPAM-SA

- The Horizon Euratom **SASPAM-SA Project**, coordinated by ENEA, investigates the **applicability of the severe accident know-how** accumulated on the operating large-LWR reactors **to the LW-SMR**
- SASPAM-SA will provide a **list of postulated severe accident scenarios** and will investigate the key elements to create a European independent point of view in the **safety of iPWRs with respect to DiD Level 4** (severe accident mitigation) and **DiD Level 5** (Offsite emergency response)

More during **Session 4.2** and
at the **Poster Session!**

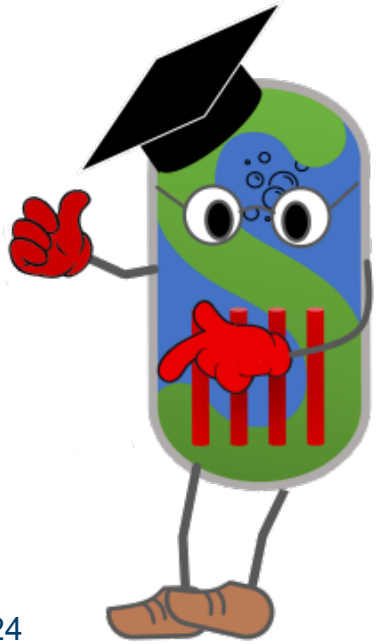

1. Background

Open-Source software for large dry PWR developed at FZJ

- Developments built on 10+ years' ANSYS CFX experience
  - Kelm, S. et al. 2016. A comparative assessment of different experiments on **buoyancy driven mixing processes** by means of CFD. Annals of Nuclear Energy. 93, (Jul. 2016), 50–57.
  - Kelm, S. et al. 2019. Development of a multi-dimensional wall-function approach for **wall condensation**. Nuclear Engineering and Design. 353, (Nov. 2019), 110239
  - Lehmkuhl, J. et al. 2016. Improvement of wall condensation modeling with suction wall functions for containment application. Nuclear Engineering and Design. 299, (Apr. 2016), 105–111.
  - Kelm, S. et al. 2019. A Review of the CFD Modeling Progress Triggered by ISP-47 on Containment Thermal Hydraulics, Nuclear Science and Engineering. 193, (Sept. 2018).
- **Tailoring OpenFOAM** for large dry containment flows
  - George, A. et al. 2023. Efficient CFD modelling of **bulk condensation, fog transport** and re-evaporation for application to containment scale. Nuclear Engineering and Design. 401, (Jan. 2023), 112067.
  - Liu, X. et al. 2022. Monte Carlo method with SNBCK nongray gas model **for thermal radiation** in containment flows. Nuclear Engineering and Design. 390, (Apr. 2022), 111689.
  - Vijaya Kumar, G. et al. 2021. Implementation of a CFD model for **wall condensation** in the presence of non-condensable gas mixtures. Applied Thermal Engineering. 187, (Mar. 2021), 116546.
- Solutions to model safety systems and technical components
  - Kelm, S. et al. 2021. The Tailored CFD Package 'containmentFOAM' for Analysis of Containment Atmosphere Mixing, **H2/CO Mitigation and Aerosol Transport**. Fluids. 6, 3 (Mar. 2021), 100.

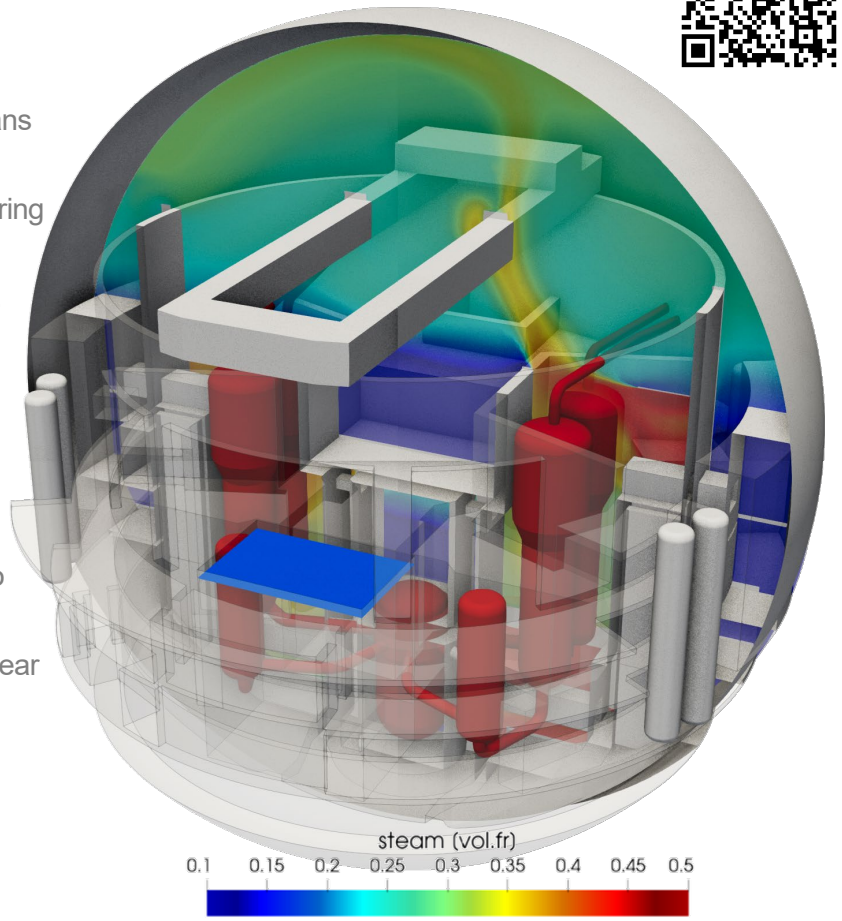

Steam distribution inside a dry PWR containment, 3D CAD Geometry by L. Serra-Lopez (UPM)

1. Background

FZJ participation in SASPAM-SA

- The **capabilities** of state-of-art European and non-European **integral SA codes** and **CFD** to simulate the key phenomena occurring in generic iPWR designs **will be evaluated in WP2**

Partners WP2	Codes Design I
GRS, IRSN	Support to the code users
EDF	**EDF-MAAP5.04**
KIT	**ASTECv3.1**
KTH	**MELCORv2.2**
PSI	**MELCORv2.2**
RATEN	Scenarios
RUB	**AC²**
SSTC NRS	**ANSYS CFX**
TRACTEBEL	**ASTECv2.2/v3.1**

Partners WP2	Codes Design II
GRS, IRNS	Support to the code users
CIEMAT	**MELCORv2.2**
ENEA	**ASTECv3.1/MELCORv2.2**
FZJ	**containmentFOAM**
JRC	**MAAP 5.06**
LEI	**AC²**
RATEN	Scenarios
UNIROMA1	**MELCORv2.2**

1. Background

FZJ participation in SASPAM-SA

- The **capabilities** of state-of-art European and non-European **integral SA codes** and **CFD** to simulate the key phenomena occurring in generic iPWR designs **will be evaluated in WP2**

WP2	Objective
GRS, IRSN	Support to the code users
KIT	**ASTECv3.1**
PSI	**MELCORv2.2**
RATEN	Scenarios
RUB	**AC²**
SSTC NRS	**ANSYS CFX**
TRACTEBEL	**ASTECv2.2/v3.1**

WP3	Objective
GRS, IRNS	Support to the code users
ENEA	**ASTECv3.1/MELCORv2.2**
JRC	**MAAP 5.06**
LEI	**AC²**
RATEN	Scenarios
UNIROMA1	**MELCORv2.2**

Where is the main added value of the use of containmentFOAM for SASPAM-SA objectives?

OUTLINE

1. Background
2. containmentFOAM for LW-SMRs
3. System coupling by FMI
4. Validation with PPOOLEX
5. Conclusions

2. containmentFOAM for LW-SMRs

A better understanding of its associated challenges via SASPAM-SA

- The containments of LW-SMR are smaller and generally have simpler geometries

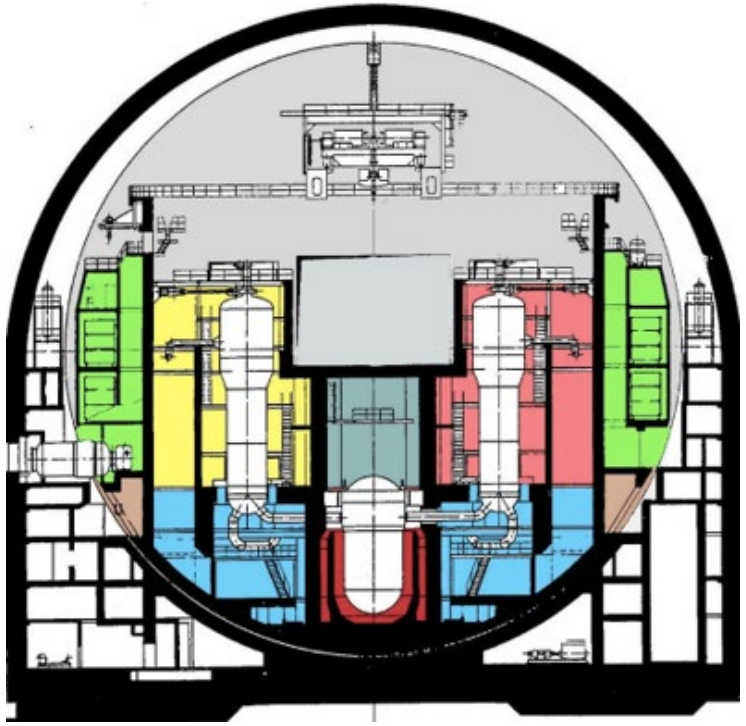

AMHYCO PWR-KWU
Free Volume **74 000 m³**

📖 L. S. Lopez et al., *AMHYCO Deliverable 2.1*

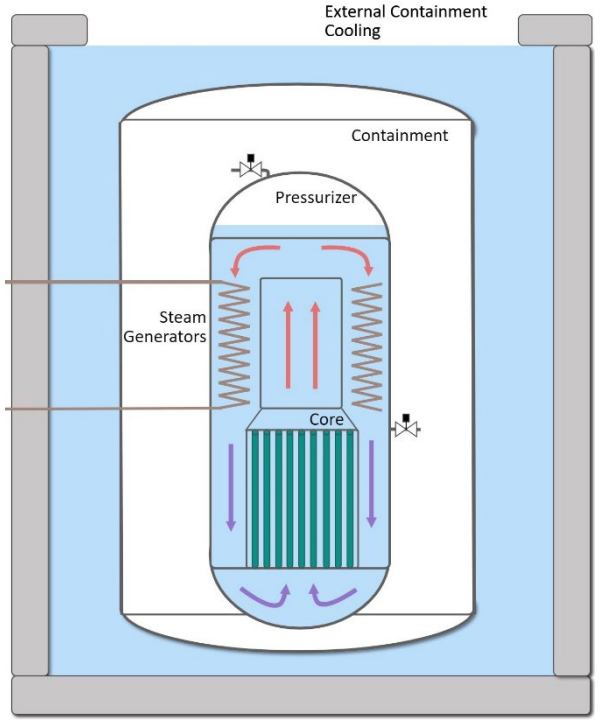

SASPAM-SA Desing 1
Free Volume **180 m³**

📖 F. Gabrielli et al., *SASPAM-SA Milestone 2.1*

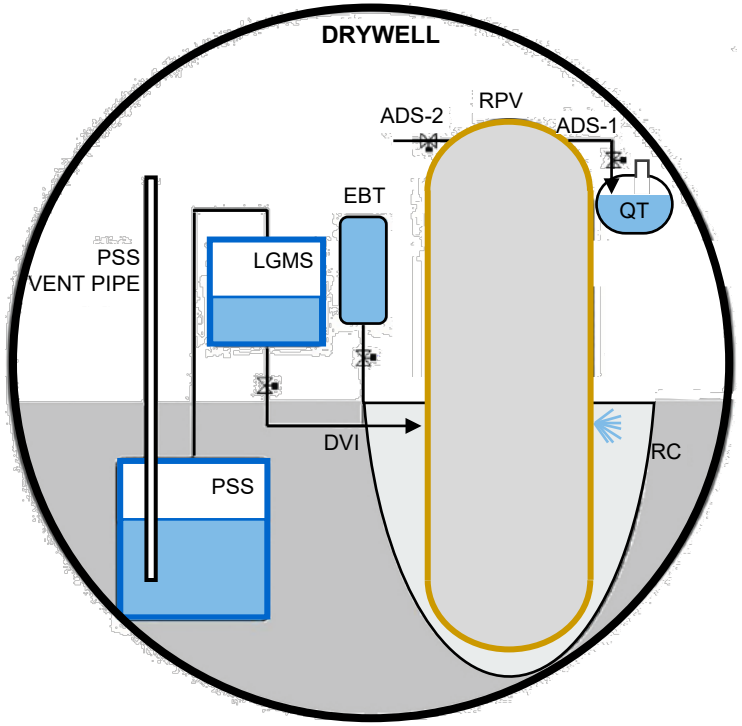

SASPAM-SA Desing 2
Free Volume **3700 m³**

📖 F. Gabrielli et al., *SASPAM-SA Milestone 2.1*

2. containment▽FOAM for LW-SMRs

A better understanding of its associated challenges via SASPAM-SA

- The **evaluation of SASPAM scenarios** improved our understanding of the modelling challenges

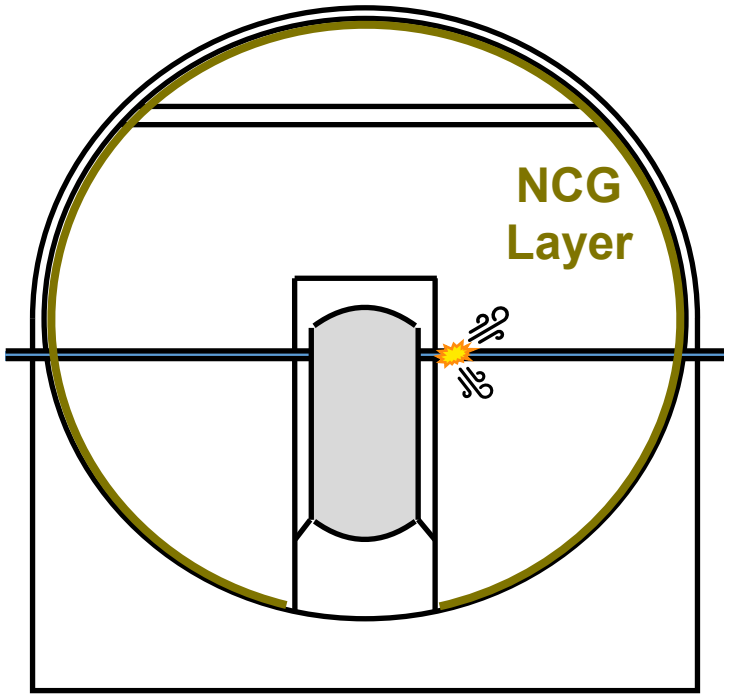

PWR-KWU

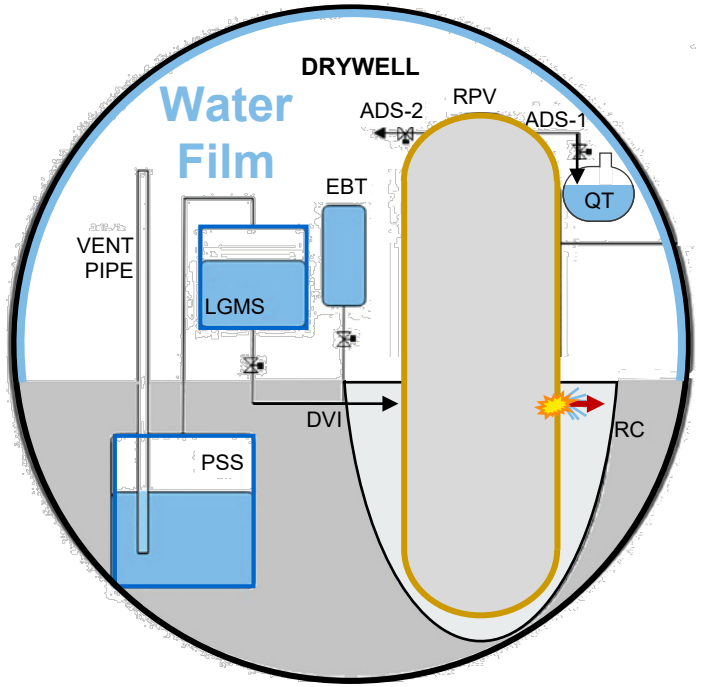

SASPAM – Design II

1. Blowdown and wall condensation

PWR-KWU

$0.05\ \frac{MWt}{m^3}$ $P_{blowdown} < 4\ bar$

SASPAM – Design I

$0.88\ \frac{MWt}{m^3}$ $P_{blowdown} < 40\ bar$

SASPAM – Design II

$0.27\ \frac{MWt}{m^3}$ $P_{blowdown} < 14\ bar$

2. containmentFOAM for LW-SMRs

A better understanding of its associated challenges via SASPAM-SA

- The **evaluation of SASPAM scenarios** improved our understanding of the modelling challenges

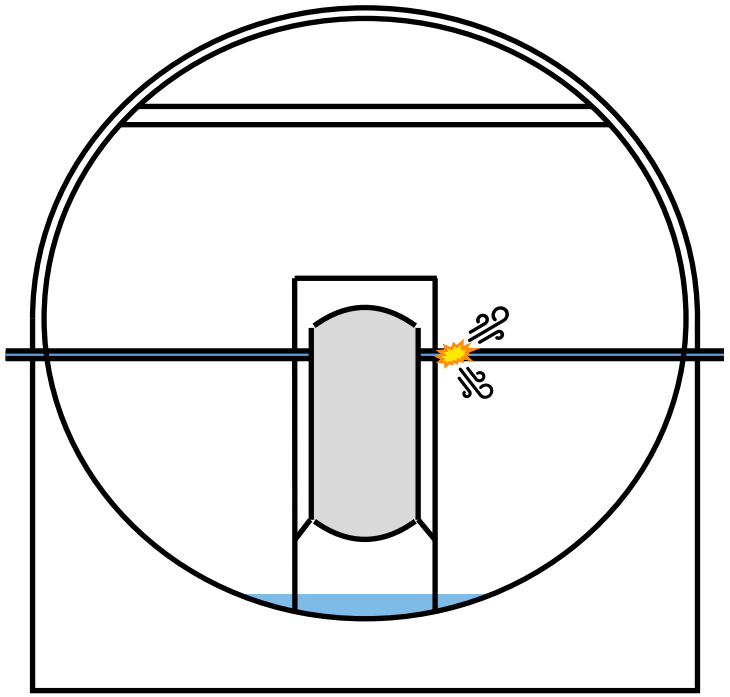

PWR-KWU

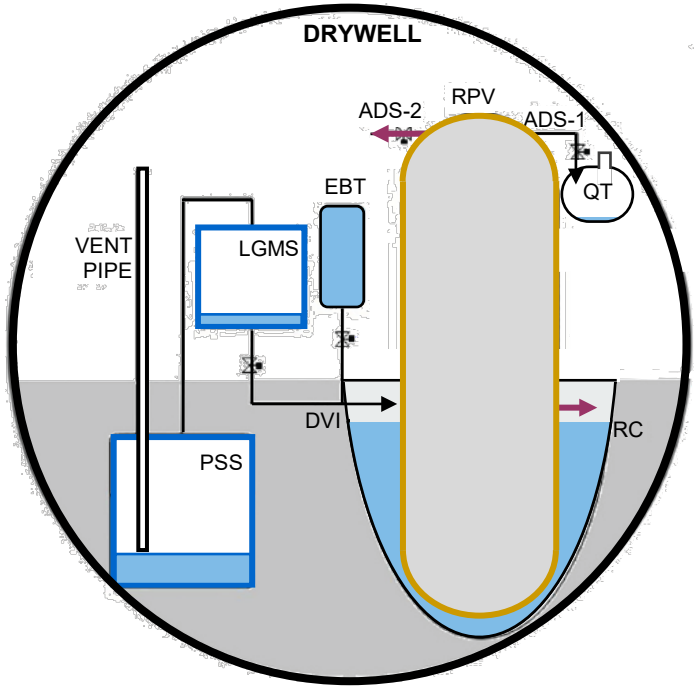

SASPAM – Design II

2. Liquid in the containment

PWR-KWU

% free volume occupied by liquid — **negligible**

SASPAM – Design I

% free volume occupied by liquid — **Up to 40 %**

SASPAM – Design II

% free volume occupied by liquid — **Up to 15%**

2. containment FOAM for LW-SMRs

A better understanding of its associated challenges via SASPAM-SA

- The **evaluation of SASPAM scenarios** improved our understanding of the modelling challenges

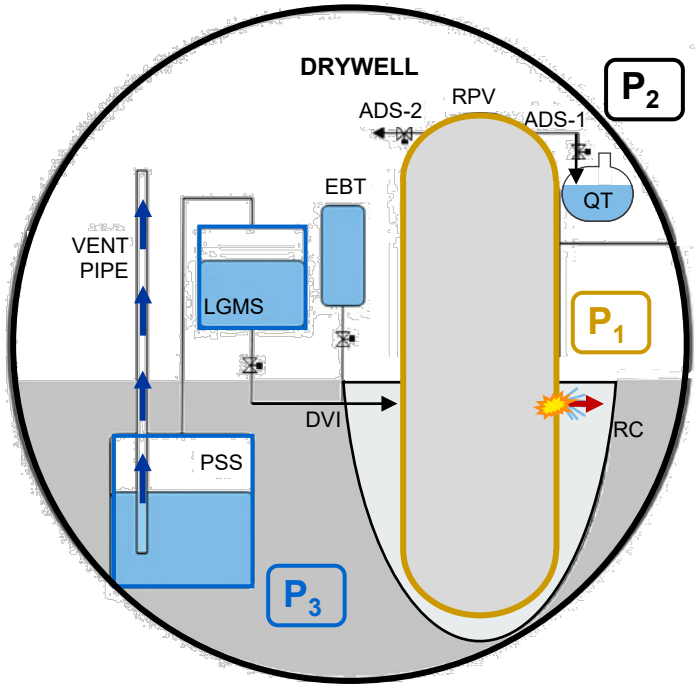

Design II – Post-blowdown

$P_3 > P_2 \approx P_1$

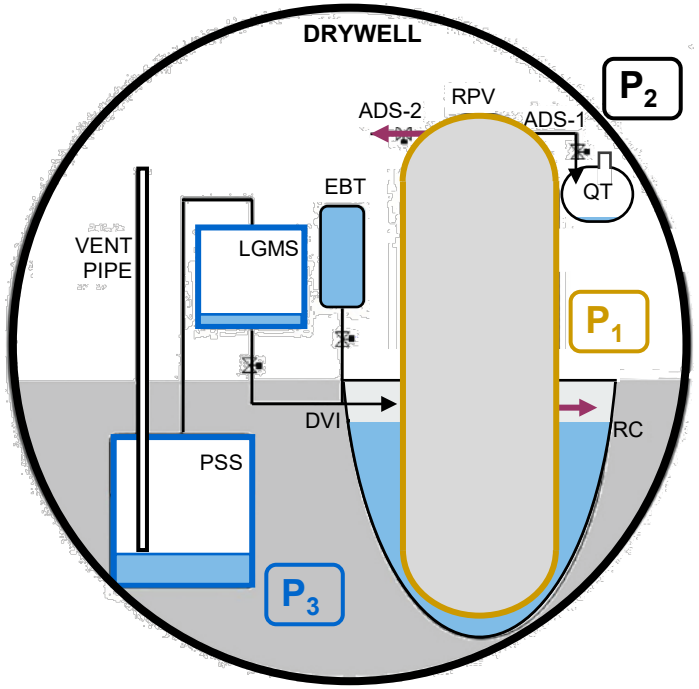

Design II – Long-term Cooling

$P_3 \approx P_2 \approx P_1$

2. Liquid in the containment

(plays a key role in the safety analysis)

2. containmentFOAM for LW-SMRs

A better understanding of its associated challenges via SASPAM-SA

- The **evaluation of SASPAM scenarios** improved our understanding of the modelling challenges

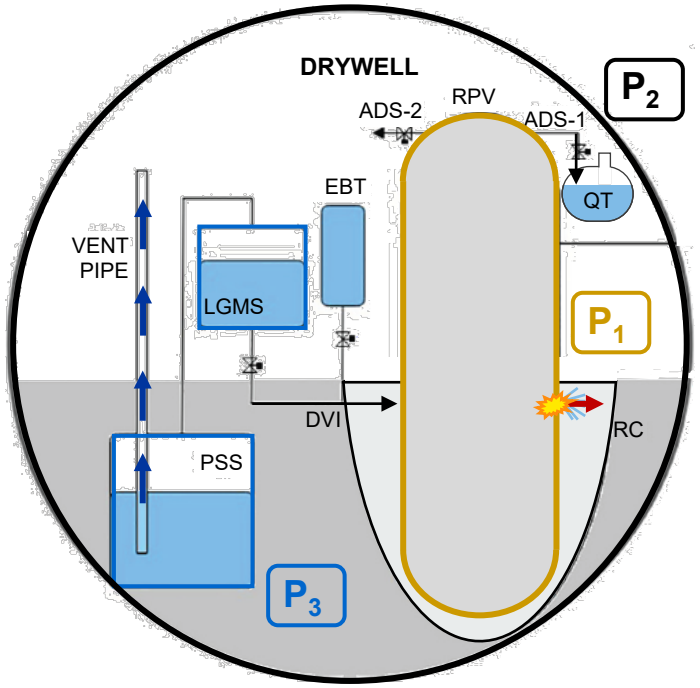

SASPAM – Design II

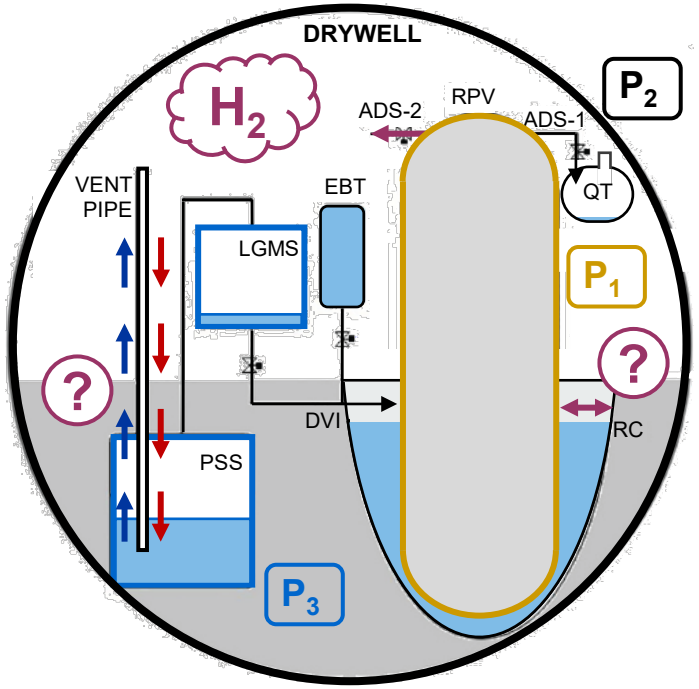

Design II – Severe accident?

$$P_3 \approx P_2 \approx P_1$$

2. Liquid in the containment

(plays a key role in the safety analysis)

↓

3. Strong coupling between the containment and the passive safety

↓

Evolution of the containment thermal-hydraulics as a key issue for the SA unfolding

2. containmentFOAM for LW-SMRs

Defining the added value of containmentFOAM to SASPAM-SA

- Where is the main added value of the use of containmentFOAM for SASPAM-SA objectives?
  - The detailed calculation of the containment thermal hydraulics using **containmentFOAM will offer complementary insights, and ideally reinforce, the SA codes predictions**

- Therefore, the **main goals of FZJ during SASPAM-SA WP2**, which should be understood as the **preparatory work before performing SA analysis (WP5)**, were:
  - Development of a CFD model of the Design-II containment based on the common databased prepared for the Severe Accident (SA) codes
  - Define a strategy to perform insightful comparisons between the LP codes and containmentFOAM
  - **Evaluating bottlenecks (if any) to model the considered SA sequences with containmentFOAM**

OUTLINE

1. Background
2. containmentFOAM for LW-SMRs
3. System coupling by FMI
4. Validation with PPOOLEX
5. Conclusions

3. System coupling by FMI

Use of OpenModelica to enable a multi-fidelity modelling approach

- Coupling containmentFOAM with OpenModelica
  - Modelica:
    - Upgrade to **ease a multi-fidelity modelling approach** with containmentFoam using **open-source** software
    - A modelling language designed for the study of engineering system dynamics
    - equation-based, modelling (DAE systems) in terms of physical/engineering principles (mass, energy and momentum balance + constitutive equation + constraints)
    - enables packaging and exporting Modelica system models as an executable simulator **(Functional Mockup Units 'FMU')** in accordance with the **Functional Mock-up Interface 2.0 (FMI2)** standard

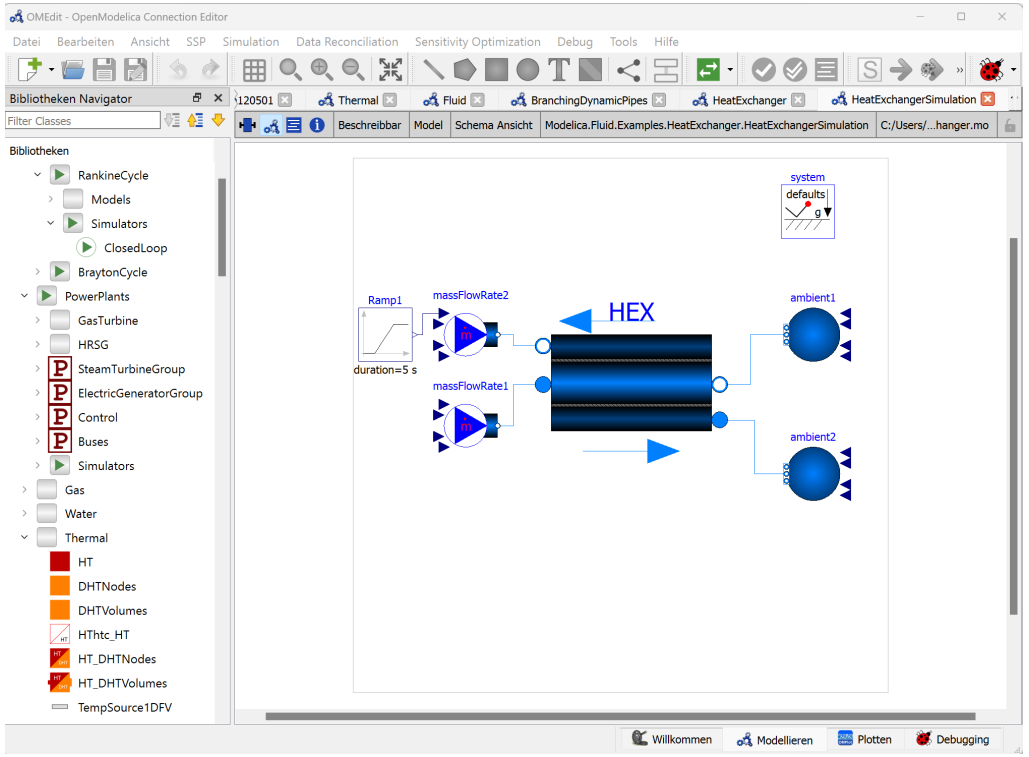

https://openmodelica.org/

P. Fritzson et al., "The OpenModelica Integrated Environment for Modeling, Simulation, and Model-Based Development," Modeling, Identification and Control: A Norwegian Research Bulletin, vol. 41, no. 4, pp. 241–295, 2020.

credits to K. Sturm

3. System coupling by FMI

Information Exchange

- Coupling containment FOAM with OpenModelica
  - Packaging FMU's for co-simulation via FMI (https://github.com/modelon-community/fmi-library)

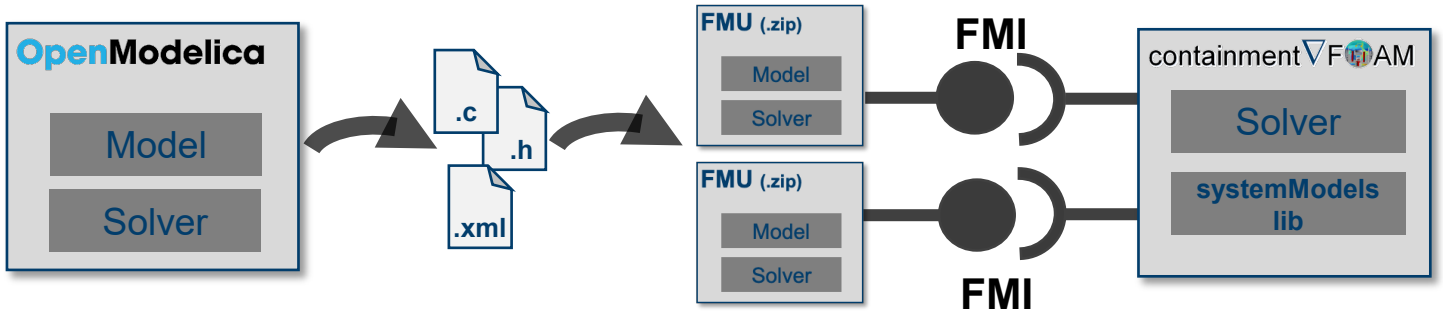

  - Well-established **code-agnostic standards** (Modelica and FMI). Any program can be packaged into FMU's and provided for coupled simulation (e.g., REKODIREKT)

🕮 https://fmi-standard.org/
https://www.samares-engineering.com/en/2021/01/21/part-9-co-simulation-of-sysml-and-other-models-through-fmi/

credits to K. Sturm

3. System coupling by FMI

Use of OpenModelica to enable a multi-fidelity modelling approach

- Coupling containmentFOAM with OpenModelica
  - `systemModels` library:
    - C++ - implementation of FMU4FOAM functionality (https://pypi.org/project/FMU4FOAM) in containmentFOAM
    - Explicit and semi-implicit coupling schemes incl. sub cycling of FMU
    - Compatible with domain decomposition and domain overlapping
    - Restarts
    - Different coupling topologies

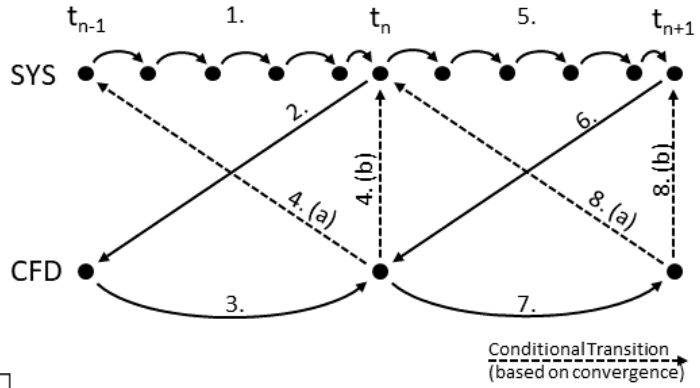

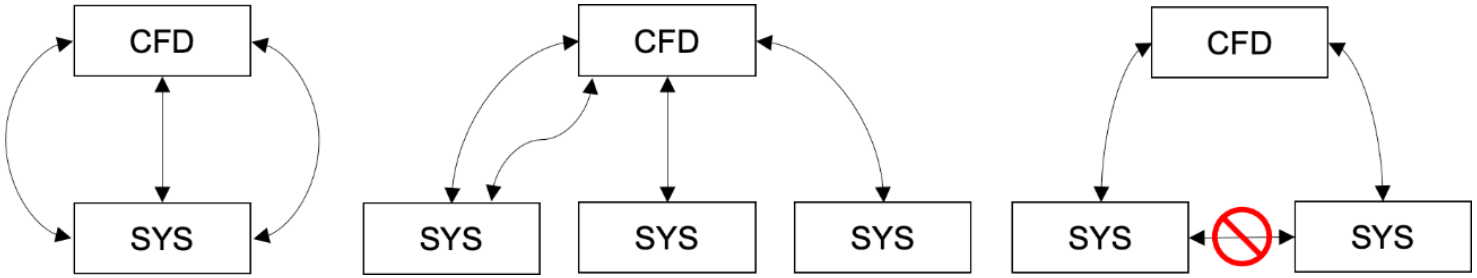

🕮 https://fmi-standard.org/
https://www.samares-engineering.com/en/2021/01/21/part-9-co-simulation-of-sysml-and-other-models-through-fmi/

credits to K. Sturm

OUTLINE

1. Background
2. containmentFOAM for LW-SMRs
3. System coupling by FMI
4. Validation with PPOOLEX
5. Conclusions

4. Validation with PPOOLEX experiments

Comparability with SASPAM-SA Issues

- The **PPOOLEX MIX series** provides a suitable database to evaluate the coupling scheme, the system model for the Pressure Suppression System (PSS) and the reformulated condensation model

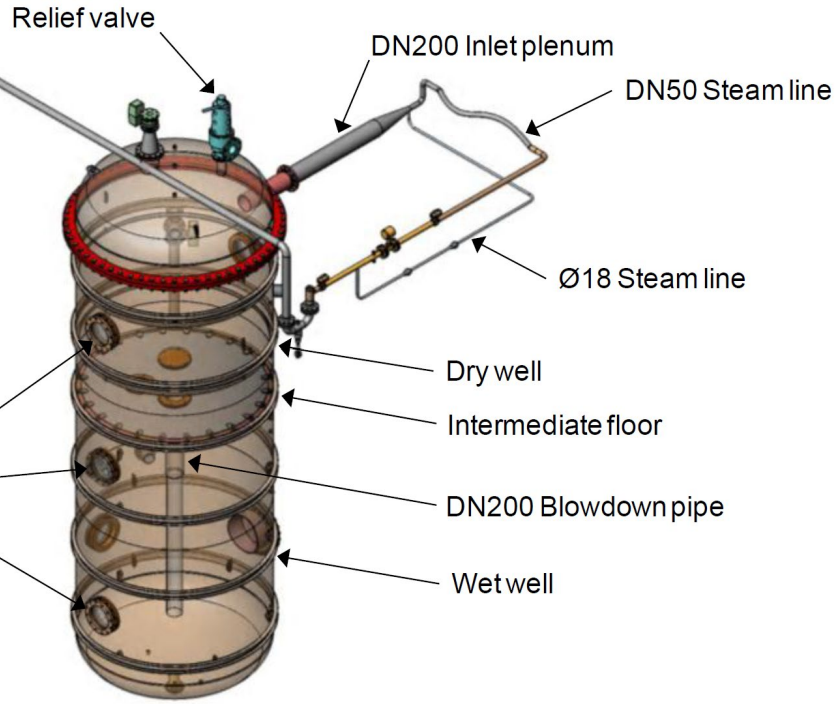

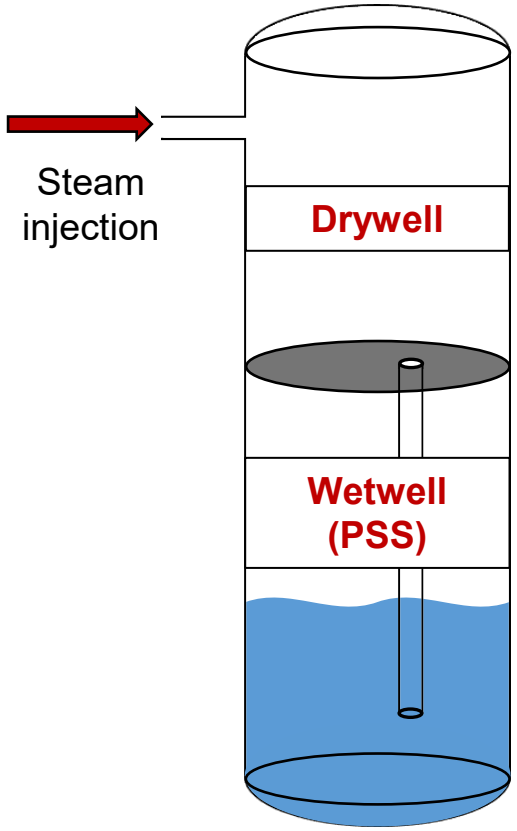

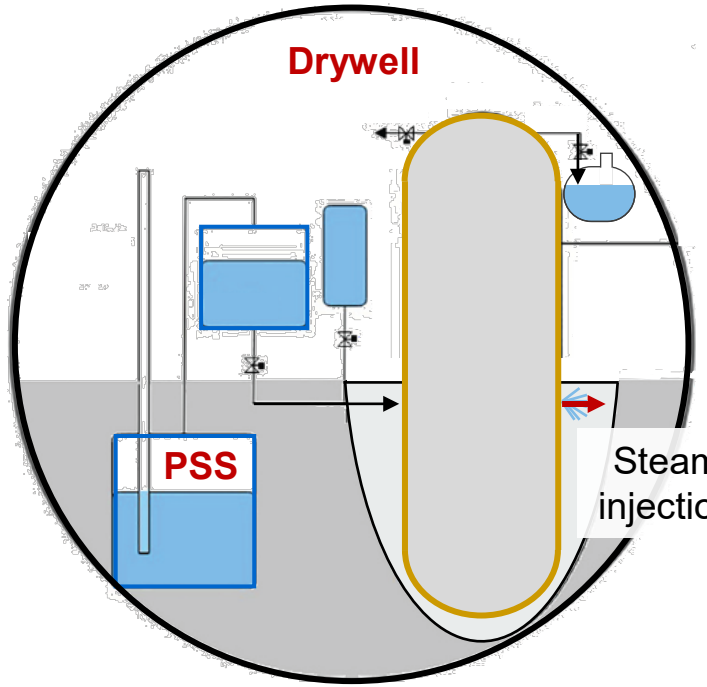

📖 J. Laine et al., *PPOOLEX experiments on the dynamics of free water surface in the blowdown pipe,* NKS-281, 2013

4. Validation with PPOOLEX experiments

Comparability with SASPAM-SA Issues

- The PPOOLEX MIX series provides a suitable database to evaluate the **coupling scheme**, the system model for the Pressure Suppression System (PSS) and the reformulated condensation model

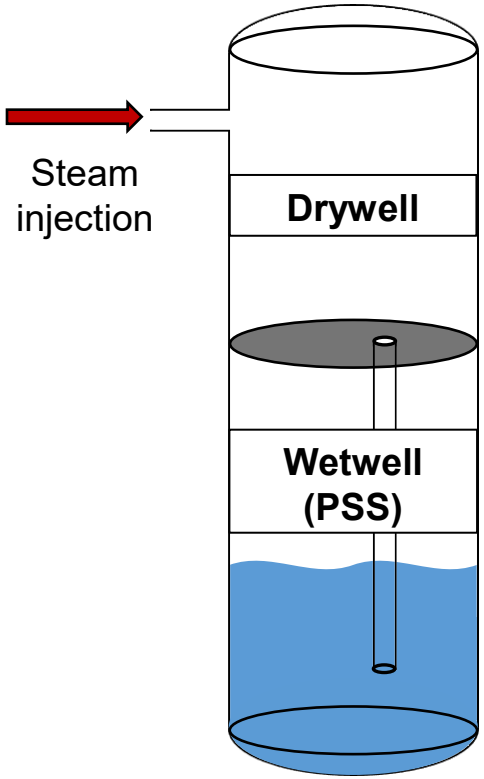

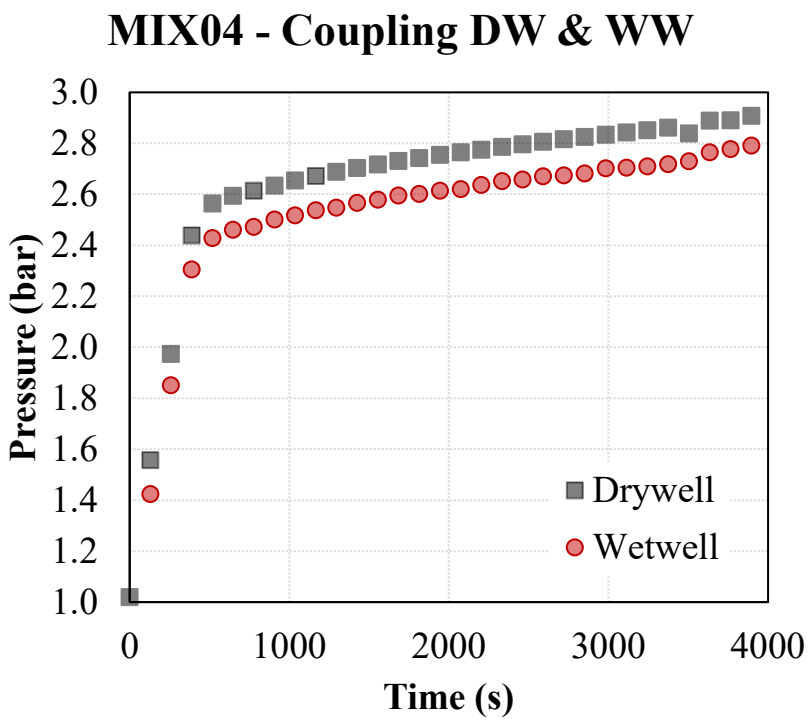

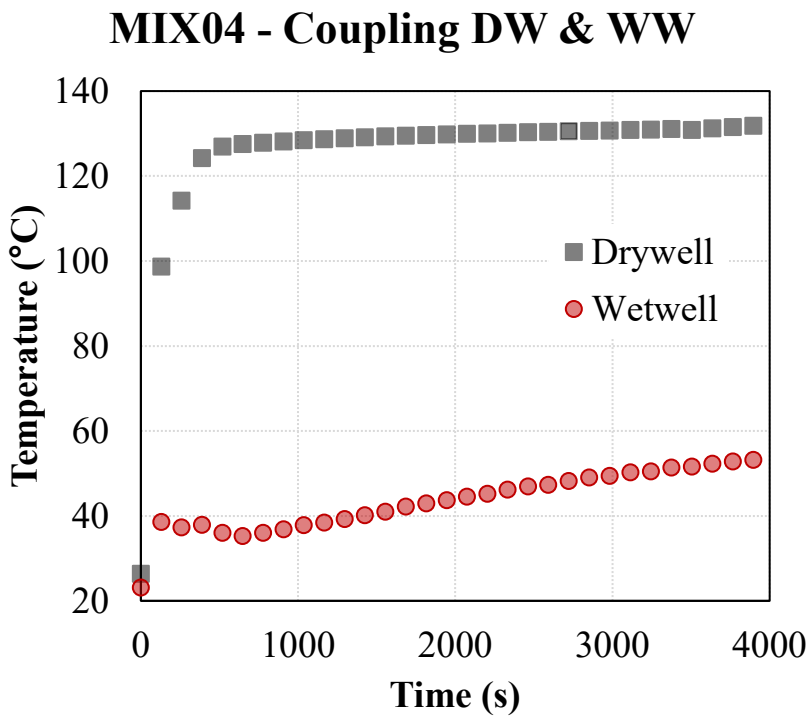

📖J. Laine et al., *PPOOLEX experiments on the dynamics of free water surface in the blowdown pipe,* NKS-281, 2013

4. Validation with PPOOLEX experiments

Comparability with SASPAM-SA Issues

- The PPOOLEX MIX series provides a suitable database to evaluate the coupling scheme, the system model for the **Pressure Suppression System (PSS)** and the reformulated condensation model

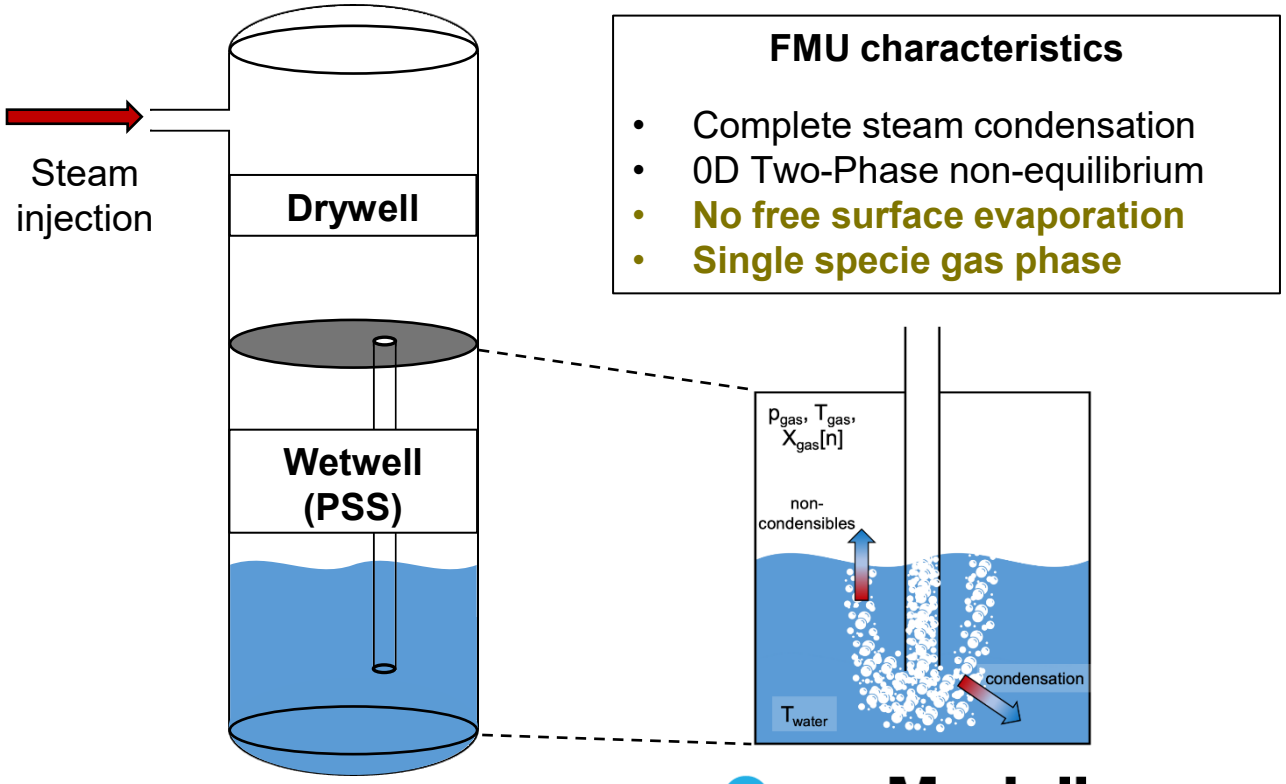

FMU characteristics

- Complete steam condensation
- 0D Two-Phase non-equilibrium
- **No free surface evaporation**
- **Single specie gas phase**

OpenModelica

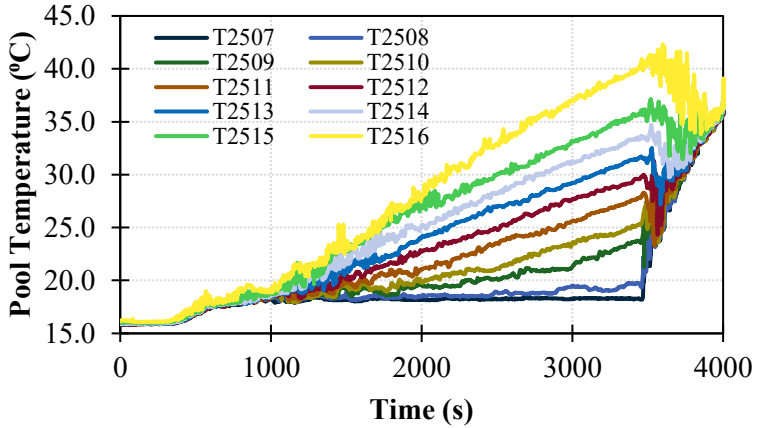

Stratified Pool

Average Temperature

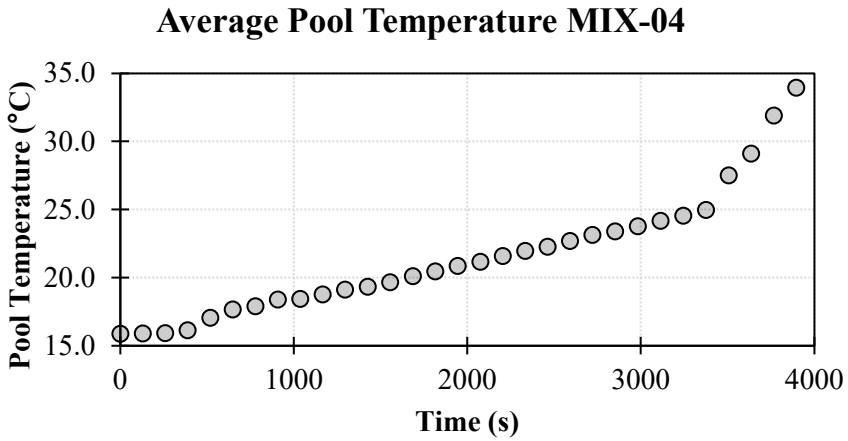

J. Laine et al., *PPOOLEX experiments on the dynamics of free water surface in the blowdown pipe,* NKS-281, 2013

4. Validation with PPOOLEX experiments

Comparability with SASPAM-SA Issues

- The PPOOLEX MIX series provides a suitable database to evaluate the coupling scheme, the system model for the Pressure Suppression System (PSS) and the **reformulated condensation model**

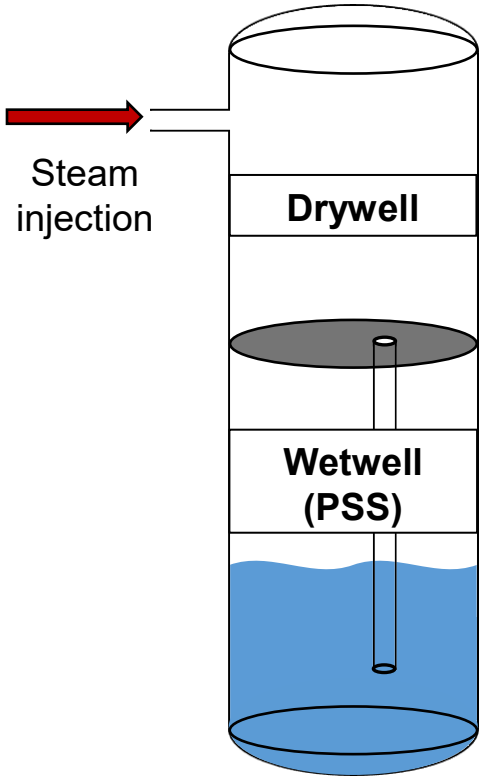

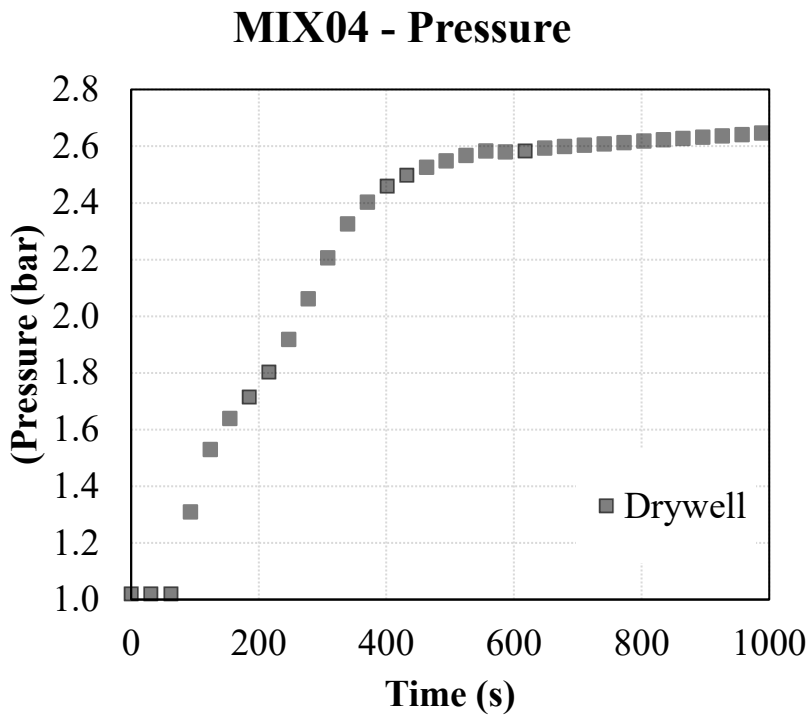

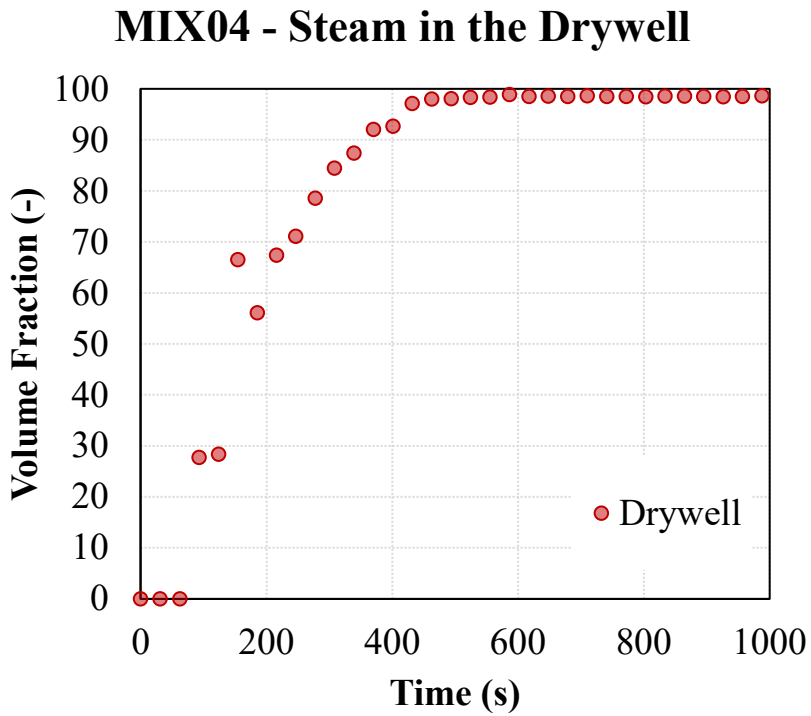

📖J. Laine et al., *PPOOLEX experiments on the dynamics of free water surface in the blowdown pipe,* NKS-281, 2013

4. Validation with PPOOLEX experiments

Strategy towards the validation of the coupling

- A **step-wise increase of the complexity** has been postulated for the validation of the coupling based on the PPOOLEX MIX Series. The **Step 1 and Step 2 have been completed** and will be presented.

RUN 1

Focused on the pressure-coupling stability
- ✓ Simple CFD model (no-wall condensation)
- ✓ Simple FMU
- ✓ Single coupling interface

RUN 2

Introducing a second coupling interface
- ✓ Simple CFD model (no-wall condensation)
- ✓ Simple FMU
- ✓ Pressure + Thermal couplings

RUN 3

Implementation of and advanced FMU
- ✓ Simple CFD model (no-wall condensation)
- ✓ Advanced FMU (including HTC correlations, heat losses, and pool evaporation)

RUN 4

Focused on condensation on the Drywell
- ✓ Improved CFD model with film-wise condensation and conjugate heat transfer
- ✓ Advanced FMU

4. Validation with PPOOLEX experiments

Modelling approach – RUN1

- The **RUN1** was focused on evaluating the **stability of the pressure-coupling** and the evolution of the **global variables** of the PPOOLEX MIX Series (pressure and pool average temperature)

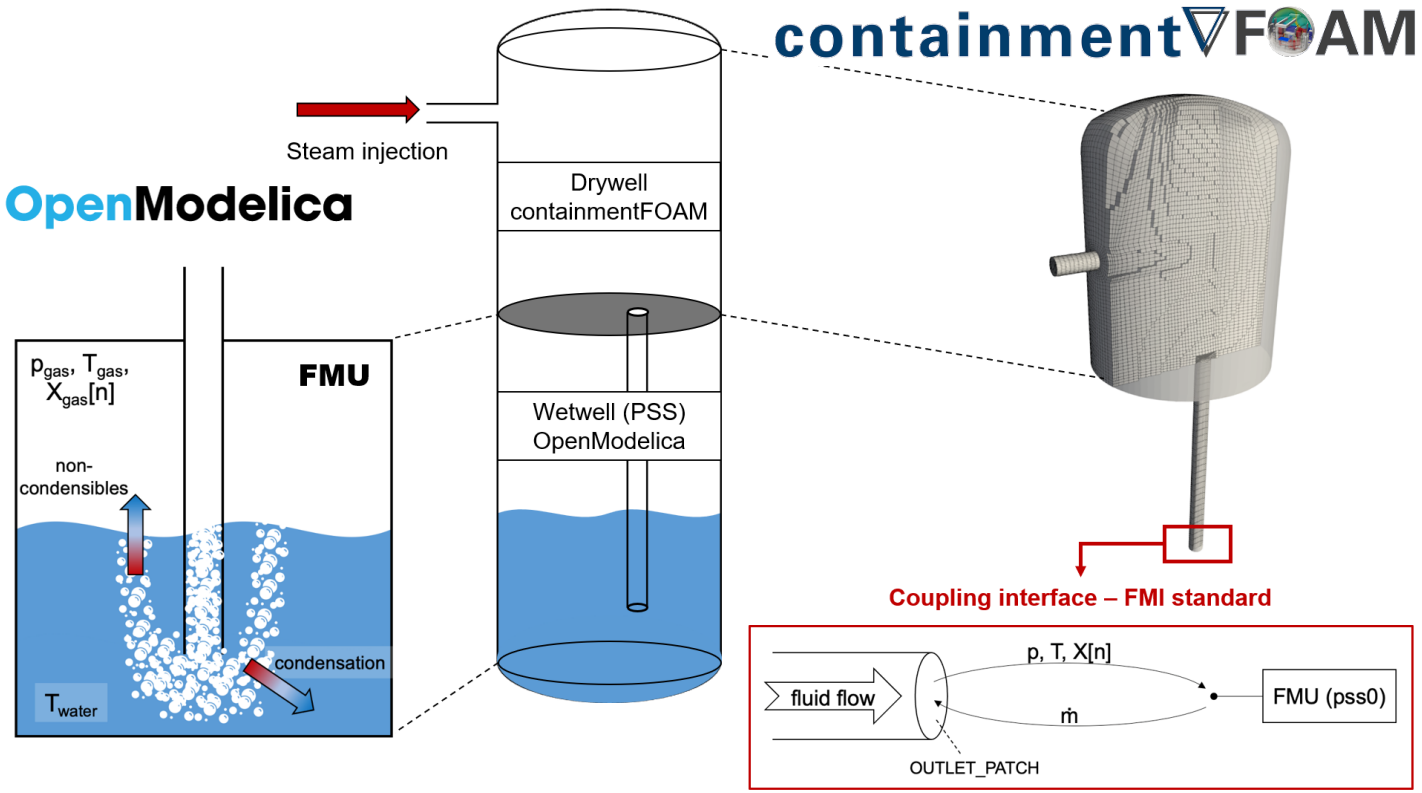

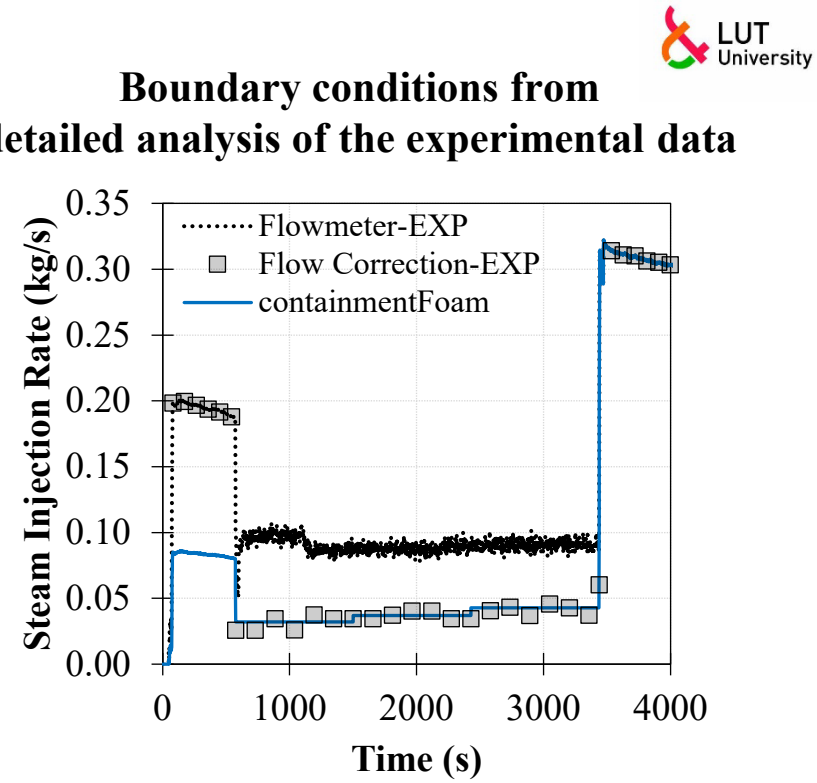

4. Validation with PPOOLEX experiments

Results RUN1

- Experimental results qualitatively reproduced. Stable **pressure-coupling with acceptable computational cost**. 16 cores → 10k fluid cells/core → simulation completed in **two days**

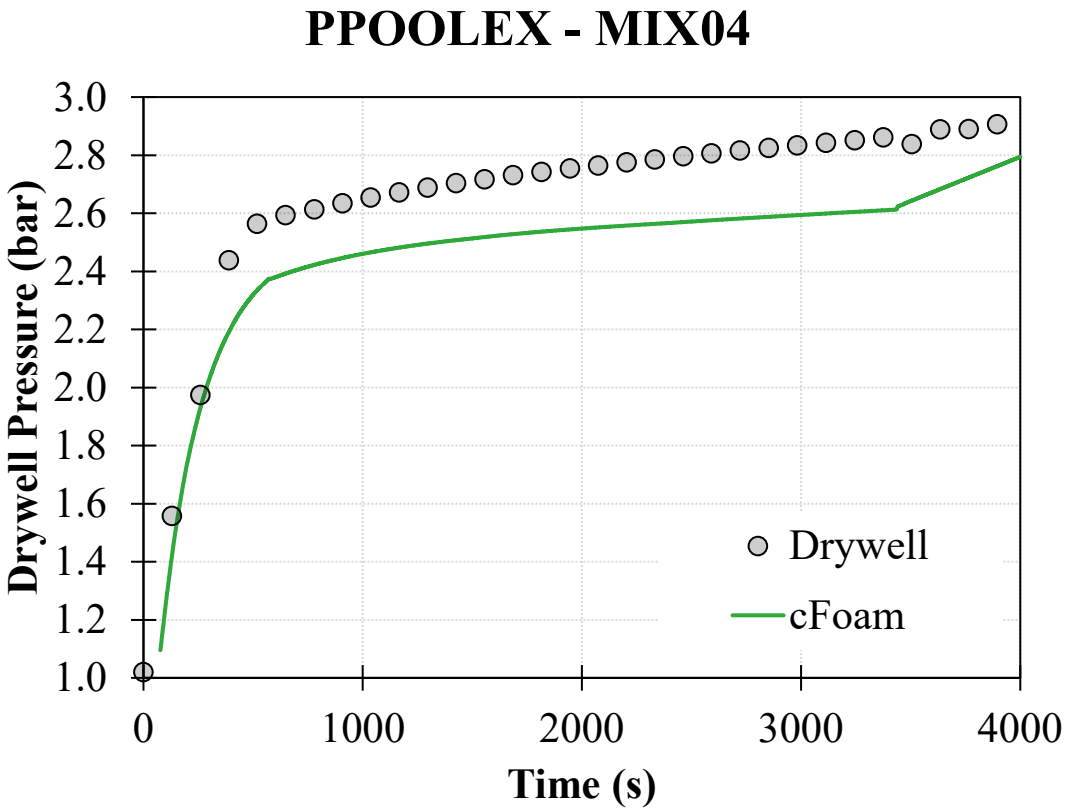

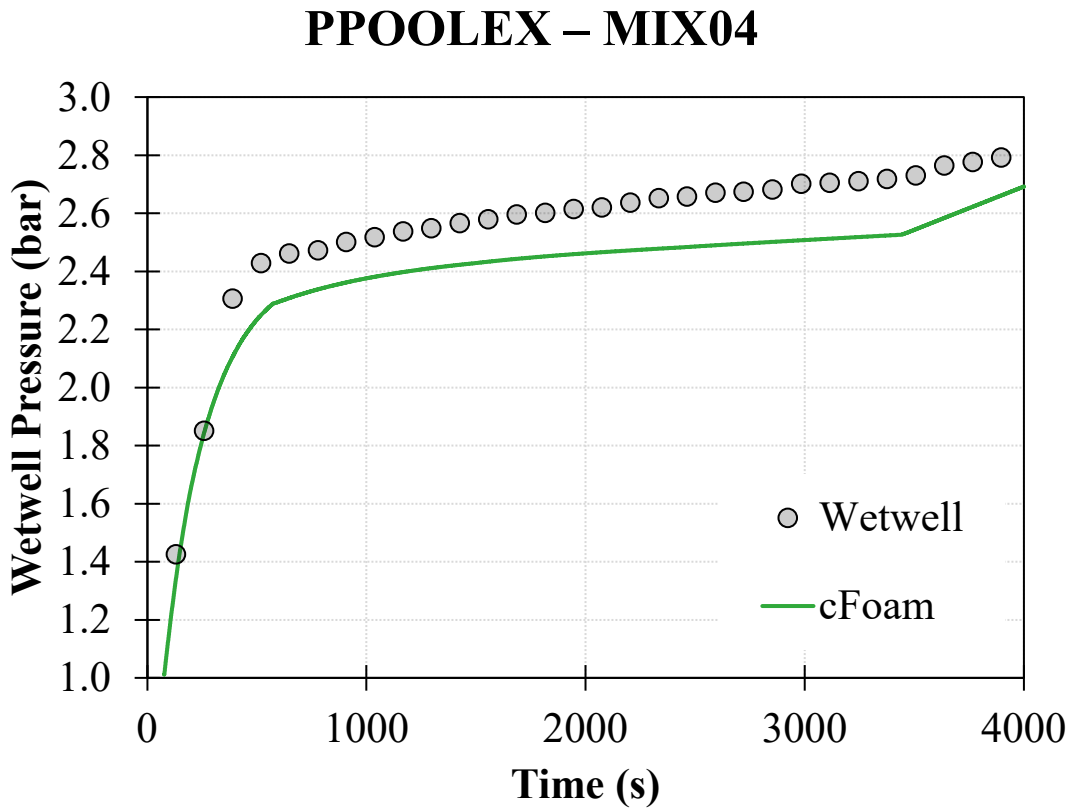

4. Validation with PPOOLEX experiments

Results RUN1

- The simple PSS model replicates the global behaviour of the suppression pool

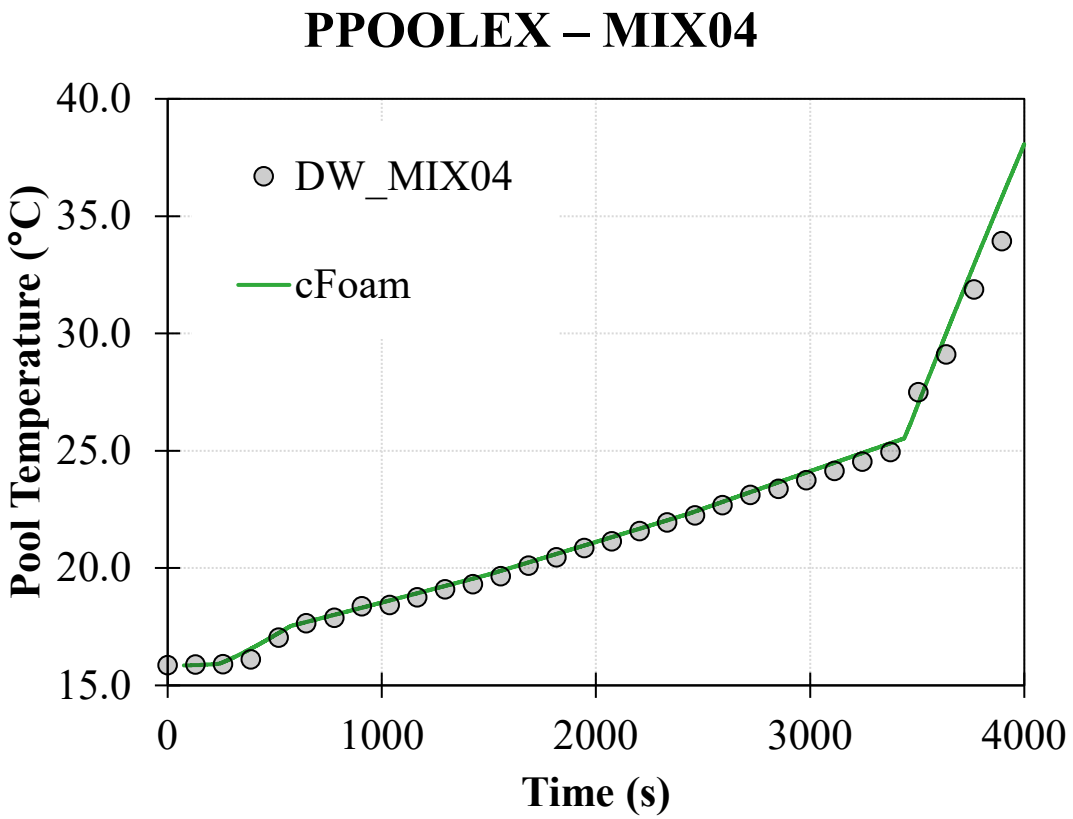

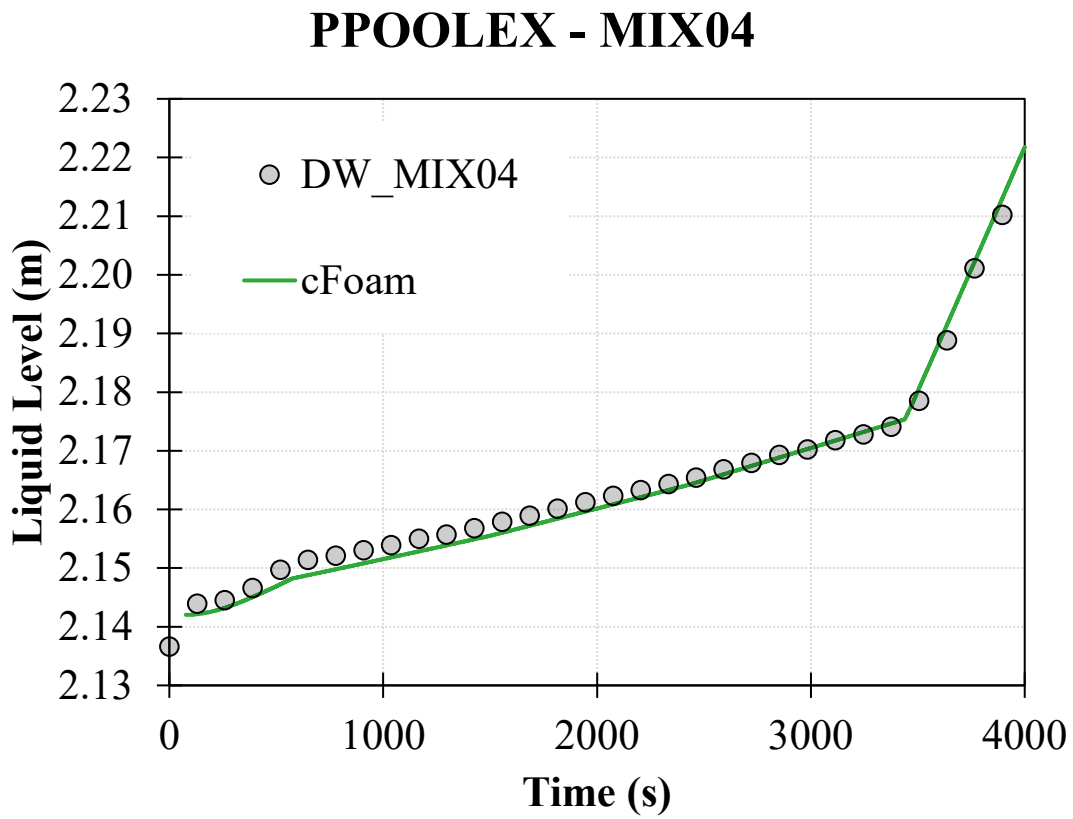

4. Validation with PPOOLEX experiments

Results RUN1

- The modelling approach has been successfully tested using different experiments of the MIX series

PPOOLEX - MIX04

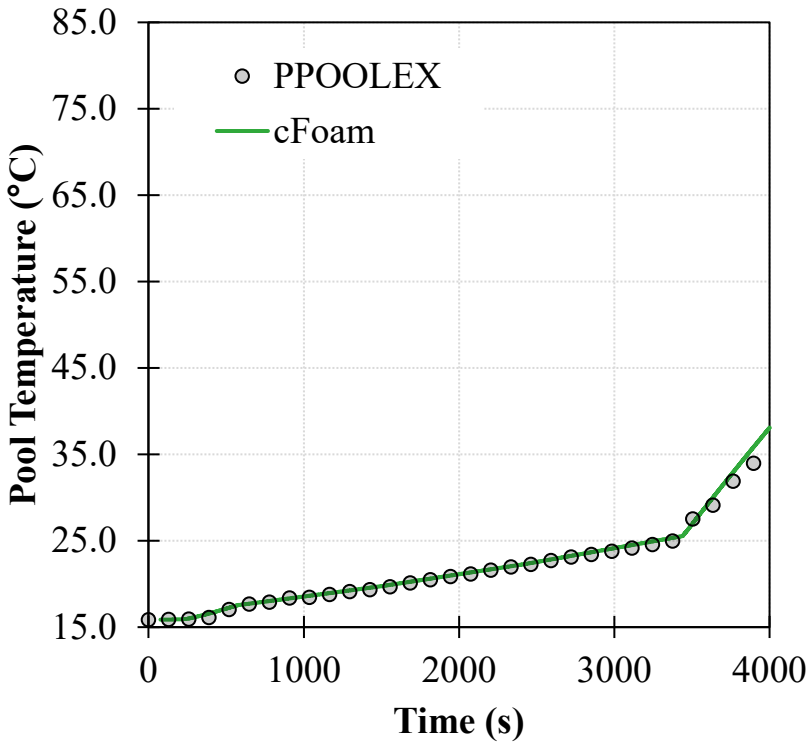

PPOOLEX – MIX05

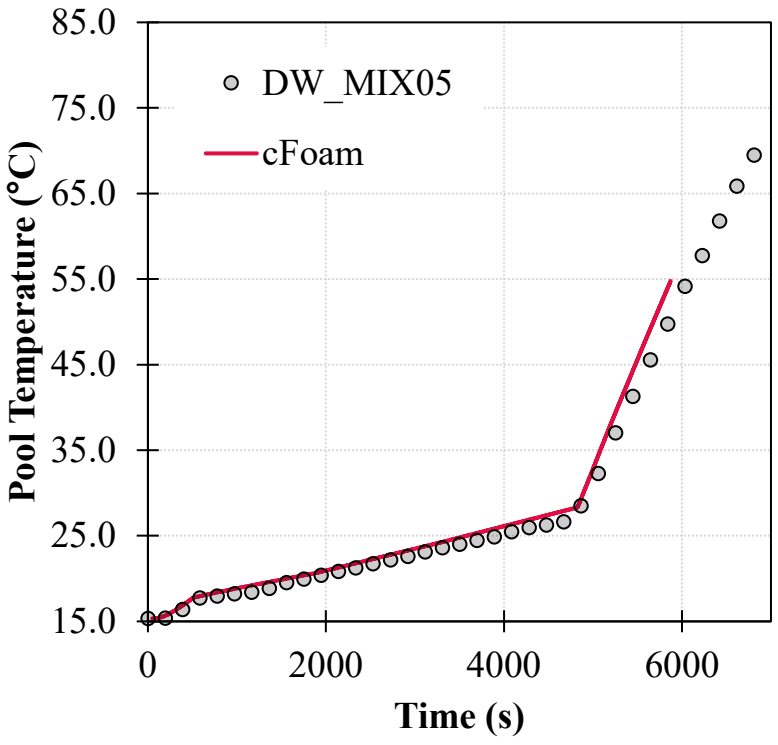

PPOOLEX - MIX06

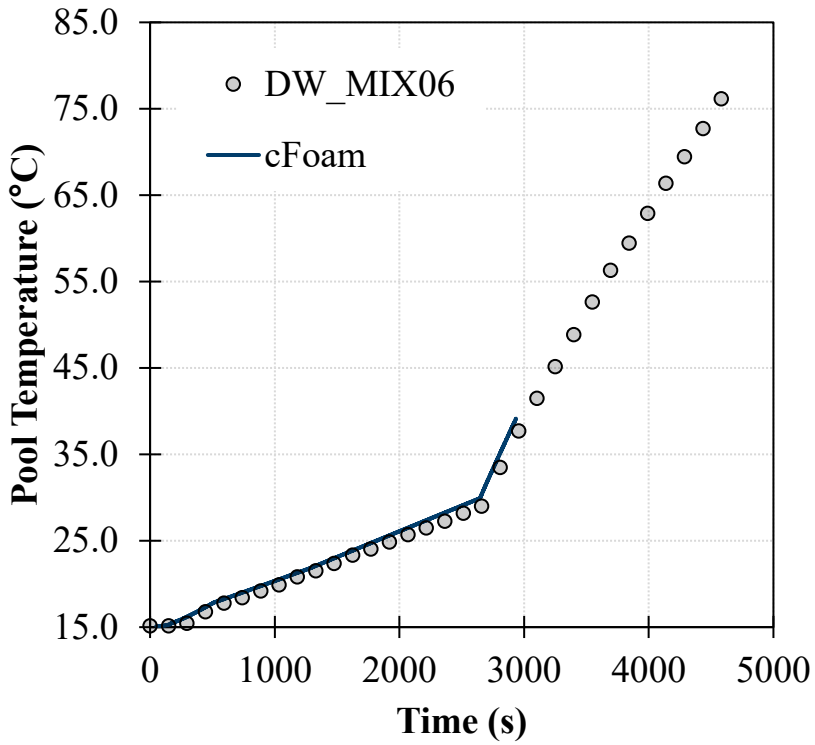

4. Validation with PPOOLEX experiments

Results RUN1

- The analyses of RUN1 revealed that the understimation of the pressure evolution could be due to the **absence of a heat flux from the Drywell to the gas space of the Wetwell**

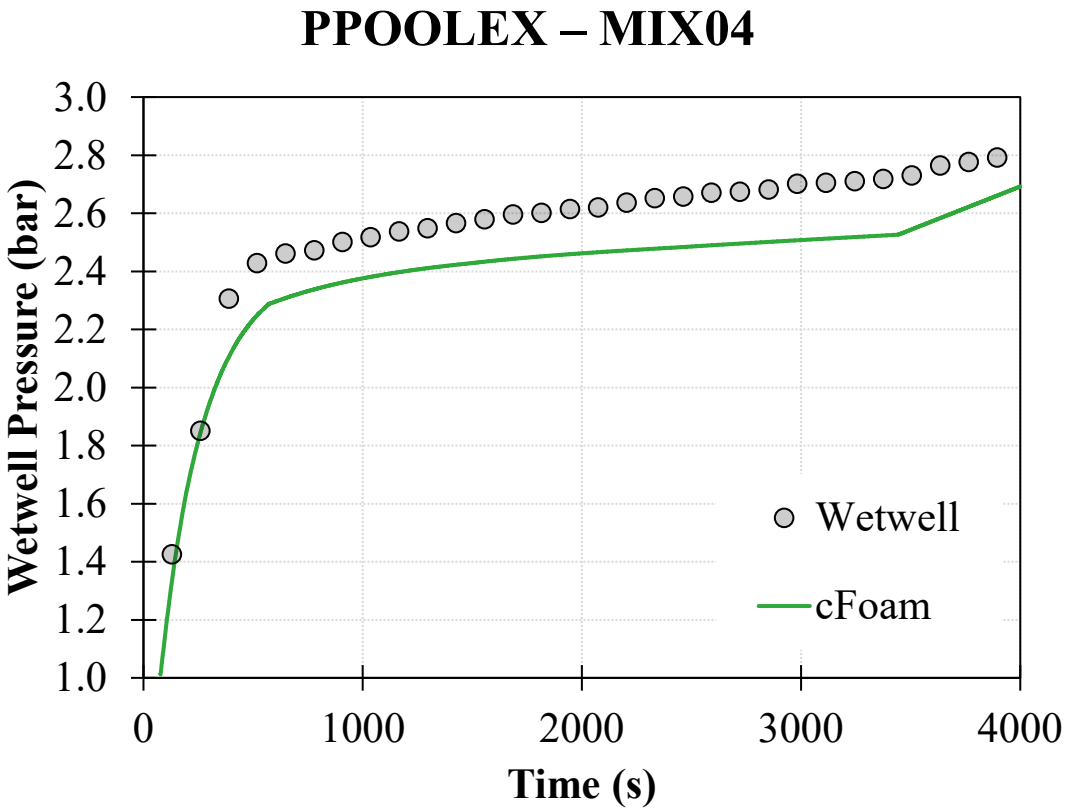

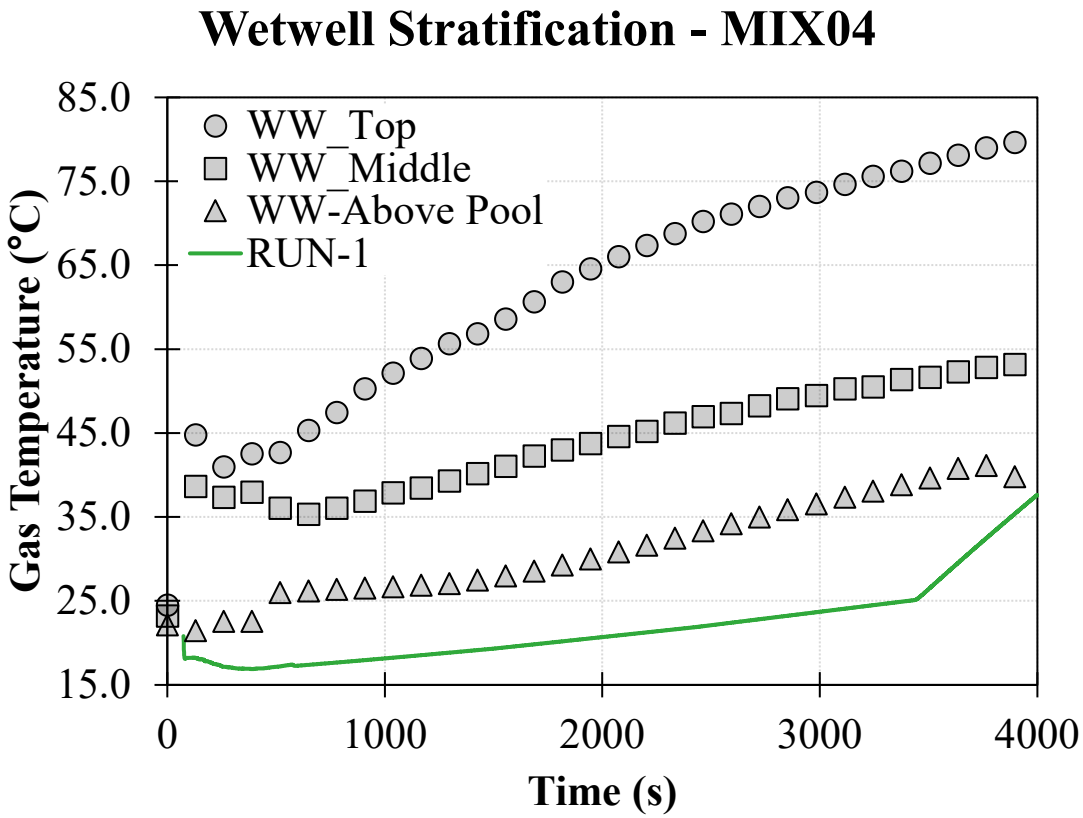

4. Validation with PPOOLEX experiments

Modelling approach – RUN2

- The **RUN2** included a second coupling interface (preliminary!) to **include the aforementioned heat flux from the Drywell to the Wetwell**.

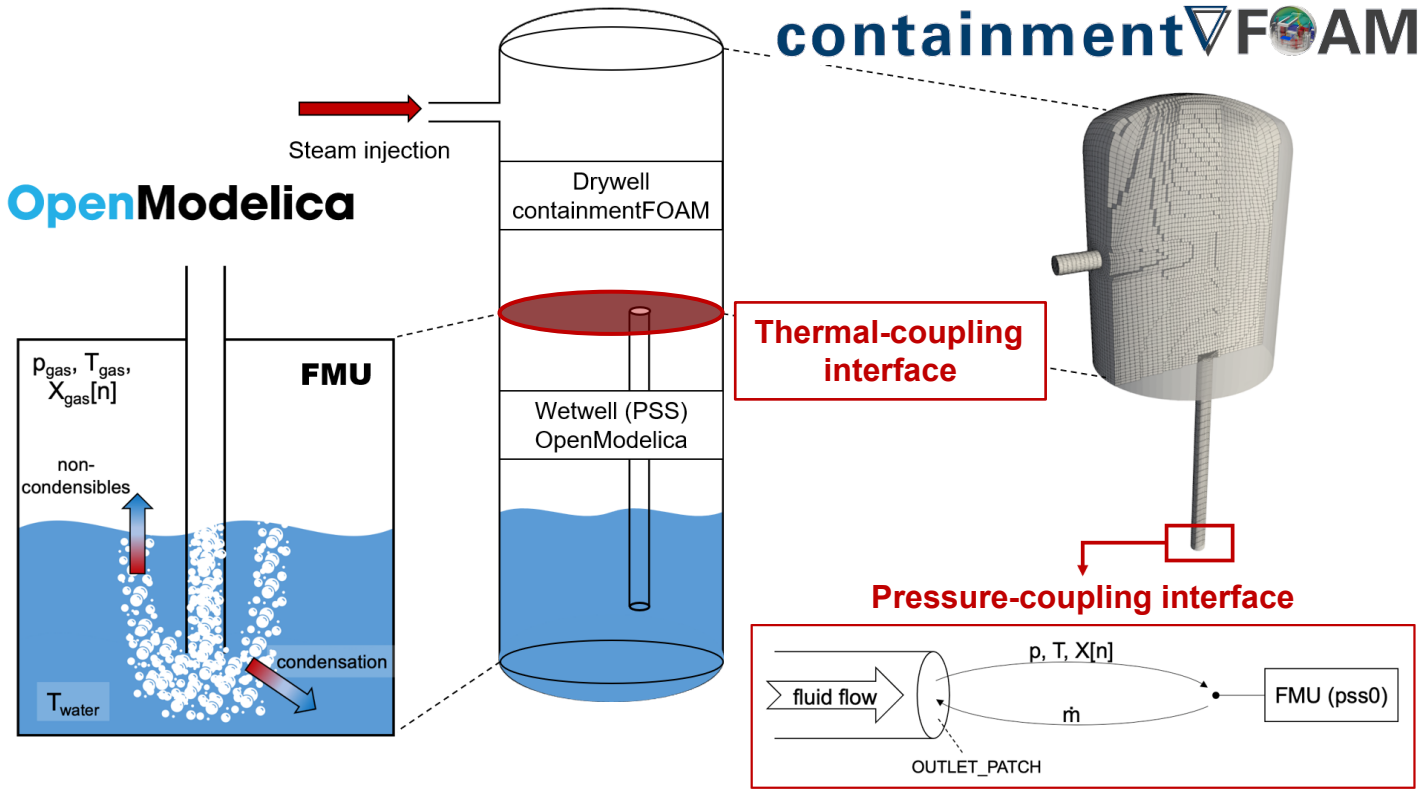

4. Validation with PPOOLEX experiments

Results RUN2

- The **pressure predictions were improved** by the inclusion of the heat transfer from DW to WW

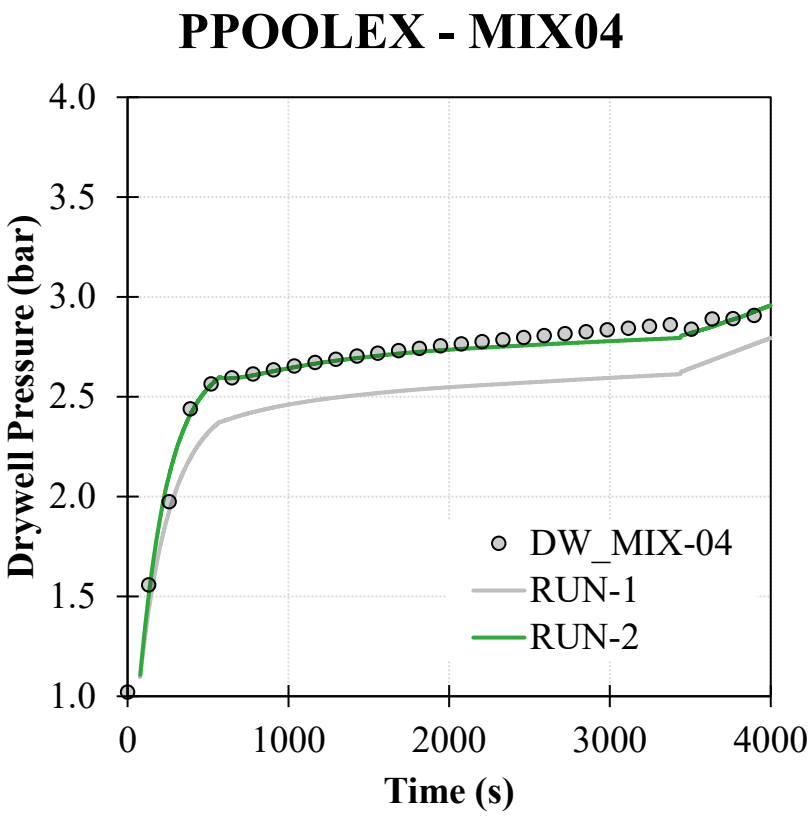

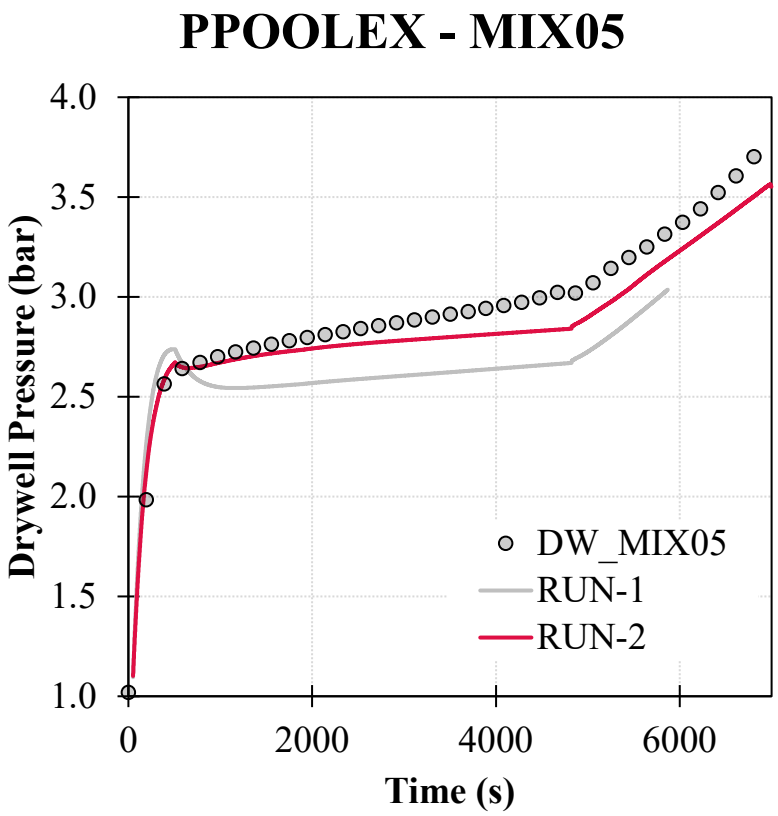

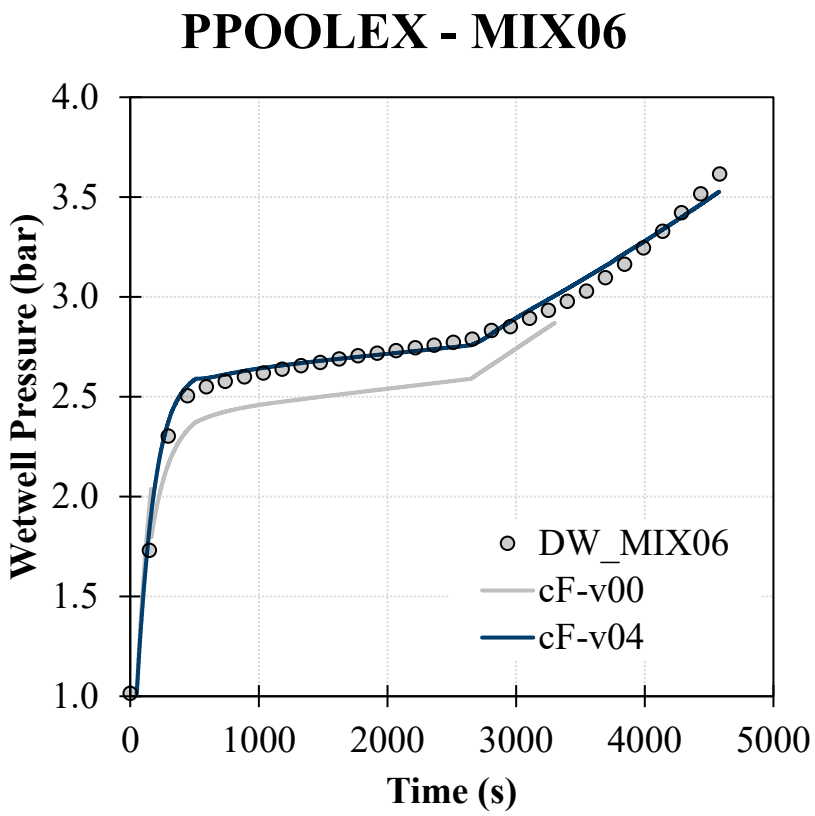

4. Validation with PPOOLEX experiments

Results RUN2

- Quantitative agreement of the average pool temperature predictions for RUN-2

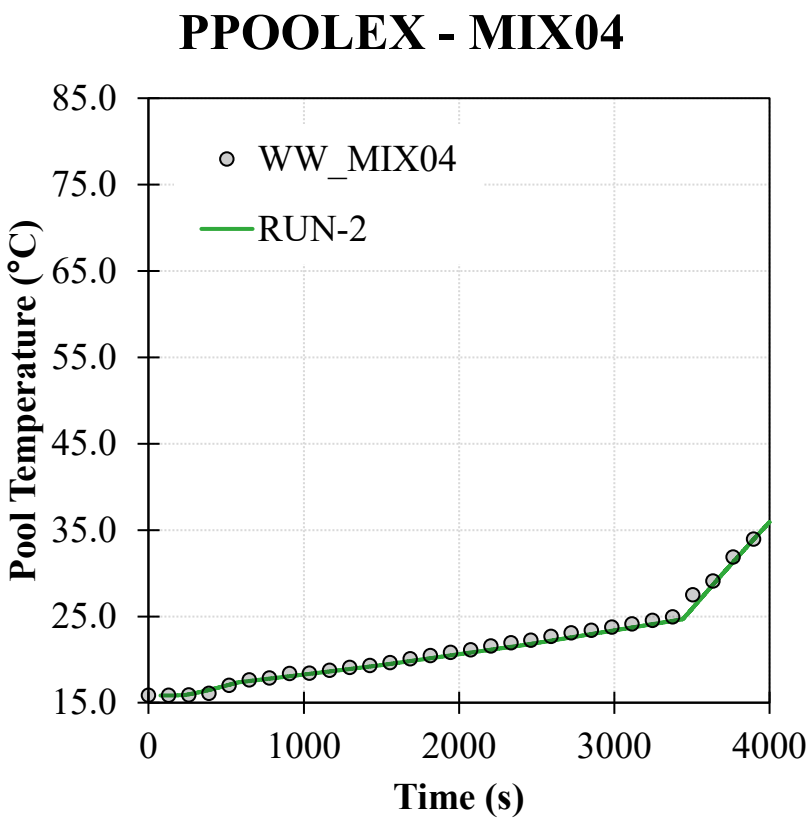

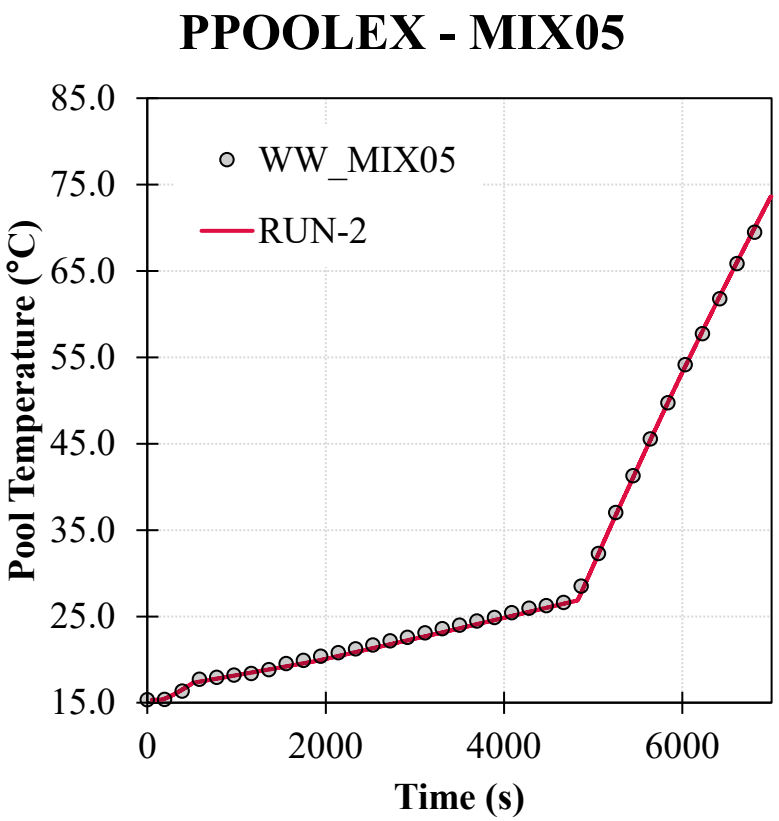

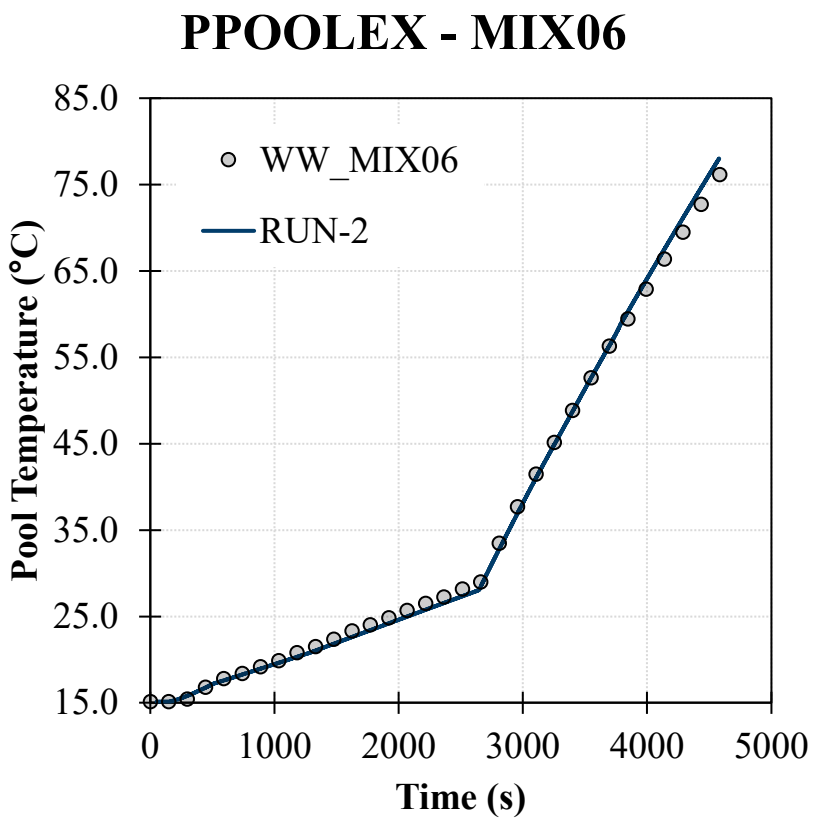

OUTLINE

1. Background
2. containmentFOAM for LW-SMRs
3. System coupling by FMI
4. Validation with PPOOLEX
5. Conclusions

5. Conclusions

- The SA sequences postulated in SASPAM-SA have been a **primary data source to identify and prioritise the R&D goals** of containmentFOAM.
- The coupling scheme has proved its **stability in the demanding domain-decomposition pressure-coupling model** used to simulate the PPOOLEX MIX Series
- The results of the multi-fidelity model of PPOOLEX showed a qualitative and quantitative agreement with the experimental data, **proving its readiness for the foreseen technical scale application** with the generic iPWR Design-II of SASPAM-SA.
- The **FMI-FMU coupling described in this paper is code agnostic** and not restricted to OpenFOAM and Modelica. Therefore, it can be used with any FMI-compatible code.

ACKNOWLEDGEMENTS (1)

Sponsors and Projects

- German Federal Ministry for the Environment, Nature Conservation, Nuclear Safety and Consumer Protection (BMUV) for funding code maintenance and integration to the national CFD reference package CF2REF (Fkz **150 1633B**) as well as the ongoing projects UQ4CFD (Fkz **150 1595**) and SETCOM-2 on wall condensation modeling (Fkz **150 1591**)
- Former German Federal Ministry of Economic Affairs and Energy (BMWi) and for funding projects related to further development of CFD for reactor safety application (Fkz **150 1407)** and the REKO experimental and model development program (Fkz **150 1308 / 150 1394 / 150 1470**) as well as the SETCOM projects (Fkz **1501404 / 1501489**)
- Becker Technologies GmbH for carefully conducting, documenting and sharing the experimental data of the national THAI programs, in particular the experiments TH2 (THAI-1, BMWi Fkz **1501218**), TH24.3 (THAI-3, BMUV Fkz **1501361**) and TH32 (THAI-VI, BMUV Fkz. **1501594**)
- **H**elmholtz **I**nterdisciplinary Doctoral **T**raining in **E**nergy and **C**limate Research (HITEC) Graduate School, the German Academic Exchange Service (DAAD) and the Chinese Scholarship Council (CSC) for funding PhD positions and student exchange
- **IAEA O**pen-source **N**uclear **CO**des for **RE**actor Analysis (**ONCORE**) initiative, a collaborative framework for the development and application of open-source multiphysics to support research, education, and training in analysis of advanced reactor designs
- Markku Puustinen and coworkers from **LUT, PPOOLEX facility**, for providing the experimental data for the validation of the PSS models
- The EU-HORIZON Euratom AMHYCO (Grant agreement ID: **945057**) and SASPAM-SA Projects (Grant agreement ID: **101059853**)

ACKNOWLEDGEMENTS (2)

Partners

- Prof. K. Arul Prakash (Indian Institute of Technology Madras) for collaborating under IITM-RWTH Joint Doctoral Program, DAAD IIT-MSP Programs.
- Dr. Berthold Schramm and Dr. Jörn Stewering (GRS) for their collaboration within the CF2REF project
- Prof. Markus Klein (Universität der Bundeswehr München), Prof. Xu Cheng (Karlsruhe Institute of Technology) and Prof. Reinhold Kneer (RWTH Aachen University) for supervising the involved PhD students and their collaboration within the UQ4CFD and SETCOM-2 projects.

- Our contributors, partners and colleagues and beta testers

- Computing time on the JURECA-DC CPU at the Jülich Supercomputing Center has been granted within the projects ‘uq4cfd’ and ‘cfrun’ (No. 26701).

And not to forget:

- The original developers, maintainers an contributors of OpenFOAM® !

- Public containmentFOAM repository
  https://go.fzj.de/containmentFOAM

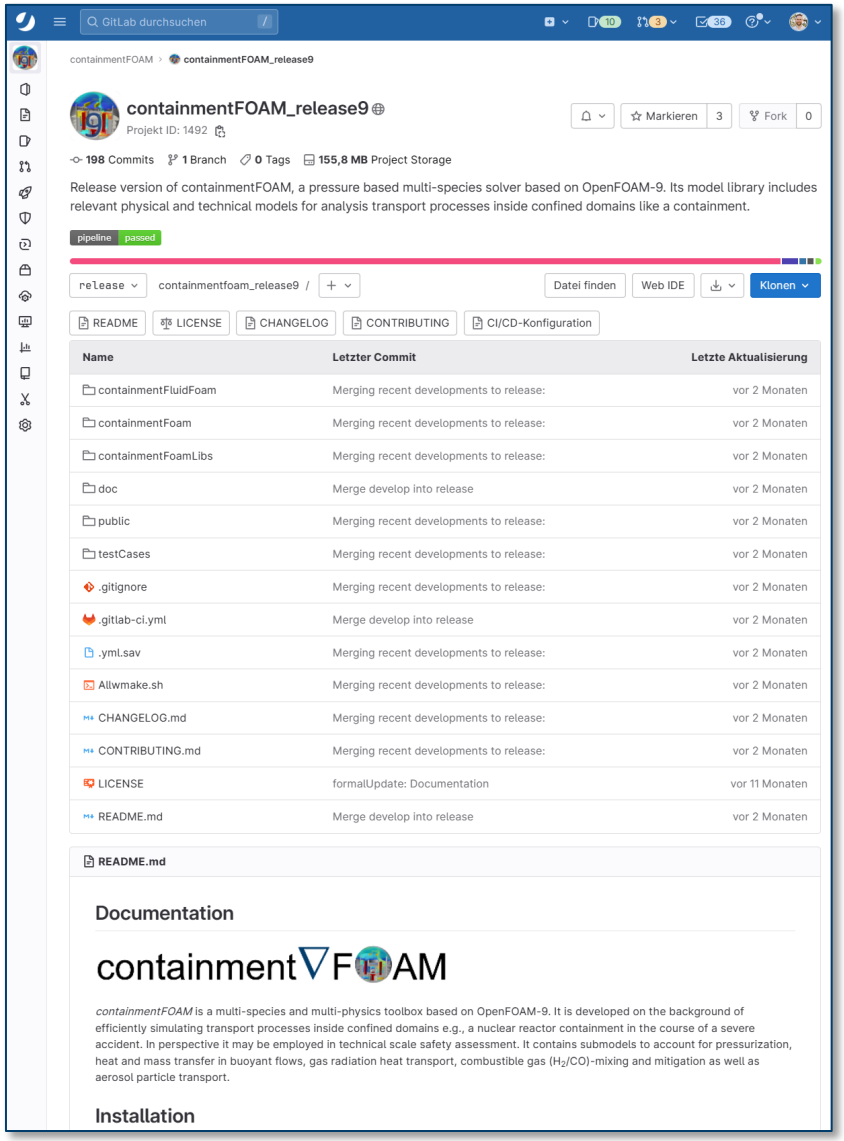

Development of containmentFOAM towards LW-SMR analyses

Carlos Vázquez-Rodríguez, Karl J. X. Sturm, Allen George, Stephan Kelm
Forschungszentrum Jülich (FZJ)

ERMSAR2024 - 11th Conference on Severe Accidents Research, May 13-16th 2024

containment FOAM

Supported by:

Federal Ministry
for the Environment, Nature Conservation,
Nuclear Safety and Consumer Protection

based on a decision of
the German Bundestag
Project No. 150 1633B

JÜLICH Forschungszentrum
Mitglied der Helmholtz-Gemeinschaft

COMPARISON OF A DBA SEQUENCE IN A GENERIC iPWR BETWEEN MELCOR AND ASTEC CODES

G. Grippo
University of Bologna
Department of Industrial Engineering (DIN), Viale del Risorgimento 2, 40136, Bologna, Italy
gianmarco.grippo2@unibo.it

P. Maccari
ENEA, C.R. Brasimone, FSN-ING-SIS
Camugnano, Italy
pietro.maccari@enea.it

G. Agnello
University of Palermo
Dipartimento di Ingegneria, Viale delle Scienze, Ed. 6, 90128, Palermo, Italy
giuseppe.agnello04@unipa.it

S. Ederli
ENEA, C.R. Casaccia
Via Anguillarese 301, 00123, Roma, Italy
stefano.ederli@enea.it

A. Bersano, F. Mascari
ENEA, C.R. Bologna, FSN-SICNUC
Via Martiri di Monte Sole 4, 40129, Bologna, Italy
andrea.bersano@enea.it; fulvio.mascari@enea.it

ABSTRACT
In view of the possible licensing needs of Small Modular Reactors (SMRs), due to the envisaged short-term deployment, the international scientific community has focused his interest in characterizing the SA integral codes capabilities in simulating SMR behavior during postulated Design Basis Accident (DBA), Beyond Design Basis Accident (BDBA) and Severe Accident (SA) scenarios. One type of SMR is the integral Pressurised Water Reactor (iPWR), which is ready to be licensed as a new build because they start from the well-proven and established large-LWR technology including moderate evolutionary design modifications to increase the inherent safety of the plant. However, despite the inherent increase of the safety of the plant with the adoption e.g. of passive safety systems and integral configuration, a sound demonstration of iPWR ability to address SA should be carried out along a safety review process. Therefore, in order to speed-up iPWR European licensing process, the Horizon Euratom project "Safety Analysis of SMR with Passive Mitigation strategies – Severe Accident" (SASPAM – SA), coordinated by ENEA (Italy), investigates the applicability and transfers of the operating large LWR knowledge and know-how to iPWRs in view of SA and Emergency Planning Zone (EPZ) European licensing analyses needs. In this framework, a code-to-code benchmark exercise between MELCOR and ASTEC integral codes has been conducted by ENEA, considering a generic 300 MWe iPWR. Due to the integral configuration a SBLOCA event has been considered; in particular a guillotine break of one Direct Vessel Injection (DVI) line has been selected as Postulated Initiating Event (PIE) of the DBA sequence. The main goal of the work is to evaluate the capability of the codes in simulating the dominant thermal-hydraulic phenomena in a generic iPWR design and assess the possible encountered discrepancies.

KEYWORDS
SASPAM-SA; SMR; DBA; MELCOR; ASTEC

1. INTRODUCTION

Integral Severe Accident (SA) codes, such as ASTEC [1][2] and MELCOR [3][4], are widely used to simulate the behavior of Nuclear Power Plants (NPPs) in transient conditions allowing to characterize the thermal-hydraulic and degradation phenomena that take place in postulated SA. Nowadays, the international nuclear community working on Deterministic Safety Analysis (DSAs) in the SA domain is currently interested to investigate the applicability of these codes to light water Small Modular Reactors (SMRs) designs due to their envisaged deployment and the consequent licensing needs. In particular, integral Pressurized Water Reactor (iPWR) are ready to be licensed as new builds because they start from the well-proven and established large Light Water Reactor (LWR) technology, incorporate their operational plant experience/feedback, and include moderate evolutionary design modifications to increase the inherent safety of the plant. Example of evolutionary modifications are the use of integral RPV (where is located the core, a compact Steam Generator – SG – and the pressurizer – PRZ –), and the use of passive safety systems for, e.g., high and low pressure injection, removing the residual core power through passive heat exchanger immersed in pool, containment cooling and pressure suppression, etc. Therefore iPWRs, as the advanced designs, are in general characterized by common features with the current operating large-LWR and by other specific features typical of their inherent evolutionary designs, providing safety advantages that reinforce the first three levels of the DiD principle. However, even if a plant is designed with advanced inherent features (through the reinforcement of the 1,2,3 DiD levels) allowing a reduction of the Core Damage Frequency (CDF), independent features for preventing and mitigating a SA sequence have to be included in its design (DiD level 4) together with the offsite emergency response (DiD level 5). Therefore, some scenarios that could lead to SAs need to be postulated and deterministically studied (More detailed information's in [7]). Therefore, it is necessary to assess the capability of internationally recognized SA code to describe the behaviour of the most promising iPWR designs during SA scenarios and to predict the resulting radiological impact on- and off-site. Therefore, state-of-art SA codes should be proven able to simulate these advanced features and the related phenomenology [5][6].In the present study, a code-to-code benchmark has been conducted to investigate the integral SA codes capabilities in simulating the main thermal-hydraulic phenomena occurring in a generic iPWR design during a DBA sequence. The aim of the activity is to gain first insights about the possible differences in predicting iPWR typical phenomena between the codes ASTEC and MELCOR. ASTEC is a European code developed by the Institut de Radioprotection et de Sûreté Nucléaire (IRSN); MELCOR is a non-European code developed by Sandia National Laboratories (SNL) for the United States Nuclear Regulatory Commission (USNRC). Subsequently, a validation against experimental could be needed to characterize the phenomena that need a further investigation, in term of qualitative and quantitative e accuracy, reducing uncertainties in the results. The present activity has been conducted in the framework of the Horizon Euratom "Safety Analysis of SMR with Passive Mitigation strategies – Severe Accident" (SASPAM-SA) project [8,9,10], coordinated by ENEA (Italy), having as a target to assess the capability of internationally recognized European and Non-European computational tools (largely used in Europe)[1] to describe the behaviour of some promising iPWR designs during SA scenarios

[1]In order to maximize the knowledge transferability and impacts of the project two generic design-concepts, characterized by different evolutionary innovations in comparison with larger operating reactor, have been selected for the analyses: a) IPWR characterized by a submerged containment and electric power of about 60 MWe, called design 1; b) IPWR characterized by the use of several passive systems, a dry containment and an electric power of about 300 MWe, called design 2. These two generic reactor concepts include the main iPWR design features, considered in the most promising designs ready to go on the European market, allowing to assess in a wider way the capability of codes (SA and CFD) to simulate the SA phenomena typical of iPWR. It is not the project's objective to assess the generic reactor designs selected but, based on the project findings, allow a more general statement on the

and to predict the resulting radiological impact on- and off-site. A generic iPWR 300 MWe reactor has been adopted as in this analysis. It is characterized by a dry containment and the use of different passive systems. Since the aim of the activity is to test the capability of ASTEC and MELCOR code in reproducing the behavior of different passive safety systems and their interaction in a SMR configuration, in order to analyze codes capability in a wider way, the following passive systems have been considered (Figure 1)2: decay heat removal, primary automatic depressurization, high and low pressure safety injection, containment pressure suppression, flooding of the Reactor Cavity (RC). Considering the characteristics of the selected design, a generic International Reactor Innovative and Secure (IRIS) SMR type has been considered in this study as reference to develop the input-deck for both codes, without using proprietary data. The main geometric data of the reactor was determined by scaling the available data of the SPES-3 experimental facility [12][13] as well as by engineering evaluation of from public general data available [11]. The ASTEC and MELCOR input-decks have been employed to simulate the same DBA sequence initiated by the Direct Vessel Injection (DVI) line double-ended guillotine break, already studied in past activities [14][15]. The reason why it has been selected this scenario is because it is the most challenging SBLOCA transient that can happen due to the lower elevation.

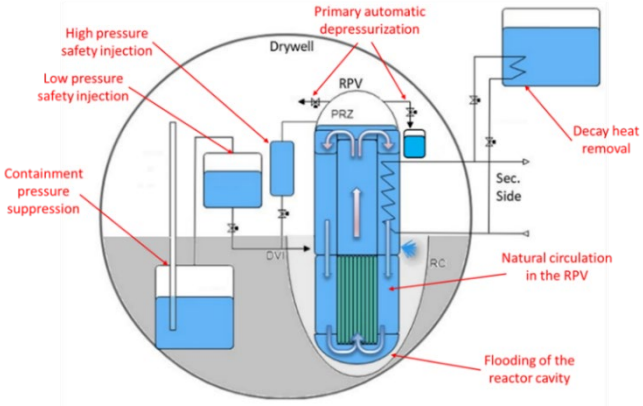

Figure 1 – Scheme of the generic iPWR design with the passive safety systems.

2. GENERIC iPWR DESIGN AND CODES NODALIZATION DESCRIPTION

code's applicability to currently favored designs under postulated SA condition. No PSA considerations will be done in the project due to the generic nature of the reactor concept considered, then the scenarios identified will be characterized in terms of severity but not in terms of probability.

[2] Passive systems are, on the one hand, an advanced solution to increase the inherent safety of the plant (e.g., there is no need of pumps), on the other hand a) they require extensive investigation for assessing the functional failure related to the thermal-hydraulic phenomena driving the operation of the systems and assess the related uncertainties, b) may still need an active initiation, and c) are characterized by very limited operational experience (to have more detailed information [7,19]). Considering this, the impact of the operation of passive systems on postulated severe accident progression is a novel topic and needs to be assessed. Considering this, the specific assessment of the code capability to simulate passive systems phenomenology is crucial. Infact, in LW-SMR reactors the BDBA/SA scenarios evolution depend from the postulated partial or total not operation of passive systems (e.g. postulate the failure of passive system valve activation). Therefore, it is necessary to analyse the capability of SA codes to predict the main thermal-hydraulic phenomena involved in the passive mitigation strategy of LW-SMR in order to adequately apply them for the design of accident management's strategy (first phase of a SA is only dominated by T-H phenomena, then in-vessel is affected by thermal-hydraulic phenomena).

2.1. Description of the generic iPWR design

In the generic iPWR considered in this study, all the RCS components, such as the PRZ, SGs and the Reactor Coolant Pumps (RCPs), are integrated into the Reactor Pressure Vessel (RPV), as shown in **Figure *1***. After flowing through the core, the primary coolant crosses the riser region (surrounded by the extended core barrel) and at the top of the riser is directed radially into the upper annular plenum, which houses the RCPs' suction region. RCPs pump the coolant inside the correspondent SGs module, where the selected iPWR design envisages the use of helical-coil SGs. After transferring the thermal power to the secondary fluid, the primary coolant flows downward along the annular downcomer region surrounding the core to the Lower Plenum (LP) and then returns up to the reactor core. The passive mitigation strategy of this iPWR design is based on several passive systems which carry out different safety functions: natural circulation in the RPV (Riser-Downcomer -RI-DC-), decay heat removal (Emergency Heat Removal System -EHRS-), primary automatic depressurization (Automatic Depressurization System -ADS-), high pressure safety injection (Emergency Boration Tanks -EBTs-), low pressure safety injection (Long-term Gravity Make-up System -LGMS-), containment pressure suppression (Pressure Suppression System -PSS- tanks), flooding of the Reactor Cavity (RC). The passive safety systems are schematized in **Figure *1***. The passive mitigation strategy envisages in case of one of the two Direct Vessel Injection (DVI) lines guillotine break and the role played by each safety system in the passive mitigation strategy are described in the following as well as in [14][15].

2.2. MELCOR nodalization description

MELCOR [3][4] is a fully integrated SA code able to simulate the thermal-hydraulic phenomena in steady and transient condition and the main SA phenomena characterizing the RPV, the RC, the containment, and the confinement buildings typical of LWR. The estimation of the source term is obtained by MELCOR code as well. The code is based on the "control volume" approach. MELCOR can be used with the Symbolic Nuclear Analysis Package (SNAP) [16] to develop the nodalization and for the post processing of data by using its animation model capabilities. MELCOR has a modular structure and is based on packages. Each package simulates a different part of the transient phenomenology. The MELCOR code version used for this analysis is MELCOR v2023. The nodalization has been developed using SNAP, with a trade-off between the computational time and a detailed prediction capability of the transient thermal-hydraulic, as well as core degradation, phenomenology.

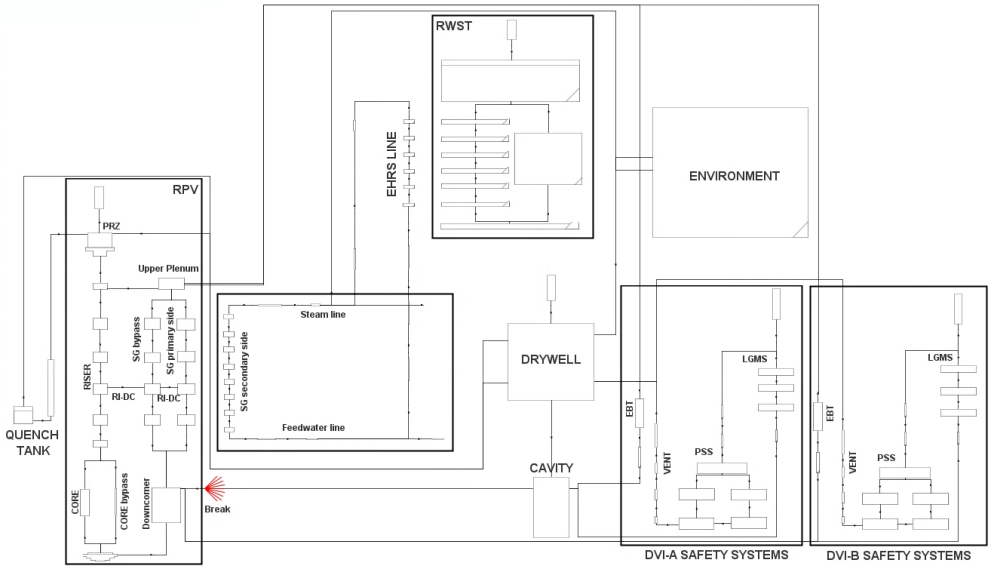

Figure 2 – MELCOR CVH nodalization.

The RPV is divided in different hydraulic regions including the LP, the reactor core, the core by-pass, the riser, the Upper Plenum (UP), the SGs and the downcomer. They have been modelled using the CVH and

FL MELCOR packages, simulating the thermal-hydraulics behavior of the system, and coupled with the HS package, modelling the heat transfer between the CVH Control Volumes (CVs). The two passive systems lines have been modelled separately. Each line includes the EBT, the PSS, the PSS-vent and the LGMS systems. To simplify the model, the SGs have been modelled as an equivalent one, with four CVH CVs on the primary side and eight CVs on the secondary side. The reactor core has been modelled by a single hydraulic CVH CV coupled with the correspondent reactor core model of the COR package. The reactor core and LP nodalization in the COR package is characterized by sixteen axial levels and six radial rings. The containment region has been modelled with one CVH volume of the RC, coupled with the correspondent CAV MELCOR package, and with one CVH volume for the DW region, thermally coupled with the environment CVH volume. In **Figure *2***, a schematic view of the MELCOR CVH and FL nodalization is presented.

2.3. ASTEC nodalization description

The ASTEC [1][2] code, aims at simulating an entire SA sequence in nuclear water-cooled reactors from the initiating event through the release of radioactive elements out of the containment. ASTEC includes several coupled modules that can deal with the different SA phenomena: thermal-hydraulics in the reactor system, core degradation and melt release, fission product release and transport, ex-vessel corium interaction, aerosols behavior and iodine chemistry in the containment, etc. The generic iPWR ASTEC model has been developed using the code version ASTEC v3.1 (study carried out with ASTEC V2, IRSN all rights reserved, [2024]). The code module CESAR is dedicated to the thermal-hydraulics of the reactor coolant system. It has been used for detailed nodalizing the upper part of the RPV, the secondary system (steam line, feedline and SGs), and most of the passive safety systems (i.e., DVIs, EBTs, PSS, LGMS, EHRS). A generic scheme of the ASTEC CESAR nodalization is reported in **Figure 3** (a). A 6-channels core model has been developed with ICARE module (4 core channels + 1 bypass channel and 1 downcomer channel), for the bottom-RPV and the core nodalization. The core internals have been realized as 2D components by employing the ICARE dedicated structures, and the models for the simulation of in-vessel core degradation phenomena are activated. The CPA module of the code, usually in charge of containment thermal-hydraulic modelling, has been used to model the DW of the continent. The dedicated insertion model of CPA is used to model the QT suppression system. The RC has been modelled with a ERVC pipe structure of CESAR to be thermally coupled with the external vessel structure of ICARE, as schematically described by **Figure 3** (b).

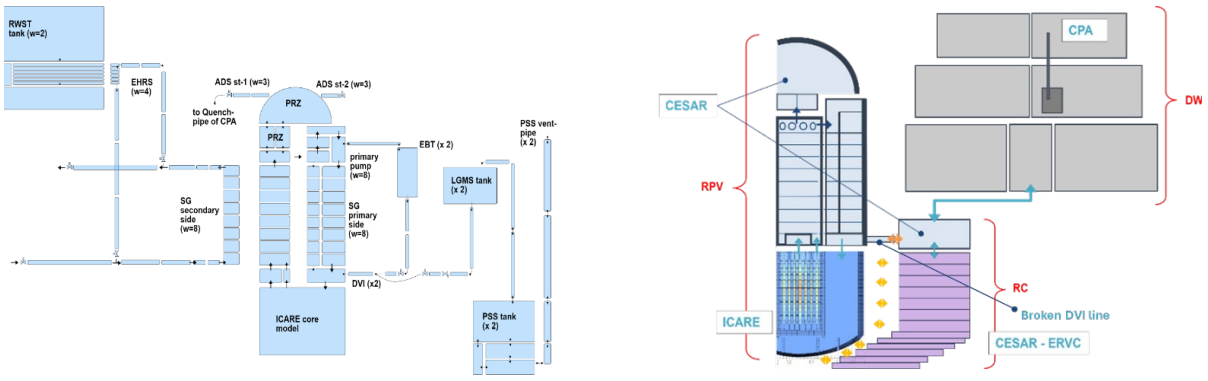

(a) (b)

Figure 3 – ASTEC CESAR nodalization [12]

3. DESCRIPTION OF THE TRANSIENT

To develop the code-to-code benchmark here presented, a DBA transient progression has been considered with the availability of all the emergency passive safety systems. The scenario under investigation is a Loss Of Coolant Accident (LOCA); the Postulated Initiated Event (PIE) is the double-ended guillotine break of one of the two DVI lines. The loss of primary coolant, caused by the opening of the break, results in a single and two-phase blowdown with the consequently RPV depressurization. Due to the

pressurization of the containment, a steam-gas mixture moves from the DW to the PSS through the PSS-vent lines increasing the pressure of the PSS-LGMS system. The RC is gradually filled with the primary coolant from the break and with the steam condensed on the metal internal surface of the DW. Once the containment high-pressure set-point is achieved, the S-Signal initiates the reactor SCRAM; due to this the isolation of the secondary side of SGs and the opening of two of the four EHRS loops occur[3]. The isolation of the SGs determines the increase of the secondary pressure. A natural circulation in the EHRS system begins, permitting the transfer of the thermal power to the water inside the RWST tanks, the cooling of the RPV and its depressurization. The low level of the coolant in the PRZ triggers the RCPs coast-down and the following automatic opening of the RI-DC check valves. These valves enable natural circulation at a lower RPV level permitting to the primary coolant to flow through a shorter path and by-passing RCP suction plenum. The LM-Signal (LOCA Mitigation) is then triggered when the PRZ pressure reaches the low pressure set-point. It determines the opening of the ADS stage-1, the start of the injection by EBTs and the opening of the two remaining EHRS system loops. The ADS stage-1 allows the steam dump from the PRZ to the QT, contributing to the RPV depressurization and acceleration of the equalization between primary and the DW pressures. The EBTs discharge borated cold water inside the RPV through the DVI lines by gravity. Whereas the intact DVI line releases water into the RPV, the broken one discharges water into the RC. At the primary and DW pressure equalization, the low RPV-DW differential pressure signal activates the LGMSs. The LGMS tank of the intact loop discharges water in the RPV by the intact DVI line while the LGMS of the broken loop discharges water in the RC. After this point, because of the steam condensation in the DW and the heat removed due to the EHRS system, the pressure in the DW decreases below the PSSs pressure. Consequently, the water inside the PSSs is forced upward through the PSS vent pipes, until filling the RC after dropping from the top end of the PSS vent pipe. This water head inside the PSS vent-pipe maintains a differential pressure between the LGMS (equal to PSS) and RPV (equal to DW) throughout the depressurization phase, which improves the LGMS water injection. Steam circulation between RPV and DW is enabled by the ADS stage-2 valves opening upon reaching the LGMS low water mass signal. The water in the RC keeps the core filled during the long-term cooling phase. The heat losses thorough the DW metal walls to the environment and the power extracted by the EHRS systems allow the cooling down of the core.

4. ANALYSIS OF THE RESULTS

4.1. Steady-state calculations

A steady-state analysis has been conducted to reach the initial reference conditions before the beginning of the transient. The values of the main steady-state parameters were compared with reference steady-state values collected and consolidated in the SASPAM-SA project and reported in [20]. Both codes have a discrepancy of less than 3% compared to the reference data. To characterize the results of the codes during the steady-state, the pressure distribution along the RPV primary side has been compared; in particular a maximum of 0.2% error is observed.

4.2. Analysis of the transient evolution

The simulation of the DBA has been investigated for 50000 s. The Start Of the Transient (SOT) has been considered at t = 0 s, with the postulated double-ended guillotine break of one of the two DVI lines. After the break, the transient is initially driven by the blowdown of the RPV. The high containment pressure set-point initiates the S-signal, which activates the SCRAM, the isolation of the SGs and the opening of the EHRS loops. Due to the SGs isolation, the SCS temporary pressure increases in both the codes. At approximately 122 s after the SOT in MELCOR and 65 s in ASTEC, the Low PRZ level signal is initiated, with the following primary pumps coast-down and RI-DC valves opening. After this phase, the mass flow rate is sustained only by natural circulation inside the RPV. The low PRZ pressure signal determines,

[3] For the analyses presented in the paper, because of the nodalizations structure (only one equivalent EHRS), the logic is simplified and only one actuation of EHRS is considered.

around 148 s in MELCOR and 158 s in ASTEC, after the SOT, triggering the opening of ADS Stage-1 and EBTs. Observing the mass flow rate through the break and the cumulative mass shown in **Figure 4**, at the SOT both the codes predict the same behavior and initial peak. The opening of the ADS 1 is practically at the same time for both (respectively 166 s ASTEC and 167 s MELCOR) and, moreover, the mass flow rate predicted by the two codes is qualitative and quantitative well represented and comparable in this first phase.

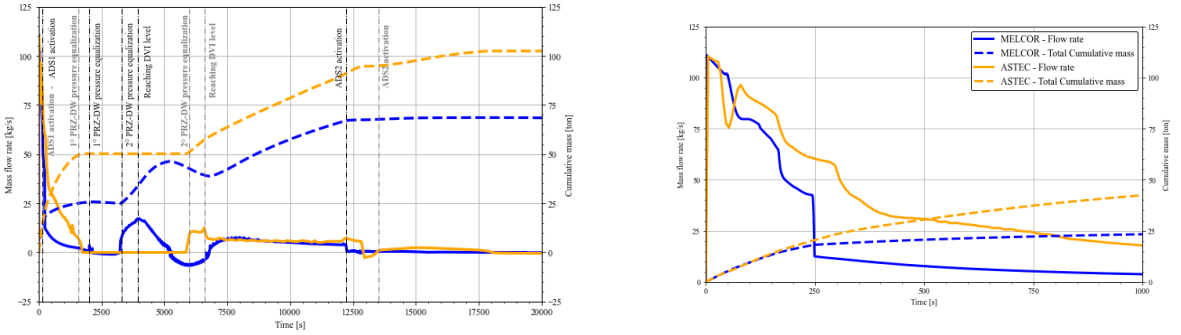

Figure 4 – Break mass flow rate and cumulative discharged mass.

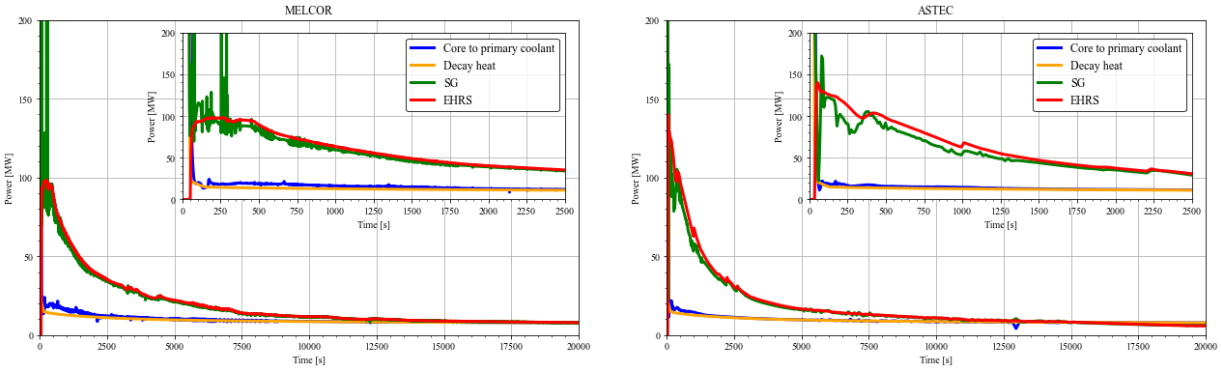

(a) (b)

Figure 5 – Decay power generated in the core, the power transmitted to the primary coolant from the core, the power transmitted from the primary system to the secondary system and the power transmitted from the secondary system to the EHRS.

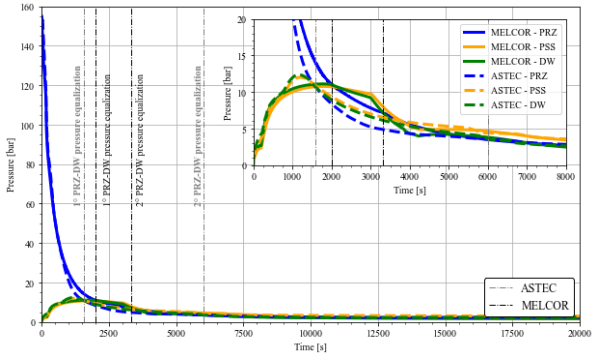

Figure 6 – Pressure behavior of the primary system and the DW

Due to that, the two codes predict an increasing of the depressurization rate in the first seconds after the ADS 1 opening. The primary pressure calculated by the two codes is comparable along the subcooled blowdown. The activation of the EHRS system allows the heat removal from the reactor core by natural

circulation, which is predicted in both codes; **Figure 5** shows the decay power generated in the core, the power transmitted to the primary coolant from the core, the power transmitted from the primary system to the secondary system and the power transmitted from the secondary system to the EHRS. While in MELCOR the EHRS power peak is about 100 MW, the ASTEC data present a higher peak of about 140 MW. Moreover, during the first 1000 s of the transient, the EHRS system removed power in ASTEC is greater than in MELCOR. This, coupled with the higher break mass flow rate in ASTEC, determines that, at about 800 s, the primary system depressurization in ASTEC is faster than MELCOR (**Figure 6**). The faster pressure decrease in ASTEC primary side determines a faster pressure increase in the DW with a consequent faster pressure equalization between the primary and the DW. It is to note that due to the higher energy removed from EHRS in ASTEC calculation, saturated blowdown is reached before in MELCOR than in ASTEC (MELCOR at 223s and ASTEC at 913s); this quantitative difference determines a higher mass flow rate in ASTEC in comparison with MELCOR, as shown in figure **Figure 4**. Observing **Figure *6***, the first ASTEC pressure equalization occurs at 1584 s while MELCOR predicts the equalization at 2000 s. Pressure equalization is followed by the increase of the DW pressure; this is due to the energy removed by the EHRS that contributes to depressurize the RPV in comparison with the DW. This phenomenology determines the stop of the break flow rate in both the codes. MELCOR code, between 2000 s (1st pressure equalization) and 3315 s (2nd pressure equalization), does not predict water injection from the break to the cavity (**Figure 4**). After the second equalization the pressure in the RPV becomes higher again and, consequently, the break flow rate start again. ASTEC code reaches the 2nd pressure equalization (**Figure 4** and **Figure *6***) at 6006 s, predicting a delayed restart of water injection through the break from the primary side to the cavity. Therefore, both codes predict the same phenomenology with different timing. Another important phenomenon to underline is the reverse flow through the break, that should take place when the level in the cavity reaches the broken DVI line and the DW pressure is higher than RPV pressure. The phenomenon is strictly related to the cavity level, **Figure *7*** and **Figure *8*** for ASTEC and MELCOR respectively; indeed both codes predict a) an increase of the break massflow rate after the 2nd pressure equalization, b) a decrease of the massflow rate when the level in the cavity reach the DVI line (respectively 6600 s ASTEC and 3950 s MELCOR). It is to note that, in this phase, only MELCOR predicts a reverse flow rate through the break (DW pressure plus head of water at the top of DVI major than RPV pressure), ASTEC code predicts the reverse flow later in the transient.

The level in the cavity depends on the a) passive systems injection through the broken DVI (EBT and LGMS), b) the water collected due to the condensation in the containment structure, c) PSS reverse flow, d) break flow rate. In **Figure *7*** and **Figure *8*** it is represented the normalized level of all the systems that contribute to the cavity level for both codes during the transient.

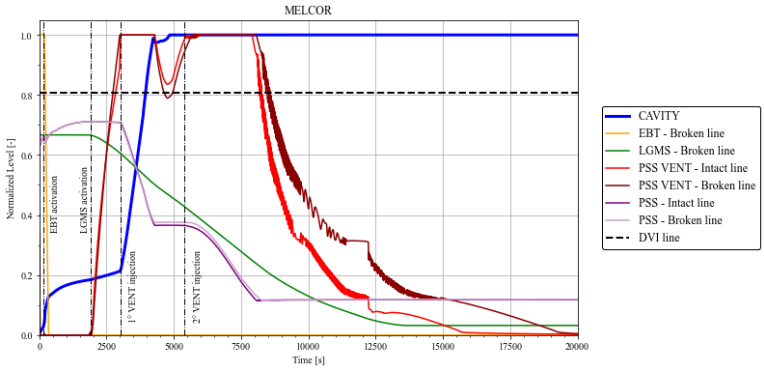

Figure 7 - Normalized collapsed cavity level, MELCOR

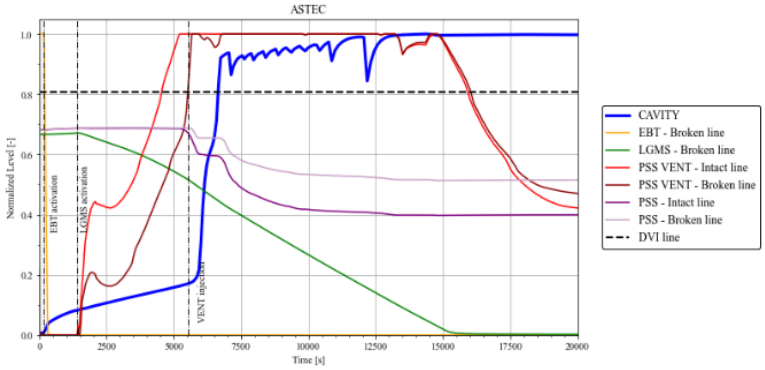

Figure 8 - Normalized collapsed level, ASTEC

The first system activated during the transient is the EBT in MELCOR, at 152 s, while, concerning ASTEC, at 160 s. Subsequently, the complete draining of this system occurs for both codes within the first 500 s of the transient, leading to a sudden rise of the cavity level. This behavior reduces its effectiveness due to the complete draining of the EBT connected to the broken line, but it is sustained by the contribution of the primary side break flow and the subsequent activation of the LGMS system. It is to note that MELCOR predicts a faster level increase in the cavity in the first phase (0s – 500s). Despite the mass flow rate through the break is higher in the ASTEC code, this MELCOR behavior is due to a major condensation in the containment structure. Due to the faster pressure decreases of ASTEC, the LGMS activation took place at 1401 s while in MELCOR at 1888 s. This injection will determine a further increase in the cavity level. In relation to the PSS reverse flow thorough the vent-pipe, it is to note a higher direct condensation of steam in MELCOR compared to ASTEC in the PSS, that determines a PSS reverse flow in MELCOR at 3010 s, and in ASTEC later at 5534 s. This determines a steeper increase of the cavity level in the MELCOR prediction in comparison with ASTEC and, as shown in **Figure *6***, a slight decrease of the DW pressure calculated by MELCOR. This phenomenon brings to the second equalization of the primary side with the DW and, consequently, to the restart of the break mass flow rate to the cavity earlier in MELCOR as described in the previous section. Therefore, in the MELCOR prediction the level of the cavity reaches the DVI level earlier than ASTEC determining the break reverse flow contributing to increase the level in the core at about 5250 s. Furthermore, the PSS vent injection predicted by the ASTEC code is less sudden than MELCOR calculation but longer over the time.

The level in the core depends on the break flow and the refilling phenomena due to the passive system activation. Initially, the level in the core decreases due to the blowdown. Indeed observing **Figure *9***, at the SOT, it is possible to notice a first decrease of level of both the codes due to the break flow rate.

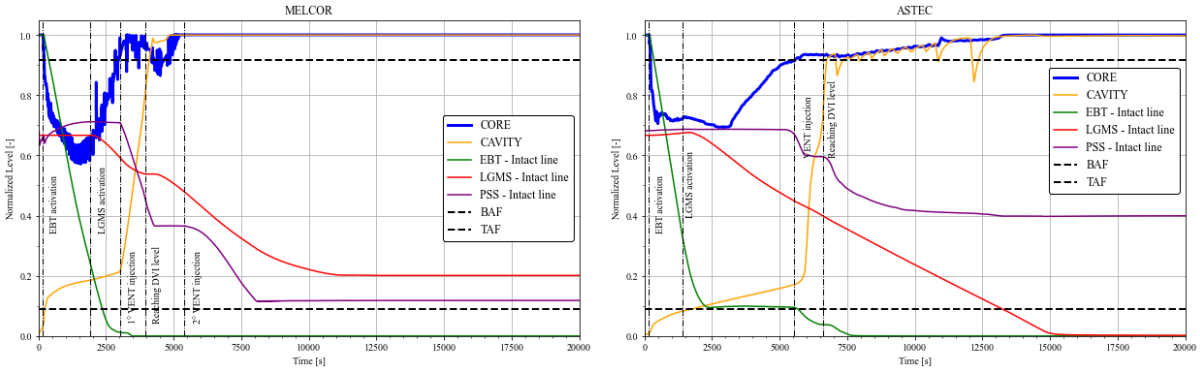

a) **b)**

Figure 9 – a) Normalized collapsed core level, MELCOR; b) normalized collapsed core level, ASTEC;

Table I. Main event characterizing the transient.

Event	MELCOR	ASTEC
Break	0	0
High Containment pressure signal (SCRAM, isolation SG, EHRS activation)	41	20
Low PRZ water level signal (Pump coast down and RI-DC opening)	122	65
Low PRZ pressure signal (ADS Stage-1 opening, EBTs opening)	148	158
Low DP RV-Containment (LGMSs opening)	1884	1398
1st RPV- DW pressure equalization	2000	1584
2nd RPV- DW pressure equalization	3315	6006
1st vent injection	3010	5534
2nd vent injection	5405	-
Core level reach the TAF	3000	5500
Cavity level reach the DVI	3950	6600
Low LGMS mass (ADS Stage -2 opening)	12265	12902

In MELCOR calculation the lower RPV water level is reached along the EBT injection: the LGMS injection starts at 1888 s and contributes to refill the core. At about 3000 s the level is recovered. After the second equalization in MELCOR it starts again the break flow that determine a small level reduction, but the reverse flow from the break restores again the level, that then remains stable. In relation to ASTEC, the EBT starts to inject at 160 s and affects the level reduction. However, comparing with MELCOR calculation, due to the longer time interval between 1st and 2nd equalization, the EBT stops to inject. While the EBT stops to inject between the two equalizations, the LGMS starts to inject affecting sensibly the level decrease that reaches the minimum at 3000 s. This phenomenon is shown in **Figure *10***; while the EBT system follows the pressure behavior of the primary side, because of the connection balance line between the top of the tank and the upper plenum of the RPV, the LGMS follows the pressure behavior of the PSS tank and, consequently, of the DW. As previously described, during the transient two pressure equalizations occur, in which, after the first equalization, the RPV pressure becomes lower than the DW one. Therefore, during this period, while the EBT stops injecting into the RPV, the LGMS keeps injecting because the higher pressure. The described phenomenon can be observed also in **Figure *6***, in which, between the 1st and the 2nd pressure equalization the level of the EBT does not decrease in both codes and remains constant.

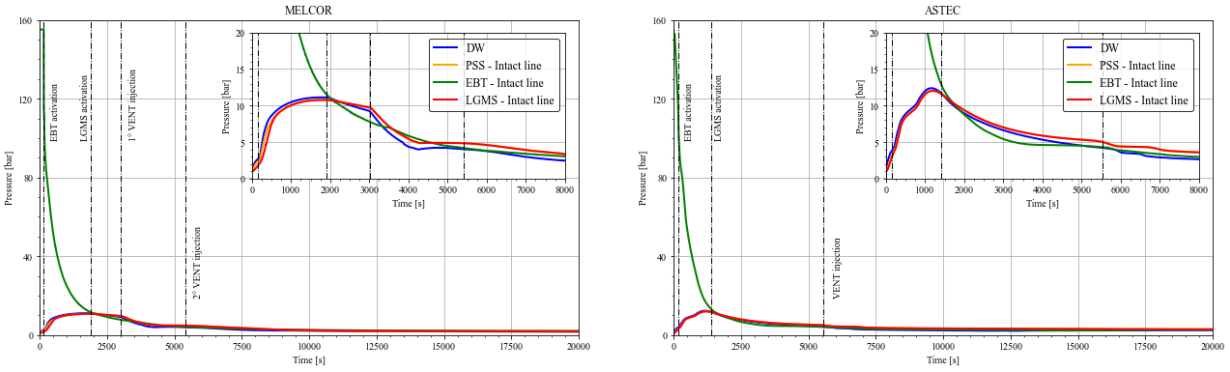

a) b)

Figure 10 – a) Pressure behavior of DW, PSS, EBT and LGMS, MELCOR; b) Pressure behavior of primary, DW, PSS, EBT and LGMS, ASTEC;

After the 2nd equalization, the LGMS together with the EBT restore the level in the core at about 5500 s. Level restored in both the simulations, the long-term cooling is well predicted by both codes. It is to note that the MELCOR code predicts a minimum normalized level of about 0.6 while ASTEC of about 0.7. The upper part of the core is uncovered in the MELCOR simulation for about 2900 s and in ASTEC for about 5400 s. The maximum cladding temperature predicted by MELCOR and ASTEC is about 622 K and

619 K respectively. No degradation core phenomena are predicted by both codes and no hydrogen is produces.

5. CONCLUSIONS

Whitin the framework of the Horizon Euratom SASPAM-SA project, the presented code-to-code benchmark exercise between the SA integral system codes MELCOR and ASTEC has been conducted considering a generic iPWR design. It is characterized by a power of about 300 MWe, the adoption of a dry containment and employs several passive systems. The double-ended guillotine break of one of the two DVI lines has been hypothesized as PIE of the DBA sequence. The analysis aimed at studying the thermohydraulic response of both codes and to investigate the discrepancies in terms of the main figure of merits of interest that drive the transients: the primary pressure, the DW pressure, the break flow rate, the level in the cavity and the level in the core. In general, the codes are able to predict the expected dominant phenomena driving the transient but some quantitative discrepancies affecting the sequence of events can be underlined. Of particular interest are the phenomena of condensation in the containment, the heat transfer in the passive heat removal systems and two-phase break flow rate. In particular, MELCOR calculation is characterized by a higher condensation in the containment and by a higher direct condensation in the PSS in comparison with ASTEC. ASTEC code is characterized by a higher heat removal from the passive heat removal systems and a higher two-phase break flow rate. More investigations are currently in progress to characterize these quantitative differences.

NOMENCLATURE

ADS: Automatic Depressurization System; **ASTEC**: Accident Source Term Evaluation Code; CV: Control Volume; **DSA**: Deterministic Safety Analysis; **DVI**: Direct Vessel Injection; **DW**: Drywell; **EBT**: Emergency Boration Tank; **EHRS:** Emergency Heat Removal System; EPZ: Emergency Planning Zone; **HX**: Heat eXchangers; **iPWR**: integral Pressurized Water Reactor; **IRSN**: Institut de Radioprotection et de Sûreté Nucléaire; **LGMS**: Long-Term Gravity Make-up System; **LOCA**: Loss Of Coolant Accident; **LP**: Lower Plenum; **LWR:** Light Water Reactor; **NPP**: Nuclear Power Plants; **PIE**: Postulated Initiating Event; **PRZ**: Pressurizer; **PSS**: Pressure Suppression System; **QT**: Quench Tank; **RC**: Reactor Cavity; **RCP**: Reactor Coolant Pump; **RCS**: Reactor Cooling System; **RI-DC**: Riser-Downcomer; **RPV**: Reactor Pressure Vessel; **RWST**: Refueling Water Storage Tank; **SA**: Severe Accident; **SASPAM-SA**: Safety Analysis of SMR with Passive Mitigation strategies – Severe Accident; **SBLOCA**: Small Break Loss of Coolant Accident; **SCS**: Secondary Cooling System; **SG**: Steam Generator; **SMR**: Small Modular Reactor; **SNAP**: Symbolic Nuclear Analysis Package; **SNL**: Sandia National Laboratories; **SOT**: Start Of the Transient; **UP**: Upper Plenum; **USNRC**: United States Nuclear Regulatory Commission

ACKNOWLEDGMENTS & DISCLAIMER

Funded by the European Union

Funded by the European Union. Views and opinions expressed are however those of the author(s) only and do not necessarily reflect those of the European Union or European Commission-Euratom. Neither the European Union nor the granting authority can be held responsible for them.

ENEA carried out the research activity with MELCOR code and SNAP, obtained in the framework of the ENEA-ISIN agreement signed on March 23rd 2020 as part of the General Arrangement between the United States Nuclear Regulatory Commission (US-NRC) and the Italian National Inspectorate for Nuclear Safety and Radiation Protection (ISIN).

REFERENCES

1. P. Chaterlard, et al., “Main Modelling features of the ASTEC V2.1 major version”, *Annals of Nuclear Energy*, **93**, pp. 83-93 (2016).

2. P. Chaterlard, et al., "ASTEC V2 severe accident integral code main features, current V2.0 modelling status, perspectives", *Nuclear Engineering and Design*, **273**, pp. 119-135 (2014).
3. L.L. Humphries, et al., "MELCOR Computer Code Manuals Vol. 1: Primer and Users' Guide Version 2.2.r2023.0", 2023.
4. L.L. Humphries, et al., "MELCOR Computer Code Manuals Vol. 2: Reference Manual Version 2.2.r2023.0", 2023.
5. "Relevant thermal-hydraulic aspects of advanced reactors design status", OECD/GD(97)8, 1996.
6. F. Mascari, et al., "Small modular reactors and insights on passive mitigation strategy modeling", *Nuclear Engineering and Design*, **401**, (2023).
7. SMR Regulators' Forum," Pilot Project Report: Considering the Application of a Graded Approach, Defence-in-Depth and Emergency Planning Zone Size for Small Modular Reactors", January 2018
8. European Commission, SASPAM-SA, https://cordis.europa.eu/project/id/101059853
9. www.saspam-sa.eu
10. ETSON, NEWS Safety Analysis of SMR with PAssive Mitigation strategies - Severe Accident (SASPAM-SA) Horizon Euratom Project, 26 Sep 2022, https://www.etson.eu/node/290
11. INTERNATIONAL REACTOR INNOVATIVE AND SECURE, IRIS Plant Overview, 2002.
12. M. Carrelli, et al., "The SPES3 experimental facility design for the IRIS reactor simulation", *Science and Technology of Nuclear installations*, **vol2009**, 579430.
13. R. Ferri, C. Congiu, "Conceptual design of SPES3-IRIS facility", SIET 01 334 RT 07 Rev.1. 2008.
14. P. Maccari, et al., "ASTEC code DBA analysis of a passive mitigation strategy on a generic IRIS SMR", *Annals of Nuclear Energy*, 156, 108194 (2021).
15. G. Agnello, et al., "DBA analysis of a generic SMR IRIS-like with MELCOR 2.2. code", *Proceedings of NUPP22*, 19-20 September 2022.
16. Applied Programming Technology, Inc., Symbolic Nuclear Analysis Package User's Manual, 2021.
17. F. Bianchi, R. Ferri, "SPES-IRIS facility RELAP5 sensitivity analyses on the containment system for design review", Report RdS/2010/61
18. A. Achilli, et al., "SPES3 Facility RELAP5 Sensitivity Analyses on the Containment System for Design Review", *Science and Technology of Nuclear installations*, **vol2012**, 173637.
19. European SMR pre-Partnership Reports, Workstream 5 –Research, Development, and Innovation Roadmap, 2023, https://snetp.eu/wp-content/uploads/2023/07/European-SMR-pre-Partnership-WS5-report-and-roadmap-30-June-2023.pdf
20. SASPAM-SA, Milestone 2.1: Generic Data on Design 1 and Design 2, Version 0.2, 04/10/2023.

SAFETY ANALYSIS OF SMR WITH PASSIVE MITIGATION STRATEGIES - SEVERE ACCIDENT

COMPARISON OF A DBA SEQUENCE IN A GENERIC iPWR BETWEEN MELCOR AND ASTEC CODES

11th European Review Meeting on Severe Accident Research Conference
13 – 16 May, Stockholm

Speaker: Gianmarco Grippo

Contributors: Giuseppe Agnello, Pietro Maccari, Stefano Ederli, Andrea Bersano, Fulvio Mascari

Outline

SAFETY ANALYSIS OF SMR WITH PASSIVE MITIGATION STRATEGIES - SEVERE ACCIDENT

- Introduction
- Design 2
  - *General view*
  - *Database*
- Selected scenario
- ASTEC input deck
- MELCOR input deck
- DBA transient
  - *Description of the transient*
  - *Balance of plant*
  - *Break massflow rate – SoT*
  - *ADS stage 1*
  - *1° Pressure equalization*
  - *2° Pressure equalization*
  - *Break massflow rate - Between 1° and 2° Pressure Eq.*
  - *PSS reverse flow*
  - *Break reverse flow*
  - *Level in the cavity*
  - *Level in the core*
  - *EBT and LGMS behaviour – Intact line*
- Results remarks
- Conclusions

Introduction

Integral Severe Accident (SA) codes, such as ASTEC and MELCOR are widely used to simulate the **behavior of NPPs in transient conditions** allowing to characterize **the thermal-hydraulic and the possible degradation phenomena**.



Investigate the **applicability of these codes to LWSMRs** designs due to their **envisaged deployment** and the **consequent licensing** needs

iPWRs are ready to be licensed as new builds

LWR technology → Operational plant experience

LWR technology → Feedback

\+ *Design modifications* to increase the inherent *safety of the plant*

Introduction

The "**safety by design**" concept must **not** be used to **justify the absence of SA management** features.

All the five levels of DiD are applied to SMR design

Reinforcement of the level 1 and 2
Implementation of specific design features

Reinforcement of the level 3 and 4
Demonstration of the safety systems effectiveness implemented to mitigate PIE and SA sequences

Reinforcement of the level 5
The mitigation of radiological consequences must be considered even if the previous levels are strengthened

Introduction

AIM OF THE ACTIVITY

A code-to-code benchmark has been conducted to investigate the **integral SA codes capabilities in simulating the main thermal-hydraulic phenomena** occurring in a generic **iPWR design** during a DBA sequence. The aim of the activity is to ***gain first insights about*** the possible ***differences*** in predicting iPWR typical phenomena between the codes ASTEC and MELCOR

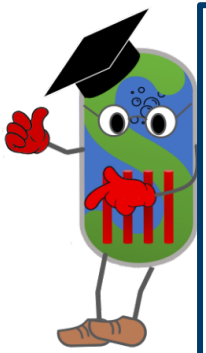

The present activity has been conducted in the framework of the Horizon Euratom **SASPAM-SA project**. The project is coordinated by ENEA and 23 organization from 14 countries are involved.

Funded by the European Union

Introduction

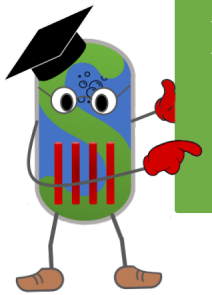

Target of the project

- Identification of **plausible postulate SA scenarios** for **iPWR** designs;
- Identification of the **conditions** in the **vessel** and in the **containment** that **characterize iPWR scenarios** and differ significantly from those in large-LWRs;
- Study the **applicability** of the **existing experimental database** to **iPWR** and identify **new experimental needs**;
- Assess the **capability** of internationally recognized **European and Non-European computational tools** (largely used in Europe) to **describe the behaviour** of the most promising **iPWR designs** during **SA scenarios** and to **predict** the resulting **radiological impact** on- and off-site.

Design 2 – General view

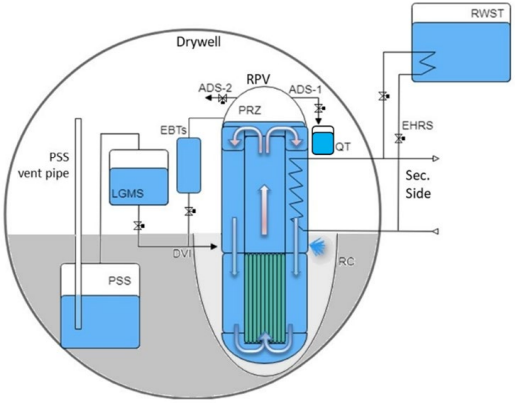

The iPWR Design-2 is characterized by the use of several passive systems and by a dry containment.

- The reactor operates in **forced circulation during normal operation** and employs a **passive mitigation strategy in accidental transients**.
- It consists of an **integral RPV**, which contains the core, a compact SG, the Control Rod Drive Mechanism (CRDM), the primary pumps and the **pressurizer included in the upper head**.
- The hot water at the core outlet **flows upward in a circular riser up** to the primary pumps suction.
- Above the riser, a perforated plate separates the riser from the PRZ, which is enclosed in the RPV upper head.

Design 2 – Database

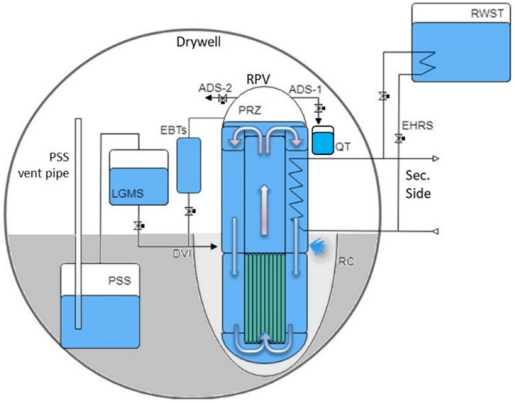

- In order to develop the **ASTEC and MELCOR input-deck**, a **reference database** was needed.
- Considering the **characteristics of Design 2 reactor type** and the selected passive systems, a **generic IRIS SMR type has been considered as reference** for this analysis.
- During the development of the MELCOR and ASTEC nodalization of the generic IRIS design, **no proprietary data have been used.**
- The **main geometric information** has been determined by **scaling the data available from the SPES-3 facility**, by **engineering evaluation** or **public general data available** for the IRIS reactor.

Selected scenario

DBA

After the qualification of the steady state, the DBA scenario selected is the guillotine break of one Direct Vessel Injection (DVI) line, considering the availability of all safety systems.

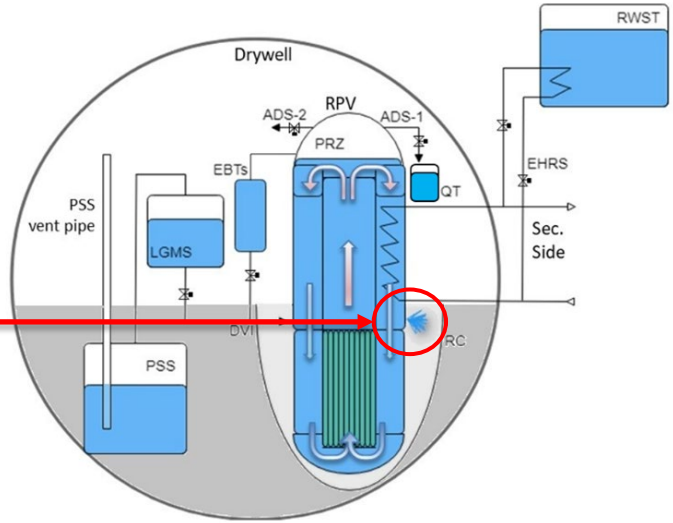

ASTEC input deck

CESAR has been used for:

- **Upper part of the RPV;**
- **The secondary system** (steam line, feedline and SGs), and most of
- The **passive safety systems**.

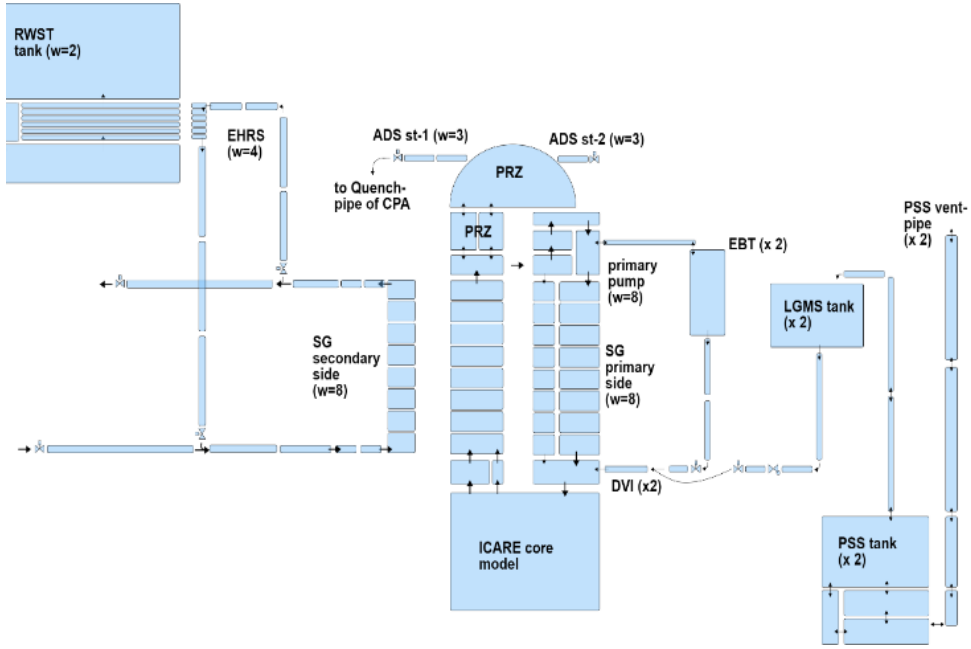

ASTEC input deck

- **ICARE** module model:
  - RPV lower part - Core (4 channels), bypass (1 channel) and downcomer channels (1 channel);
  - The core internals realized as 2D components ;
- **CPA** module used to model:
  - The DW;
  - The dedicated insertion model of CPA is used to model the QT suppression system.
- **RC** modelled **ERVC pipe structure of CESAR** to be thermally coupled with the external vessel structure of ICARE

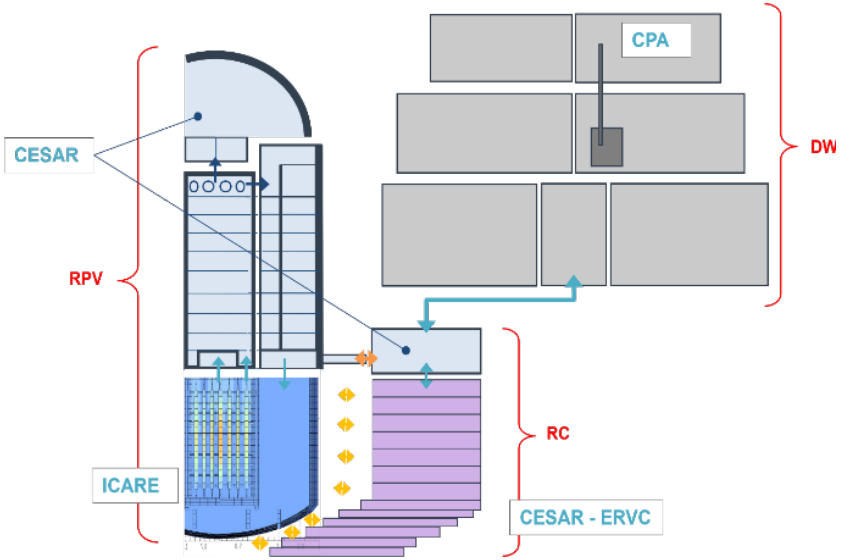

MELCOR input deck

Symbolic Nuclear Analysis Package (SNAP) to develop the **nodalization** and for the **post processing** of data by using its animation model capabilities

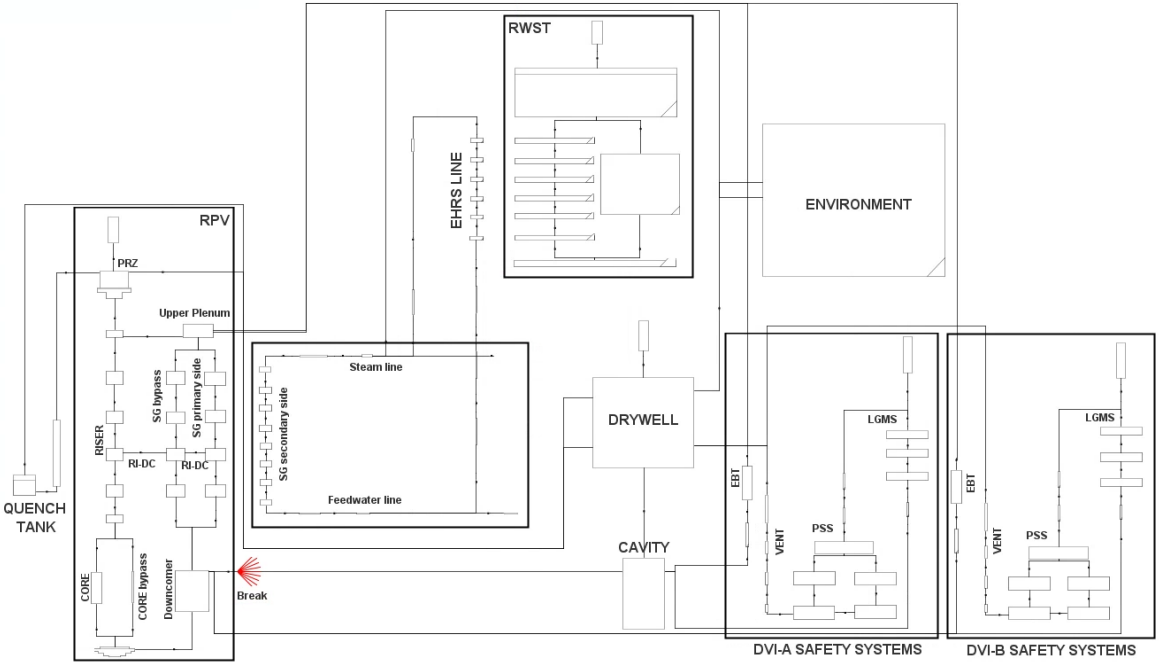

MELCOR input deck

CVH and FL packages have been used for modeling all the RPV hydraulic regions:

- LP,
- Core,
- Core bypass,
- Riser,
- UP,
- SGs
- Downcomer

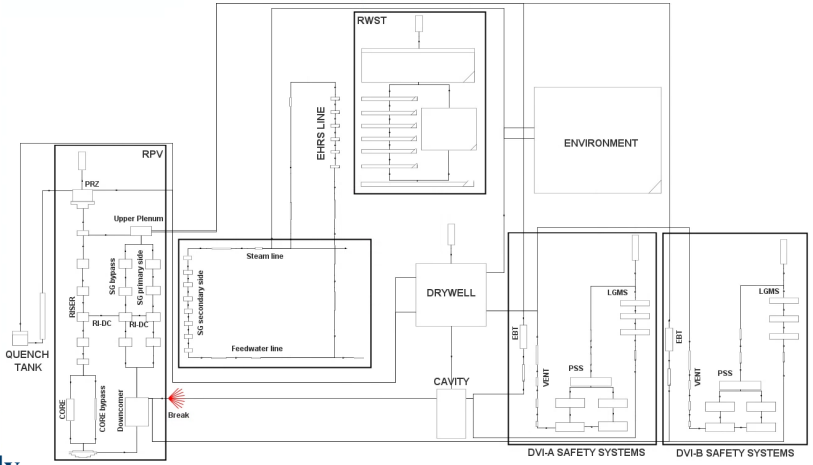

→ The **two passive systems lines** have been **modelled separately**.

→ The **SGs** (8 line), **EHRS** (4 line) and the **RWST** (2 pool) have been **modelled** as an **equivalent one**.

→ The **reactor core**, the **core bypass** and the **downcomer** has been modelled by a **single hydraulic CVH CV**

The **containment region** has been modelled with one **CVH volume of the RC**, coupled with the correspondent **CAV package**, and with **one CVH volume for the DW region**, **thermally coupled** with the **environment** CVH volume

HS package have been used, **coupled with the CVH** package, to **model the heat transfer** between the CVH Control Volumes

MELCOR input deck

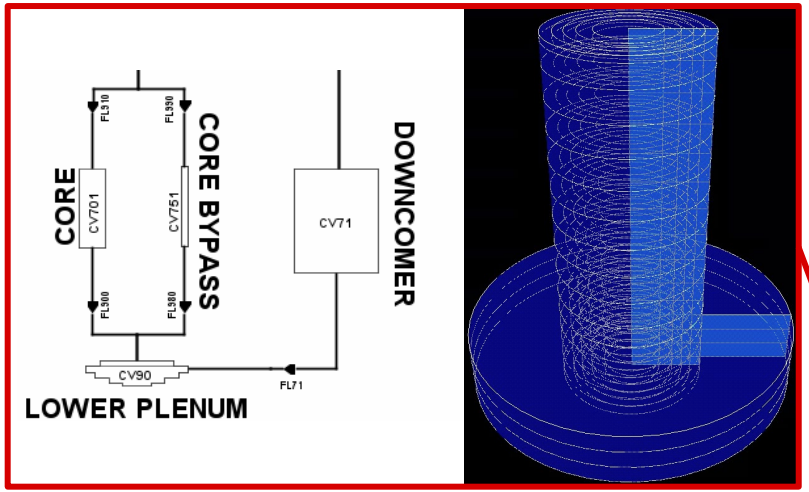

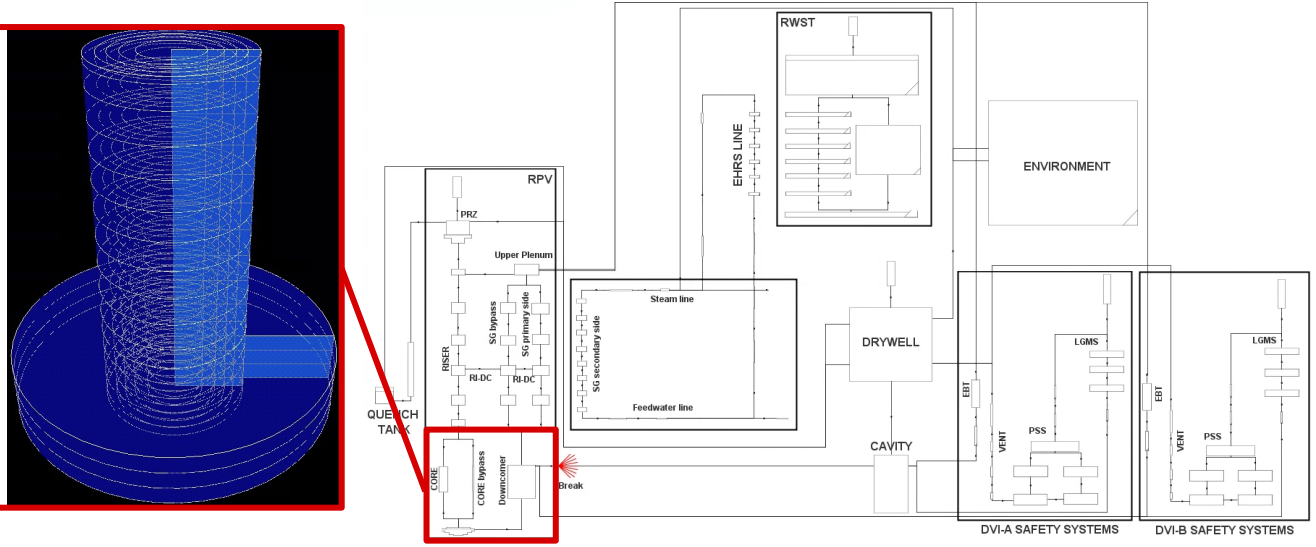

- **2D cylindrical** axial-symmetric **geometry** of the **COR package**;
- A **detailed nodalization** has been chosen for the COR package with respect to the CVH one;
- **16 axial** levels and **6** concentric **rings**;
- The **LP** is made of **one single CVH CV**, which extends to the core supporting plate;

Description of the transient

High Containment Pressure signal
- SCRAM
- Secondary system isolation
- EHRS actuation

Low PRZ pressure signal
- EBTs actuation
- ADS stage-1 actuation

Low LGMS mass signal
- ADS stage-2 actuation

BREAK OF DVI LINE

Low PRZ level signal
- RCP coastdown
- RI-DC valves opening

Low DP RPV-Containment signal
- LGMSs actuation

Balance of plant

EHRS POWER PEAK

MELCOR	100 MW
ASTEC	140 MW

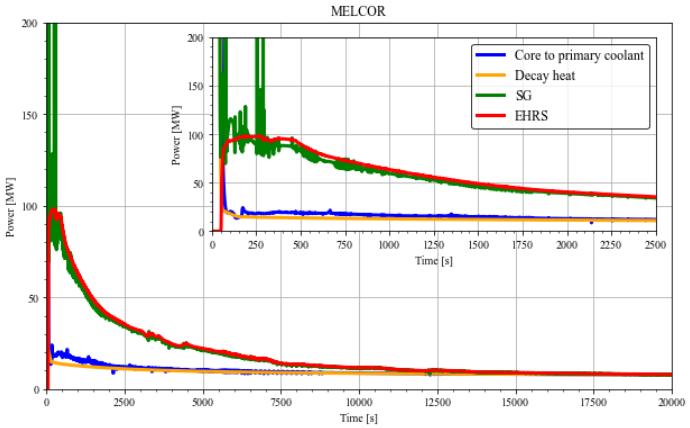

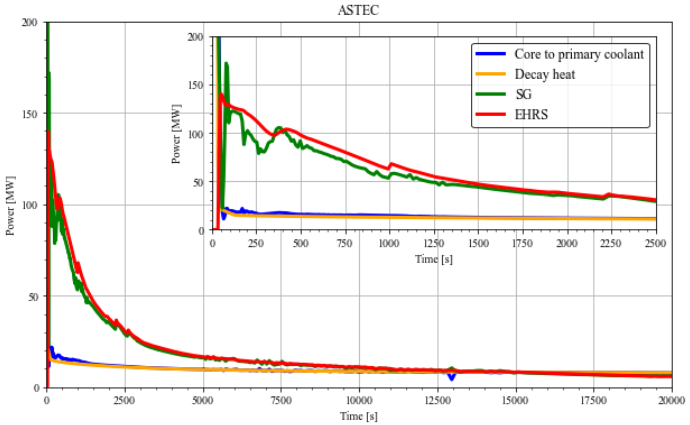

Early phase
0s - 1000s

- EHRS system's removed power in **ASTEC is greater than in MELCOR**;
- The primary system's **depressurization in ASTEC is faster than MELCOR**;
  - Faster pressure increase in the DW
  - Faster pressure equalization between the RPV and the DW;

Break massflow rate - SoT

Saturated blowdown is reached before in MELCOR than in ASTEC

- **MELCOR at 223s**
- **ASTEC at 913s**

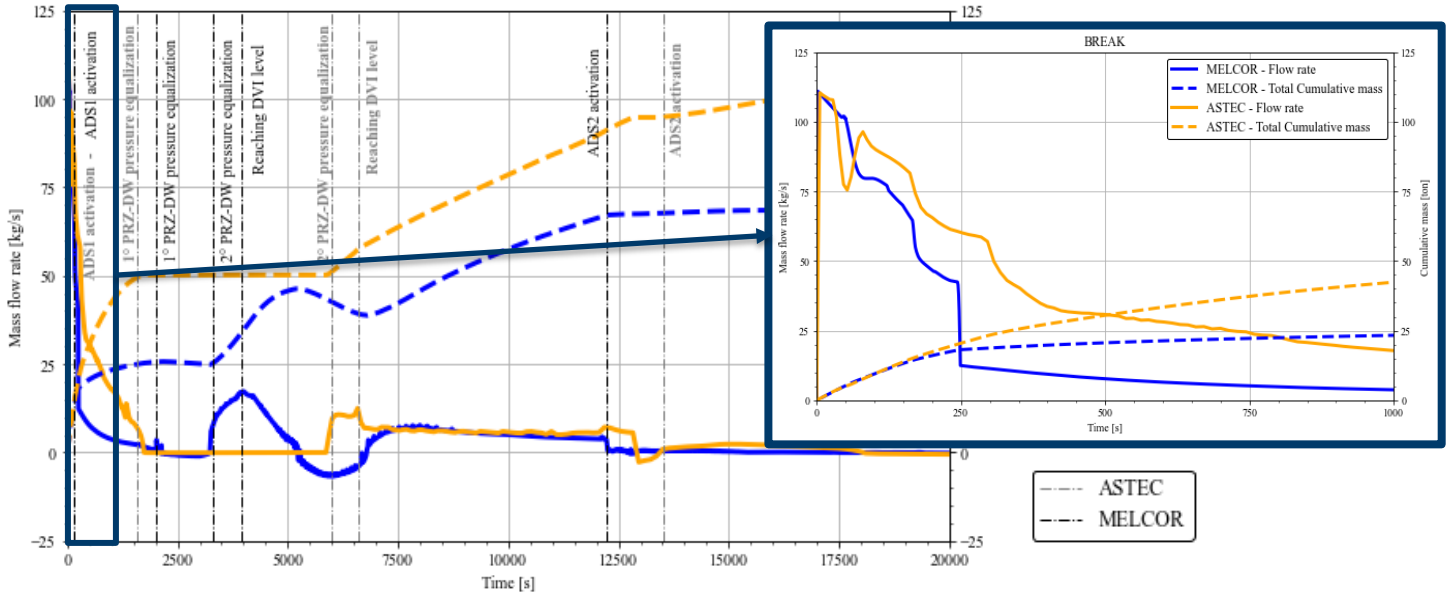

ADS stage 1

- Same predicted behavior and initial peak during **subcooled blowdown**.
- The opening of the ADS 1 is practically at the **same time**
  - 166s ASTEC
  - 167s MELCOR
- The mass flow rate predicted by the two code is **qualitative and quantitative well represented** and comparable in this first phase

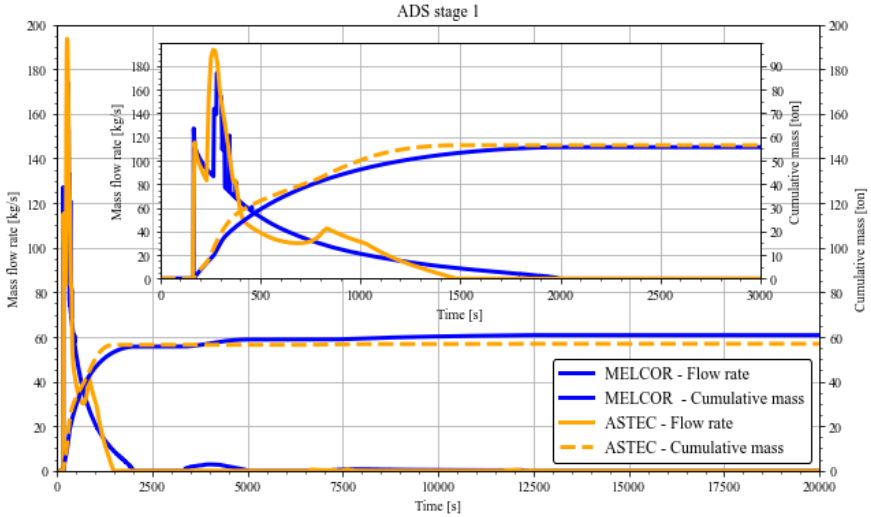

1° Pressure Equalization

1° Pressure Equalization

MELCOR	2000 s
ASTEC	1584 s

This phenomenology determines the **stop of the break flow rate** in both the codes.

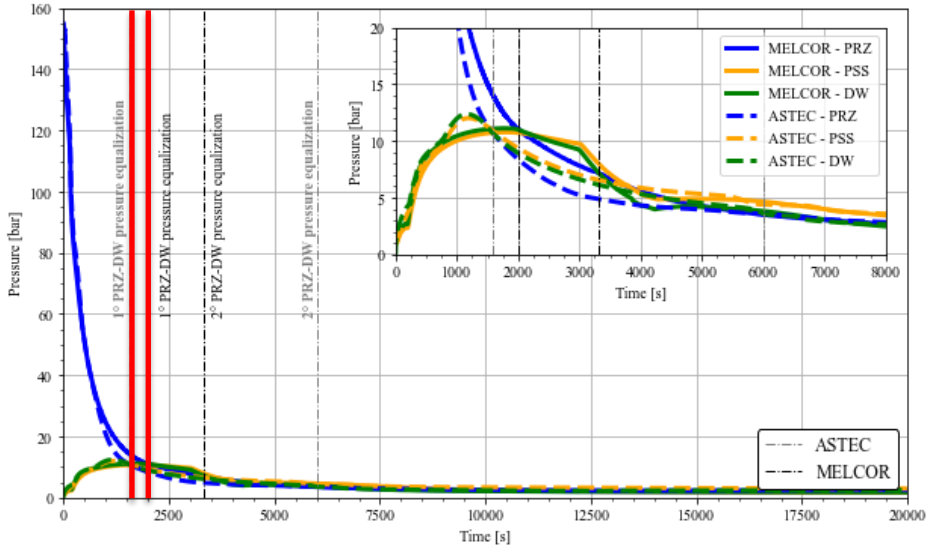

DVI BREAK — *RPV pressure decrease*
MELCOR: *0 s*
ASTEC: *0 s*

ADSs1 actuation — *RPV depressurization increase*
MELCOR: *167 s*
ASTEC: *166 s*

1° P. equalizaition
MELCOR: *2000 s*
ASTEC: *1584 s*

t [s]

2° Pressure Equalization

2° Pressure Equalization

MELCOR	3315 s
ASTEC	6006 s

The pressure in the RPV becomes higher again and, consequently, the **break flow rate start again**.

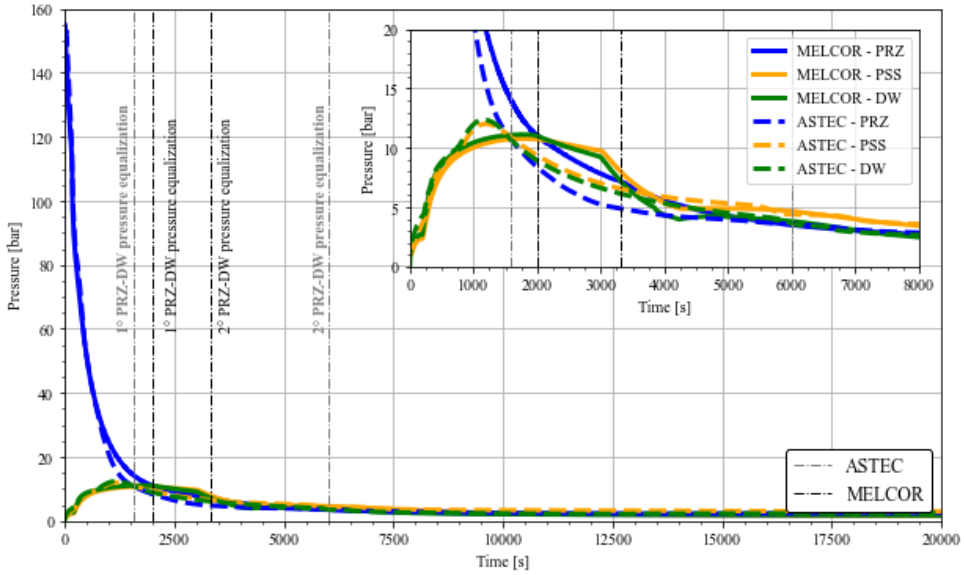

Break massflow rate – Between 1° and 2° Eq.

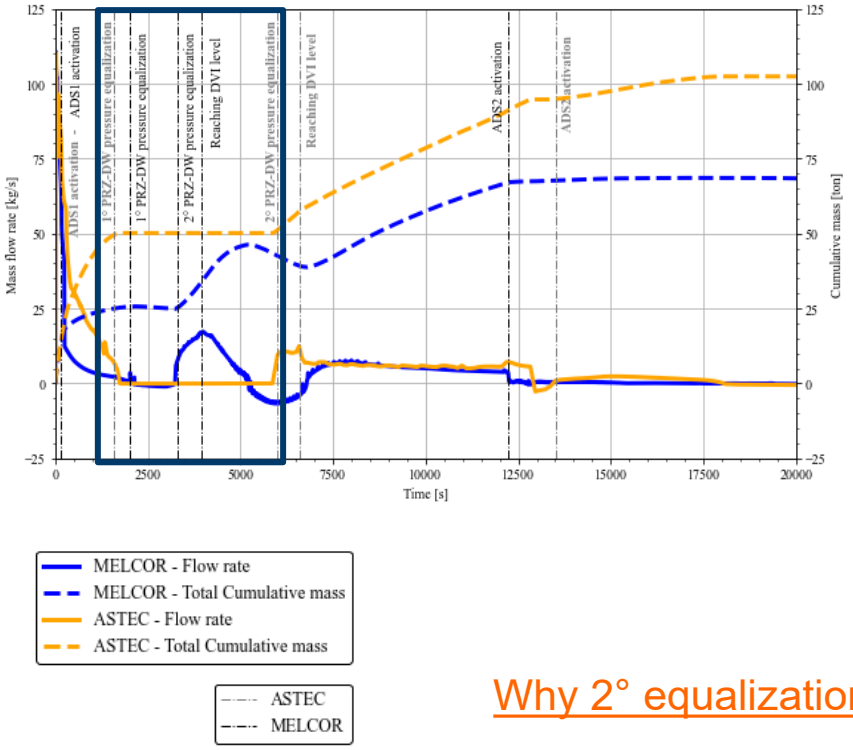

ASTEC predict a delayed restart of water injection through the break from the primary side to the cavity.

The codes predict the same phenomenology with different timing

Why 2° equalization and restart of the break massflow rate again?

PSS vent reverse flow

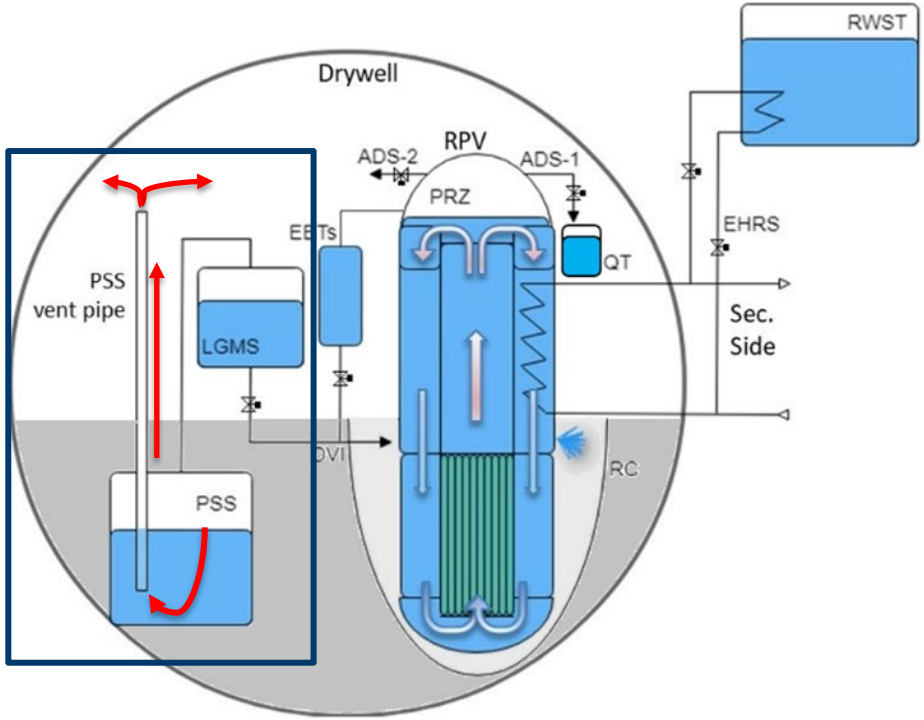

PSS vent reverse flow

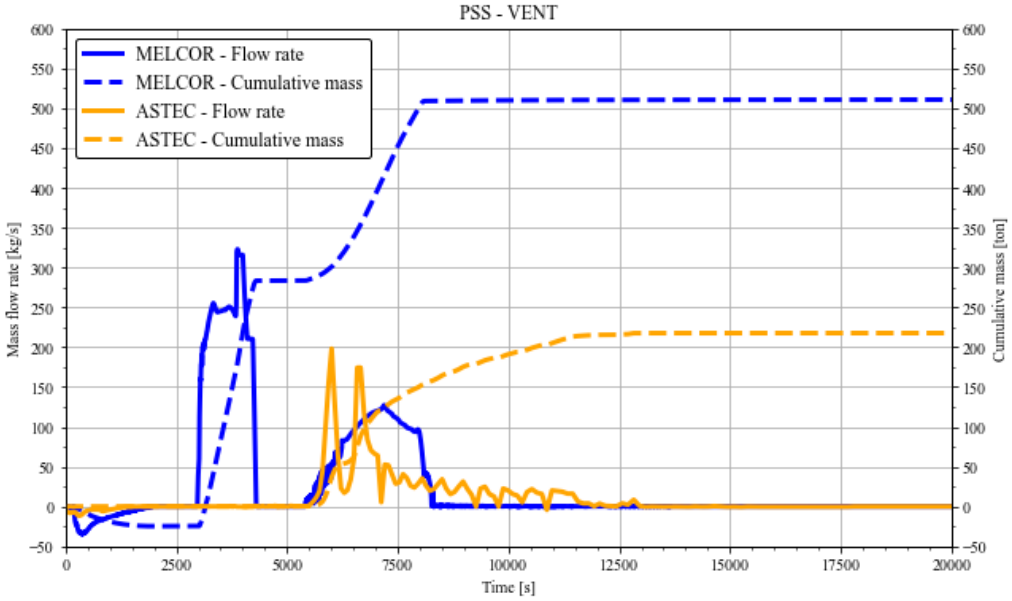

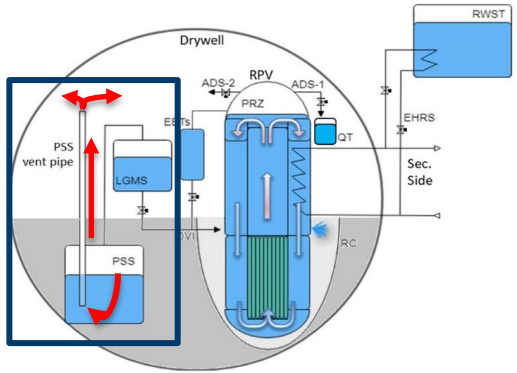

Due to:

- PSS gravity head;
- Major condensation phenomena in DW than suppression in PSS

! This phenomenon influenced the DW pressure, the restart of the BREAK massflow rate and the cavity level

PSS vent reverse flow

Reverse flow	
MELCOR	3010 s
ASTEC	5534 s

MELCOR major condensation in the DW structure.

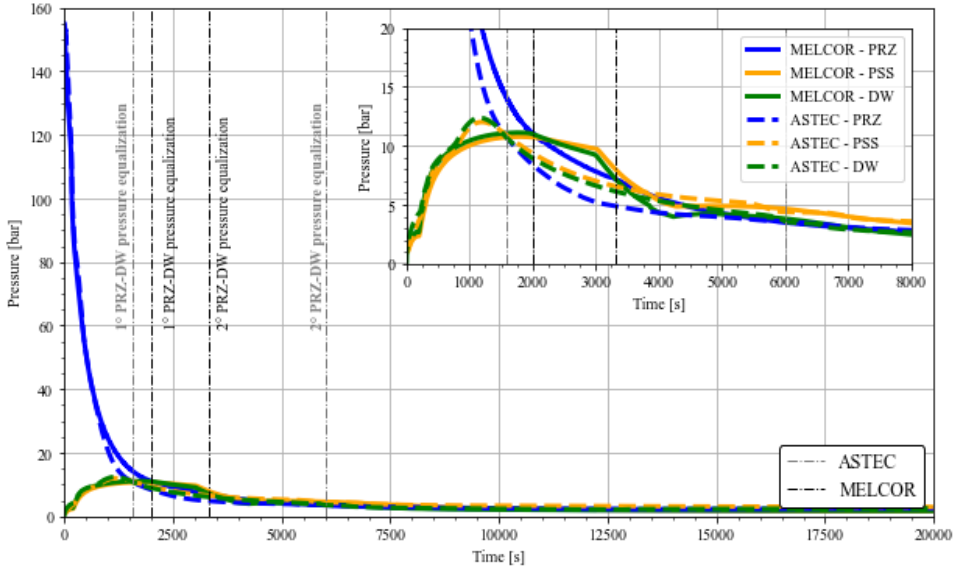

This phenomenon brings to a faster 2° pressure equalization in MELCOR than ASTEC predictions.

Break reverse flow

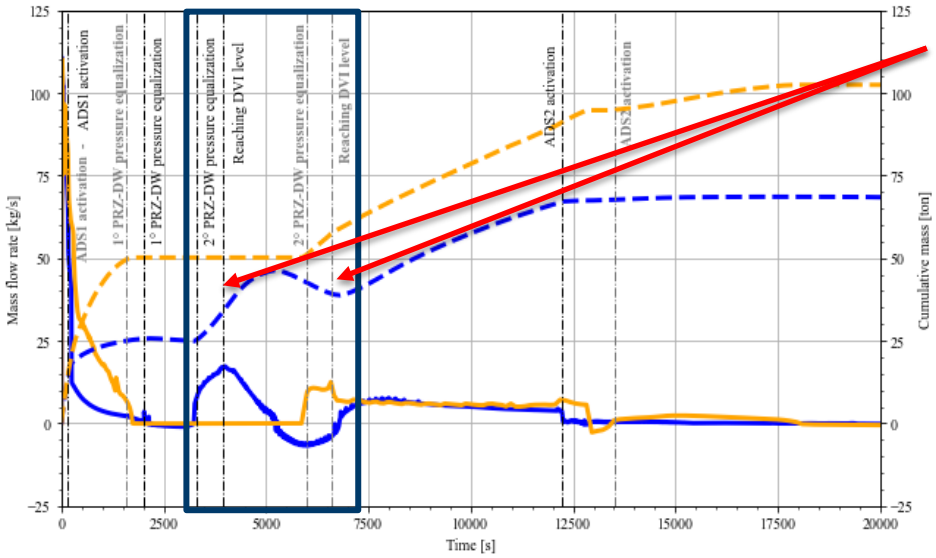

Level in the cavity reaches the DVI level

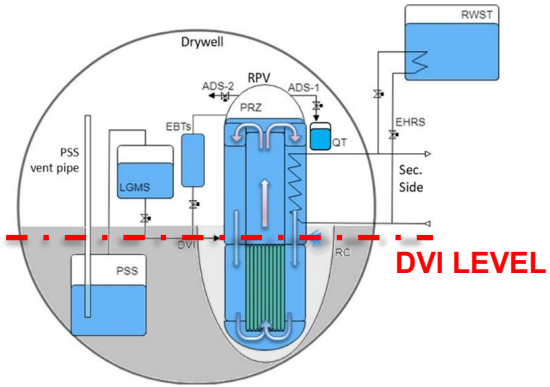

2° Pressure eq.
Restart of BREAK MFR
MELCOR: *3315 s*
ASTEC: *6006 s*

Cavity level reach DVI elevation
Inversion of BREAK MFR
MELCOR: *3950 s*
ASTEC: *6600 s*

t [s]

Level in the cavity

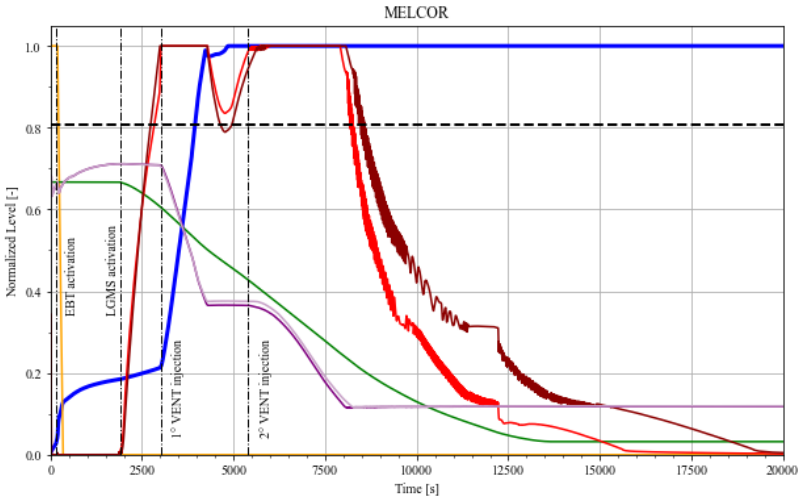

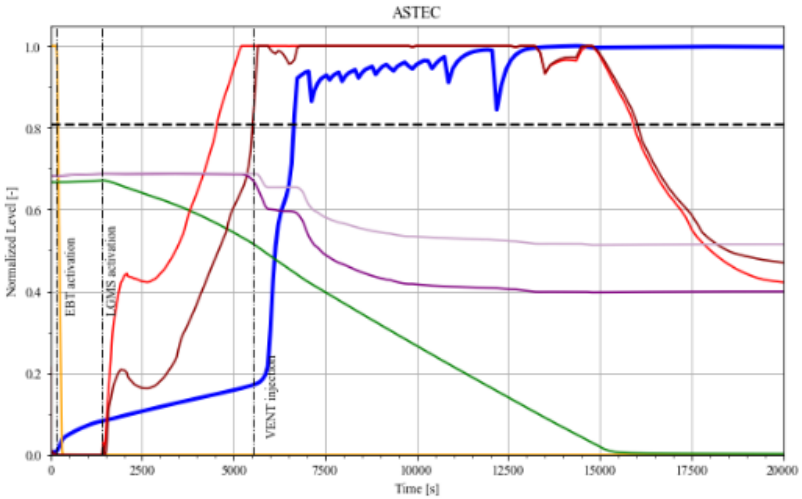

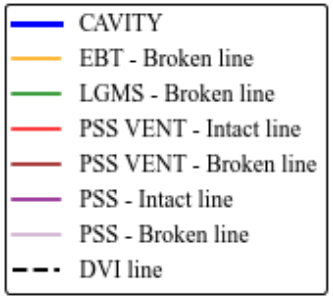

- Broken DVI passive systems
- DW condensation
- PSS reverse flow
- Break flow rate

Level in the cavity

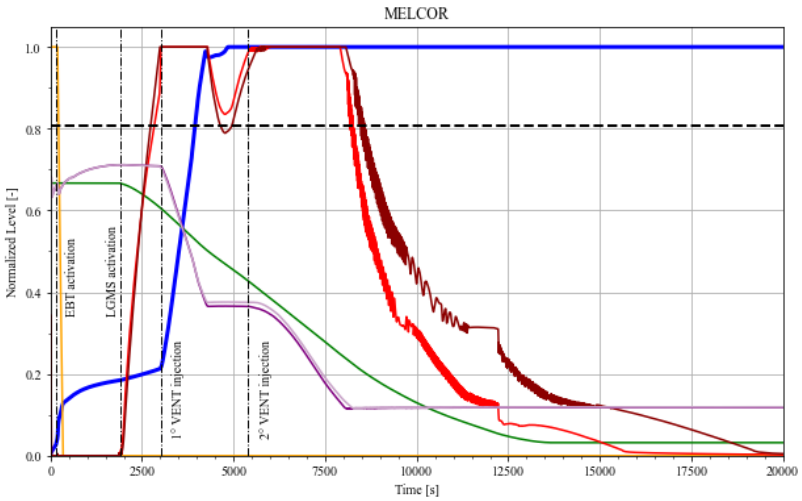

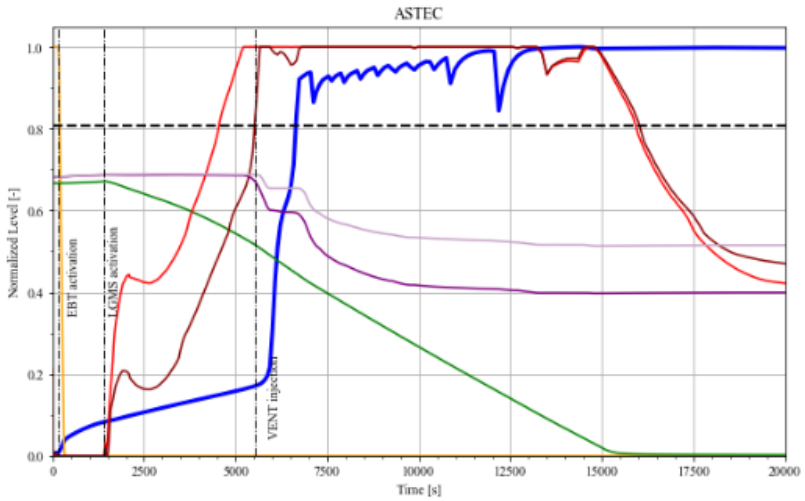

- CAVITY
- EBT - Broken line
- LGMS - Broken line
- PSS VENT - Intact line
- PSS VENT - Broken line
- PSS - Intact line
- PSS - Broken line
- DVI line

EBT activation — *Rise of CAV. level*
MELCOR: *152 s*
ASTEC: *160 s*

EBT draining completes — *Reduced level increase*
MELCOR: *652 s*
ASTEC: *660 s*

LGMS actuation
MELCOR: *1884 s*
ASTEC: *1398 s*

1° PSS reverse flow — *Cavity reaches DVI*
MELCOR: *3010 s*
ASTEC: *5534 s*

t [s]

Level in the cavity

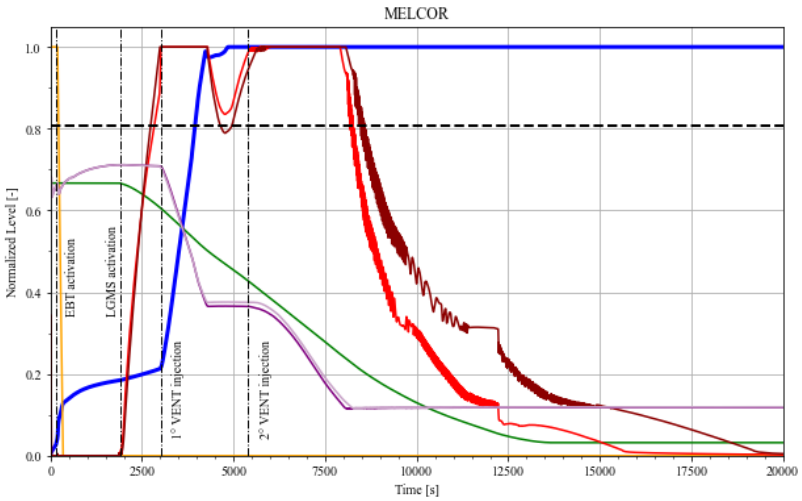

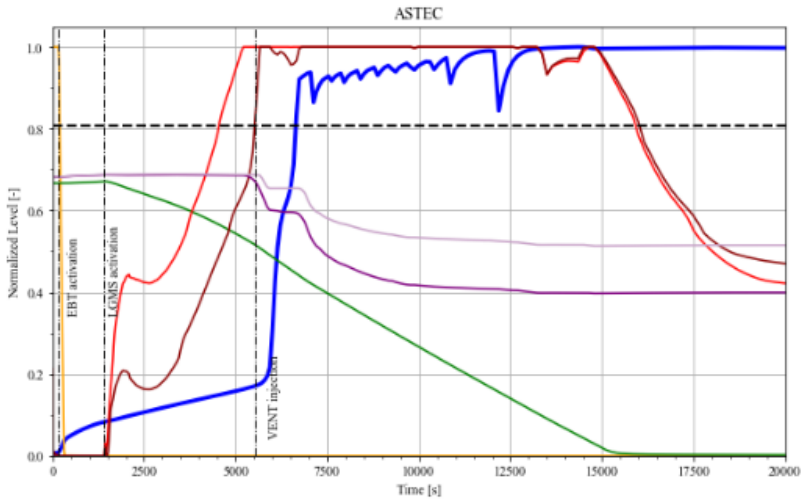

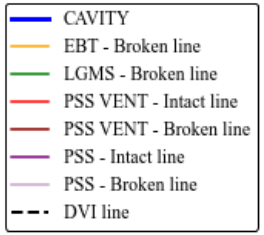

- MELCOR predicts a **faster level increase in the cavity** in the first **500s**.
- The **BREAK mass flow rate** is **higher in ASTEC**
- MELCOR behavior is due to a **major condensation in the containment** structure.

Level in the core

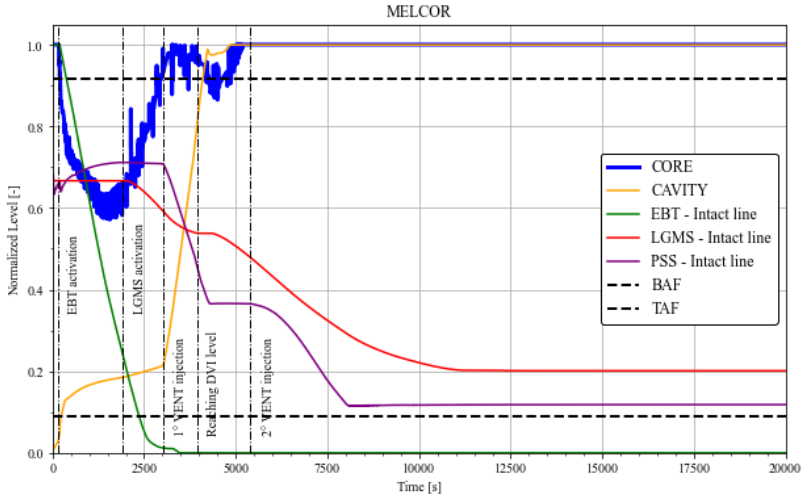

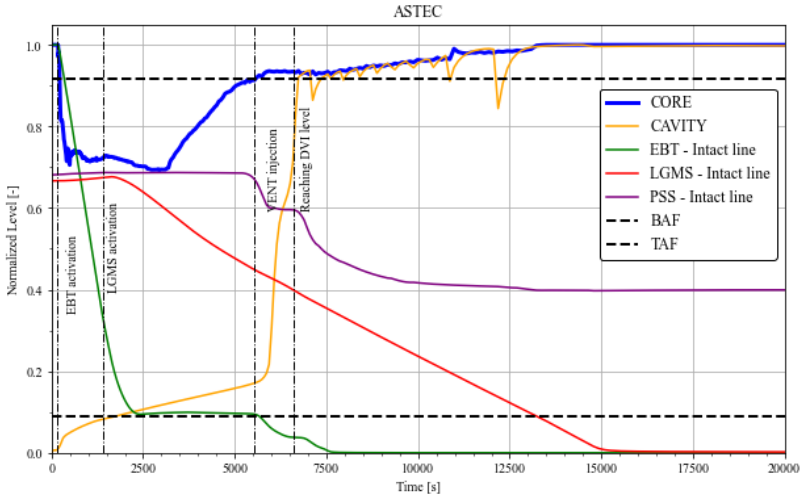

- Break flow
- Passive systems activation (Intact line)

Level in the core

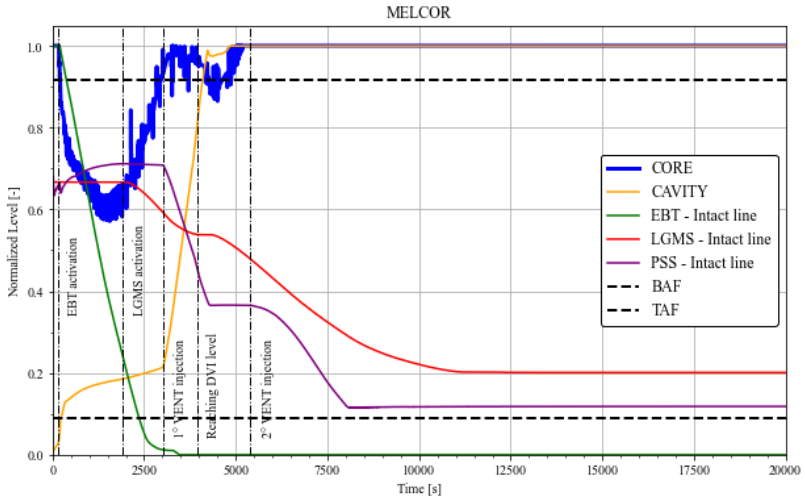

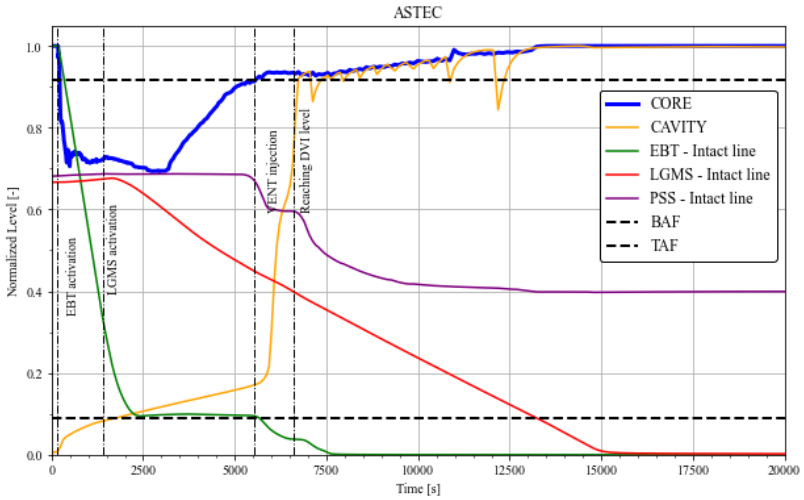

Minimum CORE level is reached

Starts again the break flow small and small level reduction is predicted

EBT activation
CORE level decreasing stop
MELCOR: *152 s*
ASTEC: *160 s*

LGMS actuation
Core level above the TAF
MELCOR: *1884 s*
ASTEC: *1398 s*

Cavity reaches DVI
Reverse BREAK flow
MELCOR: *3010 s*
ASTEC: *5534 s*

t [s]

EBT and LGMS behaviour – Intact line

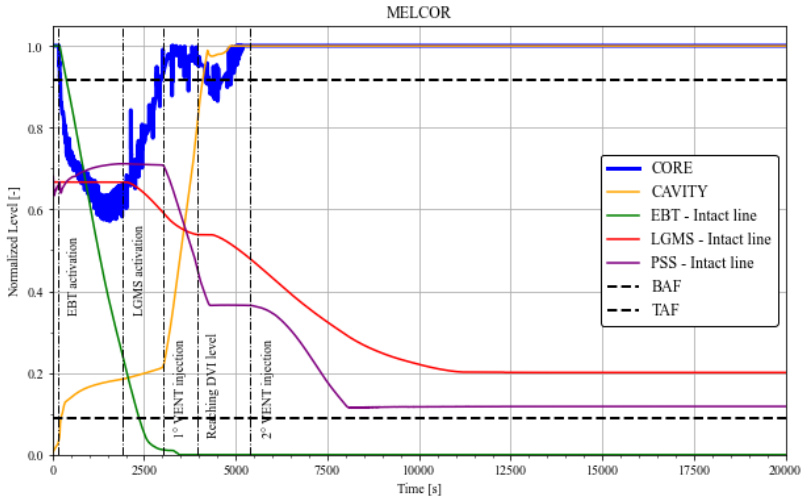

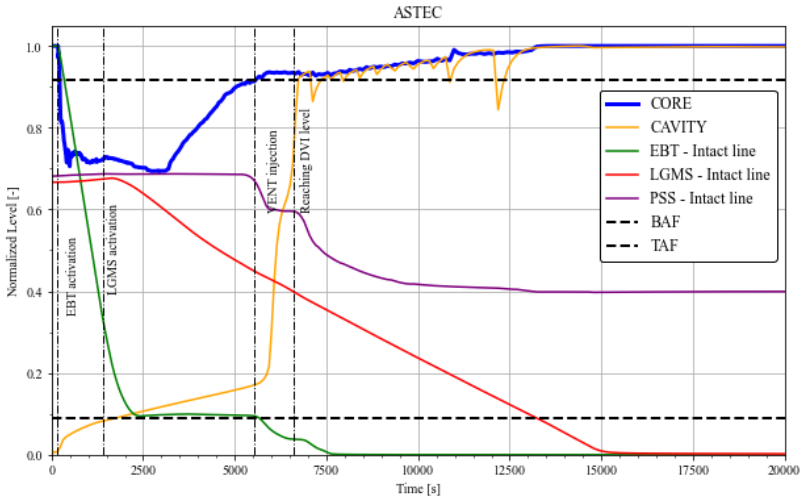

Regarding ASTEC…..

- ❑ CORE level reaches the **minimum at 3000s**
- ❑ Due to the **longer time interval** between 1° and 2° equalization, the **EBT stops to inject**. Subsequently, LGMS starts to inject affecting sensibly the level decrease

EBT and LGMS behaviour – Intact line

- EBT system follows the **pressure** behavior of the **primary side**
- the LGMS follows the **pressure** behavior of the **DW**

After the first equalization, the RPV pressure becomes lower than the DW one

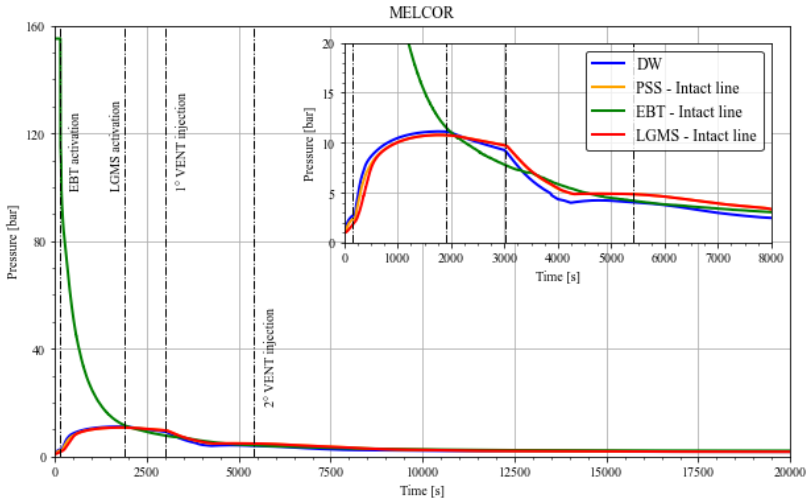

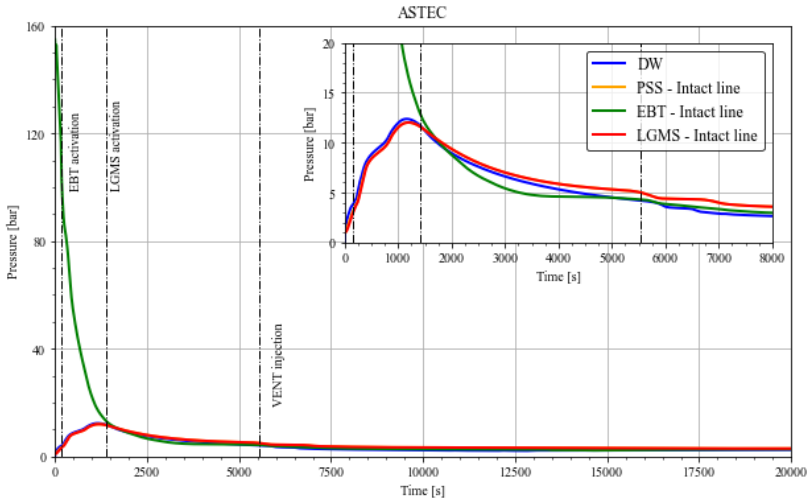

Results remarks

Event	MELCOR	ASTEC
Break	0	0
High Containment pressure signal (SCRAM, isolation SG, EHRS activation)	41	20
Low PRZ water level signal (Pump coast down and RI-DC opening)	122	65
Low PRZ pressure signal (ADS Stage-1 opening, EBTs opening)	148	158
Low DP RV-Containment (LGMSs opening)	1884	1398
1° RPV- DW pressure equalization	2000	1584
2° RPV- DW pressure equalization	3315	6006
1° vent injection	3010	5534
2° vent injection	5405	-
Core level reach the TAF	3000	5500
Cavity level reach the DVI	3950	6600
Low LGMS mass (ADS Stage -2 opening)	12265	12902

- MELCOR minimum level at about 0.6 while ASTEC at about 0.7
- The upper part of the core is uncovered in the MELCOR simulation for 2900s while ASTEC for 5400s
- The maximum cladding temperature predicted by MELCOR and ASTEC is about 622K and 619K
- No degradation core phenomena are predicted
- No hydrogen is produced

Conclusion

- The **codes** are **able to predict the expected dominant phenomena driving the transient** but some **quantitative discrepancies affecting the sequence of event** can be underlined.
- **MELCOR** calculation are characterized by a **major condensation in the containment and by a major direct condensation in the PSS** in comparison with ASTEC.
- **ASTEC** code is characterized by a **major heat removal from the passive heat removal systems** and a **major two-phase break flow rate**.
- More investigations are currently in progress to characterize these quantitative differences.

Acknowledgement/Disclaimer

SAFETY ANALYSIS OF SMR WITH PASSIVE MITIGATION STRATEGIES - SEVERE ACCIDENT



Funded by the European Union

Funded by the European Union. Views and opinions expressed are however those of the author(s) only and do not necessarily reflect those of the European Union or European Commission-Euratom.
Neither the European Union nor the granting authority can be held responsible for them.

ENEA carried out the research activity with MELCOR code and SNAP, obtained in the framework of the ENEA-ISIN agreement signed on March 23rd 2020 as part of the General Arrangement between the United States Nuclear Regulatory Commission (US-NRC) and the Italian National Inspectorate for Nuclear Safety and Radiation Protection (ISIN).

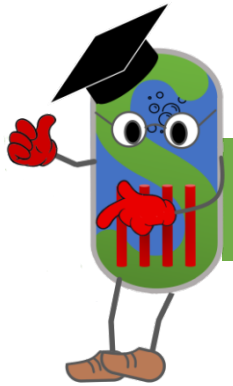

Thank you for your attention

SAFETY ANALYSIS OF SMR WITH PASSIVE MITIGATION STRATEGIES - SEVERE ACCIDENT

Gianmarco Grippo,
PhD student,
University of Bologna,
Department of Industrial Engineering (DIN), Viale del Risorgimento 2, 40136, Bologna, Italy
Email: gianmarco.grippo2@unibo.it

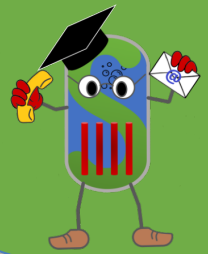

The 11th European Review Meeting on Severe Accidents Research

May 13-16, 2024, Royal Institute of Technology, Stockholm, Sweden

TECHNICAL SESSION 2.4: SEVERE ACCIDENT SCENARIOS - U&S ANALYSIS

Chairs: M. Angelucci (University of Pisa), L. E. Herranz (CIEMAT)

ID98	**Synthesis of Source Term Assessments for a Loss-Of-Cooling Accident in a Spent Fuel Pool: Uncertainty and Sensitivity Analyses and Potential Benefit of Water Injection by Spray System** O. Coindreau (IRSN)	**Paper Presentation**
ID03	**Uncertainties on Fission Product Release for a Loss-Of-Cooling Scenario in a Spent Fuel Pool with MELCOR2.2** M. Garcia (CIEMAT)	**Paper Presentation**
ID10	**Uncertainty and Sensitivity Analyses of Severe Accident Codes Using the ACE Algorithm-based Surrogate Model** Kwang-Il Ahn (KAERI)	**Paper Presentation**
ID42	**System Identification and Ranking Table (SIRT) for chemical thermodynamics of severe accidents** C. Journeau (CEA)	**Paper Presentation**

SYNTHESIS OF SOURCE TERM ASSESSMENTs FOR A LOSS-OF-COOLING ACCIDENT IN A SPENT FUEL POOL: INSIGHTS FROM UNCERTAINTY AND SENSITIVITY ANALYSES AND POTENTIAL BENEFIT OF WATER INJECTION BY SPRAY SYSTEM

O. Coindreau[1], M. Garcia[2], L.E. Herranz[2], S. Ederli[3], M. Massone[3], O. Sevbo[4], P. Groudev[5], A. Kaliatka[6], V. Vileiniškis[6], M. Malicki[7], Y. Vorobyov[8], I. Ivanov[9], M. D'Onorio[10], Y. Pontillon[11]

[1]: IRSN
Centre de Cadarache, B.P. 3 – 13115 Saint-Paul-lez-Durance Cedex, France
olivia.coindreau@irsn.fr

[2]: Nuclear Safety Research Unit, Department of Energy, CIEMAT
Avda. Complutense 40 Edificio 12-P0-13) 28040 Madrid, Spain
monica.gmartin@ciemat.es, luisen.herranz@ciemat.es

[3]: ENEA
Lungotevere Thaon di Revel 76, 00196 Roma, Italy
stefano.ederli@enea.it, mattia.massone@enea.it

[4]: Energorisk LLC
off. 141, 7 Simii Steshenkiv Str., Kyiv, 03148, Ukraine
sevbo@energorisk.com.ua

[5]: Institute for Nuclear Research and Nuclear Energy, Bulgarian Academy of Sciences (INRNE-BAS)
Tzarigradsko Chaussee 72, 1784 Sofia, Bulgaria
pavlinpg@inrne.bas.bg

[6]: LEI
Breslaujos str. 3, 44403 Kaunas, Lithuania
algirdas.kaliatka@lei.lt, virginijus.vileiniskis@lei.lt

[7]: Paul Scherrer Institut
Forschungsstrasse 111, CH-5232 Villigen PSI, Switzerland
mateusz.malicki@psi.ch

[8]: SSTC NRS
03142, 35-37 V.Stusa Street, Kyiv, Ukraine
yy_vorobyov@sstc.ua

[9]: TU-Sofia
1000 Sofia, 8, St. Kliment Ohridski Blvd., Bl. 12, Bulgaria
ivec@tu-sofia.bg

[10]: Sapienza University of Rome
DIAEE Corso Vittorio Emanuele II 244, 000186 Rome, Italy
matteo.donorio@uniroma1.it

[11] : CEA
Cadarache F-13108 Saint-Paul-Lez-Durance, France
yves.pontillon@cea.fr

ABSTRACT

The recently completed Horizon-2020 project on "Management and Uncertainties of Severe Accidents (MUSA)" has applied uncertainty and sensitivity analysis in the assessment of Severe Accidents (SA), particularly in predicting the radiological source term of reactor and Spent Fuel Pool (SFP) accident scenarios. For SFP, the two main objectives were: 1/ to determine the main uncertainties affecting the accident progression and fission product release during an accident in a SFP and 2/ to assess the possible benefits, in terms of source term reduction, of water injection by spray systems. The target of this paper is to describe the main achievements at the end of the 4 years' project, regarding SFP accident scenario. The uncertainty and sensitivity analyses were performed by eleven participants thanks to the propagation of the uncertainties of the input parameters to the output uncertainties of severe accident codes. A SFP accidental scenario was selected, uncertainty sources in models and input parameters were identified and key target variables were chosen as Figure of Merits (FOMs). It was found that spreading in SA code responses coming from the uncertainty quantification done by each participant was relatively small when compared to the variability between reference computations of all participants. It reveals that important uncertainty sources, such as the lack of modeling or the nodalization, have not been taken into account in the uncertainty quantification. The sensitivity analysis, based on statistical correlation coefficients and supported by the analysis of scatter plots, has put in light that uncertain parameters linked to aerosol phenomena in the building significantly affect the source term. It has also revealed that the relationship between the source term and uncertain parameters linked to degradation is not straightforward, due to the non-linear nature of the phenomena in play and due to cliff-edge effects. Concerning the benefits of spray systems, the mass flow rate and the injection time that can prevent cladding failure, and thus Fission Product (FP) release were determined by seven participants, thanks to ASTEC, RELAP/SCDAPSIM and MELCOR calculations. The results obtained are very preliminary and should not be considered as demonstrative, since SA codes are generally not validated to compute the cooling of an assembly by spray injection. It is thus mandatory to carry out a validation work of the thermal hydraulics and the POLCA OECD project would be an opportunity for this.

KEYWORDS: SFP, source term, uncertainty quantification, sensitivity analysis, spray system, SA codes

1. INTRODUCTION

Computer codes are widely used in nuclear industry to assess the behaviour of Nuclear Power Plants (NPPs) during postulated accidents, including SA. Since the models of these computer codes approximate the real physical behaviour, and since the data used to run these codes are also known with a limited accuracy, the code predictions are not exact, but uncertain [1]. The first way of dealing with these uncertainties in safety demonstrations is to use a conservative approach. However, due to the complexity of the phenomenology and the presence of counter-reactions, being conservative in one aspect may result in being optimistic in another aspect [2]. Consequently, a second way called "best-estimate approach" can be followed. If such

best-estimate calculations are used for safety studies, it requires quantifying the uncertainty associated to this estimation. This safety assessment approach is named Best Estimate Plus Uncertainty (BEPU). The evaluation of safety margins around the best-estimate values can be estimated thanks to uncertainty methods and benefits from the latest developments in methods and algorithms as well as the availability of computing resources. Mathematical tools for quantification of code uncertainties have thus been under development for many years for the analysis of design basis accidents [3-5], supported by the existence of many experiments, essentially focused on thermal hydraulic phenomena.

Uncertainty analysis has also been applied to SA, but less systematically, and most of the studies were performed for specific SA-phenomena. Only some of them contained an uncertainty quantification of the radiological source term. For instance, tolerance limits of source term following a severe accident were established for a French 1300 MWe PWR [6], for an accident sequence similar to the accident at Unit 2 of the Fukushima Daiichi NPP [7], and, in the framework of the US-American SOARCA study, for different NPPs and different accident scenarios [8]. To involve the Severe Accident community in the use of uncertainty methods, the Management and Uncertainties of Severe Accidents (MUSA) project was funded in HORIZON 2020 EURATOM NFRP-2018 call on "*Safety assessments to improve accident management strategies for generation II and III reactor*" [9-10]. In the framework of MUSA-WP6, uncertainty methods have been applied to the analysis of a SFP accident [11]. Indeed, a renewed interest has been paid to the safety of SFP after the accident at the Fukushima Dai-ichi Nuclear Power Plants highlighted the vulnerability of nuclear fuels that are stored in SFPs in case of prolonged loss-of-cooling accidents, even if the accident progression is slow (in comparison with reactor core accidents) [12-13]. At the same time, simulations of postulated SFP scenarios were carried out [14-19], but strong differences were found between the computations.

To get a better understanding of the SFP behaviour under accidental conditions, use has been made in MUSA-WP6 of uncertainty and sensitivity analysis. The main results obtained at the end of the project are summarized in this paper. The scenario studied is a loss-of-cooling accident, possibly mitigated by a spray system. The uncertainty sources that have been investigated are linked to modeling uncertainties and to the spray system. The uncertainty analysis has been performed by eleven participants thanks to the propagation of the uncertainties of the input parameters to the output uncertainties with three severe accident codes (ASTEC, RELAP/SCDAPSIM and MELCOR). Main outcomes resulting from the uncertainty analysis are presented. Then, results of the sensitivity analysis, that aims at evaluating the relative importance of uncertainties of the different input parameters on the output uncertainty, are discussed. In the conclusion, focus is put on the input of uncertainty and sensitivity analysis in the understanding of SFP behavior under accidental conditions, and in the identification of further R&D needs in SA codes.

2. SPENT FUEL POOL ACCIDENTAL SCENARIO and UNCERTAINTY SOURCES

2.1. Scenario, models and key target variables

The geometry for the calculations is similar to the one of the Unit 4 of the Fukushima Dai-ichi NPP, as set in the AIR-SFP NUGENIA+ project [17] and described in [11]. The main characteristics are summarized hereafter. The size of the pool is 12.2 m x 9.9 m x 11.5 m, with a total number of Fuel Assemblies (FAs) in the pool of 1535. The layout of Unit 4 was simplified for the computation as follows:

- 548 FAs (named "hot" FAs) with a fission power of 1.9 MW,
- 783 FAs (named "cold" FAs) with fission power of 0.5 MW,
- 204 FAs are fresh fuel.

The FP inventory for hot and cold FAs has been provided to the participants. The axial power profile was considered as flat in order to avoid additional complication in the modeling. It was assumed that a given

mass fraction of the initial radionuclide inventory (i.i.) is in the fuel-cladding gap at the beginning of the transient (Xe, Kr: 3% i.i., I: 1.7 % i.i., Cs: 5 % i.i., Te, Sb: 10^{-2} % i.i., Ba, Sr: 10^{-4} % i.i.). The fuel assembly type used in the calculations is a 9x9-9 assembly with a central squared water channel called STEP3B. Each FA is surrounded by a steel rack cell and the spent fuel assemblies are stored in 3x10 spent fuel racks, with 53 racks placed in the SFP. The accidental scenario is a loss-of-cooling scenario. The temporal and spatial domains are defined as follows:

- **Spatial domain**: each participant was free to decide whether including in their modeling the SFP building. Indeed, even if more representative of the real situation, the modeling of the SFP building adds variability in the simulations. In case SFP building is modeled, its free volume is supposed to be 25800 m^3 with an opening to the environment of 10 m^2.
- **Temporal domain**: the computation starts at the onset of fuel uncovery and ends at the onset of fuel melting when the fraction of relocated fuel (liquefied or debris) reaches 1-3 %.

The SFP has been modeled by 11 participants with the SA codes MELCOR [20-21], ASTEC [22-23] and RELAP/SCDAPSIM, [24-25]. The SA codes in this study were initially developed for reactor pressure vessel applications and the space meshing is thus adapted to describe axisymmetric cores or multi-channels cores. For this reason, the SFP is represented by a cylinder divided into concentric rings, inside which the FAs are placed. Main characteristics of the modeling developed by the participants are given in Table I. It can be emphasized that there are differences in the modeling. Some participants modeled the 3 different types of FAs (hot, cold, and fresh), whereas the other ones gathered cold and fresh FAs to have only 2 types of FAs. One participant modeled only one representative FA. The number of rings in the SFP also differs between the participants. In most cases, each FA type is put in a dedicated ring. In some cases, an empty ring (called by-pass channel) models the zone of the SFP that does not contain any FAs. The axial nodalization also shows some variability (more or less fine, from 8 to 26 axial meshes in the FA zone). When modeled, the SFP building is discretized in 1 to 7 meshes. In most cases, rectangular structures (water channel, channel box, rack cell and SFP concrete wall) are represented by cylinders.

Table I. List of participants, codes and nodalizations adopted for the simulations.

Organisation	SA code	Modeling of the SFP					Modeling of the building	End of the sim. **
		Nb of rings	Nb of FA types	By-pass channel*	Nb of axial meshes			
					FAs zone	above racks		
CIEMAT	MELCOR 2.2.15254	4	3	Yes	12	1	No	1 %
ENEA	ASTEC 2.2.0.1	3	2	Yes	24	5	Yes, 7 zones	1.5 %
Energorisk	MELCOR 1.8.6	2	2	Yes	10	2	Yes, 3 zones	1 %
INRNE	ASTEC 2.2.0.1	4	3	Yes	15	10	Yes, 1 zone	3 %
IRSN	ASTEC 2.2.0	3	2	Yes	24	5	Yes, 7 zones	1.5 %
LEI - A	ASTEC 2.2.0.1	3	2	Yes	10	10	Yes, 7 zones	3 %
LEI - R	RELAP/SCDAPSIM 3.4	1	1	No	8	12	No	1 %
PSI	MELCOR 2.2.18019	4	2	Yes	15	0	No	1 %
SSTC	MELCOR 2.2	3	3	No	14	1	No	1 %
TUS	ASTEC 2.2b	4	3	Yes	15	10	Yes, 1 zone	3 %
UNIRM1	MELCOR 2.2.18019	3	3	No	26	4	Yes, 6 zones	1 %

* by-pass channel corresponds to an empty ring, without any FA

** fraction of relocated fuel considered to end the computation

The following phenomena were modeled in the simulations:

- **thermal hydraulics** in the SFP (and in the SFP building when it is modeled),
- **heat transfer** by conduction in the structures, convection, and radiation. Concerning radiative heat transfers, the users faced some difficulties: the models developed for SFP-BWR type of reactor lead to

code crashes (MELCOR), or do not allow the simulation of radiative heat transfer between the steel rack cell of cold and hot FAs (ASTEC).

- **FA behaviour and degradation:** failure of fuel rods, oxidation, and eutectic reactions, melting and candling, fuel rods collapse. In MELCOR, the temperature at which claddings fail (and gap inventory is released) is a user parameter. Fuel rods collapse is given in terms of a lifetime failure function table that specifies the time remaining to collapse versus the local oxidized cladding temperature. In ASTEC, failure of the fuel rods corresponds to the burst occurrence, which is based on a stress or a strain condition. Fuel rods collapse (also named "loss of fuel rods integrity") relies on a set of criteria (temperature and cladding oxidation state). A reduced melting temperature of UO_2 - ZrO_2 is usually considered to account for eutectic reactions.
- **fission product modeling:** radionuclide release is predicted by ASTEC and MELCOR. With RELAP/SCDASIM, only cumulative releases of fission product from fuel rods could be calculated. In MELCOR, a fixed cladding temperature for gap release is set, whereas it is computed in ASTEC (and corresponds to burst occurrence as explained previously).

Since the MUSA project is focused on Source Term (ST) evaluation, the figures of merit that have been investigated are linked to FP release. Due to its inventory in the SFP, its volatility and the dose coefficients of its isotopes (Cs137, Cs134), Cs was found to be one of the elements with the greatest radiological impact. Cs release, and the onset time of FP release from fuel have thus been selected as the key target variables. Additional variables (water mass in the SFP, maximum cladding temperature) have been used to analyze the reference computation but have not been considered in the uncertainty/sensitivity analysis.

2.2. Reference computations

In lack of cooling, and due to decay heat, the pool water, which is initially at saturation temperature, evaporates and the amount of water progressively decreases (see Figure 1a). The theoretical evolution of the water level has been computed with the assumption that heat load of the immerged part of the fuel assemblies leads to the evaporation of the water. Right from the beginning, some of the computed water masses differ from the theoretical curve. Differences between the theoretical curve and the computations increase after 50 h as phenomena not accounted in the theoretical curve come into play (oxidation and heat transfer of the uncovered part of the FAs, material relocation, radiation, …). It was noticed that the water mass evolution is affected by the modeling of the SFP (axial and radial nodalization, setting of the specified decay heat, interfacial friction model) and of the SFP building.

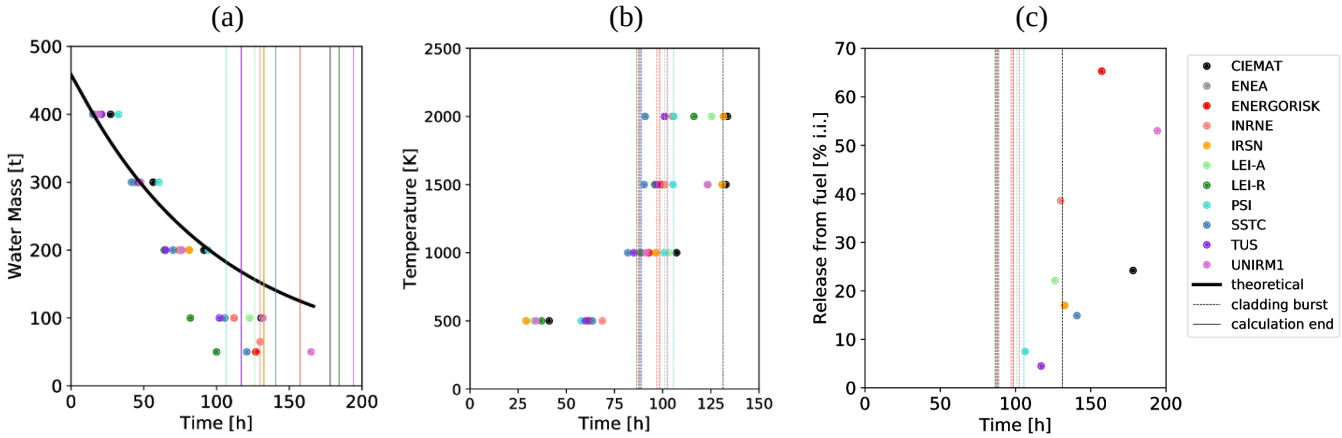

Figure 1. Reference computations. (a) Evolution of water mass in the SFP, (b) Evolution of the maximum cladding temperature, (c) Final Cs release from fuel. Lines are the ending times (fraction of relocated fuel between 1 and 3%), dotted lines correspond to cladding burst (i.e. gap release)

The maximum cladding temperature is stable until approx. 1 m of FA is uncovered (see Figure 1b). Then, the temperature of the uncovered part of the fuel assemblies increases regularly in a first time, and then more rapidly when oxidation comes into play. The maximum cladding temperature is strongly linked to the water level. So, differences in water level lead to differences in maximum cladding temperature. First FP release occurs when the cladding of hot FAs bursts, triggering the release of the fuel-cladding gap content (dotted lines in Figure 1c). This event occurs more than 80 h after the beginning of the transient, and for 10 over 11 computations, in a 20 h time-window. In some computations, the cladding of cold FAs also bursts, whereas in the other ones the cladding failure of cold FAs is not predicted. In all computations, a steep temperature rise is observed when the cladding reaches a temperature at which oxidation starts to be significant. This temperature excursion leads to the loss of cladding geometry and the relocation of either molten materials or solid debris. Depending on the amount of relocated material and on the criterion chosen to stop the computation, the computation can either end or continue. The temperature excursion initiates a fast FP release from the fuel matrix, that mostly occurs at the end of transient. However, it must be highlighted that FP release resulting from cladding burst is already very significant, given the large FP inventory in the SFP and the assumption made on the fuel-cladding gap content (see 2.1).

2.3. Uncertainty sources

The first uncertainties investigated in this study are the modeling one. As previously mentioned, the SA codes were initially developed for reactor pressure vessel applications. Even if some phenomena are close to those that occur in reactor scenarios, others are quite different due to the specificities of SFPs compared to reactor pressure vessels [12]: arrangement of the FAs (that can have very different burnup) in storage racks, flow patterns that can be three-dimensional (3D), relatively low decay power, atmospheric pressure surrounded by air, only one safety barrier (the cladding) in case the SFP is located outside the containment. Some phenomena consequently suffer from a lack of modeling in SA codes when they are applied to SFP accident conditions [26]. Uncertainties that result from modeling inaccuracies or from a modeling that has no uncertain parameters (u.p.) available to the user have not been evaluated in this study. Focus has been put on the u.p. in the existing models. The phenomena have been divided in categories, closely linked to the models developed in most SA codes. The participants have listed the u.p. available to the user in the SA codes and filled a table with their description and their Probability Density Function (PDF). Finally, each participant has selected a number of u.p., as reported in Table II. Most uncertain parameters are related to FAs' behaviour and degradation, FP release and transport and heat transfer.

Table II. modeling uncertain parameters investigated by the participants

Organisation	Nb of u.p.	TH in the pool	Heat transfer	FAs' behavior and degradation	FP release and transport	Material properties
CIEMAT	15			2	13	
ENEA	21	2		6	13	
Energorisk	8			4	3	1
INRNE	7			4	3	
IRSN	18			7	11	
LEI - A	12		2	5	4	1
LEI - R	22		10	11		1
PSI	15		5	10		
SSTC	24	5	5	8	6	
TUS	7			3	4	
UNIRM1	29	1	7	11	10	

The second type of uncertainties investigated in this study is linked to SA Management (SAM) measures. A review of existing and innovative SAM measures in the partner countries carried out during the MUSA project has shown that emergency sprays in the containment or in the spent fuel building may be used to mitigate the consequences of SFP accident. To assess the benefits of spray systems, sensitivity calculations, varying the water mass flow rate and the injection time (see Table III), were carried out to determine whether the cladding burst (and thus the onset of FP release) can be avoided within the simulation time of the reference calculation.

Table III. SAM uncertain parameters investigated by the participants

Org.	Injection time*	Water flow rate	Temperature of injected water	Injection location	Number of calculations
ENEA	2 → 14 h	0.5 → 2 kg/s	20°C	Top of the SFP	44
INRNE	1 → 16 h	1 → 2 kg/s	40°C	Top of the SFP	12
IRSN	2 → 24 h	0.75 → 2 kg/s	20°C	Top of the SFP	23
LEI - A	0 → 8 h	1 → 2 kg/s	20°C	Top of the SFP	19
LEI - R	0 → 0.5 h	0.5 → 2 kg/s	10°C	Top of the SFP	11
SSTC	5.9 → 17.9 h	0.7 → 5 kg/s	60°C	Bottom of the SFP	8
TUS	3 → 15 h	1 → 2 kg/s	40°C	Top of the SFP	8

*** before cladding failure**

3. UNCERTAINTY ANALYSIS

3.1. Methodology

The methodology developed in the frame of the MUSA project to perform uncertainty and sensitivity analysis relies on the propagation of input uncertainties which is particularly suitable for code simulation applications [27]. The method is based on the random sampling of different selected input u.p. values. The Uncertainty Tools (UTs) used in this study have the capability for pure random (Monte Carlo) and Latin Hypercube Sampling (LHS). The set of sampled values is used for running several code calculations, in which all the input uncertain parameters are sampled based on their own PDF. After the simulations are performed with the SA code, the data of interest are extracted from the result files and written in the format required by the UT to be statistically post-processed. The uncertainty analysis presented in this study is based on the following statistics indicators: minimum/maximum value, mean, standard deviation (σ). The number of simulations carried out by the participants is based on the minimum number of runs necessary to determine the two-sided tolerance interval statistics according to the Wilks' non-parametric method [28-39]. For a probability content of 95 % and a confidence level of 95 %, it corresponds to approx. 100 runs. However, it must be considered that the probability content and confidence levels cannot be ensured, since some hypotheses of Wilks' formulation [30] (identification and quantifications of all uncertainty sources, absence of calculation failures) are not met in our application. However, we consider that Wilks' formula as a valid method to estimate a "reasonable" number of runs to be performed for uncertainty analysis. It is nevertheless mandatory to do an accurate and critical analysis to identify possible misleading results.

3.2. Results and discussion

The results obtained are presented in Figure 2. In section 2.2, it was highlighted that the onset times of FP release were in relatively good agreement between the reference computations. However, the uncertainty range computed by the participants (see Figure 2a) exhibits significant differences: in the simulations where the cladding fails when a given temperature is reached, the uncertainty range is noticeable: either because

the temperature criterion is considered as an u.p. (CIEMAT, SSTC and UNIRM1) or because another u.p. influences the temperature evolution and thus the timing of gap release (PSI). In the simulations where the cladding rupture is computed by a mechanistic model implemented in the SA code, the uncertainty range is very small (only noticeable for LEI-R). Since there are uncertainties in the parametrization of the cladding burst model, this should have led to a greater uncertainty range than that observed in Figure 2a. This comes from the u.p. considered, which is the maximum hoop strain, whereas burst occurs upon another criterion (NUREG-0630 [31]). It is also probable that some uncertainties sources linked to the modeling of thermal hydraulics and heat transfer, that should influence the cladding temperature evolution and the subsequent cladding failure, are also lacking.

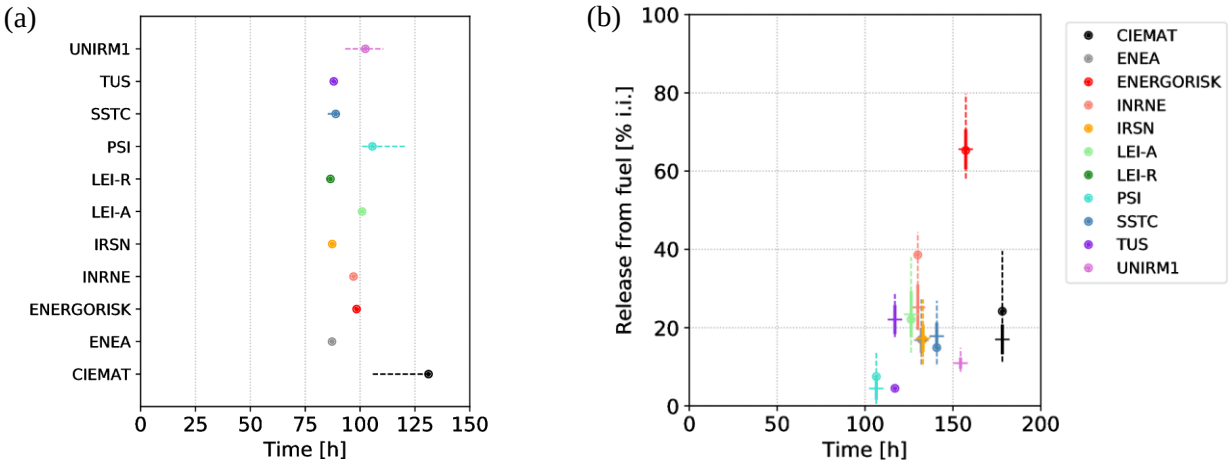

Figure 2. Uncertainty quantification. (a) onset time of FP release from fuel, (b) final Cs release from fuel. Points correspond to the reference case, dashes to the mean, dotted lines to the [minimum, maximum] range and lines to the [mean-σ, mean+σ range]

The magnitude of the first FP releases (not shown here) is computed without any uncertainty since the fuel-cladding gap inventory was set as a fixed input parameter (see 2.1). However, this parameter is not precisely known. It was estimated that the gap inventory considered in the present study (i.e. Cs: 5 % i.i) is overestimated since the global release fraction measured in the VERCORS tests RT6 and RT8 is less than 0.6 % up to 1200°C for Cs and I [32]. It would consequently be worth in further studies to take the fuel-cladding gap inventory as an u.p. Variability in FP release increases with time, when Booth diffusion model [33], that describes FP diffusion through the fuel grain to the grain surface, comes into play. Finally, the uncertainty range of Cs release at the ending computations time (see Figure 2b) is very different among participants (very small in some cases and not very large in most cases), which can be explained by the list of u.p. that have been propagated, which differ from one participant to another one. It is also noticeable that spreading in SA code responses coming from the uncertainty quantification done by each participant is relatively small when compared to the variability between reference computations of all participants. This can be attributed to the limited number of uncertainties that have been considered, i.e. only uncertainties linked to models developed in SA codes with input parameters available to the user.

Finally, it was found that a code limitation can lead to errors in FP release that exceeds the uncertainty range which has been determined by the propagation of a limited number of uncertain parameters. For instance, the distribution of a mean FPs inventory between modeled FAs according to user defined factors leads to an inaccurate radionuclides repartition. If the factors are set to correctly distribute the decay power between hot and cold+fresh FAs, the amount of some radionuclides is overestimated in hot FAs. In the configuration studied here, this is the case for Cs137 and Sr90 for instance. It leads to overestimate by a factor of 2.8 the amount of Cs in hot FAs and the subsequent Cs release when the cladding of hot FAs fails.

4. SENSITIVITY ANALYSIS

4.1. Sensitivity to modeling uncertain parameters

To carry out the sensitivity analysis, the participants have assessed the relative importance of uncertainties of the different input parameters on the output uncertainty. Methods based on Monte Carlo regression and correlation analysis [34] have been used with the following indicators for the association between the input uncertain parameters and the output: correlation coefficients on the values (Pearson) or on the ranks (Spearman), partial correlation coefficients, standardized regression coefficients. Scatterplots have also been used. One example of the results obtained is displayed in Figure 3a, with the evolution of the Spearman coefficient for Cs released from fuel, showing the association between the u.p. and the output. Correlation coefficients (absolute value) below 0.2, that corresponds to the Bravais-Pearson confidence threshold for a sample size of 100 and a confidence level of 95 %, will be considered as unsignificant.

Despite the difficulty of drawing generic conclusion, due to the diversity of modeling and u.p. considered, the following issues have been pointed out by the participants:

- The correlation coefficients between input u.p. and Cs release strongly evolve with time. An u.p. can be the most important one but only for a while. It puts in evidence that the statistical analysis at the final time only is very restrictive and can be very different from that performed during the long-lasting transient. This is especially true in the present scenario that ends during a fast increase of temperature and FP release.
- It was found that the onset time of Cs release (i.e. cladding burst) is positively correlated to the cladding failure temperature for gap release (for the simulations where the cladding fails when a given temperature is reached). It was also observed that the onset time of Cs release is correlated to u.p. that influence thermal evolution and cladding oxidation: a positive correlation with the radiative exchange factor (axial) and a negative correlation with the metallic cladding oxidation rate constant coefficients. Results of the sensitivity analysis show that oxidation cutoff temperature is correlated to the onset time of Cs release, but with 2 opposite directions: positively if the cladding fails when a given temperature is reached, negatively if a model predicts the cladding burst. It was also found that the onset time of Cs release occurs sometime before with pre-oxidized cladding. Finally, no correlation was found with u.p. linked to the cladding burst model, due to an unsuitable choice of u.p. (see 3.2).
- The sensitivity of Cs release from fuel to degradation parameters is not straightforward: u.p. that drive degradation are generally positively correlated to the maximum fuel temperature and FP release. However, after loss of integrity and fuel relocation, this is not true anymore. For this reason, correlation coefficients related to degradation parameters fluctuate significantly and their sign can change also during the degradation. At the beginning of fuel heat-up, the following correlations were found (resulting from the correlations with the onset time of Cs release): Cs release from fuel is negatively correlated with the radiative exchange factors (axial and radial) and positively correlated with the metallic cladding oxidation rate. A positive correlation with the CORSOR-Booth scaling factor for Cs was also evidenced, but no significant correlation with the fuel grain diameter. Some correlations were computed with u.p. linked to oxidation (positive correlation with the axial extension of the cracking after cladding burst for instance), and material properties.
- When the building is modeled, FP release in the environment is generally significantly affected by uncertain parameters linked to aerosol phenomena in the building. Uncertain parameters that lead to an increase of the settling velocity are negatively correlated to the Cs source term, whereas u.p. leading to a decrease of the settling velocity are positively correlated to the Cs source term. It was thus computed a positive correlation with the aerosol dynamic shape factor and a negative correlation with the particle shape factor relative to coagulation. For the mean particle density, a negative correlation has been computed (relationship as expected) by two participants, whereas one participant computed a positive correlation.

4.2. Sensitivity to spray systems

The results obtained by the 5 institutions that participated to the sensitivity analysis are displayed in Figure 3b. It represents 113 simulations performed with ASTEC, RELAP/SCDAPSIM or MELCOR, covering a large range of injection times and mass flow rates. It must be highlighted that the modeling is not completely uniform, with different temperatures of injected water and a participant who injected water at the bottom of the SFP (see Table III). In general, it was observed that:

- Within the time window investigated (i.e., later than 18 h before cladding burst), a minimum of 1 kg/s is required to prevent (or delay) cladding burst.
- Safe and failure regions have been identified. In the safe region, the conditions (injection time and mass flow rate) prevent cladding burst within the simulation time of the reference calculation for all participants. Nonetheless, in some cases, even if cladding failure was not predicted within the simulation time, it could be reached in the very long term, especially for low mass flow rate that does not compensate the evaporation flow rate. In the failure region, the conditions (injection time and mass flow rate) do not prevent cladding burst for all participants.
- Between the safe and the failure regions, a region of unclear/unreliable results emerges: a same condition (injection time and mass flow rate) prevents cladding burst in a simulation, whereas it does not in another one (for instance 1 kg/s, 8 h before cladding burst). This can be explained by differences in the thermal hydraulic and burst models.

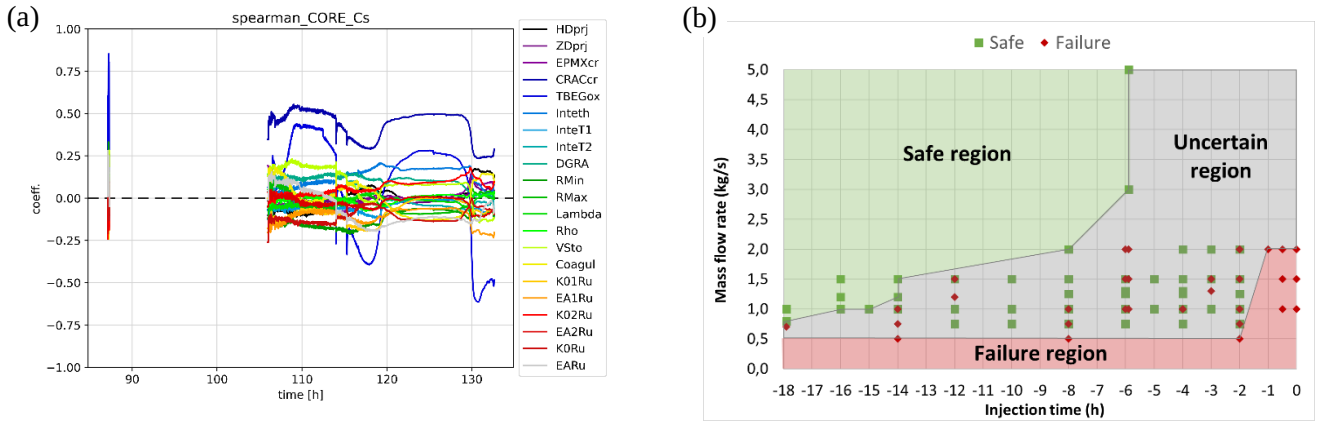

Figure 3. Sensitivity to (a) modeling uncertain parameters (evolution of the Spearman coefficient for Cs release from fuel) and (b) spray systems

The results obtained are very preliminary and should not be considered as demonstrative, since SA codes are generally not validated to compute the cooling of an assembly by spray injection. However, the work performed has shown the feasibility of such computations and the obtained results suggest that the spray system could be a very efficient mean of cooling the FAs and preventing cladding burst. To consolidate these evaluations, it is mandatory to carry out first a validation work of the thermal hydraulics and an extension of the fuel rod burst model to SFP conditions. The POLCA OECD project [35] would be an opportunity to get the experimental data needed to validate the models in existing thermal hydraulic system codes.

5. CONCLUSIONS

This paper aims at providing an overview of the uncertainty and sensitivity analyses performed by the MUSA participants on a loss-of-cooling scenario in a SFP, with two kinds of uncertainty sources

investigated: modeling uncertainties and characteristics (timing and mass flow rate) of a spray system. Despite differences in the modeling and in the list of u.p. that have been propagated the participants, the study has provided very valuable results and important lessons. Firstly, it was found that spreading in SA code responses coming from the uncertainty quantification done by each participant is relatively small when compared to the variability between reference computations of all participants. Discrepancies between reference computations come from differences in the nodalization, in the models, in the consideration or not of the building and in the criterion chosen to stop the computation (from 1 to 3% relocated fuel). The relatively small uncertainty computed by each participant reveals that there are important uncertainty sources that have not been considered in the study. Some of them were excluded from this exercise (fuel-gap inventory for instance), and it would be worth investigating them in a further study. However, a review of modeling u.p. listed by the participants has also put in evidence that some u.p. are lacking, because they are not available to the user (especially for thermal hydraulics), that there is a lack of modeling (and consequently no u.p.) or that they have not been considered as having a high impact on the ST. Consequently, the results obtained in the present study cannot be used to establish tolerance limits.

By ascertaining the relative importance of uncertainties of the different input parameters on the output uncertainty, this study has provided results in terms of sensitivity analysis. As the release of the fuel-cladding gap inventory already leads to huge radiological consequences in case of an accident in a SFP, prediction of cladding burst is of prime importance. On the one hand, it was found that the onset time of Cs release (i.e. cladding burst) is correlated to u.p. that influence thermal evolution and cladding oxidation (for instance radiative exchange factor, metallic cladding oxidation rate, and presence of a pre-oxide layer). These findings support the developments that are currently underway to adapt the radiation model to SFP geometry in SA codes and the necessity of quantifying the input uncertainty in the models developed. On the other hand, the absence of correlation with the u.p. linked to the cladding burst model in ASTEC demonstrates an unsuitable choice of u.p. and the necessity to use another set of u.p. in further studies. This study has also shown the difficulty of establishing a correlation that would last during the whole transient between the u.p. linked to the degradation models and Cs release. However, at the beginning of fuel heat-up, it was computed that Cs release is correlated to the radiative exchange factors, the metallic cladding oxidation rate, the release of Cs from the UO_2 fuel matrix, and the axial extension of the cracking after cladding burst. Cs release in the environment was found to be correlated to u.p. linked to aerosol phenomena in the building (aerosol dynamic shape factor, particle shape factor relative to coagulation and particle density), with a negative correlation for the parameters that lead to increase the settling velocity. Concerning the benefits of spray systems, the results obtained, although very preliminary, suggest that the spray system could be a very efficient mean of cooling the FAs and preventing cladding burst. The POLCA OECD project [33] would be an opportunity to get the experimental data needed to validate the models in existing thermal hydraulic system codes.

Finally, some recommendations can be made for the development of an uncertainty/sensitivity analysis with a SA code. At first, it is very important to establish a good quality reference case, as robust as possible. Then, a consistency screening of u.p. sets is highly recommended and pre-correlation should be used to avoid unphysical parameter combinations. The entire transient should be considered since just end time Figures Of Merit would miss substantial insights into models performance and key processes affecting final results. It must be kept in mind that setting tolerance limits requires some constrains that are not met in SFP calculations. But substantial insights can be gained by using sensitivity analysis: better understanding of the behaviour of a model and of its coherence, identification of interactions between processes and of the most influential parameters. If correlations found in sensitivity analyses cannot be physically supported, analysis of single realizations must be performed and eventually, code developers might be recommended to review some of the models embedded in the code if limitations or inconsistencies are found.

ACKNOWLEDGEMENTS

The MUSA project has received funding from the Euratom research and training program 2014–2018 under grant agreement No. 847441.

REFERENCES

1. E. Chojnacki and J.-P. Benoit, "The use of Monte-Carlo simulation and order statistics for uncertainty analysis of a LBLOCA transient (LOFT-L2-5)", Proceedings of Workshop on Evaluation of Uncertainties in Relation to Severe Accidents and Level-2 Probabilistic Safety Analysis, Aix-en-Provence, France, 7-9 November 2005.
2. R. Cozeret, J. Chambarel, S. Phoudiah, D. Corbin and S. Pignet, "Improvement on 900 MWe NPPs in the occasion of the 4th 10-year periodic safety review on severe accidents", *Proceedings of EUROSAFE 2019*, Cologne, Germany, November 4-5, 2019, pp. 43-51.
3. "Report on the Uncertainty Methods Study", NEA/CSNI/R(97)35 (1998).
4. "BEMUSE Phase VI Report, Status report on the area, classification of the methods, conclusions and recommendations", OECD/NEA/CSNI/R(2011)4 (2011).
5. "PREMIUM: A Benchmark on the Quantification of the Uncertainty of the Physical Models in the System Thermal-Hydraulic Codes - Methodologies and Data review", NEA/CSNI/R(2016)9 (2016).
6. K. Chevalier-Jabet, F. Cousin, L. Cantrel and C. Séropian, "Source term assessment with ASTEC and associated uncertainty analysis using SUNSET tool", *Nucl. Eng. Des.*, **272**, pp. 207-218 (2014).
7. X. Zheng, H. Itoh, H. Tamaki, Y. Maruyama, "An integrated approach to source term uncertainty and sensitivity analyses for nuclear reactor severe accidents, *Journal of Nuclear Science and Technology*, **53**, pp. 333-344 (2016).
8. S.T. Ghosh et al., "State-Of-the-Art Reactor Consequence Analyses Project: Uncertainty Analyses for Station Blackout Scenarios", *Nucl. Technol.*, **207**, pp. 441–451 (2021).
9. L.E. Herranz et al., "The EC MUSA Project on Management and Uncertainty of Severe Accidents: Main Pillars and Status", *Energies*, **14** (4473), pp. 1-11 (2021).
10. F. Mascari, "Application of Uncertainty Quantification Methods against Integral Experiments (AUQMIE) in the EU-MUSA project", ETSON news, March 2021.
11. O. Coindreau et al, "Uncertainty quantification for a severe accident sequence in a SFP in the frame of the H-2020 project MUSA: First outcomes", *Ann. Nucl. Energy*, **188** (2023).
12. "Status Report on Spent Fuel Pools under Loss-of-Cooling and Loss-of-Coolant Accident Conditions: Final Report", OECD Publishing, Paris (2015).
13. "Phenomena Identification and Ranking Table. R&D Priorities for Loss-of-Cooling and Loss-of-Coolant Accidents in Spent Nuclear Fuel Pools", NEA/CSNI/R(2017)18 (2018).
14. F. Fleurot et al, "Synthesis of spent fuel pool accident assessments using severe accident codes", *Ann. Nucl. Energy*, **74**, pp. 58–71 (2014).
15. X. Wu et al., "Analysis of the loss of pool cooling accident in a PWR spent fuel pool with MAAP5", *Ann. Nucl. Energy*, **72**, pp. 198–213 (2014).
16. X. Wu et al., "Analysis of accidental loss of pool coolant due to leakage in a PWR SFP", *Ann. Nucl. Energy* **77**, pp. 65–73 (2015).
17. O. Coindreau et al., "Severe accident code-to-code comparison for two accident scenarios in a spent fuel pool", *Ann. Nucl. Energy*, **120**, pp. 880-887 (2018).
18. K.-I. Ahn, Y.H. Jung, J.-U. Shin, W.-T. Kim, "Evaluation of an accident management strategy using an emergency water injection in a reference PWR SFP", *Ann. Nucl. Energy*, **113**, pp. 353-379 (2018).
19. K.-I. Ahn, J.-U. Shin, W.-T. Kim, "An assessment of radiological source terms for loss of cooling and coolant accidents of a PWR spent fuel pool", *Progress in Nuclear Energy*, **129**, (2020).
20. L.L. Humphries et al., "MELCOR Computer Code Manuals. Vol. 1: Primer and Users' Guide Version 2.2.14959", No. SAND2019-12536 O.

21. L.L., Humphries et al., "MELCOR Computer Code Manuals. Vol. 2: Reference Manual Version 2.2.14959", No. SAND2019-12537 O.
22. P. Chatelard et al., "Main modeling features of the ASTEC V2.1 major revision", *Ann. Nucl. Energy*, **93**, pp. 83-93 (2016).
23. P. Chatelard and L. Laborde, "ASTEC V2.2 code validation: Illustrative results and main outcomes", *Nuclear Engineering and Design*, **413** (2023).
24. C.D. Fletcher et al., "RELAP5/MOD3 code manual user's guidelines". Idaho National Engineering Lab., NUREG/CR-5535 (1992).
25. C. M. Allison et al., "SCDAP/RELAP5 Users Guide and Input Manual", NUREG/CR-6150 EGG-2720. USA, Idaho National Engineering Laboratory, Vol. 3. (1998)
26. "Phenomena Identification and Ranking Table. R&D Priorities for Loss-of-Cooling and Loss-of-Coolant Accidents in Spent Nuclear Fuel Pools", OECD Publishing, (2018).
27. G. Baroni and S. Tarantola, "A general probabilistic framework for uncertainty and global sensitivity analysis of deterministic models: a hydrological case study", *Environ. Model. Software*, **51**, pp. 26–34. (2014)
28. S.S. Wilks, "Determination of sample sizes for setting tolerance limits," *Ann. Math. Stat.*, **12**(1), pp. 91–96 (1941).
29. S.S. Wilks, "Statistical prediction with special reference to the problem of tolerance limits," *Ann. Math. Stat.*, **13**(4), pp. 400–409 (1942).
30. N.W. Porter, "Wilks' formula applied to computational tools: A practical discussion and verification", *Ann. Nucl. Energy*, **133**, pp. 129-137 (2019).
31. D. A. Powers, R. O. Meyer, "Cladding Swelling and Rupture Models for LOCA Analysis", NUREG-0630 (1980).
32. Y. Pontillon, I. Moysan, S. Bernard and M. Ledieu, "New Insight on Volatile Fission Products (I and Cs) release from high burnup UO2 fuel under LOCA type conditions", TopFuel 2018, Prague, Czech Republic (2018).
33. A. H. Booth, "A Method of Calculating Fission Gas Diffusion from UO2 Fuel and Its Application to the X-2 Loop Test", Tech. Rep. AECL-496, Atomic Energy of Canada Limited (1957).
34. J. C. Helton, "Uncertainty and Sensitivity Analysis Techniques for Use in Performance Assessment for Radioactive Waste Disposal", *Reliability Engineering and System Safety*, **42**, pp. 327-367 (1993)
35. https://www.oecd-nea.org/jcms/pl_80836/advancing-the-understanding-of-spent-fuel-pools-during-loss-of-cooling-accidents

Synthesis of Source Term Assessments for a Loss-of-Cooling Accident in a Spent Fuel Pool: Insights from Uncertainty and Sensitivity Analyses and Potential Benefit of Water Injection by Spray System

ERMSAR 2024, 13-16 May 2024, Stockholm, Sweden

Olivia Coindreau (IRSN) et al.

MUSA has received funding from the Euratom research and training programme 2014-2018 under grant agreement No 847441.

Content

- Motivation and groundwork
- Insights and results
- Conclusions

Motivation and groundwork

- To determine the main uncertainties affecting the accident progression and fission product release during an accident in a SFP, by applying UQ methodologies
- To assess the possible benefits, in terms of source term reduction, of water injection by spray systems
- Work realised in the framework of the MUSA project - grant agreement No. 847441

Insights and results – SFP scenario (1/6)

Geometry identical to the unit 4 of Fukushima Daiichi with simplifications

Dimensions: 12.2 m × 9.9 m

Heat load: 2.4 MW

1535 FA: 548 hot (3,47 kW/FA), 783 cold (0,507 kW/FA), 204 non irradiated. **FP inventory** provided to the participants

Loss-of-cooling scenario with a computation starting at the onset of fuel uncovery and ending at the onset of fuel melting. The criterion to stop the computation is a fraction of relocated (liquefied or debris) greater than 1-3 %

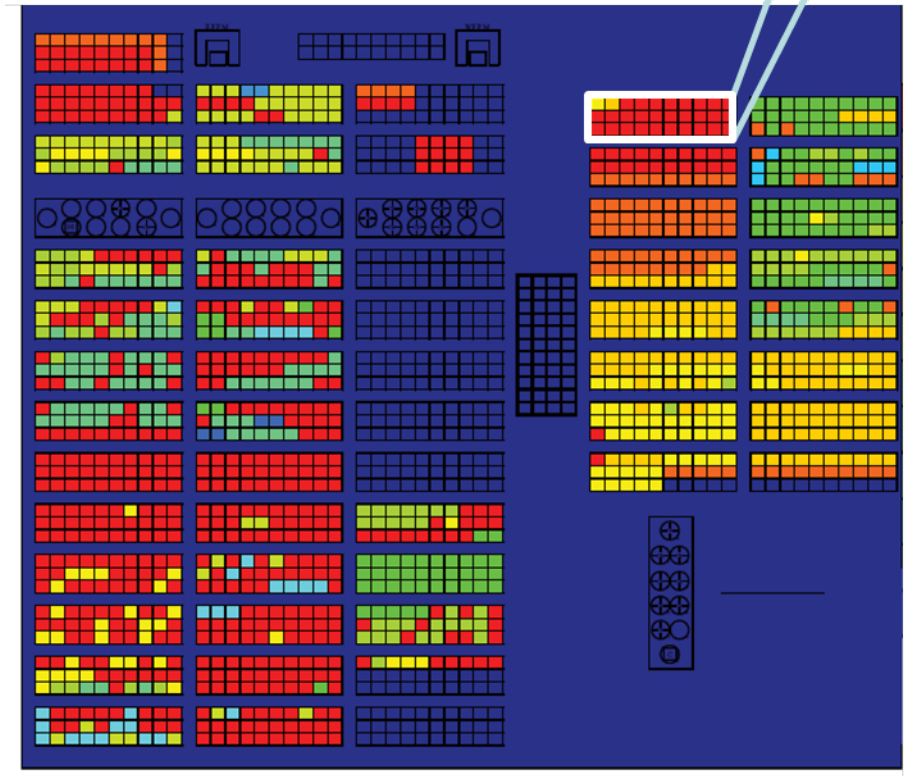

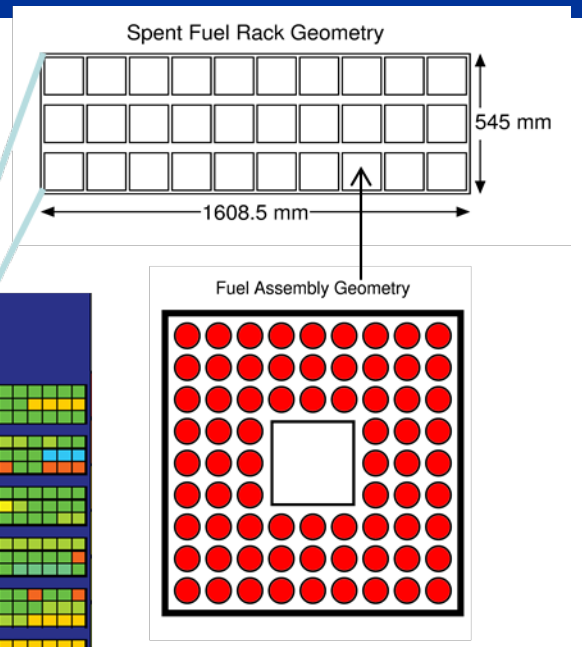

Insights and results – SFP scenario (2/6)

Modelling domain: only the pool or the pool and the building above the SFP

Org.	SA code	Uncertainty Tool
CIEMAT	MELCOR (wo containment)	DAKOTA
ENEA	ASTEC	RAVEN, Python
Energorisk	MELCOR	DAKOTA
INRNE	ASTEC	SUNSET
IRSN	ASTEC	R, Python
LEI-A	ASTEC	SUNSET
LEI-R	RELAP/SCDAPSIM (wo containment)	SUSA
PSI	MELCOR (wo containment)	DAKOTA, Python
SSTC	MELCOR (wo containment)	SUSA
TUS	ASTEC	SUNSET
UNIRM1	MELCOR	RAVEN

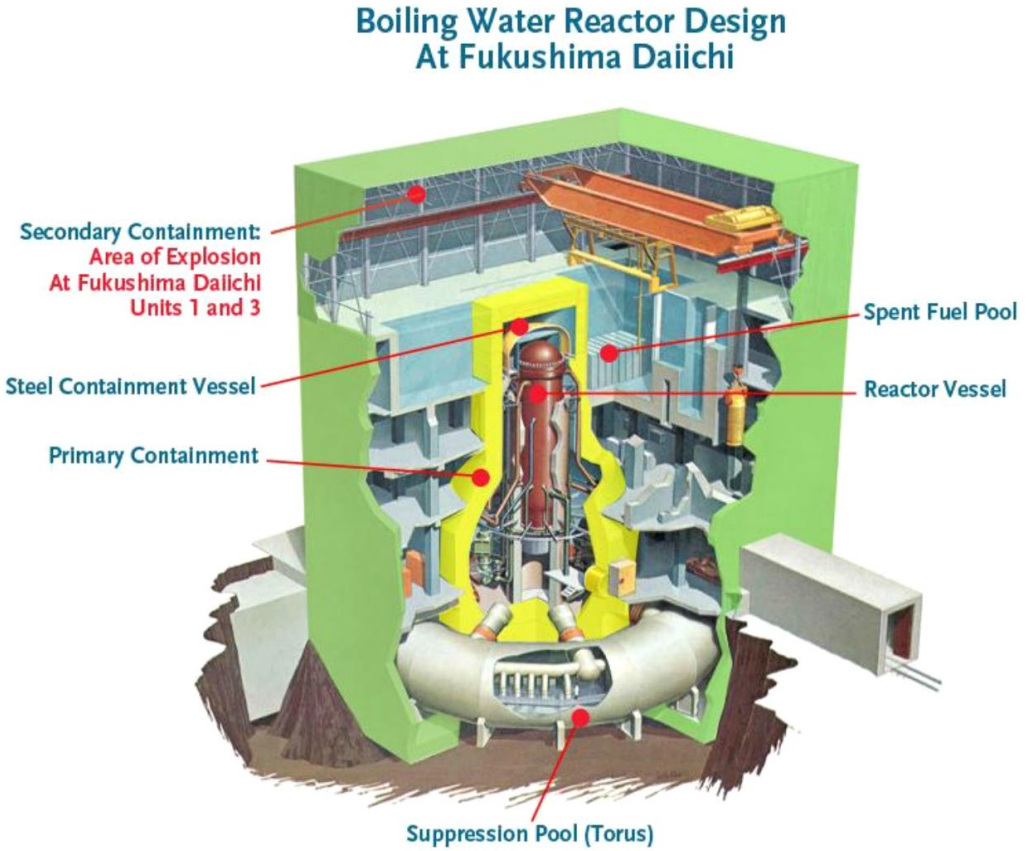

From Report INPO 11-005, Institute of Nuclear Power Operations, Atlanta, GA, USA

Insights and results – SFP scenario (3/6)

Before 50 h:

- ✓ Some results differ from the theoretical curve
- ✓ Differences can be due to **differences in heat loss and heat transfer modelling between the pool and the building**
- ✓ **Axial nodalization** can significantly impact the results
- ✓ The **use of the 5 or 6 equations modelling for diphasic thermal-hydraulics in ASTEC computations** also impact the results
- ✓ Differences were observed between **MELCOR computations carried out with different decay heat modelling**

After 50 h:

- ✓ **Increase of ≠** between the theoretical curve and the computations (oxidation, material relocation, radiation,…)
- ✓ **Differences between computations increase** as well as more phenomena come into play

Evolution of Water Mass

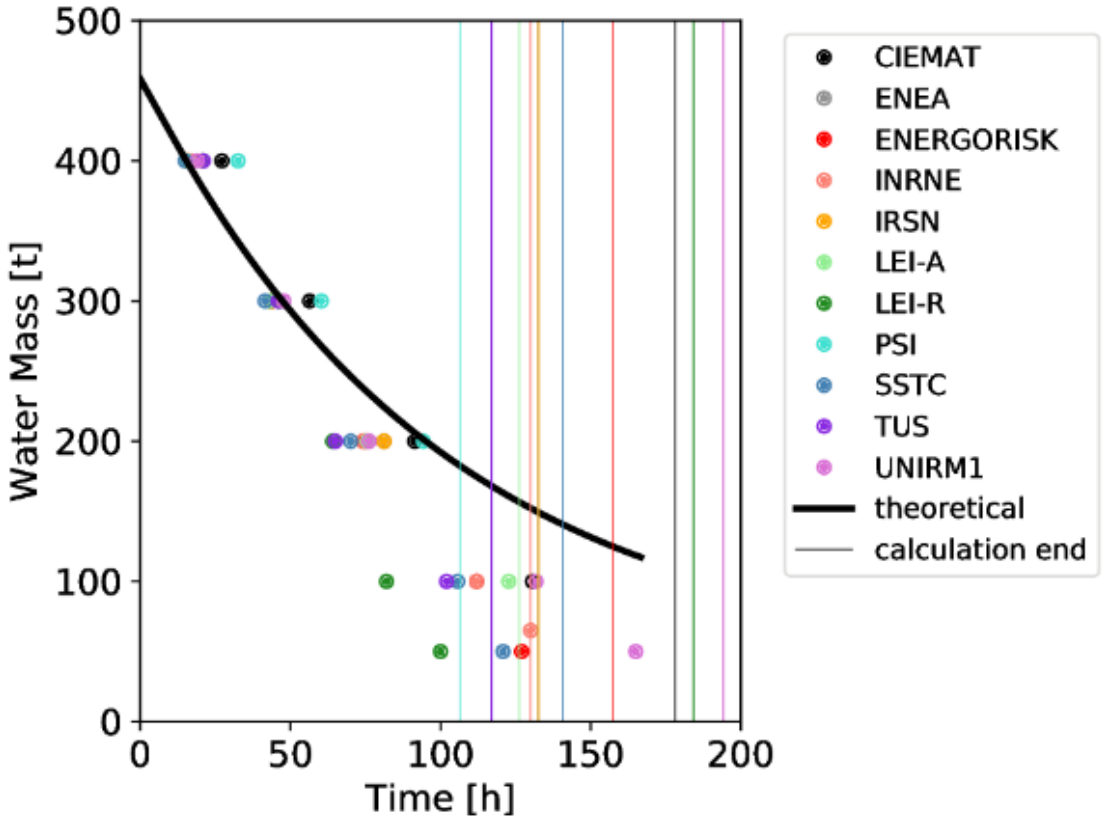

Insights and results – SFP scenario (4/6)

- ✓ The maximum **cladding temperature is stable until approx. 1 m of fuel assembly is uncovered.** Then, the temperature of the **uncovered part of the FAs increases regularly** in a first time
- ✓ **The burst of hot FAs' occurs** more than 80 h after the beginning of the transient
- ✓ The **heating of cold FAs' is strongly linked to the nodalization and radiative heat transfer** between hot and cold FAs (cladding of cold FAs burst or not)
- ✓ An **exponential temperature** rise is observed when the cladding has reached a temperature at which **oxidation starts to be significant** ⇨ loss of integrity
- ✓ Depending on the amount of relocated material and on the criterion chosen to stop the computation, the computation ends or continues ⇨ leads to **significant differences in computation end times**

Evolution of maximum cladding temperature

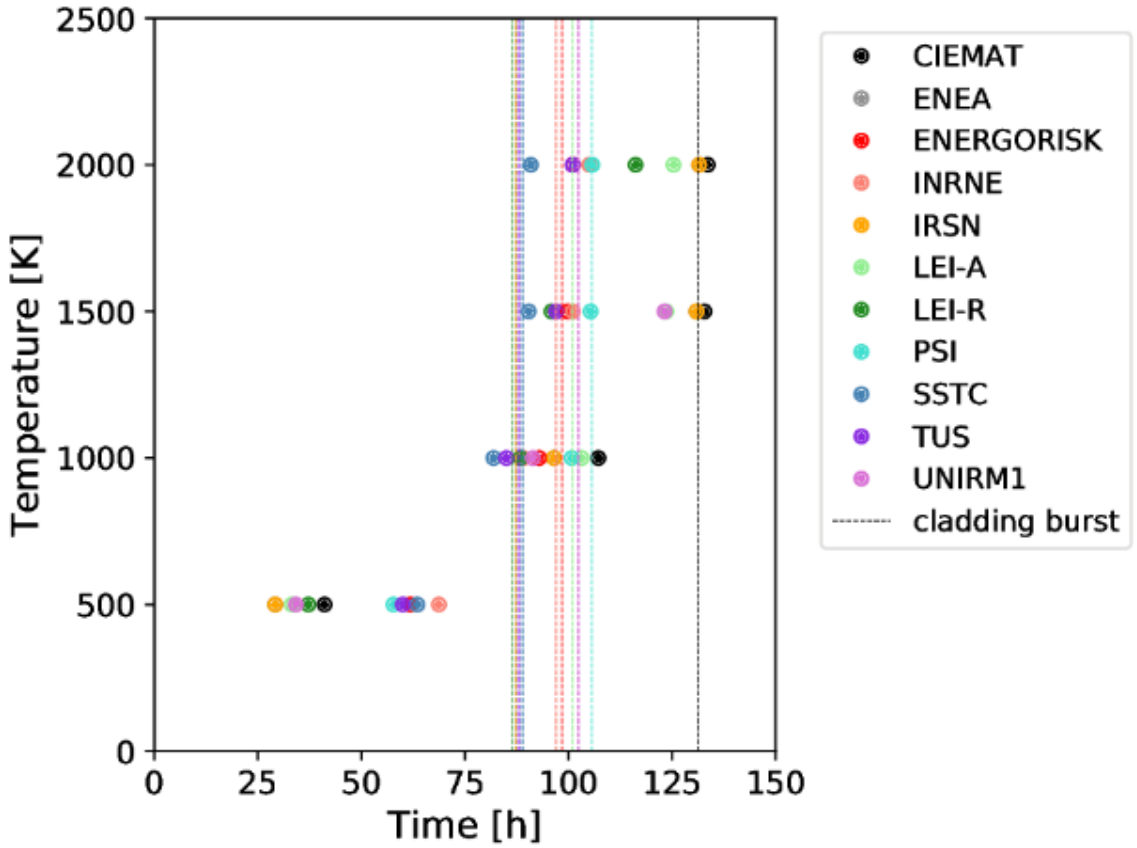

Insights and results – SFP scenario (5/6)

- ✓ **First FP release (gap release) occurs when the cladding of hot fuel assemblies' bursts** (more than 80 h after the beginning of the transient)
- ✓ **Intensity of these first releases depend on the amount of FP put in the gap and the number of failed FAs**
- ✓ **Fast FP release** from the fuel matrix when the **exponential temperature rise is observed**
- ✓ If (relatively) high temperature are maintained for a long time without reaching the criterion ⇨ leads to significant differences in releases
- ✓ **Most of release occurs at the end of transient** and the final amount is strongly impacted by the criterion chosen to stop the computation.

Final Cs release

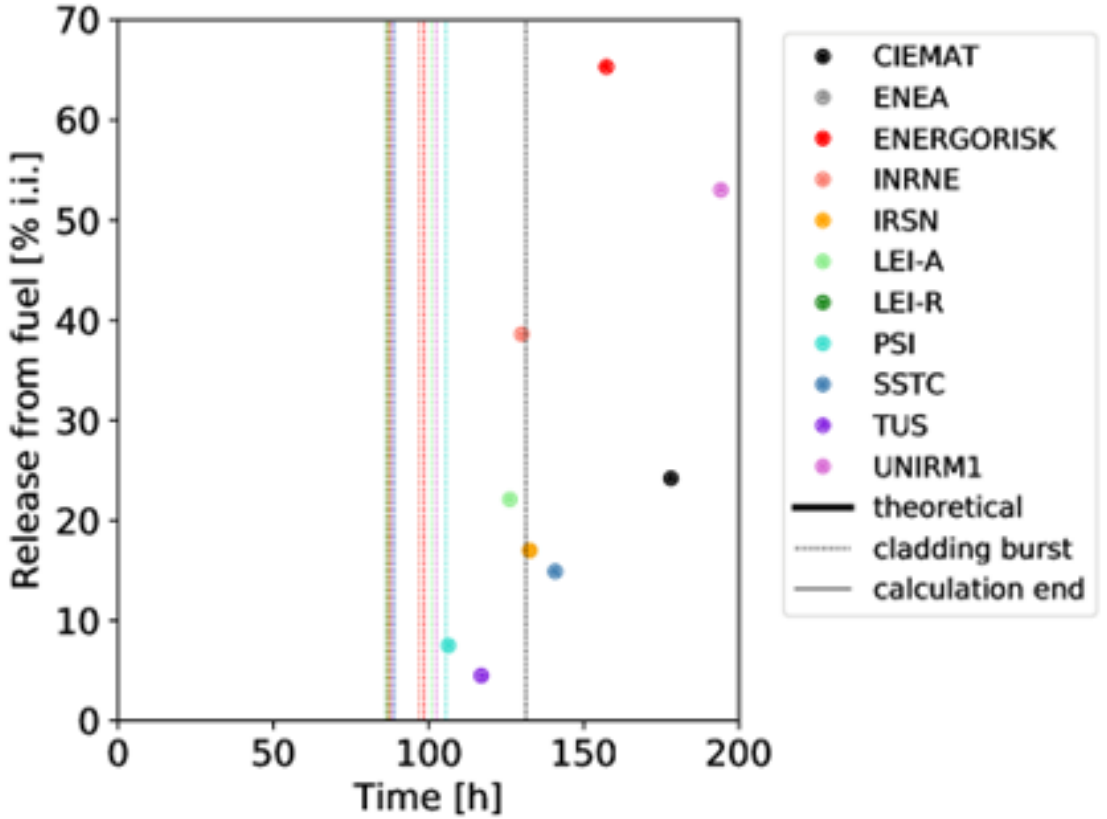

Insights and results – SFP scenario (6/6)

Conclusions:

Analysis of the reference case computations has put in evidence differences between the results:

- In the **TH behaviour**, right from the beginning
- In **FA heating & degradation,** leading to different ending times
- In **FP release**

These differences can be due to:

- **different nodalizations**: number of radial rings, number of axial meshing
- **different SA codes**
- **different physical modelling options** (within the same SA code)

⇨ **Establishing good quality reference case is an important part of UQ analysis**

⇨ **Some improvements have been done in the meantime by code developers**

Insights and results – uncertainty sources (1/2)

1. Thermal-hydraulic in the pool
2. Power generation
3. Heat transfer
4. FAs behavior and degradation
5. FP release and transport
6. Thermal-hydraulic in the SFP building
7. Material properties

Organisation	Nb of u.p.	1.	2.	3.	4.	5.	6.	7.
CIEMAT	15				*	*		
ENEA	21	*			*	*		
Energorisk	8			*	*			
INRNE	7				*	*		
IRSN	18				*	*		
LEI - ASTEC	12			*	*	*		
LEI - SCDAP	25			*	*			*
PSI	15	*		*	*			
SSTC	24	*		*	*	*		
TUS	7				*	*		
UNIRM1	25				*	*		

- **Modelling uncertainties have been investigated**
- **SA codes have strong limitations** when they are applied to SFP:
  - ✓ one mean FP inventory distributed in the modelled groups of FAs (and possibly FP grouped by classes for the MELCOR code)
  - ✓ radiation model not operational for SFP configuration
  - ✓ 3D flow patterns & stratified configurations not properly simulated
  - ✓ models developed for conditions representative of reactor scenarios and not for SFP conditions (slower temperature rise and long-standing chemical interactions)

⇨ **Only a part of the uncertainty can be evaluated**

Insights and results – uncertainty sources (2/2)

- **uncertainties linked to SA Management (SAM) measures**
- sensitivity calculations, varying the water mass flow rate and the injection time, to determine whether the cladding burst (and thus the onset of FP release) can be avoided

Org.	Injection time*	Water flow rate	Temperature of injected water	Injection location	Number of calculations
ENEA	2 → 14 h	0.5 → 2 kg/s	20°C	Top of the SFP	44
INRNE	1 → 16 h	1 → 2 kg/s	40°C	Top of the SFP	12
IRSN	2 → 24 h	0.75 → 2 kg/s	20°C	Top of the SFP	23
LEI - A	0 → 8 h	1 → 2 kg/s	20°C	Top of the SFP	19
LEI - R	0 → 0.5 h	0.5 → 2 kg/s	10°C	Top of the SFP	11
SSTC	5.9 → 17.9 h	0.7 → 5 kg/s	60°C	Bottom of the SFP	8
TUS	3 → 15 h	1 → 2 kg/s	40°C	Top of the SFP	8

* before cladding failure

Uncertainty quantification (1/3)

- propagation of input uncertainties
- random sampling of different selected input u.p. values
- the key target variables investigated are the **onset time of FP release** from fuel and **Cs release in the environment**

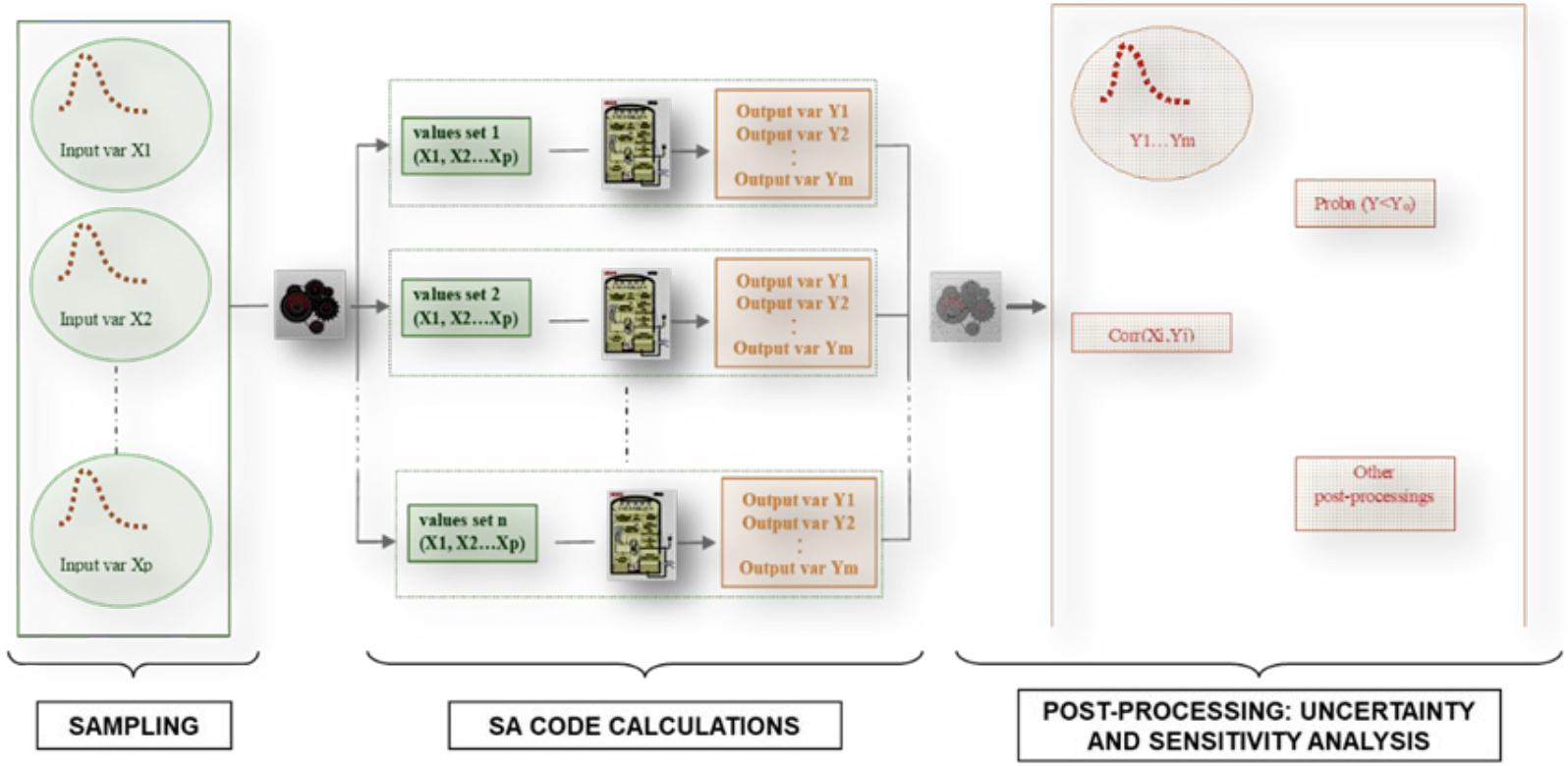

Uncertainty quantification (2/3)

Onset time of FP release

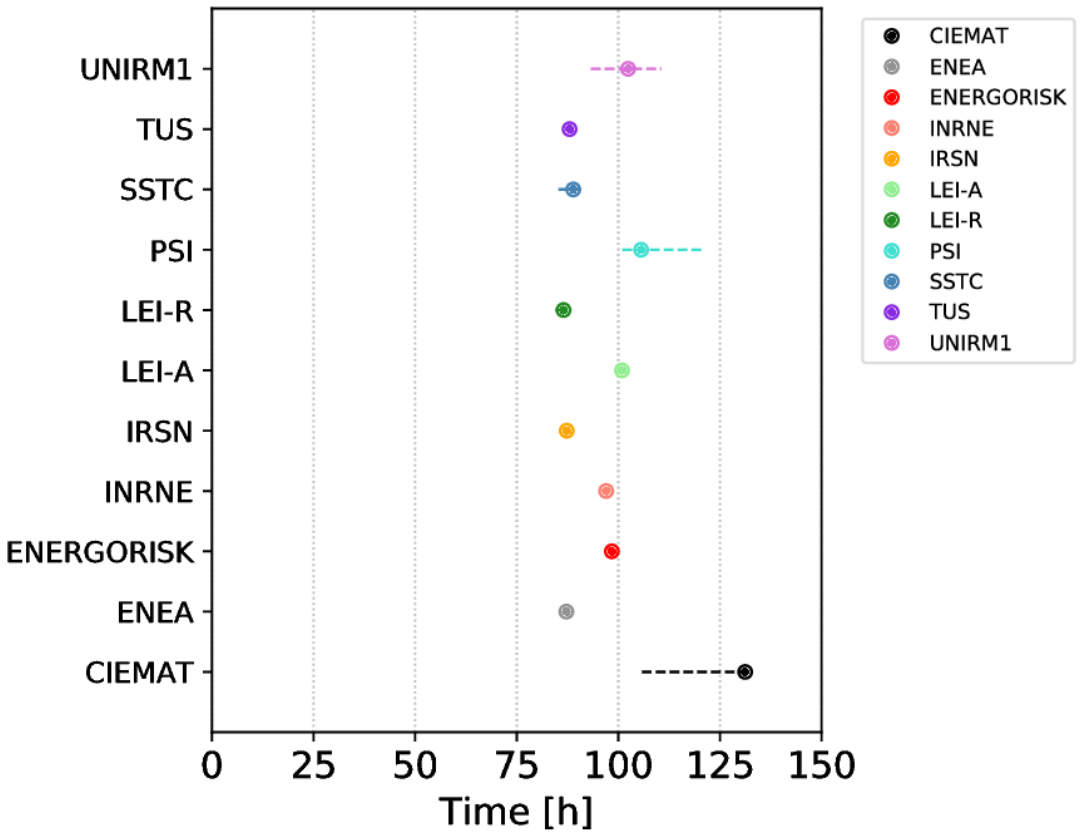

- The **onset times of FP release** for the reference case are in **relatively good agreemeent** between the computations
- **But its uncertainty range strongly differ:**
  - ✓ very small when cladding rupture is computed by the code
  - ✓ more important when cladding failure temperature is an u.p.

⇨ **Lack of some uncertainties sources linked to the modeling of thermal hydraulics and heat transfer,** that should influence the cladding temperature evolution and the subsequent cladding failure

⇨ Wrong choice of the **u.p. linked to the cladding burst modelling**

Uncertainty quantification (3/3)

Final Cs release from fuel

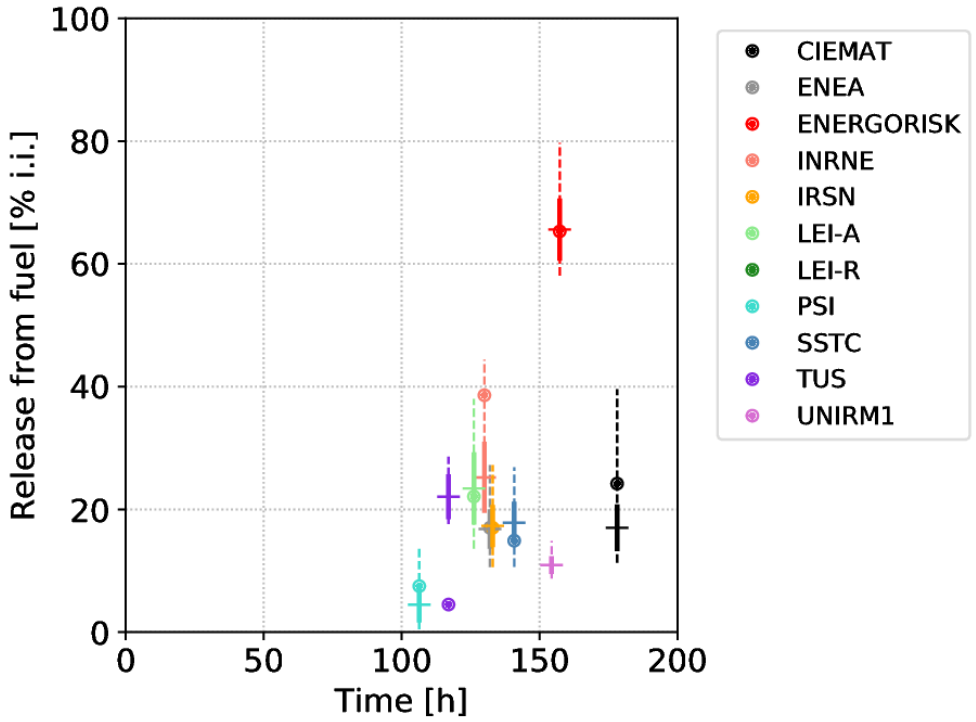

- **The uncertainty range of the final Cs release is very different among participants**, which can be explained by:
  - ✓ **the list of u.p.** that have been propagated, which differ from one participant to another one
  - ✓ the **end of the computation during fast-transient heating** and FP release
- **The uncertainty range of the final Cs release is relatively small** when compared to the variability between reference computations of all participants due to the limited number of uncertainties that have been considered
- **A code limitation (one i.i.) can lead to errors in FP release that exceeds this uncertainty range**

Sensitivity Analysis (1/2)

Spearman coefficient for Cs release from fuel (ENEA)

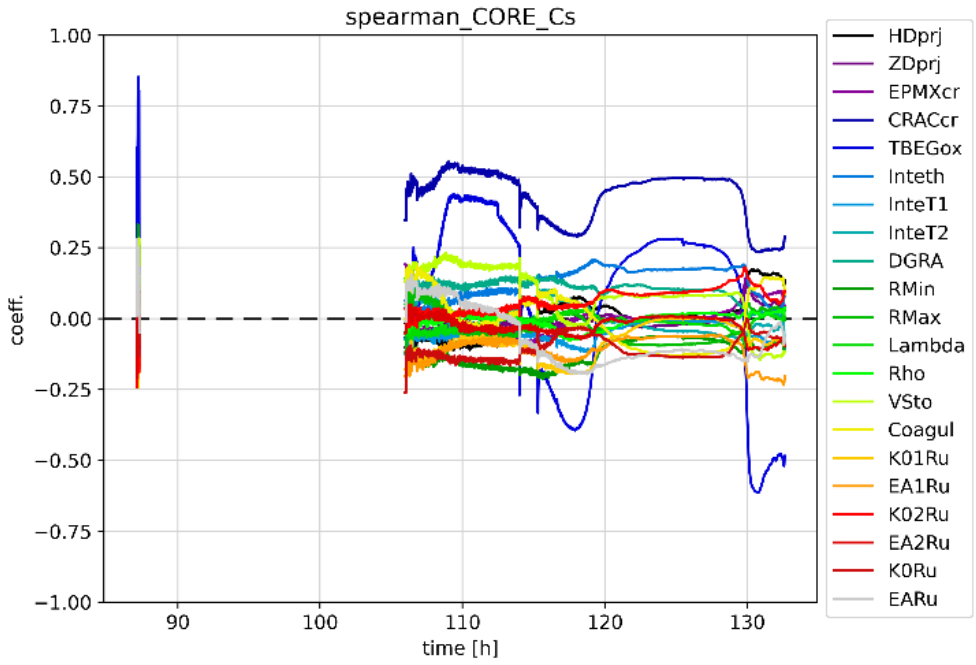

- **The correlation coefficient strongly evolves with time**
- **The onset time of Cs release** (i.e. cladding burst):
  - ✓ is positively correlated to the cladding failure temperature for gap release
  - ✓ is correlated to u.p. that influence thermal evolution and cladding oxidation (radiative exchange factor, cladding oxidation rate constant coefficients, pre-oxidation, …)
  - ✓ is not correlated to u.p. linked to the cladding burst model, due to an unsuitable choice of u.p.
- **The sensitivity of FP release from fuel to degradation parameters is not straightforward**!
- **FP release in the environment** is significantly affected by uncertain parameters linked to aerosol phenomena in the building (aerosol dynamic shape factor, particle shape factor relative to coagulation, the mean particle density)

Sensitivity Analysis (2/2)

- 113 simulations performed by 5 institutions, covering large ranges of injection time and mass flow rate
- 1 kg/s injection is required regardless of the injection time - water injection should exceed evaporation
- Safe and failure regions have been identified. Unclear/unreliable results region has also emerged

⇨ To consolidate these evaluations, a validation work of the thermal hydraulics [POLCA OECD project] and an extension of the fuel rod burst model to SFP conditions is required

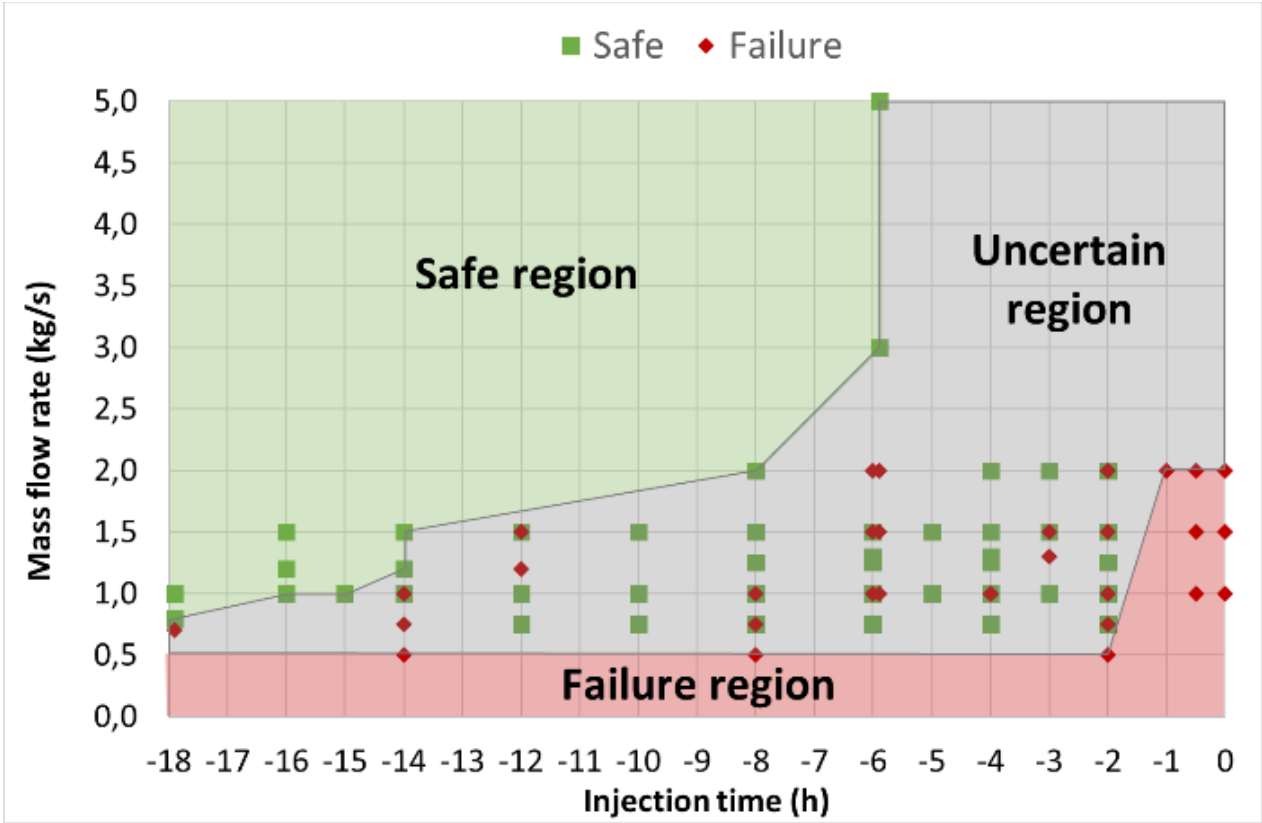

Conclusions (1/2)

The uncertainty propagation has enabled us:

- ✓ to **quantify the spreading of SA code** responses when varying some input parameters
- ✓ to see **how the dispersion evolves through the transient** and if a phenomenon gives rise to spreading
- ✓ To put in light that the **variability in FP release timing coming from the UQ** is relatively small when compared to the variability between reference computations of all participants
- ✓ To **identify important uncertainty sources that have not been considered in the study**:
  - Some were excluded from this exercise (fuel-gap inventory for instance), and it would be worth investigating them in a further study
  - Some are lacking: u.p. not available to the user, lack of modeling (and consequently no u.p.), u.p. considered as unsignificant,…

⇨The study has improved our understanding of the accident progression but the results cannot be used to establish tolerance limits

Conclusions (2/2)

The sensitivity analysis uncertainty propagation has enabled us:

- ✓ To characterize the statistical correlation between the u.p. and the FoMs thanks to **Pearson and Spearman correlation coefficients**
- ✓ To identify the uncertain input parameters responsible of outliers & to identify cliff-edge effects through the use of **Scatter plots**
- ✓ To support the analysis with **single sensitivity calculation by varying only one input parameter**

Onset time of FP release:

- ✓ is correlated to cladding oxidation rate constant coefficients and pre-oxidation of the cladding and radiative exchange factor ⇨ **supports developments already done or currently underway to adapt the radiation model to SFP geometry in SA codes**
- ✓ Should be correlated to the fuel-gap inventory and to cladding burst model parameters ⇨ **worth investigating them in a further study**

Cs release to environment strongly correlated to u.p. linked to aerosol phenomena

ST efficiently reduced by spray systems ⇨ **should be confirmed by experimental data**



Thanks for your attention,

Thanks to all participants to this study:

M. Garcia[2], L.E. Herranz[2], S. Ederli[3], M. Massone[3], O. Sevbo[4], P. Groudev[5], A. Kaliatka[6], V. Vileiniškis[6], M. Malicki[7], Y. Vorobyov[8], I. Ivanov[9], M. D'Onorio[10], Y. Pontillon[11]

2: CIEMAT, 3: ENEA, 4: Energorisk LLC, 5: Institute for Nuclear Research and Nuclear Energy, Bulgarian Academy of Sciences (INRNE-BAS), 6: LEI, 7: Paul Scherrer Institut, 8: SSTC NRS, 9: TU-Sofia, 10: Sapienza University of Rome, 11 : CEA

UNCERTAINTIES ON FISSION PRODUCT RELEASE IN A LOSS-OF-COOLING SCENARIO IN A SPENT FUEL POOL WITH MELCOR 2.2

M. Garcia, L.E. Herranz
CIEMAT
Avenida Complutense 40, 28040 Madrid (Spain)
monica.gmartin@ciemat.es; luisen.herranz@ciemat.es

M. Angelucci, S. Paci
University of Pisa
Largo Lucio Lazzarino, 56122 Pisa (Italy)
michela.angelucci@unipi.it; sandro.paci@unipi.it

ABSTRACT

After the events occurred in Fukushima in 2011, the vulnerability of the Spent Nuclear Fuel (SNF) stored in Spent Fuel Pools (SFPs) was highlighted. Subsequent studies involving accident scenario simulations in SFPs questioned the reliability of the Severe Accident (SA) codes predictions for this purpose. The present study synthesizes the main insights gained by quantifying the uncertainties and assessing outcomes' sensitivities of a SFP analysis. Inspired by the Unit 4 SFP of Fukushima-Daiichi, a Loss-Of-Cooling Accident (LOCA) was assumed with the focus on Fission Products (FPs) release. Calculations were performed with the MELCOR 2.2 code, and the uncertainty propagation was articulated through the DAKOTA statistical tool. Fifteen input uncertain parameters related to fuel rod failures, their degradation and FPs release from fuel rods were selected. By using Correlation Coefficients (CCs), some correlations between input parameters and Figures Of Merit (FOMs) were noted. As expected, Xe and Cs uncertainties were qualitatively similar, while Ru release showed its own footprints. Two outcomes of the study worth highlighting here: the relevance of a consistent choice of the input uncertainty parameters set, both number and variables, was shown to be crucial in the analysis; a thorough characterization of the FOM sensitivity will likely require more than just an individual technique.

KEYWORDS
Source Term, Severe Accident, UaSA, Spent Fuel Pool

1. INTRODUCTION

Numerical tools are widely used in the nuclear community to assess the behavior of Nuclear Power Plants (NPPs) during postulated accidents, including Severe Accidents (SAs). After the events occurred in Fukushima in 2011, the vulnerability of the Spent Nuclear Fuel (SNF) stored in Spent Fuel Pools (SFPs) was highlighted, and the reliability of the SA codes predictions when addressing SFP accident scenarios questioned.

The Management and Uncertainties of Severe Accidents (MUSA) project, funded in Euratom Research and Training Programme 2019-2023 and coordinated by CIEMAT (Spain), aims at consolidating a harmonized approach for the analysis of uncertainties and sensitivities associated with SAs focusing on Source Term (ST) [1]. In this framework, the objectives of the Innovative Management of Spent Fuel Pool Accidents (IMSFP – WP6) are to quantify and rank the uncertainties affecting accident analyses in a SFP, to review existing and contemplated SA management measures and systems, and to assess their possible benefits in terms of reduction of radiological consequences [2].

This paper summarizes the work carried out in the frame of WP6 to quantify the uncertainties affecting a SFP analysis with the SA. The focus is of particular interest since in most NPP designs SFPs are placed outside the containment; in other words, the only persisting Defense in Depth (DiD) barrier is fuel cladding, so that Fission Products Release (FPR) has a straight impact on potential radiological consequences.. In particular, Uncertainty Quantification (UQ) methodologies and sensitivity analysis techniques have been applied to the computation of a Fukushima-like scenario in a SFP. The computed scenario is a Loss-Of-Cooling Accident (LOCA) without water injection recovery, with the calculation starting at the onset of fuel uncover and ending when the amount of fuel lost from initially intact components and transferred to degraded components reaches 1%. Calculations were performed with the SA MELCOR 2.2 code [3], [4] complemented with the DAKOTA tool [5] for the statistical analysis. Major outcomes from the results are included.

2. METHODOLOGY

The Best Estimate (BE) approach has been gaining momentum in the nuclear safety community as a means to achieve more realistic calculations than the original conservative approach applied for decades. However, a single BE calculation is not enough when safety is concerned: it needs to be complemented by assessing the precision of the calculation through considering the scattering effect on estimates caused by input and code uncertainties. To do so, in the present work, the BEPU-CSA methodology [6] has been applied. This methodology, which was actually developed for containment analysis, relies on input uncertainty propagation. A number of calculations, defined by means of the Wilks formula [7], are performed with the MELCOR 2.2 code and complemented with the DAKOTA tool for the statistical analysis. The goal of the statistical analysis is the estimation of the tolerance interval of the selected Figures of Merit (FOMs), which is achieved by means of the Wilks' order statistic method [7]. In addition, a preliminary sensitivity analysis is also performed in order to highlight the input uncertainties influence, being this focused on Pearson's and Spearman's Correlation Coefficients (CCs) [8].

MELCOR is a fully integrated, engineering-level computer code that models the progression of SA. It includes a broad spectrum of phenomena, from core degradation to ST to the environment; just to mention a few: thermal-hydraulic response in the reactor coolant system, reactor cavity, containment, and confinement buildings; core heat-up, degradation, and relocation; core-concrete attack; hydrogen production, transport and combustion; FP release, transport and behavior.

The statistical tool DAKOTA was originally conceived to more readily interface simulation codes and optimization algorithms. However, latest versions include other iterative analysis methods such as UQ. In this work, the DAKOTA tool in "stand-alone" mode has been used to perform forward uncertainty propagation in which probability information for input parameters is mapped to probability information for output response functions. Several python scripts has been developed to compute the Monte Carlo (MC) sequence, to perform the pairing process of input parameters, to generate the MELCOR inputs, and to run the code automatically. The post-processing and statistical calculations with the MELCOR output-files is also managed through home-made python scripts. The whole process is governed by another python script, which follows the flow chart shown in Figure 1.

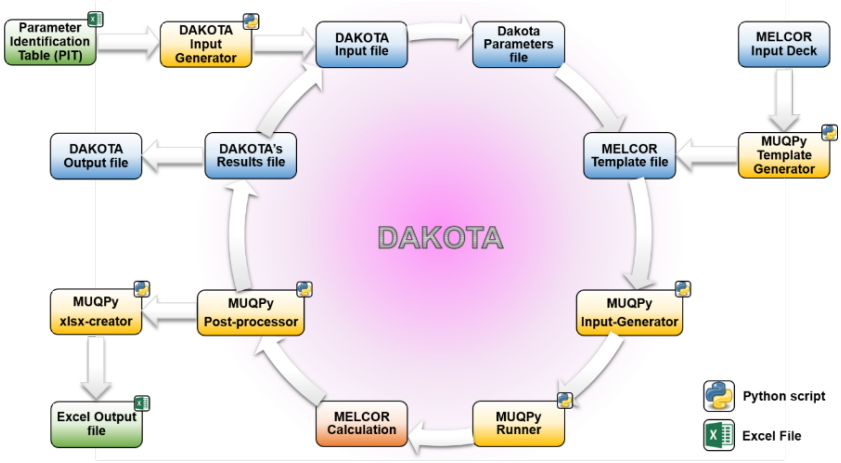

Figure 1. MELCOR/DAKOTA Coupling Scheme.

When the UQ is conducted, it is necessary to adapt the MELCOR output to the DAKOTA format. The method employed in this work consists in define the FOMs variables with Control Functions (CFs) and write them into an External Data File (EDF) with the correct format. Then, this file is used by the DAKOTA iteration algorithm to include it in the statistical analysis. In addition, a python script is also employed to perform a parallel post-processing for the statistical analysis and also to plot all the FOMs in an Excel file.

3. REFERENCE COMPUTATION

The SFP MELCOR Evaluation Model (EM) is calculated with MELCOR 2.2.15254 version. Default and sensitivity coefficients in all packages are set to those in the 2.0 standards [3], [4]. This EM is based on the SFP design, similar to that of the Unit 4 of the Fukushima Daiichi NPP and used in the AIR-SFP NUGENIA+ project [9]. According to the WP6 specifications, the accidental scenario modelled is a loss-of-cooling scenario with the computation starting at the onset of fuel uncovery (to save the computation time dedicated to the pool evaporation) and ending when the amount of fuel matter lost from initially intact components and transferred to degraded components reaches 1-3 % (1 % of degraded core as criteria to stop the calculation in this work). A detailed description of the geometry, the computation domain, the initial and boundary conditions is given in the WP6 report “WP6 – Specification of the SFP accidental scenario” [10].

3.1. Nodalization and Initial Boundary Conditions

The thermal response of the core and lower plenum internal structures is modeled in MELCOR through the COR package [3], [4]. The EM uses the SFP-PWR type core option due to failure of radiation model when the SFP-BWR type core option is used. The COR model is composed of 12 axial levels and 4 radial rings (Figure 2). Axially, the first, second and third levels correspond to the pool bottom with the rack feet, the rack’s support plate and the lower nozzle of the Fuel Assemblies (FAs) , respectively. The next 8 equally-long meshes model the active fuel region; the uppermost node includes FA holders, plugs, the tie plate and the rack’s remaining. Radially, a “cold neighbor” distribution is adopted for having potentially adverse conditions: the central ring contains the recently unloaded hot FAs (548); the second ring models the longer stored fuel (783 FAs); the third one includes the fresh FAs (204); and the fourth one is empty of FAs. The rings heat loads are 1.9 MW, 0.5 MW, 0.0 MW and 0.0 MW, respectively.

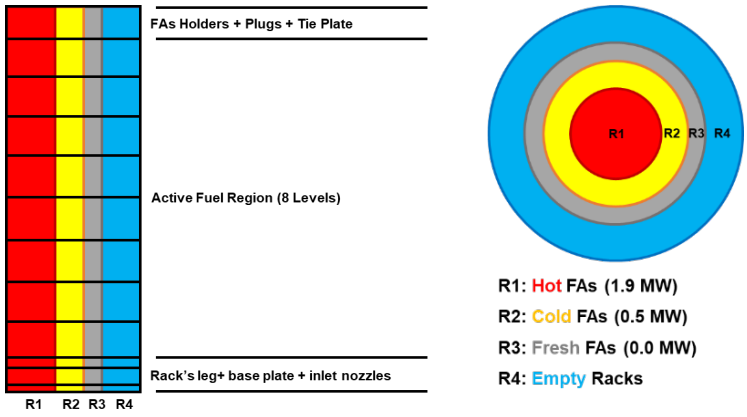

Figure 2. Core Nodalization.

The thermal-hydraulic behavior of liquid water, water vapor and gases are modeled in MELCOR code through the CVH and FL packages [3], [4]. The CVH model consists of 8 Control Volumes (CVs) (Figure 3): one CV for the support plate and the region below (CV110); for the COR active region there are four CVs, one per radial ring; each of these volumes include channel (water volume within FA) and bypass (bypass tube inside the FA, the water region between the canister and the racks and the water region between the racks) volumes. The remaining water of the pool is included in the channel and/or bypass of the fourth ring (CV240).

The rest of the SFP building is modeled with 1 CV (CV300) that includes the region above racks and the reactor building volume. A large CV is included to model the environment (CV900). In addition, a volume associated to the lower head is included (CV999).

Fifteen flow paths are included in the model. Flow direction within the pool is set to be vertical (no horizontal connections are defined). A connection between the reactor building and the environment CV is also defined. This flow path is 1 m length and friction conditions by default.

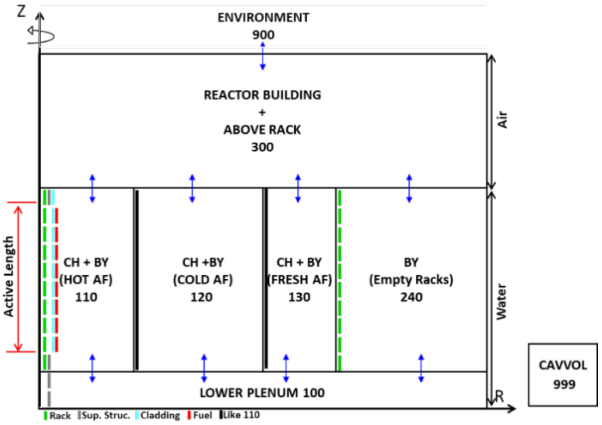

Figure 3. TH Nodalization of the SFP.

Initial boundary conditions are summarized in the next table (Table I).

Table I. Initial Boundary Conditions at SFP.

Parameter	Value

Water level (m)	4.4899 (top of racks)
Building pressure (bar)	1
Water temperature (K)	373.16
Pool concrete wall temperature (K)	373.16
Building atmosphere temperature (K)	353.16
Building atmosphere relative humidity	1
Building wall temperature (K)	353.16
Environment temperature (K)	393.16

3.2. Physical models and main assumptions

The thermal-hydraulics is modeled through the CVH and FL packages. The core active region is modeled through 4 CVs, one per radial ring, as explained in the nodalization section. Each of these volumes include channel and bypass volume. The bypass volume that includes the bypass tube inside the FA, the water region between the canister and the racks and the water region between the racks is approximated because rack's distribution within the pool is not uniform. Around each rack, it is taken a half of the minimum layer of water that separates the racks, trying to maintain the distribution as similar as possible to the Fukushima Unit 4. The remaining water of the pool is included in the channel and/or bypass of the fourth ring. The above rack region and reactor building are modeled as a single volume as the goal of this study is the in-vessel fission products release. For the flow path modeling, flow direction within the pool is set to be vertical as no canister is modeled. No more horizontal connections are defined for keeping conservative conditions. In the EM, only in-vessel phenomena are taken into account; therefore, there is no cavity model nor Molten Core Concrete Interaction (MCCI). No radiation is considered in this model as the radiation exchange activation is one of the main causes of code crashes. Regarding heat structures, as boundary condition, the pool concrete walls are set to be adiabatic in the outer side.

The FAs behavior and degradation are modeled without taking into account the effect of a reduced melting temperature of a eutectic mixture of UO_2 and ZrO_2, i.e., eutectic model is not activated. Some non-default input parameters are the fuel rod collapse temperature and the heat transfer coefficients between debris components and its associated conglomerate fuel mass. The rod collapse temperature is calculated based on a table of cladding lifetime duration as a function of the temperature to correspond to observed temperatures for which fuel rod relocation was important [11]. The candling heat transfer coefficients values for UO_2 and ZrO_2 were set by default. The default oxidation model is applied [3], [4]. The model considers the oxidation of Zircaloy by steam and oxygen and the oxidation of steel by steam. It takes place whether metals are as intact components or as conglomerate and/or particulate debris [3], [4]. The default onset temperature for oxidation is 1100 K, and the oxidation rate is calculated using a standard parabolic kinetics based on different correlations [3], [4]. For the oxidation of Zircaloy in environments containing steam and oxygen, the maximum oxidation rate calculated for the two gases is used. The default option does not permit the consumption of steam until all of the available oxygen is consumed (sequential approach). The Zircaloy air oxidation breakaway (change from parabolic kinetics to a faster linear one) is also considered.

4. RESULTS AND DISCUSSION

4.1. Reference Case Main Results

Due to the loss-of-cooling in the SFP (t=0), the pool temperature starts to increase due to the decay power. As can be observed, the water level in the channel volumes (Figure 4a) linearly decreases by evaporation up to the active core level (~ 20 h of calculation). During this period there is no heat-up regime change, water is saturated from the very beginning and all the thermal energy produced inside the pool is meant to

vaporize the water. As expected, a higher slope in the core water level is observed until the total drained of the SFP at 179.2 h. The spike at 133.6 h corresponds to the beginning of the core degradation. The mass of steam in the containment building is presented in Figure 4b. As it can be observed, a high amount of steam is generated during the first 20 h of calculation due to the evaporation of the water over the top of active fuel, from then on it decreases until slumps due to the beginning of the liquefaction of some fuel and its lost from the location which entails a sharp loss of heat surface (133.6 h). In both figures, the dashed line indicates the end time of this analysis; for the reference case this happens at 178.1 h with 1.5 % of core degraded.

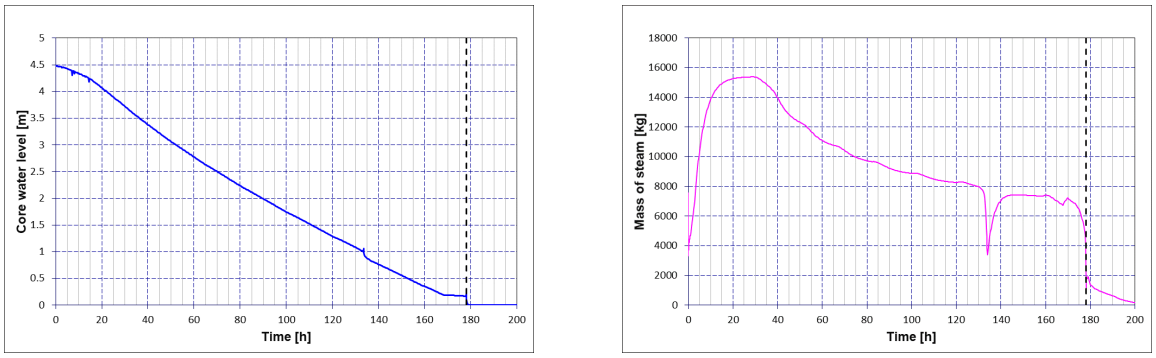

a) Core water level (m) b) Mass of steam into the RB (kg)

Figure 4. Core Water Level and Steam Amount into the Containment.

The cladding temperature of hot, cold and fresh FAs by axial level is represented in the next figure (Figure 5). It worth noting that an underestimation of cladding temperatures due to the simplification of channel and bypass in one single volume is foreseen. As it can be observed, cladding temperature increases as the pool empties, and this growth is triggered once the oxidation temperature is reached (1100 K). During the temperature excursion, the temperature in the upper levels of the hot FAs (ring 1) rises up to 2500 K and the cladding loses its geometry causing the relocation of the first axial level of hot FAs (cell 112) at 133.9 h. Meanwhile, the temperature of cold and fresh FAs also increase due to its own heat decay and the heat transfer from the hot region.

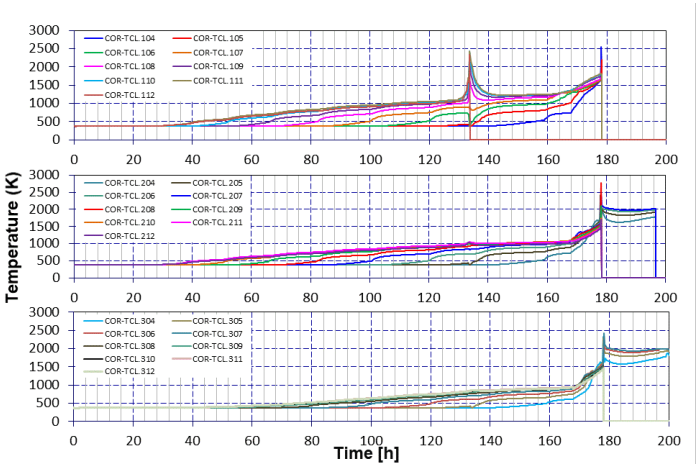

Figure 5. Cladding Temperature of Hot, Cold and fresh FAs axial levels.

In LOCAs occurred in SFPs, the oxidation reactions are key elements to understand the degradation process during the transient. In the next figure, the H_2 production evolution is presented (Figure 6). The generation

of H_2 starts when Zircaloy oxidation temperature is reached in the core cell 110 (axial level 10, ring 1) at 127.7 h. As it can be observed, the exponential temperature rise according to the breakaway oxidation model is observed approximately at 160 h. At the end time of this analysis (178.1 h), the total mass of H_2 produced is higher than 1325.7 kg: 81.4% comes from the oxidation of Zircaloy and the remaining 18.6% from the steel oxidation.

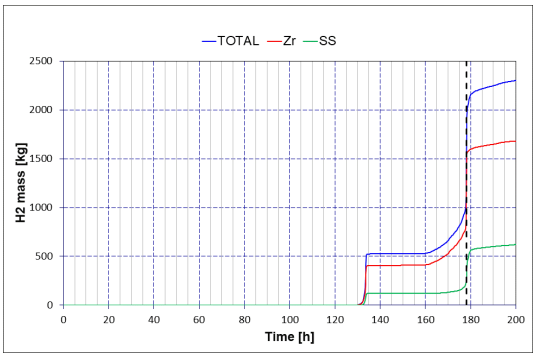

Figure 6. H_2 Mass Time Evolution in the Core.

The onset time of FPs release from fuel is set in the input deck by the cladding failure temperature (1173 K) and it occurs in the calculation at 131.22 h. In the next figure (Figure 7) the release of Xe, Cs and Ru as a fraction of the i.i. (initial inventory) is shown for the reference case. At the end of the analysis, 24.2 % of Xe and Cs are released from the core, whereas the amount released of Ru is much smaller (0.11 %) according to the figure. In all the cases, the evolution shows the inventory gap release once the clad failure temperature is reached and then a sharp increase as soon as core degradation progresses (the vertical dotted line in the plot indicates the ending time considered for the UQ in next section).

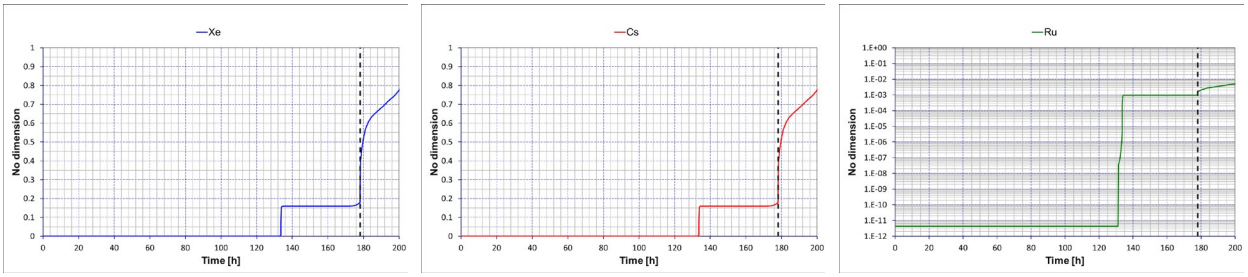

Figure 7. Main FPs Release Fraction of the i.i.

4.2. Uncertainty Quantification

The identification and characterization of uncertain input parameters is one of the most critical steps in the UQ analysis. It entails a previous assessment of the scenario under analysis to identify the phenomena governing the transient and the uncertain parameters involved.

Based on the MUSA-WP2 parameters table [1], a literature survey and the necessary expert judgment, the fifteen input uncertain selected for the analysis are the ones expected to have major impact on fuel rods failure and their degradation, and on FPs release. The CORSOR-Booth scaling factors has also been introduced as uncertain parameters to study their impact of the FPs release. These parameters are provided in MELCOR for each RadioNuclide (RN) class: multiplying Cs release rate for these scaling factors it is

possible to obtain the release rates for species other than Cs. In the case of Ru, it has been assumed to exist in the RuO_2 form, with no further oxidation modelled.

The methodology used for UQ is based on the Wilks' order statistic method [7]. Each FOM is evaluated independently assuming it is a scalar variable (neglecting time dependence). Thus, for a tolerance interval with a 95% coverage and 95% confidence, it is necessary a sample of at least 93 elements (i.e., code runs).

4.2.1. Uncertainty Analysis

The selected FOMs in this study are Xe, Cs and Ru release from fuel as a fraction of the i.i. The ending time of calculation should be the time at which there is 1.5 % of core degraded. However, the ending time is not the same for all calculations; therefore, the end time of the reference case has been chosen to do the uncertainty analysis.

Even though the main uncertainty analysis is carried out at a specific time, it is interesting to look at the time evolution of the considered FOMs. As it can be seen from the dispersion plots as presented in Figure 8, all realizations follow the same behavior over time: releases begin right after the start of core degradation (central ring, R1, at the hottest axial location of FAs), and they increase with core degradation (even affecting the cold FAs, R2, in some cases).

As expected, Xe and Cs releases show a similar time evolution. Their uncertainties spread over a narrow band. Ru release, instead, reveals a somewhat relative broader band, with few calculations presenting a slight higher release values than the bulk of the realizations. Moreover, it is worth noting the position of the BE reference case results with respect to the calculated uncertainty band: for all three FOMs, the reference case results are within the uncertainty band. However, whilst Xe and Cs reference case results are slightly higher than the mean values, Ru release from the reference case is well below them all along the entire considered time interval. This observation is confirmed also at the time in which UQ is performed (178.1 h), as it can be seen when looking at the main statistical quantities for the selected FOMs at the end time of the reference case are reported. Interestingly, even if upper bounds goes up to 44% and 40% for Xe and Cs releases, respectively, standard deviation variability is less than 4% with respect to the mean values (around 17% for both FOMs). This means that most cases end up within a narrow range around the mean (outliers could be present, though).

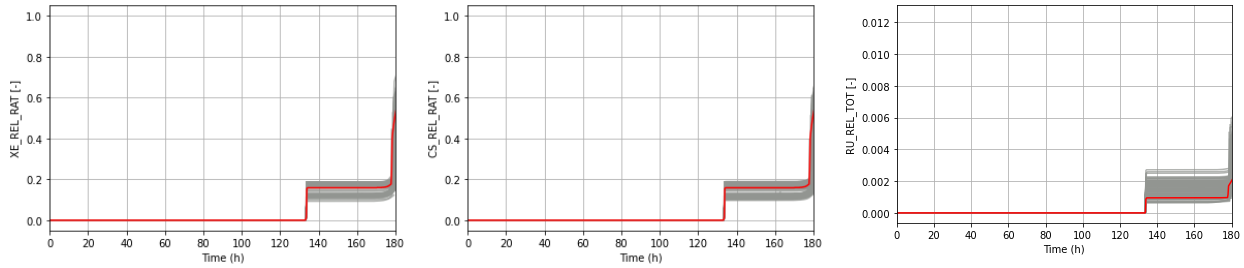

Figure 8. Dispersion plots for main FOMS.

The scatterplots and the Cumulative Distribution Functions (CDFs) for each FOM have been analyzed at the end time of calculation (Figure 9). The discussion is focused on the scatter plots, as CDFs offer the same information and, contrary to scatter plots, sometimes make outlier's identification difficult. In this case, there is a single case showing noticeably different results from the rest of the calculations (i.e., outlier).

As it can be seen, both Xe and Cs releases' plots reveal the presence of one outlier (44% and 40% release with respect to the i.i. for Xe and Cs, respectively). These high values come from the same calculation. A

close analysis of the uncertainty parameters did not reveal any particular wrong and/or unphysical combination of parameters in calculation that shows the outlier.

Most results for Xe and Cs show a similar behavior, with values going from 10% to 22% for both Xe and Cs classes. These values are consistent with the SFP modeling where the fuel is split axially and radially. Given that Cs and Xe inventories were equally split between the two irradiated-fuel rings, the results indicate that from the inventory in the central ring just around 25%-50% has been estimated to be released. The scattering observed might come from the different core damage of each case at the ending time (almost 30% of the calculations show a core damage below 1% at the selected ending time).

As for Ru, releases are about 2 orders of magnitude lower (between 0.10 % and 0.30% of the i.i.), which is consistent with the default assumption in MELCOR regarding its non-volatile chemical form (RuO_2). No outliers are noted in this case.

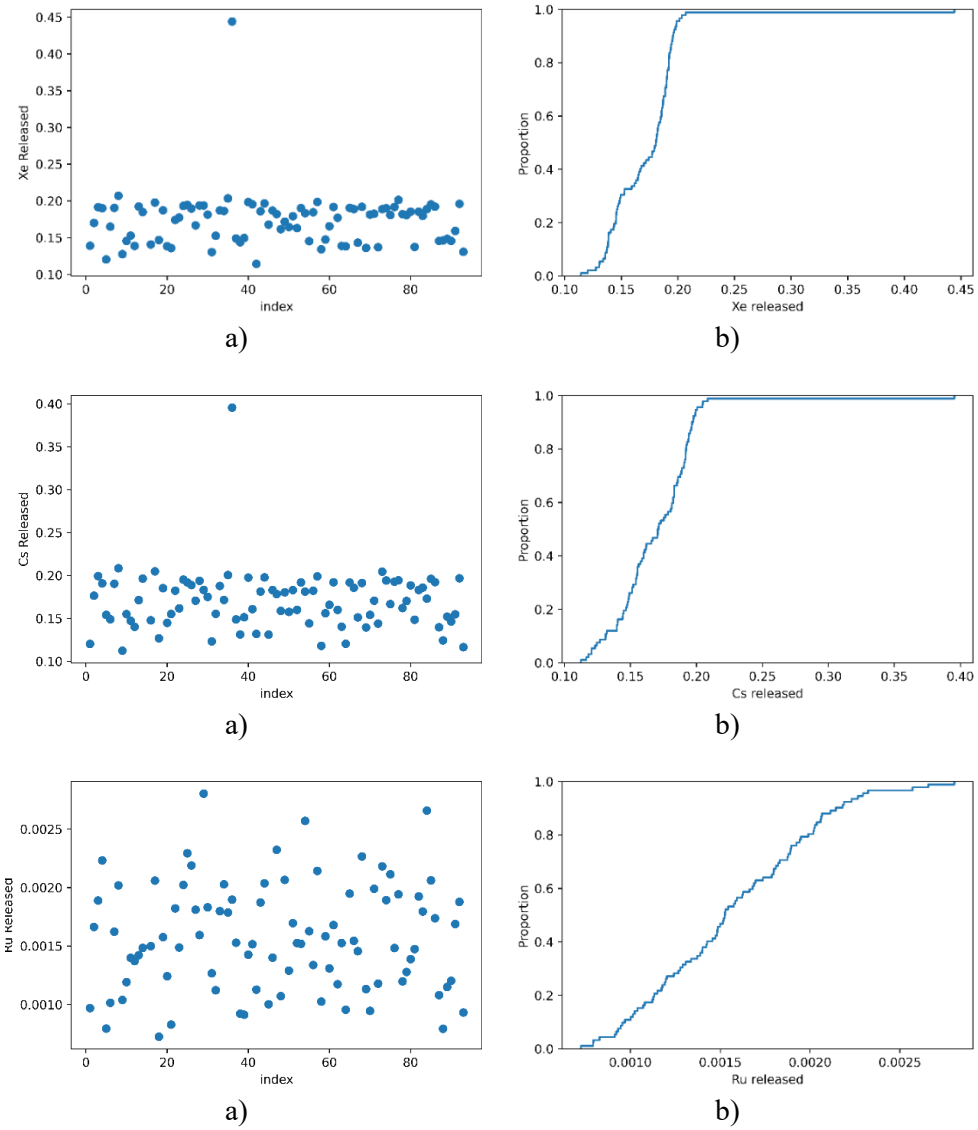

Figure 9. Scatter-plots of FOMs.

Given the relevance of the FP release onset, some attention has been given to analyze the uncertainties associated to the so called gap release onset. The main observation from a statistical analysis is the relative small standard deviation, which is less than 4% of the mean or the median of the distribution. This can be also observed in Figure 10a where significant differences are only noted for few cases, being most data in the 465000 s – 475000 s range. Interestingly, there is a clear correlation between FP release onset and cladding failure temperature (Figure 10b). As observed, FP release onset time is sensitive to the cladding failure temperature between 950 K and 1100 K, but such sensitivity vanishes for higher temperatures. In other words, once 1100 K is attained at some location of the core its heating up is fast, and the thermal sensitivity of the onset time fades away.

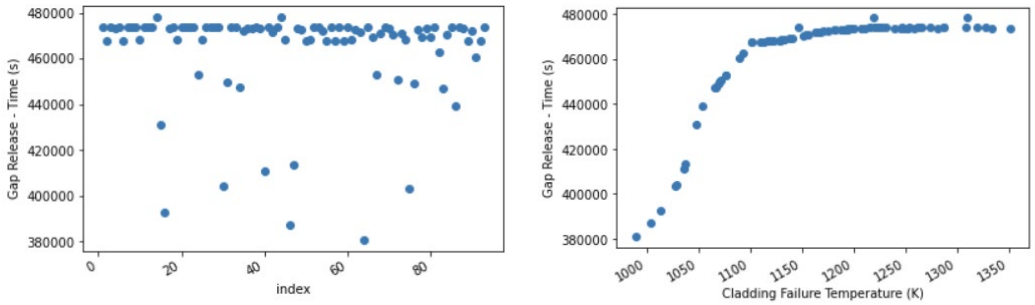

a) Gap release time (s) – Scatterplot

b) Gap release time (s) vs. cladding failure temperature (K)

Figure 10. Gap release time (s).

4.3. Sensitivity Analysis

Pearson's and Spearman's CCs have been considered as a first approach for sensitivity analysis of the 3 main FOMs at the ending time (Figure 11 and Figure 12).

When limiting the analysis to the ending time, Pearson's and Spearman's coefficients are below 0.25 for all the selected parameters: there is no indication of linear or monotonic correlations between the input uncertain parameters and the FOMs.

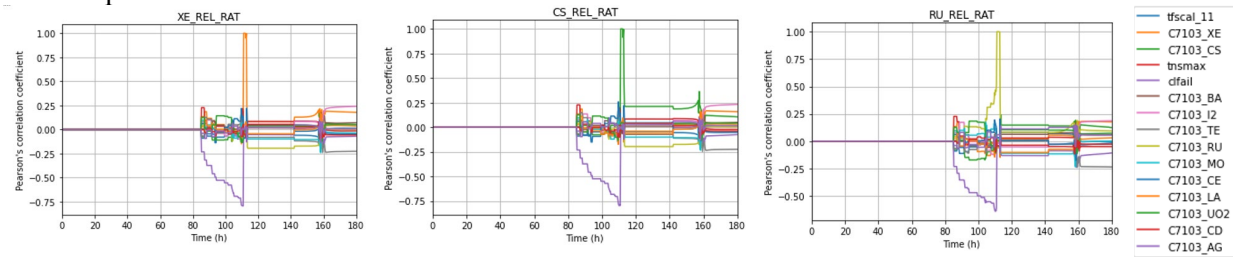

Figure 11. Pearson's coefficient for Xe, Cs and Ru releases.

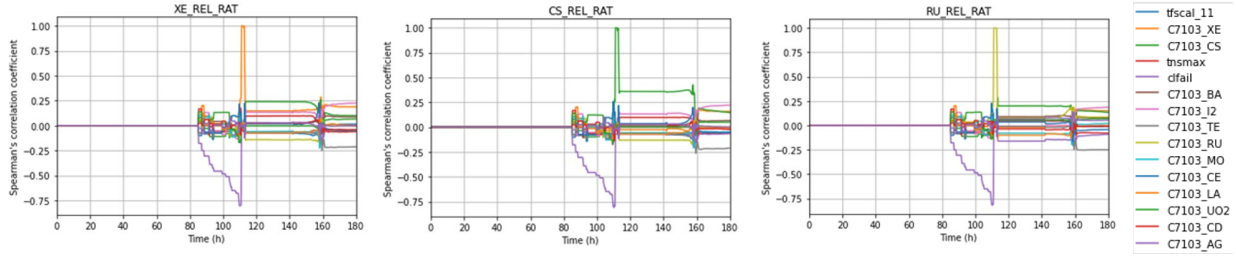

Figure 12. Spearman's coefficient for Xe, Cs and Ru releases.

5. LESSONS LEARNED AND CONCLUSIONS

Under the framework of the EU-MUSA project, focused on the application of the BEPU approach to SA analyses, a methodology for UQ has been tested against a loss-of-cooling scenario in a SFP with the focus on accident progression and FPs release. This work presents the main findings of the quantification of the uncertainties and the assessment of the sensitivity of the results through the analysis of an accidental scenario in a SFP. The accidental scenario modelled is a LOCA in the Unit 4 SFP of Fukushima-Daiichi. Calculations were carried out with the MELCOR 2.2 code and the propagation of the uncertainty performed through the DAKOTA statistical tool. Fifteen input uncertain parameters related to fuel rod failures, their degradation and FPs were selected.

From the work done, some generic observations have been settled regarding the reference case application. The scenario outlined is heavily conditioned by some hypotheses and assumptions made (i.e., the absence of "containment building" or the arbitrariness of setting 1% core melting as ending calculation time). This prevents from withdrawing meaningful final conclusions from the calculations done. Nevertheless, substantial insights have been gained from the application of UaSA to SFPs. Despite the oversimplification of the scenario, modeling SFPs with SA codes still pose challenges related to the FAs distribution in the pool (notably other than in nuclear reactors) and to the first stages of the accident, when complex steam and air flows through FAs likely occur during the FAs uncover.

Additionally, some lessons learned from this exercise might be also drawn concerning uncertainty application and sensitivity analysis:

- The selection of uncertainty parameters should consider codes and models architecture. In the case of the CORSOR-Booth model chosen for the simulations, the fact of using the Cs release as a reference for the rest of radionuclides ones by just using scaling factors, sets pre-correlations between releases that are ignored during the UQ. This might drive to misleading observations in the UQ analysis. A shorter list of uncertain input parameters might prove being more reliable.
- A consistency screening of individual cases is highly recommended. Cases where scaling factors for low-volatile radionuclide classes happen to be higher than other volatile ones, for example, should be avoided (the same would apply to cases where Xe and Cs scaling factors are set very dissimilar due to their random sampling). Not doing so might result either in code crashes or in pointless physical observations. This consistency screening should not be restricted to scaling factors, but to any pre-correlation between uncertain parameters that might affect the uncertainty propagation, like particle shape factors, for instance.
- The criterion set for the ending calculation time (1% core melting) is quite sensitive and makes hard to meet in all the uncertainty calculations. During a SA unfolding core degradation occurs pretty fast, particularly under the current approach of coarse radial and axial nodalizations of the fuel region. This makes highly unlikely that one finds same core degradation fraction at the same time in different calculations. This might strongly affect both uncertainty and sensitivity analyses, particularly when integral releases are set as FOMs.
- The variability in FP release onset due to uncertainties is relatively small (less than 4% standard deviation), but still might be significant for accident management since it might mean up to tens of hours in the case of a SFP. Cladding failure temperature seems to be associated to such variability, but just if temperatures fall below roughly 1100 K.
- Expert judgement considerations in the uncertainty parameter selection and screening of individual cases should be also present in the sensitivity analysis. Occasionally, statistical methods might highlight unphysical sensitivities that should be ruled out, or right the opposite, some sound and known correlation is missing by the statistical method. An example might be the Xe integral release correlation with the Ru scaling factor.

- There is no "silver bullet" to conduct sensitivity analysis. Scatter plots are always recommended for a first sight of uncertainty results and detection of outliers, but when coming to set correlations between FOMs and input parameters, the wiser recommendation might be use several techniques to gain some insights and make sure that any of them is physically consistent

ACKNOWLEDGMENTS

The authors thank R. Bocanegra, who actively participated in the initial stages of the work.



The work presented in this communication was done under the frame of the MUSA project. This project has received funding from the Euratom Research and Training Programme 2019-2023 under grant agreement No 847441. The content of this paper reflects only the authors' view. The European Commission is not responsible for any use that may be made of the information it contains.

REFERENCES

[1] L. E. Herranz *et al.*, «The EC MUSA Project on Management and Uncertainty of Severe Accidents: Main Pillars and Status», *Energies*, vol. 14, n.º 15, Art. n.º 15, ene. 2021, doi: 10.3390/en14154473.
[2] O. Coindreau *et al.*, «Uncertainty quantification for a severe accident sequence in a SFP in the frame of the H-2020 project MUSA: First outcomes», *Annals of Nuclear Energy*, vol. 188, p. 109796, ago. 2023, doi: 10.1016/j.anucene.2023.109796.
[3] L. L. Humphries, R. K. Cole, D. L. Louie, V. G. Figueroa, y M. F. Young, «MELCOR Computer Code Manuals. Vol. 1: Primer and Users' Guide Version 2.1.6840», Sandia National Laboratories, Albuquerque, NM, SAND2015-6691 R, 2015.
[4] L. L. Humphries, R. K. Cole, D. L. Louie, V. G. Figueroa, y M. F. Young, «MELCOR Computer Code Manuals. Vol. 2: Reference Manual. Version 2.1.6840», Sandia National Laboratories, Albuquerque, NM, SAND2015-6691 R, 2015.
[5] M. Eldred *et al.*, «DAKOTA, A Multilevel Parallel Object-Oriented Framework for Design Optimization, Parameter Estimation, Uncertainty Quantification, and Sensitivity Analysis Version 3.0 Reference Manual», jul. 2003, doi: 10.2172/798492.
[6] J. Freixa *et al.*, «Spanish contribution to the development and application of best estimate plus uncertainty methodologies: Past, present and future», *Nuclear Engineering and Design*, vol. 417, p. 112837, feb. 2024, doi: 10.1016/j.nucengdes.2023.112837.
[7] S. S. Wilks, «Determination of Sample Sizes for Setting Tolerance Limits», *The Annals of Mathematical Statistics*, vol. 12, n.º 1, pp. 91-96, mar. 1941, doi: 10.1214/aoms/1177731788.
[8] M. Mukaka, «A guide to appropriate use of Correlation coefficient in medical research», *Malawi Med J*, vol. 24, n.º 3, pp. 69-71, sep. 2012.
[9] O. Coindreau *et al.*, «Severe accident code-to-code comparison for two accident scenarios in a spent fuel pool», *Annals of Nuclear Energy*, vol. 120, pp. 880-887, oct. 2018, doi: 10.1016/j.anucene.2018.06.043.
[10] O. Coindreau, «WP6 – Specification of the SFP accidental scenario, (IRSN), Version 2». 22 de enero de 2021.
[11] US NRC, «MELCOR Best Practices as Applied in the State-of-the-Art Reactor Consequence Analyses (SOARCA) Project», NUREG/CR-7008, 2014.

GOBIERNO DE ESPAÑA
MINISTERIO DE CIENCIA, INNOVACIÓN Y UNIVERSIDADES

Ciemat
Centro de Investigaciones Energéticas, Medioambientales y Tecnológicas

Source Term Uncertainty and Sensitivity Analysis on a Loss-of-Cooling Scenario in a Spent Fuel Pool

M. Garcia*, M. Angelucci, S. Paci, L.E. Herranz

**monica.gmartin@ciemat.es*
Unit of Nuclear Safety Reseach
Departament of Nuclear Fission
CIEMAT

11th European Review Meeting on Severe Accident Research (ERMSAR2024)
KTH, Stockholm, Sweden, May 13-16, 2024

Contents:

01 Introduction

02 Motivation & Objectives

03 Methodology

04 Results & Discussion

05 Final Remarks

Introduction

MUSA – Management and Uncertainties of Severe Accidents

The Horizon 2020 MUSA project aims to stablish **an harmonized approach for the analysis of uncertainties and sensitivities associated with Severe Accident (SA) analysis** among EU and non-EU entities.



MUSA kick-off meeting in Madrid, Spain
July 10-12, 2019

MUSA Structure

- **WP1:** Coordination & Project Management
- **WP2:** Identification & Quantification of Uncertainty Sources
- **WP3:** Review of Uncertainty Quantification Methodologies
- **WP4:** Application of UQ methods against integral experiments
- **WP5:** Uncertainty Quantification in Analysis & Management of Reactor Accidents
- **WP6: Innovative Management of SFP Accidents**
- **WP7:** Communication & Results Dissemination

Motivation & Objectives

MUSA WP6: BEPU on an Accidental Scenario in a SFP

- Test the Uncertainty Quantification Methodology in Severe Accident contexts
- Test the calculation scheme between the SA code and the statistical tool
- Identify the main challenges to deal with in a SFP uncertainty analysis
- Improve the methodology and/or the calculation scheme

Figures Of Merit (FOMs)
Onset time of FP release from fuel [h]
Release of Xe, Cs, Ru from fuel [% of i.i]

Methodology

MELCOR/DAKOTA Coupling Scheme

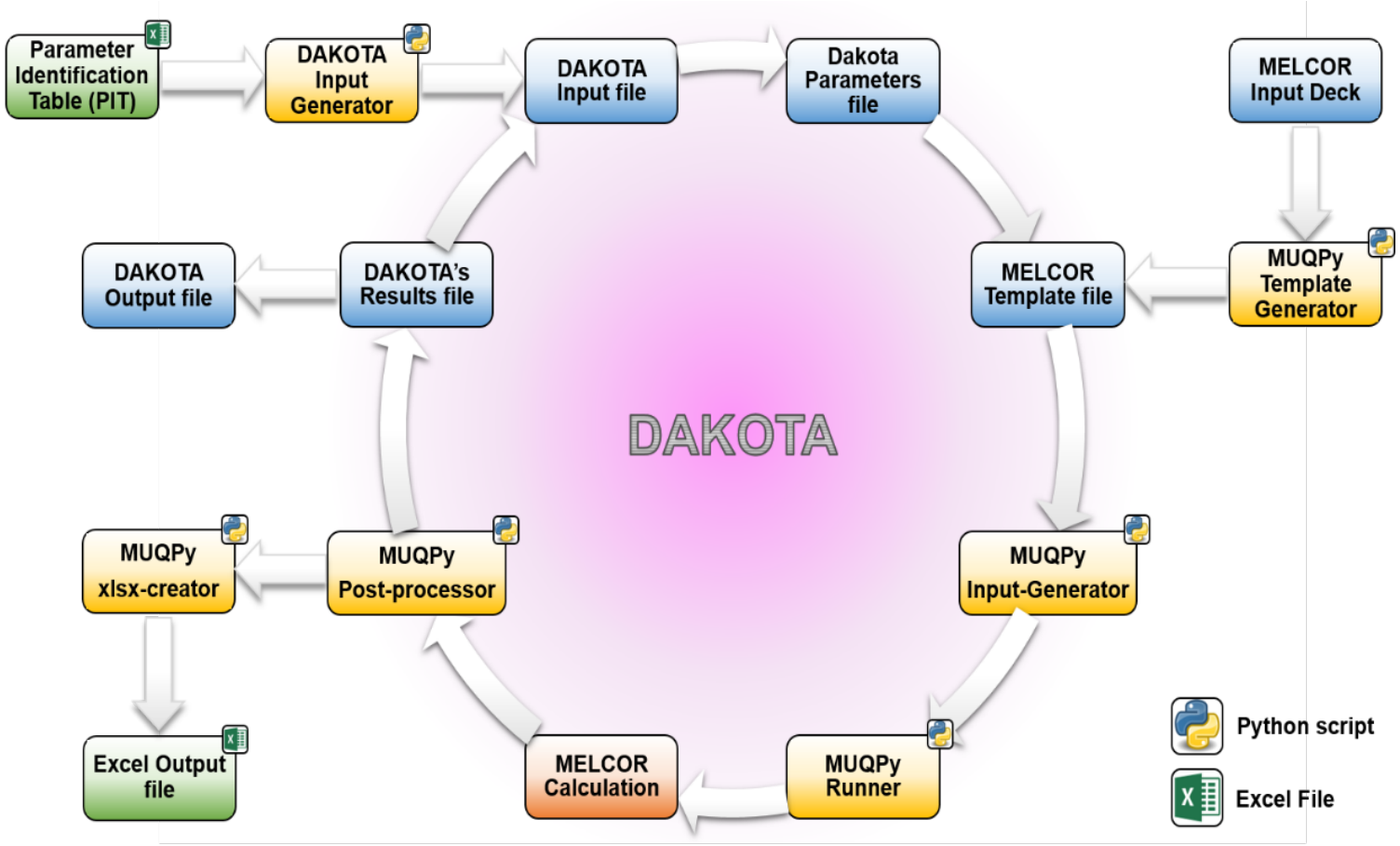

(Bocanegra & Herranz, 2022)

- Wilks – double side (95/95) – 93 runs – SRS method

Methodology

Uncertainty Methodology

Parameters Identification Table

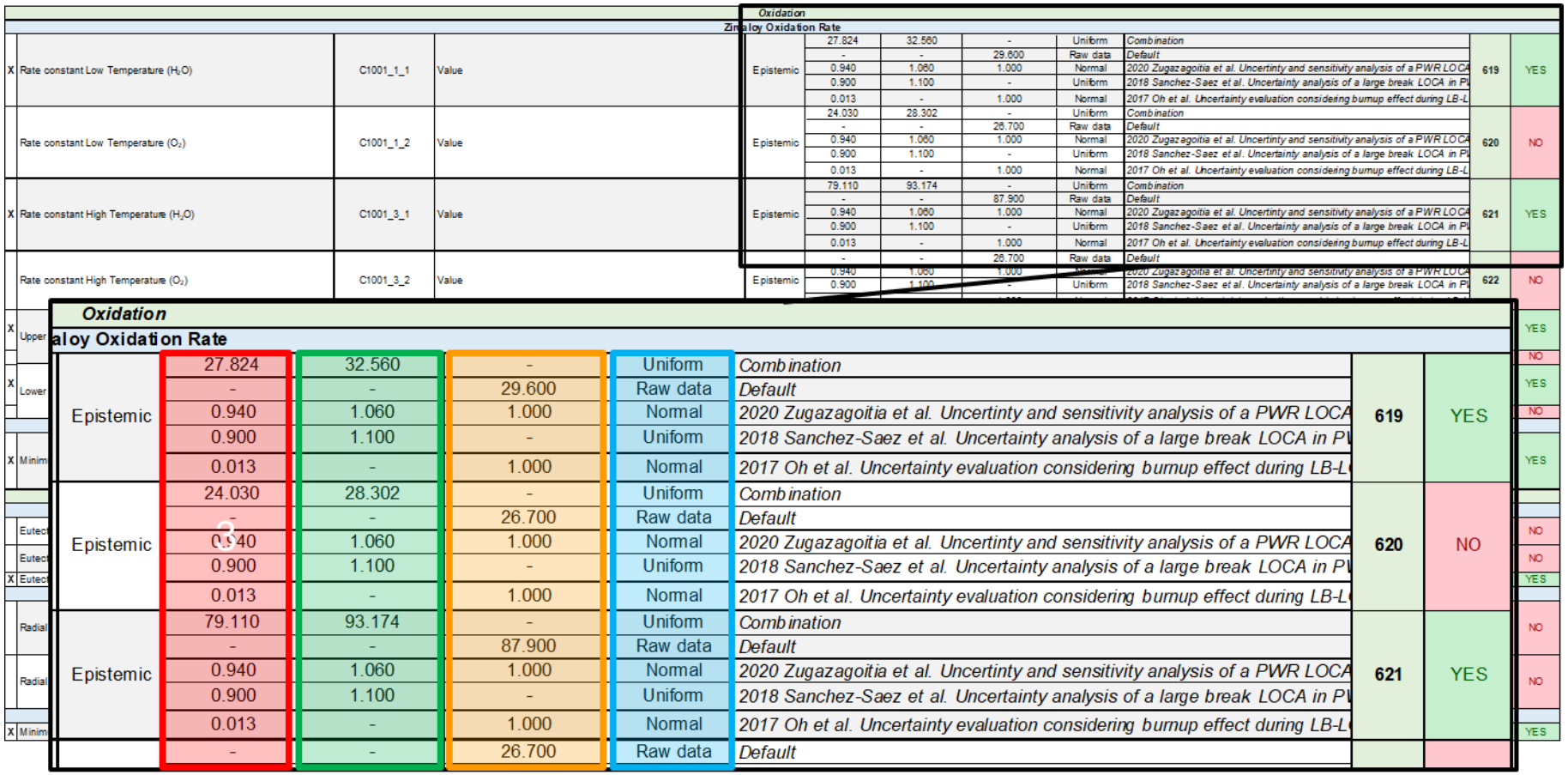

Methodology

Uncertainty Methodology

- **15 features selected :**
  - FAs behavior and degradation (2)
  - FP release Corsor-Both MELCOR model (13)

Phenomenon	Uncertain parameter	Distribution
Loss of integrity / degradation phenomena	COR_NS (TNSMAX): Temperature above which non-supporting structures collapse	Triangular distribution 1473 K – 1789 K
	COR_ROD (IRODDAMAGE): Multiplicative scale factor of cladding temperature as a function of fuel failure time	Uniform distribution Lower bound: 0.5 Upper bound: 1.5

Phenomenon	Uncertain parameter	Distribution
FP release	RN1_GAP00, CLFAIL: Gap release temperature	Triangular distribution 1173 K +/- 200 K
	RN1_CSC Xe (7103): CORSOR-Booth scaling factors	Uniform distribution Lower bound: 1 Upper bound: 2
	RN1_CSC Cs (7103): CORSOR-Booth scaling factors	Uniform distribution Lower bound: 1 Upper bound: 2
	RN1_CSC Ba (7103): CORSOR-Booth scaling factors	Triangular distribution 3.20 10-4 - 0.4
	RN1_CSC I2 (7103): CORSOR-Booth scaling factors	Triangular distribution 0.51 - 1.60
	RN1_CSC Te (7103): CORSOR-Booth scaling factors	Triangular distribution 0.51 - 1.60
	RN1_CSC Ru (7103): CORSOR-Booth scaling factors	Triangular distribution 2.50 10-3 - 4.0 10-2
	RN1_CSC Mo (7103): CORSOR-Booth scaling factors	Triangular distribution 0.05 - 0.5
	RN1_CSC Ce (7103): CORSOR-Booth scaling factors	Triangular distribution 3.20 10-8 - 4.0 10-4
	RN1_CSC La (7103): CORSOR-Booth scaling factors	Triangular distribution 3.20 10-8 - 4.0 10-4
	RN1_CSC UO2 (7103): CORSOR-Booth scaling factors	Triangular distribution 2.56 10-4 - 1.20 10-3
	RN1_CSC Cd (7103): CORSOR-Booth scaling factors	Triangular distribution 0.20 - 1.0
	RN1_CSCAg (7103): CORSOR-Booth scaling factors	Triangular distribution 0.128 - 0.8

Methodology

MELCOR Evaluation Model (v2.2.15254)

TH Nodalization

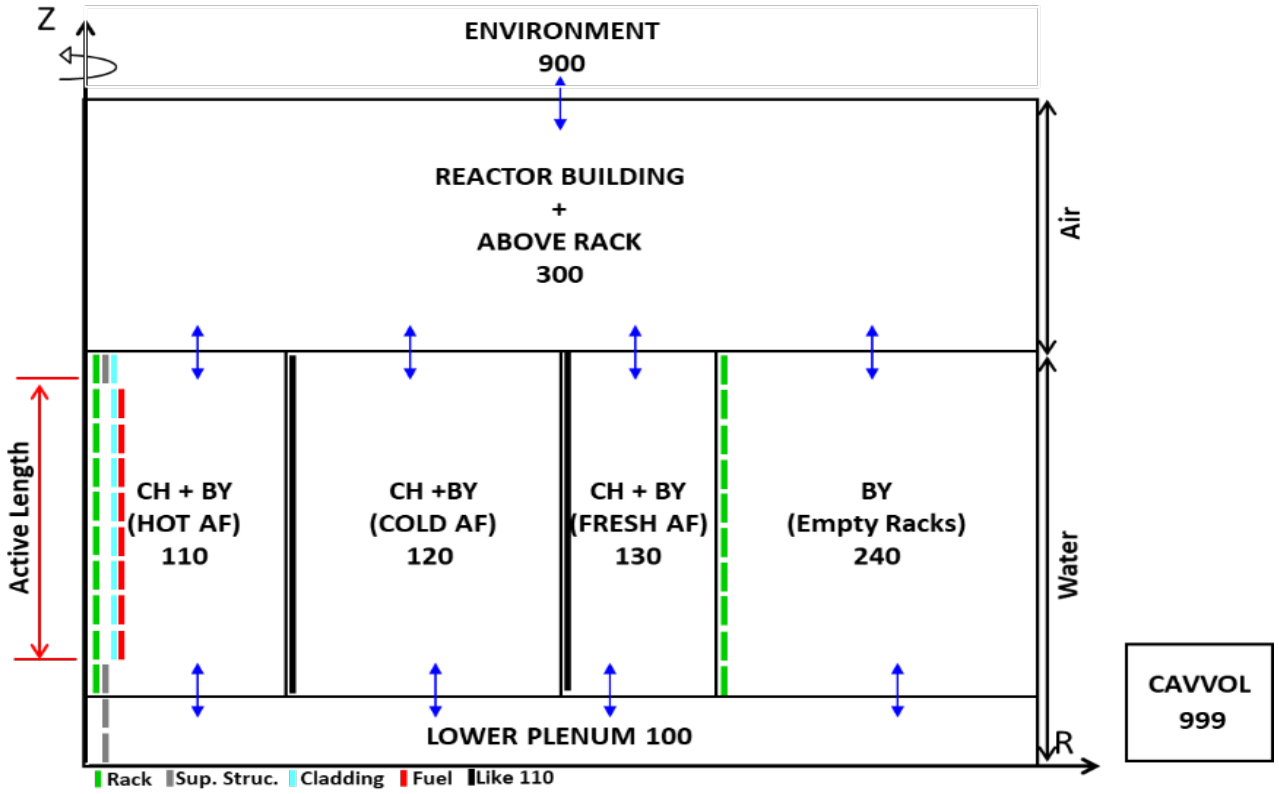

- Fukushima Unit 4 SFP based
- 8 CVs, 15 FLs
- SFP walls represented by concrete HSs (adiab. cond.) at the outer surface
- EM focused on ST
  - **FP initial masses**: WP6 specifications

  Manual input through RN package ("***RN1_FPN***" card)
- Main Initial Conditions:
  - Liquid level: over the fuel racks (~ 4.5 m)
  - Pool temperature: 373.16 K
  - Atmosphere temperature: 353.16 K
  - Pressure: 1.0 bar (1.0136E+05 Pa)
  - **Reactor Building is not modeled**
  - **1 % fuel melt (criteria to stop the calculation)**

Methodology

MELCOR Evaluation Model (v2.2.15254)

COR Nodalization

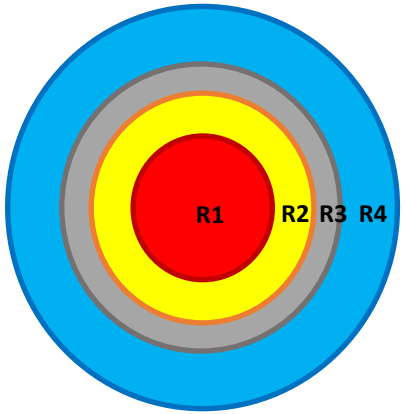

R1: Hot FAs (1.9 MW)
R2: Cold FAs (0.5 MW)
R3: Fresh FAs (0.0 MW)
R4: Empty Racks

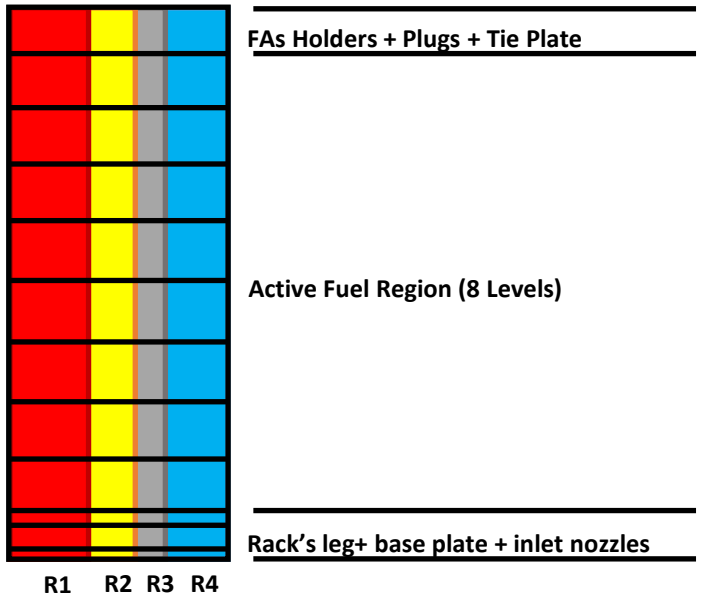

- **SFP-PWR MELCOR option**
- Racks were grouped in 4 radial rings
- **Decay Power**: 2.4 MW (1.9 Hot FAs + 0.5 Cold FAs)
  Input through control function ("***DCH_DPW***" card)
- Axial direction: the racks and the spent fuel were subdivided into 12 levels (8 levels for active fuel)

Results & Discussion

Reference Case

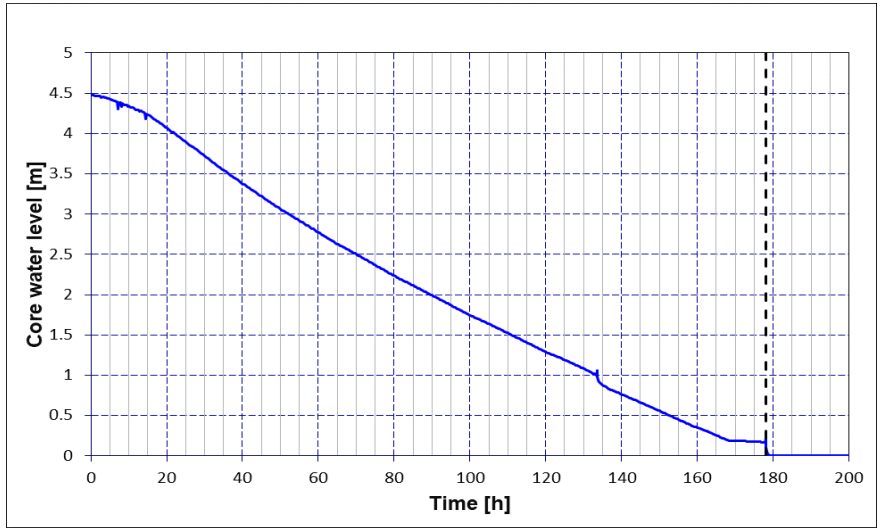

Core water level

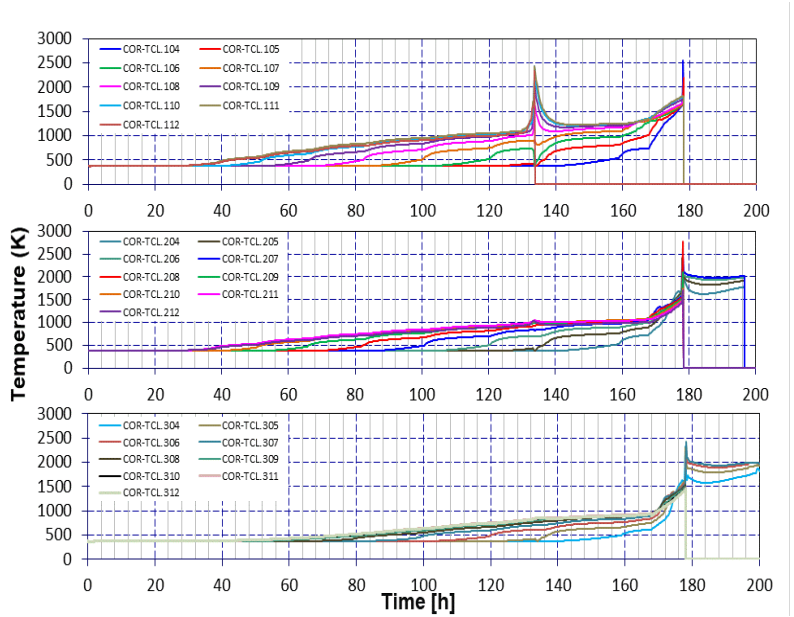

Cladding T of hot, cold and fresh FAs axial levels

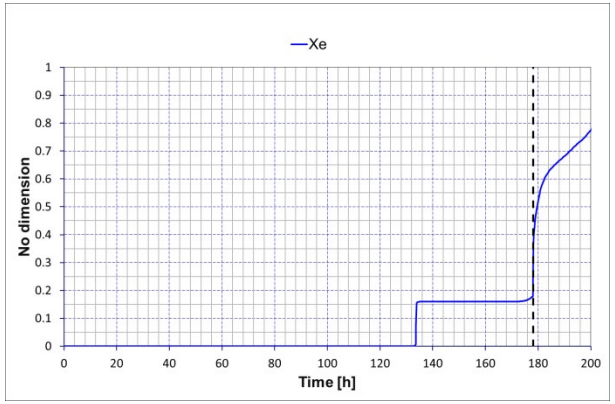

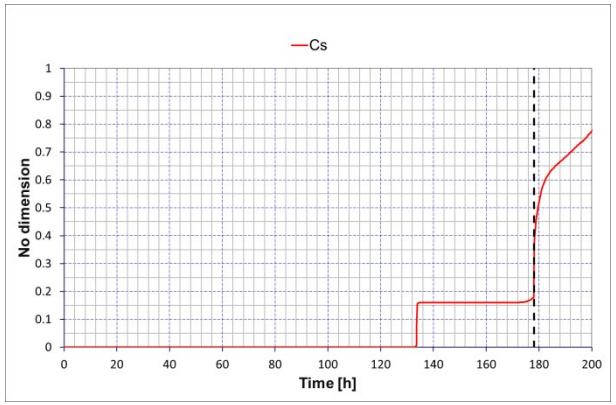

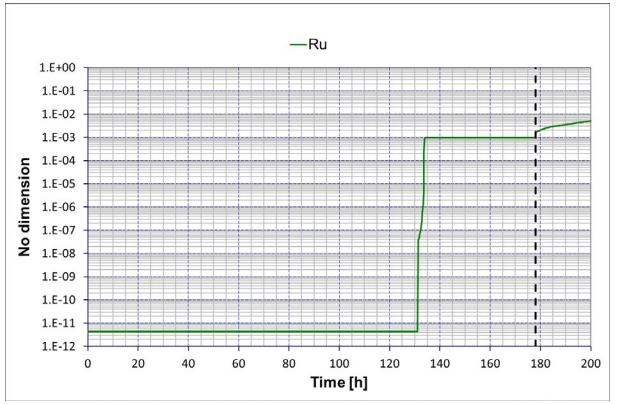

Main FPs release fraction of the i.i.

Results & Discussion

Reference Case

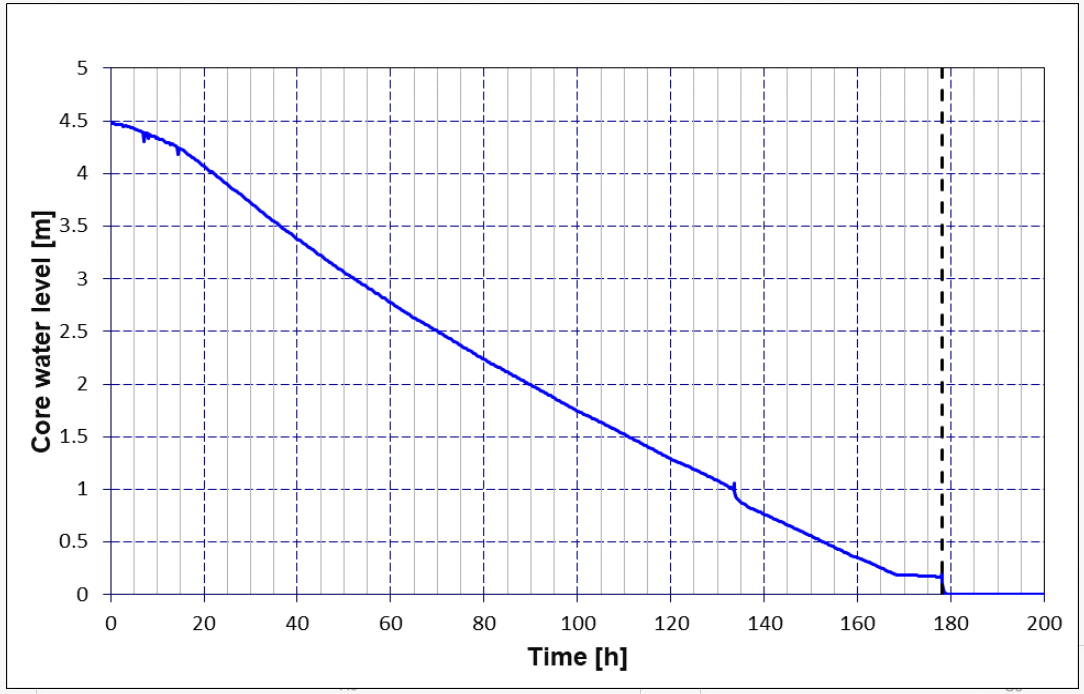

Core water level

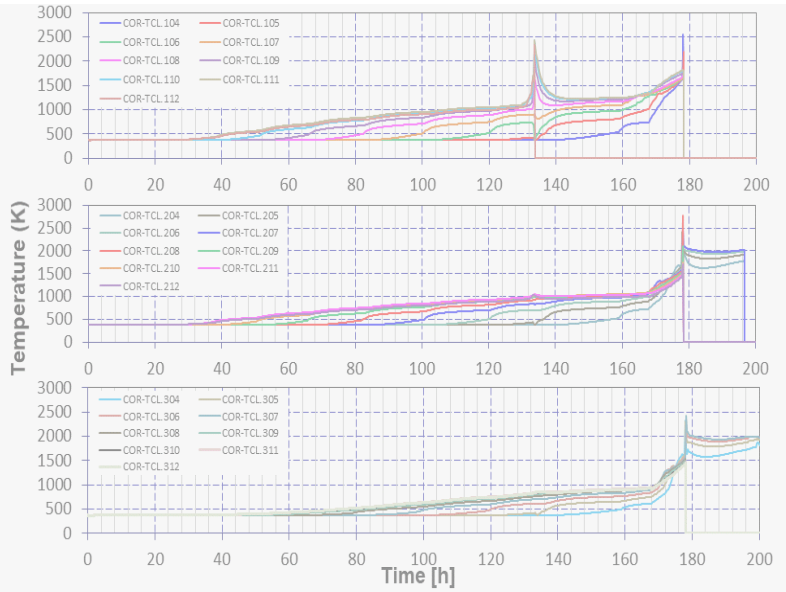

Cladding T of hot, cold and fresh FAs axial levels

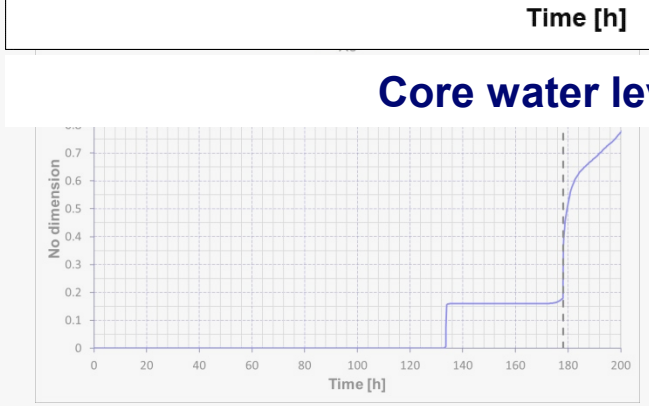

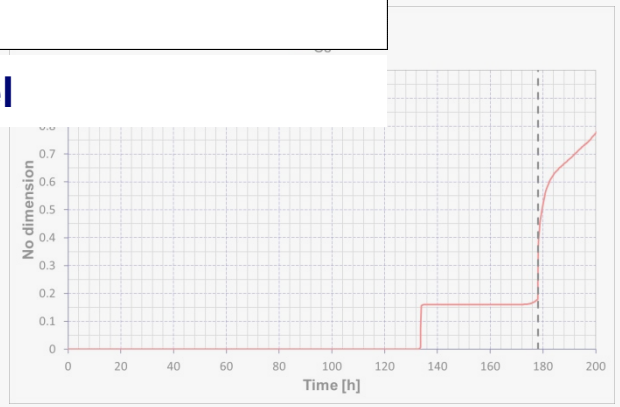

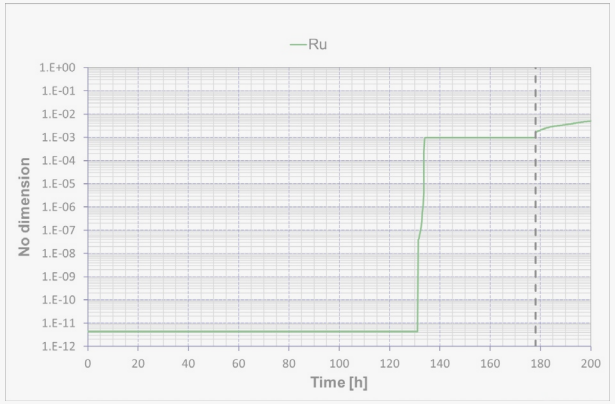

Main FPs release fraction of the i.i.

Results & Discussion

Reference Case

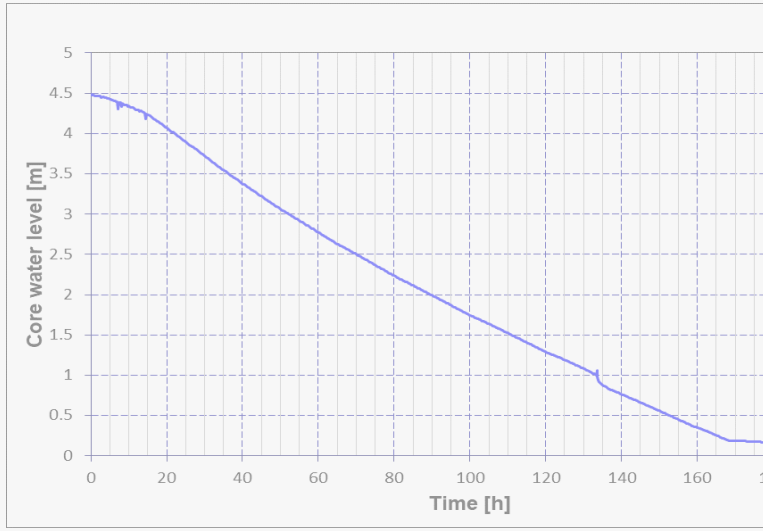

Core water level

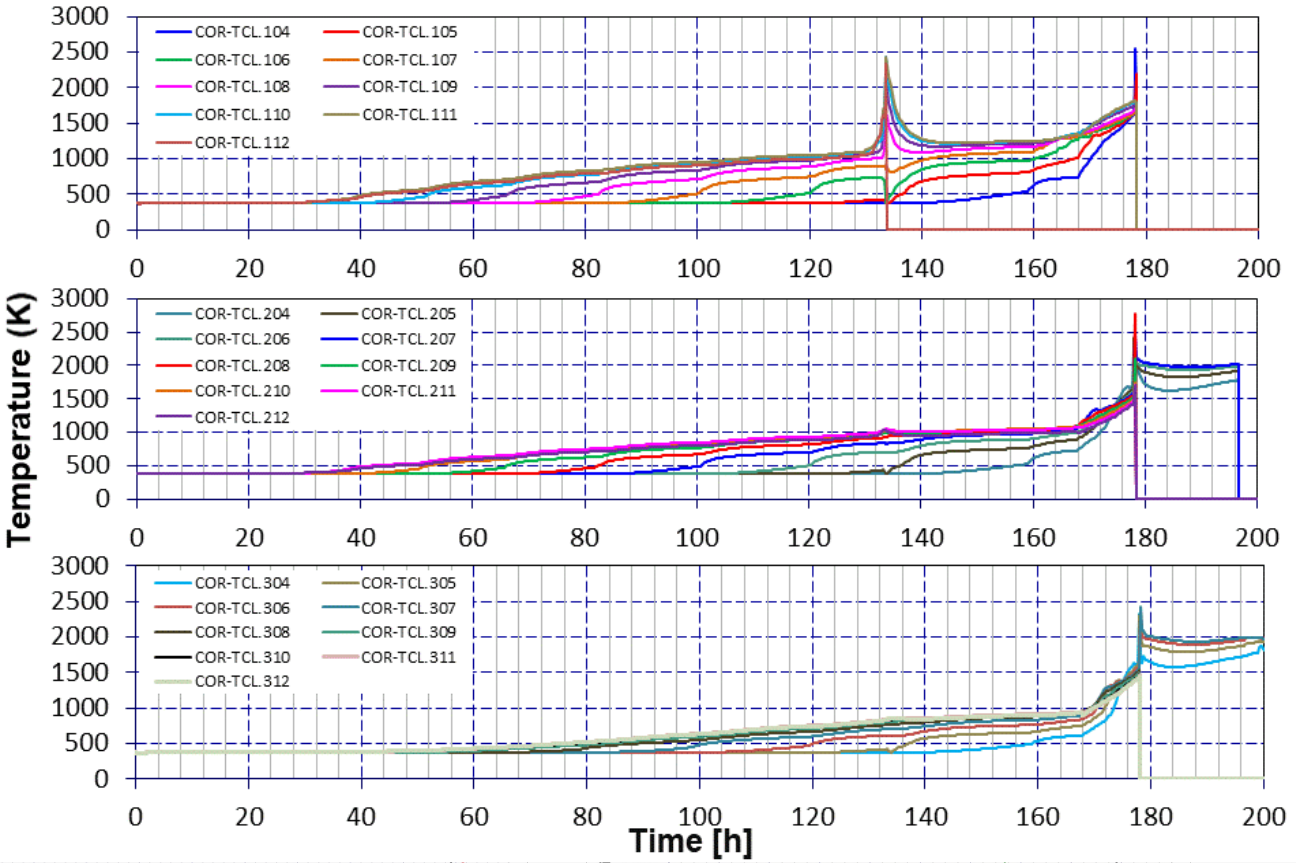

Cladding T of hot, cold and fresh FAs axial levels

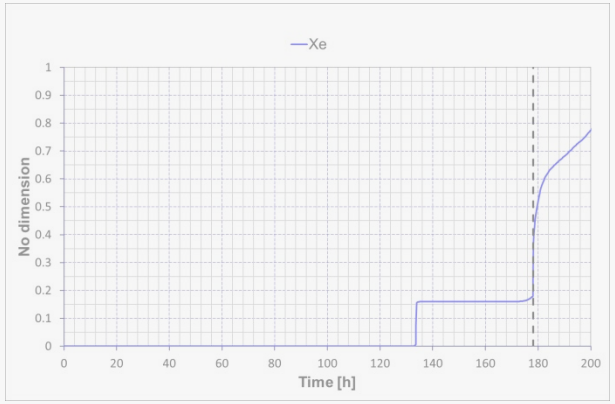

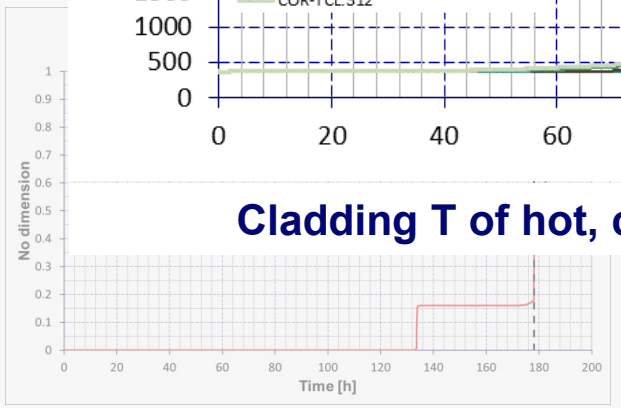

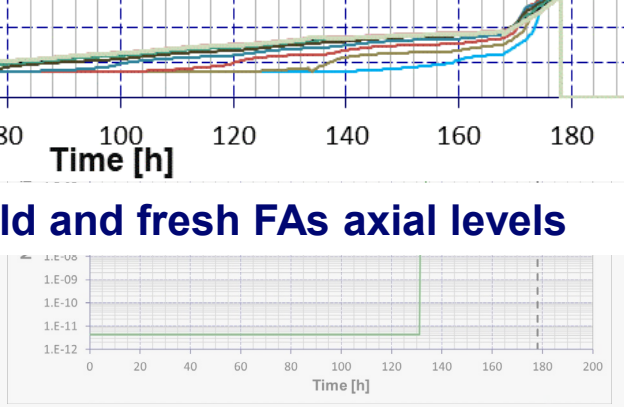

Main FPs release fraction of the i.i.

Results & Discussion

Reference Case

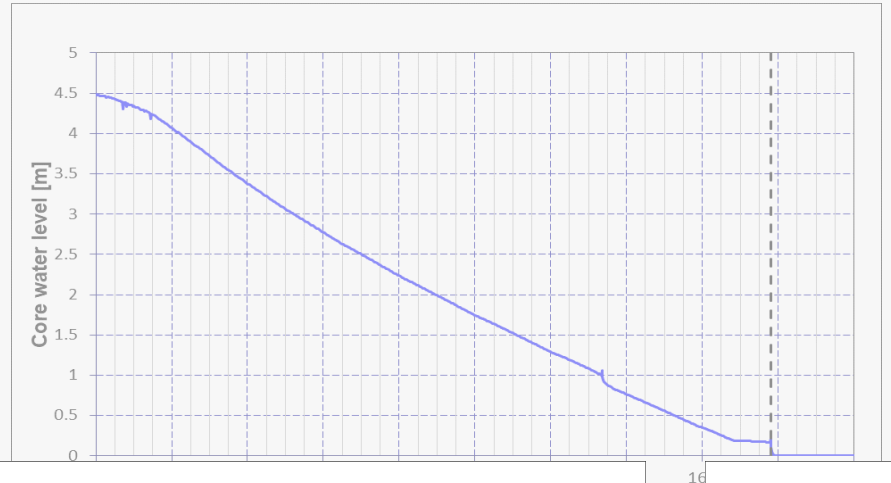

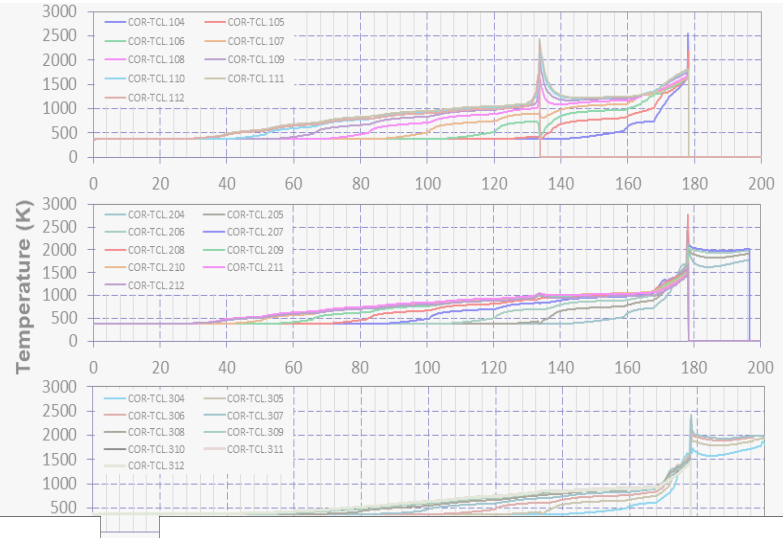

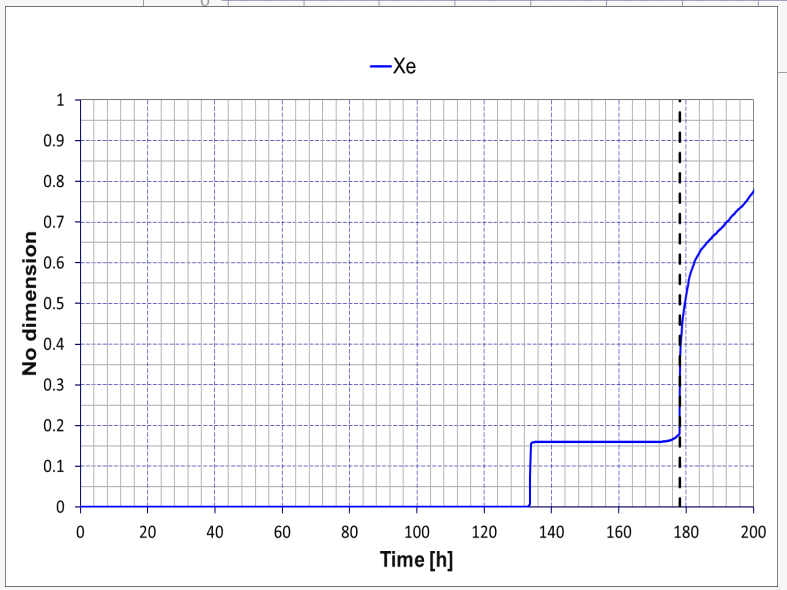

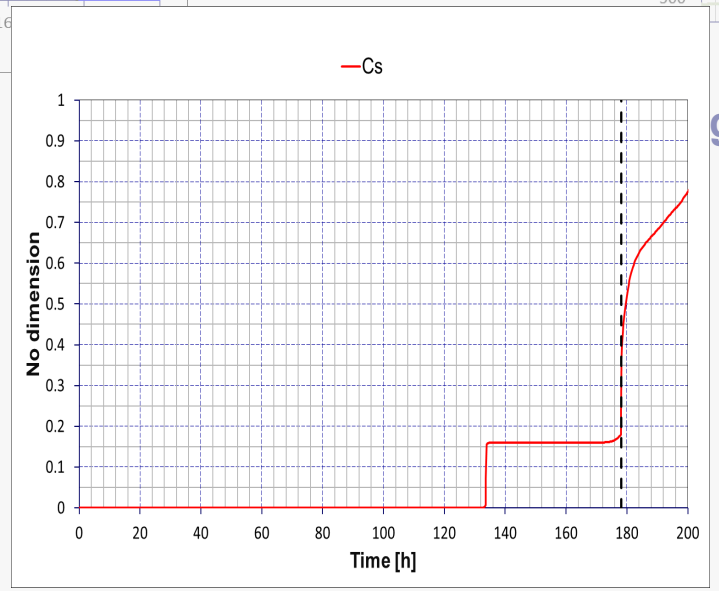

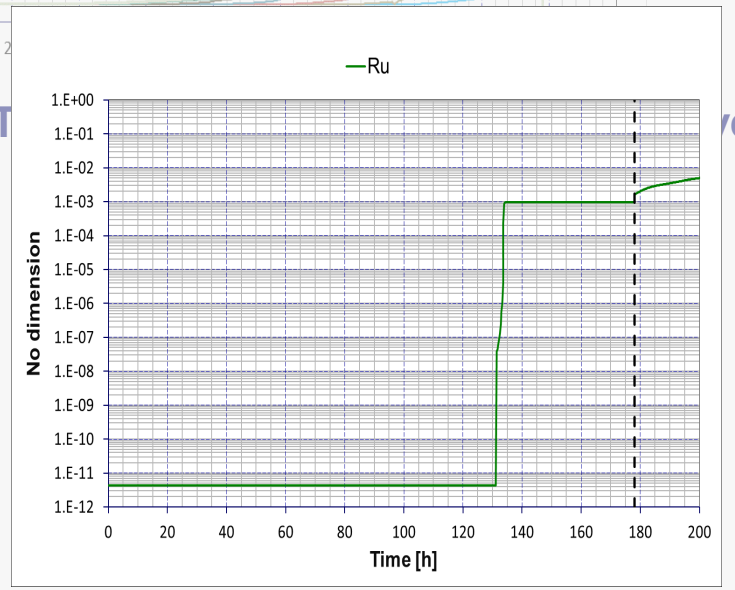

Main FPs release fraction of the i.i.

Results & Discussion

UaSA

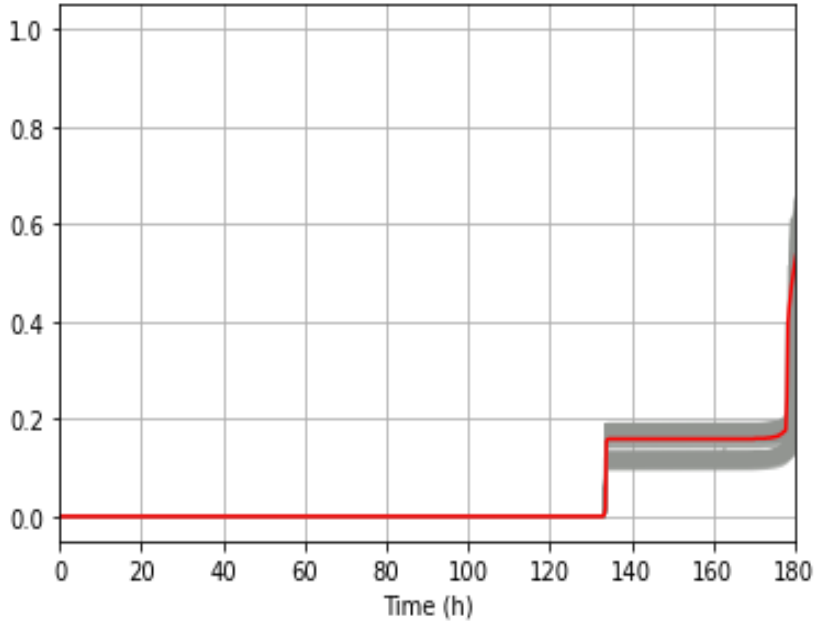

Statistical parameter	Cs
MELCOR reference case (%i.i.)	24.21
Mean (% i.i.)	17.01
Median (% i.i.)	17.10
Lower bound (% i.i.)	11.25
Upper bound (% i.i.)	39.55
Standard deviation (% i.i.)	3.43

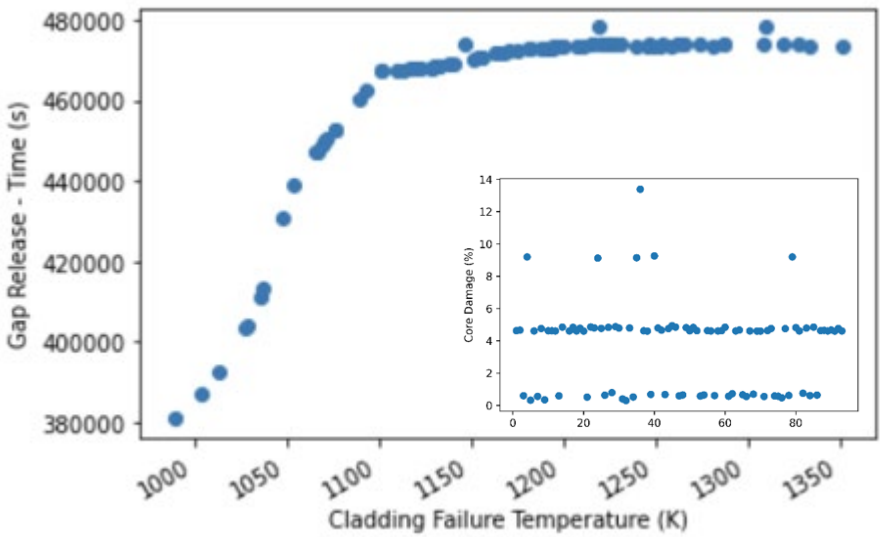

- *All dispersion plots same behavior over time (uncertainties spread over a narrow band).*
- *RC within the uncertainty band.*
- *Clear correlation between FP release onset and cladding failure T.*

Results & Discussion

UaSA

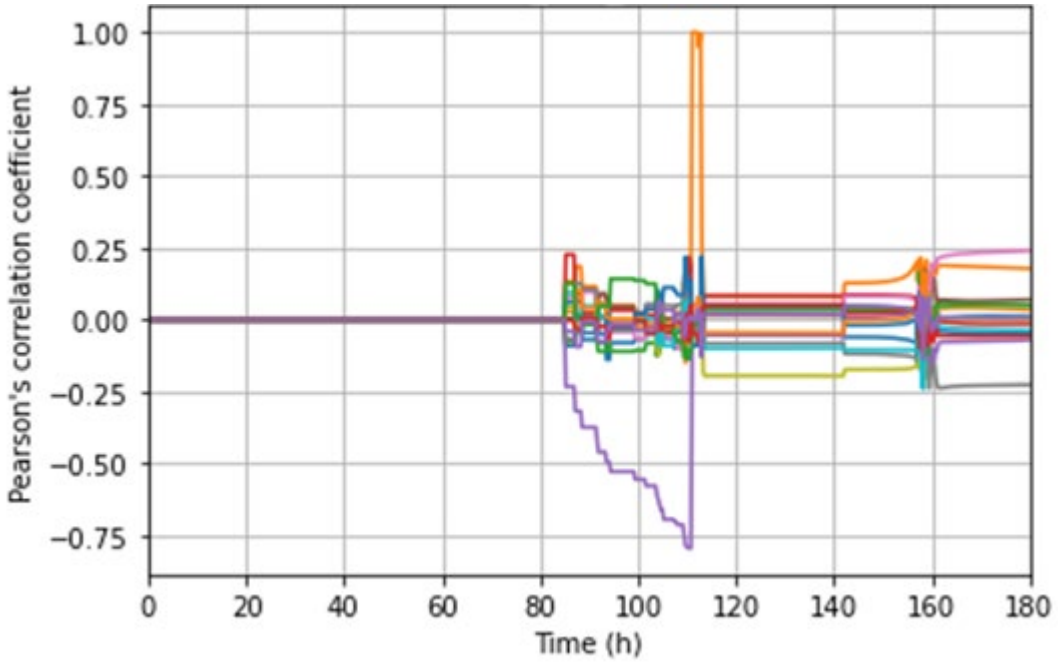

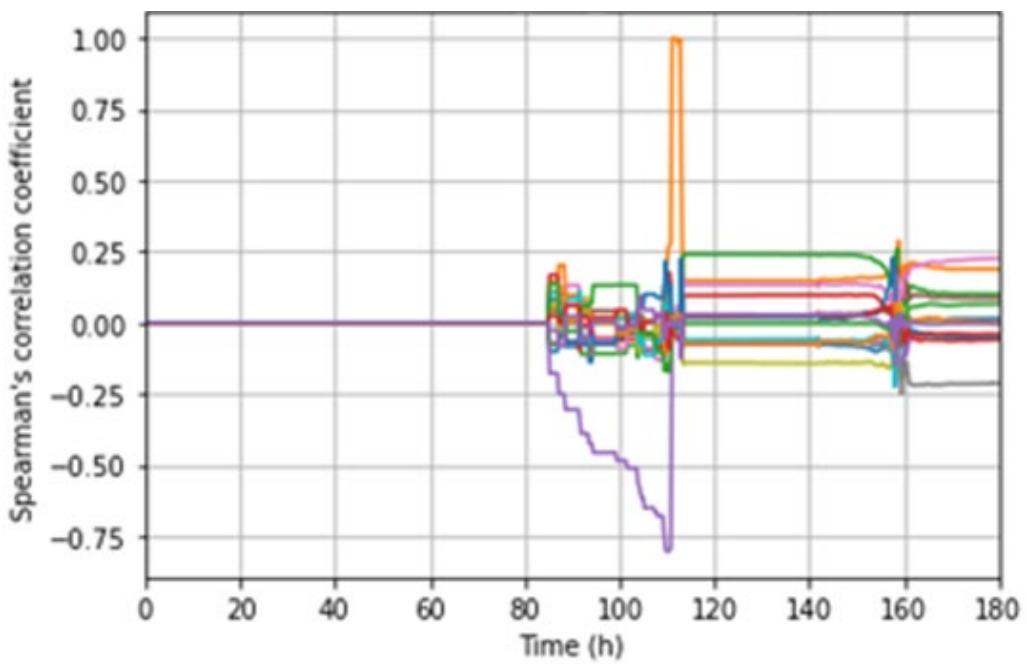



- *Pearson´s and Spearman´s CC as first approach for Sensitivity Analysis*
- *The parameter uncertainty relevance depends on time.*
- *Pearson´s and Spearman´s CC < 0.25 (ending time). Even if CCs go over 0.25, it should be point the ones close to it at the end of the time.*
- *No indication of linear/monotonic correlations between u.p.*

Take Aways

- **RC application:**
  - Given the scenario specifics, insights into dominant uncertainties cannot apply to other scenarios.
  - Modelling SFPs with SA codes still poses challenges.
  - MELCOR radiation model & SFP-BWR did not work.

- **Uncertainty application:**
  - The set of input parameters for uncertainty propagation should be optimized.
  - A consistency screening of individual cases is highly recommended.
  - Sensitivity of FOMs to IP uncertainties should be physically supported.

Acknowledgement

This MUSA project has received funding from the European Union's **EURATOM Horizon 2020** research and innovation programme **grant number 847441**.

The content of this paper reflects only the authors' view. The European Commission is not responsible for any use that may be made of the information it contains.





Thank you for your attention

Unidad de Investigación en Seguridad Nuclear
Departamento de Fisión Nuclear
CIEMAT

monica.gmartin@ciemat.es

UNCERTAINTY AND SENSITIVITY ANALYSES OF SEVERE ACCIDENT CODES USING THE ACE ALGORITHM-BASED SURROGATE MODEL

Kwang-Il Ahn
Korea Atomic Energy Research Institute (KAERI)
989-111 Daedeokdaero, Yuseong, Daejeon, 34057, Republic of Korea
kiahn@kaeri.re.kr

ABSTRACT

This paper explores the alternating conditional expectation (ACE) algorithm-based surrogate model to advance the state-of-practice in uncertainty and sensitivity methodologies for severe accident analysis. For engineering purposes, the ACE algorithm has been used as an alternative means to find the optimal functional forms of the multiple input variables and response variables of interest. Analysis results here demonstrate that compared with the reference cases the proposed surrogate model provides much higher performance in terms of the coefficient of determination (R^2) and normalized root mean square error (NRMSE), thus giving more robust insights into the relationship and correlation between the input parameters and figures of merit (FOMs) of interest. Relevant results and insights are summarized in terms of points of interest.

KEYWORDS
Severe Accident; Uncertainty and Sensitivity; Surrogate Model; ACE Method

1. INTRODUCTION

To run comprehensive plant simulations, most of the currently available integrated severe accident codes employ multiple uncertain models and parameters to represent the wide range of physico-chemical and radiological phenomena, and this makes conducting related uncertainty and sensitivity analyses a nontrivial task.

Numerous studies [1–4] have been performed to understand the uncertainties addressed in figures of merit (FOMs) of interest and to identify influential input parameters contributing to the FOMs through the correlation and/or regression analyses. The foregoing studies have relatively well quantified relevant uncertainties, including epistemic uncertainty in model parameters and to some degree aleatory uncertainty across accident progression and fission products releases; however, with Monte Carlo sampling methods, correlation and regression analyses are often problematic due to highly complex nonlinear relationships between the code inputs and the relevant FOMs. Accordingly, more sophisticated nonlinear regression models that can better capture the influences of model inputs on each relevant FOM have been required to resolve the foregoing issue.

This paper explores the alternating conditional expectation (ACE) algorithm-based surrogate model [5–7] as one of the efforts to advance the state-of-practice in uncertainty and sensitivity methodologies for severe accident analysis in water cooled reactors (WCRs). For this, a previous study [8, 9] was considered as the reference case, namely a MELCOR-based uncertainty and sensitivity analysis for a short-term station blackout (STSBO) accident of a pressurized water reactor (PWR: OPR1000) as implemented in the IAEA (International Atomic Energy Agency) CRP (Coordinated Research Project) I31033 [2, 3].

2. Methodologies

2.1. The ACE Algorithm

For a dependent (or response) variable Y and multiple independent variables (X_i, $i = 1,\ldots,p$), the ACE method [5, 6] is a generalized regression algorithm to find the optimal relations between $\theta(Y)$ and $\emptyset_i(X_i)$ that maximize the statistical correlation between $\theta(Y)$ and $\sum_i^p \emptyset_i(X_i)$. The method treats each value of the transformed dependent variable $\theta(Y)$ as the expectation of several realizations of the sum of transformed independent variables $\sum_i^p \emptyset_i(X_i)$. The resulting ACE regression model can be expressed as follows:

$$\theta(Y) = \alpha_0 + \sum_i^p \emptyset_i(X_i) + \varepsilon. \quad (1)$$

Here, θ is a function of the dependent variable Y and $\emptyset_i$ are functions of the independent variables X_i, α_0 is the regression constant, and ε is an error term that is not explained by the regression. Then the transformed variables $\theta(Y)$ and $\emptyset_i(X_i)$ after minimization of the variance of the error term (ε^2) are estimates of the optimal transformations $\emptyset_i^*(X_i)$ and $\theta^*(Y)$, leading to the following relationship:

$$\theta^*(Y) = \sum_i^p \emptyset_i^*(X_i) + \epsilon^*, \quad (2)$$

where the error term ϵ^*, which is not captured by the ACE transformations, is assumed to have a normal distribution with a mean of zero. The minimum regression error ϵ^* and maximum multiple correlation coefficient ρ^* are related by $\epsilon^{*2} = 1 - \rho^{*2}$. Once the explicit functional forms for $\emptyset_i^*(X_i)$ and $\theta^*(Y)$ are estimated using ACE-transformed data plots, we can formulate the following regression model to estimate the corresponding regression coefficients β_i:

$$\theta^*(Y) = \beta_0 + \sum_i^p \beta_i \emptyset_i^*(X_i). \quad (3)$$

With this expression, the ACE-surrogate model is given in the form of $Y = (\theta^*)^{-1}[\beta_0 + \sum_i^p \beta_i \emptyset_i^*(X_i)]$. Here, $(\theta^*)^{-1}[\cdot]$ indicates an inverse function of $\theta^*(Y)$.

The ACE method has several advantages over the traditional nonlinear regression analysis approaches [5, 6]. For instance, while traditional nonlinear regression analysis needs a priori estimates of the functional forms that attempt to accurately estimate the fitting coefficients to arrive at a converged solution, the ACE algorithm guarantees the convergence of the transformed input and output variables $\theta(Y)$ and $\emptyset_i(X_i)$. After the ACE iteration converges, a simple regression analysis can be used to generate analytical functional forms best fitted to the transformed variables. For practical engineering problems, the ACE surrogate model can be formulated through the following steps:

(1) Plot the corresponding ACE-transformed input values $[\emptyset_i(X_i)]$ against the N estimated uncertain input values (X_i) to visually inspect and find the best generalized curve between them. Typically, polynomial regression of powers ranging from 1 to 3 (or piece-wise linear regression) is good enough to fit the curve, but higher-order of powers for more complex nonlinear relations may be necessary;
(2) Plot the corresponding ACE-transformed code response values $[\theta(Y)]$ against the estimated code response values (Y) and repeat the same process as in step 1. Here, a linear regression (polynomial regression of power 1) or quadratic (quasi-linear) relation is usually good enough to fit the curve;
(3) Sum all the response values from the relationships (curves) established in step 1 to formulate Eq. (2);
(4) Input the response from step 3 into the formulation established in step 2 and perform a regression analysis for the transformed input and response variables to obtain Eq. (3);

(5) Finally, derive the optimized relationship (curve) between the code input parameters (X_i) and relevant FOM (Y) by taking the inverse function of $\theta^*(Y)$.

2.2. Problem and Work Flow

The STSBO scenario considered in the reference case, is a core damage sequence induced by a complete loss of all onsite and offsite AC power. As a result, all safety-related systems being driven by AC power are not available in this scenario. The STSBO-induced accident progression occurs relatively quickly under the postulated conditions. Table I summarizes the 25 MELCOR input parameters employed in the reference study [9, 10], whose phenomenological domain covers all phases of the severe accident progression, in-vessel, ex-vessel, containment, and behaviors of fission products, and whose uncertainties are expected to influence the severe accident results. Uncertainty analyses were performed that produced a sample set of time-dependent results, which were used for the correlation and regression analyses.

Table I. MELCOR input parameters employed in the reference study

Group	Var	Model parameter	BE (range)	PDF (Probability Density Function)
In-vessel	X_1	FCELR/ FCELA	0.1 (0.02–0.18)	Normal: μ = 0.1, σ = 0.0375
	X_2	SC1132_1 (K)	2500 (–)	Normal: μ = 2479, σ = 83
	X_3	PORDP	0.4 (0.1–0.5)	Lognormal: μ = -0.85, σ =0.32
	X_4	COR.CHT_SS (W/m^2/K)	2500 (500–8000)	Lognormal: μ = 7.9, σ = 0.83
	X_5	COR.CHT_UO2 (W/m^2/K)	7500 (2000–22000)	Lognormal: μ = 9.04, σ = 0.63
	X_6	DHYPD_LP (m)	0.02 (0.01–0.06)	Lognormal: μ = -3.68, σ = 0.5
	X_7	DHYPD_core (m)	0.01 (0.002–0.05)	Lognormal: μ = -4.34, σ =0.58
	X_8	SC1020_1 (s)	300 (100–1000)	Uniform
	X_9	SC1020_2 (s)	10 (10–100)	Uniform
	X_{10}	SC3200_1	1.0 (0.9–1.1)	Uniform
	X_{11}	SC1601_4	0.18 (0.16–0.20)	Uniform
	X_{12}	VFALL (m/s)	0.01 (0.01–1.0)	Uniform
	X_{13}	HDBH2O (W/m^2/K)	2000 (200–2000)	Uniform
	X_{14}	TPFAIL (K)	1273.15 (1273–1686)	Uniform
	X_{15}	HDBPN (W/m^2/K)	100 (100–1000)	Uniform
H-burn	X_{16}	XH2IGN (H_2 ignition criteria)	0.1 (0.04–0.09)	Discrete: 0.04=0.33, 0.06=0.33, 0.09=0.33
In-vessel	X_{17}	SC1141_2 (kg/m-s)	1.0 (0.1–2.0)	Log-triangular (mode = 0.2)
	X_{18}	FUOZR	0.2 (0.0–0.5)	Triangular (mode = 0.2)
Ex-vessel	X_{19}	XHTFCL	1.4 (1.0–2.0)	Triangular (mode = 1.4)
	X_{20}	HTRBOT	1.0 (0.9–2.0)	Triangular (mode = 1.0)
	X_{21}	HTRSIDE	1.0 (0.9–2.0)	Triangular (mode = 1.0)
	X_{22}	COND.CRUST	1.0 (1.0–5.0)	Triangular (mode = 1.0)
In-vessel	X_{23}	SC1131_2 (K)	2400 (2100–2540)	Beta (scaled): α = 3.83, β = 3.00
Fission Product	X_{24}	CHI	1.0 (1.0–5.0)	Beta (scaled): α = 1.0, β = 5.0
	X_{25}	CHEMFORM (cesium)	0.8 (0.0–1.0)	Beta: α = 9, β = 3

Taking into account the current situation in which calculation times on the order of hours per sample are required to simulate all the phases of severe accidents, Monte Carlo samples of N = 100 were simulated until 72 h after the initiation of the accident, which is the mission time for Level 2 PSA (probabilistic safety assessment). All input parameters were assumed to be mutually independent in this study.

In relation to the correlation and regression analyses between input parameters and relevant FOMs, among the seven FOMs tested in the reference study, the three given in Table II were selected for this study, namely in-vessel and ex-vessel hydrogen generation (FOMs 1 and 2) and the release of Cs to the environment (FOM 3), which respectively have moderate (0.57), low (0.29), and high (0.84) rank regression performance in

terms of the adjusted coefficient of determination (R^2). This is because the estimated degree of dependency for input and output variables might differ from the corresponding regression performance.

Table II. Three FOMs selected for the present study

FOMs	Definition	MELCOR Variable
FOM 1 (Y_1)	Mass of hydrogen generated by in-vessel Zr/steel oxidation before RPV (reactor pressure vessel) failure (kg)	COR-DMH2-TOT
FOM 2 (Y_2)	Mass of hydrogen generated by ex-vessel MCCI (molten-corium concrete interaction) after RPV failure (kg)	CAV-MEX-H2.10
FOM 3 (Y_3)	Environmental release fraction of fission product Cs through containment leakage/rupture or damaged steam generator tube (the ratio of its initial inventory)	RN1-TYCLT-x-2.ty

For reference, the coefficient of determination (R^2) (or adjusted R^2) provides an indication of how well the regression model under consideration replicates the observed results [1, 11, 12]. Correlation analysis assesses a possible linear dependence between two random variables, while regression analysis determines the importance of the input variables to the output variables of interest by examining how sensitive an output is to a given input or set of inputs. More specifically, regression analysis estimates the extent that the uncertainty in each input contributes to the variance in the output of interest, based on a mathematical relationship between input and output variables.

Based on the simulated results of $N = 100$, which were previously obtained through the reference study, FOM-relevant ACE surrogate models were formulated to explore more robust insights into the relevant sensitivity analysis results. Five types of sensitivity measures were tested in this study: Pearson correlation coefficient, Spearman rank correlation coefficient, partial rank correlation coefficient (PRCC), standardized regression coefficient (SRC), and standardized rank regression coefficient (SRRC).

The foregoing sensitivity analysis methods are superior to local sensitivity methods that examine the influence of input parameters one at a time since the above measures provide global insights into the relative importance of input parameters on the output and major sources of input uncertainty. Rank regression is a linear regression applied to rank values of two random variables using a least squares approach, which is solely used to estimate the influence of uncertainty in the input parameters on the output uncertainty and is not used for prediction. The PRCC (or PCC) is usually employed to avoid masking the effects of strong correlations that indicate the strength of an association between two variables while removing the effects of the rest [11, 12]. The degree of estimated correlation between two variables (r, $|r| \leq 1$) [13] is categorized as high (or very strong) if $|r| \geq 0.7$; moderate (or strong) if $0.3 \leq |r| < 0.7$; low (or weak) if $0.1 |r| < 0.3$; and little or no relationship if $|r| < 0.1$. The aforementioned methods, which have been used to capture the linear relationship between model inputs and outputs, have the advantage of being robust if they well represent a given model.

3. RESULTS

3.1. Formulation of the ACE Surrogate Models

Table III summarizes the three ACE-transformed regression models for 100 Monte Carlo samples of the set of code input parameters in Table I, formulated by minimizing the error term of the linear relationship between the sum of transformed code input parameters and relevant FOM through Eq. (1) to Eq. (3). Table IV and Figure 1 show that the transformed input parameters and transformed FOMs are almost linearly correlated, with coefficients approaching 1.0.

Figure 2 shows the ACE transformation for input variable x_{10} (SC3200_1, multiplier for the ANS decay heat curve), taken to find the best generalized curve. For the variable, the best curve fitting was made by applying polynomial regression of 6 powers, due to the higher nonlinear relation. Relations for the remaining input variables were also derived in a similar way. Finally, these transformed curves were inputted into Eq. (3) to derive the surrogate models for the FOM variables.

Table III. Estimated ACE surrogate models

β_i	$\theta^*(Y_j) = \beta_0 + \sum_i^p \beta_i \emptyset_i^*(X_i)$ [Eq. (3)]		
	FOM 1 ($\theta^*(Y_1)$)	FOM 2 ($\theta^*(Y_2)$)	FOM 3 ($\theta^*(Y_3)$)
i=0	–1.33E-06	3.45E-07	3.63E-06
i=1	1.07	1.1	1.09
i=2	1.0	1.19	1.17
i=3	1.02	1.01	1.23
i=4	1.53	1.14	1.09
i=5	0.933	1.09	1.02
i=6	1.13	1.46	1.77
i=7	0.978	0.799	0.972
i=8	0.87	1.73	1.16
i=9	0.95	1.57	1.47
i=10	0.959	1.0	1.01
i=11	1.22	1.55	1.09
i=12	2.26	1.02	1.2
i=13	1.16	1.05	1.02
i=14	0.973	1.11	1.14
i=15	1.05	1.17	1.15
i=16	1.58	1.24	1.45
i=17	1.13	1.07	1.18
i=18	1.22	0.992	1.01
i=19	1.29	1.1	1.04
i=20	1.2	1.01	1.08
i=21	1.31	1.01	1.14
i=22	1.17	1.35	1.37
i=23	1.03	0.998	1.07
i=24	1.06	1.22	0.967
i=25	1.45	1.0	0.953
R^2	0.96	0.92	0.98
R^2_{adj}	0.95	0.89	0.97

R^2_{adj}: adjusted R^2, reflecting the influence of the number of samples and parameters

Table IV. Performance of the estimated regression models

R^2	Linear relation between ACE-transformed variables	
	$\theta(y)$ and $\theta^*(y)$	$\theta^*(y)$ and $\sum_i^p \emptyset_i^*(x_i)$
FOM 1 (Y_1)	0.9574	0.9907
FOM 2 (Y_2)	0.9233	0.9891
FOM 3 (Y_3)	0.9811	0.9974

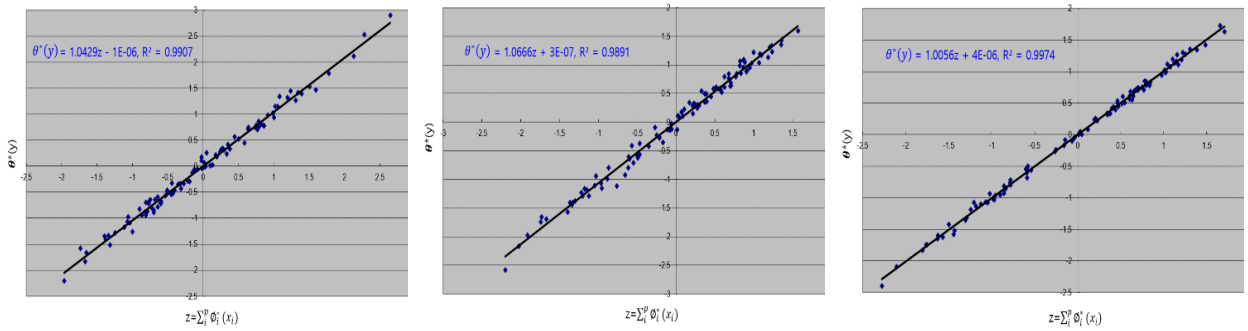

(a) FOM 1 (b) FOM 2 (c) FOM 3

Figure 1. Relation between $\sum_i^p \emptyset_i^*(x_i)$ and $\theta^*(y)$.

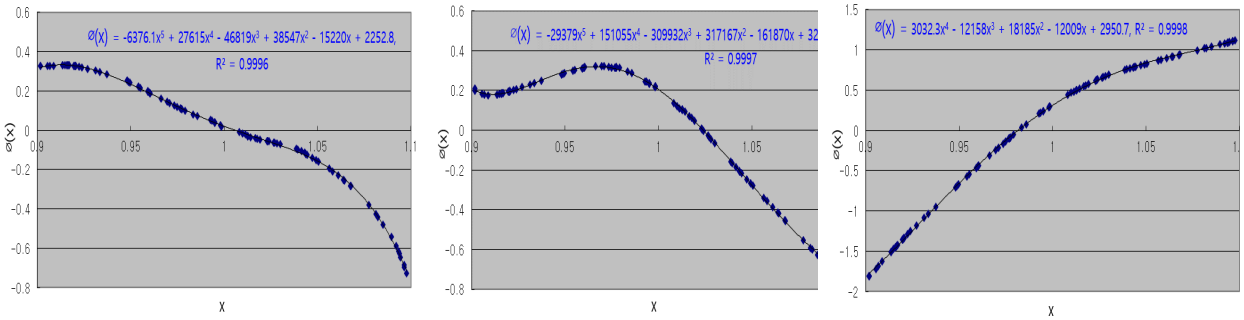

(a) FOM 1 (b) FOM 2 (c) FOM 3

Figure 2. Relation between the input x_{10} and $\emptyset_{10}(x_{10})$.

Figure 3 shows the ACE transformation for FOM variables (Y) taken to find the best generalized curve. For the three FOM variables, polynomial regression of 1 (linear) or 2 (nearly approaching a quasi-linear) powers were good enough to fit the curve. These transformed curves were also inputted into Eq. (3) to derive the surrogate models for the FOM variables.

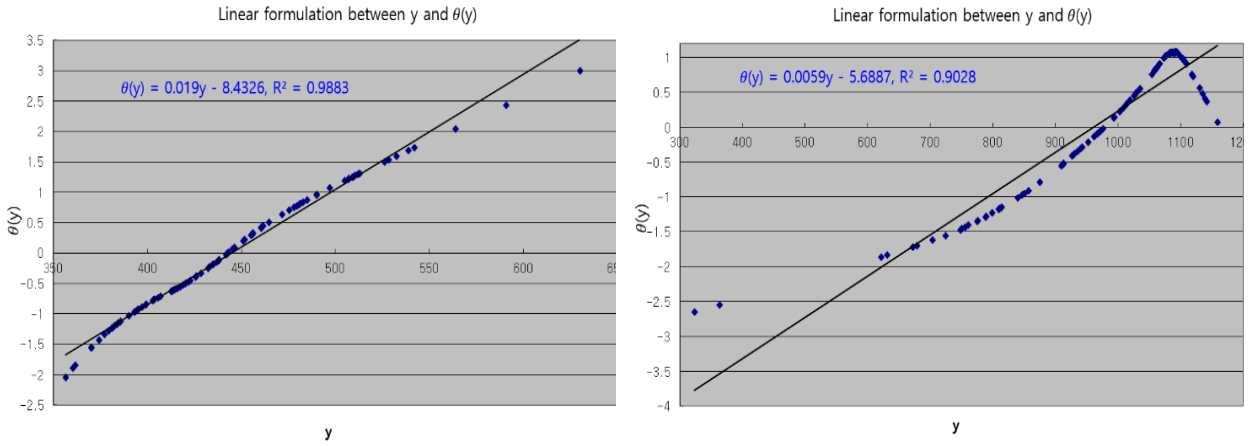

(a) FOM 1 (b) FOM 2

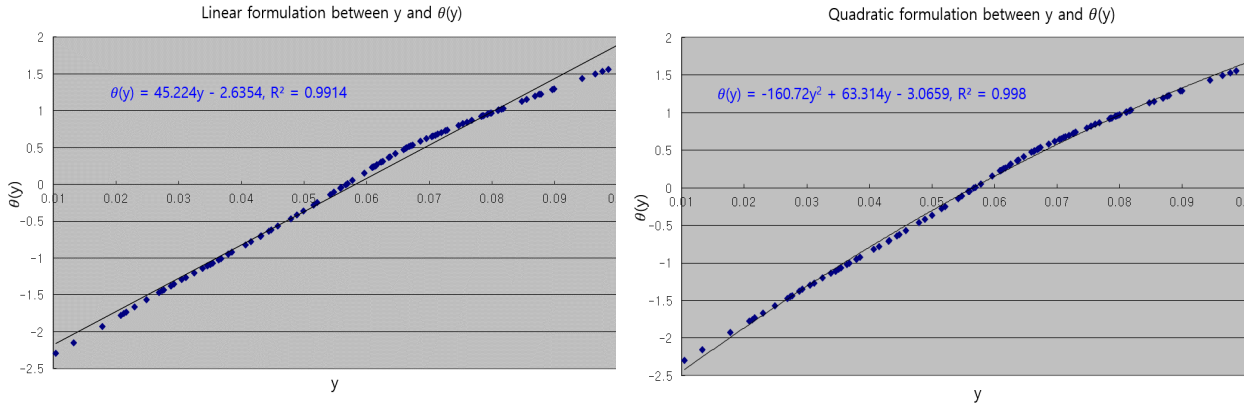

(c) FOM 3

Figure 3. Relation between y and $\theta(y)$: linear or quadratic (≈ quasi-linear).

Figure 4 and Table V summarize the ACE surrogate models (y_{reg}) for the three FOM variables and the regression performance in terms of R^2 and normalized RMS error (NRMSE), compared to the reference cases (y). As shown in the figure and table, the estimated ACE surrogate models capture well the code simulation results obtained through the reference cases, i.e., the nonlinear relationships between the code inputs and FOMs, except for FOM 2 whose regression performance was sensitive to outliers. For reference, the coefficient of determination (R^2), adjusted R^2 (R^2_{adj}), RMS error (RMSE), and NRMSE are defined as follows:

$$R^2 = \sum_{j=1}^{N}(\hat{y}_j - \bar{y})^2 / \sum_{j=1}^{N}(y_j - \bar{y})^2 \quad (4)$$

$$R^2_{adj} = 1 - (1 - R^2)(N-1)/(N-p-1) \quad (5)$$

$$\text{RMSE} = \sqrt{\sum_{j=1}^{N}(\hat{y}_j - y_j)^2 / N} \quad (6)$$

$$\text{NRMSE} = (\text{RMSE}) / (y_{\max} - y_{\min}) \quad (7)$$

Here, y_j, $\hat{y}_j$, and $\bar{y}$ denote the reference values, sampled or simulated values, and their mean, respectively. While R^2 and R^2_{adj} explain the general tendency (i.e., average behavior) of the estimated regression model, RMS error and NRMSE estimate the local variation of the regression model or observed results.

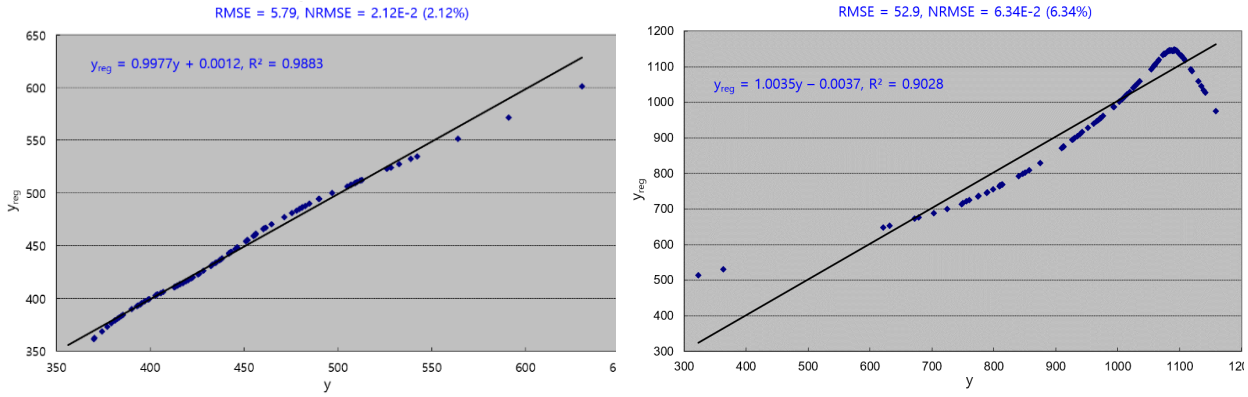

(a) FOM 1 (based on the linear $y - \theta(Y)$ relation)

(b) FOM 2 (based on the linear $y - \theta(Y)$ relation)

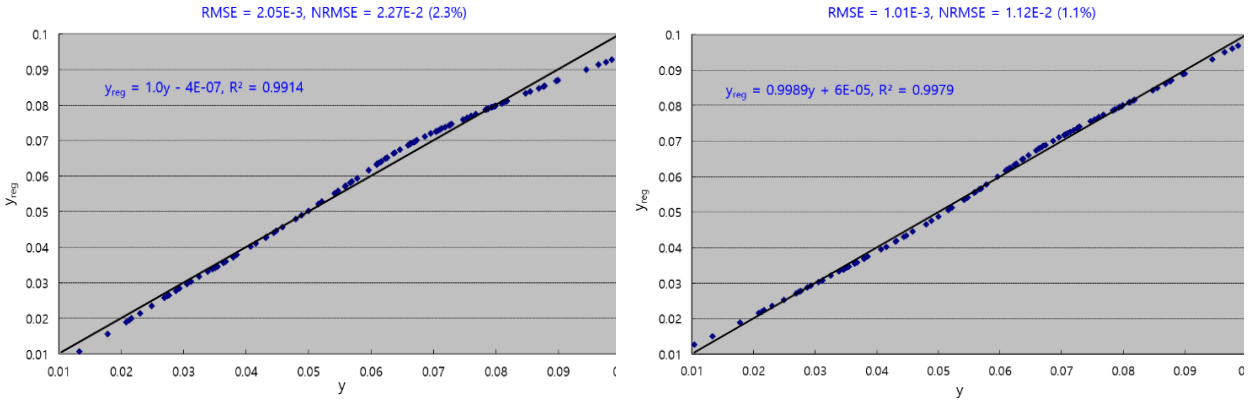

Based on the linear $y - \theta(Y)$ relation

Based on the quadratic $y - \theta(Y)$ relation ($\approx$ quasi-linear)

(c) FOM 3

Figure 4. Relation between between $y = y_{ref}$ and $y_{reg} = y_{ace}$.

Table V. Performance of the ACE models compared to the reference cases

FOMs	Based on the linear regression between y_{ref} and y_{reg}		
	$y - \theta(y)$ relation	R^2	NRMSE (%)
FOM 1 (Y_1)	linear	0.9883	2.12
FOM 2 (Y_2)	linear	0.9028	6.34
FOM 3 (Y_3)	linear	0.9914	2.30
	quadratic ($\approx$ quasi-linear)	0.9979	1.10

3.2. Correlation and Regression Analyses

In order to obtain key insights into the key contributors that are the most responsible for each of the three FOMs, the ACE surrogate models formulated for $\emptyset(x)$ and $\theta(y)$ were tested on the five types of sensitivity measures. This is because the transformed input and response variables [$\emptyset(x)$, $\theta(y)$] have a linear relationship, and when taking a linear or monotonic relation for $y - \theta(y)$, the estimated ACE surrogate models well trace the code simulation results (x, y) within a few percent error bound, as given in Table V.

Figures 5–7 show the correlation and regression analysis results for the FOMs, compared with the reference cases. According to the results, a few input inputs have much stronger correlations with particular FOMs than others, i.e., much higher importance to the relevant FOMs. For reference, Figures 8–10 illustrate data scatter plots of the code simulation results for the variables (x_{10}, y) and the corresponding ACE-transformed variables [$\emptyset(x_{10})$, $\theta(y)$], provided to visualize their relationships (Pearson correlation $\cong \sqrt{R^2}$). According to Fig. 9, it is noted that the ACE algorithm can be somewhat sensitive to outliers in the simulated data. However, even with the outliers, performances of the three ACE surrogate models formulated for the sensitivity and correlation analyses are much better than the reference cases, as shown in Table VI.

Finally, Table VII summarizes the key contributors to each relevant FOM, whose importance ranks were determined by equally weighting the five sensitivity and correlation indicators given in Figures 5–7. According to the table, the importance ranks of the input parameters to FOM 3 with the highest regression performance (R^2_{adj} greater than 0.8) were the same for the reference and ACE cases. Whereas for the

remaining two FOMs (1 and 2), the relative importance of the input parameters somewhat differed depending on the regression performance, with some of them having higher importance to a certain FOM than others. For instance, for FOMs 1 and 2, the two input parameters leading to the two highest importance ranks are the same for both cases (reference and ACE), but the remaining input parameters showed different importance ranks importance ranks: for FOM 2, 11 input parameters were ranked in the top 7, while for FOM 1, 8 input parameters were ranked in the top 7, consequently giving more robust insights into the relevant results in the case of better regression performance. Table VII demonstrates that regression models with R^2_{adj} greater than 0.8 may be good enough for the sensitivity and correlation analysis, regardless of the methods used in their formulation.

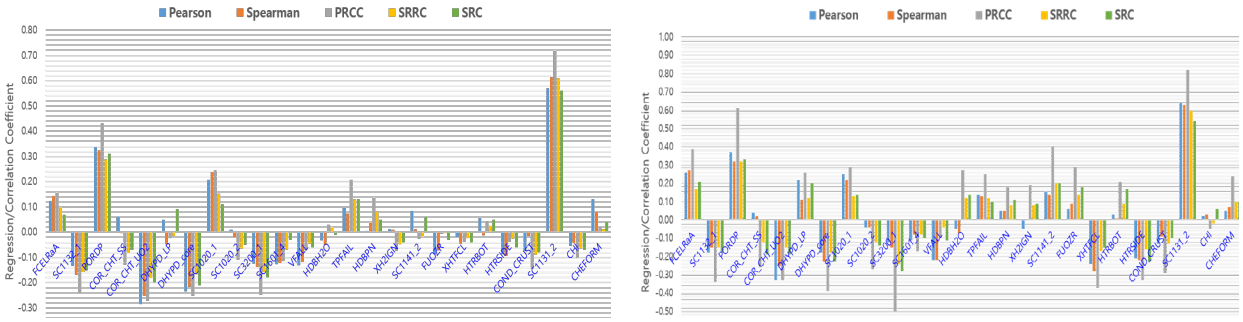

(a) Reference case (b) ACE approach

Figure 5. Correlation and regression analysis results for FOM 1.

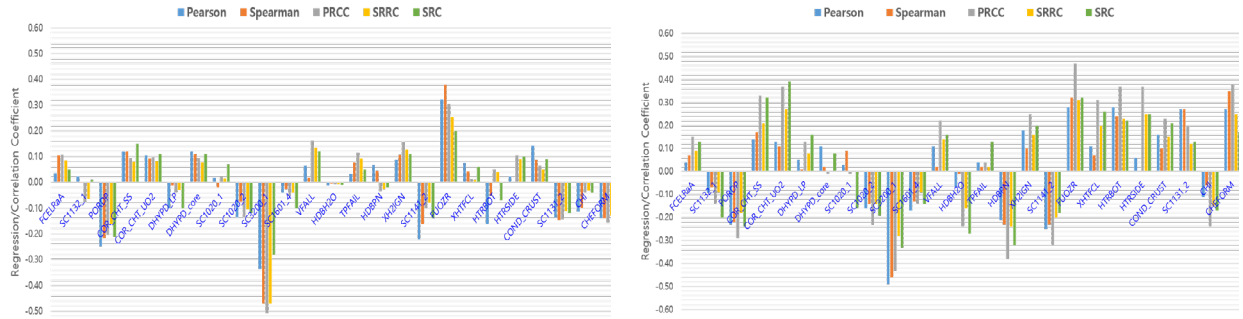

(a) Reference case (b) ACE approach

Figure 6. Correlation and regression analysis results for FOM 2.

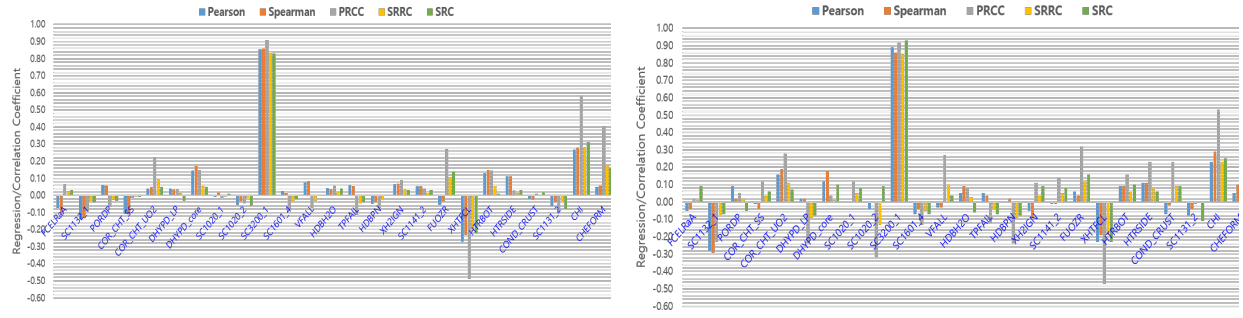

(a) Reference case (b) ACE approach

Figure 7. Correlation and regression analysis results for FOM 3.

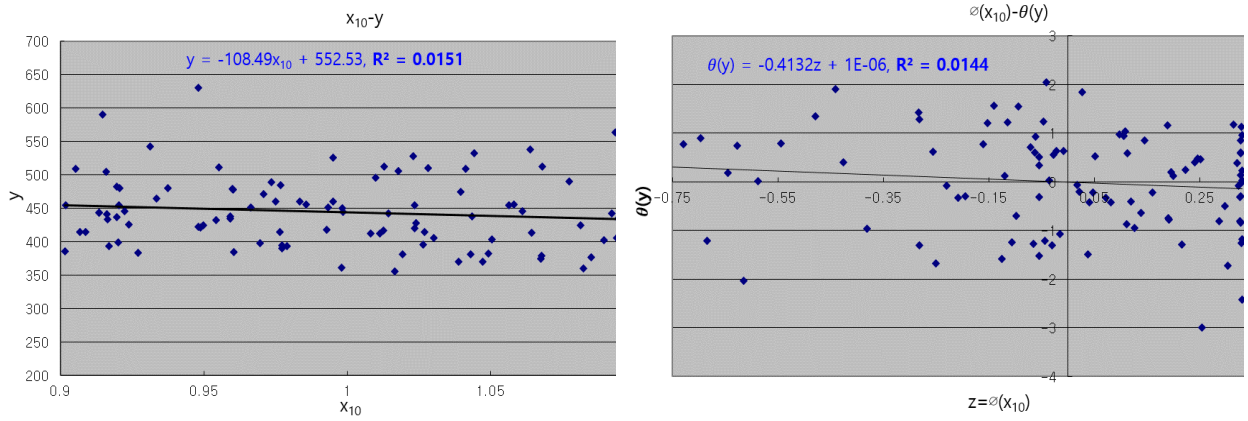

(a) Reference case (x_{10}, y) (b) ACE approach ($\emptyset(x_{10})$, $\theta(y)$)

Figure 8. Data scatter plots for FOM 1.

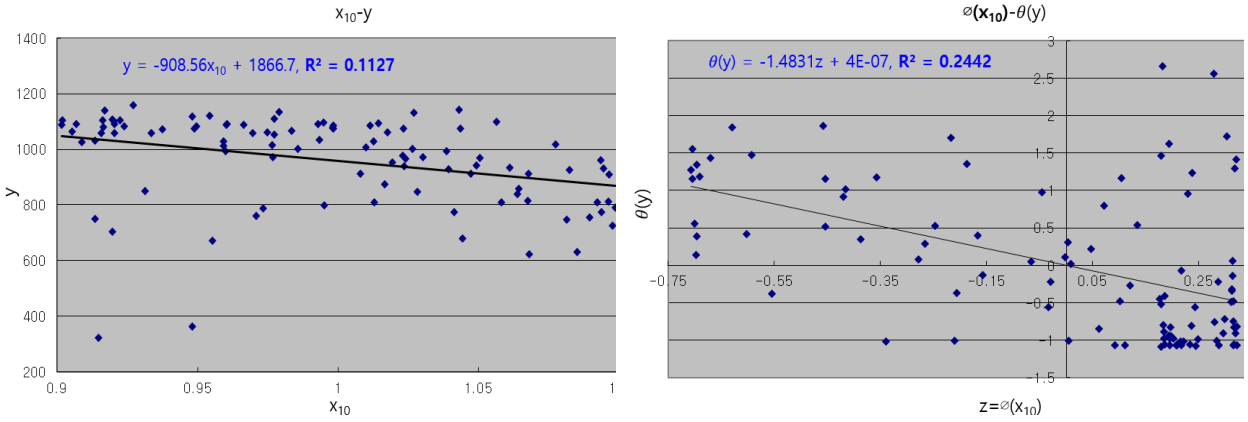

(a) Reference case (x_{10}, y) (b) ACE approach ($\emptyset(x_{10})$, $\theta(y)$)

Figure 9. Data scatter plots for FOM 2.

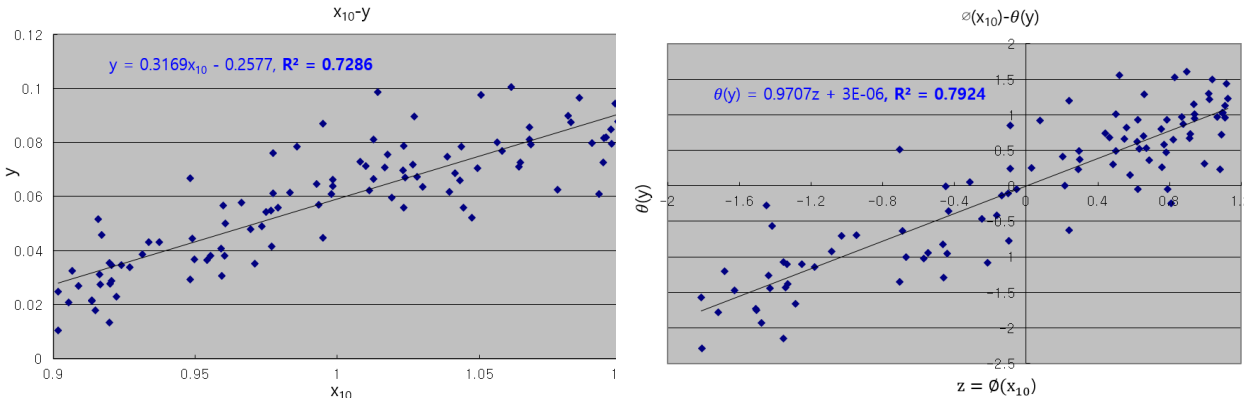

(a) Reference case (x_{10}, y) (b) ACE approach ($\emptyset(x_{10})$, $\theta(y)$)

Figure 10. Data scatter plots for FOM 3.

Table VI. Performance of the regression models used for sensitivity analysis

FOMs	R^2 (R^2_{adj})			
	Ordinary regression		Ranked regression	
	Ref.	ACE (see Table III)	Ref.	ACE
FOM 1 (Y_1)	0.66 (0.57)	0.96 (0.95)	0.68 (0.57)	0.86 (0.81)
FOM 2 (Y_2)	0.40 (0.29)	0.92 (0.89)	0.47 (0.29)	0.72 (0.63)
FOM 3 (Y_3)	0.88 (0.84)	0.98 (0.97)	0.88 (0.84)	0.90 (0.87)

Table VII. Comparison of the key contributors to each FOM

Rank	FOM 1		FOM 2		FOM 3
	Ref.	ACE	Ref.	ACE	Ref./ACE
1	SC1131_2		SC3200_1		SC3200_1
2	PORDP		FUOZR		CHI
3	COR.CHT_UO2	SC3200_1	PORDP	CHEMFORM	XHTFCL
4	DHYPD_core	FCELR/A	CHEMFORM	HTRBOT	X_{25}
5	SC1020_1	DHYPD_core	XH2IGN	HDBPN	FUOZR
6	SC1132_1	SC1132_1 COR.CHT_UO2	VFALL	COR.CHT_UO2	COR.CHT_UO2
7	SC3200_1	DHYPD_core SC1020_2	SC1020_2	HTRSIDE	DHYPD_core

4. CONCLUSIONS

In this paper, ACE algorithm–based surrogate models were explored to advance the state-of-practice in uncertainty and sensitivity methodologies for the severe accident analysis of WCRs. For this, the MELCOR–based analysis results for the OPR1000 STSBO accident were considered as the reference case.

For a feasibility study, ACE surrogate models were formulated for the three FOMs tested in the reference study, namely in-vessel and ex-vessel hydrogen generation (FOMs 4 and 5) and the release of Cs to the environment (FOM 3), which respectively have moderate, low, and high regression performance. For the three reference cases tested, the formulated ACE-based surrogate models led to much better regression performance in terms of R^2 and NRMSE than the linear regression models. Accordingly, the ACE-based surrogate models can replace the original code simulation results to reducing uncertainty to within a few percent error bound: NRMSE of approximately 2% for FOM 1; 1–2% for FOM 3; and 6% even for FOM 2, which showed a very low regression performance in the reference case.

Based on the ACE-transformed regression models formulated for the three FOM variables and 26 MELCOR input parameters tested in the reference study, five types of sensitivity analyses were performed to determine the key contributors to each relevant FOM, as implemented in the reference study. The analysis results demonstrate that ACE surrogate model–based correlation and regression analyses could give much more reliable insights into the relative importance of the input parameters with regard to the uncertainty of the results, when compared to the corresponding reference cases. However, as identified in FOM 2 and Ref. [6], the ACE algorithm may be somewhat sensitive to outliers in the simulated data. For such a situation, an

appropriate method like data screening may be needed so that relevant curve fit be more smoothed. While the methods and results employed for the present study reflected a MELCOR-specific situation, the relevant insights gained here can lead towards newly generated knowledge to be referred as one of the uncertainty and sensitivity analysis methods for severe accident codes with the intent of capturing the best practices.

ACKNOWLEDGMENTS

This work was supported by the International Atomic Energy Agency under the Coordinated Research Project award I31033 on Advancing the State-of-Practice in Uncertainty and Sensitivity Methodologies for Severe Accident Analysis in Water Cooled Reactors (RC No. 23575/R0), launched in 2019. This work was also supported by a National Research Foundation of Korea (NRF) grant funded by the Korean government (MSIT: Ministry of Science and ICT) (No. RS-2022-00143695).

REFERENCES

1. USNRC, *State-of-the-Art Reactor Consequence Analyses Project: Uncertainty analysis of the unmitigated short-term station blackout of the Surry power station*, NUREG/CR-7262, U.S. Nuclear Regulatory Commission, Washington, DC (2022).
2. F. Mascari, et al., "Overview of IAEA CRP I31033 on Advancing the State-of-Practice in Uncertainty and Sensitivity Methodologies for Severe Accident Analysis in WCRs," *The 10th European Review Meeting on Severe Accidents Research (ERMSAR 2022)*, Karlsruhe, Germany, May 16-19 (2022).
3. IAEA, *Advancing the State-of-Practice in Uncertainty and Sensitivity Methodologies for Severe Accident Analysis in Water Cooled Reactors: Final Report of a Coordinated Research Project*, TECDOC-2031, International Atomic Energy Agency, Vienna (2023).
4. L.E. Herranz et al., "The EC MUSA project on management and uncertainty of severe accidents: Main pillars and status," *Energies*, **14**(15), pp.1–11 (2021).
5. L. Breiman and J.H. Friedman, "Estimating Optimal Transformations for Multiple Regression and Correlation," *Journal of American Statistical Association*, **80**, pp.580-598 (1985).
6. D. Wang and M. Murphy, "Estimating Optimal Transformations for Multiple Regression Using the CAE Algorithm," *Journal of Data Science*, **2**, pp.329-346 (2004).
7. K.I. Ahn, B.D. Chung, and John C. Lee, "An Assessment of uncertainty on a LOFT L2-5 LBLOCA PCT Based on the ACE-RSM Approach: Complementary Work for the OECD BEMUSE Phase-III Program," *Nuclear Engineering and Technology*, **42**(2), pp.163-174 (2010).
8. K.I. Ahn, S.Y. Park, W. Choi, S.J. Kim, "Best-Practice Severe Accident Analysis for the OPR1000 Short-term SBO Sequence using MELCOR2.2 and MAAP5," *Annals of Nuclear Energy*, **160** (108350) (2021).
9. W. Choi, K.I. Ahn, S.J. Kim, "Effect of Mitigation Strategies in the Severe Accident Uncertainty Analysis of the OPR1000 Short-term Station Blackout Accident," *Nuclear Engineering and Technology*, **54**(12), pp.4534-4550 (2022).
10. L.L. Humphries, B.A. Beeny, F. Gelbard., D.L. Louie, J. Phillips, *MELCOR Computer Code Manuals, Vol. 1: Primer and Users' Guide, Version 2.2*, SAND2017-0455, Sandia National Laboratories, Albuquerque, NM, USA (2017).
11. A. Pereira and R. Broed, Methods for Uncertainty and Sensitivity Analysis. Review and recommendations for implementation in Ecolego, Dept. of Physics, AlbaNova University Center, Stockholm, Sweden (2006).
12. K.I. Ahn and S.Y. Park, "Best-practice Severe Accident Uncertainty and Sensitivity Analysis for a Short-term SBO Sequence of a Reference PWR using MAAP5," *Annals of Nuclear Energy*, **170** (108981) (2022).
13. D.J. Sheskin, *Handbook of Parametric and Nonparametric Statistical Procedures*, CRC Press, Florida, USA (2004).

Uncertainty and Sensitivity Analyses of Severe Accident Codes Using the ACE Algorithm-based Surrogate Model

Kwang-Il Ahn

KAERI, Rep. of Korea, kiahn@kaeri.re.kr

OUTLINE

- **Motivation and context**
- **Summary of ACE method**
- **Test cases and main results**
  - Formulation of ACE surrogate models
  - Surrogate model-based sensitivity analysis
- **Summary and conclusion**

1. Motivation & context

❑ State-of-practice for U&S in severe accidents

- Monte Carlo approach for UQ and correlation/regression indicators to identify a linear and/or monotonic relation between code inputs (X_i) and FOM of interest (Y), $Y = \alpha_0 + \sum_{i=1}^{p} \alpha_i X_i$.
- Formulation of surrogate models for capturing functional relationships between code inputs & FOMs.

❑ One of challenging issues

- When the relationships between the code inputs and relevant FOMs are complex and nonlinear, $Y = \beta_0 + \sum_{i=1}^{p} \beta_i f_i(X_i)$, how to formulate relevant surrogate models well capturing the relationships and the influence of X_i on Y ?

❑ The present study

- Explore ACE algorithm-based surrogate model, which can replace the original code simulation results with regard to the uncertainty.
- Propose relevant sensitivity method to capture the influence of code inputs (X_i) on FOM (Y) of interest.
- ACE algorithm: a generalized regression method to find optimal functional form between multiple input & response variables by maximizing the statistical correlation between their transformed variables.

2. ACE methodology

Formulation of the ACE surrogate model

Step	Key approach	Mathematical formulation
1	Find optimal transformations $\theta(Y)$ and $\emptyset_i(X_i)$ that maximize the statistical correlation between $\theta(Y)$ and $\sum_i^p \emptyset_i(X_i)$	$\theta(Y) = \alpha_0 + \sum_{i=1}^p \emptyset_i(X_i) + \varepsilon$
2	Treat each value of the transformed variable $\theta(Y)$ as the expectation of several realizations of the sum of transformed independent variables $\sum_i^p \emptyset_i(X_i)$	$\varepsilon^2(\theta, \emptyset_1,\ldots,\emptyset_p) = E[\theta(Y) - \sum_{i=1}^p \emptyset_i(X_i)]^2$ $Constraint: E[\theta^2\theta(Y)] = 1$
3	The minimization of ε^2 with respect to $\emptyset_1(X_1), \ldots, \emptyset_p(X_p)$ and $\theta(Y)$ is carried out through a series of single-function minimization, involving the conditional expectation and minimization	$\emptyset_i(X_i) = E[\theta(Y) - \sum_{j\neq i}^p \emptyset_j(X_j)\|X_i]^2$ $\theta(Y) = \frac{E[\sum_{i=1}^p \phi_i(X_i)\,\|\,Y]}{\|\,E[\sum_{i=1}^p \phi_i(X_i)\,\|\,Y]\,\|}$
4	Smoothing process to reduce randomness: one value $\emptyset_i(x_{i,k})$, for the jth data point, and the corresponding conditional expectation $\theta(y_j)$ has to be evaluated with its neighbouring values for some data point M	$\emptyset_i(x_{i,k})$, k=j-M, … , j+M
5	$\emptyset_i(X_i)$ and $\theta(Y)$ after the minimization are estimates of the optimal transformations, $\emptyset_i^*(X_i)$ and $\theta^*(Y)$	$\theta^*(Y) = \beta_0 + \sum_i^p \beta_i \emptyset_i^*(X_i)$
6	The ACE-surrogate model is obtained by converting the transformed input variables into functions of the original input variables (X_i, i=1,…,p)	$Y = (\theta^*)^{-1}[\beta_0 + \sum_i^p \beta_i \emptyset_i^*(X_i)]$ $(\theta^*)^{-1}[\cdot]$: an inverse function of $\theta^*(Y)$

2. ACE methodology

Work flow for its practical application

Step	Things to do
1	Plot the corresponding ACE-transformed input values ($\emptyset_i(X_i)$) against the estimated uncertain input values (X_i) to inspect visually and find the best generalized curve between them*. Usually polynomial regression or piece-wise linear relation are good enough to fit the curve.
2	Plot the corresponding ACE-transformed code response values ($\theta(Y)$) against the estimated code response values (Y)* and take the same process as step 1. Usually a linear or quadratic (quasi-linear) relation is good enough to fit the curve.
3	Sum all the code response values from the curves established from step 1 to formulate $\theta^*(Y) = \sum_i^p \emptyset_i^*(X_i) + \epsilon^*$.
4	Input the response from step 3 into the formulation established from step 2 and perform a regression analysis for the transformed input and response variables to obtain $\theta^*(Y) = \beta_0 + \sum_i^p \beta_i \emptyset_i^*(X_i)$.
5	Derive the optimized relationship (curve) between the code input parameters (X_i) and relevant FOM (Y) by taking an inverse function of $\theta^*(Y)$, $Y = (\theta^*)^{-1}[\beta_0 + \sum_i^p \beta_i \emptyset_i^*(X_i)]$.
6	Perform uncertainty and sensitivity (regression/correlation) analyses, based on the best-fitted surrogate models for the transformed variables.

(*) While traditional nonlinear regression analysis needs a priori estimate of functional forms that estimates accurately the fitting coefficients to arrive at a converged solution, the ACE algorithm guarantees the convergence of the transformed input and output variables.

3. Cases for test

Work flow of the present study

- The reference study: MELCOR-based uncertainty and sensitivity analyses for a PWR (OPR1000) STSBO, as implemented in the framework of IAEA CRP I31033(*)
- The tested three FOMs having different linear regression performance, **moderate** (0.57, FOM 1), **low** (0.29, FOM 2), and **high** (0.84, FOM 3) in terms of R^2_{adj}
- Formulation of three FOM-relevant ACE surrogate models based on the original code simulation results
- Sensitivity/correlation analyses based on the formulated ACE surrogate models: five types of sensitivity methods tested: (a) Pearson Correlation, (b) Spearman Rank Correlation, (c) Standardized Regression, (d) Standardized Rank Regression, and (e) Partial Rank Correlation.
- Cross-comparison of relevant U&S results with the corresponding reference cases.

(*) IAEA, *Advancing the State-of-Practice in Uncertainty and Sensitivity Methodologies for Severe Accident Analysis in Water Cooled Reactors: Final Report of a Coordinated Research Project*, TECDOC-2031, International Atomic Energy Agency, Vienna (2023)

3. Cases for test

❑ Reference cases explored

FOMs	Definition
FOM 1 (Y_1)	Mass of hydrogen generated by the in-vessel Zr/steel oxidation before the RPV failure (kg)
FOM 2 (Y_2)	Mass of hydrogen generated by the ex-vessel MCCI after the RPV failure (kg)
FOM 3 (Y_3)	Environmental release fraction of FP Cs through the containment leakage/rupture or damaged S/G tube (the ratio of its initial inventory)

❑ Relevant 25 MELCOR uncertainty inputs

Group	Var	Model parameter	BE (range)	PDF
In-vessel	X_1	**FCELR/ FCELA** *(radiative exchange factor for radiation (radial/axial))*	0.1 (0.02–0.18)	Normal: μ = 0.1, σ = 0.0375
	X_2	**SC1132_1** (K) *(temp. to which oxidized fuel rods can stand in the absence of unoxidized Zr in the cladding)*	2500 (–)	Normal: μ = 2479, σ = 83
	X_3	**PORDP** *(porosity of particulate debris)*	0.4 (0.1–0.5)	Lognormal: μ = -0.85, σ =0.32
	X_4	**COR.CHT_SS** (W/m²/K) *(candling heat transfer coefficient for stainless steel)*	2500 (500–8000)	Lognormal: μ = 7.9, σ = 0.83
	X_5	**COR.CHT_UO2** (W/m²/K) *(candling heat transfer coefficient for UO_2)*	7500 (2000–22000)	Lognormal: μ = 9.04, σ = 0.63
	X_6	**DHYPD_LP** (m) *(particulate debris equivalent diameter in lower plenum)*	0.02 (0.01–0.06)	Lognormal: μ = -3.68, σ = 0.5
	X_7	**DHYPD_core** (m) *(particulate debris equivalent diameter in core)*	0.01 (0.002–0.05)	Lognormal: μ = -4.34, σ =0.58
	X_8	**SC1020_1** (s) *(time constant for the relocation of solid material)*	300 (100–1000)	Uniform
	X_9	**SC1020_2** (s) *(time constant for the relocation of liquid material)*	10 (10–100)	Uniform
	X_{10}	**SC3200**_1 *(multiplier for ANS decay heat curve)*	1.0 (0.9–1.1)	Uniform
	X_{11}	**SC1601_4** *(total strain assumed to cause failure)*	0.18 (0.16–0.20)	Uniform
	X_{12}	**VFALL** (m/s) *(velocity of falling debris)*	0.01 (0.01–1.0)	Uniform
	X_{13}	**HDBH2O** (W/m²/K) *(HTC from in-vessel falling debris to pool)*	2000 (200–2000)	Uniform
	X_{14}	**TPFAIL** (K) *(failure temperature of the penetrations or lower head)*	1273.15 (1273–1686)	Uniform
	X_{15}	**HDBPN** (W/m²/K) *(HTC from debris to penetration)*	100 (100–1000)	Uniform
H-burn	X_{16}	**XH2IGN** (*(H_2 mole fraction limit for ignition without igniter)*	0.1 (0.04–0.09)	Discrete: 0.04=0.33, 0.06=0.33, 0.09=0.33
In-vessel	X_{17}	**SC1141_2** (kg/m-s) *(max. melt flow rate per unit width after breakthrough)*	1.0 (0.1–2.0)	Log-triangular (mode = 0.2)
	X_{18}	**FUOZR** *(transport parameters for UO_2 in molten zircaloy)*	0.2 (0.0–0.5)	Triangular (mode = 0.2)
Ex-vessel (Rx Cavity)	X_{19}	**XHTFCL** *(calculated atmosphere heat transfer scaling factor)*	1.4 (1.0–2.0)	Triangular (mode = 1.4)
	X_{20}	**HTRBOT** *(multiplier on the debris-to-surface HT at the bottom surface of the debris)*	1.0 (0.9–2.0)	Triangular (mode = 1.0)
	X_{21}	**HTRSIDE** *(multiplier on the debris-to-surface HTat the side surface of the debris)*	1.0 (0.9–2.0)	Triangular (mode = 1.0)
	X_{22}	**COND.CRUST** *(multiplier on the thermal conductivity of the crust)*	1.0 (1.0–5.0)	Triangular (mode = 1.0)
In-vessel	X_{23}	**SC1131_2** (K) *(maximum ZrO_2 temp. permitted to hold up molten Zr in cladding)*	2400 (2100–2540)	Beta (scaled): α = 3.83, β = 3.00
FP	X_{24}	**CHI** *(aerosol dynamic shape factor)*	1.0 (1.0–5.0)	Beta (scaled): α = 1.0, β = 5.0
	X_{25}	**CHEMFORM** (*(fraction of cesium that transformed to Cs_2MoO_4)*	0.8 (0.0–1.0)	Beta: α = 9, β = 3

3. Cases for test

❑ Uncertainty results for the reference cases (until 72 h after the start of accident)

FOM 1

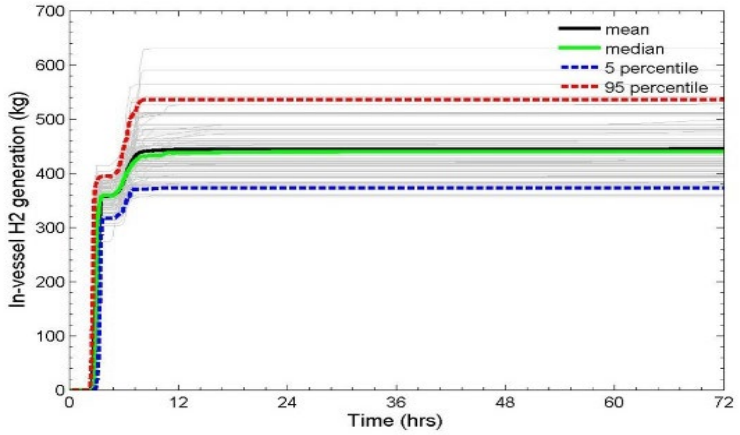

FOM 2

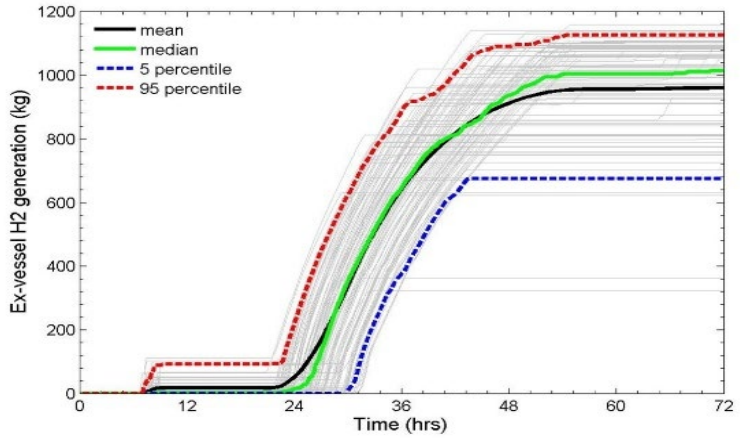

FOM 3

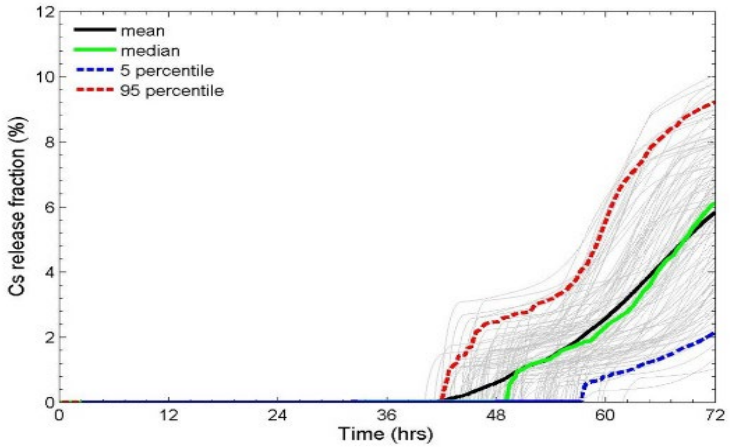

Trends with time

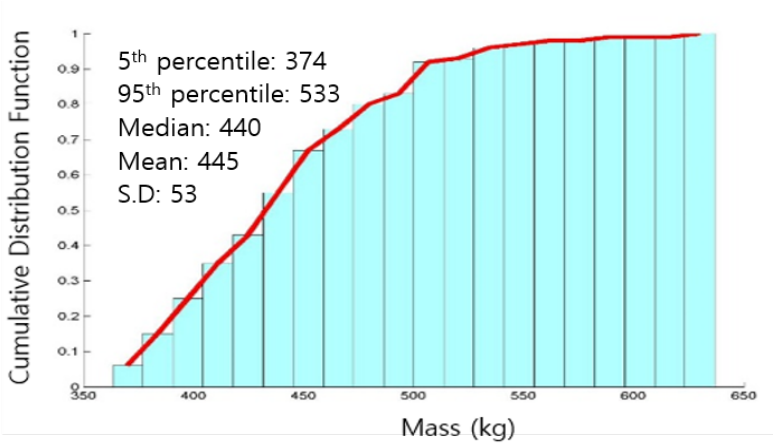

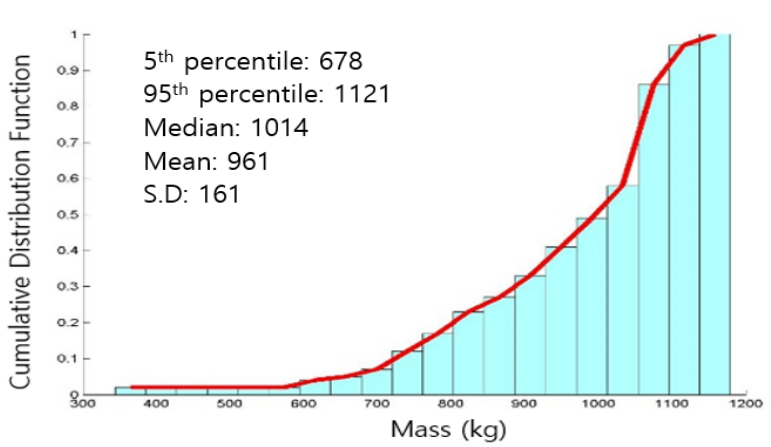

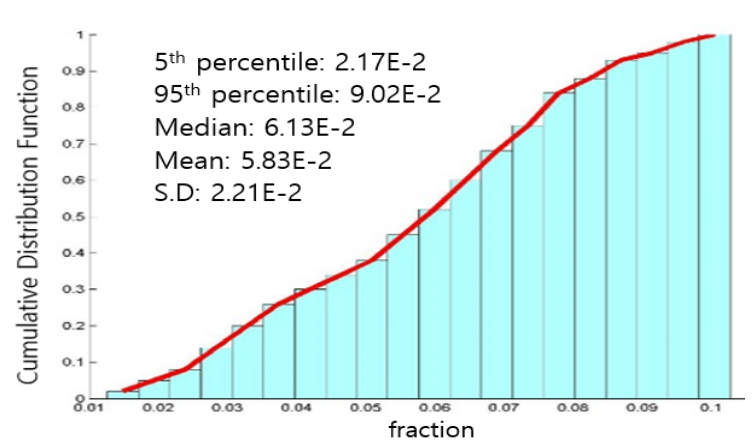

CDF at the end of of calculation (72 h)

4. Results: surrogate models

❑ The ACE surrogate model for each FOM

β_i	$\theta^*(Y_j) = \beta_0 + \sum_i^p \beta_i \emptyset_i^*(X_i)$		
	FOM 4 ($\theta^*(Y_1)$)	FOM 5 ($\theta^*(Y_2)$)	FOM 7 ($\theta^*(Y_3)$)
i=0	-1.33E-06	3.45E-07	3.63E-06
i=1	1.07	1.1	1.09
i=2	1.0	1.19	1.17
i=3	1.02	1.01	1.23
i=4	1.53	1.14	1.09
i=5	0.933	1.09	1.02
i=6	1.13	1.46	1.77
i=7	0.978	0.799	0.972
i=8	0.87	1.73	1.16
i=9	0.95	1.57	1.47
i=10	0.959	1.0	1.01
i=11	1.22	1.55	1.09
i=12	2.26	1.02	1.2
i=13	1.16	1.05	1.02
i=14	0.973	1.11	1.14
i=15	1.05	1.17	1.15
i=16	1.58	1.24	1.45
i=17	1.13	1.07	1.18
i=18	1.22	0.992	1.01
i=19	1.29	1.1	1.04
i=20	1.2	1.01	1.08
i=21	1.31	1.01	1.14
i=22	1.17	1.35	1.37
i=23	1.03	0.998	1.07
i=24	1.06	1.22	0.967
i=25	1.45	1.0	0.953
R^2	0.96	0.92	0.98
R^2_{adj}	0.95	0.89	0.97

❑ Performance of the estimated surrogate models

R^2	Linear relation between transformed variables	
	$\theta(y)$ and $\theta^*(y)$	$\theta^*(y) = \sum_i^p \emptyset_i^*(x_i)$
FOM 1 (Y_1)	0.9574	0.9907
FOM 2 (Y_2)	0.9233	0.9891
FOM 3 (Y_3)	0.9811	0.9974

❑ Best-fitted curves for the input x_{10} and $\emptyset_{10}(x_{10})$

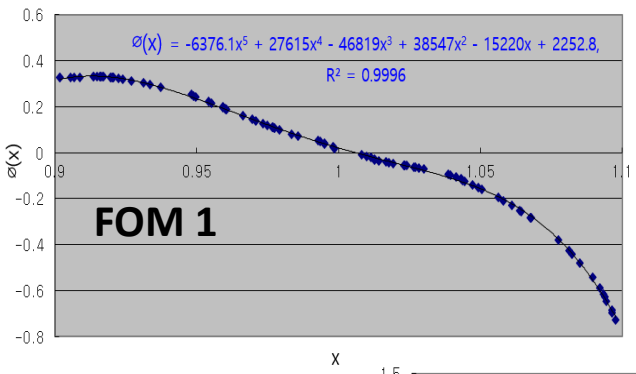

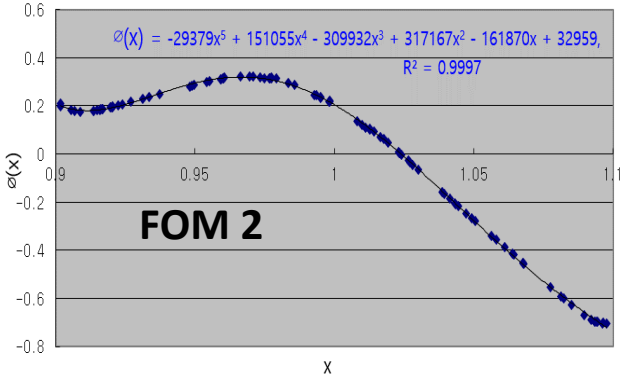

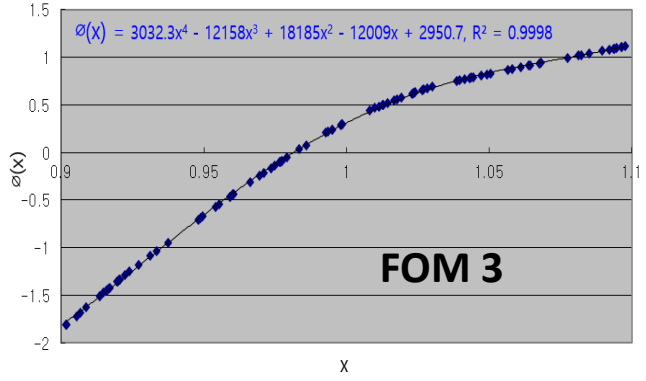

4. Results: surrogate models

❑ Linear relation between $\sum_i^p \emptyset_i^*(x_i)$ and $\theta^*(y)$

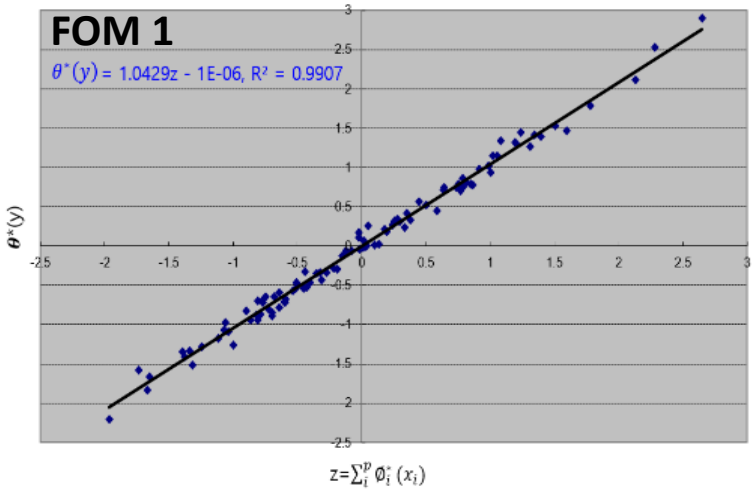

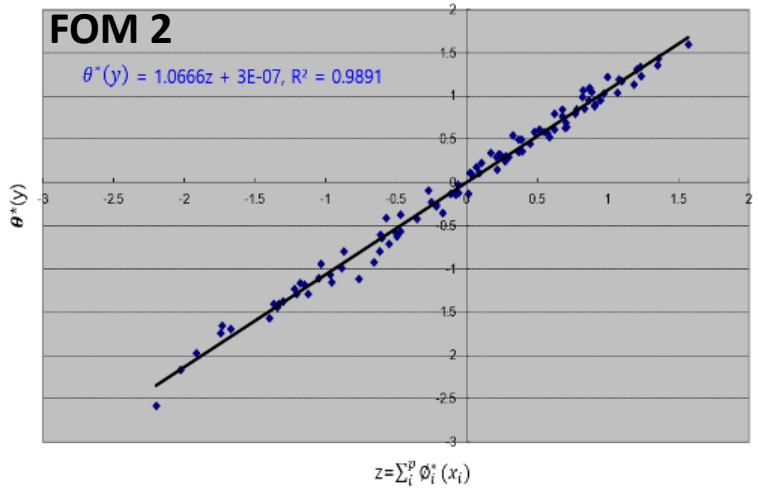

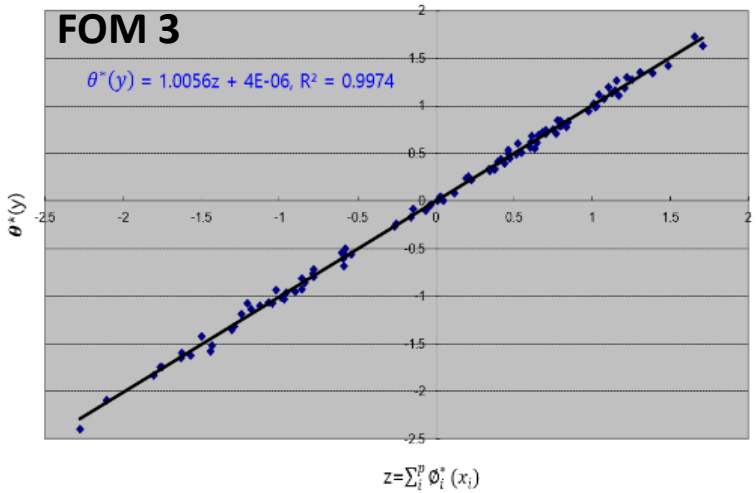

❑ Linear relation between y and $\theta(y)$

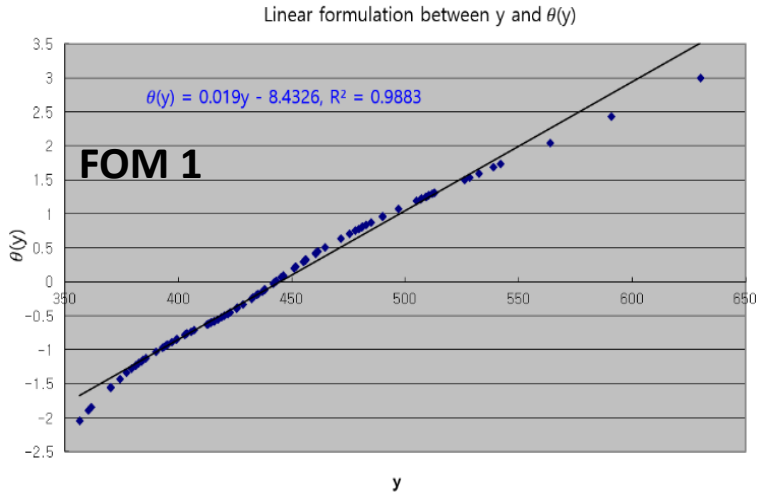

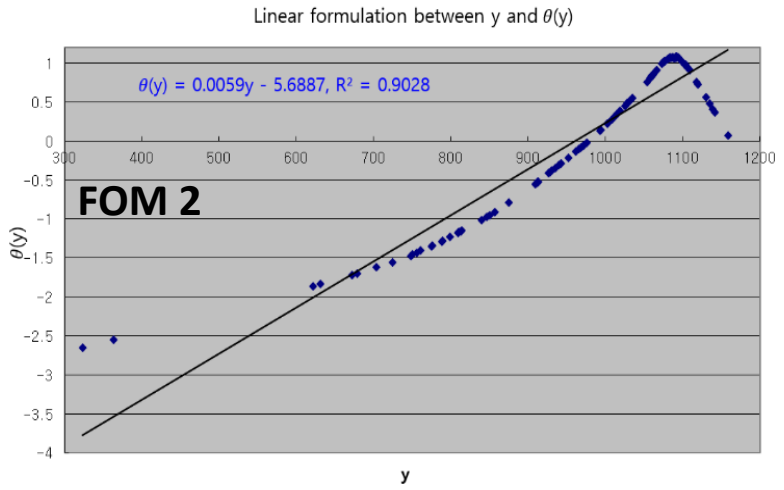

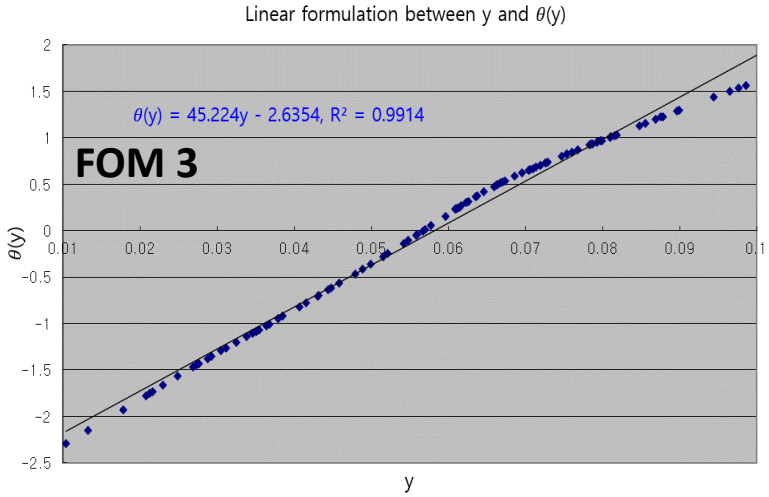

4. Results: surrogate models

❑ Based on the linear relation between $y=y_{ref}$ and y_{reg}

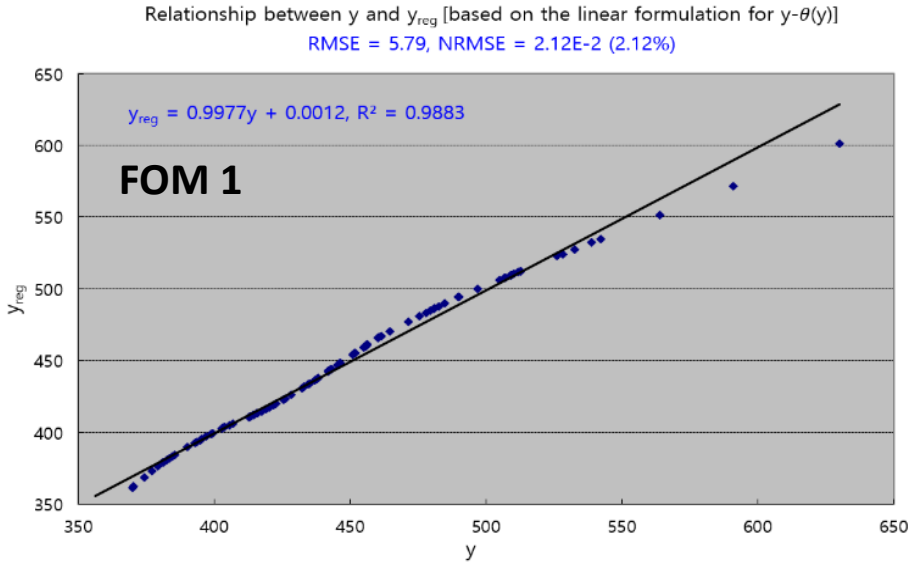

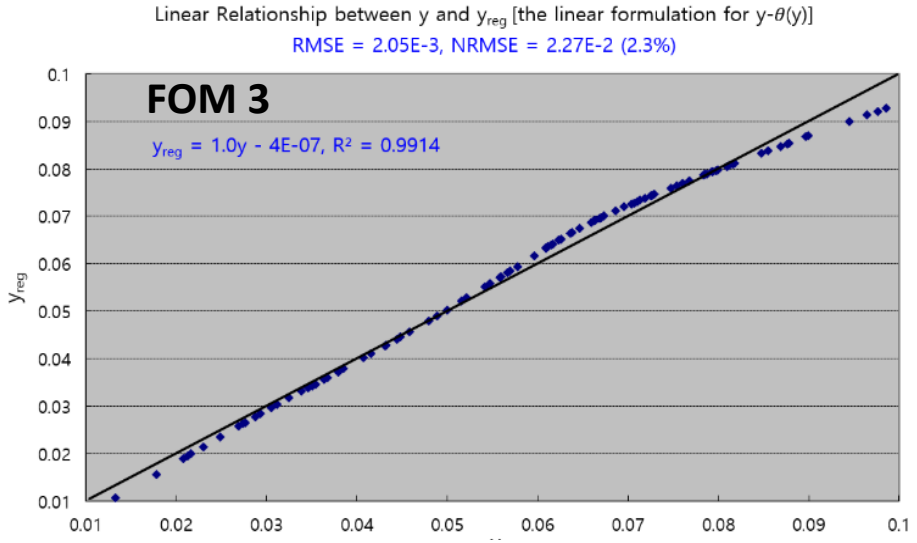

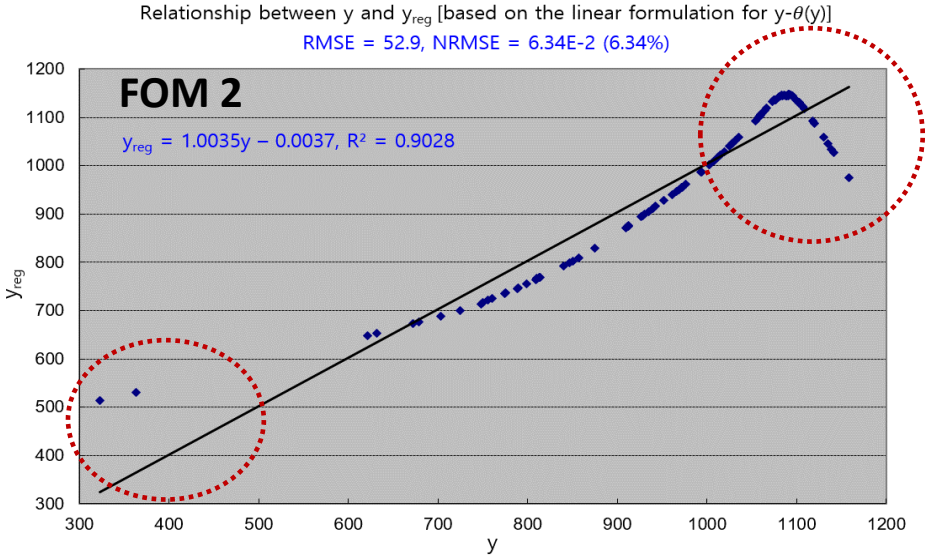

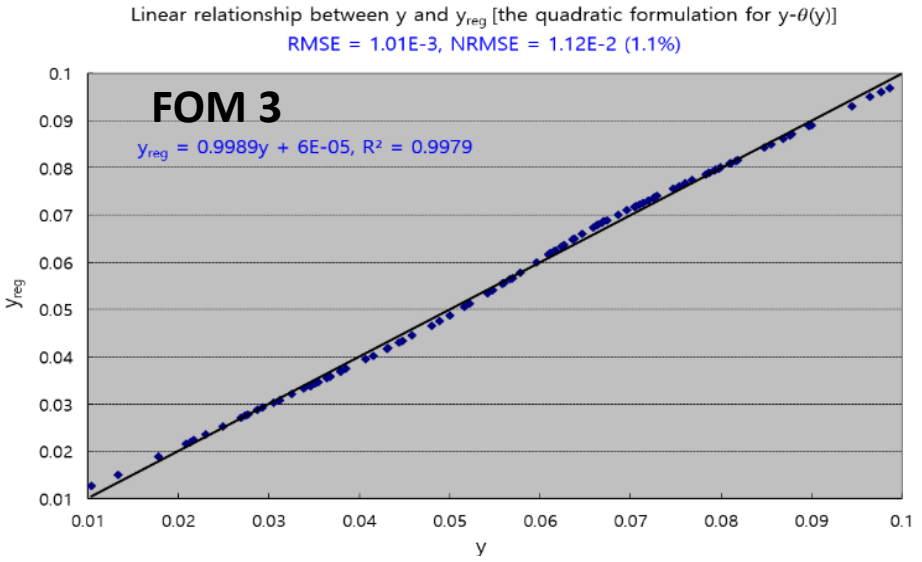

For the quadratic (≈ quasi-linear) relation between y and $\theta(Y)$

4. Results: surrogate models

❑ Difference between the ACE-based FOM values (y_{ace}) and the reference cases (y_{ref})

FOMs	Based on the linear regression between y_{ref} and y_{ace}		
	y-$\theta(y)$ relation	R^2	NRMSE (%)
FOM 1 (Y_1)	linear	0.9883	2.12
FOM 2 (Y_2)	linear	0.9028	6.34
FOM 3 (Y_3)	linear	0.9914	2.30
	Quadratic (≈quasi-linear)	0.9979	1.10

❑ Performance of the ACE-based surrogate models compared to the reference cases

FOMs	R^2 (R^2_{adj})			
	Ordinary linear regression		Ranked linear regression	
	REF	ACE	REF	ACE
FOM 1 (Y_1)	0.66 (0.57)	0.96 (0.95)	0.68 (0.57)	0.86 (0.81)
FOM 2 (Y_2)	0.40 (0.29)	0.92 (0.89)	0.47 (0.29)	0.72 (0.63)
FOM 3 (Y_3)	0.88 (0.84)	0.98 (0.97)	0.88 (0.84)	0.90 (0.87)

Root Mean Square Error (RMSE) = $\sqrt{\sum_{j=1}^{N}(\hat{y}_j - y_j)^2 / N}$; Normalized RMSE (NRMSE) = (RMSE) / $(y_{\max} - y_{\min})$

Ordinary linear regression equation: $\hat{Y} = \alpha_0 + \sum_{i=1}^{p} \alpha_i X_i$

4. Results: sensitivity analysis

❑ The ACE approach

- Based on the formulated ACE-transformed surrogate models, $\theta^*(Y_j) = \beta_0 + \sum_i^p \beta_i \emptyset_i^*(X_i)$, five types of correlation and regression analyses were carried out to identify key contributors that are most responsible for each FOM.
- The transformed variables [$\emptyset(x)$, $\theta(y)$] have a linear relationship, and when taking a linear or monotonic relation for y-$\theta(y)$, the formulated ACE surrogate models can well capture the code simulation results (x, y) within a few percent error bound.

❑ Relevant results

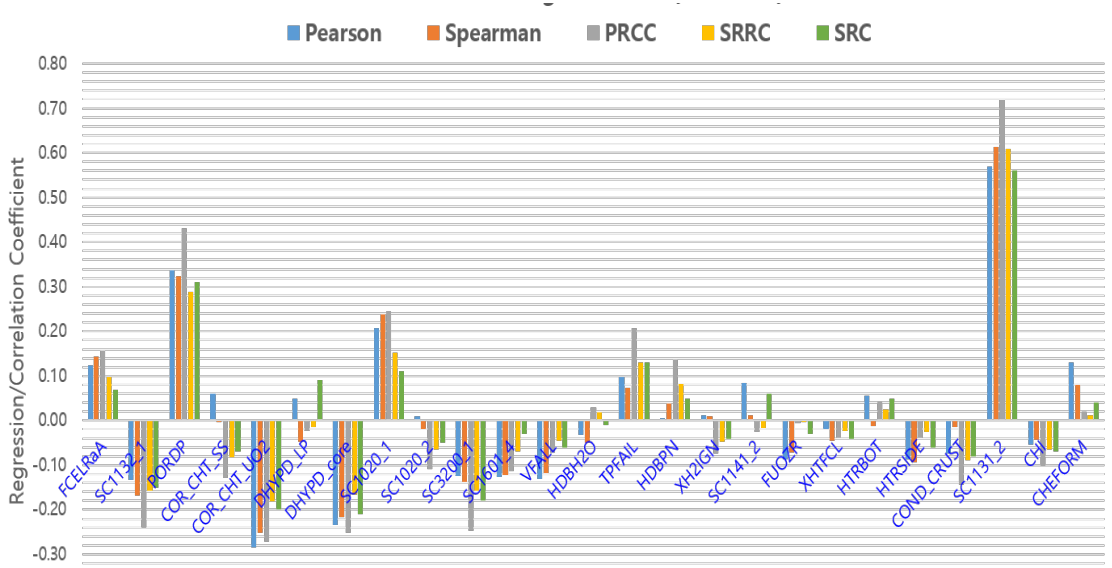

The Reference Case

FOM 1

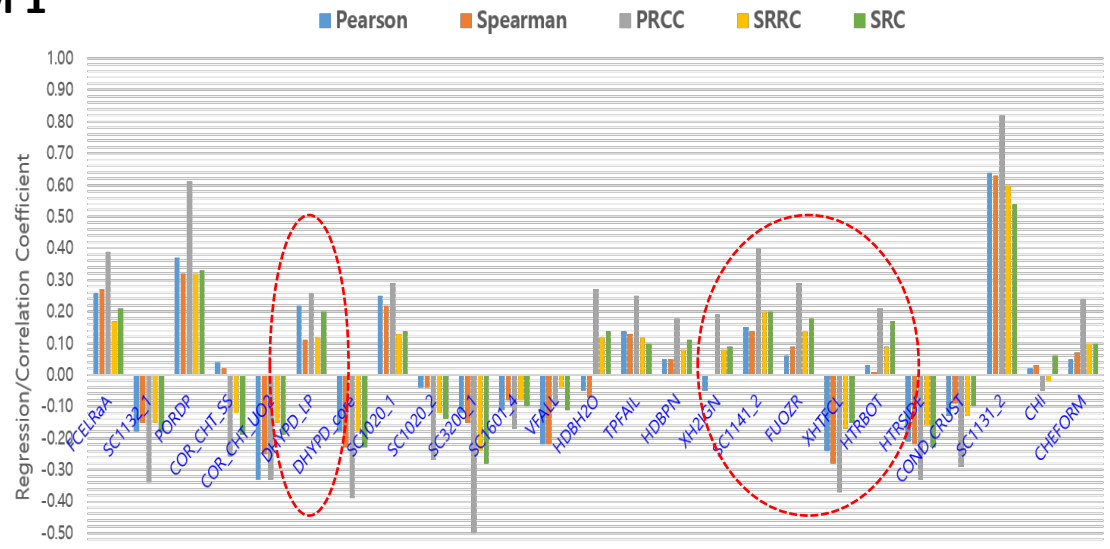

The ACE Approach

4. Results: sensitivity analysis

❑ Relevant analysis results

The Reference Case

The ACE Approach

FOM 2

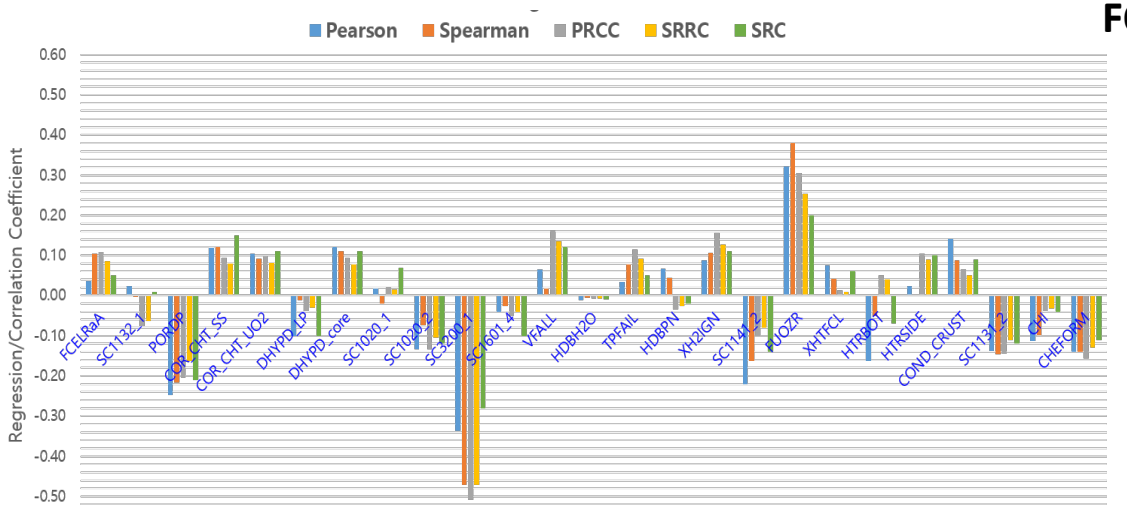

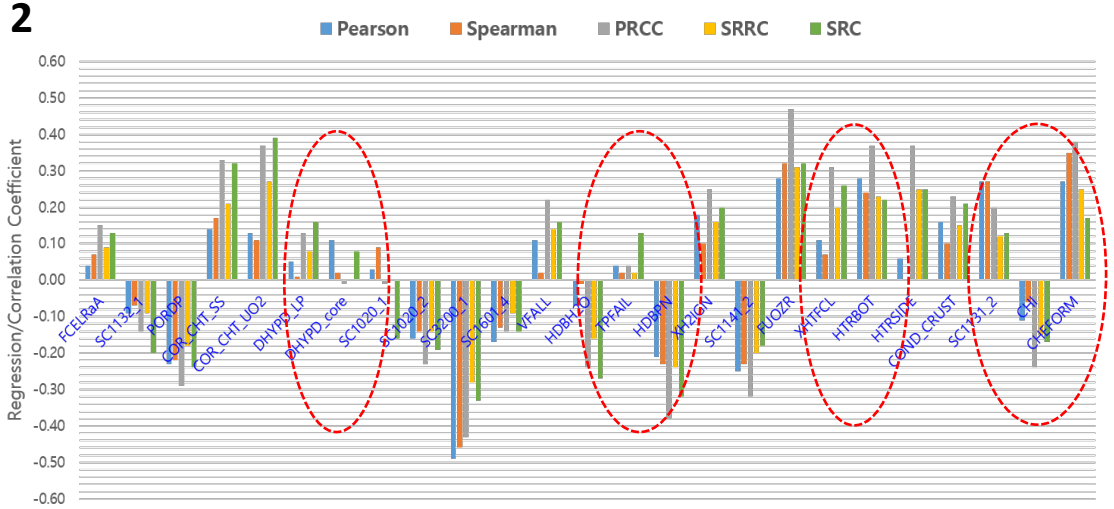

FOM 3

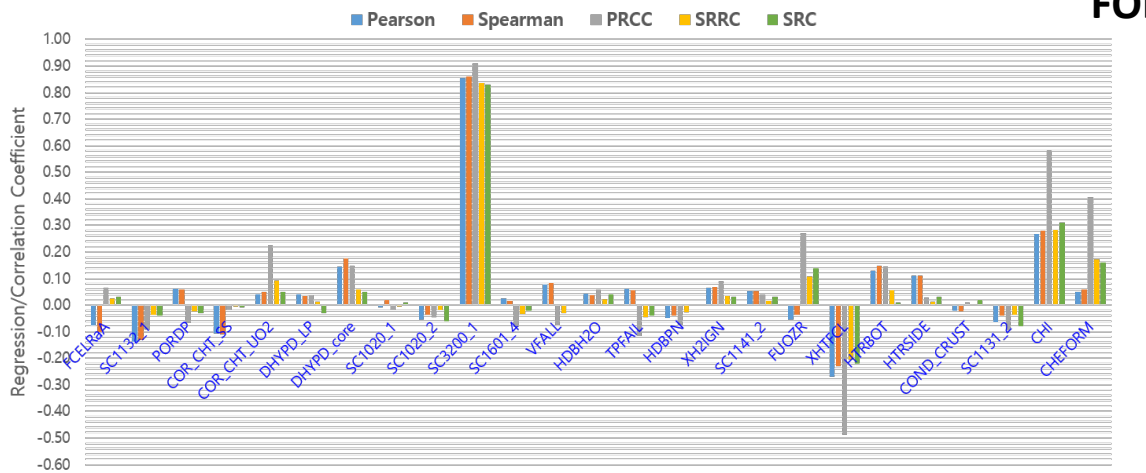

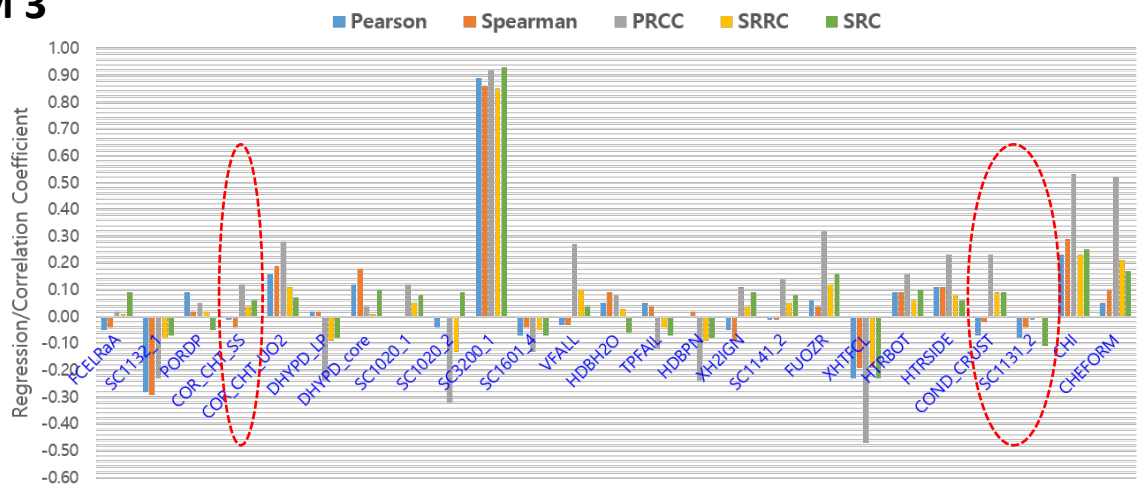

4. Results: sensitivity analysis

❑ Main contributors to each FOM (based on a weighted average of five indicators)

Rank	FOM 1		FOM 2		FOM 3
	REF	ACE	REF	ACE	REF/ACE
1	X_{23} (SC1131_2)		X_{10} (SC3200_1)		X_{10} (SC3200_1)
2	X_3 (PORDP)		X_{18} (FUOZR)		X_{24} (CHI)
3	X_5	X_{10}	X_3	X_{25}	X_{19}
4	X_7	X_1	X_{25}	X_{20}	X_{25}
5	X_8	X_7	X_{16}	X_{15}	X_{18}
6	X_2	X_2, X_5	X_{12}	X_5	X_5
7	X_{10}	X_7, X_9	X_9	X_{21}	X_7

❑ Key findings

- For FOM 3 having the highest regression performance, the importance of input parameters is almost the same for REF. & ACE cases, but for the remaining two FOMs, their importance somewhat differs depending on the regression performance.
- Relevant sensitivity indicators gave more reliable insights on the relative importance of input parameters, compared to the corresponding reference cases (based on the original code results).

5. Summary & conclusion

- The ACE algorithm-based surrogate model was explored **to advance the state-of-practice for U&S methods in the realm of severe accidents**.
- **Results explored for three reference cases demonstrate,**
  - the ACE-based surrogate models can lead to much better regression performance in terms of R^2 and NRMSE than the reference cases, consequently well capturing the original code simulation results with regard to the uncertainty within a few percent error bound.
  - the ACE surrogate model-based correlation and regression analyses could give much more reliable insights into the relative importance of the input parameters, compared to the corresponding reference cases.
  - whereas, it is noted that the ACE algorithm may be somewhat sensitive to outliers of the simulated data, as shown in FOM 2, thus necessitating appropriate methods like data screening to remove outliers before using the method.
- **Relevant approach can be used for U&S analysis of most safety analysis codes** (incl. SA and T/H) with the intent of capturing the best practices.

Thank you for your attention

SYSTEM IDENTIFICATION AND RANKING TABLE (SIRT) FOR CHEMICAL THERMODYNAMICS OF SEVERE ACCIDENTS

C. Journeau*
CEA,
IRESNE, DTN, Severe Accident Experimental Laboratory
Cadarache, F-13108 Saint-Paul-lez-Durance, France
christophe.journeau@cea.fr

S. Bechta, A. Komlev
Department of Nuclear Power Safety
KTH
Stockholm, Sweden
bechta@safety.sci.kth.se; komlev@kth.se

M. Kurata, H. Ohgi, T. Matsumoto, M. Afiqa
Japan Atomic Energy Agency
2-4 Shirakata, Tokai-mura, Naka-gun, Ibaraki, 319-1195, Japan
kurata.masaki@jaea.go.jp; ohgi.hiroshi@jaea.go.jp; matsumoto.toshinori@jaea.go.jp;
mohamad.afiqa@jaea.go.jp

M. Barrachin
IRSN
Cadarache, F13108 Saint-Paul-lez-Durance, France
marc.barrachin@irsn.fr

A. Quaini‡, C. Guéneau
Université Paris-Saclay
CEA, Service de Recherche en Corrosion et Comportement des Matériaux
F-91191, Gif-sur-Yvette, France
andrea.quaini@cea.fr; christine.gueneau@cea.fr

D. Bottomley
JRC
Karlsruhe, Germany
dboksb3@gmail.com

A. Itoh
Tokyo Institute of Technology, Laboratory for Zero-Carbon Energy
2-12-1 Ookayama, Meguro-ku, Tokyo, 152-8550, Japan
itoh.a.ae@m.titech.ac.jp

* Corresponding author

‡ Curent address : CEA, IRESNE, DER, Cadarache, F-13108 Saint-Paul-lez-Durance, France.

K. Nakamura
CRIEPI
2-6-1 Nagasaka, Yokosuka-shi, Kanagawa 240-0196, Japan
kinya@criepi.denken.or.jp

M. Steinbrück
Karlsruhe Institute of Technology
Karlsruhe, Germany
martin.steinbrueck@kit.edu

ABSTRACT

Within the second phase of the OECD/NEA project on Thermodynamic Characterisation of Fuel Debris and Fission Products Based on Scenario Analysis of Severe Accident Progression (TCOFF-2), a Systems Identification and Ranking Table (SIRT), has been derived from the usual PIRT and adapted to chemical thermodynamics and material science. Firstly, a draft list of systems of interests has been distributed to TCOFF-2 partners. After review, a final list of 154 systems has been considered. Then system ranking has been carried out. Two series of figures of merit have been considered: importance for safety including the contribution to severe accident phenomena and to fission product behaviour and source term as well as needs for further R&D, based on the lack of existing data and the needs to improve relevant existing thermodynamic databases (mostly NUCLEA and TAF-ID). Each participating organization provided ranking of the systems for these Figure of Merits. Relevance to safety has been organized in 10 columns: Classical LWR / High BU, High enrichment fuel/ Fukushima Daiichi, TMI2, Chornobyl/Near-term ATF cladding (Cr-coated Zry)/ Near-term ATF cladding (FeCrAl) /Long-term ATF cladding (SiC) /Advanced fuels (UN, U-Si) /Advanced Modular Reactors / Post-Accident Leaching). Received rankings have then been agglomerated and averaged. A dedicated finalization meeting has been held in June 2023 in which the systems having the highest relevance and the largest needs for improvement have been considered. It must be noted that some systems for which there is a rather good knowledge, like (U,O, Zr) have not been selected, nor systems in which thermodynamic results are very hard to attain due to kinetics effect such as (U,H,O). After some system grouping, consensus have been reached on a list of 20 systems (13 linked to current or near-term fuels and 7 linked to longer-term fuels) having the highest priority. They are Fe, Pu, O; PuO_2, UO_2, ZrO_2; Fe, Pu, U, Zr; CaO, SiO_2, UO_2; FeO_x, Cr_2O_3, SiO_2, UO_2, ZrO_2; Cr, Fe, Zr, O; Al_2O_3, Cr_2O_3, FeO, UO_2; Al, Cr, Fe, ; B, O, Zr; Cr, Cs, O; Cs, Si, O; B, Cs, O; Cs, O, Sr; SiC, UO_2; H_2O, SiC; PuO_2, SiC; Si, Pu, U; Cr, Si, O; N,O,U; (Eu,Sm),Zr,O.

KEYWORDS
Corium, Thermodynamic, Phase Diagrams, Ranking

1. INTRODUCTION

Within the second phase of the OECD/NEA project on Thermodynamic Characterisation of Fuel Debris and Fission Products Based on Scenario Analysis of Severe Accident Progression [1] (TCOFF-2), a Systems Identification and Ranking Table (SIRT), has been derived from the more classical PIRT (Phenomena Identification and Ranking Tables) [2] and adapted to chemical thermodynamics and material science. Instead of phenomena, it is chemical systems of interest that will be identified and then ranked in a table. This has been applied to severe accident phenomena with both current and advanced fuel materials. This work naturally took existing PIRT or priority ranking into account [3-9].

In a first section, the system identification process will be described. Then, the ranking phase will be detailed. Finally, the 20 systems with highest priority will be presented.

2. IDENTIFICATION OF SYSTEMS OF INTEREST

The objective is to identify the key thermodynamic systems to be studied to satisfactorily model the corium progression and the fission product behaviour in the various phases of a severe accident Severe accident phenomena were initially (in TCOFF-1 project [1]) divided in the expected time sequence into :

- Task Force 1 for In-Vessel Phenomena: fuel-cladding degradation, corium formation & relocation, vessel steel- corium interaction and vessel failure, and
- Task 2 for Ex-Vessel phenomena, such as corium and fission product release and molten concrete and corium interaction (MCCI).

For TCOFF-2 there were remaining early phase safety aspects: the degradation progression (fuel dissolution especially for ATF fuels (FeCrAl-cladding/UO2 fuel), hydrogen production (the effects of new systems with Fe-Cr-Al cladding). Current investigations indicate multiple vessel failure points particularly in unit 1 and the analyses from the first in-vessel corium samples will be used to improve initial calculations.
For the late phase safety such as the an accurate in-vessel corium (steel-Zr-U-O system) which is essential for the debris characterization of FDNPS accident; The current TAF-ID and NUCLEA databases need to be able accurately evaluate the expected phase relations and the theoretical solidification/liquefaction paths of concrete- fuel corium metallic/oxidic debris mixtures.
It also needed to take into account new Accident Tolerant Fuels materials (ATF; including advanced cladding and advanced control rods) where additional details of Cr-rich systems are high priority. Other new aspects include higher burn-up conventional fuels as well as advanced (Pu-containing) fuels and those of Advanced Modular Reactors. Finally, a rare earth fission product (Eu) was also included for verification of neutronic corium properties.
There was a need for further improvements in the MCCI modelling to include more additional concrete phases as well as fission product behaviour especially for volatile and /or soluble fission products (eg. Cs, Sr, Mo).
Firstly, a draft list of systems of interests has been distributed to experts from TCOFF-2 organizations. After review and introduction of missing systems, a final list of 158 systems has been considered. In particular, more fission products have been introduced in the list, more plutonium-containing systems have been proposed in view of high-burnup fuel field, as well as a small number of molten core-concrete interaction (MCCI) systems.

A series of 100 ternary systems (in alphabetical order) has been identified: (Al,Cs,O); (Al,Fe,O); (Al,Fe,U); (Al,Fe,Ni); (Al,Fe,Zr); (Al,Ni,O); (Al,O,U); (Al,O,Zr); (Al,U,Zr); (B,C,Zr); (B,Cr,Fe); (B,Cr,O); (B,Cs,O); (B,Fe,O); (B,Fe,U); (B,O,H); (B,O,Ru); (B,O,U); (B,O,Zr); (B,U,Zr); (Ba,Cr,O); (Ba,Fe,O); (Ba,La,O); (Ba,O,U); (Ba,O,Zr); (C,O,U); (C,O,Zr); (C,Si,Cr); (C,Si,Ni); (C,Si,U); (Cr,Cs,O); (Ca,Cr,O); (Ca,Fe,O); (Cr,Fe,Ni); (Cr,Fe,O); (Cr,Fe,Si); (Cr,Fe,U); (Cr,Fe,Zr); (Cr,La,O); (Cr,Ni,O); (Cr,Si,O); (Cr,Ni,Zr); (Cr,O); (Cr,O,Pu); (Cr,O,Sr); (Cr,O,U); (Cr,O,Zr); (Cr,Pu,U); (Cr,Pu,Zr); (Cr,U,Zr); (Cs,Fe,O); (Cs,Mo,O); (Cs,O,Ru); (Cs,O,Si); (Cs,O,U); (Cs,O,Zr); (Fe,La,O); (Fe,Mo,Sn); (Fe,Ni,O); (Fe,Ni,Si); (Fe,Ni,U); (Fe,Ni,Zr); (Fe,O); (Fe,O,Pu); (Fe,O,Si); (Fe,O,Sr); (Fe,O,U); (Fe,O,Zr); (Fe,Pu,U); (Fe,Pu,Zr); (Fe,U,Zr); (H,O,Zr); (H,C,Si); (H,Fe,Si); (H,Ni,O); (H,O,Si); (H,O,Zr); (La,O,Pu); (La,O,Sr); (La,O,U); (La,O,Zr); (Mo,O,Ru); (N,O,U); (N,O,Zr); (N,U,Zr); (Ni,O,Pu); (Ni,O,U); (Ni,O,Zr); (Ni,Pu,U); (Ni,Pu,Zr); (O,Pu,U); (O,Pu,Zr); (O,Ru); (O,Sn,U); (O,Sn,Zr); (O,Sr); (O,U,Zr); (Pu,U,Zr); (Si,Pu,U).

It has also been judged useful to introduce pseudobinaries, pseudoternaries and higher order systems to cover the scope of interest for severe accident phenomena and to focus future studies on specific compositional domains/sections which are set by reactor core material inventory and various material

interactions during severe accident progression, such as corium oxidation, melt interactions with different structural materials, MCCI, etc. A second list of 58 systems has been identified during this first round of the SIRT process (it also includes a few pseudobinaries). They are, in alphabetical order: (Al,Al_2O_3); (Al_2O_3,CaO,SiO_2); (Al_2O_3,CaO, FeO_x); (Al_2O_3,CaO,FeO_x,MgO); (Al_2O_3,CaO,FeO_x,SiO_2); (Al_2O_3,CaO,MgO); (Al_2O_3,CaO,Cr_2O_3,SiO_2); (Al_2O_3,Cr_2O_3,FeO,UO_2); (Al_2O_3,FeO_x,); (Al_2O_3,SiO_2,FeO_x); (Al_2O_3,SiO_2,MgO); (Al_2O_3,SiO_2,UO_2); (Al_2O_3,SiO_2,ZrO_2); (Al_2O_3,UO_2); (Al_2O_3,UO_2,ZrO_2); (Al_2O_3,ZrO_2); (Am,AmO_2); (B_4C,UO_2) ;(B_4C,ZrO_2); (Ca,CaO); (CaO,Fe_2O_3,SiO_2); (CaO,MgO,UO_2); (CaO,MgO,ZrO_2); (CaO,SiO_2,UO_2); (CaO,SiO_2,ZrO_2); (CaO,UO_2); (CaO,UO_2,ZrO_2); (CaO,ZrO_2); (Cr,Fe,Ni,O); (Cr,Fe,O,Zr); (Cr,H,O,Zr); (Cr_2O_3,FeO,UO_2), (CrO_3,Zr); (Cs,O,Sr,U); ([Eu,Sm],Zr,O); (FeO_x,SiO_2,UO_2); (FeO_x,SiO_2,ZrO_2); (FeO_x,Cr_2O_3,SiO_2,UO_2,ZrO_2); (MgO,SiO_2); (MgO,SiO_2,UO_2); (MgO,SiO_2,ZrO_2); (MgO,UO_2); (MgO,ZrO_2); (O,Sr,U,Zr); (Np,NpO_2); (Pu,PuO_2); (PuO_2,SiC); (PuO_2, UO_2, ZrO_2); (SiC,Cr_2O_3); (SiC,H_2O); (SiC,FeO), (SiC,NiO); (SiC,UO_2); (SiO_2,UO_2);(SiO_2,ZrO_2);(SiO_2,ZrO_2,UO_2); (U,UO_2); (Zr,ZrO_2).

3. RANKING OF SYSTEMS

Then system ranking has been carried out by the participating experts. It has been decided that in case of multiple experts from a partner organization, the votes shall be averaged so that there shall be one vote by organization.

Two series of Figures of Merit (FoM) have been considered: 1) importance for safety including severe accident phenomena and to fission product behavior and source term and 2) needs for further R&D, based on the lack of existing data and the needs to improve relevant existing thermodynamic databases (mostly NUCLEA [10] and TAF-ID[11]).

For the relevance to safety, 8 fields of application have been considered:

- Classical LWRs;
- High burnup, high enrichment fuel;
- Fukushima Daiichi, TMI2, Chornobyl-4 accidents;
- Near-term ATF cladding (Chromium coated);
- Near-term ATF cladding (Fe-Cr-Al);
- Long-term ATF cladding (SiC)
- Advanced fuels (UN, U-Si) ;
- Advanced Modular Reactors) ;
- Post-accident leaching.

A matrix table has been derived with a line for each identified system and a column for each domain of application. A ninth column, labelled “Other”, has been introduced to permit indicating any other application for which a system would be important. This relevance to safety is based on expert judgement informed by previous PIRT and prioritzation exercices such as [3-9]. The following ranking marks have been used to prioritize the importance to severe accident safety:

- 1: Not relevant;
- 2: Not important
- 3: Somewhat important
- 4: Very important

A second set of ranking has also been requested with respect to the level of knowledge with two columns, the first one being devoted to the existence of raw data and the second to the knowledge that has been introduced in the thermodynamic databases. The following marks have been used:

- 1: No data
- 2: Poor
- 3: Incomplete
- 4: Satisfactory

It must be noted that it has often been different experts that could vote on different columns of the ranking table, as the experts of accident scenarios are often not those of chemical system thermodynamic assessment.

In a first phase, each organization has independently conducted votes in order to fill this matrix. Marks coming from IRSN, CEA, Japanese participants, Swedish participants and JRC have been collected and averaged. As an example, Figure 1 presents the results for the 8 domains that have been given on average to some systems. For instance, system (H,O,Si) has been unanimously chosen as very important for the SiC cladding long-term ATFs but has low marks (below 2.25) for the other fields of application. The ternary (Fe,O,U) has been considered to be very important for most of the fields of application (with a slightly lower mark for post-accidental leaching issues) In particular, it is essentially important for the debris characterization of Fukushima Daiichi accident [17].

	A	B	C	D	E	F	G	H	I	J
1	Systems	Classical LWR	High BU, High enrichm	Fukushima Daiichi, TMI2, Chernobyl	Short term ATF (Cr-coa	Short term ATF (Fe	Long Term ATFs(SiC)	Advanced fuels(UN, U-Si)	Advanced Modular Reac	Post-Accident Leac
2		Importance to (severe accident) safety 1=not relevant, 2=not important, 3= somewhat important, 4 = very import								
56	Cs,O,Ru	2,00	2,00	2,00	2,00	2,00	2,00	3,00	2,00	2,50
57	Cs,O,Si	3,00	3,00	3,25	3,00	3,00	3,75	3,00	2,50	3,75
58	Cs,O,Sr	2,50	2,50	3,00	2,50	2,50	2,50	4,00	2,50	3,00
59	Cs,O,U	3,63	3,50	3,63	3,63	3,50	3,50	3,67	3,33	3,67
60	Cs,O,Zr	3,38	3,50	3,38	3,25	1,38	1,38	2,83	3,33	3,50
61	Fe,La,O	1,67	2,00	1,67	1,67	2,00	1,67	2,00	1,50	1,00
62	Fe,Mo,Sn	2,33	2,67	1,50	2,50	2,00	1,50	2,00	1,00	1,00
63	Fe,Ni,O	3,25	3,25	3,25	3,25	3,25	3,25	3,33	3,33	1,00
64	Fe,Ni,Si	2,00	2,00	2,00	2,00	2,00	2,75	2,67	1,67	1,00
65	Fe,Ni,U	3,40	3,40	3,00	3,00	3,25	2,75	3,33	3,00	1,00
66	Fe,Ni,Zr	3,75	3,75	3,75	3,50	1,88	1,38	3,17	3,67	1,00
67	Fe,O	3,50	3,50	3,75	3,50	4,00	3,00	3,00	3,67	1,00
68	Fe,O,Pu	3,75	4,00	3,75	3,75	3,75	3,75	3,75	3,67	3,50
69	Fe,O,Si	3,13	3,13	3,13	3,13	3,13	3,88	3,33	2,83	3,00
70	Fe,O,Sr	2,50	2,33	2,00	2,50	2,00	2,00	2,50	2,00	3,00
71	Fe,O,U	4,00	4,00	4,00	4,00	4,00	4,00	4,00	4,00	3,33
72	Fe,O,Zr	4,00	4,00	4,00	4,00	1,63	1,38	3,50	4,00	3,00
73	Fe,Pu,U	3,75	3,75	3,75	3,75	4,00	3,75	3,67	3,67	3,00
74	Fe,Pu,Zr	3,75	3,75	3,75	3,75	1,88	1,38	3,17	3,67	3,00
75	Fe,U,Zr	3,75	3,75	3,75	3,75	1,88	1,38	3,17	3,67	3,00
76	H,C,Si	1,75	1,67	1,67	2,25	1,67	4,00	1,50	1,50	1,00
77	H,Fe,Si	1,75	1,67	1,67	1,67	1,67	2,00	3,00	1,50	1,00
78	H,O,Si	2,00	1,50	2,33	1,50	1,50	4,00	2,00	1,50	2,00
79	H,O,Zr	3,50	4,00	3,50	4,00	1,83	1,50	1,75	2,50	2,00
80	H,Ni,O	2,50	2,00	2,50	2,00	2,00	2,00	2,50	2,00	1,00
81	La,O,Pu	3,00	3,00	3,00	3,00	3,00	3,00	3,33	3,00	2,50
82	La,O,Sr	2,50	2,33	2,00	2,00	2,00	2,00	2,50	2,00	2,50
83	La,O,U	2,67	3,00	2,67	2,67	2,67	2,67	2,50	3,00	3,00
84	La,O,Zr	2,67	3,00	2,67	2,67	1,50	1,83	2,25	3,00	3,00
85	Mo,O,Ru	2,67	2,67	2,00	2,50	2,50	2,00	3,00	2,00	1,00
86	N,O,U	1,67	1,67	2,00	1,67	1,67	1,67	4,00	1,50	1,00
87	N,O,Zr	2,67	2,67	2,75	2,67	1,50	1,83	3,50	1,50	1,00

Figure 1. An extract from the safety relevance submatrix.

Systems with average marks from 3.6 to 3.75 are highlighted in orange and those above 3.76 are highlighted in red.

Columns B: Classical LWRs, C: High Burn Up, high enrichment, D: Fukushima Daiichi, Chornobyl, Three Mile Island, E: Cr-coated ATF, F: FeCrAL ATF, G: Long Term ATF (SiC), H: SiC or U-Si, I: Advanced Modular Reactors, J: Post Accident Leaching.

Clearly, systems of high priority in terms of future experimental investigations will be those having large marks on the importance to severe accident safety and poor marks in the level of knowledge. For the (H,O,Si) ternary, the level of knowledge has received an average of 2 for the raw data and of 1 (no model) for the modelling in database. For the (Fe,O,U) example, it has received average marks of 2.5 for the raw data and 3 for the database (the apparent inconsistency arises from the fact that more people voted for the data column than for the database column).

On the other hand, a system like (O,Zr,U) has now a good knowledge (average marks of 3.3 and 3.5) due to the considerable work that have been conducted in the past years on this system. Therefore, although it received marks of 4 in 5 fields of interest, it has been decided not to rank it as the highest priority in order to concentrate on other systems of high importance but much lower knowledge.

Indeed, a SIRT table cannot be only determined by averaging the marks on such a large table. Collective expert judgement had to be introduced in the process to ensure that no system has been forgotten or unduly promoted. A dedicated one-day expert meeting has been held on June 26th at the Nuclear Energy Agency offices to discuss all the systems that had received marks above 3.6.

Some systems, e.g. (H,O,U), have not been selected despite their high importance and low knowledge, because thermodynamic factors are dominated by kinetics, and therefore the overall advantage of improving thermodynamic knowledge was considered to be small. Mostly, components of the (H,O,U) system for the severe accident analysis can be considered as U, UO_2, H_2O, O_2, H_2. It is unlikely that condensed and gas phases will be under thermodynamic equilibrium conditions during SA progression. Oxidation of UO2 fuel in steam during SA in case of cladding failure is controlled by the surface reaction, i.e. limited by the kinetic factor and the thermodynamic aspect has a lower impact [13-16].

A consensus has been reached between TCOFF-2 experts on a short list of systems having both high importance and rather poor knowledge. It included contributions from expert who had not participated to the initial ranking phase but provided some insights. After some grouping of closely related systems, a list of 20 priority systems has been adopted by the expert group. They can be grouped, depending on their respective fields of application.

3 systems are of high importance for the high burnup or MOX fuels:

1. Fe, Pu, O
2. PuO_2, UO_2, ZrO_2
3. Fe, Pu, U, Zr

Two systems of importance for Molten Core Concrete Interaction have been selected:

4. CaO, SiO_2, UO_2
5. FeO_x, Cr_2O_3, SiO_2, UO_2, ZrO_2

Two systems of importance for FeCrAl ATFs have also been selected:

6. Cr, Fe, Zr, O
7. Al_2O_3, Cr_2O_3, FeO, UO_2 and its suboxidized compositions.

It must be noted that this last system is also of interest for MCCI applications (in the case of Al_2O_3-rich concretes).

Five systems of importance for leaching and transport of radionuclides and neutron absorbers are also included:

8. B, Cs, O
9. B, O, Zr
10. Cr, Cs, O

11. Cs, O, Sr
12. Cs, Si, O

This concludes the list of highlighted systems for current fuel materials and near-term ATFs. There is also a list dedicated to longer-term materials that could affect severe accident scenarios. Three of them are linked to SiC cladding:

13. H_2O, SiC
14. SiC, UO_2
15. PuO_2, SiC

Two are linked to USi fuel:

16. Si, Pu, U
17. Cr, Si, O

One is linked to uranium nitride, UN fuel:

18. N, O, U

And, last but not least, one system linked to Accident Tolerant Control Rods (ACTRs) [12]:

19. (Eu,Sm),Zr,O

4. CONCLUSIONS

The PIRT process has been adapted to obtain a chemical System Identification and Ranking Table dedicated to severe accident phenomena in 8 fields of interest (reactor systems). This SIRT aims to improve data and extend optimisation in thermodynamic modelling of severe accidents.

Taking into account as Figures of Merits both the importance to severe accident safety studies and the knowledge of the systems (both in general and in the thermodynamic databases), a short list of 19 high priority systems has been established, 12 of which being linked to current reactor materials or short-term ATFs.

Establishing this SIRT will enable the subsequent Tasks within the TCOFF-2 project to focus their research. More generally, it is an invaluable tool to prioritize future material science research in severe accident safety studies. Finally, the new knowledge generated on these 19 systems should be introduced as soon as possible in thermodynamic databases such as TAF-ID or NUCLEA to be used in the modelling of severe accident phenomena.

ACKNOWLEDGMENTS

This work has been realized within the TCOFF-2 project of the OECD/NEA. The support of Alice Dufresne, as NEA scientific secretary of this project is gratefully acknowledged.

REFERENCES

1. M. Kurata, D. Costa, D. Bottomley, “Status of the OECD-NEA TCOFF project in support of Fukushima Daiichi Decommissioning” *Proc. HOTLAB 2019*, Mamallapuram (India), 8-12 Sep 2019.
2. G.E. Wilson, B.E. Boyack, “The Role of the PIRT Process in Experiments, Code development and Code Applications Associated with Reactor Safety Analysis”, *Nucl. Eng. Des. ,* **186**, pp. 23-37 (1998).
3. D. Magallon, A. Mailliat, J.M. Seiler, K. Atkhen, H. Sjövall, S. Dickinson, J. Jakab, L. Meyer, M. Buerger, K. Trambauer, L. Fickert, B.R. Sehgal, Z. Hozer, J. Bagues, F. Martin-Fuentes, R. Zeyen, A. Annunziato, M. El-Shanawany, S. Guentay, C. Tinkler, B. turland, L.E. Herranz Puebla, “European

expert network for the reduction of uncertainties in severe accident safety issues (EURSAFE)", *Nucl. Eng. Des.* **235** (2005) 309-346.
4. N. Sakai, H. Horie, H. Yanagisawa, T. Fuji, S. Mizokami, K. Okamoto, "Phenomena Identification Ranking Table (PIRT) for the MAAP Enhancement Project", *Proc. ICONE-21*, Chendu, China, Paper 16826 (2013).
5. S. Suehiro, J. Sugimoto, A. Hidaka, H. Okada, S. Mizokami, K. Okamoto, "Development of the source term PIRT based on findings during Fukushima Daiichi NPPs accident", *Nucl. Eng. Des.* **286**, pp. 163-174 (1015).
6. C. Journeau, V. Bouyer, N. Cassiaut-Louis, P. Fouquart, P. Piluso, G. Ducros, S. Gossé, C. Guéneau, A ; Quaini, B. Fluhrer, A. Miassoedov, J. Stuckert, M. Steinbrueck, S. Bechta, P. Kudinov, W. Ma, B.R. Sehgal, Z. Hozer, A. Guba, D. Manara, D. Bottomley, M. Fischer, G. Langrock, H. Schmidt, M. Kiselova, J. Zdarek, "SAFEST Roadmap for Corium Experimental research in Europe", *ASCE-ASME J. Risk Uncert. in Eng. Syst. B: Mech. Eng.*,**4**(3) 030901 (2018).
7. S. Bechta, W. Ma, A. Miassoedov, C. Journeau, K. Okamoto, D. Manara, D. Bottomley, M. Kurata, B.R. Sehgal, J. Stuckert, M. Steinbrueck, B. Fluhrer, T. Keim, M. Fischer, G. Langrock, P. Piluso, Z. Hozer, M. Kisselova, F. Belloni, M. Schyns, "On the EU-Japan roadmap for experimental research on corium behavior", *Ann. Nucl. Ener.*, **124**, pp. 541-547 (2019).
8. F. Fichot, L. carénini, N. Bakouta, H. Esmaili, L. Humphries, T. Laato, R. Le Tellier, L. Saas,T. Melnikov, P. Pandazis, S. Weber, R.J. Park, A. Filippov, V. Strizhov, "Elaboration of a Phenomena identification ranking Table (PIRT) for the modelling of In-Vessel retention", *Ann. Nucl. Ener.* **146**, 107617 (2020).
9. M. Khatib-Rahbar, M. Barrachin, R. Denning, J. Gabor, R. Gauntt, L.E. Herranz, R. Hobbins, D. Jacquemain, Y. Maruyama, J. Metcalf, D. Powers, S. Campbell, *Phenomena Identification Ranking Tables for Accident Tolerant Fuel Designs applicable to Severe Accident Conditions*, NUREG/CR-7282, ERI/NRC 21-204, Energy Research Inc. Rockville MD (2021).
10. S. Bakardjieva, M. Barrachin, S. Bechta, D. Bottomley, L. Brissonneau, B. Cheynet, E. Fischer, C. Journeau, M. Kiselova, L. Mezentseva, P. Piluso, T. Wiss, "Improvement of the European thermodynamic database NUCLEA", *Progr. Nucl. Ener.* **52,** pp. 84–96(2010).
11. C. Guéneau, N. Dupin, L. Kjellqvist, E. Geiger, M. Kurata, S. Gossé, E. Corcoran, A. Quaini, R. Hania, A.L. Smith, M.H.A. Piro, T. Besmann, P.E.A. Turchi, J.C. Dumas, M.J. Welland, T. ogata, B.O. Lee, J.R. Kennedy, C. Adkins, M. Bankhead, D. Costa, "TAF-ID : An international thermodynamic database for nuclear fuels applications", *Calphad*, **72**, 102112 (2021).
12. H. Ohta, K. Nakamura, T. Ogata, F. Nagase, "Development of Accident Tolerant Control Rod for Light Water Reactor", *Proc. Top Fuel 2016*, Boise ID, 11-15 Sep 2016.
13. D. S. Cox, F. C. Iglesias C. E. L. Hunt, N. A. Keller, R. D. Barrand, J. R. Mitchell, R. F. O'Connor. "Oxidation of UO2 in air and steam with relevance to fission product releases". In *Proc. Symp. Chemical Phenomena Associated with Radioactivity Releases During Severe Nuclear Plant Accidents*, NUREG/CP-0078, pp. 2–35 to 2–49, Anaheim, California, September 9-12 1986. U.S. Nuclear Regulatory Commission.
14. J. Abrefah, A. de Aguiar Braid, W. Wang, Y. Khalil, and D. R. Olander, "High temperature oxidation of UO2 in steam-hydrogen mixtures". *J. Nucl. Mater.,* **208**, pp. 98–110 (1994).
15. K. Une, M. Imamura, M. Amaya, Y. Korei. "Fuel oxidation and irradiation behaviors of defective BWR fuel rods", *J. Nucl. Mater.*, **223**, pp. 40–50 (1995).
16. M. Imamura, K. Une, "High temperature steam oxidation of UO2 fuel pellets", *J. Nucl. Mater.*, 247, pp. 131–137 (1997).
17. H. Ohgi, Y. Nagae, M. Kurata, Thermodynamic Evaluation on Solidification Path for U-Zr-Fe-O Corium, *Proceedings of the International Topical Workshop on Fukushima Decommissioning Research, FDR2022*, J-village, Japan (2022).

SYSTEM IDENTIFICATION AND RANKING TABLE (SIRT) FOR CHEMICAL THERMODYNAMICS OF SEVERE ACCIDENTS

Christophe Journeau (CEA, IRESNE), S. Bechta, A. Komlev (KTH), M. Kurata, H. Ohgi, T. Matsumoto, M. Afiqa (JAEA), M. Barrachin (IRSN), A. Quaini, C. Guéneau (CEA, ISAS), D.Bottomley (JRC), A. Itoh (Tokyo Tech), K. Nakamura (CRIEPI), M. Steinbrück (KIT)

OECD/NEA TCOFF2 project

ERMSAR 2024

11th Conference on
SEVERE ACCIDENTS RESEARCH
May 13-16, 2024 – Stockholm, Sweden

Outline

1. Context
2. System Identification
3. and Ranking Table
4. Conclusions

The OECD/NEA TCOFF-2 Project

Thermodynamic Characterization Of Fuel Debris and Fission Products

- **Task-1**: **<u>Prioritisation of the material science issues related to the severe accidents (SA) study</u>**
- **Task-2**: Improvement of the materials science knowledge regarding fuel core degradation and FP release (UO_2-Zry and ATFs)
- **Task-3**: Implementation of improved knowledge for the simulation of the accident behavior (UO_2-Zry and ATFs)
- **Task-4**: Extension of the leaching experimental database to better evaluate mid and long-term stability of degraded cores
- **Task-5**: Training and Education

This includes workshops and an International Call for Research Proposals, and sponsors students on exchanges & courses.

System Identification and Ranking Table (SIRT)

- SIRT has been derived from the more classical PIRT (Phenomena Identification and Ranking Tables)
  - adapted to chemical thermodynamics and material science.

- Instead of **phenomena**, it is chemical **systems** of interest that will be
  - **identified**
  - and then **ranked** in a **table**.
- This has been applied to severe accident phenomena
  - with both current and
  - short-term/long-term advanced fuel materials.
- This work naturally took existing PIRT or priority ranking into account
  - *Identify systems that are relevant for the priority issues*

System Identification and Ranking Table

- Figures of Merit (FoMs):
  - Importance for safety including
    - severe accident phenomena
    - Fission Product behavior and source term
  - Needs of further R&D
    - Lack of data
    - Need of improvement of database(s)
- Japanese partners preovided tables helping to fill the System Identification and Ranking Table from an analysis of severe accident phenomena for each configuration.
  - **Evaluation subjects** are: (a) accident phenomena for which improvement of materials reaction/interaction understanding is necessary, (b) relevant materials reaction/interactions, (c) relevant SA-model development, (d) thermodynamic systems to be improved and the priority, (e) current status of thermodynamic databases, (f) important lack of knowledge, and (g) expected tasks in TCOFF-2.

Schedule of work

1

February 2023

Draft identification of systems of interest send to TCOFF2 partners

2

April 2023

Inclusion of partners suggestion

Final list of 154 systems to be ranked

3

May 2023

Ranking by 5 participating organizations

1 ranking/partner

May include contributions of several experts

4

June 2023

Agglomeration of received ranks

Averaging

5

End June 2023:

Vote finalization

Consensus building to select priority systems

1. System Identification

TCOFF2 scope of interest for System Identification

8 fields of application have been considered:

- Classical LWRs;
  - Fuel degradation and hydrogen production
  - Fission Product releases
  - Late in-vessel: molten pool in lower head,…
  - Ex-vessel: MCCI,…
  - Criticality issues
- High burnup, high enrichment fuel;
- Fukushima Daiichi, TMI2, Chornobyl-4 accidents;
- Near-term ATF cladding (Chromium coated);
- Near-term ATF cladding (Fe-Cr-Al);
- Long-term ATF cladding (SiC)
- Advanced fuels (UN, U-Si)
- Advanced Modular Reactors
- Post-accident leaching.

Links with existing PIRTs and research prioritizations

Ternary systems : 100 systems identified

(Al,Cs,O); (Al,Fe,O); (Al,Fe,U); (Al,Fe,Ni); (Al,Fe,Zr); (Al,Ni,O); (Al,O,U); (Al,O,Zr); (Al,U,Zr); (B,C,Zr); (B,Cr,Fe); (B,Cr,O); (B,Cs,O); (B,Fe,O); (B,Fe,U); (B,O,H); (B,O,Ru); (B,O,U); (B,O,Zr); (B,U,Zr); (Ba,Cr,O); (Ba,Fe,O); (Ba,La,O); (Ba,O,U); (Ba,O,Zr); (C,O,U); (C,O,Zr); (C,Si,Cr); (C,Si,Ni); (C,Si,U); (Cr,Cs,O); (Ca,Cr,O); (Ca,Fe,O); (Cr,Fe,Ni); (Cr,Fe,O); (Cr,Fe,Si); (Cr,Fe,U); (Cr,Fe,Zr); (Cr,La,O); (Cr,Ni,O); (Cr,Si,O); (Cr,Ni,Zr); (Cr,O); (Cr,O,Pu); (Cr,O,Sr); (Cr,O,U); (Cr,O,Zr); (Cr,Pu,U); (Cr,Pu,Zr); (Cr,U,Zr); (Cs,Fe,O); (Cs,Mo,O); (Cs,O,Ru); (Cs,O,Si); (Cs,O,U); (Cs,O,Zr); (Fe,La,O); (Fe,Mo,Sn); (Fe,Ni,O); (Fe,Ni,Si); (Fe,Ni,U); (Fe,Ni,Zr); (Fe,O); (Fe,O,Pu); (Fe,O,Si); (Fe,O,Sr); (Fe,O,U); (Fe,O,Zr); (Fe,Pu,U); (Fe,Pu,Zr); (Fe,U,Zr); (H,O,Zr); (H,C,Si); (H,Fe,Si); (H,Ni,O); (H,O,Si); (H,O,Zr); (La,O,Pu); (La,O,Sr); (La,O,U); (La,O,Zr); (Mo,O,Ru); (N,O,U); (N,O,Zr); (N,U,Zr); (Ni,O,Pu); (Ni,O,U); (Ni,O,Zr); (Ni,Pu,U); (Ni,Pu,Zr); (O,Pu,U); (O,Pu,Zr); (O,Ru); (O,Sn,U); (O,Sn,Zr); (O,Sr,U); (O,U,Zr); (Pu,U,Zr); (Si,Pu,U).

Pseudobinaries, pseudoternaries and higher order systems: 58 systems

(Al,Al_2O_3); (Al_2O_3,CaO,SiO_2); (Al_2O_3,CaO, FeO_x); (Al_2O_3,CaO,FeO_x,MgO); (Al_2O_3,CaO,FeO_x,SiO_2); (Al_2O_3,CaO,MgO); (Al_2O_3,CaO,Cr_2O_3,SiO_2); (Al_2O_3,Cr_2O_3,FeO,UO_2); (Al_2O_3,FeO_x,); (Al_2O_3,SiO_2,FeO_x); (Al_2O_3,SiO_2,MgO); (Al_2O_3,SiO_2,UO_2); (Al_2O_3,SiO_2,ZrO_2); (Al_2O_3,UO_2); (Al_2O_3,UO_2,ZrO_2); (Al_2O_3,ZrO_2); (Am,AmO_2); (B_4C,UO_2) ;(B_4C,ZrO_2); (Ca,CaO); (CaO,Fe_2O_3,SiO_2); (CaO,MgO,UO_2); (CaO,MgO,ZrO_2); (CaO,SiO_2,UO_2); (CaO,SiO_2,ZrO_2); (CaO,UO_2); (CaO,UO_2,ZrO_2); (CaO,ZrO_2); (Cr,Fe,Ni,O); (Cr,Fe,O,Zr); (Cr,H,O,Zr); (Cr_2O_3,FeO,UO_2), (CrO_3,Zr); (Cs,O,Sr,U); ([Eu,Sm],Zr,O); (FeO_x,SiO_2,UO_2); (FeO_x,SiO_2,ZrO_2); (FeO_x,Cr_2O_3,SiO_2,UO_2,ZrO_2); (MgO,SiO_2); (MgO,SiO_2,UO_2); (MgO,SiO_2,ZrO_2); (MgO,UO_2); (MgO,ZrO_2); (O,Sr,U,Zr); (Np,NpO_2); (Pu,PuO_2); (PuO_2,SiC); (PuO_2, UO_2, ZrO_2); (SiC,Cr_2O_3); (SiC,H_2O); (SiC,FeO), (SiC,NiO); (SiC,UO_2); (SiO_2,UO_2);(SiO_2,ZrO_2);(SiO_2,ZrO_2,UO_2); (U,UO_2); (Zr,ZrO_2).

2. Ranking Table

Ranking Procedure

Relevance to safety

- 11 columns
  - Classical LWR / High BU, High enrichment fuel/ Fukushima Daiichi, TMI2, Chernobyl/ Short term ATF (Cr-coated Zry)/ Short term ATF (FeCrAl) /Long Term ATFs (SiC) /Advanced fuels (UN, U-Si) / Advanced Modular Reactors / Post-Accident Leaching/ Other
- 4 levels
  - 1=not relevant,
  - 2=not important,
  - 3= somewhat important,
  - 4 = very important

Level of Knowledge

- 2 columns
  - Raw data
  - Database
- 4 levels
  - 1:none
  - 2:poor
  - 3:incomplete
  - 4: satisfactory

Preliminary ranking made by participating organizations
Averaging, pre-selection
In-person meeting to achieve expert-judgement consensus
(possibility to amend previous votes, following discussions)

Excerpt from the table

Systems	Classical LWR	High BU, High enrichm	Fukushima Daiichi, TMI2, Chernobyl	Short term ATF (Cr-coa	Short term ATF (Fe	Long Term ATFs(SiC)	Advanced fuels(UN, U-Si)	Advanced Modular Reac	Post-Accident Leac	Other (specify)	Raw Data	Databases
	Importance to (severe accident) safety 1=not relevant, 2=not important, 3= somewhat important, 4 = very important.										Knowledge	
Cs,O,Ru	2,00	2,00	2,00	2,00	2,00	2,00	3,00	2,00	2,50	Cs ruthenates air ?2	0,00	0,00
Cs,O,Si	3,00	3,00	3,25	3,00	3,00	3,75	3,00	2,50	3,75	Cs tranport2	2,50	3,00
Cs,O,Sr	2,50	2,50	3,00	2,50	2,50	2,50	4,00	2,50	3,00	4	1,00	0,00
Cs,O,U	3,63	3,50	3,63	3,63	3,50	3,50	3,67	3,33	3,67	ATF Cr-doped UO2Cs spec	2,00	3,00
Cs,O,Zr	3,38	3,50	3,38	3,25	1,38	1,38	2,83	3,33	3,50	ATF Cr-doped UO2Cs spec	2,00	3,00
Fe,La,O	1,67	2,00	1,67	1,67	2,00	1,67	2,00	1,50	1,00	2	1,67	1,00
Fe,Mo,Sn	2,33	2,67	1,50	2,50	2,00	1,50	2,00	1,00	1,00		0,50	1,00
Fe,Ni,O	3,25	3,25	3,25	3,25	3,25	3,25	3,33	3,33	1,00	SS oxidation4	3,33	3,50
Fe,Ni,Si	2,00	2,00	2,00	2,00	2,00	2,75	2,67	1,67	1,00	Nickel minor4	0,00	0,50
Fe,Ni,U	3,40	3,40	3,00	3,00	3,25	2,75	3,33	3,00	1,00	Nickel minor4	0,50	1,00
Fe,Ni,Zr	3,75	3,75	3,75	3,50	1,88	1,38	3,17	3,67	1,00	interaction Zr/SS4	2,67	3,00
Fe,O	3,50	3,50	3,75	3,50	4,00	3,00	3,00	3,67	1,00	SS oxidation4	3,50	4,00
Fe,O,Pu	3,75	4,00	3,75	3,75	3,75	3,75	3,75	3,67	3,50	4	1,50	1,50
Fe,O,Si	3,13	3,13	3,13	3,13	3,13	3,88	3,33	2,83	3,00	4	3,00	4,00
Fe,O,Sr	2,50	2,33	2,00	2,50	2,00	2,00	2,50	2,00	3,00	4	2,00	0,50
Fe,O,U	4,00	4,00	4,00	4,00	4,00	4,00	4,00	4,00	3,33	IVR4	2,50	3,00
Fe,O,Zr	4,00	4,00	4,00	4,00	1,63	1,38	3,50	4,00	3,00	IVR4	2,67	3,00
Fe,Pu,U	3,75	3,75	3,75	3,75	4,00	3,75	3,67	3,67	3,00	IVR4	1,50	1,00
Fe,Pu,Zr	3,75	3,75	3,75	3,75	1,88	1,38	3,17	3,67	3,00	IVR4	1,50	1,00
Fe,U,Zr	3,75	3,75	3,75	3,75	1,88	1,38	3,17	3,67	3,00	IVR4	3,00	3,50
H,C,Si	1,75	1,67	1,67	2,25	1,67	4,00	1,50	1,50	1,00	2	1,33	0,50
H,Fe,Si	1,75	1,67	1,67	1,67	1,67	2,00	3,00	1,50	1,00	2	0,00	0,50
H,O,Si	2,00	1,50	2,33	1,50	1,50	4,00	2,00	1,50	2,00	SiC vapor.3	1,33	0,50
H,O,Zr	3,50	4,00	3,50	4,00	1,83	1,50	1,75	2,50	2,00	Zr oxidation4	1,50	2,50
H,Ni,O	2,50	2,00	2,50	2,00	2,00	2,00	2,50	2,00	1,00	3	0,00	0,50
La,O,Pu	3,00	3,00	3,00	3,00	3,00	3,00	3,33	3,00	2,50	3	1,50	1,00
La,O,Sr	2,50	2,33	2,00	2,00	2,00	2,00	2,50	2,00	2,50	34	1,50	0,50
La,O,U	2,67	3,00	2,67	2,67	2,67	2,67	2,50	3,00	3,00	La distribution Zr/U3	2,67	3,00
La,O,Zr	2,67	3,00	2,67	2,67	1,50	1,83	2,25	3,00	3,00	La distribution Zr/U3	2,33	1,00
Mo,O,Ru	2,67	2,67	2,00	2,50	2,50	2,00	3,00	2,00	1,00	3	0,00	0,50
N,O,U	1,67	1,67	2,00	1,67	1,67	1,67	4,00	1,50	1,00	2	0,00	0,50
N,O,Zr	2,67	2,67	2,75	2,67	1,50	1,83	3,50	1,50	1,00	Air ingress2	0,00	0,50
N,U,Zr	1,67	1,67	2,00	1,67	1,50	1,83	3,25	1,50	1,00	2	0,00	0,50

... average CEA IRSN (marks1-4) JAPAN Sweden JRC

- Average of received inputs
- Some examples:
  - system (H,O,Si) has been unanimously chosen as very important for the SiC cladding long-term ATFs but has low marks (below 2.25/4) for the other fields of application and poor mark (0.5/4) on Database knowledge.
  - system like (O,Zr,U) has now a good knowledge (average marks of 3.3 and 3.5/4) due to the considerable work that have been conducted in the past years on this system.
    - it received marks of 4/4 in 5 fields of interest,
    - Nevertheless it has been decided NOT to rank it as the highest priority in order to concentrate on other systems of high importance but much lower knowledge.
  - (Fe,O,U) has also been considered to be very important for most of the fields of application, in particular for Fukushima Daiichi fuel debris issues, but has rather good knowledge marks of 2.5-3/4, so is not selected.

19 high priority systems have been adopted by TCOFF2 expert group (1/3)

3 systems are of high importance for the high burnup or MOX fuels:

- Fe, Pu, O
- PuO_2, UO_2, ZrO_2
- Fe, Pu, U, Zr

Two systems of importance for Molten Core Concrete Interaction have been selected:

- CaO, SiO_2, UO_2
- FeO_x, Cr_2O_3, SiO_2, UO_2, ZrO_2

Two systems of importance for Cr-coated and FeCrAl ATFs have also been selected:

- Cr, Fe, Zr, O
- Al_2O_3, Cr_2O_3, FeO, UO_2 and its suboxidized compositions.

19 high priority systems have been adopted by TCOFF2 expert group (2/3)

Five systems of importance for leaching and transport of radionuclides and neutron absorbers are also included:

- B, Cs, O
- B, O, Zr
- Cr, Cs, O
- Cs, O, Sr
- Cs, Si, O

<u>For the longer-term ATFs,</u>

Three systems are linked to SiC cladding:

- H2O, SiC
- SiC, UO2
- PuO2, SiC

19 high priority systems have been adopted by TCOFF2 expert group (3/3)

Two systems are linked to USi fuel:

- Si, Pu, U
- Cr, Si, O

One that is linked to uranium nitride, UN fuel:

- N, O, U

and, one system linked to Accident Tolerant Control Rods (ACTRs) :

- (Eu,Sm), Zr, O

Conclusions

Conclusions

- PIRT process has been adapted to obtain a chemical System Identification and Ranking Table
  - Dedicated to 8 fields of interest related to severe accidents
- Taking into account as Figures of Merits both the importance to severe accident safety studies and the knowledge of the systems a short list of 19 high priority systems has been established,
  - 12 being linked to current reactor materials or short-term ATFs.
  - 7 linked to longer-term ATFs
- This SIRT enables the subsequent Tasks within the TCOFF-2 project to focus their research.
- More generally, it is an invaluable tool to prioritize future material science research in severe accident safety studies.
- Finally, the new knowledge generated on these 19 systems should be introduced as soon as possible in thermodynamic databases such as TAF-ID or NUCLEA to be used in the modelling of severe accident phenomena.

Thank you for your attention!

Any questions ?

ERMSAR 2024

11th Conference on
SEVERE ACCIDENTS RESEARCH
May 13-16, 2024 – Stockholm, Sweden

CEA CADARACHE
13108 Saint-Paul-lez-Durance
France
Christophe.journeau@cea.fr
+ 33 4 42 25 70 00

The 11th European Review Meeting on Severe Accidents Research

May 13-16, 2024, Royal Institute of Technology, Stockholm, Sweden

TECHNICAL SESSION 4.2: SEVERE ACCIDENT SCENARIOS - SMALL MODULAR REACTORS

Chairs: T. Lind (PSI), A. Bentaib (IRSN)

ID77	**Analysis of Postulated Severe Accidents in Generic Integral PWR Small Modular Reactors in the frame of the Horizon Euratom SASPAM-SA Project** F. Gabrielli (KIT)	**Paper Presentation**
ID116	**Update on Severe Accident Analysis Research at CNL for Small Modular and Advanced Reactor Designs** A. Morreale (CNL)	**Paper Presentation**
ID127	**Application of the Probabilistic Method to Propagate Input Uncertainty on a DBA Sequence in a Generic iPWR** G. Grippo (ENEA)	**Paper Presentation**
ID04	**Comparison between EDF MAAP5.04 and ASTECv3 codes on an hypothetical Severe Accident on the ELSMOR project NUWARD-Like SMR Design** J. Bittan (EdF)	**Paper Presentation**

ANALYSIS OF POSTULATED SEVERE ACCIDENTS IN GENERIC INTEGRAL PWR SMALL MODULAR REACTORS IN THE FRAME OF THE HORIZON EURATOM SASPAM-SA PROJECT

F. Gabrielli*
Karlsruhe Institute of Technology
Hermann-von-Helmholtz-Platz, 1,76344 Eggenstein-Leopoldshafen, Germany
fabrizio.gabrielli@kit.edu

F. Mascari[1], A. Bersano[1], P. Maccari[1], S. Ederli[1], G. Grippo[1,2], G. Agnello[1,3]
[1] ENEA, [2] UNIBO, [3]UNIPA, Italy
fulvio.mascari@enea.it, andrea.bersano@enea.it, pietro.maccari@enea.it, stefano.ederli@enea.it, gianmarco.grippo2@unibo.it, giuseppe.agnello04@unipa.it

M. E. Cazado, V.H. Sanchez-Espinoza
Karlsruhe Institute of Technology
Hermann-von-Helmholtz-Platz, 1,76344 Eggenstein-Leopoldshafen, Germany
mauricio.cazado@kit.edu, victor.sanchez@kit.edu

M. Di Giuli
Tractebel Engineering
Boulevard S. Bolivar 36,1000, Bruxelles, Belgium
mirco.digiuli@tractebel.engie.com

J. Bittan, N. Bakouta
Electricité de France
7 boulevard Gaspard Monge, 91120 Palaiseau, France
jeremy.bittan@edf.fr, nikolai.bakouta@edf.fr

M. Malicki, T. Lind
Paul Scherrer Institut
Forschungsstrasse 111, CH-5232 Villigen PSI, Switzerland
mateusz.malicki@psi.ch, terttaliisa.lind@psi.ch

M. Makarenko, Yu. Yesipenko, O. Zhabin, D. Gumenyuk
State Scientific and Technical Center for Nuclear and Radiation Safety
35-37 V. Stusa Street, Kyiv, 03142, Ukraine
mv_frankova@sstc.ua, jv_yesipenko@sstc.ua, oi_zhabin@sstc.ua, dv_gumenyuk@sstc.ua

C. Vázquez-Rodríguez, S. Kelm, M. Klauck, E.-A. Reinecke,
Forschungszentrum Jülich GmbH
Wilhelm-Johnen-Straße, Jülich, 52428, Germany
s.kelm@fz-juelich.de, e.-a.reinecke@fz-juelich.de, c.vazquez-rodriguez@fz-juelich.de

M. K. Koch, J. Krieger, G. Stahlberg, T. Jankowski
Ruhr-Universität Bochum, PSS
Universitätsstrasse 150, 44801 Bochum, Germany
marco.koch@pss.rub.de, julia.krieger@pss.rub.de, gregor.stahlberg@pss.rub.de, tobias.jankowski@pss.rub.de

M. Garcia Martin, L. E. Herranz
Centre for Research on Energy, Environment and Technology (CIEMAT)
Avda. Complutense 40, Madrid 28040 Spain
monica.gmartin@ciemat.es, luisen.herranz@ciemat.es

N. Reinke
Gesellschaft für Anlagen- und Reaktorsicherheit (GRS) GmbH
Schwertnergasse 1, 50677 Köln, Germany
nils.Reinke@grs.de

A. Bentaib
Institut de Radioprotection et de Sûreté Nucléaire
Avenue de la division Leclerc 31, 92262 Fontenay-aux Roses, France
ahmed.bentaib@irsn.fr

L. Carenini
Institut de Radioprotection et de Sûreté Nucléaire
Cadarache BP3, 13115 Saint-Paul-lez-Durance, France
laure.carenini@irsn.fr

J.-C. de la Rosa Blul, O. Papera Villacampa
European Commission Joint Research Centre
Westerduinweg 3, 1755 LE Petten, The Netherlands
Juan-Carlos.DE-LA-ROSA-BLUL@ec.europa.eu, Oriol.PARERA-VILLACAMPA@ec.europa.eu

A. Kaliatka, M. Valincius
Lithuanian Energy Institute
Breslaujos str. 3, 44403 Kaunas, Lithuania
algirdas.kaliatka@lei.lt, mindaugas.valincius@lei.lt

M. Constantin
Regia Autonoma Tehnologii Pentru Energia Nucleara
Street Campului 1, 115400, Mioveni, Romania
marin.constantin@nuclear.ro

M. Principato, F. Giannetti
Sapienza University of Rome
Corso Vittorio Emanuele II 244, 000186 Rome, Italy
marcello.principato@uniroma1.it, fabio.giannetti@uniroma1.it

T. Sevon
VTT Technical Research Centre of Finland
Kivimiehentie 3, Espoo, Finland
tuomo.sevon@vtt.fi

P. Groudev
Institute for Nuclear Research and Nuclear Energy, Bulgarian Academy of Sciences (INRNE-BAS)
Tzarigradsko Chaussee 72, 1784 Sofia, Bulgaria
pavlinpg@inrne.bas.bg

P. Kudinov, D. Grishchenko
Royal Institute of Technology
SE-100 44 Stockholm, Sweden
pkudinov@kth.se, dmitrygr@kth.se

ABSTRACT

Investigation of postulated SA scenarios in integral water-cooled Small Modular Reactors (SMRs) by usin g best estimate analytical tools has been not addressed in a systematic way yet. The HORIZON-EURATOM SAPSAM-SA project, coordinated by ENEA (Italy), was launched in 2022 aiming at filling this gap and at transferring the knowledge and know-how of large LWR to integral iPWRs in view of the European licensing needs with respect to Severe Accident (SA) and Emergency Planning Zone (EPZ). This paper

provides an overview of the preliminary outcomes of the large calculation campaign of postulated Design Basis Accident (DBA) and SA scenarios currently ongoing in the SASPAM-SA project performed by means of state-of-art European and non-European integral codes. The primary goal is the evaluation of such tools to predict the key physical phenomena occurring during such postulated scenarios in generic iPWR systems.

KEYWORDS
SMR, iPWR, Severe Accident, Design Basis Accidents, EU project

1. INTRODUCTION

Small Modular Reactors (SMRs) are one of the innovative Nuclear Power Plants (NPP) to be deployed in the near-term worldwide. In Europe, the technological and economical interest for SMRs has been growing for some years. Activities are going on in several member states aiming at supporting the licensing of such systems. Among the different concepts, the Integral Pressurized Water Reactors (iPWRs) are of particular interest. They are ready to be licensed as new builds, since they integrate several evolutionary features, particularly of a passive nature, to enhance even further the already inherent safety. In spite of the advantageous impact of passive safety systems on the first three levels of the Defence-in-Depth (DiD) approach, a systematic a demonstration of iPWR ability to prevent and to manage Severe Accidents (SA) needs to be done (DiD levels 4-5) [1, 2][1].

In order to fill this gap, the HORIZON-EURATOM 'Safety Analysis of SMR with PAssive Mitigation strategies - Severe Accidents' (SASPAM-SA) project, coordinated by ENEA (Italy), was launched in 2022 and takes the contribution of 23 partners from 13 European countries [3, 4, 5]. The main objective of the SASPAM-SA project is to investigate the applicability and transfer of knowledge and know-how accumulated on the operating large-LWR reactors to the iPWRs. These activities are performed in view of European licensing needs relevant to SA and Emergency Planning Zone (EPZ) analyses. SASPAM-SA therefore aims at investigating the key elements to create a European independent point of view on the safety of iPWRs with respect to DiD levels 4 and 5 [1, 2, 3]. The expected project's outcome is to support and speed-up the licensing and siting process of iPWRs in Europe. The pillars of the SASPAM-SA project are topics not addressed in other on-going iPWR initiatives. In particular, the determination of the conditions prevailing in the Reactor Pressure Vessel (RPV) and containment under postulated SA scenarios s is an essential element to support any other ongoing investigation within the project.

Two generic design-concepts are considered in SASPAM-SA. The iPWR Design 1 is characterized by a submerged containment and electric power of ~60 MWe and the iPWR Design 2 of ~300 MWe, which employs several passive systems and a dry containment. Note that it is not the project's objective to assess the design of such concepts. One of the primary goals of SASPAM-SA is the evaluation of the capabilities of integral SA codes and Computational Fluid Dynamics (CFD) tools to simulate the key phenomena occurring in generic iPWR designs. There are significant differences between iPWRs and the running reactors fleet, like the tighter interaction between the different systems of iPWRs (e.g., primary, containment, and safety systems), which might question the capability of the integral codes to predict such strong thermal-hydraulic (TH) coupling. To name a few: single and two-phase natural circulation in integral RPV, thermal stratification in large pools, primary/containment coupling, in-vessel melt retention, etc. [6, 7, 8, 9].

The paper focusses on the activities conducted within the second Work Package of the project (WP2). The WP2's objectives are three: 1) the assessment of generic, but representative, SA and CFD codes' datasets,

[1] Advanced designs, as iPWRs, are in general characterized by common features with the current operating large-LWR and by other specific features typical of their inherent evolutionary designs, providing safety advantages that reinforce the first three levels of the DiD principle. However, even if a plant is designed with advanced inherent features (through the reinforcement of the 1,2,3 DiD levels) allowing a reduction of the Core Damage Frequency (CDF), independent features for preventing and mitigating a severe accident sequence have to be included in its design (DiD level 4) together with the offsite emergency response (DiD level 5). Therefore, some scenarios that could lead to severe accidents need to be postulated and deterministically studied. More detailed information's in [1].

2) the analysis of the behavior of the generic iPWR designs during hypothetical postulated DBA and SA scenarios, 3) assessment of the codes' capability to simulate the dominant phenomena driving the accident scenarios and in particular to reproduce the behavior of the different passive safety systems and their interactions in a SMR configuration. For each iPWR design, a set of DBA and SA scenarios are postulated and analyzed. Note that since no Probabilistic Safety Analysis (PSA) assessments are done (generic designs are considered), SA scenarios are selected in terms of severity and not of probability to occur. In order to analyze code capability in a wider way the following passive systems have been considered in the work activity: decay heat removal; primary automatic depressurization; high-pressure safety injection, low pressure safety injection, containment pressure suppression, flooding of reactor cavity. Furthermore, in the frame of the project, the WP2 has the task to provide the necessary input and boundary conditions to be employed in the activities planned in the other WPs. The next sections describe the progress made so far in this venture.

2. THE GENERIC iPWR DESIGNS

The generic iPWR Design-1 and Design-2 considered in the SASPAM-SA project are shown in Figure 1. The specifications of both designs were determined in the WP2 based on open literature [10]. Such generic reactor concepts include the main iPWR design features considered in the most promising designs in the European market. Therefore, their employment in the project aims to assess more broadly the capability of codes (SA and CFD) to simulate the SA phenomena typical of iPWR.

The generic iPWR Design-1 reactor (Figure 1 – left) investigated here consists of a natural circulation iPWR composed of a shrouded reactor core and riser, an integrated Pressurizer (PRZ), and a Helical coil Steam Generator (HSG) within an integral RPV housed inside a steel containment. The containment is largely immersed in a large pool of water, serving as the ultimate heat sink. The Emergency Core Cooling System (ECCS) in the iPWR Design-1 consists of two groups of valves allowing the coolant circulation between RPV and containment during accident conditions: the Reactor Vent Valves (RVV) located at the top of the PRZ and Reactor Recirculation Valves (RRVs) located slightly above the active core[2].

The iPWR Design-2 (Figure 1, – right) is characterized by the use of several passive systems[3] and by a dry containment. The reactor operates in forced circulation during normal operation and employs a passive mitigation strategy in accidental conditions. It consists of an integral RPV, containing the core, eight HSGs, eight primary pumps, the Control Rod Drive Mechanism (CRDM), and the PRZ. The hot water at the core outlet flows upwards in a circular riser up to the primary pumps suction located above each HSGs [4].

As mentioned above, the objective of SASPAM-SA is not the assessment of the selected iPWR designs. On the contrary, the goal of the project is to investigate and proof the applicability of the state-of-art computation tools to reproduce SA conditions in generic iPWRs and identify code development needs.

[2] Even though Design-1 is generic, it includes some of the more evolutionary features of advanced SMR concepts, as integral RPV, compact SG, and natural circulation primary/containment coupling. More details on primary/containment coupling in a reactor with a submerged containment and the related experimental characterization, publicly available to the international community, are in [11].

[3] Passive systems are, on the one hand, an advanced solution to increase the inherent safety of the plant (e.g., there is no need of pumps), on the other hand a) they require extensive investigation for assessing the functional failure related to the thermal-hydraulic phenomena driving the operation of the systems and assess the related uncertainties, b) may still need an active initiation, and c) are characterized by very limited operational experience (to have more detailed information [1,12]). Considering this, the impact of the operation of passive systems on postulated SA progression is a novel topic and needs to be assessed.

[4] Considering the selected passive systems and the generic SMR features, a generic IRIS-SMR type has been considered as reference for this analysis (no proprietary data have been used); therefore, the main geometric information has been determined by scaling the data available from the SPES-3 facility, by engineering evaluation or public general data available from the IRIS reactor [13].

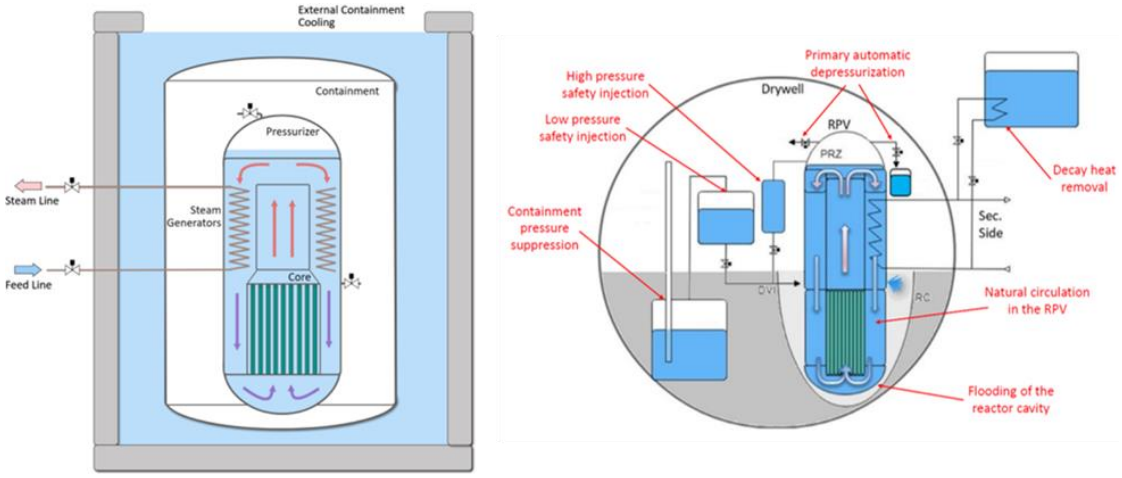

Figure 1. The generic iPWR Design-1 (left) and Design-2 (right) in the SASPAM-SA project [6].

3. DEVELOPMENT OF DATASETS OF INTEGRAL AND CFD CODES

The activities performed by the partners have been organized based on the following tasks:

1. Assessment of a common database for the iPWR Design-1 and Design-2 based on open literature to assess the iPWRs datasets;
2. Development of integral plant input decks of the two iPWR designs (SA and CFD codes);
3. Identification and analyses of DBA and SA sequences for the two iPWR designs;
4. Evaluation of a database of nuclear inventory vs. burn-up of the iPWR designs.

The full list of the partners and of the integral and CFD codes employed are given in Table I and Table II for the iPWR Design-1 and Design-2, respectively. The reference European and non-European computational tools are employed in the WP2 of the SASPAM-SA project. In order to increase the efficiency of the planned activities, some partners joined the project by sharing their own datasets, upon request. Such novel approach allowed a sensible acceleration in fulfilling the above-mentioned tasks 2 and 3, in particular. As shown in Table I and II, Tractebel and PSI made available the ASTECv2.2 and MELCORv2.2 datasets, respectively, of the iPWR Design-1.

Similarly, ENEA and ENEA/UNIROMA1 made available the ASTECv3.1and MELCORv2.2 datasets, respectively, of the iPWR Design-2. Furthermore, IRSN and GRS, as ASTEC and AC^2 developers, respectively, supported the users. New datasets of the EDF-MAAP and AC^2 codes have been developed for the iPWR Design-1 by EDF and RUB, respectively. Similarly, for the iPWR Design-2, new datasets of the MAAPv5.06 and AC^2 codes have been assessed by JRC and LEI, respectively. Concerning CFD codes, new datasets using ANSYS CFX and containmentFOAM were developed by SSTC NRS and FZJ for the iPWR Design-1 and Design-2, respectively.

Table I. iPWR Design-1: Partners and codes, and contribution

Partner	Code	Comments
EDF	EDF-MAAP5.04	New dataset
GRS		Support to the AC^2 Users
IRSN		Support to the ASTEC Users
KIT	ASTECv3.1	Contribution to a new dataset
KTH	MELCORv2.2	
PSI	MELCORv2.2	Sharing the dataset
RATEN		Support in the definition of the scenarios
RUB	AC^2	New dataset
SSTC NRS	ANSYS CFX (CFD)	New dataset
Tractebel	ASTECv2.2/ASTECv3.1	Sharing the dataset

Table II. iPWR Design-2: Partners, codes, and contribution

Partner	Code	Comments
CIEMAT	MELCORv2.2	
ENEA	ASTECv3.1/MELCORv2.2	Sharing the dataset
FZJ	CAD and containmentFOAM (CFD)	New dataset
GRS		Support to the AC^2 Users
JRC	MAAPv5.06	New dataset
IRSN		Support to the ASTEC Users
KTH	MELCORv2.2	
LEI	AC^2	New dataset
RATEN		Support in the definition of the scenarios
UNIROMA1	MELCORv2.2	Sharing the dataset

As an example of the CFD models developed, the ANSYS CFX model of the iPWR Design-1 in Figure 2 (left) and the containmentFOAM model of the iPWR Design-2 are shown in Figure 2. ANSYS CFX (left, iPWR Design-1) and containmentFOAM (right, iPWR Design-2) models mesh. (right). The ANSYS CFX model employs a preliminary mesh of about 370000 nodes for the initial round of calculations aimed at selecting and setting up the mathematical models to simulate thermal processes within the containment. Different containmentFOAM models have been developed, with preliminary meshes using between 200000 and 750000 cells for representing one quarter of the Desing-2 containment. Despite the analyses are still in progress, the preliminary results show rather stable simulations and a good qualitative assessment of the expected phenomenology.

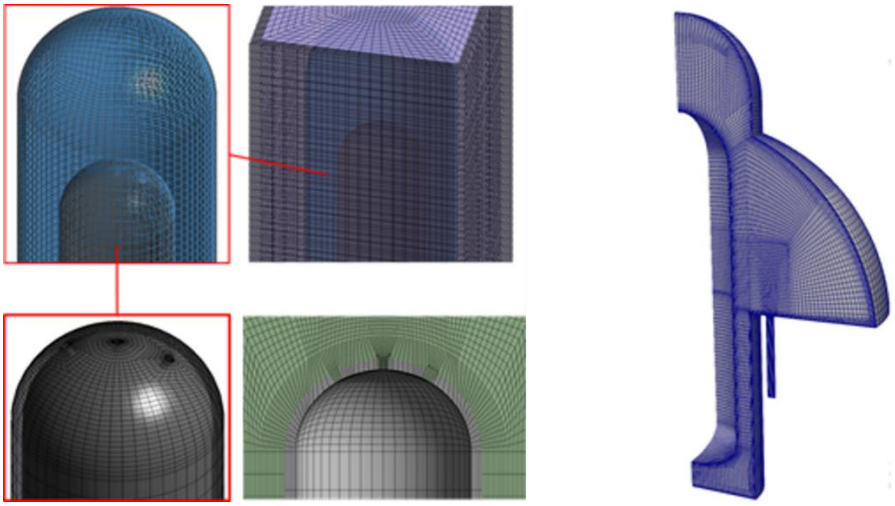

Figure 2. ANSYS CFX (left, iPWR Design-1) and containmentFOAM (right, iPWR Design-2) models mesh.

4. ASSESSMENT OF POSTULATED ACCIDENT SCENARIOS

The performance of the integral codes in Table I and II to predict the key phenomena occurring during accidental phases for the selected iPWR designs has been investigated in two phases. First, a set of DBA scenarios has been identified for each design, to evaluate the capabilities of the codes to properly analyse the key TH phenomena in DBA conditions. In a second phase, SA scenarios have been selected to assess the code performance with respect to both TH and core degradation phenomena in SA conditions. It is worth to remind that the SA scenarios were identified based on the severity of the accident consequences and not in terms of probability, since no PSA assessments were carried out in the SASPAM-SA project.

4.1. Generic iPWR Design-1

Four DBA scenarios have been postulated for the generic iPWR Design-1 triggered by opening a break of different sizes (100%, 35%, 20%, and 10% pipe section) of the Chemical and Volume Control System (CVCS) make-up line with loss of AC power supply. The CVCS discharge line is connected to the downcomer slightly above the top of the core. RVVs and RRVs are assumed available. The three SA scenarios postulated for the generic iPWR Design-1 are described as follows:

- SA-1: Break (100%) on the CVCS makeup line with loss of AC. RVVs are in operation. RRVs are postulated stuck closed;
- SA-2: Inadvertent opening (100%) of 1 RVV with loss of AC. Other RVVs are in operation. RRVs are postulated stuck closed;
- SA-3: Break (100%) on the venting line with loss of AC. RVVs are in operation. RRVs are postulated stuck closed.

4.2. Generic iPWR Design-2

One DBA scenario has been considered for the generic iPWR Design-2. The initiator is a guillotine break of one Direct Vessel Injection (DVI) line (Figure 1), while all the safety systems are available. The three SA scenarios postulated for the generic iPWR Design-2 are described as follows:

- SA-1: guillotine break of one DVI line, considering the unavailability of the Emergency Heat Removal System (EHRS) and Automatic Depressurization System (ADS)-1 (through the failure of correspondent valves to open);
- SA-2: guillotine break of one DVI line, considering the unavailability of all safety systems (through the not opening of the related valves);
- SA-3 (low pressure scenario): guillotine break of one DVI line and the unavailability of EHRS system (through the failure of correspondent valves to open).

4.3. Nuclide inventory and decay heat data

Depletion calculations have been performed for a representative 2D typical PWR fuel assembly of the iPWR Design-1 and Design-2 using CASMO5 lattice physics code, developed by Studsvik Scandpower [14]. Decay heat data and isotopic inventories have been computed from 20 MWd/kgU to 60 MWd/kgU, with a burn-up step of 2.5 MWd/kgU. For the analyses, three sets of decay heat data were used: the set calculated in the WP2 (Task 2.4), the 1973 ANS standard data, and the 1973 ANS standard data increased by 20%. The results show that after the scram, the WP2's decay power is about 30% lower than the 1973 ANS standard data.

5. SELECTED RESULTS OF POSTULATED DBA AND SA ANALYSES

Selected results of the integral codes simulations of the postulated DBA and SA scenarios are shown in the subsections below. In agreement with the schedule of SASPAM-SA, since a systematic comparison among all the results is currently ongoing, attention is paid here to provide the description of the capabilities of the codes to predict the key phenomena occurring during the transients.

5.1. Generic iPWR Design-1: results of the DBA scenarios

The ASTECv2.2 results are here shown as a matter of example. The time dependent behaviour of the pressure in the RPV and in the containment computed by the code during the postulated DBA scenarios in the iPWR Design-1 is shown in Figure 3. The results have been obtained by using the 1973 ANS standard decay heat data increased by 20%. The opening of the break in the downcomer leads to a pressure drop in the RPV and a pressure increase in the containment, labelled with straight and dotted lines, respectively (Figure 3 left).

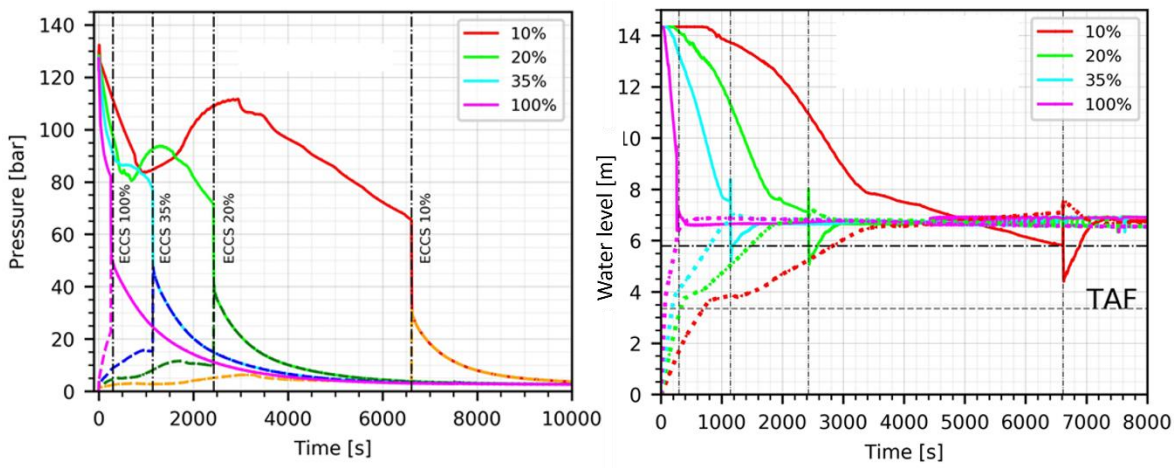

Figure 3. DBA scenarios: pressure in the RPV and in the containment (left) and water level (right) computed by ASTECv2.2.

The scenario initiated by the largest break size of the CVCS make-up line (100%) leads to a fast depressurization of the RPV and consequently to a large pressure increase containment up to about 55 bar. The scram occurs at about 4 s and the ECCS is activated at about 260 s triggering the recirculation phase and finally leading to equalize the pressure in the RPV and containment to less than 4 bar at the end of the transient. Smaller breaks of the CVCS make-up line (35%, 20%, and 10%) lead to slower initial pressure decrease in the RPV. In addition, since only part of the decay heat is evacuated through the break, there is a subsequent pressure increase in the RPV, which reaches a maximum before the ECCS activation. The peak pressure in the containment due to the ECCS intervention decreases as the size of the break decreases. However, once the ECCS is activated, the RPV pressure decreases up to the equalization with the containment at the same rate in all cases. From the phenomenological point of view, after the ECCS activation, the steam produced in the core travels along the ascending riser and exits through the RVVs; then the steam is condensed on the inner surface of the containment. The accumulated liquid at bottom of the containment is then returned to the RPV via RRVs. The energy from the containment is removed to the external pool which acts as ultimate heat sink. Figure 3 (right) shows, for the three different cases investigated, the liquid increase in the containment, and, when the ECCS valve opening, the refill of the core due to the gravity.

A preliminary comparison among the results obtained with the other integral codes used for the iPWR Design-1 (Table I) shows a good qualitative and quantitative agreement on both pressure behaviors and ECCS activation time. In particular, for the DBA scenarios initiated by 100%, 35%, and 20% break, the deviation on the timing of the ECCS activation from the AC^2, ASTEC, EDF-MAAP, and MELCORv2.2 codes ranges between 500-1000 s, while larger deviations are observed for the scenario induced by 10% break. A reasonable agreement among the codes is also observed on prediction of the values of the pressure peaks in the RPV and containment. The results show that the codes are able to predict the key TH phenomena during DBA scenarios (e.g., single and two-phase natural circulation in integral RPV, primary/containment natural circulation coupling, energy removal from the external pool, etc.).

5.2. Generic iPWR Design-1: results of the SA-1 scenario

The ASTECv3.1 results concerning the key events and parameters during the progression of the SA-1 scenario, are shown in Table III. The calculations were performed using the decay data computed in the WP2 (task 2.4), the 1973 ANS standard data (ANS73 in Table III), and the 1973 ANS standard data increased by 20% (ANS73+20% in Table III). As expected, the higher the decay heat, the faster the progression of the core degradation. The time at which the Fission Products (FP) are released ranges from 6664 s to 9099 s, and the instant of the first slump of corium into the lower plenum ranges from 21069 s to 25189 s. Finally, the total mass of corium relocated in the lower plenum varies from 5.7 tons to 10.6 tons.

Table III. Progression of the postulated SA-1 scenario (ASTECv3.1) against decay heat data

Key events/parameters	Task 2.4	ANS73	ANS73 +20%
Scram time [s]	4.3	4.3	4.3
ECCS signal [s]	934.1	933.1	950.6
Max. containment pressure [MPa]	2.65	2.75	2.81
Start of FPs release from fuel pellets [s]	9099.7	7925.8	6664.9
First material slump in the lower plenum [s]	12159.7	10725.8	9064.9
First slump of corium with FPs in the lower plenum [s]	25189.7	23850.8	21069.9
First total core uncovery [s]	32200.7	31105.8	22435.4
Total H_2 mass produced in the vessel [kg]	64	58.6	60.8
Final H_2 mass in the containment [kg]	53.9	48.9	51.3
Final aerosols mass in the containment [kg]	329.2	196	184
Total corium relocation in the lower plenum [kg]	5771	9495	10638

A preliminary comparison of the results from the different integral codes employed shows a reasonable agreement on some figure-of-merits. No RPV failure is predicted by the codes for any of the postulated SA scenarios. Going back to the SA-1 scenario, when using the same decay heat data, the deviation of the predicted time of the beginning of the material relocation to the lower plenum is about 1,000 s. Furthermore, the maximum deviation of the total amount of corium relocated to the lower plenum is about 1 ton. Finally, concerning the in-vessel hydrogen production, the deviation among the code predictions is ~20 kg.

As an example, selected EDF-MAAP5.04 and ASTECv3.1 results for the SA-1 obtained by employing the 1973 ANS standard decay data increased by 20% are shown in Figure 4. The results relevant to the hydrogen produced in the RPV (Figure 4, left) show some deviations on the instant at which the phenomenon starts (~5,500 s in ASTECv3.1 and ~7,800 s in EDF-MAAP5.04) and on the total amount of hydrogen produced (~20 kg), the latter looking mainly due different approaches to model the oxidation of stainless-steel components in the core. Further investigations on the source of such deviation are currently going-on. The EDF-MAAP5.04 and ASTECv3.1 results concerning the material relocation in the lower plenum (Figure 4, right) show a reasonable agreement on both the total mass of corium and oxidic pool.

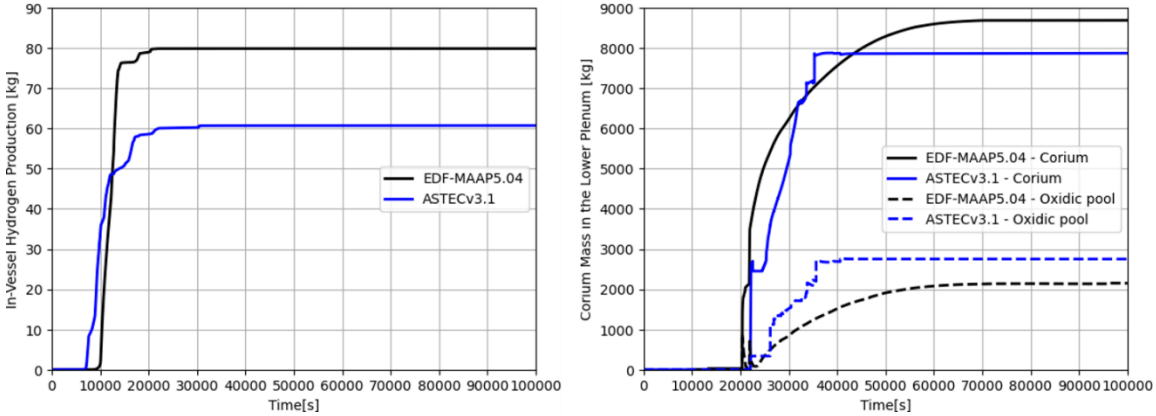

Figure 4. In-vessel hydrogen production (left) and total mass of corium and oxides relocated in the lower plenum (right) for the SA-1 computed by EDF-MAAP and ASTECv3.1.

5.3. Generic iPWR Design-2: results of the DBA scenario

The analysis of the DBA scenario in the iPWR Design-2 is rather challenging for integral codes since the system is equipped with several passive systems. The key events of the ASTECv3.1 simulation are shown in Table IV. The simulation was carried out for 100,000 seconds to include the main TH phenomena relevant in the scenario. The WP2 (Task 2.4) decay heat data were used. After the break, the transient is characterized by a fast decrease of the primary pressure and an increase of the containment pressure (Figure 5).

Table IV. Progression of postulated DBA scenario (ASTECv3.1)

Event	Time [s]
Break	0
High containment pressure signal	20
SCRAM	25
EHRS loops opening	28
Low PRZ water level signal	65
RCP coast-down	80
Natural circulation begins through RI-DC valves	84
Low PRZ pressure signal	158
ADS Stage-1 opening	166
EBTs opening	160
Low DP RV-Containment	1398
LGMSs opening	1401
Low LGMS mass signal	12902

When the high containment pressure set-point is reached (20 s), the scram signal is activated, as well as the isolation of the secondary system, and the activation of the EHRS. The peak pressure in the secondary system is reached after some seconds (~120 bar) and quickly decreases (Figure 5 – left) due to the heat removal from the Refuelling Water Storage Tank (RWST). When the low PRZ level set-point is reached (65 s), the reactor coolant pumps coast-down occurs, the riser-downcomer valves open, and the natural circulation in the RPV starts. The low-pressure set-point in the PRZ is reached at 122 s, triggering the activation of the first stage of the ADS and of the Emergency Borating Tanks (EBT), and leading to a rapid decrease of the primary and secondary pressure (Figure 5).

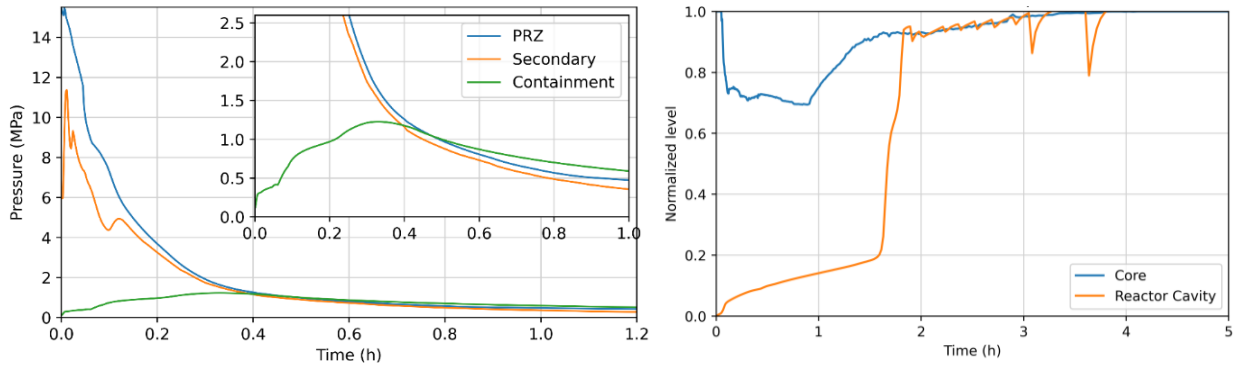

Figure 5. ASTECv3.1prediction of the pressure in the PRZ, in the secondary system, and in the drywell (left) and water level in the cavity and core (right).

The low RPV-Containment Differential Pressure signal (1401 s), activated by the RPV and drywell (DW) pressures equalization, determines the opening of the valves connecting the Long term Gravity Make-up System (LGMS) line-B to the RPV (through the intact DVI line) and the LGMS line-A to the reactor cavity (RC) (through the broken DVI line). Steam condensation on the containment walls and heat removal from the primary side due to the EHRS intervention causes the containment and the RPV pressure to decrease. When DW pressure decreases below the Pressure Suppression System (PSS) pressure, the PSS water is pushed inside the PSS vent pipes to the top end and fills the RC above the break level. When the LGMS mass reaches the low water mass signal, the ADS stage-2 valves are opened, permitting steam circulation between RPV and DW. During the long-term cooling phase, the core is kept filled and cooled by the water available from RC, the power is removed by the EHRS system, and the heat is evacuated to the environment through the DW metal surfaces. Figure 5 (right) shows the water level in the cavity and in the core predicted

by ASTEC calculations. As for the results of the iPWR Design-1, a preliminary qualitative comparison among the predictions from the different integral codes employed for analysing the iPWR Design-2 is available. The results show a general agreement with respect to the timing of the activation of the safety systems and on the behaviour of some figure-of-merits, e.g., the pressure in the different compartments. On the other hand, the first important result is that all the codes have been able to predict most of the key thermal-hydraulic phenomena occurring in the scenario (e.g., single and two-phase natural circulation in integral RPV, behaviour of passive injection and heat removal systems, long term cooling, etc).

5.4. Generic iPWR Design-2: results of the postulated SA-1 scenario

The ASTECv3.1 results concerning the total hydrogen production in the RPV, the mass in the RPV, in the containment, and in the environment during the postulated SA-1 in the iPWR Design-1 (section 4.2) are shown in Figure 6 (left). Furthermore, the spatial distribution and the temperature of the molten material in the core before core relocation to the lower plenum are shown in Figure 6 (right). Calculations have been performed using the decay heat data computed in the frame of the activities of WP2.

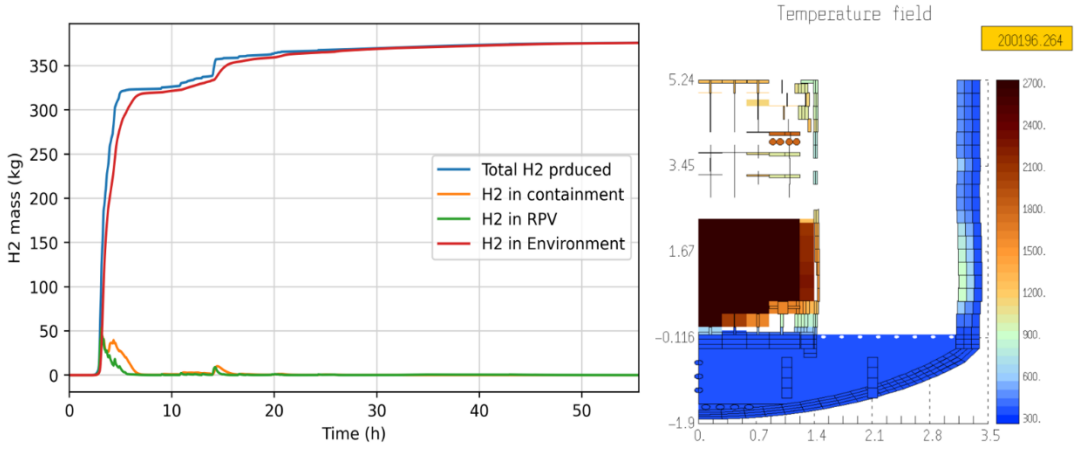

Figure 6. Total mass of hydrogen in the RPV and in the containment (left) and temperature field in the RPV (right) at the end of the simulation in the SA-1 (ASTECv3.).

The preliminary comparison of the results among the different integral codes employed in this task (Table II) shows a general qualitative agreement of the accident progression. The hydrogen production onset occurs between 1.5 and 2 h, and the core is uncovered at ~1 h after the beginning of the transient. Concerning the hydrogen production, the deviation among the codes' predictions is ~20-25%. Note that all the integral codes simulations show that no RPV lower head failure, due to the ex-vessel reactor cooling, and that the containment pressure design is reached. A deeper analysis and comparison of the results from the integral codes is currently ongoing in the framework of the SASPAM-SA WP2.

6. FINAL REMARKS

The HORIZON-EURATOM SASPAM-SA project, coordinated by ENEA (Italy), was launched in 2022 to investigate the application of the multi-decade knowledge accumulated on operating large LRW reactors to iPWRs, in view of supporting the European license needs relevant to SA and EPZ. Within the project framework, WP2, managed by KIT (Germany), focuses on developing input decks and assessing hypothetical severe accident (SA) scenarios. This involves utilizing widely adopted state-of-the-art European and non-European integral codes, along with CFD tools, to analyse postulated DBA and SA scenarios in two generic but representative iPWRs. Such systems incorporate key safety features characteristic of the most promising iPWR designs poised for entry into the European market. The main goal is to evaluate the capabilities of the target codes to predict the main phenomena and characteristics of iPWRs in accident conditions. In the framework of the WP2, DBA and SA scenarios have been postulated, the SA scenarios being assessed based on their severity and not on PSA considerations. For the analyses,

the integral codes are used. The corresponding models of the two generic designs employed in the project have been assessed by producing a common set of specifications based on open literature. Preliminary analyses indicate that the outcomes generated by various integral codes demonstrate both qualitative and quantitative consistency. Moreover, the results prove that the codes can anticipate the fundamental phenomena observed during severe accidents in iPWRs. WithinWP2, such results are the basis for the development of CFD models for a very fine analysis of the postulated scenarios. The results of the integral and CFD codes' investigations represent, in the framework of the SASPAM-SA project, the boundary conditions for developing the other research activities planned in the project and focused on the identification of existing and needed key experiments for the iPWR assessment, the in-vessel melt retention, the containment behaviour, and the characterization of the EPZ.

ACKNOWLEDGMENTS

Funded by the European Union

Funded by the European Union. Views and opinions expressed are however those of the author(s) only and do not necessarily reflect those of the European Union or European Commission-Euratom. Neither the European Union nor the granting authority can be held responsible for them.

Project funded by

Schweizerische Eidgenossenschaft
Confédération suisse
Confederazione Svizzera
Confederaziun svizra

Swiss Confederation

Federal Department of Economic Affairs, Education and Research EAER
State Secretariat for Education, Research and Innovation SERI

This work has received funding from the Swiss State Secretariat for Education, Research and Innovation (SERI).

REFERENCES

1. SMR Regulators' Forum Pilot Project Report: Considering the Application of a Graded Approach, Defence-in-Depth and Emergency Planning Zone Size for Small Modular Reactors, January 2018.
2. IAEA, "Assessment of Defence in Depth for Nuclear Power Plants," SAFETY REPORTS SERIES No. 46, Vienna (2005).
3. European Commission, "Safety Analysis of SMR with PAssive Mitigation strategies - Severe Accident - SASPAM-SA Project," https://cordis.europa.eu/project/id/101059853/de, (2023).
4. https://www.saspam-sa.eu
5. F. Mascari, "Safety Analysis of SMR with Passive Mitigation strategies – Severe Accident (SASPAM-SA) Horizon Euratom Project", ETSON NEWS, September 2022, https://www.etson.eu/node/290
6. IAEA, ''Natural Circulation Phenomena and Modelling for Advanced Water Cooled Reactors," IAEA-TECDOC-1677, Vienna (2012).
7. NEA/CSNI, ''Relevant thermal hydraulic aspects of advanced reactor design," Status Report, CSNI/R(1996)22, also referenced as: OCDE/GD(97)8, Paris (F) (1996).
8. OECD, "A state-of-the-art report on scaling in system thermal-hydraulics applications to nuclear reactor safety and design," NEA/CSNI/R(2016)14 (2017).
9. OECD, "In-vessel Code Degradation Code Validation Matrix," NEA/CSNI/R(2000)21 (2001).
10. SASPAM-SA, "Milestone 2.1: Generic Data on Design 1 and Design 2" (2023).
11. F. Mascari, et al., "Analysis of the OSU-MASLWR 001 and 002 Tests by Using the TRACE Code," NUREG/IA-0466 (2016).
12. European SMR pre-Partnership Report, Workstream 5 – Research, Development, and Innovation Roadmap, June 2023, (https://snetp.eu/wp-content/uploads/2023/07/European-SMR-pre-Partnership-WS5-report-and-roadmap-30-June-2023.pdf)
13. F. Giannetti et al., "Analyses of the MELCOR Capability to Simulate Integral PWR Using Passive Systems," Proceedings of the NURETH-20, 20-25 August, Washington, USA 2023
14. R. Ferrer, J. Hykes and J. Rhodes, "CASMO-5 Development and Applications", *Proc. Int. Conf. PHYSOR 2006*, Vancouver, BC, Canada, September 10–14 (2006).

SAFETY ANALYSIS OF SMR WITH PASSIVE MITIGATION STRATEGIES - SEVERE ACCIDENT

ANALYSIS OF POSTULATED SEVERE ACCIDENTS IN GENERIC INTEGRAL PWR SMALL MODULAR REACTORS IN THE FRAME OF THE HORIZON EURATOM SASPAM-SA PROJECT

F. Gabrielli
on behalf of the SASPAM-SA WP2 Community

Karlsruhe Institute of Technology



SASPAM-SA Consortium reserves all rights in this document and in the information contained therein.
Reproduction, use or disclosure to third party without express authorization is strictly prohibited.

SASPAM-SA Project: Motivation and Goals

SAFETY ANALYSIS OF SMR WITH PASSIVE MITIGATION STRATEGIES - SEVERE ACCIDENT

- **Systematic demonstration of iPWR ability to prevent and to manage Severe Accidents (SA) needs to be done (DiD levels 4-5)**
- 'Safety Analysis of SMR with PAssive Mitigation strategies - Severe Accidents' (SASPAM-SA) project (2022-2026), coordinated by ENEA (F. Mascari) - 23 partners from 13 European countries, including Ukraine and Switzerland
- Main objectives:
  - investigating the **applicability and transfer of knowledge and know-how** accumulated on the **operating large-LWR reactors to the iPWRs** in view of the European licensing needs related to SA and Emergency Planning Zone (EPZ) analyses
  - investigating the key elements to create a European independent point of view on the safety of iPWRs with respect to DiD levels 4 and 5

SASPAM-SA Consortium reserves all rights in this document and in the information contained therein. Reproduction, use or disclosure to third party without express authorization is strictly prohibited.

The Pillars of SASPAM-SA

SAFETY ANALYSIS OF SMR WITH PASSIVE MITIGATION STRATEGIES - SEVERE ACCIDENT

- Pillars: elements not addressed in other on-going iPWR initiatives

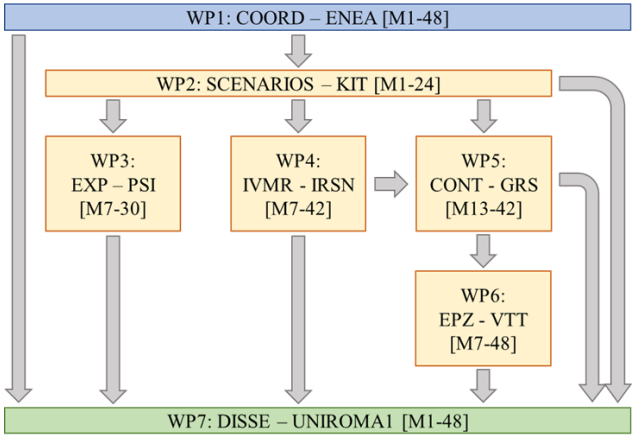

- **Input deck development and hypothetical SA scenarios assessment (SCENARIOS) (WP2)**
- Existing SA **experimental database** for iPWR Assessment (EXP) (WP3)*
- Insights into **corium retention capability** through analytical studies in iPWRs (IVMR) (WP4)
- Insights into **containment response** to a SA through analytical analysis (CONT) (WP5)
- Characterization of iPWR **EPZ** (EPZ) (WP6)
- Education and Dissemination (DISSE) (WP7)

*T. Lind, et al., '*SASPAM-SA: Assessment of the relevance and applicability of existing experimental databases to iPWR*', Session 4.1

SASPAM-SA Consortium reserves all rights in this document and in the information contained therein. Reproduction, use or disclosure to third party without express authorization is strictly prohibited.

Generic iPWR Designs

SAFETY ANALYSIS OF SMR WITH PASSIVE MITIGATION STRATEGIES - SEVERE ACCIDENT

iPWR Design-1

Submerged containment, P~60 MWe

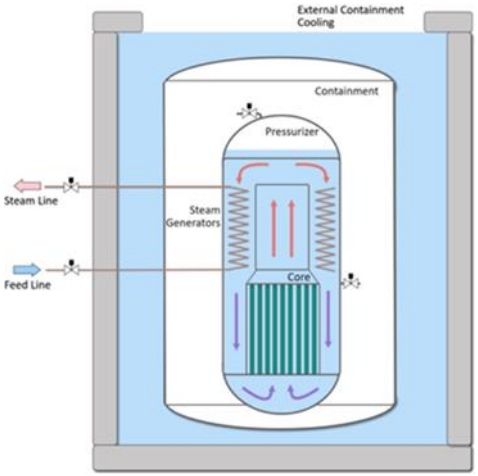

iPWR Design-2

Suppression containment, several passive systems, P~300 MWe

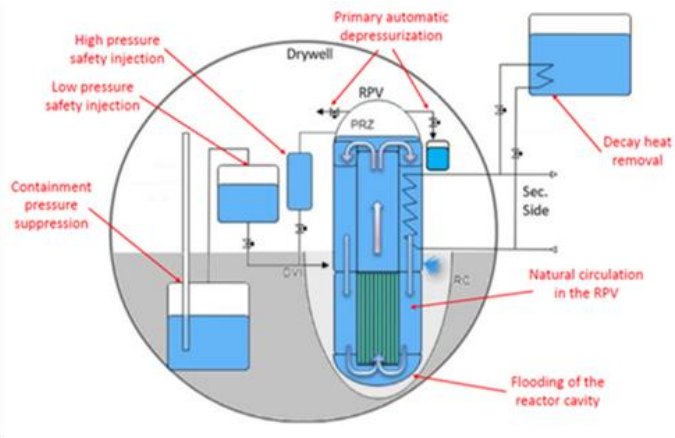

- The designs incorporate the main safety features of the most promising concepts ready for deployment in the European market

SASPAM-SA Consortium reserves all rights in this document and in the information contained therein. Reproduction, use or disclosure to third party without express authorization is strictly prohibited.

Objectives of the WP2

SAFETY ANALYSIS OF SMR WITH PASSIVE MITIGATION STRATEGIES - SEVERE ACCIDENT

- **Confirming the adaptability of state-of-art European and non-European integral SA codes to postulated SAs in generic iPWR designs and identifying conditions sine-qua-non for SA scenarios**
- **Evaluating the capabilities of CFD tools to simulate the key phenomena occurring in generic iPWR designs**
- Three main objectives:
  1. **Assessment of generic, but representative, SA and CFD codes' datasets of the iPWR Design-1 and Design-2**
  2. **Postulating DBA and SA sequences**
  3. **Analysis the postulated DBA and SA scenarios**
- **No PSA assessments employed** → SA scenarios selected in terms of severity and not of probability to occur
- Input data/Boundary conditions for the activities foreseen in the other WPs (relevant experimental data, containment, IVMR, ST and EPZ)

SASPAM-SA Consortium reserves all rights in this document and in the information contained therein. Reproduction, use or disclosure to third party without express authorization is strictly prohibited.

Input Data Preparation

SAFETY ANALYSIS OF SMR WITH PASSIVE MITIGATION STRATEGIES - SEVERE ACCIDENT

- **Common database** of the iPWR Design-1 and Design-2 **based on open literature** to assess datasets
- **Keyword: Sharing → The datasets are shared among the partners of the WP2 upon request**

- **Fuel inventory and Decay Heat**
- Depletion of a representative 2D fuel assembly of by means of CASMO5
- A database of fuel inventories from 20 MWd 60 MWd/kgU, with a burn-up step of 2.5 M composed of **300 isotopes has been ass** i.e. isotope-wise mass [kg] and activity [Bq]
- ANS73 and ANS73+20% decay data considered

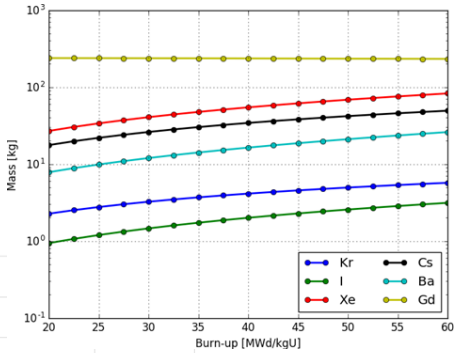

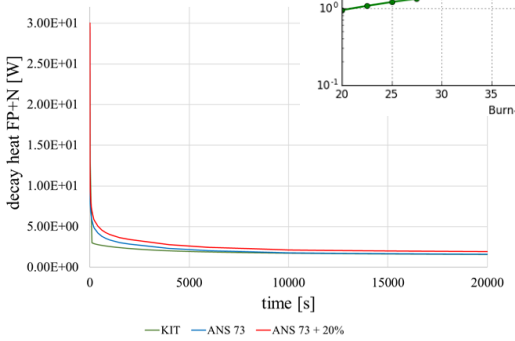

SASPAM-SA Consortium reserves all rights in this document and in the information contained therein. Reproduction, use or disclosure to third party without express authorization is strictly prohibited.

iPWR Design-1 and -2: Codes and Datasets

SAFETY ANALYSIS OF SMR WITH PASSIVE MITIGATION STRATEGIES - SEVERE ACCIDENT

iPWR Design-1

Partner	Code
EDF	EDF-MAAP5.04
GRS	Support to the AC^2 users
IRSN	Support to the ASTEC users
KIT	ASTECv3.1
KTH	MELCORv2.2
PSI	MELCORv2.2
RATEN	Scenarios
RUB	AC^2
SSTC NRS	ANSYS CFX (CFD)
TRACTEBEL	ASTECv2.2/v3.1

iPWR Design-2

Partner	Code
CIEMAT	MELCORv2.2
ENEA	ASTECv3.1/MELCORv2.2
FZJ	CAD and containmentFOAM
GRS	Support to the AC^2 users
JRC	MAAP 5.06
IRSN	Support to the ASTEC users
LEI	AC^2
RATEN	Scenarios
UNIROMA1	MELCORv2.2

SASPAM-SA Consortium reserves all rights in this document and in the information contained therein. Reproduction, use or disclosure to third party without express authorization is strictly prohibited.

CFD Models

- **ANSYS CFX model** of the iPWR Design-1
- 370,000 nodes for the initial round of calculations

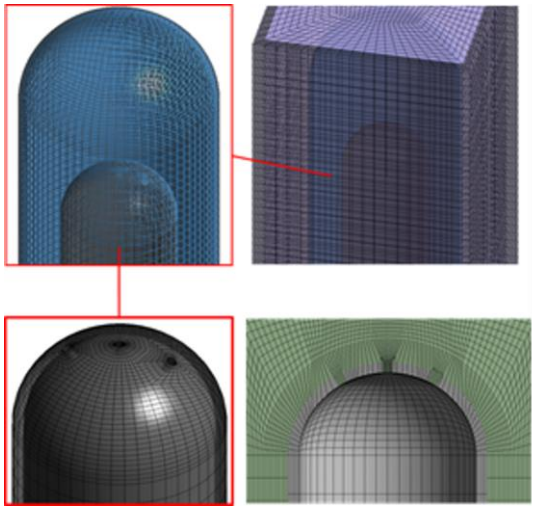

(courtesy of M. Makarenko, SSTC NRS)

- **containmentFOAM model** of the iPWR Design-2
- preliminary meshes using between 200,000 and 750,000 cells for representing one quarter of the Desing-2 containment

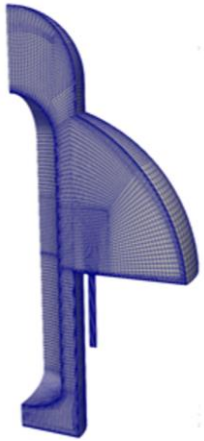

C. Vázquez-Rodríguez, et al., '*Development of a LW-SMR dry containment model with containmentFOAM*', Session 4.1

(courtesy of C. Vázquez-Rodríguez, S. Kelm, FZJ)

SASPAM-SA Consortium reserves all rights in this document and in the information contained therein. Reproduction, use or disclosure to third party without express authorization is strictly prohibited.

iPWR Design-1: DBA Scenarios

Chemical and Volume Control System (CVCS) make-up line break: with loss of AC

Opening a break of different sizes (10%, 20%, 35%, 100%)

Loss of AC occurs at t = 0 s

The transient includes:

- Loss of FDW
- Reactor SCRAM
- Isolation of the MSL
- Activation of the ECCS
  - (P_{RPV} –$P_{Cont.}$ < 62 bar) & Cont. level > 5.8 m
  - Opening of 3 RVVs and 2 RRVs

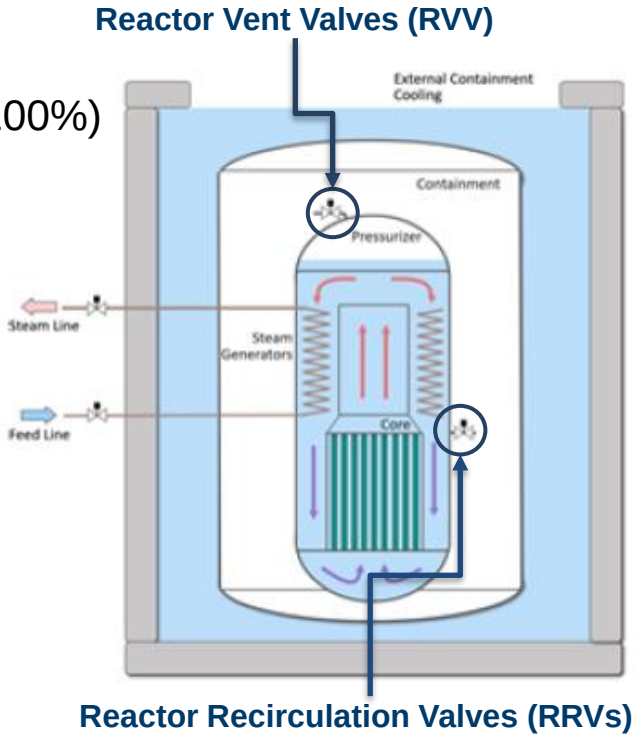

SASPAM-SA Consortium reserves all rights in this document and in the information contained therein. Reproduction, use or disclosure to third party without express authorisation is strictly prohibited.

iPWR Design-1: Postulated SA Scenarios

SAFETY ANALYSIS OF SMR WITH PASSIVE MITIGATION STRATEGIES - SEVERE ACCIDENT

3 SA cases were reproduced differing only in the initiating event

Case 1: 100% **break** on the CVCS **makeup line**

Case 2: Inadvertent opening of **1 RVV valve**

Case 3: 100% **break** on the **Venting line**

Accident progression:

Loss of AC occurs at t = 0 s

The transient includes:

- Loss of FDW and Reactor SCRAM
- Isolation of the MSL
- Activation of the ECCS
  - (P_{RPV} –$P_{Cont.}$ < 68,9 bar) & Cont. level > 5.8
  - Opening of 3 RVVs and **failure of 2 RRVs**

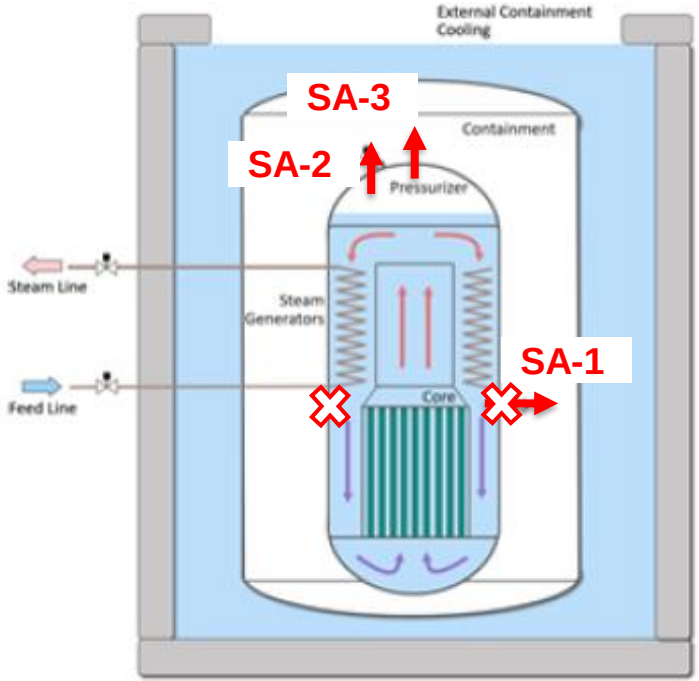

SASPAM-SA Consortium reserves all rights in this document and in the information contained therein. Reproduction, use or disclosure to third party without express authorisation is strictly prohibited.

iPWR Design-1: Results

- **Calculations performed by employing the fuel inventory from Task2.4 (a), ANS73 (b), and ANS73+20% (c)**

Scenario	ASTECv2.2 (Tractabel)	ASTECv3.1 (Tractabel)	ASTECv3.1 (KIT)	EdF-MAAP (EdF)	MELCOR (PSI)	AC2 (PSS RUB)
DBA 100%	a, b		a, b, c	a, b	b, c	a
DBA 35%	a, b		a, b, c	a, b	b, c	a
DBA 20%	a, b		a, b, c	a, b	b, c	a
DBA 10%	a, b		a, b, c	a, b	b, c	a
SA1	a, b	b	a, b, c	a	b, c	a
SA2	a, b	b	a, b, c	a	b, c	a
SA3	a, b	b	a, b, c	a	b, c	a

SASPAM-SA Consortium reserves all rights in this document and in the information contained therein. Reproduction, use or disclosure to third party without express authorization is strictly prohibited.

iPWR Design-1: DBA Scenarios results

SAFETY ANALYSIS OF SMR WITH PASSIVE MITIGATION STRATEGIES - SEVERE ACCIDENT

ASTECv3.1

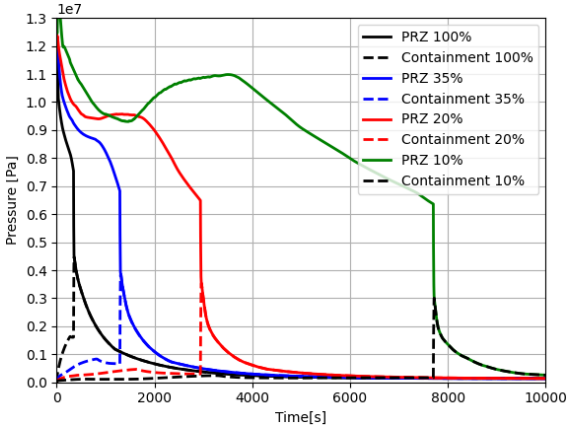

EdF-MAAP

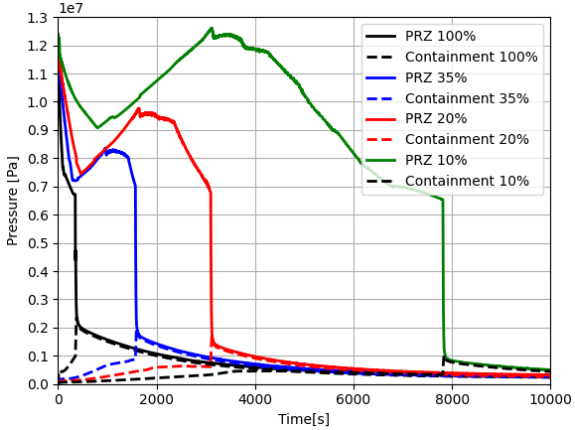

MELCOR

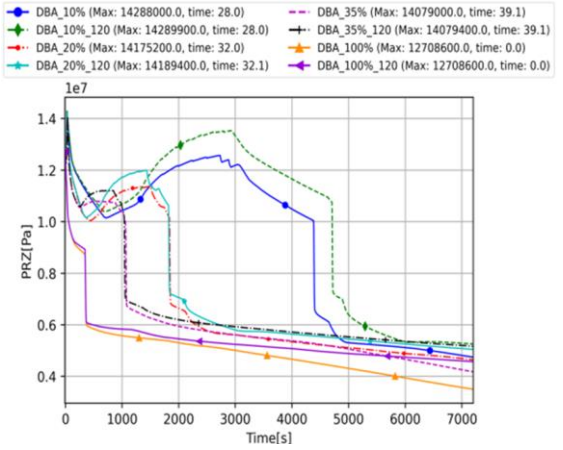

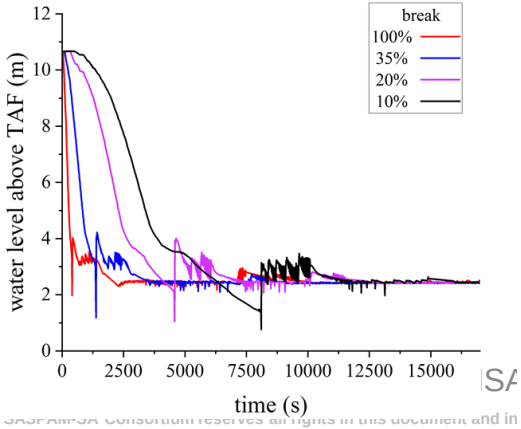

- Kinetics of the RPV depressurization depends on the break size
- Only part of the decay heat evacuated through the break → pressure increase in the RPV
- When the ECCS valve opening → core refilled by gravity
- **Timing of the ECCS activation from the AC², ASTEC, EDF-MAAP, and MELCORv2.2 codes ranges between 500-1000 s**
- **Codes are able to predict the key TH phenomena** (e.g., single/two-phase natural circulation, primary/containment natural circulation coupling, energy removal from the external pool, etc.).

SASPAM-SA Consortium reserves all rights in this document and in

iPWR Design-1: SA scenarios' results

SA-1: ASTECv3.1

key parameters	WP2.4	ANS 73	ANS 73 +20%
SCRAM time [s]	4.3	4.3	4.3
ECCS signal time [s]	934.1	933.1	950.6
Max. Press in Cont. [MPa]	2.65	2.75	2.81
Start of FPs release from fuel pellets [s]	9099.7	7925.8	6664.9
First slump of corium with FPs in LP [s]	25189.7	23850.8	21069.9
Total H_2 mass produced in the Vessel [kg]	64	58.6	60.8
Final H_2 mass in Cont. [kg]	53.9	48.9	51.3
Final aerosols mass in Cont. [kg]	329.2	196	184
Total Relocation in LP [kg]	5771	9495	10638

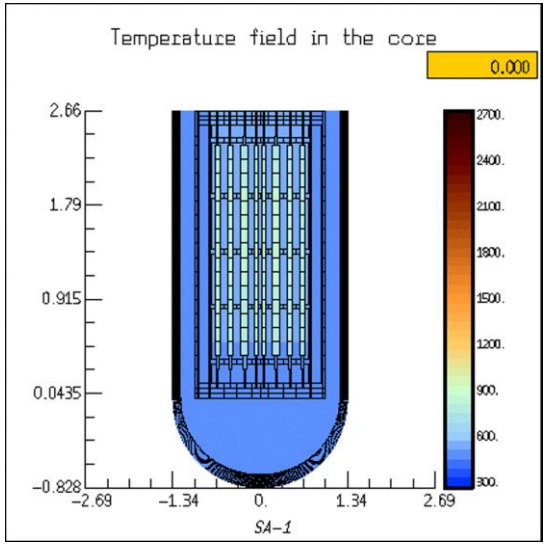

SASPAM-SA Consortium reserves all rights in this document and in the information contained therein. Reproduction, use or disclosure to third party without express authorization is strictly prohibited.

iPWR Design-1: SA scenarios' results

- Decay heat data computed inside SASPAM-SA

key parameters	SA-1	SA-2	SA-3
SCRAM time [s]	4.3	3.5	6.3
ECCS signal time [s]	934.1	2034	8453
Max. Press in Cont. [MPa]	2.65	3.88	1.16
Start of FPs release from fuel pellets [s]	9099.7	16725	24985
First slump of corium with FPs in LP [s]	25189.7	34295	42865
Total H_2 mass produced in the Vessel [kg]	64	66.5	66.6
Final H_2 mass in Cont. [kg]	53.9	64.8	51.1
Final aerosols mass in Cont. [kg]	329.2	253	325
Total Relocation in LP [kg]	5771	6662	10268

- **No lower head vessel failure due to the ex-vessel reactor cooling**

SASPAM-SA Consortium reserves all rights in this document and in the information contained therein. Reproduction, use or disclosure to third party without express authorization is strictly prohibited.

iPWR Design-1: Core degradation

SAFETY ANALYSIS OF SMR WITH PASSIVE MITIGATION STRATEGIES - SEVERE ACCIDENT

ASTECv3.1
(Decay heat SASPAM-SA)

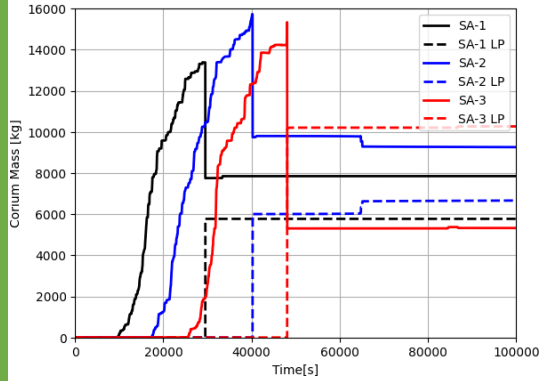

EdF-MAAP
(Decay heat ANS73)

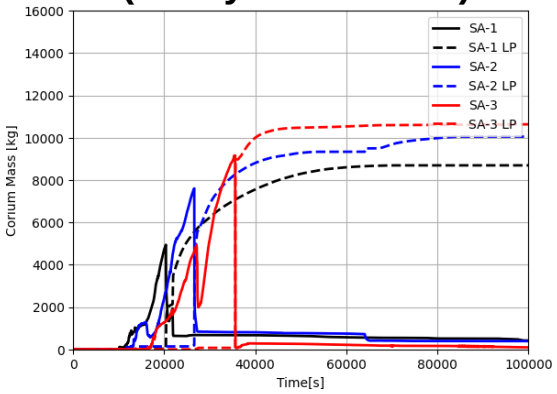

MELCOR
(Decay heat ANS73 and ANS73+20%)

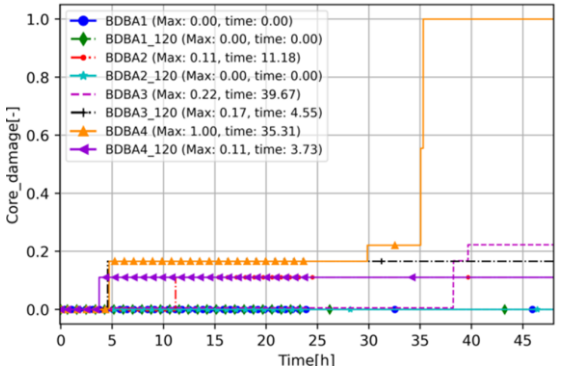

- **No RPV failure is predicted by the codes for any of the postulated SA scenarios**
- **Deviation of the timing of material relocation** to the LP is **about 1,000 s** by using the same decay heat data
- **Maximum deviation of the corium mass relocated to the LP is ~1 ton**

SASPAM-SA Consortium reserves all rights in this document and in the information contained therein. Reproduction, use or disclosure to third party without express authorization is strictly prohibited.

iPWR Design-1: Hydrogen Production

SAFETY ANALYSIS OF SMR WITH PASSIVE MITIGATION STRATEGIES - SEVERE ACCIDENT

SA-1 (ANS73+20%)

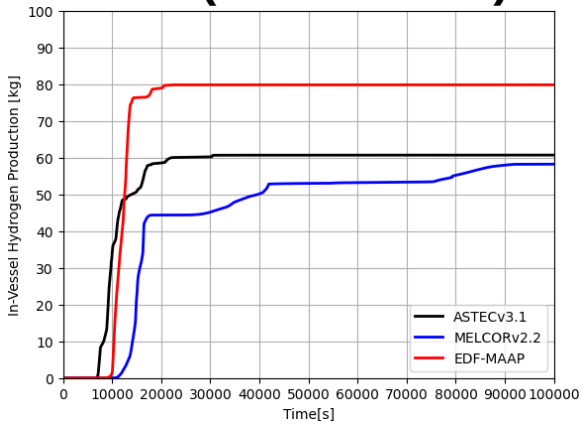

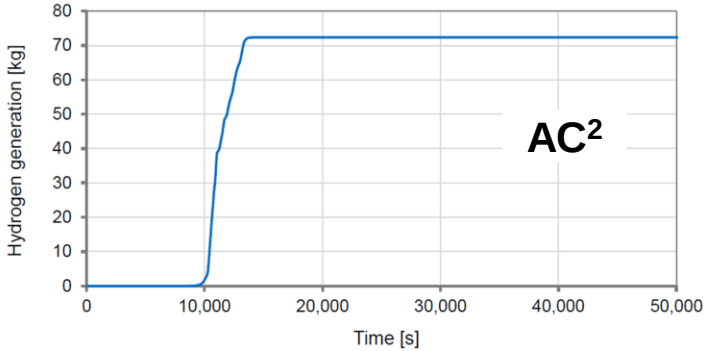

Codes and Decay Heat

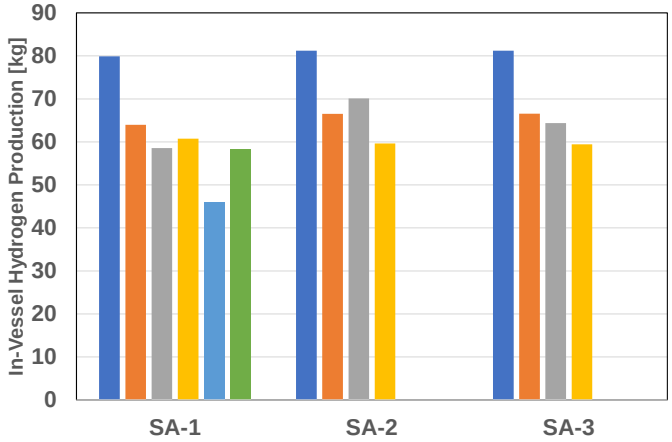

- Among the codes:
  - **Deviation on H2 onset ~ 1,000-2,000 s** by using the same decay heat data
  - **Deviation on H2 produced ~20 kg**

SASPAM-SA Consortium reserves all rights in this document and in the information contained therein. Reproduction, use or disclosure to third party without express authorization is strictly prohibited.

iPWR Design-1: SA scenario results

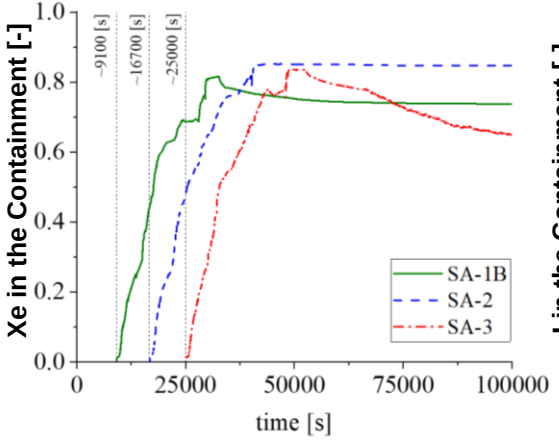

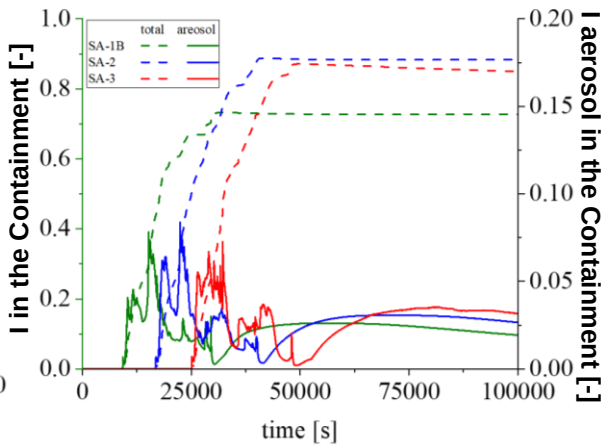

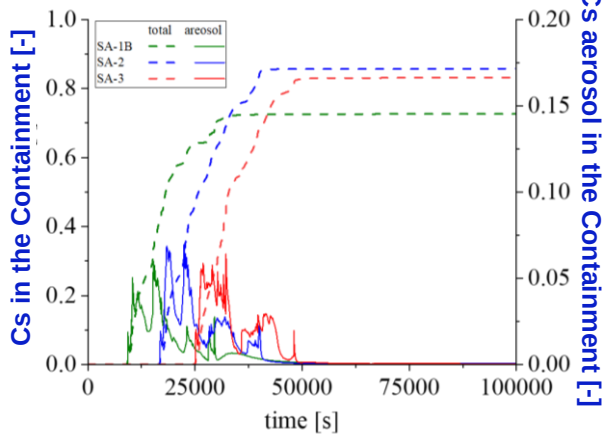

- **I and Cs aerosols released to the containment ~ 7.5% of the initial loading**
- **Maximum activity in the containment ~ 10% of the initial activity in the core (2.3E+19 Bq)**

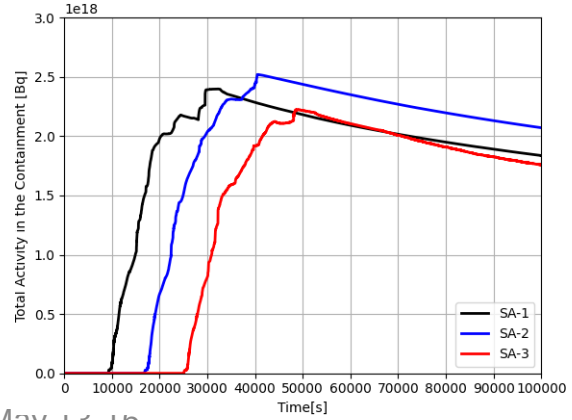

SASPAM-SA Consortium reserves all rights in this document and in the information contained therein. Reproduction, use or disclosure to third party without express authorization is strictly prohibited.

iPWR Design-1: CFD Containment Modelling

SAFETY ANALYSIS OF SMR WITH PASSIVE MITIGATION STRATEGIES - SEVERE ACCIDENT

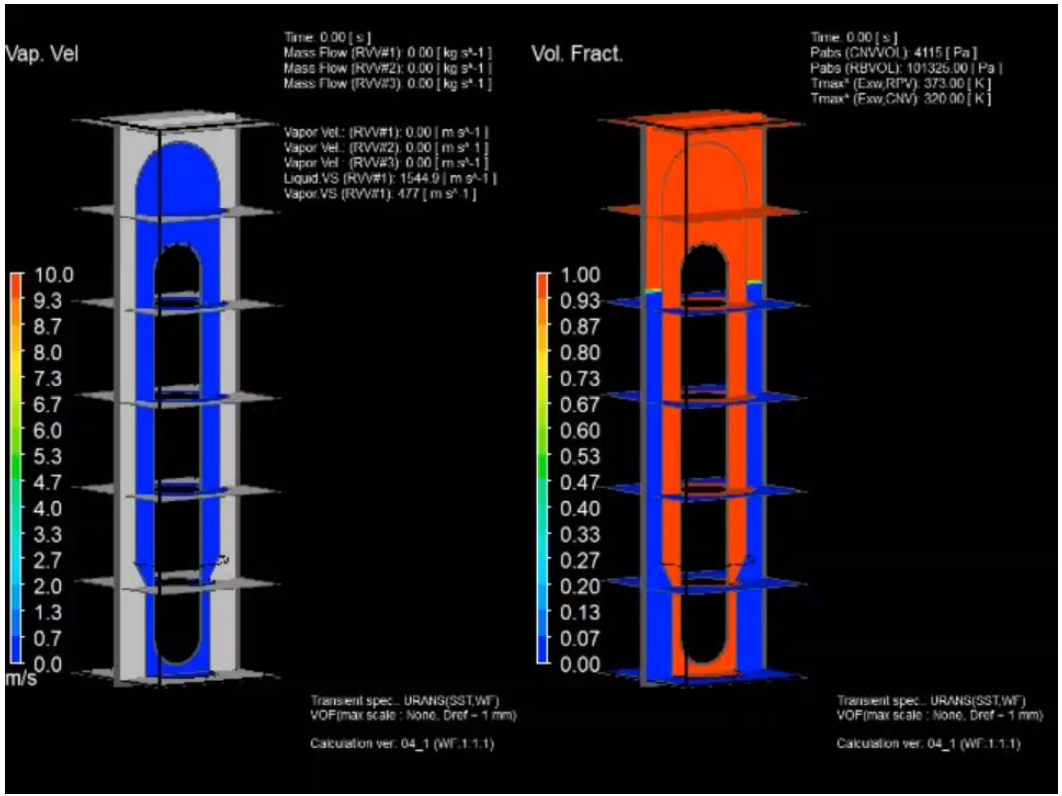

(courtesy of M. Makarenko, SSTC NRS)

- SA-2: 1000 s transient
- BCs from MELCOR (adjusted at the first 300 s to avoid choked flow)

SASPAM-SA Consortium reserves all rights in this document and in the information contained therein. Reproduction, use or disclosure to third party without express authorization is strictly prohibited.

iPWR Design-2: postulated SA Scenarios

- **DBA: Guillotine break of one Direct Vessel Injection (DVI) line**
- **Severe Accidents: DBA +**

unavailability of EHRS and ADS-1 systems (SA-1)

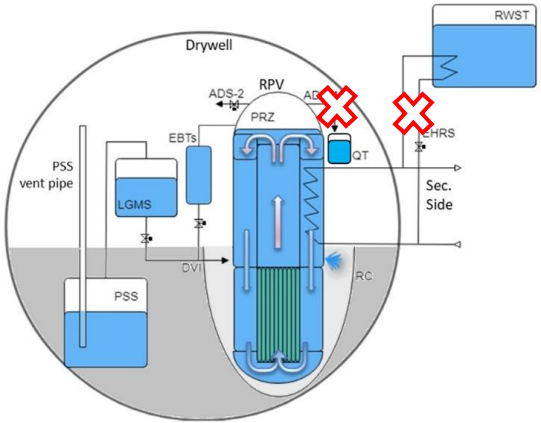

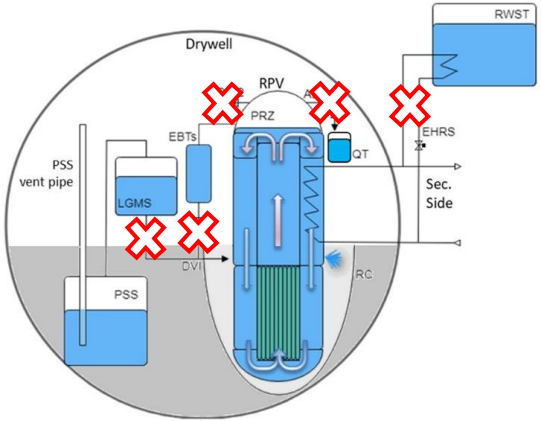

unavailability of all safety systems (SA-2)

unavailability of EHRS systems (SA-3)

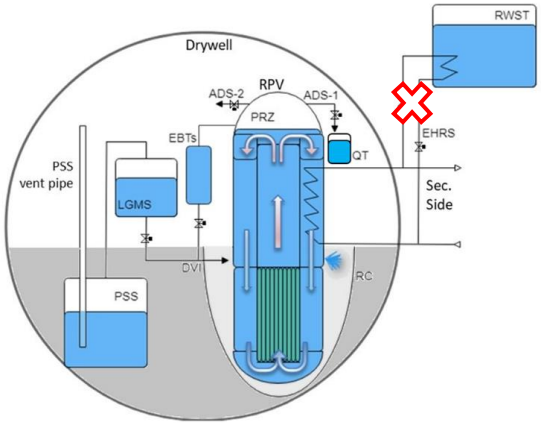

EHRS: Emergency Heat Removal System

(courtesy of A. Bersano, ENEA)

SASPAM-SA Consortium reserves all rights in this document and in the information contained therein. Reproduction, use or disclosure to third party without express authorization is strictly prohibited.

iPWR Design-2: Results

- **Calculations performed by employing the fuel inventory from SASPAM-SA**

Scenario	ASTEC v3.1 (ENEA)	MELCOR v2.2 (ENEA)	MELCOR v2.2 (UNIROMA1)	AC2 (LEI)	MAAP V5.06 (JRC)
Steady state	X	X	X	X	X
DBA	X	X	X	X	X
SA1	X	X		-	X
SA2	X	X	X	X	X
SA3	X	X		-	X

SASPAM-SA Consortium reserves all rights in this document and in the information contained therein. Reproduction, use or disclosure to third party without express authorization is strictly prohibited.

iPWR Design-2: DBA Scenario results

Event	ASTECv3.1	MAAP5.06	AC^2
Break of DVI line-A	0	0	0
High containment pressure setpoint (s)	**20**	**31**	**28**
↑SCRAM ↑Secondary system isolation ↑EHRS			
Low pressurizer level signal (s)	68	50	62
↑RCP coast-down ↑RI-DC valves opening			77
Low pressurizer pressure signal (s)	**160**	**170**	**92**
↑EBTs ↑ADS stage-1			
Low DP RPV-containment signal (s)	**1466**	**1274**	**1904**
↑LGMS			
Low LGMS mass signal (s)	**13459**	**25920**	**14301**
LGMS - Intact line empting (s)	15500		15400
Start of reverse flow in the PSS (s)	4950	5050	15400
Collapsed Maximum liquid level in the containment (m)	11.76		8.44
Collapsed Minimum level in the core from LP bottom (m)	3.84		5.54
Core TAF refilled - collapsed (s)	**5500**	**4320**	

SAFETY ANALYSIS OF SMR WITH PASSIVE MITIGATION STRATEGIES - SEVERE ACCIDENT

G. Grippo, et al., '*Comparison of a DBA sequence in a generic iPWR between MELCOR and ASTEC codes*', Session 4.1
G. Grippo, et al., '*Application of the Probabilistic Method to Propagate Input Uncertainty on a DBA Sequence in a Generic iPWR*' Session 4.2

iPWR Design-2: DBA Scenario results

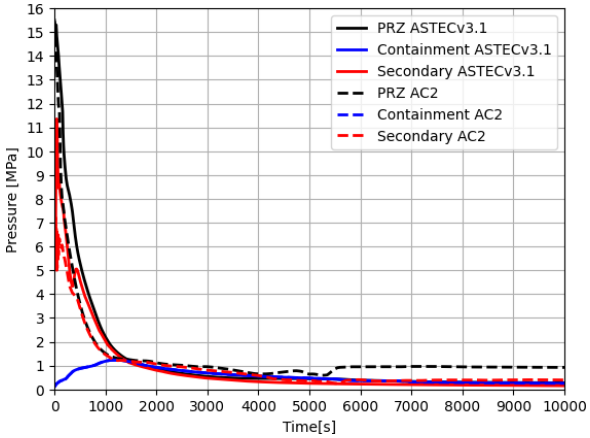

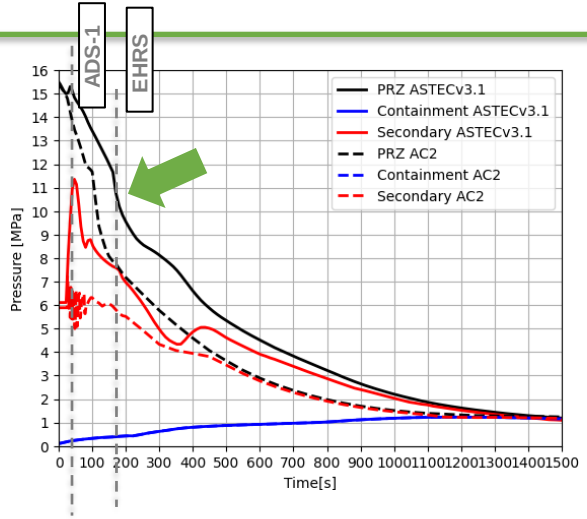

- Peak pressure in the secondary system quickly decreases (heat removal from the Refuelling Water Storage Tank (RWST))
- When the low PRZ level set-point is reached, the reactor coolant pumps coast-down occurs → **natural circulation in the RPV**
- **The low-pressure set-point in the PRZ triggers the ADS-1 → rapid decrease of the primary and secondary pressure**

SASPAM-SA Consortium reserves all rights in this document and in the information contained therein. Reproduction, use or disclosure to third party without express authorization is strictly prohibited.

iPWR Design-2: DBA Scenario results

SAFETY ANALYSIS OF SMR WITH PASSIVE MITIGATION STRATEGIES - SEVERE ACCIDENT

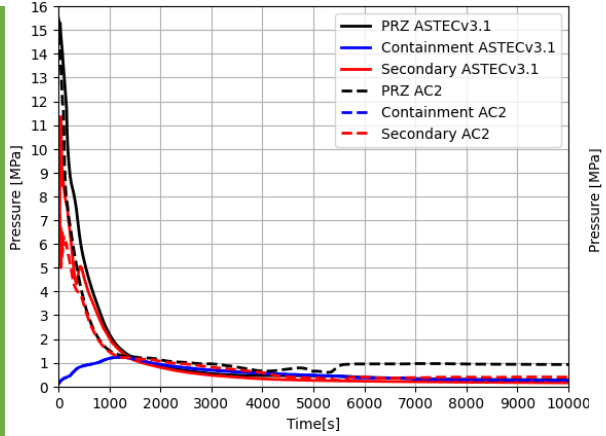

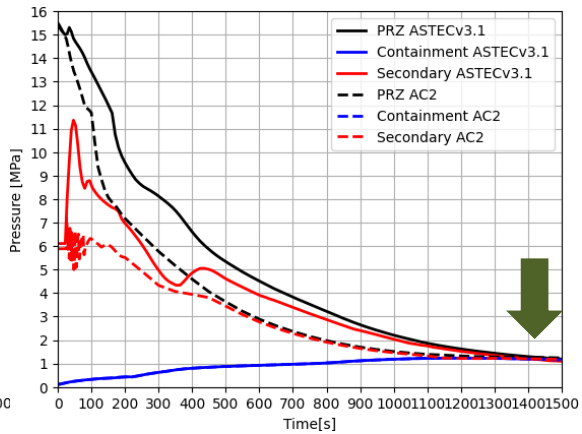

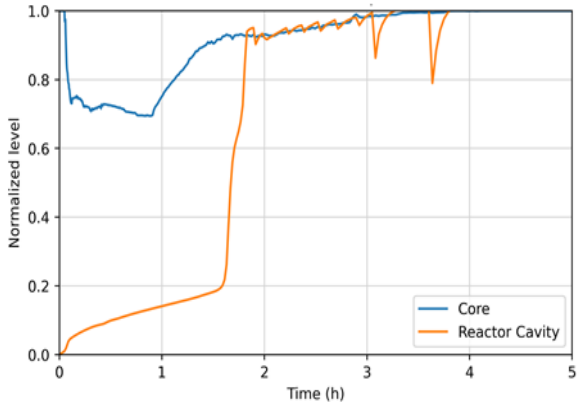

- **RPV and drywell (DW) pressures equalization → Long term Gravity Make-up System (LGMS) to the RPV and the reactor cavity**
- DW pressure decreases below the Pressure Suppression System (PSS) pressure → PSS water pushed inside the PSS vent pipes and fills the RC
- **All the codes been able to predict most of the key TH phenomena** (e.g., single and two-phase natural circulation in integral RPV, behavior of passive injection and heat removal systems, long term cooling, etc)

SASPAM-SA Consortium reserves all rights in this document and in the information contained therein. Reproduction, use or disclosure to third party without express authorization is strictly prohibited.

iPWR Design-2: SA Scenarios' results (ASTECv3.1)

Event	SA-1	SA-2	SA-3
Start of the transient (t_0)	0	0	0
High containment pressure setpoint (s)	20	20	20
Low pressurizer level signal (s)	90	90	90
Low DP RPV-containment signal (s)	45303	53532	18581
Actuation of LGMS (s)	45308	-	18586
Low LGMS mass signal (s)	133087	-	150174
Actuation of ADS-2 (s)	133087	-	150174
Containment failure	**2500**	**4020**	**800**
Start of reverse flow in the PSS (s)	2530	4060	815
RC collapsed level at DVI level (s)	2800	4300	1030
Core uncover (TAF reached), (s)	2000	5280	5830
Time of H2 production onset (s)	**8000**	**7294**	**11500**
In-Vessel H2 production [kg]	**386**	**359**	**273**
Start of FPs release from fuel (s)	9651	10386	12528
Core uncover (BAF reached), (s)	76860	72960	-
First corium slump (s)	**92900**	**74610**	**-**

SASPAM-SA Consortium reserves all rights in this document and in the information contained therein. Reproduction, use or disclosure to third party without express authorization is strictly prohibited.

iPWR Design-2: SA Scenarios' results

SAFETY ANALYSIS OF SMR WITH PASSIVE MITIGATION STRATEGIES - SEVERE ACCIDENT

Event	SA-1		SA-2			SA-3	
	ASTEC v3.1	MAAP v5.06	ASTEC v3.1	MAAP v5.06	AC^2	ASTEC v3.1	MAAP v5.06
Containment failure*	**2500**	**62192**	**4020**	**13327**	**2504**	**800**	**32700**
Core uncover (TAF)	2000	2804	5280	2675	3600	5830	2804
H2 onset	**8000**	**4762**	**7294**	**3980**	**7000**	**11500**	**4762**
H2 production [kg]	**386**	**280**	**359**	**280**	**377**	**273**	**280**
Start of FPs release from fuel	9651	19800	10386	12411		12528	19800
Core uncover (BAF)	76860	10231	72960	9955	11000	-	10231
Failure of the upper core rings	9700	10231	10386	9955	13500	12528	10231
First corium slump	**92900**	**62192**	**74610**	**13327**		**-**	**32700**

➢ **No lower head vessel failure due to the ex-vessel reactor cooling**

* Design pressure: ASTEC (1.4 MPa), MAAP v5.06 (2.4 MPa)

F. Giannetti, et al., '*MELCOR analyses of Severe Accident sequences in an integral PWR with passive systems*', Poster Session

SASPAM-SA Consortium reserves all rights in this document and in the information contained therein. Reproduction, use or disclosure to third party without express authorization is strictly prohibited.

iPWR Design-2: SA Scenario results

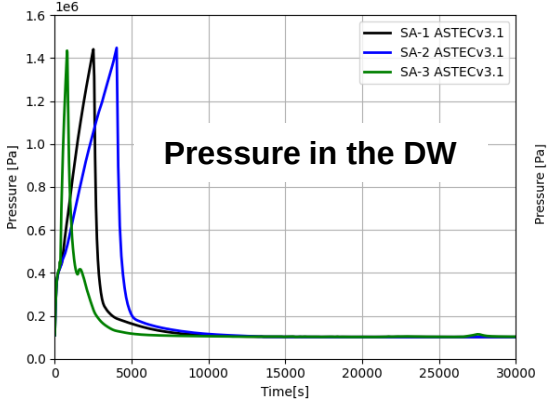

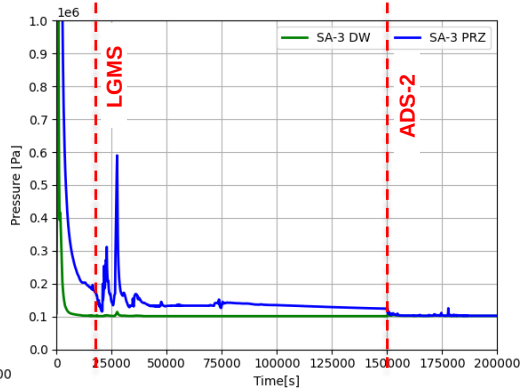

MAAP v5.06

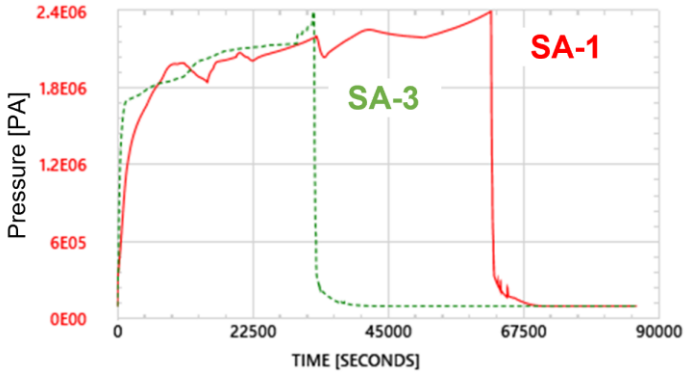

- **SA-3 case: Failure of the EHRS system**
- **EHRS Failure triggers a fast containment pressurization**, despite the 'mitigation' of the Pressure Suppression System (PSS) and Long-term Gravity Make-up System (LGMS) tanks
- As expected in the **DBA mitigation strategy**, the **containment depressurization leads to the PSS tanks water being pushed to fill the reactor cavity**
- RPV depressurization much slower than in the containment → primary system remains at higher pressure for a long period → RPV water level gradually decreases

SASPAM-SA Consortium reserves all rights in this document and in the information contained therein. Reproduction, use or disclosure to third party without express authorization is strictly prohibited.

iPWR Design-2: SA Scenario results

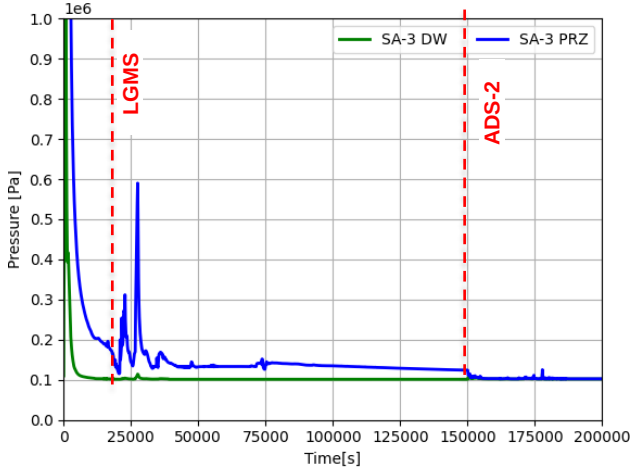

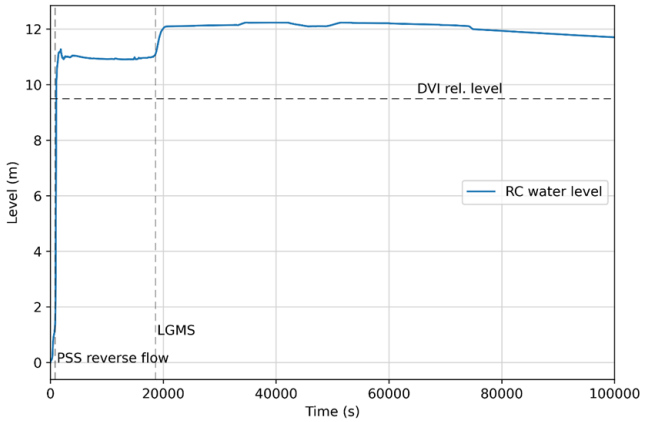

- **0 – 18000 s** → higher pressure in the RPV prevent any reverse containment/RPV flow **despite the RC is filled above the break (DVI) elevation** → RPV water level lower than the DVI level
- **25,000 s -150,000 s** → small amount of water continues to enter the RPV from the break when it depressurizes sufficiently
- **~78,000 s** → **intact LGMS slowly starts inject water into the RPV**

SASPAM-SA Consortium reserves all rights in this document and in the information contained therein. Reproduction, use or disclosure to third party without express authorization is strictly prohibited.

iPWR Design-2: SA Scenario results

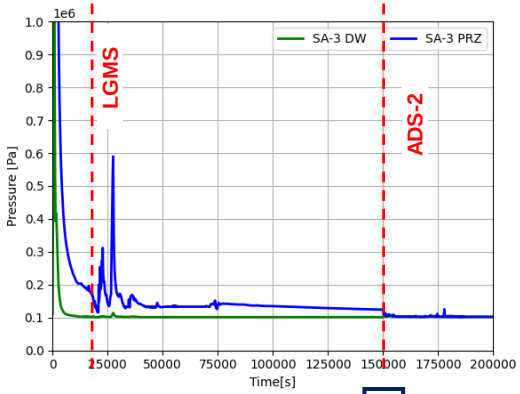

- **~ 150,000 s** → LGMS water level reached → triggering the Automatic Depressurization System-2 → RPV/containment pressure equalization
- **Water begins to re-enter from the RC though the break → core water refilling**

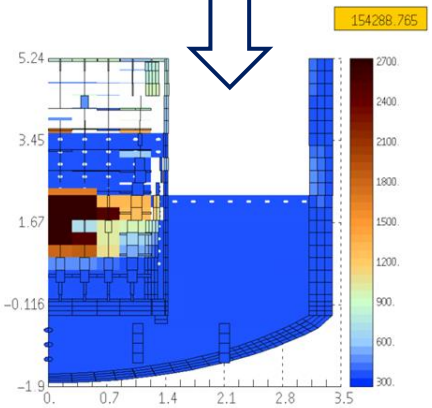

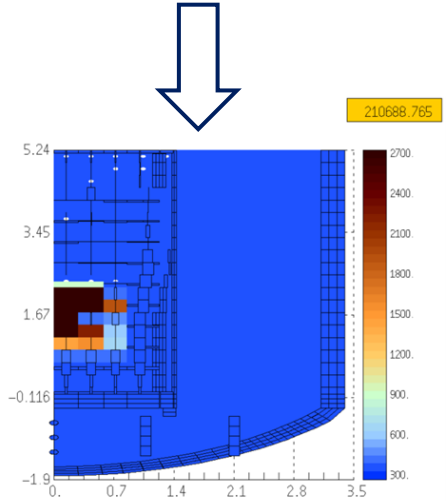

SASPAM-SA Consortium reserves all rights in this document and in the information contained therein. Reproduction, use or disclosure to third party without express authorization is strictly prohibited.

iPWR Design-2: SA Scenario results

SAFETY ANALYSIS OF SMR WITH PASSIVE MITIGATION STRATEGIES - SEVERE ACCIDENT

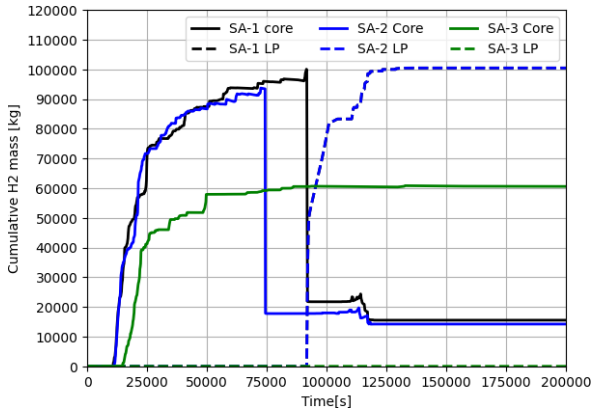

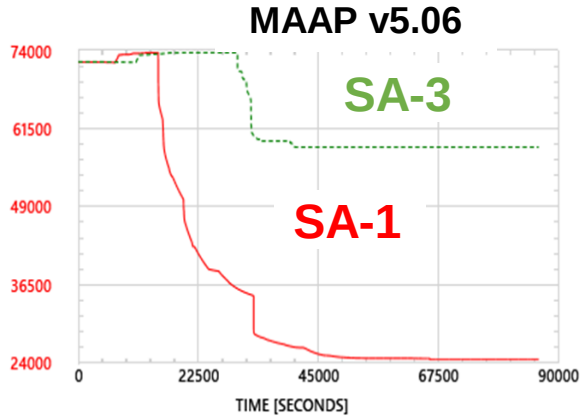

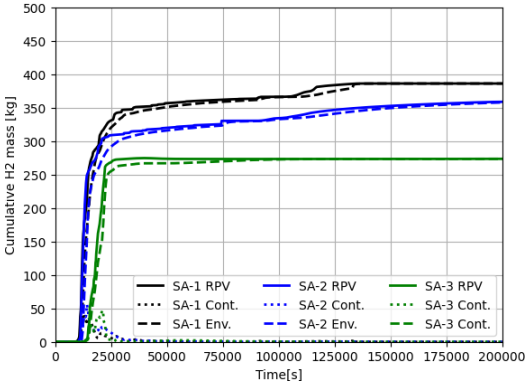

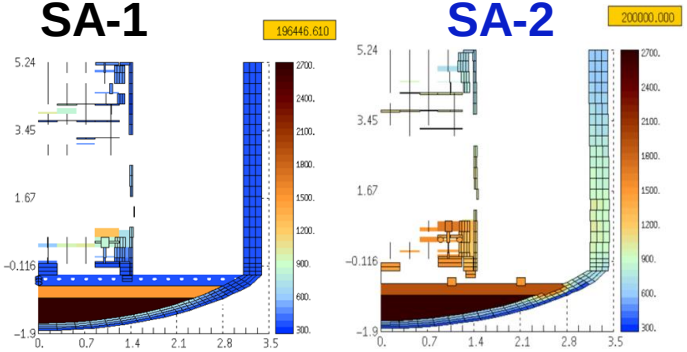

- **Increase of the systems unavailability (SA-1 and SA-2) → Increase of the severity of the core degradation conditions**
- **H2 production ranges from 250 to 375 kg**

SASPAM-SA Consortium reserves all rights in this document and in the information contained therein. Reproduction, use or disclosure to third party without express authorization is strictly prohibited.

Summary and Outlook

SAFETY ANALYSIS OF SMR WITH PASSIVE MITIGATION STRATEGIES - SEVERE ACCIDENT

- SASPAM-SA unique project on iPWRs with respect to DiD levels 4 and 5
- DBA and hypothetical SA scenarios have been postulated
- Datasets of both state-of-art European and non-European integral codes and CFD tools for two generic iPWR designs assessed
- Integral codes are able to predict the key TH phenomena occurring in iPWRs in the postulated DBA and SA scenarios
- Consistent results across the code set used in this exercise
- Datasets and results available as BCs for next investigations (e.g., IVMR, Containment, EPZ)
- Analyses of the postulated scenarios by employing ATF cladding material going to start

SASPAM-SA Consortium reserves all rights in this document and in the information contained therein. Reproduction, use or disclosure to third party without express authorization is strictly prohibited.

..finally

- The SASPAM-SA WP2‘s Community

  F. Mascari, A. Bersano, P. Maccari, S. Ederli, M. E. Cazado, V.H. Sanchez-Espinoza, M. Di Giuli, J. Bittan, N. Bakouta, M. Malicki, T. Lind, M. Makarenko, Yu. Yesipenko, O. Zhabin, D. Gumenyuk, S. Kelm, E.-A. Reinecke, C. Vázquez-Rodríguez, M. K. Koch, J. Krieger, G. Stahlberg, T. Jankowski, M. Garcia Martin, L. E. Herranz, N. Reinke, A. Bentaib, L. Carenini, J.-C. de la Rosa Blul, O. Papera Villacampa, A. Kaliatka, M. Valincius, M. Constantin, F. Giannetti, T. Sevon, P. Groudev

- Special mention to EDF (J. Bittan), ENEA (A. Bersano), and Tractebel (M. Di Giuli) for their efforts in leading the activities in the working groups

- Thunderstruck from ‘The Razors Edge’, 1990, EMI
  https://www.youtube.com/watch?v=n_GFN3a0yj0

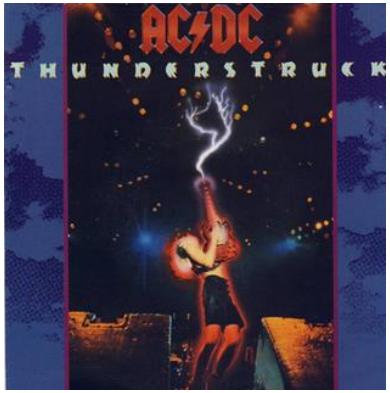

SASPAM-SA Consortium reserves all rights in this document and in the information contained therein. Reproduction, use or disclosure to third party without express authorization is strictly prohibited.

Acknowledgement/Disclaimer

SAFETY ANALYSIS OF SMR WITH PASSIVE MITIGATION STRATEGIES - SEVERE ACCIDENT



Funded by the European Union

Funded by the European Union. Views and opinions expressed are however those of the author(s) only and do not necessarily reflect those of the European Union or European Commission-Euratom.
Neither the European Union nor the granting authority can be held responsible for them.

SASPAM-SA Consortium reserves all rights in this document and in the information contained therein. Reproduction, use or disclosure to third party without express authorization is strictly prohibited.

The 11th European Review Meeting on Severe Accident Research (ERMSAR2024)
KTH, Stockholm, Sweden, May 13-16, 2024
Log Number: 116

153-126800-CONF-004656

UPDATE ON SEVERE ACCIDENT ANALYSIS RESEARCH AT CNL FOR SMALL MODULAR AND ADVANCED REACTOR DESIGNS

Andrew C. Morreale*, Luke S. Lebel, Feng Zhou, David W. Hummel, Eric Jia, John Cui, Chris I. Maxwell, Thaneshwor. P. Kaloni, Ernesto Geiger, and Garik Patterson
Canadian Nuclear Laboratories, Ltd. (CNL)
286 Plant Road, Chalk River, Ontario, K0J 1J0, Canada
andrew.morreale@cnl.ca; luke.lebel@cnl.ca; feng.zhou@cnl.ca; david.hummel@cnl.ca;
*corresponding author

ABSTRACT

The drive for carbon-free energy to combat climate change has generated increased interest in nuclear energy, specifically small modular reactor (SMR) and advanced reactor (AR) technologies. Research is conducted at Canadian Nuclear Laboratories (CNL) to support the deployment of these technologies, including modelling and experiments related to reactor safety. These efforts are part of a robust technical program supporting research, development, and licensing activities for SMR/ARs for remote (off-grid) locations and grid-level applications. Severe accident analysis and the prediction of radionuclide source terms are a major portion of this work informing design, regulatory interest, and emergency response planning. CNL has refined its generic technology-agnostic approach to focus on technologies nearest to deployment but continues to follow a progression of i) determining knowledge gaps through phenomena identification and ranking table (PIRT) exercises; ii) tailoring research projects to address these gaps, and iii) evaluating postulated accident scenarios, source terms and impacts on emergency response. Through these activities, CNL builds capabilities to support understanding of severe accidents in SMR/AR designs to service both government and industry stakeholders. The extensive experience gained in CANDU analysis, broad experimental capabilities, and innovative new test apparatus enable CNL to build this competence in SMR/AR safety analysis and severe accident assessment. Technologies under investigation include water-cooled designs (integral pressurized water reactor, iPWR; and small boiling water reactor, BWR), high temperature gas reactors (HTGR; including micro-reactor designs), molten salt reactors (MSRs), sodium fast reactors (SFRs), and heat-pipe designs. Recently completed and in-progress experimental investigations include the behaviour of fission products in small water-cooled reactor containments, air ingress into HTGR cores, passive cooling systems in water-cooled and other designs, heat pipe behaviour in operational and accident conditions, the behaviour of fission products in molten salt fuels under accident conditions (i.e., release/retention), and UO_2 corium behaviour and molten corium-concrete interaction. Modelling includes design analysis to support experiments, benchmarking activities, and integrated severe accident analysis of SMR/AR designs to determine accident progression, source terms and dose consequences. Efforts have also been made to inform criteria and procedures for emergency planning and response to potential accidents, including consideration of remote and northern operations, and the proximity to populations and/or industrial processes. Guidance on the technologies of focus and the depth and urgency of research comes from the evolution of the Canadian SMR/AR deployment landscape, such as proposed new builds and vendor design reviews by the Canadian Nuclear Safety Commission. As Canada's national nuclear laboratory, CNL's research supports industry (utilities, vendors, suppliers) and government stakeholders in deploying SMR/AR technologies in Canada.

KEYWORDS
Small Modular Reactors, source term, molten salt, high temperature gas cooled reactors (HTGR), integral PWR, small BWR

1. INTRODUCTION

The pursuit of clean energy is continuing to ramp up worldwide, and a major avenue for carbon-free generation is nuclear energy. Much of the recent development is focused on small modular designs and advanced reactors, but of late, there has also been a push for new large nuclear stations as well. The realities of climate change and the desire to increase electrification in transportation and industry are fueling this expanded interest in all sizes of nuclear energy, from micro designs (5-15 MWe) to SMRs (50-300 MWe) to large conventional reactors (1000+ MWe). Applications include remote (off-grid), industrial process applications, and small (SMR) and large on-grid power generation. Canada's historic use of nuclear energy, varied energy needs, favourable government policies and performance-based regulatory framework create excellent conditions for new deployment of all types of nuclear generation.

In the last two years, there have been several announcements for new nuclear development. For grid-scale SMRs, the siting of four GE-Hitachi BWRX-300 reactors was announced by Ontario Power Generation at the Darlington site near Toronto, and interest has been expressed in the BWRX-300 by SaskPower for builds in Saskatchewan, as well as interest in grid-scale SMR power generation by Capital Power for builds in Alberta. New Brunswick has expressed interest in two homegrown designs, the ARC Clean Technologies sodium fast reactor design and a MOLTEX molten salt reactor (MSR) design, both of which have the potential to incorporate spent fuel into their reactor fuel cycle. In terms of micro-reactors, Global First Power is currently progressing through environmental assessment and siting for an Ultra Safe Nuclear Corporation (USNC) micro-modular high temperature gas cooled (HTGR) reactor (MMR) design at the AECL (Atomic Energy of Canada Limited) Chalk River Laboratory Site and the Saskatchewan Research Council has recently launched an effort to assess the Westinghouse e-Vinci heat pipe reactor design for deployment in their province. In addition to these announcements, Bruce Power has announced plans for 4800 MWe of new large nuclear stations at its site near Kincardine, Ontario. Many jurisdictions and organizations across Canada are looking closer at how nuclear technologies can support their clean energy needs.

Canadian Nuclear Laboratories (CNL), as Canada's national nuclear laboratory and premier nuclear science and technology organization, is heavily involved in supporting the operations and deployment of nuclear energy in Canada. CNL maintains extensive knowledge and capabilities in nuclear energy as well as a robust technical program supporting research, development, and licensing activities to facilitate the deployment of new nuclear. The reactor safety program is a key component supporting the safe design and operations of nuclear reactors, which includes the analysis of reactor accident scenarios, the related phenomena, and the potential consequences in the form of the release of radionuclides to the environment (i.e., source term).

The reactor safety and severe accident research at CNL covers all types of nuclear energy, including support of the operating fleet of CANDU reactors, as well as SMR and AR technologies that are on the deployment horizon in Canada. For the purposes of this paper, we will focus on the SMR/AR related efforts, which build off the extensive experience in CANDU reactor safety developed at CNL over more than 80 years. The program encompasses both experiments (including separate effects testing and integral facilities) to improve understanding of safety and severe accident phenomena, and modelling/analysis of specific safety and accident phenomena (supporting experimental analysis, integrated safety analysis and severe accident modelling, and analysis benchmarking). This allows CNL to increase its knowledge base and enhance modelling and experimental capabilities to improve understanding of safety-related and accident phenomena for the development and assessment of SMR/AR regulatory/licensing requirements and emergency planning and response.

As discussed in a previous paper [1], CNL reactor safety efforts include i) the identification of significant phenomena and gaps in knowledge (frequently through phenomena identification and ranking table, PIRT, exercises), ii) designing experiments and modelling of the phenomena to address these gaps, iii) accident analysis for postulated scenarios and the evaluation of potential source terms, and iv) discussion of

appropriate emergency planning and response. The SMR/AR designs that are currently being investigated at CNL include water-cooled SMRs (integral pressurized water reactors, iPWR; small boiling water reactors, BWR), HTGRs, MSRs, sodium fast reactors (SFRs) and micro reactors (including heat-pipe designs). CNL maintains a continuously evolving research program with the focus narrowing to more specific technologies and deeper analysis for designs moving closer to deployment. Initially, a base knowledge level of the technology is developed, which can be expanded/deepened as technologies move towards deployment in order to meet the needs of the industry or the regulator.

This paper provides an update to the previous discussion [1] on severe accident research at CNL, discussing progress in ongoing efforts as well as forays into new areas. Experimental campaigns are discussed in Section 2, covering water-cooled, HTGR, and MSRs. Modelling and analysis, discussed in Section 3, support experimental efforts and include integral severe accident analysis of several designs (iPWR, small BWR, HTGR, and SFR) for postulated scenarios important to source terms and emergency planning. Strategic considerations of the CNL severe accident research program are presented in Section 4, which are continually updated based on Canada's deployment landscape, the regulatory needs of the Canadian Nuclear Safety Commission (CNSC), and industry customers. CNL's research program is aligned with international efforts through CNL's participation in the international community via projects and working groups run by the European Commission, the Generation IV International Forum (GIF), the International Atomic Energy Agency (IAEA) and the Organization for Economic Cooperation and Development Nuclear Energy Agency (OECD-NEA).

2. EXPERIMENTAL EFFORTS SUPPORTING SMR SAFETY

Multiple experimental campaigns are underway at CNL to support the understanding of relevant phenomena in SMR/AR severe accidents. The issues being explored were previously identified in PIRT exercises for the various SMR/AR designs as important gaps in knowledge and data. The experimental work is the progression of efforts discussed in [1] and new studies driven by emerging issues. The current severe accident experimental focus includes water cooled SMR passive safety systems (e.g., convection cooling of containment, isolation condensers, etc.), and the potential for air ingress in HTGRs. In addition, further efforts are planned in the study of fission product behaviour in molten salts.

2.1. Water Cooled Reactor Experiments

With water-cooled SMRs being some of the closest to deployment, experiments have been designed to study safety features that are novel to the designs, especially those related to passive systems that drive long term cooling and aid in fission product retention. A major focus is on pathways that can lead to the disruption of passive safety systems, and subsequent impacts on potential source terms, because are important to severe accident management and off-site emergency response as part of defence-in-depth for those facilities.

For iPWR-type SMRs with submerged containment vessels, strong condensation onto the cooled outer wall drives the passive emergency core cooling system loops. The presence of hydrogen, for example, is a cliff edge effect in that it can lead to the reduction of heat transfer coefficients and disrupt steam condensation process, but there needs to be hydrogen generation from core degradation in order to disrupt the loop in the first place. In a stronger accident condition with a "loss of containment isolation", air ingress into the containment further complicates matters, affecting the containment thermal-hydraulics while also creating a combustion risk, should hydrogen be present. In fact, given the open pathway to the environment, the final phenomenon preventing major radionuclide releases would be possible deposition on the containment walls, in part driven by strong condensation that occurs through the 'diffusiophoresis' mechanism.

These topics have been explored in experimental campaigns in the Strong Condensation Containment Apparatus (SCCA), conducted in 2021 and 2022, with some results already published [2] [3] , and others

being drafted. These topics focused on the iPWR system with condensation mainly onto a wall, but other experiments are planned for 2024 and 2025 exploring condensation onto a tube bank prototypical of a small BWR's passive containment cooling system. Data and experience from the experiments are also being incorporated into the European SASPAM-SA (Safety Analysis of SMR with Passive Mitigation Strategies – Severe Accident)[1] collaboration, in order to build up experimental databases and experience for water cooled SMR safety analysis.

The SCCA (Figure 1) is a tall rectangular volume, where steam, helium (used as an analog to hydrogen), and aerosols can be injected in from the ceiling. The left wall is maintained at a low temperature with a cooling water jacket running behind it, and the right wall can be heated with a constant heat flux. The front walls are transparent, which allows a Phase Doppler Anemometer (PDA) to be used to study the near-wall aerosol behavior. The volume was open to atmosphere via a vent near the ceiling, simulating the "loss of containment isolation" accident condition. A NaCl solution is used as the radionuclide analog, which is tracked at several aerosol sampler locations and in the condensate flows. Aerosol transport through the system was tracked either by measuring the salinity in the condensate runoff, sampling the gases at different locations and capturing aerosols in bubbler impingers (which also used liquid salinity measurements), or by evaluating the droplet size, velocity, and count concentration from the PDA measurements.

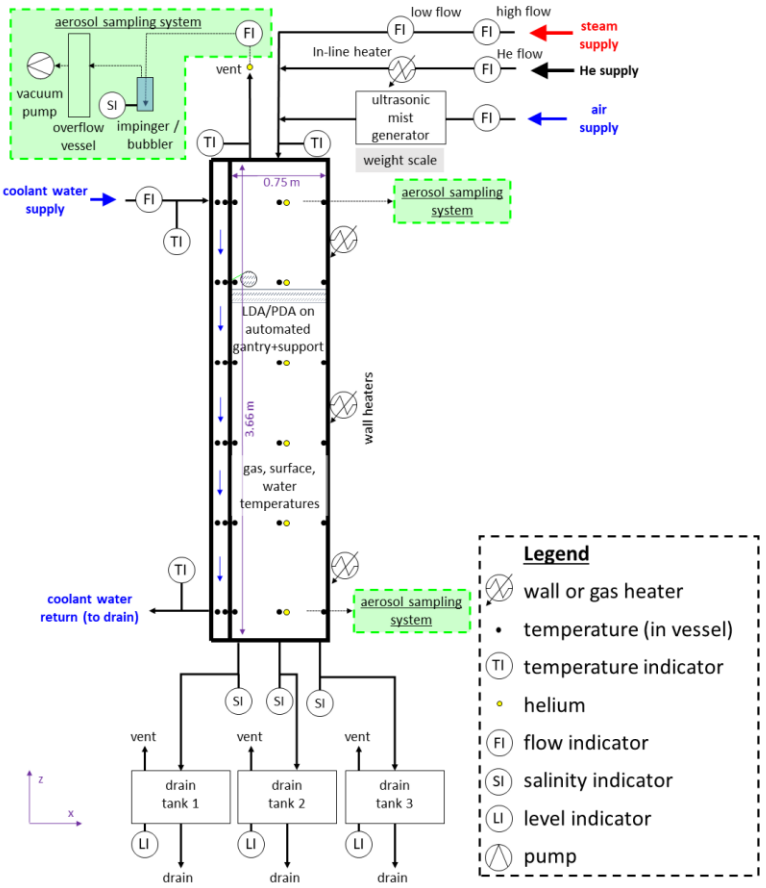

Figure 1. Schematic of the CNL Strong Condensation Containment Apparatus [3]

[1] https://www.saspam-sa.eu/

The most important observation from the point of view of the thermal-hydraulics is that, with multi-gas mixtures, and especially when there is air ingress from loss of containment isolation, there was very strong stratification between a hot upper layer and cooler under layer in the volume. At higher elevations, the environment was strongly condensing with a dense cloud of water aerosols at temperatures, but below this, there was a sharp temperature gradient at the transition to a cooler under-layer (on the order of 20°C-40°C). The maximum potential cooling capacity of the walls was in excess of the energy that is input from the steam injection, and heat transfer coefficients from steam condensation are many times higher than those for normal natural convection, so that the vast majority of heat transfer will occur in the hot upper layer. The thickness of the hot upper layer results from an equilibrium between the energy input and cooling to the wall via the surface area of the hot upper layer. When a light gas like helium (or in the reactor accident case, hydrogen) is introduced, it does not separate from the steam in the upper layer like air does because of its buoyancy, and will serve to dilute the upper layer, consequently both reducing the effective heat transfer coefficient of the upper layer [4] and causing the layer to swell. The light gas also diffuses into the lower layer where it can reach mixtures of 10-30%, which would have combustibility implications if it is hydrogen.

As far as radionuclide transport is concerned, the primary mechanisms that were observed were from diffusiophoresis, driven by steam condensation, as well as turbulent impaction driven by the fairly turbulent environment in the enclosed volume. Both of these, however, are limited primarily to the hot upper layer of the volume, with the gas stratification having an important impact on the aerosol deposition because it limits the area over which the deposition occurs. An interesting effect that can be called the “evaporative barrier” was also observed that led to the NaCl fission product tracer being effectively trapped in the upper layer. The hot upper layer is a strongly condensing environment with a thick fog, composed of water droplets on the order of 20 µm in size. In contrast, the cooler under layer is drier and less turbulent. Whereas the water droplets containing the tracer in the upper layer should have a high gravitational settling rate, if some attempt to pass from the upper layer to the lower one, they enter the drier environment, start to evaporate and shrink, which in turn slows down their settling, whereas the more turbulent environment above could re-entrain them back into the upper layer. This has implications on deposition because it keeps the concentration in the upper layer higher than it otherwise would be by both limiting the volume into which it can mix into prior to being released, limits the horizontal surface area onto which it can be removed onto, and removes one of the main deposition mechanisms noted from larger reactor containments.

2.2. High Temperature Gas Reactor Experiments

HTGR-related severe accident experimental research at CNL has been focused on the transition from stagnant flow conditions to bulk natural circulation of air within the core after a break of the helium pressure boundary. The timing of this transition is uncertain (difficult to reliably predict), and the effect of air flow on the graphite oxidation rate is significant. Originally CNL proposed to study this phenomenon with design and construction of the High Temperature Air Ingress Facility (HTAIF) inside CNL’s Large Scale Containment Facility (LSCF). However, some lessons learned from the High-Temperature Test Facility (HTTF) at Oregon State University [5] were impractical to incorporate in the HTAIF design, and considering the already high complexity and predicted expense of the facility, the decision was made to terminate the HTAIF design effort. The phenomenon will instead be studied in the relatively simpler Helium-Air Natural Convection (HANC) experimental apparatus. The geometry of the HANC experiment is an “inverted-U” shape that represents the coolant flow path within the reactor pressure vessel. Descriptions of other similarly shaped apparatus for the study of air ingress can be found in literature. However, unlike these past experimental studies, HANC will retain the full height of the core as well as the operating temperature (700°C) of the original HTAIF concept. The design of the HANC experiment is complete, and procurement of equipment and materials is ongoing. The apparatus is expected to be constructed by the end of 2024, and the first experiments are planned to take place in 2025. These experiments are intended to provide data to benchmark predictions of the onset of natural convection (ONC) in safety analysis computer codes like GOTHIC and RELAP5-3D, and potentially severe accident analysis codes like MELCOR.

2.3. Molten Salt Reactor Related Experiments

In the area of MSRs, a variety of experimental work is exploring general phenomena of molten salts (both fuel salts and coolant salts), including characterization of thermodynamic properties, corrosion, and capabilities for the production of fuel salts and simulant salts. The severe accident research focus continues to be fission product behaviour. Previous experiments on fission product releases from molten fuel salts under severe accident conditions [1] converted irradiated UO_2 to a UF-based fluoride and fluoride-chloride molten salt. These experiments yielded interesting fission product release data from the fuel salts when they were exposed to severe accident conditions (1000°C under both inert and oxidizing atmospheres). However, it was determined that further testing was needed to confirm that the conversion process from UO_2 to UF-based fuel salt was effective in producing a sample representative of a molten fuel salt reactor system. These confirmatory tests are nearing completion at CNL and utilize un-irradiated UO_2 being converted into halide salts (both fluoride and fluoride-chloride). If the confirmatory tests demonstrate the efficacy of the conversion process, the earlier fission product release results will be supported.

Future efforts at CNL in this area will be conducted with “simsalts”, which will contain actinides and fission product simulants (concentrations based on reactor physics modelling) and provide the benefit of tighter controls on purity and salt content. Part of these experiments will be the production of large (> 50 g) quantities of fluoride and fluoride-chloride salts. These simsalts would be exposed to severe accident conditions (high temperatures under an inert atmosphere, as well as air or steam in cases of fuel/coolant spill or reactor vessel breach). Multiple experimental campaigns will allow the development of experimental phase diagrams on selected halide-and oxo-halides systems. In addition, complementary modelling will be conducted, including: i) developing thermodynamic models that describe the fluoride and chloride systems under different atmospheres and ii) investigating kinetic and interface-related phenomena (such as diffusion of species or wetting behaviour of the salts). These efforts will be fundamental in future exploration of the behaviour and release of species from irradiated samples (similar to the initial tests described in [1] but with much more control on purity, content, and conditions, and with a broader test matrix), and those requiring large amounts of purified salts. This research will generate information to support deployment of MSRs and will also expand experimental capabilities required for further investigation on these technologies.

3. SEVERE ACCIDENT MODELLING AND ANALYSIS EFFORTS FOR SMR

CNL modelling and analysis efforts support the experimental programs and expand capabilities for integrated severe accident analysis and source term calculations for a variety of SMR/AR designs. The experimental benchmarking is currently aligned with aerosol behaviour in iPWR containment and the associated SCCA tests, but as more experiments are conducted and new data becomes available, new benchmarking campaigns will be developed. CNL also engages other partners, such as universities and other research organizations, in such benchmarking exercises. In terms of integral accident analysis, a generic model of the reactor design is developed based on open literature and postulated accident scenarios are assessed. In some cases, the design information is lacking, and reasonable assumptions need to be made using suitable resources from other similar designs. The overall goal at this stage is not a licensing analysis but rather building capability and exploring the important phenomena and systems involved in severe accidents in each reactor technology. The extent of the analysis needed is to follow a graded approach in line with the potential source terms and the nearness to deployment of the specific technology. Analysis models are refined periodically with the latest design details in the open literature. The ongoing integral analysis focuses on water-cooled SMRs, a grid-scale small HTGR, and the early development of SFR analysis capabilities. In addition, CNL is exploring severe accident uncertainty and sensitivity analysis and its application to SMRs. Finally, emergency response is considered, specifically methods for determining suitable emergency planning zones for various reactor technologies and applications. With these capabilities, CNL can tailor analysis to meet regulatory and licensing needs.

3.1. Water Cooled Reactor Analysis

The water-cooled SMR analysis models have focused on both iPWR and small BWRs, representing both major design threads that are being pursued in the new reactor market. As discussed, the overall theme with these models are to explore severe accident analysis and source term issues, with the main focus on pathways to severe accidents via the disruption of passive safety systems, given the strong reliance on passive safety systems in the designs and their novel aspects. The primary tool for this has been MELCOR, where CNL has developed reference models for both a generic iPWR design and generic small BWR design, both of which are discussed below. In addition, benchmarking studies are ongoing in order to use MELCOR, as well as more detailed thermal-hydraulic codes like GOTHIC and even detailed computational fluid dynamics (CFD) models, in order to ensure that phenomena are appropriately captured. Benchmarking comparisons to experimental data are underway/upcoming, such as those obtained from the SCCA campaigns and other relevant experiments from literature. With the experience and confidence being developed by exercising these safety analysis tools, they can be further employed for other studies, such as prototypical probabilistic safety analyses that can be used to inform SMR emergency planning zone development, as discussed in Section 3.6.

A model of a generic iPWR design was produced from information available in open literature, similar to the generic natural circulation iPWR MELCOR model presented by Li et al. [6], but scaled to be closer in power level and volume sizes to the NuScale design [7]. It includes models for the reactor pressure vessel (RPV) within the submerged containment vessel, as well as the outer operating pool and decay heat removal system (DHRS). Special attention was paid to systems that are part of the passive emergency core cooling (ECC) loop (facilitated by reactor vent valves, RVVs, and reactor recirculation valves, RRVs), which backs up the DHRS loop. Other highlights include containment leakage pathways, safety relief valve (SRV), and failure pathways to the environment, as well as the operating pool failure pathway; each of these play a role in different accident scenarios.

A set of accidents sequences with various initiating events have been explored, initially presented in Morreale [8], and further expanded upon in ongoing work, with some refinements to the original generic iPWR model considering an increase in availability of open literature design details. This study increases the number of sub-case permutations, explores the impacts of delays and mitigating actions, and attempts to give a more detailed picture of the potential source terms for various accident scenarios:

- Set 1 is the set of base cases, and was similar to the severe accident that was considered as part of the US NRC independent confirmatory analysis of the NuScale design [9]. It explores a station blackout with no functioning DHRS, so that the passive ECC system is triggered. Certain permutations avoid core degradation, while others lead to it, where a number of cliff edge effects relating to the water inventory in containment and presence of hydrogen have been identified. In all cases though, cooling to the overall system can be maintained even if core damage occurs, and given containment can stay intact, the overall releases to the environment are very small.
- Set 2 is an extension to Set 1 where there is also a major leak that drains the outer operating pool over a certain amount of time (with several leak rates explored). This is the same type of scenario that was considered in Li et al. [6]. The RVV still functions when the RPV reaches its design pressure, but without the outer heat sink to drive steam condensation, the passive emergency core cooling loop is interrupted. Core degradation occurs and the containment eventually over-pressurizes and vents to the environment, resulting in significant fission product releases.
- Set 3 is an alternative extension to Set 1 where following the SBO there is a small (instrument line sized) initial break in the containment vessel early into the accident, leading to a loss of containment isolation. Again, the RVV functions as designed when the RPV reaches its design pressure, and in this case there is also still a lot of steam condensation that occurs onto the containment walls, as they are still externally cooled by the still-intact large outer operating pool. However, enough steam is lost during the initial RPV blowdown that the condensate generated does not reach the level necessary to passively recirculate

back into the core (i.e. the RRVs). As such, the scenario results in significant core degradation, fission product release from the fuel, and hydrogen generation. After the core relocates to the bottom of the RPV, it is cooled through the RPV wall by the water in the containment vessel sump, which submerges the RPV lower head. During the accident, the containment break provides an open path to the environment through which fission products can be released, and air exchange back into containment can occur. Hydrogen is generated and released into containment where it can generate potentially combustible mixtures with the air.

A generic small BWR plant model in MELCOR has been developed using publicly available information, mainly with respect to the BWRX-300 [10] and referencing relevant large BWR designs [11][12]. The model, shown in Figure 2, includes a detailed RPV, the isolation condenser system (ICS), the primary containment vessel (PCV), the passive containment cooling system (PCCS), and the reactor building (RB). The relevant systems, key engineering safety features (such as fan coolers for normal containment cooling, containment inert system, and RB ventilation system) were also added along with their control logic to assist the establishment of a good steady state. The model is currently being used to explore different accident scenarios, primarily focusing on station blackout accidents (SBO) and loss-of-coolant accidents (LOCA) involving ICS and/or PCCS impairment to varying degrees. These analyses pay particular attention to the role of these natural-circulation-driven passive safety systems (i.e. the ICS and the PCCS) in severe accidents and the impact of released hydrogen on their performance. The full set of accident sequences that will be run once the model is completed is still being developed.

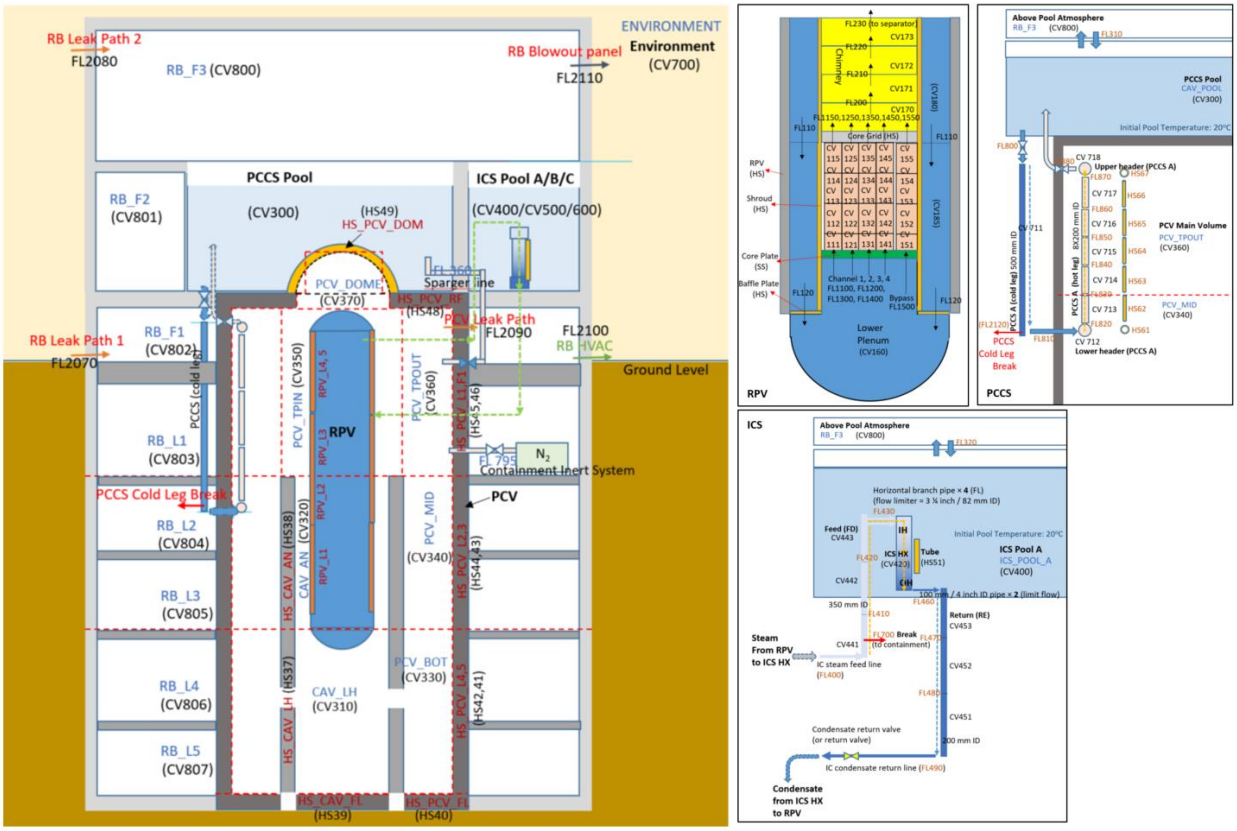

Figure 2. CNL's MELCOR model of a generic small BWR (Left: full containment and reactor building, Right – top: Reactor Pressure Vessel model and Passive Containment Cooling; Right – bottom: Isolation Condenser System)

To leverage efforts in water-cooled SMR severe accident analysis and connect with the international community, CNL is participating in the European Commission SASPAM-SA project. In this project, severe accident analysis of water-cooled SMRs and experimental data collection for the phenomena and passive safety systems involved are being conducted. CNL participation includes iPWR calculations and the contribution of data from the SCCA experiments on aerosol behaviour in iPWR containment, as well as efforts related to emergency response and near-field dose dispersion. CNL is also likely to compare small-BWR severe accident analysis efforts with a select number of SASPAM-SA partners.

3.2. HTGR Analysis

A MELCOR model of a generic 200 MW_{th} pebble bed HTGR has been constructed based on open-literature descriptions of several pebble bed reactors, including the Xe-100 [13], the PBMR [14], and HTR-PM [15]. The model includes a detailed RPV, and a simplified steam generator, housed in a below-grade vented low pressure type containment similar to the one adopted by the HTR-PM [16]. The reactor cavity is equipped with a negative pressure venting system, a simplified reactor cavity cooling system, a nitrogen injection system, and a rupture disk for over-pressure protection. The model features detailed nodalization of the RPV near the break (Figure 3) aiming to better predict air ingress and ONC. It also takes advantage of new HTGR-specific features that recently became available in MELCOR, including user-specified TRISO (i.e. tristructural isotropic) particle failure and diffusion-based fission product transport and release modelling.

Simulations have been conducted of depressurized loss of forced circulation (DLOFC) transients involving a simultaneous break of the co-axial inlet/outlet pipe entering/exiting the RPV. The predicted air ingress behaviours and the ONC were generally consistent with the current knowledge and expectations. The results highlighted the role of the global natural convection following ONC (i.e., to kick off graphite oxidation and facilitate fission product transport out of the RPV), thus highlighting the importance of knowing ONC timing. Some selected results are shown in Figure 4.

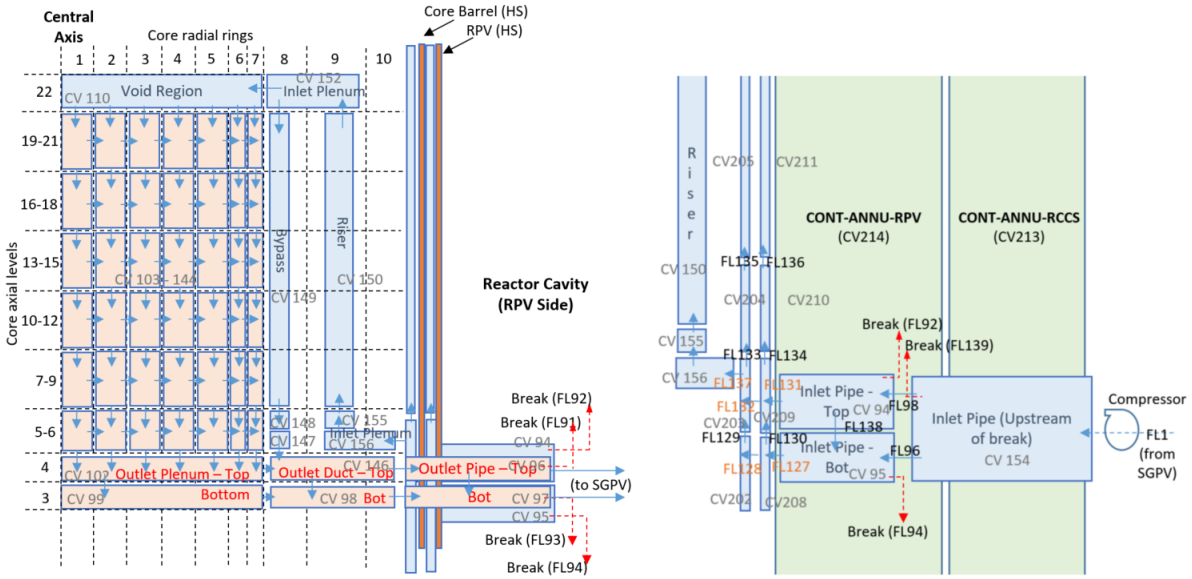

Figure 3. CNL's MELCOR model of a generic small HTGR: core and helium circulation loop nodalization (left), and zoomed cold leg (right)

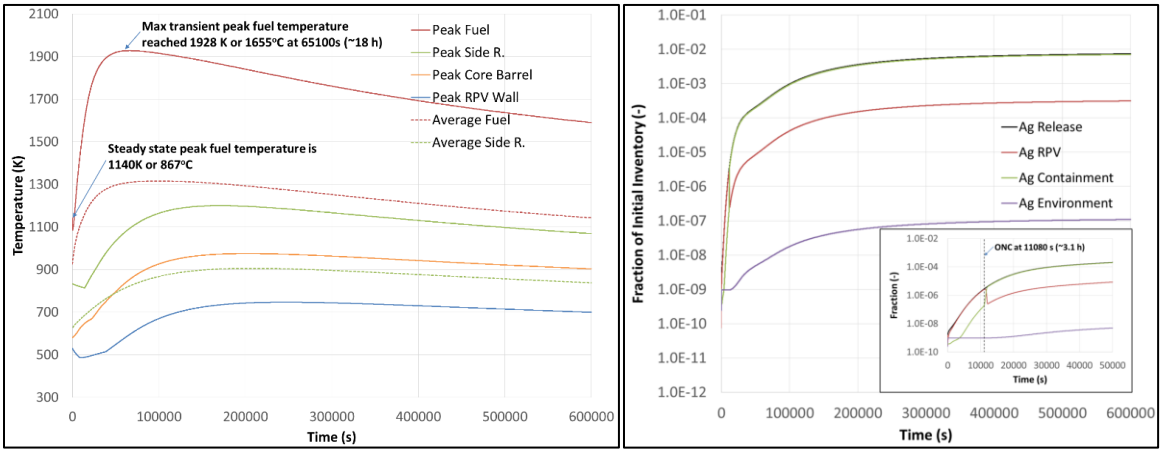

Figure 4. Preliminary results generated by CNL's small HTGR MELCOR model for a depressurized loss of forced circulation (DLOFC) accident: core/RPV temperature response (left) and fission product release behavior – silver (right)

3.3. Molten Salt Modelling (Molecular Dynamics)

As MSRs are a bit further from deployment, CNL has focused on supplementing its molten salt characterization and fission product behaviour experimental work with molecular dynamics (MD) simulations of molten salts. Interatomic potential-based MD simulations of molten salt (an example is provided in Figure 5) can be utilized either to guide future experiments or to interpret the existing experimental data. In this context, the CNL computational team has recently been working to develop the capability to be applied to the behavior of the molten salt. As such, some progress has been made on MD simulations of fission product behavior in molten salt mixtures, such as ThF4-LiF was made [17].

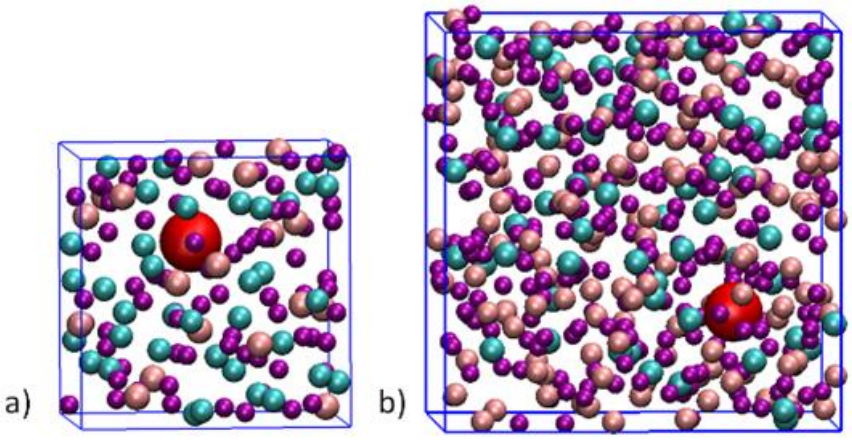

Figure 5. Solvated Cr^{2+} (Red) in FLiBe (Copper, Purple, Blue) (a) Density Field Theory and (b) MD-sized simulation cell.

In this work, the structural and dynamic characteristics of the fission products, including Cs, I, and Xe in ThF_4-LiF with different compositions were studied. This study indicated that the fission products have weak interactions with all composition ranges of fuel salt for the computational temperatures of 1200 and 1400

K. Cs, I, and Xe were found to be diffuse at similar rates, Cs^+ diffusion being slightly lower, probably due to its stronger bonding with F^-. Moreover, the presence of Cs^+ has a minor impact on the density, heat capacity, and viscosity, while significant effects were found for higher concentrations of I^+ and Xe. Currently, CNL is involved in expanding the study of interatomic potentials to include other molten salts for various properties, such as the effect of corrosion products on the properties of FLiBe, this study is expected to be completed by mid-2024.

3.4. SFR Analysis

Given recent interest in the ARC Clean Technologies ARC-100 SFR design in New Brunswick, CNL is developing knowledge and capabilities related to potential SFR severe accidents and consequences for such designs. The early effort has focused on literature reviews of past and present SFR designs, the associated severe accident phenomena, and the development of a generic SFR model with the MELCOR code. Once the generic model is developed, simulations will be conducted for postulated accident scenarios to explore the relevant phenomena and calculate potential source terms. With this baseline knowledge developed, further efforts will be considered based on the deployment landscape of this technology in Canada.

3.5. Severe Accident Uncertainty and Sensitivity Capabilities

Severe accident uncertainty and sensitivity (U&S) analysis is becoming an important research area, and CNL is developing capabilities herein to be applied to both large and small reactor systems. CNL participated in an IAEA Coordinated Research Project (CRP) I31033 – "Advancing the State-of-Practice in Uncertainty and Sensitivity Methodologies for Severe Accident Analysis in Water-Cooled Reactors" (2019-2023) [18], conducting analysis with the MAAP-CANDU severe accident and SUSA uncertainty analysis codes and leading the task focused on CANDU severe accident U&S [19]. A parallel effort has been conducted with the MELCOR severe accident code and the DAKOTA uncertainty analysis package including the development of a Python-based coupling of the two codes and deployment on the CNL ATHENA high-speed computing cluster. A preliminary analysis of a generic large PWR and a generic iPWR design were used as test cases to evaluate/refine the procedures and produce initial results. The analysis methodology will be refined for the MAAP-CANDU/SUSA and MELCOR/DAKOTA severe accident and uncertainty tools approaches, with more detailed analysis on iPWR, small-BWR and potentially other small (HTGR, SFR) or large reactor (CANDU, PWR, BWR) designs. MELCOR/DAKOTA is currently the preferred tool for non-CANDU analysis, but the applicability of SUSA to other analysis will be explored.

CNL seeks to build on the international collaboration under the IAEA CRP and will explore potential new international project proposals, for example ones similar to the MUSA (Management of Uncertainties in Severe Accidents)[2] project that ended in 2023. These efforts and capabilities allow CNL to assess the U&S effects on severe accident calculations and impacts on source terms for a variety of reactor technologies where severe accident analysis capabilities have been developed.

3.6. Emergency Planning Zones

A critical component of the response to a hypothetical severe accident at an SMR is the size of the emergency planning zone (EPZ). The EPZ is broadly defined as the region encapsulating any advanced planning areas around a nuclear power plant (NPP) where there are measures prepared to avoid or mitigate the consequences of an accident. It is commonly believed that the combination of smaller size and advanced technology will result in reduced risk and commensurately smaller EPZ compared to contemporary NPPs.

[2] https://musa-h2020.eu/

The IAEA CRP on the technical basis for SMR EPZ has concluded [20]. CNL has contributed to a technical document (TECDOC) that summarizes the work and conclusions of the research. The TECDOC is expected to be published in 2024. The IAEA is expected to publish a subsequent emergency preparedness and response (EPR) series document that provides guidance for SMRs while referencing this TECDOC.

Meanwhile, CNL published a comprehensive review of the challenges for determining SMR EPZ in Canada [21]. This review concluded that the research priorities for CNL in this area should be focused on determining the appropriate emergency planning basis, the technical criteria for determining EPZ boundaries, and creating a benchmark problem to assess different methods. According to the first two of these priorities, CNL researchers have been developing a novel framework for sizing EPZ that incorporates attributes of level 3 probabilistic safety assessment (PSA) and broader measures of public health that will enable direct comparison between the risks arising from the nuclear accident and the risks associated with protective actions. The contention is that there will be a boundary around the SMR where the health risks associated with implementing public protective actions will outweigh the risks from the radiation release, and this will inform the necessary extent of the EPZ. This framework was proposed at the 2023 workshop of the European Platform on Preparedness for Nuclear and Radiological Emergency Response and Recovery (NERIS)[3] as part of European Radiation Protection Week (ERPW) [22]. The intent is to demonstrate the application of this framework in a case study in 2024, where this may form the basis for a future EPZ benchmark problem that progresses the third and final research priority identified in the previous review.

4. CNL SEVERE ACCIDENT RESEARCH STRATEGY

As mentioned, the broad range of SMR/AR designs being proposed in Canada requires a pragmatic approach to providing support for research, development, and licensing activities. CNL maintains a flexible research program that is guided by the Canadian deployment landscape for SMR/AR and seeks to build and maintain a baseline of knowledge, skills and capabilities related to a particular technology that can be deepened/expanded as a design moves closer to deployment. The CNL strategy for severe accident research follows this guiding principle and is currently focused on water cooled SMRs, especially small BWRs, which are near deployment, along with building analysis capabilities for up and coming SMR/AR designs (e.g. HTGR and SFR) and relevant phenomena (e.g. fission product behaviour in molten salts). The experimental research programs are guided by PIRTs on the various technologies and are designed to fill in the gaps in knowledge, and generate data to support code qualification and validation activities. Thus, improving analysis tools to determine accident progression and consequences more accurately. The development of PIRTs for specific reactor technologies is another area where CNL contributes (e.g. previous PIRTs on HTGRs [23] and molten salt designs [24]) and is currently developing an open literature PIRT for design extension conditions of a BWRX-300 design for the CNSC. Such experience can be leveraged to conduct additional PIRTs for other designs/technologies in the future. In these ways, CNL ensures it has the necessary capabilities and knowledge to support industry and government stakeholders in the safe deployment of SMR/ARs in Canada.

An area being developed in earnest is micro-reactors (e.g. USNC MMR and Westinghouse e-Vinci), which have potential applications for remote communities and industry in Canada. These micro-reactors involve SMR/AR technologies as well as specialized systems (e.g. heat pipes) that should be understood. The size and potential source terms are used to dictate the needs for depth and detail of analysis when it comes to severe accidents and emergency planning. Preparations for these technologies is underway and the analysis needs are being evaluated based on the deployment landscape and regulator and vendor interest. For example, CNL is studying heat-pipe systems and assessing their operational and accident behaviour.

[3] https://eu-neris.net/

In addition to its own development of knowledge, skills and capabilities, CNL maintains interactions and collaborations with academia and other research laboratories/institutions as well as the international community. Due to the intense SMR/AR interest and plethora of technologies proposed for deployment, Canada and CNL, have taken on leadership roles in international efforts such as the OECD-NEA Expert Group on Small Modular Reactors (EGSMR), the GIF Expert Group and Reactor Safety Working Group (RSWG), and CNL plays key roles in EU and IAEA initiatives related to SMR/ARs. Bilateral cooperation includes AECL/CNL memorandums of understanding (MOU) with CEA (France) and KAERI (Korea) as well as Canada-US (NRCan-DOE) and Canada-UK (NRCan – ONR) cooperation. CNL maintains good connections with Idaho National Laboratories, Sandia National Laboratory (MELCOR developers) and the US Nuclear Regulatory Commission, specifically under the Cooperative Severe Accident Research Project (CSARP) and MELCOR Code Assessment Project (MCAP), and are developing further ties to research organizations in the Czech Republic (Centrum výzkumu Řež). Connections to the SNETP (Sustainable Nuclear Energy Technology Partnership), projects such as SASPAM-SA, and participation in the ERMSAR Conference, tie CNL and Canada to SMR development and deployment in Europe. Academic connections are forged in Canada through CNL MOUs with several key research universities (McMaster, University of Ottawa, Queens, Ontario Tech, Western, Waterloo), with more developing in the near future.

5. CONCLUSIONS

There is continuing interest in SMR/ARs in Canada to support clean energy goals and government support for their deployment. CNL operates a flexible research program, guided by the SMR/AR deployment landscape in Canada, which develops and maintains capabilities and knowledge to support industry and regulatory stakeholders in the safe deployment of these technologies. CNLs reactor safety program and its integrated severe accident research supports the development of baseline capabilities for specific SMR/AR technologies that can be deepened/expanded as they move closer to deployment. A robust reactor safety research program allows for necessary information to conduct thorough licensing reviews and supports vendors in efforts to fully demonstrate the safe operations of their reactor designs.

In terms of the CNL's reactor safety research path for SMR/ARs, the review and generation of PIRTs help determine the experimental programs, which are designed to study significant phenomena, help fill knowledge gaps, and generate data to support code qualification. Modelling and analysis supports experiments through benchmarking and develops capabilities for phenomena and integral severe accident analysis for various SMR/AR technologies near to deployment. CNL's current focus in on water cooled SMRs, including passive systems, and building capabilities for HTGRs, SFRs, and molten salt fission product retention. The needs for micro-reactor assessments are being evaluated. CNL enhances its individual efforts through international collaboration, such as EU, GIF, OECD-NEA, and IAEA efforts, along with good connections to academia and bilateral cooperation with similar research institutes in other countries. CNL's reactor safety research is continually evolving, as guided by new nuclear deployment in Canada, to support regulatory and industry needs.

ACKNOWLEDGMENTS

Much of the work discussed herein and CNL participation in various international working groups, projects and initiatives is funded through the Atomic Energy of Canada Limited (AECL) Federal Nuclear Science and Technology Program.

REFERENCES

1. A.C. Morreale, D.W. Hummel, L.S. Lebel, Y-S. Chin, R.S. Dickson, K. Stoll, and C. Maxwell, "Severe Accident Analysis Research at CNL for Small Modular and Advanced Reactor Designs", *Proceedings of the 10th European Review Meeting on Severe Accident Research (ERMSAR-2022)*, Karlsruhe, Germany, May 16-19, 2022.
2. L.S. Lebel, A.C. Morreale, K. Batten and T. Clouthier, "Aerosol retention within submerged Containment-Type iPWRs: Experiments and Modeling," *Nuclear Engineering and Design*, **Vol. 398**, p. 111994, (2022). doi: 10.1016/j.nucengdes.2022.111994
3. L.S. Lebel, A.C. Morreale, E. Jia, F. Zhou, D.W. Hummel, S. Ormiston, G. Gray. "Canadian Nuclear Laboratories Experiments and Modeling of Water-Cooled SMR Severe Accidents to Inform Level 4 and 5 Defence-in-Depth", *Proceedings of the 20th International Topical Meeting on Nuclear Reactor Thermalhydraulics (NURETH-20)*, Washington D.C., USA, August 21-24, 2023.
4. A. Dehbi, "A unified correlation for steam condensation rates in the presence of air-helium mixtures under naturally driven flows," *Nuclear Engineering and Design*, **Vol. 300**, pp. 601-609, (2016). doi: 10.1016/j.nucengdes.2016.02.009
5. M.A. André, R.A. Burns, P.M. Danehy, S.R. Cadell, B.G. Woods, and P.M. Bardet, "Velocimetry During Depressurized Conduction Cooldown Events in the HTTF", *Nuclear Engineering and Design*, **Vol. 341**, pp. 406–414 (2019). doi: 10.1016/j.nucengdes.2018.11.026
6. L. Li, T. W. Kim, Y. Zhang, S. T. Revankar, W. Tian, G. H. Su and S. Qiu, "MELCOR severe accident analysis for a natural circulation small modular reactor," *Progress in Nuclear Energy*, **Vol. 100**, pp. 197-208, (2017). doi: 10.1016/j.pnucene.2017.06.003
7. J. N. Reyes, "NuScale plant safety in response to extreme events," *Nuclear Technology*, **Vol. 178**(2), pp. 153-163, (2012). doi: 10.13182/NT12-A13556
8. A.C. Morreale, "Severe Accident Analysis of a Generic Integral Pressurized Water Reactor with MELCOR,", *Proceedings of the 4th International Conference on Generation IV & Small Reactors (G4SR-4)*, Toronto, Canada, October 3-6, 2022.
9. S. Campbell, H. Esmaili and J. Schaperow, "Independent MELCOR Confirmatory Analysis for NuScale Small Modular Reactor," Nuclear Regulatory Commission, FSCB-18-01, (2019).
10. GE Hitachi Nuclear Energy (GEH), "BWRX-300 General Description", Doc. 005N975, (2023).
11. GE Hitachi Nuclear Energy (GEH), "ESBWR Design Description", Doc. NEDC-33084, (2002).
12. GE Hitachi Nuclear Energy (GEH), "The ABWR Plant General Description", (2007).
13. E. Mulder and W. Boyes, "Neutronics Characteristics of a 165MWth Xe-100 Reactor", *Nuclear Engineering and Design*, **Vol. 357**, (2020). doi: 10.1016/j.nucengdes.2019.110415
14. OECD/NEA/NSC, ""PBMR Coupled Neutronics / Thermal-hydraulics Transient Benchmark - The PBMR-400 Core Design - Volume 1 The Benchmark Definition"", Organisation for Economic Cooperation and Development (OECD), (2013).
15. F. Chen, Z. Han, "Steady-state thermal fluids analysis for the HTR-PM equilibrium core", *International Journal of Advanced Nuclear Reactor Design and Technology*, **Vol. 3**, pp. 11-17, (2021). doi: 10.1016/j.jandt.2021.04.001
16. Z. Chen, X. Chen, et al., "Air ingress analysis of chimney effect in the 200MWe pebble-bed modular high temperature gas-cooled reactor", *Annals of Nuclear Energy*, **Vol. 106**, pp 143-153, (2017). doi: 10.1016/j.anucene.2017.03.041
17. C. I. Maxwell and T. P. Kaloni, "Molecular dynamics study of fission product behaviour in molten ThF4-LiF salt", *Annals of Nuclear Energy*, **Vol. 193**, pp. 110023, (2023). doi: 10.1016/j.anucene.2023.110023
18. F. Mascari et. al., "Overview of IAEA CRP I31033 "Advancing the State-of-Practice in Uncertainty and Sensitivity Methodologies for Severe Accident Analysis in Water Cooled Reactors", *Proceedings of the 10th European Review Meeting on Severe Accident Research (ERMSAR-2022)*, Karlsruhe, Germany, May 16-19, 2022.

19. S.M. Petoukhov, A.C. Morreale, J-H. Bae, D. Dupleac, R-M. Nistor-Vlad, T. Jevremovic, F. Mascari, A. Bersano, F. Gabrielli, D. Luxat, K.I. Ahn, L.I. Albright, J. Ortiz, J.M. Garcia, H.U. Rheman, "Uncertainty and Sensitivity Analysis of a CANDU 6 Plant by Means of Severe Accident Codes in the Framework of the IAEA CRP I31033: Preliminary Results", *Proceedings of the International Conference on Topical Issues in Nuclear Installation Safety (TIC-2022)*, Vienna, Austria, October 18-21, 2022.
20. International Atomic Energy Agency, "Development of Approaches, Methodologies and Criteria for Determining the technical Basis for Emergency Planning Zone for Small Modular Reactor Deployment," (2023). Online, available: https://www.iaea.org/projects/crp/i31029 (accessed 2024 January 29).
21. D. Hummel and L. Lebel, "Challenges in Defining Emergency Planning Zones for Small Modular Reactors and Advanced Reactors: A Review of Canadian Practices and Research at Canadian Nuclear Laboratories," *Proceedings of the International Conference on Topical Issues in Nuclear Installation Safety (TIC-2022)*, Vienna, October 18-21, 2022.
22. D. Hummel and L. Lebel, "Investigations on Small Modular Reactor Emergency Preparedness and Response Planning Basis," Proceedings of the 7th NERIS Workshop, Dublin, October 9, 2023.
23. D. W. Hummel, Y-S. Chin, A. Prudil, A. Williams, E. Masala, G. Waddington, M. Edwards, P. Yakabuskie, T. Jafri, T. Tran, Xianmin Huang, and Z. Liang, "Results of a Phenomena Identification and Ranking Table (PIRT) Exercise for a Severe Accident in a Small Modular High-Temperature Gas-Cooled Reactor", *CNL Nuclear Review*, **Vol. 8** (2), (2019). doi: 10.12943/CNR.2019.00006
24. D.W. Hummel, Y-S. Chin, A. Prudil, A. Williams, D. Cluff, D. Mancey, E. Merle, F. Adams, L. Lebel, M. Salay, R. Dickson, S. Beils, T. Jafri, T. Tran, X. Huang, "Results of a Phenomena Identification and Ranking Table (PIRT) Exercise for a Severe Accident in Molten Salt Small Modular Reactors," *Proceedings of the 4th International Conference on Generation IV and Small Reactors (G4SR-4)*, Toronto, Canada, October 3-6, 2022.

Canadian Nuclear Laboratories | Laboratoires Nucléaires Canadiens

Update on Severe Accident Analysis Research at CNL for Small Modular and Advanced Reactor Designs

Andrew C. Morreale* , Luke S. Lebel, Feng Zhou, David W. Hummel, Eric Jia, John Cui, Chris I. Maxwell, Thaneshwor. P. Kaloni, Ernesto Geiger, and Garik Patterson.

Canadian Nuclear Laboratories (CNL)

The 11th European Review Meeting on Severe Accident Research (ERMSAR-2024), KTH, Stockholm, Sweden, May 13-17, 2024



GE Hitachi BWRX-300 Single plant concept art:
- Successful bid for new SMR construction in Ontario, Canada

Outline

- Introduction
  - SMR Deployment Landscape
  - CNL's Reactor Safety Program Supporting SMR Deployment
- Experimental Campaigns Related to SMRs
  - iPWR (integral Pressurized Water Reactor) and small-Boiling Water Reactor (BWR)
  - HTGR (High Temperature Gas Reactor) Experiments
  - Molten Salt Related Experiments
- Modelling and Analysis for SMRs
  - Light Water Cooled SMR Analysis (iPWR, SCCA benchmark, and small-BWRs)
  - HTGR, SFR and Sensitivity and Uncertainty Analysis
  - Molten Salt Related Analysis
  - SMR Emergency Planning Zones
- Strategy for SMR Severe Accident Research
- Conclusions

SMR Deployment Landscape in Canada

Government support:

- Federal SMR Roadmap and SMR Action Plan
- Canadian Nuclear Safety Commission (CNSC) pre-licensing vendor design review of 12 SMRs

Industry pursuing three development streams:

1. Grid-scale (≈300 MW_e), demonstration in late 2020's
   - Ontario Power Generation (OPG) and SaskPower chose BWRX-300 (GE-Hitachi) for new-build
2. Advanced SMRs and fuel cycle development
   - New Brunswick Power is pursuing two Advanced Reactors, Moltex SSR-W and ARC-100
3. Micro-SMR (<15 MW_e), demonstration in 2020s
   - Global First Power demonstration project with USNC MMR underway at Chalk River Laboratories
   - Saskatchewan Research Council (SRC) assessment of Westinghouse e-Vinci deployment (early 2030's)

Remote Communities:

- Micro reactors for power/heat

Mining and Industry:

- Electricity, Process Heat, Hydrogen, etc.

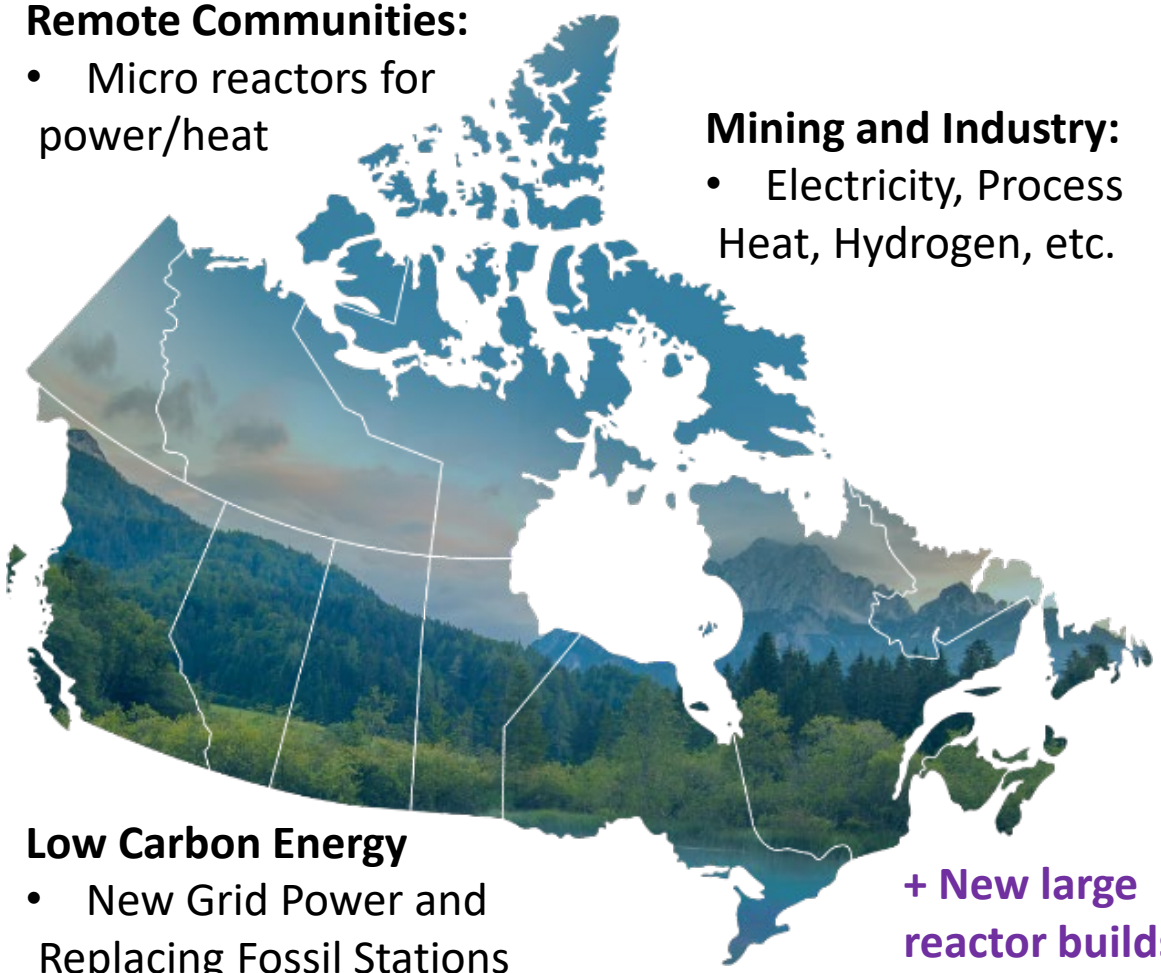

Low Carbon Energy

- New Grid Power and Replacing Fossil Stations

+ New large reactor builds planned

https://smractionplan.ca/

Introduction

- CNL has robust technical program supports SMR research, development, and deployment
  - Built upon decades of CANDU experience and recent efforts in SMR and Advanced Reactor analysis driven by the Canadian deployment landscape.
  - Support both industry and government/ regulatory stakeholders
- SMR reactor safety program: tailored research efforts to address gaps and support deployment
  - Phenomena Identification and Ranking Table (PIRT) activities
    - Identification of important phenomena and knowledge gaps, historic PIRTs and new focused PIRT efforts
  - Experiments and modelling investigate gaps and better understand phenomena including special focus on severe accident scenarios, phenomena, progression and source term
    - Containment phenomena, fission product behaviour, integrated assessment of generic SMR designs
    - Evaluation of passive safety systems and design features that impact source term and emergency response.
  - Multiple SMR/ AR are being explored (iPWR, small BWR, HTGR, SFRs, heat pipes, and molten salt behaviour) including grid-scale and micro-sized designs
- CNL leverages its research efforts with international involvement in joint projects (NEA, IAEA, EU), bilateral cooperation and industry (COG) and vendor connections (via commercial projects).

Experimental Campaigns

- Tailored experimental campaigns to address research gaps, paired with benchmarking efforts
  - Driven from PIRTs and new systems/ phenomena present in SMR/ AR designs
  - Focus on impacts on accident progression, source term and passive safety configurations
    - Important to severe accident management and off-site emergency response as part of defence-in-depth
- **Water cooled SMRs:** pathways that can disrupt passive safety systems + source term impact
  - Natural circulation + effects of small and/ or integrated containment on gas mixing and FPs
  - iPWR containment passive cooling experiments (condensation, leakage/ air ingress)
  - New experiments to study small-BWR containment cooling and isolation condensers
- **High temperature gas reactors:** studying effects of air ingress and potential for graphite oxidation.
- **Molten salt designs:** investigation of fission product (FP) behaviour/retention in the salt under accident conditions to understand the impact on fission product source term.
  - Building from preliminary FP release tests from fuel salt in hotcell (2018) and moving to use of "simsalts" (containing actinides and FP simulants)
    - Simsalt generation and purification methods, followed by tests with 1) stable isotopes; 2) potential future tests with irradiation of "simsalt" in a research reactor

iPWR Experiments

- Investigating iPWR immersed containment configurations
  - Thermalhydraulics and FP transport:
    - Gas mixing, deposition/retention of FP (e.g. diffusiophoresis), includes impact of non-condensable gas (e.g., hydrogen)
- Analogous to loss-of-containment isolation (injection of steam, NCG and aerosols into a vented vessel)
  - Phase 1 (March 2021): steam injection and wall heating
  - Phase 2 (June 2022): influence of non-condensables
    - Helium injection is analog for H2
    - Important for core damage phase of accident where H2 and radionuclides are co-released.

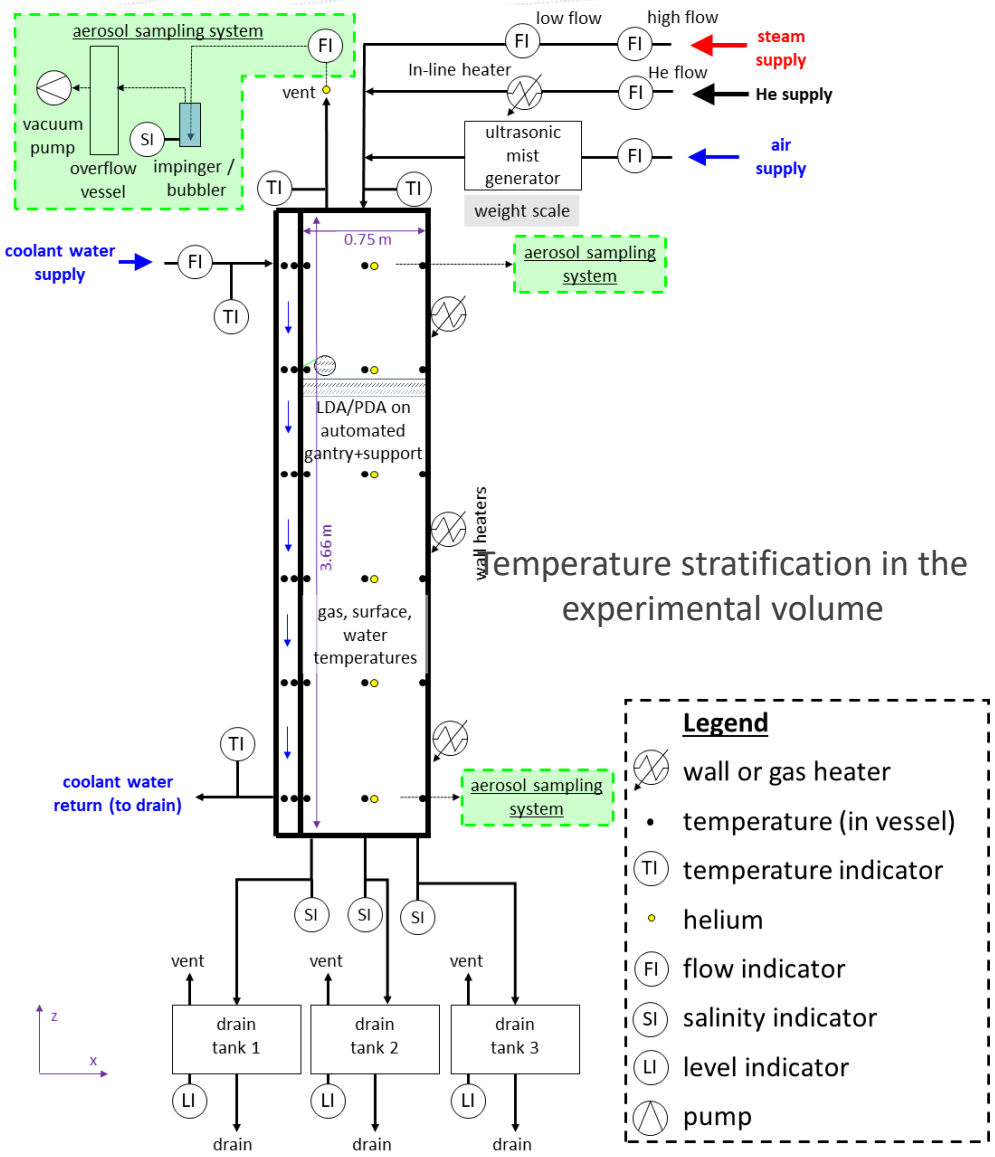

Temperature stratification in the experimental volume



Strong Condensation Containment Apparatus (SCCA)

SCCA Experiments – Key Takeaways

1) Two distinct layers (hot upper/ cooler under-layer; 20-40˚C less); thickness depends on steam injection rate
   - Condensation almost exclusively in hot upper layer due to very strong sensitivity of HTC to steam concentration
2) Helium accumulates in upper layer displacing dry air
   - Multiplies injection concentration (nearly pure steam-He system)
   - He migration to lower layer via diffusion/mixing across interface (wet concentrations >10%, up to 35% for highest gas injections)
3) Aerosols trapped in fog (in droplets) in condensation zone (upper layer; lower layer concentration 1000x less)
   - Mainly deposition by diffusiophoresis (steam condensation)
   - Turbulent deposition is a secondary process
   - Gravitational settling not possible due to stratification layers.
4) LDA/PDA Particle Measurements
   - Large size of NaCl-containing fog droplets and trapping of aerosols in upper layer confirmed (“evaporative barrier”)
   - Turbulent velocity fluctuations in upper layer are sufficient to drive secondary deposition mechanism

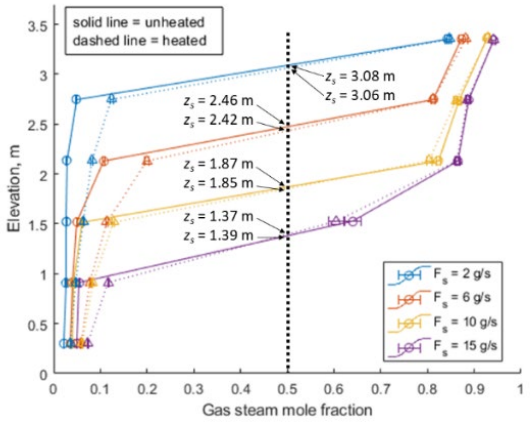

Steam stratification and layer separation with steam injection only

Helium conc.

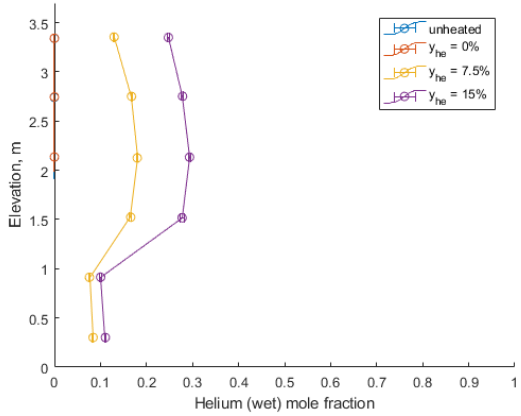

F_s = 10 g/s

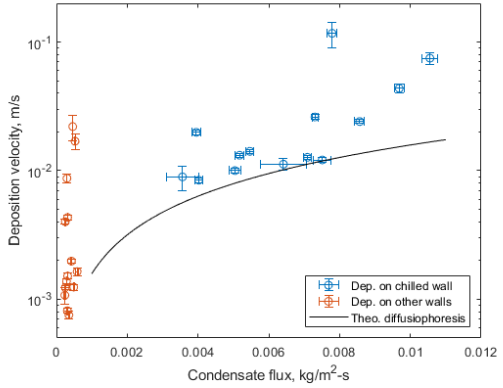

Figure: Inferred deposition velocity vs theoretical “diffusiophoresis only” value

New small-BWR Experiments

- Revamping SCCA to study small-BWR
  - Experiments are planned for 2024 and 2025
  - Exploring condensation onto a tube bank prototypical of a small BWR's passive containment cooling system.
  - Future tests on phenomena related to isolation condenser systems
- Experiments and benchmarking with multiple codes similar to SCCA iPWR tests

New configuration for SCCA small BWR tests



WC-SMR Participation in SASPAM-SA

- European SASPAM-SA (Safety Analysis of SMR with Passive Mitigation Strategies – Severe Accident) Project
  - Study of Level 4 and Level 5 of defence in depth for small WC-SMRs
  - Data and experience from iPWR (and eventually small-BWR) experiments, benchmarking and integral severe accident analysis part of broad CNL contributions to SASPAM:
    - i) severe accident modelling (source term assessment); ii) aerosol behaviour in iPWR containment; iii) atmospheric dispersion; iv) emergency preparedness and response methodologies.

HTGR Experiments

- Exploration of transition from stagnant flow to bulk natural circulation of air within the core following a postulated break of the co-axial inlet/outlet duct: **Air ingress and potential for graphite oxidation**
  - Original design revised based on lessons learned from the High-Temperature Test Facility (HTTF) at Oregon State University
- Helium-Air Natural Convection (HANC) experimental apparatus
  - "inverted-U" shape that represents the coolant flow path within the reactor pressure vessel.
  - Full core height (5 m) and operating temperature (700°C) of the original HTAIF concept.
  - Design of HANC is complete, currently procuring equipment/ materials
  - Construction by end of 2024, and first experiments in 2025.
  - Experiments are intended to provide data to benchmark predictions of the onset of natural convection (ONC)
    - GOTHIC, RELAP5-3D, and potentially severe accident analysis codes like MELCOR.
- AECL/NRCan/US DOE collaboration supported OSU HTTF interactions and data

HTGR Air Ingress - HANC

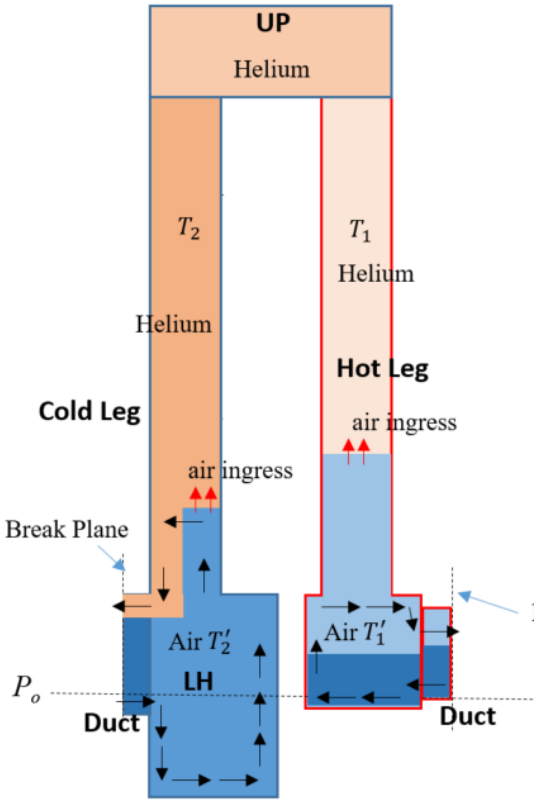

Design of scaled experimental apparatus to study air ingress in HTGRs: Helium-Air Natural Convection (HANC)

Molten Salt Experiments

- Experimental capabilities to support R&D of MSRs
  - Characterization and verification of the thermodynamic properties of salts
  - Preparation of high-purity molten salts
  - "simsalts": contain actinides + FP simulants
    - Production of large (> 50 g) quantities of fluoride and fluoride-chloride salts.
    - Exposure of simsalts to severe accident conditions
    - Seeking potential development of experimental phase diagrams on selected halide-and oxo-halides systems.
  - Complementary modelling will be conducted:
    - i) developing thermodynamic models that describe the fluoride and chloride systems under different atmospheres
    - ii) investigating kinetic and interface-related phenomena (such as diffusion of species or wetting behaviour of salts).
- Fuel salt FP behaviour accident conditions: **FP retention**
  - Builds from 2018 experiments + confirmatory studies

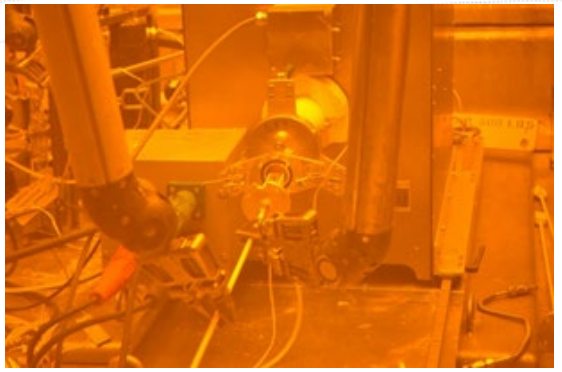



Top: Fission product release furnace in hot cell + instrument readings
Bottom: Diagram of molten salt fission product release experiment

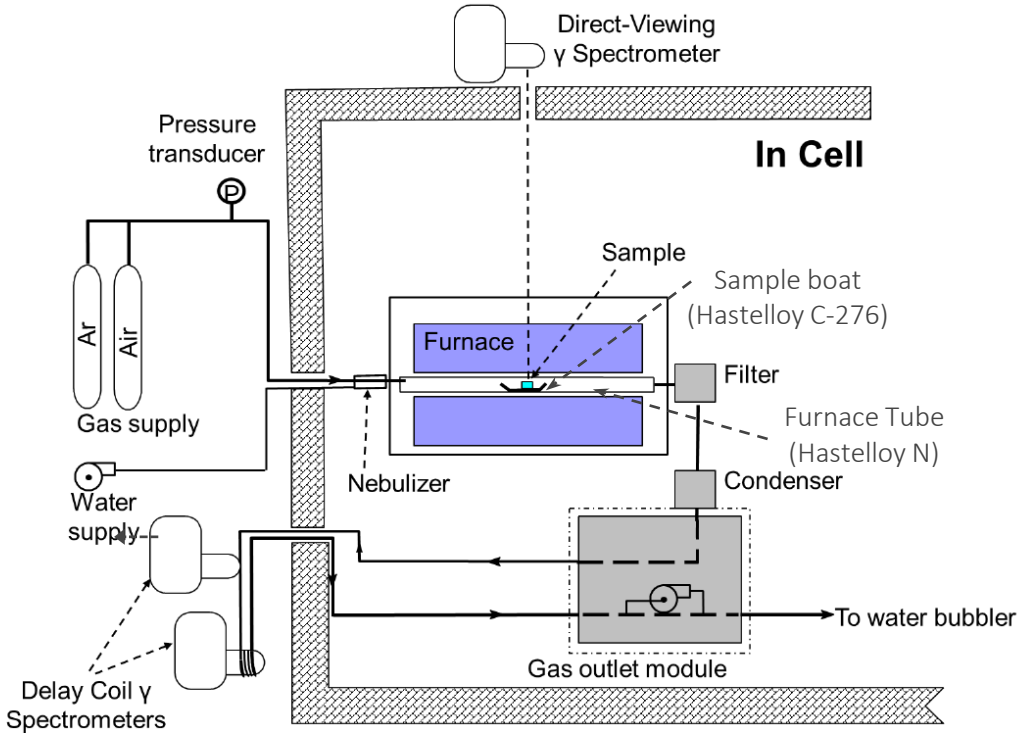

Modelling and Analysis

- Further building capabilities in analysis of beyond design basis events for SMR/AR
  - Assessments and determination of potential accident scenarios and source terms
    - Development of generic models for reactor systems nearing deployment, which are refined as new information is obtained and used to conduct integrated severe accident analysis
  - Additional efforts focused on experimental benchmarking (SCCA experiments for iPWR and soon small BWR and new HANC experiments for HTGR air ingress
    - CNL regularly engages other partners (universities, other research organizations) in such benchmarking exercises
  - Overall goal at this stage is not a licensing analysis but rather building capability and exploring the important phenomena and systems involved in severe accidents in each reactor technology.
    - Extent of the analysis needed follows a graded approach in line with potential source terms and the nearness to deployment of the specific technology.
- **Water cooled SMRs:** integral accident analysis of iPWR and small-BWR + SCCA benchmarks.
- **High Temperature Gas Reactors:** severe accident analysis of pebble bed HTGR (similar to Xe-100).
- **Sodium Fast Reactors:** building capabilities and exploring MELCOR modelling of generic SFR
- **Future:** refinement of efforts above and extending to assess heat pipe designs and possibly molten salt reactors (as they near potential deployment)

Integral PWR MELCOR Analysis

- Generic iPWR, MELCOR modeling/analysis
  - Developed model of natural circulation iPWR submerged containment design
    - Sized close to Nu-Scale design (160 MWth)
- Investigation of passive cooling/containment and impact of failures on accidents SBO + passive system/containment fail
  - Loss of SG feed water, Decay Heat Removal System (DHRS)
  - Added failure of OP heat sink (leak)
  - Case 1 plus containment break/air ingress (area = 0.001 m^2)
- Model refinement, mainly on feed water (FW) and DHRS, to support a broader study on emergency planning zone (EPZ) sizing
  - 36 subcases (12 for each of the three cases) with different FW and DHRS availability
    - Covering design-basis, beyond design-basis accidents to provide a spectrum of source terms

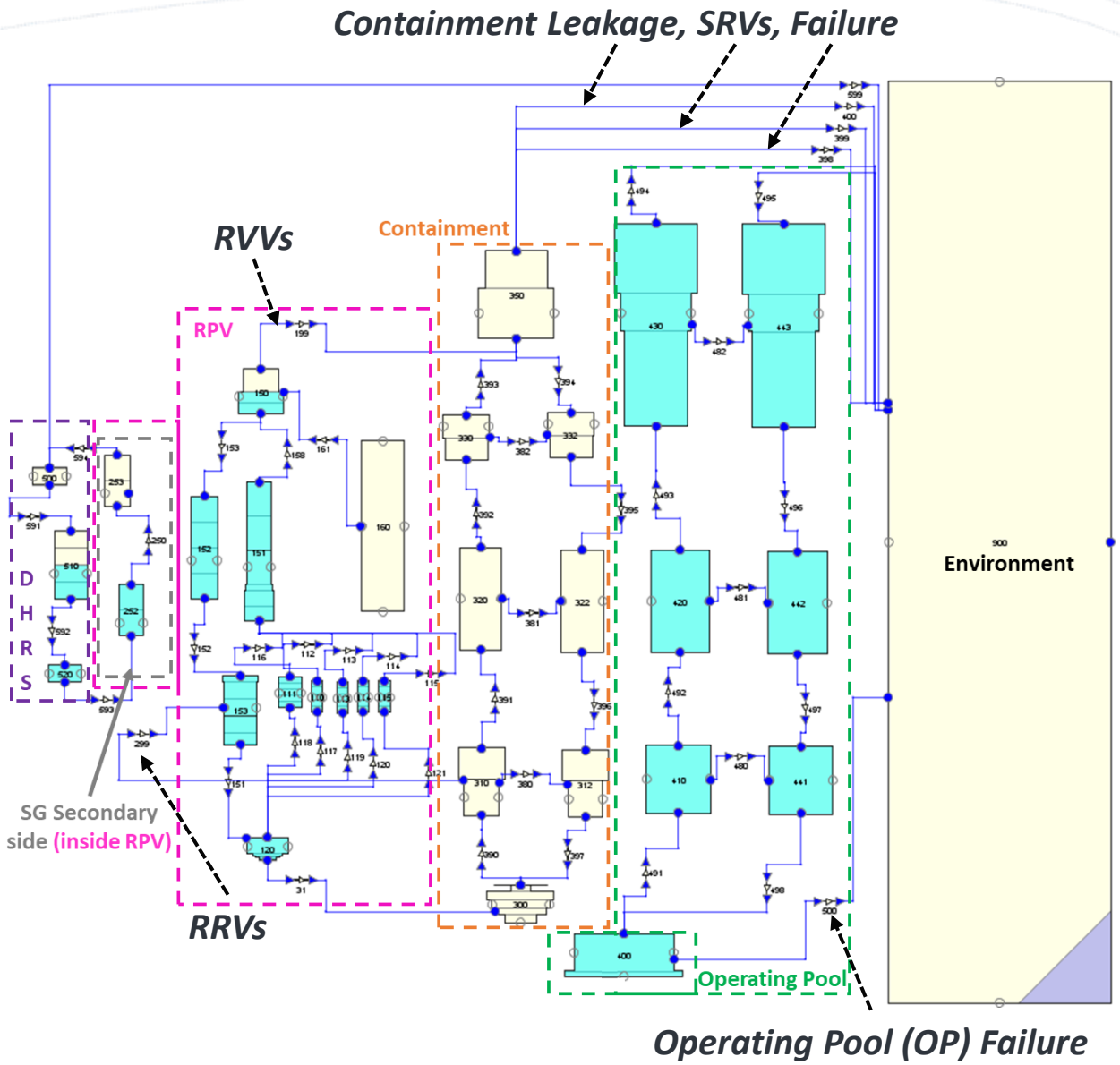

MELCOR Benchmarking of SCCA

- Benchmarking of SCCA experiments (GOTHIC, MELCOR, STAR-CCM+)
  - Phase 1 (no helium/ non-condensable injection) benchmarking completed with GOTHIC and MELCOR; CFD underway.
  - MELCOR Benchmarking of Phase 1 Experiments: Aerosol mixed with steam at varying steam injection rates w/ wo wall heating
    - Explored 3×3 and 6×3 nodalizations with radiation HT modeled among heat structures and participating gases.
    - Compared gas temperatures, steam mole fractions, wall temperatures, wall heat transfer/condensation rates, aerosol concentrations (near the vent) and aerosol deposition/release rates etc.
  - Key Observations:
    - MELCOR **predicted separation of steam (upper) and air (lower) layers as observed** which resulted in **satisfactory prediction of condensation and heat transfer rate** in certain cases.
    - However, it **failed to correctly predict the growth of steam layer as steam injection rate was increased** causing results to degrade.
    - **Wall heating effects appeared to be overestimated: strong buoyancy-induced circulation** was seen, **increased mixing** + more uniform gas temperature, steam/aerosol distributions than experiments.

SCCA MELCOR Model and Results

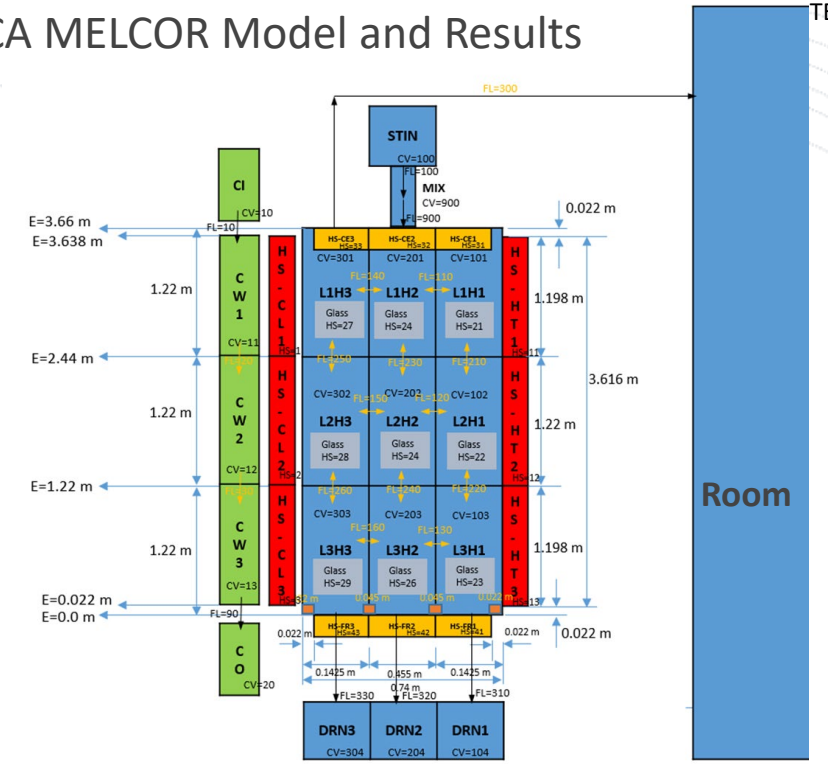

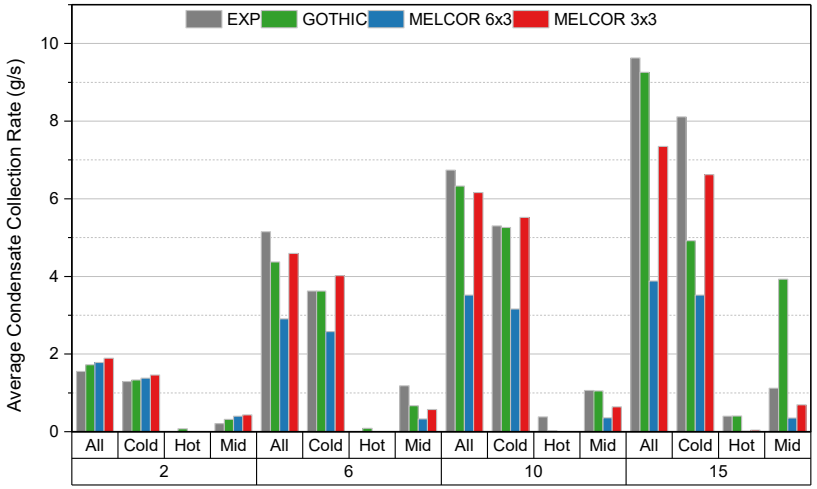

Small BWR MELCOR Analysis

- GE Hitachi BWRX-300 selected by OPG to be built at Darlington
- Generic small BWR, MELCOR model
  - Features natural-circulation-driven, model includes
    - Reactor pressure vessel (RPV)
    - Isolation condenser system (ICS)
    - Passive containment cooling system (PCCS)
    - Primary containment vessel (PCV)
    - Reactor building (RB)
- Initial analysis of SBO and SBLOCA
  - SBO with varying degree of ICS and PCCS impairment
  - SBLOCA (on 1" instrument line) – H_2 (non-condensable gas) on ICS performance

Generic Small BWR MELCOR Model

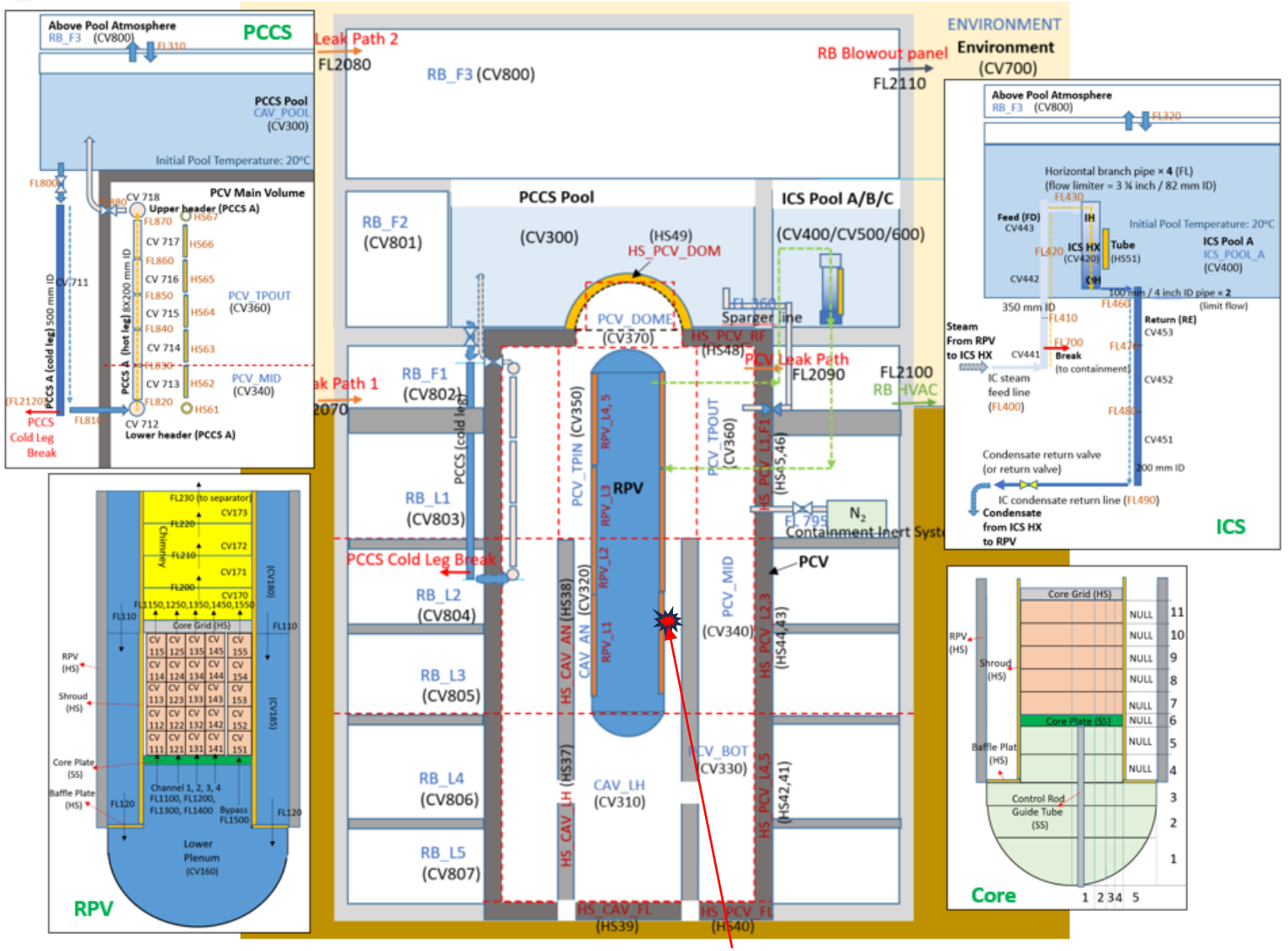

HTGR MELCOR Analysis

- X-Energy's Xe-100 in CNSC vendor design review (VDR)
- Generic pebble bed HTGR, MELCOR model developed
  - Xe-100 like (PBMR, and HTR-PM support missing design info)
    - Air ingress modeling and onset of natural circulation (ONC) prediction
    - Ventilated low-pressure containment
    - UCO-based TRISO failure curve developed from AGR (Advanced Gas Reactor) safety test data
- Depressurized loss of forced circulation (DLOFC) accident
  - co-axial inlet/ outlet pipe break
    - Includes negative pressure ventilation system (NPVS) and reactor cavity cooling system (RCCS) and sensitivity case to test nitrogen injection.

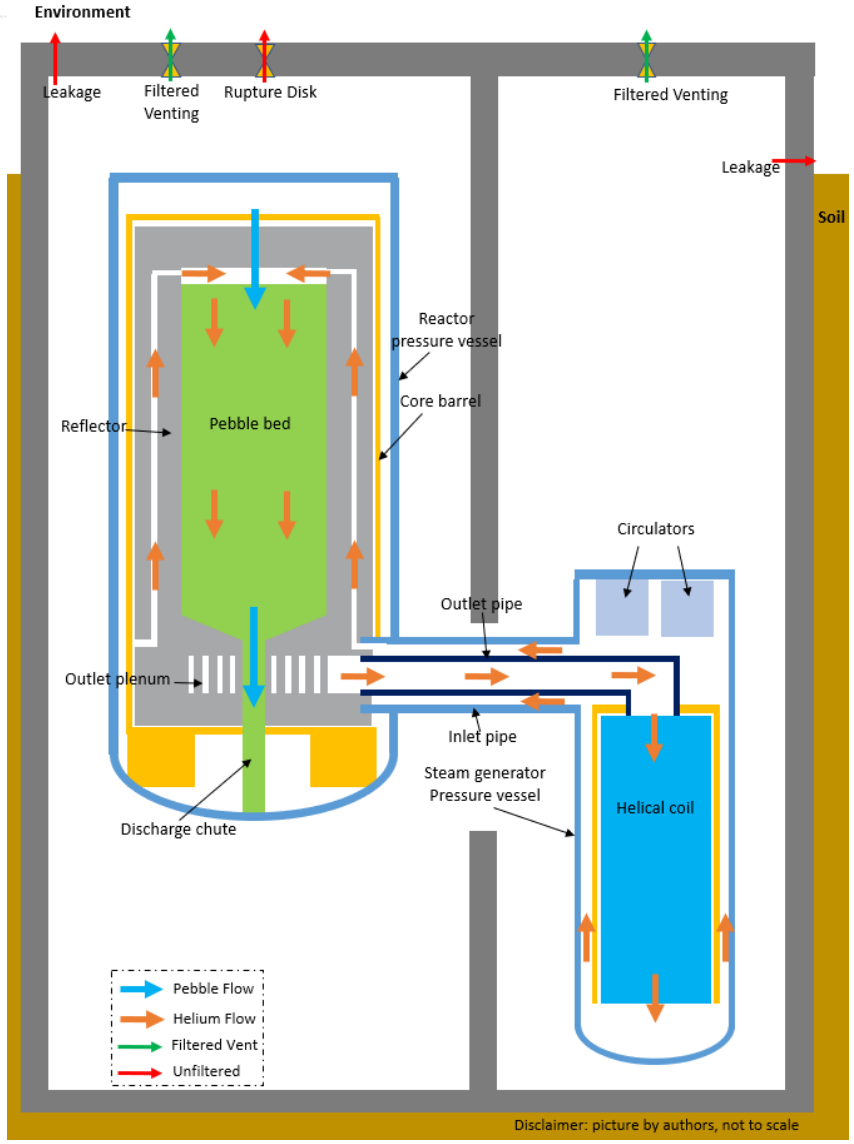

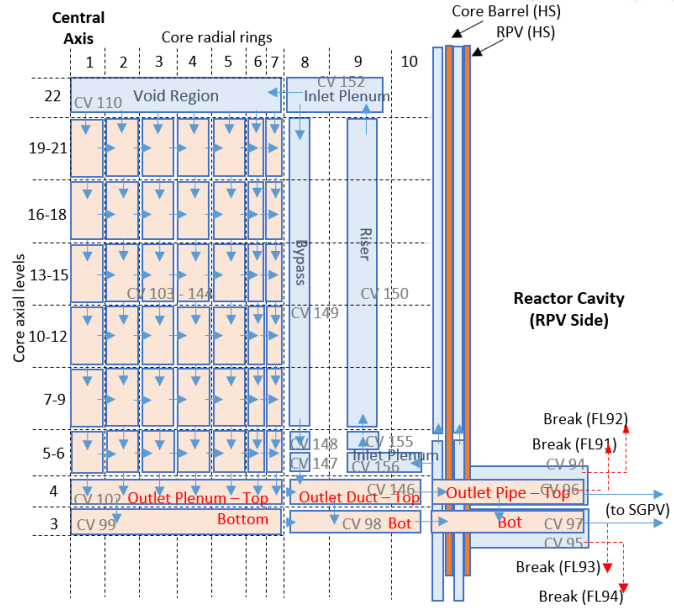

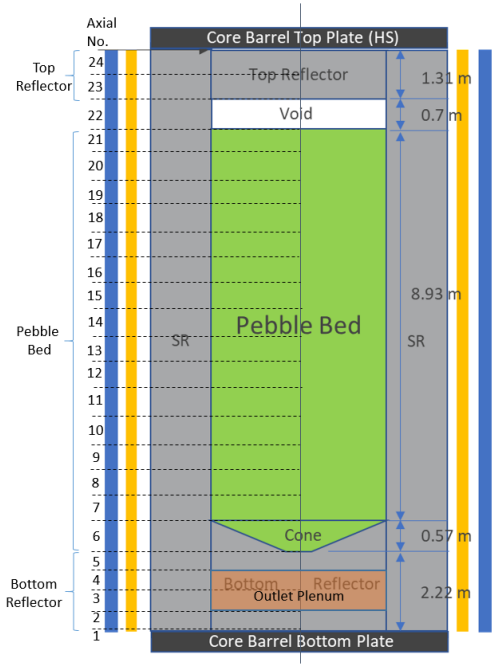

SFR MELCOR Model Development & Analysis

- ARC Canada's ARC-100 was in CNSC VDR, planned build at Point Lepreau
- Generic SFR, MELCOR model developed (analysis underway)
  - Similar to ABTR (ANL design)
    - Component data and transient results available
    - Similarities with ARC-100
- Preliminary results obtained
  - ULOFA (unprotected loss of flow accident)
    - loss of primary and secondary pump (no mitigating reactivity insertion)
  - UTOPA (unprotected transient overpower accident)
    - highest worth control rod removed
    - no mitigating reactivity insertion
  - No fuel failure in both cases; relies on inherent metal fuel reactivity feedback
  - Refining and expanding to model blocked assembly inlet scenario

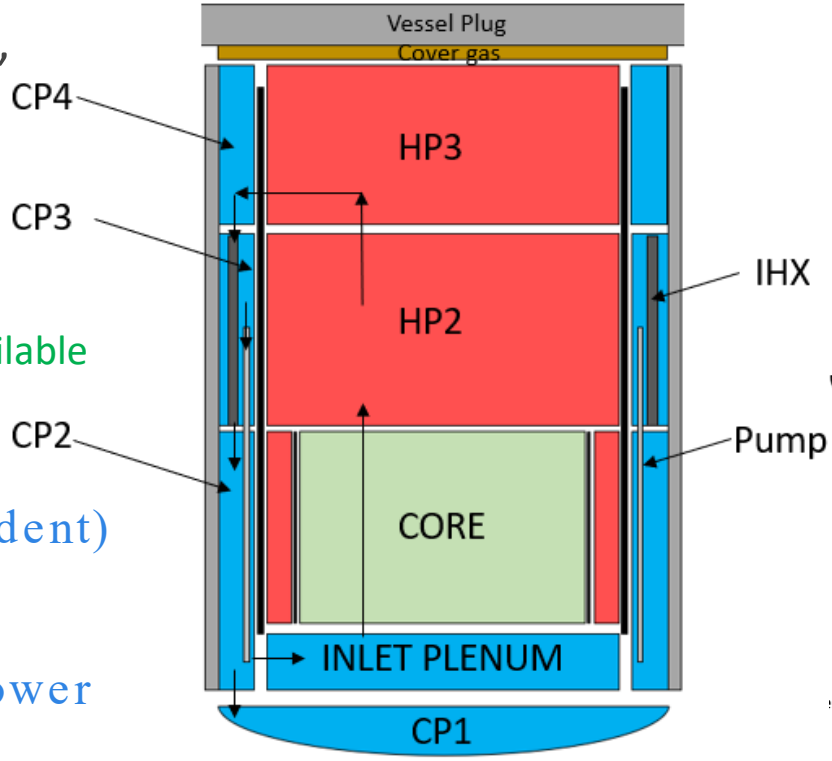

HP = hot pool; CP = cold pool
DRACS = Direct Reactor Auxiliary Cooling System

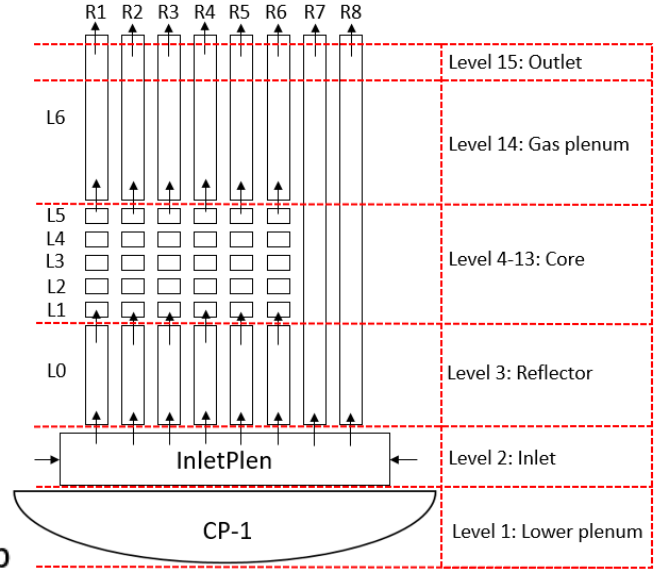

Core Nodalization

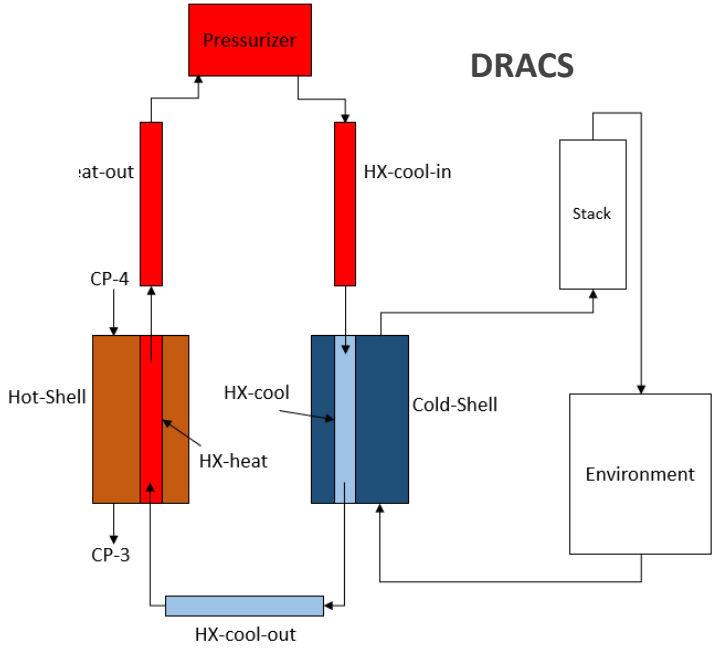

Sensitivity and Uncertainty Analysis with MELCOR-DAKOTA

- MELCOR + DAKOTA SNAP interface developed *(SNAP limited to LWR)*
  - Demonstration case study for generic PWR SBO
- MELCOR + DAKOTA coupling using Python developed
  - Procedure/ step-wise guidance
    - Support parallel runs (Windows)
    - Adaptable and user-friendly
- Demonstration case study for generic iPWR SBO
  - FOM = In-core H_2 production (H2INCORE); 15 uncertain inputs (random sampling)
  - Application to small BWR and HTGR underway

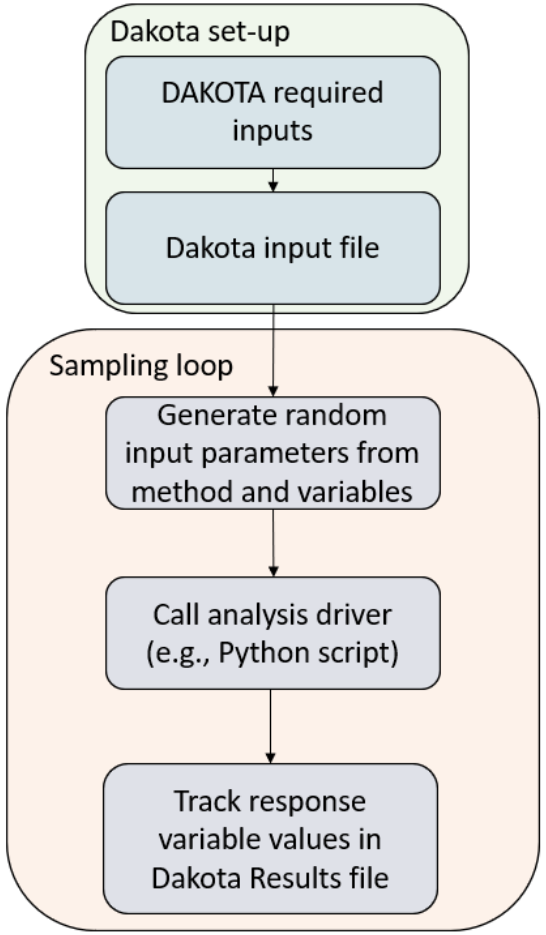

Coupling Method Flow Chart

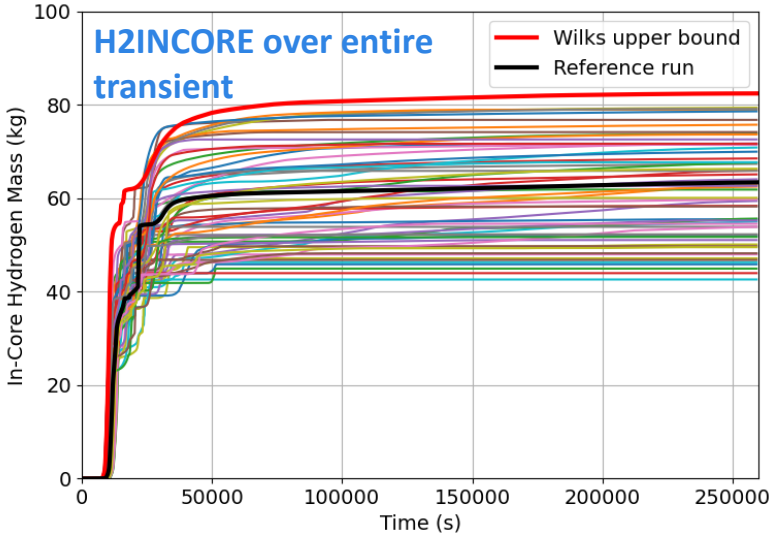

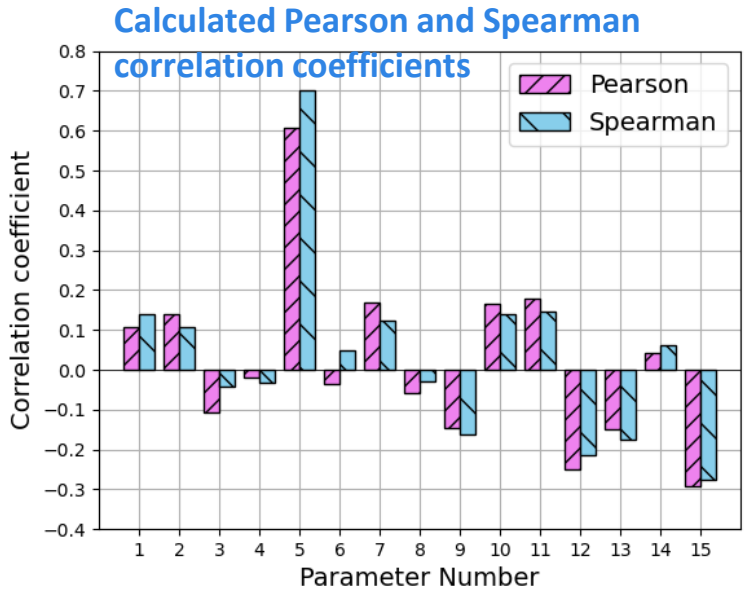

Molten Salt Modelling and Analysis

- CNL research focused on major gaps identified in PIRT (e.g. fission product behavior and retention in salts) and early investigation into MSR designs (e.g. Terrestrial IMSR)
- **Integral analysis:** Code assessment + evaluation proposed designs
  - US-NRC non-LWR analysis of pebble bed FHR (salt cooled), and MS fuel reactor
  - MELCOR supports MSR modelling; analysis will follow similar path of iPWR, HTGR
    - 1) representative generic design, 2) develop model, and 3) assess relevant severe accident scenarios.
- Molecular dynamics (MD) simulations of molten salts (salt properties + FP behaviour)
  - Supplements molten salt characterization and FP behaviour experimental work
  - Interatomic potential-based MD simulations of molten salt to guide future experiments or interpret the existing experimental data.
    - MD simulations of fission product behavior in molten salt mixtures, such as ThF4-LiF, where structural and dynamic characteristics of the fission products, including Cs, I, and Xe in ThF4-LiF with different compositions were studied.
  - Expanding study of interatomic potentials to include other molten salts for various properties, such as the effect of corrosion products on the properties of FLiBe (to be complete mid-2024).

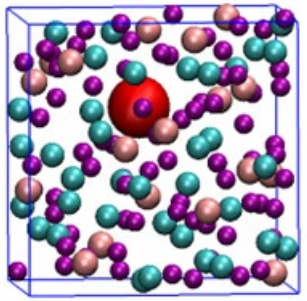

Solvated Cr^{2+} (Red) in FLiBe (Copper, Purple, Blue)

Top: Density Field Theory

Bottom: MD-sized simulation cell.

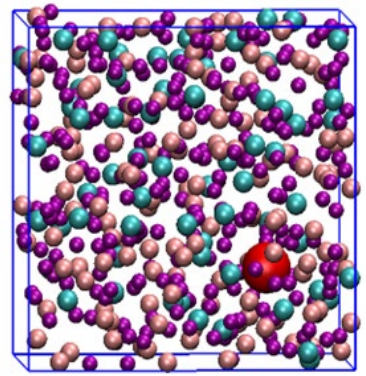

SMR Emergency Planning Zones (EPZs)

- International standards require EPZs for nuclear facilities where possible events could cause off site consequences (i.e. radiation doses) warranting urgent protective actions.
  - EPZ is the region encapsulating any advanced planning areas around a nuclear power plant (NPP) where there are measures prepared to avoid or mitigate the consequences of an accident.
  - It is commonly believed that the combination of smaller size and advanced technology will result in reduced risk and commensurately smaller EPZ compared to contemporary NPPs.
- EPZs should ensure appropriate envelope/planning basis for emergency preparedness/response
- CNL built on initial scoping-level assessment of potential postulated “limiting” reactor accidents
  - EPZ efforts furthered under IAEA CRP on technical basis for SMR EPZ (complete; TECDOC in 2024)
  - Subsequent emergency preparedness and response (EPR) series document that provides guidance for SMRs is expected (will reference EPZ CRP TECDOC).
  - Comprehensive review of challenges for determining SMR EPZ in Canada (2022)
    - **Research priorities:** i) determining appropriate emergency planning basis; ii) technical criteria for determining EPZ boundaries; and iii) creating a benchmark problem to assess different methods.
    - CNL developing framework for EPZ sizing (proposed at 2023 NERIS) and will apply to case study in 2024
    - This may form the basis for a future EPZ benchmark problem.

CNL SMR Research Strategy

- Broad range of SMRs looking to deploy in Canada requires a pragmatic approach to providing support for research, development, and licensing activities.
  - CNL maintains flexible research program guided by Canadian SMR/ AR deployment landscape
  - Build and maintain a baseline of knowledge, skills and capabilities related to a particular technology that can be deepened/ expanded as a design moves closer to deployment.
- CNL's approach to SMRs evolves as the market matures and the landscape changes
  - Current focus on water cooled SMRs near to deployment (especially small BWR)
  - Building analysis capabilities for up and coming SMR/ AR designs (e.g. HTGR and SFR) and relevant phenomena (e.g. fission product behaviour in molten salts)
  - Experimental research programs guided by PIRTs and designed to fill in knowledge gaps and generate data to support code qualification and validation activities.
  - Improving analysis tools to determine accident progression and consequences more accurately
- CNL development of PIRTs for specific reactor technologies (e.g. previous PIRTs on HTGRs and MSR)
  - Currently developing an open literature PIRT for design extension conditions of a BWRX-300
  - Experience can be leveraged to conduct additional PIRTs for other designs/ technologies

CNL SMR Research Strategy - 2

- Significant push for micro-reactors (e.g. USNC MMR and Westinghouse e-Vinci)
  - Application to remote communities and industry in Canada
  - Size and potential source terms dictate analysis needs (depth/ detail) for SA/ emergency planning.
  - Analysis needs are being evaluated (deployment landscape and regulator and vendor interest)
    - CNL is studying heat-pipe systems and assessing their operational and accident behaviour.

- CNL involvement in the international community for SMR related research
  - Leadership roles in NEA Expert Group on SMRs (EGSMR), GIF Expert Group and Reactor Safety Working Group (RSWG) + key roles in EU and IAEA initiatives related to SMR/ ARs.
  - CNL organizes Gen IV and Small Reactors Conference: G4SR-5 October 2024 in Ottawa!
  - EU project participation (SASPAM, AMHYCO, IPRESCA) and of course ERMSAR!
  - **Bilateral cooperation:** AECL/CNL MOUs with CEA (France) and KAERI (Korea), soon CVR (Czech Republic) as well as Canada -US (NRCan-DOE) and Canada -UK (NRCan – ONR) cooperation.
  - Good connections to US DOE Labs (INL, Sandia) and US NRC (CSARP/MCAP)
  - **Academia:** CNL MOUs with key Canadian research universities (McMaster, University of Ottawa, Queens, Ontario Tech, Western, Waterloo, University of New Brunswick)

Conclusions

- SMR/AR interest in Canada and abroad to support clean energy goals.
  - Canadian government support for deployment of SMRs
- CNL operates a flexible research program, guided by the SMR/AR deployment landscape in Canada
  - Develops and maintains capabilities and knowledge to support industry and regulatory stakeholders in the safe deployment of these technologies.
- Reactor safety program and integrated severe accident research develops baseline capabilities for specific SMR/AR technologies, which are deepened/expanded as they move closer to deployment.
  - Robust program allows for necessary information to conduct thorough licensing reviews and supports vendors in efforts to fully demonstrate the safe operations of their reactor designs.

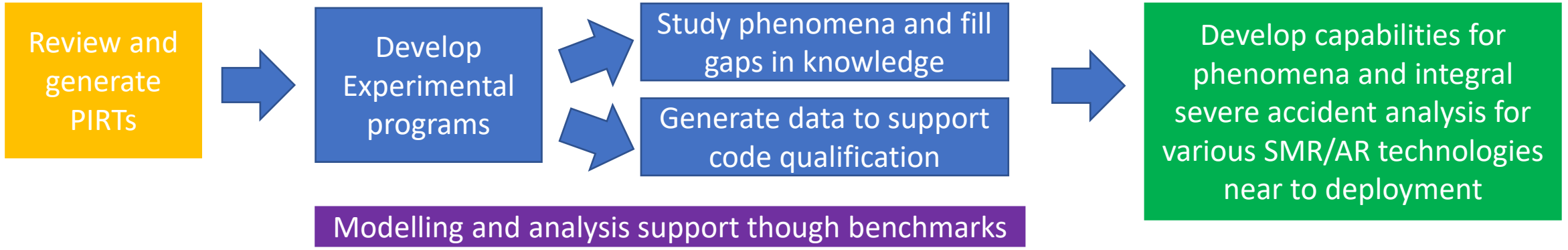

Thank you for your attention

Questions?

Acknowledgements:

- Much of the work discussed herein and CNL participation in various international working groups, projects and initiatives is funded through through the Atomic Energy of Canada Limited (AECL) Federal Nuclear Science and Technology Program

Andrew C. Morreale, PhD.

Technical Manager – Reactor Safety

Advanced Reactors Directorate

andrew.morreale@cnl.ca

APPLICATION OF THE PROBABILISTIC METHOD TO PROPAGATE INPUT UNCERTAINTY ON A DBA SEQUENCE IN A GENERIC iPWR

G. Agnello
University of Palermo
Dipartimento di Ingegneria, Viale delle Scienze, Ed. 6, 90128, Palermo, Italy
giuseppe.agnello04@unipa.it

G. Grippo
University of Bologna
Department of Industrial Engineering (DIN), Viale del Risorgimento 2, 40136, Bologna, Italy
gianmarco.grippo2@unibo.it

A. Bersano, F. Mascari
ENEA, C.R. Bologna, FSN-SICNUC
Via Martiri di Monte Sole 4, 40129, Bologna, Italy
andrea.bersano@enea.it; fulvio.mascari@enea.it

ABSTRACT

In view of the possible licensing needs of Small Modular Reactors (SMRs), the international scientific community is focusing on investigating the applicability of Severe Accident (SA) integral codes in simulating SMR response during postulated transients. Among the SMRs designs, the integral Pressurized Water Reactor (iPWR) concept, starting from the well-proven and established large Light Water Reactor (LWR) technology, is characterized by the adoption of passive safety systems and integral configuration. Within this framework, the Horizon Project "Safety Analysis of SMR with Passive Mitigation strategies – Severe Accident" (SASPAM – SA), coordinated by ENEA (Italy), is focused on investigating the applicability and transfer of operating large LWR knowledge and know-how to iPWRs in view of SA and Emergency Planning Zone (EPZ) European licensing needs. In this framework, the present study aims to provide initial insights on the application of Best Estimate Plus Uncertainty (BEPU) approach to SMR and about MECOR code uncertainties on the main thermal-hydraulic phenomena occurring in a generic iPWR..

KEYWORDS
SASPAM-SA; SMR; MELCOR; BEPU

1. INTRODUCTION

Computational integral Severe Accident (SA) codes, such as ASTEC [1] and MELCOR [2] [3], are developed to simulate the response of a Nuclear Power Plant (NPP) during mitigated and unmitigated scenarios and assess their safety. Nowadays, the international nuclear community involved in SAs is focused on investigating the applicability SA codes to light water Small Modular Reactors (SMRs), particular regarding on integral Pressurized Water Reactors (iPWRs). This SMR concept starts from the well-proven and tested Light Water Reactor (LWR) technology, incorporating operational plant experience and feedback as well as moderate evolutionary design modification to increase the inherent safety of the plant. Some of them are characterized by the adoption of an integral Reactor Pressure Vessel (RPV) containing all the Reactor Coolant System (RCS) components and the use of passive safety systems. In view of their licensing

process, state-of-the-art SA codes should be capable to simulate their advanced features and related phenomenology[1]. Within this framework, the Horizon Euratom SASPAM-SA project [4], coordinated by ENEA (Italy), aims to assess the capability of internationally recognized European and Non-European computational tools (largely used in Europe)[2] to describe the behavior of the most promising iPWR designs during SA scenarios and predict radiological impact on- and off-site. Thermal-hydraulic characterization during nominal and transient condition represent a crucial point since the phenomena that characterize them are specific to the design, phenomena related to new system components or reactor configuration[3] [5]. In this view, goal of the present work is to have a first insight about the uncertainties of the code, in terms of Figures Of Merit (FOM), on the thermal-hydraulic phenomena during a Design Basis Accident (DBA) scenario adopting a Best Estimate Plus Uncertainty (BEPU) approach [6]. Considering the iPWR mean features, a generic International Reactor Innovative and Secure (IRIS) [7] SMR type has been considered as reference to develop the MELCOR nodalization without using proprietary data but scaling the available data of the SPES-3 experimental facility [8] [9] as well as by engineering evaluation from public general data available. The probabilistic method to propagate input uncertainty [10] has been adopted to perform the uncertainty quantification analysis of a postulated Loss Of Coolant Accident (LOCA). Uncertain input parameters related to initial and boundary conditions and operation of passive safety systems have been selected based on literature and engineering judgment.

[1] Advanced designs, as iPWRs, are in general characterized by common features with the current operating large-LWR and by other specific features typical of their inherent evolutionary designs, providing safety advantages that reinforce the first three levels of the DiD principle. However, even if a plant is designed with advanced inherent features (through the reinforcement of the 1,2,3 DiD levels) allowing a reduction of the Core Damage Frequency (CDF), independent features for preventing and mitigating a severe accident sequence have to be included in its design (DiD level 4) together with the offsite emergency response (DiD level 5). Therefore, some scenarios that could lead to severe accidents need to be postulated and deterministically studied (More detailed information's in [30]). Therefore, it is necessary to assess the capability of internationally recognized SA code to describe the behaviour of the most promising iPWR designs during SA scenarios and to predict the resulting radiological impact on- and off-site.

[2] In order to maximize the knowledge transferability and impacts of the project two generic design-concepts, characterized by different evolutionary innovations in comparison with larger operating reactor, have been selected for the analyses: a) IPWR characterized by a submerged containment and electric power of about 60 MWe, called design 1; b) IPWR characterized by the use of several passive systems, a dry containment and an electric power of about 300 MWe, called design 2. These two generic reactor concepts include the main iPWR design features, considered in the most promising designs ready to go on the European market, allowing to assess in a wider way the capability of codes (SA and CFD) to simulate the SA phenomena typical of iPWR. It is not the project's objective to assess the generic reactor designs selected but, based on the project findings, allow a more general statement on the code's applicability to currently favored designs under postulated SA condition. No PSA considerations will be done in the project due to the generic nature of the reactor concept considered, then the scenarios identified will be characterized in terms of severity but not in terms of probability.

[3] Passive systems are, on the one hand, an advanced solution to increase the inherent safety of the plant (e.g., there is no need of pumps), on the other hand a) they require extensive investigation for assessing the functional failure related to the thermal-hydraulic phenomena driving the operation of the systems and assess the related uncertainties, b) may still need an active initiation, and c) are characterized by very limited operational experience (to have more detailed information [30] [31]). Considering this, the impact of the operation of passive systems on postulated severe accident progression is a novel topic and needs to be assessed. Considering this, the specific assessment of the code capability to simulate passive systems phenomenology is crucial. Infact, in LW-SMR reactors the BDBA/SA scenarios evolution depend from the postulated partial or total not operation of passive systems (e.g. postulate the failure of passive system valve activation). Therefore, it is necessary to analyse the capability of SA codes to predict the main thermal-hydraulic phenomena involved in the passive mitigation strategy of LW-SMR in order to adequately apply them for the design of accident management's strategy (first phase of a SA is only dominated by T-H phenomena, then in-vessel is affected by thermal-hydraulic phenomena).

2. GENERIC iPWR DESIGN AND MELCOR INPUT-DECK DESCRIPTION

The design here studied is characterized by a dry spherical containment and the use of different passive systems, arranged in two parallel trains and features an integral RPV containing all the RCS components such as the Pressurizer (PRZ), a compact Steam Generators (SGs) (with the adoption of helical-coil tubes) and the Reactor Coolant Pumps (RCPs). The RPV is contained in the containment composed by the Drywell (DW) and the Reactor Cavity (RC). The iPWR passive mitigation strategy is based on several passive systems, which carry out different safety functions: *natural circulation in the RPV* (Riser-Downcomer -RI-DC-), *decay heat removal* (Emergency Heat Removal System -EHRS-), *primary automatic depressurization* (Automatic Depressurization System -ADS-), *high pressure safety injection* (Emergency Boration Tanks -EBTs-), *low pressure safety injection* (Long-term Gravity Make-up System -LGMS-), *containment pressure suppression* (Pressure Suppression System -PSS- tanks), *flooding of the RC*. Except the heat sink of the decay heat removal system, all the passive systems considered in the passive mitigation strategy are supposed to be placed within the DW. A generic scheme of the iPWR layout, with the considered safety functions, is presented in Figure 1 [11].

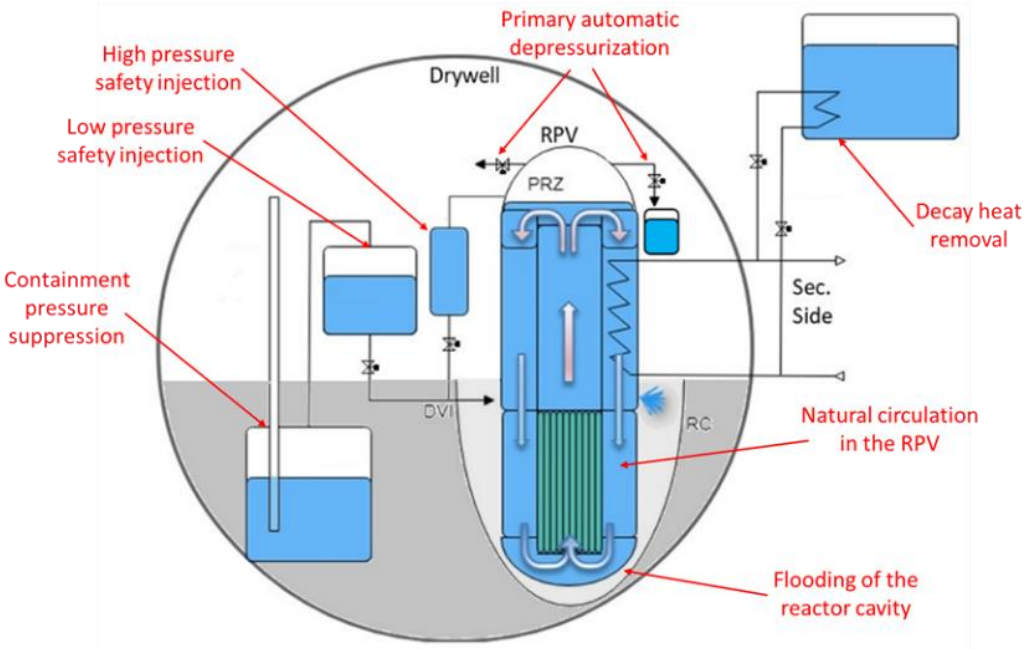

Figure 1 Scheme of the generic iPWR design with the passive safety systems [11].

MELCOR [2] [3] is a fully integrated SA code able to simulate the thermal-hydraulic phenomena in steady and transient condition and the main SA phenomena characterizing the RPV, the RC, the containment, and the confinement buildings typical of LWR. The code, which presents a modular architecture, can be used with the Symbolic Nuclear Analysis Package (SNAP) [12]. The generic iPWR MELCOR nodalization, shown in Figure 2, developed in the framework of the SASPAM-SA project using MELCOR code version v2023, combines a trade-off between the computational time and a detailed prediction capability of the transient thermal-hydraulic and core degradation phenomenology. The two passive systems cooling lines, adopted by the selected design, have been modelled separately. The RPV has been modelled in different hydraulic CVH Control Volumes (CVs), coupled with FL flow path and HS, including the Lower Plenum (LP), the reactor core, the core by-pass, the riser, the Upper Plenum (UP), the SGs and the downcomer. To simplify the model, the eight SGs have been modelled as an equivalent one, with four CVH CVs on the primary side and eight CVs on the secondary side. The reactor core has been modelled by a single CV coupled with the correspondent COR package nodalization, characterized by sixteen axial levels and six

radial rings. The containment region has been modelled with one CVH CV for the DW region, as shown previously in Figure 2, thermally coupled with the CV representing the environment, and one CV for the RC, coupled with the CAV MELCOR package.

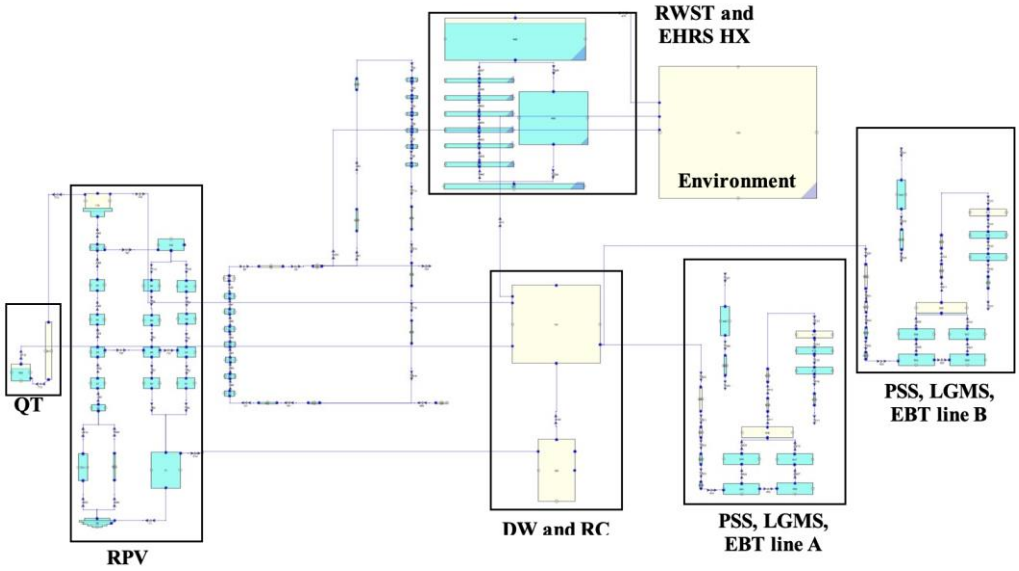

Figure 2 SNAP view of the MELCOR CVH and FL nodalization.

3. REFERENCE CASE

A LOCA accident, initiated by the double-ended guillotine break of one of the two DVI lines, has been considered as reference scenario [8] [11] [13] [14]. In general the transient starts with the break and the consequent RPV depressurization and containment pressurization. Once the containment high-pressure set-point is achieved, the S-Signal initiates the reactor SCRAM; due to this the isolation of the secondary side of SGs and the opening of two of the four EHRS loops occur[4]. A natural circulation in the EHRS system begins, permitting the transfer of the thermal power to the water inside the RWST tanks, the cooling of the RPV and its depressurization. The low level of the coolant in the PRZ triggers the RCPs coast-down and the following automatic opening of the RI-DC check valves. The LM-Signal (LOCA Mitigation) is then triggered when the PRZ pressure reaches the low pressure set-point. It determines the opening of the ADS stage-1, the start of the injection by EBTs and the opening of the two remaining EHRS system loops. At the primary and DW pressure equalization, the low RPV-DW differential pressure signal activates the LGMSs. Because of the steam condensation in the DW and the heat removed due to the EHRS system, the pressure in the DW decreases below the PSSs pressure. Consequently, the water inside the PSSs is forced upward through the PSS vent pipes, until filling the RC after dropping from the top end of the PSS vent pipe. This water head inside the PSS vent-pipe maintains a differential pressure between the LGMS (equal to PSS) and RPV (equal to DW) throughout the depressurization phase, which improves the LGMS water injection. Steam circulation between RPV and DW is enabled by the ADS stage-2 valves opening upon reaching the LGMS low water mass signal. The water in the RC keeps the core filled during the long-term cooling phase. The heat losses thorough the DW metal walls to the environment and the power extracted by the EHRS systems allow the cooling down of the core. The MELCOR simulation of the reference calculation has been performed considering an initial steady-state analysis of 2000 s to reach systems nominal conditions. Comparing the steady-state results with reference values [7], a discrepancy less than 3% has been evaluated.

[4] For the analyses presented in the paper, because of the nodalizations structure (only one equivalent EHRS), the logic is simplified and only one actuation of EHRS is considered.

The Start Of the Transient (SOT) has been considered at t=0 s with the opening of the break and the calculation has been performed for 50000 s. Table 1 reports the main phenomena characterizing the transient and predicted by MELCOR with their timings.

Table 1 Main events characterizing the MELCOR reference case.

Event	Time [s]
Break	0
High Containment pressure signal (SCRAM, isolation SG, EHRS activation)	41
Low PRZ water level signal (Pump coast down and RI-DC opening)	122
Low PRZ pressure signal (ADS Stage-1 opening, EBTs opening)	148
Low DP RV-Containment (LGMSs opening)	1884
1st RPV- DW pressure equalization	2000
2nd RPV- DW pressure equalization	3315
1st vent injection	3010
2nd vent injection	5405
Core level reach the TAF	3000
Cavity level reach the DVI	3950
Low LGMS mass (ADS Stage -2 opening)	12265

4. UNCERTAINTY QUANTIFICATION METHODOLOGY AND COMPUTATIONAL ENVIRONMENT

Among the uncertainty methodologies developed in the past to conduct uncertainty quantification analyses [6], the probabilistic method to propagate input uncertainty [10] is based, in general, on statistical approaches to correlate the input uncertainty, identified by the uncertain input parameters, to output uncertainty, expressed in the uncertainty of selected FOMs. Each uncertain input parameter is identified by a Probability Density Function (PDF), usually selected based on previous analyses, available experimental data, and engineering judgment [15]. A Monte Carlo random sampling of the uncertain input parameters is performed to define a number N of sets of values of the uncertain input parameters used to defined N input-deck used to start N code runs. The Wilks's formula [16] [17] can be used to determine the minimum number of code runs N based on the requested probability content γ and confidence level β. If multiple FOMs *p* are analysed, N is calculated using the Wald's formula [18], presented below for the *one-sided tolerance interval*:

$$\beta = \sum_{j=0}^{N-p} \binom{N}{j} \alpha^{j} (1-\alpha)^{N-j} \quad (1)$$

More details on the statistical aspects can be found in [19]. As well as assessing the uncertainty width of FOMs, the *mean*, *median*, *standard deviation* and *coefficient of variation* are calculated in this work. To have insights about the statistical correlation between the FOMs and the selected uncertain input parameters the *simple* and *simple rank correlation coefficients* are computed [20] [21] [22] [23].
The Uncertainty Tool (UT) used in this uncertainty application, shown in Figure 3, can perform all the steps needed for the development of an uncertainty analysis [24]. This tool has been developed and applied along the H2020 MUSA project, coordinated by CIEMAT(Spain) [29]. The user specifies the N number of code runs desired as well as the uncertainty parameters selected for analysis and the tool, by the sampling, creates the N sets of parameters to be replaced in an input-deck template. After executing the code runs, the tool manages the FOMs calculated data extraction by using the AptBatch executable [25] and, then, develops the statistical analysis of the results and the post-processing.

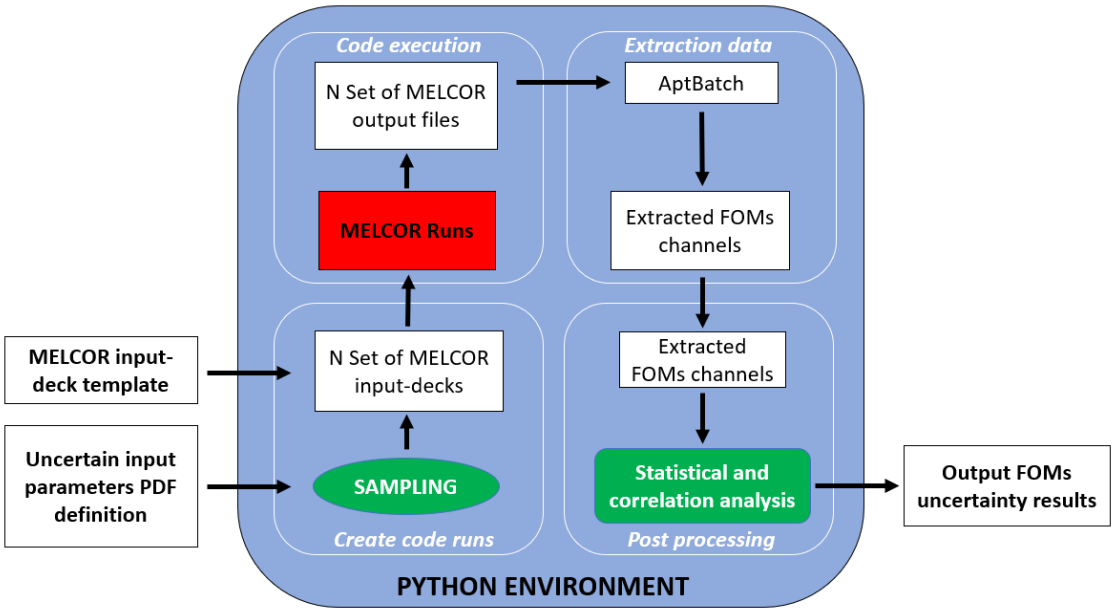

Figure 3 Workflow of the uncertainty in-house UT used with MELCOR code in a Python environment/architecture.

5. UNCERTAINTY ANALYSIS OF THE DBA SEQUENCE

Goal of the present study is not to be a comprehensive uncertainty study from the uncertain input parameters used and FOMs selected view but to develop of a full uncertainty analysis on iPWR design using the probabilistic method to propagate input uncertainty as well as to give some insights about the statistical correlation between uncertain input parameters and the FOMs. Following as done in [20], the FOMs selected for the present analysis are: peak of maximum cladding temperature (referred to as FOM_1), minimum collapsed coolant level in the core region (referred to as FOM_2) and the maximum containment pressure (referred to as FOM_3). The uncertain input parameters, listed in Table 2 have been selected and extrapolated from [26] [27] [28] and based on engineering judgment. Considering equation (1), 129 code runs are needed considering a probability γ and confidence level β of 95%. For the present application, the failed runs have not been considered and have been replaced with new ones with a different combination of the uncertain input parameters, adopting the approach mentioned in [29]. In Table 3, based on the analyses, the main statistical parameters characterizing the FOMs have been shown. A mean value of 504.74 K and an uncertainty width of 42.77 K has been estimated for FOM_1, with a standard deviation of 8.23 K. The FOM_2 is characterized by a mean value of 4.46 m with an uncertainty band of 0.7m and standard deviation of 0.16 m; The FOM_3 is characterized by a mean value of 11.37E5 Pa, with an uncertainty width of 3.76E5 Pa and a standard deviation of 0.82E5 Pa. The empirical PDFs of the FOMs have been calculated as well as the simple and simple rank correlation coefficients by means the Pearson and Spearman's correlations for each FOM and uncertain input parameters. From the statistical correlation analysis, the parameters with a significant or moderate statistical correlations with the FOM_1 are the Heat Transfer Surface of EHRS HXs (negative correlation) and the ADS Stage-1 loss coefficient (positive correlation). Regarding the FOM_2, a moderate statistical correlation with the initial DW pressure (positive correlation) and Heat Transfer Surface of EHRS HXs (negative correlation) has been underlined. A significant statistical correlation with ADS Stage-1 loss coefficient has been evaluated (positive correlation). The FOM_3 presents a moderate statistical correlation (positive correlation) with the initial DW pressure (as expected) and a significant statistical correlation with the ADS Stage-1 loss coefficient (negative correlation). From Figure 4 to Figure 9 the estimated PDF of the FOMs and the scatter plot of these parameters are shown.

Table 2 Uncertain input parameters.

Uncertain input parameter	Unit	PDF	Reference value	Lower and upper bound		Reference
Decay Power	[-] (multiplier)	Normal	1.0	Min	0.98	[27]
				Max	1.02	
Initial PRZ pressure	[Pa]	Normal	1.55E7	Min	1.54E7	[27]
				Max	1.56E7	
EBT initial temperature	[K]	Normal	321.9	Min	311.9	[27]
				Max	331.9	
LGMS initial temperature	[K]	Normal	321.9	Min	311.9	[27]
				Max	331.9	
Initial DW pressure	[Pa]	Uniform	1.013E5	Min	0.85E5	[27]
				Max	1.15E5	
RWST initial liquid level	[m]	Normal	9.0	Min	8.9390	[26]
				Max	9.0610	
RWST and environment initial temperature	[K]	Uniform	293.0	Min	283.0	[28]
				Max	303.0	
Heat Transfer Surface EHRS HXs	[-] (multiplier)	Uniform	1.0	Min	0.75	[26]
				Max	1.25	
Break Flow discharge coefficient	[-]	Uniform	0.7	Min	0.7	Engineering Judgement
				Max	1.0	
EHRS valves loss coefficient	[%]	Uniform	0	Min	-100	Engineering Judgement
				Max	+100	
EBT valves loss coefficient	[%]	Uniform	0	Min	-100	Engineering Judgement
				Max	+100	
LGMS valve loss coefficient	[%]	Uniform	0	Min	-100	Engineering Judgement
				Max	+100	
ADS Stage-1 loss coefficient	[%]	Uniform	0	Min	-100	Engineering Judgement
				Max	+100	
ADS Stage-2 loss coefficient	[%]	Uniform	0	Min	-100	Engineering Judgement
				Max	+100	

Table 3 Statistical parameters of the FOMs.

Statistical parameter	FOM_1		FOM_2		FOM_3	
	Value	Unit	Value	Unit	Value	Unit
Mean	504.74	[K]	4.46	[m]	11.37E5	[Pa]
Median	505.53	[K]	4.47	[m]	11.32E5	[Pa]
Lower Bound	483.66	[K]	4.05	[m]	9.73E5	[Pa]
Upper Bound	526.43	[K]	4.75	[m]	13.49E5	[Pa]
Standard deviation	8.23	[K]	0.16	[m]	0.82E5	[Pa]
Coefficient of variation	0.016	[-]	0.037	[-]	0.072	[-]

To characterize the uncertainty width of the code's results during throughout the transient, the values of the N cases referred to the maximum cladding temperature, core collapsed coolant level and DW pressure have been compared at each time-step to the reference case and the mean, median, upper and lower bound.

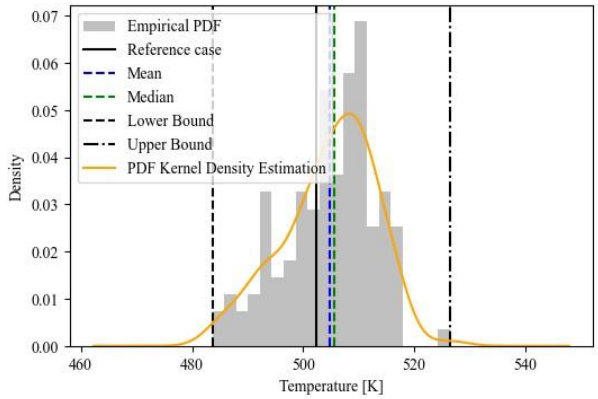

Figure 4 Empirical PDF of the FOM_1.

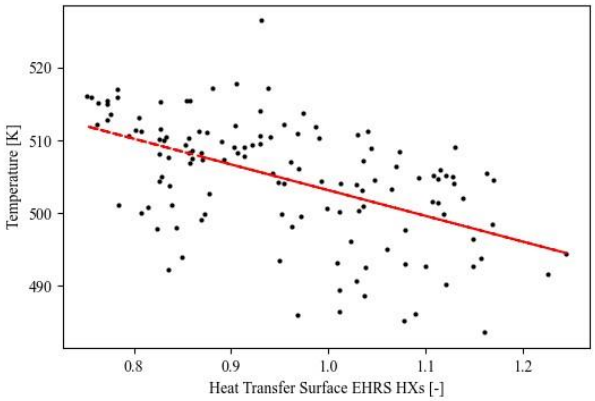

Figure 5 Scatter plot of FOM_1.

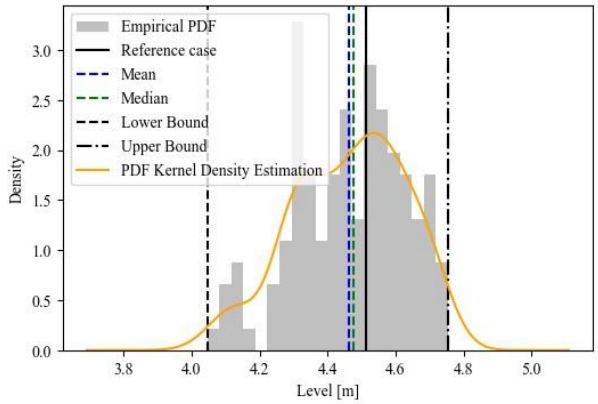

Figure 6 Empirical PDF of the FOM_2.

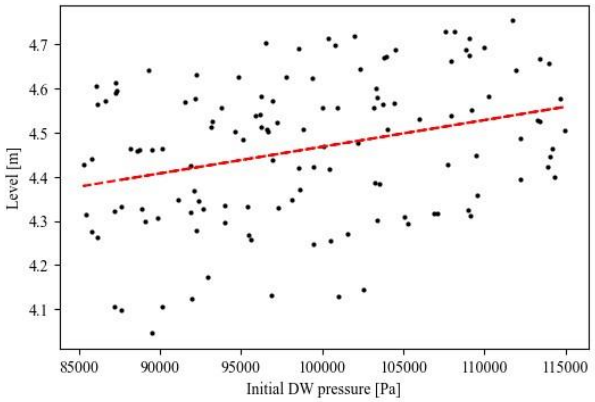

Figure 7 Scatter plot of FOM_2.

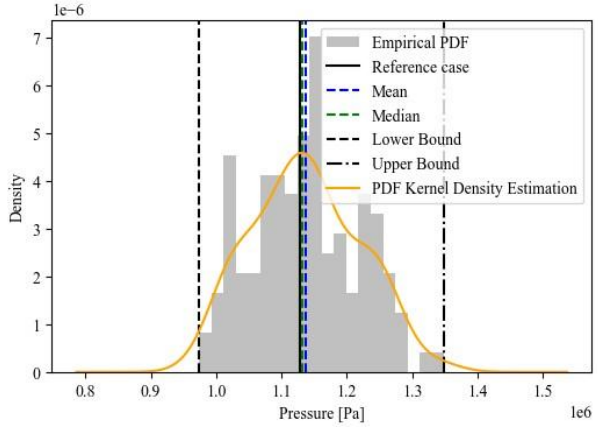

Figure 8 Empirical PDF of the FOM_3.

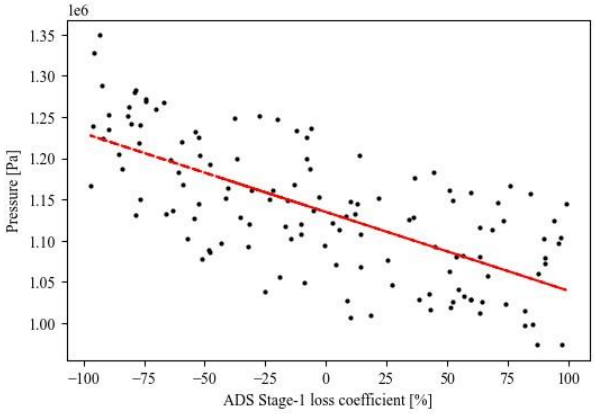

Figure 9 Scatter plots of FOM_3.

In addition, the trend of the simple correlation coefficient during the first 10000 s of the transient have been considered with respect to the uncertain input parameters previously mentioned. The maximum cladding temperature, shown in Figure 10 presents an uncertainty width of about 25 K during the first 1000 s after the SOT. Then, it increases reaching an amplitude of about 100 K, between 1000 and 2000 s. In this time region, come code runs present a peak up to 525 K. After that, the uncertainty width remains almost constant and equal to about 25 K. As highlighted in Figure 11, regarding the initial DW pressure and Heat Transfer Surface of EHRS HXs parameters, the magnitude of the correlation increases from low to moderate or significant along the transient, while the magnitude of the correlation for the ADS Stage-1 loss coefficient

parameter goes from significant to moderate along the long-term phase. The uncertainty width of the core collapsed coolant level, shown in Figure 12[5], increases its amplitude after 200 s of the SOT to a value of 1.20 m and reach its maximum value at about 3000 s after the SOT. As can be seen from Figure 12 the attainment of the TAF during the transient has a very high uncertainty width in time terms, reaching an uncertainty width of about 4000 seconds. As shown in Figure 13, the ADS-1 loss coefficient has a statistically significant correlation for the first 4000 s of the transient.

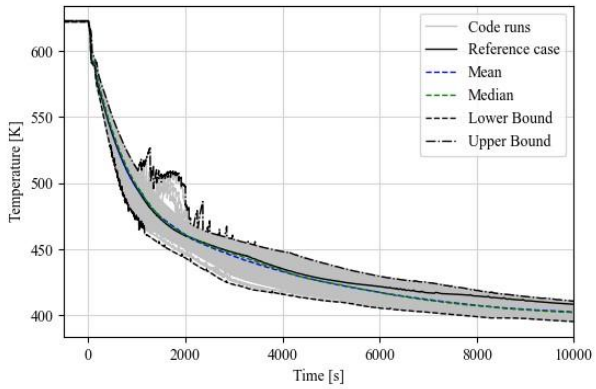

Figure 10 Uncertainty band of the maximum cladding temperature.

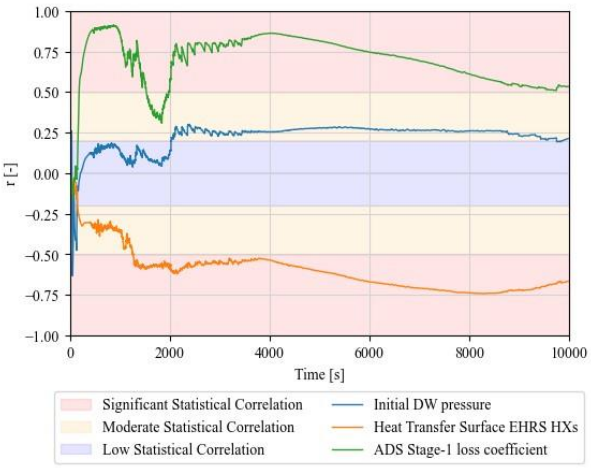

Figure 11 Simple correlation coefficient referred for the maximum cladding temperature.

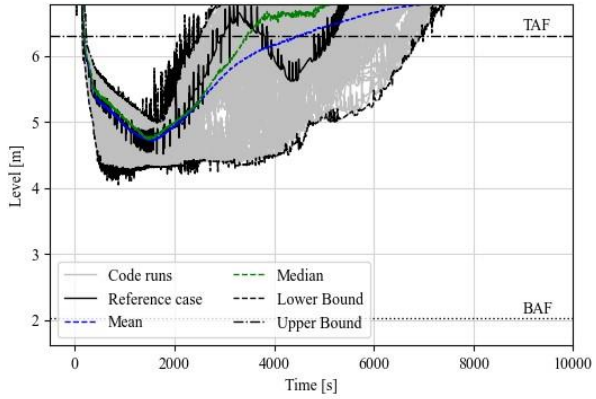

Figure 12 Uncertainty band of the core collapsed coolant level.

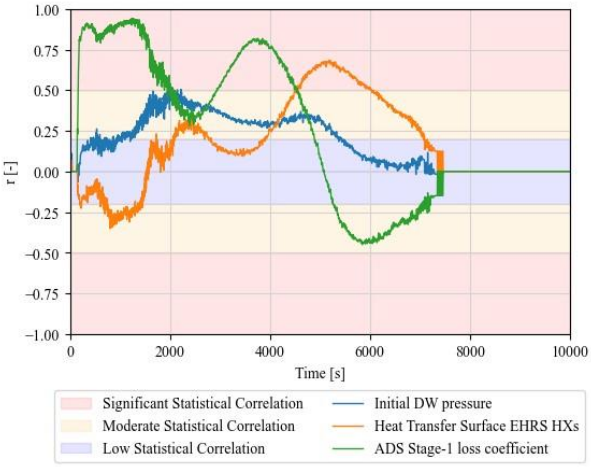

Figure 13 Simple correlation coefficient for the core collapsed coolant level.

The heat transfer surface of the EHRS HXs has a significant correlation (positive correlation) after about 4000 s. The initial pressure of the DW presents a moderate statistical correlation after about 1000 seconds after the SOT. The uncertainty width of the DW pressure, shown in Figure 14, presents a maximum value of the band at about 3000 s after the SOT and equal to about 7E5 Pa. The pressure of the DW is characterized by a statistically significant correlation with its initial value (as expected) in the first instants of the transient, and at about 1000 s from the SOT, as highlighted in Figure 15. The ADS-1 loss coefficient is also a parameter

[5] With reference to the **Error! Reference source not found.**, the uncertainty width is cut just above the TAF as only the volume representative of this region has been considered for the collapsed level.

with a significant correlation, which in the first 1000 s shows a significant statistical correlation of a negative type and then of a positive type. After the reflood phase, the heat transfer surface of the EHRS HXs shows a statistically significant negative correlation.

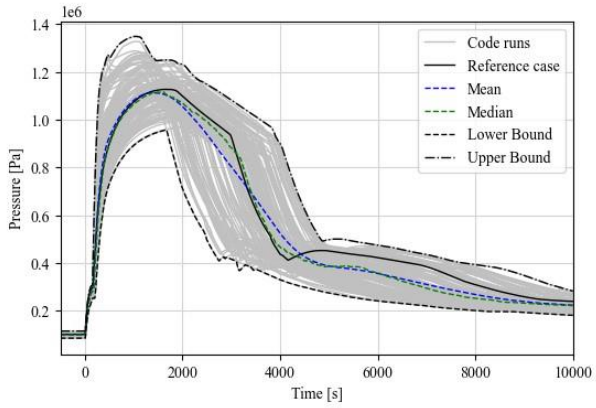

Figure 14 Uncertainty band of the FOM_3.

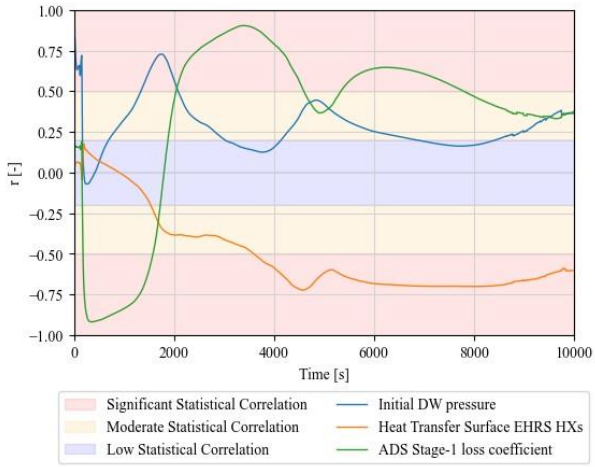

Figure 15 Simple correlation coefficient for the DW pressure.

6. CONCLUSIONS

The present work presented the uncertainty analysis of a DBA sequence in a generic iPWR. The activity has been performed, following a BEPU application, using the SA integral code MELCOR and an in-house UT developed in a Python environment/architecture. Aim of the work is to apply the probabilistic method to propagate input uncertainty in view to have some insight about the code uncertainties on the main thermal-hydraulic phenomena characterizing a mitigated transient in such scenario. Three relevant FOMs in term of plant safety and fourteen uncertain input parameters related to initial and boundary conditions and on passive safety system have been considered. The analysis gives first insights into the uncertainties of the code concerning the key TH phenomena during a mitigated transient scenario. In addition, by calculating the statistical correlation coefficients, it has been possible to identify the input uncertainty parameters with a moderate or significant statistical correlation with the FOMs. In this regard, a moderate or significant statistical correlation between FOMs and the Heat Transfer Surface of EHRS HXs, the initial pressure in the DW and the ADS-1 loss coefficient has been underlined. This study not only support but also extend the current activity done in SASPAM-SA consisting in assessing the capability of internationally recognized computational tools (largely used in Europe) to describe the behaviour of the most promising iPWR designs during mitigated and unmitigated scenarios. The next step will be to extend the uncertainty analyses to a postulated SA scenarios in order to identity the parameters that have a moderate/significant statistical correlation with SA FOMs.

NOMENCLATURE

ADS: Automatic Depressurization System; **BEPU**: Best Estimate Plus Uncertainty; **DBA**: Design Basis Accident; **DVI**: Direct Vessel Injection; **DW**: Drywell; **EBT**: Emergency Boration Tank; **EHRS**; Emergency Heat Removal System; **EPZ**: Emergency Planning Zone; **FOM**: Figure Of Merit; **HX**: Heat eXchanger; **iPWR**: Integral Pressurized Water Reactor; **IRIS**: International Reactor Innovative and Secure; **LGMS**: Long Term Gravity Make-up System; **LOCA**: Loss Of Coolant Accident; **LP**: Lower Plenum; **LWR**: Light Water Reactor; **NPP**: Nuclear Power Plant; **PDF**: Probability Density Function; **PRZ**: Pressurizer; **PSS**: Pressure Suppression System; **QT**: Quench Tank; **RC**: Reactor Cavity; **RCP**: Reactor Coolant Pump; **RCS**: Reactor Coolant System; **RPV**: Reactor Pressure Vessel; **RWST**: Refueling Water

Storage Tank; **SA**: Severe Accident; **SG**: Steam Generator; **SMR**: Small Modular Reactor; SNAP: Symbolic Nuclear Analysis Package; **SOT**: Start Of the Transient; **UP**: Upper Plenum; **UT**: Uncertainty Tool**.**

ACKNOWLEDGMENTS & DISCLAIMER

Funded by the European Union

Funded by the European Union. Views and opinions expressed are however those of the author(s) only and do not necessarily reflect those of the European Union or European Commission-Euratom. Neither the European Union nor the granting authority can be held responsible for them.

UNIPA carried out the research activity with MELCOR code and SNAP, obtained in the framework of the UNIPA-ISIN agreement signed on March 26th 2021 as part of the General Arrangement between the United States Nuclear Regulatory Commission (US-NRC) and the Italian National Inspectorate for Nuclear Safety and Radiation Protection (ISIN).
ENEA carried out the research activity with MELCOR code and SNAP, obtained in the framework of the UNIPA-ISIN agreement signed on March 23th 2020 as part of the General Arrangement between the United States Nuclear Regulatory Commission (US-NRC) and the Italian National Inspectorate for Nuclear Safety and Radiation Protection (ISIN).

REFERENCES

[1] P. Chatelard, S. Belon, L. Bosland, L. Carénini, O. Coindreau, F. Cousin, C. Marchetto, H. Nowack, L. Piar, L. Chalain, «Main modelling features of the ASTEC V2.1 major version,» *Annals of Nuclear Energy,* vol. Vol. 93, pp. 83-93, 2016.

[2] L.L. Humphries, B.A. Beeny, F. Gelbard, T. Haskin, J. Phillips, J. Reynolds, R.C. Schmidt, «MELCOR Computer Code Manuals: Vol. 1: Primer and User's Guide Version 2.2 r2023.0,» Sandia National Laboratories, Albuquerque (USA), 2023.

[3] L.L. Humphries, B.A. Beeny, F. Gelbard, T. Haskin, D. Louie, J. Phillips, J. Reynolds, R.C. Schimidt, «MELCOR Computer Code Manuals: Vol. 2: Reference Manual Version 2.2 r2023.0,» Sandia National Laboratories, Albuquerque (USA), 2023.

[4] SAFETY ANALYSIS OF SMR WITH PASSIVE MITIGATION STRATEGIES - SEVERE ACCIDENT (SASPAM-SA), [Online]. Available: https://www.saspam-sa.eu/.

[5] F. Mascari, B.G. Woods, K. Welter, F. D'Auria, A. Bersano, P. Maccari, «Small modular reactors and insights on passive mitigation strategy modeling,» *Nuclear Engineering and Design,* vol. 401, n. 112088, 2023.

[6] IAEA, «Safety Reports Series No. 52: Best Estimate Safety Analysis for Nuclear Power Plants: Uncertainty Evaluation,» Vienna, 2008.

[7] «INTERNATIONAL REACTOR INNOVATIVE AND SECURE, IRIS Plant Overview,» October 2002.

[8] M. Carrelli, L. Conway, M. Dzodzo, A. Maioli, L. Oriani, G. Storrick, B. Petrovic, A. Achilli, G. Cattadori, C. Congiu, R. Ferri, M. Ricotti, D. Papini, F. Bianchi, P. Meloni, S. Monti, F. Berra, D. Grgic, G. Yoder, A. Alamberti, «The SPES3 experimental facility design for the IRIS reactor simulation,» *Science and Technology of Nuclear installations,* vol. vol2009, n. 579430, 2009.

[9] R. Ferri, C. Congiu, «Conceptual design of SPES3-IRIS facility,» SIET 01 334 RT 07 Rev.1, Piacenza (Italy), 2008.

[10] H. Glaeser, «GRS Method for Uncertainty and Sensitivity Evaluation of Code Results and Applications,» *Science and Technology of Nuclear Installations,* vol. Volume 2008, n. 798901, 2008.

[11] P. Maccari, F. Mascari, S. Ederli, P. Meloni, S. Manservisi, «ASTEC code DBA analysis of passive mitigation strategy on a generic IRIS SMR,» *Annals of Nuclear Energy,* vol. 156, n. 108194, 2021.

[12] Applied Programming Technology Inc., «Symbolic Nuclear Analysis Package (SNAP) User's Manual,» 2021.

[13] R. Ferri, «SPES3-IRIS facility RELAP5 sensitivity analyses on the containment system for design review,» no. SIET 01 526 RT 09 Rev.0, 2010.

[14] A. Achilli, C. Congiu, R. Ferri, F. Bianchi, P. Meloni, D. Grgić, M. Dzodzo, «Integral Test Facilities and Thermal-Hydraulic System Codes in Nuclear Safety Analysis,» *Science and Technology of Nuclear Installation,* vol. Vol. 2012, n. 173637, 2012.

[15] M.E. Stephens, B.W. Goodwin, T.H. Andres, «Deriving parameter probability density funtions,» *Reliability Engineering and System Safety,* vol. 42, pp. 271-291, 1993.

[16] S.S. Wilks, «Determination of sample size for setting tolerance limits,» *The Annals of Mathematical Statistics,* vol. 12, pp. 91-96, 1941.

[17] S.S. Wilks, «Statistical prediction with special reference to the problem of tolerance limits,» *The Annals of Mathematical Statistics,* vol. 13, pp. 400-409, 1942.

[18] A. Wald, «An extension of Wilks' method for setting tolerance limits,» *Annals of Mathematical Statistics,* vol. 14, pp. 45-55, 1943.

[19] A. Guba, M. Makai, L. Pal, «Statistical aspects of best estimate method-I,» *Reliability Engineering and System Safety,* vol. 80, pp. 217-232, 2003.

[20] G. Agnello, P.A. Di Maio, A. Bersano, F. Mascari, «Cold Leg LBLOCA uncertainty analysis using TRACE/DAKOTA coupling,» *Journal of Physics: Conference Series,* vol. 2177, n. 012023, 2022.

[21] A. Bersano, F. Mascari, M.T. Porfiri, P. Maccari, C. Bertani, «Ingress of Coolant Event simulation with TRACE code with accuracy evaluation and coupled DAKOTA Uncertainty Analysis,» *Fusion Engineering and Design,* vol. 159, n. 111944, 2020.

[22] K.A. Gamble, L.P. Swiler, «Uncertainty Quantification and Sensitivity Analysis Applications to Fuel Performance Modeling,» SAND2016-4597C, 2016.

[23] J.L. Rodgers, A. Nicewander, «Thirteen Ways to Look at the Correlation Coefficient,» *The American Statistician,* vol. 42, pp. 59-66, 1987.

[24] M. Garbarini, G. Agnello, A. Bersano, F. Gabrielli, L. Luzzi, F. Mascari, «Simulation of QUENCH-06 experiment by MELCOR v2.2 with Uncertainty Analysis,» *20th International Topical Meeting on Nuclear Reactor Thermal Hydraulics (NURETH-20),* pp. 4336-4349, 2023.

[25] Applied Programming Technology, Inc., *AptPlot User's Manual,* 2021.

[26] F. Alcaro, A. Bersano, C. Bertani, F. Mascari, «BEPU analysis of a passive decay heat removal system with RELAP5/MOD3.3 and RELAP5-3D,» *Progress in Nuclear Energy,* vol. 136, n. 103724, 2021.

[27] M. Perez, et al., «Uncertainty and sensitivity analysis of a LBLOCA in a PWR Nuclear Power Plant: Results of the Phase V of the BEMUSE programme,» *Nuclear Engineering and Design,* vol. 241, pp. 4206-4222, 2011.

[28] P. Maccari, J.A. Zambaux, A. Bersano, «BEPU analysis of a 2-in DVI break in a generic IRIS SMR by ASTEC - RAVEN coupling,» *EUROSAFE Forum 2021,* Paris, France, November 22-23, 2021.

[29] F. Mascari et al., «Main outcomes of the Phebus FPT1 uncertainty and sensitivity analysis in the EU-MUSA project,» *Annals of Nuclear Energy,* vol. 196, n. 110205, 2024.

[30] SMR Regulators' Forum, «Pilot Project Report: Considering the Application of a Graded Approach, Defence-in-Depth and Emergency Planning Zone Size for Small Modular Reactors,» January 2018.

[31] 19. European SMR pre-Partnership Reports, Workstream 5 –Research, Development, and Innovation Roadmap, 2023. [Online]. Available: https://snetp.eu/wp-

content/uploads/2023/07/European-SMR-pre-Partnership-WS5-report-and-roadmap-30-June-2023.pdf.

SAFETY ANALYSIS OF SMR WITH PASSIVE MITIGATION STRATEGIES - SEVERE ACCIDENT

APPLICATION OF THE PROBABILISTIC METHOD TO PROPAGATE INPUT UNCERTAINTY ON A DBA SEQUENCE IN A GENERIC iPWR

11th European Review Meeting on Severe Accident Research Conference
13 – 16 May, Stockholm

Speaker: Gianmarco Grippo

Contributors: Giuseppe Agnello, Andrea Bersano, Fulvio Mascari

Introduction

AIM OF THE ACTIVITY

To have a **first insight about the uncertainties of the code**, in terms of Figures Of Merit (FOM), on the **thermal-hydraulic phenomena during a Design Basis Accident (DBA) scenario** adopting a Best Estimate Plus Uncertainty (**BEPU**) approach

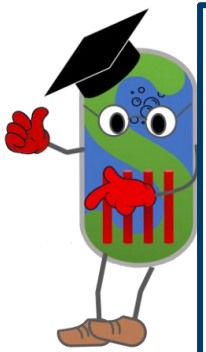

The present activity has been conducted in the framework of the Horizon Euratom **SASPAM-SA project**. The project is coordinated by ENEA and 23 organization from 14 countries are involved.

Funded by the European Union

Introduction

SAFETY ANALYSIS OF SMR WITH PASSIVE MITIGATION STRATEGIES - SEVERE ACCIDENT

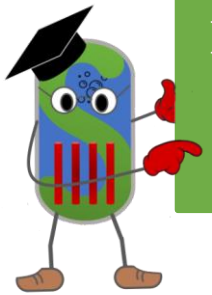

Target of the project

- Identification of **plausible postulate SA scenarios** for **iPWR** designs;
- Identification of the **conditions** in the **vessel** and in the **containment** that **characterize iPWR scenarios** and differ significantly from those in large-LWRs;
- Study the **applicability** of the **existing experimental database** to **iPWR** and identify **new experimental needs**;
- Assess the **capability** of internationally recognized **European and Non-European computational tools** (largely used in Europe) to **describe the behaviour** of the most promising **iPWR designs** during **SA scenarios** and to **predict** the resulting **radiological impact** on- and off-site.

Design 2 – General view

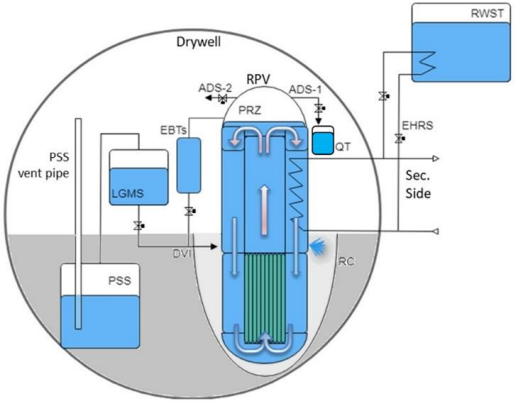

The iPWR Design-2 is characterized by the use of several passive systems and by a dry containment.

- The reactor operates in **forced circulation during normal operation** and employs a **passive mitigation strategy in accidental transients**.
- It consists of an **integral RPV**, which contains the core, a compact SG, the Control Rod Drive Mechanism (CRDM), the primary pumps and the **pressurizer included in the upper head**.
- The hot water at the core outlet **flows upward in a circular riser up** to the primary pumps suction.
- Above the riser, a perforated plate separates the riser from the PRZ, which is enclosed in the RPV upper head.

Design 2 – Database

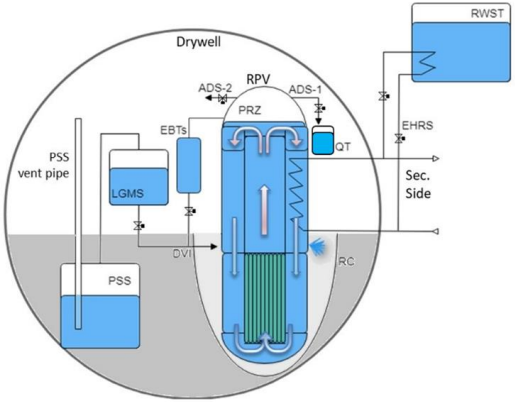

- In order to develop the **ASTEC and MELCOR input-deck**, a **reference database** was needed.
- Considering the **characteristics of Design 2 reactor type** and the selected passive systems, a **generic IRIS SMR type has been considered as reference** for this analysis.
- During the development of the MELCOR and ASTEC nodalization of the generic IRIS design, **no proprietary data have been used.**
- The **main geometric information** has been determined by **scaling the data available from the SPES-3 facility**, by **engineering evaluation** or **public general data available** for the IRIS reactor.

Selected scenario

DBA

After the qualification of the steady state, the DBA scenario selected is the guillotine break of one Direct Vessel Injection (DVI) line, considering the availability of all safety systems.

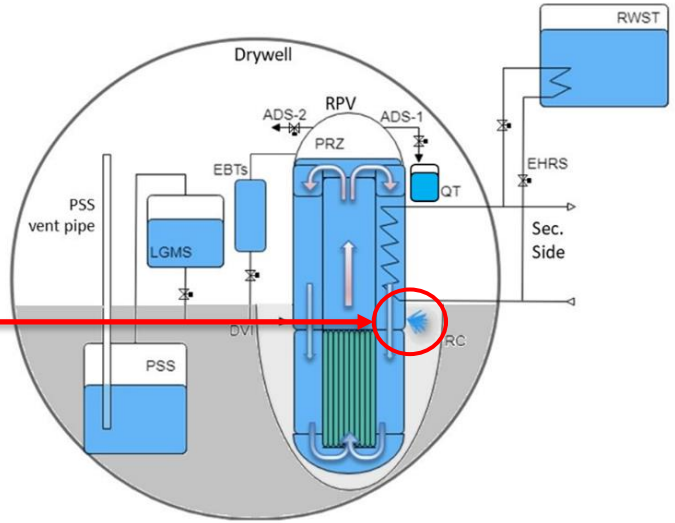

MELCOR input deck

Symbolic Nuclear Analysis Package (SNAP) to develop the **nodalization** and for the **post processing** of data by using its animation model capabilities

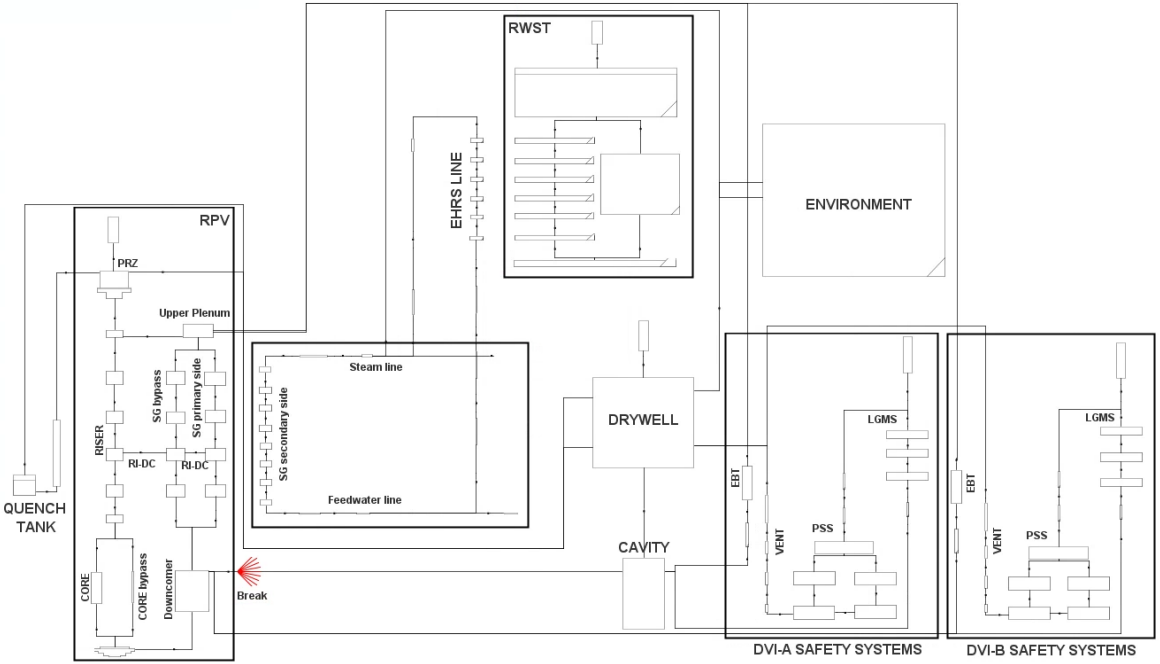

MELCOR input deck

CVH and FL packages have been used for modeling all the RPV hydraulic regions:

- LP,
- Core,
- Core bypass,
- Riser,
- UP,
- SGs
- Downcomer

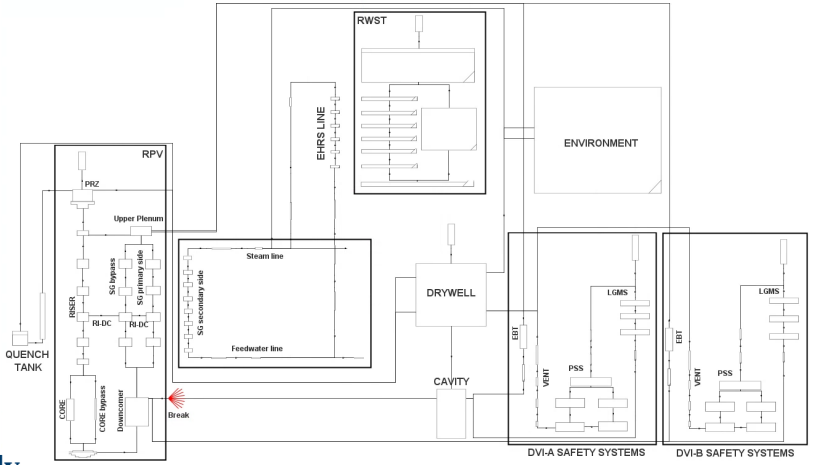

→ The **two passive systems lines** have been **modelled separately**.

→ The **SGs** (8 line), **EHRS** (4 line) and the **RWST** (2 pool) have been **modelled** as an **equivalent one**.

→ The **reactor core**, the **core bypass** and the **downcomer** has been modelled by a **single hydraulic CVH CV**

The **containment region** has been modelled with one **CVH volume of the RC**, coupled with the correspondent **CAV package**, and with **one CVH volume for the DW region**, **thermally coupled** with the **environment** CVH volume

HS package have been used, **coupled with the CVH** package, to **model the heat transfer** between the CVH Control Volumes

MELCOR input deck

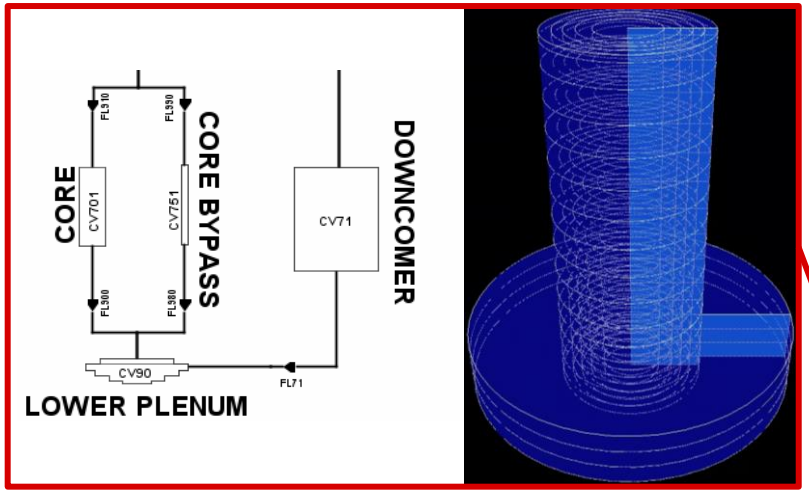

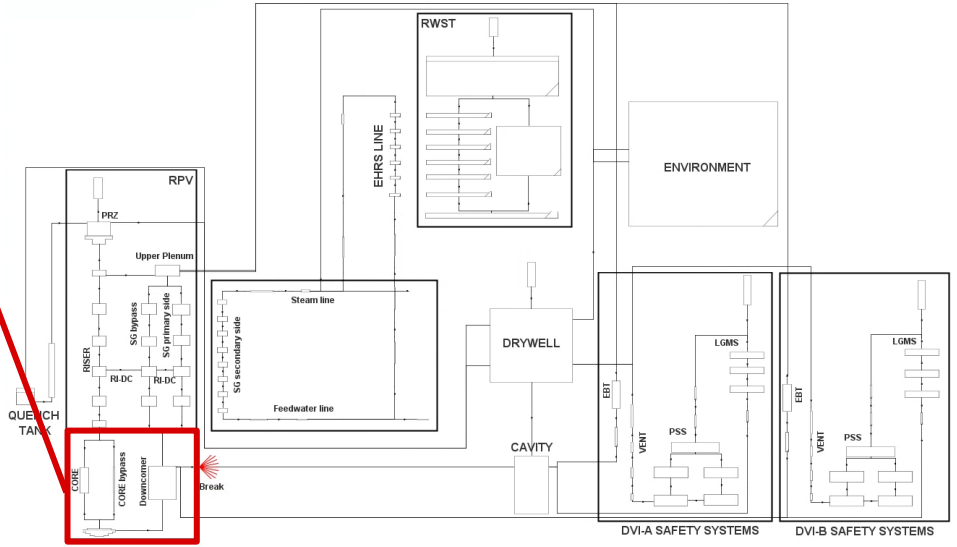

- **2D cylindrical** axial-symmetric **geometry** of the **COR package**;
- A **detailed nodalization** has been chosen for the COR package with respect to the CVH one;
- **16 axial** levels and **6** concentric **rings**;
- The **LP** is made of **one single CVH CV**, which extends to the core supporting plate;

Description of the transient

High Containment Pressure signal
- SCRAM
- Secondary system isolation
- EHRS actuation

Low PRZ pressure signal
- EBTs actuation
- ADS stage-1 actuation

Low LGMS mass signal
- ADS stage-2 actuation

BREAK OF DVI LINE

Low PRZ level signal
- RCP coastdown
- RI-DC valves opening

Low DP RPV-Containment signal
- LGMSs actuation

Reference case

Event	Time [s]
Break	0
High Containment pressure signal (SCRAM, isolation SG, EHRS activation)	41
Low PRZ water level signal (Pump coast down and RI-DC opening)	122
Low PRZ pressure signal (ADS Stage-1 opening, EBTs opening)	148
Low DP RV-Containment (LGMSs opening)	1884
1st RPV- DW pressure equalization	2000
2nd RPV- DW pressure equalization	3315
1st vent injection	3010
2nd vent injection	5405
Core level reach the TAF	3000
Cavity level reach the DVI	3950
Low LGMS mass (ADS Stage -2 opening)	12265

Probabilistic method to propagate input uncertainty

Input uncertainty

Uncertainty input parameters

Statistical approaches

Output uncertainty

Uncertainty of selected FOMs

Probability Density Function (PDF), usually selected based on:

- Previous analyses,
- Available experimental data,
- Engineering judgment

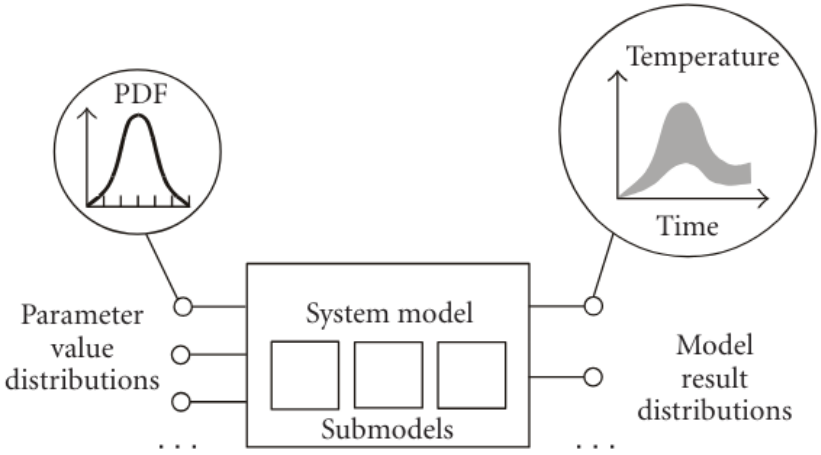

Probabilistic method to propagate input uncertainty

Input uncertainty

Uncertainty input parameters → Monte Carlo random sampling

Monte Carlo random sampling → N of sets of values of the uncertain input parameters

N of sets of values of the uncertain input parameters → N input-deck used

N input-deck used → **N code runs**

The Wilks's formula

Determine the minimum number of code runs N based on the requested probability content γ and confidence level β.

The Wald's formula

If multiple FOMs p are analysed, N is calculated using

To have **insights** about the **statistical correlation** between the FOMs and the **selected uncertain input parameters** the *simple* and *simple rank* ***correlation coefficients*** are considered

Uncertainty tool

Developed and applied along the H2020 **MUSA project**, coordinated by CIEMAT.

Funded by the European Union

Full independent in-house tool written in Python has been developed

Development of the MELCOR/DAKOTA coupling in a Python environment/architecture

- More **flexibility than** using **external software** that **requires** to manage **several scripts to interface the UT** to the code;
- Continuous **update** and **customization** of the tool according to the **user's needs**;

4 independent scripts performing all the steps needed for the development of an uncertainty analysis.

Uncertainty tool

1 *create code runs*

a.

User specification of **n° of** code **runs** N and **uncertain input parameters.**

b.

Sampling of the **uncertain input parameters** from specified **PDFs**.

c.

Creation of the N **sets** of **uncertain input parameters** to be replaced in the input-deck template.

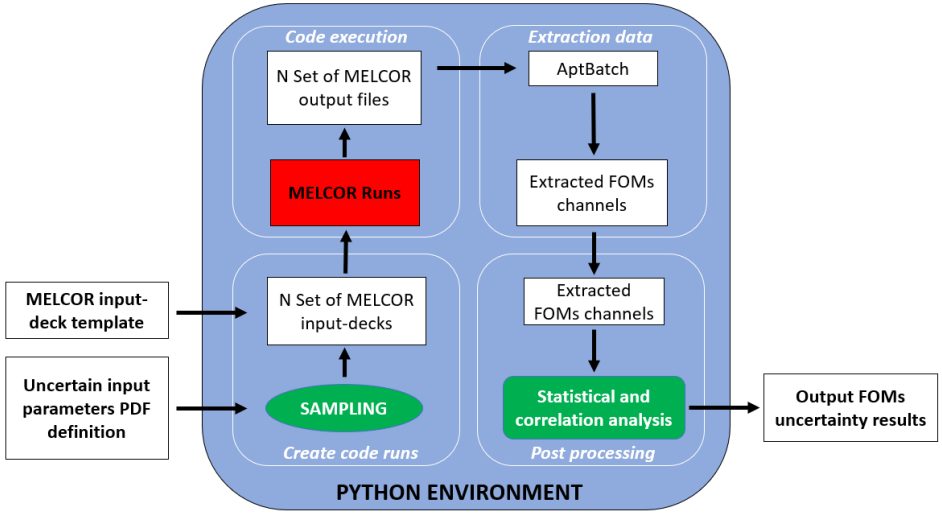

Uncertainty tool

2 *Code execution*

Through the *ProcessPoolExecutor* Python function, user select the **number P of parallel runs.**

3 *Extraction data*

Manages the **FOMs channels extraction by AptBatch** executable from the N code runs output files. The **User can set the number of parallel processes** to be divided into.

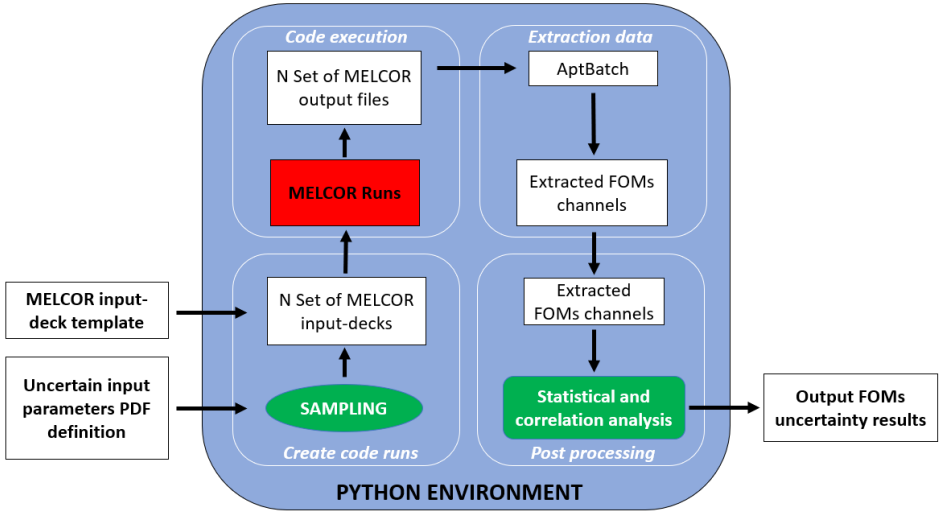

Uncertainty tool

2 *Post-processing*

Allow to **develop the statistical analysis** of the results and **the post-processing of the data**

- ❑ Mean,
- ❑ Median,
- ❑ Upper and lower bounds,
- ❑ Empirical PDF and CDF,
- ❑ Standard deviation
- ❑ Coefficients of variation of the FOMs
- ❑ Correlation coefficient

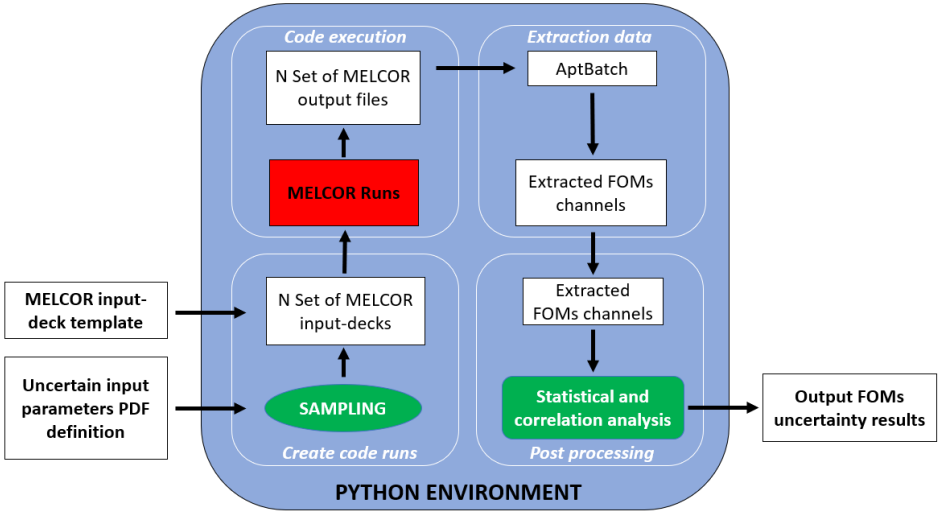

Figure of Merit and input parameter

The **FOMs** selected for the present analysis are:

- **Peak of maximum cladding temperature (FOM_1);**
- **Minimum collapsed coolant level in the core region (FOM_2);**
- **Maximum containment pressure (FOM_3).**

The **uncertain input parameters**, have been **selected** and **extrapolated** from **[1] [2] [3]** and based on **engineering judgment**. **129 code runs** are needed.

[1] F. Alcaro, A. Bersano, C. Bertani, F. Mascari, «BEPU analysis of a passive decay heat removal system with RELAP5/MOD3.3 and RELAP5-3D,» Progress in Nuclear Energy, vol. 136, n. 103724, 2021.

[2] M. Perez, et al., «Uncertainty and sensitivity analysis of a LBLOCA in a PWR Nuclear Power Plant: Results of the Phase V of the BEMUSE programme,» Nuclear Engineering and Design, vol. 241, pp. 4206-4222, 2011.

[3] P. Maccari, J.A. Zambaux, A. Bersano, «BEPU analysis of a 2-in DVI break in a generic IRIS SMR by ASTEC - RAVEN coupling,» EUROSAFE Forum 2021, Paris, France, November 22-23, 2021.

Figure of Merit and input parameter

SAFETY ANALYSIS OF SMR WITH PASSIVE MITIGATION STRATEGIES - SEVERE ACCIDENT

Uncertain input parameter	Unit	PDF	Reference value	Lower and upper bound		Reference
Decay Power	[-] (multiplier)	Normal	1.0	Min	0.98	[27]
				Max	1.02	
Initial PRZ pressure	[Pa]	Normal	1.55E7	Min	1.54E7	[27]
				Max	1.56E7	
EBT initial temperature	[K]	Normal	321.9	Min	311.9	[27]
				Max	331.9	
LGMS initial temperature	[K]	Normal	321.9	Min	311.9	[27]
				Max	331.9	
Initial DW pressure	[Pa]	Uniform	1.013E5	Min	0.85E5	[27]
				Max	1.15E5	
RWST initial liquid level	[m]	Normal	9.0	Min	8.9390	[26]
				Max	9.0610	
RWST and environment initial temperature	[K]	Uniform	293.0	Min	283.0	[28]
				Max	303.0	
Heat Transfer Surface EHRS HXs	[-] (multiplier)	Uniform	1.0	Min	0.75	[26]
				Max	1.25	
Break Flow discharge coefficient	[-]	Uniform	0.7	Min	0.7	Engineering Judgement
				Max	1.0	
EHRS valves loss coefficient	[%]	Uniform	0	Min	-100	Engineering Judgement
				Max	+100	
EBT valves loss coefficient	[%]	Uniform	0	Min	-100	Engineering Judgement
				Max	+100	
LGMS valve loss coefficient	[%]	Uniform	0	Min	-100	Engineering Judgement
				Max	+100	
ADS Stage-1 loss coefficient	[%]	Uniform	0	Min	-100	Engineering Judgement
				Max	+100	
ADS Stage-2 loss coefficient	[%]	Uniform	0	Min	-100	Engineering Judgement
				Max	+100	

FOMs' statistical parameter ans correlation coefficient

Statistical parameter	FOM_1		FOM_2		FOM_3	
	Value	Unit	Value	Unit	Value	Unit
Mean	504.74	[K]	4.46	[m]	11.37E5	[Pa]
Median	505.53	[K]	4.47	[m]	11.32E5	[Pa]
Lower Bound	483.66	[K]	4.05	[m]	9.73E5	[Pa]
Upper Bound	526.43	[K]	4.75	[m]	13.49E5	[Pa]
Standard deviation	8.23	[K]	0.16	[m]	0.82E5	[Pa]
Coefficient of variation	0.016	[-]	0.037	[-]	0.072	[-]

The empirical PDFs of the FOMs, correlation coefficients for each FOM and uncertain input parameters have been calculated.

FOM_1	▪ Heat Transfer Surface of EHRS HXs (negative correlation); ▪ ADS Stage-1 loss coefficient (positive correlation).
FOM_2	▪ Initial DW pressure (positive correlation); ▪ Heat Transfer Surface of EHRS HXs (negative correlation).
FOM_3	▪ Initial DW pressure (positive correlation); ▪ ADS Stage-1 loss coefficient (negative correlation).

Empirical PDF

SAFETY ANALYSIS OF SMR WITH PASSIVE MITIGATION STRATEGIES - SEVERE ACCIDENT

FOM_1

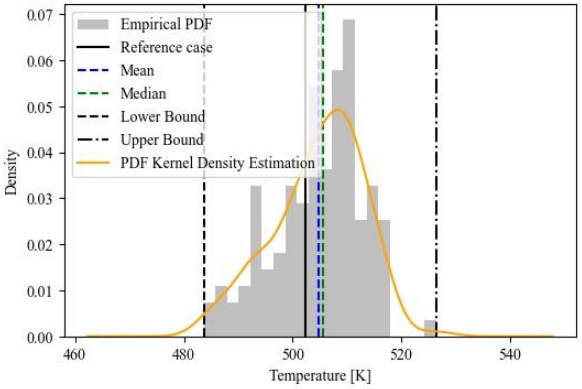

FOM_2

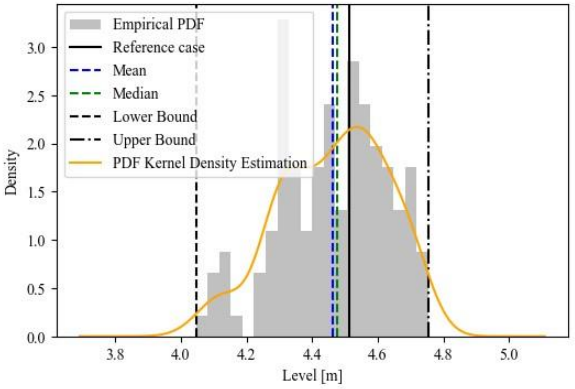

FOM_3

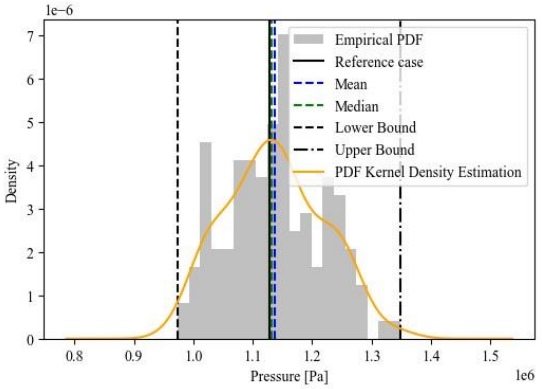

Scatter plot

FOM_1

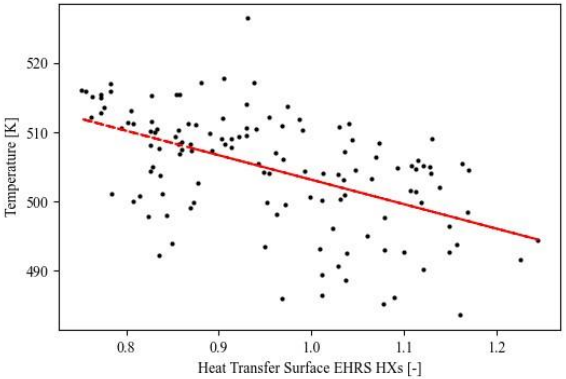

FOM_2

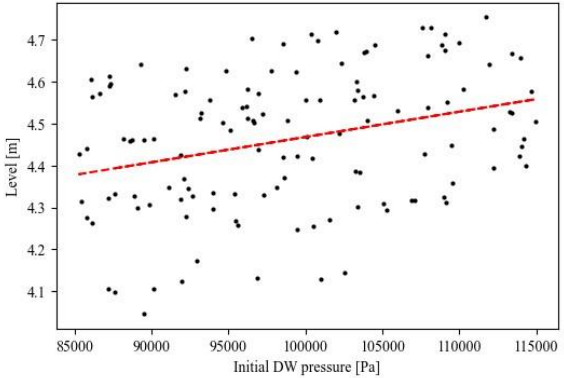

FOM_3

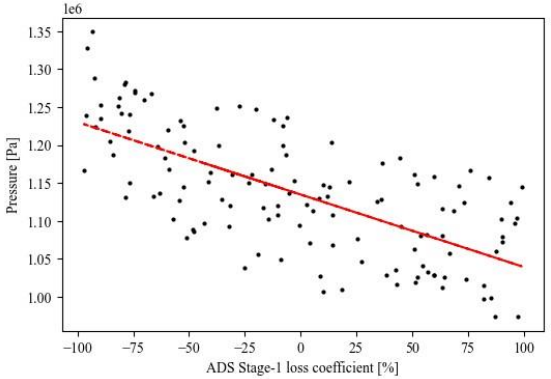

Maximum cladding temperature

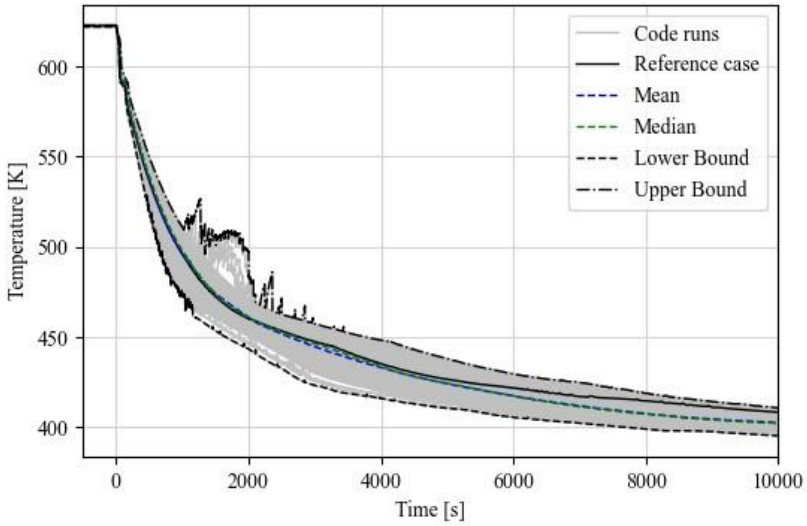

- **Uncertainty width** of about **25 K** during the **first 1000 s** after the SOT;
- **Increases** reaching an amplitude of about **100 K**, **between 1000 and 2000 s** (peak up to 525 K).
- Later the **uncertainty width remains almost constant** and equal to about 25 K.

Results

Maximum cladding temperature

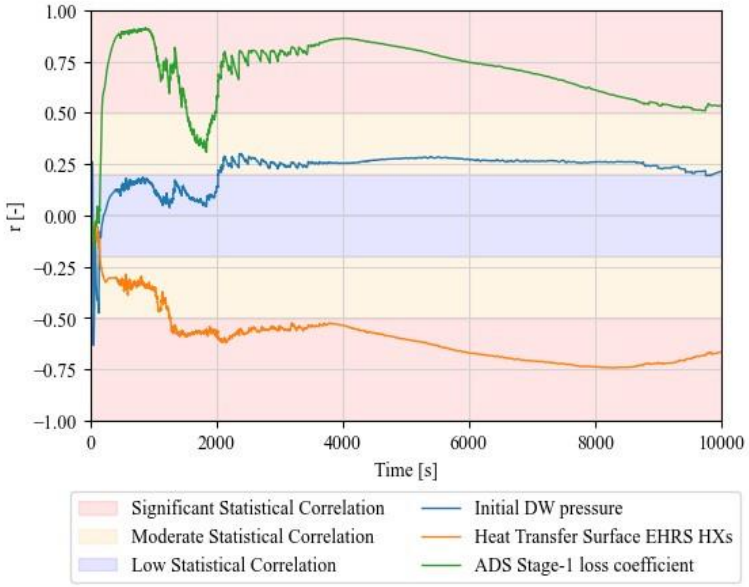

- **Initial DW pressure**: the magnitude of the **correlation increases** from low to **moderate or significant** along the transient;
- **Heat Transfer Surface of EHRS HXs**: the magnitude of the **correlation increases from low to moderate or significant** along the transient;
- **ADS Stage-1 loss coefficient**: the magnitude of the **correlation** goes **from significant to moderate** along the long-term phase.

Core collapsed coolant level

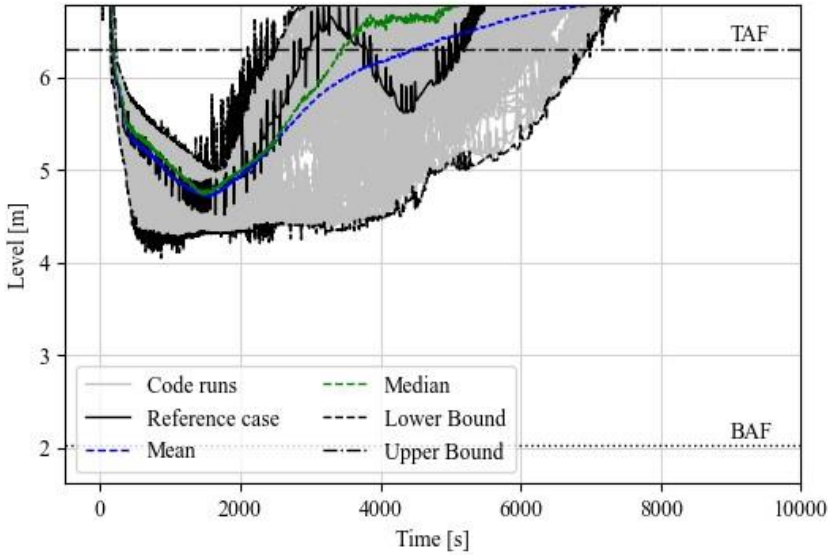

- **Uncertainty width increases its amplitude after 200 s of the SOT to a value of 1.20 m;**
- **Reach its maximum value at about 3000 s after the SOT.**
- **The attainment of the TAF during the transient has a very high uncertainty width in time terms, reaching an uncertainty width of about** 4000 seconds.

Results

Core collapsed coolant level

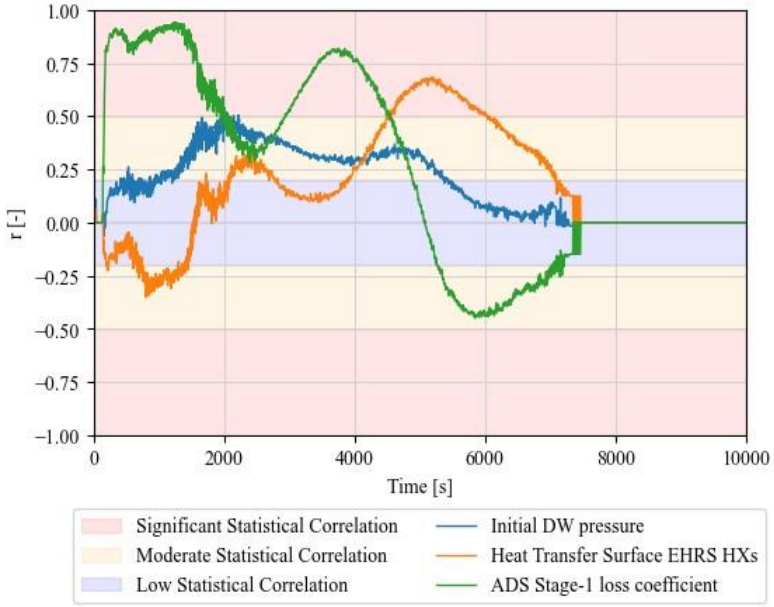

- **The ADS-1 loss coefficient** has a statistically **significant correlation for the first 4000 s** of the transient
- **The heat transfer surface of the EHRS HXs** has a **significant correlation** (positive correlation) **after** about **4000 s**.
- **The initial pressure of the DW** presents a **moderate** statistical **correlation after** about **1000 seconds** after the SOT.

Initial pressure of DW

Uncertainty width of the DW pressure, presents a **maximum value** of the **band at about 3000 s** after the SOT and equal to about 7E5 Pa.

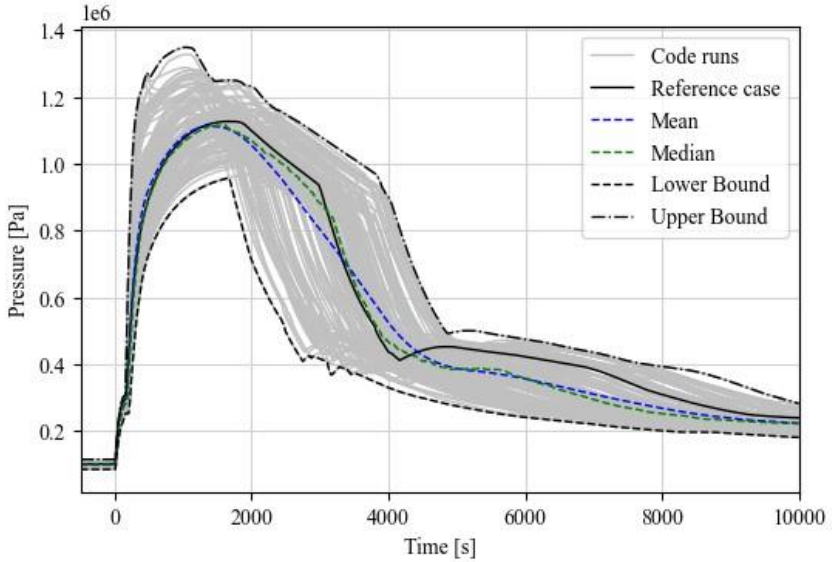

Initial pressure of DW

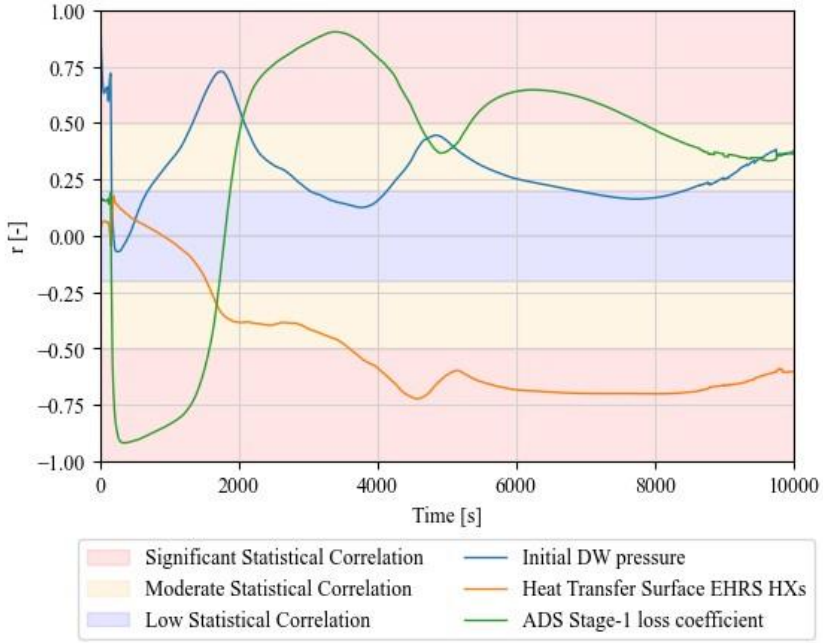

- Characterized by a **statistically significant correlation with its initial value** (as expected) in the first instants of the transient, and at about 1000 s from the SOT;
- **The ADS-1 loss coefficient**: in the **first 1000 s** shows a **significant statistical correlation** of a negative type and **then of a positive type;**
- **After the reflood phase**, the **heat transfer surface of the EHRS HXs** shows a statistically **significant** negative correlation.

Conclusions

- The analysis **gives first insights** into the **uncertainties** of the code concerning the **key TH phenomena during a mitigated transient scenario;**
- Calculating the **statistical correlation coefficients**, it has been **possible to identify** the **input uncertainty parameters** with a **moderate or significant statistical correlation** with the FOMs;
- Moderate or significant statistical correlation between FOMs and the Heat Transfer Surface of EHRS HXs, the initial pressure in the DW and the ADS-1 loss coefficient has been underlined;
- The **next step will be to extend the uncertainty analyses to a postulated SA scenarios** in order to **identity the parameters** that have a moderate/significant statistical correlation with SA FOMs.

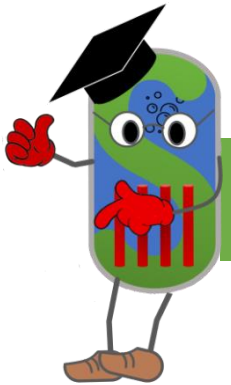

Thank you for your attention

Acknowledgement/Disclaimer



Funded by the European Union

Funded by the European Union. Views and opinions expressed are however those of the author(s) only and do not necessarily reflect those of the European Union or European Commission-Euratom.
Neither the European Union nor the granting authority can be held responsible for them.

ENEA carried out the research activity with MELCOR code and SNAP, obtained in the framework of the ENEA-ISIN agreement signed on March 23rd 2020 as part of the General Arrangement between the United States Nuclear Regulatory Commission (US-NRC) and the Italian National Inspectorate for Nuclear Safety and Radiation Protection (ISIN).

SAPAM-SA

SAFETY ANALYSIS OF SMR WITH PASSIVE MITIGATION STRATEGIES - SEVERE ACCIDENT

Gianmarco Grippo,
PhD student,
University of Bologna,
Department of Industrial Engineering (DIN), Viale del Risorgimento 2, 40136, Bologna, Italy
Email: gianmarco.grippo2@unibo.it

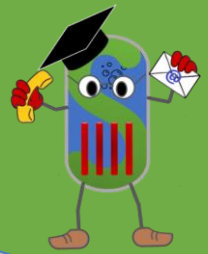

COMPARISON BETWEEN EDF MAAP5.04 AND ASTECV3 CODES ON A HYPOTHETICAL SEVERE ACCIDENT ON THE ELSMOR PROJECT E-SMR DESIGN.

Jeremy Bittan and Nikolai Bakouta
Electricité de France (EDF) Lab Paris-Saclay
7 boulevard Gaspard Monge – 91120 Palaiseau – France
jeremy.bittan@edf.fr; nikolai.bakouta@edf.fr

Julie-Anne Zambaux and Laure Carénini
Institut de Radioprotection et de Sureté Nucléaire (IRSN)
Centre de Cadarache B.P. 3 13115 St-Paul-lez-Durance Cedex– France
julie-anne.zambaux@irsn.fr; laure.carenini@irsn.fr

ABSTRACT

This paper presents a comparison between EDF MAAP 5.04 and ASTECv3 codes for a hypothetical Severe Accident leading to core degradation on the ELSMOR project proposed E-SMR (Small Modular Reactor) Design. The ELSMOR (towards European Licensing of Small Modular Reactors) project is a Horizon 2020 Euratom project. The consortium includes 15 partners from 8 European countries, involving research institutes, major European nuclear companies and technical support organizations. The 3.5-year project, launched in September 2019, investigates selected safety features of Light-Water (LW) SMRs with focus on licensing aspects. The Modular Accident Analysis Program (MAAP) is a deterministic code owned and licensed by Electric Power Research Institute (EPRI) that can simulate the response of light water moderated nuclear power plants during accidental transients for Probabilistic Risk Analysis (PRA) applications. It can also simulate severe accident sequences, including actions taken as part of the Severe Accident Management Guidelines (SAMGs). EPRI MAAP5.04 has limited capability to model SMRs: this code has been adapted by EDF (EDF MAAP 5.04) to make it compatible with the simulation of Severe Accidents transients for the ELSMOR project SMR design. ASTEC v3 is a severe accident system code developed by IRSN aiming at source term evaluation. The code is used to evaluate major nuclear accidents for different nuclear installations with a main focus on western light water reactor designs. A wide range of phenomena are represented, in particular thermal-hydraulics and core degradation while modules dealing with fission products behavior and molten corium concrete interaction are not yet used in this study. The comparison performed between EDF MAAP5.04 and ASTECv3 includes the transient evolution from the initiating event (a Station Black Out), the core degradation and hydrogen generation, the corium relocation to the Lower Plenum and the In-Vessel Melt Retention. The physical phenomena in the containment are also compared (steam condensation on the walls…). Potentiality of H_2 combustion related to the specific assumptions of the selected transient is evaluated through plotting flammability diagram and a sensitivity analysis to N_2 injection for inerting the containment is assessed.

KEYWORDS
EDF MAAP5.04, ASTECv3, SMR, Accidental transients

1. INTRODUCTION

In the frame of the H2020 European ELSMOR project [1], the analysis of accidental transients on integral Pressurized Water Reactors (iPWR) potentially leading to core degradation is of high interest. The EDF version of MAAP5.04 (including EDF developments) and the ASTECv3 code developed by IRSN are both

integral codes allowing the modeling of severe accident transients in nuclear power plants for large scale PWR and small scale iPWR. During the ELSMOR project, these codes were used to simulate the E-SMR design. This paper presents a comparison between EDF MAAP5.04 and ASTECv3 results for a Station Black-Out (SBO) transient leading to core degradation. In this configuration, the reactor is at nominal power. It is supposed that all the passive safety systems considered in Design Basis Conditions (DBC) do not work during the entire transient. An ultimate battery is considered as operable for 12 hours before full discharge. The SBO transient hence leads to a heating of the primary circuit and a progressive loss of water inventory and core degradation. The comparison includes the transient evolution from the initiating event, the core degradation and hydrogen generation, the corium relocation to the Lower Plenum (LP) and the In-Vessel Melt Retention (IVMR). Potentiality of H_2 combustion related to the specific assumptions of the selected transient is evaluated through plotting flammability diagram.

2. EDF MAAP5.04 AND ASTECv3 MODELING OF THE E-SMR REACTOR COOLANT SYSTEM (RCS) AND CONTAINMENT

A brief description of the nodalization and main characteristics of the 2 codes used for the simulation of the E-SMR design is made in this section. Main characteristics are summarized in Table I.

Table I. Characteristics of E-SMR design simulated with EDF MAAP5.04 and ASTECv3

Parameter	Reference - E-SMR dataset [1]	EDF MAAP5.04	ASTECv3	Difference MAAP vs ASTEC (%)
LP wall meshing: **Axial** **Radial**	-	 40 4	 36 13	-
Containment free volume (m^3)	1731.8	1731.8	1731.8	0.
Water wall volume (m^3)	5481	5481	5481	0.
Metallic liner condensation area (m^2)	696.3	696.3	696.3	0.
Initial mass of Zr (t)	5.3	5.4	5.2	3.7
Initial mass of UO_2 (t)	21.5	21.2	21.2	0.
Initial mass of steel in the core (t) (grids, nozzles and support plate)	6.6	6.4	6.5	1.6

2.1. EDF MAAP5.04 E-SMR Design Reactor Coolant System and Containment Modeling

The EDF version of MAAP 5.04 was used along with the SMR RCS capability developed by EPRI (the original SMR functionality alone is not operational in EPRI MAAP5.04), however the models were insufficient for the E-SMR design. EDF made some improvements to make it fully compatible and operable with the ELSMOR's design. The modifications embedded in the EDF version are both related to the geometrical nodalization as well as the physical models (Plate Steam Generators exchangers, Lower Head modeling, IVMR modeling…). Fig. 1 presents the nodalization considered in EDF MAAP5.04 for the E-SMR design. The RCS is composed of one single loop embedding the core, the upper plenum, the hot leg riser, the Compact Steam Generators (CSG) exchangers (primary side), the pressurizer, the CSG outlet, the downcomer and the lower head. There are 9 nodes called "water nodes" and 9 "flow nodes". In "water nodes" energy and mass balance calculations are performed. Flows between nodes are calculated using "flow nodes". Momentum equations are taken into account to calculate flows between "flow nodes".

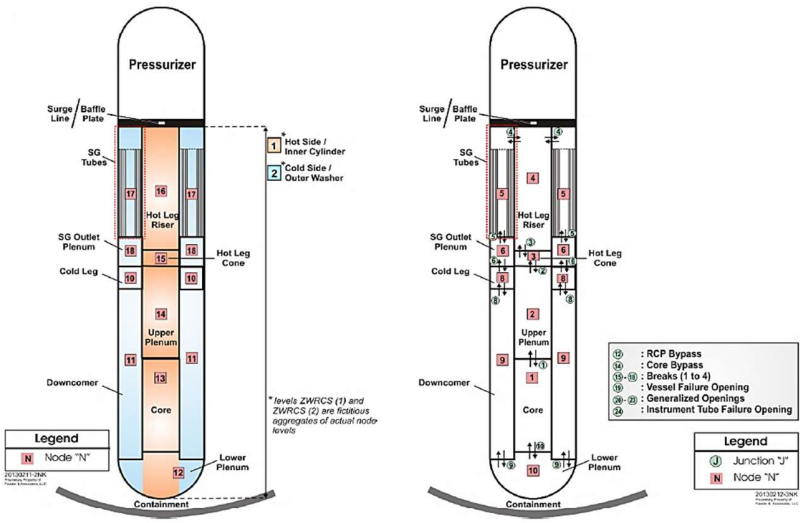

Figure 1. Nodalization in EDF MAAP5.04 for the E-SMR design – Water Nodes (left) and Flow Nodes (right) [2].

It is assumed in EDF MAAP5.04 that one CSG models the 6 CSGs of the E-SMR design. Since the CSGs have a limited impact on the evolution of the accidental transients modeled, this is considered as a reasonable approach. The ELSMOR design contains 2 safety CSGs (S-CSGs) dedicated to passive residual heat removal. The S-CSGs are not modeled since they are supposed not to work in the considered transient (cf. §2.4) leading to a severe accident. Fig. 2 presents the core nodalization and vessel structures modeled in EDF MAAP5.04 for the E-SMR design. The lower head is semi-ellipsoidal leading to a low core position compared a large-scale commercial PWR.

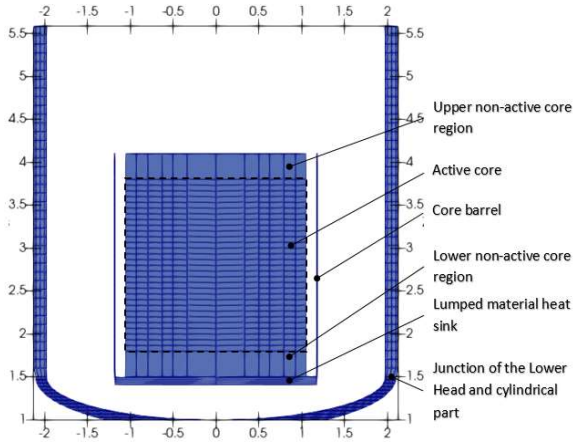

Figure 2. Core and Vessel structures in EDF MAAP5.04 for the E-SMR design

The core support plate is also meshed with 6 axial nodes, which is an improvement compared to the EPRI original version of MAAP5.04. This advanced modeling allows a better evaluation of the heat transferred from the corium pool to the support plate. Fig. 3 presents the containment and water wall submerging the containment in EDF MAAP5.04. As shown in Fig. 3, an initial level of water present in the containment

corresponds to the sparger pool involved in releases from the RCS during an accidental transient. The sparger pool and water wall are explained further in §2.2.

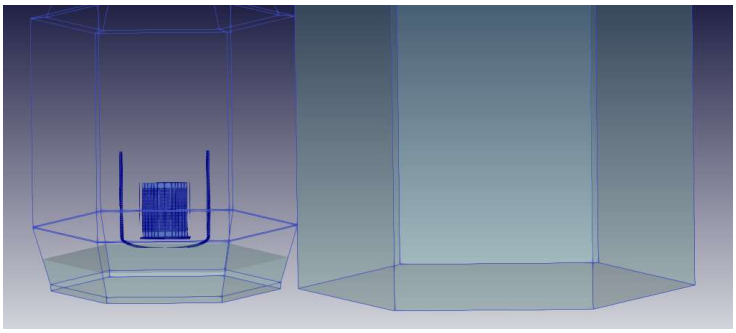

Figure 3. Containment and water wall in EDF MAAP5.04 for the E-SMR design

2.2. ASTECv3 E-SMR Design Reactor Coolant System and Containment Modeling

The ASTEC code is a system code developed at IRSN for severe accident calculation [3]. Although the ASTEC code has been mainly developed in the frame of PWR type reactors safety assessment, it has been successfully used for other light water reactor design, including SMR technologies such as the IRIS reactor design [4]. ASTEC is based on different modules for the different kind of simulated phenomena during a severe accident. These modules can be run either in a coupled mode or independently, allowing dedicated studies. In the frame of this paper, fission product release and transport were not considered as a first calculation step and a residual power law was instead imposed to the fuel.

For this study, the v3.1 of the code has been used with slight corrections, mostly regarding the coupling between the CESAR module used for the modeling of the thermal-hydraulics in the core region, the primary and secondary systems and around the vessel external surface during IVMR and the CPA module used for the modeling of the thermal-hydraulics condition in the containment and the water wall. All the corrections made for those calculations have been added to the recently released v3.1.1.

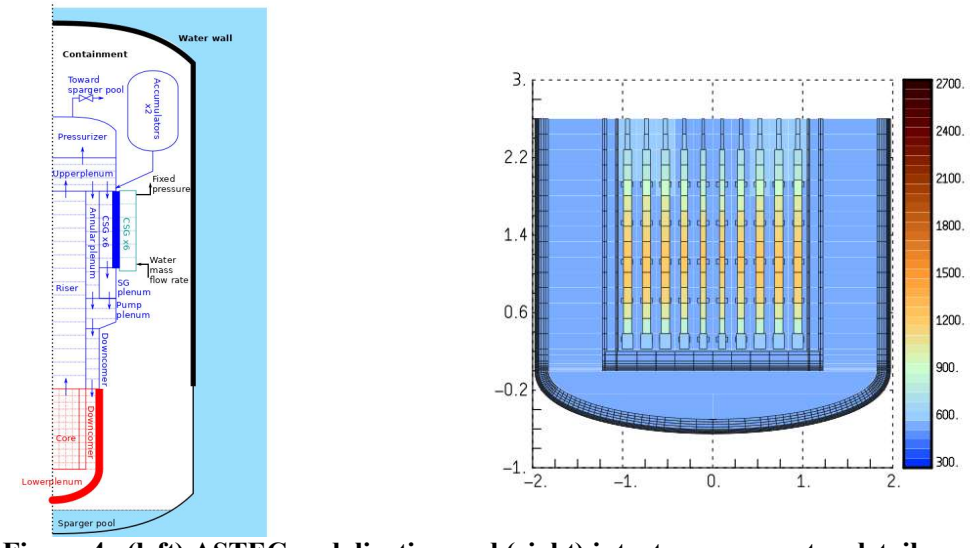

Figure 4. (left) ASTEC nodalization and (right) intact core geometry detail

Fig. 4 (left) presents a simplified representation of the proposed dataset with the chosen nodalization. In this figure, the core region where degradation is calculated is highlighted in red. The primary system is in blue while the containment is in black. A very simplified secondary system is presented here, using boundary conditions at its inlet and outlet. Thick walls on the figure represent the exchanging walls between the primary and secondary side in the steam generators, between the vessel wall and the containment and between the containment and the outside water pool. The water wall in which the containment is submerged is made of one single large water volume at one temperature. At the bottom of the containment, there is an initial volume of water (sparger pool) linked with the primary system pressure valve located at the top of the pressurizer. Initial core material inventory includes Zr, steel and UO_2 with similar mass between ASTEC and MAAP5.04. Fig. 4 (right) presents an image of the core structures with the temperature field at the end of the steady state.

2.3. Steady-States Reached with EDF MAAP5.04 and ASTECv3

Table II below presents the main parameters reached in steady state for EDF MAAP5.04 and ASTECv3. Both codes reach very close physical parameters.

Table II. Steady-states reached with EDF MAAP5.04 and ASTECv3

Parameter	E-SMR dataset [1]	EDF MAAP5.04	ASTECv3	Difference MAAP vs ASTEC (%)
Initial Core Power (MWth)	540.0	540.0	540.0	0.
Pressure in the pressurizer (bar)	150.0	149.7	150.0	-0.2
Core mean temperature (K)	588.2	585.8	586.3	-0.09
Mass flow rate in primary system (kg/s)	3700.0	3718.8	3650	1.9
Outlet Pressure in the CSGs (bar)	45.0	45.0	45.0	0.
Mass flow rate in secondary system (kg/s)	240.0	240.0	238.0	0.8
Containment sump inventory (tons)	125.0	125.0	124.8	0.2

2.4. Accidental Transient Simulated

The accidental transient simulated in this paper, and considered as the reference transient, is based on a SBO leading to a core degradation with a H_2 production and a core relocation to the lower plenum. The IVMR strategy is also evaluated. A sensitivity calculation with a N_2 injection in the containment is additionally performed. The transient described hereafter is purely hypothetical. The main purpose of this paper is to compare EDF MAAP5.04 and ASTECv3 codes on key physical phenomena occurring during the transients simulated.

The SBO transient is initiated at full power. This leads instantly to: a reactor scram, the loss of the Reactor Coolant Pumps (RCPs), the loss of the Main Feed Water (MFW) to all the CSGs (5s after the scram), the closing of the Main Steam Isolation Lines (MSIVs) concomitantly to the loss of MFW. It is considered that the passive S-CSGs fail to start, which is a highly conservative assumption. The operator initiates a primary circuit depressurization through the Pressurizer Relief Valves (RVs), one hour after noticing that the S-CSGs fail to remove any decay heat from the RCS. Two accumulators ensure core reflooding before being emptied. A DC battery enables reflooding of the reactor vessel through the water from the water wall with a constant flow of 5 kg/s. This system, called RNU, is activated on a pressure threshold in the RCS (80 bar). The large amount of water in the water wall allows delaying the core uncovery and ultimate core degradation. This

happens when the battery is fully discharged, 12 hours after the battery first solicitation, and the RCS is progressively emptied by evaporation (core decay heat removal).

3. RESULTS

Table III given below presents the figures of merit for the SBO transient for both EDF MAAP5.04 and ASTECv3. Very similar results are obtained by the 2 codes compared with only a few percents of discrepancies for most of the key events. The main discrepancy is observed on the time the core relocates to the lower plenum with around 20% discrepancy.

Table III. Comparison of key event timings between EDF MAAP5.04 and ASTECv3

Event	EDF MAAP5.04 (s)	ASTECv3 (s)	Difference MAAP vs ASTEC (%)
Reactor SCRAM and stop of RCPs	0	0	-
Secondary system isolation	5	5	0.
Pressurizer RVs fully opened	3600	3600	0.
Start of the RNU system	3803	3785	0.5
Start of accumulators' discharge	3874	3863	0.3
Accumulators are empty	4681	5348	-14.2
Stop of the RNU system	47003	46986	0.04
First cladding rupture	78130	80349	-2.8
Main material slump in lower head	133466	108869	18.4
Water wall at saturation temperature	695458	685738	1.4
End of calculation	1.3E6	1.3E6	0.

3.1 Analysis of Thermal-hydraulics in the RCS

From the initiation of the SBO accident, due to the lack of fluid circulation, the cooling of the core decay heat is hindered and pressure starts to increase in the RCS. As shown on Fig. 5 (left), pressure oscillates due to the successive activation of the RVs located at the top of the pressurizer. During that phase, the water inventory in the primary system (Fig. 5 (right)) decreases because of the subsequent mass loss. After one hour, a forced depressurization of the primary system is performed in the scenario by opening the RVs till the end of the sequence. From that point, the pressure sharply decreases. When pressure reaches 80 bars, the RNU system is started, injecting clear water from the water wall directly in the vessel, thus restoring the water inventory. At 60 bars, the two accumulators also start to discharge. The RCS water inventory gets completely restored while the RNU system is working (for 12 hours) and the water directly exits through the RVs to the containment. After the stop of the RNU system, the water inventory in the RCS starts decreasing again this time till no water is left. As the core gets uncovered, temperature increases and degradation starts. Both codes predict a close behavior for RCS thermal-hydraulics at the beginning of the scenario. The main difference observed concerns the oscillation of the water mass in MAAP when the RCS is full and the RNU system is still working (liquid entrainment at the break difference). Degradation is reached slightly earlier with MAAP due to a slightly faster water loss in the RCS when the RNU is stopped.

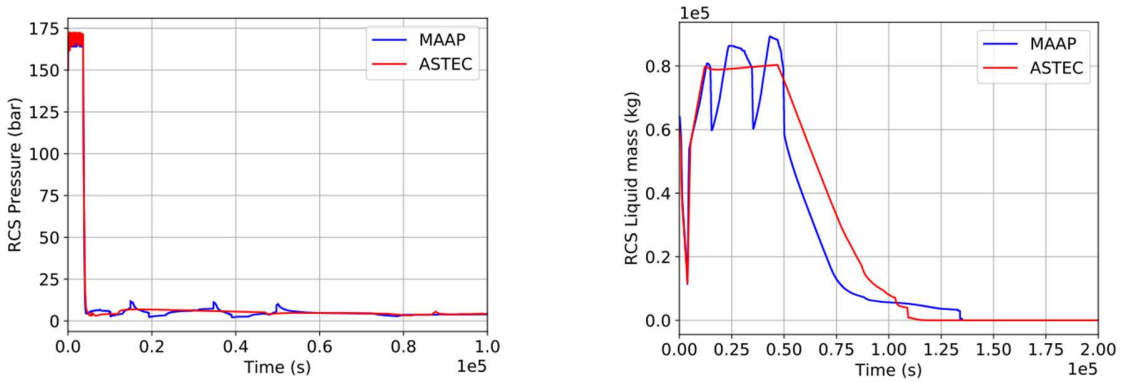

Figure 5. Evolution of (left) the pressure in the pressurizer and (right) the liquid mass in the RCS

3.2 Degradation Phase

Fig. 6 (left) presents the evolution of the total material mass in the core region along with the evolution of the molten mass (in the ASTEC calculation, the molten mass also includes re-solidified magma, which explains the non-null mass at the end of the calculation). Most of the mass initially present in the core relocates to the lower head for both codes. In ASTEC the relocation starts slightly before MAAP and is faster: all the core relocates at once. In MAAP the relocation is made of different corium slumps. This explains why in ASTEC almost all the core mass is molten before the first slump and not in MAAP (progressive slumps). The core support plate molten mass is not taken into account in the molten mass plotted in Fig. 6 in MAAP and also explains why some corium slumps in the lower head are seen without a molten mass variation (at 177000s and 211000s). This does affect the in vessel melt retention phase of the sequence.

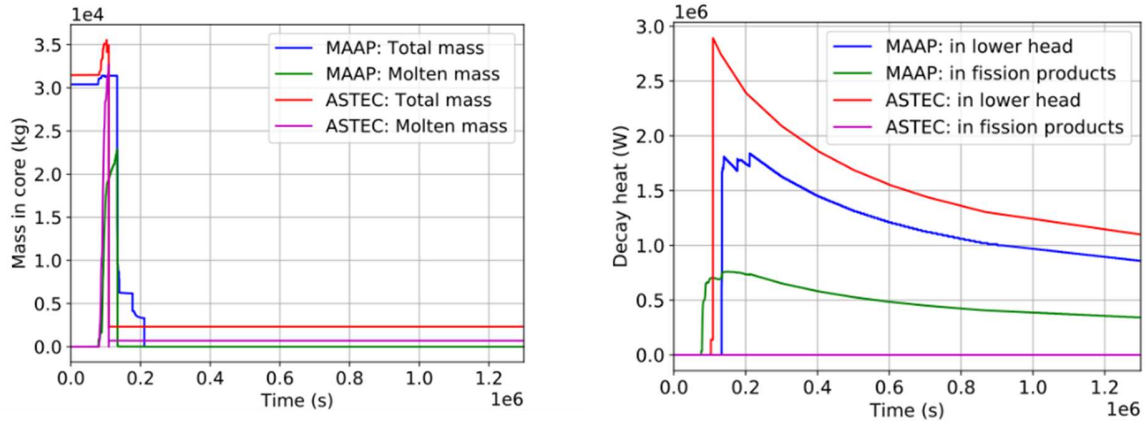

Figure 6. Evolution of (left) the remaining total and molten mass in the core and (right) the decay heat in the lower head and in the volatile fission products

Another difference between ASTEC and MAAP is highlighted on Fig. 6 (right): the decay heat in the lower head is plotted along the decay heat carried out by the fission products. In ASTEC, the volatile fission products release and transport models have not been activated. Therefore, the decay heat contained in the lower head is higher than in the MAAP calculation. In MAAP, volatile fission products correspond to around 30-35% of the decay heat and are transported and deposited elsewhere in the RCS and containment, therefore not directly participating to the IVMR part of the scenario.

3.3 Containment and external water wall behavior

Initially, pressure increases in the containment due to vapor flow from the RVs. The discharge is set at the bottom of the containment, in the sparger pool. Fig. 7 (left) presents the evolution of the pressure in the containment at the beginning of the transient. With the ASTEC code, the pressure increase is very important during the vapor release from the RVs in comparison to MAAP results. Additionally, the pressure peak is significantly higher during forced depressurization. This can be explained by a difference in modeling the direct steam condensation in the sparger pool. In the first part of the transient, highly superheated steam is injected in subcooled liquid (gas inlet is around 350°C, corresponding to the saturation temperature in the primary system while the sparger pool temperature is initially at 30°C). During the steam release, the liquid temperature increases slowly (as the initial volume is important) toward saturation while a part of the steam is condensed. This direct condensation mass flow rate is strongly underestimated in ASTEC compared to MAAP. MAAP has a dedicated model for steam jet condensation in the sparger pools while ASTEC does not and uses its regular condensation model. In this case, due to small residence time (high speed gas velocity from pressurized primary) and low void fraction in the volume (and therefore small interfacial area), the direct condensation rate is evaluated to be rather small.

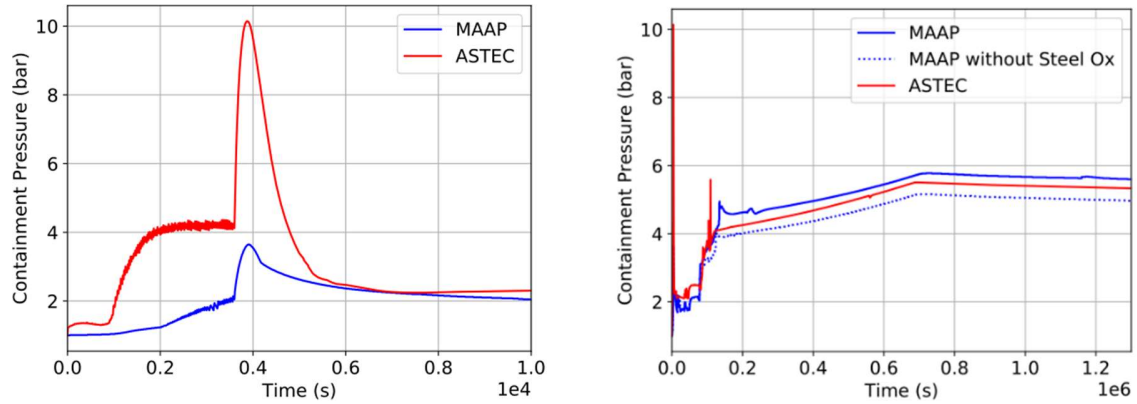

Figure 7. Evolution of the pressure in the containment: zoom at the beginning of the transient on the left

Results between MAAP and ASTEC are quite similar for both the long-term evolution of the pressure in the containment (Fig. 7 right) and of the condensation mass flow rate on the containment walls (Fig. 8 left). Once the conditions in the vessel are stabilized, the pressure in the containment keeps slowly increasing as the cooling efficiency of the external containment walls decreases. Indeed, the external water wall pool slowly heats up while extracting the decay heat. Fig. 8 (right) presents the evolution of the water wall temperature. For both codes, saturation is reached after nearly 8 days. From that point, the temperature of the pool remains constant at saturation and its level starts to decrease (vaporization). Inside the containment, when the external pool reaches saturation, pressure gets its maximum local value. It then starts decreasing as the cooling is constant while the decay heat that needs to be extracted keeps decreasing.

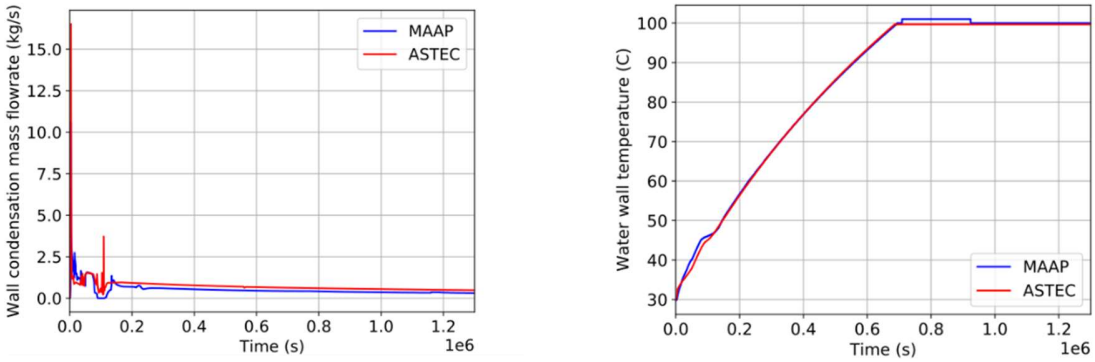

Figure 8. Evolution of (left) the condensation mass flow rate on the containment walls and (right) the water wall temperature

3.4 Hydrogen production analysis

During the degradation process, H_2 is produced through oxidation of the steel, zirconia and fuel. Fig. 9 presents the evolution of the cumulated mass of H_2 estimated by both codes and the part of H_2 produced through steel oxidation. The H_2 mass evaluated by MAAP is higher than in ASTEC and this is due to the H_2 produced by steel oxidation in core (60 kg in MAAP while it is 3 kg only in ASTEC). Results of an additional calculation performed in MAAP without activating the steel oxidation in core is presented on this same figure, showing significantly close results between both codes. ASTEC does not consider oxidation of melted steel in core since, when mixed with partially oxidized corium, oxidation is expected to involve preferentially Zr (while in MAAP, the oxidizing of melted Zr and steel are going together). The Shapiro diagram is plotted on the left of Fig. 10 for the corresponding calculations. In all the cases, the flammability region is reached, showing the need to have a system properly dealing with H_2 risk. Additional calculations have been performed with N_2 injection in the containment during the transient and no H_2 burn has been observed, as shown in the right Shapiro Diagram of Fig. 10. An increase of containment pressure to twice of the reference calculation pressure was however observed with the chosen injection parameters.

In the reference calculations, the H_2 production starts in MAAP when the steam concentration is around 30% in the containment compared to 40% in ASTEC. This is directly linked to the sparger pool condensation model discrepancy leading to a more important amount of steam in the containment of ASTEC at the time the H_2 generation starts (cf. §3.3).

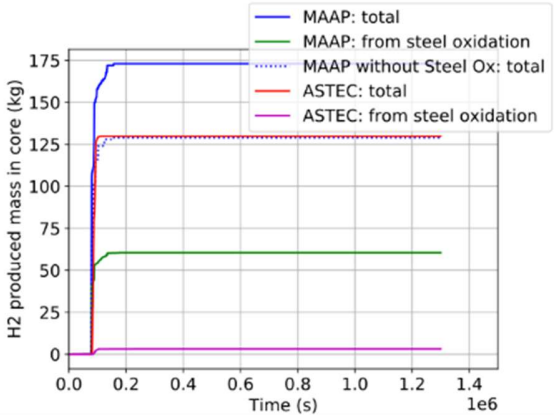

Figure 9. Time evolution of the hydrogen cumulated mass produced and its source

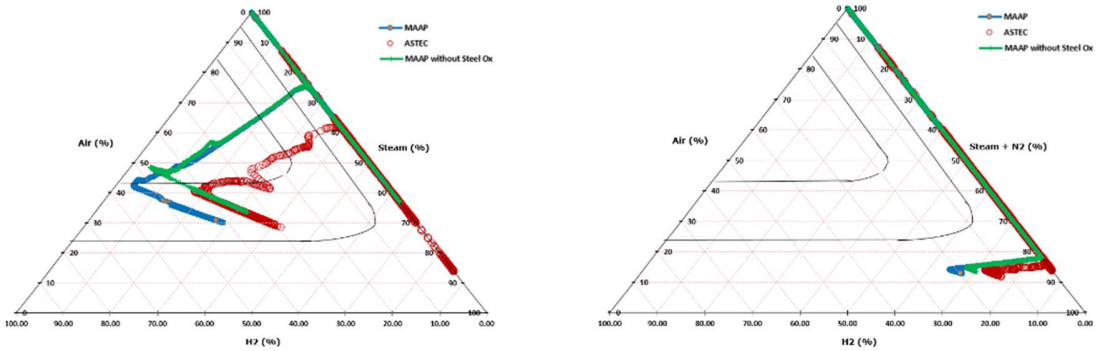

Figure 10. (left) Shapiro diagram without N_2 injection; (right) with N_2 injection

3.5 In-vessel melt retention analysis

When corium is relocated in the lower head of the vessel, due to increase of molten steel content, a gap of miscibility between oxide and metal phases leads to stratification. The metal phase can be either lighter or heavier than the oxide phase depending on its composition, leading to the possible transient formation of three different layers: light metal, oxide and heavy metal layer. Fig. 11 (top) presents a visualization of the core during the IVMR phase in ASTEC, the evolution of the mass of each layer and the wall ablation profile at the end of the calculation. In ASTEC, a thickness of more than 7 cm remains at the thinnest location of the vessel wall initially of 15 cm. Similar data obtained with MAAP are shown in Fig. 11 (bottom).

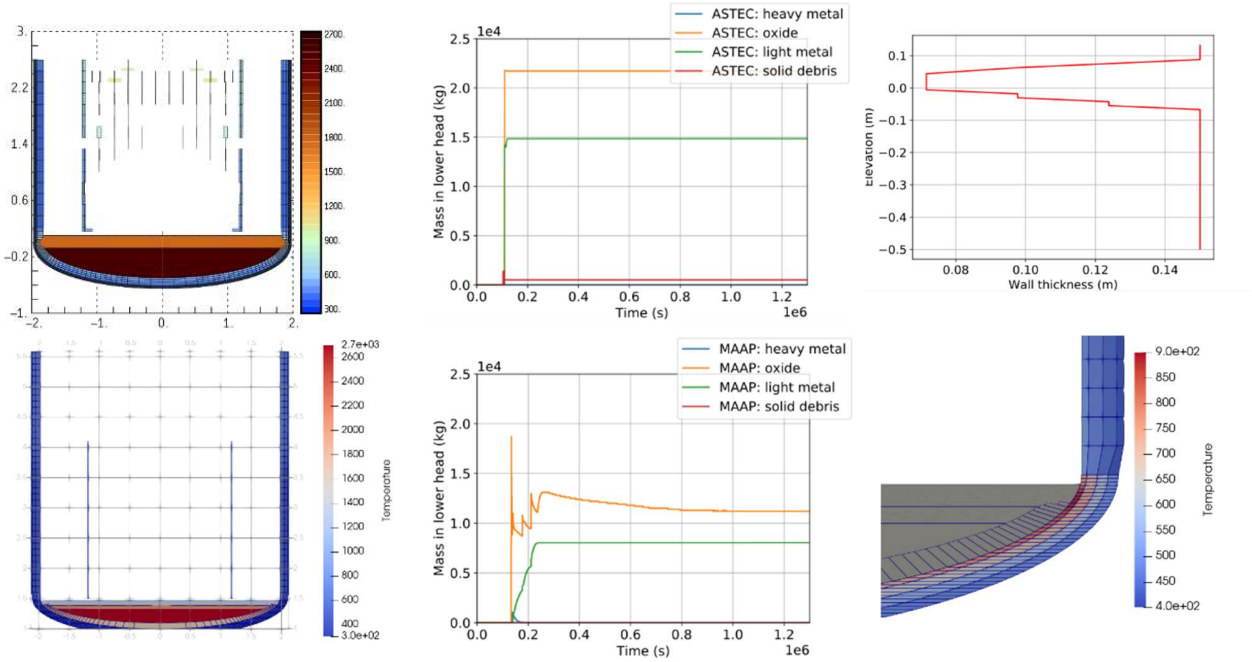

Figure 11. Top : (left) visualization of the melt in the lower head at the end of the ASTEC calculation, (center) time evolution of the cumulated mass for each material in the lower head and (right) ablation profile of the wall at the end of the calculation ; Bottom : (left) visualization of the melt in the lower head in the MAAP calculation, (center) time evolution of the cumulated mass for each material in the lower head, (right) the vessel wall temperature

The mass of the oxide layer is smaller in MAAP because of the explicit modeling of crusts surrounding the oxide pool (versus a boundary condition with fixed pool interface temperature in ASTEC). While the vessel was not ablated at all in the MAAP calculation, the temperature in some meshes reached 900 K – a threshold where steel becomes mechanically weak. Without those meshes, the residual thickness in MAAP is close to half of the initial thickness of the vessel.

To limit the discrepancy between both codes, volatile FP release was considered in an additional ASTEC calculation considering decay heat reduction of 30%, similarly to what was evaluated in the MAAP calculation. With this new assumption, the wall ablation evaluated in ASTEC is limited to 5 cm. Fig. 12 (left) presents the time evolution of the maximum external and internal heat flux on the vessel wall for both codes. For the ASTEC calculation, the reference calculation is in solid line while the adjusted power calculation is in dotted line. In both ASTEC calculations a discontinuity is observed in the power time evolution in the long term (after 550 000s - reference case in solid line) because the light metal layer is close to solidification conditions. This is not observed with current MAAP modeling.

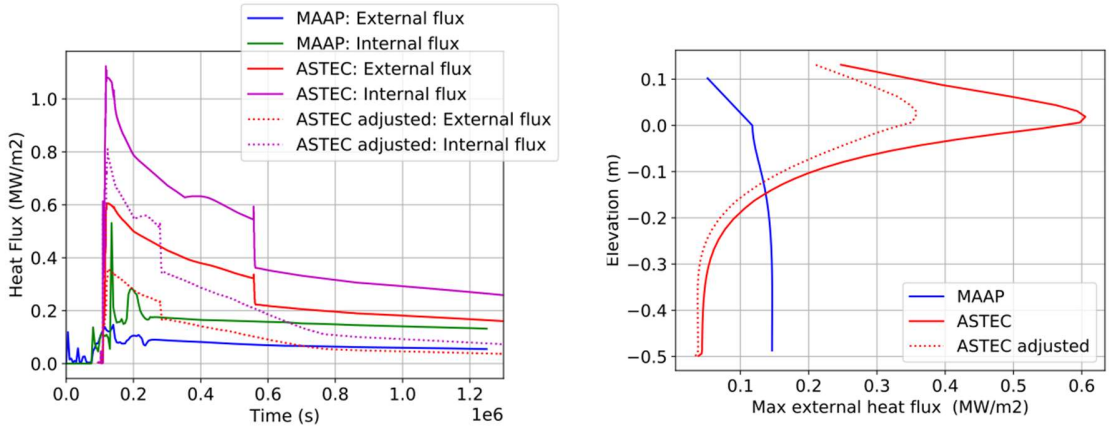

Figure 12. (left) Evolution of the external and internal wall heat flux on the lower head and (right) external heat flux profile on the wall height at the time when its maximum value is reached

Fig. 12 (right) shows the corresponding profile for the external heat flux taken at its maximum time. The 0-elevation point corresponds to the bottom point of the cylindrical part of the vessel. Negative elevations on the figure are in the semi-elliptical part. In both ASTEC and MAAP the maximum location is not located at the same height. In MAAP, it is in the elliptical part (top of the oxide) while it is just above in both ASTEC calculations (in front of the metal). The main difference lies in the value of this maximum heat flux. In the ASTEC calculations, the flux extracted from the top metal layer by radiation to the rest of the vessel is quite small (and thus the part of the heat flux going to the side wall is quite important). This is due to the conservative assumption taken in this simulation of considering radiative heat transfer from the pool in the LP only toward the core support plate. As a consequence, when this component has disappeared due to degradation (which is the case when maximum heat flux is reached), the radiation heat flux is stopped. This modeling choice has been made as it is difficult to determine which core remaining element in the magma pool would radiate in a realistic configuration when there is no more support plate. As a comparison in MAAP, the heat extracted by radiation is evaluated at maximum at 0.4 MW (around 25% of the decay heat in the debris pool) decreasing with the calculation time. At the end of the calculation the loss of the heat by radiation is estimated at 0.18MW, i.e., 18% of the decay heat in the debris pool. Therefore, no focusing effect is evaluated.

In all the performed calculations, the water level outside of the vessel, in the containment, reaches the top of the active core height. The ULPU correlation [5] used here in both codes gives a critical heat flux between 0.49 MW/m² and 1.49 MW/m² (minimum for a horizontal wall and maximum for a vertical wall). Comparing these values with Fig. 12 where the maximum external heat flux with ASTEC is obtained in the cylindrical part of the RPV wall, the external coolability of the vessel is secured, at least given the current correlation and hypothesis. This conclusion is also valid for MAAP calculation with lower heat flux.

To summarize, the higher heat fluxes with ASTEC could be explained by the higher decay heat and the different radiation heat transfer. Moreover, in ASTEC, the light metal layer includes part of the uranium and thus a part of the decay heat which is not the case in MAAP. In the long term, there is a limited discrepancy between both codes: the difference between the internal and the external heat flux is 0.1 MW/m² in the ASTEC reference calculation, 0.03 MW/m² difference in the ASTEC adjusted SBO calculation and 0.08 MW/m² difference in the MAAP calculation.

4 CONCLUSIONS

In the scope of the ELSMOR project a deep comparison between EDF MAAP 5.04 and ASTECv3 codes capacities for simulating a hypothetical severe accident in a E-SMR reactor design was performed. Results presented in this paper for one scenario allow to conclude that both codes are able to simulate the main phenomena occurring during the accident as well as the mitigation strategies like IVMR, containment inerting and reactor decay power extraction through the water wall. In general, agreement between the codes is good and this study provides the magnitude for main parameters of interest. Some modeling improvements have been performed in the frame of this study. Moreover, remaining discrepancies between codes have been discussed, therefore allowing the definition of possible improvements for future evaluations.

ACKNOWLEDGMENTS

The authors wish to acknowledge funding and support provided by the H2020 European Project ELSMOR No. 847553.

REFERENCES

1. H2020 European ELSMOR project : https://cordis.europa.eu/project/id/847553
2. Electric Power Research Institute (EPRI), 2016, "Modular Accident Analysis Program - MAAP5 v5.04 for Linux", EPRI Product ID 3002007341, September.
3. L. Chailan, L. Bosland, L. Carénini, J. Chambarel, P. Chatelard, F. Cousin, P. Drai, G. Kioseyian, S. Phoudiah, V. Topin, “Overview of ASTEC integral code status and perspectives”, *Proceedings of the 9th European Review Meeting on Severe Accident Research (ERMSAR-2019)*, Prague (Czech Republic), March 18-20 (2019).
4. P. Maccari, G. Agnello, F. Mascari, S. Ederli, “Analysis of BDBA sequences in a generic IRIS reactor using ASTEC code”, *Annals of Nuclear Energy*, Vol. 182 (2023).
5. T. G. Theofanous, C. Liu, S. Additon, S. Angelini, O. Kymäläinen, T. Salmassi, “In-vessel coolability and retention of a core melt”, *Nuclear Engineering and Design*, Vol. 169, pp. 1-48 (1997).

COMPARISON BETWEEN EDF MAAP5.04 AND ASTECV3 CODES ON A HYPOTHETICAL SEVERE ACCIDENT ON THE ELSMOR PROJECT E-SMR DESIGN

Jeremy Bittan and Nikolai Bakouta (EDF)
Julie-Anne Zambaux and Laure Carénini (IRSN)

ERMSAR – 2024, May 13-16th

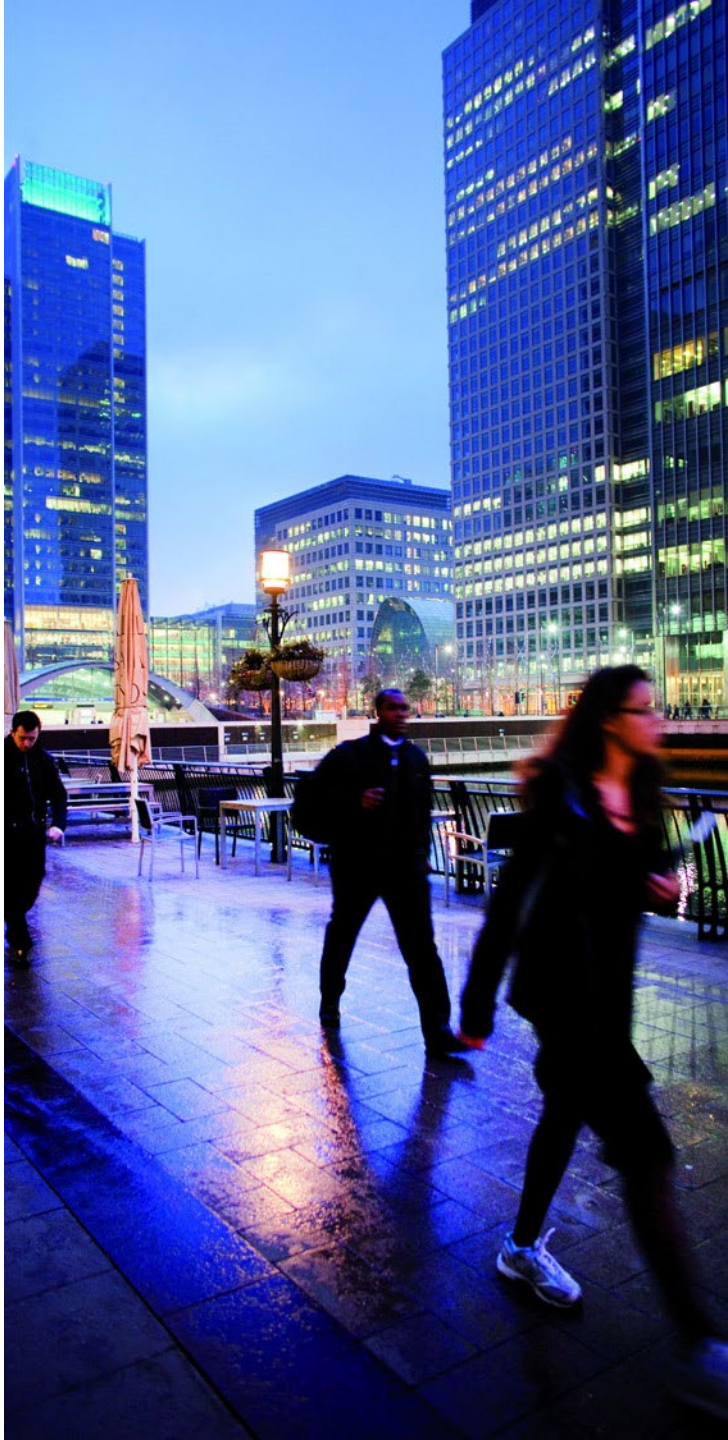

Outline

1. Context
2. Steady-state
3. Main physical parameters
4. Transient simulated
5. Results
6. Conclusions

1. Context

In the frame of the ELSMOR (Towards **E**uropean **L**icensing of **S**mall **Mo**dular **R**eactors), EU project (2019-2023), EDF MAAP5.04 has been compared to ASTECv3 on a e-SMR design

The ELSMOR RCS design has been built thanks to the use of a shared datasheet
→ Those data allow to model most of the RCS and the containment

Dataset

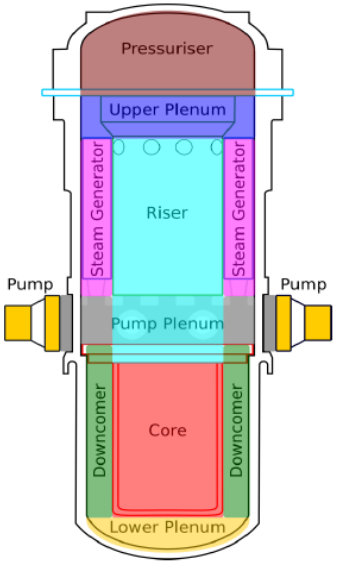

EDF MAAP5

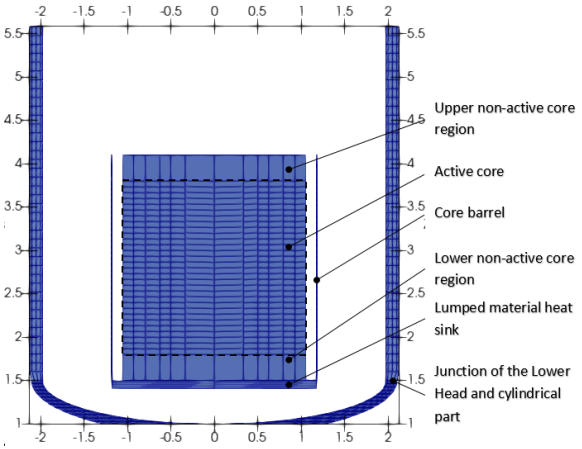

ASTECV3

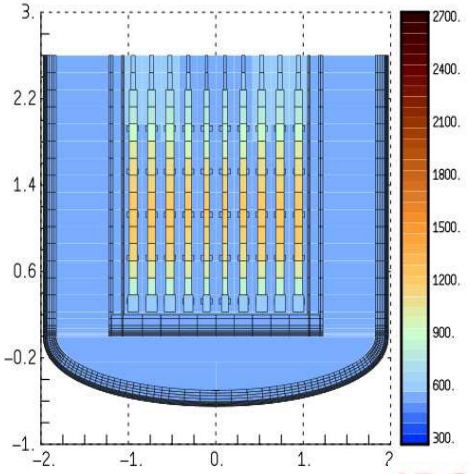

1. Context

The containment and outside “water wall” are presented below for both codes:

EDF MAAP5

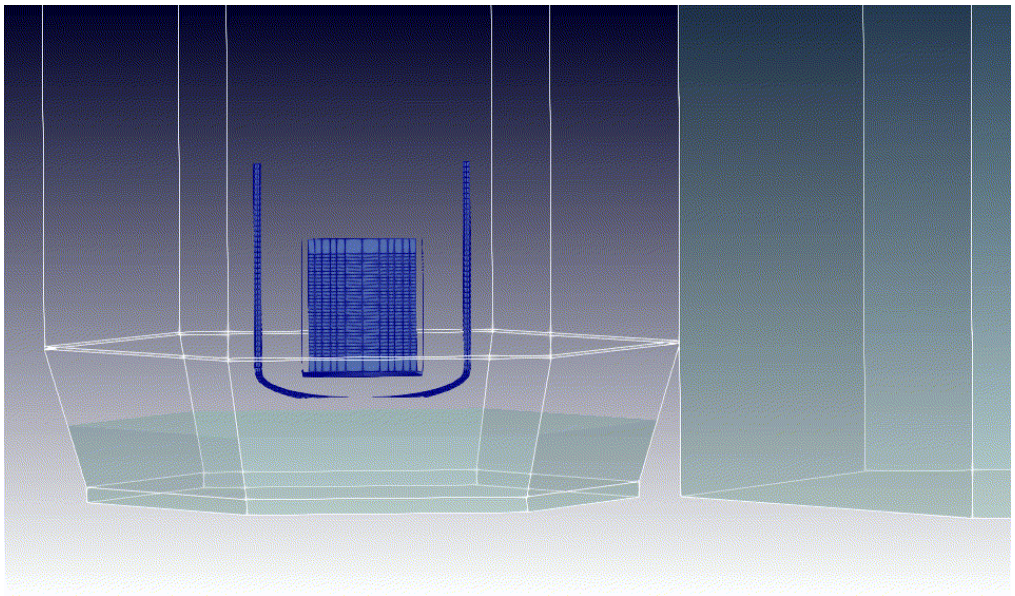

ASTECV3

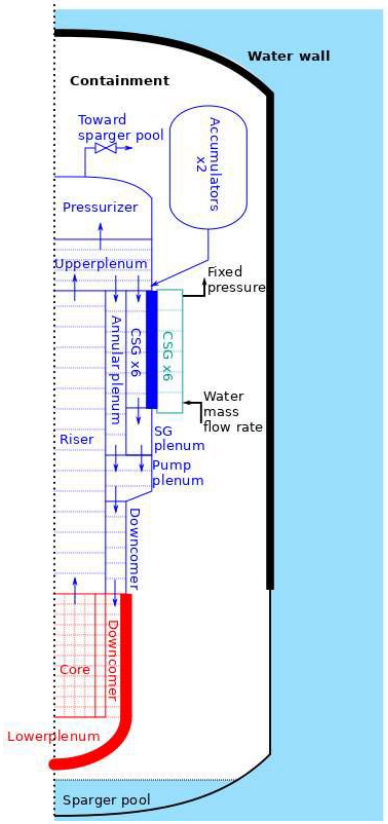

2. Steady-state

The main parameters of the reached steady state are presented below:

Parameter	E-SMR dataset [1]	EDF MAAP5.04	ASTECv3	Difference MAAP vs ASTEC (%)
Initial Core Power (MWth)	540.0	540.0	540.0	0.
Pressure in the pressurizer (bar)	150.0	149.7	150.0	-0.2
Core mean temperature (K)	588.2	585.8	586.3	-0.09
Mass flow rate in primary system (kg/s)	3700.0	3718.8	3650	1.9
Outlet Pressure in the CSGs (bar)	45.0	45.0	45.0	0.
Mass flow rate in secondary system (kg/s)	240.0	240.0	238.0	0.8
Containment sump inventory (tons)	125.0	125.0	124.8	0.2

→ Good agreement between the codes

3. Main physical parameters

The main design parameters are summarized below:

Parameter	Reference - E-SMR dataset [1]	EDF MAAP5.04	ASTECv3	Difference MAAP vs ASTEC (%)
LP wall meshing: Axial Radial	-	 40 4	 36 13	-
Containment free volume (m^3)	1731.8	1731.8	1731.8	0.
Water wall volume (m^3)	5481	5481	5481	0.
Metallic liner condensation area (m^2)	696.3	696.3	696.3	0.
Initial mass of Zr (t)	5.3	5.4	5.2	3.7
Initial mass of UO_2 (t)	21.5	21.2	21.2	0.
Initial mass of steel in the core (t) (grids, nozzles and support plate)	6.6	6.4	6.5	1.6

→ Good agreement between the codes

4. Transient simulated

The SBO (Station Blackout) transient is initiated at full power. This leads instantly to:

- a **reactor scram**,
- the **loss of the Reactor Coolant Pumps** (RCPs),
- the **loss of the Main Feed Water** (MFW) to all the CSGs (5s after the scram),
- the **closing of the Main Steam Isolation Lines** (MSIVs) concomitantly to the loss of MFW.

It is considered that the passive S-CSGs fail to start, which is a highly conservative assumption. The **operator** initiates **a primary circuit depressurization through the Pressurizer Relief Valves (RVs), one hour after noticing that the S-CSGs fail to remove any decay heat from the RCS**.

- **Two accumulators** ensure core reflooding before being emptied.
- A DC battery enables **reflooding of the reactor vessel** through the water from the water wall with a constant flow of 5 kg/s. This system, called RNU, is activated on a pressure threshold in the RCS (80 bar).

The large amount of water in the water wall allows delaying the core uncovery and ultimate core degradation. This happens when the battery is fully discharged, 12 hours after the battery first solicitation, and the RCS is progressively emptied by evaporation (core decay heat removal).

EDF

IRSN
INSTITUT DE RADIOPROTECTION ET DE SÛRETÉ NUCLÉAIRE

5. Results

Main results

Event	EDF MAAP5.04 (s)	ASTECv3 (s)	Difference MAAP vs ASTEC (%)
Reactor SCRAM and stop of RCPs	0	0	-
Secondary system isolation	5	5	0.
Pressurizer RVs fully opened	3600	3600	0.
Start of the RNU system	3803	3785	0.5
Start of accumulators' discharge	3874	3863	0.3
Accumulators are empty	4681	5348	-14.2
Stop of the RNU system	47003	46986	0.04
First cladding rupture	78130	80349	-2.8
Main material slump in lower head	133466	108869	18.4
Water wall at saturation temperature	695458	685738	1.4
End of calculation	1.3E6	1.3E6	0.

→ The results are rather similar. The main discrepancy observed is on the time of core slumping in the LH

5. Results

Thermal-hydraulics in the RCS

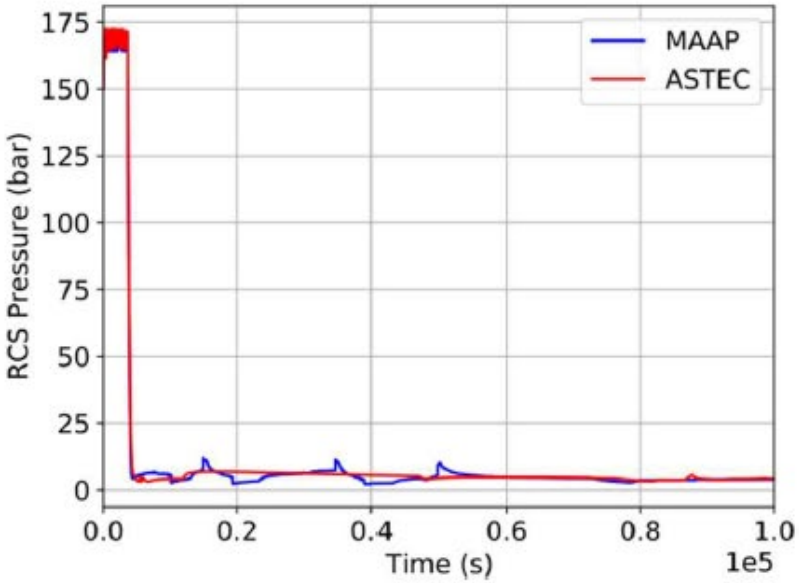

→ Similar trends

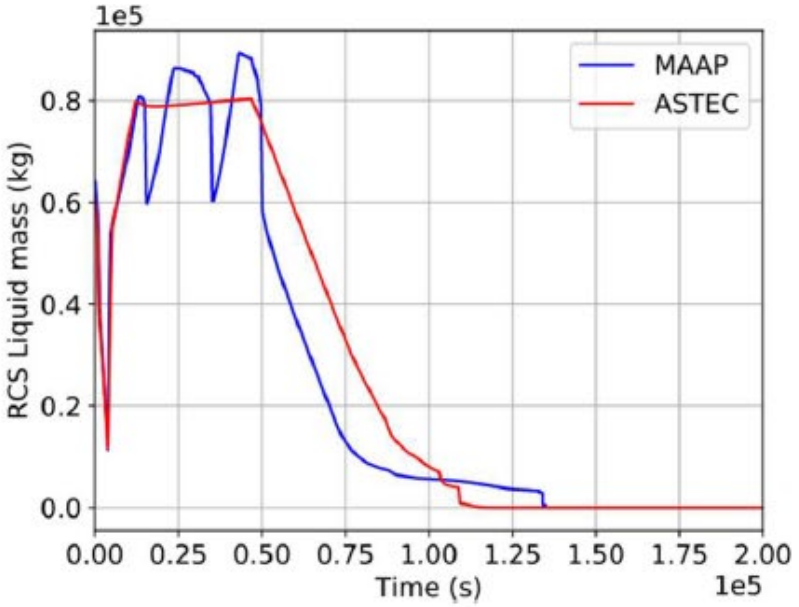

→ The discrepancy is linked to the entrainment of steam at the PZR RVs

5. Results

Degradation Phase

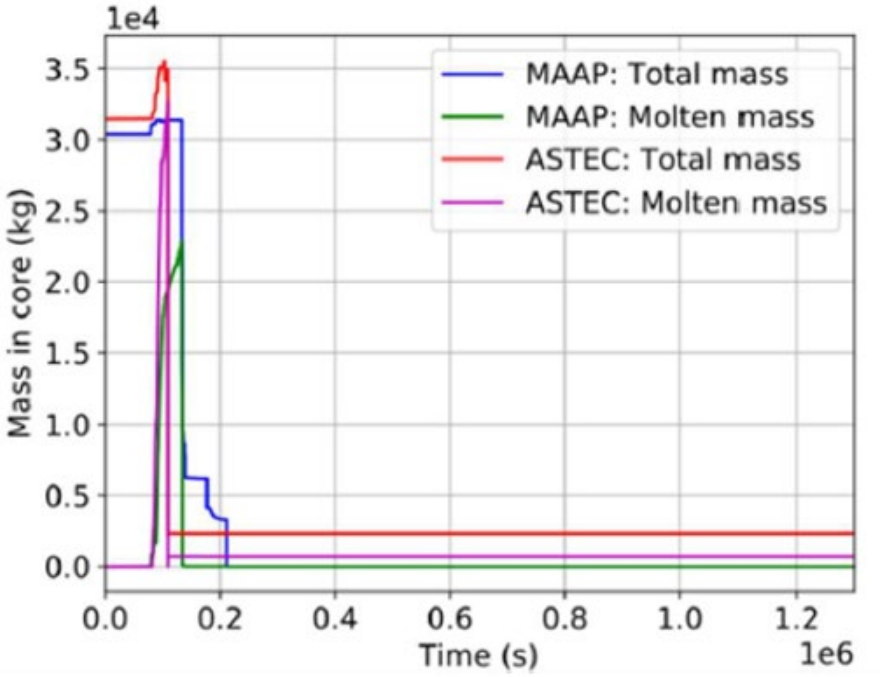

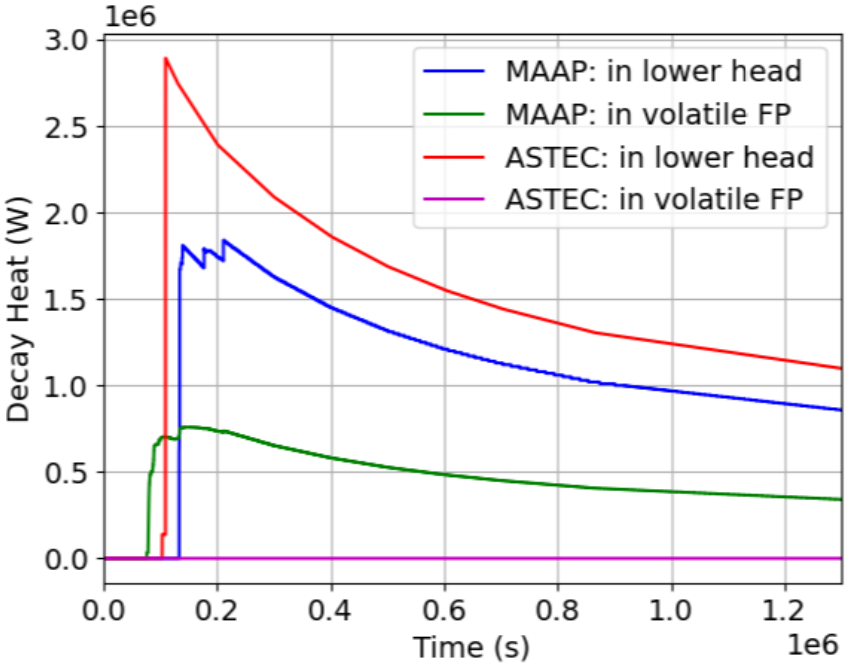

→ All the core is molten before relocation in ASTEC

→ More progressive slumps in MAAP

→ No release of volatile FPs in the reference calculation for ASTEC – a sensitivity is performed

5. Results

Degradation Phase

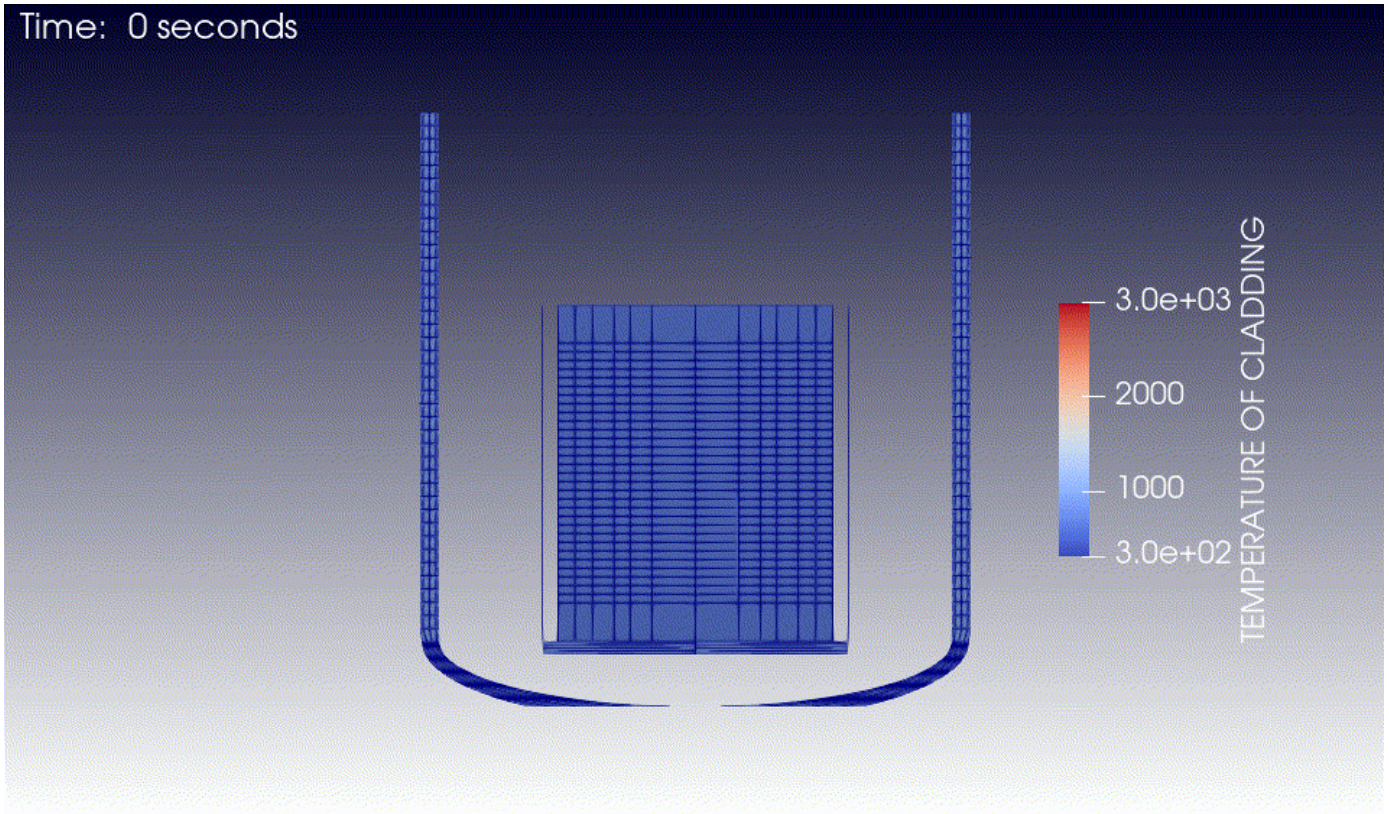

→ Example of MAAP degradation of the core and different slumps into the LH

5. Results

Containment behavior

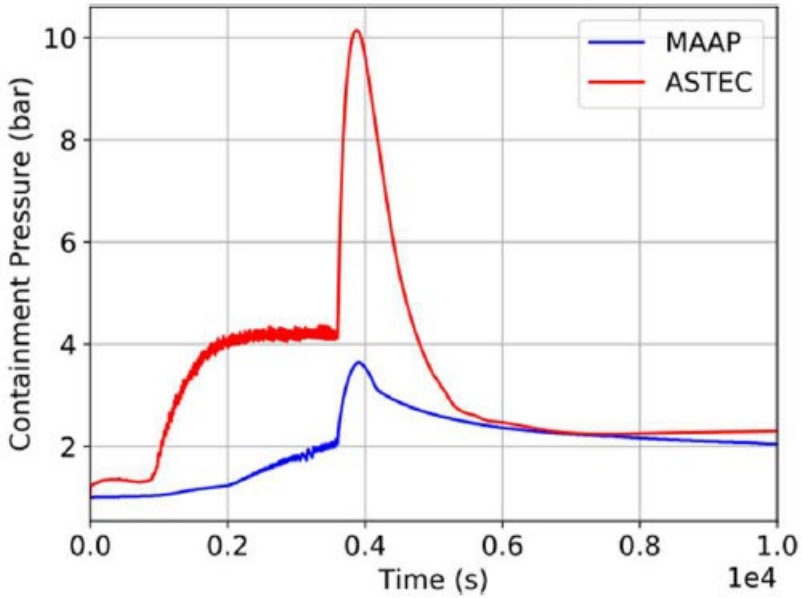

→ Condensation of steam in the sparger pool is different in the first hours of the transient (different models)

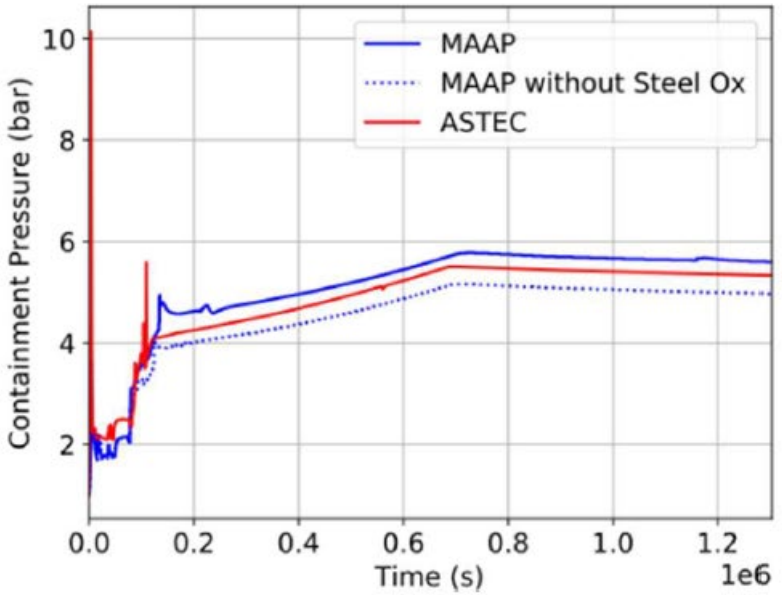

→ Except in the first hours, the containment pressure trend is similar in both codes

5. Results

Containment behavior and External water wall behavior

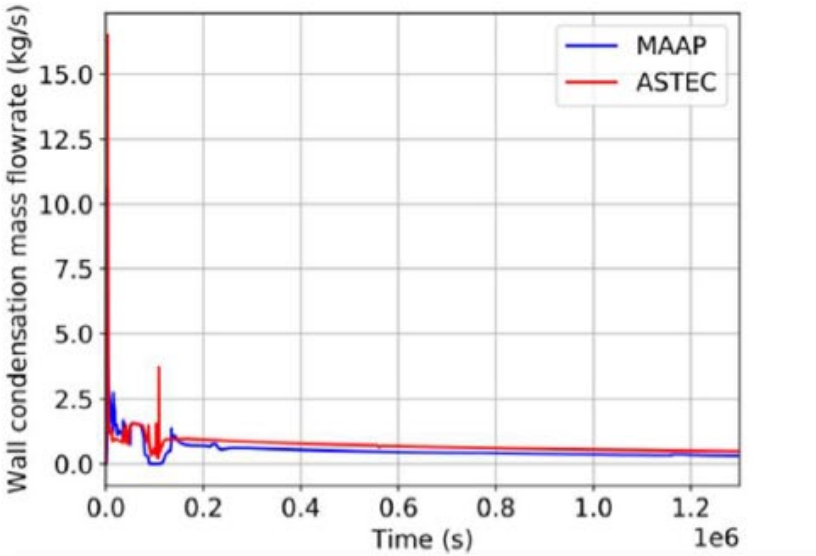

→ Long term condensation on the Stainless-steel containment wall is similar

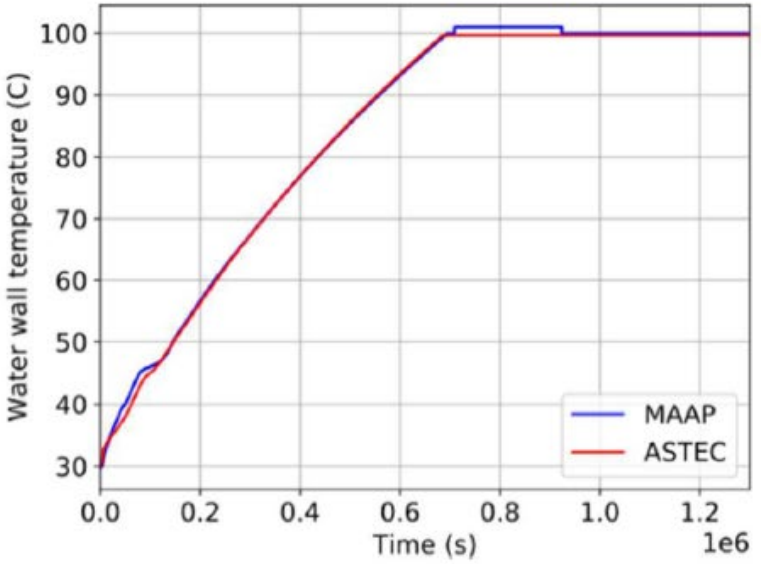

→ Evolution of the water wall temperature is almost identical

5. Results

Hydrogen production

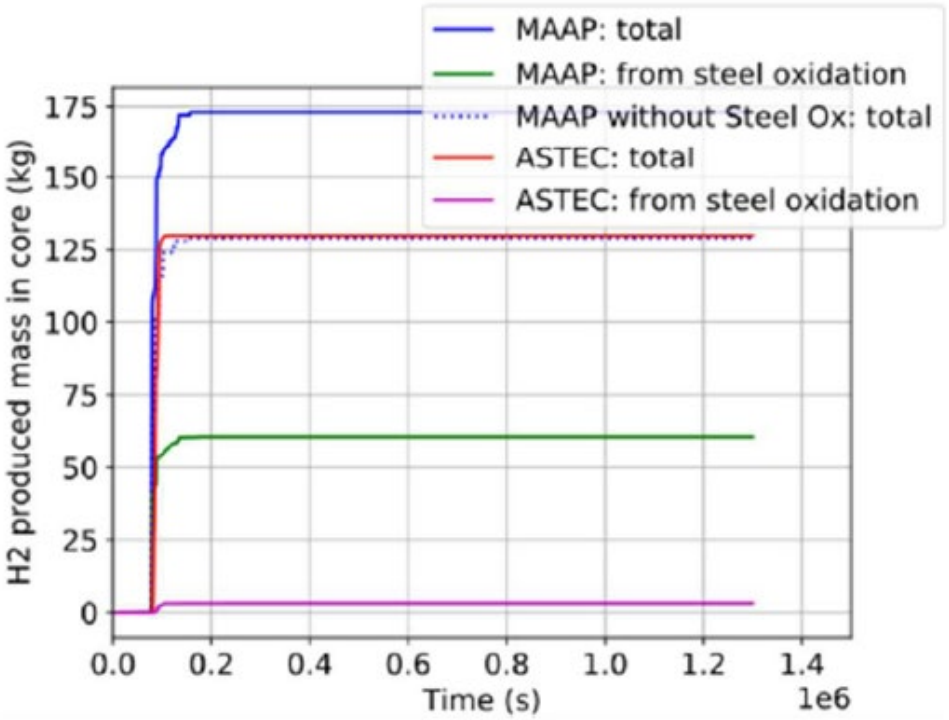

→ ASTEC does not consider oxidation of melted steel in core since, when mixed with partially oxidized corium, ASTEC assumes that oxidation is expected to involve preferentially Zr

→ A sensitivity analysis with a MAAP calculation without SS oxidation is performed leading to almost identical results between both codes (around 130 kg of H_2 generated).

5. Results

(left) Shapiro diagram without N_2 injection

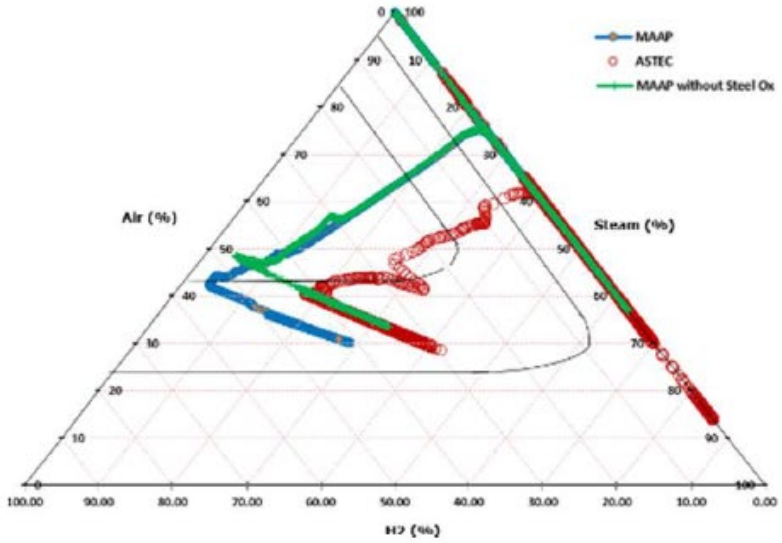

→ Reference calculation: both codes show that a potential H_2 burn in the containment cannot be excluded (H_2 burn deactivated in MAAP and ASTEC)

(right) with N_2 injection

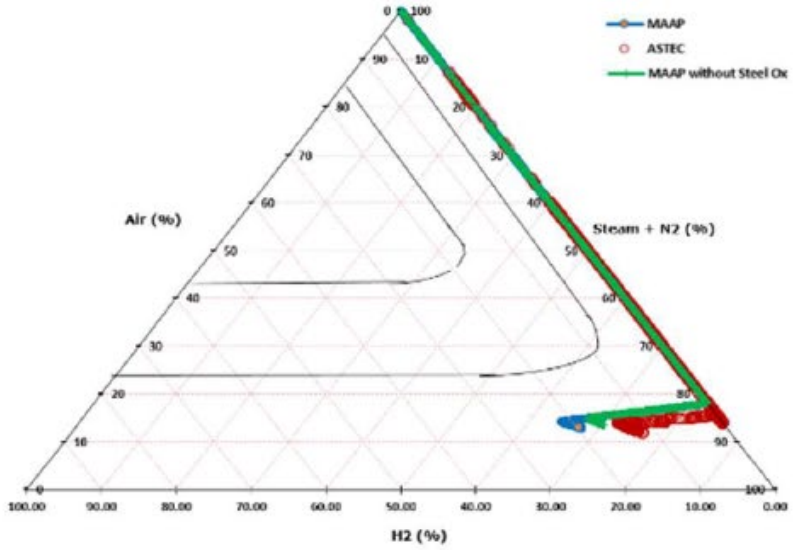

→ N_2 injection prevents from a potential H_2 burn in the containment

5. Results

In-vessel melt retention (IVMR)

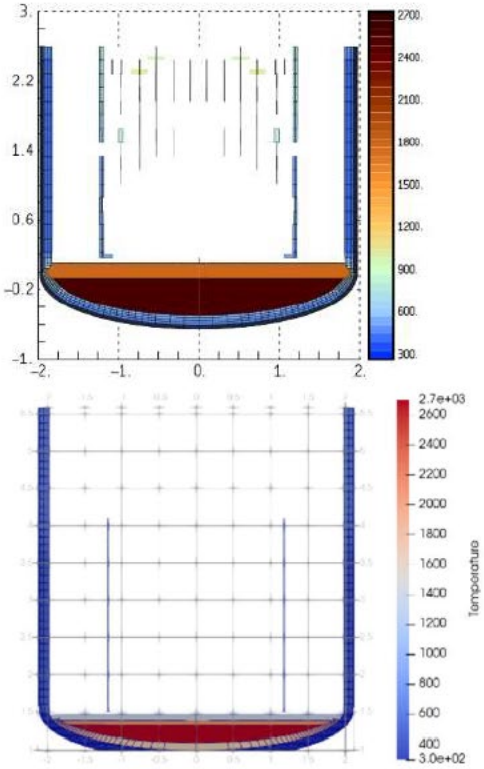

→ State of the vessel at the end of calculation (1.3e6 s)

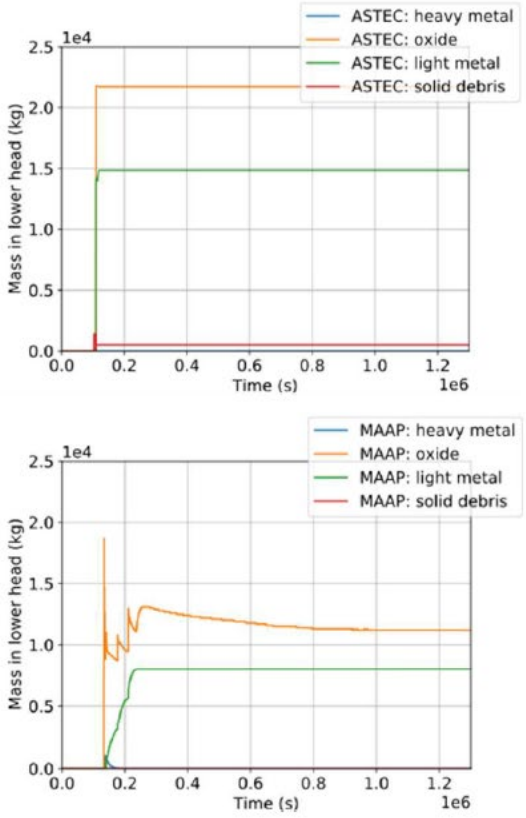

→ MAAP masses of the pool are lower than ASTEC because of the explicit modeling of crusts in MAAP

→ No heavy metal observed

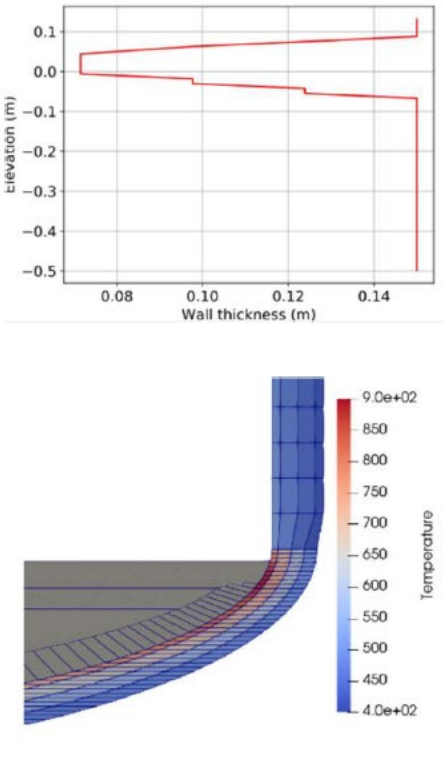

→ Vessel ablation evaluated in ASTEC (7cm left) for reference calc. (no release of volatile FPs).

→ No ablation evaluated in MAAP (radiative heat transfers discrepancy)

5. Results

In-vessel melt retention (IVMR)

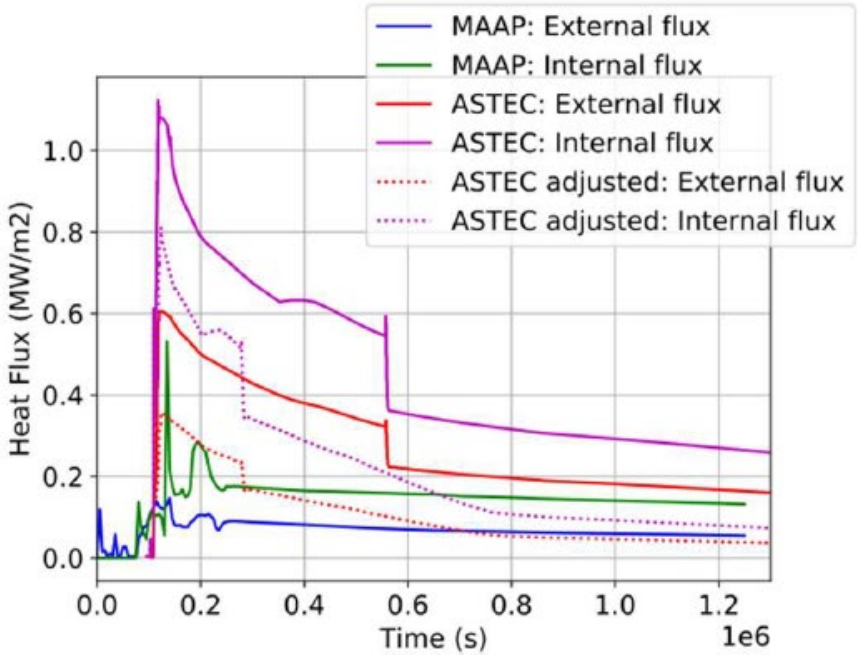

→ In the adjusted (release of volatile FPs in both codes) calculation the max heat fluxes (int/ext) are similar in MAAP and ASTEC

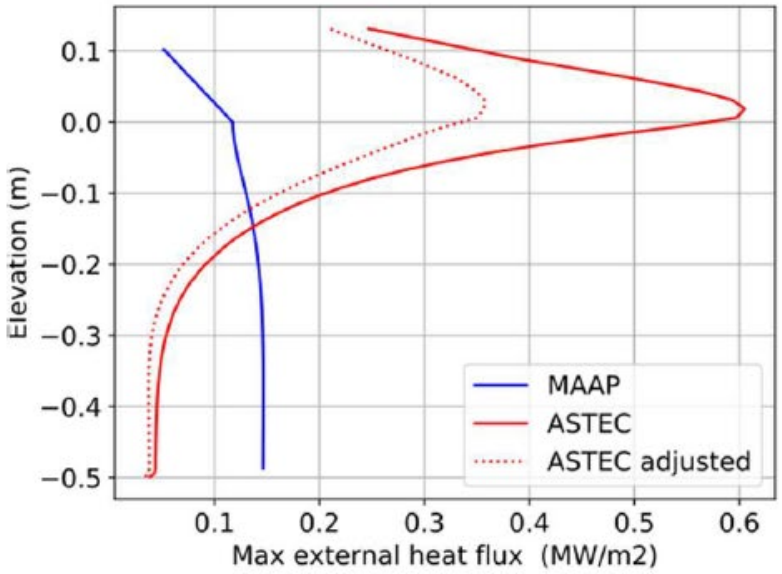

→ The maximal heat flux is in front of the steel layer in ASTEC vs oxidic layer in MAAP mostly because no radiative heat transfers are considered in ASTEC after the loss of the support plate (conservative approach)

6. Conclusions

Both EDF MAAP5.04 and ASTECv3 enable to fully model the SBO transient as well as the associated sensitivity analyses.

None of the transients lead to vessel failure except for the extremely conservative scenario with no safety systems – for both codes

Results are very similar between the codes for TH, H_2 production, and IVR especially when the same assumptions are considered (release of volatile FPs for ASTEC, no stainless-steel oxidation in the core…)

No source term evaluation (release and sedimentation) has been considered in this analysis and should be performed in the future.

Condensation models on the walls would also need some deeper validations especially for scenarios with a high fraction of non-condensable gases (with N_2 injection)

The authors wish to acknowledge funding and support provided by the H2020 European Project ELSMOR No. 847553.

EDF

IRSN
INSTITUT DE RADIOPROTECTION ET DE SÛRETÉ NUCLÉAIRE

Thank you for your attention

The 11th European Review Meeting on Severe Accidents Research

May 13-16, 2024, Royal Institute of Technology, Stockholm, Sweden

TECHNICAL SESSION 3.1: EX-VESSEL CORIUM INTERACTIONS AND COOLABILITY

Chairs: L. Carénini (IRSN), M. Hupp (Framatome GmbH)

ID06	**Results of the SSM-SICOPS melt tests in the frame of the EU-SAFEST project** G. Langrock (Framatome GmbH)	**Paper** **Presentation**
ID90	**Ex-Vessel stabilization of corium: An analysis of corium-concrete interaction with top flooding for siliceous concrete** F. Fichot (IRSN)	**Paper** **Presentation**
ID123	**Fluids Mixing Modelling with Phase Change for Molten Corium-Concrete Interaction** I. Khurshid (Khalifa University)	**Paper** **Presentation**
ID45	**Characterisation of prototypic ex-vessel fuel debris simulating MCCI at Fukushima Daiichi** C. Journeau (CEA)	**Paper** **Presentation**

Results of the SSM-SICOPS melt tests of the EU-SAFEST project

Gert Langrock*, Torsten Keim, Manfred Fischer, Sebastian Kohn, Roland Hofmann, Rainer Bezold, Martin Neumeister
Framatome GmbH
P.O. Box 1109, D-91001 Erlangen
gert.langrock@framatome.com

Sevostian Bechta
KTH Royal Institute of Technology
SE-100 44 Stockholm

Patrick Isaksson
Strålsäkerhetsmyndigheten
SE-171 16 Stockholm, Solna Strandväg 96

ABSTRACT

In the frame of the EU-SAFEST project, the Swedish Radiation Safety Authority (SSM) requested AREVA/Framatome to perform tests on molten corium-concrete interaction (MCCI) with basaltic concrete and BWR-specific corium, characterized by a higher Zr/U ratio than PWR corium.
These tests (denoted SSM-1a/2b/2c/3) were carried out in Framatome's SICOPS facility in Erlangen. Once the melt, which initially contained about 75 wt% UO2 and 17 wt% ZrO2, was generated and its interaction with the concrete had started, metallic Zr was subsequently added to the melt from the top.
All performed tests showed a fast concrete ablation, much faster than in previous experiments in the same facility and with the same concrete composition, but without Zr addition. A likely explanation for the higher erosion velocities is the now higher temperature of the melt caused by the Zr oxidation.
In addition, the absence of crusts and the even erosion profile at the bottom seen during post-test examination support the assumption of a homogeneously mixed melt pool during MCCI, consistent with the isotropic heat flux distribution observed in earlier BALI experiments with simulant fluids.
In the presence of high melt temperatures and the vivid mixing by rising concrete decomposition gases, local crusts between melt and concrete should not be stable and no evidence for them has been found in the SSM-SICOPS tests. As the formation of such crusts is seen as the main potential mechanism for anisotropic concrete ablation in the early stages of an MCCI, the investigated conditions with Zr being present in the melt can be considered capable of suppressing this effect. This is important since the core melt, after its release from the RPV, typically contains a high fraction of non-oxidized Zr.
While no crusts were found at the interface, the sampling in the late phase of the SSM-3 test revealed evidence for the formation of a kind of transition zone between melt and concrete. This conclusion was drawn based on tactile feedback during sampling from the bottom of the melt pool where a soft/viscous zone could be felt and from the appearance of the taken samples including small solid aggregates from the transition zone.
Mass spectrometric measurements during the SSM-3 test showed a significant hydrogen production, due to the reaction of water released from the concrete with the metallic zirconium. The peaks in the hydrogen production rate correlate well with the times when the measured concrete erosion velocities were highest, i.e. even at high erosion rate, the Zr in the bulk is still capable to reduce the percolating steam.

KEYWORDS
MCCI, concrete, zirconium, hydrogen production

1. INTRODUCTION

In the frame of the EU SAFEST project a number of severe accident-related experiments were proposed by various organizations for execution in dedicated test facilities provided by the project partners [1]. In this context, the Swedish Radiation Safety Authority (SSM) selected the SICOPS facility at Framatome GmbH in Erlangen to perform molten corium-concrete interaction (MCCI) experiments with BWR-type corium and basaltic concrete.

During the ex-vessel phase of a severe accident, the reactor containment is the last remaining barrier against the release of the fission products into the environment. To prevent containment failure under these conditions, the Severe Accident Mitigation strategy used at Nordic BWR's relies on ex-vessel corium debris cooling in the water-filled lower dry well. The success of this mitigation strategy relies on the (i) low risk of energetic steam explosions during ex-vessel fuel-coolant interaction (FCI) or, containment's capacity to endure energetic steam explosions and on (ii) achieving corium debris bed coolability with long-term natural circulation of water through the debris bed. In case of only partial coolability, re-melting of the debris bed can result in MCCI, specifically, melt interactions with the lower plate of the dry well. This plate separates the inside of the reactor containment from external compartments below it.

The experiments in the SICOPS facility address questions related with the impact of Nordic BWR-specific conditions, namely the combination of corium with a higher Zr/U ratio than in PWR case and basaltic concrete, on the characteristics of the MCCI. The related questions are whether non-isotropic concrete ablation or other phenomena may occur, that could require specific model adaptations.

Due to its ability to use chemically prototypic corium, the SICOPS facility allowed addressing these principal questions at medium scale, before deciding on the necessity for large-scale tests, e.g. at the VULCANO facility [2]. Though the few performed tests were not expected to adequately answer all related questions, they are nevertheless capable to indicate the direction and magnitude of the impact of both corium and concrete type.

2. EXPERIMENTAL SETUP

2.1. Skull melting at SICOPS facility

"Skull melting" uses an electromagnetic high-frequency field to create and heat an oxidic melt [3][4]. In this process a self-crucible, the so-called skull, is formed from solidifying melt due to constant water cooling of the crucible wall. As the skull consists of former molten material this method avoids the incorporation of extraneous substances from the surrounding crucible. As the induction heating can adequately simulate the radioactive decay power, this heating method is very well suited also for UO_2-containing oxidic or oxidic/metallic corium melts. At the applied high frequencies the induced energy is mainly deposited in the oxidic phase. This melting technology had already been successfully used with the SICOPS melt facility (Figure 1, left photo) in earlier research projects at Framatome/AREVA [5][6][7][8][9].

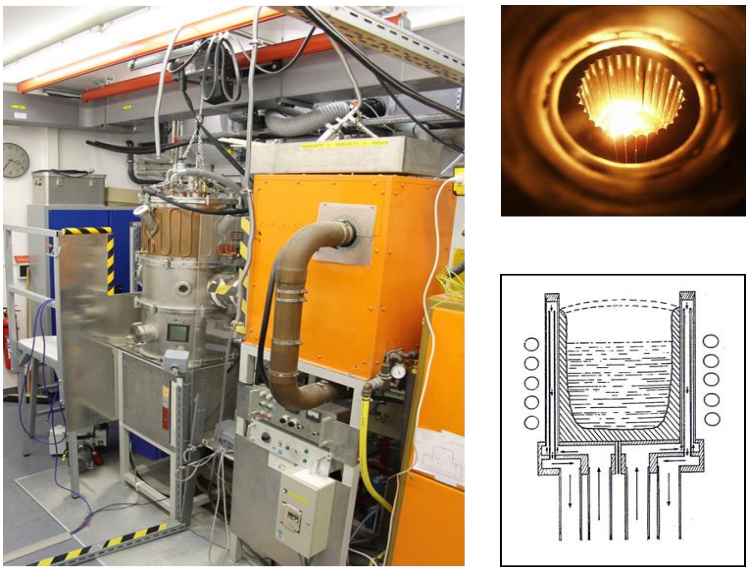

Figure 1. SICOPS melt facility (left) and cold crucible (right)

The main components of the SICOPS skull melting facility (decommissioned in 2020) were a 100 kW high-frequency generator operating at 1.3-1.9 MHz, a control unit for controlling the power and positioning of the crucible, a stainless steel vessel with the skull crucible (also known as "cold" crucible, cf. Figure 1, right photo and sketch) and inductor coil, the cooling water circuit, and the online analog data acquisition system based on LabView. The test vessel was operated with air, nitrogen, or argon atmosphere under flow-through conditions. The oxygen content was measured up- and downstream by two oxygen measuring cells (Metrotec), each connected to a flow meter (Analyt MTC/Alicat) with aerosol pre-filters.

The actual concrete erosion test took place in the skull crucible in which the concrete sample to be tested was placed on approx. 40 mm high ZrO_2 spacers above the bottom. The crucible consisted of water-cooled copper palisades (diameter 100 mm, height 300 mm, bottom surface 78.5 cm^2). The water-cooled, 65 mm high induction coil, which was specifically adapted to this type of crucible, had 4 turns and a 157 mm outer diameter. The compensating leads of the thermocouples (TCs) were routed through ceramic capillaries in the crucible bottom and connected to the data acquisition system. The recorded test data include the generator parameters (anode voltage and current), thermocouple and pyrometer readings, flow rates and the temperatures of the cooling water. The latter were used to calculate heat losses and to compare them with the generator power.

2.2. Manufacturing of instrumented concrete specimen

In the SICOPS tests self-made concrete specimen equipped with thermocouples are used. The concrete composition was based on the average composition derived from [10] for a typical basaltic concrete. The production of the specimen followed procedures established in previous projects [8][9].

To record the progress of concrete erosion, the concrete samples contain thermocouples at different elevations. Various types of thermocouples were used in the tests as illustrated in Figure 2. The applied instrumentation scheme has NiCr-Ni thermocouples (diameter 0.2 mm) along the cylinder axis (R = 0 mm) and 20 mm away from the cylinder axis (R = 20 mm). They are quickly destroyed when they come into contact with the melt. To keep consistency with previous tests, the times used to calculate the erosion velocity are those at which the thermocouples initially reach 1000 °C. This approach is valid as long as the temperature increase up to TC destruction is fast and steady, as typically during MCCI. Furthermore, WRe-W thermocouples were integrated in the sample at 10 mm distance from the axis, in order to measure

temperatures at which the NiCr-Ni thermocouples had already failed. In most cases, the ends of these WRe-W thermocouples were equipped with ZrO_2 protective caps.

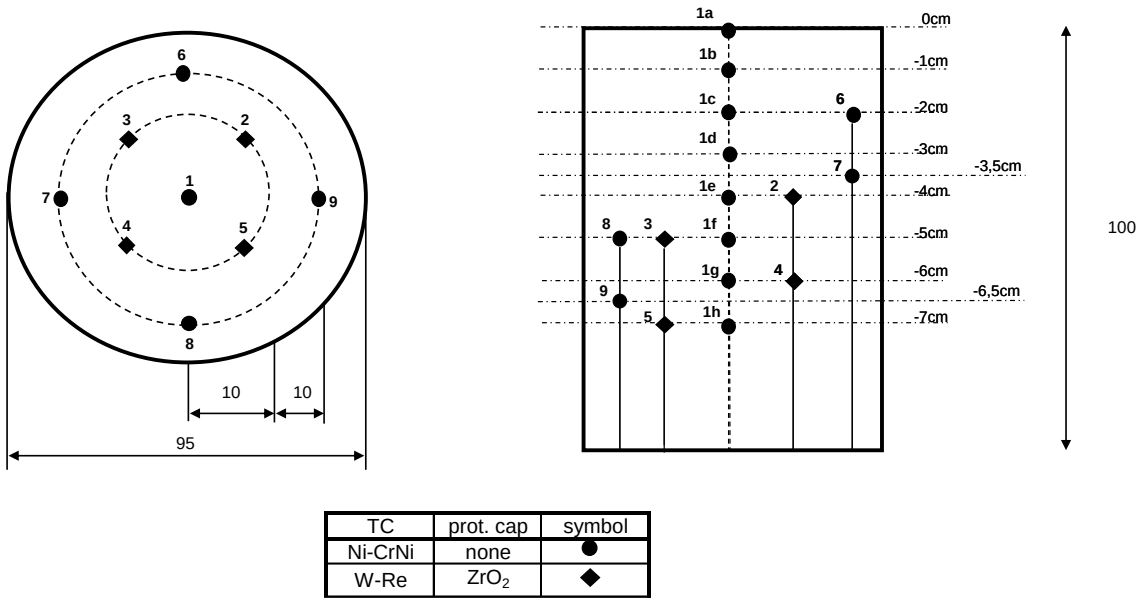

TC	prot. cap	symbol
Ni-CrNi	none	●
W-Re	ZrO_2	◆

Figure 2. Sketch of crucible instrumentation scheme "D(new)"

2.3. Test matrix

The test matrix is given in Table I. The test series included two tests (SSM-1a, SSM-3) with basaltic concrete according to the composition derived from [10]. In addition, to compare the behavior of different concretes at similar conditions, two tests with siliceous concrete (SSM-2c) and iron oxide-rich concrete (SSM-2b) were also performed. For comparison, the last column of Table I gives the specification of a former experiment (9c) performed in the same facility and with the same iron oxide-rich concrete, but without Zr addition.

Table I. Overview of tests and test conditions

Test ID	SSM-1a	SSM-2b	SSM-2c	SSM-3	AREVA 9c
Atmosphere	nitrogen				air
Concrete Type	Swedish (basaltic)	iron-oxide rich concrete (FeSI-PZ 15-8)	siliceous concrete (SI-PZ 15-8)	Swedish (basaltic)	iron-oxide rich concrete (FeSI-PZ 15-8)
Concrete water content	2.9 %	5.0 %	5.0 %	4.5 %	3.7 %
Melt	BWR specific, without steel, with reduced Zr amount	BWR specific, without steel, with reduced Zr amount	BWR specific, without steel, with reduced Zr amount	BWR specific, without steel, with reduced Zr amount	Early phase specific
Melt mass	2 kg	2.61 kg	2.67 kg	2.1 kg	1.8 kg

Test ID	SSM-1a	SSM-2b	SSM-2c	SSM-3	AREVA 9c
Initial Melt composition	74.3 % UO_2 16.9 % ZrO_2 6.4 % SiO_2 0.4 % Al_2O_3 1.9 % CaO + 3.8 % (76 g) Zr added	71.8 % UO_2 16.3 % ZrO_2 7.2 % SiO_2 0.6 % Al_2O_3 1.8 % CaO 2.2 % Fe_2O_3 + 32.2 g $BaAl_2O_4$ + 37.7 g $CsOH{\cdot}H_2O$ +4.6 % (120 g) Zr added	71.8 % UO_2 16.3 % ZrO_2 7.2 % SiO_2 0.6 % Al_2O_3 1.8 % CaO 2.2 % Fe_2O_3 + 54.4 g $BaAl_2O_4$ + 46.2 g $CsOH{\cdot}H_2O$ + 35.0 g MoO_3 + 3.0 % (80 g) Zr added	75.4 % UO_2 17.1 % ZrO_2 5.2 % SiO_2 0.4 % Al_2O_3 1.9 % CaO + 38.8 g $BaAl_2O_4$ + 25.6 g Cs_2CO_3 + 31.3 g MoO_3 +35.1 g $SrCO_3$ +4.2 % (88 g) Zr added	70 % UO_2 22 % ZrO_2 5 % SiO_2 1.8 % CaO 0.4 % Al_2O_3 no Zr added
$P_{generator,max}$	37 kW	40 kW	34 kW	36 kW	29 kW
P_{MCCI}	2.2 kW	3.6 kW	3.3 kW	1.9 kW	2.3 kW
Test duration	34 min (1340 s – 3370 s)	38 min (754 s – 3050 s)	28 min (4676 s – 6364 s)	36 min (22272 s – 24444 s)	41 min (1052 s – 3488 s)
Zr additions (time (in s) relative to start of data acquisition)	2600; 2640; 3040; 3045; (4 g each) 3085; 3125; 3160; 3220; 3260 (12 g each)	1960; 2155; 2275; 2450; 2620; 2635; 2655; 2670; 2680; 2730; 2750; 2760; 2770; 2775; 2810 (8 g each)	5517; 5567; 5657; 5722; 5777; 5792; (8 g each), 5812; 5852 (4 g each), 5865; 5892; 5922 (8 g each)	23252; 23294; 23313; 23323; 23343; 23356; 23363; 23372; 23384; 23392; 23397; 23405 (8 g each)	-

3. RESULTS

Table II summarizes measured erosion velocities and melt temperatures for all newly performed experiments.

As can be noted from Table II, not all installed thermocouples were functional, as some were destroyed during concrete pouring, storage or during the test. However, this does not obstruct the interpretation of the test results.

The destruction of thermocouple 1a at the surface of the concrete sample indicates the arrival of the melt at the concrete and the start of the MCCI.

3.1. Test SSM-1a with basaltic concrete

During the MCCI some small melt ejections and a vivid melt surface without stable crust were observed by pyrometer. Zr pellets (in total 76 g) were added to the melt from time to time during melt generation or later during the MCCI. The pellets were dissolved in the melt and a few seconds after each addition, a cloud of

aerosols occurred which became denser after each addition. After the last addition at 3260 s, a very strong aerosol release occurred, making the melt surface nearly invisible from the top (Figure 5). Since the aerosol cloud did not disappear and an overpressure in the test vessel had built up, the test was terminated at 3370 s.

Table II. Measured erosion velocities (v_{eros} in mm/min) and measured melt temperatures

		SSM-1a		SSM-2b		SSM-2c		SSM-3	
TC	Position	$t_{rel,1000°C}$ / s	v_{eros} / mm/min	$t_{rel,1000°C}$ / s	v_{eros} / mm/min	$t_{rel,1000°C}$ / s	v_{eros} / mm/min	$t_{rel,1000°C}$ / s	v_{eros} / mm/min
R = 0 mm:									
1a	0 mm	-		2610		5724		23480	
1b	-10 mm	2834		2660	12.0	5930	5.7	23556	7.9
1c	-20 mm	2947	5.3	2718	10.3	5894	9.4	23612	10.7
1d	-30 mm	3160	2.8	2793	8.0	5959	9.2	23768	3.8
1e	-40 mm	3250	6.7	2861	8.8	6043	7.1	23922	3.9
1f	-50 mm	3287	16.2	2946	7.1	6164	5.0	- *	
1g	-60 mm	-		3004	10.3	6297	4.5	24103	6.6
1h	-70 mm	-		-		-		24235*	4.5
R = 10 mm:									
2	-40 mm	3228		(2891)		-		23814	
3	-50 mm	3294	9.1	(2975)	(7.1)	6208		23932	5.1
4	-60 mm	3382	6.1	-		6358	4.0	-	
5	-70 mm	-		-				-	
R = 20 mm:									
6	-20 mm	-		2704		5896		23601	
7	-35 mm	3235		2818	7.9	6013	7.7	23721	7.5
8	-50 mm	-		2954	6.6	6159	6.2	23938	4.1
9	-65 mm	-		(3063)	(8.3)	-		24127	4.8
Melt temperatures		TC 2 (-40 mm): 2177 °C (3280 s) TC 3 (-50 mm): 2306 °C (3380 s)		-		TC 3 (-50 mm): 2030 °C (6240 s)		TC 2 (-40 mm): 2115 °C (23907s) TC 3 (-50 mm): 2086 °C (24036 s) Dip-in TC: 2254 °C (23884 s) 2006 °C (23903 s) 1996 °C (23923 s)	

**WRe-W thermocouple instead of NiCr-Ni*

The subsequent oxidation of the added Zr resulted in the formation of ZrO_2 and either H_2 or SiO. In both cases a chemical energy of about 600 kJ/mol of reacting Zr is released corresponding to about 27 kJ/pellet, or 510 kJ in total. During the first phase, lasting from 2600 s to 3085 s, 4 pellets were added. This relates to an average chemical power generation of P_{chem} = 4 * 27 kJ/485 s = 0.22 kW. In the second phase, which lasted only 185 s, 15 pellets were added. The chemical power P_{chem} = 15 * 27 kJ/185 s = 2.2 kW during this second phase of was therefore one order of magnitude higher than in the first phase and equal to the average net electric power. This must be considered when interpreting the observed course of events.

Figure 3 and Figure 4 show readings from the thermocouples. As NiCr-Ni TCs were used exclusively to detect the location of the progressing melt front, corresponding data are cut off afterwards. Data of WRe-W thermocouples were not cut off beyond their measurement range (≤ 2300 °C) which allows extracting continued information about the melt temperature even after their first contact with melt and after a possible partial melt-down. The data of TCs 1a – 1h in the central position (R = 0 mm) and the calculated erosion velocities show a fast-proceeding penetration of the concrete by the melt (Figure 3, left diagram). TCs 1b – 1f were destroyed between 2800 s and 3300 s, at an overall erosion velocity of 5.3 mm/min, cf. Table II. The erosion velocity increased clearly during Zr addition, due to the higher heat release in the melt. The measurements with the WRe-W thermocouples, arranged at R = 10 mm, provide an overall erosion velocity from TC 2 to TC 4 of 7.4 mm/min (Figure 3, right diagram). It should be noted here, that the exact position of the TC's had to be corrected afterwards based on their actual position after concrete hardening. The measurements with the TC's at R = 20 mm did not allow to extract erosion velocities due to the failure of multiple TC's (Figure 4, left diagram). In general, the erosion velocities vary in time because stationary conditions were not established during the MCCI. This is mainly due to the repeated Zr addition, which led to a periodic accelerations and related fluctuations in the concrete erosion rate.

Melt front progression can also be assessed by comparing thermocouples at the same depth but different radii. These data indicate a rather flat melt front in downward direction. This picture seems to change at the end of the test, when all thermocouples at 60 – 70 mm depth show different temperatures and melt arrival times, e.g. TC 4 vs. TC 1g (-60 mm) and TC 5 vs. 1h (-70 mm). This implies that an uneven melt front had formed.

At time 3280 s, and a few seconds after addition of the last Zr pellets to the melt, a peak temperature of 2177 °C was recorded by TC 2 (-40 mm) and 100 s later a temperature of 2306 °C by TC 3 (-50 mm), cf. Figure 4, right diagram. These temperatures are extraordinarily high, compared with own previous MCCI tests, but nevertheless reasonable and below the operational limit of the WRe-W thermocouples of 2315 °C. They were likely caused by the burning of the added Zr in the melt which produced a superheated melt with temperatures far above the liquidus temperature of the UO_2/ZrO_2-concrete mixture.
In contrast, measurement of the surface temperature of the melt with the available pyrometers provided clearly too low temperatures due to the occurrence of aerosols in the optical path between pyrometer and melt surface.

After the test, the vessel and the crucible appeared regular and dry (no coolant leakage). The inner walls of the test vessel showed wipeable fine, dust-like brown deposits. Solidified melt splatter was found on the mineral wool (Alsiflex) mat around the crucible (Figure 6, left photo). A closer look at this mat reveals some condensed, cottony matter. Something similar was observed in the ACE L6 test, where "cobweb-like" material was found around and above the melt sample [11]. A similar "cobweb-like" material was found at some tubes, coming from the vessel lid down to the melt crucible. It is assumed that it is related to the use of metallic zirconium in both experiments and its reaction with SiO_2 from the concrete according to [12]

$$\mathbf{SiO_2 + Zr \rightarrow ZrO_2 + Si} \qquad \textbf{(reaction 1)}$$

$$\mathbf{2\,SiO_2 + Zr \rightarrow ZrO_2 + 2\,SiO(g).} \qquad \textbf{(reaction 2)}$$

In principle, both reactions may occur, depending on the oxidation potential. It is nevertheless assumed, that reaction 2 is favored under the achieved experimental conditions (inert atmosphere, addition of metallic Zr, during MCCI, high melt temperature). At high release rates, the SiO aerosols may then form chain-like agglomerates.

In the pieces obtained after cutting of the sample, the melt phase appears homogeneous and with no significant gas inclusions, cf. Figure 6, right photo. The contact zone between melt and concrete shows some small gaps between the two phases and no infiltration into one of the phases.

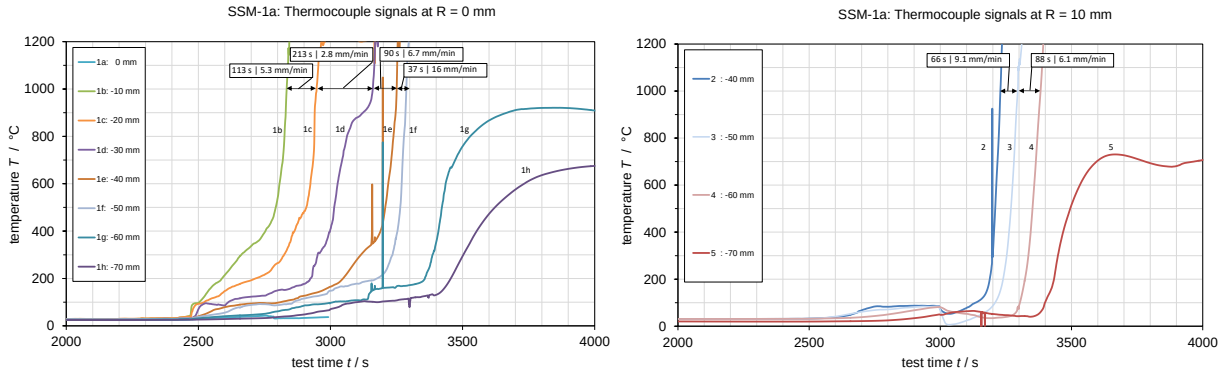

Figure 3. Thermocouple signals and erosion velocities measured with thermocouple 1b-1h (R = 0 mm, left diagram) and thermocouples 2-5 (R = 10 mm, right diagram)

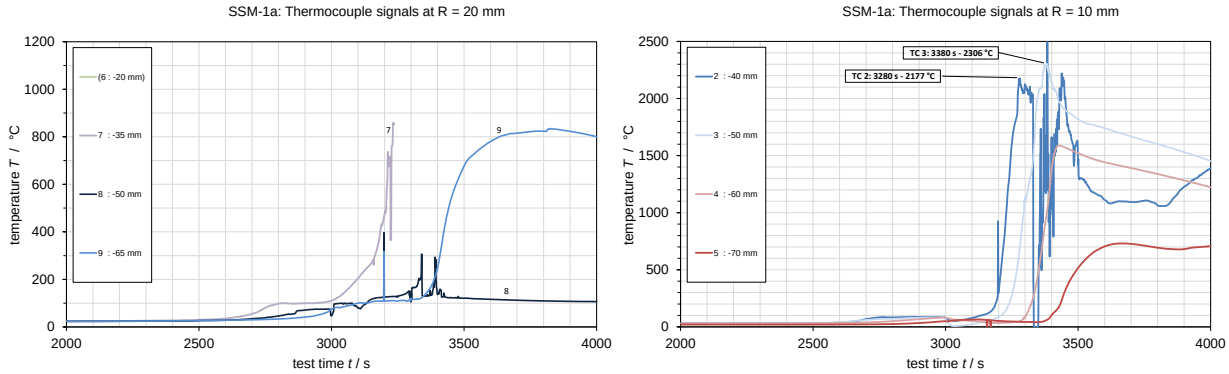

Figure 4. Thermocouple signals measured by thermocouples 6-9 (R = 20 mm, left diagram) and melt temperatures measured by thermocouples 2 and 3 (right diagram)

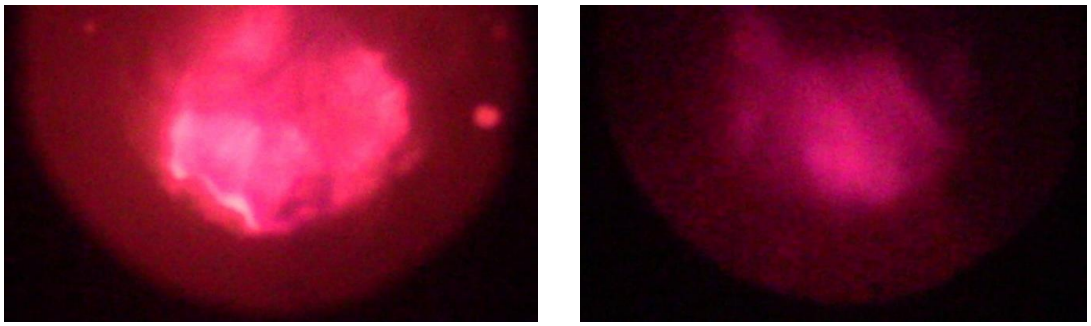

Figure 5. Strong aerosol production during MCCI (left photo), dense aerosol cloud shortly before test termination (right photo)

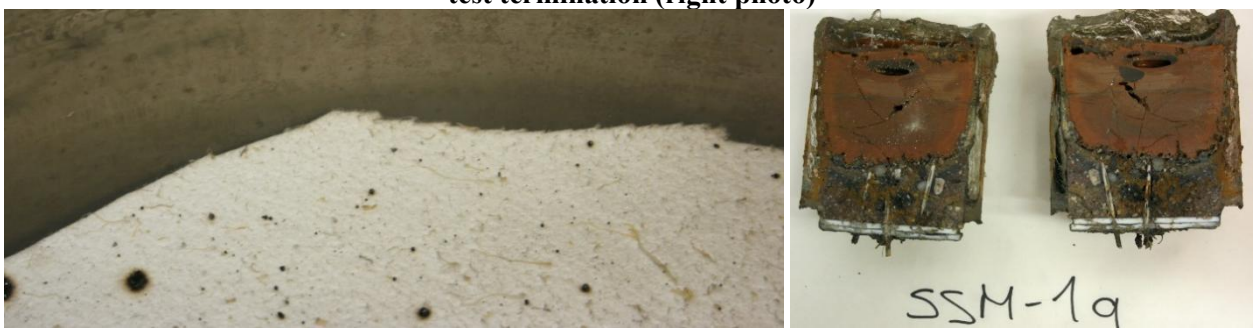

Figure 6. Condensed material and melt drops on the thermal insulation mat (left photo), melt-concrete sample after cutting (right photo)

3.2. Test SSM-2b with iron oxide-containing siliceous concrete

From the beginning of the test, a steady and – during Zr addition (120 g in total, mostly before MCCI) and the following MCCI – increasing aerosol production was observed. Later in the MCCI, melt ejections occurred at a higher rate and more aerosols were released. No stable crust formed on the surface of the melt and a vivid melt surface was observed during the entire MCCI.

The data of the TCs 1a – 1h in central position (R = 0 mm) show a rather fast vertical concrete erosion. This high erosion velocity can be attributed to the superimposition of "normal" concrete erosion by the melt (88 % UO_2+ZrO_2 at the start of the test), driven by melt cooldown and induction heating and the heat release during oxidation of the Zr. The data for the melt front velocity are confirmed by the measurement at R = 20 mm with the same type of thermocouples. The measurements with the WRe-W thermocouples at R = 10 mm generally confirm the data of the other thermocouples. Like in the SSM-1a test high, but in time-decreasing erosion velocities are derived, which temporarily accelerate during and after Zr addition. The steady decrease in the erosion velocity with depth is attributed to the admixture of concrete to the melt, changing the composition and, hence, the properties of the melt, including the liquidus temperature. When comparing the data of TC's at the same elevation an even melt front progression through the concrete during MCCI is found.

The described strong aerosol production during the whole test was confirmed by the post-test investigation. The white mineral wool mat was loaded with fine melt powder and aerosol and some solidified melt splashes. At the top of the crucible, a kind of volcanic crater with solidified lava had formed, cf. Figure 7, left photo. This is due to the high gas release during MCCI which led to the ejection and carry-over of a significant melt mass out of the crucible. The porous structure of the crater indicates that it must have formed by repeated deposition during MCCI. After cautiously removing the crater, the melt sample occurred as shown in Figure 7, middle photo. The porous sidewall crust is typical for those formed during MCCI. The melt surface itself is plane. Also, the melt/concrete interface at the bottom is rather even and only slightly convex, cf. Figure 7, right photo, and similar in shape to that of the SSM-1a test. Since during MCCI a significant melt mass was ejected, the final collapsed melt height was only about 3 cm, although the pool depth during the test was about 5-6 cm.



Figure 7. Volcanic crater with solidified lava at the top of the melt crucible and aerosol deposits and melt splashes around the crucible (left), porous melt at crucible walls formed by melt ejections during MCCI (middle), cut melt sample after the test SSM-2b (right)

3.3. Comparison with earlier test 9c

One similar test, but without the addition of metallic Zr and in air atmosphere was performed at the SICOPS facility in a previous project [8]. In this test, the concrete was dissolved at an average speed of 2.4 mm/min.

This value corresponds well to the erosion rate of 2.25 mm/min determined from the total ablation depth (approx. 4.5 cm concrete dissolved in 20 minutes). The direct comparison of the test 9c with the test SSM-2b shows: (i) The test conditions (concrete, melt composition) of both tests were similar, except for the Zr-addition. (ii) The generator power was deliberately higher in SSM-2b than in the 9c test to promote the heating of the melt. (iii) The erosion velocities were 7-9 mm/min in SSM-2b and 2.2-2.4 mm/min in test 9c, so concrete erosion was by a factor 3-4 faster in the SSM-2b test than in test 9c. (iv) The average power for concrete dissolution was 3.6 kW in SSM-2b test and 2.3 kW in the 9c test.

This proves that the use of metallic Zr significantly accelerates the concrete erosion due to the additional energy generation and the resulting superheating of the melt.

3.4. Test SSM-2c with siliceous concrete

In this test SSM-2c with siliceous concrete, Zr was added to the melt (11 additions with in total 80 g Zr) both during melt generation and after start of the MCCI. During MCCI, melt ejections occurred at an increasing rate and more and more aerosols were released. As in the former tests, no stable crust had formed on the surface of the melt during MCCI and a vivid melt surface was observed by video. However, the melt became more viscous towards the end of the test due to the increasing SiO_2 amount in the melt. The test was stopped after occurrence of a plasma arc that caused a loss of the data acquisition system.

As in the previous tests, the data of the thermocouples 1a – 1h in the central position (R = 0 mm) show a fast concrete erosion, cf. Figure 8, left diagram. The erosion velocity is somewhat lower than in the test with iron oxide-rich concrete; this is attributed to the higher silica content in the melt. SiO_2 is not as susceptible for the electrical field as iron oxide. Nevertheless, the erosion velocity is higher than in comparable tests without Zr addition. This is confirmed by the measurements at R = 20 mm with the same type of thermocouples. The data from the WRe-W thermocouples at R = 10 mm shows a similar picture. After correction of the recorded data (TC 3 and TC 5 had wrong polarity), an erosion velocity of 4.0 mm/min from -50 mm to -60 mm was calculated. This is in good agreement with the erosion velocity obtained from TC's 1f – 1g. As in the SSM-1a and the SSM-2b tests, the erosion velocities – generally high, but by time decreasing - vary as no stationary conditions had been established during MCCI. Again, it was confirmed that the Zr addition accelerates concrete erosion.

The shape of the melt front was quite even during the early phase of the MCCI. Later on, the thermocouples showed faster progression at radius R = 0 mm than at R = 10 mm than at R = 20 mm. This indicates that the melt front had become radially uneven which finally resulted in a bolus-type shape. This could be due to a higher impact of the sideward cooling on the heat transport into the concrete in case of highly viscous, siliceous melts.

In this test, TC 3 delivered a maximum melt temperature of about 2030 °C at around 6240 s. This is plausible for a superheated melt with significant SiO_2 content. The observation of the melt surface was again disturbed by the continuous production of aerosols. The right photo in Figure 8 shows the configuration of the test vessel after the test. Obviously, much aerosol was released and deposited onto the mineral wool mat. Moreover, some water must also have been condensed during or after the test, as indicated by the wetting of the mat.

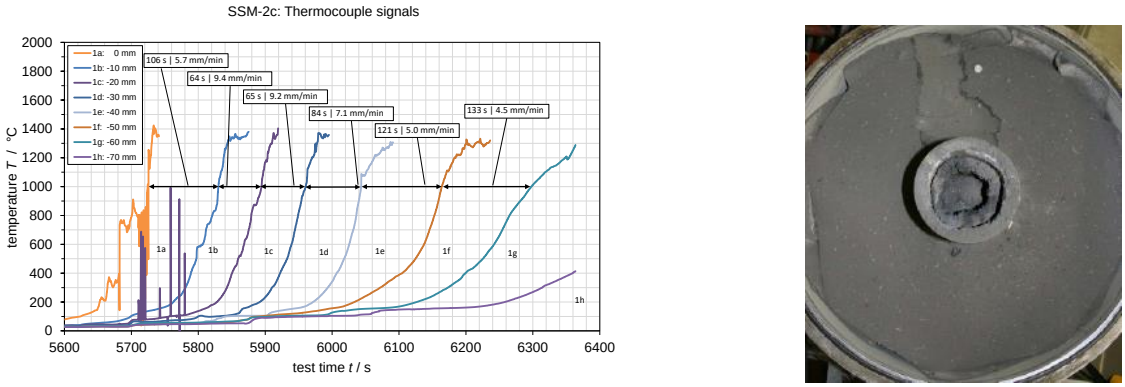

Figure 8. Thermocouple signals of TC's 1a – 1 h and calculated erosion velocities (left diagram) and aerosol deposits around the crucible after tests SSM-2c (right photo)

3.5. Test SSM-3 with basaltic concrete

This test was the last test in the SSM test series and performed with improved experimental methods. In this test, melt samplings, melt height measurements, dip-in thermocouples, aerosol suction via a cyclone and gas mass spectrometer measurement were employed.

Already during melt generation, aerosol production was observed which became very strong after addition of metallic Zr (11 additions, 8 g Zr each) to the melt shortly before the start of the MCCI (Figure 9, left photo). The correlation between Zr addition and dissolution (which leads to an additional heat release in the melt) and the increase in temperature at the concrete surface can be seen in Figure 10 (left diagram). During MCCI, only some melt ejections occurred. The release of aerosols was reduced compared to previous tests, but nevertheless considerable, especially in the two minutes after the last Zr addition. After MCCI had started, the aerosol release became less and the behavior of the melt turned into a "normal" regime, with significant void, melt depositions at the inner crucible wall (leading to an increasing wall thickness) and a vivid convective movement at the surface. The melt remained well-mixed and vivid during the entire MCCI, with a tendency to less void and higher viscous behavior towards the end of the test. This was obviously caused by the increasing amount of SiO_2 in the melt. After admixture of a significant amount of concrete, a kind of foam and gas bubbles, but no stable crust could be observed at the melt surface, cf. Figure 9, right photo.

Zr was added in this test before the start of the MCCI, hence erosion velocities were slightly different from previous tests in which some Zr had been dissolved in the melt already at the beginning of the MCCI. The data of TCs 1a – 1h in the central position (R = 0 mm) show a fast initial concrete erosion which was steadily slowing down towards the end of test. After the first 20 mm of concrete were eroded, the erosion velocity significantly decreased. From top (TC 1a) to bottom (TC 1h), the overall erosion velocity was 5.6 mm/min. This is higher than in tests with similar melts, but without addition of Zr.

Generally, the melt behavior and the characteristics of the MCCI were similar to what had been observed in the previous SSM-2c test. The measurements with the WRe-W thermocouples arranged at R = 10 mm show a consistent erosion velocity. Especially TC 3 showed some distinct changing points (Figure 10, right diagram). They seem to be correlated with the anomalies of TC 1e (-40 mm) and the end of the parallel measurement with a dip-in thermocouple at 23955 s.

During sample-taking, the tactile impression was that, between the low-viscosity melt and the hard concrete, a soft layer existed, consisting of some molten or soft, but not yet dissolved concrete. The removal of the dip-in TC may then have resulted in a change in the local conditions at TC 3. Although this single curve

should not be over-interpreted it might be a hint for the existence of a kind of mushy zone between concrete and oxide melt where the concrete has already been molten, and infiltrated by the oxide melt, and/or where some siliceous aggregates remained undissolved for some time [13]. This would also be in agreement with the findings from the sampling (Figure 11, left photo) where sticky material was found on the surface of the sampler.

The readings of TCs 6-9 at R = 20 mm confirm the above-described erosion speed measurements showing fast progression in the first phase of MCCI, which later slowed down. This sequence is also in very good agreement with the measurements of TCs 1a-1h and TC 2-3. The resulting weighted mean erosion velocity for all thermocouples is 5.4 mm/min. As in the previous tests – no stationary conditions had been established and the existence and addition of Zr was found to accelerate the concrete erosion for basaltic concrete in the same way as for the other investigated concretes.

Comparing the signals of thermocouples located at the same depth further indicates a generally even melt front progression through the concrete. Only near the end of the MCCI process, by comparing TC's 1g and 9 at 60 mm depth, some preferred ablation in the central position (R = 0 mm) can be observed compared to an outer position (R = 20 mm). This may again indicate the formation of a bolus-type melt front similar and likely caused by the same mechanism as in the previous test SSM-2c. This would not be surprising, because basaltic concrete also has a high content of silica. At the end of the test the bolus-type shape was ultimately confirmed during post-test examination, cf. Figure 11, right photo.

Melt temperatures were 2115 °C at 23907 s (TC 2, -40 mm) and 2086 °C at 24028 s (TC 3, -50 mm). Obtained from thermocouples in the concrete, they may serve as a good and plausible approximation of the melt pool temperature of a superheated 92 % (UO_2 + ZrO_2) melt with increasing concrete (especially SiO_2) content. Measurement with a dip-in TC provided a maximum melt pool temperature of 2254 °C at 23884 s. These measurements confirm the statement that the melt was superheated also during MCCI and no stationary conditions had been reached.

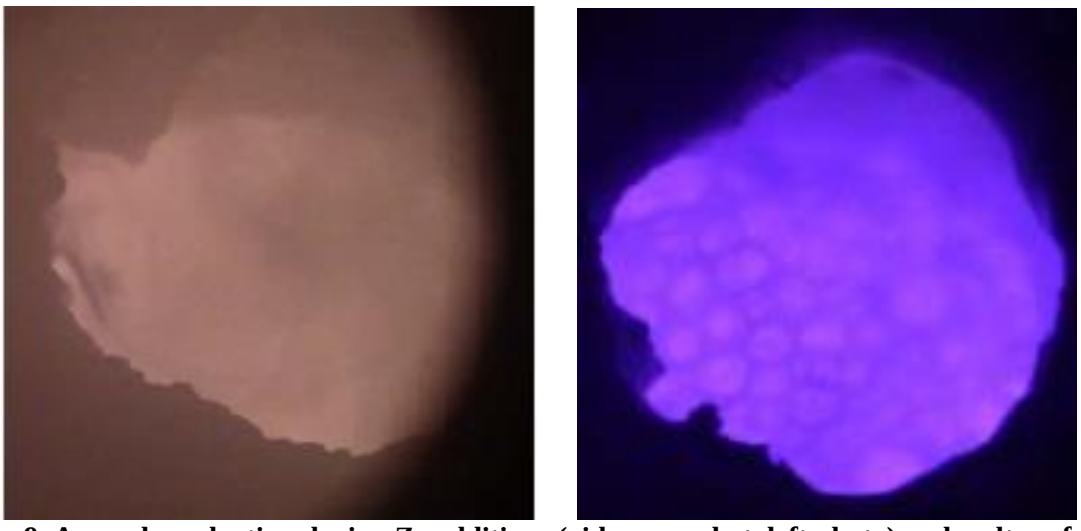

Figure 9. Aerosol production during Zr additions (video snapshot, left photo) and melt surface at 24170 s (right photo)

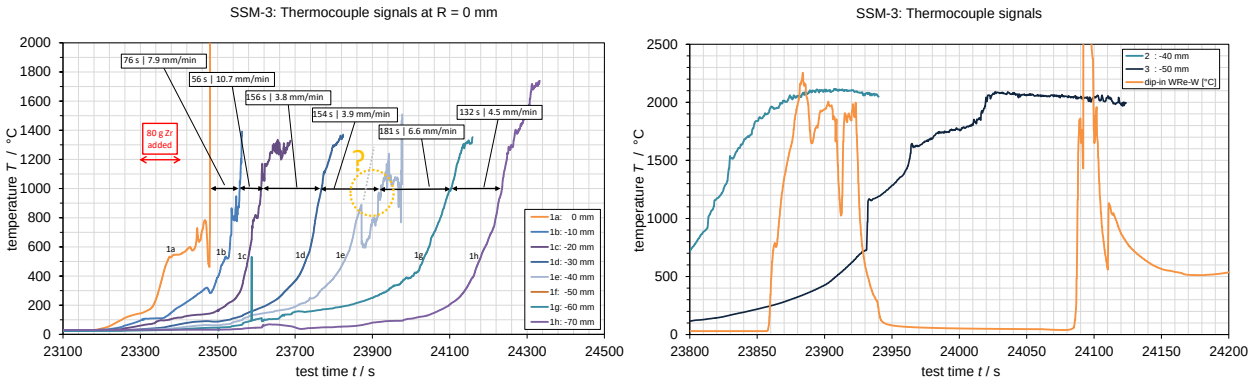

Figure 10. Thermocouple signals in central position (R = 0 mm) with erosion velocities (left diagram) and signals of dip-in thermocouple and thermocouples 2/3 with melt temperatures (right diagram)



Figure 11. Sticky material on sampler (left photo) and cut sample after test SSM-3 (right photo)

3.5.1. Mass spectrometer measurement

The results of the gas mass spectrometer measurement allow more insight into the process of the MCCI. Due to some technical constraints, the position of the measurement point was 15 cm below the vessel lid at a not fully representative position.

Figure 12 (left diagram) shows the measured ion currents on mass 18 (H_2O) and 2 (H_2). A slight increase of the water signal and a remarkable increase of the H_2 signal come with the beginning of the heating of the concrete which leads to the release of free and chemically bound water. Due to the high temperatures the water is released as gas. Inside the melt the steam can react with the metallic zirconium to produce hydrogen according to the reaction $Zr + 2\ H_2O \rightarrow ZrO_2 + 2\ H_2$. Different from steam, the generated H_2 is a non-condensable gas and thus has a different impact on the pressure build-up in the containment.

Figure 12 also shows that the H_2 production stops about 500 seconds after the last Zr addition, which is at around 23900 s. This could indicate that, at this time, all metallic Zr in the melt is consumed. The peak of the H_2 signal is measured at 23600 s when the measured concrete erosion velocities are highest (cf. Table II). This correlation is convincing because it gives more information about the process of MCCI with a Zr-containing melt:

- As long as non-oxidized Zr is present in the melt, the melt is superheated and shows high concrete erosion velocities.
- Zr is able to reduce released steam to hydrogen.
- The rate of Zr oxidation reaction obviously correlates with the concrete erosion rate.

- The H_2 measurement serves as an indicator for the consumption of Zr and for the point in time when the MCCI turns into a more "normal" regime, but still with a superheated melt.

Using a pre-test calibration, the measured H_2 concentration is up to 1.5 vol% H_2 (cf. Figure 12, right diagram). But it is difficult to draw a quantitative information from this number about the MCCI:

- For the whole period from 23400 s to 23900 s an average concentration of approx. 0.5 vol% is measured.
- With a nitrogen gas flow through the vessel of 200 SLPM, the total gas flow would be 1667 SL within 500 s, and the 0.5 vol% would then correspond to 8 SL hydrogen.
- This gives 0.37 mol H_2 produced or 0.19 mol Zr consumed. Compared to 88 g (0.96 mol) Zr that has been added to the melt, this would be about 20 % of the initial Zr amount.

It is however not clear how reliable the fraction of oxidized Zr is, since as mentioned above the sampling location was probably not fully representative.

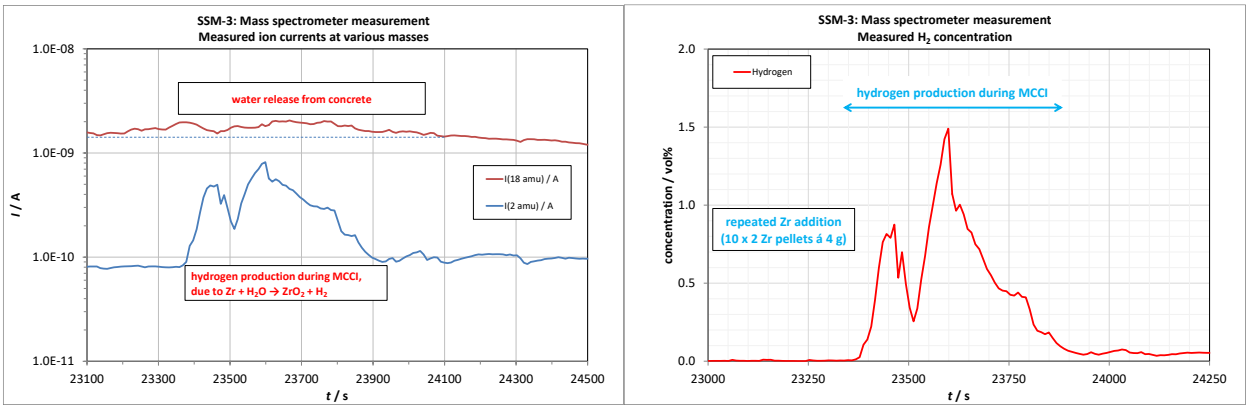

Figure 12. Measured ion currents at mass 18 amu (H_2O) and 2 amu (H_2) (left figure) and measured H_2 concentration (right figure).

4. CONCLUSIONS

All tests performed with BWR-type corium and metallic zirconium in the SSM-SICOPS series showed a very fast erosion of concrete, independent of the concrete type. Such high velocities were not observed in previous studies without added Zr.

During MCCI, the existence of a homogeneously mixed superheated melt pool was observed. Due to the superheat of the melt in the SSM-1a/2b/2c/3 tests and the vivid mixing by rising gases from the concrete decomposition, local crusts between melt and concrete and at the pool‘s upper surface have not been found. As such crusts are seen as the potential reason of non-isotropic concrete ablation in the early stages of an MCCI, the presence of Zr in the initial melt can have a damping effect on the non-isotropy of the MCCI even for the here-investigated high-silica melts. However, the sampling in the late phase of the SSM-3 test revealed evidence for the formation of a transition zone at the melt-concrete interface.

In addition to the energy input, the oxidation of the metallic zirconium during the MCCI was also found to result in an intense production of aerosols as well as the formation of condensed matters in the test apparatus in test SSM-1a. When comparing the latter with the results of the ACE L6 test [11] it is assumed that the condensed cobweb-like matter was formed from SiO agglomerates. This topic is of relevance as the strong aerosol production can potentially provide an additional release path for fission products, see the discussion

in [15]. On the contrary, a high concentration and local deposition of "sticky" non-radioactive aerosols near the MCCI surface can have an additional retaining impact on fission product aerosols.

Condensed cobweb-like matter could not be found after SSM-2b (with iron-oxide containing siliceous concrete) and SSM-2c (with siliceous concrete), but a considerable amount of deposited aerosols was nevertheless found after both tests. It is assumed that – in contrast to the SSM-1a test, where the formation of condensed matter is explained by the reaction of Zr with SiO_2 during the short phase of very high Zr-concentration and melt temperature – in the SSM-2b test a significant fraction of the Zr was likely consumed for the reduction of the iron oxides. In addition, the melt temperatures were lower, potentially also because iron oxide can act as a liquidus temperature-reducing agent.

The mass spectrometric measurement provided in SSM-3 revealed a significant hydrogen (H_2) production as long as metallic Zr was present in the melt and as soon as the temperature of the concrete started to increase above 100 °C at the melt/concrete interface. This hydrogen production is due to the reaction of water released from the concrete with metallic Zr according to $Zr + 2\ H_2O \rightarrow ZrO_2 + 2\ H_2$. Although an exact quantification of the amount of H_2 was not possible, it was estimated that at least 20 % of the added Zr was consumed for this reaction path. This raises the question on the impact of the remaining Zr. The role of Zr in an MCCI with a prototypical melt may even be more complex than expected. Besides of acting as a reductant to steam and incorporated slag within the bulk the Zr could influence the concrete erosion process not only by the superheat of the melt but also by taking part in the chemical processes right at the melt/concrete interface. If confirmed this effect would evidently be stronger for a BWR-type melt due to the higher initial Zr-fraction but, in any case, decline with the progress of the MCCI.

A comparison among the tests performed with various concretes shows that the multiple thermal and chemical effects caused by the oxidation of zirconium dominate over the effects caused by the specific (basaltic) concrete composition. The significant superheat of the melt during phases of high content of non-oxidized zirconium and the resulting enhanced ablation and mixing by concrete decomposition gases at the melt/concrete interface have the potential to suppress mechanisms that cause non-isotropic melt front progression.

NOMENCLATURE

$t_{rel,1000°C}$: time relative to start of data acquisition when thermocouple in concrete exceeds 1000 °C
v_{eros} : erosion velocity
P_{MCCI} : power for concrete erosion, calculated from difference of generator power and sum of heat losses
$P_{gen,\ max}$: maximum generator power in the corresponding test

ACKNOWLEDGMENTS

The authors gratefully acknowledge the funding by the EURATOM 7th Framework Program under Grant Agreement N° 604771 to support the work within the SAFEST project.

REFERENCES

1. A. Miassoedov, B. Fluhrer, C. Journeau, S. Bechta, Z. Hozer, D. Manara, P. D. Bottomley, M. Kiselova, T. Keim, G. Langrock , F. Belloni, M. Schyns, "The SAFEST project: towards pan-European Lab on Corium Behavior in Severe Accidents. Main Objectives and R&D priorities", 8th European Review Meeting on Severe Accident Research (ERMSAR 2017), May 2017, Warsaw
2. C. Journeau, V. Bouyer, F. Charollais, N. Chikhi, J. Delacroix, A. Denoix, H. Laffolley, C. Mattassoglio, D. Molina, P. Piluso, P. Sauvecane, S. Thilliez, B. Turquais, C. Suteau, "Upgrading the PLINIUS platform toward smarter prototypic-corium experimental R&D", Nucl. Eng. Design 386 (2022) 111511
3. W. Assmus, "Möglichkeiten und Grenzen der Skull-Schmelz-Technik", ACHEMA,1988, p. 8-13
4. W. Assmus, "Züchtung von Zirkondioxid-Einkristallen mit dem Skull-Schmelz-Verfahren", Habilitationsschrift zur Erlangung der venia legendi im Fach Physik, Frankfurt 1990
5. M. Fischer, S. Hellmann, M. Nie, "Experimentelle Untersuchungen zur Wechselwirkung von Corium-Schmelzen mit Schutz- und Opferschichten (CORESA)", Abschlußbericht des CORESA-Vorhabens, Vorhabens-Nr. 1501211, Framatome Advanced Nuclear Power GmbH, Erlangen, NGES4/2002/de/0187A, October 2002
6. S. Hellmann, M. Fischer, M. Nie, "Coriumschmelze-Beton Wechselwirkung (CORESA-Phase 3)", Abschlußbericht (Teil 2) des CORESA3-Vorhabens, Vorhabens-Nr. 1501258, Framatome Advanced Nuclear Power GmbH, Erlangen, NGTR/2004/de/0376A, December 2004
7. S. Hellmann, "Small-scale MCCI tests with prototypic oxidic corium melts", Report SAM-ECOSTAR-D33, EU ECOSTAR Project, September 2004
8. S. Hellmann, G. Langrock, "Versuche zur Untersuchung der Gesetzmäßigkeiten bei der Wechselwirkung von Kernschmelze (Oxid- und Metall-Mischschmelze) mit Beton während eines postulierten schweren Störfalls in einem KKW", Abschlussbericht des Mischschmelze-MCCI-Vorhabens, Vorhabens-Nr. 1501317, AREVA NP, PTCC-G/2011/de/0001A, January 2011
9. G. Langrock, S. Hellmann, R. Hofmann, M. Fischer, A. Fargette, "2D-Versuche zur Untersuchung der Gesetzmäßigkeiten bei der Wechselwirkung von Kernschmelze mit Beton während eines postulierten schweren Störfalls in einem KKW", Abschlussbericht des 2D-MCCI-Vorhabens, Vorhabens-Nr. 1501332, AREVA NP, PTCC-G/2012/de/0121A, March 2012
10. "SAMMANSÄTTNING AV BETONG I REAKTORINNESLUTNINGEN I SVENSKA KÄRNKRAFTVERK", Studsvik, Technical Report, Nr. 83/301
11. D. H. Thompson, J. K. Fink, ACE MCCI Test L6 – Test Data Report, Volume I – Thermal Hydraulics, ACE-TR-C26 (I), Argonne National Laboratory, August 1991
12. I. B. Wall, B. R. Sehgal, "Molten Corium Concrete Interactions - Advanced Containment Experiments (ACE) Project: Summary Report", EPRI TR-103483s, Electric Power Research Institute, December 1993
13. State-of-the-Art Report on Molten Corium Concrete Interaction and Ex-Vessel Molten Core Coolability, NEA/CSNI/R(2016)15, NEA No. 7392, OECD/NEA 2017
14. J.M. Bonnet, "Thermal Hydraulic Phenomena in Corium Pools for Ex-Vessel Situations: The BALI Experiment", Proceedings of the OECD Workshop on Ex-Vessel Debris Coolability, Karlsruhe, Germany, FZKA 6475, 15-18 November, 1999
15. J. Imoto et. al., "Cesium-Rich Micro-Particles Unveil the Explosive Events in the Fukushima Daiichi Nuclear Power Plant", Goldschmidt Abstracts 1253, 2016

framatome

Results of the SSM-SICOPS melt tests of the EU-SAFEST project

G. Langrock, T. Keim, M. Fischer, S. Kohn, R. Hofmann, R. Bezold, M. Neumeister
S. Bechta (KTH), P. Isaksson (SSM)

Stockholm, 2024-05-14

Agenda

1. Introduction
2. Experiments and main data
3. Post-Test Examinations
4. Interpretation, Conclusion
5. References

framatome

AL: N – ECCN: N © Framatome - All rights reserved

Introduction

SICOPS Melting Facility

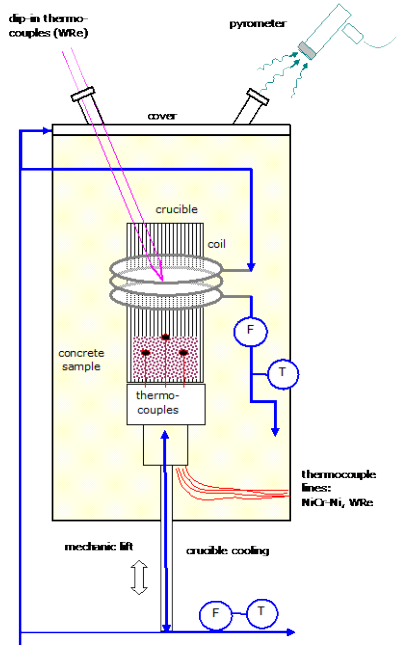

Schematic of the SICOPS facility

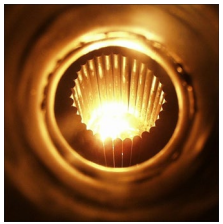

Crucible with melt

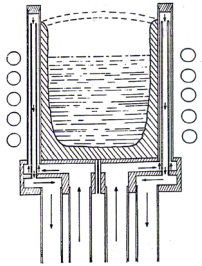

Cold crucible (schematically)

SICOPS: Simultaneous interaction of molten corium with protective and sacrificial material

Induction-melting facility for prototypic oxidic melts up to 3000°C

- **examples for application**
  - selection of sacrificial concrete and protective material for EPR reactor
  - interaction of oxide melts / concrete
  - tests with mixed metallic / oxidic melts
  - thermochemical material data
- **principle**
  - inductive high frequency heating (Skull Melting)
- **technical data**
  - frequency range: 1 - 4 MHz
  - temperature: up to 3000°C
  - maximum power: 100 kW
  - melt mass: 1 - 20 kg

AL: N – ECCN: N © Framatome - All rights reserved

Introduction

Test Objectives

SAFEST Partner: Swedish Radiation Safety Authority (SSM)

The proposed experiments in the SICOPS facility address questions related with the impact of

- BWR corium, and
- basaltic concrete (typically used in Nordic BWRs)

on the MCCI.

Such questions are:

- Can we expect anisotropy of concrete ablation, i.e. in radial and axial directions?
- Do we need specific improvement of models for BWR application?

Though the small number of tests in the series may be insufficient to answer these questions it is nevertheless expected to indicate the direction and magnitude of the impacts of both corium and concrete type.

AL: N – ECCN: N © Framatome - All rights reserved

Introduction

Test Objectives

During a real-case reactor accident: zirconium is present in the melt only during the early phase of the MCCI when the concrete content in the melt is still low and the UO_2 + ZrO_2 content correspondingly high.

Test ID	SSM-1a	SSM-2b	SSM-2c	SSM-3
Atmosphere	nitrogen (N_2)			
Concrete type	Swedish (basaltic)	iron-oxide rich concrete (FeSI-PZ 15-8)	siliceous concrete (SI-PZ 15-8)	Swedish (basaltic)
Water content	2.9 %	5.0 %	5.0 %	4.5 %
Melt	BWR specific, without steel, with reduced Zr amount			
Melt mass	2 kg	2.61 kg	2.66 kg	2.1 kg
Melt composition	74.3 % UO_2 16.9 % ZrO_2 6.4 % SiO_2 0.4 % Al_2O_3 1.9 % CaO + 3.8 % (76 g) Zr added	71.8 % UO_2 16.3 % ZrO_2 7.2 % SiO_2 0.6 % Al_2O_3 1.8 % CaO 2.2 % Fe_2O_3 + 32.2 g $BaAl_2O_4$ ($BaO{\cdot}Al_2O_3$) + 37.7 g $CsOH{\cdot}H_2O$ + 4.6 % (120 g) Zr added	71.8 % UO_2 16.3 % ZrO_2 7.2 % SiO_2 0.6 % Al_2O_3 1.8 % CaO 2.2 % Fe_2O_3 + 54.4 g $BaAl_2O_4$ + 46.2 g $CsOH{\cdot}H_2O$ + 35.0 g MoO_3 + 3.0 % (80 g) Zr added	75.4 % UO_2 17.1 % ZrO_2 5.2 % SiO_2 0.4 % Al_2O_3 1.9 % CaO + 38.8 g $BaAl_2O_4$ + 25.6 g Cs_2CO_3 + 31.3 g MoO_3 +35.1 g $SrCO_3$ +4.2 % (88 g) Zr added

AL: N – ECCN: N © Framatome - All rights reserved

Introduction

Instrumentation

For example: SSM-1a

TC instrumentation scheme "D(neu)"

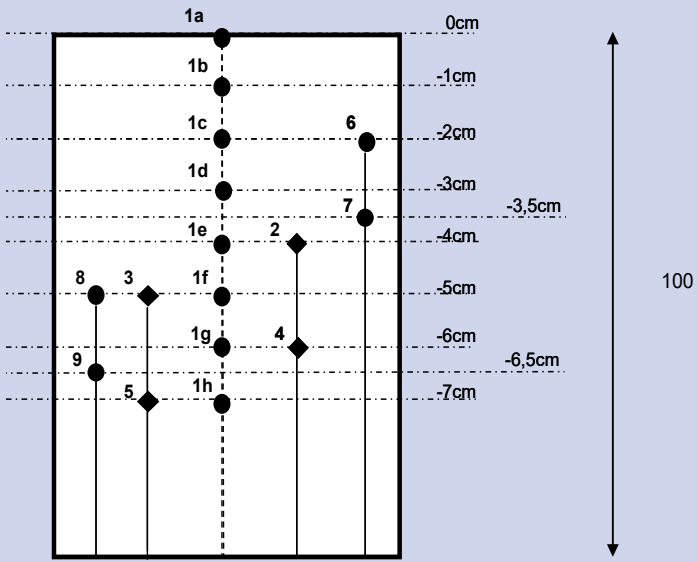

12 type K (NiCr-Ni) thermocouples:
1a – 1h at R = 0 mm;
6 – 9 at R = 20 mm
to detect erosion progression

4 type C (W5Re-W26Re) thermocouples:
2 – 5 at R = 10 mm
to measure melt temperatures and provide erosion velocities

Thermocouple 1a indicates during the test the arrival of the melt at the concrete

Usually some thermocouples are not functional; couldbe destroyed during concrete pouring, storage, installation or during the test

AL: N – ECCN: N © Framatome - All rights reserved

Introduction

Installation

For example: SSM-1a		
Installation – Top view at crucible and test vessel	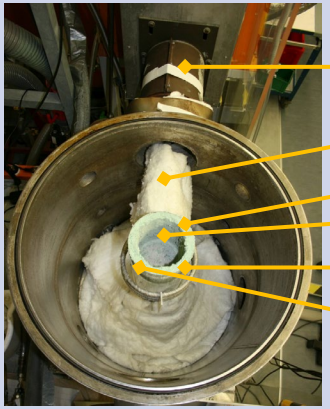	Connection between inductor coil and generator Mineral wool for protection against melt splashes ZrO_2 (ZIRCOA) protection layer at the top of the crucible palisades Top of concrete crucible Quartz tube around crucible for electrical isolation against coil and to avoid plasma arcs between coil and crucible Inductor coil with PTFE spacer
Installation – Top view at the crucible shortly before the test	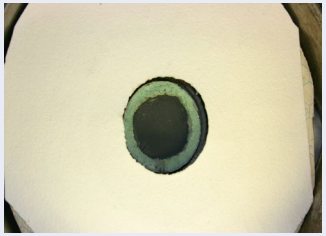	The inductor coil and the bottom of the vessel are protected by additional alumosilicate mineral wool against melt splashes. The melt powder is already placed in the crucible.

AL: N – ECCN: N © Framatome - All rights reserved

Experiments and Main Data

Electrical System and Associated Data

Measurement of voltage, current, and power of generator, comparison generator power and heat losses

For example: SSM-1a

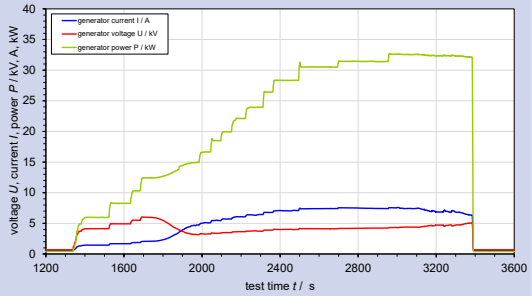

- during melt generation the generator power was increased steadily to 30 kW
- coupling with liquid pool effective at 1800 - 2000 s (crossing curves of U and I), remains very good throughout the entire MCCI phase

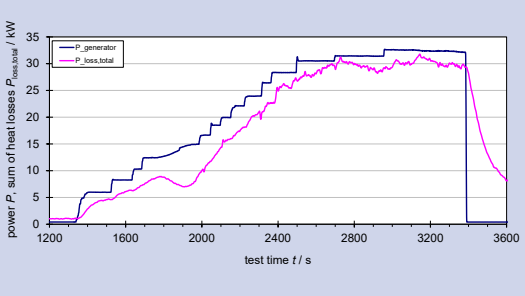

- Comparison of generator power with sum of heat losses

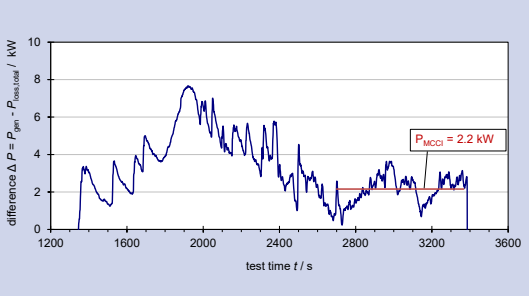

- Difference calculated from generator power minus heat losses

AL: N – ECCN: N © Framatome - All rights reserved

Experiments and main data

Course of the tests

Main parameters of the tests

Test ID	SSM-1a	SSM-2b	SSM-2c	SSM-3
$P_{generator,max}$	37 kW	40 kW	34 kW	36 kW
P_{MCCI}	2.2 kW	3.6 kW	3.3 kW	1.9 kW
Test duration	34 min (1340 s – 3370 s)	38 min (754 s – 3050 s)	28 min (4676 s – 6364 s)	36 min (22272 s – 24444 s)
Zr additions (time (in s) relative to start of data acquisition)	2600; 2640; 3040; 3045; (4 g each) 3085; 3125; 3160; 3220; 3260 (12 g each)	1960; 2155; 2275; 2450; 2620; 2635; 2655; 2670; 2680; 2730; 2750; 2760; 2770; 2775; 2810 (8 g each)	5517; 5567; 5657; 5722; 5777; 5792 (8 g each), 5812; 5852 (4 g each), 5865; 5892; 5922 (8 g each)	23252; 23294; 23313; 23323; 23343; 23356; 23363; 23372; 23384; 23392; 23397; 23405 (8 g each)

AL: N – ECCN: N © Framatome - All rights reserved

Experiments and main data

Erosion Velocities and Progression, SSM-1a

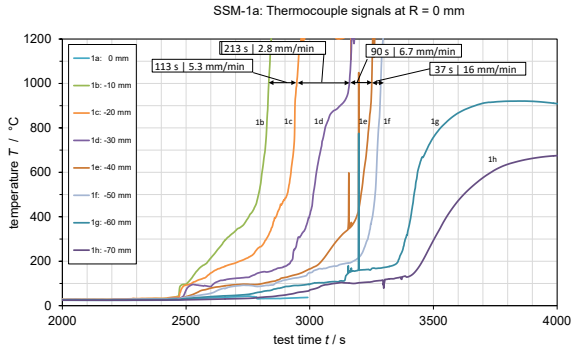

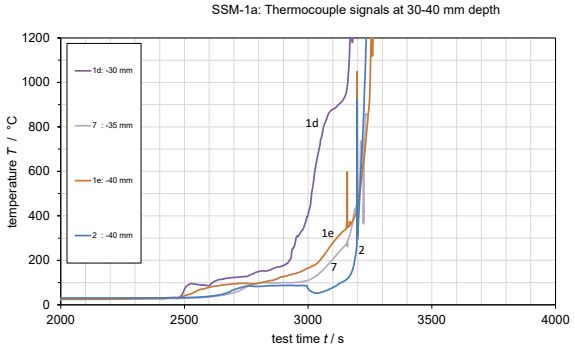

- data of the TC's 1a – 1h in the central position (R = 0 mm) show a fast penetration of the concrete by the melt
- TCs 1b – 1f indicate **average** melt front velocity of **5.3 mm/min**. Velocity increased during the phase of Zr addition, due to additional heat release in the melt ($\Delta_f H$ (Zr → ZrO_2) = -1086 kJ/mol), reaching **maximum** values of **16 mm/min**.
- Generally: During MCCI, the measured erosion velocities vary with time. Stationary conditions were not established mainly due to the repeated zirconium addition, which led to fluctuations in the concrete erosion rate.

- sorting signals of TC's by their depth in the concrete provides more information about melt progression in the crucible
- especially the destruction of TC's
  - 1e (-40 mm, R = 0 mm),
  - 2 (-40 mm, R = 10 mm),
  - 7 (-35 mm, R = 20 mm)

  at the same time indicates an **even progression of the melt front** during MCCI

AL: N – ECCN: N © Framatome - All rights reserved

Experiments and main data

Temperature Measurements

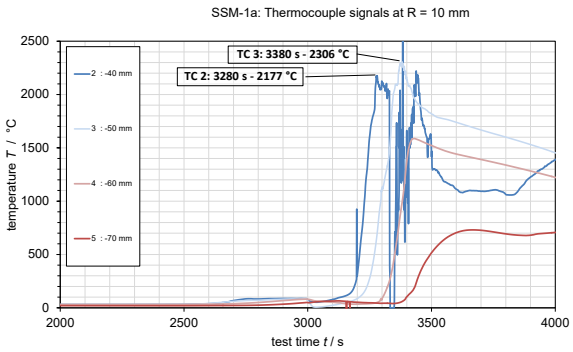

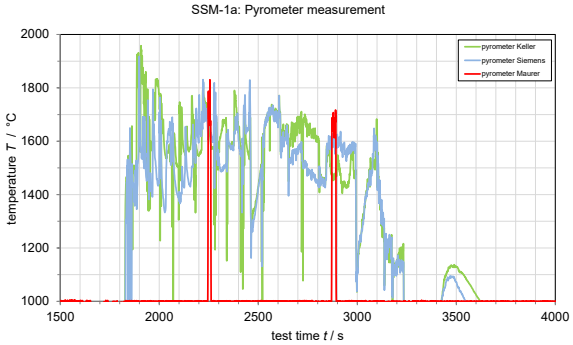

- **melt temperatures measured with thermocouples type C at R = 10 mm**
  - **SSM-1a**: peak temperatures during MCCI at 3280 s (few seconds after addition of the last Zr pellets) of 2177 °C (TC2, -40 mm) and 100 seconds later of 2306 °C (TC3, -50 mm)
    - high temperatures caused by burning of the added Zr in the melt (producing a superheated melt, temperature far above the known liquidus temperatures for such a mixture of UO_2/ZrO_2 and molten concrete)
  - **SSM-2b/2c/3:** see table

- **melt surface temperatures measured with pyrometers**
  - **SSM-1a**: readings much lower than expected
    - main reason: steadily increasing generation of smoke/aerosols which distorted the optical path between melt surface and pyrometer
    - increasing smoke production leads to decreasing pyrometer readings towards the end of the test
  - **SSM-2b/2c/3**: similar situation

AL: N – ECCN: N © Framatome - All rights reserved

Experiments and main data

Erosion velocities and melt temperatures

		SSM-1a		SSM-2b		SSM-2c		SSM-3	
TC	Position	$t_{rel,1000°C}$ / s	v_{eros} / mm/min	$t_{rel,1000°C}$ / s	v_{eros} / mm/min	$t_{rel,1000°C}$ / s	v_{eros} / mm/min	$t_{rel,1000°C}$ / s	v_{eros} / mm/min
R = 0 mm:									
1a	0 mm	-		2610		5724		23480	
1b	-10 mm	2834		2660	12.0	5930	5.7	23556	7.9
1c	-20 mm	2947	5.3	2718	10.3	5894	9.4	23612	10.7
1d	-30 mm	3160	2.8	2793	8.0	5959	9.2	23768	3.8
1e	-40 mm	3250	6.7	2861	8.8	6043	7.1	23922	3.9
1f	-50 mm	3287	16.2	2946	7.1	6164	5.0	- *	
1g	-60 mm	-		3004	10.3	6297	4.5	24103	6.6
1h	-70 mm	-		-		-		24235*	4.5
R = 10 mm:									
2	-40 mm	3228		(2891)		-		23814	
3	-50 mm	3294	9.1	(2975)	(7.1)	6208		23932	5.1
4	-60 mm	3382	6.1	-		6358	4.0	-	
5	-70 mm	-		-				-	
R = 20 mm:									
6	-20 mm	-		2704		5896		23601	
7	-35 mm	3235		2818	7.9	6013	7.7	23721	7.5
8	-50 mm	-		2954	6.6	6159	6.2	23938	4.1
9	-65 mm	-		(3063)	(8.3)	-		24127	4.8
Melt temperatures		TC 2 (-40 mm): 2177 °C (3280 s) TC 3 (-50 mm): 2306 °C (3380 s)		-		TC 3 (-50 mm): 2030 °C (6240 s)		TC 2 (-40 mm): 2115 °C (23907s) TC 3 (-50 mm): 2086 °C (24036 s) Dip-in TC: 2254 °C (23884 s), 2006 °C (23903 s), 1996 °C (23923 s)	

AL: N – ECCN: N © Framatome - All rights reserved

Experiments and main data

Gas measurement, SSM-3 – Proof of H_2 production

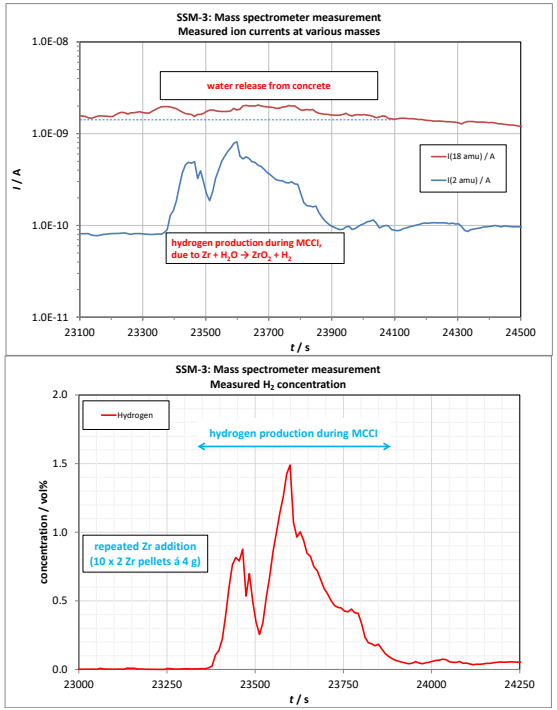

- **Gas-MS measurement**: 15 cm below vessel lid, not fully representative
- Measured ion currents of 18 amu (H_2O) and 2 amu (H_2) show an increase after heating of concrete (leads to release of free or of chemically bound water), water is released as steam.
- The steam can react with metallic zirconium acc. to $Zr + 2\ H_2O \rightarrow ZrO_2 + H_2$
- H_2 production stops ≈500 s after last Zr addition; metallic Zr is then consumed

- Peak is reached when erosion velocity is highest:
  - As long as Zr is present, melt is superheated and shows high erosion velocities
  - Rate of Zr oxidation reaction seems to correlate with erosion velocities
  - Zr is able to reduce released steam to hydrogen → H_2 is an indicator for consumption of Zr and when MCCI turns into a more “normal” regime (but still with superheated melt)

- Based on a pre-test calibration, the H_2 concentration is up to 1.5 vol%
- A rough estimation gives that (at least) approx. 20 % of the total Zr amount was consumed for the steam reduction to H_2

AL: N – ECCN: N © Framatome - All rights reserved

Experiments and main data

Strong aerosol production (video snapshots)

SSM-1a

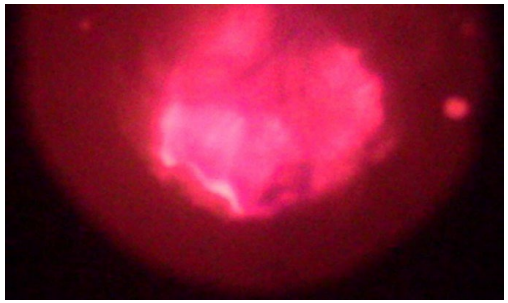

Strong aerosol production during MCCI



Dense aerosol cloud shortly before test termination

SSM-3

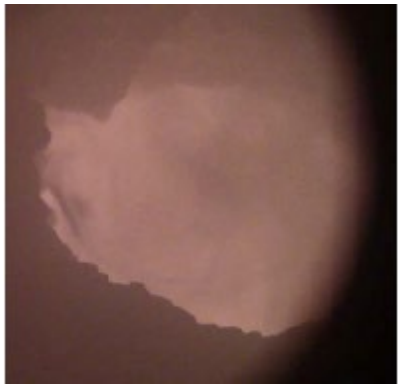

Aerosol production during Zr additions

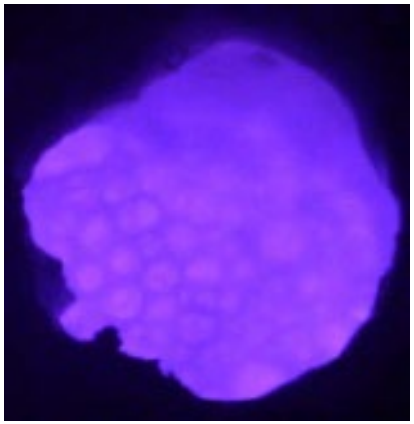

melt surface at 24170 s

AL: N – ECCN: N © Framatome - All rights reserved

Post-Test Examinations

Test Vessel and Crucible, SSM-1a





- crucible appeared regular and dry
- at inner walls of the test vessel wipeable, fine, dust-like, brown deposits
- some solidified melt splatter on the mineral wool mat around the crucible
- in addition some condensed, cobweb-like matter on the mineral wool mat (similar in the ACE L6 test [Thompson 1991])
- assumption:
  - phenomenon related to the use of metallic Zr and its reaction with SiO_2 from the concrete according to the reactions [Wall 1993]

$$SiO_2 + Zr \rightarrow ZrO_2 + Si \qquad \text{(Eqn. 1)}$$
$$2\,SiO_2 + Zr \rightarrow ZrO_2 + 2\,SiO(g) \qquad \text{(Eqn. 2)}$$

  - in principle, both reactions may occur, depending on the oxidation potential
  - reaction 2 is favored under the achieved experimental conditions (high melt temperature, inert atmosphere, metallic Zr)
  - high aerosol release, indicating other vapors/gases condensing to aerosols, may then react with SiO to form chain-like agglomerates
  - assumption to be proven in further tests and examinations

AL: N – ECCN: N © Framatome - All rights reserved

Post-Test Examinations

Test Vessel and Crucible, SSM-1a

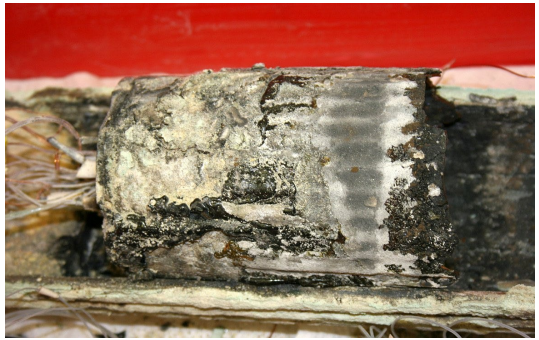

- nearly no melt found at the outside of the sample
- hence the gap between concrete und crucible was adequately closed by the applied zirconia material



- upper surface of the melt had a brown color without major irregularities
- cracks in the concrete along the sides result from cool down after the test

AL: N – ECCN: N © Framatome - All rights reserved

Post-Test Examinations

Sample After Cutting, SSM-1a

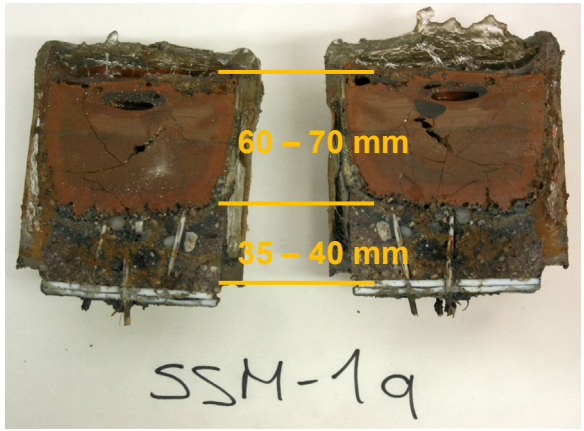

The measured height of the solidified melt is about 60 – 70 mm, while the remaining concrete is 35 – 40 mm thick.
This means the melt has eroded about 60 – 65 mm of the 100 mm initial concrete thickness, which is consistent with the TC measurements.

- melt phase appears homogeneous and without significant gas inclusions
- contact zone between melt and concrete shows some small gaps between the two phases and no mutual infiltration
- melt seemed to have "flown" around small aggregates in the concrete which were not (yet) dissolved
- concrete region near to the melt appears to have been dried out over several mm, due to the heat flux from the melt

AL: N – ECCN: N © Framatome - All rights reserved

Post-Test Examinations

Test Vessel and Crucible, SSM-2b



- white mineral wool mat is loaded with
  - fine melt powder
  - aerosols
  - solidified melt splashes
- at the top of the crucible, kind of volcanic crater with solidified lava has formed (photo bottom right):
  - this is due to the high void during MCCI
  - porous structures indicate that it must have formed during MCCI
- damaged mineral wool at the boundary to the quartz tube indicates the position where lava dropped down to the inductor coil and caused a plasma arc (photo bottom left)

AL: N – ECCN: N © Framatome - All rights reserved

Post-Test Examinations

Test Vessel and Crucible, SSM-2b



- photo of the melt sample (left) taken after removal of the crater:
  - porous sidewall crust typical for those formed during MCCI
  - plane melt surface

- even melt/concrete interface (photo below)



AL: N – ECCN: N © Framatome - All rights reserved

Post-Test Examinations

Sampler, SSM-3 – Hint for a “mushy zone”?



- In SSM-3, dip-in thermocouples and samplers were used
- The photo shows a sampler with attached aggregates – taken from the transition zone between concrete and melt
- During sampling, the tactile impression was that between the low-viscosity melt and the hard concrete a soft layer existed
- This may be a hint for the postulated “mushy zone” [SOAR 2017] between concrete and oxidic melt where concrete is being molten, infiltrated by the oxide melt and/or where some siliceous material (aggregate and cement) remained undissolved for some time

AL: N – ECCN: N © Framatome - All rights reserved

Interpretation, Conclusion

All tests with BWR-type corium and metallic zirconium showed very fast melt progression into concrete, independent of concrete type; not seen in previous studies without Zr

Homogeneously mixed superheated melt pool during MCCI, vivid mixing by rising gases

→ no local crusts between melt and concrete or crusts at the melt pool surface found
→ presence of Zr in the melt can have a damping effect for non-isotropic MCCI

Intense aerosol production in all tests, in one test (SSM-1a) condensed, cobweb-like material found, by comparison with ACE L6 concluded it was formed from SiO agglomerates

Does strong aerosol production provide an additional release path for FP's ***OR***
does high concentration and local deposition of near MCCI location retain FP's?

Zr reduces released H_2O from concrete to H_2; estimation that at least 20 % of the metallic Zr was consumed for this reaction path

AL: N – ECCN: N © Framatome - All rights reserved

Interpretation, Conclusion

Role of additional Zr in MCCI is complex:

- **Superheating of melt**
- **Strong aerosol production**
- **Reductant of H_2O from concrete, producing H_2**
- **Reducing oxidic concrete components in melt pool**
- **Participating in chemical processes right at the melt/concrete interface**

Multiple thermal and chemical effects caused by oxidation of Zr dominate over effects caused by specific concrete composition

AL: N – ECCN: N © Framatome - All rights reserved

References

[Thompson 1991] D. H. Thompson, J. K. Fink
ACE MCCI Test L6 – Test Data Report, Volume I – Thermal Hydraulics
ACE-TR-C26 (I), Argonne National Laboratory, August 1991

[Wall 1993] I. B. Wall, B. R. Sehgal
Molten Corium Concrete Interactions
Advanced Containment Experiments (ACE) Project: Summary Report
EPRI TR-103483s, Electric Power Research Institute, December 1993

[SOAR 2017] State-of-the-Art Report on Molten Corium Concrete Interaction and Ex-Vessel Molten Core Coolability, NEA/CSNI/R(2016)15, NEA No. 7392, OECD/NEA 2017

AL: N – ECCN: N © Framatome - All rights reserved

Acknowledgments

The authors gratefully acknowledge the funding by the EURATOM 7th Framework Program under Grant Agreement N° 604771 to support the work within the SAFEST project.

AL: N – ECCN: N © Framatome - All rights reserved

Additional slides

AL: N – ECCN: N © Framatome - All rights reserved

Experiments and Main Data

Erosion Velocities and Progression, SSM-2b

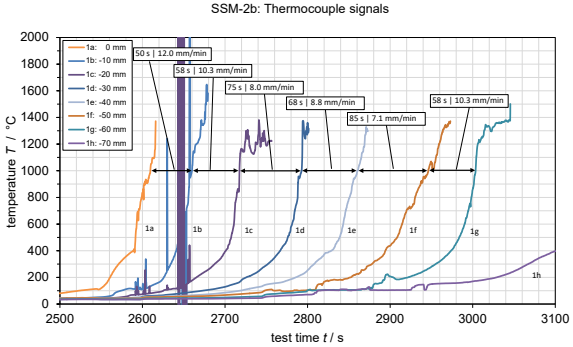

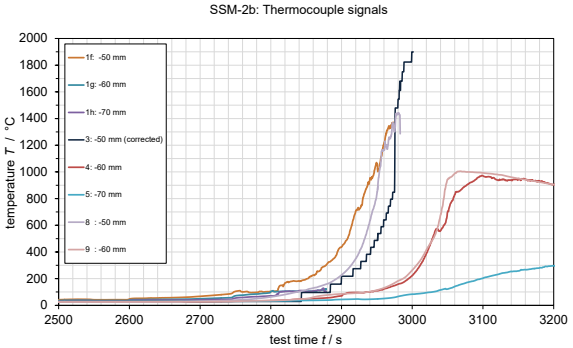

- data of the TC's 1a – 1h in the central position (R = 0 mm) show a fast penetration of the concrete by the melt
- TCs 1a – 1f indicate **average** melt front velocity of **8.9 mm/min** (**maximum** velocity TCs 1a – 1b **12 mm/min**).
- As in the SSM-1a test, erosion velocities differ as no stationary conditions had been established during MCCI. This results in high, but by time decreasing erosion velocities. It can be concluded that the Zr addition accelerates concrete erosion.

- sorting signals of TC's by their depth in the concrete provides more information about melt progression in the crucible
- **even melt front progression** through the concrete during MCCI, independent on the radial position of the thermocouples

AL: N – ECCN: N © Framatome - All rights reserved

Experiments and Main Data

Erosion Velocities and Progression, SSM-2c

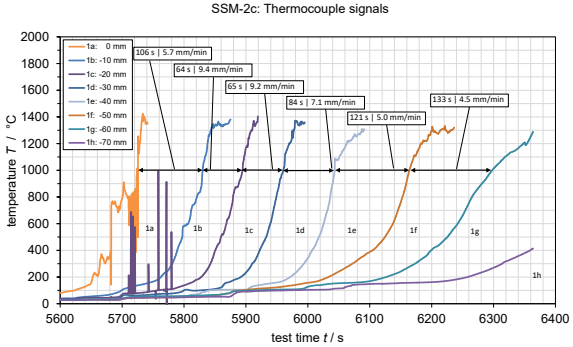

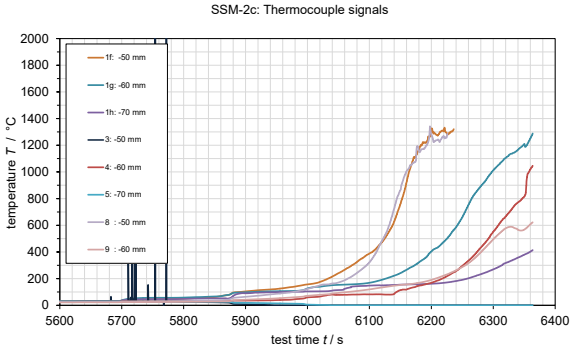

- data of the TC's 1a – 1h in the central position (R = 0 mm) show a fast penetration of the concrete by the melt
- TCs 1a – 1f indicate **average** melt front velocity of **6.8 mm/min** (**maximum** velocity TCs 1b – 1c **9.4 mm/min**).
- As in the SSM-1a test, erosion velocities differ as no stationary conditions had established during MCCI. This results in high, but by time decreasing erosion velocities. It can be concluded that the Zr addition accelerates concrete erosion.

- sorting signals of TC's by their depth in the concrete provides more information about melt progression in the crucible
- **even melt front progression** through the concrete during MCCI, independent on the radial position of the thermocouples

AL: N – ECCN: N © Framatome - All rights reserved

Experiments and Main Data

Erosion Velocities and Progression, SSM-3

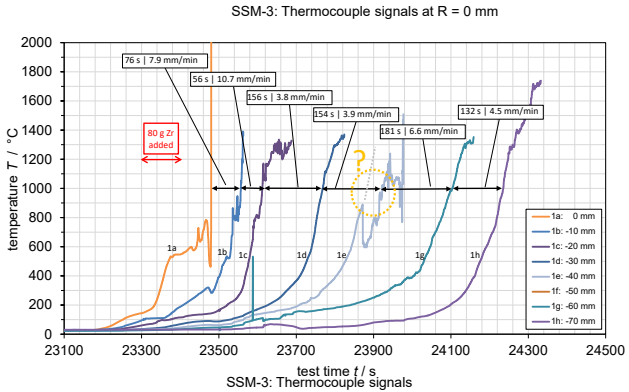

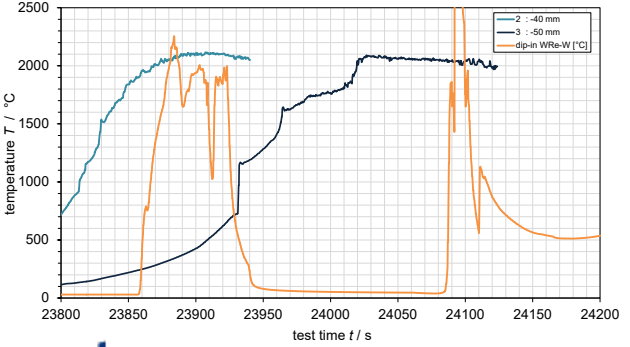

- data of the TC's 1a – 1h in the central position (R = 0 mm) show a fast penetration of the concrete by the melt
- TCs 1a – 1h indicate **average** melt front velocity of **5.5 mm/min** (**maximum** velocity TCs 1b – 1c **10.7 mm/min**).
- As in the SSM-1a test, erosion velocities differ as no stationary conditions had established during MCCI. This results in high, but by time decreasing erosion velocities. It can be concluded that the Zr addition accelerates concrete erosion.

- High melt temperatures measured during MCCI by type C thermocouples 2/3 and by a **dip-in thermocouple**

AL: N – ECCN: N © Framatome - All rights reserved

Post-Test Examinations

Test Vessel and Crucible, SSM-2c



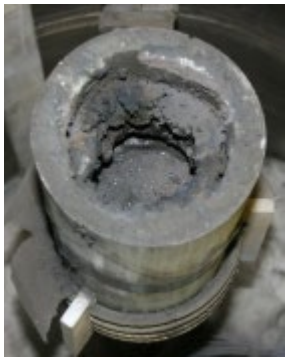



- again aerosol deposited, some melt splashes
- less losses at the crucible wall
- some frozen gas “bubbles” at the surfaces (occurs during cool down after test), indicates high void
- melt/concrete interface typical below

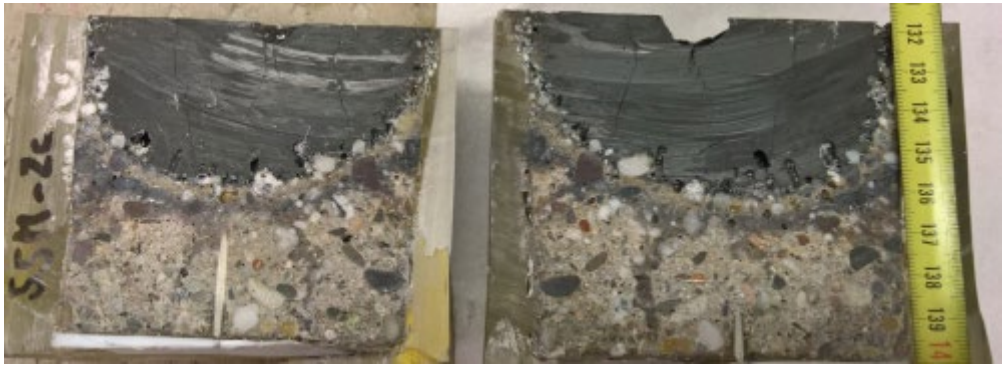

AL: N – ECCN: N © Framatome - All rights reserved

Comparison with previous test 9c

Initial melt composition: 1.8 kg, 70 % UO_2, 22 % ZrO_2, 5 % SiO_2, 1.8 % CaO, 0.4 % Al_2O_3. T_{liq} = 2380 °C

Concrete: FeSi-PZ (approx. 44 % SiO_2, 37 % Fe_2O_3), P_{gen} = 29 kW

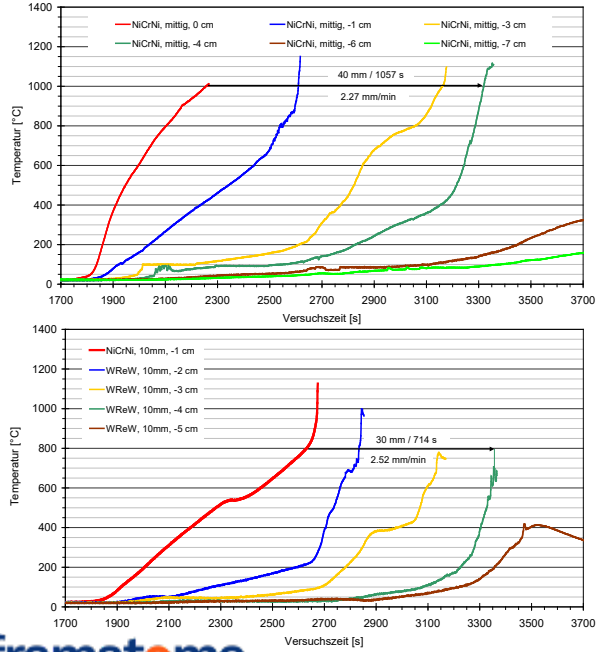

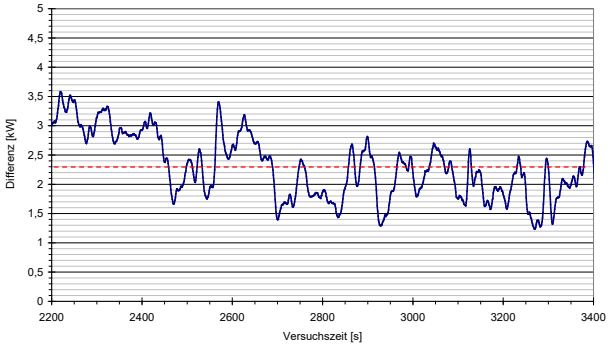



Above: P_{MCCI} = 2.3 kW
Left: v_{eros} = 2.25 mm/min
Right: pattern of the oxide melt-concrete phase boundary very similar to that of purely silicate concrete. Partially dissolved concrete grains enter the melt and only melt completely there.

AL: N – ECCN: N © Framatome - All rights reserved

Editor and Copyright 2018: Framatome GmbH – Paul-Gossen-Straße 100 – 91052 Erlangen, Germany. It is forbidden to reproduce the present publication entirely or partially without prior consent in whatever form. Legal action may be taken against any infringer and/or any person breaching the aforementioned conditions.

Subject to change and error without notice. Illustrations may differ from the original. The contained statements and information are for advertising purposes only and do not constitute an offer of contract. They shall neither be construed as a guarantee of quality or durability, nor as warranties of merchantability or fitness for a particular purpose. These statements, even if they are future-oriented, are based on information that was available to us at the date of publication. Type, quantity and characteristics of goods and services are subject to formal individual formal contracts.

AL: N – ECCN: N © Framatome - All rights reserved

framatome

Thank you!

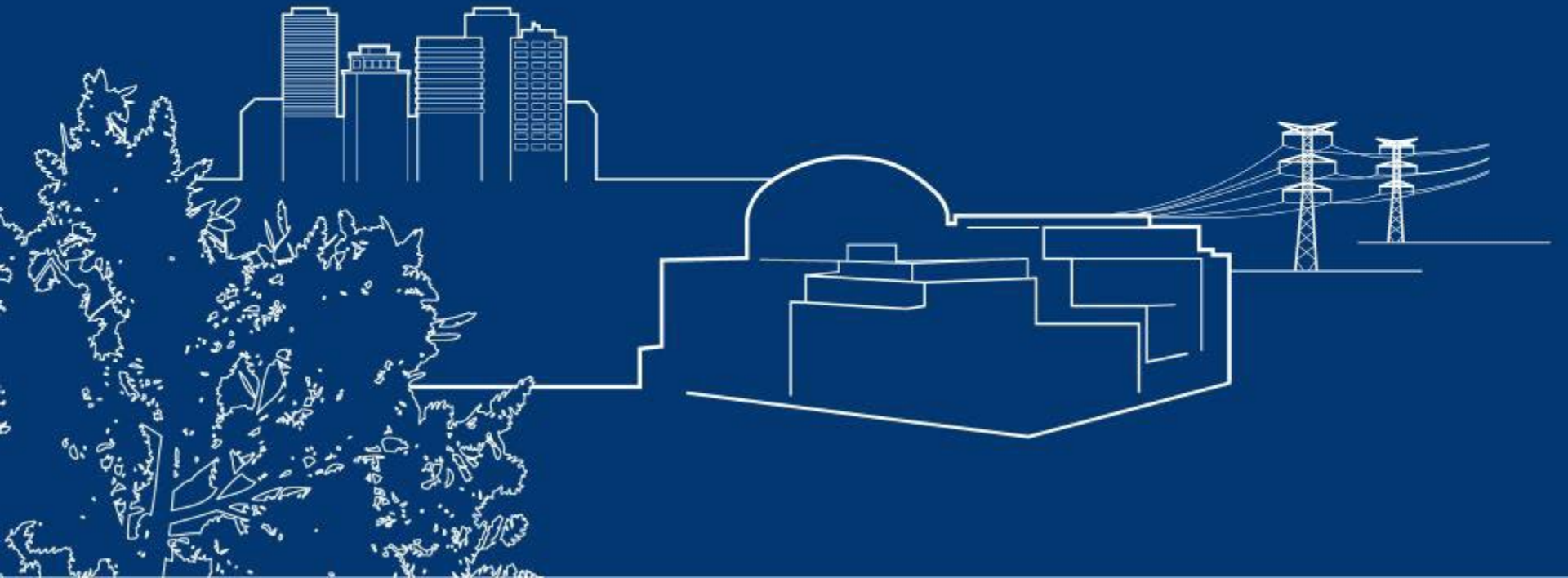

Ex-Vessel stabilization of corium: An analysis of corium-concrete interaction with top flooding for siliceous concrete.

Florian Fichot
Institute of Radiation protection and Nuclear Safety
IRSN/PSN-RES/SAM/LEPC – Cadarache Research Center (France)
florian.fichot@irsn.fr

ABSTRACT

In case of severe accident without possibility of in-vessel retention, the corium must be stabilized outside the vessel, either in a designed core-catcher or directly on the concrete basemat of the reactor building, after spreading. In this last case, the stabilization strategy must be efficient enough to avoid the progression of corium through the concrete basemat and to the environment.

In order to ensure corium stabilization, the physical processes leading to quench some part of the liquid corium must be fast enough, compared to the erosion of concrete. One of the simplest strategies consists in spreading the corium over a rather large area (i.e. the reactor pit plus one or two adjacent rooms) and flood it with water on top. Two processes have been identified experimentally for a potential quenching of corium: melt eruption and water ingression. Melt eruption is a process that is driven by the flow of gases (CO_2 and H_2O) generated by concrete erosion: the gas flow is likely to entrain droplets of corium into the overlying water, quenching the droplets quickly. Water ingression is a process where cracks are generated by the contraction of the top crust due to cooling: this process enables the flow of water into the cracks and the propagation of the cracking front deep into the corium crust. When the basemat is made of siliceous concrete, stabilization depends mostly on water ingression because there is little gas content in such concrete and melt eruption may only have a limited effect.

This paper presents the analysis of a situation where corium is spread over a rather large area (around 80 m^2) in order to reduce the corium thickness lower than 50cm after spreading. Of course, this thickness depends on the reactor design (total volume of corium divided by total spreading area). After spreading, corium is flooded with water on top. First, a sensitivity analysis is made to determine the parameters which have the largest impact on the time of stabilization. The maximum heat flux extracted by water ingression (CHF) appears as one of the most important parameters. Then, a theoretical determination of the CHF is made, as a function of the concrete content in the corium, based on the existing Lister-Epstein model and on data obtained at Argonne National Laboratory. In addition, a simple modelling of transient heat conduction through the concrete basemat is proposed, to determine a criterion of stop of erosion that can be used in a lumped-parameter code. As a conclusion, it is shown that the quenching of corium may be divided in three main stages. The first stage is characterized by a fast erosion of concrete and a significant ejection and quenching of debris. This stage lasts from half a day to a few days, depending on the type of concrete and on the model parameters. The second stage is characterized by a slower erosion of concrete and the start of water ingression. This stage may last from half a day up to a few weeks depending on the type of concrete and on the model parameters. The last stage is characterized by a very slow erosion up to the complete quenching of corium. There is a non-trivial dependence of water ingression efficiency on the potential occurrence of melt eruption at the very beginning of corium concrete interaction. Melt eruption, even if limited, is likely to significantly enhance the triggering of water ingression and favor a fast stabilization of corium.

KEYWORDS
Corium, concrete, water ingression, ex-vessel stabilization

1. INTRODUCTION

In case of severe accident without possibility of in-vessel retention, the corium must be stabilized outside the vessel, either in a designed core-catcher or directly on the concrete basemat of the reactor building, after spreading. In this last case, the stabilization strategy must be efficient enough to avoid the progression of corium through the concrete basemat and to the environment.

One of the strategies consists in spreading the corium over a rather large area including the reactor pit plus one or two adjacent rooms and flood it with water on top, as illustrated in Fig. 1.

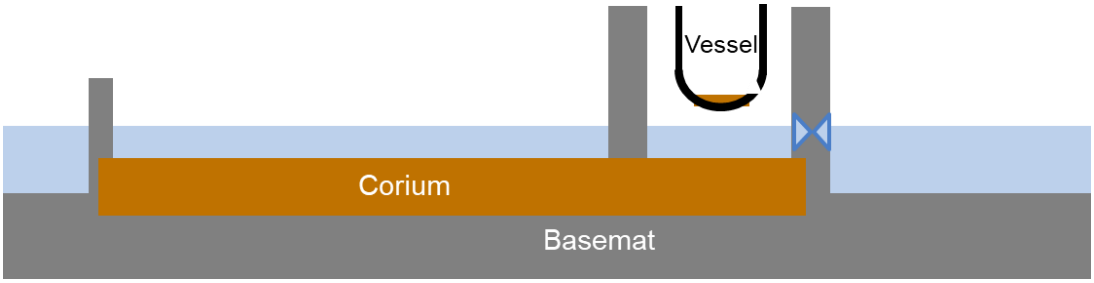

Figure 1: Schematic view of corium after spreading and flooding with water

Two processes have been identified experimentally for a potential quenching of corium: melt eruption [1] and water ingression [2,3]. Melt eruption is a process that is driven by the flow of gases (CO_2 and H_2O) generated by concrete erosion: the strong gas flow is likely to entrain droplets of corium into the overlying water, quenching the droplets quickly. Water ingression is a process where cracks are generated by the contraction of the top crust due to cooling: this process enables the flow of water into the cracks and the propagation of the cracking front may progress deeper into the corium crust. When the basemat is made of siliceous concrete, stabilization depends mostly on water ingression because there is little gas content in such concrete and melt eruption may only have a limited effect.
The issue of stabilization is mostly the competition between the ablation of concrete and the quenching of corium (either by formation of fuel-bearing debris or cracks in the crust). In this paper, the quenching rate is estimated for each of the two processes and compared to the ablation rate. After a presentation of the modelling, a sensitivity analysis is made to determine the parameters which have the largest impact on the time of stabilization. The maximum heat flux extracted by water ingression (CHF) appears as one of the most important parameters, therefore, a theoretical determination of the CHF is proposed, as an extension of the existing Lister-Epstein correlation [4,5]. Then, the role of melt eruption is explained and discussed. A criterion of end of ablation is proposed too. Finally, a simple application is presented to illustrate the interactions between the two processes.

2. A BASIC MODEL TO ANALYZE THE PHASES OF CORIUM COOLING

In this paper, a rather simple approach is chosen in order to make a clear distinction between the two cooling mechanisms and show their respective impact. Considering that the corium is spread over a total surface around 80m^2, the corium layer has an initial thickness close to 50cm. Therefore, it is reasonable to

consider that the problem is one-dimensional. The main variables are the masses (or heights) and compositions of each layer. The layers are represented in Fig. 2:

1. the concrete layer (ablated by the heat-generating corium located just above)
2. the corium layer (cooled from the top)
3. the compact crust layer (above the corium, resulting from solidification)
4. the fractured crust layer (resulting from crack formation and water ingression into the crust)
5. the debris layer (resulting for melt eruption)

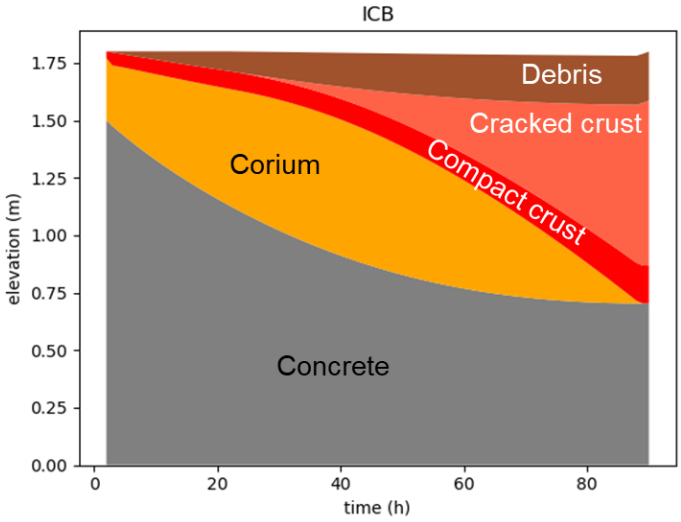

Figure 2: The five layers considered in the problem (represented here as a function of time)

An important simplification is made in the thermal analysis: it is assumed that the partitioning of residual power between the bottom and the top of the corium layer is given by a constant parameter. In general, this is not absolutely true (it evolves with time and ranges typically between 0.5 and 0.9) but this assumption makes the analysis simpler and is sufficient to get relevant orders of magnitude. With this assumption, the corium temperature plays no direct role, and it is not necessary to calculate it (of course, in the complete formulation, the corium temperature and the power partitioning coefficient are implicitly linked through the heat transfer coefficients which depend on temperature). The concrete temperature is fixed, and the debris and fractured crust layers are at the saturation temperature of water (quenched corium). The remaining unknowns are essentially the masses of fuel in the layers and the masses of concrete in the corium and crust layers.

For the fuel in the corium layer, it is depleted by debris formation and (compact and cracked) crust formation:

$$\frac{dm_f}{dt} = -\frac{dm_d}{dt} - \frac{dm_w}{dt} - \frac{dm_s}{dt} \tag{1}$$

Where the debris formation is proportional to the ablation rate and to the content of gas in concrete:

$$\frac{dm_d}{dt} = X_f k_e X_g \dot{Q}_c \tag{2}$$

And the fractured crust formation is given by the expression proposed by Epstein [4]:

$$\frac{dm_w}{dt} = \rho_f X_f \frac{\phi_{CHF} - \phi_{up}}{\Delta h + Cp(T_{sol} - T_{sat})} \tag{3}$$

At any time, the compact crust mass of fuel is:

$$m_s = \frac{X_f \rho S (T_{sol} - T_{sat})}{\phi_{CHF} - \phi_{up}} \tag{4}$$

The ablation rate is proportional to the heat flux to the bottom:

$$\dot{Q}_c = \frac{dm_c}{dt} = \frac{\phi_{dn}}{\rho_c \Delta h_{abl}} \quad (5)$$

And the partitioning of the residual power is simply written as:

$$m_f \dot{E}_f = (\phi_{dn} + \phi_{up}) S \quad (6)$$

Where:

$$\phi_{up} S = k_{up} m_f \dot{E}_f \quad (7)$$

Similar equations apply for the masses of concrete and steel in the layers. And rebars may be considered in the model by providing the mass fraction of steel in the concrete composition. However, in the experiments on melt eruption or water ingression performed up to now the effect of the presence of molten steel was not analyzed nor quantified: melt eruption depends mainly on the amount of gases in the concrete and water ingression depends mainly on the mass fraction of concrete in the corium. Therefore, we do not consider the presence of steel in this paper since it has no impact on the conclusions. But it would be straightforward to take it into account if necessary.

3. SENSITIVITY ANALYSIS

In order to determine the relative importance of the different parameters governing the problem, a sensitivity analysis is made. The range of variation of each parameter is provided in Table 1.

Table 1. Uncertain parameters and variability

Parameter	Range of variation	
$m_c \dot{E}_f$	15 – 25 MW	Residual power
S	80 – 120 m^2	Spreading surface
ϕ_{CHF}	50 – 150 kW/m^2	Critical heat flux
k_e	0.04 – 0.08	Melt eruption coefficient
k_{up}	0.5 – 0.9	Power fraction to the top
k_b	0.02 – 0.15	Fraction of corium height solidified initially (after first contact with water)

Random samples of the parameters are generated, and, for each set of parameters, calculations are run up to the stabilization of corium: the distribution of the erosion depth of concrete at the time of stabilization is represented in Fig. 3. The concrete conductivity could have been included in the variable parameters (in particular because of the presence of rebars which may increase the equivalent conductivity) but it was not considered at this stage because it plays a role only in the end of the ablation process. It will be taken into account in the next steps of this work.

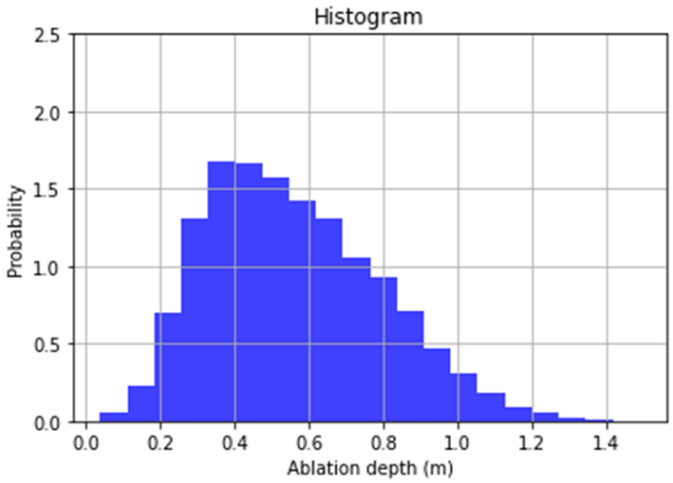

Figure 3: Distribution of the final erosion depth.

With the values selected, the average erosion depth is around 0.5m but the distribution has a noticeable tail that goes up to values of the erosion depth around 1.2-1.4m. It is also noticeable that, when all parameters are chosen for the best efficiency of quenching (lowest power, high eruption rate, high ϕ_{CHF}, largest spreading surface), there is almost no erosion of concrete (around 10cm). This shows the high sensitivity to the values of the governing parameters and the strong non-linearity of the process: the erosion depth may vary by a factor close to 15 whereas each individual parameter was varied by a factor between 1.5 and 3 only.

Looking at the Spearman coefficients, we see that the most influential parameters are the water ingression heat flux and the power partitioning coefficient. This is partly due to the rather large range of variation chosen: a factor 3 for ϕ_{CHF} and almost a factor 2 for the partitioning coefficient k_{up}.

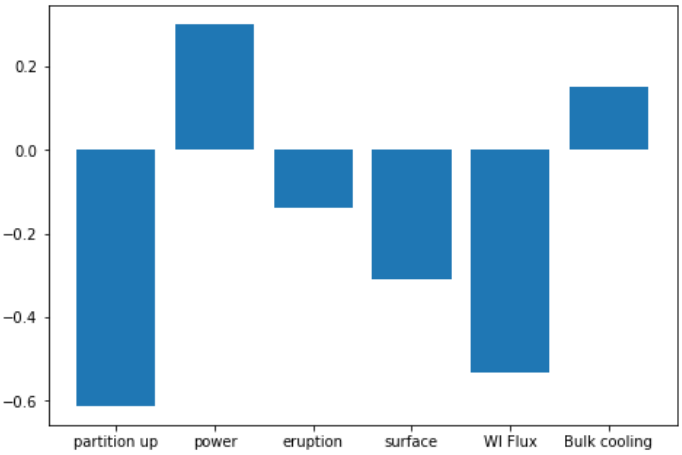

Figure 4: Spearman coefficients for each parameter.

4. A CORRELATION FOR THE WATER INGRESSION CHF

The process of crack formation and water ingression has been investigated mostly in geology. A model was proposed by Lister [5] for the quenching of hot lava. It was adapted to corium with residual power by Epstein [4]. Basically, the model consists in determining the width of the cracks and the distance between cracks, resulting from the thermal contraction due to water penetrating into the cracks: from the geometry

of the cracks, a permeability is deduced, from which the maximum heat flux (by evaporation inside the cracks) is determined.

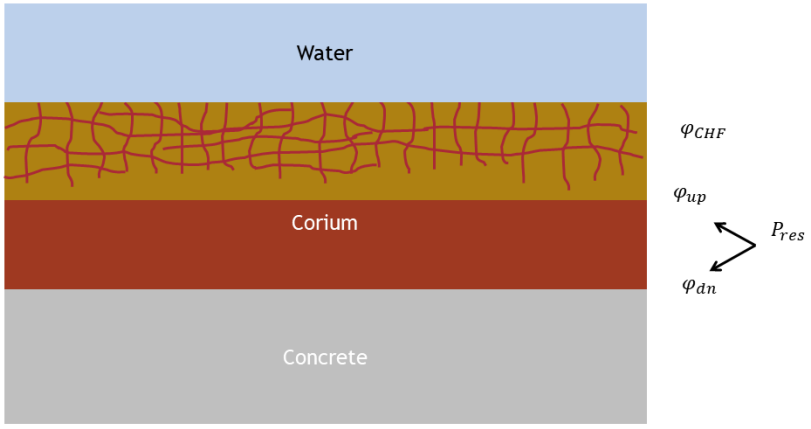

Figure 5: Schematic view of water ingression (partially cracked crust with water penetration)

In the Lister-Epstein correlation, three parameters have the most important impact: the solidification temperature, the expansion coefficient, and the heat conductivity. The other parameters may be considered as almost constant or having a small influence.

$$\phi_{CHF} = C_{CHF}\left(\Delta H_{vap}\left(\rho_l - \rho_g\right)g/\nu_g\right)^{5/13}\left(\alpha_{th}(T_{cr} - T_{sat})\right)^{15/13}\left(\frac{\lambda^2}{Cp}\frac{[\Delta h + Cp(T_{sol} - T_{sat})]^2}{\Delta h + Cp(T_{sol} - T_{cr})}\right)^{4/13} \quad (8)$$

T_{cr} is called the cracking temperature: it is a little less than 100 degrees below the solidification temperature T_{sol}, as it was estimated in [2] and measured in [6]. The determination of T_{sol} is one of the key points. In this work, we used the thermochemical database NUCLEA-ToolBox (developed by IRSN) [7] to estimate the solidification temperature of various mixtures of silicious concrete with corium. The composition of those mixtures corresponds to SSWICS tests [2] and to mixtures with more than 20 wt% of concrete.

Due to the limited size of this paper, we cannot give details about the results of the thermochemical calculations. The conclusion is that a linear correlation was found between the temperature for which the solid fraction is about 90% (almost complete solidification) and the molar ratio X between the major atoms from concrete (Si and Ca) and the major atoms from the fuel (U and Zr). This correlation is:

$$T_{sol} = T_{eut} + Max[0; X_{eut} - X](1700 - T_{eut}) \quad (9)$$

$$X = \frac{n_{Ca} + n_{Si}}{n_U + n_{Zr}} \quad (10)$$

Where X_{eut} is near the value 1.5 which is equivalent to a mass fraction of 0.3 and $T_{eut} = 1200C$.

As a result, the solidification temperature decreases linearly down to the minimum value of 1200 °C, then it is constant. This means that after this threshold value, ϕ_{CHF} decreases much more slowly.

The conductivity and the expansion coefficient both decrease with the increase of the concrete fraction because silica has a lower conductivity than fuel materials (1 W/K/m^2 compared to 2.5 W/K/m^2) and a much lower expansion coefficient (1.10^{-6} K^{-1} compared to 8.10^{-6} K^{-1}). If we calculate the conductivity of the mixture with a weighted average, and do the same for the expansion coefficient, we get the variation of ϕ_{CHF} as presented in Fig. 6. It shows that there is a strong decrease down to a threshold mass fraction (here the value 0.21 gives the best fit to experimental data, instead of 0.3) and then a slower decrease. Here the best fit is obtained with the constant $C_{CHF} = 2$. This curve differs mostly from the curve

proposed in [2] after the mass fraction 0.2. In [2], a constant extrapolation was proposed, which is not consistent with the lower conductivity and lower expansion coefficient of silica.

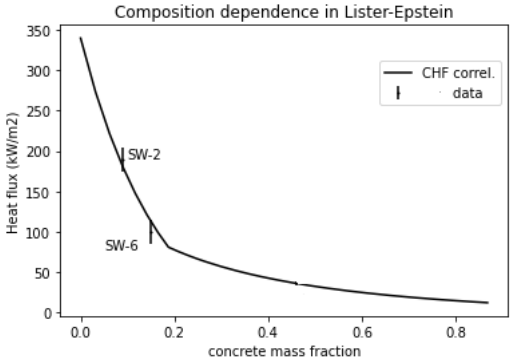

Figure 6: Comparison of the CHF correlation with experimental data (SSWICS) and proposed extension

From a practical point of view, the curve in Fig. 6 shows that, except for cases where the stabilization is reached very quickly (because of a low residual power and/or a large spreading surface) and the concrete content remains low, the CHF will be more likely around 50 kW/m^2 or even lower when stabilization is reached after several days. Lister [5] mentions that the heat flux could be estimated by Björnsson [8] during the cooling of a lava flow: it was roughly estimated at 40 kW/m^2. The model presented here would give a value between 20 and 30 kW/m^2 for a concrete mass fraction of 1, which may be considered as quite satisfactory considering all the simplifying assumptions made to derive the model. Unfortunately, there are no data for pure corium (concrete mass fraction of 0.) because such experiments are quite difficult to perform due to the very high temperature required to completely melt a mixture of UO_2 and ZrO_2. Therefore, the left part of the curve presented in Fig. 6 cannot be assessed properly. But it is not so important from a practical point of view as, in the mitigation strategy considered here, water in poured on the corium after some time of concrete erosion and the mass fraction of concrete is larger than 10% when top cooling by water starts.

5. EVOLUTION DURING THE ERUPTION-ABLATION PHASE

At first, erosion is intense, generating a strong flow rate of gas from the decomposition of concrete. The formation of quenched fuel-bearing debris leads to a decrease of the power in the corium layer. If we look at the system of equations involving only the melt ejection process, we have:

$$\frac{dm_f}{dt} = -k_e X_g \frac{m_f}{m_f + m_c} \frac{dm_c}{dt} \tag{11}$$

$$\frac{dm_c}{dt} = \left(1 - k_{up}\right) m_f \dot{E_f} / S \tag{12}$$

This set of equations may be solved analytically when $m_f$is larger than m_c, which corresponds to the beginning of concrete erosion (approximately the first few hours or even up to the first day). The solution is:

$$m_f = m_f(t=0)\, exp[A\tau(exp(-t/\tau) - 1)] \tag{13}$$

Where $A = \frac{k_e X_g (1 - \mathrm{k_{up}}) \dot{\mathrm{E}}_0}{\Delta \mathrm{h_{abl}}}$. From this equation, we can see that the mass of corium cannot decrease down to zero, but it would reach an asymptotic value, after a time equal to a few τ. This means that melt eruption alone is not sufficient to quench all the corium: melt eruption has an efficiency proportional to the constant A but it loses its efficiency with time, proportionally to $exp(-A\tau)$. It is also interesting to

notice that the ratio of the melt ejection rate to the ablation rate is proportional to the mass of fuel: hence, it decreases with time. This means that melt ejection decrease is faster than erosion decrease: the corium thickness is always growing if melt ejection is the only process considered and complete stabilization cannot be reached. This is illustrated in Fig. 7 where the corium layer (yellow) grows faster than the debris layer (brown) and where only a little part of corium is quenched after 1 day, in spite of choosing the value $k_e = 0.08$, which is the maximum recommended in [1].

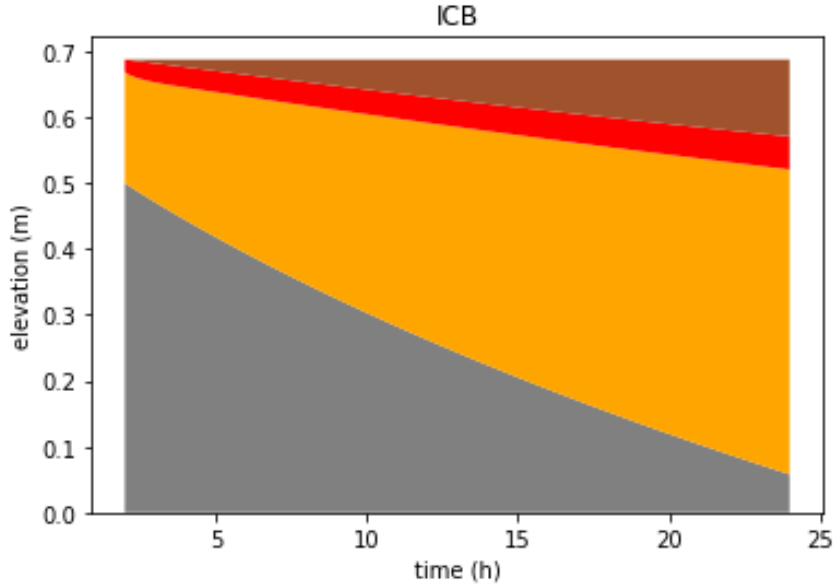

Figure 7: Example of evolution during the first day without water ingression.

To conclude, the melt ejection process should be considered as a precursor to the beginning of water injection which is the only process able to totally quench the corium. This role of precursor is very important in determining the total time for stabilization: in the first hours, melt ejection reduces the mass of fuel in the corium and therefore significantly reduces the heat flux to the top, which is a necessary condition for the onset of water ingression into the crust.

6. EVOLUTION DURING THE WATER INGRESSION PHASE

When the heat flux ϕ_{up} from the corium layer to the top crust reaches the value ϕ_{CHF}, the crust thickness becomes thick enough for the generation of cracks at the top and the penetration of water, according to the theoretical approach of Lister [5]: this corresponds to the start of the water ingression. After this initial trigger, the cracked front progresses steadily and water is able to flow into the cracks and quench the corium.

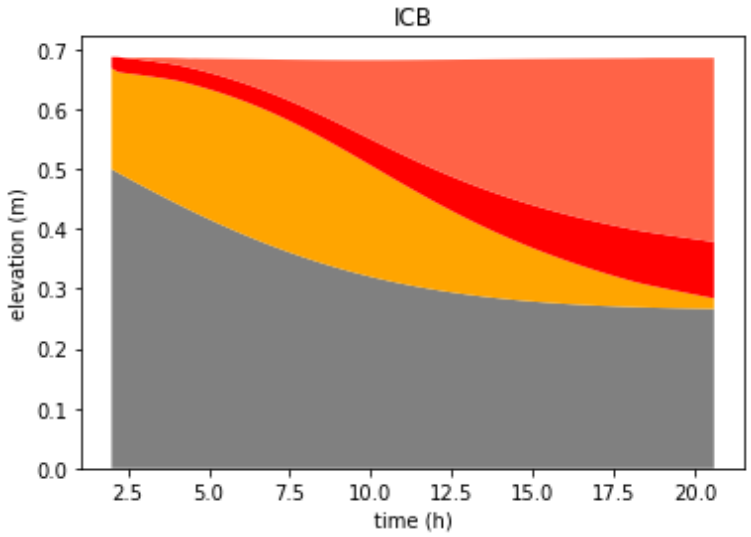

Figure 8: Example of evolution during the first day without melt eruption.

An example of evolution of corium quenching is presented in Fig. 8, where quench is examined during the first day, with water ingression only (the melt eruption is not considered). For this application, the value of ϕ_{CHF} is chosen equal to 200 kW/m^2 and does not decrease with time: it is not a realistic case but it is useful for understanding the dynamics of the process. We see that there is an acceleration of the quench front (i.e. the limit of the cracked zone moves faster downwards), followed by a progression at a quasi-steady velocity followed by a deceleration of the quench front. The initial acceleration is due to the decrease of ϕ_{up} caused by the decay of residual power and by the decrease of the mass of fuel in the corium layer: the driving force for solidification $(\phi_{CHF} - \phi_{up})$ increases. The quasi-steady progression corresponds to a period when $(\phi_{CHF} - \phi_{up})$ is approximately constant. The final deceleration is due to the accumulated power in the quenched zone which reduces the effective value of ϕ_{CHF}. This last phenomenon was not addressed by Lister because he considered only lava without internal heat generation.
It is interesting to notice that, to completely quench in one day a corium layer spread over a surface of 80m^2 and generating 15MW, it is necessary to have ϕ_{CHF}=200 kW/m^2. In most cases, the CHF will be lower, which has two implications: the onset of water ingression will occur later and the quench front velocity will be lower. As a result, the complete stabilization will be reached after a few days (or even several days in some cases). This will be illustrated in section 8.

7. DETERMINATION OF THE COMPLETE STABILIZATION

In many lumped-parameter models, the concrete basemat is represented as a layer with uniform temperature T_∞. However, in reality, there is a conductive heat transfer from the corium to the concrete and a temperature gradient near the interface. In the end of corium quenching, the downwards heat flux ϕ_{dn} decreases and eventually becomes balanced by the conductive heat flux through the concrete, which leads to stop the erosion.
For an ablation front at temperature T_{abl} moving at the velocity U_{abl} in a medium initially at temperature T_∞, the evolution of temperature is solved in Carslaw & Jaeger [9]:

$$T(z) = T_\infty + \frac{1}{2}(T_{abl} - T_\infty)\left[erfc\left(\frac{z - tU_{abl}}{2\sqrt{\alpha}}\right) + exp\left(\frac{zU_{abl}}{\alpha}\right) erfc\left(\frac{z + tU_{abl}}{2\sqrt{\alpha}}\right)\right] \qquad (14)$$

The heat flux towards the concrete layer is given by estimating the derivative at position z=0 and after a time corresponding to a quasi-steady progression

$$\phi_c = -k_c \left(\frac{dT}{dz}\right)_{z=0} = -k_c (T_{abl} - T_\infty) \sqrt{\frac{\pi}{\alpha_c t}} \tag{15}$$

This equation is valid only when the ablation velocity is close to zero and decreases faster than $1/\sqrt{t}$. Typically, this gives a heat flux of a few kW/m^2, which decreases with time.
With this result, we can write the time for which concrete erosion stops, as a function of the downwards heat flux ϕ_{dn}:

$$t_{end} = \left[\frac{k_c (T_{abl} - T_\infty)}{\phi_{dn}}\right]^2 \frac{\pi}{\alpha_c} \tag{16}$$

This evaluation is of practical interest for an implementation in a lumped-parameter model but it must be used carefully because it is only valid with the two conditions written just above. It must also be kept in mind that we used an analytical solution derived for a constant velocity of the front whereas this velocity slowly decreases in our case. To give an order of magnitude, the heat flux corresponding to the stop of erosion is represented in Fig. 9, as a function of time.

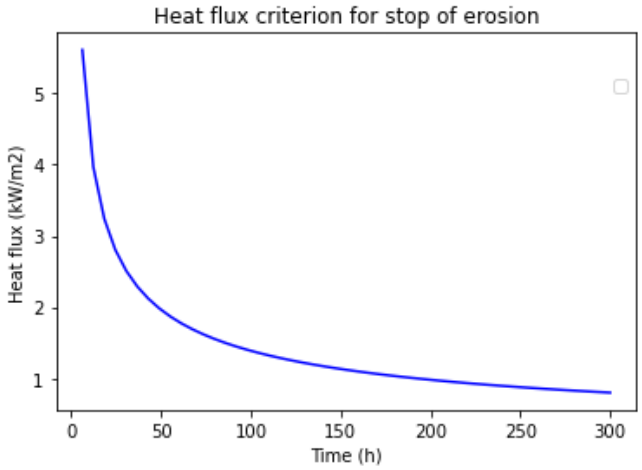

Figure 9: Bottom heat flux corresponding to the stop of concrete erosion

8. DISCUSSION ON THE COMBINED EFFETCS OF BOTH PROCESSES

In this last section, we investigate the combined effects of both quenching processes and the feedback between them. A simple case is defined, with $k_e = 0.08$ and ϕ_{CHF}=100 kW/m^2. The results are presented in Fig. 10. During the first 24h, melt ejection is the only active process because the heat flux to the top of the corium layer is too high. As a consequence, the behavior is comparable to the case shown in Fig. 7: a small layer of debris is formed, and a fast erosion leads to the ablation of approximately 50cm of corium. Then, water ingression starts because of the decrease of ϕ_{up}. This leads to a rather fast decrease of the height of the corium layer which is progressively quenched. As a consequence, the erosion of concrete strongly decreases. Another consequence is the decrease of the melt ejection. As it was explained, melt ejection has an asymptotic behavior with time: this reduction of efficiency with time is amplified by the onset of water ingression and the thickness of the debris layer remains almost constant after that. In this example, the stabilization is reached in a little more than 2 days.

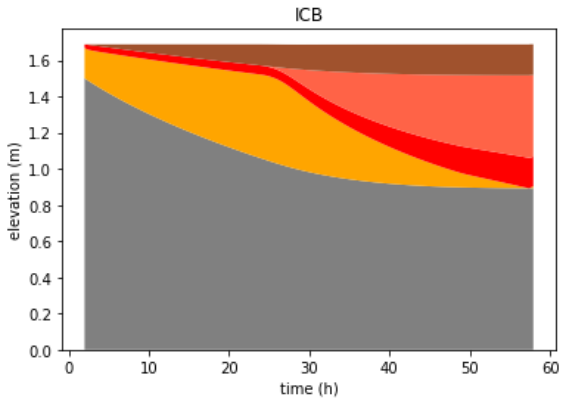

Figure 10: Example of application with both quenching processes acting simultaneously.

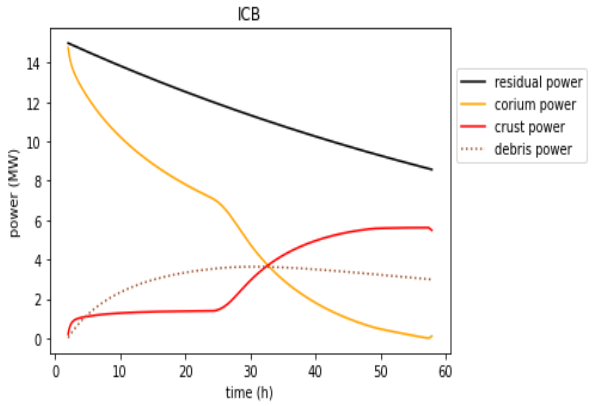

Figure 11: Distribution of power between the layers

An analysis of the powers, in Fig. 11, reveals that the debris layer, although rather thin, bears a significant part of the total power: approximately 30% of the total residual power is generated in the 15cm of debris located on top. It means that, after the first 24h, 30% of the power was already removed from the corium layer. After quenching, 70% of the power is generated in the cracked crust which is fully quenched. The onset of water ingression is clearly seen to accelerate the decrease of power in the corium layer by progressive solidification.
It is important to remind that this is only an example of application and that a variety of results may be obtained, depending on the scenario (residual power), on the spreading surface, on the type of concrete (gas content) and on model parameters. This was illustrated in the sensitivity analysis in section 3. More detailed models would also add more parameters and other dependencies (for example in the power partitioning coefficient)

9. CONCLUSIONS

The objective of this paper is to provide an insight and orders of magnitude about the quenching of molten corium spread over a siliceous concrete basemat in the containment of a nuclear reactor, since it is one of the possible strategies to mitigate the consequences of a severe accident in a GenII reactor. The case of siliceous concrete is less favorable (compared to limestone concrete) and this is why it deserves a careful evaluation. This paper does not aim at providing quantitative evaluations for specific reactor designs or specific cases. Instead, the aim is to draw the attention to the important parameters and elements of modelling that are necessary for the evaluation of a specific case.
A simple parametric model was used to investigate the problem. There are several characteristic times in the problem: the decay time of residual power, the duration of efficient melt ejection and the time of cracks progression into the crust. Those different times are not independent. The evolutions of quenching and concrete erosion may be divided in three main stages. The first stage is characterized by a fast erosion of concrete and a significant ejection and quenching of debris. This stage lasts from half a day to a few days, depending on the type of concrete and on the model parameters. The second stage is characterized by the start of water ingression and slowing down of erosion of concrete. This stage may last from half a day up to a few weeks depending on the type of concrete and on the model parameters. The last stage is characterized by a very slow erosion until the complete quenching of corium. Among the parameters governing the process, the maximum heat flux (CHF) that can be extracted (through the network of cracks that are formed in the top crust) is of crucial importance. A revised correlation is proposed for this maximum heat flux, considering the negative effect of adding silica into the corium mixture, which results

in smaller cracks and a reduced CHF. The correlation fits rather well the data obtained at Argonne National Laboratory in past and recent tests. It appears that the CHF may be significantly reduced if the concrete content in the corium is large: values lower than 50 kW/m^2 are possible, which would lead to a long time for total quenching. The problem is strongly non-linear with respect to several of the model parameters, including the CHF. An early triggering of water ingression results in a fast quenching whereas a late triggering may lead to quite long stabilization and deeper erosion of the concrete basemat (up to a couple of meters and a few weeks until complete quenching). Because of the non-linearities and because of the existence of different characteristic times, there is a non-trivial dependence of water ingression efficiency on the potential occurrence of melt eruption at the very beginning of corium concrete interaction. Melt eruption, even if limited, is likely to significantly accelerate the triggering of water ingression and favor a fast stabilization of corium. This is the reason why adding a rather thin layer of limestone concrete on top of the siliceous concrete could be a very efficient option to speed up the stabilization and limit the erosion of the basemat: with the high gas content in the limestone concrete, it would significantly enhance the debris formation in the beginning and favour a quicker onset of water ingression.

.

NOMENCLATURE

$\dot{E}_f = \dot{E}_0\, exp(-t/\tau)$	Power per unit mass of fuel materials
$\dot{E}_0$	Power per unit mass of fuel materials at $t = 0$
m_c	Mass of concrete in the corium
m_f	Mass of fuel materials in the corium
m_s	Mass of crust
m_w	Mass of fractured crust (due to water ingression)
m_d	Mass of debris (generated by melt ejection)
$\dot{Q}_c = \frac{dm_c}{dt}$	Ablation rate
X_g	Mass fraction of gas in concrete
X_f	Mass fraction of fuel materials in a layer $X_f = m_f/(m_f + m_c)$
τ	Decay time of residual power
α	Thermal diffusivity
k	Thermal conductivity
ρ	Volumetric mass
Cp	Specific heat per unit mass

REFERENCES

1. Farmer, M. T. (2006) ‘Phenomenological Modeling of the Melt Eruption Cooling Mechanism During Molten Corium Concrete Interaction (MCCI)’, in *Proceedings of ICAPP’06*.
2. Lomperski, S. and Farmer, M. T. (2007) ‘Experimental evaluation of the water ingression mechanism for corium cooling’, *Nuclear Engineering and Design*, 237(9), pp. 905–917.
3. Nayak, A. K. *et al.* (2009) ‘A numerical and experimental study of water ingression phenomena in melt pool coolability’, *Nuclear Engineering and Design*, 239(7), pp. 1285–1293.
4. Epstein, M. (1999) *Review of Water Ingression Models - EPRI Report ACEX-TR-C31*.
5. Lister, C. R. B. (1974) ‘On the Penetration of Water into Hot Rock’, *Geophysical Journal of the Royal Astronomical Society*, 39(3), pp. 465–509.

6. Lamur, A. *et al.* (2018) 'Disclosing the temperature of columnar jointing in lavas', *Nature Communications*, 9(1).
7. Bakardjieva, S. *et al.* (2014) 'Quality improvements of thermodynamic data applied to corium interactions for severe accident modelling in SARNET2', *Annals of Nuclear Energy*, 74(C), pp. 110–124.
8. Björnsson, H., Björnsson, S. and Sigurgeirsson, T. (1982) 'Penetration of water into hot rock boundaries of magma at Grímsvötn', Nature, pp. 580–581.
9. Carslaw, H. S. and Jaeger, J. C. (1959) 'Conduction of Heat in Solids'. Oxford University Press, USA.

FLUIDS MIXING MODELLING WITH PHASE CHANGE FOR MOLTEN CORIUM-CONCRETE INTERACTION

Ilyas Khurshid[1,2], Yacine Addad[1,2], Imran Afgan[1,2,3]
[1]*Department of Mechanical and Nuclear Engineering, College of Engineering, Khalifa University, Abu Dhabi, P.O. Box 127788, UAE*
[2]*Emirates Nuclear Technology Centre (ENTC), Khalifa University, Abu Dhabi, P.O. Box 127788, UAE*
[3]*Department of MACE, School of Engineering, University of Manchester, M13 9PL, United Kingdom*
ilyas.khurshid@ku.ac.ae; yacine.addad@ku.ac.ae; imran.afghan@ku.ac.ae

ABSTRACT

A severe accident in a nuclear power plant involving a reactor core meltdown could result in origination of molten corium, which is a mixture of nuclear fuel, claddings and structural components. In this paper, a new numerical mixing model is developed and implemented in OpenFOAM to comprehensively analyze the ablation of concrete during the Molten Corium-Concrete Interaction (MCCI). The model is capable of predicting the heat transfer, concrete ablation, phase change, mass transfer, mixing of concrete and corium, and natural convection. The model was tested and benchmarked against the well documented CCI-2 experiment. The imposed constant temperature boundary conditions as per the experimental setup of CCI-2, instigates ablation of concrete which progresses along both the axial and radial directions of the test configuration. Experimental results reveal that the axial and radial ablation of concrete is not same. Our model captured this effect because our model is considering the density of corium and concrete and its variation. Moreover, our results reveal that the melted concrete and corium, even though, having different densities, form a single phase/mixer which under natural convection further enhances the ablation.

KEYWORDS:

Corium ablation; fluids mixing; heat transfer; melting; phase change

1. INTRODUCTION

The growing global need for energy poses a significant obstacle to sustainable development, as a shift towards alternative energy sources has been brought about by water scarcity and depletion of fossil fuel reserves. Nuclear power is one such energy source. However, maintaining nuclear plants safely over long stretches of time can be difficult because aging materials are constantly subjected to harsh operating conditions like flow-induced creeping, thermal stresses, mechanical fatigue, etc. According to Bixler et al. [1], these difficulties alone or in combination could therefore result in a serious nuclear accident that would jeopardize a nuclear reactor's integrity and could form molten corium in the reactor pressure vessel. The molten corium which is a mixture of nuclear fuel, claddings, and structural elements has a very high temperature of over 3000°C [1, 2]. Therefore, it is extremely challenging to evaluate the molten corium concrete interaction due to its high temperature and various ubiquitous multiple processes at severe conditions. Moreover, the various thermo-chemical reactions, interaction of corium with the concrete, crust formation, has a direct impact on behavior of molten corium [3]. Therefore, reproducing these phenomena through experimentation is not only very difficult but also very expensive and risky [4, 5]. For these reasons, new and trustworthy numerical modeling tools (CFD) need to be investigated further for nuclear safety studies.

There are several computational fluid dynamics (CFD) techniques that present a viable substitute for system level codes and/or empirical correlations. In the past, both Lagrangian (Moving Particle Semi-implicit (MPS) and Eulerian

(e.g., finite volume and finite element method) approaches have been used to simulate the behavior of the various phases. To examine the mechanism of the molten corium and concrete interaction (MCCI) process, Koshizuka and Oka [6] developed the moving particle semi-implicit (MPS) method. Many researchers use the particle method known as the MPS method, which is based on the Lagrangian description, to simulate various MCCI experiments. Li and Yamaji [7] employed the MPS method to ascertain the isotropic and anisotropic ablation. Using MPS, Chai et al. [8] carried out numerical simulation of MCCI for different kinds of concrete. Li et al. [9] used MPS to predict the crust behavior and concrete erosion rate for sacrificial material impinged by a core melt jet. Chen et al. [10] used an improved MPS method to perform a three-dimensional simulation of HECLA-4. Cai et al. [11] used the improved MPS method to conduct a three-dimensional simulation study in order to ascertain the impact of sidewall crust thermal resistance. However, Euler-based strategies have also been used to good effect in the past. For example, Kucala et al. [12], Ye et al. [13], and Na et al. [14] have all studied the relocation of molten corium using computational fluid dynamics (CFD).

Aksenova et al. [15] created a multi-component environment based on a Euler method to solve the equations for mass, momentum, and energy using the conservation of separate components. Each component in their method resides in a numerical domain with defined boundaries. The ability to resolve the flow using high fidelity simulations for natural convection cases—especially when the Raleigh number rises too high—is the clear benefit of the Euler-based approaches. Regrettably, there are surprisingly few research studies in the nuclear engineering literature that simulate computational fluid dynamic modeling of the interaction between molten corium and concrete. The CFD method that was introduced by Chudanov and Bolshov [16] in 2007 was created to comprehend the interaction between molten corium and concrete. They imitated the mixture's mass and heat transfer. Their model, however, was unable to replicate the ablation of concrete during the interaction of molten corium concrete. Furthermore, a number of researchers created various numerical models, including CORFLOW, to simulate the spread of corium.

Recently, Khurshid et al. [17] and Amidu et al., [18] used multi-region approach to model the interaction of corium and concrete with considering only the transfer of heat across the regions. However, their approach doesn't have the capacity to model the mass transfer and mixing of various phases. Considering these parameters is very important to characterize the interaction of molten corium and concrete. In this study, a comprehensive numerical model is developed to investigate the molten corium and concrete interaction, heat transfer, phase change, fluid density, mixing, and natural convection. Several important parameters were considered such as the change in ablation field, temperature field, velocity field, and density field. However, this model is limited to phase change, mixing and natural convection, assuming that the concrete is not decomposing. The objective of this study was achieved by incorporating the heat transfer, phase change, mass transfer, and mixing in OpenFoam. This technique enables more robust modeling of MCCI and related damage where in most of the previous studies, mixing and mass transfer was ignored.

2. MODEL DESCRIPTION AND ANALYSIS

2.1 Modelling Concrete Melting with Molten Corium

The main challenge in modeling the interaction of molten corium and concrete is the mixing of corium and melted concrete. Khurshid et al. [17] and Amidu et al., [18] used multi-region approach to model the interaction of corium and concrete with considering only the transfer of heat across the regions. In this study for the first time to the best of authors knowledge, the mixing of concrete and corium is modelled for mixing of various phases that are concrete and corium. Where the change in various phases taking place only with the assumption that corium is a homogenous mixture of molten nuclear fuel, cladding, thermo-hydraulic and structural element. It is important to mention that molten corium has a very high viscosity, thus we considered the flow is incompressible, and laminar-creeping [19]. The developed model is customized solver and considers multi-phase, multi-component, and incompressible phases based on the volume of fluid method. This solver supports a per-phase choice of thermodynamics model, which means

that the phases share pressure and temperature. In addition to this, the employed solver supports mass and heat transfer across phases during molten corium concrete interaction.

2.1.1 Governing equations

To develop the numerical methodology for non-isothermal laminar flow of the molten corium, a solver was developed in OpenFoam using the governing equations. Molten corium has a very high viscosity and thus the flow can be considered incompressible, laminar and creeping flow. Moreover, the volume of fluid method is utilized to track the solid-liquid (concrete-corium) interface. Where a single momentum equation is shared by various phases, and the volume fraction of each phase in each computational cell in tracked throughout the domain. The volume fraction presenting the ratio of the melt volume in a cell to the volume of the cell is equal to one if the cell is completely occupied with melt and is equal to zero if the cell is totally a solid:

$$\alpha_L(x,t) = \frac{V_{melt}}{V} = \begin{cases} 0, & inside\ solid\ phase \\ 0 < \alpha_L < 1, & inside\ transitional\ region \\ 1, & inside\ melt/liquid\ \ phase \end{cases} \quad (1)$$

The density and viscosity of a single mixture phase in a computational cell are defined as follows

$$\rho = \alpha_L \rho_L + (1 - \alpha_L)\rho_s, \quad (2)$$

$$\mu = \alpha_L \mu_L + (1 - \alpha_L)\mu_s, \quad (3)$$

The continuity equation is

$$\nabla.(\rho U) = 0. \quad (4)$$

Considering the effect of gravity, the momentum equation is described as

$$\frac{\partial(\rho U)}{\partial t} + \nabla \cdot (\rho UU) = -\nabla_p + \nabla \cdot [\mu(\nabla U + \nabla UT)] + \rho g \quad (5)$$

The energy equation utilized in the model is

$$\frac{\partial(\rho E)}{\partial t} + \nabla \cdot \big(U(\rho E + p)\big) = \nabla \cdot (k\nabla T) + S_h \quad (6)$$

The Lee's model is used in the VOF method as it is used to simulate the mass transfer during melting and solidification processes and this model is applicable during the melting and solidification of a phase.

$$\frac{\partial(\alpha_s \rho_s)}{\partial t} + \nabla \cdot (\alpha_s \rho_s) = \dot{m}_{ls} - \dot{m}_{sl} \quad (7)$$

In Equation 7, the notation *s* is for solid and *l* is for liquid/melt, α_s is the solid volume fraction, ρ_s is the solid density in *kg/m³*, $\dot{m}_{ms}$ and $\dot{m}_{sm}$ are the mass transfer rates due to melting and solidification respectively and their unit is *kg/(s.m³)*.

During melting, $T_l > T_m$ which leads to the following equation

$$\frac{d\dot{m}_{ls}}{dt} = C\alpha_l \rho_l \left(\frac{T_l - T_m}{T_m}\right) \quad (8)$$

During solidification, $T_s < T_m$, which leads to the following equation

$$\frac{d\dot{m}_{sl}}{dt} = C\alpha_s \rho_s \left(\frac{T_m - T_s}{T_m}\right) \quad (9)$$

The C presents the model constant: if $C > 0$ melting will take place and if $C < 0$ solidification will occur, T_m is the melting temperature in Kelvin. It is important to mention that the multiplication of Equation 8 and 9, the rate of mass transfer and latent heat yields the source term for the energy equation.

The system of equations with boundary conditions are solved numerically using the open-source library Open-FOAM [20], which is based on the finite volume method. The coriumConcreteMultiphaseInterFoam solver is developed in this study is based on the VOF method. The pressure-velocity coupling is handled by solving the momentum equations and a pressure equation derived from a combination of the continuity and the momentum equations. Where this coupling technique is in Pimple Algorithms that is a combination of PISO and Simple algorithm. The 2nd order semi-implicit CrankNicloson scheme is employed for the time derivative discretization. While the divergence, gradient, and the Laplacian terms are approximated by the Gauss linear Upwind, the Gauss Linear, and the Gauss linear orthogonal schemes, respectively. These second-order schemes provided very good precision in the results despite their difficulty in achieving convergence. The adjustable time step is used to ensure the courant number limit to 1.

3. Model Validation

Modeling the molten corium concrete interaction is a complex and difficult as it depends on the composition of corium, composition of concrete, and thermodynamic conditions melting process is compared against the CCI-2 concrete ablation experimental data. Therefore, it is important to validate the developed model with experimental data. The detailed description of this experiment and its various boundary conditions, and data are provided in the subsequent sub-sections.

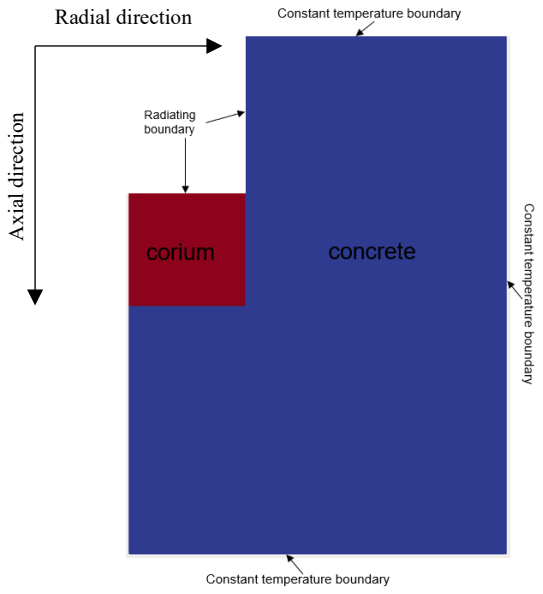

Fig. 1: Configuration of MCCI simulation domain with boundary conditions and geometry

3.1 Validation against CCI-2 experimental data

The molten corium concrete model developed in this study is tested under the same operating conditions as the CCI-2 experiment, details of the experiment can be found in Farmer et al. [21]. The CCI-2 experiment is one of the various tests performed as a part of OECD/MCCI test program conducted at Argonne National Laboratory. The experiment was conducted with a rectilinear geometry with a cavity of 50 cm^2. The mass of corium used in this test was 400 kg and the type of concrete tested was limestone/common sand concrete with BWR conditions. The molten corium

concrete analysis for this test was performed for 300 minutes under dry-cavity conditions. Recently Khurshid et al. [22] analyzed the CCI-2 model in CORQUENCH and investigated the effect of replacing Zircaloy cladding with accident tolerant silicon carbide cladding. The configuration of corium and concrete regions along the various boundary conditions were mimicked with the experimental data as shown in Figure 1.

3.1.1 Numerical Setup and Mesh Independence Study

To determine the concrete ablation and sensitivity of uncertain input parameters, three simulations were performed using coarse, medium, and fine meshes. The details of the various meshes is provided in Table 1. The results of concrete ablation, and temperature fields were compared for these three meshes. The results were compared in the radial and axial directions for the verification of the mesh sensitivity study.

Table 1: Details of mesh parameters used in the study

S. No.	Mesh Type	Number of cells (10^3)	Base/local length (mm)
1	Coarse	7,518	0.011
2	Medium	8,325	0.010
3	Fine	9,168	0.009

The computational grids were generated by changing the local base length of the cells, resulting in different refinements levels as listed in Table 2. Comparison of results from the mesh sensitivity study are shown in Fig. 2 to understand the spatial discretization errors and to determine how much the mesh is affecting the solution. Thus, we measured the temperature at various location in the radial direction and compared the percentage difference between the fine and other meshes as shown in Table 2. It can be noted that the medium mesh was within 3.3% of fine mesh predictions all noted locations. Hence, the medium mesh was used for all remaining simulations.

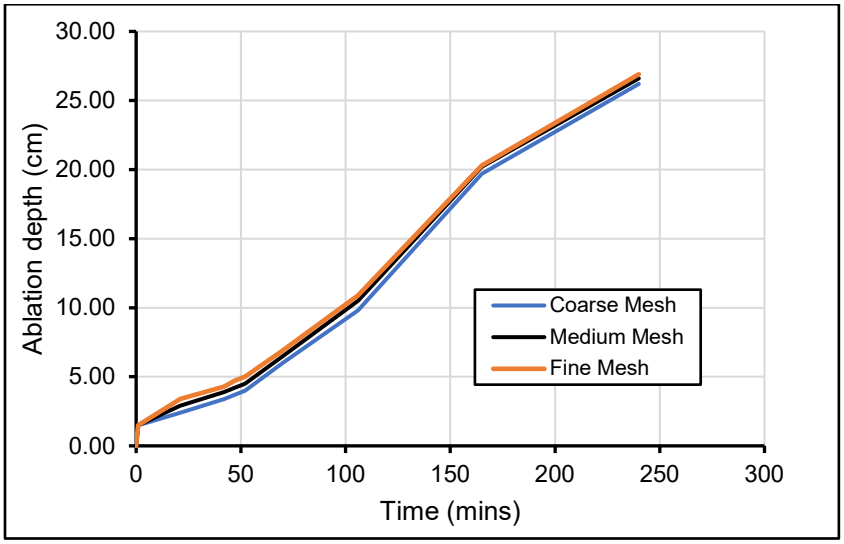

Fig. 2: Mesh sensitivity study for the comparison of axial ablation depth

All components of the molten corium and concrete and the exact thermophysical properties are used to predict the ablation of concrete. Thus, we modeled the main components of the molten corium according to the CCI-2 experiment (refer to Table 3), which is composed of 25% zirconium oxide and 61% uranium oxide by mass fraction. To shorten the amount of time needed for the simulation to reach stable conditions, the temperatures of the two phases that is molten corium and concrete were started at 2,000 K and 350 K, respectively.

Table 2: Temperature measurement at various dimensionless distances during mesh sensitivity analysis

Location in the radial direction	Coase Mesh Temperature	Medium Mesh Temperature	Fine Mesh Temperature	% Difference Coarse Mesh	% Difference Medium Mesh
0.1943	300.01	300.01	300.01	0.00	0.0000
0.3174	443.84	424.73	416.76	-6.49	-1.91
0.5244	2728.75	2624.65	2543.43	-7.28	-3.19
0.8418	2709.00	2617.77	2549.79	-6.24	-2.66
0.9993	2703.73	2604.58	2543.51	-6.29	-2.40

The various corium and concrete properties for each of the CCI-2 constituents are listed in Tables 3 and 4, and the results of the developed molten corium concrete model were compared with the experimental data in two directions. The two directions of concrete ablation measurements are axial and radial directions as mentioned by Farmer et al. [21]. The two distinct phases of corium and concrete will mix and will form a mixture composed of molten corium and concrete. The experiment was executed in a dry cavity for 300 minutes.

Table 3: CCI-2: Composition of corium and its temperature [21]

Composition of corium (kg)	Component	CCI-2
	UO_2	242.48
	ZrO_2	99.60
	Cr	25.64
	SiO_2	13.56
	CaO	12.52
	MgO	4.56
	Al_2O_3	1.64
	Zr	0
	Fe	0
	Total	400.0
Temperature (K)	Initial set molten corium temperature	2000
	Upper structure temperature	350

Fig. 3 (a) and (b) shows the comparisons of the ablation depth in the axial and radial directions between the experiments and the current CFD model. Since ablation depth is one of the primary factors that could have a direct impact on the reactor containment's integrity, it was used in the comparisons. Both of these figures show that as soon as the molten corium comes into contact with the concrete, there is an abrupt ablation of the concrete. Each simulation ran for more than 18000s, demonstrating that concrete ablation began to occur after about 250s. These figures also show that, as heat energy is consumed by concrete ablation, and the rate of concrete ablation decreases. This decrease is caused by the decrease in heat conduction to concrete. Thus, for all cases in both the axial and radial directions, the general trend is a progressive decrease in concrete ablation over time.

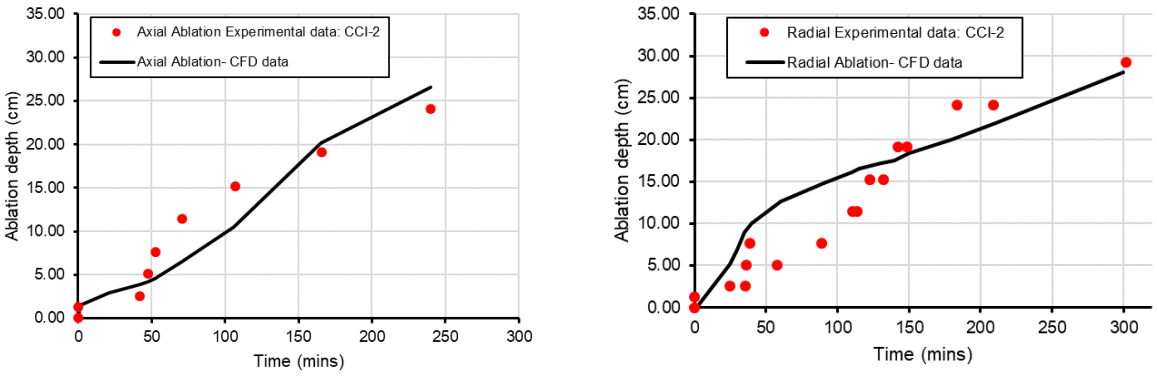

(a) (b)

Fig. 3: Comparison of ablation depth experimental data (CCI-2) with model prediction (a) axial direction (b) radial direction.

The examination of the experimental data shows that the main heat source is the high-temperature corium, thus decay heat values are used as provided by the experimental conditions; Farmer et al., [21]. The external boundary condition imposed during the modelling of concrete ablation was constant temperature at 300 K whereas the decay heat for CCI-2 was kept at 100 kW as mentioned by Farmer et al., [21]. As, the concrete ablation starts, the thickness of the concrete cavity decreases from the bottom to the upper section of the concrete geometry. It can be seen from the results that there is a slight disparity between the numerical and experimental findings as shown in Fig 3. However, the comparison of final shape of concrete ablation at the end of the experiment and our CFD model results are quite similar (marked by black arrow) as shown in Fig. 4 (a) and (b). This shows that our developed model is able to match the form of ablated cavity at the last point during the interaction of corium and concrete at the severe thermodynamic conditions.

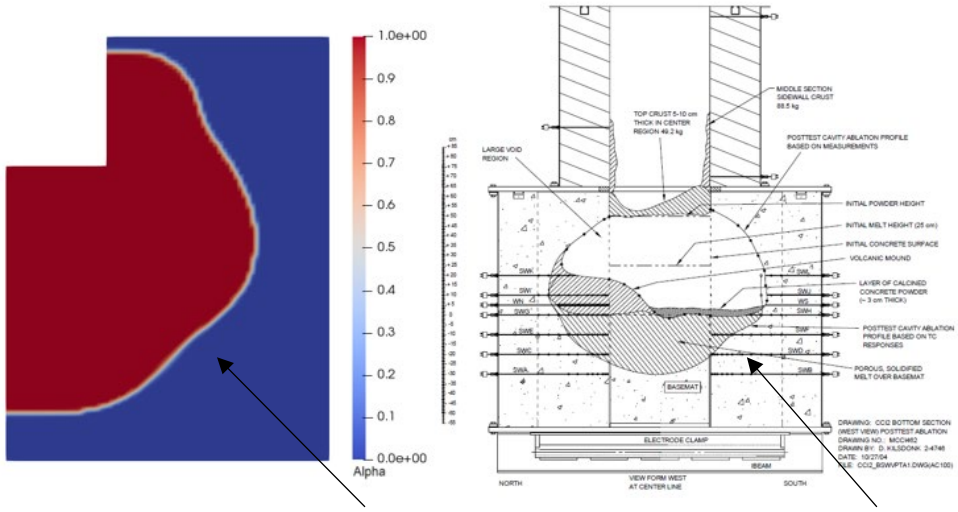

Fig. 4: Comparison of ablation results of developed CFD model with experimental ablation (a) CFD results (b) experimental results of final concrete shape

Table 4: Properties of concrete used to model molten corium concrete interaction

Thermophysical properties of concrete	
Density (Kg/m^3)	$\rho = 2330$
Thermal conductivity (W/m.K)	$\lambda = 0.302$
Expansion coefficient (1/K)	$\beta = 12.9e^{-6}$
Latent heat of fusion (J/Kg)	L = 7,200
Viscosity (m^2/s)	$\eta = 4.29e^{-7}$
Specific heat capacity (J/kg.K)	c = 837.3
Concrete solidus temperature (K)	$T_{solidus}$ = 1393
Concrete liquid temperature (K)	$T_{liquidus}$= 1568
Concrete ablation temperature (K)	$T_{ablation}$= 1500

4. Results and Discussions

After developing and validating an integrated framework to investigate the molten corium and concrete interaction, here we investigated the variation in various fields such as ablation field, temperature field, velocity field, and density field at various timesteps such as initial timestep, 150 mins and 300 minutes. We kept the values of different parameters within the typical range of experimental conditions (Tables 3 and 4) and ran all the simulations for a preset period of time. It is important to mention that the investigation of various fields will assist in determining the cumulative change in concrete ablation and related damage due to molten corium and concrete interaction.

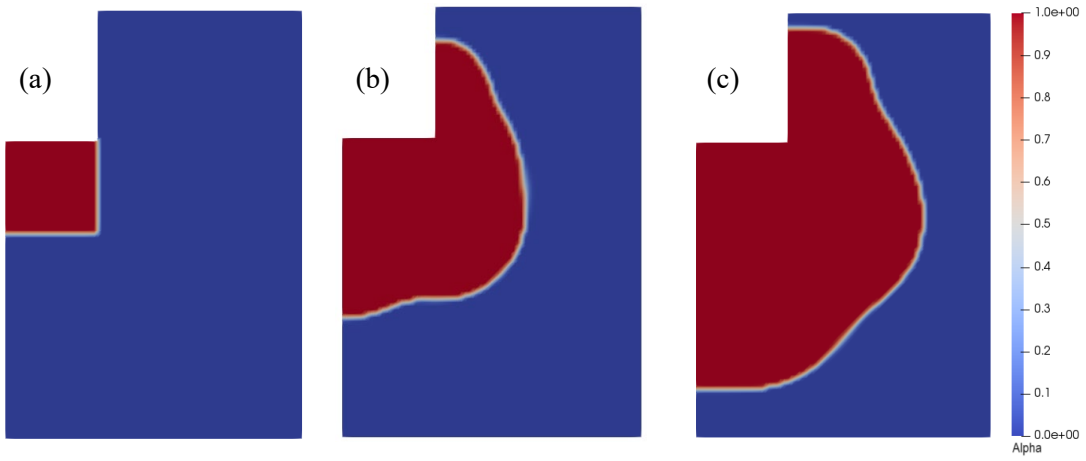

Fig. 5: Ablation Field during MCCI at different timesteps (a) Zero timestep (b) 150 minutes (c) 300 minutes

The ablation field of concrete and variation in its profile is investigated in this subsection. It is evident from the results presented in Fig. 5 (a) that initially there was just a cavity that was filled by corium. However, with the imposed constant temperature boundary conditions, the ablation take place and progresses along the axial and radial direction. Thus at 150 mins the ablation reaches to the value of 12 cm in the radial direction and 9 cm in the axial direction. The analysis of this figure reveals that the constant temperature boundary condition assisted in increasing surface flux because of the high rate of heat transfer. It can be observed from the figure that between the initial (0 timestep) and final phase (300 minutes), the ablation depth reaches to the level of 28 cm along the axial direction and 26.6 cm along the radial direction.

Fig. 6 shows the change in temperature field during the interaction of concrete and molten corium. The results presented in Fig. 6(a) reveals that the corium temperature is very high and its lies at 2200 K and the temperature of concrete is 350 K. It is important to mention that the ablation temperature of concrete is 1500 K. Accordingly, the transfer of heat from corium to concrete will increase the concrete temperature and that will lead to the initiation of concrete ablation. Therefore, this high temperature corium will ablate the concrete in all directions as shown in Fig. 5. Thus, it is evident from the results presented in Fig. 6 that concrete temperature increased to the level of concrete ablation temperature (1500 K) that lead to the ablation of concrete.

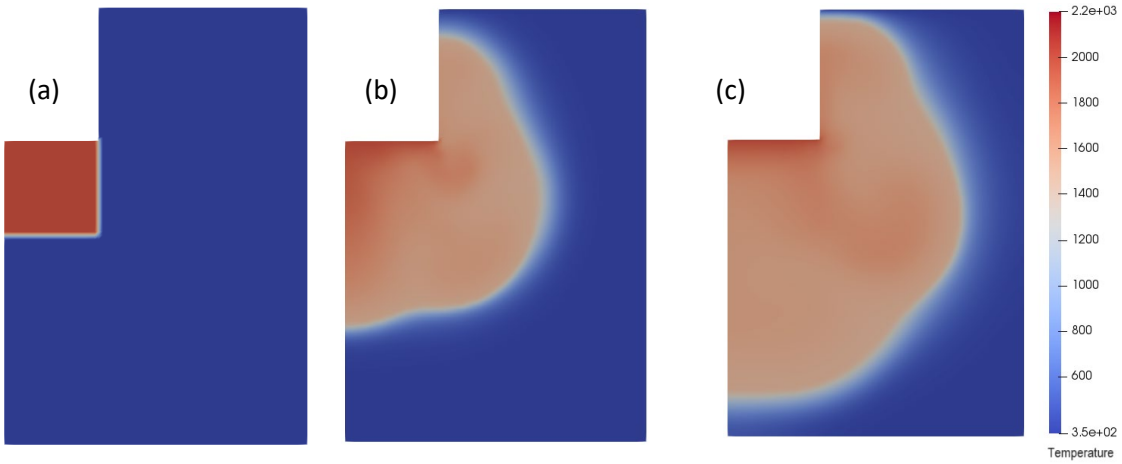

Fig. 6: Temperature field during MCCI at different timesteps (a) Zero timestep (b) 150 minutes (c) 300 minutes

Fig. 7 illustrates the variation in velocity field and its effect on ablation of concrete. The results presented in Fig. 7 (b) and (c) clearly demonstrate the vertices formed lead to natural convection and this convection become more pronounced with time. This increase in natural convection causes a decrease in ablation as shown in Fig. 3 (a) and (b), where it is evident that in the start the ablation increases exponentially. However, with the increase in natural convection and mixing of corium and concrete.

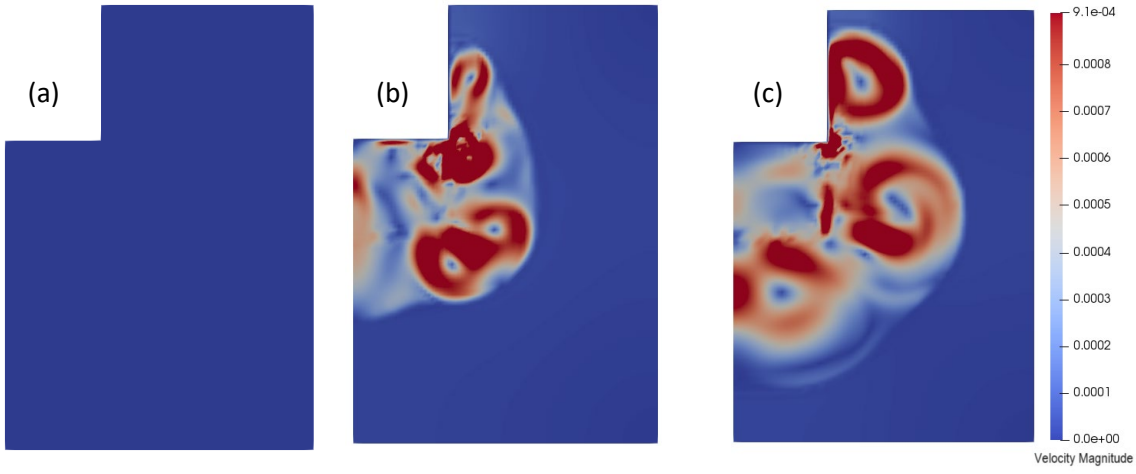

Fig. 7: Velocity field during MCCI at different timesteps (a) Zero timestep (b) 150 minutes (c) 300 minutes

The ablation of concrete decreases. Consequently, the velocity vectors exhibit greater dynamism in 7(c) compared to 7 (a) and (b). This finding suggests that the implementation of a corium mixing model reveals that the mixing of corium and concrete intensifies the natural convection motion within the melted concrete and corium. Thereby

enhancing the mixing of the corium-concrete mixer. Consequently, this phenomenon positively impacts by decreasing the ablation rate of concrete.

It is imperative to mention that the melting of concrete and mixing of corium with lead to a change in density as shown in Fig. 8. It important to mention that when a material changes its phase from solid phase to liquid phase, only volume is altered with no change in the mass. Thus, after the ablation of concrete mass will not change. Moreover, during solidification of corium-concrete mixer, will increase the spacing between the molecules (volume), but it will not change the number of molecules (mass). Therefore, the solid phase and the liquid phase during molten corium and concrete interaction will have the same mass and different density as presented in Fig. 8. Moreover, the liquid phase concentration will increase with the ablation of concrete as shown in Fig. 8 (b) and (c). Additionally, a matter of fact, the melted concrete and corium have different densities and they would separate when mixing would stop. However, due to natural convection as the results presented in Fig. 8 and it shows that the two fluids (melted concrete and corium) are continuously mixing with each other and thus they form a single phase shown as red in the Fig. 8.

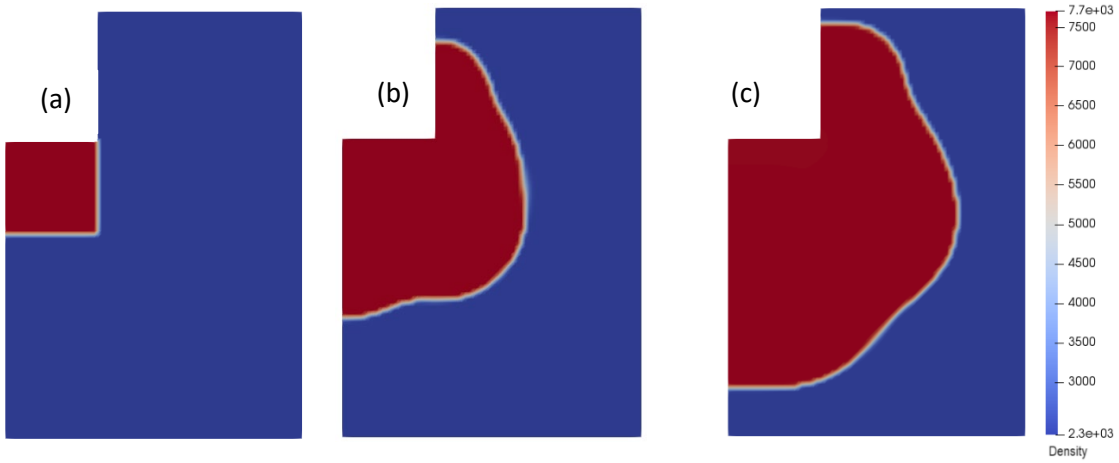

Fig. 8: Density field during MCCI at different timesteps (a) Zero timestep (b) 150 minutes (c) 300 minutes

SUMMARY AND CONCLUSIONS

In this study, a numerical model was developed which is an extension of the fluid mixing model (interfoam). The developed coriumConcreteMultiphaseInterFoam was used to simulate the heat transfer, concrete ablation (phase change) phenomena, mass transfer, density and mixing of corium and melted concrete during the Molten Corium Concrete Interaction (MCCI) for the first time. The model is implemented in OpenFoam and the numerical model is validated against the two sets of concrete ablation experimental data (along radial and axial directions) which were conducted on a limestone-based concrete. The coriumConcreteMultiphaseInterFoam proposed in this study is also able to capture the natural convection, mass transfer, density of corium and concrete, and mixing within the molten corium concrete mixture. It is found that initially there was just a cavity that was filled by corium. However, with the imposed constant temperature boundary conditions, the ablation take place and progresses along the axial and radial direction. Our results reveal that the axial and radial ablation of concrete are not same, because our model is considering the density of corium and concrete. Thus, the high temperature corium ablated the concrete and the mixing of corium and concrete intensified the natural convection along the concrete and corium interface, thereby enhancing the mixing of the corium and melted concrete. Consequently, this phenomenon positively impacts the ablation rate of the concrete by decreasing the rate of concrete ablation. The melted concrete and corium have different densities and they would separate when mixing would stop. However, we modeled only the initial transient stage of corium-concrete interaction where natural convection of the two fluids (melted concrete and corium) is simulated where the fluids are continuously mixing with each other forming a single phase.

Acknowledgments

This research was supported by ASPIRE, the technology program management pillar of Abu Dhabi's Advanced Technology Research Council (ATRC), via the ASPIRE "Award for Research Excellence program (AARE) - 2020, Award No. [AARE20-151]". The authors would also like to thank Khalifa University of Science and Technology for providing the HPC resources.

References

[1]. Bixler, N., Gauntt, R., Jones, J. 2013. Leonard, M. *State-of-the-art-Reactor Consequence Analyses Project: Volume 1*, Peach Bottom Integrated Analysis.

[2]. Sehgal, B.R., 2012. *Nuclear Safety in Light Water Reactors: Severe Accident Phenomenology* (first ed.), Elsevier/Academic Press, Amsterdam, Boston.

[3]. Farmer, M. T. 2018. *The CORQUENCH Code for Modeling of Ex-Vessel Corium Coolability under Top Flooding Conditions*, Sponsor Org.: USDOE.

[4]. Khurshid, I., Afgan, I., Amidu, M. A., Addad, Y. 2022. Influence of Corium Temperature, Concrete Composition and Water Injection Time on Concrete Ablation during MCCI: New Insights. *Progress in Nuclear Energy*, 144, 104102. https://doi.org/10.1016/j.pnucene.2021.104102.

[5]. Khurshid, I., Amidu, M. A., Addad, Y., Afgan, I., 2022. Thermochemical Modeling of Metal Composition and Its Impact on the Molten Corium–Concrete Interaction: New Insights with Sensitivity Analysis. *Energies*. 15(9), 3387. https://doi.org/10.3390/en15093387.

[6]. Koshizuka, S. and Oka, Y., 1996. Moving-particle semi-implicit method for fragmentation of incompressible fluid. *Nuclear science and Engineering*, 123(3): 421-434.

[7]. Li X., Yamaji A., 2016. A numerical study of isotropic and anisotropic ablation in MCCI by MPS method. *Progress in Nuclear Energy*, 90: 46-57.

[8]. Chai, P., Kondo, M., Erkan, N. and Okamoto, K., 2017. Numerical simulation of MCCI based on MPS method with different types of concrete. *Annals of Nuclear Energy*, 103: 227-237.

[9]. Li G., Liu M., Wang J., Chong, D., Yan, J., 2017. Crust behavior and erosion rate prediction of EPR sacrificial material impinged by core melt jet. *Nuclear Engineering and Design*, 314: 44-55.

[10]. Chen, R., Cai, Q., Zhang, P., Li, Y., Guo, K., Tian, W., Qiu, S. and Su, G.H., 2019. Three-dimensional numerical simulation of the HECLA-4 transient MCCI experiment by improved MPS method. *Nuclear Engineering and Design*, 347: 95-107.

[11]. Cai, Q., Zhu, D., Chen, R., Deng, J., Li, Y., Dong, C., Tian, W., Qiu, S. and Su, G.H., 2020. Three-dimensional numerical study on the effect of sidewall crust thermal resistance on transient MCCI by improved MPS method. *Annals of Nuclear Energy*, 144: 107525.

[12]. Kucala, A., Rao, R. and Erickson, L., 2019. A computational model for molten corium spreading and solidification. *Computers & Fluids*, 178, pp.1-14.

[13]. Ye, I.S., Kim, J.A., Ryu, C., Ha, K.S., Kim, H.Y., and Song, J.,2013. Numerical investigation of the spreading and heat transfer characteristics of ex-vessel core melt. *Nuclear Engineering Technology,* 45, 21-28.

[14]. Na, H., Kim, H.S., Lee, H.J., Kim, D.S. and Kwon, S., 2017. Preliminary feasibility study of post-flooding ex-vessel corium cooling strategy by CFD spreading simulations and concrete ablation analysis. *Progress in Nuclear Energy*, 97, pp.139-152.

[15]. Aksenova, A.E. and Chudanov, V.V., 1997. Complex of the programs for numerical modeling of experiments on interaction high-temperature melt of metals with zirconium dioxide concrete. Preprint IBRAE RAS, pp.97-19.

[16]. Bolshov, L., and Chudanov, V., 2007. CFD Approach to Modeling of Core-Concrete Interaction. Transactions, *SMiRT 19*, Toronto, Canada.

[17]. Khurshid, I., Afgan, I., Addad, Y., 2023. A CFD Approach to Mimic the Molten Corium-Concrete Interaction Phenomena: Effects of the Thermal Boundary Conditions. *Saudi International Conference on Nuclear Power*

Engineering held on 13-15 Nov, King Fahd Conference Center, KFUPM, Dhahran, KSA. https://events.kfupm.edu.sa/event/132/.

[18]. Amidu, M. A., Addad, Y., Lee, J. I., Kam, D. H., Jeong, Y. H., 2021. Investigation of the Pressure Vessel lower head potential failure under IVR-ERVC condition during a severe accident scenario in the APR1400 reactor. *Nuclear Engineering Design*, 376, 111107.

[19]. Davidy, A., 2016. CFD Analysis of Molten Core Concrete Heat Transfer Interactions during Nuclear Accidents. Proceedings of the 34th Israeli Conference of Mechanical Engineering, 21-22 Nov, Haifa Israel.

[20]. Baamrani, H.E., Bammou, L., Aharoune, A., Boukhris, A., 2021. Volume of Fluid (VOF) Modeling of Liquid Film Evaporation in Mixed Convection Flow through a Vertical Channel. *Mechanical Engineering Problems*, 2021, 9934593. https://doi.org/10.1155/2021/9934593.

[21]. Farmer, M.T., Lomperski, S., Kilsdonk, D.J. Aeschlimann, R.W. 2006. *OECD MCCI Project*. *Final Report No OECD/MCCI-20050TR06*. Nuclear Engineering Division Argonne National Laboratory Argonne IL, USA. https://doi.org/10.2172/1014859.

[22]. Khurshid, I., Addad, Y. and Afgan, I., 2024. Study on corium-concrete interaction, heat transfer, and concrete ablation: Impact of replacing Zircaloy cladding with accident tolerant silicon carbide cladding on corium characteristic. *Applied Thermal Engineering*, 243, 22569. https://doi.org/10.1016/j.applthermaleng.2024.122569.

SEAKNOT
ERMSAR 2024
11th Conference on
SEVERE ACCIDENTS RESEARCH
May 13-16, 2024 – Stockholm, Sweden

ERMSAR 2024



FLUIDS MIXING MODELLING WITH PHASE CHANGE FOR MOLTEN CORIUM-CONCRETE INTERACTION

Ilyas Khurshid[1,2], Yacine Addad[1,2], Imran Afgan[1,2,3],

[1] Khalifa University, Abu Dhabi, P.O. Box 12277, UAE
[2] Emirates Nuclear Technology Center (ENTC), UAE
[3] University of Manchester, M13 9PL, United Kingdom

جامعة خليفة
Khalifa University

مركز الإمارات للتكنولوجيا النووية
Emirates Nuclear Technology Center

Outline

- Review of Molten Corium Concrete Interaction (MCCI)
- Research Motivation and Approaches
- MCCI Model Description and Analysis
- Governing Equations to Model MCCI
- Comparison with Experimental Data
- Results and Discussion of Concrete Ablation
  - Ablation field
  - Temperature field
  - Velocity field
  - Density field

Molten Corium Concrete Interaction (MCCI)

- **MCCI refers to the interaction of concrete with melted core which is a mixture of the**
  - Molten fuel,
  - Cladding, and
  - Structural elements, originating in the reactor core after an accident.
- **This molten corium could penetrate through the**
  - Reactor pressure vessel and
  - Interacts with the concrete cemented at reactor cavity bottom and sidewalls.
- **The characteristics and behavior of molten corium varies due to a number of factors**
  - Such as Time after which the coolant (water) is introduced into the reactor vessel.
- **If the cavity of the reactor is <u>pre-filled with coolant</u> before the accident,**
  - The molten corium after its release will first interact with the coolant and then with the concrete.
- **After the molten corium-coolant interaction, the corium will experience a**
  - Fragmentation phenomenon and
  - It could break up into debris of different sizes due to various cooling mechanisms that might take place in the reactor.

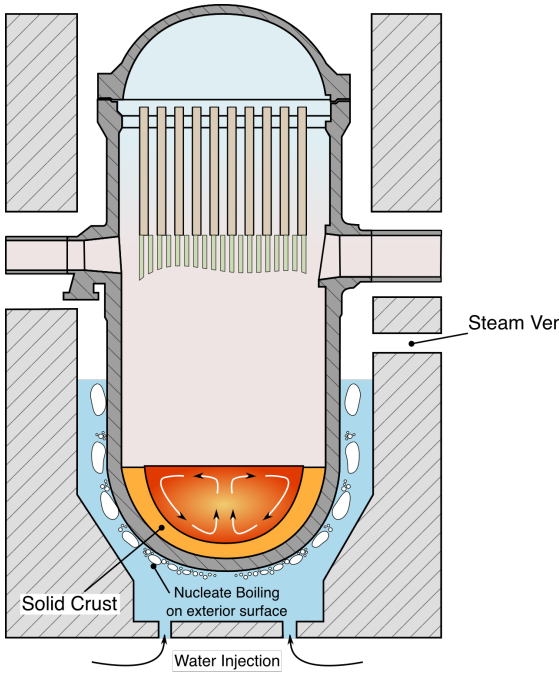

Research Motivation and Approach

- **In this research we used two approaches to**
  - Estimate and assess the different phenomena related to the **MCCI** for nuclear power plants
  - Analyze the use of Zr and SiC cladding on MCCI

1. **System Code**
2. **CFD**

- **To understand the effects of following parameters on concrete ablation**
  - Temperature
  - Concrete Composition
  - Water Injection Time
  - Corium Composition

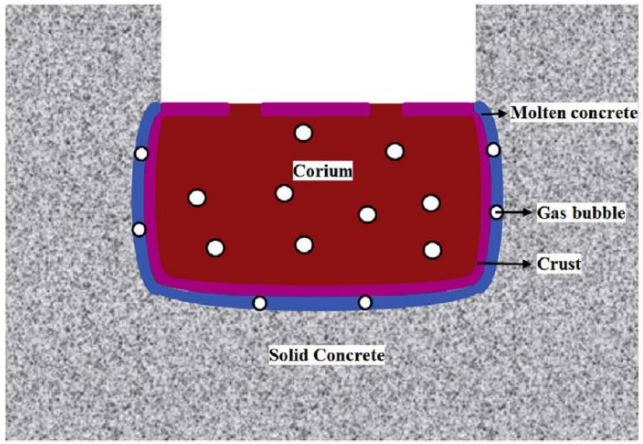

Progress in Nuclear Energy 144 (2022) 104102

Contents lists available at ScienceDirect

Progress in Nuclear Energy

journal homepage: www.elsevier.com/locate/pnucene

Influence of corium temperature, concrete composition and water injection time on concrete ablation during MCCI: New insights

Ilyas Khurshid [a,*], Imran Afgan [a], Amidu Muritala Alade [b,c], Addad Yacine [b,c]

[a] Department of Mechanical Engineering, Khalifa University, Abu Dhabi, P.O. Box 12277, United Arab Emirates
[b] Department of Nuclear Engineering, Khalifa University, Abu Dhabi, P.O. Box 12277, United Arab Emirates
[c] Emirates Nuclear Technology Center (ENTC), Khalifa University, Abu Dhabi, P.O. Box 12277, United Arab Emirates

energies

MDPI

Article

Thermochemical Modeling of Metal Composition and Its Impact on the Molten Corium–Concrete Interaction: New Insights with Sensitivity Analysis

Ilyas Khurshid [1,*], Imran Afgan [1,2] and Yacine Addad [3,4]

Governing Equations to Model Molten Corium Concrete Interaction

- **We developed a solver in OpenFoam to model phase change, concrete melting, mixing of corium and concrete and solidification using the transport, Energy and Momentum Equations.**

- **The volume fraction presenting the ratio of the melted concrete volume in a cell to the volume of the cell :**

- $\alpha_c(x,t) = \frac{V_{mc}}{V} = \begin{cases} 0, & inside\ solid\ phase \\ 0 < \alpha_{mc} < 1, & inside\ transitional\ region \\ 1, & inside\ orium\ \ phase \end{cases}$ **(1)**

- **The density and viscosity of a single mixture phase are defined as:**

- $\rho = \alpha_c \rho_c + (1 - \alpha_c)\rho_{mc},$ **(2)**
- $\mu = \alpha_c \mu_c + (1 - \alpha_c)\mu_{mc},$ **(3)**

where the subscript *c* stands for corium, and *mc* represent melted concrete

- **Considering the effect of gravity, the momentum equation is:**

- $\frac{\partial(\rho U)}{\partial t} + \nabla \cdot (\rho UU) = -\nabla_p + \nabla \cdot [\mu(\nabla U + \nabla UT)] + \rho g$ **(5)**

- **The energy equation utilized in the model is:**

- $\frac{\partial(\rho E)}{\partial t} + \nabla \cdot \big(U(\rho E + p)\big) = \nabla \cdot (k \nabla T) + S_h$ **(6)**

Numerical Model Development and Experimental Validation

Configuration of MCCI simulation domain
(a) Boundary conditions and geometry
(b) Mesh distribution of the two regions

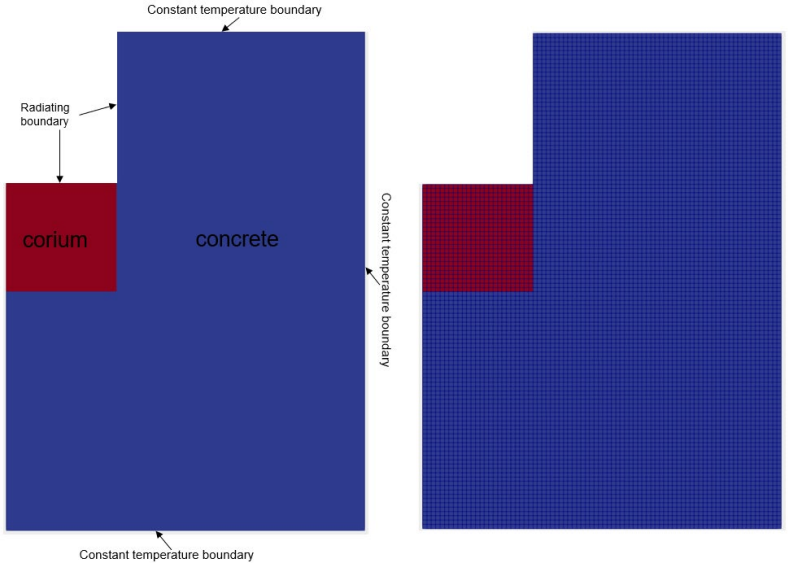

Table 4: CCI-2: Composition of corium and its temperature (Farmer, 2018)

Composition of corium (kg)	**Component**	**CCI-2**
	UO_2	242.48
	ZrO_2	99.60
	Cr	25.64
	SiO_2	13.56
	CaO	12.52
	MgO	4.56
	Al_2O_3	1.64
	Zr	0
	Fe	0
	Total	400.0
Temperature (K)	Initial set molten corium temperature	2150
	Upper structure temperature	750

Table 5: Properties of concrete used to model molten corium concrete interaction

Thermophysical properties of concrete	
Density (Kg/m^3)	$\rho = 2330$
Thermal conductivity (W/m.K)	$\lambda = 0.302$
Expansion coefficient (1/K)	$\beta = 12.9e^{-6}$
Latent heat of fusion (J/Kg)	L = 7,200
Viscosity (m^2/s)	$\eta = 4.29e^{-7}$
Specific heat capacity (J/kg.K)	c = 837.3
Concrete solidus temperature (K)	$T_{solidus} = 1393$
Concrete liquid temperature (K)	$T_{liquidus} = 1568$
Concrete ablation temperature (K)	$T_{ablation} = 1500$

Mesh Sensitivity and Experimental Validation

Mesh sensitivity study for the comparison of axial ablation depth

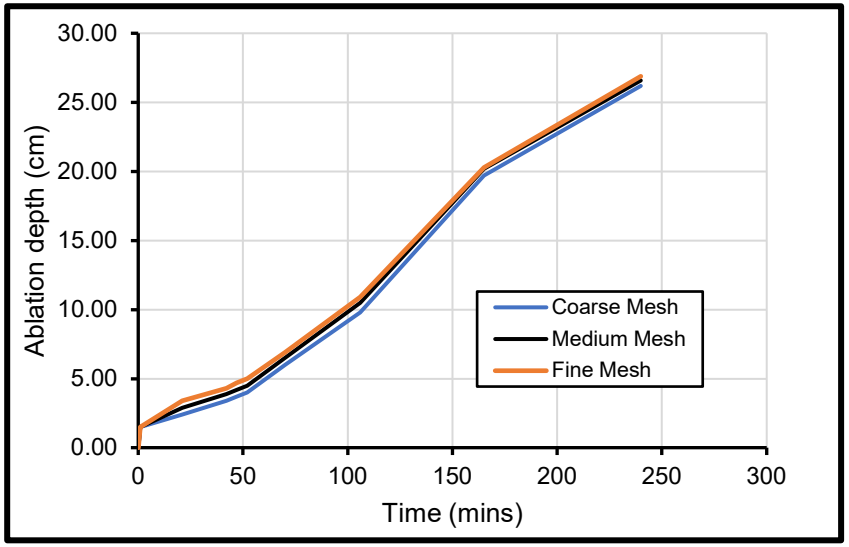

Comparison of resulting CFD model of concrete ablation with CCI-2 experimental data

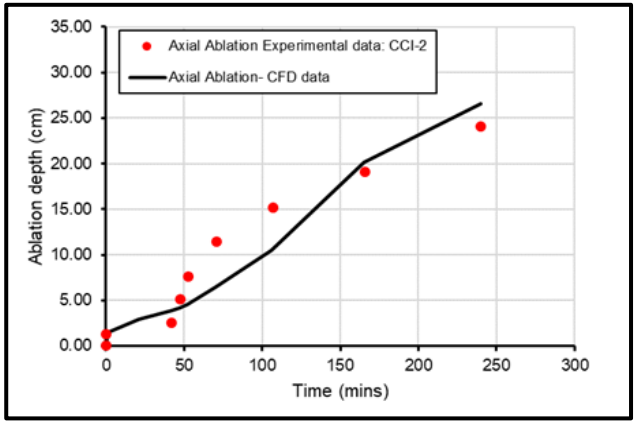

(a) Axial ablation

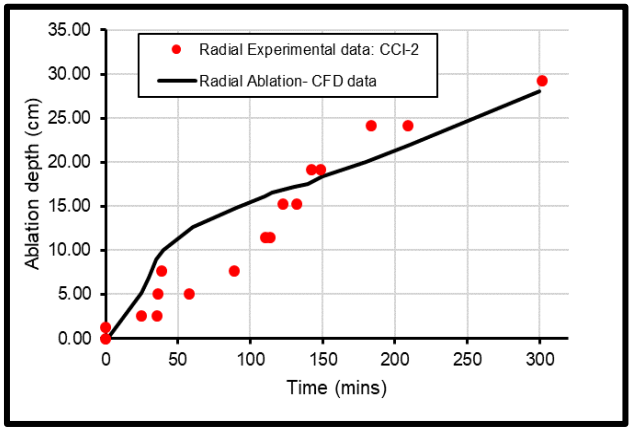

(b) Radial ablation

Comparison of ablation results of developed CFD model with experimental ablation

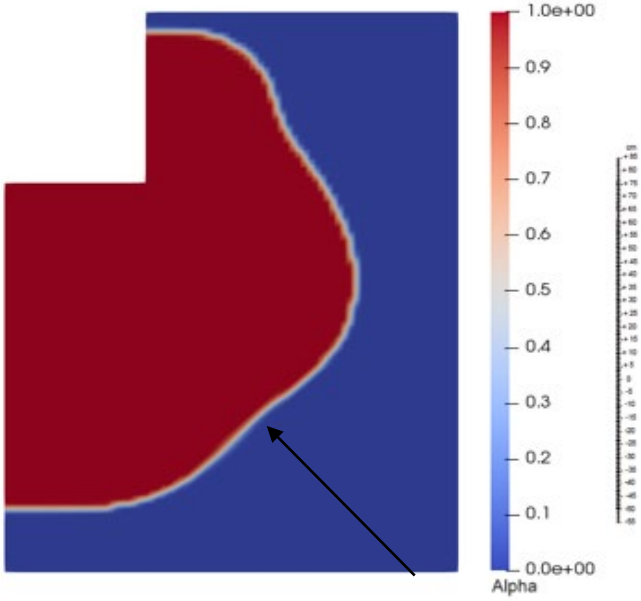

(a) CFD Results

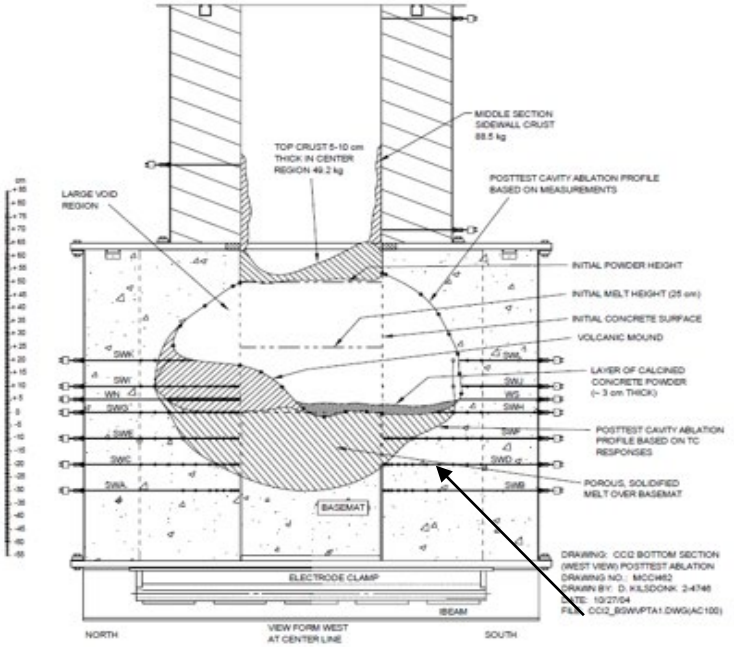

(b) Experimental results of final concrete shape

Results and Discussions of Concrete Ablation

1. Ablation field

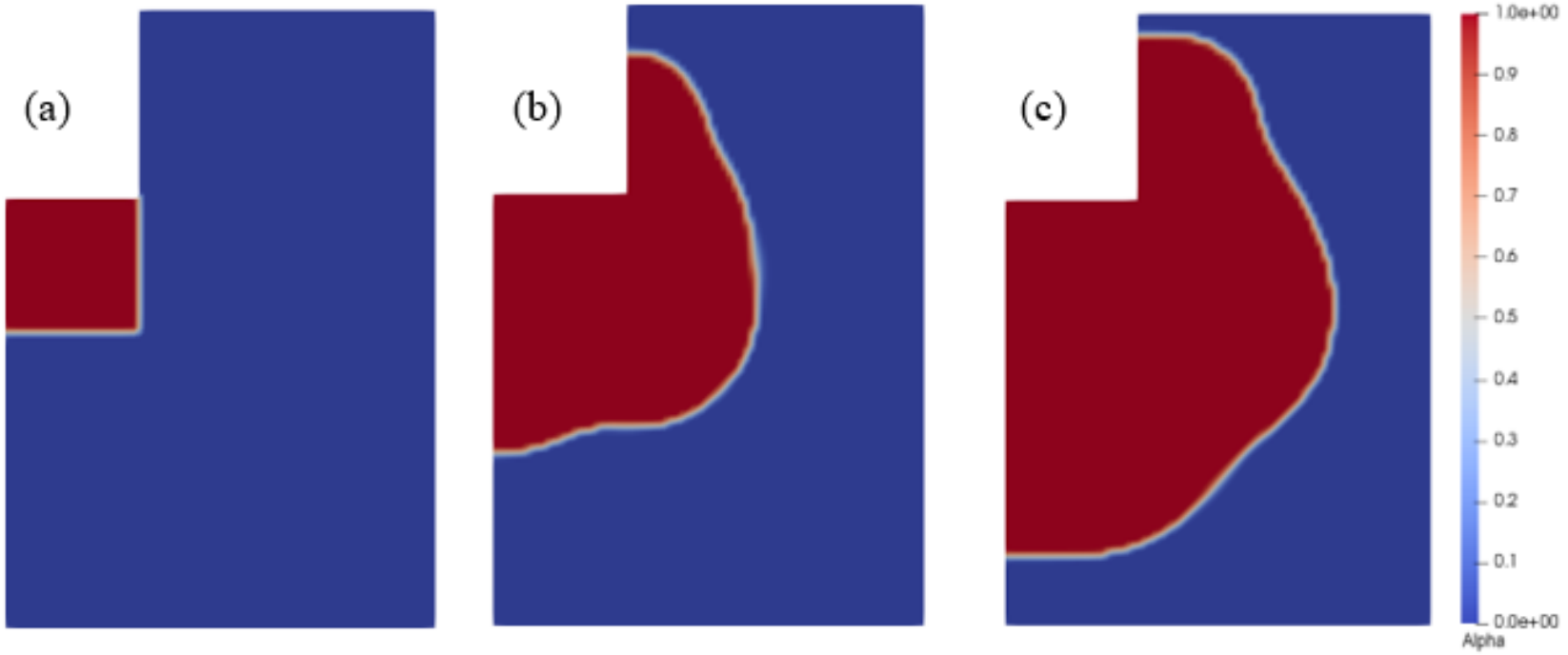

Ablation Field during MCCI at different timesteps (a) Zero timestep (b) 150 minutes (c) 300 minutes

2. Temperature field

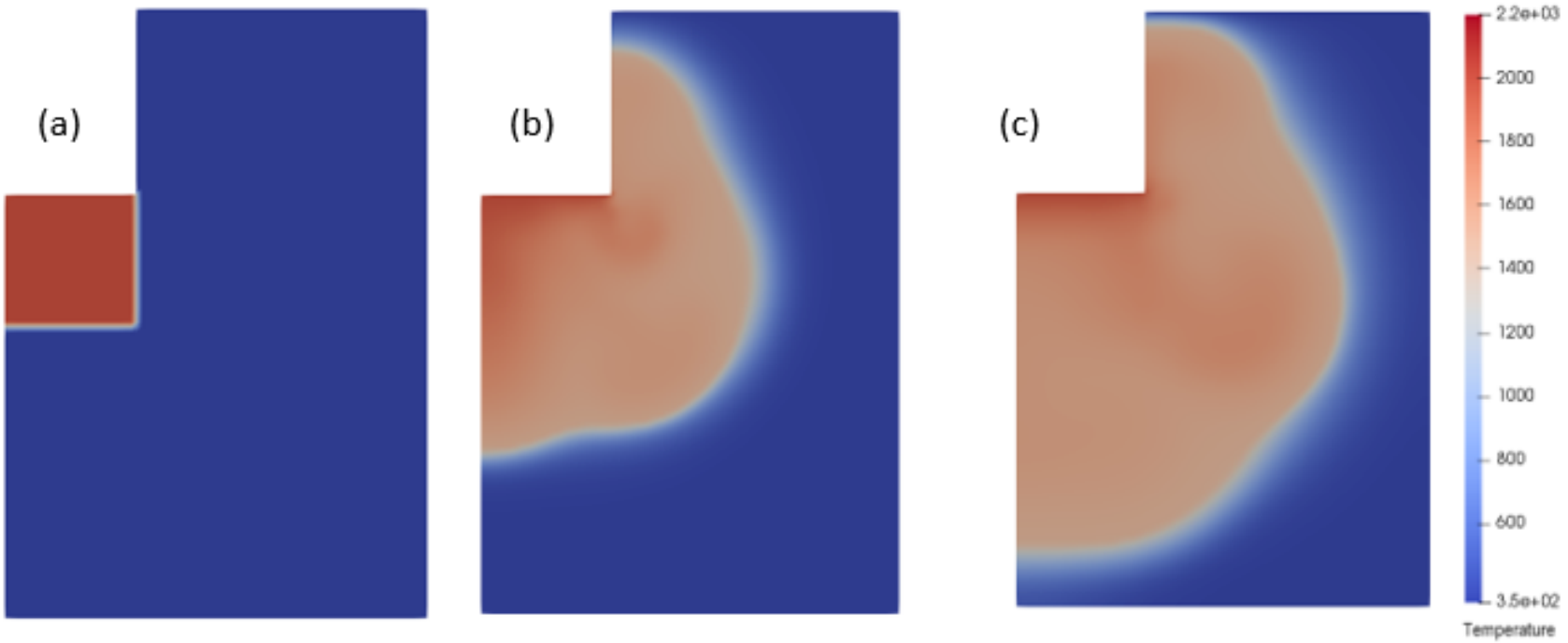

Temperature field during MCCI at different timesteps (a) Zero timestep (b) 150 minutes (c) 300 minutes

3. Velocity field

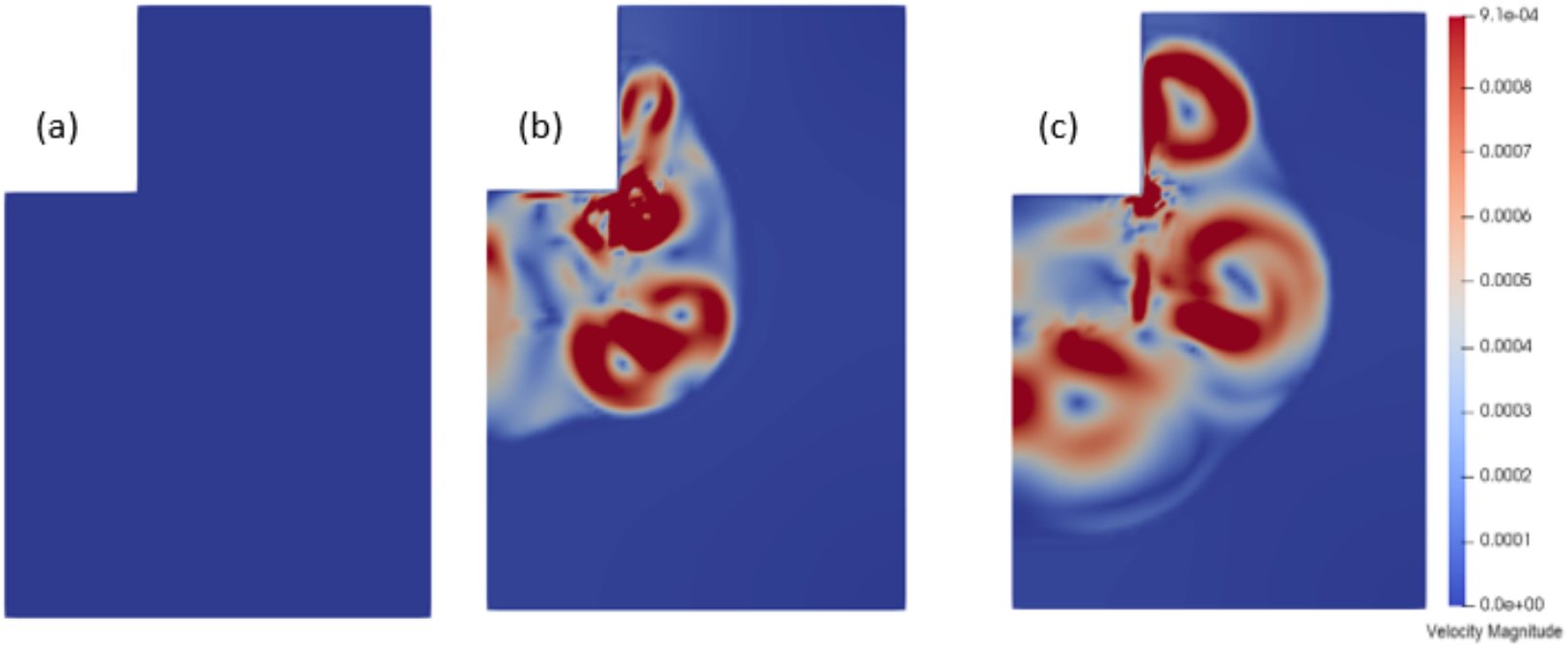

Velocity field during MCCI at different timesteps (a) Zero timestep (b) 150 minutes (c) 300 minutes

4. Density field

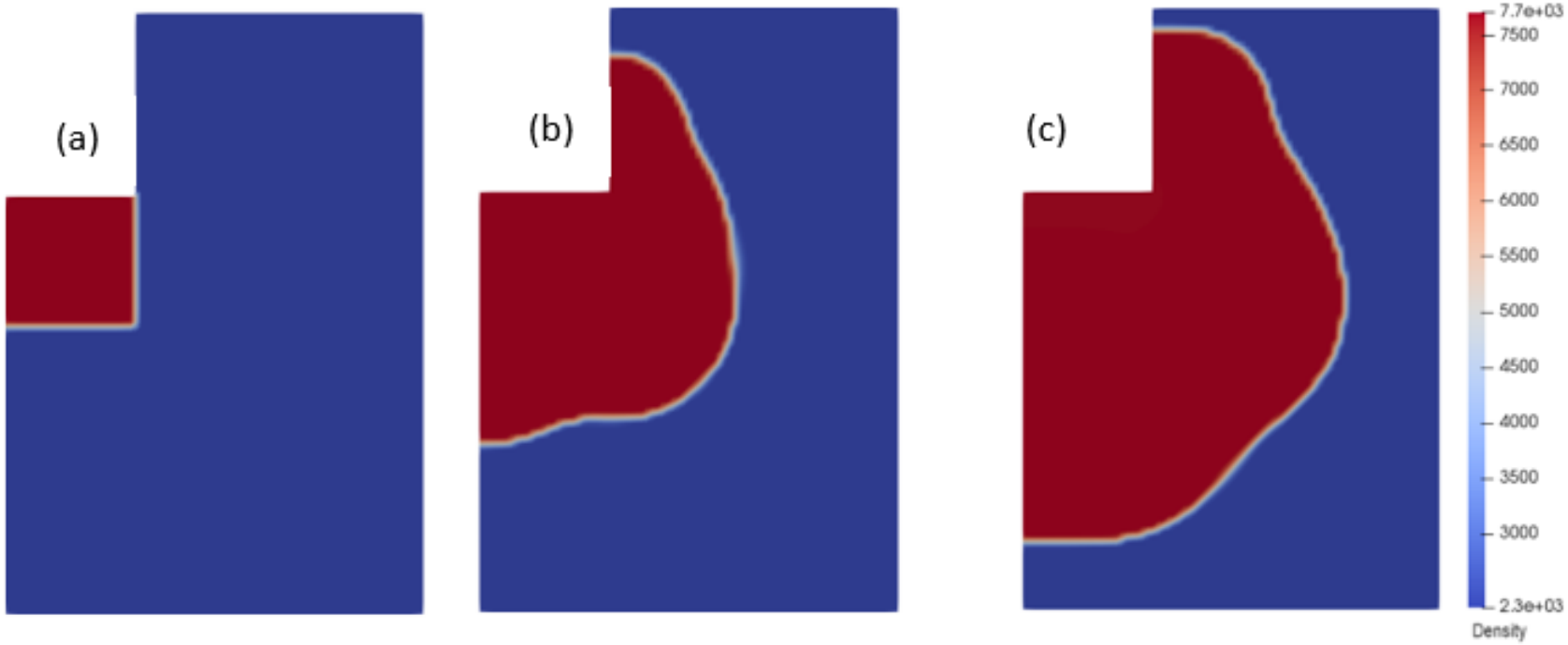

Density field during MCCI at different timesteps (a) Zero timestep (b) 150 minutes (c) 300 minutes

Conclusions

- **In this study, a numerical model was developed which is an extension of the fluid mixing model (interfoam). The model was used to simulate the**
  - Heat transfer, concrete ablation (phase change) phenomena, mass transfer, density and mixing of corium and melted concrete during the MCCI accident scenario for the first time.
- **The model is implemented in OpenFoam and the numerical model is validated against the two sets of concrete ablation experimental data**
- **The model proposed in this study able to capture the**
  - Natural convection, mass transfer, density variation of corium and concrete, and mixing within the molten corium concrete mixture.
- **Thus, the high temperature corium ablated the concrete and the mixing of corium and concrete intensified the natural convection along the concrete and corium interface,**
  - Thereby enhancing the mixing of the corium and melted concrete.
- **Consequently, this phenomenon positively impacts the ablation rate of the concrete by**
  - Decreasing the rate of concrete ablation.

- **For next stage additional physical phenomena are to be included in the model such: heat generation due to chemical reactions, crust formation, gas release,…etc.**

ERMSAR 2024

Thank you

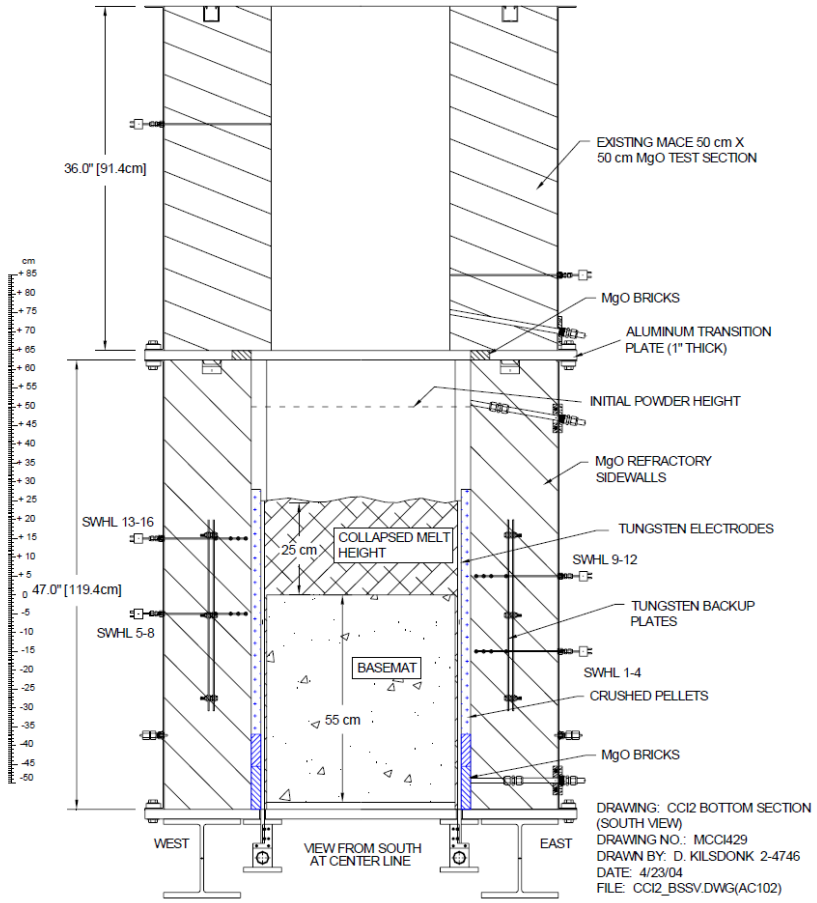
36.0" [91.4cm]
47.0" [119.4cm]
cm
+ 85
+ 80
+ 75
+ 70
+ 65
+ 60
+ 55
+ 50
+ 45
+ 40
+ 35
+ 30
+ 25
+ 20
+ 15
+ 10
+ 5
0
-5
-10
-15
-20
-25
-30
-35
-40
-45
-50
EXISTING MACE 50 cm X
50 cm MgO TEST SECTION
MgO BRICKS
ALUMINUM TRANSITION
PLATE (1" THICK)
INITIAL POWDER HEIGHT
MgO REFRACTORY
SIDEWALLS
SWHL 13-16
25 cm
COLLAPSED MELT
HEIGHT
TUNGSTEN ELECTRODES
SWHL 9-12
TUNGSTEN BACKUP
PLATES
SWHL 5-8
BASEMAT
SWHL 1-4
CRUSHED PELLETS
55 cm
MgO BRICKS
WEST
VIEW FROM SOUTH
AT CENTER LINE
EAST
DRAWING: CCI2 BOTTOM SECTION
(SOUTH VIEW)
DRAWING NO.: MCCI429
DRAWN BY: D. KILSDONK 2-4746
DATE: 4/23/04
FILE: CCI2_BSSV.DWG(AC102)

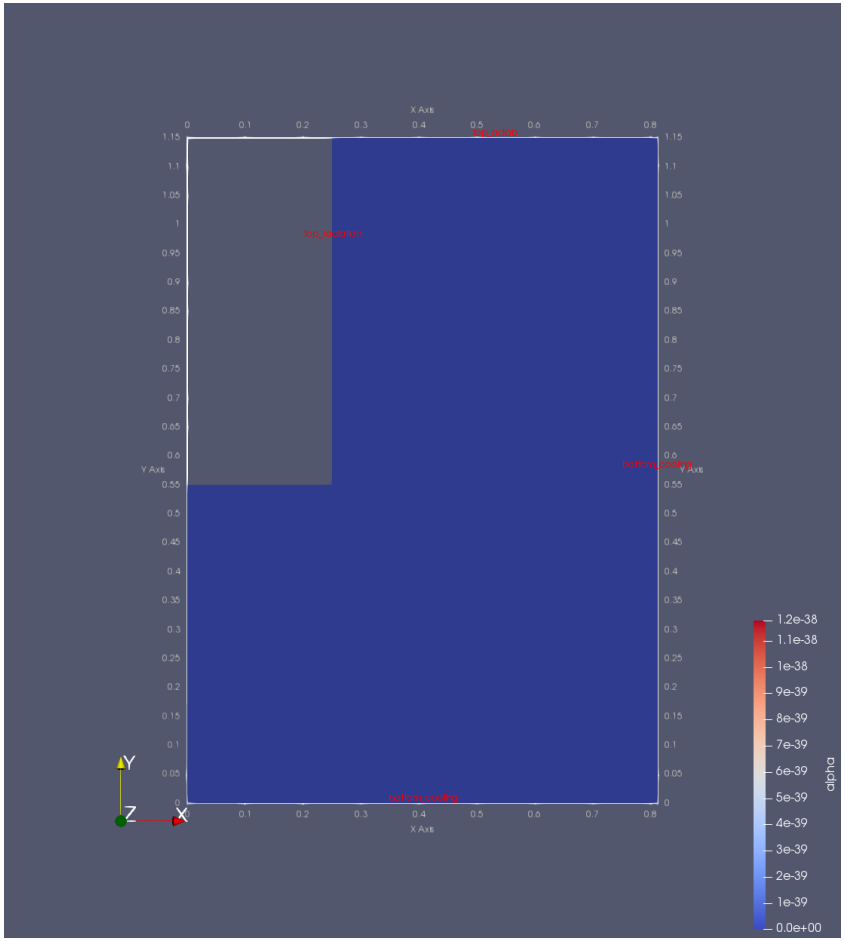
X Axis
Y Axis
top_outlet
top_inlet
bottom_outlet
bottom_inlet
alpha
1.2e-38
1.1e-38
1e-38
9e-39
8e-39
7e-39
6e-39
5e-39
4e-39
3e-39
2e-39
1e-39
0.0e+00
Y
Z
X

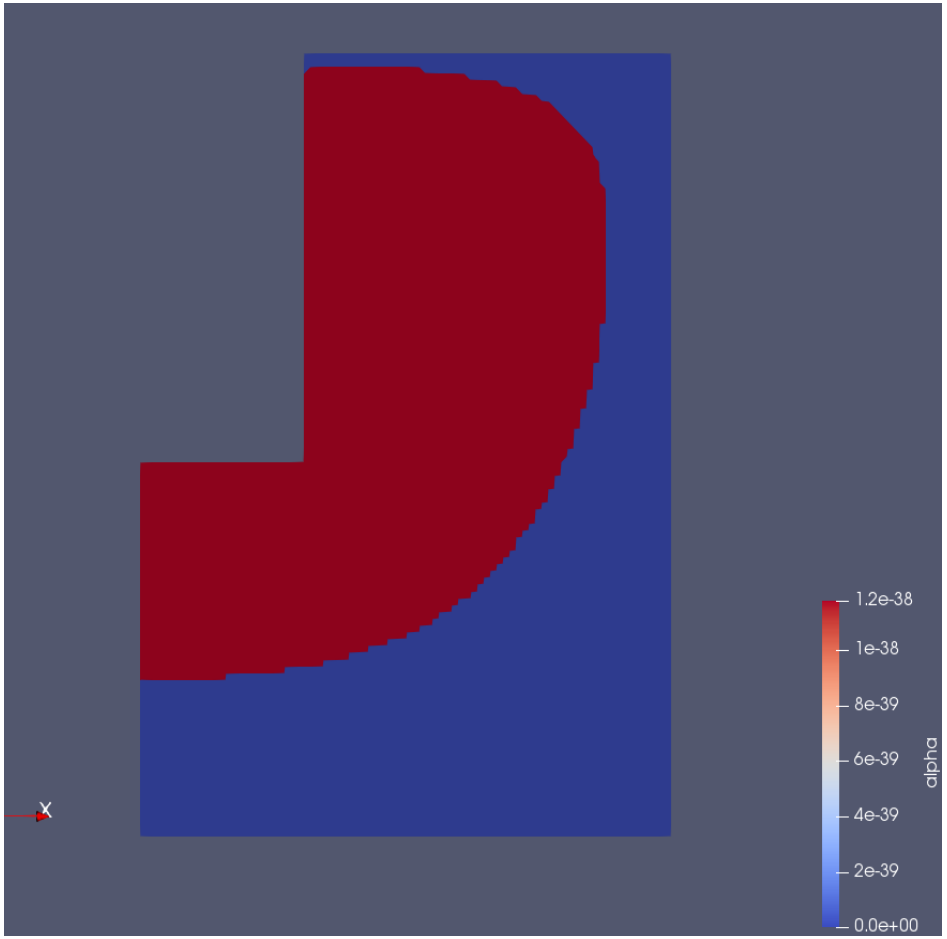
alpha
1.2e-38
1e-38
8e-39
6e-39
4e-39
2e-39
0.0e+00
X

CHARACTERISATION OF PROTOTYPIC EX-VESSEL FUEL DEBRIS INGOTS SIMULATING MCCI AT FUKUSHIMA DAIICHI

C Journeau, D Molina, V Bouyer, A Denoix
CEA, DES, IRESNE, DTN
Cadarache, F-13108 Saint-Paul-lez-Durance, France
christophe.journeau@cea.fr; diego.molina@cea.fr; viviane.bouyer@cea.fr; arthur.denoix@cea.fr

E Brackx, R Domenger,
CEA, ISEC, DRMC
Univ. Montpellier
Marcoule, France
Emmanuelle.brackx@cea.fr; renaud.domenger@cea.fr

A Ikeda-Ohno
JAEA, CLADS
Tokai-mura, Japan
ikeda.atsushi16@jaea.go.jp

ABSTRACT

Two experiments have been carried out in VULCANO facility to fabricate fuel debris representing MCCI products expected to be found in Fukushima Daiichi pedestals. VF-U1 test was an inductively-heated corium-concrete interaction experiment in which 46 kg of corium melt ablated a basaltic concrete representative of 1F concrete. In VF-U3 test, 40 kg of powders representative of the MCCI composition - estimated from unit 1 calculations and including prototypes of major fission product elements - have been mixed then melted by induction. Samples from both fuel debris prototypic experiments have been taken for analyses. Scanning Electron Micrography of samples from these fuel debris prototypes has been carried out in conjunction with Energy Dispersive Spectroscopy and X-Ray Diffraction. Quantitative phase analysis was carried out with Rietveld method. This provides insights on the composition of these debris and the large number of phases (silicate glass, uranium-zirconium oxides of various compositions, uranium-containing zirconium silicate, aluminosilicates, ferrosilicates, chromites, metallic droplets and blocks) present in them. Comparisons between these two experiments are discussed.

KEYWORDS
Fukushima Daiichi, Fuel Debris, MCCI, SEM, XRD

1. INTRODUCTION

One of the important challenges for the decommissioning of the damaged reactors of the Fukushima Daiichi Nuclear Power Station (1F) is the fuel debris cutting and retrieval. NDF Technical Strategic Plan 2023 for the Decommissioning of the Fukushima Daiichi Nuclear Power Station [1] indicates that *"it is necessary to develop fuel debris retrieval methods and safety assessment techniques for accident events"*. One of the major safety R&D issue is linked to the knowledge of radioactive dust generated by fuel debris cutting techniques.

Within the URASOL project carried out for IRID/JAEA by a French consortium (CEA, IRSN, ONET) [2], the dust production has been experimentally assessed during thermal or mechanical cutting of uranium-containing fuel debris prototypes have been fabricated at VULCANO facility in CEA Cadarache site.

Due to the expected heterogeneity of fuel debris, industrial materials such as ceramic and/or metallic pieces [3,4] are not suitable for a complete validation and it is indeed necessary to fabricate fuel debris simulants. Previously, some simulants have thus been fabricated with non-radioactive simulants [5, 6, 7]. Nevertheless, uranium oxide chemistry is very specific cannot well be simulated so that there is interest in carrying out experiments with uranium-containing prototypic fuel debris [3].

Two fuel debris prototypes (containing depleted uranium oxide) will be presented and compared. The first one, VF-U1, has been obtained from the solidification of a Molten Core Concrete experiment [8, 9] representing 3 days of MCCI at Fukushima Daiichi unit 1. The second test, VF-U3 aimed at fabricating by induction melting of a load, the composition of which has been derived from Robb et al. Fukushima Daiichi MCCI calculations [10].

In a first section, the experimental conditions will be described. Then a second section will present the material analyses carried out on these two prototypic materials. A final part will compare and discuss the results from these two experiments.

2. FABRICATION OF THE FUEL DEBRIS PROTOTYPES

The fuel debris prototypes have been fabricated in the VULCANO cell of PLINIUS experimental facility [11] within the IRESNE fission experimental platform of CEA at Cadarache.

2.1. VF-U1 MCCI test

In the VULCANO VF-U1 test [8], a uranium-containing molten core prototype has interacted with basaltic concrete. After high power melting, an average power of 38 kW has been injected by induction during 900 s (Figure 1), leading to the ablation of 9.6 dm3 of concrete corresponding to about 20 kg (Table I) by 46.4 kg of initial corium concrete mixture (Table II). Figure 1 also presents the temperature evolution until the thermocouples have been lost.

Figure 2 presents a view of the VF-U1 fuel debris prototype, still partly inserted within concrete during its removal. The bottom part is quite close to outer surface of the solidified ingot, while, as large pieces had already been removed in the top, this region is closer to the central plane of the crucible. A metallic layer is visible at the bottom [13].

Table I. VF-U1 dry concrete composition from ICP-AES analyses (oxides estimated from elemental analysis [12] and normalized to 100%)

Concrete oxide	SiO_2	CaO	Al_2O_3	Fe_2O_3	Na_2O	K_2O	MgO	TiO_2
wt%	66.3	11.2	9.5	6.6	2.7	1.6	1.5	0.7

Table II. VF-U1 corium load initial compositions [8]

	UO_2	ZrO_2 stabilized with 3.6wt% CaO	Stainless Steel (304L)	Zr
Mass (kg)	27.3	7.5	6.1	5.5
wt%	58.8	16.2	13.2	11.8

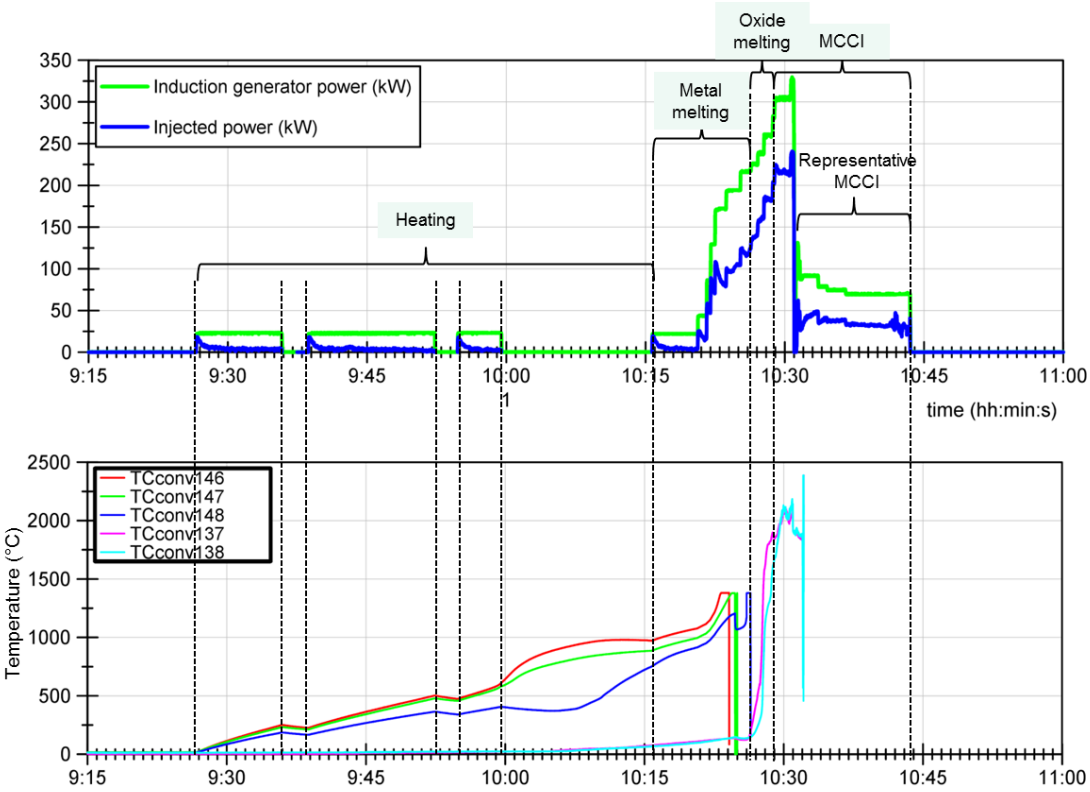

Figure 1: Power and temperature history of VF-U1 [8]

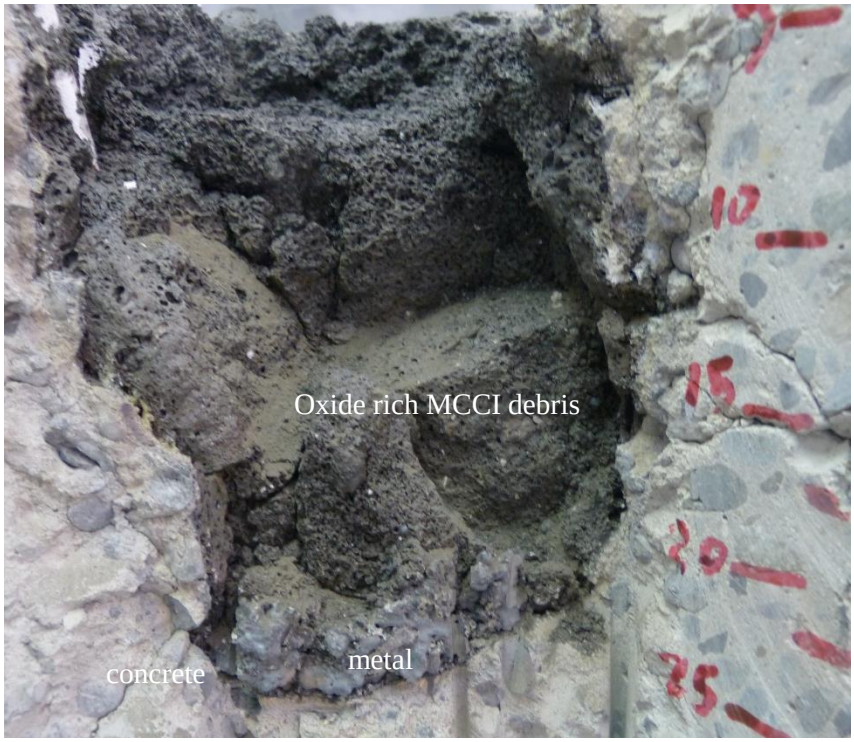

Figure 2. Post test view of VF-U1 during dismantling phase. (red scale is in cm)

2.2. VF-U3: Melting of an MCCI load

VF-U3 has been fabricated from a load (Table III) made of powders (except for stainless steel and iron that are used as susceptors to start the induction heating). The load has been introduced in a zirconia crucible (Figure 3 left). The crucible is surrounded by an induction coil. Protective sand is installed between coil and crucible as well as outside the coil.

Induction heating has been carried out for about 40 minutes with a power of the order of 40 kW. Then power has been slowly reduced. Figure 3 left presents the largest fuel debris prototype ingot that has been obtained. As for VF-U1, a metallic block has been segregated at the bottom [13]. Another oxidic block has been found at the top of the crucible, likely slightly above the initial position of the topmost metallic load (that has relocated to the bottom).

Table III: Load composition of VF-U3

	Wt%		Wt%
SiO_2	28.90%	**MoO2**	0.08%
UO_2	24.84%	**Nd_2O_3**	0.08%
ZrO_2	11.79%	**$CsOH.H_2O$**	0.06%
Fe_2O_3	11.02%	**RuO_2**	0.04%
Al_2O_3	7.21%	**BaO**	0.04%
CaO	5.87%	**La_2O_3**	0.03%
Stainless steel 304L	5.30%	**PdO**	0.02%
Fe	3.59%	**Pr_2O_3**	0.03%
Cr_20_3	0.55%	**Sm_2O_3**	0.02%
CeO_2	0.18%	**SrO**	0.02%
B_4C	0.17%	**Y_2O_3**	0.01%
SnO_2	0.15%	**TeO_2**	0.01%



**Figure 3: Left: Loading the powder and steel balls in zirconia crucible for VF-U3
Right: Post-heating side view of a 8.6 kg fuel debris prototype ingot from VF-U3**

3. MATERIAL ANALYSES

Material analyses have been carried out at CEA on samples from these blocks (excluding the metallic blocks that are described in [13]. Scanning Electron Microscopy (MERLIN from Carl Zeiss) has been carried out with Energy Dispersive X-ray spectroscopy (EDX) using an X max detector from Oxford Instruments. It is reminded, following an international round robin exercise on corium EDX analyses [15] that the uncertainties are larger for light elements - like oxygen - close to heavy elements and can account to 1/4th of the EDS measured value while the uncertainty for heavier elements is around 1/10th of the measured value.

X-ray diffraction has been obtained with a D8 ADVANCE diffractometer from BRUCKER AXS equipped with a copper cathode tube. The diffraction patterns have been quantitatively analysed Diffraction line indexing was performed with DiffracEva software from Bruker AXS with the 2020 Power Diffraction Files (PDF) international database. The X-Ray Diffraction spectra have been analysed by Rietveld refinement using the DIFFRAC.TOPAS v6 software distributed by Bruker.

3.1 Analyses of VF-U1 sample

Figure 4 presents a sample (VF-U1b) taken from the bulk of VF-U1 fuel debris, i.e. far from the concrete interfaces. Samples closer to the corium concrete interfaces are reported in [9]. This VF-U1b sample is quite heterogeneous. The differences in composition between light and dark colored areas of the SEM micrograph (Figure 4 right) were also apparent in the macrograph (Figure 4 left). This heterogeneity has been attributed to an incomplete mixing of corium and concrete leaving corium-rich (in white on micrograph) and concrete-rich (in dark on micrograph) regions.

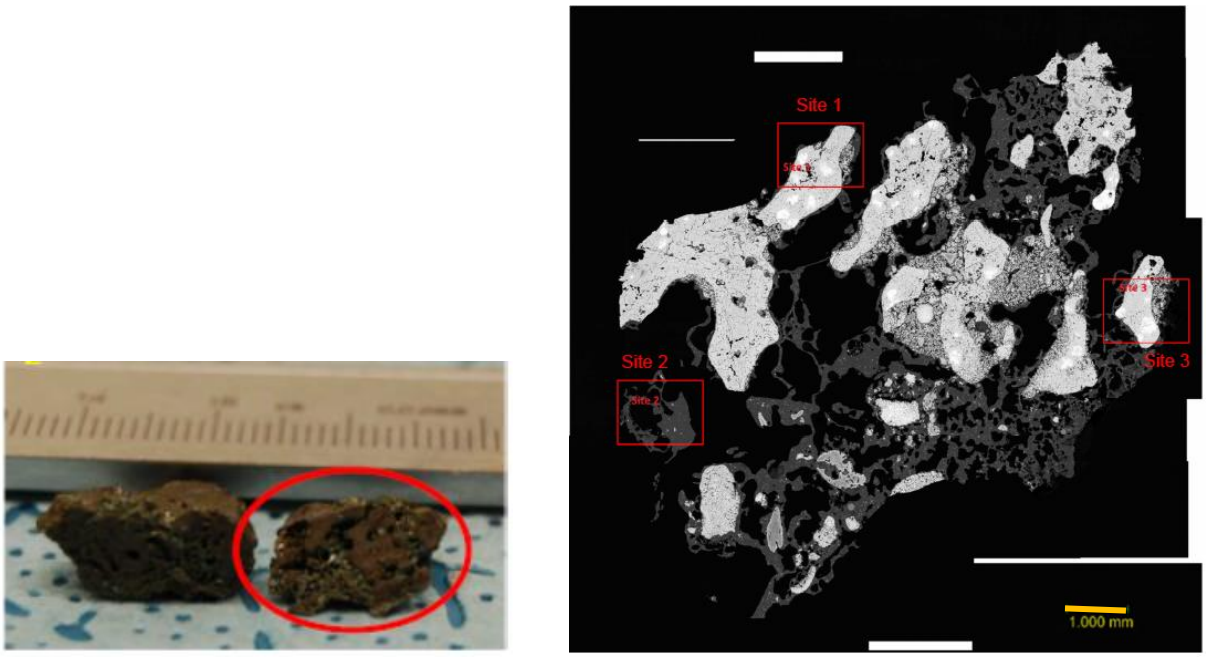

Figure 4: VF-U1 sample- Left: macrograph – Right composite SEM micrograph (scale= 1 mm)

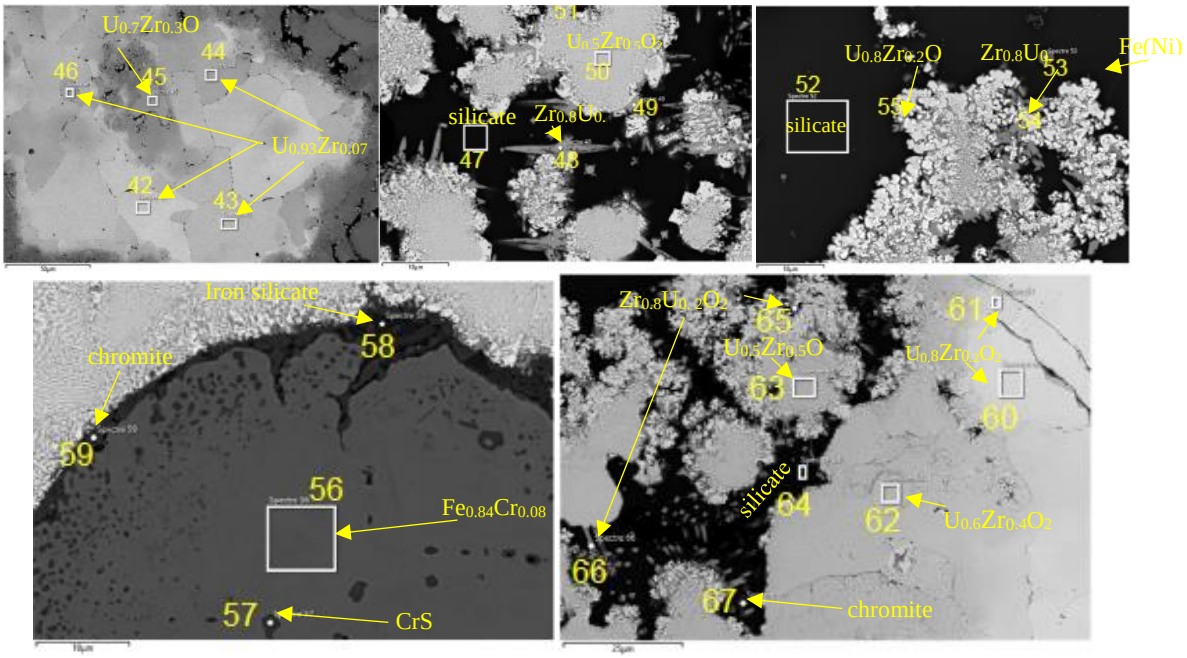

Figure 5: EDX analyses of sample VF-U1b

Figure 5 presents 5 micrographs from VF-U1b sample. Top left and top-center micrographs come from site 1, top-right from site 2 and bottom micrographs from site 3. The top left micrograph contrast has been tuned to show different shades in the uranium-zirconium oxides. Points 42, 43, 44, 46 correspond roughly to $U_{0.9}Zr_{0.1}O_2$ (average composition 33.5 at% U, 2.6 % Zr, 63.9 % O), while point 45 is close to $U_{0.7}Zr_{0.3}O_2$ (26 at% U, 12%% Zr, 62% O), point 62 is close to $U_{0.6}Zr_{0.4}O_2$ (19 at% U, 15% Zr, 66% O) and point 63 is almost $U_{0.5}Zr_{0.5}O_2$ (17 at% U, 16% Zr, 67%O). On the other micrographs, various U/Zr ratios are also observed: $U_{0.2}Zr_{0.8}O_2$ (point 48: 28 at% Zr, 8% U, 64%O; point 49: 27 at% Zr, 8% U, 66% O; point 54: 29 at% Zr, 6% U, 1% Si, 63% O; point 65: 27 at% Zr, 7% U, 1% Si, 65% O; point 66: 26 at% Zr, 6% U, 1% Si, 1% Al, 66% O); $U_{0.5}Zr_{0.5}O_2$ (point 50: 17 at% U, 16% Zr, 67% O); $U_{0.8}Zr_{0.2}O_2$ (point 55: 29 at% U, 8% Zr, 64% O

; point 60: 31 at% U, 6% Zr, 1% Al, 62% O; point 61: 27 at% U, 5%% Zr, 68% O). Some "eutectic-like patterns" have been observed in this sample. All the analyzed eutectic areas have the same average composition close to $U_{0.5}Zr_{0.5}O_2$. An explanation could be the partial transformation of a cubic $U_{0.5}Zr_{0.5}O_2$ into a cubic uranium-rich dioxide and a tetragonal zirconium-rich phase.

The uranium-zirconium oxides are surrounded by a silicate matrix rich in concrete elements (point 47: 23 at% Si, 6% Ca, 5% Al, 1% Na, 1% Mg, 1% Zr, 61% O; point 52: 23 at% Si, 5% Ca, 5% Al, 2% Na, 1% K, 1% Cr, 1% Fe, 1% Zr; point 64: 24 at% Si, 5% Al, 4% Ca, 1% Na, A% K, 1% Fe, 1% Zr). A phase close to chromite (Cr_2FeO_4) has been identified at points 67 (28 at% Cr, 13% Fe, 2% Mg, 1% Si, 57% O) and, with a Cr/Fe ratio close to 1, point 59 (18 at% Cr, 17% Fe, 2% Ca, 2% Si, 2% P, 58% O).
A metallic drop (around 50 µm diameter) has also been analysed (point 56: 84 at% Fe, 8% Cr, 7% Ni) and is less depleted in chromium and nickel than the metallic layer of VF-U1 [13]. It contains a chromium sulphide inclusion (point 57: 44 at% Cr, 7% Fe, 49% S). A phase close to ferrosilite ($FeSiO_3$) has been observed at the periphery of the metallic drop (point 58: 19 at% Si, 17% Fe, 2% Cr, 2% Ca, 1% Al, 1% Mg, 58% O). A smaller (~∅2 µm) metallic droplet has also been observed (point 53: 94 at% Fe, 3% Ni, 2% P, 1% Cu, 1% Si). It is totally depleted in chromium and more depleted in nickel than the larger drop (point 56) or the metallic collected at the bottom of the concrete crucible [13].

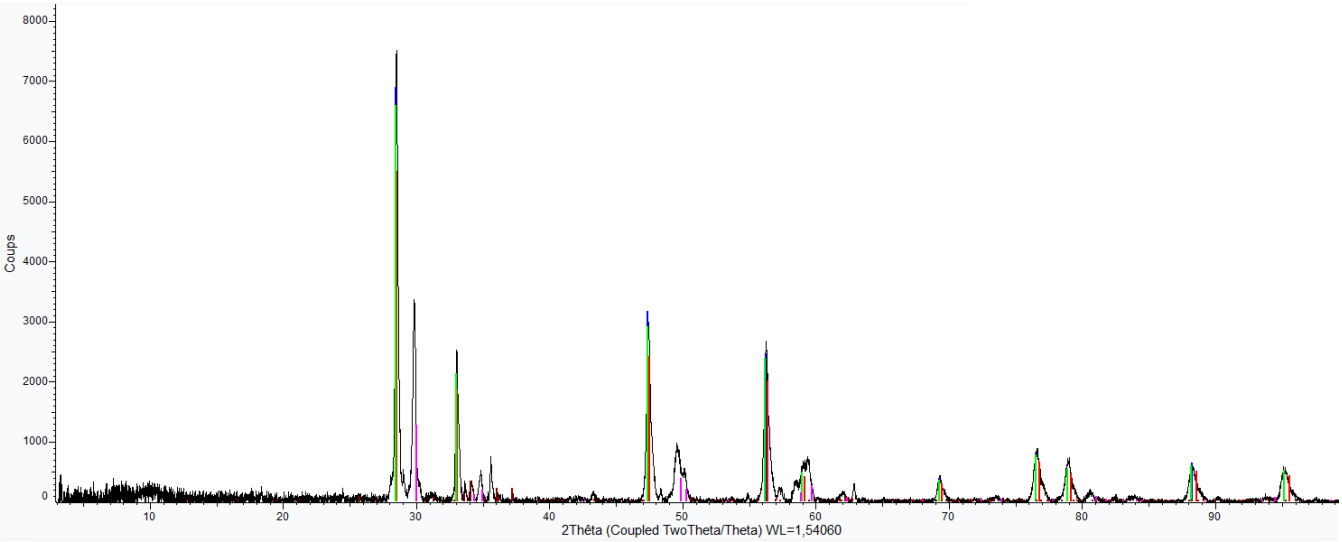

Figure 6: XRD pattern of VF-U1b sample

Reference patterns: Red: $U_{0.8}Zr_{0.2}O_2$ – Green: $U_{0.7}Zr_{0.3}O_2$ – Blue: $U_{0.5}Zr_{0.5}O_2$ – Red: $U_{0.1}Zr_{0.9}O_2$ Purple: Cr_2FeO_4

Powders crushed from sample VF-U1b have been crushed and their X-Ray diffraction pattern has been determined (Figure 10). Three phases have been identified: a uranium-rich dioxide ($U_{0.8}Zr_{0.2}O_2$), a zirconium-rich dioxide ($U_{0.1}Zr_{0.9}O_2$) and chenmingite (an orthorhombic $FeCr_2O_4$). As chenmingite is reported to be a high-pressure allotrope of chromite [14], it can be hypothesized that the presence of minor elements (Mg, Ca) observed with (Fe, Cr) oxides in EDS analyzed stabilized this phase which has a $CaFe_2O_4$-type structure. Rietveld analysis has been carried out on this pattern (Figure 6) in order to provide a quantitative best-fit of the measured spectrum. It corresponds to 68 wt% uranium-rich dioxide, 21 % zirconium-rich dioxide and 11% chromium-iron oxide. The silicate-rich matrix observed by EDS is not

detected by XRD. Brissonneau et al. [9] who observed the same effect other samples from this experiment suggests that the silicate-rich matrix is vitreous.

3.2 Analyses of VF-U3 sample

VF-U3c sample has been taken from the central part of VF-U3 larger block and has visually a fused fuel debris aspect (Figure 7 left). SEM micrograph (Figure 7 right) shows 3 sites that have been considered more in detail.

EDX analyses have been carried out on the points indicated on the micrographs of Figure 8. A series of uranium-zirconium oxides have been observed: $U_{0.9}Zr_{0.1}O_{2-x}$ is present on points 36 (32 at% U, 5% Zr, 1% Fe, 62% O), 41(33 at% U, 5% Zr, 62% O) and 47 (32 at% U, 5% Zr, 1% Fe, 63% O); $Zr_{0.6}U_{0.4}O_{2-x}$ has been found in point 42 (20 at% Zr, 15% U, 62% O); $Zr_{0.8}U_{0.2}O_{2-x}$ has been identified at points 34 (30 at% Zr, 6% U, 1% Fe, 63% O) and 39 (29 at% Zr, 7% U, 64% O); $Zr_{0.9}U_{0.1}O_{2-x}$ has been analyzed at points 45 (32 at% Zr, 5% U, 1% Fe, 63% O), 48 (29 at% Zr, 4% U, 1% Si, 1% Fe, 1% Al, 64% O) and 49 (31 at% Zr, 4% U, 1% Fe, 64% O). Zirconia is also present with some silicate in points 37 (26 at% Zr, 4% U, 3% Si, 1% Al, 65% O) and 51 (22 at% Zr, 7% Si, 3% U, 2% Al, 2% Fe, 1% Ca). Due to the phase small sizes, it is possible that the analysis is polluted by the silicate matrix surrounding it.

The black matrix is indeed a silicate (22 at% Si, 6% Al, 5% Fe, 4% Ca, traces Zr, U, 62 % O) having roughly the same composition at points 32, 38 and 43.

Points 35 (24 at% Cr, 15% Fe, 5% Al, 57% O), 40 (23 at% Cr, 14% Fe, 5% Al, 57% O) and 46 (21 at% Cr, 15% Fe, 6% Al, 58% O) are likely a spinel (chromite with some aluminum solution).

There is also amidst these oxidic phases a micronic ball of iron (point 33: 99% Fe, traces of Mo, Sn; point 44: 99 at% Fe, traces S, Sn; point 50: 96 at% Fe, 2% Mo, 1% Si, traces Al, Ca, Zr).

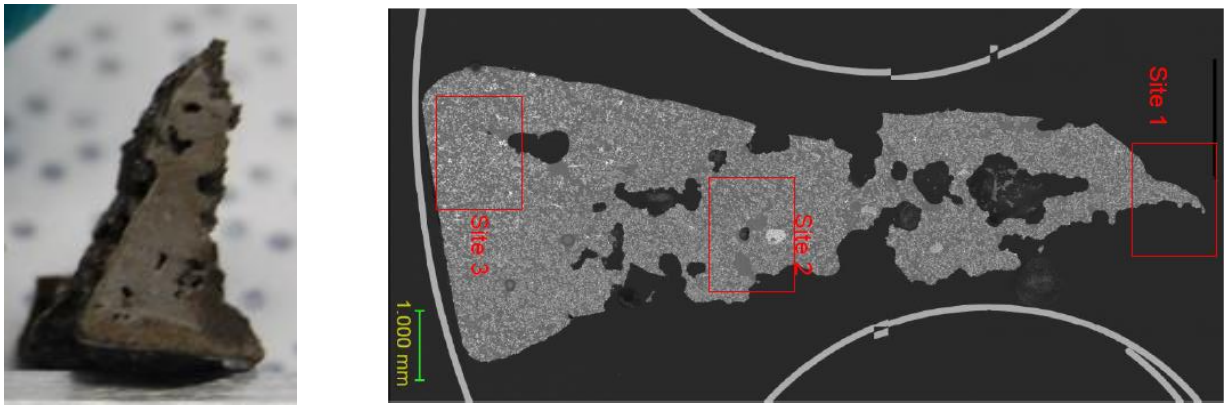

Figure 7 : Macrograph (left) and composite micrograph of sample VF-U3c

silicate

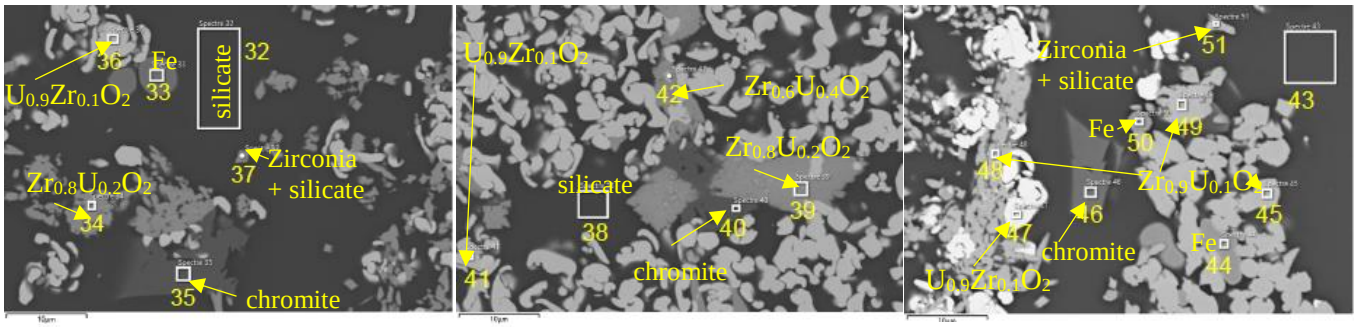

Figure 8. SEM micrographs from VF-U3c, taken, from left to right, from sites 1, 2 and 3. Scale is 10 µm.

In other samples from the VF-U3 fuel debris, as sample VF-U3a (Figure 9) coming from the top ingot, which may have experienced less interaction with the metallic load, a uranium-containing zirconium silicate (chernobylite (Zr,U)SiO_4 [16]) has been found: points 52 (16 at% Zr, 2% U, 17% Si, 64% O) and 53 (15 at% Zr, 3% U, 18% Si, 64% O). An aluminosilicate, close to anorthite, $CaAl_2Si_2O_8$, have been detected in point 54 (18 at% Si, 13% Al, 7% Ca, 1% Fe, 61% O). A ferrosilicate, close to hedenbergite ($CaFeSi_2O_6$), has been found at points 55 (19 at% Si, 12% Fe, 8% Ca, 59% O). Fayalite (Fe_2SiO_4) has also be observed in other areas of this sample. In the studied area of VF-U3a, uranium-rich oxide $U_{0.9}Zr_{0.1}O_2$ (points 56: 33 at% U, 3% Zr, 2% Fe, 2% Si, 61% O) and zirconium rich oxide (points 57: 26 at% Zr, 3% Fe, 2% Ca, 1% U,1% Al, 63% O) are here found as submicronic grains.

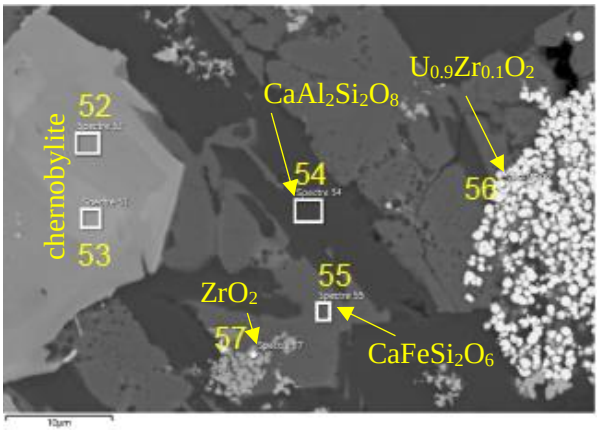

Figure 9 : Micrographs from VF-U3a.

Scale is 10 µm.

In VF-U3, fission product prototypes (having the natural isotopic composition) have been included in the load. It is thus interesting to study where these elements are present in the fuel debris phases.

- Cesium has mostly been volatilized during the melting phase. Nevertheless, about 0.1 at% has been detected in calcium iron silicates.

- Cerium (representing both Ce as a fission product and used as a surrogate of plutonium and minor actinides [19]) is found in calcium iron silicates (with concentrations up to 0.2 at% and also, once in a $Zr(U)O_2$ oxide with a 0.3 at% concentration).
- Molybdenum has been found within iron microballs (concentrations between 0.3 and 1.75 at%)
- Palladium has been observed in a (Sn, Ni, Fe) precipitate within the large metallic block.
- Tellurium has been found in iron telluride precipitates within the large metallic block.

Figure 10 presents the XRD pattern from powders obtained from VF-U3c sample. Four phases have been fitted to this pattern. Using Rietveld refinement, it has been possible to evaluate their relative proportions:

- Uranium-zirconium oxide ($U_{0.9}Zr_{0.1}O_2$): 43 wt%.
- Tetragonal zirconium oxide (ZrO_2): 33 wt%.
- Ferrous oxide (γ–Fe_2O_3): 20 wt%.
- Aluminum-iron oxide ($Fe_{0.9}Al_{1.1}O_3$): 4 wt%.

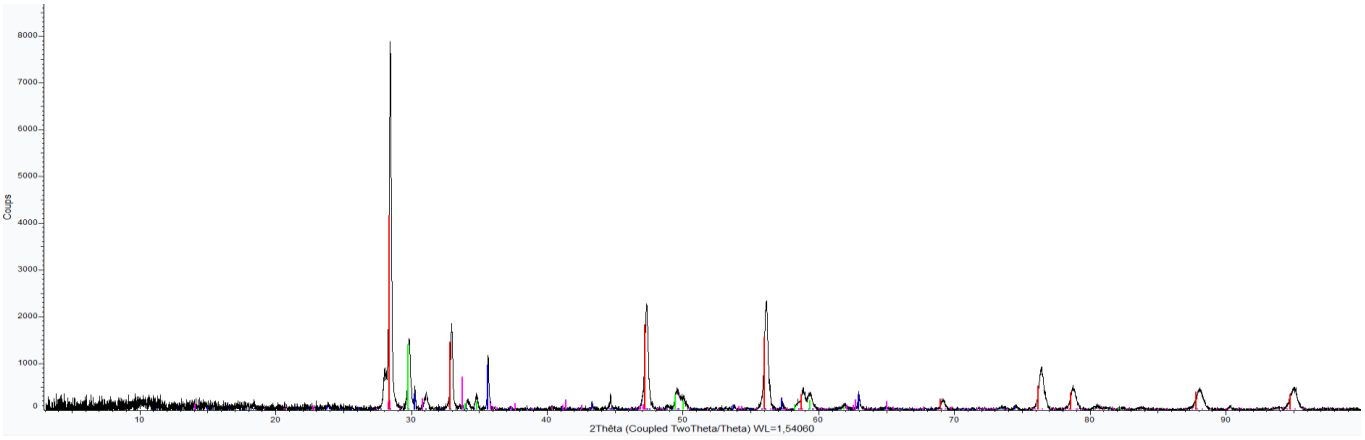

Figure 10: XRD pattern for sample VF-U3c

Reference patterns: Blue: γ-Fe_2O_3 – Green: ZrO_2 – Purple: $Fe_{0.9}Al_{1.1}O_3$ – Red: $U_{0.9}Zr_{0.1}O_2$

The major uranium-zirconium oxides have been observed in the EDX analyses. The ferrous and alumino-ferrous oxides have not been directly detected but there were many chromite phases. Finally, as for the other analyzed ex-vessel samples, there is no pattern linked to the silicate matrix, which is thus likely to be amorphous.

For the VF-U3a sample, zircon ($ZrSiO_4$) has been detected and corresponds to 1 wt% of the total mass. It is difficult to determine which of the two samples experienced the slowest cooling phase. The only sure difference is that interaction with the steel melt lasted less in VF-U3a as the metallic melt relocated downwards from the area of the top ingot from which VF-U3a has been taken.

4. COMPARISON AND DISCUSSION

In both fuel debris prototypes of MCCI, the matrix phase is a silicate. For VF-U1, its composition is around 61 at% SiO_2, 16 % CaO, 14% $AlO_{1.5}$, 3% $NaO_{1/2}$, 2% MgO, 2% ZrO_2, 2% $KO_{1/2}$, 1% FeO_x. For VF-U3, there is a larger iron oxide content in the silicate matrix with a typical composition (point 38) around: 59 at% SiO_2, 15% CaO, 13% FeO_x, 11% $AlO_{1.5}$, 1% ZrO_2 (and 0.2% UO_2). The VF-U3 composition indeed corresponds to a scenario with a larger oxidation of iron than in VF-U1.

It must be noted that the matrix has not been found in the XRD patterns. This strongly hints that the matrix is vitreous. In some cases, some crystallized silicate has been observed: ferrosilicates as ferrosilite ($FeSiO_3$), fayalite (Fe2SiO4) and hedenbergite (CaFeSi2O6) and aluminosilicates such as anorthite, CaAl2Si2O8, as well as a zirconium-uranium silicate, chernobylite $(Zr,U)SiO_4$.

Uranium and zirconium oxides form the majority of crystalline phases (89 wt% for VF-U1b and 76 wt% for VF-U3). There is a large variety of compositions from uranium-rich phases to pure zirconia, in accordance to the total miscibility at high temperature between these two oxides. An interesting feature in VF-U1 is the formation of eutectic like structures of average composition close to $U_{0.5}Zr_{0.5}O_2$. An explanation could be the partial transformation of a cubic $U_{0.5}Zr_{0.5}O_2$ into a cubic uranium-rich dioxide and a tetragonal zirconium-rich phase, which should occur around 2000 K according to the UO_2-ZrO_2 phase diagram [17]. If instead, the phase diagram of Levin and McMurdie [18] is considered, a 40 at% Zr oxide would present a 10% Zr solidus composition that could also explain the observed phases.

The separation of a uranium-zirconium oxide two series of so-called low-temperature phases (one rich in zirconium and one rich in uranium) has also been observed in uranium-containing dusts collected in Fukushima Daiichi PCVs and refueling floor [20].

Spinels mainly chromites (close to Cr_2FeO_4, but also more complex compositions as $Cr_{1.8}Fe_{1.2}Al_{0.5}O_4$). They often form polyhedral precipitates [9].

Finally, some metallic balls have been found in suspension in the oxidic fuel debris samples. It must be noted that they usually are richer in nickel (and in chromium) than the composition of the large metallic blocks found at the bottom of the test sections [13].

Cesium and Cerium have been detected by EDX in the oxidic phase (mainly in calcium iron silicates) while molybdenum, palladium and tellurium were found in metallic phases, either in metallic microballs or in the large metallic block.

In conclusion, analysis of these MCCI two fuel debris prototypes confirmed their heterogeneous nature with silicate glass, uranium-zirconium oxides of various compositions, uranium-containing zirconium silicate, aluminosilicates and ferrosilicates, chromites, metallic droplets and blocks. These results are important to evaluate the fuel debris behavior during leaching [21] or aerosol production during cutting [2].

ACKNOWLEDGMENTS

Most of this work is part of tasks by ONET/CEA/IRSN consortium contributing to the Japanese governmental subsidy program “Project of Decommissioning and Contaminated Water Management (Development of Analysis and Estimation Technology for Characterization of Fuel Debris)” organized by International Research Institute for Nuclear Decommissioning (IRID).
VF-U1 experiment has been carried out within the frame of JAEA-CEA collaboration (Specific contract DEN 4581) for a better knowledge on Fukushima-Daiichi Severe Accidents in links with the research

program entrusted to the International Research Institute for Nuclear Decommissioning (IRID) by the Agency for Natural Resources and Energy, Ministry of Economy, Trade and Industry (METI) of Japan.

REFERENCES

1. Nuclear Damage Compensation and Decommissioning Facilitation Corporation (NDF), *Technical Strategic Plan 2020 for Decommissioning of the Fukushima Daiichi Nuclear Power Station of Tokyo Electric Power Company Holdings, Inc*. NDF report (2023). https://www.dd.ndf.go.jp/files/user/pdf/en/strategic-plan/book/20231222_SP2023eFT.pdf
2. E. Porcheron, Y. Leblois, A. Bouland, C. Journeau, C. Suteau, J. Delacroix, D. Molina, R. Berlemont, Y. Lallot, D. Roulet, Y. Tsubota, A. Ikeda-Ohno, "Particle Generation Test Using Simulated Uranium Containing Debris: The URASOL project in the framework of Fukushima Daiichi dismantling", *Proc. DEM 2021 – International Conference on Decommissioning Challenges: Industrial Reality, Lessons learned and Prospects*, Avignon, France, 13-15/9/2021 (2021).
3. C. Journeau, D. Roulet, E. Porcheron, P. Piluso, C. Chagnot, Fukushima Daiichi fuel debris simulant materials for the development of cutting and collection technologies, *J. Nucl. Sci. Technol.* **55**(9), pp. 985-995 (2018).
4. K. Nomura, K. Shiihara, I. Chida, W. Kono, J. Suzuki "Evaluation of removal technologies of fuel debris using the laser processing", *Proc. 20th national symposium on power and energy systems (SPES 2015), .* Tokyo, Japan (June 2015).
5. C. Journeau, J. Monneris, B. Tormos, L. Brissonneau, E. Excoiffier, V. Testud, C. Chagnot, D. Roulet, "Fabricating Fukushima Daiichi in-vessel and ex-vessel fuel debris simulants for the development and qualification of laser cutting technique", *Proc. ERMSAR-2017 (Eur. Rev. Mtg Sev. Accident Res.)*, May 16-18 2017. Warsaw, Poland (2017).
6. M. Takano, T. Nishi, N. Shirasu, "Characterization of solidified melt among materials of UO2 fuel and B4C control blade", *J. Nucl. Sci. Technol.* **51**(7-8) pp. 859-875 (2014).
7. Q. Zhou, T. Saito, S. Suzuki, K. Yano, Sh. Suzuki, "Microparticles with diverse sizes and morphologies from mechanical and laser cutting of fuel debris simulants and geopolymer as a covering material", J. Nucl. Sci. Technol. **58** (4) pp. 461-472 (2021).
8. V. Bouyer, C. Journeau, J.F. Haquet, P. Piluso, A. Nakayoshi, H. Ikeuchi, T. Washiya, T. Kitagaki, « Large scale VULCANO Molten Core Concrete Interaction test considering Fukushima Daiichi condition, *Proc. ERMSAR-2019*, Prague, Czech Rep. (2019).
9. L. Brissonneau, H. Ikeuchi, P. Piluso, J. Gousseau, C. David, V. Testud, J. Roger, V. Bouyer, T. Kitagaki, A. Nakayoshi, S. Dubois, T. Washiya, "Material characterization of the VULCANO corium concrete interaction test with concrete representative of Fukushima Daiichi nuclear plants", *J. Nucl. Mater.* **528**, 151860 (2020).
10. K. Robb, M.W. Francis, M. T. Farmer, Ex-Vessel Core Melt Modeling Comparison between MELTSPREAD-CORQUENCH and MELCOR 2.1, Oak Ridge National Lab report ORNL/TM-2014/1 (2014).
11. C. Journeau, V. Bouyer, F. Charollais, N. Chikhi, J. Delacroix, A. Denoix, H. Laffolley, C. Mattassoglio, D. Molina, P. Piluso, P. Sauvecane, S. Thilliez, B. Turquais, C. Suteau, "Upgrading the PLINIUS platform toward smarter prototypic-corium experimental R&D", *Nucl. Eng. Des.* **386**, 111511 (2022).
12. H. Laffolley, *Synthèse de microparticules de silicate riches en césium par interaction de combustible en fusion avec du béton - Simulation expérimentale de phénomènes présents lors de l'accident de Fukushima Daiichi*, PhD thesis, IMT Atlantique, Nantes , France (2023).
13. C. Journeau, D. Molina, E. Brackx, R. Berlemont, Y. Tsubota, "Experiences from the cutting of metallic blocks from simulant Fukushima Daiichi fuel debris", *Proc. FDR2022 (Int. Topical Wkshp on Fukushima Decomm. Res.)*, J-Village, Naraha, Japan (2022).
14. C. Ma, O. Tschauner, J.R. Beckett, Y. Liu, "Discovery of chengminite, FeCr2O4 with orthorhombic CaFe2O4-type structure, a shock-induced, high-pressure mineral in the Tissint martian meteorite", *Proc. 49th Lunar Planetary Sci. Conf.*, 1464, The Woodlands, TX (2018).

15. L. Brissonneau, C. Journeau, P. Piluso, M. Kiselova, S. Bakardjieva, T. Wiss, D. Bottomley, H. Thiele, "Prototypic corium analysis : a round robin for SEM and EDS characterization", *Proc. EMAS 2011, IOP Conf. Ser.: Mater. Sci. Eng.* **32**, 012005 (2012).
16. A.A. Shiryaev, I.E. Vlasova, B.E. Burakov, B.I. Ogorodnikov, V.O. Yapaskurt, A.A. Avarin, A.V. Pakhnevich, Y. V. Zubavichus, "Physico-chemical properties of Chernobyl lava and their destruction products", *Progr. Nucl. Ener.* **92**, pp. 104-118 (2016).
17. M. Yashima, T. Koura, Y. Du, M. Yoshimura, « Thermodynamic Assessment of the Zirconiz-Urania System", *J. Am. Ceram. Soc.***79** (2), pp. 521-524 (1996).
18. W.A. Lambertson, M.H. Mueller, "Uranium Oxide Phase Equilibrium System: III, UO_2-ZrO_2", *J. Am. Ceram. Soc.* **36** (11), pp. 365-368 (1953)
19. L. Capriotti, A. Quaini, R. Böhler, K. Boboridis, L. Luzzi, D. Manara, "A laser heating study of CeO2 solid/liquid transition: challenges related to a refractory compound with a very high oxygen pressure", *High Temperatures - High Pressures*, **44**, pp. 69-82 (2014).
20. IRID, *Development of Technology for Fuel Debris Analysis and Characterization - Results for FY 2018* IRID Report, Tokyo, Japan (2019), https://irid.or.jp/_pdf/Development%20of%20technology%20for%20fuel%20debris%20characterization%20and%20analysis_FY2018_rev1.pdf
21. A. Kirishima, A. Nagatomo, D. Akiyama, T. Sasaki, N. Sato, "Study on the chemical structure and actinide leaching of MCCI debris", *J. Nucl. Mater.*, **527**, 151795 (2019).



Characterisation of Prototypic Ex-Vessel Fuel Debris Ingots Simulating MCCI at Fukushima Daiichi

C. Journeau, D. Molina, V. Bouyer, A. Denoix
CEA, DES, IRESNE, Cadarache

E. Brackx, R. Domenger, CEA, ISEC, Marcoule

A. Ikeda-Ohno, JAEA/CLADS, Tokai

IRID International Research Institute for Nuclear Decommissioning

JAEA CLADS

Outline

1. **Context**
2. **Fabrication of Prototypic Ex-Vessel Ingots**
   VF-U1, MCCI test
   VF-U3 Inductive melting
3. **Material Analyses**
4. **Comparison and Discussion**

Context

- Fuel debris cutting and retrieval is one of the major challenges for the decommissioning at Fukushima Daiichi
- Safety R&D issues include
  - Knowledge on fuel debris to be cut and their properties
  - Development of adapted cutting techniques
  - Generation of radioactive dust by fuel debris cutting techniques
  - …
- URASOL project carried for IRID/JAEA by a French consortium (CEA, IRSN, ONET)
  - Fabrication of fuel debris prototypes
  - Mechanical cutting or thermal treatment of these samples
  - Assessment of dust production/characteristics

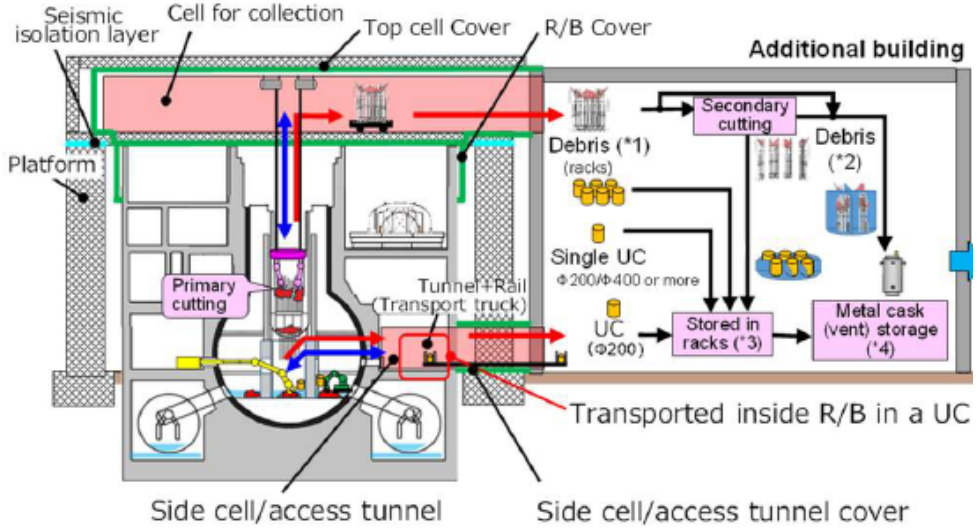

NDF Sub-committee on the Evaluation of Fuel Debris Retrieval Methods Report 2024

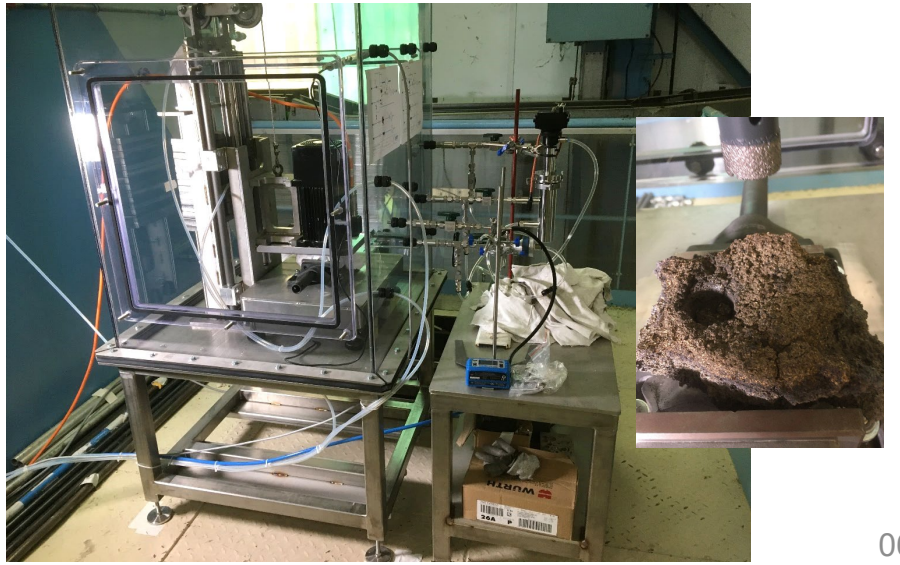

2. Fabrication of Prototypic Fuel debris Ingots

VF-U1 : Corium Concrete Interaction test

Test carried out for JAEA to simulate in VULCANO 3-day MCCI in 1F1

- **Basaltic concrete**
- **46.4 kg prototypic corium inductively melted in concrete cavity**
  - ❑ 58.8 wt% UO_2 16.2% ZrO_2, 11.8% Zr, 13.2% SS
- **Decay heat simulation (38 kW average) during 900 s lead to ablation of 9.6 dm^3 of concrete**
  - ❑ Ablated concrete/corium representative of previous plant calculations
- **Post test dismantling**
  - ❑ Large solidified pool (oxide-rich MCCI debris)
  - ❑ Presence of a metallic layer at the bottom of the solidified fuel debris pool

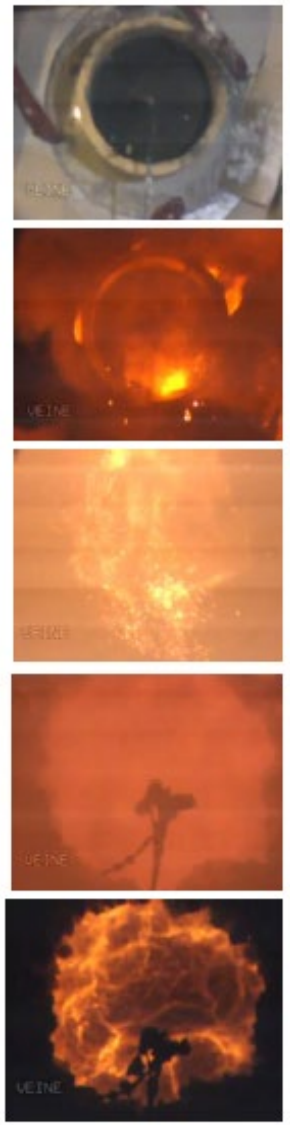





Bouyer et al. ERMSAR 2019; Nakayoshi et al. FDR 2019

VF-U3: Synthetic sample representative of 1F1 MCCI

- **VFU3 has been determined (Journeau, et al., 2017) in order to simulate a debris from interaction between the molten core and the concrete in the sump of 1F1, including fission products and other minor elements**
  - Composition with largest concrete content in Robb et al. (2014)
- **Fabrication by induction heating from a 40.5-kg load (mainly powders + steel and iron pieces)**
- **Due to large density difference between oxides and steel, a metallic debris was segregated at the bottom of crucible.**

	wt. %		wt. %
UO_2	24.84%	RuO_2	0.04%
Zr	0.00%	Nd_2O_3	0.08%
ZrO_2	11.79%	MoO2	0.08%
CeO_2	0.18%	$CsOH•H_2O$	0.06%
SnO_2	0.15%	BaO	0.04%
B_4C	0.17%	La_2O_3	0.03%
SS 304L	5.30%	PdO	0.02%
Cr_2O_3	0.55%	Pr_2O_3	0.03%
Fe	3.59%	Sm_2O_3	0.02%
SiO_2	28.90%	SrO	0.02%
Al_2O_3	7.21%	Y_2O_3	0.01%
CaO	5.87%	TeO_2	0.01%
Fe_2O_3	11.02%		



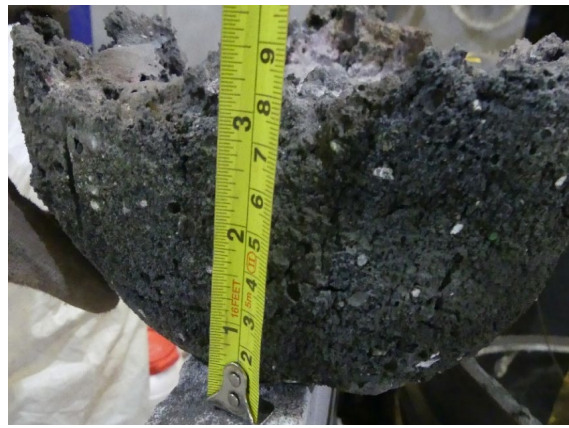

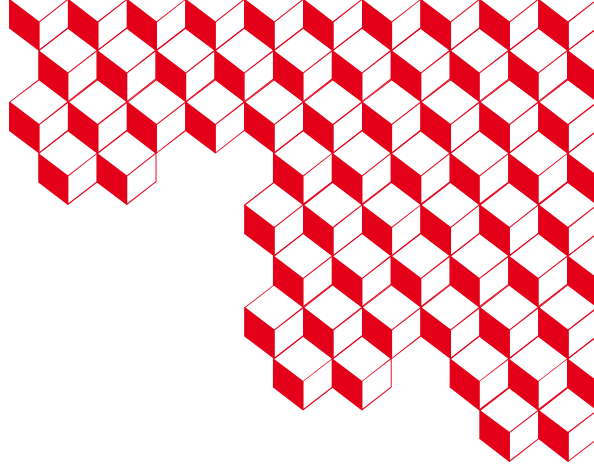

3. Material Analyses

Material analyses at CEA/LMAT Marcoule

Scanning Electron Microscopy (SEM)

Energy Dispersive X-ray spectroscopy (EDX)

- MERLIN SEM from Carl Zeis
- X max detector from Oxford Instruments
  - International round robin (Brissonneau et al., EMAS2011):
    - Discrepency on light elements like O : up to 1/4th measured value
    - Uncertainty <1/10th value for heavier elements

X-Ray Diffraction (XRD)

- D8 Advance Diffractometer from BRUCKER AXS
- Diffrac Eva software with 2020 PDF database
- DIFFRAC.TOPAS v6 software for Rietveld refinement





VF-U1b sample



SEM analysis of a VF-U1 sample

- Heterogeneous samples
  - Already in macrograph
  - More visible in BSE micrograph
    - Light linked to atomic numbers
  - Incomplete mixing of concrete and corium
    - Corium-rich regions in light colors
    - Concrete-rich regions in dark

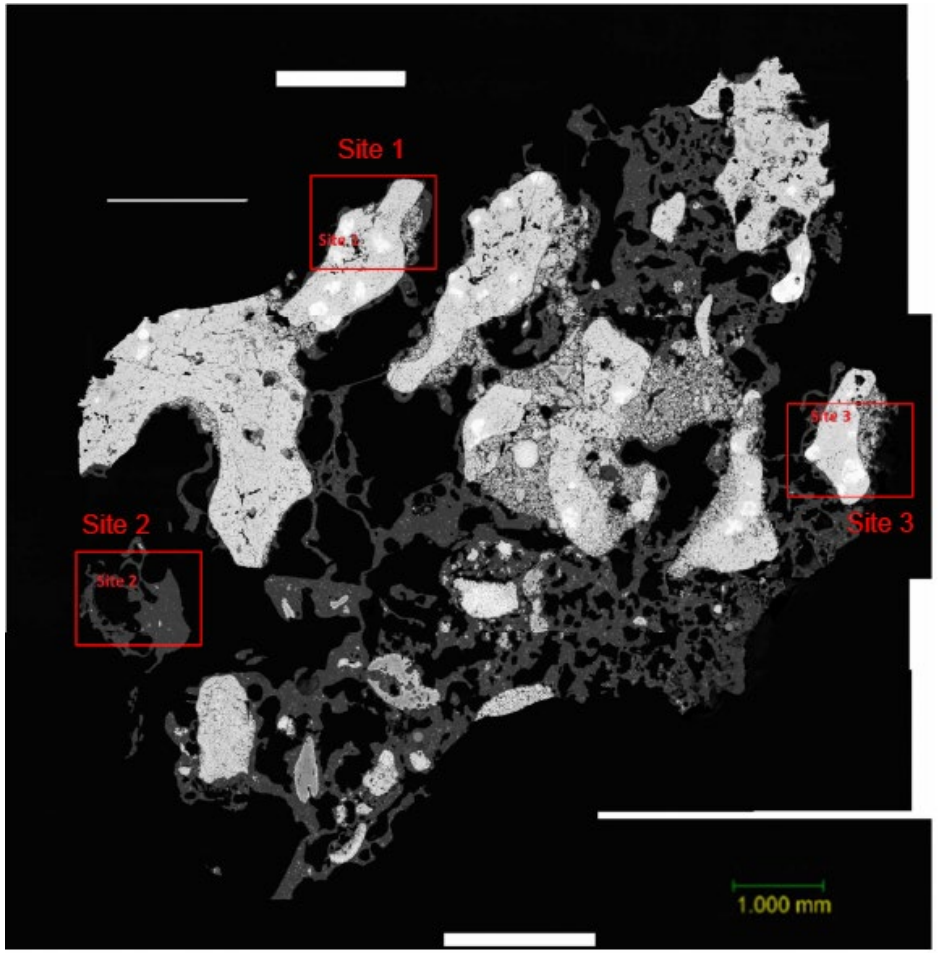

EDX analyses of VF-U1b sample

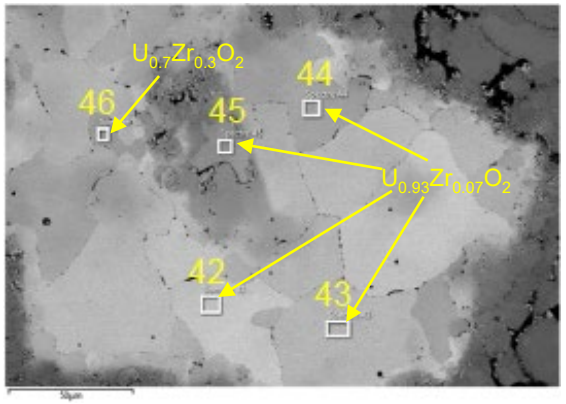

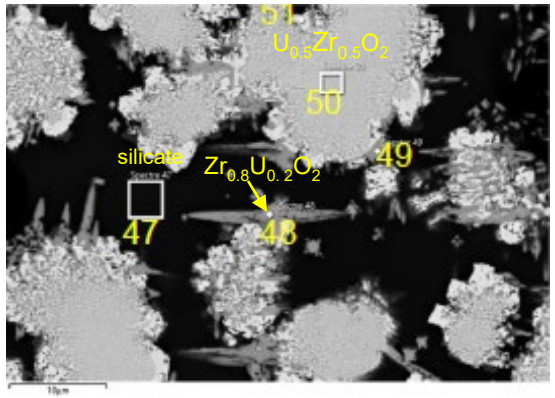

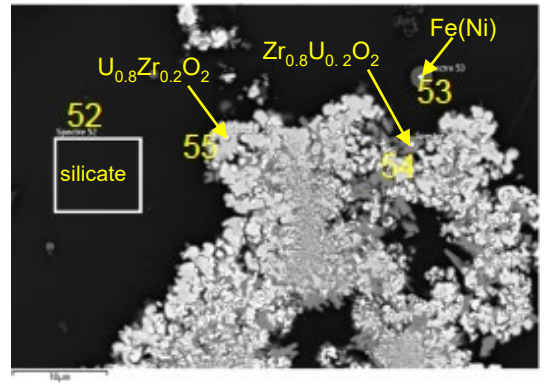

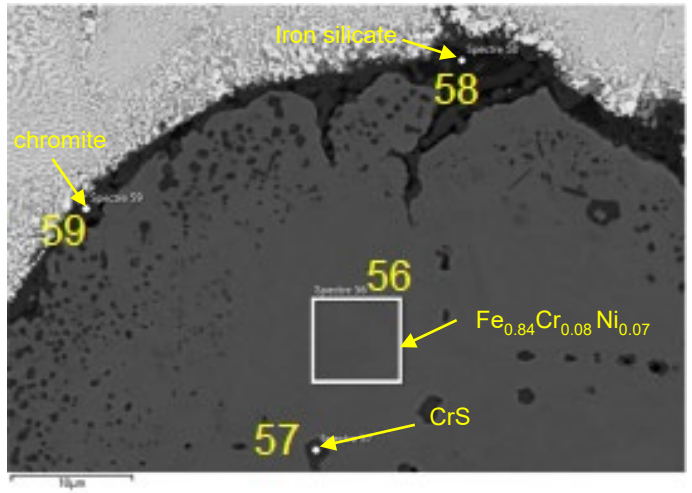

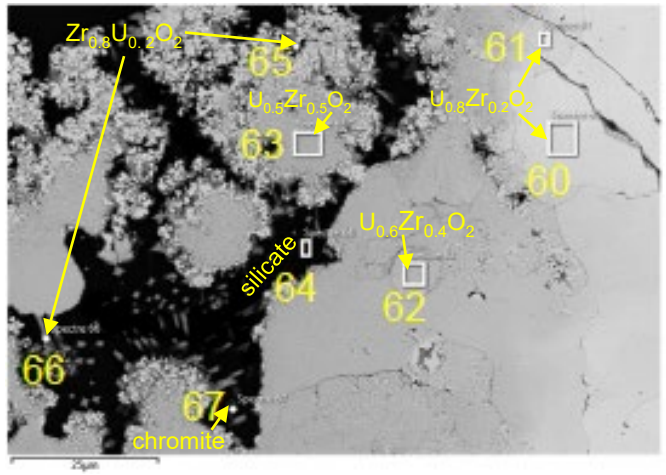

EDX Analyses of VF-U1 samples

- Uranium-zirconium oxides
  - Various U/(U+Zr) ratios : 0.9; 0.7; 0.6; 0.5; 0.2
  - Some “eutectic-looking” areas with global composition close to ($U_{.5}Zr_{.2}O_2$) have been observed that may come from the partial transformation of a cubic $U_{.5}Zr_{.2}O_2$ a cubic uranium-rich dioxide and a tetragonal zirconium-rich phase.
- Silicate matrix
  - Typically (point 47): 23 at% Si, 6% Ca, 5% Al, 1% Na, 1% Mg, 1% Zr, 61% O
- Chromite phases
  - Close to Cr_2FeO_4
  - Or with Cr/Fe ratio close to 1
- Metallic droplets (~ ∅50 µm to ∅2 µm)
  - point 56: 84 at% Fe, 8% Cr, 7% Ni
    - Less depleted in Cr, Ni than the metallic layer found below the oxidic ingot
  - Presence of chromium sulphide inclusion and ferrosilite ($FeSiO_3$)

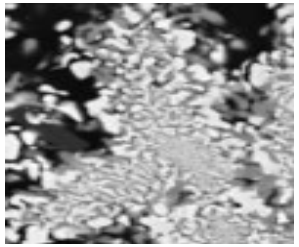

Macrograph, micrograph and EDX of VF-U3 sample



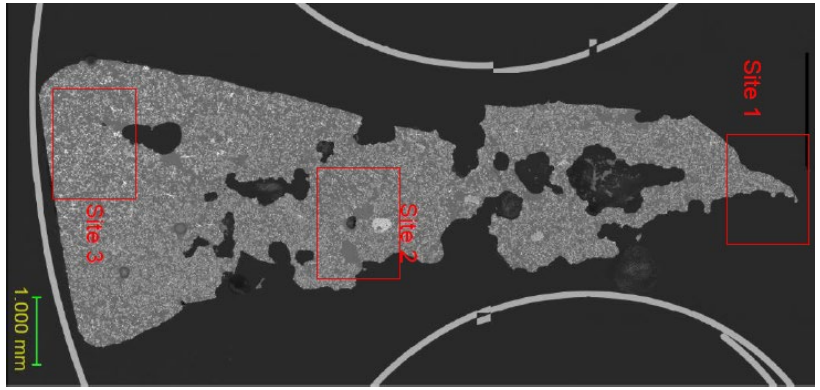

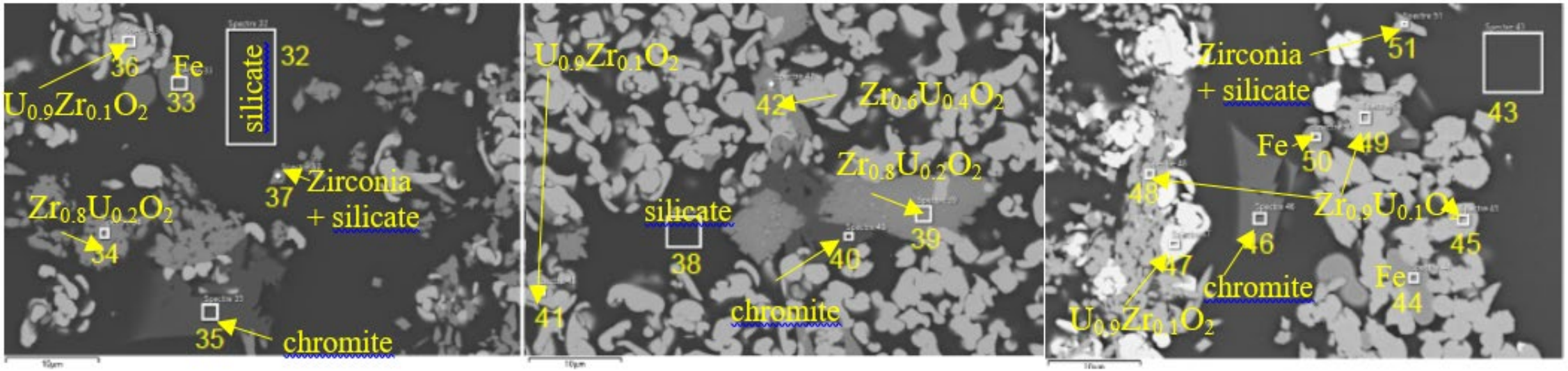

XRD of crushed VF-U1b sample

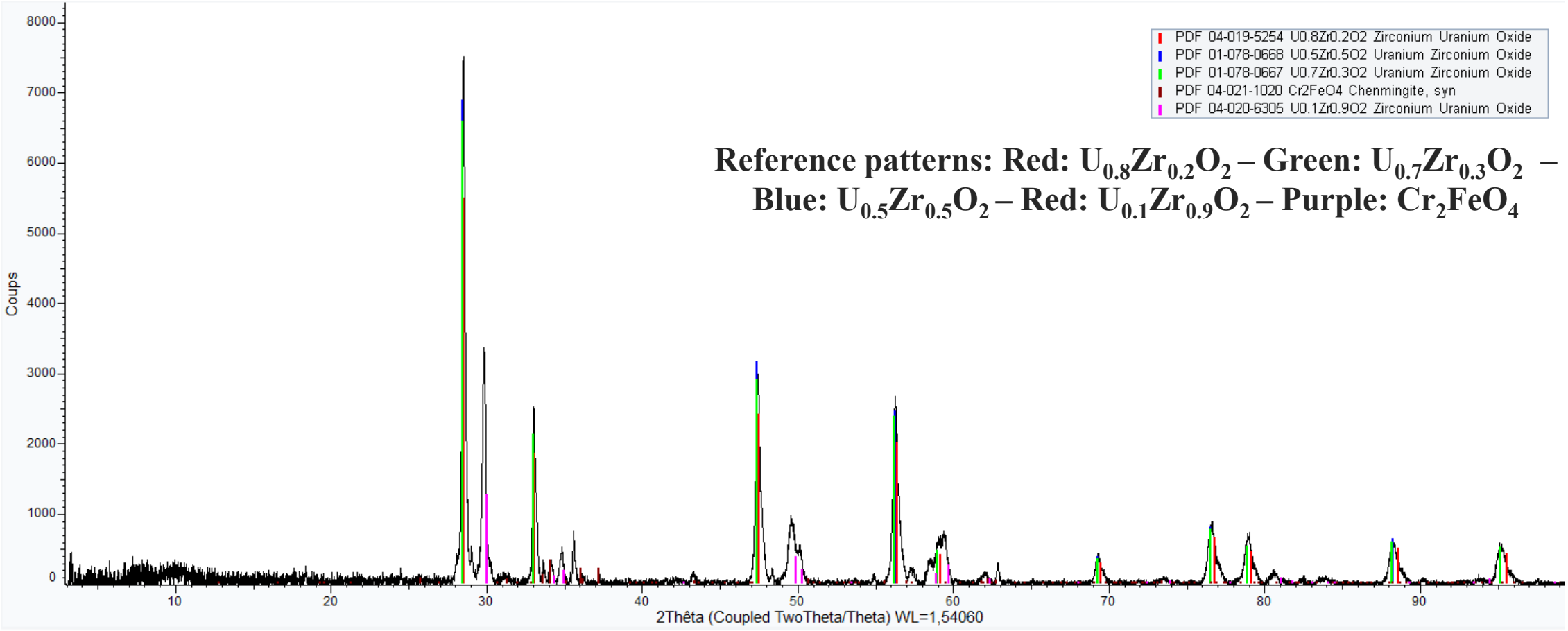

Reference patterns: Red: $U_{0.8}Zr_{0.2}O_2$ – Green: $U_{0.7}Zr_{0.3}O_2$ – Blue: $U_{0.5}Zr_{0.5}O_2$ – Red: $U_{0.1}Zr_{0.9}O_2$ – Purple: Cr_2FeO_4

Rietveld analysis of XRD patterns

VF-U1b

- 68 wt% uranium-rich dioxide
- 21 wt% zirconium-rich dioxide
- 11 wt% chromium-iron oxide

VF-U3c

- Uranium-rich dioxide: 43 wt%
- Tetragonal zirconium oxide: 33 wt%
- Ferrous oxide (γ-Fe_2O_3): 20 wt%.
- Aluminum-iron oxide ($Fe_{0.9}Al_{1.1}O_3$): 4 wt%.

Chromite phases slightly misidentified (due to presence of minor elements)
No silicate crystal detected (except 1 wt% $ZrSiO_4$ in VF-U3a)
$\Rightarrow$ silicate matrix likely to be vitreous

3. Comparison and Discussion

Main phases

- Glassy silicate matrix in both tests
  - Larger iron oxide content (~13 wt% FeO_x) in VF-U3 than in VF-U1 (~1 wt%)
    - Indeed VF-U3 corresponds to a scenario with longer oxidation of iron than VF-U1
  - A few silicate crystals observed by SEM/EDX:
    - ferrosilicates as ferrosilite ($FeSiO_3$), fayalite (Fe2SiO4) and hedenbergite (CaFeSi2O6)
    - aluminosilicates such as anorthite, CaAl2Si2O8,
    - as well as a zirconium-uranium silicate, chernobylite $(Zr,U)SiO_4$.
- Uranium and zirconium oxides form the majority of crystalline phases
  - 89 wt% for VF-U1b and 76 wt% for VF-U3
  - large variety of compositions from uranium-rich phases to pure zirconia,
    - in accordance to the total miscibility at high temperature between these two oxides
    - separation of a uranium-zirconium oxide two series of so-called low-temperature phases (one rich in zirconium and one rich in uranium) has also been observed in uranium-containing dusts collected in Fukushima Daiichi PCVs and refueling floor
- Spinels mainly chromites
  - close to Cr_2FeO_4, but also more complex compositions as $Cr_{1.8}Fe_{1.2}Al_{0.5}O_4$
  - Often in form of polyhedral precipitates
- Metallic balls rich in iron and often more concentrated in Cr, Ni than the large metallic blocks below oxides.

Fission product prototypes

- Cesium and Cerium have been detected by EDX in the oxidic phase
  - mainly in calcium iron silicates
- Molybdenum, Palladium and Tellurium were found in metallic phases
  - Either in small droplets
  - Or in large metallic block below
    - Pd found in a (Sn,Ni,Fe) precipitated within large metallic block
    - Te found in iron telluride precipitate within large metallic block

Summary

- 2 large tests have been carried out in VULCANO that provided MCCI debris simulant ingots
- analysis of these MCCI two fuel debris prototypes confirmed their heterogeneous nature
  - Silicate glass
  - uranium-zirconium oxides of various compositions,
  - uranium-containing zirconium silicate,
  - aluminosilicates and ferrosilicates,
  - chromites,
  - metallic droplets and blocks
- These results are important to evaluate the fuel debris behavior during leaching or aerosol production during cutting

Thank you for your attention!
Any questions?

Most of this work is part of tasks by ONET/CEA/IRSN consortium contributing to the Japanese governmental subsidy program "Project of Decommissioning and Contaminated Water Management (Development of Analysis and Estimation Technology for Characterization of Fuel Debris)" organized by International Research Institute for Nuclear Decommissioning (IRID).

VF-U1 experiment has been carried out within the frame of JAEA-CEA collaboration (Specific contract DEN 4581) for a better knowledge on Fukushima-Daiichi Severe Accidents in links with the research program entrusted to the International Research Institute for Nuclear Decommissioning (IRID) by the Agency for Natural Resources and Energy, Ministry of Economy, Trade and Industry (METI) of Japan.

CEA CADARACHE

13108 Saint-Paul-lez-Durance

France

Christophe.journeau@cea.fr

+ 33 4 42 25 70 00

The 11th European Review Meeting on Severe Accidents Research

May 13-16, 2024, Royal Institute of Technology, Stockholm, Sweden

TECHNICAL SESSION 6.1: HYDROGEN RISK AND CONTAINMENT BEHAVIOR

Chairs: I. Kljenak (IJS), S. Gupta (Becker Tech. GmbH)

ID94	**AMHYCO Project Overview and First Outcomes** G. Jiménez (UPM)	**Paper** **Presentation**
ID103	**Outcomes of the experimental and numerical work on the operational behavior of passive autocatalytic recombiners in the late phase of a severe accident in the framework of the AMHYCO project** E.-A. Reinecke (FZJ)	**Paper** **Presentation**
ID82	**Assessment of Unmitigated Combustion Risk in Late Phase Within the AMHYCO Project** S. Kelm (FZJ)	**Paper** **Presentation**
ID18	**Heat Removal to Large Water Pools – Macroscopic Modelling of Microscopic Phenomena in the Simulation Code AC²/COCOSYS** C. Spengler (GRS)	**Paper** **Presentation**

AMHYCO PROJECT OVERVIEW AND FIRST OUTCOMES

Gonzalo Jiménez*
Universidad Politécnica de Madrid, 28040 Madrid, Spain
gonzalo.jimenez@upm.es

Ahmed Bentaib
Institut de Radioprotection et de Sûreté Nucléaire, 92260 Fontenay Aux Roses, France
ahmed.bentaib@irsn.fr

Luis Enrique Herranz
CIEMAT, 28040 Madrid, Spain
luisen.herranz@ciemat.es

Nabiha Chaumeix
CNRS-INSIS, I.C.A.R.E., 45071 Orléans, France
nabiha.chaumeix@cnrs-orleans.fr

Stephan Kelm, Ernst-Arndt Reinecke
Forschungszentrum Juelich, 42425 Juelich, Germany
s.kelm@fz-juelich.de; e.-a.reinecke@fz-juelich.de

Matthias Braun
Framatome GmbH, Paul-Gossen-Strasse 100, D-91052 Erlangen, Germany
matthias.braun@framatome.com

Marco Koch
Ruhr-Universitaet Bochum, 44801 Bochum, Germany
marco.koch@pss.rub.de

Ivo Kljenak
Institut Jozef Stefan, 1000 Ljubljana, Slovenia
ivo.kljenak@ijs.si

Oleksandr Sevbo
Limited Liability Company Energorisk, 03148 Kyiv, Ukraine
sevbo@energorisk.com.ua

D.C. (Dirk) Visser
Nuclear Research and Consultancy Group, 1755 ZG Petten, The Netherlands
visser@nrg.eu

Zhe (Rita) Liang
Canadian Nuclear Laboratories, Chalk River, ON K0J 1J0, Canada
zhe.liang@cnl.ca

Mina Lazarevic
LGI Consulting, 75011 Paris, France
mina.lazarevic@lgi.earth

*corresponding author

ABSTRACT

A severe accident in a nuclear power plant represents a potential risk to both, humans, and the environment. To prevent and/or mitigate the consequences of such an event, it is paramount to have adequate accident management measures in place to ensure the containment integrity. During a severe accident, one of the potential threats to the containment is the release of combustible gases — especially hydrogen and carbon monoxide — leading to combustion risk in the air and steam-filled nuclear containment building. In modern plants, Severe Accident Management Guidelines (SAMG) as well as dedicated mitigation hardware are in place to minimize/mitigate this combustion risk and, thus, protect the containment integrity to avoid an unacceptable release of radioactive material into the environment.

Advancements in SAMGs are in the focus of AMHYCO, an EU-funded Horizon 2020 project (Euratom 2019/2020, GA No 945057) officially launched on October 1st, 2020. The project consortium consists of 12 organizations (from six European countries and one from Canada) and is coordinated by the Universidad Politécnica de Madrid (UPM). AMHYCO benefits from worldwide experts in combustion science, accident management and nuclear safety in its Advisory Board. Thereby AMHYCO covers the most used PWR reactor designs in continental Europe: Westinghouse-type, Siemens-KWU-type, and VVER-type.

In this paper, the progress of the first three years of the AMHYCO project is presented. A comprehensive bibliographic review has been conducted, providing a common foundation to build the knowledge gained during the project. An extensive set of accident transients was simulated, covering in-vessel as well as ex-vessel phenomena. Based on these simulations, a set of challenging sequences from the combustion risk perspective for the different power plant types was under consideration. At the same time, three generic containment models for the three considered reactor designs have been created to enable full containment analysis simulations with lumped parameter models, 3-dimensional containment codes and CFD codes. To further consolidate the modelling base, combustion experiments and performance tests on passive auto-catalytic recombiners under explosion prone H_2/CO atmospheres were performed respectively at CNRS (France) and FZJ (Germany).

KEYWORDS
AMHYCO, combustion risk, in-vessel phase, ex-vessel phase, Passive auto-catalytic recombiners, containment response, SAMGs

1. INTRODUCTION

Combustible gases generated during a severe accident are among the most serious threats to the containment integrity. An appropriate management of the associated risk is paramount to prevent the potential release of significant amounts of radioactive material to the environment. Since the Fukushima accident in Japan in 2011, various additional measures to reduce the risk of containment failure have been undertaken by nuclear power plants (NPPs) within the European Union. These measures include also dedicated severe accident mitigation hardware like Passive Autocatalytic Recombiners (PARs) and a Filtered Containment Venting System (FCVS), if not already installed previously. To this end, several projects have been recently conducted under the Organisation for Economic Co-operation and Development (OECD) Nuclear Energy Agency (NEA) framework to address remaining gaps regarding hydrogen distribution, combustion, and

efficiency of PARs to prevent combustion. On the other hand, the Severe Accident Management Guidelines (SAMGs), which guide the reactor operators on how to handle the response of the nuclear power plant against severe accidents, need to be regularly updated and include knowledge gained from international research, including recent and ongoing projects.

The main objective of the AMHYCO project is to propose innovative enhancements in the way combustible gases are managed in case of a severe accident in currently operating reactors. AMHYCO will contribute to this objective by improving the understanding of H2/CO combustion risk and incorporating this knowledge into SAMGs. To reach this main objective, the project proposes a methodology that is organized in five different technical work packages (WPs). In the next section, the AMHYCO technical WPs will be briefly described, including outcomes obtained the first three years of the project.

2. AMHYCO ADVANCES

2.1. WP1: Critical review

To identify lack of knowledge gaps related to hydrogen and carbon monoxide recombination and combustion, the first step of the AMHYCO project was to review the status of existing methodologies and practices related to gas combustion risk management in the late phase of severe accidents. Four tasks were achieved, and the main outcomes are presented in the following subsections.

2.2 WP2: Characterization of sequences with high relevant combustion risk

The identification and characterization of high relevant combustion risk sequences has proceeded in steps along the first two years of the AMHYCO project: setting figures of merit, building a sequences matrix, and achieving sequence characterization through code simulations. As an outcome, a scenario database has been developed on which experimental investigation on recombination and combustion of H_2-CO mixtures are being planned and different analytical approaches (3D vs. LP codes; LP standing for Lumped Parameter) are started to be tested.

The selection criteria to choose safety-relevant combustion scenarios were: high molar fractions of combustible gases (H_2 + CO) within flammability limits (the Shapiro diagram [1] serving as a monitor), large amounts of combustible gases, and fast in-containment release rates of H_2 or H_2+CO. Besides, some qualitative analysis was needed with a broader assessment of the entire scenario. Among the variables considered for a comprehensive description of the scenarios were: gas molar fractions, gas injection/generation rates, enthalpy and temperature associated to the incoming gases, and some others related to the compartment boundary conditions and safety systems performance. A comprehensive list was given in Reference [2].

Accident sequences with the potential to evolve in challenging combustion conditions were pooled for different PWR designs: PWR-W (different reactor sizes and variants included), PWR-VVER and PWR-KWU. Fig. 1 displays the complete matrix of sequences simulated. It should be mentioned that the thresholds set to consider a gas mixture flammable (embedded in the Shapiro diagram) have been:

- $X_{H2} + X_{CO} > 9$ vol.%
- $X_{O2} > 5$ vol.%
- $X_{H2O} < 55$ vol.%

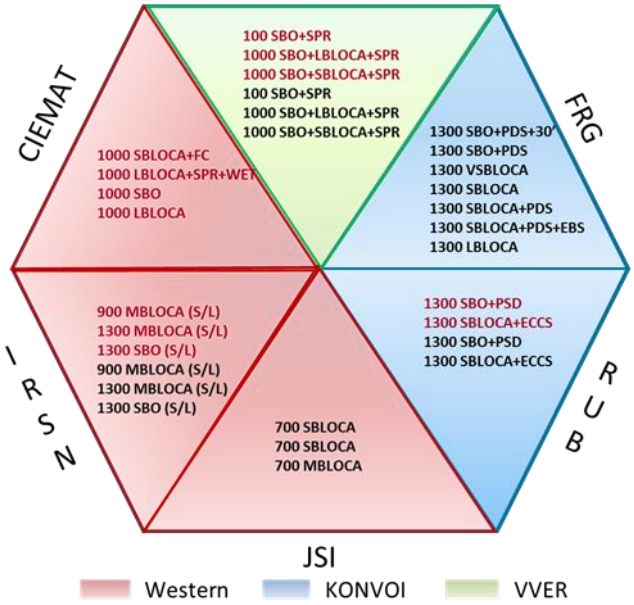

Figure 1. PWR accident sequences modelled

As an example of the type of results reported, for the Westinghouse 1000 MW_e designs , two main sequences were simulated: LOCA and SBO. The LOCA sequence was additionally varied with different pipe breach sizes (2-inch or double-ended guillotine break), and accident management actions (activating fan coolers, containment sprays, or cavity flooding). In all sequences where systems were capable of condensing steam, a higher fraction of combustible gases has been observed. Therefore, the two sequences which represent the highest risk associated with combustible gases were identified as the SBLOCA with fan coolers and the LBLOCA with spray activation and cavity flooding. Fig. 2 shows the Shapiro diagrams for these scenarios.

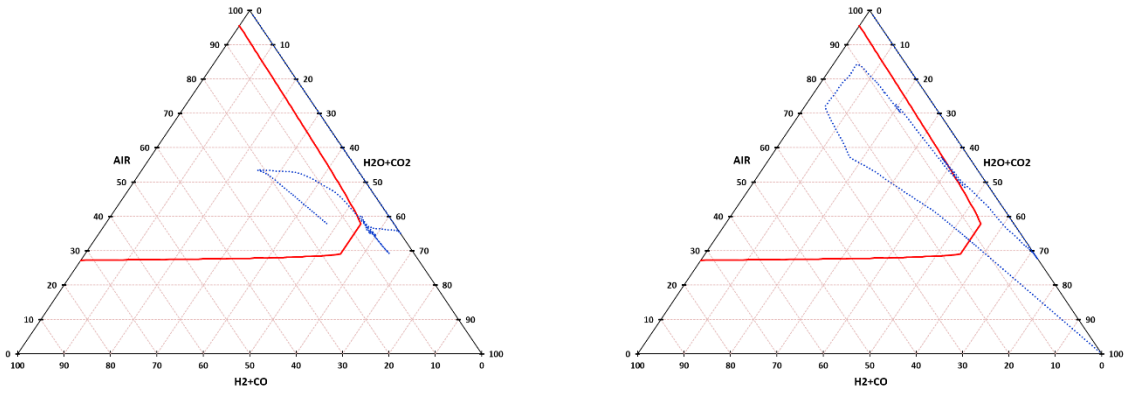

Figure 2. Shapiro diagram of PWR-W-1000 simulations (Left: SBLOCA with FC; Right: LBLOCA)

Both sequences lead to a high steam concentration at the beginning of the accident due to the flashing of the water loss from the RCS (LBLOCA) or to the release of steam directly through the circuit breach (SBLOCA). The sprays operation in the LBLOCA triggers a fast and large drop of steam content. Even though, for a short time the H_2 molar fraction reaches combustion limits set (9%) at the end of the in-vessel phase, it is in the ex-vessel phase where further release of H_2 and CO from the Core Concrete Interaction (CCI) together with the efficient condensation of steam, make combustible gas mixture attain concentration over 25% at around 20000 s. The loss of efficiency in condensation due to recirculation mode operation of sprays and the generation of CO_2 results in a progressive dilution of such high combustible gas concentration

in the long run of the sequence, but still standing over the combustion limits. For the SBLOCA sequence, the combustible gas mixture does not exceed the combustion threshold until CO is produced in the ex-vessel phase, which together with the effect of fan coolers on steam content, make it grow to higher than 20% at about 30000 s and stay at roughly that high concentration till CO_2 is released in massive amounts to reach higher than 20% of the total gas composition.

In summary, from the twenty-five PWR SA sequences simulated the main outcomes can be summarized as follows:

- The SA sequences that posed a higher risk of gas combustion (H_2 and CO) have been found to be SBLOCA and LBLOCA, for PWR-W, MBLOCA (80 cm^2) for PWR-KWU and SBO with sprays for PWR-VVER.
- A key factor heavily conditioning sequence selection is the availability of safety systems capable of condensing steam during the ex-vessel phase since they result in a boost of combustible gas content.
- Whenever PARs are modelled, O_2 starvation in the ex-vessel phase makes gas composition exit the flammable region of the Shapiro diagram in the long run, even if combustible gas content is well over 9 vol.%.

2.3 WP3: Experimental investigations

The experimental research in AMHYCO aims at obtaining knowledge and data needed for the development and validation of numerical models and simulation tools in the fields of combustion of $H_2/H_2O/CO$ mixtures in air as well as explosion risk mitigation by means of passive auto-catalytic recombiners (PARs). Following the conclusions of the review performed by WP1 and the scenarios selected by WP2, the experimental program includes separate effects, coupled effects and integral effect tests, which allow a comprehensive validation of models implemented in relevant safety tools. Based on the experimental results, numerical simulations are performed to support the development of engineering correlations to be used in safety assessment tools in WP4.

The experimental program is conducted in two laboratories: Investigations on the H_2/H_2O and $H_2/CO/H_2O$ combustion under different conditions are performed at CNRS/ICARE in Orléans/France (see Section 2.3.1), while the operational behaviour of PARs under conditions of the ex-vessel phase of a severe accident is investigated at FZJ in Juelich/Germany (see Section 2.3.2).

2.3.1 Combustion

The focus of the experimental program in Task 3.1 is on H_2/H_2O and $H_2/CO/H_2O$ combustion under different conditions, also considering the interaction with the operation of containment spray and the filtered containment venting system. In the present paper, the results on H2/CO combustion will be presented on: (i) flammability limits of a 50% H_2 / 50% CO (molar based) gas mixture at different initial pressures, (ii) combustion regimes for different initial conditions in terms of %-Fuel (50% H_2+50% CO) in air. To do so, 2 different facilities were used, BS-I, a spherical vessel (250 mm i.d., see Fig. 3-a) equipped with a central ignition and ENACCEF-II (vertical tube, 230 mm i.d. and 7.65 m high). Both facilities are coupled to different diagnostics including high speed imaging (Schlieren optical layout and high-speed cameras (Vision research V16), high frequency pressure transducers (Kistler and PCB), shock detectors (ChimieMétal), photomultiplier tubes with UG filters centred at 307 nm (OH^* detection).

For the flammability limits, 3 different initial pressures were investigated: 1, 2 and 3.5 bar (always in absolute units of pressure). The gas composition of the mixture is fixed, then the spark is created between 2 tungsten electrodes. The spark energy provided for each test is measured via a high voltage probe and a high frequency current probe placed at the electrodes ends protruding outside of the vessel. The measured energy used is 265 ± 50 mJ. Following the spark initiation, the identification of a flammable mixture is based on the recording of a successful flame propagation (Fig. 3b&c). The synchronized recording of the ignition by the high-speed imaging and the temporal profile of the pressure signal allows

to use both, the pressure and the visual criteria. The results presented in this paper will be based on the visual criterion.

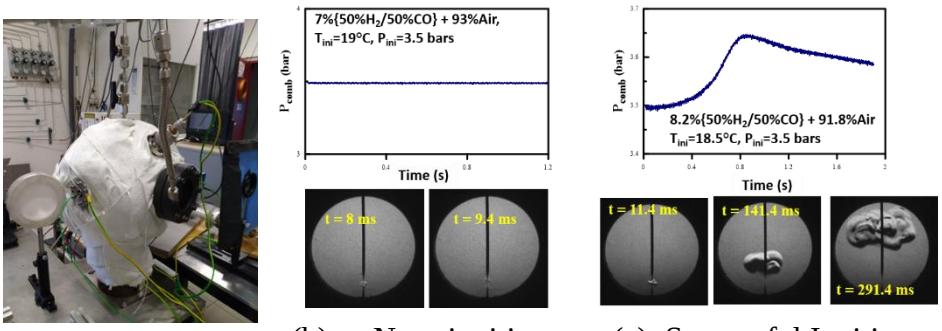

(a) (b): No ignition case (c): Successful Ignition

Figure 3. Experimental facility (BS-I) for the flammability limits study (a); examples of pressure signals and flame snapshots recorded for different runs in case of no ignition (b) and successful ignition (c).

If following the spark ignition, no sustainable flame is observed after the initial flame kernel formation, then the mixture would be identified as non-flammable. Usually, more than 100 tests are performed. The flammability limit is derived from the probability of ignition using the likelihood probability. In case of a successful ignition, the probability is given the value 1, otherwise, it will be given the value 0. The determination of the flammability limit will be based on the plot of the probability of ignition versus the molar fraction of the fuel in air (Fig. 4). Depending on the value of the probability of ignition adopted to define the flammability limits, different values are derived (summarized in Table 1). The errors derived from the 95% of confidence interval are reported as well. At 1 bar, the lower flammability limit (LFL) was found to be 6.3 % ± 0.4 % for a probability of ignition of 0.01 and increases to 7.4 % ± 0.1 % when the probability of ignition is 0.5.

These values are higher than the one determined by Kilchyk [3], but in good agreement with the recent study of Shang et al. [4] who determined a LFL of 6.5 %. For the upper flammability limit (UFL), at 1 bar, at a probability of ignition of 0.01, the experimental value is 72.4 % ± 0.6 % and decreases to 70.6 % ± 0.2 % for a probability of ignition of 0.5. These values agree with our previous work [5] and the literature [6].

As the initial pressure is increased from 1 to 2 and 3.5 bar, the flammability domain is reduced. This effect is visible at 3.5 bar at which the LFL is increased while the UFL is decreased. Jaimes et al. [7] measured the LFL for different H2/CO ratios and at different initial pressure. Their values are in a good agreement with our data.

In the ENACCEF-II facility, experiments have been performed to study the combustion regimes for the binary fuel mixture of 50 % H_2 + 50 % CO. For this study, the tube was equipped with 9 annular obstacles with a blockage ratio of 0.63. They were installed in the lower part of the tube and evenly spaced by one diameter. The flame trajectory was derived from the 27 photomultiplier tubes installed along the tube, the pressure build-up as the flame propagates in the facility is monitored via 11 pressure transducers (2 PCB and 9 Kistler). The experiments were performed for different binary fuel content in air, namely 11 %, 13 % and 15 %. The initial pressure was varied from 1 to 3 bar. Table 2 summarizes the experimental observations: the maximum flame speed observed with the maximum pressure. The theoretical maximum pressure for an isochoric adiabatic complete combustion, P_{AICC}, the speed of sound in the fresh gases, a_{GF}, and burned gases, a_{BG}, have been estimated. If, following the literature [8, 9, 10], the combustion is defined as "fast" when the ratio maximum flame speed over the speed of sound in the burnt gases is larger than 0.5, then this regime is observed only for the mixture containing 7.5 % H_2 +

7.5 % CO in air. However, as one can see in Table 2, for mixtures containing 6.5 % H_2 + 6.5 % CO in air, although the flame speed ratio is below 0.5, the maximum pressure recorded in the facility is higher than the P_{AICC} indicating that the compressibility effects are important, and shocks are formed leading to higher pressures.

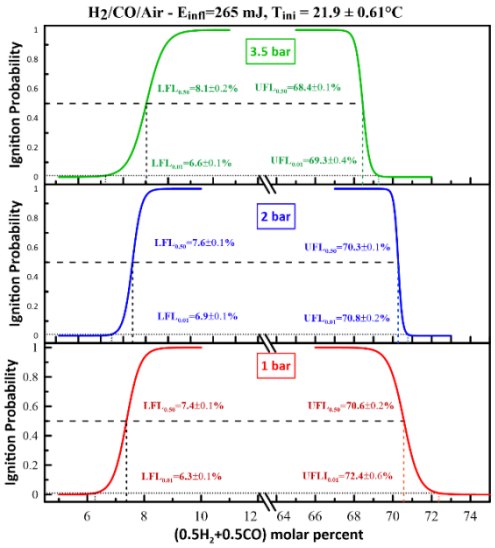

Figure 4. Probability of ignition versus the fuel/air molar percent. The binary fuel is constituted of 50 %H_2 + 50%CO. The initial temperature is 22°C and the ignition energy is 265 mJ.

Table 1. Experimental Flammability at different initial pressures for a binary mixture {50 % H_2+50 % CO) initially at 22°C.

P_{ini} (bar)	1	2	3.5
LFL at P(ignition) =0.01	6.3±0.4	6.9±0.3	6.6±0.5
LFL at P(ignition) =0.5	7.4±0.1	7.6±0.1	8.1±0.2
UFL at P(ignition) =0.01	72.4±0.6	70.8±0.2	69.3±0.4
UFL at P(ignition) =0.5	70.6±0.2	70.3±0.1	68.4±0.1

Table 2. Summary of ENACCEF-II results for a binary mixture {50%H_2+50%CO) initially at 22°C. a_{FG}: speed of sound of the fresh gases, a_{BG}: speed of sound of the burnt gases.

P_{ini} (bar)	H_2 (mol %)	CO (mol %)	$P_{exp,max}$ (bar)	$V_{flame,max}$ (m/s)	$\frac{P_{exp,max}}{P_{AICC}}$	a_{FG} (m/s)	a_{BG} (m/s)	$V_{flame,max}$ / a_{BG}
1	5.50±0.04	5.50±0.04	2.44±0.08	76±26	0.50±0.01	356.33±0.06	676.55±1.48	0.11±0.04
	6.16±0.01	6.15±0.03	4.36±0.17	230±9	0.83±0.03	357.54±0.02	702.00±0.74	0.33±0.01
	6.30±0.03	6.34±0.03	7.09±0.74	295±6	1.33±0.14	357.81±0.05	708.31±0.92	0.42±0.01
	7.25±0.04	7.25±0.08	11.96±0.51	480±26	2.06±0.09	359.57±0.07	741.63±2.01	0.65±0.03
2	5.46±0.08	5.45±0.10	5.00±0.09	72±23	0.53±0.01	356.26±0.14	674.74±3.41	0.11±0.03
	6.45±0.03	6.43±0.04	11.36±2.10	268±6.8	1.08±0.20	358.08±0.05	712.69±1.11	0.38±0.01

	7.35±0.03	7.30±0.05	20.83±1.61	482±10	1.84±0.14	359.74±0.06	744.19±1.34	0.65±0.01
	5.41±0.07	5.41±0.12	7.84±0.14	71±7.5	0.55±0.02	356.17±0.12	673.01±3.76	0.11±0.01
3	6.38±0.06	6.35±0.03	12.59±1.65	300±42	0.81±0.11	357.95±0.10	709.98±1.52	0.42±0.06
	7.21±0.09	7.25±0.15	29.21±0.54	485±19	1.72±0.03	359.49±0.17	740.72±3.78	0.65±0.02

2.3.2 Recombination

PARs are the key feature of the strategy for mitigating the hydrogen risk in many European nuclear power plants. The operational behaviour of PARs has been studied in various national and international projects in the past, starting with early test programs conducted primarily by manufacturers, such as Siemens/Germany and AECL/Canada [11]. The objective of this subtask is to provide suitable numerical PAR models which have been validated against both existing experimental data from other programs and new targeted experiments performed in the framework of AMHYCO.

PARs are supposed to continuously recombine hydrogen and oxygen once hydrogen is released into the containment. For the boundary conditions of the so-called in-vessel phase, i.e. mixtures of hydrogen, air and steam in an oxygen-rich atmosphere, numerical PAR models have proven to provide reliable results that can be confidently applied in the context of accident analyses. However, less is known about the performance of PARs in the presence of carbon monoxide. Former experimental programs have demonstrated that carbon monoxide could be converted to carbon dioxide in a heterogeneous catalytic process similar to the recombination of hydrogen. However, under certain conditions, CO has been demonstrated at different labs [12,13] to act as a catalyst poison with the potential of completely deactivating the catalyst. The boundary conditions for these different phenomena affecting the PAR performance are not yet clear.

The experimental program of sub-task allows further advancement and validation of numerical models simulating PAR operation as a function of the atmospheric boundary conditions. These models are:

- Framatome correlation, an empirical equation implemented in most of the relevant codes used for accident simulations [14]
- PARUPM (UPM), a mechanistic model involving detailed surface chemistry [15]
- REKO-DIREKT (FZJ), a mechanistic model based on a mass transfer approach [16]
- SPARK (IRSN), a 3D model involving full surface and gas phase chemistry as well as multi-species CFD [17]

The experimental setup includes three facilities located at FZJ: REKO-1 to perform scoping tests with small catalyst sheets to identify the relevant process parameters, REKO-3 to obtain experimental data in full catalyst scale providing data for project partners' model validation, and REKO-4 to investigate the effect of pressure on PAR operation. Furthermore, experimental results of the OECD/NEA THAI and THEMIS projects were analysed to broaden the database.

The analysis of the accident scenarios (as performed in WP 2) led to the test matrix being focused on oxygen-lean atmospheres. Gas temperatures were predicted to range between 70 and 150 °C while pressures were estimated to range between 1.2 and 3.7 bar. (It has to be mentioned that pressures above 2 bar cannot be realized in the present set-up). Furthermore, H_2/CO ratios between 1 and 3 need to be considered.

The scoping tests performed in REKO-1 revealed that catalyst poisoning effects are to be expected for oxygen-lean conditions. Pd-based catalysts are less susceptible to the influence of carbon monoxide. However, the effect depends significantly on the temperature, while Pt-based catalysts were showing deactivations independently from the temperature. The REKO-3 experiments have detailed these findings and have provided measurements of the temperature profile on the catalyst surface as well as

recombination rates of both hydrogen and carbon monoxide at full catalyst scale.

Fig. 5 shows two examples of the model improvements and validations that were achieved with the experimental data. The PARUPM code has significantly improved the prediction of recombination rates by adding a diffusion-based reaction model to the surface chemistry approach [15]. The graph on the left shows the comparison with experimental data before and after model enhancement. The capability to predict catalyst poisoning of the SPARK code has been advanced as shown on the right side [18]. The graph on the right shows predicted catalyst temperatures for different oxygen concentrations. Poisoning is predicted only 0.2 vol.% earlier than observed in the experiment. In a similar way, data has been used to advance REKO-DIREKT. Also the Framatome engineering correlation model which is widely used in containment codes has been significantly improved to cope especially with oxygen-starvation conditions. For this purpose, a specific database has been developed from large scale transient experiments performed in the framework of the OECD/NEA THAI projects.

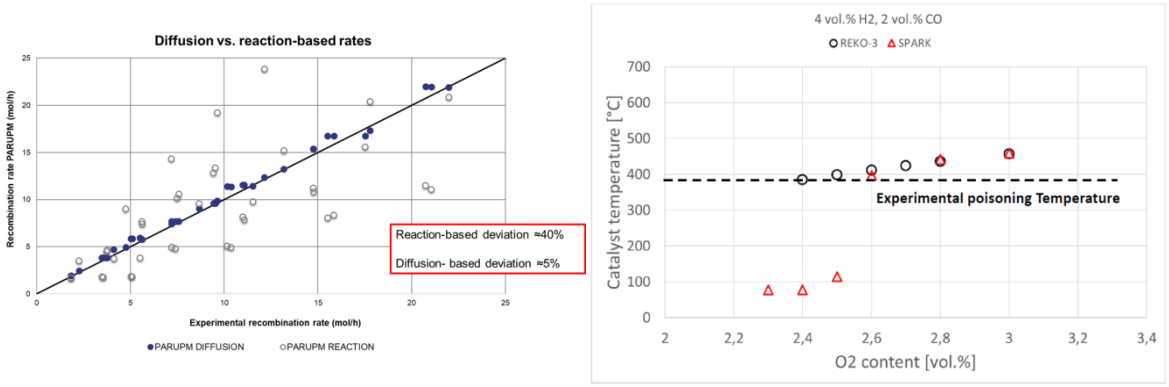

Figure 5. Examples for successful code enhancement in the framework of WP3.

Overall, the experimental program has successfully supported the further development of the computational PAR models and contributed to the availability of well-validated codes for the accident simulations in the following AMHYCO activities.

2.4 WP4: Full containment analysis

Main objective of WP4 is to employ the results obtained in WPs 1-3, to define and conduct a comprehensive analytical assessment and finally provide the insights for a review and potential extension of the SAMGs and EOPs within WP4. Following the approach of WP2, analysis is conducted for the European PWR concepts, W(estern), KWU and VVER. However, while WP2 used the available plant specific models and nodalization schemes, in WP4 generic containments and partly scaled input tables (from WP2) are employed to prepare a common open basis of the analysis, enable a certain comparability of the simulation results as well as pave the way for obtaining generic, i.e., non-plant-specific conclusions. In a nutshell, the integration of WP4 activities in the AMHYCO project is depicted in Fig. 6.

Full containment analyses are conducted in a consecutive analysis chain, consisting of three levels of increasing detail: As a basis, the identified sequences are simulated completely with lumped parameter containment models e.g., built in ASTEC or MELCOR. On this basis, the most penalizing cases will be additionally investigated by 3D models developed in GOTHIC to address potential asymmetric / 3D conditions that may lead to higher combustion risk. As a last step, relevant compartments and/or time frames identified in the 3D analysis will be simulated in detailed CFD-grade local containment studies (e.g., using containmentFOAM or ANSYS Fluent) to substantiate GOTHIC analysis and answer remaining open issues.

The increasing level of spatial details achieved with the different codes will also be utilized to assess the view on the accident from the control room (available sensors) against the full insights provided by the simulations to propose an upgrade of the SA instrumentation.

Experimental insights achieved in WP3 on combustion risk (in terms of flammability and flame propagation characteristics) as well as PAR performance under late phase conditions was transferred into engineering correlations and criteria, which can easily be implemented in the utilized codes. Within WP4 analytical work, they will be -as far as possible- compared against the State-of-the-Art summarized in WP1 to close knowledge gaps or substantiate the understanding of combustion risk, efficiency of mitigation measures and equipment survivability in the ex-vessel phase. Concluding the lessons-learned during the analysis are summarized to pave the way for subsequent work in the future.

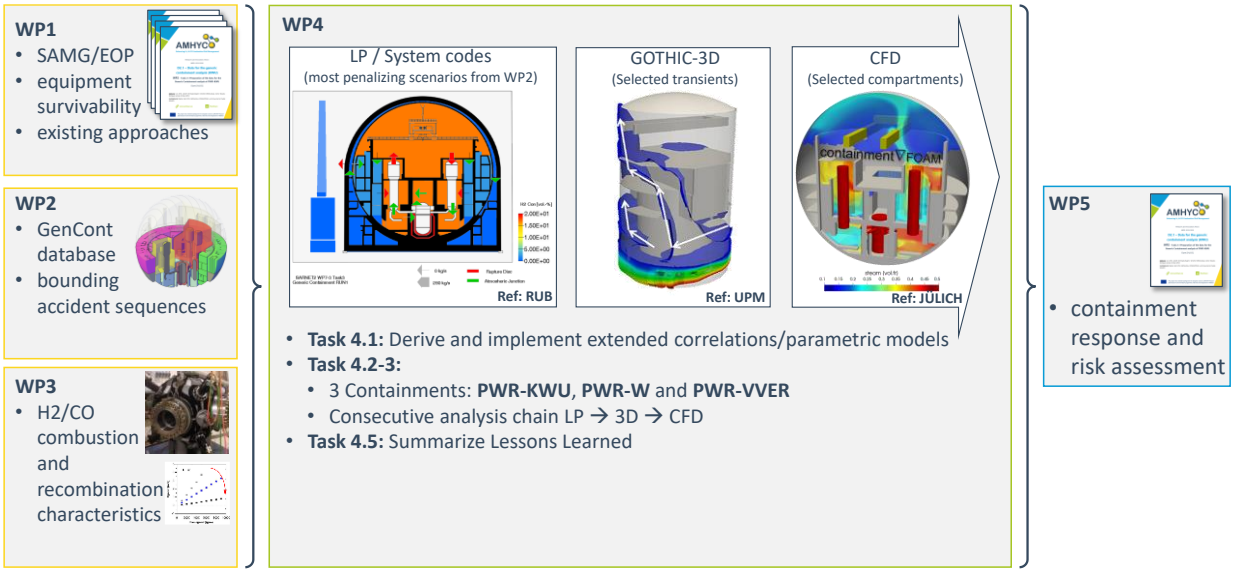

Figure 6. Integration of WP4 activities in AMHYCO

Within WP2 most penalizing accident sequences with respect to the combustion risk have been identified for the European PWR concepts. For WP4, two characteristic sequences have been selected for a detailed assessment: Unmitigated Small (S) or Medium (M) Break Loss of Coolant Accidents (LOCA) lead to a potentially flammable atmosphere in the containment and allow for studying the impact and efficiency of PARs, spray systems and fan coolers. Station Blackout (SBO) / Total loss of auxiliary power (TLAP) accidents revealed to be steam inertized throughout the transient but reach a high containment pressure up to the design limits. Thus, they enable investigating PAR efficiency at high pressure conditions, studying the effect of conducting FCVS on the combustion risk and assessing a potential recovery of emergency cooling systems in the late accident phase. A simulation matrix has been defined to systematically investigate the containment response with system codes, identify potentially challenging conditions and provide input to the subsequent analysis using 3D approaches.

2.5 WP5: Enhancement of Combustible Gas Control

The primary objectives of AMHYCO are in line with the goals described in “NFRP-02: Safety assessments for Long Term Operation (LTO) upgrades of Generation II and III reactors” of the EURATOM Work Programme 2019 with respect to the control of combustible gases present in the containment of a nuclear power plant in case of a severe accident with core damage.

When designing a combustible gas control system for a nuclear power plant, the overall system performance cannot be tested on a 1-to-1 scale due to the necessary efforts. Instead, the design and validation of the system relies on small-scale tests and full-scale numerical simulations with lumped parameter codes and CFD codes [19]. These full-scale simulations are used for optimal placement of the PAR inside the containment and determining suitable locations of the monitoring sensors. Only at these selected monitoring sensors, the main control room can “see” the gas concentration during a real accident. The operators do not have full information about the size and shape of gas clouds within the

containment. Therefore, one of the tasks of severe accident mitigation guidelines is to supply a sort of "translation" what the limited measurements available in the main control room actually tells about the real combustible gas distribution within the containment and what is the associated risk. This translation can only be gauged based on reliable containment simulations.

3. FINAL REMARKS

After three years of work in the AMHYCO project, several remarks can be shared. In WP1, after an extensive bibliographic search, several useful recommendations have been arisen for both the analytical and the experimental work of AMHYCO, giving at the same time a solid documental basement for the rest of the project. In WP2, among the accident scenario database simulated, different sequences posed the highest risk depending on PWR technology. There were several factors affecting the combustion risk: PARs performance, which significantly reduce the risk during the in-vessel phase and might condition the ex-vessel boundary conditions, particularly concerning oxygen availability; other safety systems performance (like sprays or fan-coolers), particularly whether they result in steam condensation during the ex-vessel phase; concrete composition, as it dictates the amount of CO2 resulting from MCCI; accident management actions, like cavity flooding. The final sequence selection made for further in-containment analysis was: doubled ended guillotine break (LBOCA) and station blackout (SBO) in PWR-Western; mid-size LOCA (80 cm2) with limited water injection in PWR-KWU; and, SBO with late sprays activation in PWR-VVER.

The experimental work in WP3 is going well beyond the state-of-the-art, both in the combustion side and in the recombination side (PARs). In the combustion experiments, new mixture compositions H_2/CO have been explored, with good agreement with similar work done in other research groups. On the PARs side, the soft and complex mechanism of oxygen starvation and CO poisoning have been investigated successfully, helping to validate further simulation tools such as PARUPM or SPARK.

In WP4, an innovation proposed in AMHYCO is the creation of a methodology based on new correlations to predict the combustion risk that are adapted specifically to the LP, 3D and CFD numerical codes, testing the three approaches within the WP for different safety systems actuation. Finally, the most relevant advance of the AMHYCO project will be the creation of guidelines for the SAMGs considering combustion risk management, which will be done in the second phase of the project.

ACKNOWLEDGMENTS

This project has received funding from the Euratom research and training programme 2019-2020 under Grant Agreement n°945057. The content of this paper reflects only the author's view. The European Commission is not responsible for any use that may be made of the information it contains.

REFERENCES

1. Shapiro, Z.M., and Moffette, T.R., Hydrogen Flammability Data and Application to PWR Loss-of-Coolant Accident, Report WAPD-SC-545, Bettis Plant, Pittsburgh, Pennsylvania, USA, September 1957.
2. Herranz, L.E., and Fontanet J., High combustion risk sequences. Identification and characterization, The 10th European Review Meeting on Severe Accident Research (ERMSAR2022), Log Number: 339, Karlsruhe, Germany, May 16-19, 2022.
3. Kilchyk, V., Flammability limits of carbon monoxide and carbon monoxide-hydrogen mixtures in air at elevated temperatures, Department of mechanical and manufacturing engineering, University of Calgary, Calgary, Alberta, November 2000.

4. Shang, R., Li, G., Wang, Z. and Wang, Z., Lower flammability limit of H2/CO/air mixtures with N2 and CO2 dilution at elevated temperatures, *International Journal of Hydrogen Energy*, vol. 45, n° %116, pp. 10164-10175, 2020.
5. Coudoro, K., Etude expérimentale et modélisation de la propagation de flamme en milieu confiné ou semi-confiné, Thèse de Doctorat, Université d'Orléans, Orléans, 2012.
6. Wierzba I. and Kilchyk, V., Flammability limits of hydrogen–carbon monoxide mixtures at moderately elevated temperatures, *International Journal of Hydrogen Energy*, vol. 26, n° %16, pp. 639-643, 2001.
7. Jaimes, D., McDonell, V. and Samuelsen, G., Lean flammability limits of syngas/air mixtures at elevated temperatures and pressures, *Energy & Fuels*, pp. 1 - 33, 03 septembre 2018.
8. Dorofeev, S. B., Kuznetsov, M. S., Alekseev, V. I., Efimenko, A. A., Bezmelnitsun, A. V., Yankin, Y. G. and Breitung, W., Evaluation of limits fir effective flame acceleration in hydrogen mixtures, Report FZKA-6268. Karlsruhe: Forschungszentrum Karlsruhe, preprint IAE-6127/3, 1999.
9. Bentaib, A., Bleyer, A., Meynet, N., Chaumeix, N., Schramm, B., Höhne, M., Kostka, P., Movahed, M., Worapittayaporn, S., Brähler, T., Seok-Kang, H., Povilaitis, M., Kljenak I. and Sathiah, P., SARNET hydrogen deflagration benchmarks: Main outcomes and conclusions, *Annals of Nuclear Energy*, vol. 74, pp. 143-152, 2014.
10. Ciccarelli, G., Chaumeix, N., Mendiburu, A., N'Guessan, K. and Comandini, A., Fast-flame limit for hydrogen/methane-air mixtures, *Proceedings of the Combustion Institute*, vol. 37, n° %13, pp. 3661-3668, 2019.
11. Bachellerie, E., Arnould, F., Auglaire, A., de Boeck, B., Braillard, O., Eckardt, B., Ferroni, F. and Moffett, R., Generic approach for designing and implementing a passive autocatalytic recombiner PAR-system in nuclear power plant containments, *Nuclear Engineering and Design*, 221, No. 1-3, 2003, pp. 151-165.
12. Reinecke, E.-A., Allelein, H.-J., Bentaïb, A., Chakraborty, A., Chaumeix, N., Heidelberg, D., Kelm, S., Klauck, M., Maas, L. and Steffen, P.-M., Operating behavior of passive auto-catalytic recombiners under severe accident conditions, International Severe Accident Management Conference (ISAMC), Ottawa (Ontario), Canada, October 15–18, 2018.
13. Liang, Z., Gardner, L., Clouthier, T., MacCoy, R. and Gyepi-Garbrah, S., Experimental study on H2-CO combustion and recombination in severe accidents, International Severe Accident Management Conference (ISAMC), Ottawa (Ontario), Canada, October 15–18, 2018.
14. Mimouni, S., Mechitoua, N. and Ouraou, M., CFD recombiner modelling and validation on the H2-PAR and Kali-H2 experiments, *Science and Technology of Nuclear Installations*, 2011, 574514, 2011.
15. Domínguez-Bugarín, A., Jiménez, M.-Á., Reinecke, E.-A. and Jiménez, G., PARUPM: A simulation code for passive auto-catalytic recombiners, *EPJ Nuclear Sci. Technol*, 8 32 (2022). DOI: 10.1051/epjn/2022046
16. Reinecke, E.-A., Kelm, S., Steffen, P.-M., Klauck, M. and Allelein, H.-J., Validation and Application of the REKO-DIREKT Code for the Simulation of Passive Autocatalytic Recombiner Operational Behavior, *Nuclear Technology*, 196:2, 355-366, 2016
17. Meynet, N., SPARK - Logiciel de calcul pour les recombineurs catalytiques, IRSN report PSN-RES/SAG/2015-00036, 2015.
18. Nobrega, G., Reinecke, E.-A., Bentaib, A., Maas, L., Chaumeix, N., Experimental investigation on the carbon monoxide effect on platinum- and palladium-based catalysts for passive auto-catalytic recombiners, Proc. 10th European Review Meeting on Severe Accident Research (ERMSAR2022), Karlsruhe, Germany, May 16-19, 2022.
19. Cremer, I., Tap, R. and Hupp, M., Updated Modeling and Simulation of Hydrogen Recombination in Full-scale Containment Analyses, The 19th International Topical Meeting on Nuclear Reactor Thermal Hydraulics (NURETH-19) Log nr.: 35508, Brussels, Belgium, March 6 - 11, 2022.

11TH CONFERENCE ON
SEVERE ACCIDENTS RESEARCH
May 13-16, 2024 – Stockholm, Sweden
ERMSAR 2024

AMHYCO
Enhancing H_2 & CO Combustion Risk Management

AMHYCO project overview and first outcomes

Jiménez, G. (UPM), Bentaib, A. (IRSN), Herranz, L.E. (CIEMAT), Chaumeix, N. (CNRS), Kelm, S. (FZJ), Reinecke, E.-A. (FZJ), Braun, M. (FRAMATOME), Koch, M.K..(RUB), Kljenak, I.(JSI), Sevbo, O.(ENERGORISK), Visser, D.(NRG), Liang, Z.(CNL), Lazarevic, M.(LGI)

This project has received funding from the European Union's EURATOM Horizon 2020 research and innovation programme grant number: 945057. The content of this document reflects only the author's view. The European Commission is not responsible for any use that may be made of the information it contains.

AMHYCO general data

- Full Project Name: Towards An Enhanced Accident Management Of The Hydrogen/CO Combustion Risk
- EURATOM Work Programme 2019 “NFRP-02: Safety assessments for Long Term Operation (LTO) upgrades of Generation II and III reactors”
- Project No: 945057
- Start Date: 01/10/2020
- Project Duration: 48 months
- EU contribution: 3 974 402.50 €





AMHYCO partners

#	Participant organisation name	Country
1 (Coordinator)	Universidad Politécnica de Madrid (UPM)	Spain
2	Centro de Investigaciones Energéticas, Medioambientales y Tecnológicas (CIEMAT)	Spain
3	L'Institut de Radioprotection et de Sûreté Nucléaire (IRSN)	France
4	Centre National de la Recherche Scientifique -Orleans (CNRS)	France
5	Forschungszentrum Jülich (FZJ)	Germany
6	Framatome GmbH (FRG)	Germany
7	Ruhr-Universität Bochum (RUB)	Germany
8	Jožef Stefan Institute (JSI)	Slovenia
9	Energorisk, Ltd. (ER)	Ukraine
10	Nuclear Research and Consultancy Group (NRG)	Netherlands
11	Canadian Nuclear Laboratories (CNL)	Canada
12	LGI Consulting (LGI)	France

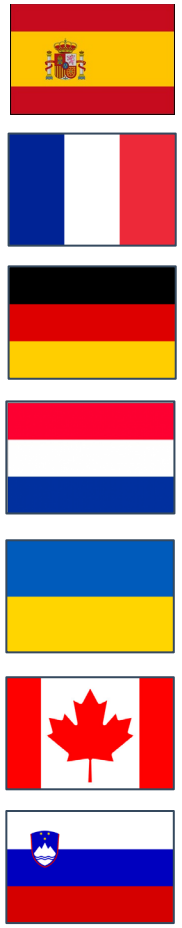

AMHYCO objectives

The AMHYCO project main objective is **to propose innovative enhancements on the way combustible gases are managed in case of a severe accident in currently operating reactors.**

To reach this main objective, the AMHYCO project has three main specific objectives:

Objective 1: To experimentally investigate phenomena that are difficult to predict theoretically: H2/CO combustion and PARs (Passive Autocatalytic Recombiners) behavior under realistic accidental conditions, taking into account their interaction with safety systems.

Objective 2: To improve the predictability of analysis tools - Lumped Parameter (LP), 3D and Computational Fluid Dynamic (CFD) codes - used for explosion hazard evaluation inside the reactor containment and providing support to SAMGs design and development.

Objective 3: To improve the Severe Accident Management Guidelines for both in-vessel and ex-vessel phases with respect to combustible gases risk management, using theoretical, simulation and experimental results.

AMHYCO workflow

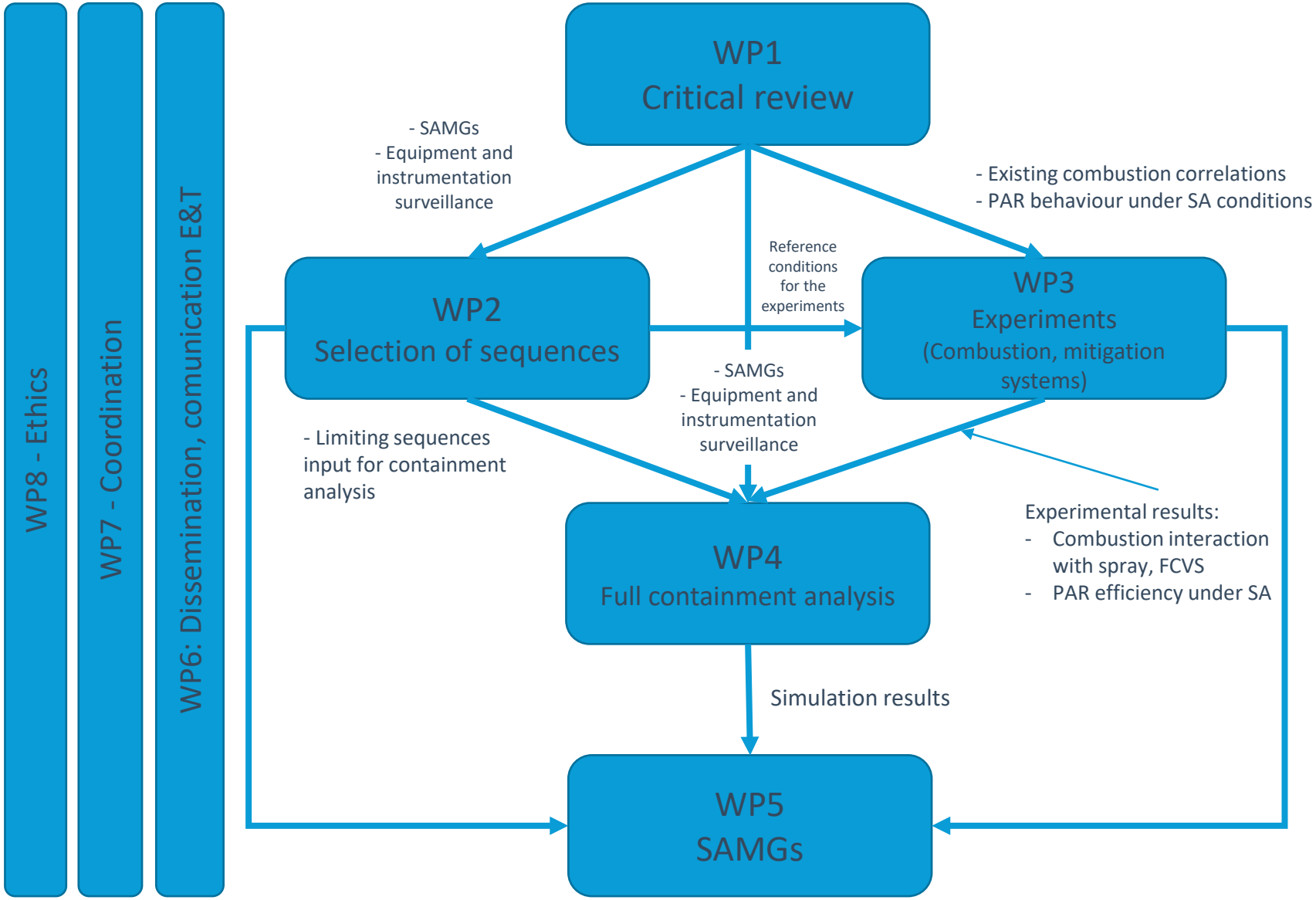

Initial schedule (October 2020 – September 2024)

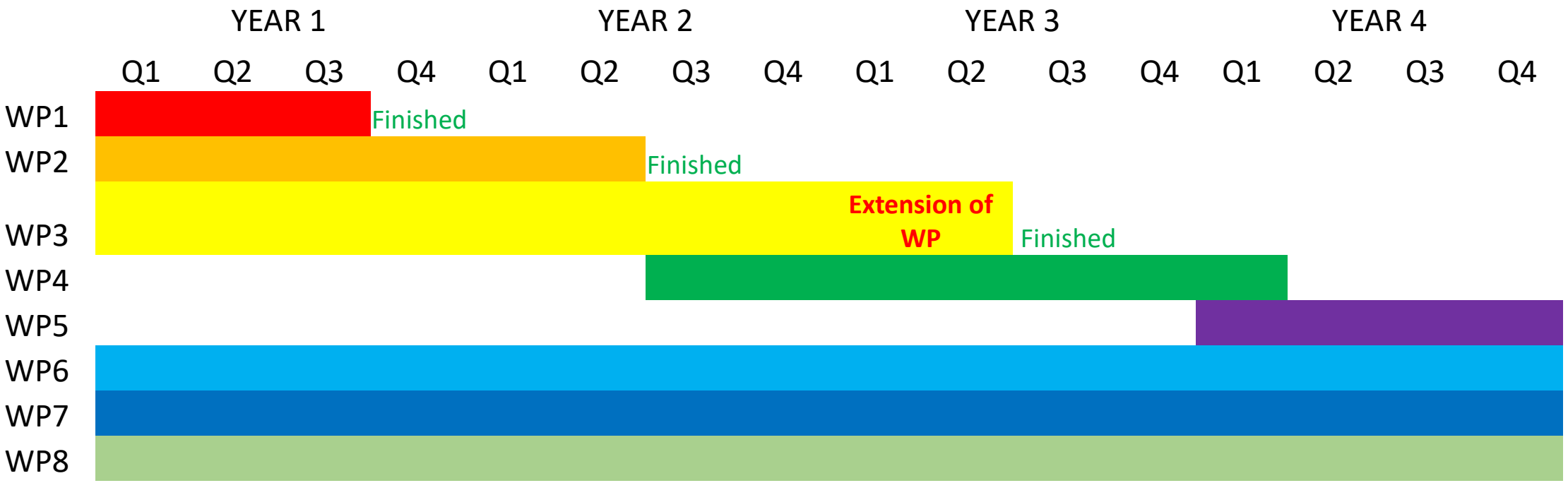

Timeline with the extension (1 Oct 2020 - 31 March 2025)

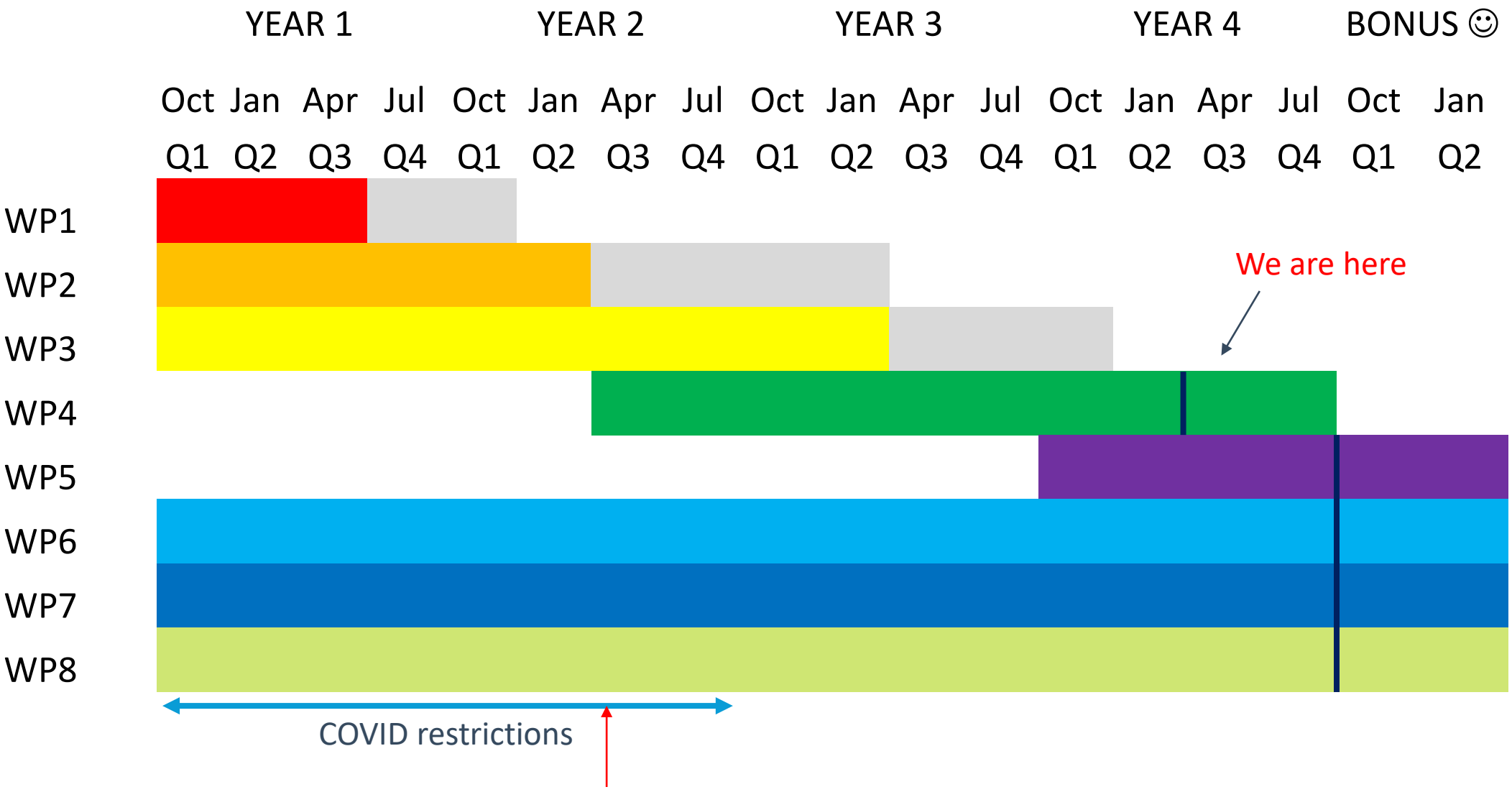

Connection with other ongoing international projects

PANDA



PAUL SCHERRER INSTITUT
PSI

NEA
NUCLEAR ENERGY AGENCY

THEMIS

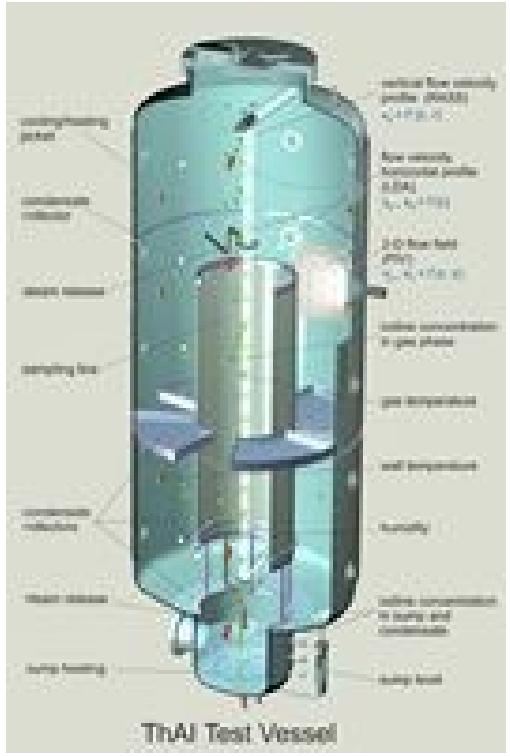

BECKER TECHNOLOGIES

SAMHYCO-NET

SAMHYCO NET

NUGENIA
Nuclear Generation II&III Alliance

WP1 – Critical review – Finished



Image credit: Pixabay

A critical review of the available literature to form the basis for the project regarding:

(1) PAR efficiency under ex-vessel conditions.

(2) Existing PWR EOPs and SAMGs regarding containment risk management.

(3) H_2/CO combustion and the available engineering correlations for combustion risk estimation.

(4) Equipment and instrumentation surveillance under SA conditions.

Review of H2/CO recombination and PAR performance under SA conditions

Until now, the conditions for the transition between H2-CO recombination regimes are unclear. Consequently, the experimental program in WP3 has to provide corresponding data regarding

- the conditions (gas composition, including oxygen starvation) leading to catalyst poisoning by CO
- the role of containment temperature and pressure on the catalyst poisoning conditions
- the sensitivity of different catalysts (e.g. platinum- or palladium-based) with regard to poisoning
- Further potential mechanisms of PAR deactivation to be investigated (e.g. cable fires) need to be deduced from analysis of relevant accident scenarios.

Review of the existing PWR SAMGs regarding containment risk management

- The adopted requirements address only in-vessel conditions. **Their extension to ex-vessel conditions need to be established for the containment and the auxiliary buildings connected to the containment,**
- The mitigation means are designed accordingly to the adopted requirements for in-vessel conditions,
- Only few countries adopt quantitative criteria for the requirement,
- Only few existing SAMG recommendations concern the use of safety systems (CHRS, spray and coolers) in case of severe accident late phases,
- The existing monitoring systems don’t measure carbon monoxide content.

Review of the H2/CO combustion and the available engineering correlations for combustion risk estimation.

- For the Flame acceleration, only two studies were relevant to ex-vessel conditions. Both of them were preliminary studies from which it was not possible to draw a clear picture on how the flame acceleration criterion can be extended from pure H_2 to a mixture of H_2/CO.
- For FA extension to ex-vessel conditions, there **is a need to determine the Zeldovich number and the effective Lewis number for a binary fuel mixture. Moreover, flame acceleration experiments should be extended to larger scales in order to adequately analyze the phenomena. The data are too scarce to address adequately this very important issue**
- A similar conclusion can be drawn for the H_2/CO detonability. Only recently, data were published on the detonation cell size of 90%H_2/10%CO mixtures with air. **These preliminary results indicate that for lean mixtures, the detonation limit may be larger for CO/H_2 mixtures than for H_2mixtures. There are not enough data to draw a clear conclusion. In this regime, larger scale experiments are desirable.**

Review of the containment equipment qualification criteria and instrumentation surveillance under severe accident conditions

It was needed to:

- Review of the principles of Survivability Assessment under SA criteria,
- Review of the regulatory frame surrounding SA survivability assessment and its connections with the EQ standards.
- Relevant plant-specific SA qualification data for temperature and pressure enveloping profiles for SA survivability assessments for a variety of PWRs and some other NPPs in several countries.
- Review some common implemented approaches and the most relevant international efforts in the field of SA equipment and instrumentation survivability under severe scenarios.

WP1: completed and available

https://amhyco.eu/wp-content/uploads/2024/02/D1_1_Critical_assessment_of_key_elements_of_combustible_gases_management_in_containment_V1.pdf

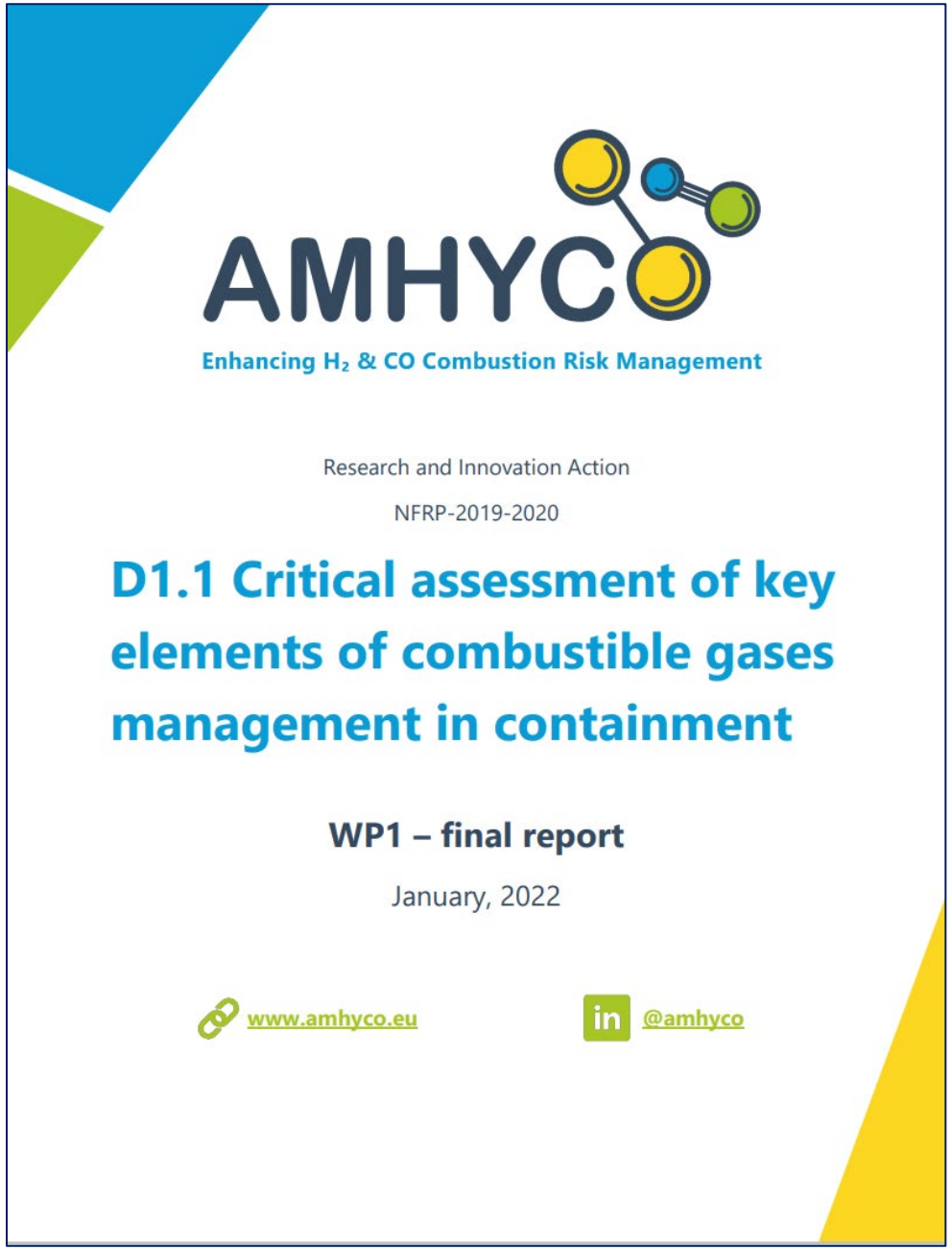

WP2 – Selection of severe accident sequences

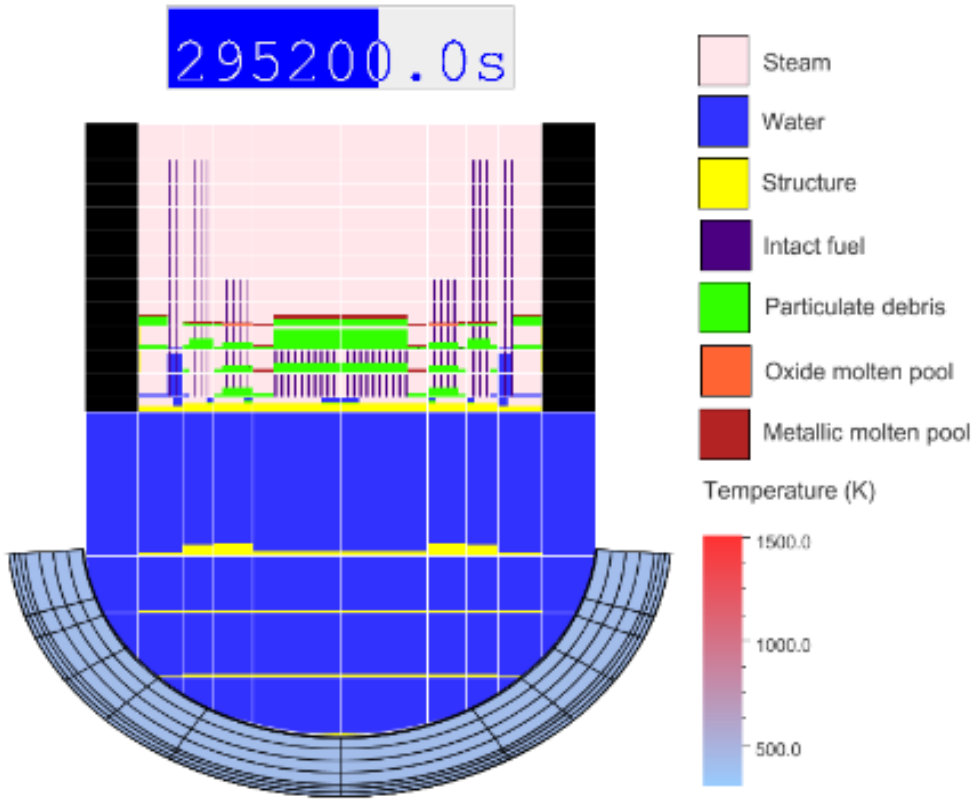

Ref: UPM

- The intention was to identify **accident sequences in which the combustible gases risk might jeopardize containment**, to establish a set of cases for evaluating the combustion risk in different scenarios later on (WP4).
- Different PWR reactor designs were addressed (**PWR-W; PWR-KWU; PWR-VVER**)
- As a result, the output of the WP was a **database with generic PWR input decks** that will feed activities to be conducted within WP4.

WP2 Selection of Severe Accident Sequences - Finished

Main deliverables and milestones achieved:

- Milestones achieved.
- Deliverables under EC approval
- Energorisk did their best despite the war in Ukraine

Generic containments have been developed (PWR-KWU, PWR-W and PWR-VVER) and severe accident sequences have been calculated.

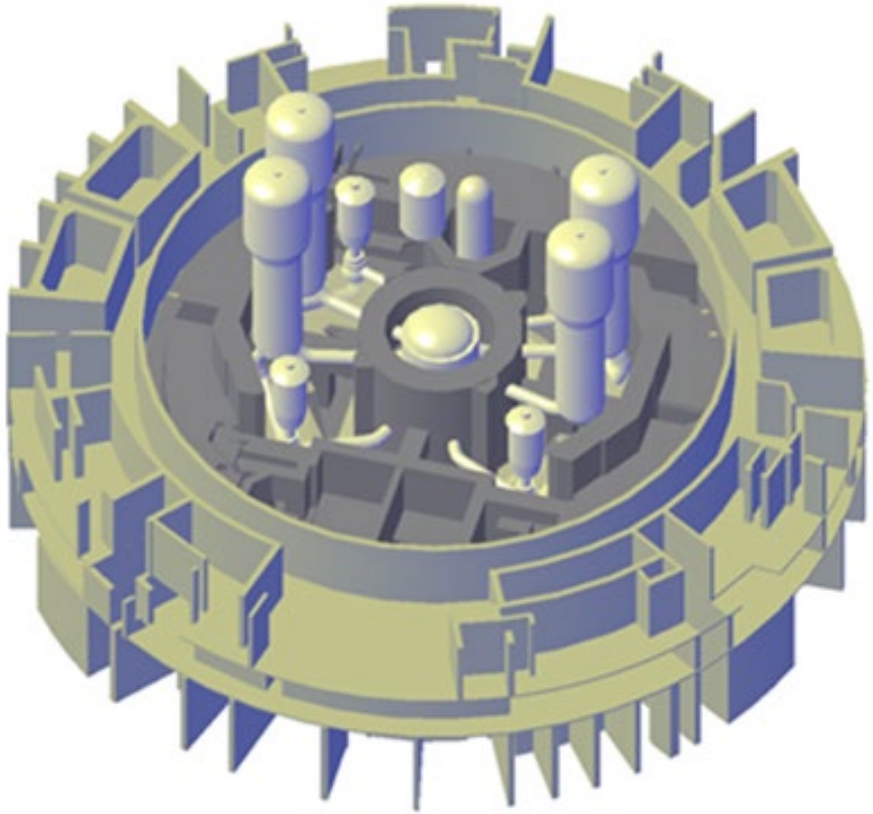

Ref: **Development of a detailed 3D CAD model of a generic PWR-KWU containment as a basis for a better assessment of H2/CO combustion risk**. Serra, Luis; Domínguez-Bugarín, Araceli; Estévez-Albuja, Samanta; Vázquez-Rodríguez, Carlos; Jiménez, Gonzalo; Kelm, Stephan and Herranz, Luis E. Proceedings of the European Nuclear Young Generation Forum ENYGF'21. September 27-30, 2021, Tarragona, Spain

Generic Containment Database (GCDb)

- GC Database (compartment volume; flow paths, structures, …)
  - Inspired by SAMHYCO GC - FZ Juelich
  - Based on CAD methodology (3D containment build)
  - Nodalizations (PWR-KWU; -W; -VVER)

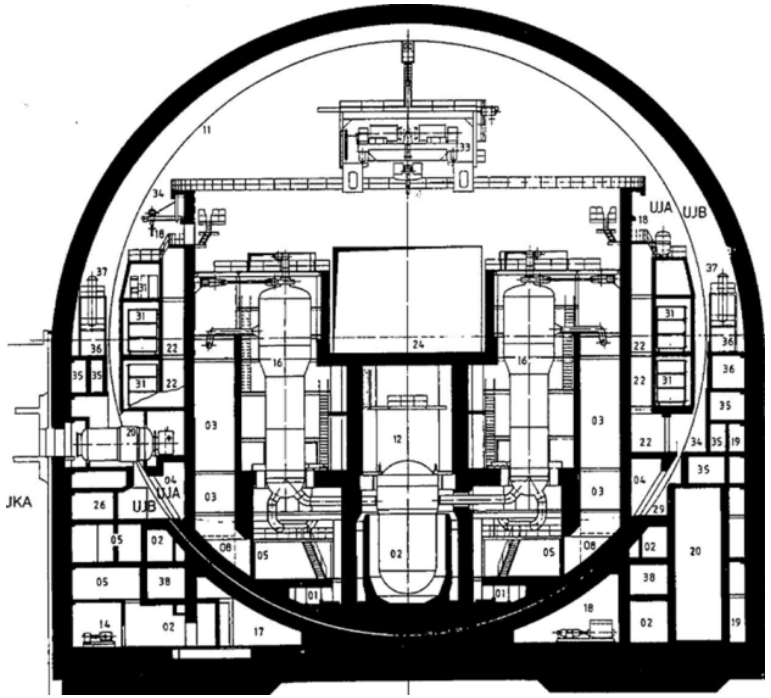

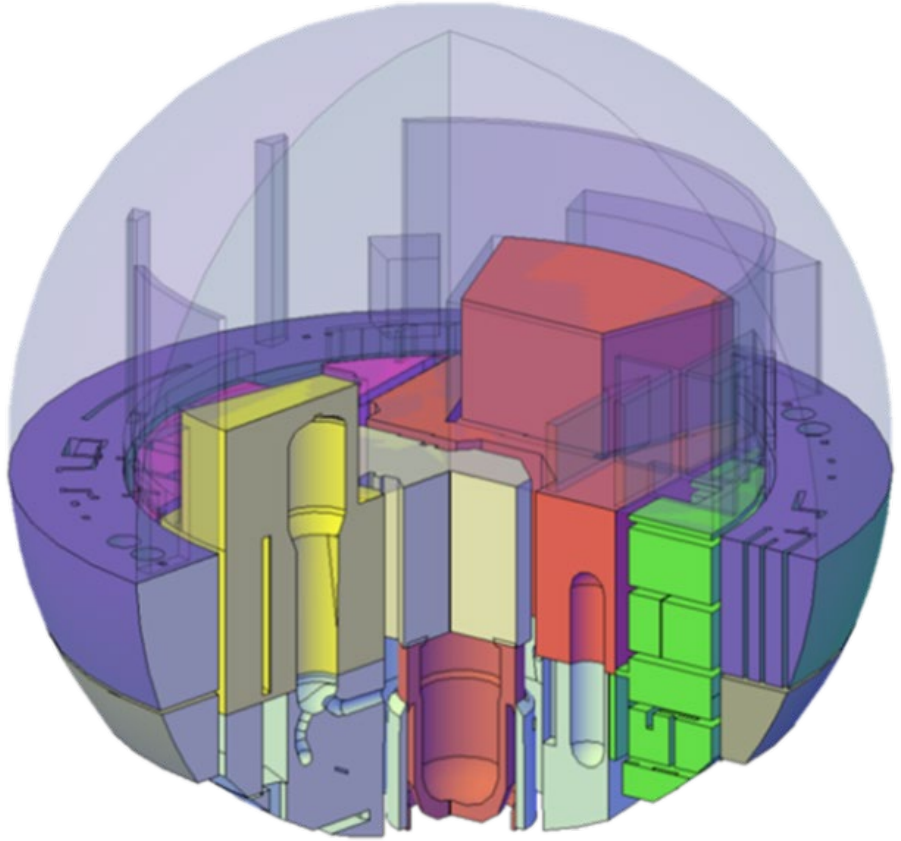

Deliverable 2.1

"Data for the generic containment analysis" (PWR-W, PWR-VVER, PWR-KWU)"

Table of Contents

1. INTRODUCTION
2. METHODOLOGY
3. GENERIC CONTAINMENT DATABASE
3.1 PWR-KWU generic containment
3.1.1 PWR-KWU 3D CAD model construction
3.1.2 PWR-KWU LP nodalization and database
3.2 .PWR-x
4. FINAL REMARKS
5. REFERENCES
ANNEX A: Heat structure data extraction methodology
ANNEX B: PWR-KWU layouts
ANNEX C: PWR-VVER layouts

- Compartment free volumes
- Concrete/steel volumes, surfaces, and thicknesses
- Flow path areas and arrangement
- Heat structures data
- Gratings, relief flaps, drainages, etc.
- Equipment and I&C location
- PAR sizing

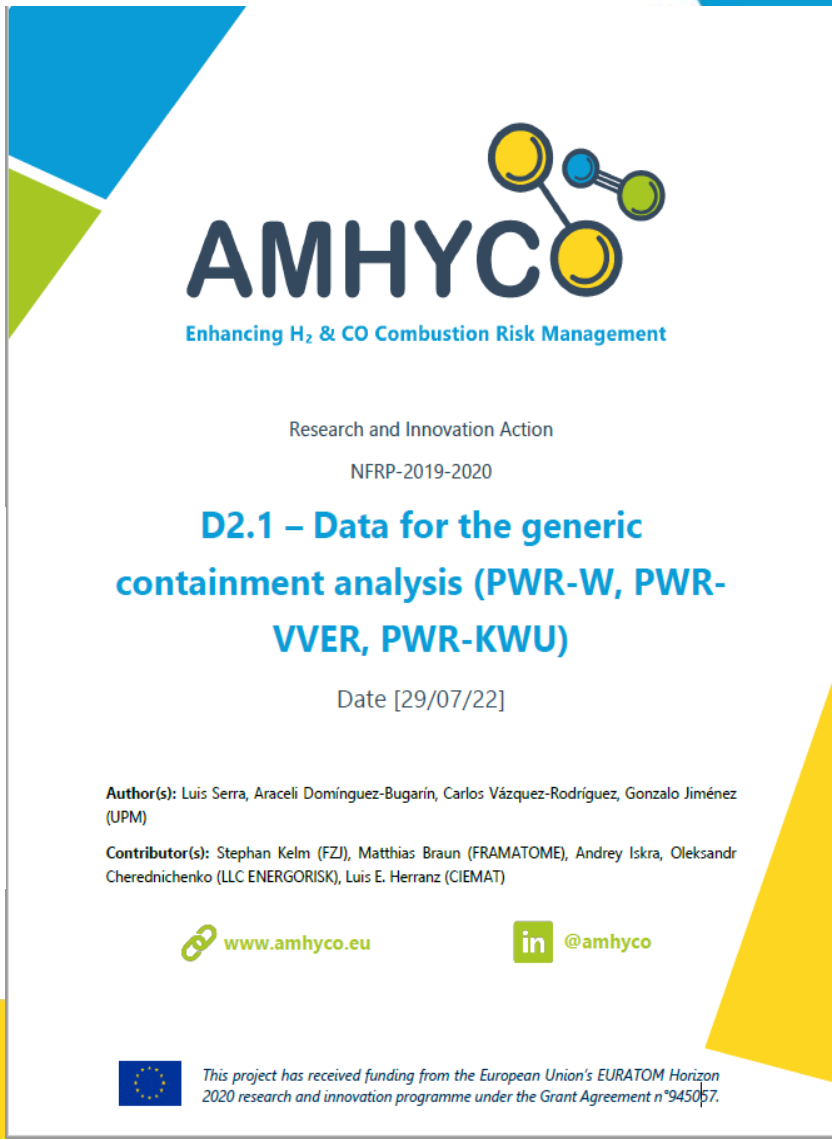

Sequence Selection Criteria

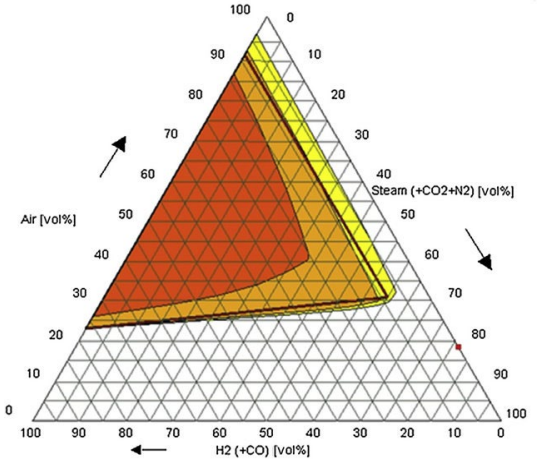

- $X_{H2}+X_{CO} > 9\%$ (Shapiro diagram) → Condition sine-qua-non
- Large mass of H_2 & CO → Flammability in big compartments
- Fast H_2 & CO injection rates → In-V injection
- **Qualitative assessment** → High P seqs.
  - Slow deflagrations might be a threat.
  - FCVS & H_2 management!
  - High pressure and steam inertization
  - Early venting for H_2 purposes

AMHYCO

Sequence Database

Western
KONVOI
VVER

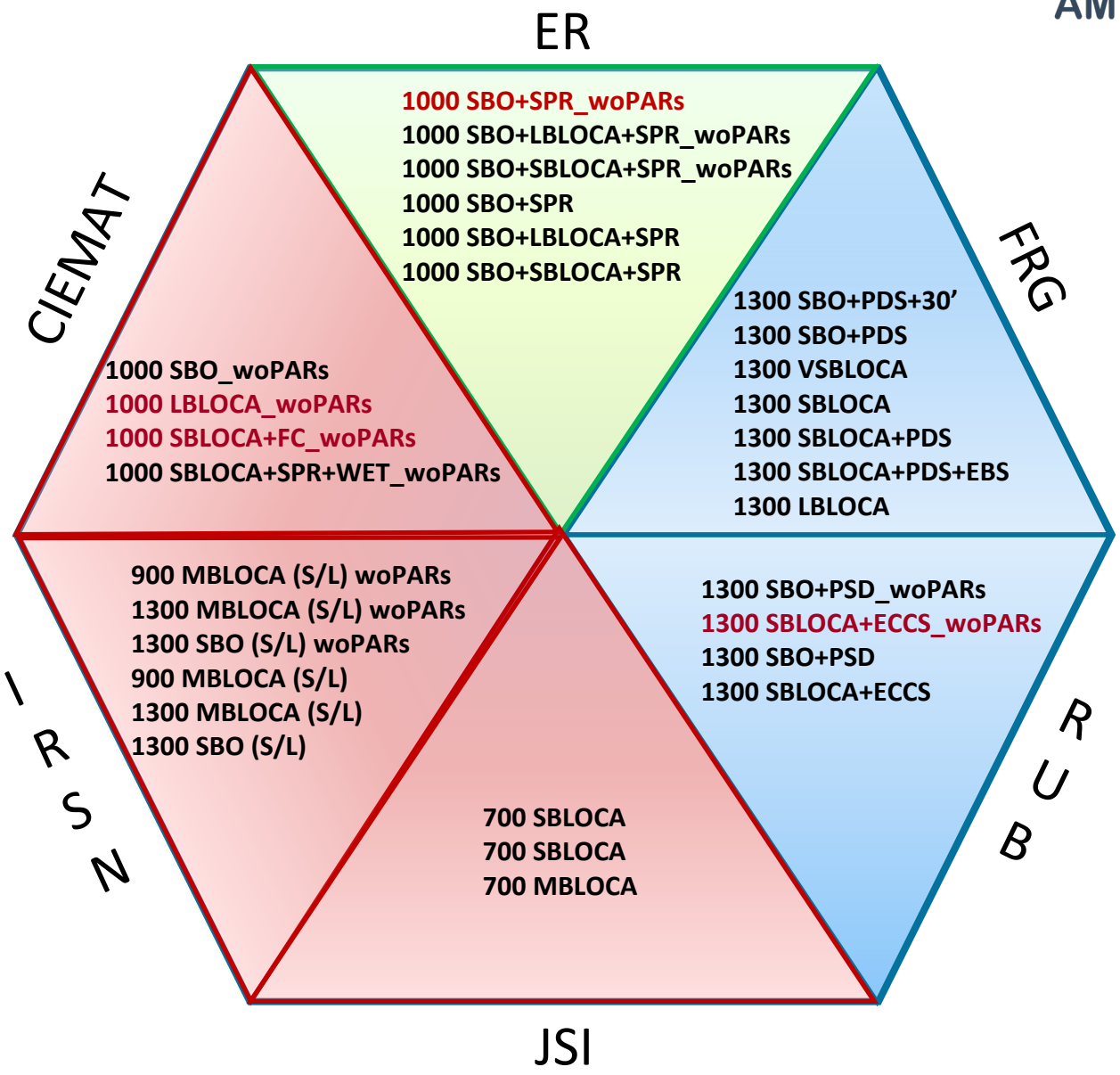

AMHYCO

Deliverable 2.2

"Identification and Analysis of accidental sequences posing high H_2/CO combustion risk (PWR-W, PWR-VVER, PWR-KWU)"

Table of Contents

1. Introduction
2. Selection criteria
3. Figures of merit
4. Results and discussion
   - 4.1. Matrixes of sequences
   - 4.2. PWR-W
   - 4.3. PWR-KWU
   - 4.4. PWR-VVER
5. Application to other WPs
   - 5.1. WP3
   - 5.2. WP4
   - 5.3. WP5
6. Conclusion

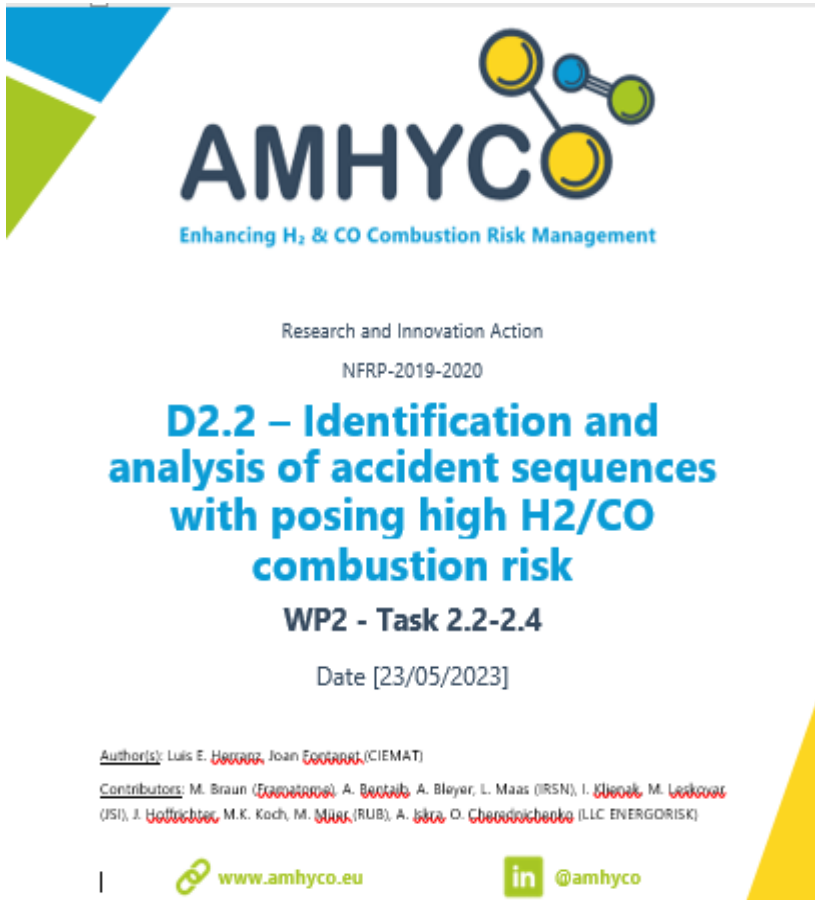

Final remarks

- **No methodology is infalible** (less if working under schedule).
- **GCDbase**, a very time consuming but **indispensable step**.
- **Sequence selection**, an uneasy task (iterative open process).
- **“Relevant combustion sequences”** identified & characterized.

WP3 – Experimental investigations - Finished

The objective of this WP· is to investigate experimentally phenomena that are difficult to predict theoretically: H2/CO/H2O combustion and PARs behavior under realistic accidental conditions, taking into account the safety systems interaction. Two main tasks:

- **Combustion of flammable H2/CO/H2O mixtures**, led by the CNRS, that will target the missing fundamental combustion parameters taking into account spray and venting with the goal to provide engineering correlations to the safety tools and improving the numerical codes;
- **PAR performance under severe accident boundary conditions** led by JUELICH

Deliverables waiting for EC approval

WP3 – Experimental investigations

CNRS: combustion experiments

- Spherical bombs:
  - BS-I: 8 l, max. pressure: 50 bar, max. temp: 100ºC
  - BS-II: 56 l, max. pressure: 50 bar, max. temp: 100ºC
  - BS-III: 93.43 l, max. pressure: 200 bar, max. temp: 250ºC
- ENACCEF-2:
  - internal diameter – 0.23 m,
  - height – 7.65 m,
  - max. pressure: 234 bar



WP3 – Experimental investigations

REKO platform (JUELICH): PAR experiments

REKO-1 (Cylindrical vertical flow channel)

- Diameter: 40..70 mm, Length: 1 m
- Performance of catalyst specimens

REKO-3 (Rectangular vertical flow channel)

- Cross section: 146 x 46 mm, Length: 1 m
- Performance of PAR catalyst section

REKO-4 (Pressure vessel)

- Diameter: 1.4 m, Height: 3.7 m
- Volume: 5.4 m^3
- Max. operating pressure: 2.3 bar @ 280 °C

REKO-Fire (Vertical flow channel)

- Combination of cylindrical flow channel with cable fire aerosol generator



WP3 Experimental Investigations

The **experimental characterization of the combustion** regimes that may occur during the late phase accident has started in BS-I, BS-III and ENACCEF-II: the flammability limits, laminar, and turbulent flames are assessed for normal air and under oxygen starvation conditions. Experiments with H2/CO with air and 6.5% O2 are carried out three H2/CO concentrations. Flame acceleration in 11-26%{H2/CO}/Air condition

The **experimental program on PAR operation** in severe accident atmosphere has started in the REKO facilities.

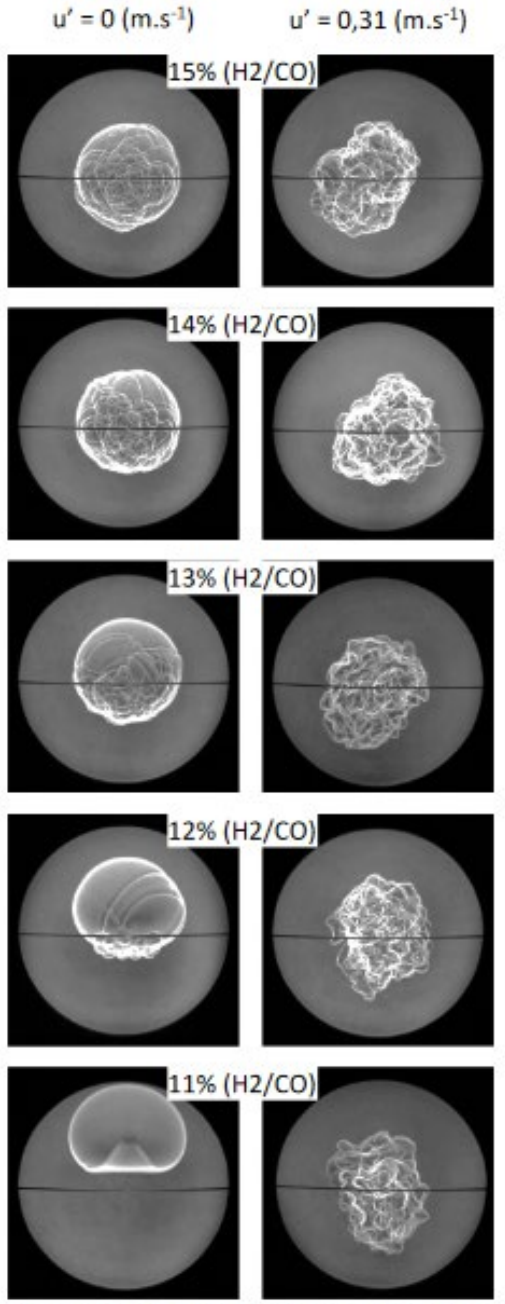

Fig. 6. Flame visualizations for a mean radius of 50 mm.

AMHYCO

REF: **Turbulent flame speed of H2-CO-Air mixtures for conditions relevant to late phase accident scenario**. Anthony Desclaux, Gustav Nyrenstedt, Mahmoud Idir, Nabiha Chaumeix, Alexandre Bleyer, Ahmed Bentaib. 19th International Topical Meeting on Nuclear Reactor Thermal Hydraulics NURETH 19. Virtual meeting | March 6-11, 2022.

WP3 – Results (examples)

PARUPM

- Chimney model
- Mass transfer-controlled reaction model
- Significant improvement of simulation results

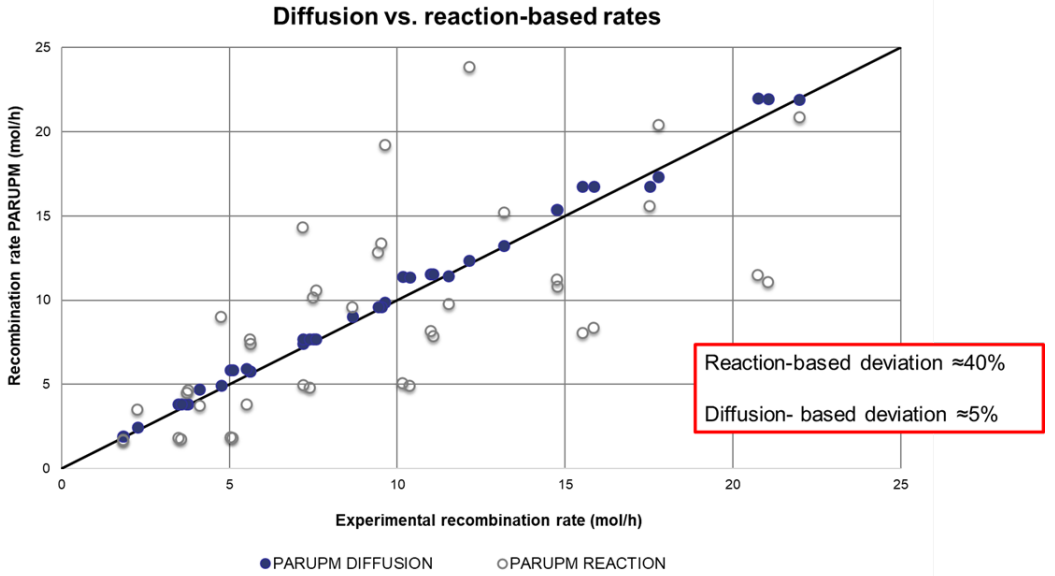

Framatome correlation

- Modified correlation proposed
- Validation against entire THAI-database
- Implementation in LP codes on-going in WP4

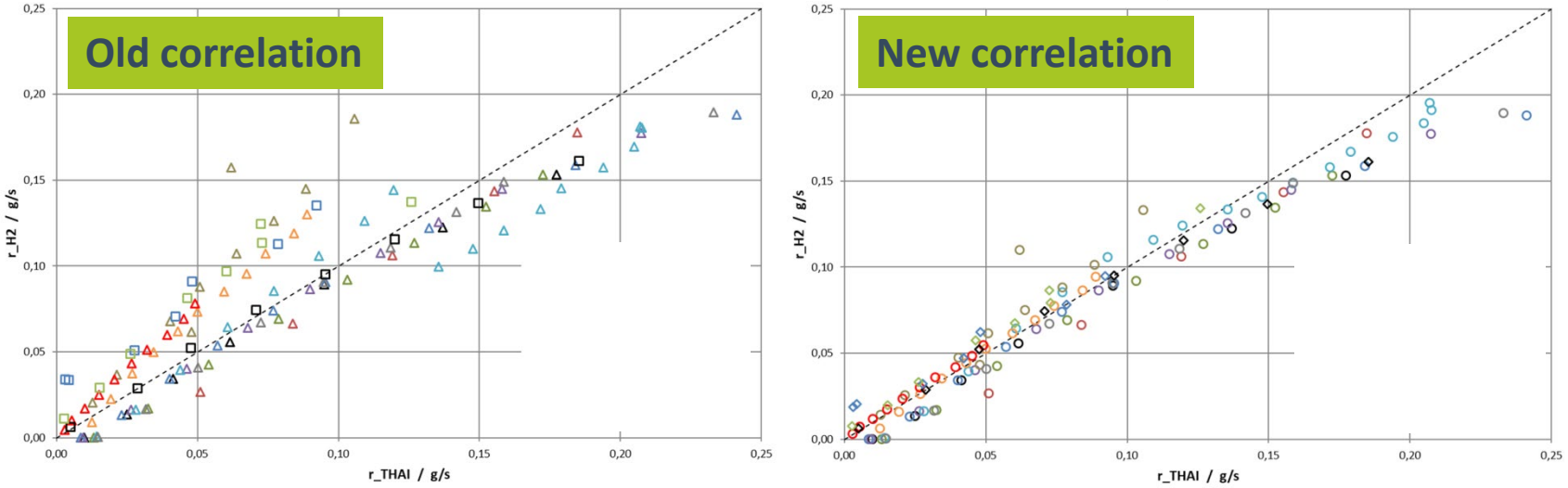

WP4 Full Containment Analysis - Ongoing

- Development and implementation of new engineering criteria and correlations
- Analysis of Containment response, combustion risk and effectiveness of mitigative measures are be conducted in three levels of detail

LP / System codes
(most penalizing scenarios from WP2)

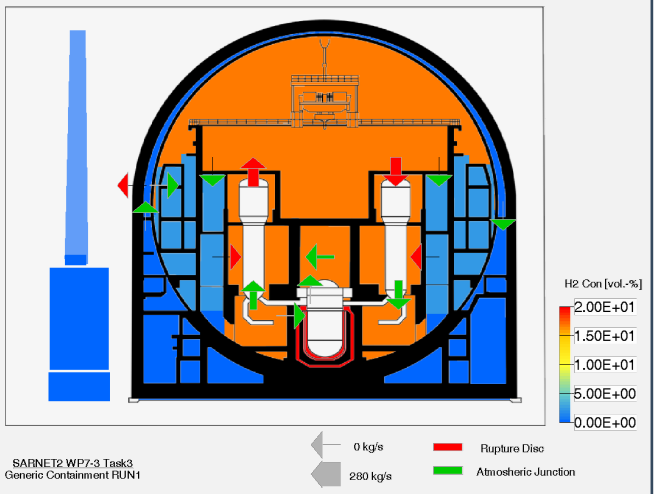

Ref: RUB

GOTHIC-3D
(Selected transients)

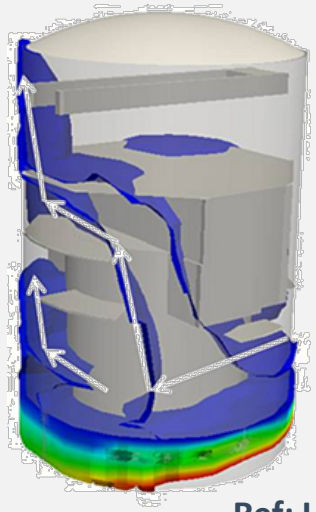

Ref: UPM

CFD
(Selected compartments)

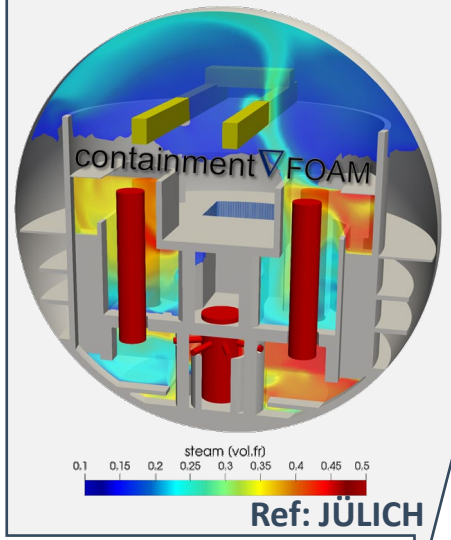

Ref: JÜLICH

- Summary of experience / lessons-learned in code specific guidelines

WP4 Full Containment Analysis

- Officially started in M19
- Needs inputs from WP2
- Preparation work began:
  - Transfer of WP3 insights to engineering models and correlations (Task 4.1)
  - Definition of a calculation matrix for PWR-KWU, PWR-W and PWR-VVER, two sequences per plant:
    - A LOCA sequence is selected to have an early ex-vessel phenomenology (high H2+CO with limited O2 starvation).
    - A SBO scenario is related to high pressure and steam concentrations for a FCVS assessment and late re-activation of the emergency cooling systems

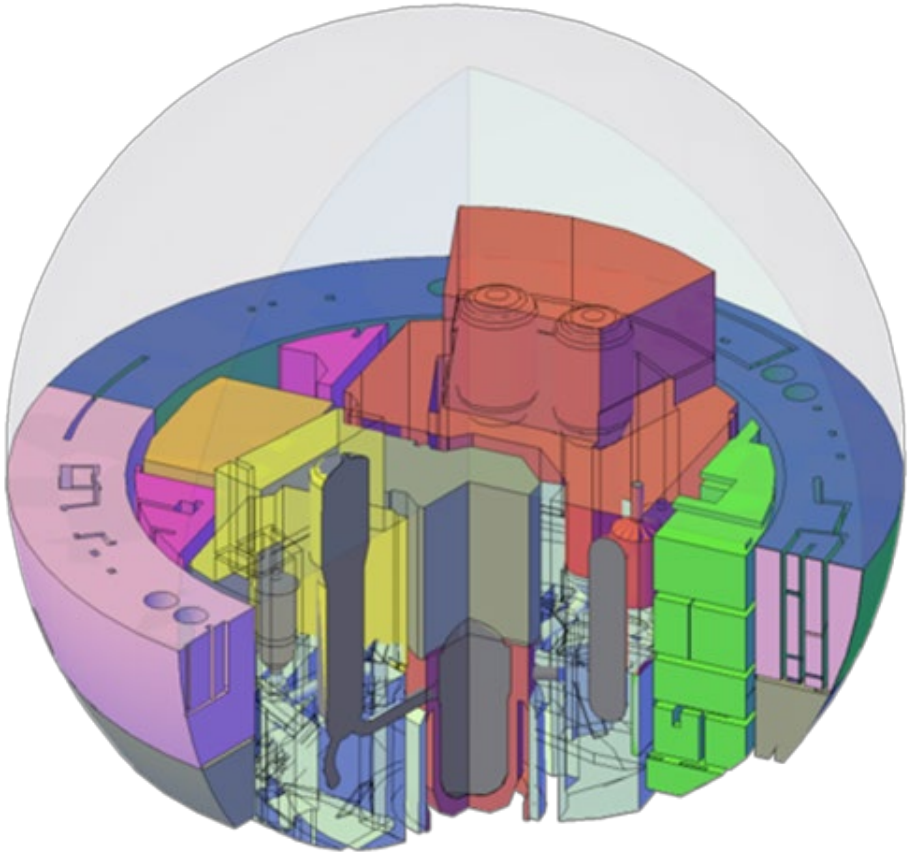

Ref: **Development of a detailed 3D CAD model of a generic PWR-KWU containment as a basis for a better assessment of H2/CO combustion risk**. Serra, Luis; Domínguez-Bugarín, Araceli; Estévez-Albuja, Samanta; Vázquez-Rodríguez, Carlos; Jiménez, Gonzalo; Kelm, Stephan and Herranz, Luis E. Proceedings of the European Nuclear Young Generation Forum ENYGF'21. September 27-30, 2021, Tarragona, Spain

WP5 – Enhancement of Severe Accident Management Guidelines – Just started



This WP aims to identify enhancements of safety procedures (e.g. EOPs) and severe accident management guidelines (SAMGs) to reduce the H2/CO combustion risks to the containment.

The output of this WP will be:

- Enhanced technical AM measures based on results achieved in the project,
- A translation into practical AM measures in which human error is minimized as far as possible,
- Recommendations for LTO upgrades to comply with the proposed AM measures above.

WP6 – Dissemination, Communication, Education and Training

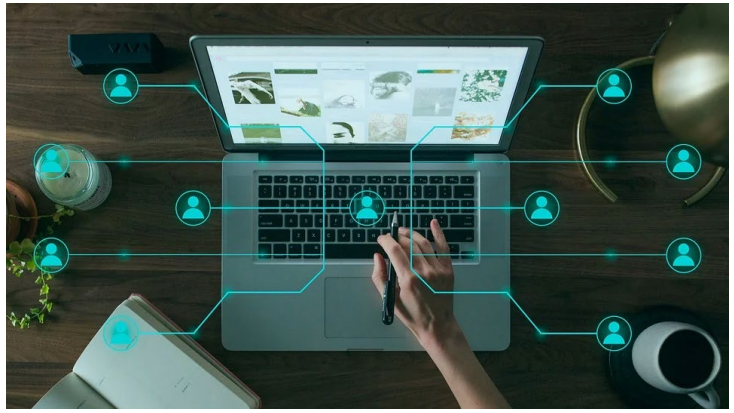



Images credit: Pixabay

- **Communication activities**: preparation of brand identity, website, poster, roll-up, newsletter, videos, and commercial brochures
- AMHYCO project will support the publication in **golden open access** approach
- The project will set up and manage an international **End-User Group** to reach out on the AMHYCO achievements, seek feedback when relevant, and attract potential future users and developers
- **Students Mobility Program**: to promote students mobility between organizations
- **Two international workshops** (M36 and M48)

WP6 Dissemination, Communication, Education, and Training - Progress



Conference papers published or in a pipeline: >25

Conferences: NURETH19, ENYGF2021, ICHS2021, FISA, ERMSAR2022, KERNETCHNIK2022, CSARP, NURETH23, ENYGF2023, SNE2021, SNE2022, SNE2023, ERMSAR2024, SNE2024

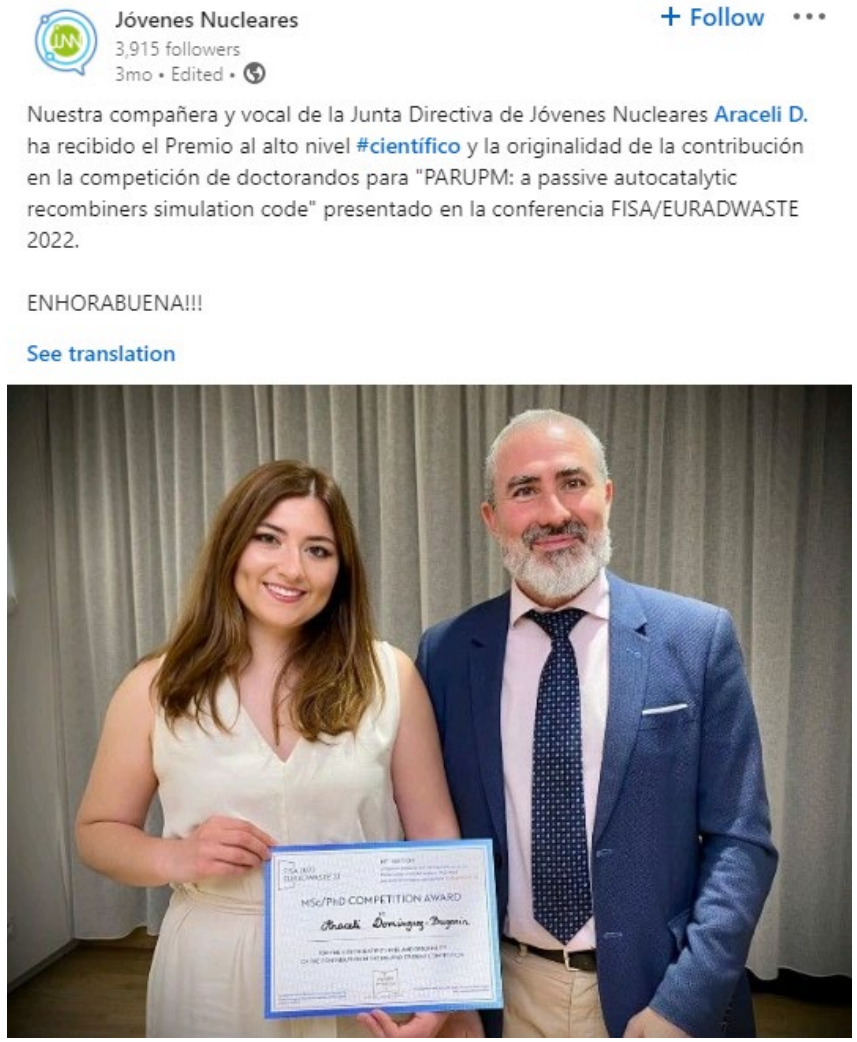

European prize for the best PhD presentation (FISA2022)

PhD mobility actions



UPM PhD students at FZJ

PhD mobility actions



RUB PhD student at UPM

11TH CONFERENCE ON SEVERE ACCIDENTS RESEARCH
May 13-16, 2024 – Stockholm, Sweden
ERMSAR 2024

AMHYCO at events

AMHYCO

International Workshop on Hydrogen Safety for Nuclear Power Plants

Fontenay-aux-Roses, France
January 19-20, 2023

Hosted by

INSTITUT DE RADIOPROTECTION ET DE SURETE NUCLEAIRE (IRSN)

31, Avenue de la Division Leclerc
92260 Fontenay-aux-Roses,
France



SNETP Sustainable Nuclear Energy Technology Platform
NUGENIA TA2 Nuclear Generation II&III Alliance
KIT Karlsruhe Institute of Technology
INR

NUGENIA TA2 Meeting
February 15th-16th, 2023

Institute for Neutron Physics and Reactor Technology (INR)
Building 521, Seminar Room
KIT, Karlsruhe, Germany



SNETP Sustainable Nuclear Energy Technology Platform

Coordinators' hub Day

14 March 2023

Maison Irène et Frédéric Joliot Curie, Auditorium, Brussels

10:00 – 16:00



AMHYCO video



https://vimeo.com/776134461

First AMHYCO journal papers



PARUPM: A simulation code for passive auto-catalytic recombiners

Araceli Domínguez-Bugarín, Miguel-Ángel Jiménez, Ernst-Arndt Reinecke and Gonzalo Jiménez

EPJ Nuclear Sci. Technol., 8 (2022) 32

Published online: 22 November 2022

DOI: https://doi.org/10.1051/epjn/2022046

Towards an optimized management of accidents

Luis E. Herranz, Gonzalo Jiménez and Francesco S. Nitti

EPJ Nuclear Sci. Technol. 8, 43 (2022)

Published online: 21 December 2022

DOI: https://doi.org/10.1051/epjn/2022019

First AMHYCO Workshop: Orleans



October 2023

Madrid final workshop



(February 2025 – specific dates TBD)

AMHYCO End-user group

- **NPP Owners:**
  - Iberdrola (co-owner of several PWRs, Spain),
  - Electricité de France (56 PWR-W, France),
  - Krško NPP (1 PWR-W, Slovenia),
  - Almaraz and Trillo NPPs (2 PWR-W, 1 PWR-KWU, Spain),
  - Ascó and Vandellós NPPs (3 PWR-W).
- **SAMGs developers**:
  - Tecnatom (PWR-W, Spain),
  - PWR Owners Group,
  - EPRI (PWR-W, USA),
  - Fortum (PWR-VVER, Finland)
- **Code developers**:
  - Zachry (USA, GOTHIC developers)



















WP7 – Project coordination and management



- **Project coordination, quality management and project secretariat.**
- Contractual & Financial Management
- **Advisory Board,** which will be constituted of high-ranking professionals from organizations in and/or outside Europe

Image credit: Pixabay

AMHYCO AB members

- **Prof. Dr. Joseph E Shepherd** (USA), C.L. “Kelly” Johnson Professor of Aeronautics and Mechanical Engineering, California Institute of Technology.
- **Dr. Juan Manuel Martín-Valdepeñas** (Spain), Senior Inspector at Probabilistic Safety Analysis, Consejo de Seguridad Nuclear (Spanish Nuclear Regulatory Body).
- **Dr. Berthold Schramm** (Germany), Expert in containment CFD modelling, Gesellschaft für Anlagen- und Reaktorsicherheit (GRS)
- **Dr. Sanjeev Gupta** (Germany), Head of Reactor Safety Research, Becker Technologies.
- **Dr. Samuel Gyepi-Garbrah** (Canada), Canadian Nuclear Safety Commission, Ottawa (CNSC)
- **Martina Adorni** (Italy), Nuclear Safety Specialist, Nuclear Energy Agency (OECD-NEA)

Caltech

CSN CONSEJO DE SEGURIDAD NUCLEAR

GRS

BECKER TECHNOLOGIES

NEA NUCLEAR ENERGY AGENCY

CNSC CCSN

WP8 – Ethics



Image credit: Pixabay

AMHYCO Partners

UNIVERSIDAD POLITÉCNICA DE MADRID

GOBIERNO DE ESPAÑA MINISTERIO DE CIENCIA E INNOVACIÓN Ciemat Centro de Investigaciones Energéticas, Medioambientales y Tecnológicas

IRSN INSTITUT DE RADIOPROTECTION ET DE SÛRETÉ NUCLÉAIRE

cnrs

JÜLICH Forschungszentrum

framatome

RUHR UNIVERSITÄT BOCHUM RUB

Jožef Stefan Institute

ENERGORISK

NRG

Canadian Nuclear Laboratories
Laboratoires Nucléaires Canadiens

LGi sustainable innovation

11TH CONFERENCE ON
SEVERE ACCIDENTS RESEARCH
May 13-16, 2024 – Stockholm, Sweden
ERMSAR 2024

Thank you from the AMHYCO family!

AMHYCO



Thank you
Connect with us for more information:

gonzalo.jimenez@upm.es

http://amhyco.eu

@amhyco



OUTCOMES OF THE EXPERIMENTAL AND NUMERICAL WORK ON THE OPERATIONAL BEHAVIOR OF PASSIVE AUTOCATALYTIC RECOMBINERS IN THE LATE PHASE OF A SEVERE ACCIDENT IN THE FRAMEWORK OF THE AMHYCO PROJECT

Ernst-Arndt Reinecke*
Forschungszentrum Jülich GmbH
52425 Jülich, Germany
e.reinecke@fz-juelich.de

Gabriela Nobrega, Ahmed Bentaib
Institut de Radioprotection et de Sûreté Nucléaire
92262 Fontenay-aux-Roses, France
ahmed.bentaib@irsn.fr

Araceli Dominguez-Bugarin, Gonzalo Jiménez
Universidad Politécnica de Madrid
28040 Madrid, Spain
araceli.dominguez@upm.es, gonzalo.jimenez@upm.es

Matthias Braun
Framatome GmbH
91052 Erlangen, Germany
matthias.braun@framatome.com

Stephan Struth, Claudia Druska, Michael Klauck
Forschungszentrum Juelich GmbH
52425 Jülich, Germany
s.struth@fz-juelich.de, c.druska@fz-juelich.de, m.klauck@fz-juelich.de

ABSTRACT

The molten core-concrete interaction in the ex-vessel phase of a severe accident in a light water reactor is a source of significant amounts of gaseous products including carbon monoxide. The European project AMHYCO addresses open issues related to the understanding of the impact of carbon monoxide on safety-relevant accident phenomena and on hydrogen mitigation measures. In order to support the simulation of accident sequences and the assessment of safety measures, Task 3.2 aimed to provide realistic models considering the influence of carbon monoxide on the operating behavior of passive auto-catalytic recombiners. The work program included conducting new experiments, analyzing existing experimental data, and further developing numerical models.

The experimental program performed within Task 3.2 involved the REKO facilities at FZJ to study the impact of predicted accident atmospheres including oxygen-lean mixtures and the presence of carbon

* corresponding author

monoxide on the hydrogen recombination efficiency of different generic catalysts. More specifically, criteria were derived to predict the atmospheric conditions leading to catalyst poisoning. At the same time, a unified database including selected datasets from the various OECD/NEA-THAI projects was developed. The available experimental data were used to further advance numerical models such as the manufacturer's engineering correlation for Framatome PARs as well as the scientific models SPARK (IRSN), PARUPM (UPM), and REKO-DIREKT (FZJ).

KEYWORDS
Severe Accident, Hydrogen Mitigation, Passive Auto-catalytic Recombiners, Carbon Monoxide

1. INTRODUCTION

The European AMHYCO project [1] aims at revising Severe Accident Management Guidelines, with focus on mitigating combustible gases in the late phase of a severe accident. In this late accident phase, the molten corium-concrete interaction (MCCI) is producing significant amounts of carbon monoxide, in combination to a further hydrogen release. The project addresses open issues related to understanding the impact of the presence of carbon monoxide on the hydrogen combustion risk and required mitigation strategies. The corresponding research activities are performed in WP3 of the project's work plan (see Fig. 1). Following the conclusions of the literature review created in WP1 and the bounding accident scenarios selected in WP2, the experimental program allows for a comprehensive validation of models implemented in relevant computational tools, which are used for scenario simulations in WP4.

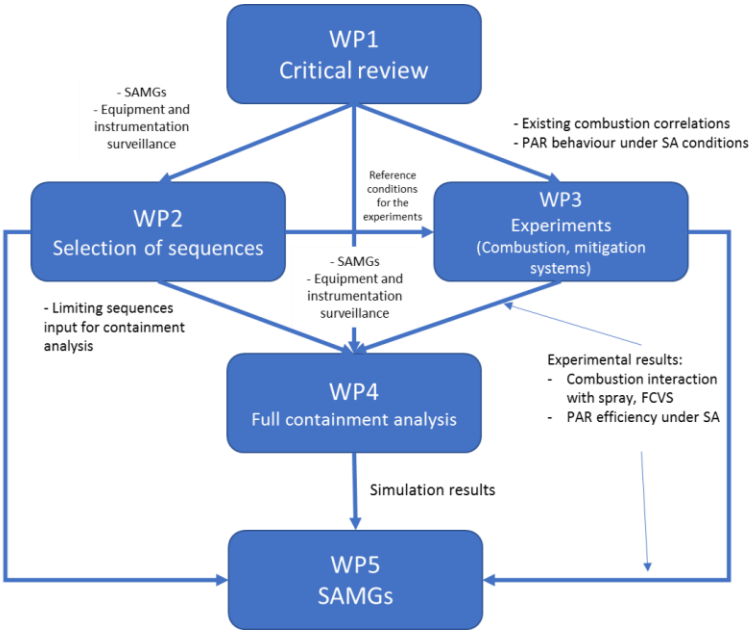

Figure 1. AMHYCO Project: Interaction of technical work packages.

Task 3.2 of WP3 has the specific objective to provide suitable numerical models describing the operation of passive auto-catalytic recombiners (PARs) in the late phase of a severe accident. These models have

been validated against both, existing experimental data from other programs and new targeted experiments carried out in the AMHYCO project. PARs are the key hardware for mitigating the hydrogen risk in many European nuclear power plants. The operational behavior of PARs has been studied in various national and international projects in the past, starting with early test programs conducted primarily by manufacturers, such as Siemens/Germany (now Framatome) and AECL/Canada [2]. Although some of the aforementioned projects were already addressing the effect of ex-vessel phenomena, such as the presence of carbon monoxide and nuclear aerosols in the containment atmosphere, an initial attempt to enhance PAR models towards the conditions in the late accident phase was made in the PAR model development exercise as part of the SAMHYCO-NET project [3]. In the framework of AMHYCO, the further development of the numerical models is based on a broader experimental database with a specific focus on severe accident sequences with high combustion risk.

2. STATE OF KNOWLEDGE AT THE START OF THE TASK

Earlier work on the effect of carbon monoxide on PAR operation has showed a complex interaction (see [4-6]), which includes regimes of unaffected/parallel or competing hydrogen-oxygen and carbon monoxide-oxygen reaction, as well as conditions where catalyst poisoning by carbon monoxide could partially or completely deactivate the catalyst.

The experiments in AMHYCO Task 3.2 focus on the influence of carbon monoxide on the operation of PARs under oxygen-lean conditions. In the context of PAR operation, “oxygen-lean” means that there is not enough oxygen available to the catalysts to allow parallel/unaffected conversion of hydrogen and carbon monoxide. In extreme cases, lean conditions can lead to a so-called poisoning of the catalyst, which is caused by persistent adsorption of carbon monoxide on the catalyst surface, thus, preventing adsorption of oxygen in a sufficient amount. In particular, the exact conditions under which the above-mentioned regimes occur, which are likely to depend on the gas composition, temperature and pressure, still need to be clarified in detail.

The analyses of the results of the accident scenario simulations performed by WP2 [7] led to the following conclusions with regard to the experimental program:

- Almost through the entire ex-vessel phase, the atmosphere is oxygen-lean with regard to PAR operation. Consequently, the experimental program and model development needs to focus on such conditions.
- PAR models should be validated for atmospheres with temperatures between 40 °C and 140 °C, pressure up to 3.7 bar and steam at saturation.
- Hydrogen fractions are typically higher than or equal to carbon monoxide fractions.
- Potential for PAR ignition should be considered in the models with corresponding criteria, if no catalyst temperature is calculated.

3. EXPERIMENTAL PROGRAM

The experimental program in Task 3.2 involves three facilities located at Forschungszentrum Jülich GmbH (FZJ), Germany. In REKO-1, scoping tests with small catalyst sheets were performed to identify the relevant process parameters. Experimental data in full catalyst scale were obtained in REKO-3, to support project partners’ model validation. Finally, the effect of pressure on catalyst poisoning was studied in REKO-4.

3.1. Scoping Tests in the REKO-1 Facility

The REKO-1 facility is a modular flow reactor which is composed of tube elements according to the test specifications and requirements (Fig. 2). The facility allows the investigation of the recombination behavior of small catalyst specimen (here: 5 x 5 cm²) under well-defined forced flow boundary conditions.



Figure 2. REKO-1: Cylindrical flow reactor (left); catalyst temperature measurement (right) [8].

Scoping tests were performed to understand the impact of parameters such as gas and catalyst temperatures, gas composition, and flow velocity on the catalyst deactivation process for both platinum- and palladium-based catalysts. Due to the small size of the catalyst samples these experiments can be carried out very efficiently in a comparatively short time, thus allowing for a large number of measurements. At the same time, the results are rather qualitative in nature, since geometry effects and heat radiation losses are not representatively mapped.

Based on these scoping tests, the following conclusions are reached:

- Platinum- and palladium-based catalysts behave differently with regard to catalyst deactivation by carbon monoxide.
- The relevant gas species for catalyst poisoning are oxygen and carbon monoxide. The amount of hydrogen in the gas mixture seems to be of secondary importance.
- The effect of the gas temperature on the catalyst deactivation needs to be considered, especially for the palladium-based catalyst.
- Catalyst deactivation needs to be studied under humid conditions as different results may be obtained compared to dry conditions.
- The flow velocity of the gas mixture has only minor effect on catalyst deactivation.

3.2. Catalyst Section Tests in the REKO-3 Facility

Using the identical peripheral set-up as REKO-1, the REKO-3 facility (Fig. 3) is equipped with a vertical modular flow tube reactor with rectangular cross section, which is composed of different elements according to the test specifications and requirements. The setup allows investigation of the recombination behavior of catalyst sheets under well-defined and steady-state forced flow boundary conditions. For the present study, four parallel catalyst sheets are exposed to stationary flows of gaseous mixtures including hydrogen, oxygen, nitrogen, steam and carbon monoxide inside a vertical flow reactor.

The tests provide steady-state data on full-scale catalyst sheets suitable for model development and validation. The resulting database has been used by the Task 3.2 partners to further advance their numerical PAR models.

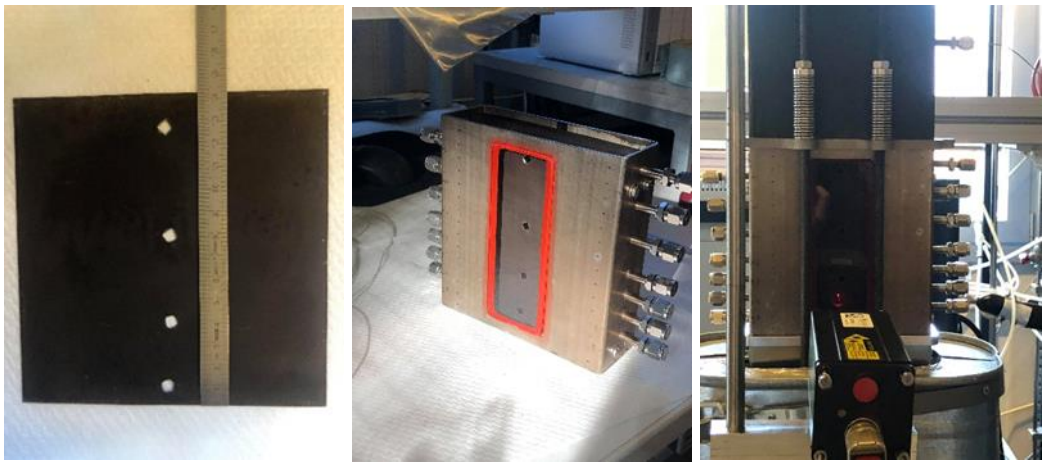

Figure 3. REKO-3: Optical measurement of the catalyst temperature [8].

Despite the complex surface processes, the experimental data allow to derive empirical criteria for catalyst poisoning with sufficient (if necessary conservative) precision, which are based on two easy to obtain parameters, i.e. the gas temperature and the oxygen concentration.

3.3. Natural Convection Tests in the REKO-4 Facility

In contrast to the previous forced-flow facilities REKO-1 and REKO-3, the REKO-4 facility (Fig. 4) simulates the geometry of an entire plate-carrier PAR, and thus operates under natural flow. The model PAR is installed inside a cylindrical steel pressure vessel, allowing to expose the PAR to a controlled atmosphere at ambient and elevated pressures.

A typical test sequence is shown in Fig. 5. The test R4-B04 starts with a pre-reduced oxygen concentration of 6.2 vol.% (black line: O2R 4.01) at a gas temperature of approx. 40 °C (green line: TR 4.16). Immediately after the hydrogen injection starts (blue line: hydrogen fraction KR-4-20), the recombination starts on the catalyst surface as indicated by the increase of the catalyst temperature (red line: TR 4-12) and the temperature inside the PAR chimney (orange line: TR 4-13). At the same time, the carbon monoxide injection starts (not represented in the graph). Due to the catalytic recombination of hydrogen and carbon-monoxide, the oxygen concentration decreases, also leading to a decrease of the catalyst temperature (as due to the oxygen-lean condition, the availability of oxygen is limiting the PAR performance).

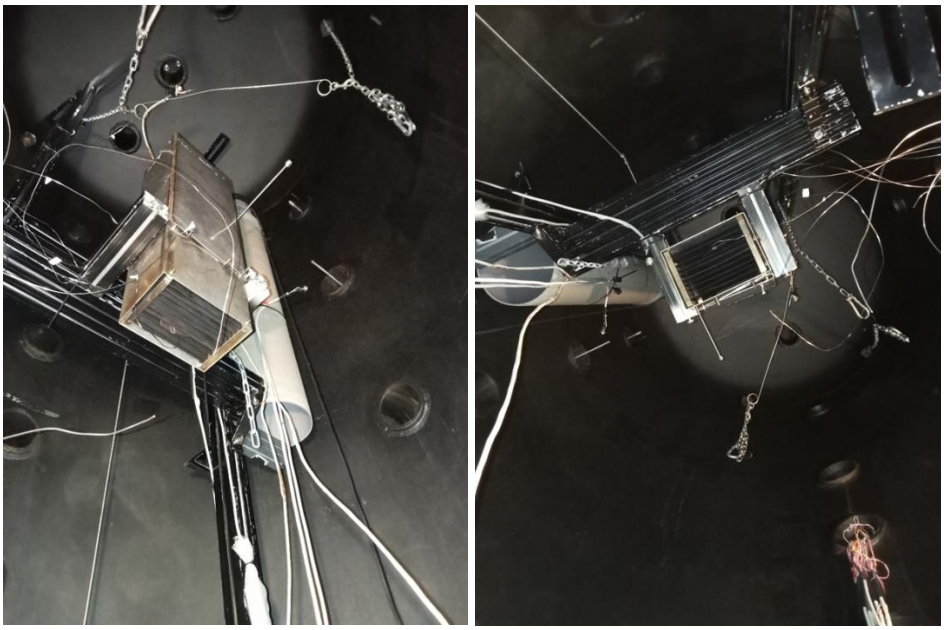

Figure 4. REKO-4: Mounting of the PAR inside the pressure vessel [8].

At approx. 3150 s (marked by the blue circle), the gradient of the catalyst temperature decrease changes rapidly, indicating an abrupt stop of the catalytic reaction. The oxygen fraction measured at the point of change of the temperature gradient is considered the poisoning concentration.

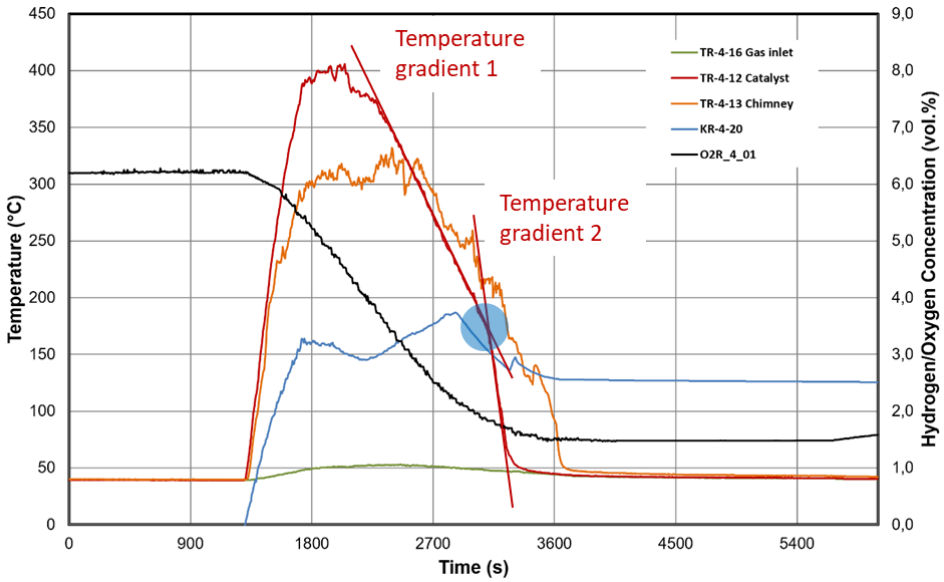

Figure 5. REKO-4 test R4-B04 as example for a typical test sequence [8].

The oxygen concentrations and the corresponding gas temperature where poisoning has been observed in the REKO-4 tests were added to the ranges of partial and full poisoning obtained from the REKO-3 experiments. For both catalysts (platinum and palladium), the results show no significant difference

between experiments performed at 1 bar and 2 bar absolute pressure. For the platinum-based catalyst, no temperature effect was observed between 20 °C and 80 °C, which corresponds with the previous findings of only minor impact of the gas temperature on the poisoning process. The obtained data for the palladium-based catalyst confirm quite accurately the significant temperature effect observed before.

3.4. Conclusions of the Test Program

Overall, the experimental results have shown a non-trivial relationship of the amount of carbon monoxide and the impact on the PAR performance. Due to the complex interaction of catalytic surface processes, mass transfer, and the catalyst and gas temperature, a precise interpretation of the experiments against the needs of manageable model complexity codes was difficult.

With due consideration of the required accuracy of full containment analysis with system codes, and considering as well the measurement uncertainties, the following empirical correlations are proposed to describe the effect of catalyst deactivation (poisoning) by carbon monoxide in the temperature range of 20 °C to 150 °C:

- For platinum-based catalysts, poisoning may occur if the oxygen fraction decreases below a value of 2.0 vol.% (conservative value: 2.5 vol.%). Poisoning occurs quite instantaneously. Partial poisoning has been observed only for a few cases.
- For palladium-based catalysts, poisoning occurs if the oxygen fraction decreases below a value which depends significantly on the gas temperature. Different approaches to derive an empirical function according to the data could be considered, for example
  $y_{O2,poison} = 2.82 - 0.016 \cdot T$ for T = 20 °C to 115 °C
  $y_{O2,poison} = 4.35 - 0.029 \cdot T$ for T = 115 °C to 150 °C
  Above 150 °C, no poisoning effects have been observed for the palladium-based catalyst.

The poisoning effects observed were independent of the pressure and didn't depend significantly on the hydrogen or carbon monoxide concentration. However, more sophisticated empirical models might consider even these effects.

Note that generic non-branded catalytic sheets were used in the experiments employing only pure catalytic metals. Catalytic materials employed in nuclear power plants may have a more complex composition which may reduce the sensitivity to carbon monoxide. Therefore, the results presented in this report can be seen as conservative enveloping.

4. NUMERICAL MODEL DEVELOPMENT

The experimental program of Task 3.2 allows further advancement and validation of numerical models simulating PAR operation as a function of the atmospheric boundary conditions. These models are:

- The empirical Framatome engineering correlation, implemented in most of the relevant codes used for accident simulation [9]
- PARUPM (UPM), a mechanistic model involving detailed surface chemistry [10]
- REKO-DIREKT (FZJ), a mechanistic model based on a mass transfer approach [11]
- SPARK (IRSN), a 3D model involving full surface and gas phase chemistry as well as multi-species CFD [12]

For model development and validation, two databases were developed, the REKO-3 database and the THAI database. Latter was generated on the basis of available data from the OECD/NEA-THAI projects [13]. The generation of a database of quasi-steady state measurement points derived from the transient

THAI experiments allows an overview of the PAR model performance for the entire experimental program rather than only comparing single transient experiments with model calculations. It is suited for both correlation model and detailed PAR models.

4.1. Framatome Correlation

The new generated THAI database has been applied to confirm existing limitations of the empirical Framatome engineering correlation in modelling PAR operation under oxygen-lean conditions. This was already identified for a single case in the SAMHYCO-NET project, the precursor to the AMHYCO project. Improvements of the correlation based on the laws of diffusion-controlled reaction kinetics have been implemented, which allow for a more consistent transition from oxygen-rich to oxygen-lean PAR operation.

Fig. 6 shows the performance of the improved engineering correlation in reproducing the PAR recombination rates observed in the THAI HR-12 experiment. The switch between oxygen-rich and oxygen-lean conditions as well as the recombination rate during oxygen starvation meets the experimental data better than before.

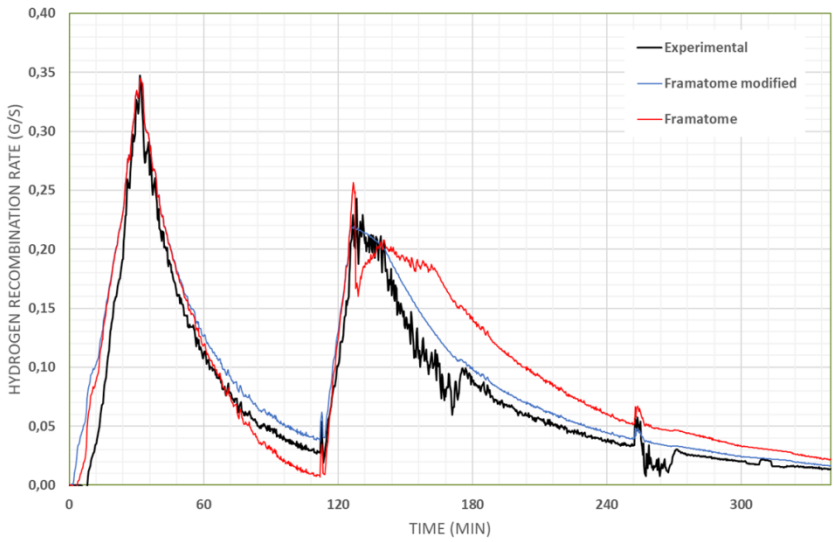

Figure 6. Original and improved Framatome correlation versus THAI HR-12 data.

The comparison of observed hydrogen recombination rates and predicted recombination rates over the entire THAI database (Fig. 7) demonstrates the successful improvement of the engineering correlation as well as the suitability of the database for model validation.

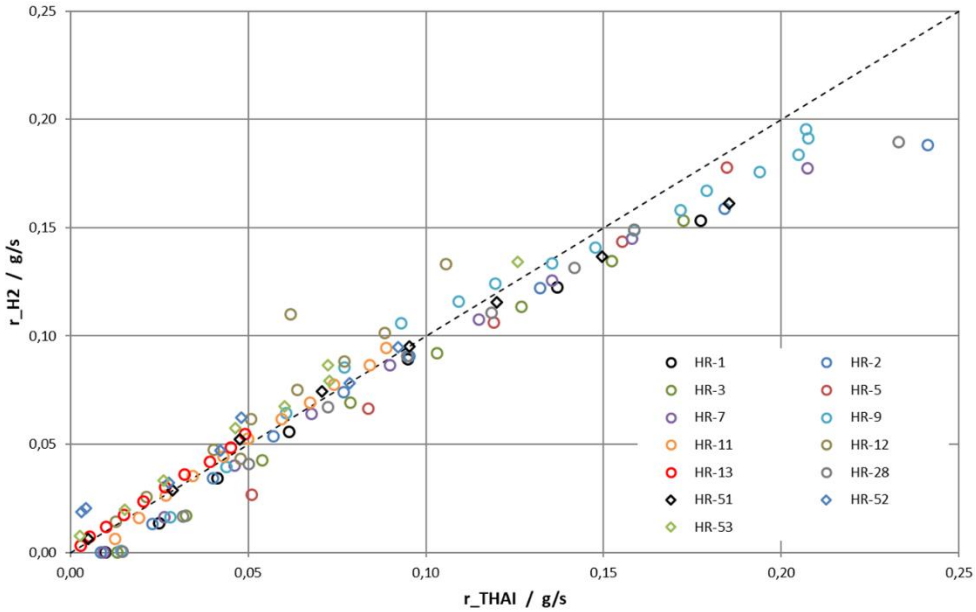

Figure 7. Comparison of the improved Framatome correlation rates with the THAI database.

The corresponding validation data for CO recombination rates, which involve new experiment from the OECD/NEA THEMIS project, cannot be shown in the present document due to contractual reasons. The new proposed engineering correlation is currently under internal review process.

4.2.2. PARUPM

Through the implementation of the linear system of differential equations that include the simplified Deutschmann mechanism, PARUPM is capable of simulating the relevant phenomena associated with the surface reactions of hydrogen and carbon monoxide on plane-parallel catalyst sheets. In the framework of Task 3.2, the PARUPM code has been further developed and validated. The most relevant enhancements include the implementation of a chimney model as well as a diffusion-based reaction model.

The transient model can approximate the PAR heating phase and its cooling down, as well as the transient changes in the boundary conditions. Fig. 8 shows the recombination rate obtained during the OECD-THAI experiment HR-1 as well as the recombination rates predicted by PARUPM, using the boundary conditions from the experiment. Apart from a moderate overprediction of the recombination rate in the first injection phase of the experiment, the only significant discrepancy between the model and the experimental recombination rates occurs at the end of the second injection phase, which is due to a PAR-induced ignition of the local vessel atmosphere causing high recombination rates during the combustion process. PARUPM doesn't contain an ignition module, thus this behavior is not analyzed by the code. Overall, the comparison with experimental data confirms that the code can simulate the behavior of a real passive autocatalytic recombiner under realistic conditions.

The validation results obtained demonstrate that the physico-chemical strategy used in the PARUPM model can simulate the behavior of the recombiner under a variety of conditions, from typical concentrations and settings to more extreme ones such as oxygen starvation, catalyst poisoning, or elevated inlet temperatures. Furthermore, the code can reproduce the behavior of a PAR in transient conditions, where pressure, temperature, and gas concentrations are constantly changing at the recombiner inlet.

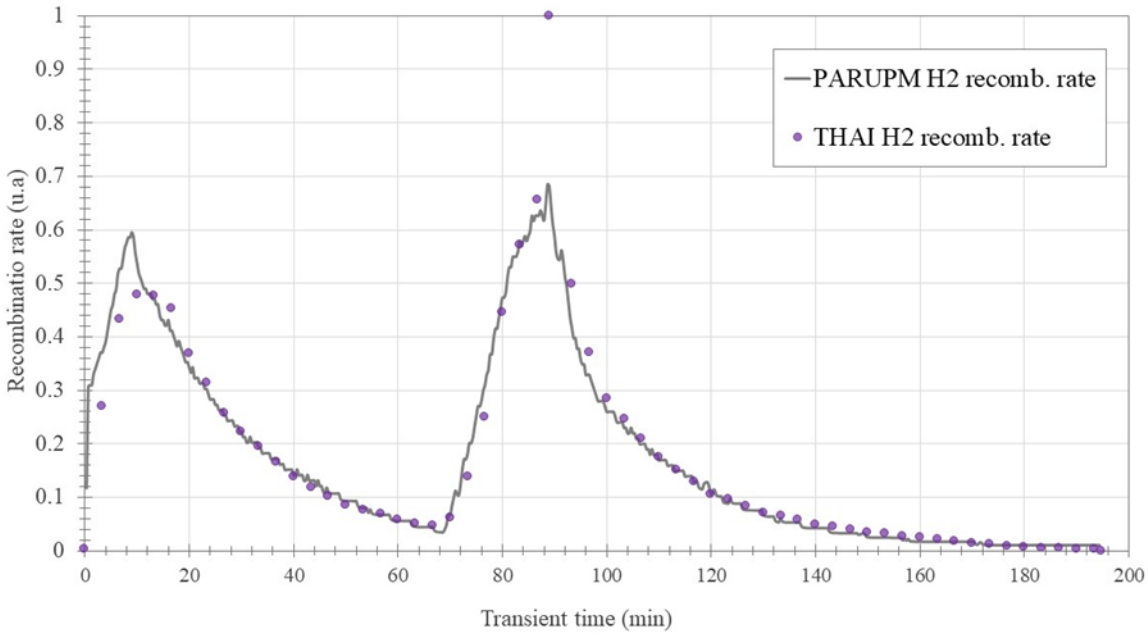

Figure 8. PARUPM: Recombination rate with PARUPM (grey line) and experimental recombination rates (purple dots) during the transient (HR-1).

More details of the PARUPM enhancement and validation have been published in [14, 15]. The PARUPM code is planned to be implemented in 3D thermo-hydraulic analysis codes, such as GOTHIC, as it was implemented in the past in lumped parameters codes like MELCOR.

4.2.3. SPARK

The further development of the SPARK code includes an update of the surface reaction mechanisms for platinum-based catalysts as well as an approach to implement a surface mechanism for palladium-based catalysts. The new Pt mechanism allows PAR simulation during deactivation conditions in the presence of carbon monoxide. The enhanced SPARK code was used for post-calculations of both REKO-1 and REKO-3 data to verify that the SPARK code is able to reproduce the experimental results.

Fig. 9 shows an example of a SPARK simulation of poisoning on a platinum catalyst for a gas mixture containing 4 vol.% hydrogen and 2 vol.% carbon monoxide. Fig. 9 (left) shows the hydrogen distribution inside the gas channel between two catalyst sheets for three different fractions of oxygen during the deactivation process. On the left, 2.6 vol.% oxygen represents the beginning of poisoning. For 2.5 vol.% oxygen, the active zone of the catalyst is moving towards the upper edge of the catalyst (middle). On the right, the catalyst is completely deactivated at 2.3 vol.% oxygen. The same effect can be observed for the carbon monoxide fraction between the catalyst sheets on the right side of Fig. 9.

The improvements and validation work performed in the framework of AMHYCO was published in [16].

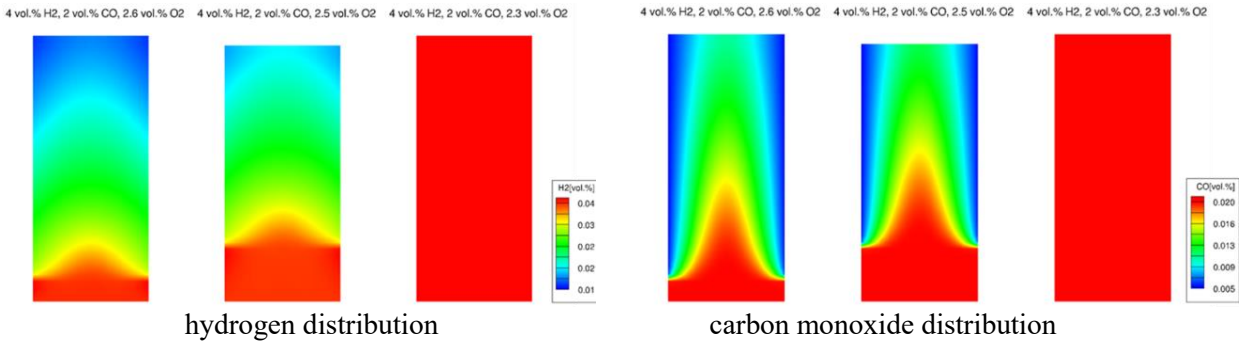

Figure 9. SPARK: Hydrogen (left) and carbon monoxide (right) distribution in the channel between two catalyst sheets for 2.6 vol.% O_2 (left), 2.5 vol.% O_2 (middle) and 2.3 vol.% O_2 (right)

4.2.4. REKO-DIREKT

Unlike in numerical codes with a detailed surface kinetics model, such as PARUPM and SPARK, the catalytic reaction inside the PAR is calculated in REKO-DIREKT with a mass transfer approach. The catalyst poisoning is represented with the empirical correlations described in Section 3.4. For this purpose, the selection of platinum- or palladium-based catalyst has been implemented in the user input.

Fig. 10 shows the predicted versus the experimentally observed hydrogen outlet concentrations and Fig. 11 the catalyst temperatures over the THAI database. The calculated hydrogen outlet concentrations agree with the experimental data very well over the entire range (Fig. 10). A specific feature of REKO-DIREKT is the calculation of the temperature profile along the catalyst sheets. A comparison of calculated and measured values is shown in Fig. 11. Again, the agreement is very good, although the calculated temperature values are systematically too high.

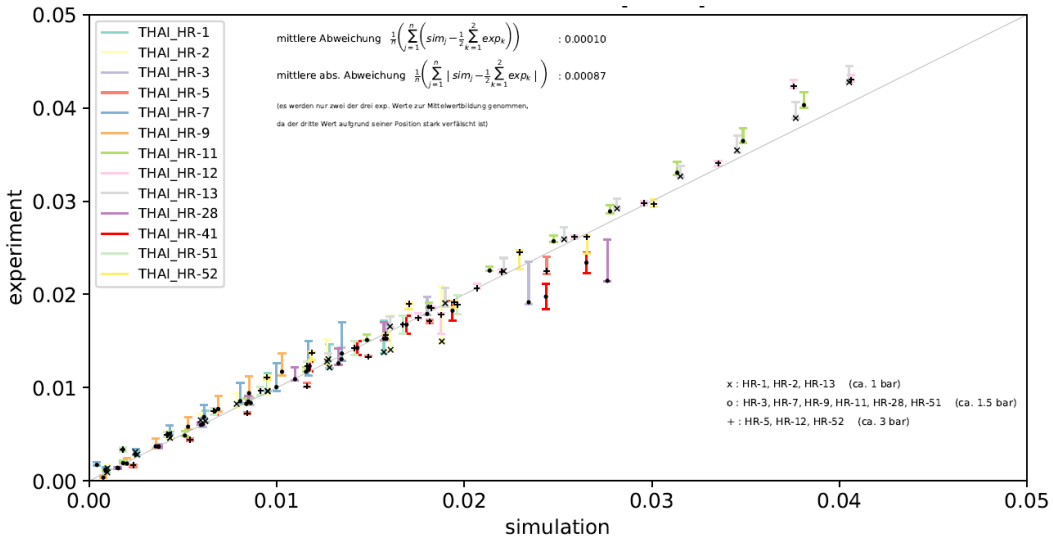

Figure 10. REKO-DIREKT: Calculated outlet hydrogen concentration compared with THAI data

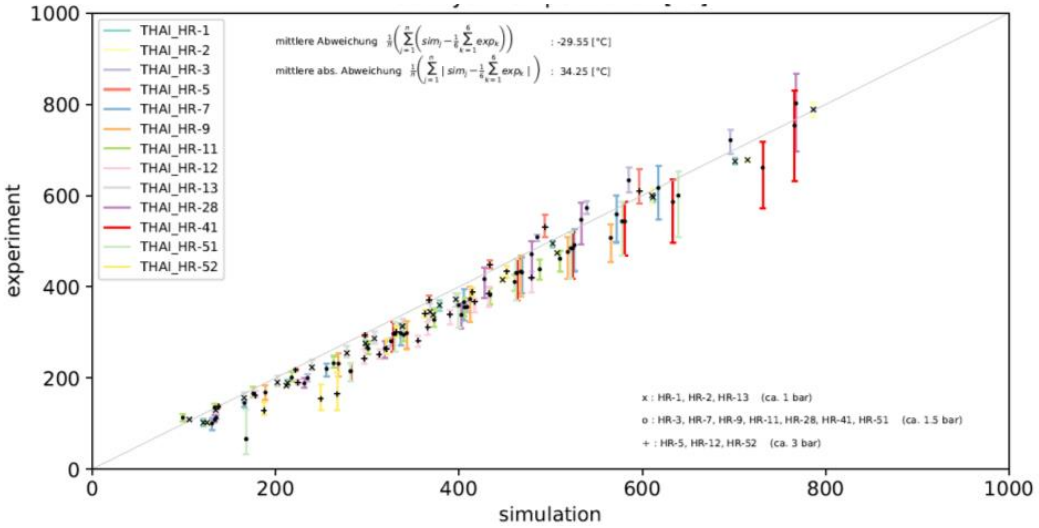

Figure 11. REKO-DIREKT: Calculated catalyst temperatures compared with THAI data

5. CONCLUSIONS

In the framework of the AMHYCO project, Task 3.2 aimed at providing realistic PAR simulations under the conditions of the late phase of a severe accident. The experimental program focused on a better understanding of the impact of carbon monoxide on the PAR performance to provide data for further developing the different numerical codes. Specifically, the effect of oxygen starvation is considered to be well understood, and the results allow to derive empirical criteria for catalyst poisoning with sufficient precision, which are based on easy to obtain parameters (gas inlet temperature and oxygen concentration) even for those PAR models that don't involve surface chemistry.

In addition to the REKO-3 database, which is especially suited for model development and validation for the PAR geometry independent mechanistic models, a second database of quasi-steady state measurement points was derived from the transient experiments performed in the framework of the OECD/NEA-THAI projects. This new database allows validation of the PAR model performance for the boundary conditions of the entire experimental program rather than only comparing single transient experiments with model calculations. It is suited for both correlation model and mechanistic PAR models.

Making use of both experimental databases, REKO and THAI, the PAR models involved (Framatome engineering correlation, PARUPM, REKO-DIREKT and SPARK) were significantly enhanced and prepared for further use in the simulation tools for accident scenarios in the further course of AMHYCO.

ACKNOWLEDGMENTS

AMHYCO has received funding from the Euratom research and training programme 2019-2020 under Grant Agreement n°945057. The content of this paper reflects only the author's view. The European Commission is not responsible for any use that may be made of the information it contains.

The authors sincerely thank the technical team, Tanja Bensberg and Dieter Maier, and the student interns and undergraduates Lydia Bucher (University Cincinnati, Ohio, USA), Pierre Houttemane (EPF Engineering School Montpellier, France), and Daniel Fausel (University of Applied Sciences Aachen/Juelich, Germany) for their dedicated assistance in the experiments conducted.

REFERENCES

1. G. Jiménez, L. E. Herranz, A. Bentaib, N. Chaumeix, A. Reinecke, S. Kelm, M. Loeffler, C. Bratfisch, I. Kljenak, O. Sevbo, D. C. Visser, R. Liang, S. Balech, "AMHYCO Project: Towards advanced accident guidelines for hydrogen safety in nuclear power plants", *Proc. International Conference on Hydrogen Safety (ICHS 2021)*, Edinburgh, Scotland, September 21-24, 2021.
2. E. Bachellerie, F. Arnould, M. Auglaire, B. de Boeck, O. Braillard, B. Eckardt, F. Ferroni, R. Moffett, "Generic approach for designing and implementing a passive autocatalytic recombiner PAR-system in nuclear power plant containments", *Nuclear Engineering and Design*, **221**(1-3), pp. 151-165 (2003).
3. E.-A. Reinecke, J. Fontanet, L.E. Herranz, Z. Liang, L. Maas, O. Mazurok, J.-S. Park, D.C. Visser, M. Hupp, S. Gupta, "PAR model development exercise in the framework of SAMHYCO-NET", *Nuclear Engineering and Design*, **399**, pp. 112035 (2022).
4. M. Klauck, E.-A. Reinecke, S. Kelm, N. Meynet, A. Bentaïb, H.-J. Allelein, "Passive auto-catalytic recombiners operation in the presence of hydrogen and carbon monoxide: experimental study and model development", *Nuclear Engineering and Design*, **266**, pp. 137-147 (2014).
5. Z. Liang, L. Gardner, T. Clouthier, "Experimental study of the effect of carbon monoxide on the performance of passive autocatalytic recombiners", *Nuclear Engineering and Design*, **364**, pp. 110702 (2020).
6. M. Klauck, E.-A. Reinecke, H.-J. Allelein, "Effect of PAR deactivation by carbon monoxide in the late phase of a severe accident", *Annals of Nuclear Energy*, **151**, pp. 107887 (2021).
7. L.E. Herranz, J. Fontanet, "D2.2 – Identification and analysis of accidental sequences posing high H2/CO combustion risk", AMHYCO Report WP2 (2022).
8. E.-A. Reinecke, A. Domínguez-Bugarín, G. Nobrega, M. Braun, "D3.2 – Synthesis and outcomes of performed experiments and numerical results related to PAR behaviour", AMHYCO Report WP3 (2023).
9. S. Mimouni, N. Mechitoua, M. Ouraou, "CFD recombiner modelling and validation on the H2-PAR and Kali-H2 experiments", *Science and Technology of Nuclear Installations*, **2011**, pp. 574514 (2011).
10. M.A. Jiménez, J.M. Martín-Valdepeñas, F. Martín-Fuertes, J.A. Fernández, "A detailed chemistry model for transient hydrogen and carbon monoxide catalytic recombination on parallel flat Pt surfaces implemented in an integral code", *Nuclear Engineering and Design*, **237**, pp. 460 (2007).
11. J. Böhm, "Modelling of processes in catalytic recombiners", Forschungszentrum Jülich Energy Technologies, **61**, ISBN 978-3-89336-473-2 (2007).
12. F. Payot, E.-A. Reinecke, F. Morfin, J.-C. Sabroux, N. Meynet, A. Bentaïb, P. March, R. Zeyen, "Understanding of the operation behaviour of a Passive Autocatalytic Recombiner (PAR) for hydrogen mitigation in realistic containment conditions during a severe light water nuclear reactor (LWR) accident", *Nuclear Engineering and Design*, **248**, pp. 178-196 (2012).
13. S. Gupta, E. Schmidt, B. von Laufenberg, M. Freitag, G. Poss, F. Funke, G. Weber, "THAI test facility for experimental research on hydrogen and fission product behaviour in light water reactor containments", *Nuclear Engineering and Design*, **294**, pp. 183-201 (2015).
14. A. Domínguez-Bugarín, M.A. Jiménez, E.-A. Reinecke, G. Jiménez, "PARUPM: A simulation code for passive auto-catalytic recombiners", *EPJ Nuclear Sci. Technol.*, **8**(32), (2022).
15. A. Domínguez-Bugarín, E.-A. Reinecke, M.A. Jiménez, G. Jiménez, "Validation of the passive autocatalytic recombiner simulation code PARUPM using experimental data from REKO-3 and THAI program tests", *Proc. European Nuclear Young Generation Forum ENYGF'23*, Kraków, Poland, May 8-12, 2023.
16. G. Nobrega, "Etude de l'empoisonnement des recombineurs auto-catalytiques passifs", PhD Thesis, Université d'Orléans (2022).

AMHYCO

Enhancing H_2 & CO Combustion Risk Management

Outcomes of the Experimental and Numerical Work on the Operational Behavior of Passive Autocatalytic Recombiners in the Late Phase of a Severe Accident in the Framework of the AMHYCO Project

ERMSAR-11, KTH, Stockholm, Sweden
May 13-16, 2024

This project has received funding from the European Union's EURATOM Horizon 2020 research and innovation programme. The content of this document reflects only the author's view. The European Commission is not responsible for any use that may be made of the information it contains.

Ernie Reinecke[1], Gabriela Nobrega[2], Ahmed Bentaib[2], Araceli Dominguez-Bugarin[3], Gonzalo Jiménez[3], Matthias Braun[4], Stephan Struth[1], Claudia Druska[1], Michael Klauck[1]

[1] FZJ, Jülich, Germany
[2] IRSN, Fontenay-aux-Roses, France
[3] Universidad Politécnica de Madrid, Spain
[4] Framatome GmbH, Germany

Outline

- Background
- AMHYCO – WP3 – Task 3.2
- Experimental program and results
- Advances in PAR modeling
- Conclusions

Background

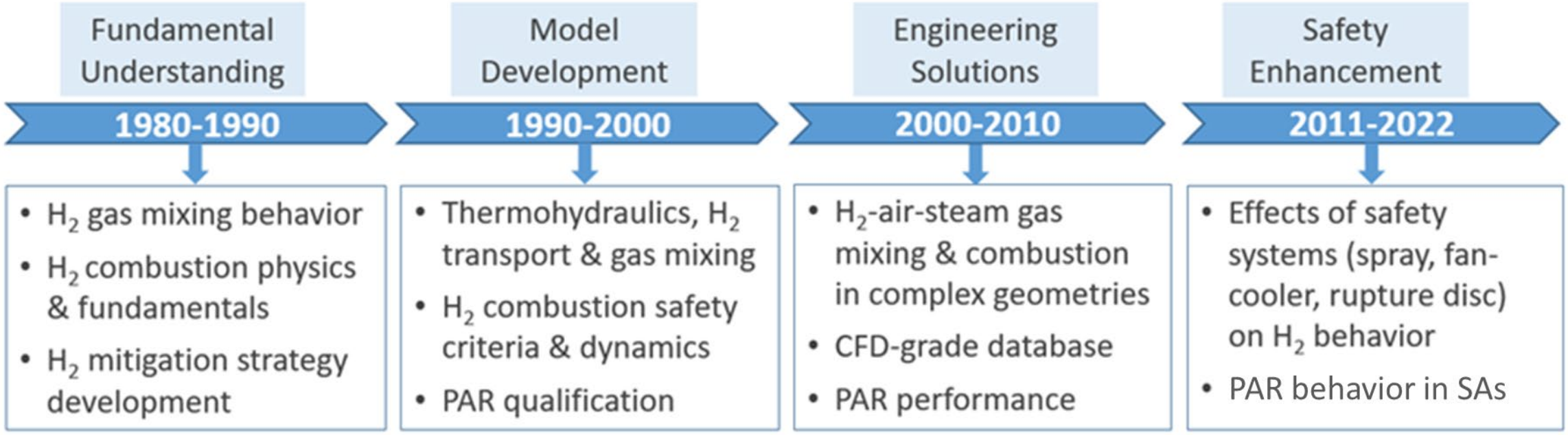

Source: Liang et al., ICHS 2023

NEA NUCLEAR ENERGY AGENCY

THAI/THEMIS

NUGENIA NUclear GENeration II & III Association

AMHYC

Task 3.2 – Overview

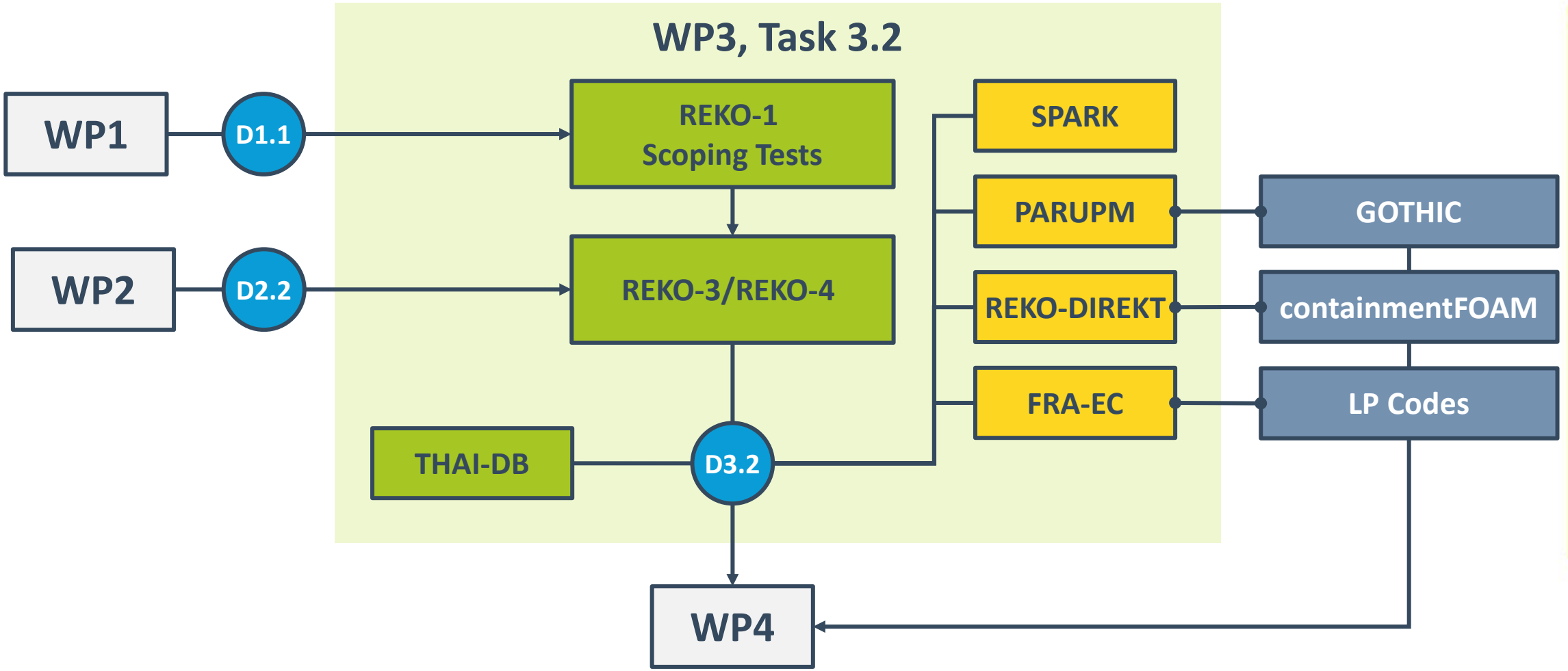

Task 3.2 – Overview

Araceli Dominguez-Bugarin, Session 6.2

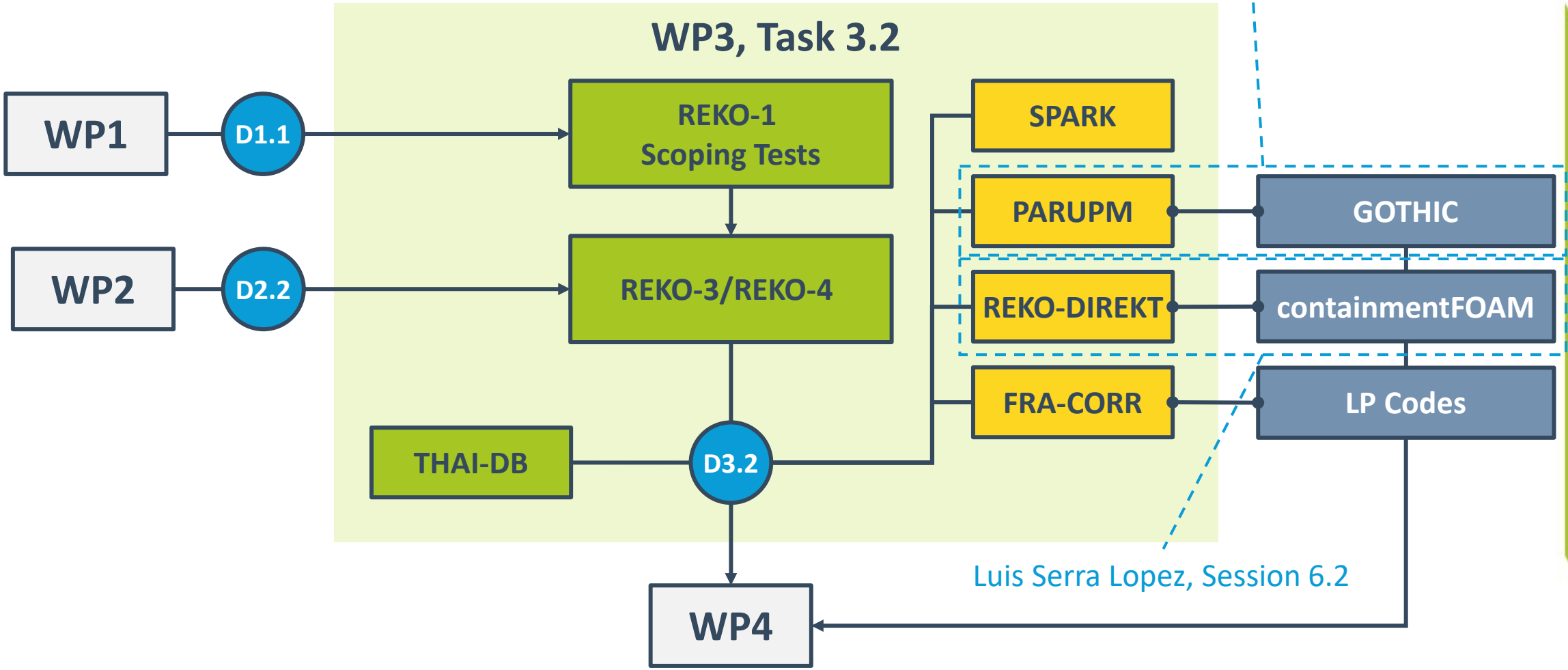

Luis Serra Lopez, Session 6.2

Scenario Analyses (WP2)

Late SA conditions

- presence of carbon monoxide

	PWR-KWU SBLOCA	PWR-W SBO	PWR-W SBLOCA	PWR-W LBLOCA
Pressure	1.7-2.3 bar	3.0-3.7 bar	1.8-2.7 bar	1.2-3.2 bar
Temperature	70-90 °C	120-140 °C	70-100 °C	40-100 °C
H_2	5-17 vol.%	6-10 vol.%	4-11 vol.%	6-13 vol.%
CO (max.)	7 vol.%	9 vol.%	11 vol.%	13 vol.%
H_2/CO ratio	**> 3**	**> 1**	**> 1**	**1**
O_2	13-9 vol.%	8-5 vol.%	12-8 vol.%	17-7 vol.%
H_2O_{vap}	15-30 vol.%	60-35 vol.%	15-60 vol.%	5-30 vol.%

Scenario Analyses (WP2)

Late SA conditions

- presence of carbon monoxide
- almost continuous oxygen starvation

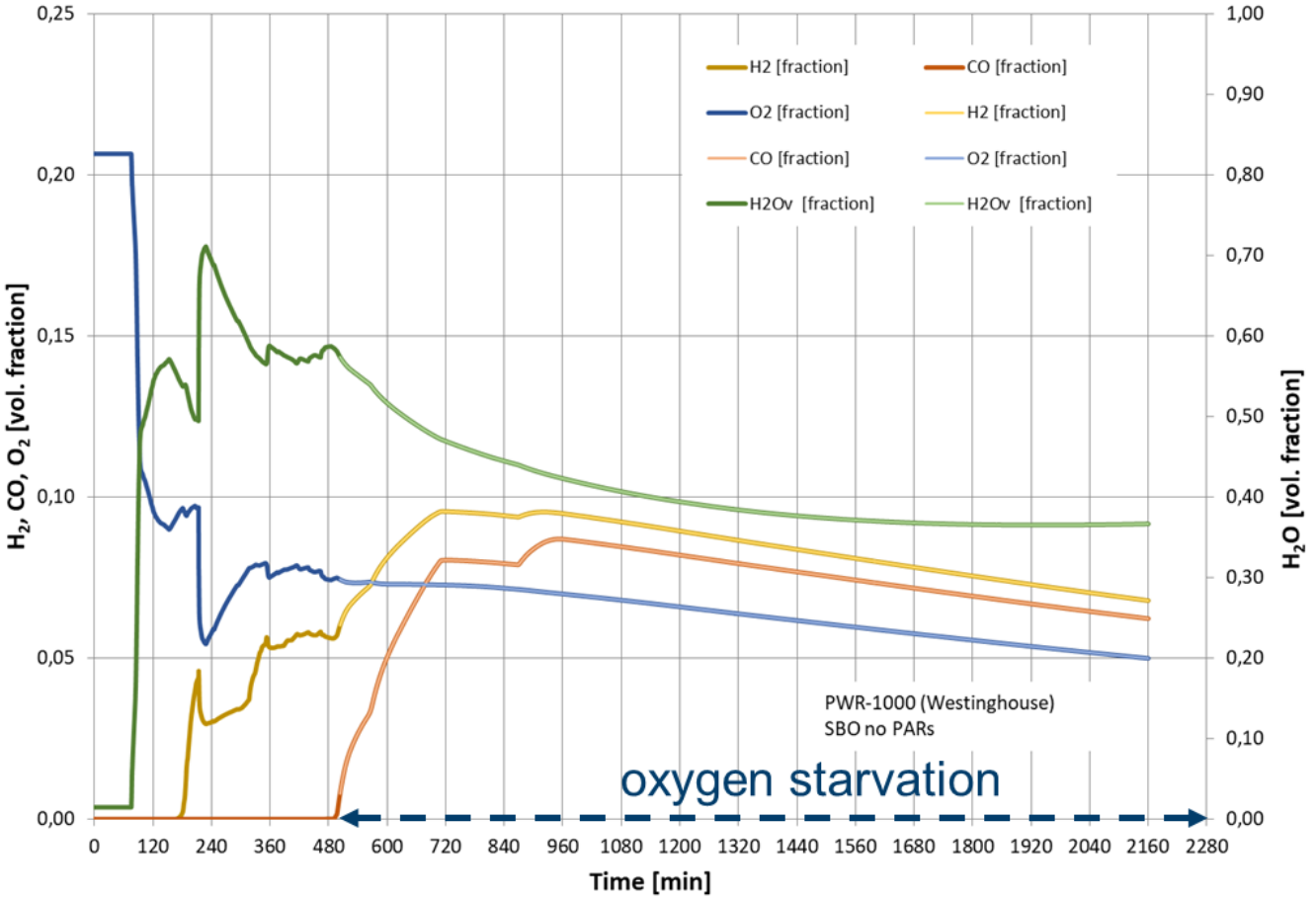

Oxygen Starvation vs. Poisoning

Oxygen starvation

- Insufficient availability of oxygen on the catalyst surface
- Limited by boundary layer diffusive flow depending on oxygen partial pressure
- No permanent effect – reversible process

Consequence for PAR operation

- Conversion rates smaller than nominal value
- Conversion rates are a function of oxygen concentration (not hydrogen conc.)

Catalyst poisoning

- Occupation of active sites on the catalyst surface by adsorbed species
- Adsorption/Desorption equilibrium depending on temperature and partial pressure of adsorbing species
- No permanent effect – reversible process

Consequence for PAR operation

- Reduced conversion efficiency up to complete deactivation

Outline

- Background
- AMHYCO – WP3 – Task 3.2
- **Experimental program and results**
- Advances in PAR modeling
- Conclusions

Experimental Strategy

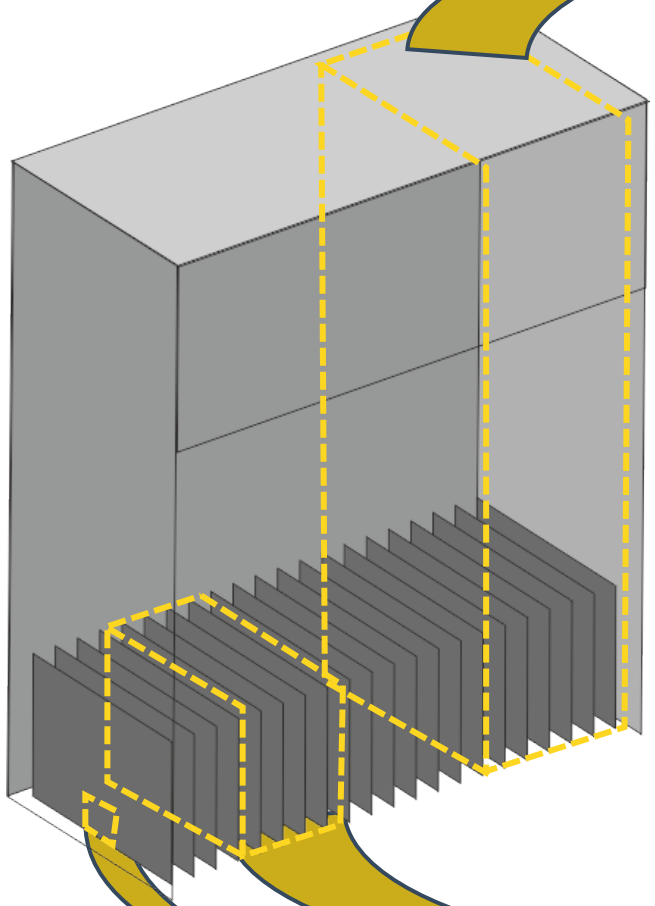

REKO-1: Scoping tests
- Basic understanding of relevant parameters

REKO-3: Catalyst
- Representative
- Steady-state data for mod

REKO-4: PAR natural flow tests
- Effect of pressure
- elopment

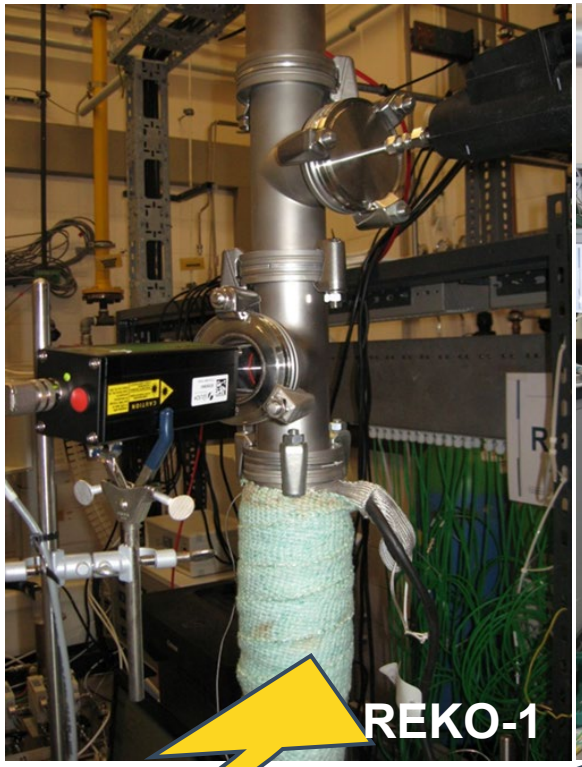





Catalyst Samples

Generic Catalysts
(5 x 5 cm² and 14.3 x 14.3 cm²)

- Manufactured by CCD, Aachen
- 50 µm stainless steel carrier
- γ-Al_2O_3 washcoat
- Pt and Pd nanoparticles (1 mg/cm²)

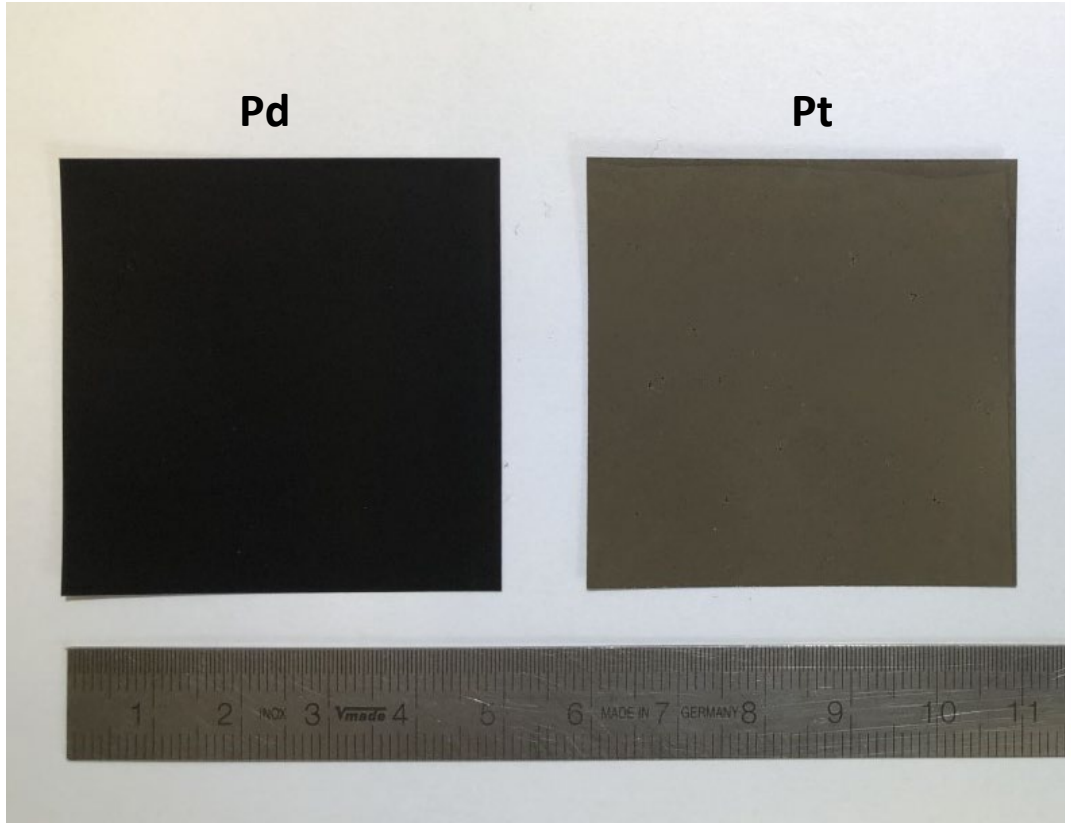

REKO-1 Experiments

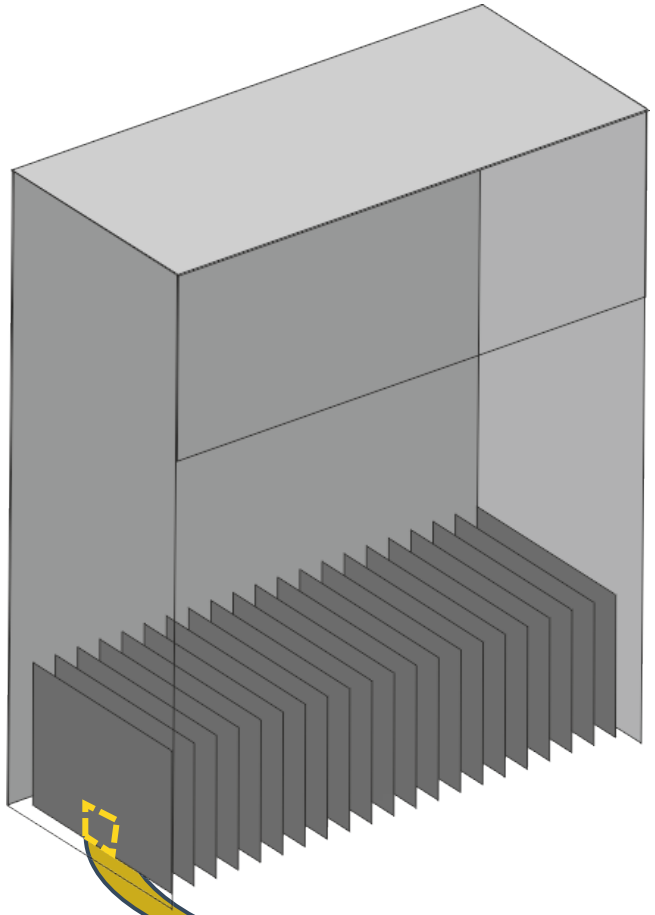

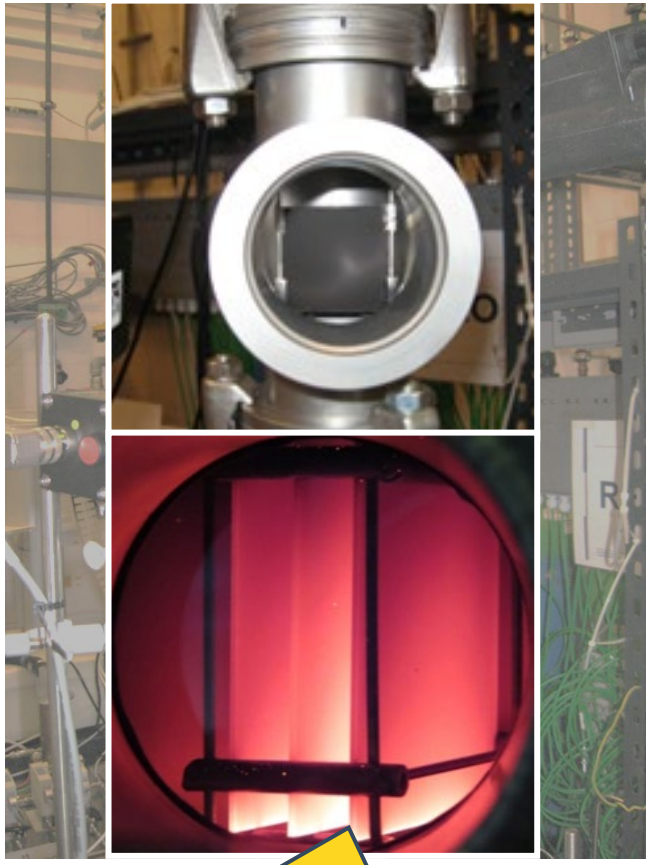

Oxygen Starvation with CO

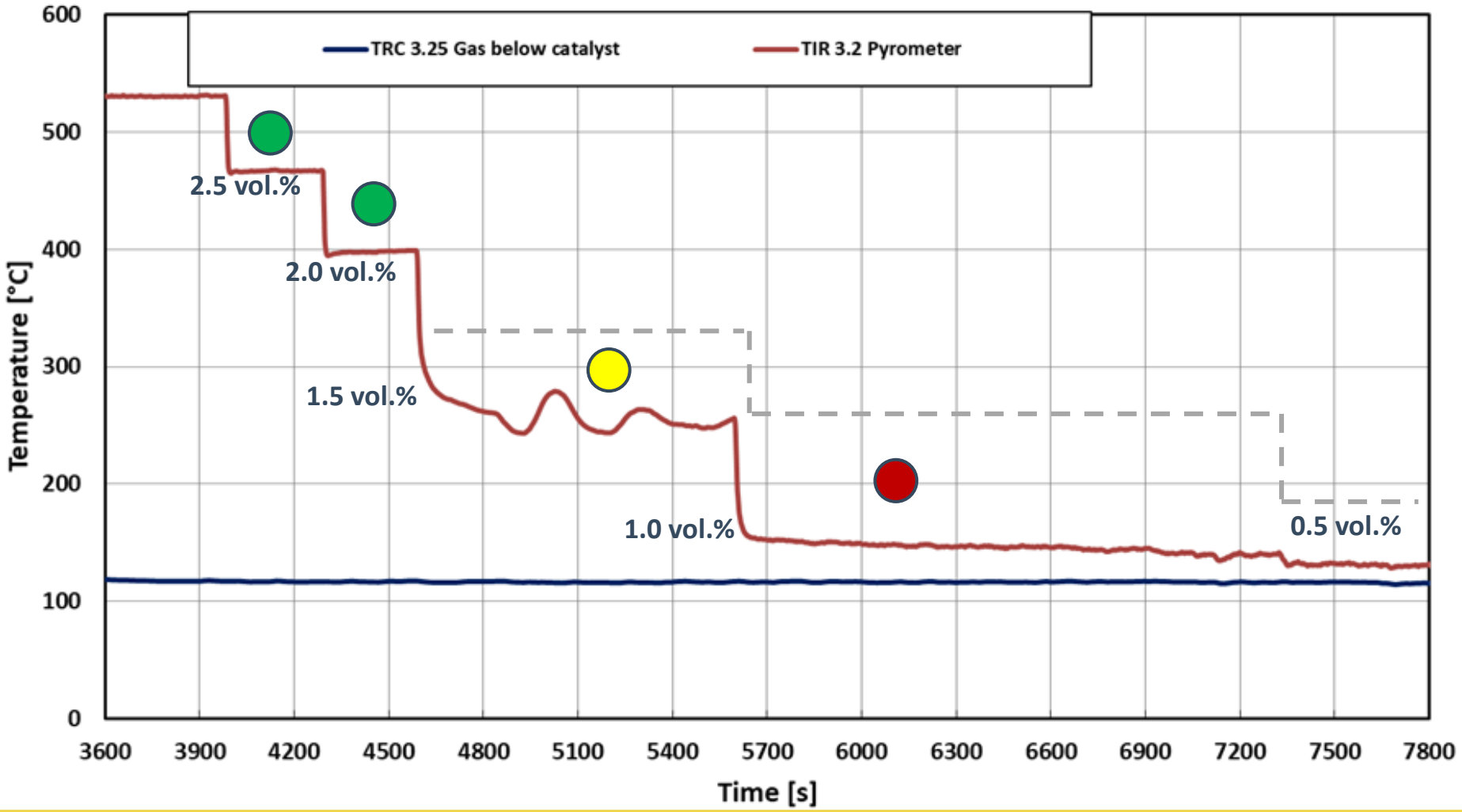

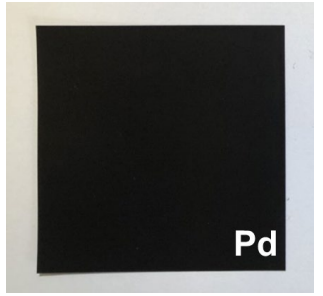

Results of Scoping Experiments

Criterion: Catalyst temperature

- Independent from test procedure

Pt-based catalyst

- Poisoning temperature
  - **independent** of gas temperature
  - **increases** for saturated conditions

Pd-based catalyst

- Poisoning temperature
  - **dependent** of gas temperature **(less sensitive to poisoning)**

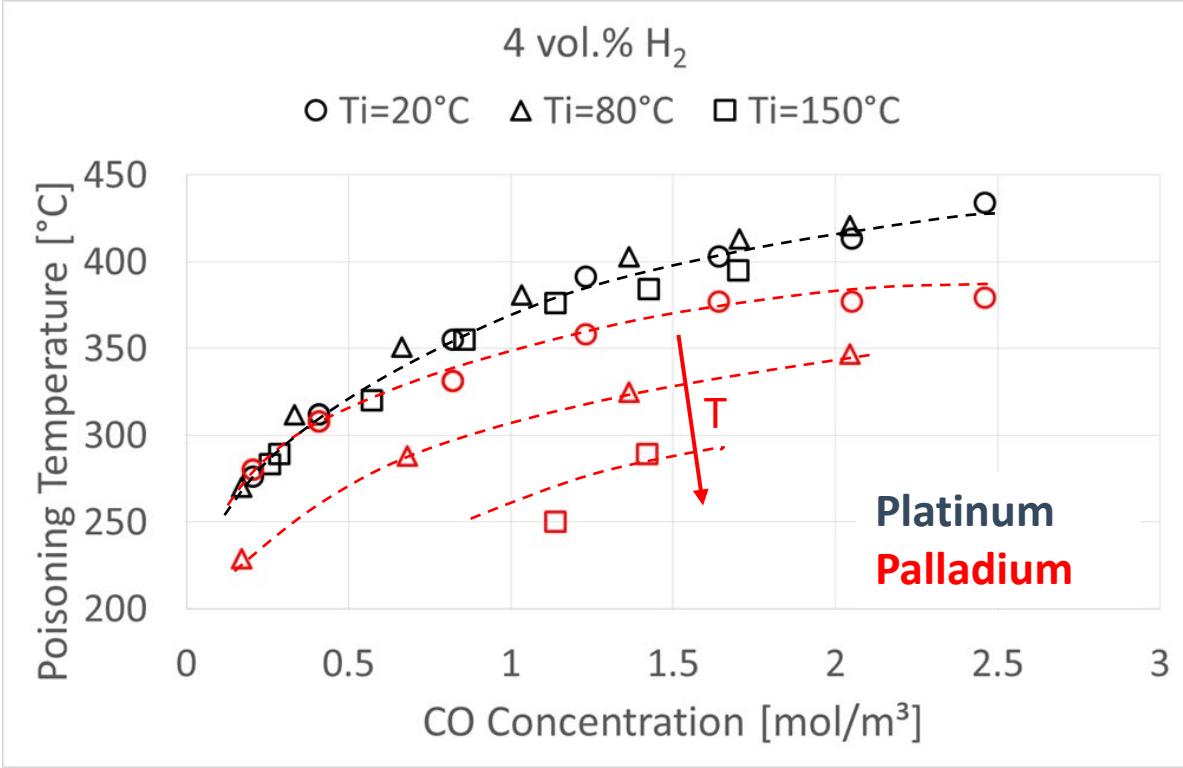

REKO-3 Experiments

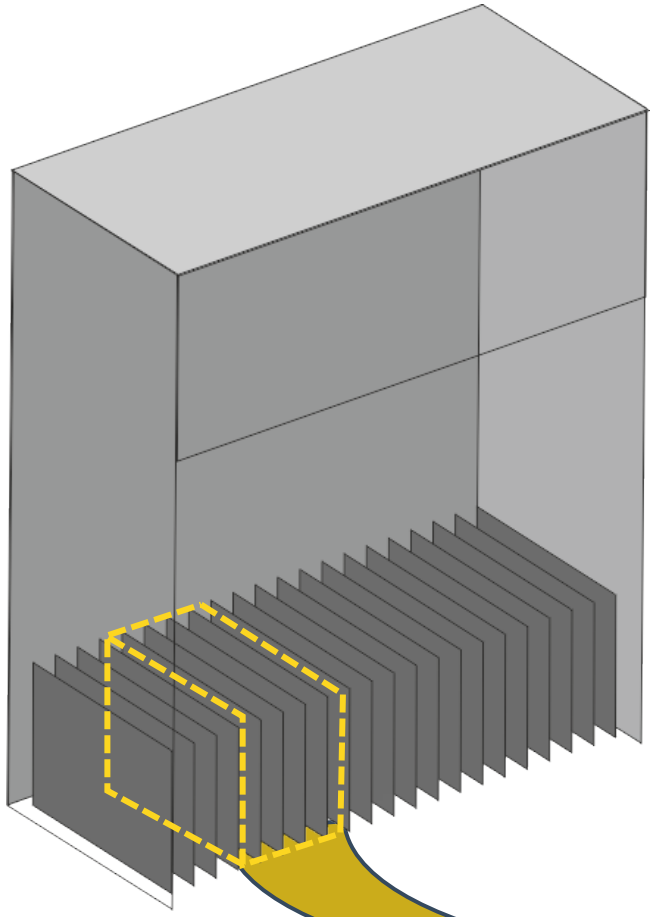



REKO-3 Experiments

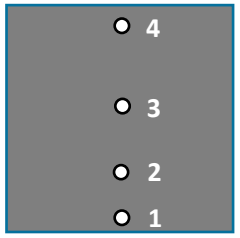

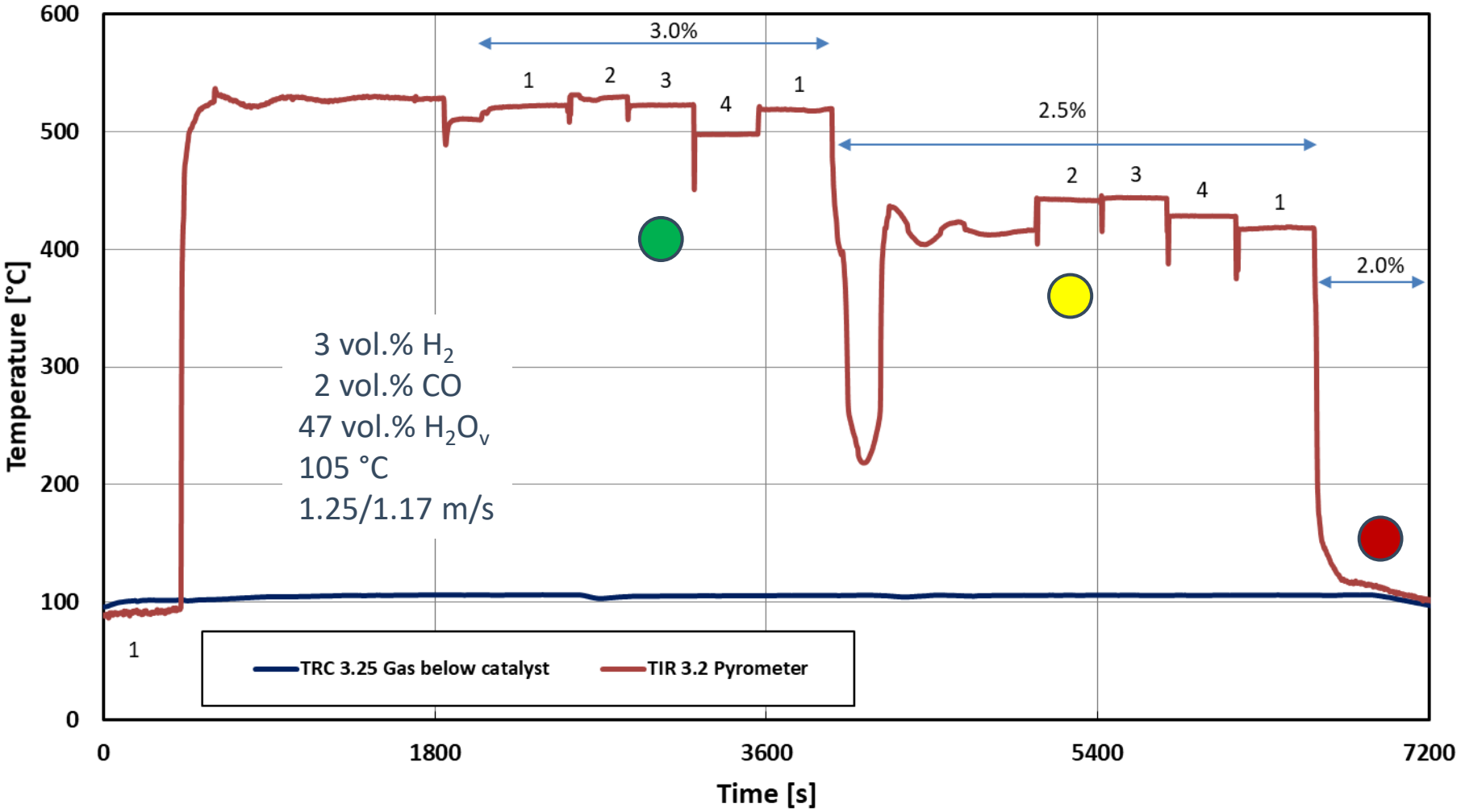

REKO-3 Results

Poisoning [Pt]

Name	Steam	H_2	CO	T	O_2						
	vol.%	vol.%	vol.%	°C	vol.%						
3%H2 0%CO	46,8	3,0	0,0	20 - 150	3,0	2,5	2,0	1,5	1,0	0,5	0,0
5%H2 5%CO	46,8	5,0	5,0	80	3,0	2,5					
3%H2 3%CO	46,8	3,0	3,0	80	3,0	2,5					
3%H2 3%CO	46,8	3,0	3,0	80	3,0	2,5					
3%H2 2%CO	46,8	3,0	2,0	80	3,0	2,5	2,0				
3%H2 2%CO	46,8	3,0	2,0	80	3,0	2,5	2,0				
3%H2 1%CO	46,8	3,0	1,0	80	3,0	2,5	2,0				
3%H2 1%CO	46,8	3,0	1,0	80	3,0	2,5	2,0				
5%H2 1%CO	46,8	5,0	1,0	80	3,0	2,5	2,0				
5%H2 5%CO	46,8	5,0	5,0	115	3,0	2,5					
4%H2 4%CO	46,8	4,0	4,0	115	3,0	2,5	2,0				
3%H2 4%CO	46,8	3,0	4,0	115	3,0	2,5	2,0				
3%H2 3%CO	46,8	3,0	3,0	115	3,0	2,5	2,0				
3%H2 3%CO	46,8	3,0	3,0	115	3,0	2,5	2,0				
4%H2 3%CO	46,8	4,0	3,0	115	3,0	2,5	2,0				
3%H2 2%CO	46,8	3,0	2,0	115	3,0	2,5	2,0				
3%H2 2%CO	46,8	3,0	2,0	115	3,0	2,5	2,0				
4%H2 2%CO	46,8	4,0	2,0	115	3,0	2,5	2,0				
5%H2 1%CO	46,8	5,0	1,0	115	3,0	2,5	2,0	1,5			
5%H2 5%CO	46,8	5,0	5,0	150	3,0	2,5	2,0				
3%H2 3%CO	46,8	3,0	3,0	150	3,0	2,5	2,0				
3%H2 3%CO	46,8	3,0	3,0	150	3,0	2,5	2,0				
3%H2 2%CO	46,8	3,0	2,0	150	3,0	2,5	2,0	1,5			
3%H2 2%CO	46,8	3,0	2,0	150	3,0	2,5	2,0	1,5			
3%H2 1%CO	46,8	3,0	1,0	150	3,0	2,5	2,0	1,5			
3%H2 1%CO	46,8	3,0	1,0	150	3,0	2,5	2,0	1,5			
5%H2 1%CO	46,8	5,0	1,0	150	3,0	2,5	2,0	1,5			

Poisoning [Pd]

Name	Steam	H_2	CO	T	O_2					
	vol.%	vol.%	vol.%	°C	vol.%					
3%H2 0%CO	46,8	3,0	0,0	20 - 150	3,0	2,5	2,0	1,5	1,0	0,5
5%H2 5%CO	46,8	5,0	5,0	80	3,0	2,5	2,0	1,5		
3%H2 3%CO	46,8	3,0	3,0	80	3,0	2,5	2,0	1,5		
5%H2 1%CO	46,8	5,0	1,0	80	3,0	2,5	2,0	1,5		
7%H2 1%CO	46,8	7,0	1,0	80	3,0	2,5	2,0	1,5	1,0	
5%H2 5%CO	46,8	5,0	5,0	115	3,0	2,5	2,0	1,5	1,0	0,5
3%H2 3%CO	46,8	3,0	3,0	115	3,0	2,5	2,0	1,5	1,0	
5%H2 1%CO	46,8	5,0	1,0	115	3,0	2,5	2,0	1,5	1,0	0,5
7%H2 1%CO	46,8	7,0	1,0	115	3,0	2,5	2,0	1,5	1,0	0,5
5%H2 5%CO	46,8	5,0	5,0	150	3,0	2,5	2,0	1,5	1,0	0,5
3%H2 3%CO	46,8	3,0	3,0	150	3,0	2,5	2,0	1,5	1,0	0,5
5%H2 1%CO	46,8	5,0	1,0	150	3,0	2,5	2,0	1,5	1,0	0,5
7%H2 1%CO	46,8	7,0	1,0	150	3,0	2,5	2,0	1,5	1,0	0,5

REKO-4 Experiments

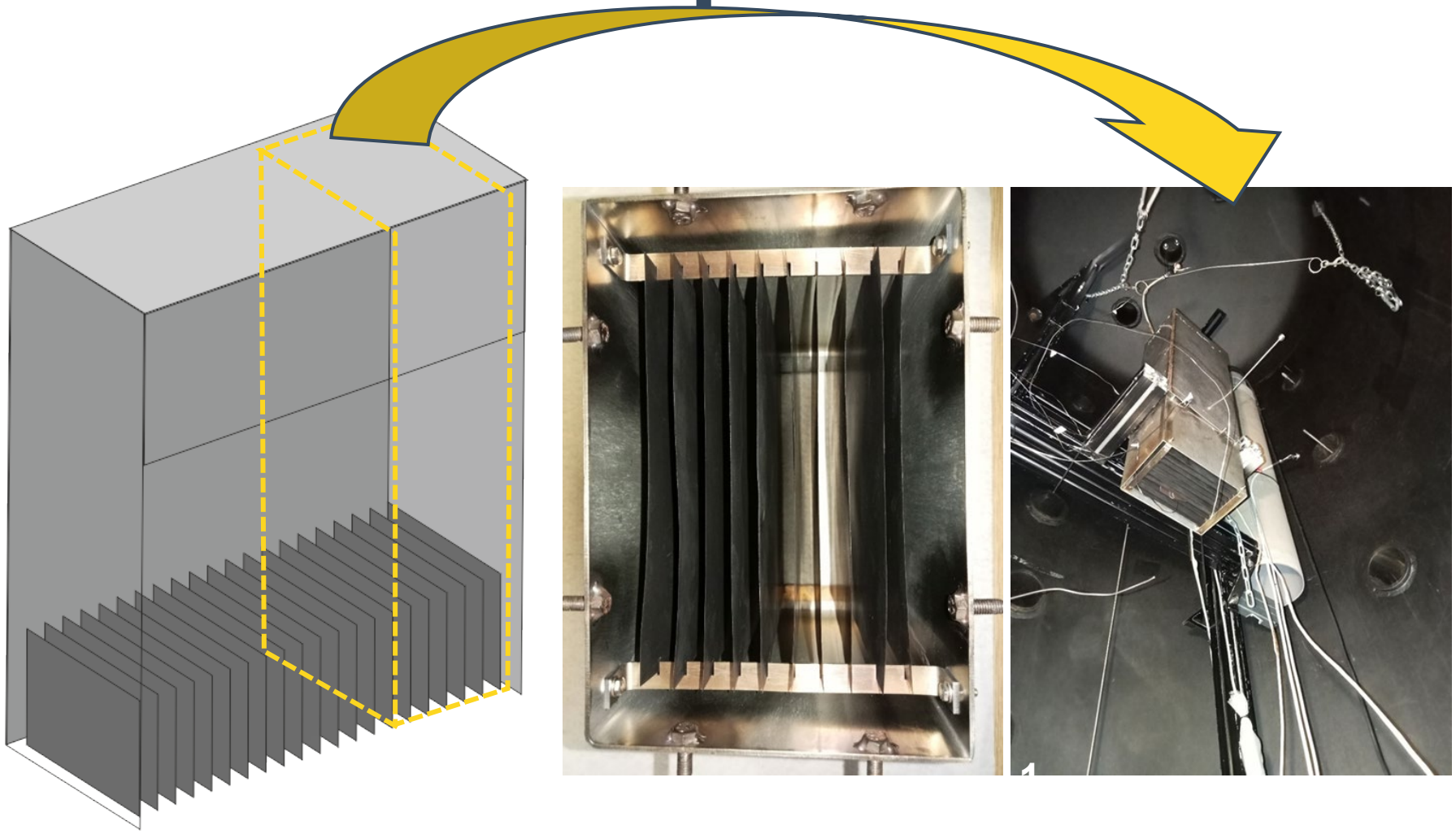

REKO-4 Experiments

Results

- Agreement with findings from REKO-3 experiments
- No pressure effect between 1 - 2 bar

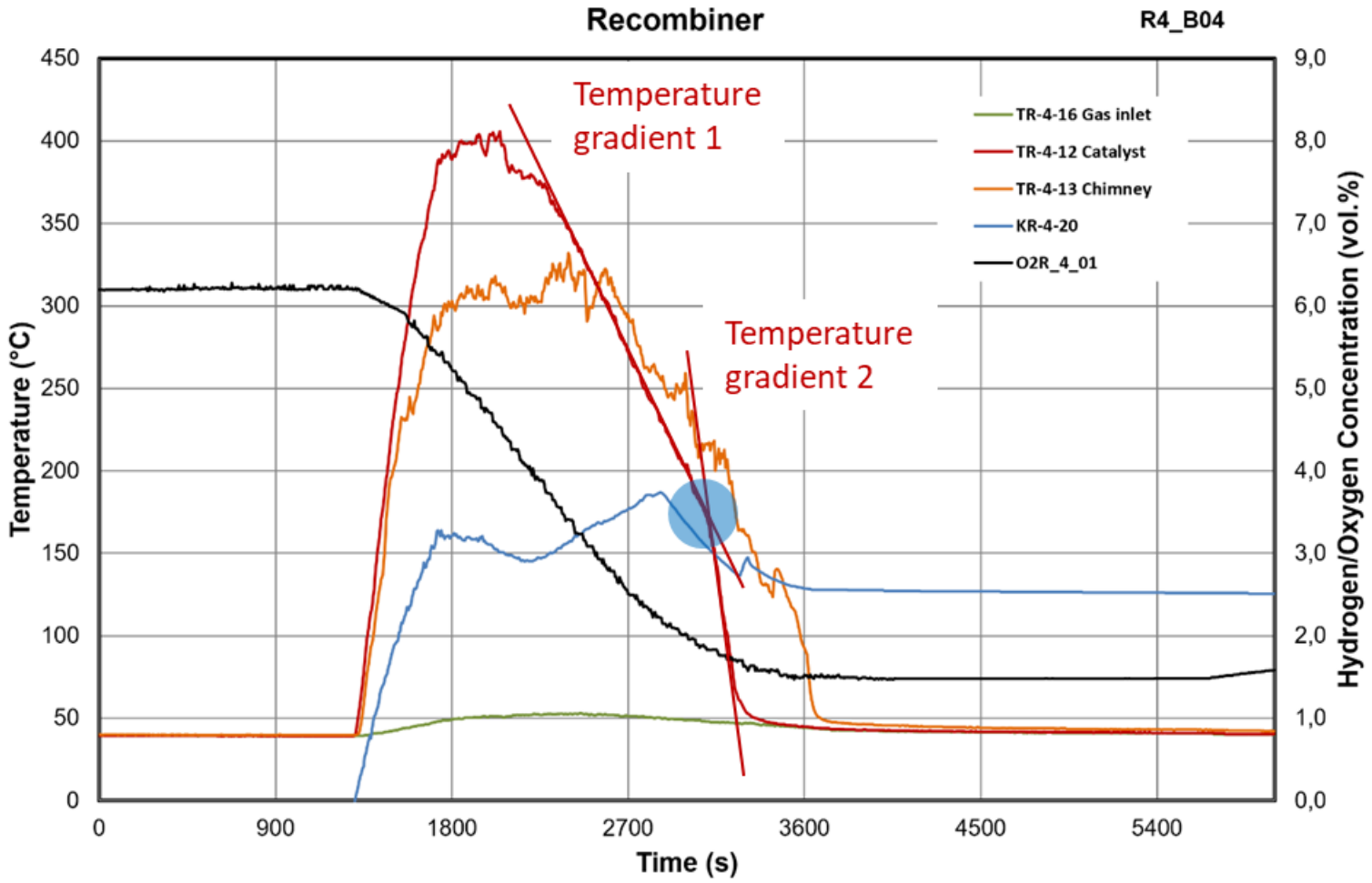

Creation of THAI Database

THAI DB

- 140 quasi-steady-states
- Estimates of uncertainties for recombination rates
- PAR model validation against the entire HR series and boundary conditions

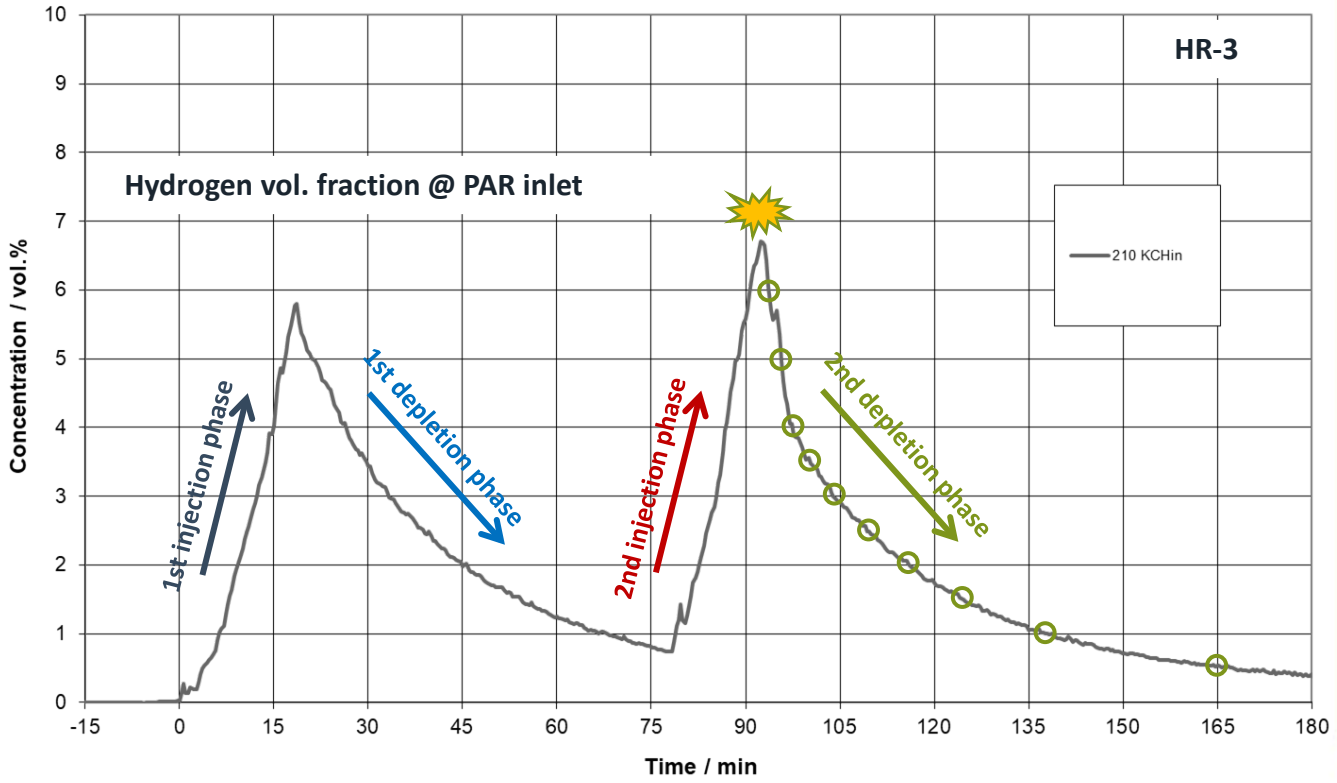

Outline

- Background
- AMHYCO – WP3 – Task 3.2
- Experimental program and results
- **Advances in PAR modeling**
- Conclusions

Advances in PAR Modelling

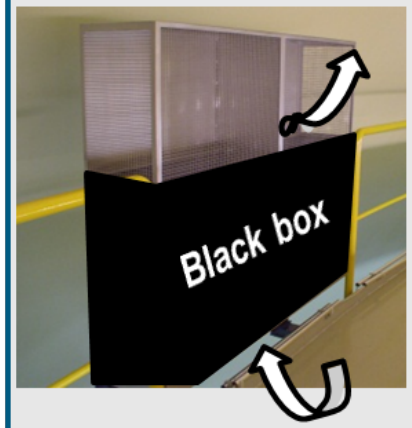

Framatome Engineering Correlation

- Integral recombination rate

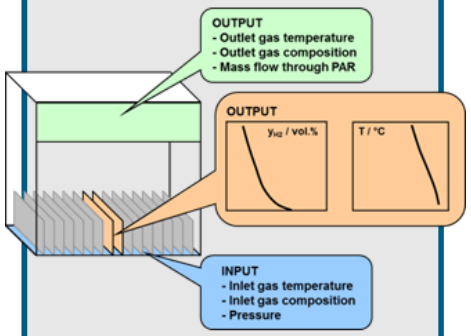

REKO-DIREKT (JÜLICH)

+ addition of
- Local recombination rate
- Local catalyst temperature
- Chimney flow

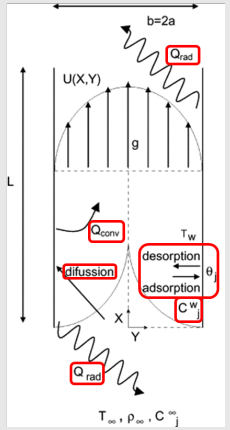

PARUPM (UPM)

+ addition of
- Surface reaction

ANSYS-CFX (JÜLICH)

+ addition of
- Temperature field
- Concentration field
- 3D flow & transport phenomena

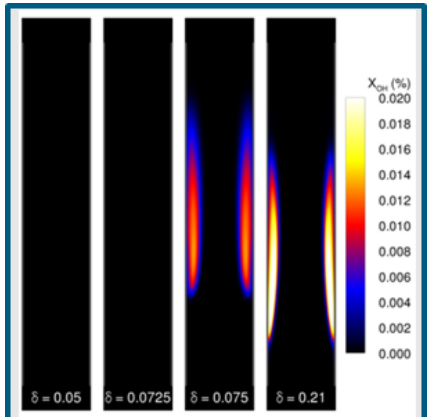

SPARK (IRSN)

+ addition of
- Gas phase chemistry
- Surface chemistry
- Multi-component transport

Framatome Engineering Correlation

framatome

Optimization

- Oxygen-starvation
- CO recombination

Enhancement

- CO poisoning

Validation

- THAI-DB

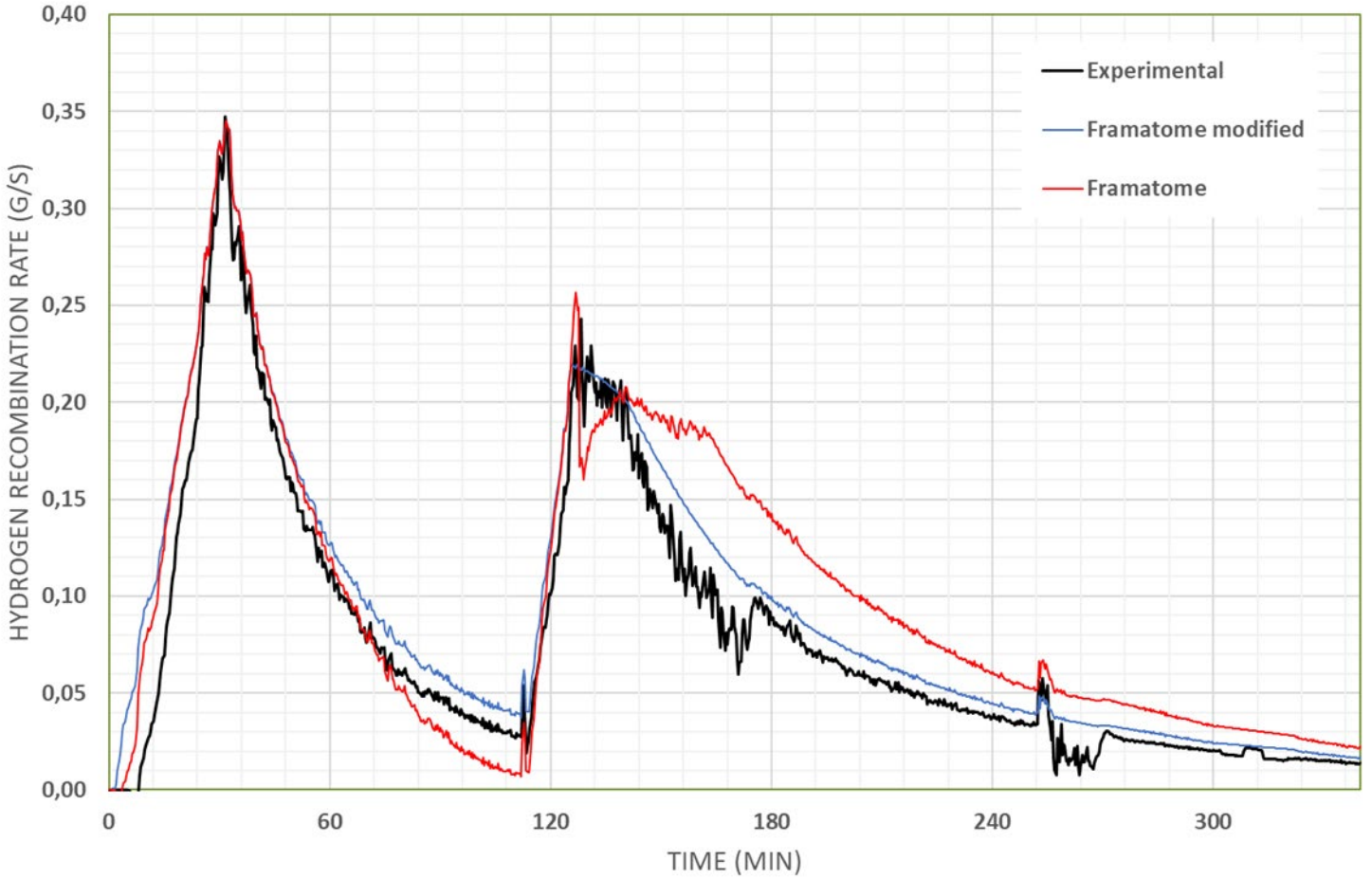

Framatome Engineering Correlation

Optimization

- Oxygen-starvation
- CO recombination

Enhancement

- CO poisoning

Validation

- THAI-DB

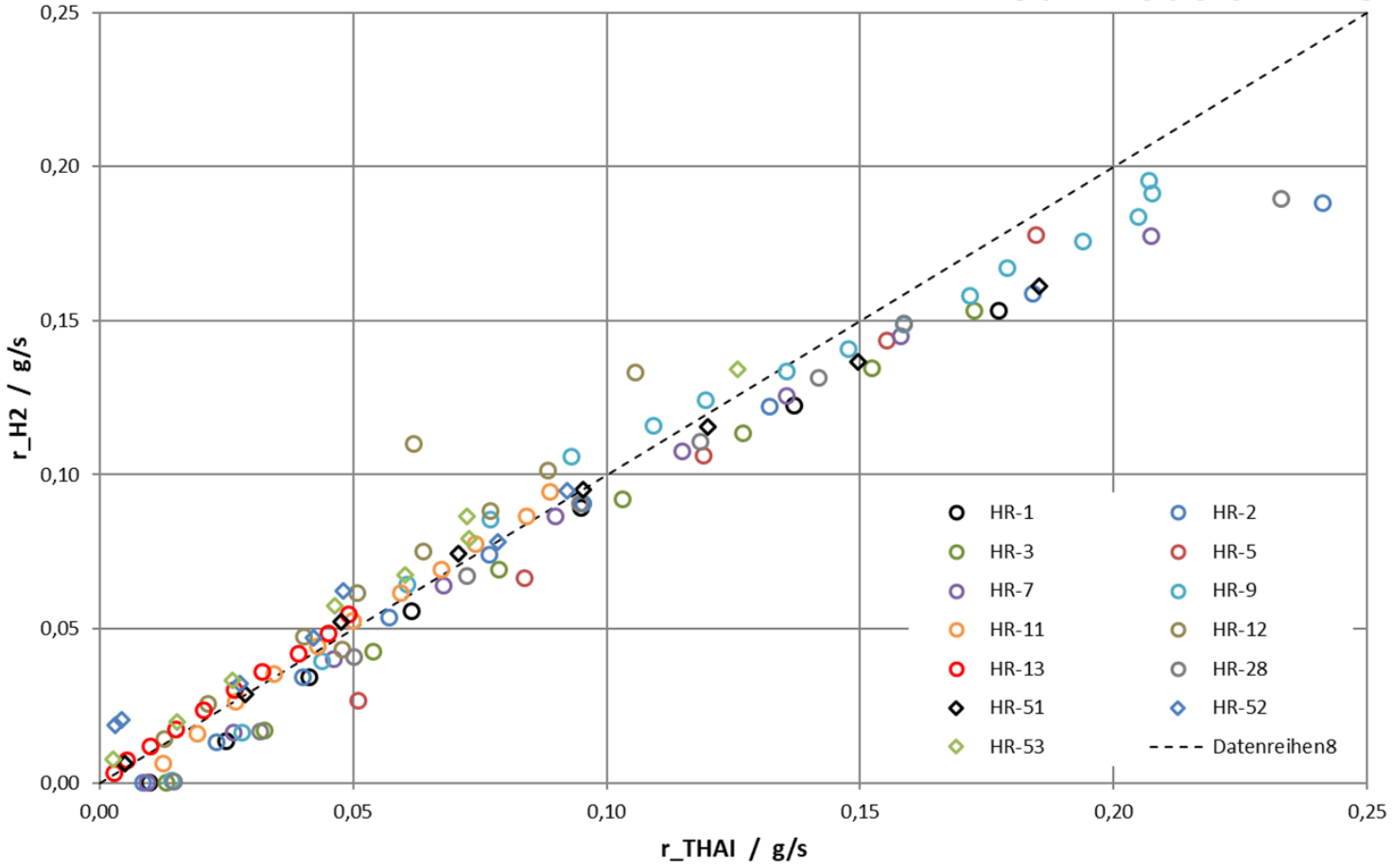

REKO-DIREKT (FZJ)

Enhancement

- CO poisoning

Validation

- THAI-DB

Implementation

- containmentFOAM

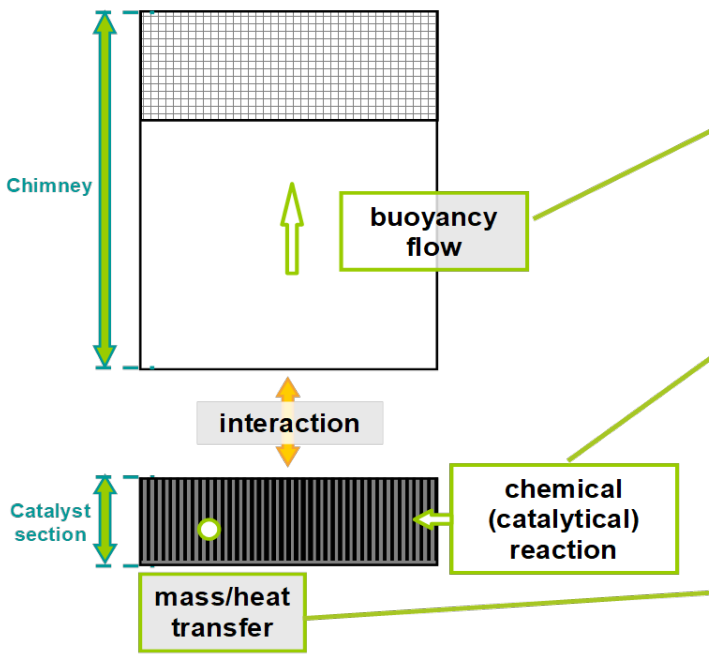

Mechanistic chimney model

$$\dot{m} = A \cdot \sqrt{\frac{g \cdot H \cdot (\rho_0 - \rho)}{\left(\frac{1}{\rho} - \frac{1}{2 \cdot \rho_0} + \underbrace{\frac{\xi \cdot H}{2 \cdot d_h \cdot \rho}}_{\omega_r}\right)}}$$

Diffusion controlled reaction kinetics: $\dot{r} = \beta \cdot \Delta C_i$

$$\beta = Sh \cdot \frac{D_{i,m}}{d_h} \qquad Sh = f(Re, Sc_i)$$

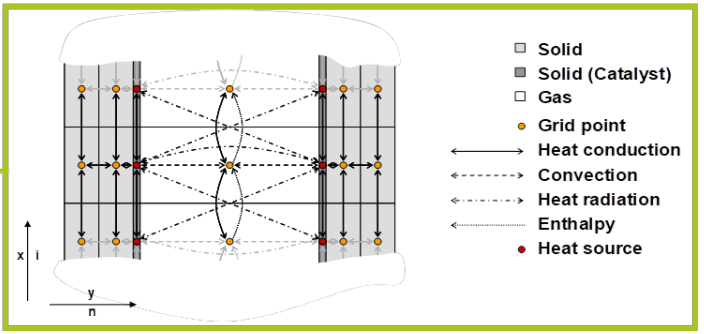

REKO-DIREKT (FZJ)

Enhancement

- CO poisoning

Validation

- THAI-DB

Implementation

- containmentFOAM

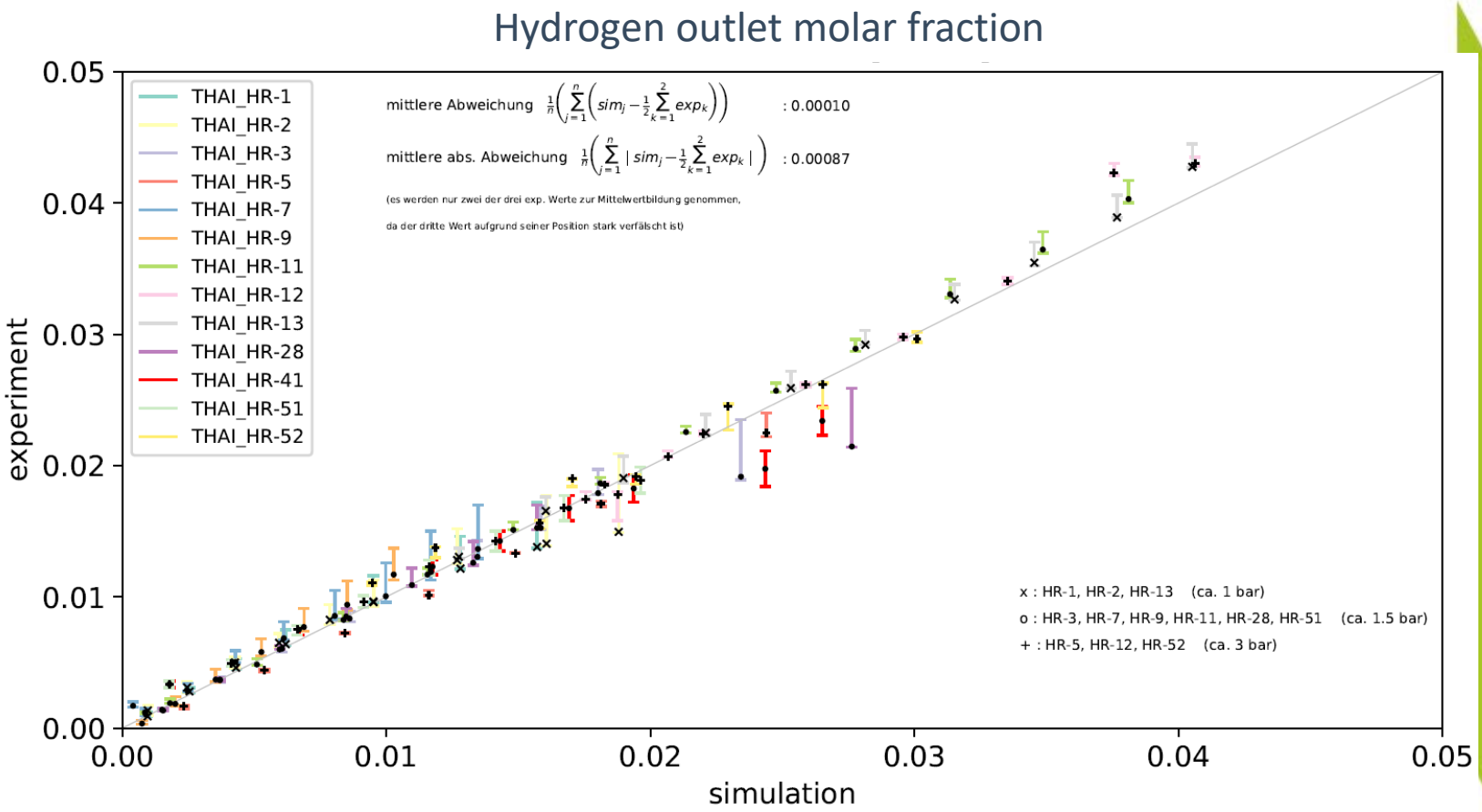

REKO-DIREKT (FZJ)

Enhancement

- CO poisoning

Validation

- THAI-DB

Implementation

- containmentFOAM

Catalyst temperature (bottom edge)

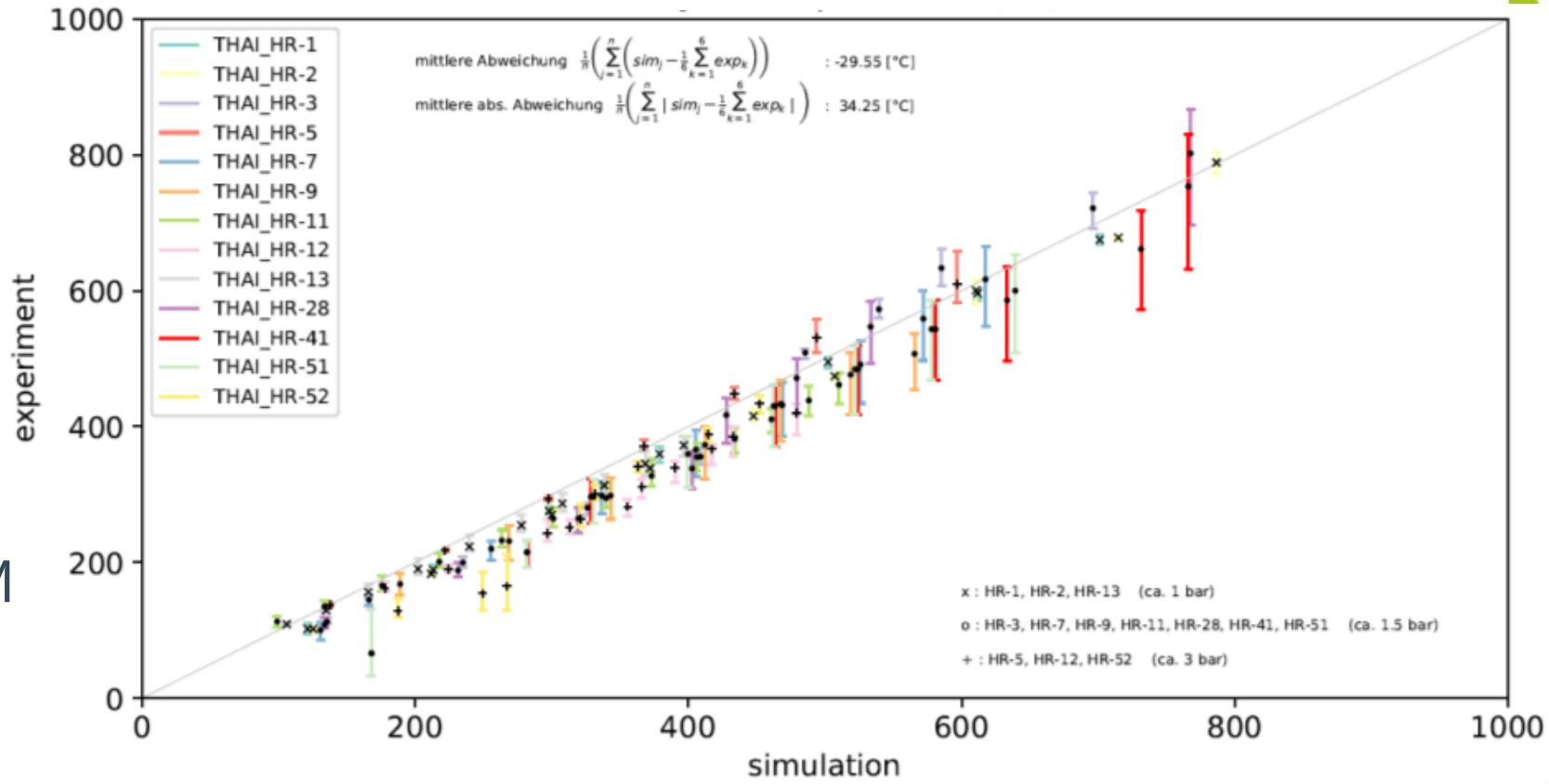

PARUPM (UPM)

Enhancement

- Chimney model
- Mass transfer-controlled reaction

Validation

- REKO-3
- Transient THAI data

Implementation

- GOTHIC

PARUPM: simulates the behaviour of a PAR device.

Mass and heat transfer between surface and flow

Adsorption/desorption of species

Surface chemical reactions

Heat realease and radiative heat **exchange**

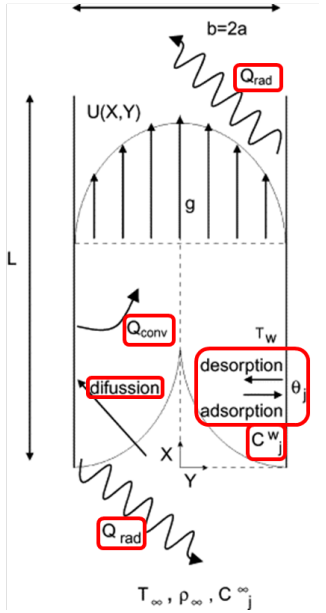

PARUPM (UPM)

Enhancement

- Chimney model
- Mass transfer-controlled reaction

Validation

- REKO-3
- Transient THAI data

Implementation

- GOTHIC

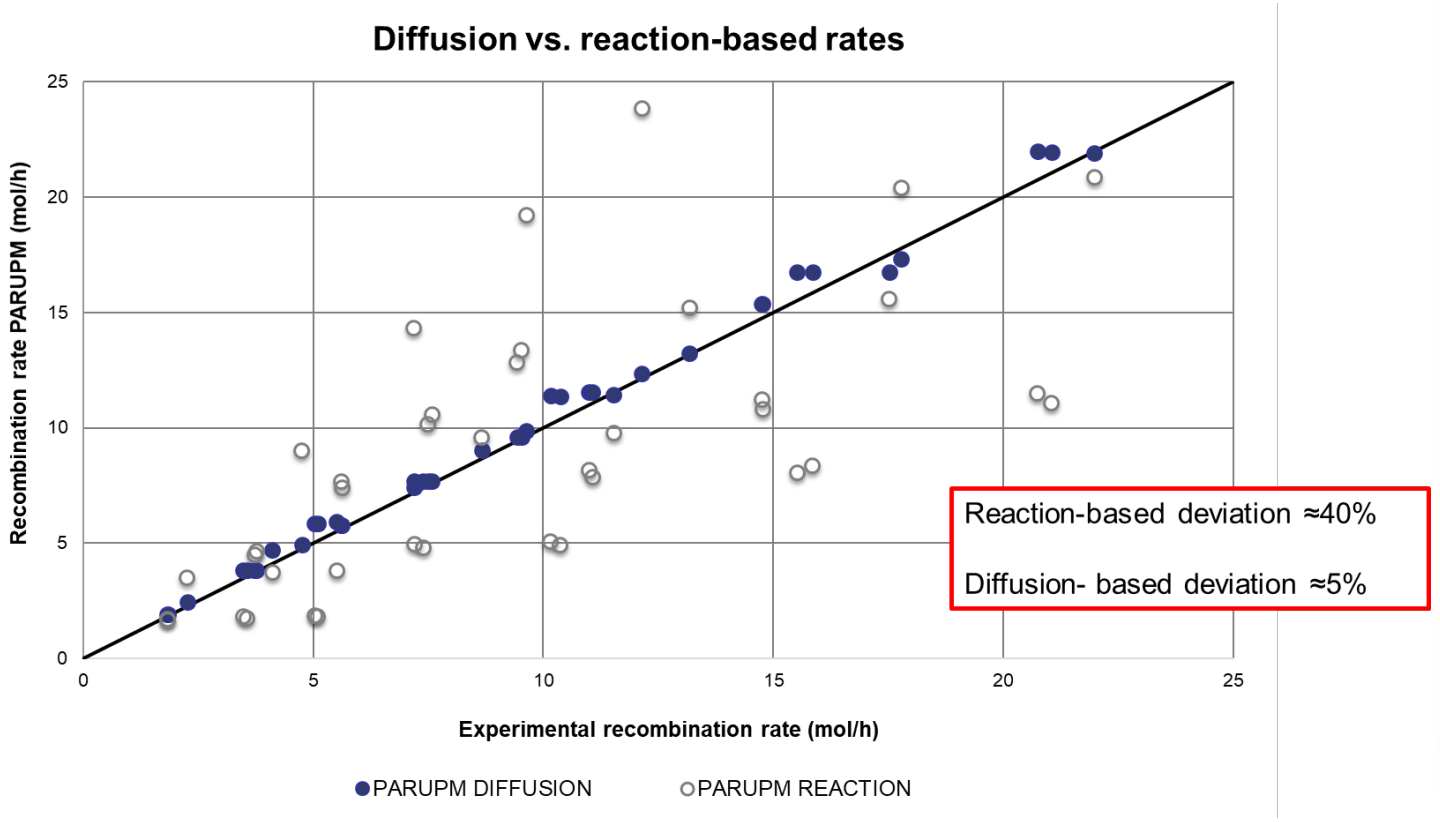

PARUPM (UPM)

Enhancement

- Chimney model
- Mass transfer-controlled reaction

Validation

- REKO-3
- Transient THAI data

Implementation

- GOTHIC

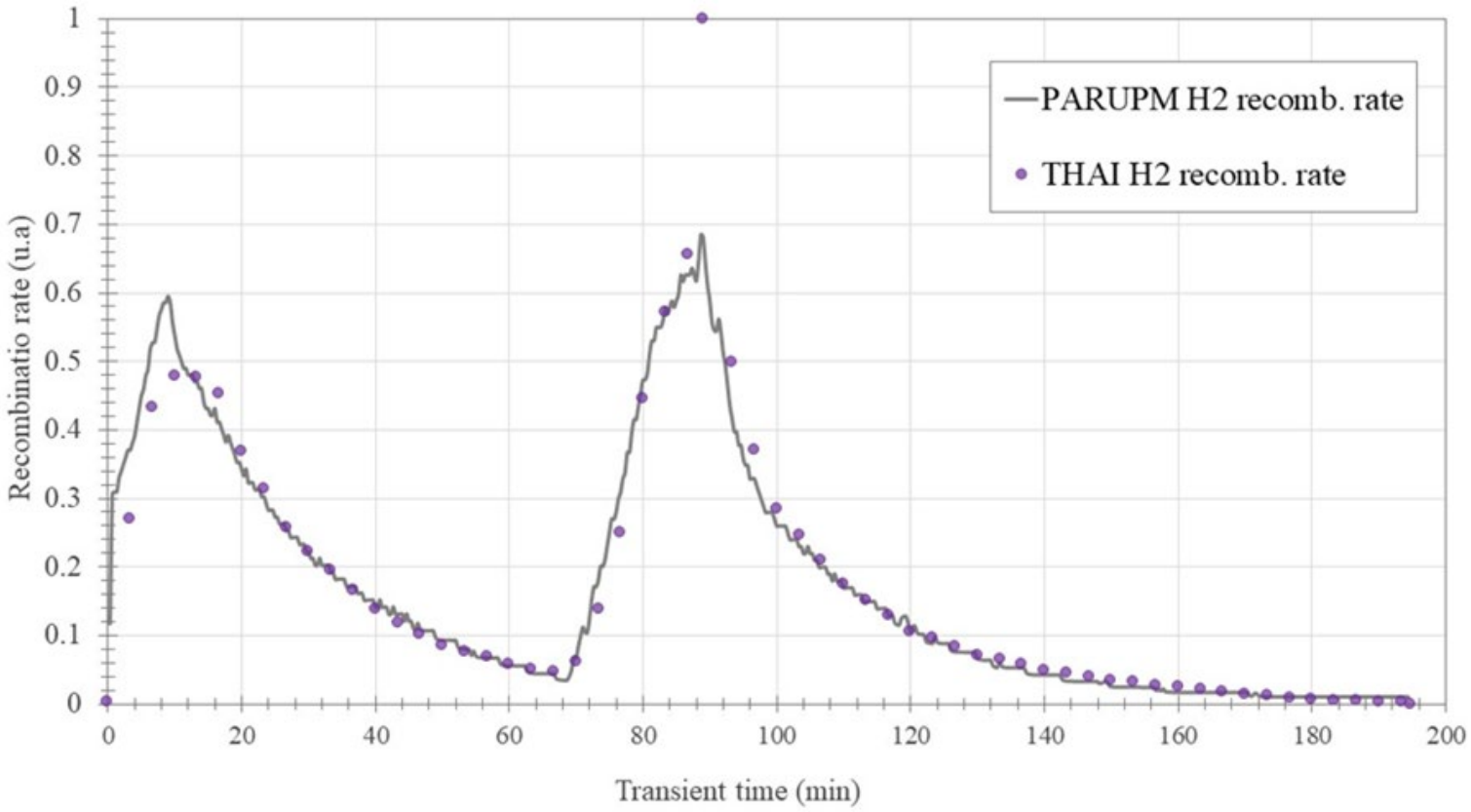

SPARK (IRSN)

Enhancement

- Implementation of enhanced reaction mechanism

Validation

- REKO-3 data
- CO poisoning (confirmation)

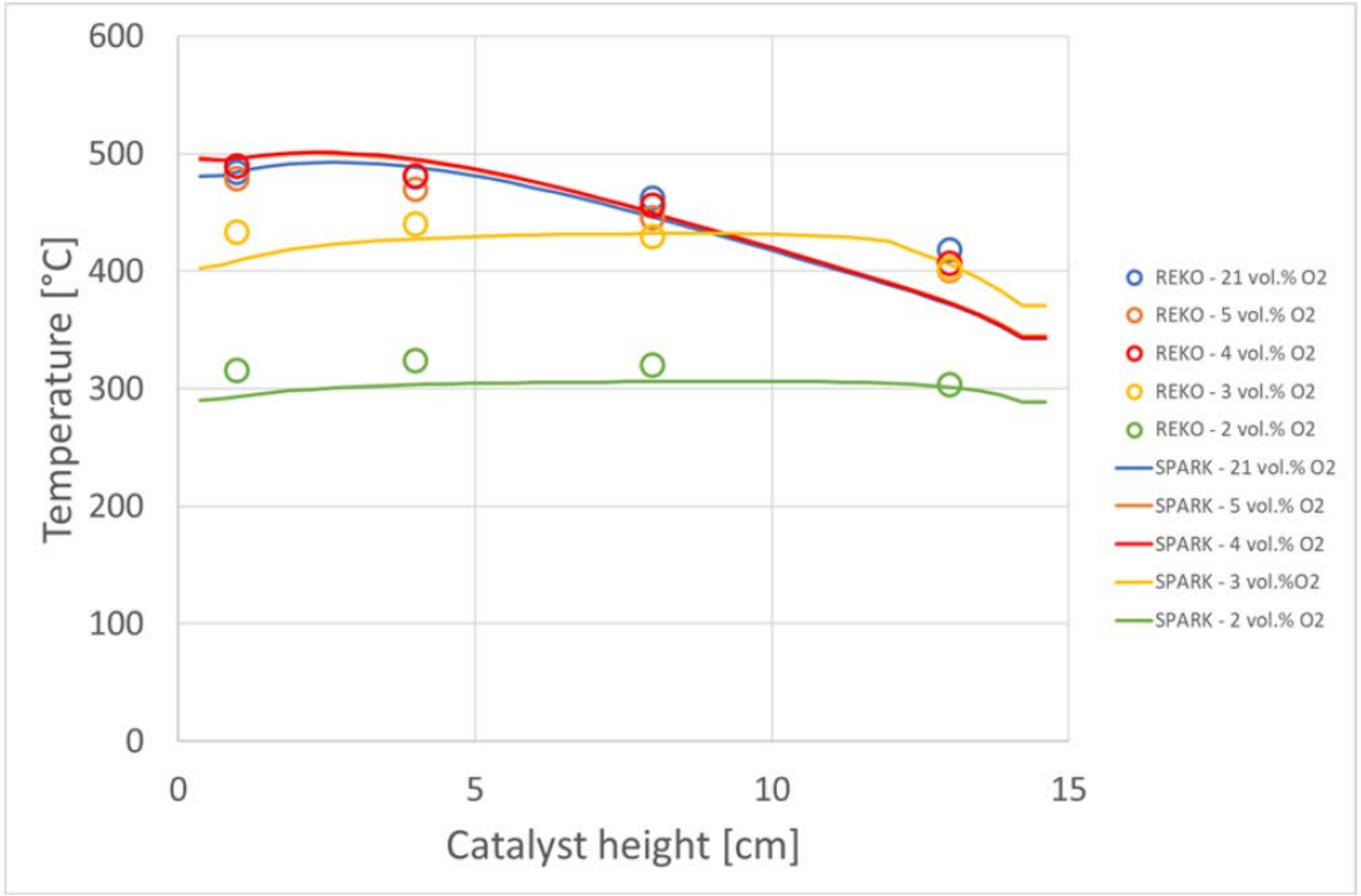

SPARK (IRSN)

Enhancement

- Implementation of enhanced reaction mechanism

Validation

- REKO-3 data
- CO poisoning (confirmation)

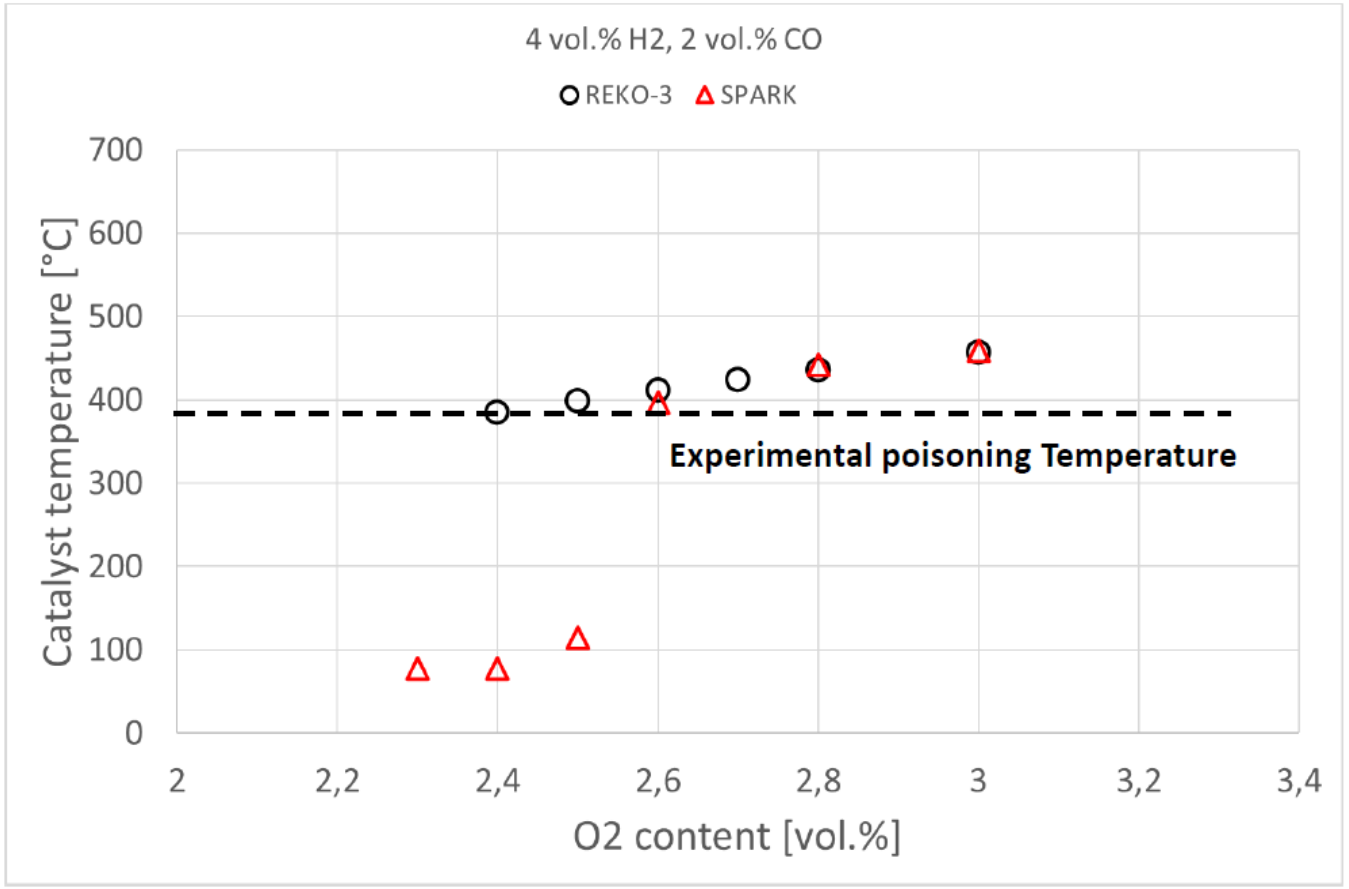

SPARK (IRSN)

Enhancement

- Implementation of enhanced reaction mechanism

Validation

- REKO-3 data
- CO poisoning (confirmation)

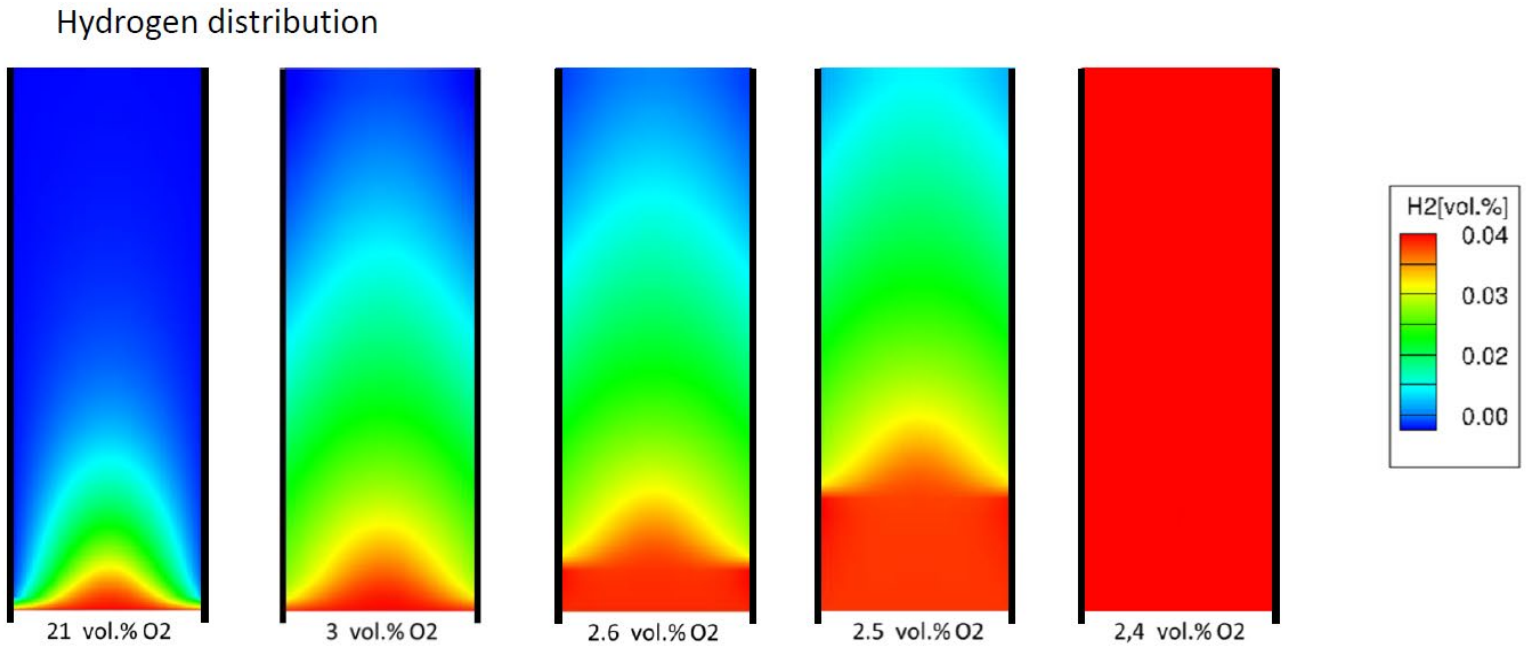

Outline

- Background
- AMHYCO – WP3 – Task 3.2
- Experimental program and results
- Advances in PAR modeling
- **Conclusions**

Conclusions

- Task 3.2 aimed at ensuring realistic PAR simulations under the conditions of the late phase of a severe accident.
  - Effect of oxygen starvation well understood
  - Results allow to derive empirical criteria for catalyst poisoning with sufficient precision, which are based on easy to obtain parameters even for PAR models without surface chemistry model
- New steady-state THAI database allows validation of PAR models for the entire range of boundary conditions of the experimental program.
- PAR models involved were significantly enhanced and prepared for the use in the simulation tools for accident scenarios in the further course of AMHYCO.

Acknowledgements

AMHYCO has received funding from the Euratom research and training programme 2019-2020 under Grant Agreement n°945057. The content of this paper reflects only the author's view. The European Commission is not responsible for any use that may be made of the information it contains.

Big Thank You…

…to the technical team, Tanja Bensberg and Dieter Maier, for their dedicated assistance in the experiments conducted.

…to student interns Lydia Bucher (University of Cincinnati, OH, USA) and Pierre Houttemane (EPF Engineering School, Montpellier, France) for their support of REKO-3 experiments.

…to undergraduate Daniel Fausel (University of Applied Sciences Aachen/Juelich, Germany) for his support of REKO-4 experiments.

Thank you
Connect with us for more information:

gonzalo.jimenez@upm.es

http://amhyco.eu

@amhyco



ASSESSMENT OF UNMITIGATED COMBUSTION RISK IN THE LATE PHASE WITHIN THE AMHYCO PROJECT

Stephan Kelm*, Michael Klauck, C. Vázquez-Rodríguez
Forschungszentrum Juelich, 42425 Juelich, Germany
s.kelm@fz-juelich.de; m.klauck@fz-juelich.de, c.vazquez-rodriguez@fz-juelich.de

Gonzalo Jiménez, Luis Serra Lopez
Universidad Politécnica de Madrid, 28040 Madrid, Spain
gonzalo.jimenez@upm.es; luis.slopez@upm.es

Luis Enrique Herranz, Joan Fontanet, Leticia Vitores-Gómez
CIEMAT, 28040 Madrid, Spain
luisen.herranz@ciemat.es; joan.fontanet@ciemat.es; leticia.vitores@ciemat.es

Ahmed Bentaib, Ludovic Maas, Alexandre Bleyer
Institut de Radioprotection et de Sûreté Nucléaire, 92260 Fontenay Aux Roses, France
ahmed.bentaib@irsn.fr, ludovic.maas@irsn.fr, alexandre.bleyer@irsn.fr

Nabiha Chaumeix
CNRS-INSIS, I.C.A.R.E., 45071 Orléans, France
nabiha.chaumeix@cnrs-orleans.fr

Matthias Braun
Framatome GmbH, 91052 Erlangen, Germany
matthias.braun@framatome.com

Johannes Hoffrichter, Miriam Müer
Ruhr-Universitaet Bochum, 44801 Bochum, Germany
johannes.hoffrichter@pss.ruhr-uni-bochum.de, Miriam.Mueer@pss.ruhr-uni-bochum.de

Ivo Kljenak
Institut Jozef Stefan, 1000 Ljubljana, Slovenia
ivo.kljenak@ijs.si

Oleksandr Sevbo, Andriy Iskra
Limited Liability Company Energorisk, 03148 Kyiv, Ukraine
sevbo@energorisk.com.ua, andriy.iskra@ukr.net

F.S.L. (Fajar) Pangukir, D.C. (Dirk) Visser
Nuclear Research and Consultancy Group, 1755 ZG Petten, The Netherlands
pangukir@nrg.eu, visser@nrg.eu

Zhe (Rita) Liang
Canadian Nuclear Laboratories, Chalk River, ON K0J 1J0, Canada
zhe.liang@cnl.ca

*corresponding author

ABSTRACT

The European AMHYCO project (Euratom 20192020, GA No 945057) aims at enhancing the understanding of H_2/CO combustion risk within the containment of a nuclear power plant in the late phase of a severe accident. The goal is to incorporate this knowledge into severe accident management guidelines and recommendations for long-term operation upgrades. Based on a critical review of existing methodologies and practices related to gas combustion risk, as well as the identification of accident sequences in which the H_2/CO combustion risk might challenge containment integrity, experimental investigations are conducted to close knowledge gaps related to combustion characteristics and the operation of passive autocatalytic recombiner under late phase conditions. To prepare the basis for the further assessment and refinement of existing SAMGs, systematic detailed analyses of the most challenging scenarios and possible mitigative measures were conducted for three generic European PWR containment designs, namely KWU, Westinghouse, and VVER. For each reactor type, one Loss of Coolant Accident and one Station Blackout scenario were selected for detailed analyses. Both scenarios cover a range of in-containment atmospheric conditions from potentially flammable at medium pressure up to a steam-inertized atmosphere at high pressure, including the late phase with an active filtered containment venting system.

This paper outlines the employed methodology using a consecutive analysis chain consisting of three levels with increasing detail (system codes, 3D GOTHIC™ and CFD) to assess containment pressurization, efficiency and/or options of individual mitigation measures with respect to H_2/CO combustion risk and equipment and instrumentation survivability. As a common basis, the system code nodalization schemes and 3D models are developed from detailed CADs and a shared geometry database. The paper discusses the status of the work with a focus on the comparative assessment of unmitigated reference cases that will be used in the future to assess the impact and effectiveness of mitigative measures (PARs, sprays, FCVS) on the combustion risk in the late phase. Concluding, challenges and lessons-learned are summarized.

KEYWORDS

AMHYCO, combustion risk, in-vessel phase, ex-vessel phase, Passive auto-catalytic recombiners, containment response, SAMG

1. INTRODUCTION

The severe reactor accident at the Fukushima Daiichi Nuclear Power Plant in 2011 has confirmed the need to develop a deeper understanding of the generation and distribution of combustible gases within the containment and connected compartments since their combustion can lead to dynamic loads on the containment structures and equipment and challenge containment integrity. While up to now primarily the risk associated with H_2 combustion during the in-vessel phase was considered [1], the European AMHYCO project (Euratom 20192020, GA No 945057) [2] aims at enhancing the understanding of H_2+CO combustion risk within the containment of a nuclear power plant both in the in-vessel (H_2) and ex-vessel (H_2+CO) phases of a severe accident (SA). Consequently, a comprehensive analytical assessment of the containment behavior is conducted in its Work Package (WP) 4 to investigate:

- the H_2/CO combustion risk, e.g., flammability or potential of flame acceleration,
- the efficiency and options/timing of individual mitigative measures, including PARs, FCVS, or spray systems activation.
- and the equipment and instrumentation survivability and ‘operators/control room view’ on the containment status.

The analysis is conducted for generic European PWR concepts, W(French and Westinghouse designs), KWU (German PWR design), and VVER (Soviet/Russian design), to provide a database for a review and potential extension of the SAMGs and EOPs within WP5. For that purpose, WP4 utilizes scenarios selected in WP2 [3], existing empirical criteria and correlations, supported by the WP1 literature review [4], and new correlations derived from experimental data on H_2/CO combustion [5] and PAR efficiency [6] in the late phase, developed in WP3. In a nutshell, the integration of WP4 in AMHYCO is depicted in Figure 1.

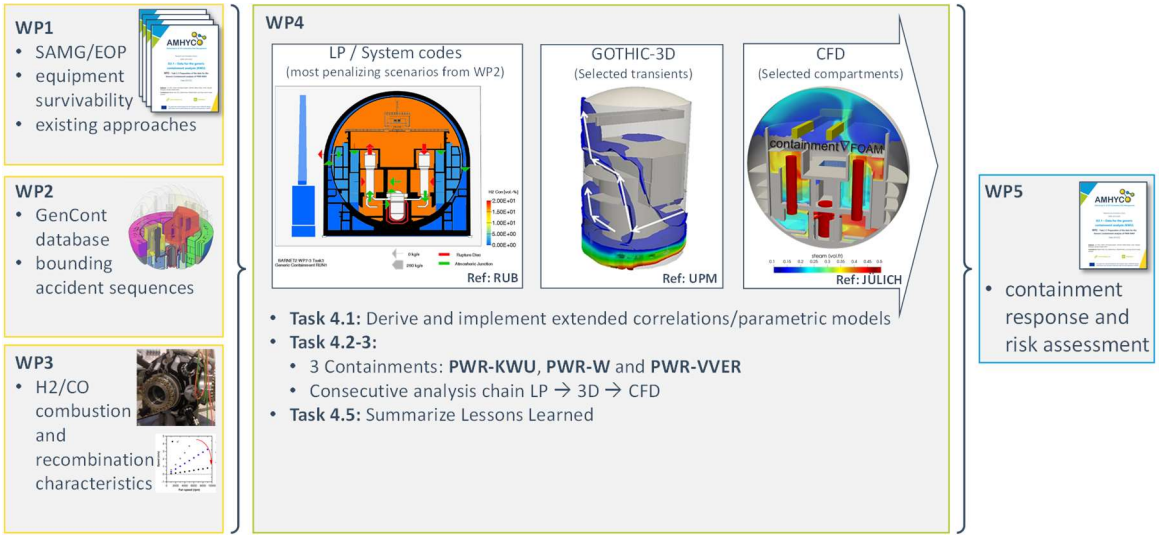

Figure 1. Integration of WP4 in the AMHYCO project

The preparative work in WP2 aimed at screening combustion risk in potential accident scenarios by using existing integral (in part non-public) plant models. As follow-up, WP4's objective is to assess the containment response in more detail, based on an open containment database. For that purpose, generalized nodalization schemes are employed, to enable a certain comparability of the simulation results as well as to pave the way for obtaining generic, i.e., non-plant-specific conclusions. Full containment analyses are conducted in a consecutive analysis chain, consisting of three levels of increasing detail:

- As basis, the identified sequences are simulated completely with lumped parameter (LP) containment models e.g., built in COCOSYS, SPECTRA, ASTEC or MELCOR.
- The most penalizing cases are additionally investigated with 3D models developed in GOTHIC™ to address potential asymmetric / 3D conditions that may lead to higher combustion risk.
- Finally, relevant compartments and/or time frames are simulated in detailed CFD-grade local containment studies to substantiate GOTHIC™ analysis and answer remaining open issues.

The increasing level of spatial resolution achieved with the different codes will also be utilized to assess the perspective on the accident from the control room (available instrumentation) against the full insights provided by the simulations to propose an upgrade of the SA instrumentation and the SA Management Guidelines (SAMG).

This paper aims to summarize the status of the work with a focus on the methodology and comparative assessment of the unmitigated reference cases. This was found to be a necessary step to ensure a consistent implementation of the generic containment nodalization schemes and definition of the mass and energy injection tables. After convergence of the unmitigated cases, they will serve as a reference for the assessment of the impact and effectiveness of mitigative measures (PARs, sprays, FCVS) on the combustion risk. Section 2 briefly introduces the characteristics of the SA scenarios selected from WP2. Within Section 3, the employed methodology and preparative steps including the comparative assessment of unmitigated reference cases are outlined. The combustion risk is assessed in Section 4 to provide a set of reference cases

that will be used in the future to assess the impact and effectiveness of the mitigative measures on the combustion risk in the late phase. Concluding, Section 5 summarized the first results and lessons learned from the analyses of unmitigated reference cases and outline the future work.

2. SCENARIOS

Within WP2, different sequences of the three European PWR designs, PWR-W, PWR-KWU, and PWR-VVER, were simulated with different system codes and hypotheses, including the nodalization schemes used. These simulations cover different initiating events and involve diverse engineered safety features and SA management measures. The simulations were screened regarding the prevailing combustion risk to identify bounding scenarios for the detailed analysis of the containment response in WP4 [3]. For each containment type, two classes of scenarios were analyzed:

(1) A Loss of Coolant Accident (LOCA) characterized by a comparably early core damage and a large H_2 release, resulting in flammable conditions in the containment with a potential of flame acceleration when no mitigative measures or hardware is in place.
(2) A Station Blackout (SBO)/Total Loss of AC Power (TLAP) sequence, which results in a delayed core damage and release of H_2.

Thereby, for the LOCA scenarios, the size and break location were varied and for the transient SBO accident, the boundary conditions like primary loop depressurization were varied to determine the accident sequence bounding with regards of hydrogen risk. Additionally, the in-vessel hydrogen release path into the containment is quite different in both types of sequences. In case of a LOCA hydrogen is released through the break location whereas for the SBO the release path is via the pressurizer release tank to the containment. After RPV lower head failure, the molten corium-concrete interaction (MCCI) generates additional H_2 and CO. The main characteristics of the selected sequences for the specific PWR designs are briefly summarized in the following [3]:

PWR-KWU design:

- Medium-break (MB) LOCA (80 cm^2, behind the main coolant pump in the cold leg of the pressurizer loop) with a limited water injection by the extra borating system (MBLOCA+ECCS). For this sequence all active emergency injection systems, which could prevent accident progression, are postulated to fail, only the hydro accumulators can inject their inventory. After the water level inside the pressurizer falls below a threshold the extra borating system starts injecting water with a limited injection rate of 4x2 kg/s over a period of 2.5 h and thus slightly delays the core uncovery but is insufficient to stop the accident. Core degradation begins after approx. 5.3 h. The delayed accident progression [7] poses a slightly higher combustion risk due to increased condensation in the containment. With a predicted RPV failure after ~6.5 h, the release of H_2 and CO by the MCCI starts. Within the transient a total amount of ~1500 kg H_2 and ~7500 kg CO are released.
- TLAP with delayed Primary System Depressurization (PSD). The primary system is depressurized 30 mins after reaching the SAMG criterion “Core Outlet Temperature >650 °C” by opening all three pressurizer safety valves. This results in a large mass of H_2 which is initially stored within the primary loop and then is released rapidly to the containment. RPV failure occurs after approx. 10 h. Within the considered problem time of 72 h a total amount of ~2300 kg H_2 and 25000 kg CO are released.

PWR-W (Framatome and Westinghouse designs):

- Large-break (LB) LOCA in the hot leg (PWR-W-1000) without availability of auxiliary feed water and safety injections, except for accumulators. Due to the fast core uncovery and depressurization of the reactor cooling system, the core degradation begins already 20 min after the initiating event.

The RPV failure occurs ~2.7 h and at about 6 h the corium in the cavity gets completely oxidized. The large water and steam release through the RCS breach leads to a sudden pressure peak. Activating the containment spray systems (fan cooler are not used in the reference case) significantly reduces the pressure before the generation of non-condensable gases by MCCI leads to a continuous pressurization. At around 2 h, the spray operation is switched to recirculation mode, which reduces their efficiency. The high release of hydrogen in the in-vessel phase and the important drop of steam molar fraction due to the actuation of the safety systems lead to flammable conditions at the end of the in-vessel phase. The further release of combustible gases during the ex-vessel phase leads to a concentration maximum at about 6 h, while the subsequent CO_2 generation results in a certain dilution of the mixture. Within the considered problem time of 48 h, a total amount of 1008 kg H_2 and 13396 kg CO are released.

- SBO with loss of all offsite power (scaled from PWR-W-1300 to the generic PWR-W-1000). All active safety systems (e.g. sprays, emergency core cooling, cavity flooding) are unavailable. Steam and hydrogen release to the containment after rupture of the pressurizer relief tank burst discs after around 2.5 h. The pressurizer relief valves lock open after approx. 4.5 h. The loss of coolant is partly compensated by accumulator injection at 4.75 h. The ex-vessel phase begins with RPV failure and melt relocation to the cavity at 11.5 h. Within the considered problem time of 48 h, a total amount of 4880 kg H_2 and 1905 kg CO are released.

PWR-VVER:

- LB LOCA at the cold line weld at the reactor pressure vessel with complete loss of power supply and failure to start all emergency diesel generators (SBO). Due to the loss of power supply, water injection from the spray system does not take place. Two of the four HA inject water into the upper plenum of the RPV, while the other two inject into the leak zone. Due to the loss of power supply, water injection from the low pressure ECCS does not take place, the core materials and water in the PRV begin to heat up rapidly and boils. Cladding oxidation and H_2 release into the containment begins after 20 min. The continuous degradation of the core leads to RPV failure and melt relocation to the cavity and MCCI. More than 2875 kg H_2 8000 kg CO are released during considered problem time to the containment.
- SBO: A complete loss of power supply and failure to start all emergency diesel generators is considered. Consequently, water injection from the high pressure ECCS does not take place. At the initial stage of the accident, heat is removed from the RPV due to the boiling off water from steam generators in 1 hour. The core materials and water in the PRV begin to heat up and relief steam to the bubbler tank and then to the containment. The bubbler tank membrane breaks in 1.7 h and release steam to the containment with moderate pressure and temperature increase in the containment. Cladding oxidation and H_2 release into the containment starts in 3.5 hours after the beginning of the accident. Continuous degradation of the core leads RPV failure and MCCI in the cavity. More than 3000 kg H_2 and 7800 kg CO are released during the simulated duration.

3. METHODOLOGY AND PREPARATIVE STEPS

The computational approach employed in WP4 is based on the experiences gained during the SARNET-II Generic Containment benchmark series [8] and its continuation in the frame of SAMHYCO-NET. Though a code-to-code benchmarking is explicitly not objective of the work, a certain consistency of the codes results is required to obtain a quantitative database for further assessment and extension of SAMG in WP5. Moreover, several codes ranging from system to CFD codes (see

Table 1) are employed and consistent transfer of the information obtained from WP2 is the fundament step.

Table 1. Codes used in WP4

Mesh	PWR-KWU	PWR-W	PWR-VVER
System codes	COCOSYS 3.1 (RUB) MELCOR 2.1 (Framatome) SPECTRA 23-12-0000 (NRG) COCOSYS 2.4 (FZJ)	ASTEC (JSI) ASTEC v2.2 (IRSN) MELCOR 2.2_r2023.0 (CIEMAT)	MELCOR 1.8.6_RL_2011 (Energorisk)
3D codes	GOTHIC8.3 Q.A (UPM)		
CFD codes	ANSYS FLUENT (IRSN)	ANSYS FLUENT (NRG) containmentFOAM (FZJ)	

For the sake of clarity, the flowing discussion focuses on the work performed for the PWR-KWU type of plants. Similar evaluations were also performed for PWR-W and PWR-VVER.

The Generic Containment nodalisation schemes were derived from 3D CAD models [9], [10] (see Figure 2), generating a consistent and freely usable data basis for all code users to develop their LP, 3D, and CFD containment models.

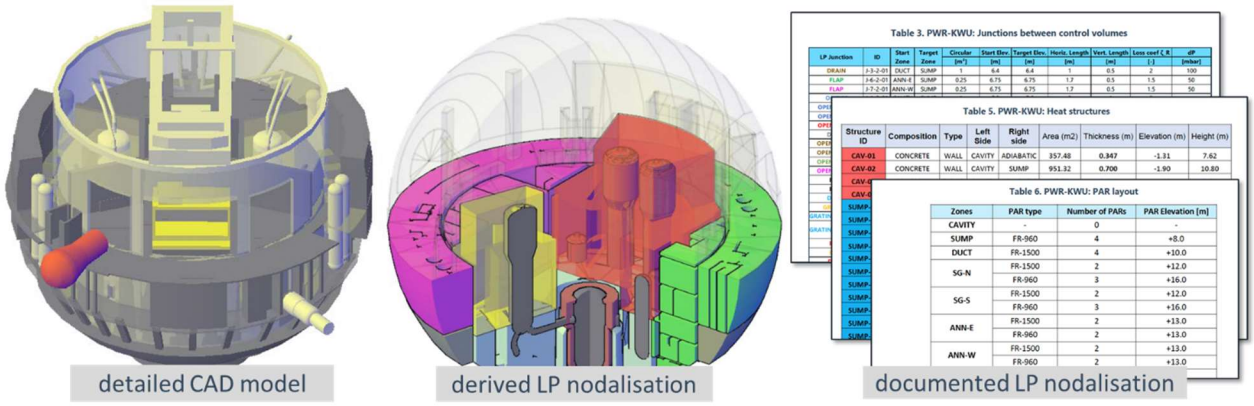

Figure 2. Definition of the generic nodalization (here PWR-KWU)

The way of extracting and documenting the nodalization scheme (surface areas, heat structure thickness, junction length etc.) still requires a 'translation' into different code input deck structures as they have deviating input requirements. This adaption led to ambiguities in the interpretation of the data. Therefore, different verification steps were taken to assess the created code input decks and ensure consistent use of the database. e.g. a comparison of the compartment volumes and the associated steel mass/surface and concrete mass/surface, see Figure 3 (as example for the PWR-KWU). In the analysis of the input verification, the identified deviations were understood and are considered as justifiable.

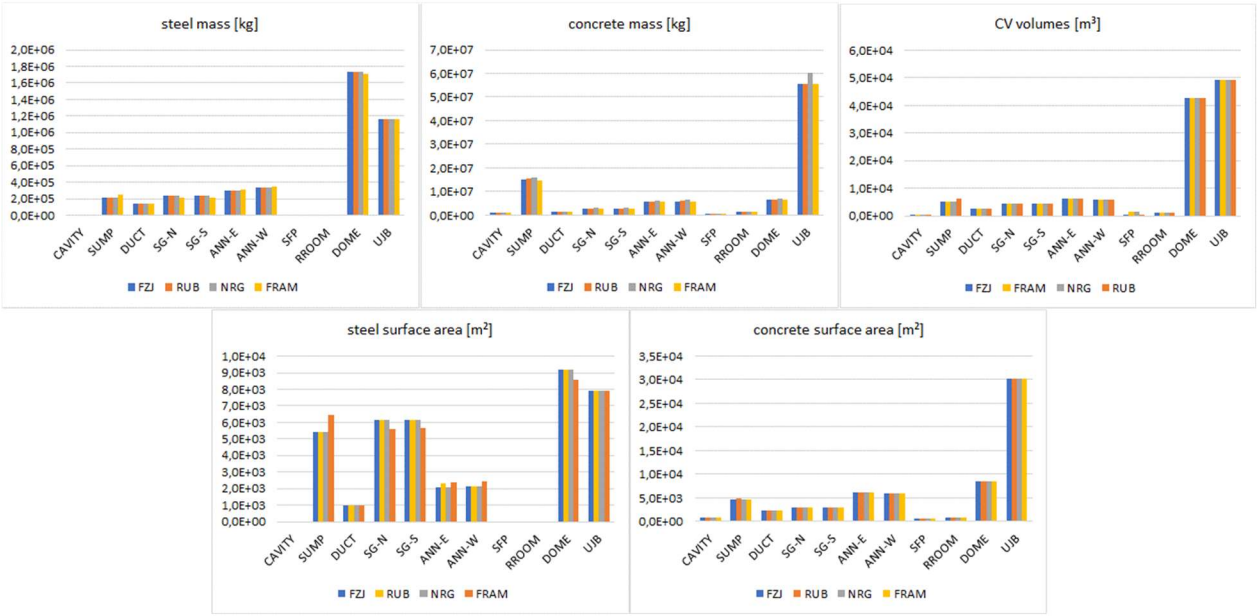

Figure 3. Comparison of the nodalization statistics for PWR-KWU

Figure 4 compares the pressure evolution obtained for the unmitigated PWR-KWU MB LOCA and TLAP squences with different codes. The predicted pressurization is generally highly consistent among the codes for the early accident phase. An increasing spread is visible over time for the late ex-vessel phase when sump water ingression leads to the cavity flooding. The same tendencies are visible for both scenarios, i.e. the strongest pressurization is predicted by MELCOR, followed by SPECTRA, and the weakest by COCOSYS The visible differences between both COCOSYS results were found to result from different versions (RUB 3.1, FZJ 2.4).

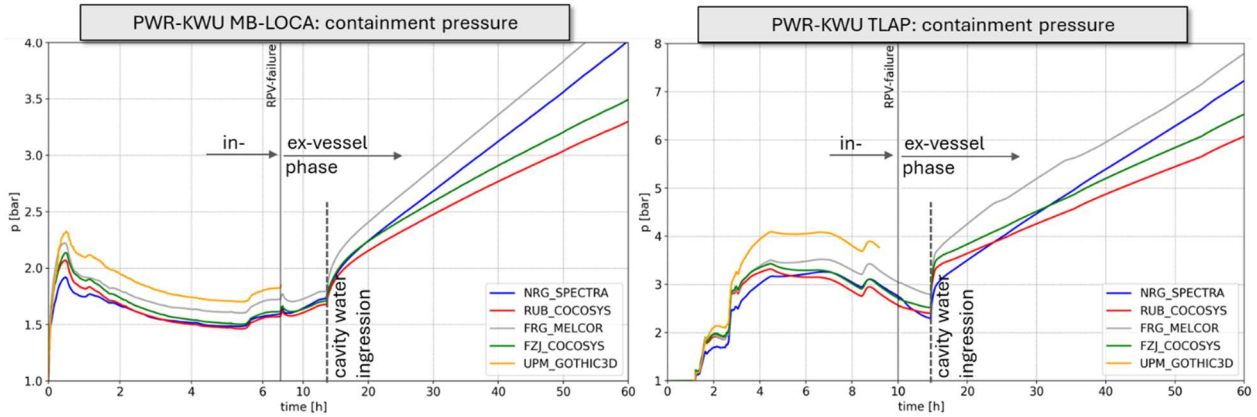

Figure 4. Pressure evolution for the PWR-KWU sequences.

The observed spreading is kind of expected, since these codes use different models for heat transfer from the gas to structures, and different models for heat conduction within these structures. The resulting differences accumulate over time so that the spreading increases with problem time. Currently, additional evaluations are ongoing to further understand the differences in containment pressurization and possibilities to reduce this uncertainty of the simulation results.

The main impact parameter for the containment pressurization turned out to be the assumed thermal conductivity of the in-containment concrete structures. The concrete structures absorb heat, and thus condense steam. After a lengthy discussion, devaluating different proposals, the common conclusion for AMHYCO was to use a best-estimate concrete density of 2500 kg/m3 - upper end of typical values due to the high rebar content of nuclear concrete, the upper limit of the concrete thermal conductivity as defined by EUROCODE 2 Chapter 3.3.3(2) [11] - to be bounding with regard to steam condensation, and a specific heat as given by EUROCODE 2 Chapter 3.3.2(1) without considering evaporation of crystal water, which is prevented by the pressurization of the containment.

Concluding, the LP code and GOTHIC™ 3D input decks are considered applicable for a quantitative assessment of the combustion risk and efficiency of mitigative measures in the further project work.

4. ASSESSMENT OF COMBUSTION RISK

Within AMHYCO WP4, combustion events are not analyzed, i.e. the combustion risk is evaluated in terms of the evolution of a flammable cloud and its potential to undergo flame acceleration in case of a combustion process. The flammability limits of H_2 derived by Martín-Valdepeñas et al. [12], using the data of Stamps and Bearman [13], are employed based on WP1 review [4].

$$x_{H2}^{LFL} \geq 0.037 + 0.011x_{H2O} - 4.16 \cdot 10^{-5}(T - 373) \quad (1)$$

$$x_{H2}^{UFL} \leq 0.772 - 1.087x_{H2O} - 2.71 \cdot 10^{-4}(T - 373) \quad (2)$$

$$x_{Inert} \leq 0.63 + 3 \cdot 10^{-4}(T - 373) \quad (3)$$

Here, x denotes molar fractions, and T is the gas temperature in Kelvin. The lower flammability limit (LFL) considers upward flame propagation conditions for the sake of conservativeness.

While the combustion of hydrogen in an air-steam mixture is well understood, the additional released of carbon monoxide due to the molten corium-concrete interaction introduces additional challenges to assess the flammability of the containment atmosphere. The usually employed conservative approach is to replace the carbon monoxide by a comparable amount of hydrogen, mostly on a molar base, and continue to employ the flammability limits of hydrogen. This approach is also used in the remaining part of this paper. However, to avoid this simplification, within AMHYCO WP3, refined criteria are developed which consider the flammability and potential of flame acceleration for a H_2+CO mixture and explicitly for late phase conditions i.e. low O_2 and high dilutant concentrations.

Based on the performed numerical simulations (compare Chapter 3), the evolution of the mixture flammability in the containment dome is evaluated in a ternary diagram in Figure 6. The involved codes provide relatively comparable trajectories in the ternary diagram. As steam is an inerting / diluting gas species, it is usually expected that the codes predicting the highest containment pressurization (see Figure 4) usually also yield the lowest flammability.

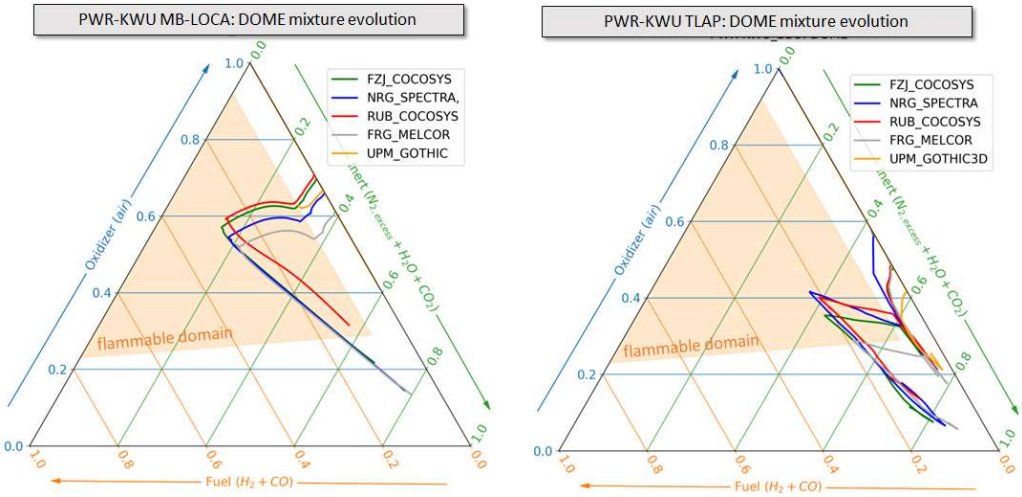

Figure 5. Shapiro-Diagram of the containment dome

To provide a more quantitative insight to the transient behavior of the flammable cloud, the flammable volume and flammable H_2 mass are integrated over all control volumes, and their transient evolution is compared in Figure 6. While the different codes generally predict the formation of a flammable cloud in the early phase of the SA quite consistently, the results spread after sump water ingress to the cavity when a large part of the containment (primarily the dome region) becomes steam inerted again, while smaller compartments close to the release remain inerted. These heterogeneities motivate a closer look with 3D and CFD models.

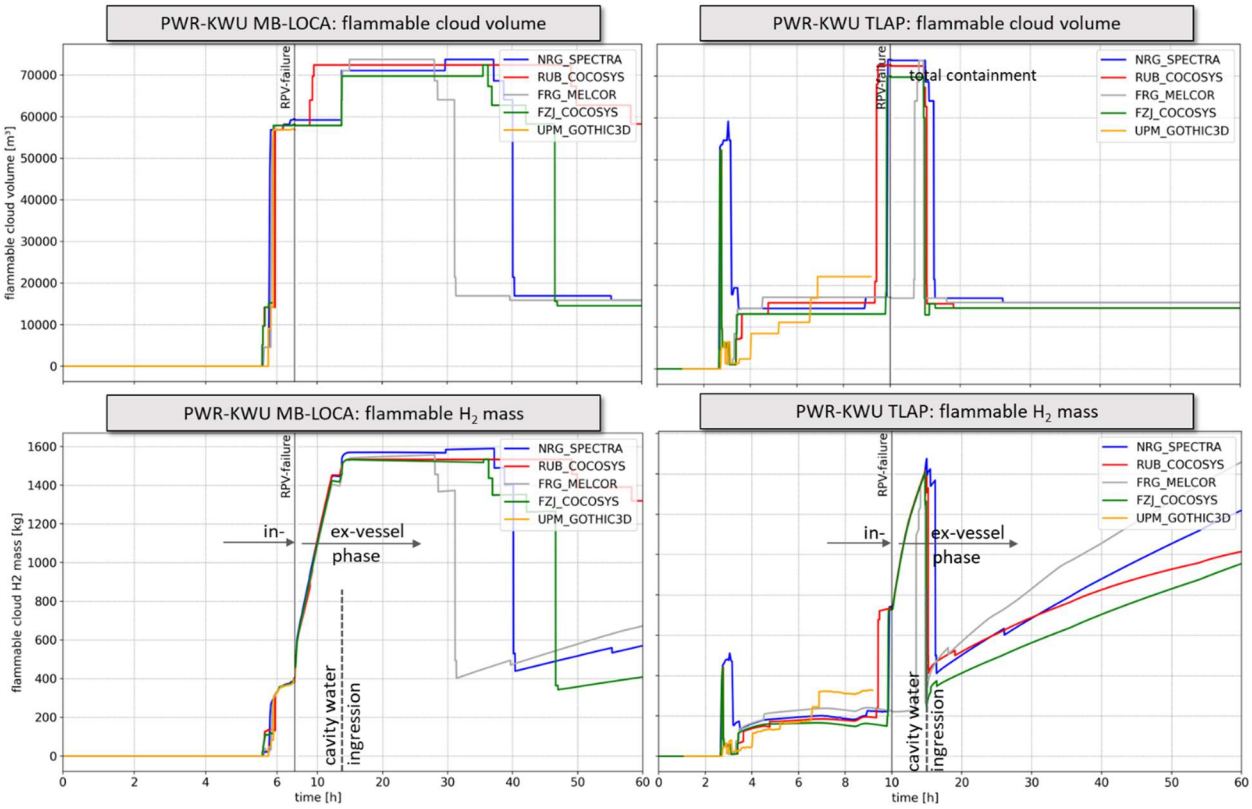

Figure 6. Evolution of the flammable cloud volume and H_2 mass for the PWR-KWU sequences

The simulations consistently show, that without any hydrogen mitigation measures, the containment atmosphere always has pockets where an ignition and flame propagation could occur. Further, the mass of combustible hydrogen increases with time due to the ongoing MCCI, see Figure 6 bottom. This emphasizes the need for combustible gas control hardware to protect the containment integrity.

In conclusion, the verification of the nodalization transfer and analyses of the unmitigated reference cases confirmed the general comparability of the input decks and simulation results, but also highlighted visible differences in the combustion risk in terms of mixture flammability. These findings need to be considered for the on-going assessment of the effect of different mitigative measures and be substantiated by 3D and CFD models. Consequently, to enable a common conclusion based on different code results, the approach considered is to involve the reference cases and evaluate a relative impact of the mitigative action instead of comparing absolute values.

5. LESSONS LEARNED AND FUTURE WORK

Even though the methodology was developed based on the experiences of the SARNET-II and SAMHYCO-NET generic containment benchmark [8], and the results discussed before already indicate a general comparability, several hurdles were encountered within the AMHYCO project up to now.

The generic containment definitions are based on a unique approach starting from a 3D CAD geometry. Nevertheless, the conversion of this database into input decks for different codes architectures (with different input requirements) caused ambiguities. Furthermore, the definition of the gas mass sources injected into the containment introduces additional uncertainties - as example the specification of an injection table in terms of mass flow rate and temperature or enthalpy does not necessarily yield the same simulation result. Only a systematic assessment and comparative evaluation of a comparably simple scenario helped to identify and clarify these issues.

Additionally, not all codes have the same capabilities to model plant -specific details, such as the sump water ingress to the cavity, require a dedicated implementation in different codes. One such example is the sump water ingress to the cavity in PWR-KWU after erosion of the Biological Shield by the core melt. Such an event requires a dedicated implementation in different codes. Another example is the representation of the core melt in a decoupled containment model, i.e. a heat source towards the atmosphere in case of dry conditions and towards the submerging water in case the melt is flooded. This is possible by a heated surface or by a volumetric energy source, each implementation possibility showing certain advantages and disadvantages. Finally, a common understanding of the material properties, especially of the concrete structures, was needed between the AMHYCO partners to obtain comparable simulation results.

These challenges required several iterations and incremental adaptions of both specification and input decks to reach the presented agreement of the containment simulations. This achievement now paves the way for a detailed and systematic assessment of the effectiveness or impact of mitigative measures like PAR, fan coolers, sprays, and filtered containment venting systems on the challenge of the flammability of the containment atmosphere.

The comparative evaluation of LP, 3D, and CFD models is expected to provide an insight into the control room view on the containment conditions based on the SA instrumentation and the full phenomenology and thus allow to review and extend the existing SAMGs and EOPs. Major advance in the Stare-of-the-Art is expected to result from the use of an extended PAR correlation that captures the effects of oxygen starvation and CO poisoning in the late phase as well as the application of new criteria for the H_2/CO combustion risk.

6. ACKNOWLEDGEMENTS

This project has received funding from the Euratom research and training programme 2019-2020 under Grant Agreement n°945057. The content of this paper reflects only the author's view. The European Commission is not responsible for any use that may be made of the information it contains.

GOTHIC™ incorporates technology developed for the electric power industry under the sponsorship of EPRI, the Electric Power Research Institute. This work was completed using a GOTHIC™ license for educational purposes provided by Numerical Advisory Solutions, LLC.

REFERENCES

[1] R. Liang, M. Sonnenkalb, M. Sangiorgi, and A. Bentaib, "Status Report on Hydrogen Management and Related Computer Codes," OECD/NEA, NEA/CSNI/R(2014)8, Jun. 2014.

[2] G. Jiménez *et al.*, "AMHYCO Project – Towards and Enhanced Accident Management of the H2/CO Combustion Risk," in *Proc. 19th International Topical Meeting on Nuclear Reactor Thermal Hydraulics (NURETH-19)*, 2022.

[3] L. E. Herranz and J. Fontanet, "Identification and analysis of accident sequences with posing high H2/CO combustion risk," AMHYCO, Deliverable D2.2, May 2023.

[4] A. Bentaib, "Critical assessment of key elements of combustible gases management in containment," AMHYCO, Deliverable D1.1, Jan. 2022.

[5] A. Desclaux, G. Nyrenstedt, M. Idir, N. Chaumeix, A. Bleyer, and A. Bentaib, "Turbulent flame speed of H2-CO-Air mixtures for conditions relevant to late phase accident scenario," in *Proc. 19th International Topical Meeting on Nuclear Reactor Thermal Hydraulics (NURETH-19)*, 2022.

[6] E.-A. Reinecke, A. Domínguez-Bugarín, and G. Nobrega, "Synthesis and outcomes of performed experiments and numerical results related to PAR behaviour," AMHYCO, Deliverable D3.2, Apr. 2023.

[7] M. Müer, J. Hoffrichter, C. Bratfisch, and M. K. Koch, "Analyses of the combustible gas release into the containment during a SBO and a SBLOCA scenario in a generic PWR using the code package AC2," in *Proc. 13th International Topical Meeting on Nuclear Reactor Thermal Hydraulics, Operation and Safety (NUTHOS-13)*, 2022.

[8] S. Kelm *et al.*, "Generic Containment: Detailed comparison of containment simulations performed on plant scale," *Ann. Nucl. Energy*, **vol. 74**, pp. 165–172, Dec. 2014, doi: 10.1016/j.anucene.2014.07.006.

[9] L. Serra, Domínguez-Bugarín, Vázquez-Rodríguez, and G. Jiménez, "Data for the generic containment analysis (PWR-W, PWRVVER, PWR-KWU)," AMHYCO, Deliverable D2.1, Dec. 2023.

[10] L. Serra *et al.*, "Development of a detailed 3D CAD model of a generic PWR-KWU containment as a basis for a better assessment of H2/CO combustion risk," in *Proc. European Nuclear Young Generation Forum (ENYGF'21), Tarragona, Spain*, 2021.

[11] The European Union Per Regulation 305/2011, "Eurocode 2: Design of concrete structures - Part 1-2: General rules - Structural fire design." Dec. 2004.

[12] J. M. Martín-Valdepeñas, M. A. Jiménez, F. Martín-Fuertes, and J. A. Fernández, "Improvements in a CFD code for analysis of hydrogen behaviour within containments," *Nucl. Eng. Des.*, **vol. 237**, no. 6, pp. 627–647, Mar. 2007, doi: 10.1016/j.nucengdes.2006.09.002.

[13] D. W. Stamps and M. Berman, "High-Temperature Hydrogen Combustion in Reactor Safety Applications," *Nucl. Sci. Eng.*, vol. 109, no. 1, pp. 39–48, Sep. 1991, doi: 10.13182/NSE91-A23843.

AMHYCO

Enhancing H_2 & CO Combustion Risk Management

Assessment of the Unmitigated Combustion Risk in within the AMHYCO Project

The 11th European Review Meeting on Severe Accident Research (ERMSAR2024)
KTH, Stockholm, Sweden, May 13-16, 2024

S. Kelm et al.

JÜLICH Forschungszentrum

This project has received funding from the European Union's EURATOM Horizon 2020 research and innovation programme. The content of this document reflects only the author's view. The European Commission is not responsible for any use that may be made of the information it contains.

Outline

- Introduction and Background
- Scenarios
- Methodology and Preparative Steps
- Assessment of Combustion Risk
- Lessons Learned and Future Work

Introduction and Background

- The European AMHYCO project aims at enhancing the understanding of H_2+CO combustion risk both in the in-vessel (H_2) and ex-vessel (H_2+CO) phases of a severe accident (SA) to substantiate / extend existing SAMGs.
- Supported by experimental work, a comprehensive analytical assessment of the containment behaviour is conducted to investigate:
  - the H_2/CO combustion risk, e.g., flammability or potential of flame acceleration,
  - the efficiency and options/timing of individual mitigative measures, including PARs, FCVS, or spray systems activation.
  - and the equipment and instrumentation survivability and 'operators/control room view' on the containment status.

➢ For the European PWR designs:
KWU (Germany), W (French + Westinghouse) and VVER.

➢ *In this talk: focus on methodology,*
illustrated by PWR-KWU as example, similar efforts for the other designs

Introduction and Background - Project Structure

WP1
- SAMG/EOP
- equipment survivability
- existing approaches

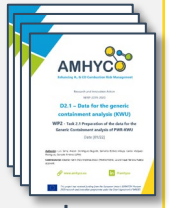

WP2
- GenCont database
- bounding accident sequences

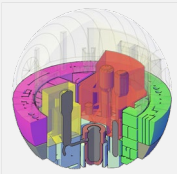

WP3
- H2/CO combustion and recombination characteristics

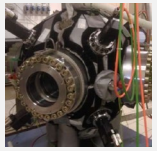

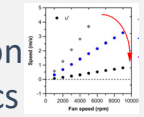

WP4

LP / System codes
(most penalizing scenarios from WP2)

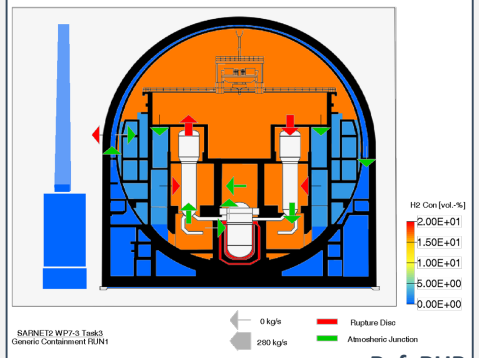

Ref: RUB

GOTHIC-3D
(Selected transients)

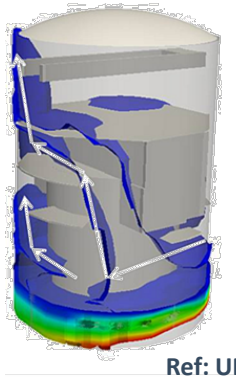

Ref: UPM

CFD
(Selected compartments)

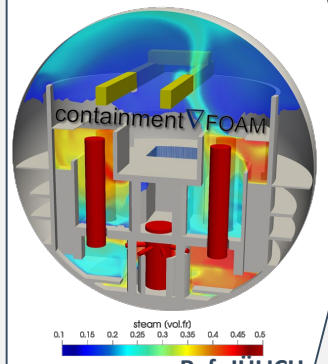

Ref: JÜLICH

- **Task 4.1:** Derive and implement extended correlations/parametric models
- **Task 4.2-3:**
  - 3 Containments: **PWR-KWU**, **PWR-W** and **PWR-VVER**
  - Consecutive analysis chain LP → 3D → CFD
- **Task 4.5:** Summarize Lessons Learned & Good Practices

Feb 2023 – Sept 2024

WP5



- containment response and risk assessment

Selected Severe Accident Scenarios

- Different sequences of the three PWR designs were simulated with
  - different system codes and hypotheses, including the nodalization schemes used,
  - different initiating events and involve diverse engineered safety features and SA management measures,
  - different release locations and flow path into the containment.

➢ The simulations were screened regarding the prevailing combustion risk to identify bounding scenarios for the detailed analysis of the containment response.

  - A Loss of Coolant Accident (LOCA) characterized by a comparably early core damage and a large H_2 release, resulting in flammable conditions in the containment with a potential of flame acceleration.
  - A Station Blackout (SBO) / Total Loss of AC Power (TLAP) sequence, which results in a delayed core damage and release of H_2.

to enable assessment of PAR performance, spray / coolers, FCVS and late re-activation of the emergency cooling systems

Methodology

- The computational approach employed is based on the SARNET-II 'Generic Containment' benchmark series and its continuation in the frame of SAMHYCO-NET.
- Though a code-to-code benchmarking is explicitly not objective of the work, a certain consistency of the (LP, 3D and CFD) codes models and results is required to obtain a quantitative database for further assessment and extension of SAMG

	PWR-KWU	PWR-W	PWR-VVER
System codes	COCOSYS 3.1 (RUB) MELCOR 2.1 (Framatome) SPECTRA 23-12-0000 (NRG) COCOSYS 2.4 (FZJ)	ASTEC (JSI) ASTEC v2.2 (IRSN) MELCOR 2.2_r2023.0 (CIEMAT)	MELCOR 1.8.6_RL_2011 (Energorisk)
3D codes	GOTHIC8.3 Q.A (UPM)		
CFD codes	ANSYS FLUENT (IRSN)	ANSYS FLUENT (NRG) containmentFOAM (FZJ)	

Methodology

- To obtain a quantitative database for further assessment and extension of SAMG
  - a consecutive analysis chain including LP, 3D and CFD codes and models is employed and
  - a certain consistency of the (LP, 3D and CFD) codes models and results is required
- Generic Containment nodalisation schemes were derived from 3D CAD models to generate a consistent and freely usable data basis
- e.g. PWR-KWU:

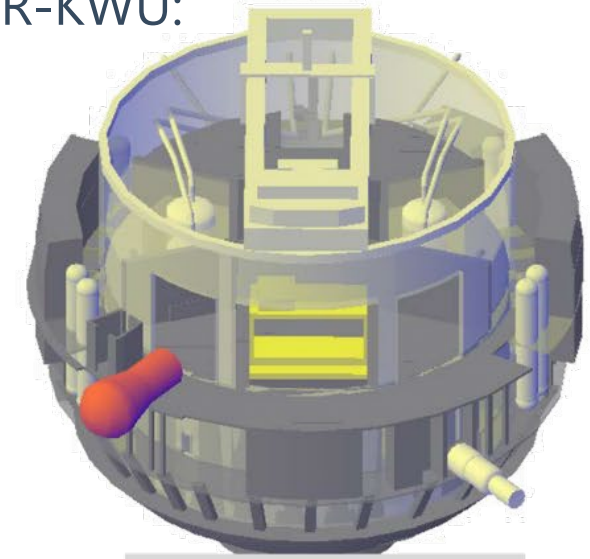

detailed CAD model

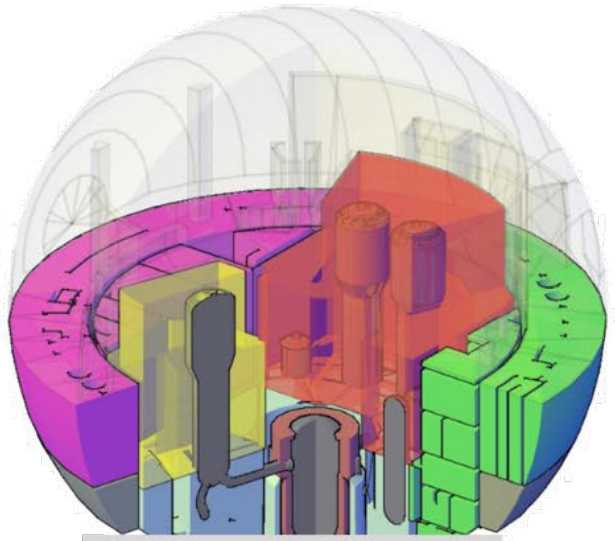

derived LP nodalisation

Table 3. PWR-KWU: Junctions between control volumes

LP Junction	ID	Start Zone	Target Zone	Circular [m²]	Start Elev. [m]	Target Elev. [m]	Horiz. Length [m]	Vert. Length [m]	Loss coef ζ_R [-]	dP [mbar]
DRAIN	J-3-2-01	DUCT	SUMP	1	6.4	6.4	1	0.5	2	100
FLAP	J-6-2-01	ANN-E	SUMP	0.25	6.75	6.75	1.7	0.5	1.5	50
FLAP	J-7-2-01	ANN-W	SUMP	0.25	6.75	6.75	1.7	0.5	1.5	50

Table 5. PWR-KWU: Heat structures

Structure ID	Composition	Type	Left Side	Right side	Area (m2)	Thickness (m)	Elevation (m)	Height (m)
CAV-01	CONCRETE	WALL	CAVITY	ADIABATIC	357.48	0.347	-1.31	7.62
CAV-02	CONCRETE	WALL	CAVITY	SUMP	951.32	0.700	-1.90	10.80

Table 6. PWR-KWU: PAR layout

Zones	PAR type	Number of PARs	PAR Elevation [m]
CAVITY	-	0	-
SUMP	FR-960	4	+8.0
DUCT	FR-1500	4	+10.0
SG-N	FR-1500	2	+12.0
	FR-960	3	+16.0
SG-S	FR-1500	2	+12.0
	FR-960	3	+16.0
ANN-E	FR-1500	2	+13.0
	FR-960	2	+13.0
ANN-W	FR-1500	2	+13.0
	FR-960	2	+13.0

documented LP nodalisation

Preparative Steps – Input Deck Verification

- The way of extracting and documenting the nodalization scheme still requires a ‘translation’ into different code input deck structures as they have deviating input requirements.
  - Potential ambiguities in the interpretation of the data.
  - Different verification steps to assess the input decks and ensure consistent use of the database:
    - (1) Nodalisation characteristics: (structure mass, surface area and volume)
      - identified deviations were understood and are considered as justifiable.
    - (2) Comparative assessment of the reference scenario

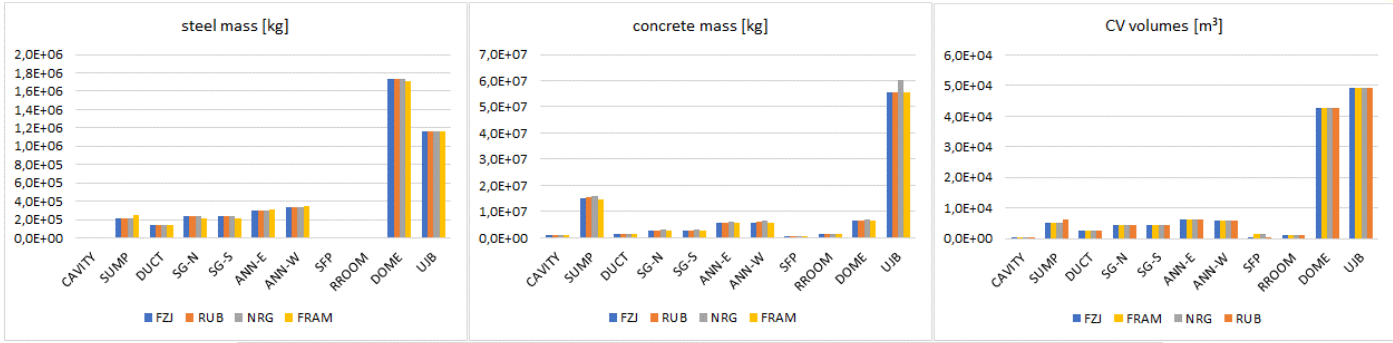

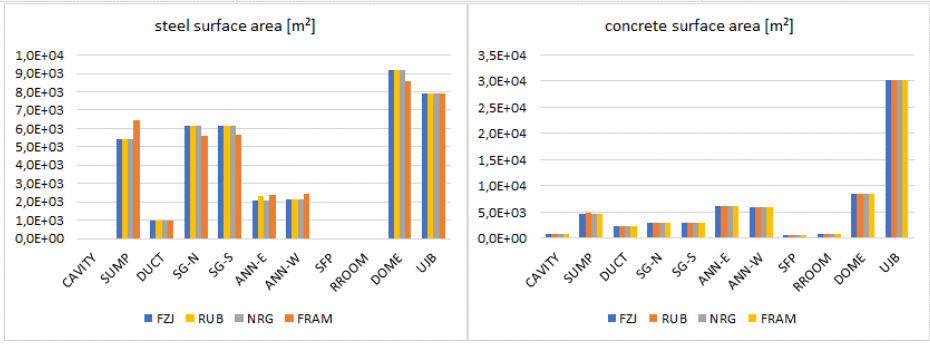

Preparative Steps – Comparative Evaluation

- Pressure evolution for the unmitigated PWR-KWU MB LOCA and TLAP sequences

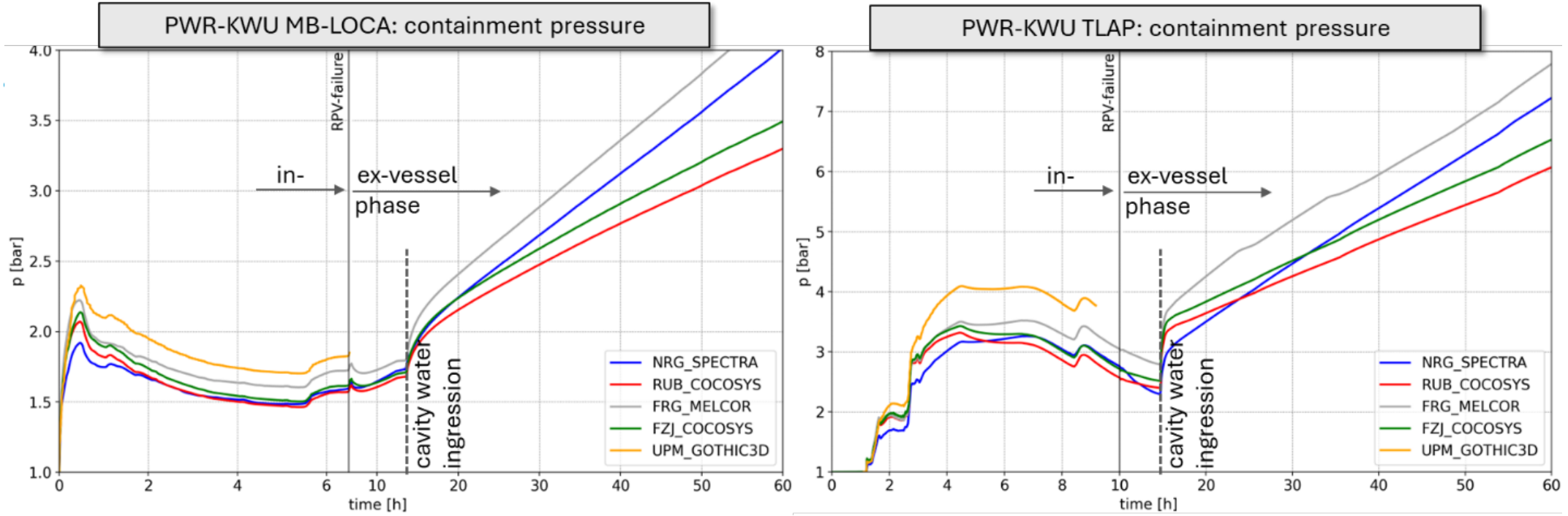

  - Generally consistent among the codes for the early accident phase, increasing spread (as expected) for the late ex-vessel phase when sump water ingression leads to the cavity flooding.

Assessment of Combustion Risk

- The usually employed conservative approach to replace the CO by an equivalent amount of H_2 and to employ the established flammability limits of H_2 is employed as first approach:
  - $x_{H2}^{LFL} \geq 0.037 + 0.011 x_{H2O} - 4.16 \cdot 10^{-5} (T - 373)$
  - $x_{H2}^{UFL} \leq 0.772 - 1.087 x_{H2O} - 2.71 \cdot 10^{-4} (T - 373)$
  - $x_{Inert} \leq 0.63 + 3 \cdot 10^{-4} (T - 373)$
- To avoid this simplification, within AMHYCO WP3, refined criteria are developed which consider the flammability and potential of flame acceleration for a H_2+CO mixture and explicitly for late phase conditions i.e. low O_2 and high dilutant concentrations

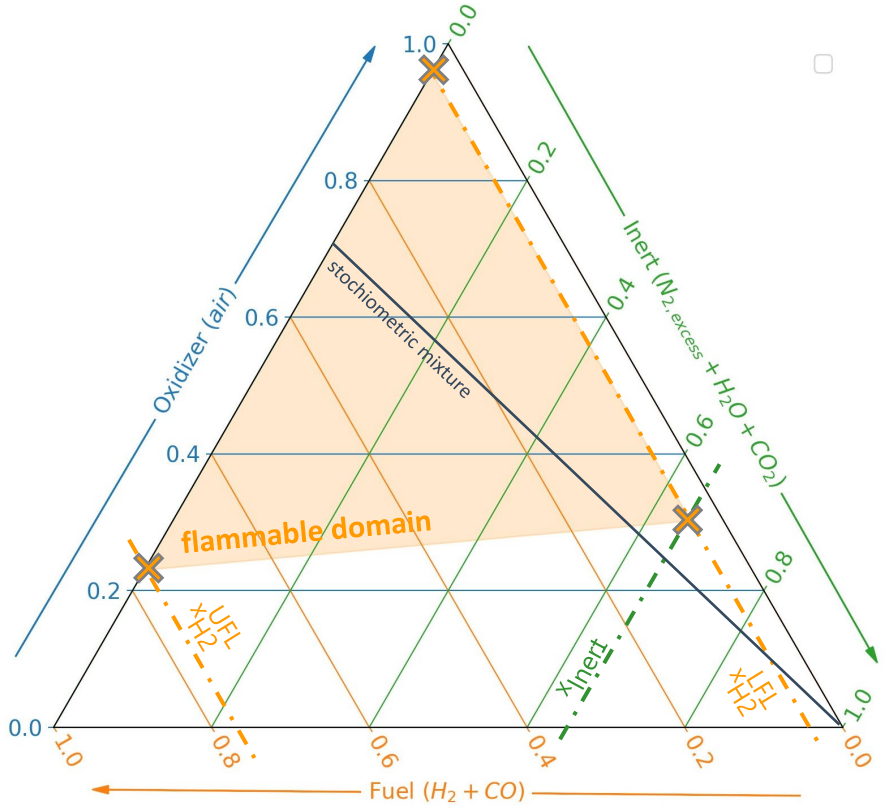

Assessment of Combustion Risk

- Mixture flammability in the dome for the unmitigated PWR-KWU sequences

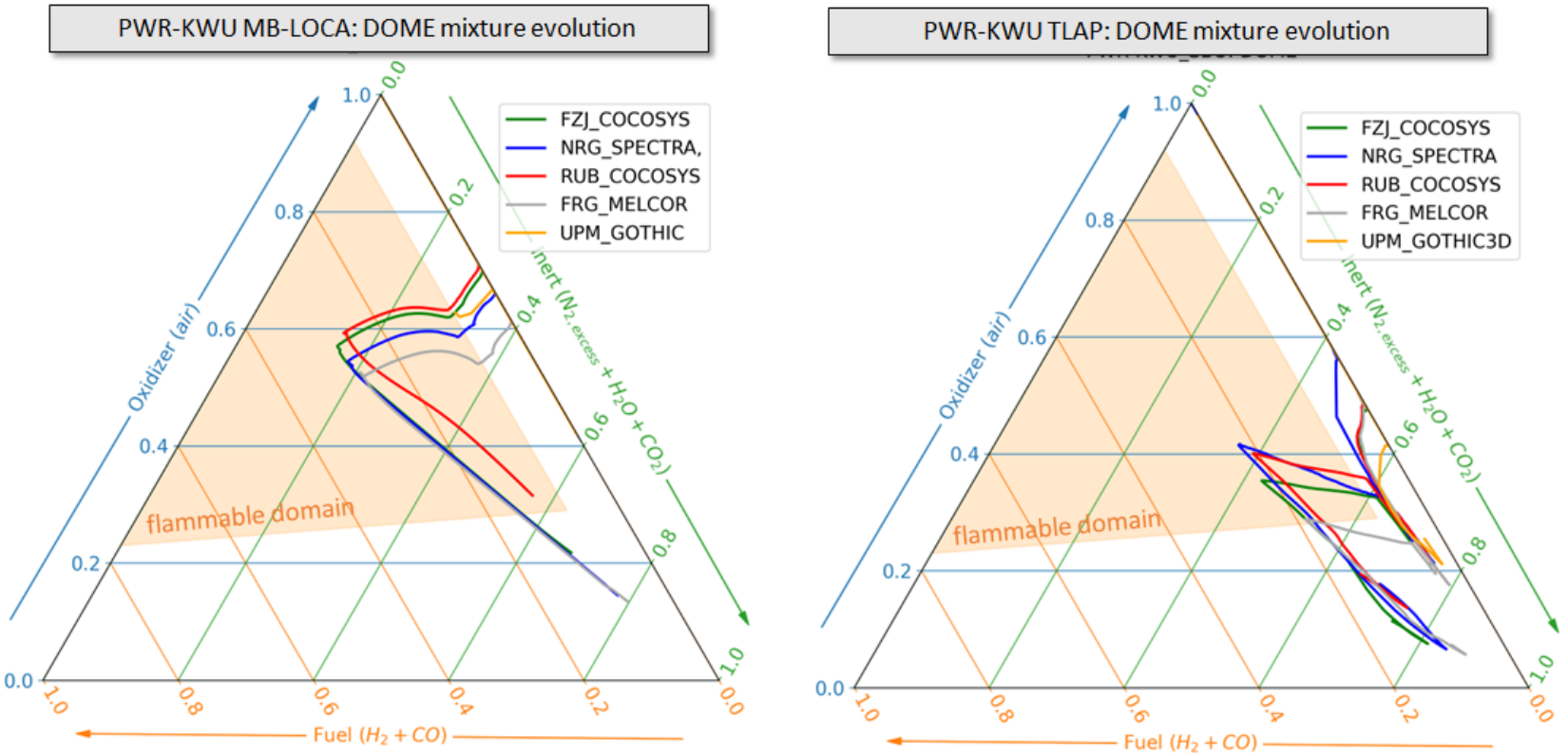

- Generally, well comparable mixture evolution

Assessment of Combustion Risk

- Evolution of the effective flammable H_2 volume and mass, integrated over all control volumes unmitigated PWR-KWU sequences
  - Consistent prediction for formation, but spread in the late phase re-inertization
  - Local heterogeneities motivate closer look with 3D methods
  - Without combustible gas control hardware mass of combustible H_2 increases with time
  - ➢ To be assessed considering different mitigative measures

➢ Differences motivate "relative evaluation"

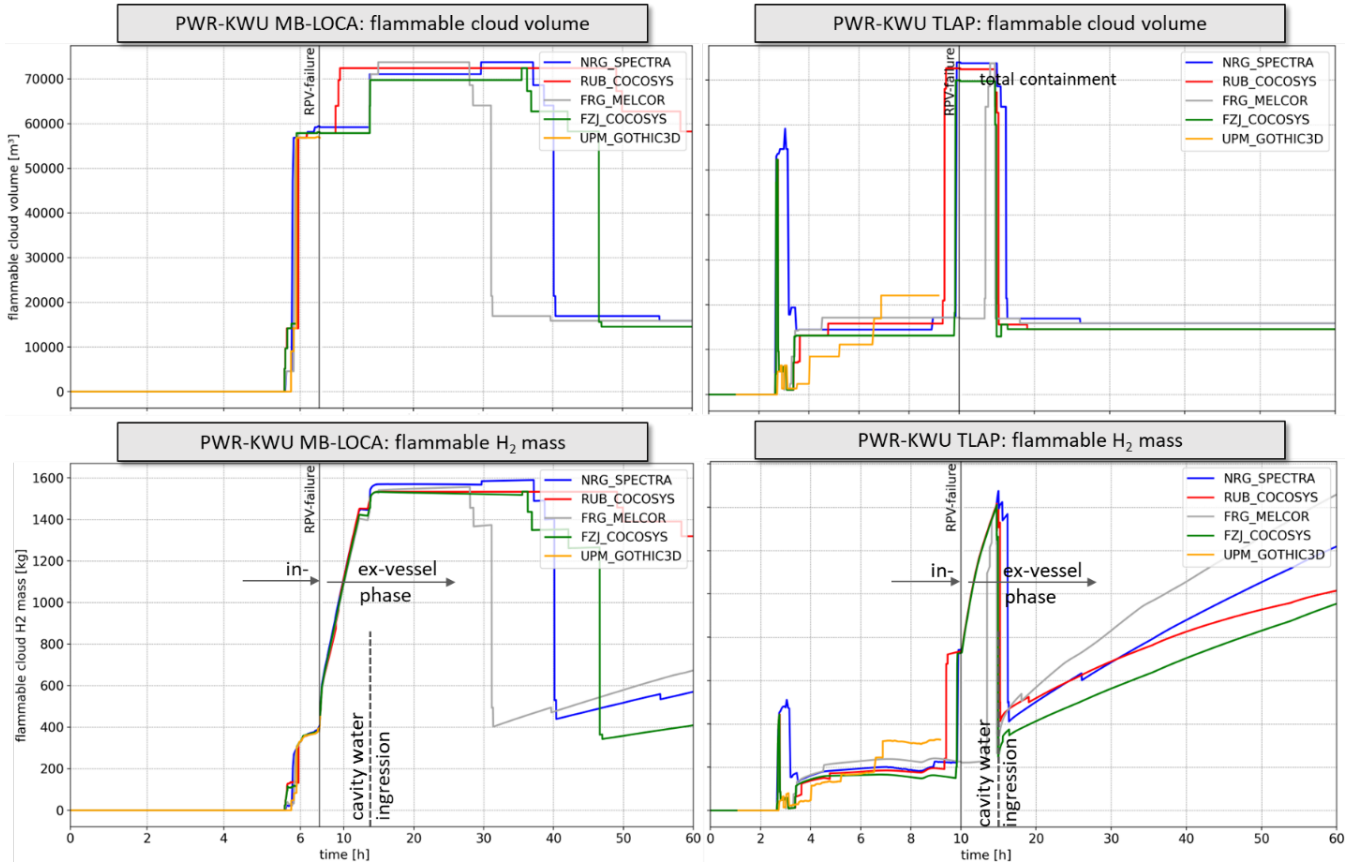

Assessment of Combustion Risk - Outlook

- "relative evaluation" for PWR-KWU sequences – e.g., effect of PAR system capacity

PWR-KWU MB-LOCA: average H_2 concentration

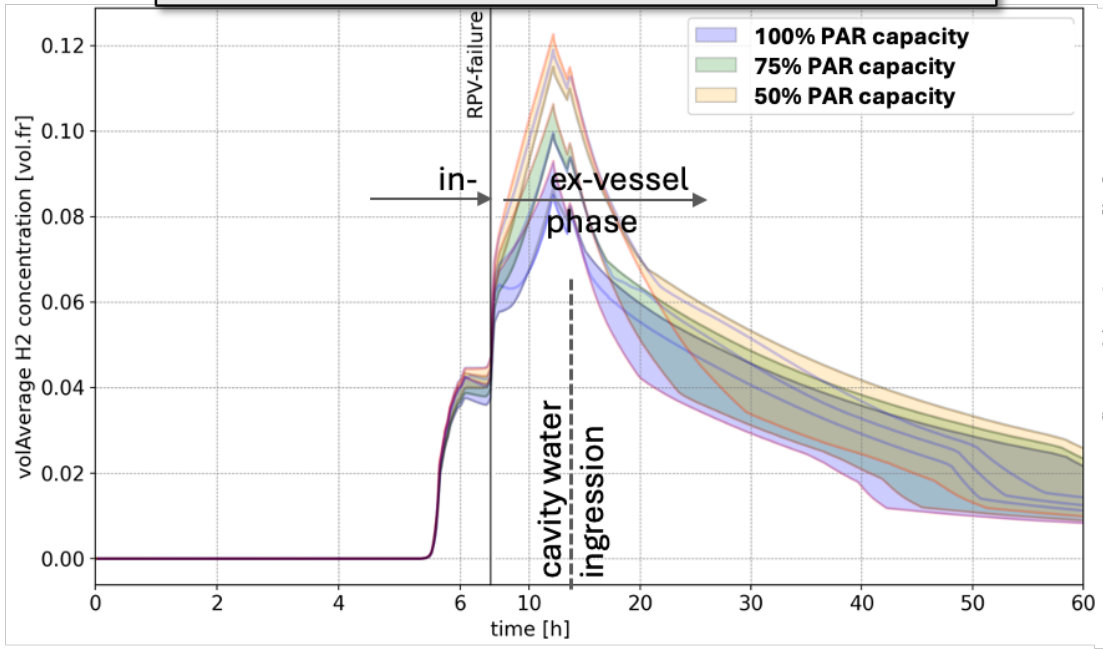

PWR-KWU MBLOCA: flammable H_2 mass

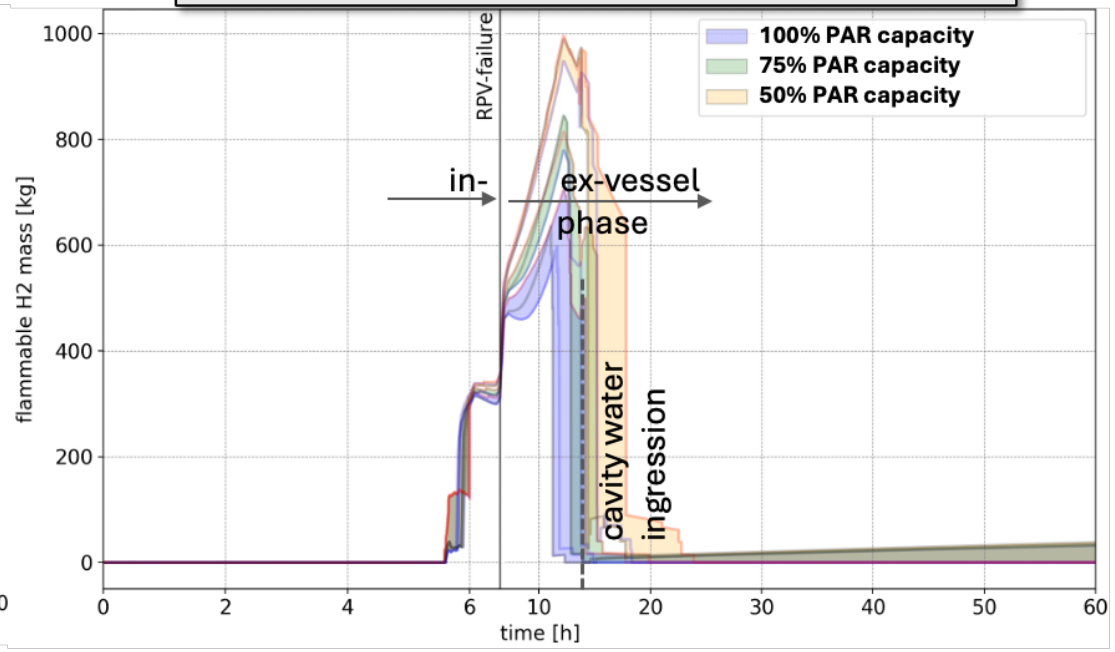

- Ongoing work, to be presented @NUTHOS
- 3D / CFD code analyses to identify 3D effects on H_2/CO distribution

Lessons Learned

- Unique and established ‘generic containment’ approach still required conversion into code input and model requirements.
  - ➢ Ambiguities and ‘interpretation bias’
- Uncertainties from derivation of the gas mass and energy sources from full system models for containment-only models, e.g.:
  - specification of injection tables in terms of mass flow rate and temperature OR spec. enthalpy
  - treatment on heat and mass release during MCCI
- Not all codes have the same capabilities to model plant-specific details. Dedicated implementations and verification exercises are needed for e.g., the sump water ingress to the cavity, extended PAR correlations
- A common understanding of the material properties, especially of the concrete structures, was needed between to obtain comparable simulation results.

➢ Several iterations and incremental adaptions of both specification and input decks to reach the presented agreement of the containment simulations.

Summary & Outlook

- Comprehensive simulation matrix and consecutive analysis chain
- Evaluation and conclusion on unmitigated reference cases
  - ✓ Verification of implementation of nodalisation and injection tables
  - ✓ Implementation of combustion risk assessment methodology
  - ✓ Identification of relevant aspects for further detailed studies
- Evaluation of mitigated scenarios
  - PAR performance in the late phase (& at high pressure)
  - Relative impact of spray/fan coolers or FCVS activation and timing on combustion risk
  - Survivability of equipment and instrumentation
  - Assessment of 'operators view'

➢ Database for improvement of SAMG (→WP5)

➢ Lessons-Learned for analyses of late phase with different codes

Thank you
Connect with us for more information:

gonzalo.jimenez@upm.es

http://amhyco.eu

@amhyco



HEAT REMOVAL TO LARGE WATER POOLS – MACROSCOPIC MODELLING OF MICROSCOPIC PHENOMENA IN THE SIMULATION CODE AC²/COCOSYS

C. Spengler, D. Iliev, I. Bakalov*, D. Eschricht, D. von der Cron
Gesellschaft für Anlagen und Reaktorsicherheit
Schwertnergasse 1, 50667 Cologne, Germany
* Kurfürstendamm 200, 10719 Berlin, Germany
claus.spengler@grs.de; dimitar.iliev@grs.de; ivan.bakalov@grs.de;
dandy.eschricht@grs.de; daniel.vondercron@grs.de

ABSTRACT

The work presented here describes the latest progress in modelling devoted to the simulation of heated water pools with AC²/COCOSYS and discusses the benefits and limitations of the pursued macroscopic approach. In the safety concepts of advanced nuclear power plants, the (temporary) decay heat removal from the reactor core to large water pools, which may be located inside or outside the containment, is provided for the prevention of postulated incidents and accidents and mitigation of their consequences. Examples include passive primary circuit cooling by heat exchangers immersed in a containment water pool, external containment cooling of small modular reactors, the in-vessel melt retention concept, and the cooling of core melt in an ex-vessel core catcher as included in reactor designs such as the EPR or VVER-1200. When analysing accident scenarios in plants equipped with the abovementioned safety systems, the code must deal with significant heat-up of large water pools. Temperature stratifications may form and have an impact on containment thermal hydraulics and other processes such as fission product transport. The software package AC² is being developed by GRS for the simulation of all relevant phenomena during normal operation, anticipated operational occurrences, design basis accidents, and design extension conditions (including core melting) in nuclear power plants. The objective of the AC² lumped-parameter code COCOSYS is to simulate all relevant phenomena and processes in the containment using a numerically fast macroscopic modelling approach. In the paper at hand, three major modelling concepts are addressed: First, the modelling of combined liquid/gas-flow junctions to consider a vertical subdivision of the pool into several COCOSYS zones is discussed. In addition to that, an extended model range for heat transfer between hot structures and water, including now nucleate boiling, film boiling and corresponding transition regimes is described. Finally, a simplified ‘plume’ approach to model an efficient upward heat transfer due to boiling is given. The newly implemented models are validated against experiments focused on heating of water in large pools (THAI SMR and PKL SACO experiments); preliminary post-test calculation results are outlined. Moreover, the new models for heat removal into water-filled containment zones are applied in test calculations using the core catcher model in COCOSYS for the simulation of core melt retention and long-term melt cooling in the event of design extension conditions in NPP with EPR. Based on the experience made with the macroscopic modelling approach, conclusions are drawn for further potential or needs of improvements. These conclusions could be beneficial also for the developers and users of other simulation codes with a similar approach to containment thermal hydraulics.

KEYWORDS
water pool, decay heat removal, boiling, stratification, COCOSYS

1. INTRODUCTION

Safety concepts of advanced nuclear power plants (NPPs) include large water pools for the (temporary) decay heat removal from the reactor core. Small modular reactor (SMR) concepts such as NuScale [1] and NUWARD SMR [2] feature containments submerged in large water pools. In-vessel melt retention (IVMR) concepts such as for VVER-1000 [3] consider flooding the reactor pressure vessel (RPV). Furthermore, the cooling of core melt with an ex-vessel core catcher submerged in water is included in reactor designs such as the EPR and VVER-1200 [4].

When analysing accident scenarios in plants equipped with the abovementioned safety systems by means of numerical simulations, the computer codes must cope with significant heat-up of large water pools and its accompanying phenomena: Temperature stratification and pool boiling may occur and have a significant impact on the thermal hydraulics in a containment, RPV or core catcher. Other processes such as fission product transport may also be very sensitive to changes in the thermal hydraulics of the system. The software package AC^2 [5] is being developed by GRS for the simulation of all relevant phenomena during normal operation, anticipated operational occurrences, design basis accidents, and design extension conditions (including core melting) in nuclear power plants. The objective of the AC^2 lumped-parameter code COCOSYS [6] is to simulate all relevant phenomena and processes in the containment using a numerically fast macroscopic modelling approach. To achieve this goal the effect of microscopic phenomena in large water pools such as departure of nucleate boiling, local film boiling, and turbulent convective flows must be modelled on a macroscopic level. In this paper, newly developed strategies used in COCOSYS to simulate the effects of microscopic phenomena in large water pools on a macroscopic level are presented.

2. NEW MODELLING FEATURES IN AC^2/COCOSYS

As AC^2/COCOSYS is a best estimate lumped-parameter system code for the simulation of all containment phenomena relevant for the assessment of reactor safety issues, it aims to cover as many physical behaviours of the complex geometries and flow patterns in the containment as possible. Due to the continuously expanding requirements for reliability and accuracy, it is necessary to continuously improve the capabilities of the code while still preserving the fast nature of the simulations.

The following COCOSYS improvements regarding heat removal to large water pools are presented in the next subsections: First, the modification of the code to allow for the simulation of zones completely filled with liquid water is described. Thereafter, an overview of the recently extended heat transfer models is given. Finally, the simplified ‘plume’ approach to model an efficient upward heat transfer in a pool due to boiling is explained.

2.1. Simulation of completely filled COCOSYS zones

One of the basic models to describe the evolution of the thermal hydraulic state of a COCOSYS zone (= computational node) allows for the co-existence of liquid water together with an atmosphere in non-equilibrium state. Here, it had originally been assumed that the liquid would cover only a smaller volume part of the zone and the larger part was occupied by the atmosphere. For the simulation of mass exchange with neighboured COCOSYS zones, it was necessary to use special atmospheric flow junctions to account for the gas flow as well as dedicated drainage or sump balance junctions for the liquid flow. Due to inherent limitations of the atmospheric junction model, this approach led to problems with simulation cases in which the liquid level inside a zone increased significantly so that a complete filling of the COCOSYS zone was reached. To circumvent the problems, the user had to revise his data set and modify the nodalisation of the respective containment parts so that a complete filling of zones was avoided. In view of future application needs, this approach was considered no longer acceptable.

For this reason, a possibility to allow the complete filling of COCOSYS zones with water via the new junction type ATM_FULL was added to COCOSYS. This new junction type allows for both atmospheric and liquid flow through the same flow path. With this concept, it is possible to start a simulation with several connected, partially flooded zones which may become completely filled during the transient simulation. As indicated by the nodalisation scheme on the left-hand side of Fig. 1, each zone is initially filled with both liquid and gas. Consequently, an initial calculation phase is required to simulate the separation of gas and liquid across the whole pool (as shown on the right-hand side of Fig. 1) and the resulting levelling of the phase interface.

Especially when simulating advanced reactor concepts with large water pools for which a sub-nodalisation is required, such an initial calculation phase would lead to undesired additional computational effort. Therefore, a new feature has recently been implemented in COCOSYS which allows to start a simulation with completely flooded zones right from the beginning. To show the benefits of this feature, in Fig. 1 the required computational time step sizes for the old COCOSYS version (allowing only the initialisation of partially flooded zones) are compared with those of the new development (fully flooded zones initialised right at the start of the simulation). A simple rectangular three-dimensional geometry of the water pool of height ~ 20 m was used in this academic test case. The levelling phase requiring many small time steps is no longer needed and during that time span, a numerically stable solution is obtained saving computational time. Furthermore, this new feature allows the use of a wider range of parameters for the numerical accuracy while still achieving a numerically stable simulation.

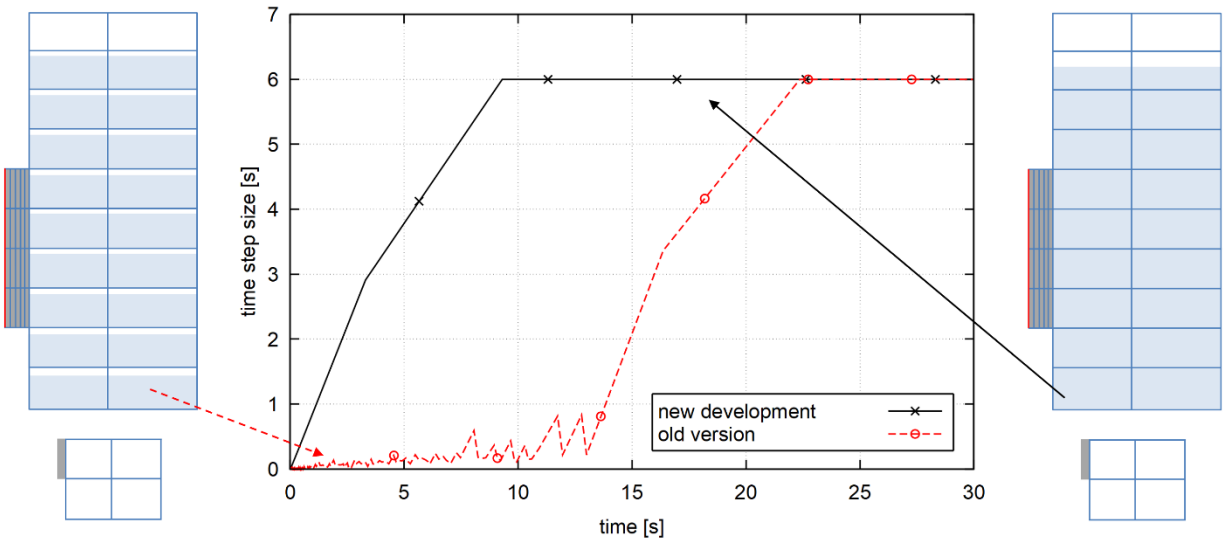

Figure 1. Time step sizes with former initialisation with partially flooded zones in the old code version (left) and for the fully flooded zones in the new development (right).

2.2. Heat transfer models at hot structures under water

Heat transfer from hot structures to water is a complex physical phenomenon which highly depends on the excess temperature ΔT, which is the difference between the temperature of the structure surface T_{wall} and the saturation temperature of water $T_{saturation}$. For low ΔT, the heat flow is dominated by free convection. If the structure is further heated up, nucleate boiling starts to set in. For even larger ΔT, dynamically distributed local areas of the surface are in contact with pure vapour during transition boiling. If the Leidenfrost point is passed, film boiling will take place. This behaviour is usually represented by

Nukiyama's boiling curve – see Fig. 2. Although the formation of vapour bubbles and the departure of those bubbles from a hot surface are local phenomena depending on the surface roughness, the purity of the water, and the local temperatures of the structure, the effect of the different heat transfer modes can be modelled accurately on a macroscopic scale.

For the modelling of the heat transfer due to predominantly free convection, in COCOSYS the interpolation curve [7] on the basis of tabulated data available in open literature is used:

$$\alpha_{\mathrm{CONV}} = \frac{e^{0.0048(\ln(Ra))^2+0.1166\ln(Ra)+0.3292}\cdot\lambda}{l_{\mathrm{char}}} \tag{1}$$

The heat transfer coefficient is denoted with α_{CONV}, Ra stands for the Rayleigh number, λ is the thermal conductivity of water and l_{char} is a characteristic length describing the convection loop size. This interpolation curve is based on a large number of physical experiments and is validated for $Ra < 10^{12}$. For larger Ra further validation is needed. More information on (1) can be found in [7].

Nucleate boiling is modelled in COCOSYS for water in contact with polished steel using the Rohsenow correlation [8]:

$$\dot{q}'' = \left(\frac{\Delta T\cdot\lambda}{0.0132\cdot h_{fg}\cdot\eta}\right)^3 \eta h_{fg}\sqrt{\frac{g(\rho_l-\rho_v)}{\sigma}} \tag{2}$$

The nucleate pool boiling heat flux is denoted with $\dot{q}''$, h_{fg} stands for the enthalpy of vaporisation, η for the dynamic viscosity of water and g is the gravitational acceleration constant. The surface tension at the liquid-vapour interface is denoted with σ, ρ_l stands for the density of the liquid water and ρ_v for the density of vapour.

To extend the capabilities of COCOSYS to transition boiling and film boiling, the correlations for film boiling of Berenson [9] and Bromley [10] were recently implemented:

$$\alpha_{BER} = 0.425\left(\frac{\lambda^3\Delta h\rho_v g(\rho_l-\rho_v)}{\eta\Delta T\sqrt{\frac{\sigma}{g(\rho_l-\rho_v)}}}\right)^{0.25} \tag{3}$$

$$\alpha_{BRO} = 0.62\left(\frac{\lambda^3\Delta h\left(1+\frac{0.4\Delta T c_p}{\Delta h}\right)^2\rho_v g(\rho_l-\rho_v)}{\eta\Delta TD}\right)^{0.25} \tag{4}$$

The heat transfer coefficients for the Berenson and Bromley correlations are denoted with α_{BER} and α_{BRO} respectively, λ represents the thermal conductivity, Δh is the enthalpy of vaporisation, η is the dynamic viscosity of the water vapour, c_p is the specific heat capacity of the vapour and D represents the hydraulic diameter of the system.

To describe the transition from free convection to nucleate boiling as well as from nucleate boiling to film boiling, a continuous and smooth interpolation was used.

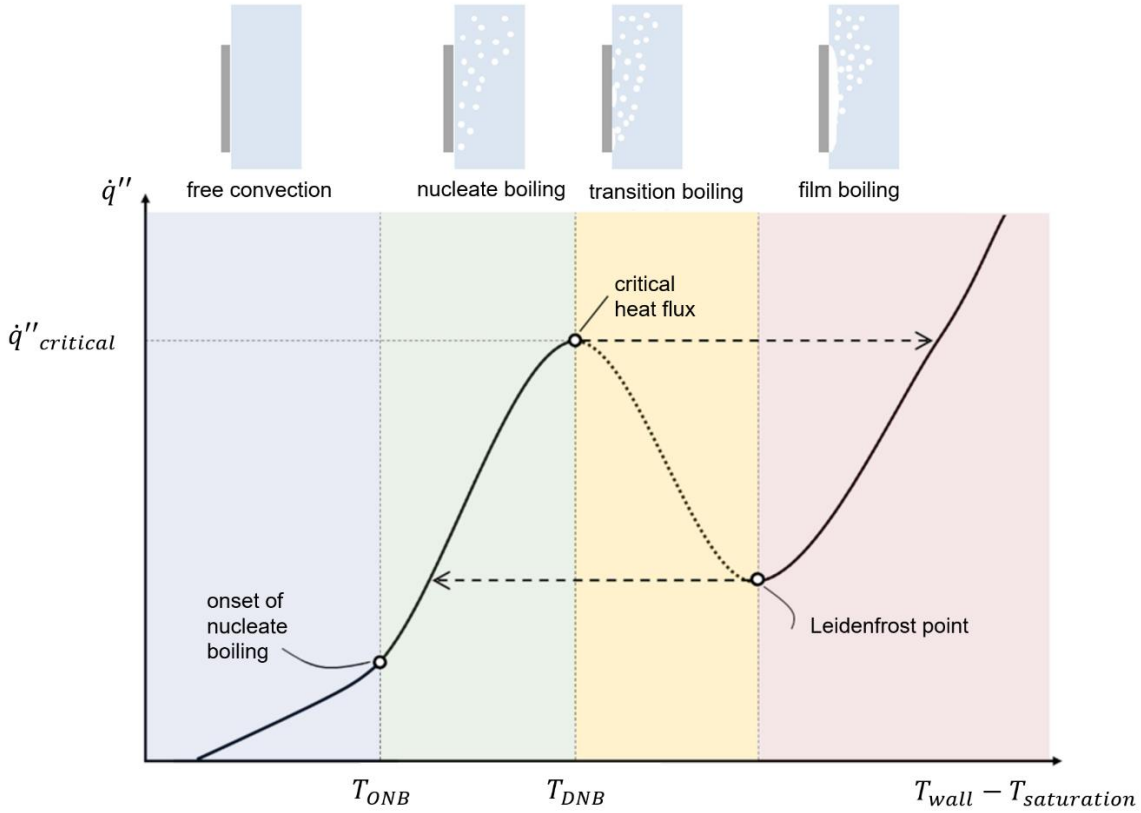

Figure 2. Sketch of Nukiyama's boiling curve.

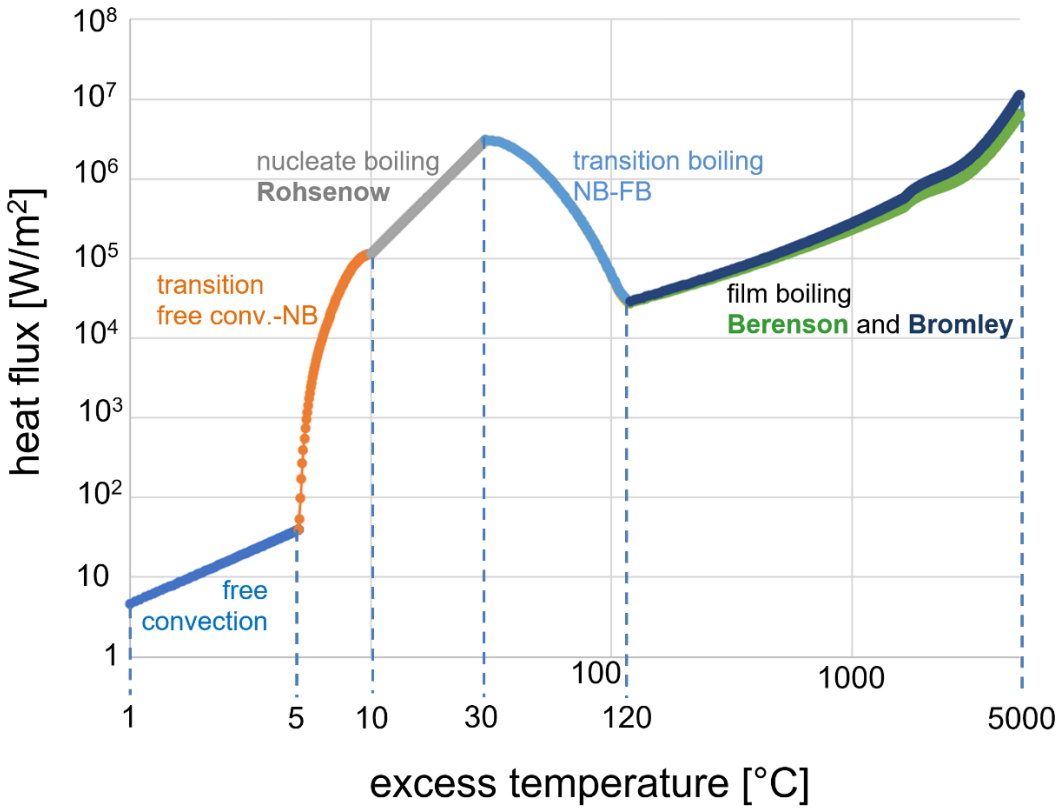

Figure 3. Nukiyama's boiling curve simulated in COCOSYS.

The utilisation of the abovementioned correlations describing the effects of the microscopic phenomena of nucleate boiling and film boiling on a macroscopic level enables COCOSYS to simulate complex transients with vast changes in structure temperatures. The simulation of Nukiyama's curve in COCOSYS for specific conditions as a function of the excess temperature is visualised in Fig. 3.

2.3. Emulation of effective upward heat transfer due to local boiling – the plume model

During nucleate boiling, transition boiling and film boiling due to heat transfer from a hot structure into water, liquid is vaporised near the structure surface. In an open pool with no major obstructions, the vapour bubbles will rise upwards. To accurately capture effects such as the superheating of liquid water near the heated surface leading to vaporisation or the transport of vapor bubbles through a pool of largely subcooled water, a simulation code would usually require a two-phase (liquid-vapour) modelling approach. Such an approach would vastly increase the complexity of the governing equations and significantly increase the computational time.

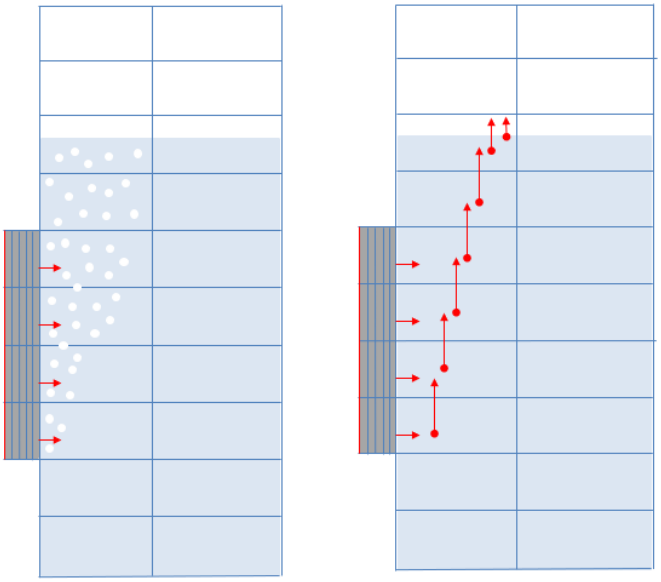

Figure 4. Vapour bubbles produced due to a heated structure (left) and graphical visualisation of the plume model in COCOSYS (right). Red arrows indicate transport of thermal energy due to the assumed vapour plume path.

A simplified approach to cope with two-phase phenomena is to model the effect of the rising vapour bubbles without accurate representation of the single bubbles or even the volume that they occupy in each zone. Concerning the upwards motion of the bubbles in a pool, a plume model has recently been implemented in COCOSYS to simulate the effect of boiling in large water pools – Fig. 4. When heat transfer from a hot structure into a flooded zone would lead to superheating, the excess heat is instantaneously (i.e., during the same COCOSYS time step) transported upwards into the neighbouring zone above (Fig. 4, right). The heated zone can thus stay in liquid state. If – as a consequence – the neighbouring zone above would be superheated now, the thermal energy is transported further upwards. When the thermal energy reaches the zone containing the free surface of the pool, the excess heat above local saturation temperature is finally used for vaporisation. Thus, the effect of the rising thermal energy is modelled on a macroscopic level without microscopic level resolution (of the bubbles). The path of the heat transport (emulating the bubble plume) is calculated automatically by COCOSYS taking into account the topology and geometry of the

zones and junctions modelled by the user. This simplified innovative approach leads to very fast computations as only a few checks for superheating are performed and there is no increase in the numerical complexity of the time-advancement algorithms used to calculate the mass and energy flows.

3. VALIDATION

In order to validate the COCOSYS code including the newly developed features described in section 2, two experiments were simulated with COCOSYS: The THAI SMR2 experiment performed by Becker Technologies aims to study the heat transport due to free convection in large water pools comparable in size to the ones used in SMR concepts [11]. The PKL SACO P1.1 experiment, conducted at the Framatome PKL test facility as part of the PASTELS program, is intended for the investigation of the heat removal capacity of the safety condenser (SACO) as a function of the water pool level.

3.1. THAI SMR2

In the THAI SMR2 experiment, a large containment simulator (CS) is submerged in a large water pool. To heat it up, steam is injected at the top of the CS. The heated structures of the CS are then cooled from the outside by the water pool. In the experiment, a stable temperature stratification in the water pool was observed, see Fig. 5 bottom right. Discretising the water pool into 18 zones with an inner and outer column shows that the trend of the temperature profiles was qualitatively captured in the COCOSYS simulation. However, the temperature stratification in the simulation is visibly smaller than in the experiment. Most likely, the high degree of freedom for the motion in a 3d water pool could not be adequately captured using the coarse grid shown in Fig. 5 left. To achieve a more accurate representation of the experimental temperatures, further studies are required: in future investigations the effects of finer grid discretisation and the role of a few relevant model parameters (convective heat transfer at large Ra, hydraulic resistances of virtual junctions inside open pool geometries, parameters for emulation of thermal convection between neighboured zones) should be considered, as well as updated knowledge from the THAI SMR test series.

3.2. PKL SACO P1.1

In the PKL P1.1 experiment, the safety condenser (SACO) is a heat exchanger integrated in a cylindrical steel vessel filled with water (water pool). The heat exchanger consists of a tube bundle with four vertical heat exchanger tubes that are completely submerged in the water pool. The SACO is connected to the secondary side of the steam generator of the PKL facility and is designed for passive decay heat removal from the reactor core.

In the COCOSYS simulations, the SACO tube bundle is subdivided into five vertical sections represented by five stacked heat conducting structures. The SACO steel vessel is modelled by six zones stacked vertically through the water pool, as shown in Fig. 6. The same figure shows a comparison of the preliminary COCOSYS calculation results versus experimental data both for the pool heat-up phase following the opening of flow through the SACO and phase A of the P1.1 experiment, starting at time point SOT (start of test). See the marking of the test phases over time in the top right of Fig. 6. In the experiment, a stable thermal stratification in the pool was observed during the heat-up of the water pool and was still visible in phase A (Fig. 6 bottom right). As can be seen, the thermal stratification in the SACO water pool is generally captured in the preliminary COCOSYS post-test simulation, albeit the temperature progression over time shows differences to the experimental data – especially for the lower zones of the pool (Fig. 6 top right). Similar to the THAI SMR2 experiment, a finer discretisation of the SACO vessel would most likely contribute to a better agreement of the calculation results with the measurement.

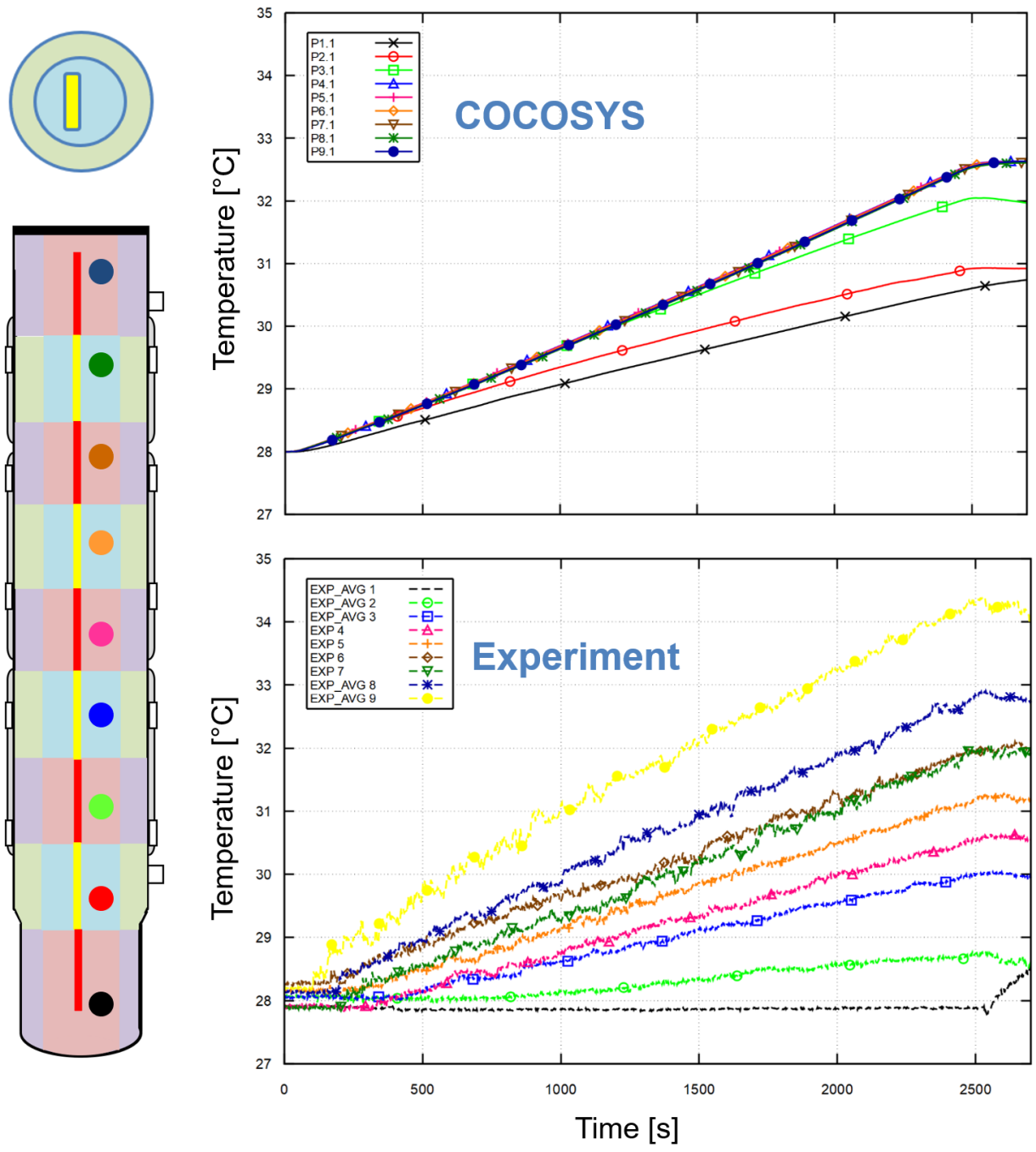

Figure 5. COCOSYS nodalisation with 18 zones for the water pool (left), COCOSYS simulated temperatures (top right) and measured temperatures (bottom right) for the THAI SMR2 experiment.

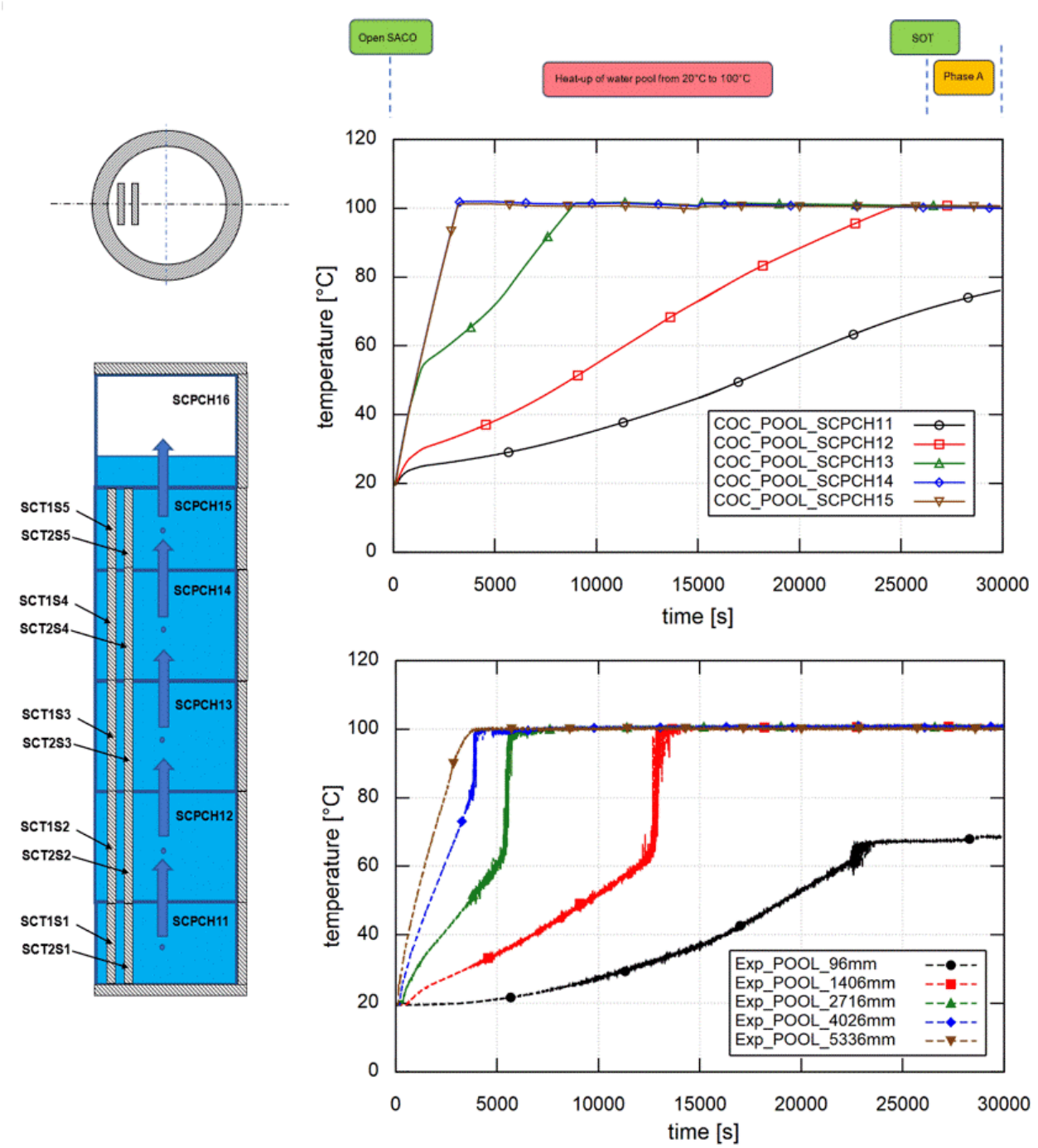

Figure 6. COCOSYS nodalisation with 6 zones for the water pool (left), water pool temperatures predicted by COCOSYS (right above), and pool temperatures measured in SACO P1.1 experiment (right below).

Steep temperature gradients measured in the experiments and visible in Fig. 6 (bottom right) are not adequately captured in the simulation. The impact of the SACO charge line on this phenomenon is currently not clear: The SACO charge line feeds the SACO tube bundle with steam during the experiment and parts of it pass through the pool and effectively heat the top volume of the water pool. This pipe was not modelled in the numerical study presented here.

4. TEST APPLICATION FOR THE SIMULATION OF AN EPR-TYPE CORE CATCHER

The effect of the plume-model (see section 2.3.) on the transport of thermal energy was also examined in a simplified model application for simulation of the core catcher in the European Pressurised Water Reactor (EPR). An important function of the core catcher is to ensure the decay heat removal from the corium pool through bottom and sidewall structures (plates) to the cooling water, which is supplied into the cooling channels beneath the bottom plate. The COCOSYS model of the core catcher spreading compartment with the water-cooled structures (bottom and sidewall plates) is presented in Fig. 7. Zone R1 represents the spreading compartment, where the corium spreading takes place. Zones R1a and R1b were introduced for modelling of the cooling channels underneath the bottom plate and behind the sidewall plate of the core catcher. The core catcher structures are subdivided into vertical (sidewall) and horizontal (bottom) plates, which are represented by single COCOSYS heat structures (HS-SIDE for sidewall and HS-BOT for bottom structure). After corium spreading, cooling water is passively supplied into the cooling channels beneath the bottom plate. Once the bottom cooling channels are filled with water, the water flows into the cooling channels behind the sidewall plate. This causes the water level in the channels to rise quickly. When the water level reaches the lower edge of the overflow, the water flows into the spreading compartment resulting in a flooding of the corium from the top.

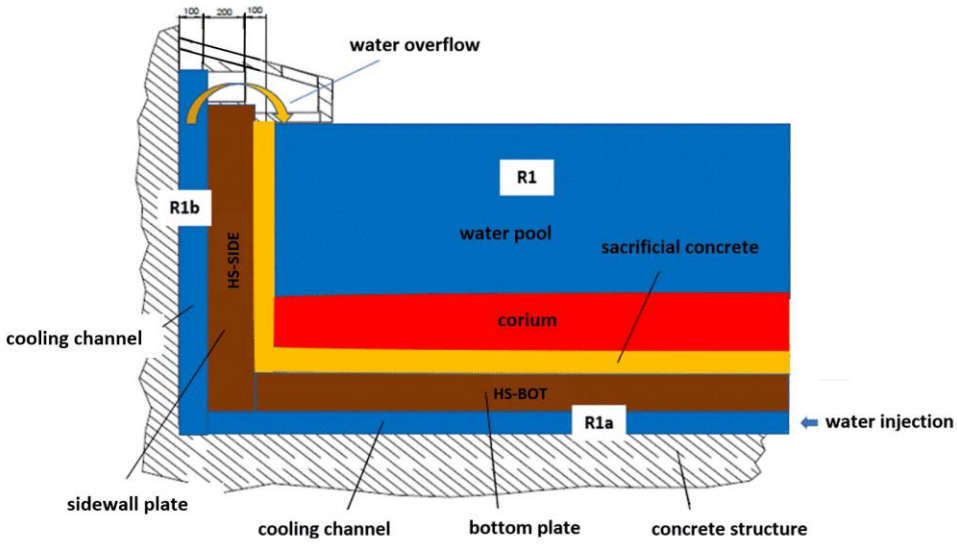

Figure 7. COCOSYS model of the core catcher spreading compartment with water-cooled steel structures (bottom and sidewall plates).

After the sacrificial concrete has been melted, the corium comes into contact with the water-cooled structures. In the test simulation, the water temperature in the cooling channels rises and reaches saturation temperature. Afterwards, boiling conditions are established leading to an intensive water evaporation both in the cooling channels and the spreading room. Fig. 8 shows a comparison of the water temperature as well as the saturation temperature in the cooling channel behind the sidewall plate for simulation cases with and without the plume-model. The comparison depicts that in the case without plume-model, the water

temperature in the cooling channels exceeds the saturation temperature at approx. 20 000 s, leading to unrealistic superheated conditions. In the case with plume-model, the excessive heat due to superheating in the water pool is effectively transported upwards and the water temperature in the cooling channel remains at saturation in the test calculation (green dashed line in Fig. 8).

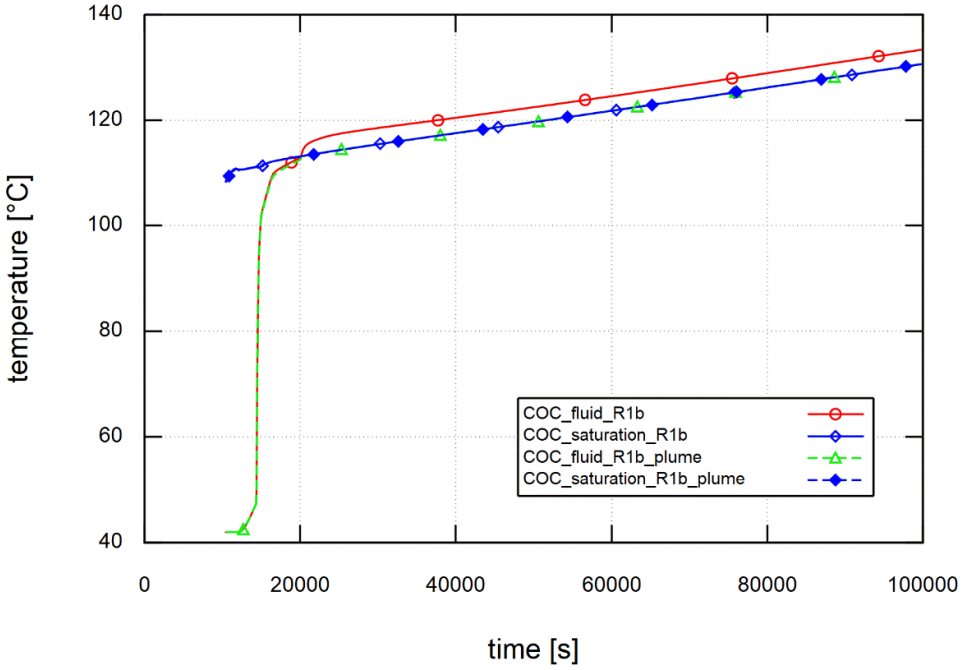

Figure 8. Fluid temperature and saturation temperature in the cooling channel behind the sidewall plate of the core catcher (with and without plume model).

5. CONCLUSIONS AND OUTLOOK

The work presented here describes the latest progress in modelling devoted to the simulation of heated water pools with AC²/COCOSYS and discusses the benefits and limitations of the pursued macroscopic approach.

The severe accident code COCOSYS was originally developed and validated for the simulation of atmospheric thermal hydraulics and the distribution of gas species, fission products, and aerosols inside the containment. For this purpose, the lumped-parameter concept as pursued in COCOSYS has several advantages for the user in comparison to more detailed approaches like methods based on CFD techniques, the most important of which is the gain in computational time in reasonable balance with remaining uncertainties and inaccuracies. However, the utilisation of large water pools inside the containment as part of safety concepts in many current Gen-3+ and SMR plant designs poses challenges to a containment code such as COCOSYS. The recent COCOSYS developments to meet these challenges are described in the paper at hand.

A first code extension of COCOSYS devoted to the handling of large water pools (the new junction type ATM_FULL) initially only allowed for the complete filling of COCOSYS zones during the problem time in an existing containment model. A necessary improvement of this feature was recently obtained, so that now it is possible to initialize a simulation with completely water-filled zones right at the start of the calculation, which results in a significant gain in computational time for the user. Furthermore, heat transfer models specific to the heating of water pools by hot structures are now available in COCOSYS. Large local heat transfer rates to the water phase at heat exchangers made it necessary to deal with efficient upward

transport of thermal energy inside the water pools due to two-phase effects which can hardly be simulated by COCOSYS on a microscopic level. For the emulation of this energy transport and release at the mixture level surface, the plume model was added. First test runs and preliminary validation calculations of the new model features show promising results. Simulations of water pool conditions including a heat-up to saturation, like in the PKL SACO P1.1 test, are possible with COCOSYS now, including the simulation of heat transfer during the transition between free convection and nucleate boiling at low excess temperatures. However, temperature stratifications in the experiments could so far not be simulated in full detail. For the case of the THAI SMR2 test, further studies are required on the effect of large Ra on convective heat transfer, grid nodalisation and the role of a few other relevant model parameters. For the case of the PKL SACO P1.1 test, most probably a more precise modelling of specific test conditions (regarding the impact of the steam charge line) is necessary.

Further analysis and developments are planned to continue improving on the capabilities of COCOSYS as a tool for fast simulations of large water pools in NPP containments, especially for SMR.

ACKNOWLEDGMENTS

The authors acknowledge the German Federal Ministry for the Environment, Nature Conservation, Nuclear Safety and Consumer Protection (BMUV) for the financial support of the projects RS1604 and RS1598 for the development of the COCOSYS code and the project 1501630 for the performance of THAI-SMR experiments. The PKL SACO P1.1 experiment was funded by the Euratom research and training programme 2019-2020 under Grant Agreement No. 945275.

REFERENCES

1. NuScale Power, L.L.C. (NuScale), *Status Report – NuScale SMR (NuScale Power, LLC)*. Status Report (2020). https://aris.iaea.org/PDF/NuScale-NPM200_2020.pdf. Accessed 22 December 2020.
2. EDF, *NUWARD SMR: Leading the way to a carbon-free world* (2023).
3. M. Jamet, C. Le Guennic, M. Buck, K. Rashkov, I. Ivanov, P. Kaleychev, A. Nieminen, S. Bajard, F. Fichot, J. Duspiva, J. Zdarek, G. Pascal, A. Grah, M. Sangiorgi, E. Alexandre, P. Grudev, P. Matejovič, N. Bakouta, V. Merkulov, I. Melnikov, L. Vyskocil, and D. Batek, *In-Vessel Melt Retention (IVMR): Analysis of a VVER-1000 NPP*, European Commission, Publications Office, Luxembourg (2016).
4. M. Fischer, "Core melt stabilization concepts for existing and future LWRs and associated R&D needs," in *NURETH-16, Chicago IL USA,* American Nuclear Society (ANS), Ed. (2015).
5. F. Weyermann, D. Eschricht, A. Wielenberg, T. Steinhoff, P. Schöffel, C. Spengler, and L. Lovasz, *AC² 2023.0 User Manual* (2023).
6. S. Arndt, S. Band, S. Beck, D. Eschricht, D. Iliev, H. Nowack, N. Reinke, C. Spengler, W. Klein-Heßling, M. Sonnenkalb, and G. Weber, *COCOSYS 3.2.0 User Manual* (2023).
7. B. Hüttermann, *Ermittlung einer universell anwendbaren Funktion für den konvektiven Wärmeübergang bei freier laminarer und turbulenter S trömung für verschieden geformte typische Sicherheitsbehälterstrukturen für den Bereich 1E-4 < Gr * Pr < 1E12*, Köln (1990).
8. W.M. Rohsenow, *A method of correlating heat transfer data for surface boiling of liquids*. Technical Report No. 5 (1951).
9. P.J. Berenson, *J. Heat Transf.*, **83**, 351 (1961).
10. L.A. Bromley, N.R. LeRoy, and J.A. Robbers, *Ind. Eng. Chem.*, **45**, 2639 (1953).
11. M. Freitag, E.W. Schmidt, B. von Laufenberg, and S. Gupta, "Experiments on Passive Heat Removal of Immersed Containments by Laminar and Turbulent Convection at very high Rayleigh Numbers," in *20th International Topical Meeting on Nuclear Reactor Thermal Hydraulics (NURETH-20),* American Nuclear Society (ANS), Ed. (2023).

HEAT REMOVAL TO LARGE WATER POOLS – MACROSCOPIC MODELLING OF MICROSCOPIC PHENOMENA IN THE SIMULATION CODE AC²/COCOSYS

C. Spengler, D. Iliev, I. Bakalov, D. Eschricht, D. von der Cron

May, 13-16, 2024 – Stockholm, Sweden

ERMSAR 2024



Short description of COCOSYS

$$AC^2 = AC^2_{ATHLET} + AC^2_{ATHLET\text{-}CD} + AC^2_{COCOSYS}$$

- COCOSYS is a lumped-parameter code developed by GRS and is part of the AC² software suite.

- More information on COCOSYS and the AC² software suite can be found in the AC² user area https://user-codes.grs.de/AC2

  or at the GRS website https://www.grs.de/en

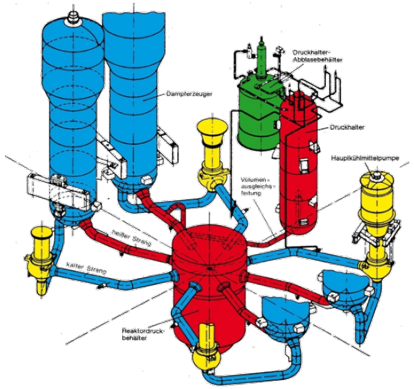

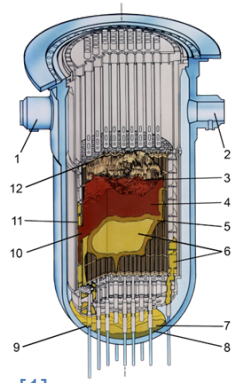

[1]

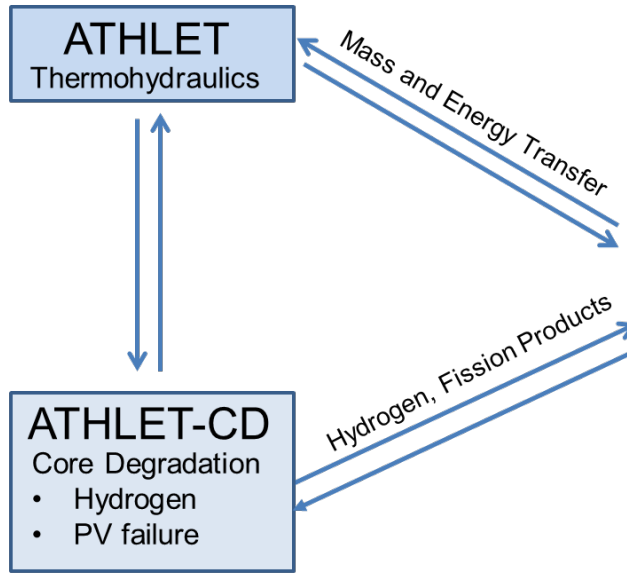

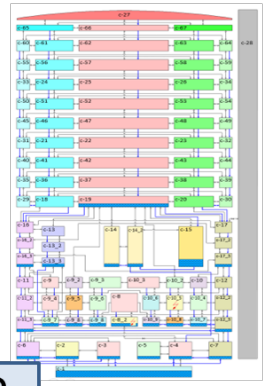

Heat removal to large water pools in modern NPP safety concepts: examples

Containment external cooling in SMR

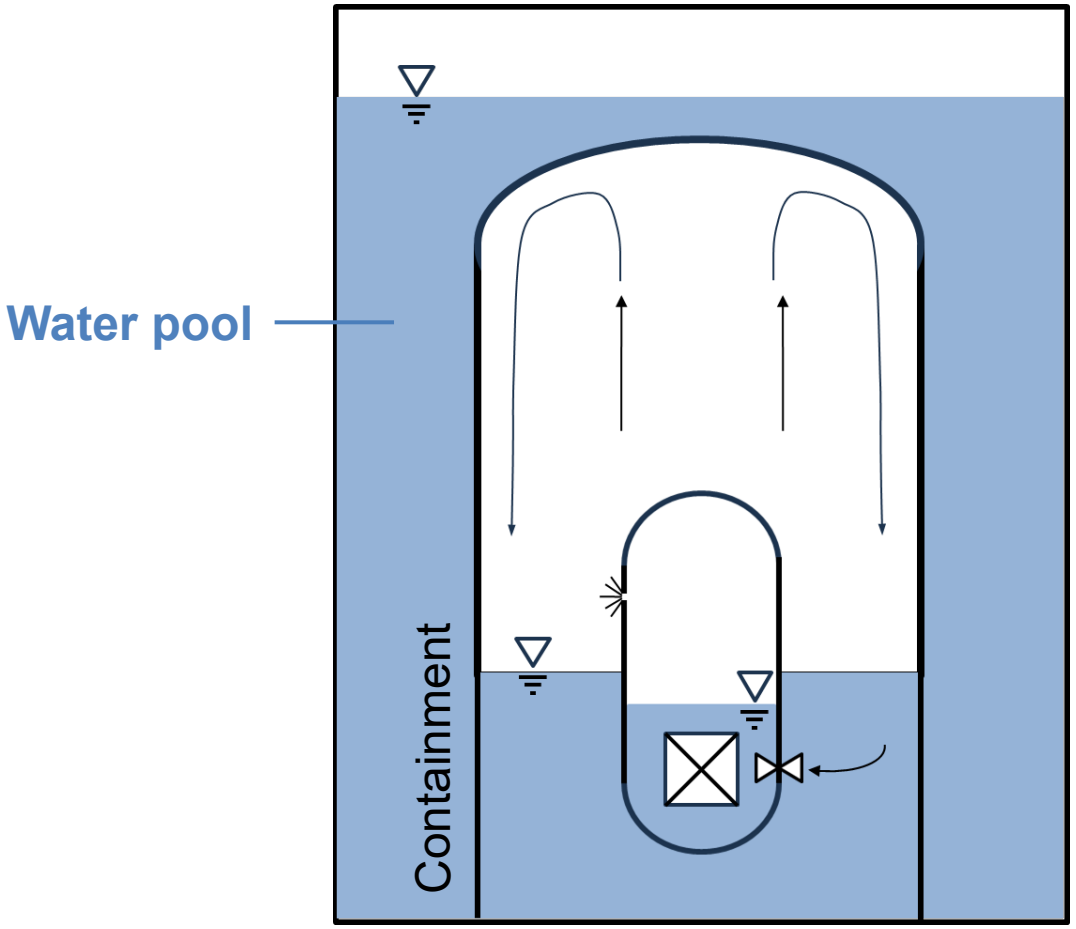

Natural circulation through emergency condensers attached to the RPV

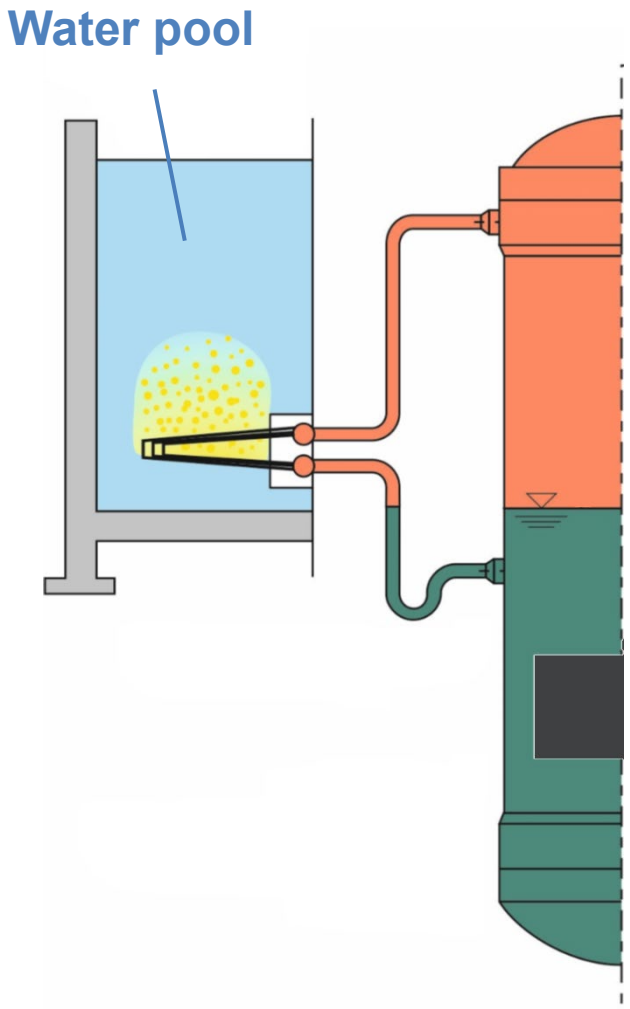

Representation of water pools in the non-equilibrium zone model in COCOSYS

- Two zone parts
  - **GAS**: atmosphere, T_{gas}
  - **FLUID**: sump (optional), T_{liquid}
  - Originally: $V_{liquid} < V_{zone}$
- Interaction at liquid surface
  - Heat and mass transfer (convection, condensation, evaporation, boiling)
- Heat transfer at structures attached to gas part and/or fluid parts
- **ATM_FULL flow junction** introduced in COCOSYS 3.0 allows complete filling of zones

Zone concept in COCOSYS thermal hydraulic module (THY)

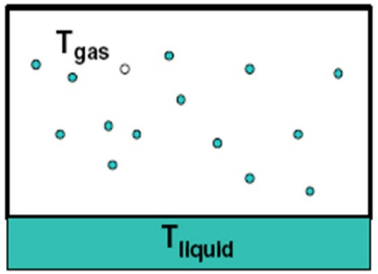

fog
steam +
non-condensable gases

liquid water

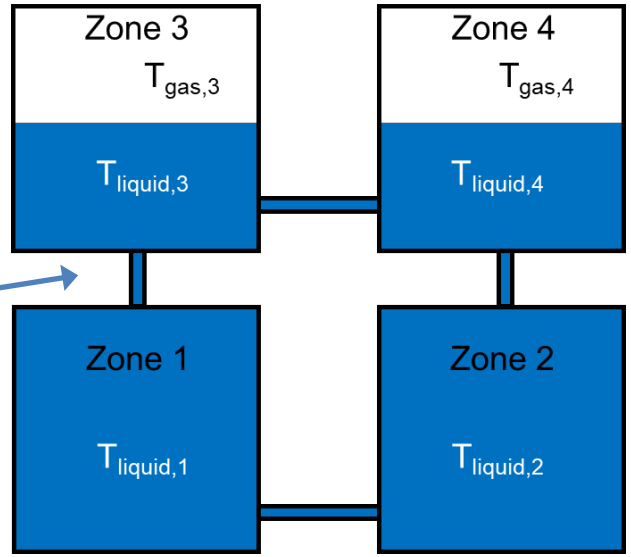

Subdivision of a heated water pool

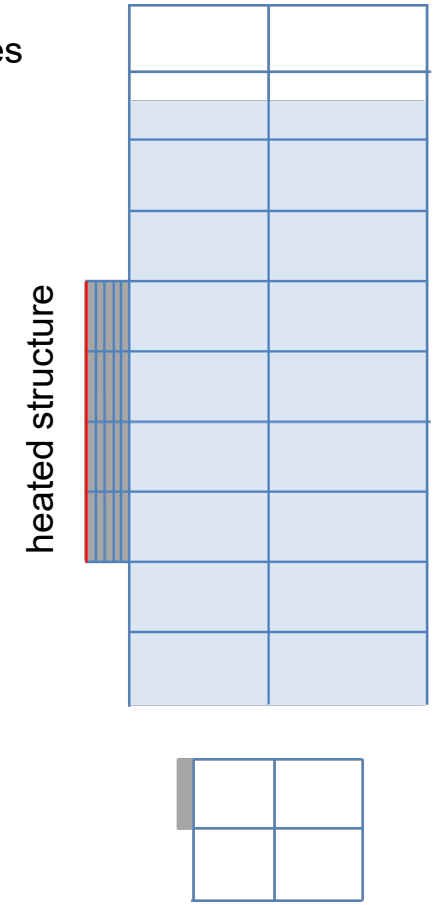

Heat transfer models at hot structures under water

- Heat transport in sumps in Gen. III and earlier NPPs can largely be modelled by accounting for free convection.

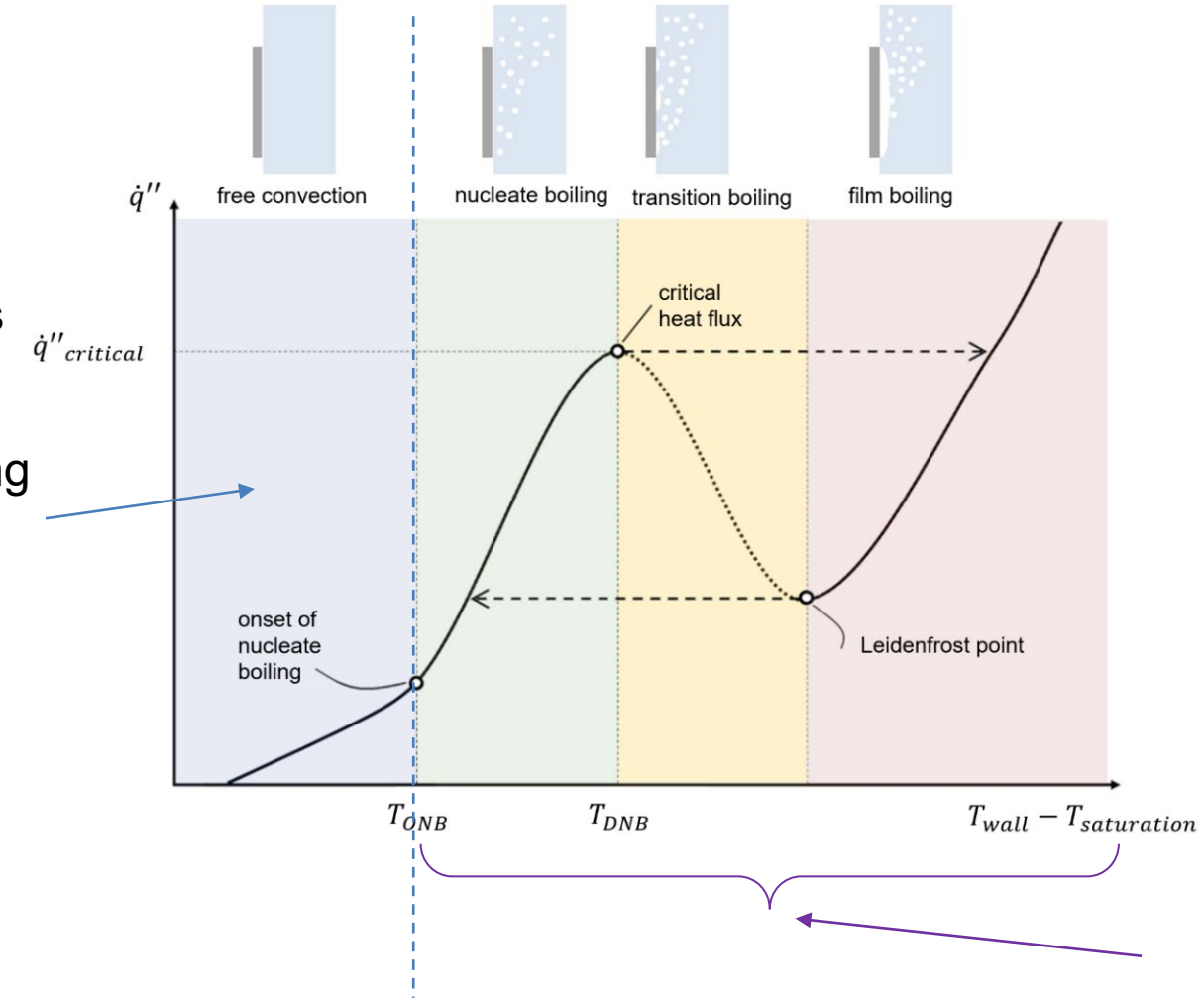

General form of the Nukiyama's boiling curve

- Large water pools in Gen. III+ and later reactor concepts including SMRs require in addition to take into account nucleate boiling, transition boiling and film boiling.

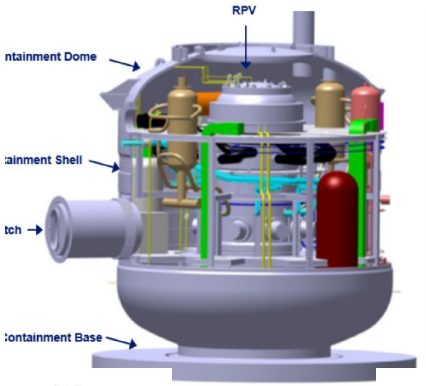

[2] NUWARD

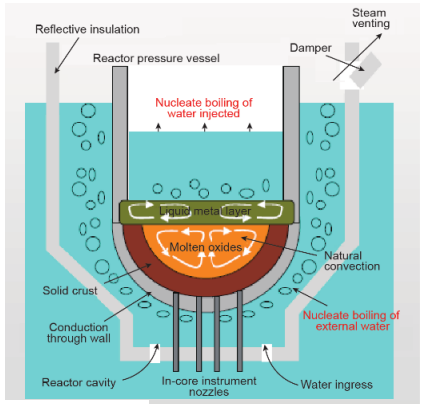

[3] APR-1400

- In order to improve the capabilities of COCOSYS without sacrificing numerical efficiency, macroscopic models were implemented to account for the heat transfer at higher excess temperatures.

Heat transfer models at hot structures under water (cont.)

- For free convection an interpolation based on a large number of experiments with $Ra < 10^{12}$ is used.
- For nucleate boiling, the Rohsenow correlation was implemented.
- For film boiling, the correlations of Berenson and Bromley are used for horizontal and vertical structures respectively.
- In the transition regimes between free convection and nucleate boiling as well as between nucleate boiling and film boiling, interpolations are used.
- Further work is planned to extend the capabilities of the code regarding the calculations of the critical heat flux and Leidenfrost point.

The Nukiyama's boiling curve in COCOSYS

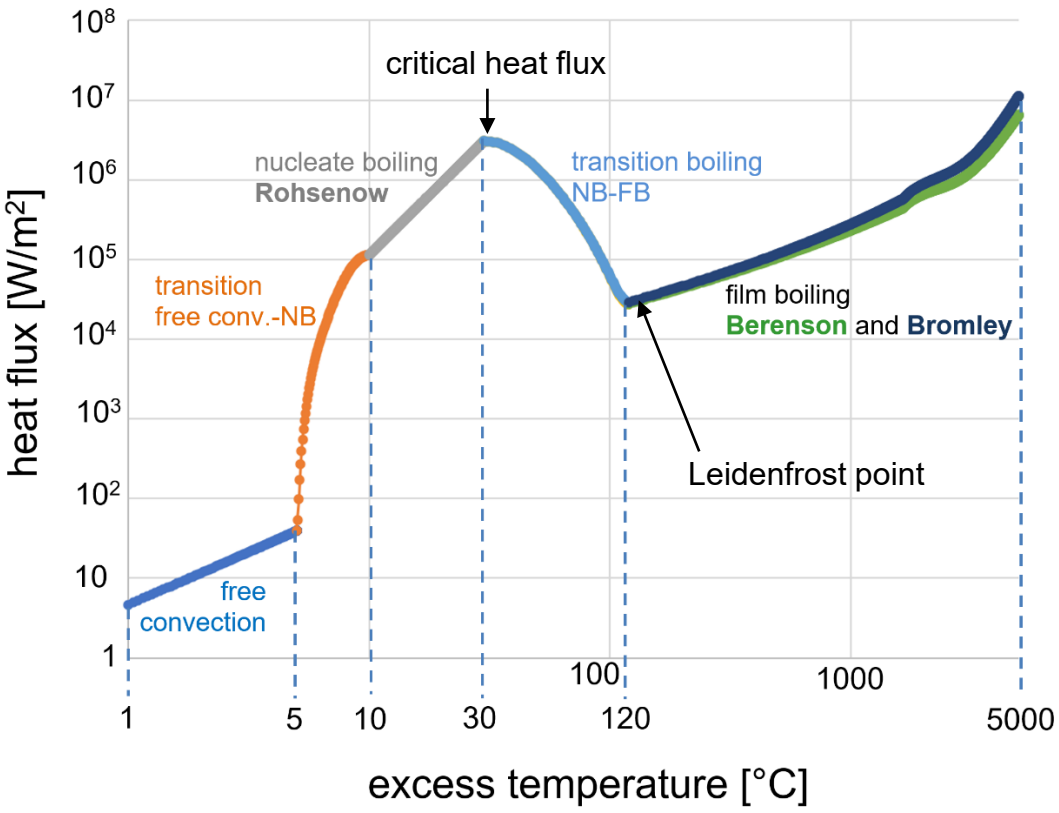

Simulation of completely filled COCOSYS zones at the start of a simulation

- The simulation of large water pools with good accuracy requires nodalisation with multiple/many zones to account for local differences in temperatures.
- New implementations in COCOSYS allow to start a simulation with completely full zones via an automatic calculation of the pressures in the initially flooded zones.
- With initially flooded zones, the numerical simulation in faster and much more numerically stable at the beginning of the numerical study.

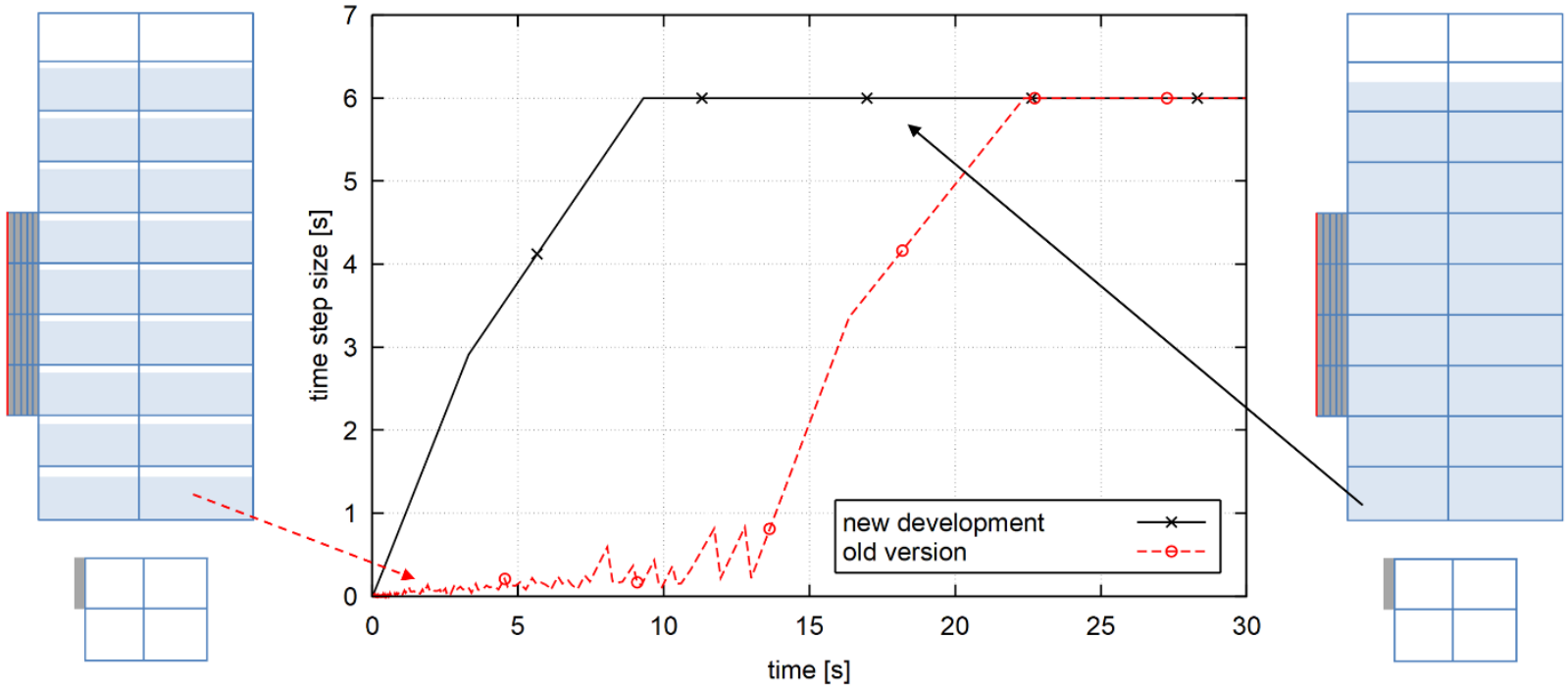

Initially not flooded zones
Requires a large number of time steps to stabilize

Initially flooded zones
Very stable numerically

Emulation of effective upward heat transfer due to local boiling (cont.)

- If the heat flow in a zone would require vaporization of the liquid water, the heat is transported upward.
- The heat eventually reaches the free surface of the water pool where liquid water is vaporized into steam as a part of the atmospheric part of this zone.
- With this approach previously numerically challenging scenarios can now be simulated and previously observed unphysical overheating of liquid water can be omitted, or in extreme cases at least minimized.

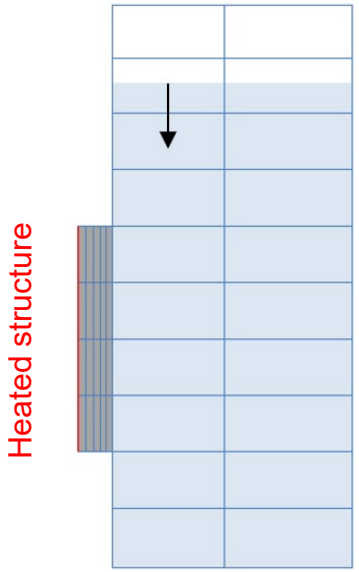

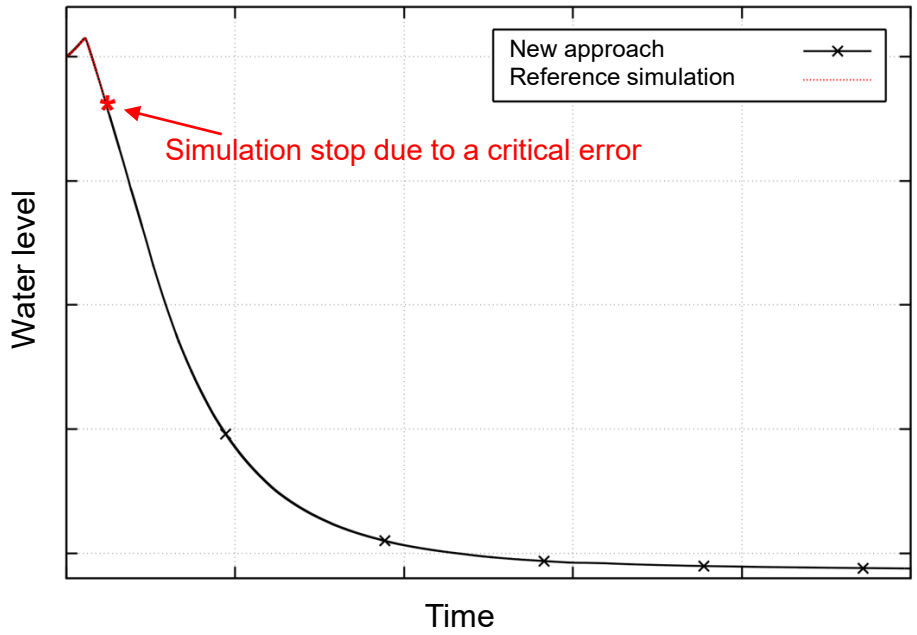

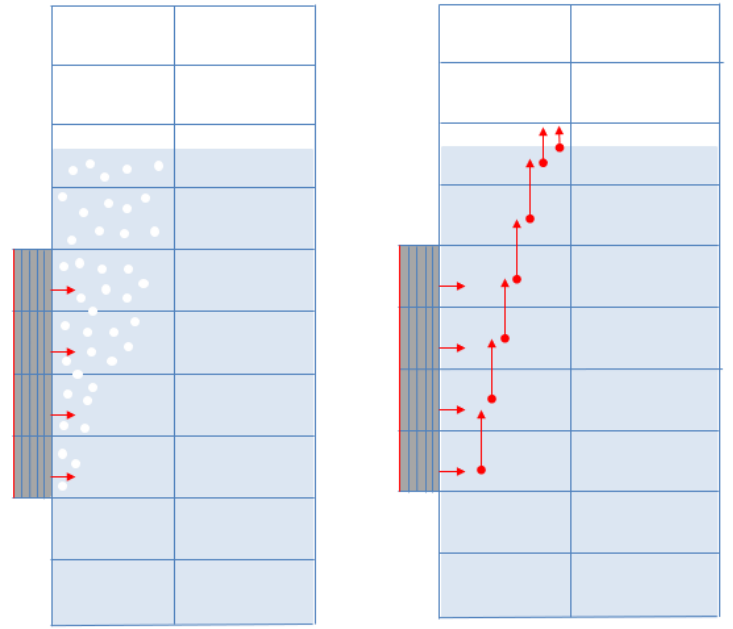

- Further developments are planned to extend the model capabilities.
- Numerical studies are planned to asses the boundaries of application.

Simulation of the THAI SMR2 experiment

- SMR concepts such as NuScale and NUWARD use large and deep water pools.
- Phenomena such as heat flow due to turbulent convection at high Rayleigh numbers may not be well captured by correlations based on experiments performed in small facilities.
- The THAI SMR experiments can be used for validation of models for heat transfer in large water pools.

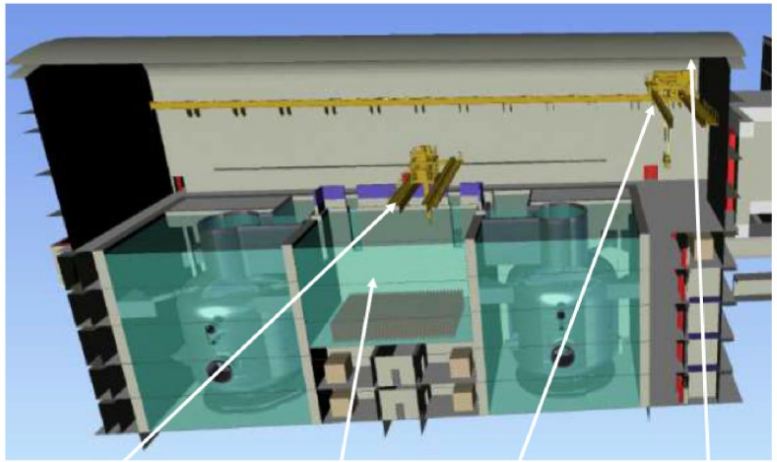

[2]

NUWARD

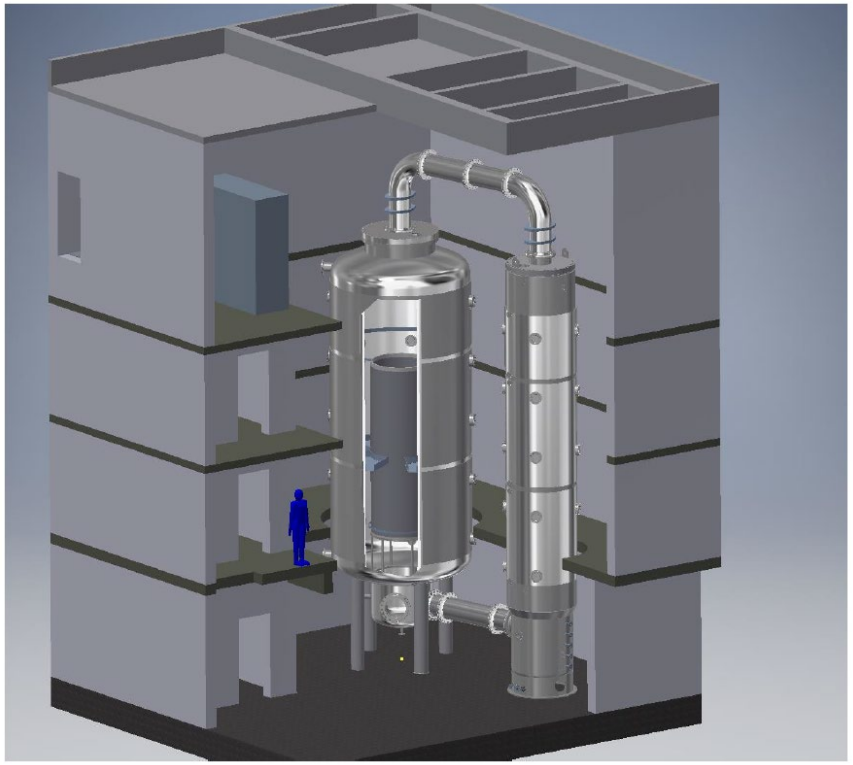

[4] The THAI+ facility at BECKER TECHNOLOGIES



Containment simulator [5] inside the PAD vessel in the THAI+ facility

Simulation of the THAI SMR2 experiment (cont.)

- Taking the measured temperatures in the inside of the containment simulator, the heat transfer to the large water pool was simulated with different nodalisations.
- All nodalisations with 1, 9 and 18 zones are a macroscopic approximation approach of the large water pool in the THAI SMR2 experiment.
- Even the nodalisation with 1 zone for the water pool captures accurately the trend of the averaged measured water temperature of the pool.

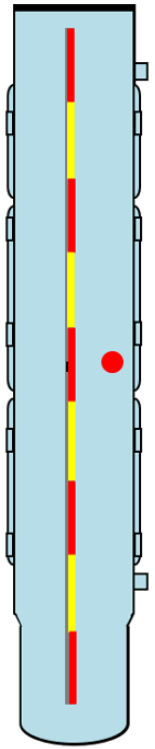

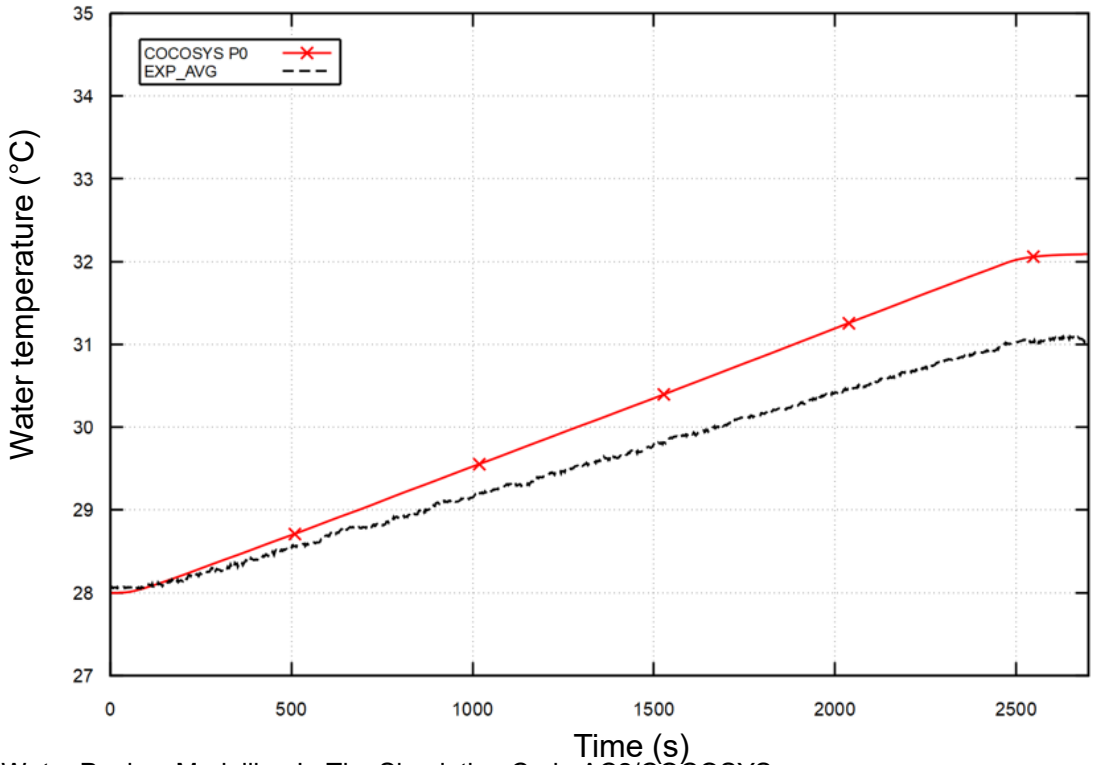

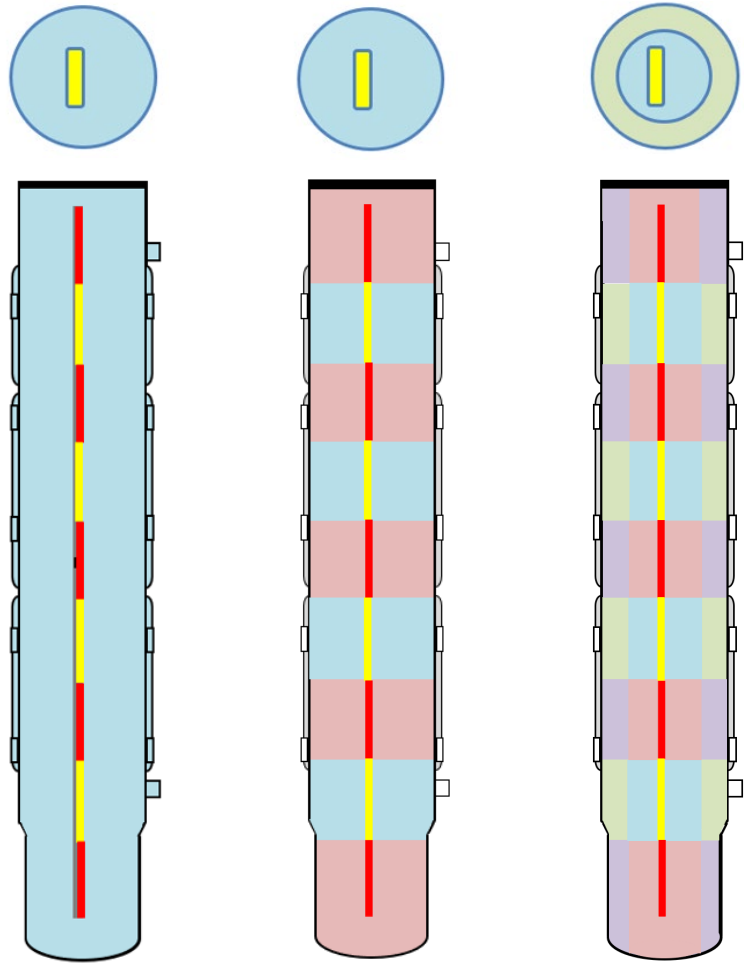

Simulation of the THAI SMR2 experiment (cont.)

- The model parameter of characteristic length for convective flow (the length of the uninterrupted thermal boundary layer) plays a significant role in the accuracy of the simulated average pool temperature.
- It is planned to test the validity of the interpolation curve used in COCOSYS against the larger dataset using more of the THAI SMR 1-12 experiments and not just THAI SMR 2.

Characteristic length = 9.0 m

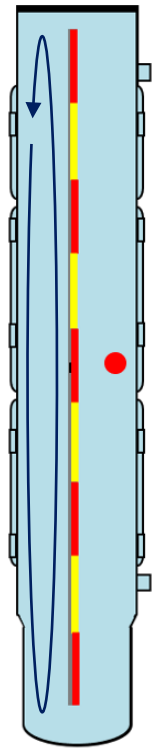

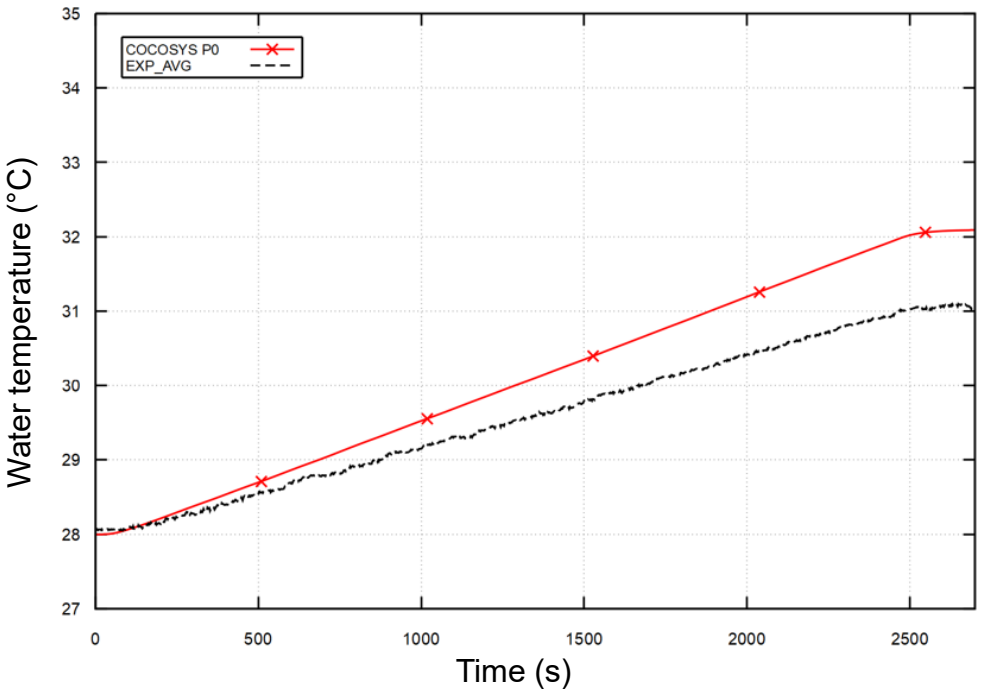

Modeling of one large convective loop

Characteristic length = 1.0 m

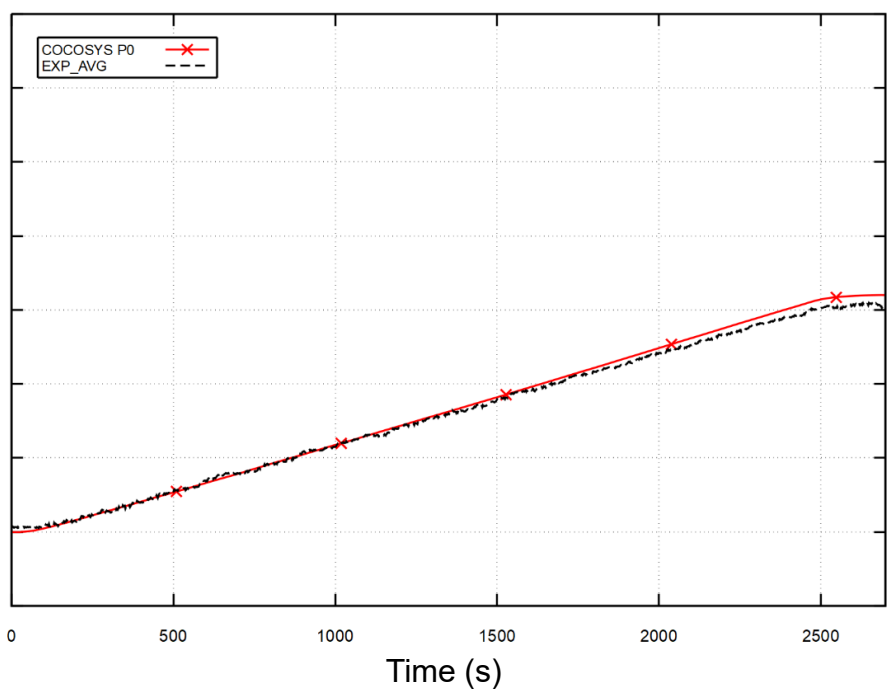

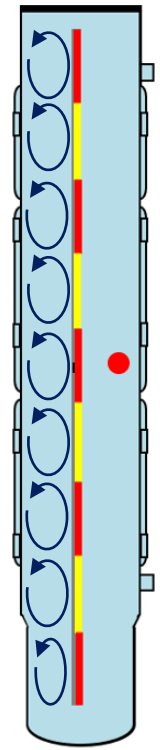

Modeling of nine smaller convective loops

Simulation of the THAI SMR2 experiment (cont.)

- The nodalisation with 18 zones shows good approximation to the average experimental temperature (especially with characteristic length of 1.0 m).
- The simulated temperature stratification is less predominant than the experimentally observed one.
- Further developments are plan to improve the predictability of thermal stratification in COCOSYS.

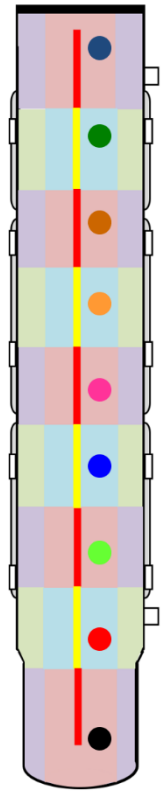

COCOSYS simulation

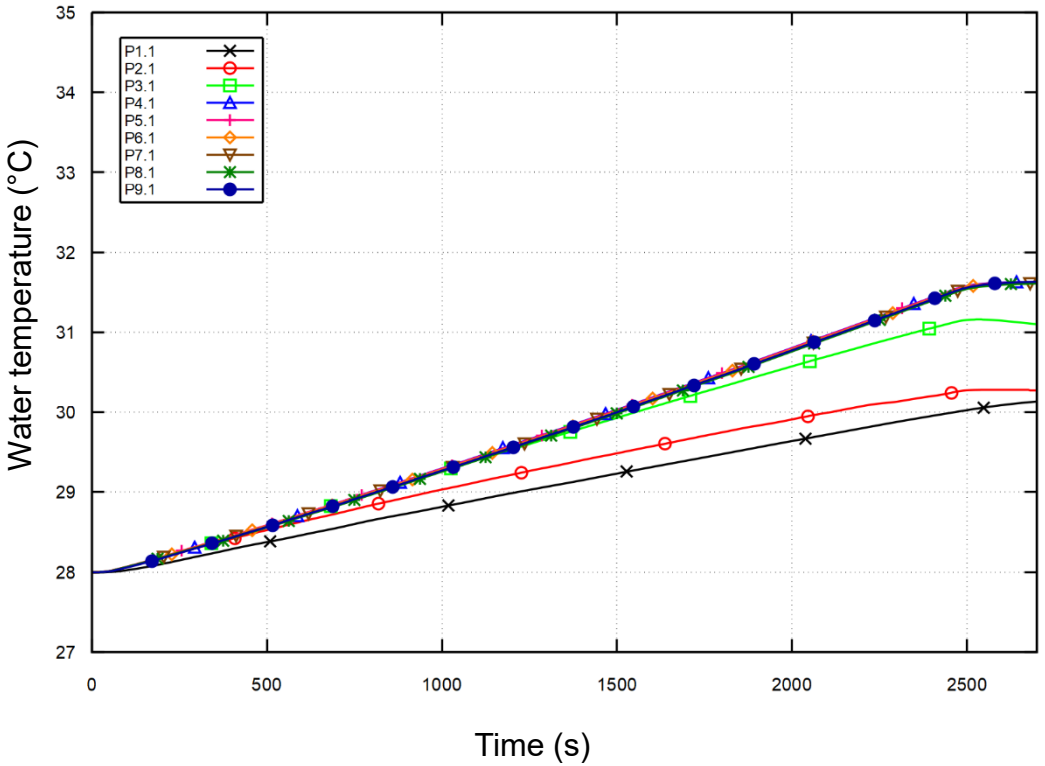

Experimental data

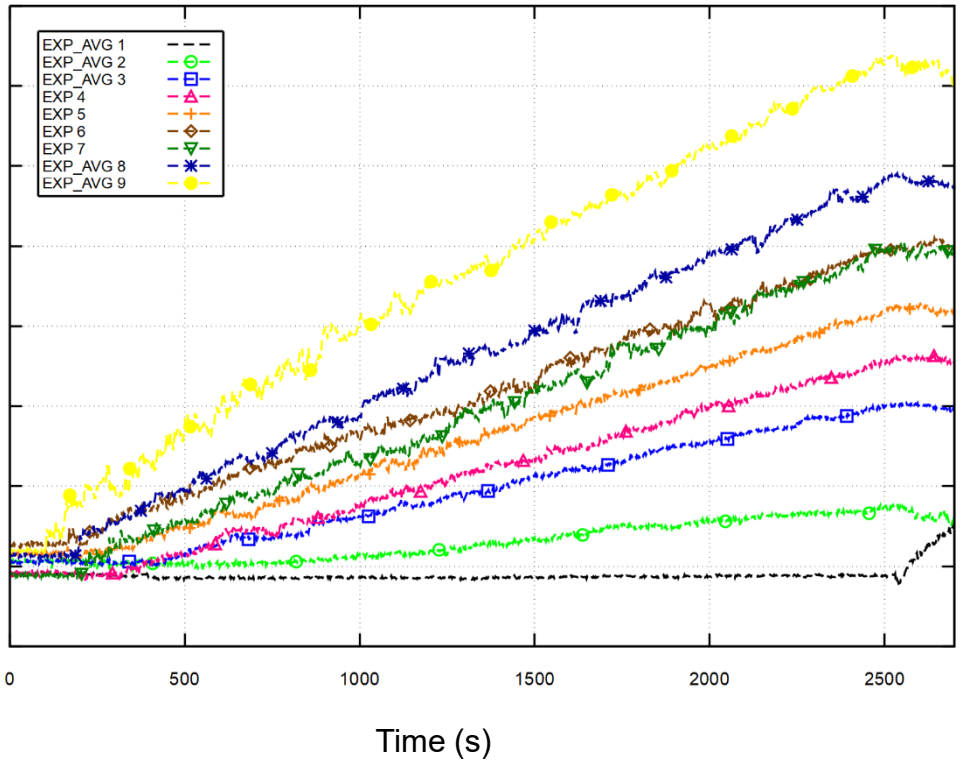

Safety condenser (SACO) passive secondary-side heat removal system in PKL test facility

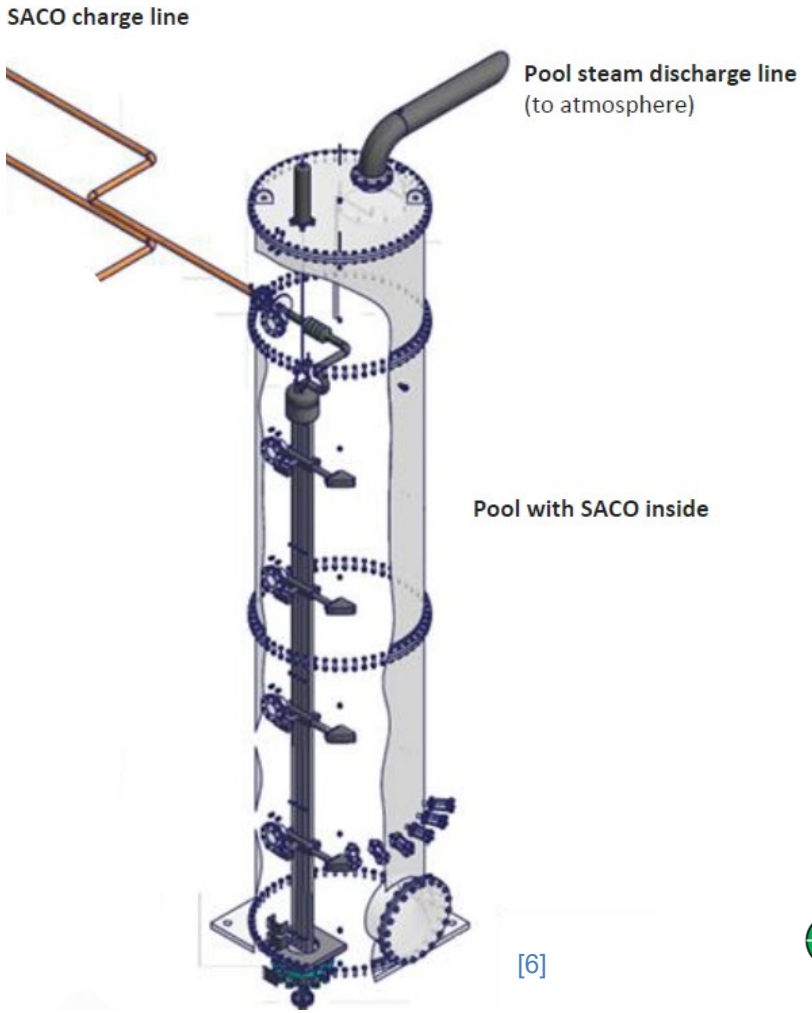

[6]

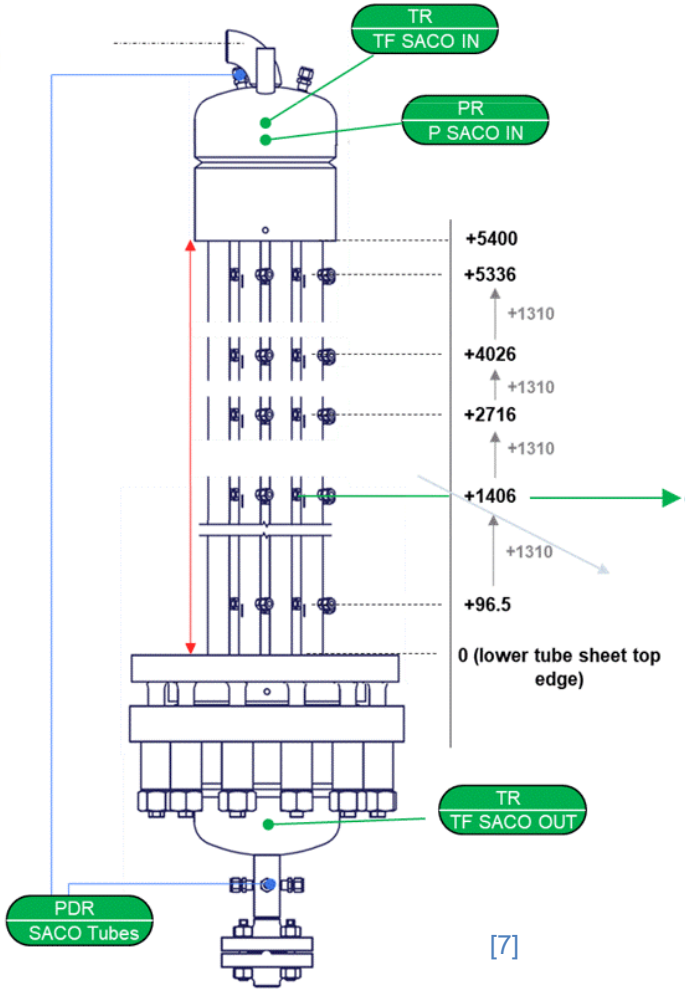

[7]

SACO steel vessel is represented by two channels.

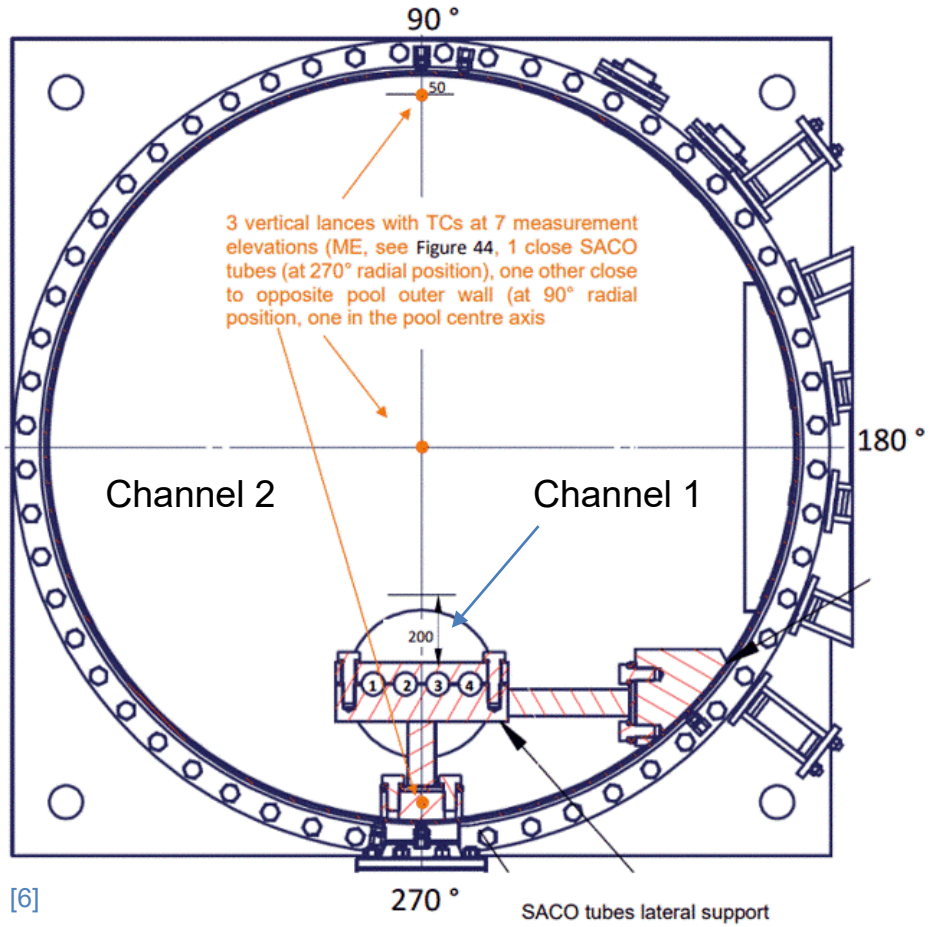

[6]

COCOSYS nodalisation of SACO in PKL P1.1 experiment

COCOSYS model with 1 channel

SACO steel vessel is represented by one channel, which is subdivided into 6 stacked zones. Each group of 2 HX tubes are modelled by 5 stacked HECU structures

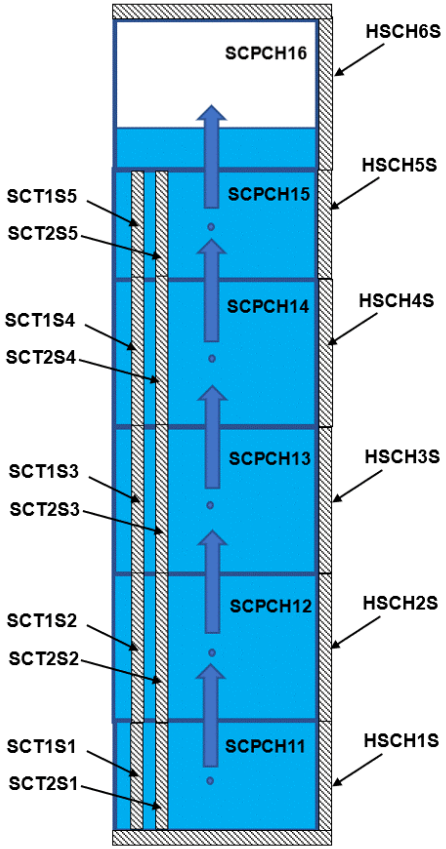

COCOSYS model with 2 channels

SACO steel vessel is represented by two channels. Each channel is subdivided into 6 stacked zones. Each group of 2 HX tubes are modelled by 5 stacked HECU structures

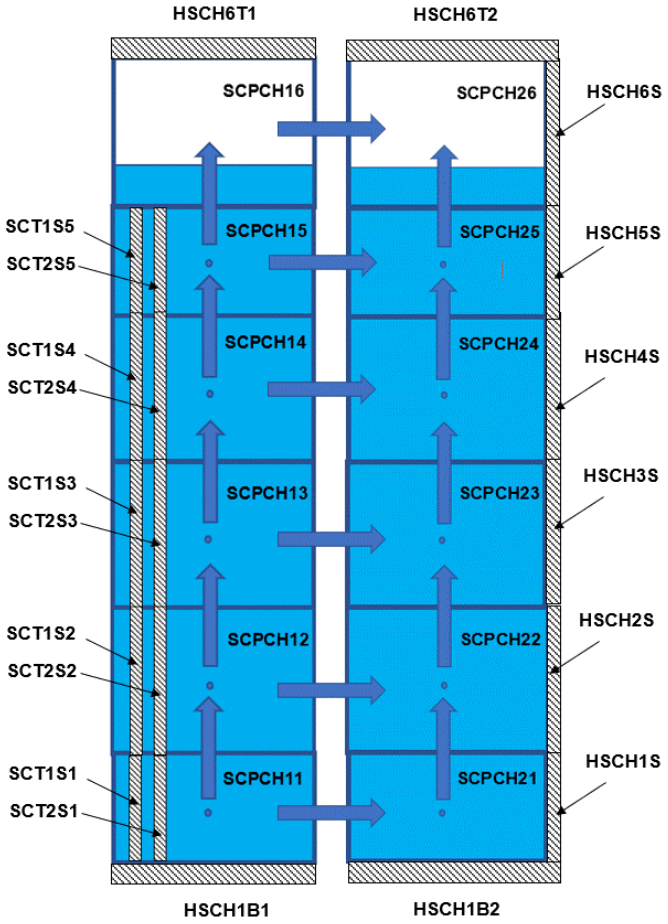

Results of COCOSYS post-test calculations of PKL P1.1 experiment

- Comparison of COCOSYS results with experiment (heat-up phase and phase A)
- Water temperature in the SACO steel vessel

COCOSYS model with 1 channel

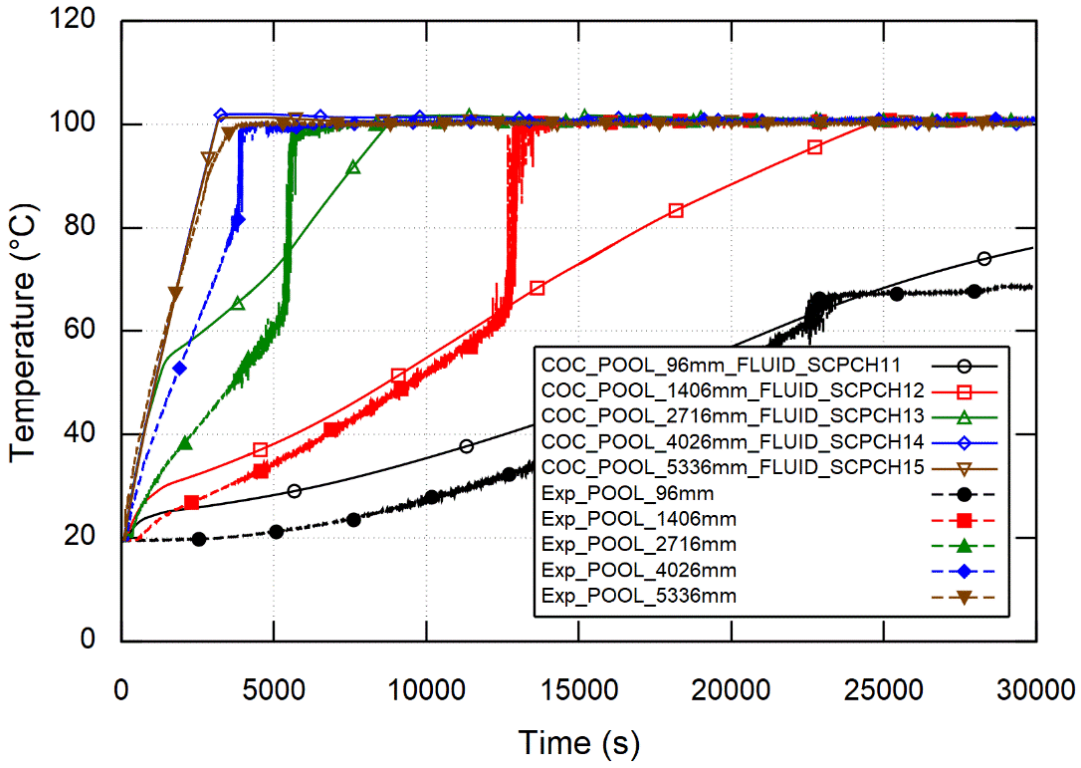

COCOSYS model with 2 channels

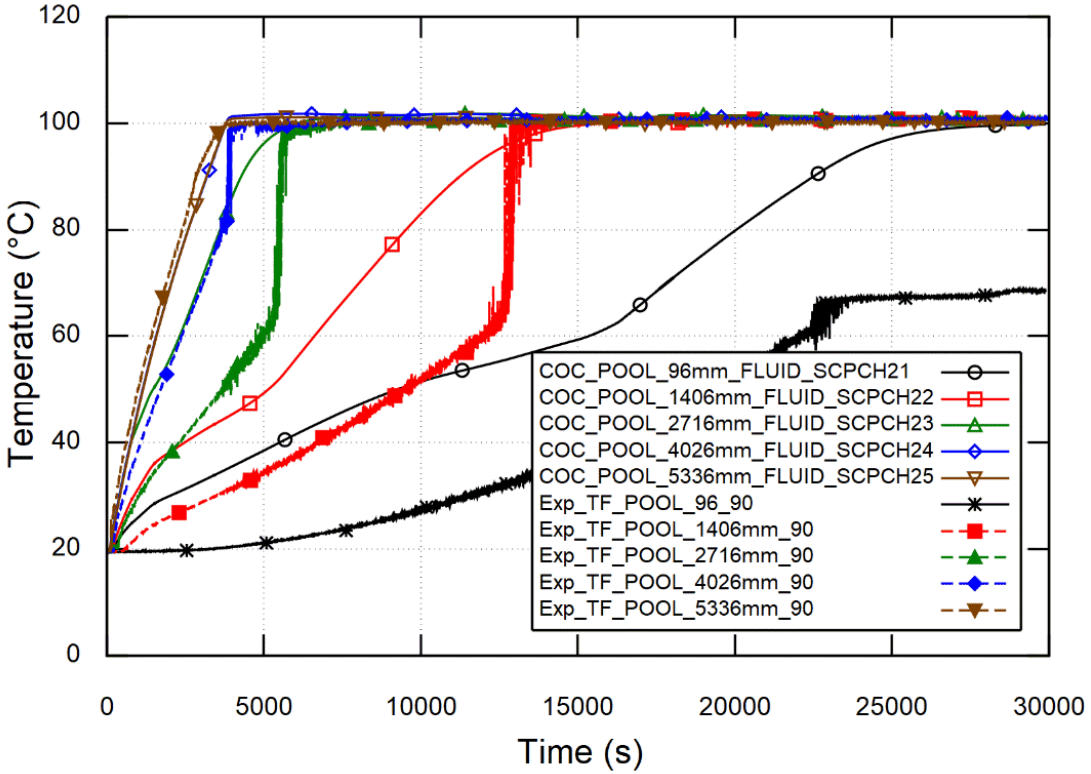

COCOSYS application for simulation of EPR core catcher

Core catcher concepts like EPR can be simulated with COCOSYS

- Localisation / Stabilization of the corium within the containment
- Evaluation of the melt spreading efficiency
- Coupling to the containment thermohydraulic

EPR core catcher

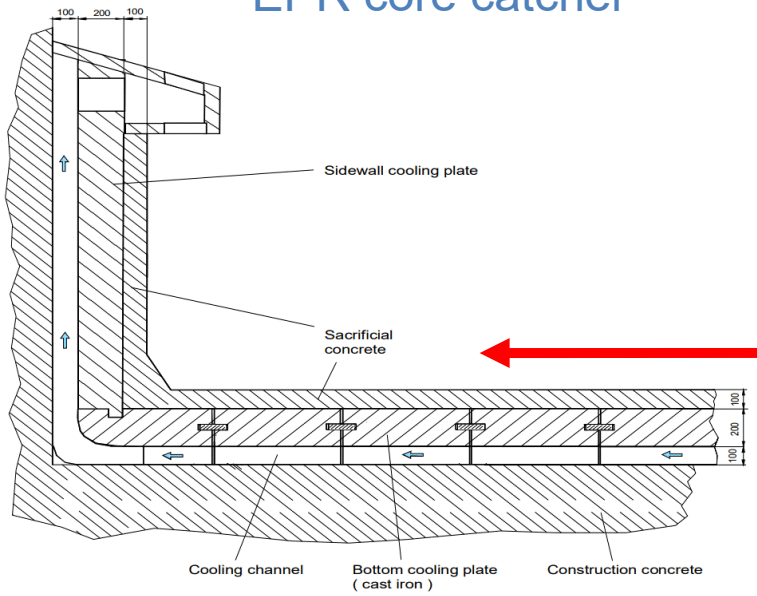

[8]

EPR melt stabilization system

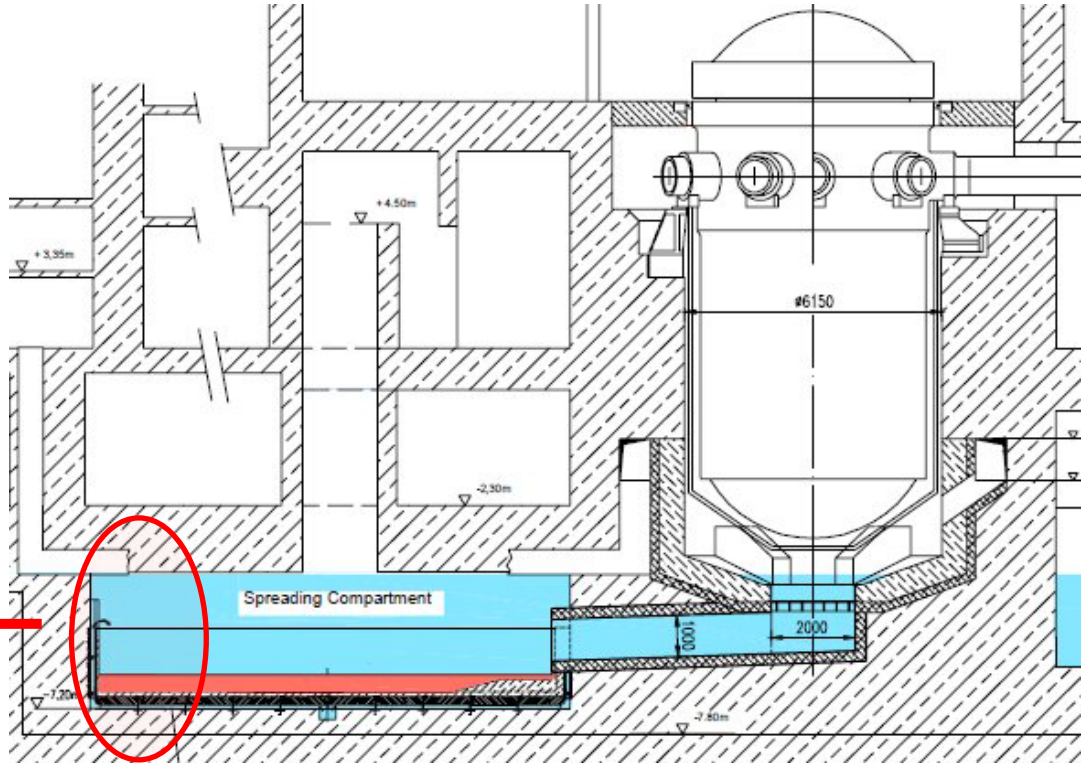

[8]

COCOSYS application for simulation of EPR core catcher

- Results of COCOSYS calculations of the thermohydraulic behavior in the cooling channels of the core catcher spreading compartment

Comparison of the water temperature with saturation temperature in R1b zone for simulation cases with and without plume-model

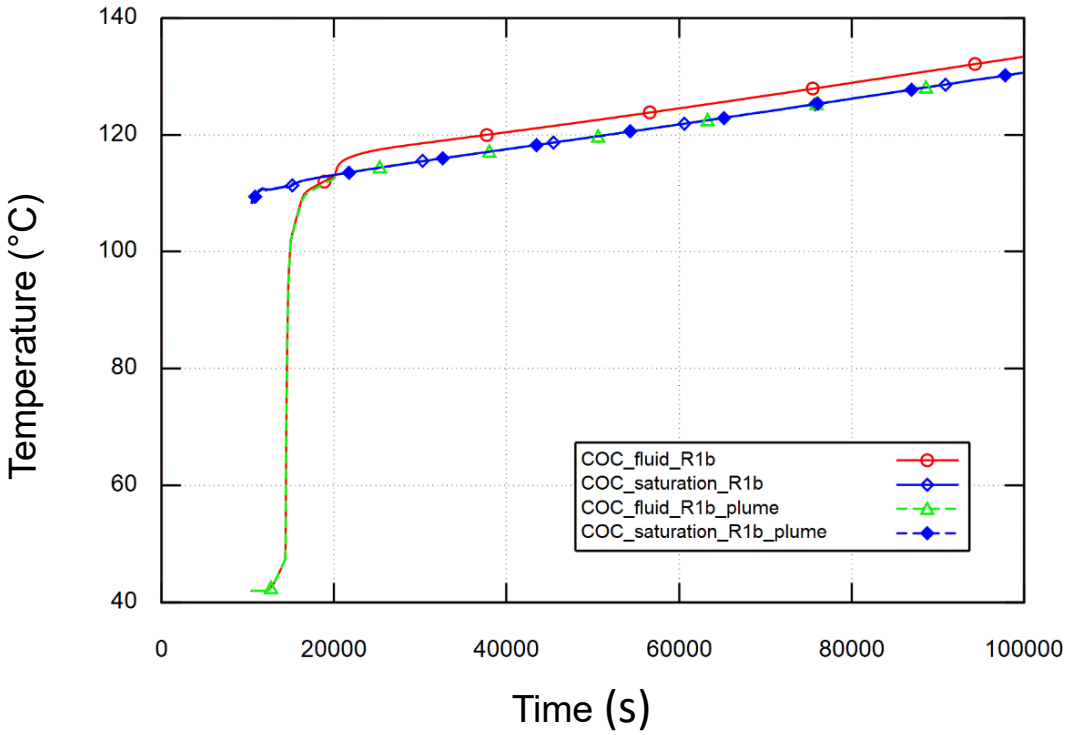

COCOSYS model of the core catcher spreading compartment with bottom and sidewall water-cooled steel structures

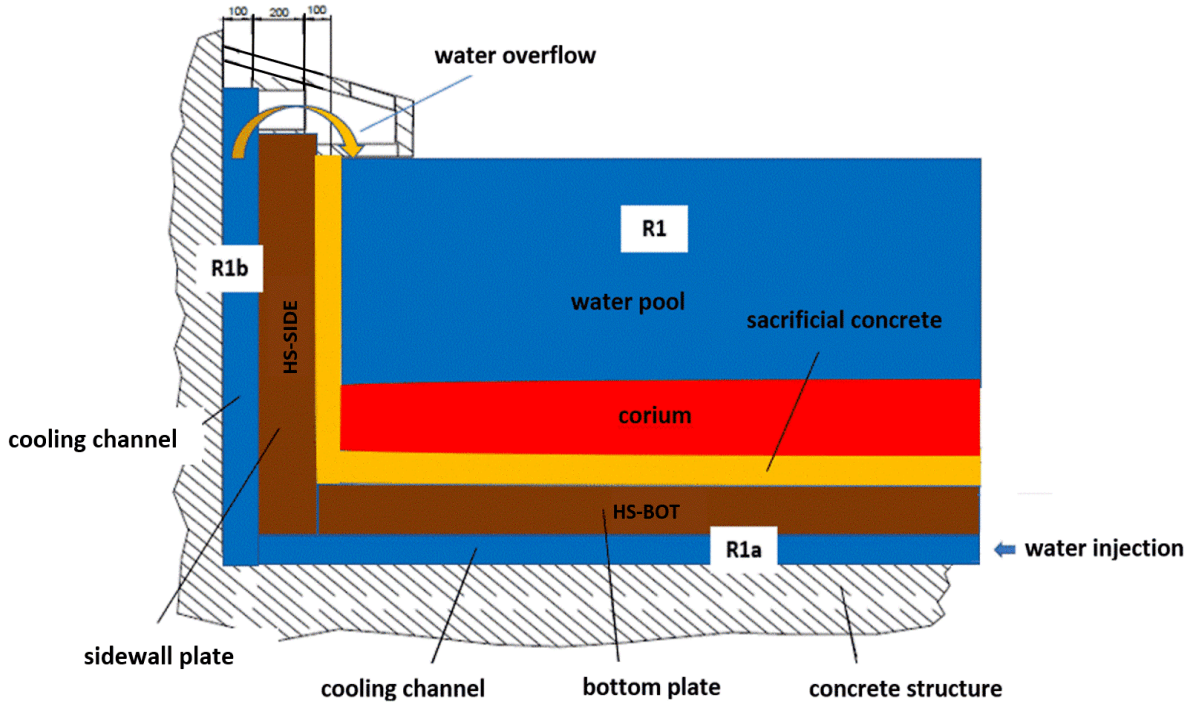

Summary and conclusions

- **Lumped-parameter concept** in COCOSYS
- **ATM_FULL junction** type introduced to **allow filling-up of a zone**
- ATM_FULL flow model was enhanced to consider **initialization of completely filled zones**
- **Heat transfer models** added for heat exchangers with **hot structures** (**Nukiyama**'s boiling curve)
- Modelling of the effect of **steam bubble transport on heat transfer** via a plume model
- First **validation** steps with COCOSYS for pool heating scenarios:
  - **THAI SMR2**: free convection at large Rayleigh numbers
  - **PKL SACO P1.1** heat-up phase up to saturation
  - **Temperature stratifications** in experiments **not simulated in full detail**.
- Open points for further work:
  - **Heat transfer at large Ra** numbers
  - Effect of **grid refinement**
  - Effect of **model parameters in lumped parameter** approach

Further analysis and developments are planned to continue improving on the capabilities of **COCOSYS as a tool for fast simulations of large water pools in NPP containments**, especially for **SMR**.

Acknowledgements

Supported by:



based on a decision of
the German Bundestag

This work is sponsored by R&D-project RS1604 financed by the German Federal Ministry for the Environment, Nature Conservation, Nuclear Safety and Consumer Protection (BMUV).

Figures

[1] https://en.wikipedia.org/wiki/Three_Mile_Island_accident#/media/File:Graphic_TMI-2_Core_End-State_Configuration.png, accessed on 07.05.2024.
[2] Francis, D. M., Beils, S.: NUWARD SMR safety approach and licensing objectives for international deployment. Nuclear Engineering and Technology, Bd. 56, Nr. 3, S. 1029–1036, DOI 10.1016/j.net.2023.12.045, 2024
[3] Weimin Ma, Yidan Yuan, Bal Raj Sehgal, In-Vessel Melt Retention of Pressurized Water Reactors: Historical Review and Future Research Needs, Engineering, Volume 2, Issue 1, (2016), pp. 103-111, https://doi.org/10.1016/J.ENG.2016.01.019.
[4] M. Freitag, B. von Laufenberg, M. Colombet, E. Schmidt, K. Dieter; Free convection heat transfer at large Rayleigh numbers, Tests SMR-1-6, Technical report, Report No. 1501630-FB/TR-SMR-1-6, 2023.
[5] Photograph from Becker Technologies GmbH, 2022.
[6] Framatome GmbH, EU-H2020 Pastels Project, Deliverable 3.1: PKL & SACO Technical Description & Design Review Report, Grant agreement No. 945275, https://www.pastels-h2020.eu/media/articles/PASTELS_D3.1_Technical-Description-Design-Review-PKL-SACO_R1..0.pdf , 2020.
[7] Framatome GmbH, EU-H2020 Pastels Project, Deliverable 3.2: PKL/SACO - phase 1 experiments, Grant agreement No. 945275, https://www.pastels-h2020.eu/media/articles/D3.2.pdf , 2020.
[8] Figures courtesy of IASMiRT: Bittermann D., Fischer M., Nie M.: Main features of the core melt stabilization system of the European Pressurized water Reactor (EPR). In: International Association for Structural Mechanics in Reactor Technology (IASMIRT): Proceedings of 18th international conference on structural mechanics in reactor technology. SMiRT 18, Beijing, China, 7. - 12. August 2005, ISBN 7-5022-3421-7, Atomic Energy Press: China, 2005.

The 11th European Review Meeting on Severe Accidents Research

May 13-16, 2024, Royal Institute of Technology, Stockholm, Sweden

PLENARY SESSION: REGULATORY PERSPECTIVE AND APPROACHES FOR SEVERE ACCIDENTS IN SMALL MODULAR REACTOR

Chairs: D. Jacquemain (OECD/NEA), A. Miassoedov (IAEA)

U.S. NRC Regulatory Perspective and Approaches for Severe Accidents in Small Modular Reactors

Jason Schaperow, (USNRC Office of Nuclear Reactor Regulation)

The Canadian Nuclear Regulatory Role, Approaches and Challenges for Severe Accidents in Small Modular Reactors

Samuel Gyepi-Garbrah (Canadian Nuclear Safety Commission)

Beyond Design Basis Analysis: Regulatory Perspective on New Reactor Designs

Ali Tehrani (Office for Nuclear Regulation, UK)

Applicability of new Swedish regulations to Small Modular Reactors – Opportunities and challenges of a performance based approach

A. O. Mowitz (Swedish Radiation Safety Authority, SSM)

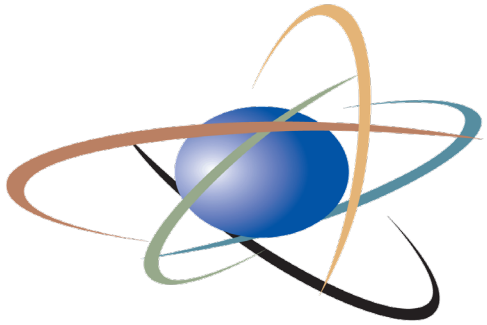

U.S.NRC

UNITED STATES NUCLEAR REGULATORY COMMISSION

Protecting People and the Environment

NRC regulatory perspective and approaches for severe accidents in SMRs

11th European Review Meeting on Severe Accidents Research (ERMSAR 2024)
May 13-16, 2024

U.S.NRC
UNITED STATES NUCLEAR REGULATORY COMMISSION
Protecting People and the Environment

Summary

- Two options for reactor licensing
  - Part 50 – Applicant first submits a preliminary design
  - Part 52 – Applicant first submits a final design
- NRC uses codes (SCALE and MELCOR) for enhanced understanding of preliminary and final designs
  - NuScale (LWR) license review
  - Hermes and Hermes 2 (non-LWR) license review
- Non-LWR source term demonstration project
  - Added phenomenological models for non-LWRs
  - Developed and demonstrated 5 non-LWR reference plant models and held public workshops
  - Continuing to enhance non-LWR modeling

Two options for reactor licensing in U.S.

- Part 50
  - Step 1 – Construction permit (preliminary design + site)
  - Step 2 – Operating license (final design + site)
  - Non-LWR applications being submitted under Part 50
  - Licensing Modernization Project (frequency/consequence curve) being used to determine non-LWR safety classification of equipment (NEI 18-04, August 2019)
- Part 52
  - Step 1 – Design certification (final design)
  - Step 2 – Combined license (final design + site)
  - Has been used for LWRs (ABWR, AP1000, ESBWR, NuScale)
  - Severe-accident-related requirements
    - PRA
    - Analysis of design features for severe accident mitigation (LWRs only)

Part 50 example 1

- Hermes construction permit
  - Test reactor (35 MWt)
  - TRISO particles in graphite pebbles with salt coolant
  - Radiator cools primary salt loop
  - NRC approved December 2023
- Severe accident issues and source term
  - Not credible to uncover fuel (SECY-23-0074, August 2023)
  - Source term – fuel failures during normal operation (fuel coating defects)
- NRC staff used MELCOR for design basis accidents (DBA) for enhanced understanding of plant response
  - DBAs for Hermes do not uncover fuel
  - SCALE for estimating decay heat, nuclide inventory, reactivity coefficients for MELCOR accident simulations

Part 50 example 1 (cont.)

Reactor coolant system (MELCOR nodalization)

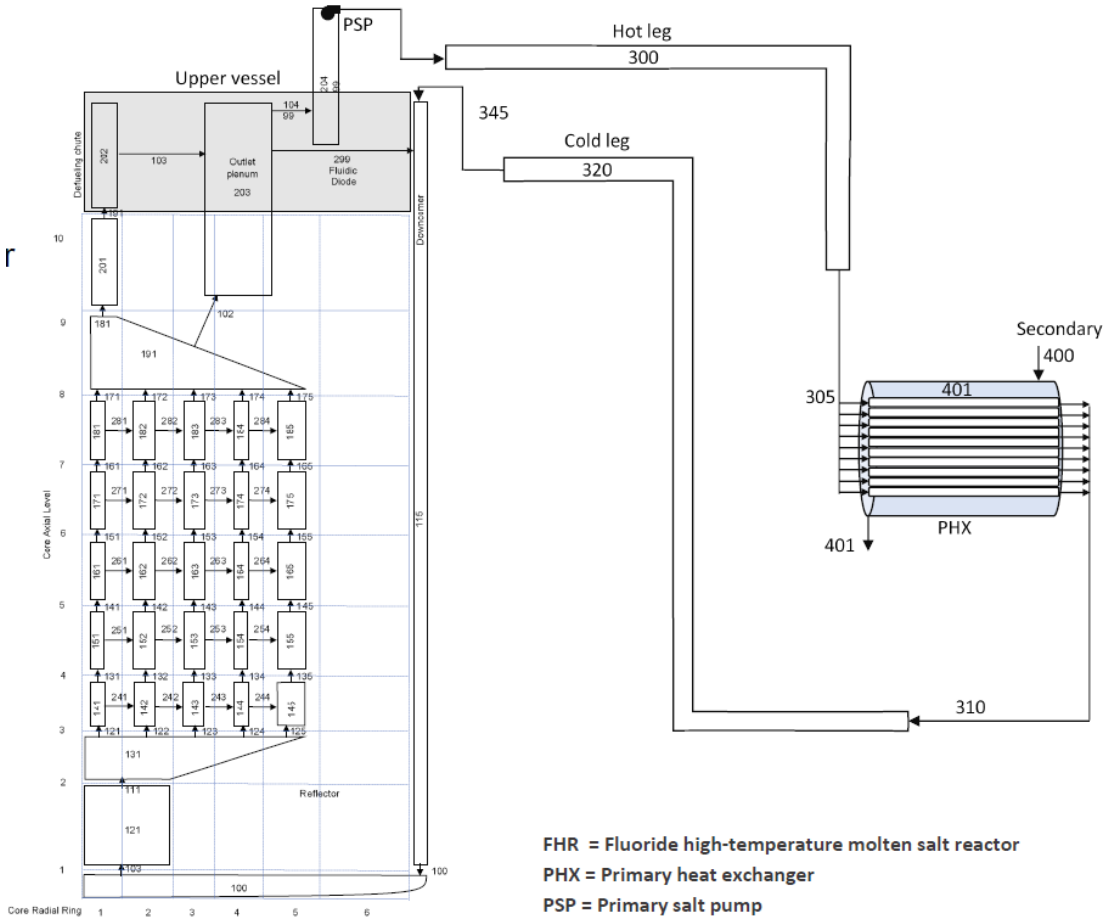

Decay heat removal system (schematic)

Figure 6.3-1: Functional Diagram of the DHRS

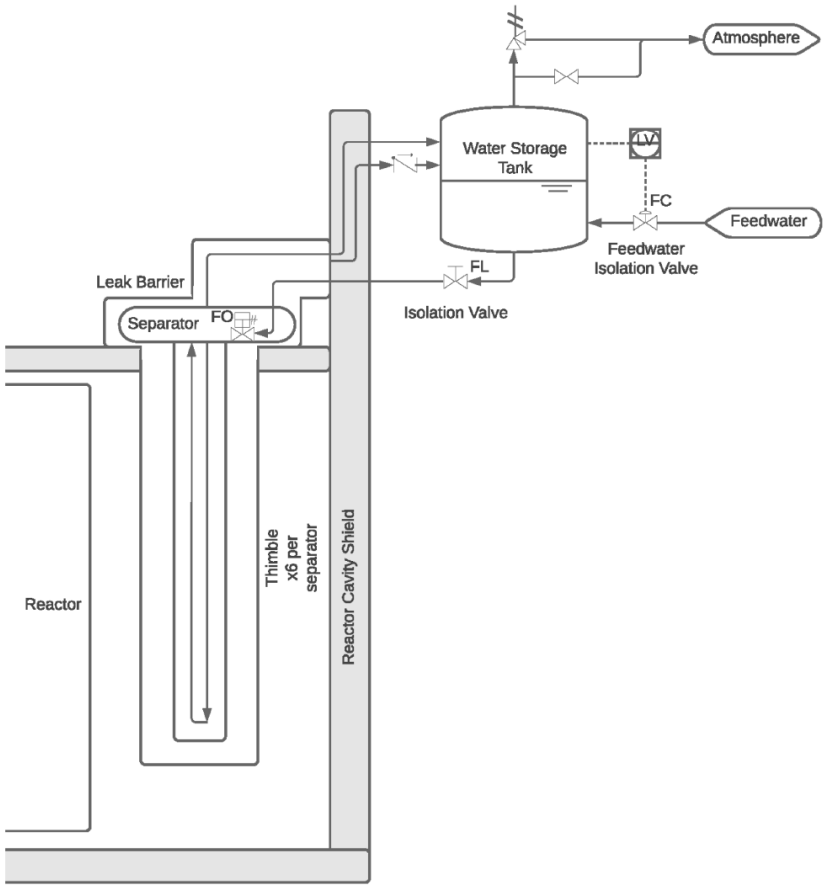

Part 50 example 1 (cont.)

MELCOR results for insertion of excess reactivity (applicant's results in upper right corner)

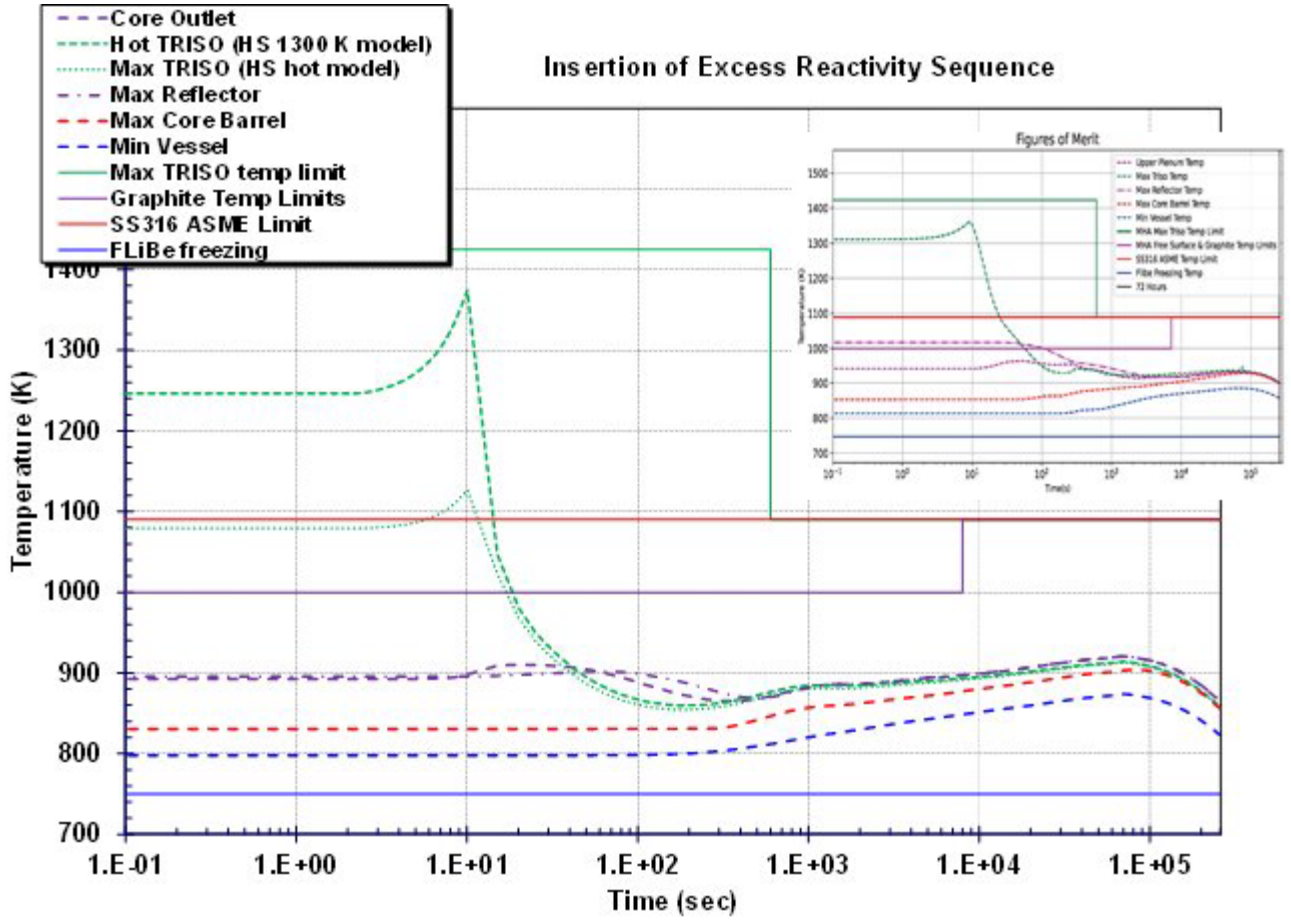

Part 50 example 2 (cont.)

- Hermes 2 construction permit
  - Facility has two reactors (each 35 MWt)
    - Same reactor design as Hermes
  - Each reactor has a secondary salt loop
  - Secondary salt loops heat a common power conversion system
  - NRC performing licensing review and developing draft Safety Evaluation
- NRC staff used MELCOR to understand differences in DBA response between Hermes and Hermes 2
  - Analysis focused on new secondary loop and power conversion system

Part 50 example 2 (cont.)

Reactor coolant system (MELCOR nodalization)

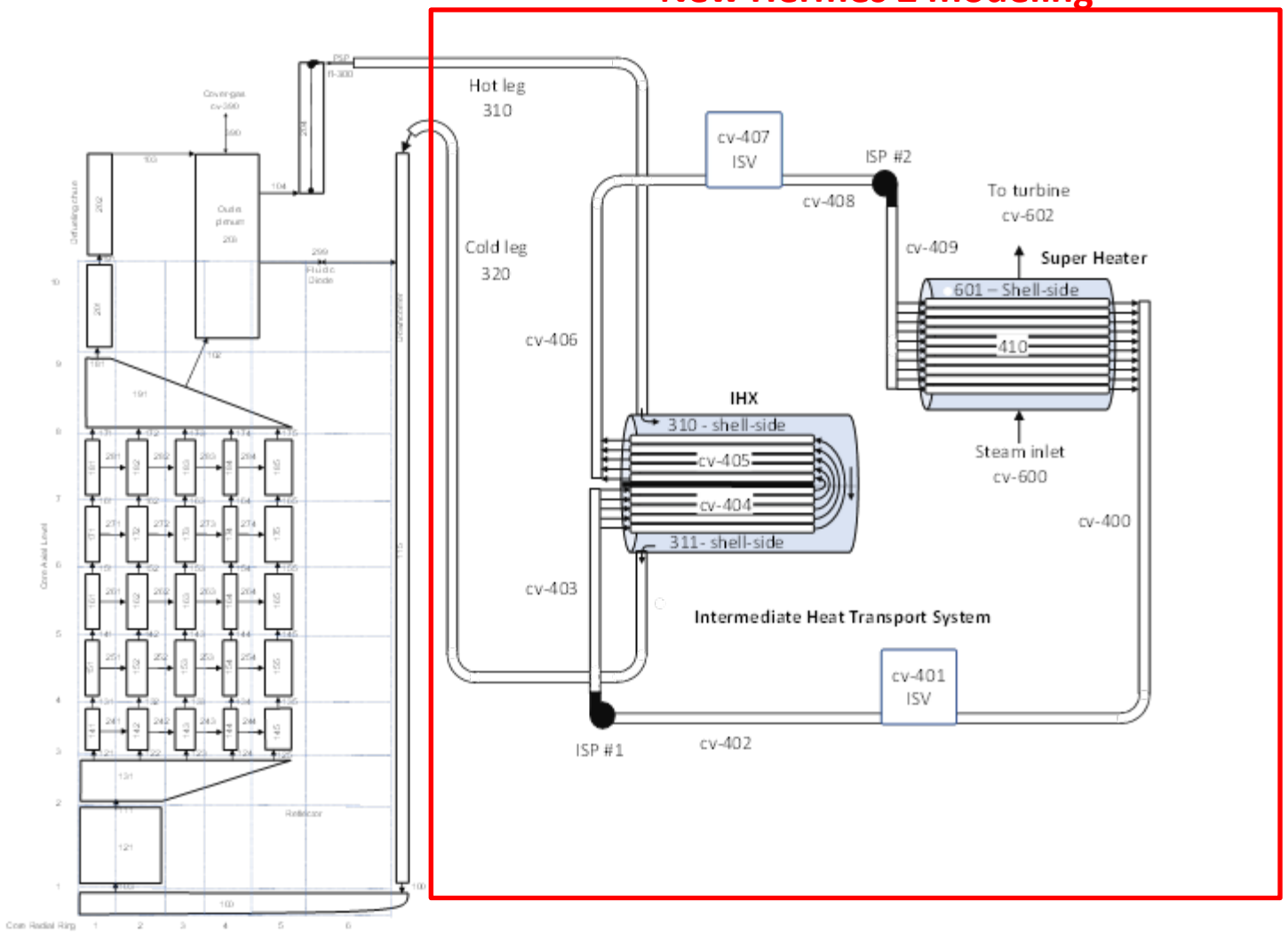

Part 52 example

- NuScale design certification
  - Integral PWR (160 MWt)
  - NRC approved January 2023
- Severe accident issues and source term
  - NuScale developed and used a MELCOR model
  - NRC staff independently developed and used a MELCOR model to independently assess safety

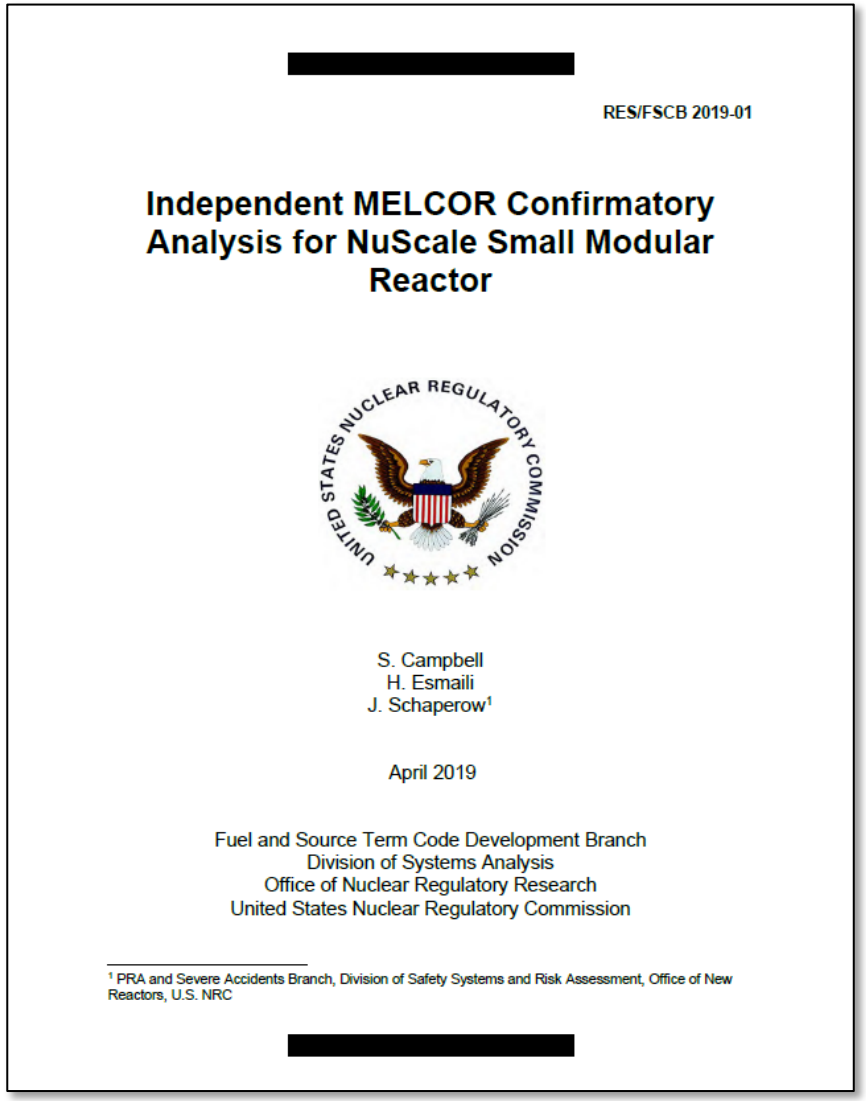

RES/FSCB 2019-01

Independent MELCOR Confirmatory Analysis for NuScale Small Modular Reactor

S. Campbell
H. Esmaili
J. Schaperow[1]

April 2019

Fuel and Source Term Code Development Branch
Division of Systems Analysis
Office of Nuclear Regulatory Research
United States Nuclear Regulatory Commission

[1] PRA and Severe Accidents Branch, Division of Safety Systems and Risk Assessment, Office of New Reactors, U.S. NRC

Part 52 example (cont.)

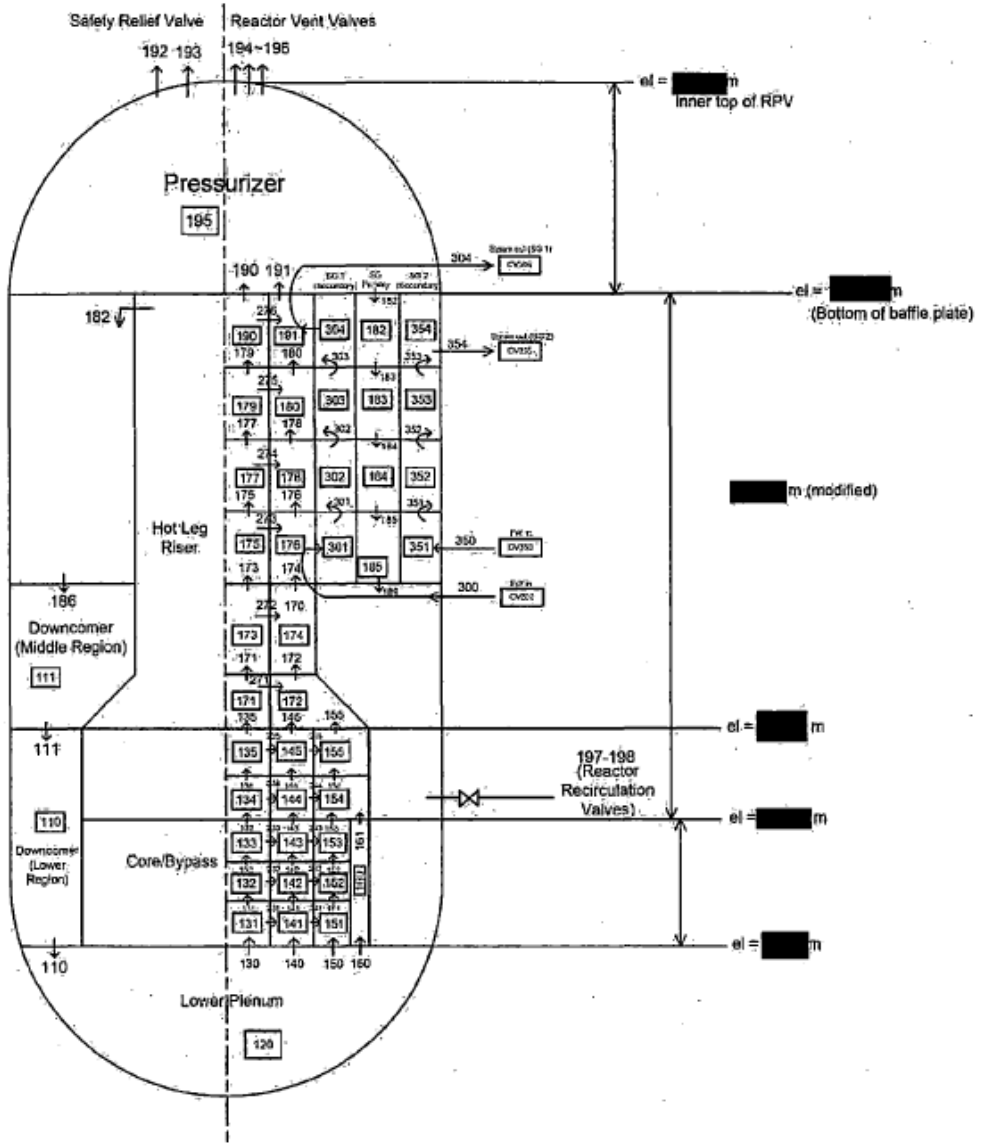

Figure 2.1 Staff's MELCOR nodalization for NuScale model – Reactor Vessel

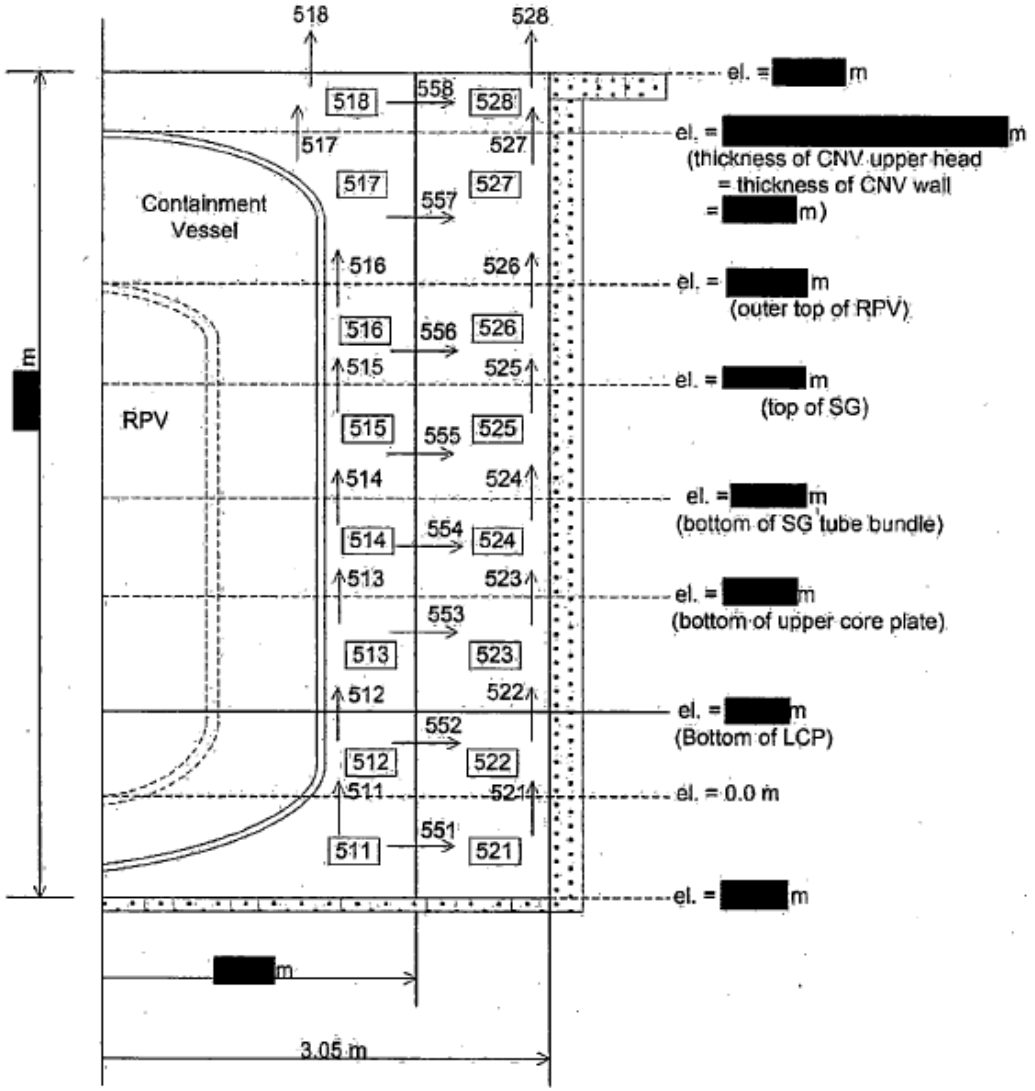

Figure 2.3 Staff's MELCOR nodalization for NuScale model – Reactor bay water pool

U.S.NRC
UNITED STATES NUCLEAR REGULATORY COMMISSION
Protecting People and the Environment

Part 52 example (cont.)

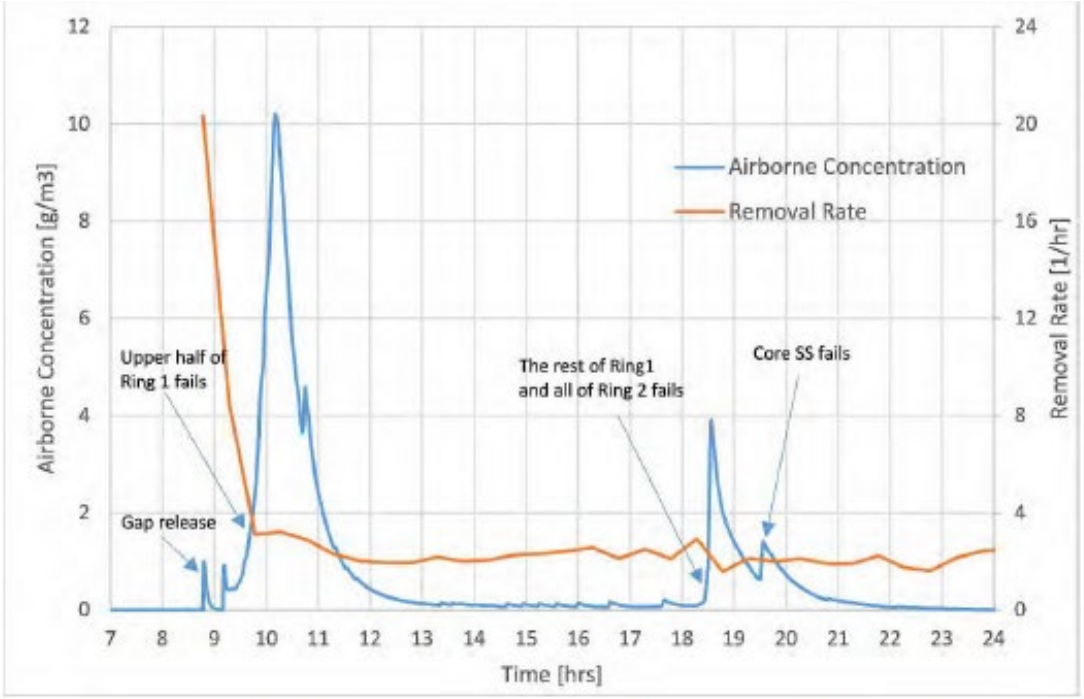

Figure 5.5 LEC-06T: Containment removal rate (averaged over 30 minute intervals) and airborne aerosol concentration.

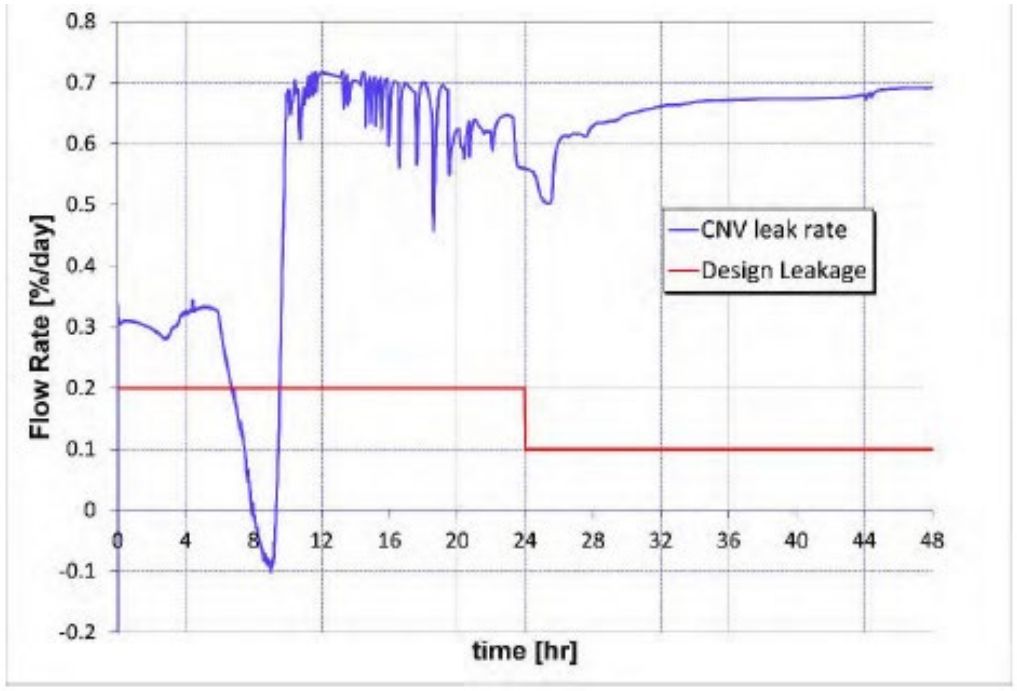

Figure 5.6 Containment leak rate calculated from staff's MELCOR calculation LEC-06T versus the applicant's assumed design leak rate.

U.S.NRC
UNITED STATES NUCLEAR REGULATORY COMMISSION
Protecting People and the Environment

Non-LWR source term demonstration project

- Objective
  - Demonstrate using SCALE and MELCOR to understand non-LWR plant response to accidents and to examine uncertainties
- Approach
  - Step 1: Build representative SCALE reactor models and MELCOR full-plant models
  - Step 2: Select scenarios to show code capabilities
  - Step 3: Perform simulations
    - SCALE – generate decay heat, core nuclide inventory, reactivity feedbacks
    - MELCOR – model thermal hydraulics, accident progression, source term
- Results
  - Developed and applied SCALE and MELCOR for 5 reference plants

Non-LWR source term demonstration project (cont.)

- Public workshops in 2021-2022
  - Heat pipe reactor – INL Design A
  - High-temperature gas-cooled pebble-bed reactor – PBMR-400
  - Molten-salt-cooled pebble-bed reactor – UCB Mark 1
  - Molten-salt-fueled reactor – MSRE
  - Sodium-cooled fast reactor – ABTR

Public workshop videos, slides, reports at advanced reactor source term webpage

SCALE input models available here.

MELCOR input models available to CSARP members.

U.S.NRC
UNITED STATES NUCLEAR REGULATORY COMMISSION
Protecting People and the Environment

Non-LWR source term demonstration project (cont.)

- Reference plant models are a starting point to develop models for NRC independent analysis for licensing
  - UCB Mark 1 → Hermes → Hermes 2
- NRC making additional enhancements to MELCOR
  - Modeling molten salt (or sodium) and water in the same simulation
    - NRC staff using this capability for Hermes 2
  - Freezing of molten salt and sodium
    - Currently modeled as subcooled liquid
  - Heat pipe reactor modeling
    - Reactor in a horizontal orientation
    - Heat-pipe failure propagation to adjacent heat pipes

U.S.NRC
UNITED STATES NUCLEAR REGULATORY COMMISSION
Protecting People and the Environment

Non-LWR source term demonstration project (cont.)

- Extended to fuel cycle facilities
  - Identify differences in potential non-LWR fuel cycles compared to LWR fuel cycle
  - Identify gaps in NRC's simulation capabilities (SCALE and MELCOR)
  - Address any gaps through code development
  - Assess, demonstrate, document through publicly available deliverables
- Public workshop materials available on advanced reactor source term webpage (links on slide 13 above)
  - High-temperature gas-cooled pebble-bed reactor
  - Sodium-cooled fast reactor

Canadian Nuclear Safety Commission | Commission canadienne de sûreté nucléaire

Canada

The Canadian Nuclear Safety Commission's Role in Facing Challenges related to Severe Accident Analysis associated with Small Modular Reactors (SMR)

Sam Gyepi-Garbrah

Reactor Behaviour Division

ERMSAR 2024, Stockholm, Sweden

May 14, 2024

Outline

- Introduction – The CNSC
- SMR Landscape
- CNSC Regulatory Framework and Processes
- CNSC Licensing Expectations
- SMR Readiness Project
- Assessing Innovative Features Against Regulatory Requirements
- Severe Accidents in SMR and Regulatory Approach to Challenges
- Conclusion

Introduction – The Canadian Nuclear Safety Commission

- CNSC is an independent regulatory quasi-judicial tribunal
- Mandate and Mission
  - regulate the use of nuclear energy and materials to protect the health, safety and security of Canadians and the environment
  - implement Canada's international commitments on the peaceful use of nuclear energy
  - disseminate objective scientific, technical and regulatory information to the public



Canada's Small Modular Reactor (SMR) Landscape

- Ontario
  - Darlington
    - LTC (Hearing, Fall of 2024)
  - Global First Power
- Saskatchewan
  - SaskPower
  - Saskatchewan Research Council Nuclear
- New Brunswick
- Position as a regulator
  - Regulating multiple reactor technologies

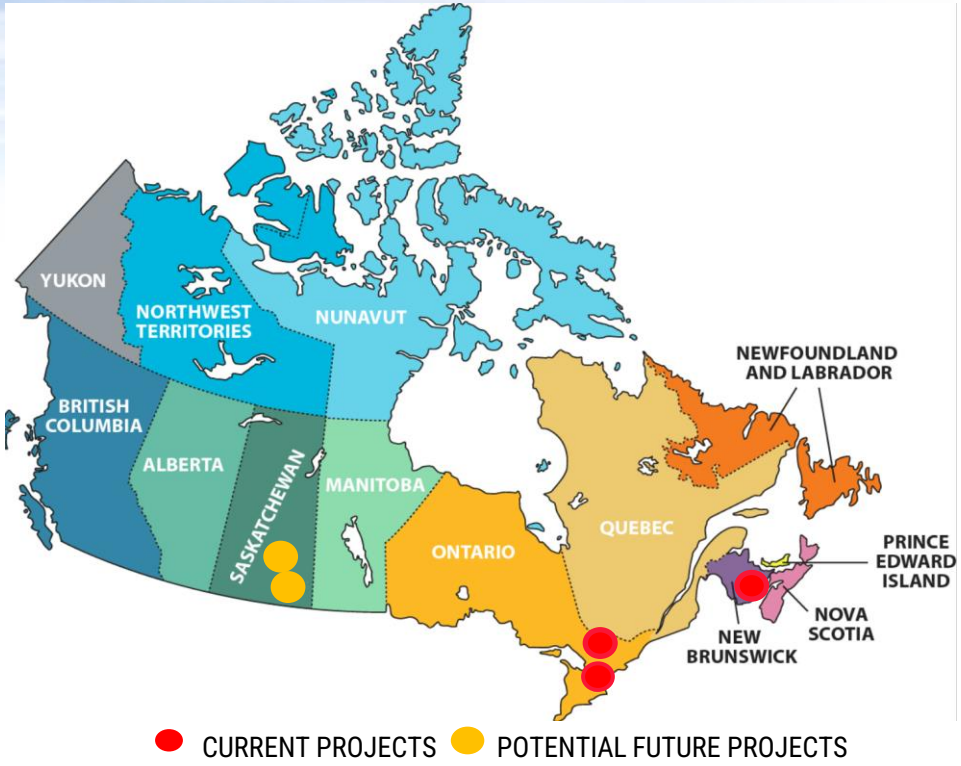

CNSC Regulatory Framework and Philosophy

- Key REGDOCS for SMR and innovative technologies:
  - REGDOC-1.1.1 *Site Evaluation and Site Preparation for New Reactor Facilities*
  - REGDOC-1.1.2 *Licence Application Guide for Construction*
  - REGDOC-1.1.5 *Supplemental Information for Small Modular Reactor Proponents*
  - REGDOC-2.5.2 *Design of Reactor Facilities*
- Other REGDOCs supporting safety analysis licensing activities:
  - REGDOC-2.4.1 *Deterministic Safety Analysis*
  - REGDOC-2.4.2 *Probabilistic Safety Assessment (PSA) for Nuclear Power Plants*
- Regulatory philosophy
  - Risk-informed, Performance-based, Technology-inclusive

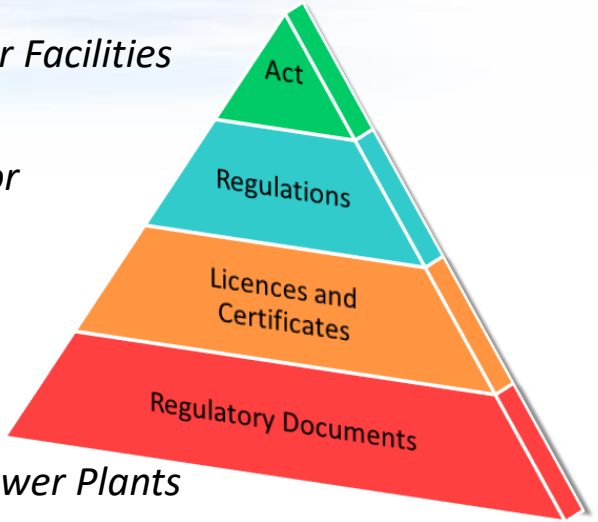

CNSC Licensing Expectations

Optional
Pre-licensing engagement

Vendor Design Review

Reactor vendor(s)
REGDOC 3.5.4, *Pre-licensing Review of a Vendor's Reactor Design*

Determining Appropriate Assessment Strategy

Potential applicant

Licensing Process

Transparent regulatory decision-making by the commission under the **Nuclear Safety and Control Act**

Licences for:

Site Preparation	Construction	Operation	Decommissioning
REGDOC-1.1.1, *Site Evaluation and Site Preparation for New Reactor Facilities*	REGDOC-1.1.2, *Licence Application Guide: Licence to Construct A Reactor Facility*	REGDOC-1.1.3, *Licence Application Guide: Licence to operate a Nuclear Power Plant*, Version 1.2	REGDOC-1.1.4, *Licence Application Guide: Licence to Decommission Reactor Facilities*

REGDOC 1.1.5, *Licence Applications Guide: Small Modular Reactor Facilities*
for all licensing stages of SMR facilities

CNSC Vendor Design Review Focus Areas

1	General NPP description – defence-in-depth, safety goals and objectives, and dose acceptance criteria	11	Pressure boundary design
2	Classification of systems, structures & components	12	Fire protection
3	Reactor core nuclear design (e.g. core physics)	13	Radiation protection
4	Fuel design and qualification	14	Out-of-core criticality
5	Control systems and facilities (main control systems, instrumentation and control, control facilities, emergency power systems)	15A 15B 15C	Robustness Security and Cyber Security Safeguards
6	Means of reactor shutdown	16	Vendor research and development program
7	Emergency core cooling and emergency heat removal systems	17	Management system of design process and quality assurance in design and safety analysis
8	Containment and safety important civil structures	18	Human factors
9	Beyond Design Basis Accident (BDBA) and severe accident prevention and mitigation	19	Incorporation of decommissioning into design considerations
10	Safety Analysis (Deterministic Safety Analysis, Probabilistic Safety Analysis, Internal and External Hazards)		

*green highlighted are objectives that directly address severe accidents

Canada's SMR Readiness

❑ Readiness project objectives

- optimize the CNSC's readiness to license and regulate SMRs
- position the CNSC as an international leader in SMR regulation
- engage Indigenous Nations and communities, and stakeholders early and often where SMRs may be located

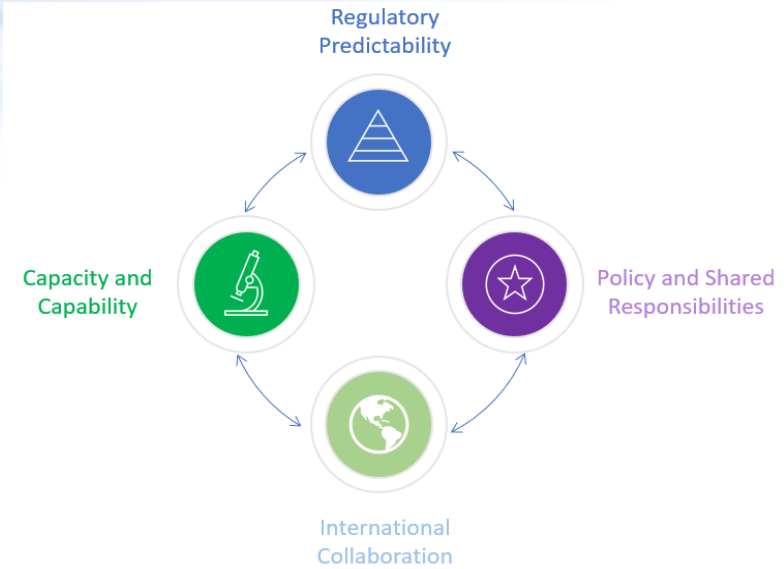

❑ Readiness will address challenges

Canada's SMR Readiness – Capacity and Capability

CAC 1: Revisit Approach to Interpretation of Requirements	CAC 8: Safeguards for ARTs and Remote Reactors	CAC 15: Separating Nuclear Island vs Balance of Plant	CAC 22: Utility, Factory, Transporter Relationship and Interconnections - 'Intelligent Customer' Roles
CAC 2: Addressing Fuel Qualification of Novel Fuels	CAC 9: Chemistry Control for Novel Technologies	CAC 16: Multi-Unit Risk Assessment - Modular	CAC 23: SMR Regulatory Research Work
CAC 3: Addressing Novel Means of Containment/Confinement	CAC 10: Addressing Novel Digital Instrumentation and Control Hardware and Software	CAC 17: Remote Monitoring and Operation	CAC 24: Knowledge Management Process
CAC 4: Addressing Novel Means of Shutdown	CAC 11: Site Security Provisions	CAC 18: Artificial Intelligence, Machine Learning, Digital Twins	CAC 25: Reg Officer Training Program
CAC 5: EPZ for SMRs and Micro Reactors	CAC 12: Robustness Requirements (civil structures)	CAC 19: Transportation of Radioactive Reactor Components	CAC 26: Establish Process to Quickly Obtain Expertise
CAC 6: Updates to Cyber Security Requirements	CAC 13: Novel Construction Materials for ARTs	CAC 20: Deconstruction Technologies	CAC 27: General Training Plan
CAC 7: Computer Codes for Safety Analysis	CAC 14: Readiness to Assess Novel Construction Techniques & Performing OPEX Review to Prepare	CAC 21: Marine-Based SMRs	

*green highlighted are objectives that "directly" address severe accident
(CAC.12/13/14 indirectly linked to severe accidents)

Technical Safety Objectives for New NPPs

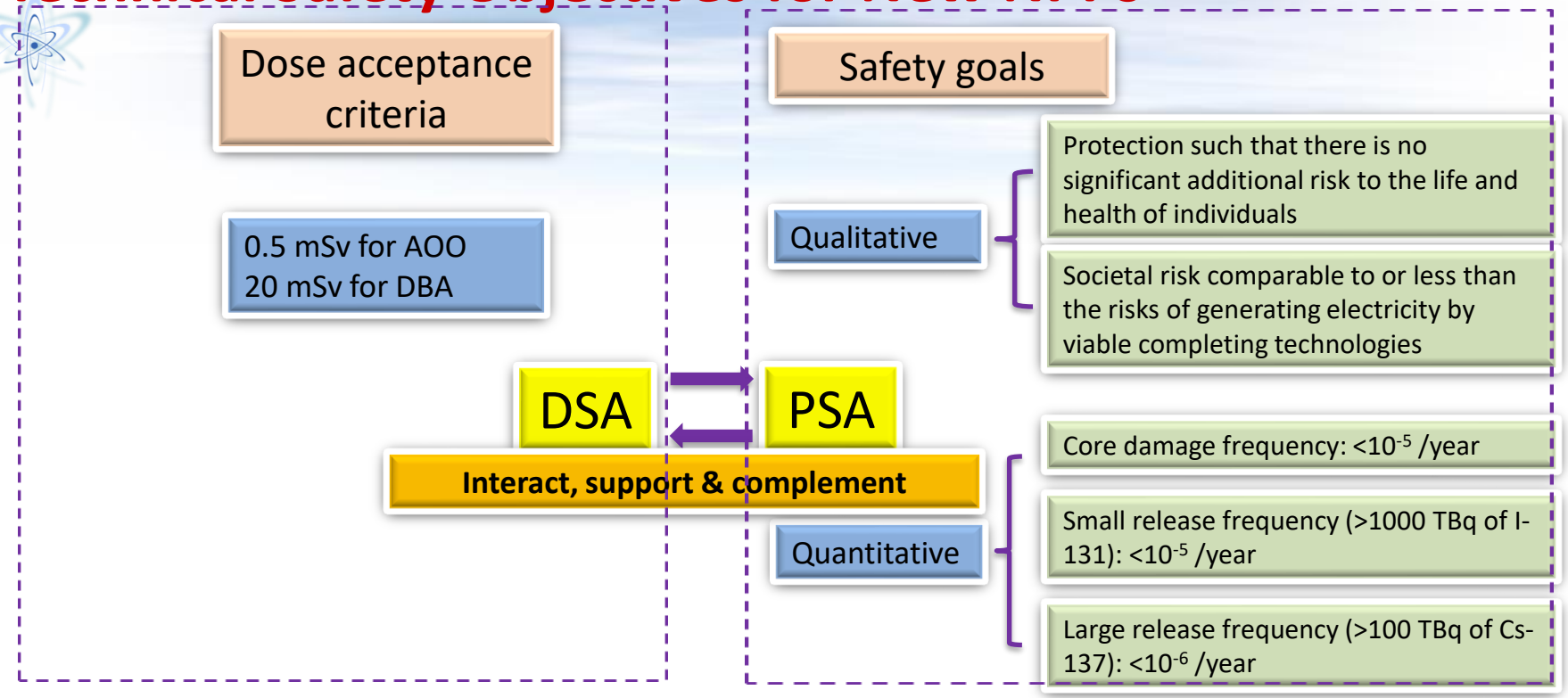

DSA and PSA Roles

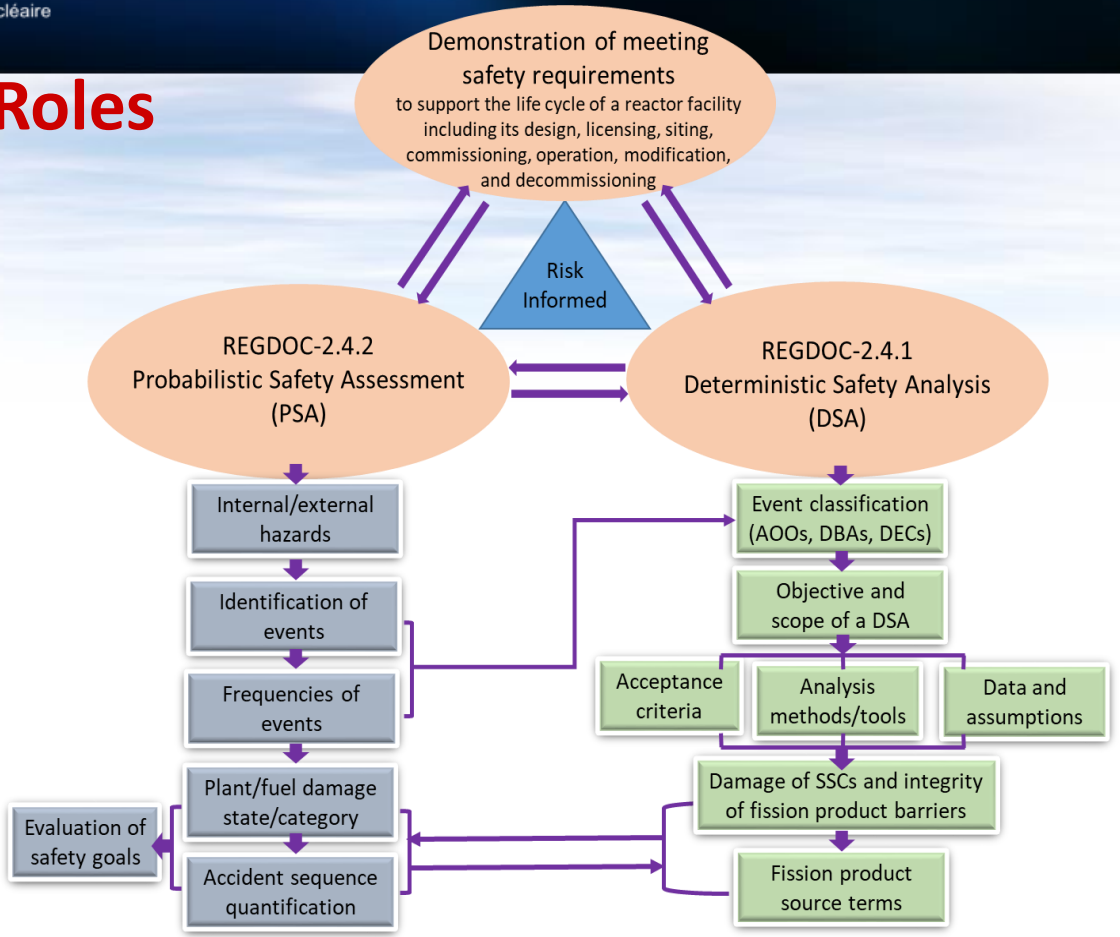

Regulatory Requirements – Accident Management and Emergency Planning Zone (EPZ)

- REGDOC 2.3.2 – Accident Management
  - establish regulatory requirements and expectations for
    - accident management including severe accidents
    - human/organizational performance
  - REGDOC required for licence to operate (LTO)
- REGDOC 2.10.1 – Nuclear Emergency Preparedness and Response
- REGDOCs 2.3.2 and REGDOC 2.10.1 linked and support each other

Regulatory Philosophy on SAM

- Accident prevention
  - prevent escalation of accident and maintain the integrity of fission product barriers
- Accident mitigation
  - terminate the accident and minimize the release of radioactive releases
  - achieve a long-term stable state
- Major lessons from Fukushima
  - ensure heat sink availability in the event of damaged SSCs for cooling
  - obtain alternate on and off-site electrical power supplies in the event of loss of power
  - install additional filtered release path (containment filtered venting system) to protect containment integrity and minimize releases
  - incorporate emergency mitigating equipment (EME) procedures into SAM

Innovative Technologies to Mitigate Severe Accidents

Specific Objectives of Accident Management

Terminate	Prevent	Maintain	Minimize	Achieve

Expectation 1 Physical and procedural barriers to cope with severe accidents are identified

Expectation 2 Equipment and Instrumentation (E&I) to mitigate accidents :

- Complementary design features
- Systems, Structures and Components (SSC) specific to mitigate accidents consequences
- SSC function extended beyond their intended function mitigate accidents consequences
- Onsite and offsite fixed and portable equipment and their points/ports

Expectation 3 E&I Operability

- E&I functions, and location (if portable) are identified
- Reasonable assurance of E&I survivability during accidents

Innovative Technologies to Mitigate Severe Accidents

Expectation 4 Potential challenges to containment are addressed:

- Design Extension Conditions (DECs) and Severe Accident scenarios that challenge containment integrity are identified
- Containment mitigative design features (active and passive systems)

Expectation 5 Radiological Shielding for DECs and Severe Accidents

- Multiple vessels
- Double containment
- Spent Fuel Pool (SFP) containment or containment-like structure

Main Challenge

Demonstrating the functionality of the suggested preventive and mitigation strategies for the design as continous and extensive R&D is required to support design and validate simulations

Application of Requirements and its Challenges

- Use of section 9 of REGDOC 2.5.2, *Alternative Approaches* for certain areas:
  - approach to addressing defence-in-depth in the design
  - means of shutdown
  - emergency core cooling and heat sinks
  - means of containment
- Issues to be addressed by CNSC in a technology neutral fashion to cover multiple technology approaches

Severe Accidents and Regulatory Challenges - Containment

CNSC Requirements

- State that an NPP shall have installed a containment structures that must be:
  - designed to be leak tight
  - classified as safety systems
  - protect against external hazards
  - provide radiation shielding

Proponents/Vendors

- To use alternatives approach to fulfill the same safety objectives:
  - engineered fuels with superior performance during plant events
  - improving retention of radionuclides such that failures of barriers will practically eliminate a large release
- CNSC proposing functional containment that satisfies the regulatory intent
  - Risk-informed functional and performance requirements

Severe Accidents and Regulatory Challenges - EPZ

- The challenge
  - Some SMR developers are seeking ways to reduce/eliminate emergency planning zones (EPZ), considering technology improvements such as passive and inherent safety systems
    - to reduce scope of level 3 and 4 defence-in-depth (for mitigating the consequences from DEC)
    - to possibly eliminate level 5 defence in depth and associated emergency preparedness requirements
- CNSC is developing a methodology for EPZ determination for licensing
  - benchmark with other regulator methodology (USNRC and ONR)
  - collaborate on alignments of EPZ determination for SMRs and advanced reactors

CNSC Regulatory Approach to Severe Accidents

- Recognize alternative approaches
- Recognize that novel techniques/features present challenges and provide opportunities to enhance safety and security
- Consider vendors/applicants claims and the evidence supporting them
- Evaluate existing requirements to document the underlying intent
- Perform proactive research development efforts including:
  - phenomena identification ranking tables (PIRT) for SMR designs, ATFs, in vessel retention (IVR) strategies, EPZ and strengthening of codes and regulation
- Collaborating with other Regulators
  - trilateral MOU with ONR and USNRC
  - develop shared approaches, collaborate on licensing, research and training

CNSC's Approach to Reviewing Innovative Features

- Three safety objectives from REGDOC-1.1.2 v2 must be met:
  - design safety objective
  - construction program objective
  - qualification objective
- Example of assessing first of a kind (FOAK) SSCs and innovative features:
  - steel concrete composite observations at DOE by CNSC and USNRC
  - Phenomenon Identification Ranking Table (PIRT) for Design Extension Conditions (DECs) (i.e., events resulting in uncovering of fuel assemblies)

PIRT for Design Extension Conditions

Phenomena Identification Ranking Table (PIRT)

- Used by CNSC as a systematic process to identify the phenomena that impact the Safety and Control Areas
- PIRT is to identify gaps in knowledge to highlight to the CNSC phenomena that need more modelling effort and/or higher level of confidence in severe accident analysis (when modelled in “Safety Analysis”)
- Identified gaps will form the basis for future research

Figure-of-Merit (FOM) *should be a continuous parameter that can be tracked through the accident phases.*

Suggested parameters:

- ✓ *Source Term*
- ✓ *Hydrogen*
- ✓ *Fuel temperature*
- ✓ *Fuel clad temperature*
- ✓ *Containment temperature*
- ✓ *Containment pressure*

Conclusion

CNSC's regulatory framework is flexible and applicable to all novel reactors including SMRs

SMR readiness project drives continuous improvement

CNSC engages in Severe Accidents Research to address challenges facing SMR deployment

International and stakeholder cooperation is key in addressing Severe Accidents in SMRs

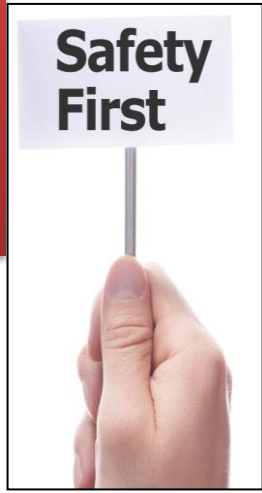

CNSC is ready to regulate innovative technologies and SMRs

Thank you!



Visit us online

Like us on Facebook

Follow us on Twitter

View us on YouTube

Subscribe to updates

Contact us

Office for Nuclear Regulation

Regulatory Perspective: Beyond Design Basis Analysis and Expectations on New Reactor Designs

Prof. Ali Tehrani

ERMSAR 24
KTH – Stockholm, Sweden
13-15 May 2024

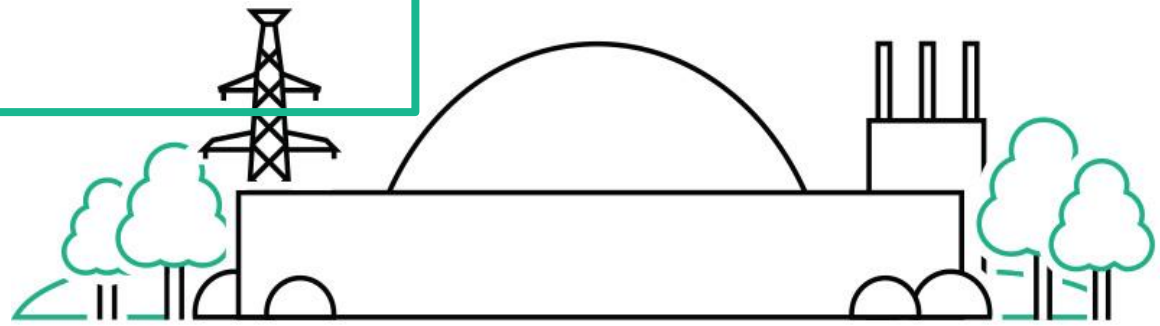

Overview

To provide a brief update and recent development relating to severe accident analysis covering;

- Post-Fukushima response and review,
- Explore and compare UK's 3 types of Fault Analysis Methods: Risk assessment→ F/S→ PSA → Severe Accidents Analysis (SAA),
- Focus of severe accident analysis and output of the analysis,
- Current designs being considered as part of GDA,
- Expectation for severe accident analysis,
- Expectations of the SAMGs, and

Stimulate thinking and discussion!

Background

- Post Fukushima – at the time - discussions with other International Regulators and ENSREG Stress Tests: It appeared that we did not all have a common understanding;



- Believe better Severe Accident Management (SAM) from better Severe Accident Analysis (SAA) will be the lasting legacy from Fukushima.

UK Post-Fukushima Response

A historic Perspective:



- Two “Weightman* Reports”
- ENSREG Stress Tests
  - Including for non-NPPs
  - Majority of UK operating plants are AGRs,
  - One operating PWR and two under construction,
    - Sizewell B (PWR) is continuing to implement the resilience enhancement measures.
- In present (SAA / SAM) context:
  - Has focussed minds on need for better SAA and SAM
  - New guidance (SAPs and TAGs)+ have incorporated the learning from Fukushima
    - New reactors submitted for the GDA would need to comply with the new guidance and standards

* Dr Mike Weightman was HM’s Chief Inspector of Nuclear Installations at the time of the Fukushima accident.

\+ Safety Assessment Principles and Technical Assessment Guides.

++ Generic Design Assessment

UK's Three Fault Analysis Methods

Guidance provided to Inspectors on risk assessment in our SAPs

[Safety Assessment Principles for nuclear facilities (onr.org.uk)]

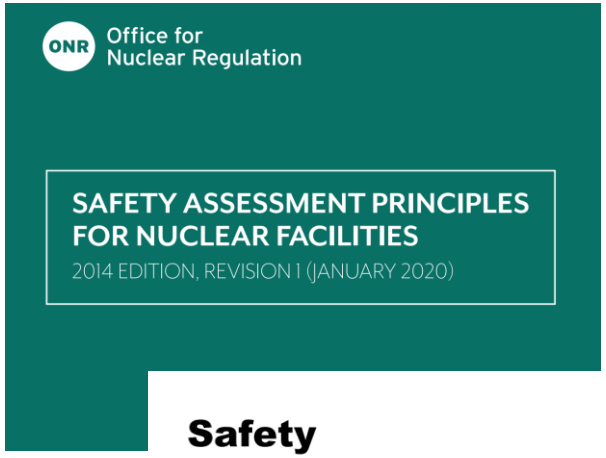

Safety Assessment Principles for Nuclear Facilities

2014 Edition, Revision 1 (January 2020)

Redgrave Court
Bootle
Merseyside
L20 7HS

General

Fault analysis: general	Design basis analysis, PSA and severe accident analysis	FA.1
Fault analysis should be carried out comprising suitable and sufficient design basis analysis, PSA and severe accident analysis to demonstrate that risks are ALARP.		

What is a Severe Accident

ONR's SAPS ***(Guidance for ONR inspectors)***

ONR's Definition:

Severe accidents are those faults with off-site consequences with the potential to exceed 100 mSv, or to a substantial unintended relocation of radioactive material within the facility that places a demand on the integrity of the remaining physical barriers.

ONR guidance is technology neutral,

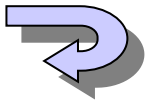

In addition to our SAPs, we predominately use IAEA's SSG2 to guide our S/A assessment of the new reactors.

IAEA SSG-54: Severe Accident Management Programme at Nuclear Power Plants:

*A Beyond Design Basis Accident comprises accident conditions more severe than a design basis accident, and may **or may not** involve core degradation. Accident conditions more severe than a design basis accident and involving significant core degradation are termed severe accidents.*

Other International Standards

- ONR's TAG includes guidance on interpretation of international expectations for consideration of 'Design Extension Conditions' (DEC) and for the 'practical elimination' of early or large releases of radioactivity.
- It is acknowledged that for NPPs the international definitions of DEC refer to two types of conditions depending on the level of fuel damage.
- Our SAA TAG focuses on fault scenarios with core melting/severe fuel damage, which is termed 'DEC B' by WENRA, although consideration of 'DEC A' as a form of deterministic analysis additional to that considered as part of DBA.
  - consistent with WENRA and SSG-2 expectations.
- ONR's TAG also recognises the role of SAA in demonstrating practical elimination of large or early releases - consistent with WENRA guidance.

DBA, PSA and SAA Compared

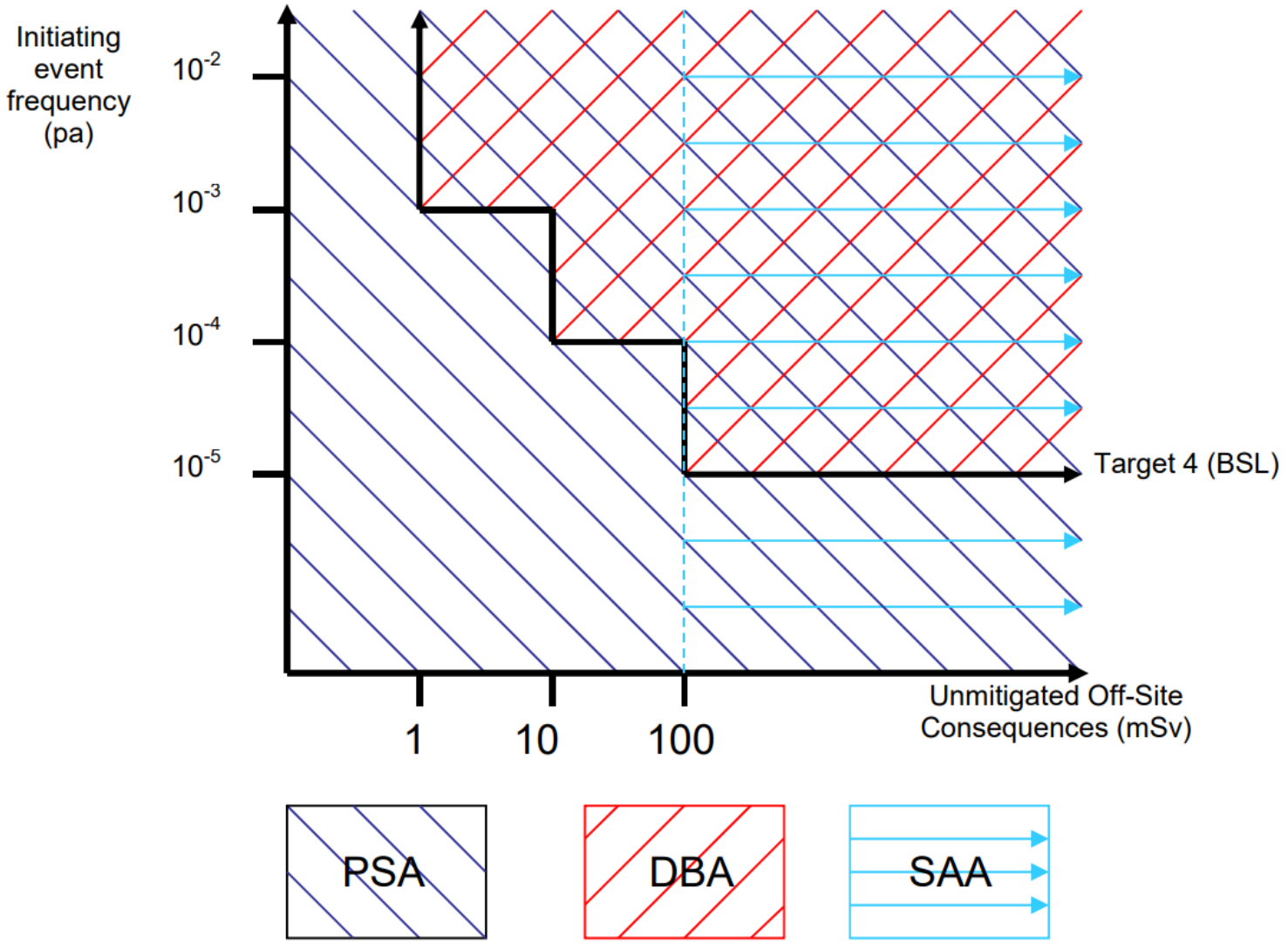

Schematic illustration; Indicative regions of applicability of different fault analysis approaches

Complementary Approach - Fault Analysis

Three complementary approaches designed to ensure nuclear Fault Analysis is adequate in its totality

- **DBA:** Design Basis Accident Analysis

  to ensure the design is robust, fault tolerant and has effective safety measures,

- **PSA:** Probabilistic Safety Analysis

  to ensure overall risks are acceptable and balanced; and to understand strengths, weaknesses and inter-dependencies in the overall design,

- **SAA:** Severe Accident Analysis

  to ensure provision of any further safety measures (defence in depth) and planning for severe but unlikely accidents.

Scopes of Each Activity

- **DBA:**
  - Sequences with IEF>10^{-5}/yr, excluding those that fail to meet consequence thresholds,
    - Natural external hazards IEF>10^{-4}/yr, conservatively designed
  - Analysis focuses on: prevention and protection
- **PSA:**
  - All sequences down to very low IEFs,
  - Analysis focuses on: protection (and mitigation)
- **SAA:**
  - Sequences leading to core melt,
  - informed by the L1 PSA
  - Analysis focuses on: mitigation and (protection)

DBA, PSA and SAA Compared

Methodologies:

- **DBA:**
  - conservative according to strict, deterministic rules;
- **PSA:**
  - best estimate, probabilistic supported by deterministic calculations;
- **SAA:**
  - best estimate deterministic calculations, supported by substantiated research outcome.

ONR – GDA – New Reactors Being Assessed

Three reactors are currently being assessed:

- Rolls-Royce SMR
- Holtec SMR-300
- GE-Hitachi BWRX-300

Early engagements with other Requesting Parties

ONR – GDA – New Reactors Being Assessed (1/3)

- Rolls-Royce SMR:
  - Three loop PWR 470MWe,
  - Safety measures include both passive and active, with emphasis on the passive measures,
    - Although the passive decay heat removal safety measure requires active systems in certain fault scenarios.
    - The emergency core cooling is passive (following initiation) with no operator action required for at least 24 hours. Based on natural circulation for decay heat removal and the volume of three redundant local ultimate heat sink vessels.
  - IVMR being proposed.

ONR – GDA – New Reactors Being Assessed (2/3)

- Holtec SMR-300
  - PWR 300MWe with 2 loop with a single steam generator,
  - Claimed safety measures are primarily passive measures, although some measure require active initiation;
    - The primary circuit includes a passive heat-exchanger cooled by an in-containment water tank, and
    - The secondary circuit that includes a passive heat-exchange penetrating through the containment into the annular reservoir,
  - Annular cooling water reservoir is claimed to provide the ultimate heat sink for primary cooling system and passive containment cooling during DBA, DEC-A and DEC-B scenarios,
  - IVMR being proposed,
  - Claimed 72 hours passive systems operations without human intervention.

ONR – GDA – New Reactors Being Assessed (3/3)

- GE-Hitachi BWRX-300
  - A BWR 300MWe natural circulation primary side direct cycle,
  - Safety measures include both passive and active, with emphasis on the passive measures, although some measure require active initiation,
    - The primary circuit includes an isolation condenser cooled by open pool positioned outside,
    - There are three redundant condenser,
    - Each condenser is capable of 7 day decay heat removal capability, and provide overpressure protection to the RPV,
    - Some similar ABWR technology safety measures are proposed.
  - The design provides containment which comprises steel concrete composite plus containment isolation valve.
  - The design does not include a wet well, nor pressure relief valve on the RPV.

Expectation for Severe Accident Analysis

Rigorous application of DBA and PSA should ensure that the predicted risks from fault sequences leading to significant radiological consequences are very low.

- The severe accident analysis should provide information to:
  - assist in the identification of any further reasonably practicable preventative or mitigating measures beyond those derived from engineering analysis, DBA and PSA;
  - form a suitable basis for accident management strategies and procedures;
  - support the preparation of emergency plans for the protection of people; and
  - support the PSA of the facility’s design and operation.

Scope of Severe Accident Analysis

ONR expect that the scope includes all possible states and configurations in which a severe accident can occur.

- The scope should include:
  - High consequence events of low frequency beyond the design basis; and
  - Design basis events where the safety provisions are assumed to fail.
- Full range of SA phenomena should be considered in the severe accident analysis;
  - Where phenomena are screened out, i.e. that the design is not specifically designed to mitigate phenomena, then appropriate arguments should be provided, and
  - This demonstration may be made through a combination of arguments which may include analyses, in-house research, international research, a demonstration that the effects have negligible impact on the progression of the transient, that uncertainties can be bound by conservatisms, or
  - That the occurrence is of low likelihood (which may also be based on PSA or the above considerations).

Expectations of the SAMGs

ONR expect that, so far as reasonably practicable, that SAMGs are based upon the SAA

- **The Key aspects where the SAA can provide input to the EOPs and SAMGs include:**
  - Identifying the symptoms that will allow the operators to identify the true state of the plant and / or imminent escalations in severity;
  - The timescales and priorities for action;
  - Appropriate points for enacting the transition from Emergency Operating Procedures (EOP) to SAMGs;
  - Identifying alternative scenarios for how the accident might escalate and an analysis of the likely effectiveness of different strategies, including the pros and cons of each;
  - Analysis of the expected radiation dose levels and means of minimising exposures;
  - Through task analysis, whether the procedures and SAMGs could reasonably be expected to be followed in the likely severely degraded plant condition following a severe accident;
    - The UK regulators looks to OPEX from emergency exercises to inform the SAMGs developments.
  - Helping to quantify the numbers of operators needed to address steps in the procedures / stages in the SAMGs;
  - Other human factors aspects of the EOPs and SAMGs; such as, the availability and use of communications systems and control structures.

Summary

Summary:

- Post-Fukushima response and review,
- Explore and compare UK's 3 types of Fault Analysis Methods,
- Review of severe accident analysis and output of the analysis,
- Designs being considered as part of GDA,
- Expectation for severe accident analysis,
- Expectations of the SAMGs, and



Questions and Thank You

Strål säkerhets myndigheten
Swedish Radiation Safety Authority

Applicability of new Swedish regulations to Small Modular Reactors

Opportunities and challenges of a performance based approach

Aino Obenius Mowitz

Swedish Radiation Safety Authority

Presentation Outline

- Swedish Regulatory Framework
- Regulation of severe accidents
- Applicability to SMRs
- Challenges and opportunities



Swedish Regulatory Framework

Summary of basic information on the national programme

- Locations of nuclear facilities and activities in Sweden
- Final repository for spent nuclear fuel approved to Forsmark site
- Encapsulation plant planned at Oskarshamn site
- Shift towards SMR/novel designs
  - New policy
  - Feasability studies etc.

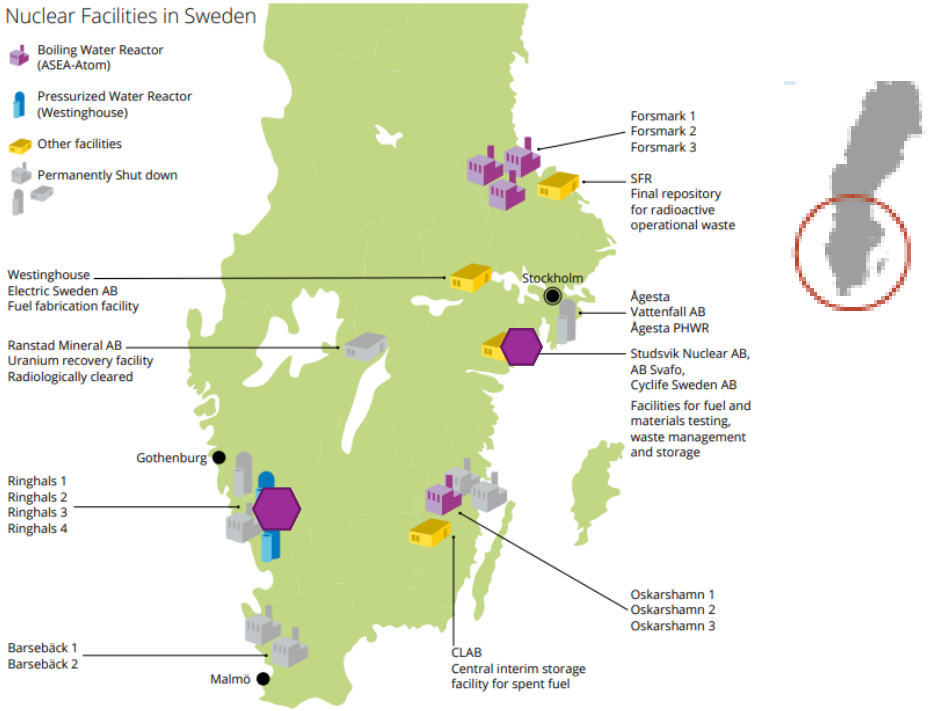

Hierarchy of the Swedish regulatory framework

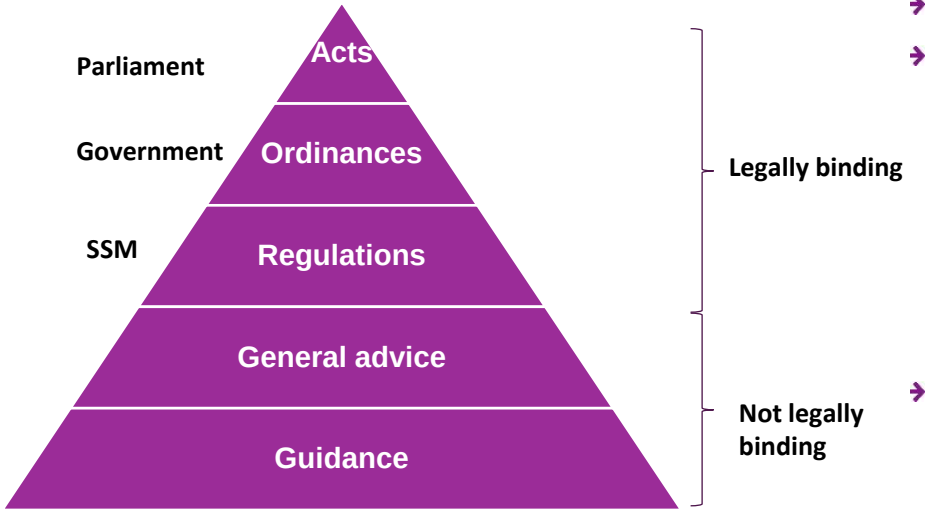

SSMs mandate to regulate

- Legally binding regulations
- General advice
  - strong recommendations on how to implement requirements
  - measures should be taken according to the general advice, or alternative measures that are justified
- Guidance
  - explanations and examples of application of requirements
  - background and motives for requirements

Schematic illustration of the new structure of regulations for nuclear facilities

- An extensive national review of the legal framework is carried out.
  - New Act on Radiation safety
  - Proposal on new Act on Nuclear Activities,
  - Level 2
    - NPP regulations in force 2022
    - Regulations for geological disposal facilities and other nuclear facilities are being developed for external consultation
  - Rev. and new ‘level 3’ regulations

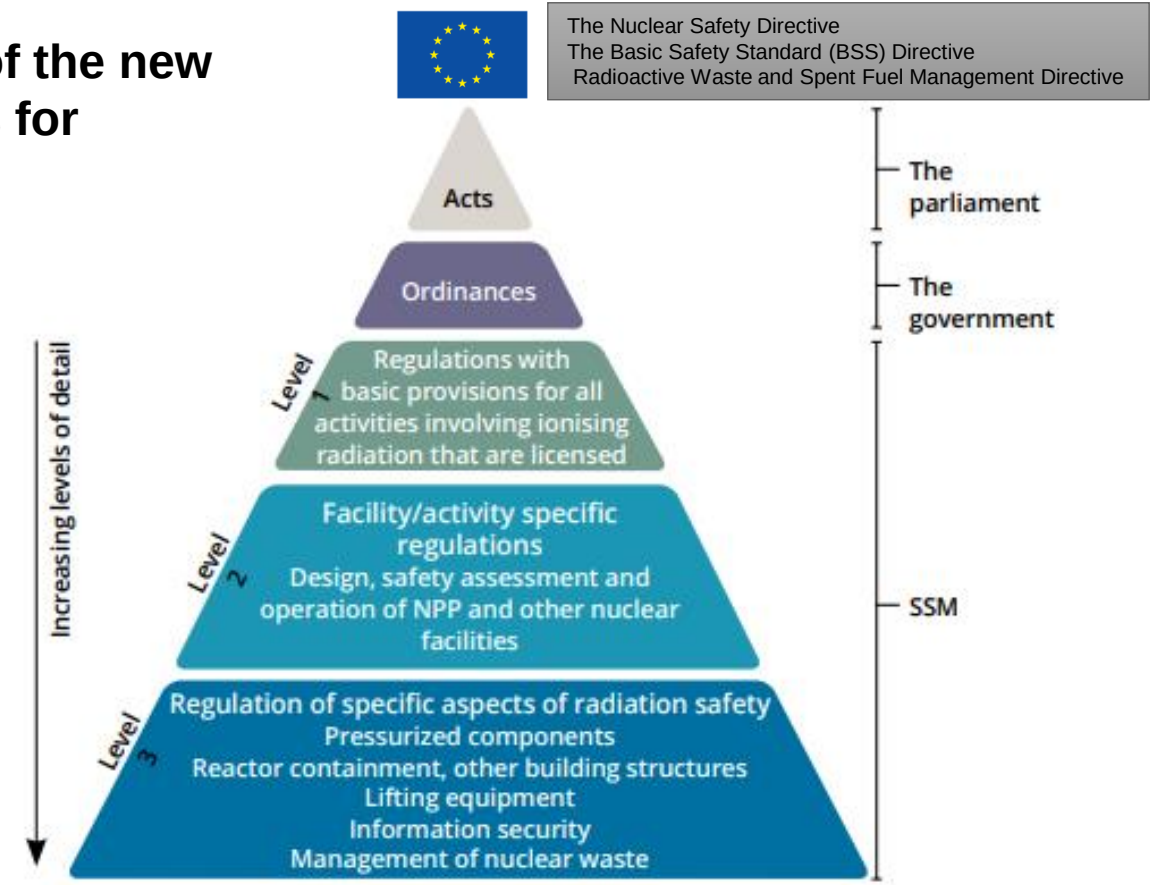

Regulation of Severe Accidents

A perspective on how the regulation of NPPs (and other nuclear facilities) has evolved over time in Sweden

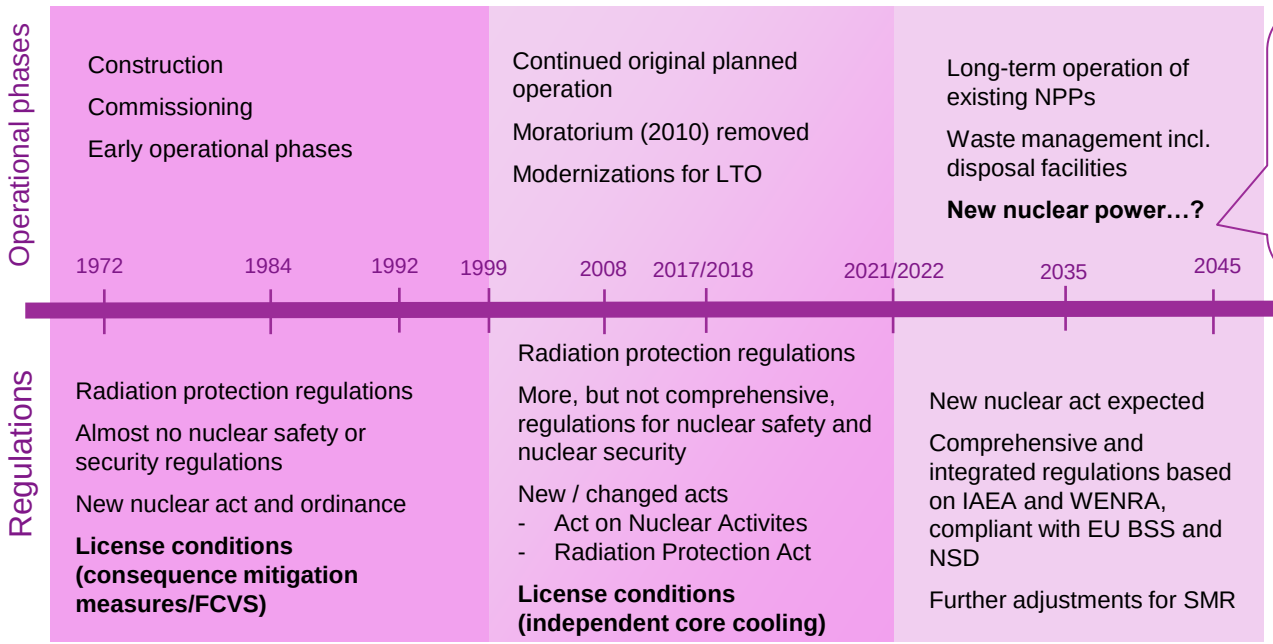

Examples of requirements relevant for SA

- **Before**: Mixture of defined terms, overall design goals and prescriptive criteria and design measures. Combination of license conditions and regulation.

- **New regulations**: Clearer ’building blocks’ of regulation as basis to identify, assess and justify the need of specific measures in design and operation;
  - *main safety functions*,
  - *events and conditions* (~*plant states:* normal operation – design extension conditions*),
  - *radiological acceptance criteria* for all *plant states*.

Examples of requirements relevant for SA (cont.)

- **Before**: Government decision defining criteria as well as prescriptive requirements, as:
  - ”No fatalities due to acute radiation syndrome”
  - ”Containment function shall be intact for the first 10-15 hours after onset of severe accident”
  - ”no permanent relocation of public population” (…)

    → Filtered Containment Venting is required for existing NPPs
- **New regulations**: Confinement functions (and other main safety functions) to be fulfilled for all *plant states.*
  - E.g. related to criteria of no off site severe deterministic effects, maximum release of 100 TBq Cs-137 (for existing reactors).
  - Plant event sequences that could lead to an *early radioactive release or a large radioactive release* shall be demonstrated to be *practically eliminated.*
  - Few prescriptive requirements related to e.g. containment and spent fuel pool, but not e.g. FCVS, core-catcher, containment spray or other ESF’s.
  - However this may be implicitly required due to the expectations on containment functions and Best Avaliable Technique, in relation to a specific reactor design and related design basis.

Applicability to SMRs

Government assignment on new nuclear

- The government assigned SSM (august 2022) to review which development of the legal framework and other measures that were needed to give preconditions to utilize both
  - existing, and
  - new nuclear power*, such as SMR.

- SSM to give suggestions on how the identified needs for new/changed preconditions could be met, e.g.
  - propose new or changed provisions within existing acts and ordinances, and identify need to review regulations (SSMFS).

*) incl. Evolutionary and Innovative Designs (EID), assessment supported e.g. by IAEA TECDOC-2010 and the IAEA Safety Report Series no. 123 (Applicability of Safety Standards to Non-Water-Cooled Reactors and Small Modular Reactors).



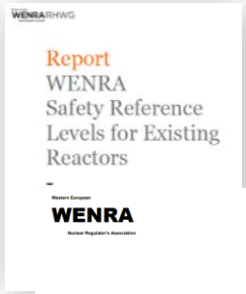

Safety Objectives
for New Power Reactors

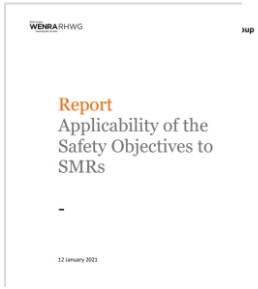

IAEA
International Atomic Energy Agency
Atoms for Peace and Development

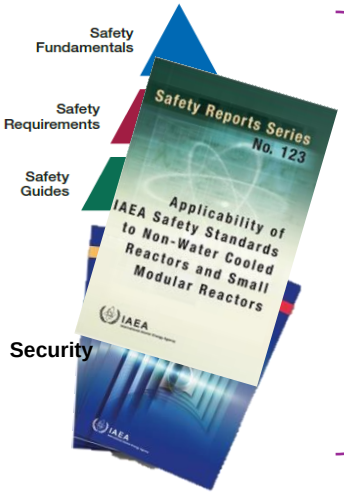



The Nuclear Safety Directive
The Basic Safety Standard (BSS) Directive
Radioactive Waste and Spent Fuel Management Directive

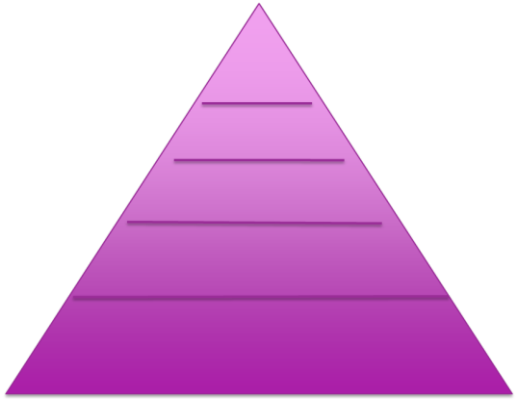

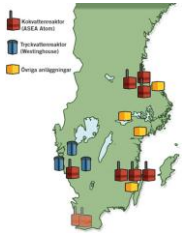

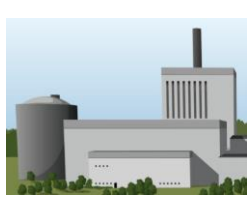



SSMFS

Results – applicability of regulations

- SSM regulations are to a high degree applicable to new nuclear power.
  - Developed mainly for light water reactors (LWR).
  - Performance based and technology inclusive approach allows for application to other designs (main safety principles apply).

- Examples of possible need for further investigation and review:
  - Radiological acceptance criteria for new nuclear (ongoing).
  - Requirements on design and organisational measures for Emergency Preparedness and Response (EPR) based on assumption that NPPs would be EPR Category 1 facilities – may not be the case.
  - Expectations and different design proposals on the need of, location and possible multi-module operation from a single Control Room.
  - Review and assessment of events and conditions and postulated events relevant for different designs may be needed (clarifying guidance, if not directly prescribed).



Inquiry on licensing of new nuclear

- Committe of Inquiry - work ongoing 2023-2026
  - Analyse and propose possible legal changes to clarify important pre-requisites and issues in the existing licensing process for nuclear power in Sweden.



- Issues to be investigated:
  - Make the licensing process more effective
  - Review the licensing fees for new nuclear power
  - Assess the national system for nuclear waste management
  - Assess the need for a graded approach for some emergency preparedness and response measures – applicability for different reactor designs?
    - Exclusion and planning zones
    - Arrangements to transfer process parameters to the authority in emergency situations

Challenges and opportunities

Conclusions

- Balance of priority
  - Planned revisions of regulations, ensuring applicability for existing and new nuclear facilities
- Application of regulatory framework to existing and new designs
  - Continuous effort to identify and manage interfaces and the application of the graded approach in implementation, licensing review and oversight etc. in a balanced way.
  - Experience from application of new regulations, new input from international cooperations etc. need to be continuously evaluated.
  - Review needs may depend on which reactor designs that may be valid for use in Sweden.
    LWR (large scale and SMR) vs. e.g. LFR.
- Knowledge and capacity building
  - International cooperation
  - Need for more knowledge, experience and guidance for new designs
  - Pre-licensing review
  - Research – extra funds for new nuclear, several proposals related to severe accidents.



Questions?
Thank you!

Credit: Patrick Isaksson & Ninos Garis



Här hittar du Strålsäkerhetsmyndigheten

E-post

registrator@ssm.se

Telefon

08 – 799 40 00

Webbplats

www.ssm.se

Sociala medier

Twitter.com/stralsakerhetsmyndigheten

Youtube.com/stralsakerhetsmyndigheten

Linkedin.com/company/stralsakerhetsmyndigheten

The 11th European Review Meeting on Severe Accidents Research

May 13-16, 2024, Royal Institute of Technology, Stockholm, Sweden

POSTER SESSION		
ID04	**MELCOR 2.2 analyses of passive systems modeling based on the PANDA facility experiments** M. Malicki (PSI)	**Paper** **Poster**
ID128	**Model Development for the Simulation of Fission Product Release from Molten Pools** F. Krist (PSS-RUB)	**Paper** **Poster**
ID14	**Severe Accident Sequence of LOCA for APR1400 using CINEMA Computer Code** Rae-Joon Park (KAERI)	**Paper** **Poster**
ID20	**Comparative Study of the Hydrogen Distribution Among Different PWR-W Lumped-Parameter and 3D Containment Models with GOTHIC 8.3 (QA)** A. García-Herranz (UPM)	**Paper** **Poster**
ID22	**Thermophysical property measurement of oxide melts using aerodynamic levitation** Y. Gong (CNPE)	**Paper** **Poster**
ID23	**PLINIUS – experimental platform for nuclear excellence** A. Bachrata (CEA)	**Paper** **Poster**
ID31	**Thermodynamic Evaluation of Liquid-Gas Surface Tension for U-O-Zr Mixtures Using the Butler Equation** A. Tourneix (CEA)	**Paper**
ID32	**Analysis of combustible gases distribution with accident management action in a generic PWR-W containment** J. Fontanet (CIEMAT)	**Paper** **Poster**
ID34	**Development of 3D view application debrisEye for decommissioning of Fukushima Daiichi Nuclear Power Plant** T. Yamashita (JAEA)	**Paper** **Poster**
ID36	**Thermal shock resistant geopolymers as refractory material for core catcher** B. Mészáros (UJV)	**Paper** **Poster**

ID38	**Investigation of New Inorganic Materials for Nuclear Industry under Severe Accident Conditions** J. Hrbek (UJV)	**Paper** **Poster**
ID41	**Modeling of pool scrubbing and sensitivity analysis using GOTHIC** X. Wang (KTH)	**Paper**
ID49	**MELCOR analyses of Severe Accident sequences in an integral PWR with passive systems** F. Giannetti (Sapienza University of Rome)	**Paper**
ID52	**Development of severe accident simulation code for sodium-cooled fast reactors: SIMMER-V (2) Development and verification of detailed fuel pin model** S. Ishida (JAEA)	**Paper** **Poster**
ID61	**Analysis of the combustion risk mitigation inside the containment during a postulated severe accident in a PWR using the code package AC2** M. Müer (PSS-RUB)	**Paper** **Poster**
ID65	**Uncertainty quantification analysis with radiological consequences for a loss of cooling accident in a spent fuel pool** M. D'Onorio (Sapienza University of Rome)	**Paper**
ID67	**THS-15 Experimental Facility: Effect of Surface Roughness on CHF Values** D. Batek (UJV)	**Paper** **Poster**
ID81	**Cooperative Nuclear Safety Research Activities at the Nuclear Energy Agency in Response to the Fukushima-Daiichi Accident** Y. Kumagai (OECD/NEA)	**Paper** **Poster**
ID87	**Filtration efficiency of electrostatic precipitator for iodine particles in different gas atmospheres simulating the severe accident scenarios** S. Basnet (University of Eastern Finland)	**Paper** **Poster**
ID91	**Study on AP1000 accident diagnosis and treatment for loss of monitoring and control** Y. Yu (China Nuclear Power Engineering Co.)	**Paper** **Poster**
ID92	**Failure modes of the reactor coolant pressure boundary in high-pressure core melt accident scenarios** C. Bläsius (GRS)	**Paper** **Poster**
ID95	**Parametric sensitivity studies for RELAP/SCDAPSIM model of QUECH-20 test** N. Elsalamouny (LEI)	**Paper** **Poster**
ID102	**Assessment of how Zr-clad oxidation affects the speciation and release of FPs under accidental conditions**	**Paper** **Poster**

	C. Riglet-Martial (CEA)	
ID105	**LPM vs. 3D Analysis of an In-Vessel LBLOCA Sequence using the ALMARAZ NPP GOTHIC Containment Model** C. Gabicagogeascoa-Cuesta (UPM)	**Paper** **Poster**
ID109	**Some results of the AMICO project** G. Langrock (Framatome GmbH)	**Paper** **Poster**
ID110	**Effect of the Stages of the Accumulators on the Hydrogen Production During LOCA+SBO in BNPP VVER-1000** A. Hosseini (Shahid Beheshti University)	**Paper** **Poster**
ID112	**Comparative Study of Two Experimental Configurations with an Internal Compartment in the PANDA Facility** S. Arfinengo-del-Carpio (UPM)	**Paper** **Poster**
ID113	**Numerical Simulation of LIVE2D Two-Layer Melt Pool Experiment** P. Guo (Tsinghua University)	**Paper** **Poster**
ID114	**Severe Accident R&D in UJV Group** P. Vácha (UJV)	**Paper**
ID117	**Investigation of IVMR Strategy for BNPP-1 VVER 1000** A. Najafi (Sharif University of Technology)	**Paper** **Poster**
ID121	**Assessment of RELAP5-3D condensation models for small modular reactor passive safety** P. K. Bhowmik (INL)	**Paper** **Poster**
ID122	**V&V of nuclear fuel oxidation behavior in sleeveless SiC-matrix during air ingress accident** Y. Nishimura (University of Tokyo)	**Paper** **Poster**
ID125	**Numerical Analyses on Melt Water Interactions with Super Absorbing Polymers Added to the Cooling Water** M. Buck (University of Stuttgart)	**Paper** **Poster**
ID130	**Study on the influence of the Core support structure on the migration process of molten material** C. Wei (Nuclear and Radiation Safety Center)	**Poster**

MELCOR 2.2 analyses of passive systems modeling based on the PANDA facility experiments

Mateusz Malicki[1] and Terttaliisa Lind[2]

[1]Paul Scherrer Institute , Forschungsstrasse 111, 5232 Villigen PSI, mateusz.malicki@psi.ch
[2]Paul Scherrer Institute , Forschungsstrasse 111, 5232 Villigen PSI, terttaliisa.lind@psi.ch

Contact email: mateusz.malicki@psi.ch

Abstract

Many new reactor designs, among them different light-water small modular reactors, rely to a large extent on passive systems in accident conditions. These passive systems are based on natural circulation and convection, which may challenge the existing safety analysis codes. That's why the verification and validation of system codes is so important for the safety of existing and licensing of new designs.

In this work, the authors analyze containment thermal-hydraulic phenomena using the MELCOR 2.2 code, based on selected experiments conducted at the Paul Scherrer Institut PANDA facility. The focus is on studying natural convection and fluid circulation under accidental conditions in a containment-type geometry. For preliminary studies, the authors have chosen the HYMERES and SAMARA-ERCOSAM experiments to investigate various aspects of the containment atmosphere, including stratification, circulation, and the impact of safety systems.

The preliminary results, which include sensitivity analyses, allow for identifying containment phenomena that are satisfactorily represented with MELCOR2.2 analysis as well as those which pose challenges to the code. This work could help develop possible future recommendations for modeling this type of phenomena.

Keywords: Passive systems, MELCOR2.2, Containment behavior

PAUL SCHERRER INSTITUT

MELCOR 2.2 analyses of passive systems modeling based on the PANDA facility experiments

11TH CONFERENCE ON SEVERE ACCIDENTS RESEARCH
May 13-16, 2024 – Stockholm, Sweden
ERMSAR 2024

M. Malicki, T. Lind,
Paul Scherrer Institute Forschungsstrasse 111, 5232 Villigen PSI, Switzerland mateusz.malicki@psi.ch, terttaliisa.lind@psi.ch

Introduction

- The COMPARE project, focuses on validation of the MELCOR containment modeling based on the data provided by the PANDA facility which is a big scale experimental facility located in PSI.
- The MELCOR is a severe accident code and like in all severe accident codes implemented numerical models need to be simplified due to the complexity of the accident phenomenology. Due to that each kind of cross-checking calculation data with experiment and validation based on experiments are valuable work for severe accident community. It can highlight areas of high uncertainty and often helps to develop good practices for future analyses.

		HP6_2	
Phase	**injection**	Start [s]	Duration [s]
Phase 1	Steam	0	5106
Phase 2	No injection	5106	2994
Phase 3	Helium	8100	580
Phase 4	No injection	8680	7320
	Total time		16000

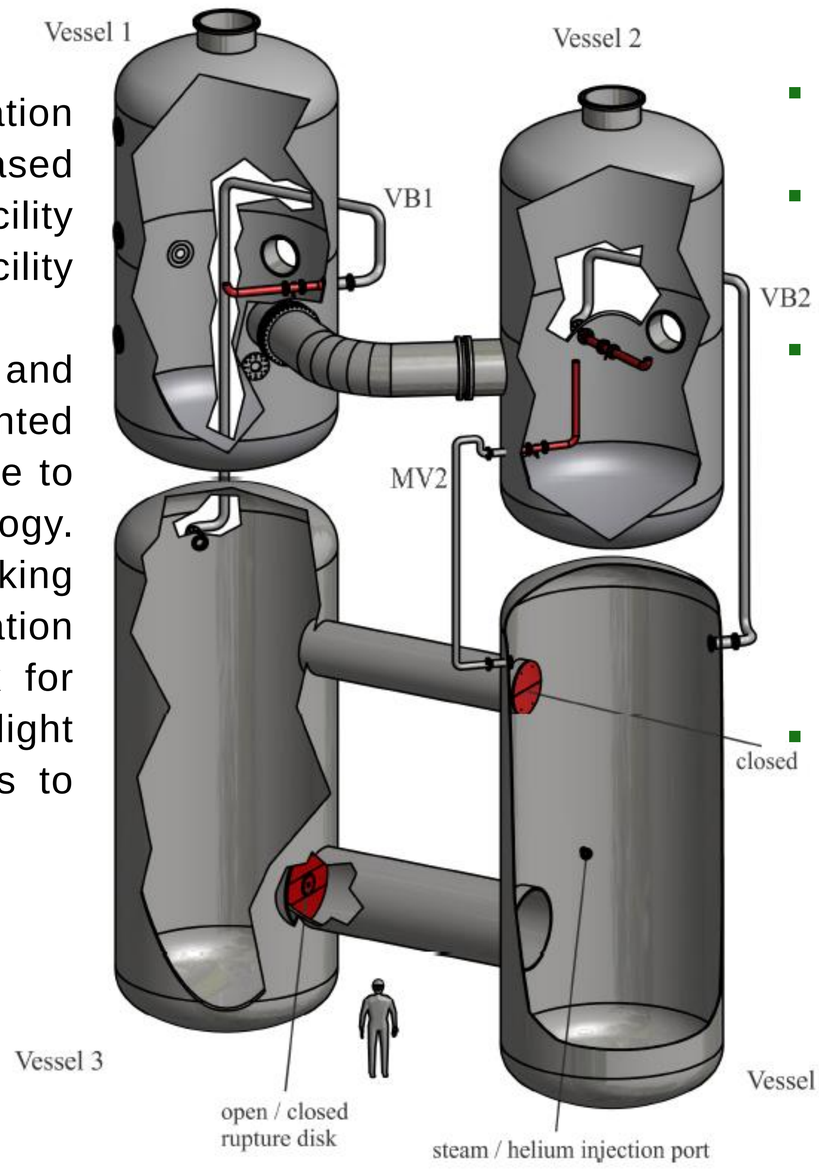

PANDA

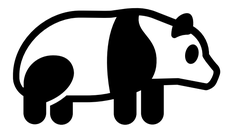

- PANDA facility is a large-scale TH facility at the Paul Scherrer Institute (PSI).
- It is 1:2 in height and 1:25 in volume and power replica of the Simplified Boiling Water Reactor,
- In the PANDA facility, both Design Basis Accident (DBA) and Beyond Design Basis Accident (BDBA) conditions can be simulated, and flexibility of the design allows to mimic conditions for BWR as well as PWRs.

HYMERES

- Following the review and focusing on applications for the Swiss reactors, it was assessed that suitable PANDA experiments for MELCOR validation would be tests related to gas distribution and natural circulation in containment. In this context, the most interesting experiments were identified as the HYMERES HP6_1 and **HP6_2** tests.

MELCOR nodalization study

One of the first actions undertaken was to conduct a sensitivity study upon nodalization. Around 70+ sensitivities were performed and the preliminary analyses shows that:

- The pipes like VB1, VB2, MV2, and interconnecting pipes need to be modeled not only by a flow path but also as volumes
- The horizontal pipes where gas and temperature stratification are expected need to be modeled as two volumes
- Dividing volumes into inner and outer regions, where outer CVHs are connected with separate HSs seems to be essential for mixing
- At the end of the Phase 4 a stratification in the experiment is maintained with temperature at the top ~ 355 K and bottom ~300 K while in MELCOR calculation it is uniform ~340 K

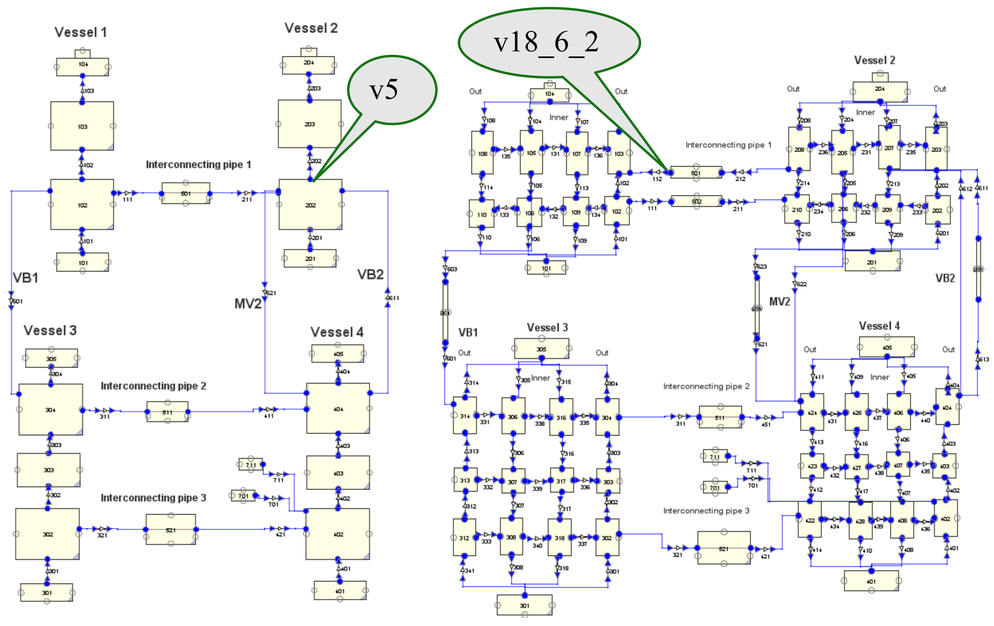

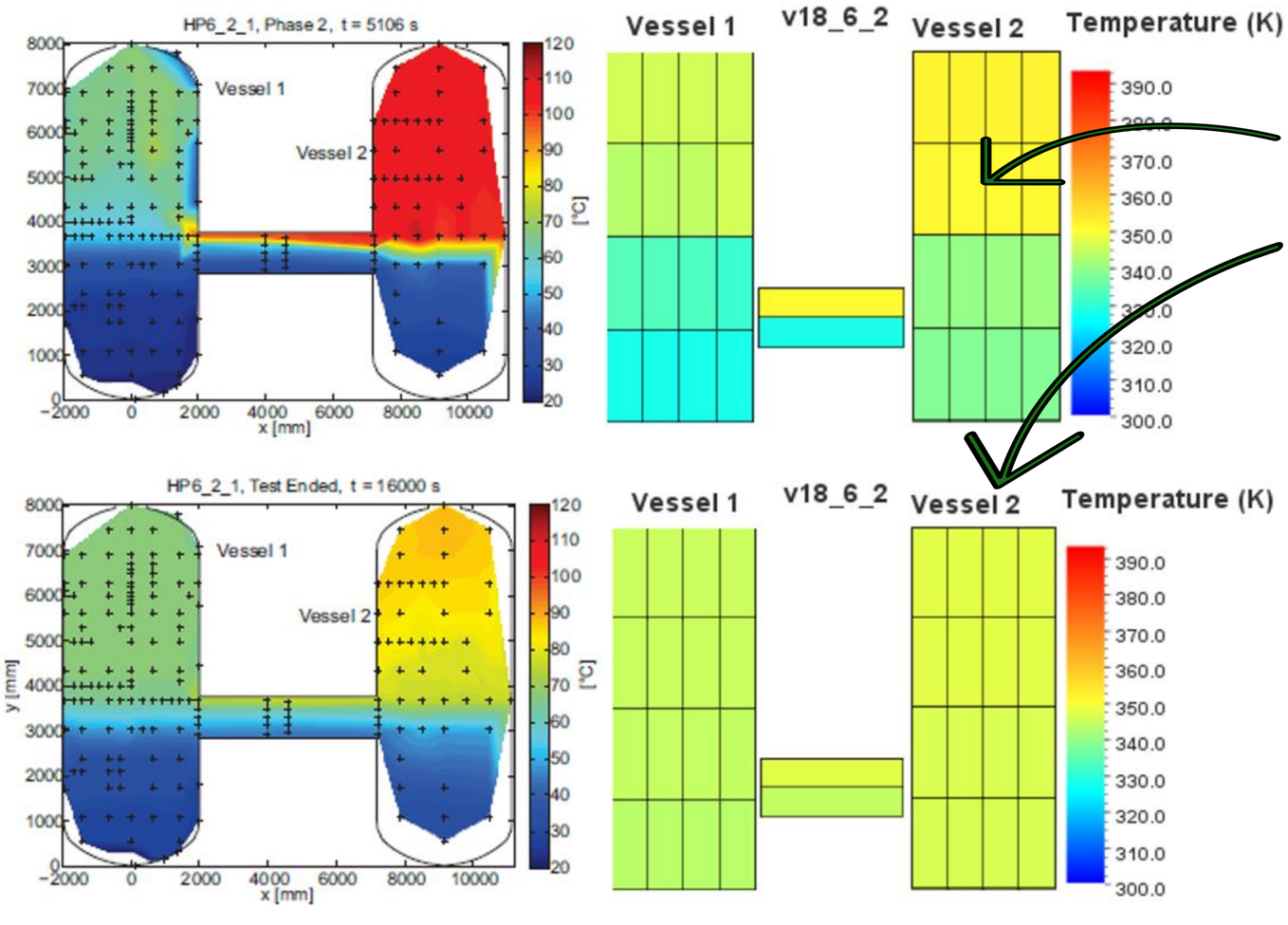

Conclusions

- Proper nodalization could significantly increase the accuracy of the results
- Calculated temperature distribution different from the experiment
- In MELCOR calculations overmixing was noticed as well as the high influence of noncondensable gasses

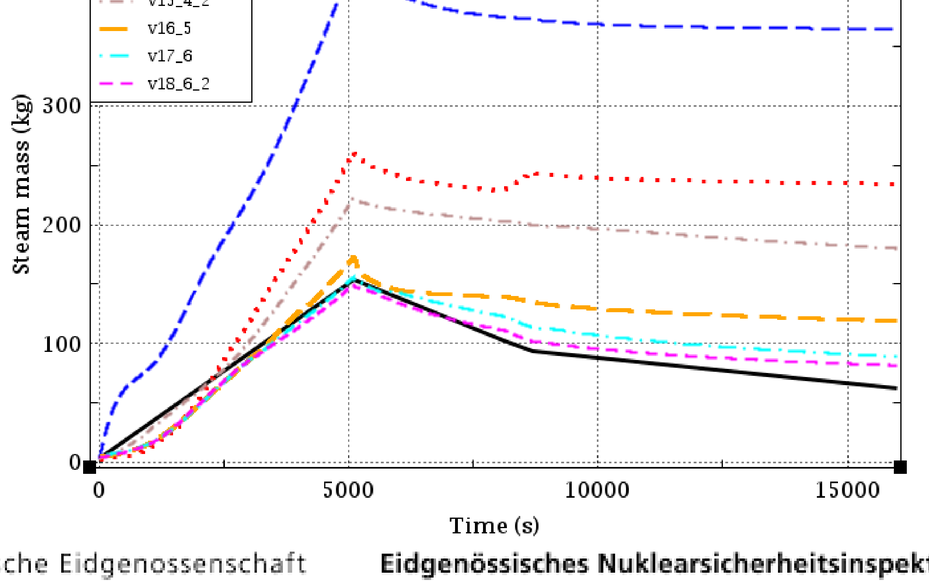

Acknowledgments

This work has received funding from the Swiss Federal Nuclear Safety Inspectorate (ENSI)

Schweizerische Eidgenossenschaft
Confédération suisse
Confederazione Svizzera
Confederaziun svizra

Swiss Confederation

Eidgenössisches Nuklearsicherheitsinspektorat ENSI
Inspection fédérale de la sécurité nucléaire IFSN
Ispettorato federale della sicurezza nucleare IFSN
Swiss Federal Nuclear Safety Inspectorate ENSI

Model Development for the Simulation of Fission Product Release from Molten Pools

Florian Krist and Marco K. Koch
Plant Simulation and Safety, Ruhr-University Bochum,
Universitätsstr. 150, 44801 Bochum,
florian.krist@pss.rub.de

Abstract

The fission product (FP) release into the primary circuit during a postulated reactor accident represents the potential primary radioactive source term for the containment. An adequate simulation of the release is therefore necessary to provide reliable initial conditions for further source term analyses. During the early accident phase, mainly volatile FP are released. With progression of the accident and liquefaction of the fuel, the transport mechanisms in the materials change. The FP move faster in the liquid phases than in the crystal structures of the solid fuel, which also favours the release of medium and low volatile FP. Further, volatile species can be formed by certain low volatile FP in oxidising conditions with significant impact on their release rates.

While established models and databases exist for the representation of the release of volatile FP from a fuel rod geometry and the release is predominantly adequately represented in current code systems, the available data on the release behaviour of less volatile FP from molten core material is very limited. Thus, there is need for improvement in the AC² code package developed by the German Gesellschaft für Anlagen- und Reaktorsicherheit (GRS) gGmbH regarding the source term contribution of a molten pool in the lower reactor plenum. The existing deficits and the necessary further developments therefore focus in this work on the release of medium and low volatile FP in the late in-vessel accident phase.

For the representation of the FP release from a molten pool in the lower plenum, a new in-house model based on the diffusion equation is being developed, which is intended to be integrated into the AC² model basis. The variables of the multicomponent system are described in an idealised way applying the Antoine equation. In order to take the influence of volatile species in an oxidising atmosphere into account new Antoine parameters are investigated. Convective mass transfer is considered by the calculation of Sherwood-Numbers. Preliminary verification analyses conducted by the simulation of experiments of the Late Phase Phenomena programme show that the release behaviour of relevant FP is plausibly represented by the new model.

This work was funded by the German Federal Ministry for the Environment, Nature Conservation, Nuclear Safety and Consumer Protection under grant number 1501629 on the basis of a decision by the German Bundestag.

The simulations were performed with the code AC², developed by GRS.

Keywords

AC², ATHLET-CD, Fission Product Release, Model Development, Molten Pools

SEAKNOT
ERMSAR 2024
11th Conference on
SEVERE ACCIDENTS RESEARCH
May 13-16, 2024 – Stockholm, Sweden

Plant Simulation and Safety
Prof. Dr.-Ing. Marco K. Koch

MODEL DEVELOPMENT FOR THE SIMULATION OF FISSION PRODUCT RELEASE FROM MOLTEN POOLS

FLORIAN KRIST AND MARCO K. KOCH
ORCID: 0000-0002-4089-5801 AND 0000-0001-7260-5250

Motivation

The fission product (FP) release into the primary circuit during a postulated reactor accident represents the potential primary radioactive source term for the containment. An adequate simulation of the release is therefore necessary to provide reliable initial conditions for further source term analyses. During the early accident phase, mainly volatile FP are released. With progression of the accident and liquefaction of the fuel, the transport mechanisms in the materials change. The FP move faster in the liquid phases than in the crystal structures of the solid fuel, which also favours the release of medium and low volatile FP. Further, volatile species can be formed by certain low volatile FP in oxidising conditions with significant impact on their release rates.

Early and late in-vessel FP release

- Established models and databases for representing the release of volatile FP from fuel rod geometry
- Limited data on the release behaviour of less volatile FP from molten core material available
- Other FP species relevant for the release from molten pools than from fuel rods
- Need for improvement in GRS AC² code package regarding the source term contribution of a molten pool in the lower reactor plenum
  - ➢ Current development focuses on the release of medium and low volatile FP in the late in-vessel accident phase

Late Phase Phenomena Experiments [1]

- Ceramic melt experiments (WP2) conducted at Rasplav-2 test facility by 2002
- Investigation of FP release sensitivity to melt temperature, composition and oxygen potential in close-to-reactor conditions
- Analyses of influence by carrier gas mass flow in pool atmosphere on release of FP and uranium oxides from UO2-ZrO2 melt
- Melt temperature and carrier gas varied in the test series. WP2-1: 2,870 K, WP2-2/2: 3,050 K
- In WP 2-1 gas feed varied during the test period and was kept at 10 l/min, 40 l/min and 70 l/min
- Suitable for validation purposes

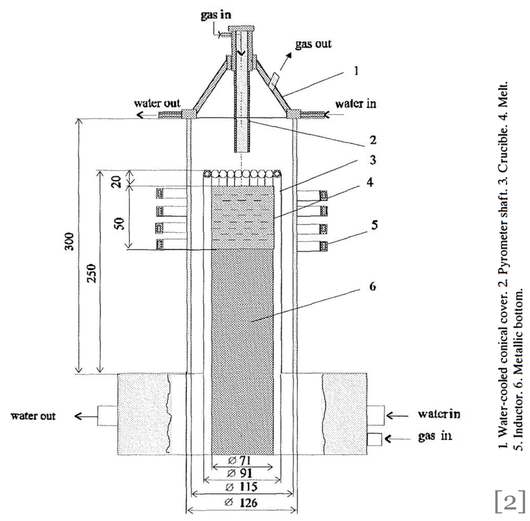

[2]

Model approach

- New in-house model being developed, based on the diffusion equation
- Variables of the multicomponent system described in an idealised way
- Assumption of strong natural convection in pool
- Concentration gradient at the boundary layer on the gas side as driving force
- Describing convective mass transfer by established correlations using Re and Sc numbers
- Calculation approach for partial pressures applying Antoine equation
- Investigation of new parameters for the representation of relevant FP oxides

$$\dot{m}_X = Sh \frac{D_{Xg}}{L_c} M_X A \left(\frac{p_{XgPh}}{RT_{Ph}} - \frac{p_{Xg\infty}}{RT_g} \right)$$

$$Sh = f(Re, Sc)$$

$\dot{m}$:	Release mass flow	X	Component
A:	Free surface area	l	Liquid
M:	Molar mass	g	Gas
R:	Universal gas constant	Ph	Phase Boundary
D_{Xg}:	Binary diffusion coefficient	∞	Bulk
L_c:	Characteristic length	Sh	Sherwood number
T:	Temperature	Re	Reynolds number
p:	Partial pressure	Sc	Schmidt number

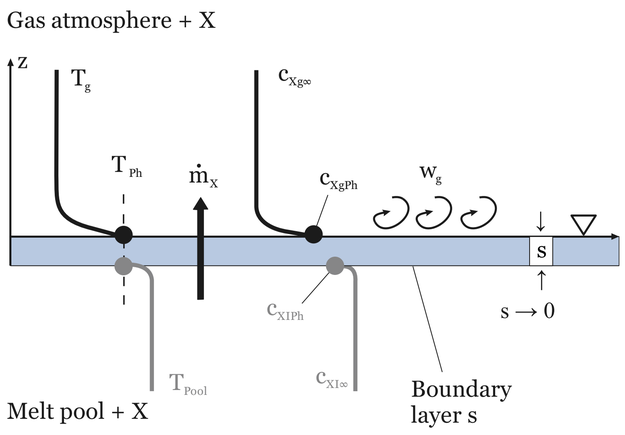

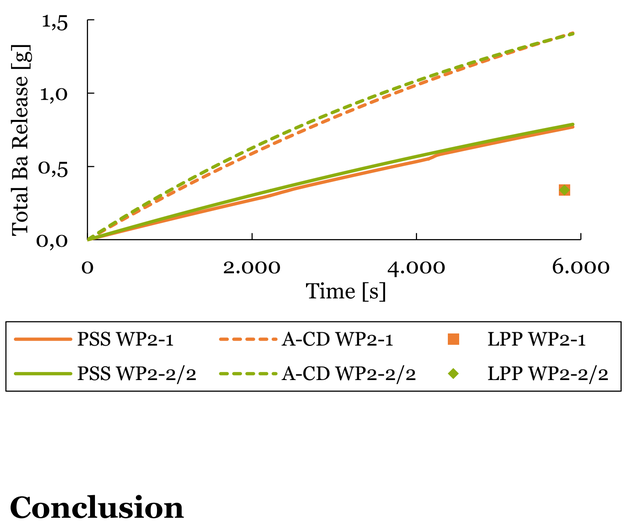

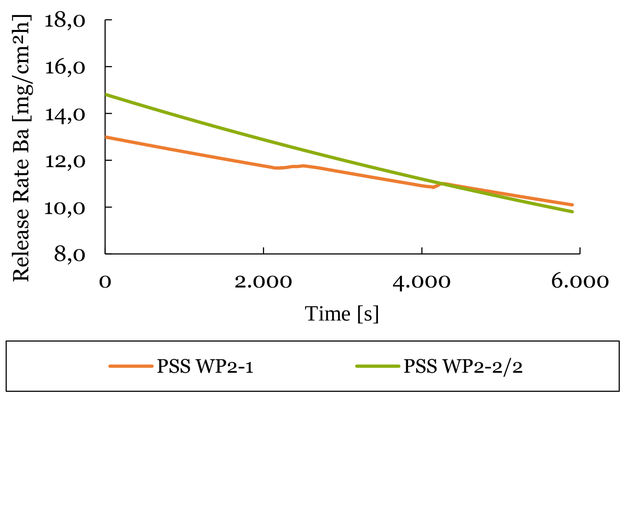

Selected Results

- Preliminary results of developed PSS model (“PSS”) in comparison with results of latest ATHLET-CD release model (“A-CD”) and experimental data
- Identical measured values for Ba in LPP experiments WP2-1 and WP2-2/2
- Overestimation of the release with both models
- Improvement can be seen with PSS model
- Slight deviations between the experiments calculated by one of the due to higher temperature in WP2-2/2
- Influence of convective mass transfer can be recognised in the course of the release rate

Conclusion

Given the limited material properties of low volatile FP on the one hand and the requirements for the development of fast-running (semi-)empirical models on the other, in particular the availability of adequate empirical coefficients and experimental data is a challenge. In this context a new FP release model is developed to address the specific requirements for the representation of late in-vessel FP release. With the development of the release model by incorporating dependencies on the thermo-fluid dynamic boundary conditions using established correlations and equations, a more comprehensive understanding of the release behaviour can essentially be achieved, thereby potentially enhancing the accuracy of modelling various FP species in different atmospheres in the lower plenum.

References

[1] Berlepsch, T. v., Kissane, M. P., Kleinhietpaß, I., Plumecocq, W., Reinke, N., Koch, M. K, “Late-Phase Source-Term Phenomena: Analysis of Experiments: Note Technique SEMAR 03/29,” IRSN, Cadarache SAM-LPP-D30, 2003. Formatierung

[2] Khabensky, V., “Late Phase Source Term Phenomena: Oxidic Melt Experiments (WP2): 5th Euratom Framework Programme 1998-2002,” SAM-LPP-D10, 2002.

Acknowledgement

Supported by:

Federal Ministry for the Environment, Nature Conservation, Nuclear Safety and Consumer Protection

based on a decision of the German Bundestag

This work was funded by the German Federal Ministry for the Environment, Nature Conservation, Nuclear Safety and Consumer Protection under grant number 1501629 on the basis of a decision by the German Bundestag.

The simulations were performed with the code AC², developed by GRS.

Florian Krist
Research Assistant
Plant Simulation and Safety Group

Ruhr-Universität Bochum
Universitätsstr. 150
44801 Bochum
Germany

Tel: +49 234 32 26909
Email: krist@pss.rub.de
Web: www.pss.rub.de

SEVERE ACCIDENT SEQUENCE ANALYSIS OF LOCA FOR APR1400 USING CINEMA COMPUTER CODE

Rae-Joon Park [1*], Jaehyun Ham[1], Dong Gun Son [1], Jaehoon Jung[1], Sang Ho Kim[1]
[1]: Korea Atomic Energy Research Institute, 1045 Daedeok-daero, Yuseong-Gu, Daejeon, Korea
[*]Email: rjpark@kaeri.re.kr

As an integrated severe accident computer code development in Korea, CINEMA (Code for INtegrated severe accidEnt Management Analysis) has been developing for a severe accident sequence analysis from an initiation event to a containment failure. The basic goal of this code development is to design a severe accident analysis code package by exploiting the existing domestic DBA (Design Basis Analysis) code system for the severe accident analysis. The CINEMA computer code are composed of CSPACE, SACAP (Severe Accident Containment Analysis Package), and SIRIUS (SImulation of Radioactive nuclide Interaction Under Severe accident), which are capable of core melt progression with thermal hydraulic analysis of the RCS (Reactor Coolant System), severe accident analysis of the containment, and fission product analysis, respectively. The CSPACE is the result of merging the COMPASS (COre Meltdown Progression Accident Simulation Software) and SPACE (Safety and Performance Analysis CodE for nuclear power plants) models, which is designed to calculate the severe accident situations of an overall RCS thermal-hydraulic response in SPACE modules and a core damage progression in COMPASS modules. For the purpose of CINEMA verification for a real power plant, severe accident sequences of LOCA (Loss Of Coolant Accident) without SI (Safety Injection) for the APR1400 has been analyzed in this study. This analysis has been performed to estimate the efficiency of the CINEMA computer code and the predictive qualities of its models from an initiating event to a containment performance during severe accidents. Best estimate calculations from the initiating events of the SBLOCA (Small Break LOCA) of 2 inch diameter and LBLOCA (Large Break LOCA) of 9.6 inch without SI (Safety Injection) have been performed by using the CINEMA computer code.

The accident was initiated by producing 2inch of the SBLOCA and 9.6 inch of the LBLOCA equivalent diameter breaks in the cold leg. The reactor and the RCP (Reactor Coolant Pump) s were assumed to be tripped at an accident initiation time. The RCS water inventory rapidly decreased and a boiling started in the core because the safety injection pumps were not actuated. The fuel began to heat up when the core was uncovered. Oxidation of the fuel cladding began when the cladding surface temperature reached 1,000K and produced an oxidation heat. The fuel cladding was failed by a sausage-type ballooning. When the cladding surface temperature reached 1,700K, oxidation of the zircaloy was accelerated as the steam was supplied from the bottom of the reactor vessel. This resulted in a rapid increase of the cladding surface temperature. At about 2,129K of the cladding surface temperature, the zircaloy inside the oxide shell began to liquefy and the outer portion of the fuel pellets was dissolved. The relatively thin ZrO_2 shell ruptured at about 2,390K because the shell strength decreased with the temperature increase. The bottom of the core dried out because a hot mixture of liquefied fuel and cladding had relocated downward. The debris formed at the bottom of the fuel rods, where the liquefied mixture had resolidified. The melting temperature of the zirconium dioxide is 2,390K, and that of the uranium dioxide is 2,400K in these calculations. The flow blockage in the lower part of the core region occurred because of a fuel melting and a cohesive debris formation. The melted core material had relocated to the lower plenum of the reactor vessel. Finally, the reactor vessel was failed by a creep through a melt thermal attack.

SEAKNOT
ERMSAR 2024
11th Conference on
SEVERE ACCIDENTS RESEARCH
May 13-16, 2024 – Stockholm, Sweden

SEVERE ACCIDENT SEQUENCE ANALYSIS OF LOCA FOR APR1400 USING CINEMA COMPUTER CODE

Rae-Joon Park[1*], Jaehyun Ham[1], Dong Gun Son [1], Jaehoon Jung[1], Sang Ho Kim[1]

[1]: Korea Atomic Energy Research Institute, 1045 Daedeok-daero, Yuseong-Gu, Daejeon, Korea

*Email: rjpark@kaeri.re.kr

1. Introduction

As a As an integrated severe accident computer code development in Korea, CINEMA (Code for INtegrated severe accidEnt Management Analysis) has been developed for a stand-alone severe accident analysis. The basic goal of this code development is to design a severe accident analysis code package by exploiting the existing domestic DBA (Design Basis Analysis) code system for the severe accident analysis. The CINEMA computer code are composed of CSPACE, SACAP (Severe Accident Containment Analysis Package), and SIRIUS (SImulation of Radioactive nuclide Interaction Under Severe accident), which are capable of core melt progression with thermal hydraulic analysis of the RCS (Reactor Coolant System), severe accident analysis of the containment, and fission product analysis, respectively, as shown in Fig. 1.

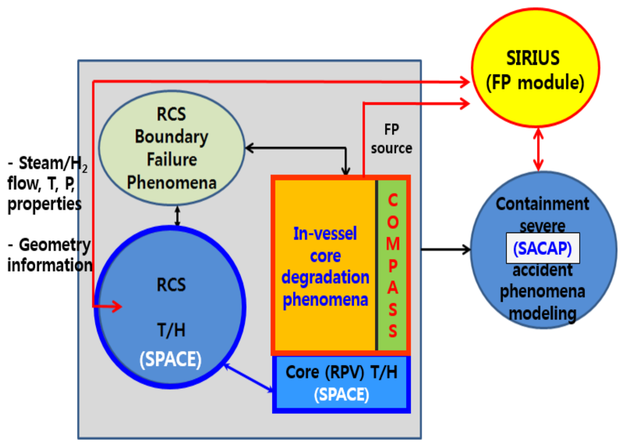

Fig. 1. CINEMA code structure.

This analysis has been performed to estimate the efficiency of the CSPACE computer code and the predictive qualities of its models from an initiating event to a core damage progression. Best estimate calculations from the initiating events of the SBLOCA (Small Break LOCA) of 2inch equivalent diameter and the LBLOCA (Large Break LOCA) of 9.6inch equivalent diameter without SI (Safety Injection) have been performed by using the CSPACE computer code.

2. CINEMA Input Model for APR1400

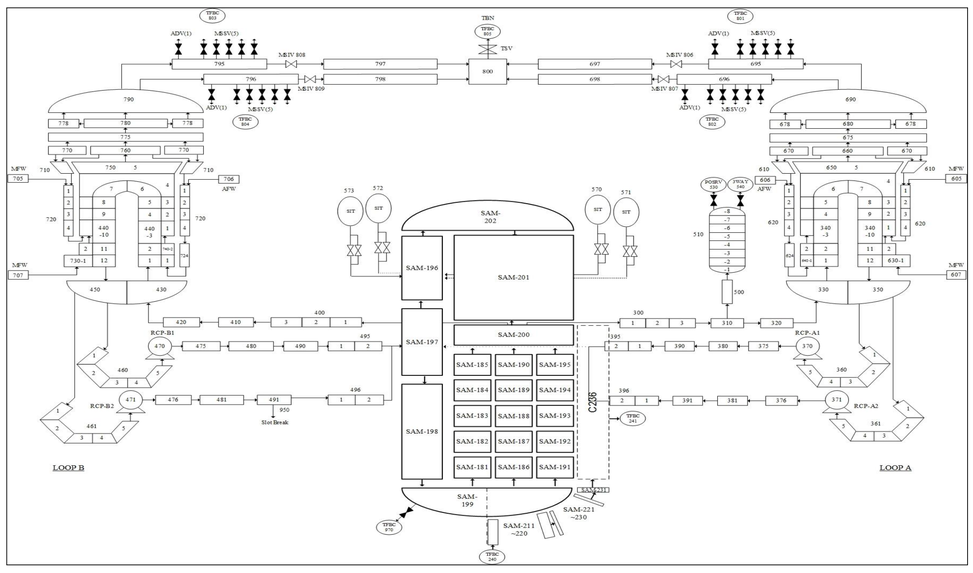

Fig. 2. CINEMA input nodalization for APR1400.

Table 1 Comparison of CINEMA steady state results with APR1400 operating data.

Parameter	Plant Operating Condition	CINEMA Results
Reactor Power (MW)	3,983.0	3,983.0
Primary System Pressure (MPa)	15.5	15.5
Hot Leg Temperature (K)	598.4	598.2
Cold Leg Temperature (K)	563.6	565.9
Core Flow Rate (kg/s)	20,378	20,465
SG Pressure (MPa)	6.86	6.86
SG Steam Temperature (K)	558.1	558.7
SG Steam Flow Rate (kg/s)	1,138.9	1,141.9

3. Results and Discussion

Table 2. Major events in the LOCA of APR1400.

Major Events	LBLOCA (sec)	SBLOCA (sec)
Transient Initiated	0	0
SIT Injection/End of SIT Injection	191/421	4,870/33,900
Core Uncovery	1,015	2,637
Initiation of Fuel Cladding Oxidation	1,650	3,197
Start of FP Gap Release (T_{clad}=1,173 K)	1,773	3,420
Core Dryout	1,953	3,718
Corium Relocation into Lower Head	3,890	65,500
Reactor Vessel Failure	6,630	74,995
End of Calculation	259,200	259,200
Total Hydrogen Generation Mass	228.4 kg	451.2 kg

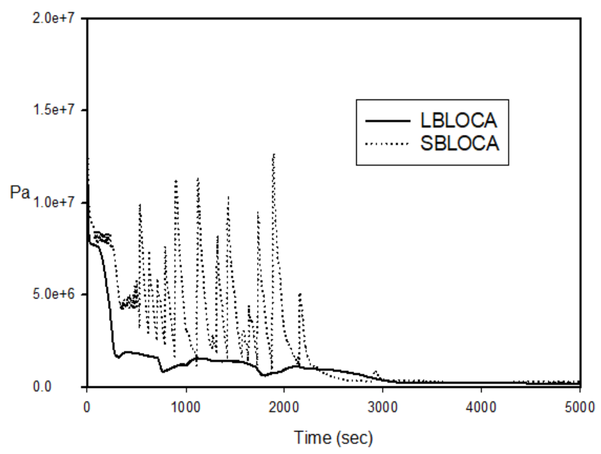

Pressure Historv

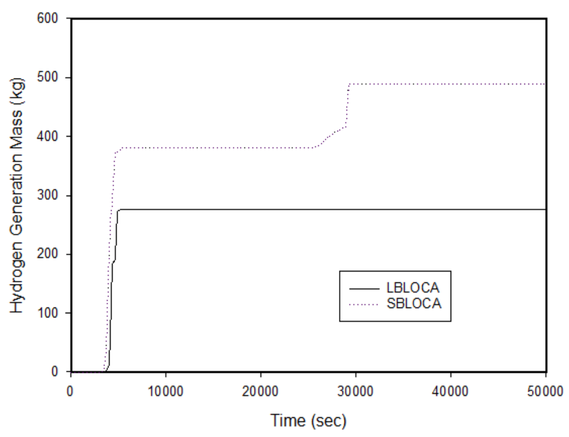

Hydrogen Generation Mass

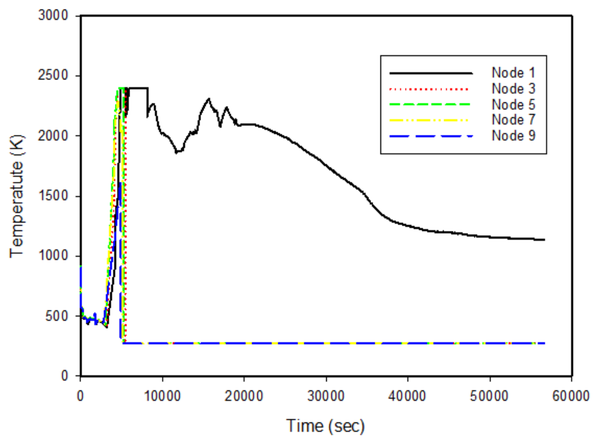

Fuel Temperature (LBLOCA)

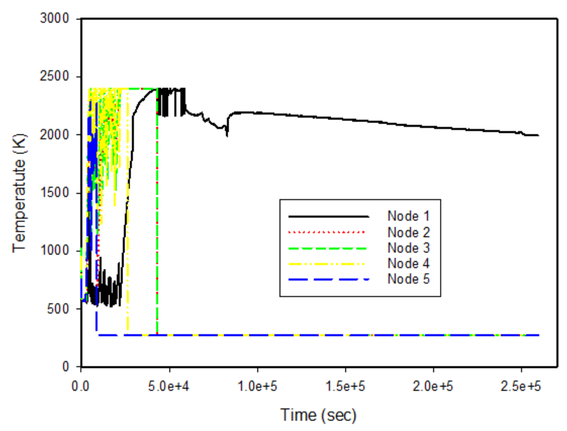

Fuel Temperature (SBLOCA)

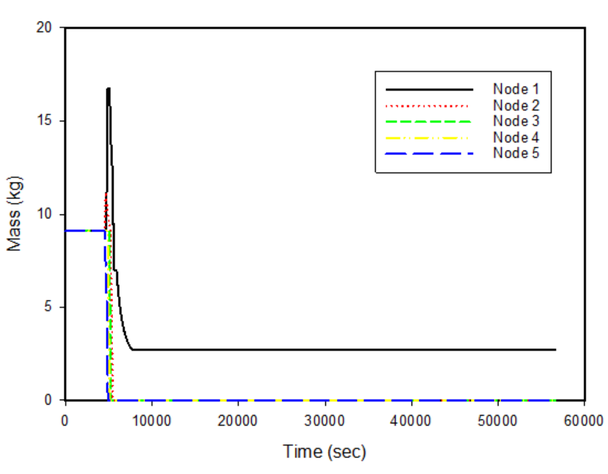

Fuel Mass Distribution (LBLOCA)

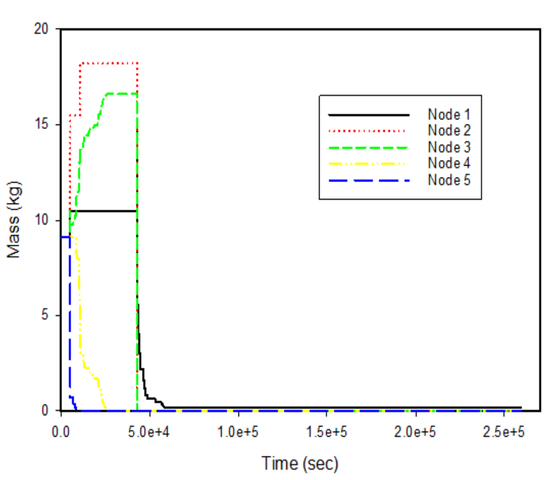

Fuel Mass Distribution (SBLOCA)

Fig. 3 CSPACE results on the LOCA in APR1400.

4. Conclusions

This analysis has been performed to estimate the efficiency of the CINEMA computer code and the predictive qualities of its models from an initiating event to a reactor vessel failure. The main results of CINEMA shows the reasonable values in the physical point. More detailed analysis is necessary to validate the CINEMA computer code in the containment performance and fission product behavior for the APR1400.

COMPARATIVE STUDY OF THE HYDROGEN DISTRIBUTION AMONG DIFFERENT PWR-W LUMPED-PARAMETER AND 3-D CONTAINMENT MODELS WITH GOTHIC 8.3 (QA)

Alberto García-Herranz, Luis Serra, Gonzalo Jiménez,
Araceli Domínguez-Bugarin, Carlos Vázquez-Rodríguez
Universidad Politécnica de Madrid (UPM)
José Gutiérrez Abascal, 2, 28006 Madrid, Spain
a.gherranz@upm.es; luis.slopez@upm.es; gonzalo.jimenez@upm.es;
araceli.dominguez@upm.es; c.vazquez@upm.es

Ignacio Molina de la Peña, Juan Manuel Martín-Valdepeñas
Consejo de Seguridad Nuclear (CSN)
Pedro Justo Dorado Dellmans, 11, 28040 Madrid, Spain
ignacio.molina@csn.es; jmmv@csn.es

EXTENDED ABSTRACT

The containment building is a key safety element in a nuclear power plant (NPP), due to its role as the last barrier against potential radioactive material releases in case of a severe accident. As a lesson learned after TMI-II and Fukushima accidents, H_2 may be accumulated in the containment building during an accident, leading to a combustion, which could increase the temperature and pressure locally above containment design limits. For this reason, a deep understanding of the thermal-hydraulic conditions inside the containment is crucial to assess its integrity against accidental scenarios.

In that line, GOTHIC thermal-hydraulic code allows, by means of lumped-parameter (LP) or 3-D Control Volumes (CVs), to simulate a variety of transients. In the framework of research projects such as GO-MERES (CSN) and AMHYCO (European Commission H2020 programme, GA nº 945057), several models of a generic PWR Westinghouse design (PWR-W) containment with GOTHIC have been developed by the ETSII-UPM group. These models have been used as the basis for this study, performed in the framework of the INTERCON3D project (ref. SN-080-2022), led by the UPM and funded by the Spanish regulator (CSN).

The present work analyzes the capabilities of different generic PWR-W LP and 3-D containment models to simulate the distribution of H_2 in the containment. The first step of the ETSII-UPM group methodology, developed throughout the last ten years to build containment models in GOTHIC, involves the creation of a detailed CAD model of the containment from public information and layouts [1]. From less to high complexity, the complex LP models of 11, 17 and 81 CVs were created following the criteria followed in [2]. The nodalization attends to: (1) compartmentalization, (2) simulation of convection loops in the containment dome, and (3) simulation of the plumes from the Steam Generator compartments, typical of a cold or hot leg LBLOCA type accident. For the 3-D PWR-W model, the “Preventive Methodology”, developed by the ETSII-UPM group during the last years, was used [3]. In this methodology, the detailed geometry is adapted to a 3-D Cartesian grid using simple shapes (wedges and cubes) to finally block cells and face surfaces in GOTHIC, ensuring the tightness of different areas of the containment. The ETSII-UPM group generated several 3-D models previously, for German PWR design [4], AP1000 design [5] and PWR-W design [1], using previous methodologies. However, the PWR-W model used for the comparison, represented in GOTHIC by a single subdivided CV with a 1x1x1.5 m grid and 70.400 cells, was adapted to the latest methodology [3].

To perform the analysis a Double-Ended Guillotine Break (DEGB) Loss of Coolant Accident (LOCA) input was implemented in GOTHIC, coming from the MELCOR UPM PWR-W model [6]. This scenario, combined with a single failure of the low-pressure injection of the Emergency Core Colling System (ECCS), led to an In-vessel Severe Accident (SA) situation. The containment initial conditions were 49 ºC, 101.35 kPa, 20 % of humidity. Computational time, performed by 4 cores of Intel Core i7-6700, shows an increasing in time with the complexity of models. For LP models, computational time threshold for a 10,000 s of transient is minutes, in particular: 1' 48" for 11 CVs, 15' 28" for 17 CVs and 29'34" for 81 CVs. In contrast, the computational time recorded for the 3-D model is 5111' 28", much longer than for the LP models.

Pressure trends show similarities between models, but the temperature distributions show relevant differences. First, about average containment pressure, 81 CV LP model and the 3-D model slightly deviates, which may be caused by the pressure difference between near rupture cells, where the gas is entering, and cells farther form the rupture. On the other hand, the average containment temperature depends on the released gas temperature and its contact with the Heat Structures (HS). For 11 and 17 CV LP models, the gas is homogenized in large cells and is instantly in contact with HS. However, 81 CV LP and 3-D models contains small cells near to the break and not in contact with HS, causing an increase on the temperature.

Towards a deep analysis of the impact of the nodalization of LP models on hydrogen distribution in a PWR-W containment, and its comparison with the 3-D approach, a visual representation was conducted. This representation of H_2 volume fraction was generated by ParaView and ProTON, a post-processing tool developed by ETSII-UPM group. Through this representation, relevant differences are observed. First, 17 and 81 CV LP models simulate the ascendant movement of H_2 throughout the containment. However, just the 81 CV volume reach similar H_2 volume fractions than 3-D model, due to the configuration of the plumes. Similarities between complex 81 CV LP and the 3-D models verify its use for test cases. Despite the similarities between 81 CV LP model and 3-D model, the finer nodalization and the limitations of the LP approach (non-conservation of fluid momentum and homogenization of properties) cause differences which justify the use of 3-D models. Those differences are relevant to identify H_2 clouds with combustion risk.

The following conclusions have been extracted from the comparison: (1) The increase of complexity in GOTHIC models implies an increase in computational time, making LP models useful for test cases; (2) Pressure trends show similarities between models, but the temperature distributions show relevant differences, caused by the introduction of hot gases into small cells; (3) The visual representation of the H_2 distribution allows to observe the similarities, as well as limitations and benefits of LP and 3-D approaches.

KEYWORDS
Containment Analysis, GOTHIC, Lumped-Parameter, 3-D Models, H_2 Combustion Risk

REFERENCES

1. R. Bocanegra, G. Jiménez, K. Fernández-Cosials. "Development of a PWR-W GOTHIC 3D model for containment accident analysis". *Annals of Nuclear Energy* **87**, pp. 547–560 (2016).
2. C. Vázquez-Rodríguez. "Desarrollo de un Modelo de Contención del Reactor AP1000 con el Código Melcor 2.1. Master Thesis". UPM. Spain (2018).
3. C. Vázquez-Rodriguez. "Advanced Implementation of the Spray Safety System into a 3D-GOTHIC PWR-W Containment Model and Its Impact on the Hydrogen Combustion Risk". PhD Thesis. UPM. Spain (2023).
4. K. Fernández-Cosials, S. Estévez-Albuja, G. Jiménez, R. Bocanegra, C. Vázquez-Rodríguez, L. Rey, J. C. Martínez-Murillo. "3D containment modeling of PWR-KWU Trillo NPP with the GOTHIC code". *Annals of Nuclear Energy* **133**, pp. 387–399 (2019).
5. S. Estévez-Albuja, K. Fernández-Cosials, C. Vázquez-Rodríguez, Z. Goñi-Velilla, G. Jiménez. "AP1000 Passive Containment Cooling System study under LBLOCA conditions using the GOTHIC code". *Nuclear Engineering and Design* **384**, 111442 (2021).
6. Bocanegra, R., Ruiz-Zapatero, M., Jiménez, G. Queral, C., 2016. "Enhanced MELCOR Models for Standard PWR-Westinghouse Design". Conference paper. *NUTHOS-11*. Korea (2016).

SEAKNOT
ERMSAR 2024
11th Conference on
SEVERE ACCIDENTS RESEARCH
May 13-16, 2024 – Stockholm, Sweden

COMPARATIVE STUDY OF THE HYDROGEN DISTRIBUTION AMONG DIFFERENT PWR-W LUMPED-PARAMETER AND 3D CONTAINMENT MODELS WITH GOTHIC 8.3 (QA)

ALBERTO GARCÍA-HERRANZ[1]

In collaboration with: Luis Serra[1], Gonzalo Jiménez[1], Araceli Domínguez-Bugarin[1], Carlos Vázquez-Rodríguez[1], Ignacio Molina de la Peña[2], Juan Manuel Martín-Valdepeñas[2].

Introduction

During a DBA (Design-Basis Accident) or SA (Severe Accident) scenario, **H_2 is generated** and accumulated increasing the combustion risk. This phenomenon may lead to a pressure and temperature increase beyond the **design conditions of the containment**. For this reason, tests, experiments and simulations have been conducted since TMI-II accident to determine the H_2 behavior inside the containment, its combustion risk and the impact of safety systems. The lack of data and the development of computer codes have led to the creation of methodologies to **evaluate the containment integrity against accidental situations** by numerical simulations. Following the inertia of national (**GO-MERES**) and international (**AMHYCO**) projects, both conducted by the **ETSII-UPM group**, the **INTERCON3D** project is introduced through this conference publication. A comparative study between **PWR-W Lumped-Parameter (LP) and 3-D models** is presented, based on the H_2 distribution in SA conditions, and using the CFD code GOTHIC 8.3 (QA).

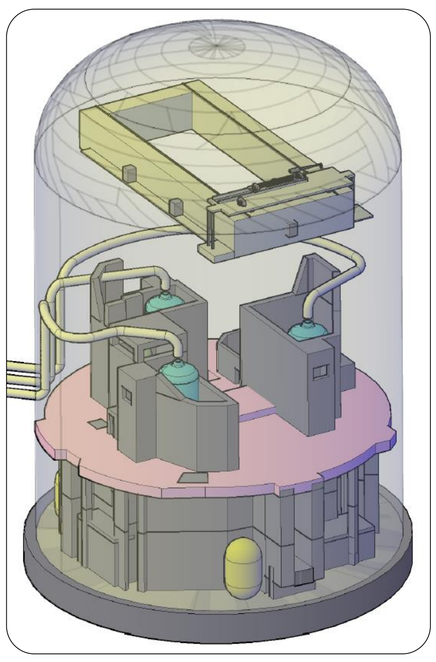

PWR-W Detailed Model

- ETSII-UPM group methodology
- Creation from public information and layouts.
- Base for 3-D and LP models.
- Making easier the heat structures area and free volume measures.
- Based in previous works of the ETSII-UPM group [1].

Computational Time

Model	Time
PWR-W-LPM-11CV	1' 48"
PWR-W-LPM-17CV	15' 28"
PWR-W-LPM-81CV	29' 34"
PWR-W-3D	5111' 28"

Post-procesing by: ParaView, ProTON

H2 Distribution

PWR 3-D Model

- Use of the "**Preventive Methodology**" (developed by ETSII-UPM) [2]. The detailed geometry is adapted to a 3-D Cartesian grid using simple shapes to ensure the hydraulic independence between compartments in GOTHIC.
- The PWR-W model used is represented in GOTHIC by a single subdivided CV with a 1x1x1.5 m grid and **70.400 cells**.
- The ETSII-UPM group have previously generated 3-D models for **German PWR design** [3], **AP1000 design** [4] and **PWR-W design** [1].

Complex PWR-W Lumped-Parameter Models

From less to high complexity, the LP models of **11, 17 and 81 CVs**; were created following the criteria collect in [5]. **The nodalization attends to**: (1) **compartmentation**, (2) simulation of **convection loops** in the containment dome, and (3) simulation of **the plumes** from the Steam Generator compartments in a LOCA type accident.

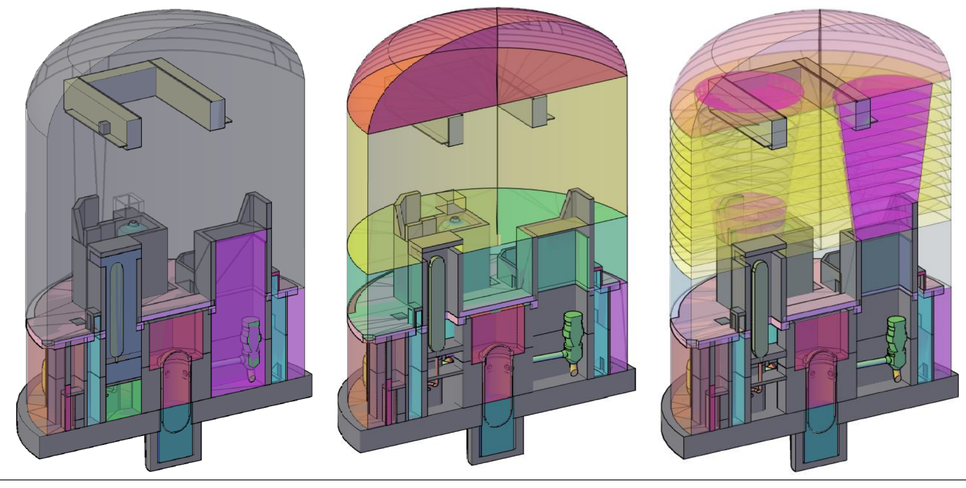

Pressure & Temperature Results

DEGB (Double-Ended Guillotine Break) **LOCA** (Loss of Coolant Accident) input were implemented in GOTHIC, from the MELCOR UPM PWR-W model [6]. This scenario, combined with a single **failure of the ECCS** (Emergency Core Colling System) **low-pressure injection**, led to an **In-vessel SA situation.** The containment initial conditions were **49 °C, 101,35 kPa, 20 % of humidity and a N_2-O_2 atmosphere**.

Computational time shows **an increasing in time with the complexity of models** (4 cores of Intel Core i7-6700).

Pressure trends show **similarities** between models, but the **temperature** distributions show **relevant differences:**

- The average containment pressure difference may be caused by the pressure difference between **near rupture cells and cells farther** form the rupture.
- The average containment temperature difference is because 81 CV LP and 3-D models contains **small cells** near to the break and **not in contact** with heat structures. These cells are **hotter**, causing an increasing on temperature.

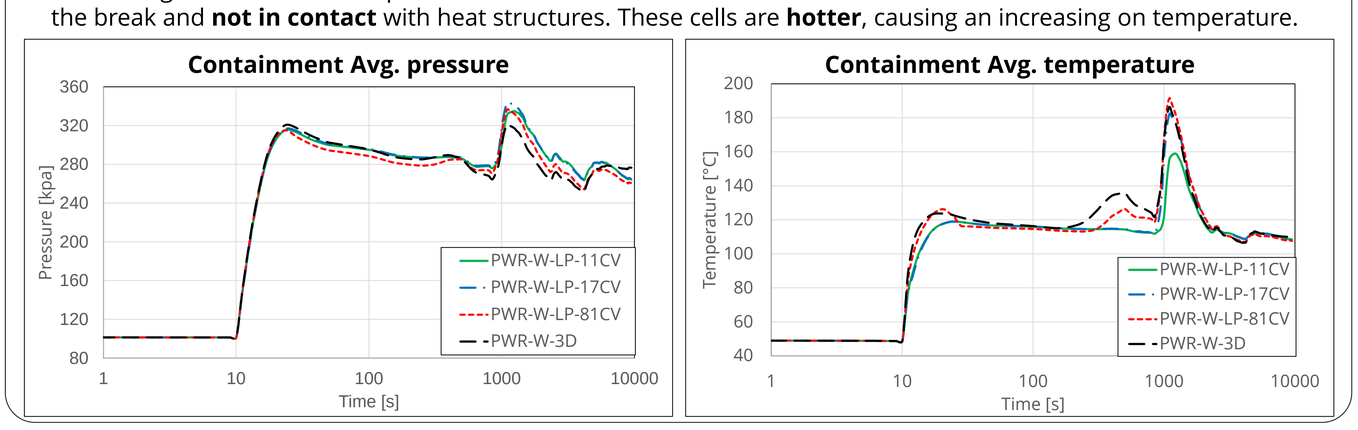

Conclusions

- The increase of complexity in LP models implies a **relevant increase in computational time**, regarding the 3-D model, longer times and similar results make **LP models useful for testing cases.**
- Pressure and temperature shows **similarities** between models, **with relevant differences** caused by the introduction of **hot gases into small cells.**
- The visual representation of the H_2 distribution allows to observe the **similarities** between 81 CVs LP and 3-D models, as well as the **limitations of the LP approach and the capabilities of the 3-D** model for the study of the control and mitigation of H_2 combustion risk.

References

[1] Bocanegra, R., Jimenez, G., Fernández-Cosials, M.K., 2016. Development of a PWR-W GOTHIC 3D model for containment accident analysis. Annals of Nuclear Energy 87, 547–560.
[2] Vázquez-Rodriguéz, C., 2023. Advanced Implementation of the Spray Safety System into a 3D-GOTHIC PWR-W Containment Model and Its Impact on the Hydrogen Combustion Risk. PhD Thesis. Universidad Politécnica de Madrid (UPM).
[3] Fernández-Cosials, K., Estévez-Albuja, S., Jiménez, G., Bocanegra, R., Vázquez-Rodríguez, C., Rey, L., Martínez-Murillo, J.C., 2019. 3D containment modeling of PWR-KWU Trillo NPP with the GOTHIC code. Annals of Nuclear Energy 133, 387–399.
[4] Estévez-Albuja, S., Fernández-Cosials, K., Vázquez-Rodríguez, C., Goñi-Velilla, Z., Jiménez, G., 2021. AP1000 Passive Containment Cooling System study under LBLOCA conditions using the GOTHIC code. Nuclear Engineering and Design 384, 111442.
[5] Vázquez-Rodríguez, C., 2018. Desarrollo de un Modelo de Contención del Reactor AP1000 con el Código Melcor 2.1. Master Thesis. Universidad Politécnica de Madrid (UPM).
[6] Bocanegra, R., Ruiz-Zapatero, M., Jimenez, G. Queral, C., 2016. Enhanced MELCOR Models for Standard PWR-Westinghouse Design. Conference paper. NUTHOS-11. Korea (2016).

IN COOPERATION WITH:

CSN CONSEJO DE SEGURIDAD NUCLEAR

Acknowledgements

GOTHIC™ incorporates technology developed for the electric power industry under the sponsorship of EPRI, the Electric Power Research Institute. This work was completed using a GOTHIC license for educational purposes provided by Numerical Advisory Solutions, LLC.

(1) ETSII, Universidad politécnica de Madrid (UPM); José Gutiérrez Abascal, 2, 28006 Madrid, Spain
(2) Consejo de Seguridad Nuclear (CSN), Pedro Justo Dorado Dellmans, 11, 28040 Madrid, Spain.

Alberto García-Herranz[1]
PhD candidate in nuclear engineering
Tel: +34 910677153
Email: a.gherranz@upm.es

SNETP Sustainable Nuclear Energy Technology Platform · NUGENIA Nuclear GENeration II & III Association · Strål säkerhets myndigheten Swedish Radiation Safety Authority · NEA NUCLEAR ENERGY AGENCY · IAEA

THERMOPHYSICAL PROPERTY MEASUREMENT OF OXIDE MELTS USING AERODYNAMIC LEVITATION

Yaopeng Gong[1,2], Li Zhang[2], Yidan Yuan[2*]
[1]Department of Engineering Physics, Tsinghua University, Beijing, China
[2]CNNC Key Laboratory for Severe Accident Research in Nuclear Power Safety, China Nuclear Power Engineering Co., Ltd, Beijing, China
yidanyuan2010@aliyun.com

ABSTRACT

Following the Fukushima incident, there has been a global focus on the safety of nuclear power plants, emphasizing the need for comprehensive research on severe accident phenomenology. A key aspect of understanding corium behavior during severe accidents is the elucidation of the thermophysical properties associated with corium components. This study is specifically dedicated to the measurement of density, surface tension, and viscosity of oxide melts by aerodynamic levitation. Aerodynamic levitation is an effective method for conducting thermophysical property measurements at elevated temperatures. This technique involves stably levitating small sample spheres through a conical nozzle, thereby eliminating interactions between the sample and crucible. By integrating laser heating technology, samples can easily reach temperatures of up to 3000K. The oscillating drop method is used to determine the resonant frequency and damping constant. Density is calculated as the ratio of mass to volume, while surface tension and viscosity are derived from the resonant frequency and damping constant using the Rayleigh and Lamb equations, respectively. The present study contributes valuable thermophysical property measurements for alumina and zirconia, demonstrating the effectiveness of the approach for the measurement of corium components.

KEWORDS
Thermophysical property, aerodynamic levitation, alumina, zirconia

1. INTRODUCTION

Historical incidents such as Three Mile Island, Chernobyl, and Fukushima have significantly impeded progress in the field of nuclear energy. To reduce the probability of severe accidents and strengthen the safety standards of nuclear power plants, it is imperative to conduct research on the phenomenology of severe accidents [1]. Thermophysical properties of corium components are necessary to accurately model and predict the behavior of corium. Integrated analysis programs, such as ASTEC [2], MAAP [3], and MELCOR [4], have been developed to simulate severe accidents in light water reactors. In these programs, density, surface tension, and viscosity stand as the three fundamental input parameters.

Due to the high melting temperatures involved, access to thermophysical data for corium remains rather limited. In particular, density and surface tension have been determined through the sessile drop method using the VITI-SD apparatus developed by CEA [5]. Surface tension measurements

of C32 were also obtained using the maximum bubble pressure method in VITI-MBP [6]. In addition, viscosity data were obtained through the oscillating drop method in VITI-GFL [7], a non-contact approach. Notably, the rotating cup method was used to measure the viscosity of C22 and C100 at the TIGEL facility in Russia [8]. The density of UO_2-ZrO_2 melt was also measured by the pycnometric method [9]. It is worth highlighting that these experiments were limited in terms of heating capabilities due to the constraints of electromagnetic induction heating, which made it challenging to achieve sample temperatures above 3000 K. In particular, with the exception of VITI-GFL, the experimental setups for VITI and TIGEL involved direct contact between the molten sample and the crucible or substrate material. This arrangement made the measurements susceptible to interactions between the samples and container walls. Furthermore, the relatively large volume of the levitated sample in the VITI-GFL resulted in significant deviations from a spherical shape, leading to measurement errors.

The primary objective of this paper is to measure the density, surface tension, and viscosity of oxide melts using aerodynamic levitation (ADL). Alumina and zirconia oxides are chosen for measurement, with alumina serving as a common material in sacrificial materials [10] and zirconia being a key component in corium [11]. ADL is a well-suited method for measuring the thermophysical properties of high-temperature oxides. This technique involves levitating samples with diameters ranging from 2 to 3 mm above a conical nozzle using gas, allowing non-contact measurements.

Compared to alternative levitation methods such as electromagnetic levitation (EML), electrostatic levitation (ESL), and acoustic levitation (AL), ADL offers notable advantages for the measurement of thermophysical properties of oxides. EML requires the sample to have good conductivity [12], while ESL requires the sample to be charged prior to levitation [13]. However, oxides typically lack conductivity and are challenging to charge at room temperature [14]. AL, on the other hand, can only establish stable levitation at lower temperatures [15]. Hybrid levitation systems, such as aero-acoustic levitation [16] or electrostatic-aerodynamic levitation [17], rely primarily on gas drag forces for levitation, while using acoustic radiation force and Lorentz force to stabilize the sample position. Although these hybrid systems have improved levitation stability, their design is complex and costly. In contrast, ADL imposes fewer constraints on the samples, making it suitable for measuring the density, surface tension, and viscosity of both metallic and non-metallic substances [18]. With certain modifications, ADL can also be used to measure enthalpy [19] and specific heat capacity [20].

This paper first presents the experimental setup designed for the thermophysical property measurements of oxide melts by aerodynamic levitation. Subsequently, the basic principles of the measurements are explained. Finally, the paper presents and discusses the measurement results for molten alumina and zirconia.

2. EXPERIMENTAL SETUP

The experimental setup, named ALSEE (Aerodynamic Levitation-laSEr hEating installation for melt properties), is shown in Fig. 1. It is designed to accurately measure the thermophysical properties of oxide melts, including density, surface tension and viscosity.

A conical converging-diverging nozzle is utilized to achieve stable levitation of a spherical sample with a diameter of 2 to 3 mm. Argon gas, stored in a high-pressure tank, is depressurized to approximately 200 KPa and directed into the nozzle to facilitate sample levitation. A gas flow controller (KOFLOC EX250SC) provides precise control of the argon gas flow rate. The samples are heated by two CO_2 laser devices (Synrad ti-100HS). These devices emit laser beams with a

wavelength of 10.6 μm and a diameter of 2 mm. The laser beams are directed onto the sample using flat mirrors and focusing lenses. Transparent ZnSe windows, which allow the 10.6 μm laser beam to pass through, are located above and below the levitator. The samples are imaged using a high-speed camera (Phantom VEO440L) equipped with a zoom lens (Movetem MAZ12.0×LZ). Backlighting for imaging can be achieved using a backlighting laser (CNI MGL-III-532) and a narrow-band filter, resulting in a white background and a black sample. A calibration process has been conducted to convert the sample diameters from pixels to standard length units using standard stainless-steel spheres with diameters ranging from 2.0 mm to 2.5 mm. The length of a pixel is 5.166 μm. A pair of bichromatic pyrometers (Sensortherm H311) is used to accurately monitor the sample temperature from 1173K to 3573K. Both pyrometers maintain a measurement uncertainty of 0.5%. The levitator is enclosed in a sealing chamber, as depicted in Fig. 2. Multiple gas washes, can effectively remove the active gas from the chamber, reducing interactions between the sample and the ambient gas.

Samples are prepared via a laser hearth melter made of either copper or aluminum alloy and possesses the capability to transform irregularly shaped objects into nearly spherical samples. Notably, the presence of induced impurities is negligible in this process [21].

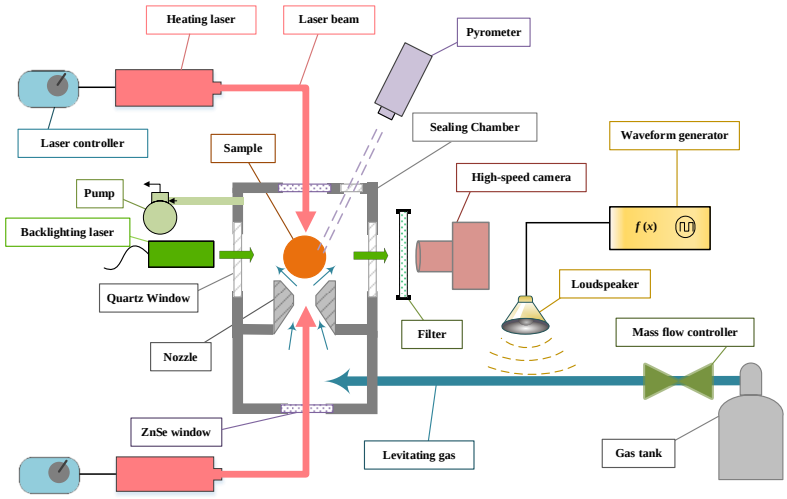

Fig. 1 Schematic view of ALSEE facility

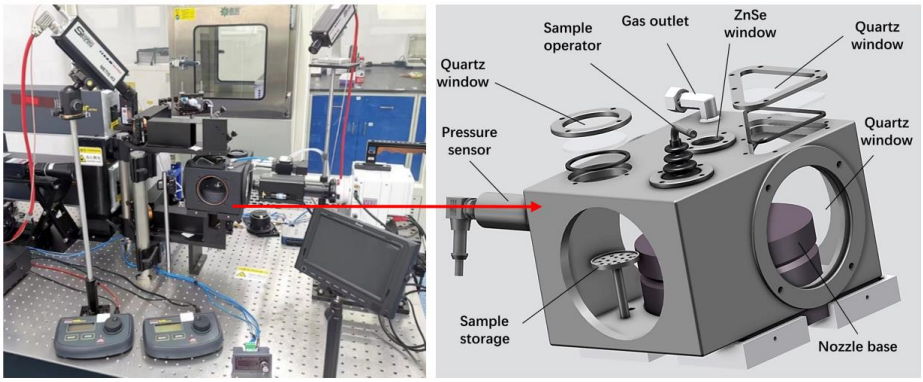

Fig. 2 Picture of sealing chamber in ALSEE facility

3. MEASUREMENT PRINCIPLE

3.1 Density

Density can be determined by the ratio of mass to volume. The volume is obtained from the image of the sample. Once the sample is levitated and heated into a drop, the drop assumes an axisymmetric ellipsoidal shape under the combined effects of gravity and the flowing gas [22]. Consequently, the volume V can be calculated using Eq. (1).

$$V = \frac{4\pi r_h^2 r_v}{3} \tag{1}$$

where r_h and r_v are the horizontal radius and vertical radius, respectively. The sample mass m can be obtained using a balance. Subsequently, the density can be calculated using Eq. (2).

$$\rho = \frac{3m}{4\pi r_h^2 r_v} \tag{2}$$

Considering the propagation law, the density uncertainty is calculated using Eq. (3).

$$\Delta\rho = \rho\sqrt{\left(\frac{\Delta m}{m}\right)^2 + 4\left(\frac{\Delta r_h}{r_h}\right)^2 + \left(\frac{\Delta r_v}{r_v}\right)^2} \tag{3}$$

3.2 Surface Tension

Surface tension is measured by the oscillating drop method. In the case of a spherical drop oscillating at a small amplitude, the surface tension of a drop is related to its resonant frequency. as described by the Rayleigh equation [23], as shown in Eq. (4).

$$\gamma = \frac{3\pi m v_r^2}{8} \tag{4}$$

where v_r is the resonant frequency. Since the drop levitated above the conical nozzle may have a slight deviation from a perfect sphere, the effect of the deviation on the resonant frequency can be considered negligible [24]. Considering the propagation law, the surface tension uncertainty is calculated using Eq. (5).

$$\Delta\gamma = \gamma\sqrt{\left(\frac{\Delta m}{m}\right)^2 + 4\left(\frac{\Delta v_r}{v_r}\right)^2} \tag{5}$$

To determine the resonant frequency, the drop can be either self-excited or acoustically excited. Millot et al. [22] analyzed the radius of self-excited drops to extract the resonant frequency. However, when the drop is stably levitated, surface oscillations may be absent, or the resonant frequency peak could be obscured by noise. Langstaff et al. [25] developed an innovative acoustic excitation system to induce drop oscillations. By sweeping through a range of frequencies, a spectrum was obtained, allowing for the analysis of the resonant frequency.

3.3 Viscosity

Damped oscillations occur when the drop is induced to oscillate at its resonant frequency through acoustic excitation and the acoustic excitation is subsequently removed. As a result, the time

evolution of the horizontal or vertical radius follows a damped oscillatory pattern, as shown in Eq. (6).

$$r_{h/v}(t) = A \cdot \exp(-\Gamma t) \cdot \sin(2\pi\nu t + \phi) + r_{av} \tag{6}$$

where A is the amplitude, Γ the damping constant, ν the response frequency, ϕ the phase and r_{av} the mean radius at rest. Then the viscosity can be calculated using the Lamb equation [26], as presented in Eq. (7).

$$\eta = \frac{\rho R^2}{5}\Gamma \tag{7}$$

where R is the equivalent radius of the drop. Since the drop is ellipsoid, the equivalent radius can be determined by mass and density, as depicted in Eq. (8).

$$R = \sqrt[3]{\frac{3m}{4\pi\rho}} \tag{8}$$

Then the viscosity can also be calculated in Eq. (9).

$$\eta = \frac{1}{5}\left(\frac{3}{4\pi}\right)^{\frac{2}{3}} m^{\frac{2}{3}} \rho^{\frac{1}{3}} \Gamma \tag{9}$$

Considering the propagation law, the viscosity uncertainty is calculated using Eq. (10).

$$\frac{\Delta\eta}{\eta} = \sqrt{\frac{4}{9}\left(\frac{\Delta m}{m}\right)^2 + \frac{1}{9}\left(\frac{\Delta\rho}{\rho}\right)^2 + \left(\frac{\Delta\Gamma}{\Gamma}\right)^2} \tag{10}$$

4. EXPERIMENTAL RESULTS AND DISCUSSION

4.1 Density

The density measurement was conducted during a cooling process. Initially, a sample was stably levitated. Lasers were used to heat the sample to an extremely high temperature. Cooling was initiated by turning off the heating lasers. Concurrently, a high-speed camera was configured to capture images of the sample. Temperature data was recorded synchronously with pyrometers.

The density of the molten alumina was measured using backlighting imaging. The ellipse's edge, semi-major axis, and semi-minor axis were determined through image processing. The temperature-dependent density is presented in Fig. 3 along with other reported data [25,27,28]. The correlation between density and temperature within the temperature range of 2550K < T < 2900K can be effectively described using Eq. (11) along with a 95% confidence interval.

$$\rho_{Al_2O_3} = -(9.606 \pm 0.625) \times 10^{-5} T + (3.105 \pm 0.017)\ (\mathrm{g/cm^3}) \tag{11}$$

The density data obtained by backlighting imaging show good agreement with reported data, considering the density uncertainty of 1.14% in the present study.

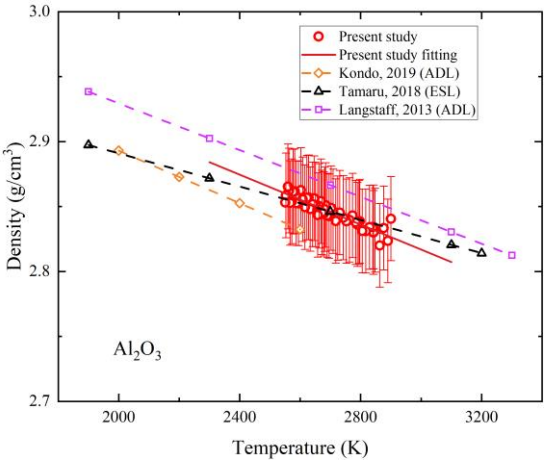

Fig. 3 Density of molten alumina

Density of the molten alumina was also measured using self-illumination imaging. The result is presented in Fig. 4 with the uncertainty of 1.44%. The correlation between density and temperature in the temperature range of 2300K < T < 3000K can be described by Eq. (12), supported by a 95% confidence interval.

$$\rho_{Al_2O_3} = -(2.421 \pm 0.089) \times 10^{-4} T + (3.493 \pm 0.0227)\ (\mathrm{g/cm^3}) \tag{12}$$

As depicted in Fig. 4, the steeper curve derived from self-illumination imaging is observed, indicating a higher temperature coefficient of density. This observation can be attributed to the significant variations in image brightness caused by self-illumination during the cooling process, resulting in an overestimation of density [29]. When the backlighting imaging was used, the background appeared bright while the drop was black. Consequently, the image brightness remained consistent regardless of the temperature variations during the cooling process.

Disparities of the alumina density between self-illumination and backlighting imaging are evident. This emphasizes the effect of the changing image brightness, especially when temperature variations are significant. In such scenarios, the utilization of backlighting imaging is recommended to ensure more accurate density measurements.

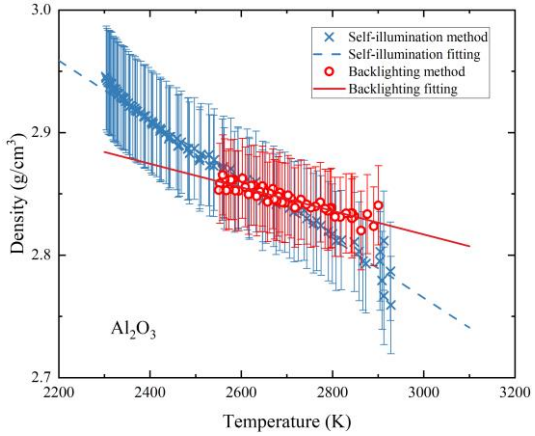

Fig. 4 Effect of imaging methods on density measurement

The density of molten zirconia was measured using the self-illumination method [30], and the temperature-dependent density data are illustrated in Fig. 5 along with other reported data [27,31,32]. The correlation between density and temperature in the temperature range of 2750K < T < 3200K can be effectively described using Eq. (13) along with a 95% confidence interval.

$$\rho_{ZrO_2} = -(7.202 \pm 1.169) \times 10^{-4} T + (6.869 \pm 0.346)\ (\mathrm{g/cm^3}) \quad (13)$$

The density uncertainty for molten zirconia is 2.33% in the present study. The present data obtained by self-illumination method also show good agreement with data obtained by Kondo et al. [27] and Denier et al. [32], who used the backlighting imaging method. Due to the control of camera shooting parameters, the brightness change of the image is not apparent, resulting in a less noticeable impact on the temperature coefficient of density. The density results of the aerodynamic levitation experiments exhibited variations, possibly duo to the different composition of the levitation gas. Kondo et al. [27] used a gas mixture of argon and oxygen, with 15% oxygen, while Denier et al. [32] used a gas mixture with 20% oxygen. Kohara et al. [31] did not specify the levitation gas, while pure argon was used in the present study.

The coefficients in Eq. (11) for alumina exhibit less uncertainty than those in Equation (13) for zirconia. This discrepancy can be attributed to the better levitation stability observed in the case of alumina. It's worth noting that the vapor pressure of molten zirconia is significantly higher (18 Pa for zirconia compared to 0.12 Pa for alumina, as calculated by Kondo et al. [27]). Consequently, molten zirconia evaporates significantly once it exceeds its melting temperature. Subsequently, the evaporated zirconia particles come into contact with the cooler nozzle walls and solidify, disrupting the symmetry of the argon gas channel. As a result, levitation stability deteriorates and measurement accuracy decreases. The temperature coefficient of density for zirconia in the present study is slightly larger than data obtained by Kohara et al. and

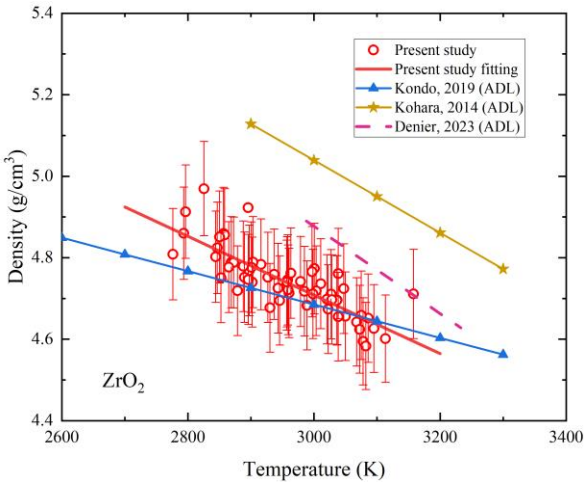

Fig. 5 Density of molten zirconia

4.2 Surface Tension

The surface tension measurement of molten alumina was conducted using acoustic excitation. It's important to note that the acoustic excitation technique is only suitable for materials with low vapor pressure. The reason is that the mass loss during the frequency sweep is minimal, and any

corresponding resonant frequency shift caused by the mass loss can be considered negligible. The obtained frequency spectrum are presented in Fig. 6 which shows less noise and more distinct peaks compared to Langstaff et al.'s [25]. In our experiments, levitation was significantly more stable, with sample position variations remaining below 10 μm for molten alumina [33]. The use of a single loudspeaker, as opposed to the multiple loudspeakers used by Langstaff et al. [25], was a deliberate choice to avoid mutual interference of acoustic signals. This approach proved to be more effective in providing better excitation of the drop. In Langstaff et al.'s spectrum, five peaks were observed that were caused by the splitting of the l=2 oscillation mode into oscillation modes (l=2, m=0, ±1, ±2). In the present study, when the sample rotation was avoided, only two or three peaks were observed, as shown in Fig. 6(a). When the experimental conditions were further improved, including the levitation stability and the acoustic excitation signal provided by one loudspeaker, the frequency spectra with only one peak were obtained, as shown in Fig. 6(b), demonstrating the elimination of the oscillation mode splitting.

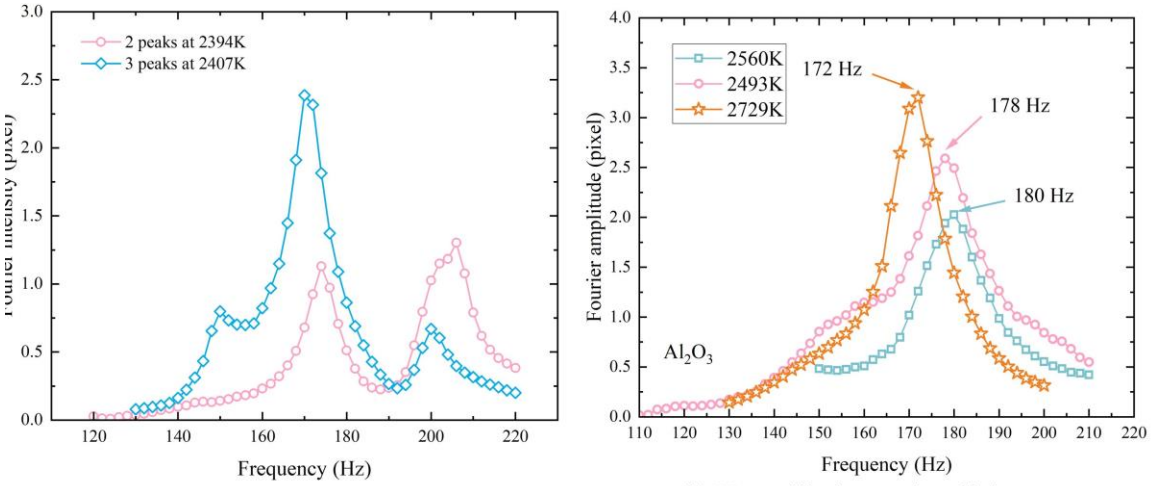

(a) Oscillation mode splitting (b) No oscillation mode splitting

Fig. 6 Frequency spectra of molten alumina

Mode splitting is typically caused by deviations from a perfect sphere and rotation of a levitated drop. When the drop rotates and deviates from a perfect sphere, the l=2 mode splits into five modes (l=2, m=0, ±1, ±2). In cases where the drop does not rotate, the l=2 mode can split into three modes (l=2, m=0, 1, 2) [34]. As the deviations from a spherical shape become less pronounced, the splitting is eliminated, resulting in only one peak in the spectrum.

Considering the frequency related to the single peak as the resonant frequency, the results for molten alumina are presented in Fig. 7, along with other published data [25,35–37]. The data in the present study are in good agreement with those reported by Langstaff et al. [25] using the sum rule developed by Cummings and Blackburn for EML [38] and those obtained by the drop impingement method [35]. The data obtained by Langstaff et al. [25] and Sun et al. [37] using the frequency of the (l=2, m=0) mode are smaller. Therefore, the conclusions drawn by Langstaff et al., which indicated that surface tension derived from the (l=2, m=0) mode may be underestimated by approximately 20%, are confirmed. Consequently, it is imperative to remain attentive to the issue of oscillation mode splitting for surface tension measurements.

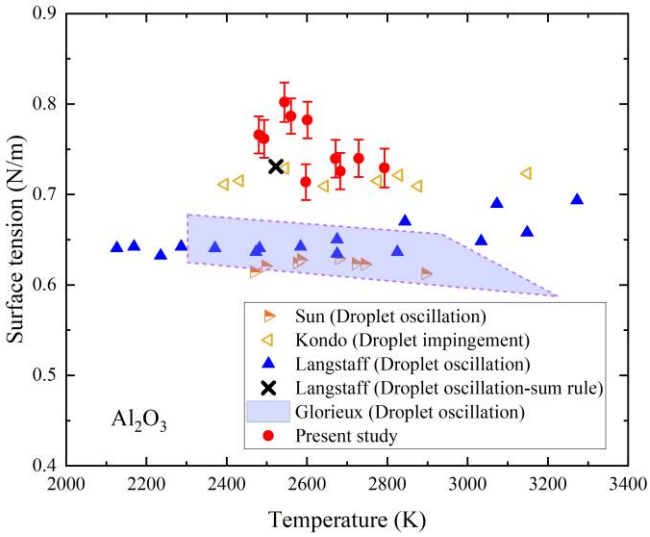

Fig. 7 Surface tension of molten alumina

Since molten zirconia exhibits significant evaporation, surface tension measurements were conducted using self-excitation to speed up the measurement process. Once the drop achieved stable levitation, disturbances were induced by abruptly changing the argon flow rate, resulting in the drop moving downward and upward from its equilibrium position while simultaneously exhibiting surface oscillations. A spectrum was obtained through the Fast Fourier Transform of the drop radius, as depicted in Fig. 8. In the spectrum, the first peak at 50 Hz corresponds to the displacement frequency, and the second peak at 170 Hz corresponds to the resonant frequency for the l=2 mode. It's worth noting that the spectrum obtained by self-excitation shows considerable noise at lower frequencies. Therefore, it is advisable to use smaller samples as the resonant frequency tends to be higher and less susceptible to noise interference.

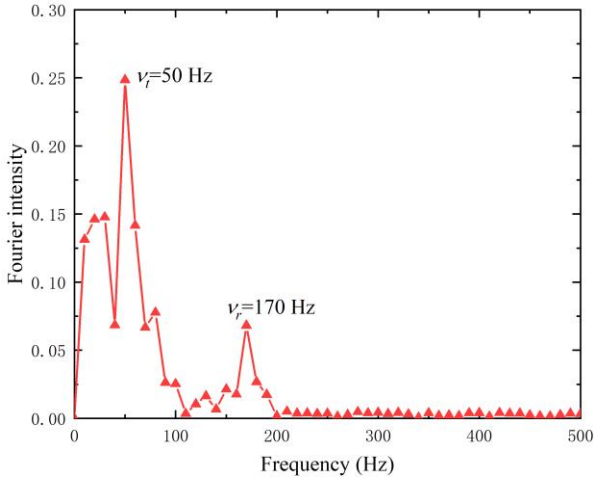

Fig. 8 Fast Fourier Transform of drop radius

The surface tension of molten zirconia is presented in Fig. 9 along with the results obtained by Kondo et al. [39] and Denier et al [32]. Uncertainty was derived using the propagation law. Notably,

the data reveals a negative temperature coefficient for the surface tension. A linear fitting gives Eq. (14) in the temperature range of 2800K to 3500K considering all published data.

$$\gamma_{ZrO_2} = -(4.376 \pm 1.022) \times 10^{-4}(T - 2988) + (0.880 \pm 0.028)\ (\mathrm{N/m}) \quad (14)$$

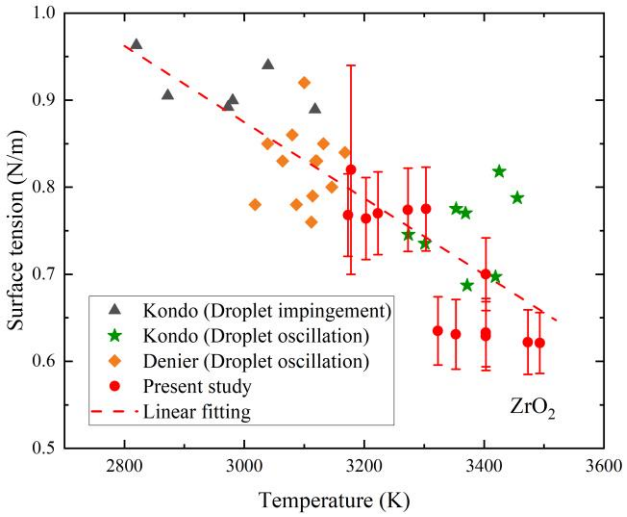

Fig. 9 Surface tension of molten zirconia

4.3 Viscosity

A damped oscillation was observed when the alumina drop, weighing 23.98 mg, oscillated at its resonant frequency of 160 Hz through the loudspeaker, and then the acoustic excitation was removed. A nonlinear fitting to Eq. (6) was conducted as shown in Fig. 10. The damping constant was then derived, and the viscosity was calculated using the Lamb equation.

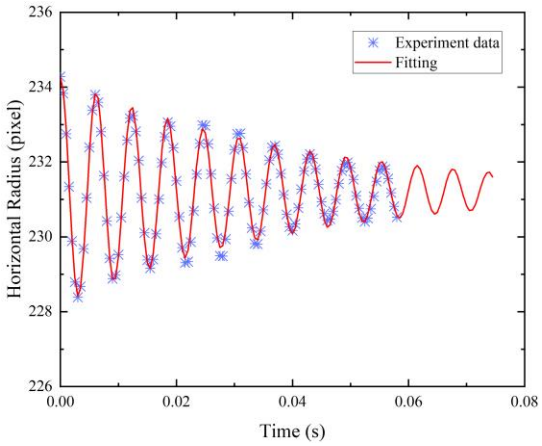

Fig. 10 Damped oscillation of molten alumina at 2571K

The obtained viscosity values for molten alumina are presented in Fig. 11 along with other reported data[25,27,40–44]. The viscosity values in the present study show good agreement with the data reported by Blomquist et al. [41], with a maximum deviation of about 20%. Similarly, a satisfactory

agreement is observed with the data reported by Glorieux et al. [43], considering the associated uncertainty of 50%. Compared to the measurements of Langstaff et al. [25], our viscosity values show deviations below 6% around the melting temperature and below 20% in the temperature range from 2336K to 2500K compared to the measurements of Kondo et al. [27]. Within the broader temperature range of 2336K to 2700K, our measured data occupy an intermediate position among the published data [25,27,40–44]. In summary, the utilization of the ALSEE facility has proven effective in providing viscosity values for molten alumina in the temperature range of 2336K to 2923K. Viscosity for molten oxides is difficult to measure due to high temperature, therefore the measurement uncertainty is high.

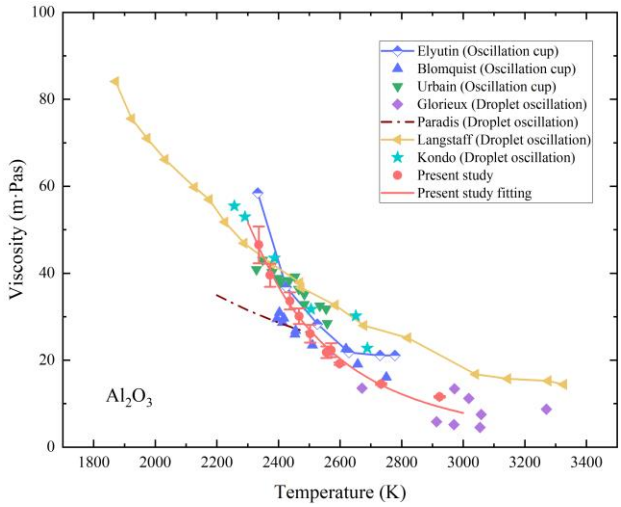

Fig. 11 Viscosity of molten alumina

The viscosity of molten alumina decreases with increasing temperature. The relationship between the viscosity and temperature is consistent with the Andrade equation [45], as depicted in Eq. (15).

$$\eta = \eta_0 \exp\left[\frac{E_a}{R_g}\left(\frac{1}{T} - \frac{1}{T_m}\right)\right] \tag{15}$$

where η_0 is the viscosity at the melting temperature, E_a the activation energy for viscous flow, R_g the gas constant (8.314 J/(mol·K)) and T_m the melting temperature. The temperature-dependent viscosity of molten alumina (2336K-2923K) can be effectively described using Eq. (16) .

$$\eta_{Al_2O_3} = (47.06 \pm 2.15) \exp\left[\frac{(1.546 \pm 0.144) \times 10^5}{R_g}\left(\frac{1}{T} - \frac{1}{2327}\right)\right] (\text{mPa} \cdot \text{s}) \tag{16}$$

The viscosity of molten zirconia was measured using the same method as alumina and the results are presented in Fig. 12. The results obtained in the present study are in good agreement with the results measured using ADL by Kondo et al. [27] and Denier et al. [32], demonstrating the high consistency of non-contact methods. Notably, the viscosity values reported by Alderman et al. [46] using molecular dynamics (MD) are significantly lower than other data. This difference can be attributed to the estimation of parameters in the Stokes-Einstein equation, which may not be accurate. In the work of Kim et al. [47], two models, CRG and Teter, were used to calculate the activation energy required in the Andrade equation. However, there is a certain level of discrepancy

between the CRG and Teter models, highlighting the sensitivity of MD calculations to the choice of model.

The temperature-dependent viscosity of molten zirconia (3183K-3420K) can be fitted into Eq. (17).

$$\eta_{ZrO_2} = (12.87 \pm 1.03)\exp[\frac{(8.035\pm2.010)\times10^4}{R_g}((\frac{1}{T}-\frac{1}{2988}))]\,(\mathrm{mPa\cdot s}) \quad (17)$$

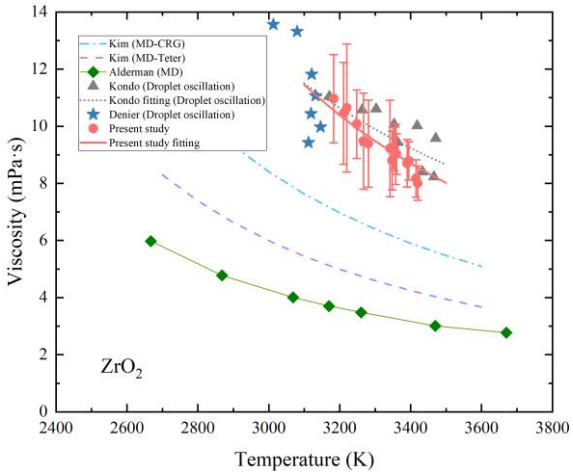

Fig. 12 Viscosity of molten zirconia

Kondo et al. and Denier et al. reported their activation energy values as E_a=$(6.4 \pm 2.0) \times 10^4$ and E_a=$(1.84 \pm 0.04) \times 10^5$ J/mol, respectively. The activation energy value in the present study falls in between these two values. Notably, the activation energy reported by Denier et al. is significantly higher. This discrepancy might be attributed to the fact that the viscosity was measured over a narrow temperature range, along with significant data fluctuations. Furthermore, the difference in activation energy between the work of Kondo et al. and the present study could be attributed to the gas composition of argon and oxygen in Kondo's experiments. Oxygen was introduced to prevent the reduction of the samples in their experiments. As a result, their samples may have undergone reduction, leading to a lower oxygen stoichiometry than zirconia.

When measuring the viscosity of molten zirconia, attention should be paid to the evaporation. Evaporated zirconia has a tendency to solidify on the low-temperature nozzle wall, causing a reduction in the flatness of the nozzle surface. Consequently, the levitation becomes unstable, which affects the damping process. Ultimately, the damping constant derived from the damped oscillation exhibits significant uncertainty.

5. CONCLUSIONS

This paper presents the ALSEE experimental setup for accurate measurements of density, surface tension, and viscosity of oxide melts by aerodynamic levitation. The obtained thermophysical properties for molten alumina and zirconia demonstrate the advantage of the ALSEE facility. Good agreement is observed with reported data for the density, surface tension, and viscosity of molten alumina and zirconia. Levitation stability is found to be the key factor for measurement accuracy. Evaporation of molten zirconia significantly deteriorates levitation stability, resulting in larger uncertainties.

ACKNOWLEDGEMENTS

This work is supported by National Key R&D Program of China (Grant No.2018YFB1900100).

REFERENCES

[1] B.R. Sehgal, Nuclear safety in light water reactors: severe accident phenomenology, Academic Press, 2011.
[2] J.P. Van Dorsselaere, C. Seropian, P. Chatelard, F. Jacq, J. Fleurot, P. Giordano, N. Reinke, B. Schwinges, H.J. Allelein, W. Luther, The ASTEC Integral Code for Severe Accident Simulation, Nucl. Technol. 165 (2009) 293–307. https://doi.org/10.13182/NT09-A4102.
[3] T.-C. Wang, S.-J. Wang, J.-T. Teng, Comparison of severe accident results among SCDAP/RELAP5, MAAP, and MELCOR codes, Nucl. Technol. 150 (2005) 145–152. https://doi.org/10.13182/NT05-A3612.
[4] R.O. Gauntt, R.K. Cole, C.M. Erickson, R.G. Gido, R.D. Gasser, S.B. Rodriguez, M.F. Young, MELCOR computer code manuals, 2000.
[5] D. Grishchenko, P. Piluso, Recent progress in the gas-film levitation as a method for thermophysical properties measurements: application to ZrO2-Al2O3 system, High Temp. - High Pressures 40 (2011) 127–149.
[6] N. Chikhi, J. Delacroix, P. Fouquart, B. Turquais, Measurement of corium surface tension using the maximum bubble pressure, Nucl. Eng. Des. 379 (2021) 111266.
[7] P.H. Haumesser, J.P. Garandet, J. Bancillon, M. Daniel, I. Campbell, P. Jackson, High temperature viscosity measurements by the gas film levitation technique: application to various types of materials, Int. J. Thermophys. 23 (2002) 1217–1228. https://doi.org/10.1023/A:1019892220523.
[8] S.S. Abalin, V.G. Asmolov, V.D. Daragan, E.K. D'yakov, A.V. Merzlyakov, V.Y. Vishnevsky, Corium kinematic viscosity measurement, Nucl. Eng. Des. 200 (2000) 107–115. https://doi.org/10.1016/S0029-5493(00)00238-7.
[9] V.G. Asmolov, V.N. Zagryazkin, E.V. Astakhova, V.Y. Vishnevskii, E.K. D'yakov, A.Y. Kotov, V.M. Repnikov, The Density of UO2–ZrO2 Alloys, High Temperature 41 (2003) 627–632. https://doi.org/10.1023/A:1026140627382.
[10] Y. Ohishi, F. Kargl, F. Nakamori, H. Muta, K. Kurosaki, S. Yamanaka, Physical properties of core-concrete systems: Al2O3-ZrO2 molten materials measured by aerodynamic levitation, J. Nucl. Mater. 487 (2017) 121–127. https://doi.org/10.1016/j.jnucmat.2017.02.002.
[11] D.W. Akers, S.M. Jensen, B.K. Schuetz, Examination of relocated fuel debris adjacent to the lower head of the TMI-2 reactor vessel, Nuclear Regulatory Commission, Washington DC, 1994.
[12] J. Etay, P. Schetelat, B. Bardet, J. Priede, V. Bojarevics, K. Pericleous, Modelling of electromagnetic levitation-Consequences on non-contact physical properties measurements, High Temperature Materials and Processes 27 (2008) 439–448. https://doi.org/10.1515/HTMP.2008.27.6.439.
[13] Y. Ohishi, K. Kurokawa, Y. Sun, H. Muta, Thermophysical properties of molten Zr1−xOx (x= 0.1, 0.2) measured by electrostatic levitation, J. Nucl. Mater. 528 (2020) 151873. https://doi.org/10.1016/j.jnucmat.2019.151873.
[14] P.-F. Paradis, T. Ishikawa, Y. Saita, S. Yoda, Non-contact thermophysical property measurements of liquid and undercooled alumina, Jpn. J. Appl. Phys. 43 (2004) 1496–1500. https://doi.org/10.1143/JJAP.43.1496.
[15] M.A. Andrade, N. Pérez, J.C. Adamowski, Review of progress in acoustic levitation, Braz. J. Phys. 48 (2018) 190–213. https://doi.org/10.1007/s13538-017-0552-6.

[16] P.C. Nordine, D. Merkley, J. Sickel, S. Finkelman, R. Telle, A. Kaiser, R. Prieler, A levitation instrument for containerless study of molten materials, Rev. Sci. Instrum. 83 (2012) 125107. https://doi.org/10.1063/1.4770125.
[17] T. Ishikawa, J. Yu, P.-F. Paradis, Noncontact surface tension and viscosity measurements of molten oxides with a pressurized hybrid electrostatic-aerodynamic levitator, Rev. Sci. Instrum. 77 (2006) 053901. https://doi.org/10.1063/1.2198787.
[18] C.J. Benmore, J.K.R. Weber, Aerodynamic levitation, supercooled liquids and glass formation, Adv. Phys.: X 2 (2017) 717–736. https://doi.org/10.1080/23746149.2017.1357498.
[19] S.V. Ushakov, A. Shvarev, T. Alexeev, D. Kapush, A. Navrotsky, Drop-and-catch (DnC) calorimetry using aerodynamic levitation and laser heating, J. Am. Ceram. Soc. 100 (2017) 754–760. https://doi.org/10.1111/jace.14594.
[20] Y. Sun, H. Muta, Y. Ohishi, Multiple-gas cooling method for constant-pressure heat capacity measurement of liquid metals using aerodynamic levitator, Rev. Sci. Instrum. 92 (2021) 095102. https://doi.org/10.1063/5.0055555.
[21] J.K.R. Weber, J.J. Felten, P.C. Nordine, Laser hearth melt processing of ceramic materials, Rev. Sci. Instrum. 67 (1996) 522–524. https://doi.org/10.1063/1.1146631.
[22] F. Millot, J.C. Rifflet, G. Wille, V. Sarou-Kanian, B. Glorieux, Analysis of surface tension from aerodynamic levitation of liquids, J. Am. Ceram. Soc. 85 (2002) 187–192. https://doi.org/10.1111/j.1151-2916.2002.tb00064.x.
[23] L. Rayleigh, On the capillary phenomena of jets, Proc. R. Soc. London 29 (1879) 71–97.
[24] J.A. Tsamopoulos, R.A. Brown, Nonlinear oscillations of inviscid drops and bubbles, J. Fluid Mech. 127 (1983) 519–537. https://doi.org/10.1017/S0022112083002864.
[25] D. Langstaff, M. Gunn, G.N. Greaves, A. Marsing, F. Kargl, Aerodynamic levitator furnace for measuring thermophysical properties of refractory liquids, Rev. Sci. Instrum. 84 (2013) 124901. https://doi.org/10.1063/1.4832115.
[26] H. Lamb, On the oscillations of a viscous spheroid, Proc. London Math. Soc. 1 (1881) 51–70.
[27] T. Kondo, H. Muta, K. Kurosaki, F. Kargl, A. Yamaji, M. Furuya, Y. Ohishi, Density and viscosity of liquid ZrO2 measured by aerodynamic levitation technique, Heliyon 5 (2019) e02049. https://doi.org/10.1016/j.heliyon.2019.e02049.
[28] H. Tamaru, C. Koyama, H. Saruwatari, Y. Nakamura, T. Ishikawa, T. Takada, Status of the electrostatic levitation furnace (ELF) in the ISS-KIBO, Microgravity Sci. Technol. 30 (2018) 643–651. https://doi.org/10.1007/s12217-018-9631-8.
[29] Y. Gong, L. Zhang, Y. Yuan, Q. Guo, W. Ma, S. Huang, Density measurement of molten drop with aerodynamic levitation and laser heating, Front. Energy Res. 10 (2022) 892406. https://doi.org/10.3389/fenrg.2022.892406.
[30] L. Zhang, Y. Gong, Y. Yuan, Q. Guo, W. Ma, Thermophysical property measurement of high-temperature oxide melt by aerodynamic levitation, Atomic Energy Science and Technology 56 (2022) 58. https://doi.org/10.7538/yzk.2022.youxian.0144.
[31] S. Kohara, J. Akola, L. Patrikeev, M. Ropo, K. Ohara, M. Itou, A. Fujiwara, J. Yahiro, J.T. Okada, T. Ishikawa, Atomic and electronic structures of an extremely fragile liquid, Nat. Commun. 5 (2014) 5892. https://doi.org/10.1038/ncomms6892.
[32] C. Denier, Z. Zhang, E. De Bilbao, J. Delacroix, P. Piluso, Thermophysical Properties of Liquid Zirconia Measured by Aerodynamic Levitation at High Temperature, Int. J. Thermophys. 44 (2023) 127. https://doi.org/10.1007/s10765-023-03230-1.
[33] Y. Gong, L. Zhang, Y. Yuan, Q. Guo, W. Ma, S. Huang, Viscosity measurement of molten alumina and zirconia using aerodynamic levitation, laser heating and droplet oscillation techniques, Heliyon 9 (2023) e22424. https://doi.org/10.1016/j.heliyon.2023.e22424.
[34] F. Millot, V. Sarou-Kanian, J.-C. Rifflet, B. Vinet, The surface tension of liquid silicon at high temperature, MSE: A 495 (2008) 8–13. https://doi.org/10.1016/j.msea.2007.10.108.

[35] T. Kondo, H. Muta, Y. Ohishi, Development of a new method to measure surface tension of molten oxides, High Temp. - High Pressures 00 (2021) 1–14.
[36] B. Glorieux, F. Millot, J.C. Rifflet, [No title found], Int. J. Thermophys. 23 (2002) 1249–1257. https://doi.org/10.1023/A:1019848405502.
[37] Y. Sun, G. Duan, A. Yamaji, T. Takatani, H. Muta, Y. Ohishi, Validating ground-based aerodynamic levitation surface tension measurements through a study on Al2O3, Npj Microgravity 8 (2022) 26. https://doi.org/10.1038/s41526-022-00213-8.
[38] D.L. Cummings, D.A. Blackburn, Oscillations of magnetically levitated aspherical droplets, J. Fluid Mech. 224 (1991) 395–416. https://doi.org/10.1017/S0022112091001817.
[39] T. Kondo, H. Muta, Y. Ohishi, Droplet impingement method to measure the surface tension of molten zirconium oxide, J. Nucl. Sci. Technol. 57 (2020) 889–897. https://doi.org/10.1080/00223131.2020.1736681.
[40] V.P. Elyutin, Properties of liquid aluminum oxide, Fiz. Aerodisper-Snykh Sist 57 (1972) 104–109.
[41] R.A. Blomquist, J.K. Fink, L. Leibowitz, Viscosity of molten alumina, Argonne National Laboratory Lemont, IL, USA, 1978.
[42] G. Urbain, Viscosity of liquid alumina, Rev. Int. Hautes Temp. Refract. 19 (1982) 55.
[43] B. Glorieux, M.-L. Saboungi, F. Millot, J. Enderby, J.-C. Rifflet, Aerodynamic levitation: an approach to microgravity, AIP Conf. Proc. 552 (2001) 316–324.
[44] P.-F. Paradis, T. Ishikawa, Surface tension and viscosity measurements of liquid and undercooled alumina by containerless techniques, Jpn. J. Appl. Phys. 44 (2005) 5082–5085. https://doi.org/10.1143/JJAP.44.5082.
[45] E.N.D.C. Andrade, XLI. A theory of the viscosity of liquids.—Part I, Philos. Mag. 17 (1934) 497–511. https://doi.org/10.1080/14786443409462409.
[46] O.L.G. Alderman, C.J. Benmore, J.K.R. Weber, L.B. Skinner, A.J. Tamalonis, S. Sendelbach, A. Hebden, M.A. Williamson, Corium lavas: structure and properties of molten UO2-ZrO2 under meltdown conditions, Sci. Rep. 8 (2018) 2434. https://doi.org/10.1038/s41598-018-20817-z.
[47] W.K. Kim, J.H. Shim, M. Kaviany, Thermophysical properties of liquid UO2, ZrO2 and corium by molecular dynamics and predictive models, J. Nucl. Mater. 491 (2017) 126–137. https://doi.org/10.1016/j.jnucmat.2017.04.030.

SEAKNOT
ERMSAR 2024
11th Conference on
SEVERE ACCIDENTS RESEARCH
May 13-16, 2024 – Stockholm, Sweden

Thermophysical Property Measurement of Oxide Melts Using Aerodynamic Levitation

YAOPENG GONG, LI ZHANG, YIDAN YUAN*
CHINA NUCLEAR POWER ENGINEERING CO.,LTD.
NO.117, XISANHUANBEILU, HAIDIAN DISTRICT, BEIJING,100840, CHINA

Introduction

Reliable modeling of corium behavior in severe accidents requires accurate thermophysical data for corium components as initial inputs, particularly density, surface tension and viscosity. Contact methods have been used to measure thermophysical properties of corium, such as sessile drop method, maximum bubble pressure method and oscillating cup method[1]. However, the results were affected by the interactions between the samples and container walls. The present study focuses on the density, surface tension and viscosity measurements of oxide melts (alumina and zirconia) using aerodynamic levitation, a non-contact method, providing accurate data for modeling of corium behavior.

Experimental Setup

The experimental setup, named ALSEE (Aerodynamic Levitation-laSEr hEating installation for melt properties), is developed at China Nuclear Power Engineering Co., Ltd for accurate density, surface tension and viscosity measurements of corium components (see Figure 1).

Aerodynamic levitation was achieved by using a conical converging-diverging nozzle, enabling the levitation of a spherical sample in the diameter range of 2 to 3 mm. Argon gas was chosen as the levitating gas due to its inert nature, ensuring minimal reactivity with the levitated samples. Sample heating was performed using two CO2 laser devices. Measurement of the sample's temperature was conducted by a pyrometer. Observations of sample behavior were performed using a high-speed camera. The acoustic excitation technique was inspired by work of Langstaff et al. [2] who used loudspeakers to induce controlled oscillations in the drop with the oscillation frequencies precisely consistent with the acoustic wave frequencies.

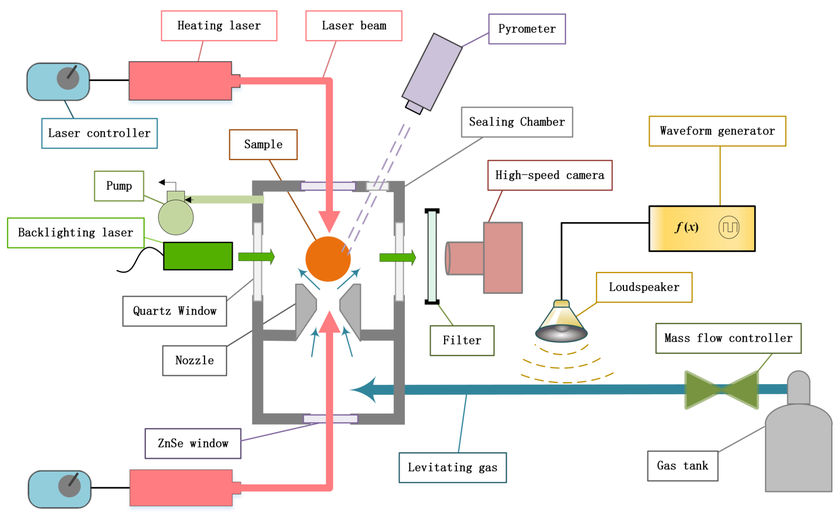

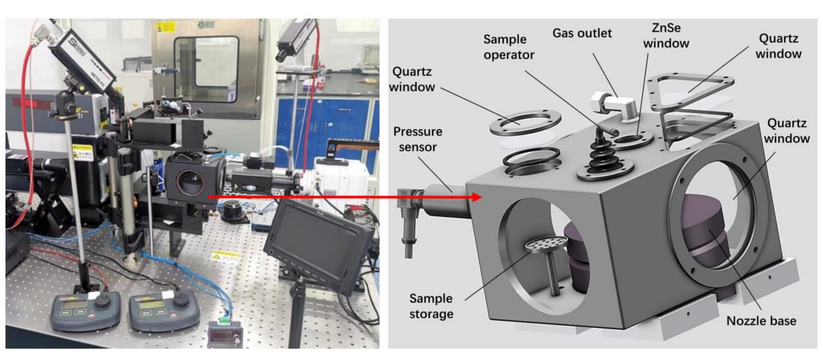

Figure 1. View of ALSEE facility

Measurement Principle

Density is determined by the ratio of mass to volume. The volume of a levitated sample is calculated based on the ellipsoid hypothesis:

$$\rho = \frac{3m}{4\pi r_h^2 r_v}$$

where m is the sample mass, r_h the horizontal radius and r_v the vertical radius.

Surface tension is measured using the oscillating drop method. The drop oscillations are self-excited or acoustically excited to obtain the resonant frequency. The surface tension is determined by the Rayleigh equation:

$$\gamma = \frac{3\pi m v_r^2}{8}$$

where v_r is the resonant frequency.

Viscosity is measured during the damped oscillation which occurs when the drop oscillation decays due to the effect of viscous forces. The time evolution of the horizontal or the vertical radius follows a damped oscillation equation:

$$r_{h/v}(t) = A \cdot \exp(-\Gamma t) \cdot \sin(2\pi\nu t + \phi) + r_{av}$$

where A is the amplitude, Γ the damping constant, ν the responding frequency, ϕ the phase and r_{av} the mean radius at rest. Viscosity is determined by the Lamb equation after the damping constant is obtained:

$$\eta = \frac{\rho R^2}{5}\Gamma = \frac{1}{5}\left(\frac{3}{4\pi}\right)^{\frac{2}{3}} m^{\frac{2}{3}} \rho^{\frac{1}{3}} \Gamma$$

where R is the equivalent radius of the drop.

Density

The density measurement was conducted during a cooling process. Initially, the sample was levitated and heated to a high temperature. Subsequently, the lasers were deactivated, initiating a rapid decrease in sample temperature. Concurrently, images and temperatures were recorded using the high-speed camera and pyrometers. For density calculation, the horizontal and vertical radii of the sample were determined by ellipse fitting.

The density of molten alumina was measured using backlighting imaging. A density equation of molten alumina (2550K-2900K) is obtained by linear fitting:

$$\rho_{Al_2O_3} = -(9.606 \pm 0.625) \times 10^{-5} T + (3.105 \pm 0.017)\ (\mathrm{g/c\,m^3})$$

The density data of molten alumina obtained by backlighting imaging (Figure 2) show good agreement with reported data [2-4], considering the density uncertainty of 1.14% in the present study.

The density of molten zirconia was measured using self-illumination-imaging. A density equation of molten zirconia (2750K-3200K) is obtained by linear fitting:

$$\rho_{ZrO_2} = -(7.202 \pm 1.169) \times 10^{-4} T + (6.869 \pm 0.346)\ (\mathrm{g/cm^3})$$

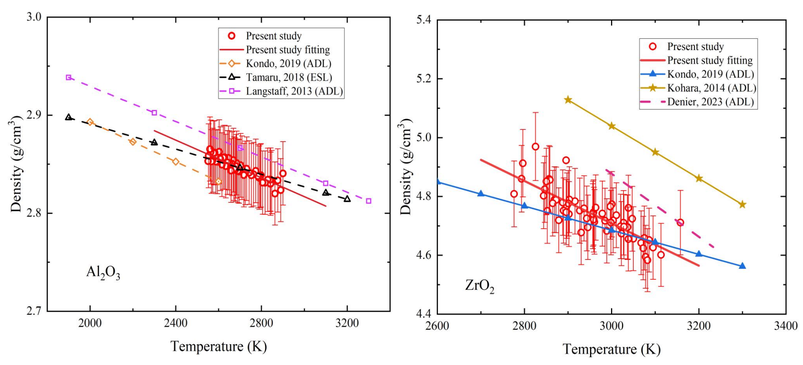

Figure 2. Density of molten alumina and zirconia

The density uncertainty for molten zirconia is 2.33% in the present study. The obtained data show good agreement with data obtained by Kondo et al. [3]. The deviations from other reported data [5-6] may be caused by the difference of the used gas composition.

The density equation of molten alumina exhibits less uncertainty compared to zirconia. This discrepancy can be attributed to the strong evaporation observed in the case of zirconia, which results in the deterioration of levitation stability.

Surface Tension

The surface tension of molten alumina was measured using acoustic excitation. A frequency sweep was performed to obtain the responding oscillation amplitude at each frequency. Resonant frequency was then determined from the resonant peak in the frequency spectrum. The results of molten alumina are in good agreements with results by Kondo et al. [7] using the drop impingement method. The deviations from other data [2,8-9] may be caused by the appearance of the oscillation mode splitting in their experiments.

The surface tension of molten zirconia was measured by self-excitation due to long duration for a frequency sweep in acoustic excitation. Otherwise, the significant evaporation of zirconia would result in a large uncertainty of mass. The obtained data shown in Figure 3 reveal a negative temperature coefficient. Taking account of all published data [3,6-7] yields (2800K-3500K) :

$$\gamma_{ZrO_2} = -(4.376 \pm 1.022) \times 10^{-4}(T - 2988) + (0.880 \pm 0.028)\ (\mathrm{N/m})$$

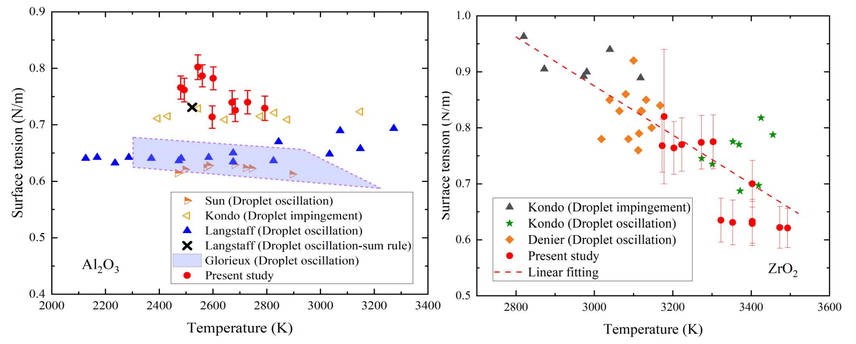

Figure 3. Surface tension of molten alumina and zirconia

Viscosity

Damping constant was obtained through a nonlinear fitting of the drop radius during the damped oscillations and then used to calculated viscosity [11]. The results for molten alumina and zirconia are presented in Figure 4.

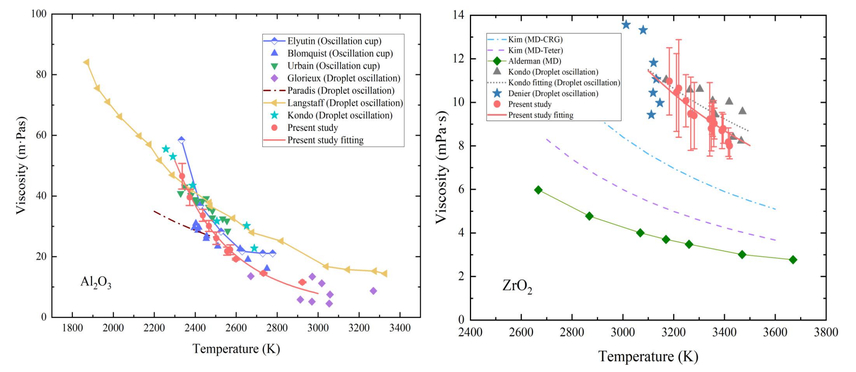

Figure 4. Viscosity of alumina and zirconia

The obtained viscosity data of molten alumina (2336K-2923K) and zirconia (3183K-3420K) are well fitted by the Andrade equation :

$$\eta_{Al_2O_3} = (47.06 \pm 2.15)\exp\left[\frac{(1.546 \pm 0.144) \times 10^5}{8.314}\left(\frac{1}{T} - \frac{1}{2327}\right)\right]\ (\mathrm{mPa \cdot s})$$

$$\eta_{ZrO_2} = (12.87 \pm 1.03)\exp\left[\frac{(8.035 \pm 2.010) \times 10^4}{8.314}\left(\left(\frac{1}{T} - \frac{1}{2988}\right)\right)\right]\ (\mathrm{mPa \cdot s})$$

Viscosity for molten oxides is difficult to measure due to high temperature, therefore the measurement uncertainty is high. Contact methods can lead to sample contamination and inaccurate measurements. Molecular dynamics (MD) calculations are strongly influenced by models and parameters, resulting in significant deviations between calculated results and experimental values [12-13]. The coefficients for molten zirconia remain a notable level of uncertainty due to the effect of evaporation.

Conclusion

ALSEE experimental setup can measure density, surface tension and viscosity of molten alumina and zirconia through aerodynamic levitation. Evaporation of molten oxides will significantly deteriorate levitation stability, hence reducing measurement accuracy.

Investigation for the corium properties is on going specifically for UO_2, UO_2-ZrO_2 and UO_2-ZrO_2-Zr-Fe mixtures.

References

[1] Y. Gong, L. Zhang, Y. Yuan, Q. Guo, W. Ma, S. Huang, Density measurement of molten drop with aerodynamic levitation and laser heating, Front. Energy Res. 10 (2022) 892406.

[2] D. Langstaff, M. Gunn, G.N. Greaves, A. Marsing, F. Kargl, Aerodynamic levitator furnace for measuring thermophysical properties of refractory liquids, Rev. Sci. Instrum. 84 (2013) 124901.

[3] T. Kondo, H. Muta, K. Kurosaki, F. Kargl, A. Yamaji, M. Furuya, Y. Ohishi, Density and viscosity of liquid ZrO2 measured by aerodynamic levitation technique, Heliyon 5 (2019) e02049.

[4] H. Tamaru, C. Koyama, H. Saruwatari, Y. Nakamura, T. Ishikawa, T. Takada, Status of the electrostatic levitation furnace (ELF) in the ISS-KIBO, Microgravity Sci. Technol. 30 (2018)

[5] S. Kohara, J. Akola, L. Patrikeev, M. Ropo, K. Ohara, M. Itou, A. Fujiwara, J. Yahiro, J.T. Okada, T. Ishikawa, Atomic and electronic structures of an extremely fragile liquid, Nat. Commun. 5 (2014) 5892.

[6] C. Denier, Z. Zhang, E. de Bilbao, J. Delacroix, P. Piluso, Thermophysical properties of liquid zirconia measured by aerodynamic levitation at high temperature, Int. J. Thermophys. 44 (2023) 127.

[7] T. Kondo, H. Muta, Y. Ohishi, Development of a new method to measure surface tension of molten oxides, High Temp.- High Pressures, 50 (2021).

[8] B. Glorieux, F. Millot, J.C. Rifflet, Surface tension of liquid alumina from contactless techniques, Int. J. Thermophys. 23 (2002) 1249–1257.

[9] Y. Sun, G. Duan, A. Yamaji, T. Takatani, H. Muta, Y. Ohishi, Validating ground-based aerodynamic levitation surface tension measurements through a study on Al2O3, Npj Microgravity 8 (2022) 26.

[11] Y. Gong, L. Zhang, Y. Yuan, Q. Guo, W. Ma, S. Huang, Viscosity measurement of molten alumina and zirconia using aerodynamic levitation, laser heating and droplet oscillation techniques, Heliyon. 9 (2023) e22424.

[12] O.L.G. Alderman, C.J. Benmore, J.K.R. Weber, L.B. Skinner, A.J. Tamalonis, S. Sendelbach, A. Hebden, M.A. Williamson, Corium lavas: structure and properties of molten UO2-ZrO2 under meltdown conditions, Sci. Rep. 8 (2018) 2434.

[13] W.K. Kim, J.H. Shim, M. Kaviany, Thermophysical properties of liquid UO2, ZrO2 and corium by molecular dynamics and predictive models, J. Nucl. Mater. 491 (2017) 126–137.

Yaopeng Gong
PhD Candidate
Tel: +86 13141317804
Email: gyp18@mails.tsinghua.edu.cn

PLINIUS – experimental platform for nuclear excellence

Andrea Bachrata[1], Caroline Billot[2], Viviane Bouyer[3], Jules Delacroix[4], Arthur Denoix[5], Christophe Journeau[6], Pascal Piluso[7] and Jean-François Villard[8]

[1]CEA IRESNE, CEA, DES, IRESNE, DTN, Cadarache F-13108 St Paul Lez Durance France , andrea.bachratakubic@cea.fr
[2]CEA IRESNE, CEA, DES, IRESNE, DTN, Cadarache F-13108 St Paul Lez Durance France , caroline.billot@cea.fr
[3]CEA IRESNE, CEA, DES, IRESNE, DTN, Cadarache F-13108 St Paul Lez Durance France , viviane.bouyer@cea.fr
[4]CEA IRESNE, CEA, DES, IRESNE, DTN, Cadarache F-13108 St Paul Lez Durance France , jules.delacroix@cea.fr
[5]CEA IRESNE, CEA, DES, IRESNE, DTN, Cadarache F-13108 St Paul Lez Durance France , arthur.denoix@cea.fr
[6]CEA IRESNE, CEA, DES, IRESNE, DTN, Cadarache F-13108 St Paul Lez Durance France , christophe.journeau@cea.fr
[7]CEA IRESNE, CEA, DES, IRESNE, DTN, Cadarache F-13108 St Paul Lez Durance France , pascal.piluso@cea.fr
[8]CEA IRESNE, CEA, DES, IRESNE, DTN, Cadarache F-13108 St Paul Lez Durance France , jean-francois.villard@cea.fr

Contact email: andrea.bachratakubic@cea.fr

Abstract

As the world embraces nuclear energy as a viable solution for sustainable development and the fight against climate change, the understanding of severe accidents becomes vital to ensure the acceptance and continued growth of the nuclear industry in a safe and responsible manner. The importance of exploring and investigating severe accidents cannot be overstated, as this knowledge serves as the foundation for developing preventive measures and effective response strategies.
The recent achievements in successfully executed experiments on PLINIUS platform at CEA IRESNE, at Cadarache in France, underline significant progress in our collective efforts to enhance nuclear safety and sustainability.
Building upon past successes, this work emphasizes the significance of current experimental capacities to simulate and study severe accidents. The presented work highlights the ongoing R&D for GENII, III and GENIV as well as ongoing R&D for dismantling needs related to Fukushima Daiichi. In 2023, three big-scale experiments are successfully performed with dedicated and high performance instrumentation.. The experiments bring insight into the corium-concrete interaction under the top flooding in MERELAVA facility and the fuel-coolant interaction phenomena in KROTOS facility. Moreover, several blocks or corium samples are being fabricated in VITI and VULCANO facility for further studies related to leaching or debris cutting for post-accidental dismantling.
Recognizing the importance of international collaboration, our platform actively engages with partners across borders to facilitate knowledge exchange and leverage global expertise in the pursuit of comprehensive severe accident understanding. The current list of our engagements and future opportunities to collaborate is presented. Moreover, the presented approach in this work encompasses a modular framework that not only addresses the immediate R&D requirements. The CEA experimental team also offers adaptability of platform to address future needs in our ongoing endeavor to mitigate the risks associated with severe accidents.

Keywords: PLINIUS, experiments, severe accidents, R&D, collaboration

SEAKNOT
ERMSAR 2024
11th Conference on
SEVERE ACCIDENTS RESEARCH
May 13-16, 2024 – Stockholm, Sweden

PLINIUS – Experimental Platform for Nuclear Excellence

A. Bachrata, C. Billot, V. Bouyer, J. Delacroix, A. Denoix, C. Journeau, P. Piluso, J.-F. Villard



Introduction

As the world embraces nuclear energy as a viable solution for sustainable development and the fight against climate change, the understanding of severe accidents becomes vital to ensure the acceptance and continued growth of the nuclear industry in a safe and responsible manner. The importance of exploring and investigating severe accidents cannot be overstated, as this knowledge serves as the foundation for developing preventive measures and effective response strategies.
The recent achievements in successfully executed experiments on PLINIUS platform at CEA IRESNE, at Cadarache in France, underline significant progress in our collective efforts to enhance nuclear safety and sustainability.

Device Spotlight

At the experimental platform PLINIUS, pioneering research on prototypic corium has been underway since 1997. This facility is notable for its focus on using **prototype materials, operating under high-temperature conditions, and conducting experiments on a large scale**. The objective is to study the interaction of corium with various materials, generating essential data to enhance R&D efforts and refine computer codes.
The overview of the present devices and their primary characteristics are as follows:

MERELAVA
- Top flooding tests of prototypic corium.
- Up to 80kg of corium.
- Molten by thermitic reaction.
- Water injection flow 3-15liters/s.
- Tests without sustained heating of corium.
- Tests with induction heating of corium.

KROTOS
- Fuel-coolant interaction.
- 3-8kg of corium.
- Up to 2700°C.
- To characterize pre-mixing & debris formation.
- To characterize steam explosion.

VITI
- Dedicated to analytical experiments.
- High temperature experiments (up to 2700°C).
- Few g to 100g.
- Prototypical corium & other materials.
- Enriching of nuclear data-base.

VULCANO
- 50-90kg of corium
- Molten core-concrete interaction
- Spreading experiments

FUJISAN : Characterizations of the aerosol released during prototypic fuel debris cutting.

Interconnectivity Snapshot

Regarding the complexities of severe accident phenomena, the interplay between devices MERELAVA, KROTOS, VITI, and VULCANO is crucial.
Each device is designed to investigate different interaction processes at different stages of severe accidents.

Notably, VULCANO and MERELAVA share a 400kW induction generator, enabling switching between the two devices. These large-scale devices use as well the thermite reaction techniques, to heat important masses of corium. The combination of thermite reaction and inductive heating techniques is a precise process that requires pre-calculations and various tests to confirm the suitability of the corium composition.

In contrast, KROTOS and VITI, are working with smaller masses and do not use thermite reaction techniques. VITI, uniquely classified as small scale, conducts numerous measurement campaigns throughout the year.

VITI measurements are often interconnected, participating in collaborative efforts with KROTOS or MERELAVA before or after campaigns to comprehensively characterize samples. Others VITI campaigns [1] focus on physical properties and interaction measurements, providing invaluable insights into the essential physical parameters required for modeling and enhancing the thermodynamic/thermophysical database.

The experiments involve numerous in-situ measurement methods (thermocouples, spectrometers, vapor flow measurements, dynamic pressure measurements), some of which are highly innovative (dynamic radiography, pyro-reflectometry...).

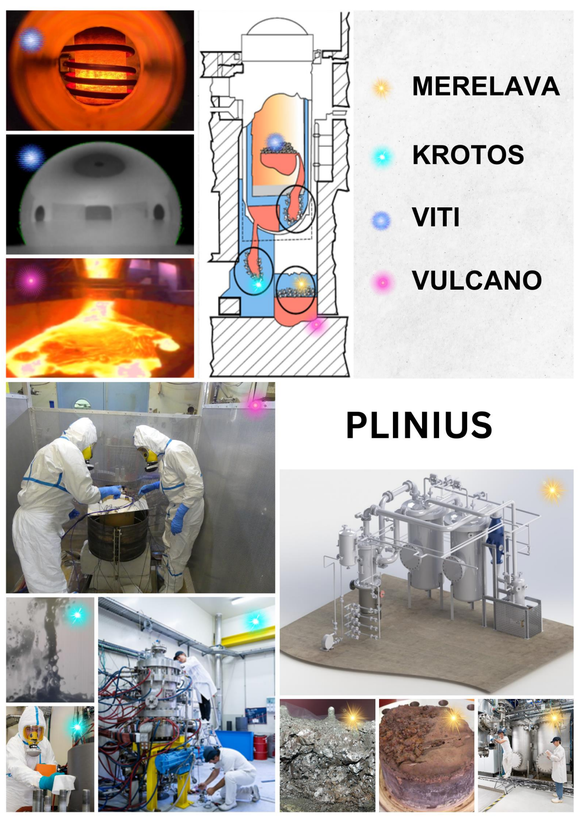

Results Snapshot

Building upon past successes, the CEA team realized successfully in 2023 different experiments at PLINIUS:

- The last two MERELAVA tests of the ANR MIT3BAR program, focusing on corium cooling through top water injection. These tests involved oxyde-metal corium, simulating residual power and concrete ablation, marking a world first.
- The final KROTOS test of the ANR ICE program, exploring corium-water interaction. Several kilograms of corium were melted and heated to over 2500°C, then released into the water, leading to steam explosion due to the interaction between the molten corium and water.
- The large quantity of corium for the cutting experiments was prepared by the CEA team in VULCANO [2], using a combination of thermitic reaction and induction heating. This corium cutting test campaign, marking a collaboration between ONET TECHNOLOGIES and IRSN, facilitates the measurement of formed aerosols, supporting the cleanup and dismantling of the Fukushima Daiichi accident-affected power plants. This collaborative effort is set to continue with a project extension until 2025.
- Numerous campaigns preparing samples for leaching experiments or measuring the physico-chemical properties of materials at very high temperatures on the VITI. VITI is the first device within the PLINIUS framework, contributing crucial data for GENIV R&D studies on severe accident mitigation. One notable aspect of its contributions involves exploring the interaction between UO2 and B4C at temperatures exceeding 2500°C. This research is conducted as part of a collaborative effort between France and Japan, focusing on sodium-cooled fast neutron reactors.

Tomorrow's Horizon

In conclusion, the PLINIUS platform has demonstrated its capability to conduct ~5 large-scale experiments and hundreds of small-scale experiments annually. These experiments are performed through collaborations within the French partnership network or are funded by various entities such as EU projects (e.g., OFFERR project from 2024), ANR projects (MIT3BAR or ICE), and OECD projects (e.g., COPS from 2024).
The facility is also open for direct collaboration with industry partners interested in financing specific experiments. Current applications predominantly focus on Fuel-Coolant Interaction (FCI), corium block preparations, corium interaction with concrete, corium reflooding and physical properties measurements.

However, effective planning is crucial, requiring a preparation phase of ~three to six months, preceding the acquisition period of consumables. Post-experiment, the analysis of results and facility restoration to its initial state may take an additional ~one to six months depending on complexity of experiment.

CEA supports R&D, innovation, and technological feasibility studies. As part of the new SAFeTY project [3], a dedicated building for severe accident studies is required for GEN2, GEN3, and GEN IV (sodium-cooled) reactors. The SAFeTY prototypic corium experimental platform is being designed to facilitate a long-term severe accident experimental research and development program spanning several decades. The experiments will involve higher corium masses and utilize modern measurement techniques.

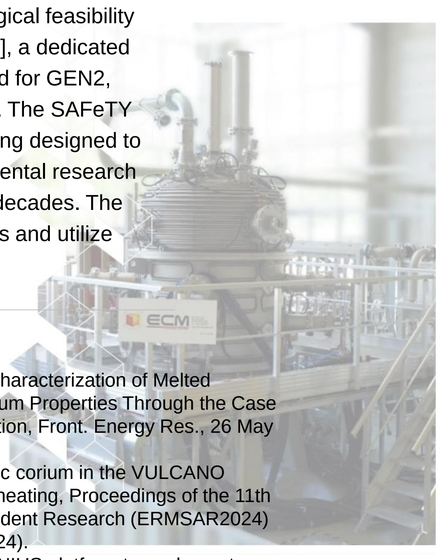

References

[1] J. Delacroix et al., High-Temperature Characterization of Melted Nuclear Core Materials: Investigating Corium Properties Through the Case Studies of In-Vessel and Ex-Vessel Retention, Front. Energy Res., 26 May 2022, Sec. Nuclear Energy, Vol. 10.
[2] A. Denoix et al., Production of prototypic corium in the VULCANO facility using uranothermite andi nduction heating, Proceedings of the 11th European Review Meeting on Severe Accident Research (ERMSAR2024) KTH, Stockholm, Sweden, May 13-16 (2024).
[3] Ch. Journeau et al., Upgrading the PLINIUS platform toward smarter prototypic-corium experimental R&D, Nucl. Eng. Des. 386 (Jan 2022) 111511.

ACKNOWLEDGMENTS

They trust us, we share our ambitions with:

CONNECT WITH US:

CEA, DES, IRESNE, DTN, Severe Accident Experimental Laboratory, Cadarache F-13108 St-Paul-lez-Durance, France

Tel: +33 6 61 85 29 03
Email: andrea.bachratakubic@cea.fr

THERMODYNAMIC EVALUATION OF LIQUID-GAS SURFACE TENSION FOR $U-O-ZR$ MIXTURES USING THE BUTLER EQUATION

A. Tourneix, C. Denier, R. Le Tellier, P. Piluso, J. Delacroix
CEA, DES, IRESNE, DTN, Cadarache
F-13108 Saint Paul-lez-Durance, France
arthur.tourneix@cea.fr; caroline.denier@cea.fr; romain.le-tellier@cea.fr;
pascal.piluso@cea.fr; jules.delacroix@cea.fr

ABSTRACT

In this work, the Butler equation is assessed for evaluating the liquid/gas surface tension for three compositions in the ternary $U-Zr-O$ system over a wide temperature range $2600-3100$ K. In this approach, the liquid phase Gibbs energy is obtained from two CALPHAD-type databases, NUCLEA and TAF-ID. Two formulations of the Butler equation make use of an ideal phase mixing hypothesis (φ being the weighting factor) with and without surface tension laws for pure components. A third formulation corresponds to the classical form of the Butler equation found in the literature where the interfacial Gibbs excess energy is assumed to be proportional to the liquid one (the multiplicative factor k_Γ being related to the ratio of broken bounds). Computed surface tensions are compared to experimental values from the literature. Three different compositions corresponding to different Zirconium oxydation degree, C0, C30 and C50 are considered. It is shown through a limited parametric analysis that the choice of the CALPHAD database affects both the slope w.r.t temperature and the level of the interfacial energy while parameters φ and k_Γ mainly affects the level and only slightly the slope. Considering pure component surface tension data has a significant impact on both and, considering the C0 composition measurements, it is shown that parameters φ and k_Γ can be successfully calibrated for reproducing these data. However, the steep variation of the interfacial energy w.r.t temperature exhibited by experimental results for the C30 composition is, in any case, not correctly captured. This shows the need for further improvement of the liquid thermodynamic modelling and a path forward is proposed.

KEYWORDS

`surface tension, corium, Butler equation, CALPHAD`

1. INTRODUCTION

Estimating the physical properties of materials involved in nuclear safety is an important aspect for the accuracy of associated simulations. This process can be particularly difficult in cases where experimental data are scarce. Corium jet fragmentation is one such example. In the event of a severe accident in a nuclear reactor, the corium resulting from core meltdown may relocate at the bottom of the reactor pressure vessel or reactor pit in case of vessel failure. The possible presence of water can lead to a fuel-coolant interaction where a high temperature corium jet fragmentates into droplets while vaporising a large amount of water due to high heat transfer [1]. In the worst case scenario, the steam film enclosing the droplets can be destabilised in such a way that the direct

contact between water and corium would lead to further fragmentations and a steam explosion. Such an event could compromise the vessel or containment integrity [2]. Fragmentation phenomena are highly dependent on the surface tension between liquid corium and water vapour as exhibited by empirical fragmentation laws based on the Weber number. However, there is little to no data on this property for liquid corium mixtures due to the very high temperature and components involved[3].
In an effort to provide such data, experimental measurements were successfully carried out recently for $U-O-Zr$ mixtures at CEA Cadarache in the VITI facility of the PLINIUS platform. Those were performed using the maximum bubble pressure method with argon gas injection into the liquid corium [4, 5]. Because of the complexity of such measurements, only a limited set of corium compositions and temperatures have been investigated. In an attempt to construct surface tension laws over a larger range of composition and temperature, the work presented in this paper makes use of a thermodynamic modelling approach using the Butler equation [6] and two different CALPHAD−type thermodynamic databases (NUCLEA [7], TAF-ID [8]) in order to evaluate surface tension between $U-O-Zr$ liquid mixtures and Argon atmosphere. Two different models are considered: on the one hand, the Butler formulation commonly applied for liquid-gas interfaces that incorporates surface tension data of pure components and, on the other hand, a more straightforward formulation of the Butler equation already used in the literature for liquid-liquid interfaces. Those models are presented in the following section 2. In section 3, the numerical solution for these models is summarized while numerical results are presented and discussed in comparison with recent experimental measurements in section 4. Finally, short conclusions and perspectives of this work are given in section 5.

2. INTERFACE MODELLING

The Butler model was chosen in this work as a full-thermodynamic approach compatible with the CALPHAD method to study surface tensions as described by Butler [6]. Its derivation from fundamental Gibbs equations has been recently revised by Kaptay in [9, 10] obtaining the equations without the monolayer approximation. In this Gibbsean approach, it is considered that the zero-volume interface can be fully characterized by an average composition. Despite its apparent simplicity and approximations[1] , the Butler equation was successfully applied to compute surface energies of various binary systems such as liquid alloys, ionic and oxide melts [12] ; also using the CALPHAD method to evaluate partial molar excess Gibbs energies [13, 14]. This model can be readily extended to $n-$components system by using $n-1$ equations as it was applied for liquid ternary $CaO-SiO_2-Al_2O_3$ [15], and quaternary $Sn-Zn-Sb-Bi$ [16]. Recently, it was successfully applied to corium systems ($U-O$ and $U-O-Zr-Fe$) for calculating the liquid-liquid interface energy in the miscibility gap region of such systems [17].

2.1. Butler equation

Let us consider a thermodynamic system of N_c components with a known temperature T (K), pressure P (Pa) and global composition written as a molar fractions vector $\boldsymbol{x}$. The Gibbs energy of this system is denoted $\mathcal{G}$ (J). We consider cases where, at equilibrium, the system contains two stable bulk phases α, β associated respectively with their Gibbs energy $\mathcal{G}_\alpha$ and $\mathcal{G}_\beta$ (J). The

[1]Santos and Reis in [11] studied its robustness and have shown that Butler equation does not take into account the composition dependency of reference state leading to slightly overestimate ($< 5\%$) surface tension values.

chemical potential $\mu_{i,\alpha}$ (J/mol) of component i in phase α (resp. β) is defined as

$$\mu_{i,\alpha} = \frac{\partial \mathcal{G}_\alpha}{\partial n_i} \tag{1}$$

Gibbs showed that at equilibrium the chemical potential of a component i is uniform over all the stable phases [18] *i.e.*

$$\mu_{i,\alpha} = \mu_{i,\beta} = \mu_i \tag{2}$$

In the Butler model, the interface is depicted as a planar phase with associated Gibbs energy $\mathcal{G}_\Gamma$, a mean composition $\boldsymbol{x}_\Gamma$ and a surface area A_Γ as seen in figure 1 as its thickness is neglected. The total Gibbs energy of the system is the sum over its stable phases of the different Gibbs energies $\mathcal{G} = \mathcal{G}_\alpha + \mathcal{G}_\beta + \mathcal{G}_\Gamma$.

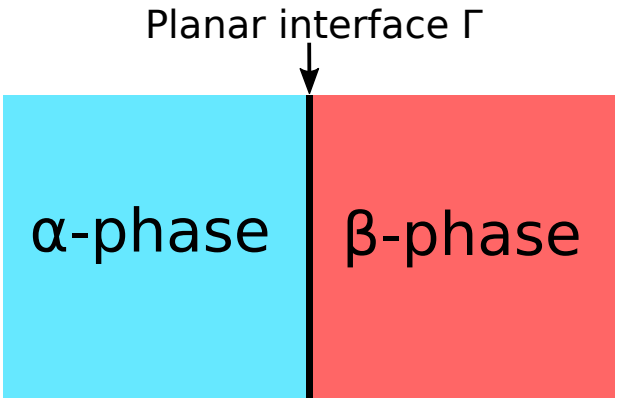

Figure 1. Schematic representation of 2 stable phases, α and β, at equilibrium with a planar interface Γ.

For the interface Γ, the chemical potential $\mu_{i,\Gamma}$ of component i is written as

$$\begin{cases} \mu_{i,\Gamma} = \mu^*_{i,\Gamma} - \omega_{i,\Gamma}\sigma_\Gamma \\ \sigma_\Gamma = \dfrac{\partial \mathcal{G}_\Gamma}{\partial A_\Gamma} \\ \mu^*_{i,\Gamma} = \dfrac{\partial \mathcal{G}_\Gamma}{\partial n_i} \end{cases} \tag{3}$$

with σ_Γ $(J.m^{-2})$ the interfacial energy, independent from the component i, and $\omega_{i,\Gamma}$ (m^2/mol) the partial molar surface of component i in interface Γ. The term $\mu^*_{i,\Gamma}$ is called the reduced chemical potential.
The equilibrium conditions (equation 1) as extended by Butler [6] lead to

$$\mu_i = \mu_{i,\Gamma} \tag{4}$$

Writing equations 3 and condition 4 for all components, the first form of the Butler equations can be deduced as, $\forall j \in [1, N_c]$

$$\sigma_\Gamma = \frac{\mu^*_{j,\Gamma} - \mu_j}{\omega_{j,\Gamma}} \tag{5}$$

The independence of the surface tension value from the components constrains the interface composition through the reduced chemical potentials and equation 5 gives a non-linear system of dimension $N_c - 1$ whose independent variables are associated with the interface composition.

The chemical potentials are usually expressed as a sum of three terms [19, 20, 21]

$$\mu_{i,\alpha} = \mu^0_{i,\alpha} + RT\ln(x_{i,\alpha}) + \Delta\mathcal{G}^E_{i,\alpha}(\boldsymbol{x_\alpha}) \tag{6}$$

$$\mu^*_{i,\Gamma} = \mu^{0,*}_{i,\Gamma} + RT\ln(x_{i,\Gamma}) + \Delta\mathcal{G}^E_{i,\Gamma}(\boldsymbol{x_\Gamma}) \tag{7}$$

where

- $\mu^0_{i,\alpha}$ (resp. $\mu^{0,*}_{i,\Gamma}$) is the chemical potential of pure component i in phase α (resp. Γ) with same temperature and pressure ;
- $RT\ln(x_{i,\alpha})$ is the entropic contribution with R $(J/(mol\cdot K))$ the universal gas constant, and $x_{i,\alpha}$ (resp. $x_{i,\Gamma}$) the molar fraction of component i in phase α (resp. in interface Γ) ;
- $\Delta\mathcal{G}^E_{i,\alpha}$ (J/mol) (resp. $\Delta\mathcal{G}^E_{i,\Gamma}$) is the partial molar excess Gibbs energy function for phase α (resp. interface Γ) at composition $\boldsymbol{x_\alpha}$ (resp. $\boldsymbol{x_\Gamma}$). This term is the deviation from an ideal solution.

A similar expression as equation 6 exists for phase $\mu_{i,\beta}$.
Using these equations 6 and 7, the Butler equation 5 can be written in its second form [10]

$$\begin{cases} \sigma_\Gamma = \dfrac{\omega^0_{i,\Gamma}}{\omega_{i,\Gamma}}\sigma^0_{i,\Gamma} + \dfrac{RT}{\omega_{i,\Gamma}}\ln\left(\dfrac{x_{i,\Gamma}}{x_{i,\alpha}}\right) + \dfrac{\Delta\mathcal{G}^E_{i,\Gamma} - \Delta\mathcal{G}^E_{i,\alpha}}{\omega_{i,\Gamma}} \\ \sigma^0_{i,\Gamma} = \dfrac{\mu^0_{i,\Gamma} - \mu^0_{i,\alpha}}{\omega^0_{i,\Gamma}} \end{cases} \tag{8}$$

where $\sigma^0_{i,\Gamma}$ is associated with the interface energy in the pure component i case.

2.2. Modelling the thermodynamic quantities

In precedent works on liquid/gas surface energies using the second Butler formulation, a hypothesis is made to solve the rightmost term of the equation 8 [12, 13, 14, 22, 10]. Considering the phase α to be the liquid phase and β the gaseous one, this hypothesis can be written as

$$\Delta\mathcal{G}^E_{i,\Gamma}(\boldsymbol{x_\Gamma}) = k_\Gamma\Delta\mathcal{G}^E_{i,\alpha}(\boldsymbol{x_\Gamma}) \tag{9}$$

where $k_\Gamma = Z_\Gamma/Z_\alpha$ is the ratio of the interface coordination number over the liquid coordination number for the components. As the components form less bonds in the surface, $Z_\Gamma < Z_\alpha$, and thus, $k_\Gamma \in [0,1]$[10].
In this work, an ideal phase mixture hypothesis was also tested to model the interface Gibbs energy such as

$$\mathcal{G}_\Gamma = \varphi\mathcal{G}_\alpha(\boldsymbol{x_\Gamma}) + (1-\varphi)\mathcal{G}_\beta(\boldsymbol{x_\Gamma}), \qquad \varphi \in [0,1] \tag{10}$$

and using equation 3, leading to

$$\mu^*_{i,\Gamma} = \varphi\mu_{i,\alpha}(\boldsymbol{x_\Gamma}) + (1-\varphi)\mu_{i,\beta}(\boldsymbol{x_\Gamma}) \tag{11}$$

This hypothesis makes use of information from the gaseous phase and the factor φ can easily be linked to k_Γ. Using equations 6, 7 and 10, it can be shown that

$$\varphi\Delta\mathcal{G}^E_{i,\alpha}(\boldsymbol{x_\Gamma}) + (1-\varphi)\Delta\mathcal{G}^E_{i,\beta}(\boldsymbol{x_\Gamma}) = k_\Gamma\Delta\mathcal{G}^E_{i,\alpha}(\boldsymbol{x_\Gamma}) \tag{12}$$

in such a way that, the two formulations are equivalent under the following constraint:

$$\varphi = \frac{k_\Gamma\Delta\mathcal{G}^E_{i,\alpha}(\boldsymbol{x_\Gamma}) - \Delta\mathcal{G}^E_{i,\beta}(\boldsymbol{x_\Gamma})}{\Delta\mathcal{G}^E_{i,\alpha}(\boldsymbol{x_\Gamma}) - \Delta\mathcal{G}^E_{i,\beta}(\boldsymbol{x_\Gamma})} \tag{13}$$

For the partial molar surfaces $\omega_{i,\Gamma}$, Kaptay has proposed to use a hard-sphere model to relate it to

partial molar volumes in the liquid phase with the relation [10]

$$\begin{cases} \omega_{i,\Gamma} = f_\Gamma V_{mi,\alpha}^{(2/3)} N_{Av}^{(1/3)} \\ f_\Gamma = 1.209 \dfrac{f_\alpha^{(2/3)}}{f_{s,\Gamma}} \end{cases} \tag{14}$$

where f_α and $f_{s,\Gamma}$ are packing fractions of phase α and interface Γ respectively and N_{av} is the Avogadro number. In the remainder, $f_\Gamma = 0.806$ is considered [10].

3. SOLVING THE BUTLER EQUATION

To solve the Butler equations presented in section 2.1, in the present work, the thermodynamic equilibrium are computed using the CALPHAD method [20, 21]. This method models the Gibbs energy of components and their phases as parameterised functions of temperature, pressure and composition. These parameters are fitted using experimental and ab initio data from various binary and ternary systems. Once assessed, they are stored in a thermodynamic database allowing to evaluate equilibrium with a Gibbs energy minimiser. In this work, the version 6 of OpenCalphad [23] software was used.
In this framework, the second Butler formulation (equation 8) was rewritten with chemical potentials using both hypotheses 10 and 9 for the interface energy. Hence, three different equation systems have been considered:

- using the first Butler formulation (equation 5) and the mixing hypothesis of equation 10, the following equation system (denoted `Butler` in the remainder) is obtained:

$$\begin{cases} \sigma_\Gamma = \dfrac{\mu_{i,\Gamma}^* - \mu_i}{\omega_{i,\Gamma}} \\ \mu_{i,\Gamma}^* = \varphi \mu_{i,\alpha}(\boldsymbol{x_\Gamma}) + (1-\varphi)\mu_{i,\beta}(\boldsymbol{x_\Gamma}) \end{cases} \tag{15}$$

- using the second Butler formulation (equation 8) and the mixing hypothesis of equation 10, the following equation system (denoted `ButlerExcess` in the remainder) is obtained:

$$\begin{cases} \sigma_\Gamma = \dfrac{\mu_{i,\Gamma}^* - \mu_{i,\alpha} + \mu_{i,\alpha}^0 - \mu_{i,\Gamma}^{*,0} + \omega_{i,\Gamma}\sigma_{i,\Gamma}^0}{\omega_{i,\Gamma}} \\ \mu_{i,\Gamma}^* = \varphi \mu_{i,\alpha}(\boldsymbol{x_\Gamma}) + (1-\varphi)\mu_{i,\beta}(\boldsymbol{x_\Gamma}) \end{cases} \tag{16}$$

- using the second Butler formulation (equation 8) and the excess hypothesis of equation 9, the following equation system (denoted `ButlerPureExcess` in the remainder) is obtained:

$$\sigma_\Gamma = \frac{k_\Gamma \mu_{i,\alpha}^*(\boldsymbol{x_\Gamma}) - \mu_{i,\alpha} + (1-k_\Gamma)(\mu_{i,\alpha}^0 - RT\ln(x_{i,\Gamma})) + \omega_{i,\Gamma}\sigma_{i,\Gamma}^0}{\omega_{i,\Gamma}} \tag{17}$$

Solving these equation systems mean finding the interface composition such that the same interfacial energy value is found for each component in the interface as seen in the equation 5. Gajavalli and Le Tellier in [17] formulated the resolution of the Butler equations as a minimisation problem allowing the use of constrained minimisation algorithms to look for the solution. The same approach has been adopted here.
In the calculations, the chemical potentials of mixed and pure phases were computed directly with the CALPHAD software. Regarding the partial molar volumes, they are evaluated from mass density laws and their possible dependency to composition is taken into account as described in [17].

4. RESULTS AND DISCUSSION

The models and resolution methodology were confronted to experimental results obtained by C. Denier in her Ph.D. thesis work [4, 5] in the VITI facility using a maximum bubble pressure technique in which argon gas is injected through a capillary tube in the liquid mixture of interest. The composition of the different liquid mixtures are given in table I (as deciphered from post-mortem analyses); they are denoted by their initial zirconium oxidation degree, C0, C30 and C50.

Table I. Compositions of the liquid phase in C. Denier measurements [5].

	U fraction	Zr fraction	O fraction	Temperature (K)	Surface tension ($J.m^{-2}$)
C0	0.20	0.24	0.56	2640 ± 50	0.706 ± 0.013
				2746 ± 50	0.693 ± 0.013
				2865 ± 50	0.677 ± 0.013
C30	0.19	0.22	0.59	2836 ± 50	0.712 ± 0.013
				2876 ± 50	0.664 ± 0.012
C50	0.21	0.17	0.62	2710 ± 50	0.670 ± 0.013

Two Calphad databases have been considered, NUCLEA [7, 24] (version 19) and TAF-ID [8] (version 11). Considering the liquid phase, the main difference between the two databases is the different underlying model used to describe the excess term of equation 6, an ionic liquid model for TAF-ID and a non-ideal associate model for NUCLEA.
The numerical results are organized as follows. First, considering only the C0 composition and the first form of the Butler equation with ideal mixing hypothesis (`Butler`, see equation 15), a comparison of the two databases along with the impact of the φ-parameter is presented in section 4.1. Then, pure component interfacial energy data are introduced in section 4.2 through the two other formulations of the Butler equation (`ButlerPure` with equation 16 and `ButlerPureExcess`, with equation 17) and the results improvement is discussed.

4.1. Effects of φ and the database in `Butler` formulation

A comparison of database and φ parameter effects was done using equation 15. Results in terms of the interfacial energy as computed over the temperature range $[2400, 3100]$K are depicted in figure 2 for both databases and multiple values of φ.
For both databases, an optimal value for φ was calculated using a least square method considering the C0 composition experimental results: $\varphi^{\star}_{nuclea} = 0.6038$ and $\varphi^{\star}_{tafid} = 0.65$ are the optimised values for NUCLEA and TAF-ID databases respectively. Considering such an optimized value, the order of magnitude of the interfacial energy can be reproduced but its variation as a function of temperature, that is mostly dependent on the database, is not the same for the databases. More precisely, it can be seen that the choice of the liquid Gibbs energy model affects both the slope and the level of the interfacial energy curve while parameter φ mainly affects the level and only slightly the slope.
The derivative of the interfacial energy w.r.t. temperature is, in absolute value, about 50% higher with the NUCLEA database, highlighting the unquantified albeit large uncertainty associated with the liquid chemical potential model when used for extrapolation out of its phase equilibria values. This is consistent with the conclusion given by Gajavalli and Le Tellier in [17] about the impact on liquid/liquid interfacial energies of the lack of thermodynamic experimental information on liquid corium systems at high temperature.
In figure 3, the element composition of the interface is depicted for the NUCLEA database and

different values of φ. It can be observed that φ mainly affects the molar ratio between U and Zr: the higher φ, the lower this molar ratio is.

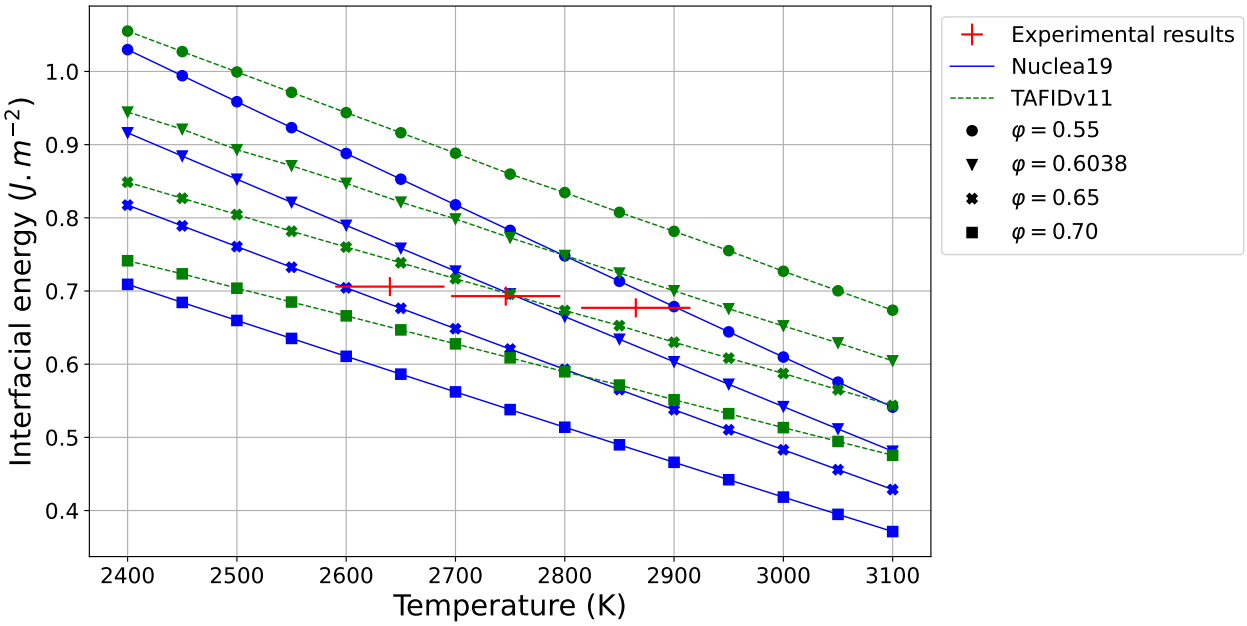

Figure 2. Interfacial energies plot using equation 15. Results obtained are shown in blue plain and green dotted curves for NUCLEA and TAF-ID respectively. Different symbols are used to show different values of φ. Experimental results are shown in red error bars.

4.2. Results improvement introducing pure component interfacial energy data

In order to improve the results, additional information coming from the knowledge associated with pure element interfacial energies are now considered along the two other Butler equation formulations (`ButlerPure` – equation 16 – and `ButlerPureExcess` – equation 17).
These data are expressed as a linear law w.r.t temperature under the following form:

$$\sigma_\Gamma(T) = \sigma_m + \frac{d\sigma}{dT}(T - T_m) \tag{18}$$

The associated parameters for the uranium and zirconium considered in this study as obtained from the open literature are given in table II.

Table II. Pure component interfacial energy laws for U and Zr.

Element	$\sigma_m(J.m^2)$	$\frac{d\sigma}{dT}$	$T_m(K)$	Reference
U	1.675	$0.34 \cdot 10^{-3}$	1405.45	[25]
Zr	1.462	$0.13 \cdot 10^{-3}$	2130.15	[26, 27, 28]

For pure oxygen, the interfacial energy was taken as an extrapolated 0 value from DFT results computed on liquid oxygen at low temperature range $(60 - 90K)$ showing a decreasing in surface tension with the temperature [29]. Indeed, the temperature involved are way above the critical temperature of pure oxygen ($T_c = 154$K) meaning that no liquid phase exist even under extreme pressure.

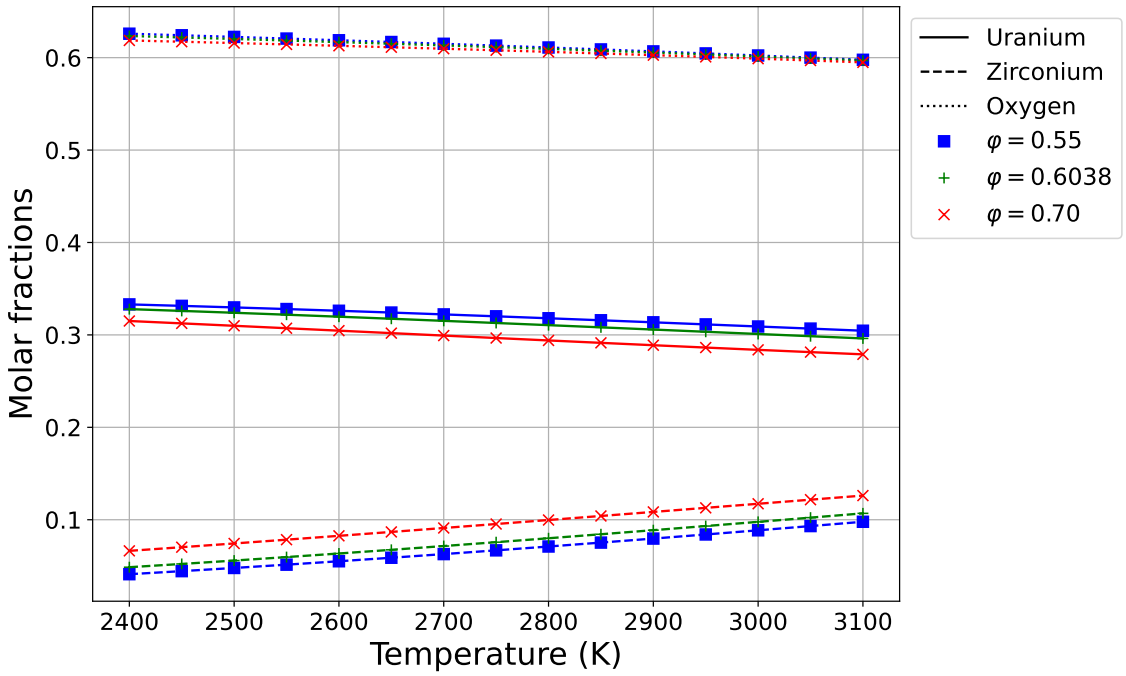

Figure 3. Interface composition computed with NUCLEA database for 3 different values of φ represented by separated symbols. Uranium, zirconium and oxygen fractions are represented by plain, dashed and dotted curves respectively.

Considering `ButlerPure` and `ButlerPureExcess` formulations, results were computed only for NUCLEA database as the ionic liquid model used in TAF-ID does not allow computations of a pure liquid oxygen phase (no vacancies in the cation sublattice).
Using the previous optimised value $\varphi_1^\star = 0.6038$ for NUCLEA, it can be seen in figure 4 that equation 16 and the use of the pure element interfacial tension data lead to an interfacial energy that is significantly lower (50% in average) than with `Butler` formulation with a derivative w.r.t to the temperature that is, in absolute value, significantly lower and closer to the experimental trend. Accordingly, a new optimised parameter was computed for the equation 16 with a value $\varphi_2^* = 0.9907$, successfully fitting the experimental results for the C0 composition. Considering the Butler equation formulation associated with equation 17, a similar optimization was carried out w.r.t. parameter $k_\Gamma^\star$ giving a value of 0.9989.
■ **Nota Bene** This value for $k_\Gamma^\star$ is higher than the value of 0.94 considered by Tanaka et al. for $k_\Gamma^\star$ for oxide melts (considering that they behave as ionic liquids) in [12] using a packing factor $f_\Gamma = 1$. Using $f_\Gamma = 1$ in our case, the optimised value of $k_\Gamma^\star$ is only slightly modified to 0.997. ■
Figure 5 depicts the comparison between the results obtained with equations 16 and 17 with these optimised parameters and the experimental measurements for the three different compositions, C0, C30 and C50. It can be observed that with an optimized value of $k_\Gamma^\star$, the results obtained with 17 are, in any case, very close to the ones obtained with equation 16 with an optimised $\varphi_2^\star$ value.
With parameters calibrated on C0 composition data, it can be seen that the single C50 composition measurement is correctly reproduced while the steepest dependency of the surface tension w.r.t. temperature exhibited for the C30 composition is not correctly captured. An attempt to optimize the parameters considering the experimental data associated with this composition was found unsuccessful. This last result highlights the need for further improvement of the liquid thermodynamic modelling (through the CALPHAD databases).

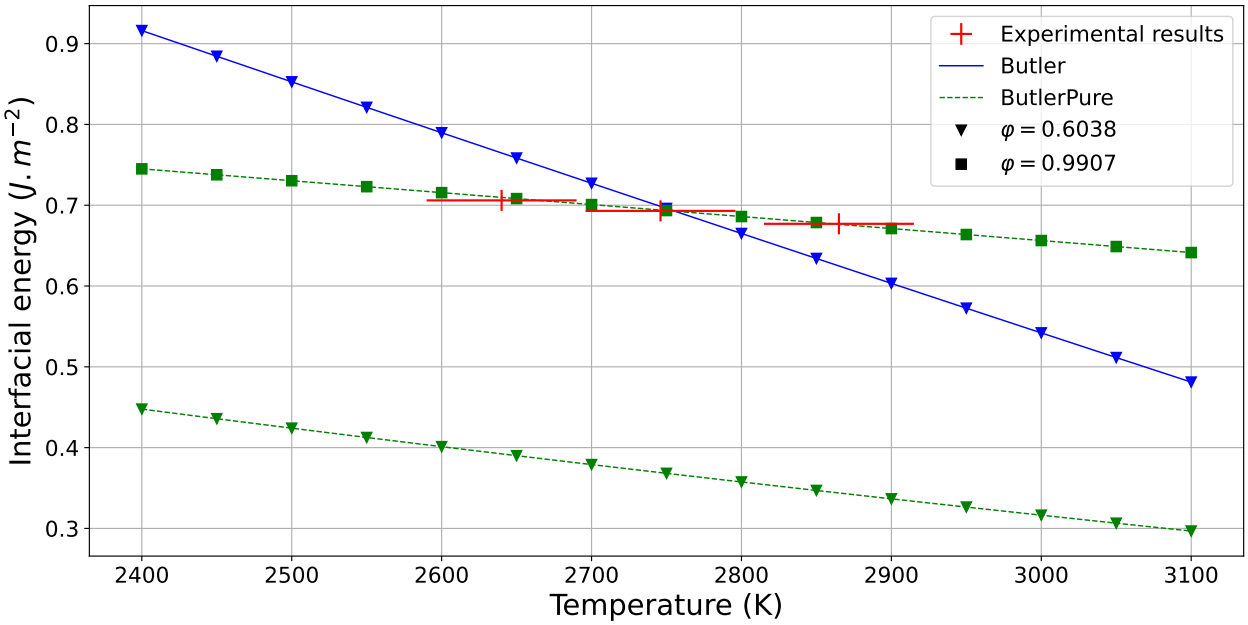

Figure 4. Interfacial energies computed with NUCLEA database with equations 15 in plain blue and 16 in dashed green. Symbols represent different φ-parameter values.

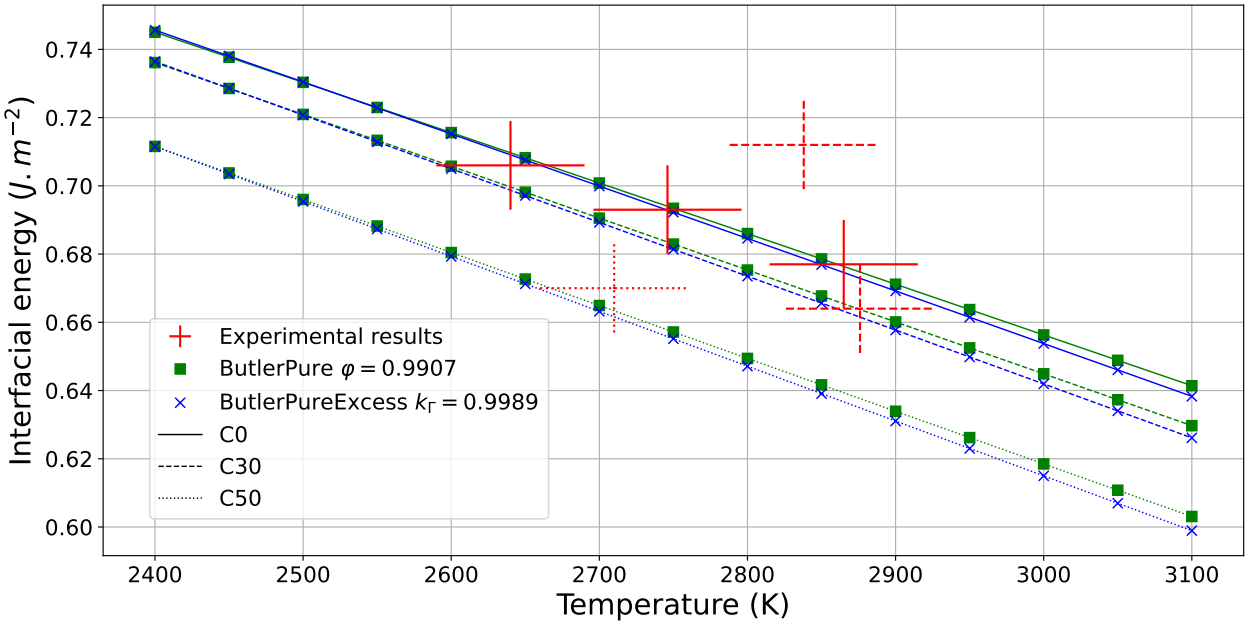

Figure 5. Interfacial energies computed with NUCLEA with equations 16 as green squares and 17 as blue cross. Plain, dashed and dotted lines represent C0, C30 and C50 compositions respectively.

5. CONCLUSIONS AND PERSPECTIVES

Different formulations of the Butler equations considering two CALPHAD databases were successfully applied to $U-Zr-O$ liquid mixtures for evaluating the associated surface tension under argon atmosphere. The impact of the database, the Butler formulation (considering or not additional information coming from pure component surface tension data) and the parameter associated with the interfacial Gibbs energy function was assessed though a comparison with experimental data. It was shown that, with a proper calibration, such a model can partly reproduce the experimental measurements and provide a valuable tool for producing surface tension laws over a wider range of composition and temperature. However, it was also found that their predictive capability is impaired by the unquantified albeit large uncertainty associated with the liquid Gibbs energy modelling in the present state of the CALPHAD databases associated with corium. Reversing the problem, considering this high sensitivity of surface tension to the underlying liquid model, surface tension data could provide valuable information on Gibbs excess energy term of the liquid phase. Accordingly, in the near future, we plan to make a proof of principle on the usage of such data in the CALPHAD assessment process.

REFERENCES

[1] Georges Berthoud. "Vapor Explosions". In: *Annual Review of Fluid Mechanics* 32.1 (2000). _eprint: https://doi.org/10.1146/annurev.fluid.32.1.573, pp. 573–611. DOI: 10.1146/annurev.fluid.32.1.573. URL: https://doi.org/10.1146/annurev.fluid.32.1.573.

[2] M. L. Corradini, B. J. Kim, and M. D. Oh. "Vapor explosions in light water reactors: A review of theory and modeling". In: *Progress in Nuclear Energy* 22.1 (Jan. 1, 1988), pp. 1–117. ISSN: 0149-1970. DOI: 10.1016/0149-1970(88)90004-2. URL: https://www.sciencedirect.com/science/article/pii/0149197088900042.

[3] Claude Brayer, Alexis Le Monnier, and Nourdine Chikhi. "Impact of corium thermophysical properties on fuel-coolant interaction". In: *Annals of Nuclear Energy* 147 (Nov. 1, 2020), p. 107613. ISSN: 0306-4549. DOI: 10.1016/j.anucene.2020.107613. URL: https://www.sciencedirect.com/science/article/pii/S030645492030311X.

[4] Caroline Denier et al. "Experimental Measurements of Thermophysical Properties of Several Corium Compositions and Influence on Fuel-Coolant Interaction". In: *PSA and Severe Accidents*. 32nd International Conference Nuclear Energy for New Europe. Portoroz, Slovenia: Nuclear Society of Slovenia, 2023, p. 707.1. ISBN: 978-961-6207-56-0. URL: https://www.djs.si/nene2023/proceedings/proceedings.

[5] Caroline Denier. *Détermination et modélisation de propriétés thermophysiques du corium pour des applications accidents graves*. http://www.theses.fr. Nov. 30, 2023. URL: http://www.theses.fr/s264877.

[6] John Alfred Valentine Butler and James Pickering Kendall. "The thermodynamics of the surfaces of solutions". In: *Proceedings of the Royal Society of London. Series A, Containing Papers of a Mathematical and Physical Character* 135.827 (Mar. 1, 1932). Publisher: Royal Society, pp. 348–375. DOI: 10.1098/rspa.1932.0040. URL: https://royalsocietypublishing.org/doi/abs/10.1098/rspa.1932.0040.

[7] S. Bakardjieva et al. "Improvement of the European thermodynamic database NUCLEA". In: *Progress in Nuclear Energy*. MAJOR ACHIEVEMENTS AFTER 4,5 YEARS OF SARNET SEVERE ACCIDENT RESEARCH NETWORK OF EXCELLENCE 52.1 (Jan. 1, 2010), pp. 84–96. ISSN: 0149-1970. DOI: 10.1016/j.pnucene.2009.09.014. URL: https://www.sciencedirect.com/science/article/pii/S0149197009001607.

[8] Christine Gueneau et al. "TAF-ID: an international thermodynamic database for nuclear fuels applications". In: *Calphad* 72 (2021), p. 102212. DOI: 10.1016/j.calphad.2020.102212. URL: https://hal-cea.archives-ouvertes.fr/cea-03118307.

[9] George Kaptay. "Improved Derivation of the Butler Equations for Surface Tension of Solutions". In: *Langmuir* 35.33 (Aug. 20, 2019). Publisher: American Chemical Society, pp. 10987–10992. ISSN: 0743-7463. DOI: 10.1021/acs.langmuir.9b01892. URL: https://doi.org/10.1021/acs.langmuir.9b01892.

[10] George Kaptay. "A coherent set of model equations for various surface and interface energies in systems with liquid and solid metals and alloys". In: *Advances in Colloid and Interface Science* 283 (Sept. 1, 2020), p. 102212. ISSN: 0001-8686. DOI: 10.1016/j.cis.2020.102212. URL: https://www.sciencedirect.com/science/article/pii/S0001868620301858.

[11] M. Soledade C. S. Santos and João Carlos R. Reis. "Examination of the Butler Equation for the Surface Tension of Liquid Mixtures". In: *ACS Omega* 6.33 (Aug. 24, 2021). Publisher: American Chemical Society, pp. 21571–21578. DOI: 10.1021/acsomega.1c02606. URL: https://doi.org/10.1021/acsomega.1c02606.

[12] Toshihiro Tanaka et al. "Application of Thermodynamic Databases to the Evaluation of Surface Tensions of Molten Alloys, Salt Mixtures and Oxide Mixtures". In: *International Journal of Materials Research* 87.5 (May 1, 1996). Publisher: De Gruyter, pp. 380–389. ISSN: 2195-8556. DOI: 10.1515/ijmr-1996-870509. URL: https://www.degruyter.com/document/doi/10.1515/ijmr-1996-870509/html.

[13] Toshihiro Tanaka, Klaus Hack, and Shigeta Hara. "Calculation of surface tension of liquid Bi-Sn alloy using thermochemical application library ChemApp". In: *Calphad* 24.4 (Dec. 1, 2000), pp. 465–474. ISSN: 0364-5916. DOI: 10.1016/S0364-5916(00)85001-4. URL: https://www.sciencedirect.com/science/article/pii/S0364591600850014.

[14] T Tanaka. "Surface properties of alloys and ionic mixtures". In: *Mineral Processing and Extractive Metallurgy* 120.4 (Nov. 1, 2011). Publisher: Taylor & Francis, pp. 229–234. ISSN: 0371-9553. DOI: 10.1179/1743285511Y.0000000021. URL: https://doi.org/10.1179/1743285511Y.0000000021.

[15] Ja-Yong Choi and Hae-Geon Lee. "Thermodynamic Evaluation of the Surface Tension of Molten CaO–SiO_2–Al_2O_3 Ternary Slag". In: *ISIJ International* 42.3 (2002), pp. 221–228. DOI: 10.2355/isijinternational.42.221.

[16] Ali Dogan and Hüseyin Arslan. "An investigation of influencing of Sb and Bi contents on surface tensions associated with Pb-free Sn-Zn-Sb-Bi quaternary and sub-quaternary solder alloys". In: *Philosophical Magazine* 99.15 (Aug. 3, 2019). Publisher: Taylor & Francis, pp. 1825–1848. ISSN: 1478-6435. DOI: 10.1080/14786435.2019.1605215. URL: https://doi.org/10.1080/14786435.2019.1605215.

[17] Kasi Gajavalli and Romain Le Tellier. "Butler-based thermodynamic modeling of interfacial energies for in-vessel corium systems". In: *Journal of Nuclear Materials* 569 (Oct. 1, 2022), p. 153935. ISSN: 0022-3115. DOI: 10.1016/j.jnucmat.2022.153935. URL: https://www.sciencedirect.com/science/article/pii/S0022311522004214.

[18] Josiah Willard Gibbs. *On the Equilibrium of Heterogeneous Substances*. Other. Volume: 2. 1879, pp. 300–320. DOI: 10.11588/heidok.00013220. URL: https://archiv.ub.uni-heidelberg.de/volltextserver/13220/.

[19] L. Kaufman and H. Bernstein. *Computer calculation of phase diagrams with special reference to refractory metals*. INIS Reference Number: 2004171. United States: Academic Press Inc, 1970.

[20] Hans Lukas, Suzana G. Fries, and Bo Sundman. *Computational Thermodynamics: The Calphad Method*. Cambridge: Cambridge University Press, 2007. ISBN: 978-0-521-86811-2. DOI: 10.1017/CBO9780511804137. URL: https://www.cambridge.org/core/books/computational-thermodynamics/255D89CDD44B83174D6F27FED432A6A2.

[21] Ursula R. Kattner. "THE CALPHAD METHOD AND ITS ROLE IN MATERIAL AND PROCESS DEVELOPMENT". In: *Tecnologia em Metalurgia Materiais e Mineração* 13.1 (2016), pp. 3–15. ISSN: 2176-1515, 2176-1523. DOI: 10.4322/2176-1523.1059. URL: http://tecnologiammm.com.br/doi/10.4322/2176-1523.1059.

[22] Shashit Yadav, Manoj Gautam, and Devendra Adhikari. "Mixing properties of Cu-Mg liquid alloy". In: *AIP Advances* 10 (Dec. 23, 2020), p. 125320. DOI: 10.1063/5.0030242.

[23] Bo Sundman et al. "The OpenCalphad thermodynamic software interface". In: *Computational Materials Science* 125 (Dec. 1, 2016), pp. 188–196. ISSN: 0927-0256. DOI: 10.1016/j.commatsci.2016.08.045. URL: https://www.sciencedirect.com/science/article/pii/S0927025616304153.

[24] B. Cheynet et al. "NUCLEA "propriétés thermodynamiques et équilibres de phases dans les systèmes d'intérêt nucléaire"". In: *Journal de Physique IV (Proceedings)* 113 (Jan. 1, 2004). Publisher: EDP Sciences, pp. 61–64. ISSN: 1155-4339. DOI: 10.1051/jp4:20040014. URL: http://dx.doi.org/10.1051/jp4:20040014.

[25] Eh.Eh. Shpil'rajn, V.A. Fomin, and V.V. Kachalov. "Density and surface tension of uranium in liquid phase". In: *Teplofizika Vysokikh Temperatur.* Plotnost' i poverkhnostnoe natyazhenie urana v zhidkoj faze 26.5 (1988). Place: USSR INIS Reference Number: 20040718, pp. 892–900. ISSN: 0040-3644.

[26] V. F. Strizhov et al. "Thermo-physical properties of corium: development of an assessed data base for severe accident applications". In: *The nuclear renaissance at work.* International congress on advances in nuclear power plants (ICAPP 2007). Nice, France: Societe Francaise d'Energie Nucleaire (SFEN), July 1, 2007. ISBN: 978-1-60423-871-6. URL: https://www.osti.gov/etdeweb/biblio/21078181.

[27] Takehiko Ishikawa et al. "Viscosity measurements of molten refractory metals using an electrostatic levitator". In: *Measurement Science and Technology* 23.2 (Jan. 2012). Publisher: IOP Publishing, p. 025305. ISSN: 0957-0233. DOI: 10.1088/0957-0233/23/2/025305. URL: https://iopscience.iop.org/article/10.1088/0957-0233/23/2/025305.

[28] Yuji Ohishi et al. "Thermophysical properties of molten Zr1-xOx (x=0.1, 0.2) measured by electrostatic levitation". In: *Journal of Nuclear Materials* 528 (Jan. 1, 2020), p. 151873. ISSN: 0022-3115. DOI: 10.1016/j.jnucmat.2019.151873. URL: https://www.sciencedirect.com/science/article/pii/S0022311519310542.

[29] Scott D. Bembenek. "Calculation of the surface tension of oxygen using molecular-dynamics simulations". In: *The Journal of Chemical Physics* 124.1 (Jan. 5, 2006), p. 014709. ISSN: 0021-9606. DOI: 10.1063/1.2136872. URL: https://doi.org/10.1063/1.2136872.

ANALYSIS OF COMBUSTIBLE GASES DISTRIBUTION WITH ACCIDENT MANAGEMENT ACTION IN A GENERIC PWR-W CONTAINMENT

Joan Fontanet, Leticia Vitores-Gómez, Luis E. Herranz
Unit of Nuclear Safety Research (CIEMAT)
Av. Complutense 40, 28040 Madrid (Spain)
joan.fontanet@ciemat.es; leticia.vitores@ciemat.es; luisen.herranz@ciemat.es

EXTENDED ABSTRACT

In a Severe Accident (SA) in a Light Water Reactor (LWR), hydrogen can be mainly generated by oxidation reactions inside the Reactor Pressure Vessel (RPV) or by the Molten Core-Concrete Interaction (MCCI) in the cavity pit, where, in addition, carbon monoxide can be produced. Both gases are released towards the containment and, depending on containment thermal-hydraulics, they can accumulate and eventually reach flammable concentrations. Aimed to improve severe accident management concerning the minimization of the in-containment combustion risk, the AMHYCO project has been launched in the frame of the Euratom program.

In the present work, within AMHYCO, a generic Western PWR containment is modelled with MELCOR v2.2 to analyze the effect of the safety systems and Passive Autocatalytic Recombiners (PARs) in the evolution of combustible gases concentrations with a special focus on the ex-vessel phase of the accident. Two scenarios have been evaluated. The first one is a Large Break LOCA (LBLOCA), representing a double-ended guillotine break of a hot leg pipe. The containment sprays are available in injection mode until the Refueling Water Storage Tank (RWST) is depleted. Then, the spray system switches to recirculation mode. The second scenario is a Station Black-Out (SBO) with late recovery of sprays at different times into the accident.

Only the containment has been modelled following the specifications discussed and defined within the project. This containment (free volume of 61,000 m^3) gets divided into 11 control volumes connected by 32 flow paths. Forty Passive Autocatalytic Recombiners (PARs) of two types (FRAMATOME FR-1500 and FR-960) are considered within the containment. Correlations for H_2 and CO recombination rates have been specifically developed within the project and are implemented through so-called control functions in the MELCOR code. The release of fluids into the containment is modelled as boundary conditions (i.e., external sources) taken from full plant simulations. The LBLOCA is characterized by a fast release of water and steam into the steam generator chamber from both sides of the guillotine break followed by the hydrogen generated in the vessel. After RPV failure (~3 h), H_2, CO, steam and CO_2 are released by the MCCI directly into the cavity atmosphere. The SBO has a delayed release of gases into the annulus compartment from the pressurizer relive tank. The RPV failure, and thus, the beginning of the MCCI, is predicted at ~11 h. Additionally, a heat source is defined into the cavity to model the corium-to-cavity atmosphere heat transfer of both scenarios after the failure of the RPV.

For the LBLOCA, PARs significantly reduce the molar fraction of combustible gases (H_2 and CO) and avoid conditions of uncontrolled combustion in the in-vessel phase but not for some hours during the ex-vessel phase (Fig. 1), mainly due to the large amount of CO generated by the MCCI combined with the lower PARs efficiency to remove CO compared to H_2. Another parametric case has been studied in which the cooling of the containment is provided by fan coolers and sprays do not have a heat exchanger in the recirculation

mode. In this case, the pressure is 0.3 bar higher in the ex-vessel phase since fan coolers have a milder heat removal capacity than the spray system. The impact on the combustible gases concentration is however low, and therefore, flammability conditions can also be reached in the ex-vessel phase.

For the SBO, PARs are able to prevent the mixture from reaching flammable conditions along the whole sequence, even if a PAR efficiency reduction of 50% is postulated. PARs have a moderate effect on increasing the pressure and temperature. Regarding spray recovery, as expected, a strong effect in reducing the steam molar fraction, and therefore in the pressure, is observed. In all cases, PARs prevent uncontrolled combustion in the dome, but in the annulus (the release compartment), the mixture reaches the flammability limits for short periods in the in-vessel phase if sprays are activated at the earliest times considered, 4.5 hours (Fig. 2).

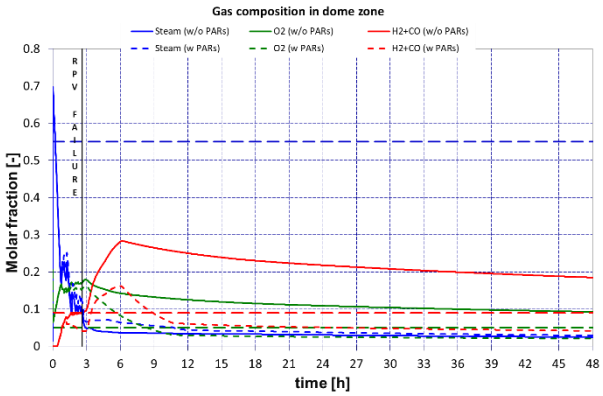

Fig. 1. Gas molar fraction in the dome for the LBLOCA. Comparison of simulations with PARs and without PARs

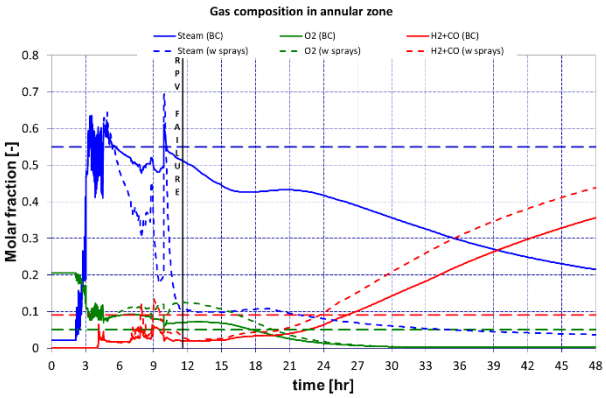

Fig. 2. Gas molar fraction in the annulus for the SBO. Comparison of the base case simulation and with sprays recovered at 4.5 h.

The two scenarios analysed have very different conditions in pressure and steam concentration mainly due to the operation of the sprays in the LBLOCA unlike the SBO scenario. In both sequences, PARs strongly reduce the risk of combustion by decreasing the concentration of combustible gases and depleting O_2 in the containment atmosphere. Nonetheless, attention has to be paid to the early activation of sprays since, if the PARs do not have time to sufficiently remove the combustible gases or the O_2, the sprays can greatly increase the risk of flammability. In addition, the CO generation in the ex-vessel phase can represent a significant risk if the steam concentration is low, even if PARs are used as a passive mitigation measure.

The AMHYCO project, coordinated by the UPM (Universidad Politécnica de Madrid) has received funding from the Euratom research and training programme 2019-2020 under Grant Agreement n°945057. The content of this paper reflects only the authors' view. The European Commission is not responsible for any use that may be made of the information it contains.

SEAKNOT
ERMSAR 2024
11th Conference on
SEVERE ACCIDENTS RESEARCH
May 13-16, 2024 – Stockholm, Sweden

Analysis of Combustible Gases Distribution with Accident Management Action in a Generic PWR-W Containment

JOAN FONTANET, LETICIA VITORES & LUIS E. HERRANZ

Introduction

- Hydrogen and carbon monoxide, both flammable gases, can be generated in a severe accident.
- Those gases can accumulate into the containment building and reach flammable conditions.
- The AMHYCO project (Euratom program) was launched to improve severe accident management focusing on the in-containment combustion risk.

Scope

- Plant: PWR-Westinghouse 1000 MWe
- Code: MELCOR v.2.2
- Scenarios: SBO & LBLOCA

Approach & model

- Generic containment-stand alone model developed within the AMHYCO project [1].
- Fluid release modelled as boundary conditions (i.e., external sources).
- Framatome design PARs (FR-1500 and FR-960)
- Recombination correlation developed in AMHYCO

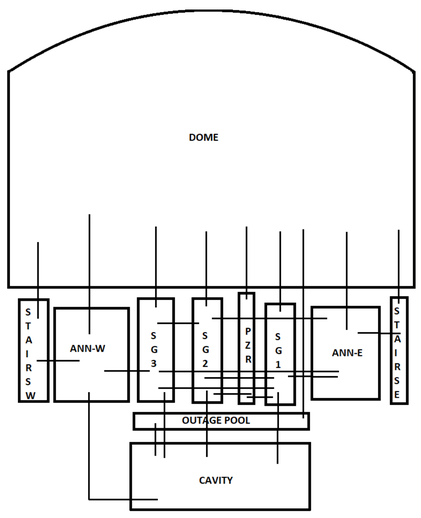

LBLOCA scenario

- Double ended guillotine break in the hot leg.
- Release into the SG room.
- Availability of containment sprays.
- Limestone concrete.

Event	Time
Hot leg break	0.0
Sprays injection	4.1 s
Sprays recirculation	2.1 h
RPV failure	2.9 h

Parametric cases

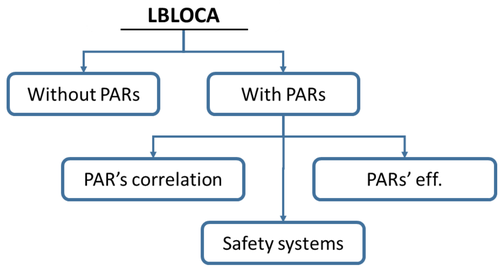

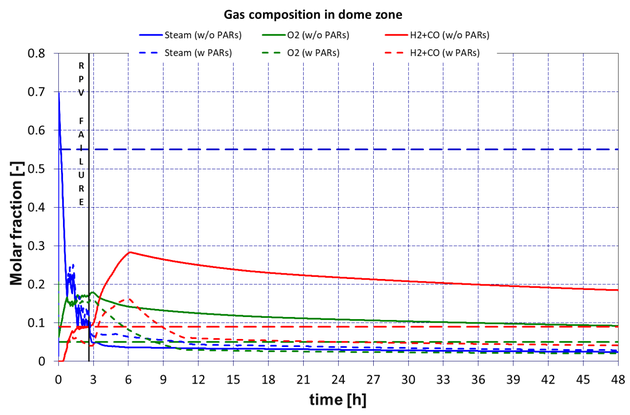

- PARs significantly reduce X_{H2+CO} but cannot avoid the possibility of deflagration in the ex-vessel phase.
- Effect of fan coolers is very low.

SBO scenario

- Total loss of safety systems.
- Release into the annular compartment.
- Siliceous concrete.
- Recovery of power supply.

Event	Time
Loss of power	0.0
Sprays injection	$t_{recovery}$
Sprays recirculation	$t_{recovery}$+2.1 h
RPV failure	11.5 h

Parametric cases

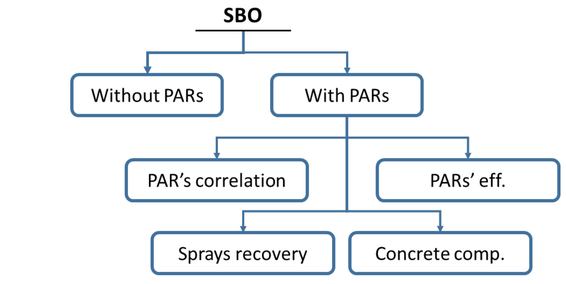

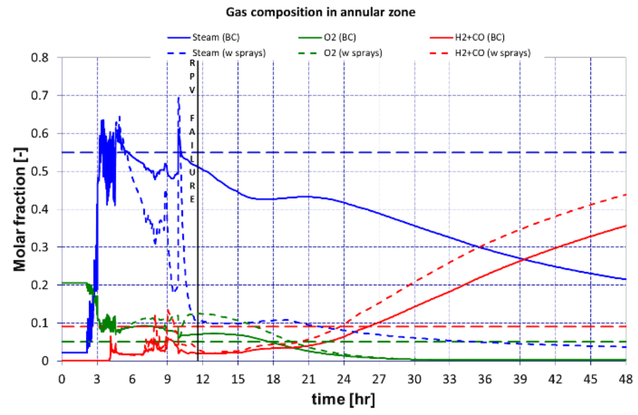

- PARs prevent flammable mixtures even considering a 50% eff.
- Strong effect of sprays recovery. Flammable conditions if sprays are recovered at 4.5 h.

Conclusions

PARs strongly reduce the flammability risk by decreasing H_2 & CO concentration and depleting O_2.

Attention must be paid to the early activation of sprays since PARs have no time to deplete H_2 & CO or O_2.

The gas generation in the ex-vessel phase can represent a significant risk if steam concentration is low, even if PARs are used as a mitigation measure.

IN COOPERATION WITH:

This work has been carried out in the frame of the AMHYCO Project. This project is funded from the **Euratom research and training programme** 2019-2020 under Grant Agreement No. 945057

References

[1] Serra, L., 2023. *D2.1 – Data for the generic containment analysis (PWR-W, PWR-VVER, PWR-KWU)*. AMHYCO project deliverable NFRP-2019-2020

Centro de Investigaciones Energéticas, Medioambientales y Tecnológicas
Avenida Complutense, 40
E28040 Madrid (Spain)
Tel: (+34) 91 346 65 77
Email: joan.fontanet@ciemat.es

Development of 3D view application debrisEye for decommissioning of Fukushima Daiichi Nuclear Power Plant

Takuya Yamashita*
Japan Atomic Energy Agency (JAEA)
4002, Oarai-machi, Ibaraki, Japan
yamashita.takuya38@jaea.go.jp

Kenta Shimomura, Yuji Nagae
Japan Atomic Energy Agency (JAEA)
790-1, Tomioka-machi, Fukushima, Japan
shimomura.kenta@jaea.go.jp, nagae.yuji@jaea.go.jp

Eiichi Nagai
Prometech Software, Inc.
3-34-3 Hongo, Bunkyo-ku, Tokyo, Japan
nagai@prometech.co.jp

Tomohiro Yasumatsu
NDD Corporation
2-46-2 Hon-cho, Nakano-ku, Tokyo, Japan
tomohiro.yasumatsu@nddhq.co.jp

Satoru Nakashima, Shoya Ogino
Tokyo Electric Power Company Holdings (TEPCO)
22 Aza Kitahara Oaza Ottozawa, Okuma-machi, Futaba-gun, Fukushima, Japan
nakashima.satoru@tepco.co.jp, ogino.shoya@tepco.co.jp

Shinya Mizokami
Tokyo Electric Power Company Holdings (TEPCO)
1-1-3 Uchisaiwai-cho, Chiyoda-ku, Tokyo, Japan
mizokami.shinya@tepco.co.jp

ABSTRACT

Internal investigations of the Fukushima Daiichi Nuclear Power Plant (1F) have been conducted, and the internal situation is gradually becoming clearer. In addition, trial debris removal has been conducted and much information is being obtained. The information obtained from the trial debris removal is managed in the decommissioning fundamental research database (debrisWiki), which was established by JAEA and TEPCO. However, it is difficult to understand the entire accident progress only from individual data. Therefore, we developed a 3D view application (debrisEye) for 1F decommissioning. debrisEye was created by Unity. For the CG displayed in debrisEye, pre- and post-accident conditions were constructed. The pre-accident status was created using design information and point cloud data from periodic inspections. The

post-accident status was created mainly from the results of the internal investigation. For areas where internal investigations have not yet been obtained, the information in the estimation diagram was reflected. CG displayed on debrisEye can be viewed from any viewpoint and angle using the functionality contained in debrisEye. It is also possible to clipping at any cross section and to show or hide each part. debrisEye can be linked to and used with debrisWiki to write information in any location, thus displaying the analysis results and location of the debris collected. Visual linking of debris analysis results with on-site information is expected to facilitate understanding of accident progress and improve efficiency of decommissioning work.

KEYWORDS
Fukushima Daiichi, Severe accident, Decommissioning, debrisEye

1. INTRODUCTION

Internal investigation of the Fukushima Daiichi Nuclear Power Plant (1F) has been conducted, and the internal situation is gradually becoming clearer. In addition, experimental debris retrieval has been conducted and a lot of information has been obtained. The information obtained from the experimental debris retrieval is stored in the decommissioning research fundamental database (debrisWiki) [1], which was set up by the Japan Atomic Energy Agency (JAEA) and the Tokyo Electric Power Company (TEPCO).

However, it is difficult to grasp the accident progress and plant status only from individual data. In order to simply the grasp of the 1F situation, estimation diagrams were prepared [2-4]. For reference, latest version of the estimation diagram for Unit 2 is shown in Figure 1.

Although estimation diagrams were visually easy to grasp the 1F status, it is necessary to provide more detailed information in order to contribute to decommissioning in the future. Therefore, three dimensional (3D)−estimation diagrams have been developed by using the results of internal investigations, design information, information from inspections, etc., and constructed with computer graphics (CG). there are many view applications that only display the developed 3D-estimation diagrams, it is necessary to develop a corresponding 3D view application in order to utilize it for decommissioning studies.

The 3D view application (debrisEye) was developed to interactively display the 3D-estimation diagrams. The debrisEye is also linked to the debrisWiki. By utilizing these application, debris analysis results and on-site information will be visually linked, and it is expected to enhance the grasp of the 1F status and the understanding of accident progress. This paper focuses on the development of the debrisEye and introduces the development status of the debrisWiki and the 3D-stimation diagrams.

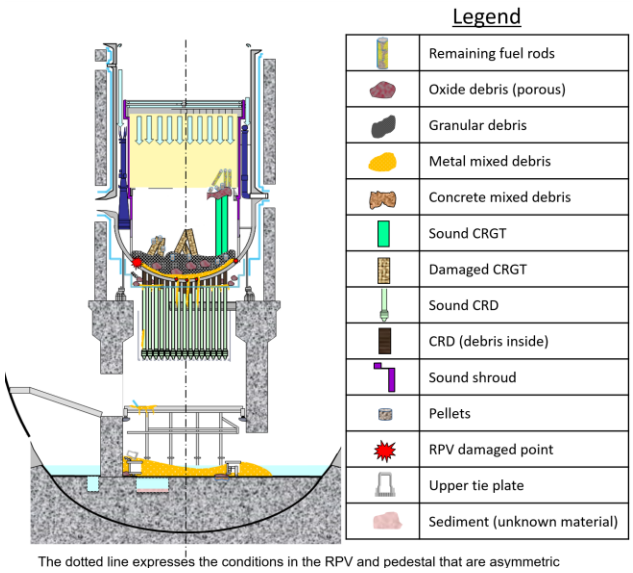

Figure 1. The estimation diagram for Unit 2.

2. debrisWiki

More than 10 years have passed since the accident at the 1F, and much on-site information and research results have been obtained. A reliable and easy-to-use database with this information is needed to efficiently examine debris retrieval and equipment design. JAEA and TEPCO are collaborating to establish the debriWiki [1]. Figure 2 shows a sample of the debrisWiki page. The information and functions contained in the debrisWik are as followings:

- The 1F Database (Search public documents)
- The estimation diagrams
- Accident progression scenarios
- Debris analysis data, etc.

Providing this information to researchers in an easy-to-understand manner will enhance their understanding of severe accident research as well as the decommissioning of the 1F.



Figure 2. debrisWiki (in Japanese).

3. debrisEye

More information will be accumulated on the debrisWiki at the start of debris retrieval in earnest. Nuclear power plants are huge and complex structures. It is difficult even for nuclear engineering experts to determine the origin and relocation path of collected debris. Therefore, a tool is needed to visually grasp the status of the entire plant as well as the location of debris collection. To achieve these aims, the debrisEye was developed to create computer graphics (CG) models of the entire plant and to store information on the debris collected at each location. The debrisEye was developed by Unity 2020.3.30.f1. The debrisEye runs as a Windows application and interactively displays CG models of the 1F 3D-estimation diagrams, as shown in Chapter 4. The debrisEye has the following Functions:

(a) Stores debris information in pin (Figure 3)
(b) Show/hide function for each object (Figure 4)
(c) Object clipping (Figure 5)
(d) Switching viewpoints in east-west, north-south, and west-north (Figure 5)

For function (a), pin icons are displayed in the 3D-estimation diagrams and information is stored in the debrisEye. Although it is possible to store information in the debrisEye itself, it is mainly designed to be linked with the debrisWiki to acquire information. This is because if a huge amount of information such as graphics and videos are stored in a single application, operation becomes heavy, and users need to prepare a high-spec PC. The function in (b) was designed to avoid complex reactor structures and piping, etc., and to view the targeted location. In addition, by indicating the name of each object in a detailed list, it is possible for users to understand the name of the object they want to grasp. The function in (c) was designed for the need to check the cross-section of an object by clipping in order to grasp the internal state of the 3D-estimation diagrams. For function (d), a compass function is provided so that it is easy to see from which direction the object is being viewed when handling the 3D-estimation diagrams. In addition to these, the debrisEye has measurement and other functions, but these functions are restricted for general users because detailed plant design information is involved.

The developed the debrisEye is already being used by TEPCO in its ongoing internal investigation studies. [5]

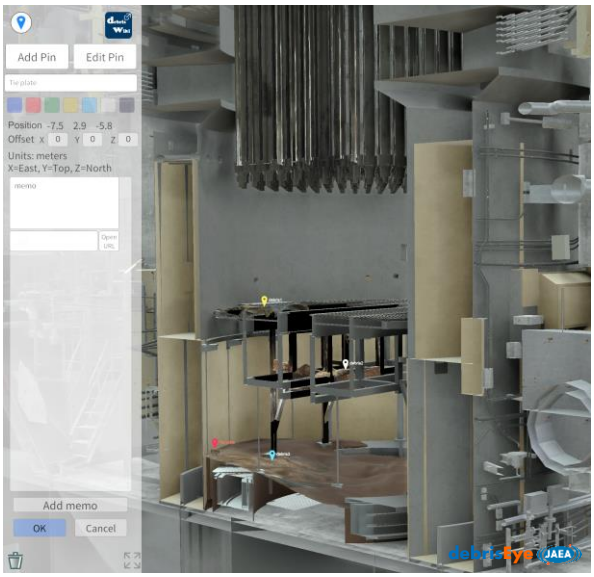

Figure 3. Stores debris information in pin.

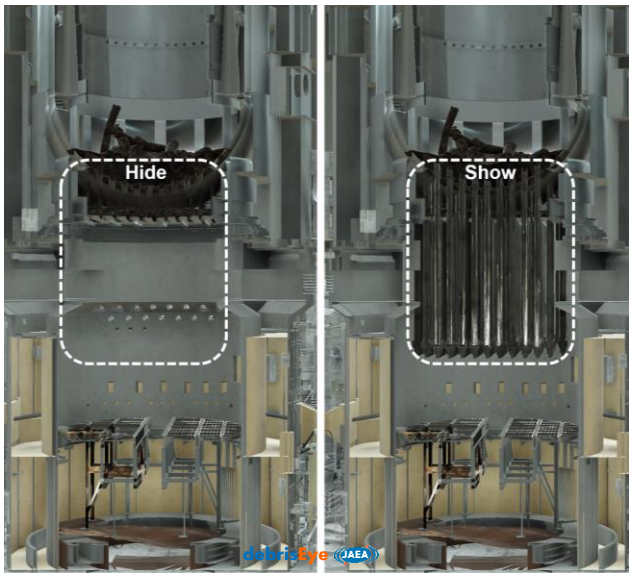

Figure 4. Show/hide function for each object.

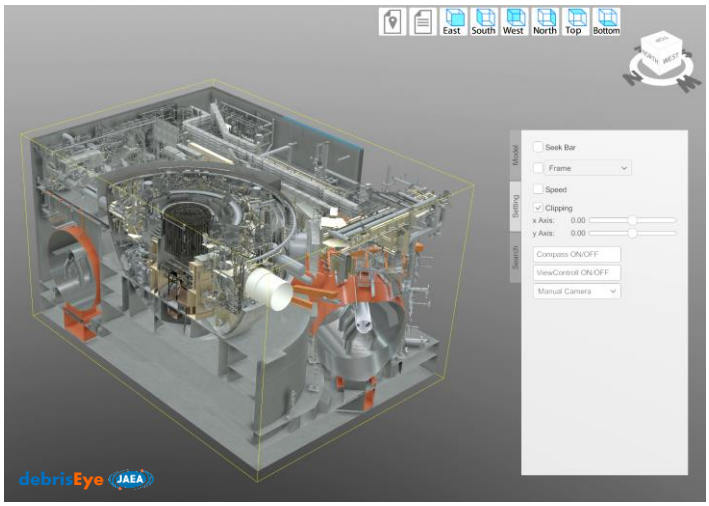

Figure 5. Object clipping and switching viewpoints.

4. 3D estimation diagram

The 3D-estimation diagrams were developed based on the information shown in Table I. Details of the status of information reflected in each unit were described in Sections 4.1-4.3. In common with each unit, the following procedure was used to develop the 3D-estimation diagrams.

i. Create 3D-computer aided design (CAD) models from design information.
ii. Convert 3D-CAD models to CG models.
iii. For the areas where point cloud data was available, priority was given to reflecting the point cloud data converted to CG models, CG models created with ii. was merged.
iv. For the areas where clear photos were obtained from the internal investigation results, the photos were pasted onto CG models. For locations for which clear photos were not available, the texture was created by taking into account the results of the internal investigation and the photos taken before the accident.
v. For locations for where internal investigation results were not yet available, the results of analysis and simulated tests were comprehensively evaluated and reflected in CG models.
vi. Replace with data from v. when detailed internal investigation results are available.

After i. and ii. are done to prepare the base of the 3D-estimation diagrams, the process of iii.-vi. will be repeated and updated according to the progress of the internal investigation.

Table I. Status of information reflected in the 3D−estimation diagrams.

		Unit1	Unit2	Unit3
(A)	CG was created from point cloud data of the reactor building obtained from 2012 to 2015.	X	X	X
(B)	CG was created from point cloud data obtained from internal investigation results			X
(C)	CG was created from RPV and PCV design drawings.	In progress	X	In progress
(D)	Texture information from internal investigation results reflected.	In progress	In progress	In progress
(E)	CG reflected the results of the estimation, which was comprehensively evaluated based on analysis, experiments, etc.		X	

4.1. Unit 1

As for the Unit 1, (A) in Table I has already been reflected. The 3D-estimation diagram for the Unit 1 is shown in Figure 6. The reactor building, the S/C, part of the PCV, and the RPV were reflected in the Unit 1 model. Regarding (C), a 3D-CAD of the reinforcing steel of the pedestal was being created as shown in Figure 7 to reflect the results of an PCV internal investigation conducted on March 28-31, 2023 [6]. In the future, a CG model will be created to match the internal investigation in Figure 8[6], comparing a 3D-CAD in Figure 7 with the results of the internal investigation, and (D) will be performed as appropriate.



Figure 6. The 3D-estimation diagram for the Unit1.

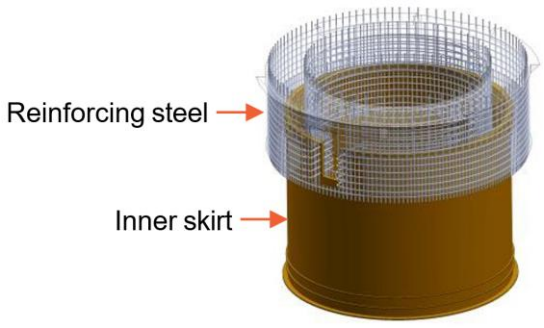

Figure 7. Reinforcing steel of the pedestal.



Figure 8. Status of pedestal opening [6].

4.2. Unit 2

As for the Unit 2, (A), (C) and (E) in Table I have already been reflected. The 3D-estimation diagram for the Unit 2 is shown in Figure 9. Regarding the Unit 2, (A) has been conducted in a wider area than Unit 1. Therefore, together with (C), a 3D-estimation diagram reflected the inside of the RPV and all areas other than those for which internal investigation results have not yet been obtained. For areas where internal investigation results were not available and (E) was not conducted, design information before the accident was reflected.

Presently, (E), which was conducted only for the Unit 2, reflected the results of the Development of Analysis and Estimation Technologies for Characterization of Fuel Debris (Development of Estimation Technologies of RPV Damaged Condition, etc.) project (RPV PJ) [7]. In the RPV PJ, severe accident analysis by MAAP code[8], RPV failure simulated tests[9], evaluation of high-temperature strength of RPV material[10], RPV failure evaluation by thermal-structural coupled analysis[11-12], and core material relocation behavior evaluation by moving particle simulation method (MPS) analysis[13-16] were conducted, and the results obtained were comprehensively evaluated to estimate RPV failure and debris discharge from the RPV. As a result, The 3D-estimation diagram for the Unit 2 reflected a breached point on the lateral part of the RPV and debris accumulated between the RPV and the insulation material, which had not yet been confirmed by the results of the internal investigation.

The amount of debris accumulated in the lower plenum of the RPV was arranged in reference to the muon measurement results as shown in Figure 10. The debris shape of some fuel rods was based on the results of CMMR tests [17]. The amount of debris accumulated in the lower plenum of the RPV was estimated to be approximately 12.51 m^3(calculated without porosity).

The debris accumulated on the pedestal floor was placed at the height described in Figure 11, as judged from the videos and photos obtained by the internal investigation. The amount of debris placed on the pedestal floor was approximately 7.94 m^3(calculated without porosity).

For the areas mentioned above, where photos were clearly obtained, the photos were pasted onto CG models.

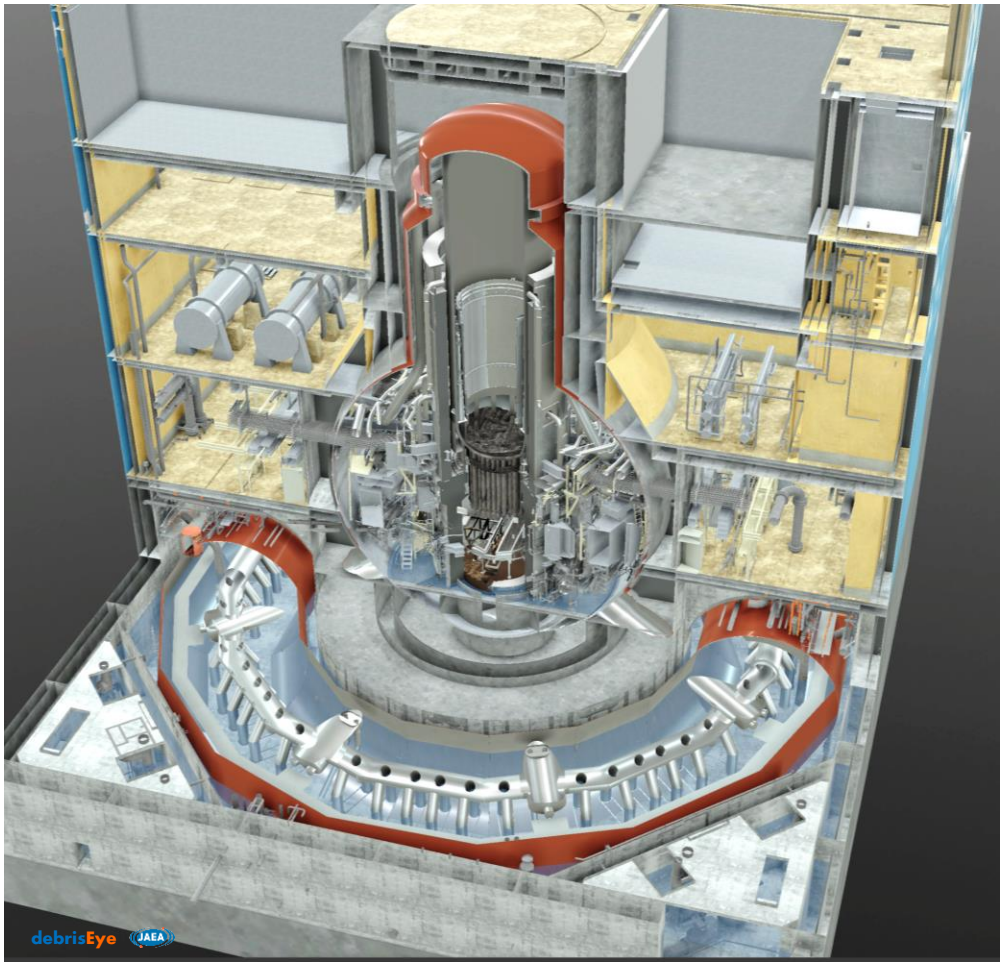

Figure 9. The 3D-estimation diagram for the Unit2.

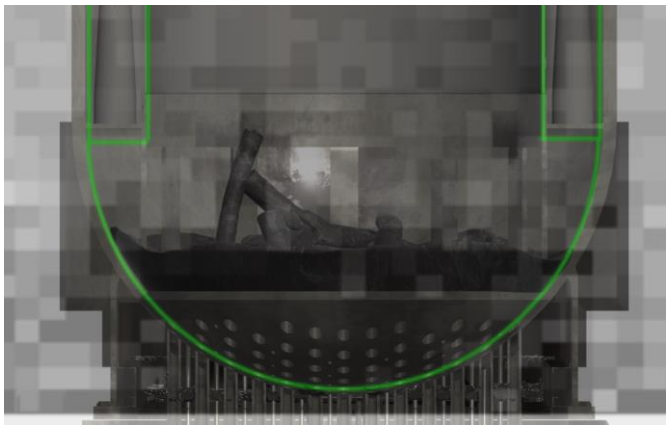

Figure 10. The muon measurement results compared to the 3D-estimation diagram for the Unit2.

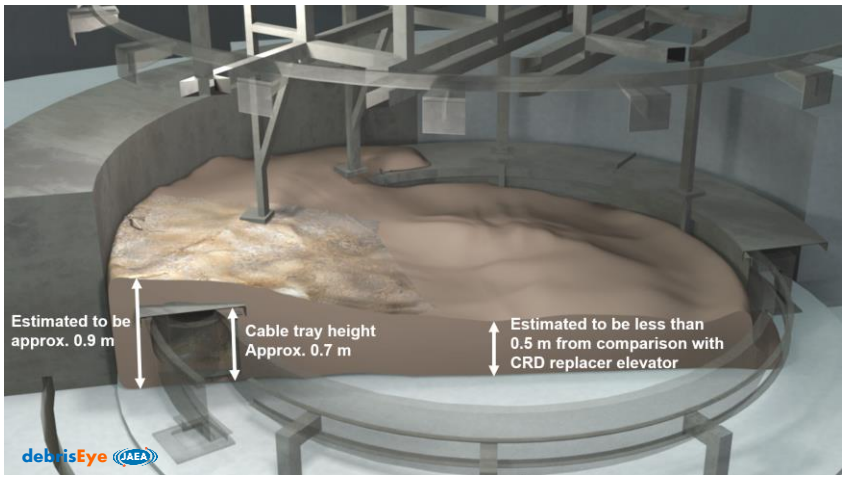

Figure 11. The debris accumulated on the pedestal floor.

4.3. Unit 3

As for the Unit 3, (A) and (B) in Table I have already been reflected. The 3D-estimation diagram for the Unit 3 is shown in Figure 12 and 13. Regarding the Unit 3, The information in (A) was obtained in almost the same area as in the Unit 2. Underwater ROV investigations inside the PCV were conducted in July 2017; Structure from Motion (SfM) captured the entire pedestal [18]. As shown in Figures 14 and 15, there are two kinds of structures: those that were recovered by confirming the video images and those estimated and recovered based on design information because they cannot be confirmed in the video images. The approximate height of the sediment accumulated on the pedestal floor was estimated from the pedestal opening and some rail support, as shown in Figure 15 [18]. The recovered information was converted to CG models and reflected in The 3D-estimation diagram.

In the future, the areas for which clear images are acquired from the internal investigation results will be pasted into CG models and (D) will be performed as appropriate.

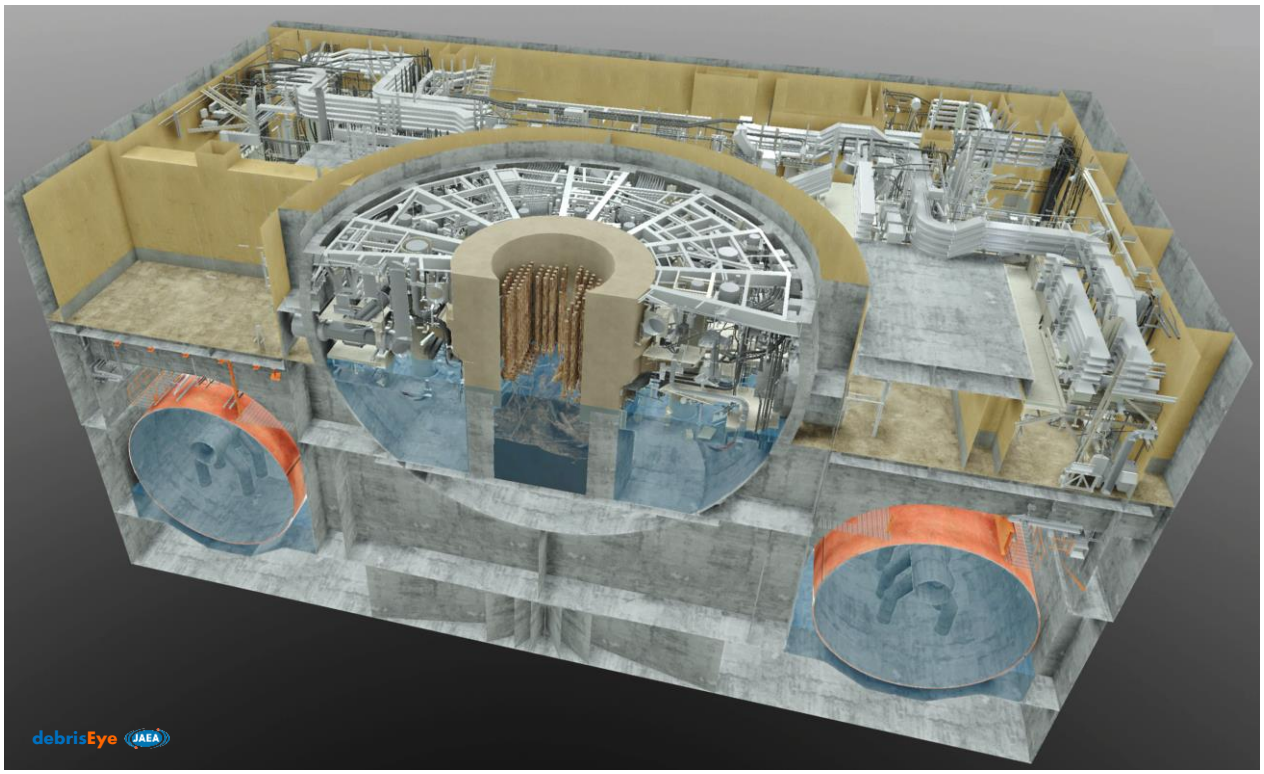

Figure 12. The 3D-estimation diagram for the Unit3.

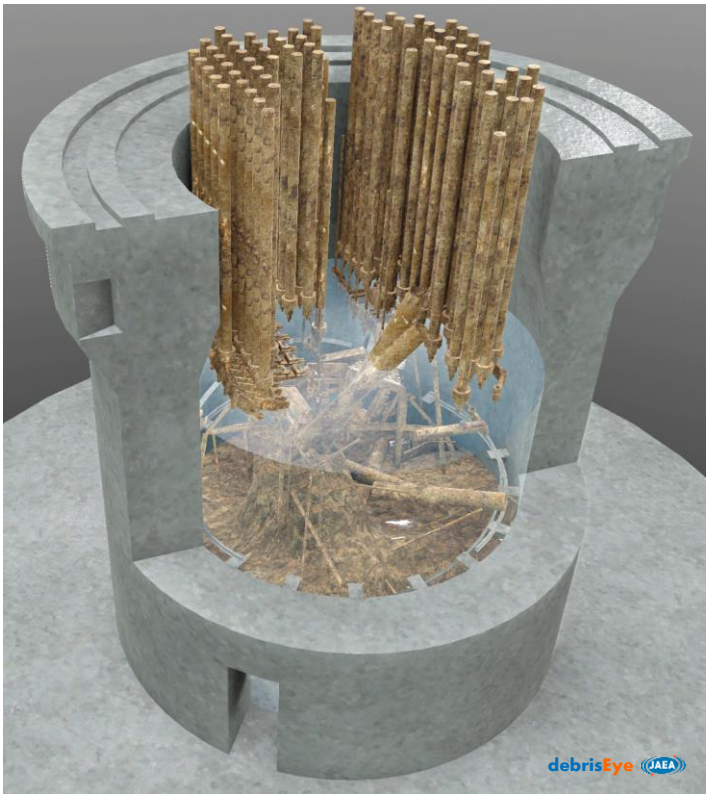

Figure 13. The 3D-estimation diagram for the Unit3 pedestal 3Dmodel.

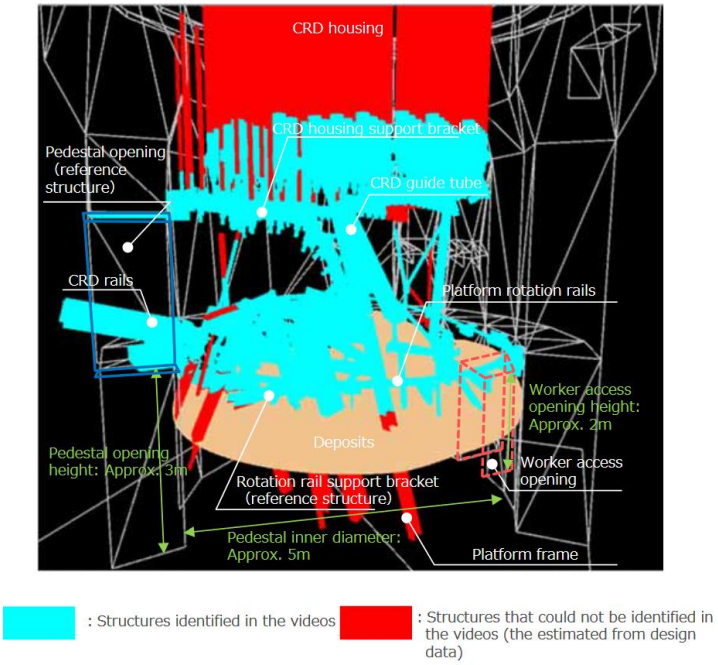

Figure 14. Scope of structures identified. [18]

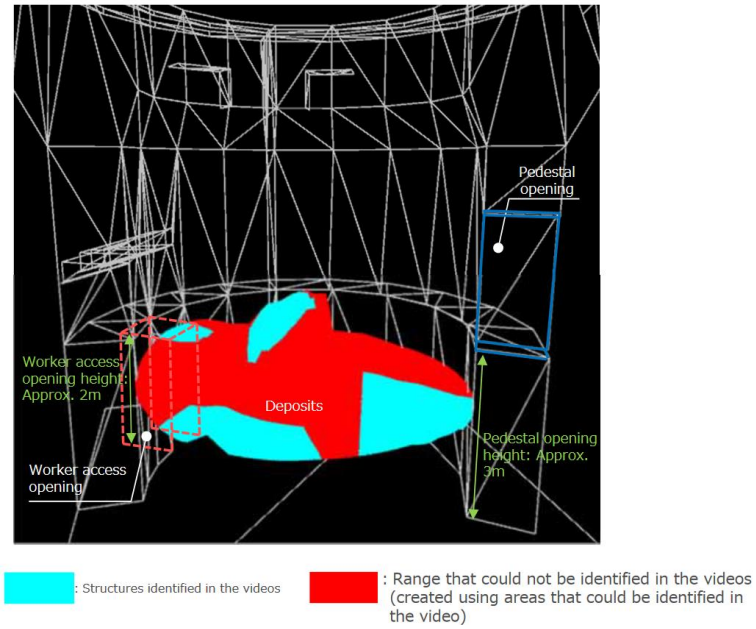

Figure 15. Scope of deposit identified. [18]

5. Conclusions

As for the debrisEye, we will continue to add functions to this application to grasp the situation on the 1F in an easy-to-understand manner. In addition, the 3D−estimation diagrams to be contained in the debrisEye

has been developed by optimizing the information presently obtainable, but it includes a large uncertainty. It will be updated as the decommissioning progresses.

ACKNOWLEDGMENTS

This study has been partly performed by the funds from the Japanese Ministry of Economy, Trade and Industry as The Subsidy Program “Project of Decommissioning, Contaminated Water and Treated Water Management (Development of Analysis and Estimation Technologies for Characterization of Fuel Debris".

REFERENCES

1. “debrisWiki,” https://fdada-plus.info/
2. T. Yamashita et al., “Comprehensive Analysis and Evaluation of Fukushima Daiichi Nuclear Power Station Unit 2,” Nuclear Technology. 206(10), pp. 1517-1537 (2020).
3. T. Yamashita et al., “Comprehensive Analysis and Evaluation of Fukushima Daiichi Nuclear Power Station Unit 3,” Nuclear Technology. 209(6), pp. 902-927 (2023).
4. “TEPCO HD,” https://www.tepco.co.jp/decommission/information/accident_unconfirmed/pdf/20210719.pdf
5. “TEPCO HD,” https://www.tepco.co.jp/decommission/information/newsrelease/reference/pdf/2023/2h/rf_20231120_2.pdf
6. “TEPCO HD,” https://www.tepco.co.jp/decommission/information/newsrelease/reference/pdf/2023/1h/rf_20230404_1.pdf
7. “Management Office for Project of Decommissioning Contaminated Water and Treated Water Management,” https://dccc-program.jp/wp-content/uploads/20231019_JAEA.pdf
8. S. Mizokami et al., “Fukushima Daiichi Nuclear Power Plant unit 2 evaluation of containment behavior under the severe accident condition,” 2024 Annual meeting of AESJ (in Japanese)
9. K. Shimomura et al., “RPV lower head penetration failure test due to eutectic reaction ELSA 3,” 2024 Annual meeting of AESJ (in Japanese)
10. K. Shimomura et al., “Formulation of material property formula for calculation of damage in reactor pressure vessel during accident evaluation,” Proceedings of ERMSAR2024
11. K. Sakae et al., “Evaluation of temperature behavior of CRD Housing of Unit 2 during accident progress,” 2024 Annual meeting of AESJ (in Japanese)
12. T. Yamashita et al., “Thermal-structural coupled analysis for estimating RPV damage in FDNPS unit 2,” Proceedings of ICEM2023
13. Y. Bando et al., “MPS method simulation for estimating fuel debris distributions under the damaged reactor pressure vessel of 1F Unit-2,” Proceedings of ICEM2023
14. A. Yamaji et al., “Evaluation of the Core Material Relocation Behavior,” 2024 Annual meeting of AESJ (in Japanese)
15. L. Xin et al., “Numerical simulation of core material relocation behavior in the RPV lower head region,” 2024 Annual meeting of AESJ (in Japanese)
16. I. Sato et al., “Clarification of boundary conditions for evaluation of the core material relocation behavior,” 2024 Annual meeting of AESJ (in Japanese)
17. T. Yamashita et al., “Post-Test Analyses of the CMMR-4 Test,” ASME J. of Nuclear Rad Sci. NERS-21-1055, 8(2), p.021701(14 pages) (2022).
18. “TEPCO HD,” https://www.tepco.co.jp/en/nu/fukushima-np/handouts/2018/images/handouts_180426_03-e.pdf

SEAKNOT
ERMSAR 2024
11th Conference on
SEVERE ACCIDENTS RESEARCH
May 13-16, 2024 – Stockholm, Sweden

Development of 3D view application debrisEye for decommissioning of Fukushima Daiichi Nuclear Power Plant

Takuya Yamashita, Kenta Shimomura, Yuji Nagae (JAEA)
Eiichi Nagai (Prometech)
Tomohiro Yasumatsu (NDD)
Satoru Nakashima, Shoya Ogino, Shinya Mizokami (TEPCO)

debrisEye [1]

Internal investigations of the Fukushima Daiichi Nuclear Power Plant (1F) have been conducted, and the internal situation is gradually becoming clearer. In addition, trial debris removal has been conducted and much information is being obtained. The information obtained from the trial debris removal is managed in the decommissioning fundamental research database (debrisWiki), which was established by JAEA and TEPCO. However, it is difficult to understand the entire accident progress only from individual data. Therefore, we developed a 3D view application (debrisEye) for 1F decommissioning. debrisEye was created by Unity. For the 3D-estimation diagram displayed in debrisEye, pre- and post-accident conditions were constructed. The pre-accident status was created using design information and point cloud data from periodic inspections. The post-accident status was created mainly from the results of the internal investigation. For areas where internal investigations have not yet been obtained, the information in the estimation diagram was reflected. The 3D-estimation diagram displayed on debrisEye can be viewed from any viewpoint and angle using the functionality contained in debrisEye. It is also possible to clipping at any cross section and to show or hide each part. debrisEye can be linked to and used with debrisWiki to write information in any location, thus displaying the analysis results and location of the debris collected. Visual linking of debris analysis results with on-site information is expected to facilitate understanding of accident progress and improve efficiency of decommissioning work.

debrisWiki

More than 10 years have passed since the accident at the 1F, and much on-site information and research results have been obtained. A reliable and easy-to-use database with this information is needed to efficiently examine debris retrieval and equipment design. JAEA and TEPCO are collaborating to establish the debriWiki.

Estimation diagram (Unit 2) [3]

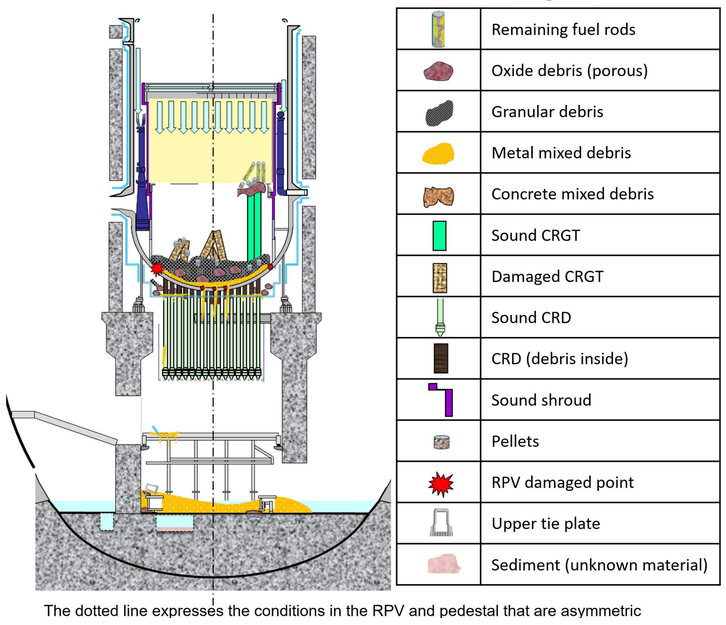

The dotted line expresses the conditions in the RPV and pedestal that are asymmetric

3D-estimation diagram

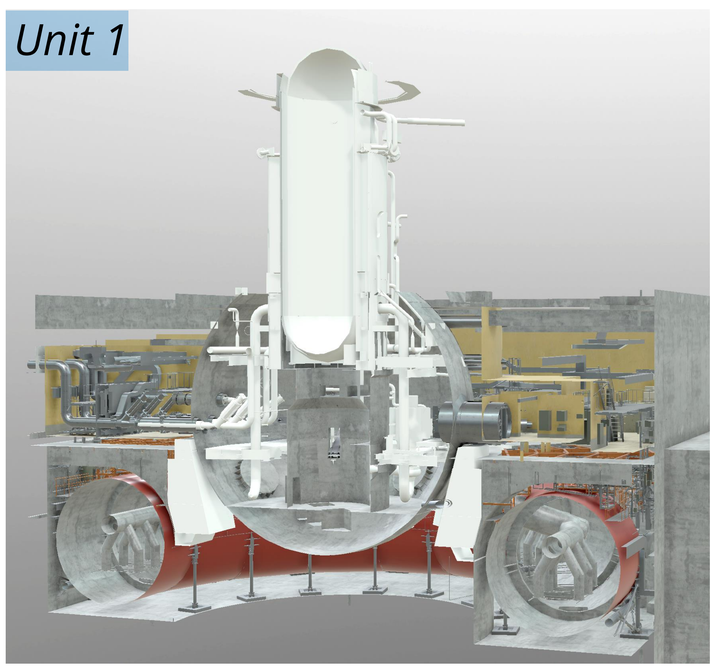

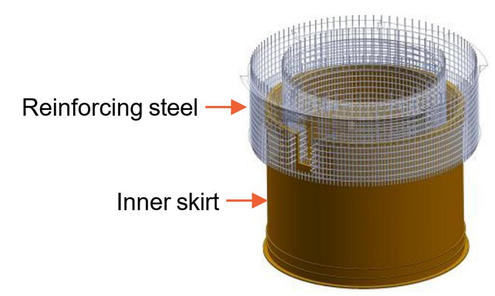



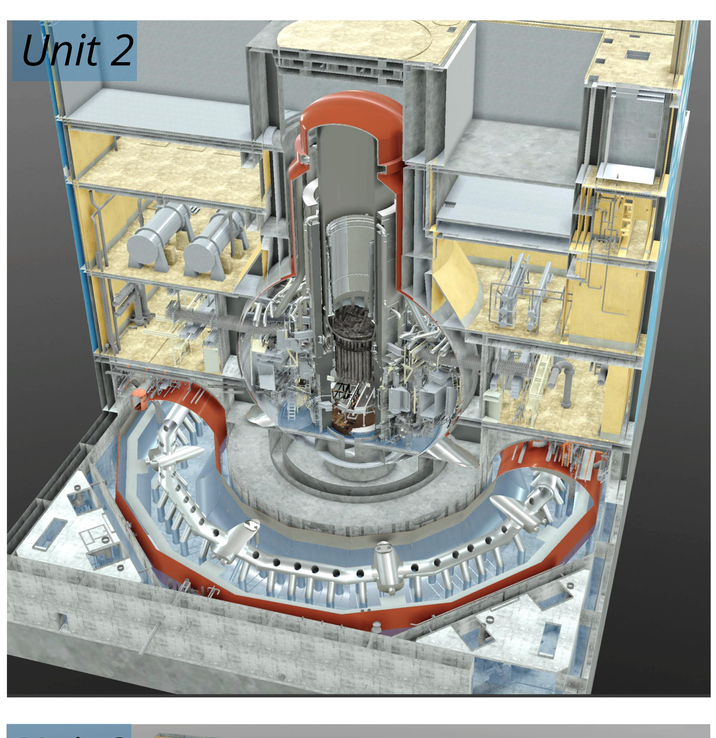

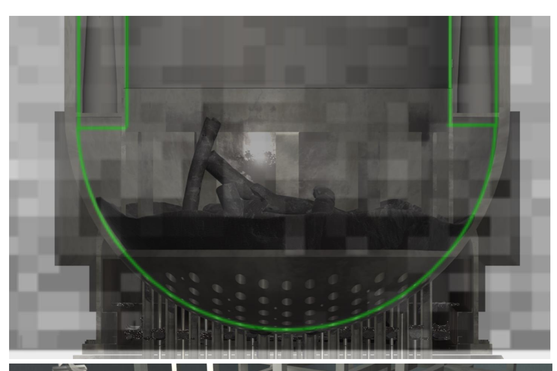

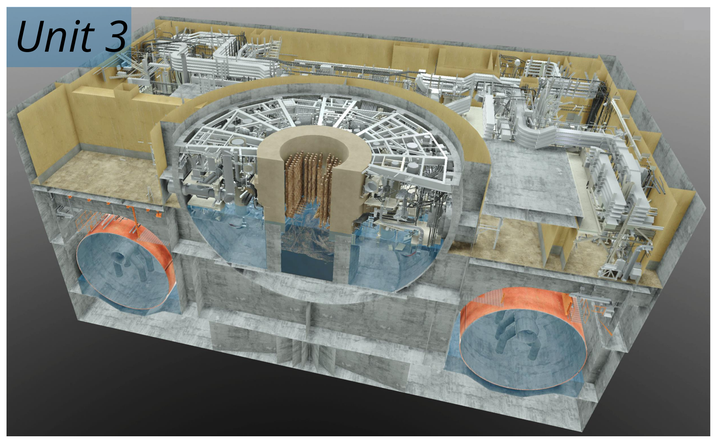

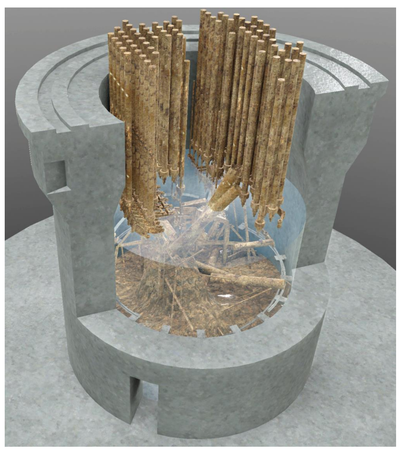

		Unit1	Unit2	Unit3
(A)	CG was created from point cloud data of the reactor building obtained from 2012 to 2015.	X	X	X
(B)	CG was created from point cloud data obtained from internal investigation results			X
(C)	CG was created from RPV and PCV design drawings.	In progress	X	In progress
(D)	Texture information from internal investigation results reflected.	In progress	In progress	In progress
(E)	CG reflected the results of the estimation, which was comprehensively evaluated based on analysis, experiments, etc.		X	

References

[1] "debrisWiki," https://fdada-plus.info/wiki/index.php?title=ERMSAR2024
[2] "TEPCO HD," https://www.tepco.co.jp/decommission/information/newsrelease/reference/pdf/2023/1h/rf_20230404_1.pdf
[3] "Management Office for Project of Decommissioning Contaminated Water and Treated Water Management," https://dccc-program.jp/wp-content/uploads/20231019_JAEA.pdf

IN COOPERATION WITH:

Takuya Yamashita **4002, Oarai-machi, Ibaraki, Japan** **Email: yamashita.takuya38@jaea.go.jp**

Thermal shock resistant geopolymers as refractory material for core catcher

Bence Mészáros, Jan Hrbek, Mykhaylo Paukov
Research Centre Řež
Hlavní 130, Řež, 250 68 Husinec, Czech Republic
bence.meszaros@cvrez.cz; jan.hrbek@cvrez.cz; mykhaylo.paukov@cvrez.cz

Václav Tyrpekl
Department of Inorganic Chemistry
Faculty of Science, Charles University
Hlavova 2030, 128 00 Prague, Czech Republic
vaclav.tyrpekl@natur.cuni.cz

Zbyněk Černý, Pavlíva Rosypal
Institute of Inorganic Chemistry of the Czech Academy of Sciences
250 68 Husinec- Řež, Czech Republic
cerny@iic.cas.cz, novakovap@iic.cas.cz

ABSTRACT

Geopolymers have been intensively studied for immobilization of radioactive waste, but they can be beneficial in other applications. These materials show strong resistance to radiation, low moisture content and possibility of incorporation of various additives to modify their properties. This universality makes them a potential sacrificial, structural, or refractory component in passive or active safety systems in nuclear power plants (NPPs). [1] This may enhance the safety of NPPs and help to mitigate the severe accident consequences.

This paper presents a scoping interaction test of a geopolymer refractory material with prototypic corium melt. The corium mixture was achieved by induction skull melting technology and poured on a geopolymer refractory plate with high MgO content. The results suggest a good resistance of geopolymers to corium impact and minimal interaction observed through post-test analysis.
The good thermal shock resistance and low thermal conductivity make this material interesting for application in first contact layers, refractory sacrificial materials etc.

KEYWORDS
corium, severe accident, geopolymer, refractory ceramics, core catcher

ACKNOWLEDGMENTS

The presented results have been financially supported by the Technology Agency of the Czech Republic (TA CR) - the project TK01030130, and they were obtained using the CICRR infrastructure, which is financially supported by the Ministry of Education, Youth and Sports - project LM2023041.

REFERENCES

1. Z. Černý, T. Černoušek, P. Vácha, K. Sihelská, V. Tyrpekl, “Development of geopolymer based sacrificial materials for GEN IV severe accident mitigation,” *J. Nucl. Mater.*, **553**, 153024 (2021).

SEAKNOT
ERMSAR 2024
11th Conference on
SEVERE ACCIDENTS RESEARCH
May 13-16, 2024 – Stockholm, Sweden

Thermal shock resistant geopolymers as refractory material for core catcher

BENCE MÉSZÁROS,
Jan Hrbek, Mykhaylo Paukov, Václav Tyrpekl, Zbyněk Černý, Pavlína Rosypal

Abstract

Geopolymers have been intensively studied for immobilization of radioactive waste, but they can be beneficial in other applications. These materials show strong resistance to radiation, low moisture content and possibility of incorporation of various additives to modify their properties. This universality makes them a potential sacrificial, structural, or refractory component in passive or active safety systems in nuclear power plants (NPPs). [1] This may enhance the safety of NPPs and help to mitigate the severe accident consequences.

This poster presents a scoping interaction test of a geopolymer refractory material with prototypic corium melt. The corium mixture was achieved by induction skull melting technology and poured on a geopolymer refractory plate with high MgO content. The results suggest a good resistance of geopolymers to corium impact and minimal interaction observed through post-test analysis.
The good thermal shock resistance and low thermal conductivity make this material interesting for application in first contact layers, refractory sacrificial materials etc.

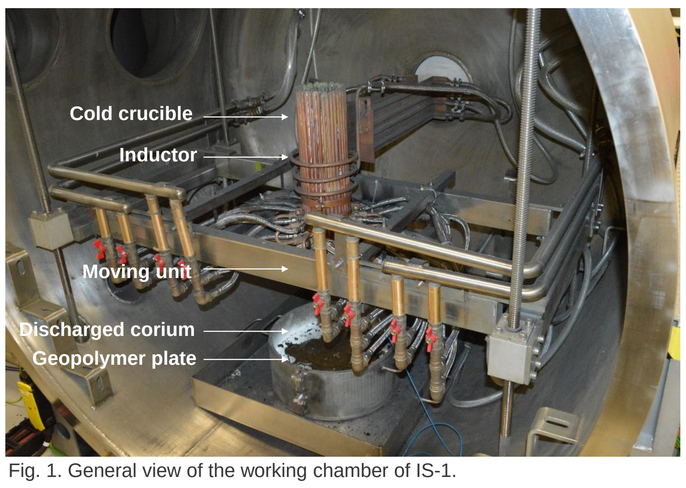

Fig. 1. General view of the working chamber of IS-1.

Introduction

- Geopolymers, inorganic materials formed by polymerization of a binding matrix and filler powders, offer properties superior to concrete, for example, increased radiation stability, low water content and the ability to insert various filling materials to modify their physicochemical properties. [2,3]
- Potential applications in nuclear power plants (NPPs) as sacrificial, construction, or refractory materials in safety systems.
- **Goal of study:** a scoping interaction test of geopolymer refractory material with prototypic corium melt to verify the material's ability to resist thermal shocks and to study the corium melt-plate interaction.

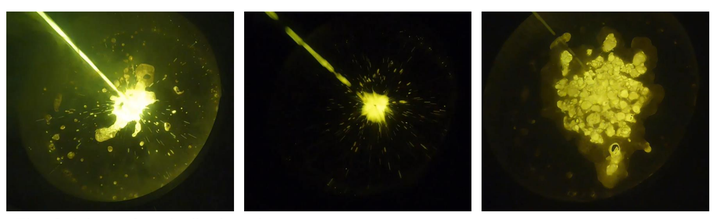
Fig. 2. View of melt discharging.

Experimental design

- Corium melt was created using induction skull melting technology.
- The IS-1 is a high-frequency generator for melting oxides with a 1.5–1.7 MHz frequency, and an output power of 160 KW was used. (Fig. 1)
- Two experimental steps: 1) Melting UO_2 with geopolymer sacrificial material (corium), and 2) Fast interaction with the refractory geopolymer plate after the discharging of the melt.
- Refractory plate composition: high MgO content and geopolymer matrix with specific mol% compositions of Na_2O, SiO_2, Al_2O_3, MgO, CaO, and Fe_2O_3.

Table 1. Composition of the corium

Material	Weight [g]	Weight %
UO_2	2250	50
Geopolymer with Gd_2O_3	1125	25
Geopolymer with Fe_2O_3	1125	25
Total mass	4500	100
Fe_3O_4 (starting material)	10	

Results

- Macro and microanalysis demonstrated good impact resistance of geopolymer with no cracking and minimal interaction zone.
- Limited solubility of uranium and gadolinium in the silicate matrix, forming solid solutions after solidification.
- Melting temperature reached up to 2000 ˚C when discharged.
- Corium remained liquid for approx. 10 seconds, forming a thin layer with bubbles from escaping gasses.
- Refractory plate resisted thermal shock without macroscopic cracking; minimal ablation observed.



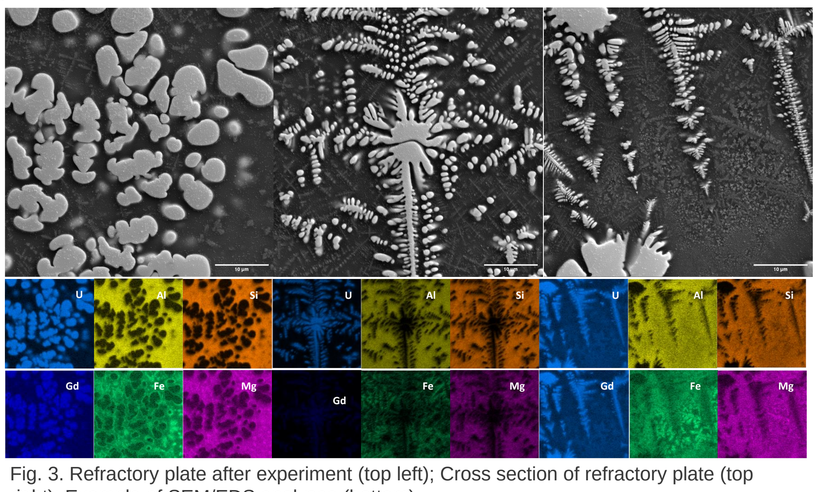

Fig. 3. Refractory plate after experiment (top left); Cross section of refractory plate (top right); Example of SEM/EDS analyses (bottom).

Conclusion

- MgO-rich geopolymer demonstrated good resistance to the first impact of corium melt.
- Chemical analysis revealed the formation of aluminosilicate melt dissolving the MgO filler. UO_2 and Gd_2O_3 formed a solid solution, reducing the re-criticality probability.
- Study supports the qualification of MgO-rich geopolymer as a refractory sacrificial material for severe accident mitigation or high-temperature applications.

Acknowledgments

The presented results have been financially supported by the Technology Agency of the Czech Republic (TA CR) - the project TK01030130, and they were obtained using the CICRR infrastructure, which is financially supported by the Ministry of Education, Youth and Sports - project LM2023041.

References

[1] Z. Černý, T. Černoušek, P. Vácha, K. Sihelská, V. Tyrpekl, "Development of geopolymer based sacrificial materials for GEN IV severe accident mitigation," *J. Nucl. Mater.*, **553**, 153024 (2021).
[2] Liew, Y.-M., Heah, C.-Y., Mohd Mustafa, A.B., Kamarudin, H., 2016. Structure and properties of clay-based geopolymer cements: A review. Prog. Mater Sci. 83, 595–629.
[3] Mehta, A., Siddique, R., 2016. An overview of geopolymers derived from industrial byproducts. Constr. Build. Mater. 127, 183–198.

IN COOPERATION WITH:

Mgr. Bence Mészáros
Hlavní 130, Řež, 250 68 Husinec, the Czech republic
Tel: +420 266 172 147
Email: bence.meszaros@cvrez.cz

INVESTIGATION OF NEW INORGANIC MATERIALS FOR NUCLEAR INDUSTRY UNDER SEVERE ACCIDENT CONDITIONS

Jan Hrbek, Mykhaylo Paukov, Bence Mészáros
Research Centre Řež
Hlavní 130, Řež, 250 68 Husinec, Czech Republic
jan.hrbek@cvrez.cz; mykhaylo.paukov@cvrez.cz; bence.meszaros@cvrez.cz

Václav Tyrpekl
Department of Inorganic Chemistry
Faculty of Science, Charles University
Hlavova 2030, 128 00Prague, Czech Republic
vaclav.tyrpekl@natur.cuni.cz

Zbyněk Černý, Pavlína Rosypal
Institute of Inorganic Chemistry of the Czech Academy of Sciences
250 68 Husinec- Řež, Czech Republic
cerny@iic.cas.cz, rosypal@iic.cas.cz

ABSTRACT

Geopolymers can show superior properties than concrete in nuclear reactor severe accident applications, helping to increase safety and mitigate consequences. Scientists study geopolymers primarily for usage in radioactive waste immobilization due to their polymeric structures and advantageous properties. With these properties, such as high gamma radiation resistance, low water content, and the ability to incorporate various elements to enhance physicochemical properties, geopolymers may be sacrificial materials in GEN IV reactors [1]. In present study we conducted a geopolymer interaction experiments with molten corium and studied the physicochemical properties at extreme temperatures to contribute to their qualification and application. Based on our research, geopolymers with Gd_2O_3 additive as a neutron absorber and Fe_2O_3 additive as a liquidus lowering agent of the mixture indicated as functional sacrificial materials for GEN IV reactors, exhibiting advantageous physicochemical properties for use as sacrificial material and commonly used concrete.

KEYWORDS
Geopolymer, corium, sacrificial material, severe accident

ACKNOWLEDGMENTS

The presented results have been financially supported by the Technology Agency of the Czech Republic (TA CR) - the project TK01030130, and they were obtained using the CICRR infrastructure, which is financially supported by the Ministry of Education, Youth and Sports - project LM2023041.

REFERENCES

1. Z. Černý, T. Černoušek, P. Vácha, K. Sihelská, V. Tyrpekl, “Development of geopolymer based sacrificial materials for GEN IV severe accident mitigation,” *J. Nucl. Mater.*, **553**, 153024 (2021).

SEAKNOT
ERMSAR 2024
11th Conference on
SEVERE ACCIDENTS RESEARCH
May 13-16, 2024 – Stockholm, Sweden

Investigation of New Inorganic Materials for Nuclear Industry under Severe Accident Conditions

JAN HRBEK

Mykhaylo Paukov, Bence Mészáros, Václav Tyrpekl, Zbyněk Černý, Pavlína Rosypal

Abstract

Geopolymers can show superior properties than concrete in nuclear reactor severe accident applications, helping to increase safety and mitigate consequences. Scientists study geopolymers primarily for usage in radioactive waste immobilization due to their polymeric structures and advantageous properties. With these properties, such as high gamma radiation resistance, low water content, and the ability to incorporate various elements to enhance physicochemical properties, geopolymers may be sacrificial materials in GEN IV reactors [1]. In present study we conducted a geopolymer interaction experiments with molten corium and studied the physicochemical properties at extreme temperatures to contribute to their qualification and application. Based on our research, geopolymers with Gd_2O_3 additive as a neutron absorber and Fe_2O_3 additive as a liquidus lowering agent of the mixture indicated as functional sacrificial materials for GEN IV reactors, exhibiting advantageous physicochemical properties for use as sacrificial material and commonly used concrete.

Experimental

The experimental setup uses induction melting in a cold crucible to reach high temperature and prevent melt contamination. The cold crucible walls and bottom are intensively water-cooled; thus, the sample is not melted in the contact area with the cold crucible and thin solid-state layer is formed. This solid-state layer is called the skull. The induction melting in the cold crucible allows to reach melt temperature up to 3200 °C. The surface temperature of the melt is measured using a pyrometer. A working chamber allows the melting of materials in an inert atmosphere or vacuum. The experimental setup with the cold crucible and inductor is shown in Fig. 1.

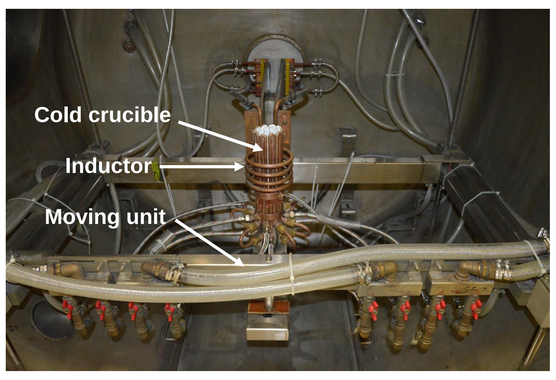

Fig. 1. A view into the working chamber with the cold crucible and inductor

The purpose of the experiments was to study behavior of molten corium with geopolymers (Gd_2O_3 geopolymer and Fe_2O_3 geopolymer) potentially usable as a sacrificial material, Fe, and also with B_4C in Case 2. The corium had only one component - UO_2. The composition of mixtures used in the experiments is shown in Tab. 1.

Table 1: Composition of the mixtures

	Composition (wt. %)	
Material	Case 1	Case 2
UO_2	50	48
Geopolymer with Gd_2O_3	20	20
Geopolymer with Fe_2O_3	20	20
Fe	10	10
B_2C	-	2

Fig. 2 shows a view of the melt surface during one of the experiments and the halved ingot casted in resin. No significant adverse effects occurred during melting (melt spouting, etc.).

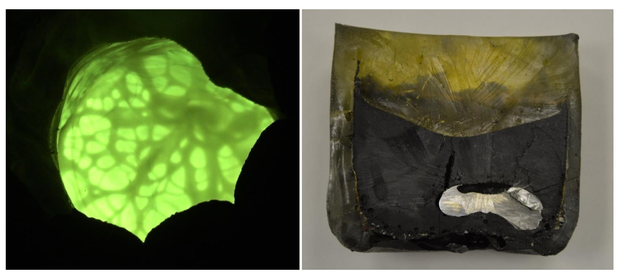

Fig. 2. A view of the melt surface during the experiment (left) and the halved ingot encased in resin (right)

After the end of the experiments, the ingots were removed from the cold crucible, cast in resin, cut in half, and then samples were taken from them. The samples were prepared in a standard way - cutting and polishing and then analyzed using SEM/EDS.

Results

Maps obtained using SEM/EDS from one sample are shown in Fig. 3. As seen in Fig. 3, the higher concentration of Gd_2O_3 can be found in the same places in the ingot as UO_2. Ca shows a similar effect, but other elements do not interact with UO_2.

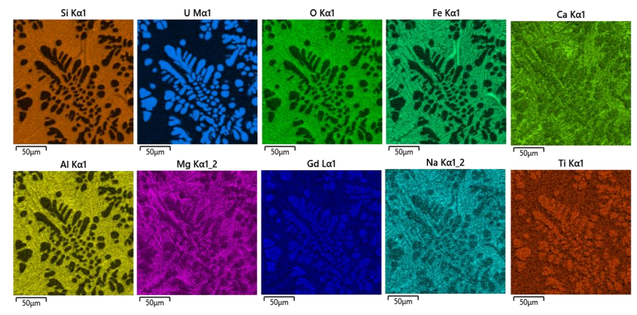

Fig. 3. Illustrative example of sample maps obtained by SEM/EDS

Conclusion

The interaction of UO_2 with geopolymers with Gd_2O_3 and Fe_2O_3 additives was investigated during the experiments. The results show that UO_2 does not interact with most of the elements from the geopolymer matrix. The exception is Ca, which overlaps with UO_2 in some parts of the ingot. The higher concentration of Gd_2O_3 was always found in the same places in the ingot as UO_2. It is a positive phenomenon expected from sacrificial material.

When interacting with corium, the investigated geopolymers show beneficial properties for possible use in the nuclear industry. However, further research of new inorganic materials based on geopolymers will bring additional knowledge about their properties and behavior, and the area of their potential use may be broad.

Acknowledgments

The presented results have been financially supported by the Technology Agency of the Czech Republic (TA CR) - the project TK01030130, and they were obtained using the CICRR infrastructure, which is financially supported by the Ministry of Education, Youth and Sports - project LM2023041.

References

[1] Z. Černý, T. Černoušek, P. Vácha, K. Sihelská, V. Tyrpekl, "Development of geopolymer based sacrificial materials for GEN IV severe accident mitigation," *J. Nucl. Mater.*, **553**, 153024 (2021).

IN COOPERATION WITH:

Jan Hrbek
Hlavní 130,
Řež, 250 68 Husinec
Tel: +420 606 470 063
Email:
jan.hrbek@cvrez.cz

Modeling of pool scrubbing and sensitivity analysis using GOTHIC

Xicheng Wang[1], Dmitry Grishchenko[2] and Pavel Kudinov[3]

[1]Royal Institute of Technology, KTH, Roslagstullsbacken 21 - Stockholm, xicheng@kth.se
[2]Royal Institute of Technology, KTH, Roslagstullsbacken 21 - Stockholm, dmitrygr@kth.se
[3]Royal Institute of Technology, KTH, Roslagstullsbacken 21 - Stockholm, pkudinov@kth.se

Contact email: xicheng@kth.se

Abstract

Pool scrubbing referred as the process of the retention of fission products in a water pool, is a mitigation measure to avoid leaking of radioactive fission products into the environment during severe accidents. Aerosol particles accompanied by gaseous mixtures (e.g., steam and non-condensable gas) can be injected through multi-hole spargers or vents into a large water pool during different scenarios. The amount of aerosols captured by the pool is governed by the transport processes of aerosols inside the bubbles and the dynamic characteristics of the gas-liquid interface. Decontainment factor (DF) defined by the ratio of injected aerosols over escaped aerosols is used to evaluate the efficiency of the pool scrubbing. Several codes (e.g., BUSCA, SUPRA, SPARC-90, SPARC-B/98) have been developed to evaluate the DF during pool scrubbing. In the latest update of the containment system code GOTHIC (v8.4), the pool scrubbing feature derived from SPARC-90 is enabled. The motivation of goal of this work is to investigate the modeling capability of GOTHIC with respect to pool scrubbing and develop and implement GOTHIC models to provide analytical support of experiments conducted in THAI facility.

Keywords: Pool scrubbing, aerosol deposition, THAI, GOTHIC,

MELCOR analyses of Severe Accident sequences in an integral PWR with passive systems

Fabio Giannetti[1], Marcello Principato[2], Matteo D'Onorio[3], Giuseppe Agnello[4], Gianmarco Grippo[5], Andrea Bersano[6] and Fulvio Mascari[7]

[1]Sapienza University of Rome, DIAEE, Corso Vittorio Emanuele II, 244, 00186 Rome, Italy, fabio.giannetti@uniroma1.it
[2]Sapienza University of Rome, DIAEE, Corso Vittorio Emanuele II, 244, 00186 Rome, Italy, marcello.principato@uniroma1.it
[3]Sapienza University of Rome, DIAEE, Corso Vittorio Emanuele II, 244, 00186 Rome, Italy, matteo.donorio@uniroma1.it
[4]Università degli Studi di Palermo /ENEA, Viale delle Scienze 6, Palermo, 90128, Italy, giuseppe.agnello04@unipa.it
[5]ENEA FSN-SICNUC, Via Martiri di Monte Sole 4, Bologna, 40129, Italy, gianmarco.grippo@enea.it
[6]ENEA FSN-SICNUC , Via Martiri di Monte Sole 4, Bologna, 40129, Italy, andrea.bersano@enea.it
[7]ENEA FSN-SICNUC, Via Martiri di Monte Sole 4, Bologna, 40129, Italy, fulvio.mascari@enea.it

Contact email: fabio.giannetti@uniroma1.it

Abstract

The SASPAM-SA Horizon Euratom project is investigating the maximization of the knowledge transferability and impacts of the project two generic design concepts, characterized by different evolutionary innovations in comparison with larger operating reactors, with a focus on the ability of Severe Accident (SA) programs to mimic integral Pressurized Water Reactors (iPWRs) during SA sequences. The effectiveness of the MELCOR system code in simulating severe accident scenarios that might occur in an iPWR is the main topic of this study.

The selected design, referred to as Design 2 in the SASPAM-SA project, is a 300 MWe iPWR characterized by passive safety systems and a dry spherical metallic containment. As a result, Design 2 serves as a general-purpose reactor design that may be representative of relevant reactor concepts like IRIS and SMART. In this framework, a MELCOR input deck was prepared by Sapienza University of Rome in collaboration with ENEA and CIEMAT using MELCOR 2.2 18019, developed by Sandia National Laboratories (SNL) for the USNRC, with the aim to assess DBA and BDBA code prediction capability.

The selected initiating event analyzed in this study is a small break Loss of Coolant Accident (SBLOCA) due to a double guillotine rupture of the Direct Vessel Injection line. This could be considered the only plausible LOCA in the primary circuit since integral reactor layouts intrinsically avoid Large break LOCAs because the reactor's main components, such as the Steam Generator and the pressurizer, are inside the Reactor Pressure Vessel (RPV). The developing SA scenario involves the failure of every passive safety system installed: the Emergency Heat Removal System, the Emergency Borated Tanks, the Long-term gravity makeup systems and the Automatic Depressurization Systems. This extremely unlikely scenario was selected as the worst case only to test the code prediction capability.

Transient analysis results highlighted that the MELCOR code captures the predominant phenomena driving the transient evolution of accidental scenarios, starting from a thermal-hydraulic behavior and including the core degradation, and material relocation in the RPV lower head. This preliminary study serves as a base for future developments in SASPAM-SA WP4, which will focus on more detailed simulations to predict the key phenomena, associated uncertainties, and mitigation strategies during In-Vessel-Melt-Retention in such iPWR.

Keywords: SMR, Passive systems, iPWR, SASPAM-SA

Development of severe accident simulation code for sodium-cooled fast reactors: SIMMER-V (2) Development and verification of detailed fuel pin model

Shinya Ishida, Hirotaka Tagami, Yasushi Okano, Hidemasa Yamano, and Shigenobu Kubo
Japan Atomic Energy Agency
4002 Narita-cho, Oarai-machi, Higashi-ibaraki-gun, Ibaraki-ken, Japan
ishida.shinya@jaea.go.jp; tagami.hirotaka@jaea.go.jp; okano.yasushi@jaea.go.jp; yamano.hidemasa@jaea.go.jp; kubo.shigenobu@jaea.go.jp

Yoshiharu Tobita
Japan Atomic Energy Agency (present affiliation: Karlsruhe Institute of Technology)
Hermann-von-Helmholtz-Platz 1, 76344 Eggenstein-Leopoldshafen, Germany
yoshiharu.tobita@kit.edu

ABSTRACT

The new detailed fuel pin model has been developed as a part of the SIMMER-V code to simulate thermal and mechanical behavior of the fuel pin from accident initiation to fuel pin failure. The SIMMER-III and SIMMER-IV codes have been developed mainly to simulate the event progression in transition phase (TP), and the initiating phase (IP) was simulated by the SAS4A code. Calculated results of IP are taken as the initial conditions of a TP analysis. In this data transfer from SAS4A to SIMMER, the differences in computational geometries and models can cause discontinuity in calculated event progression. In particular, the standard fuel-pin model of SIMMER-III and SIMMER-IV is too simple to represent the complex behavior necessary for simulating the IP. To solve these problems, an improved and detailed fuel-pin model has been developed at JAEA as a part of a new SIMMER-V code, a joint research program being conducted in collaboration with CEA. To develop the new model, the key physical phenomena relevant to fuel pin failure were extracted. They include: thermal behavior, fission gas release, fission gas swelling, mechanical deformation, and in-pin fuel motion. Each of these phenomena was modeled as a module, which was then incorporated to SIMMER-V. Considering the applicability of the model to wider range of core and fuel designs, it is necessary to simulate in detail the fuel motion in a central hole of the annular fuel pellet and the fuel ejection from the fuel pin cavity to the coolant channel. In order to simulate these phenomena and obtain numerical stability, the in-pin fuel motion was modeled based on the multi-phase fluid-dynamics algorithm of SIMMER-III. In addition, the model enables the multi-cavity formation for an axially heterogeneous core design. A verification matrix was constructed to check the performance of the new model, and test cases were prepared, focusing on verifying individual modules. Since the new detailed fuel-pin model has been developed to simulate the physical phenomena occurring in the IP, the calculated results are compared with SAS4A, to check the capability of the model. This study verified the performance of individual modules of the new detailed fuel-pin model of SIMMER-V.

KEYWORDS
SFR, SIMMER-V code, detailed fuel pin model, verification

1. INTRODUCTION

In a severe accident (SA) of a sodium-cooled fast reactor (SFR), the event progresses on various scales from fuel pin failure within a fuel subassembly to fuel motion on a whole core scale. In current accident evaluation practice, the accident sequence is divided into several phases and the most appropriate computer code is applied to each phase in order to accurately analyze the event progression. An initiating phase (IP) is the first stage of a SA, in which damaged core regions are still contained in the wrapper tubes. In a transition phase (TP), the damaged core region expands to form a molten fuel pool due to the failure of the wrapper tubes. The SIMMER-III and SIMMER-IV codes (called only as SIMMER-III hereinafter since the two codes have essentially the same models except for spatial dimensions) [1] have been developed mainly to simulate the event progression in a TP, and an IP is simulated by the SAS4A code [2, 3]. The calculated results of SAS4A are transferred to SIMMER-III as initial conditions of the TP. In this data transfer, the difference in computational geometries and physical models can cause discontinuity in calculated event progression. In particular, the standard fuel-pin model of SIMMER-III is too simple to represent the complex behavior necessary for simulating the IP. In addition, complex reactor core geometry, such as the annular fuel pellet and the axial heterogeneous core, which are also being considered for future SFRs, have to be considered. To solve these problems, an improved and detailed fuel-pin model (hereinafter referred to as the new pin model) has been developed at JAEA as a part of a new SIMMER-V code [4], a joint research program being conducted in collaboration with CEA. The model enables a continuous (or once-through) analysis from IP to TP in the future SFRs. In this paper, the physical modules of the new pin model are briefly described and the verification test matrix and the results are presented.

2. NEW DETAILED FUEL PIN MODEL

The SIMMER-III code, which comprehensively analyzes the neutronics and thermal-hydraulics of a disrupted core, consists of three fundamental modules: the fluid-dynamics module, the structure module, and the neutronics module. A standard fuel-pin model included in the structure module is very simple and models only two radial temperature nodes in fuel pellet and a fuel failure criterion is based on thermal condition (melt fraction). It is still possible to calculate the behavior of the fuel pins from intact state to failure, especially in a loss of coolant flow transient. The behavior of the fuel pins is such that after coolant boiling, the cladding heats up and loses its mechanical strength, resulting in fuel pin disruption. On the other hand, in an overpower transient, the fuel pellets heat up to mechanically load the cladding caused by fuel thermal expansion and fission gas swelling, leading to fuel pin mechanical failure. SIMMER-III is unable to deal with the latter mode of fuel pin failure. In the SIMMER-V code, a joint research program being conducted by JAEA and CEA, a new pin model has been developed to evaluate the mechanical failure behavior. The development of this model would allow us to consistently evaluate the fuel pin behavior up to the fuel pin failure in the IP and the subsequent event progression in the TP.

2.1. Identifying key physical phenomena

To develop the new pin model, elementary phenomena related to fuel pin failure are analyzed, and the key physical phenomena are identified. A schematic representation of the elementary phenomena related to fuel pin failure is shown in Fig. 1. As the reactor power increases, the fuel pellet temperature rises and a molten cavity is formed in the center of the fuel pellet column as the fuel melts. At the same time, fission gas bubbles in the fuel pellet grow and swell the fuel pellet (fission gas swelling), while fission gas is released when the bubble connects to the free surface of the pellet. In addition, temperature increase also cause thermal expansion of the fuel pellet. This deformation causes pellet-cladding mechanical interaction (PCMI), which leads to fuel pin failure when the circumferential stress exceeds the ultimate cladding strength. In the molten cavity, a multiphase mixture of liquid fuel and fission gas flows axially inside the fuel pin. If the fuel pin fails and the molten cavity becomes connected to the coolant channel through the failure site, a mixture of liquid fuel and fission gas is ejected to the coolant channel due to the pressure difference. In the coolant

channel, heat exchange between liquid fuel and sodium causes rapid vaporization due to fuel-coolant interaction (FCI), and the fuel is dispersed in a vertical direction. Such fuel behaviors can cause large reactivity changes and are important phenomena that can also influence the subsequent core disruption behavior [5, 6].

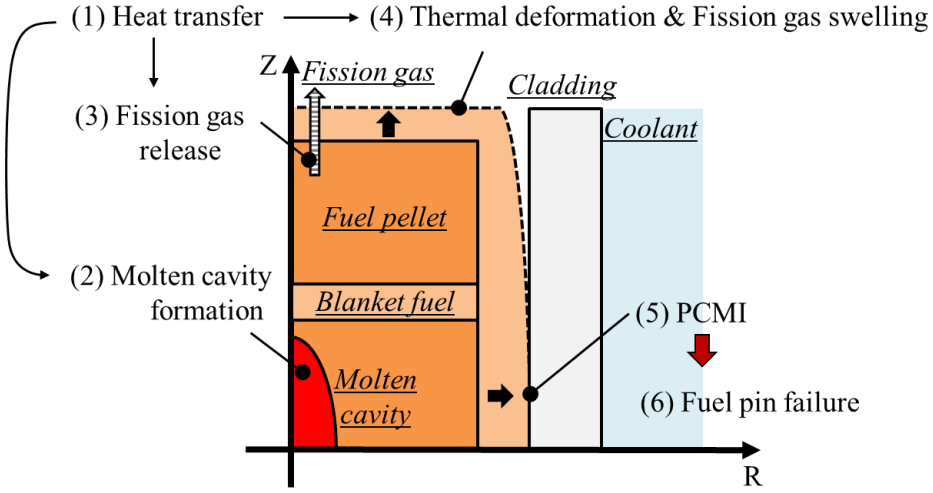

a) From accident initiation to fuel melt

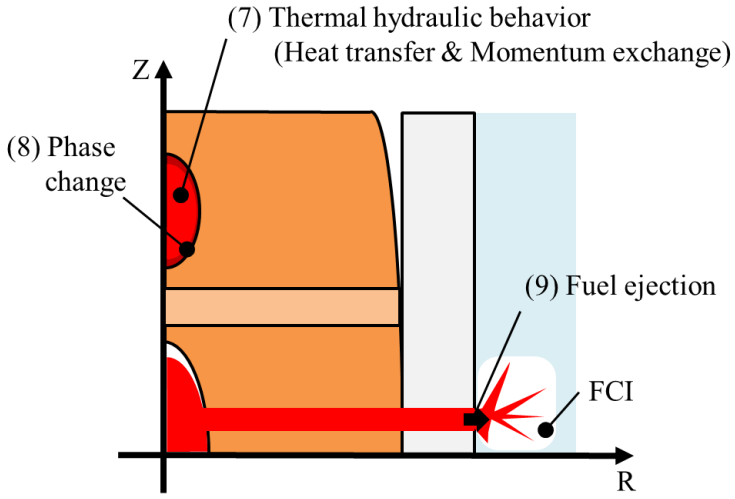

b) From fuel melt to fuel pin failure

Fig. 1. Elementary phenomena related to fuel pin failure.

Figure 2 summarizes the relationships among the elementary phenomena, which are then analyzed to extract key physical phenomena. In the figure, the area indicated by the colored frames corresponds to each ley physical phenomenon. Heat transfer and related behaviors are expressed as “thermal behavior”. The release behaviors of fission gas from the fuel pellet into the fuel pin gap or gas plenum are expressed as “fission gas release”. The fuel pellet expansion behaviors due to the fission gas swelling are expressed as “fission gas swelling”. The behavior related to fuel pellet and cladding deformation is described as “mechanical deformation behavior”, which is a phenomenon directly related to fuel pin failure. Thermal-hydraulic behavior in the molten cavity and fuel ejection behavior into the coolant channel are collectively expressed

as “in-pin fuel motion behavior”. The mechanical strength of the cladding is also important in simulating fuel pin failure, although it is not regarded as key physical phenomenon. The cladding mechanical strength depends mainly on its temperature and is weakest slightly above the midplane. On the other hand, the mechanical stress of the cladding depends on axial power distribution and is higher near the midplane of the fuel. Since the failure site is determined by this strength-stress relationship, the failure site is generally above the midplane in the case of mechanical failure. Since liquid fuel in the fuel pin is ejected through the failure site into the coolant channel, a mid-plane failure causes axial fuel compaction in the cavity, increasing reactivity. A failure site also affects post-failure behavior, such as fuel motion in the channel and cooling voiding due to FCI.

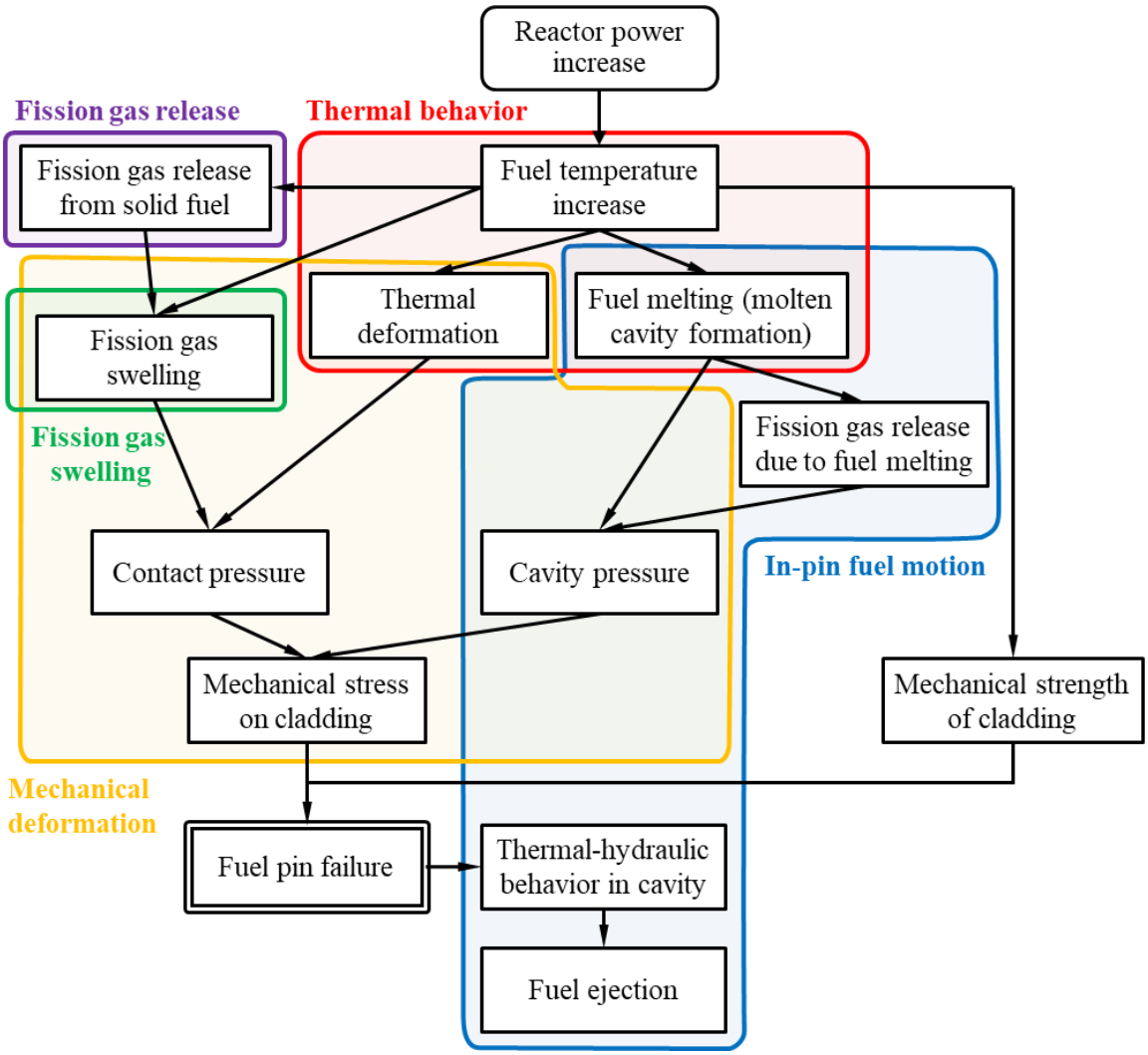

Fig. 2. Inter-relationship of elementary phenomena related to fuel pin failure and extracted key physical phenomena.

2.2. Modeling key physical modules

Based on the discussion in the previous section, the following five key physical phenomena were modeled as modules in the new pin model: the thermal behavior, mechanical deformation behavior, fission gas release behavior, fission gas swelling behavior, and in-pin fuel motion behavior. These modules are applied to the

structure module of the SIMMER-V and treat the fuel pellet, the cladding, and fission gas contained in the fuel pin. The behavior of the materials ejected into the coolant channel is calculated in the fluid-dynamics module, not in the structure module.

For the thermal behavior, the one-dimensional radial heat conduction in the fuel pellet and cladding and the gap conductance between the fuel pellet and cladding are considered. The heat generation is given by a neutronic module in the SIMMER-V and the heat transfer between cladding and coolant is treated as a boundary condition between the new pin model and the fluid-dynamics module. The mechanical deformation behavior is expressed by the relational expressions between stress and strain, strain and deformation and the balance equation for stress to get stress, strain and deformation. Thermal expansion is also considered for fuel pin deformation. The fission gas is released from the fuel pellets according to a temperature-dependent time constant. Since the fission gas swelling is a similar phenomenon to fission gas release, a volume expansion rate was assumed to be the same as the time constant of the fission gas release. The in-pin fuel motion behavior is expressed by a one-dimensional two-phase flow, which consists of fission gas, liquid fuel, and fuel vapor, in a molten cavity and a central hole. The liquid fuel and fission gas are ejected to the coolant channel due to the pressure difference between the molten cavity and the coolant channel. Considering the applicability of the model to wider range of core and fuel designs, it is necessary to simulate in detail the fuel motion through a hole in the center of the annular fuel pellet [7] and through the liquid fuel ejection outside the fuel pin through the failure site of the cladding. In the molten cavity and the central hole, a two-phase flow and a very narrow path flow can occur. In order to simulate the above complex phenomena and obtain numerical stability, the model for analyzing in-pin fuel motion was developed according to the thermal-hydraulic computational algorithm of SIMMER-III that calculates the two-phase flow. In addition, in an axially heterogeneous core, the blanket fuel is located at the axial center of the fuel pin and may have two axial power peaks. This may result in simultaneous formation of multiple cavities that has been modeled.

3. VERIFICATION

3.1. Verification Matrix

A verification matrix was constructed to check the performance of the new pin model, as shown in Table I. In the matrix, the five key physical phenomena, corresponding to the five modules of the new pin model, are listed in rows, and the calculational elements are listed in columns. The relationship between the calculational elements and the key physical phenomena was already shown in Fig. 2. Test cases have been prepared for each of the key physical phenomena that corresponds to the modules of the new pin model. Since the new pin model has been developed to simulate the key physical phenomena during the IP, the calculated results are compared with SAS4A, which has been extensively validated with results of the CABRI and TREAT in-pile experiments [3, 8, 9], and has been widely applied to reactor analyses [5, 10].

3.2. Verification Results

Verification analyses were performed based on the matrix, and the modules related to the individual key physical phenomena were verified by comparing with the analyses by SAS4A. The calculation condition was made as simple as possible, and the initial condition is based on the fuel pin condition used in the CABRI test because many experimental analyses have been conducted using SAS4A with this fuel pin thus far. For the comparisons between SIMMER-V and SAS4A calculations, the calculational conditions of SAS4A and SIMMER-V should be made consistent as much as possible. Thus, the thermophysical property model in SIMMER-V was installed in SAS4A because the thermal calculation is largely influenced by this model.

As a result of these analysis, it was confirmed that the all key physical phenomena were almost consistently calculated between SIMMER-V and SAS4A. The results of the test case related to mechanical deformation, which is a phenomenon directly related to fuel pin failure, and the test case related to fuel ejection, which greatly affects the post-failure behavior, are shown below as the main cases.

Table I. Verification matrix for the new pin model

	Calculational elements											
	Thermal calculation			Fuel pin failure calculation					In-pin fuel motion calculation			
Key physical phenomena (Modules)	Heat transfer	Thermal deformation	Molten cavity formation	Fission gas release	Fission gas swelling	Stress calculation	Contact pressure	Cavity pressure	Heat transfer in cavity	Momentum exchange	Phase change	Fuel ejection
Thermal behavior	O		O									
Fission gas release	X		X	O								
Fission gas swelling	X		X	X	O							
Mechanical deformation	X	O	X	X	X	O	O	O				
In-pin fuel motion	X	X	X	X	X	X	X	X	O	O	O	O

"O" indicates the calculational element to be verified in the relevant test case.
"X" indicates the calculational element that has already been verified in the other test case.

3.2.1. Test case for cladding deformation behavior

The deformation calculation module evaluates thermal expansion and stress deformation for fuel and cladding. To simulate mechanical fuel pin failure, it is necessary to evaluate PCMI that can be evaluated by checking the cladding deformation behavior. In this test case, the fuel pellet is expanded by increasing the power, the fuel pellet and the cladding are brought into contact, and the cladding is deformed by the PCMI to check the cladding deformation behavior. Transient power conditions include increasing the power by 5% of the initial power per second between 5 s and 15 s and by 70% between 15 s and 20 s. At the end state of the analysis, the power was increased to five times the initial power.

The fuel and cladding deformation and fuel temperature of each fuel and cladding node were checked for verification (Figs. 3 and 4). The fuel and cladding temperature evolutions are almost in good agreement between the two codes, and this means the temperature increase with the power increase is adequately simulated by SIMMER-V. The fuel temperature in the center reaches its melting point, about 3000 K, in about 17 s, forming a molten cavity. In both the analyses, fuel melting starts when the cell temperature reaches the solidus temperature, and the fuel is completely melted when it reaches the liquidus temperature. Thus, the rate of temperature increase becomes slow at about 17 s and faster again in at about 18 s. The fuel

melting behavior is also in good agreement between the two codes. As for deformation behavior, the fuel outer radius gradually increases as the fuel expands due to the temperature increase, and the fuel contacts the cladding at about 18 s. Then, the cladding is mechanically loaded by the fuel expansion, and the cladding also is deformed significantly outward. Comparing the results of SAS4A and SIMMER-V, the fuel outer radius and cladding inner radius are both slightly larger in SIMMER-V. Because of the difference in the heat transfer coefficients between cladding and coolant of the SAS4A and SIMMER-V thermohydraulic models, the fuel temperature is about 10 K higher in SIMMER-V. Although there is small difference in the fuel and cladding deformation, the overall deformation behaviors are almost consistently calculated between SIMMER-V and SAS4A.

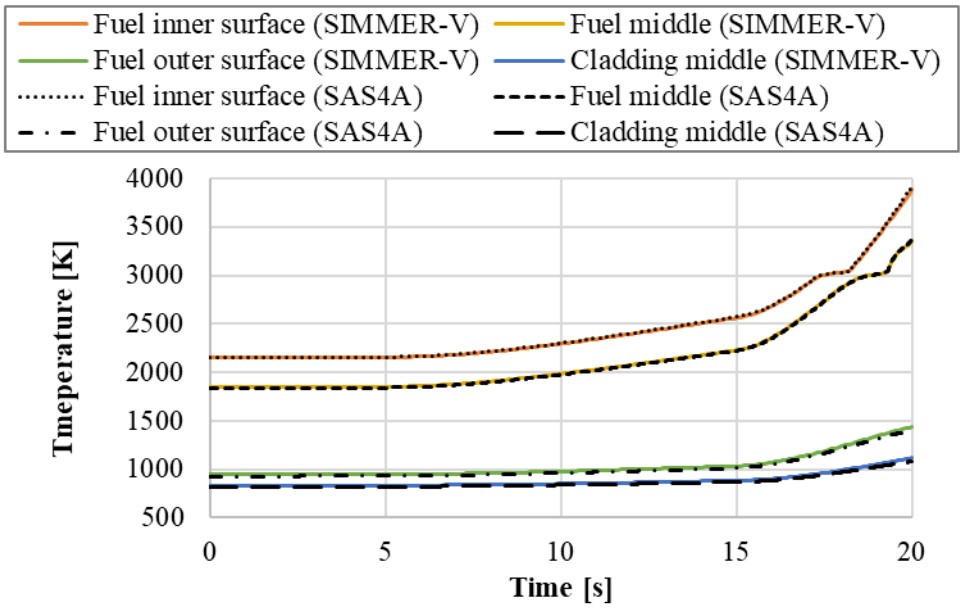

Fig. 3. Temperature changes in different temperature nodes at core midplane.

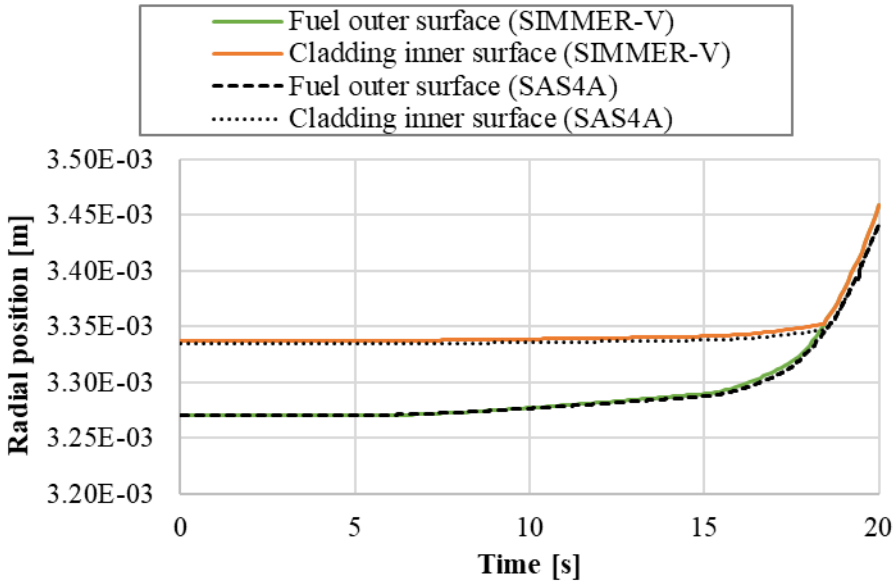

Fig. 4. Fuel and cladding deformation behavior.

In conclusion, it was confirmed that the mechanical deformation module has been verified by comparing with SAS4A and that the module has been appropriately introduced to SIMMER-V.

3.2.2. Test case for fuel ejection behavior

In this test case, to analyze the fuel motion behavior in a fuel pin at the fuel pin failure, the power was increased to melt the fuel pellet, and then the fuel pin was forced to fail at a certain axial position. The test case is to check the fuel ejection behavior into the coolant channel through the cladding failure site. Figure 5 shows the condition of the fuel pin at the time of artificial fuel pin failure. The fuel pin was failed at an axial node 25. The behavior of fuel ejection into the coolant channel is driven by the pressure difference between the molten cavity and the coolant channel and the whole fuel ejection behavior was compared with SAS4A. Since the channel pressure buildup due to FCI may also influence the fuel ejection behavior, the two parametric cases were set up by changing the liquid fuel radius: Case 1 with the minimum droplet radius of 0.05 mm and Case 2 with 0.5 mm. The larger the radius becomes in Case 2, the smaller the heat transfer from fuel to sodium, resulting in lower FCI pressure buildup.

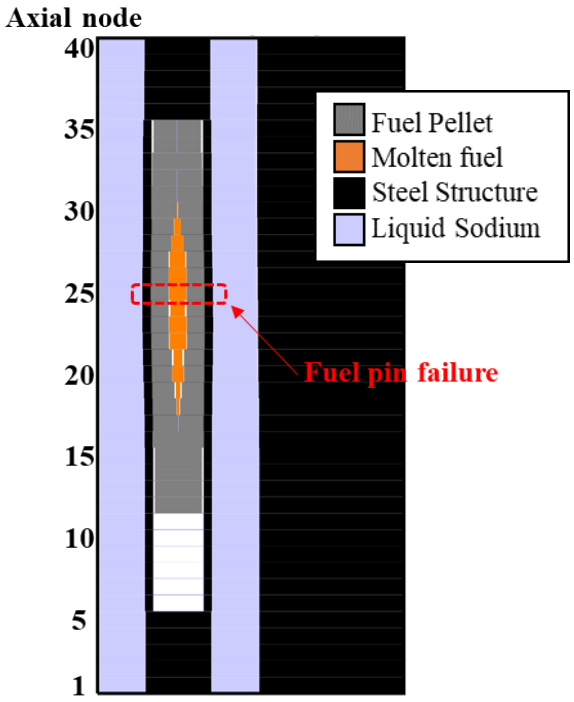

Fig. 5. Fuel pin condition at the time of artificial fuel pin failure.

Figure 6 shows the results of the fuel mass ejected into the coolant channel. In the case of SAS4A, fuel was ejected into the coolant channel until approximately 50 ms after the fuel pin failure. In the SIMMER-V Case 1, the evolution of the fuel ejection mass is similar to that in SAS4A; however, the fuel ejection rate immediately after the fuel ejection is smaller than that in SAS4A. The fuel is ejected into the coolant channel and then axially dispersed, causing a decrease in reactivity, so the fuel ejection rate is an important parameter that can influence the subsequent event progression. In the SIMMER-V Case 2, when the radius of the liquid fuel droplets was set larger, the fuel ejection rate was also similar to that of SAS4A. The pressure decrease

in the coolant channel increases the pressure difference between the molten cavity and the coolant channel, which is the driving force for fuel ejection. Therefore, it is physically consistent that the fuel ejection rate increases as a result of the larger liquid fuel particles. As the objective of this study is to check the performance of the new pin model, the verification was focused on the model. However, the behavior of the fluid-dynamics module is also important in the SIMMER-V IP analysis, as the coolant channel pressure influences the fuel ejection behavior, so it will be necessary to check the capability of SIMMER-V against the whole IP analysis in the future.

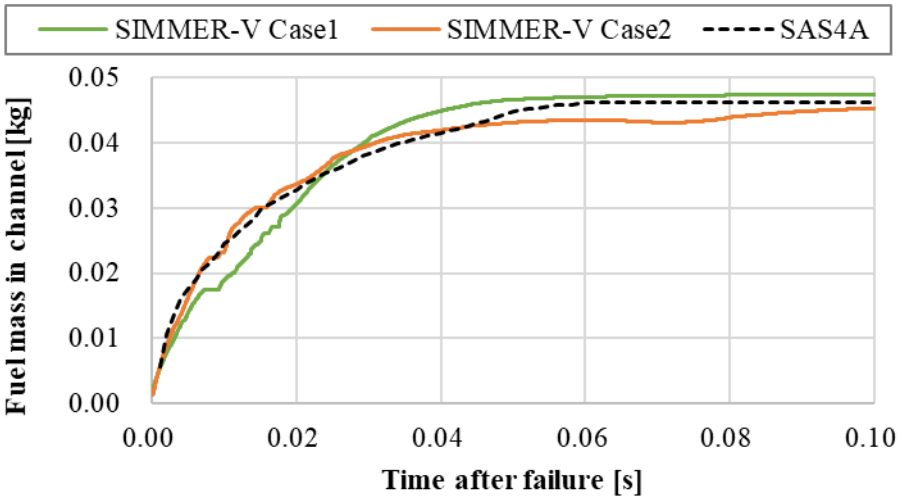

Fig. 6. Fuel mass ejected to the coolant channel.

In conclusion, it was confirmed that the in-pin fuel motion module can simulate the results of SAS4A and that the analytical results are physically consistent, as seen in the relationship between pressure conditions and fuel ejection behavior. Therefore, it can be said that the necessary functions for the simulation of the fuel ejection have been introduced to SIMMER-V.

4. CONCLUSIONS

For the evaluation of a SA of SFRs, the new pin model has been developed as part of SIMMER-V to impro ve the capability for once-through analysis from the IP to the TP of the SA and to be applicable to wider range of core and fuel designs for future SFRs. The verification analysis for each module was performed based on the verification matrix by comparison with the existing analytical code, mainly SAS4A, and it was confirmed that physically consistent results were obtained. This allowed the new pin model to simulate the fuel pin behavior from the start of an accident with the fuel pin failure in the IP to the subsequent TP by SIMMER-V.

The verification analysis focused on the evaluation of individual key physical phenomena. To confirm the whole behavior of the new pin model, it will be necessary to analyze available in-pile test data where mechanical failure behavior has been confirmed to validate the model. In addition, to demonstrate that the model is capable of once-through analysis from the IP to the TP, which is the purpose of the development of this model, it will also be necessary to perform accident analyses on an actual reactor and to investigate the applicability of the new pin model to the actual reactor conditions.

ABBREVIATION

FCI	Fuel-Coolant Interaction
IP	Initiating Phase
PCMI	Pellet-Cladding Mechanical Interaction
SA	Severe Accident
SFR	Sodium-cooled Fast Reactor
TP	Transition Phase

ACKNOWLEDGMENTS

The authors express their sincere gratitude to Mr. Katsuhiko Takahashi and Mr. Masaaki Sugaya of NESI Inc. for their enormous programming and computational supports. The paper includes the results of technical development program on a fast reactor for demonstration entrusted to JAEA by Ministry of Economy, Trade and Industry.

REFERENCES

1. S. Kondo, et al., "SIMMER-III and SIMMER-IV: Computer Codes for LMFR Core Disruptive Accident Analysis," *Japan Atomic Energy Institute research report*, (to be published) (2024).
2. A. M. Tentner, et al., "The SAS4A LMFBR whole core accident analysis code", *Proceedings of the International Topical Meeting on Fast Reactor Safety*, Knoxvill, USA, April 21-24, pp. 989-997 (1985).
3. S. Ishida, Y. Fukano, "Study on initiating phase of core disruptive accident (Validation study of SAS4A code for the unprotected transient overpower accident)," Transactions of the JSME (in Japanese), 88(911), pp. 1-11 (2022).
4. H. Tagami, et al., "Development of severe accident simulation code for sodium-cooled fast reactors: SIMMER-V", *Proceedings of the 11th European Review Meeting on Severe Accident Research (ERMSAR2024)*, KTH, Stockholm, Sweden, May 13-16, (2024).
5. T. Suzuki, et al., "A preliminary evaluation of unprotected loss-of-flow accident for a prototype fast-breeder reactor", *Nuclear Engineering and Technology*, **47**(3), pp. 240-252 (2015).
6. I. Sato, et al., "Safety Strategy of JSFR Eliminating Severe Recriticality Events and Establishing In-Vessel Retention in the Core Disruptive Accident", *Journal of Nuclear Science and Technology*, **48**(4), pp. 556-566 (2011).
7. Y. Fukano, Y. Onoda, I. Sato, "Fuel Pin Behavior up to Cladding Failure under Pulse-Type Transient Overpower in the CABRI-FAST and CABRI-RAFT Experiments", *Journal of Nuclear Science and Technology*, **47**(4), pp. 396-410 (2010).
8. T. E. Kraft, et al., "Simulations of an unprotected loss-of-flow accident with a 37-pin bundle in the sodium loop safety facility", *Proceedings of the International Meeting on Fast Reactor Safety Technology*, Vol. 2, pp. 896-904 (1979).
9. J. A. Morman, A. M. Tentner, and D. J. Dever, "SAS validation and analysis of in-pile TUCOP experiments", *Proceedings of the International Topical Meeting on Fast Reactor Safety*, Knoxvill, USA, April 21-24, pp. 797-801 (1985).
10. I. Sato et al., ''Development of severe accident evaluation technology (Level 2 PSA) for sodium-cooled fast reactors (2) Identification of dominant factors in initiating phase of unprotected events,'' *Proceedings 2009 International Congress on Advances in Nuclear Power Plants (ICAPP '09)*, Tokyo, Japan, May 10-14, Paper 9132 (2009).

SEAKNOT
ERMSAR 2024
11th Conference on
SEVERE ACCIDENTS RESEARCH
May 13-16, 2024 – Stockholm, Sweden

Development of severe accident simulation code for sodium-cooled fast reactors: SIMMER-V (2) Development and verification of detailed fuel pin model

Shinya Ishida, Hirotaka Tagami, Yasushi Okano, Hidemasa Yamano, Shigenobu Kubo and Yoshiharu Tobita

I. INTRODUCTION

- ✓ In the current severe accident (SA) evaluation of a sodium-cooled fast reactor (SFR), the accident sequence is divided into several phases and the most appropriate analytical code is applied to each phase, but the data transfer between codes can cause discontinuity in calculated event progression due to difference in computational geometries and physical models.
- ✓ A SIMMER code, which have been developed mainly to simulate the event progression in transition phase (TP), has limitations to deal with complex reactor core geometry, such as the annular fuel pellet and the axial heterogeneous core, which are also being considered for future SFRs.
- ✓ To solve these issues, an improved and detailed fuel-pin model has been developed at JAEA as a part of a new SIMMER-V code, a joint research program being conducted in collaboration with CEA.

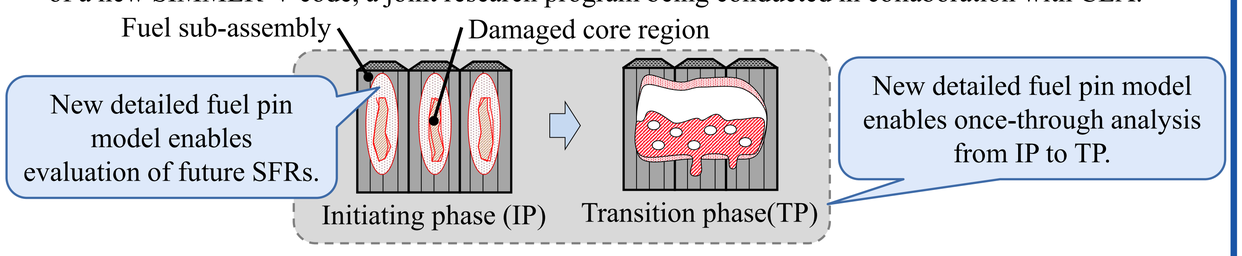

Event progression of SA in SFRs

II. NEW DETAILED FUEL PIN MODEL

II-1. Organizing physical phenomena

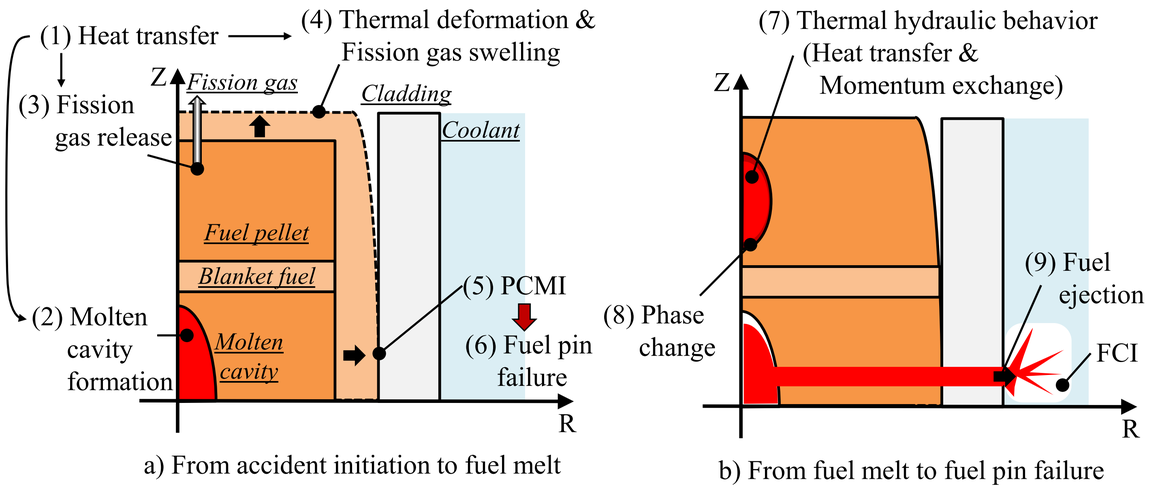

Elementary phenomena related to fuel pin failure.

II-2. Modeling physical modules

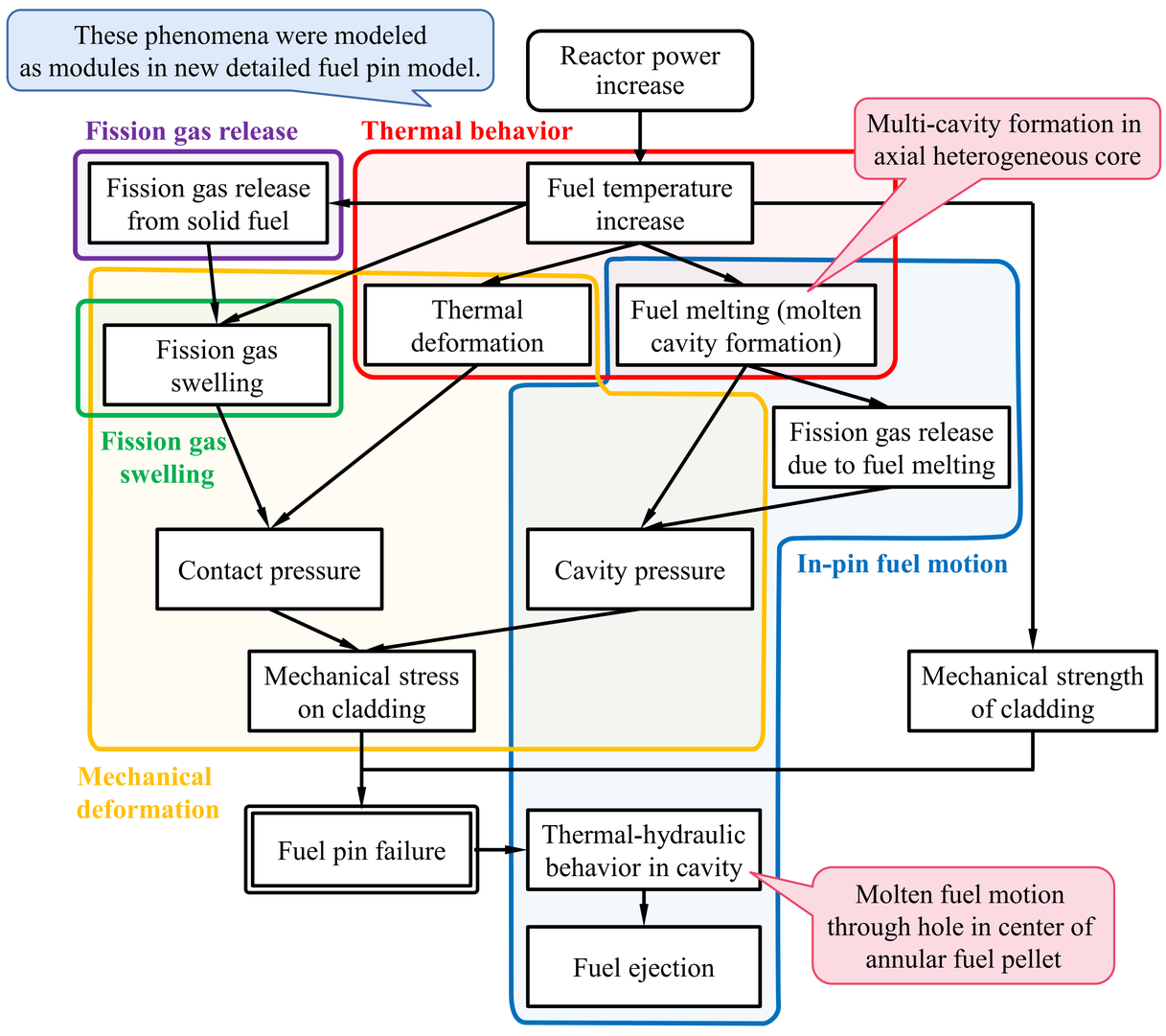

Inter-relationship of elementary phenomena related to fuel pin failure and extracted key physical phenomena

III. VERIFICATION

III-1. Verification Matrix

Verification matrix for the new fuel pin model.

	Calculation elements											
	Thermal calculation			Fuel pin failure calculation					In-pin fuel motion calculation			
Key physical phenomena (Modules)	Heat transfer	Thermal deformation	Molten cavity formation	Fission gas release	Fission gas swelling	Stress calculation	Contact pressure	Cavity pressure	Heat transfer in cavity	Momentum exchange	Phase change	Fuel ejection
Thermal behavior	O		O									
Fission gas release	X		X	O								
Fission gas swelling	X		X	X	O							
Mechanical deformation	X	O	X	X	X	O	O	O				
In-pin fuel motion	X	X	X	X	X	X	X	X	O	O	O	O

"O" indicates the calculational element to be verified in the relevant test case.
"X" indicates the calculational element that has already been verified in the other test case.

III-2. Verification Result 1: Test case for cladding deformation behavior

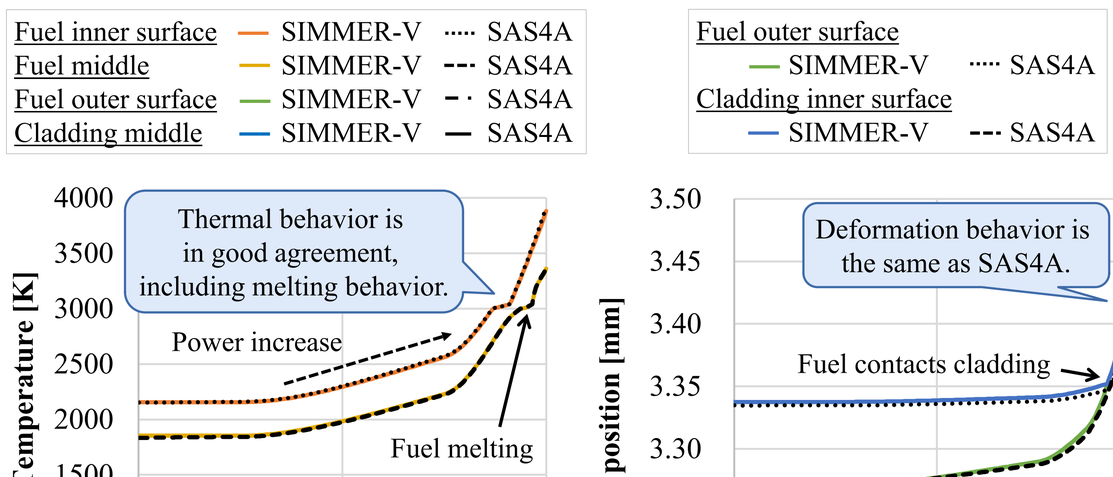

Temperature changes in different temperature nodes at core midplane.

Fuel and cladding deformation behavior.

III-3. Verification Result 2: Test case for fuel ejection behavior

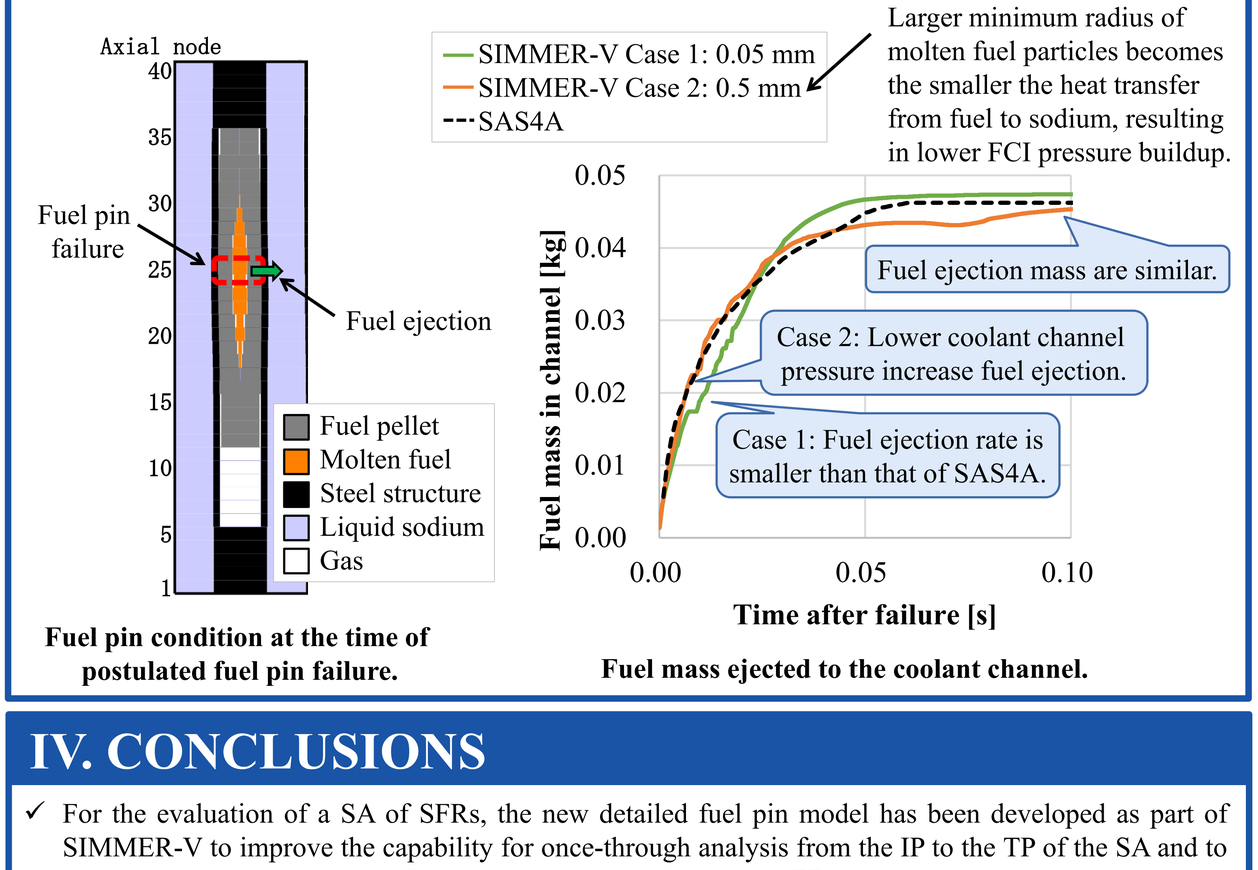

Fuel pin condition at the time of postulated fuel pin failure.

Fuel mass ejected to the coolant channel.

IV. CONCLUSIONS

- ✓ For the evaluation of a SA of SFRs, the new detailed fuel pin model has been developed as part of SIMMER-V to improve the capability for once-through analysis from the IP to the TP of the SA and to be applicable to wider range of core and fuel designs for future SFRs.
- ✓ The verification analysis for each module was performed based on the verification matrix by comparison with the existing analytical code, and it was confirmed that physically consistent results were obtained. This allowed the new detailed fuel pin model to simulate the fuel pin behavior from the start of an accident with the fuel pin failure in the IP to the subsequent TP by SIMMER-V.

Acknowledgments: Present study includes the results of technical development program on a fast reactor for demonstration entrusted to JAEA by Ministry of Economy, Trade and Industry.

Analysis of the combustion risk mitigation inside the containment during a postulated severe accident in a PWR using the code package AC²

Miriam Müer and Marco K. Koch
Ruhr-Universität Bochum (RUB)
Plant Simulation and Safety Group (PSS)
Universitätsstr. 150, 44801 Bochum, Germany
Miriam.mueer@pss.rub.de and marco.koch@pss.rub.de
ORCID-ID: 0000-0002-5124-828X and 0000-0001-7260-5250

ABSTRACT

In the framework of the European research project "AMHYCO" the combustion risk inside the containment is investigated. Therefore, different severe accident scenarios are simulated and analyzed. A new nodalization for a generic containment of a pressurized water reactor (PWR) type KWU has been created within the project. Furthermore, different combustion mitigation measurements are postulated and the influence on the composition of the containment atmosphere is investigated.

A loss of coolant accident (LOCA) with a postulated failure of almost all active safety systems is conducted. During the in-vessel phase of the accident around 600 kg hydrogen are produced and released to the containment. During the ex-vessel phase of the accident additional 800 kg hydrogen and 7,000 kg carbon monoxide are released by molten corium concrete interaction. Both, the rising pressure inside the containment due to the steam release as well as the potential combustion risk due to the presence of combustible gases, may jeopardize the containment integrity.

The PWR KWU containment is divided into 12 zones, of which the dome zone with 42,654 m^3 is the largest zone. The break during the LOCA accident is postulated to occur on the cold leg at the pressurizer loop in the north-sided steam generator room. The compartments are connected with each other either via doors, flaps or open connections to enable both gas and liquid transportation. To reduce the hydrogen concentration inside the containment, 40 generic box-type passive autocatalytic recombiners (PARs) are installed all over the compartments. To investigate the PAR efficiency several simulations with different PAR performance rates (0 %, 50 %, 75 %, 100 %) are conducted. The varying PAR performance rate is intended to simulate the case that recombiners are not fully available, for example due to poisoning or maintenance. The PARs catalytically recombine H_2 and CO in presence of oxygen. In the framework of the AMHYCO project, a new generic correlation which coFconcentransiders low-oxygen and CO-rich atmospheres is developed and used for the simulations. The PARs work passively, which leads to an immediate recombination after the onset of H_2 and CO from the in-vessel circuit to the containment.

The results show, that even with only 50 % PAR performance the H_2 and CO volumetric concentration in the dome compartment decrease from 18.9 % respectively 6.7 % to 14 % respectively 6.1 % at the highest peak. With increasing PAR performance up to 75 % and 100 % the H_2 concentration decreases further to 12 % and 10 %. The CO concentration shows a similar decrease to 5.5 % (75 % PAR performance) and 5.2 % (100 %). (Figure 1 and 2)

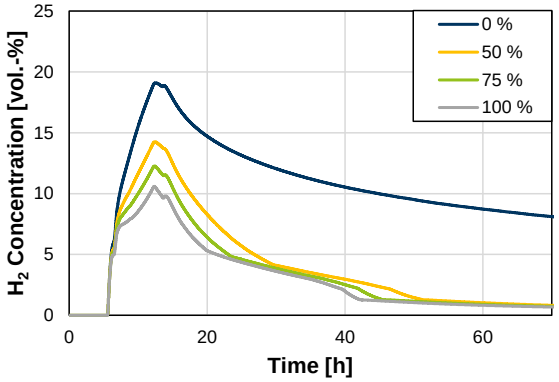

Figure 1: H_2 Concentration in Dome

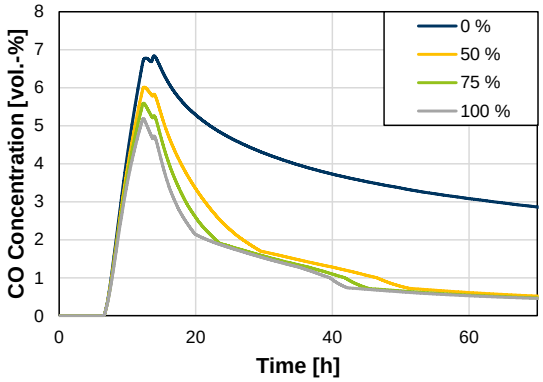

Figure 2: CO Concentration in Dome

As a result of the recombination, the total mass of the substances in the dome, due to its largeness used as the reference zone, decreases significantly. At the peak point, right after the melt in the cavity is flooded, the H_2 mass is halved from 1,000 kg without recombiners to 480-680 kg, depending on the performance. At the same time the present CO mass is lowered from 1,100 to 1,850 kg of CO. With ongoing accident progression, the burnable gas masses further decrease significantly to a minimum of 62 kg (H_2) and 550 kg (CO). (Figure 3 and 4)

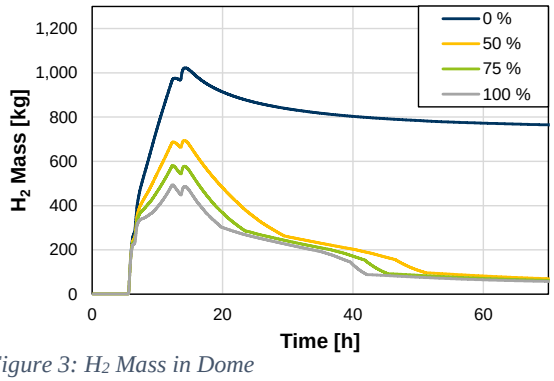

Figure 3: H_2 Mass in Dome

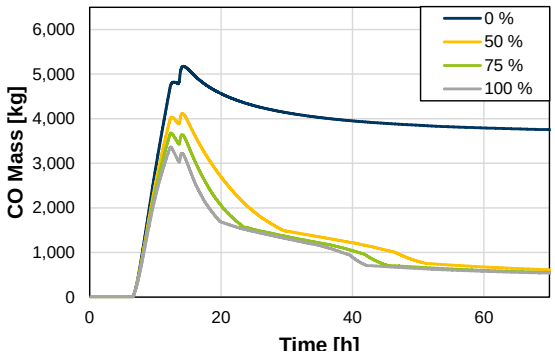

Figure 4: CO Mass in Dome

A comparison of the Shapiro diagrams (Figure 5 a-d) clearly shows that the flammability risk is strongly reduced. While the gas mixture in the dome during the unmitigated scenario remains in the detonation region as well as the burning region for a long period of time, the flammability in the mitigated scenarios is highly reduced. While the detonation region is still touched when only 50 % of the available PAR capacity is used, the 75 % and 100 % variants have a very similar progression. Here, the gas mixture is only in the combustion zone for a relatively short period of approximately 8 hours.

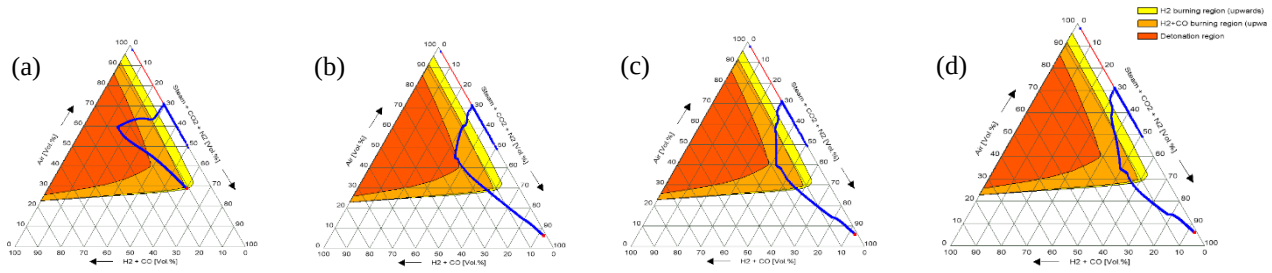

Figure 5 a-d: Shapiro Diagrams for 0 % (a), 50 % (b), 75 % (c) and 100 % (d) PAR Performance

The simulations are performed using the code package AC² 2021.1 containing the accident analysis codes COCOSYS developed by GRS.

KEYWORDS: *AC², Plant Simulation, Combustion Risk, Hydrogen, Passive Autocatalytic Recombiners*

Acknowledgement:

AMHYCO has received funding from the Euratom research and training programme 2019-2020 under Grant Agreement n°945057. The content of this paper reflects only the author's view. The European Commission is not responsible for any use that may be made of the information it contains.

SEAKNOT
ERMSAR 2024
11th Conference on
SEVERE ACCIDENTS RESEARCH
May 13-16, 2024 – Stockholm, Sweden

Plant Simulation and Safety
Prof. Dr.-Ing. Marco K. Koch

Analysis of the combustion risk mitigation inside the containment during a postulated severe accident in a PWR using the code package AC²

MIRIAM MÜER
Supervised by Marco K. Koch

Introduction

In the framework of the European research project "AMHYCO" the combustion risk inside the containment is investigated. Therefore, different severe accident scenarios are simulated and analyzed. A new nodalization for a generic containment of a pressurized water reactor (PWR) type KWU has been created within the project to provide comparability between different simulation codes. Furthermore, different combustion mitigation measurements are postulated and the influence on the composition of the containment atmosphere is investigated.

Accident Scenario

- Loss of Coolant Accident (LOCA) with postulated failure of nearly all active safety systems
- Core uncovery and damage leads to RPV failure
- H_2 and CO release from in-vessel oxidation and ex-vessel MCCI to containment atmosphere
- Rising containment pressure due to large steam mass release
- Combustion risk increases due to presence of combustible gases
- Containment integrity may be jeopardized

Containment Build Up [1]

- Proposed generic containment with 12 compartment zones
- ~ 75.000 m³ volume
- 40 generic box type passive autocatalytic recombiner (PARs) distributed over the containment rooms
- New generic AMHYCO correlation for PARs considers low-oxygen and CO-rich atmospheres

Simulations

- Investigation of PAR influence on containment atmosphere
- 4 Simulations with varying PAR performances to consider unavailability caused by poisoning or maintenance
- 0 % (unmitigated), 50 %,75 % and 100 % (40 PARs fully available) PAR perfomance

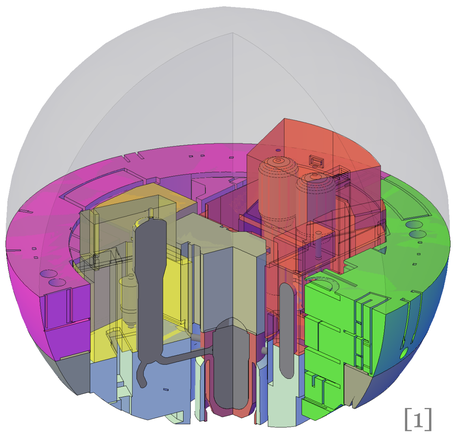

[1]

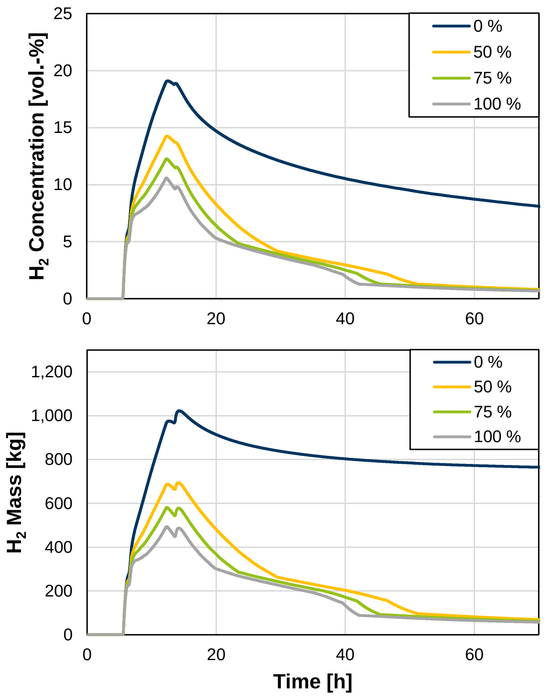

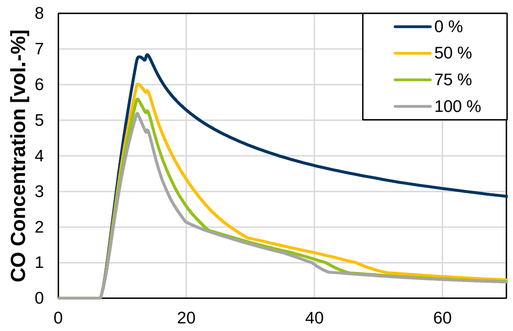

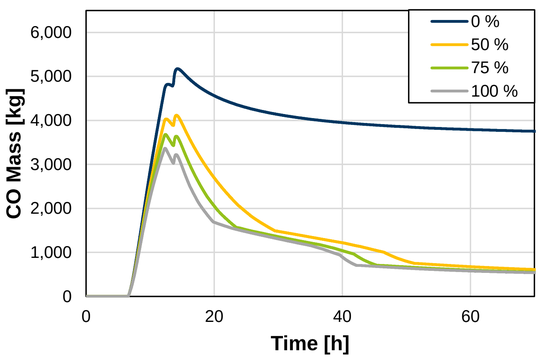

Selected Results

- Measurement zone: Dome as largest compartment
- The higher the PAR performance, the lower the H_2 and CO concentrations and masses
- Additionally, the containment pressure drops about half a bar in the late phase progression
- Shapiro diagrams show a strongly reduced flammability risk

- The simulations are performed using the code package AC² 2021.1 containing the accident analysis codes COCOSYS developed by GRS.

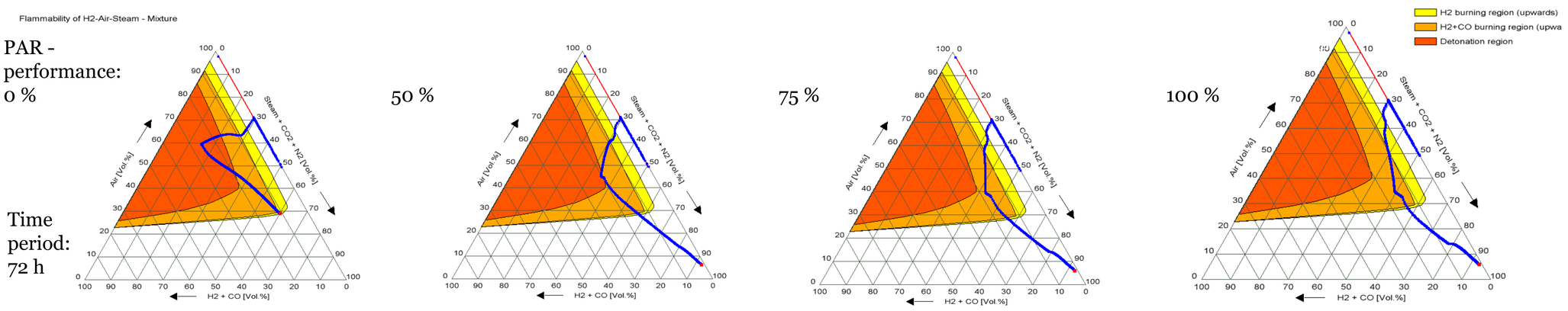

Conclusion

While the gas mixture in the dome during the unmitigated scenario (0 %) remains in the detonation region as well as the burning region for a long period of time, the flammability in the mitigated scenarios is highly reduced. With 50 % PAR availability the detonation region is still slightly reached. Even with higher PAR performances the burning region is touched, but only for a shorter period of around 8 h, after that the combustion risk in the containment atmosphere is fully mitigated.

IN COOPERATION WITH:

AMHYCO
Enhancing H_2 & CO Combustion Risk Management

AMHYCO has received funding from the Euratom research and training programme 2019-2020 under Grant Agreement n°945057. The content of this paper reflects only the author's view. The European Commission is not responsible for any use that may be made of the information it contains.

References

[1] L. Serra et al., "Development of a detailed 3D CAD model of a generic PWR-KWU containment as a basis for a better assessment of H2/CO combustion risk," in Proc. European Nuclear Young Generation Forum (ENYGF'21), Tarragona, Spain, 2021.

Miriam Müer
PhD Student
Plant Simulation and Safety Group
Ruhr-Universität Bochum
Universitätsstr. 150
44801 Bochum
Germany
Tel: +49 234 32 29417
Email: mueer@pss.rub.de
ORCID-iD: 0000-0002-5124-828X

Uncertainty quantification analysis with radiological consequences for a loss of cooling accident in a spent fuel pool

Matteo D'Onorio[1], Tommaso M. Glingler[2], Fabio Giannetti[3] and Gianfranco Caruso[4]

[1]Sapienza University of Rome, C.so Vittorio Emanuele II 244, 00186, Rome, Italy, matteo.donorio@uniroma1.it
[2]Sapienza University of Rome, C.so Vittorio Emanuele II 244, 00186, Rome, Italy, tommaso.glingler@uniroma1.it
[3]Sapienza University of Rome, C.so Vittorio Emanuele II 244, 00186, Rome, Italy, fabio.giannetti@uniroma1.it
[4]Sapienza University of Rome, C.so Vittorio Emanuele II 244, 00186, Rome, Italy, gianfranco.caruso@uniroma1.it

Contact email: matteo.donorio@uniroma1.it

Abstract

In the current field of analyzing severe accidents in nuclear reactors, incorporating a robust methodology for quantifying uncertainties has become essential. The intricacies of the physical phenomena occurring during a severe accident give importance to acknowledging and addressing the inherent unpredictability and variations that can influence outcomes.

The presented uncertainty quantification analysis has contributed to the Management and Uncertainties of Severe Accidents (MUSA) project, where a dedicated work package was devoted to quantify uncertainties affecting accident analyses in a Spent Fuel Pool. This effort also involved the evaluation of the potential advantages that can arise from quantifying these uncertainties in reducing radiological consequences.

A detailed modeling of a boiling water reactor spent fuel pool has been developed using the MELCOR code. Radionuclide classes have been duplicated to model decay heat distribution between hot and cold fuel assemblies. The effects on the accident progression of physical phenomena, such as core degradation, heat transfer, and radionuclide transport, are investigated by selecting 29 uncertain input parameters. Using the RAVEN tool, a random Montecarlo sampling strategy has been adopted to propagate uncertainties all over the input space. The source term and the selected uncertainty parameters are examined in a post-processing phase with a sensitivity study to evaluate and rank possible correlations.

The accident sequence designated for the analysis is a loss of cooling accident. All emergency and mitigation systems are unavailable, resulting in the degradation of fuel racks containing fresh, hot, and cold fuel and irradiated core internals. The MACCS code software, developed to assess the repercussions of severe accidents on neighboring environments, has been used for dispersion modeling and dose rate computations.

The study's primary findings on uncertainty quantification, combined with other MUSA project outcomes, can significantly enhance the assessment's reliability. This is achieved through a comprehensive grasp of potential risks and vulnerabilities, empowering decision-makers with informed insights for proactive risk mitigation and management strategies.

Keywords: SFP, Uncertainty Quantification, Sensitivity, Radiological Consequences, RAVEN

THS-15 Experimental facility: Effect of Surface roughness on CHF values

David Batek, Jiri Zdarek, and Miroslav Kotouc
UJV Rez, a.s.
Hlavni 130, 25800 Husinec-Rez
David.batek@ujv.cz; Jiri.zdarek@ujv.cz; Miroslav.kotouc@ujv.cz

SUJB (owner/user of described results)
Czech National Regulatory Body
Senovazne namesti 1585/9, 11000 Praha
Sujb.cz; podatelna@sujb.cz

ABSTRACT

The THS-15 (Thermal-Hydraulic Stand, est. design 2015) test facility was built in ÚJV Řež in 2018 to perform thermo-hydraulic experiments to verify the cooling capacity of the VVER-1000 reactor during a severe accident using the In Vessel Melt Retention (IVMR) strategy. As part of the international IVMR project under H2020 (IVMR - Grant Agreement 662157), a series of experiments have been performed on the THS-15 facility. In the first phase of the experiments, tests were performed to confirm that the reactor pressure vessel can be cooled from the outside under the conditions expected in the final phase of a severe accident (e.g., no boiling crisis, no pressure above the limit, etc.). These experimental conditions were initially determined thanks to analytical support and the results of severe accident calculations. The experiments of the first phase were successful in terms of the functionality of the IVMR strategy (for VVER-1000), and therefore the second phase of the tests was started, in which the critical heat flux (CHF) was studied according to specific conservative conditions. When comparing the CHF and the heat flux distribution around the RPV, it was possible to establish the so-called “safety margin to the CHF.”
As the CHF values during the IVMR depend on many factors, possible improvements were considered for the third phase of the tests in order to increase the CHF values (through technical measures). The first measure assessed was to perform experiments with a deflector (a structure along the RPV that allows the intensification of the coolant flow). The results of the CHF values obtained during the experiments with the deflector were on average 20% higher than in the tests with the configuration without deflector.
As part of the following national project (named "Increasing the Safety Margin of IVMR Strategy Applications for VVER 1000", number TITSSUJB830) - the influence of another factor on the CHF values was investigated, namely the effect of different roughness of the RPV surface. The CHF values measured during the experiments in the original device configuration and then on the device where the RPV surface roughness was increased were compared.

KEYWORDS
Critical Heat Flux (CHF), pool boiling, In Vessel Melt Retention (IVMR), External Reactor Vessel Cooling (ERVC)

1. INTRODUCTION

The objective of the national (TITSSUJB830) project was to perform analytical, experimental and engineering activities to evaluate the applicability of the IVMR strategy to the VVER-1000 reactor. The summary report concluded that IVMR could not be implemented on an operating plant, or that technological modifications would be too expensive, and that the resources to ensure long-term operation to assure the

safety of the nuclear unit could be used more efficiently. The situation is different when the plant (VVER-1000) is in the design or construction phase. In this case, appropriate modifications to safety systems can ensure the success of the IVMR strategy. [1]
The main activities of the above-mentioned project can be divided into three parts. Analytical activities to specify the boundary conditions of the experiments and to validate the computational models based on the experimental data. Experimental activities to verify the effectiveness of ERVC and compare CHF values for untreated surface/surface (treated with Sponge Jet technology) with higher surface roughness. Overall assessment of the applicability of IVMR on the VVER-1000 (including a Feasibility Study of Sponge Jet application to the RPV surface).
This paper mainly presents the results of the experimental activities, assuming the effect of RPV surface roughness on CHF values: in the case of low void fraction in the coolant, an increase in the surface roughness of the RPV leads to an increase in the initiation sites for nucleate boiling. Increased heat removal efficiency leads to an increase in CHF values. However, if the RPV surface is cooled by a developed boiling process with a high fraction of steam, the increased surface roughness may disturb the water film on the RPV surface and cause earlier dry-out. Thus, the effect of increased surface roughness on CHF values can be both positive and negative, depending also on other parameters affecting CHF. [2], [3]
All experimental work was performed on the THS-15 device, see Figure 1 and 2 for a schematic.

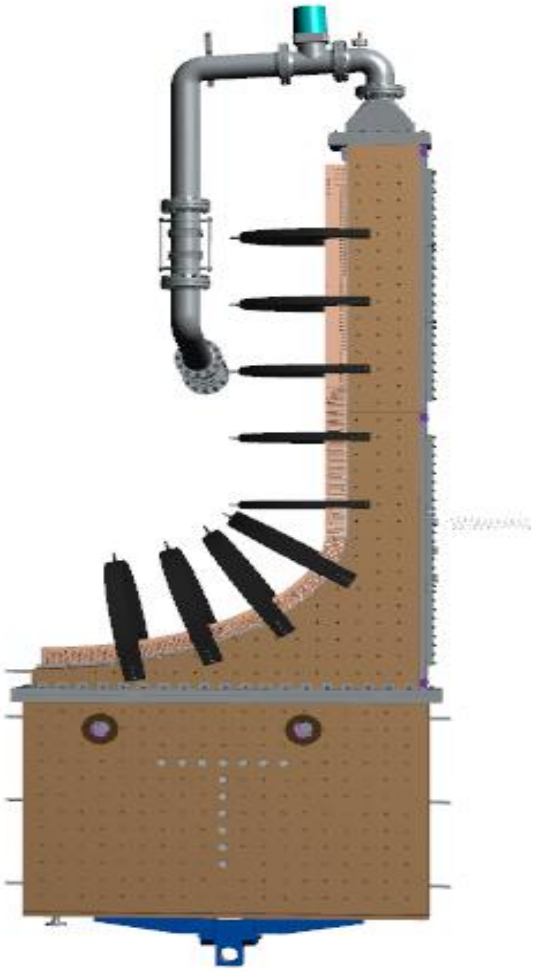

Figure 1. 2D model of THS-15 experimental facility

Experimental channel (in original non-modified configuration) consists of two main parts connected by a flange. Lower part (approx. 6 tons) is representing the cavity under the WWER-1000 RPV. Upper part (approx. 12 tons) represents the RPV and its external surface and a gap between RPV and side wall of a cavity. Heat flux from the melted corium to the vessel wall and to the water in a cavity is generated by heating panels. Heating panels are made from copper blocks explosively welded with RPV steel and then welded to the construction of experimental channel. Copper matrix is filled with electric cartridge heaters. Shaped heating panel is divided into 19 heating sections where each section can be regulated separately. Parameters of heating panels are summarized in Table I below.

Table I. Sample table: accuracy of nodal and characteristic methods

Parameter	Value
Number of heating segments	19
Number of heating cartridges	1212
Installed electric power	1,5 MW
Reachable heat flux	1,6 – 2,2 MW/m^2
Thickness of copper	150 mm
Thickness of RPV steel	3 mm
Effectiveness of heaters (electric → thermal power)	Min. 92 %

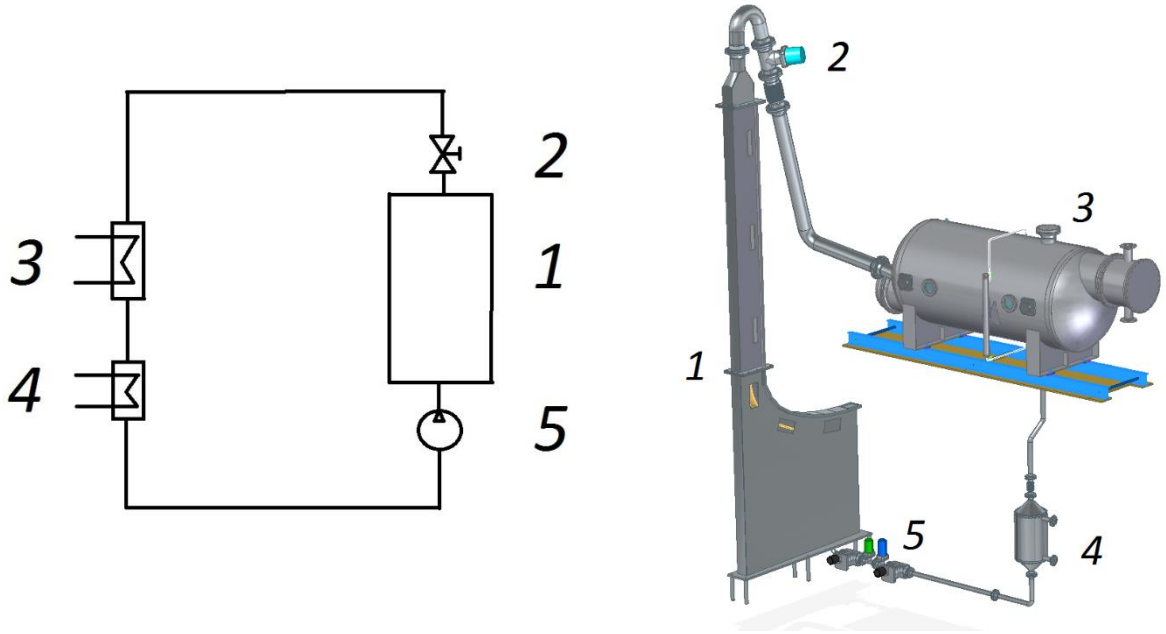

Figure 2. Basic scheme and 3D model of THS-15 experimental facility.

In reactor cavity model /1/, water circulates on the natural circulation principle. Part of the water evaporates and goes through the valve /2/ into the condenser /3/ - this part simulates the steam release around the supporting parts of the reactor into the containment. At the same time, the condenser serves as a reservoir for the cooling medium of the primary - experimental circuit. The condensate goes to the sub-cooler /4/, where it can cool down from the saturation temperature to 20°C - 30°C. The cooled water is transported by the primary pump /5/ back to the reactor cavity model /1/.

The experimental channel is designed so that, as much as technologically possible, it corresponds to the actual conditions of the space under the semi-elliptical bottom of the RPV in terms of the inlet and outlet of the cooling medium, in terms of size and volume, in the chosen width of the section. The height of the pressure vessel therefore corresponds to the proportions in the RPV cavity of the VVER 1000 reactor in a ratio of 1:1. The width of the pressure vessel corresponds to half the diameter of the real space in the cavity. The width of the cutout (width of the channel) was chosen for technological reasons to be 150 mm. Demineralized water is usually used as a coolant, with a maximum possible pressure of 0,6 MPa and a temperature of 200 °C [4].

2. ANALYTICAL SUPPORT AND EXPERIMENTAL RESULTS [1]

2.1. Summary of the results of the computational analyses

The structure or sequence of the analytical work is represented by the following 5 consecutive points:

1. Perform ASTEC code calculation of severe accident (SA) scenarios of the large LOCA or SBO type with a fixed boundary condition on the outer surface of the RPV (constant temperature and heat transfer coefficient) in order to fix the maximum heat flux achieved. This maximum is obtained in the form of an axial heat flux profile and is used to input the temperature (power) profile to the THS-15 facility to perform a set of confirmatory experiments.
2. ASTEC code check recalculation of the calculated maximum heat flux, performed by the Fluent code. The CFD code Fluent contains detailed flow models, including a corium in which it simulates turbulent flow using approximation models. By recomputing with the fine and detailed Fluent code, it is verified that the heat flux calculated by the ASTEC code excludes locally or temporally constrained heat flux peaks that significantly exceed the heat flux maximum generated by the ASTEC code simulation. See Figure 3.
3. Validation of the ASTEC code, or its thermo-hydraulic module CESAR, on the experiment performed on THS-15. Validation of the calculation of the thermo-hydraulic behavior is carried out by comparing the measured and calculated temperatures from thermocouples located below the surface of the welded steel plate on the copper heated block forming the base of the THS-15 facility. See Figure 4
4. Finding a suitable parameter to simulate the changing heat transfer coefficient on the RPV surface during refrigerant cleaning and surface roughening. This parameter turned out to be the thermal conductivity λ ($W/m^2.K$) of the outer layer of steel on the RPV surface. Tuning of this parameter was again done by tuning the ASTEC code (by modifying λ) to the thermocouple outputs from measurements made on the THS-15 with clean coolant and applied surface roughening using Sponge jet technology (SJ30).
5. Performing an integral, i.e., "coupled" calculation with the ASTEC code for the less favorable (i.e., envelope) SA sequence, which appeared to be a large LOCA. The scenario development into SA was computed in variants with and without the application of SJ30, respectively, to appreciate the benefit of surface roughening specifically. This integral envelope scenario was used to verify the applicability of the IVMR strategy for the VVER-1000/320 reactor (Temelín NPP).

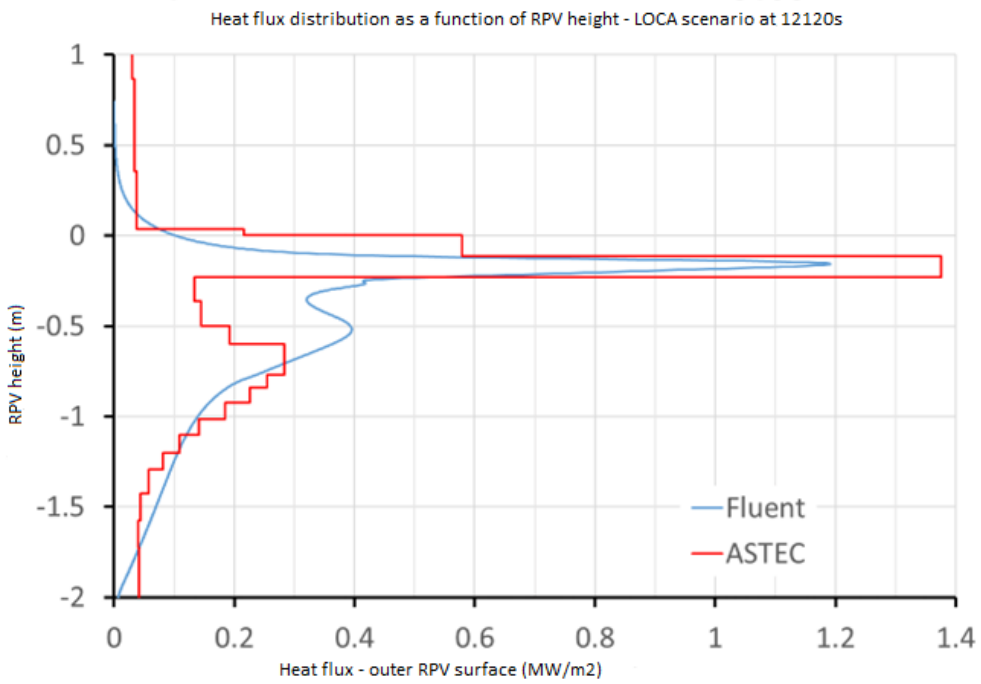

Figure 2. Heat flux profile on the outside of the reactor vessel

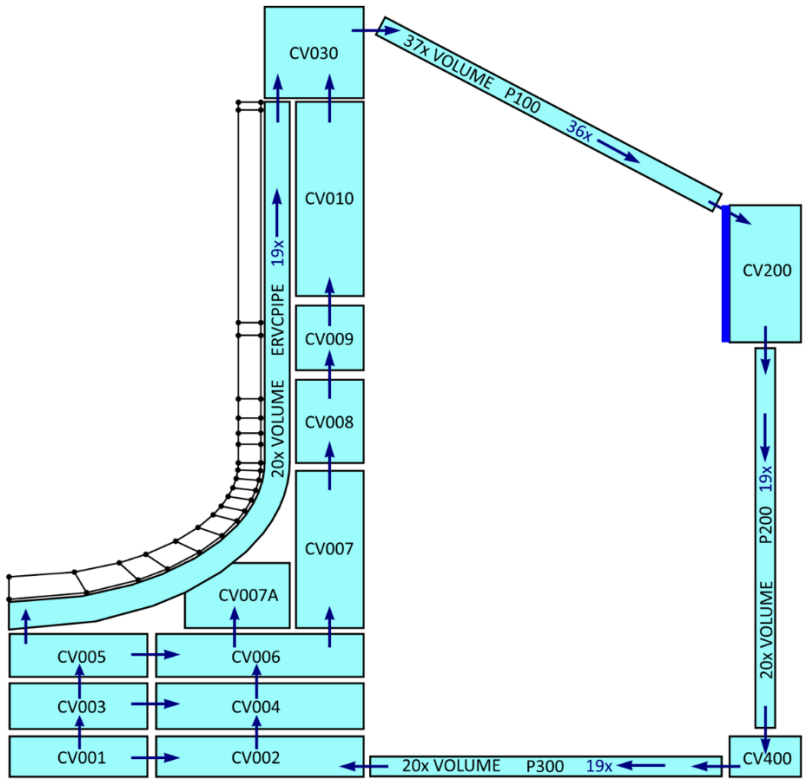

Figure 4. Nodalization of the task (experiment performed on THS-15) prepared to verify the thermo-hydraulic capability of the ASTEC code to model two-phase flow around RPV in a flooded reactor cavity when applying the IVMR strategy. The individual rectangles represent the spatial discretization nodes of the THS-15 facility.

2.2. Summary of the experimental results

2.2.1. Boundary conditions for experiments

The problem of achieving the critical heat flux and obtaining the CHF rank is quite complex and is usually verified experimentally according to the specific application (e.g., calculations of steam generators, cooling of fuel rods, etc.). A number of factors affect the achievement of the critical heat flux (the heat flow at which the boiling crisis occurs) CHF, and the following conditions are particularly important for determining the CHF values under IVMR:

- Geometry of the space for external cooling of the RPV – dimensions and shape of the RPV, geometry of the reactor cavity.
- Conditions and solutions for coolant inlet and steam release in the reactor cavity, pressure in the system.
- Specific scenario of a severe accident, heat flux density distribution along the RPV, etc.

Other factors affecting the CHF values can be, for example, the condition and roughness of the RPV surface, the presence of impurities (solid, chemically bounded) in the coolant, etc. In general, it can be assumed that CHF values are influenced by the roughness value of the RPV surface in addition to other factors. The surface of a material with a higher roughness slightly increases the total area from which heat is removed to the coolant, but in particular more effectively disrupts the formation and formation of large bubbles, or so-called vapor film, which cause a boiling crisis. A similar effect (preventing the formation of large bubbles and vapor layers at the RPV surface) can be achieved by suitable additives to the coolant. However, it is necessary to control the amount and composition of additives quite precisely because undesirable components or high concentrations (sediments, impurities) can reduce CHF values.
THS-15 boundary conditions set (see Figure 5):

- Heat flux density profile along RPV.
- Pressure in experimental circuit.
- Inlet water temperature
- State of the RPV surface - without treatment, cleaned (from corrosion), with increased roughness.

For the experiments, the result of the calculations, performed by the ASTEC code, considering the LOCA accident scenario was used. The development of a severe accident, as well as the heat flux (HF) density profile, changes over time, and therefore the HF at a specific time was used for the experiments, which is interesting from the point of view of checking the maximum value (peak) of the HF. Concretely, the development of HF from the RPV to the cooling water at a time of 12,120 s was used, with the maximum peak of the HF being located in the cylindrical part of the RPV, with a value close to 1.4 MW/m^2.

THS-15 heating system consists of 19 separate heating sections, the analytically calculated HF needs to be appropriately converted according to the capabilities of the experimental facility. The power profile (referred to the area of the RPV sample) across the height of the vessel thus consists of 19 partial power units set as close as possible to the conditions according to the calculation results. The total delivered heat output transferred from the heating panels to the coolant respects the values of the heat flux peaks and at the same time the ratio of the residual output that is generated inside the RPV at the given time. The setting of the HF to the individual heating panels is carried out by setting the electrical input for each panel with a known size of the RPV sample area (the area in contact with the coolant). Due to heat losses, the thermal output is 8% lower than the value of the set electrical input.

Due to the technical capabilities of the experimental facility, the heat flux profile from the calculation was modified for the experiments so that the peak of the HF was simulated at a lower level than calculated peak (see Figure 5).

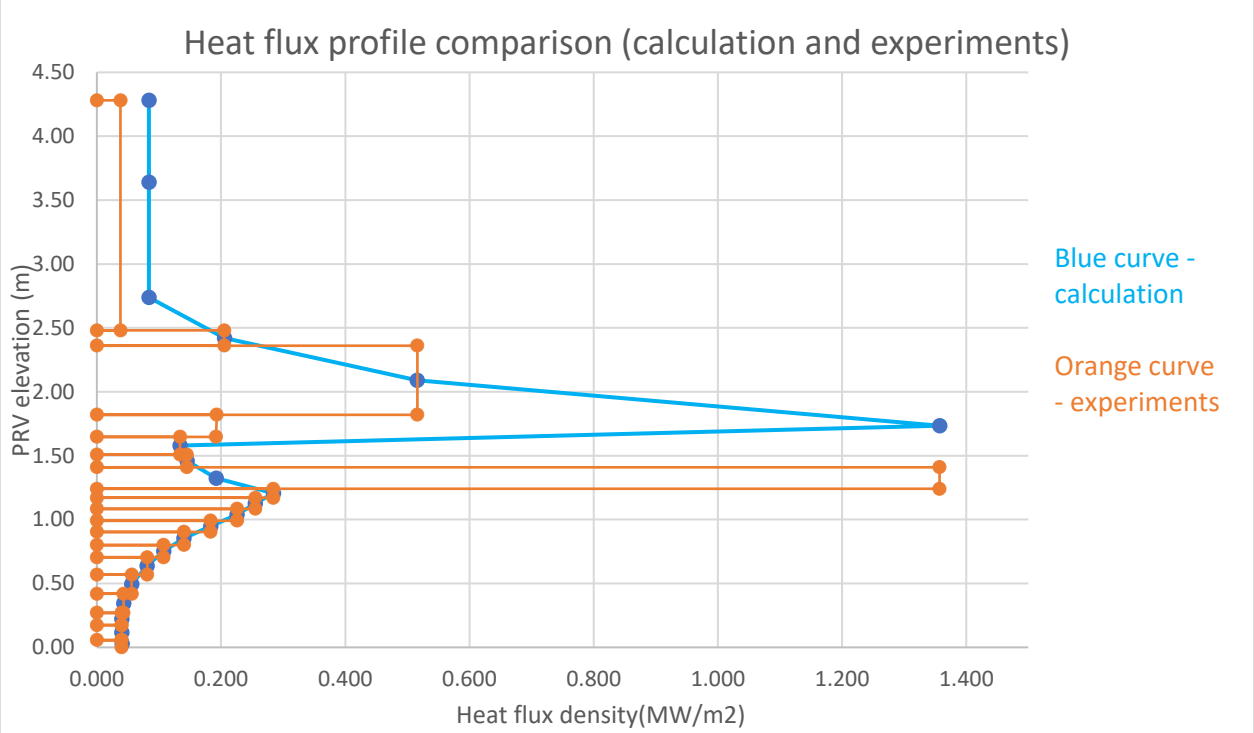

Figure 5. HF distribution (ASTEC calculation and experimental set comparison)

To obtain the most possible conservative CHF values during the experimental measurements, other boundary conditions were also set (in addition to the HF profile) for testing.

Pressure in the system: for the main phase of the experiments, the atmospheric pressure of the cooling medium at the outlet of the experimental channel was maintained. The position of regulation valve determining the flow area for steam release from the experimental channel was set to 100% open so that there was no pressure increase at the exit from the experimental channel.

No sub-cooling: The temperature of the coolant at the entrance to the experimental channel was not regulated and during the experiments it was usually around 70-90 °C. Demineralized water was used as the coolant.

State of RPV surface treatment: The RPV surface condition was modified during the experimental program - from the original surface condition after 2 years of previous experimental projects (corroded surface), through the "cleaned" surface condition (using the SJ80 technology) to the final surface condition with increased roughness (using the SJ30 technology). At the start of operation of THS-15 (in 2018), the surface roughness of the steel was in accordance with the design documentation of the RPV VVER-1000, at Ra 6.3. However, during operation, surface corrosion of the RPV steel gradually occurred and for the first experiments (Experiment E1) in this project an average surface roughness of Ra = 12 was measured. The aim of the application of Sponge Jet 80 technology was to clean the RPV surface of corrosion but without modifying the surface roughness, and so during Experiments E2 and E3 the average surface roughness remained at Ra = 12. Subsequently, Sponge Jet 30 technology was used to increase the surface roughness and an average RPV surface roughness of Ra = 16 was measured in experiments E4 to E6.

2.2.2. Safety margin to the CHF

One of the basic physical conditions for the success of the IVMR strategy is not to exceed the critical heat flux during the cooling of the outer wall of the RPV:

$$HF < CHF \tag{1}$$

From the ratio of HF and CHF values, the so-called Safety margin to the CHF (SMCHF [%]) can then be evaluated (for a given RPV position, according to the same initial and boundary conditions), while the following applies:

$$SM_{CHF} = \frac{CHF*100}{HF} - 100 \tag{2}$$

Example: If the value of the heat flux of 1 MW/m^2 was calculated at a given RPV location and the value of the critical CHF heat flux of 1.5 MW/m^2 was experimentally determined under the same conditions, then the SM_{CHF} value is 50 %.

2.2.3. Summary of performed experiments

In total, 6 experimental campaigns were carried out as part of Project (under Czech technology agency, No. TITSSUJB039), of which 5 campaigns were carried out according to the boundary conditions resulting from the results of analytical works (performed within above mentioned project) and 1 final additional experimental campaign according to the boundary conditions of the analyzes processed thanks to a European grant project (IVMR, EC Project Horizon 2020 No. 662157). During the experimental program, 3 surface states of the RPV sample were examined (originally corroded, cleaned by the SJ80 method, and roughened by the SJ30 method), with the main goal of evaluating the effect of the change in the surface state (or surface roughness Ra) on the CHF values. Important CHF values from 3 experimental campaign are shown in Table II below:

Table II. Important CHF values measured during the experimental program

	Heat flux	**Exp. 1**	**Exp. 2**	**Exp. 4**
Conditions	HF calculated by ASTEC	Corroded RPV surface, Ra 12	Cleaned RPV surface by SJ80, Ra 12	Roughened RPV surface by SJ30, Ra 16
Heating section	**HF value (MW/m^2)**	**CHF value (MW/m^2)**	**CHF value (MW/m^2)**	**CHF value (MW/m^2)**
1	0,04	0,42	0,42	0,47
2.1	0,04	0,53	0,51	0,57
3	0,04	0,65	0,61	0,65
5	0,08	1,00	0,87	1,00
9	0,23	1,35	1,50	1,89
13	0,15	1,92	2,15	2,33*

Note: If the value of (C)HF is marked * in the table, it is the maximum achievable heat flux value when the heating panel output was 100% and at the same time the CHF was not reached. The CHF value is realistically higher in the given case, but it cannot be accurately verified under THS-15 conditions.

From the point of view of the interpretation of experimental part of this project, the most important measured results are the CHF values obtained during the 1st and 4th experimental campaigns (comparison of tests on the original untreated surface of the RPV sample with the results of the sample after the final surface treatment with the Sponge Jet 30 technology, when the RPV surface´s roughness was increased). The data from these two experimental sets were therefore selected from the table of all important CHF measured values, which are supplemented in the Table III below with data on the approximate position of the measured location on the RPV (inclination, elevation from the bottom of the RPV). The Table III also evaluates the safety margin to the CHF. See also Figure 6.

Table III. Important CHF values and safety margin to the CHF

	RPV inclination	RPV elevation	HF	Experiment E1		Experiment E4		CHF ratio
Cond.			HF by ASTEC	Corroded RPV surface, Ra 12		Roughened RPV surface, Ra 16		
Heating section	**α (°)**	**H (m)**	**HF value (MW/m²)**	**CHF value (MW/m²)**	**SM_{CHF} (%)**	**CHF value (MW/m²)**	**SM_{CHF} (%)**	**E4/E1 (%)**
1	0-10	0,1	0,04	0,42	950	0,47	1075	+11,9
2.1	15	0,2	0,04	0,53	1225	0,57	1325	+7,5
3	25	0,4	0,04	0,65	1525	0,65	1525	0
5	45	0,7	0,08	1,00	1150	1,00	1150	0
9	70	1,1	0,23	1,35	487	1,89	722	+40
13	90	1,5	0,15	1,92	1180	2,33*	1453*	+21,4*
12 (peak)	90	1,4	1,35	1,92	42,2	2,33*	72,6*	+21,4*

Note: If the value of (C)HF is marked * in the table, it is the maximum achievable heat flux value when the heating panel output was 100% and at the same time the CHF was not reached. The CHF value is realistically higher in the given case, but it cannot be accurately verified under THS-15 conditions.

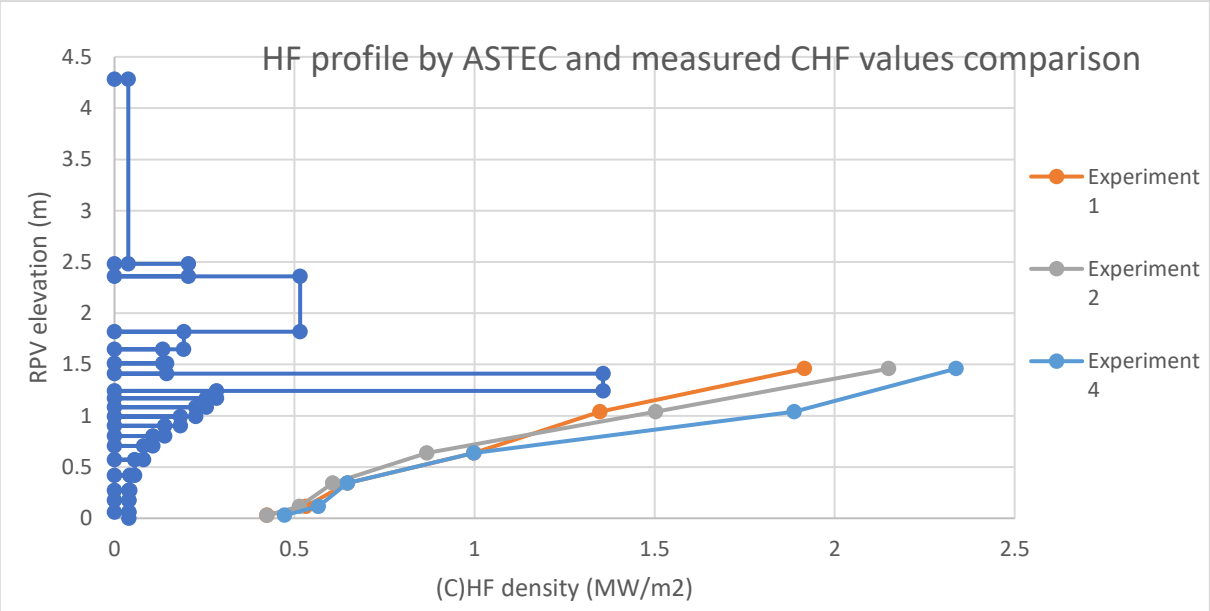

Figure 5. HF profile (ASTEC) and measured CHF values comparison

3. CONCLUSIONS

Experimental results showed that under the conditions of the THS-15 tests, changing the surface roughness (while maintaining the other boundary conditions of the tests) has an effect on the CHF values. The most important conclusions:

- Experiments show that the HF profile according to the ASTEC calculation can be cooled by the IVMR strategy with high reserves - safety margin to the CHF.
- At the critical point according to ASTEC calculation and simulation on THS-15, safety margin to the CHF measured was approx. 42 % during experiments with an untreated RPV surface and approx. 73% during tests with a roughened RPV surface.
- In the area of the elliptical part of the RPV, an increase of safety margin to the CHF was not clearly demonstrated.
- In the area of the cylindrical part of the RPV, an increase safety margin to the CHF was demonstrated by increasing the cooling efficiency by min. 20 %.

ACKNOWLEDGMENTS

Results of this work were funded thanks to Technology Agency of the Czech Republic, under the TACR Beta framework program – project No. TITSSUJB830.

REFERENCES

1. D. Batek, J. Zdarek and M. Kotouc, “In Vessel Melt Strategy Application for VVER 1000 reactor with modified roughness surface - Final Technical Report”, National TACR project No. TITSSUJB830, UJV Rez, 2022.
2. A. Walunj and A. Sathyabhama, “Effect of Surface Roughness on Pool Boiling Characteristics under Variable Heat Supply,” *Twelve International Conference on Thermal Engineering: Theory and Applications*, Gandhinagar, India, February 23-26, 2019.
3. B. Qiu, X. Liu et.al., “Effects of surface alteration on CHF related to IVR accident scenarios: A review,” *Elsevier*, Progress in Nuclear Energy 159 (2023).
4. D. Batek, J. Zdarek, V. Krhounek et.al., “Final report on full scale tests,” EC project Horizon 2020 No. 662157, Deliverable 4.4, UJV Rez 2019.

SEAKNOT
ERMSAR 2024
11th Conference on
SEVERE ACCIDENTS RESEARCH
May 13-16, 2024 – Stockholm, Sweden

THS-15 Experimental facility: Effect of Surface Roughness on CHF Values

DAVID BATEK, JIRI ZDAREK, MIROSLAV KOTOUC ET.AL.

Supervised by V. Krhounek

1. INTRODUCTION

The objective of the national (TITSSUJB830) project was to perform analytical, experimental and engineering activities to evaluate the applicability of the IVMR strategy to the VVER-1000 reactor. [1]
The main activities of the project can be divided into three parts. Analytical activities to specify the boundary conditions of the experiments and to validate the computational models based on the experimental data. Experimental activities to verify the effectiveness of ERVC and compare CHF values for untreated surface/surface (treated with Sponge Jet technology) with higher surface roughness. Overall assessment of the applicability of IVMR on the VVER-1000 (including a Feasibility Study of Sponge Jet application to the RPV surface).
This poster mainly presents the results of the experimental activities, assuming the effect of RPV surface roughness on CHF values: in the case of low void fraction in the coolant, an increase in the surface roughness of the RPV leads to an increase in the initiation sites for nucleate boiling. Increased heat removal efficiency leads to an increase in CHF values. However, if the RPV surface is cooled by a developed boiling process with a high fraction of steam, the increased surface roughness may disturb the water film on the RPV surface and cause earlier dry-out. Thus, the effect of increased surface roughness on CHF values can be both positive and negative, depending also on other parameters affecting CHF. [2], [3]
All experimental work was performed on the THS-15 device, see Figure 1.

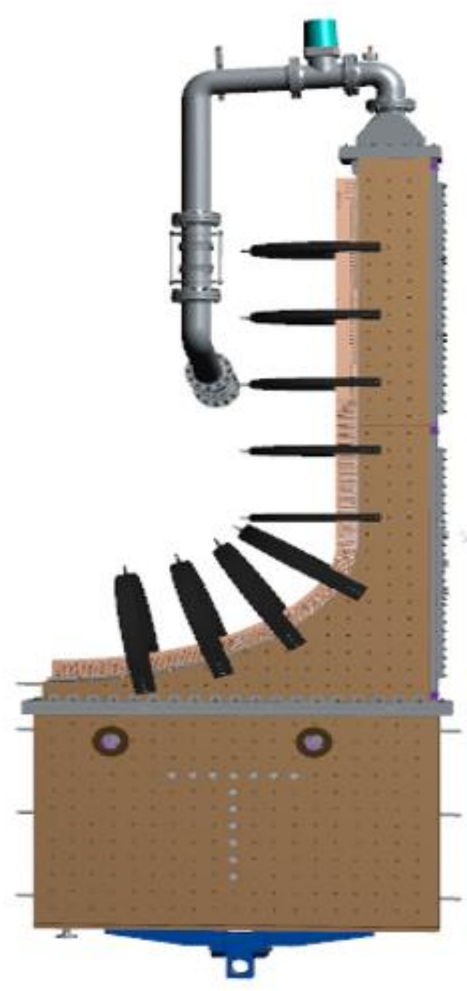

Figure 1. 2D model of THS-15 experimental facility

2. ANALYTICAL SUPPORT

The structure or sequence of the analytical work is represented by the following 5 consecutive points:

- Perform ASTEC code calculation of severe accident (SA) scenarios of the large LOCA or SBO type with a fixed boundary condition on the outer surface of the RPV (constant temperature and heat transfer coefficient) in order to fix the maximum heat flux achieved.
- ASTEC code check recalculation of the calculated maximum heat flux, performed by the Fluent CFD code. See Figure 2.
- Validation of the ASTEC code, on the experiment performed on THS-15.
- Finding a suitable parameter to simulate the changing heat transfer coefficient on the RPV surface during surface roughening. This parameter turned out to be the thermal conductivity λ (W/m².K) of the outer layer of steel on the RPV surface.
- Performing an integral, i.e., "coupled" calculation with the ASTEC code for the less favorable LOCA SA sequence. The scenario development into SA was computed in variants with and without the application of SJ30, respectively, to appreciate the benefit of surface roughening specifically. This integral envelope scenario was used to verify the applicability of the IVMR strategy for the VVER-1000/320 reactor (Temelín NPP).

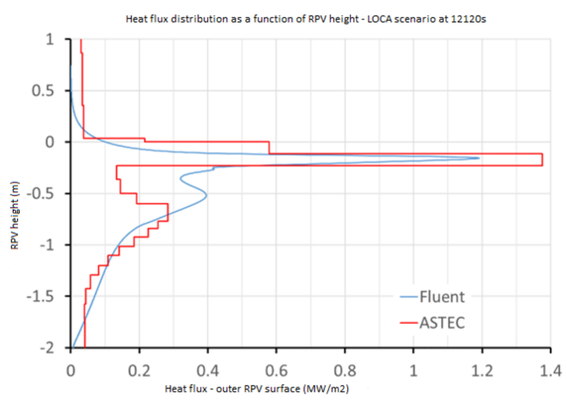

Figure 2. Heat flux profile on the outside of the reactor vessel

3. EXPERIMENTAL RESULTS

Boundary conditions for experiments
A number of factors affect the achievement of the critical heat flux (the heat flow at which the boiling crisis occurs) CHF, and the following conditions are particularly important for determining the CHF values under IVMR:

- Geometry of the space for external cooling of the RPV – dimensions and shape of the RPV, geometry of the reactor cavity.
- Conditions and solutions for coolant inlet and steam release in the reactor cavity, pressure in the system.
- Specific scenario of a severe accident, heat flux density distribution along the RPV, etc.

THS-15 boundary conditions set:

- Heat flux density profile along RPV → Figure 2
- Pressure in experimental circuit → atmospheric
- Inlet water temperature → 70-90 °C
- State of the RPV surface - without treatment, cleaned (from corrosion), with increased roughness.

Safety margin to the CHF
One of the basic physical conditions for the success of the IVMR strategy is not to exceed the critical heat flux during the cooling of the outer wall of the RPV:

$$HF < CHF \qquad (1)$$

From the ratio of HF and CHF values, the so-called Safety margin to the CHF (SM_{CHF} [%]) can then be evaluated (for a given RPV position, according to the same initial and boundary conditions), while the following applies:

$$SM_{CHF} = \frac{CHF*100}{HF} - 100 \qquad (2)$$

Example: If the value of the heat flux of 1 MW/m² was calculated at a given RPV location and the value of the critical CHF heat flux of 1.5 MW/m² was experimentally determined under the same conditions, then the SM_{CHF} value is 50 %.

During the experimental program, 3 surface states of the RPV sample were examined (originally corroded, cleaned by the SJ80 method, and roughened by the SJ30 method), with the main goal of evaluating the effect of the change in the surface state (or surface roughness Ra) on the CHF values. Important CHF values from 3 experimental campaign are shown in Table I below:

Table I. Important CHF values measured during the experimental program

	Heat flux	Exp. 1	Exp. 2	Exp. 4
Conditions	HF calculated by ASTEC	Corroded RPV surface, Ra 12	Cleaned RPV surface by SJ80, Ra 12	Roughened RPV surface by SJ30, Ra 16
Heating section	**HF value (MW/m²)**	**CHF value (MW/m²)**	**CHF value (MW/m²)**	**CHF value (MW/m²)**
1	0,04	0,42	0,42	0,47
2.1	0,04	0,53	0,51	0,57
3	0,04	0,65	0,61	0,65
5	0,08	1,00	0,87	1,00
9	0,23	1,35	1,50	1,89
13	0,15	1,92	2,15	2,33*

The most important measured results are the CHF values obtained during the 1st and 4th experimental campaigns (comparison of tests on the original untreated surface of the RPV sample with the results of the sample after the final surface treatment with the Sponge Jet 30 technology, when the RPV surface´s roughness was increased from Ra 12 to Ra 16). The data from these two experimental sets were therefore selected from the table of all important CHF measured values, which are supplemented in the Table II below with data on the approximate position of the measured location on the RPV (inclination, elevation from the bottom of the RPV). The Table II also evaluates the safety margin to the CHF. See also Figure 3.

Table II. Important CHF values and safety margin to the CHF

	RPV inclination	RPV elevation	HF	Experiment E1		Experiment E4		CHF ratio
Cond.			HF by ASTEC	Corroded RPV surface, Ra 12		Roughened RPV surface, Ra 16		
Heating section	**α (°)**	**H (m)**	**HF value (MW/m²)**	**CHF value (MW/m²)**	**SM_{CHF} (%)**	**CHF value (MW/m²)**	**SM_{CHF} (%)**	**E4/E1 (%)**
1	0-10	0,1	0,04	0,42	950	0,47	1075	+11,9
2.1	15	0,2	0,04	0,53	1225	0,57	1325	+7,5
3	25	0,4	0,04	0,65	1525	0,65	1525	0
5	45	0,7	0,08	1,00	1150	1,00	1150	0
9	70	1,1	0,23	1,35	487	1,89	722	+40
13	90	1,5	0,15	1,92	1180	2,33*	1453*	+21,4*
12 (peak)	90	1,4	1,35	1,92	42,2	2,33*	72,6*	+21,4*

3. CONCLUSIONS

- Experiments show that the HF profile according to the ASTEC calculation can be cooled by the IVMR strategy with high reserves - safety margin to the CHF.
- At the critical point according to ASTEC calculation and simulation on THS-15, safety margin to the CHF measured was approx. 42 % during experiments with an untreated RPV surface and approx. 73% during tests with a roughened RPV surface.
- In the area of the elliptical part of the RPV, an increase of safety margin to the CHF was not clearly demonstrated.
- In the area of the cylindrical part of the RPV, an increase safety margin to the CHF was demonstrated by increasing the cooling efficiency by min. 20 %.

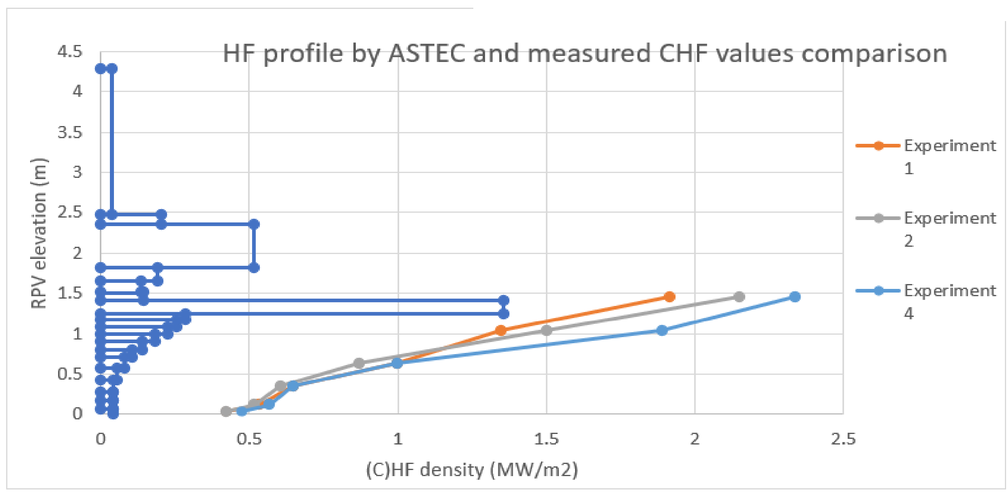

Figure 3. HF profile (ASTEC) and measured CHF values comparison

Acknowledgement

Results of this work were funded thanks to Technology Agency of the Czech Republic, under the TACR Beta framework program – project No. TITSSUJB830.

References

1. D. Batek, J. Zdarek and M. Kotouc, "In Vessel Melt Strategy Application for VVER 1000 reactor with modified roughness surface - Final Technical Report", National TACR project No. TITSSUJB830, UJV Rez, 2022.
2. A. Walunj and A. Sathyabhama, "Effect of Surface Roughness on Pool Boiling Characteristics under Variable Heat Supply," *Twelve International Conference on Thermal Engineering: Theory and Applications*, Gandhinagar, India, February 23-26, 2019.
3. B. Qiu, X. Liu et.al., "Effects of surface alteration on CHF related to IVR accident scenarios: A review," *Elsevier*, Progress in Nuclear Energy 159 (2023).
4. D. Batek, J. Zdarek, V. Krhounek et.al., "Final report on full scale tests," EC project Horizon 2020 No. 662157, Deliverable 4.4, UJV Rez 2019.

David Batek
Jiri Zdarek
Miroslav Kotouc

UJV Rez
Hlavni 130
250 68
Husinec-Rez

Email:
david.batek@ujv.cz
Jiri.zdarek@ujv.cz
Miroslav.kotouc@ujv.cz

IN COOPERATION WITH:

STATE OFFICE FOR NUCLEAR SAFETY

TA CR Technology Agency of the Czech Republic

Cooperative Nuclear Safety Research Activities at the Nuclear Energy Agency in Response to the Fukushima-Daiichi Accident

Yuji Kumagai, Didier Jacquemain (NEA)

Since the 2011 Tōhoku earthquake and tsunami which hit the Fukushima Daiichi Nuclear Power Station (FDNPS), the Nuclear Energy Agency (NEA) is conducting nuclear safety research activities involving wide international collaborations to gain insights for a safe decommissioning of the FDNPS and for safety enhancements of NPPs in general. These activities are conducted under the auspices of the WGAMA (Working Group of Accident Management and Analysis) of the Committee of the Safety of Nuclear Installations (CSNI) and in joint nuclear safety research projects, with some dedicated directly to collecting insights from on-site investigations, to the analysis of the accident and to the preparation of the damaged plant decommissioning such as the BSAF (Benchmark Study of the Accident at the Fukushima Daiichi Nuclear Power Plant) Project, the PreADES (Preparatory Study on Analysis of Fuel Debris) project, the ARC-F (Analysis of Information from Reactor Building and Containment Vessel and Water Sampling in Fukushima Daiichi NPS) project and the TCOFF (Thermodynamic Characterisation of Fuel Debris and Fission Products Based on Scenario Analysis of Severe Accident Progression at Fukushima-Daiichi Nuclear Power Station) project. A number of other joint nuclear safety research projects are also investigating safety issues related to the FDNPs accident. Insights learnt from these research activities have been considered worldwide to improve nuclear safety.

As the most recent activities, the FACE (Fukushima Daiichi Nuclear Power Station Accident Information Collection and Evaluation) project has begun in July 2022, and aims to address key technical issues identified in recent investigations into the damaged plant, to improve understanding of the accident and to support the decommissioning activities.

There are still immense challenges ahead related to the FDNPs long term management. International collaboration should be continued, first through the on-going FACE project, to further inform decommissioning and to value more the insights from the accident analyses for severe accident management both for operating and future reactors. In order to provide directions for future research in the accident management area, NEA is organizing in September 2024 an international workshop on future research to enhance accident management in operating and future reactors, informed by Fukushima Daiichi insights.

FILTRATION EFFICIENCY OF ELECTROSTATIC PRECIPITATOR FOR IODINE PARTICLES IN DIFFERENT GAS ATMOSPHERES SIMULATING SEVERE ACCIDENT SCENARIOS

Satish Basnet and Anna Lähde
University of Eastern Finland
Department of Environmental and Biological Sciences, FI-70211, Kuopio, Finland
satish.basnet@uef.fi; anna.ladhe@uef.fi

ABSTRACT

In pursuit of carbon-neutral energy sources, the relevance of nuclear power plants (NPPs) has been increasing, requiring improved NPP safety. In the event of severe accidents (SA), the release of radioactive aerosols and the potential for hydrogen (H_2) explosions pose significant challenges. This study aims to enhance NPPs' safety by addressing the challenges of radioactive aerosol emissions and H_2 during SA.
The preliminary experiment investigating the secure removal of H_2 during the venting scenarios was conducted with the Electrostatic Precipitator (ESP) in the FunktioMat laboratory (https://sites.uef.fi/fine/front-page/funktiomat/). ESP was used with Formier (5%) and nitrogen gas at room temperature. The residual gas was collected from the ESP outlet and analysed with the microGC (Agilent 490) for traces of H_2. Though the final concentration of H_2 was reduced (~ 25%), in an inert atmosphere, the corona discharge in the ESP alone was unable to fully oxidise H_2. Extensive experiments with detailed atmospheric conditions and varying settings with different ESPs are needed to conclude our findings.
The study further aims to examine the effectiveness of ESP on the filtration of radioactive aerosols emitted during hypothetical SA. A particular focus will be applied to the chemistry and behaviour of iodine species. Gaseous iodine and iodine oxide particles are passed through an ozone feed, oxidising these particles, and filtered through the ESP. ESP-based filtration employs a humidified inlet for aerosol flow, enabling particle growth and enhanced particle charging for improved collection in the electric field.

KEYWORDS
Electrostatic precipitators, Nuclear power plants, severe accidents, hydrogen mitigation

SEAKNOT
ERMSAR 2024
11th Conference on
SEVERE ACCIDENTS RESEARCH
May 13-16, 2024 – Stockholm, Sweden

Filtration efficiency of ESP for iodine particles in different gas atmospheres simulating the severe accident scenarios

SATISH BASNET

Supervised by Prof. Anna Lähde and Prof. Olli Sippula

Background and Objective

In the event of severe accidents (SA) in Nuclear power plants (NPPs), the potential for hydrogen (H_2) explosions and the release of radioactive aerosols, especially iodine, pose significant challenges. This study aims to offer solutions to enhance NPPs' safety by:

- developing new filtration techniques utilising the highly efficient Electrostatic precipitator (ESP) for radioactive aerosol emissions.
- understanding the complex iodine chemistry involving several different iodine species (elemental, ionic, organic, particulate) that can exist during a hypothetical SA.
- developing an efficient and safe hydrogen mitigation system that will ensure controlled removal and combustion of H_2 from the reactor building while using the ESP.
- applying the developed technologies under the simulated SA scenarios to demonstrate their suitability and efficiency for such scenarios.

Methods and Preliminary Results

- Formier (5%) with Nitrogen was passed through the ESP at room temperature.
- The residual gas was collected and analysed with microGC.
- The corona discharge alone in an inert atmosphere was unable to fully oxidize H_2 in ESP, resulting in a ~25% reduction in its final concentration.
- The corona discharge in conjunction with ozone may further reduce the H_2 concentration.
- Extensive experiments with varying H_2 concentrations in different atmospheric conditions are needed to conclude our findings.
- The effectiveness of ESP on the filtration of radioactive aerosols emitted during hypothetical SA will employ a humidified inlet for aeroslo flow, enabling particle growth and enhanced particle charging for improved collection in the electric field.

Experimental Setup and instrumentation

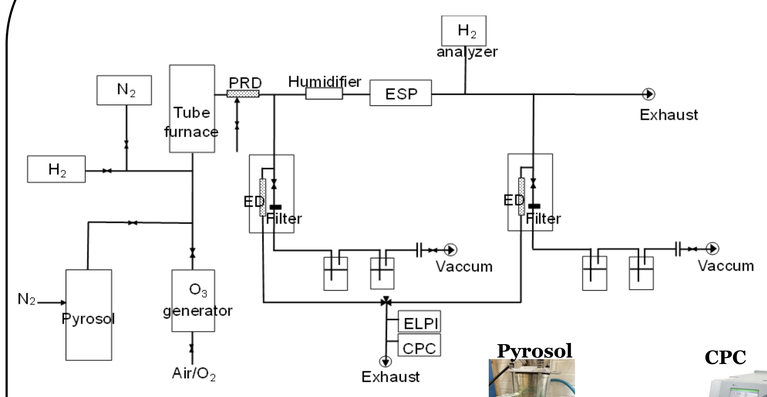



ESP

Filtration



Tube Furnace

Reaction



Pyrosol

Aerosol generation



CPC



ELPI

Particle number size distribution

Probable outcome

- for hydrogen mitigation experiment

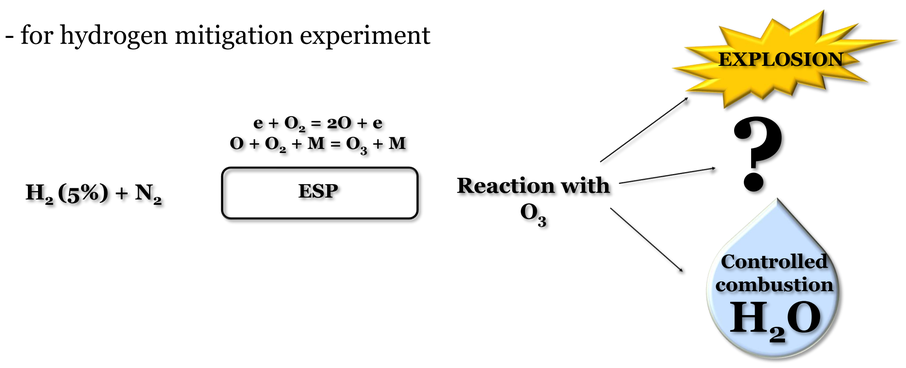

- for source term experiment

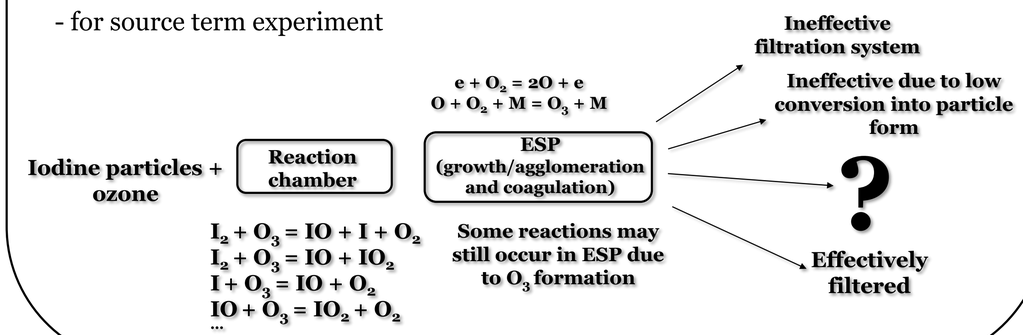

IN COOPERATION WITH:

SAFER 2028

- The Doctoral Education Network under SAFER2028 (DENSE) project (VYR REST2028, grant no. 29350001281).

Forename Surname
Satish Basnet

Yliopistonranta 8,
70210, Kuopio

Tel: +385 417 483 935
Email: satish.basnet@uef.fi

Study on AP1000 accident diagnosis and treatment for loss of monitoring and control

Yun Yu[1]

[1]China Nuclear Power Engineering Co., Ltd., No.117 Xisanhuanbeilu, Haidian District, Beijing, China, yuyun09@163.com

Contact email: yuyun09@163.com

Abstract

The Fukushima nuclear accident showed that extreme external events may cause the loss of monitoting and control of control rooms (including main control room and remote shutdown station), because the previous emergency operating procedures (EOP) and severe accident management guidelines (SAMG) of nuclear power plants did not consider the loss of control room monitoring and control scenario, in order to improve the accident management system of nuclear power plants, it is necessary to study the accident diagnosis and treatment method for conditions where the control rooms lose monitoring and control. The SSG-54 (Accident Management Programs for Nuclear Power Plants) released by IAEA in 2019 clearly states that the scenario of instrument failure and loss of command and control should be considered in the management of severe accidents at nuclear power plants. NRC in 2019 issued the requirement to mitigate beyond-design-basis external events (MBDBE) in regulation 10CFR50.155, which proposes that nuclear power plants should set up mitigation strategies for such scenarios caused by extreme external events. In order to ensure the AP1000 nuclear power unit's ability to respond to loss of control room monitoring and control, this article carries out the following analysis: (1) reactor and spent fuel pool states monitoring method for loss of monitoring and control scenario by analyzing AP1000 instrumentation and control system from 0th layer to the 2nd layer; (2) prevention and mitigation strategies for AP1000 nuclear power units to deal with severe accidents based on accident mitigation objectives and AP1000 design features; (3) Study local operation methods for mitigation strategies when the control room is unavailable; (4) determine the diagnosis and treatment logic of loss of monitoring and control conditions. By studying the accident management methods of AP1000 NPPs for loss of monitoring and control condition, the ability of nuclear power plants to respond to extreme external events will be further improved, and the depth defense system and safe operation level of nuclear power plants will be enhanced.

Keywords: AP1000, nuclear power units, accident management, loss of monitoring and control

Failure modes of the reactor coolant pressure boundary in high-pressure core melt accident scenarios

Christoph Bläsius[1], Jürgen Sievers[2] and Stefan Weihe[3]

[1]GRS gGmbH, Schwertnergasse 1, 50667 Cologne, christoph.blaesius@grs.de
[2]GRS gGmbH, Schwertnergasse 1, 50667 Cologne, juergen.sievers@grs.de
[3]MPA Stuttgart, Pfaffenwaldring 4, 70569 Stuttgart, stefan.weihe@mpa.uni-stuttgart.de

Contact email: christoph.blaesius@grs.de

Abstract

In light water reactor core melt accident scenarios with an unsuccessful pressure relief, the persisting mechanical loads in the reactor coolant pressure boundary become superimposed by increasing thermal loads from hot gas flows generated in the core melt process. Location, time and size of the failure and subsequent depressurization can have substantial implications on the further course and consequences of the accident. The failure location determines not only the location of release of hydrogen and radionuclides, but also the risk of bypassing the containment as a last barrier for radioactivity. Recent investigations of the events at Fukushima Daiichi emphasize the importance of this issue and its cliff-edge nature.

The modeling of severe accident phenomena has been improved over the years by further development of lumped parameter system codes as well as by the use of mechanistic codes, such as computational fluid dynamics. The modeling of mechanical failure has been concentrated on specific components such as the reactor pressure vessel. Failure modes of other components, which may fail much earlier in the described scenario, are often not considered, or their assessment is based on expert judgment or questionable relations borrowed from other fields of application. This is not least because of the complexity of the reactor coolant pressure boundary, which includes a variety of components with several failure modes that in addition differ considerably from those at operational conditions. Furthermore, as failure times of different components are assumed very close, modeling effort must be equally distributed and failure modes should not be overlooked. For each failure mode, the knowledge of the exact phenomenology and connected uncertainties must be put in front of a proper quantitative modelling.

The work provides an overview of identified failure modes and their associated particularities. Where appropriate, deduced approaches for a practical failure assessment are briefly presented. A first group includes failure modes resulting from mechanical interactions between the system's components or with adjacent structures, e. g. by thermal expansion. A second group encompasses failure modes of single components, such as large piping, elbows, junctions, steam generator tubes, nozzles, penetrations, pre-damaged components, pumps, flanges, and valves. In a third group, failure modes at material level are described, which includes failure modes based on macroscopic deformation, such as buckling, kinking, plastic instability, or creep necking, as well as failure modes based on loss of internal cohesion and the associated characteristic types of microstructural damage.

The paper is based on results from the research projects RS1520, RS1555 and RS1602 of the reactor safety research program sponsored by the Federal Ministry for the Environment, Nature Conservation, Nuclear Safety and Consumer Protection.

Keywords: high-pressure core melt, HPME, C-SGTR, reactor coolant pressure boundary, failure modes

SEAKNOT
ERMSAR 2024
11th Conference on
SEVERE ACCIDENTS RESEARCH
May 13-16, 2024 – Stockholm, Sweden

Failure modes of the reactor coolant pressure boundary in high-pressure core melt accident scenarios

C. BLÄSIUS[1], J. SIEVERS[1], S. WEIHE[2]

[1] Gesellschaft für Anlagen- und Reaktorsicherheit (GRS) gGmbH, Cologne, Germany

[2] Materials Testing Institute (MPA), University of Stuttgart, Germany

Introduction

In postulated high-pressure core melt accident scenarios, persisting inner pressure and increasing thermal loads from circulating hot gases from core melt processes at some point unavoidably induce a failure of the reactor coolant pressure boundary.

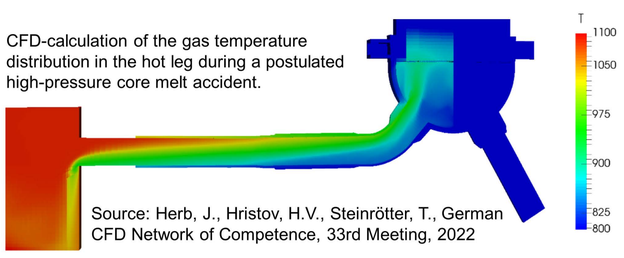

Location, time and size of the failure and subsequent depressurization can have substantial implications on the further course and consequences of the accident, e.g. in terms of containment-bypass scenarios (HPME/DCH[1], C-SGTR[2], Pipe-Whip, ...).

Analyses of such scenarios require mechanical failure models, which currently often rely on simple analytical methods, e.g. Larson-Miller type relations. A detailed mechanistic approach can validate and enhance those models and allow the investigation of further locations and more complex failure modes.

Ballooning failure of hot leg or surge line

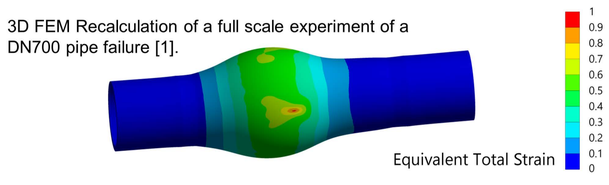

Hot leg or surge line failure is a probable outcome due to the high thermal loading. Nevertheless, current models do not take into account the effect of the deformed state onto the original load situation, which could be either accelerating or stabilizing.

Accelerating: Deformed geometry acts back on stress as driver of further deformation.

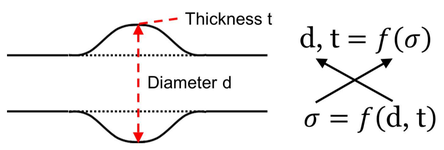

Stabilizing: Contact with double pipe can prevent further ballooning and failure.

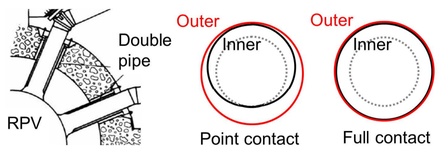

Complex geometry and loading situations

Piping under thermal gradients or complex geometry (elbows, T-junctions, ...) can be replaced by models of straight pipes by introducing a stress factor as long as the failure mode does not change [2].

Cracked Steam Generator Tubes

Induced steam generator tube failure is associated with containment-bypass and must be precluded. Although experiencing lower thermal load, they have smaller thermal inertia and may be pre-damaged.

FE-Analyses show that tubes with notches or abrasion are more likely to fail than tubes with cracks due to allowing creep-necking, which accelerates failure [3].

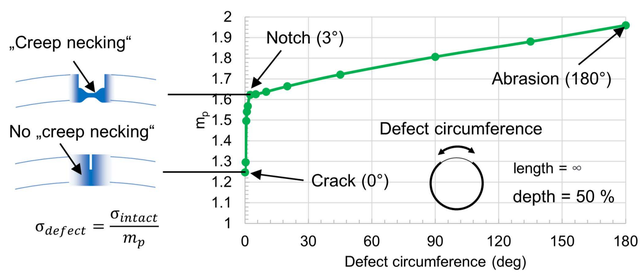

Constrained thermal expansion of large piping

Thermal stresses and localized strains induced by constrained thermal expansion of large piping can be quantified and assessed concerning failure. They are self-limiting and will relax at higher temperatures [4].

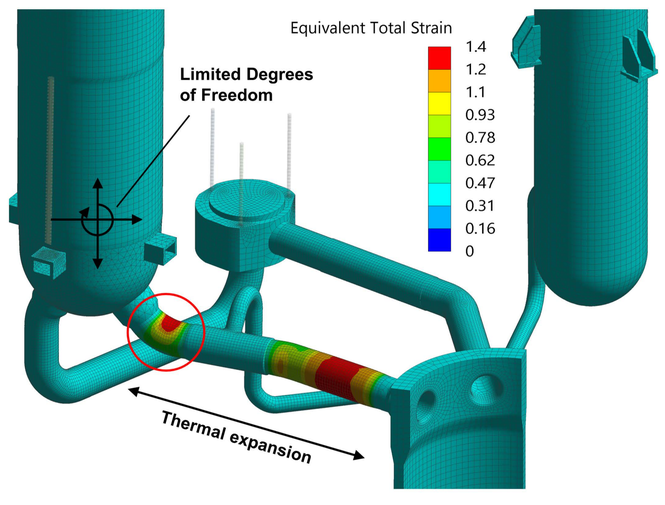

Penetrations

The failure mode of penetrations differs from pipe failure and can encompass weld failure, ejection or creep buckling depending on the design. Especially in Boiling Water Reactors, an early failure is probable due to the high number of penetrations.

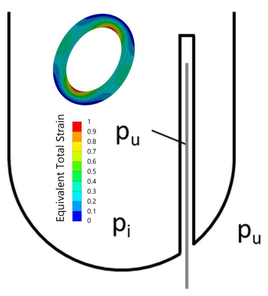

SRM/IRM[4] Instrumentation

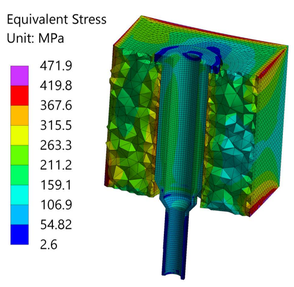

Steam generator drainage nozzle

Flanges

Flanges at connections, manholes or blind flanges can leak and subsequently fail under extreme loading conditions. Depending on the design a loss of bolt preload or a “rotation” of the flange body is found responsible for failure [5].

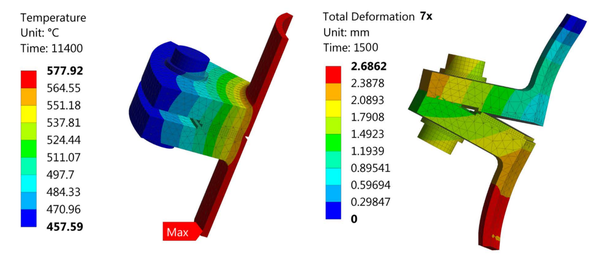

Safety and Relief Valves

Valves are complex components with different designs and failure modes. A survey among experts revealed jamming as a candidate for the predominant failure mode. Experiments on a surface mock-up shows that under high temperature, surfaces can stick but also loosen under force or at further temperature increase.

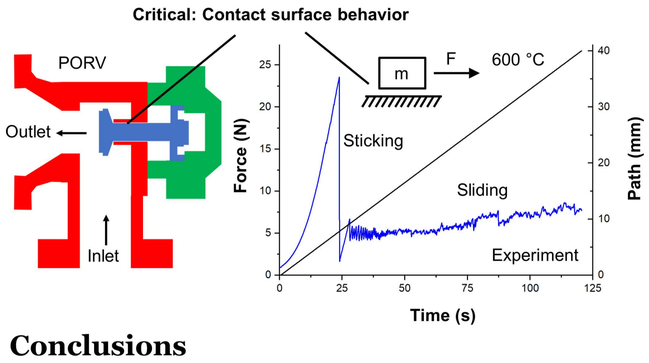

Conclusions

A mechanistic approach to the mechanical failure of the reactor coolant pressure boundary in high-pressure core melt accident scenarios allows to better understand accident sequences and failure modes of components. Further it helps to design future plants to be able to mitigate consequences.

Footnotes

1. High Pressure Melt Ejection/Direct Containment Heating
2. Consequential Steam Generator Tube Rupture
3. Source Range/Intermediate Range Neutron Flux Monitor

References

[1] OECD/NEA (2018). Components and Structures under Severe Accident Loading (COSSAL), NEA/CSNI/R(2019)2
[2] Bläsius, C., Sievers, J., Weihe, S. (2023). Failure modes of the reactor coolant pressure boundary in high-pressure core melt accident scenarios, 47th MPA-Seminar, Stuttgart, Germany
[3] Bläsius, C., Sievers, J., Weihe, S. (2024), Under-Recognized Phenomena and Uncertainties in the Integrity Assessment of the Reactor Coolant Pressure Boundary in High-Pressure Core Melt Accident Scenarios, SMiRT-27 Conference, Tokyo, Japan
[4] Bläsius, C., Sievers, J. (2021). Assessment of NPP pressure boundary under severe accident loading, Nuclear Engineering and Design, Vol. 374, 111050
[5] Simonovski, I., Bläsius, C., Andersson, D., Local Failure of a Flange Connection, NENE-27, Portoroz, Slowenia

Christoph Bläsius
GRS gGmbH
Schwertnergasse 1
50667 Cologne
Tel: +49(221)2068-743
christoph.blaesius@grs.de

Parametric sensitivity studies for RELAP/SCDAPSIM model of QUECH-20 test

Elsalamouny N, Kaliatka T *
Lithuanian Energy Institute
Breslaujos g. 3 LT-44403 Kaunas, Lithuania
Noura.Elssalamouny@lei.lt;Tada.kaliatka@lei.lt

ABSTRACT

The QUENCH-20 test was the first experiment equipped with a BWR fuel bundle conducted at the QUENCH facility in Karlsruhe Institute of Technology in 2019. The objective of the test was to understand the effect of B_4C and its stainless-steel cladding on BWR fuel assembly degradation during strong heat-up and subsequent flooding processes. One of the main aspects of this test is hydrogen generation and overall degradation of the BWR fuel bundle at the mentioned conditions.
For the numerical investigation of the QUENCH-20 test, the severe accident code RELAP/SCDAPSIM was used. The developed RELAP/SCDAPSIM model which uses the "PWR control rod" component to simulate absorber blades and the "Shroud" component for modeling the structural elements of the fuel bundle (fuel channel box, water channel box, and water wings) gives close calculation results to the experimental data. The calculated cladding and shroud temperatures showed ~5 % lower values (~50 degrees in the pre-oxidation phase and ~100 degrees in the quench phase) compared to experimental data.
Calculation results of hydrogen generation are less by ~10 % (~5 g) compared to measurements taken at the end of the QUENCH-20 test. Thus, it could be concluded that the results of the calculations show that the thermal behaviour is qualitatively and quantitively predicted in good agreement with the experiment, but some discrepancies need to investigate in more detail. For this reason, it was decided to perform the parametric sensitivity studies. These studies investigate the influence of parameters related to initial, boundary conditions, and radiation heat transfer in the SCDAP modeling part. This poster presents the results of described parametric sensitivity studies. In addition, different values of the radiation view factors were varied. Evaluation of the radiation view factors showed that even small changes could cause the Cliff-edge effect on the calculation results.

KEYWORDS
QUENCH-20, BWR, RELAP/SCDAPSIM, parametric studies, hydrogen generation.

ACKNOWLEDGMENTS

This work is done as a part of the International Atomic Energy Agency (IAEA) Coordinated Research Project (CRP), titled "Advancing the State-of-Practice in Uncertainty and Sensitivity Methodologies for Severe Accident Analysis in Water Cooled Reactors", launched in 2019.

SEAKNOT
ERMSAR 2024
11th Conference on
SEVERE ACCIDENTS RESEARCH
May 13-16, 2024 – Stockholm, Sweden

LITHUANIAN ENERGY INSTITUTE
http://www.lei.lt

Parametric sensitivity studies for RELAP/SCDAPSIM model of QUECH-20 test

NOURA ELSALAMOUNY

Supervised by; T. KALIATKA

- QUENCH-20 test (with BWR bundle) was modeled using RELAP/SCDAPSIM severe accident code.
- Parametric sensitivity studies of the most influencing parameters for the calculation results were performed.
- Different radiation view factors for complex/asymmetric QUENCH-20 test bundle were investigated.

DESCRIPTION QUENCH-20 TEST

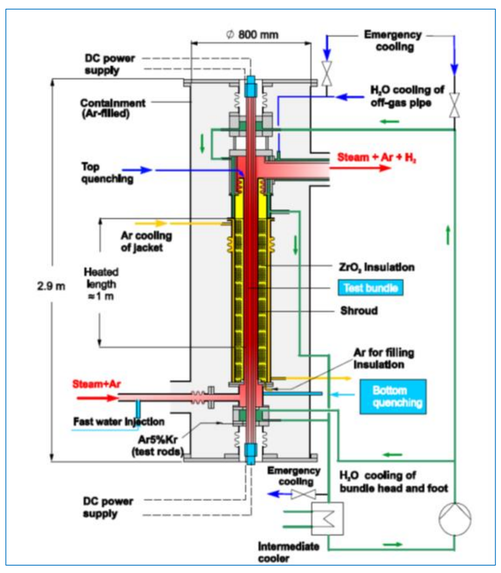

Schemic view of QUENCH facility

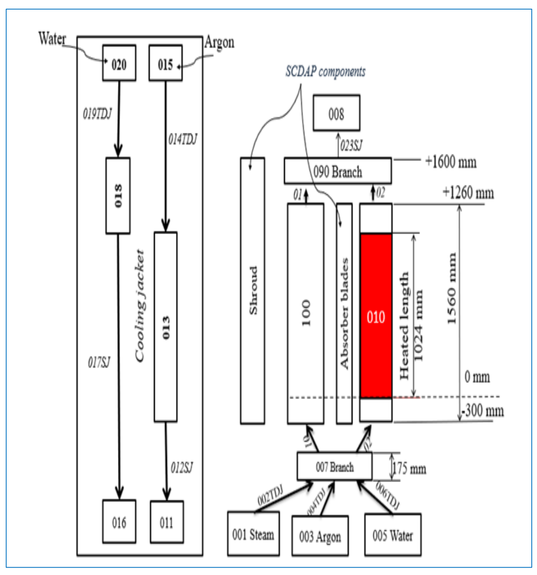

Nodalization of RELAP part

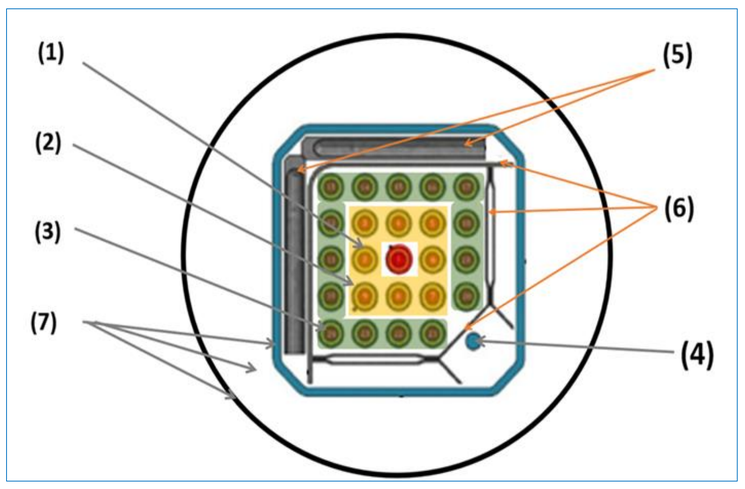

Nodalization of SCDAP part: (1) the central rod, (2) inner ring, (3) outer ring, (4) corner rod, (5) Absorber blades, (6) Water channel box, fuel channel box and water wings, (7) shroud.

Selected parameters

Taking the modeling experience of LEI scientists previous work done in QUENCH and PHEBUS tests, the most influenced parameters were selected:

Parameter	Reference value	Range
Contact resistance, ohm	0.006825	+-3%
Steam injection, kg/s	0.003	+-2%
Quench water injection, kg/s	0.05	+-2%

PARAMETRIC SENSITIVITY STUDIES

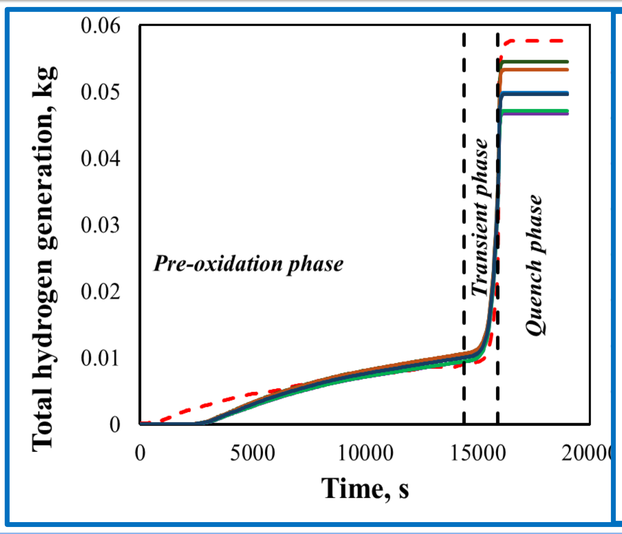

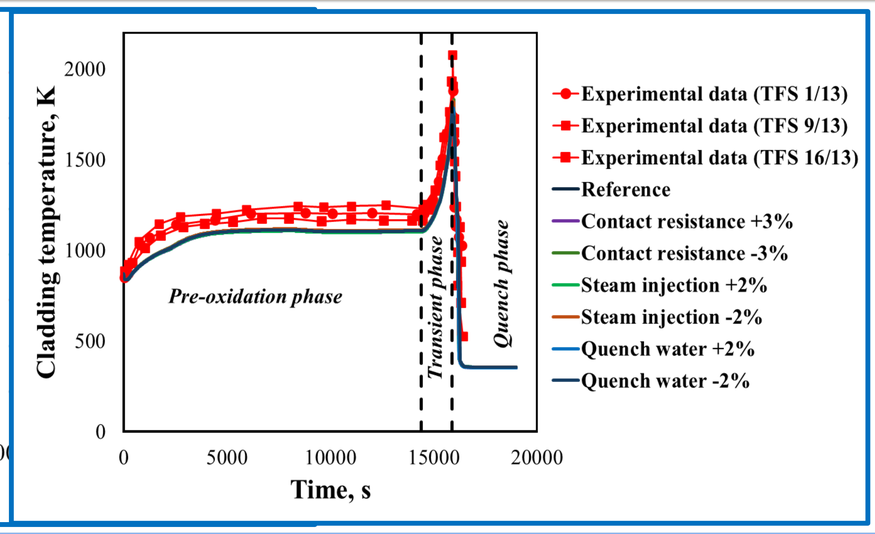

FFTBM was used to perform the accuracy factor (calculation results/Experimental data) of the calculation results for the QUENCH-20 test.

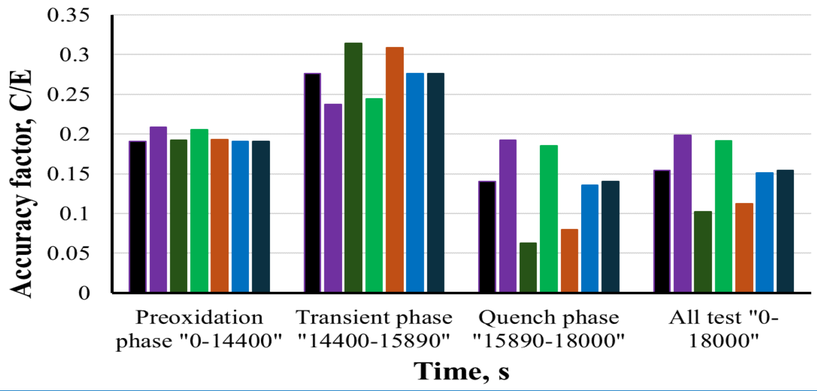

RADIATION VIEW FACTORS

Schematic view of radiation transfer to QUENCH-20 test bundle. Shroud takes direct radiation transfer from component 6.

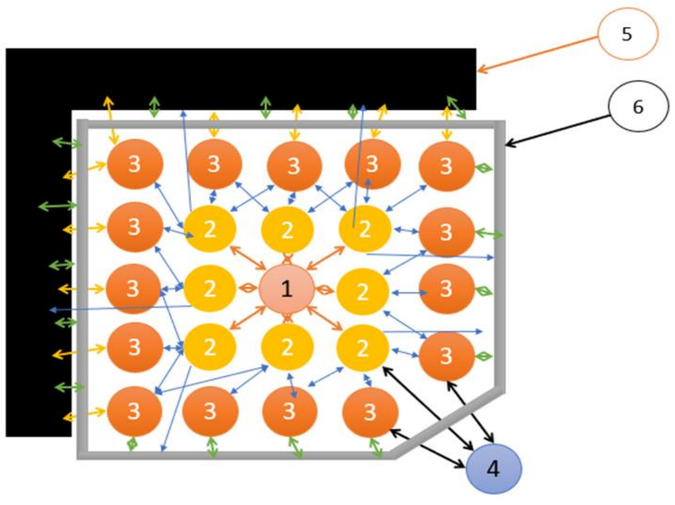

- Case 1: an increase in radiation heat transfer from component 3 (rods in the outer ring) to component 5 (absorber blades) by 10% and a reduction in radiation heat transfer from component 3 to component 6 (water channel box, fuel channel box, and water wings) by 10%.
- Case 2 is the opposite.

Case 1; $F_{35}\uparrow$ and $F_{36}\downarrow$ Case 2; $F_{35}\downarrow$ and $F_{36}\uparrow$

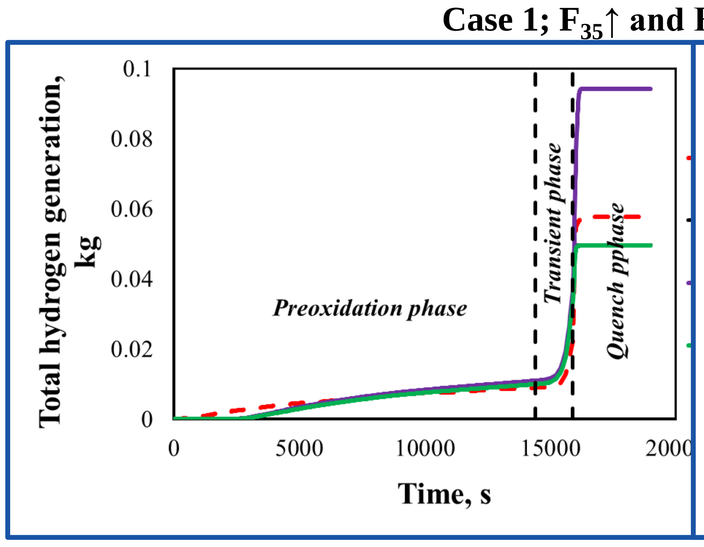

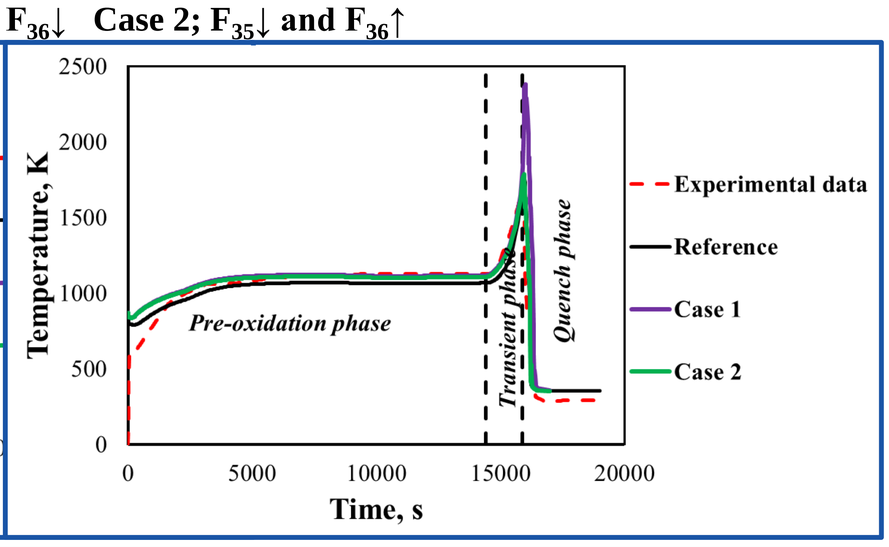

CONCLUSIONS

- The most influenced parameters were selected based on the previous experience in modeling of QUENCH and PHEBUS tests.
- Varying the selected parameters did not have a significant effect on the temperature and hydrogen generation for pre-oxidation and transient phases.
- Reduction of contact resistance by 3% gives better agreement with experimental data compared to reference case calculations.
- Due to the asymmetric QUENCH-20 test bundle the modeling of the radiation transfer is complicated. Thus, it was decided to vary the radiation view factors in order to investigate their influence on calculation results. Even small changes in radiation view factors could cause the "cliff-edge" effect in the calculation results.

ACKNOWLEDGMENT

This work is done as a part of the International Atomic Energy Agency (IAEA) Coordinated Research Project (CRP), titled "Advancing the State-of-Practice in Uncertainty and Sensitivity Methodologies for Severe Accident Analysis in Water Cooled Reactors", launched in 2019.

Tadas Kaliatka — **Lithuanian Energy Institute, Kaunas, Lithuania** — **+37060540008** — Tadas.Kaliatka@lei.lt

ASSESSMENT OF HOW Zr-CLAD OXIDATION CAN AFFECT THE SPECIATION AND RELEASE OF FPs UNDER SEVERE ACCIDENT CONDITIONS

Chantal RIGLET-MARTIAL, Morgane ROCHEDY
Commissariat à l'Energie Atomique et aux Energies Alternatives
CEA, DES, IRESNE, DEC, SESC, LM2C, Cadarache, F-13108 Saint-Paul-lez-Durance, France
chantal.martial@cea.fr, morgane.rochedy@cea.fr

ABSTRACT

Temperature and oxygen partial pressure (i.e. oxygen potential) are key parameters governing the speciation and release of fission products (FPs) from nuclear oxide fuels. Under severe accident conditions, large variations in oxygen potential are expected to occur within the fuel due to both temperature increase and oxidation of Zr-clad by water.
In this paper, a quantitative assessment of how Zr-clad oxidation can affect the speciation and release of fission products under accidental conditions is carried out using experimental feedback collected at CEA within the VERCORS and VERDON programs.
During the tests, total oxidation of the Zircaloy cladding occurs in the temperature range [600 °C - 1500 °C] and results in a strong release of di-Hydrogen, which causes a more or less significant reducing perturbation on the carrier gas (Air/H_2O/O_2) coming into contact with the fuel sample.
The magnitude of the reducing perturbation highly depends on the composition of the carrier gas. It is very large under un-buffered humid conditions (H_2O gas) whereas it can be much weaker, or even become non-existent, if the incoming carrier gas is initially buffered in O_2, using a H_2O/H_2 gas mixture. As soon as the Zr-oxidation stage is over, the oxygen potential suddenly increases to the level imposed by the incoming carrier gas.
The strong oxydo-reducing perturbation experienced by the gas interacting with the fuel is likely to significantly modify the speciation of volatile FPs (Mo, Cs, I) usually released in the temperature range where the cladding oxidation occurs.

KEYWORDS
Fission products, oxide fuel, zircaloy cladding, severe accident conditions, Hydrogen, source term

1. INTRODUCTION

Over the past few decades, Source Term Evaluation for Pressurized Water Reactors (PWRs) has been the subject of a number of research programs in the field of severe reactor accidents. The evaluation of the impact of a severe accident (SA) on the environment requires a thorough knowledge of FPs behavior at high temperature and in highly oxidizing conditions (steam) ([1] to [5]).
The items of major concern in assessing the consequences of off normal operating conditions are i) the chemical affinities of the FPs ii) the speciation and release kinetics of the FPs from the fuel iii) the re-deposition of released FPs when cooling.
Temperature and oxygen partial pressure (i.e. oxygen potential) are key parameters governing the speciation and release of fission products (FPs) from nuclear oxide fuels. Under severe accident conditions, large variations in oxygen potential are expected to occur within the fuel due to both temperature increase and oxidation of Zr-clad by water.

The present study focuses on how the Zr-clad oxidation, and the consequent di-Hydrogen production, can affect the speciation and release of volatile FPs under accidental conditions. The main outcomes concerning Caesium, Iodine and Molybdenum, which are likely to release from the fuel during the clad-oxidation stage, are discussed.

2. THERMOCHEMICAL FEATURES OF THE VERCORS AND VERDON TESTS

The thermal tests performed within the VERCORS and VERDON programs aim at quantifying the release of fission products (FPs) and actinides from irradiated nuclear ceramics during a severe accident. From 1989 onwards, extensive and invaluable data were collected about i) the released fraction and release rates of FPs from irradiated fuels ii) the nature and chemical composition of the vapors and aerosols emitted and iii) the degradation mechanisms of the fuel.
Full descriptions of the experimental set-ups and detailed analyses of the data collected in various temperature and redox conditions are given in references [1] to [5] (and related references). To summarize, the fuel samples are composed of sections of a PWR fuel rod, containing two or three UO_2 (or MOX) pellets in their original zircaloy cladding. Before thermal testing, the samples are generally re-irradiated at low linear power (in Material Testing Reactor) in order to rebuild the inventory of short-lived fission products. the applied experimental sequence is divided into three phases. First comes Phase 1, dedicated to the conditioning of the loop, which takes place below 400°C under neutral atmosphere. Then comes Phase 2, dedicated to the oxidation of the cladding, which takes place in the range 400 - 1500°C under H_2O/He or H_2O/H_2 atmosphere. Finally comes Phase 3 consisting in a high temperature ramp (sometimes with intermediate temperature plateaus) under controlled redox conditions (steam, O_2/H_2O or H_2O/H_2 mixtures, H_2) until the end (i.e. collapse of the sample most often).

The present study refers specifically to Phase 2 of the VERCORS/VERDON tests, dedicated to the oxidation of the cladding, with the objective to assess the impact of the Zr-clad oxidation on i) the oxido-reducing properties of the carrier gas (depending on its initial composition) and potentially ii) the release of FP gaseous species from the fuel.

Experimental conditions typical of phase 2 in the VERCORS/VERDON tests are given in table I. In fact, two main types of carrier gases are used during the cladding oxidation phase. One, named VER-Phase2-BA, refers to an oxygen Buffered Atmosphere (BA) such as (H_2O/H_2) mixture. The other, named VER-Phase2-unBA, refers to an un-Buffered Atmosphere (unBA) such as H_2O gas or (H_2O/He) gas mixture.

Table I. Thermohydraulic experimental conditions typical of the clad oxidation stage (Phase 2) in VERCORS/VERDON tests.

Test reference	Fuel Burn-up	Carrier gas composition			Experimental sequence
		H_2O	H_2	He	
	GWj/tM	g/min	g/min	g/min	
VER-Phase2-BA (Buffered Atmosphere)	30 to 60	1.5	0.027	0.054	- Ramp from 400°C to 1200°C - 17 min. plateau at 1200°C - Ramp from 1200°C to 1500°C - 9 min. plateau at 1500°C
VER-Phase2-unBA (unBuffered Atmosphere)	30 to 60	1.5	0	0.108	- Ramp from 400°C to 1200°C - 15 min. plateau at 1200°C - Ramp from 1200°C to 1500°C - 10 min. plateau at 1500°C

Then, the main difference in the experimental conditions (cf. Table I) between VER-Phase2-BA and VER-Phase2-unBA tests is that the initial carrier gas is a (H_2O/H_2) gas mixture in case of VER-Phase2-BA whereas it is a (H_2O/He) gas mixture in case of VER-Phase2-unBA. This implies that the buffer (H_2O/H_2) sets constant the O_2 partial pressure of the incoming carrier gas in case of VER-Phase2-BA. In contrast, the carrier gas is not buffered in O_2 in case of VER-Phase2-unBA;

During all VERCORS/VERDON tests, total oxidation of the Zircaloy cladding occurs in the temperature range [600 °C – 1500 °C], which results in a strong release of di-Hydrogen. Typical release curves of H_2(g) measured during the oxidation phase of the Zr-cladding are given in Figures 1 and 2, in case of VER-Phase2-BA and VER-Phase2-unBA respectively. Each figure gives the measured flow-rate of H_2 created during the whole oxidation stage as well as the total volume of H_2 produced. The volume of H_2 produced is obtained by integration of the H_2 flow-rate over the total duration of H_2 production. For comparison, a theoretical volume is calculated considering total oxidation of a Zr-cladding of same dimensions as that of the fuel sample. In both cases, the measured H_2-volume fits quite well with the theoretical one estimated from the reaction $Zr + 2H_2O = ZrO_2 + 2H_2$. This confirms that the clad oxidation phase was fully completed, before moving to the next high temperature stage.

Temperature and oxygen partial pressure (i.e. oxygen potential) are key parameters governing the speciation and release behavior of FPs from nuclear oxide fuels. However, as the release of some volatile PFs (such as Cs or I) usually begins before the end of the clad oxidation stage, the production of H_2 following the cladding oxidation is likely to modify the release kinetics and speciation of these gaseous species of fission products.

The objective in the following section is therefore to estimate the O_2 partial pressure (or oxygen potential) of the gas in contact with the sample during the tests, in taking into account the release of H_2 resulting from the Zr-clad oxidation. The methodology is developed in consistency with the known experimental features of the selected tests (cf. Table I, cf. Figures 1 and 2) assuming thermodynamic equilibrium is achieved, as naturally expected at such high temperature conditions.

3. FUNDAMENTALS IN THERMODYNAMICS

3.1. The equilibrium O_2 partial pressure

Oxidation of the zircaloy cladding, according to the reaction (1) gives rise to di-Hydrogen in significant amount, which is likely to modify the oxido-reducing properties of the gas in contact with the sample.

$$Zr(s) + 2H_2O(g) \rightarrow ZrO_2(s) + 2H_2(g) \quad (1)$$

Let us note:
- h_2o, h_2, o_2 : flow-rate of $H_2O(g), H_2(g), O_2(g)$ in the incoming carrier gas (in molar scale)
- $D_{H_2O}, D_{H_2}, D_{O_2}$: flow-rate of $H_2O(g), H_2(g), O_2(g)$ in the gas (including H_2-produced in contact with the sample (in molar scale)

Considering the equilibrium (2), the O_2 partial pressure of a (H_2O/H_2) gas mixture may be estimated from the relation (3).

$$2H_2O(g) \underset{\leftarrow}{\overset{\rightarrow}{}} 2H_2(g) + O_2(g) \qquad \text{Equilibrium constant } K_p(T) \quad (2)$$

$$pO_2 = K_p(T) * \left(\frac{pH_2O}{pH_2}\right)^2 \quad (3)$$

In the current study, the pressure unit chosen for all gaseous species is the Bar, in consistency with the standard state pressure of one Bar, as recommended by the International Union of Pure and Applied Chemistry IUPAC [6]. In theory, the constant $K_p(T)$ has no unit. In practise, relative to the 1 Bar reference state, the constant $K_p(T)$ is expressed in Bar.

The data of $K_p(T)$ constants (Bar unit) are taken from the SGPS pure substances database (v13.1, revised 2019), developed by the Scientific Group Thermodata Europe (SGTE) and available within the FactSage software version 8.3 [7], which is used in the current study for thermochemical calculations.

3.2. Application to the gas in contact with the sample (including H_2 from the clad oxidation)

Based on equation (3), the O_2 partial pressure of the gas mixture in contact with the sample is given by relation (4), in consistency with the perfect gas law.

$$pO_2 = K_p(T) * \left(\frac{D_{H_2O}}{D_{H_2}}\right)^2 \quad (4)$$

The H_2 flow rate D_{H_2} is estimated from the relation (5).

$$D_{H_2} = (D_{H_2} - h_2) + h_2 \quad (5)$$

The amount $(D_{H_2} - h_2)$ is directly obtained from the measurements of H_2 produced from the clad oxidation given in Figures 1 and 2. The amount h_2 refers to that of H_2 initially present in the carrier gas, if any (VER-Phase2-BA). The quantity h_2 is deduced from the experimental conditions given in table I.

From equation (1), the principle of conservation of the matter imposes:

$$h_2o \approx D_{H_2O} + (D_{H_2} - h_2) \quad (6)$$

which gives:

$$D_{H_2O} \approx h_2o - (D_{H_2} - h_2) \quad (7)$$

The quantity h_2o is deduced from the experimental conditions given in table I. The quantity $(D_{H_2} - h_2)$ is obtained from the experimental data given in figures 1 and 2.
The O_2 partial pressure of the gas in contact with the sample is therefore estimated using equation (4).

The O_2 potential is deduced using relation (8).

$$\mu O_2 = \mu O_2^{\circ} + R\,T \ln(pO_2) \quad (8)$$

The O_2 potential at the standard state (1 Bar pressure) is $\mu O_2^{\circ} = 0$.
The constant R is 8.314 J/mol/K.
In equation (8), the units are as follows: μO_2 in J/mol O_2, T en K, pO_2 in Bar.

3.3. Application to the entering carrier gas (before the clad oxidation)

Based on equation (3), the O_2 partial pressure of the carrier gas entering the furnace is given by the relation (9), in consistency with the perfect gas law.

$$pO_2 = K_p(T) * \left(\frac{h_2o}{h_2}\right)^2 \quad (9)$$

In case of VER-Phase2-BA, the carrier gas is a (H_2O/H_2) gas mixture circulating at flow rates of h_2o and h_2 respectively. The quantities h_2o and h_2 are deduced from the experimental conditions given in table I. The O_2 partial pressure of the carrier gas is estimated using equation (9) and the oxygen potential using equation (8).

In case of VER-Phase2-unBA, the carrier gas is a (H_2O/He) mixture flowing under a total gas pressure of 1 Bar. The H_2O and He flow rates (in molar scale) are h_2o and he respectively.

As $h_2 \ll o_2 \ll h_2o$, the H_2O partial pressure at equilibrium writes:

$$pH_2O \approx P_w \approx \frac{1}{1+\frac{he}{h_2o}} \quad (10)$$

The H_2 partial pressure in the carrier gas meets the relation (11) in consistency with the perfect gas law.

$$pH_2 = \frac{h_2}{h_2o} * pH_2O \approx \frac{h_2}{h_2o} * P_w \quad (11)$$

At equilibrium, equation (2) gives $h_2 = 2o_2$, that is:

$$pO_2 = \frac{1}{2} * pH_2 \approx \frac{1}{2} * \frac{h_2}{h_2o} * P_w \quad (12)$$

Combining equations (9) and (12) leads to:

$$\frac{1}{2} * \left(\frac{h_2}{h_2o}\right) * P_w \approx K_e(T) * \left(\frac{h_2o}{h_2}\right)^2 \quad (13)$$

$$\frac{h_2}{h_2o} \approx \left(\frac{2 * K_p(T)}{P_w}\right)^{\frac{1}{3}} \quad (14)$$

Combining equations (12) and (14) gives then:

$$pO_2 = \frac{1}{2} * pH_2 \approx \left(\frac{K_p(T)}{4}\right)^{\frac{1}{3}} * P_w{}^{\frac{2}{3}} \quad (15)$$

In equation (15), the units are as follows: pO_2, $K_e(T)$, P_w in Bar.
In VER-Phase2-unBA, the O_2 partial pressure in the carrier gas is estimated using equation (15) assuming the test is carried out under a total gas pressure of 1 Bar. The oxygen potential is estimated using equation (8).

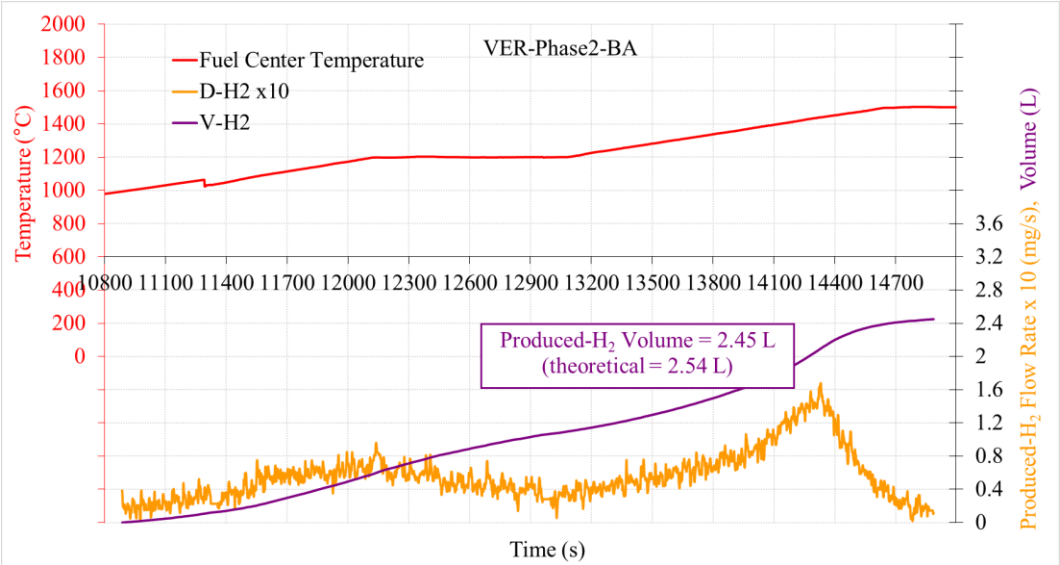

Figure 1. VER-Phase2-BA test: Experimental measurements of the H_2 flow-rate produced by the Zr-clad oxidation between 1000°C and 1500°C.

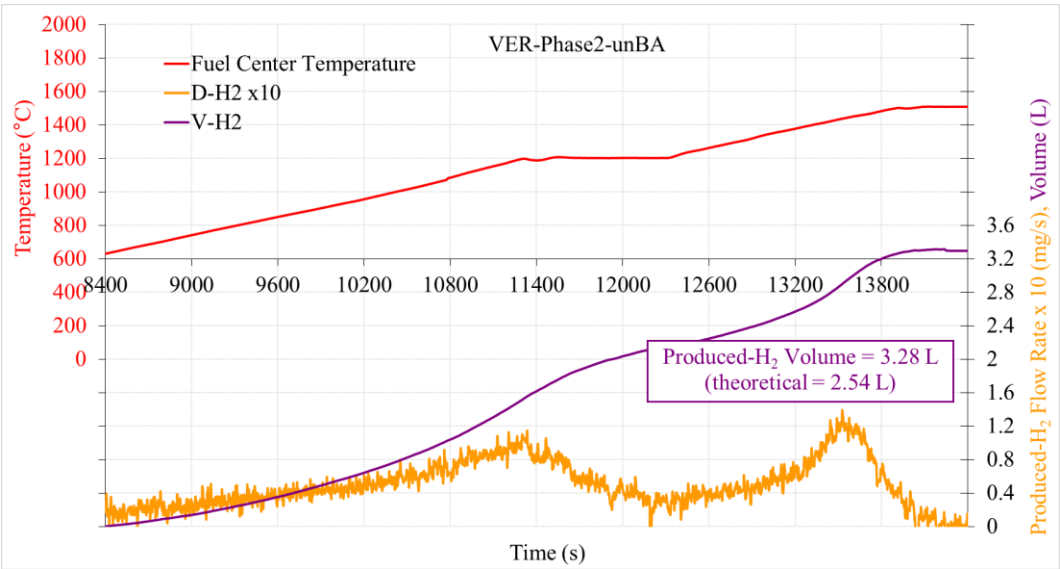

Figure 2. VER-Phase2-unBA test: Experimental measurements of the H_2 flow-rate produced by Zr-clad oxidation between 600°C and 1500°C.

The assumption underlying the estimation of the O_2 partial pressure using equations (4), (9) and (15) is that all H-containing gaseous species such as H(g) or OH(g) other than H_2 (cf. equation (2)) are insignificant in the gas phase at any temperature. In fact, this assumption may be invalid at very high temperature depending on the composition of the system. For 100% H_2O for example, we observed that H-containing gaseous species other than H_2 introduce a bias in the estimation of the O_2 partial pressure greater than 20% above 2000°C. This results in an error in the estimation of the oxygen potential ranging from 4% to 10% between 2000°C and 2500°C.
However, since this difference is not essential for the purposes of the present study, equations (4), (9) and (15) were applied in the calculations throughout the whole temperature range of interest.

4. RESULTS AND DISCUSSION

4.1. Oxygen potential profiles

The oxygen potential profiles of the gas in interaction with the sample taking into account the H_2 release resulting from the clad oxidation are given in Figures 3 and 4 for the VER-PHASE2-BA and VER-Phase2-unBA tests respectively. Calculations were carried out using the equations detailed in §. 3. For ease of analysis, O_2 potential profiles for (H_2O, 0 or 8.17% He), (H_2, 0.02%H_2O) and (MoO_2, Mo) were added in Figures 3 and 4. The reasons are as follows: i) The (H_2O, 0 or 8.17% He) and (H_2, 0.02%H_2O) profiles delimit the whole electro-activity domain experimentally accessible for each test. The oxidizing limit is estimated from a carrier gas consisting mainly of steam (> 92%). The reducing limit is estimated from a pure H_2 gas including 0.02% of residual H_2O traces. ii) the oxygen potential for an irradiated fuel is expected to be in the vicinity of the (MoO_2/Mo) redox buffer in normal operating conditions at approximately 1000°C.

In case of VER-Phase2-BA test, the incoming gas consists in a mixture (H_2O/H_2) with a molar (or pressure) ratio H_2O/H_2 of 6.2. The production of H_2 resulting from the clad oxidation takes place in the range [1000°C, 1500°C]. In that range, the molar (or pressure) ratio H_2O/H_2 of the gas in contact with the sample, including the H_2 produced, decreases down to 5.5 +/- 1.6 throughout the clad oxidation phase. As shown in Figure 3, the production of H_2 from clad oxidation does not affect significantly the oxygen potential of the gas in contact with the sample. Indeed, as the (H_2O/H_2) carrier gas is already buffered in O_2 at the entrance of the furnace, the redox perturbation resulting from the clad oxidation is greatly attenuated in the atmosphere around the sample. In the experimental conditions of the test, the amount of H_2 produced is not sufficient to induce a significant variation in the oxygen potential of the atmosphere. Therefore, the oxygen potential is still controlled by the incoming carrier gas during the clad oxidation phase.

In contrast, in case of VER-Phase2-unBA test, the carrier gas, consisting of a mixture (H_2O/He), is not buffered in O_2 at the furnace entrance: Its H_2 and O_2 contents are controlled by the H_2O dissociation only. As a result, the initial H_2 content of the carrier gas is very low (molar $H_2O/H_2 > 100$ at $T < 1300$°C). As shown in Figure 4, the production of H_2 resulting from the clad oxidation takes place in the range [600°C, 1500°C]. Then, the molar (or pressure) ratio H_2O/H_2 of the gas in contact with the sample, including the produced H_2 drastically decreases in the range [1 – 13] throughout the clad oxidation phase. The rather large variations in H_2O/H_2 are directly linked to the variations in the H_2 release from the clad, as the carrier gas is not buffered initially (contrary to the VER-Phase2-BA test). Consequently, in the experimental conditions of VER-Phase2-unBA, the production of H_2 resulting from the clad oxidation causes an intense reducing perturbation in the atmosphere. The oxygen potential of the gas in contact with the sample is therefore controlled by the H_2 produced by the clad oxidation, and not by the incoming carrier gas (as in case of VER-Phase2-BA).

By comparing Figures 3 and 4, it is shown that the oxygen potential of the gas in contact with the sample ranges between -350 and -250 kJ/mol O_2 during the clad oxidation stage, for both tests VER-Phase2-BA and -unBA. The range of variation of μO_2 is in fact the same for both tests, though the initial composition of the carrier gas is different. However, the redox conditions are much better controlled in case of VER-Phase2-BA (smaller fluctuations), where the carrier gas is initially buffered in O_2 when entering the furnace.

In both tests, the oxygen potential during the clad oxidation stage is not far from the (MoO_2/Mo) redox buffer, but rather on the oxidising side of the buffer (MoO_2 stability area). However, as shown in Figure 4 for VER-Phase2-unBA, the oxygen potential can decrease until reaching the reducing side of the buffer (stability zone Mo) when the H_2 flow-rate reaches its maximum.

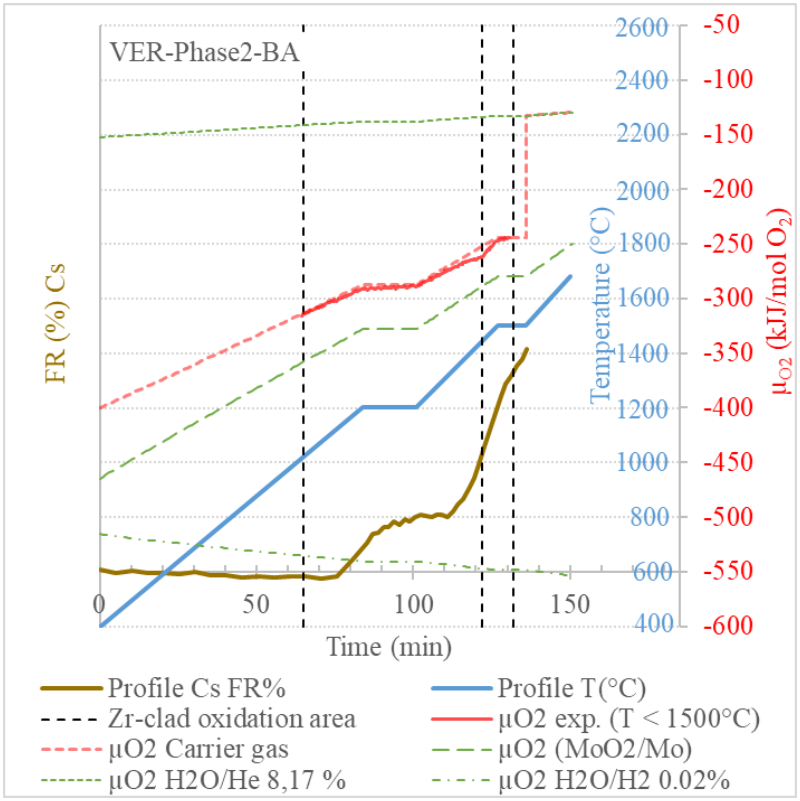

Fig. 3a. Cesium release profile in VER-PHASE2-BA test

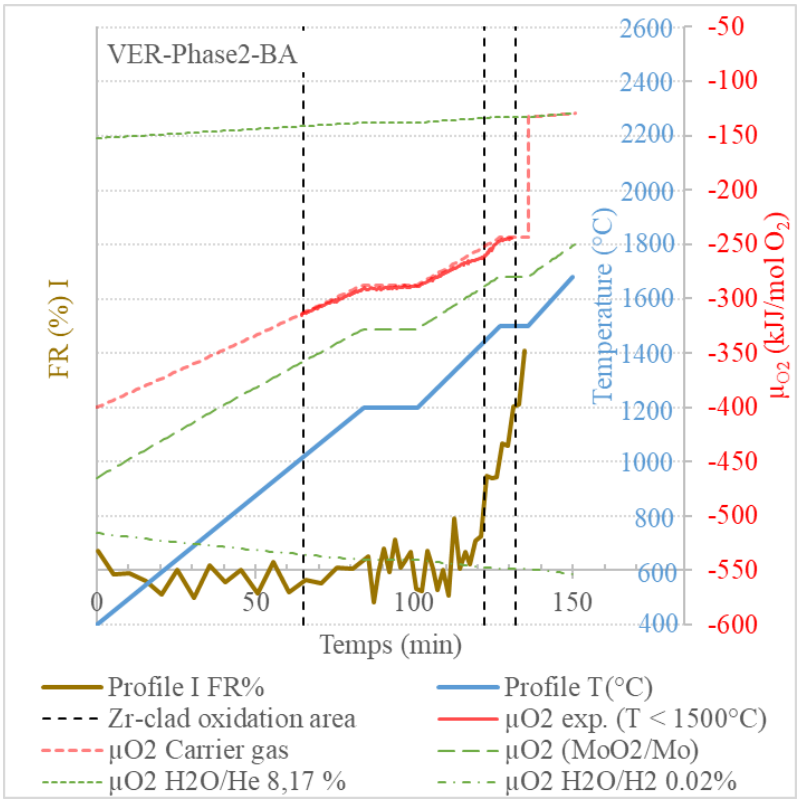

Fig. 3b. Iodine release profile in VER-PHASE2-BA test

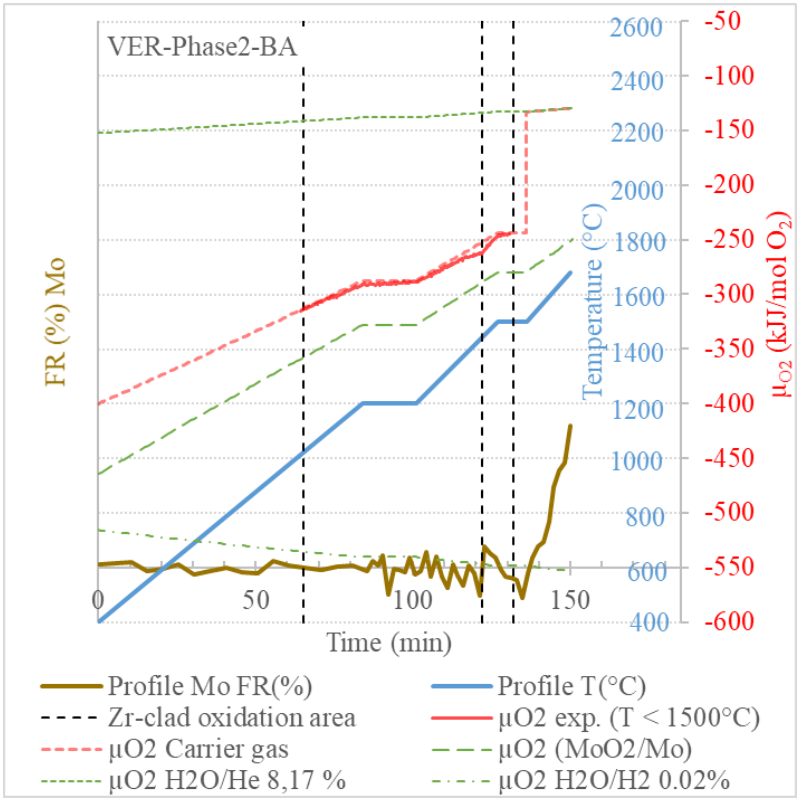

Fig. 3c. Molybdenum release profile in VER-PHASE2-BA test

Figure 3. VER-Phase2-BA test: Release profiles of Cs, I and Mo compared to temperature and oxygen potential profiles

4.2. Speciation of volatile FPs released during the clad oxidation stage

As the variation ranges of T and μO_2 during the clad oxidation stage are similar for both tests, similar release kinetics and speciation of the volatile FPs freed from the samples (Cs, I and Mo) in the temperature range of interest are expected.

By superimposing the release profiles of Cs, Mo and I with the relevant O_2 potential profiles for each test, one observes (cf. Figures 3a, 3b, 3c, cf. Figures 4a, 4b, 4c) that the releases of these three FPs begins either during or at the end of the clad oxidation stage.

Thus, for both VER-Phase2-BA and VER-Phase2-unBA tests:

- Caesium is released first from about 1200°C (cf. Figures 3a and 4a). The oxygen potential is then in the range [-320; -300] kJ/mol O_2. The most stable gaseous species of Caesium at this point is Cs(OH)(g) and Cs(g) to a lesser extent.

- Iodine is released second from 1350°C (cf. Figures 3b and 4b). The oxygen potential is then about -275 kJ/mol O_2. At this point, Cs and I are released together. The most stable gaseous species are CsI(g), Cs(OH)(g) and Cs(g).

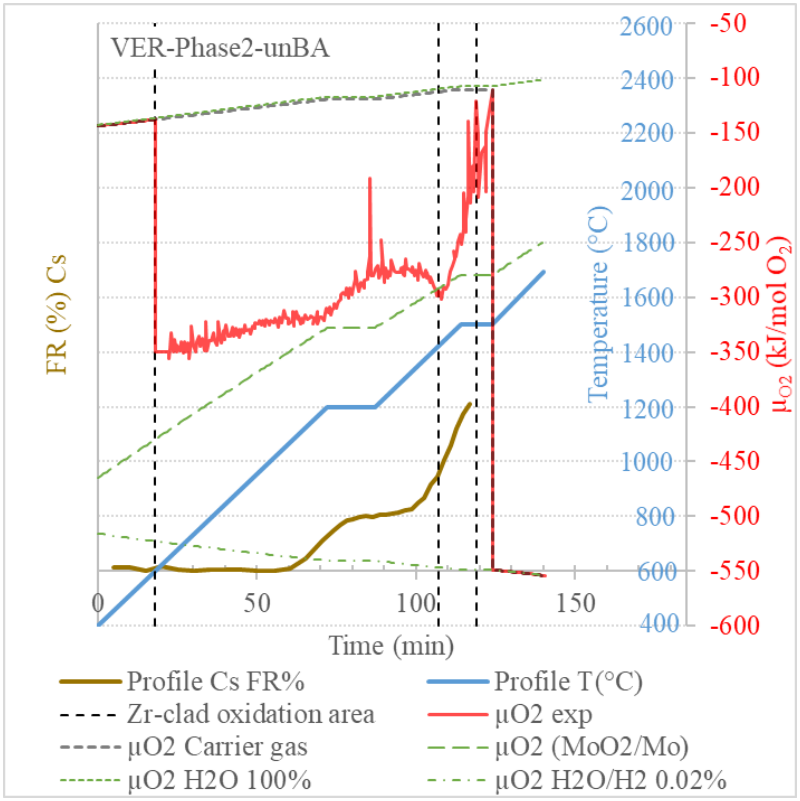

Fig. 4a. Cesium release profile in VER-Phase2-unBA test

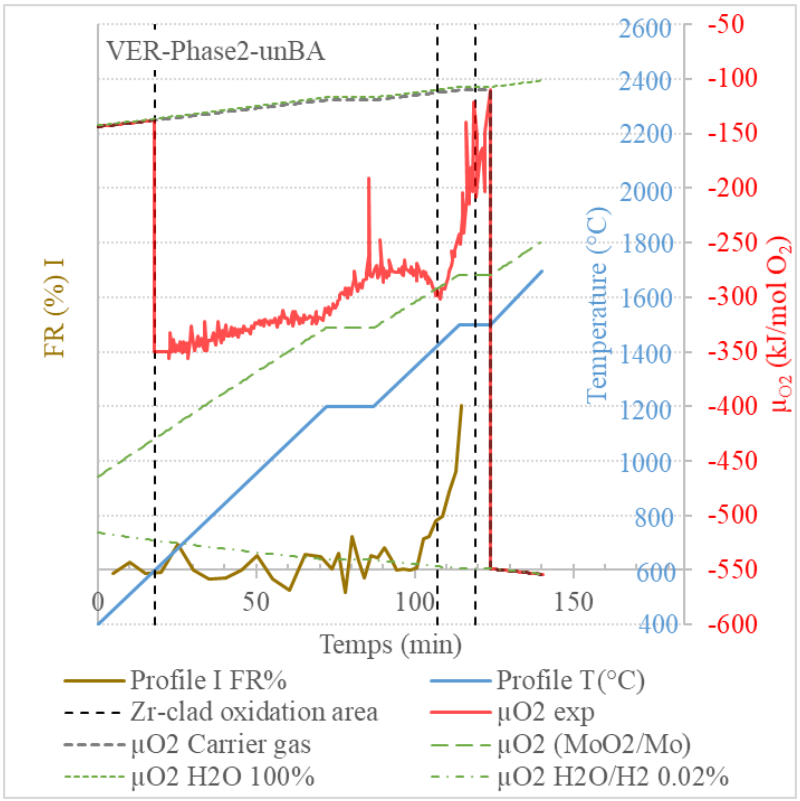

Fig. 4b. Iodine release profile in VER-Phase2-unBA test

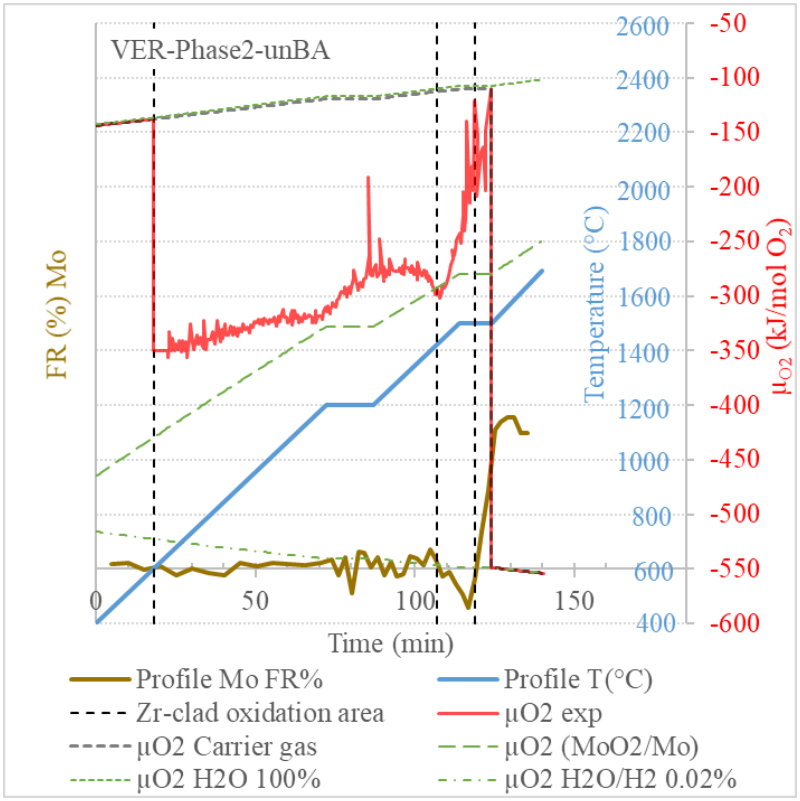

Fig. 4c. Molybdenum release profile in VER-Phase2-unBA test

Figure 4. VER-Phase2-unBA test: Release profiles of Cs, I and Mo compared to temperature and oxygen potential profiles

- Molybdenum is last released from the temperature plateau of 1500°C (cf. Figures 3c and 4c) as soon as the oxygen potential exceeds that of the buffer system (MoO_2/Mo). In reverse, as shown in Figure 4c for VER-Phase2-unBA test, the release of Mo stops once the O_2 potential drops below the potential threshold of the (MoO_2/Mo) redox buffer. This is consistent with the fact that in reducing conditions, Mo is stabilized in metal form Mo(sc) of low volatility, which results in the immediate stop of its release.
From this point, Mo, Cs and I are released together from the fuel sample. The most stable species are i) CsI(g), Molybdenum oxides of type MoO_x(g) and Caesium molybdates of type $Cs_2Mo_nO_{3n+1}$(g) (n = 1, 2) in oxidising conditions ii) CsI(g) and Cs(g) in reducing conditions (no Mo-containing gaseous species).

5. CONCLUSION

A quantitative assessment of how Zr-clad oxidation can affect the speciation and release of FPs under accidental conditions has been carried out using the experience feedback collected at CEA within the VERDON program. Redox equilibrium calculations of the (H_2O/H_2) system have shown that the H_2 produced by the Zr-clad oxidation under humid conditions can cause a more or less significant reducing perturbation on the carrier gas (He/H_2O/H_2) coming in contact with the fuel sample.

The magnitude of the reducing perturbation was found to depend on the composition of the initial carrier gas. It is very large under un-buffered humid conditions (H_2O gas) whereas it can be much weaker, or even become non-existent, if the incoming carrier gas is initially buffered in O_2, using a H_2O/H_2 gas mixture. As soon as the Zr-oxidation stage is over, the oxygen potential of the gas in contact with the sample suddenly increases to the level imposed by the initial carrier gas.

In the experimental conditions of the VERCORS/VERDON tests, the oxygen potential of the gas during the clad oxidation taking place in the range [600°C-1500°C], turned out to be close to that of (MoO_2/Mo) redox buffer, within the stability area of MoO_2. It was predicted therefore that the most stable gaseous species of volatile FPs released from the fuel at this stage were i) Cs(OH) (g) and Cs(g) from ~1200°C ii) CsI (g), Cs(OH) (g) and Cs(g) from ~1350°C iii) CsI, gaseous Molybdenum oxides and gaseous Caesium molybdates at the temperature plateau of 1500°C. Release of Molybdenum stops once the oxygen potential drops below that of the (MoO_2/Mo) redox buffer. In these later conditions, Cs(g) and CsI(g) are the only major gaseous species of FPs likely to release.

This work demonstrates that the reducing perturbation resulting from the Zr-clad oxidation under SA conditions is likely to modify the thermodynamic parameters, which governs the speciation and release of some volatile FPs. It is therefore essential to consider this phenomenon when modelling the FPs speciation and release kinetics as well as when assessing the FPs Source Term under SA conditions.

These conclusions are in line with previous simulations of SA tests performed on UO_2 fuel rods [8] and imply that the clad oxidation kinetics must be integrated in SA codes to model precisely the changing external conditions during the tests.

NOMENCLATURE

SA	:	Severe Accident
PWR	:	Pressurized Water Reactor
FP	:	Fission Product
FR (%) X	:	Released Fraction (in %) of the Fission Product X
(g)	:	(gas)
(sc)	:	(solid compound)

ACKNOWLEDGMENTS

The authors wish to thank their colleagues Yves Pontillon, Jérôme Sercombe and Jacques Léchelle for careful review of the article and valuable suggestions to improve the manuscript.

REFERENCES

1. Y. Pontillon *et al.*, “Behaviour of fission products under severe PWR accident conditions VERCORS experimental programme”, *Nuclear Engineering and Design*, **240** (7), pp. 1843-1852 ;1853-1866 ;1867-1881 (2010)
2. Y. Pontillon *et al.*, “Fission products and nuclear fuel behaviour under severe accident conditions”, *Journal of Nuclear Materials*, **495**, pp.49-57 ; 291-298 ; 363-384 (2017)
3. A. Gallais-During *et al.*, “Overview of the VERDON-ISTP Program and main insights from the VERDON-2 air ingress test”, *Annals of Nuclear Energy*, **101**, pp. 109-117 (2017)
4. C. Le Gall *et al.*, “Fission product speciation in the VERDON-3 and VERDON-4 MOX fuels samples”, *Journal of Nuclear Materials*, **530**, 151948 (2020)
5. C. Le Gall *et al.*, “MOX fuel microstructural evolution during the VERDON-3 and 4 tests”, *Journal of Nuclear Materials*, **531**, 152015 (2020)
6. *“Compendium of Terminology in Analytical Chemistry”*, IUPAC Orange Book, prepared for publication by D Brynn Hibbert, The Royal Society of Chemistry, 2023
7. *“FactSage”*, https://www.factsage.com/
8. A. Germain *et al.*, “Coupled modelling of irradiated fuel thermochemistry and gas diffusion during severe accidents”, *Journal of Nuclear Materials*, **560**, 153429 (2022)

LPM VS. 3D ANALYSIS OF AN IN-VESSEL LBLOCA SEQUENCE USING THE ALMARAZ NPP GOTHIC CONTAINMENT MODEL

Carlota Gabicagogeascoa-Cuesta*, Sofía Arfinengo-del-Carpio, Carlos Vázquez-Rodríguez
Gonzalo Jiménez
Universidad Politécnica de Madrid
C. de José Gutiérrez Abascal, 2, 28006 Madrid
c.gcuesta@alumnos.upm.es; s.arfinengo@upm.es; c.vazquez@upm.es; gonzalo.jimenez@upm.es

Luis Rey
Iberdrola Generación Nuclear
c/ Tomás Redondo, 1, 28033 Madrid

Juan Carlos Martínez-Murillo
Centrales Nucleares Almaraz-Trillo
Av. de Manoteras, 46, 28050 Madrid

ABSTRACT

Thermal-hydraulic codes are used to simulate possible accident scenarios in a nuclear power plant (NPP) containment building. However, its configuration is very large and complex and involves a wide range of different types of phenomena. Therefore, the thermal-hydraulics calculations in these types of simulations lead to a very demanding and challenging task, due to the difficulty of developing an optimal model that accurately represents the geometry while maintaining an affordable computational time, especially for 3D models.

Traditionally, Lumped Parameters (LP) models have been extensively used for licensing and severe accident analysis, as the models have proved to adequately represent average pressure and temperature trends with an affordable computational cost. However, they have limitations when it comes to simulating three-dimensional flow patterns, not being able to capture local effects caused by the containment geometrical constraints. Due to the increase of computational resources, these limitations can be overcome through the complementary use of 3D models, which provide a more detailed level of geometrical information, positioning them as a useful tool for the study of the 3D thermal-hydraulics inside the containment of a NPP.

GOTHIC is a thermal-hydraulic code with 3D capabilities, which uses a Cartesian mesh. It formulates the conservation equations using the porous media approach, which means that the geometry is constructed by defining simple solid shapes in the fluid domain. The solids, also known as blockages, can partially or completely occupy the cell volume and cell faces, meaning that the liquid and solid phases are allowed to coexist in the same cell unlike most of the CFD codes.

For this study, two GOTHIC models of the containment building of the Almaraz NPP have been compared. The first model is a single node LP type and the second one is a three-dimensional integral model, where all the rooms and compartments are represented using a single control volume.

In previous works carried out by the Universidad Politécnica de Madrid (UPM), the integral model of the Almaraz NPP was designed following a new methodology called “preventive methodology”(Vázquez-Rodríguez 2023). This methodology attempts to preventively avoid the appearance of problematic

configurations that lead to convergence errors and even the simulation interruption, such as the connection of two cells with significantly different free volumes. Therefore, this methodology consists of adapting the models geometrically to the Cartesian mesh, thereby decreasing the computational cost. The modelling process consists of developing a detailed CAD geometry from plant layouts, then simplifying the geometry in CAD in such a way that it complies with GOTHIC's modelling and domain discretization particularities.

The single node LP model has been developed from the 3D model, and particular attention has been paid to ensure the consistency of all parameters in both models. As a result, the free volume, material properties, thermal structures and boundary conditions are identical for both models.

The analyzed severe accident transient consists of a mass and energy release coming from a double-ended guillotine-break LOCA obtained from the UPM PWR-Westinghouse MELCOR model (Bocanegra et al. 2016) and the consequences of the transient evolution are unmitigated.

Subsequently, the results obtained from the LP and the 3D model of the Almaraz NPP were compared. Firstly, the averaged pressure and temperature values comparison shows a first pressure peak in both models almost identical (353 kPa), while the second pressure peak, caused by the zirconium oxidation, is slightly higher in the 3D model (36.861 kPa higher). This pressure difference can be explained by looking at the temperature evolution in each room of the 3D model, where, in certain rooms, the maximum temperature peak in that instant, exceeds the average temperature values.

This pressure and temperature difference might be caused by the nature of a single node LP model, in which, once the mass and energy are released, the vapor immediately interacts with all the thermal structures. As a result, the steam condensation occurs instantaneously, leading to an early cooling of the free volume and preventing the generation of sharp temperature peaks. In contrast, in the 3D model, there may be a time delay between the release of mass and energy and the interaction between the vapor and the containment structures. It is important to mention that it is possible to represent the temperature heterogeneity with LP models to a certain level by using a more complex nodalization.(Carlos Vazquez-Rodriguez et al. 2009)

Regarding the hydrogen concentrations, the LP model could only obtain an average value, not being able to reach the required local detail necessary to accurately predict the performance of hydrogen management systems. Meanwhile, the 3D distribution of the hydrogen demonstrates that locally, hydrogen concentration values are higher than the one obtained in the lumped model.

References

Bocanegra R, Ruiz-Zapatero M, Jimenez G, Queral C (2016) Enhanced MELCOR models for standard PWR-Westinghouse design.

Carlos Vazquez-Rodriguez, Rafael Bocanegra, Gonzalo Jiménez, Luis Rey, Andrea Cadenas, José María Posada, Juan Carlos Martínez-Murillo (2009) Toward Conservatism in Containment Design Basis Accident Analyses. Lumped parameters and 3D Approaches. Journal of the Atomic Energy Society of Japan 51: 702–702. https://doi.org/10.3327/jaesjb.51.9_702

Vázquez-Rodríguez (2023) ADVANCED IMPLEMENTATION OF THE SPRAY SAFETY SYSTEM INTO A 3D-GOTHIC PWR-W CONTAINMENT MODEL AND ITS IMPACT ON THE HYDROGEN COMBUSTION RISK.

KEYWORDS
GOTHIC, THERMAL HYDRAULICS, CONTAINMENT ANALYSIS.

SEAKNOT
ERMSAR 2024
11th Conference on
SEVERE ACCIDENTS RESEARCH
May 13-16, 2024 – Stockholm, Sweden

LPM vs. 3D analysis of an in-vessel LBLOCA sequence using the Almaraz NPP GOTHIC containment model

CARLOTA GABICAGOGEASCOA CUESTA

In collaboration with: Sofía Arfinengo del Carpio (ETSII UPM), Gonzalo Jiménez (ETSII UPM), Carlos Vázquez-Rodríguez (ETSII UPM), Luis Rey (Iberdrola Generación Nuclear), Juan Carlos Martínez-Murillo (CNAT)

INTRODUCTION

- Computational codes are the most used tool to simulate possible accident scenarios in a nuclear power plant (NPP) containment building
- **Lumped Parameters** (LP) models have been thoroughly validated, and the models have proved to **accurately represent average pressure and temperature** values with an affordable computational effort. However, they have limitations when it comes to simulating three-dimensional flow patterns, not being able to capture local effects.
- **3D computational codes** provide a **detailed level of geometrical information**, positioning them as a fundamental tool for the study of the 3D thermal-hydraulics inside the containment of a NPP.

GOTHIC CODE

- 3D capabilities.
- Cartesian mesh
- Porous media approach

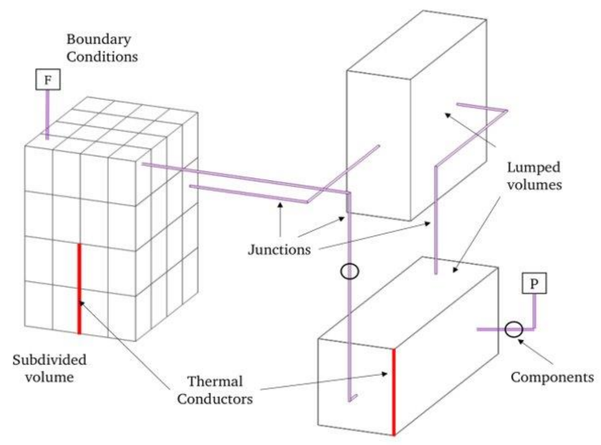

MODELLING PROCESS

3D Almaraz NPP model

Modelling decisions

- **Integral model** (single control volume)
- 1 meter side cubic homogeneous mesh

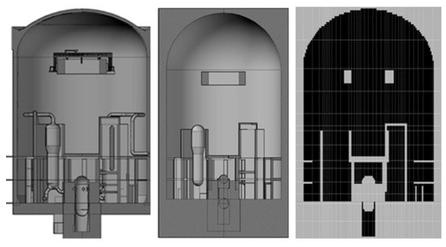

Model development process:

- **Detailed CAD geometry** from plant layouts
- **Simplified CAD geometry**, which suits GOTHIC's modelling and domain discretization particularities.
- **Model geometry in GOTHIC**.

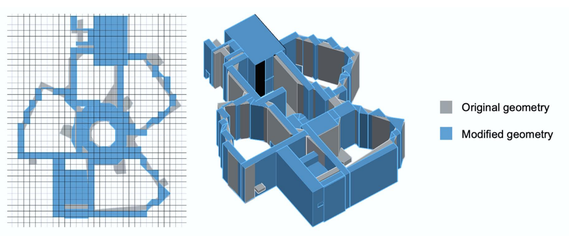

Single-node LP Almaraz NPP model

Model development process:

- The **free volume matches** the 3D model.
- All the thermal structures have been accounted for and grouped by types, while keeping the total area.

An in-vessel **severe accident sequence** triggered by a **LBLOCA** (large break loss of coolant accident) with no spray actuation has been simulated and analyzed for both models

RESULTS

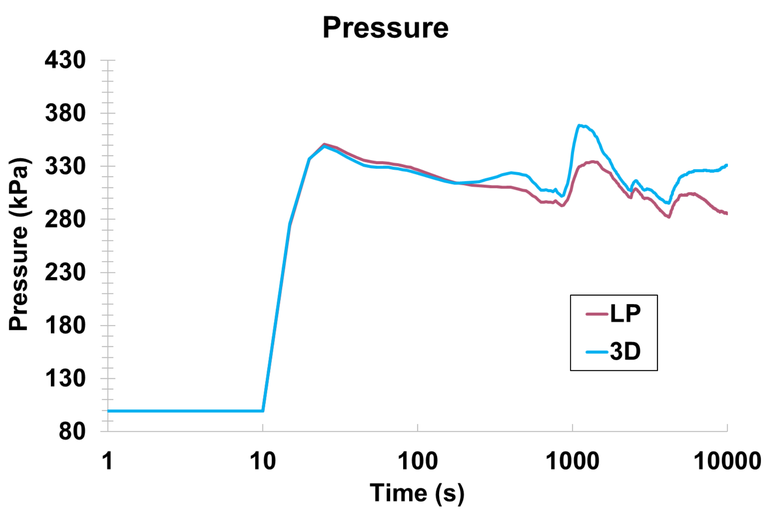

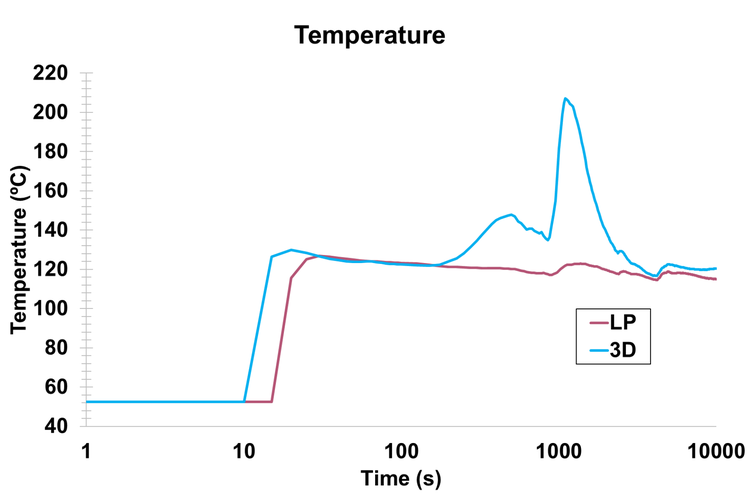

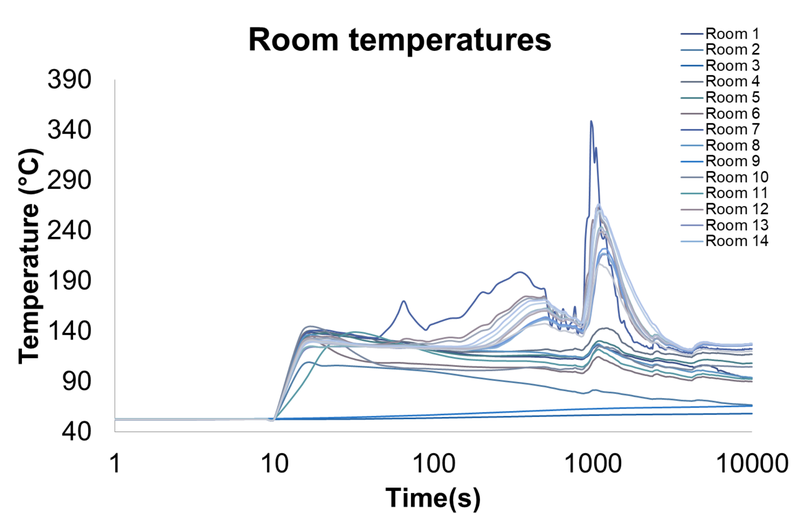

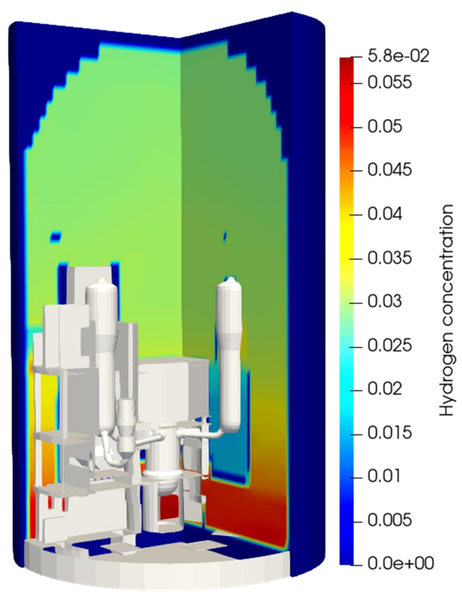

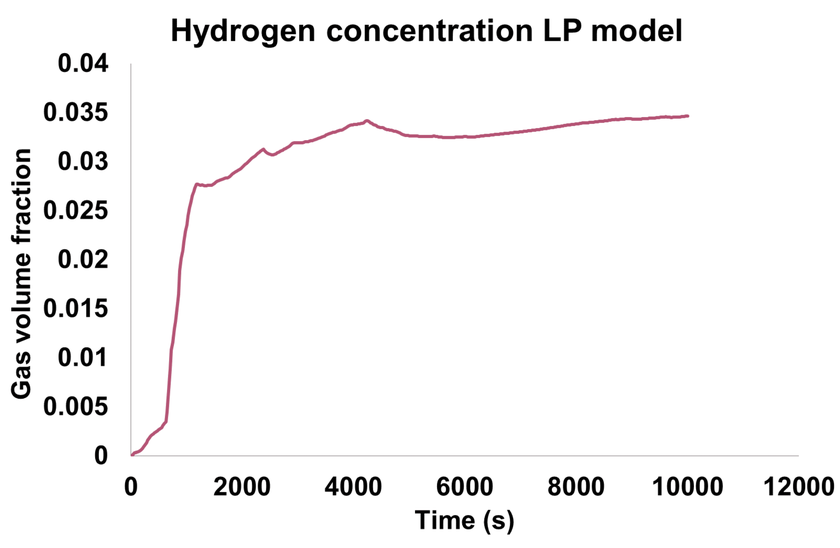

CONCLUSIONS

- The averaged pressure and temperature values were calculated and studied. The first pressure peak in both models is almost identical (**353 kPa**), while the second pressure peak, caused by the zirconium oxidation, is **slightly higher in the 3D model (37 kPa higher).**
- This difference might be caused by **the nature of a single node lumped model**, in which, once the mass and energy are released, **the vapor immediately interacts with all the thermal structures**. As a result, the steam condensation occurs instantaneously, leading to an early cooling of the free volume and preventing the generation of sharp temperature peaks.
- Regarding the hydrogen concentrations, the lumped model can only obtain an average value. **Meanwhile the 3D distribution of the hydrogen demonstrates that locally, hydrogen concentration values are higher than the one obtained in the lumped model** (0.034% vol.)

GOTHIC™ incorporates technology developed for the electric power industry under the sponsorship of EPRI, the Electric Power Research Institute. This work was completed using a GOTHIC license for educational purposes provided by Numerical Advisory Solutions, LLC.

References

- (Carlos Vazquez-Rodriguez et al. ICAP'09: 2009 International Congress on Advances in Nuclear Power Plants. "Toward Conservatism in Containment Design Basis Accident Analyses. Lumped parameters and 3D Approaches."

Carlota Gabicagogeascoa
PhD candidate in Nuclear Engineering
ETSII UPM; José Gutiérrez Abascal, 2, 28006 Madrid, Spain
Tel: +34 910677153
Email: c.gcuest@upm.es

SOME RESULTS OF THE AMICO PROJECT

Gert Langrock*, Mohammed Bendiab, Friedhelm Funke
Framatome GmbH
P.O. Box 1109, D-91001 Erlangen
*gert.langrock@framatome.com

ABSTRACT

In the R&D project „Analyses for the modelling of the iodine behaviour in containment (AMICO)“, co-funded by the German BMUV (project number 1501562), analytical work and COCOSYS calculations were carried out on different aspects of the fission product and especially the iodine behaviour in a severe accident. As part of AMICO Work Package (WP) 1.1 (Long-term development of the airborne iodine activity), the THAI test Iod-31 was calculated with COCOSYS V3 and the NewAFP module. In this experiment, after injecting iodine into the THAI test vessel, a water spray was activated for six defined time periods. This water spray transferred iodine from the atmosphere into the sump. Aim of the COCOSYS calculations was to reproduce the test results, especially the impact of the spray on the airborne iodine. It proved advantageous to define separate mass transfer coefficients (MTC's), which describe the exchange of iodine between aqueous phase and gas phase, for the spray system. MTC's which tend to be higher than the standard coefficients in COCOSYS and the simulation of the fixation of dissolved iodine in the sump proved to be suitable. Uncertainties result from experimental features that are difficult to model in the code, e.g. the short fall time of spray droplets, uncertainties about the surface of the vessel wetted by the spray cone and the iodine speciation in the sump. This affects the calculated reaction rates of iodine species in the gas phase, on dry and wet steel walls and in the sump. The COCOSYS calculations appear plausible overall, and yield indications for further experimental investigations to further validate the spray model in the code.

In a second step, the findings from the Iod-31 simulation on the effects of different mass transfer coefficients for the spray system were applied to a full-scale PWR containment simulation. As reference scenario, a large-break loss of coolant scenario was chosen, which, due to the assumed safety system failures, escalates into a nuclear accident with core damage. Three calculations were performed, each using a different set of pre-defined mass transfer coefficients for the spray system. The higher the resulting mass transfer coefficients for I_2 and for organic iodine (RI), the higher the predicted amount of airborne iodine. The increase of the RI in the variation calculations was higher than that of the I_2, making RI the dominant airborne iodine species. The higher amounts of RI and I_2 also lead to a stronger radiolytic formation of IO_x aerosols, which are washed out by the spray system and thus only accounted for about one percent of the airborne activity. This very clear result requires further analyses and evaluations.

In AMICO WP 1.2 and 1.3 (iodine modelling) various analytical and modelling work was carried out. For this purpose, a large number of new experimental data from national and international projects was evaluated and the existing modelling of the reaction with paint and steel, radiolytic iodine release from paint, radiolytic formation and decomposition of organic iodine in the gas phase and radiolytic nitric acid formation in the containment were checked and revised. Results of the AMICO WP 2 (CoPool modelling of a deep sump) and WP 3 (Iodine Uncertainty and Sensitivity Analysis) are not subject to this contribution.

KEYWORDS
iodine, organic iodine (RI), spray, mass transfer, modelling

1. INTRODUCTION

For the description of the fission product behavior in a light water reactor containment in severe accidents with fission product release from the primary circuit, the containment code system COCOSYS has been developed by GRS for many years and has been validated with the participation of several other institutions. The calculated fission product distribution in the containment is an essential basis for the calculation of the fission product release into the environment and the assessment of the radiological consequences.

COCOSYS is used for safety analyses, retrofitting or new construction projects. However, modern plant calculations require increasingly reliable calculations of

- the fission product source term to the environment with regard to compliance with regulatory limits;
- the distribution of the fission products in the containment as dose rate and decay heat sources regarding the stability of the materials used in the containment or the functionality of the installed instrumentation.

The modelling of fission product behavior in COCOSYS is subject to continuous development, by adding new phenomena or by refining, extending, or revising models of already considered phenomena. The need for further development of models arises, for example, from plant calculations, uncertainty and sensitivity studies, or from experimental findings. The continuous code improvement implies the need for continuous code validation.

The Framatome R&D project AMICO (Analysis for the modelling of the iodine behaviour in containment), co-funded by the German BMUV aimed at supporting the further development of COCOSYS by performing several tasks related to modelling and analyses of iodine behavior.

With the COCOSYS code version 3.0, the fission product module in COCOSYS was started to be restructured [1], leading to the evolution of the AFP (Aerosol and Fission Products) module into the NewAFP module, which has been incorporated in the most recent COCOSYS versions [2,3]. NewAFP contains also the Advanced Iodine Model (AIM) describing iodine chemistry. New models for the I_2/paint reaction [4] and for the wash-off of insoluble aerosols [5] have been integrated. In this form, COCOSYS was already used by Framatome (previously AREVA) in the preceding fission product project 1501457 [6], where the influences of containment-relevant phenomena on the fission product distribution were investigated. Beside other results, the AIM validation work in this preceding project helped to revise the model of the iodine/paint reaction in the gas phase [4].

COCOSYS simulations of the THAI experiment Iod-31 for iodine washout during spraying showed room for improvement in the treatment of spray systems. Therefore, further work on this topic was performed in AMICO WP 1.1, “Long-term development of airborne iodine”. The capabilities of the revised spray model in the NewAFP module was investigated by post-test calculations of the THAI Iod-31 test. The found optimization was then evaluated in a full-scale simulation of a PWR containment.

The validation work on the iodine model AIM in COCOSYS [6] was an additional reason for model improvements on the part of GRS, especially on the iodine/paint reaction. The latter had to be further optimized, based on newly produced data or new experiments. Ongoing international experimental projects, e.g. BIP-3, STEM/STEM-2, ESTER, THAI/OECD-3 and THEMIS [7-9], have also yielded new data on the iodine behaviour in containment, which can be used for analyses and, if necessary, for the further development of AIM. The AMICO WP 1.2/1.3, “Contributions to the development and validation of the AIM-4 model”, revised these analytical and modelling work.

2. POST-TEST CALCULATIONS OF THE THAI IOD-31 TEST ON IODINE SPRAYING

The THAI Iod-31 test was performed at the THAI facility at Becker Technologies in April 2016. It aimed at the investigation of the iodine wash-out from the gas atmosphere by a spray system. It was performed over two days. The detailed data are described in [10]. After a short summary of the Iod-31 test, the developed COCOSYS model will be briefly described, followed by selected results of a parametric study to explore well-suited simulation parameters to describe the test.

2.1. THAI Iod-31 test

In the Iod-31 test, gaseous iodine (I_2), labelled with radioactive I-123 ($t_{1/2}$ = 13.2 h) was injected into the dome of the THAI test vessel (TTV), a 60 m^3 steel (stainless steel, 1.4571) vessel. The TTV was connected to the PADvessel, a 20 m^3 test vessel (parallel attachable drum, 1.4571) via a lower and an upper inter-connection pipe. For a schematic depiction, see Figure 1. A full cone whirl spray nozzle (BETE, model no. 3/4WL 1230) was installed in the PAD at +3.5 m elevation. The spray was operated for six dedicated phases during the test. The first spraying was performed with fresh water, the other five sprayings were performed with recirculated water from the PAD sump ("recirculation spraying"). The sump of the PAD was initially filled with 200 l of deionized water (pH 4.5). It was be recirculated and cooled by an external cooler. With the vessel heating mantles, the temperatures were kept between 85 °C and 90 °C in the TTV and around 85 °C in the PAD vessel, with negative peaks during the spray phases. The vessel pressure was initially at 1.16 bar, with time increasing due to water evaporation from the sump and decreasing during the spray phases. The spray water flow rate was 0.8 l/s. Temperatures of the PAD sump water and of the gas atmosphere near the sump surface exhibited a more complex pattern: After the start of the test, the stagnant sump revealed a height-dependent temperature gradient from 65 °C to 18 °C. After starting the sump recirculation pump, temperatures became uniform with some peaks during and after spraying. After switching-off the recirculation pump at 11.25 h, a temperature gradient started to re-establish until the sump recirculation was switched on again, leading to uniform temperatures in the sump.

Iodine was measured in the gas phase by the well-established gas scrubber technique. Samples from the sump provided total iodine concentrations in the sump water. A direct concentration measurement by an iodide sensitive electrode to determine the amount of I_2 and I^- in the water failed. In addition, two online detectors measuring iodine deposition on two steel coupons (one has been previously used in THAI tests and represents the steel of the TTV-vessel, one fresh steel coupon represents the steel of the then new PAD-vessel) were used, complementing the gas scrubber measurements.

The main test program is summarized in Table I. Main test results, thermal-hydraulic data, and iodine measurements, are given in Chapter 2.3 together with the COCOSYS simulation results.

2.2. COCOSYS model

To perform post-test simulations of the Iod-31 test, the THAI facility was modelled in the COCOSYS code. These post-test simulations shall allow for code validation and especially the examination and optimization of the iodine modelling. Of particular interest was the question how with the experimentally observed spray effect, i.e. the wash-out and revolatilization of fission products, can be dealt and whether the IVO spray model [1, 11], recommended for the use with COCOSYS, and the modelled iodine mass transfer between gas and water phase can represent the experimental results adequately.

For this purpose, a multi-zone nodalization of the THAI facility was developed for the COCOSYS code, see Figure 1. The TTV-vessel is divided into 10 zones R0-R9, the PAD-vessel into 7 zones PR0-PR6 (with

PR0 for the lower part of the PAD vessel including the sump zone) and two zones consider the interconnecting pipes on top and bottom. Zones at the same elevation have the same volume and represent 120° segments of the axially symmetric vessels. Zones R7-R9 and PR 4-PR6 describe the upper parts of the vessels, R4-R6 and PR1 – PR4 the middle part of the vessels and R1-R3 the lower part of the TTV.

Table I. Chronological list of phases of the THAI Iod-31 experiment

***t* / h**	**Experimental Event**
0.000 – 0.167	Injection of gaseous I_2 (10 min), 0.96 g
3.000 – 3.455	1. Spray phase: Spraying with fresh water, V_{Sump} increased from 200 l to 1116 l
3.883 – 4.383	2. Spray phase: Recirculation spraying (from PAD-Sump)
4.800 – 5.3000	3. Spray phase: Recirculation spraying
11.250 – 20.000	Temporary switch-off of the PAD sump recirculation pump
21.000 – 23.000	Increase of pH in PAD sump from 4.5 to 11 with NaOH
23.383 – 23.533	4. Spray phase: Recirculation spraying (with alkalized sump water)
24.167 – 24.417	5. Spray phase: Recirculation spraying
25.333 – 25.933	6. Spray phase: Recirculation spraying
27.100 forward	Shutting-down vessel heating, sump cooling, recirculation pump

The detailed COCOSYS model including geometric data is described in [6] and [13]. In the simulations, the IVO spray model was used. A helpful new feature of more recent COCOSYS versions is the possibility to define separate mass transfer coefficients for the global mass transfer ("global" means it is applied in the simulation for all water/gas boundaries) and the mass transfer in sprays and to vary them over time. Moreover, it is possible to calculate chemical reactions in spray droplets. This may become relevant for spray systems in full-containment analyses, where the large containment height leads to long droplet drop times from the dome towards the sump.

The mass transfer is described in COCOSYS with the help of the "two film theory" describing the diffusion of a volatile species through the interface between a gaseous and an aqueous phase [1] where a partition coefficient P is used to describe the equilibrium distribution of a species between both phases. The total mass transfer coefficient of I_2 (in COCOSYS denoted as k_{35}) or of organic iodine (k_{36}) is calculated as described in Equation (1), where k_W is the water-side mass transfer coefficient (parameter name in COCOSYS is KMTWAS), k_G is the gas-side mass transfer coefficient (KMTGAS), $P(I_2)$ the partition coefficient for I_2 and $P(RI)$ for organic iodide (RI), and the water temperature T_W in K (with omitted units). Recommended values for COCOSYS application are $k_G = 1.4 \cdot 10^{-3}$ m/s and $k_W = 1.0 \cdot 10^{-5}$ m/s.

$$\frac{1}{k_{35}} = \frac{1}{k_W} + \frac{P(I_2)}{k_G} \qquad \frac{1}{k_{36}} = \frac{1}{k_W} + \frac{P(RI)}{k_G}$$
$$with\ P(I_2) = 10^{(9.132E5 \cdot T_w^{-2} - 4.1E3 \cdot T_w^{-1} + 5.404)} \qquad P(RI) = e^{-6.97 + \frac{2641}{T_W}} \tag{1}$$

The impact of the iodine mass transfer on the gaseous I_2 concentration is calculated according to Equation (2), with $S_{W/G}$ as the surface area of the water/gas interface (sump surface or spray droplet surface), V_G as the gas volume, and $[I_2(g)]$ and $[I_2(w)]$ as the I_2 concentrations in gas and water:

$$\frac{d([I_2(g)])}{dt} = k_{35} \cdot \frac{S_{W/G}}{V_G} \cdot ([I_2(w)] - [I_2(g)] \cdot P(I_2)) \qquad (2)$$

After test calculations with a base case (ID: T31L-50, with standard parameters, no separate mass transfer coefficients for the spray system), systematic variations of relevant model parameters were performed:

- variation of global mass transfer coefficients (MTC's)
- variation of the MTC's for the spray system, independently of the global MTC's
- pH of the sump
- variation of the rate constant of the Fe/I_2 reaction on steel immersed in water to treat the possible conversion of I_2 to I^- in the water phase

of which some relevant results are presented. The calculations were performed with a COCOSYS developer version 3.1beta (rev. 8125:8137M) with the improved NewAFP module on a 64 bit Windows PC.

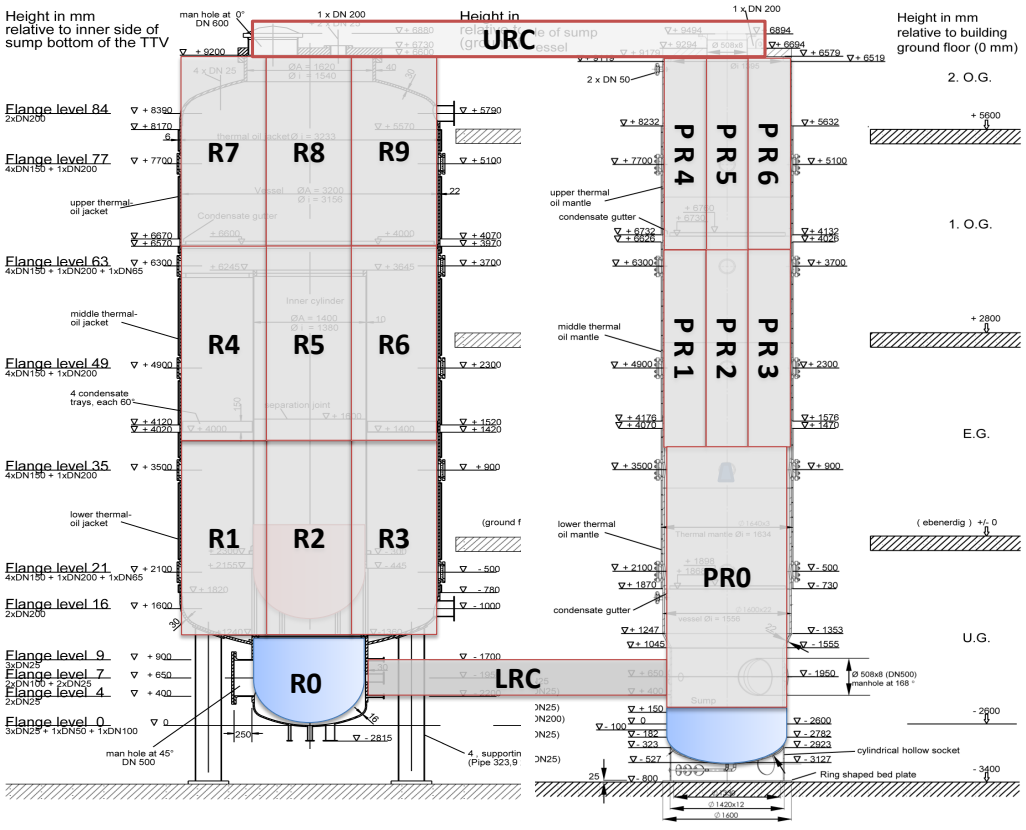

Figure 1. COCOSYS nodalization of the THAI+ facility for the test Iod-31

2.3. Results of the parametric study

The performed COCOSYS calculations were able to reproduce the thermal-hydraulic conditions of the THAI Iod-31 test very well. Figure 2 provides as example the gas temperatures in the PAD-vessel from the base case. Experimental temperatures (averaged temperatures from several measuring points, denoted as

Mitt_T in the figures) were well reproduced in the fluid (upper part, left figure) and in the lower part (above the PAD sump, right figure). The temperature decreases during spraying were visible with a tendency to a slight overestimation of the gas cooling by few Kelvin in COCOSYS. Figure 3 provides the sump temperatures (left figure) and the system pressure (right figure), showing generally a good agreement between simulation and experiment.

Different sets of MTC's were used in the following cases, one set for the global mass transfer and a different set for the spray system. To match the slow I_2 entrainment to the sump in the time between iodine injection (0 h) and the first spraying phase (3 h), low MTC were chosen with k_G = 1.4E-4 m/s and k_W = 1.0E-6 m/s, giving a total MTC of k_{35} = 7.3E-7 m/s. For case (ID) T31L-59, no separate MTC's were defined for the spray system. As can be seen in Figure 4, with these standard values, the impact of spraying on the iodine entrainment to the sump is predicted far too low, in comparison to the experiment, leading to an under-estimation of the sump iodine content by an order of magnitude.

For the next simulation case (ID: T31L-60), a separate set of MTC's was defined for the spray with k_G = 1.1E-1 m/s and k_W = 7.0E-5 m/s, resulting in k_{35} = 6.8E-5 m/s. These values are based on recommendations in [12]. As can be seen in Figure 4, this change significantly increases the initial iodine transfer from the atmosphere to the sump in the simulation. However, as I_2 is volatile, it can evaporate from the sump and the spray droplets, and since the pH of 4.5 favours the dominance of I_2 over its hydrolysis products HOI, I^- and IO_3^-, the I_2 cannot be retained in the water phase and is released back into the atmosphere. Only after alkalization, the iodine increase in the sump becomes irreversible during the 4th to 6th spray phases. This calculated behaviour is not consistent with the experimental finding of a quick and strong fixation of iodine in the sump even at pH 4.5. It was assumed that the experimentally observed iodine fixation is to a significant extent due to the reaction of I_2 with the steel walls of the PAD sump. The COCOSYS rate constant k_{55} for this reaction was therefore arbitrarily increased by a factor 100 (case T31L-62). The calculated iodine behaviour is then significantly improved (Figure 5) with a quick formation of iodide as the main species in the sump water. However, the extent of the iodine transfer to the sump by spray is still not reproduced. This led to another calculation (T61L-63) with increased spray MTC's. The MTC's for the spray were chosen according to [Reinke 2019]. In this calculation, the pH of the sump was set to 7.0 to enforce the formation of the non-volatile hydrolysis products I^-, HOI, IO_3^- whereas k_{55} was set to standard value (Figure 6, left). The extent of iodine entrainment in the sump is perfectly met for the first spray, telling that this is a good set of MTC's for the investigated spray system. However, for the later course of the test, COCOSYS does not reproduce the 4th to 6th spray phases, very likely due to the volatile intermediate volatile species HOI. The iodine concentrations in the gas phase (see Figure 6, right) mirrors this picture with a good agreement between experimental and calculated values during the first 15-20 hours of the test, while after alkalization of the PAD sump they are calculated conservatively high.

To conclude, numerous COCOSYS calculations of the THAI test Iod-31 have shown that the improved NewAFP spray model is able to demonstrate the impact of spray systems on iodine in the gas phase ("spray effect"). The wash-out of iodine from the gas phase can be well reproduced with the chosen set of mass transfer coefficient. It is advisable to use mass transfer coefficients for sprays higher than the standard values of COCOSYS (which actually describe a stagnant sump) to properly describe the take-up of iodine in the spray droplets and its transfer to the sump. It was difficult to reproduce the iodine increase in the sump during the 4th to 6th spray phases of the test after sump alkalization. Based on a more detailed analysis and discussion in [13] it is believed that this is mainly due to some experimental specifics of the test where probably also wet walls led to a higher iodine deposition on dry and wet steel walls and part of the iodine increase in the sump can be attributed to the wash-down of iodine from the steel walls. Without further elucidation and modelling of these phenomena, the two chosen sets of spray MTC's with 7.0E-5/1.1E-1

m/s and 3.0E-4/1.1E-1 m/s (and values in between) seem to be suitable for the application for spray systems. Both demonstrate the spray effect clearly.

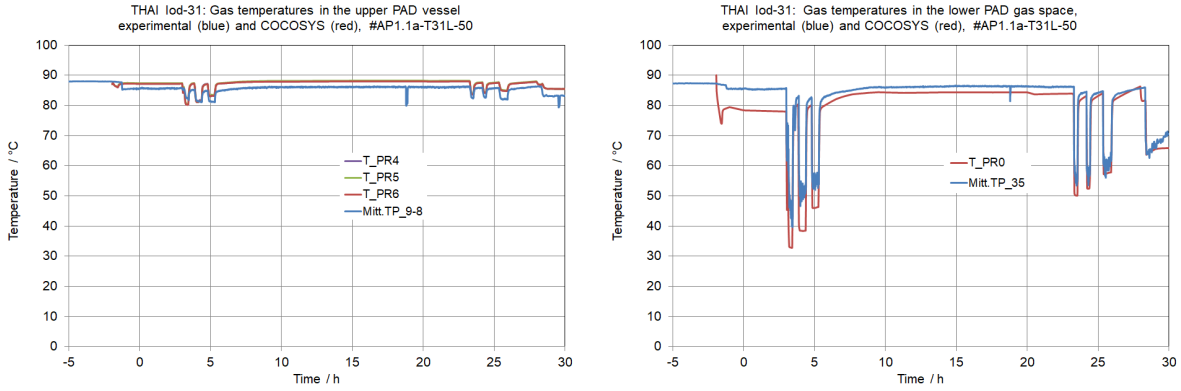

Figure 2. Experimental ("Mitt.TP_9-8") and calculated gas temperatures in the upper (left figure) and lower (right figure) part of the PAD vessel during the THAI test Iod-31

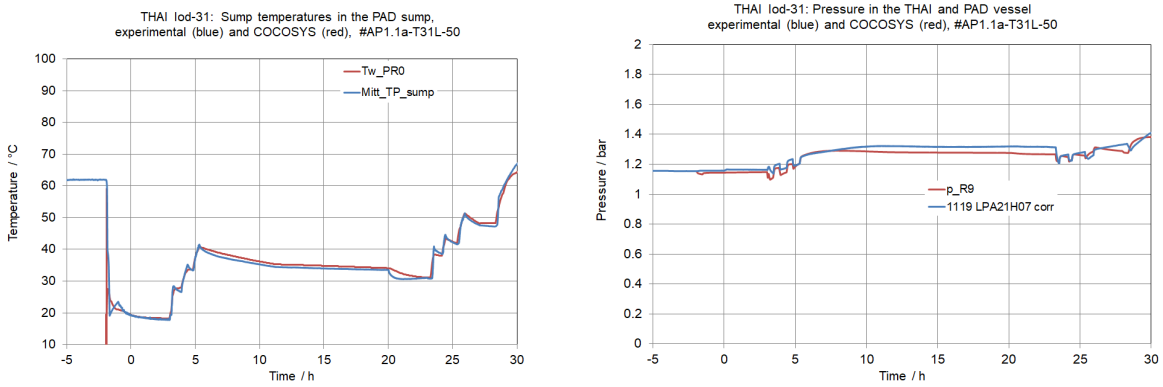

Figure 3. Experimental (averaged, "Mitt_TP_sump") and calculated water temperatures in the PAD sump (left figure) and pressure during the THAI test Iod-31

Table II. Calculation cases and varied parameters of some of the performed post-test calculations

Case (ID) T31L-	Parameters										
	Global MTC's			Spray-MTC's			pH sump	pH spray			Chem-istry
	k_G / m/s (KMTGAS)	k_W / m/s (KMTWAS)	k_{35} / m/s (35 °C)	k_G / m/s (KMTGAS)	k_W / m/s (KMTWAS)	k_{35} / m/s (35 °C)	PAD	1.	2./3.	4.-6.	
59	1.4E-4	1.0E-6	7.3E-7	-	-	-	4.5 / 11.0	7.0	7.0	11.0	
60	1.4E-4	1.0E-6	7.3E-7	1.1E-1	7.0E-5	6.8E-5	4.5 / 11.0	7.0	7.0	11.0	
62	1.4E-4	1.0E-6	7.3E-7	1.1E-1	7.0E-5	6.8E-5	4.5 / 11.0	7.0	7.0	11.0	k_{55} ↑
63	1.4E-4	1.0E-6	7.3E-7	1.1E-1	3.0E-4	2.6E-4	7.0 / 11.0	7.0	7.0	11.0	

NB: The mass transfer constants k_{35}/k_{36} are calculated for a temperature of 35 °C

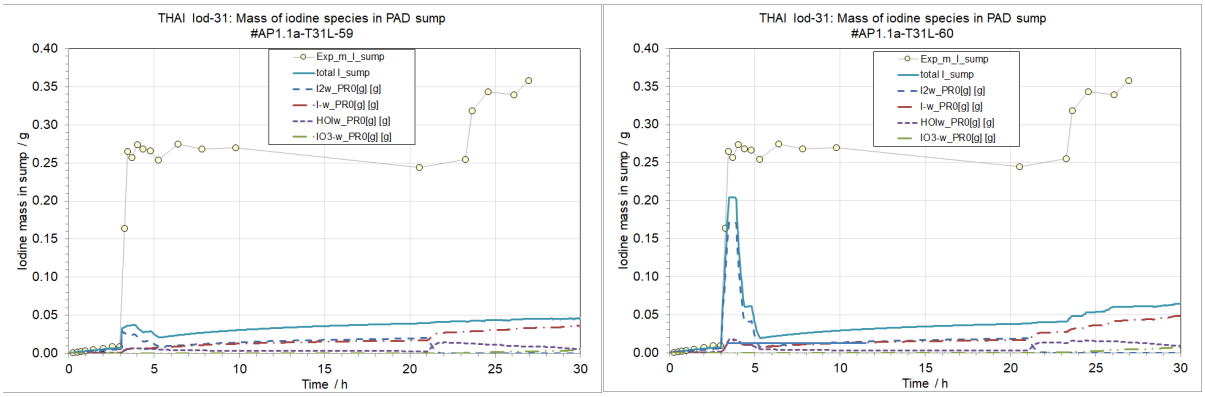

Figure 4. Experimental and calculated iodine species concentrations in the PAD sump during the THAI test Iod-31. Case T31L-59 (left figure) and T31L-60 (right figure)

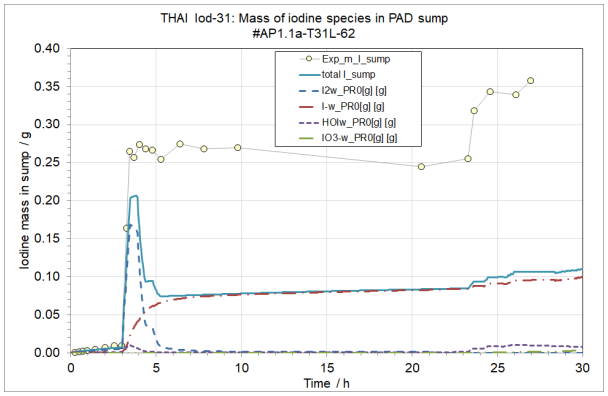

Figure 5. Experimental and calculated iodine species concentrations in the PAD sump during the THAI test Iod-31. Case T31L-62

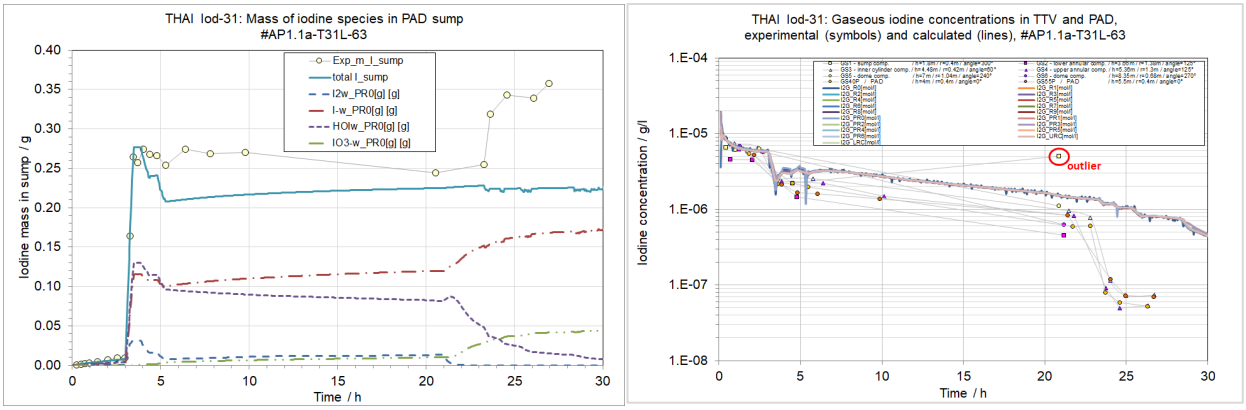

Figure 6. Experimental and calculated iodine species concentrations in the PAD sump (left figure) and iodine gas phase concentrations (right figure) during the THAI test Iod-31. Case T31L-63

3. PLANT CALCULATIONS

Based on the described findings of the THAI Iod-31 calculations, the impact of different mass transfer coefficients on the iodine source term was further investigated for a full-scale PWR containment.

3.1. Input and investigated scenario

For this purpose, 3 cases were calculated, one with the COCOSYS default values ("V3.0", base case), and two ("V3.0_(3)", "V3.0_(4)") with the above investigated sets of mass transfer coefficients for sprays, cf. Table III. These three cases cover a wide range (factor 30) of mass transfer constants for the spray system, while the global mass transfer coefficients were kept at their default values. A developer version of COCOSYS V3.0 with NewAFP was used for these calculations.

The calculations were performed for a Large Break Loss of Coolant Accident (LBLOCA) scenario for a generic PWR containment model. This scenario is considered as conservatively enveloping with regard to fission product release from the core and pressure surge in the containment. It is characterized by a sequence of events, which are reflected in the containment pressure (Figure 7). The initiating event is a surge line break without safety injection. A large amount of water and steam is then released to the containments, resulting in high pressure and temperature. The scenario considers the loss of core cooling, start of oxidation and later meltdown of the core, RPV failure and transfer of the melt to the reactor pit with quenching of the melt at a later point in time. After several hours, the containment heat removal system (CHRS) is activated and sprays start to remove decay heat from the atmosphere and wash down aerosols and gaseous fission products for many hours. The spray is fed from the sump and operated as a recirculated spray. This means that after the initial spraying with clean water, the spray is then contaminated by fission products washed out from the atmosphere.

Table III. Performed calculations of a commercial PWR and chosen mass transfer coefficients

Case	$P(I_2)$	$P(RI)$	Mass transfer coefficients (m/s)							
			global				Spray system			
			k_G	k_W	k_{35}	k_{36}	k_G	k_W	k_{35}	k_{36}
V3.0	*21*	*2.6*	1.4E-03	1.0E-05	8.7E-06	9.8E-06	1.4E-03	1.0E-05	8.7E-06	9.8E-06
V3.0_(3)	*21*	*2.6*					1.1E-01	7.0E-05	6.9E-05	7.0E-05
V3.0_(4)	*21*	*2.6*					1.1E-01	3.0E-04	2.8E-04	3.0E-04

NB: The partition coefficients P and the mass transfer constants k_{35}/k_{36} are calculated for a temperature of 60 °C

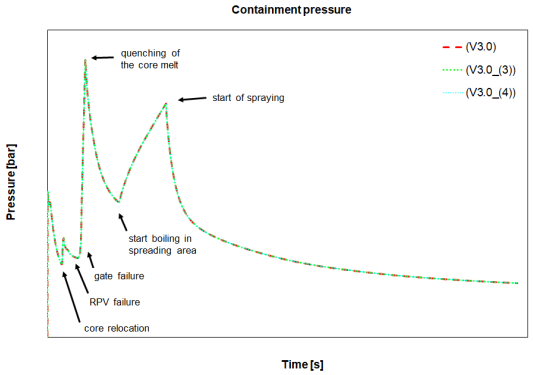

Figure 7. Course of the containment pressure in the LBLOCA scenario of a commercial PWR for all three performed calculations

3.2. Results of the calculations

Since data of a commercial PWR were used, the following figures are given only without numbers at the axes. The y-axis of the figures below has a logarithmic scale, the x axis a linear one and all figures are scaled to the same time to allow comparison. Results are compared qualitatively or given as relative information. However, this will not negatively affect the findings concerning the use of different mass transfer coefficients for the spray system.

The calculated total iodine in the sumps and in the atmosphere of the plant indicates no significant differences between the three cases for the iodine mass in the water phase (which contains the large majority of iodine). But a significant increase of the volatile iodine of up to 60-72 % for the cases with increased MTC's (Figure 8) was calculated. This is mainly due to the changes of molecular iodine (I_2) and organic iodine (RI) concentrations.

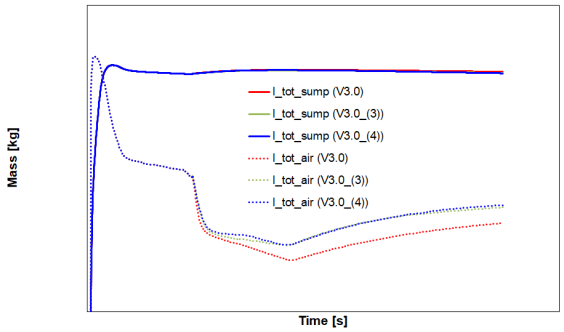

Figure 8. Total iodine masses in atmosphere and sumps in the plant calculations for a LBLOCA scenarios in three cases with different mass transfer coefficients

A complex scheme unfolds for the I_2 behaviour (Figure 9, left):

- With the start of the spray, some iodine is transferred from the sump to the atmosphere by evaporation from spray droplets and leads to a small peak of the gaseous I_2. Afterwards, I_2 is efficiently washed out from the atmosphere, leading to different I_2 concentrations in the sump for the three cases. The logarithmic scale hides that the delta of sump and gas atmosphere in each case correspond to each other, proving this is indeed due to mass transfer processes.
- But during spraying, radiolytic processes in water and gas continue (not at least radiolytic formation of I_2 from iodide or iodate in water or from iodine oxides or caesium iodide aerosols in the atmosphere). This keeps up the I_2 concentration level, despite a slightly alkaline spray water. Towards the end of the computed scenario, the I_2 sump concentrations reach similar levels for all three cases.
- The differences in the atmosphere are explained by different mass transfer coefficients.
- While in the short term, I_2 is depleted after spray start for several hours, there is an increase in the long term. This is due to the higher I_2 sump concentrations and also the stronger evaporation of I_2 from spray water droplets. The two cases "V3.0_(3)"/"V3.0_(4)" provide finally 41/57 % higher I_2 concentrations in the atmosphere than the base case.

The case for organic iodine (RI, Figure 9, right) as the other major volatile species is somewhat different. A strong RI formation on painted surfaces submerged in water phases is calculated already before spraying. Organic iodine then evaporates from the sumps and leads to a high RI level in the atmosphere. With the start

of the spray, RI is efficiently washed out from the gas phase (with a peak in the two variations, similar to the I_2 peak). In the long term, the calculated RI concentrations start to increase again. This is explained by the increase of RI in the sump and subsequent mass transfer of RI to the gas phase during spraying (evaporation from droplets), but also by the ongoing production of RI in the sump by its reaction with painted surfaces. The higher mass transfer in the spray in the two variations "V3.0_(3)" and "V3.0_(4)" leads to higher concentrations in the atmosphere and a depletion of RI in the sump, compared to the base case ("V3.0"). The calculated concentration level of gaseous organic iodine is by approximately one order of magnitude higher than for molecular iodine, thus, the iodine source term becomes dominated by organic iodine.

It is also interesting to note that for both gaseous I_2 and gaseous RI the calculated curves show a tendency to reach a nearly constant value. This would be the equilibrium of both species between aqueous and gas phase.

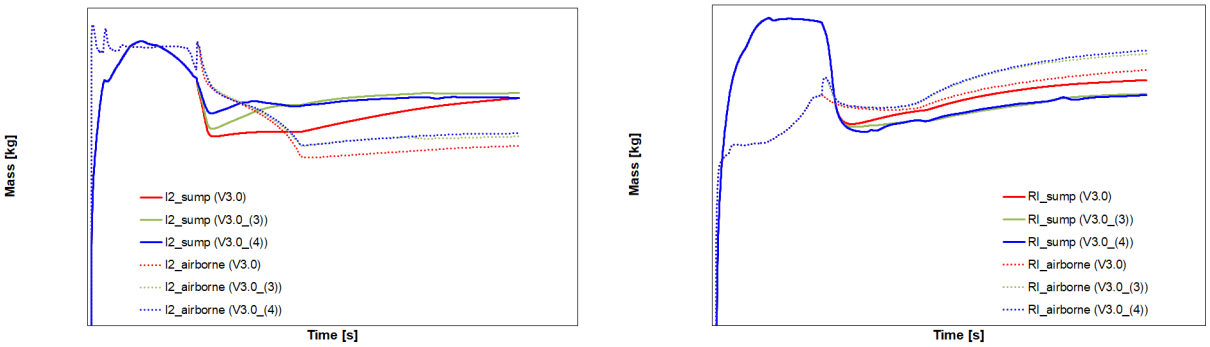

Figure 9. Molecular iodine (I_2, left figure) and organic iodine (RI, right figure) masses in atmosphere and sumps in the plant calculations for a LBLOCA scenarios in three cases with different mass transfer coefficients

Table IV. Percentage change of the masses of several iodine species in water and gas phase at the end of the computed scenario, calculation cases "V3.0_(3)" and "V3.0_(4)" compared to base case "V3.0"

Water phase			Atmosphere		
Species	**V3.0_(3) / V3.0**	**V3.0_(4) / V3.0**	**Species**	**V3.0_(3) / V3.0**	**V3.0_(4) / V3.0**
Total iodine	- 4 %	- 4 %	**Total iodine**	+60 %	+ 72 %
Iodide (I^-)	-10 %	-11 %	**Iodide (I^-) (CsI aerosols)**	+ 1 %	+ 1 %
Iodate (IO_3^-)	+25 %	+24 %	**Iodine oxide ("IO_3^-" = IO_x)**	+16 %	+ 19 %
Iodine (I_2)	+20 %	0 %	**Iodine (I_2)**	+41 %	+ 57 %
Organic iodine (RI)	-39 %	-42 %	**Organic iodine (RI)**	+78 %	+102 %
Hypoiodous acid (HOI)	+51 %	+25 %	**On containment surfaces**		
Silver iodide (AgI)	+ 4 %	+ 5 %	**Deposited iodine**	+ 3 %	+ 3 %

Table IV provides a comparison for all calculated iodine species in all phases (water, gas, surfaces) and is given as the percental change between each of the variation case over the base case. It underlines that the choice of more realistic coefficients for the iodine mass transfer in sprays leads in accident simulations to significantly higher amounts of volatile iodine in the containment atmosphere.

To conclude, the possibility to define separate mass transfer constants for a spray system in COCOSYS overcomes the limitation of the use of one global set of mass transfer coefficients for a whole plant and is a major step towards the realistic modelling of the impact of spraying on the in-containment iodine source term. The presented results show that with higher and more realistic mass transfer coefficients more volatile iodine is found in the gas phase during spraying. However, the further development of the underlying models of sprays, but also of iodine chemistry, and their validation by new experimental results is still essential to ensure reliable accident simulations.

4. CONTRIBUTIONS TO IODINE MODELLING

In the frame of the AMICO project, also various analytical and modelling work on various aspects of severe accident chemistry was performed. The results are described in [14], but due to the use of proprietary information and data from the BIP-1/2/3, STEM/STEM-2, THAI-OECD projects, they shall be only outlined here.

Numerous data from the Canadian OECD BIP Project lab tests were analyzed for the I_2/paint reaction. In combination with the iodine data from the large-scale THAI test facility and the THAI-6-TIP lab tests, it was concluded that the I_2 deposition on painted surfaces in the containment is limited by the mass transfer. Based on THAI data, the previous AIM model of I_2 deposition on paint can be used for containment calculations at a slightly reduced speed, the formulated dependence on the water vapour concentration remains as before. The values of the other model parameters were also adjusted.

This model, which was initially only developed for dry paint surfaces, was extended to wet paint surfaces by coupling it with the Stefan Flow model to account for thermophoresis. A corresponding proposal with an enhancement factor dynamically determined in COCOSYS as a function of the condensation rate is given in [14].

For the I_2/steel reaction, new analyses were necessary in the course of the analyses of the I_2/paint reaction, also due to the now even broader THAI data base. The main result is that in all relevant THAI tests without paint, condensate or other surfaces, I_2 is distributed in half on the steel surface and in the gas phase. This results in a determination of the ratio of adsorption and desorption velocity for AIM. This is less relevant for containment calculations, but it is important for the analysis of THAI tests carried out in steel vessels.

The AIM model of the radiolytically induced iodine release of paint was tested using data from the OECD-STEM projects. While it overestimates the organic iodine release, this is conservative regarding the containment source term. A refinement of the organic iodine release model has been canceled because it is not consistent based on the existing data.

As a new phenomenon, the radiolytically induced I_2 release from paint was modelled at the same rate as the RI release in AIM. It is recommended to add a kinetic term analogous to the RI release as a robust option for containment calculations. This reaction should only be used for paint surfaces in the gas phase.

For the formation of organic iodine in the gas phase from elemental and organic matter, which has not yet been considered in AIM, a new provisional model was proposed. This will enable analyses of the data of

the current OECD-ESTER project, which will generate experimental data for this phenomenon, and will lead to a refinement of the provisional model.

The concentration of organic substances as a source for organic iodine is required for the analysis of the current OECD-ESTER project as well as for containment calculations. Initial values for organic substances are recommended for containment calculations in gas and water phases. These are each 1E-5 mol/L, whereby for the starting value of organic substances (R) in water also the option to overwrite this initial value should be foreseen, depending on the situation considered (e.g., organic residues in the coolant, organic from paint coats, organic from decomposition/destruction processes of organic materials).

The radiolytic nitric acid formation in the gas phase in COCOSYS was checked, a reduction of the formation rate by a factor of 5.4 is required. For periods of one year, the pH value can drop significantly below 2 if the substances present in the containment, which partially increase the pH value, are not taken into account.

5. CONCLUSIONS

In the R&D project AMICO, analytical and modelling work and COCOSYS calculations were carried out on different aspects of the fission product and especially the iodine behaviour in a severe accident.
In the THAI test Iod-31, six consecutive spraying periods transferred gaseous iodine from the atmosphere to a sump. Post-test calculations with an improved COCOSYS version V3 aimed at the simulation of the iodine wash-out by sprays. It was possible to obtain a good representation of the experimental results by using a new COCOSYS feature that allows to define specific mass transfer coefficients for the spray. The chosen mass transfer coefficient allowed to better represent the experimental results than previously.
Two identified sets of suitable parameters were then used in simulations with COCOSYS V3 for a full-scale PWR containment. a LBLOCA scenario. The calculations were performed for a Large Break Loss of Coolant Accident (LBLOCA) scenario for a generic PWR containment model. It was shown by comparison with a calculation without dedicate mass transfer coefficient that the improved treatment of the impact of spraying by separate mass transfer constants leads to significantly higher calculated concentrations of organic iodine as dominant species and molecular iodine in the containment atmosphere, i.e. to a higher volatile iodine source term. This very clear result requires further analyses and evaluations.
Various analytical and modelling work on several aspects of severe accident chemistry was carried out by evaluating a large number of new experimental data from national and international projects was evaluated. The existing modelling of the reaction with paint and steel, radiolytic iodine release from paint, radiolytic formation and decomposition of organic iodine in the gas phase and radiolytic nitric acid formation in the containment were checked and revised.

ACKNOWLEDGMENTS

The authors gratefully acknowledge the funding of AMICO by the German Federal Ministry for the Environment, Nature Conservation, Nuclear Safety and Consumer Protection (BMUV (project number 1501562). The authors acknowledge the permission to use data of the THAI Iod-31 test from the THAI project (project number 1501455) for AMICO as well. The support of AMICO by GRS, especially Holger Nowack, Sara Beck, Claus Spengler, Dimitar Iliev, Dandy Eschricht, and their continuous support and collaboration was highly appreciated.

REFERENCES

1. W. Klein-Heßling, COCOSYS V3.0 Program Reference Manual, Revision 0, GRS, November 2015
2. N. Reinke, S. Arndt, I. Bakalov, S. Band, S. Beck, S. Buchholz, D. Eschricht, W. Klein-Heßling, D. Iliev, H. Nowack, C. Spengler, J. Stewering, M. Sonnenkalb, "Validierung & Verifikation der Rechenprogramme COCOSYS und ASTEC", GRS report, GRS-551, August 2019
3. C. Spengler, S. Arndt, S. Beck, D. Eschricht, D. Iliev, H. Nowack, "Modellentwicklung zu Vorgängen im Containment für das GRS-Codesystem AC² (ATHLET/CD/COCOSYS)", GRS Report GRS-629, March 2021
4. S. Beck, G. Weber, "Das neue Iod/Farbe-Modell in AIM-3 für trockene Bedingungen und die Validierung an THAI-Versuchen", Technische Notiz GRS-V- RS 1532 -1/2015, September 2015
5. G. Weber, "Ein neues Abwaschmodell für unlösliche Aerosole (AULA)", Technische Notiz WEG-01/2011, GRS, August 2011
6. F. Funke, M. Bendiab, G. Langrock, "Analyse des Einflusses containment-typischer Phänomene auf die Spaltproduktverteilung", Abschlussbericht Reaktorsicherheitsforschung Vorhaben Nr. 1501457, June 2017, AREVA Report DTICC-G/2017/de/0093A
7. C. Mun, L. Bosland, L. Cantrel, J. Colombani, O. Leroy, M.-N. Ohnet, T. Albiol, "OECD/STEM project and its follow-up STEM2", Proceedings of the International OECD-NEA/NUGENIA-SARNET Workshop on the Progress in Iodine Behaviour for NPP Accident Analysis and Manage-ment, 2015 - Marseille (France)
8. "Behavior of Iodine Project 3 - Final Summary Report", NEA/CSNI/R(2020)14, February 2023
9. L. Bosland, S. Beck, S. Dickinson, H. McKenzie, Y. Lee, A. Nieminen, H. Nowack, H. Roebuck, P. Yakabuskie, G. Glowa, L. Oury, T. Van Rompuy, G. Langrock, W. Klein-Hessling, K. Kentaro, S. Tietze, "Recommendations from BIP-3 and STEM-2 Analytical Working Groups (AWG)", Rapport IRSN/2023-00085, 2023
10. F. Funke, S. Gupta, G. Weber, G. Langrock, A. Kühnel, E. Schmidt, M. Freitag, B. von Laufenberg, "Iodine Washout from Containment Atmosphere by Spray - Test ID: Iod-31", Technical Report 1501455 TR Iod 31, Reactor Safety Research Project No. 150 1455, September 2016
11. IVO Power Engineering Ltd. (Finnland), Description of the inside spray model (short description of the spray model implemented in RALOC Mod 2.2 Version), internal note Nov 9th, 1993
12. Interim Report on Task 4 – Specifying Useful Mass Transfer Models, ACE Extension Project, 1995
13. G. Langrock, M. Bendiab, F. Funke, "Analyses on modelling of iodine behaviour in the containment (AMICO)", Final Report, Reactor Safety Research Project No. 1501562, Framatome report D02-ARV-01-222-666, August 2023
14. F. Funke, "AMICO-Beiträge zur Entwicklung und Validierung des AIM-4-Modells", Framatome report D02-ARV-01-168-209 (restricted), October 2020

SEAKNOT
ERMSAR 2024
11th Conference on
SEVERE ACCIDENTS RESEARCH
May 13-16, 2024 – Stockholm, Sweden

Some results of the AMICO project

G. LANGROCK, M. BENDIAB, F. FUNKE

The AMICO project

In the R&D project „Analyses for the modelling of the iodine behaviour in containment (AMICO)“, co-funded by the German BMUV (project number 1501562), analytical work and COCOSYS calculations were carried out on different aspects of the fission product and especially the iodine behaviour in a severe accident. AMICO was divided into 3 work packages of which results of WP 1 are presented here:

WP 1: Long-term development of the airborne iodine activity
WP 2: CoPool modelling of a deep sump
WP 3: Iodine Uncertainty and Sensitivity Analysis

WP 1.1a: Post-test calculations of THAI Iod-31 test (I_2 spray test)

The THAI test Iod-31

The test was performed in the THAI+ facility in April 2016. ^{123}I labelled I_2 was injected into the 60 m^3 THAI test vessel (TTV, 60 m^3), connected via an upper and lower inter-connecting line to a second vessel (PAD, 20 m^3) with a sump (pH 4.5, 200 l initial volume) at the bottom and a spray nozzle at +3.5 m elevation.

Vessel temperatures were 85-90 °C. The sump was filled with 200 l fresh, cold water shortly before the test and sump recirculation started. After measuring the I_2 distribution in the two vessels for 3 hours, the first spraying was performed with fresh water. The other 5 spray phases were performed with sump water (recirculation spraying). The pH of the spray water was ~4.5 on the first day of the test and ~11 on the second day.

Iodine was measured in the gas phase by gas scrubbers. Total iodine in the sump was measured from water samples. Two online detectors observed steel coupons, providing direct measurements of iodine deposition on steel.

t / h	Experimental Event
-1.93 – -1.65	Filling of sump with fresh cold water (200 l)
0.00 – 0.17	Injection of gaseous I_2 (10 min), 0.96 g
3.00 – 3.46	1. Spray phase: Spraying with fresh water, V_{Sump} 200 l → 1116 l
3.88 – 4.38	2. Spray phase: Recirculation spraying (from PAD-Sump)
4.80 – 5.30	3. Spray phase: Recirculation spraying
11.25 – 20.00	Temporary switch-off of the PAD sump recirculation pump
21.00 – 23.00	Increase of pH in PAD sump from 4.5 to 11 with NaOH
23.38 – 23.53	4. Spray phase: Recirculation spraying (with alkalized sump water)
24.17 – 24.42	5. Spray phase: Recirculation spraying
25.33 – 25.93	6. Spray phase: Recirculation spraying
27.10 forward	Shutting-down vessel heating, sump cooling, recirculation pump

COCOSYS post-test calculations

The post-test simulations shall allow for code validation and especially the examination and optimization of the iodine modelling. Of particular interest was the question how with the experimentally observed spray effect, i.e. the wash-out and revolatilization of fission products, can be dealt and whether the IVO spray model, recommended for the use with COCOSYS, and the modelled iodine mass transfer between gas and water phase can represent the experimental results adequately.

A COCOSYS developer version with the restructured NewAFP module was used. It allowed to define iodine mass transfer coefficients (MTC's), which describe the exchange of iodine between aqueous phase and gas phase, globally for the whole simulated system, but also separately and time-dependent for a spray. Mass Transfer is treated in COCOSYS according to the “two film theory”:

$$\frac{1}{k_{35}} = \frac{1}{k_W} + \frac{P(I_2)}{k_G} \qquad \frac{1}{k_{36}} = \frac{1}{k_W} + \frac{P(RI)}{k_G}$$

$$with\ P(I_2) = 10^{(9.132E5 \cdot T_W^{-2} - 4.1E3 \cdot T_W^{-1} + 5.404)} \qquad P(RI) = e^{-6.97 + \frac{2641}{T_W}}$$

Several cases were calculated, e.g.:

Case (ID) T31L-	Parameters										
	Global MTC's			Spray-MTC's			pH sump	pH spray			Chem -istry
	k_G / m/s (KMTGAS)	k_W / m/s (KMTWAS)	k_{35} / m/s (35 °C)	k_G / m/s (KMTGAS)	k_W / m/s (KMTWAS)	k_{35} / m/s (35 °C)	PAD	1.	2./3.	4.-6.	
59	1.4E-4	1.0E-6	7.3E-7	-	-	-	4.5 / 11.0	7.0	7.0	11.0	
60	1.4E-4	1.0E-6	7.3E-7	1.1E-1	7.0E-5	6.8E-5	4.5 / 11.0	7.0	7.0	11.0	
62	1.4E-4	1.0E-6	7.3E-7	1.1E-1	7.0E-5	6.8E-5	4.5 / 11.0	7.0	7.0	11.0	k_{55} ↑
63	1.4E-4	1.0E-6	7.3E-7	1.1E-1	3.0E-4	2.6E-4	7.0 / 11.0	7.0	7.0	11.0	

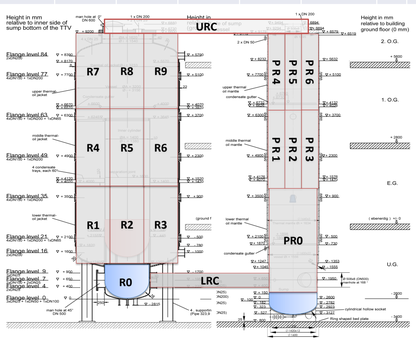

Multizone COCOSYS nodalization of the THAI+ facility

The calculations revealed a strong impact on iodine wash-out by sprays by the choice of iodine mass transfer coefficients for spray systems. Higher coefficients lead to a higher transfer of airborne iodine to the sump water. While the iodine was not revolatilized in the experiment, calculations provide some revola-tilization, that could be suppressed in the calculation by either an increase of the reaction rate of I_2 with steel in the water, leading to a significant formation of non-volatile iodide (I^-), or by an increase of the sump pH enhancing hydrolysis and formation of non-volatile I^-, HOI, IO_3^-.

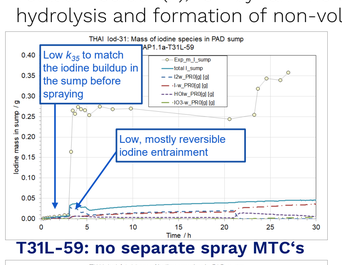

T31L-59: no separate spray MTC's

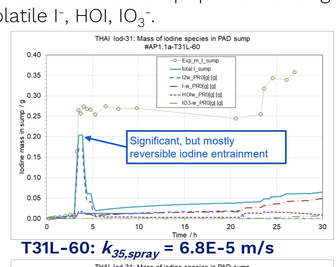

T31L-60: $k_{35,spray}$ = 6.8E-5 m/s

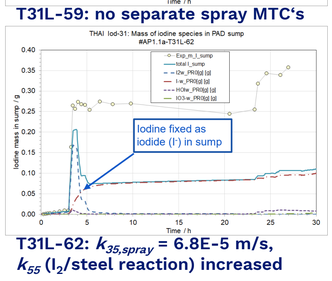

T31L-62: $k_{35,spray}$ = 6.8E-5 m/s, k_{55} (I_2/steel reaction) increased

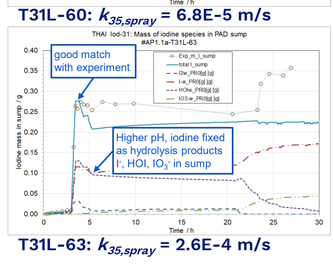

T31L-63: $k_{35,spray}$ = 2.6E-4 m/s

WP 1.1b: Transfer of the findings to a full-scale PWR simulation with a new COCOSYS version

The impact of the choice of dedicated MTC's for the spray system was further investigated in simulations for a full-scale PWR and for a Large Break Loss of Coolant (LBLOCA) scenario, with a recirculated spray system that is fed by a sump.

Three sets of parameters were tested:

Case	$P(I_2)$	$P(RI)$	Mass transfer coefficients (m/s)							
			global				spray system			
			k_G	k_W	k_{35}	k_{36}	k_G	k_W	k_{35}	k_{36}
V3.0	21	2.6	1.4E-03	1.0E-05	8.7E-06	9.8E-06	1.4E-03	1.0E-05	8.7E-06	9.8E-06
V3.0_(3)	21	2.6					1.1E-01	7.0E-05	6.9E-05	7.0E-05
V3.0_(4)	21	2.6					1.1E-01	3.0E-04	2.8E-04	3.0E-04

The results provided significantly higher concentrations of airborne iodine , namely organic iodine (RI) and molecular iodine (I_2), for the calculation cases with increased iodine mass transfer coefficients (cases „V3.0_(3)“ and „V3.0_(4)“ compared to case „V3.0“). This is explained by stronger exchange of RI and I_2 between spray droplets and the atmosphere as described by the mass transfer coefficients. Organic iodine was found to be the dominant species.

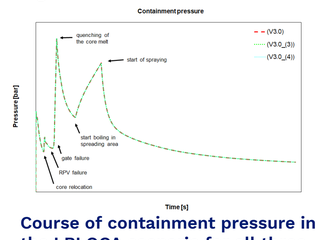

Course of containment pressure in the LBLOCA scenario for all three performed calculations

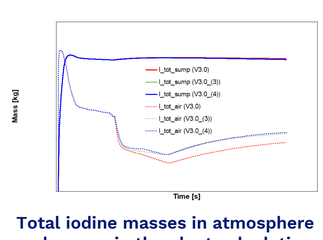

Total iodine masses in atmosphere and sumps in the plant calculations

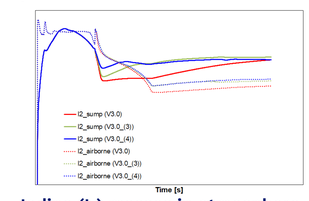

Iodine (I_2) masses in atmosphere and sumps in the plant calculations

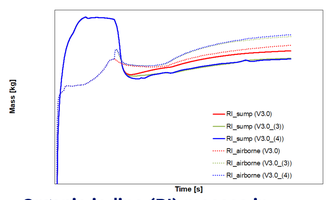

Organic iodine (RI) masses in atmosphere and sumps in the plant calculations

WP 1.2/1.3: Contributions to iodine modelling

Based on an extensive analysis of (partly proprietary) experimental data, various analytical and modelling work was performed, especially concerning models used in COCOSYS.

Some major findings and recommendations were:

- Gaseous I_2 deposition on dry painted surfaces in the containment is limited by mass transfer. An extension also for wet painted surfaces with coupling with the Stefan Flow model to account for thermophoresis was proposed.
- For the formation of organic iodine from elemental and organic matter, a new provisional model was proposed for COCOSYS.
- For the concentration of organic substances (R) as a source for organic iodine (RI), initial values of 1E-5 mol/l in gas and water phases are recommended for containment calculations.
- Radiolytic HNO_3 formation in the gas phase in COCOSYS was checked, a reduction of the formation rate by a factor of 5.4 seems to be necessary.

On behalf of:

Federal Ministry
for the Environment, Nature Conservation,
Nuclear Safety and Consumer Protection

of the Federal Republic of Germany

Gert Langrock **P.O. Box 1109** **Tel: +49 9131 900-97665**
Framatome GmbH **D-91001 Erlangen** **gert.langrock@framatome.com**

Effect of the Stages of the Accumulators on THE Hydrogen Production During LOCA+SBO in BNPP VVER-1000

Alireza Hosseini[1], Mahdi D. Zangian[2], Amir Saeed D. Shirani[3], Alireza Najafi[4] and Roya Tahmasebi[5]

[1]Shahid Beheshti University, Faculty of Engineering, Shahid Beheshti University, Shahriari Sq, Velenjak, Tehran, Iran., seyedali.hosseini@mail.sbu.ac.ir
[2]Shahid Beheshti University, Faculty of Engineering, Shahid Beheshti University, Shahriari Sq, Velenjak, Tehran, Iran., m_zangian@sbu.ac.ir
[3]Shahid Beheshti University, Faculty of Engineering, Shahid Beheshti University, Shahriari Sq, Velenjak, Tehran, Iran., a_shirani@sbu.ac.ir
[4]Sharif University of Technology, Department of Energy Engineering, Taymouri Alley, Ghasemi Street, Habibollahi St., Azadi Avenue, Tehran, Iran, alireza.najafi@energy.sharif.edu
[5]Shahid Beheshti University, Faculty of Engineering, Shahid Beheshti University, Shahriari Sq, Velenjak, Tehran, Iran., r_tahmasebi@sbu.ac.ir

Contact email: m_zangian@sbu.ac.ir

Abstract

VVER reactors are Russian-designed PWRs and they are widespread over Asia, and Eastern Europe. Bushehr NPP, located in Iran includes one VVER-1000 V446 (Unit-1) in operation and two VVER-1000 V528 (Unit 2&3) under construction. BNPP unit-1 is somehow a unique VVER, as it is a combination of a German KWU design and a Russian VVER. One of the key features of the BNPP Unit-1 is related to its accumulator stages. The first stage of accumulators is VVER-dedicated and includes four tanks connected to the RPV. The second-stage accumulators are indeed a part of the KWU design and include eight tanks, connected to the loops. According to the plant configuration, second stage accumulators are activated only in Design Extension Conditions (DECs)BNPP-1 is the first VVER in the world, with two stages of accumulators, and some subsequent VVER models are equipped with two or even three stages of accumulators. Some research has been performed to assess the effectiveness of the second stage. These stages have different setpoints for the injection, the first stage injects at 5.88 Mpa, and the second stage at 2.5 Mpa. This paper aims to investigate the effect of the accumulators, especially the second stage on Hydrogen Production during various LOCA sizes, combined with SBO.

These Scenarios are modeled by MELCOR 1.8.6. Prior to accident modeling, the steady-state is developed based on the engineering handbook of the plant. The Steady-state calculated parameters (e.g. cold/hot leg temperature, pressurizer pressure, primary pressure/level, bypass flow rate, primary flow rate, secondary pressure, secondary flow rate, and core pressure loss) have shown acceptable errors in comparison with the design values. The LOCA+SBO is modeled for some SBLOCA sizes (25mm, and 45mm), and the effect of the first/ second-stage accumulators on Hydrogen is being investigated in these break sizes. The next step is to model MBLOCA, and LBLOCA while considering different situations for the accumulators to achieve the amount of produced Hydrogen.

Keywords: VVER, Accumulators, Hydrogen, LOCA, SBO

COMPARATIVE STUDY OF TWO EXPERIMENTAL CONFIGURATIONS WITH AN INTERNAL COMPARTMENT IN THE PANDA FACILITY

Sofía Arfinengo-del-Carpio*, Carlota Gabicagogeascoa-Cuesta, Carlos Vázquez-Rodríguez, Gonzalo Jiménez
Universidad Politécnica de Madrid
C. de José Gutiérrez Abascal, 2, 28006 Madrid
s.arfinengo@upm.es; c.gcuesta@alumnos.upm.es; c.vazquez@upm.es; gonzalo.jimenez@upm.es

Michele Andreani, Domenico Paladino
Paul Scherrer Institut
Forschungsstrasse, 111, 5303 Villigen, Switzerland
michele.andreani@psi.ch; domenico.paladino@psi.ch

Juan Manuel Martín-Valdepeñas
Consejo de Seguridad Nuclear
C/ Pedro Justo Dorado Dellmans, 11, 28040 Madrid
jmmv@csn.es

ABSTRACT

The containment building of a nuclear power plant is the last physical barrier preventing a radioactive leakage to the environment in the unlikely event of a severe accident, following the defense in depth principles [1]. Therefore, the evaluation of the different phenomena that could threaten the containment integrity, such as hydrogen accumulation, acquires crucial importance [2]. For this reason, several efforts have been made to experimentally recreate hydrogen risk scenarios in international collaborative frameworks such as the OECD/NEA HYMERES (Hydrogen Mitigation Experiments for Reactor Safety), HYMERES-2 or PANDA projects [3].

In these projects, experiments have been conducted at the large-scale PANDA facility at Paul Scherrer Institut (Switzerland) during the past years, allowing to extend the experimental database and to help validating the simulation codes used for safety analyses under severe accident conditions. These efforts are currently being extended within the framework of the OECD/NEA PANDA project, which includes two series (identified as P1A1 and P1A3) addressing the interaction of flow with complex structures, such as steam generator compartment models (representing the compartment where the steam generator is located), and activation of a spray phase during the experiment. The goal of the P1A1 and P1A3 experiments is to study how complex flow obstructions affect hydrogen distribution phenomena (e.g. mixing, stratification, natural circulation, etc.) and the modeling needs (physical models, mesh resolution, etc.) to analyze the experimental phenomena.

The steam generator compartment model for the P1A1 and P1A3 series was obtained through a scaling process based on a typical PWR containment building configuration. The test scenarios include different phases, namely: release of steam, injection of helium (used to simulate hydrogen) inside the steam generator compartment model and later activation of the spray system in the upper dome of PANDA Vessel 1. During the experiment, the containment is first pressurized (due to the steam and helium release) and later depressurized due to spray activation.

The difference between both configurations is purely geometrical: the P1A1 series includes one steam generator compartment model, as a first step to represent the interaction of the flow with typical PWR containment structures. Then, the P1A3 series adds a second compartment to its proposed configuration, with a connection between both structures. These modifications serve as a step forward to representing the containment building configuration with a higher level of detail, allowing the study of the interaction of the flow with additional structures, compared to P1A1, as well as its behavior through the interconnection. Both geometries have been modeled using GOTHIC, a thermal-hydraulic code for containment safety analysis. It solves the conservation equations for mass, momentum and energy for multicomponent, multiphase compressible flow, with the possibility of using both lumped parameters and/or multi-dimensional geometries, for three phases: vapor, continuous liquid and droplets [4]. Thereafter, both models have been compared to assess the impact of the addition of the second compartment on the model thermal hydraulics.

For both cases, pressure significantly increases in the PANDA vessel during the steam injection phase and remains nearly stagnant while helium is injected in the compartment, as the injected mass flow rate is not high enough to compensate the effect of the steam condensation. Lastly, the vessel is depressurized through the effect of the spray system activation. Although the values are very similar for both models, the pressure peak is slightly lower for the P1A3 series, due to the addition of the second compartment and the connecting tunnel. The introduction of additional metallic structures provides extra surface for steam condensation, consequently reducing the pressure peak.

In addition to the analysis of global magnitudes, the effect of the configuration modification was studied locally. The observation of the flow through the model suggests that the injected gases flow upwards, towards the upper compartment openings, and enter the vessel with enough momentum to induce mixing patterns, starting at the upper levels of the vessel dome and progressively descending to the lower parts of the vessel. To furtherly study this mixing effect, a criterion for defining the thermal stratification front was defined and calculated for every time step. As a result, it was observed that, this front is located at lower heights as the transient advances, confirming the presence of descending mixing patterns. The location of the stratification front is somewhat lower for the P1A3 series at every time step, implying that the presence of the second compartment promotes the mixing of the PANDA vessel atmosphere.

Subsequently, upon the close observation of the helium distribution during the helium injection phase, it was corroborated that the two compartments configuration presents rather lower local concentration values, in line with the theory of the enhanced mixing scenario. However, the observed differences are not significant and do not justify the need of performing the P1A3 experiments with the configuration proposed during the scoping calculations. Some modifications will be further studied, such as the increase of the injection flows, that would make the presence of the second compartment more relevant, as well as diverse geometrical modifications that allow the experiments to provide additional useful information for the experimental database, while still being representative of a generic containment configuration.

References

[1] B. R. Sehgal, *Nuclear Safety in Light Water Reactors - Severe Accident Phenomenology*. Academic Press, 2012.
[2] IAEA, *Mitigation of hydrogen hazards in severe accidents in nuclear power plants*, IAEA-TECDOC-1661. Vienna, Austria, 2011.
[3] M. Andreani, D. Paladino and D. Papini, «Multi-step planning calculations with the GOTHIC code used for the design of complex experiments in the PANDA facility», *Nucl. Eng. Des.*, vol. 339, pp. 116-125, dic. 2018, doi: 10.1016/j.nucengdes.2018.09.005.
[4] EPRI, «GOTHIC Thermal Hydraulic Analysis Package, Version 8.3(QA). EPRI Palo Alto, CA.» 2018.

KEYWORDS
PANDA, GOTHIC, HYDROGEN DISTRIBUTION, CONTAINMENT ANALYSIS, SPRAY SAFETY SYSTEM

SEAKNOT
ERMSAR 2024
11th Conference on
SEVERE ACCIDENTS RESEARCH
May 13-16, 2024 – Stockholm, Sweden

Comparative study of two experimental configurations with an internal compartment in the PANDA facility

SOFÍA ARFINENGO-DEL-CARPIO[1]

In collaboration with: Carlota Gabicagogeascoa-Cuesta[1], Carlos Vázquez Rodríguez[1], Gonzalo Jiménez[1], Michele Andreani[2], Domenico Paladino[2], Juan Manuel Martín-Valdepeñas[3]

[1]Universidad Politécnica de Madrid (UPM), [2]Paul Scherrer Institut (PSI), [3]Consejo de Seguridad Nuclear (CSN)

BACKGROUND

- **Defense in depth** principle: the **containment building** is the last physical barrier preventing a radioactive leakage in case of a severe accident
- The evaluation of phenomena such as **hydrogen risk** is crucial to preserve containment integrity
- Several international projects (OECD/NEA HYMERES, HYMERES2, PANDA) have been developed to recreate severe accident scenarios and validate the simulation codes used for severe accident analysis.

EXPERIMENTAL SERIES

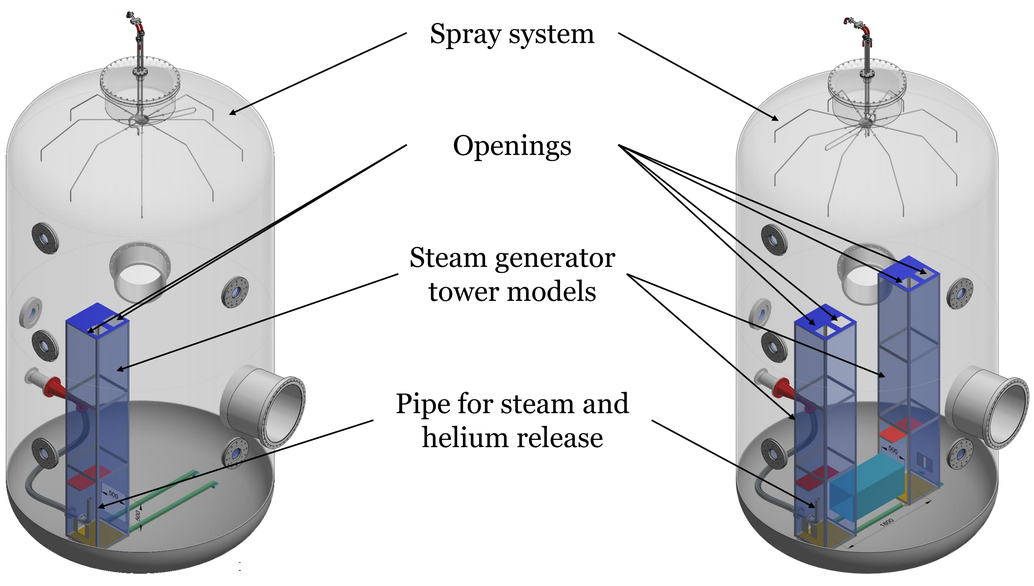

Large-scale PANDA facility at Paul Scherrer Institut (Switzerland)

Both series address the interaction of flow with complex structures, representative of typical containment geometric configurations

MODELING PROCESS

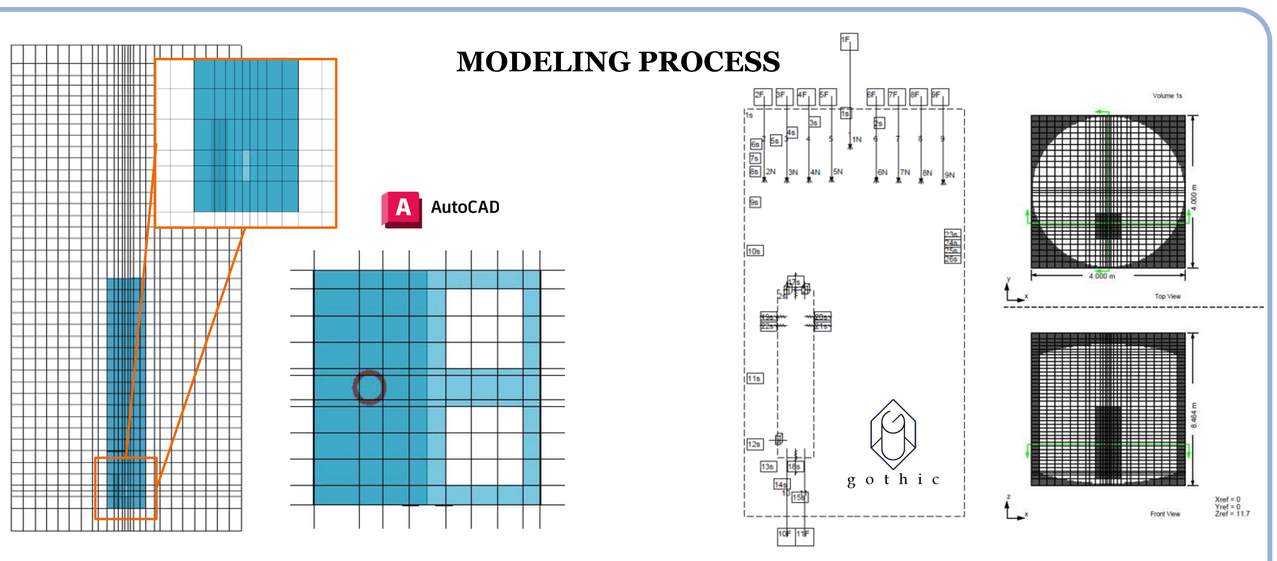

- CAD software is used as the main working environment for model development, for gathering and tracing all the geometric information.
- Model development process:
  1. **Detailed CAD geometry** of the experimental facility.
  2. **Simplified CAD geometry**, which suits GOTHIC's modelling and domain discretization particularities.
  3. Model geometry in **GOTHIC**.

RESULTS

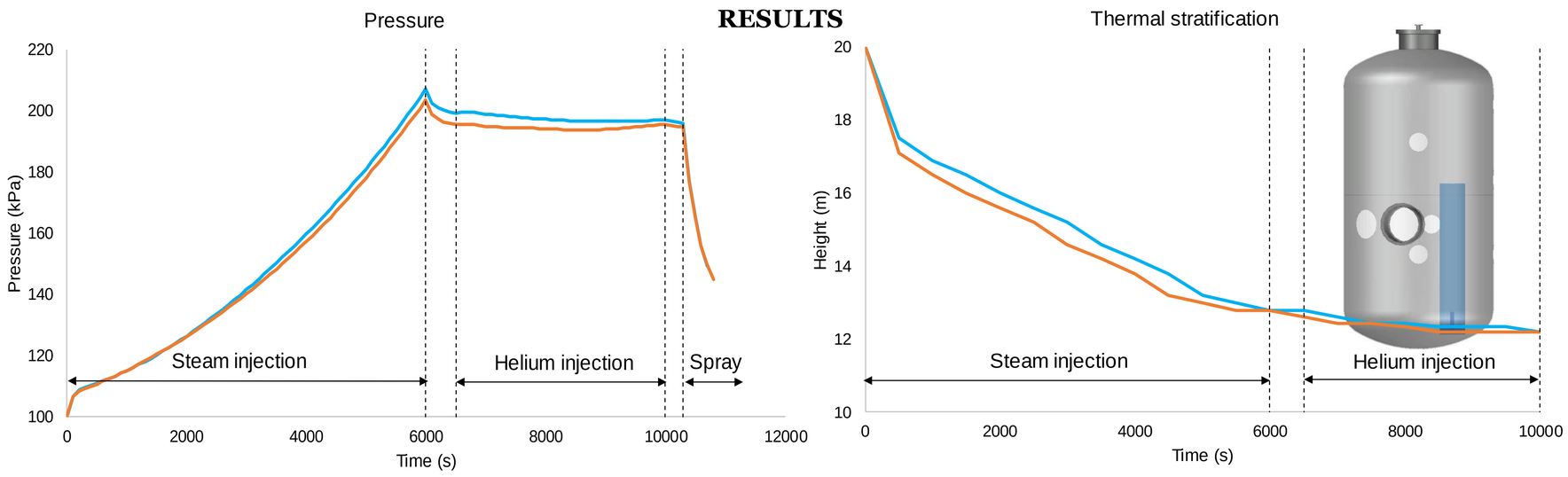

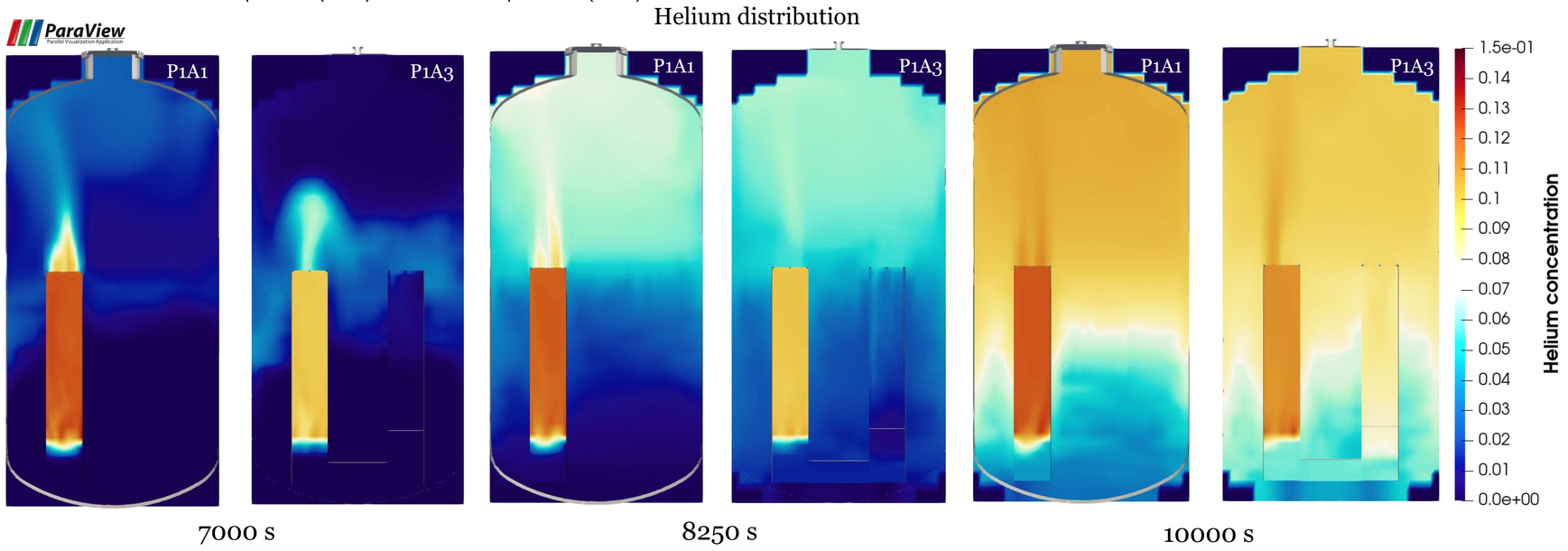

CONCLUSIONS

- The addition of the second compartment seems to **promote mixing** in the PANDA vessel
- However, both scenarios present **similar phenomenology** regarding pressure and temperature average evolution
- Further scoping calculations will be performed for analyzing new cases to define **alternative test conditions**

REFERENCES

[1] B. R. Sehgal, Nuclear Safety in Light Water Reactors - Severe Accident Phenomenology. Academic Press, 2012.

[2] IAEA, Mitigation of hydrogen hazards in severe accidents in nuclear power plants, IAEA-TECDOC-1661. Vienna, Austria, 2011.

[3] M. Andreani, D. Paladino, y D. Papini, «Multi-step planning calculations with the GOTHIC code used for the design of complex experiments in the PANDA facility», Nucl. Eng. Des., vol. 339, pp. 116-125, dic. 2018, doi: 10.1016/j.nucengdes.2018.09.005.

[4] EPRI, «GOTHIC Thermal Hydraulic Analysis Package, Version 8.3(QA). EPRI Palo Alto, CA.» 2018.

IN COOPERATION WITH:

GOTHIC™ incorporates technology developed for the electric power industry under the sponsorship of EPRI, the Electric Power Research Institute. This work was completed using a GOTHIC license for educational purposes provided by Numerical Advisory Solutions, LLC

Sofía Arfinengo-del-Carpio
PhD candidate in sustainable energy, nuclear, and renewables

ETSII UPM; José Gutiérrez Abascal, 2, 28006 Madrid, Spain

Tel: +34 910677153
Email: s.arfinengo@upm.es

Numerical Simulation of LIVE2D Two-Layer Melt Pool Experiment

Pengya Guo[1], Peng Yu[2], Fengyang Quan[2], and Yidan Yuan[2*]
[1]Department of Engineering Physics, Tsinghua University, Beijing, China
[2]CNNC Key Laboratory on Severe Accident in Nuclear Power Safety, China Nuclear Power Engineering Co., Ltd, Beijing, China
gpy20@mails.tsinghua.edu.cn; yupenga@139.com; 499804996@qq.com;
yidanyuan2010@aliyun.com

ABSTRACT

During a severe accident, the molten core migrates to the lower head of the reactor pressure vessel, eventually forming a melt pool. To ensure the in-vessel retention (IVR) of molten material within the reactor, it is necessary to maintain the heat flux of the melt pool sidewall below the critical heat flux at any angle. However, the RASPLAV experiment indicates that the stratification of the melt pool may pose a threat to the feasibility of IVR. Therefore, it is necessary to conduct experiments and simulations specifically for two-layer melt pools. This study simulates LIVE2D two-layer experiments under two different top boundary conditions. This study utilizes computational fluid dynamics (CFD) software Fluent for numerical simulations, incorporating models such as the WMLES turbulence model, the Solidification and Melting model, and the Volume of Fluid (VOF) multi-phase flow model. Due to the immiscibility, density stratification, and crusting formation requirements between the two materials, heat transfer oil and a eutectic salt mixture of 50% KNO3 and 50% NaNO3 are chosen as the materials for the LIVE2D two-layer experiments. In conclusion, the simulation results align well with the LIVE2D experimental data, validating the capability of CFD to simulate two-layer melt pools accurately. This approach establishes a solid foundation for simulating two-layer melt pools under corium materials in future studies.

KEYWORDS
In-vessel retention; Two-layer melt pool; Computational fluid dynamics (CFD); Interlayer crust; LIVE2D

1. INTRODUCTION

The concept of IVR was first introduced in 1989 by Theofanous for the VVER-440 at the Loviisa nuclear power plant[1] and has been widely implemented to ensure the long-term stability of light water reactors over the past two decades. Serving as an innovative approach to Severe Accident Management (SAM), the critical strategy of IVR involves arresting and confining the corium in the lower head of the Reactor Pressure Vessel (RPV). An effective IVR technique is External Reactor Vessel Cooling (ERVC) technology, which involves injecting water into the cavity of a pressurized water reactor (PWR) or the dry well of a boiling water reactor (BWR), submerging at least the lower head of the RPV, and utilizing boiling heat transfer to dissipate decay heat (Ma et al., 2016). The IVR-ERVC strategy is currently utilized in various reactor designs, including VVER440 [1], [2], AP600 [3], AP1000 [4]–[6], APR1400, and Aerva Group 1000MWe boiling water reactor design. Moreover, IVR has been widely adopted in most advanced nuclear power plants (NPPs) in China, such as ACPR1000, CAP1400, and HPR1000 [7].

However, when dealing with a two-layer melt pool, the IVR strategy may encounter challenges. According to the IVR technique, the angular heat flux (q_w) imposed by the melt pool on the vessel wall at any point around the lower head should not exceed the critical heat flux (CHF) at any angle. The RASPLAV project, using UO2-ZrO2 material, confirmed that the corium pool experienced density

stratification between metal and oxide, resulting in the formation of a two-layer melt pool [8]. A concentration of heat flux occurs along the upper layer, which is known as the "focusing effect." And 'Focusing factor' can be used to describe the ratio of local heat flux to the average sidewall heat flux. The focusing factor is affected by the thickness of the layer [9]. The probability of failure in the lower head is highest during the early stage of the formation of the two-layer melt pool due to the rapidly increasing focusing effect. For instance, a thermal analysis of the AP1000 suggests that the heat load on the sidewall, as a thin stratified upper layer overlying the ceramic pool, may exceed CHF and lead to lower head failure [4]. The measurement of CHF can be achieved through prototype experiments, but it is challenging to directly measure the heat flux of the prototype core material melt pool. Additionally, the behavior of the melt pool during severe accidents is uncertain. Therefore, it is necessary to conduct heat transfer experiments and simulations on two-layer melt pools.

In recent years, a variety of two-layer melt pool experiments have been conducted, broadly categorized into three groups. The first category focuses on separate analyses of the upper layer and the lower layer in the two-layer melt pool, such as MALAD, BALI-metal, HELM, and HELM-LR. The second category involves using a metal sheet to separate the simulation working medium to achieve a stratification effect, as demonstrated by LIVE-L6, SIMECO, COPO II, and COPRA[10]–[12]. The third category pertains to density stratification according to different densities. An example of this is Gaus-Liu's selection of heat transfer oil and nitrate as simulators in LIVE2D to maintain density stratification based on density variations, enabling the observation of the crust [13].

$$Ra' = RaDa = GrPrDa = \frac{g\beta q_v H^5}{\alpha v \lambda} \quad (1)$$

In computational fluid dynamics (CFD) simulations, the Large Eddy Simulation (LES) model is widely used to calculate natural convection melt pools with internal heat sources. The Rayleigh number (Ra) is a dimensionless parameter associated with free convection. A higher Rayleigh number indicates a more significant contribution to heat convection compared to heat transfer. Horvat et al. utilized the LES Smagorinsky model to conduct a two-dimensional simulation of an internal heat square cavity. They observed the flow transition and heat transfer at Ra=10^6~10^{11} [14]. Liu et al. used the lattice-BGK (LBGK) model based on Large Eddy Simulation (LES) to calculate at Ra up to 10^{16}. The k-ε model and LES model were used to simulate and evaluate the BALI melt pool experiment with Ra=1016 in the PHOENICS software [15]. Zhang et al. conducted validation of the WMLES model using three typical melt pool heat transfer experiments: BALI, LIVE, and COPRA [16]. Zhang et al. (2018) also employed WMLES to calculate the three-dimensional single-layer and two-layer melt pools of HPR1000 with corium material[17].

This paper explores the simulation of experimental investigations on the two-layer melt pools LIVE2D, incorporating density stratification for the two materials. The model's effectiveness is validated by comparing flow and heat transfer data, and the behavior of stratified melt pools is summarized by comparing it with experimental results. It provides reliable support for predicting the temperature and heat flux of the corium material, contributing to a better understanding of IVR reliability.

2. CFD Calculation Method

ANSYS Fluent was used for the computational fluid dynamics (CFD) analysis, and the WMLES turbulence model was employed. The main advantage of the WMLES formulation is the improved Reynolds number scaling. By simulating the inner boundary layer and precisely resolving the outer boundary layer regions, the WMLES model avoids the need for high mesh resolution near the wall. In addition, the Volume of Fluid (VOF) multiphase flow model and the Solidification and Melting model were utilized to simulate the molten salt scenario.

2.1. Wall Modeled LES (WMLES) Turbulence Model

The WMLES model is based on the LES model. In the LES method, a filtering function distinguishes between large and small vortices. Large eddies, which show stronger dependence on the specific problem, are directly resolved using the Navier-Stokes equation. Meanwhile, smaller eddies are commonly addressed through subgrid-scale modeling. Applying the Boussinesq hypothesis, the N-S governing equations after filtration for the large eddy simulation are described as follows [15]:

$$\frac{\partial \bar{u}_i}{\partial x_i} = 0 \tag{2}$$

$$\frac{\partial \bar{u}_i}{\partial t} + \frac{\partial \bar{u}_i \bar{u}_j}{\partial x_j} = -\frac{1}{\rho_0}\frac{\partial \bar{p}}{\partial x_i} - \frac{\partial \tau_{ij}}{\partial x_j} + \frac{\partial}{\partial x_j}[\mu(\frac{\partial \bar{u}_i}{\partial x_j} + \frac{\partial \bar{u}_j}{\partial x_i})] - g_i \beta \bar{\phi} \tag{3}$$

$$\frac{\partial \bar{\phi}}{\partial t} + \frac{\partial \bar{u}_j \bar{\phi}}{\partial x_j} = -\frac{\partial h_j}{\partial x_j} + \frac{\partial}{\partial x_j}(\alpha \frac{\partial \bar{\phi}}{\partial x_j}) \tag{4}$$

$$\tau_{ij} = \bar{u_i u_j} - \bar{u}_i \bar{u}_j \tag{5}$$

$$q_j = \bar{u_j \phi} - \bar{u}_j \bar{\phi} \tag{6}$$

The sub-grid scale turbulent stresses are computed from

$$\tau_{ij} - \frac{1}{3}\tau_{kk}\delta_{ij} = -2\mu_t \bar{S}_{ij} \tag{7}$$

$$\bar{S}_{ij} = \frac{1}{2}(\frac{\partial \bar{u}_i}{\partial x_j} + \frac{\partial \bar{u}_j}{\partial x_i}) \tag{8}$$

$$q_j = -\frac{\mu_t}{\sigma_t}\frac{\partial \phi}{\partial x_j} \tag{9}$$

where τ_{ij} is the sub-grid scale stress; μ_t is the sub-grid scale turbulent viscosity; $\bar{S}_{ij}$ is the rate-of-strain tensor for the resolved scale; q_j is the sub-grid scale flux and ϕ is the sub-grid scale turbulent flux of a scalar.

To better account for near-wall gradient effects, Shur et al. proposed an algebraic Wall Modeled LES (WMLES) model [18]. This model combines a mixing length model and a modified Smagorinsky model [19], and integrates Piomelli's wall-damping function [20]. In the WMLES model, the eddy viscosity is calculated using a hybrid length scale:

$$v_t = \min[(\kappa d_w)^2, (C_{Smag}\Delta)^2] \cdot S \cdot (1 - e^{-(\frac{y^+}{25})^3}) \tag{10}$$

$$\Delta = \min[\max(C_w d_w, C_w h_{\max}, h_{wn}), h_{\max}] \tag{11}$$

where C_{Smag} = 0.2; S is the strain rate; $y^+$is the normal to the wall inner scaling; $h_{\max}$ is the maximum edge length of the cell; h_{wn} is the wall-normal grid spacing; C_w is constant 0.15 here.

2.2. Volume of Fluid (VOF) Model

The Volume of Fluid (VOF) model can simulate two or more immiscible fluids by solving a single set of momentum equations while tracking the volume fraction of each fluid across the computational domain. The interface is constructed by calculating the phase fraction of each grid element. The volume fraction of the fluid signifies the proportion of the phase's volume to the total volume of the grid.

- $\alpha_q = 0$: The cell is empty (of the qth fluid}.
- $\alpha_q = 1$: The cell is full(of the qth fluid).
- $0 < \alpha_q < 1$: The cell contains the interface between the qth fluid and one or more other fluids.

For the qth phase, the phase equation has the following form:

$$\frac{1}{\rho_q}[\frac{\partial}{\partial t}[\alpha_q\rho_q] + \nabla\cdot[\alpha_q\rho_q\vec{v}_q] = S_{\alpha_q} + \sum_{p=1}^{n}(\dot{m}_{pq} - \dot{m}_{qp})] \quad (12)$$

where $\dot{m}_{pq}$ is the mass transfer from phase q to phase p and $\dot{m}_{qp}$ is the mass transfer from phase p to phase q. By default, the source term S_{α_q} is zero.

The momentum equation is given by:

$$\frac{\partial}{\partial t}(\rho\vec{v}) + \nabla\cdot(\rho\vec{v}\vec{v}) = -\nabla p + \nabla\cdot[\mu(\nabla\vec{v} + \nabla\vec{v}^T)] + \rho\vec{g} + \vec{F} \quad (13)$$

The presence of the component phases in each control volume determines the properties in the transport equations. For an n-phase system, the volume-fraction-averaged density (ρ) is given by:

$$\rho = \sum\alpha_q\rho_q \quad (14)$$

All other properties, such as viscosity, are computed similarly.

2.3. Solidification and Melting Model

An enthalpy-porosity technique is used in Ansys Fluent to model the solidification/melting process. In this method, the liquid fraction, which represents the fraction of the cell volume in liquid form, is calculated at each iteration based on an enthalpy balance. When the material has fully solidified in a cell, the velocities drop to zero. Sink terms are incorporated into the momentum and turbulence equations to accommodate the pressure drop and decreased porosity in the solid regions.

The enthalpy of the material is computed as the sum of the sensible enthalpy. h and the latent heat, ΔH:

$$H = h + \Delta H \quad (15)$$

where

$$h = h_{ref} + \int_{T_{ref}}^{T} c_p dT \quad (16)$$

h_{ref} = reference enthalpy, T_{ref} =reference temperature, and c_p = specific heat at constant pressure

The liquid fraction, β,can be defined as

- $\beta = 0$ if $T < \mathrm{T}_{solidus}$.
- $\beta = 1$ if $T > \mathrm{T}_{solidus}$
- $\beta = \frac{T - T_{solidus}}{T_{liquidus} - T_{solidus}}$ if $T_{solidus} < \mathrm{T} < \mathrm{T}_{liquidus}$

The latent heat content can now be written in terms of the latent heat of the material, L:

$$\Delta H = \beta L \quad (17)$$

The latent heat content can vary between zero (for a solid) and L (for a liquid).

For solidification/melting problems, the energy equation is written as

$$\frac{\partial}{\partial t}(\rho H) + \nabla\cdot(\rho\vec{v}H) = \nabla\cdot(k\nabla T) + S \quad (18)$$

where H = enthalpy, ρ = density, $\vec{v}$ = fluid velocity, and S = source term.

The momentum sink due to the reduced porosity in the mushy zone takes the following form:

$$S = \frac{(1-\beta)^2}{(\beta^3+\varepsilon)} A_{mush}(\vec{v} - \vec{v}_p) \quad (19)$$

where β is the liquid volume fraction, ε is a small number (0.001) to prevent division by zero, A_{mush} is the mushy zone constant, and $\vec{v}_p$ is the solid velocity due to the pulling of solidified material out of the domain (also referred to as the pull velocity).

In all of the turbulence equations in the mushy and solidified zones, sinks are added to account for the presence of solid matter:

$$S = \frac{(1-\beta)^2}{(\beta^3+\varepsilon)} A_{mush}\varphi \quad (20)$$

where φ represents the turbulence quantity being solved (k, ε, ω, , and so on).

3. Simulation of LIVE2D Stratified Experiment

3.1. Experiment Design

The LIVE2D test vessel, designed in a semi-circular slice geometry, replicates the geometry of the RPV lower head, as depicted in Figure 1, at a reduced linear scale of 1:5 [13]. This vessel has an inner diameter of 1 meter and a width of 12 centimeters. It is made of stainless steel and has an approximate wall thickness of 24 millimeters. The curved vessel wall is surrounded by a water-cooling channel. The rear vertical surface of the test vessel is insulated, while the entire front side is equipped with two glass plates, allowing for direct observation of the melt pool.

Notably, two distinct boundary conditions are implemented on the upper surface of the melt pool: a hot boundary (SO1 test) and a rigid cooled boundary (SOTC test). The hot boundary is created by placing a metallic plate over the top edge of the vessel, which forms a hot air atmosphere above the surface of the melt. Conversely, the rigid cooling boundary involves placing a water-cooled steel lid directly onto the surface of the melt. The decay heat is simulated using nine planes of independently controlled electrical resistance heating wires [13].

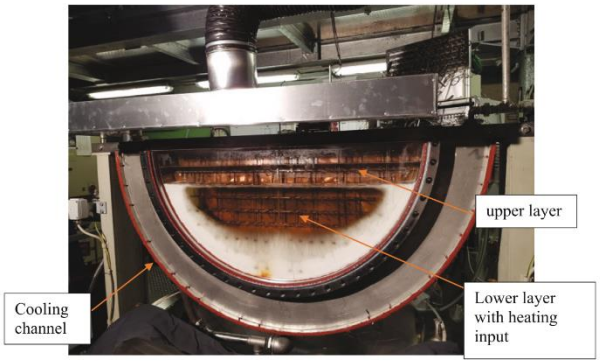

Figure 1 LIVE2D test facility with a hot upper boundary in SO1 test [13]**.**

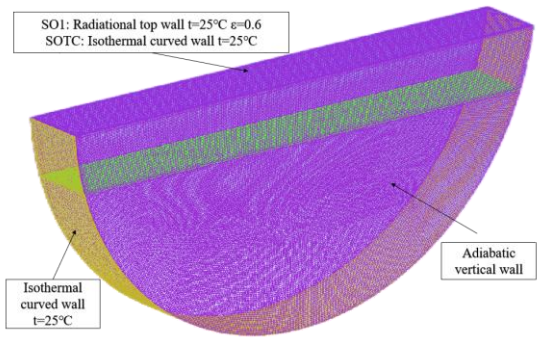

Figure 2 Boundary condition of LIVE2D simulation

3.2. Simulation Conditions

Table 1 SO1 and SOTC tests in the simulation

Test	Height of layer, mm	Heating phase, W	Boundary condition

	Upper layer	Lower layer		Top surface
SOTC	35	340	4300	Water cooled
	75	340	4300	
	110	340	4300	
SO1	110	340	1400	Hot air
	75	375	1300	
	35	415	1300	

In the simulation, six cases of SO1 and SOTC with different heights are calculated (Table 1). The mesh and the specified boundary condition are illustrated in Figure 2. The height of the boundary layer mesh is less than 0.5mm. The vertical front and back walls remain adiabatic, while the curved wall is isothermally cooled to 25°C with a steel boundary of 24 mm. In the SO1 test, a radiation heat transfer condition is applied to the upper section with a radiation heat transfer coefficient of 0.6. In the SOTC test, the upper section is maintained at 25°C with a 5mm steel boundary. According to the experiment, it is assumed that the heat loss in SOTC is 15% and that of SO1 is 20%. The physical property parameters of a 50% NaNO3-50% KNO3 mixture and heat conduction oil are presented in Table 2 [21].
Table **3** presents data that are all input using pointwise-linear interpolation.

Table 2 Physical parameters of 50%-50% NaNO3-KNO3

Temperature/℃	0	224 [21]	260 [21]	300 [22]	350 [22]
Density (kg/m3)	2260	1964	1937	1903	1869
Cp (specific heat) (j/kg-k)	947.4	1290	1310	1320	1320
Thermal Conductivity (w/m-k)	0.4	0.48	0.47	0.459	0.443
Viscosity (kg/m-s)	10	5.42E-03	4.32E-03	3.20E-03	2.32E-03
Pr		14.5	12.0	9.18	6.89
solid-liquid phase line/℃	223.8				

Table 3 Physical parameters of heat transfer oil in LIVE2D [13]

Temperature /℃	140	220
Density (kg/m3)	755	540
Cp (specific heat)(j/kg-k)	1700	1830
Thermal Conductivity (w/m-k)	0.15	0.15
Viscosity (kg/m-s)	8.31E-03	4.86E-03
Pr	94	59

3.3. Results Discussion

3.3.1. Simulation of LIVE2D SOTC tests

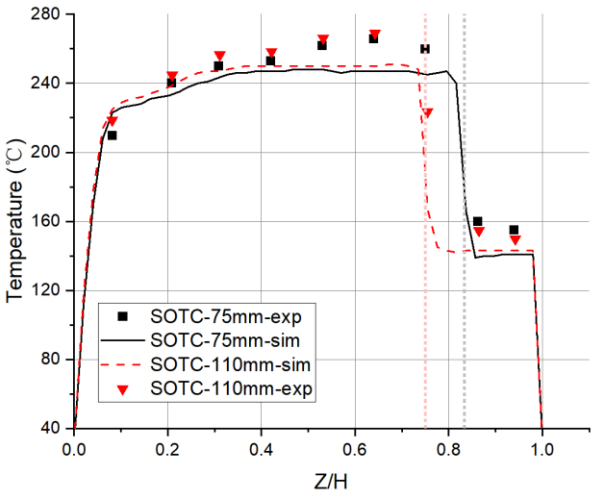

Figure 3 Comparison of two layers of temperature distributions in simulation and experimental results of LIVE2D SOTC tests

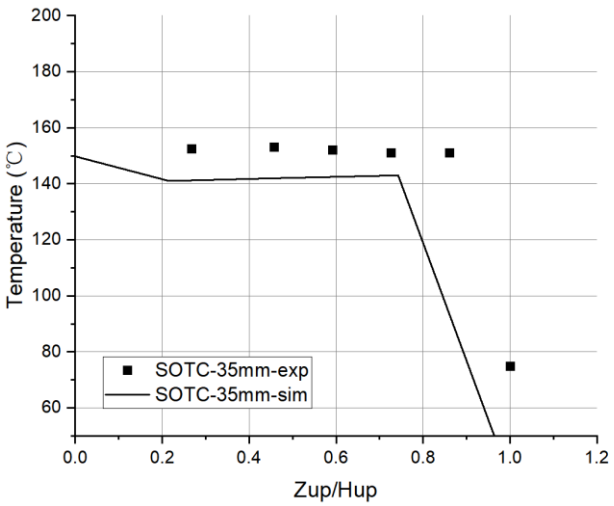

Figure 4 Comparison of upper layer temperature distributions in simulation and experimental results of LIVE2D SOTC tests

Figure 3 and Figure 4 both compare the LIVE2D SOTC temperature distribution in simulation and experi ment results. The simulated temperature distribution of the melt pool closely matches that of the experime ntal results, including the crust region at the bottom and the interface. In Figure 3, when the height of the u pper layer is 110mm, the volume of the lower layer is smaller than that when the height of the upper layer is 110mm, and the power density under the same power is increased, resulting higher lower layer temperat ure. The heat transfer area of the upper layer side wall is reduced, and the upper layer temperature is slight ly decreased. The upper layer data in Figure 4, compared with experiment data measured with thermocoup les in the melt and under the cooling lid, demonstrates that the temperature of the upper layer is relatively uniform.

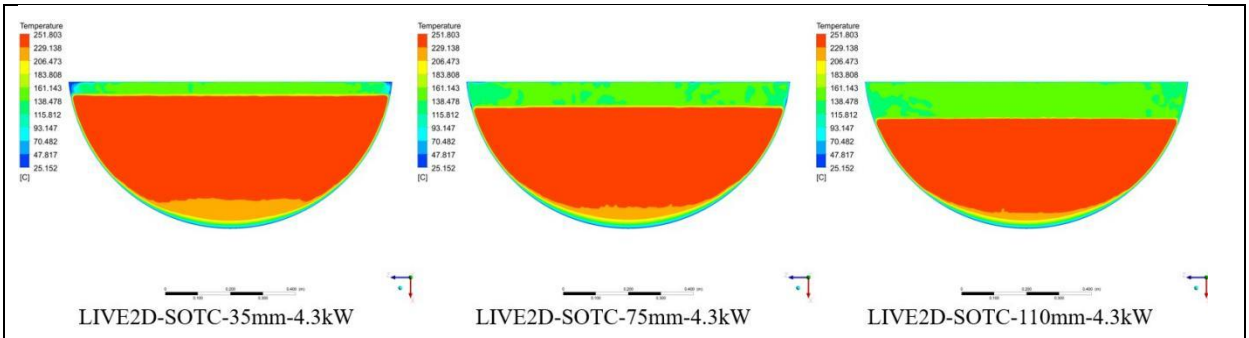

Figure 5 Temperature contours of LIVE2D SOTC simulation results

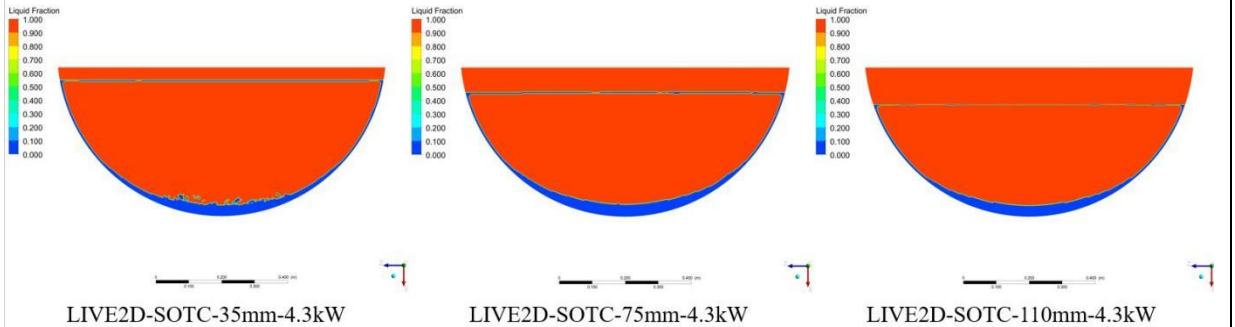

Figure 6 Liquid Fraction contours of LIVE2D SOTC simulation results

In SOTC tests, the top cooling condition causes the temperature difference (**Figure 5**) and enhances the integrity of the interlayer crust (Figure 6). The temperature distribution and the integrity of th e interlayer crust also interact with each other. The uneven temperature caused by top cooling causes interl ayer crust, and the interlayer crust further enhances the temperature difference between the two layers. Wit h the increase of the upper layer height, the power density in the lower layer increases, causing the bottom area to warm up and the crust thickness gradually to be thinner

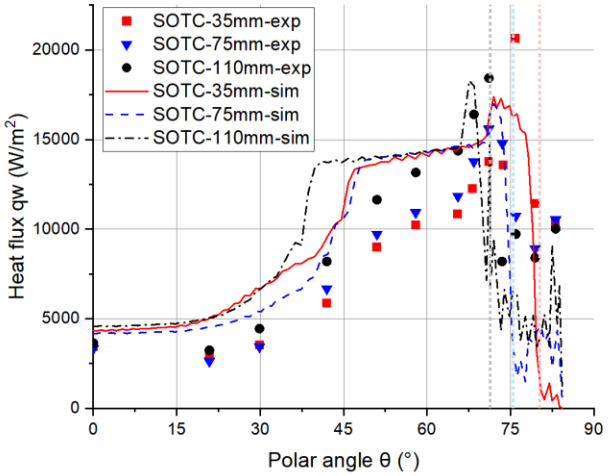

Figure 7 Comparison of heat flux distributions in simulation and experimental results of LIVE2D SOTC tests

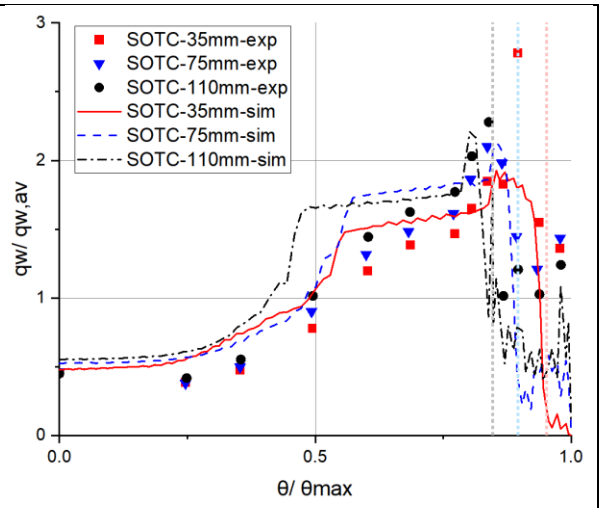

Figure 8 Comparison of focusing factor distributions in simulation and experimental results of LIVE2D SOTC tests

Under SOTC conditions, the two layers' simulated heat flux (Figure 7) and focusing factor (Figure 8) are also roughly consistent with the experimental results. The peak heat flux value appears below the interface in SOTC both in the experiment and simulation. In the simulation results, the temperature at the left and right boundary of the upper layer (especially when the thickness is 35mm) decreases significantly due to the cooling of the top and side walls (see Figure 5), so the heat flux of the upper side wall is smaller compared to the experiment data.

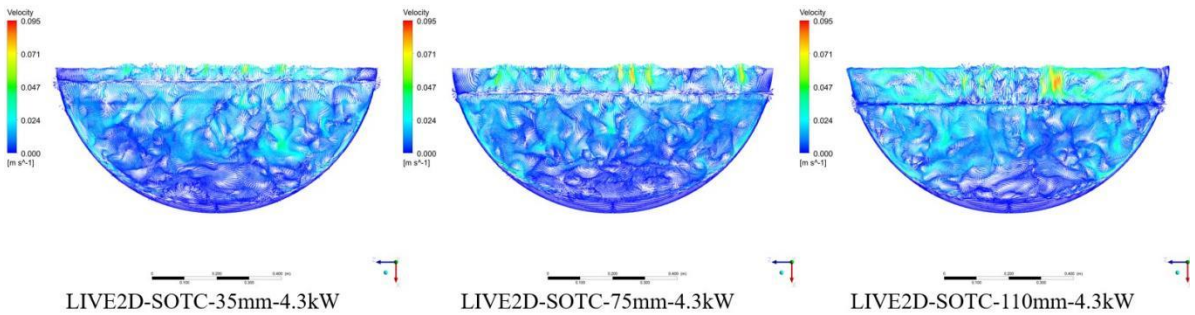

Figure 9 Velocity vectors of LIVE2D SOTC simulation results

Similar to the results of a single-layer molten pool, the velocity of both layers is larger than that of the top radiation and the flow is more intense in the top cooling, as indicated by the velocity vectors in Figure 6. In the case of strong cooling at the top, the flow of the top upper layer is similar to Rayleigh–Bénard convection with alternative uprising and descending flows, resulting in multiple convection cells[23].

3.3.2. Simulation of LIVE2D SO1 tests

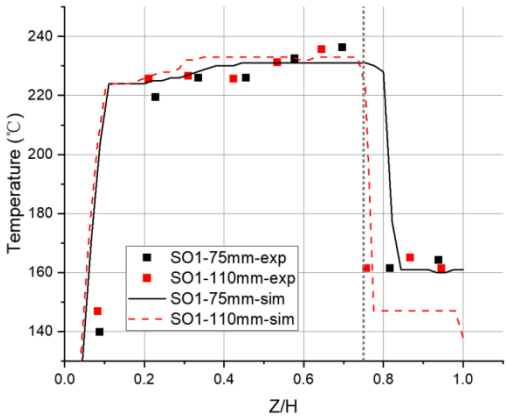

Figure 10 Comparison of two layers of temperature distributions in simulation and experimental results of LIVE2D SO1 tests

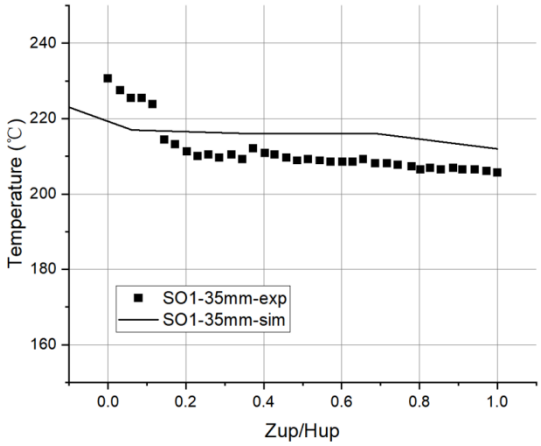

Figure 11 Comparison of upper layer temperature distributions in simulation and experimental results of LIVE2D SO1 tests

Figure 10 and Figure 11 both compare the LIVE2D SO1 temperature distribution in simulation and experi ment results. The simulated temperature distribution of the melt pool is also close to that of the experiment al results. In contrast to the SOTC cases, the lower layer height remains constant in the SO1 cases, resultin g in a fixed power density. As the height of the upper layer decreases in Figure 10, the temperature of the l ower layer changes minimally, while the temperature of the upper layer increases significantly. The upper l ayer data is also comparable to the experiment data measured with mobile lance in Figure 11.

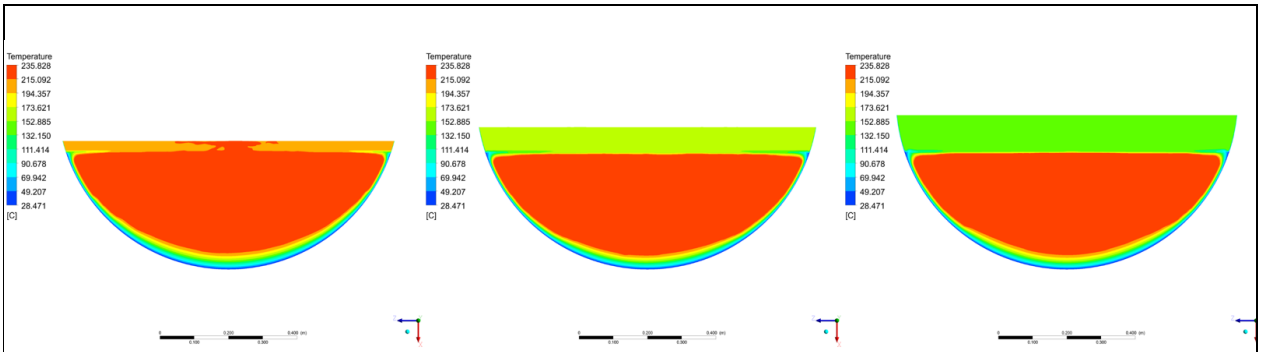

Figure 12 Temperature contours of LIVE2D SO1simulation results

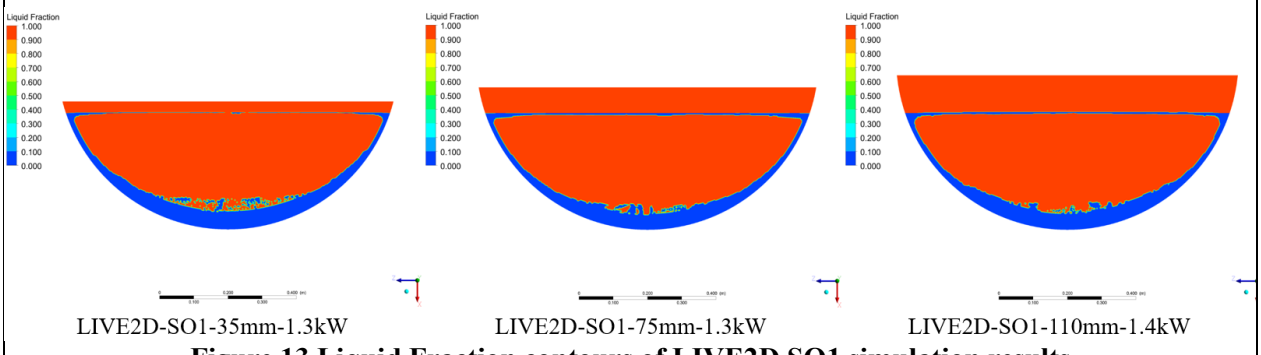

Figure 13 Liquid Fraction contours of LIVE2D SO1 simulation results

In LIVE2D SO1 tests, the temperature of the upper layer changed with its height. The variation of upper la yer temperature with upper layer height can be visually observed in Figure 12. Correspondingly, the interl ayer crust also becomes thicker with the decrease of the upper layer's temperature.

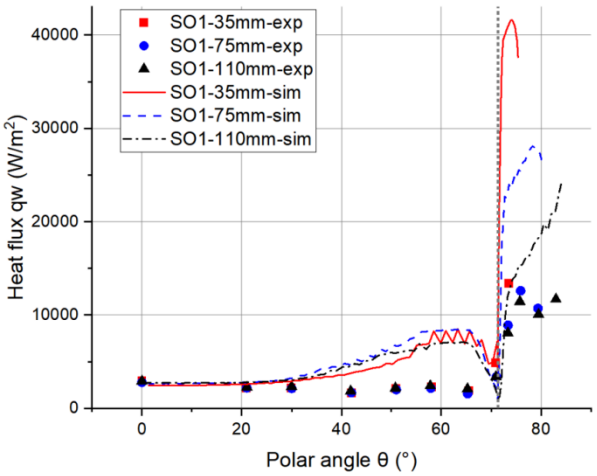

Figure 14 Comparison of heat flux distributions in simulation and experimental results of LIVE2D SO1 tests

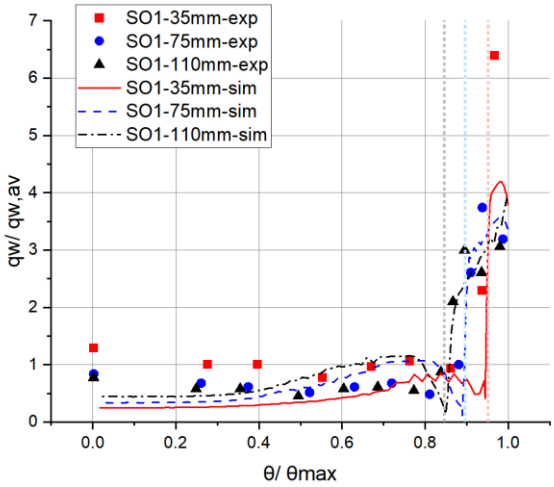

Figure 15 Comparison of focusing factor distributions in simulation and experimental results of LIVE2D SO1 tests

Under SO1 conditions, the heat flux obtained by simulation is greater than that obtained by experiment (Fig. 14), but the focusing effect is less evident in the SO1-35mm case (Fig. 15). The primary reason is that the heat flux measured is relatively low in the SO1 experiments, while the heat flux spike is prone to occur near the wall in the Fluent calculation. The top layer of the metal dissipates little heat, causing the heat flux peak to appear in the upper layer in SO1 and creating the 'focusing effect'.

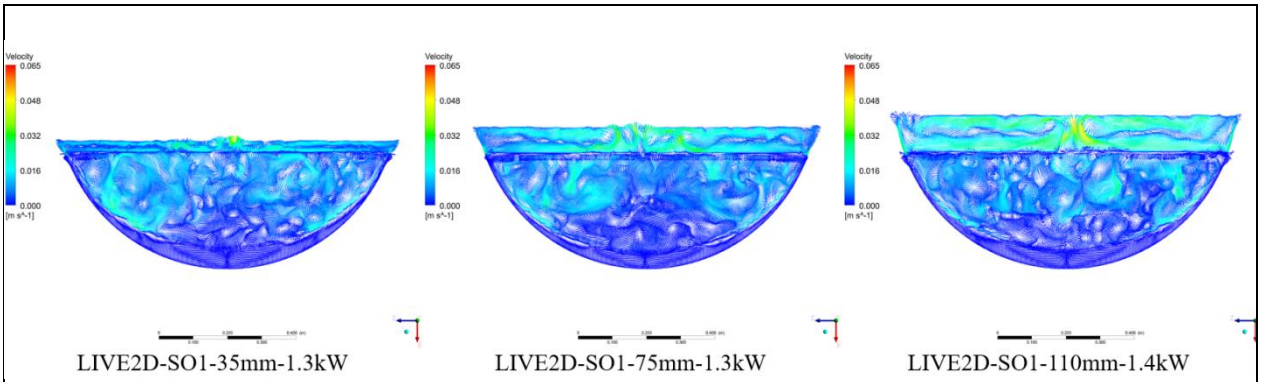

Figure 16 Velocity vectors of LIVE2D SO1 simulation results

Without top cooling, the velocity of both layers in SO1 is lower, exhibiting a weaker flow compared to the SOTC tests, as depicted by the velocity vectors in Figure 16. Simultaneously, under the influence of intense side cooling, convection characterized by horizontal flow at the upper and bottom boundaries. Consequently, the flow in the upper layer is predominantly governed by two convection cells.

4. CONCLUSIONS

This paper focuses on the two-layer melt pool experiment LIVE2D under density stratification, validates the effectiveness of the Fluent model, and summarizes the law of stratified melt pool through a comparison with experimental results. In this study, the WMLES turbulence model, VOF model, solidification, and melting models in Fluent are used for numerical simulation. The conclusions are listed below.

Firstly, after comparing the flow and heat transfer simulation results with the LIVE2D experiment, the feasibility of simulating the two-layer melt pool experiment with Fluent has been preliminarily verified.

Secondly, in comparison to the scenario with top radiation, the temperature of the metal layer remains relatively stable at different heights under the top cooling condition, and the peak heat flux occurs in the bottom layer region.

Thirdly, this study demonstrates that with strong cooling at the top, the convection exhibits behavior similar to Rayleigh-Bénard convection.

ACKNOWLEDGMENTS

This work was financially supported by the National Key R&D Program of China (Grant No. 2018YFB1900100).

REFERENCES

[1] O. Kymäläinen, H. Tuomisto, and T. G. Theofanous, "In-vessel retention of corium at the Loviisa plant," *Nucl. Eng. Des.*, vol. 169, no. 1–3, pp. 109–130, 1997, doi: 10.1016/s0029-5493(96)01280-0.

[2] F. Fichot *et al.*, "Some considerations to improve the methodology to assess In-Vessel Retention strategy for high-power reactors," *Ann. Nucl. Energy*, vol. 119, pp. 36–45, 2018, doi: 10.1016/j.anucene.2018.03.040.

[3] T. G. Theofanous, C. Liu, S. Additon, S. Angelini, O. Kymäläinen, and T. Salmassi, "In-vessel coolability and retention of a core melt," *Nucl. Eng. Des.*, vol. 169, no. 1–3, pp. 1–48, 1997, doi: 10.1016/S0029-5493(97)00009-5.

[4] H. Esmaili and M. Khatib-Rahbar, "Analysis of In-Vessel Retention and Ex-Vessel Fuel Coolant Interaction for AP1000," *Nureg/Cr-6849, Eri/Nrc 046201*, 2004.

[5] J. L. Rempe, D. L. Knudson, C. M. Allison, G. L. Thinnes, C. L. Atwood, and M. J. Cebull, "Potential for AP600 In-Vessel Retention through Ex-Vessel Flooding," no. December, p. 128, 1997.

[6] T. G. Theofanous, C. Liu, S. Additon, S. Angelini, O. Kymalainen, and T. Salmassi, "IN-VESSEL COOLABILITY AND RETENTION OF A CORE MELT," vol. 1, no. October, p. 441, 1996.

[7] Y. Zhiyi, Z. Ningna, Z. Dahuan, D. Chao, S. Mingqiang, and X. Hong, "IVR design and review of advanced NPPs in China: Issues and perspectives," *Int. J. Adv. Nucl. React. Des. Technol.*, vol. 3, no. June, pp. 97–101, 2021, doi: 10.1016/j.jandt.2021.06.006.

[8] V. G. Asmolov and A. V. Merzliakov, "OECD RASPLAV Project: Phase I results." 1998. Accessed: May 24, 2023. [Online]. Available: http://inis.iaea.org/Search/search.aspx?orig_q=RN:29060098

[9] F. Fichot *et al.*, "Chemical Interactions of Molten Steel with (U-Zr-O) Corium: Main Outcomes of the CORDEB Program," *Nucl. Eng. Des.*, vol. 388, no. January, p. 111588, 2022, doi: 10.1016/j.nucengdes.2021.111588.

[10] A. A. Gubaidullin and B. R. Sehgal, "Simeco tests in a melt stratified pool," *Int. Conf. Nucl. Eng. Proceedings, ICONE*, vol. 4, pp. 935–945, 2002, doi: 10.1115/ICONE10-22709.

[11] A. Palagin *et al.*, "Analysis and interpretation of the LIVE-L6 experiment," *5th Eur. Rev. Meet. Sev. Accid. Res.*, no. March, pp. 21–23, 2012.

[12] Y. Zhou *et al.*, "Experimental research on heat transfer behavior of large scale two-layer salt melt pool based on COPRA facility," *Ann. Nucl. Energy*, vol. 138, 2020, doi: 10.1016/j.anucene.2019.107166.

[13] X. Gaus-Liu, T. Cron, B. Fluhrer, and T. Wenz, "Experimental study and analytical analysis on the global heat transfer of stratified corium in LWR lower head," *Nucl. Eng. Des.*, vol. 372, no. November 2020, p. 110999, 2021, doi: 10.1016/j.nucengdes.2020.110999.

[14] A. Horvat, I. Kljenak, and J. Marn, "Two-dimensional large-eddy simulation of turbulent natural convection due to internal heat generation," *Int. J. Heat Mass Transf.*, vol. 44, no. 21, pp. 3985–3995, 2001, doi: 10.1016/S0017-9310(01)00066-7.

[15] M. Fukasawa, S. Hayakawa, and M. Saito, "Thermal-hydraulic analysis for inversely stratified molten corium in lower vessel," *J. Nucl. Sci. Technol.*, vol. 45, no. 9, pp. 873–888, 2008, doi: 10.1080/18811248.2008.9711489.

[16] L. Zhang, S. Luo, Y. Zhang, W. Tian, G. H. Su, and S. Qiu, "Large eddy simulation on turbulent heat transfer in reactor vessel lower head corium pools," *Ann. Nucl. Energy*, vol. 111, pp. 293–302, 2018, doi: 10.1016/j.anucene.2017.08.055.

[17] L. Zhang *et al.*, "Large eddy simulation for the thermal behavior of one-layer and two-layer corium pool configurations in HPR1000 reactor," *Appl. Therm. Eng.*, vol. 145, no. September, pp. 38–47, 2018, doi: 10.1016/j.applthermaleng.2018.09.019.

[18] M. L. Shur, P. R. Spalart, M. K. Strelets, and A. K. Travin, "A hybrid RANS-LES approach with delayed-DES and wall-modelled LES capabilities," *Int. J. Heat Fluid Flow*, vol. 29, no. 6, pp. 1638–1649, 2008, doi: 10.1016/j.ijheatfluidflow.2008.07.001.

[19] J. Smagorinsky., "General Circulation Experiments with the Primitive Equations. I. The Basic Experiment," *Mon. Wea. Rev.*, vol. 91, no. 3, pp. 99–164, 1963, doi: 10.1126/science.12.306.731-a.

[20] P. M. and J. H. F. U. Piomelli, "Model consistency in the large eddy simulation of turbulent channel flows," *Phys. Fluids*, vol. 31, pp. 1884–1894, 1987, doi: 10.2514/6.1987-1446.

[21] X. Gaus-Liu, T. Cron, B. Fluhrer, T. Wenz, and A. Miassoedov, "Experimental Study on the Behaviour of in-Vessel Two-Layer Melt Pool in Live2D Facility," pp. 1–14, 2019.

[22] S. Luo, Y. Zhang, Y. Zhou, W. Tian, G. H. Su, and S. Qiu, "COPRA experiment and numerical research on the behavior of internally-heated melt pool with eutectic salt," *Appl. Therm. Eng.*, vol. 140, no. January, pp. 313–324, 2018, doi: 10.1016/j.applthermaleng.2018.05.041.

[23] D. Villers and J. K. Platten, "Coupled buoyancy and Marangoni convection in acetone experiments and comparison with numerical simulations," *J. Fluid Mech.*, vol. 234, pp. 487–510, 1992, doi: 10.1017/S0022112092000880.

SEAKNOT
ERMSAR 2024
11th Conference on
SEVERE ACCIDENTS RESEARCH
May 13-16, 2024 – Stockholm, Sweden

Numerical Simulation of LIVE2D Two-layer Melt Pool Experiment

PENGYA GUO, PENG YU, FENGYANG QUAN, YIDAN YUAN*

Introduction

The success of the In-Vessel Retention (IVR) strategy depends on the principle that the angular heat flux (q_w) imposed by the melt pool on the Reactor Pressure Vessel (RPV) lower head does not exceed the critical heat flux (CHF) [1]. However, as observed in the RASPLAV experiment, the formation of a double-layer melt pool could lead to a concentration of wall heat flux in the top metal layer region, known as the 'focusing effect' [2]. And 'Focusing factor' can be used to describe the ratio of local heat flux to the average sidewall heat flux. The most challenging situation for vessel integrity may occur in the early stage of the formation of the two-layer melt pool due to a drastic increase in the focusing effect [3]. To accurately predict the wall heat flux and assess the effectiveness of the IVR strategy, it is crucial to study the thermal behavior of the two-layer melt pool.

Simulation Methods

ANSYS Fluent is used for the computational fluid dynamics (CFD) simulation, and the WMLES turbulence model is employed. In addition, the Volume of Fluid (VOF) multiphase flow model and the Solidification and Melting model are utilized in the simulation.

LIVE2D Experiment Design

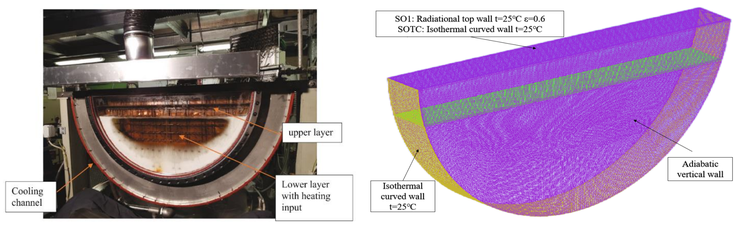

Fig.1 LIVE-2D experiment and simulation conditions

The LIVE2D test vessel, designed in a semicircular slice geometry, replicates the geometry of the reactor pressure vessel (RPV) lower head at a reduced linear scale of 1:5 [4]. Two distinct boundary conditions were applied to the upper surface of the melt pool: a hot boundary (LIVE2D-SO1 test) and a rigid cooled boundary (LIVE2D-SOTC test). The physical property parameters of a 50% NaNO3-KNO3 mixture and heat conduction oil were obtained from the experiment [5]. Based on the experimental data, the heat loss is estimated to be 15%-20%.In the simulation, six cases of SO1 and SOTC with different layer heights are calculated.

Table 1 SO1 and SOTC tests in the simulation

Test	Height of layer, mm		Heating phase, W	Boundary condition
	Upper layer	Lower layer		Top surface
SOTC	35	340	4300	Water cooled
	75	340	4300	
	110	340	4300	
SO1	110	340	1400	Hot air
	75	375	1300	
	35	415	1300	

Results and discussions

1. Simulation of LIVE2D SOTC tests

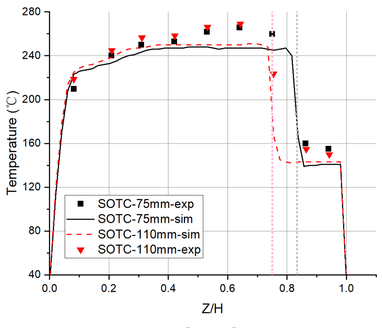

Fig. 2 Temperature distributions in LIVE2D SOTC tests

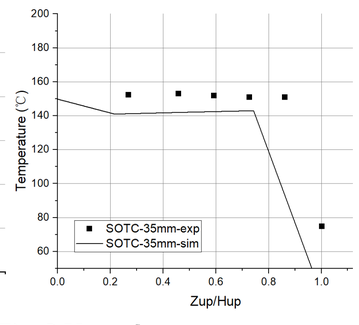

Fig. 3 Upper layer temperature distributions in LIVE2D SOTC tests

In LIVE2D SOTC tests, the simulated temperature distribution of the melt pool closely matches the experimental results, including the crust region at the bottom and the interface. The temperature in the upper layer is relatively uniform.



Fig.4 Temperature contours of LIVE2D SOTC simulation results

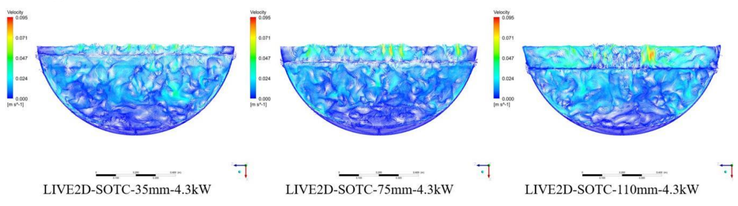

Fig.5 Liquid Fraction contours of LIVE2D SOTC simulation results

The top cooling condition results in a temperature difference (see Fig. 4) and improves the integrity of the interlayer crust. In the case of strong cooling at the top, the flow of the upper layer is similar to Rayleigh–Bénard convection with alternating upward and downward flows [6]. , resulting in multiple convection cells (Fig. 5).

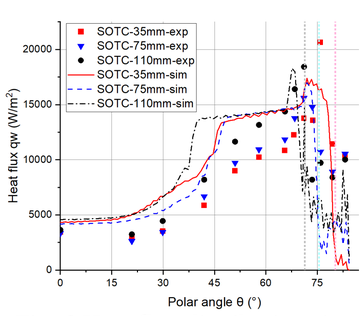

Fig. 6 Heat flux distributions in LIVE2D SOTC tests

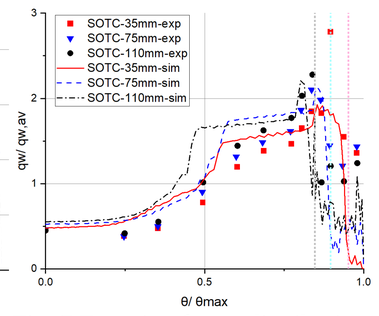

Fig. 7 Focusing factor distributions in LIVE2D SOTC tests

The two layers' simulated heat flux and focusing factor are also approximately consistent with the SOTC experimental results. The peak heat flux value appears below the interface both in the SOTC experiments and simulations.

2. Simulation of LIVE2D SO1 tests

In LIVE2D SO1 tests, the temperature of the upper layer changed with its height. In contrast to the SOTC cases, the lower layer height remains constant in the SO1 cases, resulting in a fixed power density. As the height of the upper layer decreases, the temperature of the lower layer changes marginally, while the temperature of the upper layer increases significantly, as depicted in Fig. 10, too. The data from the upper layer is also comparable to the experimental data.

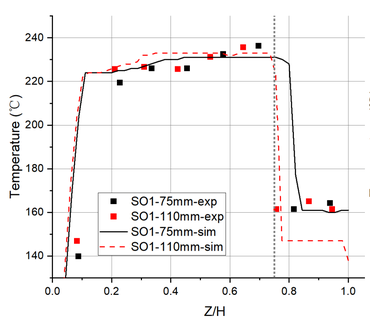

Fig. 8 Temperature distributions in LIVE2D SO1 tests

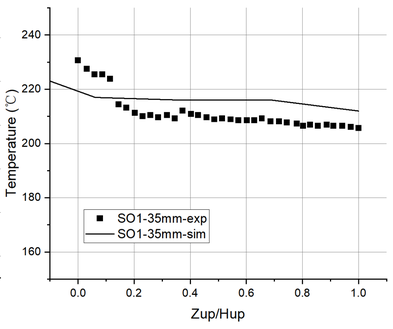

Fig. 9 Upper layer temperature distributions in LIVE2D SO1 tests

Without top cooling, the velocity of both layers in SO1 is lower, exhibiting a weaker flow compared to the SOTC tests, as depicted by the velocity vectors in Fig. 11. Simultaneously, under the influence of intense side cooling, convection characterized by horizontal flow at the upper and bottom boundaries. Consequently, the flow in the upper layer is predominantly governed by two convection cells.

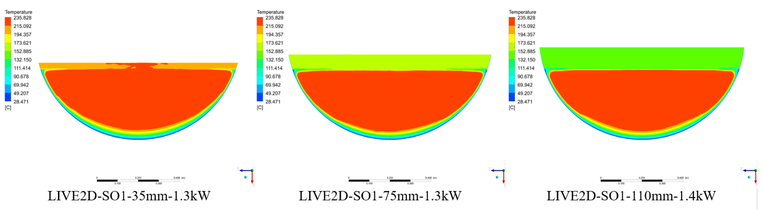

Fig.10 Temperature contours of LIVE2D SO1 simulation results

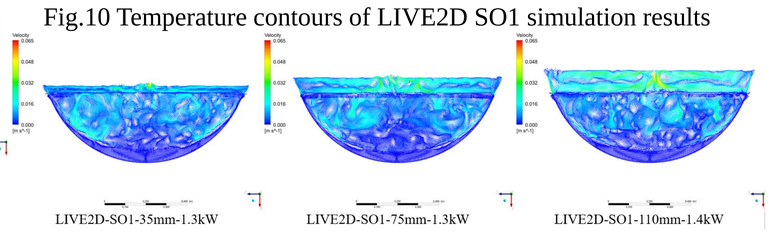

Fig.11 Liquid Fraction contours of LIVE2D SO1 simulation results

Under SO1 conditions, the heat flux obtained by simulation is greater than that obtained by experiment (Fig. 12), but the focusing effect is less evident in the SO1-35mm case(Fig. 13). The primary reason is that the heat flux measured experimentally under SO1 is relatively low, while the heat flux spike is prone to occur near the wall in the Fluent calculation. The top layer of the metal removes little heat, causing the heat flux peak to appear in the upper layer in SO1 and creating the 'focusing effect'.

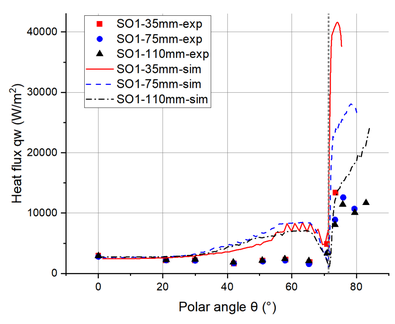

Fig. 12 Heat flux distributions in LIVE2D SO1 tests

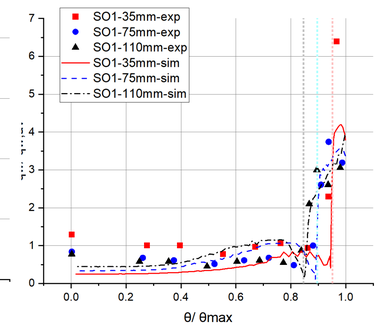

Fig. 13 Focusing factor distributions in LIVE2D SO1tests

Conclusions

1. After comparing the simulation results with the LIVE2D experiment, the feasibility of simulating the two-layer melt pool experiment with Fluent has been preliminarily validated.
2. In comparison to the scenario with top radiation, the temperature of the metal layer remains relatively stable at different heights under the top cooling condition, and the peak heat flux occurs in the bottom layer region.
3. With strong cooling at the top, the convection exhibits behavior similar to Rayleigh-Bénard convection.

References

[1] Ma, W., Yuan, Y., Sehgal, B.R., 2016. In-Vessel Melt Retention of Pressurized Water Reactors: Historical Review and Future Research Needs. Engineering 2, 103–111. https://doi.org/10.1016/J.ENG.2016.01.019

[2] Fichot, F., Michel, B., Almjashev, V., Le Guennic, C., Bakouta, N., Le Tellier, R., Piluso, P., Keim, T., 2022. Chemical Interactions of Molten Steel with (U-Zr-O) Corium: Main Outcomes of the CORDEB Program. Nuclear Engineering and Design 388, 111588. https://doi.org/10.1016/j.nucengdes.2021.111588

[3] Esmaili, H., Khatib-Rahbar, M., 2004. Analysis of In-Vessel Retention and Ex-Vessel Fuel Coolant Interaction for AP1000. Nureg/Cr-6849, Eri/Nrc 046201.

[4] Gaus-Liu, X., et al., 2013. LIVE-3D and LIVE-2D experimental results on melt pool heat transfer with top cooling conditions. In: 6th European Review Meeting on Severe Accident Research (ERMSAR 2013), Avignon, F, October 2-4, 2013.

[5] Gaus-Liu, X., Cron, T., Fluhrer, B., Wenz, T., 2021. Experimental study and analytical analysis on the global heat transfer of stratified corium in LWR lower head. Nuclear Engineering and Design 372, 110999. https://doi.org/10.1016/j.nucengdes.2020.110999

[6] D. Villers and J. K. Platten, "Coupled buoyancy and Marangoni convection in acetone experiments and comparison with numerical simulations," J. Fluid Mech., vol. 234, pp. 487–510, 1992, doi: 10.1017/S0022112092000880.

Pengya Guo **Tel: +86 18801359598**
PhD Candidate **Email: gpy20@mails.tsinghua.edu.cn**
***yidanyuan2010@aliyun.com**

SEVERE ACCIDENT R&D IN UJV GROUP

Petr Vacha, Miroslav Kotouc, Jan Komrska
UJV Rez, a. s.
Hlavni 130, Husinec-Rez, 250 68, Czechia
petr.vacha@ujv.cz; miroslav.kotouc@ujv.cz; jan.komrska@ujv.cz

Tomas Cernousek, Jan Hrbek, Bence Meszaros
Centrum Vyzkumu Rez, s. r. o.
Hlavni 130, Husinec-Rez, 250 68, Czechia
Tomas.cernousek@cvrez.cz; jan.hrbek@cvrez.cz; bence.meszaros@cvrez.cz

ABSTRACT

The presented work summarizes the latest advancements in the ex-vessel corium interactions and cooling research and development (R&D) program carried out by the UJV Group – UJV Rez and its daughter company Research Centre Rez. The goal of this work is to provide the context of these activities, their synergies and interconnections, and to put them into the wider framework of development of nuclear energy in the Czech Republic. The high-level overview is provided in the first chapter. The R&D targeting GENII reactors focus mainly on severe accident research of VVER-1000 type of reactors and serves mainly to enhance the safety of the Czech VVER-1000 reactors in operation. An ex-vessel cooling strategy has been formulated and supported by a number of computational and experimental studies. The main outcomes are summarized in the second chapter. Part of the GENII program overlaps issues specific to new builds featuring GENIII and GENIII+ reactors. New materials, that can replace concrete in its applications inside the containment, resilient to high temperatures, radiation, and even chemical interactions with acids has been under development, based on geopolymer matrices. Results of all the test carried out so far show excellent behavior of these materials in prototypic conditions. An overview of these results is provided in the third chapter. In R&D focused on severe accidents in GENIV reactors, the gas-cooled fast reactor (GFR) concept is the main technology that has been developed. Ex-vessel strategy for this type of reactor was established, and a core catcher with innovative sacrificial materials has been under development, targeted to mitigate the consequences of a severe accident specifically in GFR with its unique corium compositions. Chapter four provides an overview of these activities.

KEYWORDS
Severe accidents, ex-vessel, core catcher, cold crucible

1. INTRODUCTION

UJV Group (namely UJV Rez and its daughter company CVR) has a long and rich tradition in both the in-vessel retention (IVR) and ex-vessel corium research. UJV Rez is primarily an engineering company providing wide range of services, including design, and engineering activities in the fields of energy, industry, and health. CVR is a research center dedicated to R&D in energy research with a wide range of state-of-the-art experimental infrastructure, including the LVR-15 and LR-0 research reactors, and various

technology loops. The goal of this work is to provide context for the part concerning the R&D related to ex-vessel phenomena.

The IVR research is focused on large-scale experiments using the THS-15 facility and has been very well documented in recent years [1][2]. In the part of the program focused on the ex-vessel phenomena, the corium spreading and interactions with solid materials – concrete or newly developed functional/sacrificial materials are the main areas of focus. The activities span several national R&D projects and are supported by active participation of both the organizations of UJV Group in various international R&D projects within the framework of Euratom and OECD NEA. The goal is to keep and broaden the knowledge base of the Group and to contribute to expanding the boundaries of the state of the art in the field.

The goals of these R&D activities differ based on the generation of nuclear power plants (NPPs) the solution is intended for. The program spans projects for NPPs under operation (GEN II), innovative light water reactor designs of GENIII and GENIII+, as well as innovative concepts of advanced reactors of GENIV. However, all the activities are interconnected, and solutions found for, on first sight, unrelated technologies, can be often adopted to a completely different generation and type of reactors. One such example is given in Chapter 3.

For GENII reactors under operation, the main focus of the ongoing research in UJV Group is on development of a reliable ex-vessel corium stabilization strategy for VVER-1000 reactors. This activity includes a variety of numerical simulations using various computational tools, such as MELCOR, ASTEC, MELTSPREAD and CORQUENCH codes, as well as the CFD approach and computational materials engineering code Thermo-calc. To validate the computational analyses, a number of experiments has been conducted in-house by the UJV Group, and UJV Rez is also a partner in OECD NEA projects ROSAU and COPS. Development of a special new geopolymer-based sacrificial material is also a part of these activities. More on this topic is available in Chapter 2. Severe accident research for new builds of GENIII and GENIII+ reactors is closely related to both the GENII and GENIV part, as shown in Chapter 3.

The GENIV severe accident R&D in the UJV Group is focused on the Gas-cooled Fast Reactor technology (GFR). This technology has been developed in the Group over the last almost 15 years, and severe accident research is a part of the effort to bring the technology ever closer to building a demonstration unit.

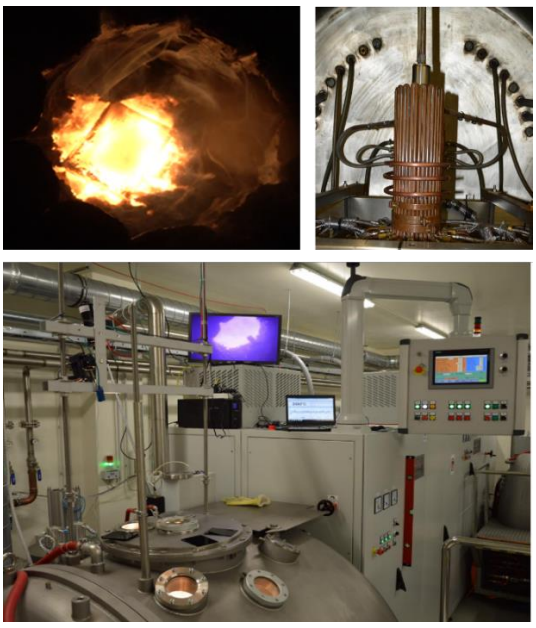

Figure 1. The cold crucible laboratory of CVR [3]

2. Ex-vessel strategy for reactors under operation

The ex-vessel corium spreading and stabilization strategy for VVER-1000/v320 reactors is a part of efforts leading to further enhancing safety of this design to stay compliant with the ever more stringent safety requirements and standards. The general strategy and the computational part of the analyses are elaborated in detail in [4].

In brief, the main idea is to let the RPV lower head fail (in case that every other mean either preventing or mitigating a severe accident during the in-vessel phase fails), let the corium evacuate to the Reactor shaft, where one of the walls are intentionally weakened to make sure it fails due to MCCI first in the exact point. The adjacent room of the containment will be prepared for spreading the corium onto a pre-defined surface (a sort of retroffited core catcher) and stabilize it using water cooling from the top.

In order for this proposed strategy to be viable and reliable, and the resulting design of the newly proposed system to be optimized, a number of requirements have to be met and a lot of data has to be collected:

- First, it needs to be confirmed, that the corium ejected from the RPV is, in all the sequences leading to a severe accident reaching the ex-vessel phase, is in a state allowing the intended spreading, i. e. it is not too viscous and near the solidus line.
- It needs to be confirmed, that the bottom of the Reactor shaft can withstand the impact and the subsequent heat-up before the cavity wall fails and corium starts to spread.
- It needs to be confirmed, that the corium will spread to all of the designated area in the room adjacent to the Reactor shaft, and that the proposed top-cooling system is capable to stabilize the resulting melt, preventing uncontrolled MCCI or unacceptable damage to the containment structure.

Concerning the first and the third set of problems, a long-term activity to confirm the fulfillment of the requirements has been underway in UJV Rez for the past almost a decade. Since the phenomena involved in this phase of a severe accident are very complex and not yet fully understand in general, UJV Rez relies on active participation in both international and national R&D projects aiming at broadening of understanding of ex-vessel melt spreading, most recently the OECD NEA ROSAU and COPS projects.

Various analytic and computational tools have been used to analyze and predict the behavior of corium ex-vessel in VVER-1000/v320 design. These tools include the MELTSPREAD and CORQUENCH codes, in

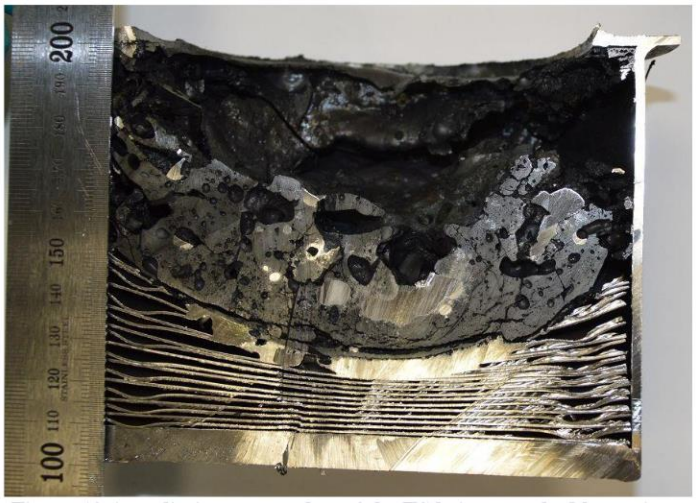

Figure 2. Results of corium ejection onto the thermal shielding

Table I. Gases produced by MCCI/interactions with geopolymer (CORQUENCH analysis)

Basemat material	Total [kmol]	Total [kg]	Total H2 [kmol]	Total H2 [kg]	Total CO2 [kmol]	Total CO2 [kg]
VVER-1000 concerete	604.4	1218.5	604.4	1218.5	0.0	0.0
Geopolymer	142.6	3068.0	35.6	71.8	106.9	2996.2

which in-house models of the relevant parts of the containment have been developed, and subsequent validation of the tools and the models, using data from the R&D projects. Latest addition in these activities is use of the Thermo-calc software with its databases of material data, which is planned to be directly coupled to the numerical analyses in the near future.

For the second requirement, the main open question is whether the corium ejected from the RPV penetrate deeply into the structures on the bottom of the Reactor shaft or not. The bottom of the Reactor shaft is lined with a shielding structure made from layered sheet steel. This structure is the first part of the bottom of the Reactor shaft to interact with the corium.

The fulfillment of the second requirement has been experimentally tested in the cold crucible laboratory of CVR. [4] A batch of prototypical corium from a severe accident of VVER-100/v320 was prepared using the cold crucible and then poured onto a structure with the same design as the shielding present in the Reactor shaft of the real reactor. The results of the experiment showed that the penetration of corium into the steel structure is very limited, the impact and the subsequent thermal damage did not breach the structure completely, and soon, a crust is formed at the interface. This means, that in the real situation, corium in the reactor shaft is ready to be spread on the pre-prepared surface in the adjacent room.

Multiple new experiments using prototypical corium compositions of VVER-1000/v320 are underway under the governance of the “national center of excellence” project called CANUT2. The cold crucible laboratory of CVR will be further equipped and enhanced to be able to simulate melt spreading with decay heat simulation, evaluation of MCCI, and more precise measurements of the properties of the melt, including temperature dependence of melt viscosity.

A part of the efforts to develop and prove the viability of the ex-vessel melt stabilization strategy for the VVER-1000/v320 is development of a new sacrificial material that could be used as a liner in the designated corium spreading area. It is envisaged that this multipurpose material will produce a significant amount of CO2 and minimum hydrogen during its interaction with corium, thus helping with the top-cooling by cracking the crust layer on top, and its use would reduce the amount of flammable gases from MCCI. Comparison between the predicted production of gases from MCCI and from interaction with the geopolymer sacrificial material modeled with CORQUENCH after spreading the melt into the designated containment compartment of VVER-1000/v320 is shown in Table 1. More on these materials and their development follows in the next chapter and in [5].

3. Material research and development for new builds

Within the Czech national targeted R&D project MATPRO, new materials suitable for replacement of concrete in the most loaded parts of containment internals has been under development. The new materials are based on geopolymer matrices with various filler materials, tailoring their properties to their intended



Figure 3. Visual comparison of geopolymer (A) and CEM1 concrete (B) samples after 10 000 h.

purpose. The geopolymer materials are superior to concrete in several ways – they contain minimum of chemically bound water; thus they exhibit resistance to elevated temperatures without changing its properties (up to 500°C for a short periods of time, below 200° C indefinitely) as well as resistance to gamma radiation, all this while achieving mechanical properties at the level of a high-performance concrete. This combination of properties makes it an ideal material for the reactor shaft, where no additional shielding material would be needed. The geopolmyers used in the project were designed and manufactured by the Institute of Inorganic Chemistry of the Czech Academy of Sciences (IIC CAS).

One of the very favorable properties of the newly developed materials is their resilience to acidic environment, as was found out during the project. [5] Long-term exposures to boric acid in high concentrations (equivalent to shutdown concentration in the reactor or in the spent fuel pool) shows vastly superior response of the geopolymer structure and better retention of its original properties and structure compared to concrete. This can play a major role in preventing long-term deterioration of concrete under the steel liner of the spent fuel pool in case of leakages. While it is not a direct prevention or mitigation of a severe accident, potential use of the material can help in both extending the plant life, and as a prevention to accidents induced by deterioration of concrete structures around the SFP. Visual comparison of the two materials after the exposure experiment (10 000 hours, stable temperature 40 °C and boric acid concentration 12 g/l) are shown in Figure 3. More information is available in [5].

4. Research on severe accidents in advanced reactors

The part of the severe accident R&D on advanced reactors in UJV Group is focused on the GFR technology. For the ALLEGRO demonstration unit, which is envisaged to be a first-of-a-kind (FOAK) GFR reactor, there is a plan to include core catcher into the design, although the safety analyses performed so far show that a severe accident with large-scale core melting and possible breach of the RPV lower head has very low probability and thus is practically eliminated. However, for a FOAK unit, all the uncertainties in all types of analyses are significantly higher, and employing a strategy for corium stabilization even as a residual risk elimination is considered reasonable by the developer of ALLEGRO, the V4G4 CoE consortium.

In UJV Group, this task has been tackled within two national targeted R&D projects – NOVA, in which an innovative sacrificial material for GFR core catcher had been successfully developed and tested, and ALLEGRO, where the design of the core catcher and its cooling system is being elaborated. These activities

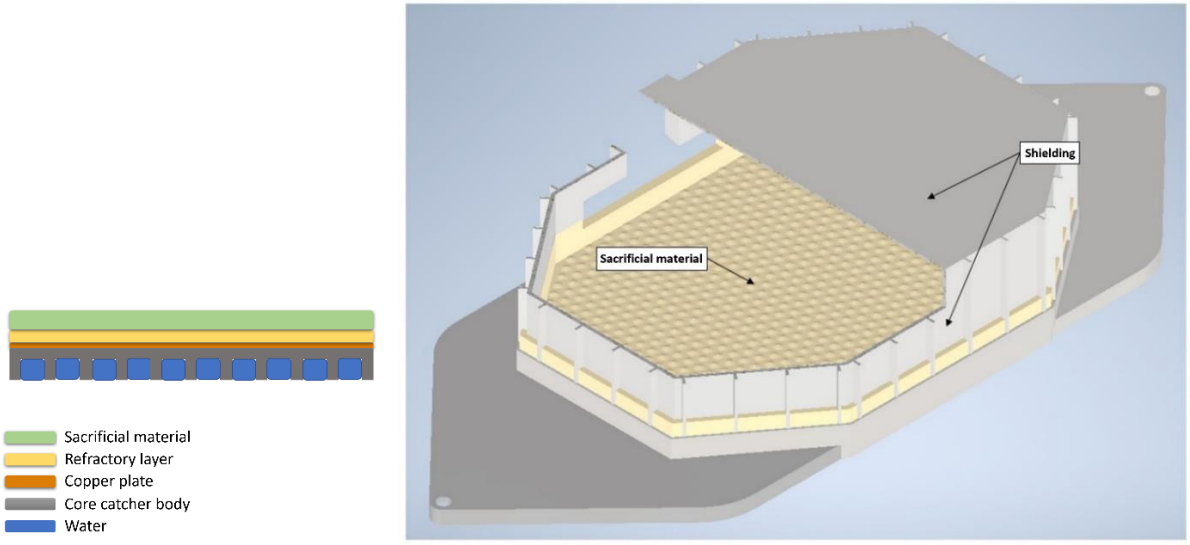

Figure 4. Conceptual design of the ALLEGRO core catcher

utilize multiple synergies with the other parts of the severe accident R&D program, utilizing the experience in modelling and analyzing ex-vessel phase of severe accidents in PWRs.

The core catcher is designed to first spread the corium into a relatively thin layer, mix it with several layers of sacrificial materials, and stabilize it using indirect cooling through channels in the bottom and sides of the core catcher vessel filled with water in a closed cooling loop. The design of the core catcher can be seen in Figure 4 on the left side, the individual layers in a cross-section in Figure 4 on the right side.

The main challenges in designing the core catcher are:

- Correct prediction of corium spreading
- Composition of sacrificial materials
- Correct prediction of long-term cooling after interaction with the sacrificial materials

The second part was the aim of the NOVA project, and more on this topic can be found in [6] and [7]. For the first and third part, a complex three step computational analysis had been devised. First, the amount, composition, and main physical properties of corium at the entrance to the core catcher are established through analyses of severe accidents using the MELCOR code [6] [8]. The spreading itself is evaluated using in-house developed CFD models, that are under development within the ALLEGRO project, and preliminary results are shown for example in [9]. The subsequent phase of interaction with the sacrificial material will be analyzed using the CORQUENCH code, modified to include the newly developed sacrificial materials properties, and, as the third and final step, the long-term cooling will be analyzed again using CFD approach, utilizing UJV's experience with CFD analyses of corium cooling in various IVR-related R&D projects.

5. CONCLUSIONS

This paper summarized the latest advancements in the ex-vessel corium interactions and cooling research and development program carried out by the UJV Group – UJV Rez and its daughter company Research Centre Rez. UJV Group is the leading entity in nuclear engineering and R&D in the Czech Republic, and severe accident research belongs to the long-term priorities of the Group.

The R&D program covers a wide range of applications, from safety enhancement and retrofitting of safety systems in GENII reactor under operation, through development potentially suitable for new builds of GENIII and GENIII+ lightwater reactors, to complex material and phenomenological research for use in advanced GENIV reactors of the GFR type.

The part of the program oriented to GENII reactors is aimed at the VVER-1000/v320 design. The main idea is to let the RPV lower head fail (in case that every other mean either preventing or mitigating a severe accident during the in-vessel phase fails), let the corium evacuate to the Reactor shaft, where one of the walls are intentionally weakened to make sure it fails due to MCCI first in the exact point. The adjacent room of the containment will be prepared for spreading the corium onto a pre-defined surface (a sort of retrofitted core catcher) and stabilize it using water cooling from the top.

In research oriented to GENIII and GENIII+ reactors, new materials suitable for replacement of concrete in the most loaded parts of containment internals has been under development. The new materials are based on geopolymer matrices with various filler materials, tailoring their properties to their intended purpose. The geopolymer materials are superior to concrete in several ways – they contain minimum of chemically bound water; thus, they exhibit resistance to elevated temperatures without changing its properties (up to 500°C for a short period of time, below 200° C indefinitely) as well as resistance to gamma radiation, all this while achieving mechanical properties at the level of a high-performance concrete.

The part of the severe accident R&D on advanced reactors in UJV Group is focused on the GFR technology. For the ALLEGRO demonstration unit, which is envisaged to be a first-of-a-kind (FOAK) GFR reactor, there is a plan to include core catcher into the design. In UJV Group, this task has been tackled within two national targeted R&D projects – NOVA, in which an innovative sacrificial material for GFR core catcher had been successfully developed and tested, and ALLEGRO, where the design of the core catcher and its cooling system is being elaborated.

ACKNOWLEDGMENTS

Parts of the presented work has been co-sponsored by the Technology Agency of the Czech Republic (TACR) within the THETA program, namely the ALLEGRO (TK01030116), NOVA (TK01030130), MATPRO (TK03020188) and CORIUM(TK03020149) projects.

REFERENCES

1. J. Zdarek et al: "*Final report on full scale tests*", Deliverable D4.4 of H2020 IVRM project (Grant Number 662157), (2019)
2. D. Batek et al.: "*Experimental studies to support IVMR strategies for WWER 1000 reactors*", International Severe Accident Management Conference (ISAMC) Synthesis report, 2023
3. I. Pznyak, J. Hrbek, M. Marecek, B. Meszaros: *"Final report on the large-scale cold crucible experiments*", Deliverable D3.17 of H2020 IVRM project (Grant Number 662157), (2019)
4. M. Kotouč, et al.: "*Assessment of Ex-Vessel Corium Coolability in the Containment of the VVER-1000 Reactor as a Measure of Severe Accident Mitigation*," Proceedings of the 2022 10th European Review Meeting on Severe Accident Research, Karlsruhe, Germany, May 16-19, 2022
5. T. Cernousek, J. Komrska, P. Vacha: "*TK03020188 – MATPRO project overview* GFR topical seminar, Rez, February 7, 2024
6. V. Tyrpekl et al.: "*Development of geopolymer based sacrificial materials for GENIV severe accident mitigation*", Journal of Nuclear Materials **553**, (2021)
7. P. Vacha et al.: "*TK01030130 – Main results of the NOVA project*", GFR topical seminar, Rez, February 7, 2024

8. P. Vácha and L. Belovsky: "*Analyses of Severe Accidents in GFR Demonstrator ALLEGRO with MELCOR 2.1,*" Proceedings of the 2016 24th International Conference on Nuclear Engineering ICONE24, June 26-30, 2016, Charlotte, North Carolina, (2016)
9. J. Komrska, et al:, "*Mesh Sensitivity Analysis of the CFD Model of the Core Catcher of the ALLEGRO Reactor*", Proceedings of the 20th International Topical Meeting on Nuclear Reactor Thermal Hydraulics (NURETH 20), Washington D.C., USA, August 20-25, 2023

Investigation of IVMR Strategy for BNPP-1 VVER 1000

Alireza Najafi[1], Seyed Ali Hosseini[2], Athena Shahsavand[3] and Amir Saeed Shirani[4]

[1]Sharif University of Technology, Department of Energy Engineering, Taymouri Alley, Ghasemi Street, Habibollahi St., Azadi Avenue, Tehran, Iran, alireza.najafi@energy.sharif.edu
[2]Polytechnic University of Milan (POLIMI), Department of Energy, Politecnico di Milano, Via La Masa 34 (Building B12), 20156 Milano, Italy., seyedali.hosseini@polimi.it
[3]Sharif University of Technology, Department of Energy Engineering, Taymouri Alley, Ghasemi Street, Habibollahi St., Azadi Avenue, Tehran, Iran, athena.shahsavand@energy.sharif.edu
[4]Sahid Beheshti University, Faculty of Engineering, Shahid Beheshti University, Shahriari Sq, Evin, Tehran, IRAN, a_shirani@sbu.ac.ir

Contact email: alireza.najafi@energy.sharif.edu

Abstract

Bushehr-1 NPP, located in Iran is a VVER-1000 (type V-446) reactor that has some different features in comparison with other VVER-1000s, and even its reference plant i.e., VVER-1000 (Type V-320). These differences stem from the fact that BNPP-1 is a combination of VVER and KWU reactors. Some important features that may affect accident progression include different containment shape (spherical), different cavity, and more units of accumulators in BNPP-1. Bushehr-1 is operating since 2011, and currently, the most safety efforts for this plant is focused on SAMGs, and emergency plans development. According to the features mentioned above, SAM activities should be modeled dedicatedly for this plant, and other VVER-1000s severe accident modeling may not be sufficiently reliable.

In Vessel Melt Retention (IVMR) is considered as a strategy to maintain the molten material within the vessel during severe accidents. During the IVMR, the reactor cavity is filled with water, and the heat from the molten material inside the vessel is transferred to this amount of water through the vessel wall. This strategy is incorporated mostly for small-size reactors (<500 Mw), and if it is aimed to perform this strategy for high-power reactors, it should be modeled more carefully. The important phenomena that should be analyzed in this strategy are related to heat fluxes from the molten material to the vessel, and the heat flux from the vessel wall to the outer water. The CHF limit is the determinant in the success of the IVMR. Currently, different strategies within SAMGs are being developed, and modeled for Bushehr NPP-1, and IVMR is a controversial one. This paper aims to perform a preliminary assessment of the IVMR strategy for BNPP-1 VVER 1000, by considering it's dedicated features, especially the number of accumulators, and the cavity shape. BNPP-1 VVER 1000 incorporates two stages of accumulators. The first stage includes four borated water tanks with a setpoint of 5.88 Mpa, injecting the water directly into the vessel. The second stage includes eight tanks with setpoint of 2.5 Mpa, and injecting to the hot-legs, and cold-legs only during severe accidents. In comparison to BNPP-1 VVER 1000, the previous models have only the first stage, and most of the subsequent models have more than one stage of accumulators (two or even three stages). Most of the subsequent models also benefit from a core catcher which eliminates the need for IVMR strategy. In this research, the MELCOR code is used to analyze different LOCA sizes that are considered representative of SB/MB/LB LOCAs with SBO. The main goal is to calculate the heat fluxes, induced to the water, to conclude the effectiveness of IVMR, in different scenarios, and according to the second-stage accumulators. The additional water, provided by the accumulators can play an important role in increasing the inner vessel heat transfer and reducing the heat flux on the vessel wall.

Keywords: In-Vessel retention, VVER-1000, Severe Accidents

Assessment of RELAP5-3D condensation models for small modular reactor passive safety

Palash Kumar Bhowmik[1]

[1]Idaho National Laboratory, Idaho 83415, PalashKumar.Bhowmik@inl.gov

Contact email: PalashKumar.Bhowmik@inl.gov

Abstract

This paper presents the RELAP5 condensation heat transfer models for small modular reactor (SMR) safety systems. The passive safety systems of advanced SMRs are designed such that steam released from the reactor vessel is condensed at the containment vessel by transferring heat to the outside cooling water pool. This heat removal system is referred to as a passive containment cooling system (PCCS). The steam condensation performance becomes greatly deteriorated due to the presence of non-condensable gases such as air. Previous experimental studies on PCCSs used small tube sizes for separate effects testing and large containment for integral effects testing. However, no study has considered scaling its evaluation with supportive data to validate the correlations and models for condensation that are suitable for SMRs. In this study, scaled geometry and representative test data were used to verify the scaling performance of RELAP5 condensation models in order to improve SMR thermal-hydraulics and safety analyses.

Keywords: Small modular reactor, passive safety, condensation heat transfer, RELAP5-3D, scaling

V&V of nuclear fuel oxidation behavior in sleeveless SiC-matrix during air ingress accident

Yosuke Nishimura[1], Avadhesh K. Sharma[2], Anna Gubarevich[3], Katsumi Yoshida[4] and Koji Okamoto[5]

[1]The University of Tokyo, 7-3-1, Hongo, Bunkyo-Ku, Tokyo, Japan, nishimura-y@g.ecc.u-tokyo.ac.jp
[2]The University of Tokyo, 7-3-1, Hongo, Bunkyo-Ku, Tokyo, Japan, avdhruva@gmail.com
[3]Tokyo Institute of Technology , 2-12-1 Ookayama, Meguro-ku, Tokyo, hubarevich.h.aa@m.titech.ac.jp
[4]Tokyo Institute of Technology , 2-12-1 Ookayama, Meguro-ku, Tokyo, k-yoshida@zc.iir.titech.ac.jp
[5]The University of Tokyo , 7-3-1, Hongo, Bunkyo-Ku, Tokyo, okamoto@n.t.u-tokyo.ac.jp

Contact email: nishimura-y@g.ecc.u-tokyo.ac.jp

Abstract

As an advanced technology of high-temperature gas-cooled reactors (HTGRs), a direct cooling method has been proposed between a sleeveless fuel compact and helium coolant in the core. One crucial problem is air-ingress event following Depressurized-Loss-Of-Forced-Coolant (DLOFC) accidents associated with severe fuel oxidation at high temperatures. Preventing unacceptable fuel degradation and minimizing risk of radioactive release to the environment, the fuel matrix needs resistance to oxidation. For reactor safety assessment, V&V study of the fuel oxidation behavior is needed; however, the experiments and modeling have not been fully developed. Thus, a long-term evaluation of fuel oxidation during the postulated accidental scenarios is poorly understood. To address this issue, this work focused on the investigation of oxidation behavior of silicon carbide, a promising candidate for fuel matrix, in air up to 1400 ℃. Based on the preliminary experiments, an empirical model for SiC oxidation kinetics was determined. To achieve the V&V of fuel safety assessment during the accidents in the HTGRs, validation tests were additionally conducted using real-sized High Temperature Test Facility (HTTF) at The University of Tokyo. The detailed experimental results, the proposed model, and V&V discussion will be presented at the conference.

Keywords: V&V, oxidation, high-temperature gas-cooled reactor, air ingress accident, sleeveless fuel compact

Numerical Analyses on Melt Water Interactions with Super Absorbing Polymers Added to the Cooling Water

Michael Buck[1]

[1]Institute for Nuclear Technology and Energy Systems (IKE), University of Stuttgart, Pfaffenwaldring 31, 70569 Stuttgart, Germany, michael.buck@ike.uni-stuttgart.de

Contact email: michael.buck@ike.uni-stuttgart.de

Abstract

The majority of the operating Nuclear Power Plants (NPPs) have not been designed to withstand a severe accident with core melting. Flooding of the cavity below the reactor pressure vessel (RPV) is one of the few options to mitigate an accident at a late stage. However, this has only been adopted by some of the operators of NPPs since success is not guaranteed and the melt water interaction bears the risk of an early containment failure due to strong steam explosions. Recently, an innovative potential solution to this problem was proposed, based on adding super absorbing polymers (SAP) to the coolant water in the cavity. The SAP material can take up water volumes orders of magnitude larger than their initial size and forms pools consisting of water and water-saturated particles. First scoping experiments have indicated the capability of the concept to enhance melt jet fragmentation and to suppress energetic interactions between melt and water. Additional experimental and analytical research is required to further develop and promote this promising concept.

However, current computational models for melt water interactions are presently not readily applicable for the simulation of coolant containing SAP. In a first step, the present paper discusses the properties of water/SAP coolant, which distinguishes it from pure water, and how these properties should affect the likelihood and potential strength of steam explosions. Then, the codes COCOMO-3D and IDEMO-3D, which are being developed at IKE, Stuttgart to model the premixing and explosion stages of steam explosions, have been partly enhanced and applied in parametric studies to investigate some of the effects under discussion, such as strongly increases apparent viscosity. The results are discussed considering their preliminary character due incomplete modelling. Further steps for developing FCI codes towards more realistic simulations of SAP/water pools are proposed.

Keywords: Severe Accidents, Fuel-Coolant-Interactions, Accident Mitigation, Multiphase Flow, Modelling

Study on the influence of the Core support structure on the migration process of molten material

Nuclear and Radiation Safety Center

Chao WEI，Chun LI

2024.05

Content



- Background
- Core support structure type
- The influence of the core support structure in the process of melt migration
- Conclusion

Background

- With the development of nuclear power technology and the continuous improvement of the single reactor power of the third generation pressurized water reactor, the core support structure has changed greatly.
- As an important channel for the core melt to enter the lower chamber of the RPV from the active zone, the core support structure is the main metal source of the lower chamber molten pool. The structural differences will change the hindering characteristics of the core melt flow migration, and different behaviors may occur during the migration process, affecting the accident process, and increasing the uncertainty of the final molten pool material composition and the thermal load analysis of the lower head molten pool.
- It may lead to a decrease in the safety margin of the In-Vessel Retention (IVR) mitigation measures originally used for low-power reactors, affecting its effectiveness.

Background

- In this paper, according to the different design concepts and structural characteristics of the core support structure in the third generation PWR, combined with the failure modes of each structure in the reactor, the influence of different core support structures on the melt migration process and the mechanism leading to structural failure are analyzed.
- The dangerous weak links affecting the effectiveness of IVR are revealed, and the uncertainty of IVR effectiveness analysis is effectively reduced, which provides technical reference for the research of severe accident mitigation measures and nuclear safety review.

Core support structure type

- In the third generation of pressurized water reactor nuclear power units, the core support structure is mainly divided into three categories.

- Difference
  - the structure
  - the secondary support structure
  - the flow distribution

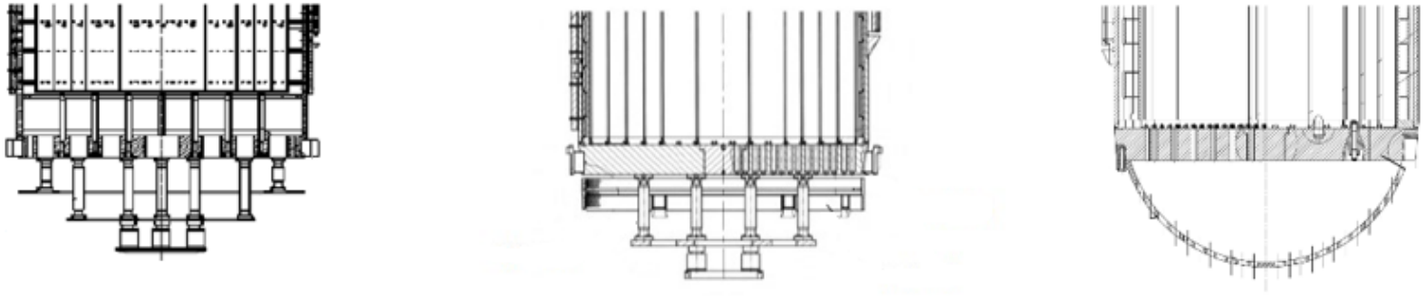

（a）A　　（b）B　　（c）C

Fig. 1 Structure type of Core support structure

Table 1 Comparison of different types of Core support structure

Type	Thickness of lower support plate（mm）	Lower chamber flow distribution device	Secondary support member of reactor core	Lower core plate and support column structure	Number of radial support keys
A	450-500	√	√	√	4
B	400-410	√	√	×	4
C	415	√	×	×	8

The influence of the core support structure in the process of melt migration

- In the whole process of core melt migration in severe accident, the bearing capacity of core support structure is gradually lost due to the influence of high temperature, water level of pressure vessel and interaction of different molten materials.
- The core support structure (stainless steel) is the most important source of metal components in the steady-state molten pool of the lower chamber. Its failure mode and mechanism of action at different stages of the melt migration process play an important role in the effectiveness of IVR mitigation measures for severe accidents.

The influence of the core support structure in the process of melt migration

Core melting and initial migration stage

- Under the action of the core support structure, with the development of the core heating process, metal melts such as control rods, grids, and unoxidized zirconium claddings with lower melting points will first flow down to the low temperature area of the core support structure to solidify, plug the water channel on the support plate, and form a metal blocking layer on the top of the support plate.

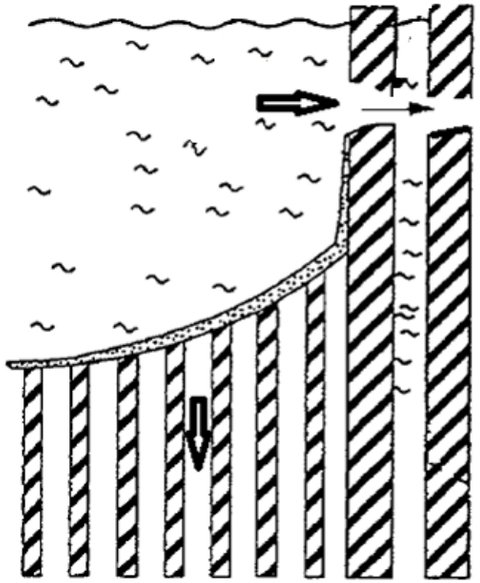

- Subsequently, the fuel and the zirconium oxide cladding melt and migrate, and the upper part of the metal blocking layer is cooled to form an oxide hard shell layer. The thickness of each layer and the water level of the pressure vessel will directly determine the boundary conditions of the bowl-shaped molten pool inside the core.

- As the bottom of the internal molten pool gradually forms a stable oxide hard shell that can be cooled, the downward heat load of the molten pool is smaller than that of the side wall, and the maximum heat load will act on the side wall hard shell, resulting in the continuous radial expansion of the molten pool in the internal molten pool, resulting in the lateral migration of the molten pool.

The influence of the core support structure in the process of melt migration

Core melting and initial migration stage

- For A structure, the size of the lower core plate water hole (70mm) is smaller than the support plate water hole (140-240mm), and the thickness is thinner (45mm). In the core melting stage, when the initial molten metal passes through the water hole of the lower core plate, it will solidify at the hole wall, and gradually form a metal blocking layer and an oxide hard shell layer on the lower core plate. With the development of the accident process, the water level of the pressure vessel continues to decline, and the internal molten pool continues to expand. Under the action of high temperature, the support column may undergo local instability, causing the core to collapse before the subsequent secondary migration, affecting the subsequent melt migration process.

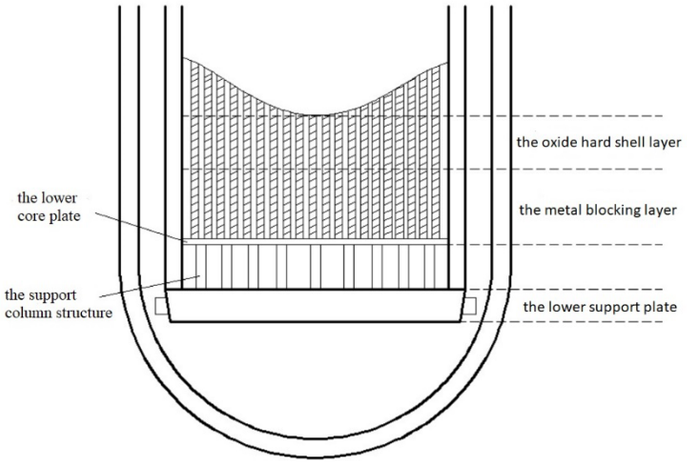

- For B and C structures, the thickness of the metal blocking layer and the oxide hard shell layer depends on the water level height in the pressure vessel and the oxidation rate of the cladding under different accident conditions. Assuming that the remaining coolant in the core area is all involved in the zirconium water reaction, and the peripheral fuel assembly melts only half of its exposed height before the initial migration, the ratio of the thickness of the support plate, the metal blocking layer and the oxide hard shell layer is about 1.5 : 2 : 1.

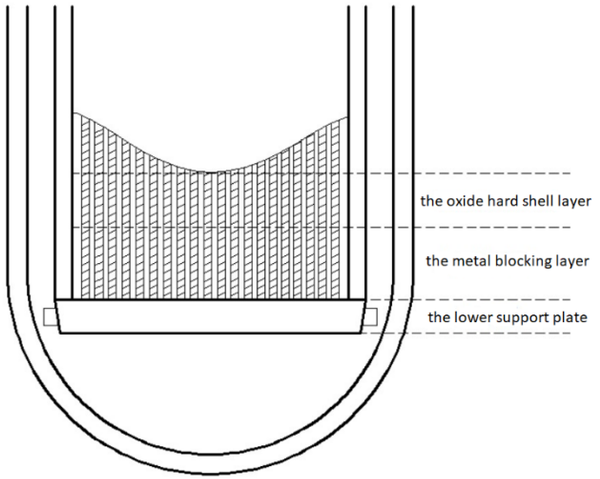

The influence of the core support structure in the process of melt migration

Secondary migration stage

- In the initial migration stage, there is less molten material entering the lower chamber, and it will not contact the lower surface of the support plate to form direct heating. Then the development of the secondary migration process of the melt is directly related to the real-time water level in the pressure vessel.
- If the water level is higher than the support plate area, the support plate and the upper retained layered material can be cooled, the internal molten pool expands slowly downward, and the molten material is still dominated by lateral migration.
- If the water level is lower than the edge of the support plate, the support plate will lose direct cooling, and the oxide hard shell debris will re-heat to an overheated state under the action of decay heat. The lateral migration process of the internal molten pool is weaker than the vertical migration, and the molten material gradually gathers at the bottom of the molten pool. The bowl-shaped molten pool gradually deepens and continues to heat the metal blocking layer and the support plate structure below. Under the action of upper and lower high temperatures, the supporting plate structure will soon be melted through, and the molten material enters the lower chamber through vertical migration.

The influence of the core support structure in the process of melt migration

Secondary migration stage

- The class A support plate is higher than the class B and C from the bottom of the pressure vessel.
- In the subsequent secondary migration process of the molten material, the molten pool formed by the melting of the debris bed particles in the lower head will have a strong radiation heat transfer effect on the support plate structure upward after the water in the lower chamber is evaporated.
- In the case of support plate losing support, the outer edge will directly contact with the pressure vessel wall, thus completely blocking the flow channel between the lower chamber and the upper molten material. If the molten material in the lower chamber has not yet touched the support plate, the contact area between the pressure vessel wall and the support plate may partially melt and produce stress concentration under high temperature conditions, threatening the integrity of the pressure vessel.

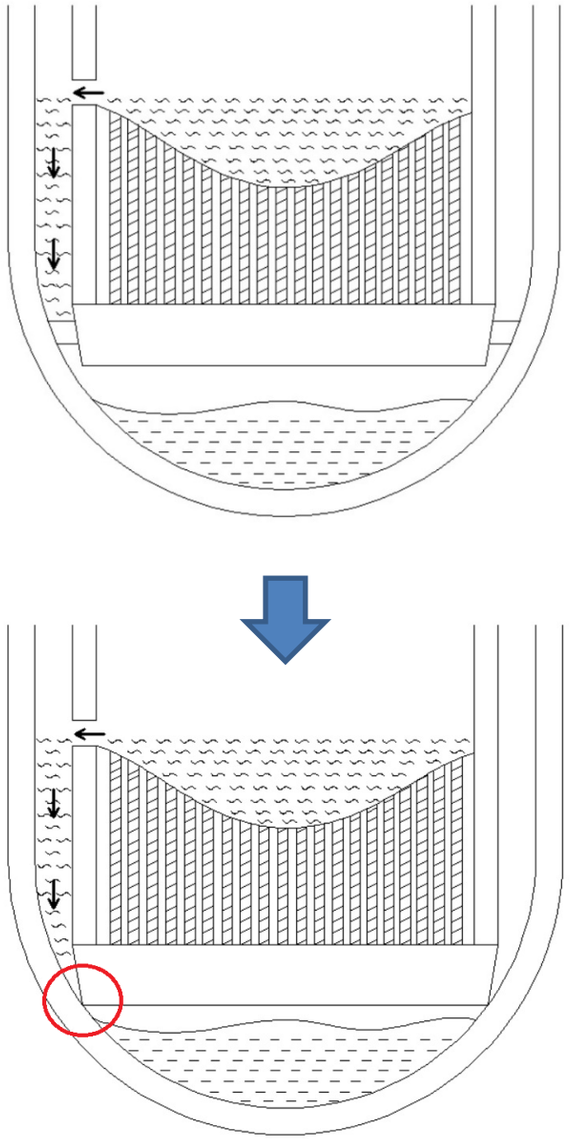

Conclusion

The design of the core support structure and its related components not only affects the positioning, bearing and flow distribution of the core components, but also has a certain impact on the severe accident process and the effectiveness of IVR mitigation measures. The main conclusions are as follows :

- （1）The melting time and failure mode of the three main types of core support structures in China 's third-generation nuclear power plants are different in the process of melt migration. As the most important source of the metal composition of the lower chamber molten pool, if the support plate and the upper metal blocking layer structure cannot be melted in time, the metal composition of the lower chamber molten pool will be difficult to meet the requirements, resulting in thermal focusing effect and affecting the effectiveness of IVR.

Conclusion

- （2）The water level change in the pressure vessel under different accident conditions and the assumed melting ratio of the core material will determine the boundary conditions of the bowl-shaped molten pool inside the core, which in turn affects the subsequent migration process of the molten pool.
- （3）In the secondary migration stage of the melt, under the dual action of high temperature and lateral melt, some radial support keys may melt, and the side edge of the collapsed support plate will directly contact with the pressure vessel wall, completely blocking the flow channel. Under high temperature conditions, the contact position may produce stress concentration, which threatens the integrity of the pressure vessel.

Thank you for your attention

The 11th European Review Meeting on Severe Accidents Research

May 13-16, 2024, Royal Institute of Technology, Stockholm, Sweden

TECHNICAL SESSION 3.2: EX-VESSEL CORIUM INTERACTIONS AND COOLABILITY

Chairs: S. Bechta (KTH), P. Piluso (CEA)

ID62	**Production of prototypic corium in the VULCANO facility using uranothermite and induction heating** A. Denoix (CEA)	**Paper** **Presentation**
ID68	**Overview of Ex-Vessel Severe Accident Scenarios Simulations at UJV Rez** J. Komrska (UJV)	**Paper** **Presentation**
ID120	**Simulations of FLOAT debris quenching experiments** M. Uršič (JSI)	**Paper** **Presentation**

Production of prototypic corium in the VULCANO facility using uranothermite and induction heating.

A. Denoix, V. Bouyer, C. Journeau, A. Balland-Longeau
CEA, DES, IRESNE, DTN
Cadarache, F-13108 Saint-Paul-lez-Durance, France
arthur.denoix@cea.fr; viviane.bouyer@cea.fr; christophe.journeau@cea.fr; alexia.ballandlongeau@cea.fr

ABSTRACT

VULCANO is the advanced facility of the PLINIUS severe accident platform of the CEA, enabling the melting of up to 90 kg of UO2-containing prototypic corium. The facility is equipped with several standard cameras, a thermal camera, pyrometers, weighing scales and the possibility to have up to 150 type-K thermocouples and 20 type-C thermocouples. In VULCANO, two melting technics can be used separately or combined: uranothermite and induction heating.

Since the end of 2014, the team installed a new induction generator on the PLINIUS platform. The nominal power is 400 kW, and the frequency can be set between 80 and 300 kHz. The device was already used to directly melt the corium in several tests.

Since 2016, the team installed a thermite workshop inside the PLINIUS platform. It allows the fabrication of up to 100 kg of uranothermite, in 2 kg batches, under a controlled atmosphere. A large variety of composition has been fabricated and used inside VULCANO and others PLINIUS facilities.

Both induction and thermite have advantages and drawbacks for melting corium. However, combining the two processes, one may be able to pull the advantages of both. It means that the quick increase of the temperature of the corium with the uranothermite reaction can be followed by induction heating (to simulate the decay heat or continue to increase the temperature for example).

After production of the corium melt, several kinds of experiments can be done in VULCANO facility. For example: let it cool to fabricate a fuel debris block, maintain the induction heating to simulate a molten core concrete interaction or spread the molten corium on a surface.

In this paper, the temperature measurement results, dismantling observation of the solidified ingot for experiments with uranothermitic heating and uranothermitic and induction heating that have been done in the VULCANO facility will be highlighted.

KEYWORDS
Fuel Debris, Corium, Uranothermite, Induction

1. INTRODUCTION

Whether to study the mitigation of corium, test cutting tools for dismantling, carry out molten core concrete interaction or spreading experiment, all corium experiments study request to succeed in obtaining a corium melt. In practice this means successfully raising several kilograms of chemical compounds to a high temperature (usually above 1750K). This has been done using uranothermitic reaction (containing depleted uranium oxide) within the PLINIUS installation within the IRESNE fission experimental platform at CEA in Cadarache for many years. But the compositions were until now limited to corium compositions with

mass fractions of concrete less than 10% and mass fractions of metal less than 10%. However, during a serious accident in a nuclear power plant, corium composition is not limited to these compositions. Several tests have been carried out in VULCANO in recent years to determine what variety of corium compositions could be obtained by uranothermitic reaction.

The first section will present the results of thermite tests which were carried out to try to obtain corium compositions by uranothermitic reaction with new compositions. The second part will present how the addition of induction heating to the uranothermitic reaction makes it possible to obtain a block of molten corium of several centimeter where the uranothermitic reaction alone does not allow it.

2. URANOTHERMIC HEATING

Thermite is a self-sustained and self-propagating exothermic reaction between a metal oxide and a metal. Uranothermite is therefore a thermite which has uranium oxide as one of its reactants [1]. It allows to melt several dozen kilograms of corium in just a few minutes.

The fabrication process is the same for all the uranothermites. All the powders are weighted and mixed in a gloves box under argon with less than 100 ppm of oxygen and less than 100 ppm of H_2O. The mixing is realized in a mixer with same time and speed for each 2 kg batch. This parameter has been determined in past experiments to obtain a homogenous mixture.

The uranothermite is ignited by a Pyrofuze® wire (Sigmund Cohn 304WR020). It is wound into a spiral and placed on top of the powder loaded in a crucible. The electric current which allows the Pyrofuze® wire to be melted is supplied by a DC power supply

3. INDUCTION HEATING

The induction system is composed of:

- A CELES (MP 400) HF generator of maximum power 400 kW (500V - 1240A), frequency between 80 and 300 kHz. For this study the frequency was 134kHz,
- A CELES impedance matching box,
- A copper induction line connecting the matching box to the inductor,
- Cooling systems (with flowmeters and thermocouples for thermal balance), and
- A copper inductor, made of a cylindrical coils which surround the crucible.

4. TEST OF URANOTHERMITE

Several new compositions of uranothermite have been tested in VULCANO cell of PLINIUS in the past years. The goal is always the same: find a thermite composition that allows the temperature to rise high enough to obtain a molten block. We present here two tests above all, one with a high content of concrete, the other with a high content of metal.

4.1. Experimental setup

The reaction is carried out in a zirconia crucible (ZIRCOA S-105-12.5) with an internal diameter of 165 mm and an internal height of 300 mm. The test is instrumented with (Figure 1):

- One type C thermocouple (tungsten-rhenium with maximal measured temperature of 2572 K) sheathed with molybdenum tube (external diameter 1.78 mm, inside diameter 1.07 mm, isolated with HfO_2). It is placed vertically in the center of the crucible approximately 20 mm from the bottom. It is used to measure the temperature reached during the uranothermitic reaction.

- One type K thermocouple (chromel-alumel) sheathed with Inconel tube which is placed horizontally at the bottom of the crucible. It is used to detect the arrival of the reaction front at the bottom of the crucible.

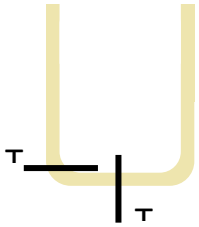

Figure 1: Scheme of the installation of the thermocouples (T) in the crucible.

4.2. DEV-01-04 test

The goal of this uranothermite test is to obtain a corium with 60 wt% of siliceous concrete. Its composition is given in Table I. In this uranothermite the oxidizing reactants are U_3O_8 and CrO_3. There is also a high proportion of non-reactive SiO_2 because of the stoichiometry of the chemical reaction. Uranothermite and corium characteristics have been calculated using thermodynamic database NUCLEA-22-1 [2] and thermodynamic software Thermo-Calc 2020a. The calculated reaction temperature is 1967 K (heat release of 8324 kJ/kg), the liquidus temperature is 2024 K and there is 90 wt% of liquid phase at the reaction temperature.

Table I: Composition of the uranothermite and the corium after the uranothermite reaction for DEV-01-04.

Chemical Compound	Uranothermite (wt%)	Corium (wt%)		Chemical Compound	Uranothermite (wt%)	Corium (wt%)
U_3O_8	21.83	0.00		Si	6.15	0.00
UO_2	0.00	21.00		SiO_2	37.25	50.40
Zr	6.66	0.00		Al	0.81	0.00
ZrO_2	0.00	9.00		Al_2O_3	0.00	1.53
CrO_3	19.23	0.00		CaO	8.07	8.07
Cr	0.00	10.00		Total	100	100

The uranothermite completely reacted in 225.3 sec and the type C thermocouple measured a maximum temperature of 1933 K (Figure 2) which is a little bit lower than the calculated temperature. After the end of the reaction, the corium is cooled for 24 h. Then, the experimental setup is dismantled to observe the corium (Figure 3). The corium is green which is not common because corium is usually black. It could be the high proportion of chromium (10 wt%) which could have oxidized in Cr_2O_3. The corium can be separated into three distinct parts. First part is powder that is on top and against the walls of the crucible for 20 wt% of total mass. Second part is from the top to around 70 mm from the bottom of the crucible. It is made of agglomerated powder and has a cavity inside for 39 wt%. The last part is the corium ingot for 41 wt%; it looks like molten corium, 50 mm thick in the middle and 70 mm thick on the sides. It was broken into two parts during dismantling which revealed pores between 1 mm and 3mm in diameter inside the block.

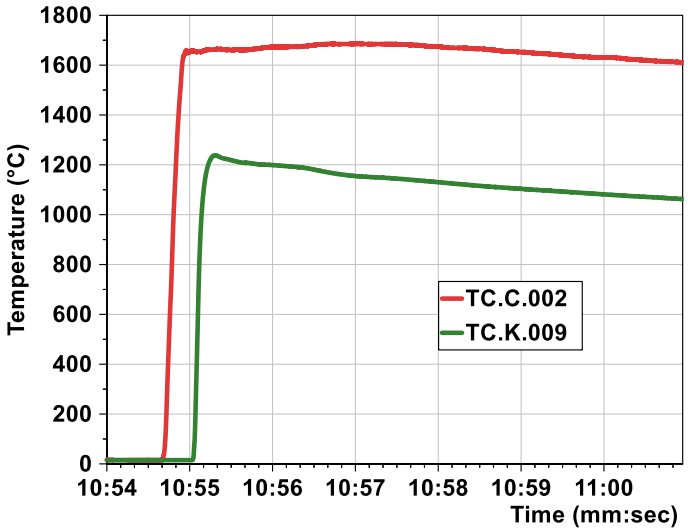

Figure 2: DEV-01-04 temperature measurements for type C and type K thermocouples. Focus on the start of temperature increase.



Figure 3: Pictures of the dismantling of the corium of DEV-01-04. Left: corium after removing the crucible. Middle and right: inside of the two parts corium ingot at the bottom of the crucible.

In this test, the maximum temperature measured is close to the calculated reaction temperature. At this temperature there is 90 wt% liquid phase. However, the ingot only represents 40 wt% of the total mass of corium. One explanation would be the thermal losses at the walls of the crucible which, added to the slow propagation of the reaction, would greatly reduce the temperature of the corium during the reaction. This prevents it from reaching a sufficient temperature to obtain a molten appearance on the walls of the crucible. The corium at the heart of the crucible would be liquid enough to relocate to the bottom of the crucible and form the ingot.

4.3. DEV-02-02 test

The goal of this uranothermite test is to obtain a corium with 30 wt% of metal (metal composition: 80 wt% of Fe and 20 wt% of Cr). Its composition is given in Table II. In this uranothermite, the oxidizing reactants are U_3O_8, Fe_2O_3 and CrO_3. There is also a high proportion of non-reactive Fe because of the stoichiometry of the chemical reaction. The uranothermite and corium characteristics have been calculated using NUCLEA-22-1 and Thermo-Calc 2020a. The calculated reaction temperature is 2452 K (heat release of 2075 kJ/kg), the liquidus temperature is 2569 K and there is 67.8 wt% of liquid phase at the reaction temperature.

Table II: Composition of the uranothermite and the corium after the uranothermite reaction for DEV-02-02.

Chemical Compound	Uranothermite (wt%)	Corium (wt%)		Chemical Compound	Uranothermite (wt%)	Corium (wt%)
U_3O_8	47.30	0.00		Cr	0.00	6.00
UO_2	0.00	45.50		Si	1.96	0.00
Zr	14.44	0.00		SiO_2	0.00	4.20
ZrO_2	0.00	19.50		Al	0.07	0.00
Fe_2O_3	0.08	0.00		Al_2O_3	0.00	0.13
Fe	23.94	24.00		CaO	0.67	0.67
CrO_3	11.54	0.00		Total	100	100

In this test, the type K thermocouple was reached by the melting front 5.8 sec before the type C thermocouple so the reaction duration is given by the type C thermocouple which is 20 mm from the bottom of the crucible. The type K thermocouple failed at the same time after exceeding a measurable temperature. The explanation of this discrepancy was given during the dismantling: a liquid metallic phase relocated to the bottom of the crucible during the uranothermitic reaction before the end of the propagation of the reaction front. The uranothermite completely reacted in 53.8 sec and the type C thermocouple measured a maximum temperature of 2257 K (Figure 4) which is 195 K lower than the calculated reaction temperature (2452 K).

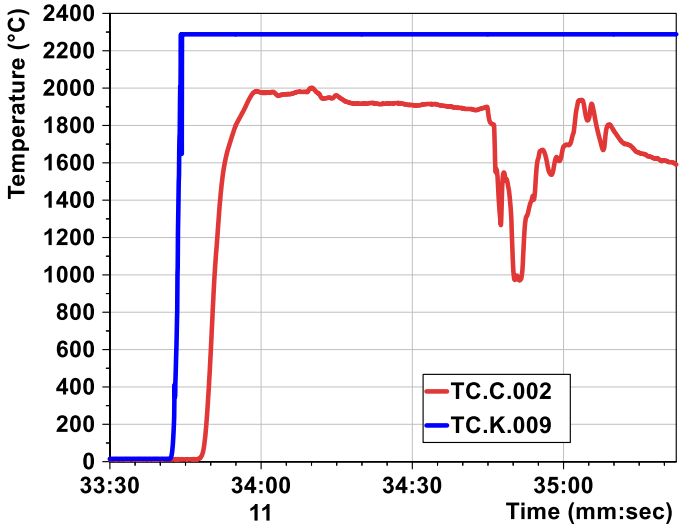

Figure 4: DEV-02-02 temperature measurement. Focus on the start of temperature increase.

After the end of the reaction, the corium is cooled for 24h. Then, the experimental setup is dismantled to observe the corium. The corium is black/grey and can be separated into four distinct parts. First part is composed of debris/powder on top of the block (Figure 5 left) for 5.2 wt% of total mass. Second part is the crust on the wall of the crucible for 20 wt% of total mass (Figure 5 left). It is very fragile and crumbly. Third part is the corium ingot (Figure 5 right) for 74.8 wt% of total mass which looked like molten corium. It has a minimum thickness of 35 mm in the middle and a maximum of 56 mm on the sides. The entire block is magnetic. It has numerous pores with a size between less than 1 mm and 5 mm. Several magnetic metal balls from 1 mm to 5 mm in diameter are present in the block. At the bottom is a magnetic metal plate measuring 90 mm by 110 mm and 5 mm to 10 mm thick (Figure 6).



Figure 5: DEV-02-02. Left: Picture of debris/powder from top of the block and crust on the crucible. Right: Picture of inside of one part of corium ingot at the bottom of the crucible



Figure 6: DEV-02-02. Picture of magnetic metal plate at the bottom of the corium ingot.

Since the maximum measured temperature is much lower than the calculated reaction temperature, the corium block should not represent such a large mass fraction of the total and it should not have such a molten appearance. An explanation could be that the corium was oxidized in contact with air, which modified its composition and therefore its liquid mass fraction at the reaction temperature.

4.4. Comparison and discussion

Both tests were successful in obtaining a block that looked molten at the end of the uranothermite reaction. But the mass fraction of the block does not in any case corresponds to what it should be at the maximum temperature measured. Each time the explanation could come from an artefact due to the experimental setup. For the first test it is a lack of thermal insulation and for the second the presence of air during the reaction.

5. FABRICATION OF FUEL DEBRIS PROTOTYPES

The fuel debris prototypes have been fabricated in the VULCANO cell of PLINIUS experimental facility [3]. The objective is to produce a few kilograms of fuel debris prototypes with a composition representative of the Fukushima Daiichi Unit 2 lower head debris.

5.1. Uranothermic reaction

The Figure 7 describes the experimental setup of the VULCANO CRIEPI-FD#7-01. The crucible (Zircoa S-50-14.0 composition 3001) dimensions are 145 mm inside diameter, 165 mm outside diameter, 356mm outside height and 336 mm inside height. A metallic cylindrical shell is put around the crucible with sand

between them. A cellular concrete plate is put above the metallic cylindrical shell. This plate has a square hole (150 mm x 150 mm) just above the crucible to allow fumes and hot gas from the uranothermite reaction to escape. There is a continuous gas flow of argon inside the experimental setup through a metallic tube. This configuration makes it possible to both limit thermal losses at the walls of the crucible and to limit the presence of air in contact with the corium.

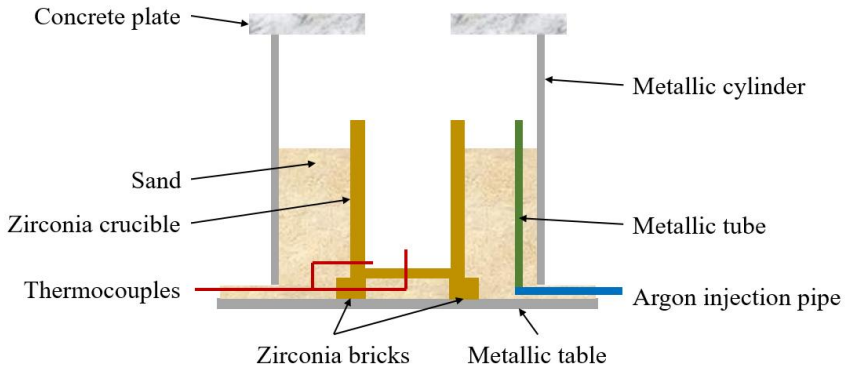

Figure 7: scheme of experimental setup for VULCANO CRIEPI-FD#7-01

The experimental setup is instrumented with 3 thermocouples:

- One type K (chromel-alumel) thermocouple sheathed with Inconel tube at the side-bottom of the crucible to detect the end of the uranothermite reaction (height 0 mm, radius 42 mm).
- Two type C (tungsten-rhenium with maximal measured temperature of 2572 K) thermocouples sheathed with molybdenum tube (external diameter 1.78 mm, inside diameter 1.07 mm, isolated with HfO_2) at the center of the bottom of the crucible respectively at 20 mm and 40 mm height from the bottom. They measure the temperature of the corium.

The crucible is filled to the top with uranothermite. Its composition and the composition of the corium after the uranothermite reaction are given in Table III.

Table III: Composition of the uranothermite and the corium after the uranothermite reaction for VULCANO CRIEPI-FD#7-01.

Chemical Compound	Uranothermite (wt%)	Corium (wt%)		Chemical Compound	Uranothermite (wt%)	Corium (wt%)
U_3O_8	38.26	0.00		Nd_2O_3	0.11	0.11
UO_2	0.00	36.81		MoO_2	0.09	0.09
Zr	44.22	25.41		$CsOH.H_2O$	0.06	0.06
ZrO_2	0.00	25.41		BaO	0.04	0.04
CrO_3	3.74	0.00		La_2O_3	0.03	0.03
Cr	0.00	1.95		PdO	0.03	0.03
Fe_2O_3	11.13	0.00		Pr_2O_3	0.03	0.03
Fe	0.00	7.79		Sm_2O_3	0.01	0.01
CeO_2	0.20	0.20		SrO	0.02	0.02
SnO_2	0.90	0.90		Y_2O_3	0.01	0.01
B_4C	1.00	1.00		TeO_2	0.03	0.03
RuO_2	0.06	0.06		Total	100	100

Uranothermite and corium characteristics have been calculated using different thermodynamic softwares (GEMINI2 and Thermo-Calc) and databases (NUCLEA14_1 and TAF-ID14 [4]) (Table IV). The solid fraction in mass at the temperature of reaction is very different between the calculations. It varies from 20 wt% to 59 wt%. The highest solids fraction suggest little block formation.

Table IV: Uranothermite and corium characteristics for VULCANO CRIEPI-FD#7-01

	GEMINI2 + NUCLEA14_1	Thermo-Calc + NUCLEA21_1	Thermo-Calc + TAF-ID14
T reaction (K)	2567	2610	2510
T liquidus (K)	2626	2628	2583
ΔT liquidus- reaction	41	18	73
wt% solid phase at T reaction	59	20	46

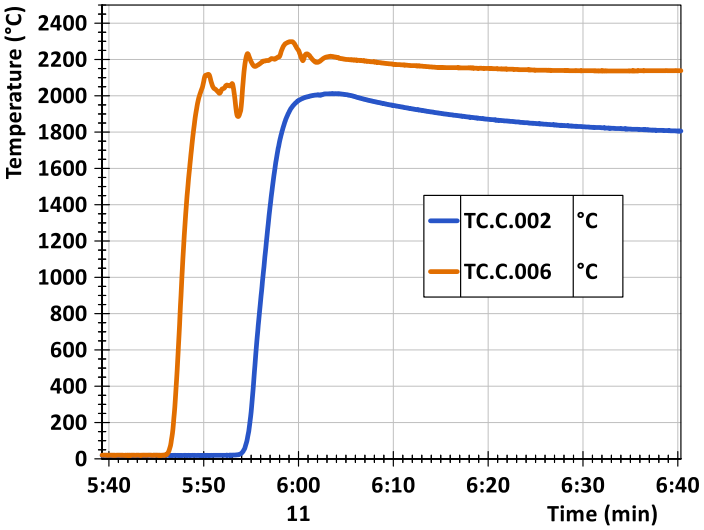

Figure 8: VULCANO CRIEPI-FD#7-01 temperature measurement for type C thermocouple. TC.C002 at 20 mm and TC.C.006 at 40 mm from the bottom of the crucible.

The uranothermite completely reacted in 82.4 sec and the type C thermocouple measured a maximum temperature of 2571 K (TC.C.006 at 40 mm) and 2285K (TC.C.002 at 20 mm) (Figure 8). After the end of the reaction the corium is cooled for 48 h. Then, the experimental setup is dismantled to observe the corium. The corium looks black with a few small gold dots on the top (Figure 9). The crucible is completely broken. After removing a side of the crucible, the corium seems agglomerated with some sand at the side which came from the sand around the crucible through the cracks of the crucible. After removing the crucible, almost all the corium comes into powder. Only the bottom of the corium remains agglomerated. Despite the fact that the uranothermite reacted completely, it did not melt the corium. This confirms the results of calculations with GEMINI2 + NUCLEA14 and Thermo-Calc + TAF-ID14 which respectively gave 59 wt% and 46wt% as solid fraction at the reaction temperature. It therefore seems necessary to use an additional heating method such as induction heating to successfully melt the corium.



Figure 9: Pictures of the dismantling of the corium of VULCANO CRIEPI-FD#7-01. Left: side of the corium after dismantling of the crucible. Right: corium at the bottom of the crucible.

5.2. Uranothermic reaction and induction heating

The objective of the test VULCANO CRIEPI-FD#5-02 is to couple the uranothermite reaction of VULCANO CRIEPI-07-01 with induction heating. The composition and characteristics of thermite and corium i this test are exactly the same as the previous one (Table III and Table IV). Because of induction heating, the experimental setup is different from the WULCANO CRIEPI-07-01 (Figure 10). The crucible (Zircoa S-105-12.5 composition 3001) dimensions are 165 mm inside diameter, 192 mm outside diameter, 320mm outside height and 300 mm inside height. It is reinforced with a special mortar (around 29 mm on the side and 30 mm at the bottom). Around the mortar there is sand which is held by several zirconia rings. Above the top zirconia ring, an aerated concrete plate is placed with a square hole (200 x 200 mm) just above the crucible. A hole is made in the top zirconia ring to pass the argon injection pipe. The inductor coil is outside the zirconia rings with an inside diameter of 500 mm.
The experimental setup is instrumented with several thermocouples:

- One type K thermocouple (chromel-alumel) sheathed with Inconel tube at the side-bottom of the crucible to detect the end of the thermite reaction (height 0 mm, radius 42 mm).
- One type K thermocouple (chromel-alumel) sheathed with Inconel tube below the crucible between the bottom and the mortar (height 20 mm, radius 42 mm) to detect breach of the crucible.
- Two type K thermocouples (chromel-alumel) sheathed with Inconel between the wall of the crucible and the mortar (96 mm radius) at 20 mm and 40 mm height from the bottom.
- Two type C thermocouples (tungsten-rhenium with maximal measured temperature of 2572 K) sheathed with molybdenum tube (external diameter 1.78 mm, inside diameter 1.07 mm, isolated with HfO_2) at the center of the bottom of the crucible respectively at 20 mm and 40 mm height from the bottom. They measure the temperature of the corium.

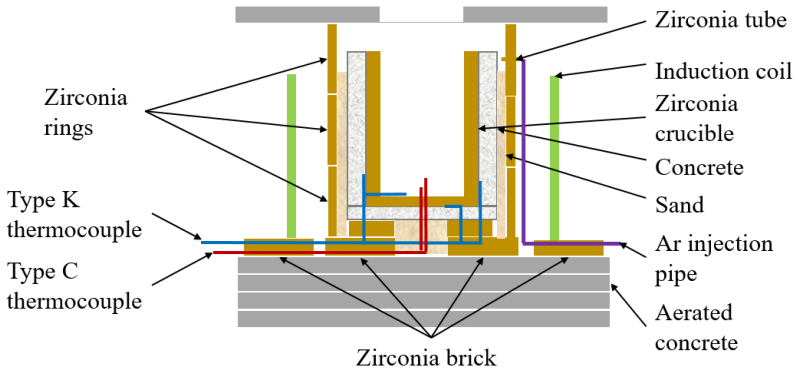

Figure 10: Scheme of experimental setup for experiment VULCANO CRIEPI-FD#5-02.

The thermite completely reacted in 72.4 sec and the type C thermocouple measured a maximum temperature of 2572K (TC.C.002 at 40 mm) and 2485K (TC.C.006 at 20 mm) (Figure 11). 7 seconds after the start of uranothermite reaction, induction is set at 3% of maximal power. When the uranothermitic reaction reaches the bottom of the crucible, the power is set at 40%. TC.C.006 (height: 20 mm) reached a maximum before the TC.C.002 (height: 40 mm). It might be because of the heating of the induction. As the temperature continued to decrease we decided to increase the power up to 42% (212 sec). This had no effect, so we increased it again up to 44% (333 sec). We kept this power until the end of the test for 59 sec. The induction is stopped because of excess of flame and fumes production from the test section.

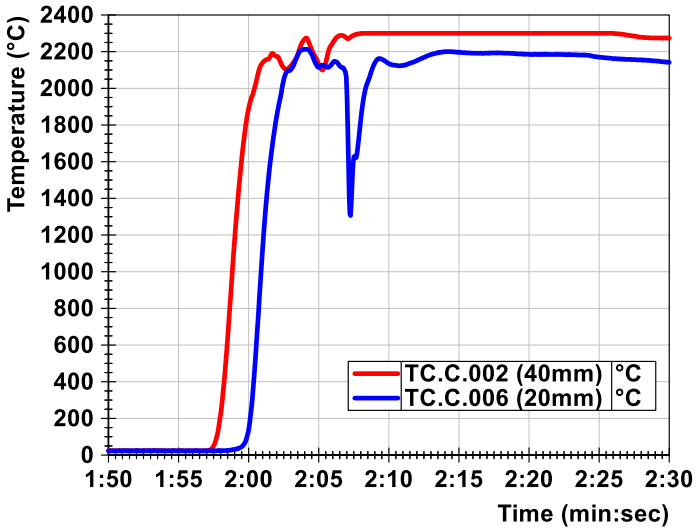

Figure 11: Temperature measurement for type C thermocouples for VULCANO CRIEPI-FD#5-02. Focus on the start of temperature increase.

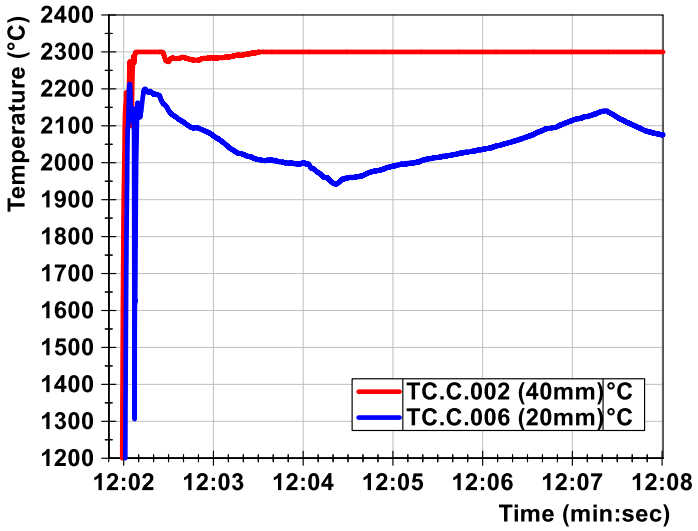

Figure 12: Temperature measurement for type C thermocouples for VULCANO CRIEPI-FD#5-02. Focus from the start of the temperature increase until the induction is stopped.

After the end of the reaction, the corium is cooled for 48 h. Then, the experimental setup is dismantled to observe the corium. The top of the corium shows a crust located at the level of the thermite before reaction

(Figure 13 left). There is a cavity below the crust and a part of it has fallen on the corium ingot below (Figure 13 right). The zirconia crucible is completely broken and have crust on the inside wall in the cavity. The inside of the zirconia crucible is partially melted, and it is impossible to differentiate between molten zirconia and corium at this level (Figure 13 right). The corium ingot is composed of several parts:

- The top layer from 70 mm to 110 mm. It is composed of powder and molten debris.
- The middle layer from 30 mm to 70 mm with blocks of molten corium (Figure 14 left) and powder. The largest blocks are approximately 70 to 80 mm high and 40 to 50mm wide. The smallest blocks are approximately 40 to 50 mm high and wide.
- The bottom layer from 0 mm to 30 mm with blocks of molten corium and powder (Figure 14 right). There is a large block approximately 100 mm long and 80 mm wide. The other blocks are between 40 mm and 50 mm high and wide.



Figure 13: Pictures of the dismantling of the corium of VULCANO CRIEPI-FD#5-02. Left: top of the crucible with corium crust. Right: top of the corium pool with crust on the crucible wall.



Figure 14: Pictures of the dismantling of the corium of VULCANO CRIEPI-FD#5-02. Left: Corium blocks localised between 30 mm and 70 mm from the bottom of the crucible. Right: Corium blocks localised between 0 mm and 30 mm from the bottom of the crucible.

The coupling of the uranothermitic reaction with induction heating therefore made it possible to increase the temperature inside the pool and to obtain corium blocks. The use of induction alone also allows this result [4] but the coupling with the uranothermitic reaction allows the heating time to be drastically reduced few minutes versus half an hour to more than an hour.

6. CONLUSION

The uranothermitic reaction therefore is a very powerful process that allow to obtain corium blocks with very different compositions from those obtained in the past (60 wt% of concrete or 30 wt% of metallic phase). However, using simple experimental device reaction results are sensitive to lacked thermal insulation and atmosphere. With subsequent improvement, the results of the tests are greatly enhanced.

However, we have seen that despite this, for certain corium compositions the uranothermitic reaction alone may not be enough to obtain a block of corium due to lack of energy. The coupling of the uranothermitic reaction with induction heating is a very efficient process to provide the missing energy to obtain a molten block, while reducing the duration of the induction heating. This innovative technic can be used for MCCI for example. This avoids the risk of starting to ablate the concrete while the corium is not completely melted when heating only by induction.

7. ACKNOWLEDGMENTS

A part of this work has been carried out within the frame of CEA/IRSN/FRAMATOME/EDF collaboration.

A part of this work has been carried out within the frame of ONET/CEA/IRSN collaboration contribution to the Project “Development of Safety System (Acquisition of Dust Dispersion Data)” led by CRIEPI (Central Research Institute of Electric Power Industry)), which were carried out as a subsidy program of METI, “Project of decommissioning, contaminated water and treated water management”, of Japan..

8. REFERENCES

1. P. Piluso, K. Mwamba, C. Journeau, “Uranothermic reaction as an efficient SHS process to synthesize severe accident nuclear materials” *International Journal of Self-Propagatig High-Temperature Synthesis*, **18,** No 4, 241-251 (2009)
2. S. Bakardjieva, M. Barrachin, S. Bechta, D. Bottomley, L. Brissonneau, B. Cheynet, E. Fischer, C. Journeau, M. Kiselova, L. Mezentseva, P. Piluso, T. Wiss, Improvement of the European thermodynamic database NUCLEA, Progress in Nuclear Energy, **52**, No 1, 84-96 (2010) https://doi.org/10.1016/j.pnucene.2009.09.014.
3. C. Journeau, V. Bouyer, F. Charollais, N. Chikhi, J. Delacroix, A. Denoix, H. Laffolley, C. Mattassoglio, D. Molina, P. Piluso, P. Sauvecane, S. Thilliez, B. Turquais, C. Suteau, “Upgrading the PLINIUS platform toward smarter prototypic-corium experimental R&D”, *Nucl. Eng. Des.* **386**, 111511 (2022).
4. Guéneau, C., Dupin, N., Kjellqvist, L., Geiger, E., Kurata, M., Gossé, S., Corcoran, E., Quaini, A., Hania, R., Smith, A.L., Piro, M.H.A., Besmann, T., Turchi, P.E.A., Dumas, J.C., Welland, M.J., Ogata, T., Lee, B.O., Kennedy, J.R., Adkins, C., Bankhead, M., Costa, D., 2021. TAF-ID: An international thermodynamic database for nuclear fuels applications. Calphad, 72, 102212. https://doi.org/10.1016/j.calphad.2020.102212.
5. C. Journeau, D. Molina, V. Bouyer, A. Denoix, “Characterisation of prototypic ex-vessel fuel debris simulating MCCI at Fukushima Daiichi” *Proceedings* of t*he 11th European Review Meeting on Severe Accident Research (ERMSAR2024)* KTH, Stockholm, Sweden, May 13-16 (2024)

Production of prototypic corium in the VULCANO facility using uranothermite and induction heating

Arthur DENOIX, Viviane BOUYER, Christophe JOURNEAU, Alexia BALLAND-LONGEAU

ERMSAR – May 13-16, 2024 – Stockholm, Sweden

Outline

1. **Corium heating technologies in VULCANO facility**
   - Uranothermic heating
   - Induction heating
2. **Tests with uranothermic reaction heating**
   - DEV-01-04
   - DEV-02-02
   - VULCANO-CRIEPI-FD#7-01
3. **Tests with uranothermic reaction and induction heating**
   - VULCANO-CRIEPI-FD#5-02

Corium heating technologies in VULCANO facility

Uranothermic heating

- Thermite is a self-sustained and self-propagating exothermic reaction between a metal oxide and a metal.
  - Uranothermite ➔ U_3O_8, is one of the reactants
  - Allows several kg of corium to be heated between 1500°C and 3000°C in a few minutes

- The maximum temperature and duration of the reaction depend of the composition
  - Non reactive component ↗ temperature reaction ↘
  - Not all the corium compositions are possible: sometime temperature reaction is not high enough to melt corium

Corium heating technologies in VULCANO facility

Induction heating

- In PLINIUS it is composed of:
  - A CELES (MP400) high frequency generator of maximum power of 400 kW (500 V – 1240 A), frequency between 80 and 300 kHz
  - A cooling systeme with flowmeters and thermocouples for thermal balance
  - A copper inductor which surround the crucible.

- Corium needs to be conductive :
  - Needs of metal part in corium at room temperature
  - If corium is mostly oxide : only at high temperature

Tests with uranothermic reaction heating

Experimental device

- In Plinius thermite is ignited by a pyrofuze wire.
- The pyrofuze wire is put a few mm below the surface powder
- Instrumentation is:
  - 1 type K thermocouple to measured the duration of the reaction front propagation
  - 1 type C thermocouple to measured the maximum temperature of the corium.

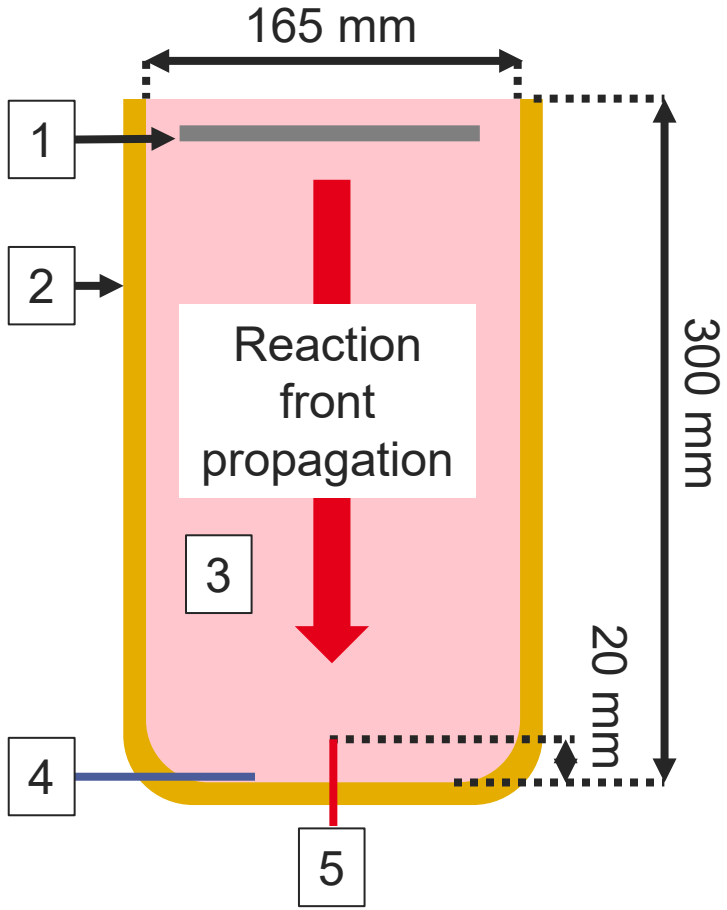

1. Pyrofuze wire
2. Zirconia crucible
3. Thermite
4. Type K thermocouple
5. Type C thermocouple

Tests with uranothermic reaction heating

Chemical Compound	Uranothermite (wt%)	Corium (wt%)	Chemical Compound	Uranothermite (wt%)	Corium (wt%)
U_3O_8	21.83	0.00	Si	6.15	0.00
UO_2	0.00	21.00	SiO_2	37.25	50.40
Zr	6.66	0.00	Al	0.81	0.00
ZrO_2	0.00	9.00	Al2O3	0.00	1.53
CrO_3	19.23	0.00	CaO	8.07	8.07
Cr	0.00	10.00	Total	100	100

DEV-01-04

- Goal: obtain a corium with 50 wt% of silicieous concrete
  - 37,25 wt% of SiO2 : non reactive component

Databased + Software	NUCLEA-22-1 + Thermo-Calc 2020a
Liquidus temperature (jellow dots)	1750°C
Reaction temperature (blue dots)	1694°C
Liquid fraction at reaction temperature	90 wt%

- Results
  - Max temperature : 1660 °C
  - Reaction duration : 225,3 sec

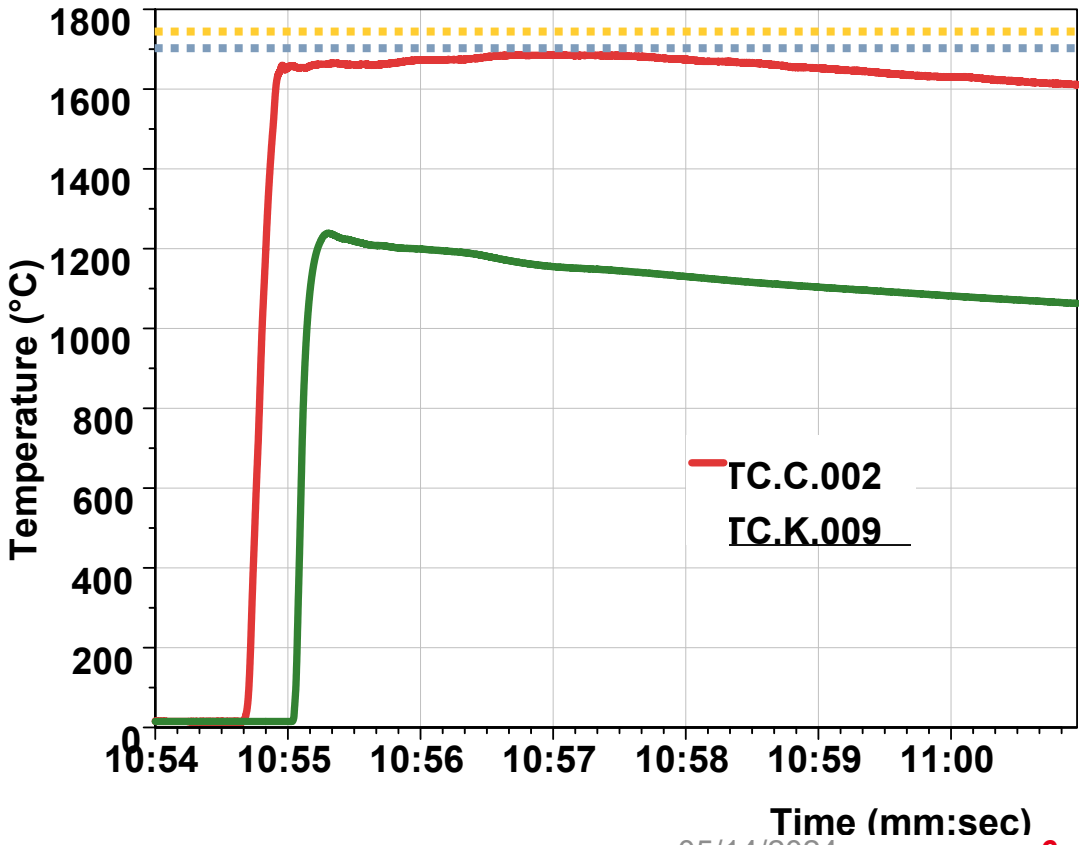

Tests with uranothermic reaction heating

DEV-01-04 dismantling

1. Powder 20 wt%
2. Agglomarated powder 39 wt% (top to 70mm)
3. Corium ingot 41 wt% with height between 60 – 70 mm

- Maximum temperature ≈ Reaction temperature
- But we don’t observe 90 wt% of molten corium
- Could be the lack of insulation of the crucible with very long duration of the reaction

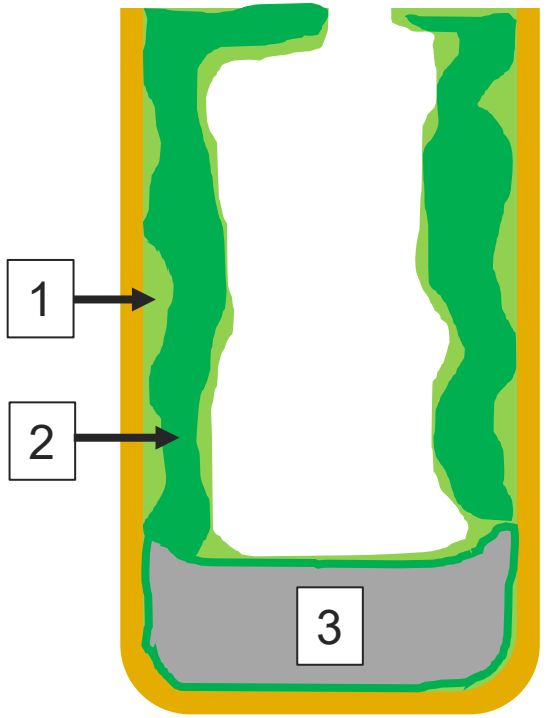

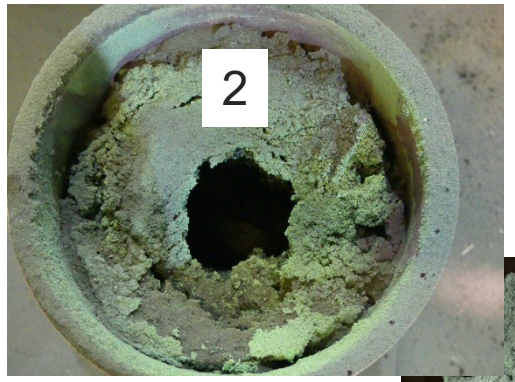



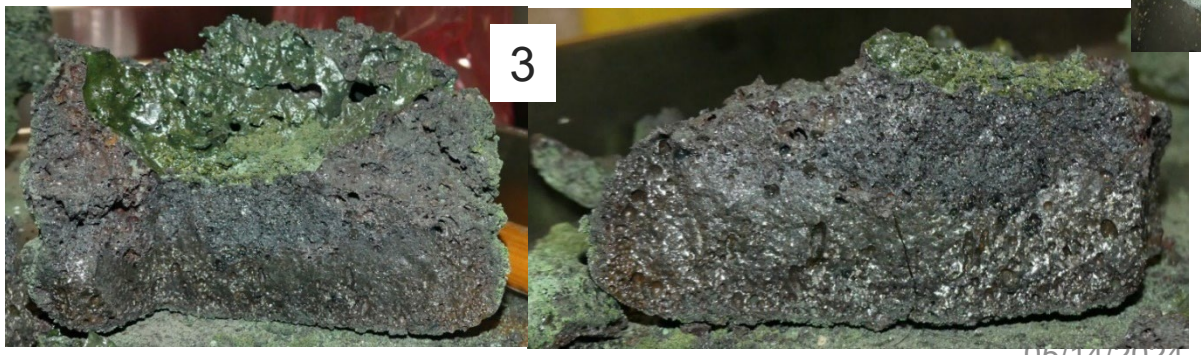

Tests with uranothermic reaction heating

Chemical Compound	Uranothermite (wt%)	Corium (wt%)		Chemical Compound	Uranothermite (wt%)	Corium (wt%)
U_3O_8	47.30	0.00		Cr	0.00	6.00
UO_2	0.00	45.50		Si	1.96	0.00
Zr	14.44	0.00		SiO2	0.00	4.20
ZrO_2	0.00	19.50		Al	0.07	0.00
Fe_2O_3	0.08	0.00		Al2O3	0.00	0.13
Fe	23.94	24.00		CaO	0.67	0.67
CrO_3	11.54	0.00		Total	100	100

DEV-02-02

- Goal: obtain a corium with 30 wt% of metal (80 wt% Fe and 20 wt% Cr)
  - ≈24 wt% of Fe : non reactive component

Databased + Software	NUCLEA-22-1 + Thermo-Calc 2020a
Liquidus temperature (jellow dots)	2296°C
Reaction temperature (green dots)	2179°C
Liquid fraction at reaction temperature	90 wt%

- Results
  - Type K is reached by melted metal before type C is reached by corium
  - Max temperature : 1984°C
  - Reaction duration : 53,8 sec (from Type C thermocouple)

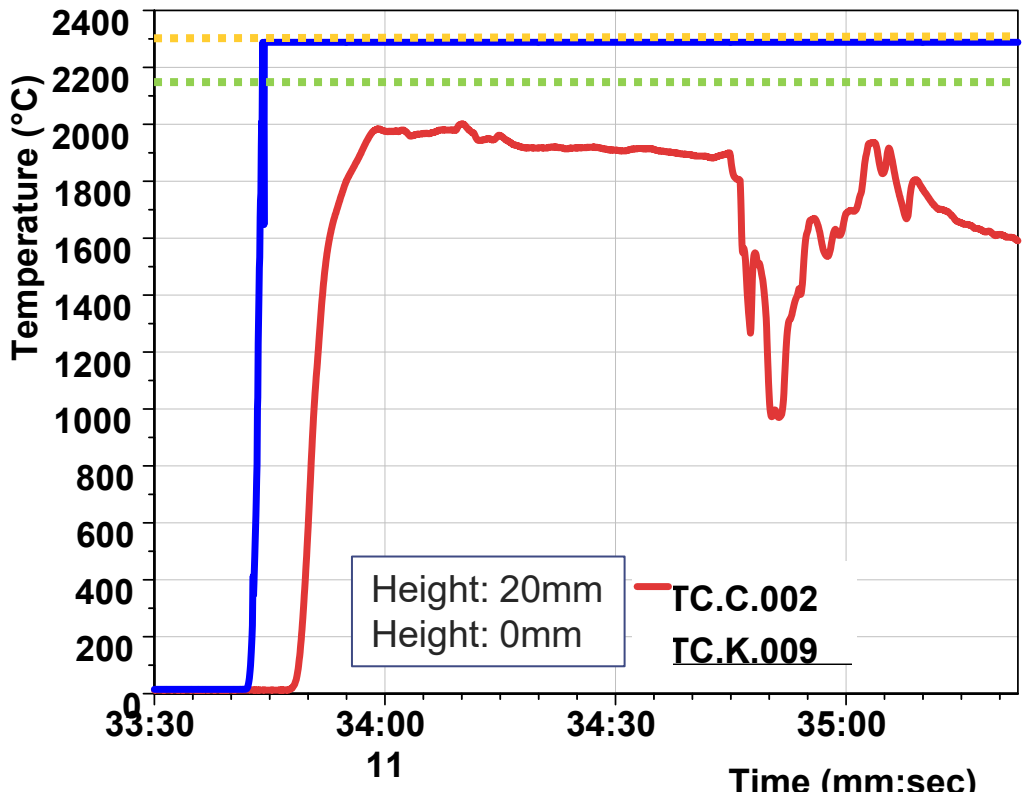

Tests with uranothermic reaction heating

DEV-02-02 dismantling

1. Debris/powder 5.2 wt%
2. Crust 20 wt%
3. Ingot 74,8 wt% height between 35 mm and 56 mm
4. Metal plate

- Maximum temperature < Reaction temperature and Liquidus temperature
- But we observe a molten corium?
- Could be oxydation by oxygen

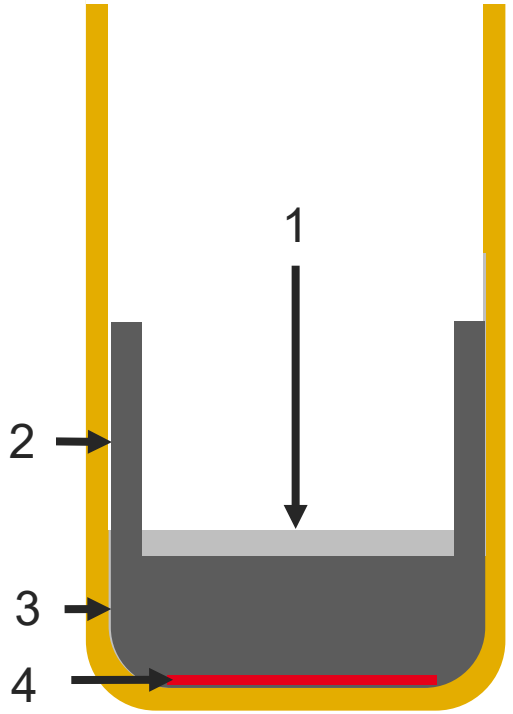





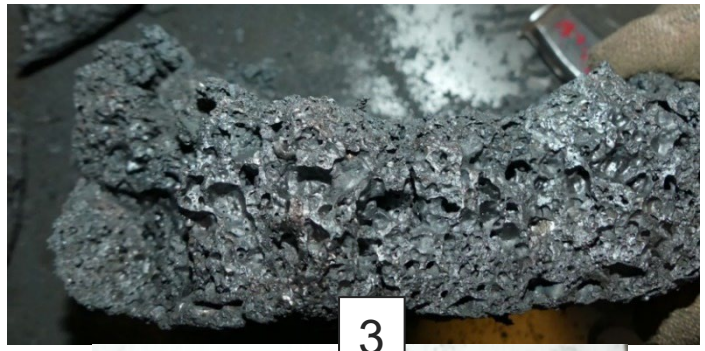

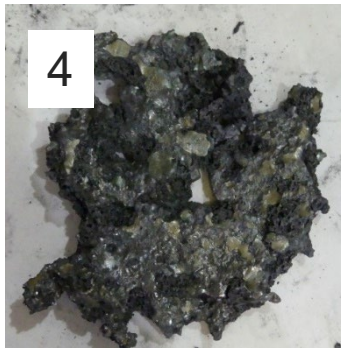



Tests with uranothermic reaction heating

VULCANO-CRIEPI-FD#7-01

- Objective:
  - Argon atmosphere
  - Increase crucibe insulation
- Dimensions
  - Height = 336 mm
  - Diameter = 145 mm
- Instrumentation
  - 2 type C : 20 mm and 40 mm from the bottom of the crucible
  - 1 type K at the bottom of the crucible

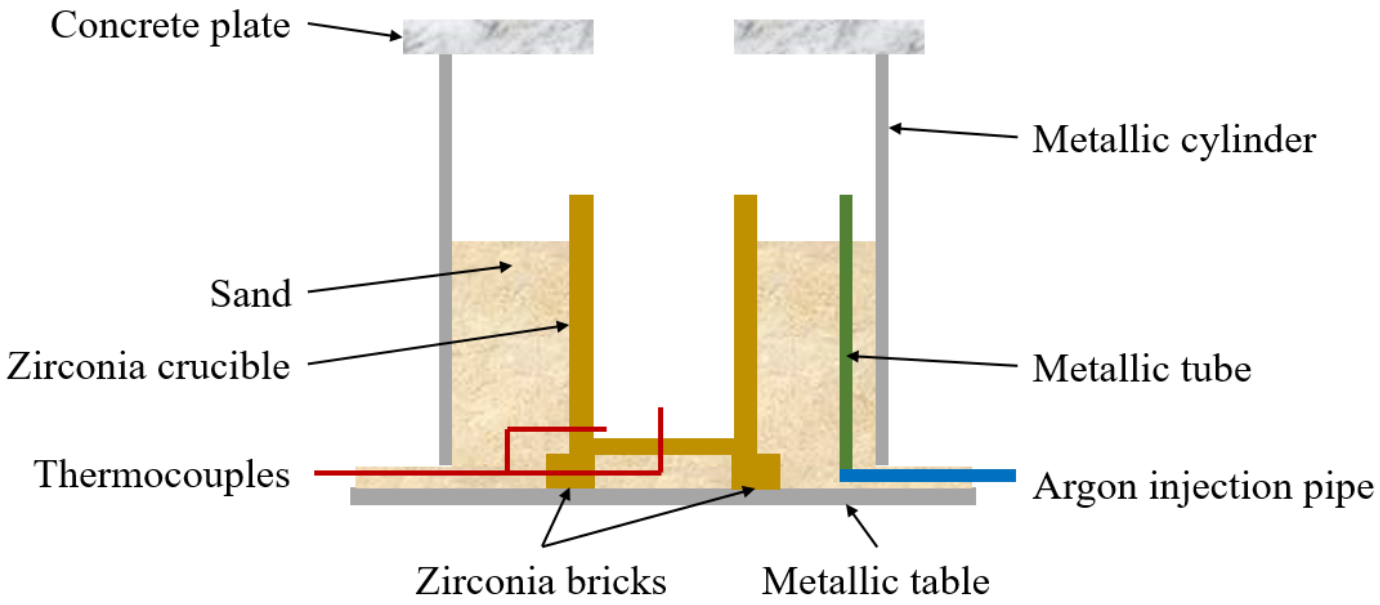

Tests with uranothermic reaction heating

Chemical Compound	Uranothermite (wt%)	Corium (wt%)		Chemical Compound	Uranothermite (wt%)	Corium (wt%)
U_3O_8	38.26	0.00		Nd2O3	0.11	0.11
UO_2	0.00	36.81		MoO2	0.09	0.09
Zr	44.22	25.41		CsOH.H2O	0.06	0.06
ZrO_2	0.00	25.41		BaO	0.04	0.04
CrO_3	3.74	0.00		La2O3	0.03	0.03
Cr	0.00	1.95		PdO	0.03	0.03
Fe_2O_3	11.13	0.00		Pr2O3	0.03	0.03
Fe	0.00	7.79		Sm2O3	0.01	0.01
CeO_2	0.20	0.20		SrO	0.02	0.02
SnO_2	0.90	0.90		Y2O3	0.01	0.01
B_4C	1.00	1.00		TeO2	0.03	0.03
RuO_2	0.06	0.06		Total	100	100

VULCANO-CRIEPI-FD#7-01

- Objective: Fabrication of fuel debris prototypes
  - Fukushima Daiichi Unit 2 lower head debris
  - Presence of simulant of FP

Software + Databased	GEMINI2 + NUCLEA14_1	Thermo-Calc + NUCLEA21_1	Thermo-Calc + TAF-ID14
T reaction (°C)	2294	2337	2237
T liquidus (°C)	2353	2625	2310
wt% solid phase at T reaction	59	20	46

- Results
  - Maximum temperature : 2298°C
  - Reaction duration: 82,4 sec

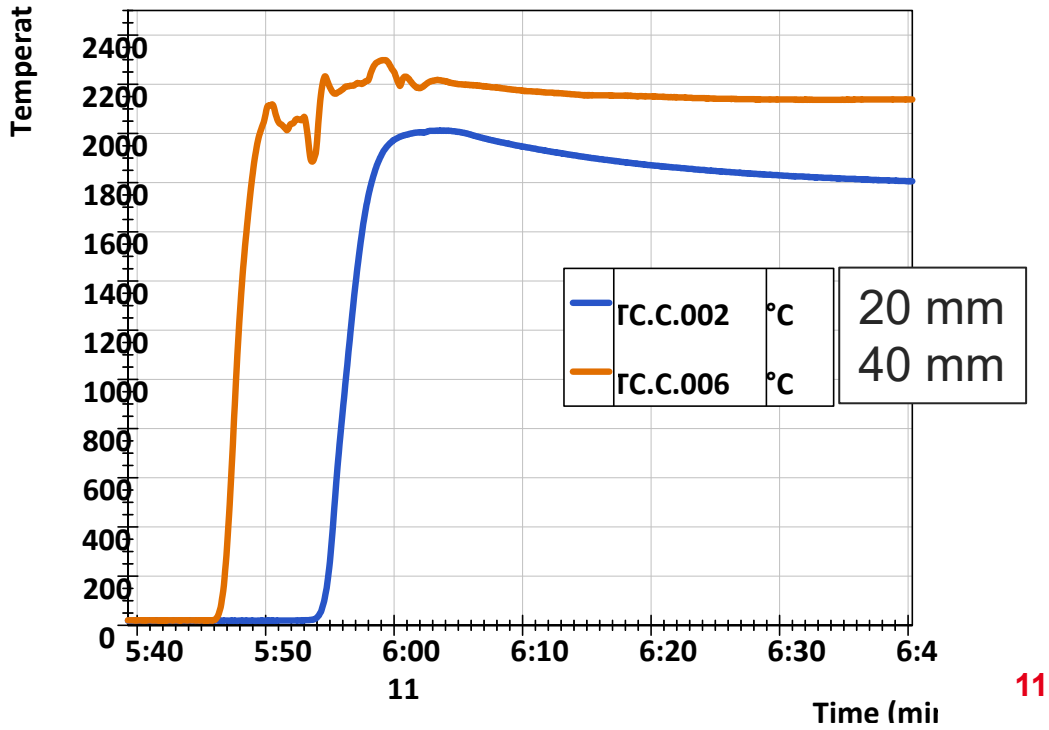

Tests with uranothermic reaction heating

VULCANO-CRIEPI-FD#7-01

dismantling

1. Powder from the top to 50 mm from the bottom
2. Agglomerated powder from the bottom to 50 mm

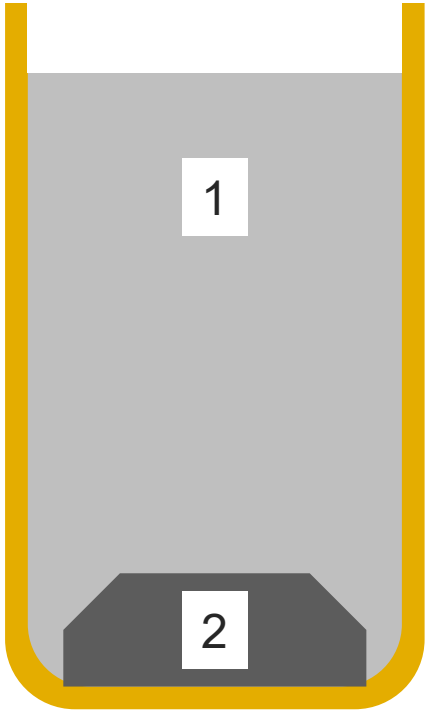



- Dispite the improvement of the experimental setup we are unable to melt the corium
- That is in this type of case when induction heating is interesting



Tests with uranothermic reaction and induction heating

VULCANO-CRIEPI-FD#5-02

- Objective:
  - Thermite + Induction heating
  - Argon atmosphere
  - Increase the crucible insulation
- Dimensions
  - Height = 300 mm
  - Diameter = 165 mm
- Instrumentation
  - 3 type K thermocouples for security outside of the crucible
  - 1 type K thermocouple at the bottom of the crucible
  - 2 type C thermocouples 20 mm and 40 mm from the bottom of the crucible

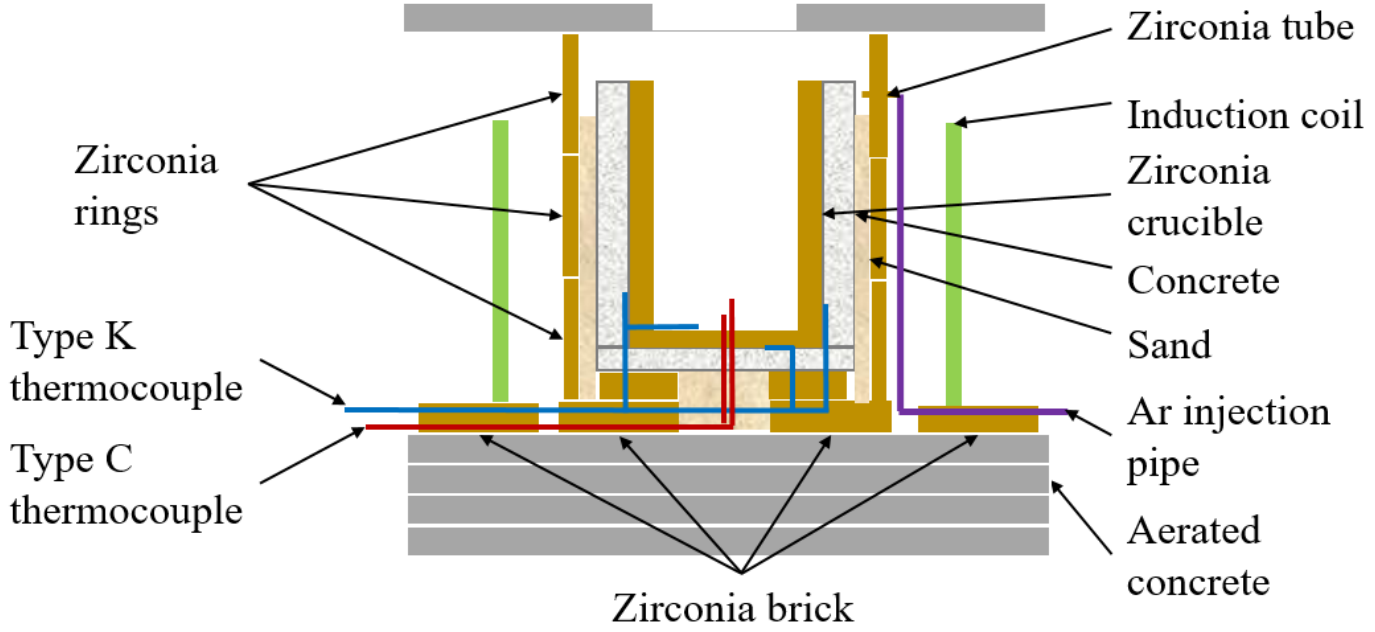

Tests with uranothermic reaction and induction heating

VULCANO-CRIEPI-FD#5-02

- Same composition as VULCANO-CRIEPI-FD#7-01

- Induction heating
  - Induction is switched on 72 sec after the biginning of the reaction (1)
  - Induction is stopped after 320 sec of heating (2) because of ablation of the crucible

- Maximum temperature : 2299 K
  - Maximum measurable temperature of type C thermocouple

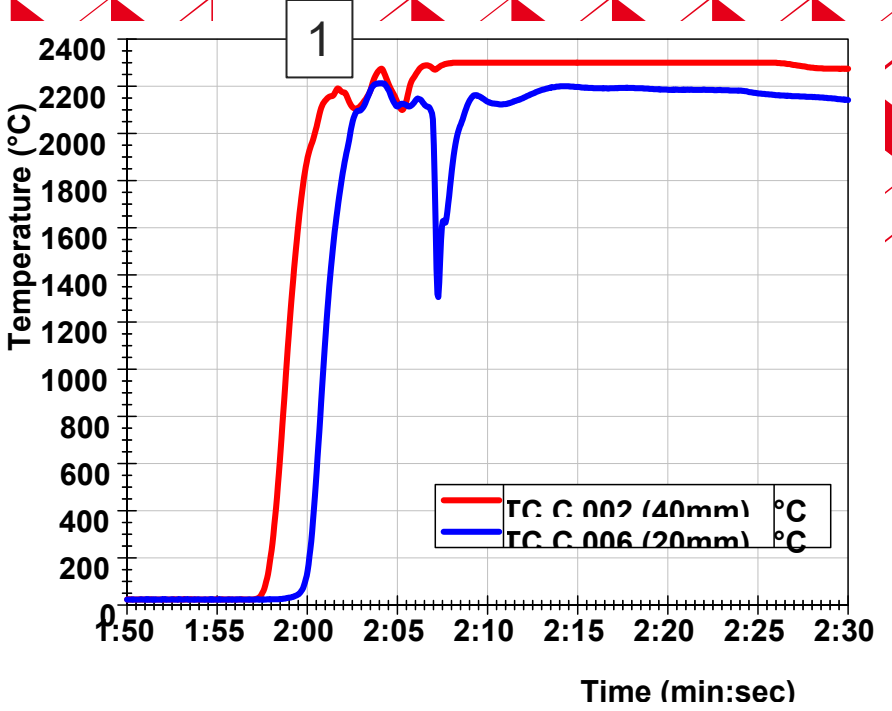

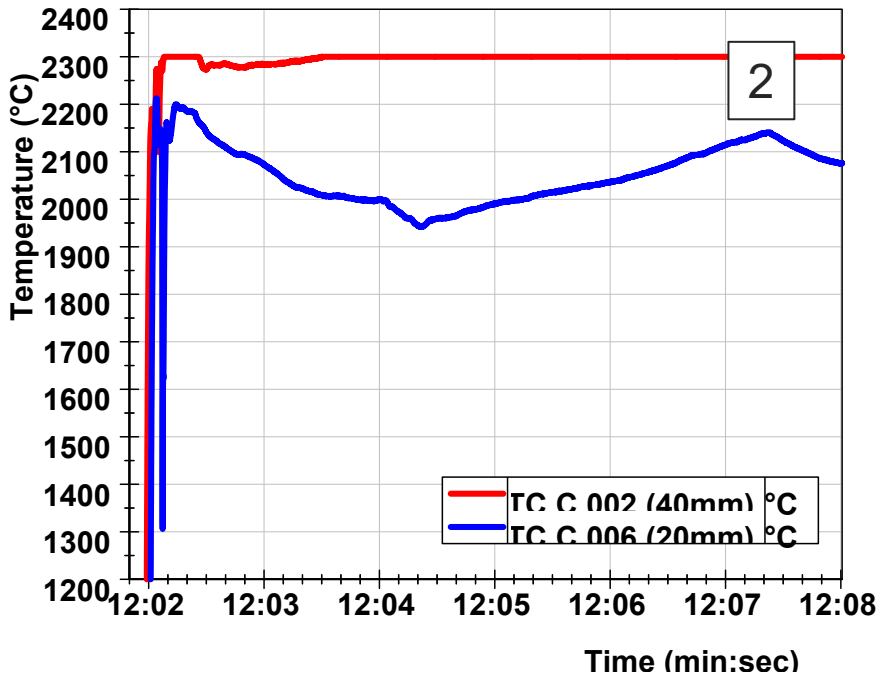

Tests with uranothermic reaction and induction heating

VULCANO-CRIEPI-FD#5-02 dismantling

1. Crust
2. Cavity and crust on the wall
3. Powder and molten debris : 70 – 110mm
4. Molten corium blocks and powder : 30 – 70 mm
5. Molten corium blocks and powder : 0 – 30 mm

- Couplingin duction heating with uranthermic heating makes it possible to obtain blocks of molten corium

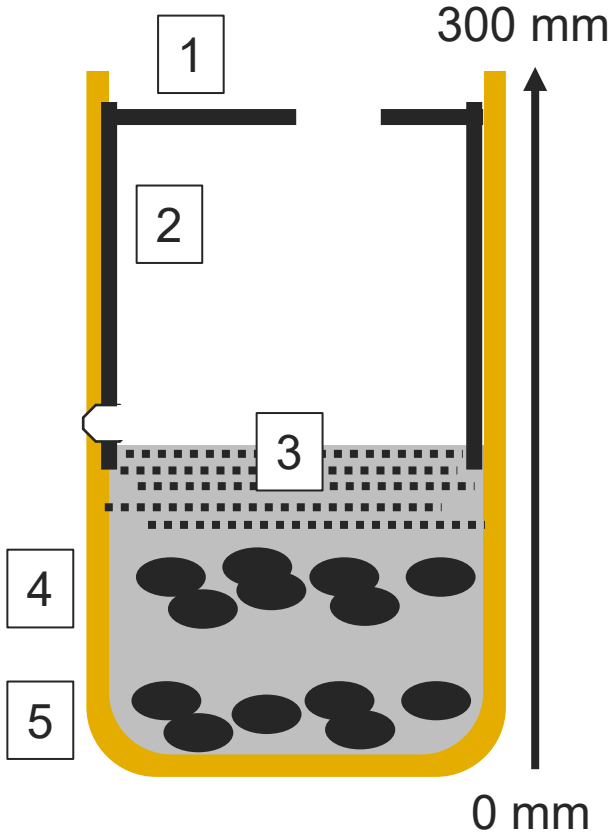

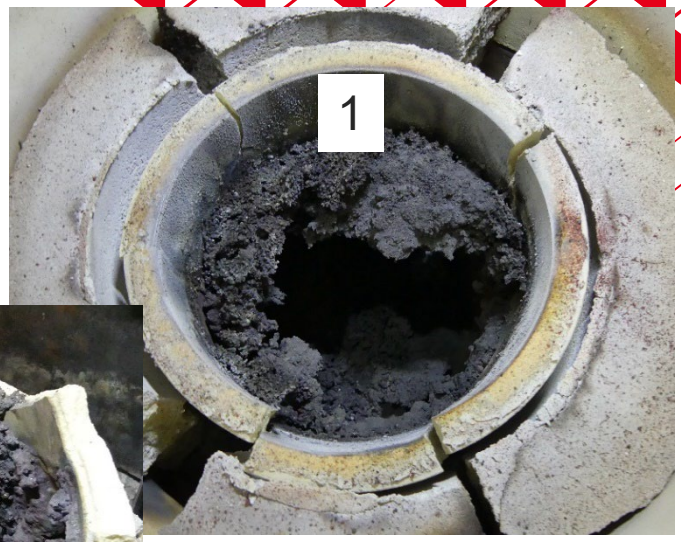

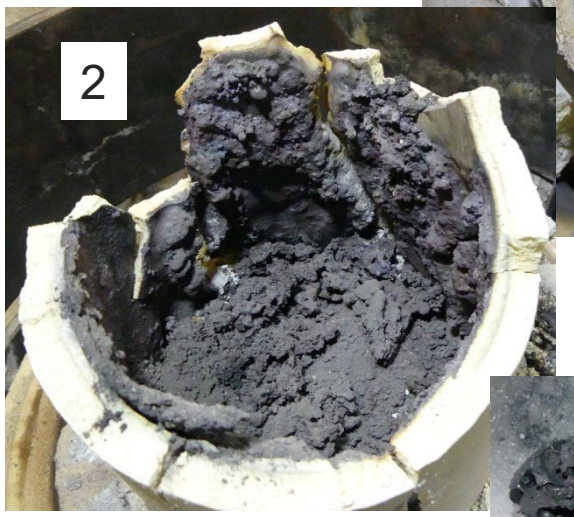





Conclusion

- Uranothermite is a powerfull tool to obtain corium
  - Make the reaction under argon atmosphere
  - Insulate the crucible
  - Not all the composition are possible

- Uranothermite can be coopled with induction
  - Reaction temperature should be high enough for the corium to be conductive
  - Be careful with possible ablation of the crucible

- This innovative technique has been used in PLINIUS for:
  - Molten Core Concrete Interaction in VULCANO (1)
  - Molten Core Concrete Interaction with water top flooding in MERELAVA (2)

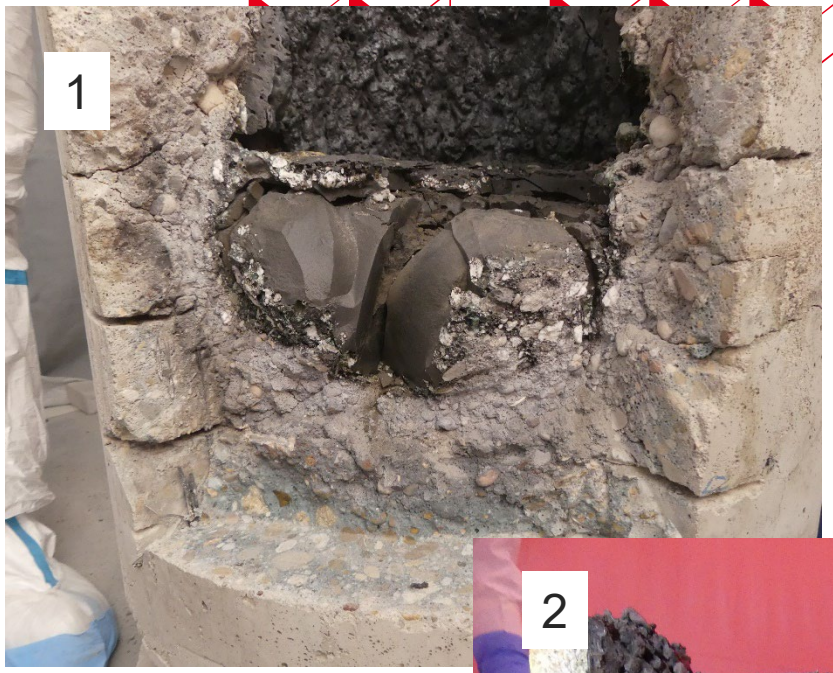



Thank you for your attention

A part of this work has been carried out within the frame of CEA/IRSN/FRAMATOME/EDF collaboration.

A part of this work has been carried out within the frame of ONET/CEA/IRSN collaboration contribution to the Project “Development of Safety System (Acquisition of Dust Dispersion Data)” led by CRIEPI (Central Research Institute of Electric Power Industry), which were carried out as a subsidy program of METI, “Project of decommissioning, contaminated water and treated water management”, of Japan.

Arthur DENOIX
CEA
DES/IRESNE//DTN/SMTA/LEAG
Cadarache, Building 219
131108 Saint-Paul-Lez-Durance
France
Arthur.denoix@cea.fr

Overview of Ex-Vessel Severe Accident Scenarios Simulations at UJV Rez

Jan Komrska, Tomas Janda and Petr Vokac
ÚJV Řež, a. s.
Hlavní 130, Řež, 250 68, Husinec, Czech Republic
jan.komrska@ujv.cz, tomas.janda@ujv.cz, petr.vokac@ujv.cz

ABSTRACT

Severe accidents (SA) at nuclear power reactors may be mitigated in an in-vessel phase of their progression (e.g., by means of in-vessel melt retention by external reactor vessel cooling, IVMR-ERVC), or after vessel failure by ex-vessel corium localization and cooling. A SA in the ex-vessel phase demands huge attention, as such a scenario may lead to breaching the final barrier for fission products (FP) hold-up – the containment (CTMT). Some NPPs rely on the so-called wet cavity strategy, which consists of flooding the reactor cavity prior reactor pressure vessel breach; the ejected corium is thus fragmented, which promotes its cool ability. On the other hand, the risk of steam explosion, which could jeopardize CTMT integrity, exists. The wet cavity strategy is also applicable only for reactors with very deep cavities. Therefore, some NPPs opt for a dry cavity configuration, which allows for corium spreading and its consequent cooling by water top-flooding. As breaching of the CTMT basemat would lead to large radioactivity release into the environment, which shall be practically eliminated, investigations of ex-vessel corium spreading and cooling phenomena are in the spotlight of analytical and experimental research of UJV Rez. Numerical simulations using a variety of mechanistic SA analysis codes - e.g., MELTSPREAD, CORQUENCH) were employed to assess corium spread-ability and cool-ability in the reactor cavity and adjacent rooms. Moreover, CFD-grade codes were used to perform simulations to further investigate corium spreading in more detail. The initial conditions for corium spreading, namely acquisitions of corium mass, composition, temperature, and decay power, were assessed using various integral SA codes (ASTEC, MELCOR, MAAP). Besides analytical and numerical investigations, several experimental programs, partially funded by the government grant, were launched to further support analytical and numerical work. These projects are aimed at studying corium properties at elevated temperatures, interaction of corium with RPV internals or layered steel structure at the reactor cavity floor or investigating of the possibility of using innovative materials (such as geopolymers) as a suitable reactor cavity lining, replacing concrete basemat and promoting thus ex-vessel SA mitigation. These national experimental projects are in conjunction with the broader international OECD project ROSAU, which aims to experimentally investigate large-scale corium spreading and cooling. A comprehensive overview of UJV Rez's most recent findings on ex-vessel corium behavior is presented in the proposed article, considering all the progress that has been made both in analytical activities and experimental programs, in which UJV Rez actively participates. The final goal of those investigations is to support long-term safe operation of Czech nuclear fleet.

KEYWORDS
Ex-Vessel Retention, Corium, Severe Accident, UJV, Numerical Simulations

1. INTRODUCTION

The aim of this paper is to present work done by researchers from UJV Rez that concern mostly ex-vessel behavior of corium in various phases of a postulated severe accident scenario with reactor core melt down. Typically, severe accident scenarios are simulated using either integral codes for complex problems or mechanistic codes for specific problems. For corium flow simulation, there are mechanistic codes like MELTSPREAD or CORFLOW [1, 2]. Quite recently, various corium flow simulations are being done using CFD simulations [3, 4]. CFD simulations offer a valid option for simulating corium flow, especially for complex geometries and full 3-D corium flow cases.

In this paper we present an updated version of previous work done for VVER 1000/V320 ex-vessel scenarios with new versions of MELTSPREAD and CORQUENCH. Following with MELTSPREAD simulation and preliminary evaluation of corium spreading experiments under preparation within CANUT project in cooperation with Research Centre Rez. And finally, a preliminary 3-D simulation of corium flow and cooling in a core catcher of a proposed GFR reactor demonstrator ALLEGRO.

In the presented work mostly MELTSPREAD, CORQUENCH, MELCOR severe accident codes are used, as well as CFD software Ansys Fluent for 3-D CFD corium spreading simulations in a core catcher.

2. OVERVIEW OF EX-VESSEL SEVERE ACCIDENT SCENARIOS SIMULATIONS AT UJV REZ

2.1. Updates on VVER 1000/V320 Ex-Vessel Corium Coolability

New version of MELTSPREAD [5] code released in mid of 2023 allows to simulate no-slip condition at the interface of spreading corium and side walls. Other improvement is an option to categorize molten Zirconium as part of oxidic molten corium This terminology arrangement allows to use a user defined solid fraction table not only for oxides, but for the whole mixture of UZrO. In MELTSPREAD code the simulated corium is composed of two components, oxidic and metallic. These components are treated as well mixed and have the same temperature. During the first minutes of corium spreading after RPV failure, the corium temperature is above the liquidus temperature of metallic component, that means that all the metallic content is liquid. The viscosity of corium is calculated based on volumetric solid fraction of well mixed volumes of metallic and oxidic components (using e.g., Ramacciotti correlation [6]). In well mixed corium, assumed large amount of molten metals significantly decreases corium effective viscosity. However, release of well mixed corium from the failed vessel cannot be considered as the only possible scenario. Cases with flow of corium with some extent of components separation may lead to much lower initial spreading, at least of the oxidic component. An approach to investigate such cases is under initial preparation.

New version of CORQUENCH [8] code allows simulation of corium on the basemat from refractory materials. Model of heat transfer in molten corium pool is not interlinked to the production of gasses that are sparging through molten pool to surface and are mixing the molten pool and thus forcing the convective heat transfer. The new model of convective heat transfer is now able to simulate situations in whose corium interacts with material where no gas sparging occurs. Among other new models there is a model of heat transfer from completely solidified corium. This model allows to calculate remelting of completely solidified corium after loss of cooling water.

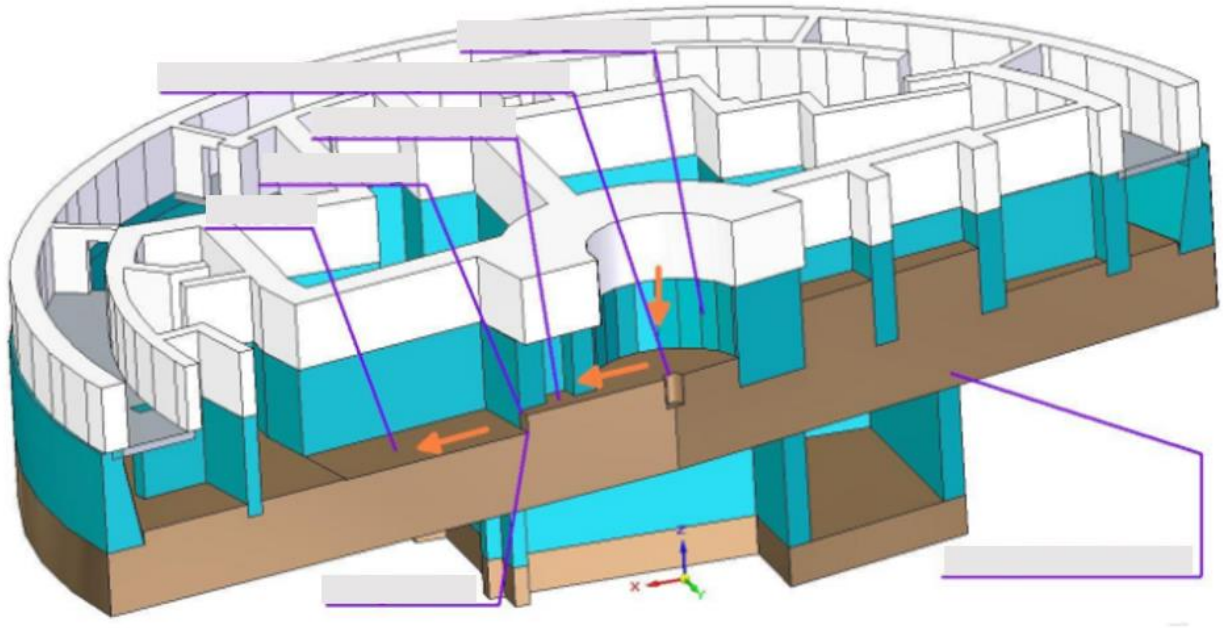

Figure 1: Corium Spreading path in the VVER 1000/V320 Containment [9]

2.2. CANUT Experiments Pretest Calculations

Small scale corium spreading experiments are under preparation in CV Rez in the frame of national CANUT project. Prototypical corium will be prepared in the cold crucible and poured into the predefined dry spreading channel. Preliminary calculations of the CANUT spreading experiments were focused on finding the optimal geometry of the spreading channel and the initial parameters of the corium, i.e., the initial temperature and velocity of the discharge. The preliminary design considered a straight rectangular channel of inert material.
The calculations were carried out using the MELTSPREAD 3.01 program. Detailed preliminary calculations for channel geometries of 10x60 cm, 15x60 cm and 20x60 cm were considered. The experiment will involve the preparation of a fully oxidized corium of composition UO2+ZrO2 in a cold crucible. The weight of the corium will be about 10 kg. The melt volume of 10 kg can thus be estimated at 1.3 to 1.4 liters. It is assumed that at least this amount of corium will be discharged into the spill channel.

Following variants of corium compositions with defined ratio of U/Zr were calculated:

- S1: U/Zr(at) = 0.552. According to the composition of thermite #16 used in the ROSAU experiments, after subsequent complete oxidation of the remaining Zr. It corresponds to the corium of a typical BWR reactor severe accident scenario. For safety reasons, since metallic uranium cannot be used in the thermite, the higher U/Zr values of the corium prepared by burning the thermite can be achieved.
- S2: U/Zr(at) = 1.252. This corresponds to Corium created during severe accident of the typical VVER-1000 PWR reactor.

The objective of the two experiments conducted with different composition of the corium will be:

1. to test the transferability of the ROSAU experimental results to the evaluation of the VVER-1000 corium spill
2. to check the repeatability of the CANUT small scale spill experiments (the experimental results should not be qualitatively different).

The MELTSPREAD code calculates only 1-D corium spill. For a relatively narrow channel of 10 cm width, an almost "rectangular" nodalisation was chosen. In this case, however, the corium in the model flows out of the crucible into selected nodes that occupy the entire width of the channel. For a channel width of 10 cm, this simplification was considered acceptable. However, in the case of a 20 cm wide channel, a uniform discharge over the entire width of the channel is no longer realistic.

As part of the calculations an alternative "concentric" nodalisation was created by moving the virtual center of the nodalisation circles to the axis of the cold crucible drain opening. The area receiving the corium discharge from the cold crucible is marked in red. In both cases the corium discharge is directed uniformly to the selected nodes.

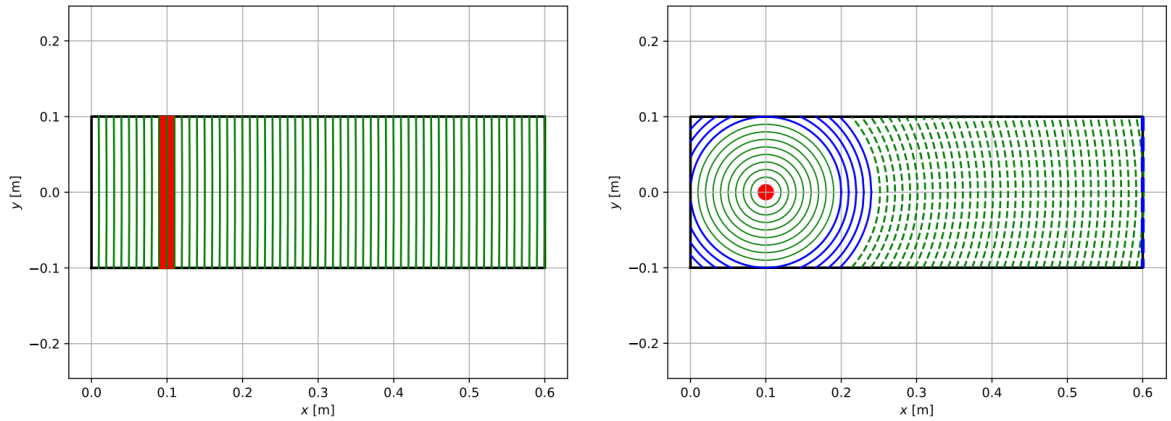

Figure 2: Rectangular and Concentric Nodalisation

2.3. ALLEGRO Core Catcher CFD simulation

ALLEGRO is a gas-cooled fast reactor demonstrator unit. It is being developed by the V4G4 CoE (Visegrad 4 for Generation IV Centre of Excellence). Main goal of the ALLEGRO demonstrator is to serve as an experimental platform for research and development needs for future development and operation of commercial nuclear reactors based on the GFR technology.

One of the systems developed specifically for ALLEGRO is a core catcher. This specialized system is used for stabilization and localization of corium in case of a severe accident with reactor core meltdown. Its main purpose is to retain and cool down the corium, and, therefore, to protect the concrete baseplate of the containment from melting through and to eliminate risk of a large radionuclide release. It is designed as a dry spreading ex-vessel core catcher with extensive use of sacrificial materials.

Presented simulation of the early ex-vessel phase of a severe accident in the ALLEGRO reactor is a part of a broader scope of core catcher design. Simulations are done for verification of the core catcher functionality and to simulate the behavior of corium in the core catcher. The presented early ex-vessel phase analysis is divided into two phases, solved in different codes.

The first phase of the simulations was performed using the integral code MELCOR 2.2 and CORQUENCH 4.1. The results obtained in the first phase were used as input conditions for the corium spreading simulation in the core catcher. The second phase of the corium spreading simulations in the ALLEGRO core catcher were performed in CFD code ANSYS Fluent.

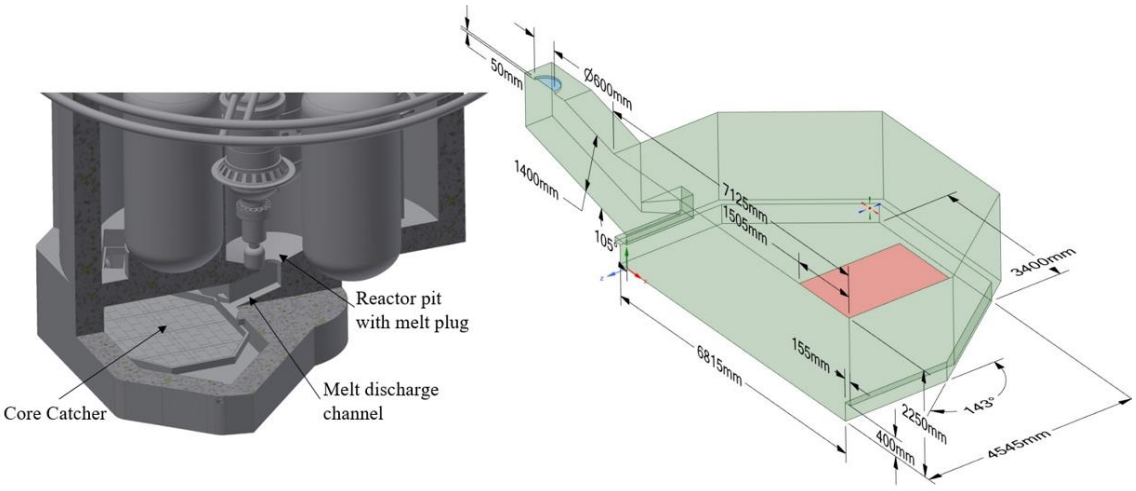

Figure 3: Model of the Core Catcher geometry used for CFD Calculations

For the CFD simulation, several simplifications were made for the corium flow in the core catcher. As the scenario only includes the initial very dynamic part of the corium spread, neither the crust formation on the corium surface nor the ablation process of the walls and floors of the core catcher were considered. Properties of N_2 atmosphere were assumed as constant. To reduce the computational complexity, axisymmetry was used in the geometry of the core catcher vessel. For the corium spreading simulation, the multiphase VOF model and Eulerian Multi-Fluid VOF model were used. Results for these models are compared in the conclusions. Basic numerical model setup parameters and solvers are based on previous studies [10, 11], except for inlet mass flow, which was changed 880 kg/s for the first 7.31 seconds of the simulation. Currently radiative heat transfer model was neglected for these initial simulations, as further work concerning sensitivity analysis for the various radiation models will be done soon and the optimal radiation model will be selected for use in combination with the Eulerian multiphase model.

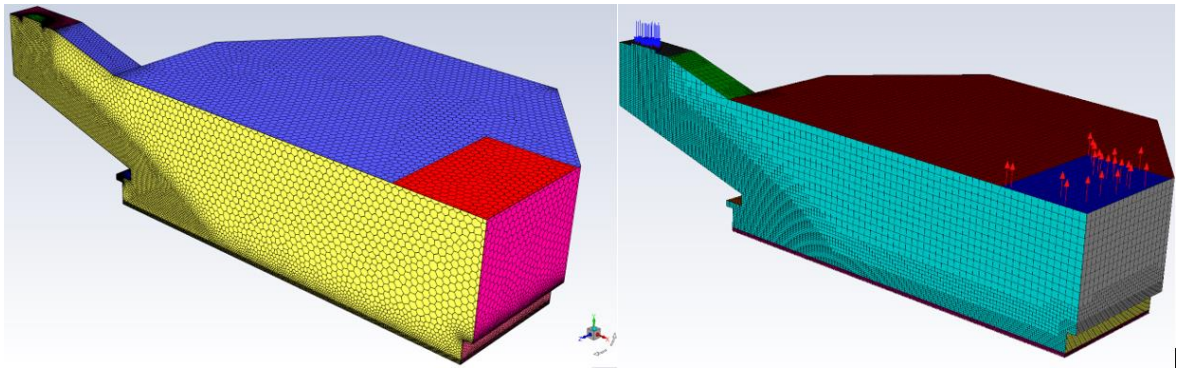

Figure 4: Polyhedral and CutCell Volume mesh

Based on the mesh sensitivity analysis [11], a computational mesh of the entire core catcher geometry was created. Entire core catcher floor has area of 54.2 m^2. For the VOF model the standard polyhedral volume mesh was used. For the Eulerian Multi-fluid model CutCell volume mesh was used, as during testing it was found that Eulerian model was divergent for polyhedral, or hex-core types of volume meshes. In total there were 809655 cells for the polyhedral VOF model with minimum orthogonal quality of 0.202. For the Eulerian cutcell mesh, the total number of cells was 826751 with minimum orthogonal quality of 0.15. These qualities of mesh were found to be satisfactory for the CFD simulation.

3. RESULTS

3.1. Updates on VVER 1000/V320 Ex-Vessel Corium Coolability

As discussed in chapter 2.1 by adding the Corium-Wall interface no-slip condition and option to categorize molten zirconium as part of oxidic molten corium are major two improvements in quality of corium spreading modeling and have significant influence on corium spread ability results [9]. A flow of corium through concrete door aperture was not successful therefore an aperture size must have been increased. Even the increased aperture (designated in Table 1. with Otv) did not permit an occupation of full spreading surface available in the adjacent room next to the reactor cavity (room designated in table 1 as GA302). The amount of corium that was able to escape reactor cavity and to spread into neighboring room was smaller, compared to the calculations with previous version of MELTSPREAD.

In the calculations performed in 2020 there was a complete melt spill into the adjacent room [9]. The new version of the MELTSPREAD code contains mainly frictional losses of the corium against the walls and the heat exchange of the corium with the walls. The new version of the code and the modified model predict that the full corium spreading won't be achieved. It reflects the remaining significant uncertainty of the assessment.
Importantly, while validation against the MST-0 experiment showed that within the uncertainties the MELTSPREAD calculation provides a correct estimate of the spill distance, it underestimates the melt front velocity. This may be the reason that the presented VVER-1000 geometry spill calculation predicted less favorable spreading.

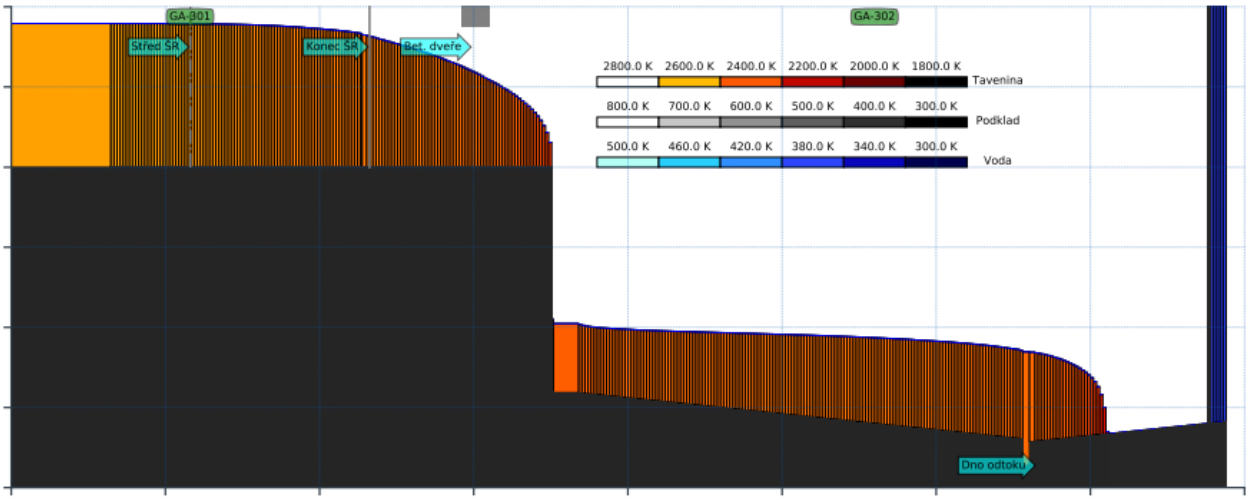

Figure 5: Example of MELTSPREAD visualisation for SBO Otv scenario at 310 seconds

Table 1: Results of the MELTSPREAD Calculations for Various Severe Accident Scenarios

SA Scenario	Corium volume [m^3]			Corium volume [%]	
	RS+CS	GA302	Total	RS+CS	GA302
G-LOCA	12.21	6.86	19.07	64	36
G-LOCA Otv	8.63	10.12	18.75	46	54
SBO	23.17	0	23.17	100	0
SBO Otv	12.58	10.49	23.07	55	45

The corium spill is considered successful when at least 50% of the corium leaves the reactor shaft (RS), while travelling through connecting shaft (CS) and moves to adjacent room to the reactor cavity, thus lowering the level of the corium in the RS and allowing the corium in the RS to cool down after the corium has been flooded with water.

For the water to flow into the RS, the level of the corium must be below the top edge of the aperture in the hermetic door (there must be a gap for water to flow back into the RS). With the original aperture in the hermetic door, the corium spill was not successful for the SBO scenario. With the enlarged aperture in the hermetic door only 45% of the corium moved into adjacent room to the reactor shaft in the SBO Otv scenario. Only successful scenario was the G-LOCA with enlarged aperture. For these reasons, it is recommended that the aperture be enlarged even more and further analyses will be conducted for this new variant.

The CORQUENCH improvements described in chapter 2.1 now allow to calculate scenarios where corium interacts with 27mm thick layer of stainless steel, that is installed on the concrete floor of reactor cavity in form of so-called thermal shielding, a special sheet metal layered structure. A coolability study of corium in reactor cavity was assessed, reactor cavity had its floor covered with thermal shielding and the corium was top flooded with water. A mass of corium in reactor cavity corresponded to the mass of corium left in cavity at the end of corium spreading calculation. This new scenario set up proved that thermal shielding layer did not complicate corium cooling. Gas sparging that developed after dissolving thermal shielding stainless steel layer helped to cool down corium and solidify it.

The new version of the CQ allows to use a new setting of the water ingression (WI) phenomenon into the crust of the corium and thus to improve the prediction of the cooling of the corium during MCCI in RS and the adjacent room after the completion of the corium spill. Previous models from the corium calculations performed in 2020 by the CQ code were adapted and a study was performed for the same variants as for the MELTSPREAD code.

The new version of the CQ has made it possible to perform calculations with a layer of steel on the floor surface, where no gases are generated during ablation of the underlying material. This gives qualitatively different results for the cooling of the corium in the RS+CS space on the surface of the heat shield. It is shown that due to the 27 mm thick stainless-steel layer, there was no decrease in the solidus temperature and no increase in the volume of the corium since the corium did not mix with the ablation products of the concrete but was only mixed with the iron.

On the contrary, it was found that there may be a problem with corium cool-ability and retention if the corium is not spilled over the entire prepared spill area and has an extra high decay heat. A solution to the corium retention problem may be to place a geopolymer sacrificial concrete on the floor of the room, but this requires further study.

3.2. CANUT Experiments Pretest Calculations

For the first part of the calculations the rectangular geometry was considered for the 10x60 and 15x60 cm channel dimensions. The floor of the channel is modelled as a 1.5 cm thick layer of siliceous concrete. The floor is divided into 15 vertical nodes each 1 mm thick. Walls are not modelled in the basic model.

Corium discharge is placed in the 5th node (see Figure 2). Time of 0 seconds corresponds to the moment when corium is dropped on the spill channel floor. Various corium discharge options were assessed. The first was fast drop of 10 kg of Corium in 1 second at a constant rate. Then the flow rate from the crucible was evaluated for orifice ø12 mm and ø20 mm assuming initial load of about 14 kg of corium in the crucible

and simplified formulas for viscous or inviscid flow through the orifice. For the corium viscosity calculation, the Ramacciotti correlation was used [6]. For the first part of calculations a total of 11 simulations were performed with different initial temperature of the corium between the solidus temperature and the liquid. The spreading simulation is calculated for a total of 15 seconds.

On Figure 6 and Figure 7 are results of the pretest calculations of the CANUT spreading experiments. Figure 8 represents the results of the comparison of various channel dimensions. Included in these calculations were varying dimensions of the cold crucible outlet (d2 dimension) and viscid/inviscid behavior of the flow through the crucible outlet.

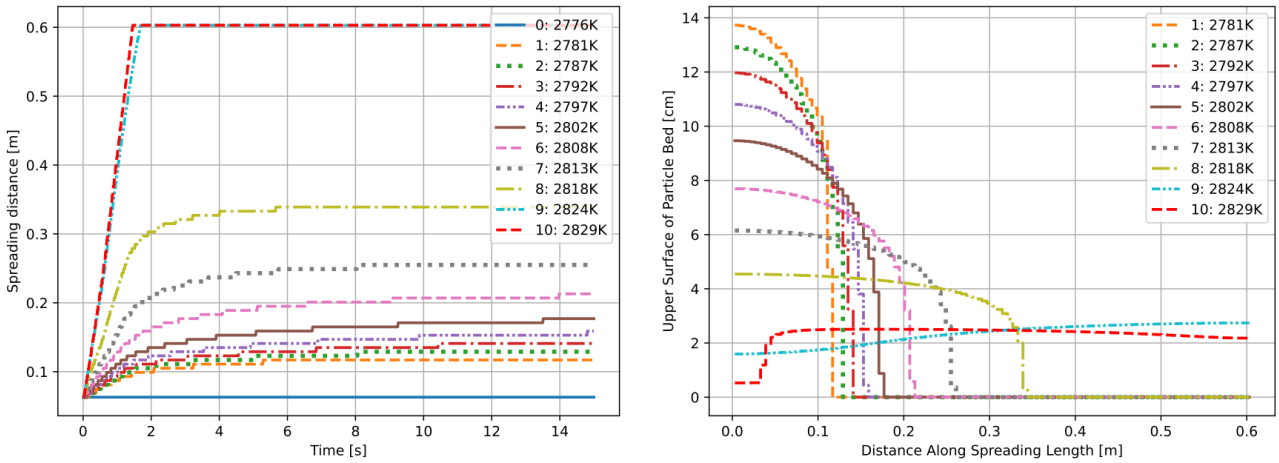

Figure 6 –Spreading distance along the Channel 10x60 with S1 Corium Composition

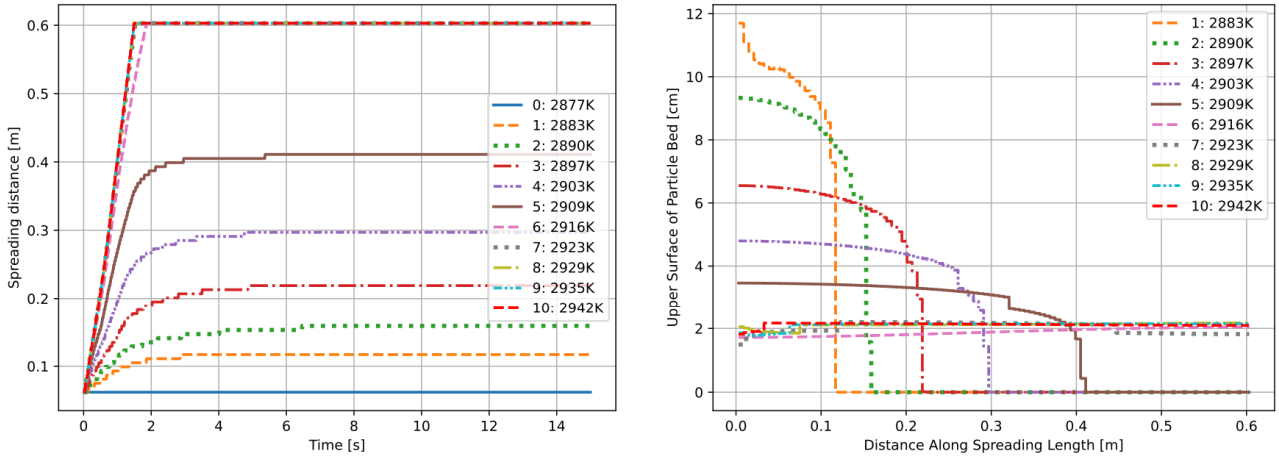

Figure 7 – Spreading Distance along the Channel 10x60 with S2 Corium Composition

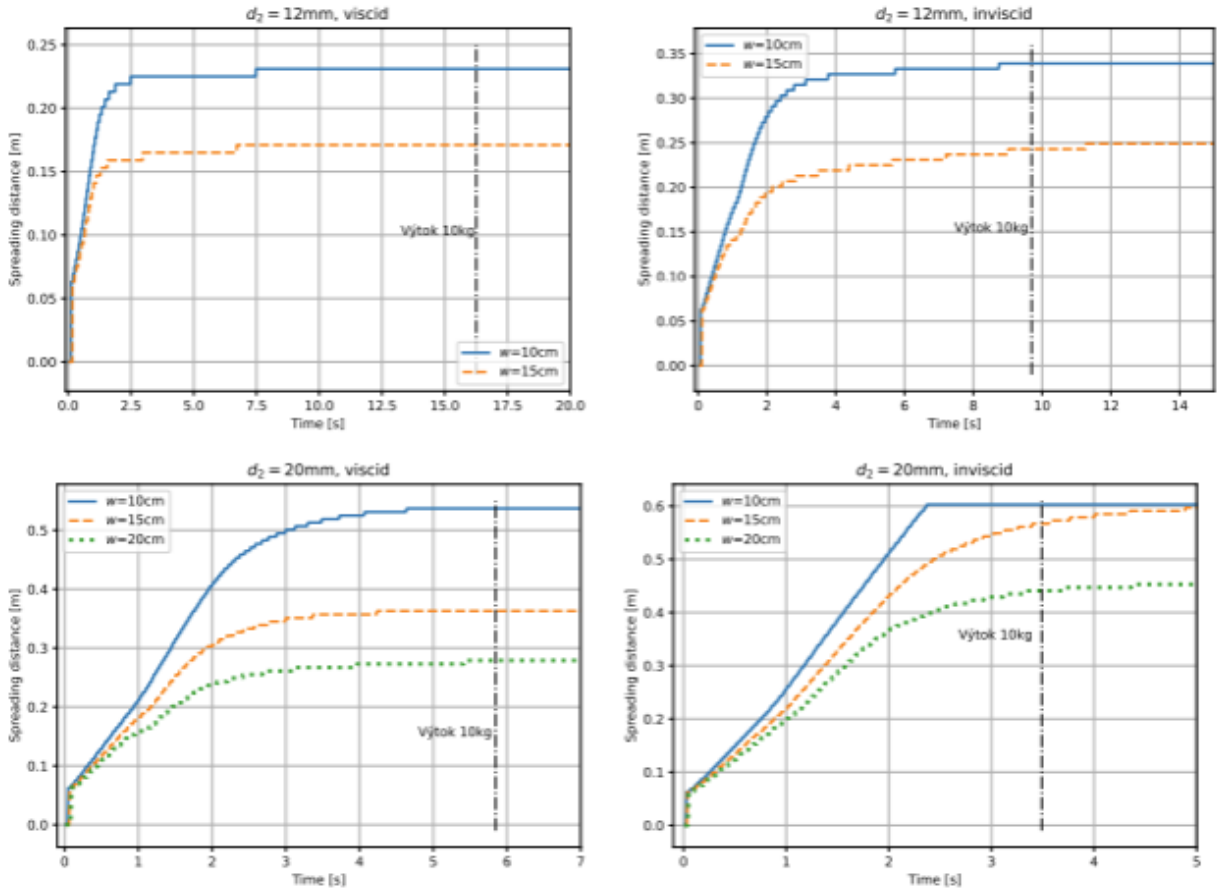

Figure 8 – Corium Spreading Distance as a Function of Channel Width

Finally, comparative calculations were made for varying nodalisations for the 20x60 cm channel variant (See Figure 1). Calculation was performed for inviscid variant with 20 mm opening and S2 corium composition.

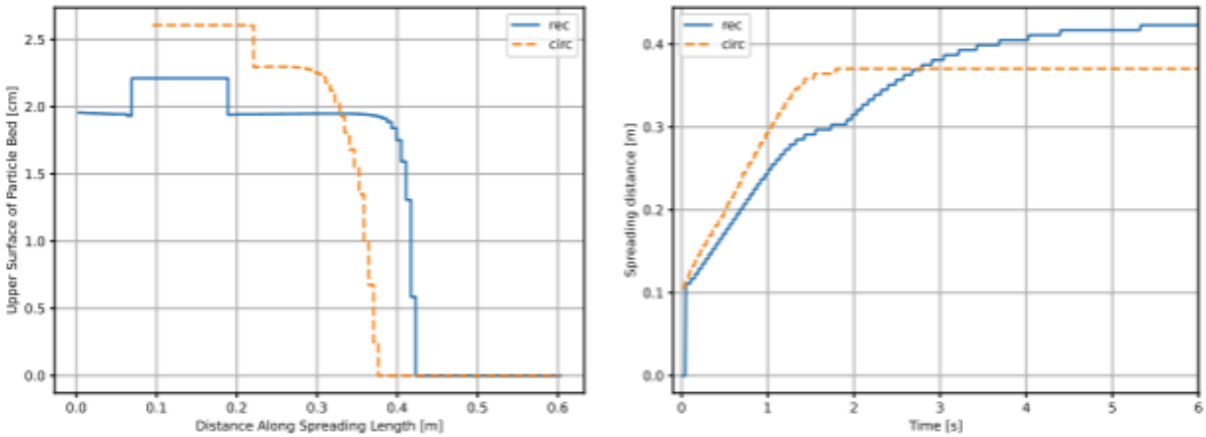

Figure 9 – Comparison Calculation for Rectangular and Concentric nodalisation

The proposed CANUT experiments assume the use of a fully oxidized UO2-ZrO2 melt. This system is characterized by a small temperature interval between solidus and liquidus. Major changes in material properties of the material under study therefore take place in a small temperature interval.

MELTSPREAD calculations are burdened by large uncertainties. The uncertainties apply more for small amounts of melt. This is related to the fact that, that the surface-to-volume ratio increases as the melt volume decreases. This introduces more uncertainty in the estimation of heat loss from the melt. For small quantities of melt, the temperature gradient at the melt surface and the neglect of crust formation in the simulation are also more pronounced. The uncertainty also increases with the duration of the spreading, again because heat loss from the corium has more time to take effect.

For channel dimensions of 20x60 cm, the total spreading area is already sufficient to avoid reflection at realistically achievable discharge rates from the cold crucible of the corium melt from the end of the channel. On the other hand, with a channel width of 20 cm, the 2D nature of the spillage cannot be neglected when the melt is discharged from a hole up to ø2 cm. For the lowest discharge rate of the corium from the cold crucible, the predicted resulting area under solidified melt is limited to an area of approximately 20x20 cm below the crucible.

3.3. ALLEGRO Core Catcher

Since the corium spill is a very dynamic process, the CFD program ANSYS Fluent was chosen for this calculation. The aim of this calculation was to simulate the spillage of corium after the melt plug rupture, followed by the actual discharge of corium first into the connecting shaft of the core catcher and then into the core catcher structure itself. Figure 10 illustrates a comparison between the two models used for the corium spreading simulation in the core catcher. In the figure, a volume with at least 50 % of the corium phase is visualized in the time sequence.

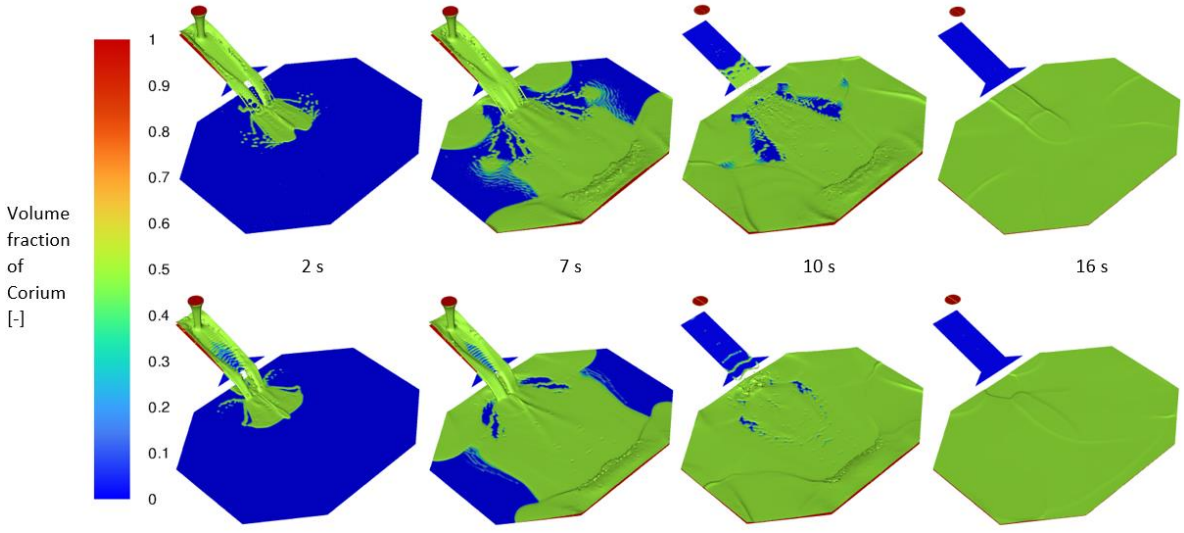

Figure 10. Corium Spreading Simulation in the Core Catcher (Top -VOF, Bottom – Eulerian)

Figure 11 shows the progress of the corium spill on the floor of the core catcher. Full flooding occurs at approximately 16 s from the start of the simulation for the VOF model and 18 seconds for the Eulerian model. For the VOF model the approximate simulation time of 0.01 seconds was found to be 1 minute and 6 seconds and approximate data size of solution .dat files was 330 MB.

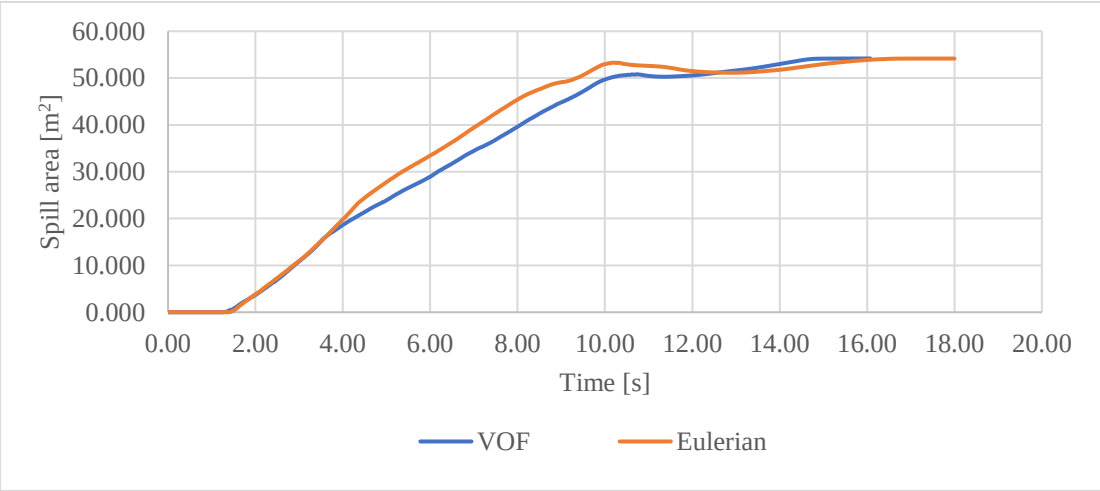

Figure 11. Graph of Corium Spreading on the Core Catcher Floor

For the Eulerian model VOF model the approximate simulation time of 0.01 seconds was found to be around 40 seconds and approximate data size of solution .dat files was 360 MB. Figure 12 illustrates a comparison between the two models used for the corium spreading simulation in the core catcher. In the figure, a total temperature is visualized in the time sequence.

Further simulations will continue with the Eulerian model, as it allows us to define several different phases that can be simulated.

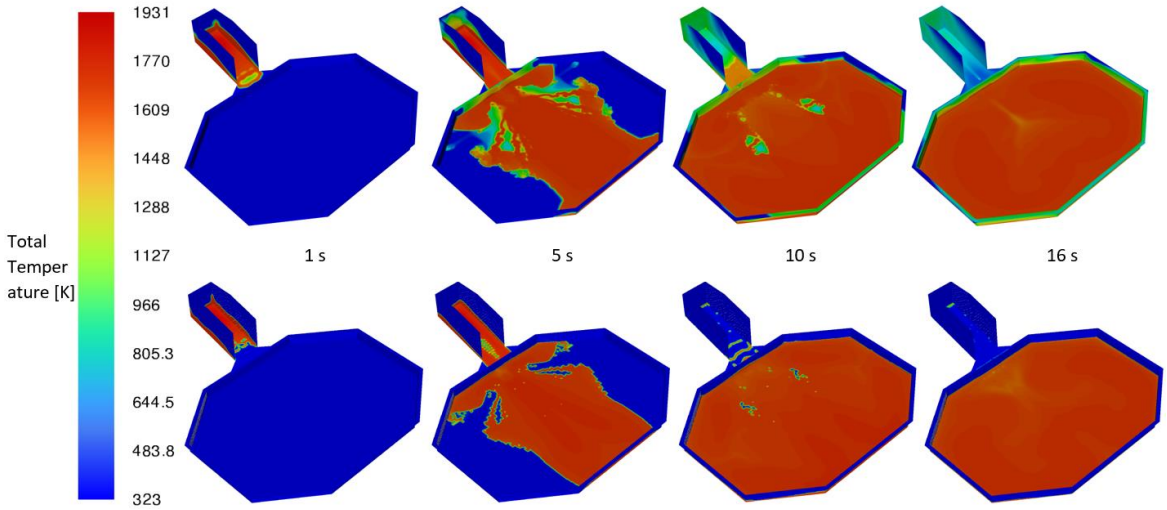

Figure 12. Temperature field in the Core Catcher (Top -VOF, Bottom – Eulerian)

CONCLUSIONS

The main conclusion of VVER 1000 Simulation is that it is important to delay the failure of the bottom of the reactor pressure vessel. The lower the decay heat, the greater the chance of subsequent melt retention on the floor. On the other hand, it is necessary to consider the effect of measures to delay RPV bottom failure on the spread-ability of the corium. These aspects will be considered in further analyses.

For the CANUT experiment simulations the final choice of the geometry of the channel depends a lot on whether the CANUT experiments can be done with the bottom opening of the cold crucible with at least ø2 cm diameter. If the effective diameter of the outlet opening is smaller, the spill area can be reduced. Another recommendation for the experiments can be to add appropriate material to the corium mixture to lower the viscosity of the final mixture, thus enabling better corium spreading in the channel.

For the simulation of the corium spill in ALLEGRO core catcher, the future use of Eulerian model will allow for a multiphase composition of the atmosphere-oxide corium-metallic corium composition to be defined and simulated. This Eulerian multiphase model will be used for the full simulation of corium spill, with the gradual addition of all, for now simplified features in the models described in this paper.

ACKNOWLEDGMENTS

The work carried out on the VVER-1000-like corium, including simulations of its spreadability and coolability assuming newly measured thermo-physical corium properties and taking into account the outcomes from the tests of its interaction with solid in-vessel structures was done under the auspices of the Technology Agency of the Czech Republic, programs THETA TK03020149 “Corium properties at high temperatures” and CANUT II PB_01_02_03 “Nuclear fuel behavior in severe accident conditions”. The work carried out on the ALLEGRO core catcher was done under the auspices of the Technology Agency of the Czech Republic, program TK01030116 ALLEGRO “Model of the core catcher system for CFD calculations”.

REFERENCES

1. M.T. Farmer, “Melt Spreading Code Assessment, Modifications, and Applications to the EPR Core Catcher Design,” Nuclear Engineering Division, Argonne National Laboratory, USA (2019)
2. I.S. Ye, et al., “Numerical investigation of the spreading and heat transfer characteristics of ex-vessel core melt,” Nuclear Engineering and Technology, 45 (1), pp. 21-28 (2013)
3. W.S. Yeon, et al., “CFD analysis of core melt spreading on the reactor cavity floor using ANSYS CFX code,” Nuclear Engineering and Design, 249, pp. 90-96 (2012)
4. S. Yamashita, T. Ina, Y. Idomura, H. Yoshida, “A numerical simulation method for molten material behavior in nuclear reactors,” Nuclear Engineering and Design, 322, pp. 301-312 (2017)
5. M. T. Farmer, “The MELTSPREAD Code for Modeling of Ex-Vessel Core Debris Spreading Behavior, Code Manual”, Argonne National Laboratory, USA (2023)
6. M. Ramacciotti, et al., “Viscosity models for corium melts” Nuclear Engineering and Design, 204, pp. 377-389 (2001)
7. S. Bakardjieva, et al., “Improvement of the European thermodynamic database NUCLEA”, Progress in Nuclear Energy, 52, pp 84-96 (2010)
8. M. T. Farmer, “The CORQUENCH Code for Modeling of Ex-Vessel Corium Coolability under Top Flooding Conditions Code Manual, Argonne National Laboratory, (2023).
9. M. Kotouč, et al., “Assessment of Ex-Vessel Corium Coolability in the Containment of the VVER-1000 Reactor as a Measure of Severe Accident Mitigation,” *Proceedings of the 2022 10th European Review Meeting on Severe Accident Research*, Karlsruhe, Germany, May 16-19, 2022
10. P. Zácha and V. Železný, “CFD modeling and sensitivity analysis of ex-vessel core melt process,”*Proceedings of the 18th International Topical Meeting on Nuclear Reactor Thermal Hydraulics (NURETH 2019),* Portland, USA, August 18-23, 2019
11. J. Komrska, et al., “Mesh Sensitivity Analysis of the CFD Model of the Core Catcher of the ALLEGRO Reactor”, *Proceedings of the 20th International Topical Meeting on Nuclear Reactor Thermal Hydraulics (NURETH 20),* Washington D.C., USA, August 20-25, 2023

NUCLEAR RESEARCH INSTITUTE

Overview of Ex-Vessel Severe Accident Scenarios Simulations at UJV Rez

ERMSAR 2024
Stockholm, 13-16 May

Jan Komrska
Tomáš Janda
Petr Vokáč

UJV Group
PEOPLE | INNOVATION | TECHNOLOGY

INTRODUCTION

- The aim of this presentation is to present work done by researchers from UJV Rez that concern mostly ex-vessel behavior of corium in various phases of a postulated severe accident scenario with reactor core melt down

- Presented work consists of:

  - Updated version of previous work done for VVER 1000/V320 ex-vessel scenarios with new versions of MELTSPREAD

  - MELTSPREAD simulation and preliminary evaluation of corium spreading experiments under preparation within CANUT project in cooperation with Research Centre Rez

  - Preliminary 3-D simulation of corium flow and cooling in a core catcher of a proposed GFR reactor demonstrator ALLEGRO using CFD software Ansys Fluent

UPDATES ON VVER 1000/V320 EX-VESSEL CORIUM COOLABILITY

- Simulation of corium spill in the VVER 1000/V320 reactor shaft and adjacent rooms using MELTSPREAD code

- The new version of the MELTSPREAD code contains mainly frictional losses of the corium against the walls and the heat exchange of the corium with the walls
  - no-slip condition at the interface of spreading corium and side walls
  - categorize molten zirconium as part of oxidic molten corium
    - Two major improvements with huge impact on corium spreadability

- The corium spill is considered successful when at least 50% of the corium leaves the reactor shaft (RS), while travelling through connecting shaft (CS) and moves to adjacent room to the reactor cavity

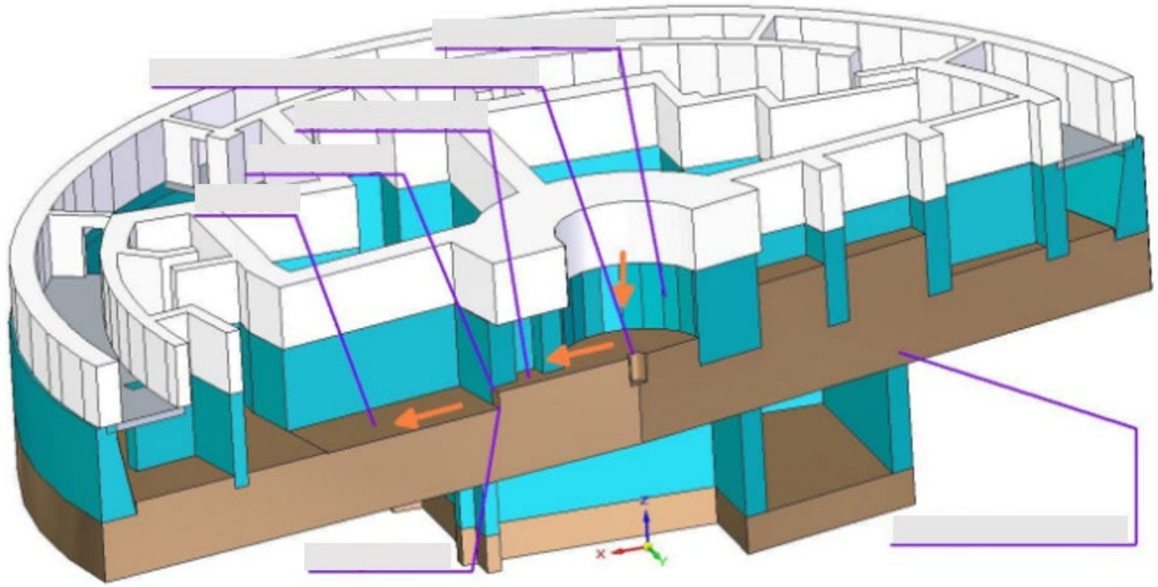

UPDATES ON VVER 1000/V320 EX-VESSEL CORIUM COOLABILITY

- In the calculations performed in 2020 there was a complete melt spill into adjacent room (GA302) for both SBO and G-LOCA scenarios

- Using the newer version of MELTSPREAD with the original aperture in the hermetic door, the corium spill was not successful for the SBO scenario
  - Larger aperture for corium spill into adjacent room was calculated
    - SBO scenario still unsuccesful
    - Only successful scenario was the G-LOCA with enlarged aperture.

- For these reasons, it is recommended that the aperture be enlarged even more and further analyses will be conducted for this new variant.

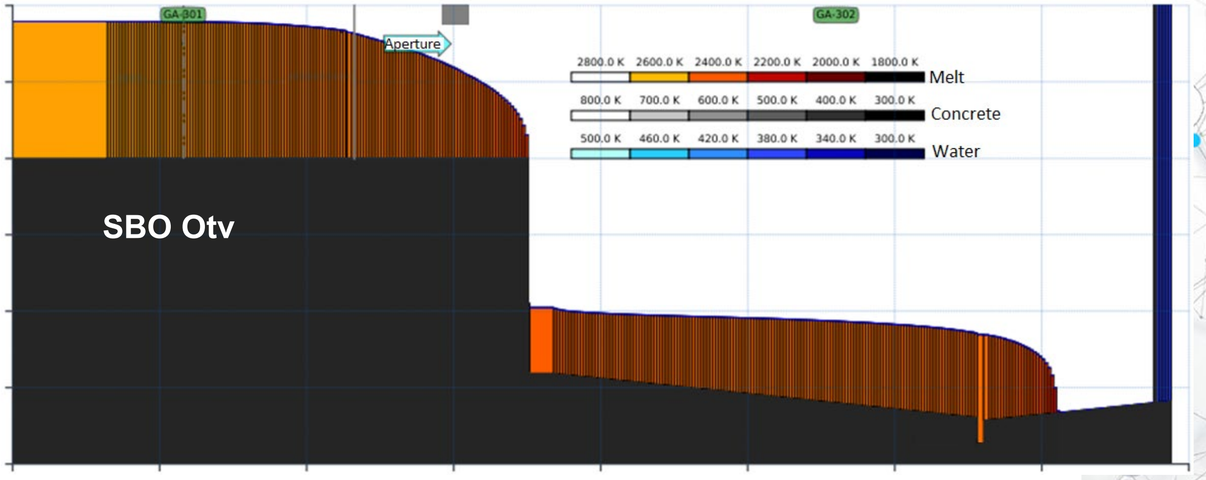

SA Scenario	Corium volume [m^3]			Corium volume [%]	
	RS+CS	GA302	Total	RS+CS	GA302
G-LOCA	12.21	6.86	19.07	64	36
G-LOCA Otv	8.63	10.12	18.75	46	54
SBO	23.17	0	23.17	100	0
SBO Otv	12.58	10.49	23.07	55	45

CANUT EXPERIMENTS PRETEST CALCULATIONS

- Small scale corium spreading experiments are under preparation in Research Centre Rez Cold Crucible facilities in the frame of czech national CANUT project

- Prototypical corium will be prepared in the cold crucible and poured into the predefined dry spreading channel

- The objective of the two experiments conducted with different composition of the corium will be:
  - 1. to test the transferability of the ROSAU experimental results to the evaluation of the VVER-1000 corium spill
  - 2. to check the repeatability of the CANUT small scale spill experiments (the experimental results should not be qualitatively different).

- Presented preliminary calculations of the CANUT spreading experiments were focused on finding the optimal geometry of the spreading channel and the initial parameters of the corium

- The calculations were carried out using the MELTSPREAD 3.01 program.

CANUT EXPERIMENTS PRETEST CALCULATIONS

- Detailed preliminary calculations for channel geometries of 10x60 cm, 15x60 cm and 20x60 cm were considered

- The weight of the corium will be about 10 kg, It is assumed that at least this amount of corium which can be estimated at 1.3 to 1.4 liters

- Following variants of corium compositions with defined ratio of U/Zr were calculated:
  - **S1: U/Zr(at) = 0.552**
    - According to the composition of thermite #16 used in the ROSAU experiments, after subsequent complete oxidation of the remaining Zr.
    - Typical BWR reactor severe accident scenario corium
  - **S2: U/Zr(at) = 1.252**
    - Typical VVER-1000 PWR reactor corium.

- For narrow 10x60 cm channel a rectangular geometry was chosen
- For wider 20x60 cm channel a concentric geometry of corium spill was chosen

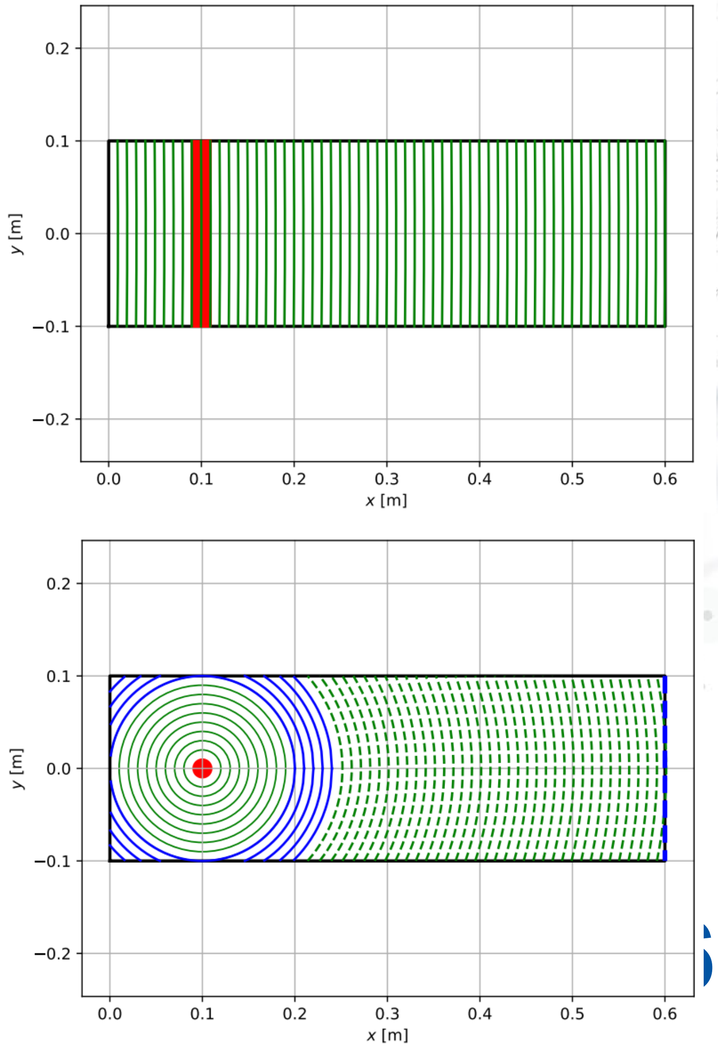

CANUT EXPERIMENTS PRETEST CALCULATIONS

- S1 and S2 corium in 10x60 cm rectangular geometry
- 11 calculations performed for various initial corium melt temperatures between solidus and liquidus temperatures
- Ramaciotti correlation used for melt viscosity calculation
- Full spreading of 60 cm achieved at highest temperatures nearing or above liquidus temperature

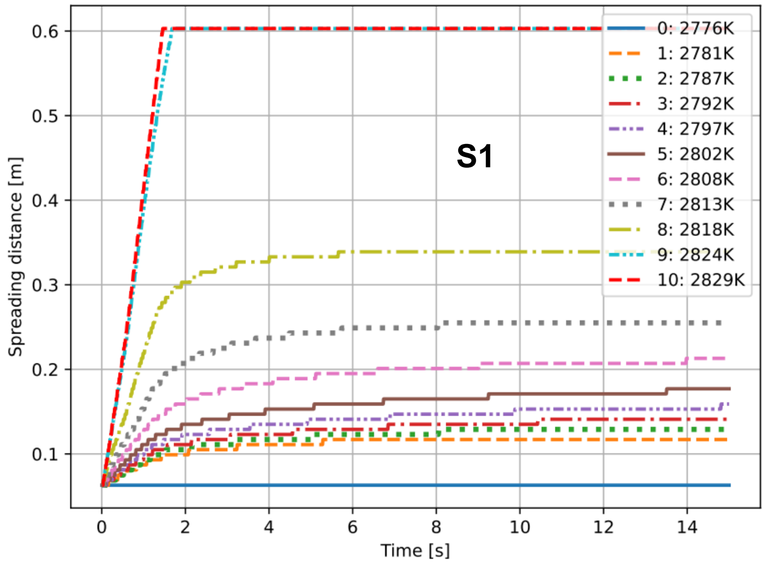

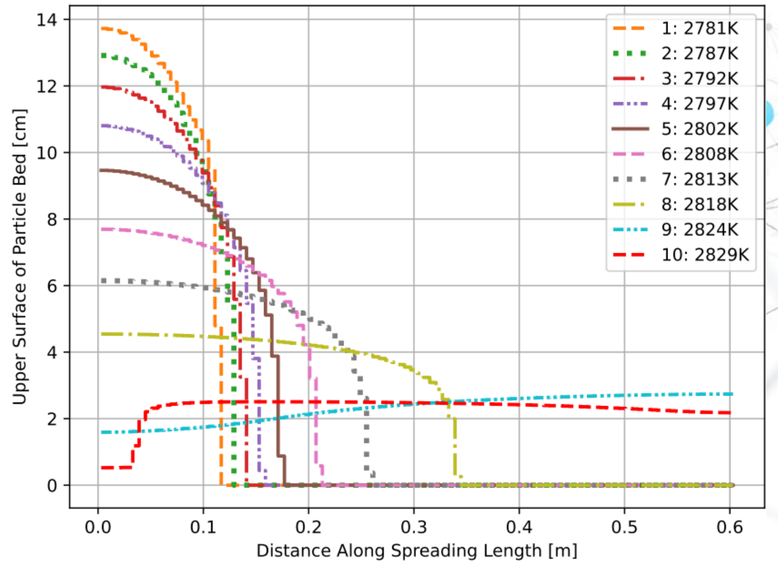

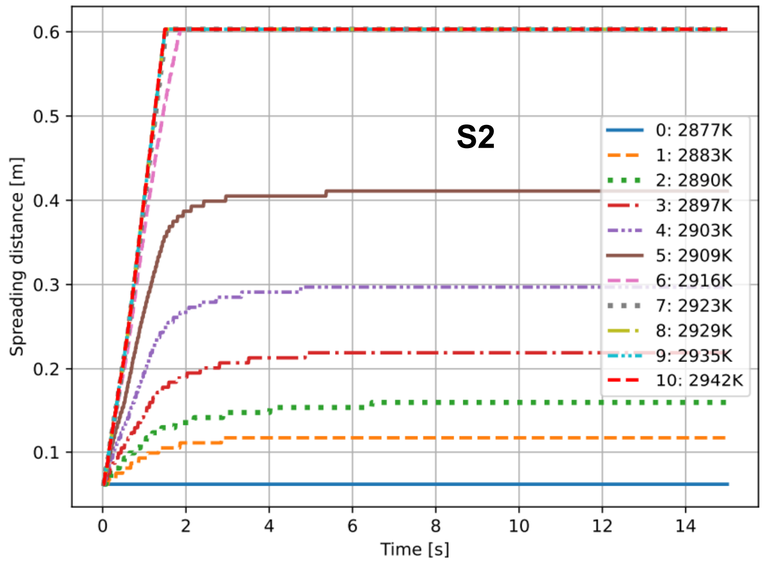

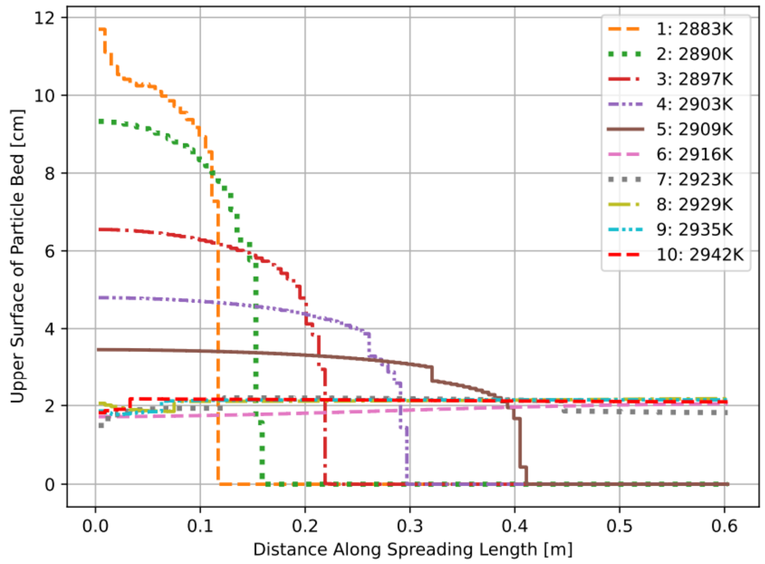

CANUT EXPERIMENTS PRETEST CALCULATIONS

- Additional pretest calculations with varying cold crucible outlet dimension (12 or 20 mm) for all rectangular geometries
  - Initial corium melt weight of 10 kg
  - Initial temperature at liquidus (~3000 K)
  - Full spread of 60 cm is not reached

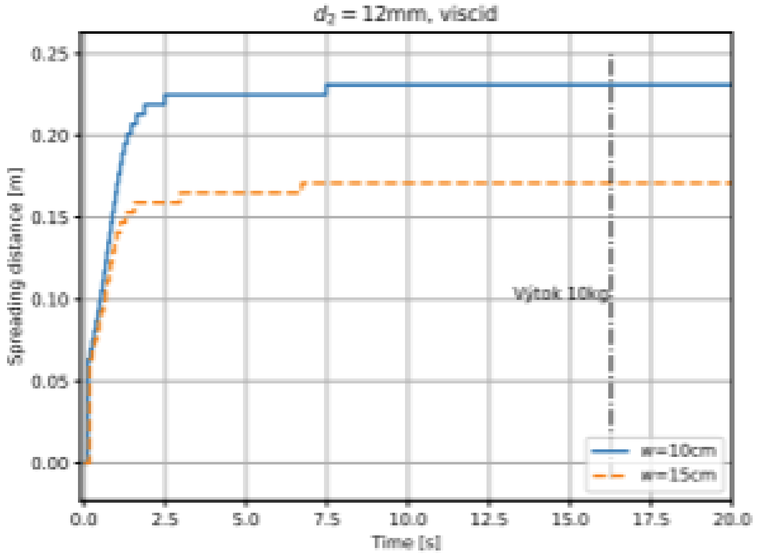

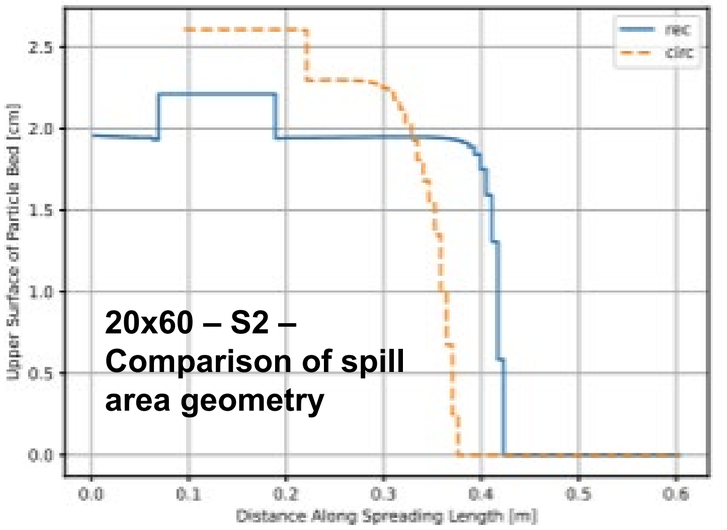

- Pretest calculations for comparison of rectangular and concetric geometries for 20x60 cm channel geometry
  - Full spread of 60 cm is not reached for either variant
  - Initial temperature at liquidus (~3000 K)
  - Concentric variant faced with reflecting corium „waves“ -> lower spreading

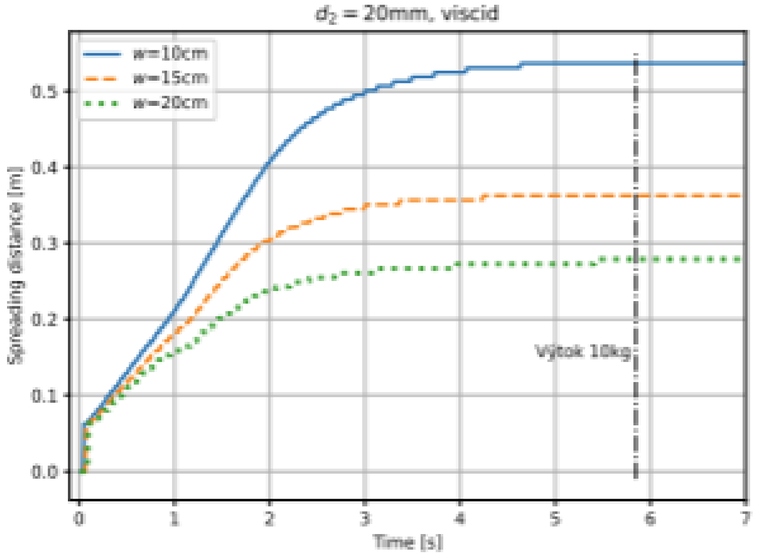

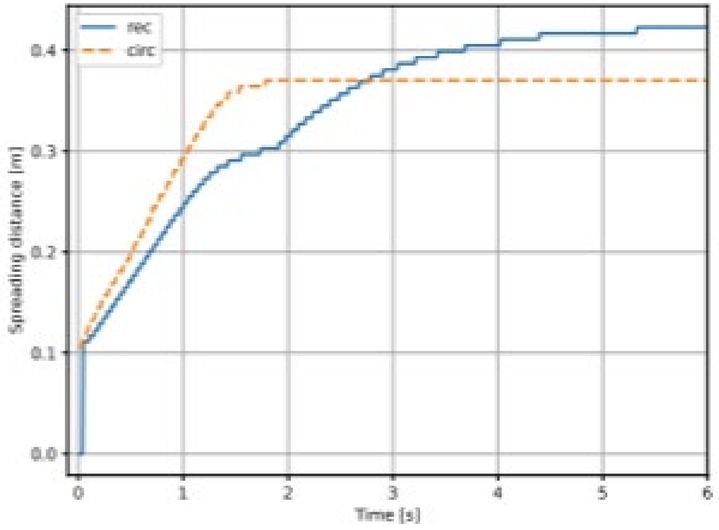

ALLEGRO CORE CATCHER CFD SIMULATION

- ALLEGRO is a gas-cooled fast reactor demonstrator unit. It is being developed by the V4G4 Centre of Excellence
- Main goal of the ALLEGRO demonstrator is to serve as an experimental platform for research and development of GFR
  - One of the systems developed specifically for ALLEGRO is a core catcher
- Presented simulation of the early ex-vessel phase of a severe accident in the ALLEGRO

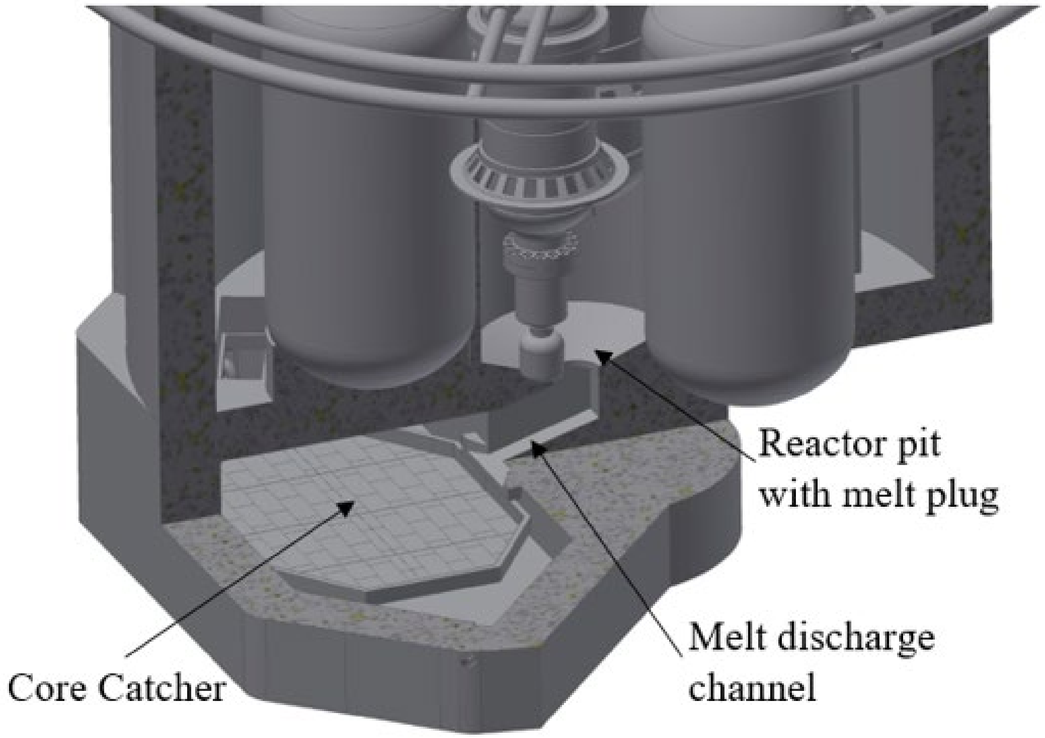

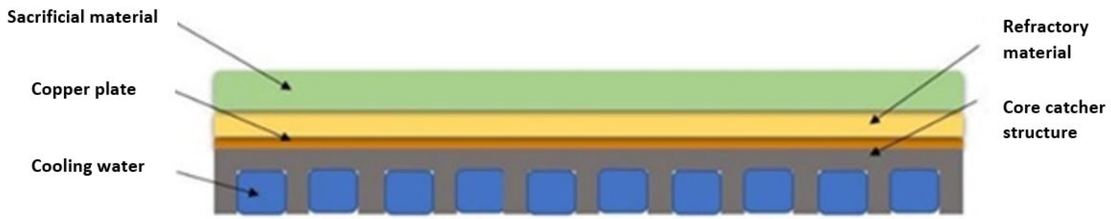

ALLEGRO CORE CATCHER CFD SIMULATION

- Simulations for verification of the core catcher functionality and to simulate the behavior of corium in the core catcher

- Initial and boundary conditions for the CFD simulation of Corium are taken from results of MELCOR and CORQUENCH simulations:
  - Viscosity, specific heat capacity as a function of temperature of corium
  - Corium made up of UO2, SS, Fe2O3 (geopolymer sacrificial material)

- Due to complexity of corium spreading simulation there were several simplifications used:
  - Constant properties of N2 atmosphere
  - Axisymmetry
  - Crust formation and ablation simulated as added heat transfer to floor and walls

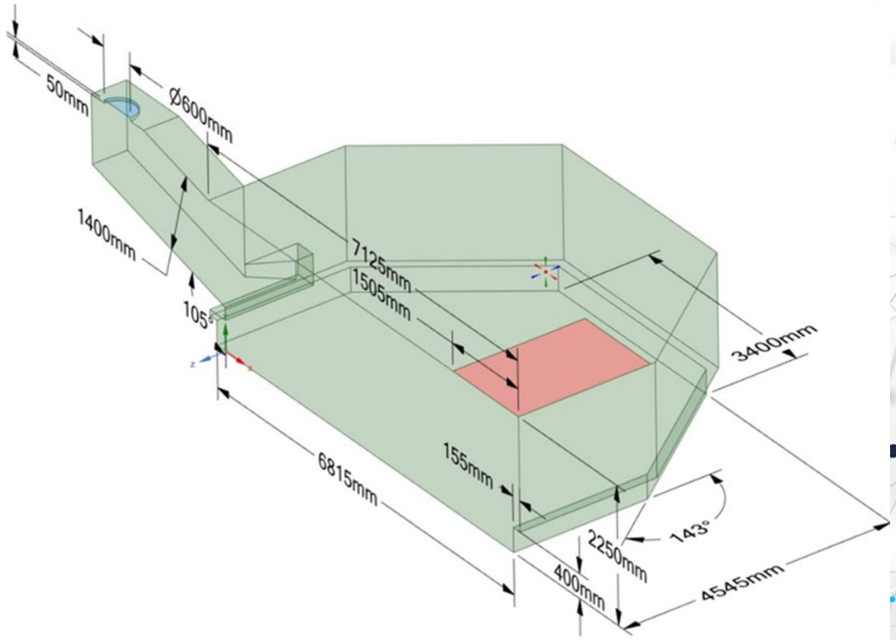

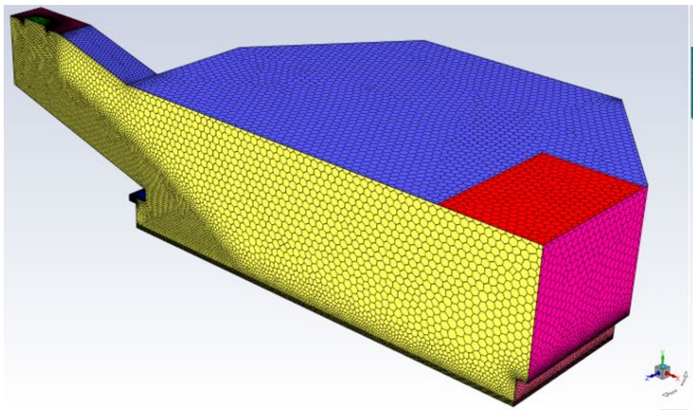

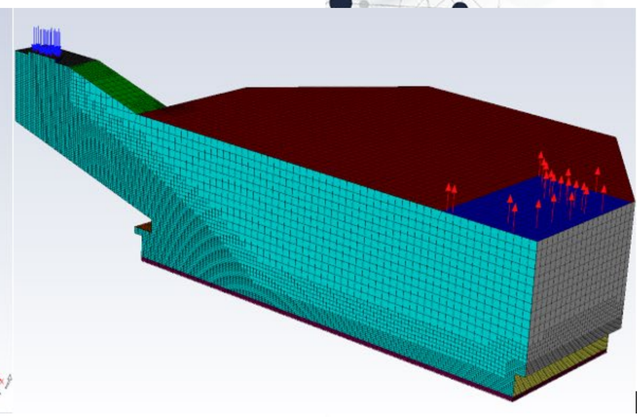

ALLEGRO CORE CATCHER CFD SIMULATION

- Simulation of corium spillage after melt plug rupture
  - Corium discharge through melt discharge channel onto the core catcher floor
- VOF and Eulerian VOF multiphase models used

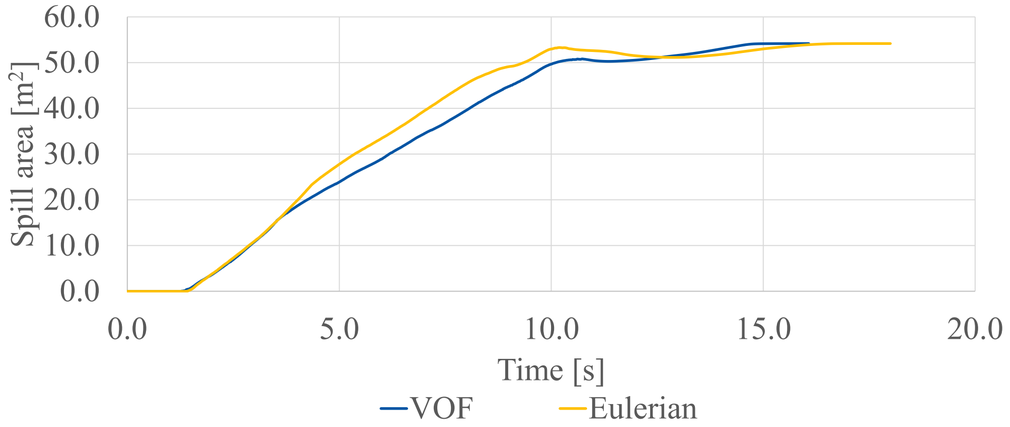

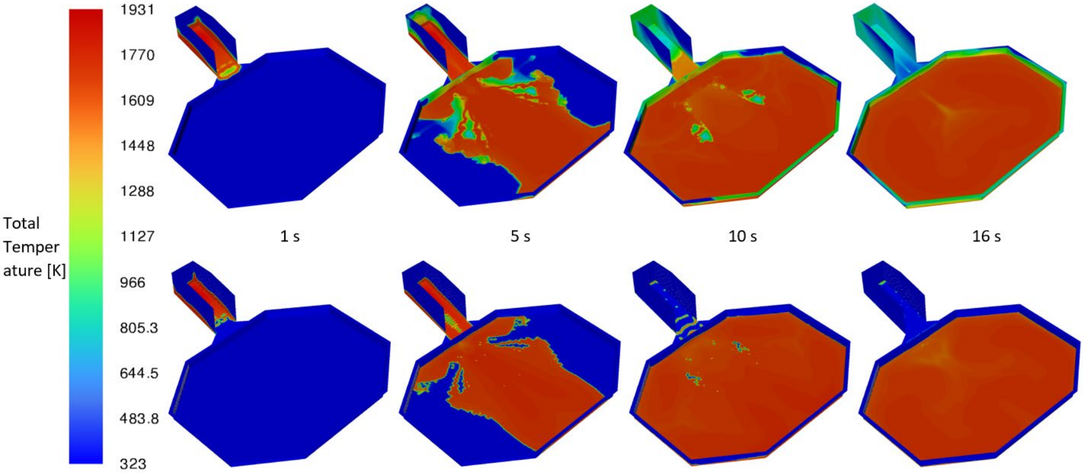

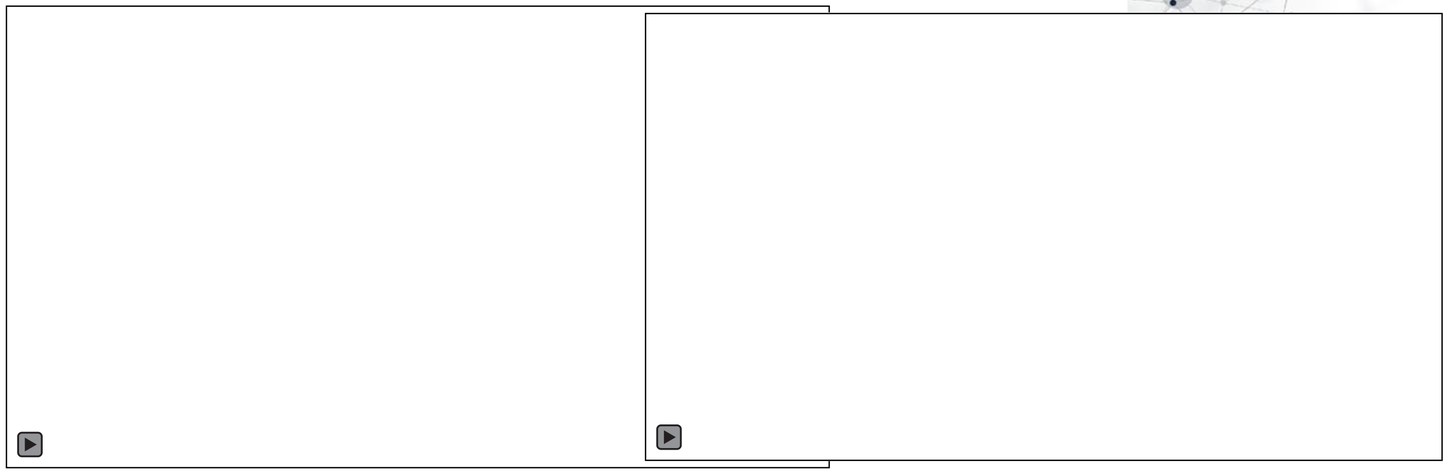

CONCLUSIONS

- The presented work is part of ongoing projects and work done by UJV in the field of ex-vessel severe accident scenarios

- **VVER 1000 Simulation:**
  - It is important to delay the failure of the bottom of the reactor pressure vessel
  - The lower the decay heat, the greater the chance of subsequent melt retention on the floor
  - Problems with corium cool-ability and retention if the corium is not spilled over the entire prepared spill area and has an extra high decay heat
    - Solution to the corium retention problem may be to place a geopolymer sacrificial concrete on the floor of the room, but this requires further study

- **CANUT Pretest Calculations:**
- Final choice of the geometry of the channel depends a lot on whether the CANUT experiments can be done with the bottom opening of the cold crucible with at least ø2 cm diameter
  - If the effective diameter of the outlet opening is smaller, the spill area is reduced
- Another recommendation for the experiments can be to add appropriate material to the corium mixture to lower the viscosity of the final mixture, thus enabling better corium spreading in the channel

- **Core Catcher simulations:**
  - Since the corium spill is a very dynamic process, the CFD program ANSYS Fluent was chosen for this calculation
  - Full flooding of the Core Catcher occurs at approximately 16 s from the start of the simulation for the VOF model and 18 seconds for the Eulerian model
  - Further simulations will continue with the Eulerian model, as it allows us to define several different phases that can be simulated

ACKNOWLEDGMENTS

- The work carried out on the VVER-1000-like corium, including simulations of its spreadability and coolability assuming newly measured thermo-physical corium properties and taking into account the outcomes from the tests of its interaction with solid in-vessel structures was done under the auspices of the Technology Agency of the Czech Republic, programs THETA TK03020149 “Corium properties at high temperatures” and CANUT II PB_01_02_03 “Nuclear fuel behavior in severe accident conditions”.

- The work carried out on the ALLEGRO core catcher was done under the auspices of the Technology Agency of the Czech Republic, program TK01030116 ALLEGRO “Model of the core catcher system for CFD calculations”.

Thank you for your attention !

Questions ?

NUCLEAR
RESEARCH
INSTITUTE

ÚJV Řež, a. s.
Hlavní 130, Řež
250 68 Husinec, Czech Republic

e-mail: jan.komrska@ujv.cz
www.ujv.cz

UJV Group
PEOPLE I INNOVATION I TECHNOLOGY

SIMULATIONS OF FLOAT DEBRIS QUENCHING EXPERIMENTS

Mitja Uršič, Tim Kelhar, Janez Kokalj, Matjaž Leskovar, Leon Cizelj
Jožef Stefan Institute
Jamova cesta 39, SI-1000 Ljubljana, Slovenia
mitja.ursic@ijs.si; timy.kelhar@gmail.com; janez.kokalj@ijs.si; matjaz.leskovar@ijs.si; leon.cizelj@ijs.si

Markus Petroff, Rudi Kulenovic, Jörg Starflinger
Institute of Nuclear Technology and Energy Systems (IKE), University of Stuttgart
Pfaffenwaldring 31, D-70569 Stuttgart, Germany
markus.petroff@ike.uni-stuttgart.de; rudi.kulenovic@ike.uni-stuttgart.de; joerg.starflinger@ike.uni-stuttgart.de

ABSTRACT

Recently, a series of tests have been performed at the FLOAT experimental facility (IKE, Germany). The purpose of the facility is to investigate the debris bed coolability during top-flooding or bottom-flooding conditions, at different initial debris bed temperatures, and at the presence of air inflow from the bottom. The aim of the air injection at the bottom of the debris bed is to simulate the possibility of the release of non-condensable gases during the molten corium concrete interaction. In the paper, two top-flooding FLOAT tests are presented, analyzed, discussed, and simulated with the MC3D computer code (IRSN, France). Selected tests were performed at similar temperatures of particles in the debris bed, similar water flow injection rates, and with or without air inflow. A 2D computational domain is developed and it is considered reasonable because of the rotational symmetricity of the FLOAT facility and because at the selected tests the preferential penetrating channel of water was in the central region of the debris bed. The simulation and test results are in good qualitative agreement. The observed discrepancy could be attributed to the establishment of other penetrating channel(s) at the edge of the debris bed that could not be covered with 2D simulations.

KEYWORDS
severe accidents, debris bed coolability, computer simulation

1. INTRODUCTION

Severe accidents in nuclear power plants can result in the reactor core degradation. Incapability of severe accident management strategies to ensure adequate decay heat removal may result in significant core melting with its relocation to the bottom of the reactor vessel causing further ablation and creeping. In case of lower pressure within the reactor vessel at the time of the loss of the reactor vessel integrity, the core melt is moved towards the reactor cavity in the form of one or several melt jets. In the case of wet cavity strategy, the melt jet fragments in contact with water, and finally after the fragment settlement the debris bed is formed. Due to elevated temperatures of the fragments, the debris bed may initially become dry. Later the quenching of the debris bed is caused by penetration of the surrounding water. In case of inadequate coolability of the debris bed, parts of the melt fragments may re-melt and form a melt cake. The melt cake possibly interacts further with the underlying concrete. The melt cake may also form due to incomplete jet

fragmentation in a cavity filled with a shallower level of water. During the melt interaction with concrete, non-condensable gases are formed. A safety-relevant question is whether the debris bed geometry is coolable in the presence of molten corium concrete interaction.

In the presented research, we are interested in the conditions inside the cylindrically shaped debris bed during the water penetration from the top and at the inflow of non-condensable gases at the bottom. First, several experimental investigations revealed that the initial temperature pattern of the debris bed governs the quenching process. In case of a homogeneous temperature pattern, the water could penetrate through several preferential channels [1, 2]. The existence of several penetrating channels of water is commonly seen during the penetration of water in a porous medium and is referred to as a Saffman-Taylor instability [2]. With heterogeneous temperature pattern, preferential penetrating channels exist in regions where the debris bed initial temperature is lower [2]. Further, the presence of several penetrating channels could be also attributed to the water flow downward blocked by the steam flowing upward [3]. Additionally, lower porosity near the debris bed edge promotes penetration of water [3]. Second, experiments revealed that the quenching occurs in two stages, i.e., a downward quenching stage (partial debris bed quenching during water penetrating downwards) and an upward quenching stage (relatively homogeneous debris bed quenching by water raising [4]). The quenching front velocity decreases with increasing debris bed temperature and decreasing debris particle diameter [1, 2]. Third, the presence of non-condensable gases inhibits quenching [5], [6].

Recently, a series of experiments have been performed at the FLOAT experimental facility (IKE, Germany) with a focus on the effect of the debris bed temperature and the air flow rate on the debris bed coolability [5]. Performed tests revealed, that in many cases, the preferential penetrating channel of water existed in the near-wall region where the porosity was higher, and the temperatures of the debris bed were lower due to nonuniform inductive heating and heat losses towards the environment. In some tests, the preferential penetrating channel was in the central region of the debris bed. Investigation on test repeatability showed important deviations in total quenching times at larger debris bed temperatures and higher air flow rates. Larger deviations were attributed to the existence of random effects favoring the formation of initial penetrating channels. Non-condensable gases reduce quenching capabilities and have smaller effects on the downward quenching stage duration than on the upward stage. Some tests were simulated with the COCOMO computer code (IKE, Germany) that aims to study the dry out and quenching behavior of debris bed [7]. For all conducted simulations, the water primarily penetrated downwards through a preferential penetrating channel developed at the central part of the debris bed. Experimentally seen preferential penetrating channels in the near-wall region and local reheating of the debris bed could not be obtained with the performed 2D simulations.

This paper is dedicated to the applicability of the MC3D computer code (IRSN, France) for predicting thermo-hydraulic conditions inside the debris bed during top-flooding conditions and in the presence of non-condensable gases. The MC3D computer code is devoted to fuel-coolant interaction simulations including debris bed coolability issues, and its ability to adequately cover both quenching stages and the presence of several penetrating channels was already demonstrated [8-10]. In this paper, the goal is to discuss the quenching front propagation simulation results in respect to the FLOAT test data. The 2D simulation results are presented and discussed in respect to the observed 3D nature of FLOAT tests. Here the aim is to use insights from simulations for understanding the processes during quenching.

2. FLOAT TESTS

Several tests have been performed at the FLOAT experimental facility (IKE, Germany) and reported [5, 7]. In this section, experimental data on two tests (F.32 and F.33) are presented and analyzed in more detail with some comparison with the trends from the other experimental tests.

2.1. Experimental facility and selected tests

As seen in Fig. 1, the FLOAT experimental facility enables top-flooding and bottom-flooding tests in combination with air injection [5]. In the top-flooding configuration, uniform distribution of water over the debris bed area is enabled with the use of a spray head. The injected rate is measured with a water flow meter having uncertainty of $\pm 4.7 \cdot 10^{-2}$ l/min. Air is uniformly injected at the bottom of the debris bed through ceramic spheres using the air flow control unit having maximal uncertainty of $\pm 1.8 \cdot 10^{-3}$ kg/min. At the top of the test section, a steam mass flow meter is installed with a maximal uncertainty of $\pm 4.5 \cdot 10^{-2}$ kg/s. The debris bed diameter and height are 200 mm and 300 mm, respectively. The debris bed is composed of stainless-steel spheres with a diameter of 6 mm and average permeability of $\sim 4.3 \cdot 10^{-8}$ m^2 (applying the Ergun model [10]). It is volumetrically preheated by the inductive coil. Temperatures within the debris bed are measured with 42 thermocouples. Those thermocouples are placed on selected positions at seven different heights (equidistantly between 20 mm and 260 mm), at three different radial locations (0 mm, 50 mm, and 90 mm), and at six different angular locations (between 0° and 300°). Three more thermocouples are in the central position 20 mm below (within the layer of ceramic spheres), on the top of the debris bed, and 20 mm above the debris bed. The maximal uncertainty of thermocouples measurement is ±2.8 K for temperatures up to 700°C. The test section is insulated to minimize thermal losses.

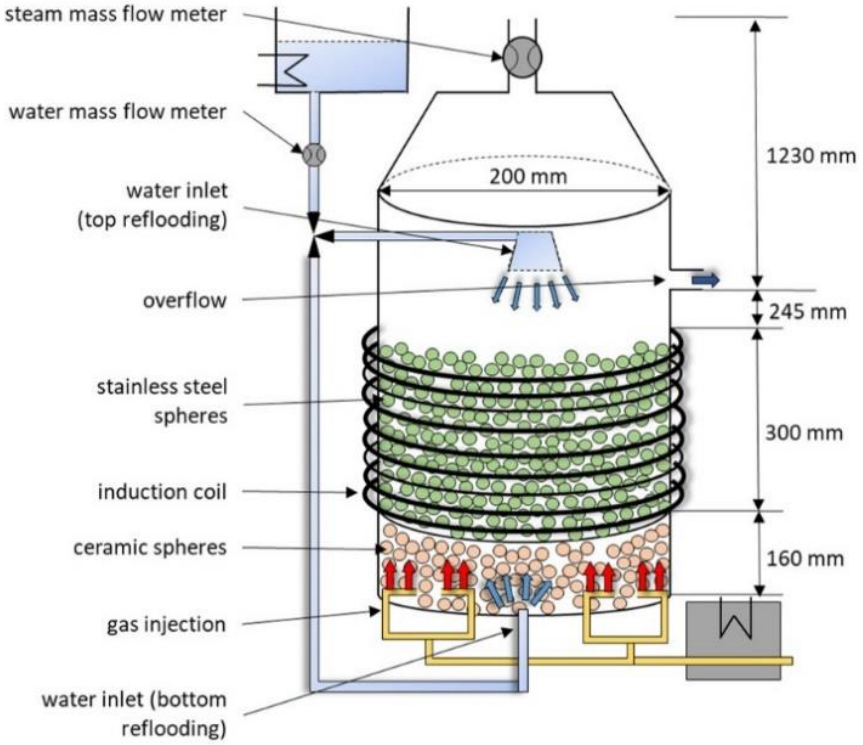

Figure 1. Schematic presentation of the FLOAT experimental facility.

Table I gives basic information on the selected top-flooding F.32 and F.33 tests. In both tests the 7 mm ZrO_2 ceramic spheres were used (average permeability of $\sim 5.8 \cdot 10^{-8}$ m^2). As seen in the table the key difference is in the air flow rate, which was provided only in the F.32 test. To minimize thermal losses, the injected air was preheated to 100°C [5]. The flow rate is defined to correspond to the gas measurements during the COMET L3 oxide melt concrete interaction experiment [5]. The initial debris bed temperatures of selected experiments were the highest among performed experiments [5].

Table I. Initial and boundary conditions for the F.32 and F.33 tests.

		F.32	F.33
Debris bed	Mass (kg)	44.2	44.1
	Initial average temperature (°C)	501	515
Water	Flow rate (l/min)	4.3	4.5
	Average temperature (°C)	88	88
Air	Flow rate (kg/min)	0.18	0
	Temperature (°C)	100	N.A.

2.2. Analysis with discussion

Fig. 2 shows the quenching front propagation for both tests. The time of quenching at the specific location is defined as the time when the corresponding thermocouple within the debris bed was cooled to the water's saturation temperature (with a considered threshold of 1°C). If a later increase in the thermocouple's temperature is seen for more than one time step it is considered for redefining the quenching time.

In Fig. 2 the downward and upward quenching stages are clearly seen. The minor increase in the total quenching time at the test with air inflow cannot be attributed only to the lower water flow rate and the lower initial average temperature (see Table I). Namely, the analyses of 21 FLOAT tests clearly showed that the total quenching time and its standard deviation noticeably increase with increasing debris bed temperature, i.e., due to increased internal heat to be removed during the quenching process, and increasing air flow rate, i.e., due to increased friction force on a penetrating channel(s) of water [5]. More specifically, for the F.24 and F.25 tests performed at similar initial average temperatures as the F.32 and F.33 tests, the presence of air inflow significantly increased the total quenching time from 179 s to 245 s [5]. Although part of the increase is attributed to the lower water flow rate for the test with air injection (6.5 l/min vs. 5.4 l/min), the increase could be related to the presence of air inflow as well. Thus, the discrepancy in the total quenching time between the experimental observation and the common expectation might be related to the experimentally seen trend on the standard deviations. For tests performed at initial average temperatures around 365°C and water flow rates around 6.9 l/min, the standard deviation was assessed to be around 8 % for tests without air inflow and 16 % for tests with an air flow rate of 0.18 kg/min [5]. Standard deviations were attributed to random effects favoring the formation of preferential penetrating channels [5].

As shown in Fig. 2, at the initial period of the downward quenching stage the upper part of the debris bed is quenched in a wider area. From there the water penetrates through a preferential penetrating channel established around the center of the debris bed in a narrower area. Later another penetrating channel closer to the edge of the debris bed is established around the angle with lower initial temperature of stainless-steel spheres. The establishment of another penetrating channel and the potentially partial or total redistribution of the water flow might relate to the seen temporary decrease of the quenching front propagation velocity. This might be promoted by higher initial stainless-steel spheres temperatures in the center of the debris bed. Similar was seen for the F.24 (without air inflow) test where the quenching front propagation during the downward stage was slowed down [5]. Further at the F.25 (with air inflow) test the quenching propagation was stopped for around 30 s and was reestablished from the bottom once the ceramic spheres were flooded by water from the penetrating channel(s) established near the debris bed edge [5].

In Fig. 2, the transition from the downward to the upward quenching stage could be marked with the time of quenching of thermocouples at an elevation of 20 mm. The observed time delay in quenching of the lowest thermocouples should be importantly attributed to the difference between the time of the central

thermocouple cooled by the water of the preferential penetrating channel during the downward stage and the time necessary for the water to flood the ceramic spheres and the lower part of the debris bed during the upward stage.

As seen in Fig. 2, during the upward quenching stage the quenching front propagation velocity is approximately constant. During this stage all still non-quenched thermocouples placed at the same height are quenched at similar times, the span being up to 20 s. The time span is larger for the test with air inflow and might be also attributed to the water foaming due to air injection. An additional penetrating channel was formed during this stage for the test with air inflow as indicated by two earlier quenched thermocouples placed at the edge and positioned at 180°. Further, for both tests quenching is slower at the edge of the upper two-thirds of the debris bed than in the middle. This could be attributed to the gas flow established closer to the debris bed edge and so inhibiting the cooling of the debris bed in that area. Nevertheless, the quenching behavior could be approximated as 1D for both tests.

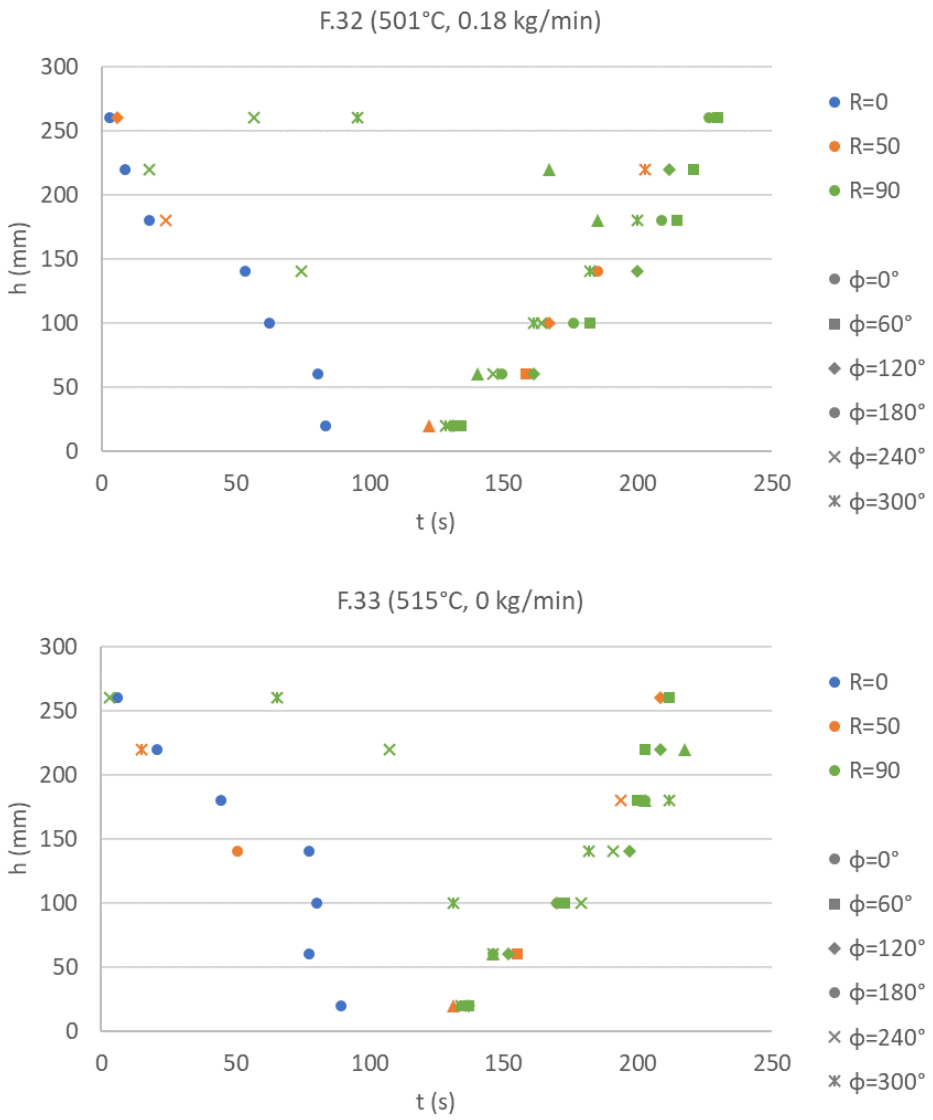

Figure 2. Quenching front propagation for the F.32 (top) and F.33 (bottom) tests. Legend: R for radial direction in mm and Φ for angle.

3. SIMULATIONS WITH MC3D

The simulation results for the F.32 and F.33 tests are shown and discussed. Simulations are performed with the MC3D computer code version 3.10 [9, 10]. For the simulations, the 2D geometry is selected and considered reasonable because of the rotational symmetric setup of the test section (see Fig. 1) and because at the selected tests the main preferential penetrating channel of water was in the central region of the debris bed (see discussion in Section 2.2). It is worth noting that the F.33 test was also simulated in 2D geometry with the COCOMO computer code [7].

3.1. Calculation model

Fig. 3 shows the applied computational domain. The domain is divided into the support zone, debris bed zone, and upper zone. Dimensions of the domain and zones correspond to the experimental setup up to the location of overflow (see Fig. 1).

The applied 2D mesh is axial symmetrical and cylindrical coordinates are used. The mesh size of 20 x 166 cells is selected. The selection of mesh is based on convergence analyses where we followed the integral steam production at different mesh sizes until the mesh did not give any greater differences in the simulation results compared to the selected mesh. In the radial direction, the cell width is set to 5 mm. The heights of the cells in the support, debris bed, and upper zones are set to 10 mm, 2.5 mm, and 10 mm, respectively.

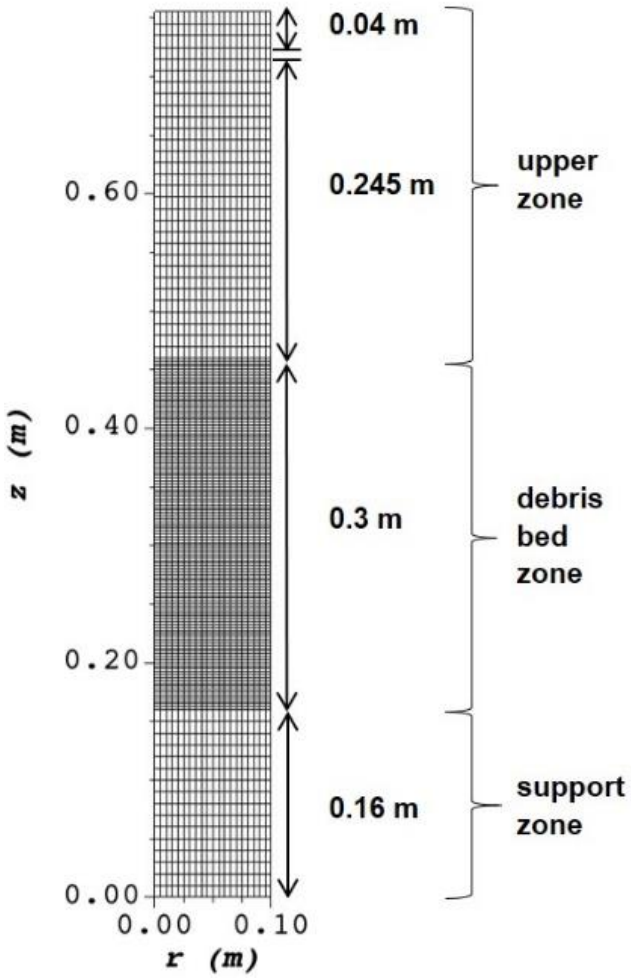

Figure 3. Computational model.

The initial conditions in the zones are set as follows:

- The air is initially considered for the upper zone.
- In the debris bed zone stainless steel spheres of 6 mm in diameter are considered. Porosity is defined by preserving the mass of the stainless-steel spheres (see Table I). Additionally, the porosity shall vary and increase in radius for the area close to the test section edge [11]. Thus, for the cells, except the one at the edge, the porosity is set to 0.37. At the edge cell, the porosity is set to 0.63. It is worth noting that the average porosity of FLOAT tests was in the range from 0.37 to 0.42 [5]. Further, the debris bed zone was divided into 21 subzones based on the 42 thermocouple locations. Fig. 4 shows the initial temperatures of subzones set based on the thermocouple's values. The temperatures are similar for both tests. The effect of thermal losses towards surroundings is clearly visible.
- In the support zone glass spheres of 7 mm in diameter are considered. Glass has similar volumetric heat capacity as ceramic used in the tests. The porosity is the same as in the debris bed zone, i.e., the porosity is set to 0.37 in the inner cells and to 0.63 at the edge cell. The initial temperature for the upper 40 mm of the support zone is set based on the thermocouple measurements at that location to 197°C (F.32) and 212°C (F.33). The temperature at the bottom 120 mm of the support zone is set to 85°C based on the temperature provided by air flow control unit.

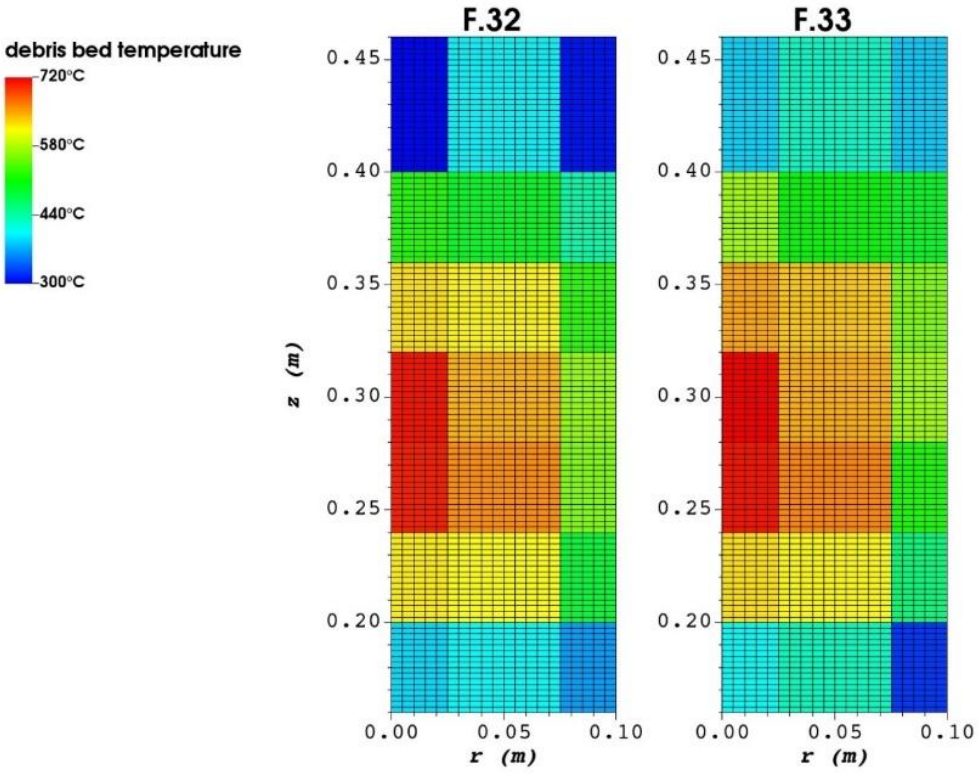

Figure 4. Temperatures within the debris bed zone for the F.32 (left) and F.33 (right) tests at the beginning of simulations.

The boundary conditions are set as follows:

- The water inflow is set as a boundary condition on the upper edge of the computational domain. The water in the tests is gravitationally driven and thus the injection velocity is set by considering the difference in the height between the computational domain and the water tank in the

experimental facility (see Fig. 1). In the tests the spray head had a diameter of 90 mm. To consider radial water spreading the water inflow radius is set to 60 mm. The same inflow radius was also applied for the COCOMO simulations [7]. The water mass flow rates and temperatures are set based on the test values (see Table I).

- The gas (i.e., steam and air) outflow is enabled through an area between 60 mm and 100 mm on the upper edge of the computational domain. The pressure boundary condition is set to 0.1 MPa.
- The air inflow is set as a boundary condition on the entire bottom edge of the computational domain. The experimentally set flow rates and temperatures are considered (see Table I).
- In the experiment the water overfilling above the debris bed is limited by an overflow (see Fig. 1). The overflow in the simulations is considered by applying the pressure boundary condition set to 0.1 MPa at the side close to the top of the upper zone.

In the MC3D computer code phases are described with the Eulerian approach [2, 8, 10]. A porous media is considered for the debris bed if its volume fraction is above 0.4. The Schulenberg and Müller friction model is used for diphasic flow inside the porous media in the performed simulations. The heat transfer in the convection regime is computed by the convection correlation for a single drop. For the film boiling, the Sakurai correlation is considered. The modelling depends on a flow map, which is based on the relative volume fraction of gas and liquid.

3.2. Simulation results with discussion

Fig. 5 shows simulated timeseries of the temperature and water distribution inside the debris bed zone. The calculated temperature in the debris bed zone decreases in the presence of water. Hereafter the quenched area within the debris bed zone stands for locations with temperatures below 100°C.

In Fig. 5, areas significantly filled only with water are seen for both tests during the downward quenching stage. For the case without air inflow the propagation of the preferential penetrating channel of water in the central part of the debris bed zone is clearly seen and is synchronized also with the quenched area propagation. This is opposite to the test results where another penetrating channel was developed later near the edge of the debris bed (see Fig. 2). The quenched area in the simulation is wider in the upper part of the debris bed as was also seen in the tests by some of the quenched thermocouples at a radius of 50 mm earlier during the downward stage (see Fig. 2). For the case with the air inflow the area filled with water is synchronized with the quenched area only at the beginning of the simulation and it seems to be physically limited in downward direction with the subzones of higher initial temperatures (see Fig. 4). The effect of temperature jump between subzones on simulation results might be numerical. Nevertheless, it is worth mentioning that a similar stop in quenching propagation, but at lower debris bed locations, was also seen at the F.25 test that was performed at similar initial temperatures and with air inflow [5]. In the simulation of the F.32 case the quenching area propagation velocity in this initial period is lower compared to the F.33 case. After that, the initial area of accumulated water starts to disintegrate by the counter-current flow of gas and its entrapment. The result shows the complexity of two-phase flow modelling in porous media in the presence of counter-current conditions that might also depend on the selection of friction models. The disintegration of the wider area of water promotes the progression of the quenched area in the radial direction in the upper part of the debris bed and reduces the width of the leading edge of the quenched area in the central part. Such a process might be a potential trigger for other penetrating channels in the test. Overall, the change between the downward and upward stages occurs later in the case with air inflow.

As seen in Fig. 5, during the upward quenching stage quenching is delayed at the edge of the debris bed zone. As shown by the figure, this could be attributed to the establishment of the gas flow at the edge of the zone decreasing the cooling performance. Even more, stronger gas flow at the edge of the debris bed zone that is heated up at the lower part of the debris bed is heating the upper part as observed at the initial times

of the simulations. A similar delay in the quenching time at the same height during the upward stage was seen also in tests (see Fig. 2). In the tests and simulations with a developed preferential path at the center of the debris bed such delay could be attributed to the lower porosity at the edge of debris bed and wider preferential penetrating channel at the upper part of the debris bed both affecting the gas flow direction.

In Fig. 5 strains with a higher fraction of water (relative fraction of around 0.5) are seen in the quenched part of the debris zone with otherwise relatively homogenous lower fraction of water (relative fraction of around 0.3) for both simulation cases. The strains are initiated either by local disintegration of the preferential water channel caused by counter-current flow of gas or more globally by vaporization around the interface of rising water. The strains penetrating towards the hotter part of the debris zone disappear due to the water vaporization. The impact of observed strains on the main simulation conclusions is assessed to be negligible.

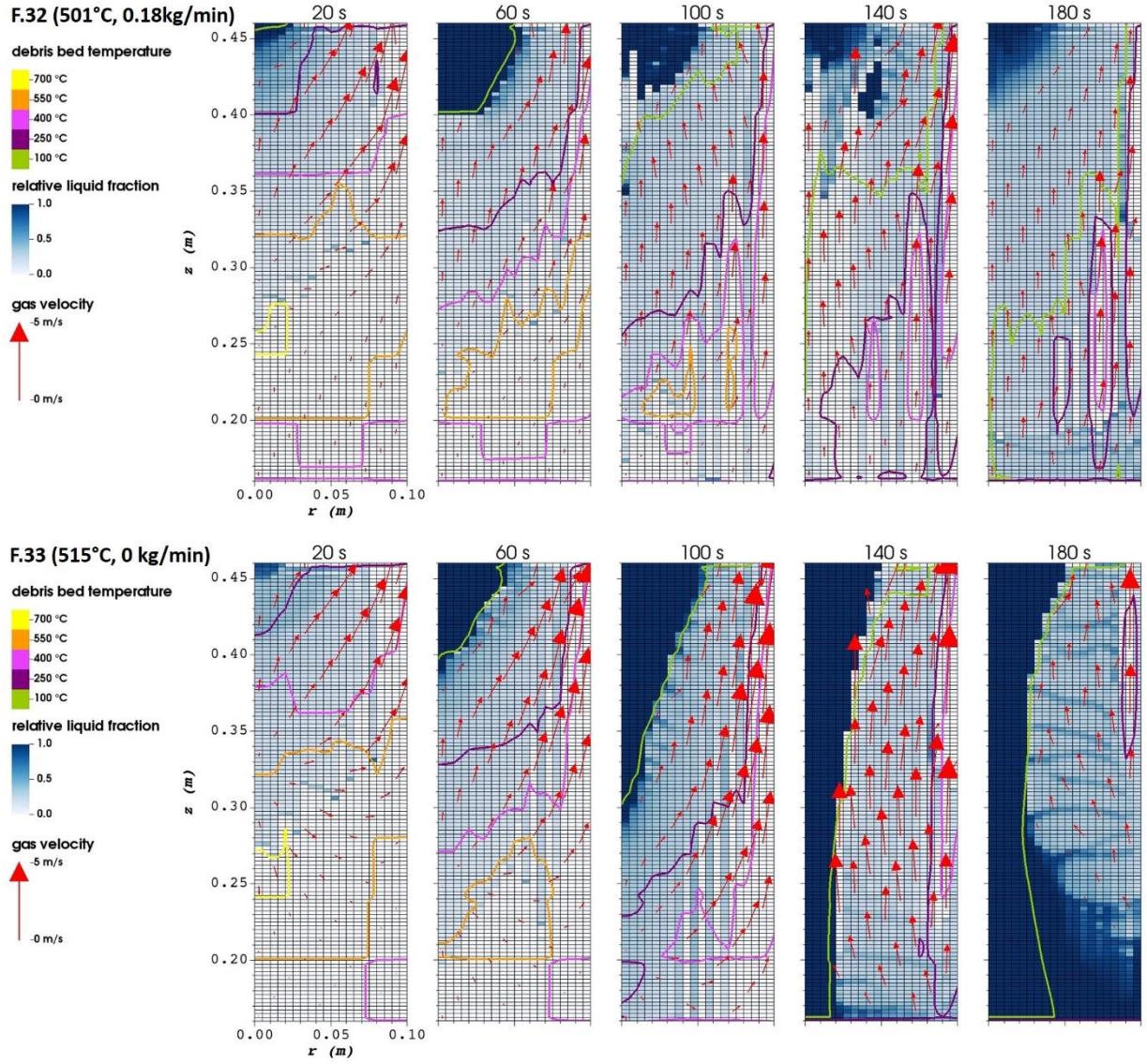

Figure 5. Snapshots of the F.32 (top) with gas injection and F.33 (bottom) without gas injection test simulations at various times within the debris bed zone. Legend: gas velocity (vectors), relative liquid fraction (field), and debris bed temperature (curves).

Finally, in Fig. 6 we show a direct comparison of the quenching front propagation between the test values (Fig. 2) and the simulation results (Fig. 5). As seen in the figure, the simulation results are followed at the same radial locations as in the tests and are shifted in time to be synchronized with the quenching time of the first thermocouple within the debris bed. With this time shift we compensate the differences in time for the water flow reaching the upper part of the debris bed and potential differences in time before the beginning of the water penetration into the debris bed.

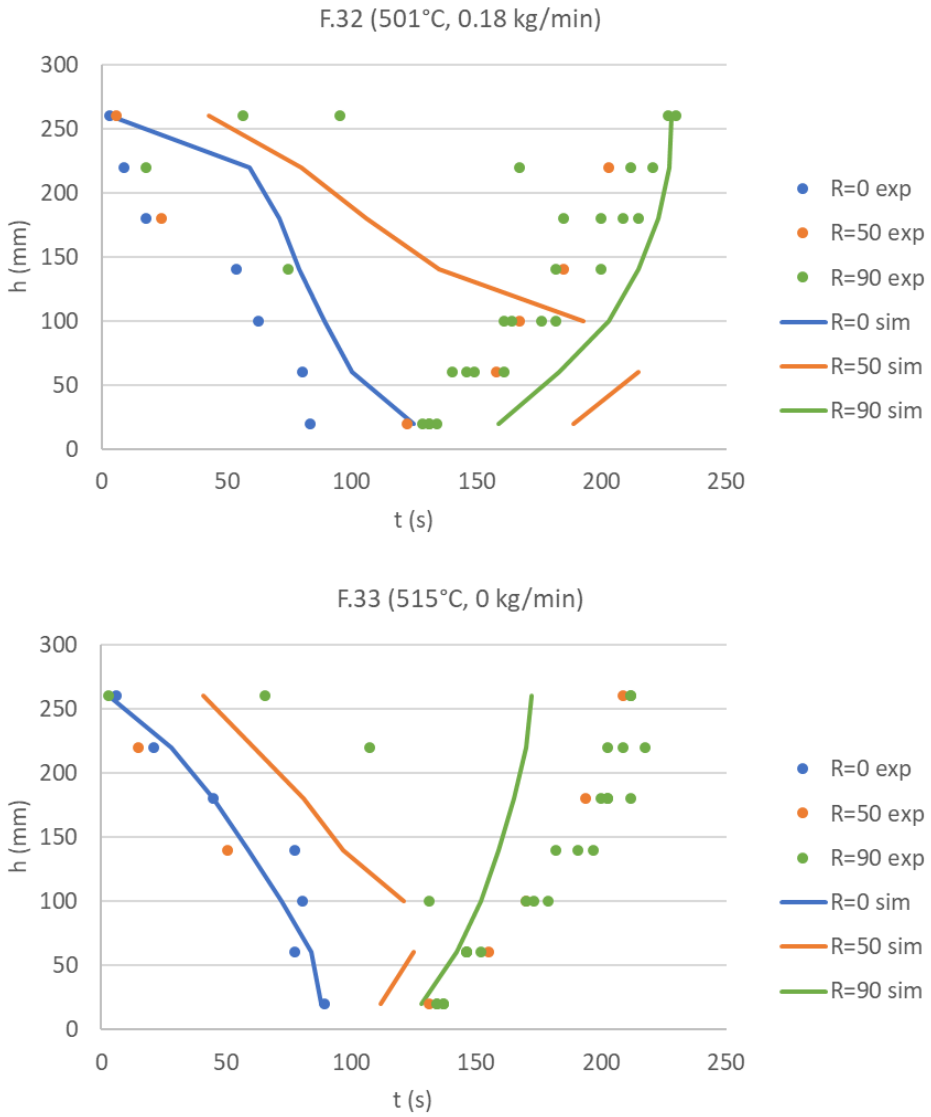

Figure 6. Comparison of simulation and test results for quenching front propagation for the F.32 (top) and F.33 (bottom) tests. Legend: R for radial direction, experimental results (dots), and simulation results (line).

In Fig. 6, the effect of the air inflow on the total quenching time increase is seen in simulations. The simulated and test total quenching times are in good agreement for the case with air inflow. For the case without air inflow, the simulated total quenching time is underestimated, if compared to the experimental

value. However, following the discussion in Section 2.2, the observation in the simulation is in line with the observed trend for similar other FLOAT tests, and thus part of the simulation underestimation might be attributed to the experimentally shown higher standard deviation in total quenching times at higher debris bed temperatures.

As seen in Fig. 6, the simulated quenching front propagation velocity during the downward quenching stage is in better agreement for the test without air inflow. For the test with air flow, the observed decrease in the progression velocity occurs at different times and the potential reasons are already discussed above. The progression velocity agrees once the disintegration of the water by the counter-current flow of gas starts in the simulation. The simulated quenching front propagation velocity during the upward stage is in good agreement with experiments for both cases at the initial period of the water level rise. As discussed above the average propagation velocity for the F.33 test without air inflow could be assessed as overestimated when compared to the other FLOAT tests.

To summarize, the simulation results with the MC3D code are in quantitative agreement with the test results, i.e., both quenching stages are covered. Further, the simulations showed the influence of the established gas flow on the inhibition of the quenching front propagation as generally observed also in experiments. Considering the observed uncertainties for the total quenching time in the FLOAT tests, the simulation results are in reasonable qualitative agreement with the tests. Additional mesh refinements, more detailed consideration of porosity near the wall and improvement of the initial temperature of the debris bed would quantitatively affect the results. Indeed, the recent detailed numerical investigation showed the sensitivity of the penetrating channels to the permeability, the initial temperature, the temperature heterogeneity, and the boundary conditions with the overlying water pool [2]. Finally, in the test observed penetration channel(s) near the edge of the debris bed could not be reproduced with the 2D modelling approach, as azimuthal dependences cannot be described. Thus, for situations with dominating non-central penetration channel(s) the 3D modelling approach shall be applied.

4. CONCLUSIONS

A safety-relevant question is whether the debris bed geometry is coolable in the presence of molten corium concrete interaction. Recently performed FLOAT tests (IKE, Germany) can be considered as a relevant source of experimental data supporting investigations related to the debris bed coolability in conditions of top-flooding and with simultaneous bottom injection of air. Some tests were already used for the validation of the COCOMO computer code (IKE, Germany). In the presented research also the applicability of the MC3D computer code (IRSN, France) is shown.

The comparison of test data and the simulation results proved that the simulations could provide valuable insights into the experimentally seen particularities. The MC3D simulations show that, in general, the quenching front propagation is well reproduced except for the experimentally seen periods of slower water propagation that could be attributed to one or several contributions, i.e., establishment of other penetrating channels near the debris bed edge, water channel disintegration by the counter-current flow of gas and inhibiting of water propagation in regions of higher debris bed temperatures. Finally, the simulations showed the influence of the established gas flow on the quenching front propagation. The total quenching time is prolonged with the presence of air inflow.

In the simulations, the existence of other penetrating channels might be seen only if a 3D calculation model is applied. The establishment of the penetrating channel(s) would be primarily affected by the initial temperature distribution inside the debris bed and might be promoted by the differences in the debris bed porosity.

ACKNOWLEDGMENTS

The Jožef Stefan Institute authors acknowledge:

- The financial support from the Slovenian Research Agency (research core funding No. P2-0026).
- The financial support from the state budget by the Slovenian Research Agency and the Slovenian Nuclear Safety Administration (project No. V2-2375).
- IRSN (France) and the MC3D development team.
- University of Stuttgart, Institute of Nuclear Technology and Energy Systems who have developed the original FLOAT test data. The results of the FLOAT tests are available at the Jožef Stefan Institute within the written agreement.

REFERENCES

1. Ginsberg, T., et al., *Transient core-debris bed heat-removal experiments and analysis. [PWR; BWR]*, in *Conference: International meeting on thermal nuclear reactor safety, Chicago, IL, USA, 29 Aug 1982; Other Information: Portions of document are illegible*. 1982: United States. p. Medium: ED; Size: Pages: 16.
2. Villarreal Larrauri, A., *Analysis and modeling of ex-vessel underwater cooling processes of debris bed and molten corium pool in interaction with concrete*. 2020, Université de Lorraine: Université de Lorraine, France. p. 219.
3. Starflinger, J., et al., *Recent numerical simulations and experiments on coolability of debris beds during severe accidents of light water reactors.* Nuclear Engineering and Design, 2015. **294**: p. 153-160.
4. Rashid, M., et al., *Quenching Experiments: Coolability of Debris Bed.* Nuclear Technology, 2013. **181**(1): p. 208-215.
5. Petroff, M., R. Kulenovic, and J. Starflinger, *Experimental Investigation on Debris Bed Quenching With Additional Non-Condensable Gas Injection.* Journal of Nuclear Engineering and Radiation Science, 2022. **8**(4).
6. Nayak, A.K., B.R. Sehgal, and A.V. Stepanyan, *An experimental study on quenching of a radially stratified heated porous bed.* Nuclear Engineering and Design, 2006. **236**(19-21): p. 2189-2198.
7. Petroff, M., R. Kulenovic, and J. Starflinger, *Experimental and Numerical Investigation on Debris Bed Quenching with Additional Injection of Non-Condensable Gas.* Proceedings of 2021 28th International Conference on Nuclear Engineering (Icone28), Vol 2, 2021.
8. Kokalj, J., et al., *Modelling of debris bed reflooding in PEARL experimental facility with MC3D code.* Nuclear Engineering and Design, 2018. **330**: p. 450-462.
9. Meignen, R., et al., *The challenge of modeling fuel–coolant interaction: Part I – Premixing.* Nuclear Engineering and Design, 2014. **280**: p. 511-527.
10. Raverdy, B., et al., *Capabilities of MC3D to investigate the coolability of corium debris beds.* Nuclear Engineering and Design, 2017. **319**: p. 48-60.
11. Benenati, R.F. and C.B. Brosilow, *Void fraction distribution in beds of spheres.* AIChE Journal, 1962. **8**(3): p. 359-361.

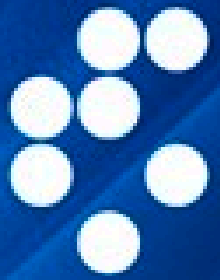

Jožef Stefan
Institute

R4

Reactor
Engineering
Division

Simulations of FLOAT debris quenching experiments

Mitja Uršič, Tim Kelhar, Janez Kokalj, Matjaž Leskovar, Leon Cizelj, Markus Petroff, Rudi Kulenovic, Jörg Starflinger

ERMSAR2024, KTH Royal Institute of Technology, Stockholm, Sweden, May 13-16, 2024

Motivation

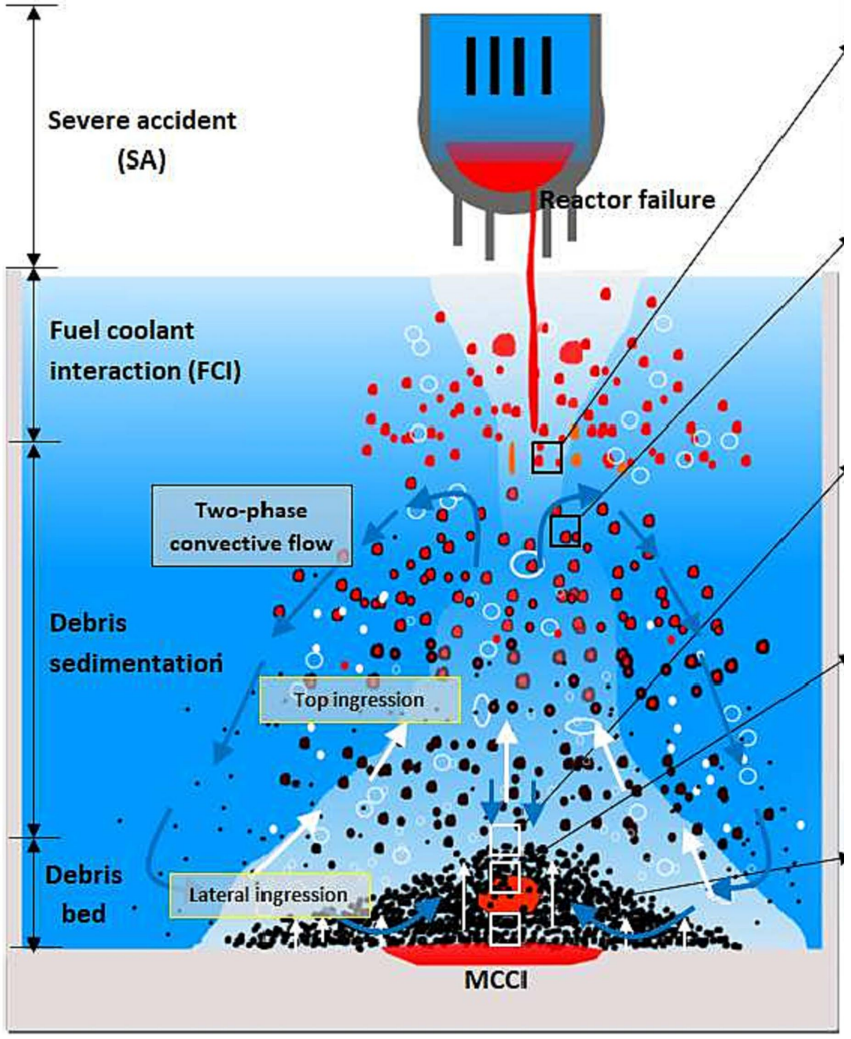

Adapted from M. Modak, V. V. Nirgude, H.S. Park, Y.J. Choi, M.R. Seo, Experimental investigation of quenching phenomena in high temperature conical debris bed – Part 1: MONET tests, Nuclear Engineering and Design, Volume 402, 2023, 112102.

Outline

FLOAT tests by IKE

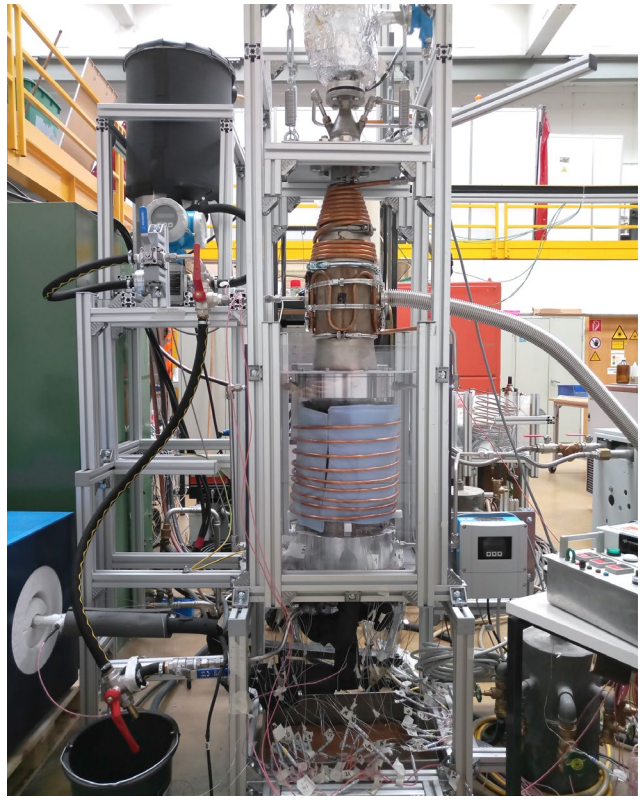

Adapted from M. Petroff, R. Kulenovic, J. Starflinger, Experimental Investigation on Debris Bed Quenching With Additional Non-Condensable Gas Injection. Journal of Nuclear Engineering and Radiation Science, 2022. 8(4).

FLOAT simulations by JSI

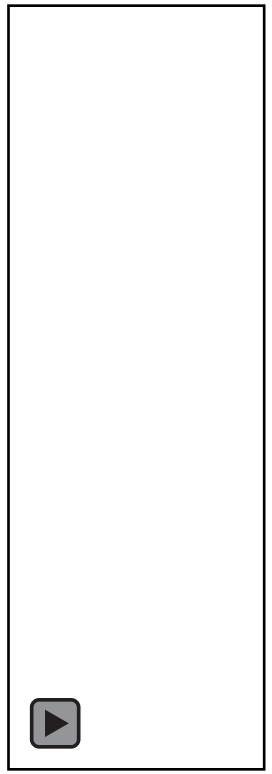

Adapted from T. Kelhar, MsC thesis defense, 2023.

Introduction

- Quenching in top-flooding conditions occurs in two stages
  - downward quenching stage (partial debris bed quenching during water penetrating downwards)
  - upward quenching stage (relatively homogeneous debris bed quenching by water raising)
- Quenching velocity decreases with
  - decreasing debris size
  - increasing debris bed temperature
  - increasing non-condensable gas rates

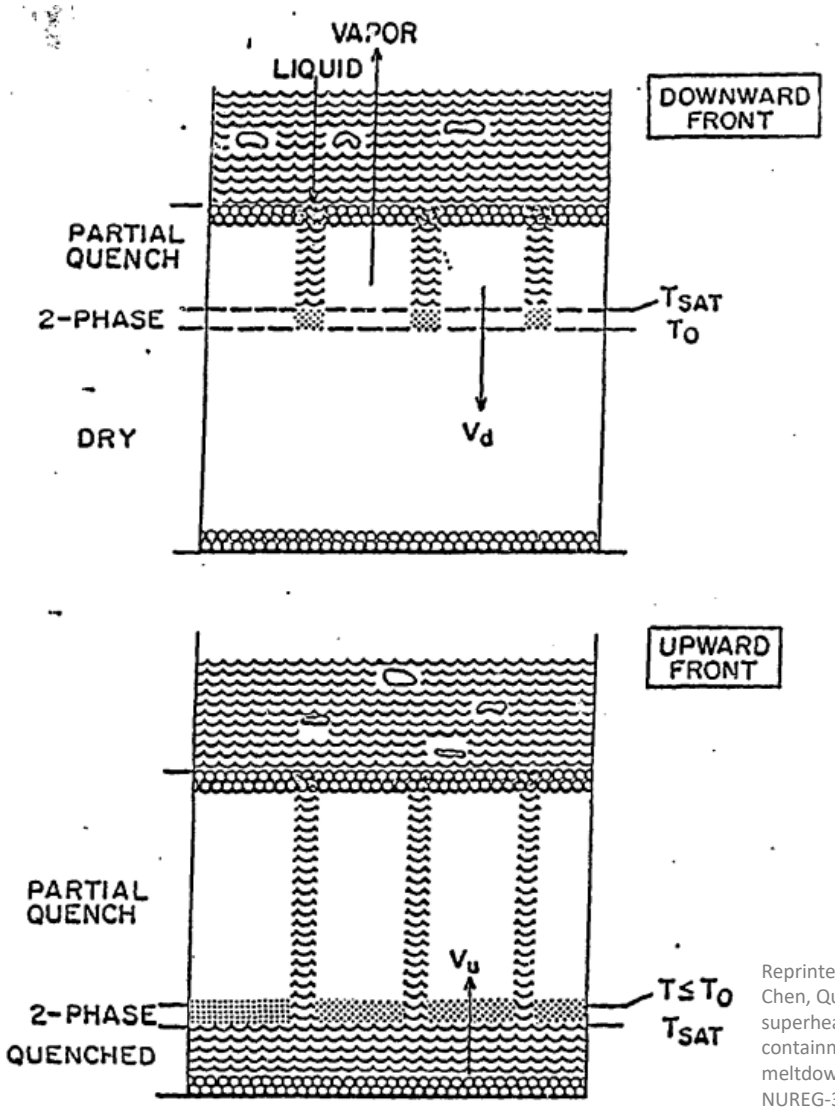

Reprinted from T. Ginsberg, J.C. Chen, Quench cooling of superheated debris beds in containment during LWR core meltdown accidents, BNL-NUREG-34655.

Introduction

Effect of initial debris bed temperature pattern

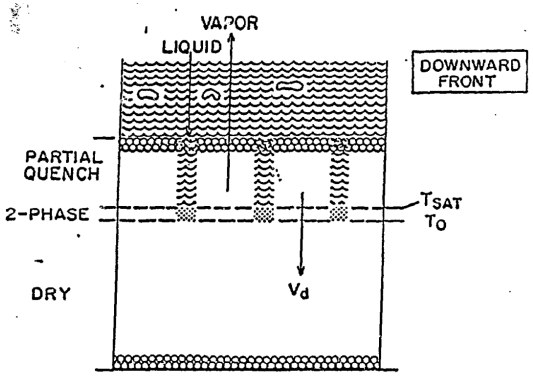

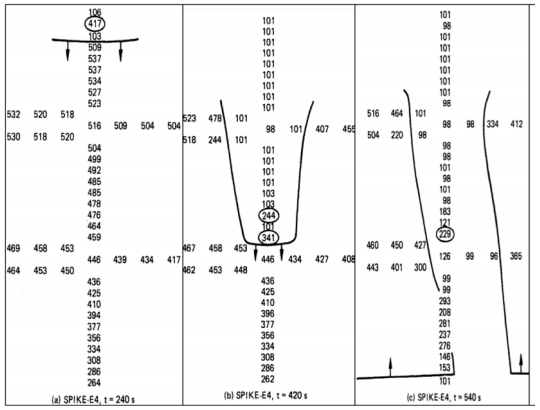

Adapted from T. Ginsberg, J.C. Chen, Quench cooling of superheated debris beds in containment during LWR core meltdown accidents, BNL-NUREG-34655.

Adapted from D.H. Cho, D.R. Armstrong, S.H. Chan, On the Pattern of Water Penetration into a Hot Particle Bed, Nuclear Technology, vol. 65, no. 1, pp. 23–31, Apr. 1984.

Effect of steam flow and porosity

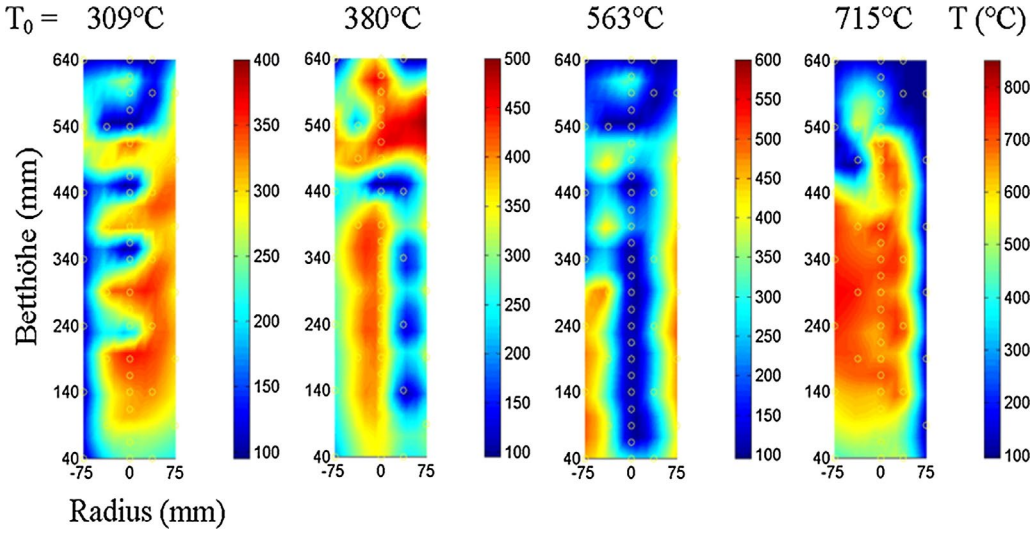

Reprinted from J. Starflinger, M. Buck, A. Hartmann, R. Kulenovic, S. Leininger, S. Rahman, M. Rashid, Recent numerical simulations and experiments on coolability of debris beds during severe accidents of light water reactors, Nuclear Engineering and Design, Volume 294, 2015, Pages 153-160.

FLOAT in general

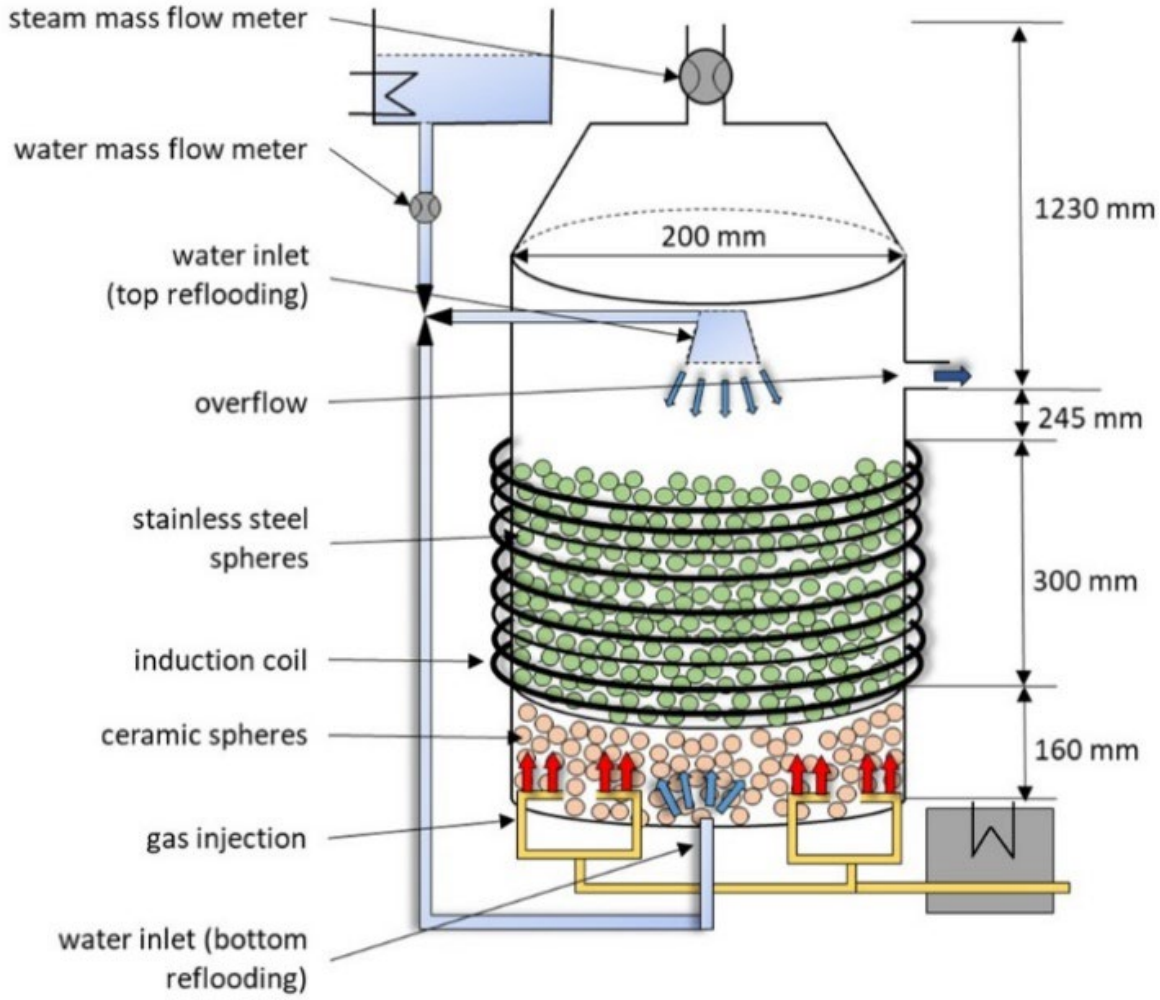

Water
- Flow: ~4 l/min – ~8 l/min
- Temperature: ~100°C

Debris bed
- Diameter: 6 mm
- Porosity: 0.37 – 0.42
- Initial temperature: 300°C – 700°C

Air
- Flow: 0 kg/min – 0.18 kg/min
- Temperature: ~100°C

FLOAT in general

Thermocouples in test section

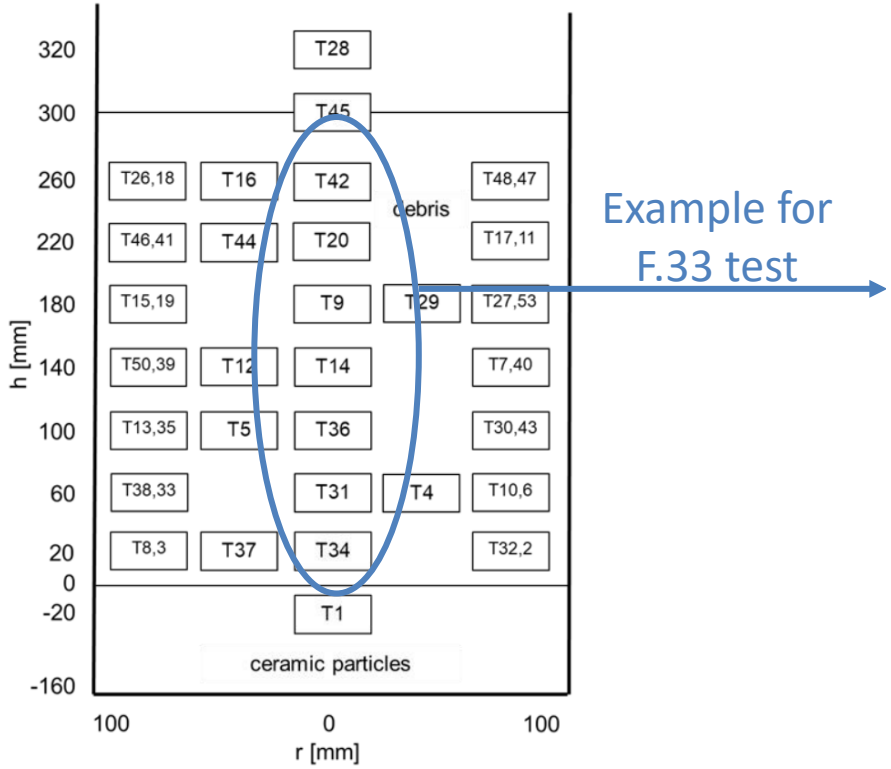

Example for F.33 test

Thermocouples measurements

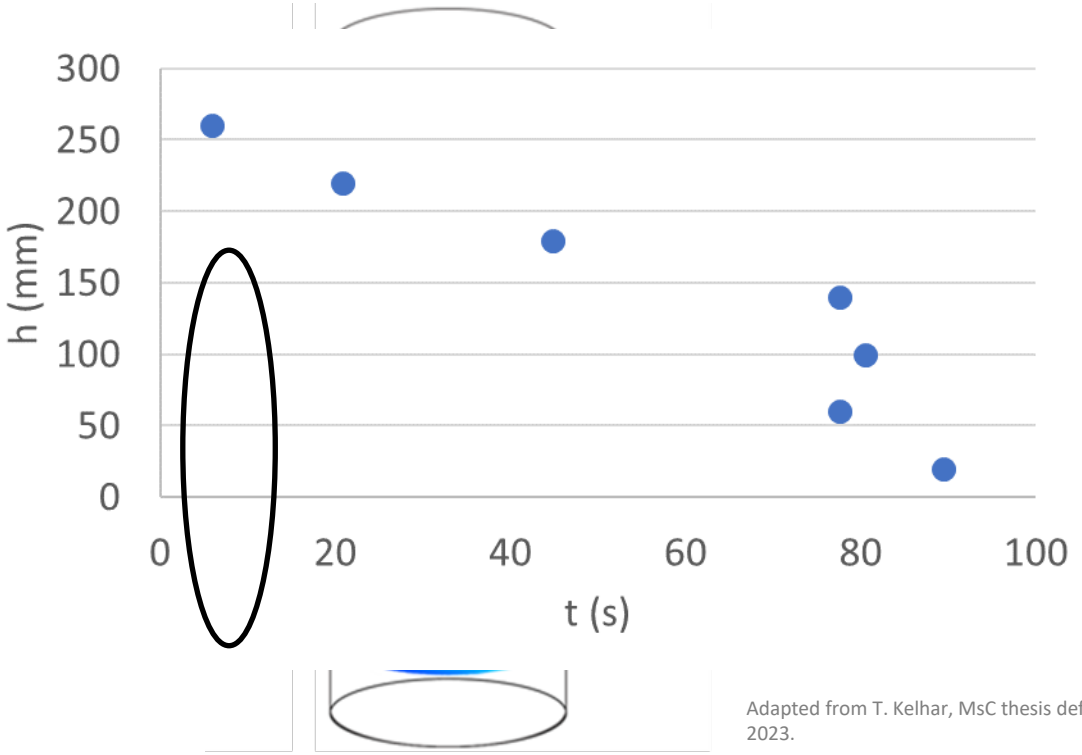

Reprinted from M. Petroff, R. Kulenovic, J. Starflinger, Experimental Investigation on Debris Bed Quenching With Additional Non-Condensable Gas Injection. Journal of Nuclear Engineering and Radiation Science, 2022. 8(4).

Adapted from T. Kelhar, MsC thesis defense, 2023.

FLOAT in general

- Preferential penetrating channel of water
  - in many cases existed in the near-wall region
    - higher porosity
    - lower temperatures
      - nonuniform inductive heating
      - heat losses towards the environment
  - in some tests in the central region
- Test repeatability
  - important deviations in total quenching times at larger debris bed temperatures and higher air flow rates
  - existence of random effects favoring the formation of initial penetrating channels
- Non-condensable gases reduce quenching capabilities

Selected FLOAT tests

Tests with the highest initial temperature

Preferential penetrating channel of water was developed in the central region

		F.32	F.33
Debris bed	Mass (kg)	44.2	44.1
	Initial average temperature (°C)	501	515
Water	Flow rate (l/min)	4.3	4.5
	Average temperature (°C)	88	88
Air	Flow rate (kg/min)	0.18	0
	Temperature (°C)	100	N.A.

Corresponds to the gas measurements of the COMET L3 oxide melt concrete interaction test

Selected FLOAT tests

Initially the debris bed is quenched in a wider area

Preferential penetrating channel established around the center

Another penetrating channel closer to the edge of the debris

Temporary decrease of preferential penetrating channel (might be attributed to higher debris bed temperature and/or establishment of another channel)

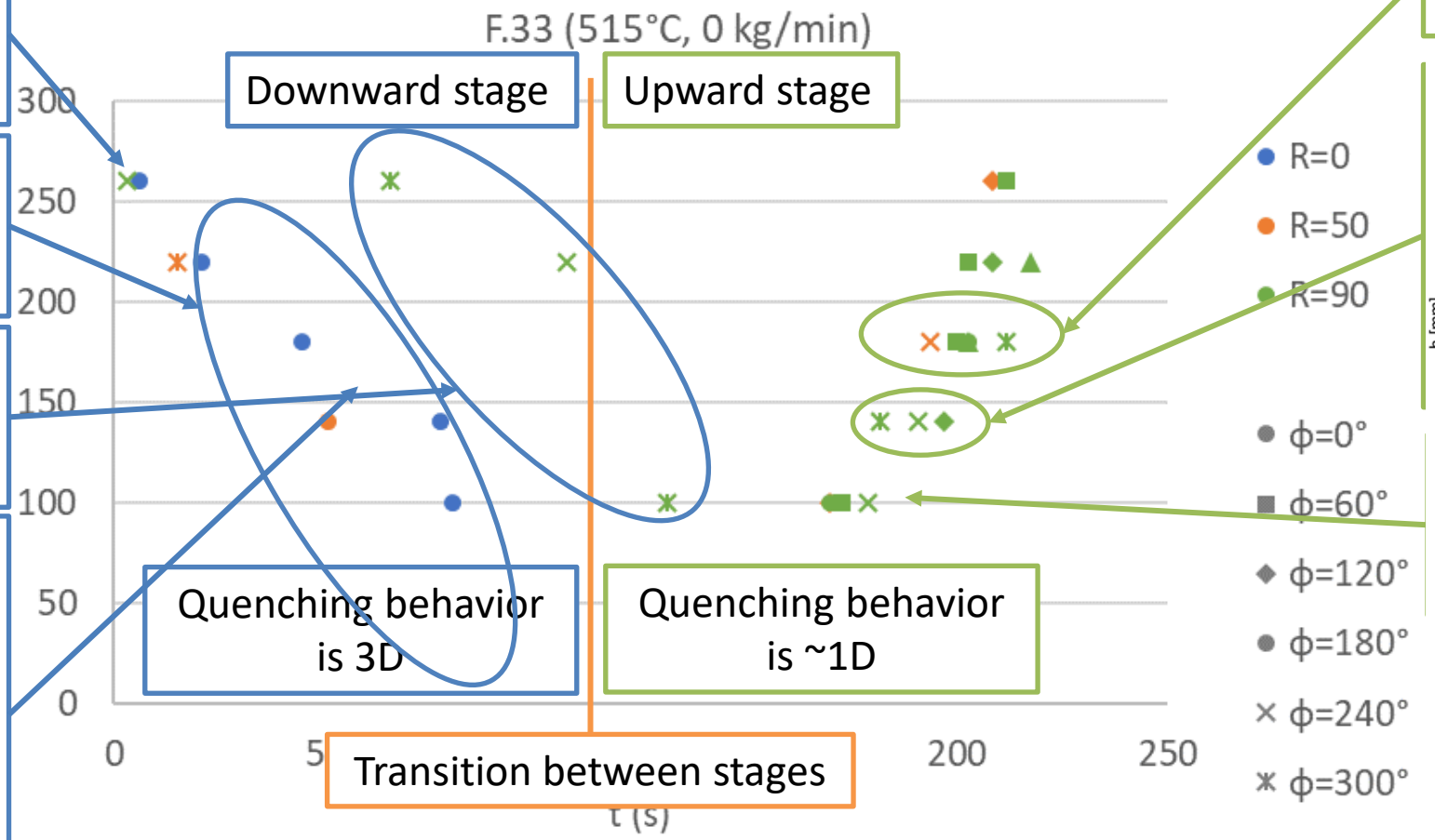

Quenching is slower at the edge

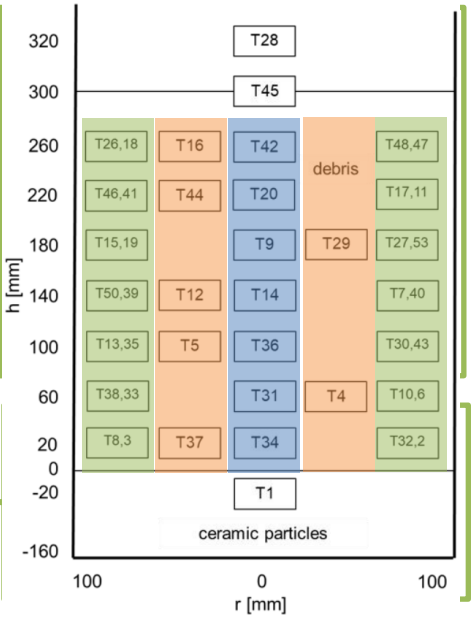

Selected FLOAT tests

- Similar tests showed that air flow significantly increases the total quenching time
- Observed discrepancy in total quenching time might be related to the experimentally seen trend on the standard deviations
  - larger at higher debris bed temperatures and air flows
    - e.g. ~16 % @365°C and air flow
  - time also depends on the random effects favouring the formation of initial penetrating channels during the downward quenching stage

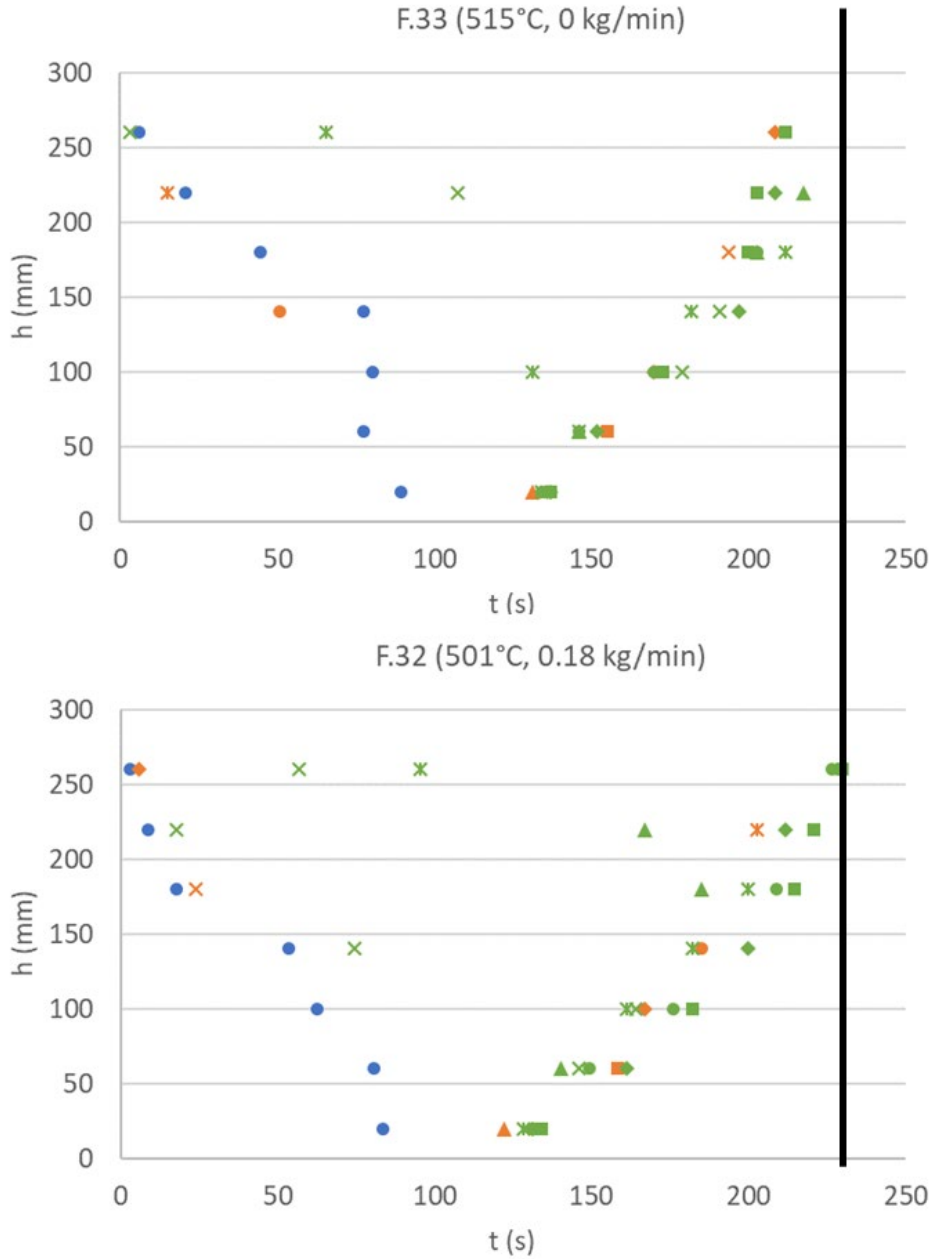

Simulations

About

- MC3D computer code (IRSN, France)
- 2D geometry
- FLOAT F.32 and F.33 data to define
  - domain and zones dimensions
  - boundary conditions
  - initial conditions

Computational model (left)
Initial debris bed temperature (right)

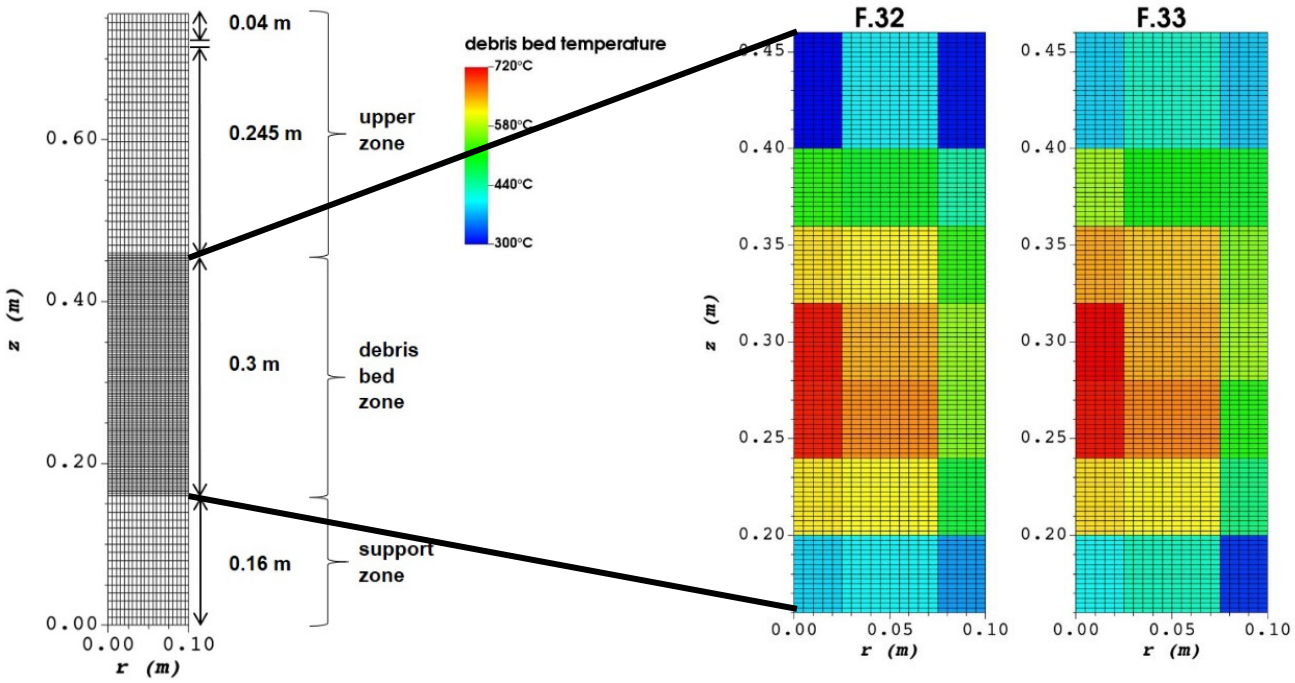

Simulations

Quenched area

Gas flow effects cooling capabilities at the edge

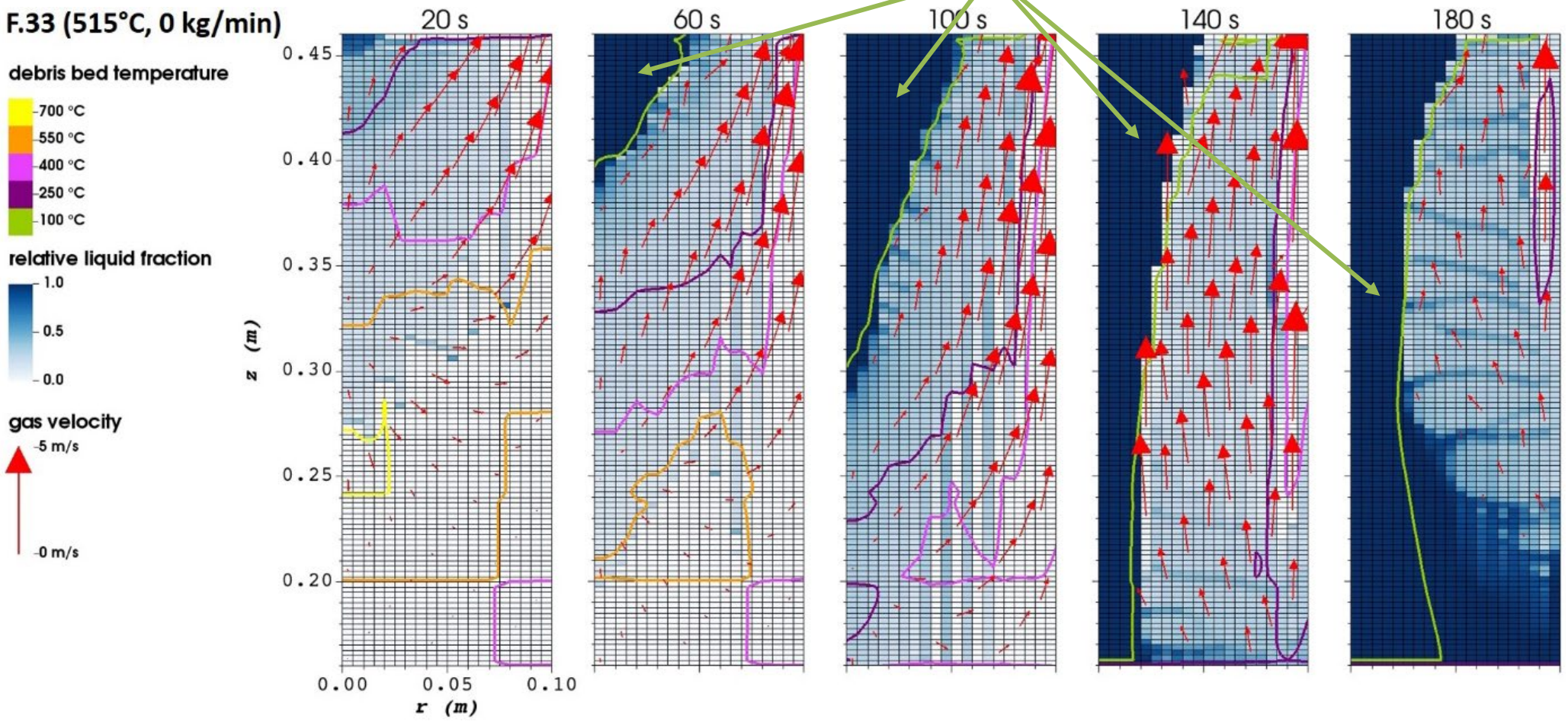

Simulations

Progression velocities are in good agreement

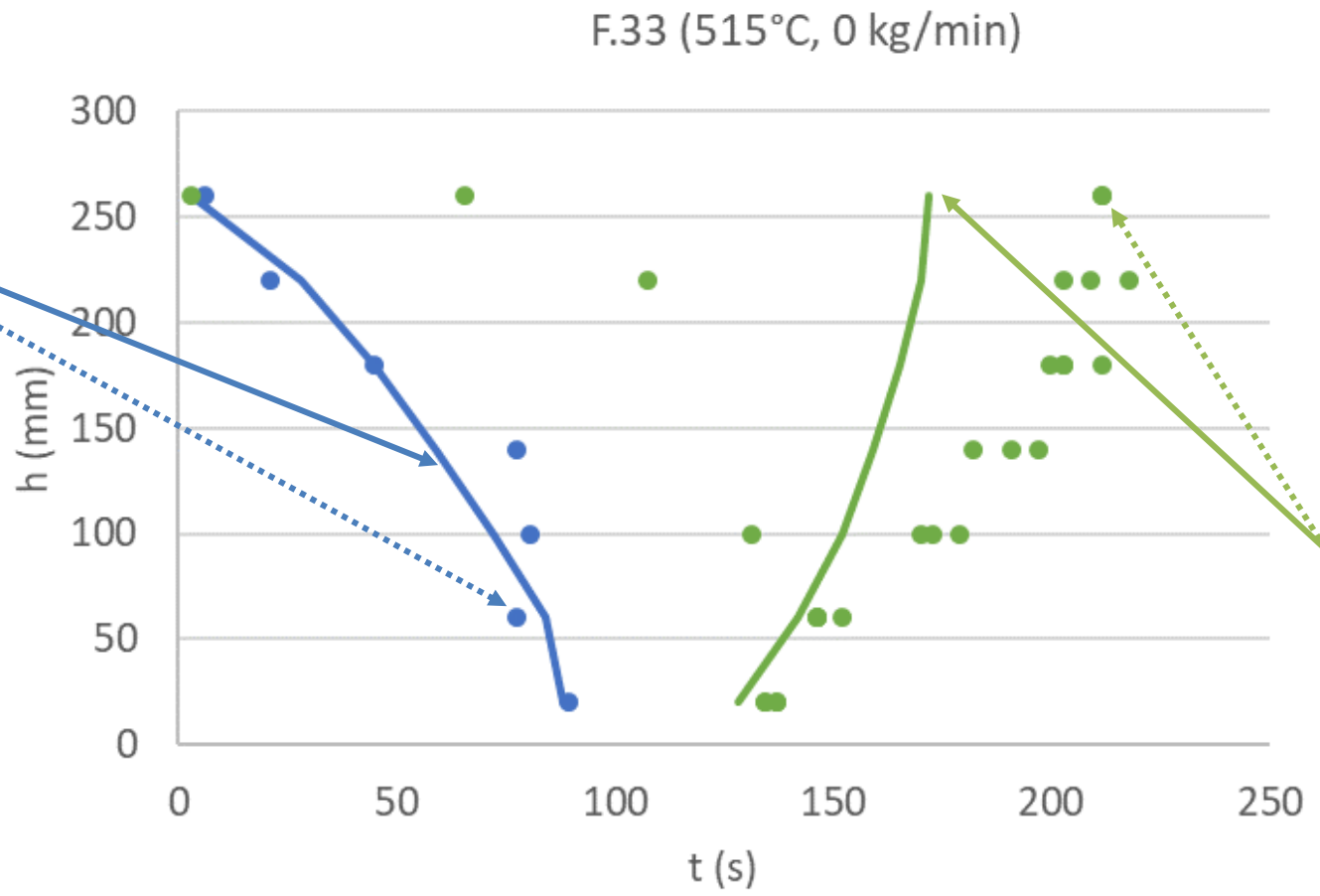

The simulated total quenching time is underestimated, if compared to the experimental value. However, the observation in the simulation is in line with the observed trend for similar FLOAT tests.

Simulations

Decrease in the progression velocity occurs at different times (might be attributed to debris bed temperature setup, friction models, flooded area) and affects on the end of downward stage

Progression velocities are in good agreement

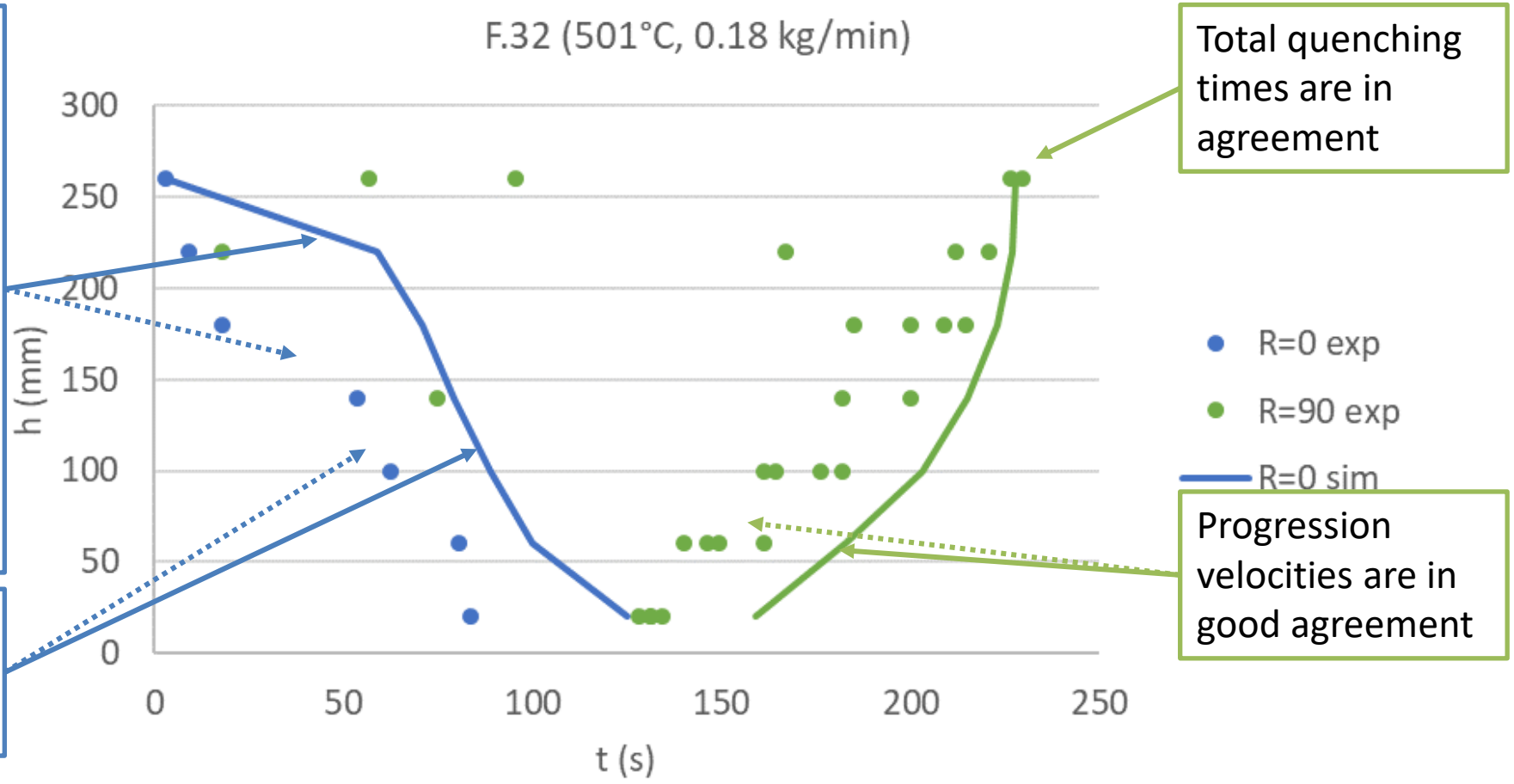

Total quenching times are in agreement

Progression velocities are in good agreement

Conclusions

- Simulation results with MC3D code
  - in quantitative agreement with test results
    - both quenching stages are covered
    - quenching is prolonged with the presence of air flow
  - in reasonable qualitative agreement with tests (considering the observed uncertainties in the FLOAT tests) regarding total quenching time
- Potentials for improvements
  - mesh refinements
  - more detailed consideration of porosity near the wall
  - improvement in zoning the initial temperature of the debris bed
  - 3D modelling approach (especially for situations with dominating non-central penetration channel(s))

Acknowledgment

- The Jožef Stefan Institute authors acknowledge:
  - The financial support from the Slovenian Research Agency (research core funding No. P2-0026) and from the state budget by the Slovenian Research Agency and the Slovenian Nuclear Safety Administration (project No. V2-2375)
  - IRSN (France) and the MC3D development team
  - University of Stuttgart, Institute of Nuclear Technology and Energy Systems, who have provided the original FLOAT test data

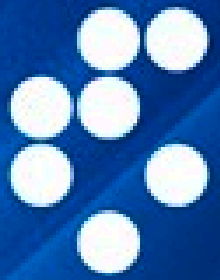

Jožef Stefan
Institute

R4

Reactor
Engineering
Division

The 11th European Review Meeting on Severe Accidents Research

May 13-16, 2024, Royal Institute of Technology, Stockholm, Sweden

TECHNICAL SESSION 5.1: SEVERE ACCIDENT SCENARIOS - MODEL DEVELOPMENT AND VALIDATION

Chairs: M. Angelucci (University of Pisa), F. Gabrielli (KIT)

ID53	**Formulation of material property formula for calculation of damage in reactor pressure vessel during accident evaluation** K. Shimomura (JAEA)	**Paper** **Presentation**
ID60	**Correlation Development for the Determination of Aerosol Particle Retention in Liquid Pools** J. Rehrmann (PSS-RUB)	**Paper** **Presentation**
ID43	**In Vessel Melt Retention 0D model for integral Pressurized Water Reactors** M. Principato (Sapienza University of Rome)	**Paper** **Presentation**

FORMULATION OF MATERIAL PROPERTY FORMULA FOR CALCULATION OF DAMAGE IN REACTOR PRESSURE VESSEL DURING ACCIDENT EVALUATION

Kenta Shimomura[1], Takuya Yamashita[2], Yuji Nagae[1]
Japan Atomic Energy Agency (JAEA)
[1]:790-1, Tomioka-machi, Fukushima, Japan
[2]:4002, Oarai-machi, Ibaraki, Japan
shimomura.kenta@jaea.go.jp, yamashita.takuya38@jaea.go.jp, nagae.yuji@jaea.go.jp

ABSTRACT

From the results of the internal investigation of Fukushima Daiichi Nuclear Power Station Unit 2, it was confirmed that part of the fuel assembly (upper tie plate) had fallen to the bottom of the pedestal periphery. From this result, it could be presumed that RPV (Reactor Pressure Vessel) has a hole large enough for the upper tie plate to drop. One of failure mode of the RPV lower head would be assumed to be “mechanical failure”. In the mechanical failure, it is assumed that the RPV lower head will be damaged due to the accumulation of creep damage caused by core material above the creep temperature of the RPV substructure materials falling into the lower plenum. Such damage evaluation is performed by thermohydraulic-structure coupled analysis. Such analysis requires RPV material properties from the creep temperature range to near the melting point. In this study, we obtained the strength data of RPV material including welded joints form the creep temperature range to near the melting point and formulated the material property formulas (elastoplastic stress-strain formula, creep strain formula, creep rupture formula) necessary for mechanical failure evaluation.

KEYWORDS
Fukushima Daiichi Nuclear Power Station, Reactor Pressure Vessel, Material Property, Tensile, Creep,

1. INTRODUCTION

Decommissioning works is currently underway in response to Fukushima Daiichi Nuclear Power station accident that occurred in March 2011. According to the internal investigation results of Unit 2, it was confirmed that part of the fuel assembly (upper tie plate) had fallen to the bottom of the outer periphery of the pedestal. Based on this result, it is estimated that there may be a hole in the RPV (Reactor Pressure Vessel) that may be large enough for the upper tie plate to fall though. However, an internal investigation does not reveal whether there is a hole somewhere at the bottom of the RPV. “Mechanical failure” is assumed to be one of the failure modes of the RPV lower head. In terms of mechanical failure, it is assumed that core material with a temperature higher than the creep temperature of the RPV lower structure material falls in the lower plenum, causing creep damage to accumulate and damage to the RPV lower head. This type of damage evaluation is performed using thermal-hydraulic-structural interaction analysis. Such analysis requires material property data in the creep temperature range of RPV material including welded joints. In this case, since it is considered that the temperature rises to a point where each material melts, it is assumed that the temperature exceeds the creep temperature range of each material. During such severe accidents, high temperature material data for RPV material including welded joints is required. Since the RPV lower head part is welded and welded data is necessary. Past material data [1]-[7] of RPV material acquired by others are up to approximately 1473 K for the base metal. And past material data [6] of the

welded joints including submerged arc process and shielded arc process is up to approximately 873 K. According to phase diagram of Fe-C system, a phase change occurs from the ferrite phase to the austenite phase at the A1 transformation point and the phase becomes completely austenite at the A3 transformation point. The A1 transformation should lead to change not only the specific heat and thermal expansion coefficient but also strength at the specified carbon value of the material equivalent to the actual RPV material (JIS SQV2A). it is necessary to formulate material property formulas according to the temperature category. In this study, we acquired strength data of RPV material including welded joints form the creep temperature to the vicinity of the melting point (1723 K) and developed material property formula (elasto-plastic stress-strain formula, creep strain formula, creep rupture formula) that can be applied to mechanical failure evaluation. In addition, although RPV has welded parts, material data on the creep temperature range of welded parts is scarce, and it is said that the strength of welded parts is generally lower than that of the base metal, so the necessity of welding strength reduction factor was investigated through comparison with base metal data.

2. RPV material

In this study, we used JIS SQV2A (equivalent to ASTM SA533B), which is used as RPV material. As shown in Table I, sample of the plate material was meet the JIS standard values.

Table I. Specification of SQV2A

	Chemical composition %												
	C	Si	Mn	P	S	Cu	Ni	Cr	Mo	Nb	V	Ti	B
Sample	0.17	0.25	1.42	0.006	0.001	0.01	0.66	0.15	0.57	0.00	0.00	0.00	0.0002
JIS*	≤ 0.25	0.15 ~ 0.40	1.15 ~ 1.50	≤ 0.020	≤ 0.020	≤ 0.40	0.40 ~ 0.70	≤ 0.30	0.45 ~ 0.60	≤ 0.02	≤ 0.03	≤ 0.03	≤ 0.00010
* JIS G3120:2018[8] Heat treatment conditions: Quenched 1153 K,10 min. Tempered 953K, 120 min.													

The structure of this material starts to change from ferrite phase to austenite phase at the A1 transformation point. It is known that this structural change changes the tendency of thermal properties (thermal expansion coefficient). Therefore, the test was conducted in a temperature range (873 to 1673 K) that includes the A1 transformation point. As a result of the transformation point measurement (Formaster measurement) performed on a test piece obtained from the same material used in this test, the transformation points were A1=993 K, A3=1103 K.

Using JIS SQV2A equivalent materials used as RPV materials and low hydrogen welding rods, welded joints simulating the actual machine were fabricated (Figure 1). After welding, heat treatment was performed that reasonably simulated the information of the actual machine (Figure 2). Test specimens were taken from the manufactured welded joints and material tests were conducted (Figure 3).

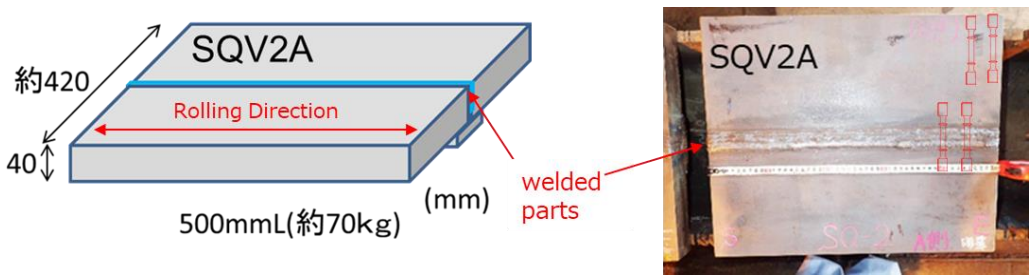

Figure 1. Appearance of the welded joint

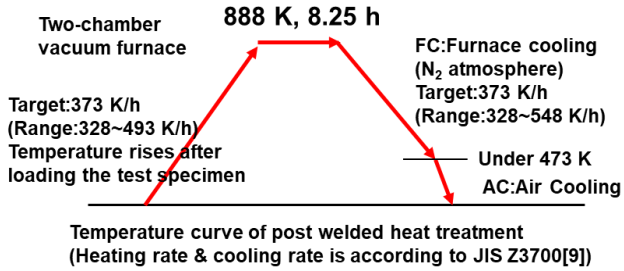

Figure 2. Post welded heat treatment conditions

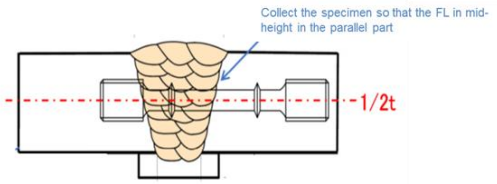

Figure 3. Test specimen collection position

3. EXPERIMENT

3.1. TENSILE TEST

The tensile test specimen was taken from the RPV material including welded joints, and the tensile test was conducted. Tensile test was conducted on the base metal and welded joints at room temperature and in 100 K increments from 973 K to 1673 K following JIG G0567[10]. The shape of the tensile test specimen is shown in Figure 4. Type A specimens were used up to 1273 K, and Type B specimens were used above 1273 K. Tensile test specimens were taken from the plate in a direction perpendicular to the rolling direction. Tensile tests were conducted in Ar at high temperatures to prevent oxidation during the high temperature tests.

Temperature	Shape of specimen	Appearance of specimen
$T \leq 1273$ K	Unit : mm R5 M12 30 50 80 Type A	Temperature :1273 K SBT-03 Base metal Temperature :1273 K SWT-09 Welded
$T > 1273$ K	R40 6Φ Unit : mm 15Φ 30.0 180~220 Type B	Temperature: 1673 K SWT-19 Welded

Figure 4. Tensile test specimen

Figure 5 shows relationship between temperature and 0.2% proof stress. There was no large variation between the test results and the reference data, and the data for the base metal and joint showed almost the same values. Figure 6 shows strain-stress curve of tensile test results. We compared between base metal and welded data at room temperature and 1273 K, there were no difference between these data. From the above, it was found that there was no difference in tensile strength between base metal and welded. Additionally, observation after the test, metal thinning was about 0.1 mm at 1673 K and maximum metal thinning was about 0.6 mm at 1273 K (Figure 7). In this case, 0.2 % proof stress was 19 MPa and including metal thinning for calculated 0.2% proof stress, this value become 23 MPa. This value was within the margin of error, so there was little effect of oxidation during the test.

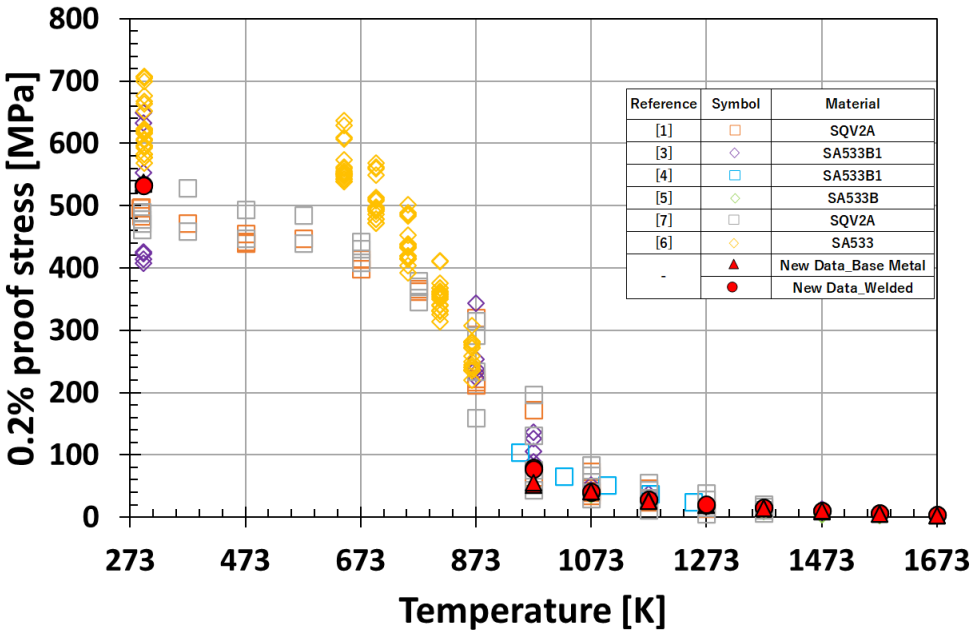

Figure 5. Relationship between temperature and 0.2% proof stress

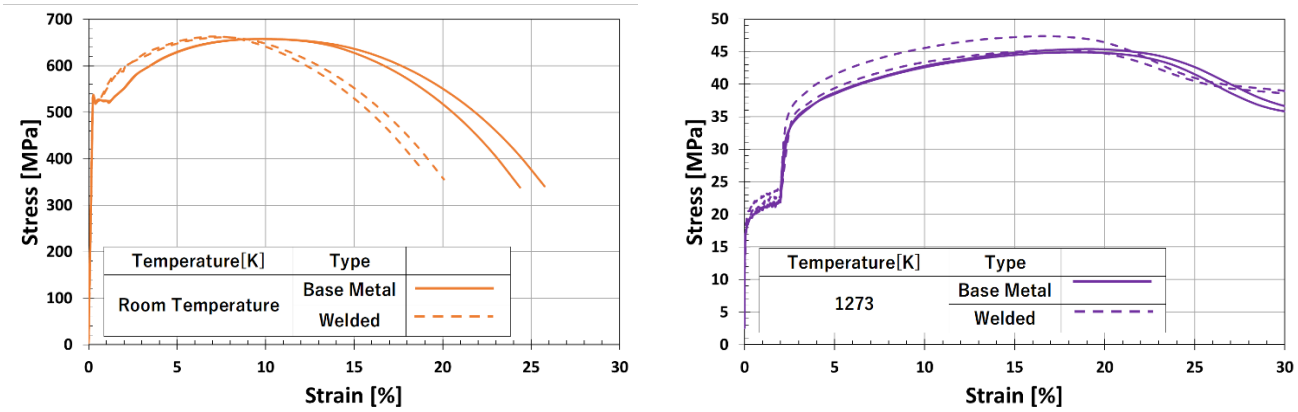

a) Room temperature **b) 1273 K**

Figure 6. Tensile test results (strain-stress curve)]



(a) 1673 K **(b) 1273 K**

Figure 7. Observation after tensile test at 1673 K and 1273 K

3.2. CREEP TEST

The creep test was taken from the RPV material including welded joints, and the creep test was conducted. For the base metal, tests were conducted at 923K, 973 to 1273K in 100K increments, and 1373K and 1673K, and for welded joints, tests were conducted in 100K increments from 973 to 1273K following JIS Z2271[11]. The shape of the creep test specimen is shown in Figure 8. Type A specimens were used up to 1273 K, and Type C specimens were used above 1273 K. Creep test specimens were taken from the plate in a direction perpendicular to the rolling direction. Creep tests were conducted in Ar at high temperatures to prevent oxidation during the high temperature tests.

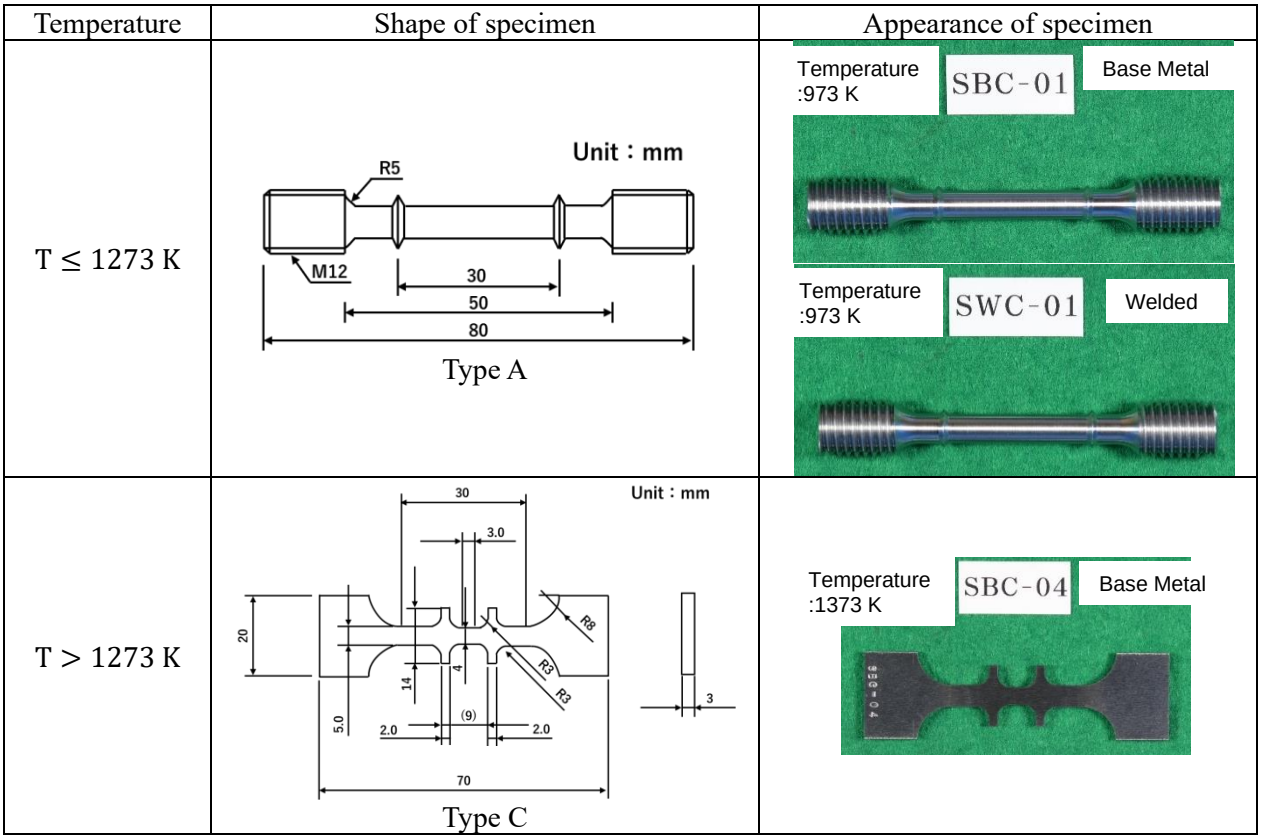

Figure 8. Creep test specimen

Figure 9 shows relationship between rupture time and stress. The time to rupture tends to be shortened with high stress and high temperature. And we compared test data and reference data, they were no difference between these data. And we compared between base metal and welded data, there were no difference between these data. From the above, it was found that there was no difference in creep strength between base metal and welded. Additionally, observation after the test, metal thinning was very little at 1673 K and metal thinning was 0.7 mm (Figure 10). In this case, using stress was 7 MPa and including metal thinning for calculated stress, this value become 9 MPa. This value was within the margin of error, so there was little effect of oxidation during the test.

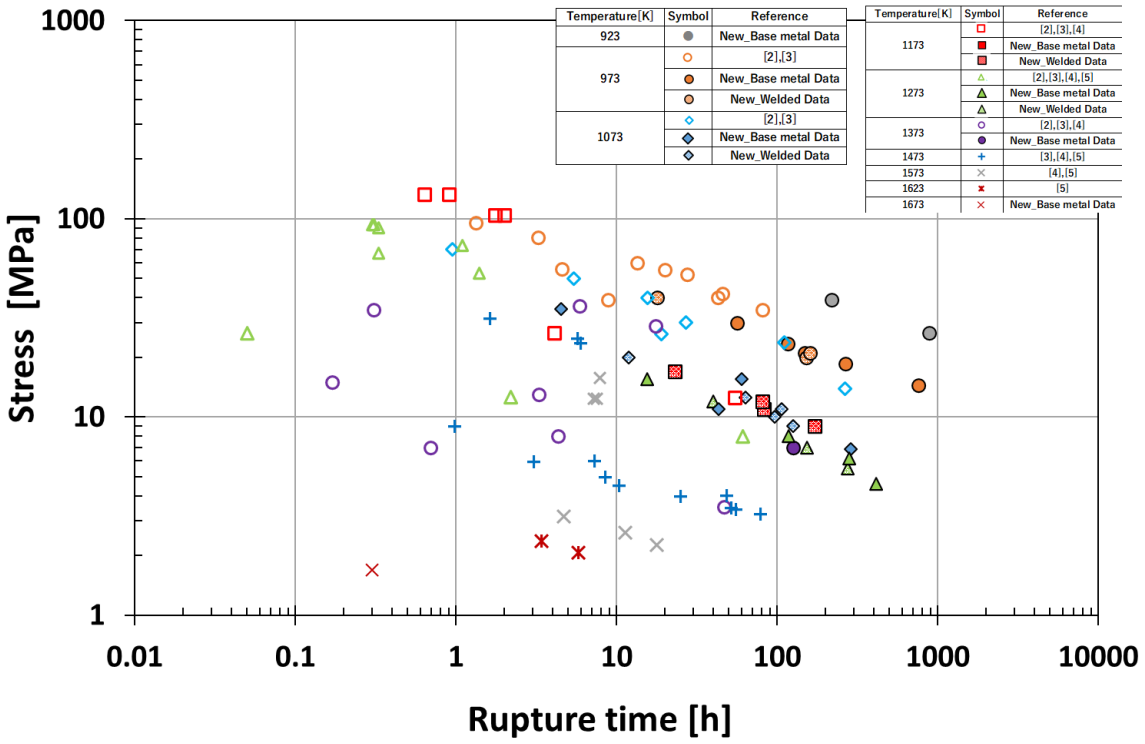

Figure 9. Relationship between rupture time and stress

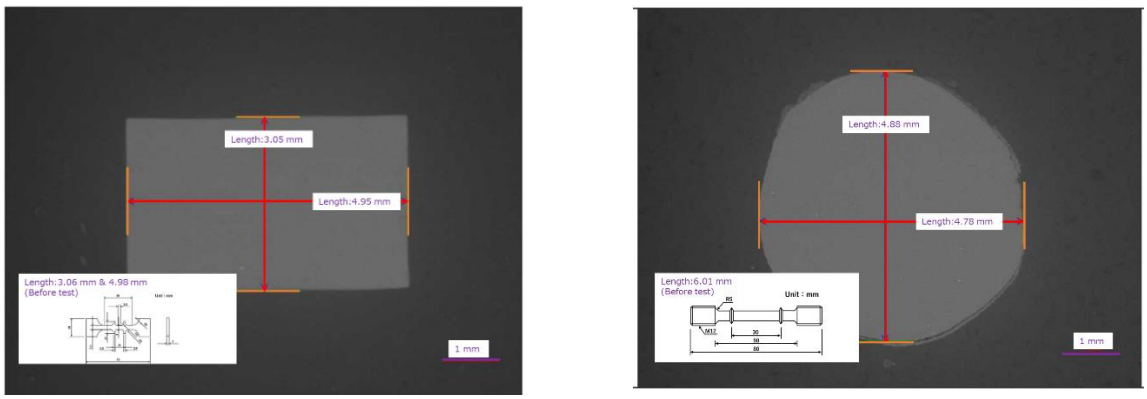

(c) 1673 K **(d) 1273 K**

Figure 10. Observation after creep test at 1673 K and 1273 K

4. FORMULATION OF MATERIAL PROPERTY FORMULA

4.1. ELASTOPLASTIC STRESS-STRAIN FORMULA

In structural analysis evaluation, the elasto-plastic stress-strain formula is required to calculate elastic strain and plastic strain. In this study, the elasto-plastic stress-strain formula of bilinear approximation was applied. The applied formula is shown below. And diagram of two-line approximation is shown in Figure 11.

$$\sigma \leq \sigma_y \therefore \sigma = \frac{\varepsilon}{E} \quad (1)$$

$$\sigma > \sigma_y \therefore \sigma = \sigma_y + K\varepsilon \quad (2)$$

σ	:	Stress	[MPa]
σ_y	:	Yield Stress	[MPa)
ε	:	Strain	[-]
E	:	Young modulus	[GPa]
K	:	Tangent modulus	[GPa]

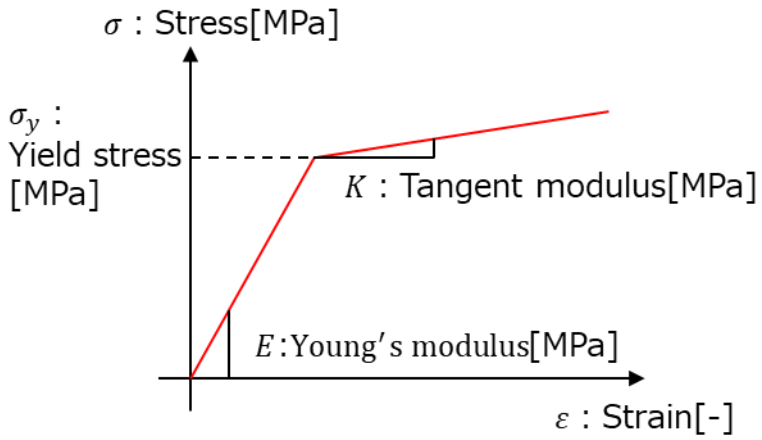

Figure 11. Diagram of elasto-plastic stress-strain formula (two-line approximation)

Each parameter (Young's modulus, Tangent modulus, Yield stress) was calculated based on the data obtained this study and past knowledge. Figure 12 shows the calculated parameters. Figure 13 shows the elsto-plastic stress-strain formula of two lines approximation from setting each parameter considering transformation temperature.

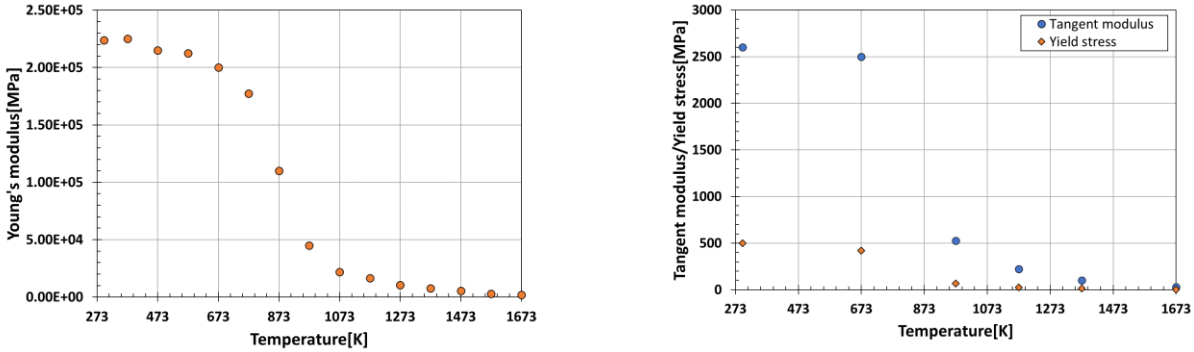

Figure 12. Relationship between temperature and Young's modulus, yield stress/tangent modulus

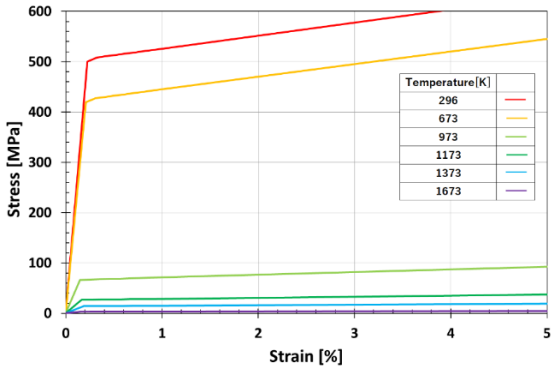

Figure 13. Elasto-plastic stress-strain formula

4.2. CREEP STRAIN FORMULA

Structural analysis that takes creep into account requires a creep strain formula that can be applied up to high temperatures to determine creep strain. Since tertiary creep becomes noticeable in high temperature range, we applied the Kachanov-Rabotonov (K-R) model, which can evaluate up to tertiary creep. The applied formula is shown below. And K-R model calculation procedure is shown in Figure 14.

$$d\omega_i = B\frac{\sigma^k}{(1-\omega_{i-1})^l} \times dt \quad (3)$$

$$\omega_i = \omega_{i-1} + d\omega_i \times (t_i - t_{i-1}) \quad (4)$$

$$d\varepsilon_i = A\left(\frac{\sigma}{1-\omega_i}\right)^n \times dt \quad (5)$$

$$\varepsilon_i = \varepsilon_{i-1} + d\varepsilon_i \times (t_i - t_{i-1}) \quad (6)$$

ω	:	Damage coefficient	[-]
t	:	Time	[h]
σ	:	Stress	[MPa]
ε	:	Strain	[-]

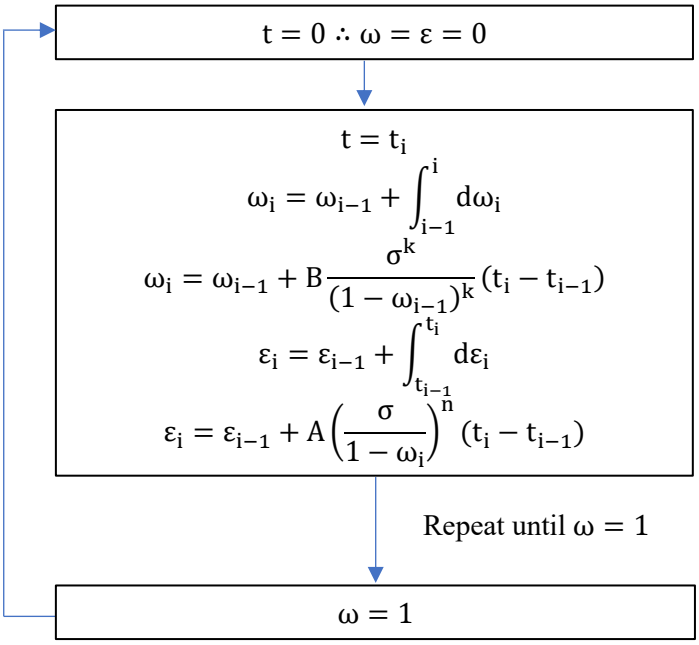

- Calculate the damage coefficient at each time
- Calculate creep strain form the calculated damage coefficient

Figure 14 K-R model calculation procedure

Each parameter was set based on the creep strain behavior obtained in the test. Table II shows the parameter of creep strain (K-R model). Regarding temperature classification, the classification was done taking into account the transformation point. Figure 15 shows comparison calculated data and test data, each data was almost same.

Table II. Parameter of creep strain (K-R model)

	A	B	n	k	l
T ≤993 K	5.417×10^{60} $\exp(-1.280 \times 10^{6}/RT)$	4.599×10^{36} $\exp(-8.0267 \times 10^{5}/RT)$	2.525	2.774	2.774
993 < T ≤ 1103 K	1.205×10^{3} $\exp(-1.340 \times 10^{5}/RT)$	1.977×10^{3} $\exp(-1.812 \times 10^{5}/RT)$	3.130	3.18	3.18
T > 1103 K	1.620 $\exp(-1.334 \times 10^{5}/RT)$	3.354×10^{-2} $\exp(-8.292 \times 10^{4}/RT)$	3.324	3.045	3.045

* T:Temperature (K), R:Gas constant (J/mol/K)

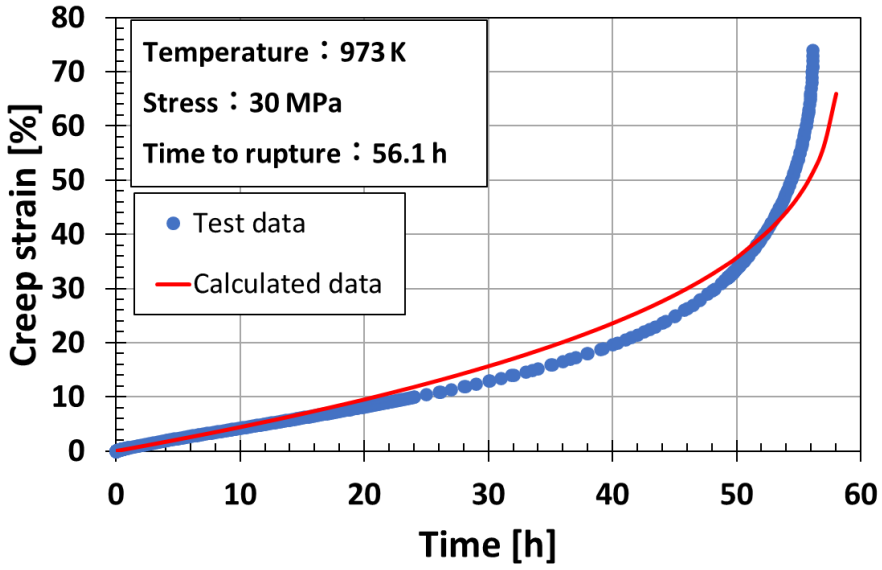

Figure 15. Comparison calculated data and test data

4.2. CREEP RUPTURE FORMULA

As a mechanical failure evaluation of RPV, evaluation using creep damage Dc has been carried out. Dc is calculated below:

$$Dc = \sum \Delta t / t_r \tag{7}$$

tr is rupture time and the rupture time required for this failure evaluation is calculated using the Larson-Miller-Parameter (LMP) (creep rupture formula).

$$LMP = T(C + \log t_r) = A + B\log\sigma + D(\log\sigma)^2 \tag{8}$$

T	:	Temperature	[K]
t_r	:	Time to rupture	[h]
σ	:	Stress	[MPa]
C	:	Property of the material	[-]
A, B, D	:	Constant	[-]

Each of the above parameters was calculated from the data obtained this time and the relationship between rupture time and stress based on past knowledge. In addition, considering the regression nature of long-term data, we adopted a quadratic equation this time. The temperature classification was set taking into consideration the transformation pointe temperature of carbon steel. Table III shows the material properties for LMP and Figure 16 shows the relationship between rupture time and stress.

Table III. Material properties for LMP

	$T \leq 993$[K]	993[K] $< T \leq 1103$[K]	1103[K] $< T$
C	20.05	2.69	8.70
A	21882.45	7366.37	17274.83
B	1743.35	-732.30	-4648.61
D	-1491.68	-971.87	78.46

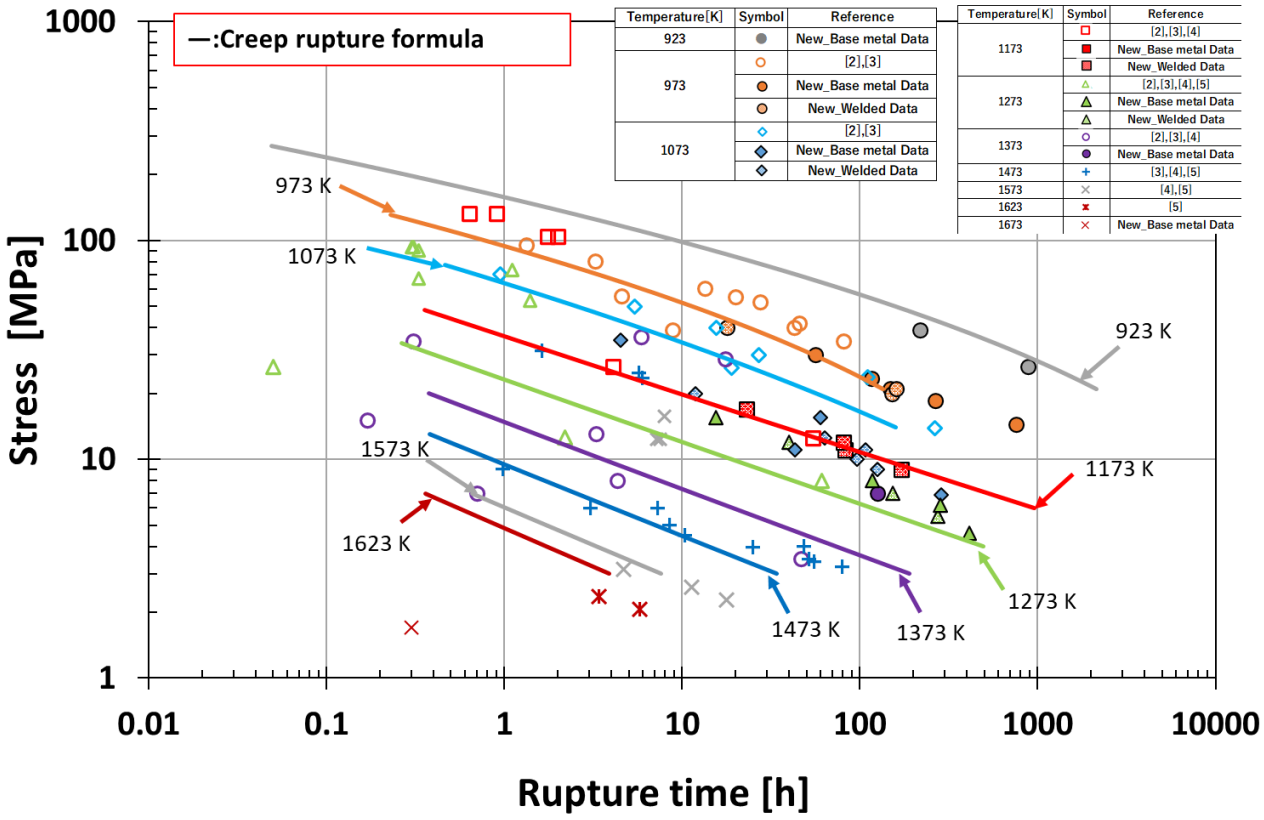

Figure 16. Relationship between rupture time and stress

LMP is used for creep damage evaluation in severe accident analysis codes. The formula of MELCOR is shown below and Table IV shows default material properties for LMP functions in MELCOR [12].

$$t_R = 10^{\left(\frac{P_{LM}}{T} - C\right)} \tag{9}$$

t_R	:	Time to rupture	[s]
T	:	Temperature	[K]
P_{LM}	:	Larson-Miller parameter	[-]
C	:	Property of the material	[-]

$$P_{LM} = \min[a_1 \log_{10}(\sigma_e) + b_1, a_2 \log_{10}(\sigma_e) + b_2] \quad (10)$$

σ_e : Effective stress [MPa]

Table IV. Default material properties for LMP function in MELCOR[12]

Material Type	a_1[K]	b_1[K]	C	a_2[K]	b_2[K]
A-508, class 2 carbon steel	-5335	62291.3	16.44	-	-
SS-316, 316 stainless steel	-7400	81088.4	16.44	-35555.5	322036.2
INC-600, Inconel 600	-6296	67129.96	11.44	-	-
SA533B1, LH-Steel, Default LH Steel	-4730	4.81E+04	7.042	-	-
SC1604, SS-Steel, Default COR SS Steel	-7500	8.10E+04	16.44	-	-

In addition, a comparison with the formulated formula is shown in the Figure 17. LMP is a linear equation, and the rupture time tends to be shorter than actual data. At temperatures below the A1 transformation point, there is a large difference at the same stress, and between the A1 and A3 transformation points, both show equivalent values, but after the A3 transformation point, the same stress differs by about 1/10. Therefore, it is considered better to use data based on actual data regarding LMP.

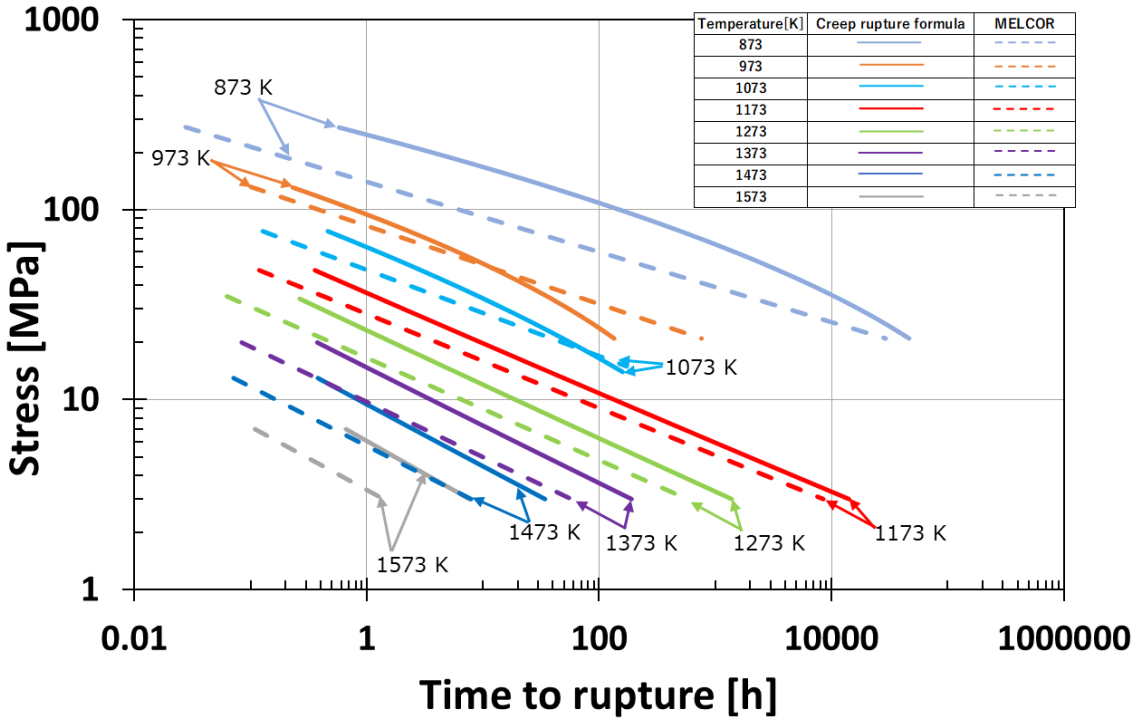

Figure 17. Comparison MELCOR and creep rupture formula

5. CONCLUSIONS

It was found that at high temperatures, there is no difference in strength between the base metal and the joint, they are equivalent, and can be evaluated by applying the same characteristic formula. A high

temperature material property formula for RPV material including welded joints was formulated based on newly acquired data and past knowledge. This formula can be useful for mechanical failure evaluation. By formulating a characteristic formula that takes into account the A1 and A3 transformation points, the formula more closely reproduces actual data. It is thought that applying this formula to severe accident analysis codes will result in more valid evaluations.

ACKNOWLEDGMENTS

- This study has been performed by the funds from the Japanese Ministry of Economy, Trade and Industry as The Subsidy Program “Project of Decommissioning, Contaminated Water and Treated Water Management (Development of Analysis and Estimation Technologies for Characterization of Fuel Debris (Development of Estimation Technologies of RPV Damaged Condition, etc.)".
- This study has been performed by the funds from Japanese Ministry of Economy, Trade and Industry as the Subsidy Program " Project of Decommissioning, Contaminated Water and Treated Water Management (Development of Analysis and Estimation Technologies for Characterization of Fuel Debris)"

REFERENCES

1. Japan Nuclear Energy Safety Organization, “Project of Integrity Assessment of Flawed Components with Structural Discontinuity (IAF) Material Properties Data Book at High Temperature for dissimilar metal welding in Reactor Pressure Vessel”, JNES-RE-2012-0024(2013)
2. J.L. Rempe, S.A. Chavez, G.L. Thinnes, C.M. Allison, G.E. Korth, R.J. Witt, J.J. Sienicki, S.K. Wang, L.A. Stickler, C.H. Heath, S.D. Snow, “Light Water Reactor Lower Head Failure Analysis”, NUREG/CR-5642(1993)
3. D.R. Diercks, L.A. Neimark, “Results of Mechanical Tests and Supplementary Microstructural Examinations of the TMI-2 Lower Head Samples”, NUREG/CR-6187(1994)
4. L.L. Humphries, T.Y. Chu, J. Bentz, R. Simpson, C. Hanks, W. Lu, B. Antoun, C. Robino, J. Puskar, P. Mongabure, “OECD Lower Head Failure Project Final Report”, NEA/CSNI/R(2002)
5. Y. Yamaguchi, J. Katsuyama, Y. Kaji, M. Osaka, Y. LI, “Expansion of high temperature creep test data for failure evaluation of BWR lower head in severe accident”, Mechanical Engineering Journal Vol.7, No.3(2020)
6. H.E. McCoy, “TENSILE AND CREEP PROPERTIES OF SA533 GRADE B CLASS 1 STEEL”, DOE-HTGR-88383(1989)
7. Y. Takahashi, “Development of accurate inelastic analysis models for materials constituting penetrations in reactor vessel”, Q14016(2015)
8. JIS G3120:2018, “Manganese-molybdenum and manganese-molybdenum-nickel alloy steel plates quenched and tempered for pressure vessels”
9. JIS Z3700:2009, “Methods of post weld heat treatment”
10. JIS G0567:2020, “Method of elevated temperature tensile test for steels and heat-resisting alloys”
11. JIS Z2271:2019, “Metallic materials-Uniaxial creep testing in tension-Method of test”
12. L.L. Humphries, B.A. Beeny, F. Gelbard, D.L. Louie, J. Phillips, “MELCOR Computer Code Manuals”, SAND2017-0455 O(2017)

The 11th European Review Meeting on Severe Accident Research (ERMSAR2024)
KTH, Stockholm, Sweden

FORMULATION OF MATERIAL PROPERTY FORMULA FOR CALCULATION OF DAMAGE IN REACTOR PRESSURE VESSEL DURING ACCIDENT EVALUATION

May 13-16, 2024

*Kenta Shimomura, Takuya Yamashita, Yuji Nagae
Japan Atomic Energy Agency (JAEA)

This study has been performed by the funds from the Japanese Ministry of Economy, Trade and Industry as The Subsidy Program “Project of Decommissioning, Contaminated Water and Treated Water Management (Development of Analysis and Estimation Technologies for Characterization of Fuel Debris (Development of Estimation Technologies of RPV Damaged Condition, etc.)".

Outline

1 Introduction

2. Experiment

3. Material Test
   3.1 Tensile test
   3.2 Creep test

4. Formulation of material property formula
   4.1 Elasto-plastic stress-strain formula
   4.2 Creep strain formula
   4.3 Creep rupture formula

5. Conclusions

1. Introduction

- Estimated situation inside the reactor of Fukushima Daiichi Nuclear Power Plant(1F) Unit 1~3
  - It is estimated that there is a hole in the Reactor Pressure Vessel (RPV)
- Mechanical failure (creep failure) of RPV
  - Core material at a temperature higher than the creep temperature of the RPV substructure material falls int the lower plenum

Although RPV has welded parts, material data on the creep temperature range of welded parts is scarce, and it is said that the strength of welded parts is generally lower than that of the base metal, so the necessity of welding strength reduction factor was investigated through comparison with base metal data.

Estimated situation inside the reactor of Unit 1※

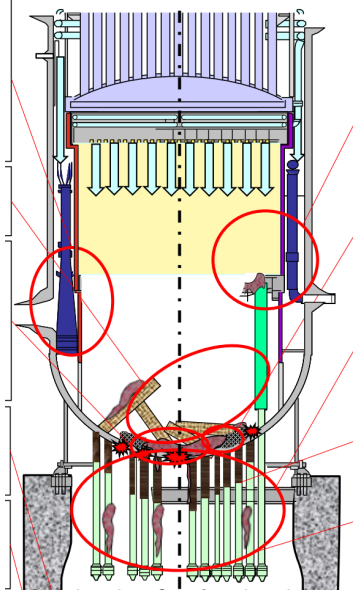

Estimated situation inside the reactor of Unit 2※

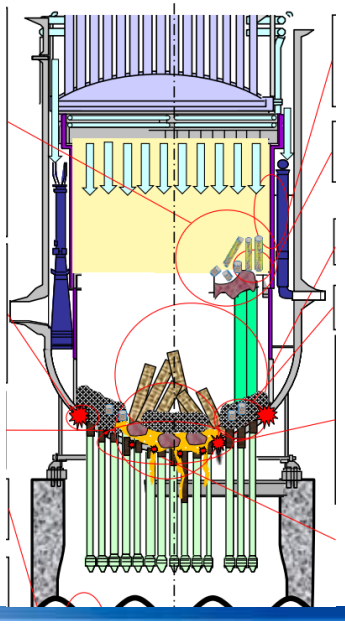

Estimated situation inside the reactor of Unit 3※

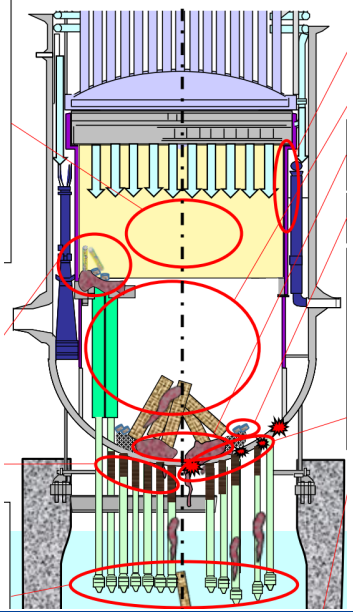

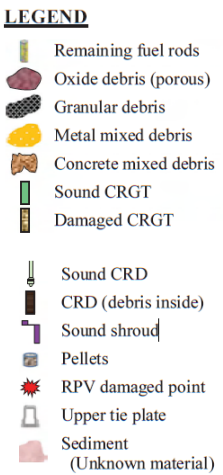

※ debriswiki
https://fdada-plus.info/wiki/index.php?title=%E7%82%89%E5%86%85%E7%8A%B6%E6%B3%81%E6%8E%A8%E5%AE%9A%E5%9B%B3#.E3.83.87.E3.83.96.E3.83.AA.E5.88.86.E5.B8.83.E3.83.BBRPV.E3.83.BBPCV.E7.8A.B6.E6.85.8B.E3.81.AE.E6.8E.A8.E5.AE.9A.E5.9B.B3

2. Experiment

2. Experiment

Implementation content

- Using JIS SQV2A equivalent materials used as RPV materials and low hydrogen welding rods, welded joints simulating the actual machine were fabricated. After welding, heat treatment was performed that reasonably simulated the information of the actual machine.
- Test specimens were taken from the manufactured welded joints and material tests were conducted

Appearance of the manufactured welded joints

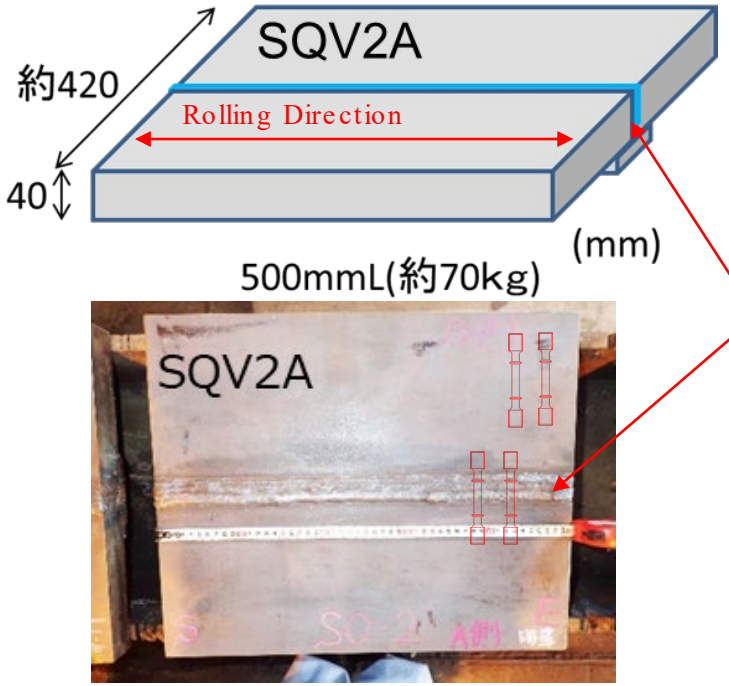

Test specimen collection position

test specimen including welded parts

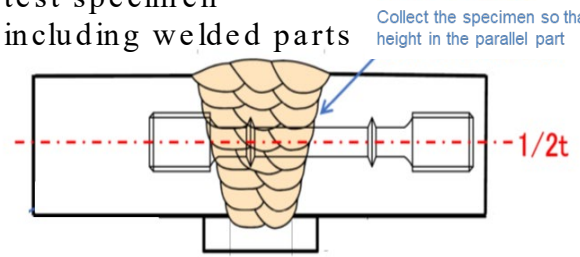

Test specimens containing only the base metal were collected from the base metal of the manufactured welded joints

Post welded heat treatment conditions

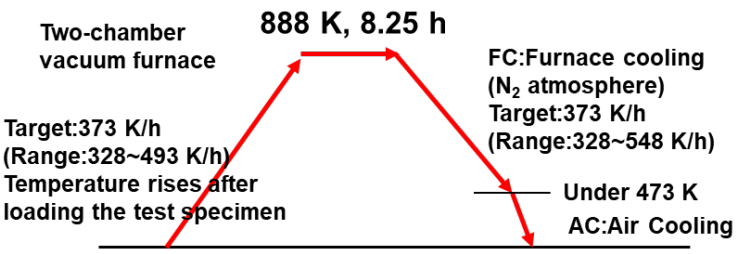

Temperature curve of post welded heat treatment
(Heating rate & cooling rate is according to JIS Z3700)

3. Material test

3.1 Tensile test

Implementation content

- Previous knowledge of tensile test data including welded joints is lacking beyond 873 K, so we considered the A1 transformation point (993 K) & A3 transformation pint(1103 K) and where the thermal properties of RPV material (carbon steel) change, conducted tensile tests on welded joints and expanded the data. In addition, for comparative study, base material data was acquired at room temperature and 1273 K.

Appearance of test piece　□Φ6×30mm Round bar with brim□

Temperature	Shape of specimen	Appearance of specimen
T≦1273 K	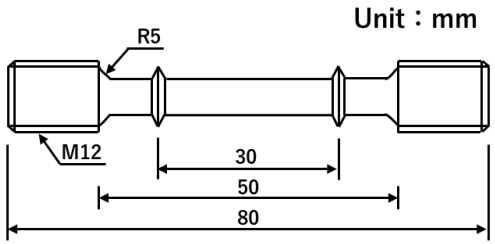	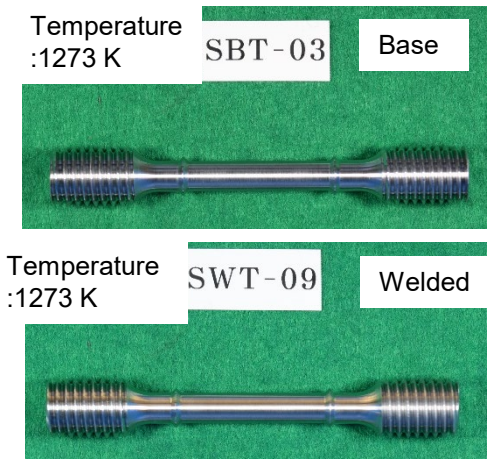
T>1273 K	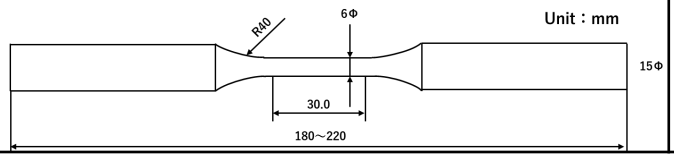	

3.1 Tensile test

Test results

- The tensile test results showed that the stress-strain behavior of the base metal and welded joints was almost the same at room temperature and 1273 K.

Tensile test results
(strain-stress curve)

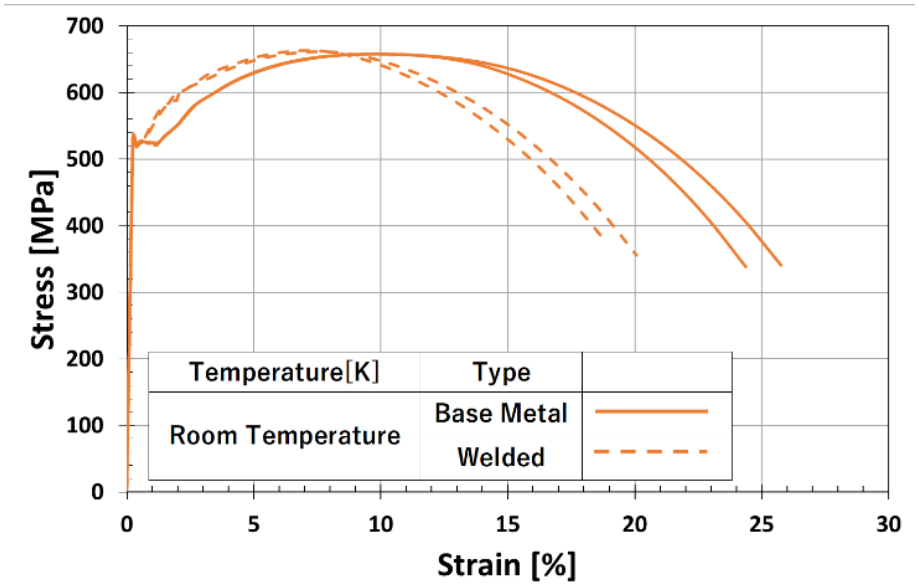

a) Room temperature

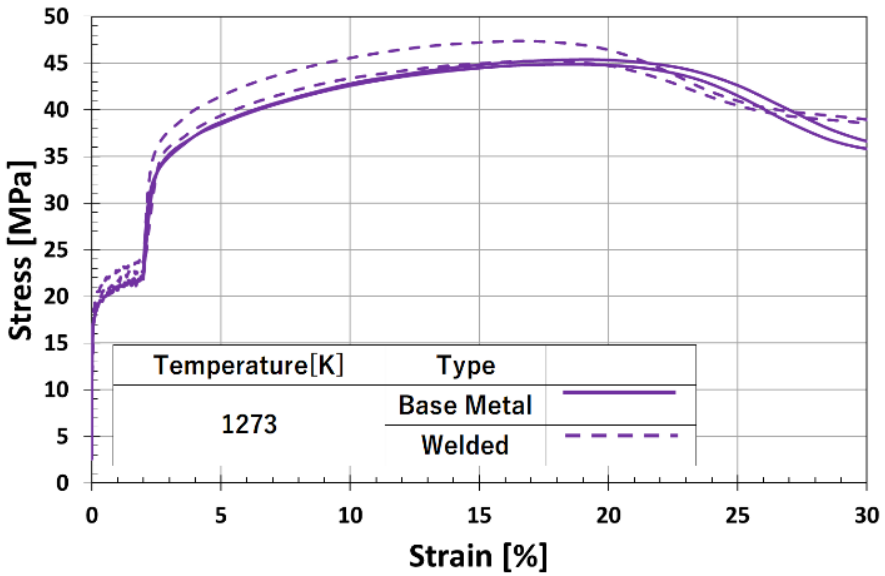

b) 1273 K

3.1 Tensile test

Test results

- In addition, the 0.2% proof strength of the base metal and welded joint was approximately the same as previous findings. From the above, it was found that the base metal and the welded joints had the same tensile strength.

Tensile test results：relationship between temperature and 0.2% proof strength：

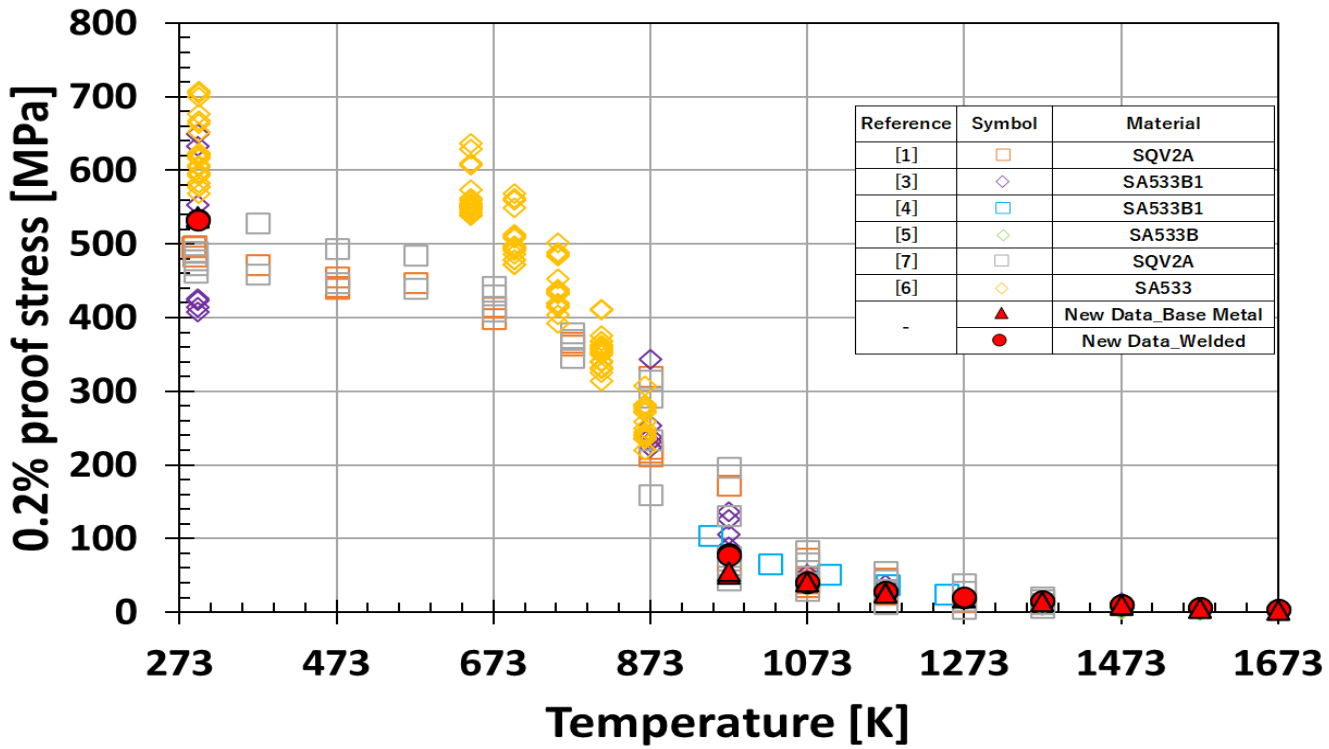

3.2 Creep test

Implementation content

- Previous knowledge of creep test data that includes welded joints is lacking beyond 873 K, so we considered temperatures above 873 K and the A1 transformation point (993 K) & A3 transformation pint(1103 K) where the thermal properties of RPV material (carbon steel) change , and expanded the data. We also acquired base metal data at 973 K and expanded base metal data for temperatures above 1273 K.

Appearance of test piece

Temperature	Shape of specimen	Appearance of specimen
T≦1273 K	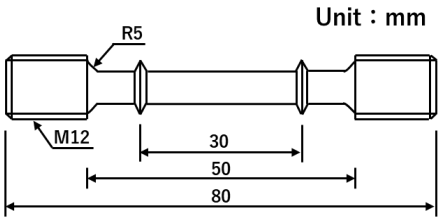	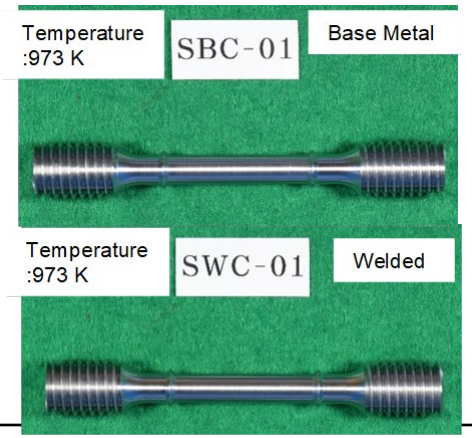
T>1273 K	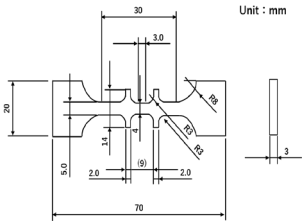	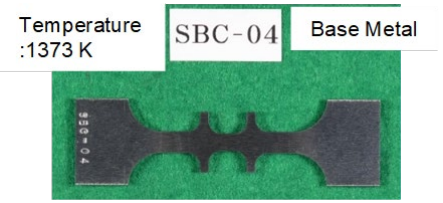

3.2 Creep test

Test relts

- From the relationship between rupture time and stress, there was no difference in strength between the base metal and the welded joints, and the values were comparable. From the above, it was found that the base metal and the welded joints had the same degree of creep strength.

Creep test results (relationship between rupture time and stress)

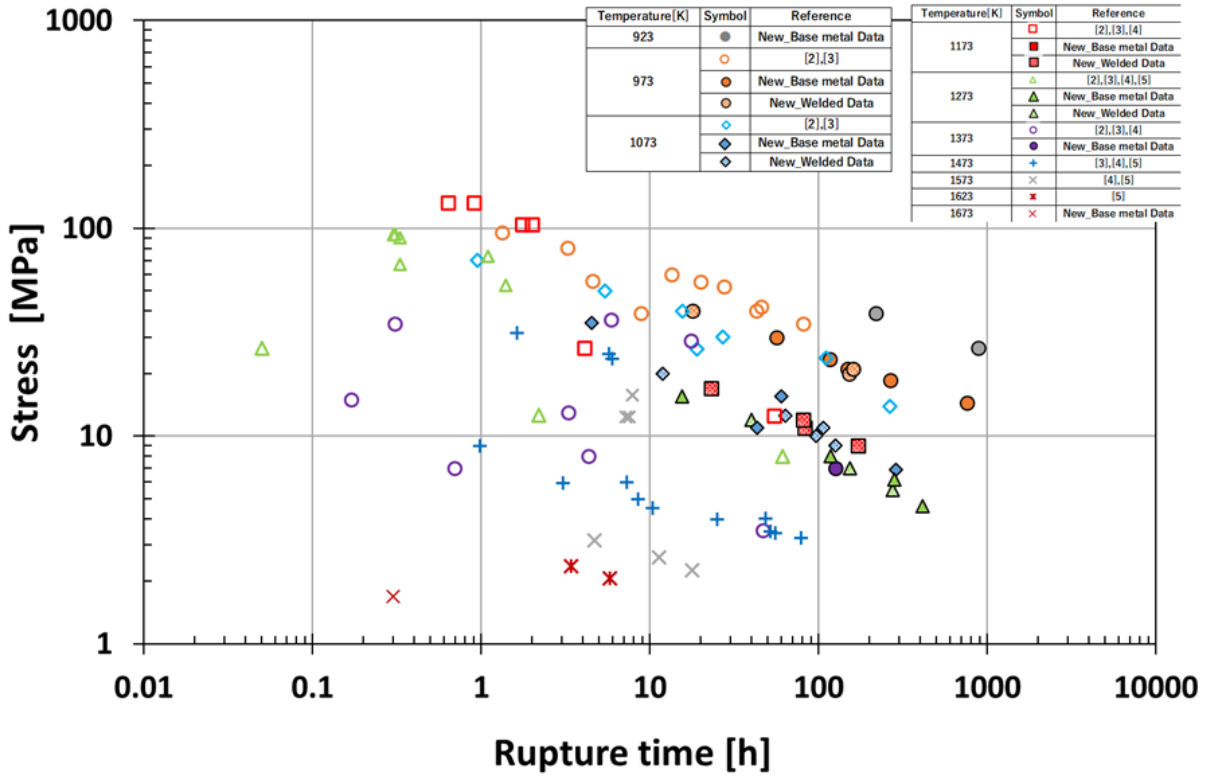

Appearance of test specimen after test

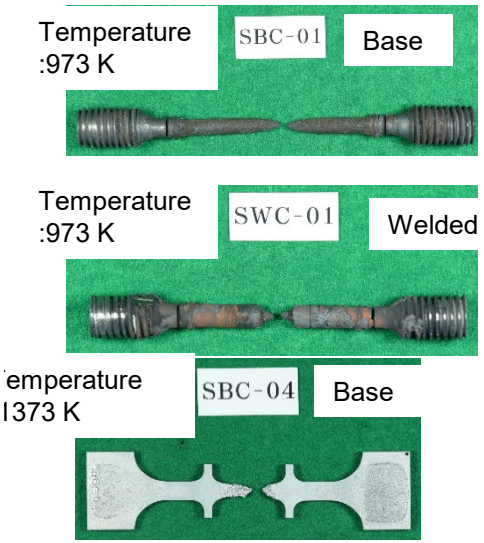

4. Formulation of material property formula

4.1 Elasto-plastic stress-strain formula

Implementation content

- Based on past knowledge and newly acquired data, we formulated an elasto-plastic stress-strain formula to be applied to structural analysis. This time, we adopted two-line approximation and set the values of each parameter.

Elasto-plastic stress-strain formula (two-line approximation)

$$\sigma \leq \sigma_y \therefore \sigma = \frac{\varepsilon}{E}$$
$$\sigma > \sigma_y \therefore \sigma = \sigma_y + K\varepsilon$$

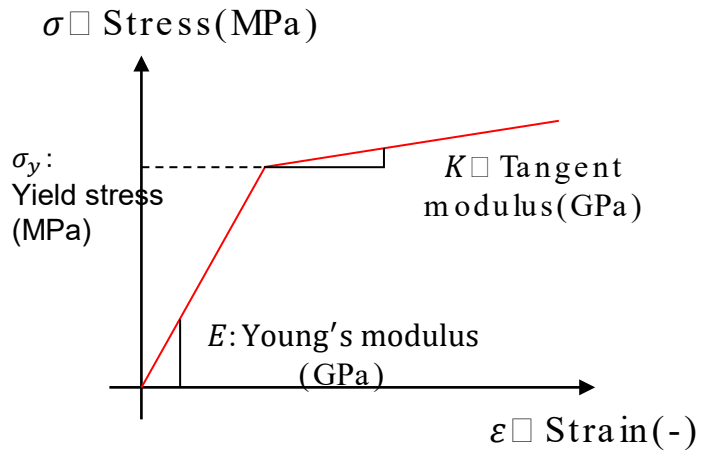

Used elasto-plastic stress-strain formula

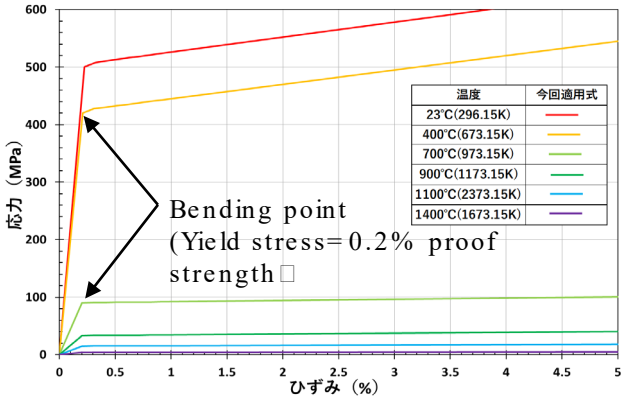

Relationship between temperature and Young's modulus

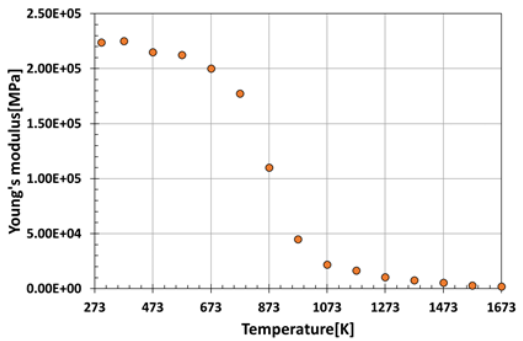

Relationship between temperature and yield stress/tangent modulus

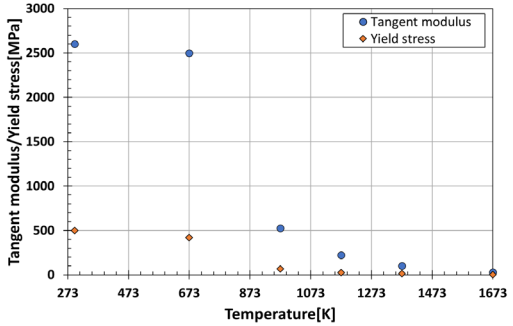

4.2 Creep strain formula

Implementation content

- The creep strain formula is required to perform structural analysis that takes creep into account. In analyzes that take severe accident in consideration, the material will be exposed to the creep temperature range. In high-temperature regions, tertiary creep, where creep strain accelerates, tends to become more pronounced, so we decided to adopt the Kachanov-Rabotonov formula, which can take even tertiary creep into account

Creep strain calculation using K-R model

$$t = 0 \therefore \omega = \varepsilon = 0$$

$$t = t_i$$

$$\omega_i = \omega_{i-1} + \int_{i-1}^{i} d\omega_i$$

$$\omega_i = \omega_{i-1} + B\frac{\sigma^k}{(1-\omega_{i-1})^k}(t_i - t_{i-1})$$

$$\varepsilon_i = \varepsilon_{i-1} + \int_{t_{i-1}}^{t_i} d\varepsilon_i$$

$$\varepsilon_i = \varepsilon_{i-1} + A\left(\frac{\sigma}{1-\omega_i}\right)^n (t_i - t_{i-1})$$

Repeat until $\omega = 1$

$$\omega = 1$$

Calculate the damage coefficient at each time

Calculate creep strain form the calculated damage coefficient

Creep Strain ε□ -□

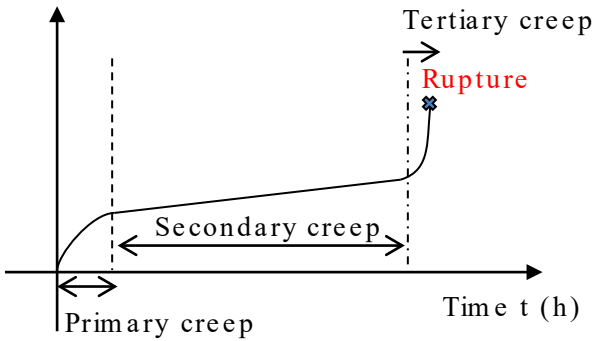

Each parameter set

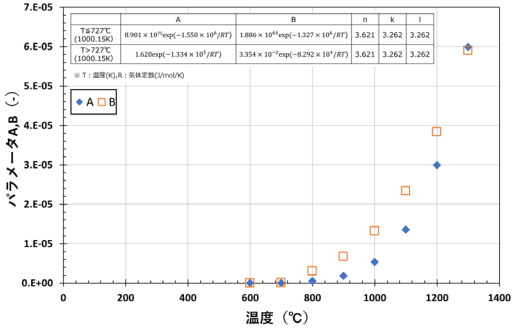

Comparison with test results

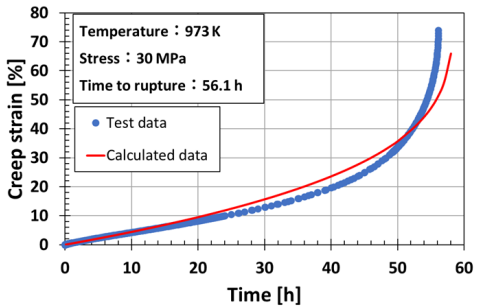

	A	B	n	k	l
T ≤993 K	5.417×10^{60} $\exp(-1.280 \times 10^6/RT)$	4.599×10^{36} $\exp(-8.0267 \times 10^5/RT)$	2.525	2.774	2.774
993 < T ≤ 1103 K	1.205×10^3 $\exp(-1.340 \times 10^5/RT)$	1.977×10^3 $\exp(-1.812 \times 10^5/RT)$	3.130	3.18	3.18
T > 1103 K	1.620 $\exp(-1.334 \times 10^5/RT)$	3.354×10^{-2} $\exp(-8.292 \times 10^4/RT)$	3.324	3.045	3.045

t□ time(s),σ□ Stress(MPa),
ε□ Strain(-),ω□ Damage coefficient(-)

4.3 Creep rupture formula

Implementation content

- As a mechanical failure evaluation, evaluation using creep damage Dc(=∑Δt/tr) has been carried out. The rupture time tr required for this failure evaluation is calculated using the Larson-Miller-Parameter(LMP)(creep rupture formula). LMP is defined by the following formula

$$LMP = T(C + logt_r) = A + Blog\sigma + D(log\sigma)^2$$ Temperature:T(K), Stress:σ(MPa)

Each parameter in the above formula was calculated from the data obtained this time and the relationship between rupture time and stress based on past knowledge. In addition, considering the regression nature of long-term data, we adopted a quadratic equation this time.

Relationship between rupture time and stress

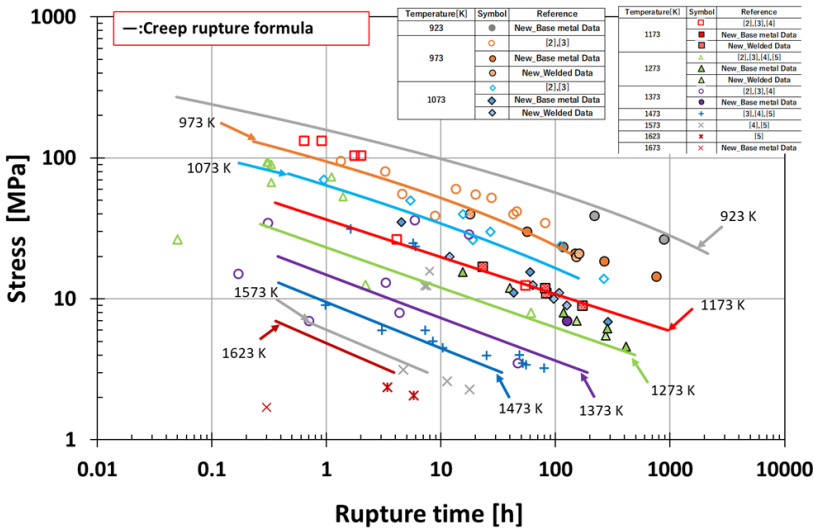

	T ≤ 993[K]	993[K] < T ≤ 1103[K]	1103[K] < T
C	20.05	2.69	8.70
A	21882.45	7366.37	17274.83
B	1743.35	-732.30	-4648.61
D	-1491.68	-971.87	78.46

4.3 Creep rupture formula

Implementation content

- LMP is a linear equation in MELCOR, and the rupture time tends to be shorter than actual data. At temperatures below the A1 transformation point, there is a large difference at the same stress, and between the A1 and A3 transformation points, both show equivalent values, but after the A3 transformation point, the same stress differs by about 1/10. Therefore, it is considered better to use data based on actual data regarding LMP.

Comparison MELCOR and creep rupture formula

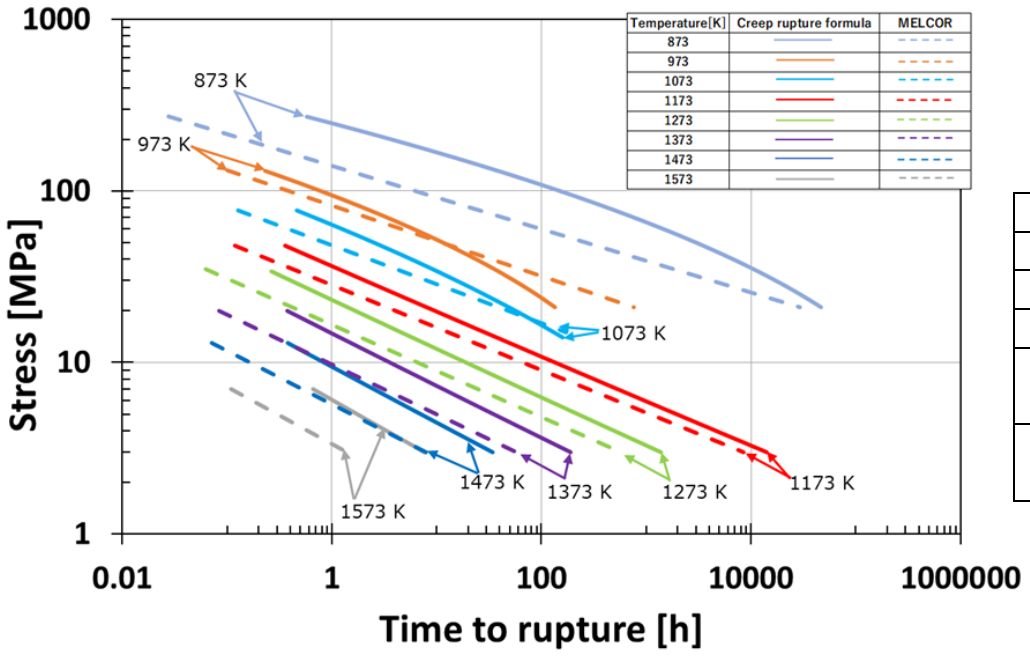

$$t_R = 10^{\left(\frac{P_{LM}}{T} - C\right)}$$

$$P_{LM} = \min[a_1 \log_{10}(\sigma_e) + b_1, a_2 \log_{10}(\sigma_e) + b_2]$$

Material Type	a_1[K]	b_1[K]	C	a_2[K]	b_2[K]
A-508, class 2 carbon steel	-5335	62291.3	16.44	-	-
SS-316, 316 stainless steel	-7400	81088.4	16.44	-35555.5	322036.2
INC-600, Inconel 600	-6296	67129.96	11.44	-	-
SA533B1, LH-Steel, Default LH Steel	-4730	4.81E+04	7.042	-	-
SC1604, SS-Steel, Default COR SS Steel	-7500	8.10E+04	16.44	-	-

1. L.L. Humphries, B.A. Beeny, F. Gelbard, D.L. Louie, J. Phillips, "MELCOR Computer Code Manuals", SAND2017-0455 O(2017)

5. Conclusions

Results

- Including the data acquired this time and past knowledge, we formulated material property formulas (elasto-plastic stress-strain relationship formula, creep strain formula, and creep rupture formula) for RPV material.
- Based on the currently available data, the welded joints and the base metal have the same strength, so it is considered unnecessary to set a welded joint reduction factor.

REFERENCES

1. Japan Nuclear Energy Safety Organization,"Project of Integrity Assessment of Flawed Component with Structural Discontinuity (IAF) Material Properties Data Book at High Temperature for dissimilar metal welding in Reactor Pressure Vessel", JNES-RE-2012-0024(2013)
2. J.L. Rempe, S.A. Chavez, G.L. Thinnes, C.M. Allison, G.E. Korth, R.J. Witt, J.J. Sienicki, S.K. Wang, L.A. Stickler, C.H. Heath, S.D. Snow,"Light Water Reactor Lower Head Failure Analysis", NUREG/CR-5642(1993)
3. D.R. Diercks, L.A. Neimark, "Results of Mechanical Tests and Supplementary Microstructural Examinations of the TMI-2 Lower Head Samples", NUREG/CR-6187(1994)
4. L.L. Humphries, T.Y. Chu, J. Bentz, R. Simpson, C. Hanks, W. Lu, B. Antoun, C. Robino, J. Pusk P. Mongabure,"OECD Lower Head Failure Project Final Report", NEA/CSNI/R(2002)
5. Y. Yamaguchi, J. Katsuyama, Y. Kaji, M. Osaka, Y. LI,"Expansion of high temperature creep test data for failure evaluation of BWR lower head in severe accident", Mechanical Engineering Journal Vol.7, No.3(2020)
6. H.E. McCoy, "TENSILE AND CREEP PROPERTIES OF SA533 GRADE B CLASS 1 STEEL ", DOE-HTGR-88383(1989)
7. Y. Takahashi, "Development of accurate inelastic analysis models for materials constituting penetrations in reactor vessel", Q14016(2015)

Correlation Development for the Determination of Aerosol Particle Retention in Liquid Pools

Jonas Rehrmann, Tobias Jankowski and Marco K. Koch
Ruhr-Universität Bochum (RUB)
Plant Simulation and Safety Group (PSS)
Universitätsstr. 150, 44801 Bochum, Germany
jonas.rehrmann@pss.rub.de, tobias.jankowski@pss.rub.de and marco.koch@pss.rub.de
ORCID: 0000-0002-3870-7058; 0000-0001-5506-0498, 0000-0001-7260-5250

ABSTRACT

For the estimation of the particle retention in a liquid pool, a correlation is under development that is suitable to be implemented in the software package AC² developed by the Gesellschaft für Anlagen- und Reaktorsicherheit (GRS) gGmbH. Within AC², the Containment Code System COCOSYS is used for the simulation of ex-vessel phenomena in the frame of postulated severe accident scenarios in light water reactor containments. As a lumped parameter code COCOSYS is characterized by a low simulation time compared to other simulation methods such as CFD. Validation work shows a significant underestimation of the retention efficiency by the pool scrubbing model implemented in COCOSYS compared to experimental data. Therefore a new model is being developed.
Considering that the quantification of the contribution of individual deposition mechanisms to the particle retention in pool scrubbing is not concluding solved due to a lack of measurement options, analytical methods and evaluation procedures were conducted to determine the dependence of retention efficiency on different boundary conditions. The work indicates a high dependence of the retention efficiency on particle diameter and submergence of the aerosol injection in the liquid pool. Essential boundary conditions can be reproduced via dimensionless numbers, so that interacting effects can be taken into account. The input parameters of the new correlative approach are provided by COCOSYS and a calculation of the particle retention is possible without significant user influence. The correlation was developed on experiments with different types of test facilities, injection devices and boundary conditions, so that the approach is not limited to any specific configuration. First calculation results show high agreement with experimental data.

KEYWORDS
Pool Scrubbing, Particle Retention, COCOSYS, Correlation, Validation

1. INTRODUCTION

Pool scrubbing describes the retention of aerosol particles from a gas flow that is directed into a liquid pool. Pool scrubbing can occur in numerous places in the event of accidents in nuclear power plants with the release of fission products. For example, in an SGTR (Steam Generator Tube Rupture), flooded MCCI (Molten Core Concrete Interaction) or in the condensation chamber of a boiling water reactor. Pool scrubbing is quantified using the retention efficiency η, that can be calculated using the fission product inlet mass flow $\dot{m}_{in}$ and the fission product mass flow $\dot{m}_{out}$ leaving the liquid pool,

$$\eta = \frac{\dot{m}_{in} - \dot{m}_{out}}{\dot{m}_{in}} \tag{1}$$

or the decontamination factor DF:

$$DF = \frac{\dot{m}_{in}}{\dot{m}_{out}}. \quad (2)$$

Pool scrubbing is determined in accident analysis codes using various models such as SPARC90 (MELCOR) or SPARC-B/98 (COCOSYS). The models show high uncertainties in validations and tend to underestimate the retention efficiency. In addition to the models described, there are also correlative approaches that are characterized by low user influence and a small number of input parameters. The applicability of correlative models is generally very limited. To determine pool scrubbing without major user influence and without restriction to specific plant geometries, a model is developed on the basis of a large number of different experiments, which is suitable for implementation in accident analysis codes.

2. EXPERIMENTS TAKEN INTO ACCOUNT

For the development of the present model, experiments from the test series ACE, LACE-España, Poseidon-II, RCA, SAAB-I, SAAB-II and THAI WH25-27 are used, for the most following the recommendations in [1]. The experimental investigations focus on nozzle geometries with a round outlet, placed in downward, horizontal, or upward orientations. No experiments with installations or additives in the liquid pool are included in the development. A comprehensive description of the facilities and experiment-specific boundary conditions can be found in Rehrmann et al. [2].
Within the ACE project, particle retention for three different substances of a mixture is analysed in four experiments. The resulting data are included into the correlation development for individual substances, resulting in twelve considered retention efficiencies. The injection was carried out using a quencher with 51 orifices, each with a diameter of 9.525 mm diameter. The main parameters varied are the gas mass flow, the steam fraction, the pool temperature and the submergence of the quencher. The ACE experiments predominantly determine high retention efficiency ($\eta > 0.99$). [3]
The LACE-España project, conducted by the LACE-España consortium consisting of CIEMAT, CSN, ENUSA, TECNATOM, UNESA and UPM at the "LACE-España Project facility", contribute seven experiments to the model development, exclusively using experiments with a single horizontal orifice. Among other things, the steam mass fraction is varied in the experiments, while the submergence remains constant. [4]
The focus of the 17 POSEIDON-II experiments conducted at the Paul Scherrer Institute (PSI) is to investigate the particle retention by condensation and inertia, therefore the dependence of the DF on the submergence, the steam fraction and the particle diameter is analysed. The Poseidon II experiments show a linear relationship between retention efficiency and submergence, with particle retention additionally favoured by steam fraction and injection velocity. [5]
As part of the RCA program, four experiments are conducted to investigate particle retention and nine hydrodynamic experiments are carried out in the PECA test facility. The experiments RCA1, RCA2, RCA3 and RCA4 investigating the particle retention are used for modelling. The investigations focus on the effect of the submergence, the pool temperature, the steam mass flow and the weber number. The carrier gas used is nitrogen with an inlet pipe diameter of 0.01 m. [6]
As part of the SAAB-I project, 14 experiments are carried out to analyse particle retention. The submergence, the particle concentration in the gas flow, the feed volume flow rate, the steam fraction in the gas flow and the orientation of the orifice in the liquid pool are varied. Six experiments from the SAAB-I project are included in the development. [7]
The SAAB-II experiments show a dependence between retention efficiency and submergence. In addition to the retention efficiency of an averaged particle diameter, the retention efficiency for different cut-off diameters is also provided. The retention efficiency for the entirety of size classes is derived from the average cut-off diameters.
The THAI test series are conducted by Becker Technologies. The THAI WH25-27 experiments are oriented towards the conditions of a condensation chamber of an SWR 72 and include a scaled-downcomer (1:3 regarding the size). The test series are carried out in the PAD tank of the THAI+ test facility and comprise 13 individual experiments in which the particle retention is determined for different steam mass fractions from 0 to 0.73. [8]

3. ANALYTICAL METHODS

3.1. Identification of relevant boundary conditions

As part of the first work package of the APVOR project, an analysis based on the PIRT (Priority Identification and Ranking Table) method is carried out and documented in the first technical report of the project [2]. The goal of the procedure based on PIRT is the systematic identification of influencing parameters that are considered by experts to be of high importance for particle retention. Eight participants have assessed the relevance of the parameters as "l" (low), "m" (medium) or "h" (high) based on their understanding and knowledge of pool scrubbing. The relevance is calculated based on the number of votes *n* as follows [9]:

$$Relevance_i = \frac{1{,}0n_h + 0{,}5n_m + 0{,}0n_l}{n_h + n_m + n_l} \tag{3}$$

The relative standard deviation for the scattering of votes $Scattering$ is calculated as follows [9]:

$$Scattering = \frac{Scattering_i}{max(Scattering_i)} \tag{4}$$

where $Scattering_i$ is the standard deviation of n_h, n_m and n_l for a parameter. The value $max(Scattering_i)$ refers to the standard deviations of the entire table.
For the analysis, the pool is subdivided into the injection zone (Table I.), the quasi-stationary bubble rise zone (Table II.) and the bubble burst zone at the surface (Table III.). Sub-PIRTs are created for the individual areas and relevant parameters influencing pool scrubbing processes are identified. Table II and III are shortened for the sake of improved visualization. The complete tables can be found in [2].

Table I. Relevance of individual parameters in the injection zone

Injection zone					
Parameter	**l**	**m**	**h**	**Relevance**	**Scattering**
Injection velocity	0	0	7	1.000	1.000
Density of the particles	1	1	5	0.786	0.571
Surface tension	1	2	5	0.750	0.515
Particle diameter	1	1	4	0.750	0.429
Nozzle diameter	2	0	6	0.750	0.756
Steam mass fraction	0	3	3	0.750	0.429
Nozzle geometry	1	1	3	0.700	0.286
Fluid temperature	1	3	4	0.688	0.378
Submergence	2	0	4	0.667	0.495
Gas pressure	2	0	4	0.667	0.495
Density of the gas	1	2	2	0.600	0.143
Particle concentration	2	1	3	0.583	0.247
Big bubble diameter	1	3	2	0.583	0.247
Condensability of the gas	3	0	4	0.571	0.515
Temperature of the gas	2	2	3	0.571	0.143
Orientation of the nozzle	2	3	3	0.563	0.143
Fluid pressure	1	4	1	0.500	0.429

Injection zone					
Parameter	**l**	**m**	**h**	**Relevance**	**Scattering**
Nozzle diameter / pool diameter / -height ratio	3	2	2	0.429	0.143
Pool diameter / -height	3	2	1	0.333	0.247
Big bubble rise velocity	4	3	1	0.313	0.378
Fluid viscosity	3	1	1	0.300	0.286
Residence time of the large bubble	5	1	1	0.214	0.571
Pool diameter	5	2	0	0.143	0.623
Solubility	3	1	0	0.125	0.378
Bubble geometry	5	1	0	0.083	0.655

Table II. Relevance of individual parameters in the Quasi-stationary bubble rise zone

Quasi-stationary bubble rise zone					
Parameter	**l**	**m**	**h**	**Relevance**	**Scattering**
Residence time	0	0	8	1.000	1.000
Submergence	0	0	7	1.000	0.875
Surface tension	0	1	6	0.929	0.696
Bubble rise velocity	1	0	7	0.875	0.820
Bubble size of the swarm bubbles	0	2	5	0.857	0.545
Fluid temperature	1	1	6	0.813	0.625

Table III. Relevance of individual parameters in the bubble burst zone at the surface

Bubble burst zone at the surface					
Parameter	**l**	**m**	**h**	**Relevance**	**Scattering**
Gas exit velocity	0	2	6	0.875	0.950
Humidity of the atmosphere	1	2	4	0.714	0.475
Surface tension	2	1	5	0.688	0.648
Gas bubble size	1	3	3	0.643	0.359
Density of the particles	3	0	5	0.625	0.783
Steam mass fraction	2	1	3	0.583	0.311

The consortium considers particle size and density as well as the injection velocity and the surface tension to be highly relevant influencing factors for pool scrubbing in the injection zone. The steam mass fraction is also considered by the consortium to be of medium to high relevance to particle retention. In the bubble rise zone, the residence time of the particles in the water pool is rated as highly relevant by all participants. The gas exit velocity and the humidity of the atmosphere are considered important in the bubble burst zone at the surface with a low scattering of results.

3.2. Pearson coefficient

The Pearson coefficient shows the linear correlation between two data series. It assumes values between -1 and 1. For -1, there is a completely negative linear correlation between the data series. For +1, there is a completely positive linear correlation. There is no linear correlation for a Pearson coefficient of 0. Table IV shows the Pearson coefficient between various boundary conditions and the retention efficiency of the selected experiments. The results should be seen in the consideration that not only the

investigated parameters are changed in the experiments. Even if the method is not ideal for finding dependencies, since relationships can be exponential or different, for example, it still gives a first rough impression.
The hydrostatic pressure and the density of the gas mixture are calculated as a function of the submergence and show a high linear correlation to the retention efficiency. In addition to the submergence, a high Pearson coefficient is also determined for the particle diameter. In contrast to the PIRT-based method, the Pearson coefficient of the selected experiments for the injection velocity suggests that this has a negative influence on the retention efficiency: The injection velocity is calculated from the mass flow rate, the nozzle cross-sectional area and the gas density. With a high submergence (high retention efficiency), the hydrostatic pressure and therefore the density of the gas increases. With a constant mass flow rate, the injection velocity decreases. The retention efficiency therefore increases for low injection velocities, as these often result from a high submergence. It cannot therefore be said that the injection velocity itself has a negative effect on particle retention. The retention efficiency is high for a high injection velocity and a high submergence.

Table IV. Pearson Coefficient of individual parameters of selected experiments

Parameter	Pearson Coefficient
Submergence	0.494
Hydrostatic pressure	0.485
Particle diameter	0.371
Density of the gas mixture	0.221
Stokes number	0.140
Carrier gas pressure	0.105
Nozzle diameter	0.092
Pool temperature	0.081
Gas mass flow	0.075
Steam mass fraction	0.005
Pool pressure	-0.012
Dynamic viscosity of the fluid	-0.030
Surface tension	-0.089
Density of the fluid	-0.111
Density of the particles	-0.180
Gas temperature	-0.188
Weber number	-0.259
Dynamic pressure	-0.286
Injection velocity	-0.325

3.3. Analysis of trends

To determine trends, the retention efficiency of the selected experiments is shown below as a function of boundary conditions that were considered as influential in the PIRT method. It should be noted that many other boundary conditions were changed in the experiments in addition to the boundary condition shown.
In Figure 1, the particle-specific boundary conditions of density and diameter are illustrated.

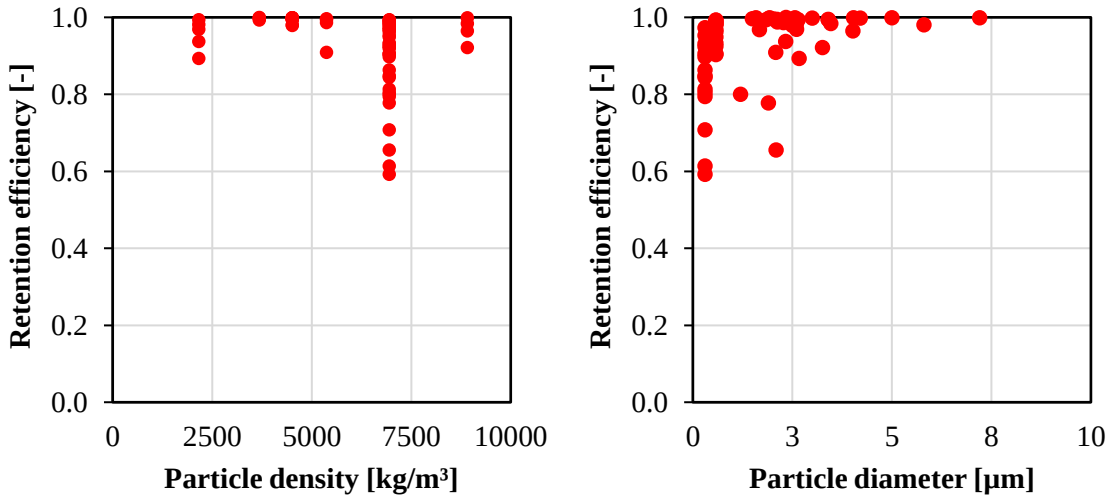

Figure 1. Retention efficiency for particle density and diameter of the investigated experiments

No trend is observed for particle density. The shown density corresponds to the pure substance and not the density of the processed, injected material, as this information is often not provided in the documentation of experiments. As the particle diameter increases, the retention efficiency improves. For lower limit values (minimum value of the y-axis for each x-value), the retention efficiency as a function of diameter can be described using a logarithmic function. In Figure 2, the submergence of the outlet geometry and gas velocity is shown. Similar to the particle diameter, a logarithmic trend is observed for the lower limit values of submergence. The gas velocity is a variable typically derived from the mass flow rate, nozzle cross-sectional area and gas density. In numerous experiments, the collection efficiency is high at low injection velocities, potentially resulting from a high steam mass fraction, submergence or large particles. It should be noted that the gas velocity can have a positive influence on the retention efficiency, but as the injection velocity increases, the residence time of the particles in the liquid and thus the retention efficiency decreases. Therefore, no clear trend can be identified.

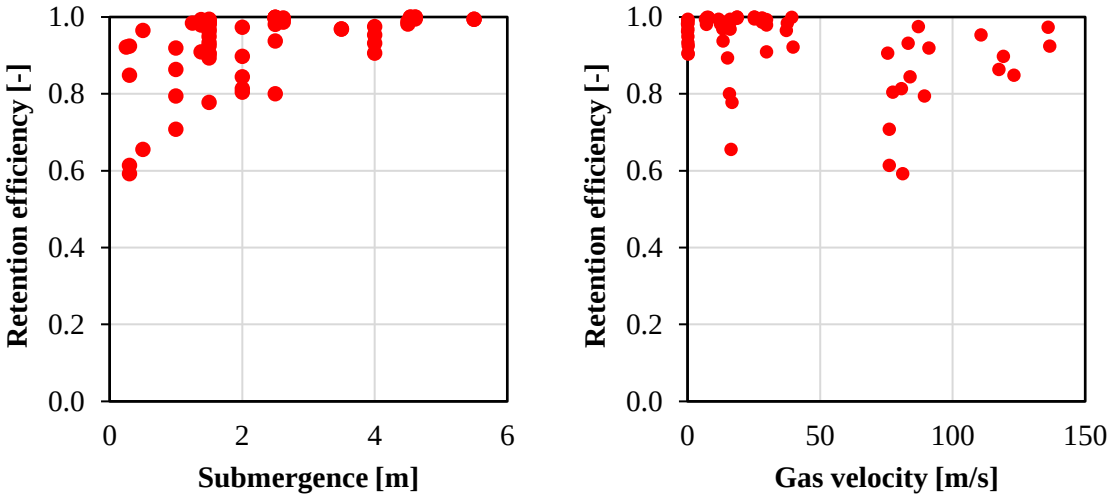

Figure 2. Retention efficiency for submergence and gas velocity of the investigated experiments

Since an analysis of retention efficiency based on isolated boundary conditions neglects the mutual influences of these conditions, the following discusses the relationships between retention efficiency and dimensionless numbers that combine relevant parameters (As shown in Figure 3).

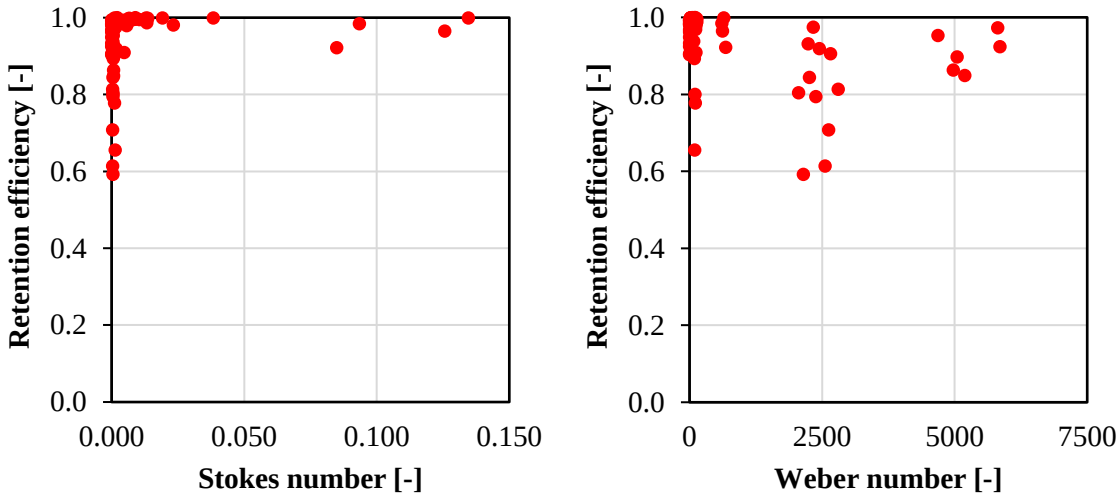

Figure 3. Retention efficiency for stokes number and weber number

For Stokes numbers Stk greater than 0.005 the retention efficiency converges to $\eta = 1$, with few exceptions. The trend of lower limit values for $Stk < 0.005$ shows similarities to a logarithmic function. The retention efficiency tends to increase with the Weber number. This is attributed, on one hand, to the rising gas velocity (which, as previously discussed, must be considered differentially) and, on the other hand, to the decreasing surface tension.

4. AGREEMENT WITH THE EXPERIMENTS USED

To determine the retention efficiency η, the penetration Pt, i.e. the proportion of particles that are not retained, is determined. With $\eta_i = 1 - Pt_i$ the retention efficiency η can be calculated as follows:

$$\eta = 1 - (1 - \eta_1) \cdot (1 - \eta_2) \cdot (\dots) \cdot (1 - \eta_i). \tag{5}$$

The coefficients η_i are employed to calculate the retention efficiencies of various pool scrubbing phenomena. The function comprises three coefficients η_i, which depend on the Stokes number, Weber number and a submergence parameter. Additionally, the model considers the impact of condensation on particle retention. The approach is taken from Uchida et al. [9]. Furthermore, a factor is incorporated to account for different nozzle orientations. The coefficients are based on a logistic function:

$$y = \frac{1}{1 + exp\,(-x)} \tag{6}$$

The logistic function can be divided into three distinct sections: an initial exponential growth phase, followed by a linear phase and a saturation phase. By adjusting different function constants, functional properties such as the gradient can be adjusted. In the context of pool scrubbing experiments, an overall retention efficiency is determined. Due to limitations in development and validation, it is not feasible to adjust the correlation constants for individual coefficients η_i. Consequently, these correlation constants are determined as a whole. To achieve this, the sum of the absolute deviation between the experimental retention efficiency η_{exp} and the calculated retention efficiency η_{calc} is minimized across all experiments by simultaneously modifying all correlation constants.
Figure 4 shows the retention efficiency of the calculation as a function of the retention efficiency of the experimental series used to develop the correlation.

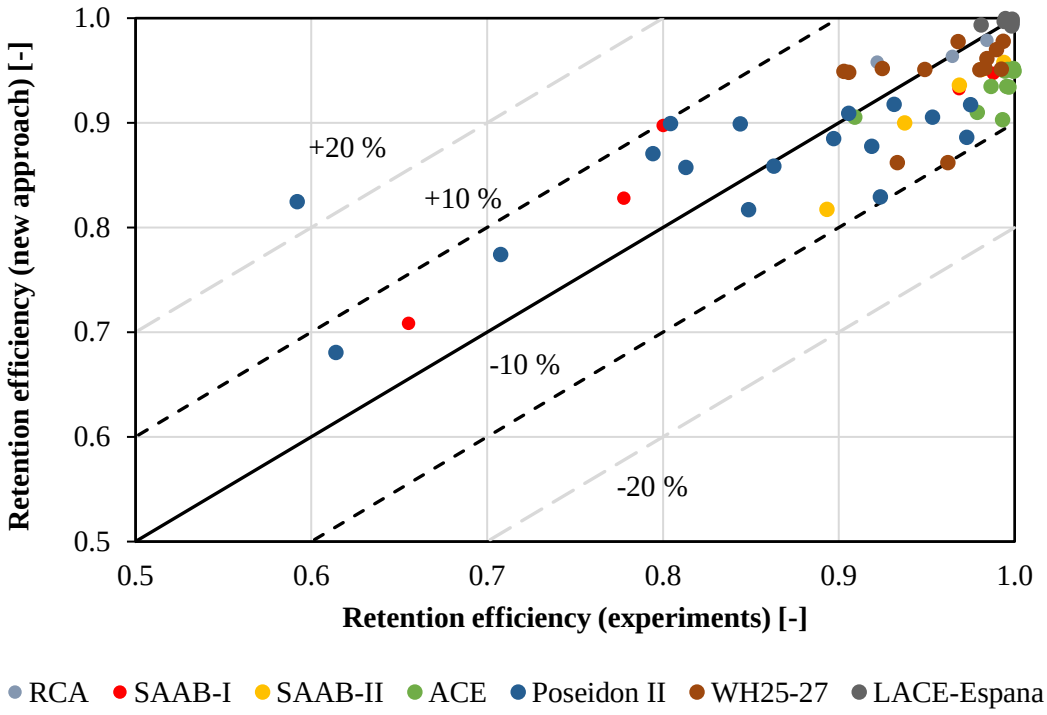

Figure 4. Retention efficiency of the calculation as a function of the retention efficiency of the selected experiments

With the exception of an experiment within the Poseidon II test series, the deviation of the calculated retention efficiency from the measured retention efficiency in all test series is less than ±10%. Additionally, the calculations accurately capture the trend observed in the experimental data. In the low particle retention range (η < 85%), the model tends to overestimate the retention efficiency. For high particle retention (η > 85%), there is a tendency toward a slight underestimation.
For the Poseidon II - PA21 experiment with an experimentally determined retention efficiency of η = 0.59, particle retention due to condensation is significantly overestimated (η_{Cond} = 0.778, see Figure 4) because of the elevated steam mass fraction of x = 0.7. It is possible that due to the low submergence (H = 0.3 m), the steam is not fully condensed. The approach taken from Uchida et al. [9] for determining the condensation influence on particle retention needs to be adjusted accordingly.

5. CONCLUSION

The analytical methods involve various steps, including identifying influential factors through a PIRT-based procedure, using the Pearson coefficient to investigate linear relationships between boundary conditions and retention efficiency and a trend analysis. Results indicate that submergence and particle diameter positively influence particle retention. The trend analysis for individual boundary conditions yielded no clear trends for most parameters, as the influence on retention efficiency often depends on multiple conditions collectively considered. For this reason, additional dimensionless numbers were examined and included in the development.
The developed model incorporates various coefficients considering influences such as particle size, submergence, gas velocity and condensation. To account for the influence of condensation on particle retention, a model by Uchida et al. is tested. Apart from a single experiment within the Poseidon II test series, the difference between the calculated and measured retention efficiencies is consistently within ±10% across all experimental series. In future work, the correlation must be validated with appropriate experiments.

ACKNOWLEDGMENTS

Supported by:

Federal Ministry
for the Environment, Nature Conservation,
Nuclear Safety and Consumer Protection

based on a decision of
the German Bundestag

This work was funded by the German Federal Ministry for the Environment, Nature Conservation, Nuclear Safety and Consumer Protection under grant number 1501618 on the basis of a decision by the German Bundestag.

The simulations were performed with the code AC², developed by GRS.

REFERENCES

1. L. E. Herranz, F. Sánchez, S. Gupta: "Validation Matrix for Pool Scrubbing Models." *Nuclear Technology,* Vol. **209**., pp. 1523-1536, (2022).
2. J. Rehrmann et al.: „Bewertung der verfügbaren Datenbasis zur Partikelrückhaltung in Flüssigkeitsvorlagen. Technischer Fachbericht zum Vorhaben BMUV 1501618: Analytische und experimentelle Untersuchungen zur Partikelrückhaltung in Flüssigkeitsvorlagen (APVOR)“, Ruhr Universität Bochum, Arbeitsgruppe Plant Simulation and Safety, Germany (2022).
3. L.W. He: “Investigation on Aerosol Pool Scrubbing Model During Severe Accidents”, *Frontiers in Energy Research*, Vol. **9**., (2021).
4. M. J. Marcos Crespo et al.: “LACE-ESPANA Experimental Programme on the Retention of Aerosols in Water Pools”, Centro de Investigaciones Energeticas Medioambientales Y Tecnologicas, Spain (1994).
5. A. Dehbi et al.: “Aerosol retention in low-subcooling pools under realistic accident conditions”, *Nuclear Engineering and Design*, Vol. **203**., pp. 229–241, (2001).
6. V. Peyres et al.: “Pool scrubbing and hydrodynamic experiments on jet injection regime”, *Informes Tecnicos Ciemat*, Vol. **27**., (1995).
7. H.J. Allelein et al.: „Aerosolverhalten bei schweren Störfällen. Abschlussbericht - Reaktorsicherheitsforschung – Vorhaben-Nr.: 1501454“, RWTH Aachen (2018).
8. M. Freitag et al.: „Aerosolrückhaltung in einer Wasservorlage - Pool Scrubbing - Versuchsserie WH-25–WH-27. Experimentelle Untersuchungen zur Spaltproduktrück-haltung und Wasserstoffbeherrschung bei Stör- und Unfallabläufen im Sicherheitsbehälter (THAI-VI) - 1501547 – FB/TR – WH25-27“, Becker Technologies, Germany (2018).
9. M. Adorni et al.: “Phenomena Identification and Ranking Table. R&D Priorities for Loss-of-Cooling and Loss-of-Coolant Accidents in Spent Nuclear Fuel Pools”, OECD; NEA, (2018).
10. S. Uchida et al.: “Temperature dependent fission product removal efficiency due to pool scrubbing”, *Nuclear Engineering and Design*, Vol. **298**., pp. 201–207, (2016).
11. L. E. Herranz; F. Sánchez: "New pool scrubbing correlations based on reliable data." *Annals of Nuclear Energy*, Vol. **183**., (2023).



RUB

RUHR-UNIVERSITÄT BOCHUM

Correlation Development for the Determination of Aerosol Particle Retention in Liquid Pools

Jonas Rehrmann, Tobias Jankowski and Marco K. Koch

ERMSAR | Stockholm | May 13th - 16th, 2024

PSS Plant Simulation and Safety
Prof. Dr.-Ing. Marco K. Koch

Outline

- Introduction
- Analytical methods
- Modelling approach
- Results
- Conclusion and Outlook

- Jonas Rehrmann, M. Sc.
  - Research Associate
  - Plant Simulation and Safety at Ruhr-Universität Bochum, Germany



INTRODUCTION

- Model development to determine the retention efficiency for pool scrubbing
- The work is part of the BMUV APVOR project *(Completed; report in progress)* and my dissertation *(Publication planned for 2026)*
- Aim of the current development:
  - A fast running algorithm with easy to define input parameters
  - Low user influence
  - General applicability
- Future Objective:
  - Extension with regard to specific accident boundary conditions

ANALYTICAL METHODS

PIRT BASED METHOD

- To determine the influence of various boundary conditions on the retention efficiency
- Eight participants from different institutions:
  - Becker Technologies, Forschungszentrum Jülich, GRS, Plant Simulation and Safety - Ruhr Universität Bochum
- Three tables for different Zones:
  - Injection Zone
  - Bubble Rise Zone
  - Pool Surface
- Rating of the influence from low (l) to medium (m) to high (h)

Injection zone					
Parameter	**l**	**m**	**h**	**Relevance**	**Scattering**
Injection velocity	0	0	7	1.000	1.000
Density of the particles	1	1	5	0.786	0.571
Surface tension	1	2	5	0.750	0.515
Particle diameter	1	1	4	0.750	0.429
Nozzle diameter	2	0	6	0.750	0.756
Steam mass fraction	0	3	3	0.750	0.429
Nozzle geometry	1	1	3	0.700	0.286
Fluid temperature	1	3	4	0.688	0.378
Submergence	2	0	4	0.667	0.495
Gas pressure	2	0	4	0.667	0.495
Density of the gas	1	2	2	0.600	0.143
Particle concentration	2	1	3	0.583	0.247
Big bubble diameter	1	3	2	0.583	0.247
Condensability of the gas	3	0	4	0.571	0.515
Temperature of the gas	2	2	3	0.571	0.143
Orientation of the nozzle	2	3	3	0.563	0.143
Fluid pressure	1	4	1	0.500	0.429
Nozzle diameter / pool diameter / -height ratio	3	2	2	0.429	0.143
Pool diameter / -height	3	2	1	0.333	0.247
Big bubble rise velocity	4	3	1	0.313	0.378
Fluid viscosity	3	1	1	0.304	0.156

ANALYTICAL METHODS

PIRT BASED METHOD

- General findings: → High importance of the surface tension

- **Injection Zone:** → Particle specific boundary conditions
  → Injection velocity
  → Properties of the nozzle

- **Bubble Rise Zone:** → Submergence → Residence time

- **Pool Surface:** → Gas exit velocity
  → Higher Scattering of the votes

ANALYTICAL METHODS

EXPERIMENTS USED FOR DEVELOPMENT

- ACE
- LACE-España
- RCA
- Poseidon-II
- SAAB-I (FZJ)
- SAAB-II (FZJ)
- THAI WH25-27 (Becker Technologies)

„QfV“ → Qualified for validation

PROGRAM	# TESTS	QfV	UfU	NoU
UKAEA (1965-1966)	>47			X
GE (1982)	18		X	
EPRI (1982-1986)	>151		X	
EPSI (1983-1991)	>7			X
POSEIDON-I (1987)	>100		X	
JAERI (1987)	~70		X	
ACE (1988-1992)	9	X		
LACE-España (1990-1992)	11	X		
SPARTA (1992)	1			X
RCA (1995)	4	X		
POSEIDON-II (1998)	17	X		
AASC-PS (1999-2000)	4	X		
SG-Experiments (2000-2012)	9	X		
PASSAM-RSE (2013-2017)	6	X		
PASSAM-CIEMAT (2013-2017)	7	X		
PASSAM-AREVA (2013-2015)	>21		X	
TOTAL # TESTS	>482	67	>360	>55

Herranz, L. E.; Sanchez, F.: “Critical Assessment of the Pool Scrubbing Database”, 3rd Meeting of the IPRESCA Project, 2019

Use for future development and validation

Analytical methods

Pearson Coefficient

- Represents linear relationships between two Datarows
  - Data row 1: Boundary Condition
  - Data row 2: Retention Efficiency

Parameter	Pearson Coefficient
Submergence	0.494
Hydrostatic pressure	0.485
Particle diameter	0.371
Density of the gas mixture	0.221
Stokes number	0.140
Carrier gas pressure	0.105
Nozzle diameter	0.092
Pool temperature	0.081
Gas mass flow	0.075



- First impression of significantly influential boundary conditions
- Fast analysis of large amounts of data



- Exponential relationships are often assumed
- More experiments needed for more reliable results

ANALYTICAL METHODS

DATA EVALUATION

- Possible progression of submodels

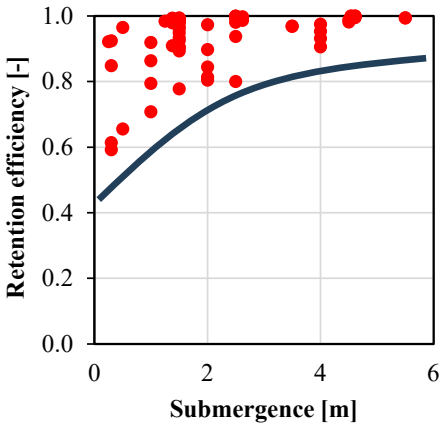

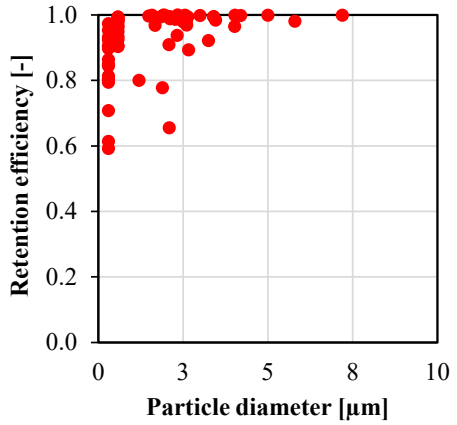

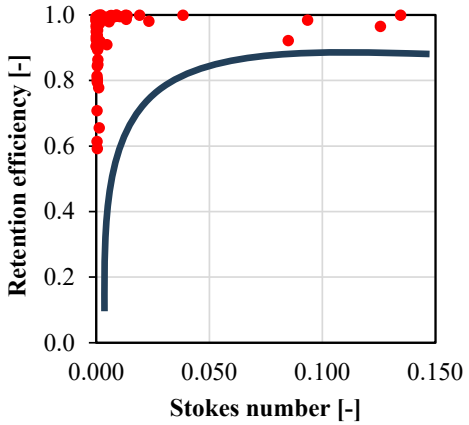

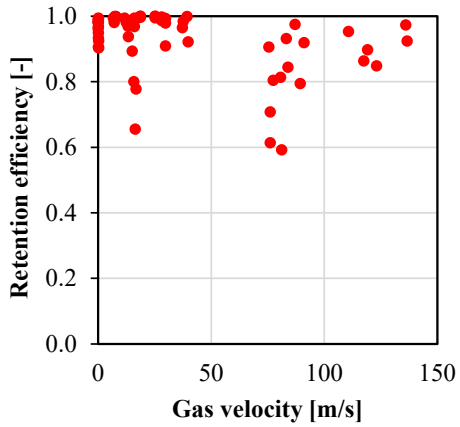

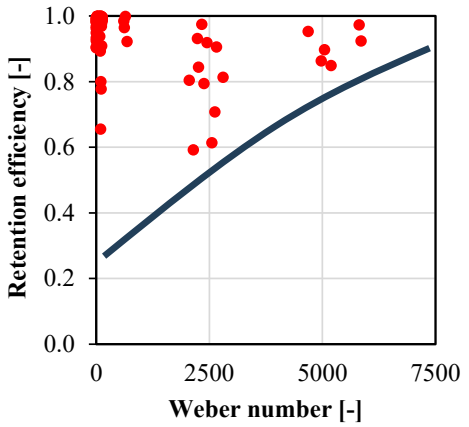

MODELLING APPROACH

STRUCTURE

- Basic structure
  - $\eta = 1 - (1 - \eta_1) \cdot (1 - \eta_2) \cdot (\dots) \cdot (1 - \eta_i)$

- Submodels and functions used:
  - Model based on stokes number
  - Model based on weber number
  - Submergence parameter
  - Third party condensation model
  - Factor for nozzle directions



- Correlative Approach
  - …without using input parameters that are difficult for the user to determine
  - …without calculation of thermal-hydraulic parameters, which are hard to validate

MODELLING APPROACH

MODIFYING OF THE FUNCTION PARAMETERS

- Submodels are based on a logistic function $y = \frac{1}{1+exp(-x)}$
- The sum of the absolute deviation between the experimental retention efficiency and the calculated retention efficiency is minimized by modifying all correlation constants at once

The model becomes more accurate the more different experiments are included in the procedure.

In this way, the model can be continuously improved through newly available experiments

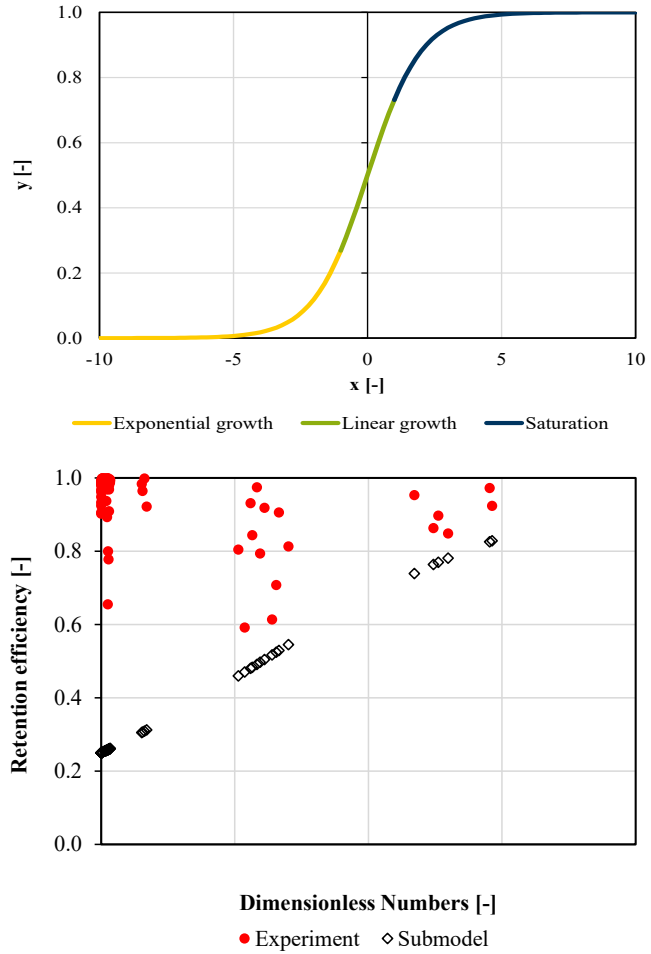

RESULTS

AGREEMENT WITH ALL EXPERIMENTS USED

- With the exception of one experiment the deviation in all test series is less than ±10%.
- For η < 85 % the model tends to overestimate the retention efficiency.
- For η > 85 % there is a tendency toward a slight underestimation.
- For the Poseidon II - PA21 experiment the particle retention due to condensation is significantly overestimated (η_{Cond} = 0.778).

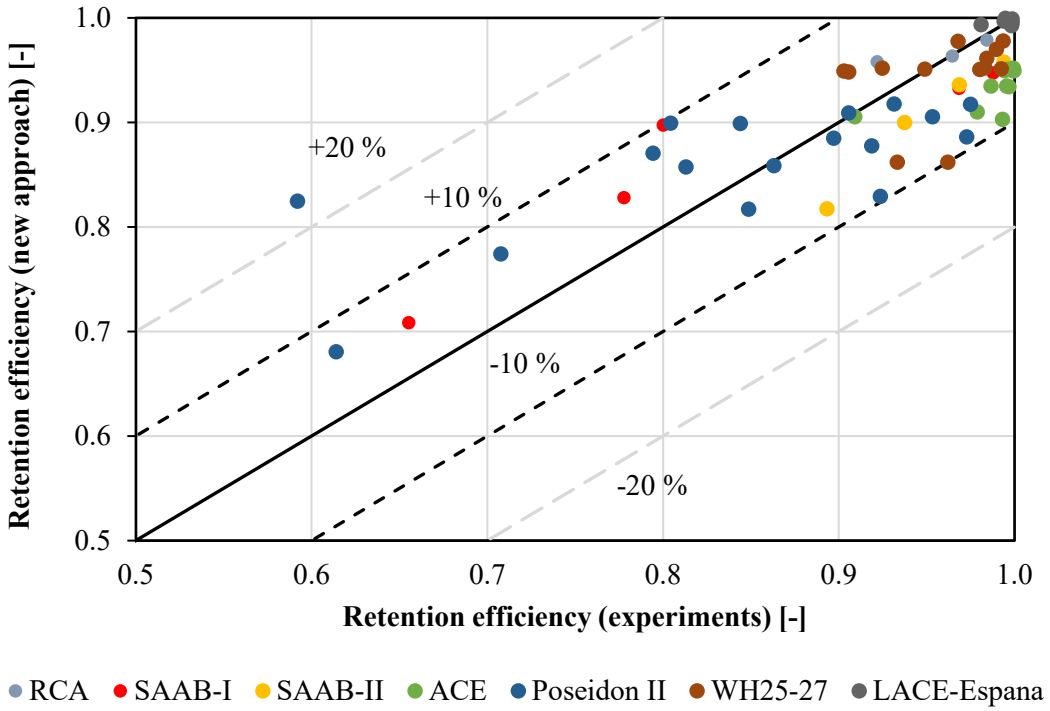

RESULTS

FIRST LOOK AT THE VALIDATION WITHOUT EXPERIMENTS USED FOR DEVELOPMENT

- The deviation is less than ±10 % for 36 of the 40 EPRI experiments.
- For the four experiments outside this range, the particle retention is overestimated due to the submergence.
- For $\eta > 0.99$ the deviation is less than 3.7 % for all 19 experiments.

→ Also small deviations for other experimental series

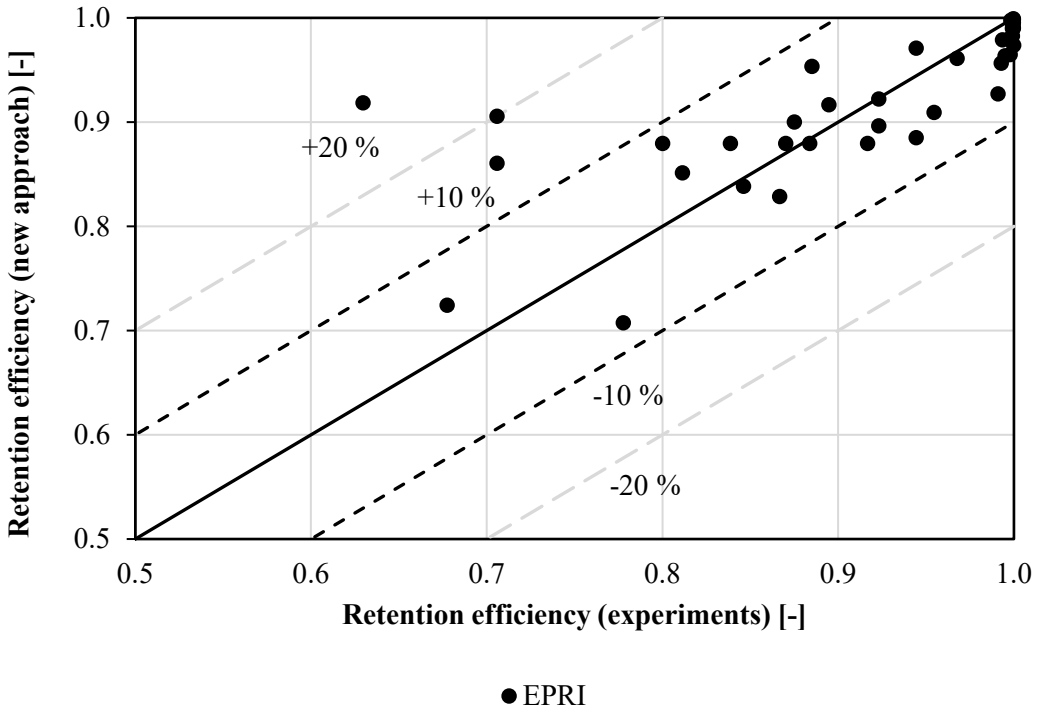

Conclusion and Outlook

Conclusion

- Various analytical methods were carried out to determine the main factors influencing pool scubbing
- On the basis of the main factors a first correlative approach was developed
- The model has easy to define input parameters
- It has not yet been improved for any specific application case
- Apart from a single experiment, the difference between the calculated and measured retention efficiencies is consistently within ±10% across all experimental series
- An initial validation shows good agreement with experimental data

Conclusion and Outlook

Outlook

- In future work, the validation of the model will be shown with appropriate experiments
- Previous results show potential for improvement:
  - Improvement of the condensation term for low submergence
  - Revision of the factor to take into account the nozzle direction
- The correlation is to be optimized for possible accident typical boundary conditions

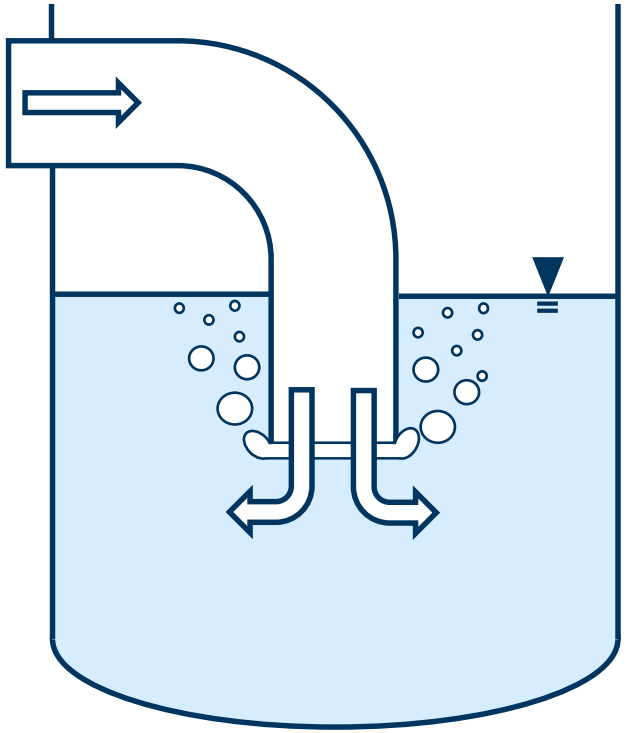

Based on M. Freitag, E. Schmidt, M. Colombet, B. von Laufenberg „Aerosol retention in water pools - Pool Scrubbing"; 2018

ACKNOWLEDGEMENT

This work was funded by the German Federal Ministry for the Environment, Nature Conservation, Nuclear Safety and Consumer Protection (BMUV) under the contract number 1501618.

Supported by:

Federal Ministry
for the Environment, Nature Conservation,
Nuclear Safety and Consumer Protection

based on a decision of
the German Bundestag



Thank you for your interest!

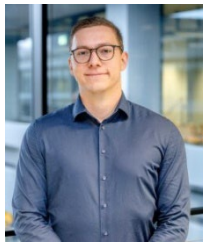

Jonas Rehrmann
rehrmann@pss.rub.de



Dr.-Ing. Tobias Jankowski
jankowski@pss.rub.de



Prof. Dr.-Ing. Marco K. Koch
koch@pss.rub.de

IN VESSEL MELT RETENTION 0D MODEL FOR INTEGRAL PRESSURIZED WATER REACTORS

M. Principato, C. Ciurluini, F. Giannetti
Sapienza University of Rome, Department of Astronautical, Electrical and Energy Engineering
Corso Vittorio Emanuele II, 244, 00186 Rome, Italy
marcello.principato@uniroma1.it; cristiano.ciurluini@uniroma1.it; fabio.giannetti@uniroma1.it

L. Carénini, F. Fichot
IRSN Institut de Radioprotection et de Sûreté Nucléaire
Cadarache research centre, 13115 Saint-Paul-Lez-Durance, France
laure.carenini@irsn.fr ; florian.fichot@irsn.fr

ABSTRACT
The In Vessel Melt Retention (IVMR) strategy developed for Light Water Reactors (LWR) is an appealing solution for the mitigation of many Severe Accident (SA) scenarios. Allowing the corium to remain in the Reactor Pressure Vessel (RPV), significantly reduces the stresses on the containment. This approach is typical of innovative reactors like the AP1000 and the Hualong One, both GW-size Pressurized Water Reactors (PWR). In this paper, the IVMR application for integral PWR (iPWR) is investigated. These kinds of reactors are characterized by an electrical power output generally lower than 300 MWe, an integral layout and the use of passive safety systems. During a postulated accidental sequence that leads to fuel melting, the molten corium relocates down to the lower plenum of the RPV. By flooding the reactor cavity where the RPV is immersed, the external face of the vessel is cooled, and corium is maintained inside the lower head. The overall phenomenology occurring during the IVMR in an iPWR is similar to the phenomenology in a high-power LWR, but a few differences can be highlighted due to the different design features. Among the differences, it is interesting to notice that the molten pool is rather shallow and does not occupy a full hemisphere. This has an impact on the heat flux profile along the vessel wall. Another difference is the rather thick oxide crust, for which the modelling approach is adapted with respect to what is usually done for the analysis of high-power reactors. The purpose of this paper is to develop a 0D model for the steady-state analysis of idealized cases in an iPWR. It has been developed in the framework of the SASPAM-SA Horizon Euratom project. It is part of the preliminary activities of Work Package 4, which examines the evaluation of the safety margin for several existing iPWR designs, considering available data and plausible assumptions for the unknown parameters. The aim of this model is to include the specific features of iPWRs and provide first estimates of safety margins. Heat transfer correlations depending on the aspect ratio H/R are used to consider the shallow geometry of the pool. The absence of a designed channel or baffle around the vessel requires the use of pool boiling correlations for the external cooling. This work will also prepare the next steps of SASPAM-SA, which is the identification of models in SA codes needing some improvements. Integral reactor calculations focused on the IVMR are also planned: they will be compared to the results of the present 0D approach. Finally, we mention that the developed model is not design specific: it may be easily adapted to various designs by changing some geometrical or material parameters. The 0D model was implemented in Python. This tool will be made available for other partners for applications to other designs of interest.

KEYWORDS
SMR, SA, IVMR, Integral PWR, SASPAM-SA

1 INTRODUCTION

Climate change implications, growing energy demand, and the present emphasis on energy safety and independence have sparked a renewed interest in nuclear energy and more sophisticated reactor designs. Small Modular Reactors (SMR) are one of the most viable options for the deployment of the next generation reactors [1]. They seek to achieve the major objectives of higher inherent safety and enhanced economic efficiency by contemporarily cutting capital costs and building times. Among SMRs, integral Pressurized Water Reactors (iPWR) stand out and seem very attractive since based on the previous generation Light Water Reactor (LWR) technology. Their key aspects are the relatively low electrical power output, a Reactor Pressure Vessel (RPV) integral design and the installation of many passive safety systems. Among the possible safety procedures needed to mitigate Severe Accident (SA) scenarios, In Vessel Melt Retention (IVMR) has been studied thoroughly in the context of High-Power Reactors (HPR). Indeed, many designs share the application of IVMR, like the AP1000 [2] and the HPR1000 [3]. This strategy is also very captivating for iPWR, whose analyses are being carried out in the framework of the Horizon Europe - Euratom Safety Analysis of SMR with Passive Mitigation strategies – Severe Accident (SASPAM-SA) project [4] [5], coordinated by ENEA (Italy). Among its major goals, SASPAM-SA aims to determine plausible postulated SA scenarios for iPWRs[1], to examine the applicability of existing experimental databases to iPWRs and to identify gaps of knowledge needed to be filled with new experiments. Other key objectives are: the evaluation of the capability of state-of-the-art international computational tools to reproduce the behaviour of the most promising iPWR designs during SA scenarios; the prediction of the radiological impact on and off-site, considering special SA mitigation and management strategies. Two generic iPWR designs are considered in the project[2], named Design 1 and Design 2. The iPWR Design 1 is a 160 MWth natural-circulation PWR with a compact steam generator and a submerged containment, in a large pool of borated water. Design 2 on the other hand has a thermal power of around 1000 MWth, a dry spherical containment, and utilizes several passive systems for accident protection. Both designs share similar layouts within the RPV and SA mitigation, based on IVMR strategy. In the SASPAM-SA Work Package 4, coordinated by IRSN, the IVMR is investigated considering both Design 1 and 2. As part of the overall research effort, a 0D model has first been developed by the Nuclear Engineering Research Group of Sapienza University of Rome, in collaboration with IRSN, for the steady state analysis of IVMR in iPWRs. The purpose of this 0D model is to identify specificities of iPWRs with respect to HPRs in terms of IVMR configurations and make available to the partners a fast-running tool giving the magnitude of expected results for a wide range of steady state configurations. It will be useful for identification and definition of model improvements in SA codes. It will also provide references for comparison with SA codes, also

[1] Advanced designs, as iPWRs, are in general characterized by common features with the current operating large-LWR and by other specific features typical of their inherent evolutionary designs, providing safety advantages that reinforce the first three levels of the DiD principle. However, even if a plant is designed with advanced inherent features (through the reinforcement of the 1,2,3 DiD levels) allowing a reduction of the Core Damage Frequency (CDF), independent features for preventing and mitigating a severe accident sequence have to be included in its design (DiD level 4) together with the offsite emergency response (DiD level 5). Therefore, some scenarios that could lead to severe accidents need to be postulated and deterministically studied. More detailed information's in [6].

[2] To maximize the knowledge transferability and impacts of the project, two generic design-concepts, characterized by different evolutionary innovations in comparison with larger operating reactor, have been selected for the analyses. These two generic reactor concepts include the main iPWR design features, considered in the most promising designs ready to go on the European market, allowing to assess in a wider way the capability of codes (SA and CFD) to simulate the SA phenomena typical of iPWR. It is not the project's objective to assess the generic reactor designs selected but based on the project findings, allow a more general statement on the code's applicability to currently favored designs under postulated SA condition. No PSA considerations will be done in the project due to the generic nature of the reactor concept considered, then the scenarios identified will be characterized in terms of severity but not in terms of probability.

planned within this project, in which transient effects will have to be considered. This paper is focused on the description of the 0D model, in particular its methodology and assumptions, together with its preliminary results and identification of specificities of iPWRs compared to HPRs.

2 IVMR 0D MODEL

The 0D model is composed of various modules and considers a steady state configuration of corium in the lower plenum. Its main purpose is to provide quantitative elements to identify the most relevant parameters and phenomena that should be investigated further with integral reactor calculations. During a SA scenario, core and vessel internals melt and relocate at the bottom of the RPV. The model deals with a stabilized phase after a transient evolution when a stratified two-phase liquid pool is formed.

2.1 Thermochemical Module and Corium properties

2.1.1 Thermochemical Module and densities

The main constituents of the stratified pool are Uranium (U), Zirconium (Zr), Oxygen (O) and steel (Fe). Two phases are present: an oxidic one composed by Zr and U oxides and a metallic one made up by elemental U, Zr and Fe [7][8]. Their equilibrium compositions are needed to compute their densities and thermophysical properties. To achieve that, the analytical model from [9] has been considered. It is based on three assumptions: oxygen is present only in a bounded state inside the oxide pool, Fe presence in the oxide pool is neglected and the ratio of U to Zr atoms remains unchanged in oxide and metal pools after separation. The inputs given to this module are the molten masses of fuel, Zirconium, and steel internals. Then, it computes the initial U/Zr and Fe/Zr atomic ratios and the Zr degree of oxidation, labeled C_{ox}. The model outputs are the molar fractions of every species in both pools, which are used to compute the pools volumes, masses, densities and thermal properties. The oxide and liquid metal pools relative positions strongly affects the IVMR heat transfer problem. For this reason, the relative densities were estimated to precisely identify the region of existence of the pool disposition selected for the current 0D model (i.e., oxide pool below, Liquid Metal (LM) layer above) and to compare it with the parameter ranges of interest for the considered reactor design. This kind of analysis is generic, and it was repeated for different reactor layouts, i.e., iPWR Design 1 and Design 2 of SASPAM-SA project and a generic PWR of 1000 MW_e as considered in [10], referred to High Power Reactor HPR in the rest of this paper. The input mass of steel (up to the maximum steel inventory corresponding to the complete melting of the core support plate) and the Zirconium degree of oxidation were varied, and the corresponding densities of oxide pool and LM layer were computed according to the thermochemical model presented above. The results are shown in Figure 1, where the lines of equal density are shown for the three aforementioned designs[3]. Cases corresponding to a lighter LM layer are located above the curves. It may be seen that for the two iPWR designs, lower steel mass ratios are possible compared to HPR case, leading to situations where the heavy metal configuration (i.e., LM layer denser than the oxide pool) is the most probable. In addition, in Design 2, the UO_2/Zr mass ratio in the fuel rods is lower compared to Design1 and HPR and this leads to a lower density of the oxide phase. When this ratio is reduced, the density of the oxide phase becomes very close to the density of the LM layer, and it is more difficult to get a light metal. This explains why the Design 2 curve is above the two other designs in Figure 1. These preliminary considerations are based on the outcomes of equilibrium calculations only and they must be confirmed by transient integral code calculations. It may be concluded that, for the designs studied, stratification inversion is very likely to occur during the evolution of the molten pool in the lower plenum. This justifies the need of studying IVMR phenomenology further with dedicated transient codes able to simulate corium pool oxidation and transient steel addition. If densities of the two phases are very close, it may even be assumed that the molten pool is not stratified, and that metal and oxide phases are mixed. This will be done in the future steps of SASPAM-SA project.

[3] Higher steel mass fractions may be obtained for design 1 and for HPR (up to 0.8) and are not represented since those situations will lead to light metal layer formation even for low Zr oxidation degree.

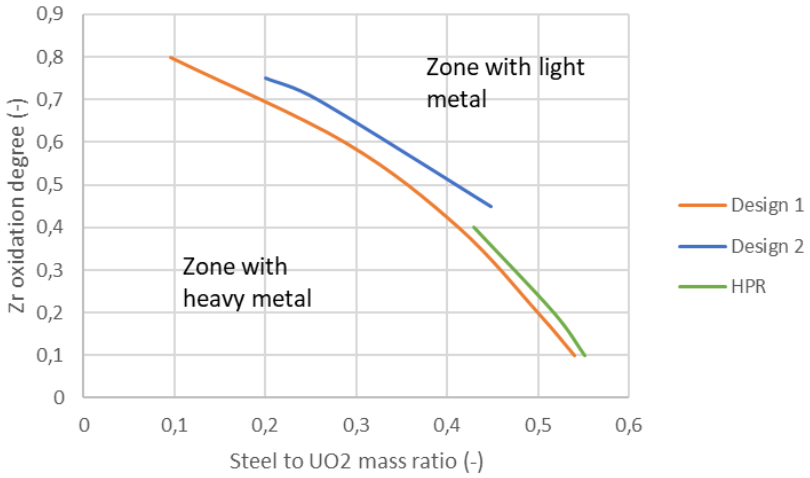

Figure 1: Pools iso-density lines for the considered reactor designs.

2.1.2 Corium properties

The LM layer and oxide pool thermal properties are computed according to formulas and correlations available in [8]. Except for the viscosity, every property is computed as a weighted average, with the weight varying for each property: for density the weight is the volumetric fraction, for thermal conductivity it is the molar fraction, for heat capacity it is the mass fraction. A more accurate discussion on the pool properties can be found in [8]. Finally, this module distributes the decay power in the oxide pool and in the LM layer, based on the atomic Uranium content, derived from the molar fractions yielded by the previous calculations.

2.2 Geometrical Module

An accurate evaluation of the system's geometry is crucial for the overall reliability of the code since the layers' shapes (i.e., height over diameter) strongly influence the heat transfer calculations and power flow paths. In the reference scenario considered, the oxide pool lies at the bottom of the Lower Head (LH), while the metal layer lies on top of it. The overall system is depicted in Figure 2. Further considerations on this aspect are present in section 1.1. For the metal layer geometry, the module considers the partial ablation of the vessel thickness due to the focusing effect (labeled ΔR in Figure 2). In addition, the presence of the crust inside the oxide pool is also considered. It is assumed that both elements (pool and crust) have the same atomic composition. The purpose of the geometrical module is to evaluate the height of both pools and to calculate the ablated vessel thickness while doing so. This is achieved through a system of 3 equations in 3 unknowns, reported below, that has been obtained considering the geometrical formulas of the spherical cap. The unknowns in the system are h_{oxy}, h and ΔR which represent respectively the height of the oxide pool, the total combined height, and the ablated vessel thickness. All the volumes in Eq.s (1), (2) and (3) are input data and can be assessed starting from the outputs of the thermochemical model, i.e., layers' masses and densities. Moreover, combining the height of both pools, the geometrical module evaluates Θ_p, the angle identifying the top of the pool as illustrated in Figure 2, which will be used in the heat transfer module (see next section).

$$V_{oxy}=\pi h_{oxy}^2\left(R_{LH}-\frac{h_{oxy}}{3}\right) \quad (1)$$

$$V_{lm}-V_{ablated}+V_{oxy}=\pi h^2\left(R_{LH}-\frac{h}{3}\right) \quad (2)$$

$$\left\{\pi(h+\Delta R)^2\left[(R_{LH}+\Delta R)-\frac{(h+\Delta R)}{3}\right]\right\}-\left\{\pi\left(h_{oxy}+\Delta R\right)^2\left[(R_{LH}+\Delta R)-\frac{\left(h_{oxy}+\Delta R\right)}{3}\right]\right\}=V_{lm} \quad (3)$$

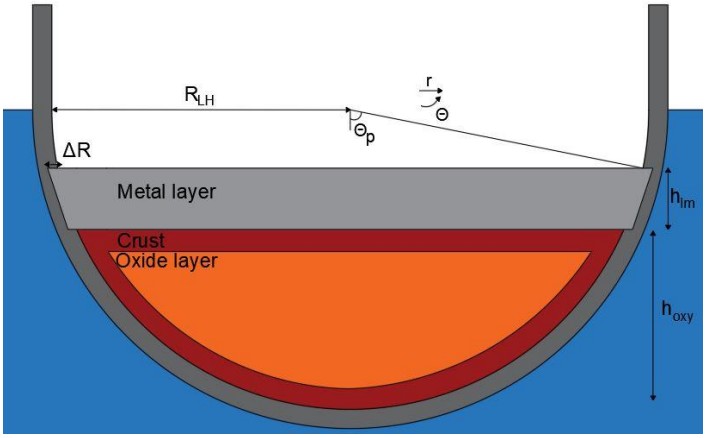

Figure 2: Lower Head schematization for the geometric module.

2.3 Heat Transfer Module

The heat transfer module has been developed starting from models and considerations presented in [10][8]. As already discussed, the reference scenario considers the oxide pool surrounded by an oxidic crust. The interface between these two elements is assumed to be at the oxide liquidus temperature. The latter, which is one of the boundary conditions for the problem, is postulated to be equal to 2800 K, according to the indications provided by [11]. The liquid metal layer on the other hand finds itself on top of the oxidic one, and for these analyses a top radiative boundary condition has been chosen. The radiative heat transfer mode has been selected following the results of the preliminary calculations, reported in section 3. They hint that, for the iPWR design considered, the metal layer is very thin with a height of around 15 cm. As stated by [12], for a thin liquid metal layer the adiabatic condition becomes very conservative. For this, the radiative heat transfer has been included in the module. Surrounding the lower head there is the water flooded cavity, which is assumed to be at saturation temperature for conservative reasons. The heat transfer module is conceptually divided into three steps: evaluation of the oxide pool bulk temperature, power balance in the oxide pool and power balance in the LM pool. The first step requires the evaluation of the internal Rayleigh number (Ra) of the oxide pool, and the evaluation of the Nusselt number in the upward (Nu_{up}) and downward (Nu_{dn}) directions. Many correlations derived from experimental facilities are available in literature. In this model, the focus has been on the ones that possess the dependence on the aspect ratio of the oxide pool (H/R) for the downward heat transfer. Also, only correlations deriving from experiments considering the hemispherical geometry have been selected. The correlations have the following form:

$$Nu_{dn}=ARa^{a}\left(\frac{H}{R}\right)^{b} \quad (4)$$

$$Nu_{up} = BRa^{c} \quad (5)$$

The coefficients vary for each correlation, and they are reported in Table 1.

Table 1 : Heat transfer correlations implemented to evaluate the oxide pool thermal transfer.

Correlation	A	a	B	B	C	Ra_{min}	Ra_{max}
ACOPO [8]	0.1857	0.2304	0.25	2.4415	0.1772	1.00E+13	1.00E+17
BALI 2D [13]	0.116	0.25	0.32	0.383	0.233	1.00E+13	1.00E+17
BALI3D [13]	0.131	0.25	0.19	0.383	0.233	1.00E+13	1.00E+17
Mini ACOPO[14]	0.0038	0.35	0.25	1.95	0.18	1.00E+11	7.00E+14
ASFIA [15]	0.54	0.2	0.25	0.403	0.226	2.00E+10	1.10E+14

After determining the Nu numbers for both directions, to get the oxide pool temperature (T_{pool}), the expression below is adopted. It accounts for the repartition of the total residual decay power (P_{res}). For SASPAM-SA design 2, this latter parameter has been derived from [16] and it is approximately 4.4 MW:

$$T_{pool}=T_{liq}+P_{res}\frac{H}{k_{ox}}\left(Nu_{dn}S_{dn}+Nu_{up}S_{up}\right)^{-1} \quad (6)$$

Where the height H[4] and the downward (S_{dn}) and upward (S_{up}) surfaces are computed by the geometrical module. Once the temperature of the oxide pool is found, the model moves on to evaluate the thermal field along the LH section in contact with the oxide pool itself, and to estimate the crust's thickness. The LH region contacting the oxide pool is divided into N polar regions, over which the heat balance will be solved. For the most relevant parameters notation, refer to Figure 3.

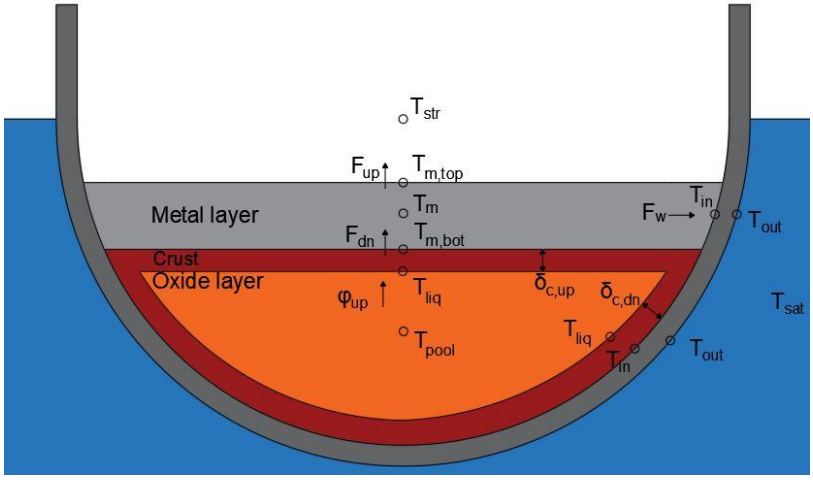

Figure 3 : 0D model Heat transfer visual schematization.

For the heat balance of each polar region, a spherical one-dimensional conduction problem is solved. The formulas to be implemented are derived from [17]. This allows for a better representation of the LH actual geometry and thermal field. The heat flux profile in the downwards direction and the correlation to be used to assess the Critical Heat Flux (CHF) for the cavity water have been selected from literature [13][14][15][18]. The former is used to distribute the average heat flux in the downwards direction (that can be derived reverting Eq. 6 once T_{pool} is known) along the polar coordinate, computing $\varphi_{dn}(\theta)$, which is a boundary condition for the conduction problem. The distribution is based on weights calculated by considering the LH internal surface associated with each polar mesh. The selected experimental internal heat flux profiles have different shapes but all increase as the polar coordinate approaches the top of the pool. The evaluation of the water CHF, which is achieved through Cheung correlation [18], is crucial to determine the heat transfer mode to be used to compute the associated heat transfer coefficient (HTC, h_w), that is another boundary condition to the conduction problem. If the heat flux to the external water is lower than the CHF, nucleate pool boiling is assumed at the LH external surface and Rohsenow correlation [19] is used for the heat transfer coefficient. Instead, if the heat flux exceeds the CHF, film pool boiling regime is assumed and Bromley correlation is adopted [20]. The resulting system of equations that is solved for each θ coordinate along the vessel is:

[4] It should be noted that H corresponds to the height of the liquid part of the oxide pool and is thus dependent on the results of the heat transfer evaluation allowing to estimate the crust thicknesses. Thus, calculations are repeated in an iterative way until all the parameters involved converge (i.e., relative differences are below the selected tolerances).

$$\varphi_{dn}(\theta) - \frac{k_c}{\delta_{c,dn}}\left(T_{liq}-T_{in}\right)\left(\frac{R_{LH}}{R_{LH}-\delta_{c,dn}}\right)+\frac{q'''_c}{2}\delta_{c,dn}\left(1+\frac{\delta_{c,dn}}{3(R_{LH}-\delta_{c,dn})}\right)=0 \quad (7)$$

$$\frac{k_v}{\delta_v}(T_{in}-T_{out})\frac{R_{LH,ext}}{R_{LH}} - \frac{k_c}{\delta_{c,dn}}\left(T_{liq}-T_{in}\right)\left(1-\frac{\delta_{c,dn}}{R_{LH}}\right) - \frac{q'''_c}{2}\delta_{c,dn}\left(1-\frac{\delta_{c,dn}}{3R_{LH}}\right)=0 \quad (8)$$

$$\frac{k_v}{\delta_v}(T_{in}-T_{out})\frac{R_{LH}}{R_{LH,ext}} - h_w(T_{out}-T_{sat})=0 \quad (9)$$

Where R_{LH} and $R_{LH,ext}$ represent the internal and external vessel radiuses, δ_v the vessel thickness, $\delta_{c,\,dn}$ the crust thickness, q'''_c the volumetric power inside the crust, which is equal to the oxide pool one since we assumed the same composition for both. The thermal conductivities for the oxidic crust and the vessel (k_c and k_v) are estimated through extrapolation functions derived from [8]. The unknowns in Eq.s (7), (8) and (9), are the crust thickness in the downward direction $\delta_{c,\,dn}$, and the LH internal and external temperatures T_{in}, T_{out}. At the current stage, the model does not assume vessel wall ablation in front of the Oxide crust. Once the system is solved, the model checks if the total power in the downwards direction corresponds to the sum of the power transmitted through every polar coordinate. For the metal layer heat balance, as already mentioned, a top radiative boundary condition has been selected, with a metal layer emissivity of 0.38 [10] and an average core internal structures temperature of 1100 K. This last value comes from MELCOR preliminary integral calculations performed in SASPAM-SA and related to Design 2. It is not to be considered as a definitive value since the overall simulation activity is in progress. To solve the heat balance, a non-linear system of 9 equations and 9 unknowns has been derived. In this case, in first approximation, only a single polar coordinate is considered. For this, a one-dimensional slab approach has been selected to solve the conduction problem in the vessel. The implemented formulas are reported below:

$$F_{dn}=h_{dn}(T_{m,bot}-T_m) \quad (10)$$

$$F_{up}=h_{up}(T_m-T_{m,top}) \quad (11)$$

$$F_{up}=\varepsilon\sigma(T^4_{m,top}-T^4_{str}) \quad (12)$$

$$F_w=h_{wall}(T_m-T_{in}) \quad (13)$$

$$F_w=\frac{k_v}{\delta_v}(T_{in}-T_{out}) \quad (14)$$

$$F_w=h_w(T_{out}-T_{sat}) \quad (15)$$

$$\varphi_{up}=\frac{k_c}{\delta_{c,up}}\left(T_{liq}-T_{m,bot}\right)-\frac{q'''_c}{2}\delta_{c,up} \quad (16)$$

$$F_{dn}=\frac{k_c}{\delta_{c,up}}\left(T_{liq}-T_{m,bot}\right)+\frac{q'''_c}{2}\delta_{c,up} \quad (17)$$

$$F_{dn}S_{dn}+q'''_m V_m=F_{up}S_{up}+F_w S_w \quad (18)$$

The unknowns in Eqns (10) to (18) are: the metal layer heat fluxes in the downwards (F_{dn}), upwards (F_{up}), and lateral (i.e., wall, F_w) directions; the metal layer pool temperature (T_m); the metal layer bottom ($T_{m,\,bot}$) and top ($T_{m,\,top}$) surfaces temperatures; the oxide crust upwards thickness ($\delta_{c,\,up}$); the vessel external temperature (T_{out}). The heat transfer module also calculates the residual thickness of the vessel (δ_v). An outer iteration is thus performed between the various models presented so far (i.e., thermochemical, geometrical and heat transfer) until the δ_v computed allows to obtain a vessel internal temperature (T_{in}) equal to the vessel's melting temperature (set to 1600 K according to [8]). The heat transfer mode assumed for the metal layer is natural convection. The Rayleigh number is used to compute the heat transfer coefficients in three directions: upwards (h_{up}), downwards (h_{dn}) and through the vessel wall (h_{wall}). Globe-Dropkin correlation [21] is selected for the first two directions, while for the latter, Chawla-Chan correlation has been chosen [22].

2.3.1 Influence of the oxide pool aspect ratio H/R

As previously hinted, one of the criteria for the correlations selection for oxide downwards heat transfer, is the dependance on the oxide pool aspect ratio. The influence of this parameter on the power repartition is depicted in Figure 4. On the y-axis we have the fraction of the oxide total power that goes in the upwards direction X_{up}, computed for each correlation, while on the x-axis lies the oxide pool aspect ratio. The black dotted vertical lines represent the test cases discussed in this paper. The calculations for X_{up} are performed using average corium properties, otherwise the aspect ratio would not have been an independent parameter. The curves are cut considering the Ra validity range for each correlation (see Table 1). This evaluation highlights that for decreasing oxide pool aspect ratio, regardless of the used correlation, X_{up} increases. Higher X_{up} deviations are observed for low H/R values, while the correlations are more consistent at high aspect ratios. The increase in upwards heat flux is clearly more relevant for iPWR with respect to HPR, since the former present shallower oxide pools, hence a higher upwards surface area with respect to the downwards one. In this paper, the BALI-3D correlation was used.

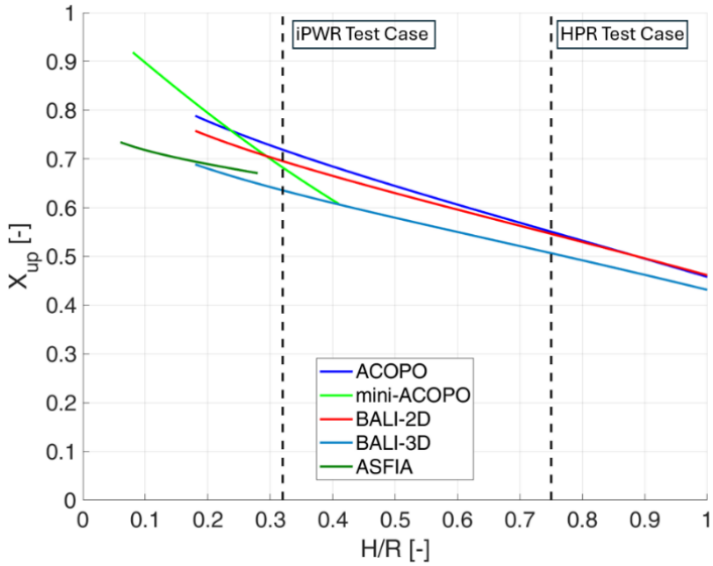

Figure 4: Oxide pool aspect ratio influence on power partitioning.

3 SIMULATION RESULTS

3.1 Verification Case (HPR)

Firstly, to assess the appropriateness of the developed 0D model, it was tested with the steady state case studied in the IVMR benchmark [10]. The detailed inputs and results are not presented here but preliminary results well reproduce the benchmark results of [10]. The most important difference is the heat flux from the LM layer to the vessel wall, which is higher in the 0D model case. This is because the geometrical model does not consider the LH geometry transition from hemispherical to cylindrical shape. Indeed, it has been developed expecting shallow pools in iPWR. So, the height of metal is underestimated for this HPR case.

3.2 Input data for the application to iPWR cases.

Once verified the suitability of the 0D model, preliminary calculations corresponding to the SASPAM-SA Design 1 and 2 have been performed, whose input data are reported in Table 2. Note that the masses data refer to the initial masses which are supposed to be later molten during degradation.

Table 2: Input parameters for the 0D model test cases

PARAMETER	UNITS	SASPAM-SA Design 2 [23]	SASPAM-SA Design 1
LH radius	m	3.11	1.4
LH thickness	m	0.25	0.12
LH height	m	1.27	0.7
UO_2 mass	tons	58	9
Zr mass	tons	19.4	2.5
Steel mass	tons	22.2	4
C_{ox} (Zr oxidation degree)	-	0.70	0.45
Decay power	MW	4.4	1.7
Core structure temperature	K	1100	1100
Metal emissivity	-	0.38	0.38

3.3 Results and comparison of designs

The main results for the two iPWR designs are summarized in Table 3. The partitioning of the overall decay heat (see Table 2) among the different elements constituting the stabilized phases is presented in Figure 5, and compared to the HPR case [10].

Table 3: Main results associated with the Design 1 and 2 test cases.

PARAMETER	UNITS	DESIGN 2	DESIGN 1
Oxide superheating	K	36.4	43.9
Metal superheating	K	26.	50.
Average $\delta_{c,\,dn}$	cm	6.5	4.4
Residual Vessel thickness in LM layer	cm	22.1	8.7
Radiative power fraction in LM layer	-	0.872	0.662
Power to LM layer fraction in liquid oxide	-	0.657	0.655
Heat flux from LM layer to vessel (F_w)	MW/m^2	0.133	0.335
Oxide layer H/R	-	0.28	0.33
LM layer H/R	-	0.09	0.146

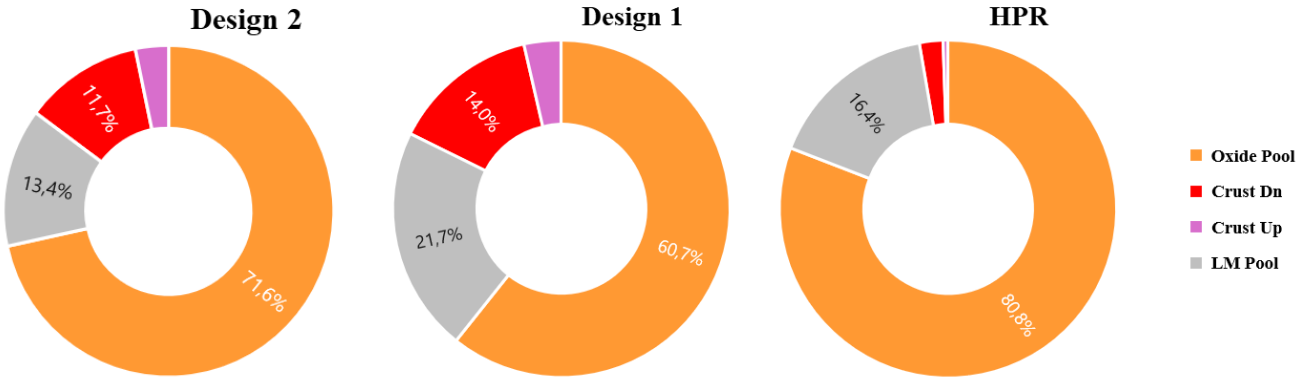

Figure 5: Distribution of the overall decay power between the main volumes.

As visible, in all the considered reactor designs most of the power is generated within the molten oxide pool (more than 60%). However, in iPWR designs a significant fraction is also produced within the oxide crust

(above 11%). In Design 2, where a high oxidation degree of the Zr (70%) is considered, this fraction is even comparable to the one corresponding to the LM layer (13%). On the contrary, in the HPR design, the contribution of the oxide crusts is negligible. The comparison of the oxide crust profiles is presented in Figure 6. At the top of the oxide pool the crust thickness is about 4-5 cm in both iPWR design, whereas it is about 0.5 cm in a typical existing PWR. In Design 2, a thick crust of more than 14 cm is evaluated at the bottom of the pool, due to the very large vessel radius related to this reactor layout (cf. Table 2).

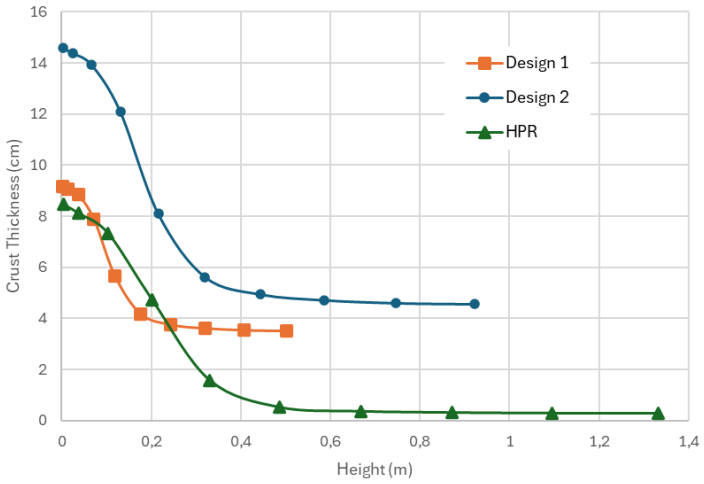

Figure 6: Profile of crust thickness around the oxide pool.

The power fraction transferred the top of the oxide pool (i.e. to the metal layer) is about 66% in both iPWR designs (see Table 3), which is much higher than the value corresponding to a typical existing high-power PWR (50%). This is due to the very low value of the oxide pool aspect ratio, as explained in the previous section (cf. Figure 4). In Figure 7, the relative contributions of the different power flow paths are compared. Referring to the LM layer, the fraction of power lost by radiative heat transfer is quite large in iPWR designs compared to HPR: between 34% and 51% of the total power vs 13% in HPR. Also in this case, this is due to the very low value of the LM layer aspect ratio (see Table 3). This leads to a very large ratio between the top flat surface and the lateral surface of the metal. Consequently, the focusing effect is limited and the level of maximum heat flux is lower than the predicted CHF at all angles along the vessel. The minimum residual vessel thicknesses are evaluated equal to 22 cm for Design 2 and 9 cm in Design 1, which is comparable to the VVER440 case (about 10cm). Much lower values (2-3cm) are obtained for a typical high-power reactor.

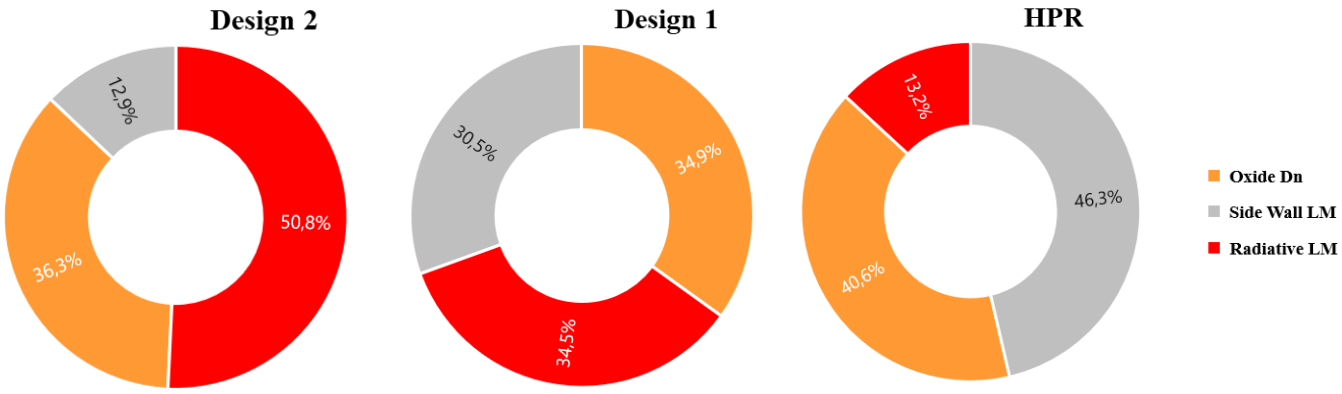

Figure 7: Relative extent of the different power flow paths leaving the global system.

4 CONCLUSIONS

In the framework of SASPAM-SA project WP4, a 0D model for steady state IVMR was developed, with the aim of identifying the necessary model improvements and providing preliminary estimates for integral reactor codes users. Its development was first made for iPWRs at the current stage. Two designs were studied in this paper. The model was also assessed by comparison to a high-power PWR benchmark case. As expected, the first results show that in-vessel retention strategy appears feasible, with a good safety margin. However, detailed data and complete calculations would be necessary to go further. Some specific features of IVMR in iPWRs appear: a larger fraction of power transferred to the top of the oxide pool because of the low aspect ratio (shallow pool), the existence of a rather thick oxide crust and the occurrence of a thin metal layer but a limited focusing effect because of a large fraction of power lost by radiative heat transfer. Also, it is expected that, in many cases, density inversion would occur in transient conditions, starting with a heavy metal. It may even be possible to have a well-mixed pool instead of stratification. Regarding the oxide crust thickness, results yield average values of one order of magnitude higher than for HPR. All these specific features have to be considered in models. The impact of aspect ratio H/R can be treated by simply selecting correlations which already include the H/R parameter, and some of those correlations are listed in the paper. The presence of thick oxide crusts requires a modification of existing models which usually neglect the crust. A model was proposed in the paper. The existence of a heavy metal layer at the beginning of the transient, leading to a stratification inversion, is a more difficult issue: first it requires a heat transfer model for the heavy metal layer (such model was not developed yet) and second it requires a transient calculation of stratification inversion, which is not available in all system codes. Finally, a more accurate analysis of top radiative heat transfer must be done as it appears to be significant for the evaluation of focusing effect and the maximum heat flux to the vessel. Some of those issues will be addressed in the next steps of SASPAM-SA WP4, by developed new models and/or performing transient calculations of the stratified pool.

ACKNOWLEDGEMENTS

Funded by the European Union

Funded by the European Union project SASPAM-SA, Grant n° 101059853. Views and opinions expressed are however those of the author(s) only and do not necessarily reflect those of the European Union or European Commission-Euratom. Neither the European Union nor the granting authority can be held responsible for them.

5 REFERENCES

[1] IAEA, “Advances in small modular reactor technology developments”, 2022 Edition, in IAEA advanced reactor information system (ARIS), Vienna (2022).

[2] Esmaili H., Khatib-Rhabar M, “Analysis of in-vessel retention and ex-vessel fuel coolant interaction for AP-1000”, NUREG/CR-6849, ERI/NRC 04-201 (2004).

[3] Xing, J., Song, D., Wu, Y., Engineering, “HPR1000: advanced pressurized water reactor with active and passive safety” 2(1), pp. 79–87 (2016).

[4] European Commission, Safety Analysis of SMR with PAssive Mitigation strategies - Severe Accident - SASPAM-SA Project, (2023), available online on https://cordis.europa.eu/project/id/101059853.

[5] Horizon Euratom SASPAM-SA project website. https://www.saspam-sa.eu/

[6] SMR Regulators’ Forum Pilot Project Report, Considering the Application of a Graded Approach, Defence-in-Depth and Emergency Planning Zone Size for Small Modular Reactors. SMR Regulators’ Forum, January 2018. https://www.iaea.org/sites/default/files/18/01/smr-rf-report-29012018.pdf

[7] Bal Raj Sehgal et al., Nuclear Safety in Light Water Reactors, Severe Accident Phenomenology, page 128 chapter 2.3.2, Elsevier, Waltham, MA, USA (2012).

[8] Theofanous, T.G., Liu, C., Addition, S., Angelini, S., Kymälainen, O., Salmassi, T," In-vessel coolability and retention of core melt", Nuclear Engineering and Design, 169 (1997).
[9] S. Nandan, F. Fichot, B. Piar, "A simplified model for the quaternary U-Zr-Fe-O system in the miscibility gap", Nuclear Engineering and Design, 364, 110608 (2020).
[10] Carénini L. et al.," Main outcomes from the IVR code benchmark performed in the European IVMR project", Annals of Nuclear Energy,146, 107612, (2020).
[11] K. Ross et al., MELCOR Best Practices as applied in the State-Of-the-Art Reactor Consequence Analyses (SOARCA) Project, NUREG/CR-7008, U.S. NRC (2014).
[12] Carénini L., Fichot F., Seignour N., "Modelling issues related to molten pool behaviour in case of In-Vessel Retention strategy", Annals of Nuclear Energy, 118 (2018).
[13] Bonnet J.M., Seiler J.M., "Thermal hydraulic phenomena in corium pools: the BALI experiment", 7th international Conference on Nuclear Engineering (ICONE), Tokyo, Japan (1999)
[14] Theofanous T.G. et al., "Natural convection experiments in a hemisphere with Rayleigh numbers up to 10(15)", Proceedings 1995 National Heat Transfer Conference, Portland, Oregon (1995).
[15] Asfia F.J., Dhir V.K., "An experimental study of natural convection in a volumetrically heated spherical pool bounded on top with a rigid wall", Nuc. Eng. Des., 163 (3), pp. 333-348 (1996).
[16] Maccari P. et al., "ASTEC code DBA analysis of a passive mitigation strategy on a generic IRIS SMR", Annals of Nuclear Energy, 156, 108194 (2021).
[17] A. Bejan, A.D. Kraus, Heat Transfer Handbook, chapter 3.4.3 pp.182-193, John Wiley & Sons, Inc., Hoboken, New Jersey (2003).
[18] F.B. Cheung et al., "Critical Heat Flux (CHF) Phenomenon on a Downward Facing Curved Surface", NUREG/CR-6507, U.S. NRC (1997)
[19] I. L. Pioro, W. Rohsenow, and S. S. Doerffer, AECL-CONF-1415 (2001)
[20] L.A. Bromley, "Heat Transfer in Stable Film Boiling", 1949. Available online at: https://escholarship.org/uc/item/0pj1211q
[21] S. Globe, D. Dropkin, "Natural convection heat transfer liquids confined by two horizontal plates and heated from below", Journal of Heat Transfer, 81, pp-24-28 (1959).
[22] T.C. Chawla, S.H. Chan, "Heat transfer from vertical/inclined boundaries of heat generating boiling pools", Journal of Heat Transfer, 104, pp.1323-1329 (1982).
[23] IRIS Plant Description Document, WCAP-16062-NP Revision 0, Westinghouse Non-Proprietary, March 21, 2003. https://www.nrc.gov/docs/ML0336/ML033600112.pdf

SAPIENZA UNIVERSITÀ DI ROMA

IRSN
INSTITUT DE RADIOPROTECTION ET DE SÛRETÉ NUCLÉAIRE

SEAKNOT
ERMSAR 2024
11th Conference on
SEVERE ACCIDENTS RESEARCH
May 13-16, 2024 – Stockholm, Sweden

In Vessel Melt Retention 0D Model for Integral Pressurized Water Reactors

M. Principato, C. Ciurluini, F. Giannetti, L. Carénini, F. Fichot

Sapienza University of Rome, IRSN

Outline

- SASPAM-SA project
- 0D Model objectives
- Modules description
- Results for iPWR
- Conclusions and future perspectives

SASPAM-SA project

SAFETY ANALYSIS OF SMR WITH PASSIVE MITIGATION STRATEGIES - SEVERE ACCIDENT

Overall objectives:

- Identification & analysis of SA scenarios in iPWR;
- Availability and/or needs of experimental databases to iPWR;
- Suitability of state-of-the-art numerical tools to study the phenomena occurring during & after a SA scenario;
- 2 Generic iPWR designs considered;

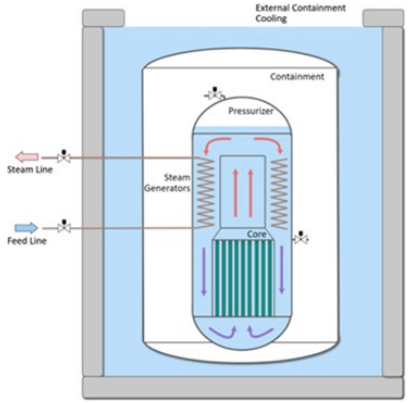

The presented activity is part of IVMR WP:

- Molten pools formation and potential stratification;
- Potential differences with respect to High Power Reactors;
- Suitability of state-of-the-art numerical tools to study the phenomena occurring during & after a SA scenario;

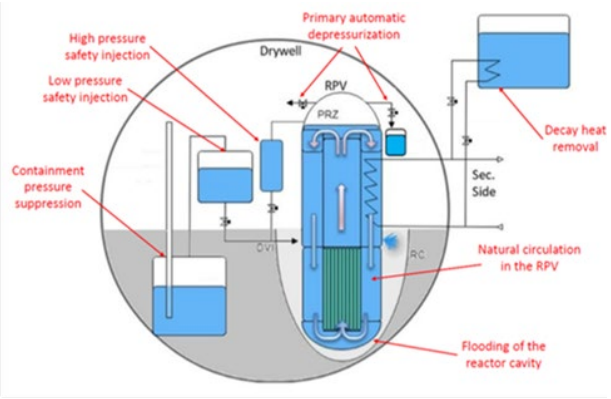

Framework

- A **0D Corium Model** was developed to preliminary investigate the **In-Vessel Melt Retention** (**IVMR**) phenomenon for **integral Pressurized Water Reactors** (**iPWR**).
- So far, the prepared model allows the calculation of **corium composition** and **heat transfer performances**.
- The main aim of the technical activity related to SASPAM-SA WP 4.1 task is setting up a **steady-state simplified model of IVMR** able to be used for:
  - ❖ Identify specificities of iPWRs in terms of IVMR parameters;
  - ❖ Provide the partners a fast-running tool giving the magnitude of expected results for a wide range of steady state configurations;
- The outcomes of this simplified model will provide a feedback on the most relevant parameters/phenomenologies to be investigated with 'complete' reactor calculations.

Model Assumptions

- The physical model considers the **IVMR in an advanced state**, where the core and vessel internals are molten and located in the bottom of the vessel.
- At this phase of the transient evolution, **a two-phase pool is formed**, whose main constituents are **U, Zr, O and Fe**. To calculate heat transfer data and evaluate the bulk temperature of the pool, the equilibrium composition of the mixture is needed.
- The thermochemical model [1], is based on three main assumptions:
  - ❖ Oxygen is present only in a bounded state inside the oxide pool;
  - ❖ Fe presence in the oxide pool is negligible;
  - ❖ The ratio of U to Zr atoms remains unchanged in oxide and metal pools after separation.

Thermochemical model

Thermochemical model [1]:

1) Global data:

$$C_{uz},\ C_{ox},\ C_{sz}$$

2) Calculate:

$$m = m^{ref}\frac{1+C_{uz}^{ref}}{1+C_{uz}}$$
$$b = n_o^{st} - m$$

3) Set:

$$N_z = 1$$
$$N_u = C_{uz}$$
$$N_o = 2(C_{uz} + C_{ox})$$
$$N_s = C_{sz}$$
$$N_{tot} = N_z + N_u + N_o + N_s$$
$$n_i = N_i/N_{tot}\ (i = o, s)$$

4) Calculate the fit function $f(y)$:

$$f(y) = y + \sqrt{y^2 + bmn_s}$$

where:

$$y = \tfrac{1}{2}(n_o + mn_s - b)$$

5) Calculate thermochemical equilibrium parameters:

$$n_s^m = \frac{f(y)}{m}$$
$$n_s^m = \frac{mn_s}{f(y)}$$
$$n_o^{ox} = b + f(y)$$

Nomenclature:

- C_{uz}: Initial U/Zr atomic ratio.
- C_{sz}: Initial Fe/Zr atomic ratio.
- N_i: Normalized Mole Numbers, normalizing factor is the number of Zr moles.
- n_o^{ox}: molar fraction of Oxygen in the oxide pool;
- n_s^m: molar fraction of Iron in the metal pool;
- n_m: molar fraction of Metal layer atoms.

1) S. Nandan, F. Fichot, B. Piar, "*A simplified model for the quaternary U-Zr-Fe-O system in the miscibility gap*", Nuclear Engineering and Design, 364, 110608 (2020).

Pool properties

Property	Oxide Pool [2]	Liquid Metal Pool [2]	Unit
$T_{liquidus}$	2800	1600	K
Density (ρ)	$\frac{\sum_i \rho_i * V_i}{\sum_i V_i}$	$\frac{\sum_i \rho_i * V_i}{\sum_i V_i}$	kg/m^3
Thermal Conductivity (k)	$\sum_{i=1,2} \varkappa_i * k_i - 0.4 * \varkappa_1 * \varkappa_2$	$\sum_{i=1,2} \varkappa_i * k_i - 0.4 * \varkappa_1 * \varkappa_2$ (SS and Zr)	W/m*K
Th. Exp. Coeff. (β)	$\frac{\sum_i \beta_i * V_i}{\sum_i V_i}$	$\frac{\sum_i \beta_i * V_i}{\sum_i V_i}$	K^{-1}
Heat Capacity (C_p)	$\frac{\sum_i C_{p,i} * M_i}{\sum_i M_i}$	$\frac{\sum_i C_{p,i} * M_i}{\sum_i M_i}$	J/kg*K
Th. Diffusivity (α)	$k/(C_p{}^*\rho)$	$k/(C_p{}^*\rho)$	J/m^{3}K
Viscosity (μ)	$A * \exp\left(\frac{B}{RT}\right)$ $A = \frac{5.7*10^{-5}*(T_m*\bar{M})^{0.5}}{\exp\left(\frac{B}{RT_m}\right)*V_m^{2/3}}$ $B = 2.65 * T_m^{1.27}$	$A * \exp\left(\frac{B}{RT}\right)$ $A = \frac{5.7*10^{-5}*(T_m*\bar{M})^{0.5}}{\exp\left(\frac{B}{RT_m}\right)*V_m^{2/3}}$ $B = 2.65 * T_m^{1.27}$	Pa*s

2) Theofanous, T.G., Liu, C., Addition, S., Angelini, S., Kymälainen, O., Salmassi, T," *In-vessel coolability and retention of core melt*", Nuclear Engineering and Design, 169 (1997).

Stratification analysis

Oxide and Metal pools **relative positions strongly influence heat transfer**, hence a study on densities has been performed through the thermochemical model:

- Design 1, Design 2 and a generic 1000 MWe PWR (HPR) [3] have been considered;
- Inputs: Stainless Steel (SS) mass and Zr degree of Oxidation (C_{ox})

Iso-density curves are shown:

- Lower steel mass ratios are possible in iPWR; ***This leads to scenarios where the heavy metal configuration is the most probable***;
- In Design 2, a lower UO_2/Zr mass leads to lower oxide density;
- **Stratification inversion is likely to occur! (To be confirmed by transient integral code calculations)**

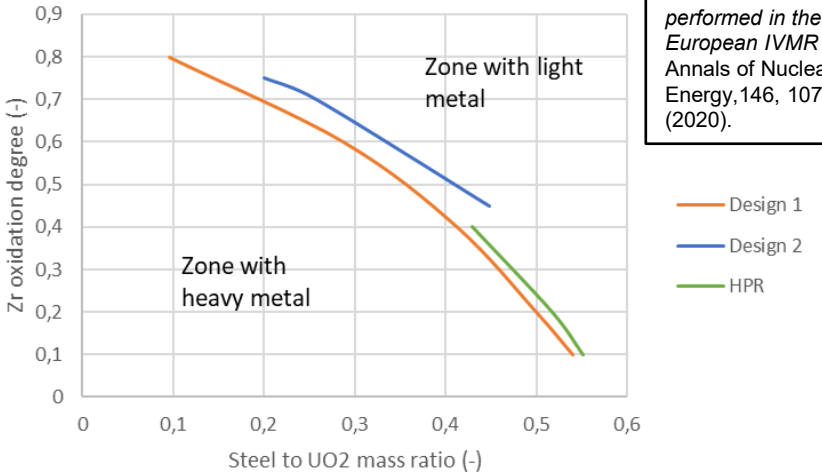

Higher steel mass fractions may be obtained for design 1 and for HPR (up to 0.8) and are not represented since those situations will lead to light metal layer formation even for low Zr oxidation degree.

3) Carénini L. et al.," *Main outcomes from the IVR code benchmark performed in the European IVMR project*", Annals of Nuclear Energy,146, 107612, (2020).

Geometrical Module

Geometrical configuration ($\boldsymbol{\rho_{oxi} > \rho_m}$):

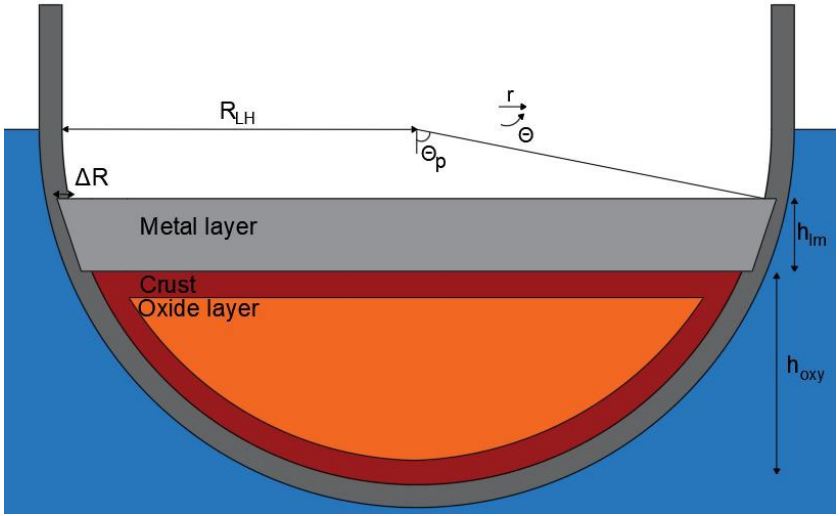

= Unknowns

1. $V_{oxi} = \pi * h_{oxi}^2 * \left(R_{LH} - \frac{h_{oxi}}{3}\right)$
2. $V_{LM} - V_{ablated} + V_{oxi} = \pi * h^2 * \left(IR_{LH} - \frac{h}{3}\right)$
3. $\left\{\pi * (h + \Delta R)^2 * \left[(R_{LH} + \Delta R) - \frac{(h+\Delta R)}{3}\right]\right\} - \left\{\pi * (h_{oxi} + \Delta R)^2 * \left[(R_{LH} + \Delta R) - \frac{(h_{oxi}+\Delta R)}{3}\right]\right\} = V_{LM}$

$\rightarrow h_{LM} = h - h_{oxi}$

Heat Transfer module

- The Heat Transfer (HT) calculation strongly depends on the pool geometry obtained by the precedent considerations. **So far, the light metal configuration was considered based on [3].**
- The HT module developed is articulated in three consecutive steps:

1. Evaluation of the Oxide pool temperature (named T_{pool});
2. Power balance in the oxide pool;
3. Power balance in the LM pool.

- The reference geometry and the adopted nomenclature are shown in the figure nearby.

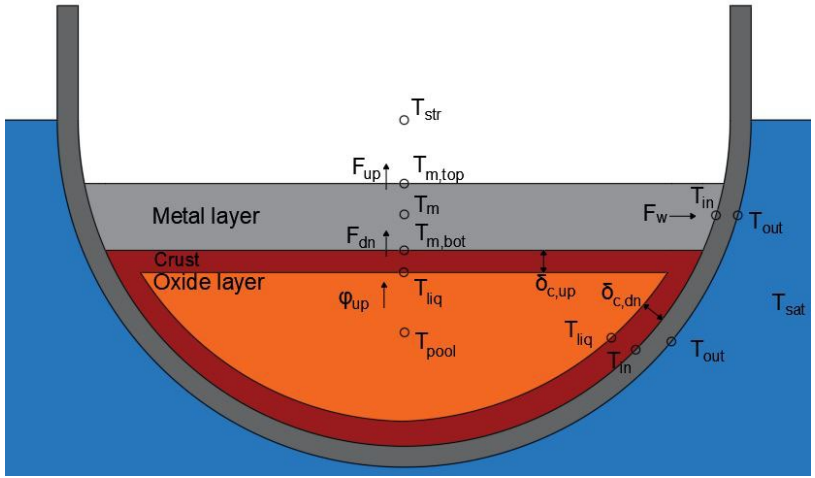

Heat Transfer module

Evaluation of the Oxide pool temperature (named T_{pool});

Updated at every iteration, to account for the crust thickness

$$T_{pool} = T_{liq} + P_{res}\frac{H}{k_{ox}}\left(Nu_{dn}S_{dn} + Nu_{up}S_{up}\right)^{-1}$$

$$Nu_{dn} = ARa^{a}\left(\frac{H}{R}\right)^{b}$$

$$Nu_{up} = BRa^{c}$$

Many correlations are available in literature, differentiating one another for the coefficients adopted and the Rayleigh (Ra) number range of validity.

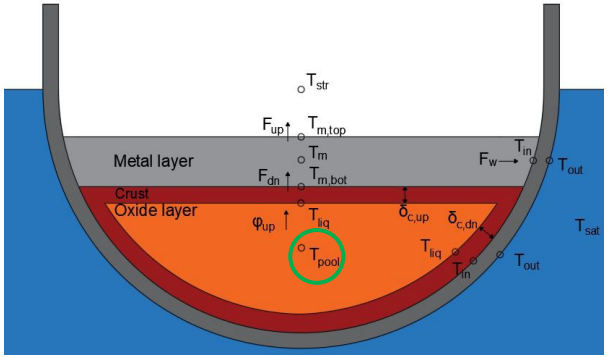

= from geometrical model

= property derived from thermochemical model

= Input

Heat Transfer module

Evaluation of the Oxide pool temperature (named T_{pool});

$$Nu_{dn} = A Ra^{a} \left(\frac{H}{R}\right)^{b}$$

$$Nu_{up} = B Ra^{c}$$

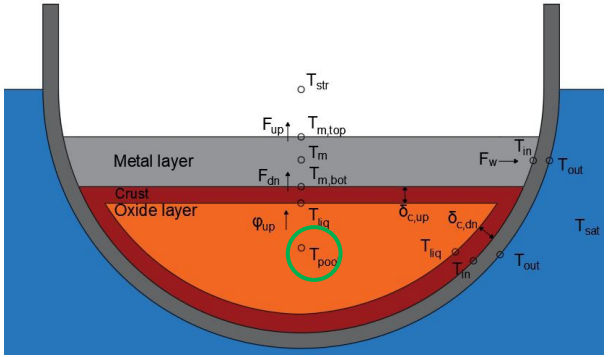

Correlation	A	a	b	B	c	Ra_{min}	Ra_{max}
ACOPO [2]	0.1857	0.2304	0.25	2.4415	0.1772	1.00E+13	1.00E+17
BALI2D [4]	0.116	0.25	0.32	0.383	0.233	1.00E+13	1.00E+17
BALI3D [4]	0.131	0.25	0.19	0.383	0.233	1.00E+13	1.00E+17
miniACOPO [5]	0.0038	0.35	0.25	1.95	0.18	1.00E+11	7.00E+14
ASFIA [6]	0.54	0.2	0.25	0.403	0.226	2.00E+10	1.10E+14

Influence of the oxide pool aspect ratio

- One of the criteria for correlation selection was the dependance on Oxide Pool aspect ratio (**H/R**);
- Each correlation is plotted in its Ra range;
- The fraction of the oxide total power going in the upwards direction (X_{up}), increases for low aspect ratios regardless of the correlation
- **The increase in X_{up} is more relevant in iPWR**, since they present **shallower corium pools**, i.e., higher upwards (flat) surface area w.r.t. downwards (hemispherical)

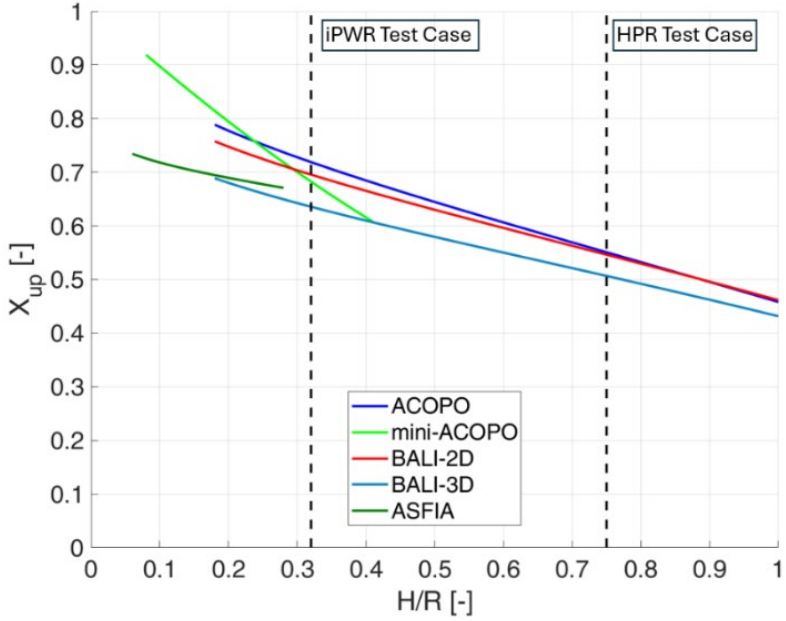

BALI 3D correlation was preliminary selected for the following calculations!

Heat Transfer module

Power balance in the oxide pool;

$$\begin{cases} \varphi_{dn}(\theta) - \dfrac{k_c}{\delta_{c,dn}}\left(T_{liq} - T_{in}\right)\left(\dfrac{R_{LH}}{R_{LH} - \delta_{c,dn}}\right) + \dfrac{q'''_c}{2}\delta_{c,dn}\left(1 + \dfrac{\delta_{c,dn}}{3(R_{LH} - \delta_{c,dn})}\right) = 0 \\ \dfrac{k_v}{\delta_v}(T_{in} - T_{out})\dfrac{R_{LH,ext}}{R_{LH}} - \dfrac{k_c}{\delta_{c,dn}}\left(T_{liq} - T_{in}\right)\left(1 - \dfrac{\delta_{c,dn}}{R_{LH}}\right) - \dfrac{q'''_c}{2}\delta_{c,dn}\left(1 - \dfrac{\delta_{c,dn}}{3R_{LH}}\right) = 0 \\ \dfrac{k_v}{\delta_v}(T_{in} - T_{out})\dfrac{R_{LH}}{R_{LH,ext}} - h_w(T_{out} - T_{sat}) = 0 \end{cases}$$

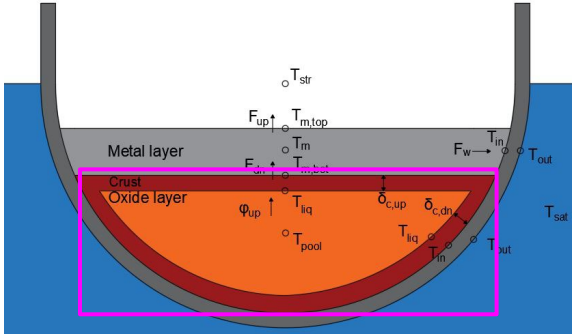

= Unknowns

Notes:

- R_{LH} and $R_{LH,ext}$ internal and external vessel radiuses, δ_v vessel thickness, $\delta_{c,\,dn}$ crust thickness in dn direction, q'''_c volumetric power inside the crust, equal to the oxide pool (same composition for both).
- Heat flux distribution $\varphi_{dn}(\theta)$ derived from the corresponding correlation's experimental data.
- The system is solved for every polar mesh, obtaining a profile for all unknowns.

Heat Transfer module

Power balance in the oxide pool;

LH steel and crust thermal conductivities were derived from [2];

$$\begin{cases} \varphi_{dn}(\theta) - \dfrac{k_c}{\delta_{c,dn}}(T_{liq} - T_{in})\left(\dfrac{R_{LH}}{R_{LH} - \delta_{c,dn}}\right) + \dfrac{q'''_c}{2}\delta_{c,dn}\left(1 + \dfrac{\delta_{c,dn}}{3(R_{LH} - \delta_{c,dn})}\right) = 0 \\ \dfrac{k_v}{\delta_v}(T_{in} - T_{out})\dfrac{R_{LH,ext}}{R_{LH}} - \dfrac{k_c}{\delta_{c,dn}}(T_{liq} - T_{in})\left(1 - \dfrac{\delta_{c,dn}}{R_{LH}}\right) - \dfrac{q'''_c}{2}\delta_{c,dn}\left(1 - \dfrac{\delta_{c,dn}}{3R_{LH}}\right) = 0 \\ \dfrac{k_v}{\delta_v}(T_{in} - T_{out})\dfrac{R_{LH}}{R_{LH,ext}} - h_w(T_{out} - T_{sat}) = 0 \end{cases}$$

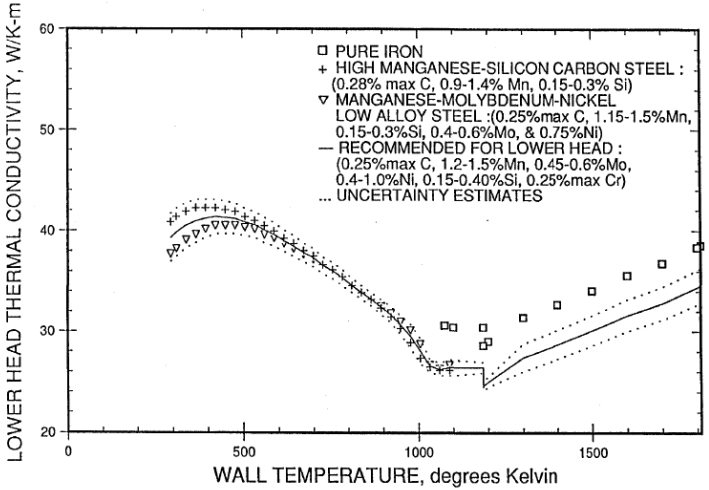

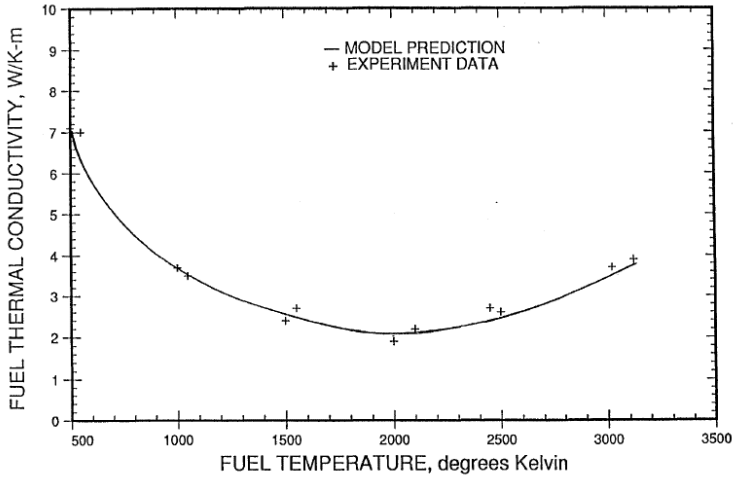

Heat Transfer module

Power balance in the oxide pool;

Pool boiling HTC was evaluated based on CHF condition, estimated with **Cheung** correlation:

- If the heat flux is lower than the CHF, nucleate pool boiling is assumed and h_W is evaluated by using **Rohsenow** correlation;
- If the heat flux exceeds the CHF, film pool boiling regime is assumed and **Bromley** correlation is adopted.
- T_{sat} evaluated with IF-97 Steam tables starting from the input pressure considered for the containment.
- As a first guess, $\mathbf{p_{containment} = p_{design}}$ for both Designs.
- This value could be refined by adding a dedicated containment model or by using the outcome of the integral code simulations.

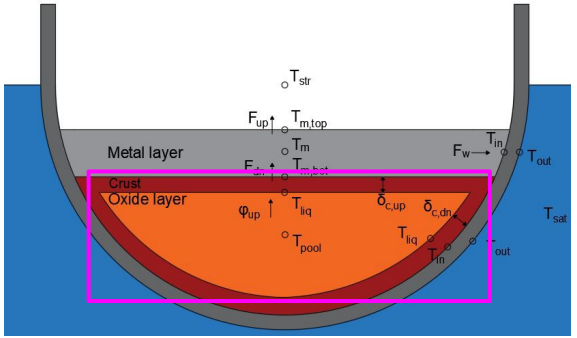

$$\begin{cases} \varphi_{dn}(\theta) - \frac{k_c}{\delta_{c,dn}}\left(T_{liq} - T_{in}\right)\left(\frac{R_{LH}}{R_{LH} - \delta_{c,dn}}\right) + \frac{q'''_c}{2}\delta_{c,dn}\left(1 + \frac{\delta_{c,dn}}{3(R_{LH} - \delta_{c,dn})}\right) = 0 \\ \frac{k_v}{\delta_v}(T_{in} - T_{out})\frac{R_{LH,ext}}{R_{LH}} - \frac{k_c}{\delta_{c,dn}}\left(T_{liq} - T_{in}\right)\left(1 - \frac{\delta_{c,dn}}{R_{LH}}\right) - \frac{q'''_c}{2}\delta_{c,dn}\left(1 - \frac{\delta_{c,dn}}{3R_{LH}}\right) = 0 \\ \frac{k_v}{\delta_v}(T_{in} - T_{out})\frac{R_{LH}}{R_{LH,ext}} - h_w(T_{out} - T_{sat}) = 0 \end{cases}$$

Heat Transfer module

SAFETY ANALYSIS OF SMR WITH PASSIVE MITIGATION STRATEGIES - SEVERE ACCIDENT

Power balance in the LM pool;

$$
\begin{cases}
F_{dn} = h_{dn}(T_{m,bot} - T_m) \\
F_{up} = h_{up}(T_m - T_{m,top}) \\
F_{up} = \varepsilon\sigma(T_{m,top}^4 - T_{str}^4) \\
F_w = h_w(T_m - T_{in}) \\
F_w = \dfrac{k_v}{\delta_v}(T_{in} - T_{out}) \\
F_w = h_w(T_{out} - T_{sat}) \\
\varphi_{up} = \dfrac{k_c}{\delta_{c,up}}(T_{liq} - T_{m,bot}) - \dfrac{q'''_c}{2}\delta_{c,up} \\
F_{dn} = \dfrac{k_c}{\delta_{c,up}}(T_{liq} - T_{m,bot}) + \dfrac{q'''_c}{2}\delta_{c,up} \\
F_{dn}S_{dn} + q'''_m V_m = F_{up}S_{up} + F_w S_w
\end{cases}
$$

The HT module calculations iterate on δ_{vessel} until $T_{in} = T_{melt,LM}$

It also considers the ablated thickness.

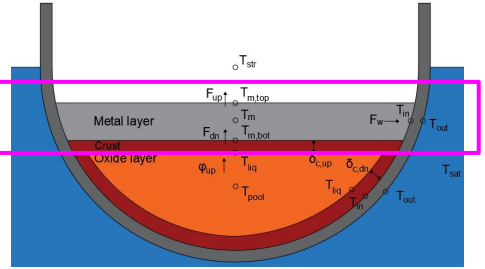

= Unknowns

= from geometrical model

Notes:

- Top cooling heat transfer is radiative. The key parameters are the LM pool emissivity (ε) and the core internals temperature (T_{str}), provided as inputs;
- q'''_m → the overall Decay Heat is distributed among the LM and oxide pool according to the relative content (i.e., moles) of Uranium.

Case II: Pool Heat Transfer

Power balance in the LM pool;

From literature, the following correlations were selected:

$$Nu_{up,\,down} = 0.069\, Ra^{\frac{1}{3}}\, Pr^{0.074}$$, Globe-Dropkin

$$Nu_{wall} = 0.076\, Ra^{\frac{1}{3}},$$ Chawla-Chan

$$Ra = a\Delta T L^3, \text{ with } L = \begin{cases} H \text{ for up, down} \\ R \text{ for wall} \end{cases}$$

$$a = \frac{g\beta}{\alpha \upsilon}$$

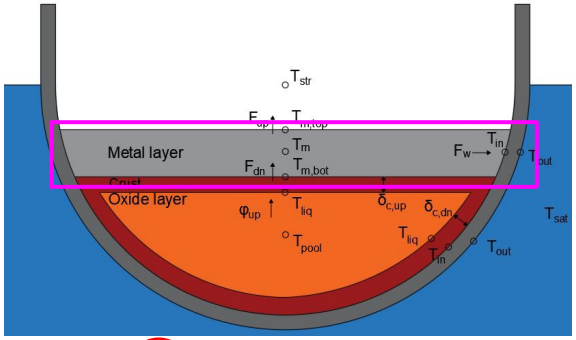

$$\begin{cases} F_{dn} = h_{dn}(T_{m,bot} - T_m) \\ F_{up} = h_{up}(T_m - T_{m,top}) \\ F_{up} = \varepsilon\sigma(T_{m,top}^4 - T_{str}^4) \\ F_w = h_w(T_m - T_w) \\ F_w = \frac{k_v}{\delta_v}(T_w - T_{ext}) \\ F_w = h_{pb}(T_{ext} - T_{sat}) \\ \varphi_{up} = \frac{k_c}{\delta_{c,up}}(T_{liq} - T_{m,bot}) - \frac{q'''_c}{2}\delta_{c,up} \\ F_{dn} = \frac{k_c}{\delta_{c,up}}(T_{liq} - T_{m,bot}) + \frac{q'''_c}{2}\delta_{c,up} \\ F_{dn}S_{dn} + q'''_m V_m = F_{up}S_{up} + F_w S_w \end{cases}$$

Test Case: Input Data

Parameter	Unit	Design 1	Design 2	HPR [3]
LH Radius	m	1.4	3.11	2
LH Thickness	m	0.12	0.25	0.15
LH Height	m	0.7	1.27	2
UO_2 Initial Mass	t	9	58	68
Zr Initial Mass	t	2.5	19.4	20
SS Initial Mass	t	4[1]	22.2[1]	60
C_{ox}	-	0.45	0.7	0.63
Decay Power	MW	1.7	4.4	14
$T_{core\ internals}$	K	1100	1100	950
Metal emissivity	-	0.38	0.38	0.38

[1] : The SS Mass does not consider the contribute coming from the partial ablation of LH thickness.

C_{ox} value selected based on considerations in slide 9.

BALI 3D correlation selected based on considerations in slide 14.

Test Cases: Outcomes

SAPAM-SA

SAFETY ANALYSIS OF SMR WITH PASSIVE MITIGATION STRATEGIES - SEVERE ACCIDENT

PARAMETER	UNITS	DESIGN 2	DESIGN 1	HPR
Oxide superheating	K	36.4	43.9	108.2
Metal superheating	K	26.	50.	85.35
Average δc, dn	cm	6.5	4.4	0.52
LH residual thickness	cm	22.1	8.7	4.8
Xrad in LM layer	-	0.872	0.662	0.222
Xup in Oxide pool	-	0.657	0.655	0.515
Fw	MW/m^2	0.133	0.335	0.62
Oxide layer H/R	-	0.28	0.33	0.69
LM layer H/R	-	0.09	0.146	0.405

Preliminary results fairly reproducing the ones in [3], no LH transition yet implemented, major difference being Fw (lower H LM, higher Fw)

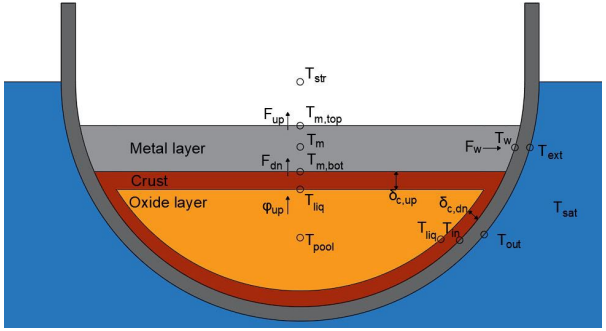

- **Small aspect ratios cause high heat transfer in the upwards direction!**
- In LM layer, this limits the focusing effect. The residual vessel thickness is much higher w.r.t. to the one obtained for HPR (4-5 cm).

Test Cases: Outcomes

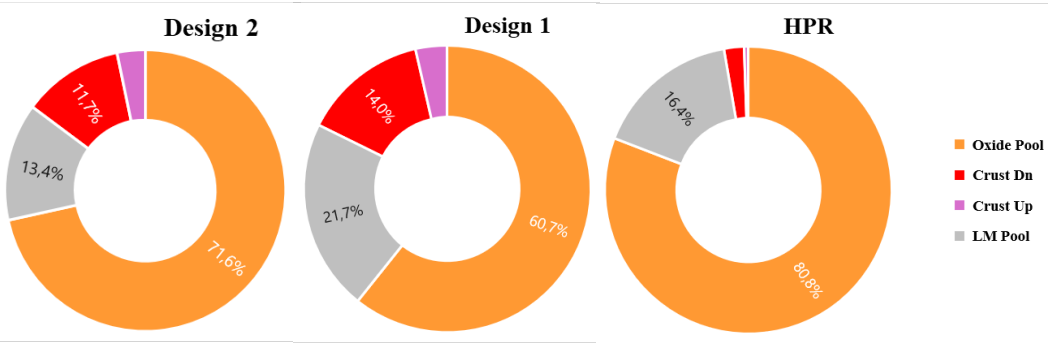

Distribution of decay power between the main volumes

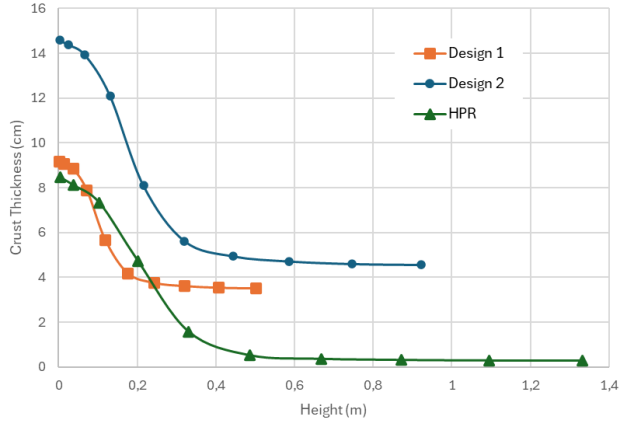

Crust thickness distribution with oxide pool height

- In iPWR, a significant fraction is produced in the oxide crust. In Design 2 it is even comparable to LM power.
- Indeed, the crust profiles indicate an average thickness of 4-6 cm for iPWR, one order of magnitude higher than HPR (5 mm).
- A thick crust of more than 14 cm at the bottom of Design 2 is registered due to its large vessel radius.

Test Cases: Outcomes

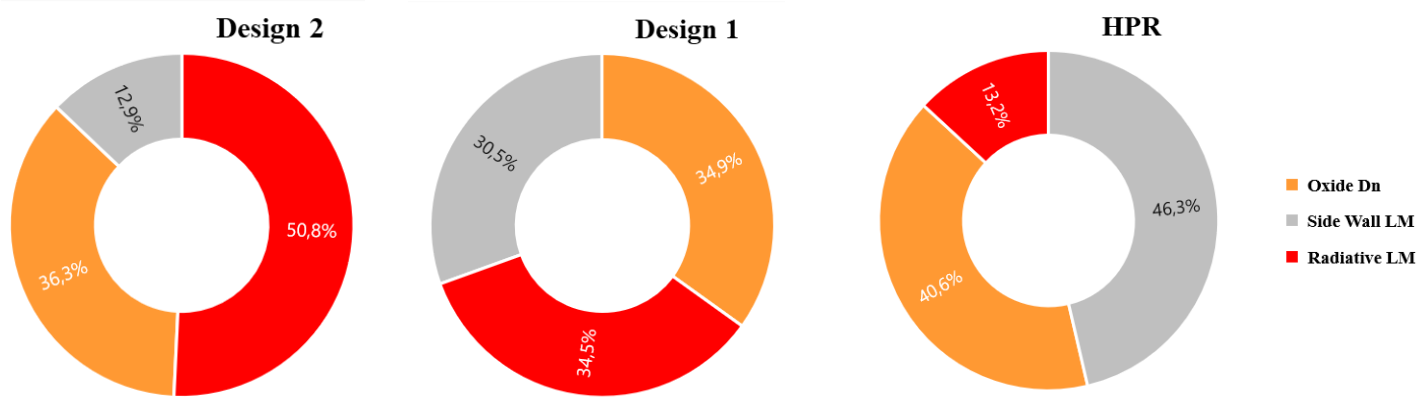

Power flow paths leaving the global system

- Referring to the LM layer, the fraction of power lost by radiative heat transfer is quite large in iPWR designs compared to HPR: between 34% and 51% of the total power vs 13% in HPR. As previously stated, this reduces the focusing effect.

- Thanks to the low focusing effect, the maximum heat flux to water is lower than the predicted CHF at all angles along the vessel (no thermal crisis is expected).

Conclusions

SAFETY ANALYSIS OF SMR WITH PASSIVE MITIGATION STRATEGIES - SEVERE ACCIDENT

Specific iPWR features identified, possibly to be considered in integral codes:

- Larger X_{up} due to low aspect ratio (can be treated by implementing H/R depending correlations).
- Rather thick oxide crust (usually neglected in HPR calculations, a model is proposed to account for it).
- Occurrence of a thin metal layer and a limited focusing effect because of a large fraction of power lost by radiative heat transfer; More accurate analyses are required for radiative heat transfer, due to its relevant impact on results.
- Expected stratification inversion in transient conditions, starting with heavy metal or mixed pools. This issue should require a model for the heavy metal layer heat transfer (not implemented in the 0D model), and a transient calculation for stratification inversion (not available in all system codes).
- Some of those issues will be addressed in the development of SASPAM-SA WP4 (new models and/or performing transient calculations of the stratified pool).

Acknowledgement/Disclaimer

SAFETY ANALYSIS OF SMR WITH PASSIVE MITIGATION STRATEGIES - SEVERE ACCIDENT



Funded by the European Union

Funded by the European Union. Views and opinions expressed are however those of the author(s) only and do not necessarily reflect those of the European Union or European Commission-Euratom.
Neither the European Union nor the granting authority can be held responsible for them.

SAFETY ANALYSIS OF SMR WITH PASSIVE MITIGATION STRATEGIES - SEVERE ACCIDENT

Marcello.principato@uniroma1.it
Cristiano.ciurluini@uniroma1.it
Fabio.giannetti@uniroma1.it
Laure.carenini@irsn.fr
Florian.fichot@irsn.fr

Thank you for listening!



The 11th European Review Meeting on Severe Accidents Research

May 13-16, 2024, Royal Institute of Technology, Stockholm, Sweden

PLENARY SESSION: LOOKING AHEAD IN SA RESEARCH

Chairs: L. Carénini (IRSN), S. Gupta (Becker Technologies GmbH)

Incoming Euratom Research funded Projects on Severe Accident and Nuclear Safety

A. Iorizzo (European Commission)

Recent IAEA Activities Related to Severe Accidents

A. Miassoedov (IAEA)

Status and Perspectives in NEA Joint Nuclear Safety Research Projects in the Severe Accident Area

D. Jacquemain (OECD/NEA)

11th European Review Meeting on Severe Accident Research Conference (ERMSAR 2024)

13-16 May 2024
KTH, Stockholm

Incoming Euratom Research funded Projects on Severe Accident and Nuclear Safety

Angelgiorgio IORIZZO
Unit C.4–Euratom Research
DG RTD Research & Innovation
European Commission

Outline

1. **Policy context Severe Accident and Nuclear Safety**
   I. Commissioner for innovation, research, culture, education and youth.
   II. Declaration on EU SMR 2030 – Safety, R&I, E&T
   III. EC DG ENER (RTD, JRC) European SMR pre-Partnership
   IV. EC DG ENER (GROW, RTD, JRC) European Industrial Alliance on Small Modular Reactors

2. **EC RTD Euratom Reserch on Severe Accident and Nuclear Safety**
   I. Horizon Europe & Euratom
   II. Selection procedure for the Euratom Research funded Projects
   III. Euratom research and training programme RTD (2021-'25)
   IV. Euratom research and training programme WP 2023-2025
   V. Incoming projects on Severe Accident and Nuclear Safety- Euratom Work Programme 2023-25
   VI. Safety of light water small modular reactors (LW-SMRs)
   VII. Euratom Research cooperation with International Organizations on Severe Accident and Nuclear Safety

Commissioner for innovation, research, culture, education and youth.

- Ms. Iliana Ivanova Commissioner for innovation, research, culture, education and youth since 18 September 2023.



Declaration on EU SMR 2030 – Safety, R&I, E&T

- **Stressed the R&I needs for SMRs**
- **Committed to jointly continue R&I, E&T**
- **Full brochure with the Declaration (in EN, FR and DE) and the key messages from the speakers**

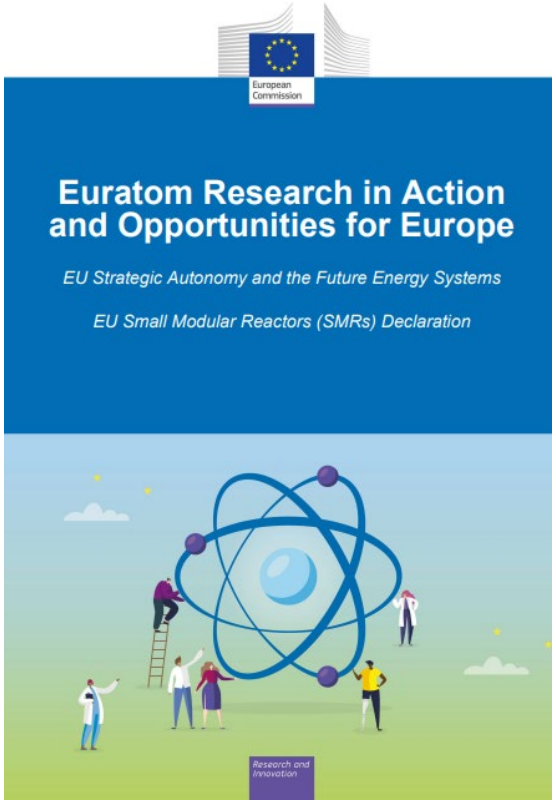

European SMR pre-Partnership

European SMR pre-Partnership - nuclearеurope

- In June 2021, in response to the call of the European nuclear industry and the R&D&I community, the EC organized the first EU Workshop on Small Modular Reactors (SMRs).
- **European SMR pre Partnership**:

  SC:
  - one member from ENSREG,
  - one member from nuclearеurope,
  - one member from SNETP,
  - the nominated Chairs of the five WSs

  5 WSs:
  1. Market integration and deployment
  2. Licensing
  3. Financing & partnership
  4. Supply Chain adaptation
  5. Innovation, research and development
- In October 2023 "Stakeholders' Forum" was held in Bruxelles and paved the way for the **European Industrial Alliance on SMRs**

European Commission

[European Industrial Alliance on Small Modular Reactors - European Commission (europa.eu)]



nuclearеurope

SNETP
Sustainable Nuclear Energy Technology Platform

European Industrial Alliance on SMRs
Main Objective

The main objective of the European Industrial Alliance on SMRs **is to facilitate and accelerate the development, demonstration, and deployment of the first SMRs projects in Europe in the early 2030s**, by assisting emerging SMRs projects to reach the demonstration and deployment phase.

European Industrial Alliance on Small Modular Reactors - European Commission (europa.eu)

Timeline

6 February 2024 — Communication on 2040 climate target and climate neutrality by 2050

9 Februay 2024 — Open call for membership launched

22 March 2024 — SMR Industrial Alliance dissemination event

Organised in the margins of the Nuclear Energy Summit in Brussels.

12 April 2024 — Deadline for applications

29-30 May 2024 — First General Assembly

European Industrial Alliance structure

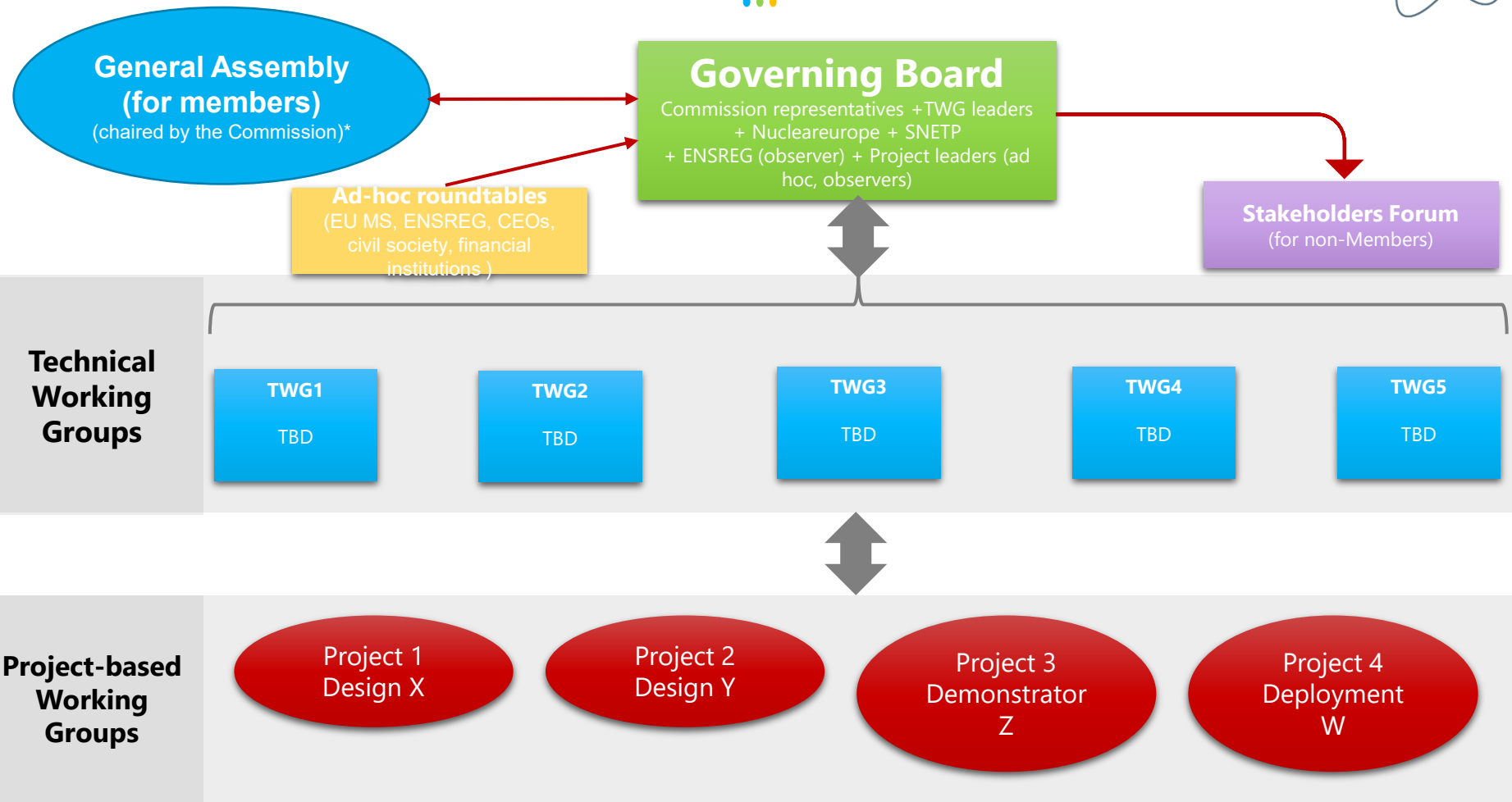

*: The three Commissioners for Energy, for Internal Market, and for Innovation, Research, Culture, Education and Youth will co-chair the General Assembly meetings.

European Industrial Alliance structure

Technical Working Groups

- Groups for policy reflection and action in important aspects for which further work is needed (project development, project finance, supply chain, financing, safety research, public engagement, waste management, etc.) or not yet touched upon.
- Will be nourished by projects' feedback experience and will disseminate best practices across projects
- Will directly interact with EU & National decision-makers.

Project-based Working Groups

- Will be assisted under the SMR Alliance
- Will gather interested stakeholders through specific agreements.
- Depending on project nature & objectives, they could fall under different categories (IPCEIs, PPP, SRIA, etc,)
- Will run under strict commercial protection / non-disclosure agreements

Working Methods – Technical Working Groups

INDICATIVE LIST

Project development	Project finance	Supply chain	Public engagement
Radioactive waste and spent fuel management	Research & Innovation	Skills	Safety, Security, and Safeguards

- Technical Working Groups assigned tasks by the Governing Board.
- Stakeholder collaboration: developers, vendors, utilities, research institutes, financial institutions, supply chain representatives, training centres, and civil society.
- European Commission could provide technical support, including research on safety, security and safeguards for SMRs.
- Working Groups may meet multiple times a year.
- Administrative support provided by an entity designated by the industry in agreement with the European Commission.

Horizon Europe & Euratom

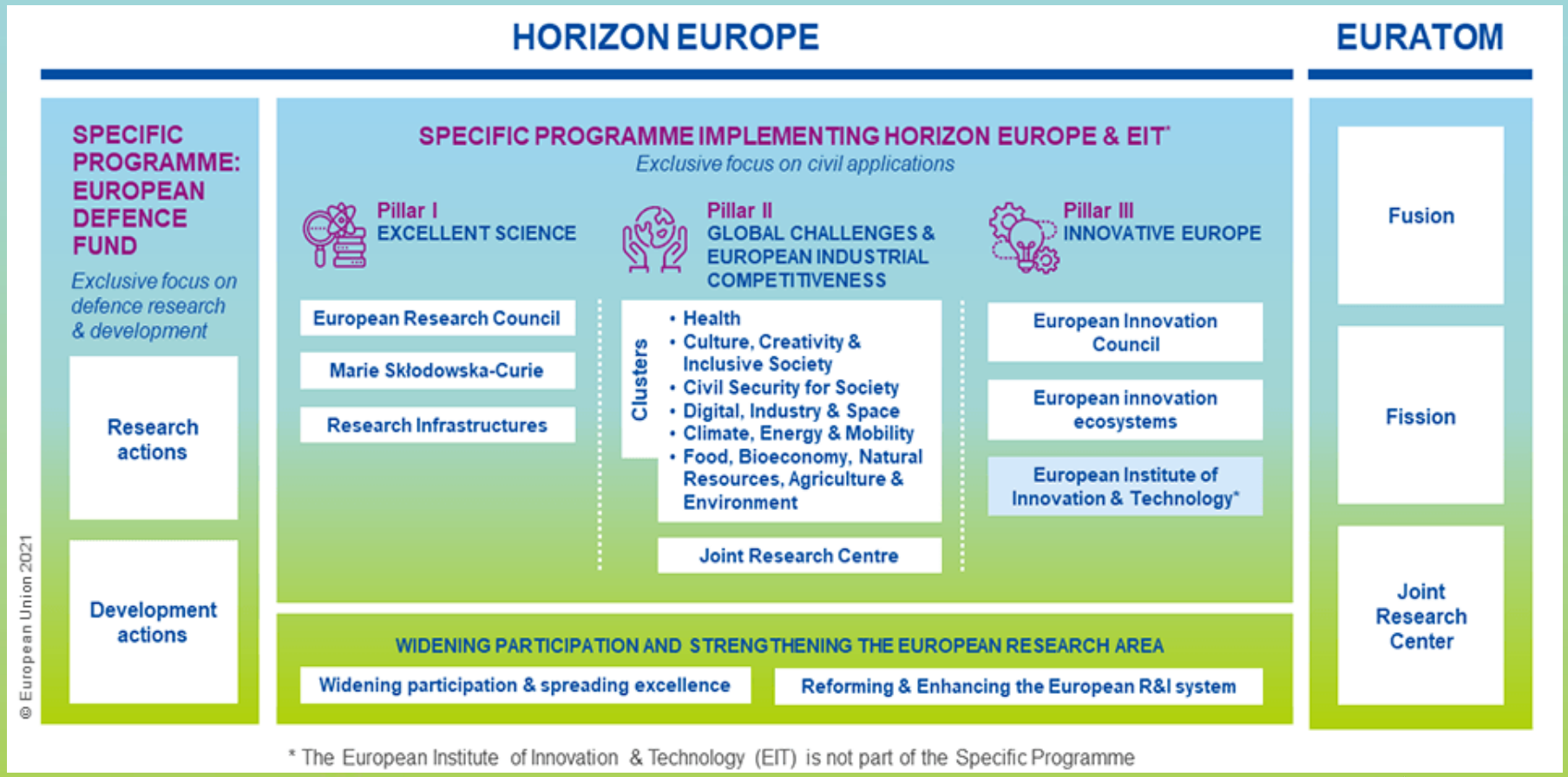

European Commission

Selection procedure for the Euratom Research funded Projects

The Euratom Research funded Projects are selected via a competitive process:

- The EC-DG RTD representing Euratom drafts a Euratom Research and Training Programme (5+2 years) containing topics of research
- Potential beneficiaries apply with proposals for research Projects
- These research Projects are evaluated by independent Experts panels
- Euratom Work Programme 2023-2025 proposals were evaluated in January 2024
- The selected Projects should start indicatively from mid-2024

Euratom research and training programme RTD (2021-'25)



EU adopted Euratom Research and Training Programme on 12 May 2021

The programme has a budget of €1,38 billion for 5 years (€1,98 b. in 7 y. MFF)

€583 million for indirect actions in fusion research and development

€266 million for indirect actions in nuclear fission, safety and radiation protection

€532 million for direct actions undertaken by the JRC

Euratom research and training programme WP 2023-2025



Euratom WP 2023-’25

EUR 132 Millions

Incoming projects on Severe Accident and Nuclear Safety

Euratom Work Programme 2023-25

- **HORIZON-EURATOM-2023-2025-NRT-01-01: Safety of operating nuclear power plants and research reactors. Total indic. budget EUR 20.00 m.**
- **HORIZON-EURATOM-2023-25-NRT-01-02: Safety of Light Water Small Modular Reactors (LWR-SMRs). Total indic. budget EUR 15.00 m.**
- **HORIZON-EURATOM-2023-25-NRT-01-03: Safety of advanced and innovative nuclear designs and fuels. Total indic. budget EUR 12.00 m.**
- HORIZON-EURATOM-2023-25 NRT-01-04: Co-funded European Partnership for research in nuclear materials. Total indic. budget EUR 20.00 m.
- HORIZON-EURATOM-2023-25 NRT-01-05: Partitioning and Transmutation of minor actinides towards industrial applications. Total indic. budget EUR 5.00 m.
- **HORIZON-EURATOM-2023-25 NRT-01-06: Improved nuclear data for the safety of energy and non-energy applications of ionising radiation. Total indic. budget EUR 4.00 m.**

Euratom Work Programme 2023-25

- HORIZON-EURATOM-2023-25-NRT-01-07: Innovative technologies for safety and excellence in decommissioning including robotics and AI. Total indic. budget EUR 4.00 m.
- HORIZON-EURATOM-2023-25-NRT-01-08: Safety of low enriched fuel for research reactors - securing the supply of medical radioisotopes. Total indic. budget EUR 7.00 m.
- HORIZON-EURATOM-2023-25-NRT-01-09: Nuclear and radiation techniques for EU strategic autonomy, circular economy and climate change policies. Total indic. budget EUR 7.00 m.
- **HORIZON-EURATOM-2023-25-NRT-01-10: Harnessing innovation in nuclear science, technology and radiation protection. Total indic. budget EUR 7.00 m.**
- HORIZON-EURATOM-2023-25-NRT-01-11: Preparatory phase for a European production capability to secure a supply of High-Assay Low Enriched Uranium Fuel (HALEU). Total indic. budget EUR 1.00 m.

DISCLAIMER

- Currently the GAP phase is ongoing.
- The Grants are not yet signed!
- The information provided in this presentation is **INFORMAL** as based only on the ranking list.
- The ranking list does not guarantee the signature of the grants cf. Financial and Legal verifications on the consortia, etc.

Topic	Funding Scheme	Acronym
1. Safety of operating nuclear power plants and research reactors	RIA	**FIND**
1. Safety of operating nuclear power plants and research reactors	RIA	**SOCRATES**
1. Safety of operating nuclear power plants and research reactors	RIA	**Magic-RR**
1. Safety of operating nuclear power plants and research reactors	RIA	**EVEREST**
2. Safety of Light Water Small Modular Reactors (LWR-SMRs)	IA	**EASI-SMR**
3. Safety of advanced and innovative nuclear designs and fuels	RIA	**ENDURANCE**
3. Safety of advanced and innovative nuclear designs and fuels	RIA	**TREASURE**
3. Safety of advanced and innovative nuclear designs and fuels	RIA	**LESTO**
6. Improved nuclear data for the safety of energy and non-energy applications of ionising radiation	RIA	**APRENDE**
10. Harnessing innovation in nuclear science, technology and radiation protection	IA	**SANE**

FIND

topic 1

- Future Instrumentation and coNtrol based on innovative methods and Disruptive technologies for higher safety level
- *Keywords: Structural health management, instrumentation, digital twin, accident management, material ageing, long-term Operation.*

Abstract:

The Long-Term Operation of Nuclear Power Plants (NPPs) calls for innovative methods to monitor the ageing of safety systems. New instrumentation will also lead to improve decision-making in accidental conditions thanks to additional information, complementing the material and organisational modifications decided after the Fukushima accident.

The project FIND aims first to adapt innovative technologies deployed in other industries to prevent the failure of metallic pipes. FIND will work on Structural Health Monitoring technologies (ultrasonic guided waves and acoustic emission) to detect defects in real time during plant operation, even in inaccessible locations. In addition, Digital Twins will be developed to better predict degradation phenomena, with combination of detailed mechanical models and real plant data (strain, temperature and vibration measurements). Tests in experimental and industrial conditions (including NPPs) will be performed, representative of the following phenomena:

- Local corrosion and large deformations of raw service water pipes,
- Stress corrosion cracking and fatigue on the primary circuit,
- Flow accelerated corrosion on the turbine extraction line.

Concerning accidental instrumentation, FIND will first develop systems to track water movements during a loss-of-coolant accident. This will include localisation of breach thanks to heated thermocouples and data science approaches. FIND will evaluate feasibility to monitor progression of severe accidents, thanks to analysis of fission products in containment, either by gamma ray spectroscopy or physicochemical analysis.

Technologies developed in FIND are low intrusive and cost effective. They will help to anticipate maintenance, and will complete or replace some Non-Destructive Testing. This will result in higher availability of NPPs, lower operator dosimetry, and reduced costs, which will foster their adoption. FIND is led by IRSN, French public expert for nuclear risks and encompasse

SOCRATES

topic 1

- Assessment of Liquid Source Term for Accidental Post Management Phase
- *Keywords: LTO, waste management, SAM, severe accident, liquid source term, fission product, experiments, modelling, mitigation, recommendations*

Abstract:

The SOCRATES project addresses critical gaps in our understanding of the liquid source term during severe nuclear accidents and offers innovative solutions to mitigate and monitor the release of radionuclides into the environment. The project contributes to the mid-to-long-term management of nuclear power plants after a severe accident by enhancing safety, environmental protection, safe waste management and public well-being. The main contributions of the topical project are:

- Enhanced understanding of liquid source term
- New computer models for the liquid source term phenomena
- Innovative absorbent materials to effectively trap key radionuclide species, particularly Cs and Sr
- Miniature size radiochemical laboratory for radionuclides
- Education and training for nuclear safety
- Recommendations for long-term operations, waste management and severe accident management strategies.

The management of possible leakages of contaminated water, which may happen more frequently due to aging of reactor components and joints, will gain new remedies from SOCRATES results to tackle and mitigate the contaminants inside the plant. The project's research on the liquid source term directly impacts a majority of existing and new nuclear reactors, encompassing diverse reactor designs and technologies. Recommendations based on SOCRATES results will support nuclear community on international scale by giving guidelines how to manage liquid source term. Developed computer models for the analysis of liquid source term phenomena will benefit industry, safety authorities and research community in the safety assessments of NPPs. The models developed in SOCRATES will be implemented in severe accident analysis codes, such as AC2 and ASTEC. When the design of new sorbent materials for radionuclides will be performed with computer simulations, it will enhance the digitalization of safety developments, and enable considerations of multiple sorbent composition variations with low cost.

Magic-RR topic 1

- Research on Materials Ageing and Structural Integrity of Research Reactors
- *Keywords: Irradiation damage in Al alloys, Corrosion, Transmutation, Ageing of research reactors, Small specimen techniques, Surveillance testing, continued safe operation (CSO), Multi-scale modelling.*

Many of the existing Research Reactors (RR) in Europe are very old (>60 years operation). Only few initiatives are taken (PALLAS and JHR) to partially replace this capacity. Continued operation of these RRs is mandatory (at least until the new reactors come to operation) to maintain the EU excellence in development and qualification of nuclear materials for advanced reactor concepts and to maintain the supply of medical isotopes. License extensions for continued safe operation (CSO) requires ageing management review (AMR) and time limited ageing analysis (TLAA) of critical structures and components. However, there is limited understanding of damage mechanisms and lack of materials data on RR materials at relevant operating conditions for long term operation of RRs. In addition, there is a shortage of surveillance specimens for extending the operational life for some RRs. Lastly, sharing of knowledge and operational experience is crucial in this relatively small RR community.

Magic-RR addresses aforementioned issues by leveraging (1) available archive materials and data from the existing research reactors, e.g. from surveillance programs and shut down reactors, (2) operational experience of research reactor operators and (3) advanced characterization and modelling techniques at universities and nuclear research centers.

To achieve this goal Magic-RR focuses on the following topics in order to CSO of European RRs:

- Improved understanding on irradiation induced damage in RR structural materials (specifically Al alloys) at high fluence conditions
- Application of advanced multi-scale modelling methods for prediction of irradiation influence on mechanical properties
- Investigation of corrosion mechanisms and its prevention/mitigation
- Assessment of sub-size testing for surveillance programs
- Sharing knowledge on reactor operation and Providing guidelines on best practices
- Structural integrity assessment of critical components of RRs to support CSO of RRs

European Commission

EVEREST topic 1

- Experiments for Validation and Enhancement of the REactor preSsure vessel fluence assessment
- *Keywords: Vessel fluence estimation of VVER and PWR; multi-physics (neutron transport, fluid flow and heat transfer) validation; high resolution experimental data;*

The safety of a nuclear reactor relies heavily on modelling. In the last two decades, making use of the increased computer power available, advanced multi-physics solvers have been developed to reduce the level of conservatism when simulating pressurized water reactors. These tools rely on a first-principles based approach and produce solutions with a much finer spatial resolution. However they are seldom used in practice due to, amongst other things, the lack of dedicated experimental data for validation, especially when it comes to their improved spatial resolution.

The EVEREST project intends to address this issue by quantifying the impact of using advanced MP models for the modelling of a VVER reactor ("usefulness"); by demonstrating the accuracy of their results, especially the improved resolution through the production of dedicated experimental data (“trustworthiness”); and by promoting them to key groups of the nuclear engineering community (students, utilities, regulators). The consortium is built around the necessary research facilities and expertise from all the required actors of the nuclear industry, both within Europe and outside.

In terms of impact, the project will produce scientific knowledge towards producing electricity using a climate-neutral energy system, in a safe and efficient way. The advanced models will provide more accurate and detailed information about the current safety margins in nuclear reactors enabling more informed decisions on setting the regulatory limits; and resulting in an improvement of the plant safety as a whole. A better understanding of the safety margins for a nuclear power plant could also allow power uprate. The same approach can be envisioned for research reactors and allow more users to carry out research activities. Finally, the EVEREST project will have a long-term impact on knowledge preservation through the organization of a summer school and trainings as well as the funding of mobility grants.

EASI-SMR topic 2

- Ensuring Assessment of Safety Innovations for SMR
- *Keywords: SMR, Passive safety system, streamlined licensing, code-validation, reliability assessment, nuclear physics*

The EASI-SMR project intends to address the safety issues related to the LW-SMR in order to provide advances that should support implementation of such technologies as soon as possible. The EASI SMR project activities are aimed at ensuring that these reactors will be designed, constructed, commissioned and operated in the safest possible way and in accordance with existing regulations. The consortium was carefully chosen so that the research entities can provide the necessary research teams and support facilities across the European Continent and beyond.

EASI-SMR will address the safety issues associated with major LW-SMR innovations:

- Passive systems
- Soluble Boron-free cores
- Co-generation and hybridation
- Additive manufacturing to improve compactness of Nuclear Steam Supply System
- Multi-units operation

The work aims to provide insights for European LW-SMR projects, in particular:

- NUWARD SMR, a French design of a reactor generating 170 MW of electricity production
- LDR-50, a Finnish design of a district heating reactor of 50 MW

EASI-SMR is closely linked with NUGENIA TA6 and the European SMR pre-Partnership's WS5.

ENDURANCE topic 3

- EU kNowleDge hUb foR enAbling MolteN Salt ReaCtor safety development and dEployment
- *Keywords: Molten Salt Reactors, Fuel salt chemistry, MSR experimental evidence, Safety of MSR system, Modelling, Sustainable energy, Energy transition*

The ENDURANCE project (EU kNowleDge hUb foR enAbling MolteN Salt ReaCtor safety development and dEployment) aims at supporting the safe operation and the technological development of MSR in Europe, through the knowledge advancement in different fields of the MSR research, connecting the design developers and industry needs with the university and research centre capabilities and the regulator requirements. This EU knowledge hub will gather seven universities, eight research centres, four European startups working on MSR design, one industry, one technical and support organization to improve the maturity of relevant Critical Technology Elements (CTEs) that are key enablers for the industrial deployment of the MSR technology. The five CTEs in which the ENDURANCE project will contribute are: i) the chemistry of fuel salt and structural materials in reactor environment; ii) the experimental evidence on safety related phenomena; iii) the modelling preparedness for safety assessment and licensing; iv) the sustainability and safeguards compliance of MSR fuel cycle; v) the demonstration of (safe) MSR adaptability in future decarbonized energy scenario. The environment created by the project will allow to promote cross-fertilization of ideas, solutions of technological issues, discussion about the regulatory framework of the MSR. The outcomes of the project on the different CTEs will be analysed to define a technological and scientific roadmap for the future development and deployment of MSR technology in Europe.

TREASURE topic 3

- Towards reliable and safe GFR
- *Keywords: GFR, Safety, ALLEGRO, Decay Heat Removal, Core Physics, Innovative Nuclear Fuel, Proliferation Resistance, Thermal-hydraulics, High-temperature Chemistry*

Gas-cooled fast reactor (GFR) is considered as one of the six most promising advanced nuclear reactor technologies, supported worldwide by the Generation IV International Forum and ESNII in Europe, with concepts under development in Europe and the USA. It excels in versatility, combining very high core outlet temperatures and the possibility to close the fuel cycle, allowing for very efficient and sustainable electricity and industrial heat production, replacing burning fossil fuels.

The TREASURE proposal presents a Research and Innovation Action aiming at connecting European developers of GFR demonstrator ALLEGRO (V4G4 Centre of Excellence) with expert organizations with experience in GFR and HTR research, who will utilize their unique expertise and knowledge and bring fresh ideas to the GFR development. It is divided into 6 Work Packages, four of them dealing with open research and development problems of GFRs, namely the Core operation and safety optimization (WP1), Experimental validation of the DHR concept (WP2), GFR as industrial heat and power source (WP3), Enhancing GFR safety (WP4). Dissemination and outreach activities are included in WP5, alongside with communication activities with regulators and relevant international organizations, and education and training activities. WP6 ensures smooth management and execution of the project.

The main objectives of the TREASURE project are:

- Further optimization of the GFR fuel design and fuel cycle.
- Exploring possibilities to further reduce produced waste and to further enhance proliferation resistance in GFRs.
- ALLEGRO safety concept demonstration, including large-scale experimental verification.
- Optimization of operation flexibility and performance of GFRs, using intermediate heat storage system, cogeneration, and hydrogen production.
- Further enhancing ALLEGRO safety via use of passive and redundant safety systems.
- Attracting students and young professionals to work on GFR development.

LESTO topic 3

- LEad fast reactor Safety design and Tools
- *Keywords: LFR, H2 generation, integration with RES, passive safety systems, advanced materials, code validation*

Shortening the time-to market of the LFR technology is an ambitious, but undeniably important factor to attract additional investments, thanks to the lower initial risk, added flexibility, and faster return of experience. Industries and utilities sharing the vision of a competitive LFR of a small and medium-size with modular features will be attracted by the compressed deployment roadmap, and will play a leverage role at national and European level, strengthening synergies and creating public–private–partnership opportunities. In this context, the European community working on the LFR development and deployment assumed the commitment, among others, to highlight the technical open issues and existing research infrastructures, aiming to support the R&D phase through European, national and in-kind contribution of the involved partners. The aim of the LESTO project is moving on along the depicted roadmap, aiming at further developing the LFR technology, supporting the demonstration that LFRs can be designed, sited, constructed, commissioned and operated in line with the requirements of the actual safety standards, with particular focus on their safety features and passive safety systems. Along the project the most relevant facilities in Europe and UK will be adopted to implement a large and very comprehensive experimental database for code validation, safety assessment and component/system demonstration. Among the others, it is worth to mention the large-scale pool type ATHENA facility, being commissioned in Romania, the CIRCE pool in Italy, as well as MELECOR in UK. These facilities, with the support of research infrastructure in Belgium, Germany and Sweden represent the state of art for the LFR R&D. Large emphasis will be devoted to transient analysis in large pools, allowing the community to cross the death valley from laboratory to industry scale.

APRENDE topic 6

- Addressing PRiorities of Evaluated Nuclear Data in Europe

The conception, development, optimization, and safety evaluation of a broad range of nuclear energy (fission and fusion) and non-energy applications (radiation protection, radionuclide production, health, geosciences, space research, security, and industry) require reliable and accurate simulation tools. Such tools critically rely on accurate nuclear decay and reaction data. APRENDE has the ambition to improve nuclear data for modelling and simulation (M&S) tools used by European stakeholders in the application areas of the European Union and its member states that currently have the highest priority. The priority application areas identified by stakeholders of nuclear data and by national, European, and international projects and consultations are:

A. All aspects of spent nuclear fuel (SNF),
B. Reactor operational characteristics such as reactivity versus burnup, transients, and margins,
C. Advanced reactor and fuel cycle development including small modular reactors (SMR) and GenIV systems based on lead and sodium coolants, molten salts, or an accelerator like MYRRHA,
D. Criticality safety and shielding for safety assessments and safety assessment methodologies,
E. Non-Energy applications, radiation protection.

This ambition requires a comprehensive approach involving the eight objectives stated above, and a methodology and impact pathway as detailed below. The combination of this ambition, objectives, methodology and our pathway to create impact is what the proposers believe to be not only the best, but also an excellent response to the HORIZON-EURATOM-2023-NRT-01-06 call 'Improved nuclear data for the safety of energy and non-energy applications of ionising radiation'. In the following, we break down and explain our ambition by each of the priority application areas.

SANE **topic 10**

- Safety Assessment of Non-Electric uses of nuclear energy
- *Keywords: Nuclear energy, hydrogen, non-electric uses, process heat, safety, risk communication*

Safety Assessment of Non-Electric uses of nuclear energy (SANE) project investigates the potential of non-electric usage of nuclear energy, the safety aspects of reactors designed for non-electric use as well as the safety implications of the end use. As many of the applications are novel, their use needs to be properly communicated to various stakeholders, and for this the project includes work on risk communication.

Non-electric uses are identified in EU SMR pre-Partnership as one of the high level R&D needs, and the understanding of the potential applications and their limitations as well as the challenges in integration of nuclear energy to end use were seen as important issues to be studied. Non-electric uses will be an important way to diversify the income streams of nuclear plants, as the electricity production will become more and more competitive. Nuclear has unique advantages in non-electric uses as it can produce lot of energy locally for large local uses

.

SANE aims to review potential future uses of nuclear energy in order to facilitate their implementation in the near future. This project aims to provide information for both industrial applications retrofitted to operating nuclear power plants, as well as for novel reactors dedicated for non-electric uses. Information needs for appropriate risk communication is studied with case studies in several countries, and a specific study on communications during abnormal situations is done based on the events that transpired in Ukraine during Russia's invasion.

Euratom Research cooperation with International Organizations on Nuclear Safety

- **NEA-OECD Committee on the Safety of Nuclear Installations CSNI**

  - Next 75th CSNI Meeting 4-6 June 2024 Gréoux-les-Bains, France - video conference.

European Commission



Thank you for your attention!

IAEA
International Atomic Energy Agency
Atoms for Peace and Development

Recent IAEA Activities Related to Severe Accidents

Presented by A. Miassoedov

The 11th European Review Meeting on Severe Accident Research KTH Royal Institute of Technology, Stockholm, Sweden
May 13-16, 2024

Outline

- IAEA short information
- Technical meetings
- Coordinated Research Projects
- Publications, education and training
- IAEA activities related to AI for nuclear power

Nuclear Power Technology Development Section
Division of Nuclear Power
Department of Nuclear Energy





Nuclear Power Engineering Section

The Section supports countries operating nuclear power plants or expanding their existing programmes to improve engineering, performance, management systems, human resource management, stakeholder involvement and technical infrastructure. It shares best engineering practices and innovations consistent with the global objectives of nuclear safety, security and non-proliferation. Read more →



Nuclear Power Technology Development Section

Fostering information exchange and collaborative research and development for advanced nuclear reactor technologies, this Section provides information to the IAEA's Member States on technology status and development trends for advanced reactor systems and their applications. Read more →



Nuclear Infrastructure Development Section

This Section is responsible for coordinating IAEA assistance to Member States considering or embarking on nuclear power programmes. It supports capacity-building, conducts review missions and offers guidelines, standards and workshops on developing the infrastructure for a safe, secure and sustainable nuclear power programme. Read more →



International Project on Innovative Nuclear Reactors and Fuel Cycles Section

The Section coordinates the activities of the membership-based International Project on Innovative Nuclear Reactors and Fuel Cycles (INPRO) to increase international cooperation on global nuclear energy sustainability, long term strategies and institutional and technical innovations for nuclear energy development and deployment. Read more →

Outline

- IAEA short information
- Technical meetings
- Coordinated Research Projects
- Publications, education and training
- IAEA activities related to AI for nuclear power

Technical Meeting on Advanced Technologies and Systems for Containment Preservation in Accident Conditions (11–13 October 2022)

- Presently, R&D focuses on advancing and assessing active and passive safety systems, along with monitoring systems for accident mitigation
- Containment R&D involves various phenomena and scales, requiring high-resolution CFD-scale measurements
- Optimizing experimental infrastructure in Member States, including scaling considerations and expanding databases for representative conditions
- *Potential collaborative activity: utilizing diverse methodologies to extrapolate experimental findings to reactor scale for analyzing containment behaviour during accidents.*

Technical Meeting on Reliability Assessment of Passive Heat Removal Systems Used in Advanced Reactor Designs (25–28 April 2023)

- Assess uncertainties in passive system operation before integrating into emerging advanced reactor technologies
- Discuss achievements and future directions in reliability analysis of passive heat removal systems
- Identify R&D needs for deploying passive heat removal systems in advanced reactor designs
- *Recommendation: develop an IAEA publication analyzing advancements in passive heat removal from reactor core and containment during transient/accident conditions*

Consultancy Meeting on Preparation of the TECDOC on Advances in Knowledge and Technology Related to the Ex-Vessel Corium Behaviour and Cooling in WCRs (15–17 May 2023)

- Exchange of information on ongoing activities in Member States related to ex-vessel corium behaviour and cooling in WCRs
- Preparation of the IAEA publication on the analysis of the latest advances in knowledge and technology related to the ex-vessel corium behaviour and cooling in WCRs. Title, draft content, and implementation schedule defined
- Developing a training course on application of severe accident codes to ex-vessel scenarios
- Discussing scope and objectives of proposal for International Collaborative Standard Problem (ICSP) or CRP on ex-vessel corium behaviour and cooling

Outline

- IAEA short information
- Technical meetings
- Coordinated Research Projects
- Publications, education and training
- IAEA activities related to AI for nuclear power

IAEA Coordinated Research Activities

- Provide opportunities to engineers and scientists in developing and developed Member States to collaborate on research topics of common interest

- Results of research activities supported by the Agency are disseminated to all Member States through national, international and IAEA scientific and technical publications, and other communications media



http://cra.iaea.org/cra/index.html

Developing a Phenomena Identification and Ranking Table (PIRT) and a Validation Matrix, and Performing a Benchmark for In-Vessel Melt Retention (2020 – 2024)

23 participating organizations from 14 Member States

Research objectives:

1. To develop a PIRT for IVMR
2. To develop a validation matrix for IVMR and to identify relevant high-quality experimental data requested for the validation of computer codes for IVMR simulation
3. Benchmark involving code-code comparison and comparison with experimental data on individual phenomena
4. To carry out an analytical benchmark on an IVMR comprehensive scenario exercise

International Collaborative Standard Problem (ICSP) or a CRP on ex-vessel corium behaviour and cooling

- Discuss scope and objectives
- Suggest employing open data and a wide range of codes and code users in a two-step approach
- Analyse open results (e.g. MCCI and/or melt spreading tests conducted at the VULCANO facility in CEA, France) under Fukushima-specific conditions
  - Freedom to select parameters that best capture the results
- In the second step, conduct a Fukushima-based scenario in two phases: spreading and MCCI
  - Use the same parameters and correlations and conduct sensitivity analysis
- Tentatively timeline: preparation phase 2024-2025, start in 2026

Outline

- IAEA short information
- Technical meetings
- Coordinated Research Projects
- Publications, education and training
- IAEA activities related to AI for nuclear power

Publications under development

- TECDOC Advances in Severe Accident Simulation and Modelling for Pressurized Heavy Water Reactors (2024)
- Reliability Assessment of Passive Heat Removal Systems in Advanced Nuclear Reactor Designs (2025)
- TECDOC Modelling of Severe Accidents in Water Cooled Reactors with Accident Tolerant Fuels (end 2025)
- TECDOC Modelling and Simulation of Severe Accidents for Liquid Metal-Cooled Fast Reactors: Status of Knowledge and Challenges (2025)
- TECDOC (or NES) Ex-vessel Phase of Severe Accidents in Water Cooled Reactors (2026)

IAEA SAMG-D toolkit

SAMG-D

Severe Accident Management Guideline Development toolkit

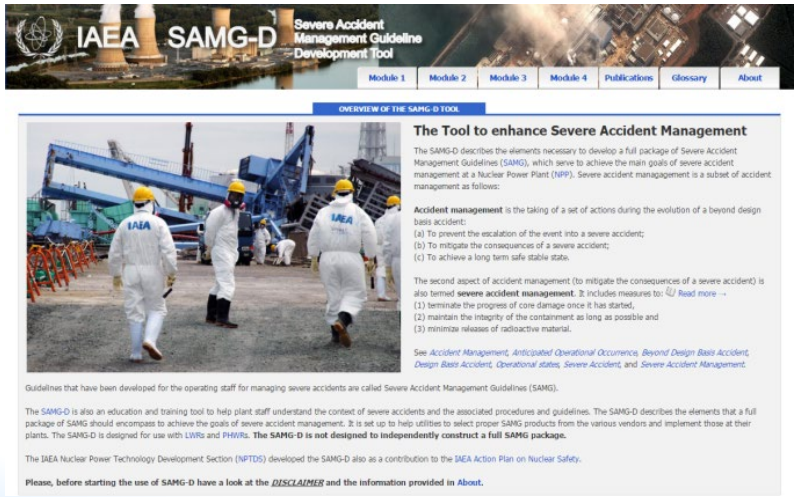

Module 1
Fundamentals of reactor safety

Module 2
Severe accident challenges and mitigation strategies

Module 3
Severe accident management guidelines

Module 4
Implementation, requirements and infrastructure

IAEA SAMG-D toolkit activities

Seven Training Workshops

Toolkit revision in 2019-2020

- Review the toolkit ensuring coherency with IAEA Specific Safety Guide SSG 54
- Review and update the toolkit with information for BWRs, including practical examples of SAMG for BWRs
- Include additions or changes regarding CANDU reactors
- Review and update the sections focusing on computer codes used for the accident analysis
- Update the toolkit based on advances in the state-of-the-art (mainly the phenomenology of severe accidents, Module 2), revision of the list of references

Toolkit revision in 2025-2026 under discussion

Next training workshop: 2-6 December 2024, Vienna (in-person)

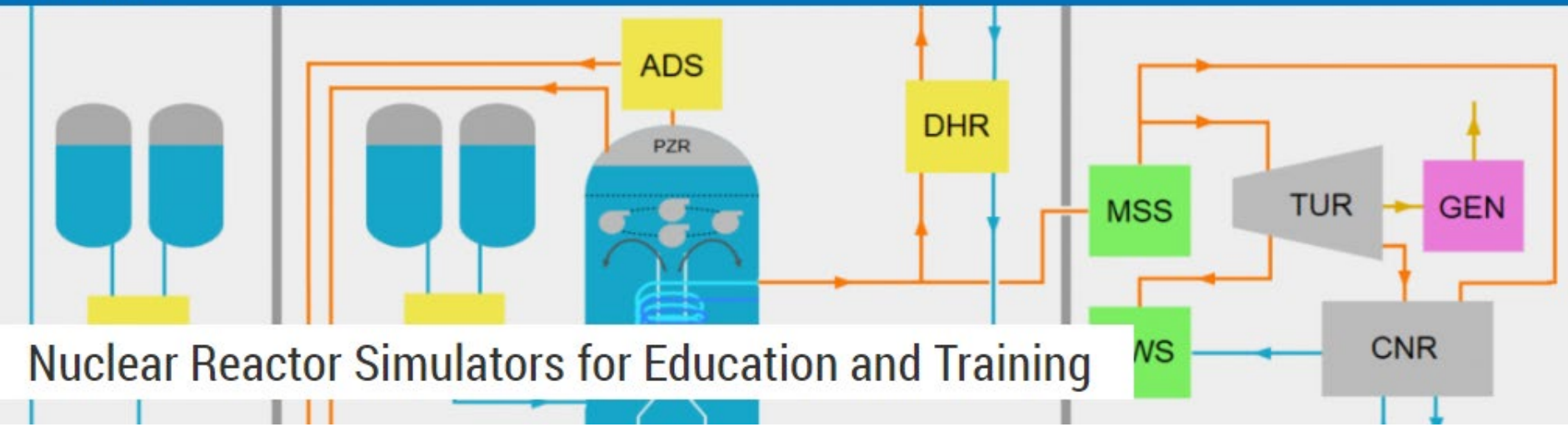

Nuclear Reactor Simulators for Education and Training

Pressurized Water Reactor (PWR) Simulators

- Advanced PWR: Two-Loop Large PWR (Korean-OPR 1000)
- Russian-type PWR (VVER-1000)
- Advanced Passive PWR (AP-600)
- Integral Pressurized Water Reactor (SMR)

Boiling Water Reactor (BWRs) Simulators

- Conventional Boiling Water Reactor with Active Safety Systems (BWR)
- Advanced BWR with Passive Safety Systems (ESBWR)

Pressurized Heavy Water Reactor (PHWR)

- Conventional Pressurized Heavy Water Reactor (PHWR)
- Advanced PHWR (ACR-700)

Part-Task Simulator

- Micro-Physics Nuclear Reactor Simulator

Under Development

- High Temperature Gas Cooled Reactor (HTGR)
- Sodium Cooled Fast Reactor (SFR)

Educational hypothetical Severe Accident Simulator (ESAS)

- Advanced PWR with active and passive safety systems
- Normal operation mode (incl. malfunctions) and severe accident mode
- Completion of documentation
- Access to Member States: 2024

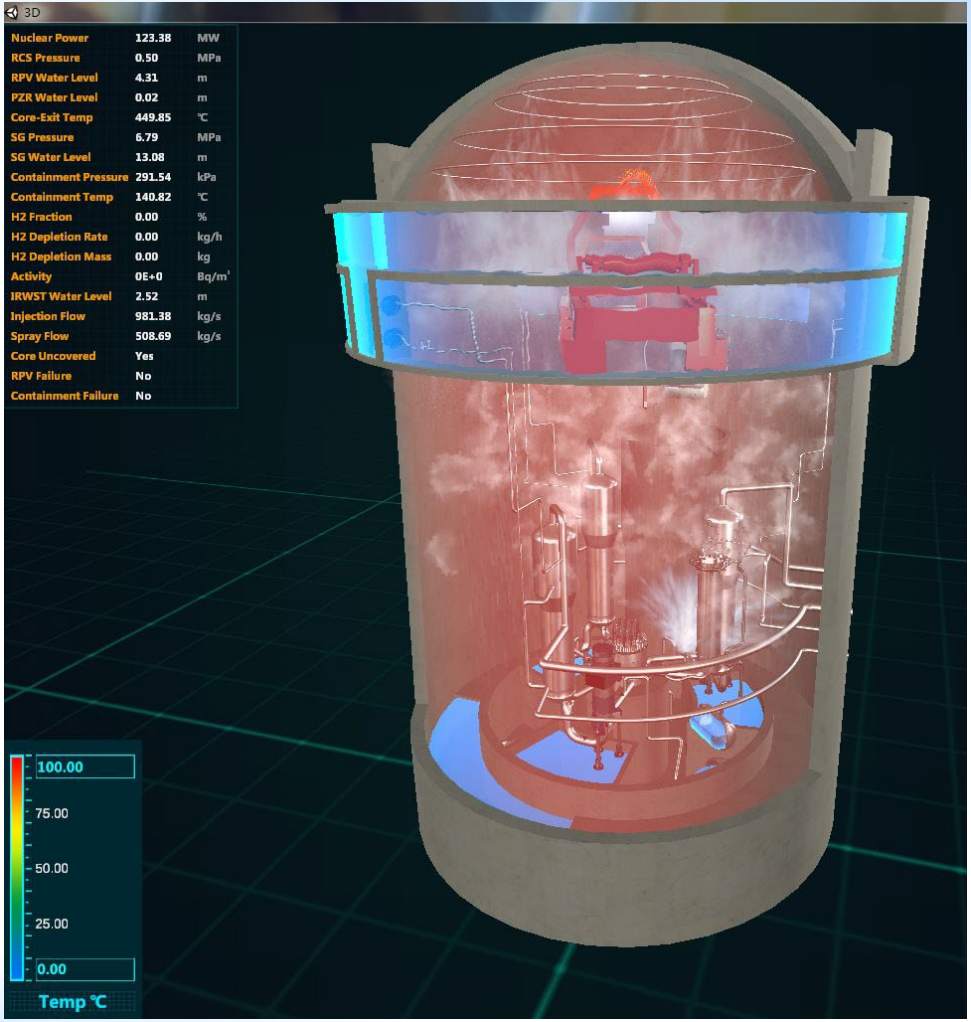

Outline

- IAEA short information
- Technical meetings
- Coordinated Research Projects
- Publications, education and training
- IAEA activities related to AI for nuclear power

IAEA Collaborating Centre on AI with Center for Science of Information at Purdue University (2023-2027)



- **Facilitate programmatic activities and knowledge sharing** in AI for nuclear power (AI4NP) to advance reactor designs and support industrial deployment of AI solutions at operating NPPs
- **Develop validation approaches for AI concepts** in reactor technology, real-time operation, maintenance, design optimization, safety analysis, and accident management
- **Support human capacity building** with training and educational courses on AI basics, opportunities, challenges, and applications for nuclear power software development, safety analysis and accident management

Technical Meeting on AI, 4-7 November 2024, Vienna

- Second meeting scheduled for 2024 on AI in nuclear engineering and technology
- First meeting held on 18–21 March 2024, titled "TM on Deployment of AI Solutions for Nuclear Power Industry" at NRC Headquarters, USA. Aim: finalize new IAEA TECDOC for Member States interested in AI deployment in nuclear plants
- November meeting aims to thoroughly discuss and explore AI analysis's role in accelerating nuclear reactor design. Goals: identify collaboration opportunities, offer suggestions for future IAEA activities, involve broader participation from operating plants, include evolutionary and innovative designs.

Joint IAEA-ICTP School on AI in nuclear engineering and technology in 2025

- Gain a **comprehensive understanding of AI and ML** concepts and applications in nuclear engineering
- **Learn about knowledge-based and data-based AI**, ML paradigms, and decision support for optimal design, operation, maintenance, safety analysis, and risk assessment in nuclear technology
- **Explore various ML approaches**, including decision trees, tree ensembles, artificial neural networks, and data analytics
- **Engage in hands-on exercises** with datasets to apply AI and ML in nuclear engineering problems
- **Gain confidence in utilizing AI** to solve real-world nuclear technology issues and assess the reliability and effectiveness of these techniques

Acknowledgments

IAEA activities related to severe accidents involve close collaboration between the Department of Nuclear Energy and the Department of Nuclear Safety and Security.

The help of Colleagues in preparing this presentation is greatly appreciated.

IAEA
International Atomic Energy Agency
Atoms for Peace and Development

Thank you!

NEA
NUCLEAR ENERGY AGENCY

Session : Looking ahead in Severe Accident Research

Status and perspectives in NEA joint nuclear safety research projects in the severe accident area

Didier Jacquemain, NEA, Nuclear Safety Technology and Regulation Division



© 2024 OECD/NEA

Outline

Overview of NEA co-operative nuclear safety research projects.



Insights from NEA joint nuclear safety research projects.

Enhancing nuclear safety research cooperation and capabilities to accelerate safe deployment of new technologies.

© 2024 OECD/NEA

1. Overview of NEA co-operative nuclear safety research projects

© 2024 OECD/NEA

The NEA: A Worldwide Co-operation Forum for Nuclear Countries

- Founded in 1958, HRP and DRAGON (HTGR) projects launched the same year
- Currently 34 member countries and 2 strategic partners
- 8 standing technical committees and 1 management board
- 74 working parties and expert groups*
- 28 on-going joint nuclear safety research projects (several projects in other NEA expertise areas)





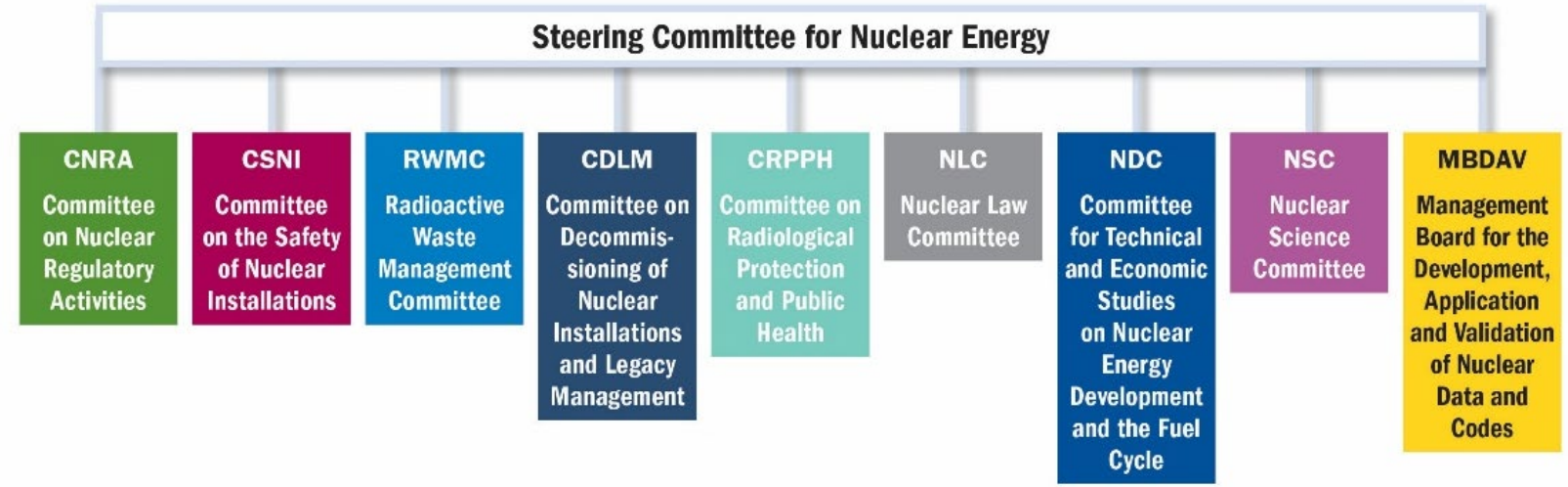

* As of December 2021

© 2024 OECD/NEA

NEA Joint Nuclear Safety Research Projects



Cooperation through projects

Share world-wide expertise on safety topics and experimentation

Share resources, leveraging investments and facilities

Maintain key research facilities and competencies, support operating agents, contribute to education

Facilitate cooperation between countries and various stakeholders



Applications and perspectives

Understand phenomena that affect safety (e.g. data for assessing accident management)

Quantify and reduce uncertainties

Obtain high quality data for safety code validation, benchmark safety codes

Be ready for the future

- **License renewal of existing reactors**
- **New reactor applications (light water, non-light water, SMRs)**

Nuclear Energy Agency (NEA) - Nuclear Safety Research Joint Projects (oecd-nea.org)

© 2024 OECD/NEA

28 On-going Joint Nuclear Safety Research Projects

- **Fuel and cladding behavior, fuel safety, including in-reactor, storage and transport**
- **Reactor Technology**
- **Thermal hydraulics data, models and tools**
- **Severe accident management and post-Fukushima Daiichi lessons**
- **Fire propagation, fire events high energy electrical faults**
- **LTO, structural component ageing and harvesting research, operational experience**
- **Human and Organisational aspects of Safety**

CABRI CIP | SCIP-4 | Halden F&M

FIDES II JEEPs (5) | Quench-ATF (DBA)

LOFC (HTGR)

ATLAS-3 | ETHARINUS | RBHT-2 | POLCA (SFP)

ROSAU | THEMIS | ESTER | PANDA | COPS

FACE | TCOFF-2 | Quench-ATF (BDBA)

FAIR | FIRE-7 DB | HEAF-2

Halden (structure mat.) | FIDES II JEEPs (2)

SMILE | CODAP-4 DB | ICDE-9 DB

Halden HTO, phase 2

© 2024 OECD/NEA

28 On-going Joint Nuclear Safety Research Projects

Several new projects discussed with focus on advanced designs and LTO

JP timeline
(3 operational data base projects not included)

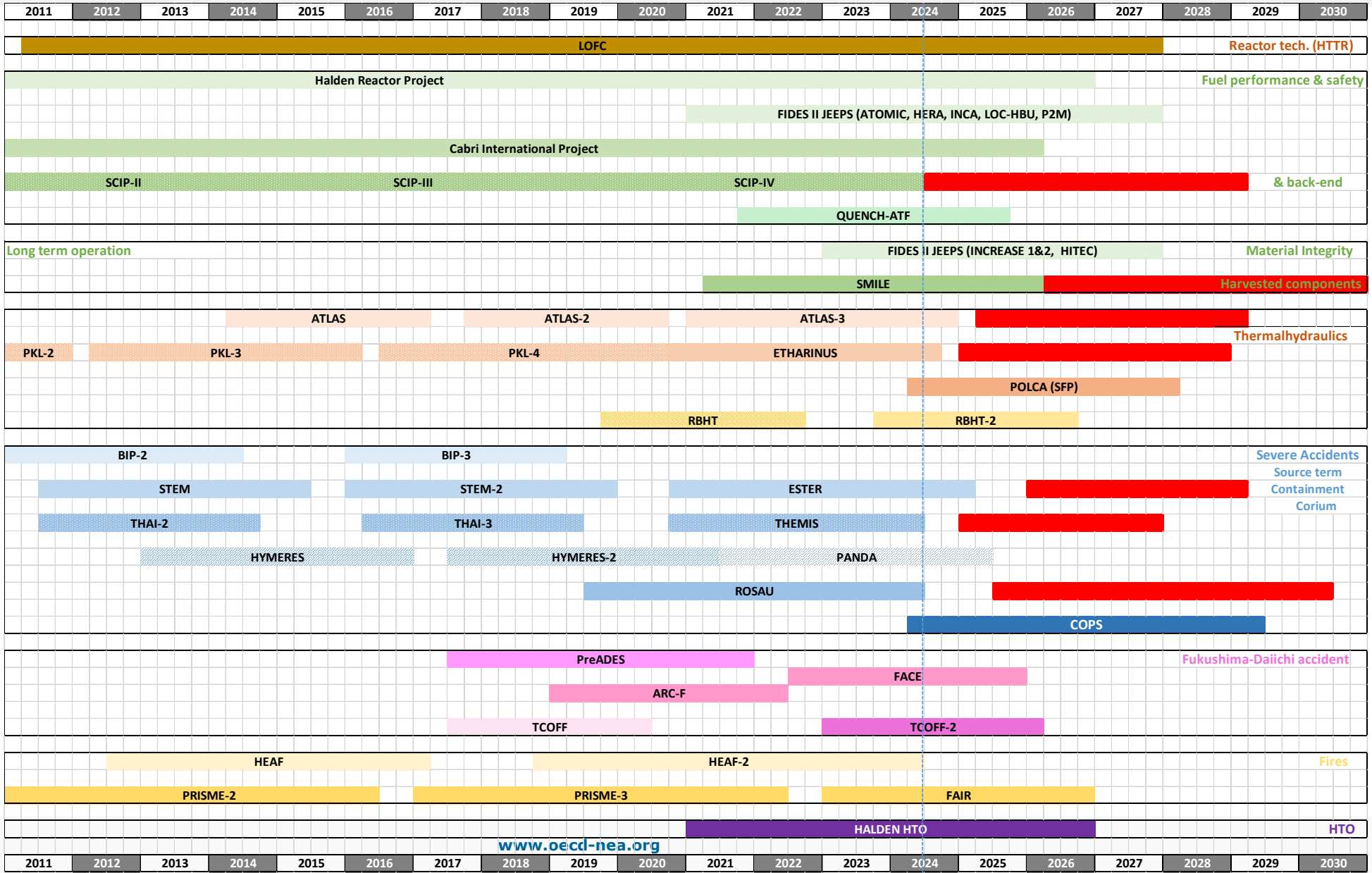

© 2024 OECD/NEA

2. Insights from NEA joint nuclear safety research projects

© 2024 OECD/NEA

Insights from joint Nuclear Safety Research projects

Halden reactor



Courtesy IFE

Major resources used in safety analyses, as well as in safe technological developments, e.g.:

- Fuels and claddings safety criteria evaluation, LOCA and RIA transient analysis
- Analyses of ageing and durability of structure materials, with the development of a data base for harvested components
- RCS and containment TH transients' analyses, including efficiency and reliability of conventional and modern safety systems, with passive ones, and of operating procedures
- Assessment of management of H_2 combustion risk with efficiency of operating procedures and mitigation systems (e.g., PARs, spray)
- Source term analysis for severe accidents
- Use of insights from the Fukushima-Daiichi accident analyses for accident management (and for decommissioning)
- Fire risk analysis in nuclear facilities and assessment of mitigation measures and systems
- HTO studies
- Etc.

© 2024 OECD/NEA

Insights from joint Nuclear Safety Research projects

Joint projects contributed to the development of frameworks:

- to preserve and develop core research capabilities and expertise
- to establish a broad partnership to share common technical bases and funding
- to contribute to education, training and dissemination of knowledge
- to preserve and disseminate high quality data

Need to enhance nuclear safety research cooperation and capabilities to accelerate safe deployment of new technologies

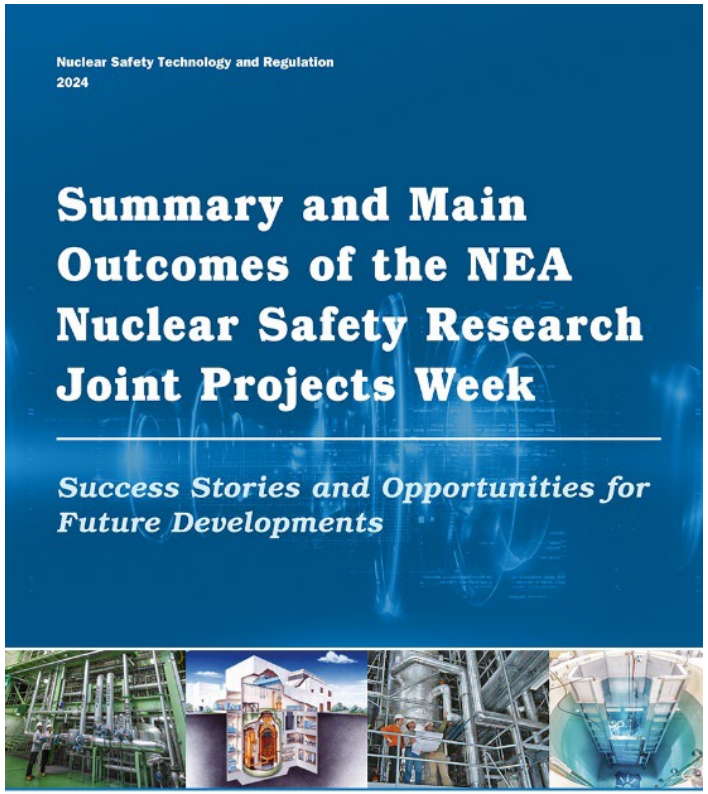

Nuclear Energy Agency (NEA) - NEA Nuclear Safety Research Joint Projects Week: Success Stories and Opportunities for Future Developments (oecd-nea.org)

3. Enhancing nuclear safety research cooperation and capabilities to accelerate safe deployment of new technologies

© 2024 OECD/NEA

NEA's views regarding the goal of tripling nuclear energy by 2050 announced at COP28

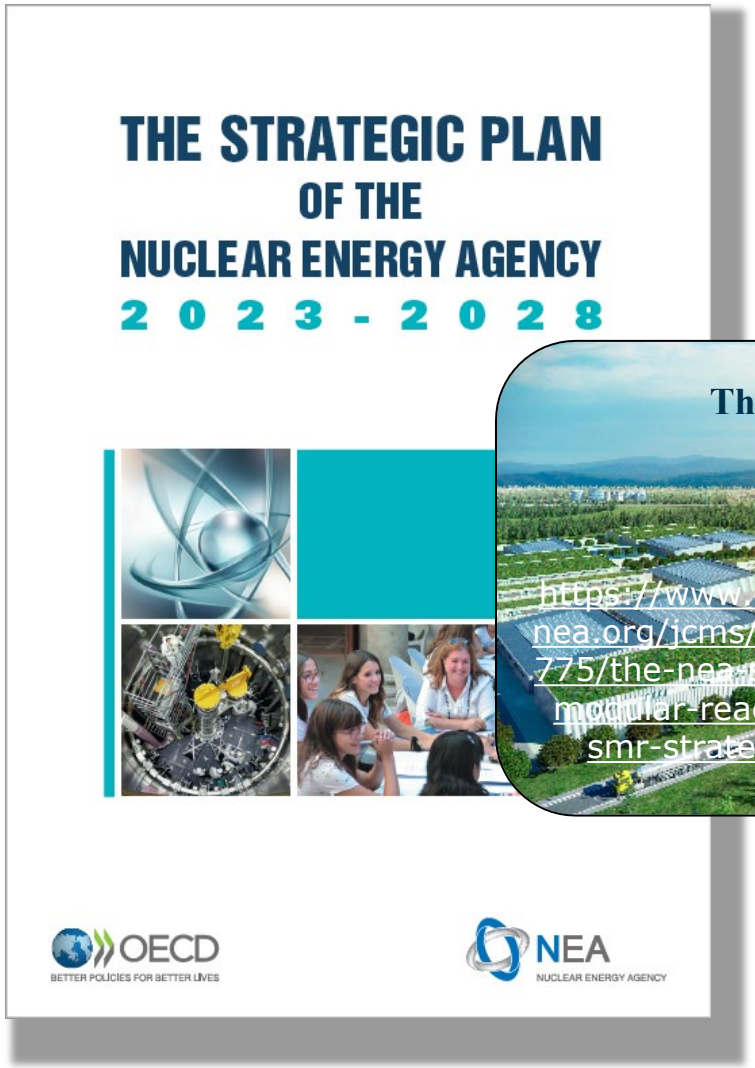









Towards a high-level nuclear safety research roadmap

PIRTs for innovative designs and phenomena related to LTO issues

Organise a R&D and databases framework model

Establish a safety research board roadmap

Engage with policy making bodies

Safety research capabilities

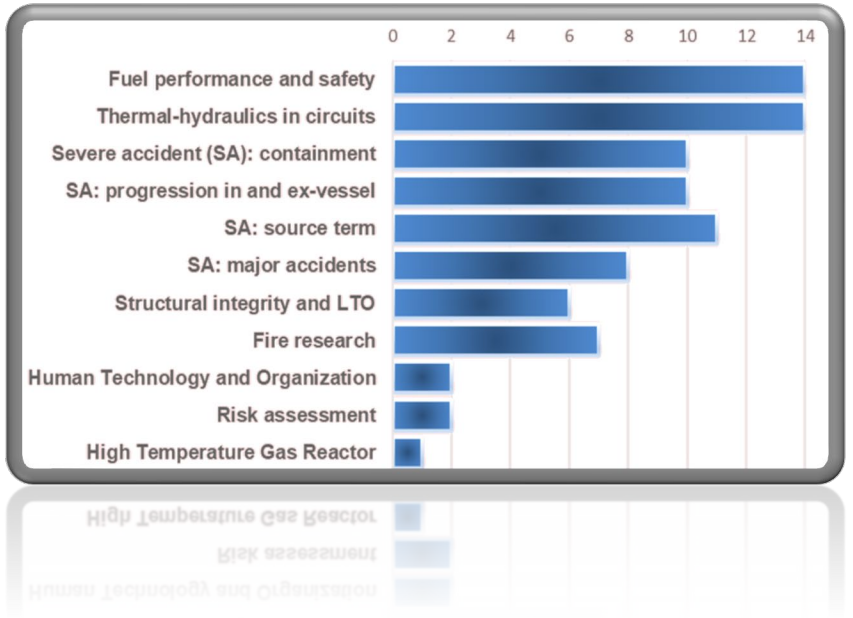

Balance to be reviewed considering long-term perspectives

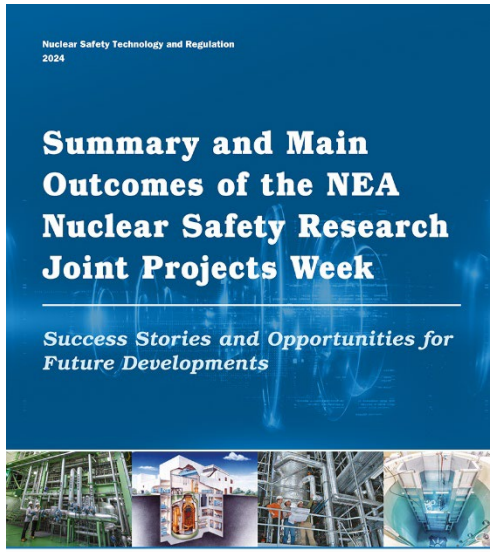

Nuclear Energy Agency (NEA) - NEA Nuclear Safety Research Joint Projects Week: Success Stories and Opportunities for Future Developments (oecd-nea.org)

© 2024 OECD/NEA

Roadmap for nuclear safety research under development

Identify research priorities and draft recommendations to ensure adequate funding, infrastructure and international mechanisms for research cooperation to support sustainable nuclear safety research.

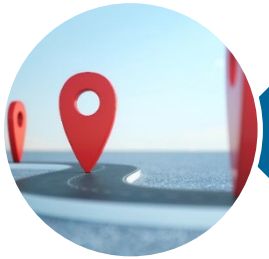

Providing ***broad long-term perspectives***

- regulators key messages on nuclear safety research needs and challenges
- deeper technical insights and overall schedule on priority research needs in key technical areas (considering industry insights).



Facilitating timely ***collaborative actions*** to sustain research infrastructures, expertise, and safety research programmes capabilities that will need to be developed by governments and industry over the coming decades to meet evolving regulatory needs.

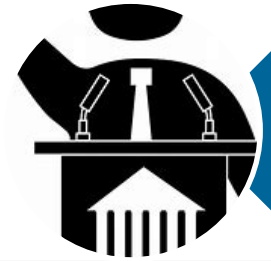

Addressing major stakeholders: ***policy-makers, research operators, industry and other relevant international institutions***

© 2024 OECD/NEA

NEA Thematic Research Platforms (including SMRs specific topics)

involving



Fuel and structure material: FIDES II

TH platforms





Component ageing Platform

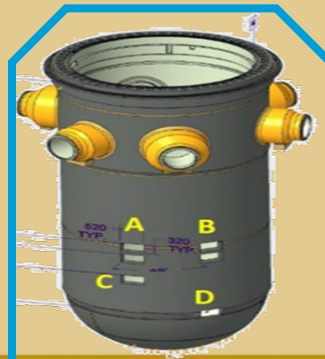

SA platform

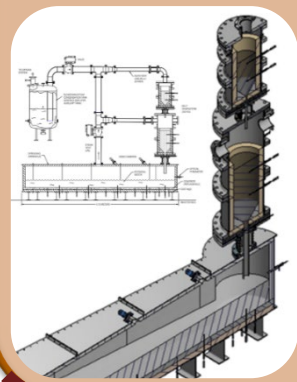



Figure sources: ANL, BECKER Technologies, KAERI, KIT, Studsvik

© 2024 OECD/NEA

FRAME Workshop: reviewing perspectives in TH and SA research



DOE logo coming soon (under approval)

EPRI

NEA
NUCLEAR ENERGY AGENCY

U.S.NRC
United States Nuclear Regulatory Commission
Protecting People and the Environment

© 2024 OECD/NEA

Conclusion



Co-operative nuclear safety research still needs to be widely supported for the development and durability of the nuclear sector



Addressing all the envisioned new technologies requires accelerating the development of research capabilities and expexpertise



NEA is working on setting up adequate frameworks with a wider support from stakeholders

© 2024 OECD/NEA



Thank you for your attention

didier.jacquemain@oecd-nea.org

© 2024 OECD/NEA

The 11th European Review Meeting on Severe Accidents Research

May 13-16, 2024, Royal Institute of Technology, Stockholm, Sweden

TECHNICAL SESSION 7.1: SOURCE TERM

Chairs: I. Kljenak (IJS), S. Gupta (Becker Tech. GmbH)

ID119	**The Reduction of Radiological Consequences of design basis and extension Accidents: re-assessment of calculation results and main outcomes of the R2CA project** N. Girault (IRSN)	**Paper Presentation**
ID124	**Progress in understanding fission products remobilization behaviour and hydrogen risk in water cooled reactors under severe accident conditions: OECD/NEA THAI-3 project** S. Gupta (Becker Technologies GmbH)	**Paper Presentation**
ID88	**Source Term Assessment for a VVER-1000 Reactor Equipped with Filtered Venting: Sensitivity Study of the Impact of Different Forms of Iodine in the Containment** M. Kotouc (UJV)	**Paper Presentation**
ID97	**Source Term Dispersion Analysis and Construction of the Risk Map around the Peach Bottom Unit-2 Plant Using the ASTEC and JRODOS codes** O. Murat (KIT)	**Paper Presentation**

The Reduction of Radiological Consequences of design basis and extension Accidents: re-assessment of calculations and main outcomes of the R2CA project

N. Girault[1], K. Chevalier-Jabet[1], T. Taurines[1], F. Mascari[2], N. Muellner[3], A. Berezhnyi[4], M. Cherubini[5], A. Malkhasyan[6], F. Parmentier[6], T. Kaliatka[7], P. Foucaud[8], A. Arkoma[9], Z. Hozer[10], M. Jobst[11], L. Luzzi[12], A. Kecek[13], D. Gumenyuk[14], L. E. Herranz[15]

[1]: Institut de Radioprotection et de Sûreté Nucléaire (IRSN), 13115 Saint-Paul-lez-Durance, France
[2]: Agenzia Nazionale per le Nuove Tecnologie, L'Energia e lo Sviluppo Economico Sostenibile (ENEA), 40129 Bologna, Italy
[3]: University of Natural Ressources and Life Sciences (BOKU), 1190 Wien, Austria
[4]: Analytical Research Bureau for NPP Safety (ARB), Kiev, Ukraine
[5]: Nuclear and Industrial Engineering (NINE), 759 Lucca, Italy
[6]: Bel V, 1070 Brussels, Belgium
[7]: Lithuanian Energy Institute (LEI), Breslaujos g. 3, Kaunas, Lithuania
[8]: Tractebel Engineering (TE), 1000 Brussels, Belgium
[9]: VTT Technical Research Centre of Finland, 02044 Espoo, Finland
[10]: Centre for Energy Research (EK), 1121 Budapest, Hungary
[11]: Helmholtz-Zentrum Dresden-Rossendorf, D-01328 Dresden, Germany
[12]: Politecnico di Milano (POLIMI), 20156 Milan, Italy
[13]: Ustav Jaderneho Vyzkumu (UJV), Rez, Czeh Republic
[14]: State Scientific & Technical Centre for Nuclear and Radiation Safety (SSTC-NRS), 03142 Kiev, Ukraine
[15]: Centro de Investigationes Energética, Medioambientales y Tecnologicas (CIEMAT), 28040 Madrid, Spain

ABSTRACT

The 4-year H2020 R2CA (Reduction of Radiological Consequences of design basis and extension Accidents) project was intended to propose guidelines to harmonize the safety analysis methods through the development of generic methodologies for best estimate evaluations of the radiological consequences (RC). It was dedicated to Design Basis Accidents (DBA) and accidents in the Design Extension Condition domain without significant fuel melting (DEC-A). The project addresses a broad scope of LWR designs (BWR, EPR, PWR, VVER) from Gen II, III and III+ focusing on bounding scenarios of Loss Of Coolant Accidents (LOCA) and Steam Generator Tube Rupture (SGTR) transients.

The work performed within the project intends to reduce some of the conservatisms currently used in safety studies and/or licensing calculations, which are necessary to help a better quantification and consideration of the potential changes to come in the operation conditions (e.g. increase of fuel burn-up, usage of ATF). In doing so, some potential higher risks exhibited by knowledge improvements (e.g. clad embrittlement through secondary hydriding, increased fission product releases from high-burn-up or MOx fuels, etc.) were also highlighted. Finally, it was beneficial to the development of innovative measures or tools to prevent these accidents (i.e. algorithms, AI based tools, etc.) as well as to strengthen their management.

This article summarizes the main outcomes of the R2CA project presenting the most relevant improvements in simulation tools and calculation methodologies therein. LOCA and SGTR calculation results in DBA and DEC-A domains are discussed. In addition, some insights are given on tools/methods that could be further used to increase the NPP safety based on exploratory innovative work performed within the project. Finally, in conclusion, preliminary guidelines are given for a better estimation of the RC of the considered scenarios.

KEYWORDS
LOCA, SGTR, DBA, DEC-A, Radiological Consequences

1. INTRODUCTION

The 4-year R2CA project (Reduction of Radiological Consequences of design basis and extension Accidents) launched within the NUGENIA network and funded by the European Commission was dedicated to the improvements of methodologies for assessing the environmental radiological source terms of accidents under DBA and DEC-A conditions. It covered two main types of accidental scenarios (LOCA and SGTR identified as the most penalizing ones from PWR level 2 Probabilistic Safety Assessments) and a wide range of LWR concepts (PWR, VVER, BWR). Its main goals were:

- To provide more realistic evaluations of the environmental radiological source terms of these NPPs, then of their associated safety margins under these accidental conditions through improvements in models, simulation tools and calculation chains,
- To increase the NPP safety levels through optimizations of their emergency operating procedures and the development of innovative methods (based on artificial intelligence) for anticipated diagnosis/prognosis of specific accidental situations.

The reason for the project - to focus on DBA and DEC-A conditions mainly raised from the Fukushima Daichii Accident (FDA). In fact, the substantial Research & Development (R&D) efforts made in modelling and source term evaluations of Severe Accidents (SA) after FDA, led to reduce the risks associated to all main categories of SA conditions and consequently also highlighted the overly conservative risk assessments of DBA. These latter, covering uncertainties, unknown or poorly understood phenomena, prevent from anticipating NPP responses for other configurations (i.e. other types of fuel (ATF), fuel with increased burn-up or Pu content…). It also prevents from extending with confidence such evaluations to other NPP concepts such as Small Modular Reactor (SMR) for which realistic radiological source term assessments will be even more crucial due to their potential proximity to homes and population. Furthermore, FDA also highlighted the need to further increase the existing and future NPP safety by including in their design accidental scenarios slightly more severe than DBA and for which specific safety provisions must be implemented to prevent from a further evolution into SA (DEC-A scenarios).
The R2CA project represented a major opportunity for improving models and simulation tools all along the calculation chain used when assessing the radiological source term. It concerned, fuel rod thermomechanics and fission products (FP) releases up to FP physicochemical behaviour within the third containment barrier (i.e. containment vessel or failed Steam Generator (SG). In this article the main modelling improvements and outcomes of the environmental radiological source term re-evaluations are reported, as well as the main results gained from innovative work performed regarding accident management and prevention (i.e. EOP optimization, development of a neural network-based tool for defective fuel rod diagnosis).

2. RE-ASSESSMENTS OF ENVIRONMENAL SOURCE TERM FOR DBA & DEC-A

The approach used for LOCA and SGTR analyses was identical. After each partner has identified transients of interest (depending on reactor type, safety studies etc...), two series of calculations were carried out using the same transients: the initial one generally using current practices in their own countries for DBA and DEC-A studies, and the final one taking advantage of the improvements made during the project. The benefits due to improvements in calculation chains, from core to environmental FP release modelling, were analyzed and highlighted through the environment source term and radiological consequence evaluations.
The first set of reactor calculations was used to identify the needs in terms of model, simulation tool and/or calculation chain improvements to be made to minimize conservatisms as much as possible and avoid the decoupling factors currently used, for Design Basis Accidents, in safety studies. A specific database was then developed (incl. more than 200 tests at different scales and NPP measurements) [1-].

2.1. LOCA: Modelling improvements and source term re-assessments

To calculate properly the radiological source term of LOCA DBA or DEC-A accidents the main phenomena to be considered are related to:

- Thermal-hydraulic (in core, primary vessel, coolant circuits, containment…),
- Thermo-mechanics (in fuel rods),
- FP behaviour/chemistry (in fuel, primary circuit, containment).

Initial calculations originating from a very different context and background greatly varied, then improvements were needed. The results of source term evaluations were consequently rather scattered [2-]. Some of them use rather deterministic and conservative assumptions, especially for DBA studies, and decoupled approaches between fuel studies and source term evaluation. For example, failed rod ratio in the core, directly impacting the radiological source, was sometimes assumed but it greatly varied (from 10 to 100%). Thus, the needs to evaluate this ratio more accurately according to fuel assembly (FA) characteristics (i.e., burn-up, location, internal pressure, etc.) to which they belong, through fuel rod thermomechanical calculations were clearly pointed out.

Then, although significant improvements have been made regarding transient FP release from fuel during a LOCA (mainly through the upgrading of fuel performance such as TRANSURANUS [21-] and FP behaviour codes [3-],[22-] and their coupling enhancement [4],[5-]), the main modelling improvements that have benefited radiological source term re-assessments have concerned fuel rod thermomechanics and core modelling.

2.1.1. Modelling improvements: fuel rod burst & core model

During the project, the ballooning and burst failure data of various Zr-based alloys (i.e., E110, Zr-4…) were re-assessed. It allowed the re-fitting of plastic deformation model of the FRAPTRAN tool and the reduction of its calculation uncertainties. Above all, from a thorough re-assessment of the very large existing database related to clad burst failure, several new clad burst criteria were proposed (**Figure 1**, **Figure 2**) as:

1- Simple envelopes on engineering burst hoop stress (i.e. including minimum, mean and maximum),
2- A temperature criterion depending on clad heating rate and engineering stress.

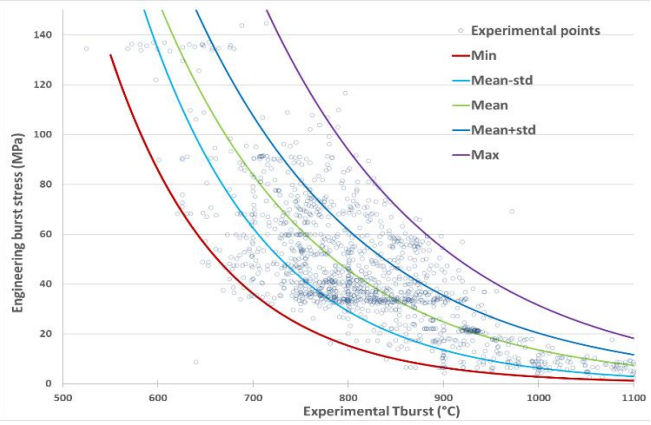

Figure 1. Engineering burst stresses vs burst temperatures: exponential models compared to experimental points from [6-]

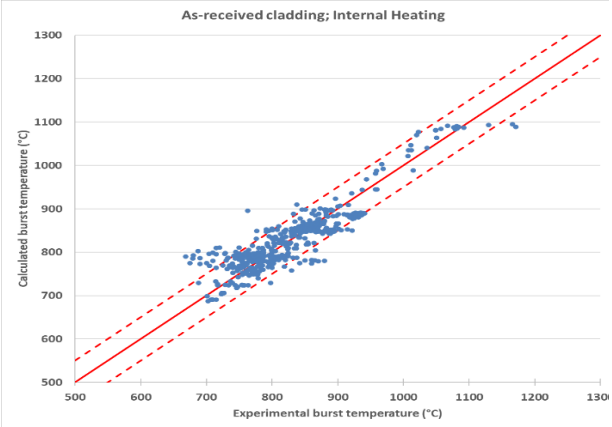

Figure 2. Calculated burst temperatures with temperature criterion vs experimental ones (dashed lines correspond to ±50°C) [6-]

All these new criteria are more specifically dedicated to clad burst occurrence prediction for radiological source term evaluation of LOCA under DBA and DEC-A conditions. They were further implemented in different simulation tools (ASTEC [10-], DRACCAR [11-], FRAPTRAN [23-]) and used in source term re-assessments. From these studies, it was recommended to test a large panel of burst criteria, as the choice of burst criteria is of first order when evaluating the fuel rod burst ratio and the uncertainties associated to these criteria remains high (±50°C for the temperature criterion).

In addition, specific 3D methodologies of core modelling were developed. These methods are the most accurate in terms of describing as best as possible the different characteristics of fuel rods in a core directly impacting their thermomechanical behaviour (i.e. rod internal pressure, burn-up, power…) and then of calculating the number of failed fuel rods. More especially, two different approaches were built both using an integral code coupling thermal-hydraulic to fuel rod thermomechanics [9-]:

1- A full RPV and 3D core model with ATHLET-CD [12-] tool simulating each fuel assembly (i.e., 193),
2- A 3D eighth core model with DRACCAR tool simulating each fuel assembly (i.e., 26).

These most advanced 3D core modelling were more suitable to capture the 3D heterogeneities in a core due to its non-symmetrical heat-up during LOCA and to heterogeneities in fuel assembly power distribution. They are generally very challenging in terms of computational costs which limits their use to specific study and make them inappropriate for instance for uncertainty analyses requiring many simulations. To do so, it will be necessary to balance detailed core description vs computational effort and use specific calculation methods.

2.1.2. LOCA source term re-assessments

LOCA source term re-assessments benefited from three types of improvements related to:

1. The code modelling: i.e. use of more appropriate thermomechanical models for clad ballooning and burst, of new clad burst criteria…,
2. The core models: i.e. use of more detailed 3D T/H core models, or core models updated based on results from parametric analyses or from more detailed (mechanistic) fuel performance code …,
3. The calculation chains: i.e. use of detailed (mechanistic) fuel performance codes not only as a support of less-detailed tools, but also as an integral part of the chain for a better coupling of thermohydraulic and thermomechanical models at the subchannel level; use of new simulation tools in the chain….

LOCA DBA transients were analyzed by 8 partners providing 16 calculations and analyzing different kinds of reactor concepts (2 for VVER, 2 for PWR and 1 for EPR). Main improvements made between 1st and 2nd set of calculations are related to fuel rod burst (**Figure 3**). For VVER this involves the use of thermomechanical models instead of the very conservative assumptions if all fuel rods would fail during the transient. For Konvoi also the 10% failed rod ratio issued from regulatory practices were replaced by thermomechanical calculations of fuel clad behaviour. For PWR-900, improvements of both clad burst models/criteria and core modelling were provided. Finally, for EPR, in addition, new cladding creep and phase transformation laws for M5 clad materials were used for updated calculations [24-]. Finally, some partners, by using new tools in their calculation chains, improved their core modelling or the modelling of FP releases from fuel and transport up to containment. Thanks to this, the number of burst fuel rods in the core was generally reduced for all reactor concepts (especially for VVERs) except for two cases: one PWR-900 calculation where the number of failed fuel rods were similar and EPR calculation where a slightly higher number of fuel rods were calculated to fail due to the introduction of a more stringent cladding failure criterion.
In analyzed scenarios, as only containment design leakages were considered, the environmental activity was constantly increasing, due to pressure differences between containment and environment. Furthermore, as there have been no changes in thermal-hydraulics nor major modifications in the modeling of FP transfer in primary circuit (except for Konvoi) and containment vessel, the changes in burst fuel rod ratios directly influence the activity releases in the environment (**Figure 4**). That is why significant differences in environmental activities between the two sets of calculations were observed for VVER. For Konvoi, the significant reduction in

environmental releases (about 3 orders of magnitude) is mainly due to the consideration of FP decay. In the end, the relative reduction in environmental activity releases is ranging from 80 to 100% for all NPP concepts.

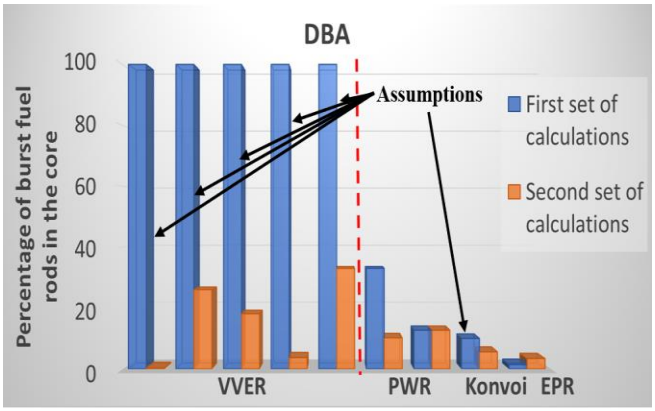

Figure 3. Rod burst ratio in LOCA DBA

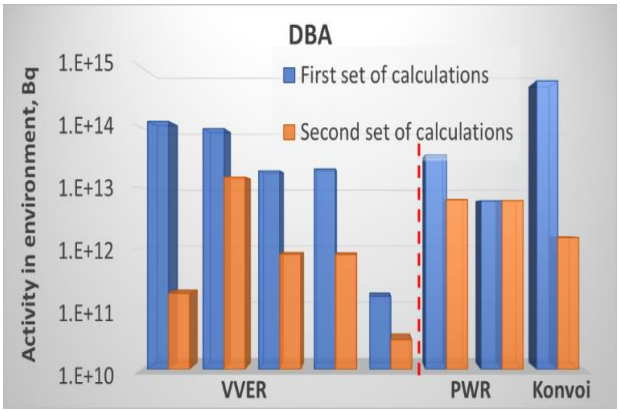

Figure 4. Activity releases in LOCA DBA

Thanks to improvements the discrepancy between released activity in environment (2 order of magnitude difference between minimum and maximum) was reduced by a factor of 2. The remaining discrepancy can be explained by differences still in initial/boundary conditions, modelling and NPP operation in LOCA… (i.e. gap inventory, design containment leakages, CSS operation and efficiency, and for iodine (differences in iodine form fraction, consideration of iodine chemistry or not), list of isotopes considered…). The conservatism and decoupled approaches have been reduced as much as possible in the updated calculations, nevertheless in very few of them due to low calculated PCT and no clad failure predicted some of them had to be retained.

LOCA DEC-A scenarios were analyzed by 5 partners, providing 13 calculations, and analyzing different kinds of reactor concepts (2 for VVER, 2 for PWR and 1 for BWR). In general, as recommended, realistic initial and boundary conditions were used for both sets of calculations. As for DBA, the main improvements made between 1st and 2nd set of calculations are related to fuel rod burst (**Figure 5**). For VVER this involves the use of thermomechanical models instead of the very conservative assumptions there all fuel rods would fail during the transient. For PWR-900, improvements of both clad burst models/criteria and core modelling were provided, while for BWR only the core ring nodalization was refined based upon information from detailed fuel performance code analyses. Finally, as for DBA, some partners, by using new tools in their calculation chains, improved their core modelling or the modelling of FP releases from fuel and transport up to containment. Thanks to this, as for DBA, the number of burst fuel rods in the core was generally reduced for all reactor concepts (especially for VVERs) except for the PWR cases where the number of failed fuel rods were either similar or increased. For PWR cases, the core modelling was refined in two different ways. The case using a 3D core modelling led to a slight increase of the failed rod number with a more accurate prediction of the clad burst as a function of the fuel assembly characteristics (burn-up, location, etc.). In comparison, the case using a more refined core modelling by just increasing the number of representative FA in each ring channels did not lead to any variations compared to initial results.

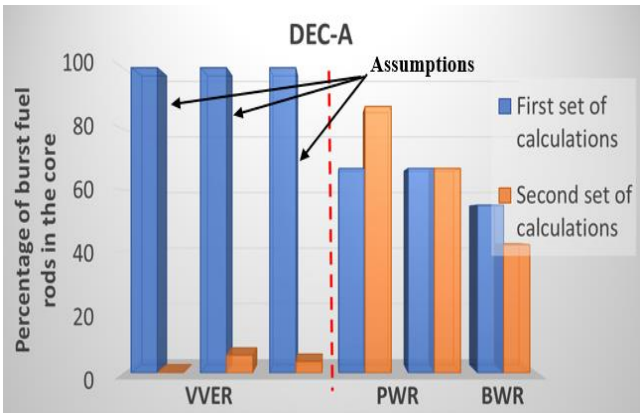

Figure 5. Rod burst ratio in LOCA DEC-A

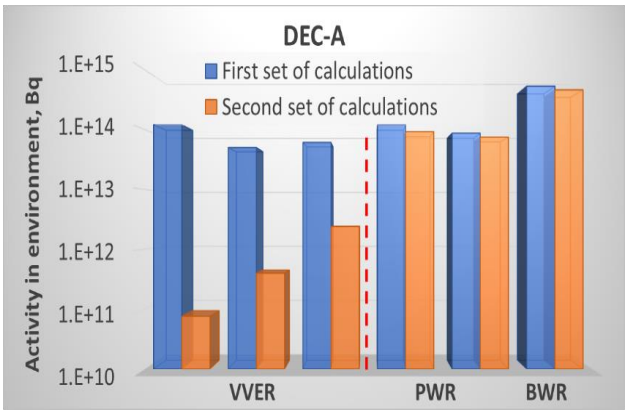

Figure 6. Activity releases in LOCA DEC-A

As for DBA, changes in burst fuel rod ratios directly influence the FP releases in the environment (**Figure 6**). That is why significant differences in environmental activities between the two sets of calculations were observed for VVER (2 to 3 order of magnitude difference). For PWR, the environment releases are quite similar, despite for one case a higher fuel rod burst ratio. This is due to more realistic assumptions regarding the containment leaking rates, where, for final calculations part of the containment leakages was considered recovered in the auxiliary buildings instead of fully direct containment leakages. In the end, the reduction in activity releases in the environment ranges from about 13 % (PWR, BWR) to 99% for VVER.
Due to the significant reduction in fuel burst ratio and FP releases in VVER, the differences between the different concepts (i.e. VVER/PWR) are finally more marked in final than in the initial calculations (4 orders of magnitude difference between minimum and maximum activity releases vs 1 respectively).
Radiological consequences (thyroid equivalent and total effective doses) evaluated for both sets of calculations are consistent with what is observed with the activity calculated in the environment: for most calculations, especially for VVER, radiological consequences are reduced in the second set of calculations compared to the first one.

2.2. SGTR: Modelling improvements and source term re-assessments

The presence of leaking fuel rods in normal operation, due to defects, is one of the main bases of the considered source term in SGTR. Occurrence of these defects, depending on NPPs, is detected by primary circuit contamination measurements, where sometimes several orders of magnitude of specific FP activities were observed between situations without or with leaking fuel elements. The occurrence of defective fuel rods, becoming today rarer, primary circuit contamination is reduced.
To calculate properly the radiological consequences of SGTR DBA or DEC-A transients, the main phenomena to be considered are related to:

- Thermal-hydraulic (in coolant circuits, safety injection systems, SGs…),
- FP releases from defective fuel rods,
- FP transfer from primary-to-secondary coolant systems,
- FP transfer between gas and liquid phases in the failed SG (incl. flashing/atomisation/partitioning…).

As for LOCA, initial calculations originating from different backgrounds greatly varied, then improvements were needed. The results of initial source term evaluations were consequently rather scattered [2-. Varying degree of conservatism, arbitrariness or empiricism were used, including for DEC-A scenarios, to compensate the lack of models and/or measurements (i.e. primary coolant activity in normal operations, spiking activities during SGTR and iodine gas-liquid transfer in failed SG…). Also, iodine speciation in RCS (then gaseous iodine fraction), directly impacting the source term evaluation, was always imposed.

Then, although significant improvements have been made regarding transient FP release from fuel during a SGTR [7-], the main modelling improvements that have benefited radiological source term re-assessments have concerned the iodine spiking in RCS and flashing/partitioning in the failed SG.

2.2.1. Modelling improvements: iodine spiking in RCS & transport in failed SG

The release of FP, particularly iodine, from defective fuel rods and its transport into the secondary side of the failed SG were considered as areas where further improvements might have a significant impact on environmental activity releases as generally conservative and/or empirical assumptions were currently used to take them into account. Amongst these improvements, the refinement of spiking models (i.e. enhanced transient releases of FP gap inventory during a transient) appears of upmost importance whatever SGTR scenarios (overflowing or non-overflowing). The improvements made during the project, for the most part, were based on legacy or new NPP measurements (**Figure 7**) and concerned especially iodine. They were made in different types of code (i.e T/H, Severe Accident codes…) considering not only the reactor power & primary pressure variations but also the time point in the fuel cycle as influent parameters and greatly differed in complexity (ranging from simple correlations to more mechanistic models where the latter appears more appropriate to be easily extending to any operating NPP concept).

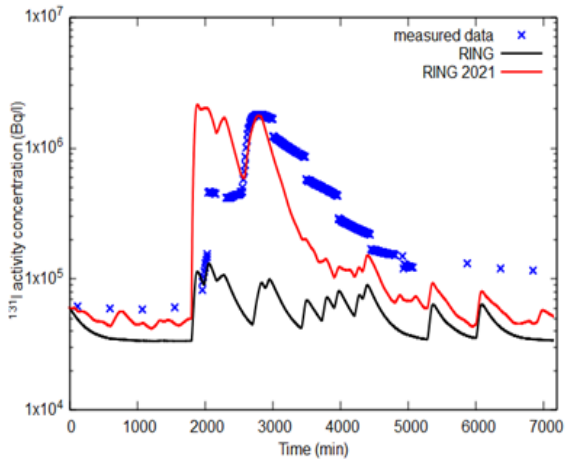

Figure 7. I-131 spike in RCS during SGTR: RING code results vs measurements

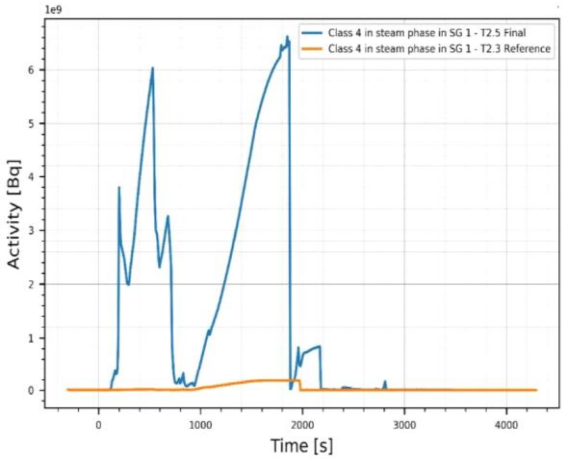

Figure 8. I_2 partitioning in failed SG: MELCOR code initial vs final calculations [8-]

The modelling of the FP (particularly iodine) transport within conditions representative of failed SG was also especially enhanced, as, often, no specific models were available. The scarcity of relevant data addressing those phenomena (such as flashing, atomization, partitioning) under the prevailing conditions made this more complex and uncertain. The main modelling improvements used in re-assessments concerned iodine flashing and partitioning (**Figure 8**). They often led to higher iodine source term in the failed SG gas phase, thus potentially a further increase in environmental activity releases.

2.2.2. SGTR source term re-assessments

SGTR source term re-assessments benefited from two types of improvements related to:

1. The code modelling: i.e. use of models for FP dilution, transport in RCS, use of updated FP (mostly iodine) spiking models, use of updated or new FP transport models in failed SG (such as for partitioning, flashing and atomization also mainly for iodine), use of refined T/H models for SG relief/safety valve releases …,

2. The calculation chains: i.e. use of new modules/simulation tools, used of mechanistic codes in support of less detailed codes… For SGTR calculations, both detailed T/H and integral codes were used.

In addition, implementation and application of new optimized EOPs were performed in some calculations.

DBA transients were analyzed by 8 partners, providing 23 calculations. Main improvements made by the partners between 1st and 2nd set of calculations are all related to RCS radionuclide inventory and transport aspects both in RCS and failed SG, except for one partner, who also improved the SG relief/safety valves thermohydraulic correlations. Thanks to this, partners achieved a 23% to 80% reduction of the activity releases in the environment (**Figure 9**), except for one partner, whose environmental radiological releases are two times greater in the final calculations than in initial ones. This partner used a new calculation chain including a new module for FP transport in RCS and failed SG directly impacting the pre-spiking RCS contamination and spiking, as well as the FP distribution between the liquid and gaseous phase in the failed SG. Finally, this partner also used a detailed code in support for predicting the iodine speciation in RCS and then better calculate the iodine flashing rates in the failed SG.

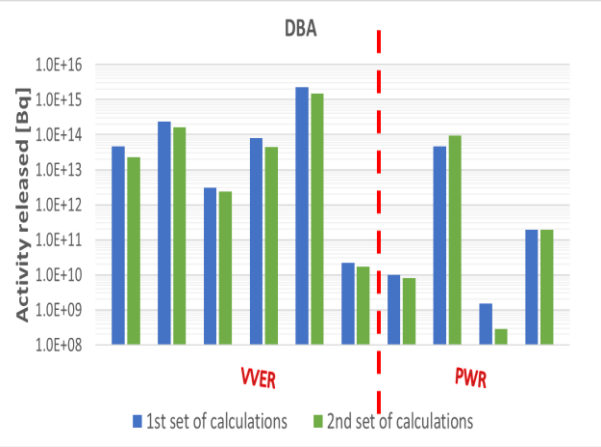

Figure 9. Activity releases in SGTR DBA

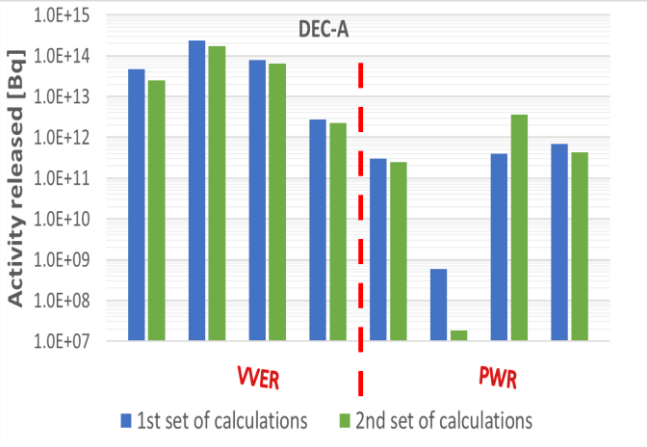

Figure 10. Activity releases in SGTR DEC-A

Large discrepancies between the activity releases (up to 7 orders of magnitude difference between minimum and maximum) can be observed even for the updated calculations. There are several reasons for this, such as: differences on the thermohydraulic evolution during the transient (due to break size, operators' actions, initial conditions, thermohydraulic code and correlations considered etc.), differences in the assumptions regarding the initial RCS FP inventory (including spiking), differences on the list of isotopes considered, differences in the modeling (i.e. on FP dilution in RCS, on FP transport phenomena considered in the failed SG (such as atomization, flashing, partitioning, scrubbing), or sometimes also differences in the consideration of activity releases (from steam only or from both liquid/steam phases). In the end, some partners tend to be more conservative while others may be more realistic (i.e. the highest releases calculated by one partner in both sets of calculations due to maximum allowable RCS activity considered, a slow RCS and SG depressurization leading to a break flow rate that doesn't cancel out in time and continuous activity release to environment through the relief valve). Conservatisms have been however as much as possible reduced in the updated calculations through model/calculation chain refinements. Nevertheless, despite such improvements, discrepancies between partners are in the second set of calculations as high as in the first ones.

DEC-A scenarios were analyzed by 6 partners, providing 21 calculations. As for DBA, the main improvements made by the partners between 1st and 2nd set of calculations were all related to RCS radionuclides inventory and transport aspects in RCS and failed SG, except for one partner, who considered optimized EOPs for

operators' actions to depressurize RCS as fast as possible. Thanks to this, partners achieved a 17% to 97% reduction of the activity releases in the environment (**Figure 10**), except for one partner, whose environmental radiological releases are greater in the final calculations than in initial ones due to the consideration of activity release through the liquid pathway in addition.
As for DBA, there is also a large discrepancy between the partner results (up to 7 orders of magnitude difference between minimum and maximum activity releases) for the same reasons. Even though more realistic conditions were generally used for DEC-A, the discrepancies were even greater. This is mainly due to the results of one partner who, unlike the others, have considered a SGTR + isolable Steam Line Break which led to stop the releases to the environment very early during the transient.
Eventually, radiological consequences (thyroid equivalent and total effective doses) were evaluated for both sets of calculations. The results are consistent with what is observed with the activity releases to the environment: for most partners, radiological consequences are reduced in the second set of calculations compared to the first one, except for two SGTR transients.

3. MAIN PROGRESSES IN ACCIDENT MANAGEMENT AND PREVENTION

Several studies were performed during the project to cope with SGTR radiological consequences, resulting through containment by-pass in direct FP releases to the environment.

3.1. AMP optimization

The general approach of optimizing an Accident Management Procedure (AMP) [14- using the Downhill Simplex method [15-, earlier applied to a station blackout in VVER1000 [13-, was refined in the frame of the R2CA project and applied to a DEC-A SGTR scenario for a generic PWR 3750 MW_{th}. In this scenario, the Safety Relief Valve (SRV) of the affected SG was assumed to remain stuck open after the first opening (direct release path) and that none of the trains of Low-Pressure Injection System (LPIS) was working due to technical failure.
The AM strategy for such events aims at reducing the primary system pressure as fast as possible to prevent further loss of coolant to the secondary system (i.e through cooling down of the primary system with the three remaining intact steam generators, actuation of the pressurizer spray system, opening of the pressurizer relief valve (PORV) and finally safety injection switch off). In this analysis, it is further assumed that the operator would then initiate cool down of the primary via depressurization of the secondary and that two trains of the High-Pressure Injection System (HPIS) would be disconnected. The Simplex method was the used to optimize the timing of three further operator actions: opening the PORV, disconnecting train 3 of HPIS, and finally train 4 while reconnecting the make-up system.
The simplex method provides a very robust numerical algorithm to find a local minimum of a function $F:\mathbb{R}^n \rightarrow \mathbb{R}$. First step is to create an initial, arbitrary simplex in $\mathbb{R}^n$ (i.e. the simplest geometrical shape, e.g. a triangle in $\mathbb{R}^2$ or a tetraeder in $\mathbb{R}^3$). The function F is then evaluated at each corner of the simplex. The highest point is moved according to the algorithm and a new simplex is constructed, the function is again evaluated, and so on. The series of simplexes slowly converges to a local minimum. To use the simplex method for AM optimization, the independent parameters of the function were chosen to be the timing of the three above mentioned operator actions. Then, a thermal hydraulic system code (the function) evaluated the plant response. As dependent variable, a figure of merit was constructed, that evaluated the AM-Measures based on a.) the radioactive releases to the environment, b.) the primary pressure at the end of the transient and c.) the water level in the reactor core. The simplex method was then applied to find the optimum timing for the operator actions. After thirteen iterations, the algorithm converged to a minimum. The results showed that the opening of the PORV is most efficient later in the transient, while shutting down one HPIS early, and the second one late in the transient, provides good results. Overall, the iodine release to environment could be significantly reduced through optimization of the timing of investigated operator actions (**Figure 11**).

3.2. Development of Neural networks for earlier diagnosis

During NPP normal operations, the fuel rod cladding may be damaged due to various phenomena. Such deterioration and subsequent activity releases having safety and economic consequences, the early detection of defective fuel rod is of primary importance. Different approaches to this end have been developed over the years, based mostly on physical considerations [16-.
On another hand, the improvement of data-driven methods led to their successful use as anomaly detectors in various fields of industry. These were consequently tested in the framework of R2CA project: since the occurrence of a defect leads to a change of primary activity compared to an activity level labeled as normal, the efficiency of autoencoders shaped as Recurrent Neural Networks [17- (RNN), Gated Recurrent Units [18- (GRU) networks, or Long Short-Term Memory networks (LSTM) [19-], fitted for time related variables, were tested. As no experimental data were available, a workflow was established to build artificial data.
First, a simple physical model was built [20-, physically relevant enough to render various situations such as the opening of a defect, a pre-existing defect, no defect at all among others. The physical model considers the release from a fuel pellet by diffusion or recoil, a generalized diffusion and first-order kinetic model for the fission products in the gap region, and a first-order kinetic model in the coolant region. Considering that the use of physical model can be CPU intensive, a fast surrogate model was built, based on a moderate sized physical database, taking as input parameters both literature values and TRANSURANUS [21- calculations results. The surrogate model turned out to be precise as the maximum relative error was about 2.6%, and less CPU intensive by a factor 1000 than the physical reference model. This allowed the generation of several tens of thousands of activity sequences in a small amount of time. Finally, all tested anomaly detectors gave 100% satisfactory results (**Figure 12**), and the difference between them relied in learning speed.

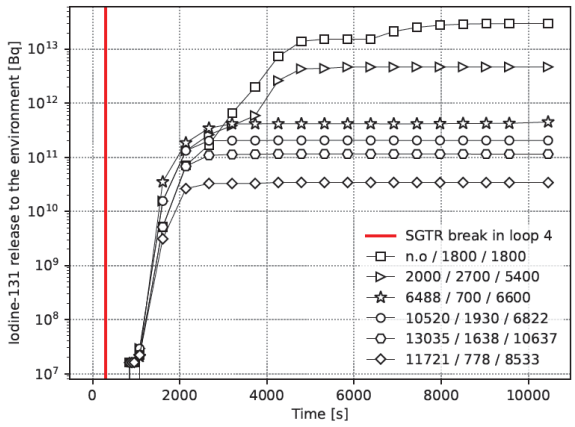

Figure 11. I-131 release in environment as a function of operator action timing

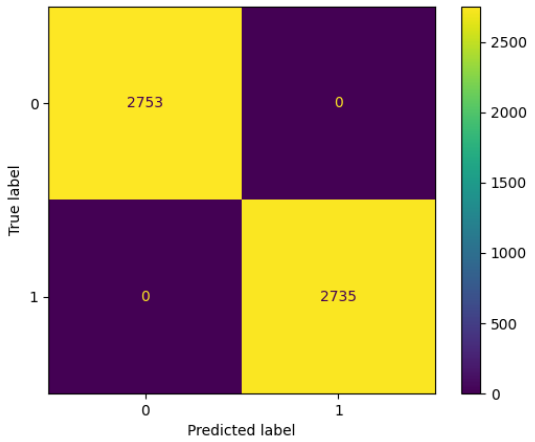

Figure 12. Anomaly detector performance

4. FINAL REMARKS

Thanks to the developments/improvements of models, simulations tools and calculations more realistic RC evaluations of both LOCA and SGTR scenarios within DBA and DEC-A conditions have been provided that led to reduce some conservatisms. This represents a first step towards best estimate evaluations. These latter needed to be associated to systematic Sensitivity Analyses an Uncertainty Quantifications were beyond the scope of the project. However, from the updated evaluations, the parameters having the most impactful effect on results were identified and some recommendations formulated as:

For LOCA transients:

- Better prediction of failed fuel rods is of first importance. To do so, expressing specific fuel rod initial conditions (i.e., burn-up, internal rod pressure, specific power…) for thermomechanical calculations (incl. axial gas communication) and use refined criteria of cladding burst temperature and strain, specific to DBA and DEC-A conditions is important.
- To have a coupling between T/H and thermomechanical calculations. To this end, the use of a detailed 3D core modelling allowing for better differentiation of FA characteristics (power distribution) could be beneficial. It also allows to consider the asymmetric character of LOCA transient. However, the level of details in the model must be balanced with computational capabilities.
- Refine the FP gap inventory calculations by considering differences between fuel rods/assemblies (i.e., provide multi-inventory, 3D burn-up distribution…) is also recommended.
- Regarding FP behaviour in containment, use of a dedicated calculation tool/module for modelling the complex and time dependent iodine behaviour/chemistry is necessary.

For SGTR transients:

- Initial RCS contamination and spiking is of first importance. Real NPPs data can be preferred to be more realistic but it will be difficult to extend them to other operating or future NPPs (i.e. for different types of fuel, operating conditions…). Then, the development of more complex mechanistic models was recommended, at least in support of less detailed codes.
- All transport phenomena through SGTR break and in failed SG (atomization, flashing, partitioning, scrubbing) should be simulated based on feedbacks from the TH part. Iodine speciation in primary circuit conditions also (determining its volatility) as it could impact its flashing fraction at SGTR break and its partitioning from secondary liquid phase.
- For transfer to environment, as consequences of activity releases in liquid water or in steam phases are not the same, each phase must be considered separately in failed SG. In addition, for non-overflowing scenarios, aerosol retention in upper SG structure (size-dependent) must be calculated or deduced from the use of existing test facility results.

In parallel, many other modelling improvements were made (generally more mechanistic), not reflected in the re-evaluation of the scenarios, which will be of benefit in future reactor calculations (i.e. internal clad secondary hydriding, FP releases from fuel during transients, high burn up structure and releases...). Regarding code improvements, enhanced couplings of fuel performance code (such as TRANSURANUS) with FP codes were also performed and their capabilities extended to study new fuel types in the future, such as near-term accident tolerant fuels (ATF).

Finally, exploratory work on AMP showed that the increased capabilities of numerical tool and the use of expert methods could be advantageously used to increase the NPP safety.

REFERENCES

1- Hózer, Z. and al., 2023, "Review of experimental database to support nuclear power plant safety analyses in SGTR and LOCA domains", *Annals of Nuclear Energy*, R2CA special issue, **193**, 110001. https://doi.org/10.1016/j.anucene.2023.110001.

2- Girault, N. and al., 2022, "The R2CA project for evaluation of radiological consequences at design basis accidents and design extension conditions for LWRs: Motivation and first results", *10th European Review Meeting on Severe Accident Research* (ERMSAR 2022), Karlsruhe, Germany, May 16-19.

3- Zullo, G. and al, 2022, "Towards grain-scale modelling of release of radioactive fission gas from oxide. Part I: SCIANTIX", *Nuclear Engineering and Technology*, **54**, 2771-2782. https://doi.org/10.1016/j.net.2022.02.011.

4- Zullo, G., and al., 2022, "Towards grain-scale modelling of the release of radioactive fission gas from oxide fuel. Part II: Coupling SCIANTIX with TRANSURANUS", *Nuclear Engineering and Technology*, 54, 4460-4473. https://doi.org/10.1016/j.net.2022.07.018.

5- Zullo, G. and al., 2023, "Towards simulation of fuel rod behaviour during severe accidents by coupling TRANSURANUS with SCIANTIX and MFPR-F", *Annals of Nuclear Energy*, R2CA special issue, **190**, 109891. https://doi.org/10.1016/j.anucene.2023.109891.
6- Taurines, T. and al, 2024, "New burst criteria for Loss Of Coolant Accidents Radiological Consequences Assessments", *Annals of Nuclear Energy*, R2CA special issue, to be issued.
7- Giaccardi, L. and al, 2024, "Towards modelling defective fuel rods in TRANSURANUS: Benchmark and assessment of gaseous and volatile radioactive fission product release", *Annals of Nuclear Energy*, R2CA special issue, **197**, 110249. https://doi.org/10.1016/j.anucene.2023.110249.
8- Foucaud, P. and al, 2024, "Iodine source term assessment as result of iodine spiking and mass transfer phenomena during a SGTR transient using MELCOR 2.2 and CATHARE 2 codes" (DEC-A)", *Annals of Nuclear Energy*, R2CA special issue, **198**, 110305. https://doi.org/10.1016/j.anucene.2023.110305.
9- Belon, S. and al, 2024, "Advances from R2CA project on reactor simulations for burst rod number evaluation during LOCA", *Annals of Nuclear Energy*, R2CA special issue, to be issued.
10- Chatelard, P. and al, 2016, "Main modelling features of ASTEC v2.1 major version", *Annals of Nuclear Energy*, **93**, pp. 83-93. https://doi.org/10.1016/j.anucene.2015.12.026.
11- Glantz, T. and al, 2018, "DRACCAR: A multi-physics code for computational analysis of multi-rod ballooning, coolability and fuel relocation during LOCA. Part one: General modeling description", *Nuclear Engineering and Design*, **339**, pp. 269-285. https://doi.org/10.1016/j.nucengdes.2018.06.022.
12- Lovasz, L. and al, 2021, "ATHLET-CD 3.3 User's Manual, GRS-P-4/Vol. 1 Rev. 8., Ges. für Anlagen- und Reaktorsicherheit (GRS).
13- Cherubini, M. and al, 2008, "Application of an optimized procedure during a SBO in VVER-1000", *Nuclear Engineering and Design,* **238**, pp. 74–80. https://doi:10.1016/j.nucengdes.2007.04.016.
14- Muellner, N. and al, 2007, "A procedure to optimize timing of operator actions of AM procedures", *Nuclear Engineering and Design*, **237**, pp. 2151–2156. https://doi:10.1016/j.nucengdes.2007.03.011.
15- Nelder, J. and al., 1965, "Simplex method for function minimization", *The Computer Journal,* **7**, 308–313.
16- Lewis, B. J. and al, 2017, "Fission product release modelling for fuel-failure monitoring and detection", *Journal of Nuclear Materials*, **489**, pp. 64–83. https:// doi: 10.1016/j.jnucmat.2017.03.037.
17- Kieu, T. and al, 2019, "Outlier detection for time series with recurrent autoencoder ensembles", *IJCAI Int. Jt. Conf. Artif. Intell.*, vol. 2019-August, 2725–2732. https://doi: 10.24963/ijcai.2019/378.
18- Cho K. and al., 2014, "Learning Phrase Representations using RNN Encoder-Decoder for Statistical Machine Translation", [Online]. Available: http://arxiv.org/abs/1406.1078.
19- Hochreiter, S. and al, 1997, "Long Short-Term Memory", *Neural Comput.*, **9**, pp. 1735–1780. https://doi.org/10.1162/neco.1997.
20- Verma, L. and al, 2023, "Defective fuel rods detection and characterization using an Artificial Neural Network", *Progress in Nuclear Energy*, **160**, 104686. https://doi.org/10.1016/j.pnucene.2023.104686.
21- Lassmann, K., 1992, "TRANSURANUS: a fuel rod analysis code ready for use" in *Nuclear Materials for Fission Reactors*, Elsevier Oxford (UK), 295–302. https://doi.org/10.1016/B978-0-444-89571-4.50046-3.
22- Veshchunov, M.S. and al., 2006, "Development of the mechanistic code MFPR for modelling fission-product release from irradiated UO2 fuel", *Nuclear Engineering Design,* **236**, pp. 179-200. https://doi.org/10.1016/j.nucengdes.2005.08.006.
23- "FRAPTRAN: A computer code for the transient analysis of oxide fuel rods (NUREG/CR-6739, vol. 1) NRC.gov", 2022. https://www.nrc.gov/reading-rm/doc-collections/nuregs/contract/cr6739.
24- Dif, B. and al, 2023, "Reassessment of FRAPTRAN's cladng failure criteria in LOCA in R2CA project", *WRFPM Proceedings*, July 17-21, Xi'an, China, 97-107. https://doi.org/10.1007/978-981-99-7157-2_10.

ACKNOWLEDGMENTS

This paper has been possible thanks to the work of all the project partners hereby thanked.
R2CA project received funding from the Euratom research and training programme 2014-2018 under grant agreement No 847656.

REDUCTION OF RADIOLOGICAL ACCIDENT CONSEQUENCES

The EU H2020 R2CA project: Main Outcomes

Reduction of Radiological Consequences of Accidents

N. Girault, K. Chevalier-Jabet, T. Taurines, F. Mascari, N. Muellner, A. Berezhnyi, M. Cherubini, A. Malkhasyan, F. Parmentier, T. Kaliatka, P. Foucaud, A. Arkoma, Z. Hozer, M. Jobst, L. Luzzi, A. Kecek, D. Gumenyuk, L. E. Herranz

ERMSAR 2024, May 13-16, Stockholm

IRSN

Commission européenne

This project has received funding from the Euratom research and training programme 2014-2018 under grant agreement No 847656.

Motivation

REDUCTION OF RADIOLOGICAL CONSEQUENCES OF DESIGN BASIS & DESIGN EXTENSION ACCIDENTS

H2020 projet (certified by NUGENIA) gathered 17 organisations from 11 countries (Sept 19-Dec 23)

- Provide more realistic evaluations of radiological consequences of LOCAs and SGTRs in DBA (DEC-A) conditions for **Gen II, III & III+ NPPs**
  - Decrease of conservatisms (model parameters, assumptions, I&B conditions) & decoupling factors (Fuel/FP behaviour)
  - Improvements of models/simulation tools & calculation methodologies

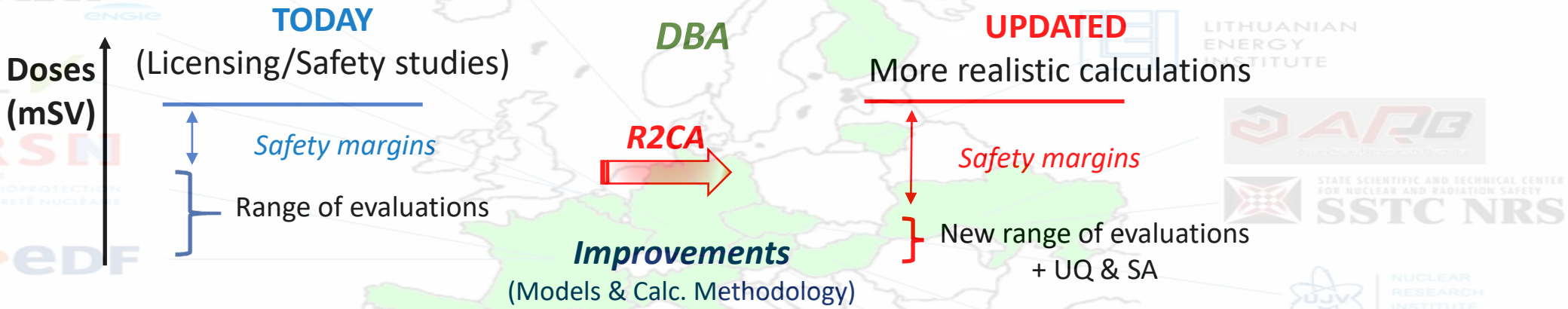

- Increase NPP safety (worldwide request)
  - Consideration of situations more severe than those integrated in plant designs (DEC-A ↔ complex sequences, multiple failures)
  - Optimization of Emergency Operating/Accident Management Procedures
  - Development of prototypical tool based on ML for abnormal situation diagnosis (defective rods)

Motivation

REDUCTION OF RADIOLOGICAL CONSEQUENCES OF DESIGN BASIS & DESIGN EXTENSION ACCIDENTS

- Help better quantification/consideration of potential changes to come in operating conditions (fuel **BU increase**, **ATF** …)
- Highlight potential risks exhibited by knowledge/model improvements (clad embrittlement through II^{ary} hydriding, higher FP releases from high burn-up …)
- Prepare development and safety assessments of **SMRs** for which providing realistic evaluations of RC will be more crucial (vicinity of homes and population)
- Support development of innovative measures, devices (incl. ATFs) or tools to prevent these accidents and/or strengthen their management

R2CA main Achievements

REDUCTION OF RADIOLOGICAL CONSEQUENCES OF DESIGN BASIS & DESIGN EXTENSION ACCIDENTS

- **E**xtensive dedicated exp. database (DBA & DECA): ~200 tests, different scales (NPP data)
- **S**ignificant "modelling" improvements for both LOCA & SGTR phenomena at different levels
  - ✓ Upgrading or development of models
  - ✓ Improvements of simulation tools at different scales for most impacting processes in RN releases
  - ✓ Enhancement of tool coupling (i.e. Fuel performance and FP behaviour…)
  - ✓ Updating of calculation chains/RC evaluation methodologies
- **A**nalyses and RC evaluations of a large variety of LWR concepts/scenarios
  - ✓ Calculation results archived and formatted for easy database input on NPP calculation results
- **R**ecommendations for more realistic/harmonisation of RC evaluation methodologies (NUGENIA TA2)
- **O**ptimisation of AMP (SGTR) (i.e. through application of an optimisation algorithm)
- **F**OAK of an "expert" system for early diagnosis of rod defect
- **E**valuation of some near-term **ATF** with updated methodologies

LOCA : main modelling improvements

REDUCTION OF RADIOLOGICAL CONSEQUENCES OF DESIGN BASIS & DESIGN EXTENSION ACCIDENTS

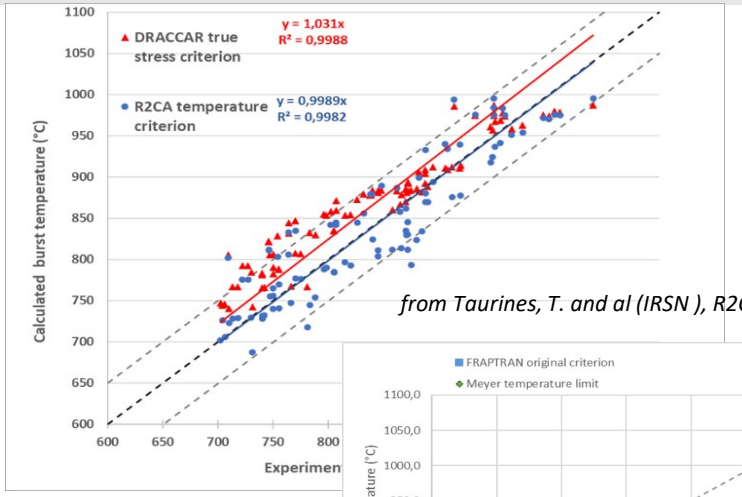

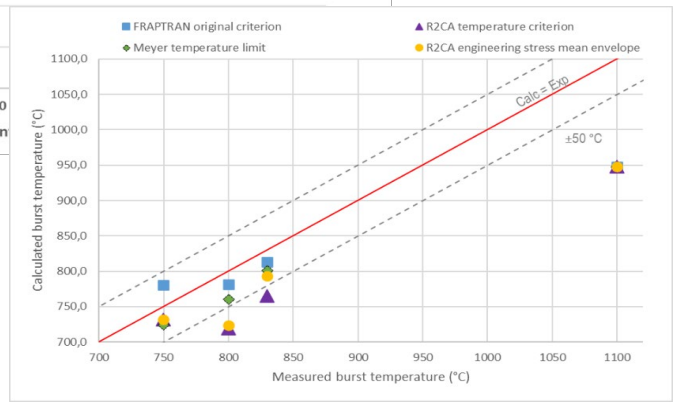

from Taurines, T. and al (IRSN), R2CA T3.2 technical report

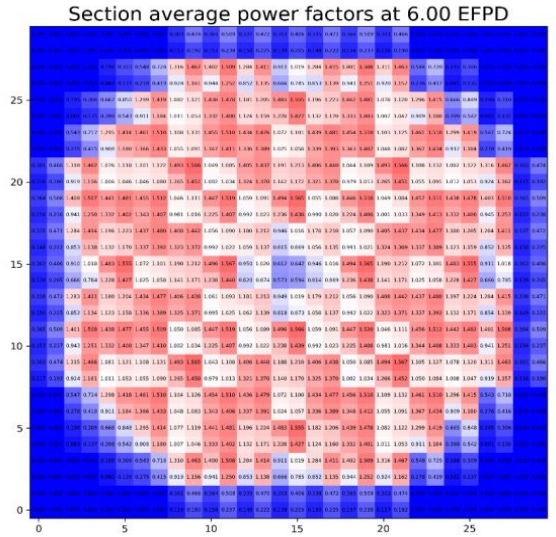

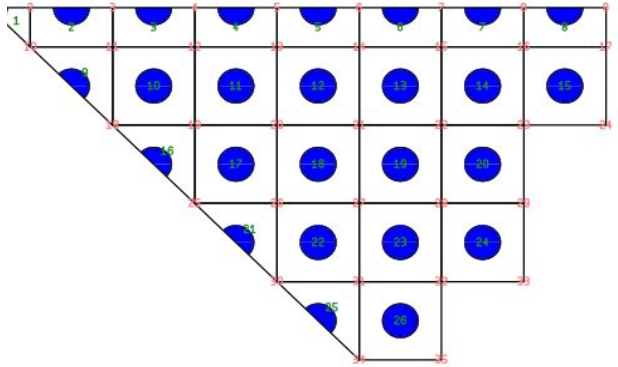

from Belon, S. and al (IRSN), ANE special issue

- Clad burst & creep models
  - ✓ New burst criteria for RC evaluation implemented in several tools (ASTEC, DRACCAR, FRAPTRAN…)
  - ✓ Thermomechanical model update in some tools (FRAPTRAN..) & new models for M5 (TU)

- 3D core model (core T/H coupled to fuel T/M)
  - ✓ Core T/H with 3 D model (@FA scale): possibility to capture non symetric behaviour for full core model
  - ✓ Several representative rods (average, hot rod…) per FA: with 1- ≠ rod powers 2- ≠ initial states & FP inventories
  - ✓ Necessary compromise between CPU and model details

- New calculation chains (for fuel & FP behaviour in core/circuits) developped

LOCA : other modelling improvements

REDUCTION OF RADIOLOGICAL CONSEQUENCES OF DESIGN BASIS & DESIGN EXTENSION ACCIDENTS

- Higher degree of mechanistic modelling in fuel performance simulations though database reassessmt, code extensions, upgraded/new coupling of fuel & FP codes (better estimate of gap building inventory, RIP…)
  - ✓ Axial gas communication (prototype stand alone model)
  - ✓ Plug-in modules for coupling mesoscale FP codes to integral FPC codes (TRANSURANUS, FRAPTRAN) ①
  - ✓ Refined models in FP detailed codes (SCIANTIX, MFPR-F) for FG releases from HBU fuel (refined modelling of HBU zone formation and FG releases from grain boundaries with power ramps (②, ③)

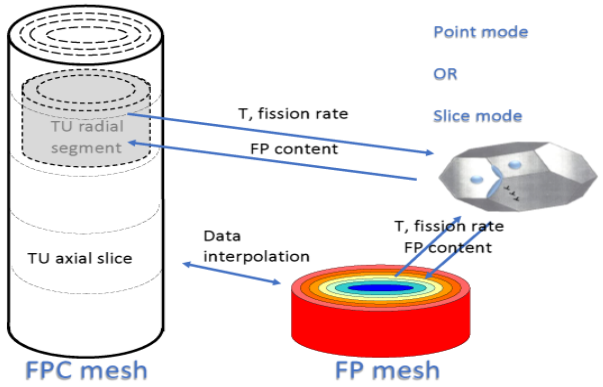

①

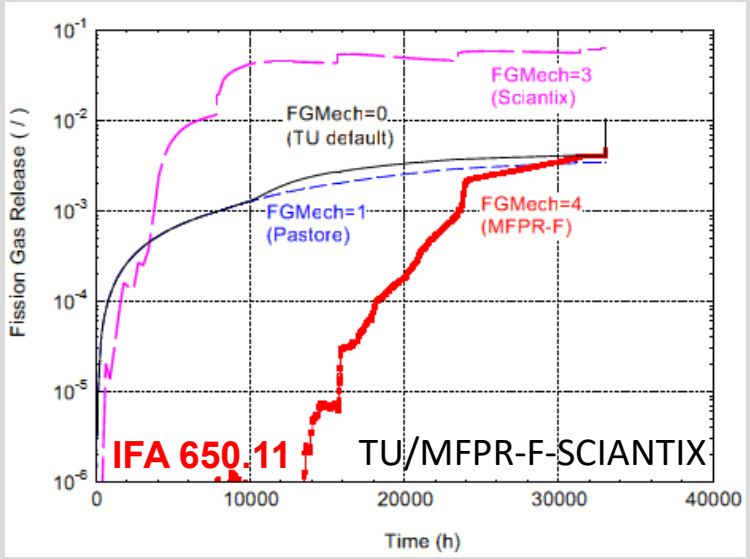

from Schubert, A. and al. (JRC), R2CA T3.3 technical report

②

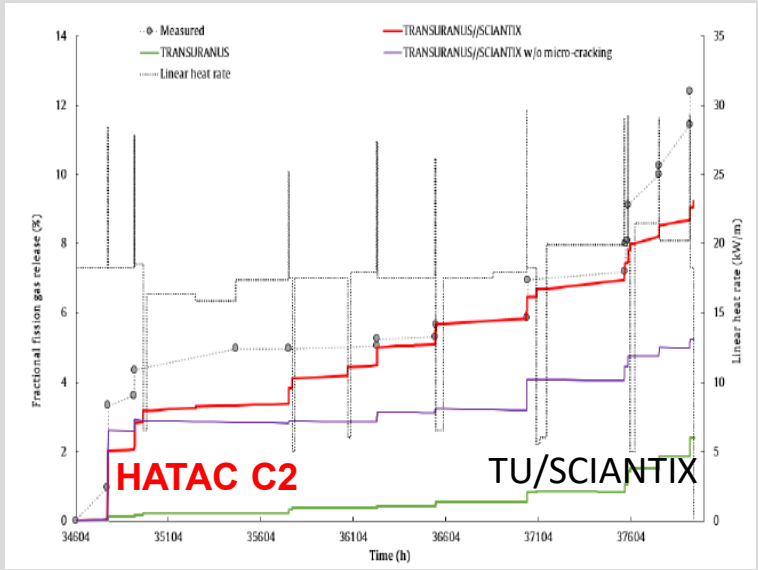

from Zullo. and al. (POLIMI), R2CA T4.2 technical report

③

- Extension of code capabilities for ATF evaluations (Hastelloy-N, Cr-coated Zr..)

LOCA RC re-evaluations

REDUCTION OF RADIOLOGICAL CONSEQUENCES OF DESIGN BASIS & DESIGN EXTENSION ACCIDENTS

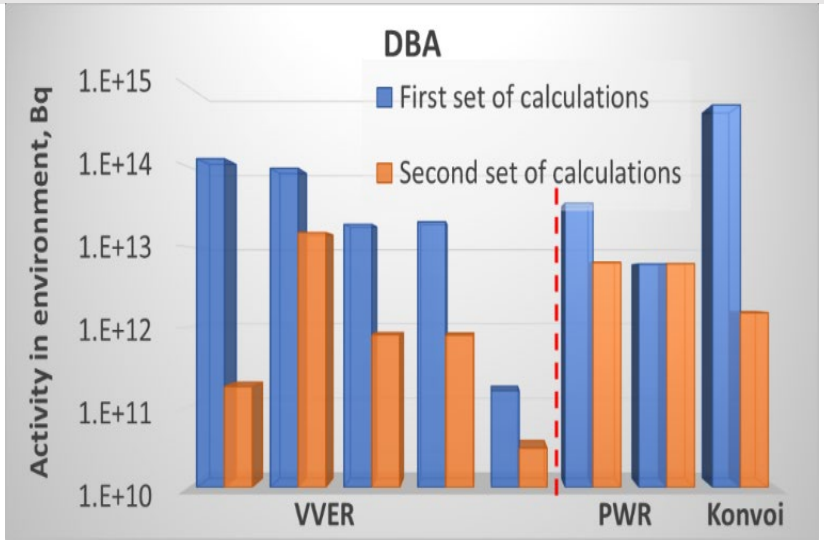

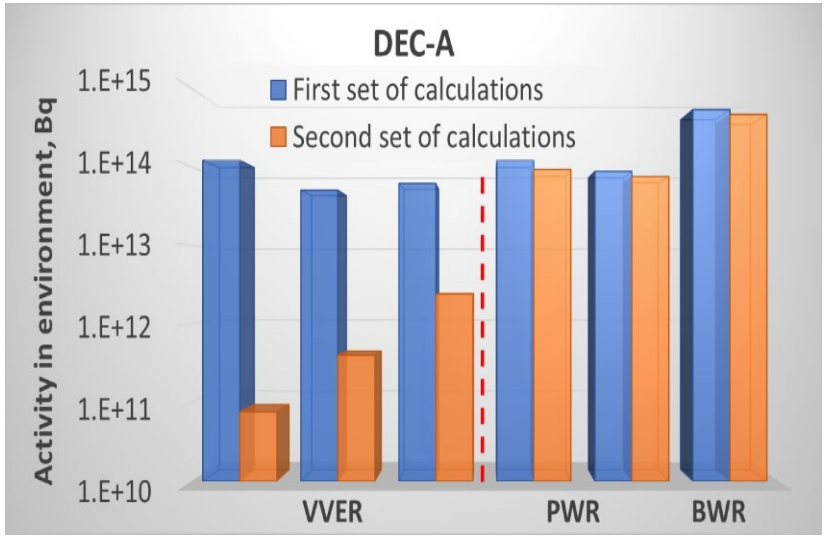

7 LWR designs, 2 scenarios,~ 30 reactor calc.

- Updated calculations used different methodologies
  - ✓ RBR evaluation : chaining T/H system (core + RCS) & fuel performance codes or coupled integral approaches (with core ring or 3D modelling)
  - ✓ FP behaviour: FP SA modules chaining, integral approaches (based on SA codes)….: few improvements integrated only

- Reduction of environmental releases
  - ✓ Mostly due to a decrease of failed fuel fraction in DBAs (no more assumptions on failed fuel fractions, core model refinement)
  - ✓ For VVERs larger discrepancies between updated calc. results (> 2 orders of magnitude linked to ≠ in RBR (failure criteria)
  - ✓ Impact of core modelling
    - ✓ No significant differences with refined core ring modelling (averaged T/H)
    - ✓ 3D core modelling (better FA differentiation) lead to decrease or increase of RBR
  - ✓ R2CA burst criteria (slightly more stringent but somewhat hidden) could be more important considering uncertainties in its determination (± 50°C)

SGTR : main modelling improvements

REDUCTION OF RADIOLOGICAL CONSEQUENCES OF DESIGN BASIS & DESIGN EXTENSION ACCIDENTS

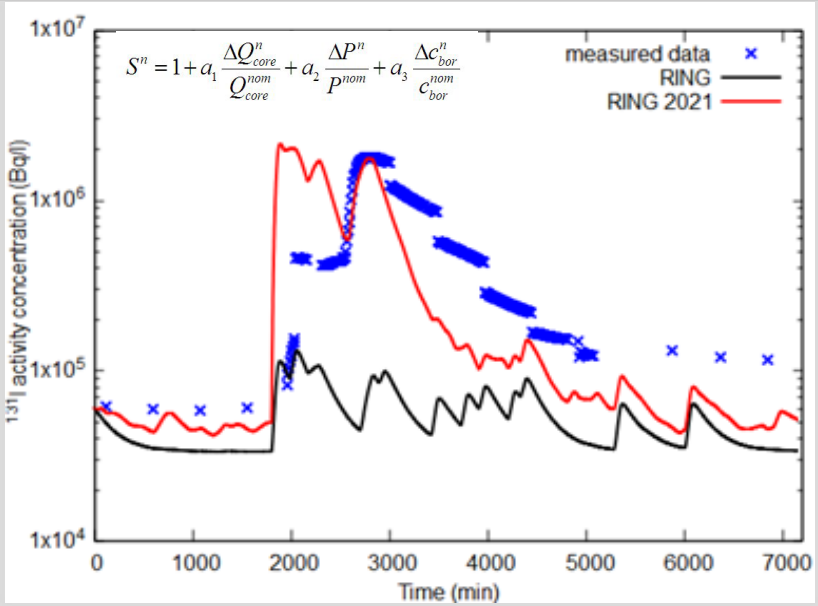

from Hozer, Z. and al (EK), R2CA T4.2 technical report

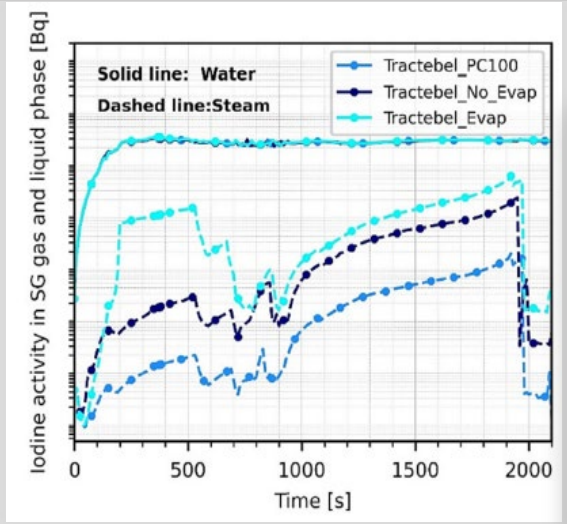

from Foucaud, P. and al (TE), R2CA ANE special issue

from Dieschbourg, K. and al (IRSN), T2.5 technical report

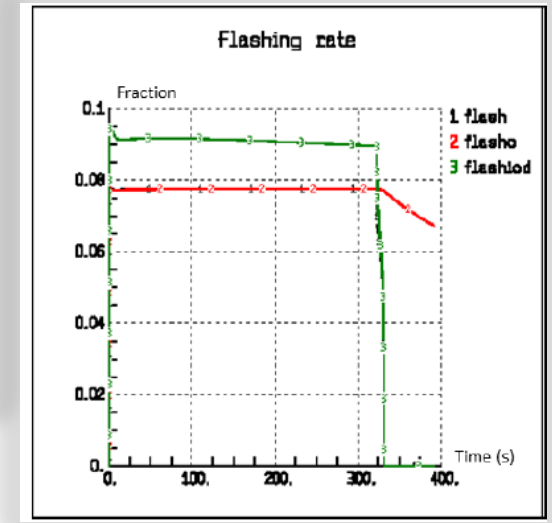

- FP spiking releases from defective rods
  - ✓ Updated IS empirical models (new NPP data) incl. Cs & I
  - ✓ Different IS models (=f(power, P_{prim}, [B], fuel BU…), further enhancements limited by data availability
  - ✓ Future improvements expected from extended fuel perf . Code, multiscale approaches (meso-scale models informing fuel perf. codes

- FP transfer in failed SG from liquid-to-gas phase
  - ✓ Enhanced partitioning model (considering diffusion & convection processes in PC determination, T_{liq})
  - ✓ New or enhanced flashing/atomisation models (incl. iodine speciation in some cases)
  - ✓ Only scarce exp. adressing transfer & individual phenomenon contributing

- Updated calculation chains (for FP behaviour/transport from primary-to-secondary systems) developped

SGTR : other modelling improvements

REDUCTION OF RADIOLOGICAL CONSEQUENCES OF DESIGN BASIS & DESIGN EXTENSION ACCIDENTS

- Clad secondary hydriding simulations from water ingress to blister formation through database reassessmt (incl. new data from R2CA, model devpt/upgrade, code extensions (better estimate of blister thickness then clad failure
  - ✓ New experimental data for H_2 uptake on Zr-based @ 300-400°C ① & extension of H_2 uptake modelling @ low temperatures
  - ✓ Hydrogen diffusion/precipitation (blister formation): model update or implementation, different H redistribution models ② leading to slight differences in predicted blister thickness ③ (defect can be "through wall" in NO)
  - ✓ Failure criteria from fracture mechanical theory could be applied providing remaining uncertainties (kinetics of clad internal oxidation, of H pick-up from H_2/H_2O mixtures…) are adressed

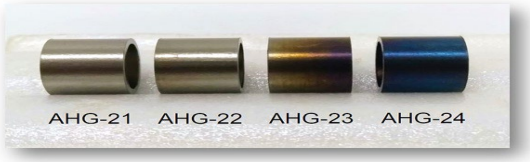

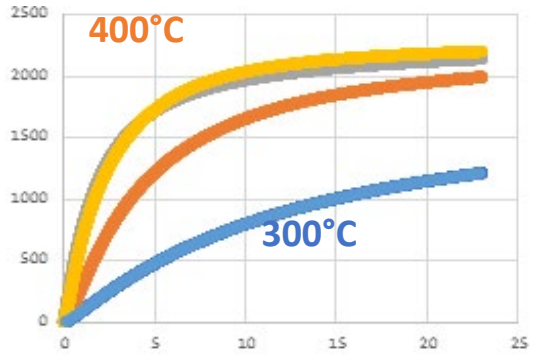

H content (wppm) = f(t-mn)

①

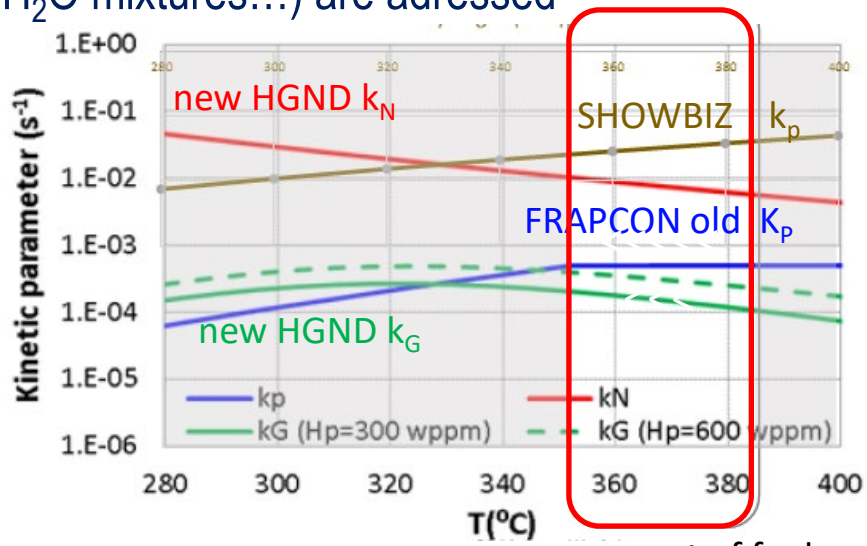

upper part of fuel rods

enhanced in-clad H model
(@ FRAPCON) (HNGD model)

②

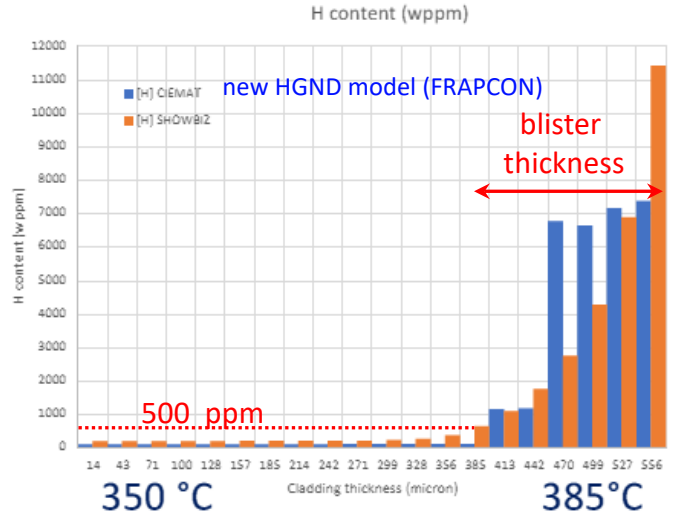

in-clad H distribution
(HNGD model vs precipitation model)

③

SGTR RC re-evaluations

REDUCTION OF RADIOLOGICAL CONSEQUENCES OF DESIGN BASIS & DESIGN EXTENSION ACCIDENTS

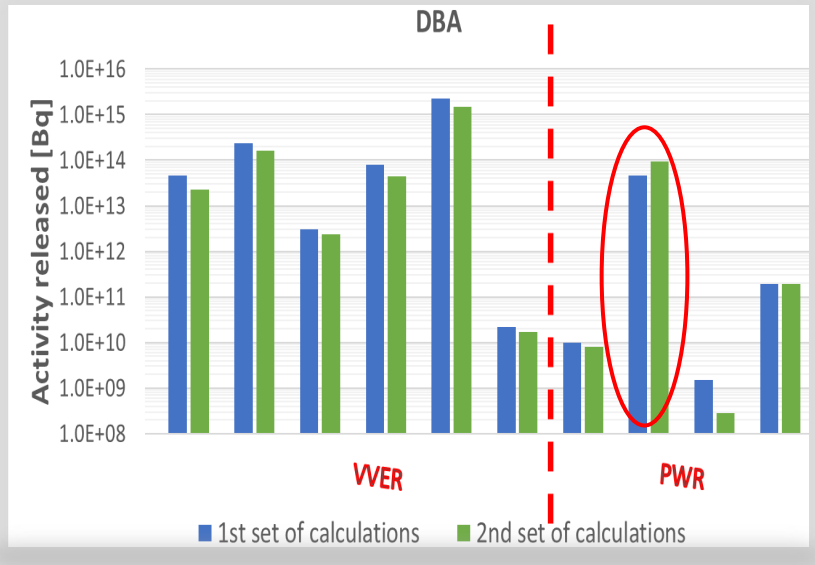

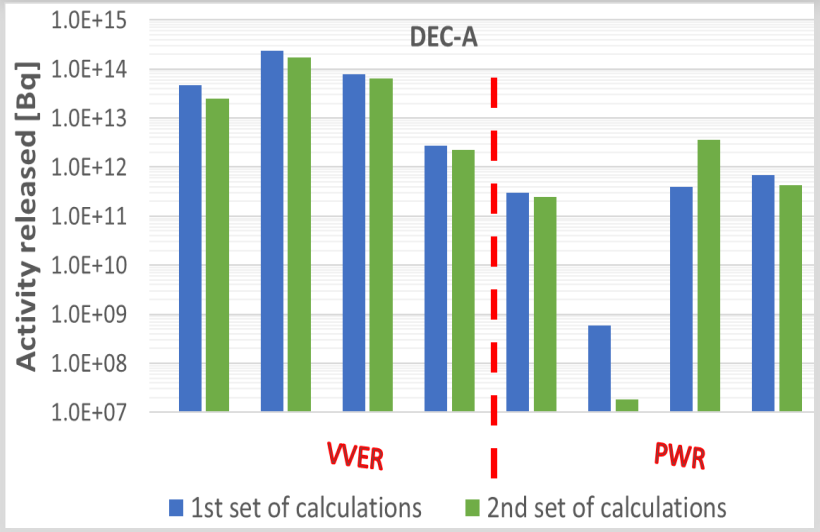

5 LWR designs, 2 scenarios, ~ 45 reactor calc.

- Updated calculations used different methodologies
  - ✓ FP (iodine) releases from defective rods/transport: with T/H system (incl. FP transport models or coupled with dedicated codes) or integral approaches (SA codes)
  - ✓ Liquid-to-gas transfer in failed SG (uncovery breaks): empirical coefficients, integral SA codes enhanced with dedicated models or dedicated new modules: only few improvts made (flashing/partitioning)

- Reduction of environmental releases
  - ✓ Mostly due to a decrease of RCS radionuclide inventory and transport aspects in RCS & failed SG (dilution in RCS, pool scrubbing, IS model…)
  - ✓ For PWRs larger discrepancies between updated calc. (> 5 orders of mag.) linked to ≠ in spike modelling, FP transfer modelling improvements
  - ✓ Transport aspects combined with FP chemistry in primary RCS led in one case to a slight increase of environmental release

Accident Management & Prevention

REDUCTION OF RADIOLOGICAL CONSEQUENCES OF DESIGN BASIS & DESIGN EXTENSION ACCIDENTS

- **O**ptimisation of **A**ccident **M**anagement **P**rocedures (apply to SGTR)
  - ❑ **Downhill-SIMPLEX** Method used to determine best timing of operator's actions to limit the releases of primary coolant to the secondary system and further to the environment.
    - ✓ Provide a robust numerical algorithm to find a local minimum of a function
    - ✓ Timing of (3) operator's actions & T/H system used to evaluate plant response
    - ✓ AM measures evaluated from 3 independant parameters (I-131 release, P_{prim}, water level in core) combined in a function in a way that the value of the function is a good measure of the operator's actions
  - ❑ Highlight importance of timing for a specific procedure to reduce environmental releases
    - ✓ High reduction of I-131 releases by switch off 3 HPIS trains early & opening PORV at later stage

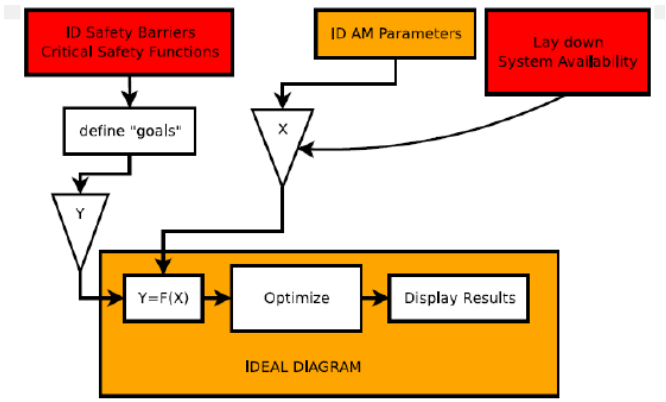

1.) Safety Barriers/ Critical Safety Functions
2.) Identify AM Parameters
3.) Fix system availability
4.) Optimization and "Ideal Diagram"

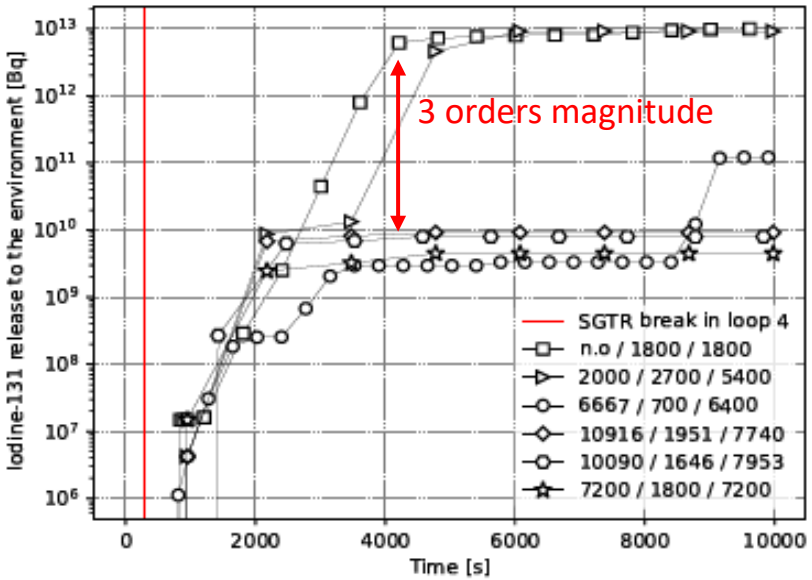

Accident Management & Prevention

REDUCTION OF RADIOLOGICAL CONSEQUENCES OF DESIGN BASIS & DESIGN EXTENSION ACCIDENTS

- FOAK of an **expert tool** for early **diagnosis of defective fuel rods**
  - ✓ Develpts of a physical model relevant for activity release from fuel to coolant
    Isotope decays (30 isotopes, 8 decay chains) & transport equations considered
  - ✓ Generation of a sample dataset (computational database considering 16 input parameters)
    Model parameter space randomly sampled: some parameters calc. with Fuel Perf. Code (TU)
    Identification of most influential parameters (8) on activity with Pearson Correlation Coefficients
  - ✓ Design of 2 ANNs for coolant activity & defect formation prediction
    Surrogate of the physical model (8 most influential input parameters): ~50000 sequences generated
    Anomaly detector (autoencoder trained only on normal situations wo defect): RNN, GSU, LSTM tested

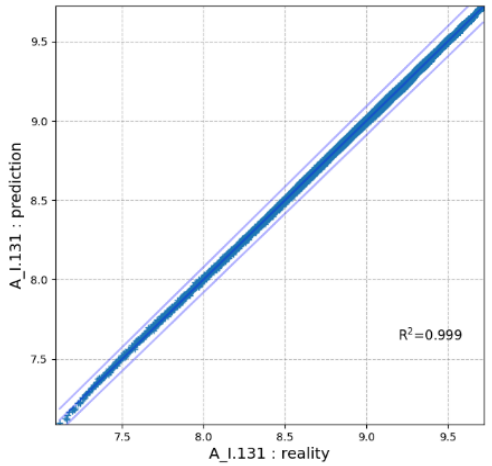

High accuracy of the surrogate model
(max. relative error ~ 2,6%)

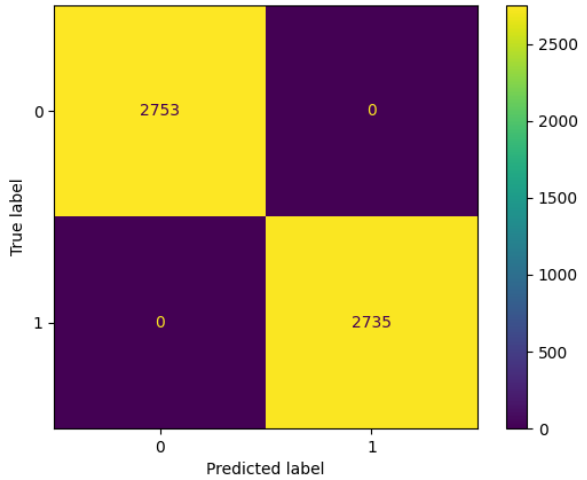

100% satisfactory results for all anomaly detectors
(differences in learning speed)

Final remarks

REDUCTION OF RADIOLOGICAL CONSEQUENCES OF DESIGN BASIS & DESIGN EXTENSION ACCIDENTS

- Significant improvements made in LOCA/SGTR modelling (refinement/development of models or external functions, built of new calculation chains…) decreasing the level of conservatisms, then Radiological Consequences, but not eliminating all
- Updated validated numerical tools in support to a more realistic evaluation of DBA/DEC-A accident risks (ST evaluation) in design phase of future NPP concepts (incl. evaluation of some ATFs & new AMPs)
- Though still large room for additional improvts, comparisons between initial/final calc. allowed to provide some recommendations for SGTR/LOCA RC evaluations
- Demonstrations made that increased capabilities of numerical tools and use of "Expert" methods could be advantageously used to fill the data gaps and increase NPP safety (SGTR AM optimisation and early diagnosis of defective fuel rods)

Some issues for the future

REDUCTION OF RADIOLOGICAL CONSEQUENCES OF DESIGN BASIS & DESIGN EXTENSION ACCIDENTS

- **Database extension** (exp. data too sparse for some phenomena (FP chemistry), or to be completed for more prototypical conditions (clad burst) or few new types of materials (ATF …)
- **Missing Phenomena, partially or not well modelled** (FP chemistry in fuel/primary circuit, retention in SG UP, liquid-gas distribution, others for DEC-A?…)
- **Calculation schemes** (multi-physics/multi-scale code coupling, CPU optimisation…)
- **Systematic SA/UQ** (influent parameters & uncertainty bounds) for **BEPU** evaluations
- **Methodology extension/application** to other kinds of fuel (**MOX, high burn-up, ATFs…**) & to foreseen innovative NPP technologies (LW-**SMRs**…)
- **Harmonisation** of RC evaluation methodology in a context where national regulations vary greatly from one country to another
- **Advanced technology** (devices, tools) for improving transient **diagnosis/prognosis** (early realistic estimation of ST…) to better prevent/reduce their consequences
- …..

Thank you!!!

R2CA archives & publications

https://r2ca-H2020.eu

https://zenodo.org/

Annals of Nuclear Energy/R2CA special issue

This project has received funding from the Euratom research and training programme 2014-2018 under grant agreement No 847656.

PROGRESS IN UNDERSTANDING FISSION PRODUCT REMOBILIZATION AND HYDROGEN RISK IN WATER-COOLED REACTORS: OECD/NEA THAI-3 PROJECT

S. Gupta, M. Freitag, E. Schmidt, M. Colombet, B. von Laufenberg
Becker Technologies GmbH
Rahmannstr.11, Eschborn, Germany
gupta@becker-technologies.com; freitag@becker-technologies.com;
eike.schmidt@becker-technologies.com; colombet@becker-technologies.com;
von.laufenberg@becker-technologies.com

G. Langrock, F. Funke
Framatome GmbH
Paul-Gossen-Straße 100, Erlangen, Germany
gert.langrock@framatome.com; friedhelm.funke@framatome.com

ABSTRACT

OECD/NEA THAI-3 project aimed to investigate hydrogen risk and source term related issues with specific emphasis on representative boundary conditions as expected during a severe accident in light water reactors. The project was conducted between 2016 and 2019, hosted by Germany and supported by signatories from 16 countries. The experimental program was conducted in the technical-scale THAI$^+$ facility, comprising two interconnected vessels with a total volume of 80 m^3.

The hydrogen combustion tests investigated the impact of varying initial flow conditions, gas composition, and burn direction on pressure buildup, flame front propagation, and jet-ignition effects during H_2-deflagration. The test HD-44 served as a benchmark for validating combustion models. Hydrogen recombiner tests provided data on recombination onset, recombination rate, and hydrogen depletion efficiency under counter-current flow conditions, with the test HR-49 used for benchmark code calculations. The source term related experiments examined the re-entrainment of fission products (CsI, I_2) from water pools, showing CsI re-entrainment increased tenfold in the case of water pool with reduced surface tension. The results of fission product resuspension tests revealed significant resuspension of fission products from paint and steel surfaces during hydrogen deflagration with the potential to remain gasborne over a long time ("fine particles"), with notable release of organic iodine and decomposition of CsI to I_2 in the high-temperature environment.

This paper summarizes the key findings of the project and emphasizes their significance for mitigating hydrogen risk and source term issues. It also highlights the use of project results for code validation and reactor analyses to manage and mitigate severe accidents in LWRs.

KEYWORDS
THAI, severe accident, H_2 risk, source term, mitigation, validation database

1. INTRODUCTION

The experimental investigations conducted as part of the previous OECD/NEA THAI and THAI-2 projects have significantly contributed to understanding hydrogen and fission product related challenges in water-cooled reactor containment during accidental conditions [1, 2]. The experiments were conducted in the technical-scale THAI (Thermal-hydraulics, Hydrogen, Aerosols, and Iodine) containment test facility. Based on the selected experiments, code benchmark activities were conducted, such as on hydrogen distribution (OECD/NEA THAI HM-2 code benchmark), Passive Autocatalytic Recombiner (PAR)

performance (OECD/NEA THAI-2 HR-35 code benchmark), and an international standard problem involving THAI hydrogen combustions test HD-22 (ISP-49) [3].

The OECD/NEA THAI-3 project aimed to cover open issues related to hydrogen risk and source term, including those identified based on the Fukushima Daiichi accident analysis conducted in the frame of various European and other international activities, e.g. OECD/NEA SAREF [4], European Stress Test [5]. The THAI-3 experimental program benefitted from the extended technical capabilities of the THAI$^+$ facility, which provided higher flexibility in containment safety-related investigations with two inter-connected vessels.

The OECD/NEA THAI-3 project was conducted between February 2016 and July 2019. The project consortium included signatories from technical safety organizations, research centers, regulatory bodies, industry, and universities from 16 countries, namely: Belgium (Bel V), Canada (CNL), China (SNPSDC), Czech Republic (UJV Rez), Finland (VTT), France (IRSN, EDF), Germany (BT, FZJ, Framatome, RUB, GRS, KIT), Hungary (NUBIKI, MVM PAKS), India (AERB, BARC, NPCIL), Japan (NRA), Korea (KAERI, KINS, KHNP), Luxembourg (MESR), Slovak Republic (UJD), Sweden (SSM), Switzerland (PSI), and UK (ONR).

The present paper provides a synthesis of the main experimental outcomes and highlights the progress achieved in understanding hydrogen risk and source term related issues in the containment of water-cooled reactors. Application of project results for analytical activities towards modelling improvement and reactor application is highlighted with the selected examples.

2. WORK PROGRAM

In the OECD/NEA THAI-3 project, the following test series/tests were part of the work program:

- Hydrogen deflagration tests in two-vessel geometry (HD-40 to HD-45),
- Hydrogen recombiner (PAR) tests (HR-46 to HR-50),
- Re-entrainment of dissolved CsI from a heated/boiling water pool without and with impurities (WH-24 & WH-28),
- Release of volatile iodine from a boiling pool (Iod-32),
- Resuspension of aerosol deposits from surfaces by hydrogen deflagration (HD-46)
- Resuspension of iodine from "decontamination paint"[1] by H_2 deflagration (Iod-34).

In the OECD/NEA THAI-3 project, the Analytical Working Group (AWG) was formed, comprised of voluntary contributions from project partners, with a primary focus on enhancing and validating advanced Lumped Parameter (LP) and Computational Fluid Dynamics (CFD) codes. The AWG evaluated test results to improve the predictive capabilities of advanced simulation codes, selecting experimental data from hydrogen deflagration test HD-44 and hydrogen recombiner test HR-49 for blind and open post-test calculations as part of code benchmark exercises. Additionally, tests from the THAI National project (phase V), namely HD-36, HD-38, and HR-43, were shared with OECD/NEA THAI-3 partners to support analytical activities by providing reference or complementary data for OECD/NEA THAI-3 experiments [6].

3. TEST FACILITY AND THE EXPERIMENTAL CONFIGURATIONS

The experimental program was conducted in the extended THAI$^+$ test facility, which has the same design limiting conditions (i.e. 14 bar at 180°C) as in the original THAI test facility and also retains its unique experimental features, e.g. use of hydrogen and iodine I-123 tracer (half-life of 13.5 h), differential wall heating/cooling, etc. The extended THAI test facility, which includes the second smaller vessel called PAD

[1] Decontamination paint utilized in nuclear power plant containment features epoxy resin formulations fortified with radiation-absorbing additives, ensuring easy cleaning, radiation mitigation, and long-term surface protection.

(parallel attachable drum) was built and qualified in the frame of the THAI national program before the start of the OECD/NEA THAI-3 project [7]. The various test configurations employed in the OECD/NEA THAI-3 project for the experimental investigations are shown in Figure 1.

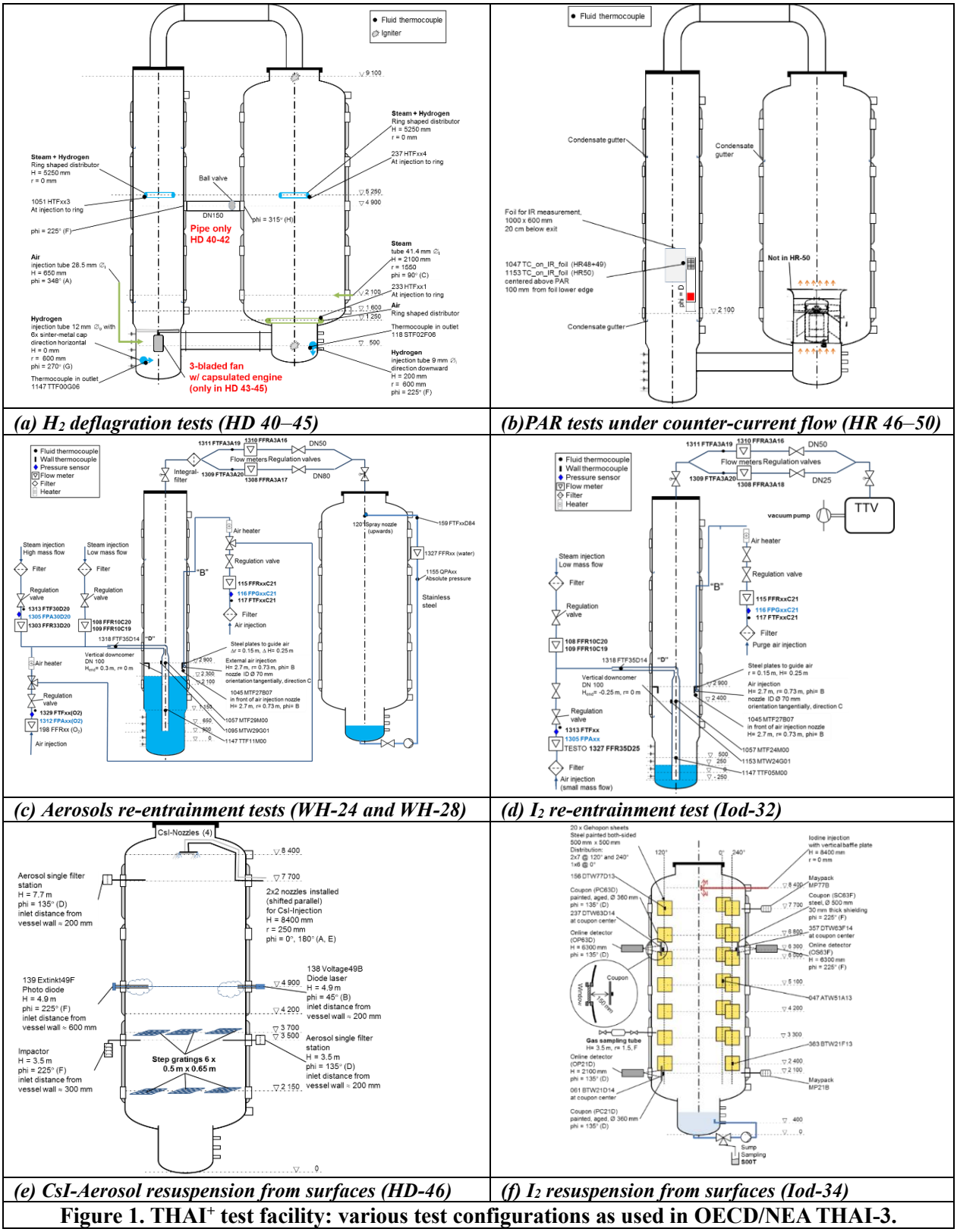

(a) H_2 deflagration tests (HD 40–45)

(b)PAR tests under counter-current flow (HR 46–50)

(c) Aerosols re-entrainment tests (WH-24 and WH-28)

(d) I_2 re-entrainment test (Iod-32)

(e) CsI-Aerosol resuspension from surfaces (HD-46)

(f) I_2 resuspension from surfaces (Iod-34)

Figure 1. THAI+ test facility: various test configurations as used in OECD/NEA THAI-3.

As per the experimental requirement, the THAI$^+$ configuration was adopted to perform the experiments in a single vessel configuration alone, i.e. original THAI test vessel (TTV) or new PAD vessel or in the new THAI$^+$ two-room configuration consisting of both. The main dimensions of the TTV are 9.2 m height, 3.2 m diameter, and 60 m³ volume. The main dimensions of the PAD vessel are 9.8 m height, 1.6 m diameter, and 18 m³ volume. The vessels are optionally connected at the top and bottom by large diameter pipes (ID = 478 mm). The cylindrical parts of both vessels are equipped with three independent heating/cooling jackets over the height for controlled wall temperature conditioning using external thermal oil circuits.

To provide a relevant database, advanced instrumentation, and data acquisition systems were installed for monitoring the relevant physical quantities with high spatial and time-related resolution. Selected measurement techniques installed for the experiments conducted in the frame of the OECD/NEA THAI-3 project are mentioned below:

- Gas flow velocity by vane wheels (turbine flow meters) in vessel gas atmosphere and at PAR inlet
- A grid of "fast" sheathed thermocouples (outer diameter 0.5 mm), installed at 13 different elevations in the test vessel to monitor flame propagation ("flame front arrival") and flame temperature during hydrogen combustion
- Strain gauge type "fast" pressure transducers (1 kHz) to monitor the transient deflagration pressure
- Bulk filters for aerosol concentration measurement
- Integral filter installed in the vessel exhaust line to measure the aerosol release
- Laser light extinction for on-line aerosol concentration measurement
- Cascade impactors for aerosol particle size distribution measurement
- Gas scrubbers for gaseous iodine concentration measurement
- Maypack filter stations for the discrimination of the iodine species in the vessel atmosphere
- Scintillation detectors for monitoring the iodine activity on deposition coupons or in gas phase
- Online iodine measurement system LASI (Light Absorption System for I_2 using spectroscopy)

4. MAIN OUTCOMES OF THE EXPERIMENTAL PROGRAM

4.1. Hydrogen Deflagration and Flame Propagation in a Two-Compartment System

The hydrogen deflagration (HD) test series aimed to address uncertainties in predicting slow hydrogen deflagration behaviour in multi-compartment geometries, where technical-scale experimental data are limited in the open literature. Furthermore, the HD tests assessed the impact of initial turbulence in the gas atmosphere on flame propagation behaviour, alongside the multi-compartment effect. The test series comprised six experiments in stratified (HD 40–42) and pre-mixed (HD 43–45) conditions, Table I. In experiments involving a homogeneous gas atmosphere, initial turbulence was induced using a blower. One of the two installed igniters initiated either an upward or downward flame propagation according to the specified test conditions, (Fig 1a). The reference tests HD-36 (THAI$^+$ configuration) and HD-22 (TTV alone) were conducted in the initially quiescent atmosphere with an igniter position at the TTV bottom.

Concerning the geometric effect, no pressure difference was noted in OECD/NEA THAI-3 tests during combustion between the two interconnected vessels of the THAI$^+$ facility. Hence, any potential augmentation in peak pressure, such as that from a larger scale or from interacting flame fronts in the dual-vessel setup, was not identified. Comparison between THAI$^+$ and single THAI vessel tests revealed slightly lower peak pressures in two-vessel geometry compared to a single-vessel that could occur due to higher heat transfer in THAI$^+$ (surface/volume ratio = 2.2) than the single THAI vessel (1.67 ratio).

In contrast to single-vessel THAI tests, flame acceleration has been observed in the OECD/NEA THAI-3 HD tests particularly inside the lower and upper connection pipes, caused by diameter change ahead of the expanding flame and increased turbulence in the connecting pipes. The most pronounced flame acceleration occurred in the lower connecting pipe in test HD-41 (H_2-concentration 12 vol-% in the pipe, quasi no steam, relatively low temperature), with a flame speed of approximately 50 m/s. However, no additional or faster

pressure increase was observed due to flame acceleration. Furthermore, jet-ignition has also been observed, which occurs exclusively in a compartmentalized geometry and observed in other test facilities, such as the 640 m^3 Battelle Model Containment (BMC) [8], when the unburnt hydrogen gas mixture from an upstream compartment is rapidly displaced into a downstream compartment.

Table I. Specified test conditions in HD 40–45 tests

Test ID	Test Parameters				
	H_2 concentration	***Steam concentration***	***Temperature***	***Initial gas flow***	***Igniter position***
	[vol-%]	***[vol-%]***	***[°C]***		
HD-40	12 top 6 bottom	47 top 3 bottom	90 top 30 bottom	none	TTV bottom
HD-41	6 top 12 bottom	47 top 3 bottom	90 top 30 bottom	none	TTV bottom
HD-42	10 top 10 bottom	47 top 3 bottom	90 top 30 bottom	none	TTV bottom
HD-43	10	25	90	low (0.61 m^3/s)	TTV bottom
HD-44	10	25	90	high (1.2 m^3/s)	TTV bottom
HD-45	10	25	90	high (1.2 m^3/s)	TTV top

Figure 2a shows the flame front propagation in premixed THAI+ HD 43-45 tests together with tests HD-36 and HD-22. The jet-ignition type combustion mode has been observed in tests HD-40, HD-41 (not shown in Figure 2a), and also in HD-36 as rapid downward combustion in the upper half of the PAD. Notably, the test HD-36 characterized by a higher average H_2 concentration of 10.3 vol.-% with superheated steam, compared to tests HD-40 and HD-41, demonstrates the most pronounced jet-ignition behaviour. The weak jet ignition was also observed for test HD-42, with rapid flame travel consuming over 1/3 of PAD's mixture inventory within 100 ms.

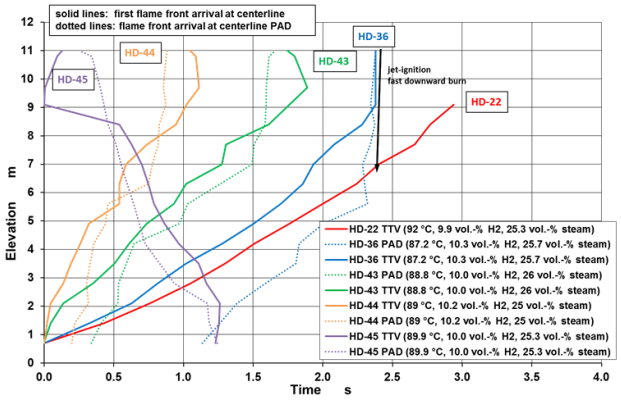

(a) Flame front propagation in HD 43-45 tests and comparison with HD-36 (THAI+) and HD-22 (TTV)

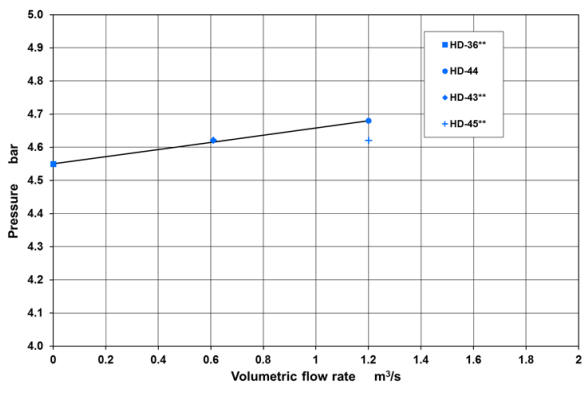

(b) Peak pressures for different initial flows as a function of volumetric flow

Figure 2. Results of hydrogen deflagration tests.

The tests conducted with initial convection revealed a higher flame speed in the upper connecting pipe with downward directed jet ignition into the upper half of the PAD indicating a significant effect of initial convective flow on combustion behaviour. The peak pressure increases slightly with an increase in initial volumetric flow, with HD-44 showing a 0.11 bar/(m^3/s) increase in peak pressure for ignition triggered at TTV bottom, Figure 2b. Due to the slight difference in initial conditions of the tests shown in Figure 2b, the

peak pressures have been extrapolated to H_2 concentration of 10.2 vol.-% (HD-44) using the slope of the adiabatic isochoric complete combustion (AICC) pressure for an initial pressure of 1.5 bar and an initial steam content of 25 vol.-%.

On the safety significance of HD tests, results revealed that the peak pressures in all tests remained below adiabatic isochoric complete combustion (AICC) pressures resulting from non-adiabatic real thermodynamic process with heat transfer to structures. Peak pressures were highest for tests with homogeneous H_2 distribution (steam concentration and temperature still stratified) due to the higher mean H_2 concentrations and complete combustion for these tests compared to the stratified conditions.

4.2. PAR Operation under Counter-Current Flow Conditions

PAR tests conducted in previous OECD/NEA THAI and THAI-2 projects [1, 2] provided crucial data about the performance of PARs coming from different manufacturers, namely AREVA (now Framatome), AECL, and NIS. The focus of these tests was on investigating PAR performance behaviour under a broad range of accident conditions, such as onset behaviour, recombination rates, depletion efficiency, PAR-induced ignition behaviour, and performance in oxygen-lean conditions. All experiments were conducted under initially quiescent atmospheric conditions. Investigating PAR operation under pre-existing flow conditions became a focus of the OECD/NEA THAI-3 project, with reference data from prior OECD and national THAI programs under similar initial thermal-hydraulic conditions but without preexisting flow conditions. A total of 5 tests were conducted in the OECD/NEA THAI-3 project using PAR units provided by NIS and AREVA (Table II).

Table II. Test conditions as specified for the HR test series

Test #	P_0 [bar]	T_0 [°C]	c_{Steam} [vol-%]	PAR unit	Flow velocity in the vicinity of PAR	Effect obtained by test
HR-46	1.5	75	25	NIS 1/8th full module	≈ 0.5 m/s	Counter-current flow
HR-47	1.5	75	25	NIS 1/8th full module	≈ 0.5 m/s	Reduced chimney height
HR-48	1.5	75	25	AREVA 0.5 x FR-380	≈ 1.0 m/s	Strength of counter current flow
HR-49	3.0	117	60	AREVA 0.5 x FR-380	≈ 1.0 m/s	Pressure and temperature
HR-50	1.5	75	25	AREVA 0.5 x FR-380	natural convection	PAR exposed to natural convection

In tests, HR 46-49, counter-current flow velocities were established between 0.5 m/s and 1 m/s near the PAR outlet using a blower installed in the TTV. The test PAR unit had been installed in the PAD vessel, Figure 1b & Figure 3a. Test HR-50 established natural convection through the differential wall heating and cooling of the TTV and PAD vessels. Additionally, the effect of PAR chimney height was investigated, with a 1/4th reduction in HR-47 compared to HR-46, to assess its effect on PAR performance under counter-current flow conditions.

In general, the results indicate that the onset of hydrogen recombination occurs sooner under counter-current flow conditions compared to the initially quiescent atmosphere. As an example, in the case of NIS-PAR (Tests HR-46 & 47), the onset occurred below 0.4 vol.-% as compared to 1.5 vol.-% for initially quiescent atmosphere in tests HR-14 & HR-15 conducted earlier in OECD/NEA THAI project [1]. In the HR-49 test conducted with AREVA-PAR at elevated pressure and temperature conditions, the onset of recombination occurred below 0.6 vol.-% compared to 1.3 vol.-% for the initially quiescent atmosphere in test HR-12 [1].

The two PARs used for the experiments differed in design and responded differently to the investigated counter-current flow conditions, Figure 3a. The AREVA PAR, featuring a top-covered chimney with three lateral outlets, effectively shielded the PAR from adverse effects caused by counter-current flow conditions. Apart from the influence on onset behaviour, no measurable effect on AREVA-PAR performance was determined under the investigated counter-current flow conditions.

On the other hand, the NIS PAR unit used for the OECD/NEA THAI-3 experiments had an open-top chimney (NIS-PARs are also available with top covered chimney). For this PAR unit, the counter-current flow induces flow oscillations, mainly observed at low concentration levels (below 2.0 vol.-% in HR-46). The flow oscillations also had a negative influence on the PAR performance (recombination rate and depletion efficiency) but only under conditions where no stable upward directed flow has been established and flow oscillations are still present, Figure 3b. For hydrogen concentrations above 2 vol.-%, the hydrogen depletion efficiency of HR-46 matches the results of HR-14 and HR-15 [1] with values between 50 and 60 %. The shortening of chimney height results in a reduced PAR internal flow showing slightly increased efficiency (about 10%), which could be related to the increasing hydrogen residence time at catalytic cartridges due to reduced PAR internal flow. In the case of the reduced chimney height, PAR becomes even more susceptible to external counter-current flow, inducing flow oscillations even at low hydrogen concentrations compared to full chimney height as investigated in HR-46.

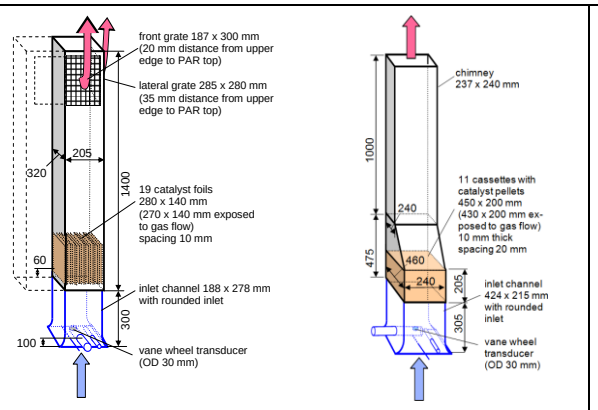

(a) Test PAR units: ½ FR-380 size AREVA PAR (left), full-scale 1/8th NIS PAR (right)

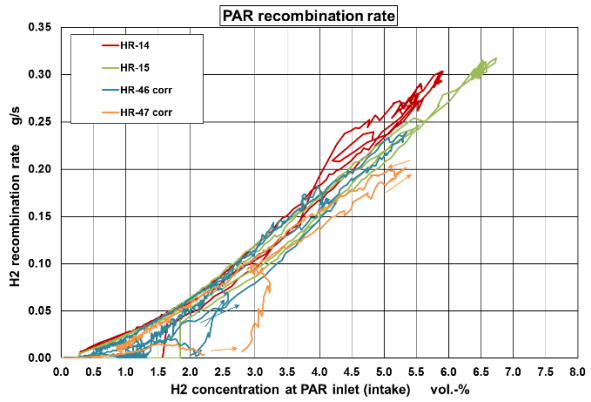

(b) H_2 recombination rate

Figure 3. Dimensions of the PAR units and results of NIS-PAR tests.

4.3. Fission Products Re-Entrainment from Water Pools

4.3.1 Re-entrainment of the dissolved CsI aerosols from a water pool

Two tests WH-24 and WH-28 were conducted to investigate the re-entrainment behaviour of dissolved CsI aerosols from heated water pools. While both tests shared similar initial thermal-hydraulic conditions, WH-24 used decalcified water while WH-28 introduced a surfactant to reduce surface tension, simulating the impurities effect under severe accident conditions.

Compared to the previous re-entrainment tests conducted in THAI and elsewhere [9], the OECD/NEA THAI-3 tests (WH-24 & WH-28) offered valuable data on aerosol re-entrainment under elevated pressure conditions and different injection geometries in water pool. Three distinct phenomenological categories were studied, providing comprehensive insights for code development and model validation under varied accident scenarios, namely:

a) Particle re-entrainment from a heated pool by injection of air and steam/air mixtures,
b) Particle re-entrainment from boiling pool by injection of steam and steam/air mixtures,
c) Particle re-entrainment from flashing pool induced by venting-induced depressurization.

Table III provides the specified test conditions for WH-24 and WH-28 tests consisting of 12 test phases using the injection of air, steam, and a mixture of steam and air injection into the vessel sump through a scaled-down DN100 downcomer pipe. The test phases a) and b) were performed at stationary pressure conditions of 2.5 bar. The depressurization rates used in test phase c) referred to accident-typical conditions during a filtered containment venting operation of a BWR (i.e. German SWR-72 or Japanese BWR Mark-I type), as well as those typical for PWR with large containment volume.

Table III. Specified test conditions for the phases of tests WH-24 and WH-28

Test phase	Air injection flow rate (kg/h)	Steam injection flow rate (kg/h)	Water temperature (°C)	Purge air flow rate (kg/h)	Depressurization rate
a1)	80	-	46	0	
a2)	80	-	60	0	
a3)	19	70	60	145	
a4)	19	70	90	145	
a5)	19	70	120	145	
b1)		70	boiling	145	
b2)		210	boiling	145	
b3)		350	boiling	145	
b4)	19	210	boiling	145	
c1)	-	-		-	BWR type 1 bar/5 min
c2)	-	-		-	BWR type 1 bar/ 15 min
c3)	-	-		-	PWR type 0.1 bar/30 min

In both tests, quantification of aerosol re-entrainment relied on measuring CsI particle concentrations released into the PAD gas atmosphere from the sump. The vessel walls were heated to 138°C to create a superheated atmosphere, essential for drying the aerosol particles released by entrained water droplets. Superficial velocities across all tests ranged from 0.01 to 0.12 m/s, encompassing the transition from fully developed bubbly flow to the initial domain of churn turbulent flow regime.

In the WH-24 test, an extensive examination of water pool hydrodynamics was conducted using high-speed cameras. Comparison with literature, including EPRI tests [10] and the THAI test [11], revealed significant disparities in bubble dynamics. Unlike previous studies showing cascaded reduction of bubble sizes, WH-24 observed a complete breakup of primary bubbles within 3–4 times their diameter, diverging from phenomena recorded in some pool scrubbing codes like SPARC-90 [12]. Key differences between WH-24 and EPRI tests [10] stemmed from varying temperature and pressure, with WH-24 conducted at elevated pressure/temperature conditions, manifesting in non-spherical bubble shapes deviating from observations in ambient pressure tests. Another important insight obtained was concerning the bubbles close to the pool surface. The average bubble diameter in the test WH-24 ranged from about 1.5 mm up to 3.5 mm during the test phases. The bubble diameters close to the water surface showed an increase with increasing Weber numbers. The previous THAI tests [11] conducted at ambient pressure conditions (also using a downcomer for gas discharge in the pool) showed an average bubble diameter in the range of about 4 mm. This might be explained by the higher vessel pressure in test WH-24 which increases the density inside the gas bubbles as compared to tests at atmospheric conditions. The shape classification of bubbles in WH-24 was based on Eötvös (ranging between 0.03 to about 50) and Reynolds numbers, with detected bubbles encompassing spherical, ellipsoidal, and wobbling types [13], Figure 4b.

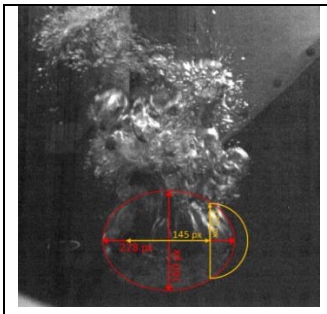

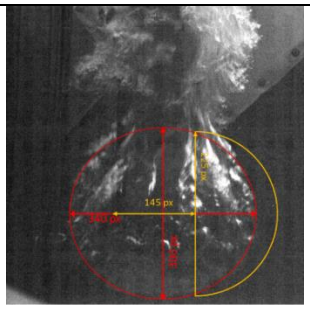

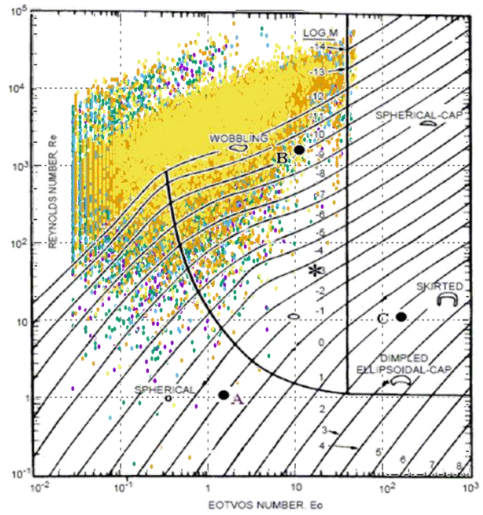

(a)Primary bubbles leaving the downcomer during phases of low non-condensed (left) and with steam-only flow (right)

(b) Classification of the detected bubbles of all test phases close to the water surface, following Grace [13]

Figure 4. WH-24 test results.

For the determination of the re-entrainment factor, aerosol measurements were taken independently using filters and gas scrubbers. Impactor measurements revealed very small particles with a mass median diameter (MMD) of approximately 0.5 microns, relevant for long-term airborne considerations inside containment in case of a severe accident. Entrainment values in the WH-24 test ranged between $E = 5\times10^{-6}$ and $E=7\times10^{-5}$. Increasing superficial velocities correlate with increased entrainment rate, particularly in bubbly flow regime. But at higher superficial gas velocities belonging to the transition regime and onset of churn turbulent flow regime, a decrease in entrainment rate was determined.

The WH-28 test was conducted with the reduced surface tension of water by adding Borchi GOL 1375 and Carl Roth® silicone anti-foaming emulsion to suppress the foaming tendency of the liquid, released larger aerosol particles compared to WH-24, resulting in bimodal size distributions. Entrainment values in WH-28 were about one order of magnitude higher than in WH-24, varying between $E=3\times10^{-6}$ and $E=3\times10^{-3}$. The size of the aerosol particles was determined using a low-pressure cascade impactor showing bimodal distribution, exhibiting a mass median diameter of about 0.1–0.2 µm and 1.2–2 µm. The reduction of the surface tension in WH-28 favored the release of larger particles compared to WH-24 but on the other hand, also a high number of tiny particles have been released generating bimodal distributions.

4.3.2 Release of volatile iodine from a boiling pool

The test Iod-32 aimed to investigate the volatile iodine release from a boiling sump. The test was mainly conducted in the PAD vessel, while the THAI vessel served as a pressure relief tank, Figure 1d. The test procedure for test Iod-32 consisted of a preconditioning phase followed by the main test phases as listed in Table IV.

After establishing the designed thermal-hydraulic conditions in the PAD vessel, during the reference phase (Phase 1) under non-boiling conditions, 0.73 g of molecular iodine (I_2) labelled with I-123 was injected into the PAD sump water (T = 108 °C, pH = 3, V = 1.09 m³). Within 2.5 hours, a small fraction of I_2 (between 0.5 % and 5 %) was released into the PAD atmosphere. The majority of the aqueous I_2 converted into non-volatile iodine due to reaction with the sump's steel wall, limiting further releases of volatile iodine to the gas atmosphere.

For the subsequent test Phase 2, another 0.73 g of fresh I_2 was injected into the PAD sump. Boiling was initiated through a 5-minute depressurization followed by steam injection into the sump water to maintain boiling. Gas from the PAD was vented to the TTV during both depressurization and steam injection phases, resulting in a release of 0.21 g I_2 (14 %) from the sump water. This release was about ten times higher than under non-boiling conditions. The gas-phase I_2 concentration increased by a factor of 100 after boiling compared to the end of the reference phase, Figure 5. Nevertheless, it is imperative to cautiously assess this value for reactor implementation, as the circumstances of the Iod-32 test could impact the outcome. Factors such as I_2 adsorption/desorption from the steel walls within the PAD gas atmosphere, along with potential stratification of the gas atmosphere near the sump-gas interface, could potentially lead to an underestimation of iodine gaseous concentration, particularly under non-boiling conditions. Concerning the effect of venting-induced depressurization on I_2 release from the pool, online detectors indicated a stronger I_2 release during depressurization than during steam injection into the boiling sump water.

Table IV. Specified test conditions in the PAD vessel

Test phase	P (bar)	T (°C)	Steam conc.(vol%)	PAD-sump
Pre.	2.5	117 (gas) 110 (water)	72 (satur.)	Initial filling deionized water 1028 L, H= 0.25 m inside PAD Conditioning to pH= 3
1	2.5 (reference phase)		up to 90	Injection of ~1 g radio-labelled I_2 Activity ~0.5 GBq
2	1.3 bar after depressurization		up to 90	Injection of ~1 g radio-labelled I_2 Activity ~ 0.5 GBq Steam injection mass flow rate 5 g/s, injection duration 10 min
3	1.3 bar after depressurization		up to 90	NaOH injection to reach pH = 8, Steam injection mass flow rate 20 g/s, injection duration 10 min

The Phase 3 was conducted under alkaline conditions with a pH of 8. No volatile iodine was released from the sump during this phase, confirming that any volatile iodine present had already been consumed in the previous phase. Furthermore, Phase 3 revealed no release of non-volatile iodine, specifically as droplet-bound iodine. Post-test vessel cleaning confirmed that the overall iodine mass balance at the end of the test was essentially closed (91 %), including inventories in the PAD and the TTV.

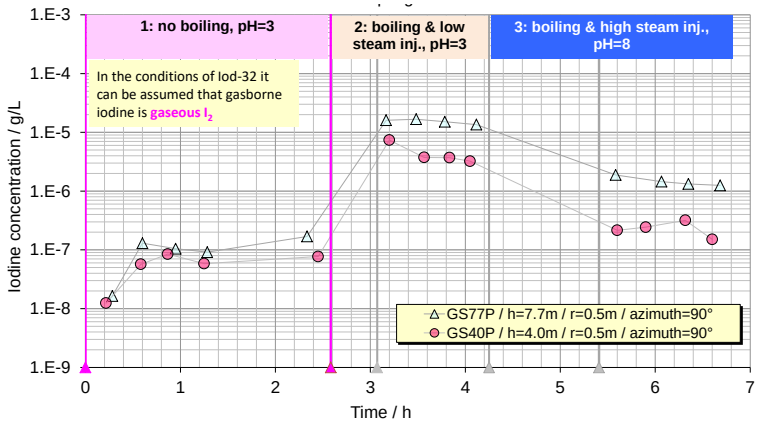

Figure 5. Gasborne iodine concentrations in PAD atmosphere.

4.4. Fission Product Resuspension from Surfaces

4.4.1 Resuspension of CsI aerosols from containment typical surfaces

During the HD-46 test, CsI particles were injected into the THAI vessel and deposited over four days on various surfaces, with the majority accumulating on vertical walls and gratings (Figure 1e, and Figure 6). The surface loading achieved after the deposition phase was 27 g/m^2 on horizontal, 0.2 g/m^2 on vertical, and 7.8 g/m^2 on grating surfaces. The deposited particles were resuspended by the deflagration of a gas atmosphere consisting of 23.6 vol.-% steam and 10.1 vol.-% H_2. The intensity of the hydrogen deflagration was according to the reference test HD-22 with peak gas temperatures above 900 °C and peak pressure of about 4.86 bar. About 4% of the previously deposited aerosol was resuspended. A comparison of HD-46 test results with the VANAM M4 test conducted in the BMC facility and AER tests conducted in THAI [14, 15], revealed that despite similar aerosol settling behaviour in the deposition phase, the resuspended fraction was much higher in HD-46 compared to the aforesaid BMC and THAI tests.

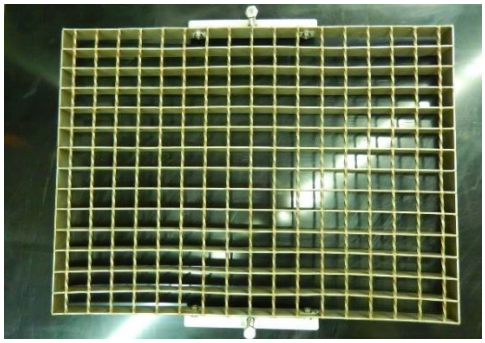

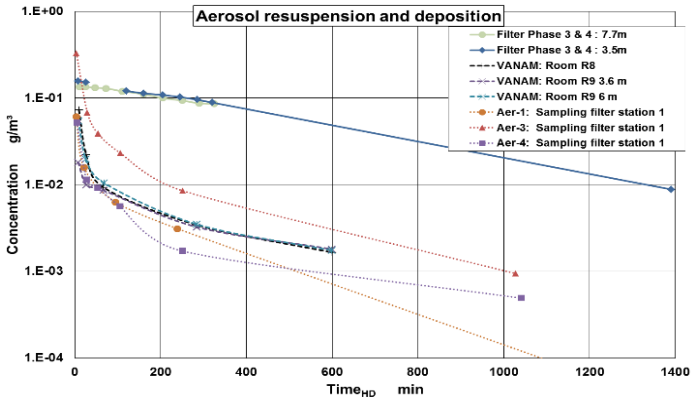

Figure 6. Test HD-46: (left) Grating surfaces, (right) Aerosol resuspension and deposition behaviour as observed in HD-46, comparison with other tests from the literature [14, 15].

One of the main differences noted in BMC M4 and THAI AER tests was that measurements show a large fraction of particles with MMD larger than 1.5 µm, probably due to the high shear stress of the considered flow mechanism for resuspension. The MMD of the resuspended particles representing the major mass fraction in test HD-46 was determined to be in the range of ~ 0.5 – 0.7 µm, hence particles are much finer and feature much slower settling velocities, approximately 0.9 m/h, compared to 2.8 m/h during the deposition phase, Figure 6 (right). The release of finer particles is likely due to relatively small shear velocities generated by the vertically upward propagated deflagration not sufficient enough to resuspend large particles primarily deposited at the vessel bottom.

The gaseous iodine release due to thermal decomposition of CsI particles was also observed in the HD-46 test. The corresponding conversion factor which quantifies the thermal decomposition of CsI by relating the released molar concentration of gaseous iodine to the initial molar concentration of CsI is about 2 %. The I_2 concentration decayed rapidly due to the physisorption of gaseous I_2 on CsI particles or the steel walls of the vessel.

4.4.2 Revolatilization of gaseous iodine from containment typical surfaces

The Iod-34 test aimed to explore the revolatilization behaviour of molecular iodine on painted surfaces and to determine the speciation of released iodine (Figure 1f). It utilized 10.65 m² of epoxy-type paint

representative of German NPP containment areas, with painted coupons inside the TTV establishing the surface area. All painted surfaces were artificially pre-aged by thermal treatment for 21.1 h at 160 °C in an air atmosphere, which follows a THAI standard procedure [16].

During the initial phase of the experiment, 1.0 g of I_2, labeled with radiotracer I-123, was introduced into the THAI vessel. Within five hours, gaseous iodine concentrations decreased significantly due to deposition onto painted and steel surfaces. Subsequent sprayings aimed to remove unfixed ("physisorbed") iodine on painted surfaces, with 70% of initially injected iodine remaining on vessel surfaces, primarily on painted surfaces.

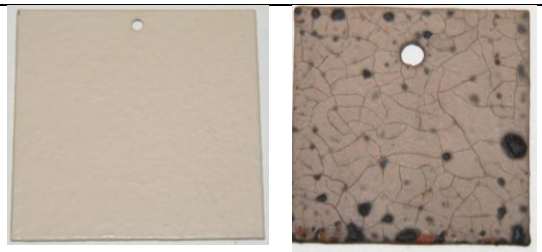

(a)Photographs of painted coupons, before deflagration (left), after deflagration (right)

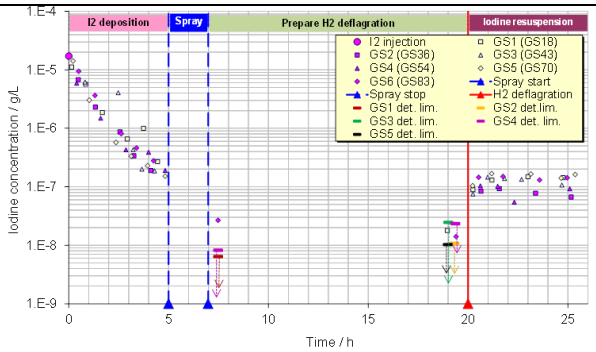

(b)Gasborne iodine concentrations from gas scrubbers

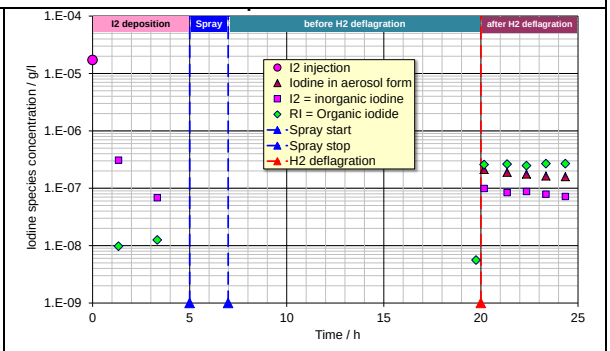

(C) ***Gasborne iodine species from Maypacks***

Figure 7. Iod-34 test results.

Before the hydrogen deflagration, gas-phase iodine concentrations were exceptionally low (measuring at 1E-8 g/l), indicating iodine fixation on painted surfaces. The deflagration resulted in peak gas temperatures of 950°C and led to significant degradation of painted surfaces, observed through flaky paint structures, blistering, and cracks. Although degradation was relatively uniform, increased damage was noted at the edges of painted coupons (Figure 7a, right).

The hydrogen deflagration resulted in the release of iodine fractions ranging from 4 to 9 % of the pre-deposited inventory, Figure 7b. Analysis revealed that half of the released iodine existed as aerosol iodine, while the other half was in gaseous organic iodide form, Figure 7c. Persistent observation of gas-borne iodine concentration allowed for interpretations regarding remaining iodine, indicating potential future experimental needs in this area.

5. APPLICATION OF PROJECT RESULTS TO MODELLING IMPROVEMENT AND REACTOR CASE

The majority of the experiments conducted in the OECD/NEA THAI-3 project have been subjected to analytical activities by the project partners. The safety analysis codes based on both LP- and CFD-modelling approaches were employed for validation and further modelling improvement based on OECD/NEA THAI-3 project results, Table V.

Table V. Summary of analytical activities based on OECD/NEA THAI-3 experiments

Subject	Organization – Code used – THAI tests
Hydrogen deflagration in a multi-compartment geometry	CNL (Canada) – GOTHIC – HD 43 - 45 RUB (Germany) – AC^2/COCOSYS – HD-44 KIT (Germany) – GASFLOW-MPI – HD-44 GRS (Germany) – AC^2/COCOSYS – HD-44 NPCIL (India) – FLUIDYN-MP – HD-44 VKI (Belgium) – OpenFOAM – HD-44 KINS (Korea) – ANSYS FLUENT – HD-44 IRSN (France) – ANSYS FLUENT & P2REMIC – HD-44 KHNP (Korea) – STAR-CCM+ – HD-44 NUBIKI (Hungary) – AC^2/COCOSYS -HD-44 UJD SR (Czech Republic) AC^2/COCOSYS – HD-44 VTT (Finland) – FLUENT – HD-44
PAR operation under counter-current flow conditions	GRS (Germany) – AC^2/COCOSYS – HR-49 GRS (Germany) – OpenFOAM – HR-43 UJV (Czech Republic) – MELCOR – HR-46 KINS (Korea) – ANSYS FLUENT – HR-49 IRSN (France) – ANSYS FLUENT – HR-49 PSI (Switzerland) – GOTHIC – HR49 AERB (India) – FLUENT – HR49
Aerosols and Iodine re-entrainment from a water pool without and with impurities	IRSN (France) – ASTEC- Iod-32 RUB (Germany) – AC^2/COCOSYS – WH-24 & WH-28 GRS (Germany) – AC^2/COCOSYS/AIM – Iod-32
Aerosols and gaseous iodine resuspension from surfaces by H_2 deflagration	Analytical activities by several partners – need for modelling improvement, particularly for iodine identified

The hydrogen deflagration test series provided an important database for model development and validation in the areas of "multi-compartment effects" and "hydrogen combustion under pre-existing convective flows". Regarding the consequence of hydrogen combustion on the source term, it was shown that elevated temperatures associated with slow deflagration might lead to the destruction of decontamination paint. In the code benchmark conducted based on the HD-44 test, during blind simulation, only a few simulations were able to predict the fast flame propagation as observed in the experiment [17]. The possible reason for that was considered to be due to uncertainty in predicting the turbulence level generated due to blower operation or flame-induced. By improving turbulence modelling during the deflagration phase and adequate modelling of thermal radiation and convection, partners showed significant improvement both in the deflagration and cool-down phases [18].

In the PAR benchmark based on the HR-49 test, the simulations addressed the internal behaviour of the PAR, recombination rates, and the influence of the PAR on counter-current atmospheric flow [19]. While simulations generally captured flow distribution and PAR behaviour reasonably well, discrepancies were noted in predicting recombination rates, particularly under different hydrogen concentration scenarios and counter-current flow conditions. Overall, the benchmark highlighted the importance of accurately modelling PAR behaviour and its interaction with containment conditions during hydrogen release accidents. The data have been extensively used for validation of CFD codes among others, e.g. [20].

For the fission product re-entrainment tests (WH-24, WH-28 and Iod-32), and fission product resuspension tests Iod-34 and HD-46, post-test calculations have been performed by the partners. The THAI re-entrainment experimental results also provided feedback in an IRSN analysis performed to study the impact of aerosol re-entrainment from pressure suppression pools on the source term of the Fukushima Daiichi accident with ASTEC. Resuspension tests have yielded crucial data regarding safety concerns associated with the formation of "fine" resuspended aerosols in the sub-micron range. These particles pose challenges for filter retention. Furthermore, the sustained iodine concentration over an extended period, as well as the

presence of a significant amount of organic iodide provides useful insights and data for assessing the performance of installed mitigation and safety measures in containment.

6. CONCLUSIONS

During a core-melt accident, apart from hydrogen radioactive gases and aerosols are released into the containment, the behaviour of which is of great importance for the radiological source term. The investigation of their behaviour is the subject of the OECD/NEA THAI-3 project.

Two code benchmarks based on hydrogen deflagration and hydrogen recombiner tests provided important insights. Data on PARs have also provided more confidence in PARs functioning under adverse conditions. In the case of hydrogen deflagration tests, the outcomes of the tests show that flame acceleration and jet-ignition-similar combustion modes were observed at relatively low H_2 concentrations, which underlines the importance of considering the geometry effect (in addition to the H_2 concentration) on the transition of combustion regimes from laminar to turbulent. The tests also provide valuable input for source-term calculations, e.g. contribution of airborne "fine" aerosol particles on volatile iodine behaviour in a containment atmosphere and suitable data to assess continuous fission products releases from water pools. Data on fission products re-entrainment from boiling pools have been used in severe accident code calculations of the Fukushima-Daiichi accident in the assessment of continued releases in the days following the accident.

In summary, the OECD/NEA THAI-3 experiments not only shed light on severe accident-related phenomena but also provide crucial data for validating predictive models, thus providing support in enhancing safety measures in nuclear power plants. Remaining open issues concerning ex-vessel phases of a severe accident with H_2/CO mixtures, and the presence of fine aerosols (iodine oxides and aerosols resulting from remobilization phenomena) are included in the work program of the ongoing OECD/NEA THEMIS project.

ACKNOWLEDGMENTS

THAI experimental research program is funded by the German Federal Ministry for the Environment, Nature Conservation, Nuclear Safety and Consumer Protection (BMUV), on the basis of a decision of the German Bundestag. The financial support by the countries that participated in the OECD/NEA THAI-3 project is greatly acknowledged.

REFERENCES

1. OECD/NEA, "Summary report of the OECD/NEA THAI Project: Hydrogen and Fission Product Issues Relevant for Containment Safety Assessment under Severe Accident Conditions", *NEA/CSNI/R(2010)3*, June 2010.
2. S. Gupta, et al., "Main Outcomes of OECD/NEA THAI-2 project and its use for code validation and containment safety assessment under accident conditions", Proceedings of 20th International Topical Meeting on Nuclear Reactor Thermal Hydraulics (NURETH-20), *doi:10.13182/NURETH20-40948*.
3. NEA, ISP-49 on Hydrogen Combustion 2012, Report, Nuclear Safety NEA/CSNI/R(2011)9, Paris.
4. NEA, Safety Research Opportunities Post-Fukushima: Initial Report of the Senior Expert Group, Nuclear Safety NEA/CSNI/R(2016)19, February 2017.
5. ENSREG, Post-Fukushima NAcP - STATUS REPORT, Report number HLG_p(2022-48)_183, European Nuclear Safety Regulators Group, 2022.
6. S. Gupta, et al., "Single- and Multi-Compartment tests on fission-product and hydrogen behaviour in the containment – THAI-V". Final Project Report 1501455-FR, Becker Technologies GmbH, Eschborn, April 2017.

7. M. Freitag, A. Kühnel, G. Langer, "Extension of the THAI Test Facility by a Second Vessel: PAD", Technical Report - Reactor Safety Research - Project No. 1501455. 1501455-FB/TR-THAIPLUS, Becker Technologies GmbH, Eschborn, 2016.
8. T. F. Kanzleiter, "Hydrogen Deflagration Experiments Performed in a Multi-compartment Containment", Transactions of the 12th International Conference on Structural Mechanics in Reactor Technology; Stuttgart (Germany); 15-20 August 1993.
9. M. Ouallal, S. Leyer, S. Gupta, "Literature survey of droplet entrainment from water pools", *Nuclear Engineering and Design*, Vol. 379, 2021, doi.org/10.1016/j.nucengdes.2021.111188.
10. D.D. Paul et al., "Radionuclide scrubbing in water pools. Volume 2: Gas-liquid hydrodynamics with full-scale downcomers and horizontal vents", *Report EPRI NP-4154-L*, Vol. 2, October 1991.
11. B. Balewski, S. Gupta, K. Fischer, G. Poss, "Experimental Investigation of air bubble flows in a water pool", In: Proceedings of 14th International Topical Meeting on Nuclear Reactor Thermal hydraulics (NURETH-14), paper 036, Toronto, Ontario, Canada, September 25-30, 2011.
12. P.C. Owczarski, and K.W. Burk: "SPARC-90: a Code for Calculating Fission Product Capture in Suppression Pools". *NUREG/CR-5765, PNL-7723*, 1991.
13. J. R. Grace, "Shapes and velocities of bubbles rising in infinite liquids", *Trans. Inst. Chem. Eng*. 51, pp. 116-120, 1973.
14. T, Kanzleiter, "Experiments on the aerosol behaviour within a multi-compartment containment ("VANAM Tests")", Final report BIeV-R67.098-01, Battelle-Institut, Frankfurt, Germany, March 1995
15. S. Gupta, G. Langer, "Experimental research on hydrogen deflagration in multi-compartment geometry and application to nuclear reactor conditions", *Nuclear Engineering and Design*, Vol. 343,2019.
16. F. Funke, S. Gupta, G. Weber, G. Langrock, G. Poss, "Interaction of gaseous I_2 with painted surfaces and aerosols in large-scale THAI tests", OECD/NEA International Iodine Workshop Full Proceedings, Nuclear Safety NEA/CSNI/R(2016)5 May 2016.
17. Freitag, M., Sonnenkalb, M., "Comparison Report for Blind and Open Simulations of HD-44. Hydrogen combustion and flame propagation in two-compartment system with initial convective flow", Report No. 1501516-CR HD44, Becker Technologies GmbH, Eschborn, Germany, September 2019.
18. F. Wang, J. Xiao, S. Gupta, M. Freitag, M. Kuznetsov, S. Rui, S. Zhou, T. Jordan, "Numerical and experimental investigations of hydrogen-air-steam deflagration in two connected compartments with initial turbulent flow", *Process Safety and Environmental Protection*, Vol 184, 2024, Pages 248-259.
19. Freitag, M., Sonnekalb, M., "Comparison Report for Blind and Open Simulations of HR-49. Passive autocatalytic recombiner operation under counter-current flow conditions". Report No. 1501516-CR-HR49, Becker Technologies GmbH, Eschborn, Germany, April 2018.
20. Y. Halouane, A. Dehbi, "CFD prediction of hydrogen passive autocatalytic recombiner performance under counter-current flow conditions", *International Journal of Hydrogen Energy*, Volume 45, Issue 16, 2020, Pages 10247-10256, https://doi.org/10.1016/j.ijhydene.2020.01.189.

11th Conference on Severe Accidents Research
May 13-16, 2024, Stockholm, Sweden (ERMSAR-2024)

PROGRESS IN UNDERSTANDING FISSION PRODUCT REMOBILIZATION AND HYDROGEN RISK IN WATER-COOLED REACTORS: OECD/NEA THAI-3 PROJECT

S. Gupta, M. Freitag, E. Schmidt, M. Colombet, B. von Laufenberg
Becker Technologies GmbH, Germany

G. Langrock, F. Funke
Framatome GmbH, Germany

Outline

- ❑ Background & Introduction
- ❑ Experimental facility
- ❑ Main experimental outcomes
- ❑ Data application for code validation & reactor application
- ❑ Main highlights

Introduction

Objectives

✓ to address open questions concerning the **behaviour of hydrogen, iodine and aerosols under severe accident typical conditions** in the containment of water-cooled reactors.

✓ to contribute to the **validation and further development of advanced Lumped Parameter (LP) and Computational Fluid Dynamics (CFD) codes** used for reactor applications

Project partners

- 16 countries, > 22 organizations
- Host country: Germany
- Operating agent: Becker Technologies GmbH

Project period

- February 2016 – July 2019
  (Non-disclosure period ended in June 2023)

Signatories	Country
The Bel V	Belgium
The Canadian Nuclear Laboratory (CNL)	Canada
The State Nuclear Power Software Development Center (SNPSDC),	China
The ÚJV Řež, a. s. Czech Republic	Czech Republic
The Teknologian tutkimuskeskus VTT Oy	Finland
The Institut de Radioprotection et de Sûreté Nucléaire (IRSN) jointly with Electricité de France (EDF)	France
Gesellschaft für Anlagen- und Reaktorsicherheit (GRS) gGmbH Becker Technologies GmbH	Germany
The Nuclear Safety Research Institute (NUBIKI), jointly with the MVM Paks Nuclear Power Plant Ltd.	Hungary
The Atomic Energy Regulatory Board (AERB) jointly with the Bhabha Atomic Research Centre (BARC), and the Nuclear Power Corporation of India Ltd. (NPCIL)	India
Nuclear Regulation Authority (NRA)	Japan
The Korea Atomic Energy Research Institute (KAERI) jointly with Korea Hydro and Nuclear Power Co., Ltd (KHNP) and Korea Institute of Nuclear Safety (KINS)	Korea
Ministère de l'Enseignement Supérieur et de la Recherche (MESR)	Luxembourg
Nuclear Regulatory Authority of the Slovak Republic (ÚJD SR)	Slovak Republic
The Strålsäkerhetmyndigheten (SSM)	Sweden
Paul Scherrer Institut (PSI)	Switzerland
Office for Nuclear Regulation (ONR)	United Kingdom

Introduction

LWR safety research and related issues: “Containment[1]“ and “Source Term[2]“

Fukushima accident related projects, e.g.
- ✓ OECD/NEA BASAF project
- ✓ EC/PASSAM

Specialist workshops
- ✓ **Iodine workshop(2015)** *NEA/CSNI/R(2016)5*
- ✓ **Source Term workshop (2019)** *NEA/CSNI/R(2020)4*

Status reports, e.g
- ✓ Hydrogen Management and related computer codes

NEA/CSNI/R(2014)8

Source Term
- ✓ Delayed releases: remobilization of fission products (Aerosols, gaseous iodine)
  - Re-entrainment from water pools
  - Resuspension from surfaces, e.g. due to energetic events such as Hydrogen deflagration

Safety and Mitigation systems (H_2 risk and Source term)
- ✓ Performance of safety/mitigations systems under accident conditions, e.g. Hydrogen Recombiners (PARs), Spray, FCVS

Extrapolation to reactor scale

Representative boundary conditions (e.g. P/T, impurities effect)

Experimental work programme

Combustible gas risk and mitigation (recombination)

Topic 1: **Hydrogen Deflagration** tests in two-vessel geometry (HD 40-45)

Topic 2: Hydrogen **Passive Autocatalytic Recombiner tests** (HR 46-50)

Fission product release from water pools

Topic 3: **Release of gaseous iodine from a sub-cooled and boiling pool** (Iod-32)

Topic 4: **Release of CsI aerosol from a sub-cooled and boiling pool** (WH-24 & WH-28) – ***impurities effect***

Fission product remobilization from surfaces

Topic 5: **Resuspension of pre-deposited molecular iodine from decontamination paint** by hydrogen deflagration (Iod-34),

Topic 6: **Resuspension of aerosol deposits from containment surfaces** by hydrogen deflagration (HD-46)

Additional data from THAI National project on Hydrogen deflagration (HD-36 & HD-38) and Recombiner tests (HR-43) offered to THAI-3 partners (*"Reference tests"*)

Overall project scope

Experimental work programme

Analytical Working Group (AWG)

- Code benchmarks
- Extrapolation of results to reactor scale (reactor analysis)

→ ***Final project seminar took place in 2021***

Young Scientists/Experts

- **Korea Atomic Energy Research Institute (KAERI):** Support in design of technical scale test facilities, instrumentation/measuring systems
- **Atomic Energy Research Board (AERB), India:** Validation of CFD tools for hydrogen mitigation strategy in Indian PHWRs
- **China Institute of Atomic Energy (CIAE):** Uncertainty calibration of aerosol measurement system

Education & Training

- Partners involved several PhDs (Hydrogen combustion (**VKI/BeI-V, Belgium**), Hydrogen mitigation by PARs (**AERB, India**), Fission product re-entrainment (**RUB, Bochum**), Hydrogen combustion (**RUB Bochum**), Aerosols re-entrainment (**University Luxembourg**), etc.

THAI+ – multi-compartment test facility

THAI+: Thermal-hydraulics, Hydrogen, Aerosols, Iodine, + Multi-compartment

	THAI	PAD
Height	9.2 m	9.8 m
Diameter	3.2 m	1.6 m
Volume	60 m^3	18 m^3
Upper and lower connecting pipes: DN 500		

- Configurable sub-compartments
- Large top openings to install test components
- Pressure resistant for (slow) H_2-deflagrations
- Licensed for use of radiotracer I^{123}

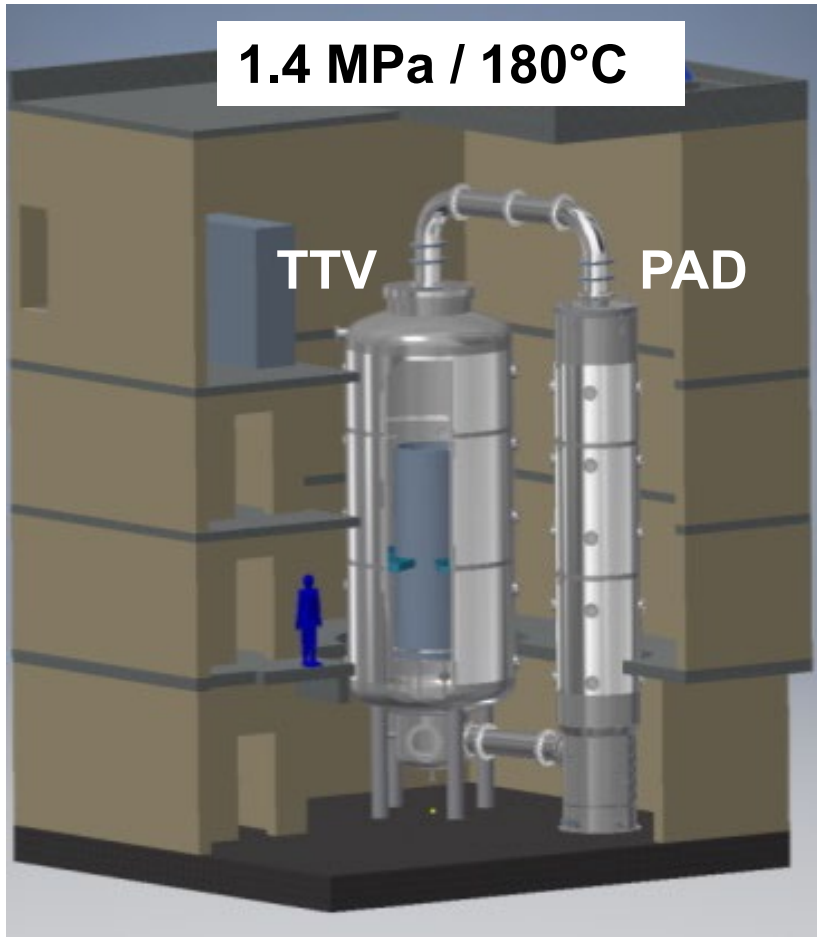

TTV: THAI Test Vessel
PAD: Parallel Attachable Drum



Recent upgrades:

- Extension to two-vessel system (+PAD) (2015)
- Licensed to perform tests with Carbon Monoxide (2019)
- Provisional arrangements to perform first LW-SMR tests (2021)

Supporting test facilities

- **Test loop***
  - Designed for FCVS operation conditions
    → 10 bar, 200 °C, 2 kg/s steam
  - Moderate and high Reynold number flows
  - Development and qualification of measurement techniques



- **TRIPAC** (**T**est **R**ig for **I**nstrument and **P**roduct performance testing under **A**ccident **C**onditions)
  - Designed for H_2 – safety investigations
  - Application H_2 and aerosol generation qualification



* Acknowledgement: The Test Loop has been constructed in the framework of a project funded by Framatome GmbH

Main results

Hydrogen deflagration tests

- Previous THAI experimental database on hydrogen deflagration considers initial “quiescent” atmosphere

- Hydrogen deflagration research at THAI facility consists of
  - Peak pressure and temperature response measurements
  - Effect of spray on combustion
  - Effect of hydrogen and steam concentration
  - Effect of uniformly mixed/stratified gas atmosphere

→ **Database for validation of combustion models under a broad range of conditions**

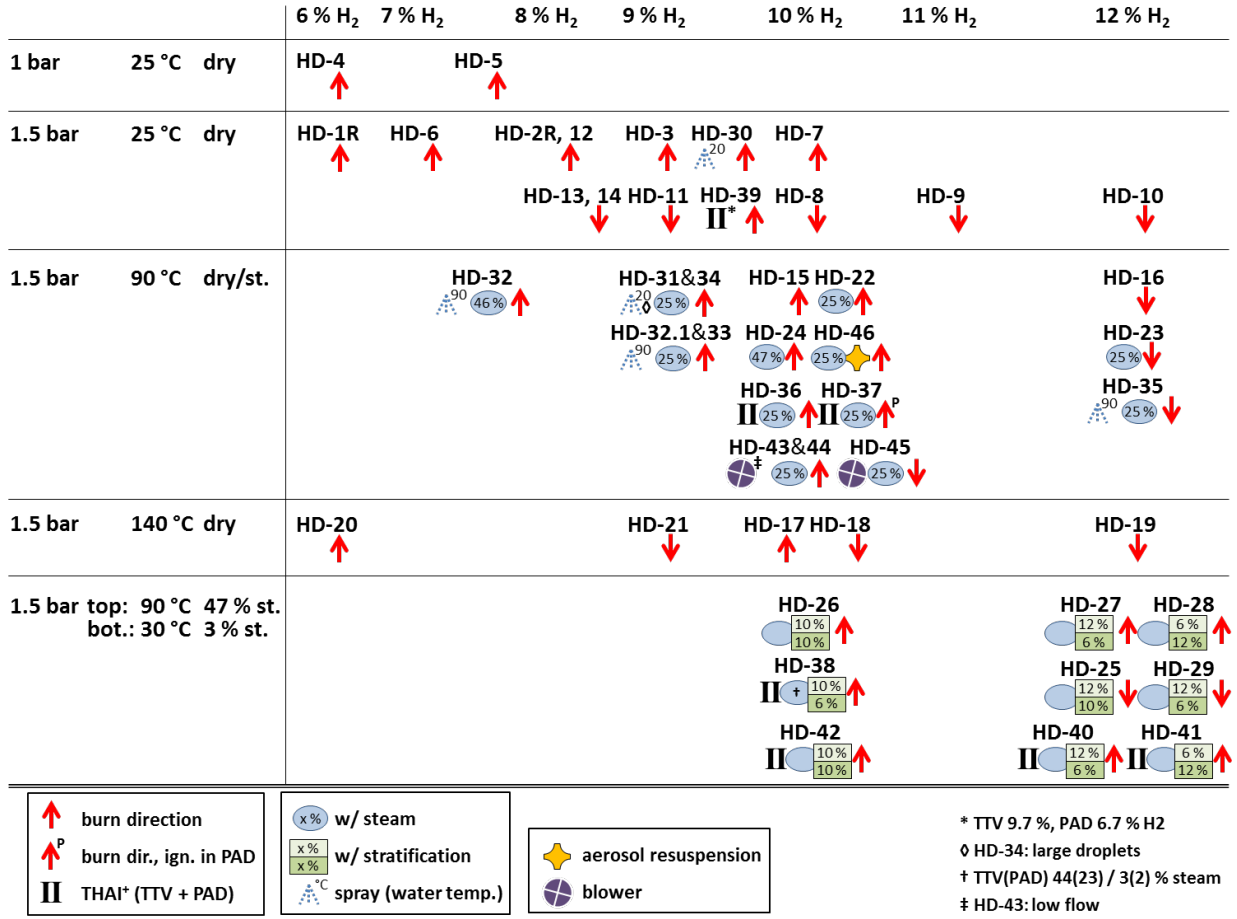

Hydrogen deflagration tests – Main results

Objective

- Effect of initial turbulence (superimposed flow) on flame propagation behaviour
- Flame propagation in pre-mixed/stratified gas atmosphere
- Multi-compartment geometry effect

Test details

- Gas composition: H_2-steam-air
- H_2 concentration: 10 vol. % (premixed), upto12 vol. % (stratified)
- Positive or negative H_2 gradient
- Initial flow variation (blower installed)
- Burn direction: upward and downward

Main outcomes

- ✓ ***New insights and data for code validation/further development purpose*** - particularly on “initial turbulence” and “multi-compartment” effects on H_2 deflagration behaviour
- ✓ ***Safety relevance*** - flame acceleration and jet-ignition-similar combustion modes at relatively low H_2 conc. (Geometry effect)

Example: HD 39 (H_2-gradient vessel-to-vessel)

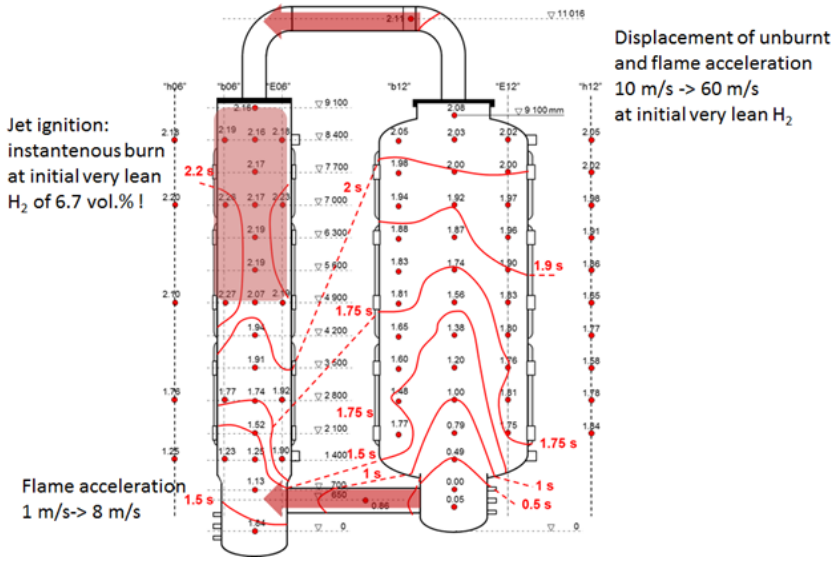

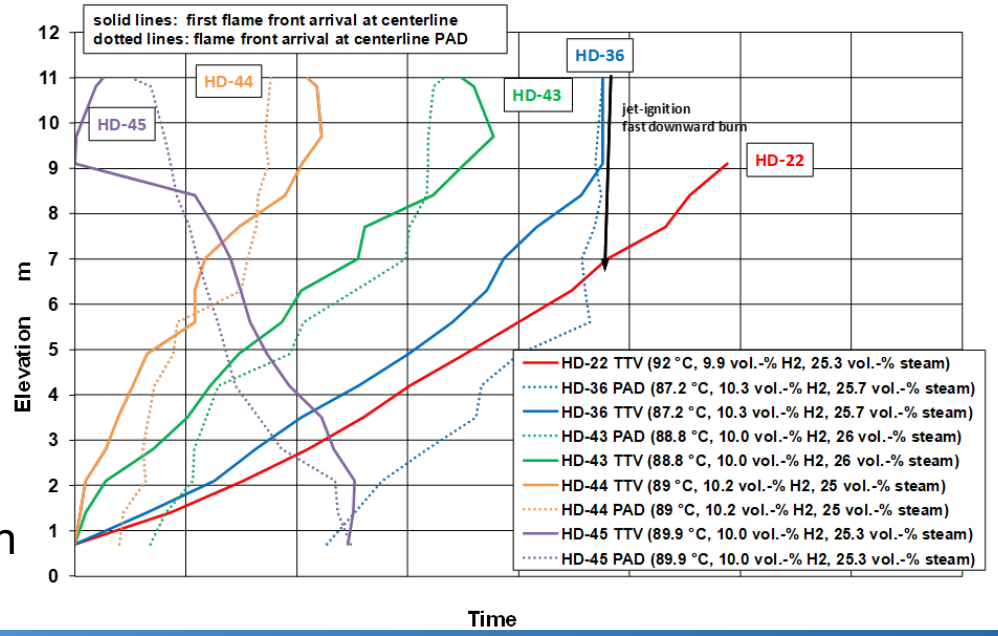

Previous THAI PAR database

Start phase

Accident progression

Sufficient O_2 surplus (air-filled), H_2 release starts

- varying thermal-hydraulics, gas composition

Elevated H_2 concentration?

- risk of combustion?

Fission product interaction

- PAR poisoning ? (“cold catalyst”)
- additional I_2 source term (“hot catalyst”)

Late phase

O_2 lean atmosphere, presence of CO

- Performance degradation

Framatome
FR-150 (full scale)
1/2 FR-380



AECL
(1/2 scale)

Plate type PARs

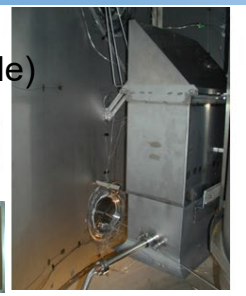

NIS
Full scale

Pellet type PARs



			Areva 0.5 × FR-380	NIS 1/8 module	0.52 × AECL
1 bar	25 °C	dry	HR-1 HR-2		HR-23
	86 °C	60 % st.	HR-13		
1.5 bar	25 °C	dry	HR-3 HR-28 HR-27† HR-51		HR-17 HR-18
	70 °C	N_2/20 % st.	HR-36		
	74 °C	25 % st.	HR-6 HR-7 HR-8	HR-14 HR-15* HR-16*	HR-19
	75 °C	25 % st.	HR-43 HR-44 HR-45 HR-48 HR-50	HR-46 HR-47‡	
	90 °C	47 % st.	HR-9 HR-10		HR-20
	91 °C	N_2/30 % st.	HR-37*		
	97 °C	60 % st.	HR-11 HR-29**		HR-22
	105 °C	N_2 dry	HR-33		
	117 °C	dry		HR-40*	
2 bar	105 °C	N_2/40 % st.	HR-34	HR-38 HR-41*	
2.2 bar	25 °C	dry	HR-4		HR-24 HR-25 HR-26†
	95 °C	40 % st.	HR-32#		
	108 °C	N_2◊/34 % st.			HR-21
	140 °C	60 % st.	HR-31~		
3 bar	25 °C	dry	HR-5		
	117 °C	60 % st.	HR-12 HR-30** HR-49 HR-52 HR-53		
	117 °C	N_2/60 % st.	HR-35	HR-39 HR-42*	

Test objectives
- onset of recombination
- recombination rate
- oxygen starvation
- steam influence
- ignition potential
- influence of aerosol
- co-current w/ blower
- counter-cur. w/ blower
- counter-cur. nat. conv.
- 2× 2 PAR behavior
- influence of CO

* no or only minor ignition effect observed
** steam cont. decr. (by cond.) for ignition
† w/o bellmouth
‡ short chimney
◊ 2 % O_2 initially in test HR-21
high CsI & SnO_2 load on PAR
~ CsI decomposition

Recent tests (THEMIS) at 4.5 bar, 136 °C, 70 vol.% steam

THAI-3 PAR tests

- ❑ Extensive experimental database on PAR performance considering **"quiescent atmosphere"** exists
- ❑ THAI-3 test: PAR performance under counter-current flow conditions in containment
  → *E.g. counter-current flow due to condensation induced flow, air coolers, sprays*

- ➢ Tests with PAR units provided by PAR vendors Framatome & NIS
- ➢ Counter-current flow generated by a blower installed in TTV, flow velocity up to 1 m/s in the PAR outlet vicinity
- ➢ **Reference tests** HR-6/HR-7/HR-8 (AREVA/Framatome), HR-14/HR-15/HR-16 (NIS)

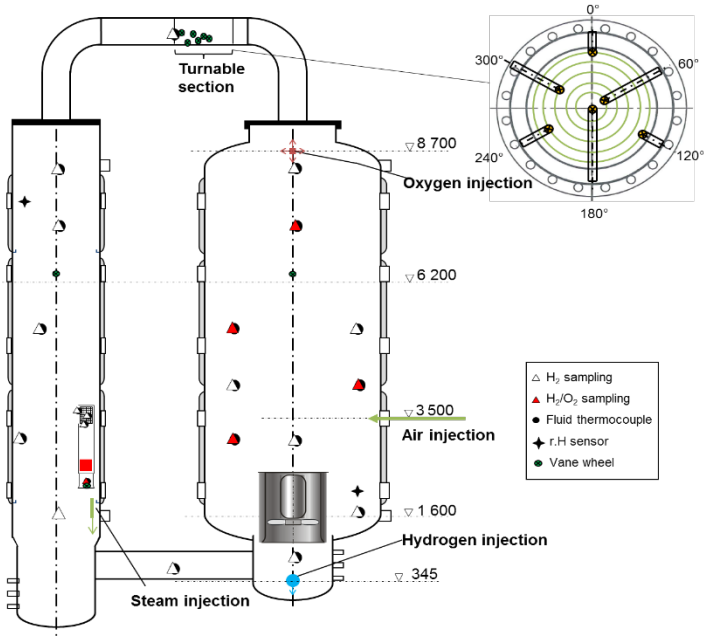

Test	P_0 [bar]	T_0 [°C]	C_{steam} [vol.-%]	PAR unit	Blower Setting	Effect obtained by test
HR-46	1.50	77.2	27.2	NIS	Low	Counter-current flow
HR-47	1.50	77.8	27.8	NIS	Low	Chimney effect in counter-current flow
HR-43**	1.5	77	27	AREVA**	Low	Counter-current flow
HR-48	1.50	77.6	26.9	AREVA**	High	Strength of counter current flow
HR-49	3.00	119.0	61.6	AREVA**	High	Pressure and temperature
HR-50	1.51	100.8	17.1	AREVA**	No blower	PAR exposed to natural convection

*** national THAI project** **** Framatome**

Main results – H_2 recombiner (PAR) tests

Main outcomes

- ✓ ***New data for code validation/further development purpose*** - particularly on PAR performance under counter-current flow at elevated pressure/temperature conditions & data on PAR/containment atmosphere interaction
  - (Counter-current effect): PAR recombination rate at similar level as reference Tests HR-14/HR-15. Flow oscillations observed at low H2 concentrations (< 2 vol. %)
  - (Chimney effect) shortened chimney reduces recombination rate by about 10-15 %

- ✓ ***Safety relevance –*** feedback for the PAR installation methodology assessment (e.g. numbers, location inside a containment building)

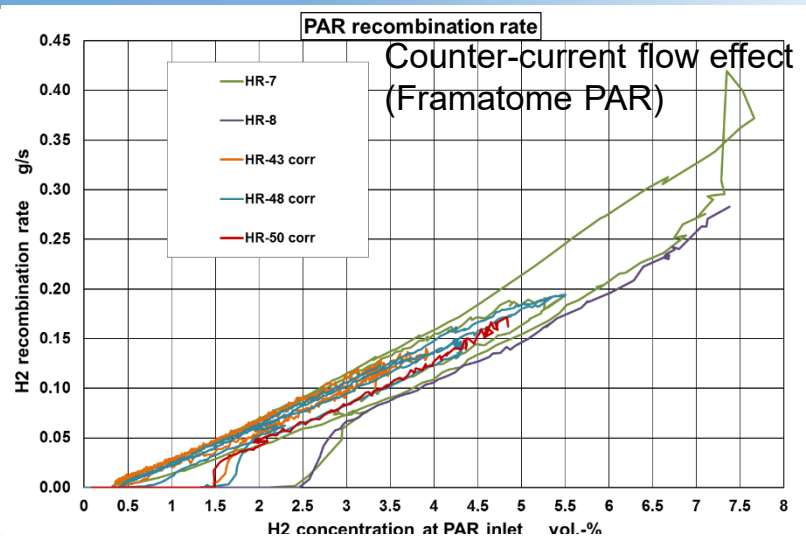

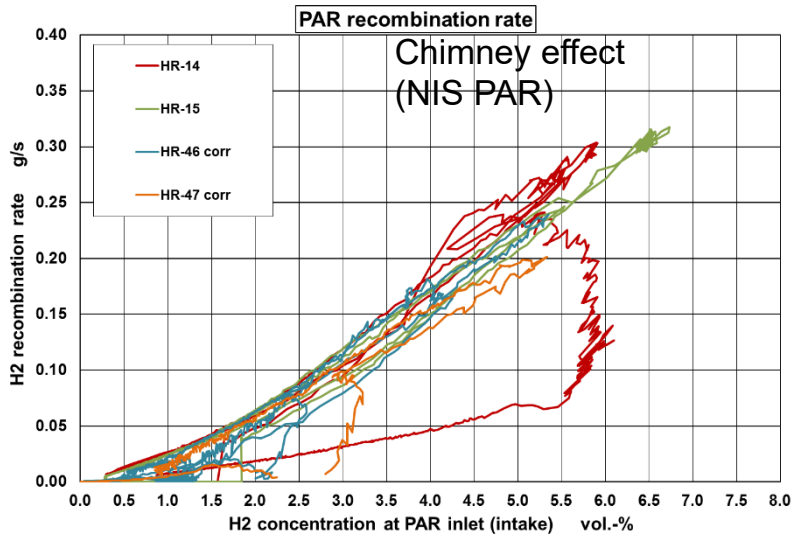

Fission product re-entrainment

Objective

- To investigate **aerosol/iodine re-entrainment from water pool** due to:
  - continuous heat-up of the pool,
  - due to depressurization (venting) induced boiling → ***FCVS operation***
- **Impact of impurities** (reduced surface tension of water) on aerosol re-entrainment behaviour

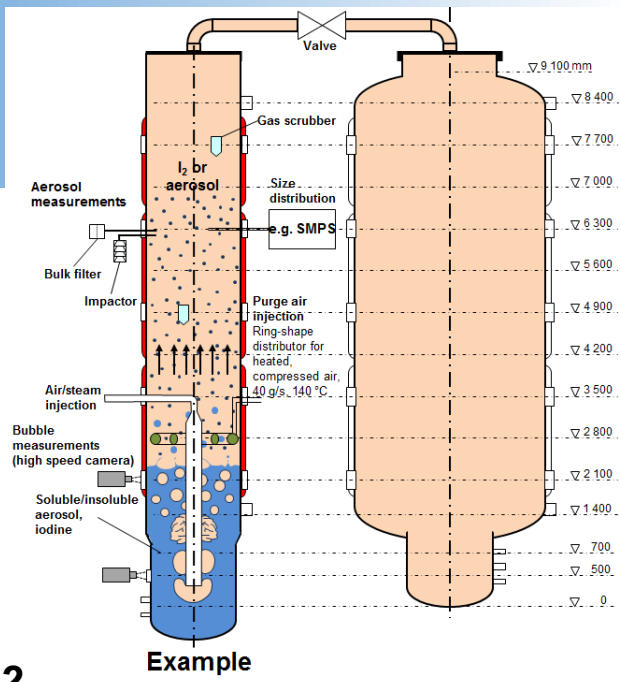

Example

CsI aerosols: WH-24 (decalcified water) & WH-28 (reduced surface tension

Test phase	Air injection flow rate (kg/h)	Steam injection flow rate (kg/h)	Water temperature (°C)	Purge air flow rate (kg/h)	Depressuriza-tion rate
a1)	80	-	46	0	
a2)	80	-	60	0	
a3)	19	70	60	145	
a4)	19	70	90	145	
a5)	19	70	120	145	
b1)		70	boiling	145	
b2)		210	boiling	145	
b3)		350	boiling	145	
b4)	19	210	boiling	145	
c1)	-	-		-	BWR type 1 bar/5 min
c2)	-	-		-	BWR type 1 bar/ 15 min
c3)	-	-		-	PWR type 0.1 bar/30 min

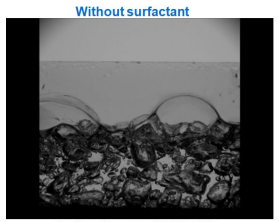

Surface tension: 25-30 mN/m

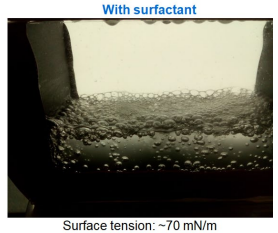

Surface tension: ~70 mN/m

Molecular I_2: Iod-32

Test phase	P (bar)	T (°C)	Steam conc.(vol%)	PAD-sump
Pre.	2.5	117 (gas) 110 (water)	72 (satur.)	Initial filling deionized water 1028 L, H= 0.25 m inside PAD Conditioning to pH= 3
1	2.5 (reference phase)		up to 90	Injection of ~1 g radio-labelled I_2 Activity ~0.5 GBq
2	1.3 bar after depressurization		up to 90	Injection of ~1 g radio-labelled I_2 Activity ~ 0.5 GBq Steam injection mass flow rate 5 g/s, injection duration 10 min
3	1.3 bar after depressurization		up to 90	NaOH injection to reach pH = 8, Steam injection mass flow rate 20 g/s, injection duration 10 min

Results example: Fission product re-entrainment

Main outcomes

- ✓ ***New insights/data for code validation/development:***
  - ***(WH-24 and WH-28, CsI aerosols)*** increased aerosol re-entrainment in case of reduced surface tension of the water pool;
    - no cascade reduction as assumed in pool scrubbing codes like SPARC-90 (complete breakup of primary bubbles within 3–4 times their diameter)
    - bubble size near water surface 1.5 – 3 mm
  - **(Iod-32):** compared to non-boiling pool, boiling increase gasborne I_2 concentration significantly (10 times higher!).

- ✓ ***Safety relevance:*** input for source-term calculations, e.g. contribution of airborne "fine" aerosols on volatile iodine concentration, suitable data to assess continuous FPs releases from water pools as observed in Fukushima accident analyses.

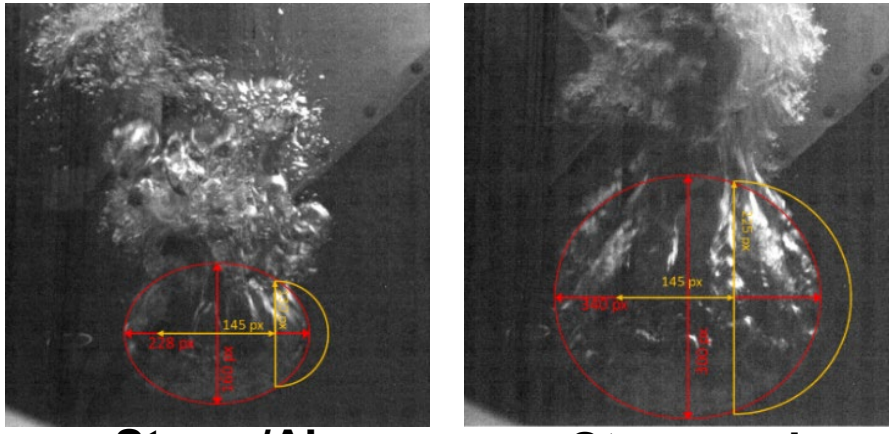

Steam/Air **Steam-only**

Measurement of bubble dynamics in tests

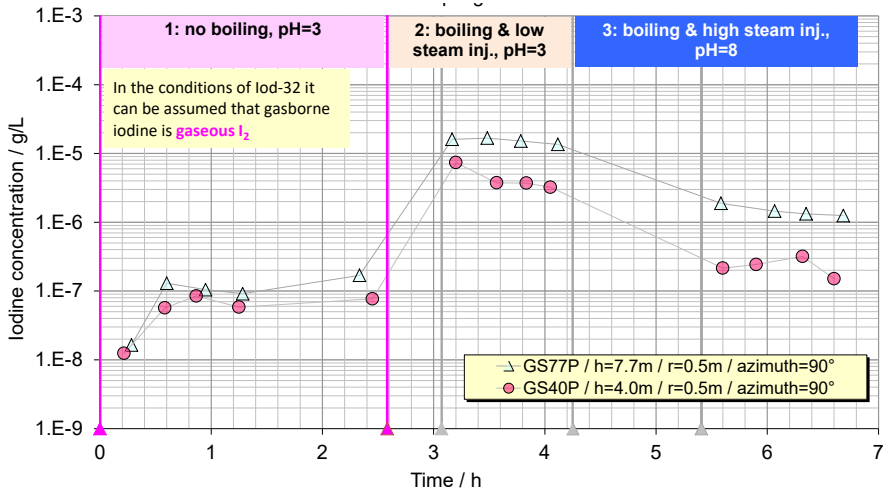

Fission product resuspension from surfaces

Objective

Aerosol and iodine re-suspension from deposits by hydrogen deflagration

Additional I_2 source term due to thermal oxidation of metal-iodide aerosols, degradation of painted surfaces by combustion

Test details

Two tests conducted,

- Iod-34: pre-deposited iodine on painted surfaces
- HD-46: pre-deposited aerosols (CsI) on test-vessel surfaces and containment typical step gratings (installed for this experiment)

→H_2 deflagration: reference THAI test without I_2/aerosols (10 vol. % H_2 in air-steam mixture) → 1000 °C

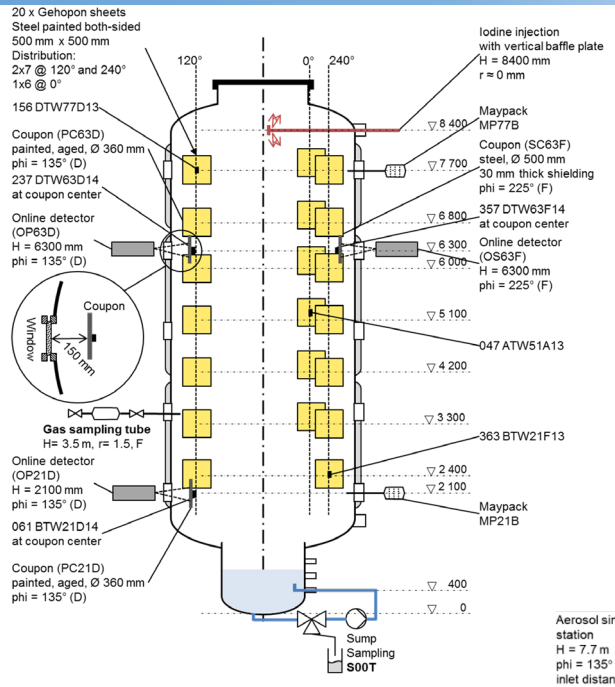

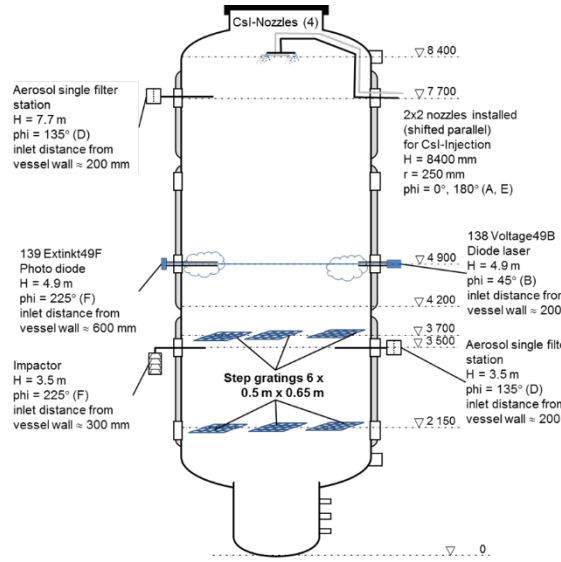

Test Iod-34

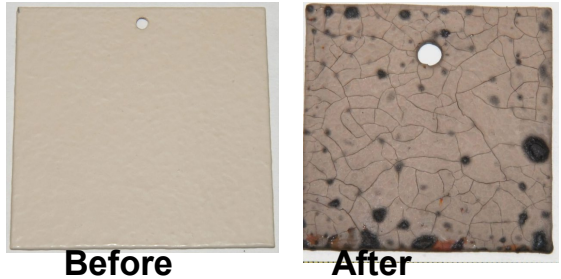

Before deflagration **After deflagration**

Test HD-46

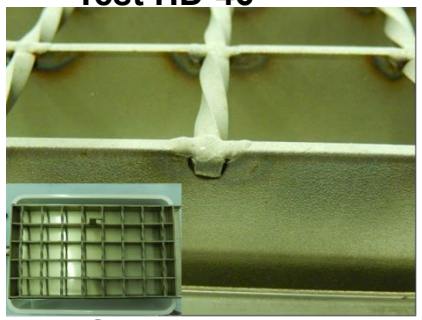

Step gratings

Main results – Fission product resuspension

Main outcomes

- ✓ ***New insights/data for code validation/development:***
  - → Persistence concentration over long time of fine particles both in aerosol and iodine tests
  - → Significant release of Org-I in containment atmosphere
  - → Destruction (pyrolysis) of painted surfaces observed

- ✓ ***Safety relevance:*** resuspended aerosols consist of fine particles (challenge for filter-retention), constant iodine concentration over long time period (Org-I, ultra fine particles)

HD-46 (CsI)

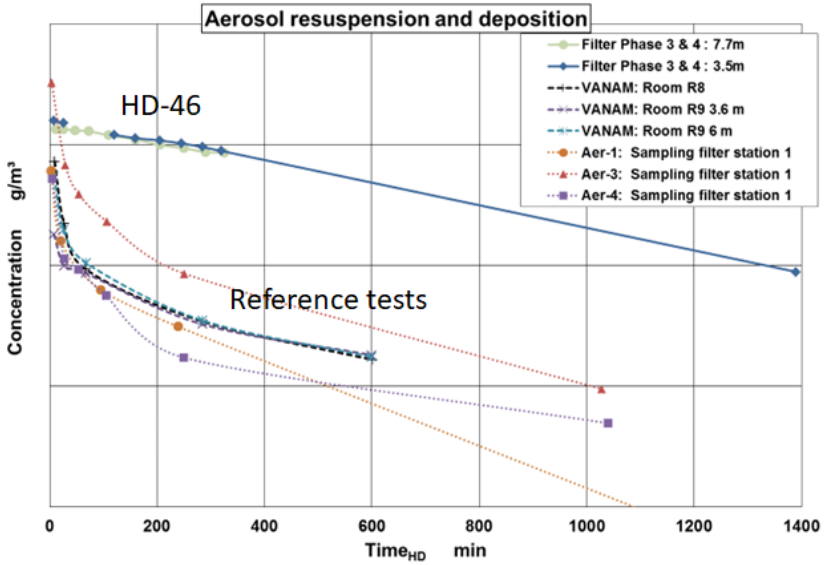

Iod-32 (I_2)

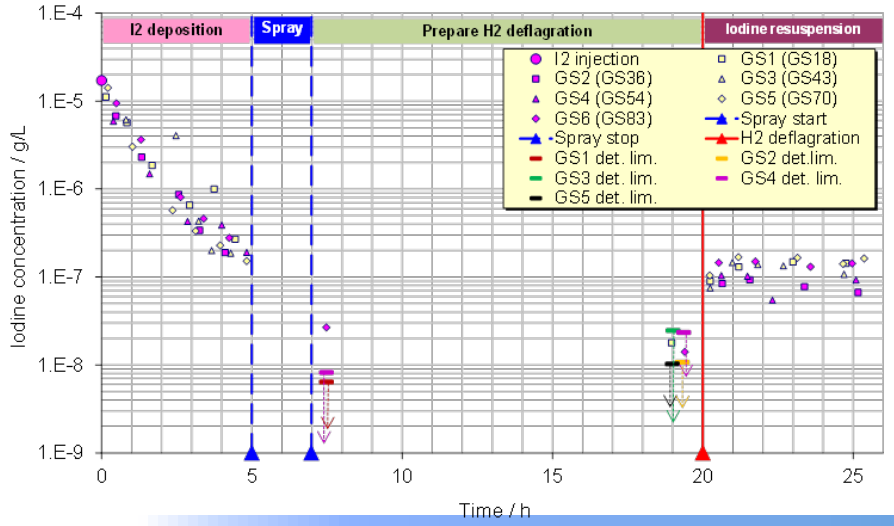

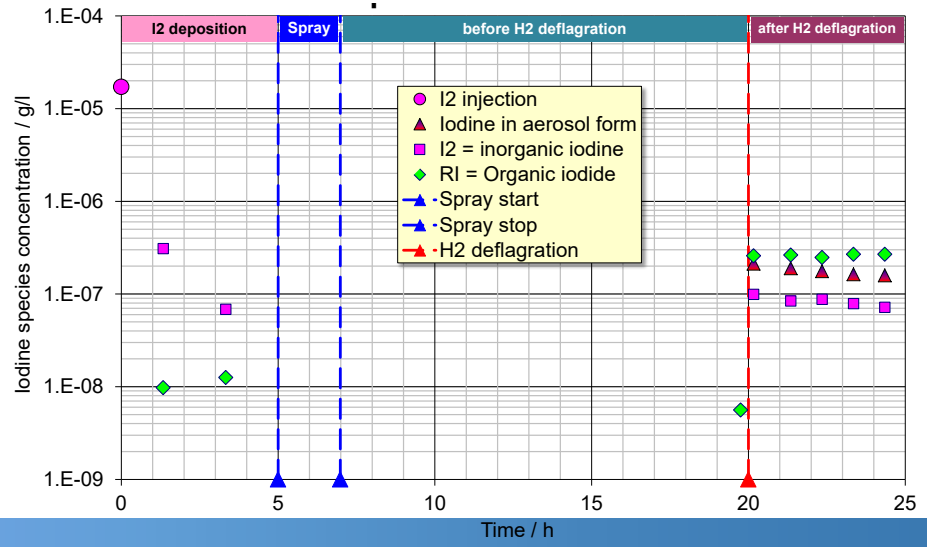

Analytical activities

Analytical activities

- **Code calculations for pre-test assessments, result evaluations, benchmarking of codes and extrapolation of results to reactor conditions:**
  - ✓ Lumped parameter and CFD codes
  - ✓ "Blind" and "open" **code benchmark** exercises based on H_2 recombiner (HR-49), and H_2 deflagration (HD-44) tests (see figures)
  - ✓ Fission product re-entrainment tests results used in assessment of continued releases observed in the days following the **Fukushima Daiichi accident**

Subject	Organization – Code used – THAI tests
Hydrogen deflagration in a multi-compartment geometry	CNL (Canada) – GOTHIC – HD 43 - 45 RUB (Germany) – AC²/COCOSYS – HD-44 KIT (Germany) – GASFLOW-MPI – HD-44 GRS (Germany) – AC²/COCOSYS – HD-44 NPCIL (India) – FLUIDYN-MP – HD-44 VKI (Belgium) – OpenFOAM – HD-44 KINS (Korea) – ANSYS FLUENT – HD-44 IRSN (France) – ANSYS FLUENT & P2REMIC – HD-44 KHNP (Korea) – STAR-CCM+ – HD-44 NUBIKI (Hungary) – AC²/COCOSYS -HD-44 UJD SR (Czech Republic) AC²/COCOSYS – HD-44 VTT (Finland) – FLUENT – HD-44
PAR operation under counter-current flow conditions	GRS (Germany) – AC²/COCOSYS – HR-49 GRS (Germany) – OpenFOAM – HR-43 UJV (Czech Republic) – MELCOR – HR-46 KINS (Korea) – ANSYS FLUENT – HR-49 IRSN (France) – ANSYS FLUENT – HR-49 PSI (Switzerland) – GOTHIC – HR49 AERB (India) – FLUENT – HR49
Aerosols and Iodine re-entrainment from a water pool without and with impurities	IRSN (France) – ASTEC- Iod-32 RUB (Germany) – AC²/COCOSYS – WH-24 & WH-28 GRS (Germany) – AC²/COCOSYS/AIM – Iod-32
Aerosols and gaseous iodine resuspension from surfaces by H_2 deflagration	Analytical activities by several partners – need for modelling improvement, particularly for iodine identified

Analytical activities (Example)

HD-44: H_2 deflagration with initial convection

- Multicompartment geometry
- Relevance of scale for flame acceleration effects
- Test indicate strong increase of flame propagation speed
  - Fast flame propagation challenges containment integrity
  - Faster combustion increases thermal load for passive safety systems

Benchmark summary

- 15 participants with 9 codes (CFD and LP)
- Uncertainty in predicting the turbulence level generated by blower/flame
- Lack of chemistry-turbulence interaction in the models
- Improvements: turbulence modelling during the deflagration phase and adequate modelling of thermal radiation and convection.

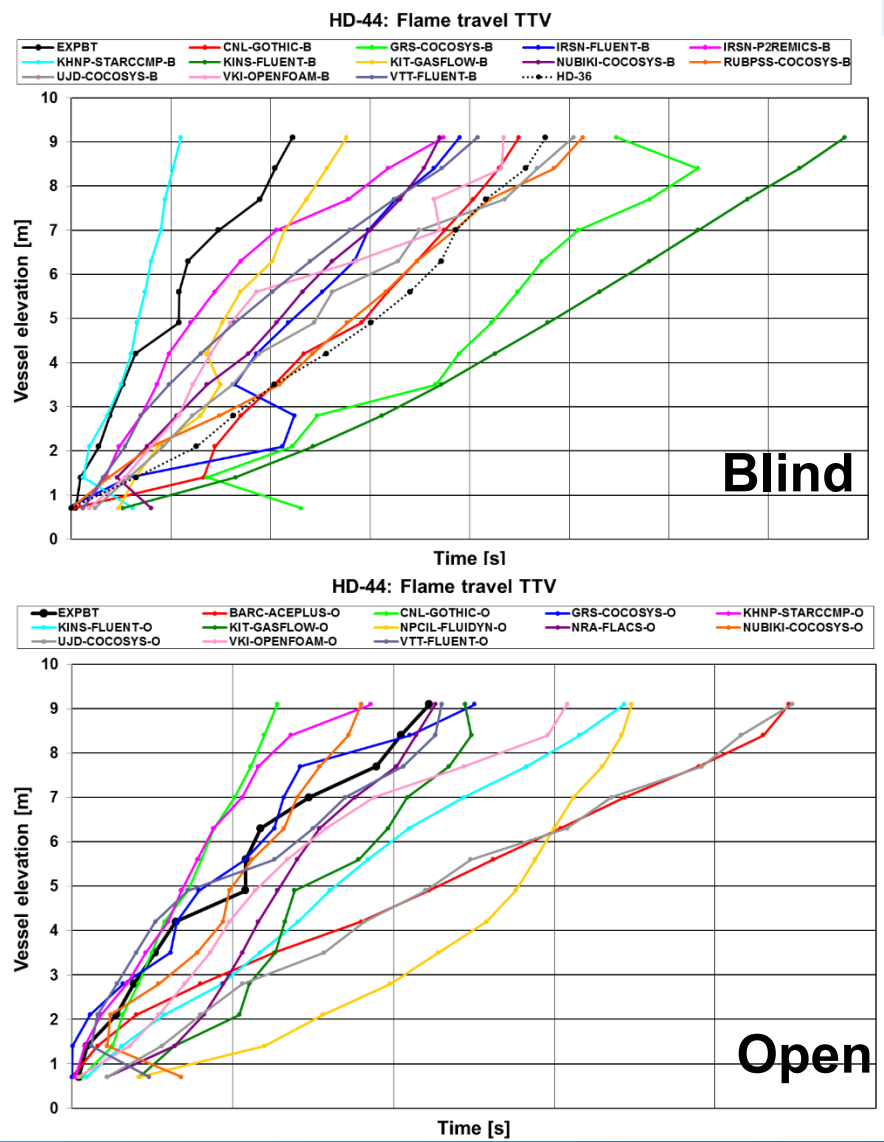

Main highlights

- THAI-3 project aimed to investigate open questions concerning **hydrogen risk and source term in containments of LWRs: C**ombustion, PARs, FPS remobilization from water pools and surfaces

- The experimental work scope included **investigations on safety and mitigation systems, namely, Spray and PARs** under typical accident conditions

- In addition to phenomenological understanding, experiments provided suitable database for **validation and application of LP- and CFD-codes** towards containment safety analyses. Two code benchmarks were organized: Combustion, PAR

- Significant use of experimental database for **Education & Training purposes**, e.g. in PhD framework

- **Project final seminar** organized in 2021 allowed to further discuss the use of **THAI-3 project data for modelling and reactor application** by the project partners

- The currently ongoing **OECD/NEA THEMIS** project focuses on **hydrogen risk and source term related issues for ex-vessel phase of a severe accident with H_2/CO mixtures**.

OECD/NEA THEMIS follow-up project – in preparation

Feedback received on the proposed list of topics

Country	Organisation
Sweden	Swedish Radiation Safety Authority
Canada	CNL
China	CNPRI, CIAE
Spain	CSN, CIEMAT, UPM
France	IRSN
Finland	VTT
Germany	FZJ, GRS, Framatome, BT
Korea	KAERI
Czech Republic	UJV
Slovak Republic	UJD SR (Nuclear Regulatory Authority of the Slovak Republic)
Switzerland	PSI

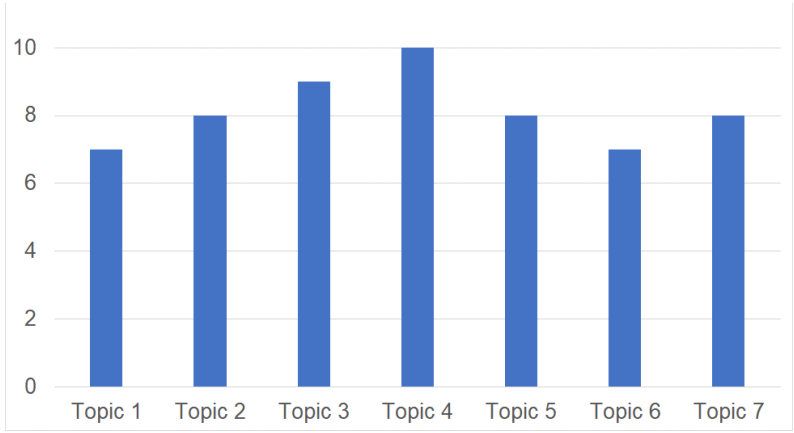

"THEMIS follow-up: *Consider topics for both current fleet of LWRs and SMRs*"

Topic 1: Heat removal in large water bodies

Topic 2: Passive Safety systems performance

Topic 3: Effect of (strong) wall cooling in water submerged SMR containments, gas release scenarios

Topic 4: FPs remobilization behavior from water pools and containment surfaces

Topic 5: Containment atmosphere (Aerosol washodown-SMR)

Topic 6: Combustion (compact geometries - LW-SMRs)

Topic 7: Mitigation by PARs

→Next meeting foreseen in September 2024

Experimental infrastructure for future tests

- **Relocation of existing experimental infrastructure to a new site**
- **Extension of experimental infrastructure towards Passive systems/SMR related investigations**
- **Dimensions of the proposed SMR facility:**

  - ✓ **Pool with concrete casting : D= 7 m, H= 14 m**
  - ✓ **Pressure-resistant or vacuum-maintaining containment vessel**
  - ✓ **P= -1.0 / +64.0 bar, 250 °C (D= 2.3 m, H= 12 m)**
  - ✓ Reference THAI: 14 bar/180 °C or 10 bar/250 °C

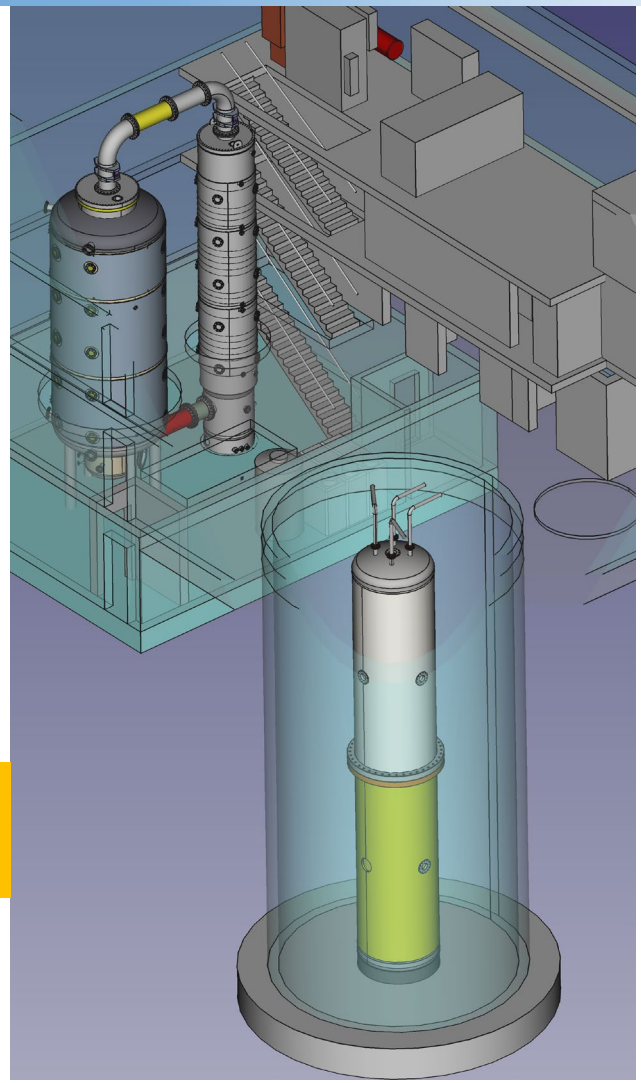

- ***Construction and qualification planned in a THAI national project***
- ***Available for THEMIS-follow up project - 2026/2027***

ACKNOWLEDGMENT

- The financial support by the countries participating in the OECD/NEA THAI-3 project
- The financial support by the German Federal Ministry for the Environment, Nature Conservation, Nuclear Safety and Consumer Protection (BMUV) to the THAI programme



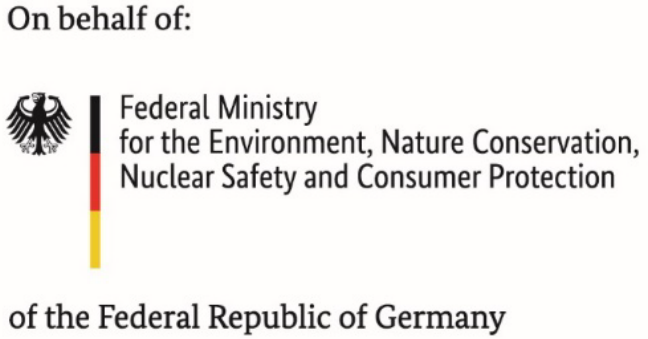

SOURCE TERM ASSESSMENT FOR A VVER-1000/V320 REACTOR EQUIPPED WITH FILTERED VENTING: SENSITIVITY STUDY OF THE IMPACT OF DIFFERENT FORMS OF IODINE IN THE CONTAINMENT

Miroslav Kotouč, Adam Kecek
ÚJV Řež
Hlavní 130, Husinec-Řež, 250 68
miroslav.kotouc@ujv.cz; adam.kecek@ujv.cz

ABSTRACT

After the Fukushima accident, both Czech NPPs Dukovany and Temelin have been enhancing their safety with regard to severe accidents (SA). As a measure of preventing containment (CTMT) over-pressurization, filtered containment venting system (FCVS) is to be implemented at the Temelin NPP (equipped with 2 VVER-1000/V320 reactors). In order to specify its design requirements, SA analyses were conducted to assess the amount of fission products (FP) to be drawn onto the FCVS filters while in operation. Results of such analyses are extremely sensitive to the radionuclides' (RN) speciation within the CTMT, especially iodine. The integral code MELCOR considers iodine in the form of CsI by default. However, certain fraction of iodine remains in the molecular (and thus gaseous) form (I_2). To best-estimate such fraction, a CTMT analysis with the dedicated COCOSYS code was performed and the integral MELCOR simulation was afterwards refined by setting a deduced fixed percentage of I_2 among iodine forms in the CTMT. A sensitivity study was finally performed to assess the effect of the form of iodine on the source term (ST) onto the FCVS filters.

KEYWORDS
Iodine form, MELCOR code, COCOSYS code, filtered containment venting system, source term

1. INTRODUCTION

Since the Fukushima accident, continuous effort has been made to further enhance the safety of Czech nuclear fleet, especially with respect to SAs. Numerous systems, belonging to the 4th level of defense-in-depth (e.g. passive autocatalytic recombiners, in-vessel melt retention provisions, alternative ultimate heat sink, etc.) have already been implemented, some other systems recently accomplished their design phase (e.g. dedicated system for primary circuit depressurization, FCVS or alternative CTMT heat removal system). These systems, currently undergoing licensing approvals, must be supported with appropriate safety analyses.

The Czech NPP Temelin, consisting of 2 VVER-1000/V320 reactors, is equipped with a large dry CTMT. For this plant, the ex-vessel corium cooling is considered as one of the possible measures for maintaining the CTMT integrity. Cooling of the corium produces large amount of vapor, the ongoing molten-core concrete interaction is responsible for production of non-condensable gases. Hence, without any system of heat removal from the CTMT, the CTMT would be over-pressurized (within a few days).

Two systems are currently being designed to evacuate heat from the CTMT: diverse CTMT atmosphere spraying system and FCVS. The latter was analyzed with the integral SA analysis code MELCOR, focusing on the ST onto the FCVS filters – especially iodine. However, as the representation of iodine is rather simple

in the MELCOR code (iodine, by default, is allowed to form cesium iodide, which behaves as aerosol at the thermal-hydraulic conditions during a SA within the CTMT), the analyses had to be performed in 2 steps. First, sensitivity analyses with the aim of investigating expected iodine forms in the CTMT were performed with the aid of the CTMT-analysis code COCOSYS, equipped with advanced iodine chemistry models. For this purpose, the MELCOR code was employed only to estimate sources of Cs, I, CsI and Ag[1] into the CTMT. Second, based on the COCOSYS results, the iodine was adequately divided between the CsI (i.e. aerosol) form and the I_2 (i.e. gaseous) form for a refined MELCOR integral analysis. A sensitivity study was moreover carried out to assess the effect of iodine speciation on the ST into the FCVS (and further on into the environment).

A note must be made on the form of results' presentation: the aim of this study was to assess the sensitivity of iodine representation on the ST; the goal is to show how important the knowledge of I form in the CTMT is, as different forms (aerosols vs. gas) exhibit very different physical behavior, affecting its release onto the FCVS filters. Therefore, although concrete values and parameters related to the VVER-1000/V320 reactor were considered in the performed analyses, the results are presented only *relatively* to each other and only the orders of magnitude are provided. However, it does not attenuate the presented outcomes.

2. AUXILIARY ANALYSIS OF IODINE SPECIATION

In order to estimate and substantiate the fixed ratio of molecular (i.e. gaseous) iodine I_2 among all iodine forms for the best-estimate integral calculation performed with the MELCOR code, a detailed analysis performed with the CTMT-analysis code COCOSYS was performed first.

2.1. MELCOR input model and definition of sources into the CTMT

The integral, lumped parameter code MELCOR ([1], [2]) of the latest available release r2023.0.6 was used to carry out integral SA analyses; first, as the "1st phase" calculation to define the sources into the CTMT for the COCOSYS analysis, and, consequently, to perform the refined (in terms of redefined iodine forms in the CTMT, proportioning I_2 vs. CsI) "2nd phase" analysis of a SA course with foreseen FCVS operation and ongoing Molten Core Concrete Interaction (MCCI), which otherwise could not be properly accounted for with the stand-alone COCOSYS simulation. The MELCOR code was given credit for the ST from the RCS to the CTMT as it is a largely validated SA integral code ([3]). The ST is somewhat pre-determined taking into account the fact that both Cs and I are highly volatile and that their speciation is given by the NUREG-1465. Thus, the MELCOR in-vessel phase calculation defines mainly the timing of RNs' releases and thermo-hydraulic conditions for the CTMT.

As the focus of this article is on the forms and speciation of iodine, the input model description limits to the nodalization scheme of the core/reactor pressure vessel (RPV, Figure 1); discretization of the reactor coolant system (RCS, shown in Figure 3). CTMT nodalization prepared for the MELCOR code is somewhat finer, but comparable to that shown for the COCOSYS code (in Figure 4).

A schematic view of the possible sources of mass, enthalpy and FPs, provided for the COCOSYS CTMT analysis, is shown in Figure 3. All possible pathways for thermodynamic materials (water, steam, non-condensable gases), their corresponding enthalpies and FPs were identified and set to be recorded (via ASCII

[1] As the focus was on the iodine speciation, it was concluded, from [5], that the main factors affecting iodine chemistry in the CTMT were the pH, dose rate and steel/painted/concrete surfaces. Hence only those 4 species were recorded during the in-vessel MELCOR simulation. The control rods being made of B_4C, only small amount of Ag was tracked. However, for the sake of completeness and having in mind that I reacts with Ag, the ‚AG' class was provided for the COCOSYS analysis.

data files) throughout the MELCOR calculation. For the station blackout (SBO) scenario, the breach from the RCS is through the pressurizer relief tank and through the breached RPV. For the loss of coolant accident (LOCA) scenario, the breach is either from the 2-ended guillotine break of the primary pipeline or from a single breach from the primary pipeline; the RPV-pathway is naturally applicable too. For the ex-vessel phase, when the concrete ablation process sets in, sources from the cavities are also collected (though mainly for thermal-hydraulic conditions estimation, as most of the RNs must already have escaped the fuel/debris).

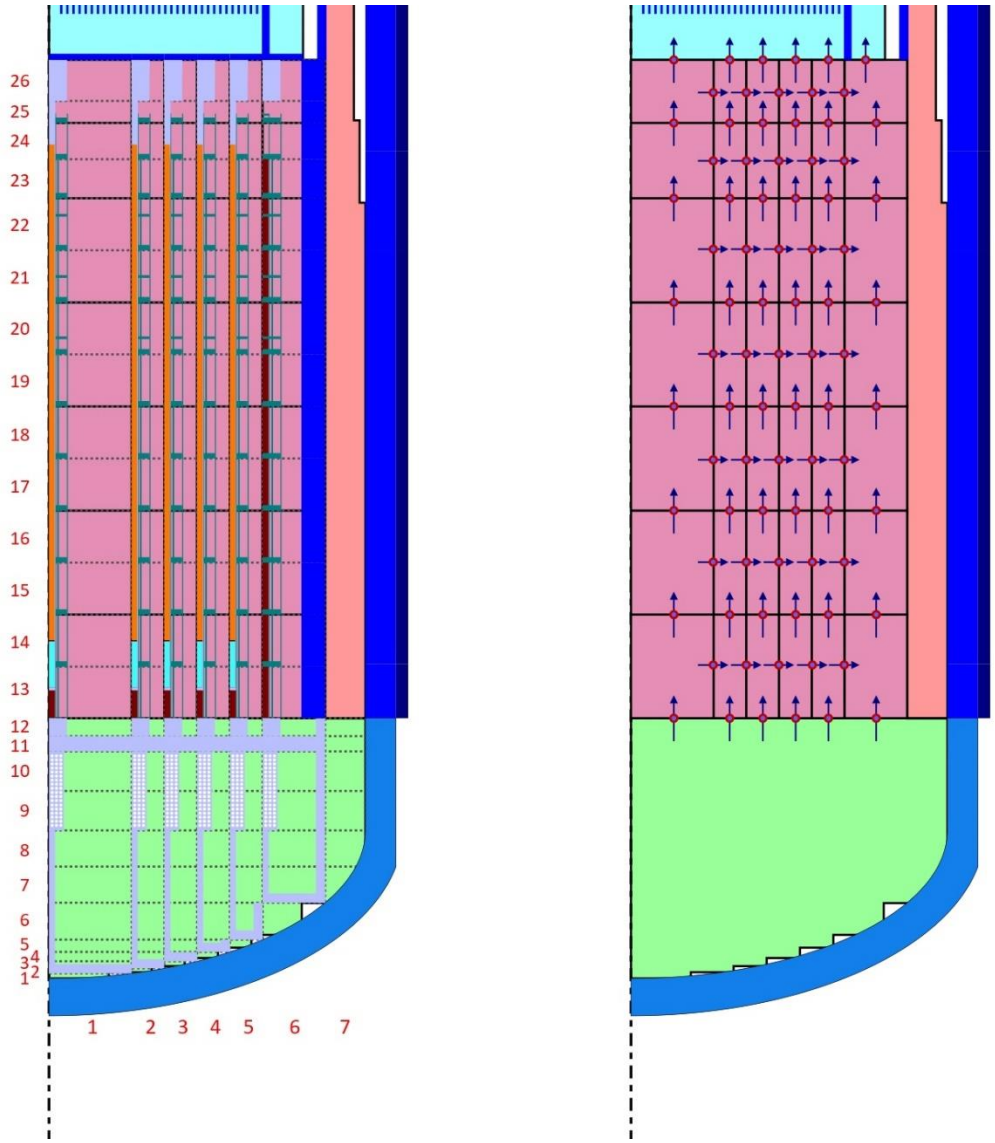

Figure 1. Nodalization scheme of the RPV: core cells and components (left), control volumes and flow paths (right).

2.2. COCOSYS simulation

The COCOSYS code ([4]) includes models for detailed iodine speciation in the CTMT, including chemical reactions both in the atmosphere and sumps and on different surfaces (painted, concrete or steel) under various conditions, including dose rate and acidity effect. The list of chemical reactions considered would

be exhaustive, therefore a schematic view of possible reactions, which are very similar to those considered in the ASTEC code ([5]; both codes have the same origins), is shown in Figure *5*. As already stated before, boundary conditions for the iodine speciation-focused COCOSYS analysis were provided by the MELCOR code (the so-called "1st phase" of MELCOR calculation).

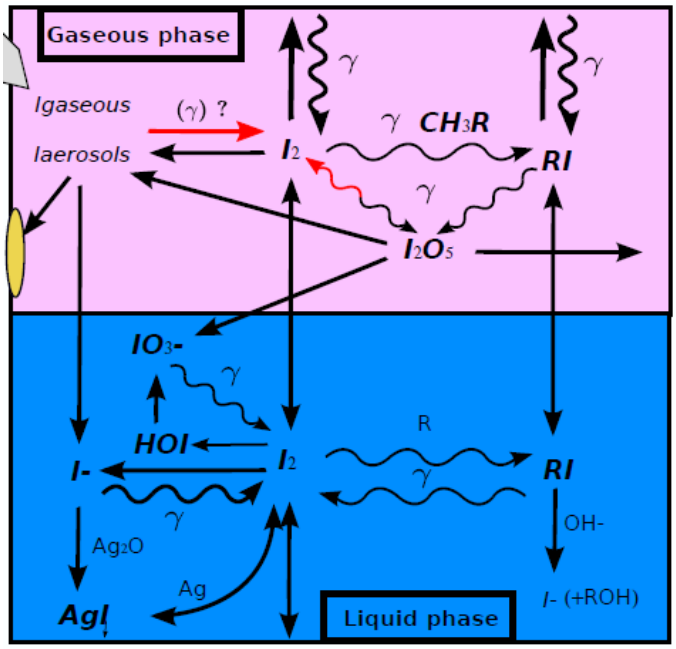

Figure 2 Thermal, radiolytic and mass transfer reactions with iodine considered in the COCOSYS simulation; the base is the same as for the ASTEC code ([5]).

The COCOSYS simulation was performed using a simplified model of the CTMT, the nodalization of which is shown in Figure 4. Among the fission products, only Cs, I, CsI and Ag had to be utilized from the identified sources (as iodine reacts mainly with those elements, forming the compounds AgI and CsI). As the MELCOR RN classes (e.g. noble gases, halogens, chalcogens, alkali metals...) contain all elements chemically similar (e.g. F, Cl, Br, I, At for halogens), it is necessary to define the fraction of Cs, I and Ag within their respective RN classes. Those are: 89.1 % of class 'CS'[2] are isotopes of Cs, 90.5 % of class 'I2' are isotopes of I and 53.1 % of class 'AG' are isotopes of Ag.

For the initial speciation in the MELCOR code (for the calculation defining sources into the CTMT), iodine was assumed to exist in the halogens ('I2') class to the extent of 5 % (according to [7]); this was done to avoid entering of the iodine solely as CsI into the COCOSYS CTMT calculation (as MELCOR automatically combines Cs and I). The SA scenario simulated to obtain the sources for the COCOSYS analysis was an unmitigated SBO, with pathways into the CTMT through pressurizer relief tank, through the failed RPV and from cavities being ablated by corium). The SBO scenario was investigated for 3 days. Later on, sensitivity analyses were performed and also a large break LOCA scenario was simulated, the sources of which were consequently input into the COCOSYS stand-alone CTMT simulation (in a way similar to the SBO scenario case). It was found that for both scenarios, SBO and LB LOCA, the resulting amount of I_2 in the CTMT, seen by the COCOSYS code, was very similar (see later).

[2] In the present study, The MELCOR RN classes are denoted in capitals and enclosed in single quotes (e.g. 'I2', 'CS', 'CSI'); this distinguishes the classes, containing also other elements from the same chemical group, from the elements and compounds; those are denoted without single quotes and in normal letters, e.g. Cs, I_2, CsI.

Specific conditions for the COCOSYS simulation had to be set: the acidity in the sumps was assumed to be conservative (from the point of view of I_2 release from the sump), yet still realistic: pH=5 was assumed. The dose rate was estimated to reach 2 kGy/h, according to previously performed calculations with the MAVRIC code; such analyses are regularly being carried out at ÚJV Řež to assess the dose rates onto equipment (and, possibly, also personnel) during SAs. The method consists of 1. computing the masses of RNs nearby the equipment to be assessed for dose rates and 2. carrying out analyses using the MAVRIC sequence of codes from the ORIGEN/SCALE package. More details on the methodology can be found e.g. in ([6]).

The COCOSYS analysis was carried out also for 3 days. The main result was the acquirement of the amount of gaseous iodine (mainly in the form of I_2 or CH_3I; other gaseous species are of much lower magnitude) in the CTMT in a long term (i.e. within the order of days). The main outcomes from the iodine forms-investigation simulation with the COCOSYS code is the evolution of iodine forms in the CTMT (averaged over modeled compartments, see Figure 5). The COCOSYS code considers iodine in the following forms:

- AER … aerosol forms of iodine (mainly CsI, AgI, IO_3^-)
- ELE … molecular iodine I_2 (as gas)
- ORG … organic forms of I (practically only CH_3I)
- IOD … iodine in the aqueous form – trapped in the sumps

From the graph in Figure 5 it can be deduced that in a long term (after 3 days into the accident), the gaseous forms of iodine (i.e. ELE+ORG) constitute roughly 1.56 % of I in the CTMT. Hence, roughly this value shall be used for the best-estimate integral analyses performed with the MELCOR code to properly account for iodine not being uniquely in the form of aerosols (which. contrarily to gas, gravitationally settle and deposit). This approach still exhibits uncertainties, but undoubtedly is qualitatively more correct than considering the iodine as CsI. Realistic approach, without any shortcuts, to the iodine representation in the CTMT is of special importance for FCVS analyses, where the filters must be designed to hold-up the expected inflow of gaseous iodine.

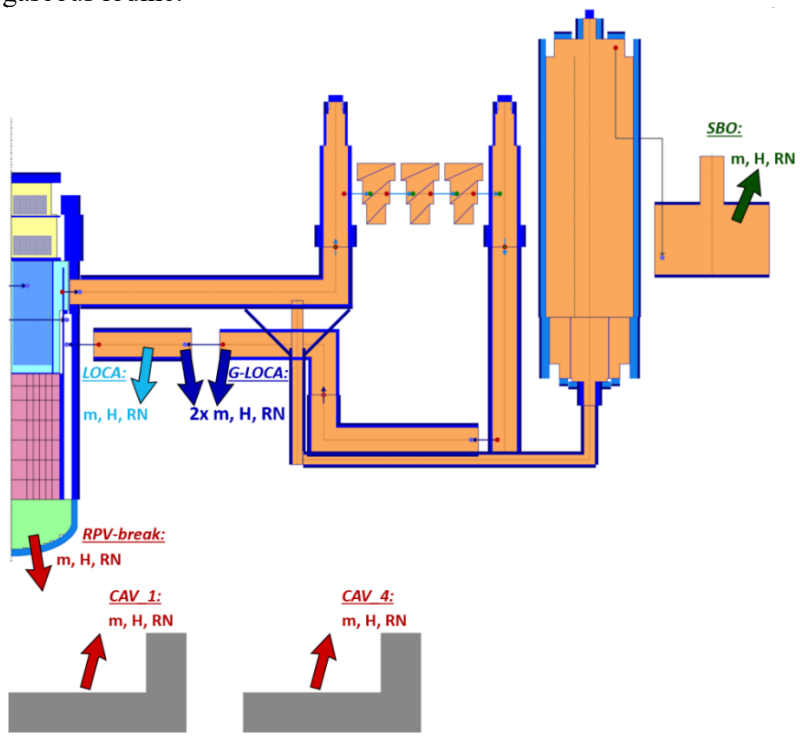

Figure 3. Sources of mass, enthalpy and FPs from the integral MELCOR calculation to the COCOSYS CTMT calculation.

The COCOSYS-calculated value is in good agreement of a parallel study, carried out also with the MELCOR code (for the "2nd phase" – after fixing the amount of gaseous iodine, [8]). The authors consider not only the fixed amount of I_2, but also the fixed amounts of CsI and Cs_2MoO_4. The estimated fixed fraction of I_2 was 1.7 %, which means 98.3 % of I was bound to Cs. The remaining Cs was distributed among the Cs_2MoO_4 (80 %) and the CsOH (20 %) compounds.

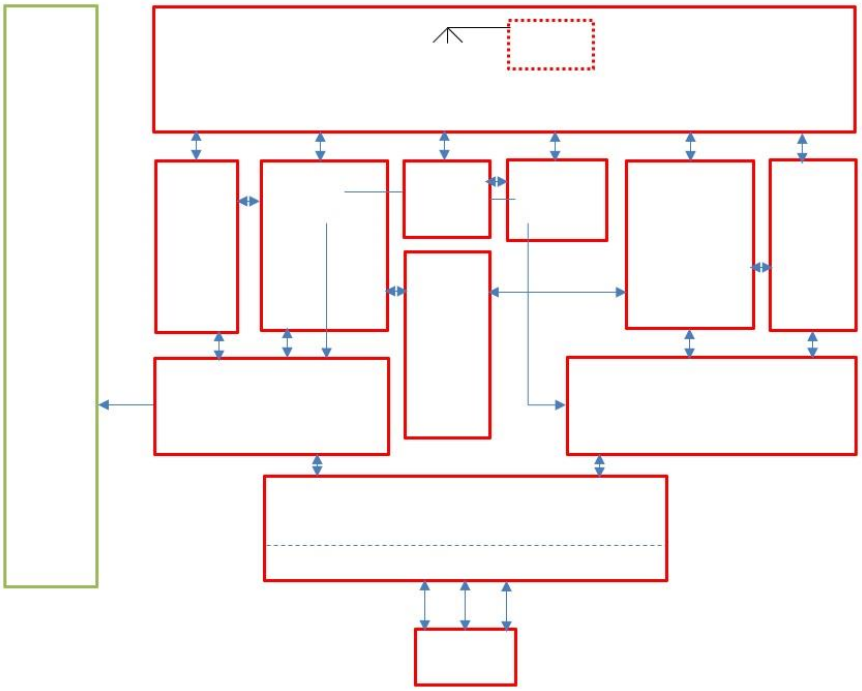

Figure 4. CTMT nodalization for the iodine speciation-focused COCOSYS analysis.

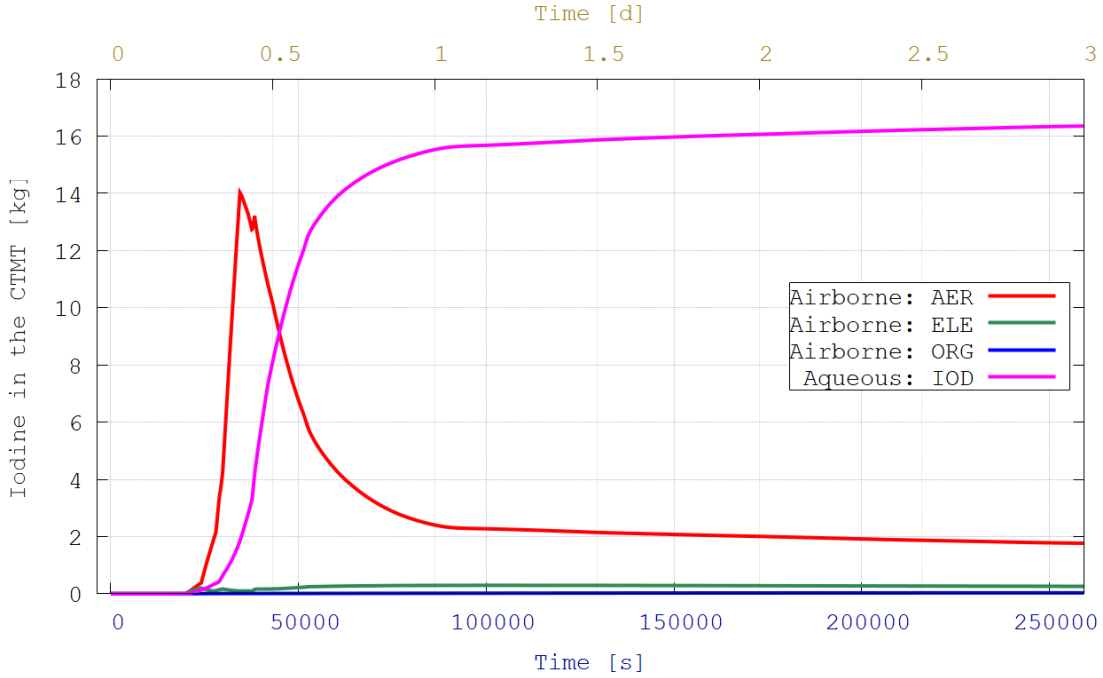

Figure 5. Forms of iodine averaged in the CTMT, estimated by the COCOSYS calculation.

3. RESULTS OF THE INTEGRAL MELCOR ANALYSIS

After the amount of gaseous iodine was estimated by the COCOSYS analysis, the MELCOR integral simulation was relaunched, as a "2nd phase" calculation, with the COCOSYS-estimated fixed fractions of I_2. The remaining I was envisaged to form CsI (the amount of which was also fixed).

The MELCOR input model, presented in Subsection 2.1, was used to launch several simulations of 2 qualitatively different SA scenarios: a guillotine-break LOCA (G-LOCA) sequence and an SBO sequence, respectively. For the sake of simplicity and legibility, only the **G-LOCA scenario** results are presented. In the scenario, as a SA management measure to avoid CTMT over-pressurization, FCVS is actuated before the CTMT pressure limit is reached.

According to the findings presented in Subsection 2.2, the fixed amount of gaseous iodine (as I_2, i.e. belonging to the class 'I2') was set to 1.56 %[3] of all the iodine initial inventory (i. i.). The remainder of I was forced to recombine with Cs to form CsI (i.e. class 'CSI'). Moreover, to further assess the effect of iodine speciation on the ST calculated by an integral code, 2 additional cases – from both sides of the spectrum – were studied:

- iodine being freely allowed to react with cesium and form thus CsI, and
- iodine in the fixed form as I_2 representing 3.12 % (i.e. the double) of the overall initial iodine mass.

Similar study to the present one is provided in [13], where the fixed amount of gaseous 'I2' was, according to the NUREG-1465, fixed to 5 % (more details are given in Subsection 3.2). To substantiate the choice of I speciation in the sensitivity analyses, one has to examine the best-practices reported for the MECLOR code. Representation of I primarily as CsI is recommended in the U.S.NRC.'s NUREGs 1935, 7008 and 7245, respectively ([9], [10] and [11]). It is in line with the observations provided in [12] and [7], where it is stated that the estimated upper limit for gaseous iodine, entering the CTMT from breached RCS, is roughly 5 %.

For the 2 simulations with the fixed I_2 amount, the automatic creation of CsI was forbidden. This was done by omitting the RN1_CLS record in the input deck. The initial (and fixed, throughout the calculation) CsI amount was input so that remaining I, i.e. not being I_2, constituted the CsI initial mass. Remaining Cs was allowed to freely form the Cs_2MoO_4 compound (denoted as 'CSM' class), leaving the rest of Cs to remain within the 'CS' class as CsOH. The user also had not to forget to define specific decay power for the new CI element within the 'CSI' class. The RNs in the core and in the fuel-cladding gap were distributed not per unit mass of fuel, but in absolute values ([kg]); the gap inventory considered was between 0.7 and 2.2 %, according to the burn-up (which differs from ring to ring, Figure 1).

3.1. Results of the in-vessel phase of the integral MELCOR calculation

Before the results are presented, a note on the results' representation is made. To avoid abundant text in the graphs' legends and repeating the titles of simulated cases, the following convention on the curves' colors in the graphs was made; the following 3 bullets also clearly present the 3 cases simulated:

- **Red curves in the graphs**: automatic CsI formation is allowed, automatic Cs_2MoO_4 formation is allowed; remaining I resides in the 'I2' class[4], remaining Cs resides in the 'CS' class.

[3] This percentage is rather too precise to be considered as the „correct" value; the authors, aware of vast uncertainties accompanying both MELCOR and COCOSYS simulations, prefer stating „approximately 1.5 %".

[4]It was found that for the option of automatic creation of CsI, non-negligible amount of I remains in the halogens ('I2')

- **Green curves in the graphs**: fixed amount of I in the 'I2' class (1.56 % of the i. i.) and in the 'CSI' class (98.44 % of the i. i.) throughout the whole simulation; automatic Cs_2MoO_4 formation is allowed; remaining Cs resides in the 'CS' class.
- **Blue curves in the graphs**: fixed amount of I in the 'I2' class (3.12 % of the i. i.) and in the 'CSI' class (96.88 % of the i. i.) throughout the whole simulation; automatic Cs_2MoO_4 formation is allowed; remaining Cs resides in the 'CS' class.

The legend in the graphs then describes only the plotted parameter (or more parameters), the used color is red (though being applicable to all of the 3 cases). The time of RPV rupture is indicated by a vertical line with corresponding color; for the late-phase graphs, the vertical lines represent time of FCVS opening. As the purpose of this study is to investigate the impact of iodine speciation on the ST onto the FCVS filters, no table of events is provided for the in-vessel phase of the accident; however, marking events are distinguishable from the vertical colored lines (RPV failure time and CTMT venting onset).

First, illustration of the G-LOCA scenario progression for the SA phase until RPV failure is demonstrated in graphs in Figure 6 to Figure 8. Although the influence of Cs/I speciation on the core degradation was not expected, it turned out that non-negligible differences were observed for the 3 simulated cases even in the in-vessel phase. The most visible difference is the time of RPV failure, the FPs release from fuel occurring approximately at the same period. One reason for such sensitivity of core degradation progress to the I_2/CsI ratio is most likely the different dynamics of iodine/cesium/cesium iodide release from fuel: different species have different vapor pressures and thus the dynamics of their release differs. However, the differences in iodine species are rather tiny between the 3 investigated cases and the scatter of results indicates rather the inherent sensitivity of integral SA codes to the input parameters. This observation applies also for the water level in the core (Figure 7) and mass of particulate debris/molten pool in the lower plenum (Figure 8).

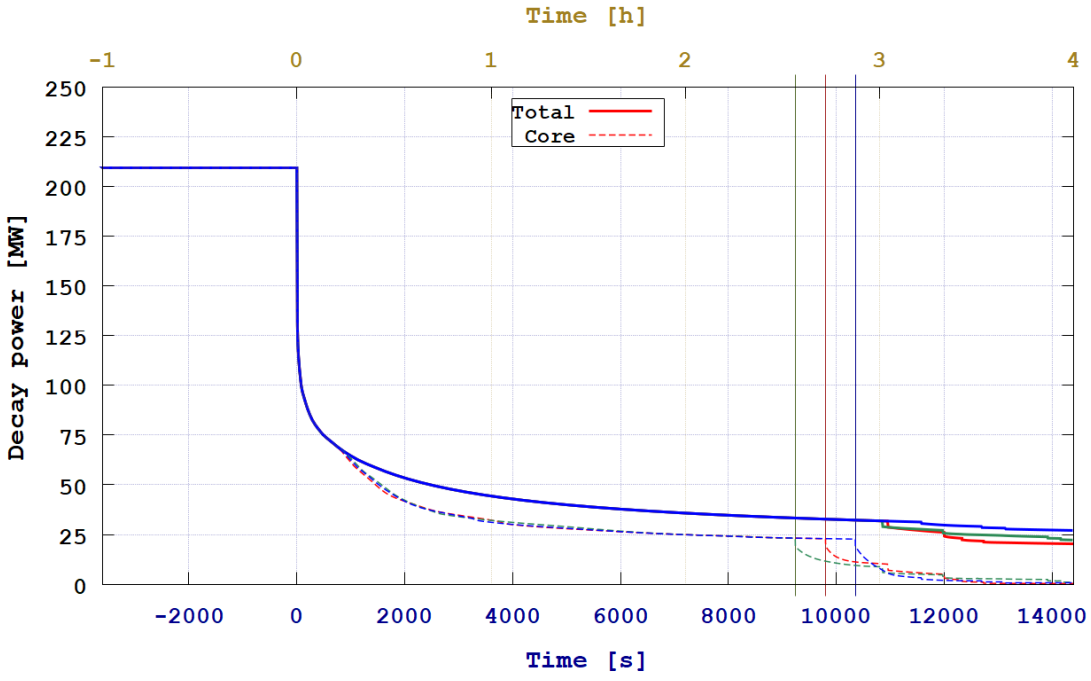

Figure 6. Decay power indication cladding rupture and FPs release, as well as RPV failure.

class, even though the I initial mass is about 10 times lower than the Cs initial mass.

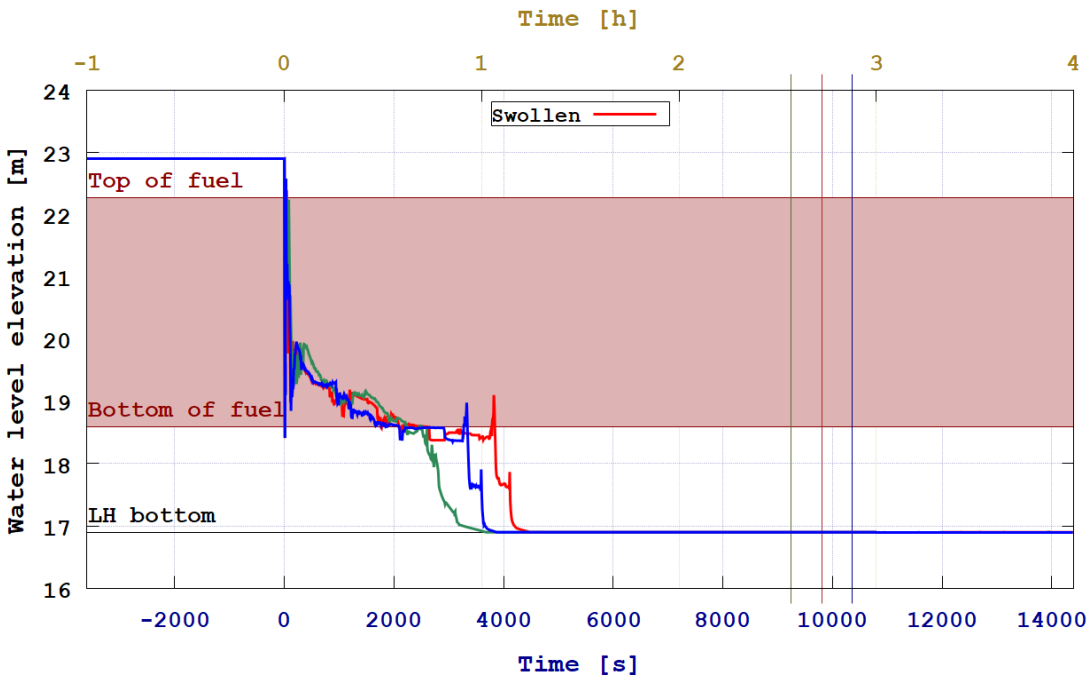

Figure 7. Swollen water level in the core and lower plenum.

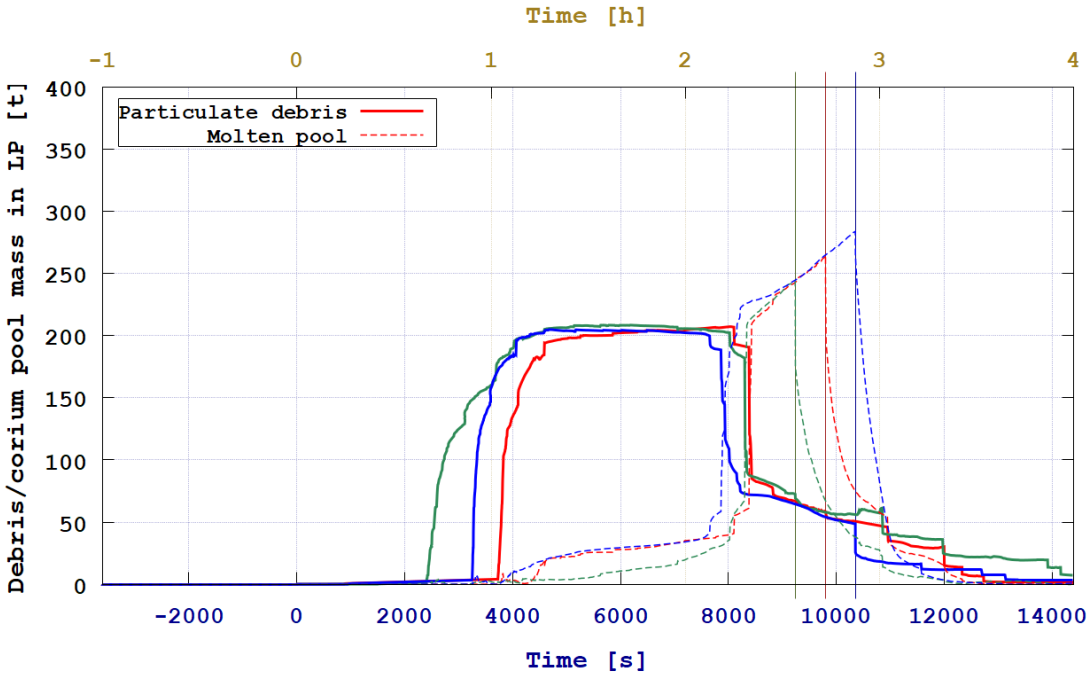

Figure 8. Mass of solid debris and molten corium in the lower plenum.

3.2. Results of the CTMT-phase of the integral MELCOR calculation

The graph in Figure 9 indicates the rate of CTMT pressurization, until the limit for FCVS opening is reached. Here the behavior is monotonic: less I2 (volatile) in the CTMT atmosphere leads to slower trend of CTMT pressurization. However, the difference between 1.56 and 3.12 % of 'I2' class seems to be too tiny to influence the decay power in the atmosphere. After further investigation, it was found that the total decay power, seen by the RN package, is not conserved (which can be proven by the fact that the solid lines in Figure 6 deviate, after RPV failure, from an exponential decrease) and thus different amounts of residual power are transferred into the cavity. Hence, the objective reason for accelerated pressurization for larger amount of 'I2' class is the more pronounced MCCI process in the cavity, generating gases. This issue is being tackled with the MELCOR code developers.

Figure 10 shows the amount of: (i) overall release of CsI from fuel, (ii) CsI present in the CTMT (i.e. not residing in the core, RPV or RCS), (iii) airborne CsI in the CTMT, and (iv) CsI released onto the FCVS filters. The trend is as expected: with more CsI allowed to be formed (the most for the CsI automatic creation case and the least for the case of 3.12 % of I fixed into the 'I2' class), more CsI is released from fuel. Within the CTMT, CsI aerosols settle and/or are dissolved in the water sumps. Thus, only tiny mass of airborne CsI exists and consequently, only small amount of CsI is released onto the FCVS filters.

The situation is different for molecular iodine I_2, Figure 11. The 'I2' class behaves almost like the noble gases class, i.e. it is in the form of non-condensable gases. However, the small deviation of the airborne mass from the total CTMT mass (and also released mass) indicates that some chemisorption is ongoing. But the most important results is the release of I_2 onto the FCVS filters: practically all non-chemisorbed iodine is release through the filters into the environment, which underlines the necessity of adequate I_2 representation in the integral SA analyses.

A similar study was carried out and presented in [13], with similar conclusions: it is extremely important that the speciation of I/Cs is considered, as it directly affects the source term. This speciation has to be made by the user at the start of the simulation and the species of I and Cs remain the same throughout the whole simulation, as the chemistry models are not incorporated in the MELCOR code. Thus, the user must use its chemical and physical knowledge to estimate, before-hand, the foreseen forms of iodine. Or a more advanced stand-alone tool such as COCOSYS may be used for this purpose.

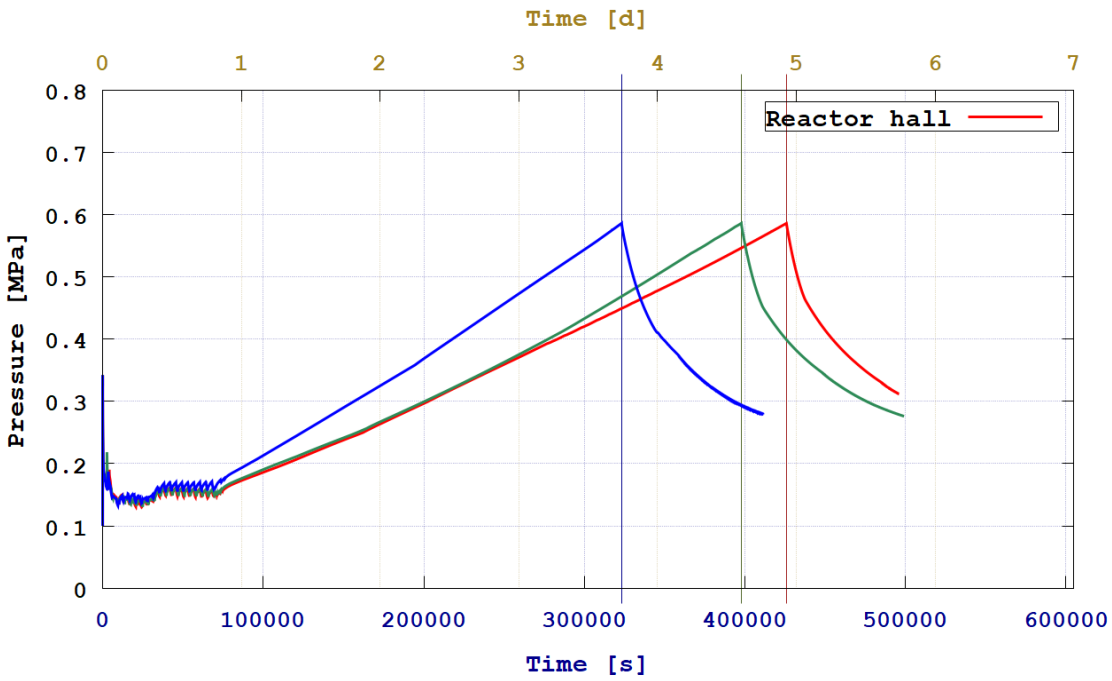

Figure 9. CTMT pressure indicating the instant of FCVS opening.

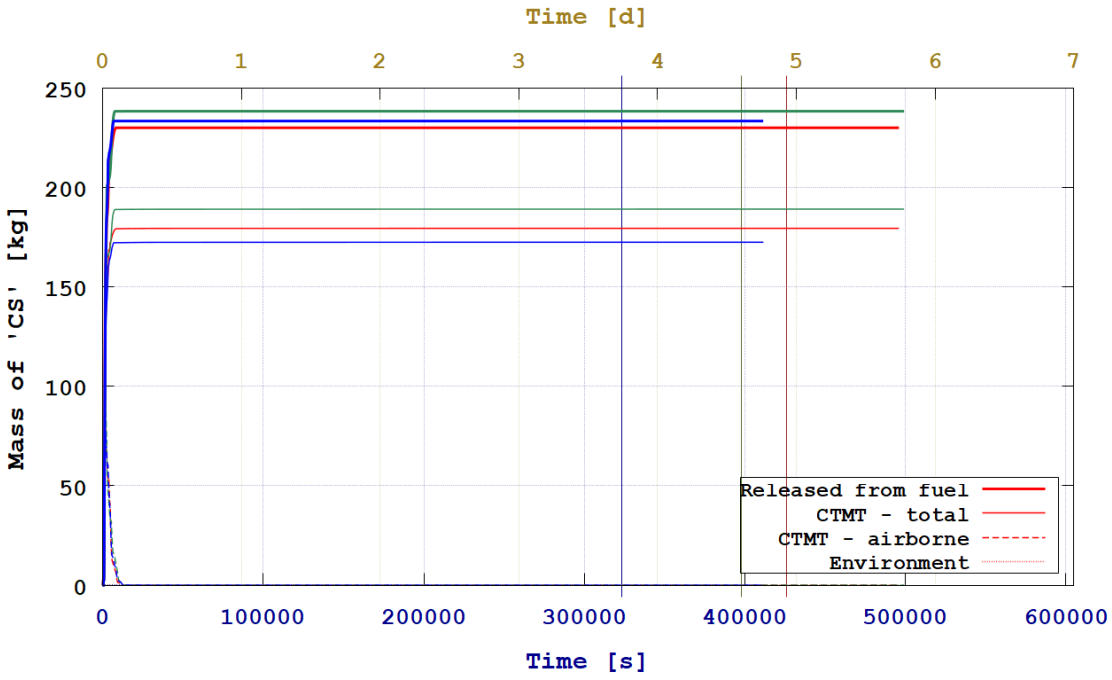

Figure 10. Mass of cesium iodide released from fuel, present in the CTMT (distinguished if it is airborne) and released into the environment (via FCVS filters).

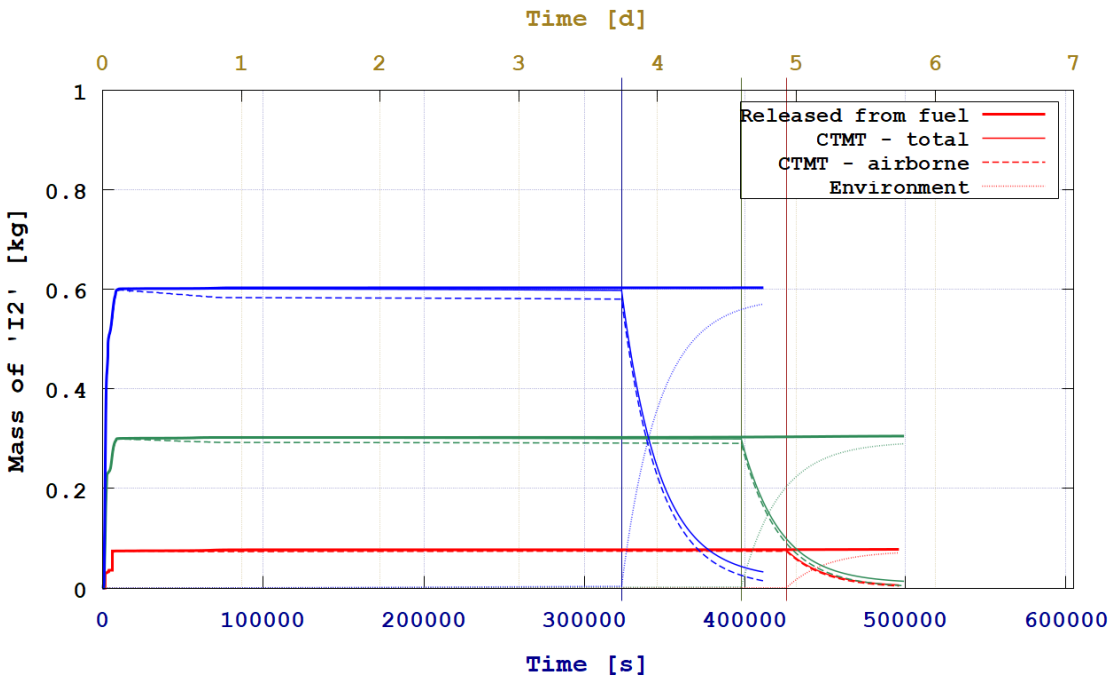

Figure 11. Mass of molecular iodine released from fuel, present in the CTMT (distinguished if it is airborne) and released into the environment (via FCVS filters).

4. CONCLUSIONS

The presented parametric study of different forms of iodine, present in the CTMT in a long-term during a SA, showed the importance of iodine speciation. For the integral code MELCOR, which is not equipped with detailed iodine chemistry models, the user may either use the default option of letting I react with Cs or fix the portion of iodine to be in the form of molecular I_2 throughout the calculation. The first way of representing iodine is too optimistic, as CsI is an aerosol (at typical thermal-hydraulic conditions in the CTMT during a SA) which gravitationally settles (or dilutes in the sumps) and hence does not contribute to the ST from the CTMT. The second way of treating iodine is to fix its gaseous portion (input as 'I2' class). This approach is more realistic, on the other hand it demands the user of the code to properly estimate the exact amount of I_2 as it directly influences the ST (the 'I2' RN class behaves in the CTMT almost as the noble gases class 'XE' with the exception of possibilities of chemisorption). Hence, without setting the fixed I_2 amount with care, the user can easily over-estimate gaseous iodine release from the CTMT. An attempt was thus made to best-estimate the portion of iodine in the form of I_2 in the late-phase of a SA, using the CTMT-analysis code COCOSYS (equipped with detailed iodine chemistry models and accounting for pH and dose rate effects). The resulting fraction of I_2 among other forms of iodine was found to be ~1.5 %. A parametric study was finally carried out to show the influence of the amount of gaseous iodine I_2 on the ST. Because of its nature, the user-defined I2 fixed mass directly, almost linearly, affects the calculated ST and, through radiological analyses, the impact on the public health (via mainly the isotope I-131).

The authors are aware of the uncertainties present in the study, both for the MELCOR integral simulations and the COCOSYS CTMT stand-alone simulation. Scatter of results for the in-vessel phase (Figure 6 to Figure 8) indicate rather high sensitivity of the input model to change of parameters, therefore uncertainty and sensitivity analyses should be carried out for any simulated sequence serving as an outcome of deterministic safety analysis. Nevertheless, the purpose of this work is to provide a best-estimate value for

the fixed amount of the 'I2' class to be used in integral MELCOR simulation involving CTMT response. The effect of different forms of iodine visible for the ex-vessel phase of the accident (CTMT response and the resulting source term) is, on the other hand, clear: the more iodine in the form of 'I2' is considered, the worse the ST – in terms of radiological consequence cause to the thyroid – would be. With this in mind, the main source of uncertainties is the COCOSYS CTMT stand-alone analysis and the consequent radiological analysis. To reduce the COCOSYS-related uncertainties, the lowest plausible acidity of the sump (pH=5) was set. The uncertainty stemming from the MELCOR simulation only concerns the timing of CTMT failure. Unfortunately, the present version of MELCOR exhibits an inexplicable behavior with regard to the decay power transferred into the cavity: the total decay power, seen by the RN package, is not conserved (see the description above).

REFERENCES

1. L. L. Humphries et al., *MELCOR Computer Code Manuals, Vol. 1: Primer and Users' Guide, Version 2.2 r2023.0*, Sandia National Laboratories, Albuquerque, NM, USA (2023).
2. L. L. Humphries et al., *MELCOR Computer Code Manuals, Vol. 2: Reference Manual, Version 2.2 r2023.0*, Sandia National Laboratories, Albuquerque, NM, USA (2023).
3. L. L. Humphries et al., *MELCOR Computer Code Manuals, Vol. 3: MELCOR Assessment Problems*, Sandia National Laboratories, Albuquerque, NM, USA (2015).
4. W. Klein-Hessling et al., *COCOSYS V2.4v5*. Revision 29, GRS, Köln, Germany (2018).
5. L. Bosland, Presentation of Iodine chemistry in containment with SOPHAEROS module in ASTEC V3.1.1, *Proceedings of the ASTEC Training Course*, Aix-en-Provence, France, January 15-19 (2024).
6. S. Nývlt, EVALUATION OF CONTAINMENT DOSE RATE DURING POSTULATED SEVERE ACCIDENT FOR THE TEMELIN NPP, Proceedings of the International conference VVER 2019, November 11-12 2019, Prague, Czech Republic.
7. L. Soffer et al., *Accident Source Terms for Light-Water Nuclear Power Plants. Final Report*, NUREG-1465, U.S.NRC, Washington, DC, USA (1995).
8. M. Leskovar, "Uncertainty Analysis of Severe Accident Scenario in Krško NPP," *Proceedings of the International Conference Nuclear Energy for New Europe*, Portorož, Slovenia, September 11-14 (2023).
9. R. Chan et al., *State-of-the-Art Reactor Consequence Analyses (SOARCA) Report*, NUREG-1935, Sandia National Laboratories, Albuquerque, NM, USA (2012).
10. K. Ross et al., *MELCOR Best Practices as Applied in the State-of-the-Art Reactor Consequence Analyses (SOARCA) Project*, NUREG/CR-7008, Sandia National Laboratories, Albuquerque, NM, USA (2014).
11. S. T. Ghosh, *State-of-the-Art Reactor Consequence Analyses (SOARCA) Project: Sequoyah Integrated Deterministic and Uncertainty Analyses*, NUREG/CR-7245, Sandia National Laboratories, Albuquerque, NM, USA (2019).
12. E. C. Beahm et al., *Iodine Chemical Forms in LWR Severe Accidents: Final report*, NUREG/CR-5732, Oak Ridge National Laboratory, Oak Ridge, TN, USA (1992).
13. A. Rýdl and G. Mazzini, "Cesium and Iodine Source Term Analyses with New VVER-1000 MELCOR Input Deck," *Proceedings of the 19th International Topical Meeting on Nuclear Reactor Thermal Hydraulics (NURETH-19)*, Brussels, Belgium, August 29 - September 3 (2021).

NUCLEAR RESEARCH INSTITUTE

SOURCE TERM ASSESSMENT FOR A VVER-1000/V320 REACTOR EQUIPPED WITH FILTERED VENTING: FORMS OF IODINE & DOSE RATE EVALUATION

Miroslav Kotouč
Adam Kecek
Sebastian Nývlt

UJV Group
PEOPLE | INNOVATION | TECHNOLOGY

The 11th European Review Meeting on Severe Accident Research (ERMSAR2024)
KTH, Stockholm, Sweden, May 13-16, 2024

MOTIVATION & OUTLINE

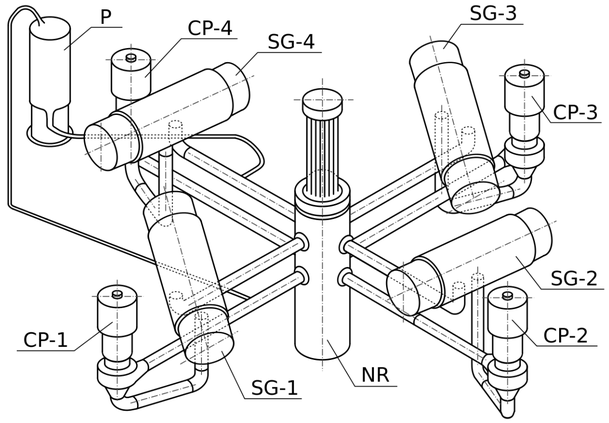

- Goal of the present study:

1. Evaluate *realistic* ST onto the FCVS filters for the Temelin NPP (VVER-1000/320)
   - Dry Filter Method (DFM) filtering unit was used

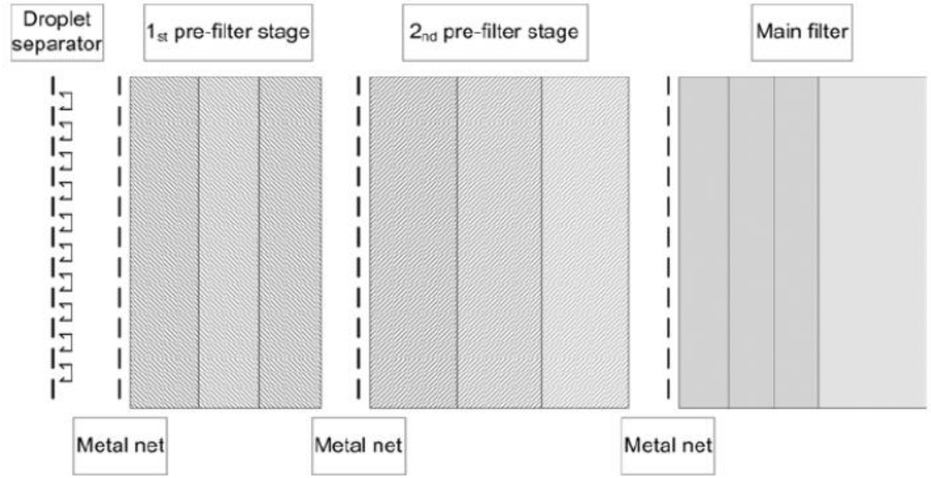

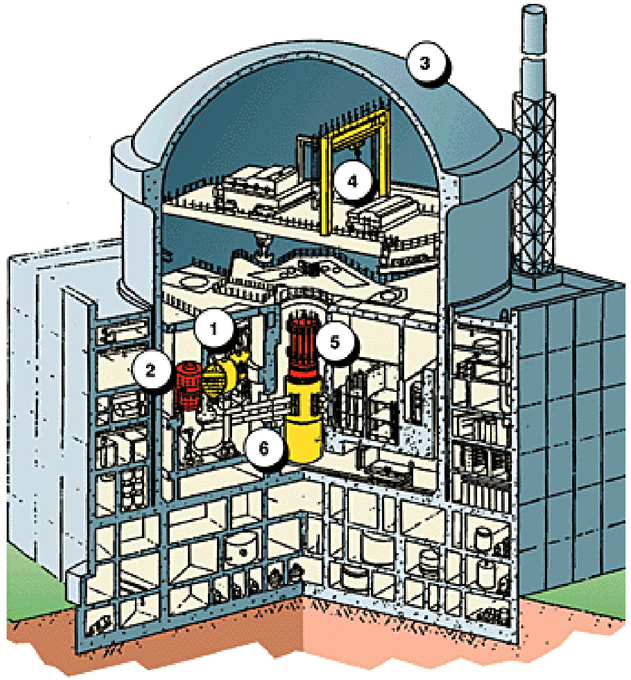

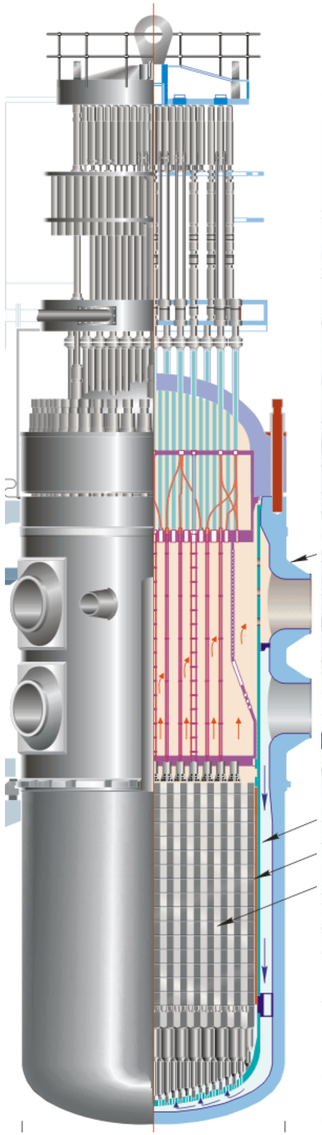

2. Assess the possibility of *manual* FCVS opening

NUCLEAR RESEARCH INSTITUTE

1. IODINE REPRESENTATION IN MELCOR

FORMS OF IODINE IN MELCOR

~hundreds of kg ~tens of kg

- MELCOR default: RN class combination ‘CS’ + ½*’I2’ => ‘CSI’
- => practically all ‘I2’ class transfers into the ‘CSI’ class, which might bias the ST results in the following ways:
  - CsI (aerosols) gravitationally settle
    - MELCOR does not allow for *mechanistic* remobilization of RNs from water sumps
  - Filters of FCVS are more efficient for aerosols (DF~10^4) than for gaseous forms of iodine (DF~10^2)
  - Correct speciation is important also for radiological consequences assessment
- NUREG-1465 estimated the approximate amount of CsI => CTMT:

> The results from Ref. 18 indicate that iodine entering the containment is at least 95% CsI with the remaining 5% as I plus HI, with not less than 1% of each as I and HI. Once the iodine enters containment, however, additional reactions are likely to occur. In an aqueous

- I.e., up to ~5 % of iodine shall be treated as *gaseous* in the CTMT
- Proposal: to fix the percentage of ‘I2’ class in the MELCOR simulation
  - What amount? As iodine undergoes several reactions in the CTMT…

Class	Class Name	Chemical Group	Representative	Member Elements
1	XE	Noble Gas	Xe	He, Ne, Ar, Kr, Xe, Rn, H, N
2	CS	Alkali Metals	Cs	Li, Na, K, Rb, Cs, Fr, Cu
3	BA	Alkaline Earths	Ba	Be, Mg, Ca, Sr, Ba, Ra, Es, Fm
4	I2	Halogens	I_2	F, Cl, Br, I, At
5	TE	Chalcogens	Te	O, S, Se, Te, Po
6	RU	Platinoids	Ru	Ru, Rh, Pd, Re, Os, Ir, Pt, Au, Ni
7	MO	Early Transition Elements	Mo	V, Cr, Fe, Co, Mn, Nb, Mo, Tc, Ta, W
8	CE	Tetravalent	Ce	Ti, Zr, Hf, Ce, Th, Pa, Np, Pu, C
9	LA	Trivalents	La	Al, Sc, Y, La, Ac, Pr, Nd, Pm, Sm, Eu, Gd, Tb, Dy, Ho, Er, Tm, Yb, Lu, Am, Cm, Bk, Cf
10	UO2	Uranium	UO_2	U
11	CD	More Volatile Main Group	Cd	Cd, Hg, Zn, As, Sb, Pb, Tl, Bi
12	AG	Less Volatile Main Group	Ag	Ga, Ge, In, Sn, Ag
13	BO2	Boron	BO_2	B, Si, P
14	H2O	Water	H_2O	H_2O
15	CON	Concrete	CON	- – -
16	CSI	Cesium iodide	CsI	CsI
17	CSM	Cesium Molybdate	CsM	CsM

FINDING REALISTIC IODINE SPECIATION

- Study performed in 3 steps:
  1. ***MELCOR*** integral SA analysis => sources of *m/H/RN*
     - In-vessel phase of the accident; *assuming 5 % of iodine as 'I2' (NUREG-1465)*
  2. ***COCOSYS*** CTMT analysis <= sources of *m/H/RN*
     - Account for *chemical reactions*, *pH* in the sumps, *dose rate* and *wet/dry painted/steel/concrete surfaces*
  3. ***MELCOR*** integral analysis with the *COCOSYS*-calculated long-term 'I2' class mass
     - Complete SA analysis, accounting for MCCI

***MELCOR* integral analysis**

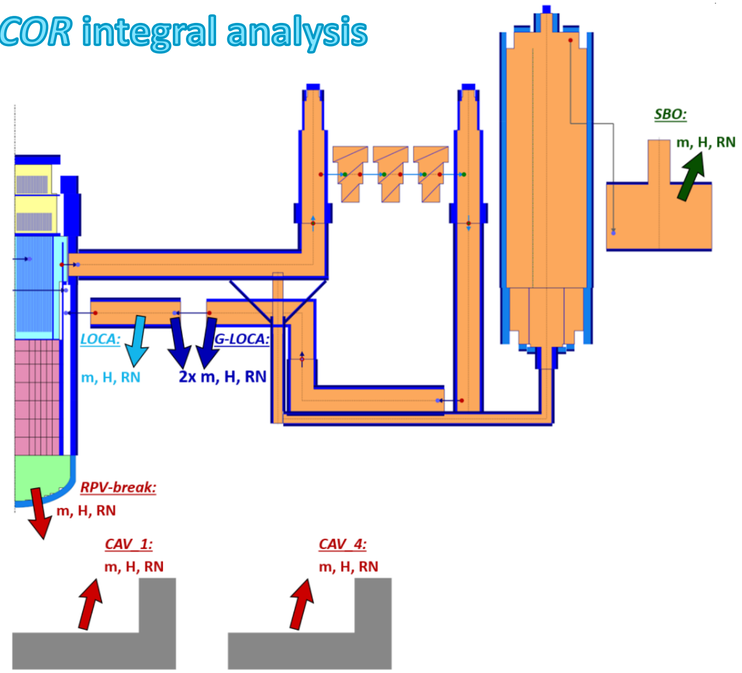

1-2

2-3

***COCOSYS* CTMT stand-alone analysis**

- pH=5; P=2 kGy/hr

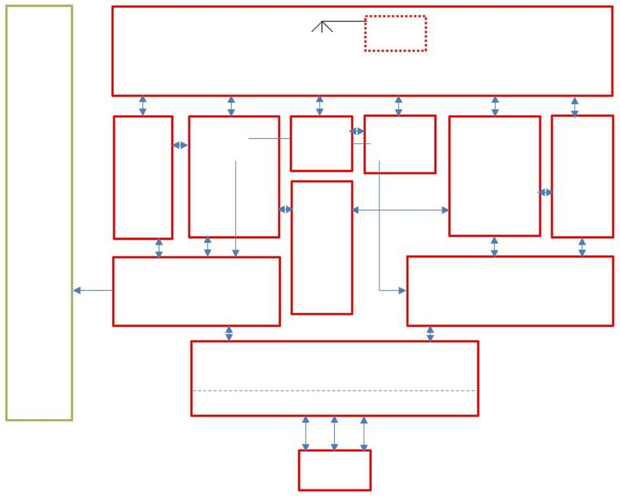

COCOSYS CTMT RESULTS

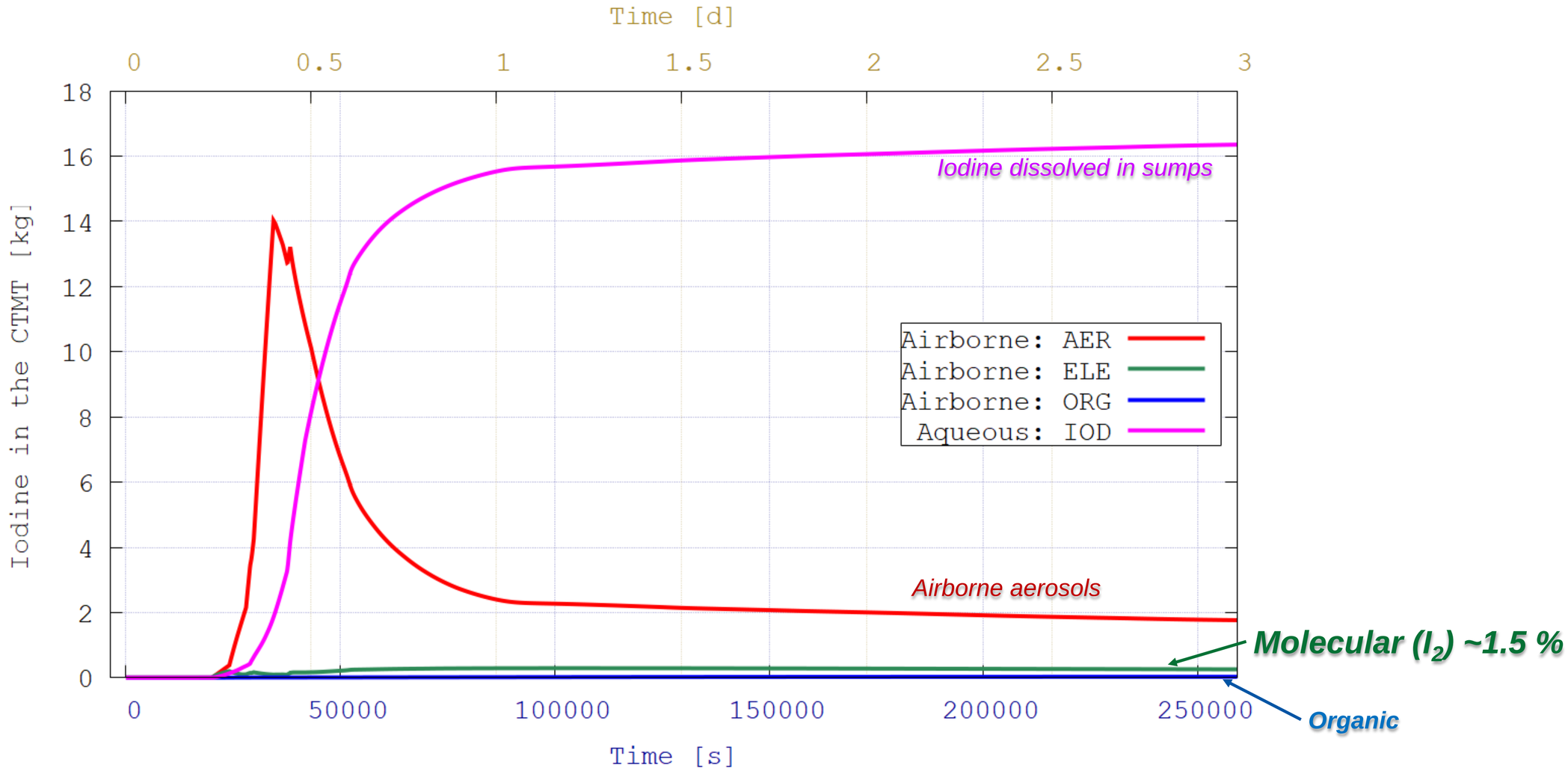

- => best-estimate: **~1.5 %** of iodine in the ‘I2‘ class!

MELCOR SENSITIVITY STUDY

- Scenario: Guillotine-Break LOCA + SBO
- FCVS opens after reaching 0.5865 MPa(abs)
- 3 cases for iodine representation:

1. **„CsI“** (red curves in the graphs)
   - automatic CsI formation is allowed
   - automatic Cs_2MoO_4 formation is allowed
2. **„1.5 of I2“** (green curves in the graphs)
   - 1.5 % of iodine => ‘I2’ class
   - 98.5 % of iodine => ‘CSI’ class
   - automatic Cs_2MoO_4 formation is allowed
3. **„3 of I2“** (blue curves in the graphs)
   - 3 % of iodine => ‘I2’ class
   - 97 % of iodine => ‘CSI’ class
   - automatic Cs_2MoO_4 formation is allowed

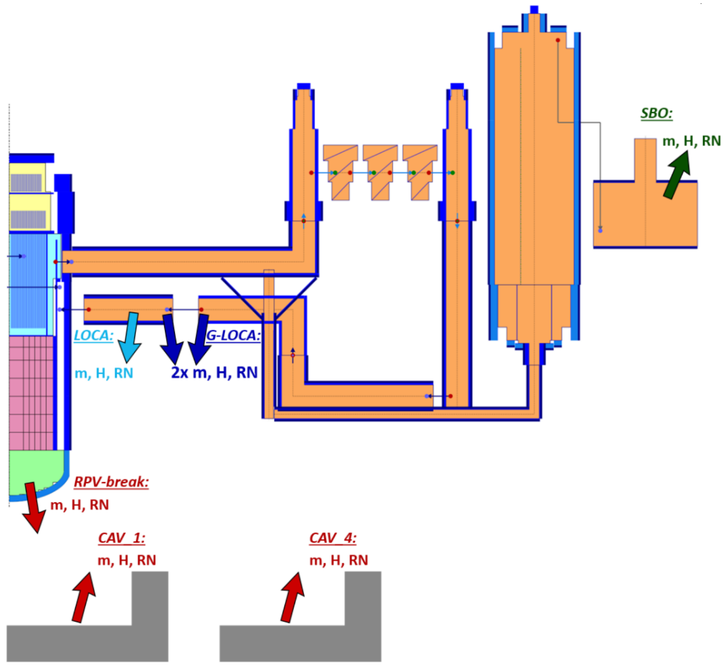



DECAY HEAT

CsI
1.5I2
3I2

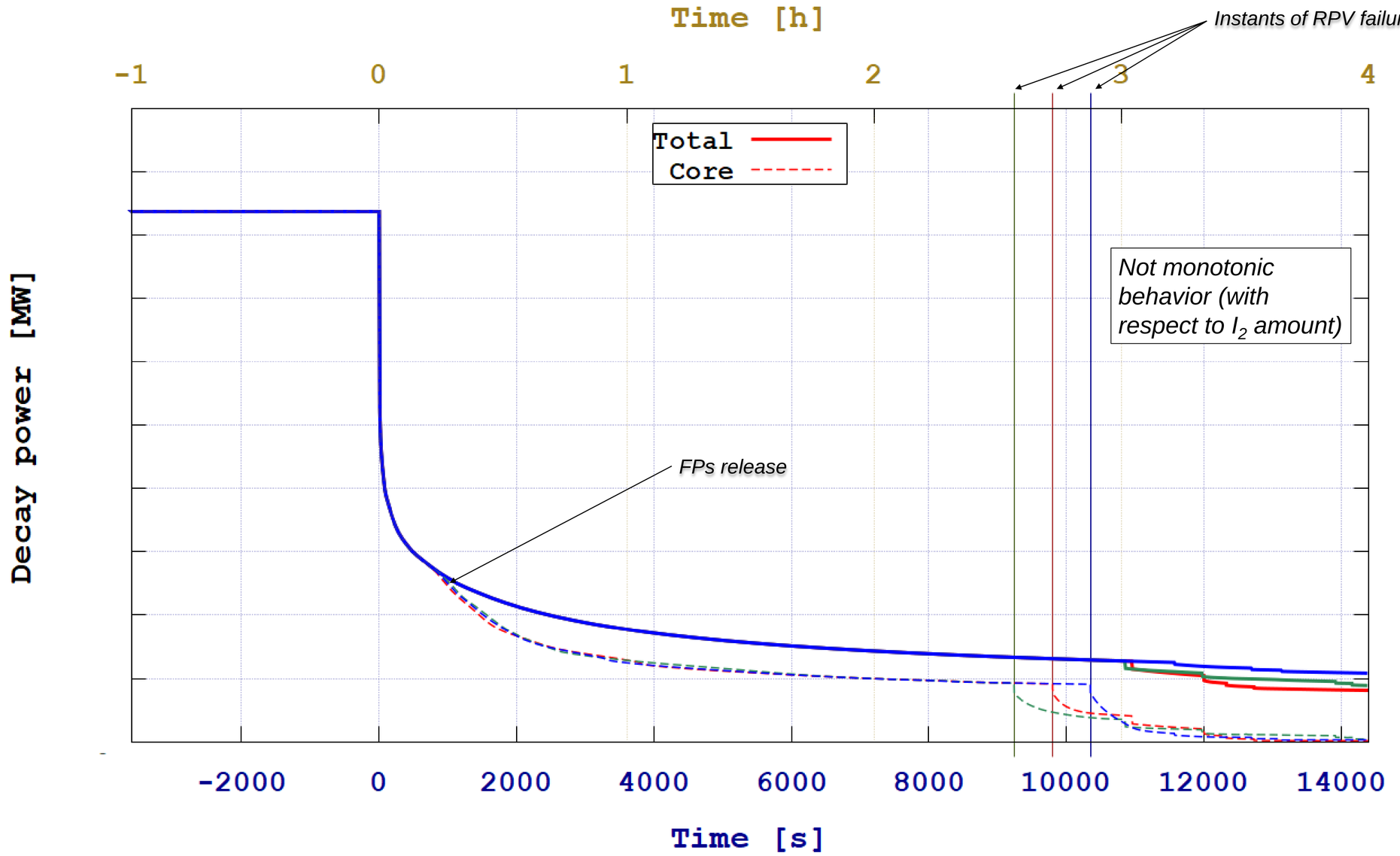

RPV WATER LEVEL

CsI
1.5I2
3I2

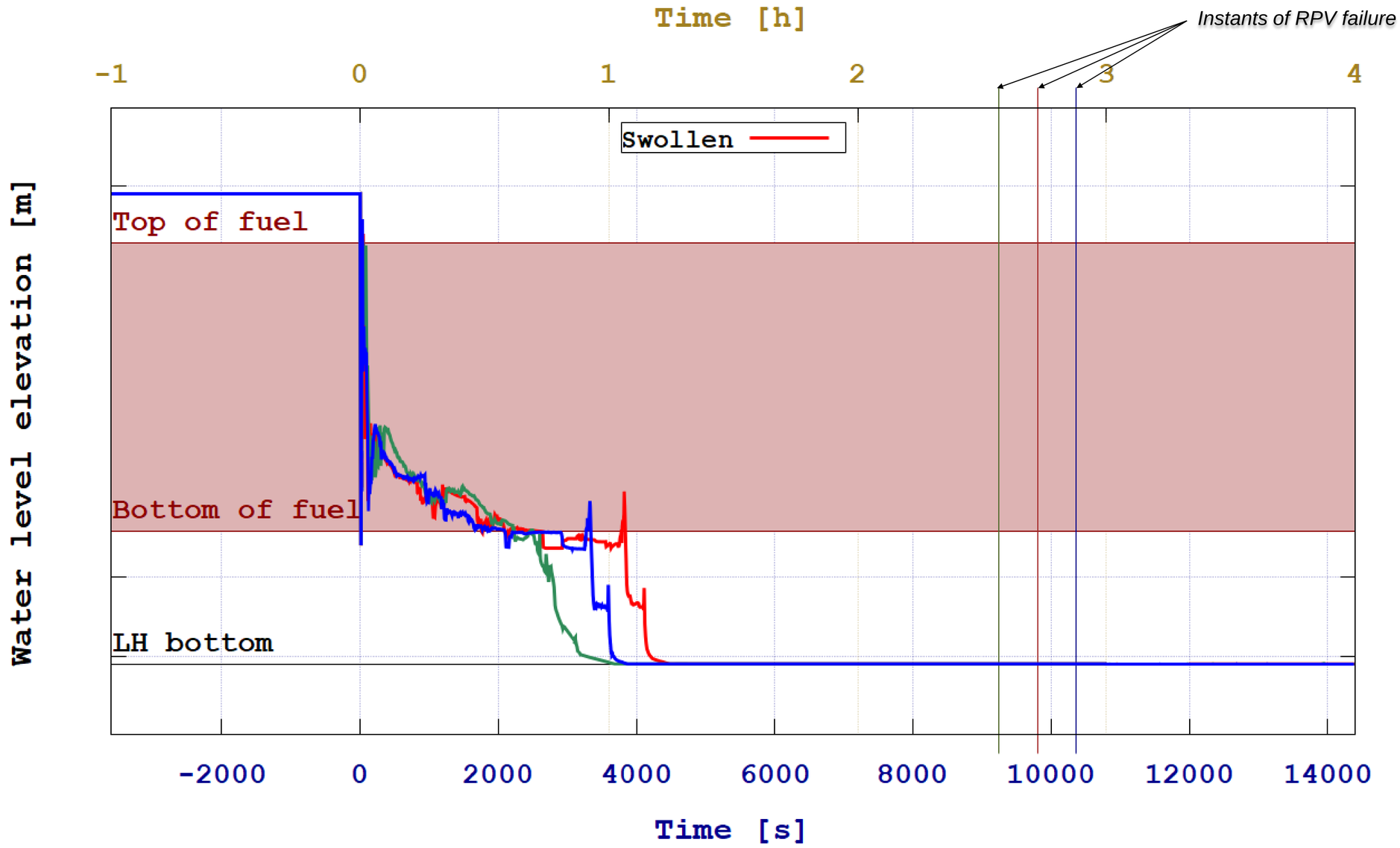

CORE EXIT TEMPERATURE

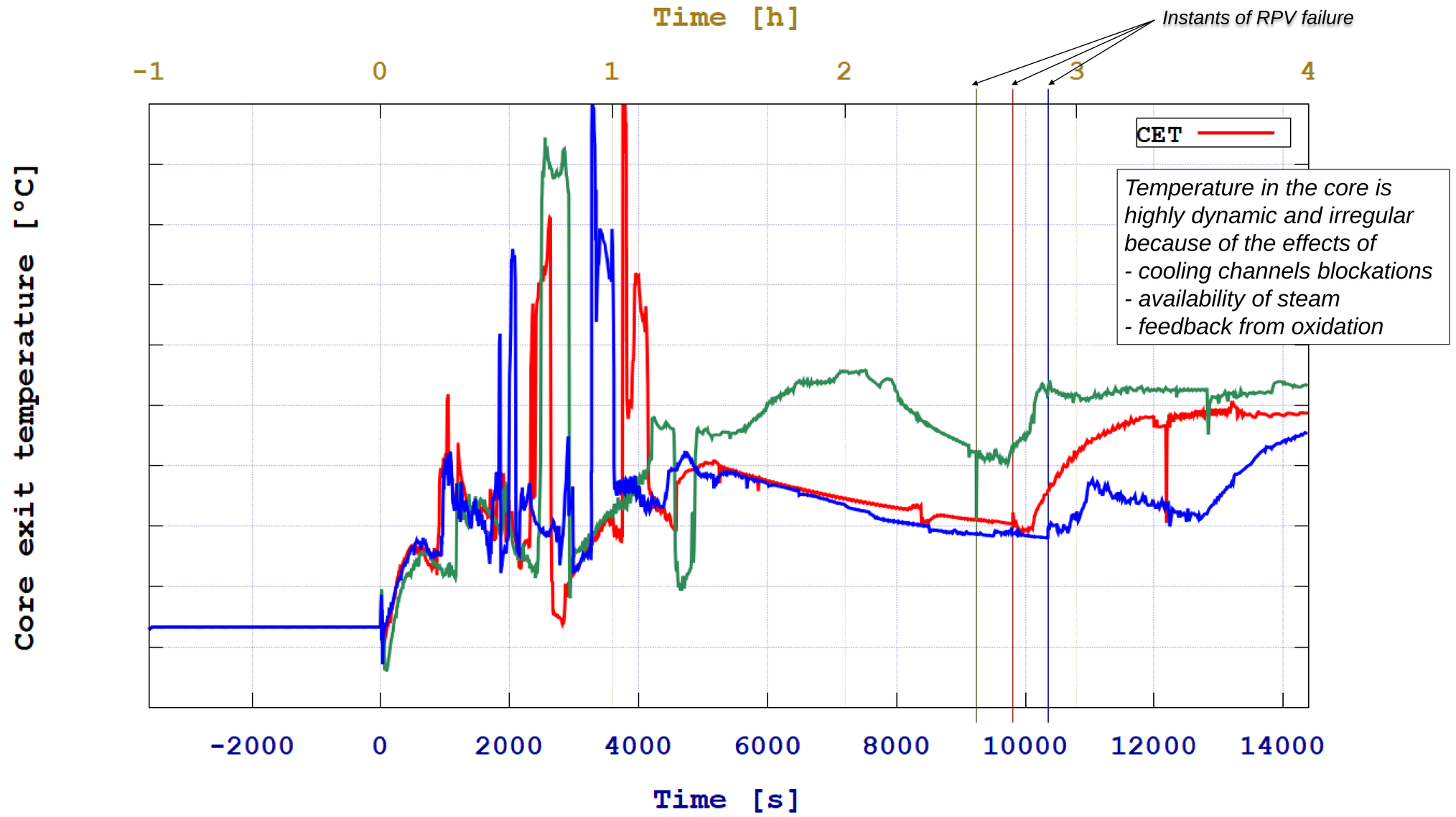

PD/MP IN LOWER P.

CsI
1.5I2
3I2

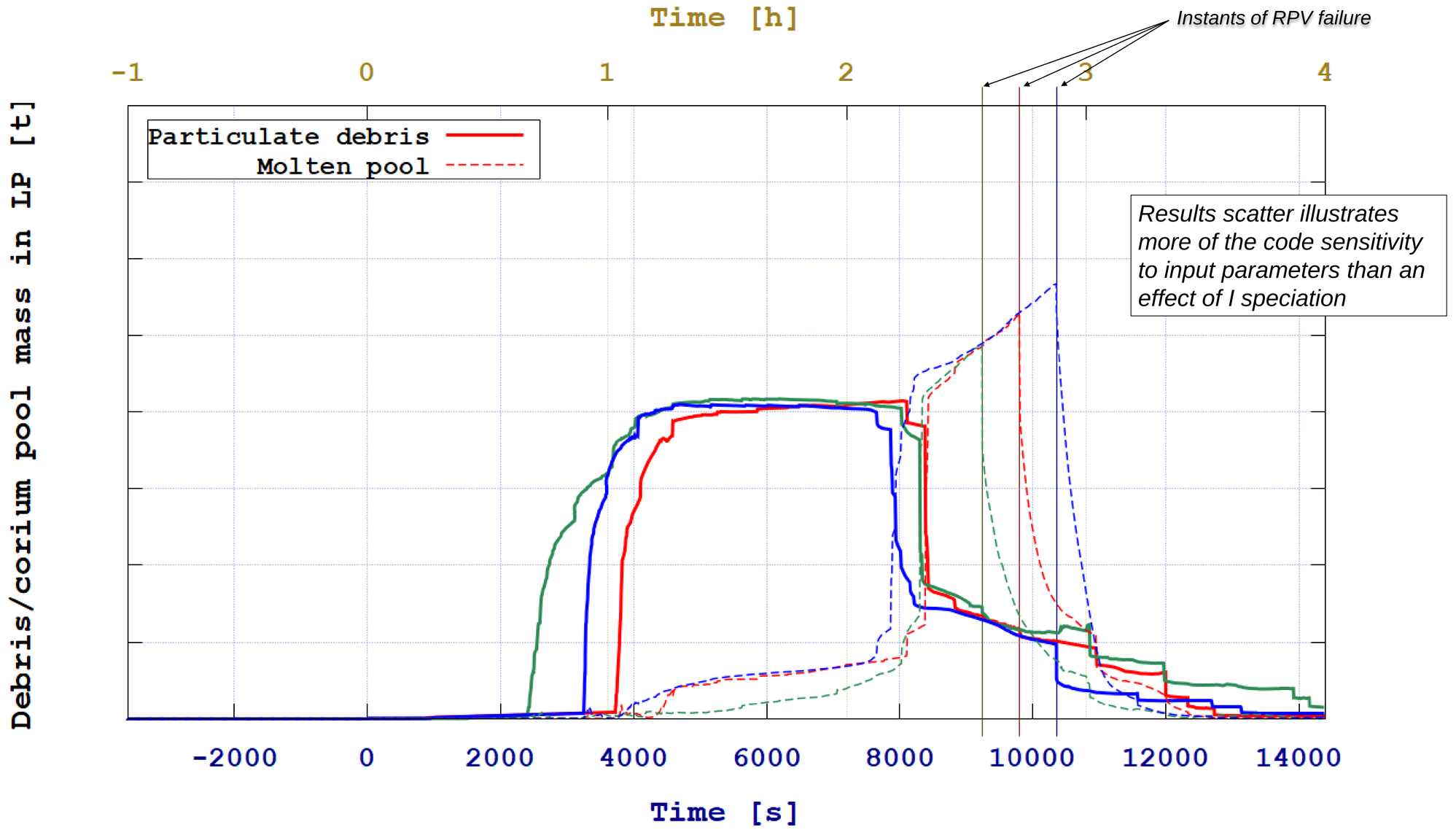

CTMT PRESSURE

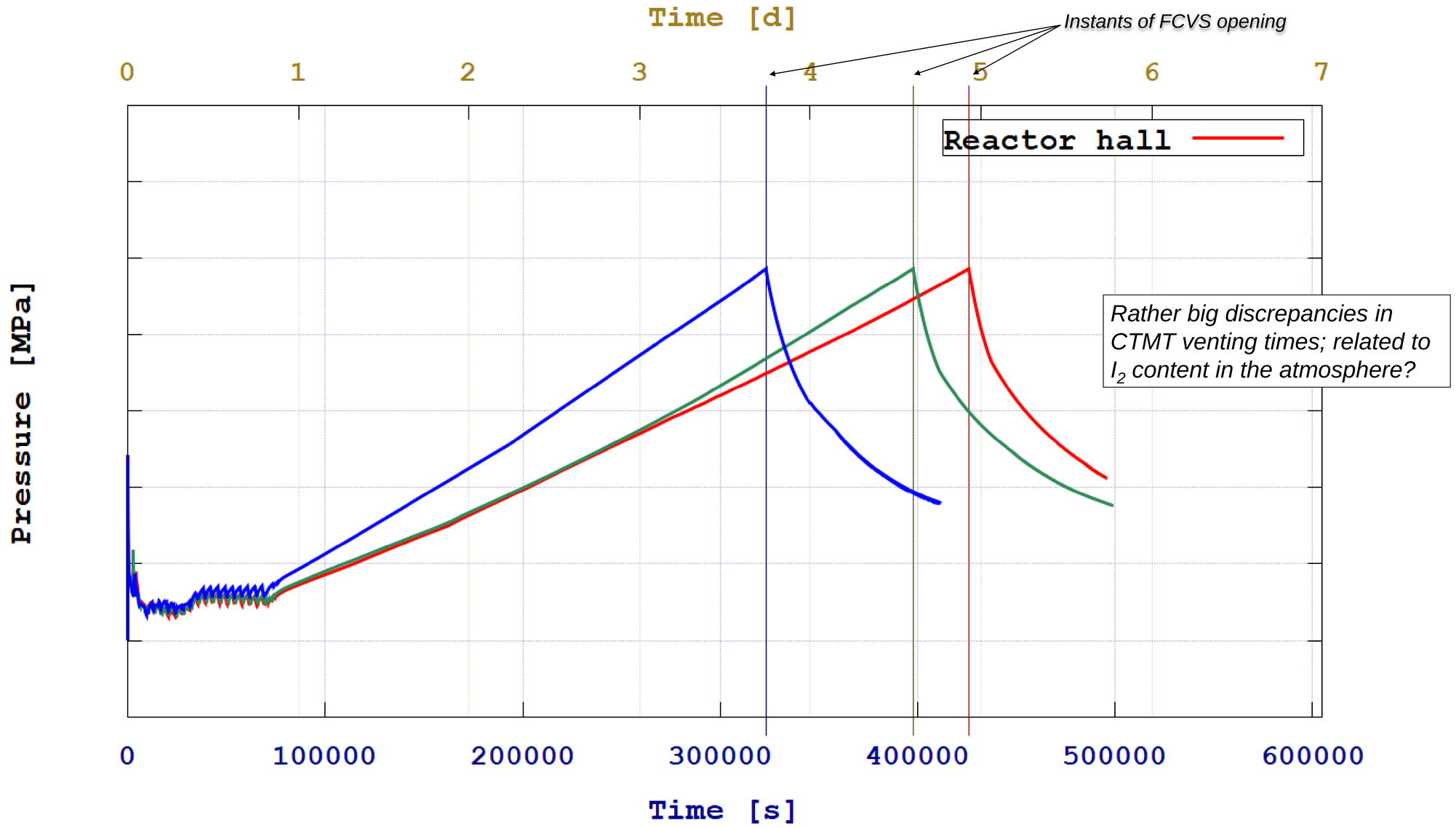

Rather big discrepancies in CTMT venting times; related to I_2 content in the atmosphere?

CAVITY DECAY POWER

CsI
1.5I2
3I2

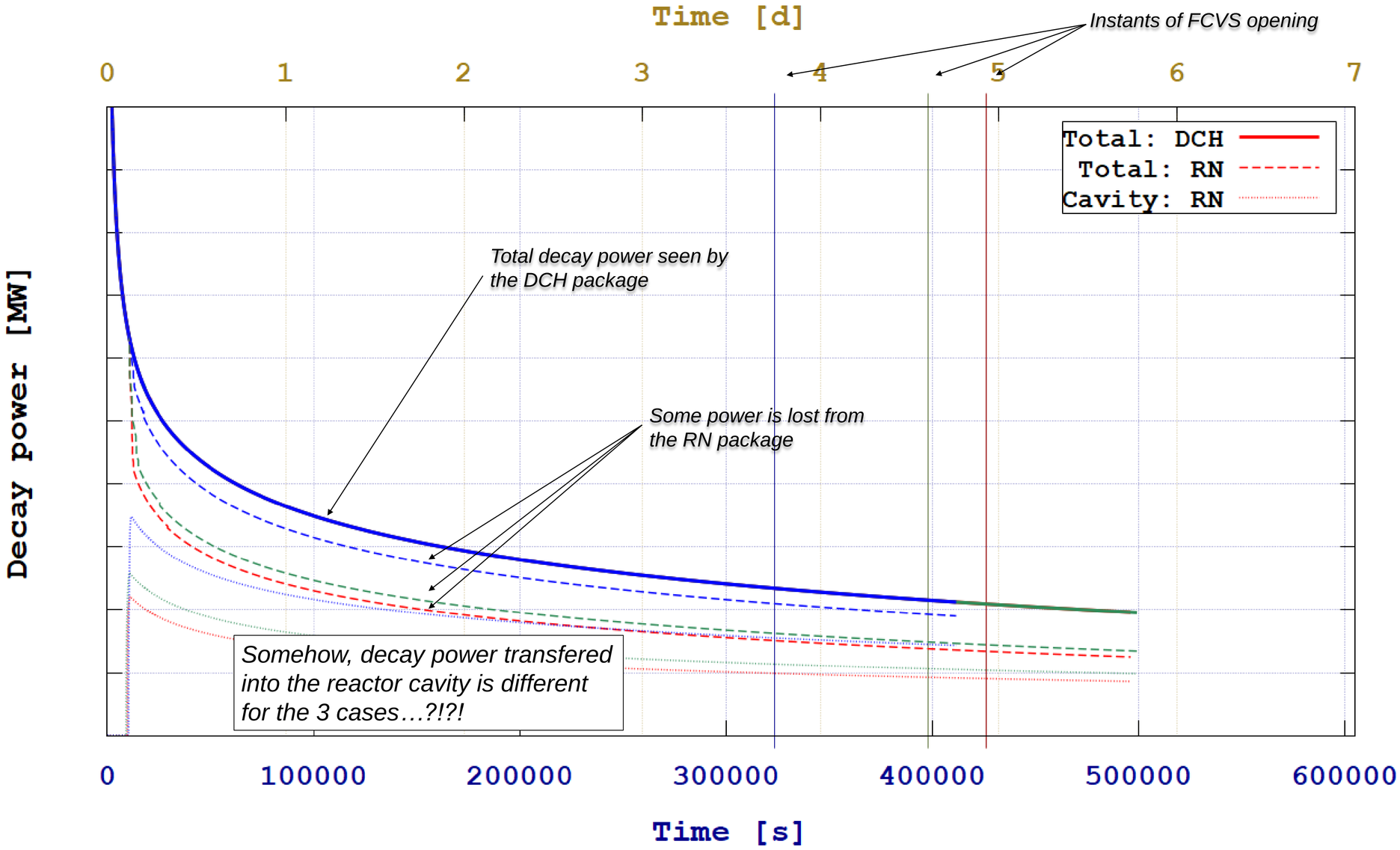

‘XE‘ RELEASE

CsI
1.5I2
3I2

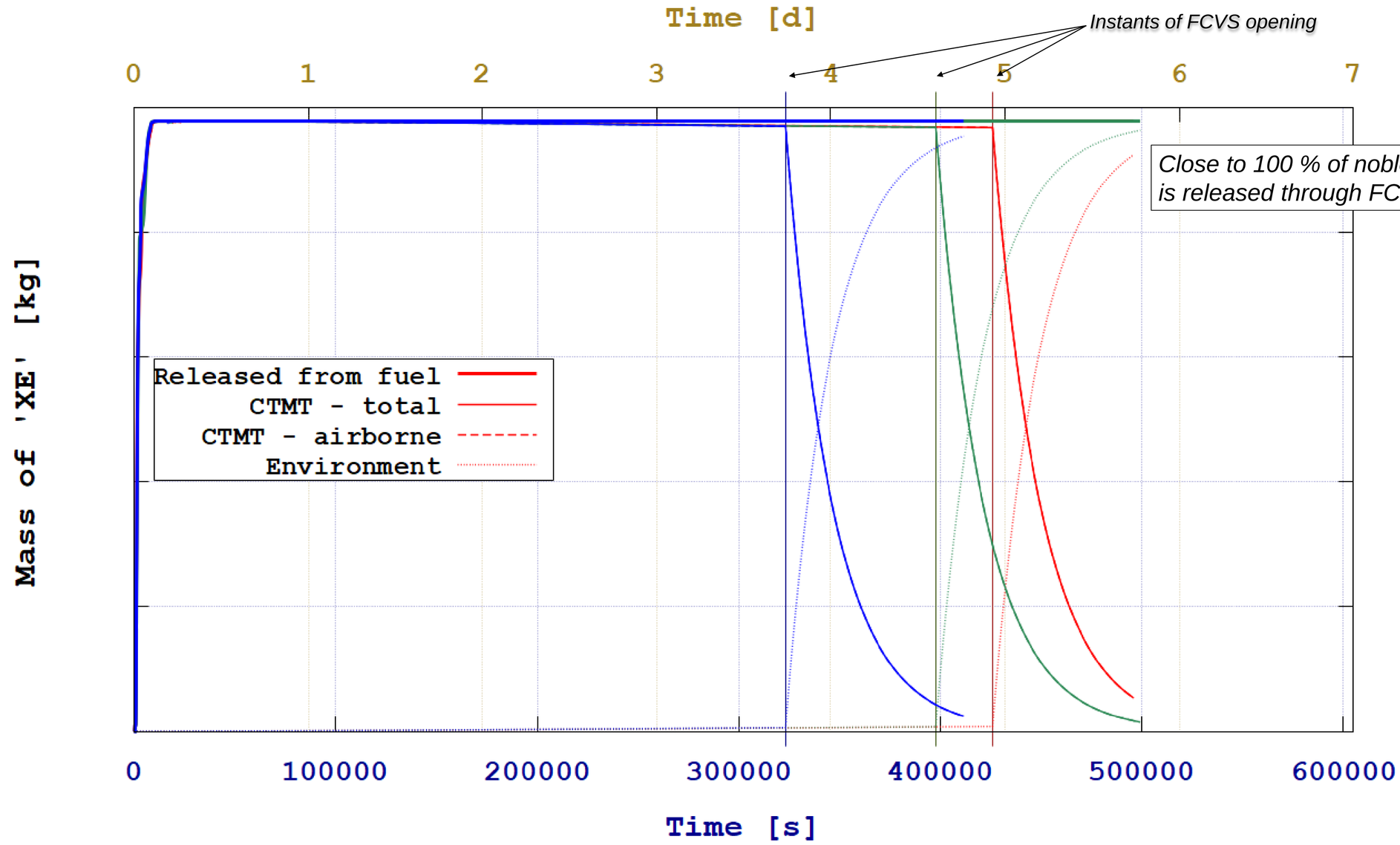

‘I2‘ RELEASE

CsI
1.5I2
3I2

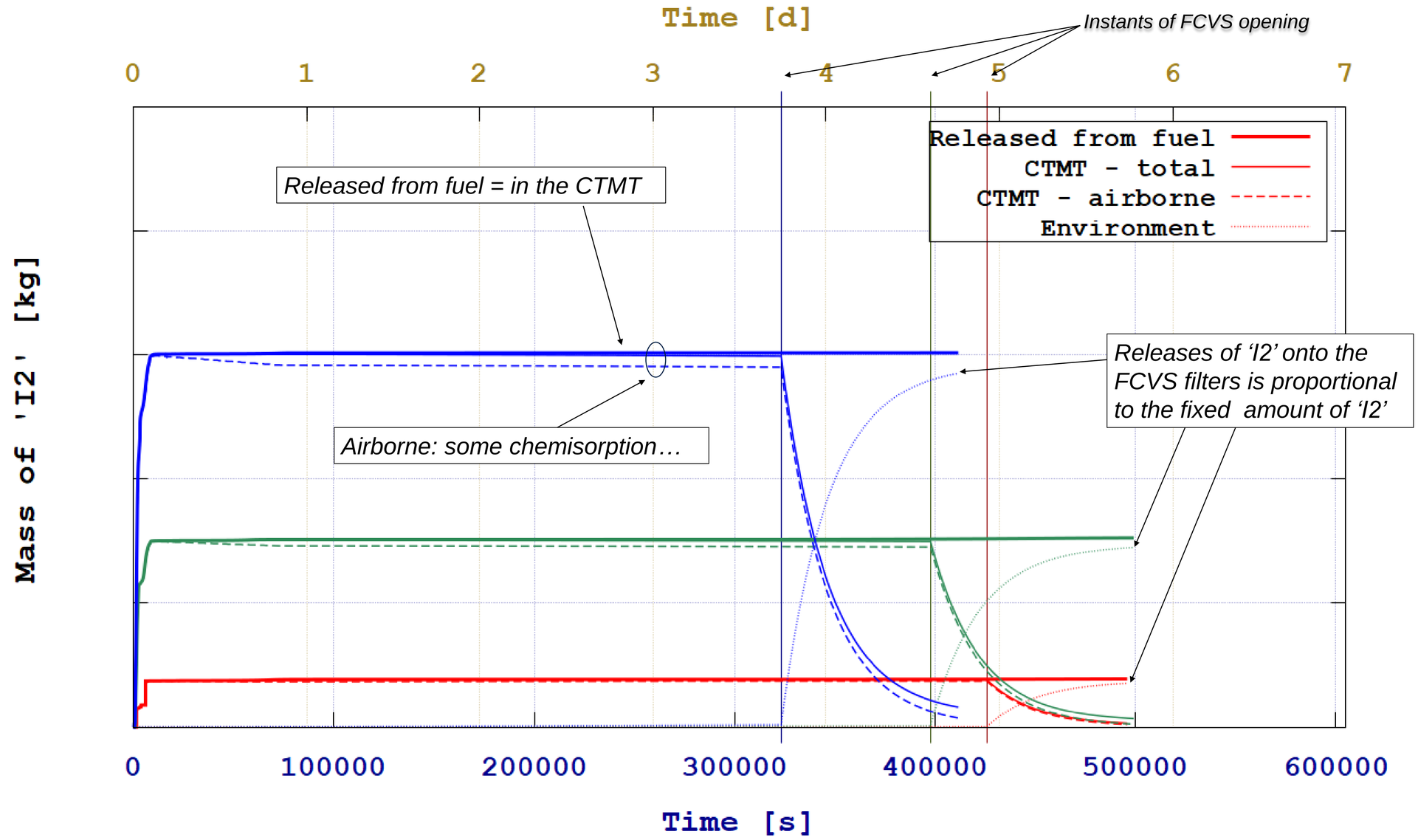

‘CSI‘ RELEASE

CsI
1.5I2
3I2

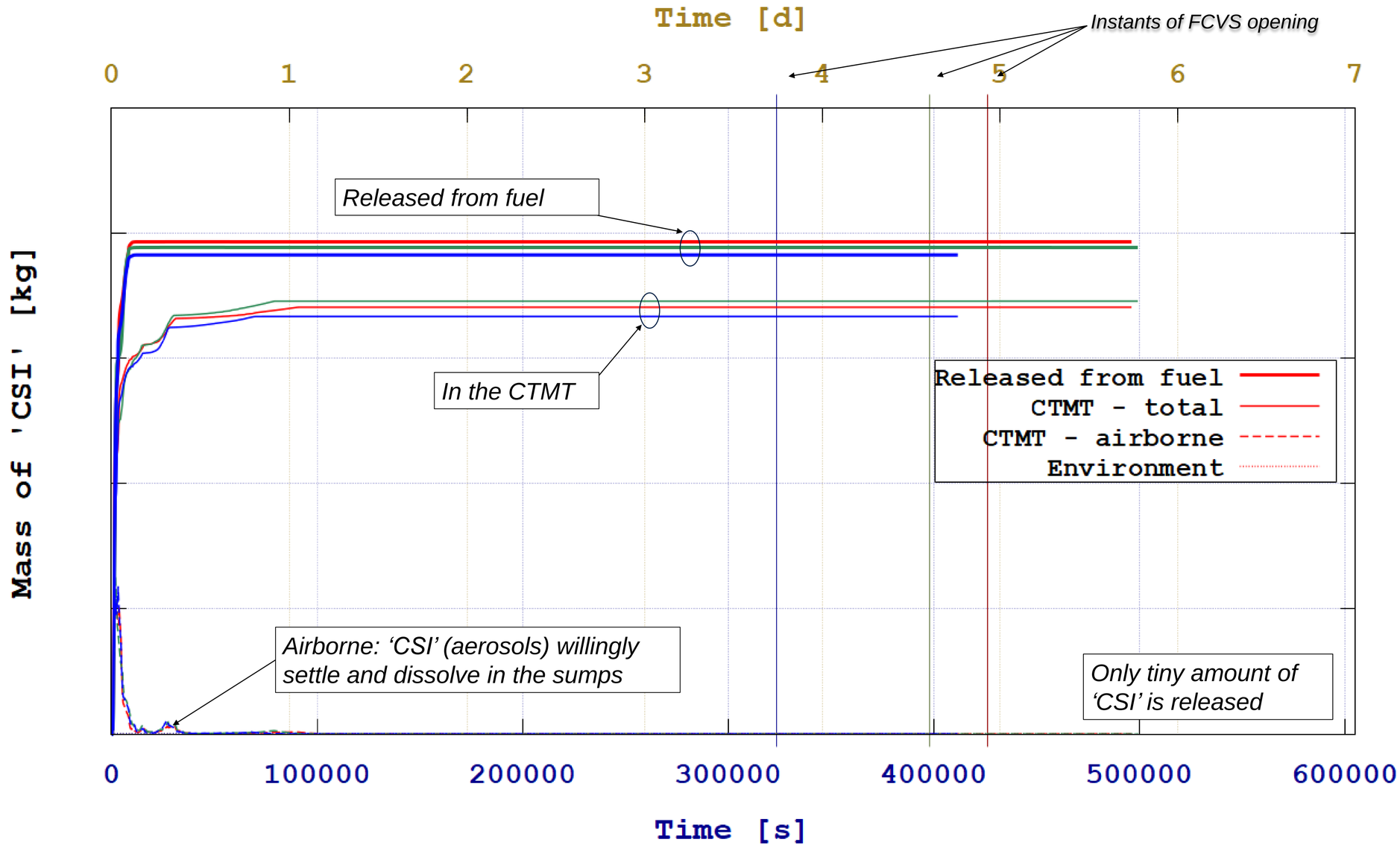

NUCLEAR RESEARCH INSTITUTE

2. DOSE RATE EVALUATION IF FCVS IS MANUALLY OPENED

FCVS: OPENING

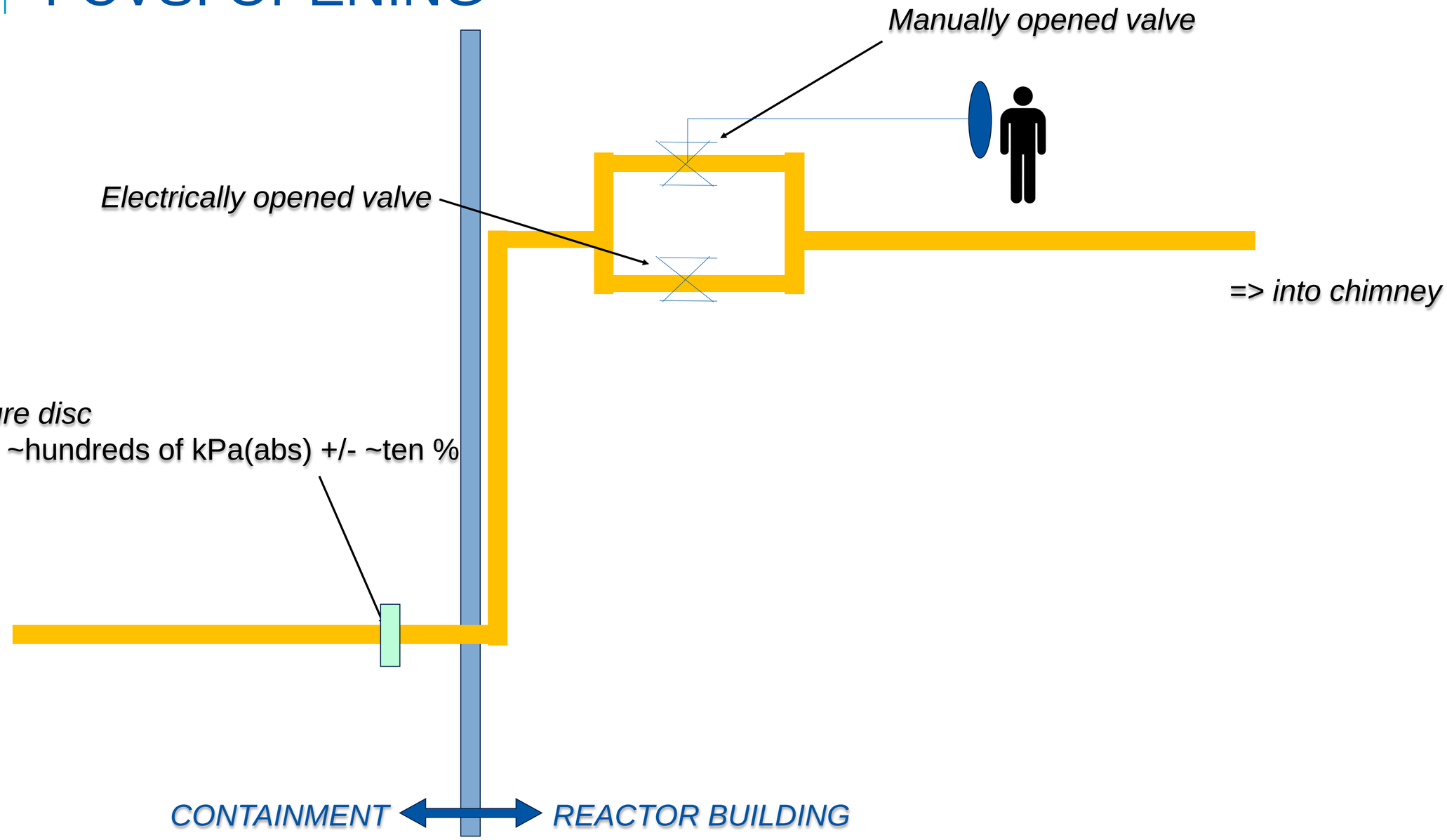

FCVS: DETAILED MODEL

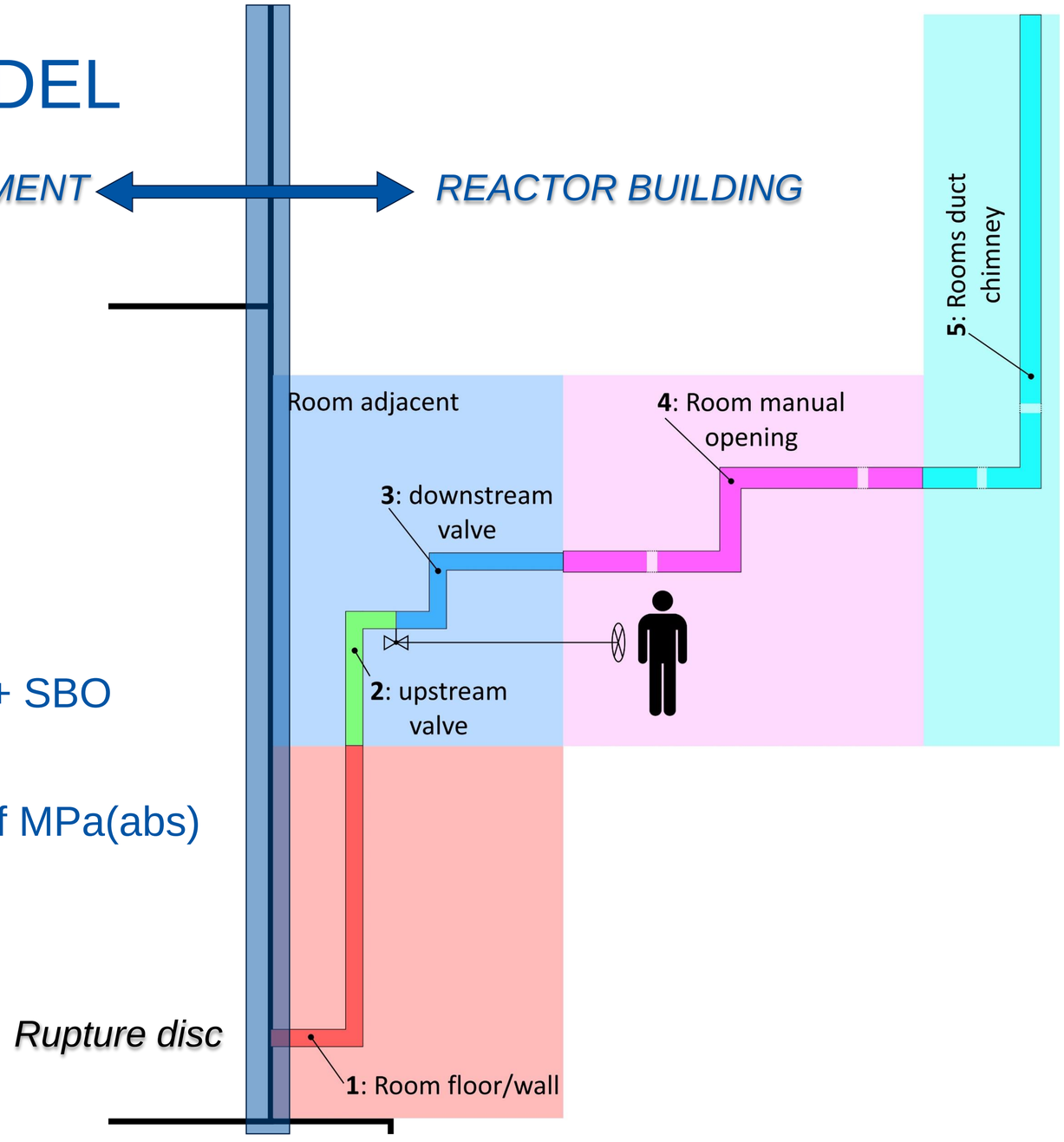

- MELCOR integral calculation: G-LOCA + SBO
- Iodine: **1.5 % in ‘I2‘**
- Opening pressure (rupt. disc): ~tenths of MPa(abs)
- Manual opening:
  - hrs to „take the action“
  - mins to „turn the hand-wheel“

FCVS: PRESSURE IN THE CTMT

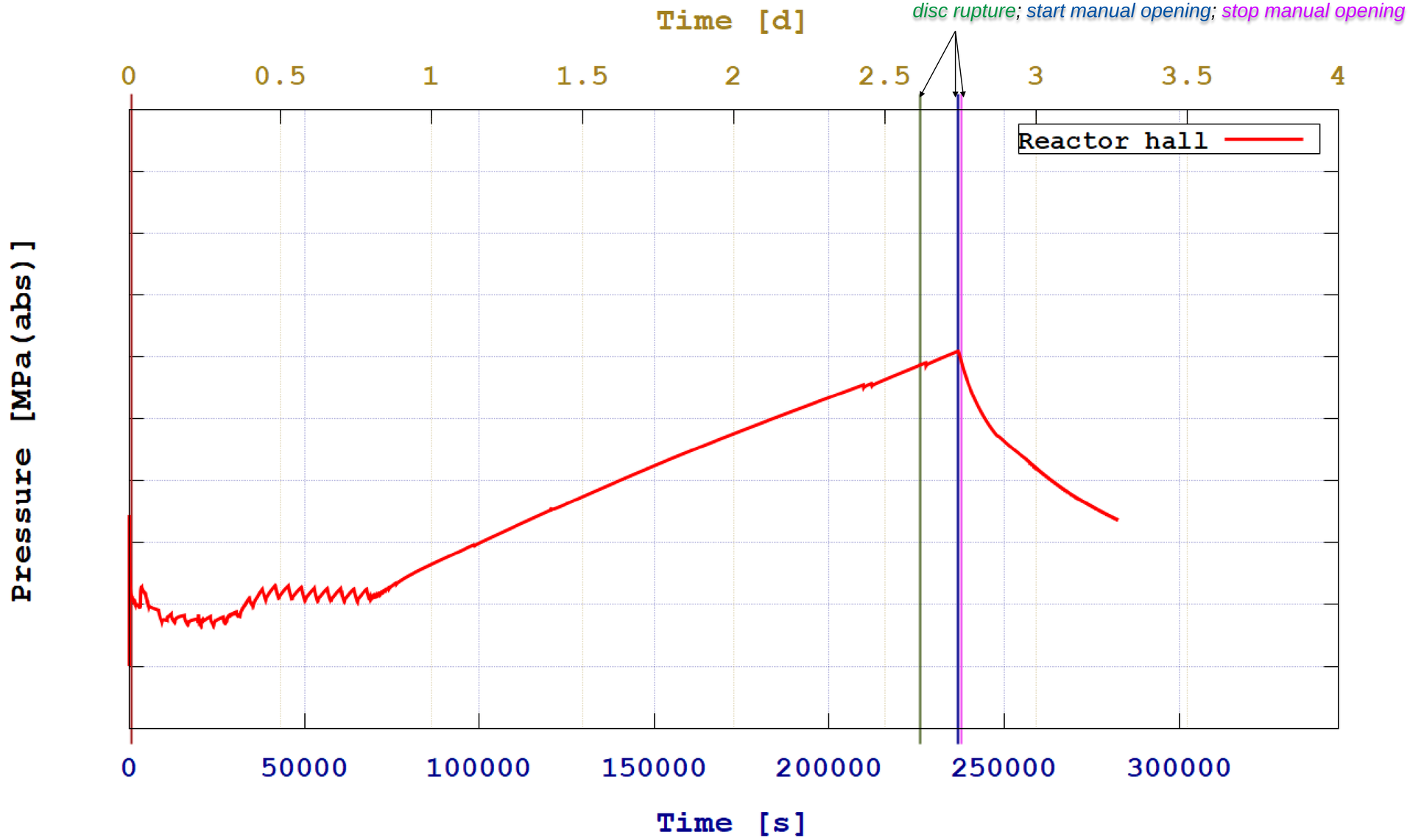

FCVS: PRESSURE IN THE CTMT

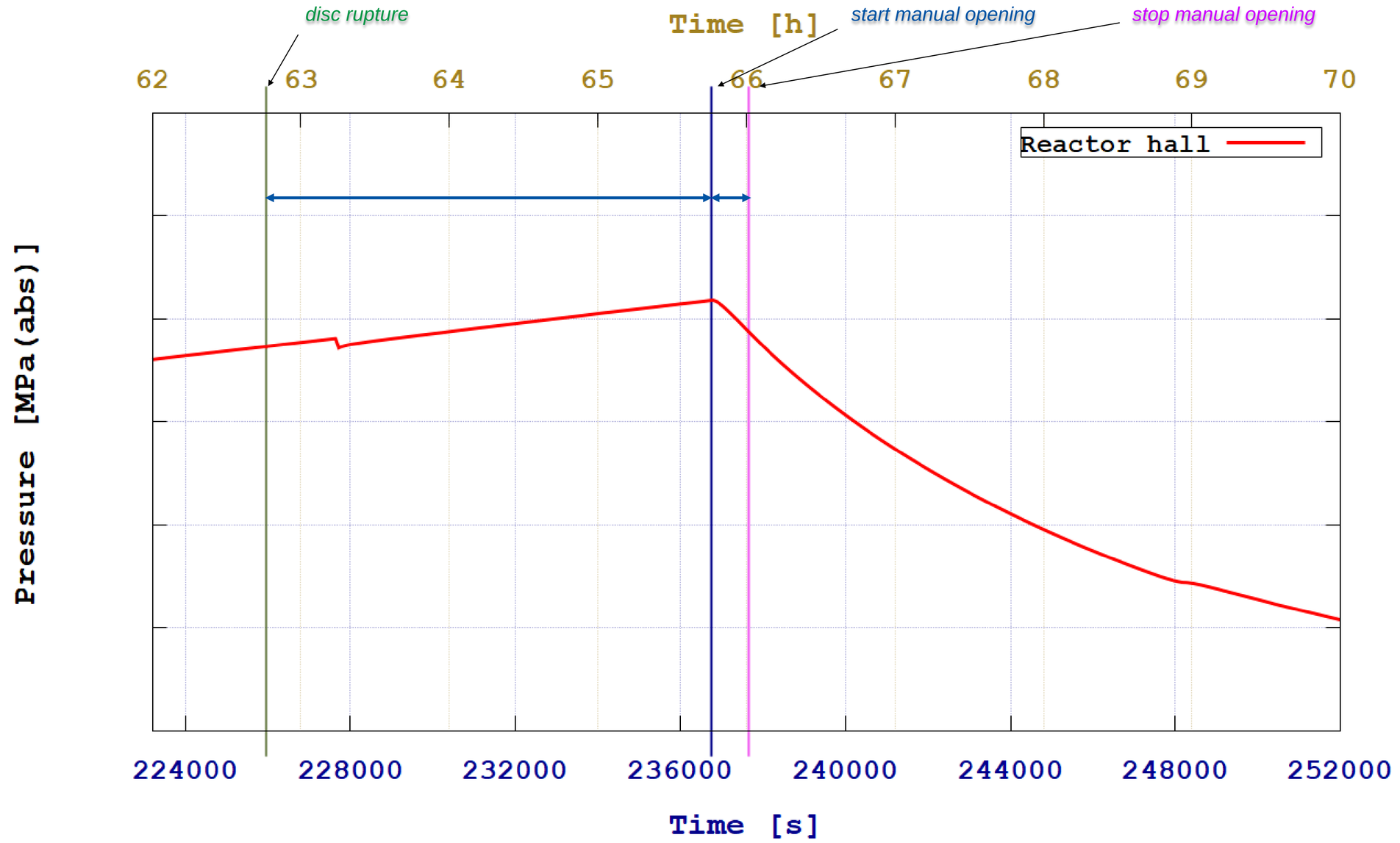

FCVS: PRESSURE IN THE DUCT

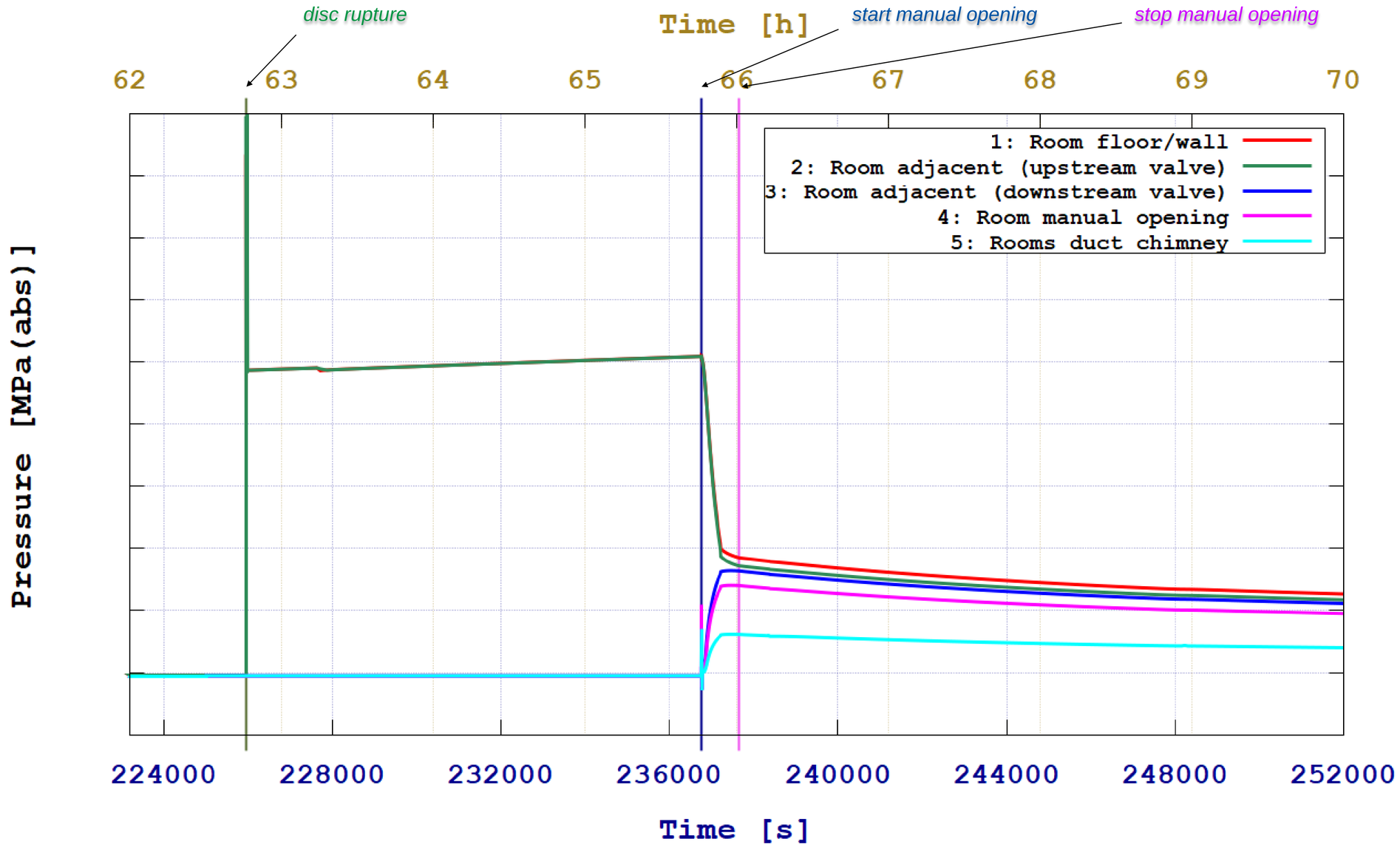

FCVS: FLOW RATE THROUGH THE DUCT

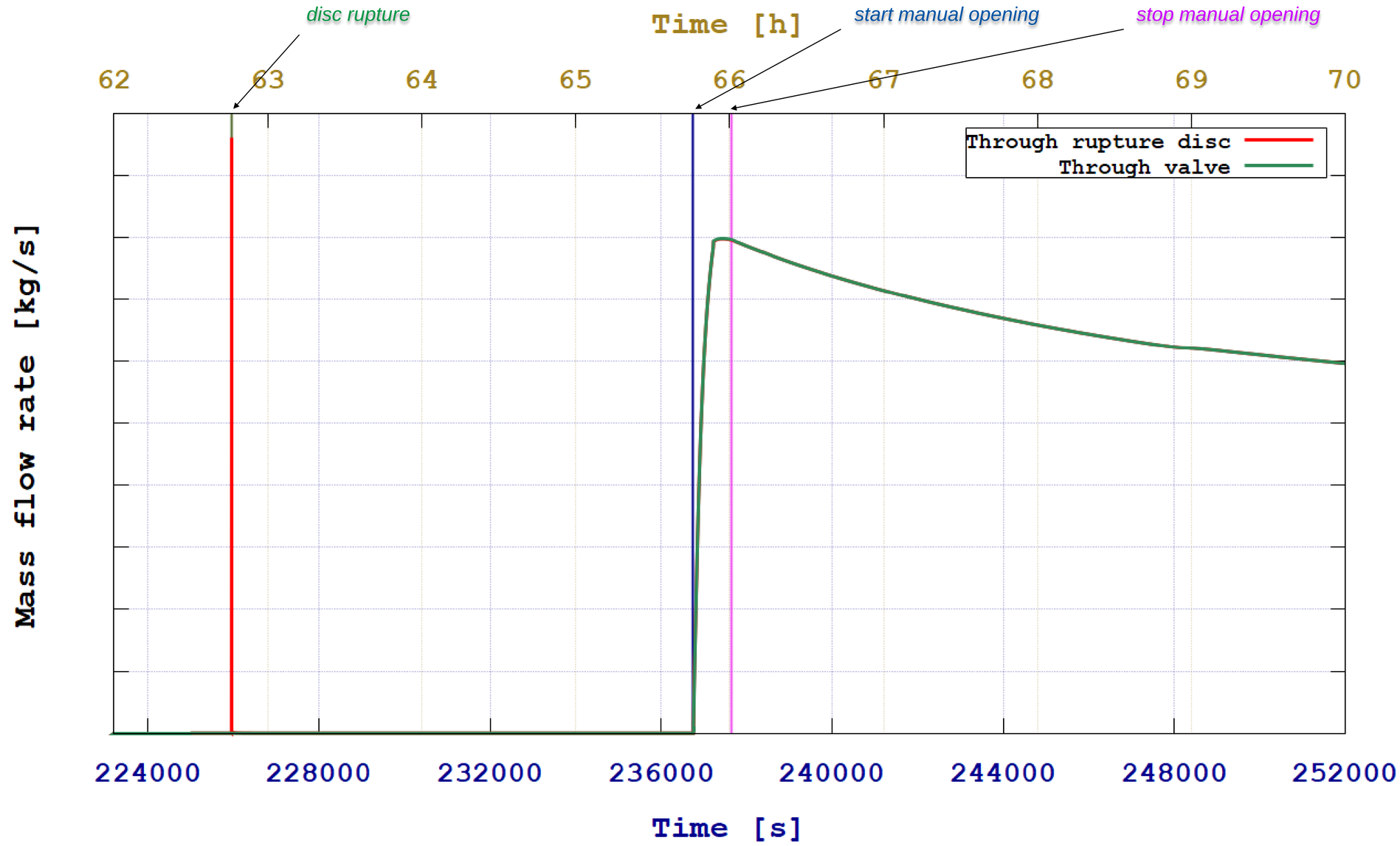

FCVS: AIRBORNE AEROSOLS

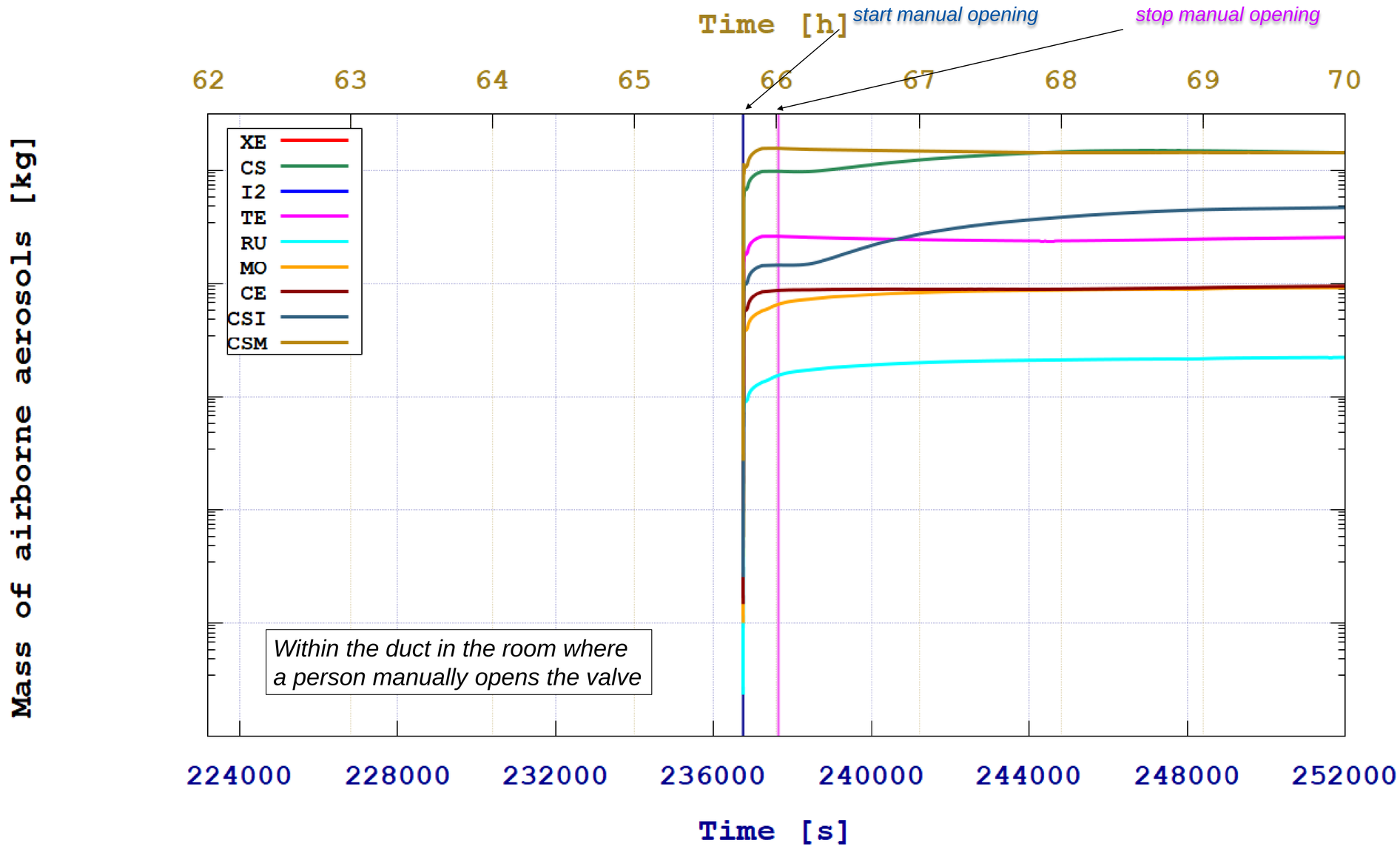

FCVS: VAPOURS

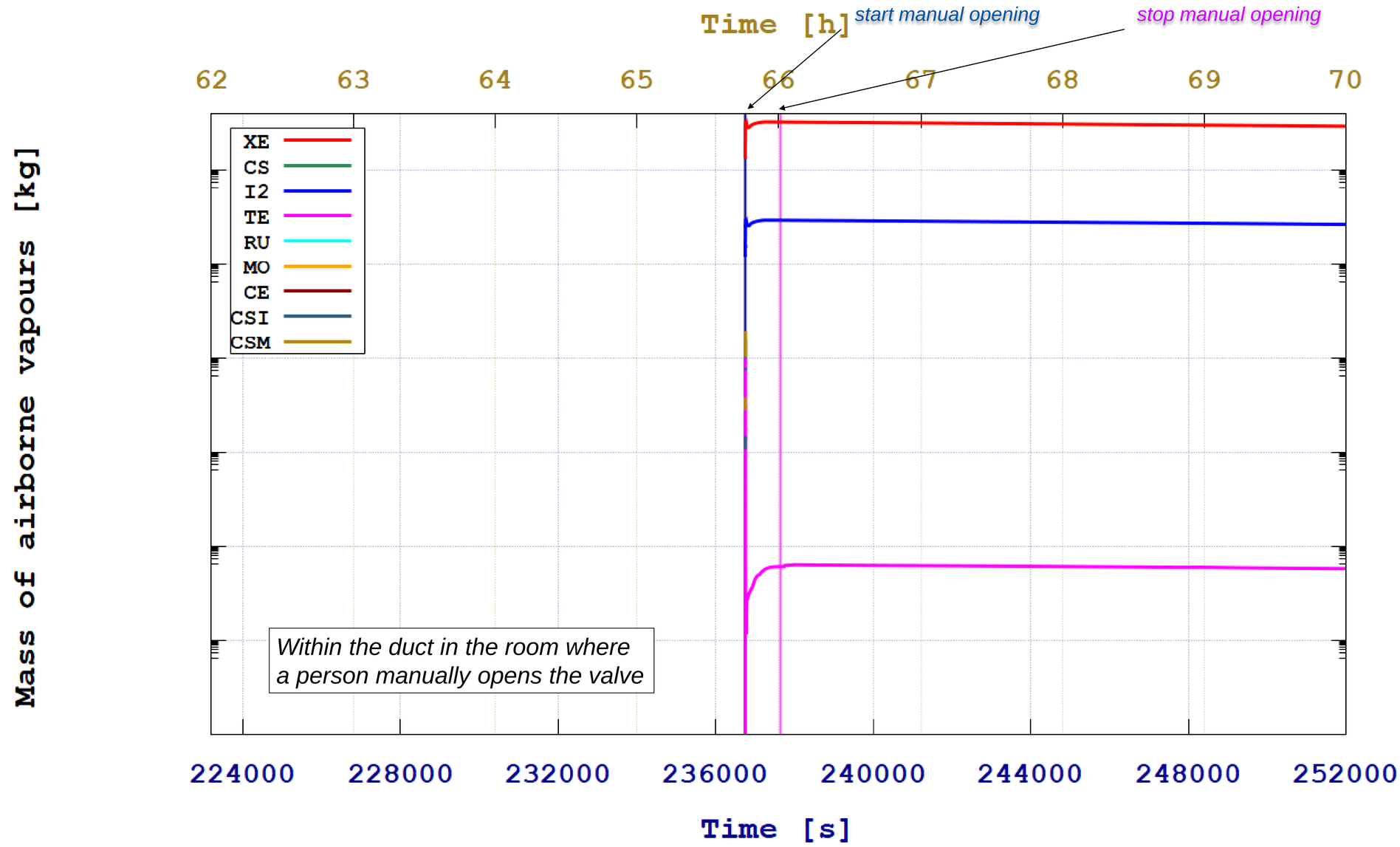

FCVS: DEPOSITED AEROSOLS/COND. VAPOURS

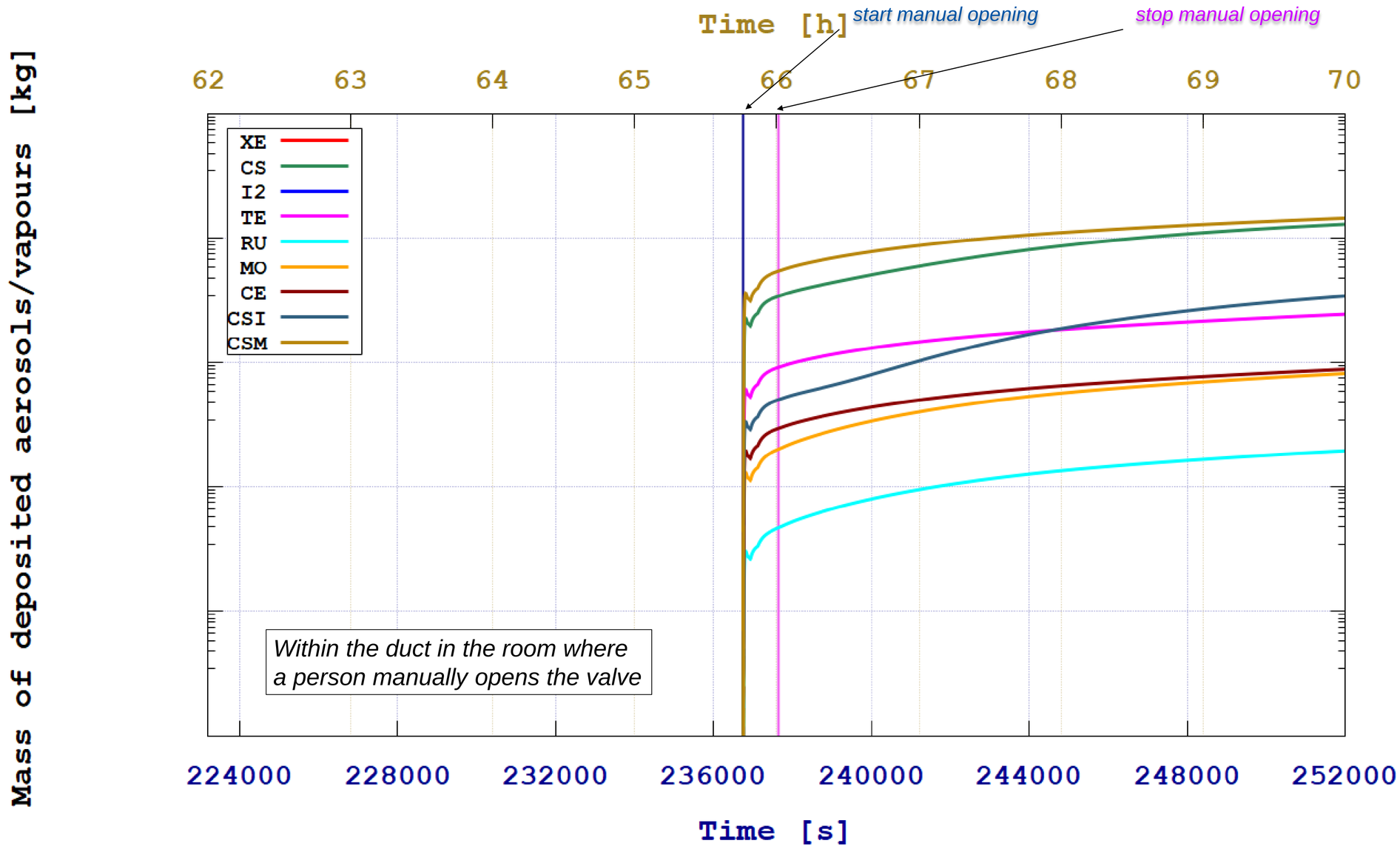

FCVS: EFFECTIVE DOSE RESULTS

- The sequence of codes MAVRIC/SCALE was employed
- Only γ-radiation was evaluated

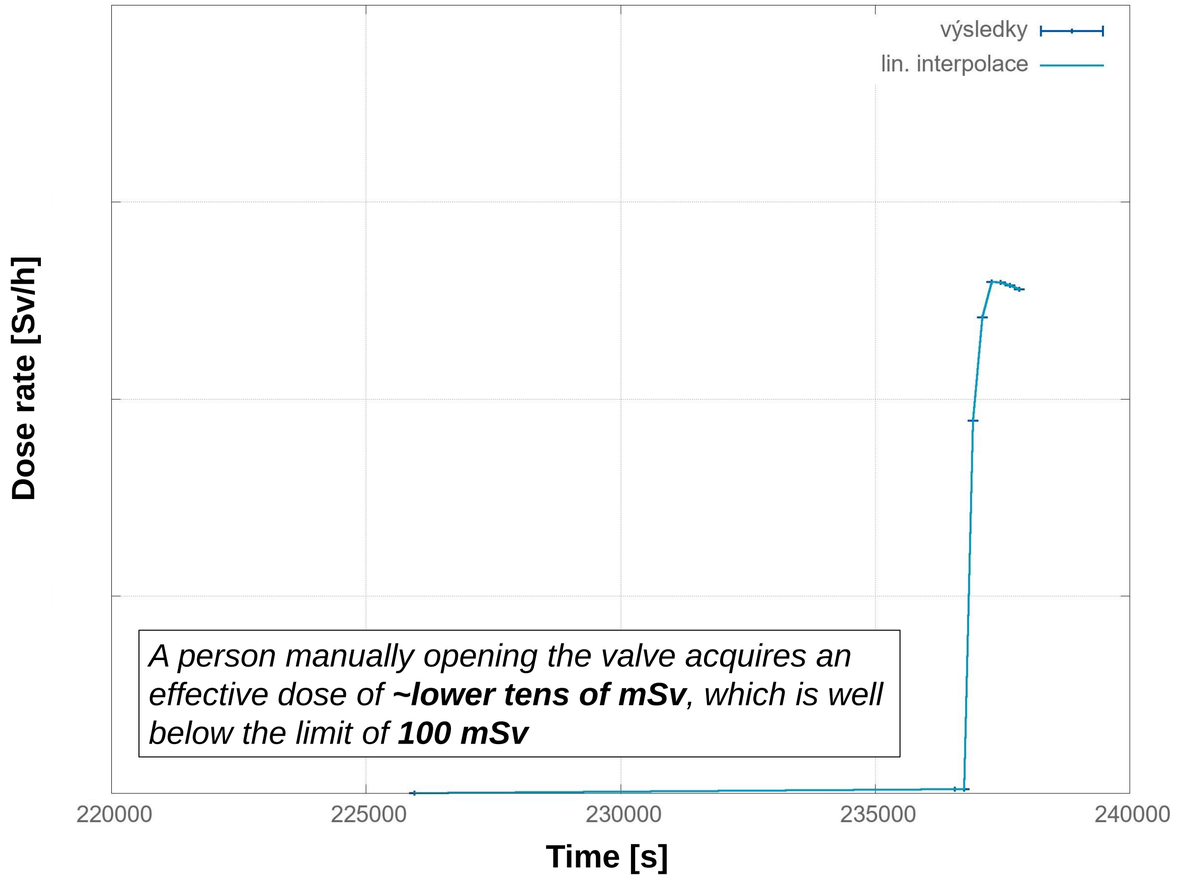

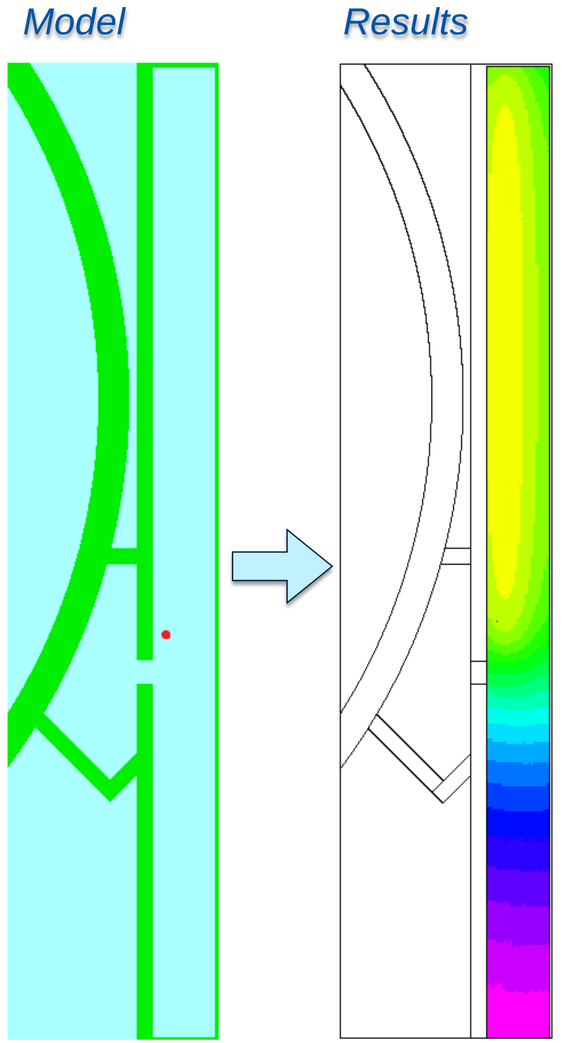

CONCLUSIONS

- Is is important to consider the iodine to remain also in the ‘I2’ class
  - To properly estimate the ST onto the FCVS filters
  - To properly account for iodine forms for radiological consequences analyses
- It was confirmed that manual opening of the FCVS valve is feasible
  - Even for the action taking 15 min, the acquired dose of ~lower tens of mSv < 100 mSv (limit for SAs)

Thank you for your attention!

NUCLEAR
RESEARCH
INSTITUTE

ÚJV Řež, a. s.
Hlavní 130, Řež
250 68 Husinec, Czech Republic

e-mail: sales@ujv.cz
www.ujv.cz

UJV Group
PEOPLE I INNOVATION I TECHNOLOGY

Source Term Dispersion Analysis and Construction of the Risk Map around the Peach Bottom Unit-2 Plant Using the ASTEC and JRODOS codes

Onur Murat, Fabrizio Gabrielli, Victor Hugo Sanchez Espinoza
Karlsruhe Institute of Technology
Hermann-von-Helmholtz-Platz 1, Eggenstein-Leopoldshafen, Germany
onur.murat@kit.edu, fabrizio.gabrielli@kit.edu, victor.sanchez@kit.edu

ABSTRACT

National regulators and Emergency and Preparedness teams require accurate source term predictions to protect the public from abnormal radiological emergency events like severe accidents (SA) in Nuclear Power Plants (NPPs). Therefore, reliable evaluations of the radiological consequences of hypothetical SAs in a NPP are mandatory. With this goal, a robust first-of-its-kind platform of codes has been developed at Karlsruhe Institute of Technology (KIT) in order to evaluate best estimate source term data and the corresponding radiological consequences following a SA in a NPP. In the platform, the fuel inventory loaded in the reactor core is computed by means of the CASMO5 code and the European reference Accident Source Term Evaluation Code (ASTEC), developed by IRSN, is employed to analyze the SA sequence from the initiation up to the fission product release to the environment. Finally, the source term results computed by ASTEC are employed by the JRODOS code, developed by KIT, to evaluate the radiological consequences of the dispersion of the fission product in the environment.
In this paper, the abovementioned calculation platform is employed to analyze the radiological consequences of an anticipated station blackout scenario (SBO) in a generic Peach Bottom Unit-2 NPP. Fuel inventory has been computed based on the real plant operation history and the ASTEC generic model of the plant has been assessed. The isotope-wise activity released to the environment during the investigated SBO scenario computed by ASTEC is then provided to JRODOS for performing the corresponding dispersion analyses. The 'usual' approach for JRODOS analyses consists of selecting 'representative' dates to evaluate the radiological effects of the source term dispersion. In principle, for a precise evaluation of the radiological risk, one should perform such analyses for each part of each day of the year because of the detailed meteorological data available nowadays, which would take a nonrealistic amount of calculation time.
In order to solve this issue, a methodology was developed to evaluate the radiological consequences of the SA in each geographical mesh around the NPP. A series of analysis, coming from about 60000 JRODOS calculations, have been carried out in each season by assuming that the SA occurs in randomly sampled days and hours. As a result, sample groups of JRODOS results in each mesh grid are obtained. For each mesh grid, the probability distribution of the radiological consequences is computed by employing the average values of each sampling group, the central limit theorem being employed. Finally, a risk map for each season of a full year is constructed to visualize, i.e., the average total effective gamma dose rate for each mesh as a consequence of the SBO SA scenario computed by ASTEC in the generic Peach Bottom Unit-2 NPP. In this way scope of the considered accident over the domain pictured in detail to able to address proper planning for early and intermediate phases of the accident. Therefore, the proposed methodology has the potential to provide meaningful and detailed information for the assessment of the Emergency and Preparedness actions in response to a SA event in an NPP. In the paper, the results for the SBO scenario in a generic Peach Bottom Unit-2 NPP will be shown and discussed.

KEYWORDS
ASTEC, JRODOS, BWR, Source term, Radiological Analysis

1. INTRODUCTION

Severe accident (SA) consequences carry significant risks on the public health and environment. Experienced severe accidents which resulted with large amount of radiological release to the environment, e.g., Chernobyl and Fukushima Daiichi, triggered the importance of the assessment of the SA analysis to support an adequate response planning in order to establish public safety.
Having this in mind, a first-of-its-kind calculation platform has been developed at KIT to perform radiological dispersion investigations following a SA in a NPP based on the employment of state-of-art codes for a best-estimate evaluation of the source term (ST) during an accident scenario. The CASMO5 code [1] is employed to evaluate the fission product (FP) inventory loaded in the core. Such data are used for the assessment of the model of the NPP and for the analysis of the postulated SA scenario from the intuition up to the FP release to the environment by employing the European reference ASTEC code [2], developed by IRSN. Finally, the ASTEC source term results are employed by the JRODOS code [3], developed by KIT, to evaluate the radiological consequences of the FP dispersion in the environment. The calculation platform has been applied in previous studies [4-5] to evaluate the radiological consequences of an anticipated station blackout scenario (SBO) in a generic Peach Bottom Unit-2 NPP. It is important to emphasize the results of the severe accident analysis in terms of public safety since the action plans during the accidents can be developed based on taking into account possible consequences of the severe accidents.
In order to identify the uncertainties on the radiological releases resulted by SA scenarios, the EU CONFIDENCE (Oping with uNcertainties For Improved modelling and DEcision making in Nuclear emergenCiEs) Project has been performed (2017-2019) [6]. The main purpose of the project was to improve the decision-making process to help protect public and environmental safety against the severe accident consequences. For this reason, certain parameters, which carry the main uncertainties for dispersion period and for the longer term after the accident, were identified. During the release of the radioactive isotopes, wind direction, atmospheric stability, magnitude of the source term, and timing of the event were identified as major drivers for the uncertainties.
Another study [7] about the decision-making process for the transition phase after a severe accident, which corresponds to the turning back to the normal living conditions after accident occurs, pointed out that the actions and the decisions during the emergency phase of the accident have strong connection for the transition phase. For this reason, the assessment of the emergency phase and of the construction of proper response plans are required to establish better conditions for public and environmental safety.
Such requirements for improved emergency response planning triggered the research summarized in the current paper, which focusses on a further extension of the above-mentioned calculation platform developed at KIT aiming at the construction of a risk map approach and at the assessment of a large JRODOS database. As study case, a generic Peach Bottom Unit-2 is considered here with short-term station blackout accident transient. Released amount of radionuclides to the environment described as source term in the JRODOS to simulate emergency phase of the accident. Simulation of the radionuclide release repeated to build up database of the risk map. In the paper, a brief description of the ASTEC model of the NPP and the evaluation of the fuel inventory is provided in chapter 2. Then, in the third section of the paper, the risk map creation approach which is based on the statistical analysis is described and results are provided and discussed.

2. ASTEC MODEL AND FUEL INVENTORY OF THE PEACH BOTTOM UNIT-2

The model of a generic Peach Bottom Unit-2 NPP was constructed on the ASTEC European reference severe accident code and depletion analysis was accomplished by using CASMO5 code in order to determine radionuclide inventory in the fuel material. Modern BWR type fuel assembly GE14 10x10 has been selected for the analysis and the discharge burnup of 46.47 MWd/t has been achieved. The determination of the discharge level and burning period of the fuel assembly has been made based on the experimental studies on the ENRESA samples which are from the same type of GE14 10x10 BWR fuel assembly [8-10]. It has been assumed that core is loaded with the fuel assemblies which are at the same discharge burnup level.

The plant model details, such as vessel dimensions, volumes, and connections, are extensively covered in the previous studies [4-5]. Updates to modern fuel assembly and notable differences have been expressed in the level of fuel assembly design and power plant level. The core includes 764 assemblies distributed across radial meshes, with a new GE14 10x10 fuel assembly design. Water rods in the BWR fuel assemblies enhance neutron moderation, impacting accident progression by increasing Zircaloy material and coolant availability in the active region. Subchannel definition within fuel assemblies aids understanding the new design's behavior under SAs. Containment and reactor building zones, along with primary containment failure modes, remain unchanged. The two failure modes involve ruptures between wetwell-torus and drywell-refueling bay, respectively. Reactor pressure vessel and connection between containment section including the failure modes and general layout is given in Figure 1. The short-term station blackout (SBO) has been selected for the analysis, since such scenario is one of the highest core damage frequency accident transients for the BWR type Peach Bottom Unit-2 NPP [11]. The ASTECv3.1.1 has been employed for the analysis of the progression of the SA scenario and for the source term evaluation.

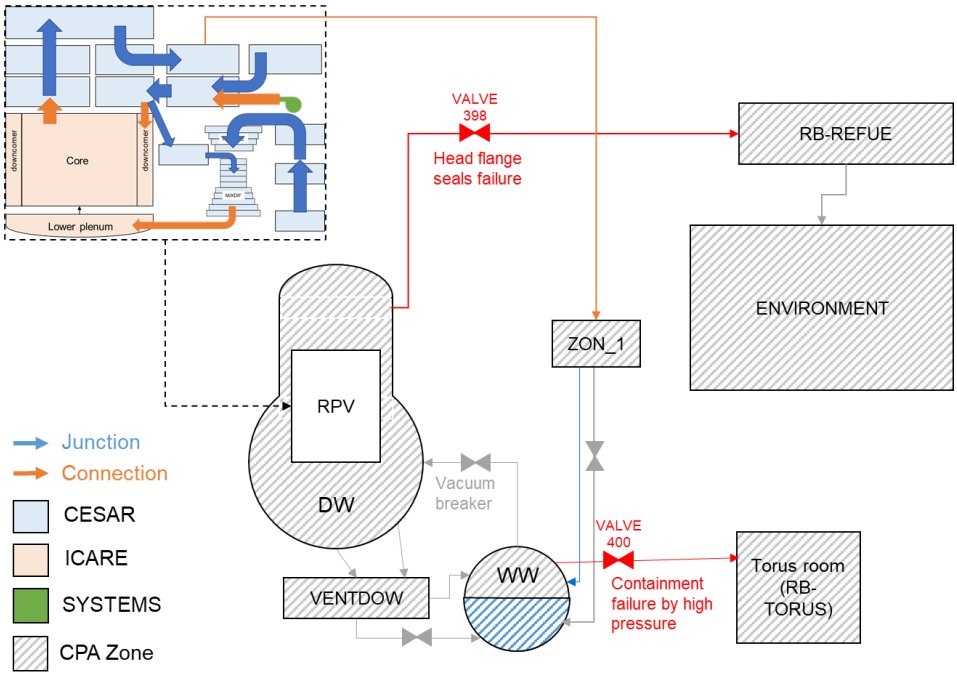

Figure 1. Simplified representation of the ASTEC Model layout of the Peach Bottom Unit-2 NPP [5].

After the failure of the head flange seals failure connection between drywell zone and refueling bay is activated. In this way, radioactive isotopes are transfered from refueling bay domain to the environment and release starts. At the end of the short-term station blackout simulation, 2.19E18 Bq activity released to the environment. In order to compare the magnitude with experienced severe accidents in the past, Chernobyl and Fukushima Daichi has total radioactivity release to the atmosphere around 14.0E+18 Bq [12] and 6.3E+17 Bq [13] respectively. Total radioactive isotope release to the environment took 20.68 hours. At the end of the transient, the ASTEC results concerning amount radioisotopes released to the environment are given in Table I.

Table I. Total released activities of radioactive isotopes to the environment at the end of short-term station blackout accident [5].

Isotope	Half life	Release (Tbq)	Isotope	Half life	Release (TBq)
Kr-85	10.7 y	1.686×10^4	Mo-99	2.8 d	13.65×10^2
Sb-125	2.8 y	27.11	Rh-105	35.5 h	1.813
Sb-127	3.8 d	152.4	Ba-140	12.8 d	452.5
I-131	8.0 d	7.986×10^4	Sr-90	28.6 d	3.341
Te-132	3.2 d	1.266×10^3	Sr-91	9.5 h	3.177
I-132	2.3 h	12.34×10^3	Y-92	3.7 h	<<
Xe-133	5.2 d	1.732×10^3	Ru-103	39 d	115.9
I-133	20.8 h	7.094×10^4	Ru-105	4.4 h	1.145
I-134	0.9 h	5.698×10^{-5}	Ru-106	1.0 y	53.52
Cs-134	2.1 y	681.6	La-140	1.7 d	196.2
I-135	6.6 h	9.014×10^3	Ce-141	32 d	126.4
Xe-135	9.1 h	25.03×10^4	Ce-143	1.4 d	79.7
Cs-137	30.1 y	470.4	Ce-144	284 d	128.5

3. STATISTICAL ANALYSIS AND CONSTRUCTION OF THE RISK MAP

The implementation of the radionuclide release from the plant to the environment, computed by ASTEC, is the step to determine the consequences of the severe accident in terms of public and environmental safety by means of the JRODOS code. The one can select possible starting time point of the release in the calendar year. Depending on the selected time period, meteorological conditions over the region could have different wind direction, temperature, precipitation rate etc..

In order to picture the possible consequences of the radiological dispersion analysis, example cases have been constructed. Release rate, amount of released fission product has been kept constant. Differences between the cases are only the starting time of the release to the environment. As it can be seen in Figure 2, depending on the selected year, month, day, the dispersion results around the NPP site might have very dispersed consequences compare to each other. Not only the day by day but also considering the start of the release at different time of the same exact day could have different results in terms of dispersion direction and total affected area and dose rates. The one considers that example cases in Figure 2 only given for representative purposes and they are not related with fission product inventory given in Table I.

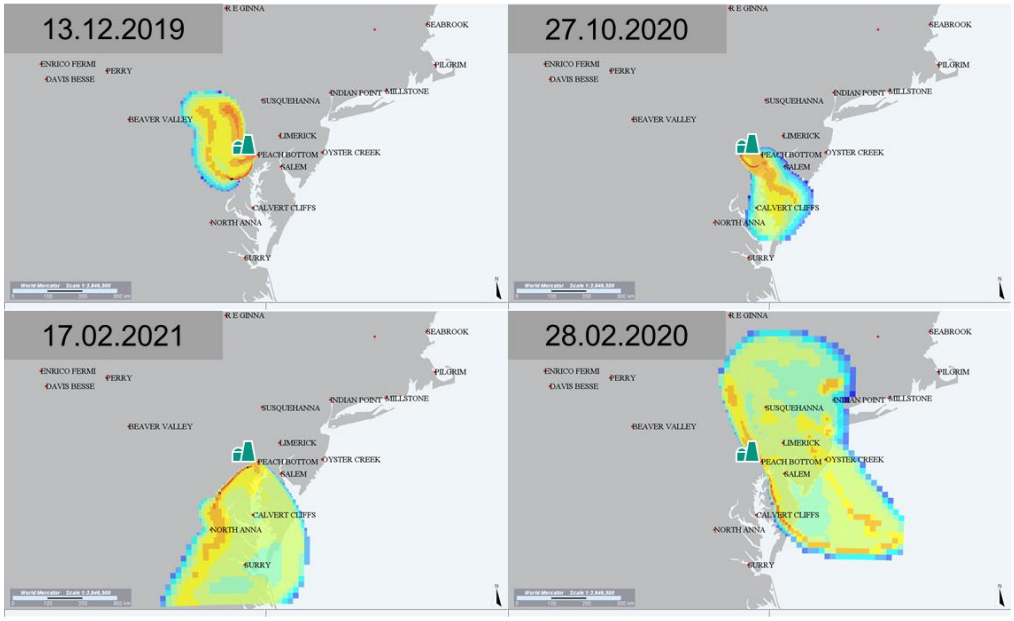

Figure 2. Example of the possible dispersion consequences in terms of total gamma dose rate resulted by short-term station blackout accident in the Peach Bottom Unit-2 NPP.

In order to understand the possible outcomes of the calculated radionuclide dispersion over the considered domain, a statistical analysis approach has been taken into account in the previous studies [4-5]. Same approach has been followed in this study as well. Construction of the grid selected as default in the JRODOS options which corresponds 8056 square meshes in 5 concentric rings around the plant location point. Most outward ring radius adjusted as 400 km. Meteorological data over the considered spatial domain has been provided by the American NOMAD servers which are hosted by the U.S: National Oceanic and Atmospheric Administration under the U.S. National Weather Service Office. Atmospheric dispersion model of the RIMPUFF puff model is selected for the analyses. Simulations have been carried out for 24 hours, which covers the total 20.68 hours of release duration from the power plant. Time resolution of the simulation has been selected as 30 minutes. Released activity has been divided into equal parts of 30 minutes to implement the time dependent source term release computed by ASTEC to the environment in JRODOS analyses. Selection of the time dependent source allow the analysis more realistic, as the release of the all activity in the plant is not expected to be occur instantaneously.

All the days in the considered calendar years have been taken into account and the release starting points have been selected randomly to simulate radiological dispersion analysis. Among all the results, the highest recorded gamma dose rate has emphasized the potential of the radiological release by considering worst case scenario including specific meteorological conditions. Since the regime of the weather conditions is not stable during the year, month and even days the one need to check every possible starting point in order to understand what possible consequences the dispersion could create for the public and environment. In order to do that, the analysis needs to be performed by using 1-minute steps which is the time resolution of the JRODOS code.

The simulation of the statistical analysis in the previous study [5] includes 3 calendar years and 24 hours analysis has been performed for each day of the years. Analysis was completed with total cpu time of one day. Including every possible starting time point for the statistical analysis requires 1440 simulation analysis for a day and the total cpu time requirement of the 3 years statistical analysis could result about 4 years, which is unrealistic to be performed. Furthermore, the conducted analysis based on the fission product releases from the short-term station blackout accident took 21 hours. Other potential accidents that could result in core damage and the release of radioisotopes to the environment may have a longer duration of fission product release. It could even require even higher cpu times to complete a dispersion analysis taking into account every starting time point.

In order to overcome this issue and extract valuable information from the large database of JRODOS results coming from analyses of 1-minute of time step over the years domain, the central limit theorem has been employed. As known, the theorem states that regardless of its shape of the population distribution, the distribution of the mean of the samplings from that population will approximate to the normal distribution [14]. Over the population of time points in the year 2021, sample groups have been created and the sample group mean distribution has been established to obtain the population mean. Sample groups and investigations have been carried out for each season separately. For each season, 30 starting time points have been selected randomly, radiological dispersion analyses with JRODOS have been conducted, and total gamma dose rates have been computed and stored. One group of samples is created at each of the 30 selections and finally 500 sampling groups have been established. The mean value of the total gamma dose rate of each group has been calculated and finally 500 sample mean values (one for each group of samples) have been collected for every mesh point over the domain. As an example, the distribution of the average total gamma dose rate of the sample groups on a mesh is given in Figure 3. Assumption has been made for all the meshes over the domain that the distribution of the average of the sample groups will follow a normal distribution and that the mean of the average sampling distribution equals to the population distribution, which is equivalent to the seasonal average of the total gamma dose rate on the mesh.

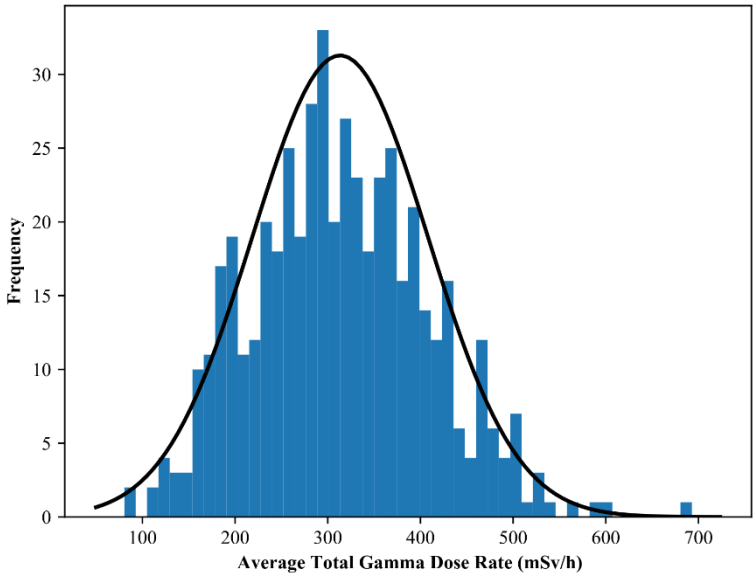

Figure 3. Average of a random sampled groups example on a mesh for the spring season.

The simulation of the 500 groups, which consist of 30 sample simulations, have been concluded for each season and a database of results from 60000 JRODOS simulations has been constructed for the year 2021. The total simulation time for the 60000 analyses was approximately 25 days of CPU time. The mean values of the total gamma dose rate in the winter and spring are shown in Figure 4, while the results for summer and autumn seasons are shown in Figure 5. Scale of the figure legends are set to up to 50 mSv/h which is the radiation annual limit for the radiation workers in the U.S. [15]. In case of public individual annual limit is decided 1 mSv/h for a whole year. Since each season has their characteristic weather conditions, construction of the sample groups and risk maps divided into four seasons.

The largest dispersion of dose rate is observed in the winter time in Figure 4 among the all the seasons and the main branches of the distribution located on the south, south-east and south-west locations. In general, it is in favor of public safety that not only in winter but also in spring and autumn seasons have strong dispersion tendency to the Atlantic Ocean due to the average weather conditions. On the direction of the south-west, cities of Baltimore, Washington D.C., and Richmond are located and a wide spread of the average total gamma dose rate is observed not only in the winter risk map but also in the spring and autumn.

In addition to that, another strong dispersion along the north-east direction has potential to reach the peninsula where New York City is located. Hills and mountains in range extending from the southwest to the northeast between Peach Bottom Plant and Perry Nuclear Power Plant prevents the spread of radioactive isotopes from progressing northward and westward.

Especially during the summer season average, the computed total gamma dose rate exceeds the public individual limit in a larger area around the plant than to the other seasons. Due to the average weather conditions, summer season produced larger high dose rate domains and, from power plant site location to the around 38 km up to north direction, recorded total gamma dose rates are above the 50 mSv/h. In order compare with previous experienced accidents which resulted radiological release to the environment, Three Mile Island and Fukushima Daiichi accidents can be considered. Beginning of the Three Mile Island accident evacuation around the plant started considering 8 km of radius from the plant and the evacuation plan was enlarged by considering 32 km of radius area in the following days. A similar plan was followed up at the Fukushima Daiichi NPP and at the first evacuation order was made first 2 km radius and following evacuation planning by the government decided to increase the radius first 10 km and then 20 km. The reason of the extension of the evacuated area is that planned emergency actions and pre-defined evacuated and sheltering zones in the regulations did not consider the extent of the accident and the magnitude of the radiological release [16]. However, the implementation of the risk map concept for each plant by considering the worst-case scenario and the radiological release, it can be used to determine the extent of a radiological release over the domain and based on this, appropriate emergency plans can be introduced. Effectiveness of the communication and number of the emergency personnel in the field and logistic capabilities are key factors to be able to follow the constructed plan. Since blackout condition at the Fukushima also disrupted communications between local and central government and this prevented the application of the evacuation plan in desired way and time.

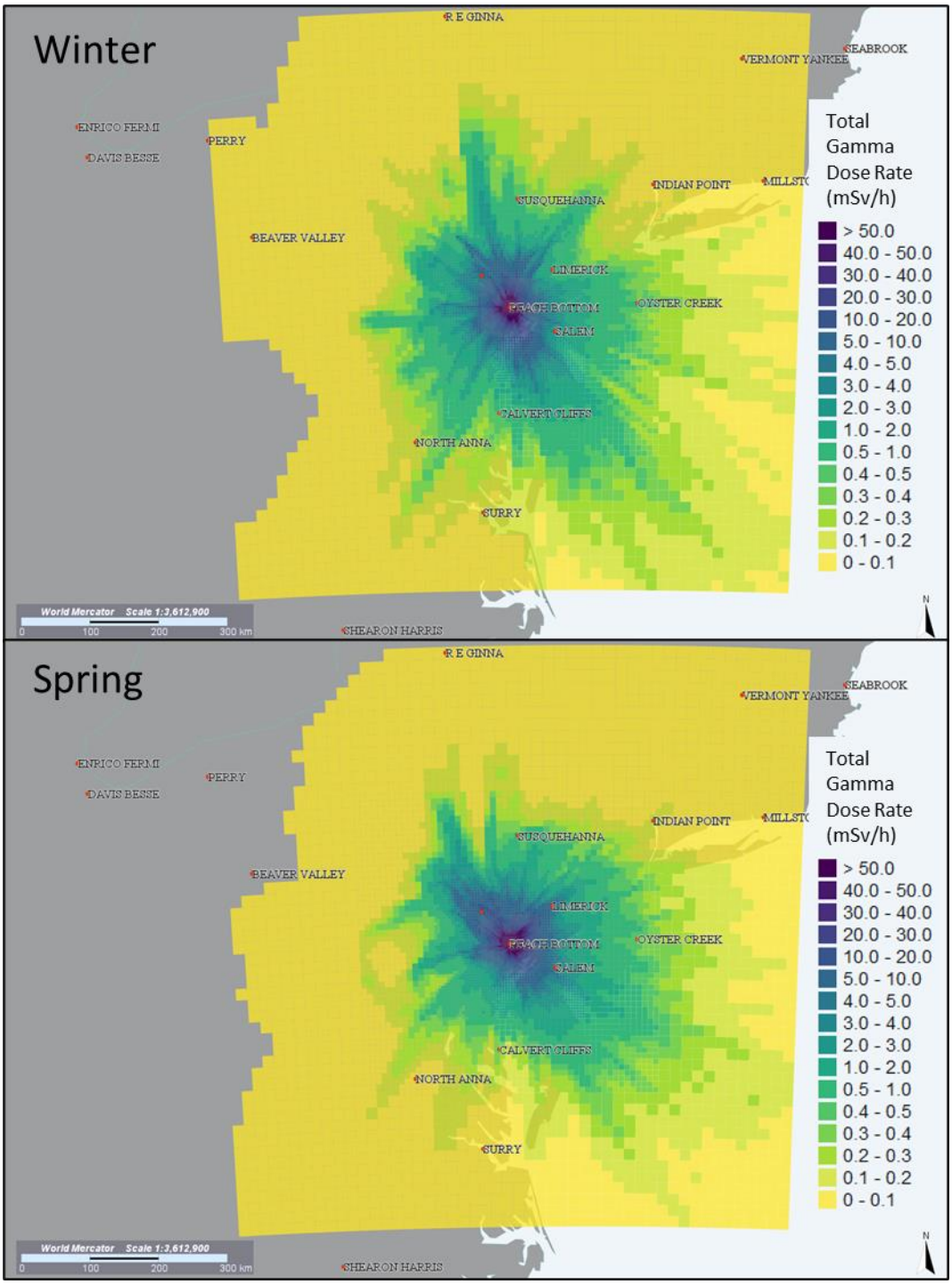

Figure 4. Risk map of short-term station blackout accident in Peach Bottom Unit-2 NPP including seasons of 2021 winter and spring.

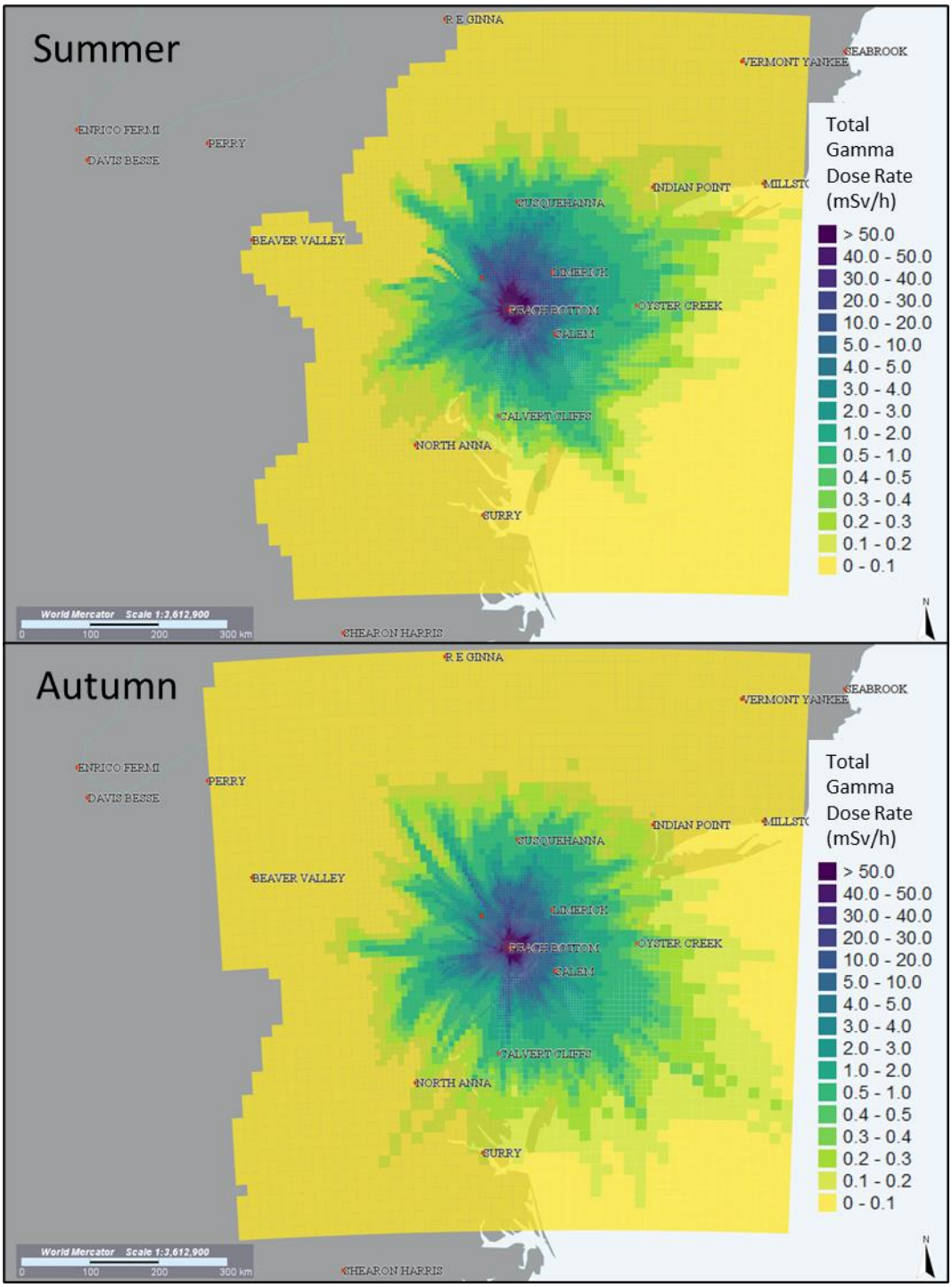

Figure 5. Risk map of short-term station blackout accident in Peach Bottom Unit-2 NPP including seasons of 2021 summer and autumn.

4. CONCLUSIONS

The issue raised by the Fukushima accidents was that we needed to improve the reliability of our predictions to support the emergency plant actions. To address this issue, a calculation approach was developed to establish the risk map and to examine accidents with high core damage frequency with the final goal of expanding the emergency planning database and enabling the creation of up-to-date plans. The study was conducted as a next step of previous studies where source term calculation and severe accident assessment have been done by using ASTEC, and statistical analyses of the fission product dispersion have been performed by using JRODOS code for the short-term station blackout scenario in a generic Peach Bottom Unit-2 Power Plant. In order to draw a general picture of possible outcomes, the total gamma dose rate parameter has been selected. However, in order to analyze the radiological consequences more in detail around the plant site, deterministic effects, distribution of the iodine tablets, evacuation and relocation of the residents around, long terms effects, total deposition of the iodine and aerosols and economical costs can be included. In this way, the constructed database can be adopted to update emergency planning and countermeasure actions.

In this study, database of 60000 JRODOS scenarios have been stored. The sample group size of 500 may provide sufficient data for some mesh points where radiological dispersion frequently occurs. However, some points, particularly those located far from the plant, do not receive fission product transfer and dose rate readings in every randomly selected time frame. In very rare conditions, some points do not receive any measurements at all. To strengthen the assumption of a normal sampling distribution, the sample size can be increased. Additionally, the mesh grid around the plant has been selected within a 400 km radius. After a distance of approximately 300 km from the plant, the average total gamma dose rates recorded during different seasons drop rapidly. This indicates that the number of days dose received is not high. Therefore, the construction of the mesh grid around the plant can be reduced to 200 km to decrease computational time and establish better average sampling distributions for each mesh.

It needs to be stressed that construction of risk map and assessment of the possible outcomes is plant-, accident scenario, and plant location specific. Considering the same design and accident or equivalent source term release in terms of activity and release rate could differ on the different geographical location. Establishing risk map analyses on a fleet of a power plants on nationwide could be used to identify regions, where potentially higher risk in terms of public safety.

Methodology described in the article will be applied to other generic severe accident scenarios and different NPP designs.

REFERENCES

1. J. D. Rhodes, R. M. Ferrer and J. M. Hykes, "CASMO5 A Fuel Assembly Burnup Program User's Manual," SSP-07/431 Rev. 21, Idaho Falls, Idaho (2022).
2. P. Chatelard, S. Belon, L. Bosland, L. Carénini, O. Coindreau, F. Cousin, C. Marchetto, H. Nowack, L. Piar and L. Chailan, "Main modelling features of the ASTEC V2.1 major version," *Annals of Nuclear Energy*, **vol. 93**, pp. 83-93 (2016).
3. I. Ievdin, D. Trybushnyi, M. Zheleznyak and W. Raskob, "RODOS re-engineering: aims and implementation details," *Radioprotection*, **vol. 45**, pp. 181-189 (2010).
4. O. Murat, V. Sanchez-Espinoza, F. Gabrielli, R. Stieglitz and C. Queral, "Analysis of Short Term-Station Blackout accident at the Peach Bottom Unit-2 reactor with ASTEC including the estimation of the radiological impact with JRODOS," *Nuclear Engineering and Design*, **vol. 406** (2023).
5. O. Murat, V. Sanchez-Espinoza, F. Gabrielli, S. Wang, R. Stieglitz and C. Queral, "Improved Analysis of the Short-Term Station Blackout Accidents of the Peach Bottom Unit-2 Reactor with ASTEC Including Radiological Impact and Statistical Analysis with JRODOS," *Nuclear Engineering and Design*, **vol. 420**, p. 113012 (2024).

6. W. Raskob, N. Beresford, T. Duranova, I. Korsakissok, A. Mathieu, M. Montero, T. Müller, C. Turcanu and C. Woda, "CONFIDENCE: project description and main results," *Radioprotection*, **vol. 55**, pp. 7-15 (2020).
7. E. D. v. Asselt, C. J. Twenhöfel, T. Duranova, R. C. Smetsers, J. Bohunova and T. Müller, "Facilitating the Decision-Making Process After a Nuclear Accident: Case Studies in the Netherlands and Slovakia," *Integrated Environmental Assessment and Management*, **vol. 17**, pp. 376-387 (2020).
8. D. Rochman, A. Vasiliev, H. Ferroukhi, A. Munoz, M. V. Antolin, M. B. Torres, C. C. Sanchez, T. Simeonov and A. Shama, "Analysis of ENRESA BWR samples: nuclide inventory and decay heat," *Nuclear Science and Technologies*, **vol. 8**, no. 9 (2022).
9. I. Gauld and U. Mertyurek, "Margins for the Uncertainty in the Predicted Spent Fuel Isotopic Inventories for BWR Burnup Credit, NUREG/CR-7251," U.S. Nuclear Regulatory Commission, Oak Ridge, TN (2018).
10. J. Martinez, B. Ade, S. Bowman, I. Gauld, G. Ilas and W. Marshall, "Impact of Modelling Choices on Inventory and in-Cask Criticality Calculations for Forsmark 3 BWR Spent Fuel," Charlotte, North Carolina (2015).
11. U.S. Nuclear Regulatory Commission, "Severe Accident Risks: An Assessment for Five U.S. Nuclear Power Plants, NUREG-1150," United States Nuclear Regulatory Commission, Washington (1990).
12. Organisation for Economic Co-Operation and Development - Nuclear Energy Agency, Chernobyl: assessment of radiological and health impacts, Nuclear Energy Agency of the OECD (NEA): ISBN: 92-64-18487-2 (2002).
13. INPO, "Special Report on the Nuclear Accident at the Fukushima Daiichi Nuclear Power Station, INPO 11-005," [Online]. Available: https://www.nrc.gov/docs/ML1134/ML11347A454.pdf. (2011)
14. Y. Dodge, "Central Limit Theorem," in The Concise Encyclopedia of Statistics, New York, NY, Springer New York, pp. 66-68 (2008).
15. U.S. Nuclear Regulatory Commission, "Radiation Dose Limits for Individual Members of the Public (Subpart D), 10 C.F.R. § 20.1301," [Online]. Available: https://www.ecfr.gov/current/title-10/chapter-I/part-20/subpart-D/section-20.1301 (1991)
16. T. Ohba, K. Tanigawa and L. Liutsko, "Evacuation after a nuclear accident: Critical reviews of past nuclear accidents and proposal for future planning," *Environment International*, **vol. 148**, p. 106379 (2021).

Karlsruhe Institute of Technology

ERMSAR 2024
KTH, Stockholm, Sweden
13-16 May 2024

Source Term Dispersion Analysis and Construction of the Risk Map around the Peach Bottom Unit-2 Plant Using the ASTEC and JRODOS codes

Onur Murat, Fabrizio Gabrielli, Victor Hugo Sanchez Espinoza

Karlsruhe Institute of Technology, Institute for Neutron Physics and Reactor Technology, Hermann-von-Helmholtz Platz 1, D-76344 Eggenstein-Leopoldshafen

Institute for Neutron Physics and Reactor Technology





Content

- Peach Bottom Unit-2 NPP
- CASMO Model of the Fuel Assembly
- ASTEC Model of the Plant
- Selected Transient : ST-SBO and Results
- ST-SBO Radiological Impact with JRODOS
- Extension of the Statistical Analysis to Risk Map
- Conclusion and Outlook

Peach Bottom Unit-2 Nuclear Power Plant

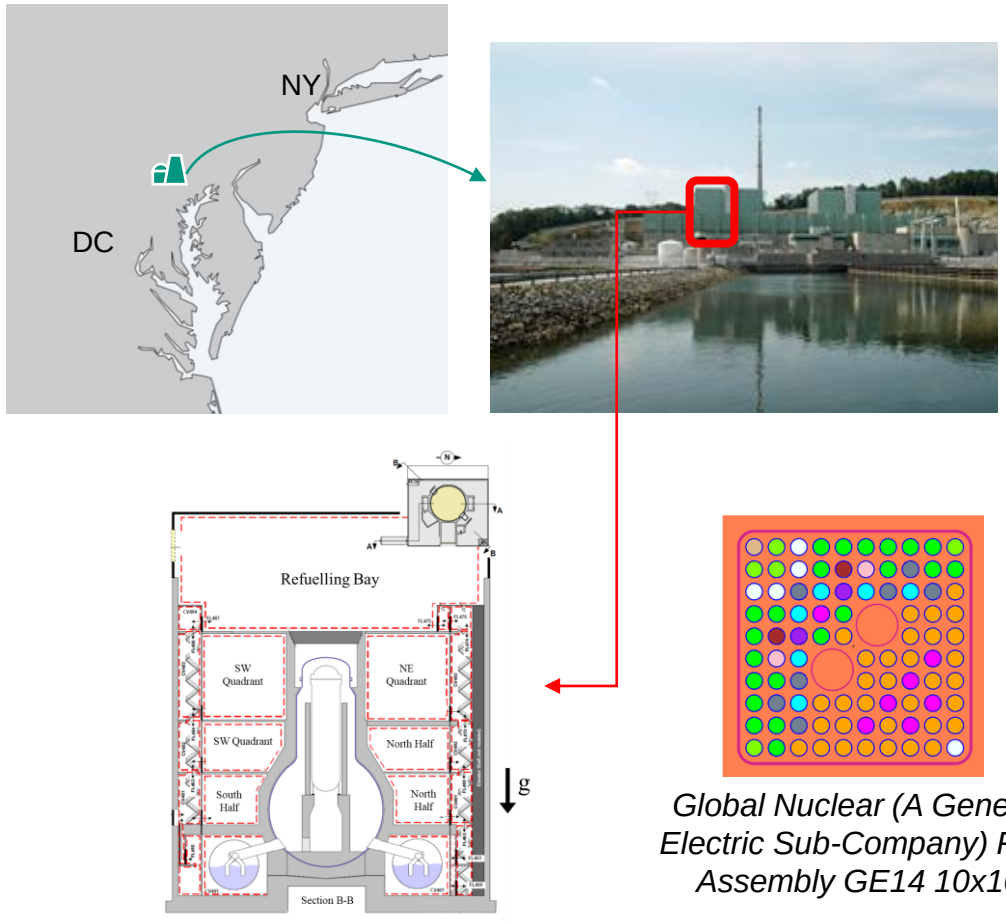

Global Nuclear (A General Electric Sub-Company) Fuel Assembly GE14 10x10

- The Plant is located on East Coast of the U.S.
- General Electric BWR4 Mark-1 Design.
- Operational licence received in 1973.
  - First Authorized Power level 3293 MWth
  - Power upgrade (1994) 3458 MWth
  - Power upgrade (2014) 3951 MWth
  - Power upgrade (2017) 4016 MWth
- Reference study* by U.S.NRC states GE14 10x10 was used for the analysis of the Peach Bottom (in 2013).
- In portfolio of Global Nuclear Company GE14 10x10 is still most recent 10x10 assembly for BWRs.

*Bixler, N., Gauntt, R., Jones, J., Leonard, M., State-of-the-Art Reactor Consequence Analysis Project, Volume 1 Peach Bottom Integrated Analysis, NUREG/CR-7110, 2013

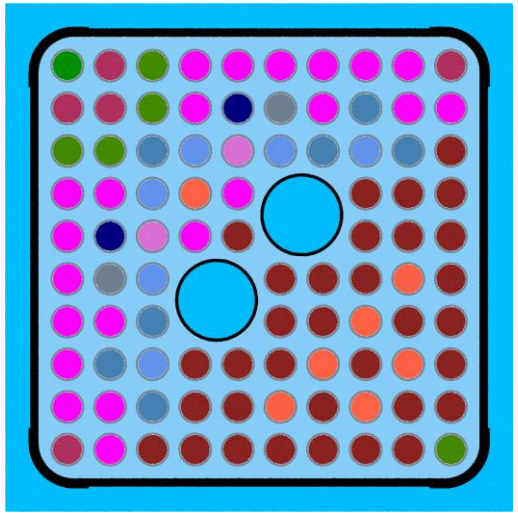

CASMO Model of the GE14 10x10 Fuel Assembly

Computational Tool: CASMO

- Advanced lattice physics code for light water reactors.
- Multigroup, two dimensional transport code for the burnup analysis.
- Symmetric and anti-symmetric layout of the light water reactor fuel assemblies can be handled.
- The code has flexibility for storage pool and transportation cask criticality analysis as well.

Studsvik

CASMO

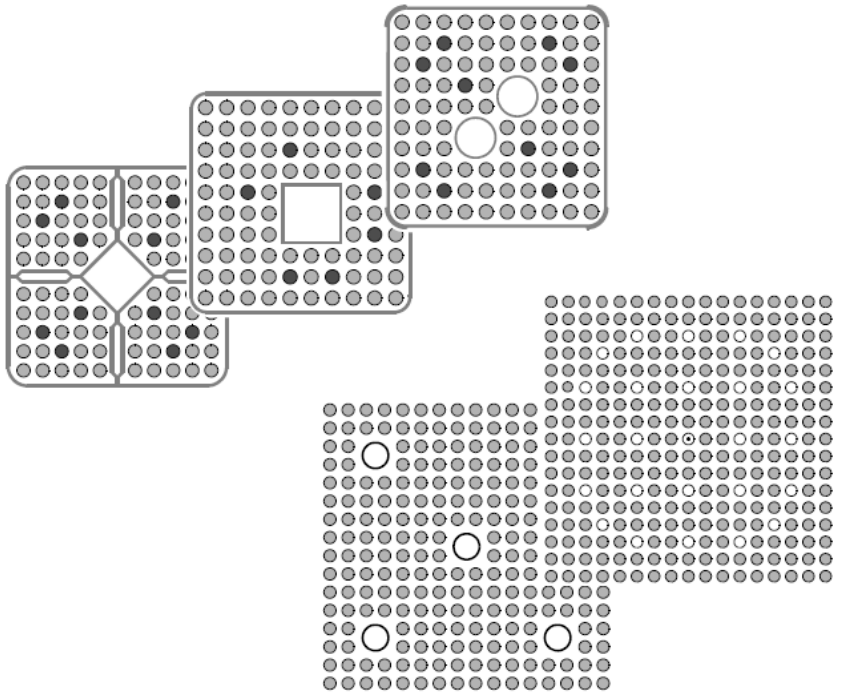

CASMO Model of the GE14 10x10

- Between July 2000 – 28 May 2005 one GE14 10x10 fuel assembly was burned in Forsmark 3 NPP.
  - 1792 Days (from 1st of July)
  - 5 Cycles (Beginning of Cycle 16 → end of cycle 20)
  - Rod avg. Burnup 41 MWd/kgU
  - Peak Burnup 56 MWd/kgU
- Extracted one fuel rod from the assembly and samples from the rod investigated (ENRESA samples)
- Based on the known informations of the ENRESA samples, and GE14 10x10 design CASMO input deck was constructed.
  - Assumptions have been made on the void fraction profile, specific power of the assembly and burning period.

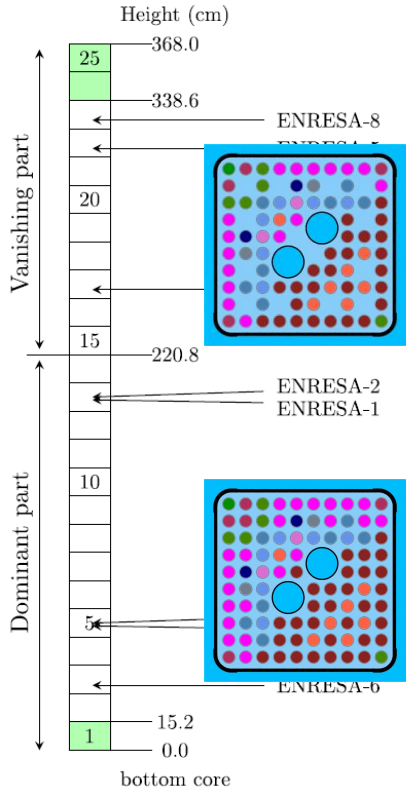

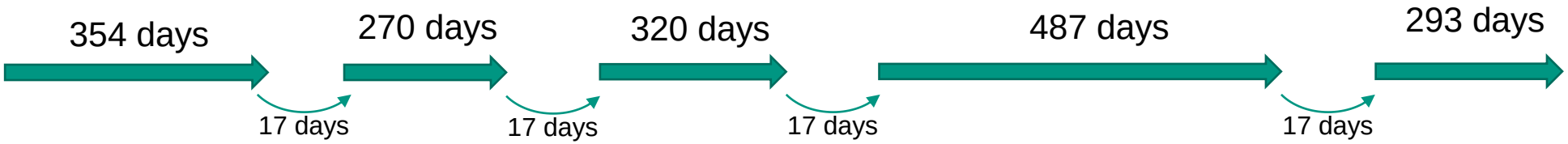

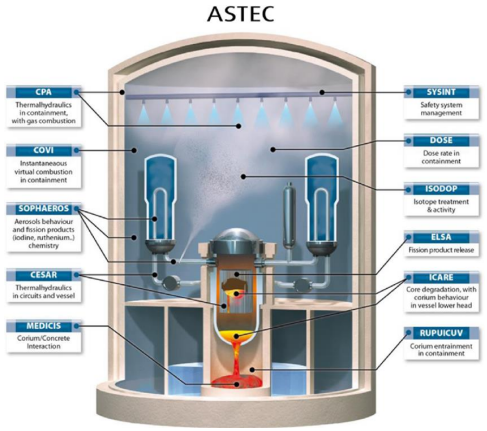

ASTEC Model of Peach Bottom Unit-2 with GE14 10x10 BWR Fuel Assembly

Computational Tool: ASTEC

- Accident Source Term Evaluation Code (ASTEC)
- European reference severe accident analysis tool.
- Mechanistic approach of the code allows modular structure of different zones of the plant.
- Starting from the reactor scram up to fission product release to the environment can be handled with the code.



ASTEC Model of the Peach Bottom Unit-2 Updated Core

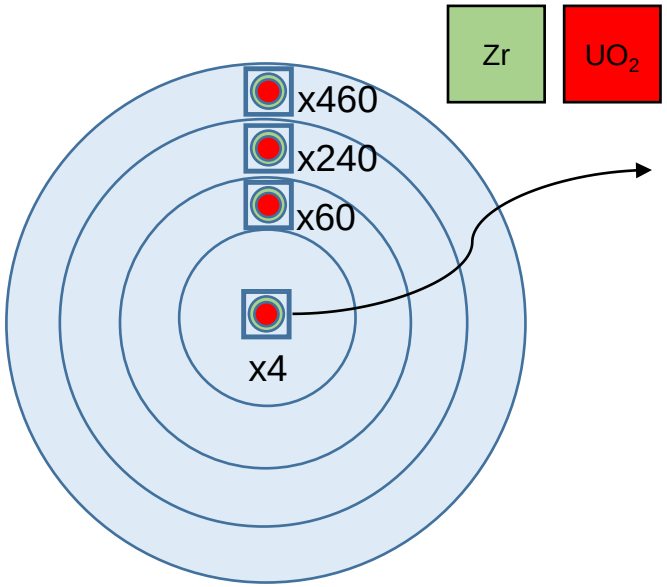

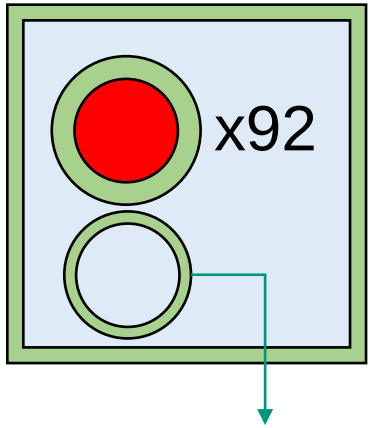

Water rod covers 8 fuel rods area

There are part length rods in the GE14 10x10 model but all rods considered as full length.

```
STRU NT_HEAT
     UNIT …
     PNOM …

     SR1 POWER
     …
     …
     SR1 PROF
     …
     …
```

Allowed only one NT_HEAT structure

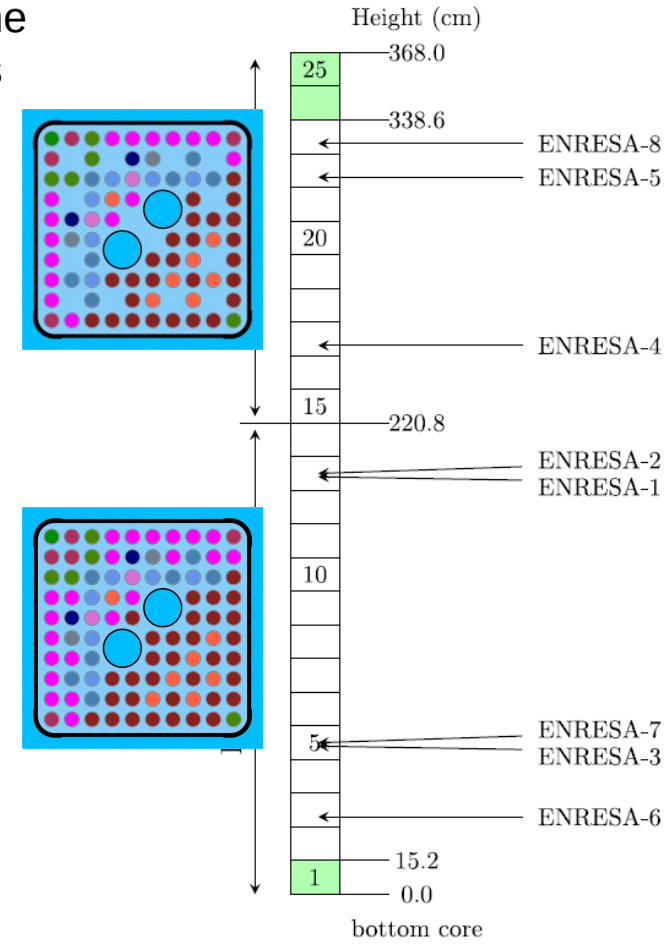

- Number of Fuel Assembly = 764
- Radius of fuel pellet = 4.38 mm
- Clad internal radius = 4.47 mm
- Clad external radius = 5.13 mm
- Water rod internal diameter = 23.21 mm
- Water rod external diameter = 25.21 mm
- Fuel channel inner length side = 134.06 mm
- Canister length = 4119.0 mm

ASTEC Model of the Peach Bottom Unit-2 Updated RPV

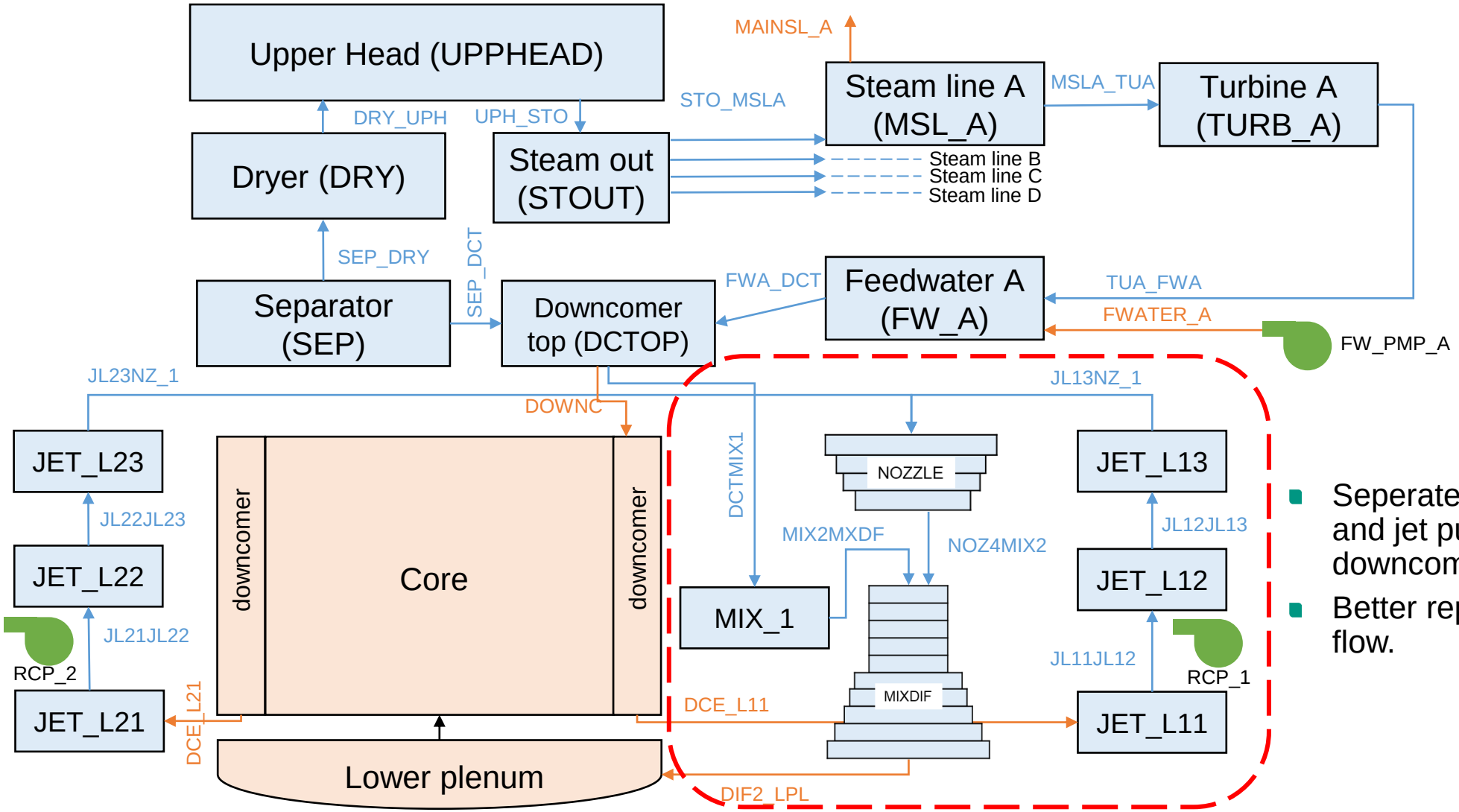

Junction
Connection
CESAR
ICARE
SYSTEMS

- Seperated flow to recirculation and jet pump from the downcomer.
- Better representation of the water flow.

ASTEC Model of the Peach Bottom Unit-2 Containment

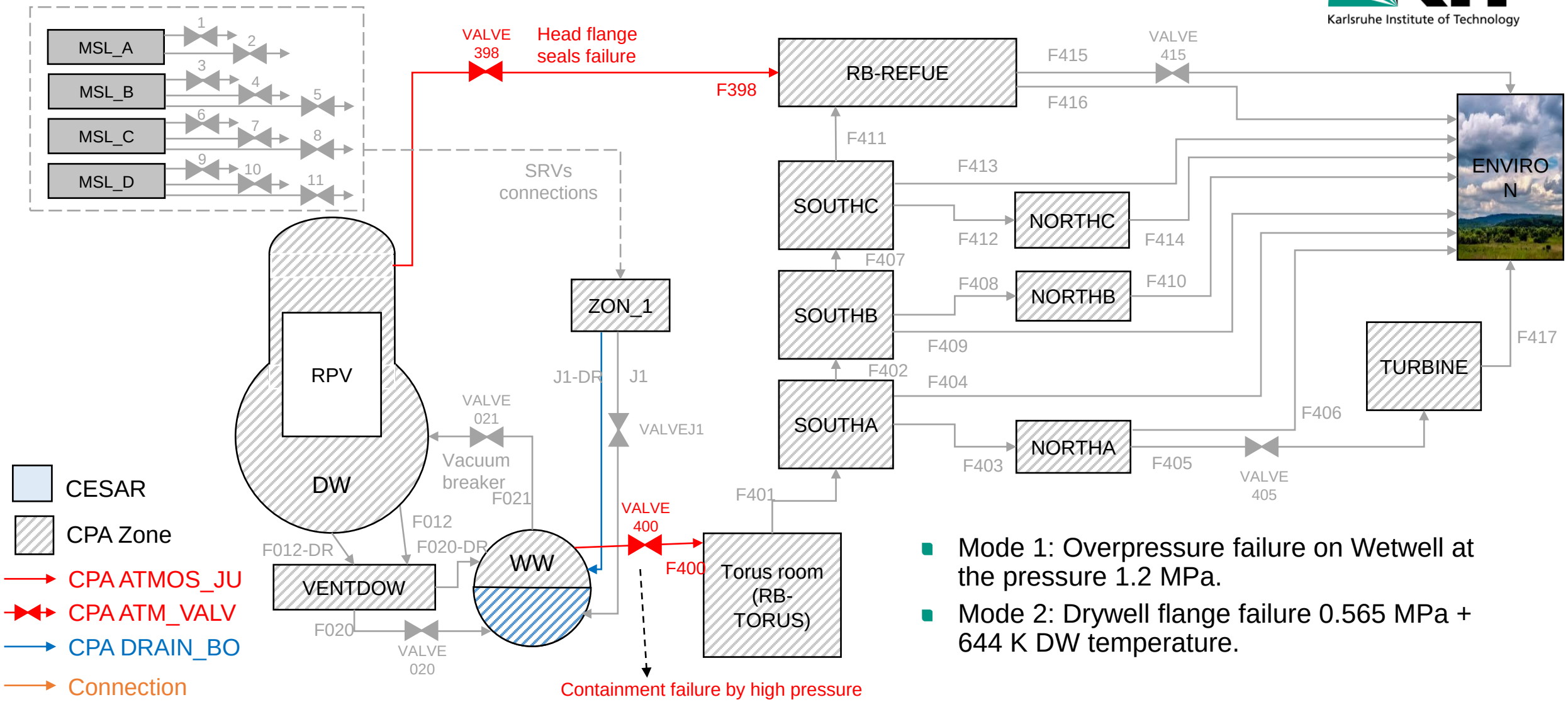

- Mode 1: Overpressure failure on Wetwell at the pressure 1.2 MPa.
- Mode 2: Drywell flange failure 0.565 MPa + 644 K DW temperature.

Selected Transient : Short Term Station Blackout and Results

Sequence of Events PB2 ASTEC Model ST-SBO Scenario

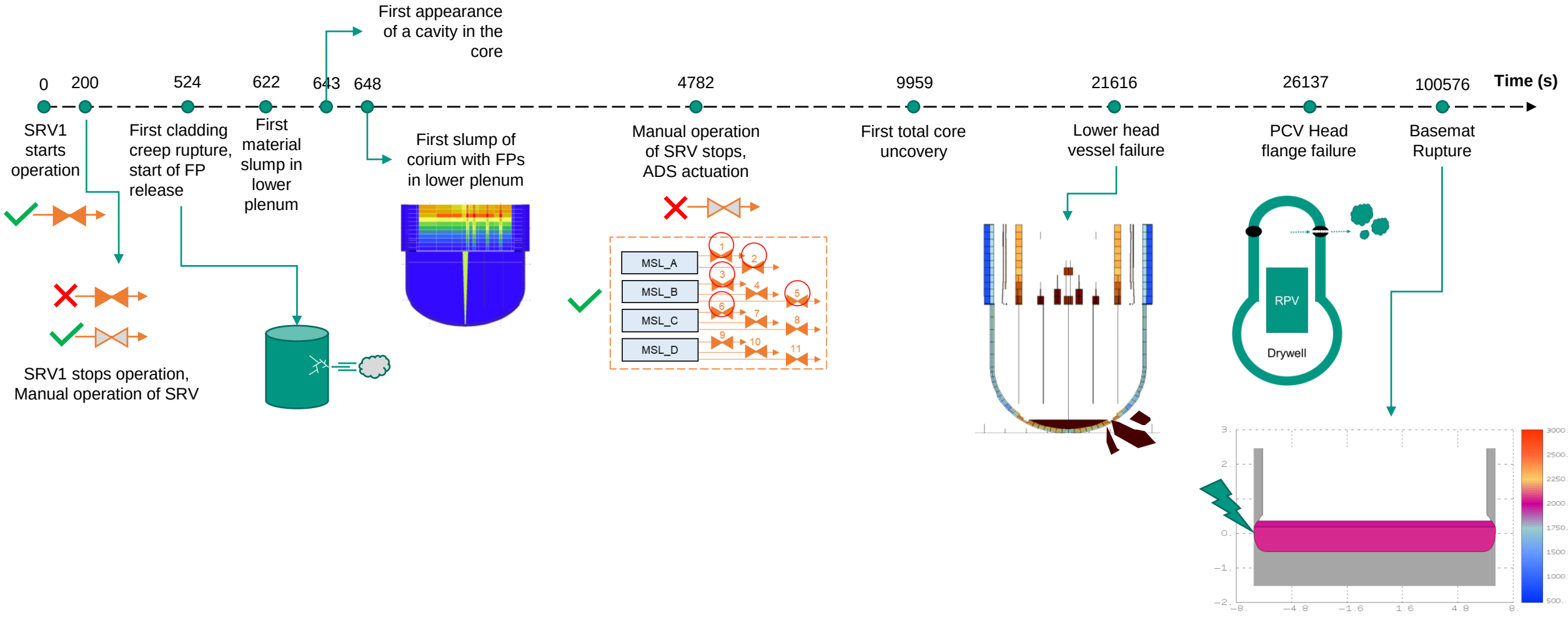

Fission Product Inventory and Retention Fractions

Elements	Inventory (kg)	Primary	Containment	Environment
Kr	68.60	0.105	0.499	0.264
Xe	1025.79	0.105	0.499	0.264
I	36.66	0.172	0.664	0.025
Sb	2.81	0.115	0.572	5.38E-4
Te	93.41	0.141	0.449	3.95E-4
Ag	7.30	0.206	0.657	5.53E-4
Cs	556.56	0.185	0.698	6.77E-4
Rh	79.54	9.85E-5	2.02E-4	1.66E-8
Mo	644.51	0.096	0.402	2.78E-4
Ba	290.09	0.230	0.323	8.08E-5
Sr	166.72	0.152	0.029	6.59E-6
Y	87.65	9.72E-5	1.98E-5	6.21E-8
Nb	3.80	0.0	0.0	0.0
Ru	479.17	0.088	0.160	1.98E-5
Ce	502.68	0.128	0.115	2.71E-5
La	236.88	0.067	0.031	7.09E-6
Eu	27.98	0.049	0.021	4.24E-6

At the end of the simulation released activity to the environment = 2.190E+18 Bq

Fukushima = ~ 6.3E+17 Bq
Chernobyl = ~ 14E+18 Bq

Source term for JRODOS

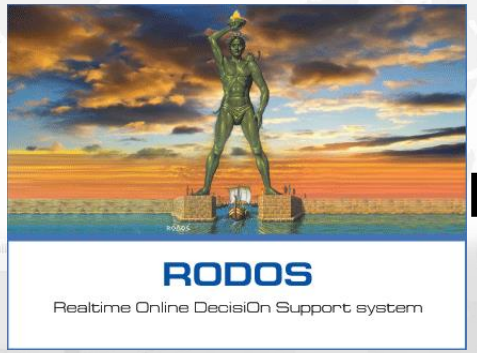

Radiological Dispersion Analysis with JRODOS

Computational Tool: JRODOS

- Java Based Realtime Online Decision Support (JRODOS) System.
- System provides the necessary information to take action to protect society and the environment.
- Starting from the fission product release and exposing the public in possible transport paths for short term and longer term effects can be assessed.
- Regional, national and international emergency management decision can be build by joint efforts.

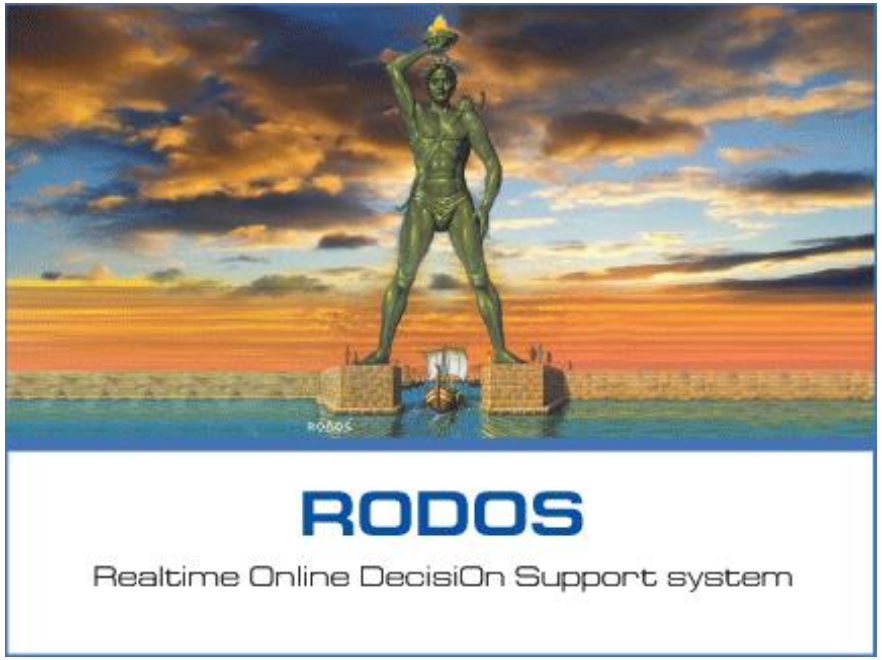

JRODOS Dispersion Model (ST-SBO) 1/2

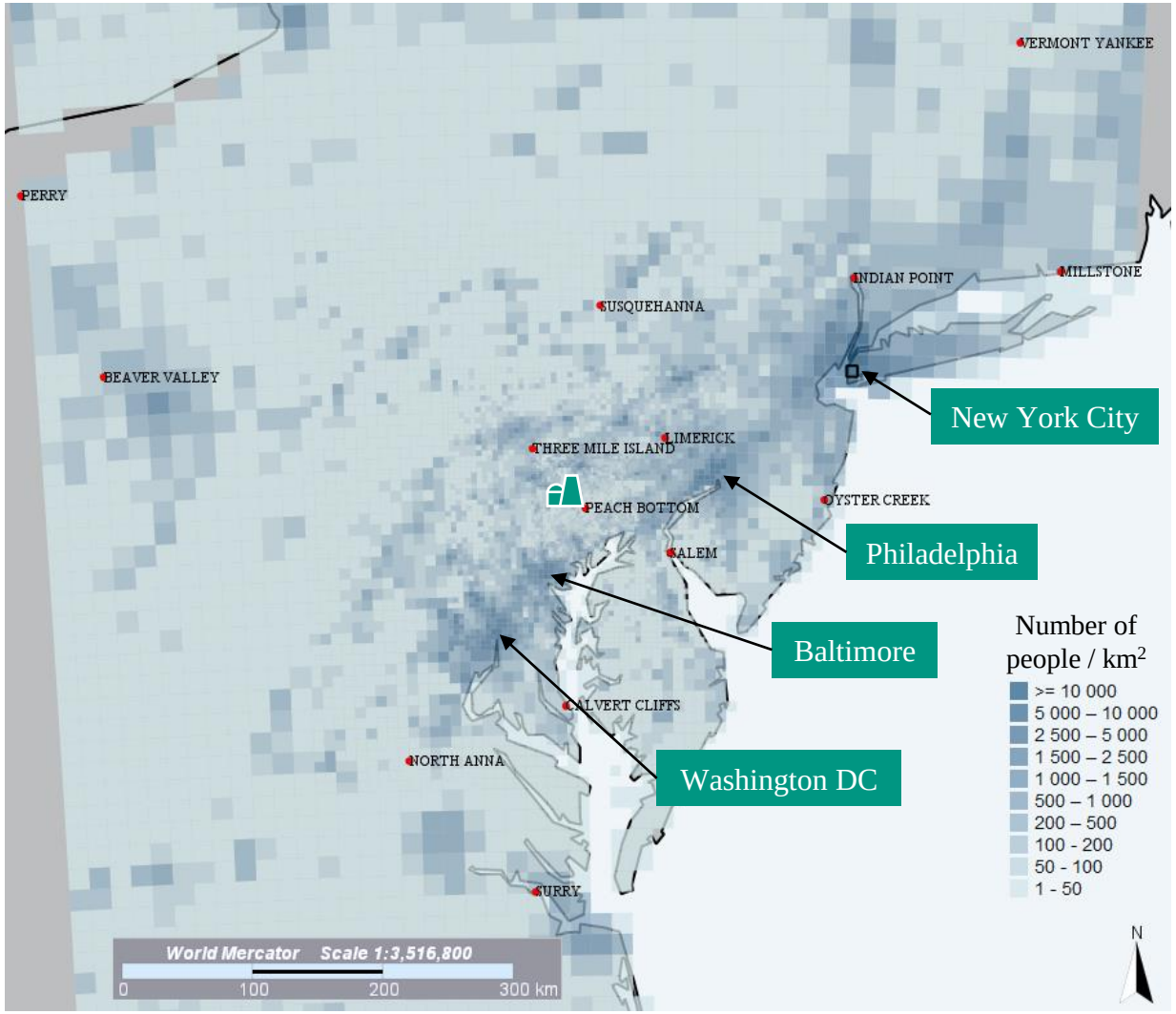

- Mesh construction around the plant for radius of 400 km.
- 24 hours calculation.
- No emergency countermeasures taken into account.
- Source term taken from ASTEC simulation environment release results.

WHERE to look at?

- Most populated cities around:
  - **New York City** : meshes 5554, 5606, 5658, 5607, 5771
  - **Philadelphia** : meshes 3209, 3240, 3241
  - **Baltimore** : mesh 2594
  - **Washington DC** : mesh 2064, 2065

JRODOS Dispersion Model (ST-SBO) 2/2

WHEN is the correct time for a simulation?



- Same source term for the examples.
- Results are highly disperse.
- There is no correct time to consider among the interested meshes.
- How to proceed?

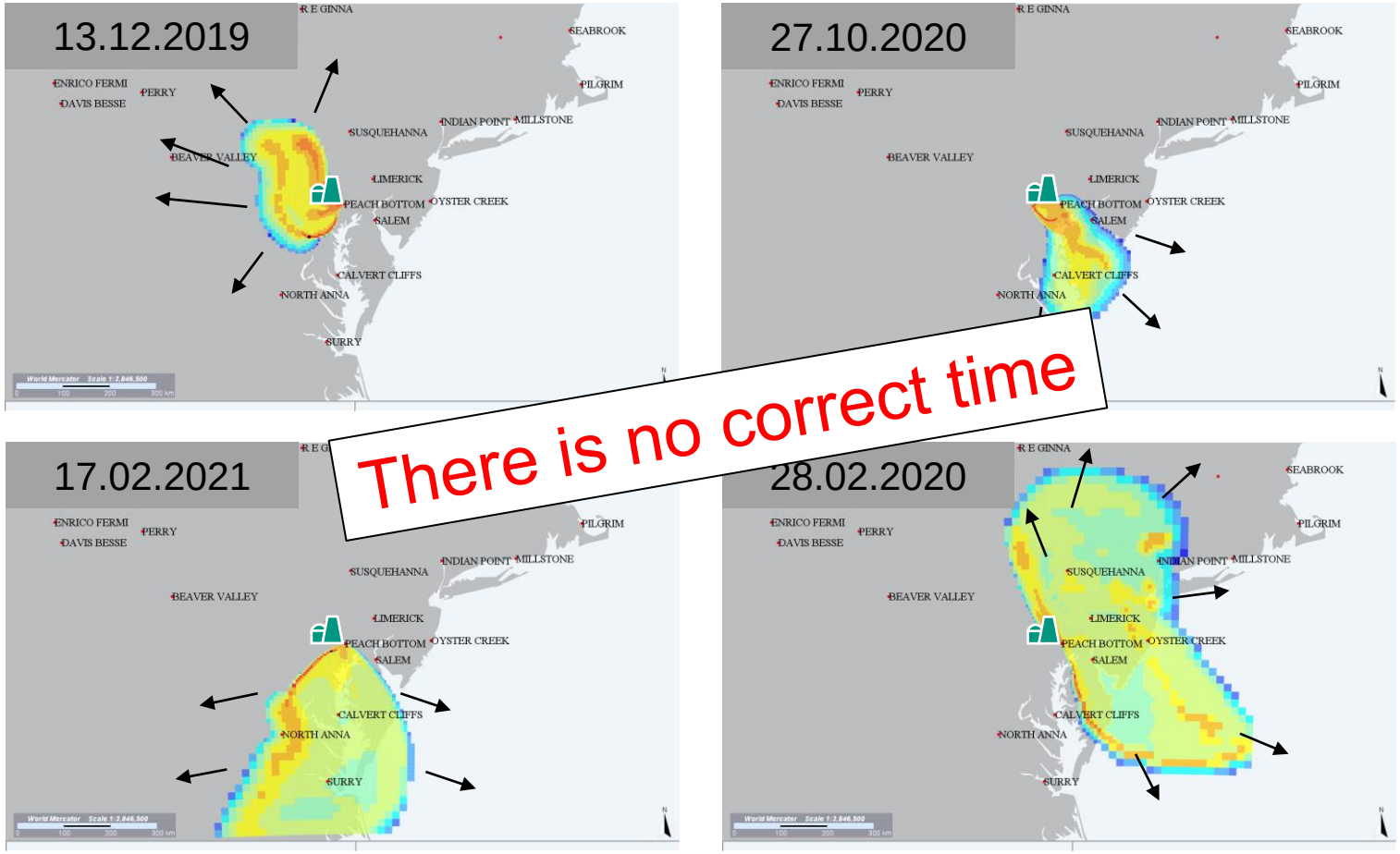

Statistic Sampling of Source Term with JRODOS 1/3

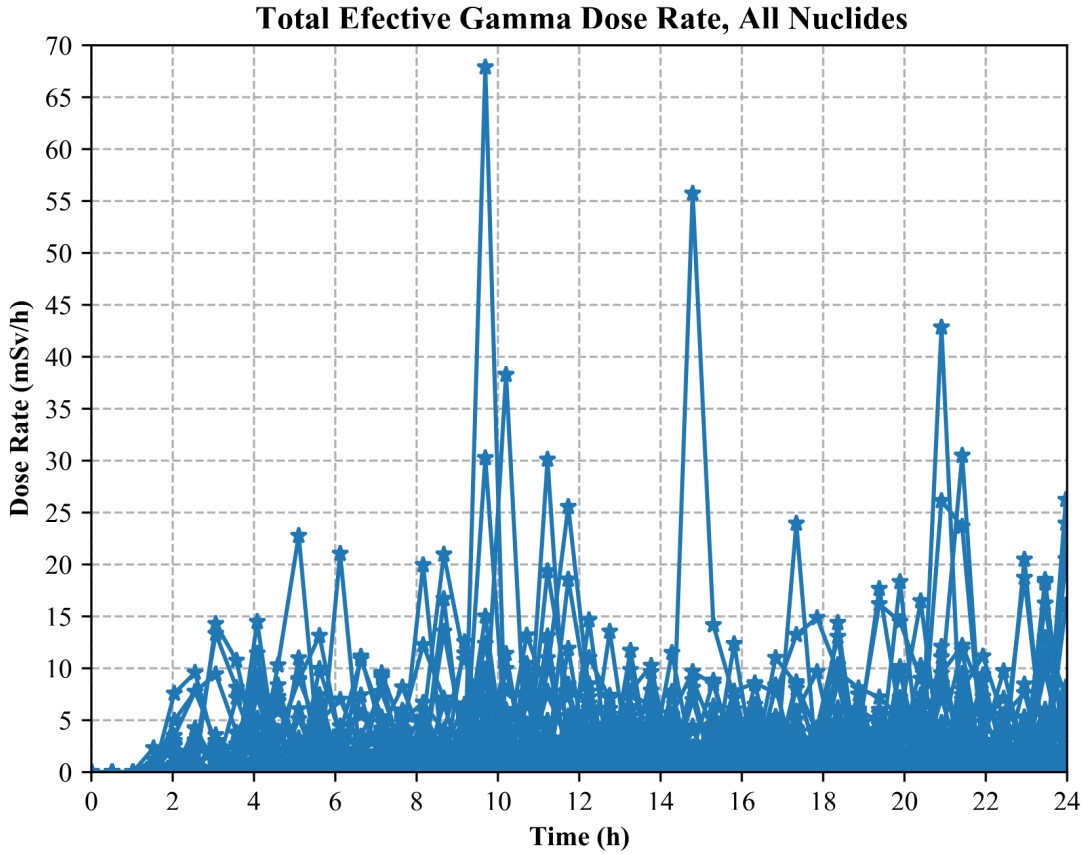

U.S. annual limit for whole body total effective dose (*10 CFR 20*)

Radiation worker	*Member of public*
50 mSv/yr	1 mSv/yr

- Making large set of simulation instead of one.
- Multiple runs of 24 hours analysis carried out:
  - 3 years (01.01.2019 – 31.12.2021) = 1095 simulations
- Starting time for the analysis of each day is selected randomly.
- The highest dose rate was recorded:
  - Cell = 2594 (Baltimore)
  - Value = 67.89 mSv/h
  - Release Start Date = 13.12.2019 20:41

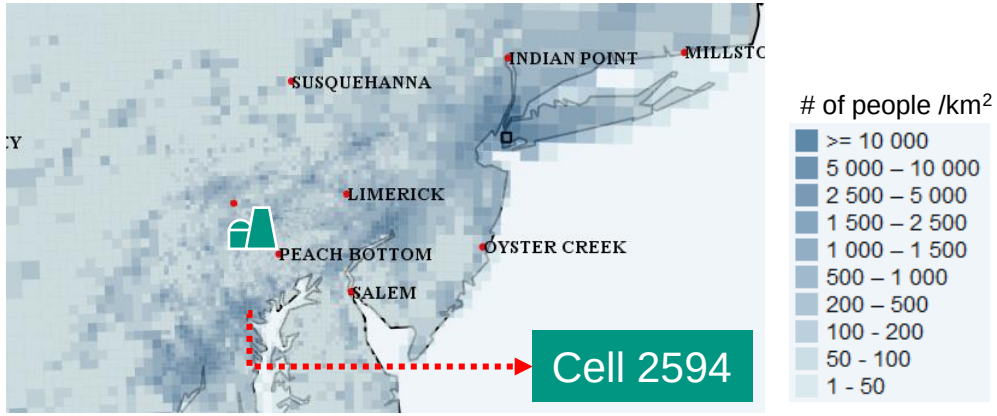

Statistic Sampling of Source Term with JRODOS 3/3

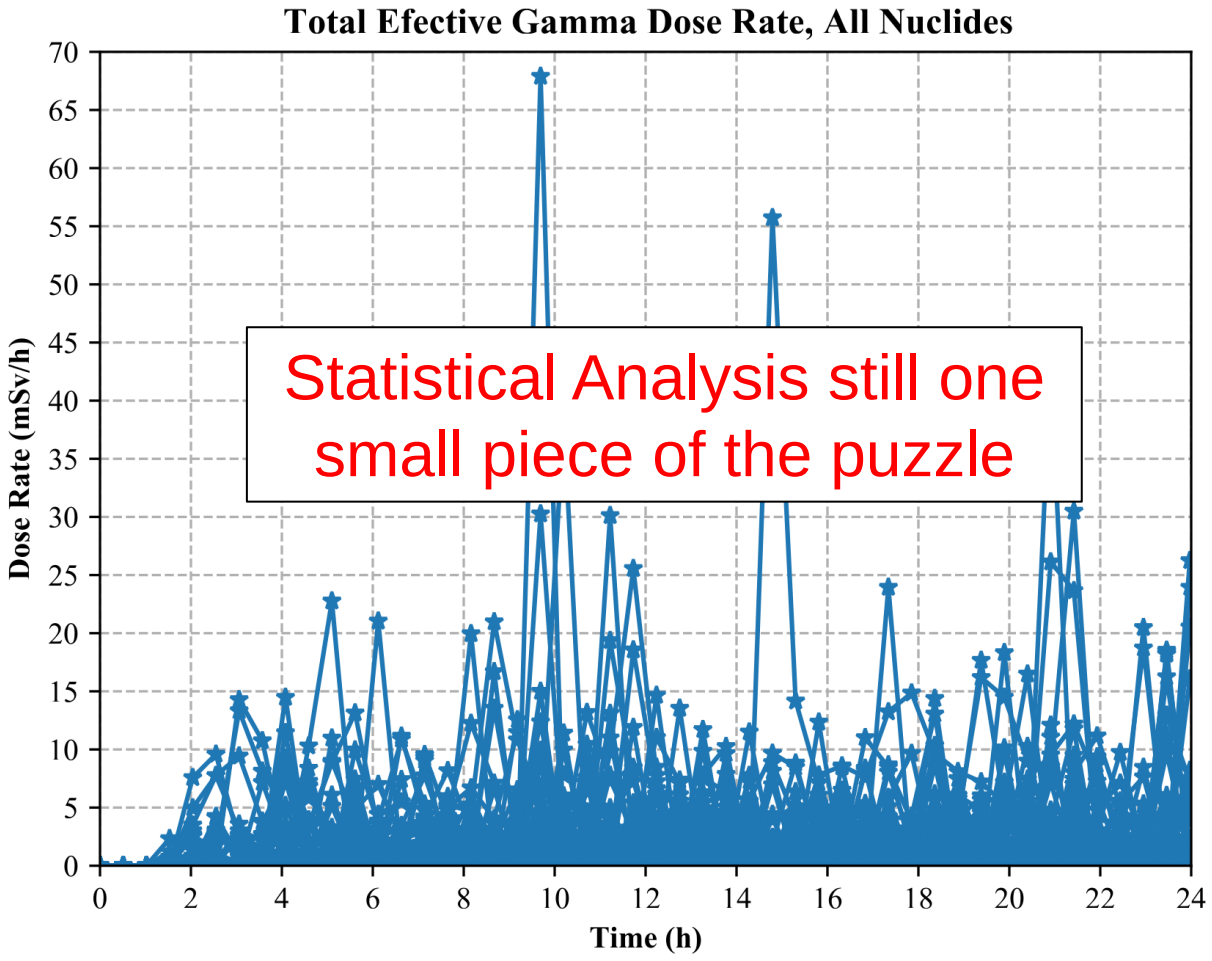

24h calculation each day for 3 Years (01.01.2019-31.12.2021)

Highest dose rate was recorded:

Cell = 2594 (Baltimore)

Value = 67.89 mSv/h

Release Start Date = 13.12.2019 20:41

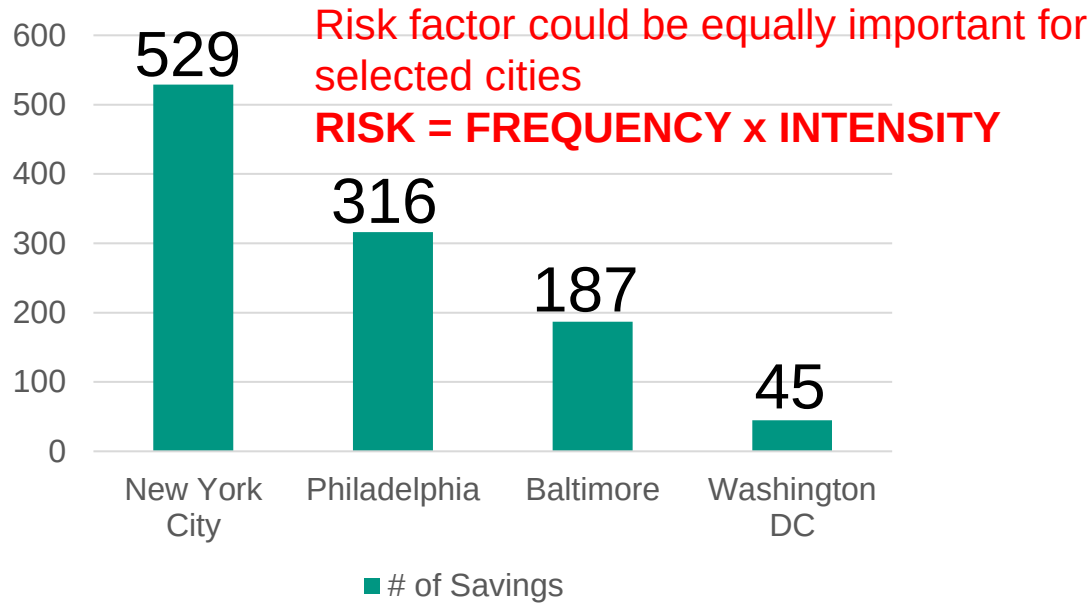

Randomness over Statistical Results of JRODOS 1/2

A sample statistical analysis

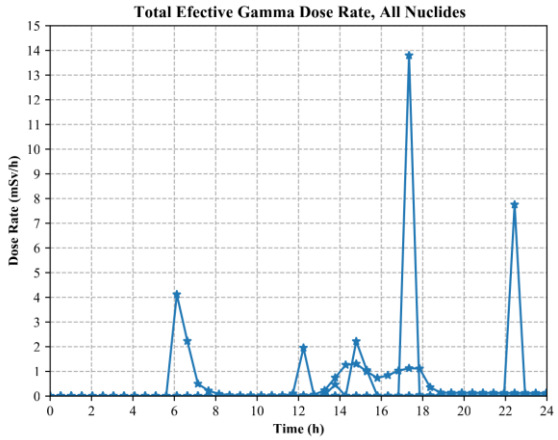

- Month of February.
- One day simulations for each 28 days of the month.
- Randomly selected the starting point of the release.
- Only one mesh is considered to keep the analysis simple.

Reproducing the statistical result with same input:



- Depending on the random selection, maximum recorded dose rates can vary more than 100%.
- The one can not conclude a possible consequences without considering all possible scenarios.

Randomness over Statistical Results of JRODOS 2/2

WHAT DO WE HAVE?

- Statistical analysis over the 3 years.
- Random selected starting time for each day.
  - Statistical analysis needs to be enlarged.

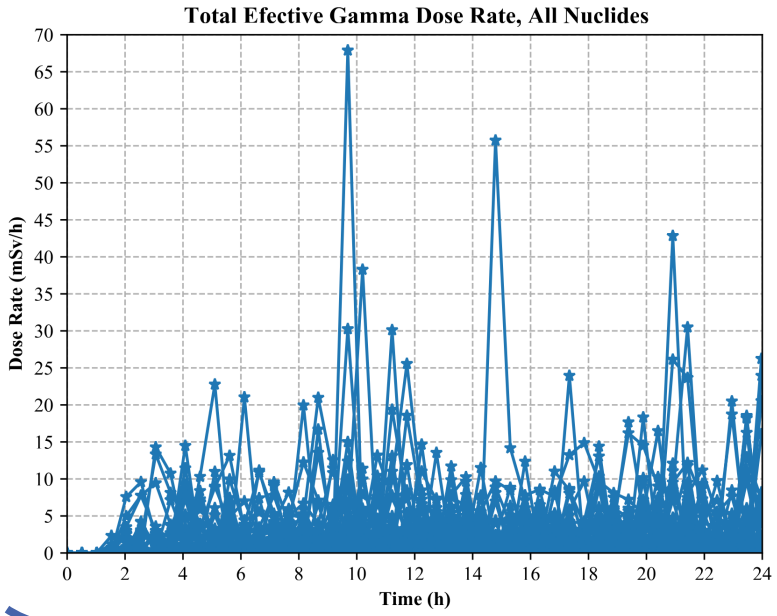

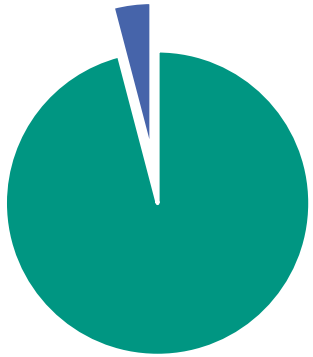

All possible scenarios

HOW TO EXPAND THE DATABASE?

- Resolution of the JRODOS is a minute.
  - One day = 1440 minutes
  - There are 1440 possible starting points in a day.
- Implementing every possible starting point is highly expensive in terms of cpu time.
  - 3 years of statistical analysis run takes about 24 hours.
    - Each day 1 starting point.
  - Considering every possible starting point requires 1440 times of repeating one day simulations.
  - 24 hours x 1440 ≅ 4 years of cpu time
  - Cases which considers longer duration of releases would take longer cpu time.

Central Limit Theorem Application

- 24 hours x 1440 ≅ 4 years of cpu times is expensive in terms of resource and time and deals with very large amount of data.

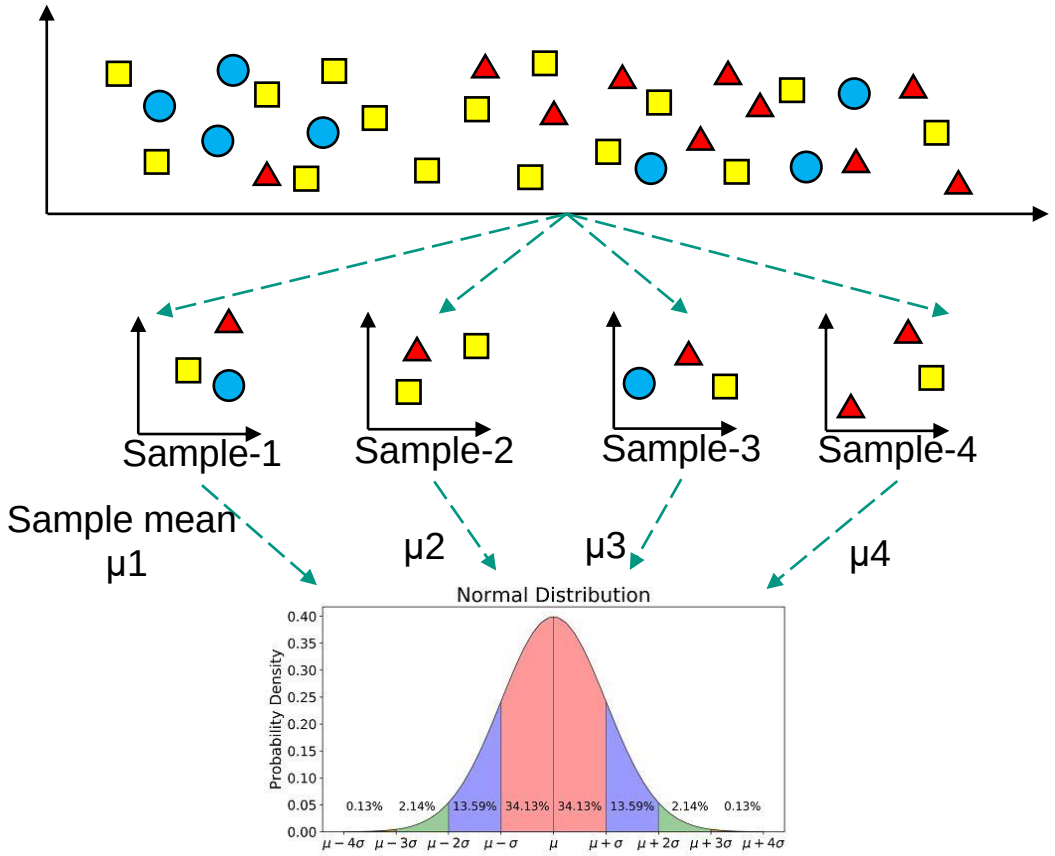

- How to estimate an information about a large dataset by using smaller sizes of samples?

  Central Limit Theorem

- Collect samples from the population → combine the informations from samples to draw conclusion about the population.
- Sample mean distributions of any population (regardless of its shape) will approximate to normal distribution.
- Estimation of the average value of large dataset by using smaller samples.
- If the sampling is large enough:
  - Mean of the sampling distribution = population mean

Production of Sampling Mean Distribution

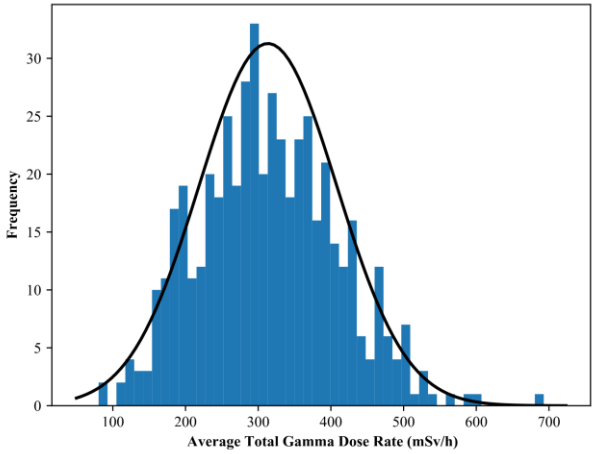

Sampling average distribution on an example mesh

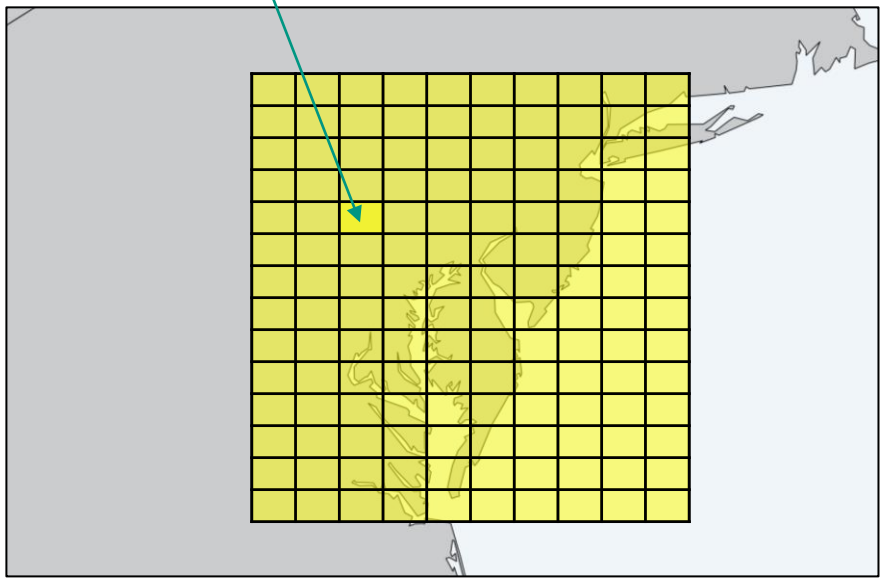

- Year 2021 was selected.
- Each season seperately considered.
  - Winter, Spring, Summer and Autumn have distinctive weather conditions.
  - 500 groups each contains 30 sample simulation for each season.

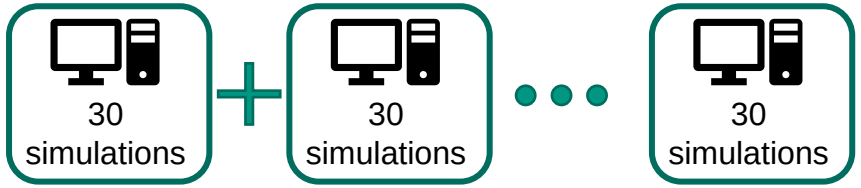

  - 15.000 simulation for each season → 60.000 simulations for a year.
- Assumed to be perfect normal distribution which means:

Mean of the average sampling distribution
=
Mean of the population distribution

- For each mesh same assumption followed and mean value recorded to create the map.

Peach Bottom NPP Risk Map 1/2

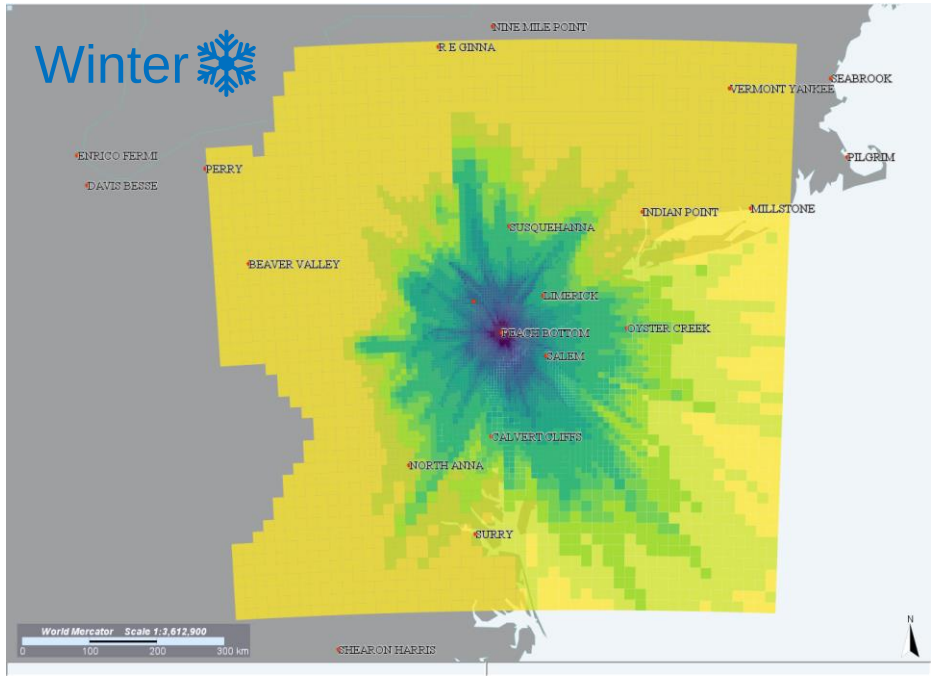

Total Gamma Dose Rate (mSv/h)

- > 50.0
- 40.0 - 50.0
- 30.0 - 40.0
- 20.0 - 30.0
- 10.0 - 20.0
- 5.0 - 10.0
- 4.0 - 5.0
- 3.0 - 4.0
- 2.0 - 3.0
- 1.0 - 2.0
- 0.5 - 1.0
- 0.4 - 0.5
- 0.3 - 0.4
- 0.2 - 0.3
- 0.1 - 0.2
- 0 - 0.1

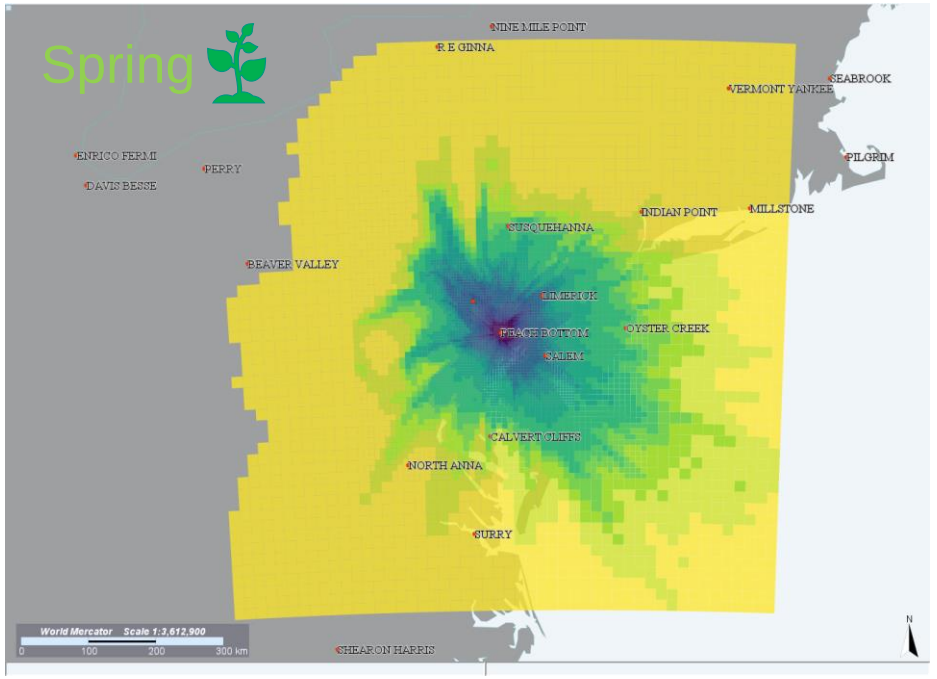

- Winter season has largest span and branches of calculated average total gamma dose rates.
  - Having the largest spread will reduce the average value, but it will require a larger area to be covered in terms of evacuation.
- All major cities: NY, Washington DC, Baltimore and Philadelphia are in the range of the calculated average total gamma dose rates.
- Tendency of the dispersion mostly to West and South-West. Dispersion towards to East is quite limited compare to other directions.

Peach Bottom NPP Risk Map 2/2

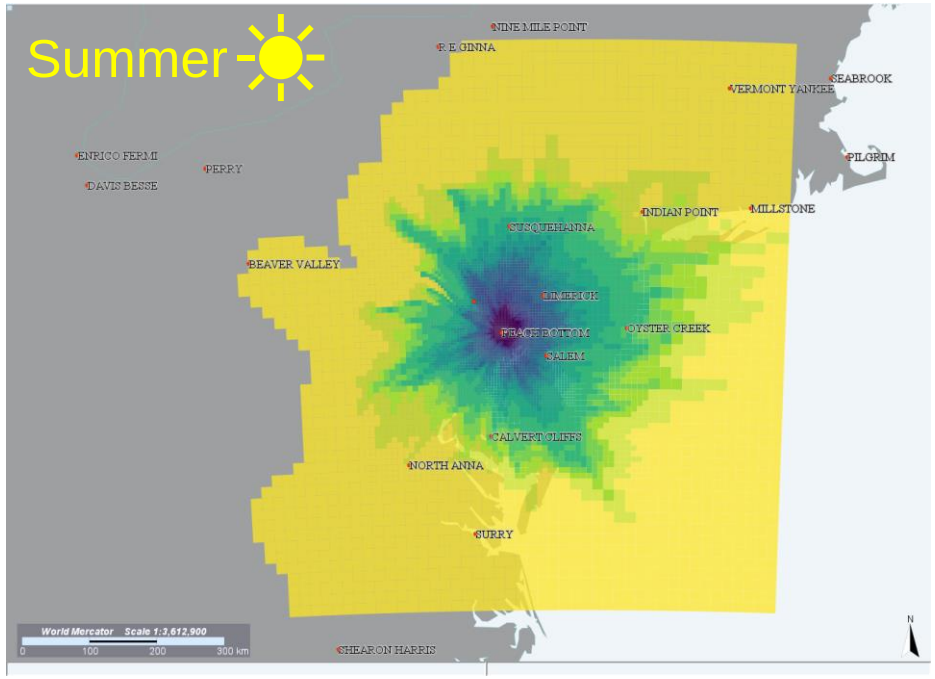

Total Gamma Dose Rate (mSv/h)

> 50.0
40.0 - 50.0
30.0 - 40.0
20.0 - 30.0
10.0 - 20.0
5.0 - 10.0
4.0 - 5.0
3.0 - 4.0
2.0 - 3.0
1.0 - 2.0
0.5 - 1.0
0.4 - 0.5
0.3 - 0.4
0.2 - 0.3
0.1 - 0.2
0 - 0.1

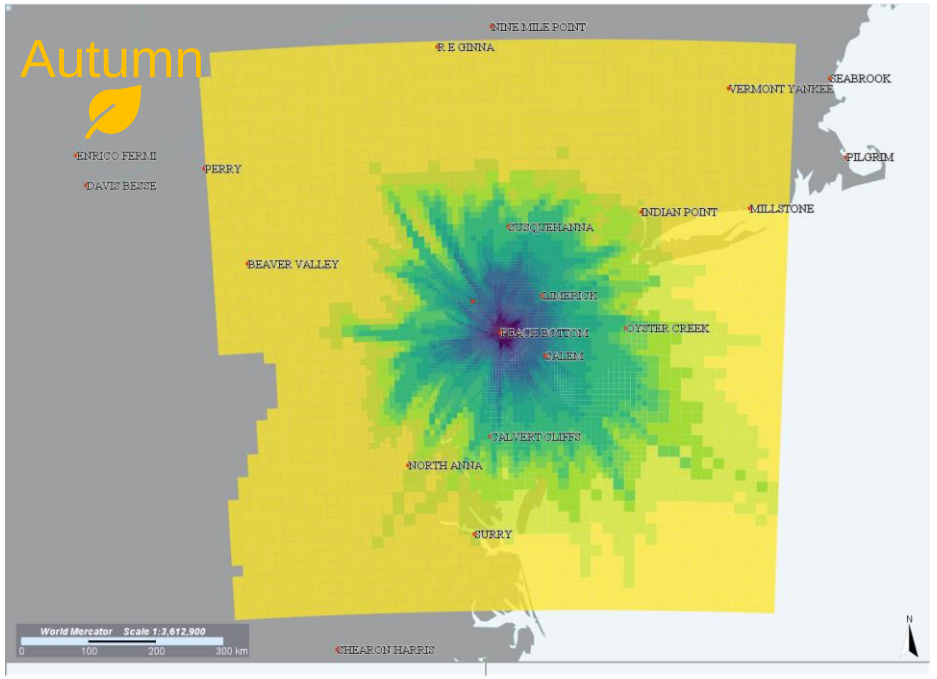

- Summer season has largest area of exceeded dose limit due to weather conditions (Up to 38 km from the plant in North direction).
  - Based on the current results highest risk in terms of public safety having a dispersion in Summer season.
- All major cities NY, Washington DC, Baltimore and Philadelphia are in the range of the calculated average total gamma dose rates.
- There is a tendency of the dispersion to the West and South-West considering all seasons.
  - Geographic obstacles and based wind regime directs the overall trend.

Conclusion and Outlook

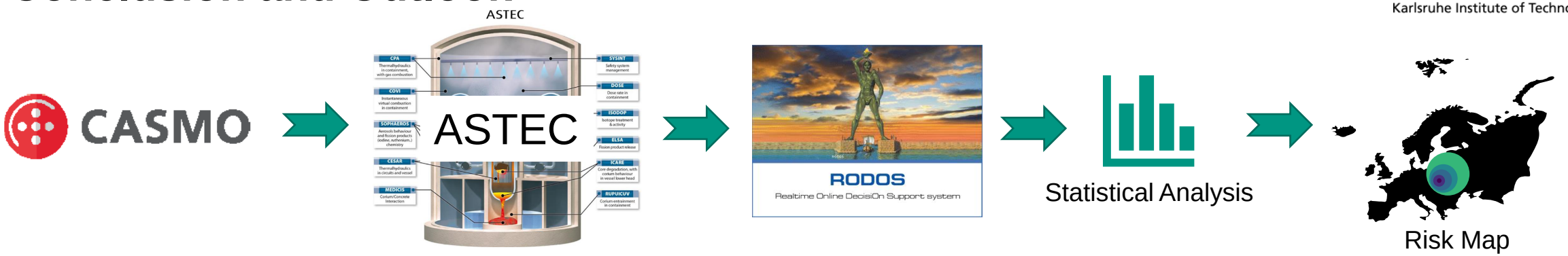

- More information in one picture than simple dispersion map → Frequency, dose rate, regime, range etc.
- Considering sampling mean distribution and central limit theorem helps to achieve the results *much faster*.
  - 25 days of cpu time << 4 years of cpu time
- Counter measures and evacuation actions will be taken in action to extent the analysis.
  - Can be major pillar to support emergency planning.
- Smaller mesh grid and increased number of the simulation will be performed to achieve better normal distribuation approximation over the all the meshes.
- Approach can be applied new smaller NPP design since the sitings might be closer to the settlements.
- Experince of KIT on performing AI implementation of weather forecasting can improve speed and analysis scope.

Thank You for Your Attention

Onur Murat
onur.murat@kit.edu

Dr. –Ing. Fabrizio Gabrielli
fabrizio.gabrielli@kit.edu

Dr. –Ing. Victor Hugo Sanchez Espinoza
victor.sanchez@kit.edu

The 11th European Review Meeting on Severe Accidents Research

May 13-16, 2024, Royal Institute of Technology, Stockholm, Sweden

TECHNICAL SESSION 5.2: SEVERE ACCIDENT SCENARIOS - MODEL DEVELOPMENT AND VALIDATION

Chairs: A. Stakhanova (KIT), T. Hollands (GRS)

ID126	**Assessment of pH-values in water pools during severe accidents in PWR using the lumped parameter code COCOSYS** L. Anschuetz (Framatome GmbH)	**Paper** **Presentation**
ID99	**Modeling of oxidation behavior of Accident Tolerant Fuel by using AC²** G. Stahlberg (PSS-RUB)	**Paper** **Presentation**
ID40	**ASTEC validation of SFP Dewatering using Results from the DENOPI project** L. Laborde (IRSN)	**Paper** **Presentation**
ID39	**A review of correlations of stainless steel oxidation in steam, and modeling the reaction with MELCOR** T. Sevón (VTT)	**Paper** **Presentation**

Assessment of pH-values in water pools during severe accidents in PWR using the lumped parameter code COCOSYS

Leon Anschütz, Mohammed Bendihab
Framatome GmbH
P.O. Box 1109, D-91001 Erlangen
Leon.anschuetz@framatome.com, mohammed.bendihab@framatome.com

Holger Nowack
Gesellschaft für Anlagen und Reaktorsicherheit | GRS
Schwertnergasse 1, 50667 Cologne
Holger.Nowack@grs.de

ABSTRACT

The pH-value in water pools during a severe accident has an important influence on the release and consequential distribution of iodine in the containment. Additionally, its correct determination in severe accident analyses improves iodine distribution assessments, which facilitates equipment qualification, development of operating procedures and quantification of potential releases. Additionally, the pH-value plays a major role in the degradation of materials in contact with water.

The paper delves into the analysis of pH-values in large water pools and puddles within the containment during severe accidents. Focusing on the utilization of the lumped parameter code COCOSYS, that is part of the integral code system AC² developed at Gesellschaft für Anlagen- und Reaktorsicherheit (GRS) [1], the paper presents its capabilities in calculating pH-values by integrating detailed distributions of pH-relevant species for a generic GenIII+ PWR. Most of these species are released from the primary circuit and corium, such as boron, lithium, cesium. Other species are created during the severe accident such as CO_2 or HNO_3. A primary emphasis is placed on the role of HNO_3, generated through radiolysis throughout the duration of the accident. The creation of HNO_3 contributes to lower pH-values in water pools for a long duration, thereby becoming a major species influencing long-term pH within the containment.

The paper demonstrates the influence of several key events in the accident sequence (e.g., start of mass and energy release, reactor pressure vessel failure, corium quenching, boiling of the water pool above the corium and containment spraying), on local pH-values. Furthermore, it illustrates the capability of COCOSYS to assess pH-values on compartment level, providing an understanding of the pH dynamics induced by the presence of different pH-relevant species, without delving into the specific calculation equations of the pH in water pools or the formation and deposition of the species.

The paper shows the nature of pH variations in water pools during severe accidents as a result of the distribution of different species, highlighting the role of HNO_3 and demonstrating the capability of the lumped parameter code COCOSYS in predicting pH-values in severe accidents in the short and long term.

KEYWORDS
pH, COCOSYS, Lumped Parameter

1. INTRODUCTION

During a severe accident with core melting the containment and the systems and components therein are exposed to different types of loads (thermal, mechanical, and chemical loads). Systems and components needed to mitigate the consequences of the severe accident must be able to withstand these loads. This on one hand requires the knowledge about the expectable loads and on the other side the qualification of these systems to withstand the expected loads.

In long term scenarios such as large break loss of coolant (LB-LOCA) scenarios the containment is cooled by the spray system. The spray system ensures that the containment pressure remains below the design pressure. The system draws water from the in-containment refueling water storage tank (IRWST) and pumps it into spray nozzles located in the containment dome. The water spray leads to increased steam condensation and cooling of the atmosphere in the containment, which decreases the pressure in the containment. The water pump as well as other important instrumentation are directly exposed to the IRWST pool water. An acidic water pool may lead to increased material degradation of the pump and pipe materials, which may lead to decreased efficiency or failure of the spray system in the long term. Additionally, an acidic water pool is detrimental with respect to bound radioactive iodine [2]. Therefore, it is important to evaluate the possible pH ranges of the water in the containment to know what pH conditions the spray system will be exposed to during the long-term accident progression. With that knowledge, the right specifications for the system components can be deduced, and/or grace periods can be defined to initiate countermeasures to bring the pH-value within acceptable ranges.

Up until now different assumptions have been made to estimate the pH-value progression during severe accidents, however for the short- and long-term no detailed analysis for the whole containment have been made using a containment code. The code COCOSYS (COntainment COde SYStem) has been equipped with a model, able to calculate the distribution of different pH-active species and thereby the pH of puddles and pools within the containment over the whole accident sequence [3]. The code can calculate the distribution of fission products and chemicals that are released into to containment, in the gas and the fluid phase. Based on the concentration of these species in the water pools, the pH-value for the pools and puddles in the containment can be calculated for each time step. The goal of the report is to demonstrate the capabilities of COCOSYS in this regard.

2. COCOCSYS PH CALCULATION

The software program COCOSYS is used in this work. It is a lumped parameter code that enables a thermal hydraulics analysis, i.e., calculation of the pressure, temperature, and gas composition of local containment zones as well as wall temperatures and flow rates between the zones. Furthermore, COCOSYS features advanced models for the simulation of the fission product (FP) behavior inside the containment including the transport and the wash out behavior of FPs considering the typical behavior within the containment (hygroscopy and solubility) and the decay heat linked to the FP distribution within the containment (atmosphere, deposition on structures and in the sumps). Using a well-defined containment model, this code can be used to calculate the pH-values in different zones that consist of lumped rooms. When sumps are referred to in this document, the water volumes in every zone regardless of their size is meant. To demonstrate the capabilities of the code, a simplified generic GenIII+ PWR containment model for a LB-LOCA scenario has been used. The used COCOSYS version is COCOSYS v3.2 with some modification to handle the species transport by the containment spray.

2.1. PH-active species

This section describes the pH-active species modeled in COCOSYS. The pH-value (potential for hydrogen) is a measure of the acidity or alkalinity of an aqueous solution. The pH scale ranges from 0 to 14, with 7 being neutral. Different pH-active species are modelled in the COCOSYS code. These are listed in table I [4].

Table I. pH-active species modelled in COCOSYS

Molecule	Source	Influence on pH
HNO_3 Nitric acid	- Radiolytically formed in the containment atmosphere and washed down into the sump - Also formed radiolytically from air dissolved in the sump	↓ Strong acid
H_2CO_3 Carbonic acid	Formed by molten corium-concrete interaction - One part is directly released into the sump - The other part is released to the atmosphere and by mass transfer from there into the sump and pools	↓ Weak acid
H_3BO_3 Boric acid	Additive to primary coolant to reduce reactivity of fresh fuel	↓ Weak acid
LiOH Lithium hydroxide	Additive to increase pH of primary coolant (corrosion prevention, compensation of boric acid)	↑ Strong base
NH_3 Ammonia	Formed in primary coolant from hydrazine (N_2H_4), which is used for oxygen mitigation	↑ Weak base
CsOH Cesium hydroxide	Fission product Cs injected as aerosol (CsI, CsOH und Cs_2MoO_4) into containment and washed down into sump. (Only CsOH is considered)	↑ Strong base

CsOH is treated as an aerosol by COCOSYS. Therefore, it is transported by atmospheric flows, as drainage flows into other compartments. CsOH can be deposited and onto structures and washed down into the compartment sump by condensate flows. Lithium hydroxide (LiOH), boric acid (H_3BO_3) and ammonia (NH_3) are treated as a chemical species bound to the liquid phase. Therefore, they are not transported by atmospheric flows or released into the atmosphere by water evaporation. They can only be transported with the liquid phase by e.g., pumps or drainage flows. Carbonic acid is created when CO_2, created during the MCCI reacts with the water in the zone sump. CO_2 is released into the containment and transported by atmospheric flows. The CO_2 sump concentration in the zone sump is determined by the henrys law.

HNO_3 is treated like a gaseous and liquid species by COCOSYS. It is created in the gas and sump part of a zone by radiolysis. Nitric acid is created in the sump by radiolysis of the water molecules and subsequent reaction with nitrogen dissolved in the water phase. In the gas phase HNO_3 is produced by creation of NO_x by radiolysis and subsequent reaction with reaction with water molecules contained water droplets of the atmosphere. The atmospheric production of HNO_3 is derived from the MELCOR model for HNO_3 production [5]. Atmospheric formation of HNO_3 is the main source of HNO_3 during a severe accident as identified in [2] [6] (according to rate of production due to irradiation). Gaseous HNO_3 can be transported into the zone sump by two mechanisms. The first mechanism is direct mass transfer to the water surface. The second transport mechanism is by deposition of HNO_3 on structures by condensation and subsequent wash down of the deposited HNO_3, when a sufficient condensation rate is achieved. Deposited HNO_3 cannot be re-released into the atmosphere. Once HNO_3 has reaches any sump, it is bound to the liquid phase and cannot be resuspended by evaporation or dry out of a containment sump [4]. COCOSYS models the dissociation of every pH-active species, by calculating temperature and concentration dependent dissociation equilibrium for each dissociation stage [3]. Strong acids and bases usually influence the pH more strongly as they dissociate strongly.

2.2. Geometric containment model

The containment model consists of multiple zones which are a result of lumping of rooms that are functionally and geometrically connected. The containment is divided into the two main room classes, equipment (Eq) rooms and annular (Ann) rooms. Equipment rooms are rooms containing the main equipment of the primary circuit such as the steam generators, pumps, the reactor compartment, as well as additional zones directly connected to these zones, such as the spreading room and the IRWST. The Ann and Eq rooms are divided along three levels lower, middle, and upper rooms. The lower rooms represent the ground floor level of the containment. The middle and upper rooms represent the next two floor levels above the ground level. Figure 1 shows a simplified depiction of the nodalization of the containment, including the main water drainage paths (blue lines). The spray system pumps water from the IRWST pool through a cooler and then injects the water as spray into the containment dome to condense steam and reduce containment pressure during the ex-vessel phase. The spray water and condensate flow downwards trough the upper Ann and Eq rooms downwards to the lower rooms. From there, the water is drained into the IRWST surface, which mixes with the IRWST pool water during the operation of the spray. Finally, the spreading room is connected with the IRWST pool to enable a flooding of the corium during the ex-vessel phase.

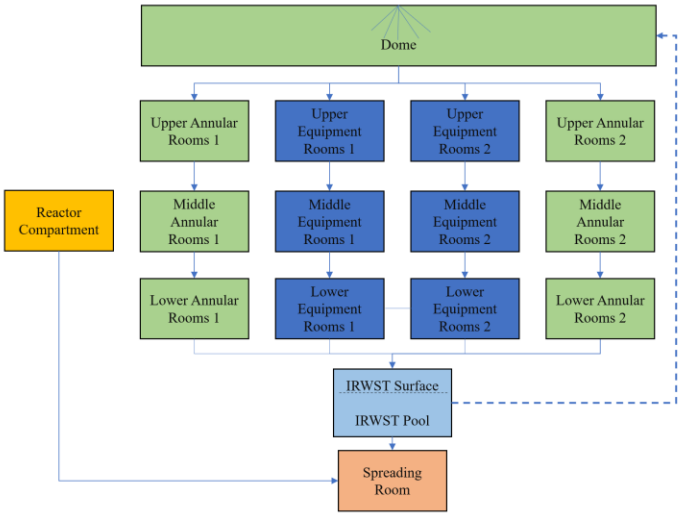

Figure 1: Simplified nodalization of the containment model including main fluid flow paths

Figure 2 shows the main atmospheric flow paths between the COCOSYS compartments. The figure shows, that the Eq rooms are connected by atmospheric openings The reactor compartment is connected to the lower and upper Eq rooms. The annular rooms and equipment rooms are atmospherically connected by the dome and the IRWST. Annular rooms on the same level are connected with each other as well.

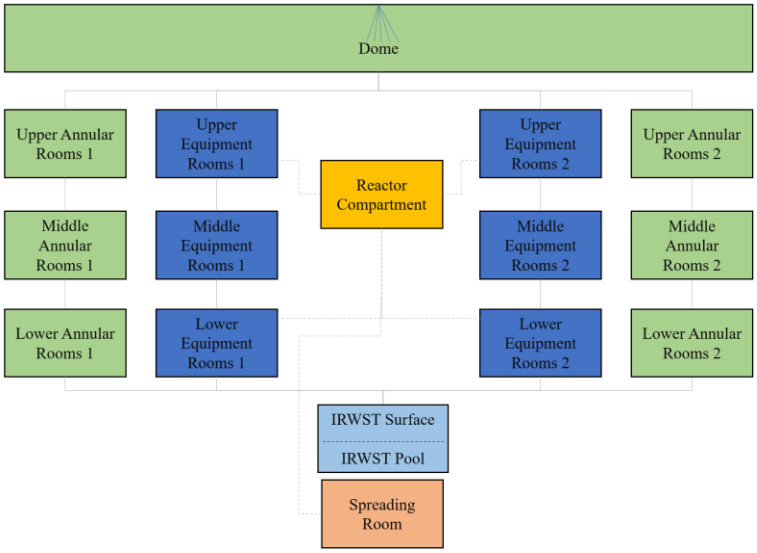

Figure 2: Simplified nodalization of the containment model including main gas flow paths

2.2. LB-LOCA scenario

The considered accident sequence is a large break loss-of-coolant-accident (LB-LOCA) at the hot leg located in the lower equipment rooms 2 compartment. Some important events are referenced to in the figures of the results chapter which are shortly described here. During the accident sequence different pH-active species are released into the containment. At the beginning of the scenario, fission products are released from the break into the lower equipment rooms 2. During the RPV failure fission products are released from the reactor compartment into the equipment rooms. After the RPV failure hot corium is relocated to the spreading room. Afterwards the hot corium is flooded by water from the IRWST (Quench). During the initial quenching phase, a large amount of the water is rapidly evaporated. After some time, the core is sufficiently cooled so that a stable water level is established in the spreading room. The spreading room is continuously fed by IRWST water, so that a constant cooling of the corium is ensured. After some time, the subcooled water in the spreading room starts to boil (Boiling). Later, the spray system is activated (Spraying). The spray system pumps water from the IRWST pool zone through a cooler and then injects it into the dome as spray. The spray system condenses steam in the containment and decreases the containment pressure. As there are no sources and sinks for the water, the containment water is cycled by the spray system.

3. RESULTS

3.1. Phase of initial event until start of containment spraying

Figure 3 shows the short-term and intermediate-term pH-values predicted for the LB-LOCA scenario. The abbreviation for the figure legends follows the scheme as shown in in Figure 1. Figure 3 shows that different water pools exhibit different pH-values until spraying. During the initialization of the calculation, there are some fluctuations of the pH due to the low water mass in all zones. The pH then increases during the initial release of mass and energy from the large break. Fission products, steam and water are released at the lower

equipment (Eq) rooms first and then in the reactor compartment during RPV failure. LiOH and H_3BO_3 are dissolved in the primary circuit water and are therefore released at the break location. These species are only transported by the liquid phase and therefore follow the drain flow paths (see Figure 4). A figure for boric acid is not provided, as it shows the same behavior at different concentration levels. Initially the concentration of LiOH and H_3BO_3 increases in the water pool of the lower Eq Rooms as it is the zone where the species are released to (species contained in steam are allocated to the water phase). The figure shows an initially fast and then slow decrease of the species concentration over time. This is a result of the pool water mixing with pH-neutral condensate. After the initial release peak, steam condenses along the height of the Eq Rooms and flows downwards until the water reaches the IRWST. Initially the condensate flows are high, which leads to the fast decrease in species concentration. Later the condensate flows decrease but do not stop, leading to a slow decrease in the concentrations in the lower Eq rooms 2. Accumulated pH-active species are therefore washed down from the upper containment levels down into the IRWST.

During the quenching phase water from the IRWST is fed to the spreading area, where it is rapidly evaporated. The pH-active species (except carbonic acid and CsOH to a very low degree) are bound to the water phase in COCOSYS and are therefore not released into the atmosphere along with the steam. This leads to the peak of the species concentrations in the spreading room (see Figure 4). After the initial quenching, the water in the spreading area has cooled the corium to the point where a stable water level can be established above the corium. As a result, the pH-active species concentration in the spreading room decreases (dilution by water). These findings apply to the other species as well (Except carbonic acid).

During the boiling phase, steam from the spreading room enters the lower Eq rooms and is distributed throughout the containment. This steam condenses and flows downwards into the IRWST via the drainage paths. Along with the condensate, the pH-active species are transported downwards, which leads to the slow decrease in the sump concentrations as seen in Figure 4 for the lower Eq rooms 2. As the IRWST pool is the final zone in the drain path, species concentrations can increase there as a result of the condensate flows.

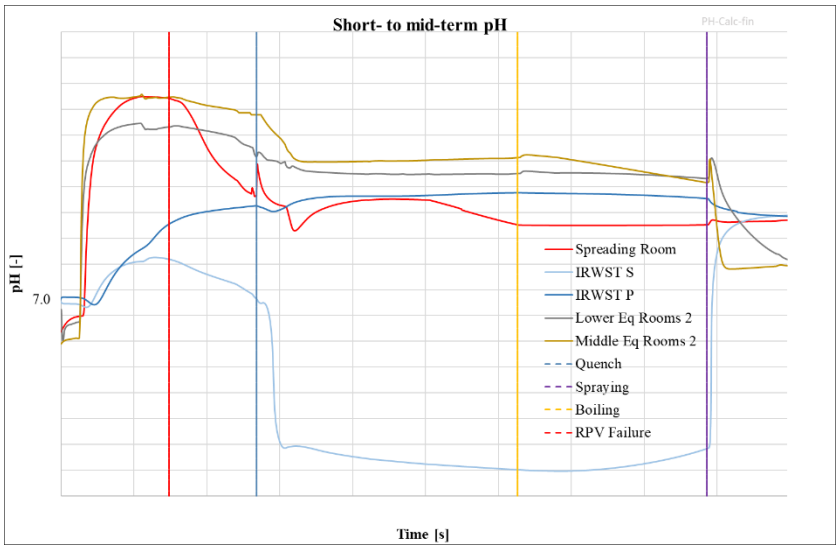

Figure 3: Short-term pH of main pools and puddles on different containment levels

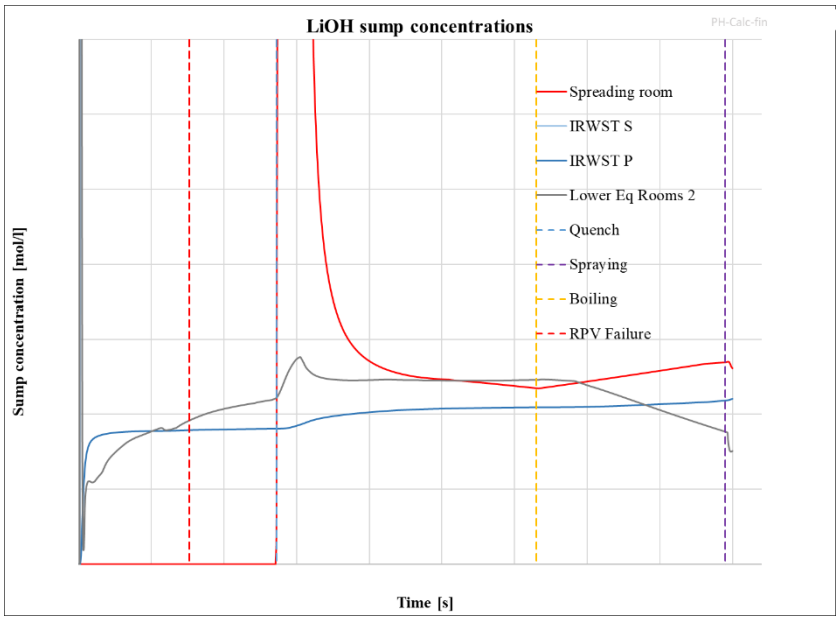

Figure 4: Sump concentration of LiOH on different containment levels

Fission products are transported throughout the containment either via the water drain routes or via atmospheric flows. Cesium is initially released from the break and later by the RPV failure. Figure 5 and Figure 6 show the atmospheric and sump concentration of CsOH. It is transported into all zones via atmospheric flows. After the release, CsOH is deposited on walls and dissolved into the water phase of the respective zone. This can be seen in the rapid decline of atmospheric CsOH, which is reduced to almost zero after 20000 s and the rise of the sump concentrations (see Figure 6). This causes the pH of the respective sumps to rise, leading to alkaline pH-values.

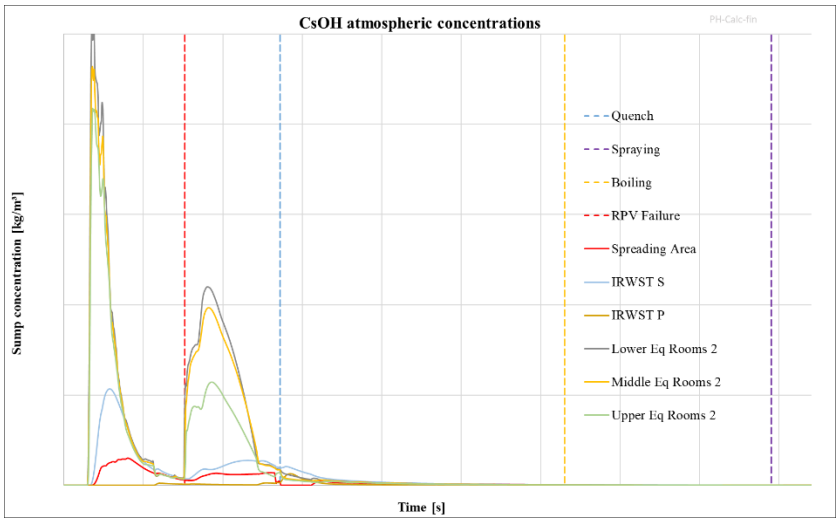

Figure 5: Atmospheric concentration of CSOH on different containment levels

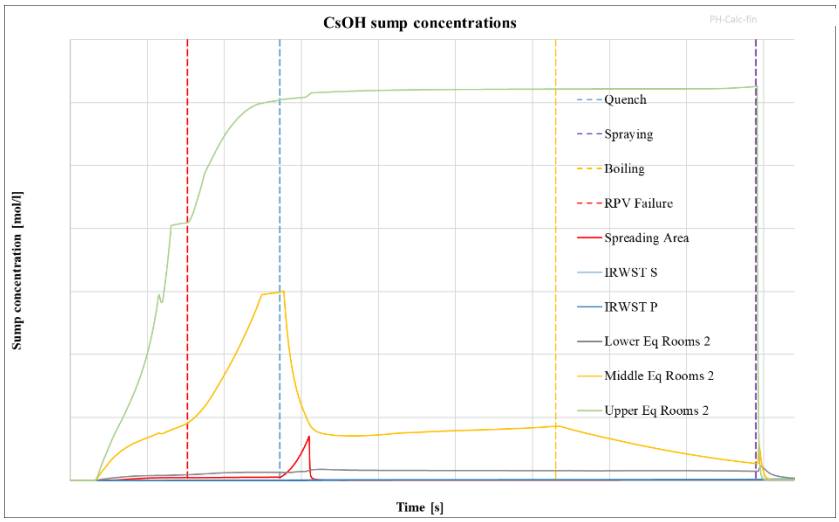

Figure 6: Sump concentration of CSOH on different containment levels

Injections of small amounts of species can lead to big changes of the pH in small water pools due to their low amount of water. Similarly, a wash down of water from another zone may lead to visible changes in the pH as a relatively low amount of water is able to replace all the water in a small sump. This can be seen in CsOH concentrations in the middle and upper Eq rooms 2. Even though the atmospheric concentration in these zones is smaller than in the lower Eq rooms, the sump concentrations are much higher (low amount of water). Big water pools such as the IRWST are less affected by small changes of species within the water pool, which is why the change in species concentration and pH is less pronounced in the IRWST pool or the lower Eq Rooms (much larger water pool than in the upper Eq Rooms).

As fission products are released into the containment, the dose rate in the containment is established. This enables the production of HNO_3 in the atmosphere and the sump. Figure 7 and Figure 8 depict the atmospheric, sump and structure deposited concentrations of HNO_3 in the IRWST surface zone. It can be seen, that with the establishment of the dose rate, the HNO_3 concentrations begin to rise. This is a result of the creation of HNO_3 in the air and subsequent direct deposition into the sump and structures of the respective zones (HNO_3 is also created in the sump). Atmospheric HNO_3 is transported and deposited on structure surfaces as a result of of steam condensation on the respective structure. Figure 9 shows the condensation rate for the IRWST zone and the amount of deposited HNO_3 on the structures of the IRWST. The figures show that the deposition rate of HNO_3 increases at higher condensation rates. The deposited HNO_3 is washed down into the sump at different times in the calculation. During the quenching phase, a high mass of steam is released into the containment. This steam condenses on the structures, resulting in an increased deposition of HNO_3. The deposited HNO_3 is then washed down from the structures into the zone sump. Figure 10 shows the HNO_3 concentrations of sumps on different levels in the containment. The figure shows a strong increase of HNO_3 concentrations for the zones during the quenching. This is a caused by the deposition and wash down of HNO_3 from the structures. After the quenching, the concentration of HNO_3 decreases in the upper zones, while the concentration in the lower rooms continue to increase. This is a result of the wash down of HNO_3 by condensate drainage. The mechanisms for creation, deposition and wash down described for this zone apply to the other zones as well.

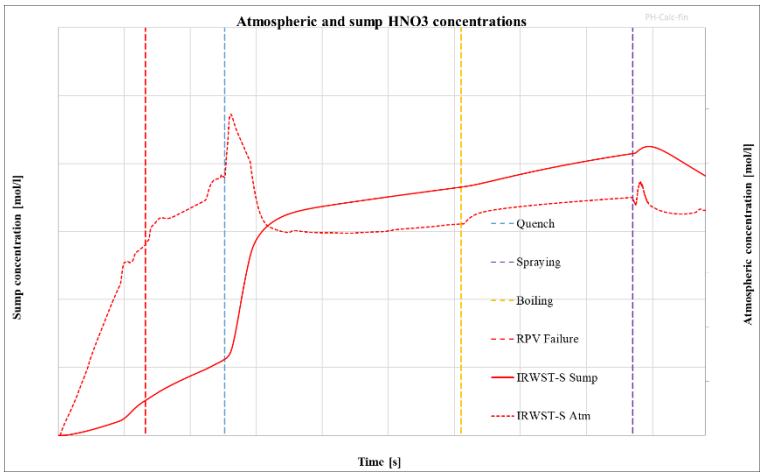

Figure 7: Sump and atmospheric concentration of HNO_3 in the IRWST

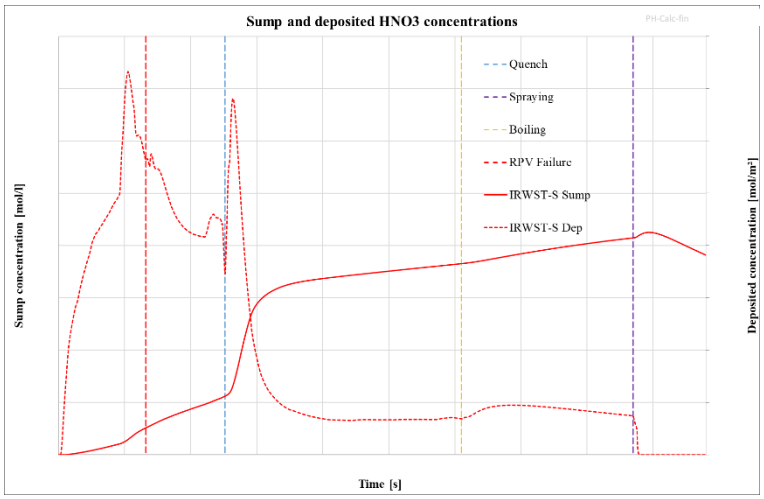

Figure 8: Sump and deposited concentration of HNO_3 in the IRWST

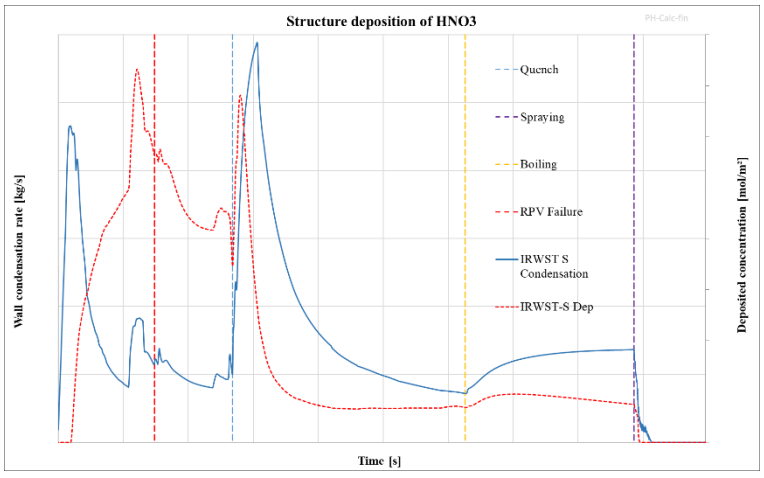

Figure 9: Deposited concentration of HNO_3 in the IRWST and condensation rate

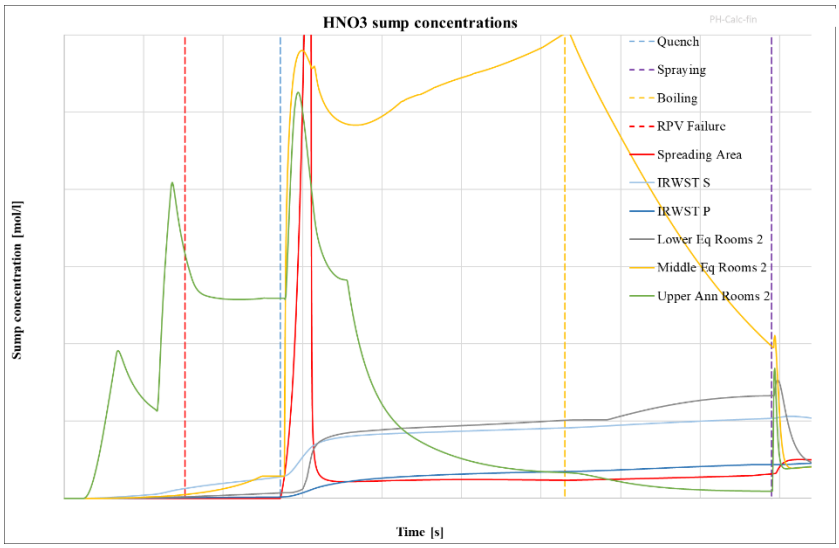

Figure 10: Sump concentration of HNO_3 on different containment levels

Carbon monoxide and carbon dioxide are released into the reactor compartment and spreading room after RPV failure. The effect of CO on the pH is negligible in comparison to CO_2. Therefore, only CO_2 is considered in the COCOSYS pH model. Atmospheric CO_2 is transported into the sump phase according to the water-gas equilibrium, using temperature dependent Henry's law. Figure 11 shows the sump and atmospheric concentration of CO_2. The sump concentration follows the atmospheric concentration. The sump concentration of CO_2 is calculated in COCOSYS by assuming an equilibrium between the atmospheric and sump CO_2. CO_2 is transported only by the gas phase, not the liquid phase. This means that, once the atmospheric concentration in one zone changes, the sump concentration changes to the respective equilibrium concentration. This leads to some differences in the pH-values between the lowest containment zones and all other zones as the atmospheric CO_2 concentrations are lower in the lower zones. As a result, the effect of carbonic acid on pH is overestimated in the other zones and underestimated in the IRWST and spreading room.

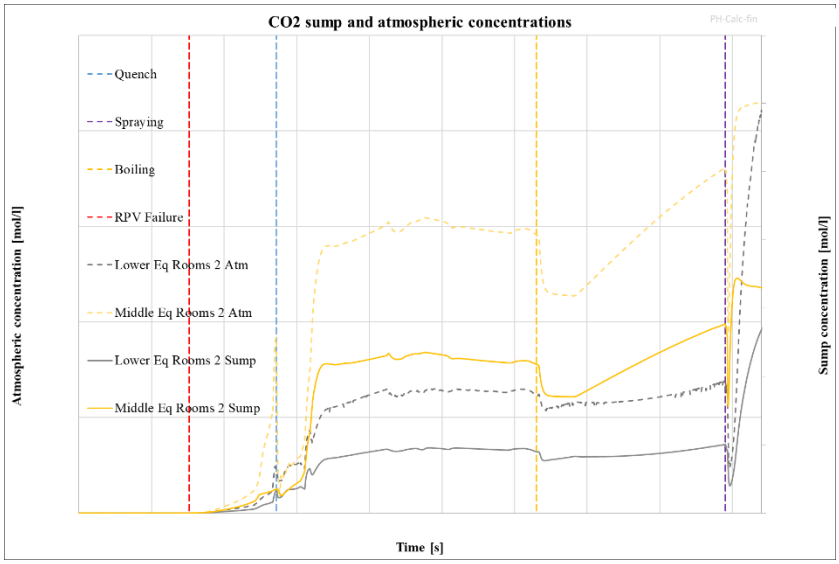

Figure 11: Atmospheric and sump concentration of CO_2 on different containment levels

3.2. Phase of start of containment spraying until the end of the calculation

After the initiation of the spray, the long-term phase of the calculation begins. The spray system injects water from the IRWST pool into the containment dome as spray. This water condenses steam, and washes deposited species on walls down into the respective one sump. This leads to a rapid change of the pH-value of different water pools, as after the spray initiation due to the fast exchange of the current water inventory with IRWST water as well as wash down of deposited HNO_3 into the containment sumps. This can be seen in Figure 12 as an initial dip in the pH of the Eq Rooms. After the initial dip the pH of the pools approach the pH-value of the IRWST pool with some difference. This difference is caused by the presence of carbonic acid as described in the previous section. From this point on without the production of HNO_3 the pH-values of the water pools would stay approximately on the same level. Finally, Figure 13 shows the long-term pH of the lower Eq rooms 2 and heir HNO_3 concentration only, as there are no visible differences between the different zones at low pH-values. It can be seen that changes in the pH directly correlate with changes in the HNO_3 concentration in the long-term. The s-curve form of the pH indicates that the pH of the pools becomes acidic in the long term.

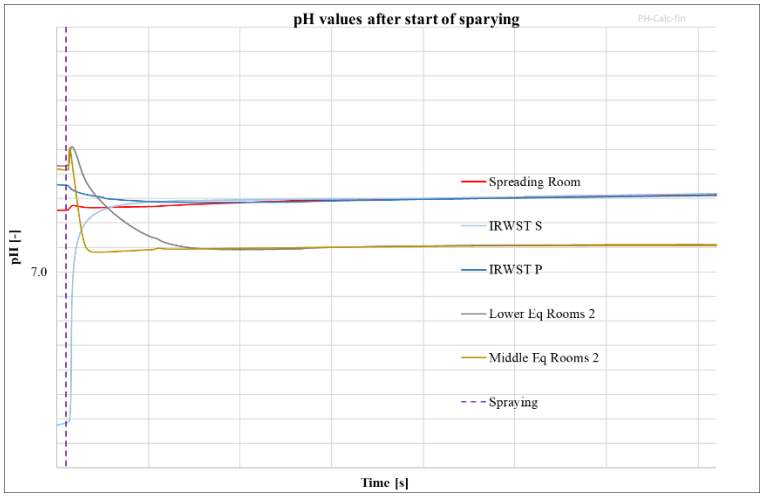

Figure 12: PH-values of different pools after the initiation of the containment spray

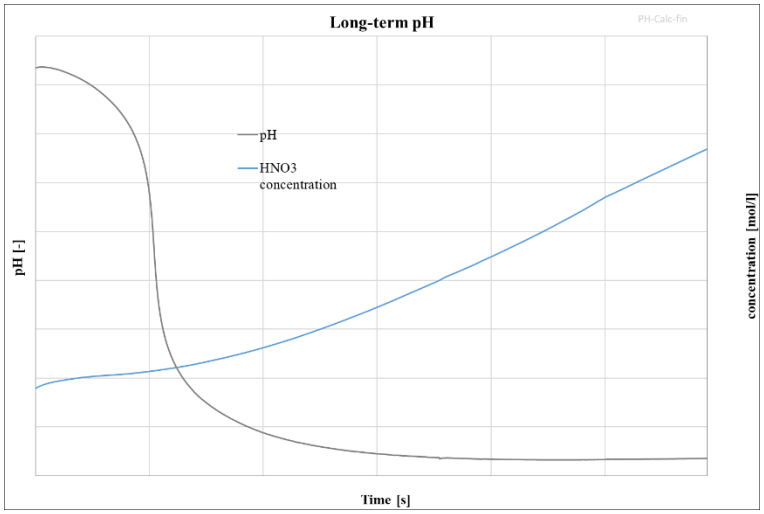

Figure 13: PH value of the lower Eq Rooms and HNO_3 concentration in the long-term

4. CONCLUSIONS

This report has shown that the lumped parameter code COCOSYS can model the production, release and transport of various pH-active species within the containment and predicting the associated changes in pH of water pools and puddles. With its fast computation time, COCOSYS is suitable for assessing the short- and long-term effects of different pH-active species on water pools, as well as the long-term effect of radiolitic HNO_3 production on pH-values. With some additions to the code additional processes can be modelled. In the current state of the COCOSYS pH model, species dissolved in the liquid phase cannot be rereleased in the atmosphere (except for CsOH and CO_2) by evaporation or other processes. Therefore, a re-release of these species during e.g., boiling of the spreading room cannot be directly assessed. Another useful improvement would be a remodeling of the deposition of CO_2 in the sump phase, so that it is transported within the water phase. Finally, the addition of more pH-active species and models for acid-structure interactions could allow a more detailed assessment of material degradation and the effect of countermeasures.

ACKNOWLEDGMENTS

The authors would like to acknowledge the funding of the R&D department of FRAMATOME GmbH and the support of GRS in this work.

REFERENCES

1. Weyermann, Spengler, Schöffel, Buchholz, Steinhoff, Sonnenkalb, Wielenberg, Schaffrath, "Development of AC2 for the simulation of advanced reactor design of Generation 3/3+ and light water cooled SMRs" Kerntechnik, **Vol. 84**, no. 5, 2019, pp. 357-366. https://doi.org/10.3139/124.190068
2. Beahm, Weber, Kress, Parker, “Iodine Chemical Forms in LWR Severe Accidents, Oak Ridge National Laboratory”, Oak Ridge (1992)
3. Arndt, Eckel, Klein-Heßling, Spengler, Schwarz, Nowack, Pelzer, “COCOSYS V2.4v6 User’s Manual”, Rev 37, Cologne (2021)
4. Arndt, Beck, Eckel, Klein-Hessling, “Weiterentwicklung der Rechenprogramme COCOSYS und ASTEC”, GRS-358, Cologne (2014)
5. R.O. Gauntt et al., “MELCOR computer code manuals / Reference Manuals, Version 1.8.6 September 2005", NUREG/CR-6119, **Vol. 2** Rev. 3, SAND 2005-5713.
6. S. Dicksinson , H. Sims, E. Belval-Haltier, D. Jacquemain, C. Poletico, F. Funke, Y. Drossinos, E. Krausmann, B. Herrero, T. Routamo, B. Handy, "Iodine chemistry", Proceedings FISA-99: EU Research in Reactor Safety, Luxemborg, 29 November - 1 December 1999, EUR 19532 EN (1999)

framatome

ERMSAR 2024

Assessment of pH-values in water pools during SA using the lumped parameter code COCOSYS

Leon Anschütz

May 15, 2024

C1 - Framatome Restricted, Framatome know-how
Export Control – AL: N / ECCN: N

Content

1. Motivation
2. Theoretical Background
3. COCOSYS Code and Model
4. Calculation Scenario
5. Calculation Results
6. Conclusions

1. Motivation

- Severe accident management objectives:
  - Ensure long-term containment integrity
  - Minimize/prevent release of radioactive species
- Achieved through:
  - Containment integrity
  - Functionality of mitigation features
- pH has a major influence on:
  - Material degradation
  - Atmospheric iodine concentration



Goal:

A good prediction of pH evolution allows the assessment of expected effects on material and the dimensioning of pH mitigation measures

Confidentiality Framatome (external) – AL: N – ECCN: N © Framatome - All rights reserved

2. Theoretical Background

- Acidic and basic species are released during severe accidents
- Short-term pH-values depend on the distribution of Cs, B, Li, CO_2
- HNO_3 is formed radiolytically throughout the duration of the accident
- Long-term pH values depend on the formation of HNO_3

Air/Steam
- HNO_3

Primary circuit
- Boron (H_3BO_3)
- Lithium (LiOH)

Core
- Cesium (CsOH)

Concrete
- CO_2 (H_2CO_3)

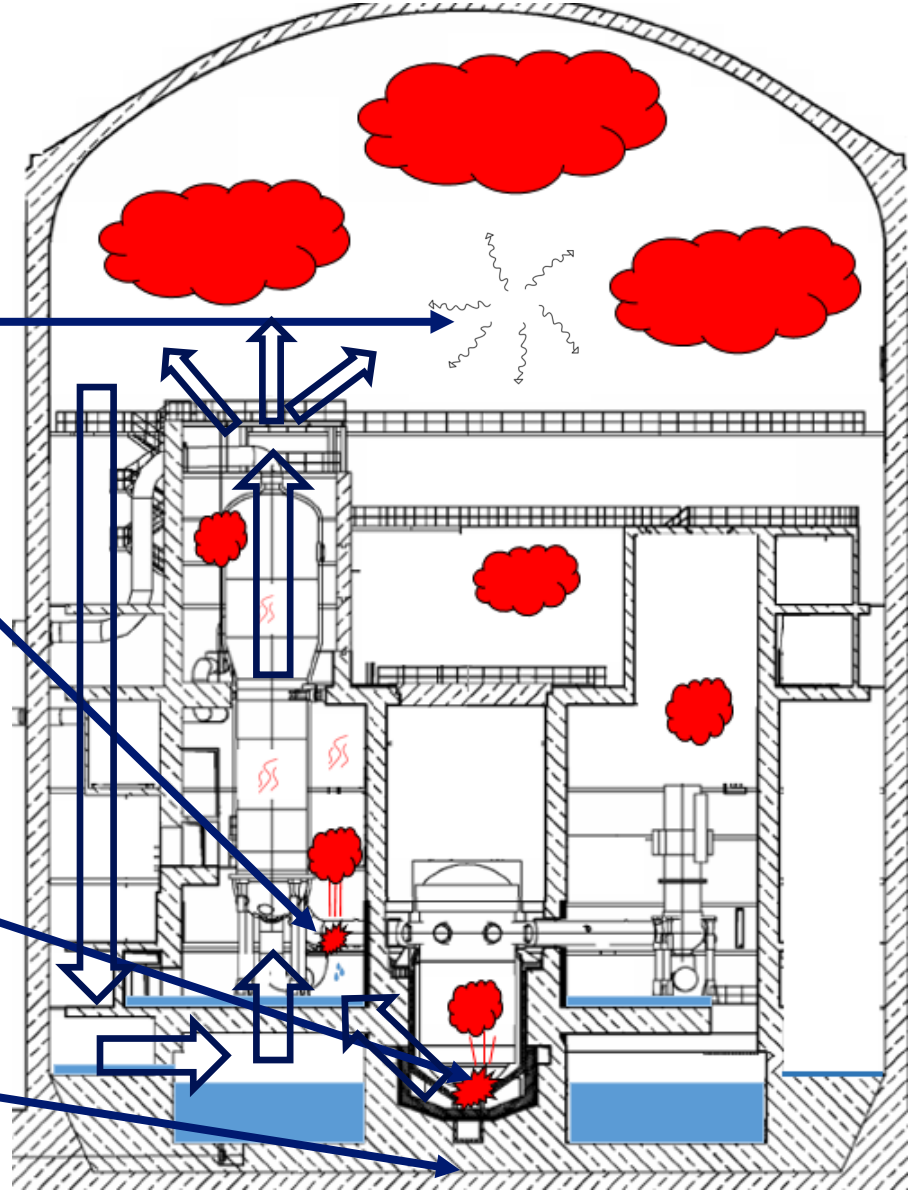

Confidentiality Framatome (external) – AL: N – ECCN: N © Framatome - All rights reserved

3. COCOSYS (Code and Containment Mod.)

Lumped parameter code for calculation of:

- Thermohydraulic (e.g. temperature, pressure, gas distribution, flows, heat transfer to structures, condensation)
- Fission product behavior (Transport, Deposition, Agglomeration, Resuspension)
- Iodine behavior (e.g. Iodine chemistry, Iodine distribution)

- **Transport and distribution of pH-active species**
- **Dissociation reactions of pH-active species**
- **Calculation of the pH**

Confidentiality Framatome (external) – AL: N – ECCN: N © Framatome - All rights reserved

3. COCOSYS (Code and Containment Mod.)

Molecule	Source	Modelling
HNO_3 - Nitric acid	- Formed radiolytically in the containment atmosphere and washed down into the sump - Also formed radiolytically from air dissolved in the sump	- Gas/liquid carried species - Deposition on structures and wash down - Direct deposition to sump
H_2CO_3 - Carbonic acid	CO_2 released by molten corium-concrete interaction is dissolved in sumps to form carbonic acid	- Gas carried species - Sump concentration calculated by Henry's law - No liquid phase transport
H_3BO_3 - Boric acid	Additive to primary coolant to reduce reactivity of fresh fuel	- Carried by the liquid phase only
LiOH - Lithium hydroxide	Additive to increase pH of primary coolant (corrosion prevention, compensation of boric acid)	- Carried by the liquid phase only
NH_3 - Ammonia	Formed in primary coolant from hydrazine (N_2H_4), which is used for oxygen mitigation	- Carried by the liquid phase only
CsOH - Cesium hydroxide	Fission product Cs injected as aerosol (CsI, CsOH und Cs_2MoO_4) into containment and washed down into sump. (Only CsOH is considered)	- Modelled as an aerosol

Confidentiality Framatome (external) – AL: N – ECCN: N © Framatome - All rights reserved

3. COCOSYS Generic Gen III+ PWR Model

Fluid connections

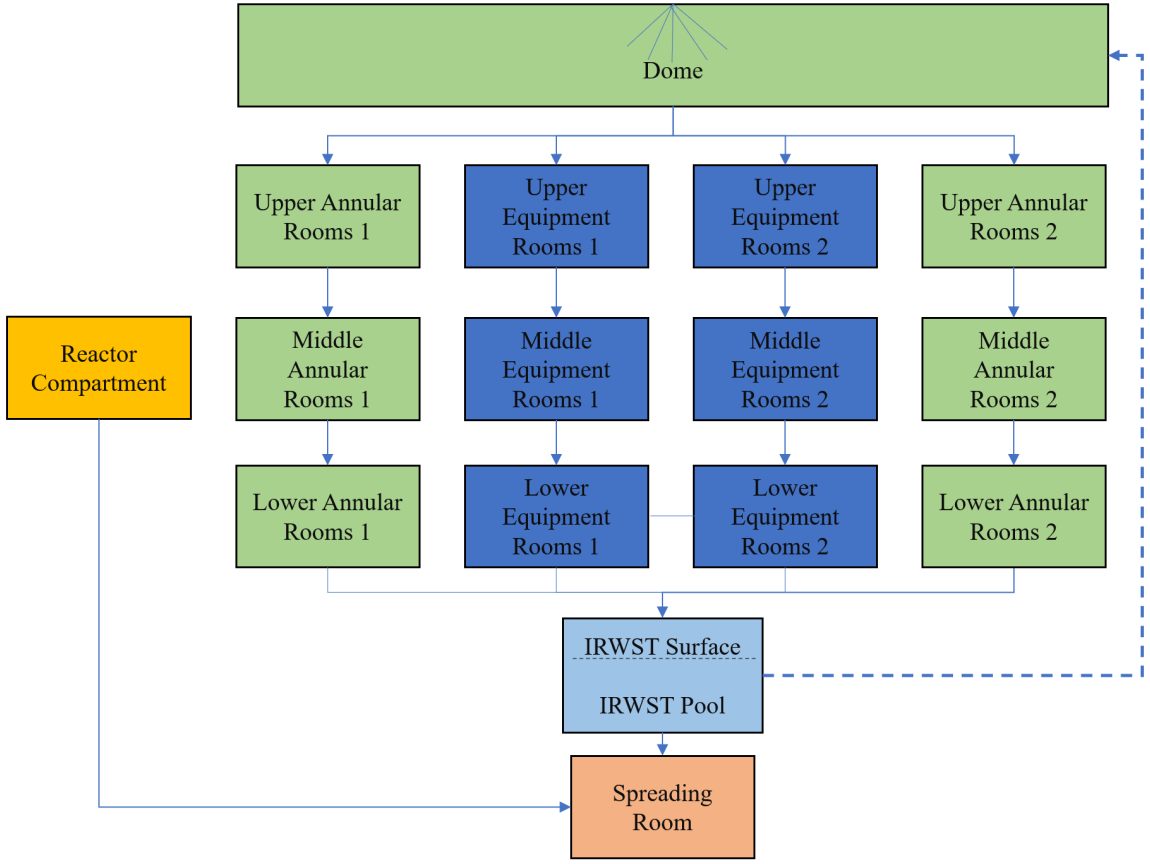

Atmospheric connections

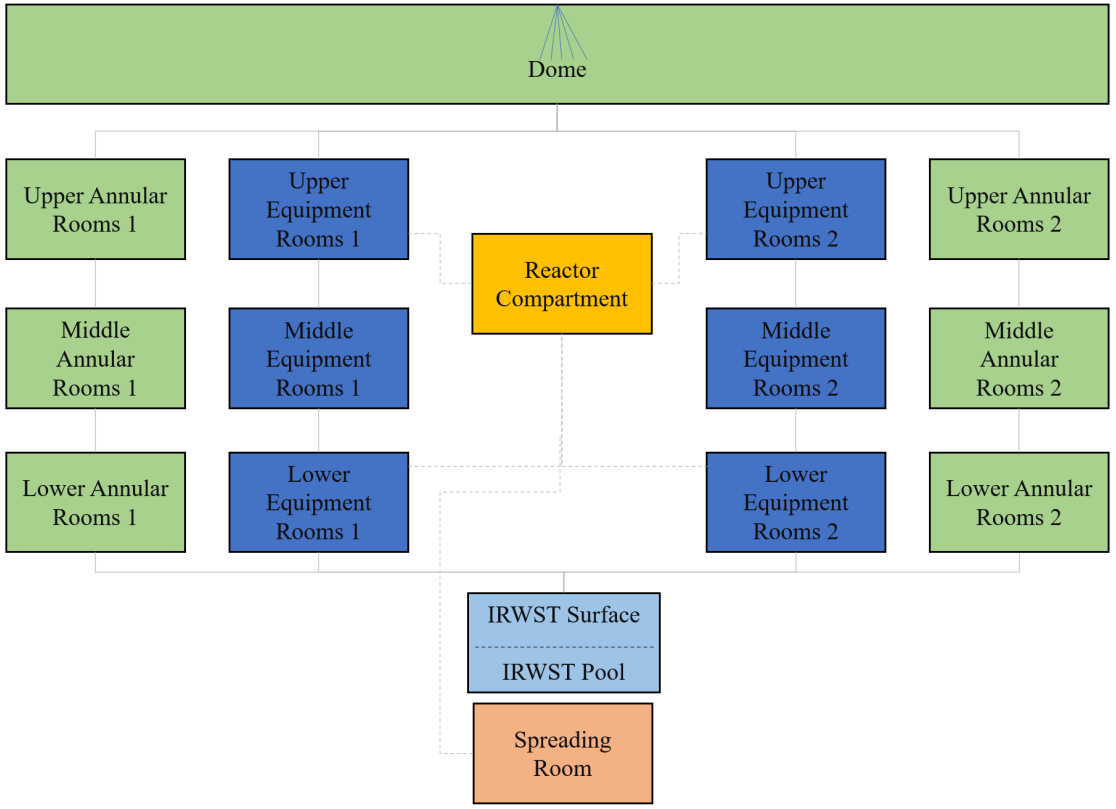

Confidentiality Framatome (external) – AL: N – ECCN: N © Framatome - All rights reserved

4. Calculation Scenario

Large Break Loss-Of-Coolant-Accident (LB-LOCA)

- Release of water/steam/fission products in lower Equipment Rooms 2 during the initial phase
- Release of water/steam/fission products in the Reactor Compartment/Spreading Room at RPV failure
- Quenching of the corium in the spreading room with IRWST water
- Boiling of the water in the spreading room
- Start of containment spraying

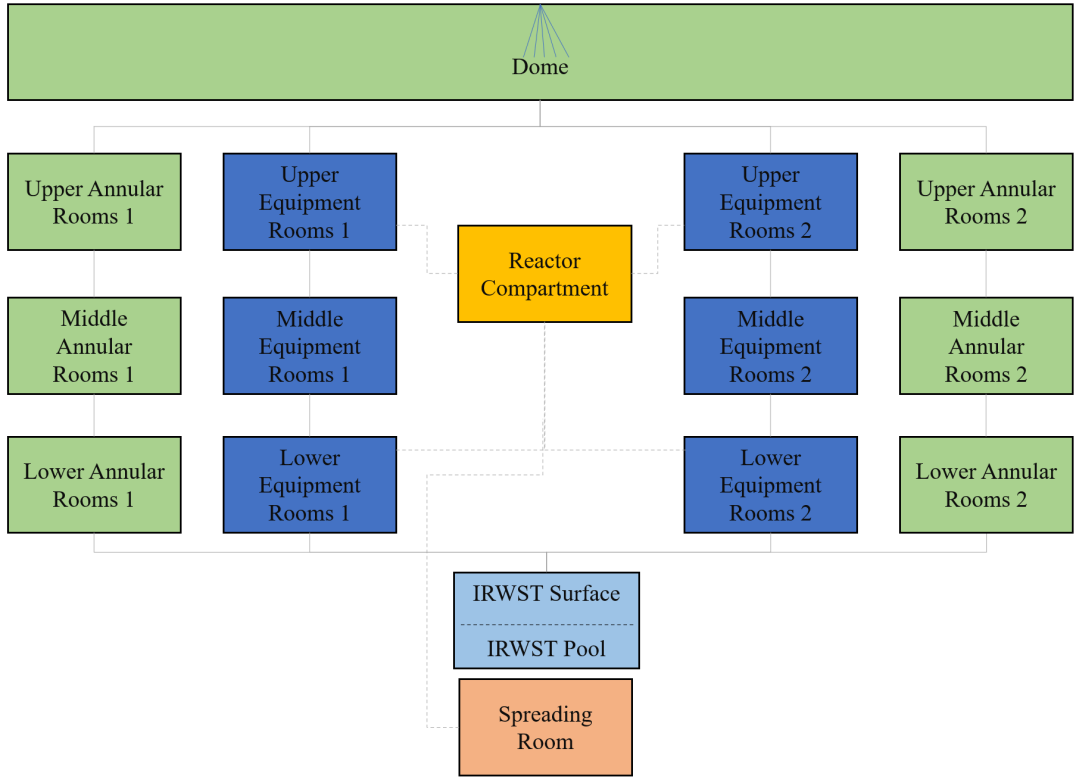

Confidentiality Framatome (external) – AL: N – ECCN: N © Framatome - All rights reserved

5. Calculation Results

Phase until containment spraying LiOH / H_3BO_3

- Rapid increase in the release compartment
- Rapid dilution by condensate
- Wash down into IRWST
- Rapid increase during quenching in spreading room

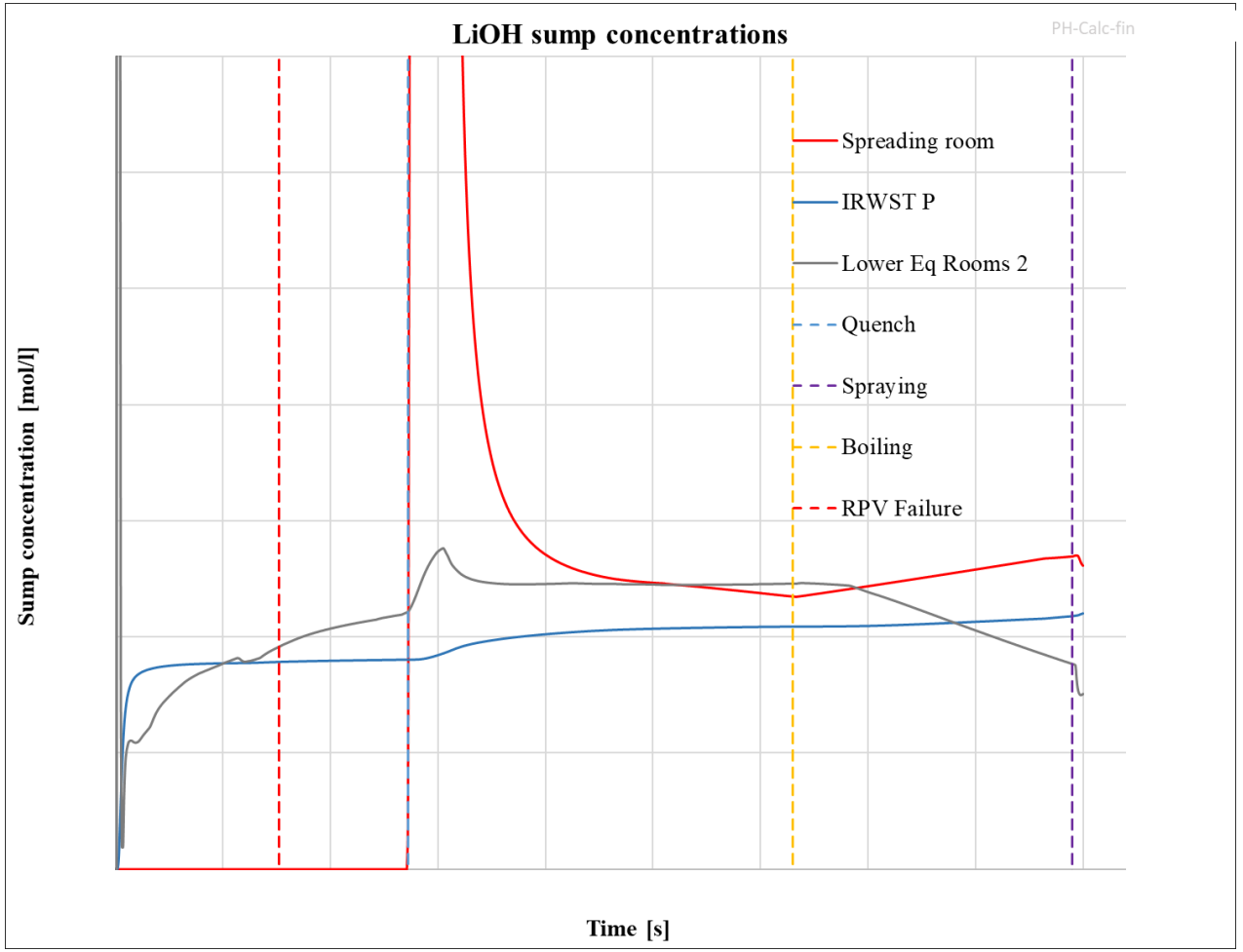

Confidentiality Framatome (external) – AL: N – ECCN: N © Framatome - All rights reserved

5. Calculation Results

Phase until containment spraying CsOH

- CsOH released during RPV failure and initial break in the lower levels
- Transported upwards by atmospheric flows
- Deposition into sumps
- Increase of pH in respective sumps (strong base)

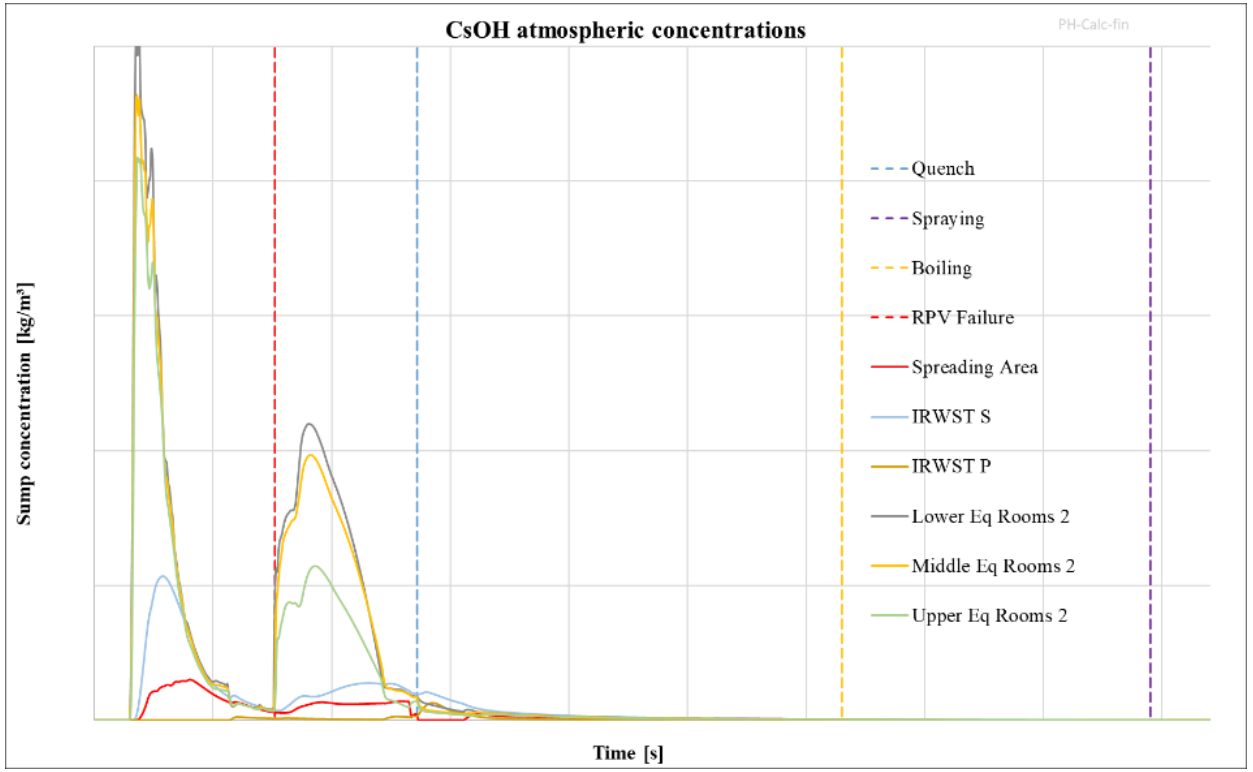

Confidentiality Framatome (external) – AL: N – ECCN: N © Framatome - All rights reserved

5. Calculation Results

Phase until containment spraying CsOH

- CsOH in sumps increases after CsOH release
- Higher CsOH sump concentrations at high elevation
- Low water mass at upper levels lead to stronger fluctuations in concentrations

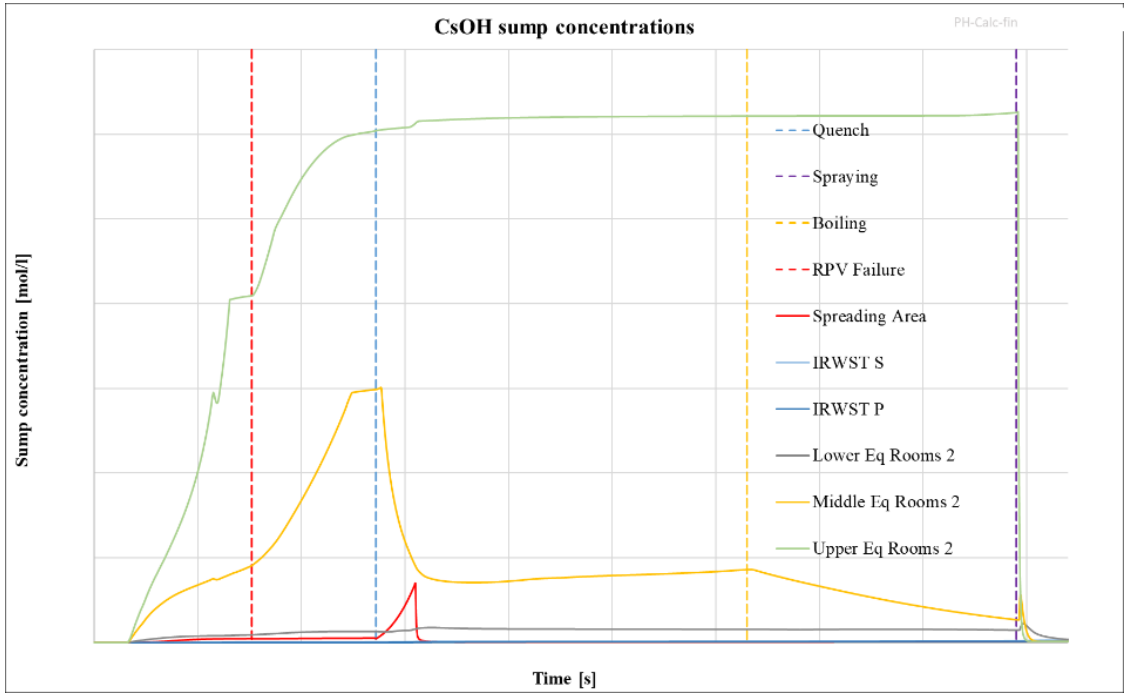

Confidentiality Framatome (external) – AL: N – ECCN: N © Framatome - All rights reserved

5. Calculation Results

Phase until containment spraying HNO_3

- Sump and atmospheric HNO_3 created once dose rate is established by FP release
- Drop in atmospheric concentration as a result of deposition into sump/structures
- Sump concentration increases until spraying

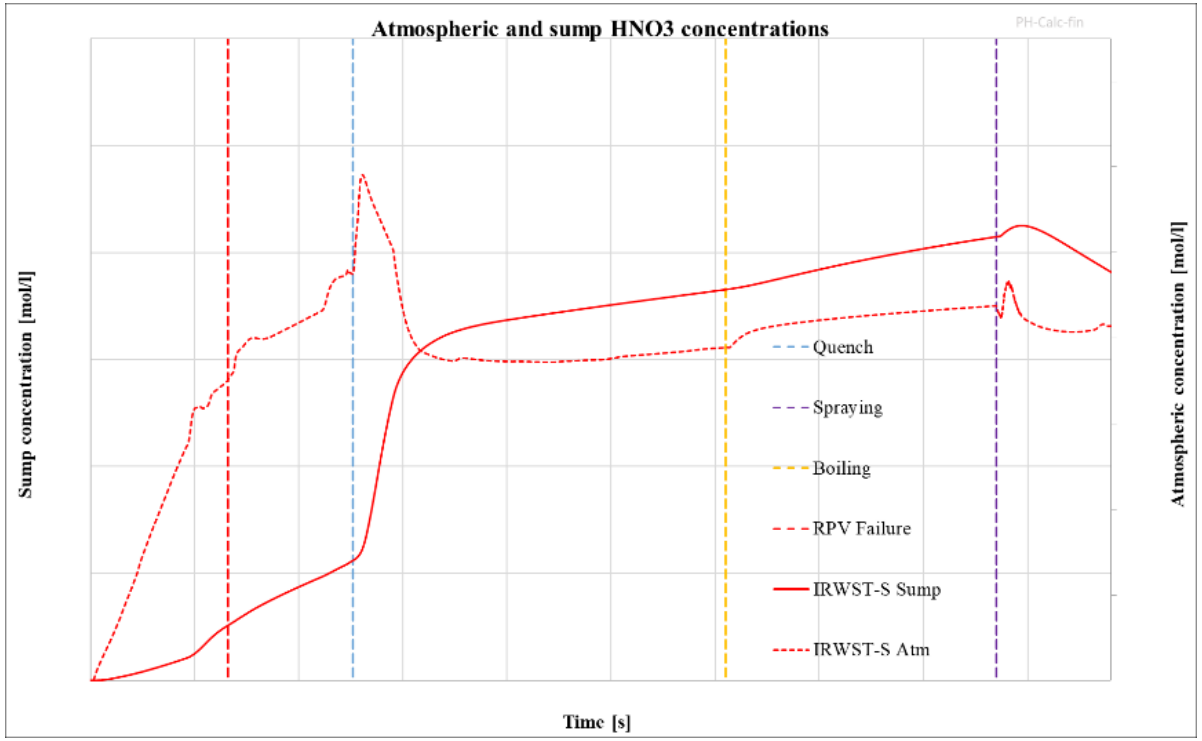

FP...fission product

Confidentiality Framatome (external) – AL: N – ECCN: N © Framatome - All rights reserved

5. Calculation Results

Phase until containment spraying HNO_3

- Atmospheric HNO_3 carried to structures by condensation
- Wash down of deposited HNO_3 by condensation
- Evaluation for each structure

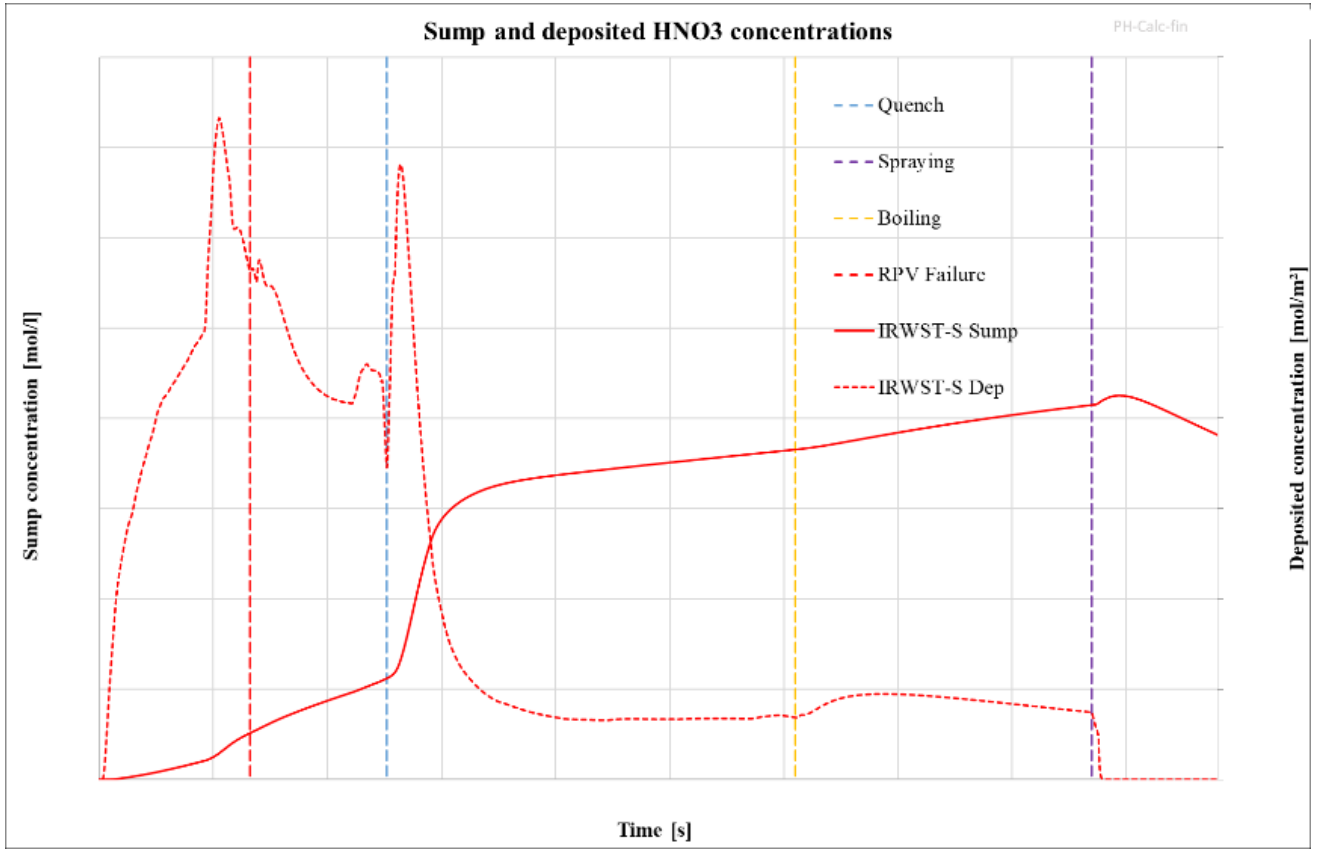

Confidentiality Framatome (external) – AL: N – ECCN: N © Framatome - All rights reserved

5. Calculation Results

Phase until containment spraying HNO_3

- Upper levels exhibit higher concentrations (lower water masses)
- High concentrations in IRWST surface
- Wash down of HNO_3 by condensate into lower levels

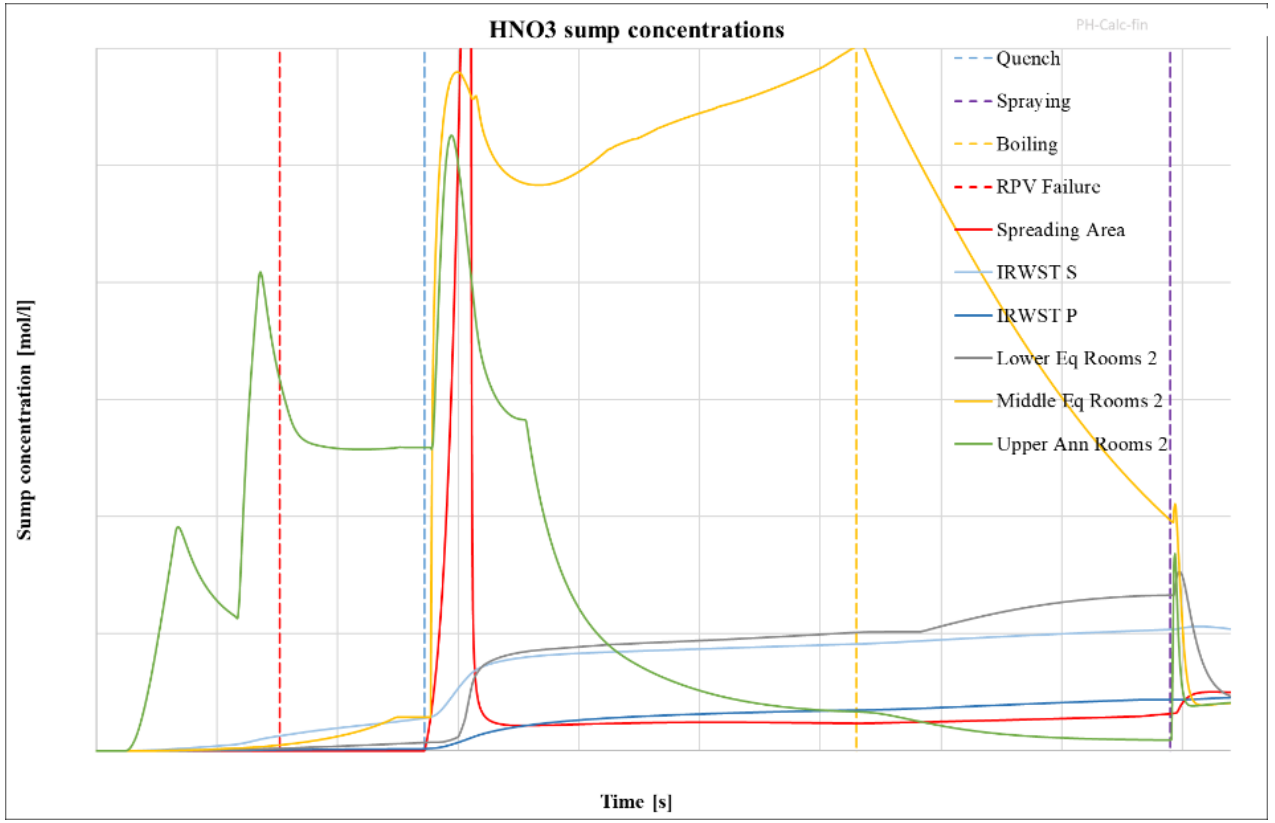

Confidentiality Framatome (external) – AL: N – ECCN: N © Framatome - All rights reserved

5. Calculation Results

Phase until containment spraying CO_2

- Release of CO_2 during MCCI
- CO_2 sump concentration follows atmospheric concentration (Henry's Law)

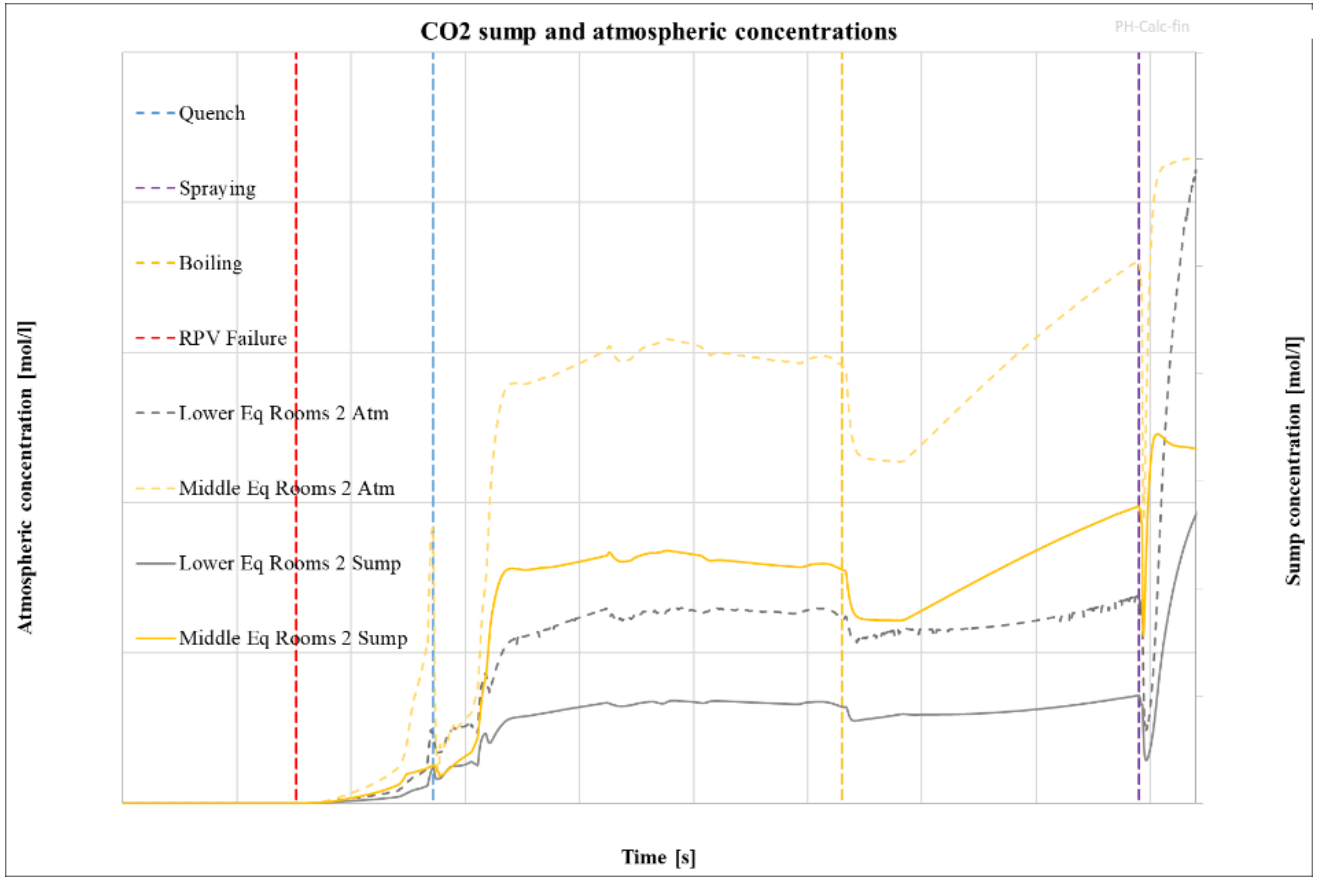

Confidentiality Framatome (external) – AL: N – ECCN: N © Framatome - All rights reserved

5. Calculation Results

Phases until containment spraying pH

- Initial increase of pH due to CsOH
- Slow decrease of pH due to HNO_3 buildup and wash down of CsOH
- Faster decrease during by wash down of HNO_3 into sumps (quenching phase)
- Lower pH-values in IRWST surface due to high HNO_3 concentration

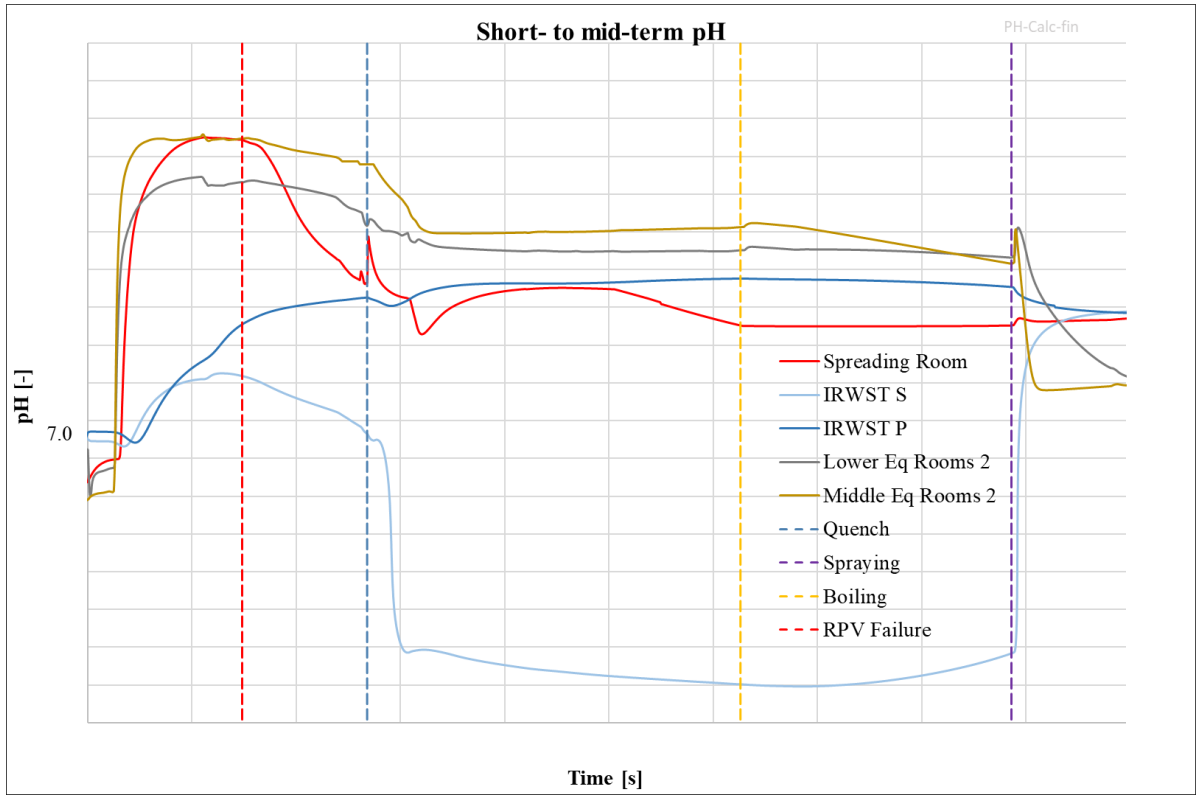

Confidentiality Framatome (external) – AL: N – ECCN: N © Framatome - All rights reserved

5. Calculation Results

Phase after containment spraying pH

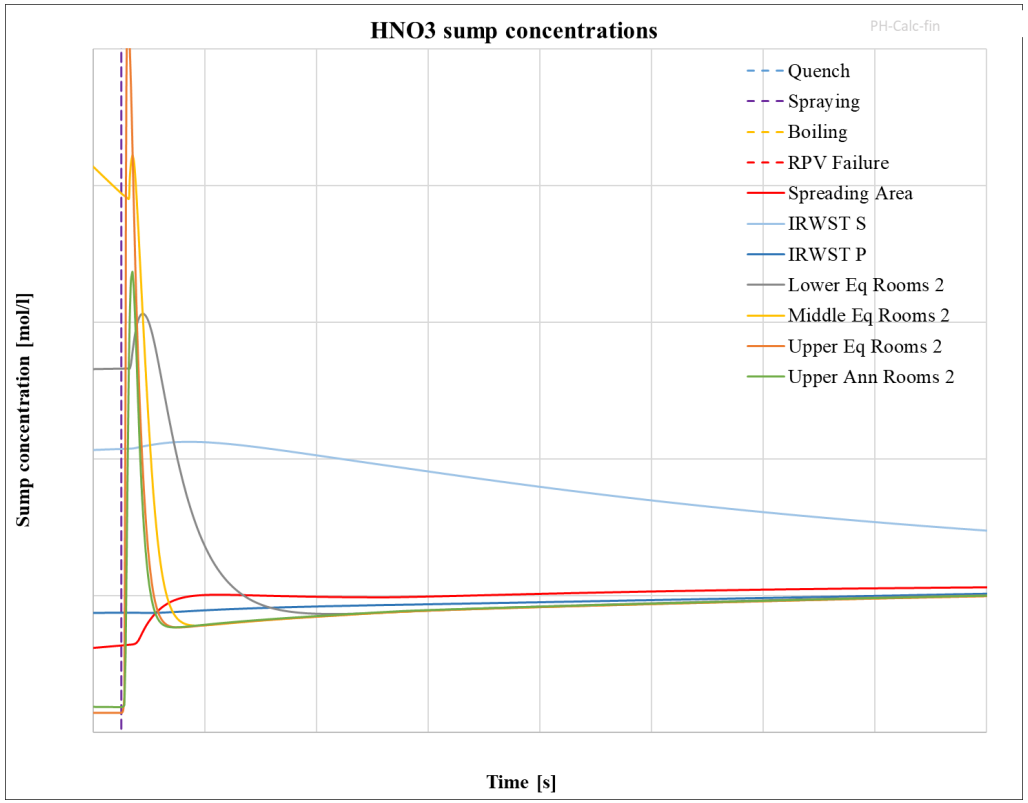

- Containment spraying leads to equalization of sump concentrations in the long term
- Sump concentrations of all pools converge to IRWST concentration levels (mixing)
- Small water sumps exhibit fast changes, while bigger sumps exhibit slower changes
- Only small differences of pH in the long-term

Confidentiality Framatome (external) – AL: N – ECCN: N © Framatome - All rights reserved

5. Calculation Results

Phase after containment spraying pH

- HNO_3 formation is the main influence on long-term pH values
- pH reaches low values in the long-term
- Increased degradation due to low pH can be expected in the long-term

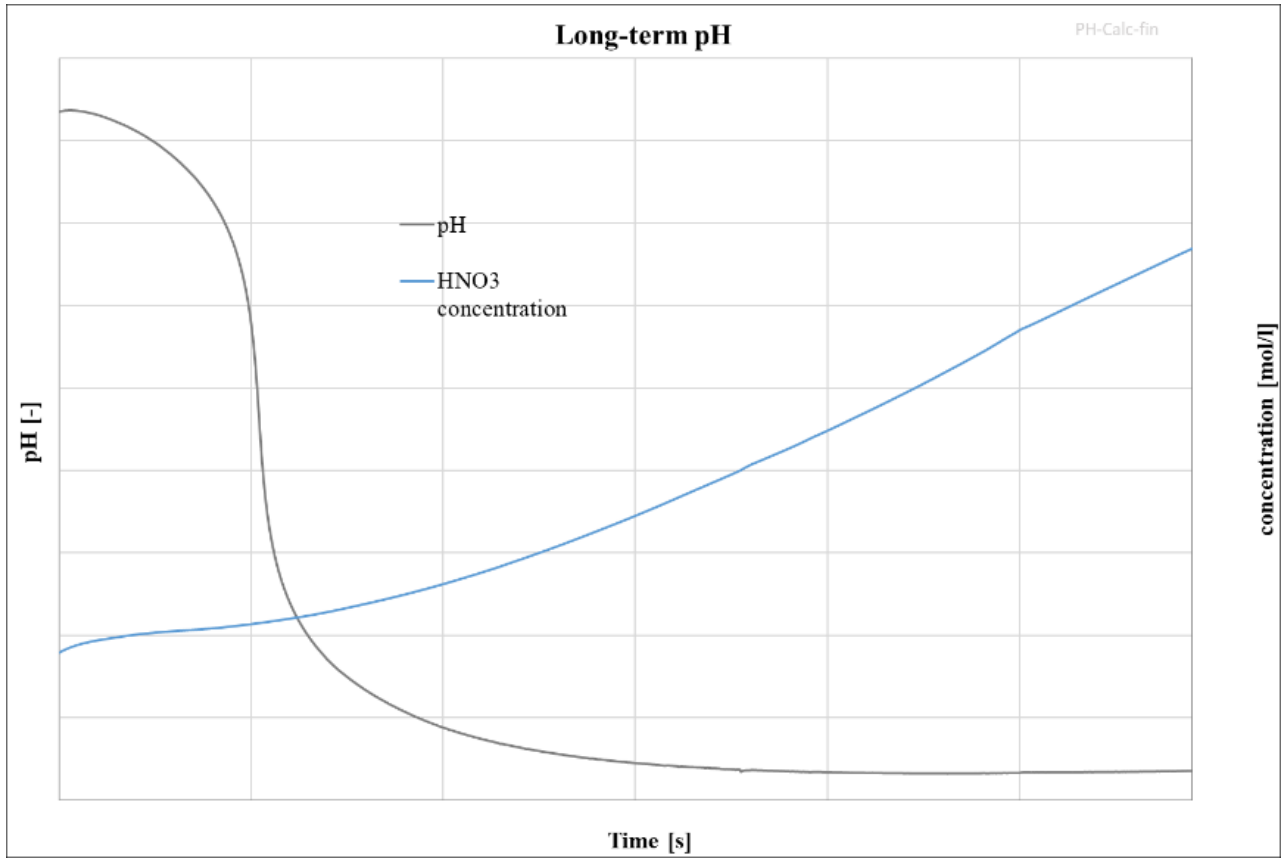

Confidentiality Framatome (external) – AL: N – ECCN: N © Framatome - All rights reserved

6. Conclusions

COCOSYS pH model

- The most important pH active species are modelled in COCOSYS
- Assessment of species distribution on compartment level is possible
- The COCOSYS pH model can predict the release and distribution of the most important pH-active species during a severe accident
- Plausible results for short- and long-term pH
- Best estimate approach instead of conservative approach

Some open points remain

- Reactions between acidic water and steel/paint
- Evaporation/Entrainment of dissolved species

Framatome Solution: Severe Accident Long-Term (SALT) Containment Condition Control Processes

Confidentiality Framatome (external) – AL: N – ECCN: N © Framatome - All rights reserved

framatome

Thank you

To discover more about how we can help, visit us at
http://www.framatome.com/solutions-portfolio

Legal Notice

Editor and Copyright 2024: Framatome GmbH – Paul-Gossen-Straße 100 – 91052 Erlangen, Germany. It is forbidden to reproduce the present publication entirely or partially without prior consent in whatever form. Legal action may be taken against any infringer and/or any person breaching the aforementioned conditions.

Subject to change and error without notice. Illustrations may differ from the original. The contained statements and information are for advertising purposes only and do not constitute an offer of contract. They shall neither be construed as a guarantee of quality or durability, nor as warranties of merchantability or fitness for a particular purpose. These statements, even if they are future-oriented, are based on information that was available to us at the date of publication. Type, quantity and characteristics of goods and services are subject to formal individual formal contracts.

Confidentiality Framatome (external) – AL: N – ECCN: N © Framatome - All rights reserved

Modeling of Oxidation Behavior of Accident Tolerant Fuel by using AC²

Gregor T. Stahlberg and Marco K. Koch
Ruhr-Universität Bochum (RUB)
Plant Simulation and Safety Group (PSS)
Universitätsstr. 150, 44801 Bochum, Germany
Gregor.Stahlberg@pss.rub.de and Marco.Koch@pss.rub.de
ORCID-ID: 0000-0001-6250-3971 and 0000-0001-7260-5250

ABSTRACT

Postulated and unmitigated accidents in a nuclear power plant could endanger the facilities integrity due to escalating temperatures, rising pressures and released combustible gases. Regarding the barriers of the defense-in-depth concept, the fuel cladding could be a major contributor affecting the accident progression. Although the commonly used alloys based on Zirconium (Zr) provide excellent performance under long-term operational conditions, its limited beneficial behavior at higher temperatures under accident conditions may lead to a fast accident progression along with high hydrogen production. Several studies have shown that other materials could partially improve the claddings behavior under accident conditions. Currently, there are several accident-tolerant concepts that are leading the development of Accident Tolerant Fuels (ATF), like e.g. Iron-Chromium-Aluminum alloys (FeCrAl), claddings based on silicon carbide (SiC-SiC composites) or the coating of existing and widely used Zr-alloys.

In this paper modeling the oxidation resistance is the focus of the extension of AC², a system code package for simulating various phenomena as well as complete accident sequences of nuclear power plants, developed by the Gesellschaft für Anlagen- und Reaktorsicherheit (GRS) gGmbH. The major outcome is a first newly developed in-house ATF model at the PSS Group at RUB regarding the oxidation of Chromium (Cr)-coated claddings. The main motivation is its increased international use in reactors to qualify market readiness as well as new experimental investigations at Karlsruhe Institute of Technology (KIT) during the QUENCH-ATF project. Within a nationally funded research project regarding model development for system codes by PSS, the scope of ATF, among others, is therefore of particular interest with regard to the potential benefit by upgrading existing plants or projected reactors.

There are currently two modeling options for FeCrAl available in AC². One for the calculation of a fixed composition and the other with flexible input for own FeCrAl related correlations. The corrosion resistance of both concepts depends highly on thermodynamically stable oxides, mainly Al_2O_3 for FeCrAl and Chromium oxide (Cr_2O_3) for Cr-coated Zr-alloy, which are formed during oxidation. New findings resulted in further developed FeCrAl correlations, with different dominant kinetics in various temperature regions. This correlation by KIT is implemented in an PSS in-house version of AC².

Regarding Cr-coating, sensitivity studies and the comparison with experimental data resulted in various suggestions for improvements of the in-house Cr-coating model. The oxidation process relies on different influential parameters like coating quality, thickness and degradation phenomena. The diffusion of oxygen into the binary system of Cr/Zr as well as diffusion processes between the coating and substrate result in a loss of protectiveness of the coating, eventually enhancing the oxidation kinetics. Furthermore, mechanical stresses arising from external factors, such as thermal expansion and mechanical loading, play a crucial role in coating failure. Pressure induced ballooning can lead to cracking, ultimately resulting in local coating failure at e.g. burst regions.

KEYWORDS
AC², ATHLET-CD, ATF, Cr-coating, Oxidation, In-Vessel

1. INTRODUCTION

The field of nuclear energy is constantly evolving, with ongoing research and development aimed at enhancing the safety and efficiency of nuclear reactors. In this regard, ATF are presumed to withstand accident conditions potentially better than conventional fuels. Two promising ATF concepts being explored as alternatives to Zircalloy (Zry) claddings are Cr-coated Zry and FeCrAl claddings. Despite its low neutron capture cross-section and good mechanical properties, Zry can rapidly oxidize in accident scenarios, leading to significant hydrogen generation and temperature increase. To address this, Cr-coated Zry has been proposed as an enhanced cladding concept. FeCrAl alloys are another promising ATF solution, exhibiting excellent oxidation resistance in high-temperature steam, a key aspect of any accident tolerant concept. Overall, the potential benefit could be the reduction of hydrogen and heat release during accident scenarios, thereby increasing the coping time for accident management measures. Facilities like QUENCH at the KIT provide the necessary platform for rigorous testing and significant contribution to the validation database for system codes by conducting large-scale bundle tests. These tests were carried out to demonstrate the properties of these new concepts. [1] [2]

In this context, the QUENCH-ATF project investigates the chemical, mechanical, and thermal behavior of Cr-coated claddings in Design Basis Accident and Beyond Design Basis Accident scenarios applied to bundle tests. [3] Furthermore, the QUENCH-19 test was already conducted using FeCrAl alloys for relevant components [4]. To reflect and analyze the ATF concepts more accurately, the German severe accident code AC² is being assessed regarding ATF. Due to missing options, a new model for Cr oxidation was implemented in an in-house version of AC² [5], [6]. For FeCrAl, built-in correlations are additionally used along with a new correlation in preliminary test calculations.

2. OXIDATION BEHAVIOR OF VARIOUS CLADDING MATERIALS

In this section the oxidation behavior of candidate ATF materials is described, focusing on failure characteristics which could affect the oxidation kinetics. Each modelled oxidation approach is shortly summarized in section 2.3, highlighting the used oxidation kinetics in the conducted simulations.

2.1. Chromium-Coated Zircalloy Oxidation

The oxidation of Cr-coated Zry in steam atmospheres involves the interaction between the protective Cr coating and the Zry substrate. Cr coatings are presumed to significantly mitigate the rapid oxidation of Zry by applying a protective layer that slows down the diffusion of oxygen. The corrosion resistance of the formed chromium(III) oxide layer (Cr_2O_3) is characterized by a low weight gain. It is furthermore influenced by several parameters including the coating microstructure, layer thickness, and degradation phenomena (such as eutectics). Additionally, the transient boundary conditions, such as the heating rate, the peak cladding temperature (PCT) and the oxidation duration, are relevant for the protectiveness. [2] [7]
The manufacturing process determines the dense or columnar microstructure. Currently, cold spray (CS) or physical vapor deposition (PVD) are common deposition techniques. By using CS, chromium particles in powder form are accelerated to high speeds and applied to the substrate. Applying a coating by PVD is done in a high-vacuum environment accelerating Cr-atoms towards a target material where they condense and form a thin film. [8] [9]

Furthermore, the thickness of the chromium layer can influence the absorption of neutrons. On the one hand, a thicker chromium layer could potentially absorb more neutrons. This negatively affects the neutron economy. On the other hand, a layer that is too thin might not provide sufficient protection against corrosion. The applied layer thickness is in the order of several microns, e.g. 5 to 20 µm. Experimental investigations in [10] show that the dense 4.5 µm-thick Cr coating with higher activation energy of 202 kJ/mol provides better oxidation resistance up to 1,100 °C than thicker columnar coatings with slightly lower values (177–183 kJ/mol). But at 1,200°C, only the 9 µm coating offered a longer diffusion path for oxygen into the Zr

substrate. A thicker coating of at least 9 µm was therefore recommended for the presented investigations. [10] The effect of heating rate on the oxidation behavior of Cr-coated Zry is equally relevant, as it influences the kinetics of the oxidation process. Higher heating rates lead to faster oxidation, but the coating has a reduced time to form a protective dense layer. For different heating rates, the weight gain of Cr-coated specimens are overall significantly lower than that of uncoated specimens until the occurrence of the Zr-Cr eutectic above 1,300 °C and the successive failure of the coating. [11] [12]

The degradation of the Cr/Zr system during oxidation is depicted in Figure 1. At first, the coating is exposed to steam and an initial dense Cr_2O_3 layer is formed in this atmosphere, limiting oxygen diffusion into the substrate. The ongoing oxidation is dominated by the outward diffusion of chromium cations (red). As temperatures rise, an intermetallic layer is formed due to a reaction of Cr (orange) and Zr (dark blue). This indicates the beginning of microstructural changes that can affect the integrity and protective capabilities of the coating. Additionally, a small amount of oxygen diffuses (yellow) to the inner coating and substrate via grain boundaries, eventually reacting with outward diffusing Zr (light blue) at higher temperatures. ZrO_2 precipitates are formed. [13]

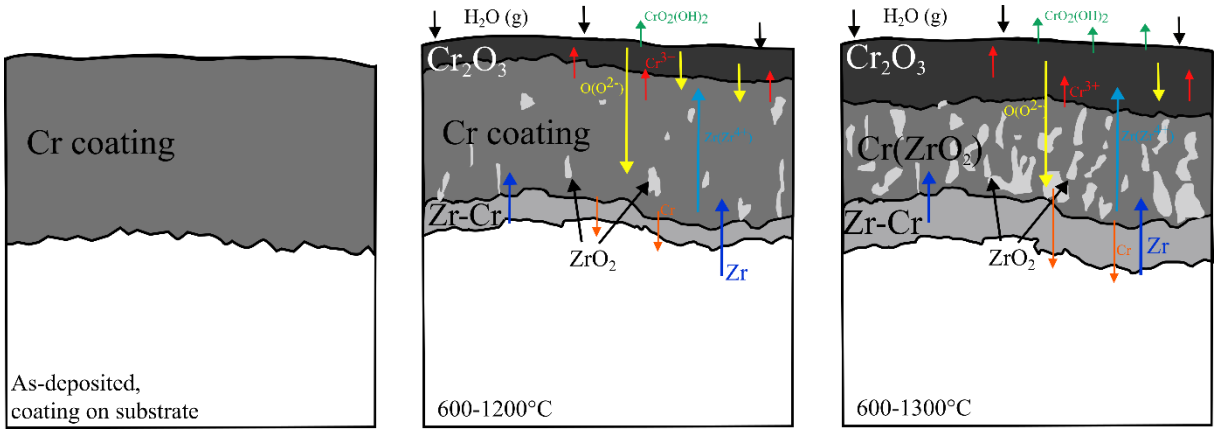

Figure 1. Degradation mechanisms of Cr-coated cladding, adapted from [13].

Once the eutectic temperature of ~1,332 °C is exceeded, it is assumed that the Zr reduces the chromium oxide to Cr metal and further ZrO_2 is formed. This leads to an additional reduction in thickness of the protective Cr scale. These processes collectively lead to the rapid oxidation of both the coating and the substrate, highlighting the limitations of Cr coatings in extremely high-temperature steam environments.
To conclude, coating failure occurs due to several processes. These are mainly the eutectic Zr-Cr interaction, the Zr-Cr inter-diffusion and the precipitation of ZrO_2 along non-oxidized Cr grain boundaries as well as the thickness decrease of the outer Cr_2O_3 layer. The failure of the coating and the resulting rapid oxidation of the coating and substrate occurs at 1,300-1,350 °C the latest. [13]

2.2. FeCrAl-alloy Oxidation

The oxidation mechanism of FeCrAl alloys is investigated. At lower temperatures, some findings of investigated nuclear-grade tubes indicate an external oxide layer containing Al, Cr and Fe at 800 °C. Additionally, current investigations showed mostly Fe and therefore higher Fe kinetics at even lower temperatures like 600 °C. As the temperature increases, the oxidation behavior changes. In high-temperature steam environments, FeCrAl alloys form a protective alumina film, which is crucial for their oxidation resistance. Above 1,350-1400 °C, the oxide layer fails and Fe oxides are formed accompanied by strong oxidation kinetics. [14] [15]
A current study indicates different dominant kinetics of the FeCrAl oxidation (Figure 4). For this purpose, two relevant alloys B136Y3 and C26M2 were examined. Both alloys contain lower Cr content compared to

commercial FeCrAl/Kanthal alloys to mitigate embrittlement issues. The oxidation tests from 500 °C to 1,500 °C in steam atmosphere revealed different oxide layer compositions on the FeCrAl alloys after test conduct. Below 1,000 °C, the formation of transient θ-Al results in faster oxidation kinetics. Within the range of 1,000 °C to 1,300 °C the slower α-Al formation kinetics are observed. Above 1,300 °C the kinetics significantly increase. During the isothermal tests, catastrophic oxidation occurs due to the failure of the protective alumina layer, leading to the formation of Fe-rich oxides. The catastrophic oxidation also causes a liquid phase in Fe-rich oxides. However, transient test results showed slightly better results in contrast to the isothermal investigations. The catastrophic oxidation did not occur until ~1,500 °C and mechanical behavior regarding ballooning is slightly better as well. This might have positive implications for severe accidents. [15]

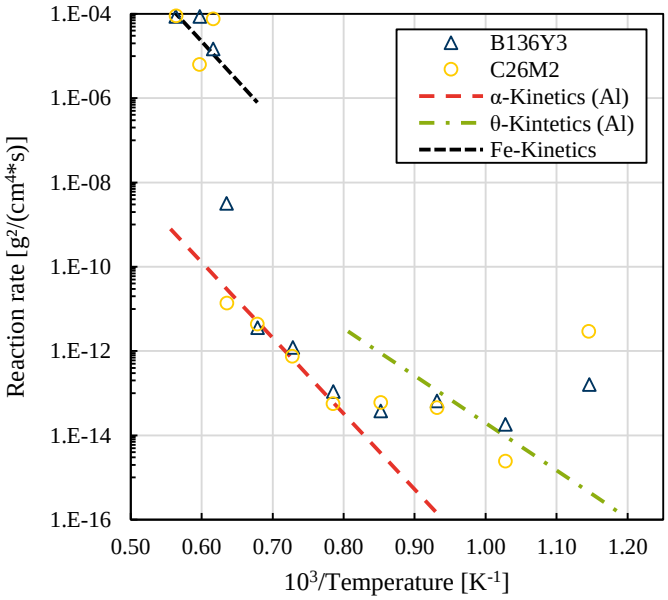

Figure 2. Oxidation rate constants of alloys B136Y3 and C26M2 during the isothermal oxidation of FeCrAl alloys, adapted from [15].

Besides the influence of the temperature ranges on the kinetics, the oxidation of FeCrAl alloys depends on their composition. For example, high Cr and Al contents are beneficial for corrosion and oxidation resistance, but high Al content can make steels brittle, complicating the production of thin cladding tubes. Additionally, high Cr content also makes alloys vulnerable to thermal and irradiation embrittlement. The aluminum content (e.g.) has furthermore significant implications for the alloy's protective properties. When the aluminum content is 3 wt% or less, a mixture oxide containing Fe_2O_3, Cr_2O_3, $FeCr_2O_4$, and Al_2O_3 is formed. The alloy cannot develop a continuous oxide layer quickly. Consequently, Fe and Cr form a loose oxide film that inhibits oxygen penetration at the early stages of oxidation. Additionally, Fe oxide form a continuous but porous film which is less effective at limiting oxygen diffusion, leading to a less protective scale. In contrast, when the aluminum content is above 4 wt%, the main phase becomes the protective α-Al_2O_3, which is due to the higher oxidation rate of aluminum compared to Fe and Cr at 1,200 °C. [15] [16]

Therefore, a sufficient aluminum content allows for the formation of a continuous Al_2O_3 layer. This slows down the oxidation rate effectively, providing better protection. These findings indicate that the formation of protective oxide films is highly dependent on the composition of the alloy, particularly the aluminum content. Alloys with higher aluminum content form denser and more continuous Al_2O_3 films, which improve oxidation resistance and reduce the oxidation rate. [16]

2.3. Oxidation Modeling for Cr-coated Zry and FeCrAl

The used oxidation kinetics within steam atmosphere for FeCrAl and the new Cr-coating oxidation option are modeled using an Arrhenius approach shown in Figure 3. Here, K_p is the oxidation rate constant, T the temperature in [K], A_x the pre-exponential coefficient and E_x the activation energy. Table I depicts the values for A_x and E_x for specific temperature regions.

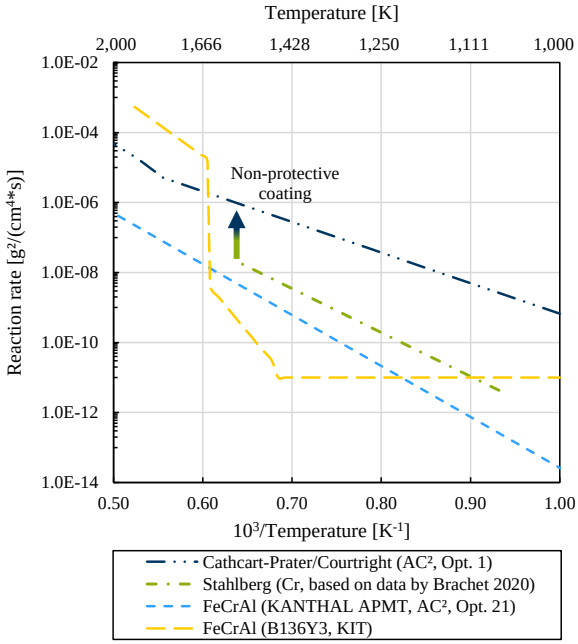

Cr-coating Oxidation

$$K^{m}_{p,Stahlberg}\left[\frac{g^2}{cm^4 s}\right] = \begin{cases} A_{Cr}\exp\left(\frac{-E_{Cr}}{RT}\right), T < 1{,}573K \\ A_{Zr}\exp\left(\frac{-E_{Zr}}{RT}\right), T \geq 1{,}573K \end{cases}$$

$$A_{Zr}:\ AC^2, \text{Opt. 1 for Zry, Cathcart} - \text{Prater/Courtright}$$

FeCrAl Oxidation

$$K^{m}_{p,KIT}\left[\frac{g^2}{cm^4 s}\right] = \begin{cases} 9.62 \times 10^{-12}, & T \leq 1{,}473K \\ A_B \exp\left(\frac{-E_B}{RT}\right), & 1{,}473K < T < 1{,}648K \\ A_{Fe}\exp\left(-\frac{E_{Fe}}{RT}\right), & T \geq 1{,}648K \end{cases}$$

$$K^{m}_{p,AC^2,Opt.21}\left[\frac{g^2}{cm^4 s}\right] = A_{Opt.21}\exp\left(\frac{E_{Opt.21}}{RT}\right),\ \forall\ T$$

Figure 3. Oxidation kinetics for Cr-coating and FeCrAl cladding materials.

For the oxidation of Cr, there are several proposed correlations, e.g. in [17], [18]. However, the author derived an own correlation from experimental data on the oxide layer growth, which are presumed to provide the best agreement with the behavior of current coating generations. The correlation for oxide growth presented in [5] and [7] is then converted to mass gain due to the code specifications of AC² using [18]. It is implemented and used in a model option which considers a simple coating failure approach after which Zr kinetics are active. Currently, Zr kinetics are assumed above 1,300 °C. The heat of oxidation depends on the active correlation, i.e. the temperature region. The correlation itself is verified against publicly available data and the model under development is used in benchmark calculations of the QUENCH-ATF-1 bundle test within a OECD/NEA project. For comparative assessment, additional correlations were derived by the author from available mass gain data. [12] [5] [6]

Table 1. Coefficients for Arrhenius equations in Figure 2.

Correlation	Pre-exponential Coefficient [g²/cm⁴s]	Activation Energy [J/mol]
Cr-coating	$A_{Cr} = 207.1$	$E_{Cr} = 240{,}000$
FeCrAl (KIT)	$A_B = 3.0 \times 10^9$	$E_B = 594{,}354$
	$A_{Fe} = 2.4 \times 10^6$	$E_{Fe} = 352{,}513$
FeCrAl (AC², Opt. 21)	$A_{Opt.\ 21} = 300 \times (3.1 \times 10^{-2})$	$E_{Opt.\ 21} = 278{,}500$

3. APPLICATION TO QUENCH EXPERIMENTS

This section contains an overview of the QUENCH facility, which is used for validation calculations. For this purpose, the experimental boundary conditions are implemented into the respective input deck and the simulation results are investigated. The experiments considered are briefly described and section 3.3 contains the simulation results. The experimental data for comparison are kindly provided by KIT.

3.1. QUENCH facility and relevant experiments

The QUENCH Program is a key research program to improve the safety and understanding of nuclear reactors under (severe) accident conditions. It focuses on reflooding, i.e. a critical accident management measure. The large-scale bundle facility (Figure 4) consists mainly of a test section with an electrically heated rod bundle, a surrounding containment and insulation. Among others, thermocouples, flow meters, pressure sensors and a mass spectrometer allow experiments to be properly monitored. [19]

In Figure 5 the developed simulation model for AC² is shown. The thermo-fluid objects are positioned to ensure a flow path for injected fluids (INPIPE), such as steam or quenchwater, through the BUNDLE and BYPASS, where the rods are located. Using the AC² module ATHLET-CD, rod groups are modelled using concentric core sections representing the electrically heated rods. The cross-sections of the bundle on the right-hand side show the bundle configuration for the calculated experiments QUENCH-19 (Q-19), QUENCH-ATF-1 (ATF-1) and QUENCH-L3HT (L3HT).

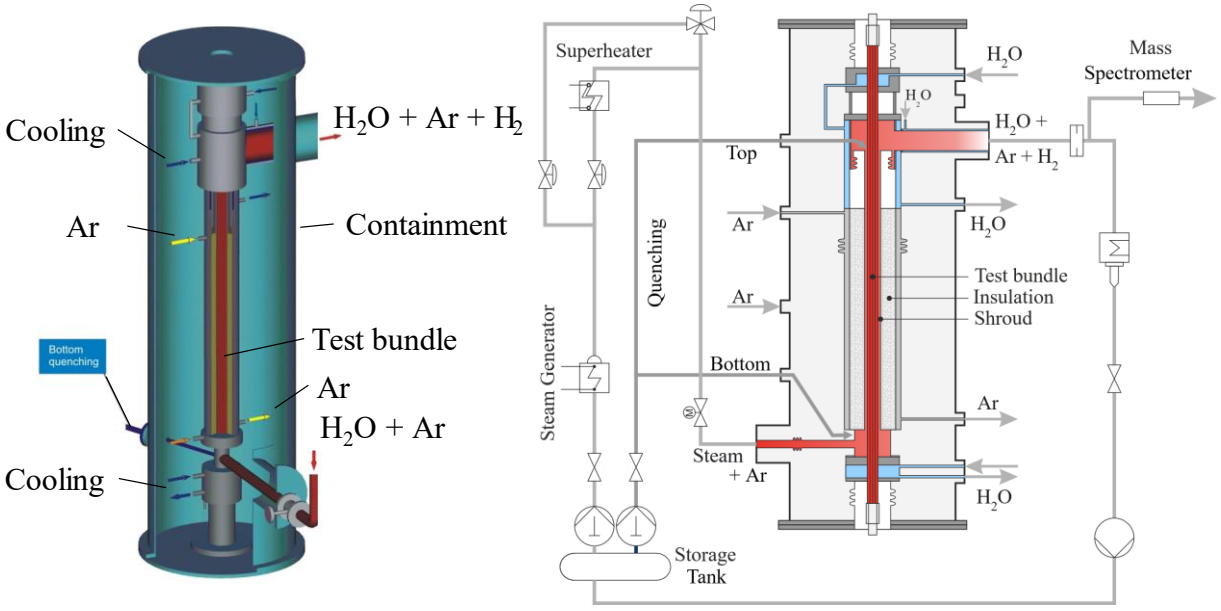

Figure 4. QUENCH facility at KIT, adapted from [19].

Additionally, the bundle has corner rods and is surrounded by the shroud. By adjusting the coolant channel area with corner rods, the QUENCH experiments can more accurately simulate the thermal-hydraulic conditions that would be present during an accident scenario. The mass spectrometer is located at the bundle outlet, represented by OFFPIPE. Here, gases like hydrogen (H_2) as well as steam are measured.

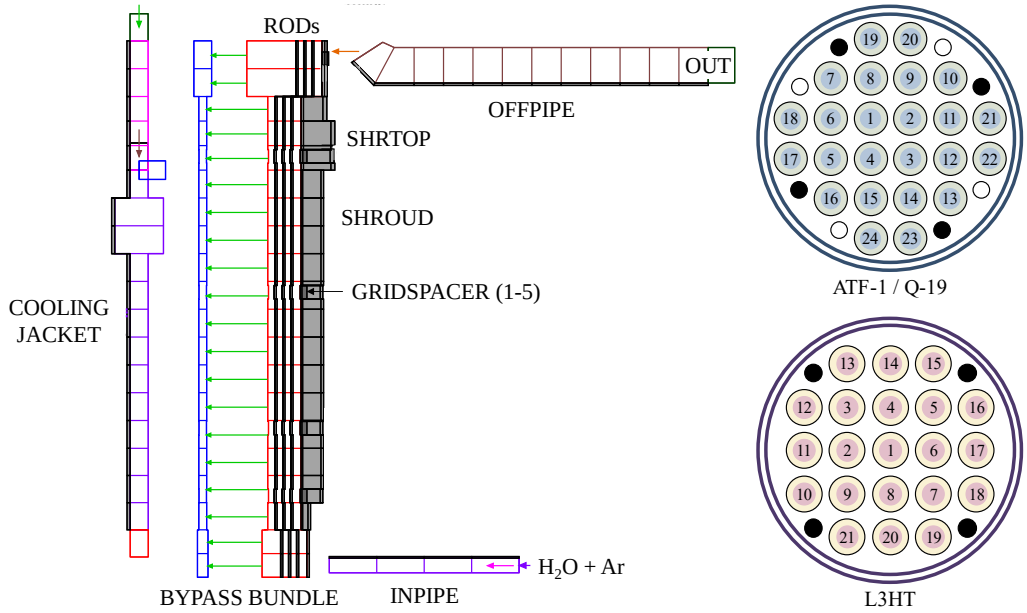

Figure 5. Simulation model of the QUENCH facility [5] and cross section of bundle.

QUENCH-L3HT / QUENCH-ATF-1: Cr-Coated Zircalloy

The QUENCH-LOCA test series aims to investigate the influence of secondary hydriding on the applicability of cladding embrittlement criteria under loss of coolant (LOCA) conditions. The experiment L3HT is part of the LOCA program and is conducted according to a LBLOCA transient with a heat-up rate of max. 7.5 K/s. Due to the high PCT and planned as a transient with design basis conditions, the experiment L3HT is used as the reference test for the first large-scale bundle test ATF-1 with Cr-coated claddings. However, ATF-1 is designed with extended LOCA conditions, reaching potentially even slightly higher temperatures. The intended PCT in L3HT is moderate with approximately 1,500 K, but in any case lower than the eutectic temperature of Cr/Zr. However, technical irregularities lead to a slight temperature escalation, resulting in a unique and not prototypical experimental sequence. A thermocouple (TC) on rod #7 at 850 mm e.g. registers locally ~1,600 K, while other TCs at this height are considerably lower with 1,400 -1,500 K and below. Figure 6 depicts the experimental sequence of L3HT and Q-19. Steam as well as argon as carrier gas are used to simulate the environment within a reactor during an accident. A separate inlet at the bottom of the test section allows for water injection, representing the emergency cooling process. [7] [19] [20]

QUENCH-19: FeCrAl-alloy

Q-19 is designed to simulate accident conditions followed by water quenching an ATF bundle, specifically focusing on the performance of FeCrAl cladding under severe accident conditions. The primary purpose of this experiment was to compare the behavior of this ATF concept to conventional Zr-based cladding (QUENCH-15) under similar electrical power and gas flow conditions. The transient includes pre-oxidation and transient stages with a specific electrical power applied during these phases (Figure 6). The test aimed to reach a maximum power of ~18 kW. Compared to Zr, the results from Q-19 indicate that the FeCrAl cladding is favorable in terms of H_2 release. During Q-19 about 9.2 g H_2 were released compared to 47.6 g in Q-15. Additionally, the maximum temperature which is measured by intact TCs of 1,455 °C (Q-19) was lower than ~1,880 °C in Q-15. Additionally, the two experiments differ regarding the maximum power supply period of 18 kW, which was maintained for around 2,000 s in Q-19. [4] [21]

As summarized in the technical report [4], the rods are widely damaged at elevations between 850 and 1,000 mm. Among others, circumferential cracks, high-temperature inner oxidation as well as the formation of molten FeO are to be highlighted. However, as stated by [21], the FeCrAl concept might improve the

cladding behavior during an accident due to the still protective oxide layer on intact rod sections and lower H_2 release despite a longer maximum power input period.

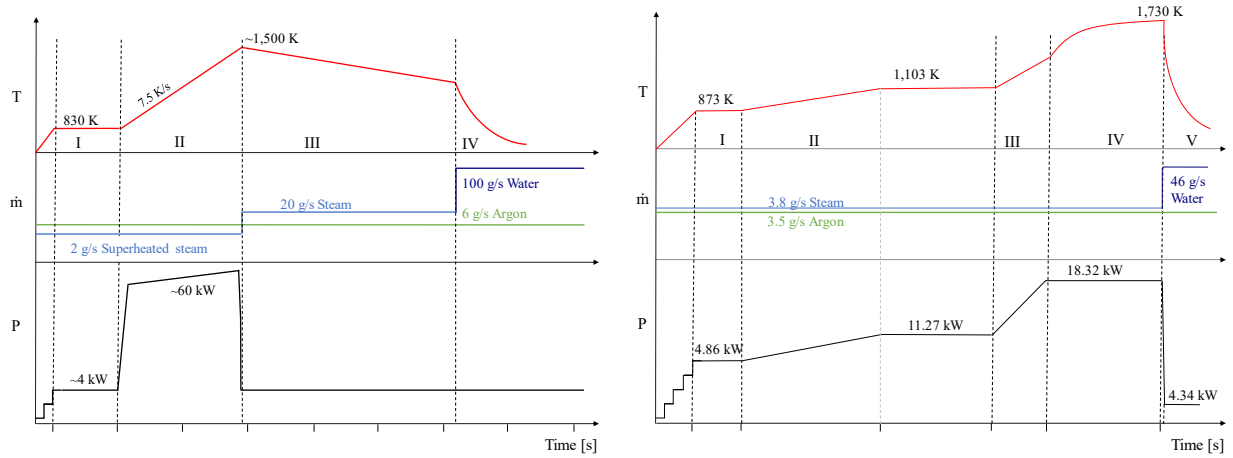

Figure 6. QUENCH-L3HT (left) and QUENCH-19 (right) test characteristics.

3.2. SIMULATION RESULTS

This section contains simulation results of relevant QUENCH experiments. As the results of the QUENCH-ATF test series are not yet publicly available during the project period, only simulation results of ATF-1 that have already been approved are shown. No quantitative results are shown due to the non-disclosure policy set on project results. For further assessment, additional calculations are conducted using the Cr-oxidation model under development applied to the L3HT sequence. For this purpose, a dataset is modified with L3HT boundary conditions, assuming a Cr-layer on critical components i.e. implementing relevant material properties and using the preliminary model option. Regarding Q-19, the available model option Opt. 21 is used. Additionally, preliminary results using an in-house version with a new correlation are shown.

Assessment of QUENCH-L3HT / QUENCH-ATF-1

Figure 7 shows selected results of the calculated ATF-1 transient. The transient can be divided into stationary, heat-up, steam cooling and quenching phase like L3HT (compare to Figure 6). As can be seen, the TCs at 950 mm of rod #2 and #4 are depicted besides two simulation runs Sim. (1) and (2). These runs differ in terms of the number of parallel fluid channels for the bundle [5]. The different bundle modeling with a second channel in (2) leads to partly higher temperatures which results in higher H_2 values. Overall, the thermal behavior at 950 mm of the transient is calculated mostly in good agreement with the experimental values.

Differences can be seen for both runs during the heat-up phase as the cladding bursts (small drop in temperature progression). This is not reproduced by the code, as it might be due to the potentially different mechanical behavior of Cr-coated claddings which is not taken into account. Additionally, the temperature increase right before the steep temperature drop due to quenching is underestimated. Despite the widely correct reproduction of the temperature progression and PCT, the amount of H_2 released is underestimated. Although better reproduced with the second run (2), especially the H_2 release during steam cooling is not calculated accurately. This results in an integral H_2 of app. 65% of the experimental value.

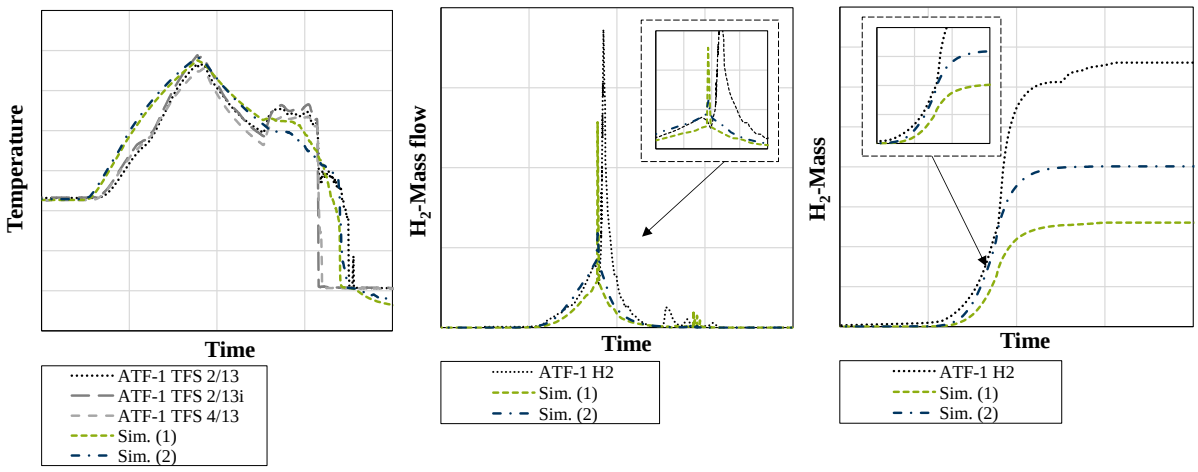

Figure 7. ATF-1 temperature progression at 950 mm and H_2 release, adapted from [5].

Additional calculations are carried out using the modified input deck using the same boundary conditions set in the L3HT simulations but assuming a Cr-layer on relevant components. The calculated L3HT results are also depicted below. Figure 8 shows the temperature progression at 950, 850 and 650 mm. For a comparative analysis, the available oxidation models for Zr oxidation (Sim. (Opt. 1/3)) as well as Cr oxidation (Sim. (Cr)) are shown. When analysing the simulation results, it is evident that some measured temperatures, like e.g. the TCs on 850 and 650 mm, cannot be reproduced accurately by the simulation model. Especially at 850 mm, the technical issues during the experiment affecting parts of the bundle are visible as an unusual slow cooling phase in saturated steam. Among others, the measured temperatures at 950 mm are, however, reproduced qualitatively well. As expected, the simulation using Cr shows even lower maximum temperatures due to the reduced oxidation heat.

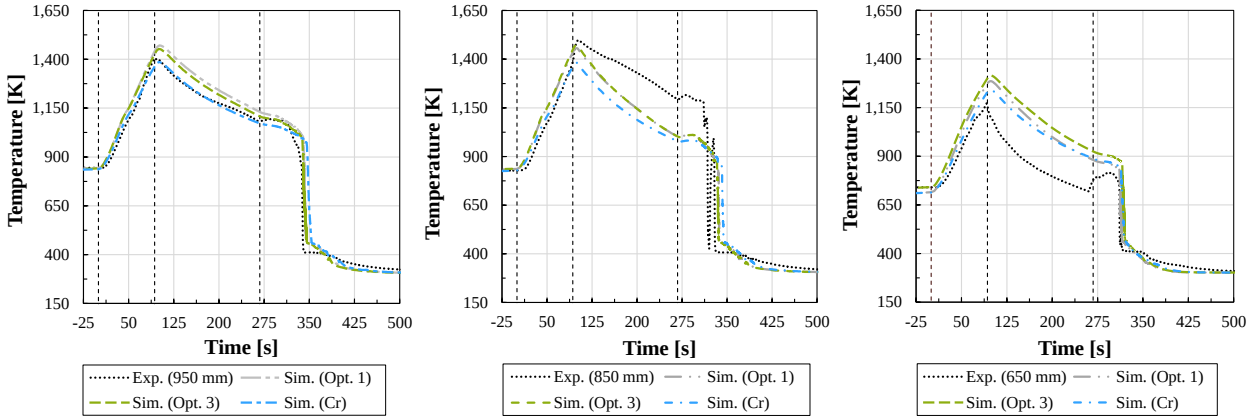

Figure 8. L3HT temperature progression at 950, 850 and 650 mm.

The calculated integral H_2 qualitatively and quantitatively corresponds mostly to the measured values when using Opt. 3 in AC² (Figure 9). This corresponds to the correlation after Leistikow & Prater/Courtright. Although the temperatures are partially overestimated compared to the measurement of L3HT, the hydrogen is accurately calculated, if not slightly underestimated. The hydrogen mass flow is qualitatively better reproduced with Opt. 1, except for the steam cooling phase. As the calculated temperatures are well below 1,400 K, the released hydrogen when assuming Cr oxidation is significantly lower. Additionally, Figure 9 shows the quench phase in detail. The overall progression of the quenchfront is calculated well for all runs. There is one noticeable difference in the simulation using the Cr model, as the values after 325 s are

marginally lower compared to the runs using Opt. 1/3. This indicates a slower quenching of the bundle, as can be seen at the temperature calculation.

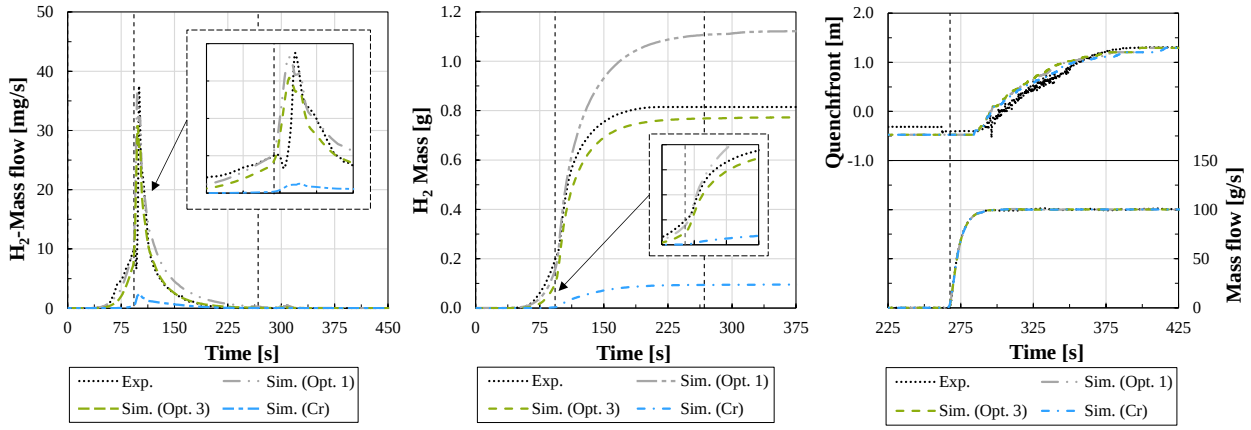

Figure 9. L3HT quenching phase and hydrogen release.

Assessment of QUENCH-19

The calculated results of Q-19 are shown in Figure 10 for different heights. Regarding the thermal behavior, no significant discrepancies are visible when using the various model options for oxidation. It has to be mentioned that the heat of oxidation released had to be significantly reduced for Sim. (mod.) compared to the value implemented in AC², as otherwise an unreasonable temperature progression was calculated. This must be examined in future research und underlines the preliminary character of the results with the new correlation. Overall, the measured values of the selected TCs are reproduced well with each run, except for the PCT at each height. Furthermore, the temperatures are partly lower with Sim. (mod.) than with Opt. 21.

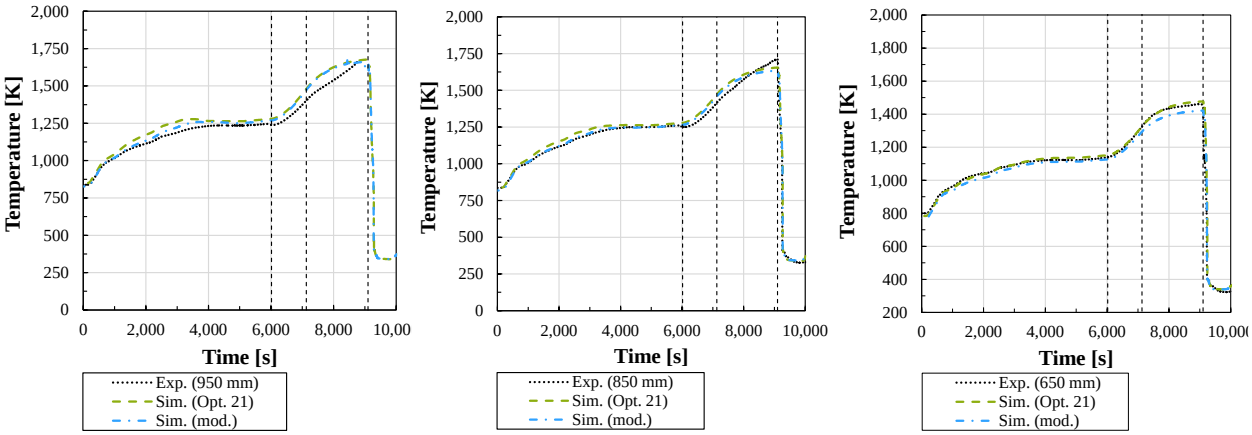

Figure 10. Q-19 temperature progression at 950, 850 and 650 mm.

In terms of steam and H_2 release, Figure 11 reveals deviations for all runs when compared to the measured data. In the first picture the generated steam due to quenching is shown next to the quenchfront in the upper left corner. The quenching is calculated accurately but the initial steam generation is underestimated. This might be due to lower calculated PCT in both simulations right before quenching starts. Furthermore, some aspects such as the melt formation during the experiment cannot be accurately considered which might influence the quenching. Regarding H_2, the Opt. 21 calculates approximately 50% of the integral value assuming α-Al kinetics for all temperature regions. Considering this simplification, the calculated values

are well reproduced although neglecting the FeCrAl composition. By using the modified version with the new correlation, it is evident that no smoothed transition of the different dominant kinetics is modelled currently. The integral value is, however, calculated well. The kinetics of the material are not adequately reproduced by either simulation.

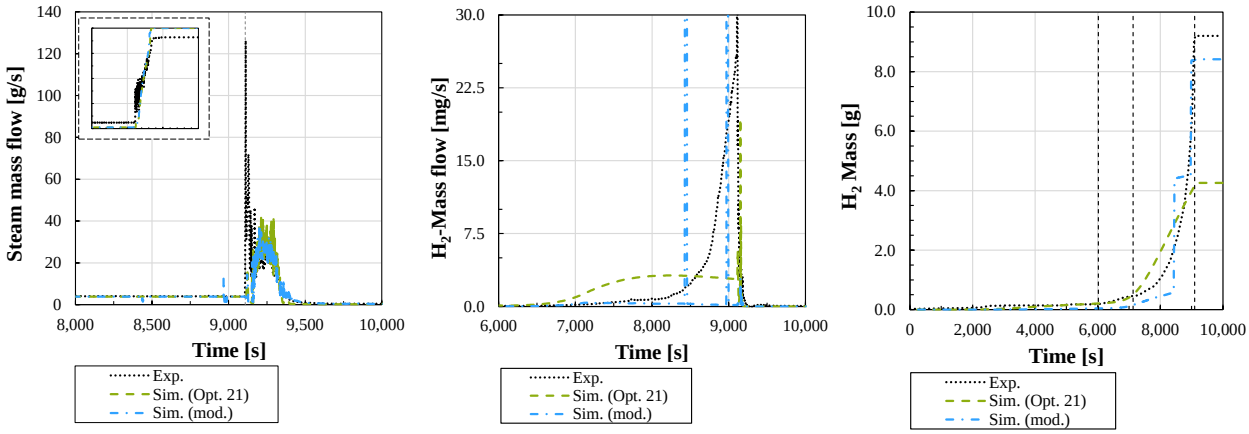

Figure 11. Q-19 steam and hydrogen release.

4. CONCLUSIONS

The near-term ATF solutions, FeCrAl and Cr-coating, as well as their behavior under conditions beyond normal operations, were analysed. Additionally, this work considers the numerical modeling of their oxidation kinetics. For this purpose, a simulation model of the QUENCH facility was prepared and assessed with experimental data. Different QUENCH experiments were taken into account, such as the QUENCH series with (severe) accident conditions as well as the LOCA program with design basis conditions. The integral H_2 mass at L3HT is found to be better represented using Opt. 3 in AC². Using Opt. 1 results in significantly overestimated H_2 mass due to the temperatures during the steam cooling phase. The selected TCs of the Q-19 transient are reproduced well. However, the oxidation process is currently not modelled accurately. Considering the thermal behavior, the simulation results for each experiment show noticeable results regarding the H_2 generation. Although the temperatures are overestimated at nearly all bundle heights, the H_2 generation is calculated accurately, albeit slightly underestimated. Overall, the analyses show plausible results in terms of validation of AC². The new model for coating oxidation was assessed against the bundle test ATF-1 and applied to the L3HT experiment. Further investigation into the failure of the coating is a viable direction for future development. Various influencing parameters, such as the heating rate and coating cracks, could be taken into account. It is important to note that the simulations using ATF correlations do not account for different mechanical behaviors of the rods. Currently, this aspect is not modeled for any materials other than the standard Zr-based cladding in AC².

ACKNOWLEDGMENTS

Supported by:
Federal Ministry for the Environment, Nature Conservation, Nuclear Safety and Consumer Protection
based on a decision of the German Bundestag

This work is funded by the German Federal Ministry for the Environment, Nature Conservation, Nuclear Safety and Consumer Protection (BMUV) under grant number 1501629 based on a decision by the German Bundestag. Responsibility for the content lies with the authors.

The results were obtained using an in-house version at PSS of the GRS software package AC² 2021 and the GRS software package AC² 2021.1.

REFERENCES

[1] Zinkle, S. J. et al.: Accident tolerant fuels for LWRs: A perspective. Journal of Nuclear Materials 448, 2014. DOI 10.1016/j.jnucmat.2013.12.005
[2] Terrani, Kurt A.: Accident tolerant fuel cladding development: Promise, status, and challenges. Journal of Nuclear Materials 501, 2018. DOI 10.1016/j.jnucmat.2017.12.043
[3] OECD NEA: QUENCH-ATF project. https://www.oecd-nea.org/jcms/pl_36597/quench-atf-project, accessed on 18. January 2024.
[4] Stuckert, J. et al.: Results of the bundle test QUENCH-19 with FeCrAl claddings. 2022. DOI 10.5445/IR/1000148370
[5] Stahlberg, G. T. et al.: Comparative analyses of the QUENCH experiments L3HT and ATF-1 on high temperature oxidation mechanisms using AC². Proceedings of the NURETH-20, Washington, D.C., S. 5450–5461, 2023. DOI 10.13182/nureth20-39989
[6] Stahlberg, G. T.; Koch, M. K.: Development of a preliminary model for Cr-coated Claddings for System Codes. 28th International QUENCH Workshop Proceedings. 2023. DOI 10.5445/IR/1000165938
[7] Stahlberg, G. T. et al.: Preliminary simulation results of the experiments QUENCH-L3HT and QUENCH-ATF-1 regarding high-temperature oxidation mechanisms using the system code AC². 27th International QUENCH Workshop Proceedings, 2022, DOI 10.5445/ir/1000152245.
[8] Geelhood, K. G.; Luscher, W. G.: Degradation and Failure Phenomena of Accident Tolerant Fuel Concepts: Chromium Coated Zirconium Alloy Cladding. Pacific Northwest National Laboratory, U.S. Department Of Energy, PNNL-28437 Revision 1, Washington, 2019.
[9] Yuan, G. et al.: In situ X-ray computed micro-tomography imaging of failure processes in Cr-coated Zircaloy nuclear fuel cladding materials, Materials & Design 234, 2023. DOI 10.1016/j.matdes.2023.112373
[10] Kashkarov, E. B. et al.: Oxidation kinetics of Cr-coated zirconium alloy: Effect of coating thickness and microstructure. Corrosion Science 175, 2020. DOI 10.1016/j.corsci.2020.108883
[11] Kim, D. et al: Eutectic reaction and oxidation behavior of Cr-coated Zircaloy-4 accident-tolerant fuel cladding under various heating rates. Journal of Nuclear Materials 583, 2023. DOI 10.1016/j.jnucmat.2023.154538
[12] Brachet, J. C. et al.: High temperature steam oxidation of chromium-coated zirconium-based alloys: Kinetics and process. Corrosion Science 167, 2020. DOI 10.1016/j.corsci.2020.108537
[13] Liu, J. et al.: Transient experiments on oxidation and degradation of Cr-coated Zircaloy in steam up to 1600 °C. Corrosion Science 192, 2021. DOI 10.1016/j.corsci.2021.109805.
[14] Rebak, R. B.et al.: Oxidation Characteristics of Two FeCrAl Alloys in Air and Steam from 800°C to 1300 °C. JOM Volume 70, 2018. DOI 10.1007/s11837-018-2979-9
[15] Kim, C. et al.: Oxidation mechanism and kinetics of nuclear-grade FeCrAl alloys in the temperature range of 500 °C-1500 °C in steam. Journal of Nuclear Materials 564, 2022. DOI 10.1016/j.jnucmat.2022.153696
[16] Yingjie Qiao, et al.: Mechanism of Al on FeCrAl steam oxidation behavior and a dynamics simulations, Journal of Alloys and Compounds 828, 2020, DOI 10.1016/j.jallcom.2020.154310.
[17] Feng, T. et al.: Quantification of the effect of Cr-coated-Zircaloy cladding during a short term station black out. Nuclear engineering and design 363, 2020. DOI 10.1016/j.nucengdes.2020.110678
[18] Khatib-Rahbar, M. et al.: Review of Accident Tolerant Fuel Concepts with Implications to Accident Progression and Radiological Releases. NUREG/CR-7282, Energy Research Inc., 2020.
[19] Stuckert, J. et al.: Results of the LOCA bundle test QUENCH-L3 with optimized ZIRLO™ claddings (SR-7737), 2018. DOI 10.5445/IR/1000083087.
[20] Stuckert, J. et al.: First results of the high temperature bundle test QUENCH-L3HT with optimized ZIRLO™ claddings, 20th International QUENCH Workshop Proceedings, KIT, Karlsruhe, 2014. ISBN 978-3-923704-88-0
[21] Doyle, P. et al.: Analysis of iron-chromium-aluminum samples exposed to accident conditions followed by quench in the QUENCH-19 experiment. Journal of Nuclear Materials 580, 2023. DOI 10.1016/j.jnucmat.2023.154433



RUB

FOR INTERNAL USE ONLY
CONFIDENTIAL

RUHR-UNIVERSITÄT BOCHUM

Modeling of Oxidation Behavior of Accident Tolerant Fuel by using AC²

Gregor T. Stahlberg, Marco K. Koch

11th European Review Meeting on Severe Accidents Research | KTH, Stockholm | May 13 – 16, 2024

PSS Plant Simulation and Safety
Prof. Dr.-Ing. Marco K. Koch

MOTIVATION AND OBJECTIVE

Postulated plant accidents with fuel damage

- Assessment of simulation models of a PWR using ASTEC and AC²

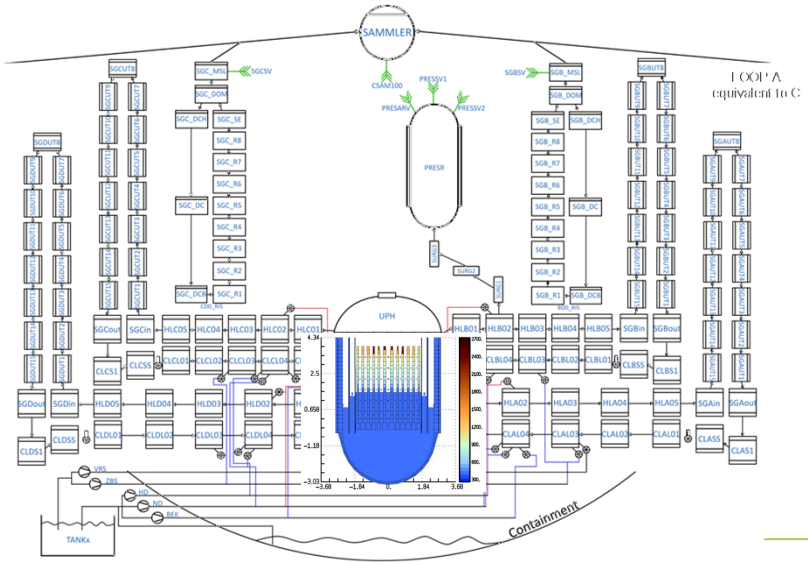

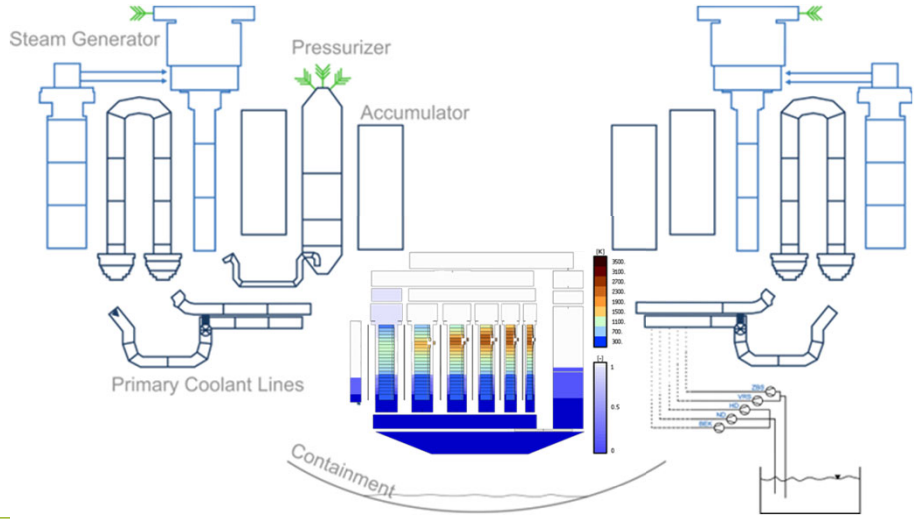

© PSS RUL

PSS Plant Simulation and Safety
Prof. Dr.-Ing. Marco K. Koch
RUHR UNIVERSITÄT BOCHUM
RUB

MOTIVATION AND OBJECTIVE

Postulated plant accidents with fuel damage

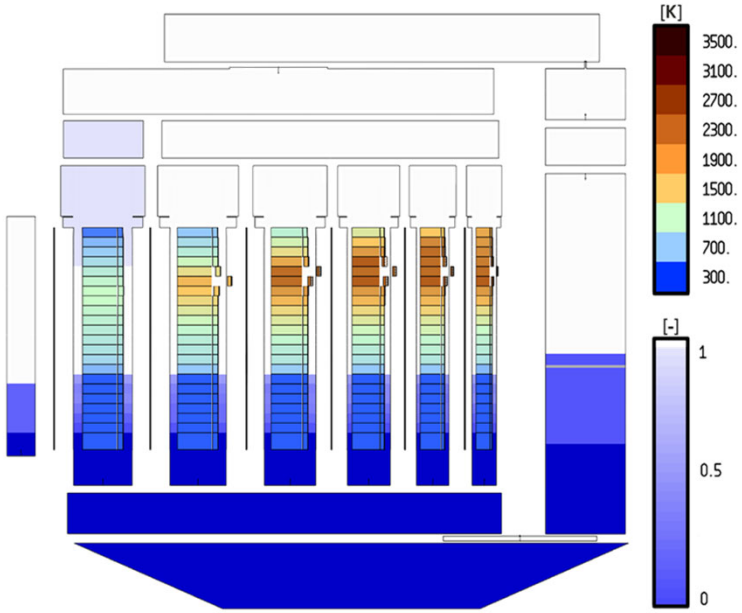

How to increase the coping time?

Advanced Technology / Accident Tolerant Fuel?

ADVANCED TECHNOLOGY / ACCIDENT TOLERANT FUEL?

FeCrAl alloy | Cr-Coated Zr-alloy

- Analysis of technologies that specifically target improved accident behavior
- Reduce potential hydrogen and heat release, that must be removed by cooling systems (i.e. Emergency Core Cooling System) in the event of incidents or accidents → coping time!
  - Testing of new correlations for **FeCrAl alloy** based on publications by KIT
  - Development of preliminary model for oxidation of **Cr-coated claddings** available as new option for AC² at RUB PSS (ongoing development)

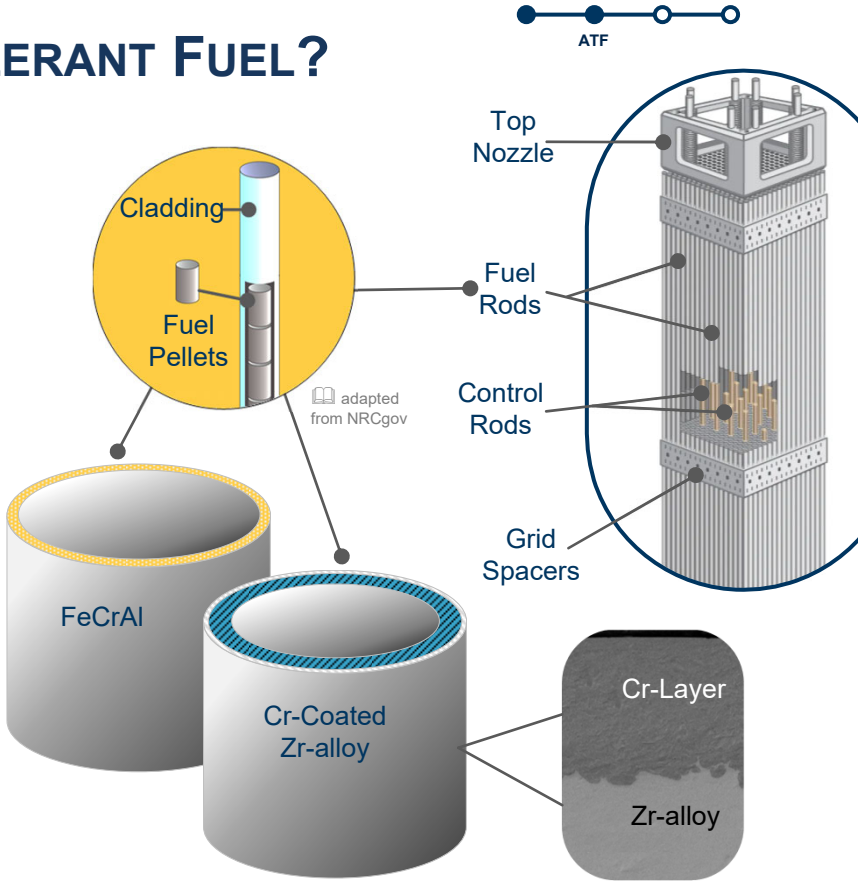

PSS Plant Simulation and Safety
Prof. Dr.-Ing. Marco K. Koch
RUHR UNIVERSITÄT BOCHUM
RUB

ACCIDENT TOLERANT FUEL

FeCrAl alloy | Cr-Coated Zr-alloy



- Oxidation behavior of FeCrAl alloys is dependent on their composition, particularly the concentrations of Cr, Al and other alloying elements

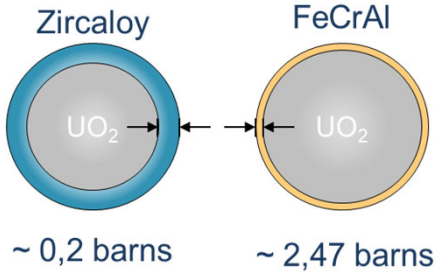

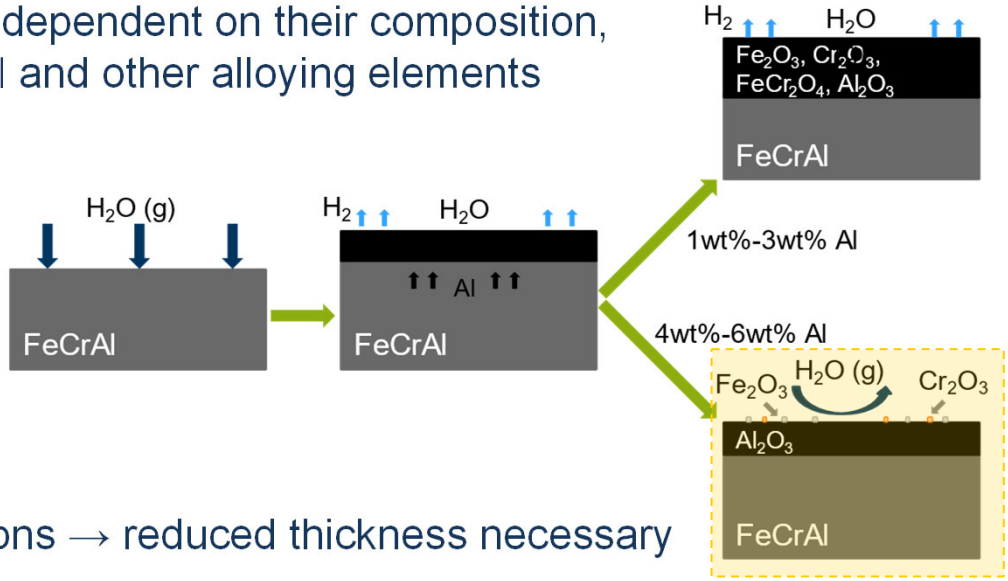

- Higher neutron absorption cross-sections → reduced thickness necessary
- Different kinetics depending on temperature level → strong oxidation above ~1350°C

adapted from Y. Qiao et al. 2020

ACCIDENT TOLERANT FUEL

FeCrAl alloy | Cr-Coated Zr-alloy

ATF

- Coating as diffusion barrier, protecting substrate material (e.g. Zr-based alloy)
- Chromium (III) oxide layer (Cr_2O_3) is characterized by low weight gain
- Corrosion resistance / protective scale influenced by several parameters
  - Coating quality (deposition, microstructure, thickness, …)
  - Transient boundary conditions (PCT, heating rate, …)

  → Degradation of the coating

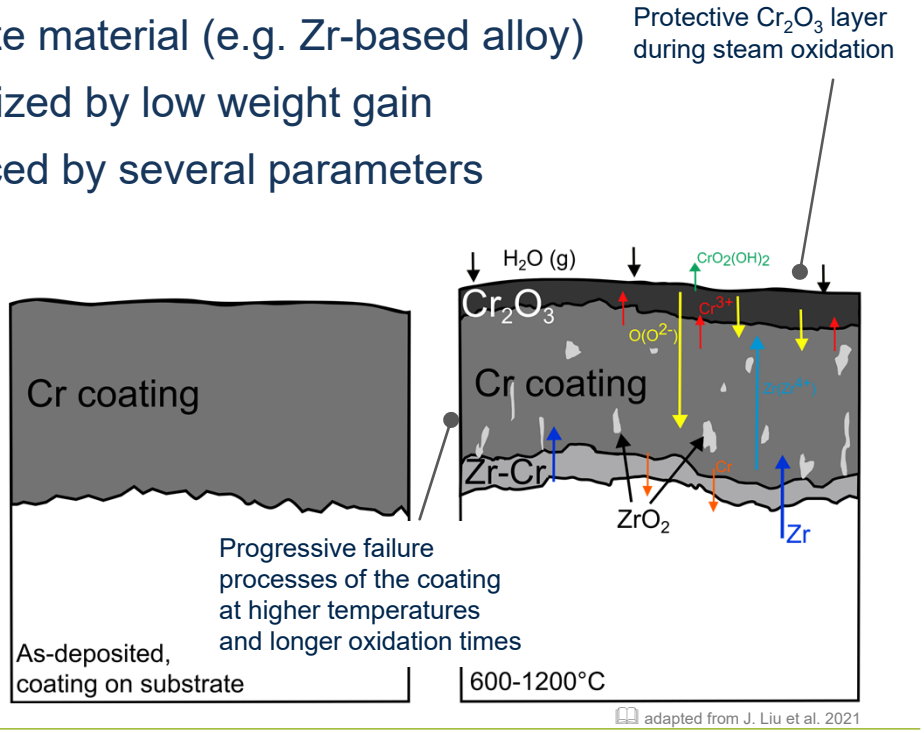

adapted from J. Liu et al. 2021

Modeling

MODELING

Current approaches under development

Current improvements see T. Hollands

- FeCrAl Correlation
  - α-Al Oxidation (AC², Opt. 21)
  - Different kinetics depending on temperature
  - ✘ Heat of oxidation → limited for testing

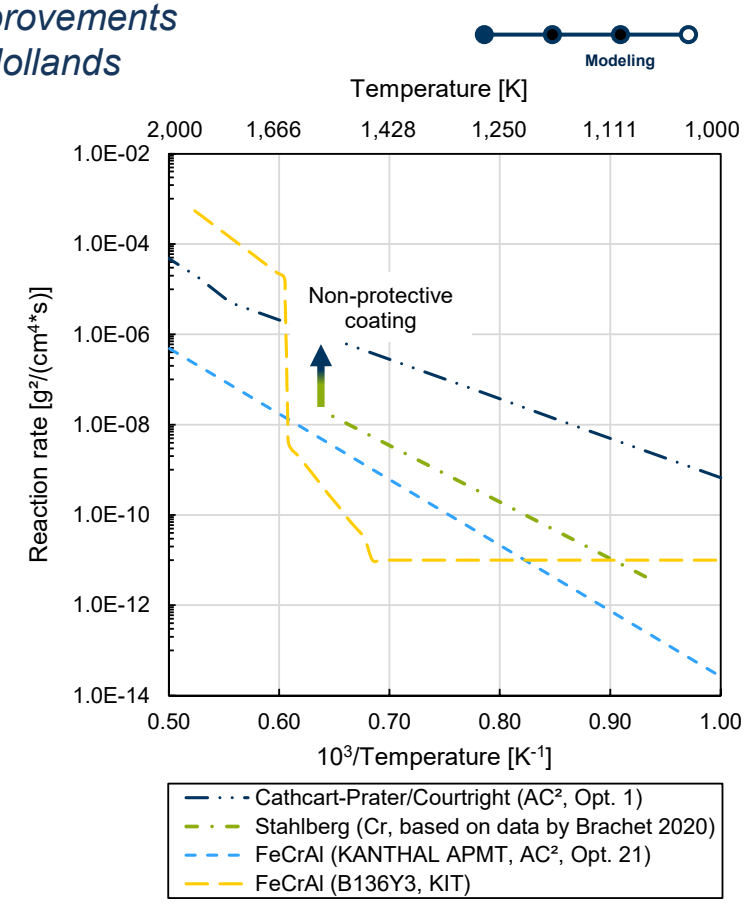

PSS Plant Simulation and Safety
Prof. Dr.-Ing. Marco K. Koch
RUHR UNIVERSITÄT BOCHUM
RUB

MODELING
Test facility model with AC²

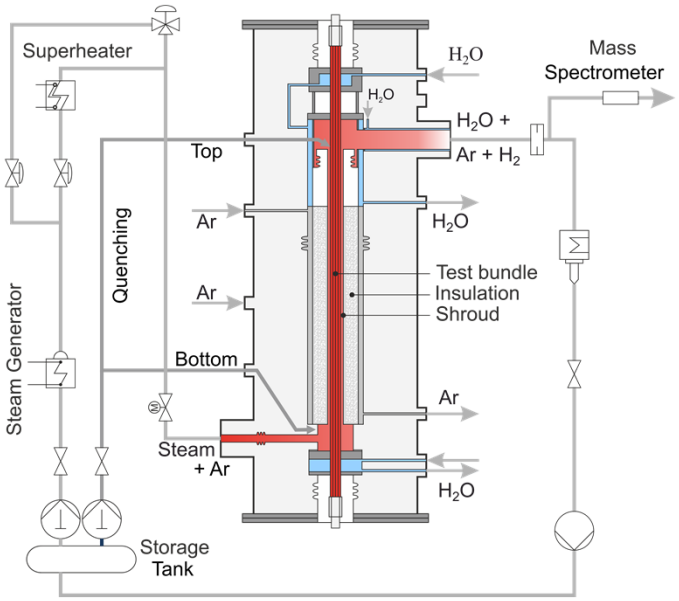

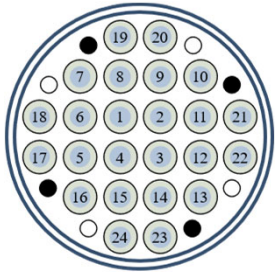

QUENCH-19 / ATF-1

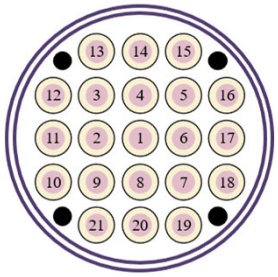

QUENCH- L3HT

COOLING
JACKET

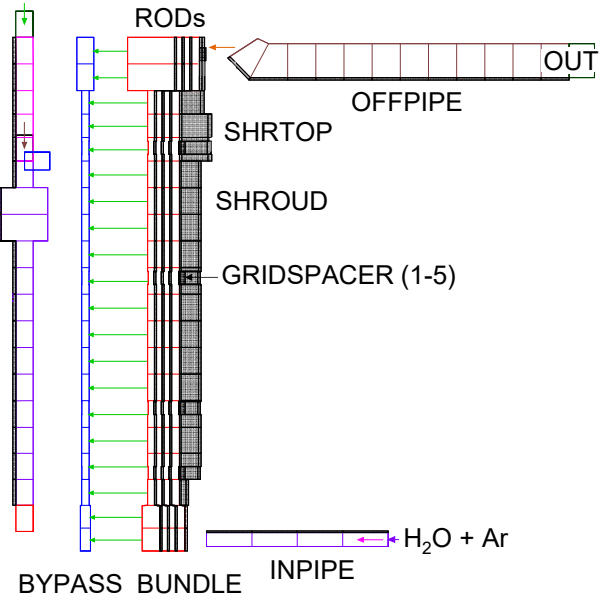

MODELING
Experimental characteristics

- LOCA Series – “QUENCH-L3HT”

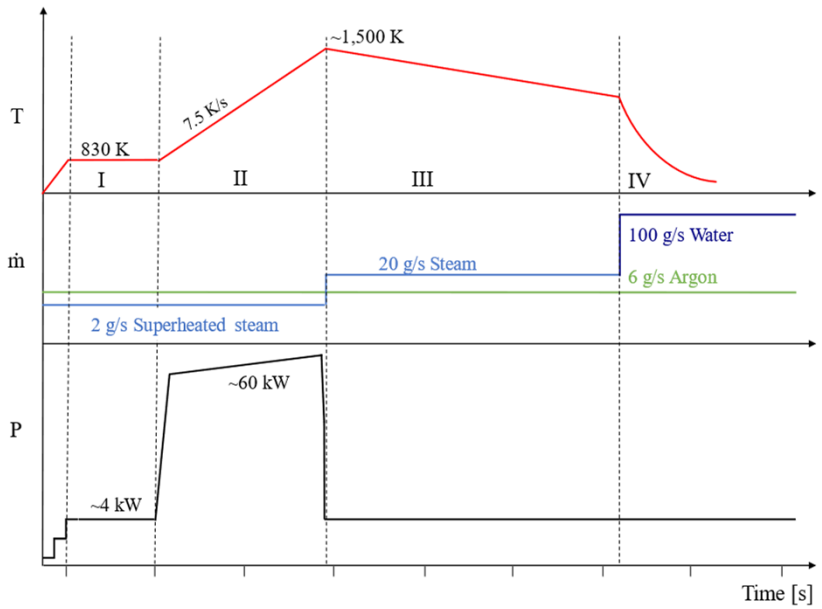

- QUENCH Series – “QUENCH-19”

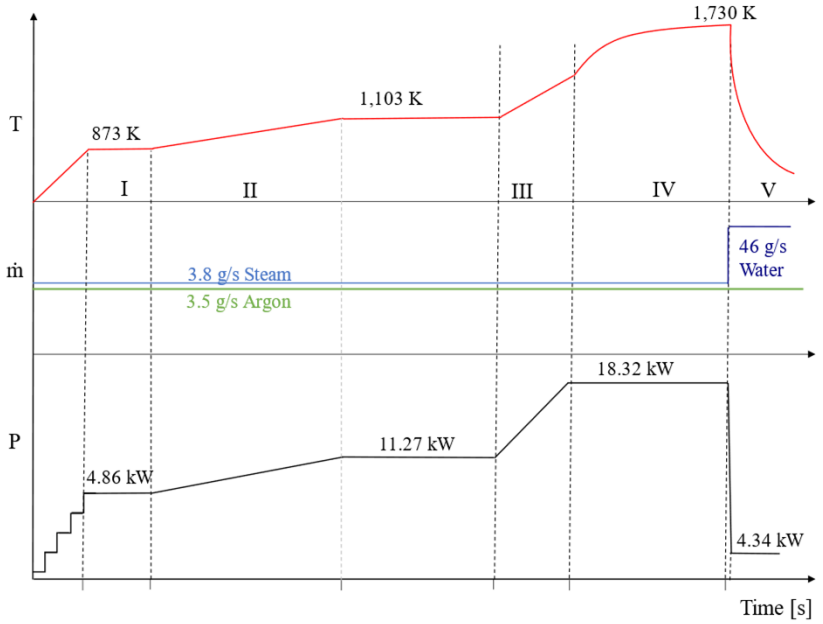

Verification and Application

VERIFICATION
Correlation for Cr, 1200°C

- Calculated mass gain curve shows good agreement at 1200°C
  - Calculated mass gain tends to be slightly overestimated; most data are captured adequately (few outliers like Kim15)
  - Coating failure seems to occur for some tests after ~5000 s

Different experimental settings (e.g. isothermal / transient) and different deposition technologies may involve uncertainties.

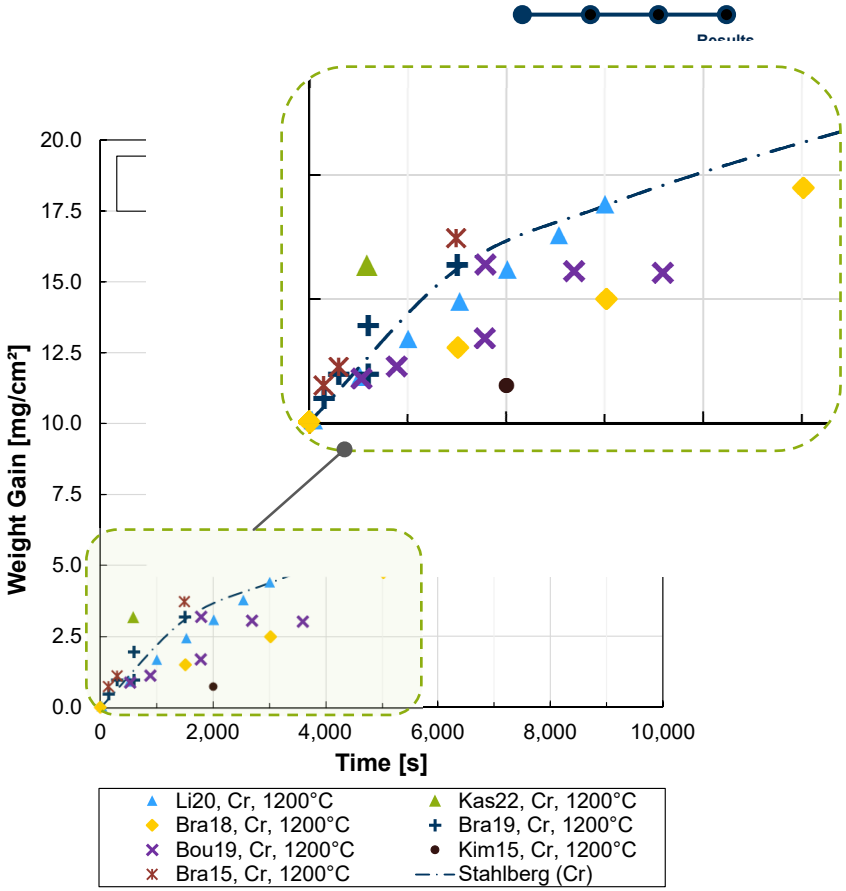

APPLICATION
QUENCH-19

- Overall, the measured values of the selected TC at 950 mm are reproduced well, except for the PCT
- The temperatures are partly lower with mod. version
- Sim. (Opt. 21) shows approximately 50% of the integral H_2
- Preliminary: No smooth transition of H_2 for Sim. (mod.) with new correlation

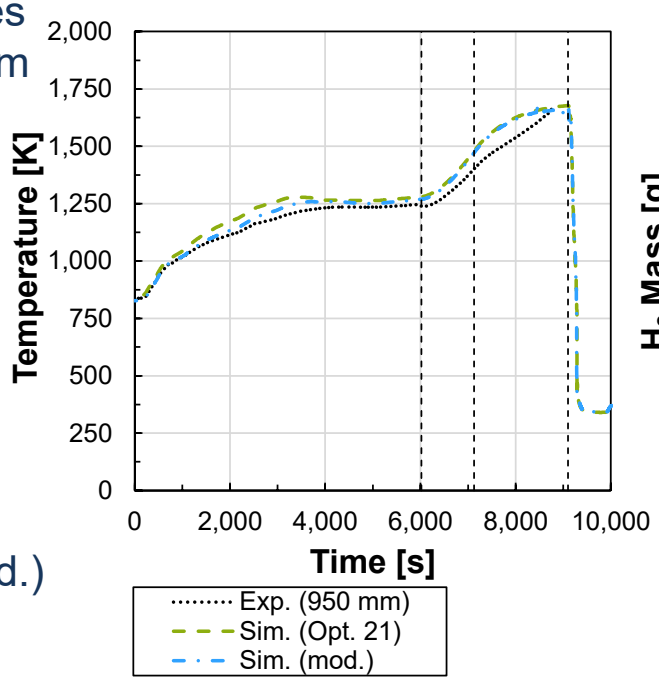

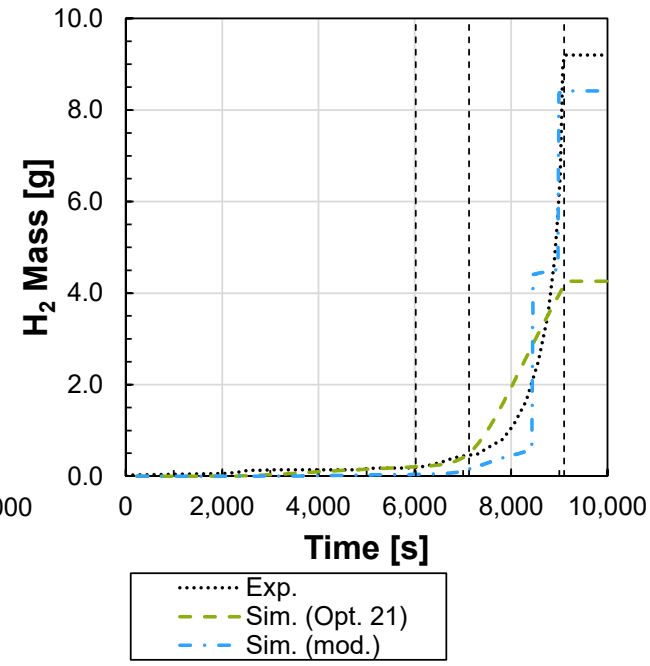

APPLICATION
QUENCH-ATF-1 / -L3HT

- Calculated values of TC at 950 mm is overestimated, but qualitatively well
- Application of Cr-coated cladding shows lower Temperatures, as expected
- Variation: models for Zr oxidation (Opt. 1/3) as well as Cr oxidation are shown
- Comparing Opt. 1 and 3 reveals differences of H_2 and maximum temperatures

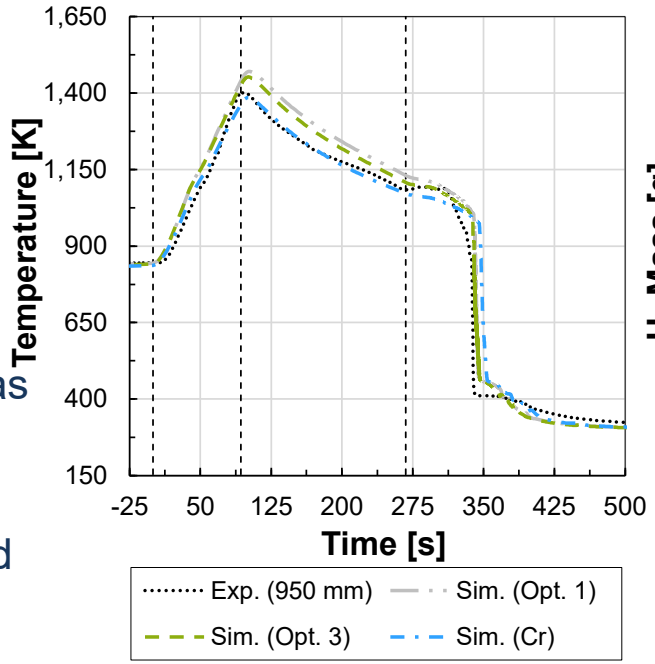

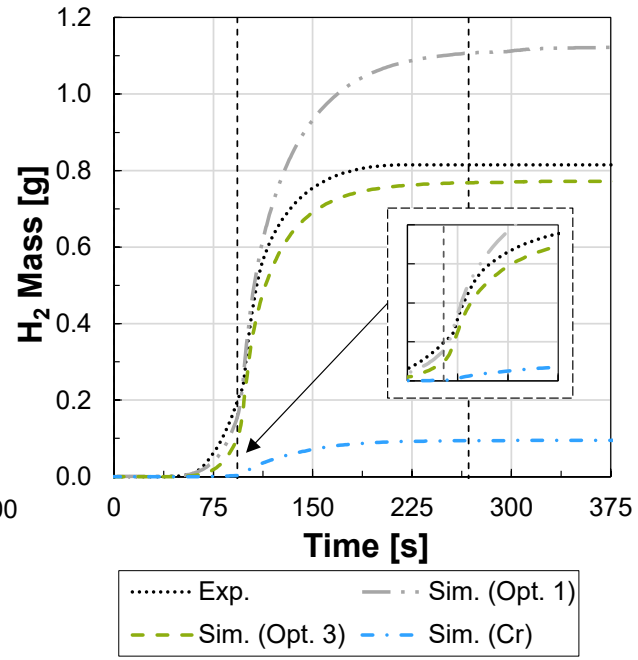

APPLICATION
QUENCH-ATF-1 / -L3HT

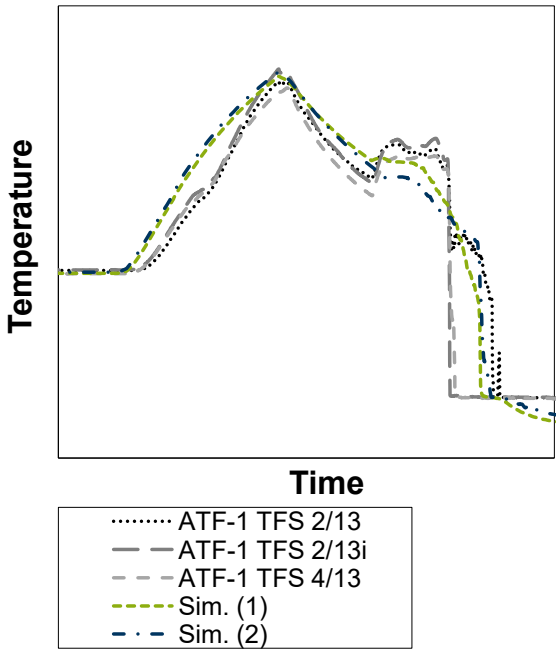

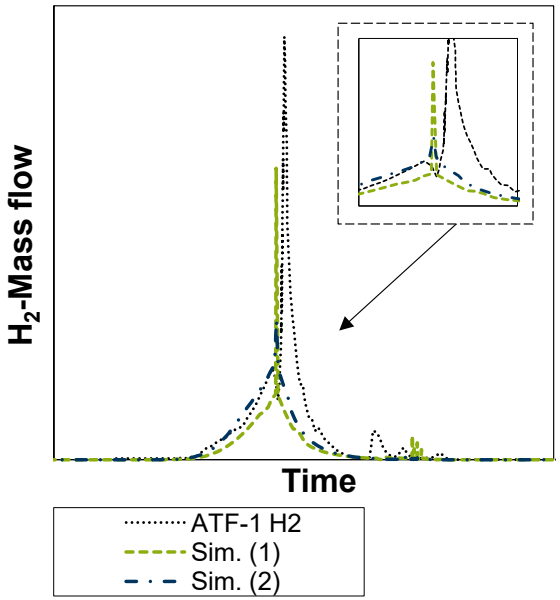

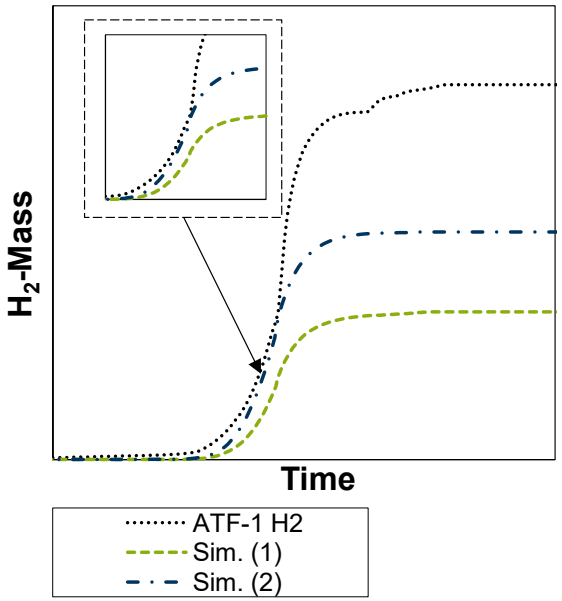

adapted from G. Stahlberg et al. 2023

CONCLUSION

- Modeling and assessment of oxidation kinetics: simulation model of the QUENCH facility was prepared and assessed with experimental data of different experiments
  - Q-19 transient is reproduced well, but the oxidation process is currently not modelled accurately, highlighting the preliminary modelling as well as necessary further development
  - Q-L3HT transient has partly overestimated temperatures. The integral H_2 is better represented using Opt. 3 in AC² → Overall it seems that Opt. 3 underestimates H_2 at lower temperatures
  - Q-ATF-1 is mostly reproduced, however the integral H_2 is underestimated. A possible contributor could be an earlier than modeled / anticipated local failure of the coating. Further development of the numerical approach might also improve the results.
- Further application of Cr-coating to other Experiments (e.g. CODEX-ATF) and preliminary assessment during plant application is planned. Further extension is currently under investigation in a proposed national funded project.

ACKNOWLEDGEMENT

This work is funded by the German Federal Ministry for the Environment, Nature Conservation, Nuclear Safety and Consumer Protection (BMUV) under grant number 1501629 based on a decision by the German Bundestag.

Responsibility for the content lies with the authors.

The results were obtained using the GRS software package AC² 2021.1 and an in-house version at PSS of the GRS software package AC² 2021.0.

Supported by:

Federal Ministry
for the Environment, Nature Conservation,
Nuclear Safety and Consumer Protection

based on a decision of
the German Bundestag

Thank you for your attention!

Gregor Stahlberg

Gregor.Stahlberg@pss.rub.de



Marco K. Koch

Marco.Koch@pss.rub.de



RUHR-UNIVERSITÄT BOCHUM

PSS Plant Simulation and Safety
Prof. Dr.-Ing. Marco K. Koch

Building: IC | Floor 2
Universitätsstr. 150
D-44801 Bochum

pss.rub.de

REFERENCES (EXCERPT)

[Bou19] Bourdon, Gauthier; Ševecek, Martin; Krejčí, Jakub; Cvrček, Ladislav: HIGH-TEMPERATURE STEAM AND AIR OXIDATION OF CHROMIUM-COATED OPTIMIZED ZIRLO™. Acta Polytechnica CTU Proceedings, 24, 2019. DOI: 10.14311/APP.2019.24.0001.

[Bra15] Brachet, Jean-Christophe; Le Saux, Matthieu; Le Flem, Marion; Urvoy, Stephane; Rouesne, Elodie; Guilbert, Thomas; Cobac, C.; Lahogue, F.; Rousselot, J. L.; Tupin, Marc; Billaud, Pierre; Hossepied, Charles; Monsifrot, Eric: On-going studies at CEA on chromium coated zirconium based nuclear fuel claddings for enhanced accident tolerant LWRS fuel, cea-02492582, Top Fuel 2015 - Reactor Fuel Performance Meeting, Zurich, Switzerland, 2015.

[Bra18] Brachet, Jean-Christophe; Guilbert, T.; Le Saux, Matthieu; Rousselot, J.; Nony, G.; Toffolon-Masclet, C.; Michau, Alexandre; Schuster, Frederic; Palancher, Herve; Bischoff, Jeremy; Augereau, J.; Pouillier, Edouard: BEHAVIOR OF Cr-COATED M5 CLADDINGS DURING AND AFTER HIGH TEMPERATURE STEAM OXIDATION FROM 800°C UP TO 1500°C - LOSS-OF-COOLANT ACCIDENT & DESIGN EXTENSION CONDITIONS, Top Fuel 2018 - Reactor Fuel Performance, Prague, Czech Republic, 2018.

[Bra19] Brachet, Jean-Christophe; Idarraga-Trujillo, Isabel; Le Flem, Marion; Le Saux, Matthieu; Vandenberghe, Valérie; Urvoy, Stephane; Rouesne, Elodie; Guilbert, Thomas; Toffolon-Masclet, Caroline; Tupin, Marc; Phalippou, Christian; Lomello, Fernando; Schuster, Frédéric; Billard, Alain; Velisa, Gihan; Ducros, Cédric; Sanchette, Frédéric: Early studies on Cr-Coated Zircaloy-4 as enhanced accident tolerant nuclear fuel claddings for light water reactors. Journal of Nuclear Materials, 517, S. 268–285, 2019. DOI: 10.1016/j.jnucmat.2019.02.018.

[Bra20] Brachet, Jean-Christophe; Rouesne, Elodie; Ribis, Joël; Guilbert, Thomas; Urvoy, Stéphane; Nony, Guillaume; Toffolon-Masclet, Caroline; Le Saux, Matthieu; Chaabane, Nihed; Palancher, Hervé; David, Amandine; Bischoff, Jérémy; Augereau, Julien; Pouillier, Edouard: High temperature steam oxidation of chromium-coated zirconium-based alloys: Kinetics and process. Corrosion Science, 167, 2020. DOI: 10.1016/j.corsci.2020.108537.

[Kas22] Kashkarov, E. B.; Sidelev, D. V.; Pushilina, N. S.; Yang, J.; Tang, C.; Steinbrueck, M.: Influence of coating parameters on oxidation behavior of Cr-coated zirconium alloy for accident tolerant fuel claddings. Corrosion Science, 203, S. 110359, 2022. DOI: 10.1016/j.corsci.2022.110359.

[Kim15] Kim, Hyun-Gil; Kim, Il-Hyun; Jung, Yang-Il; Park, Dong-Jun; Park, Jeong-Yong; Koo, Yang-Hyun: Adhesion property and high-temperature oxidation behavior of Cr-coated Zircaloy-4 cladding tube prepared by 3D laser coating. Journal of Nuclear Materials, 465, S. 531–539, 2015. DOI: 10.1016/j.jnucmat.2015.06.030.

REFERENCES (EXCERPT)

[Li20] Li, Guangbin; Liu, Yanhong; Zhang, Yingchun; Li, Huailin; Wang, Xiaojing; Zheng, Mingmin; Li, Yusha: High Temperature Anti-Oxidation Behavior and Mechanical Property of Radio Frequency Magnetron Sputtered Cr Coating. Metals, 10, S. 1509, 2020. DOI: 10.3390/met10111509.

[Liu21] Liu, Junkai; Tang, Chongchong; Steinbrück, Martin; Yang, Jianqiao; Stegmaier, Ulrike; Große, Mirco; Di Yun; Seifert, Hans Jürgen: Transient experiments on oxidation and degradation of Cr-coated Zircaloy in steam up to 1600 ℃. Corrosion Science, 192, 2021. DOI: 10.1016/j.corsci.2021.109805.

[Sha18] Shah, Hemant; Romero, Javier; Xu, Peng; Oelrich, Robert; Walters, Jorie; Wright, Jonathan, Gassmann, William: Westinghouse-Exelon EnCore® Fuel Lead Test Rod (LTR) Program including Coated cladding Development and Advanced Pellets, WAAP-10756, Top Fuel 2018 - Reactor Fuel Performance, Prague, Czech Republic, 2018.

[Sta22] Stahlberg, Gregor, T., et al.: Preliminary Simulation Results of the Experiments QUENCH-L3HT and QUENCH-ATF-1 Regarding High-Temperature Oxidation Mechanisms Using the System Code AC^2, 27th International QUENCH Workshop, KIT, Karlsruhe, 2022. https://doi.org/10.5445/ir/1000152245

[Sta23] Stahlberg, Gregor T., et al.: Comparative analyses of the QUENCH experiments L3HT and ATF-1 on high temperature oxidation mechanisms using AC^2, in Proceedings of NURETH-20 - International Topical Meeting on Nuclear Reactor Thermal Hydraulics, pp. 5450–5461, 2023. https://doi.org/10.13182/nureth20-39989

RÉPUBLIQUE FRANÇAISE
Liberté
Égalité
Fraternité

IRSN
INSTITUT DE RADIOPROTECTION ET DE SÛRETÉ NUCLÉAIRE

ASTEC VALIDATION OF SPENT FUEL POOL (SFP) DEWATERING USING RESULTS FROM THE DENOPI PROJECT

Laurent Laborde, Benoît Migot

IRSN/FRM-296 ind. 06

Outline

- Motivations
- MIDI experimental device and main results
- ASTEC modelling of the MIDI facility: first results and current limitations
- Conclusions and perspectives

Motivations

- Studying SFP severe accidents with a system code like ASTEC requires a satisfactory calculation of the SFP dewatering

- However, natural convection flow in large water pool (SFP or immersed heat removal system of SMR) is **highly turbulent**: detailed analysis usually requires a CFD tool

- Feedback of MUSA Horizon 2020 project: difficulties in computing SFP dewatering with ASTEC

- ***Is a system code like ASTEC able to capture the main features of an SFP accident initial phases?***
  1. Dewatering before fuel uncovery
  2. Fuel uncovery before degradation

The DENOPI project (2013-2023)

Experimental project launched by IRSN to improve the understanding of SFP accidents:

MIDI

Large-scale study of SFP dewatering **before fuel uncovery**

ASPIC

Mid-scale observation of assembly uncovery before fuel degradation

OXIDATION

Small-scale analysis of fuel cladding oxidation under air flow

The MIDI mock-up

MIDI Overview

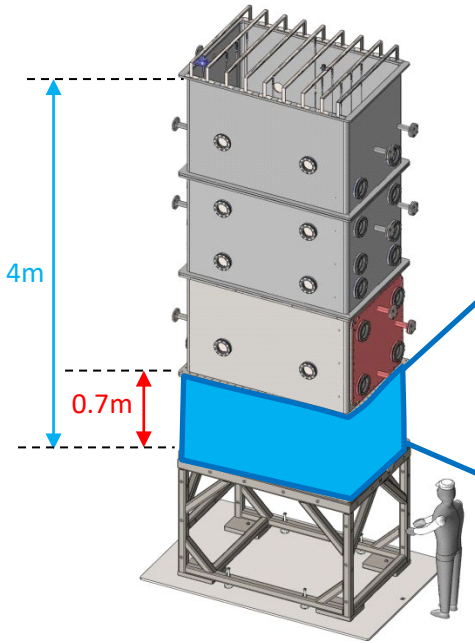

Storage rack:

- 21 racks with 3x3 heating elements inside
- No possible crossflows between racks
- Bypass between the storage rack and the basin

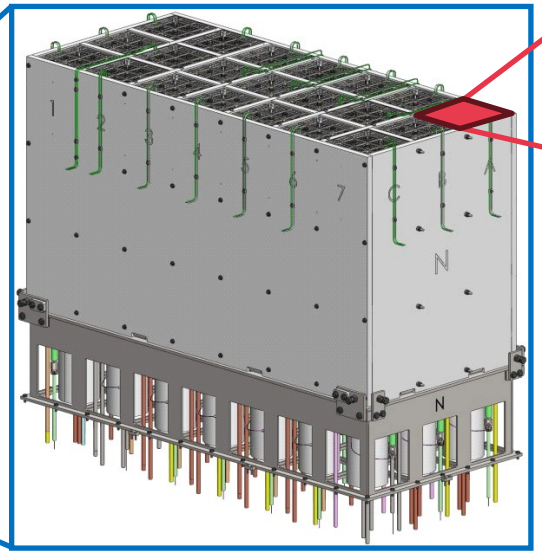

3x3 heating rods

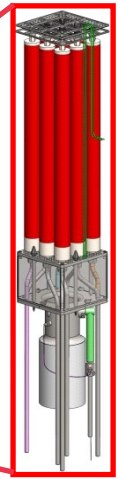

Main instrumentation:

- Temperatures in pool and racks
- Mass flow rate in racks
- Water level
- Cameras

MIDI experiments

- Test matrix parameters:
  - 4 different arrangements (*loading patterns*) of hot and cold racks
  - 4 overall heating power: 50, 90, 220 or 300 kW
  - initial water level: 4 m or 2 m.

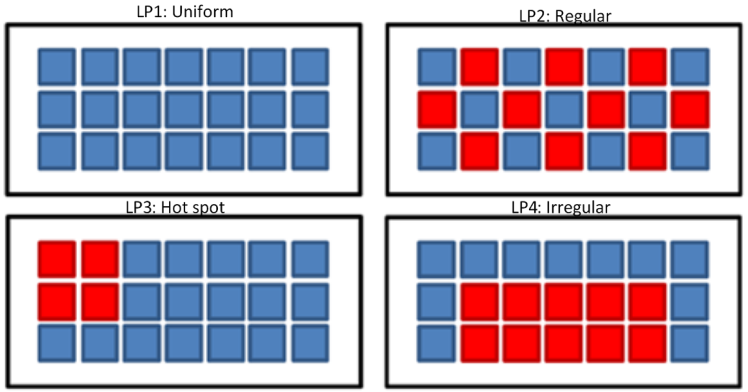

- 9 tests, 5 of them repeated twice to check (with success) repeatability

- Experimental protocol:
  - Basin is filled up to the target level water level (2m or 4m)
  - Water and structures are heated up to 50°C by full power with forced convection
  - Test: forced convection is stopped, selected power and loading pattern are applied

Main results

- Strong mixing → homogeneous pool temperature
- **Behaviour weakly dependent on loading pattern**, except hot spot
- **3 consecutive phases corresponding to 3 vaporization modes**

3 vaporization modes depending on local temperature compared to local Tsat

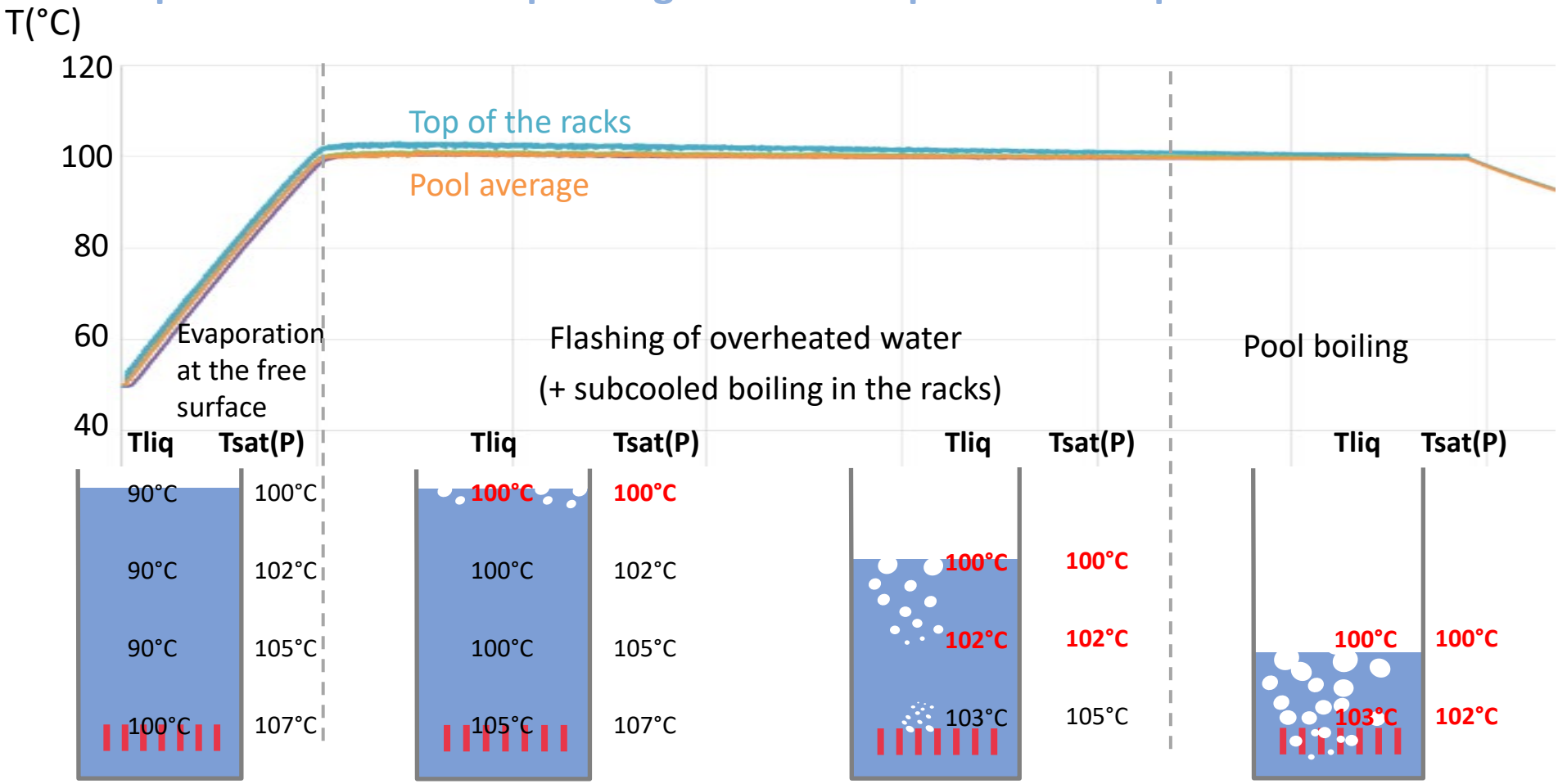

MIDI experiments: illustration of phase 2 (flashing + subcooled boiling)

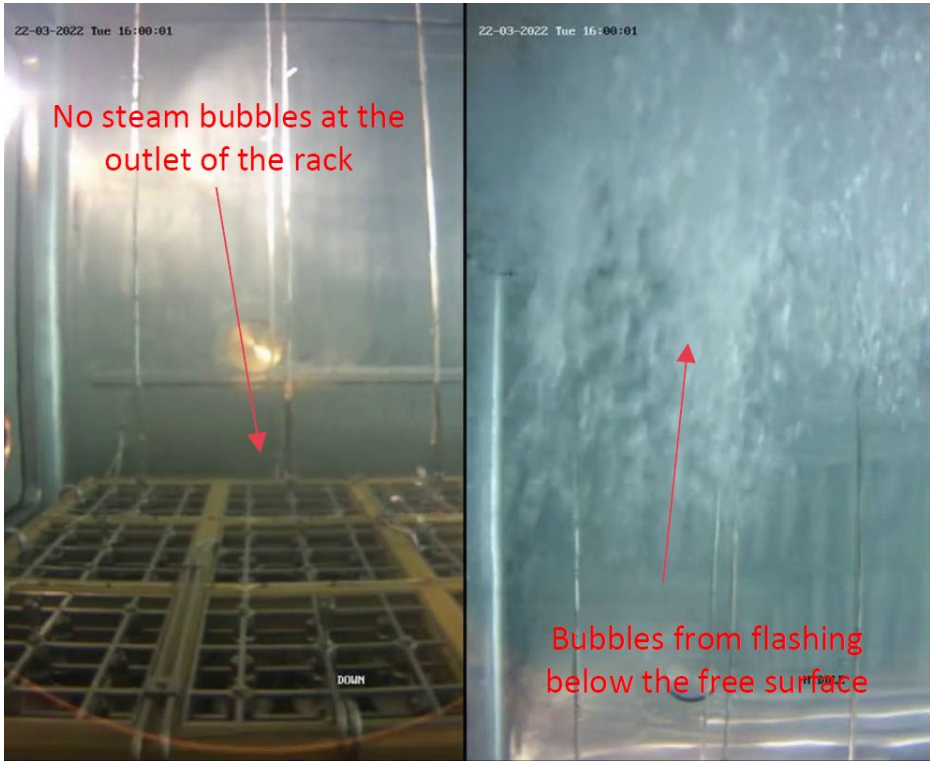

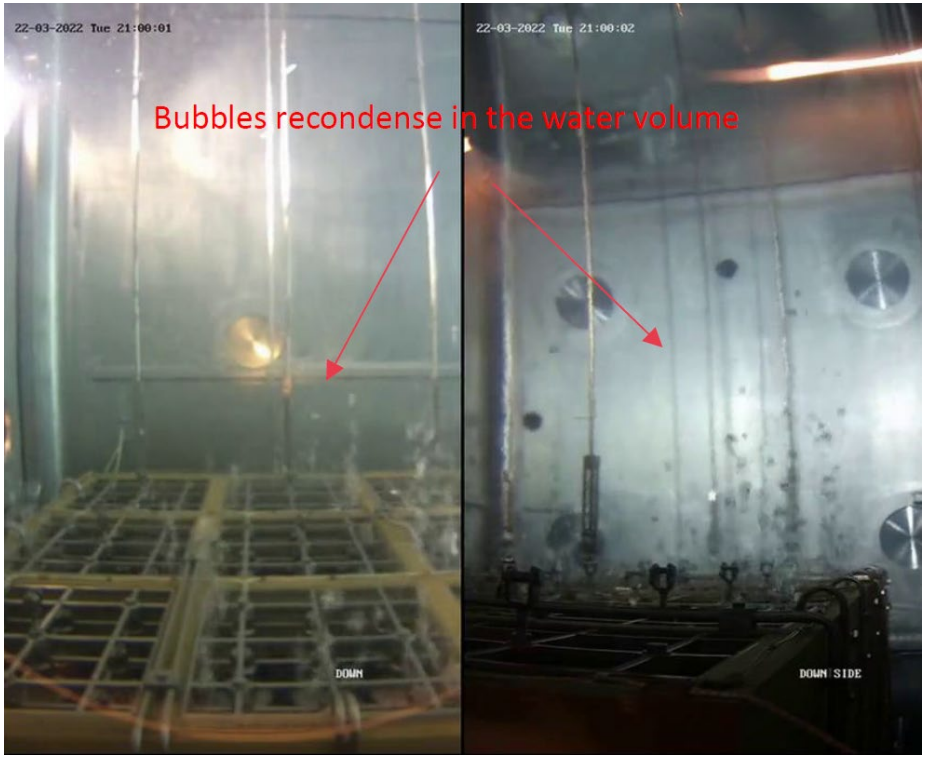

ASTEC V3.1 thermal hydraulics module (CESAR)

- 1D description in circuits, 2D in vessel (or SFP)

- 6 equations (mass, energy, and momentum conservation equations for liquid and gas)
  + up to 8 non condensable gases

- Validated in conditions close to LWR conditions:
  - Circuits or bundle (intact or degraded) configuration
  - High heat flux, flow rate and pressure

- Applied for several years to SFP loss of cooling and loss of coolant accidents:
  - Large open regions above the fuel assemblies
  - Low heat flux, flow rate and pressure

→ First comparison of ASTEC results with SFP-like experiments

MIDI representation with ASTEC

- Two groups of fuel assemblies: hot group and cold group

- Weight of each group adapted to each test:

Uniform Pattern | Regular Pattern | Hot spot

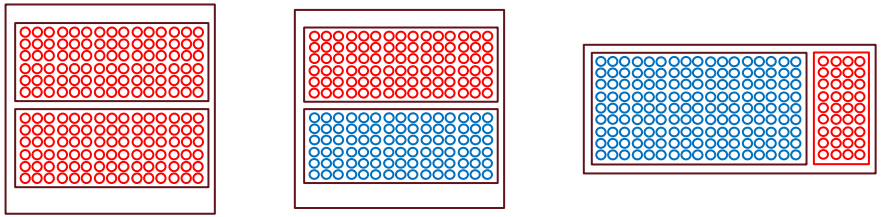

- Main parameters are respected:
  - Surfaces, fluid section, power, pattern, racks porosity

- Boundary and initial conditions as in experiment:
  - Constant atmospheric pressure at the top
  - Thermal losses on external vertical faces of the basin (T_{ext}=25°C)
  - Initial temperature: 50°C

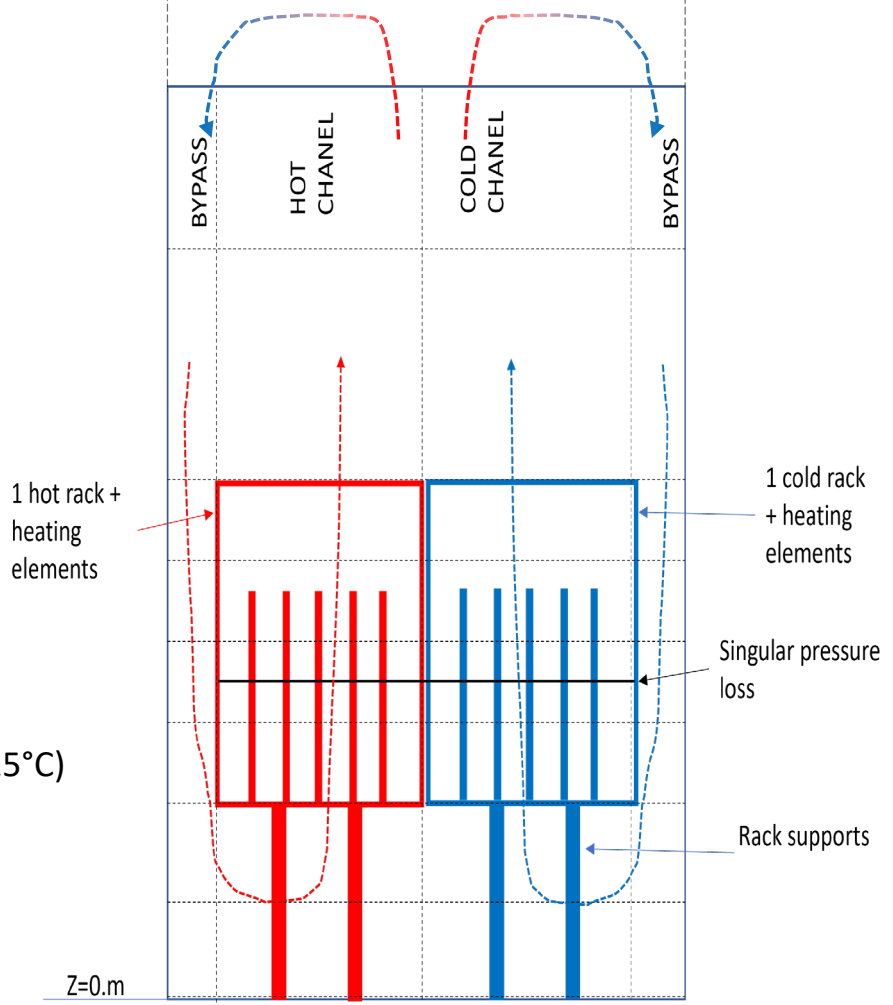

Results at low power with uniform loading pattern (same power in hot and cold racks)

90 kW

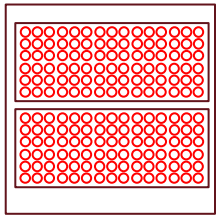

- First check:
  - correct energy balance
  - good calibration of thermal losses (20% of the injected power at 90 kW)

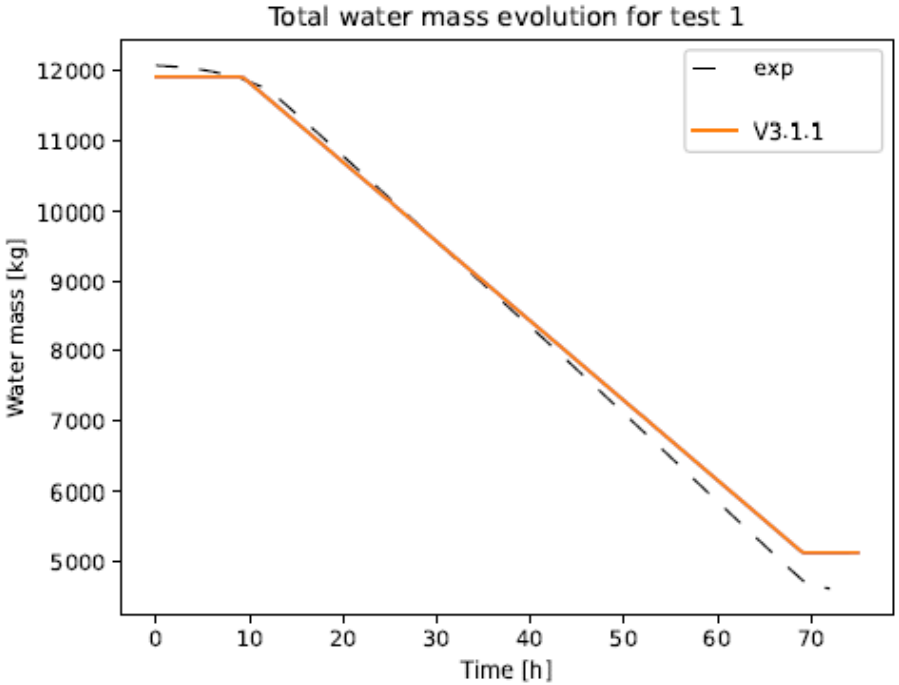

Results at low power with uniform loading pattern (same power in hot and cold racks)

- Simple representation ≠ complexity of real flowpath in the racks
  → Pressure losses are underestimated

- First calculation: rack mass flow rates overestimated by a factor 2

- Singular pressure loss coefficient (k=32) at mid-height of heating elements:
  fitted to match experimental mass flow rate, **conserved for all other tests**.

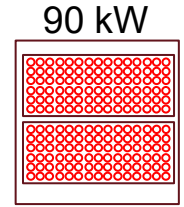

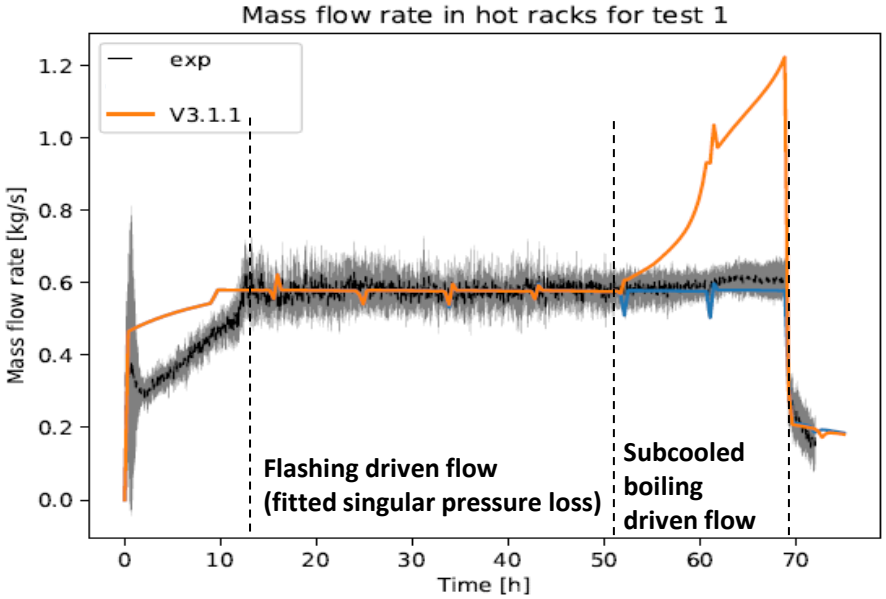

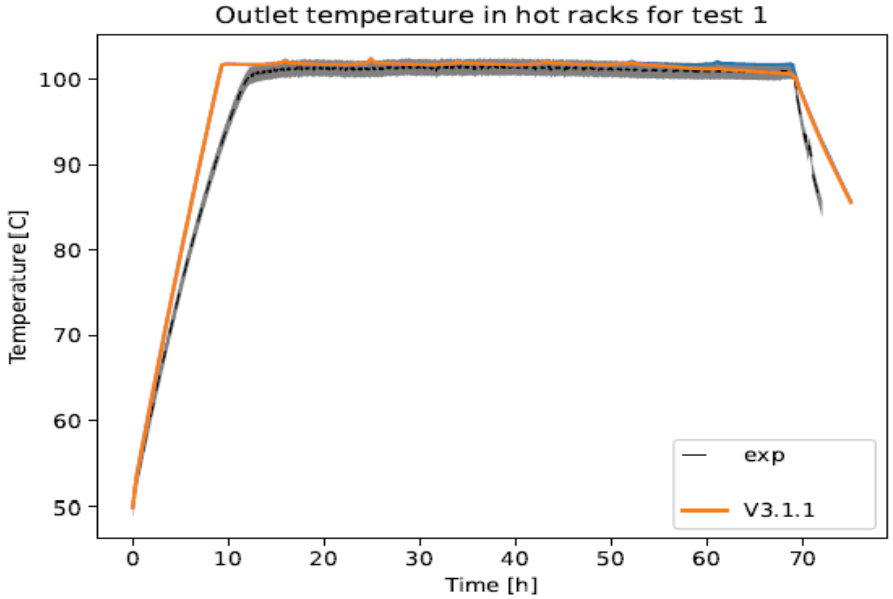

Subcooled boiling modelling

Based on partitioning the total heat flux φ extracted from a wall:

- $\varepsilon\ \varphi$ → vaporization
- $(1-\varepsilon)\ \varphi$ → liquid heat up

Model name in ASTEC	ε
No subcool	$\varepsilon=0$ if $T_{liq}<T_{sat}$ $\varepsilon=1$ otherwise
V3.1.1	$(T_{liq}-T_{sat})\ Pe\ St\ /\ D_{liq}$

Sensitivity to the subcooled boiling model

- All these models have been established at high heat flux and mass flow rate compared to MIDI conditions

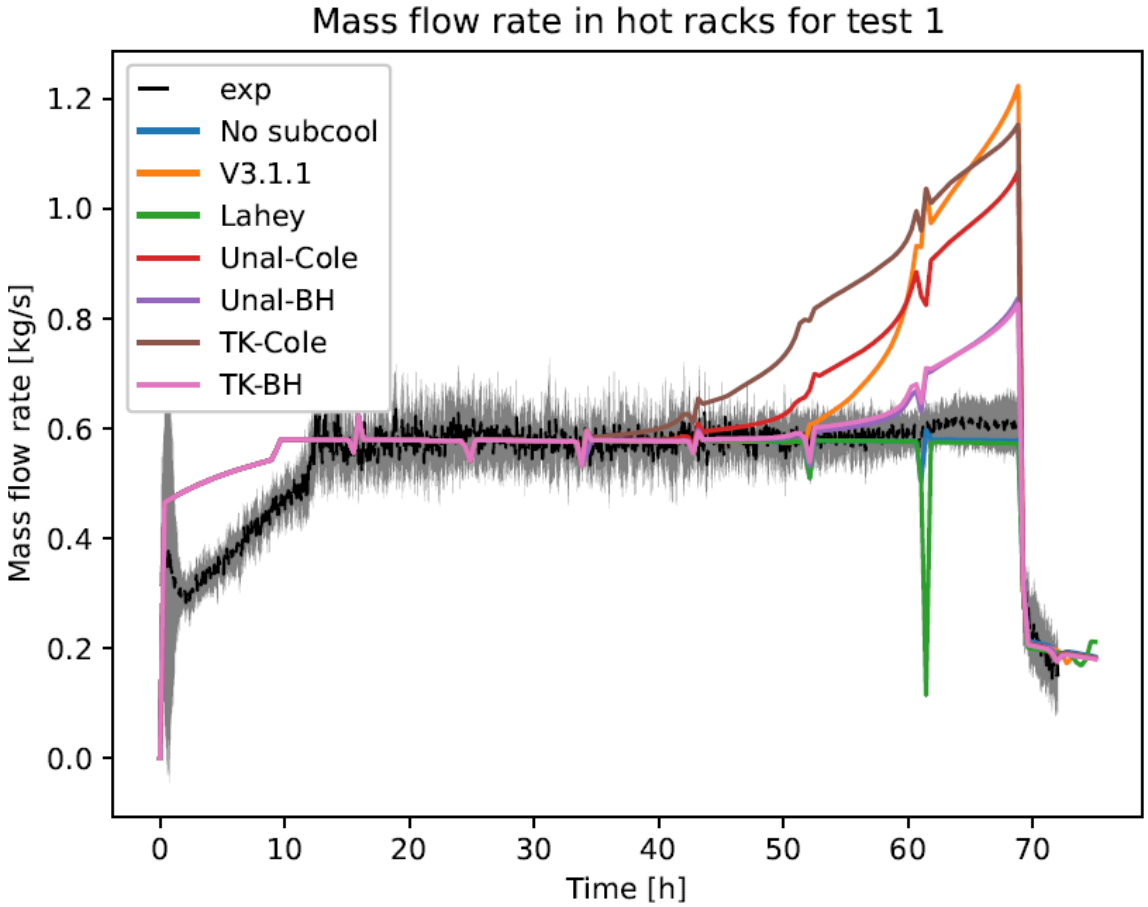

Example of results with other powers and patterns

Test 5:
P=300 kW
Strong heat exchanges between hot and cold racks in experiments
→deviations in computed flows

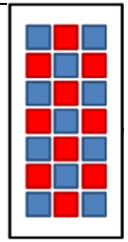

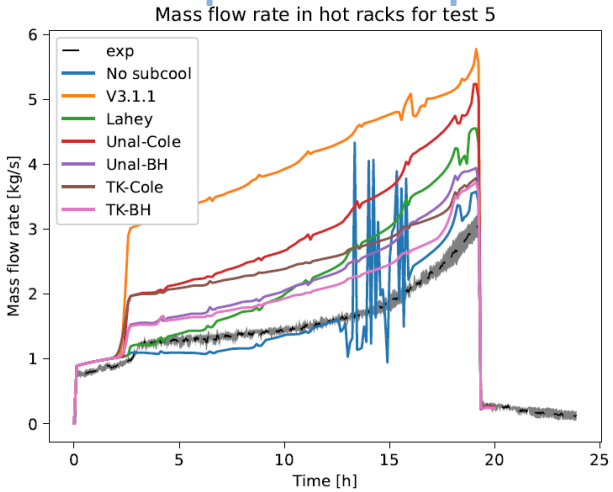

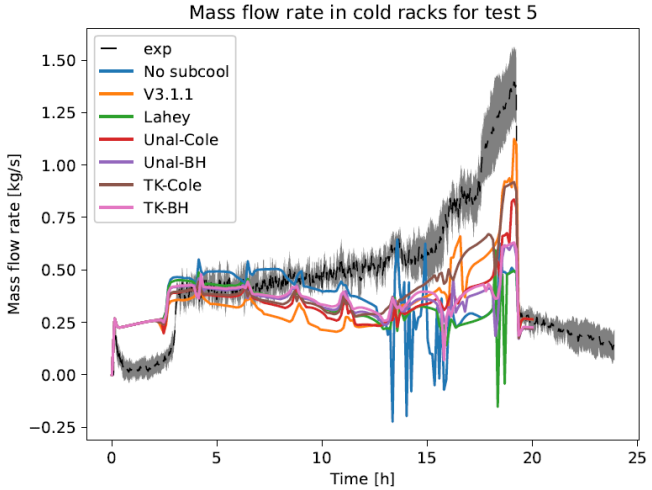

Test 8:
P=219 kW
Isolated hot spot: reduced heat exchanges between hot and cold racks
→ reduced deviations

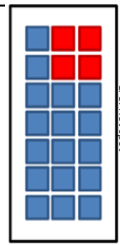

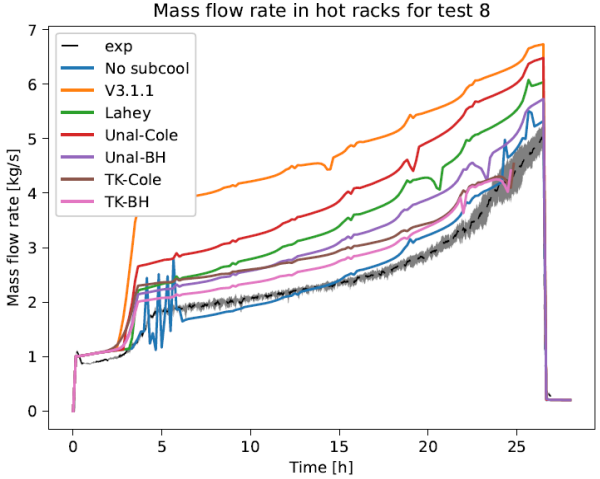

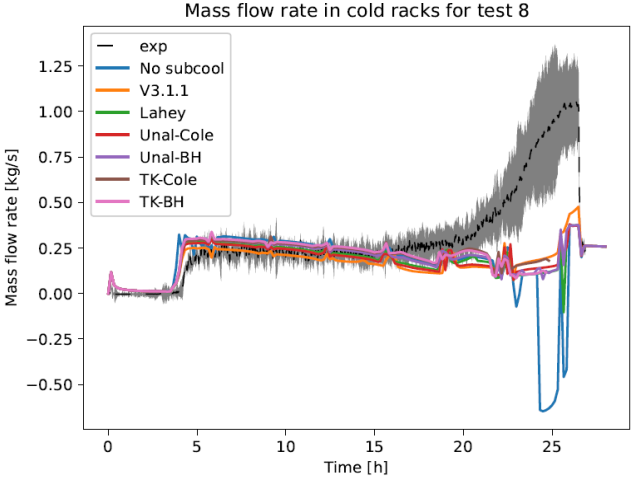

Is subcooled boiling really needed?

- Without subcooled boiling:
  - too hot temperature (i.e. local Tsat) at the outlet of hot racks
  - when saturation is reached, violent vaporization

→strong peaks on mass flow rate
→many events of reversed flows not observed in experiment
+ small time steps

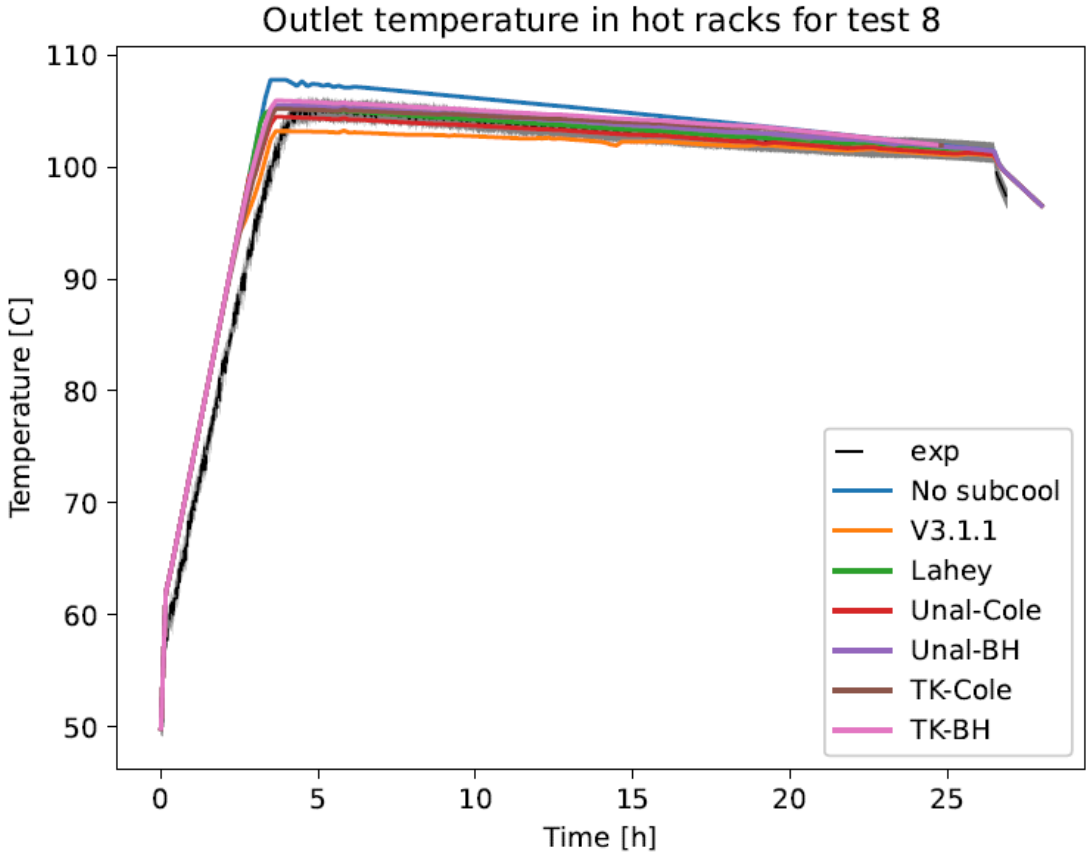

Summary

First step of ASTEC assessment against pool dewatering under natural circulation

Main phenomena reproduced:

- temperature evolutions well reproduced in the pool and in the racks
- 3 phases of vaporization modes: evaporation, flashing and boiling
- increase of racks mass flow rate during boiling phase

Current limitations:

- Homogeneous temperature profile in the pool: enough mixing in ASTEC. Too much?
  → compare ASTEC flows to CFD results
- Too intense subcooled boiling
  → deviation of mass flow rate when approaching saturation
- No direct heat exchange between hot and cold racks in ASTEC
  → tendency to overestimate the difference between hot and cold racks
  → new test planned at high power with uniform pattern
  → assessment of the different subcooled boiling models
- Numerical issues: discontinuous heat flux when water level crosses axial nodalization
  → heat flux and mass flow rate “peak” (emphasized during assembly uncover in MUSA project)

Perspectives

- Next step towards ASTEC assessment for SFP accidents analysis and mitigation: ASTEC validation against assembly uncovery, with and without spray (ASPIC device)

- POLCA project (OECD NEA) started in April 2024:
  - Additional tests in MIDI and ASPIC
  - Benchmark of system codes and CFD codes against MIDI and ASPIC results
    Nuclear Energy Agency (NEA) - Assessing the safety of spent fuel pools during a loss of cooling accident (oecd-nea.org)

- Progress in such modelling also relevant to immersed passive Heat Removal Systems of SMR (EASI project starting in 2024)

Thank you for your attention !

MIDI test matrix

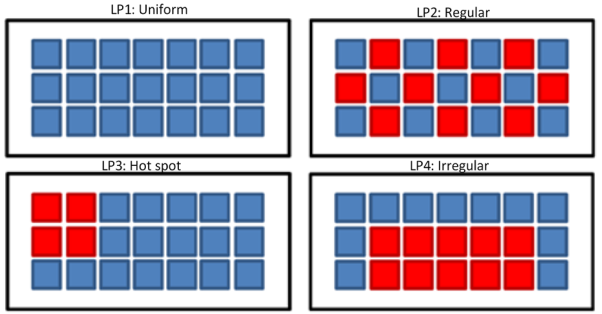

Tests	Loading pattern	Overall heating power	Number of hot racks / Power in hot racks	Number of cold racks / Power in cold racks	Initial pool level
1_1	LP1	90.1 kW	21 / 4.3 kW	0 / 0 kW	4 m
2_1	LP2	92.2 kW	10 / 8.4 kW	11 / 0.7 kW	4 m
5_1	LP2	299.5 kW	10 / 27.3 kW	11 / 2.5 kW	4 m
7	LP2	300. kW	10 / 27.3 kW	11 / 2.5 kW	2 m
8	LP3	218.7 kW	4 / 50.0 kW	17 / 1.1 kW	4 m
9_0	LP3	55.0 kW	4 / 11.4 kW	17 / 0.6 kW	4 m

Additional subcooled boiling models introduced in ASTEC

Kurul and Podowski models (mostly used in CFD codes):

$$Q_E = L_{LG}\,\rho_G\,\frac{\pi}{6}\,d_W^3 f N$$

Model name in ASTEC	Origin of the model	Correlations used in Kurul and Podowski model		
		d_W=bubbles size at detachment	f = bubbles detachment frequency	N=nucleation site density
No subcool	No subcooled boiling model: bubbles cannot appear if water is subcooled.	Not applicable		
V3.1.1	Model similar to Saha-Zuber [21] but fitted to KIT experimental data. Valid at P>2 bar.	Not applicable		
Lahey	Lahey [22] model with liquid enthalpy at bubble detachment from [21]. Used in TRACE V5 code [23].	Not applicable		
Unal-Cole	Kurul and Podowski [17]	[24]	[26]	[28]
Unal-BH	Kurul and Podowski [17]	[24]	[27]	[28]
TK-Cole	Kurul and Podowski [17]	[25]	[26]	[28]
TK-BH	Kurul and Podowski [17]	[25]	[27]	[28]

ASTEC VALIDATION OF SFP DEWATERING USING RESULTS FROM THE DENOPI PROJECT

Laborde L. and Migot B.
Institut de Radioprotection et de Sûreté Nucléaire (IRSN),
Centre de Cadarache B.P. 3, 13115 Saint-Paul-lez-Durance Cedex, France
laurent.laborde@irsn.fr; benoit.migot@irsn.fr

ABSTRACT

Loss of cooling in a Spent Fuel Pool (SFP) of a nuclear power plant can lead to the melting of fuel assemblies and to strong radiological consequences to the environment. In order to study the first phases of such accidents, up to the fuel assemblies uncovery, the DENOPI project was launched by the French Institute for Radiation Protection and Nuclear Safety (IRSN) supported and funded by the French Government and partners. Among the different facilities developed in the project, the MIDI facility aims at studying the complex thermal-hydraulics phenomena occurring in a large water pool heated from the bottom by electrical rods arranged in dedicated racks. MIDI is scaled by homothety to a typical French SFP. Different assembly arrangements (loading patterns) have been tested at different power levels, with either uniform power repartition, or hot and cold cells. In each test, the water level and temperatures at different elevations are followed, as well as mass flow rate entering each fuel rack. These experimental results also provide relevant data for the analysis and understanding of large natural convection loops that are expected in immersed passive heat removal systems of Small Modular Reactors. The forthcoming OECD/NEA POLCA project aims to extend such results database, in particular to assess the capability of thermal-hydraulics codes to reproduce the main tendencies of these experimental results.
The ASTEC code developed by IRSN is a system code dedicated to the simulation of major accidents in nuclear facilities that may lead to the release of radiological material. Recent works within the MUSA European project have shown the importance of reducing models uncertainties in the first phases of the accident, during the pool dewatering. In this paper, first simulations of MIDI tests are performed with ASTEC in order to assess and improve the capability of ASTEC to simulate the dewatering of a large water pool such as a SFP during a loss-of-cooling accident. Simulations are performed for a selection of MIDI tests with different heating patterns and power levels. Different models of subcooled boiling models from the literature are tested in ASTEC, stressing the key role of these models for an accurate prediction of the experimental flow.

KEYWORDS
Spent Fuel Pool, Loss-of-Cooling, ASTEC, subcooled boiling, natural convection.

1 INTRODUCTION

Since the Fukushima Daiichi accident that occurred in Japan in 2011, nuclear safety in Spent Fuel Pools (SFP) has become a major issue. Among the main concerns are Loss-of-Cooling Accidents (LOCA) which can lead to the dewatering of the pool and, without any mitigation, to the fuel assemblies uncovery and degradation, with a large release of fission products to the environment. In order to improve our understanding of such accidents, the Organisation for Economic Cooperation and Development (OECD) launched several research activities and published in 2018 a Phenomena Identification Ranking Table (PIRT) [1] identifying the physical phenomena that are of high importance and high uncertainty. A recent

update of the progresses performed after this PIRT can be found in [2]. One of the identified priorities is to improve the capability of computer codes to simulate such accidents, and in particular the first phase of the accident, up to the fuel assemblies uncovery. Due to the turbulent nature of the natural convection-driven flow in the large open region above the fuel, such calculations are usually performed using Computational Fluid Dynamic (CFD) codes [3, 4, 5]. However, such calculations are very expensive, in particular when it comes to two-phase flows. Therefore, studies are also performed with 1D thermal-hydraulic system codes [6, 7] which provide much faster but less accurate results, due to the rough nodalizations and approximations applied in these codes.
Recent works have also tested the ASTEC severe accident code in a 2D application to model the water evaporation of a small container [8], stressing the difficulty to use these codes to model such turbulent flow in open regions.
In addition, recent simulations performed with severe accident codes like ASTEC or MELCOR in the MUSA project [9] also underlined difficulties in modelling the fuel assembly uncovery phase: in such stratified flows with a very thin two-phase region due to the low decay heat, periodic increases of the evaporation mass flow rate were observed, in relation with the nodalization, which led to periodic fuel cooling, delaying in some cases the fission products release.
Beyond these current difficulties, one of the main limitations of these simulation tools for SFP applications comes from the lack of relevant validation data: these codes are in general applied in conditions corresponding to reactor transients, with high pressure and high heat fluxes, for which the codes are well validated. In contrast, SFP transients occur close to the atmospheric pressure with very low decay heat, so that the validation of these tools to this low pressure and heat flux range is of crucial importance.
Therefore, to extend the validation database of thermal-hydraulic codes and to improve the understanding of phenomena involved in SFP accidents prior to the severe accident phase, the DENOPI project was launched in 2013 by IRSN. Funded by the French Government, the project consists in experimental work organized in three axes corresponding to different scales and consecutive phases of the accident [10]:

- large-scale study of SFP dewatering before fuel uncover (MIDI device);
- mid-scale observation of assembly uncovery before fuel degradation (ASPIC device);
- small-scale analysis of fuel cladding oxidation in SFP-LOCA.

The current paper is focused on the first axis and makes use of data recently obtained in the MIDI mock-up located at Cadarache (France). First, the MIDI experimental device is quickly described, together with the series of tests and main results. Then, calculations using the severe accident code ASTEC are presented, for different loading patterns and power levels. The influence of several subcooled boiling models from the literature is also presented. The objective of this work is two-fold: to improve the modelling and results of current version of ASTEC for SFP applications, and to identify the limitations and needs for further experimental data and models, with the idea to apply ASTEC to more generic open regions applications like immersed passive heat removal systems of Small Modular Reactors.

2 MIDI EXPERIMENTAL DEVICE

2.1 Description of the MIDI mock-up

The MIDI mock-up consists in a large rectangular basin of water representing a typical French PWR SFP, with a 1/36 ratio for the free surface and 1/3 ratio for pool height. A scheme of the MIDI device is represented in Figure 1 and the main characteristics of the installation are indicated in Table I. The basin is heated by 21 heating elements located at the bottom of the device, representing 21 cells of a storage rack, each element being composed of a 3x3 electrically heated rod bundle. The 21 cells are separated by solid walls representing the racks, so that horizontal flows between cells are not possible in the heated region. Further details of the facility can be found in [10]. One key feature of MIDI is the possibility to modulate the heating power of each cell individually, simulating different arrangements of hot and cold assemblies in a SFP. The

four loading patterns already tested are indicated in Figure 2. Above the pool, a ventilation hood extracts the steam outside the building.

MIDI is equipped with a large number of sensors to characterize the flows in the racks and in the pool. Temperatures are measured at different elevations of the pool (with uncertainties below 1 degree), above hot and cold assemblies and at the inlet and outlet of the cells. Mass flow rates are measured in each heated cell using vane wheel flow sensors (with an accuracy of 7.5% and a sensitivity limit of 0.5 kg/s) while the water level is recorded using a pressure gauge and a guided level–radar probe. The flow in the pool can be visualized and recorded thanks to cameras looking through dedicated optical windows at several elevations of the tank. The atmosphere of the pool, maintained at 1 bar, is also monitored: gas temperature, total pressure and relative humidity above the free surface are measured.

The current MIDI test matrix is built on varying the following parameters:

- Overall heating power up to 300 kW (with a local maximum power of 50 kW per cell);
- Loading pattern as indicated in Figure 2;
- Initial water level: 4 m or 2 m.

Each test follows a 3-phases protocol: basin fill-up to the required level, heat up of the pool to 50°C by the heating elements with a forced convection, stop of the forced convection and start of the experimental test by application of the loading pattern. Tests are stopped when the remaining collapsed level reaches 50 cm above the top of the racks.

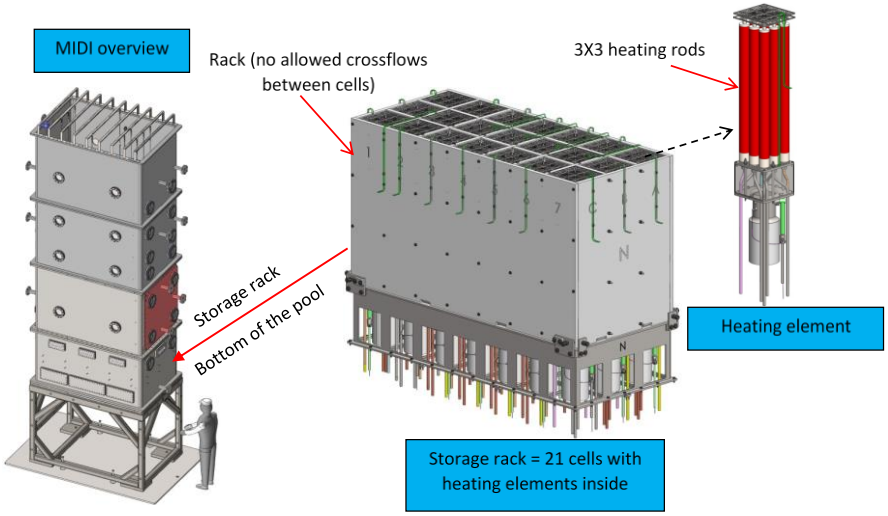

Figure 1: MIDI facility

Table I: Main parameters of the MIDI facility

Parameters	MIDI facility
Maximum water level (m)	4.0
Bundle active length (m)	0.7
Basin width (m)	1.35
Basin length (m)	2.10
Overall rack flow section (m^2)	0.65
Free surface area (m^2)	2.835
Bundle width (m)	0.225
Bundle porosity (-)	0.61
Number of cells (-)	21 (7 X3)
Power range (kW)	[50;300]
Max. power per bundle (kW)	50
Volumetric power (kW/m^3)	[4.2;25.1]

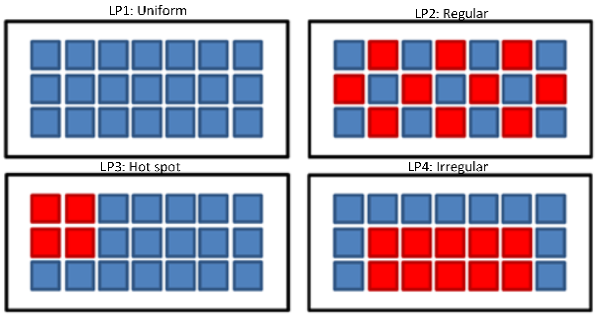

Figure 2: Loading patterns applied in MIDI tests.

2.2 Main Results of MIDI Experiments

The first MIDI campaign included nine different tests, of which 5 have been run twice, successfully checking the repeatability of the tests. Only the main conclusions of the tests are reported in this section, while time evolutions of temperature and mass flow rate in the cells are provided in the next section, together with ASTEC results. The tests have put in evidence a phenomenology consisting in three consecutive phases corresponding to three vaporization modes.

At first, while the temperature at the pool surface is below saturation, vaporization is driven by evaporation at the free surface. Then, as soon as the pool temperature reaches the local saturation temperature, flashing of uprising overheated water occurs. During this phase, the water temperature at the rack outlet is significantly lower than the saturation temperature at the top of the racks, due to the hydrostatic pressure above the racks, preventing water boiling in this region. At this stage, local boiling may appear on the heated elements, but bubbles quickly recondensate when water is mixed with cooler liquid above the racks. When the water level approaches 1m above the top of the racks, the local saturation temperature has decreased down to the temperature at the outlet of the cells, so that the boiling phase starts, with a continuous bubble plume from the top of the racks to the free surface.

It was observed that the effect of the loading pattern was only significative in the vicinity of the cells or inside the racks. With the “Hot spot” pattern, the presence of a significantly hotter plume above the heating zone was reported, promoting the formation of vapor bubbles by flashing in this zone. For other patterns, the temperature in the pool is homogeneous except at the outlet of cells with power higher than 4 kW.

3 ASTEC MODELLING OF MIDI TESTS

3.1 Main Characteristics of ASTEC V3.1.1 Code

The severe accident integral code ASTEC [11, 12] developed by IRSN aims at simulating an entire severe accident sequence in nuclear facilities, from the initiating event up to the release of radioactive elements in the atmosphere. Compared to the last versions of the V2 series, the current V3 series of ASTEC covers additional applications like accidents in fuel reprocessing facilities, while previous applications related to water-cooled reactors remain globally unchanged. The software is organized in modules in charge of different regions and physics of the represented nuclear facility. In this work, the only ASTEC relevant modules are ICARE, in charge of heat transfers and degradation in a reactor core or SFP, and CESAR, which deals with the thermal-hydraulics in the core and circuits. The CESAR module [13] is a two-phase 6 equations system code using a 2D description of the vessel (or SFP pool) and a 1D meshing of circuits in a finite volume approach. It is implicitly coupled with the ICARE module to compute the heat transfers from the vessel structures to the fluid.

3.2 Representation of MIDI with ASTEC

The geometry of the ICARE module is based on imbricated axisymmetric objects, like cylinders in pressurized water reactors, but also squared objects like canisters in boiling water reactors or SFP racks. This last feature is used in the current work to represent the MIDI facility: the rectangular basin is represented by a squared structure with real fluid section (thus with deviation on the wet perimeter), containing two squared racks representing the set of grouped hot and cold racks, and a bypass channel. For each test, the hot rack and the cold rack contain the number of cylindric heating elements according to Table I, and their dimensions and surface are defined accordingly. This approach ensures a correct representation of the fluid section and porosities in hot and cold cells as well as in the bypass surrounding the racks, at the price of a small approximation on the area of the vertical surfaces delimiting the racks. The four loading patterns indicated in Figure 2 are thus simulated by the three configurations indicated in Figure 3 (as the ASTEC representation of two squares in a larger square could not be drawn in a satisfactory manner, the squares have been replaced by rectangles in the figure). It must be noticed that the loading patterns LP2 and LP4 are represented by the same ASTEC geometry since hot and cold racks are put all together.

The ASTEC axial nodalization (see Figure 3) is made of 2 meshes below the racks, 4 meshes inside the racks, and 9 meshes above. All elements of the pool (water and structures) are initiated at 50°C and a boundary condition imposes the atmospheric pressure at the top of the pool. Thermal losses along the basin are represented by a constant external temperature of 25°C associated to a heat exchange coefficient assessed from the energy balance of each test (average value 10 W/m^2/K).

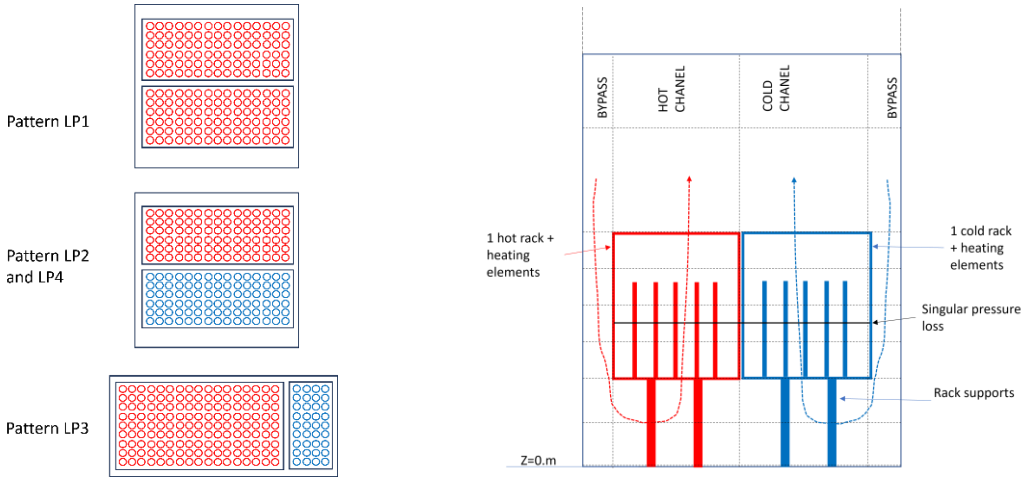

Figure 3: Representation of loading patterns in ASTEC (number of rods and cells geometry are not respected: cells are always squared in ASTEC) and scheme of the ASTEC meshing (upper basin part is not shown).

Table II: List of MIDI tests computed with ASTEC

Tests	Loading pattern (see Figure 2)	Overall heating power	Number of hot cells / Power in hot cells	Number of cold cells / Power in cold cells	Initial pool level
1_1	LP1	90.1 kW	21 / 4.3 kW	0 / 0 kW	4 m
2_1	LP2	92.2 kW	10 / 8.4 kW	11 / 0.7 kW	4 m
5_1	LP2	299.5 kW	10 / 27.3 kW	11 / 2.5 kW	4 m
7	LP2	300. kW	10 / 27.3 kW	11 / 2.5 kW	2 m
8	LP3	218.7 kW	4 / 50.0 kW	17 / 1.1 kW	4 m
9_0	LP3	55.0 kW	4 / 11.4 kW	17 / 0.6 kW	4 m

Since this simple geometry cannot take into account the complexity of the real geometry of the cells and the real fluid flowpath, the pressure losses along the cells are underestimated and must be corrected as they play a crucial role in such natural circulation flows. Indeed, mass flow rates obtained in test 1_1 without any additional pressure loss are too high by nearly a factor of 2. The calibration of the pressure loss is done once and for all using the test 1_1 where a uniform loading pattern was applied: a singular pressure loss is introduced in the cells, at mid-height of the heating structures, and the value of its coefficient k is adjusted to reproduce the measured mass flow rate obtained in the plateau of the test (see Figure 4). The obtained value $k=32$ has then been conserved for all other simulated tests.

3.3 Results of ASTEC V3.1.1 with Uniform Pattern

Results obtained with ASTEC V3.1.1 for test 1_1 after the calibration of the singular pressure drop are indicated in Figure 4. The evolution of the water inventory is well reproduced, indicating a correct energy balance and a good calibration of thermal losses which represent around 20% of the injected power.

The experimental outlet cell temperatures and mass flow rates have been averaged over the 21 cells, and the grey shaded area around the corresponding black curves represent the experimental standard deviation over the 21 cells. The initial temperature rise in the cell outlet is too fast in the ASTEC calculation, reaching 100°C in 8.7 h, to be compared with 11.9 h in the test. The mass flow rate evolution is also overestimated by ASTEC during this evaporation phase (while the pool stays subcooled, so up to 11.9 h). It is reminded that the mass flow rate during the plateau (from 11.9 h to 50 h) is fitted with ASTEC thanks to the calibration of the singular pressure drop. From 50 h, ASTEC predicts a strong increase of the mass flow rate due to the start of a boiling phase in the pool with the reduced hydrostatic pressure. This behaviour, not detected in the experiment, reveals the deficiency of the subcooled boiling model of ASTEC V3.1.1 applied to this configuration. The responsibility of the subcooled boiling model is checked by running ASTEC without any subcooled boiling model: in this case (blue lines in Figure 4), the final mass flow rate excursion is not predicted. This crucial point is studied in more details hereafter.

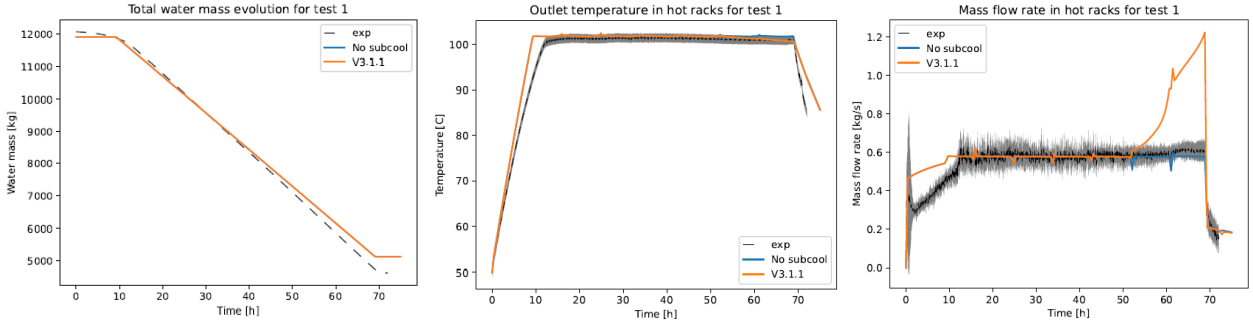

Figure 4: Evolution of pool water mass, temperature and mass flow rate, at the cell outlet in test 1. Grey shaded regions represent the uncertainties of experimental mass flow rate and temperature.

3.4 Introduction of Additional Subcooled Boiling Models in ASTEC

The modelling of subcooled boiling has been an intensive topic of research during the last decades. A review of such models is out of the scope of this paper but the reader can refer to [14, 15] for a short presentation of the topic. Most current models are based on the flux partitioning approach introduced by Kurul and Podowski [16, 17]. In this approach, the wall to fluid heat flux is partitioned between single-phase convection with liquid, quenching, and evaporation. The general expression of the evaporation term is:

$$Q_E = L_{LG}\,\rho_G\,\frac{\pi}{6}\,d_W^3 f N$$

where L_{LG} is the latent heat, ρ_G is the gas density, d_W is the bubble size at detachment, f is the bubble detachment frequency, and N is the nucleation site density. The last three parameters can be obtained from correlations established from dedicated experiments in specific conditions: pressure and heat flux range, pool boiling, forced convection, micro-channels…
The introduction of such correlations in CFD [18] or other thermal-hydraulic codes [19] has been reported to significantly improve the code predictions, in particular at low void fraction regimes. However, many of these correlations were established in conditions (pressure, subcooling, heat flux) close to in-reactor ones, whereas few studies have been performed in low pressure [20] and low heat flux conditions met in SFP.

In order to investigate the impact of such models on ASTEC modelling of MIDI tests, some recent or widely used subcooled boiling models adapted to pool boiling configurations have been introduced in ASTEC. Several ASTEC runs have been performed using models indicated in Table III, in addition to the previous cases presented in section 3.3.

Table III: Description of subcooled boiling models tested in ASTEC simulations of MIDI tests

Model name in ASTEC	**Origin of the model**	**Correlations used in Kurul and Podowski model**		
		d_W=bubbles size at detachment	**f = bubbles detachment frequency**	**N=nucleation site density**
No subcool	No subcooled boiling model: bubbles cannot appear if water is subcooled.	Not applicable		
V3.1.1	Model similar to Saha-Zuber [21] but fitted to KIT experimental data. Valid at P>2 bar.	Not applicable		
Lahey	Lahey [22] model with liquid enthalpy at bubble detachment from [21]. Used in TRACE V5 code [23].	Not applicable		
Unal-Cole	Kurul and Podowski [17]	[24]	[26]	[28]
Unal-BH	Kurul and Podowski [17]	[24]	[27]	[28]
TK-Cole	Kurul and Podowski [17]	[25]	[26]	[28]
TK-BH	Kurul and Podowski [17]	[25]	[27]	[28]

The results obtained on MIDI test 1_1 with each of these models introduced in ASTEC are presented in Figure 5 (water mass and temperatures at cell outlet are not displayed since all models lead to the results of Figure 4). It appears that the current V3.1.1 model leads to the largest deviation of mass flow rate, while the Lahey model seems to predict no subcooled boiling in this case. Other models based on Kurul and Podowski approach give intermediate results, with best predictions (among this family of models) for cases referred as “Unal-BH” and “TK-BH” which both use the bubbles detachment frequency from [27]. This better agreement could be expected since the Cole correlation [26] is simpler and depends only on gas and liquid densities and bubble detachment size, whereas the more recent correlation from Brooks and Hibiki [27] is based on 4 dimensionless parameters fitted with a large validation database.

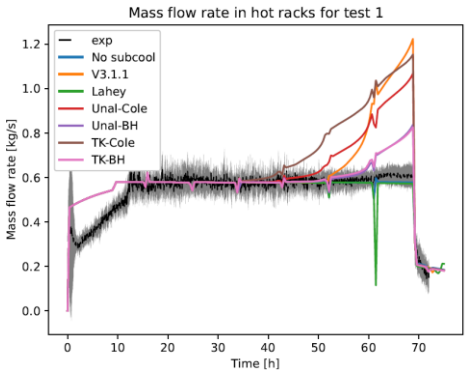

Figure 5: Comparison of several subcooled boiling models in ASTEC simulation of MIDI test 1_1.

3.5 Results with Different Patterns

The same process is now applied to other MIDI tests listed in Table II, investigating the influence of power levels, loading patterns and initial water level on the phenomenology. In all cases, the water level matches the experimental one and is not shown here. For most MIDI tests, the temperature at the cell outlet computed by ASTEC has the same behaviour as in Figure 4 which is model-independent. The exception is the test 8 which is the only test where the maximum power has been applied in hot cells: in this case, different levels of water subcooling can be observed in Figure 6 at the end of the heating phase (3 h). As expected, the calculation without any subcooled boiling model leads to the highest water temperature, corresponding to the saturation temperature at 3.2m below the water surface, i.e. 107°C. Consistently with the too strong subcooled boiling reported in section 3.4, the ASTEC V3.1.1 model computes subcooled boiling at too low temperatures, more than 2 degrees below the experimental value. Other models predict outlet temperatures close to experimental ones and within the measurement accuracy.

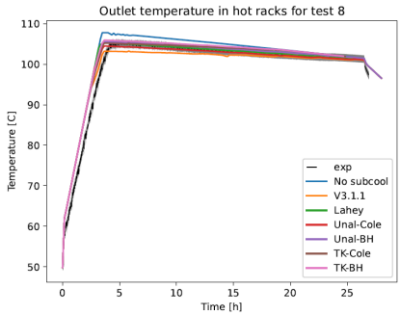

Figure 6: Evolution of temperature at the hot cell outlet in test 8.

Mass flow rates in hot and cold cells obtained for each test and model are indicated in Figure 7. At first look, ASTEC is able to capture the increase of the mass flow rate in hot cells with increasing power. It can also be remarked that the agreement with experimental results increase with the power level in hot cells: best and worst results are obtained with tests 8 and 9_0 respectively, corresponding to the highest power in hot cells and lowest overall power. This can be explained by the thermal influence of hot cells on neighboured cold ones in the experiment, while there is not direct heat exchange between hot or cold cells in ASTEC calculations. From this point of view, test 8 is best reproduced thanks to the limited influence between hot and cold cells due to the loading pattern. This thermal influence, not represented in ASTEC, also explains the fact that hot cell flows are always overestimated by ASTEC while cold flows are always underestimated (except in test 2 where the measured cold mass flow rate is below the 0.5kg/s sensitivity of the sensor).
Looking at the different subcooled boiling models, it appears from hot cell flows evolution that best overall results are obtained with Lahey and TK-BH models. More precisely, the Lahey model looks very well

adapted to low heat fluxes (tests 2_1 and 9_0), while the TK-BH model gives better predictions at higher heat flux (tests 5_1,7 and 8). Again, this must be related with the range of parameters that were considered when building these correlations. In particular, it has been identified that the Jakob number reached in test 8 (highest heat flux of 50 kW/m^2) was close to 1.0x10^{-3}, which is an order of magnitude smaller than the lower bound of the Brooks and Hibiki [27] correlation for bubble detachment frequency. Other tests with lower heat flux have even lower Jakob number, hence a weaker agreement.

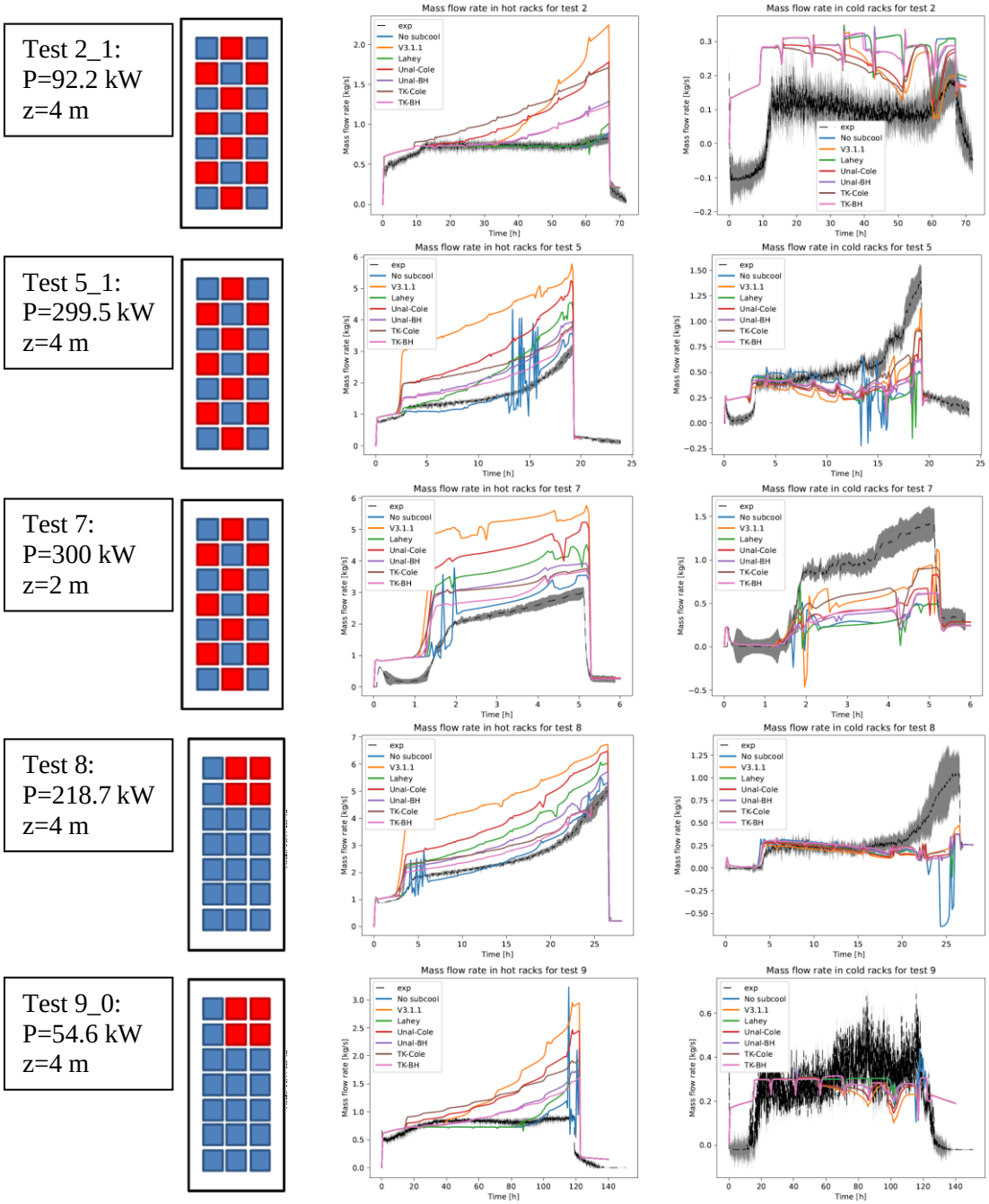

Figure 7: Mass flow rates in hot (left) and cold (right) cells for 5 MIDI tests.

3.6 Alternative ASTEC Modelling using Weighted Channels

In order to provide ASTEC users with modelling best-practices, an alternative modelling of the MIDI tests has been tested. Instead of grouping all together hot racks and cold racks in two large racks, a single hot rack and a single cold rack are represented, with their real geometry, but with a weight corresponding to the number of hot and cold racks of each test. Actually, this approach looks more natural than the previous one but was not yet validated against dewatering tests, by lack of experimental data. Simulations of same MIDI tests, with same subcooling models, have produced very similar results as the ones exposed in previous section, with similar CPU time, thus validating that both approaches were equivalent. As an illustration, hot cells mass flow rate from test 8 are indicated for the previous grouped (left) and weighted approach (right).

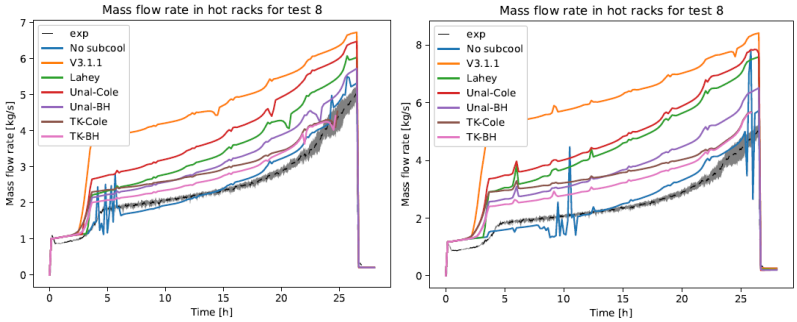

Figure 8: Hot cells mass flow rate from test 8 for the grouped (left) and weighted approach (right).

3.7 Numerical aspects

Figure 7 and Figure 8 indicate that best results are obtained without any subcooling models. However, such simulations are not satisfactory for two reasons: first because of numerical issues related to the violent water vaporization when saturation is reached, leading to very small time steps, and second to associated possible reverse flows (not observed experimentally) as for instance on cold racks mass flow rate on test 8.

In addition to models improvement, one of the objective of this work was to study some numerical issues previously reported during SFP dewatering [9]: due to the different wall to fluid heat flux models applied when a mesh is nearly full of water or nearly empty, some discontinuities appear when the water level switches from an axial level to a lower one. During fuel assemblies uncovery, things can get worse since these discontinuities can have a strong impact on the flow (sudden vaporization), and hence on the fuel cladding temperature which suddenly drops. Such behaviour can also be observed here on mass flow rate evolutions, for instance in case V3.1.1 of Figure 8 with the weighted approach (equidistant small peaks) and on-going activities are focused on the reduction of these features, thanks to MIDI validation data. This topic will be also further studied in ASPIC tests (assembly dewatering, [10]) modelling that will start in 2024.

4 CONCLUSION AND PERSPECTIVES

Simulations of MIDI tests have been performed with ASTEC to assess the capability of the code to predict natural circulation flows occurring during a SFP dewatering transient. It was shown that current V3.1.1 model, validated for high pressures, predicts a too intense subcooled boiling in the racks which leads to mass flow rates much higher than in the experiment. Several subcooled boiling models from the literature have been tested to improve the results. Best agreement was found with models referred as Lahey and TK-BH for low and high heat flux respectively. Additional investigations are ongoing to further improve the results, like introducing a model of temperature for the onset of nucleate boiling. Further works are also needed to correct numerical issues related to the axial nodalization.

This work confirms that such system codes can be used for first order calculations of natural circulation in open regions, provided that singular pressure losses in the heated region can be characterized.

However, it must be stressed that the validity of the flows computed by ASTEC above the racks is still to be assessed: the uniform temperature field observed in the experiment was reproduced by ASTEC, indicating an efficient mixture of the fluid, but this is not sufficient to really assess the predicted flow which may be too intense. In the near future, ASTEC calculations will be compared to results of the SATURNE-CFD code in order to check the validity of the flow computed by ASTEC in the pool region.
It is also planned to model with ASTEC the ASPIC experimental tests, related to the second axis of the DENOPI project and dedicated to the uncovery of a SFP assembly in its storage cell with or without spray to check the coolability of an assembly. Then, additional tests will also be run in MIDI and ASPIC within the new project POLCA launched by OECD in 2024 to consolidate these validation tasks. Benchmark activities involving different thermal-hydraulics codes will also be conducted. Beyond SFP activities, these works also provide relevant data for the understanding of large natural convection loops that are expected in immersed passive heat removal systems of Small Modular Reactors that ASTEC should address.

5 ACKNOWLEDGMENTS

The authors wish to thank S. Morin, J. Martin, G. Brillant and P. Ruyer for fruitful discussions in preparing this work. The present work has been performed using part of the experimental results of DENOPI research program on SFP-LOCA ended in 2022. The French Government and the National Research Agency are gratefully acknowledged for their interest and financial support (contract reference: ANR 11 – RSNR 006).

6 REFERENCES

1. OECD NEA, "*Phenomena Identification and Ranking Table. R&D Priorities for Loss-Of-Cooling and Loss-Of-Coolant Accident in Spent Nuclear Fuel Pools*", Report NEA n°7443 (2018).
2. J. Martin, N. Trégourès, "OECD/NEA R&D priorities for loss-of-cooling and loss-of-coolant accidents in Spent-Fuel-Pools", *Nuclear Engineering and Design*, **410** 112380, ISSN 0029-5493 (2023), https://doi.org/10.1016/j.nucengdes.2023.112380.
3. S.R. Chen, W.C. Lin, Y.M. Ferng, C.C. Chieng, B.S. Pei, "CFD simulating the transient thermal–hydraulic characteristics in a 17×17 bundle for a spent fuel pool under the loss of external cooling system accident", *Annals of Nuclear Energy*, **73**, pp. 241-249, ISSN 0306-4549 (2014), https://doi.org/10.1016/j.anucene.2014.06.054.
4. Ronald Oertel, T. Hanisch, E. Krepper, D. Lucas, F. Rüdiger, J. Fröhlich, "Two-scale CFD analysis of a spent fuel pool involving partially uncovered fuel storage racks", *Nuclear Engineering and Design*, **341**, pp. 432-450, ISSN 0029-5493 (2019), https://doi.org/10.1016/j.nucengdes.2018.10.014.
5. T. Someya, H. Chitose, S. Watanabe, Y. Nemoto, Y. Kaji, "Study on Loss-of-Cooling and Loss-of-Coolant Accidents in Spent Fuel Pool (8)Safety Margin of Spent Fuel in Large LOCA Event by the Simple Assessment Method", *The Proceedings of the International Conference on Nuclear Engineering (ICONE)*, Vol.2019.27, pp.1153, (2019), https://doi.org/10.1299/jsmeicone.2019.27.1153.
6. A. Kaliatka, A. Graževičius, T. Kaliatka, "Analysis of loss of cooling accidents in the spent fuel pools using system thermal hydraulics and computational fluid dynamic codes", *Nuclear Engineering and Design*, **412** 112447,ISSN 0029-5493 (2023), https://doi.org/10.1016/j.nucengdes.2023.112447.
7. S. Carlos, F. Sanchez-Saez, S. Martorell, "Use of TRACE best estimate code to analyze spent fuel storage pools safety", *Progress in Nuclear Energy*, **77**, pp. 224-238, ISSN 0149-1970 (2014), https://doi.org/10.1016/j.pnucene.2014.07.008.
8. J-A Zambaux, L. Laborde and P. Ruyer, "Calculating steam-water flows at large non-condensible gas concentration with severe accident code ASTEC V2.2", *Proceedings of the 19th International Topical Meeting on Nuclear Reactor Thermal Hydraulics (NURETH-19)*, Brussels, Belgium (2022).
9. O. Coindreau, L.E. Herranz, R. Bocanegra, S. Ederli, P. Maccari, F. Mascari, O. Cherednichenko, A. Iskra, P. Groudev, P. Vryashkova, P. Petrova, A. Kaliatka, V. Vileiniškis, M. Malicki, T. Lind, O. Kotsuba, I. Ivanov, F. Giannetti, M. D'Onorio, P. Ou, L. Feiye, P. Piluso, Y. Pontillon, M. Nudi,

"Uncertainty quantification for a severe accident sequence in a SFP in the frame of the H-2020 project MUSA: First outcomes", *Annals of Nuclear Energy*, **188** 109796 (2023).
10. B. Migot, G. Brillant, J. Martin and S. Morin, "DENOPI project devoted to spent fuel pool accidents: overview on the thermal hydraulics experimental facilities", *Proceedings of the 19th International Topical Meeting on Nuclear Reactor Thermal Hydraulics (NURETH-19)*, Brussels, Belgium (2022).
11. L. Chailan, L. Bosland, L. Carénini, J. Chambarel, P. Chatelard, F. Cousin, P. Drai, G. Kioseyian, S. Phoudiah, V. Topin, "Overview of ASTEC integral code status and perspectives", *Proceedings of the 9th European Review Meeting on Severe Accident Research (ERMSAR-2019)*, Prague, Czech R., (2019).
12. P. Chatelard and L. Laborde, "ASTEC V2.2 code validation: Illustrative results and main outcomes", *Nuclear Engineering and Design*, **413** 112547, ISSN 0029-5493 (2023), https://doi.org/10.1016/j.nucengdes.2023.112547.
13. T. Glantz, T. Taurines, O. De Luze, S. Belon, G. Guillard, F. Jacq, "DRACCAR: A multi-physics code for computational analysis of multi-rod ballooning, coolability and fuel relocation during LOCA transients Part one: General modeling description", *Nuclear Engineering and Design*, **339**, pp. 269-285, ISSN 0029-5493 (2018), https://doi.org/10.1016/j.nucengdes.2018.06.022.
14. A. Rabhi, "*Numerical Modelling of Subcooled Nucleate Boiling for Thermal Management Solutions Using OpenFOAM*", Licentiate Thesis, Mälardalen University, School of Business, Society and Engineering, Future Energy Center (2021).
15. H. Hoang, I. C. Chu, D. J. Euh, and C. H. Song, "On the Application of Wall Boiling Models to prediction of subcooled flow boiling using EAGLE code", *Proceedings of the 16th International Topical Meeting on Nuclear Reactor Thermal Hydraulics (NURETH-16)*, Chicago, USA (2015).
16. N. Kurul and Michael Z. Podowski. "Multidimensional effects in forced convection subcooled boiling." *International Heat Transfer Conference Digital Library*. Begel House Inc. (1990).
17. N. Kurul. "On the modeling of multidimensional effects in boiling channels.", *ANS. Proc. National Heat Transfer Con. Minneapolis*, Minnesota, USA (1991).
18. E. Krepper and R. Rzehak, "CFD for subcooled flow boiling: Simulation of DEBORA experiments", *Nuclear Engineering and Design,* **241** (9), pp. 3851-3866, ISSN 0029-5493 (2011). https://doi.org/10.1016/j.nucengdes.2011.07.003.
19. V. Kumar and R. K. Salko Jr, "Implementation of a new wall boiling model in CTF", *ANS Winter Meeting and Nuclear Technology Expo 2020*, Chicago, USA, Vol. 123, 1728-1731 (2020).
20. J.Y. Tu, G.H. Yeoh, "On numerical modelling of low-pressure subcooled boiling flows", *International Journal of Heat and Mass Transfer*, **45** (6), pp. 1197-1209, ISSN 0017-9310 (2002), https://doi.org/10.1016/S0017-9310(01)00230-7
21. P. Saha and N. Zuber, "Point of net vapor generation and void fraction in subcooled boiling", *Proceedings of the 5th International Heat Transfer Conference*, Tokyo, Japan, Vol. 4, 175-179 (1974).
22. R. T. Lahey, Jr., "A Mechanistic Subcooled Boiling Model", *Proceedings of the 6th International Heat Transfer Conference*, Toronto, Canada, Vol. 1, 293-297 (1978).
23. US NUCLEAR REGULATORY COMMISSION, "*TRACE V5.840 Theory Manual: Field Equations, Solution Methods, and Physical Models*", Tech. rep., US Nuclear Regulatory Commission (2013).
24. H.C. Unal, "Maximum bubble diameter, maximum bubble growth time and bubble growth rate", *Int. J. Heat Mass Transfer*, **19**, pp. 643-649 (1976).
25. V.I. Tolubinsky and D.M. Kostanchuk, "Vapour bubbles growth rate and heat transfer intensity at subcooled water boiling". *Proceedings of the 4th International Heat Transfer Conference*, Paris-Versailles, France, Vol. 23. (1970).
26. R. Cole, "A photographic study of pool boiling in the region of the critical heat flux". *AIChE Journal*, **6** (4), pp. 533–538 (1960).
27. C.S Brooks and T. Hibiki, "Wall nucleation modeling in subcooled boiling flow". *International Journal of Heat and Mass Transfer*, **86**, pp. 183–196 (2015).
28. M. Lemmert and J.M Chawla, "Influence of flow velocity on surface boiling heat transfer coefficient", *Heat Transfer in Boiling*, pp. 237–247, Academic Press and Hemisphere, New York and Washington DC (1977).

A REVIEW OF CORRELATIONS OF STAINLESS STEEL OXIDATION IN STEAM, AND MODELING THE REACTION WITH MELCOR

Tuomo Sevón
VTT Technical Research Centre of Finland
Kivimiehentie 3, Espoo, Finland
tuomo.sevon@vtt.fi

ABSTRACT

Metals oxidize in contact with steam in severe accident conditions. A lot of research has been conducted on the oxidation of zirconium, but less attention has been paid to the oxidation of stainless steel. However, it has been observed in many MELCOR simulations that steel oxidation can generate significant amounts of hydrogen. The steel oxidation correlation in the MELCOR code is from the year 1966.

Five sets of separate effect tests on stainless steel oxidation in steam above 900 °C were found in the literature. Each of the published oxidation correlations is based on a single set of experiments. In this work, a new correlation was developed by fitting the Arrhenius equation to 14 experiments from four different test facilities. The constants of the new correlation are $A = 4.3\times10^7$ kg_{steel}^2/m^4s and $B = 37\ 800$ K. These can be entered into MELCOR by changing the sensitivity coefficient 1002. The correlations were tested by modeling the separate effect tests and the Fukushima unit 1 accident with MELCOR.

None of the correlations is clearly better than the others. Generally, each correlation can reproduce well those experiments, based on which it has been developed. The MELCOR default correlation is conservative. It gives the highest oxidation rate among all the correlations, and it overestimates the oxidation in all tests, except the Bittel test, based on which it has been developed. The new correlation, developed in this study, can be considered as the best fit to all the published data, overestimating the oxidation in some experiments and underestimating it in others. In the Fukushima calculation, the new correlation gave 24 % less steel oxidation and 6 % less total in-vessel hydrogen generation than the default correlation. These are average values of seven calculations with each correlation, perturbed by small changes to see the effect of the numerical noise.

KEYWORDS
Stainless steel, oxidation, MELCOR

1. INTRODUCTION

Hydrogen is generated when hot metals oxidize in contact with steam during a severe accident in a light-water reactor. Oxidation of zirconium is much more important than oxidation of stainless steel. However, it has been observed in many MELCOR simulations that steel oxidation can generate significant amounts of hydrogen [1]. The steel oxidation correlation used by the MELCOR code is from the year 1966 [2]. The objective of this report is to review if the old correlation is still state-of-the-art, or if some better correlation is available.

Stainless steel consists mostly of iron, chromium and nickel. When hot stainless steel is in contact with steam, it oxidizes and forms hydrogen. At least the following four reactions can occur:

$$Fe + H_2O \rightarrow FeO + H_2$$
$$3Fe + 4H_2O \rightarrow Fe_3O_4 + 4H_2$$
$$2Fe + 3H_2O \rightarrow Fe_2O_3 + 3H_2$$
$$2Cr + 3H_2O \rightarrow Cr_2O_3 + 3H_2$$

MELCOR does not model Fe, Cr and Ni separately. Instead, the Core package of MELCOR has a material called *stainless steel*, which can oxidize to form *stainless steel oxide*. The same concerns the oxidation experiments found in the literature: they did not measure the oxidation reactions separately. Instead, they measured the weight gain of the steel sample, or the thickness of the metal oxidized, or the mass of hydrogen generated.

Chapter 2 of this paper presents a literature review of separate effect tests on stainless steel oxidation in severe accident conditions. Chapter 3 reviews existing correlations of the oxidation rate, and develops a new correlation by fitting to measurements from four test facilities. Chapter 4 tests the correlations by modeling oxidation experiments with MELCOR. Chapter 5 investigates the effect of the steel oxidation correlation in a full plant calculation of the Fukushima unit 1 accident. A preliminary version of this work was reported in the Finnish national SAFER2028 research program [3].

2. A LITERATURE REVIEW OF OXIDATION EXPERIMENTS

A literature search was performed to find experiments of oxidation kinetics of stainless steel in steam at temperatures above 900 °C. Five sets of separate effect tests at different test facilities were found (Table I). In all the tests, small steel samples of a few grams were kept in a furnace at a constant temperature, while steam was flowing through the furnace.

Table I. Steel oxidation tests found in the literature.

Name of first author	Year of publication	Institute	Steel type	Temperature range (°C)	Measured quantity	Ref.
Bittel	1969	General Electric	304L	1000–1375	Weight gain	[4]
Leistikow	1985	Kernforschungszentrum Karlsruhe	1.4970	600–1300	Weight gain	[5]
Ishida	1986	Japan Atomic Energy Research Institute	304	900–1350	Thickness of metal oxidized	[6]
Tang	2020	Karlsruhe Institute of Technology	348	1100–1300	Hydrogen generation	[7]
Avelar	2020	Universidade de São Paulo	348	1100–1350	Weight gain	[8]

The experiments employed four types of austenitic stainless steel. The chromium and nickel contents of the samples are collected in Table II. The compositions are very similar, except for the 1.4970 steel, used by Leistikow, which has significantly less chromium and more nickel. Chromium may protect the steel from oxidation at lower temperatures. The lower chromium content may be the reason why Leistikow measured higher oxidation rates at low temperatures than the other researchers.

Table II. Chromium and nickel contents of the steel samples in the oxidation experiments.

	Cr (%)	Ni (%)
Bittel 304L	18	10.95
Leistikow 1.4970	14.9	15
Ishida 304	18.57	9.68
Tang 348	18	7
Avelar 348	17.45	10.94

It might be possible to develop different oxidation models for different steel types. However, this could be impractical because the exact composition of the steel components in the reactor is often unknown, and there may be several different types of steel in the same reactor. In the following, the Leistikow experiments, and the correlation that they developed, are not considered because the steel composition and the measured oxidation rates differ so much from the other four experiments.

3. CORRELATIONS FOR STEEL OXIDATION

The oxidation rate is modeled with the Arrhenius equation:

$$\frac{dW^2}{dt} = A \exp\left(\frac{-B}{T}\right), \quad (1)$$

where t is time (s), T is the steel temperature (K), and A and B are experimentally determined constants. W is the cumulative oxidation per surface area, but its exact definition varies. In MELCOR, W is the mass of steel oxidized per unit surface area (kg_{steel}/m^2). In many correlations, W is the weight gain of the steel sample, i.e. the mass of oxygen participating in the reaction (kg_O/m^2), probably because it is easier to measure. Conversion between kg_{steel} and kg_O depends on the reaction product (FeO, Fe_3O_4, Fe_2O_3, Cr_2O_3, or their mixture). The exponent 2 in the equation means that the oxidation follows parabolic kinetics, i.e. the reaction slows down as an oxide layer develops on the surface.

The measured oxidation as a function time was digitized from figures published in [4], [6], [7] and [8], using WebPlotDigitizer. The measured quantity was the mass gain in most experiments, the thickness of metal oxidized in the Ishida experiments [6], and the hydrogen generation in the Tang experiments [7]. To be compatible with the MELCOR definition of W, the data was converted to the mass of metal oxidized, assuming that the reaction product is Fe_3O_4 and the stainless steel density is 7 930 kg/m^3.

In the parabolic model of equation (1), the cumulative oxidation is proportional to the square root of time. Therefore, the mass of metal oxidized was plotted as a function of the square root of time ($time^{0.5}$). An example of such a plot is in Fig. 1. A linear function was fitted to the data. Zero oxidation at time zero was used as one data point, but the line was not forced through the origin. For the Bittel test at 1200 °C, the correlation coefficient R is 0.995, which confirms that the oxidation followed parabolic kinetics very accurately. The slope of the line is 0.0242 $kg_{steel}/m^2s^{0.5}$. The oxidation rate constant (right side of equation (1)) is the second power of the slope, equaling 5.86×10^{-4} kg_{steel}^2/m^4s.

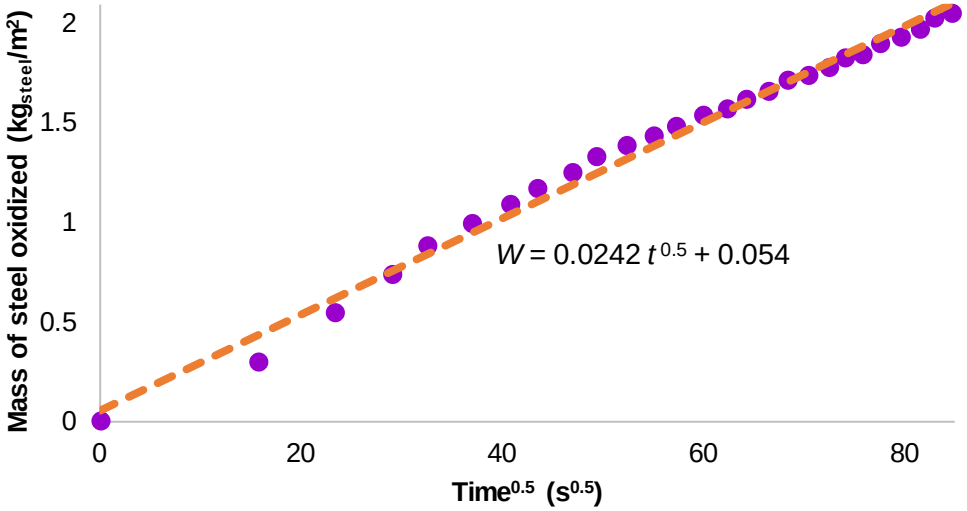

Figure 1. Fitting equation (1) to the data of Bittel [4] at 1200 °C.

The same fitting procedure was repeated with 16 oxidation experiments from [4], [6], [7] and [8]. The oxidation rate constants as a function of temperature are plotted in Fig. 2. The Ishida tests at 1200 and 1250 °C are outliers, so they were excluded from further analysis. The *A* and *B* constants of equation (1) were fitted to the remaining 14 points. The result, along with four other correlations from the literature, are plotted in Fig. 3. The numerical values of the constants are listed in Table III.

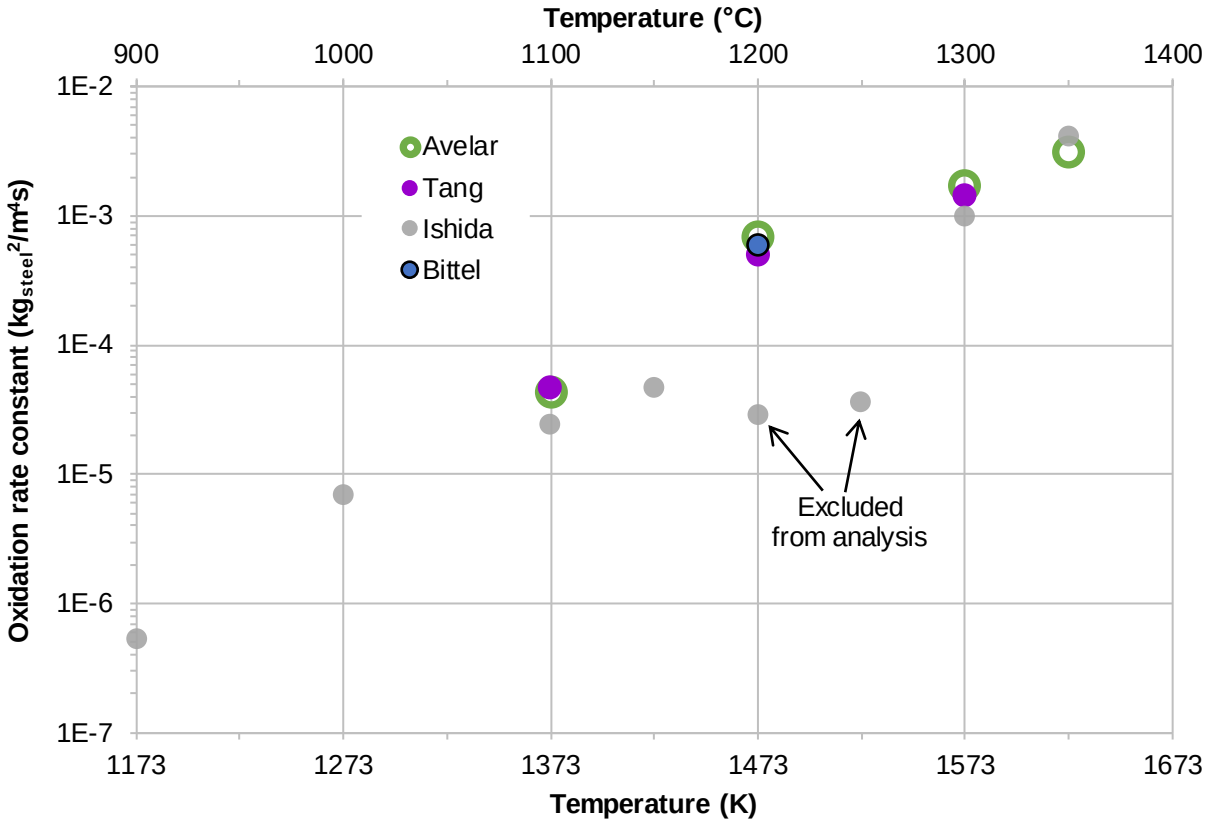

Figure 2. Oxidation rate constants, derived from 16 experiments.

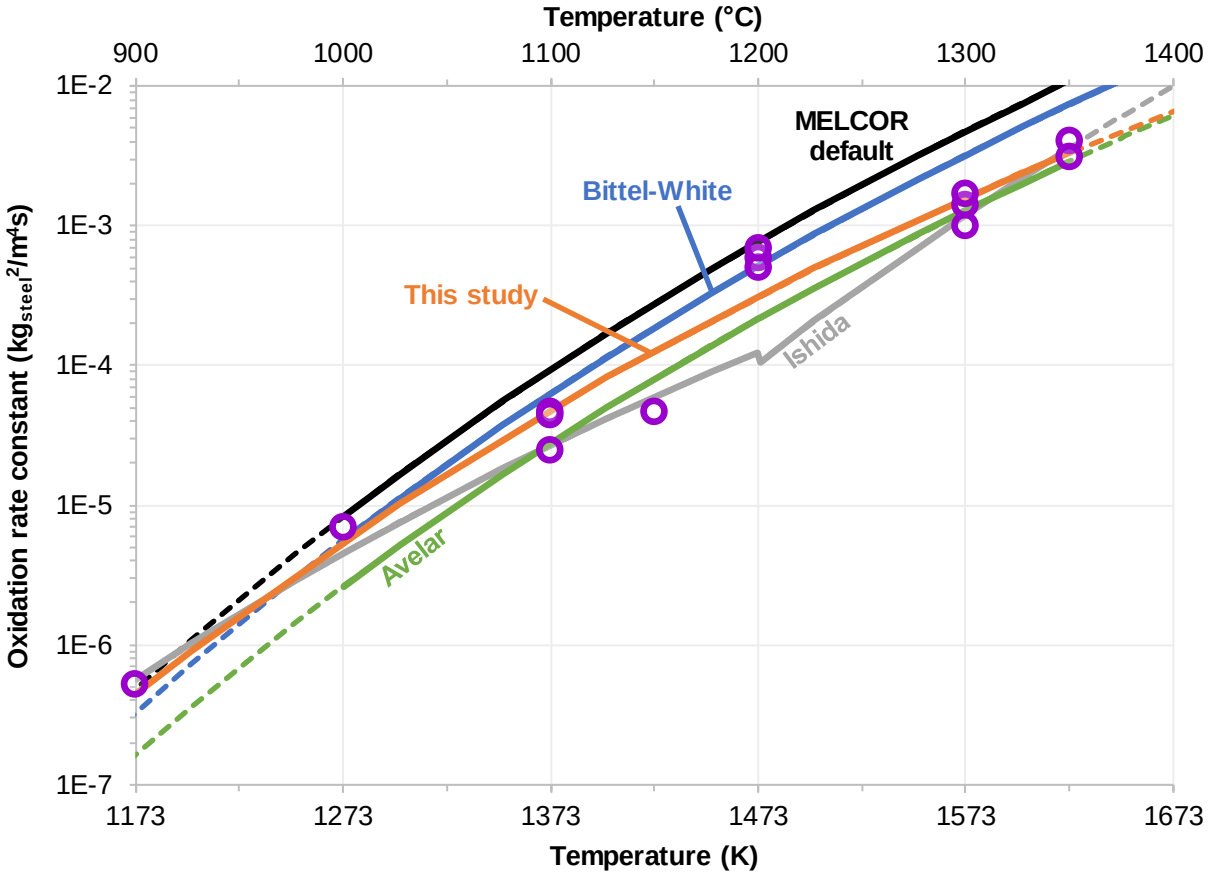

Figure 3. Oxidation rate constants derived from 14 experiments (purple circles), and five correlations. The validity range of each correlation is shown with the solid line, and the extrapolated part with the dashed line.

Table III. Constants of the oxidation correlations, equation (1).

Correlation	A (kg$_{steel}$^{2}/m^{4}s)	B (K)	Ref.
MELCOR default	2.42E9	42 400	[2]
Bittel-White	1.64E9	42 400 ± 1 200	[4]
Ishida, T = 900–1200 °C	1.80E5	31 070 ± 2 267	[6]
Ishida, T = 1200–1350 °C	4.59E12	56 460 ± 3 336	[6]
Avelar	3.32E8	41 338 ± 1 257	[8]
This study	4.30E7	37 800	

The MELCOR default correlation gives higher oxidation rate than the other correlations. It is based on the same experiments as the Bittel-White correlation, but the A constant is different because the original publication [4] uses the mass of oxygen, and apparently MELCOR developers have assumed some mixture of reaction products when converting from kg$_O$ to kg$_{steel}$. The A value of 1.64×10^9 kg$_{steel}^2$/m^{4}s corresponds to Fe_3O_4 as the reaction product. The value would be 2.92×10^9 for FeO, 1.3×10^9 for Fe_2O_3, and 1.13×10^9 for Cr_2O_3. In the current study, Fe_3O_4 (magnetite) was assumed because it gives an intermediate value for the A constant. Fe_3O_4 was observed in post-test examinations of all the oxidation tests.

4. MODELING OF OXIDATION EXPERIMENTS WITH MELCOR

In order to test the oxidation correlations, four of the five test facilities in Table I were modeled with MELCOR 2.2 revision 15254. The Leistikow facility was excluded because they used a substantially different steel type. Four of the five correlations in Table III were tested by changing the *A* and *B* constants with sensitivity coefficient 1002. The Ishida correlation cannot be entered into MELCOR without changing the source code because it is a piecewise-defined function. All the 14 experiments in Fig. 3 were calculated, and four representative examples of the results are shown in section 4.2.

4.1. Model Description

The nodalization of the MELCOR model is illustrated in Fig. 4. It consisted of five control volumes, connected with flow paths. The time-independent Steam source volume provided steam to the furnace. (In the Tang experiments, the gas source was 55 % steam and 45 % argon. The argon was needed as a reference gas to measure the hydrogen production with a mass spectrometer.) The flow path from Steam source to the Inlet volume was time-specified, with a constant flow velocity, corresponding to the flow rate in each experiment. The results were not sensitive to variations of the flow rate. The time-independent Steam sink volume kept the system at 1 bar pressure and received the exhaust steam and hydrogen.

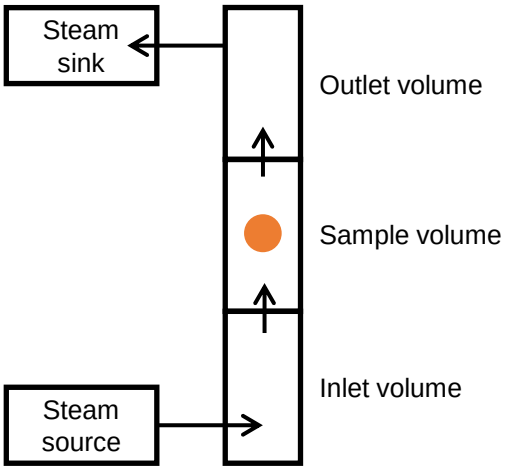

Figure 4. Nodalization of the MELCOR model.

In the Core package, the system was modeled with one radial ring and three axial levels. The three core cells were linked to the Inlet, Sample, and Outlet volumes, respectively. The sample was modeled as a supporting structure. The minimum component thickness was set to zero, ensuring that the structure does not collapse to particulate debris even if it oxidizes completely.

The temperature of the system was adjusted with boundary conditions. The Inlet volume corresponds to the lower plenum in the Core package. The outer surface of the lower head was interfaced with a time-independent control volume, containing steam at the specified temperature. The walls of the Sample and Outlet volumes were modeled as heat structures, and their outer surfaces were set to the constant temperature used in each test. The radiation heat transfer exchange factors in the Core package and the emissivities of the heat structures were set to unity. These settings ensured that the heat transfer between the sample and the walls was efficient, and the sample temperature was maintained at each experiment's specified value ±3 °C during the entire simulation.

4.2. Results

The weight gain in the Bittel test [4] at 1200 °C, compared with the four oxidation correlations, is plotted in Fig. 5 left. All the correlations underestimate the oxidation, but the MELCOR default correlation is very close to the measured weight gain. This is not surprising, since the default correlation was developed from the Bittel experiments. The Avelar correlation underestimates the oxidation by over 50 %. The new correlation, developed in this study, is closer to the measurements than Avelar. Bittel et al. [4] published the oxidation as a function of time only for one test, at 1200 °C, even though they performed tests at several temperatures.

The thickness of the metal oxidized in the Ishida test [6] at 1100 °C, compared with the four oxidation correlations, is plotted in Fig. 5 right. The thickness of the metal oxidized is not directly available as a MELCOR plot variable, so it was calculated from the mass of steel oxidized, using the stainless steel density 7 930 kg/m^3 and the sample surface area. The results are as expected from the correlation plot (Fig. 3): the best result is given by the Avelar correlation, which is closest to the Ishida correlation at 1100 °C.

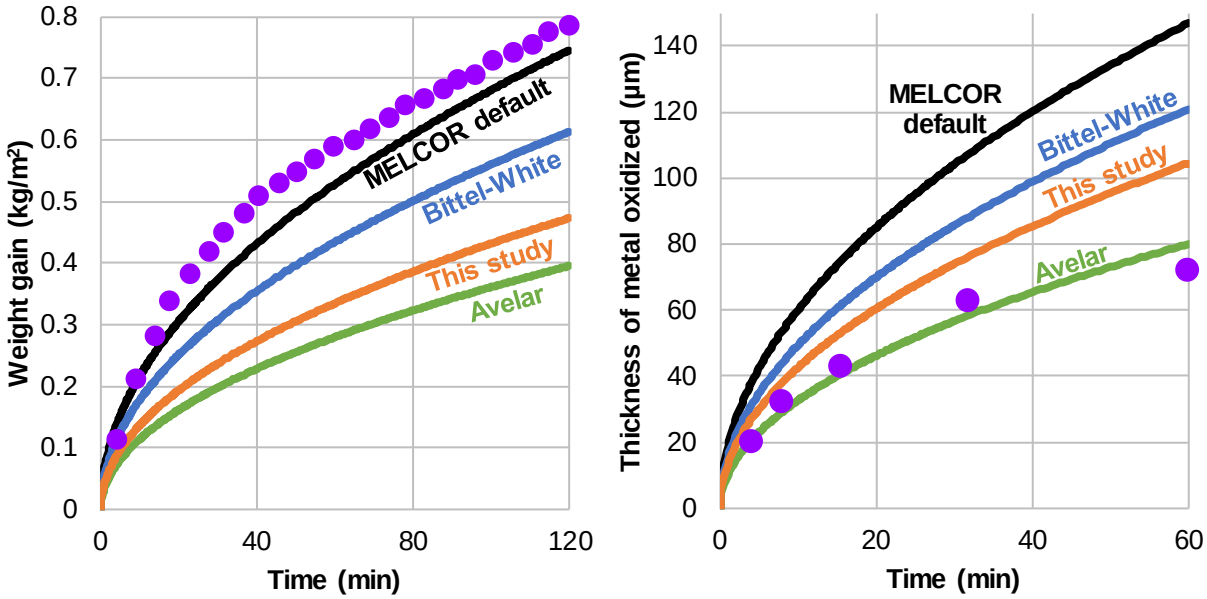

Figure 5. Left: Bittel experiment [4] at 1200 °C. Right: Ishida experiment [6] at 1100 °C. Measured data (purple circles), compared with MELCOR calculations using four different oxidation correlations.

The hydrogen production in the Tang test [7] at 1100 °C, compared with the four oxidation correlations, is plotted in Fig. 6 left. The calculated curves are in the same order as in the Ishida test at the same temperature (Fig. 5 right), but the test results are now closer to the Bittel-White correlation and the new correlation of this study.

The weight gain in the Avelar test [8] at 1300 °C, compared with the four oxidation correlations, is plotted in Fig. 6 right. The Avelar correlation gives good results of the experiments, based on which it was developed. The new correlation of this study is slightly above the Avelar correlation at 1300 °C. The MELCOR default and the Bittel-White correlations grossly overestimate the oxidation in this test.

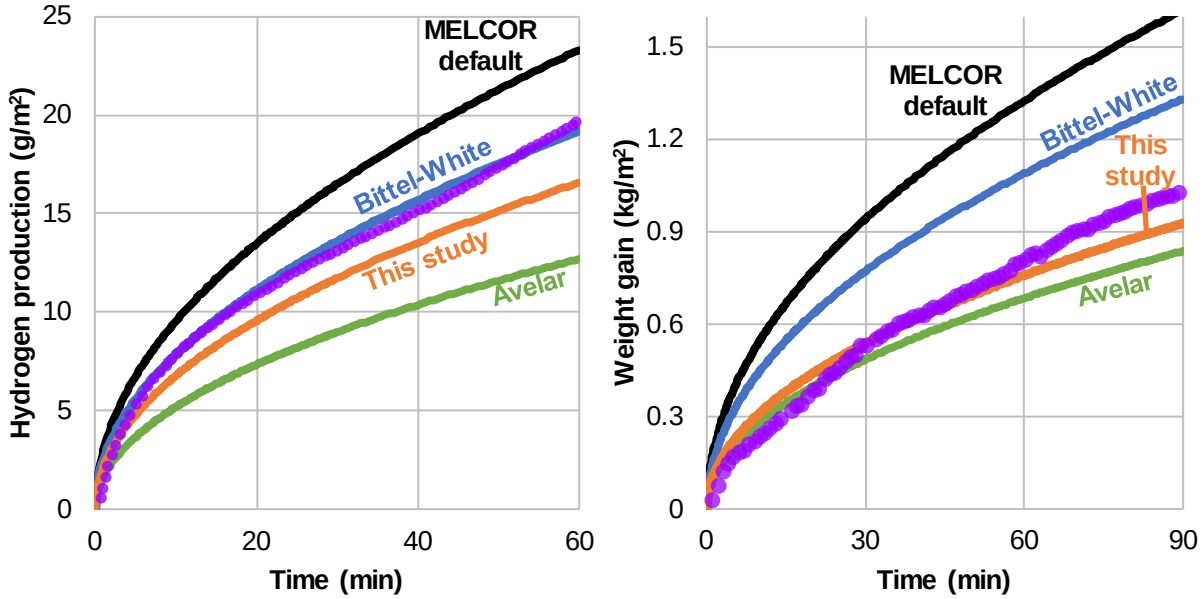

Figure 6. Left: Tang experiment [7] at 1100 °C. Right: Avelar experiment [8] at 1300 °C. Measured data (purple circles), compared with MELCOR calculations using four different oxidation correlations.

5. EFFECT OF THE STEEL OXIDATION CORRELATION IN A PLANT CALCULATION

The previous chapter showed that the different steel oxidation correlations give significantly different results when modeling separate effect oxidation tests. This is not necessarily the case in full-plant simulations. In order to test the significance of the steel oxidation correlation in a plant calculation, the Fukushima unit 1 accident was calculated with the four correlations. The plant model is described in [9].

Differences between two MELCOR calculations are often caused by "numerical noise" or "numerical sensitivity" [10], not by real physical effects. Very small changes to the model have significant impacts on the results when modeling core degradation. The scatter is caused by small differences in core component temperatures, causing different relocation timings, after which the calculations start to bifurcate. Numerical noise was not an issue when modeling the separate effect tests because the geometry of the samples did not change during the tests.

In order to discern real physical differences from numerical noise, small perturbations were added by varying the decay heat curve within ±0.1 %. This variation is so small that its effect on the results represents only noise, not any physical effect. Seven calculations with the small perturbations were performed with each of the four oxidation correlations.

The numerical noise is demonstrated in Fig. 7, which presents the in-vessel hydrogen generation from steel oxidation in the seven calculations with the MELCOR default oxidation correlation. The only difference between the models is the very small perturbation of the decay heat curve. The oxidation begins at the same time, but the results begin to diverge an hour later, when the core geometry begins to change.

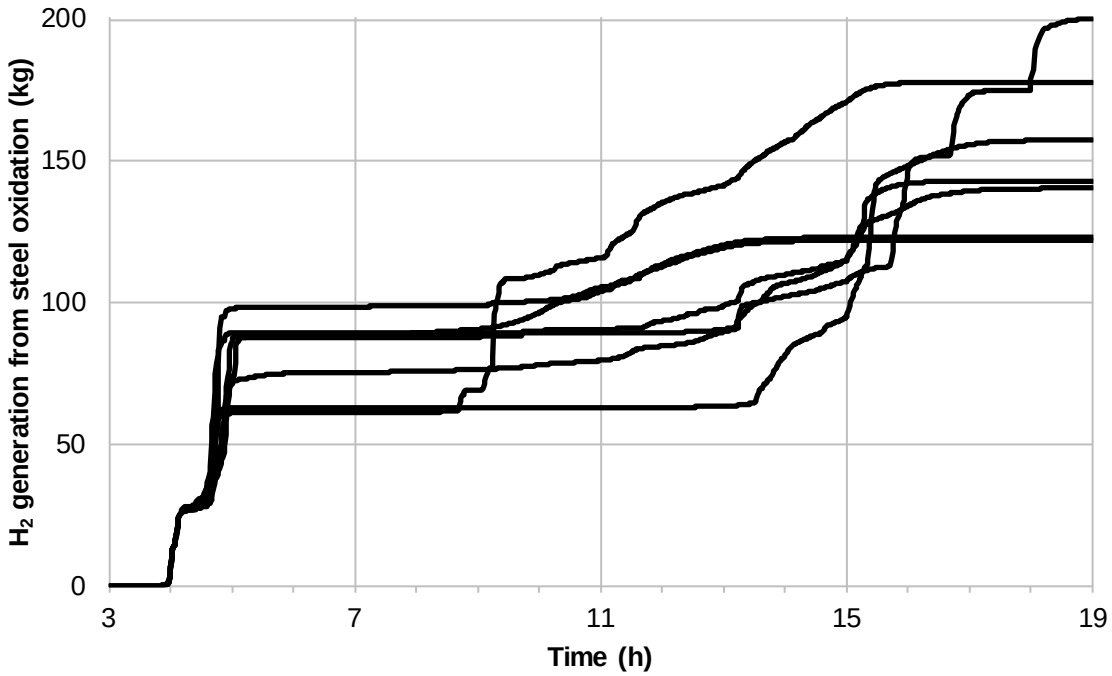

Figure 7. Effect of the numerical noise on the hydrogen generation from steel oxidation in the Fukushima unit 1 accident. The default oxidation correlation was used, and the decay heat was varied within ±0.1 %.

The average hydrogen generation from steel oxidation and in total is presented in Fig. 8, along with the population standard deviations of the seven perturbed calculations, representing numerical noise. The standard deviation is 17 % of the average for steel oxidation and 7 % for the total hydrogen generation, in the case of the default correlation. On the average, the MELCOR default correlation gives the greatest hydrogen generation, both from steel oxidation and in total. This was the expected result, as Fig. 3 shows that the default correlation has the highest oxidation rate constant.

Because of the numerical noise, the significance of the differences between the correlations has to be investigated with statistical methods. The Student's t-test is appropriate for this task. The computation was made with the Excel function T.TEST, using two-tailed distribution and unequal variances between the data sets. The null hypothesis is that the different correlations would calculate equally much oxidation.

The correlation developed in this study gave, on the average, 24 % less steel oxidation than the default correlation. The statistical test gave the p-value of 0.027. This can be interpreted as 97.3 % probability that the null hypothesis can be rejected and that these two correlations give different amounts of steel oxidation. P-values less than 0.05 are generally considered statistically significant. Also the Avelar correlation gave significantly less steel oxidation than the default correlation, with the p-value of 0.036. On the contrary, the Bittel-White correlation did not show a statistically significant difference to the default correlation: the p-value is 0.36.

The correlation developed in this study gave, on the average, 6 % less total in-vessel hydrogen generation than the default correlation. The p-value is 0.13, which is not statistically significant. For the Avelar correlation, the p-value is 0.09, and for the Bittel-White correlation, 0.31. Thus, the differences in the total hydrogen generation are not statistically significant, due to the numerical noise. It is possible that a larger number of calculations would have shown statistically significant differences.

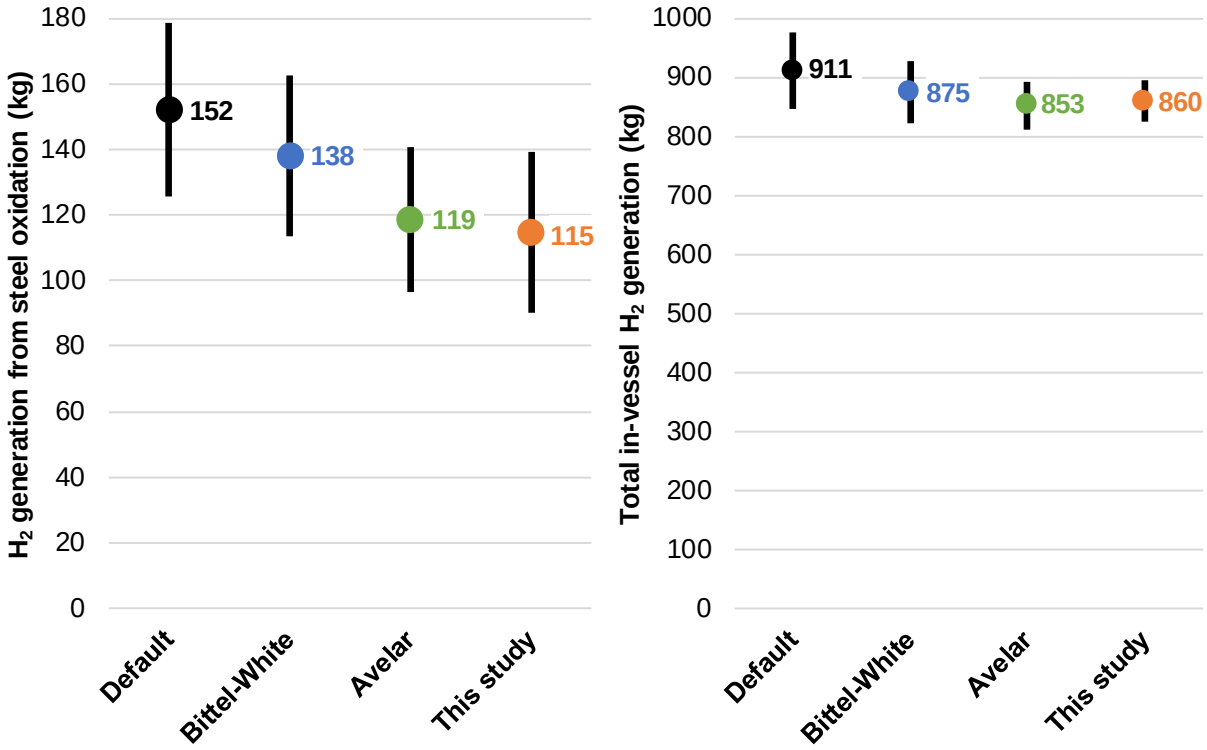

Figure 8. In-vessel hydrogen generation from steel oxidation (left) and in total (right) in the Fukushima unit 1 accident, calculated with four oxidation correlations. The circles show the average results of seven calculations. The black bars show the standard deviations, caused by the numerical noise, brought out by perturbing the decay heat within ±0.1 %.

6. CONCLUSIONS

Five sets of experiments and five correlations on oxidation kinetics of stainless steel in steam at temperatures above 900 °C were found in the literature. The MELCOR default oxidation correlation gives higher oxidation rate than the other correlations. The Leistikow experiments and correlation [5] were excluded from further analysis because they were made with a different steel type than the others. Oxidation rate constants were derived from experiments in the other four facilities. A new correlation was developed by fitting the Arrhenius equation (1) to the measurement data from 14 experiments. The best fit was obtained by setting the constants $A = 4.3\times10^7$ kg_{steel}^2/m^4s and $B = 37\ 800$ K.

The oxidation correlations were tested by modeling the 14 experiments in the four facilities with MELCOR. The correlations can be entered into MELCOR by changing the sensitivity coefficient 1002, except for the Ishida correlation [6] because it is a piecewise-defined function.

None of the correlations is clearly superior to the others. In general, each correlation gives the best results with those experiments, based on which that correlation has been developed. The new correlation developed in this study can be considered as the best fit to the available data, overestimating the measured oxidation in some tests and underestimating it in other tests. It can be recommended when best-estimate results are desired. The MELCOR default correlation is conservative: it overestimates the oxidation in all the tests, except the Bittel test [4], based on which it has been developed. Using the default correlation can be recommended when conservative results are required.

The effect of the steel oxidation correlation in a full-plant simulation was tested by calculating the Fukushima unit 1 accident. Because of the random variation ("numerical noise") that is always seen in MELCOR simulations of core degradation, several calculations are needed for comparing the models. Seven calculations were performed with each correlation, perturbing the decay heat within ±0.1 %, in order to show the magnitude of the numerical noise. The new correlation of this study gave, on the average, 24 % less steel oxidation and 6 % less total in-vessel hydrogen generation than the default correlation. The statistical t-test showed that the difference in the steel oxidation is statistically significant, but the difference in the total hydrogen generation is not.

In addition to the correlation, the oxidation is influenced by the contact area between the steel and the steam. The area is precisely defined in the intact core geometry. However, as the core degrades, the area changes. Modeling the evolution of the contact area introduces significant additional uncertainty, potentially surpassing the impact of selecting the correlation. Investigating this aspect experimentally is challenging and falls beyond the scope of the present study.

ACKNOWLEDGMENTS

This work was funded by SAFER2028, the Finnish national nuclear safety and waste management research program. The method for taking into account the numerical noise when comparing models was developed in the EU MUSA project (Management and Uncertainties of Severe Accidents).

REFERENCES

1. T. Räihä, “MELCOR analyses for Loviisa NPP: Results and effect of steel oxidation,” *11th Meeting of the European MELCOR User Group (EMUG)*, Villigen, Switzerland, April 3–5, 2019.
2. L.L. Humphries et al., “MELCOR computer code manuals, Vol. 2: Reference manual, version 2.2.14959,” Sandia National Laboratories, SAND2019-12537 O (2019).
3. T. Sevón, “Modeling steel oxidation in steam with MELCOR,” VTT Technical Research Centre of Finland, VTT-R-00689-23 (2023).
4. J.T. Bittel, L.H. Sjodahl and J.F. White, “Oxidation of 304L stainless steel by steam and by air,” *Corrosion* **25**(1), pp. 7–14 (1969).
5. S. Leistikow, G. Schanz and Z. Zurek, “Comparison of high temperature steam oxidation behavior of zircaloy-4 versus austenitic and ferritic steels under light water reactor safety aspects,” Kernforschungszentrum Karlsruhe, KfK 3994 (1985).
6. T. Ishida, Y. Harayama and S. Yaguchi, “Oxidation of 304 stainless steel in high-temperature steam,” *Journal of Nuclear Materials* **140**(1), pp. 74–84 (1986).
7. C. Tang, M. Steinbrueck and M. Grosse, “Round robin high temperature oxidation tests at KIT,” In: Analysis of options and experimental examination of fuels for water cooled reactors with increased accident tolerance (ACTOF), IAEA-TECDOC-1921 supplementary files (2020).
8. A.M. Avelar et al., “Oxidation of AISI 304L and 348 stainless steels in water at high temperatures,” *Materials Research* **23**(6) (2020).
9. T. Sevón, “Analyzing reactor water level measurements in the Fukushima Daiichi 1 accident,” *Progress in Nuclear Energy* **160** (2023).
10. Sandia National Laboratories, “Fukushima Daiichi Unit 1 accident progression uncertainty analysis and implications for decommissioning of Fukushima reactors – Volume I,” SAND2016-0232 (2016).

A review of correlations of stainless steel oxidation in steam, and modeling the reaction with MELCOR

Tuomo Sevón

ERMSAR, May 13–16, 2024, Stockholm, Sweden

VTT – beyond the obvious

Introduction

- Hydrogen generated in severe accidents when metals oxidize in steam
- Oxidation of Zr most important and most researched because strongly exothermic
- Oxidation of stainless steel less intensive, and only slightly exothermic
  - But, in some MELCOR calculations a lot of hydrogen from steel oxidation
- Steel oxidation correlation in MELCOR from 1966
- Objective: review if the old correlation still state-of-the-art

Literature review

- Found five sets of experiments for stainless steel oxidation in steam above 900 °C
- Steel samples of a few grams kept in a furnace at constant temperature in flowing steam
- Measured sample mass gain, or thickness of metal oxidized, or hydrogen generation
- Leistikow experiments not analyzed because steel composition significantly different from others

	Cr (%)	Ni (%)
Bittel 1969	18	10.95
Leistikow 1985	14.9	15
Ishida 1986	18.57	9.68
Tang 2020	18	7
Avelar 2020	17.45	10.94

Stainless steel oxidation model in MELCOR

- $Fe + H_2O \rightarrow FeO + H_2$
  $3Fe + 4H_2O \rightarrow Fe_3O_4 + 4H_2$
  $2Fe + 3H_2O \rightarrow Fe_2O_3 + 3H_2$
  $2Cr + 3H_2O \rightarrow Cr_2O_3 + 3H_2$
- MELCOR does not model Fe, Cr and Ni separately
- MELCOR has material called *stainless steel* that oxidizes to form *stainless steel oxide*
- Reaction rate: $\frac{dW^2}{dt} = A \exp\left(-\frac{B}{T}\right)$
- *W* = mass of steel oxidized per unit surface area (kg_{steel}/m^2)
- *A* and *B* experimentally determined constants

Oxidation correlations

- Existing correlations based on a single test facility
- Digitized measured oxidation of 16 experiments in 4 test facilities
- Converted the measured quantity to mass of metal oxidized, the same as MELCOR definition, assuming reaction product Fe_3O_4
- Plotted as a function of square root of time
- Fitted linear functions, determining the oxidation rate constant

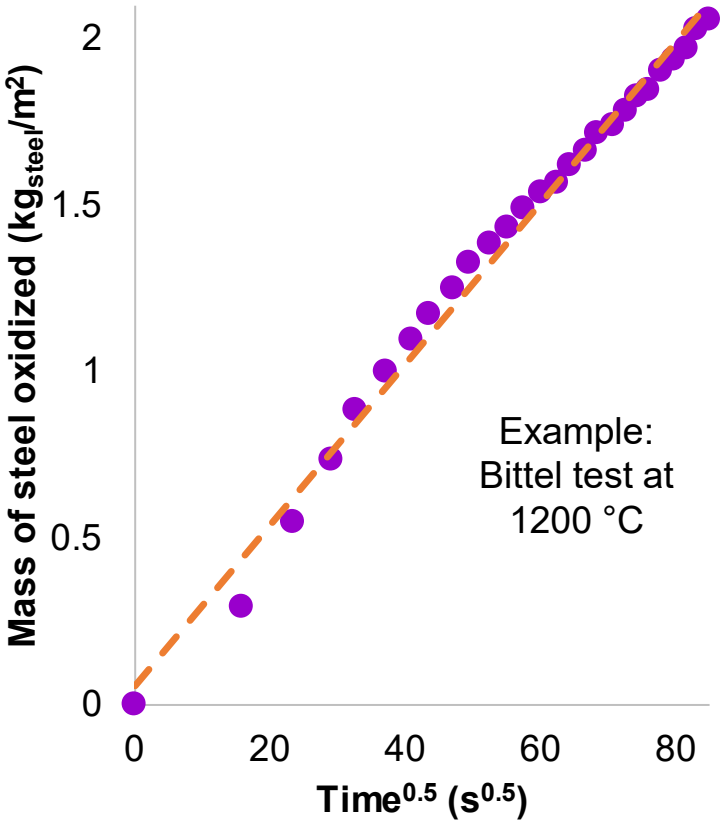

Oxidation rate constants, derived from 16 experiments

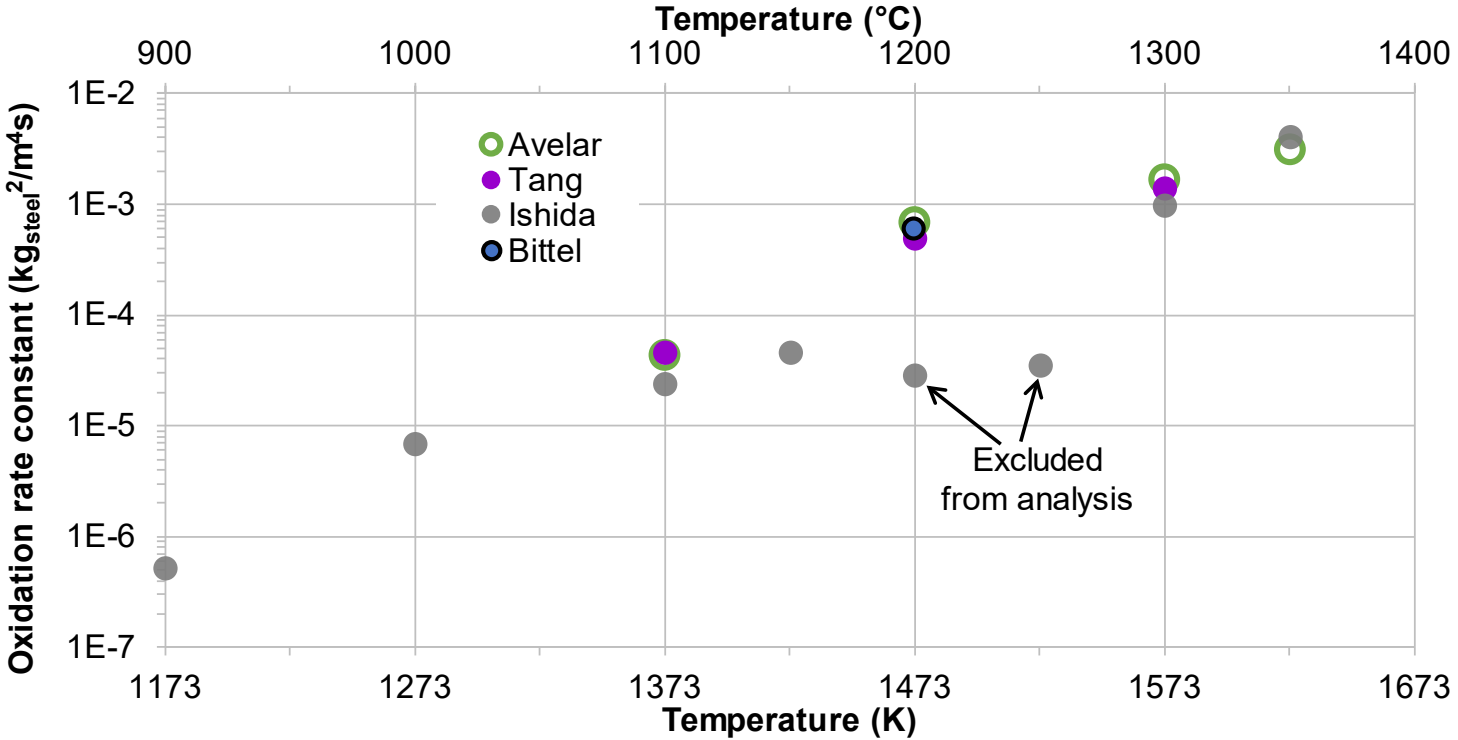

Oxidation rate constants from 14 experiments, and 5 correlations

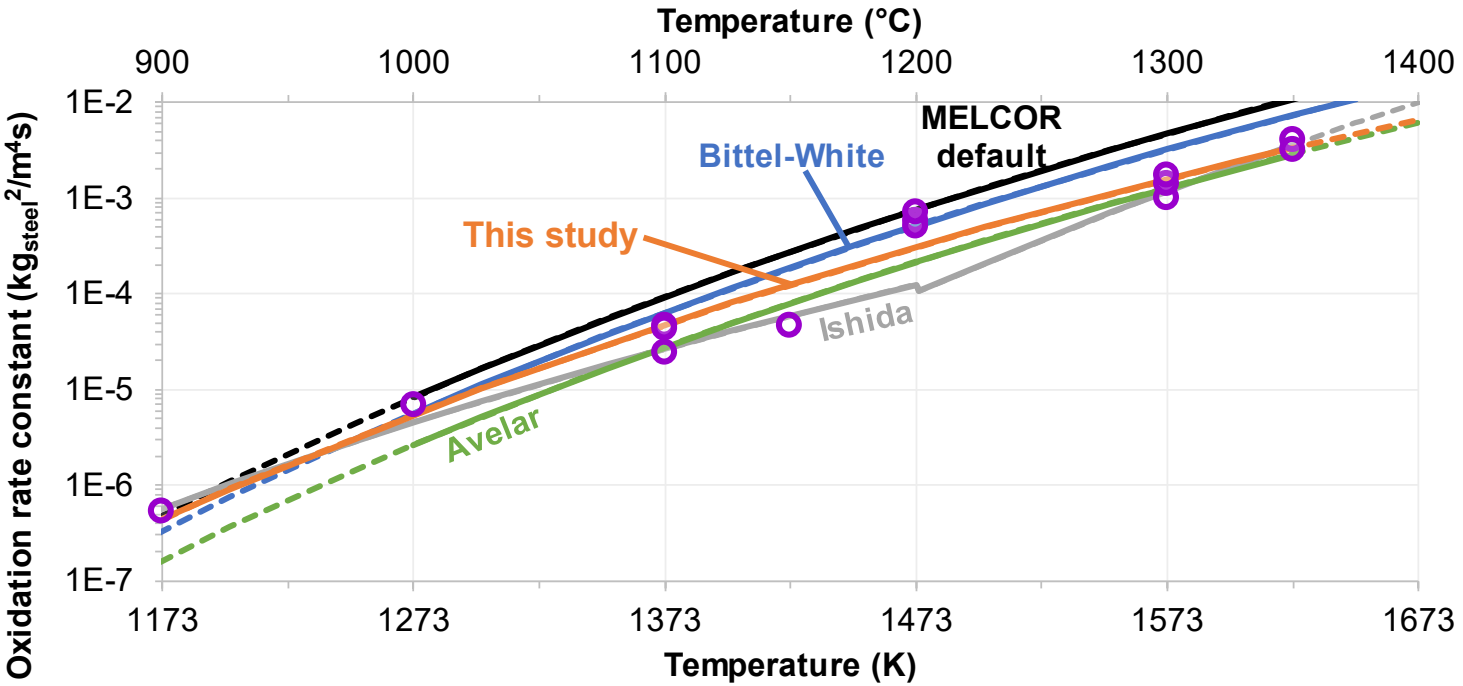

Modeling the oxidation tests with MELCOR

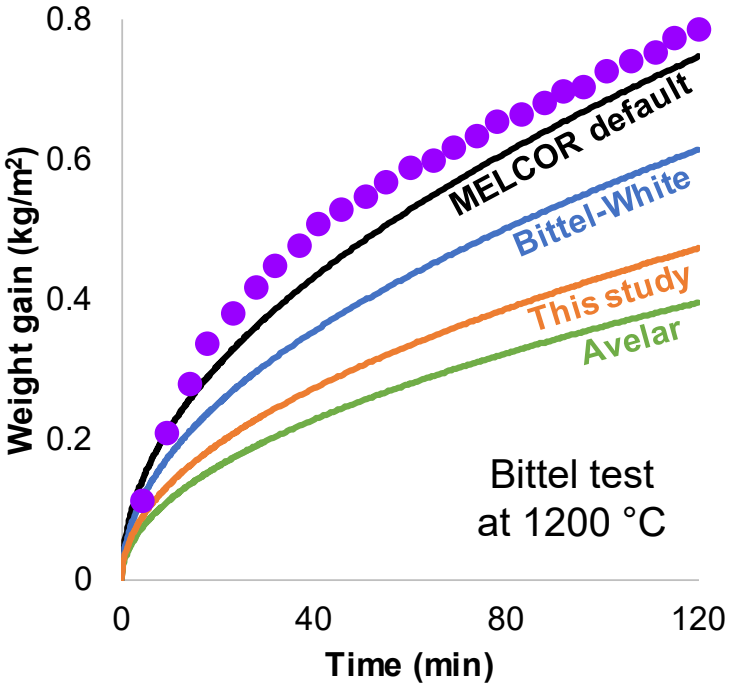

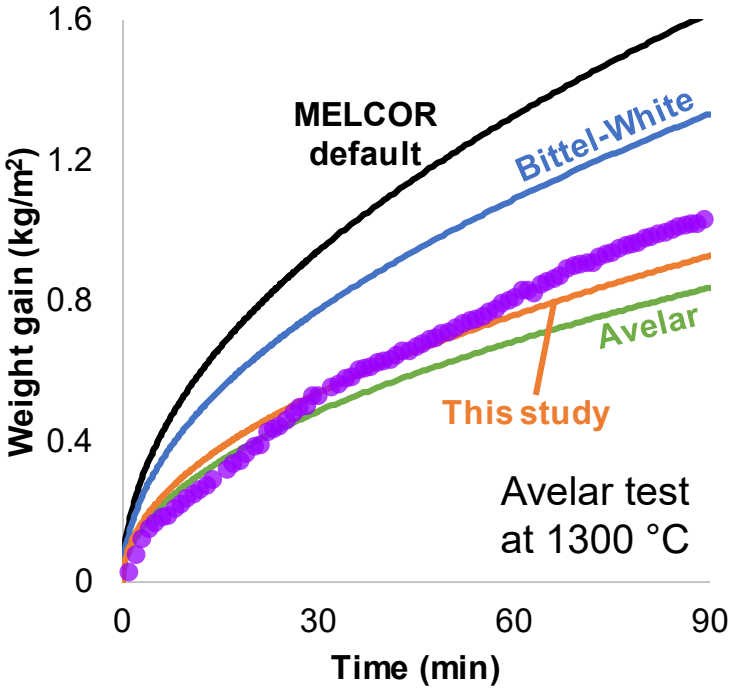

Effect of the correlation in a full plant calculation

- Calculated Fukushima unit 1 accident with MELCOR using different oxidation correlations
- Comparing results of full-plant calculations not straight-forward because of numerical noise:
  - Any small change in the model causes significant changes in results
  - Slightly different timing of core component collapse → results begin to bifurcate
- Seven calculations with each correlation, perturbing decay heat by ±0.1 %, to quantify the numerical noise

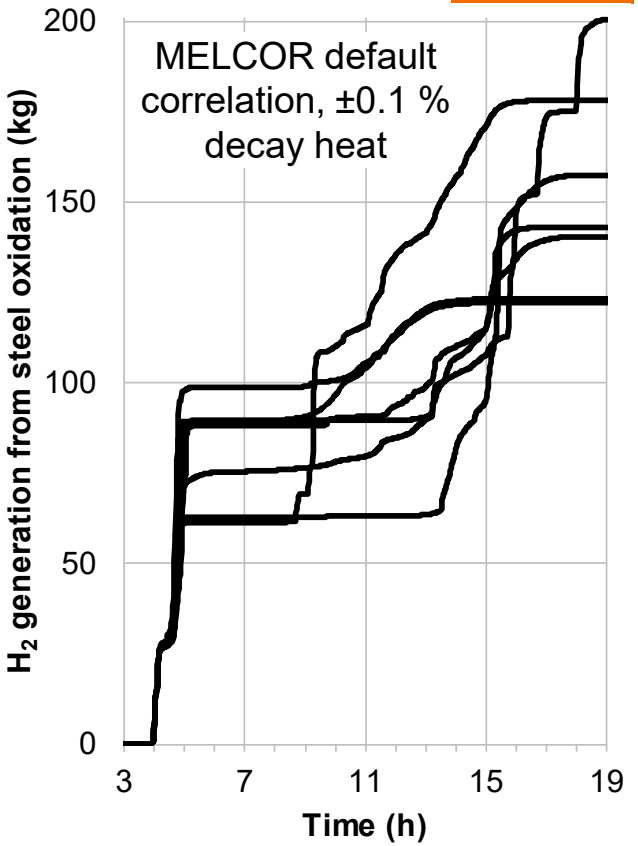

Fukushima simulations: 7 runs with 4 correlations

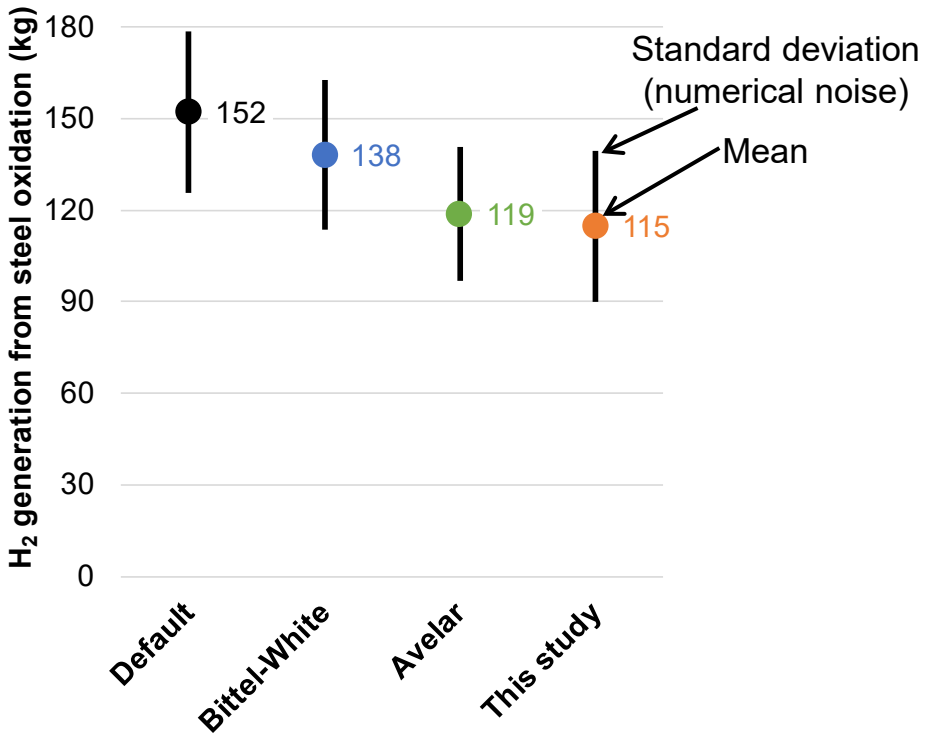

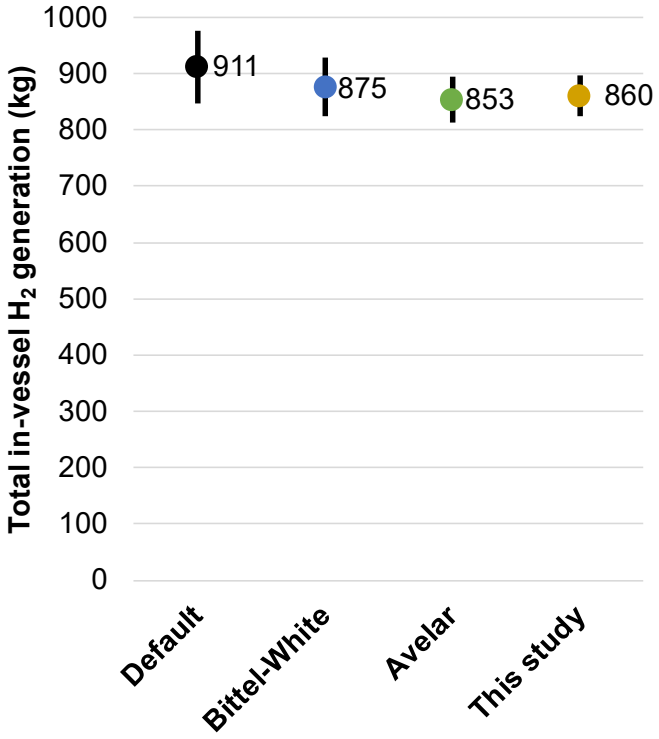

Conclusions

- None of the steel oxidation correlations is clearly better than others
- Each correlation good for those tests, from which it was developed
- The MELCOR default correlation
  - results in faster oxidation than any other correlation
  - overestimates oxidation in all experiments, except the Bittel test
- Developed a new correlation by fitting to data from several facilities
- In Fukushima accident, changing the correlation had:
  - a significant effect on steel oxidation
  - a minor effect on the total hydrogen generation
- Oxidation depends also on the contact area between steel and steam
  - Major uncertainty during core degradation, but difficult to study

The 11th European Review Meeting on Severe Accidents Research

May 13-16, 2024, Royal Institute of Technology, Stockholm, Sweden

TECHNICAL SESSION 7.2: SOURCE TERM

Chairs: L. E. Herranz (CIEMAT), S. Gupta (Becker Tech. GmbH)

ID80	**Effect of Boric Acid on Fission Product Tellurium and Iodine in Severe Accident-Like Conditions: Analysis with X-Ray Photoelectron Spectroscopy** F. Börjesson Sandén (Chalmers University of Technology)	**Paper** **Presentation**
ID15	**Local measurements on particle mass transfer in gas-liquid flows** A. Ramos Perez (PSI)	**Paper** **Presentation**
ID29	**New Experimental Devices for Severe Accident Study: a Laser Based Approach** Y. Pontillon (CEA)	**Paper** **Presentation**
ID33	**On the progress made in source terms evaluation and possible open issues relative to advanced technologies** L. Cantrel (IRSN)	**Paper** **Presentation**

EFFECT OF BORIC ACID ON FISSION PRODUCT TELLURIUM AND IODINE IN SEVERE ACCIDENT-LIKE CONDITIONS: ANALYSIS WITH X-RAY PHOTOELECTRON SPECTROSCOPY

Fredrik Börjesson Sandén[1*], Anna-Elina Pasi[2], Teemu Kärkelä[2], Christian Ekberg[1]

[1]Chalmers University of Technology, Kemivägen 4, SE-412 96 Gothenburg, Sweden, @chalmers.se
[2]VTT Technical Research Centre of Finland Ltd, P.O. Box 1000, FI-02044 VTT, Espoo, Finland, @vtt.fi

ABSTRACT
Tellurium is a volatile fission product with a rich and complex chemistry. In a severe nuclear accident it will be released alongside a variety of other chemical compounds such as fission products and structural material, and be exposed to a variety of atmospheres. By virtue of its chemistry, tellurium can potentially take the forms of aerosols, organic tellurides or other forms during the accident scenario, and understanding its interaction with common materials becomes important from an accident management perspective. In this work, the interactions between tellurium and boric acid, used as a chemical shim to control fission reaction in pressurized water reactors are investigated. Furthermore, the impact of iodine vapor on this system is investigated. The method involves heating tellurium to its melting point and transporting the vapor in a flow of oxidizing, inert or reducing gas to a reaction furnace where droplets of boric acid solution and/or fission products are added. The gas stream is then directed through a filter. Analysis focuses on XPS (X-ray photoelectron spectroscopy) analysis of this filter in an attempt to determine the aerosolized chemical species that may be present in an accident.
The results indicate that there is little direct interaction between tellurium and boric acid, but the degree of oxidation appears to change with the presence of boric acid. Furthermore, tellurium appears to interact with hydrogen, forming H_2Te, and with iodine to form tellurium iodides.

KEYWORDS
Volatile Fission Products, Containment Chemistry, Boric Acid

1. INTRODUCTION
Severe nuclear accidents make for complex chemical environments. Due to the fission products, the number of elements included is large. The temperature ranges from above a thousand degrees inside the reactor to ambient temperature outside of the power plant. Light-water reactors (LWRs) includes a significant volume of water which may evaporate or result in the evolution of hydrogen gas, and boiling water reactors (BWR) may be filled with nitrogen gas. Different atmospheres result different chemical environments. Additionally, the structural materials of the reactor building will also become part of the accident chemistry, including concrete, steel, paint, cables etc.
Studies of severe accidents can be broadly categorized into three types: post-accident research, which would include the research conducted in the aftermath of a real accident, such as Fukushima. This would also include the analysis of data from the accident process, as well as measurements of contamination inside and outside of the plant. Second is so called combined effect tests. These are large programmes aimed to simulate an accident in a realistic manner and investigate the combined effects of multiple interactions and phenomena all working in tandem. This type of research allows for a specific, well-known starting state of

the accident, and allows for careful data collection. Finally, there are separate effects tests, which are aimed at investigating some specific facet of severe accident chemistry.
This study is a separate effect test, and aims to investigate the impact of boric acid, a common chemical in nuclear reactor operations, upon tellurium and iodine, both of them volatile fission products. The study is specifically aimed to communicate the results of the XPS (X-ray photoelectron spectrometry) analysis preformed as part of a larger study, partially reported in [1], and compare them.

2. THEORY AND BACKGROUND

2.1. Tellurium

Tellurium is a metalloid element with 52 protons in the nucleus. It belongs to the chalcogen family of elements, same as oxygen, sulfur, selenium, and polonium, and is the heaviest stable such element. Chemically it is not unlike several of the other chalcogens in that it adopts the same principal oxidation states as sulfur, -II, 0, +II, +IV and +VI. Another similarity to sulfur is the existence of organic tellurium compounds, though there are much fewer than for sulfur. Incidentally, organic tellurides also have a pungent smell, much like sulfur. The melting point of tellurium is around 450ºC, though it volatizes earlier than that, at 430ºC [2].

Owing to its many oxidation states, tellurium has a variable chemistry. This can be seen in the context of severe nuclear accidents, where it is postulated to exist in several different forms and forming compounds with multiple other elements. One intuitive species is the analogue of water, H_2Te, which can be formed as depicted in Reaction 1.

$$Te + H_2 \rightleftharpoons H_2Te \quad (1)$$

This reaction necessitates a high partial pressure of hydrogen, and hydrogen telluride itself is prone to decompose at temperatures below 623 ºC, especially in the presence of water vapor [3]. The species may still be relevant in the context of severe accidents, however, as the necessary hydrogen may be generated through the oxidation of zirconium alloy by water, as described by Reaction 2.

$$Zr + 2H_2O \rightleftharpoons ZrO_2 + 2H_2 \quad (2)$$

This reaction begins at about 900 ºC, and produces heat. At 1300 ºC, the reaction becomes autocatalytic [4]. The formation of H_2Te is therefore possible, but it will likely decompose quickly [2].

Aside from TeH_2, there are two more broad classes of tellurium species of interest for severe accidents: organic tellurides, and oxides. The organic tellurides are mostly a curiosity, though they have been demonstrated in circumstances similar to those in a real accident [5]. They are interesting especially because of their low boiling point, potentially making tellurium more volatile and altering the chemistry in relation to the other forms of tellurium.

When heated in ambient conditions, tellurium forms TeO_2 [6] This species also forms on metallic tellurium by atmospheric oxygen at low rates. The same also happens is aerated waters, making TeO_2 an important and expected species in nuclear accident scenarios. The volatility of TeO_2 is lower than the metallic form, melting at 732 ºC and boiling at 1245ºC. It is not very soluble in water, except for at high and low pH [2].

2.2. Iodine

Iodine is arguably the most important, and most thoroughly researched fission product. Iodine is more volatile than tellurium, melting at 113 ºC, and undergoing sublimation at only gentle heating. Biologically,

iodine is taken up by humans and accumulated in the thyroid gland. From a nuclear safety perspective, this is important as radioactive iodine also will accumulate, giving a prolonged, local radiation dose.
Chemically, iodine belongs to the halogen group of elements, which also includes fluorine, chlorine, bromine and the radioactive astatine.
In a nuclear accident, iodine has been calculated to mostly occur as CsI aerosols, with small contributions of HI, or I_2. The same study also remarks that boric acid may influence the iodine speciation by reacting with CsI according to Reaction 3 [7].

$$CsI(c) + B(OH)_3(g) \leftrightharpoons CsBO_2(c) + HI(g) + H_2O \quad (3)$$

Iodine can also interact with tellurium to form tellurium iodides. The principal reaction is seen in Reaction 4.

$$I_2(g) + Te(g) \leftrightharpoons TeI_2 \quad (4)$$

Several tellurium iodides have been characterized, including TeI_4, TeI_2 (which only exist in the gas phase) and subhalides [8].

2.3. Boric Acid

Boric acid is included in the pressurized water reactor (PWR) as a chemical shim; that is, a way to moderate the reactor by introduction of the strongly absorbing nuclide ^{10}B. It can also be used as part of the emergency reactor shutdown in the same way [9], both for BWR:s and PWR:s. It is therefore likely that boric acid, or species derived from it, will be part of the chemistry of a severe nuclear accident. Boric acid dehydrates when heated to ultimately form B_2O_3, at about 327°C. The process is depicted in Reaction (5).

$$2B(OH)_3 \leftrightharpoons B_2O_3 + 3H_2O \quad (5)$$

2.4. X-ray Photoelectron Spectroscopy (XPS)

XPS is a surface analysis method based on the photoelectric effect. In principle, any electron exposed to electromagnetic radiation of sufficient energy will be ejected from its corresponding atom by absorbing the energy from the radiation. The kinetic energy of the electron will be equal to the difference in electron binding energy and the energy of the incoming radiation. As the binding energy of each electron in turn depends on the makeup of the atom it belongs to, this means that every element will generate electrons of different energies allowing for different elements in the sample to be identified [10]. What's more, the energies of the electrons around an atom is also changed when the atom forms bindings with other atoms. This change can also be detected, allowing XPS to determine the chemical environment and bindings of a sample. Furthermore, as each element generates electrons with a distinct energy, the ratio of elements present in the sample can also be determined. This, however, requires knowledge about the relative ease of detection for different electrons. This information is tabulated for different XPS machines as "sensitivity factors". The ones used in this paper are tabulated in Table I, and the equation to calculate the chemical abundance is seen in Equation 1.

Table I: Sensitivity factors for the relevant elements.

Element	Signal	Sensitivity factor
Te	4d	1.721
B	1s	0.171
O	1s	0.733
C	1s	0.314

The technique is dependent on detecting the ejected electrons. These are easily screened by the sample itself, or by gases around the sample. The latter is counteracted by XPS always being performed in high vacuum, which imposes certain restrictions on what samples can be analyzed, whereas the latter means that only the very surface of the sample can be probed.

$$C_x = \frac{\frac{I_x}{S_x}}{\sum_i \frac{I_i}{S_i}} \quad Equation\ 1$$

"I" is the measured peak area, "S" is the peak sensitivity factor, "x" is for the species of interest, "i" implies every species in the sample, and C is the calculated abundance.

3. Method

The experiments took place by heating the tellurium precursor (5 g) to 540ºC inside a tube furnace. The carrier gas consisted of synthetic air, 5% H_2 in Ar, or N_2. It flows through the furnace at a rate of 3L/min. Boric acid (0,2 M aqueous solution, aerosolised) and/or iodine vapour is added to the gas stream after the furnace, and the mixture of carrier gas, tellurium aerosols, iodine and/or boric acid is fed to a reaction furnace. This feed is made with the same carrier gas, and introduces another 4.2 L/min of gas. The reaction furnace is held at 650 ºC. Following this second furnace, there a Polytetrafluoroethylene filter is placed to capture any solid particles. Following the filter, a liquid trap containing 100 ml 0.1M NaOH captures any volatile species formed. This paper focuses on the subsequent XPS analysis of the filters, and excludes the oxidizing conditions as these give a coating of TeO_2 regardless of the system. Thus for the context of this paper, these experiments are not discussed further.
The experimental conditions relevant to this paper are described in Table II.

Table II: experimental conditions

Atmosphere	Injected through atomizer	Fission products
Reducing (Ar/H_2)	-	Te
Reducing (Ar/H_2)	H_2O, $B(OH)_3$	Te
Reducing (Ar/H_2)	-	I, Te
Reducing (Ar/H_2)	H_2O, $B(OH)_3$	I, Te
Inert (N_2)	-	Te
Inert (N_2)	H_2O, $B(OH)_3$	Te
Inert (N_2)	-	I, Te
Inert (N_2)	H_2O, $B(OH)_3$	I, Te

All of the reducing, inert, and oxidizing atmospheres can be of relevance in nuclear chemistry, at least to some degree. Oxidizing atmospheres are what can be expected in case of a break of the reactor pressure

vessel, wherein ambient air enters the reactor. Experiments in inert atmosphere is relevant in BWR reactors, as their atmosphere can be relatively inert. Reducing atmosphere may become locally interesting in case of fuel cladding oxidation, which releases hydrogen gas. The temperature chosen was 650ºC, as to be comparable to the hot-leg of the steam generator in a LWR.
Tellurium and iodine are supplied in their elemental forms, which are not expected to be the main species in a real accident. Iodine tends to appear mostly in the form of CsI [11], though some amount of iodine gas is also expected. Te is speculated to interact with zirconium in the zircalloy cladding and form a ZrTe phase. Upon oxidation of the cladding, tellurium is liberated, in principle as Te_2, but reactions with fission products (such as Cs, to form various forms of CsTe) or other cladding materials (to form SnTe) are expected [12]. For simplicity's sake, Te is chosen as the precursor in this experiment.

4. RESULTS

The filter surface compositions as determined by XPS are summarized in Table III.

Table III: Elemental ambiance in the different samples, as measured by XPS.

Species present	Atmosphere	Tellurium [%]	Oxygen [%]	Iodine	Boron [%]
Te	Ar/H_2	51	49	-	-
Te	N_2	37	63	-	-
H_2O, $B(OH)_3$, Te	Ar/H_2	54	35	-	11
H_2O, $B(OH)_3$, Te	N_2	54	42	-	4
I, Te	Ar/H_2	Uncertain	Uncertain	Uncertain	-
I, Te	N_2	Uncertain	Uncertain	Uncertain	-
H_2O, $B(OH)_3$, Te, I	Ar/H_2	51	1	32	16
H_2O, $B(OH)_3$, Te, I	N_2	89	5	2	5

Overall, it can be said that the most prevalent elements are tellurium and oxygen, whereas boron is more scarce. Iodine is difficult to generalize due to the experiments containing only Te and I could not effectively be probed by XPS. However, from the experiments involving Te, I and boric acid solution, there is a clear influence of the carrier gas atmosphere on the iodine behavior.

It is worth pointing out that of the analyzed elements, boron has a very low sensitivity factor compared to the others, meaning it is difficult to detect. In principle this is compensated for with the sensitivity factor, but in practice it makes the signal-to-noise ratio significantly worse for boron than for the other elements. The abundancy of boron is therefore less certain than for the other elements.

The difficulty with the Te-I experiments is due to the interaction between tellurium and iodine to form tellurium iodides, which are volatile species and thus not likely to interact with the filter. In the XPS spectrum this was seen as very weak Te and I signals, but with large influences from carbon and fluoride.

This then means that the polytetrafluorethylene filter itself was probed, in turn revealing the coating on the filter to be extremely thin.

4.1. Results- Only Tellurium

As can be seen from the "reference experiment" involving only tellurium, tellurium is indeed volatized from the precursor and transported through the system. However, as it sticks to the filter rather than passing through, it is likely transported in the form of aerosols rather than as a gaseous species.
The presence of oxygen is partially due to the time between the experiment and the measurement. This time was four days, during which the filter was exposed to the open atmosphere and ambient temperature. Some oxidation is expected. It is also possible that there is some leaking in the system. The tellurium energy spectrum is presented in figure 1.

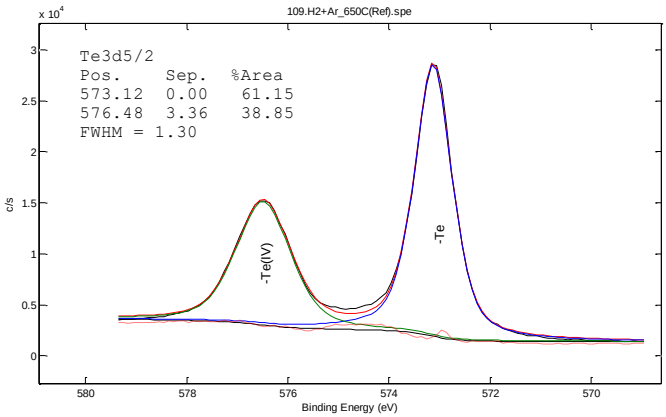

Figure 1: Tellurium XPS spectrum for the reference condition in reducing atmosphere, with annotated oxidation states.

As only tellurium and oxygen are detected on the filter in substantial amounts, the surface most likely consists of TeO_2, and metallic Te.

As for the same system under inert atmosphere, the elemental composition analysis states that the surface is more oxidized. In fact, according to the composition analysis, the ratio of tellurium to oxygen is close to one to two, implying a complete coverage of TeO_2. The spectrum presented in figure 2 shows the tellurium speciation in this case. Indeed, the surface is oxidized to a larger extent in this case, but compared to what the elemental composition predicts, the surface is still less oxidized than what would be expected.

Ideally, the oxidation in these samples should be the same, and derive from the exposure to the ambient atmosphere after the experiment. This would imply no leaking of oxygen. Presumably, if oxygen leaks into the reducing system, it will react with hydrogen and form water, rather than with tellurium. In the inert system, on the other hand, there is no hydrogen which makes the oxidation of tellurium a likely reaction. The fact that the inert system is more strongly oxidized does imply that the system does have some leaking.

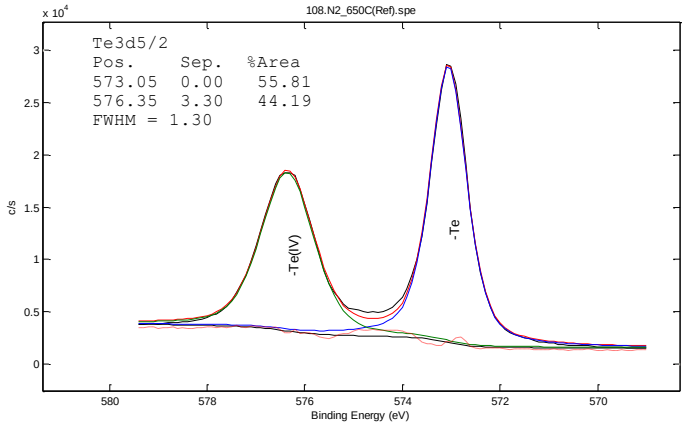

Figure 2: Tellurium XPS spectrum for the reference condition in inert atmosphere, with annotated oxidation states.

4.2. Results- Tellurium with Boric Acid

Compared to the same system but with boric acid solution added, the filter surface contains significantly less oxygen, as well as a relatively small fraction of boron. It appears that the presence of the boric acid solution has effectively hindered the oxidation of the tellurium. As the temperature of the system was 650°C, it is likely that the boron on the filter will have undergone dehydration and is present in the form of B_2O_3, meaning that the oxygen present on the filter is largely bound to boron, rather than to tellurium, which is then a large difference compared to the reference case. The corresponding spectrum, presented in Figure 3, confirms this hypothesis, as the share of oxidized tellurium has decreased significantly. However, there are no new tellurium energy signals. Both signals present can still be assigned metallic tellurium and the Te-O bond. There is no indication that a Te-B bond has formed on the filters.

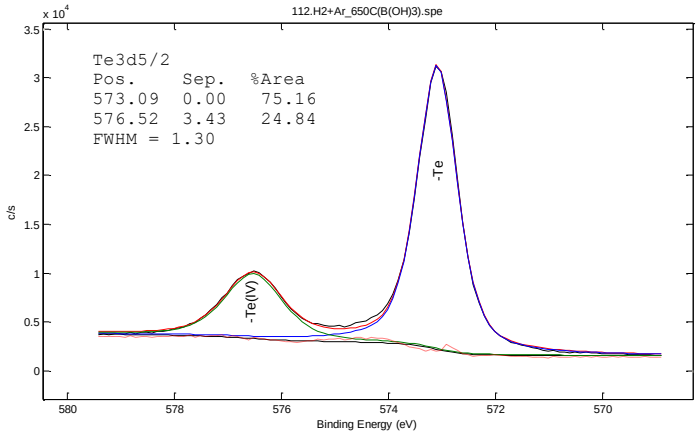

Figure 3: Tellurium XPS spectrum for the system including tellurium and boric acid solution in reducing atmosphere, with annotated oxidation states.

As for the system in inert atmosphere, the tellurium speciation spectrum, as seen in Figure 4, looks almost identical to the one in reducing atmosphere, with just a few percent less oxidation.

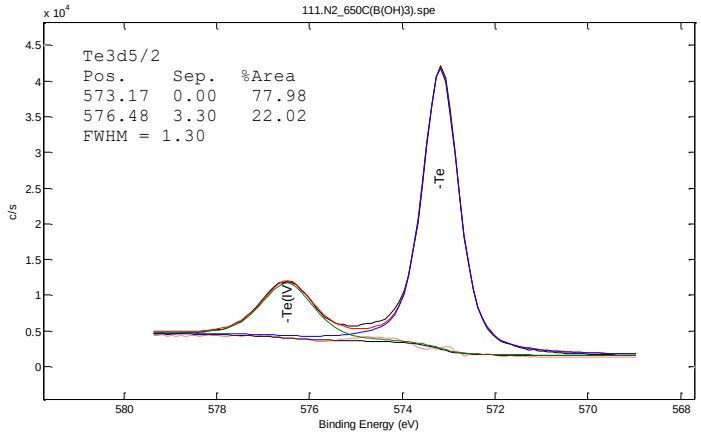

Figure 4: Tellurium XPS spectrum for the system including tellurium and boric acid solution in reducing atmosphere, with annotated oxidation states.

It appears from the comparisons between the spectra presented in the Figures 1-4, that boric acid does influence the tellurium behaviour. However, this effect does not include direct interaction between boron and tellurium. Instead, it appears that boric acid prevents, to some degree, the oxidation of the tellurium metal. As tellurium metal is more volatile than tellurium dioxide, this has some implications in the wider accident context.

4.3. Results- Tellurium with Iodine

Both the experiments involving iodine and tellurium together are difficult to assess using XPS. The signals form those filters are very weak and display a significant portion of fluoride. Fluoride is, of course, not added to the system during the experiment, but is part of the PTFE-filter itself. For it to be visible in the XPS spectrum, the substrate of the filter must be extremely thin. The spectra collected from these two filters should be considered with this in mind.

The spectra are very similar, with nearly all the tellurium giving the energy signal of 576.5 eV, implying TeO_2. While oxygen was not part of the experiment itself, the hypothesis behind these signals is that due to the small amount of tellurium present, it was very quickly oxidized by the ambient atmosphere during the time between the experiment and the XPS measurement.

However, this result is interesting, since it is a strong indicator of a volatile species forming when iodine and tellurium are both present in the system. This species would then be able to penetrate the filter. An option would be tellurium iodide.

4.4. Results- Tellurium with Iodine and Boric Acid

The system including both iodine and boric acid together with tellurium is the system with the largest discrepancy between the inert and reducing atmospheres. The reducing case shows a significant amount of iodine present on the filter, very little oxygen, and a relatively large portion of boron. Both the boron and the iodine are interesting. Iodine is a volatile species, and the filter casing was hot during the experiments, being placed ca. 10 cm downstream from the furnace (with the temperature of 650 °C). Pure iodine would not have condensed on the filter in those conditions, meaning that the iodine is bound either to boron or to tellurium. The tellurium energy spectrum is presented in Figure 5.

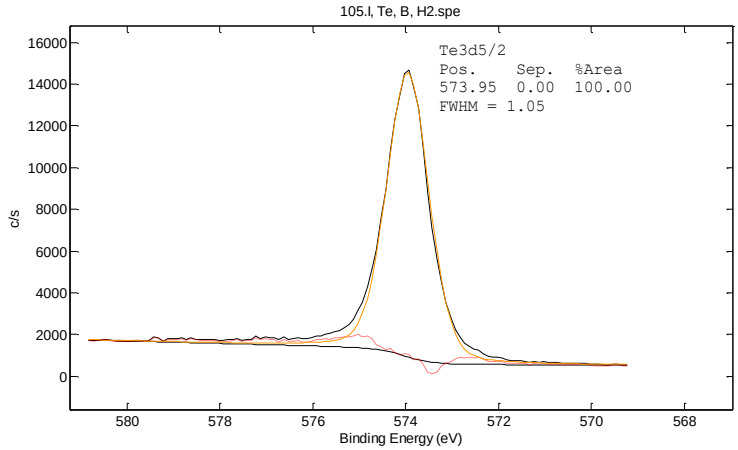

Figure 5: Tellurium XPS spectrum for the system including tellurium, iodine, and boric acid solution in reducing atmosphere.

The spectrum, as could be expected, shows only one signal. However, it is unlikely to indicate metallic tellurium. In figures 1-4, metallic tellurium has consistently had the signal between 573.05-573.17 eV. The signal in Figure 5 is at 573.95 eV. It was suspected that this signal derives from the Te-I bond, so samples of tellurium iodides were prepared by heating a stoichiometric (one atom of tellurium per two atoms of iodine) mixture of tellurium and iodine in an evacuated ampule up to 400 ºC. The result was characterized as tellurium iodide with the help of PXRD. Measuring this sample gave the signal 373.67 eV, which is not a perfect match, but relatively close.

This, however, leaves the boron unaccounted for. There is only one signal in the tellurium species spectrum and in the iodine spectrum, meaning neither of them can be bound to boron. Very little oxygen is detected in the filter, meaning the boron cannot be in the form of B_2O_3, which would otherwise be the expected species. Finally, pure boron will not form in these conditions. The boron speciation spectrum is impossible to determine with certainty due to a poor signal-to-noise ratio. Given these premises, the most likely answer is that the measurement overestimates the boron content.

The lack of oxygen in this filter is probably due to the tellurium iodide forming during the experiment and remaining stable against ambient oxidation.

The final experiment involves tellurium, iodine, and boric acid solution in inert atmosphere. By the abundancy analysis, this filter contains almost solely tellurium, with small inclusions of oxygen and boron, and hardly any iodine. The tellurium speciation again seems to consist of one single signal, with the energy 573.68 eV, as seen in Figure 6.

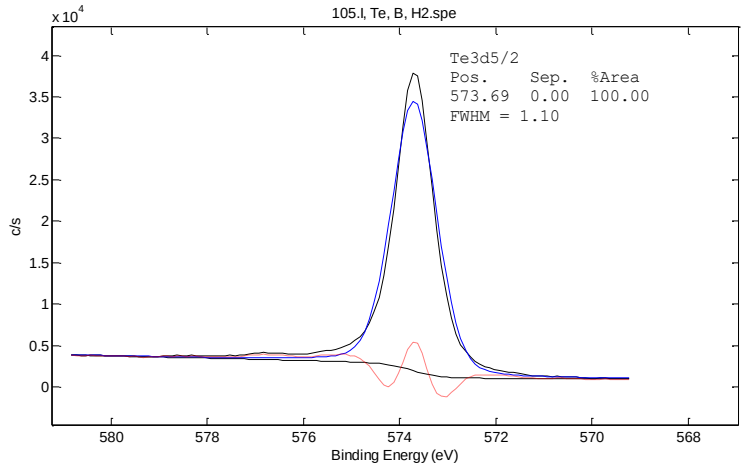

Figure 6: Tellurium XPS spectrum for the system including tellurium, iodine, and boric acid solution in reducing atmosphere.

This signal matches the measured TeI_2 sample very well. However, this is not congruent with the abundancy analysis, as there is hardly any iodine present in the sample. While it would be possible for some tellurium to be present in the form of tellurium iodide, the entire sample surface cannot. In fact, given the abundancy analysis gives almost 90% of the surface as tellurium, the most likely conclusion is that the surface consists of mostly metallic tellurium, and that the signal has shifted slightly compared to the samples containing only Te or Te and $B(OH)_3$. This is possible, as the samples with Te, I and $B(OH)_3$ were measured a few weeks after the others.

This experiment, however, may add to the credibility of boric acid preventing oxidation of the tellurium surface. If the lack of oxygen in the reducing conditions was due to tellurium iodide, then the same reason does not apply in inert conditions. Still, there is very little oxygen present. Potentially, this is because of the boron protecting the surface.

This paper has investigated the interaction between tellurium and iodine in conditions similar to a severe accident. However, there are certain discrepancies between the simulated environment and a real accident environment. For instance, the lack of radiation, and the lack of several other volatile or semi-volatile fission products, such as cesium (a volatile fission product), technetium and/or silver (both of them semi-volatile) [13]. As such, the results of these paper must be reported with these constrictions in mind, and the question of weather or not tellurium iodide is likely to form is still largely unanswered, as it is known that cesium influences the iodine speciation, for instance, which is likely to affect the tellurium speciation as well. Furthermore, the release kinetics of the different fission products have not been considered, which may also affect the chemical form of the fission products. Fission products that release from the fuel at similar times are more likely to interact than those who release at different times. The release times themselves depend largely on the accident progression.

However, the results do imply that the formation of tellurium iodide is not impossible and deserves to be investigated further to gain clarity in whether it forms, and if so, its effects on the speciation of other fission products.

5. CONCLUSIONS

XPS is a useful tool for surface analysis. In many cases, a relatively certain assessment can be made about the species present on the surface. However, it should ideally be complemented by additional techniques, for instance SEM-EDX and/or PXRD to verify the abundance analysis. There is also the possibility of

overlapping signals in more complex samples, or different species can contain the same chemical bonds, making them very difficult to distinguish with XPS alone, for instance B_2O_3 and $B(OH)_3$, both containing the B-O bond.
Boric acid seems to affect tellurium indirectly by preventing the oxidation of tellurium metal to tellurium dioxide. This probably does not happen by direct interaction, however, as there are no indications of a Te-B bond in the samples. Instead, the protection may be due to a passive layer of B_2O_3.

Tellurium also interacts with iodine, likely to form tellurium iodide, which is a volatile species. This is implied to happen especially in reducing conditions, while being less certain in inert conditions.

ACKNOWLEDGMENTS

This template was adapted from the template for ERMSAR 2019 posted on the Internet. APRI11, and NKS (Nordic nuclear safety research) are acknowledged for funding the project. Eric Tam is acknowledged for their assistance with running the XPS.

6. REFERENCES

[1] F. Börjesson Sandén, A-E. Pasi, T. Kärkelä, T. Kajolinna, C.Ekberg, "Interactions between volatile tellurium and boric acid in severe accident conditions", submitted to *Annals of Nuclear Energy* at 2023-12-14.

[2] D. Medina-Cruz, W. Tien-Street, A. Vernet-Crua, B. Zhang, X. Huang, A. Murali, J. Chen, Y. Liu, J. Miguel Garcia-Martin, J. L. Cholula-Díaz, T. Webster, edited by : B. Li, T. Fintan Moriarty, T. Webster, M. Xing, *Racing towards the Surface- Antimicrobial and Interface Tissue Engineering*, pp 729-763, Springer Nature, Cham, Switzerland, 2020, ISBN 978-3-030-34470-2, https://doi.org/10.1007/978-3-030-34471-9, retrieved 2023-05-16

[3] F. Garisto, "Thermodynamic behaviour of Tellurium at high temperatures", INIS report nr: AECL—10691, Canada, retrieved 2023-05-30

[4] J.M. Schwantes, C.R. Orton, R.A. Clark, "Analysis of a Nuclear Accident: Fission and Activation Product Releases from the Fukushima Daiichi Nuclear Facility as Remote Indicators of Source Identification, Extent of Release, and State of Damaged Spent Nuclear Fuel", *Environmental science and technology*, **vol 46** (16),pp 8621-8627 (2012), https://doi.org/10.1021/es300556m, retrieved 2023-12-18.

[5] Pasi, A.-E., Foreman, M.R.St.-J., Ekberg, C. "Organic Telluride Formation from Paint Solvents Under Gamma Irradiation", *Nuclear Technology*, **vol 208** (11), pp 1734-1744, (2022) https://doi.org/10.1080/00295450.2022.2061258

[6] Edward C. Beahm, "Tellurium Behavior in Containment under Light Water Reactor Accident Conditions", *Nuclear Technology*, **vol 78** (3), pp 295-302 (1987), DOI: 10.13182/NT87-A15995, retrieved 2021-12-01

[7] T.S. Kress, E.C. Beahm, C.F. Weber, G.W. Parker, "Fission Product Transport Behaviour", *Nuclear Technology*, **vol 101** (3), pp 262-269, (1993), DOI: 10.13182/NT93-A34789, Retrieved 2022-08-26

[8] R. Kniep, A. Rabenau, "Subhalides of tellurium", *Physical and Inorganic Chemistry, Topics in Current Chemistry*, **vol 111** (1983), https://doi.org/10.1007/3-540-12065-3_3, retrieved 2023-12-21

[9] J. Wiesman, *Elements of Nuclear Reactor Design*, pp 1-47, Elsevier Scientific Publishing Company, 1977, Printed in Amsterdam, The Netherlands, (1977)

[10] F. A. Stevie, C.L. Donley, "Introduction to X-ray Photoelectron Spectroscopy", *Journal of Vacuum Science & Technology A*, **vol. 38** (6), (2020), DOI: 10.1116/6.0000412, retrieved 2023-011-08

[11] T.S. Kress, E.C. Beahm, C.F. Weber, G.W. Parker, "Fission Product Transport Behaviour", *Nuclear Technology*, **vol.101** (3), (1993), DOI: 10.13182/NT93-A34789, Retrieved 2022-08-26

[12] J.McFarlane, J.C.LeBlanc, "Fission product Tellurium and Cesium Telluride Chemistry Revisited", *No. AECL-11333, Atomic Enegry of Canada Ltd.*, 1996, retrieved 2021-10-11

[13] Y. Pontillon, G. Ducros, "Behaviour of fission products under severe PWR accident conditions- The VERCORS experimental programme—Part 2: Release and transport of fission gases and volatile fission products", *Nuclear Engineering and Design*, **vol.240,** (2010), DOI:10.1016/j.nucengdes.2009.06.024, retrieved 2021-08-11

ERMSAR 2024-

Interactions between volatile fission products and Boric Acid

Fredrik Börjesson Sandén, Anna-Elina Pasi, Teemu Kärkelä, Christian Ekberg



Presented by: Fredrik Börjesson Sandén, Chalmers University of Technology

Severe Nuclear Accident Research…



Severe Nuclear Accident Research…



I CLAIM THAT…

The combination of tellurium, iodine and boric acid, all together, increases the volatility of tellurium significantly.

The formation of Tellurium iodide is likely involved in the process.

XPS analysis does not indicate a Te-B bond being formed.

Let us talk about some chemistry…

- Iodine, Caesium and Tellurium all are volatile fission products

- BP (I)= 184°C

- MP (Cs)= 29°C
- BP (Cs)= 671°C

- MP (Te)= 450°C
- BP (Te)= 990°C



Spread of Te-132 after the Fukushima-Daiichi Accident

Estimated spread; see the reference:

K. Tagami, S. Uchida, N. Ishii, J. Zheng, *Estimation of Te-132 Distribution in Fukushima Prefecture at the Early Stage of the Fukushima Daiichi Nuclear Power Plant Reactor Failures*, *Environmental Science and Technology*, vol 47, 10, 5007-5012, 2013, DOI: 10.1021/es304730b, retrieved 2023-08-15

Used with permission from the publisher.

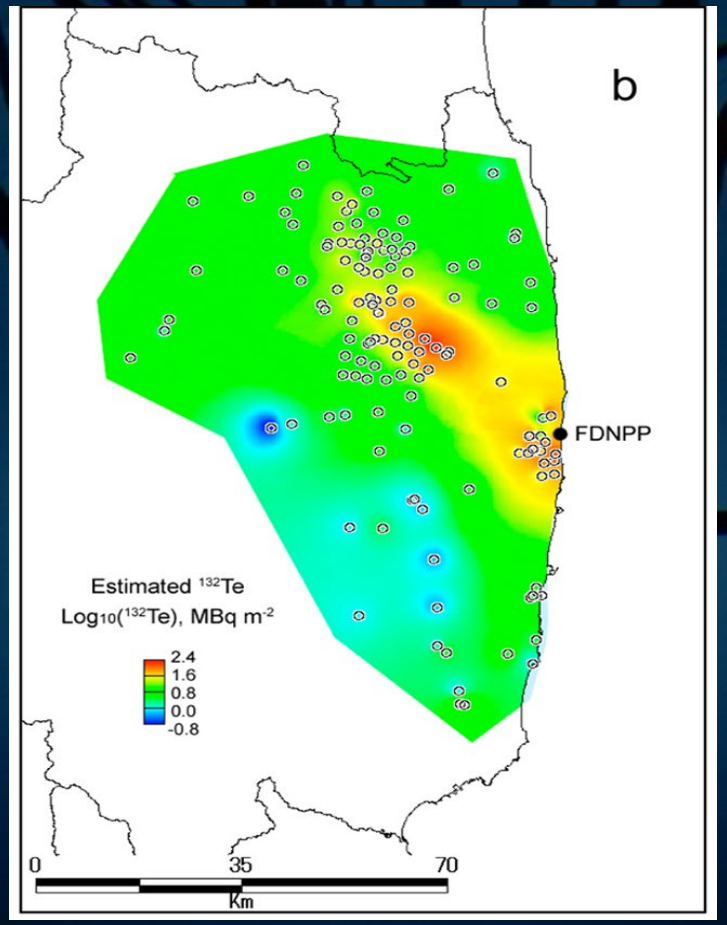

SEVERE ACCIDENT CHEMISTRY

Boric acid contains boron of two isotopes (^{10}B and ^{11}B)

^{10}B is extremely reactive to thermal neutrons, which cause nuclear fission in light water reactors.

Boric acid is therefore used as part of the emergency shutdown system.

This, in turn, makes its interaction with tellurium in such scenarios worth studying.

Experimental Setup

Precursor

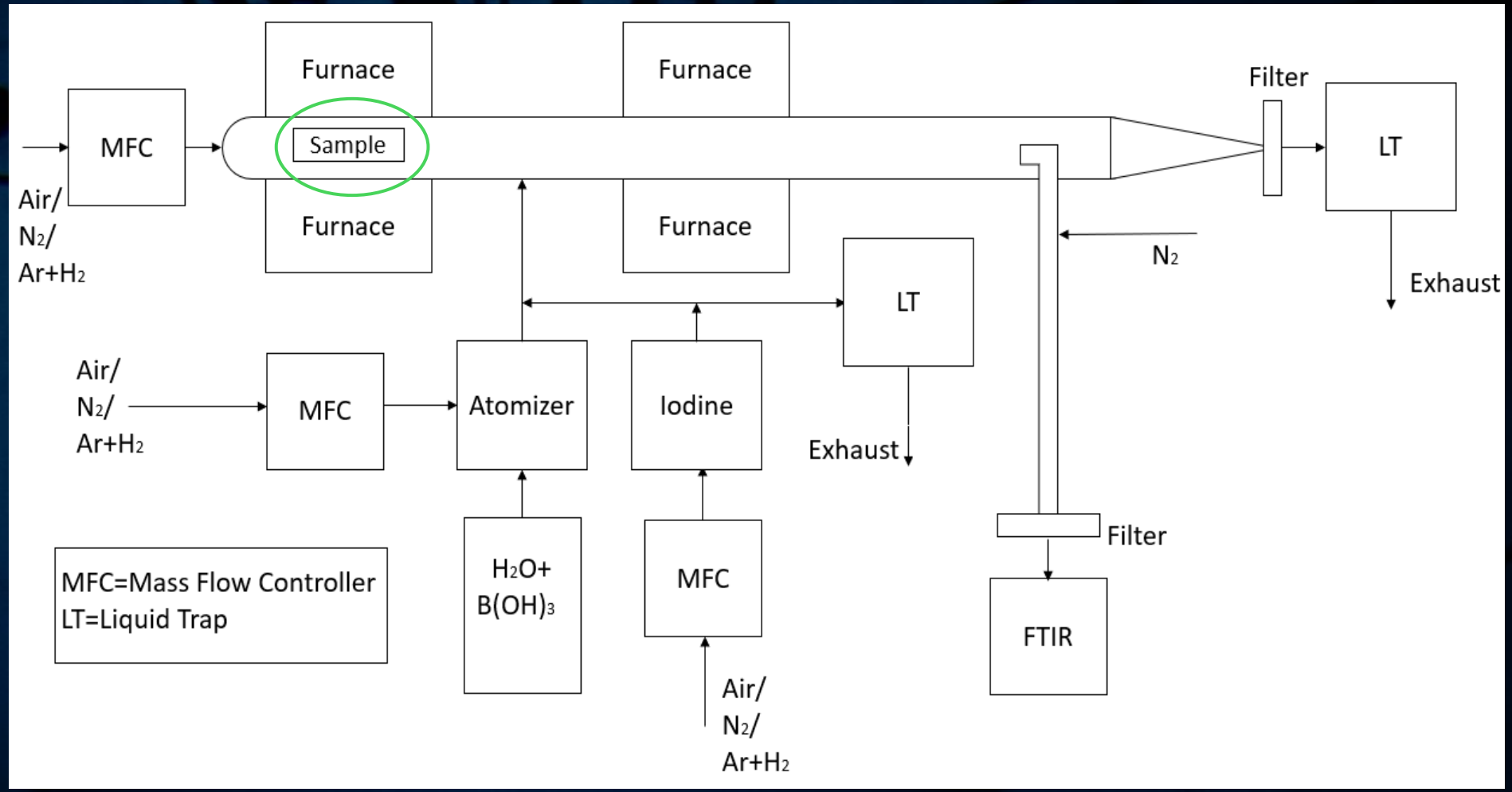

Experimental Setup

Precursor

Iodine+ dissolved species

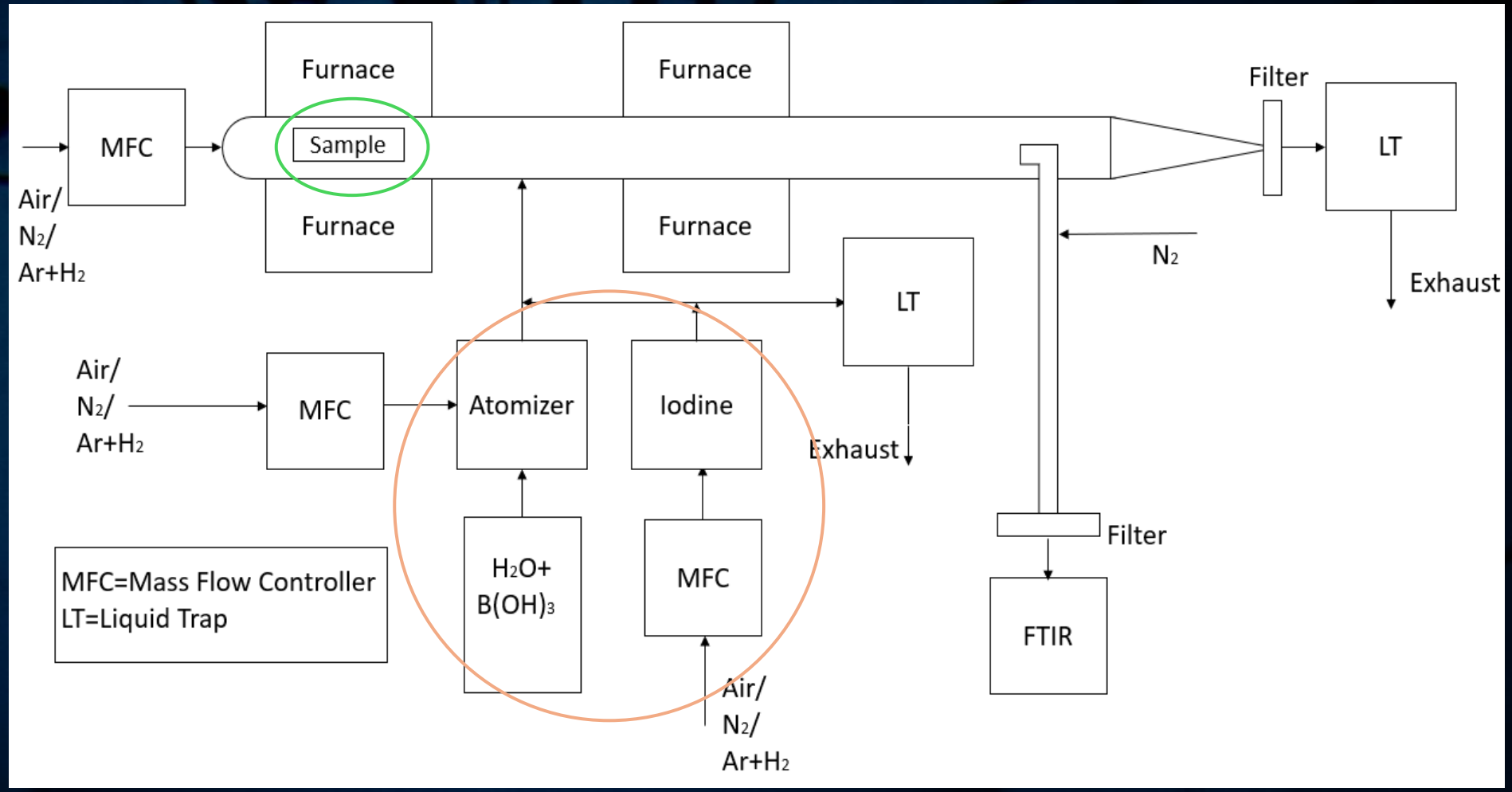

Experimental Setup

Precursor

Iodine+ dissolved species

Reaction Furnace (650°C)

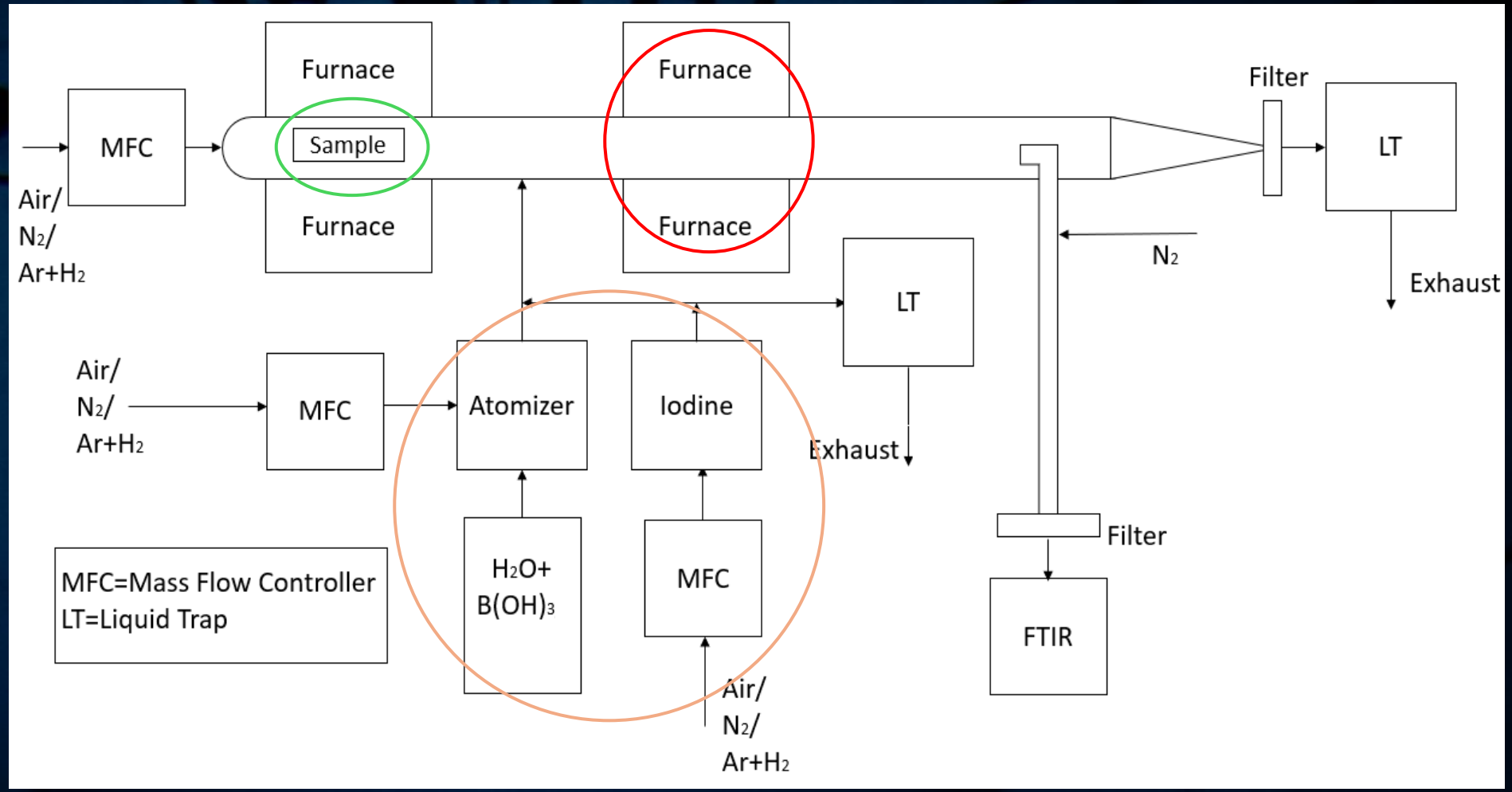

Experimental Setup

Precursor

Iodine+ dissolved species

Reaction Furnace (650°C)

Filter

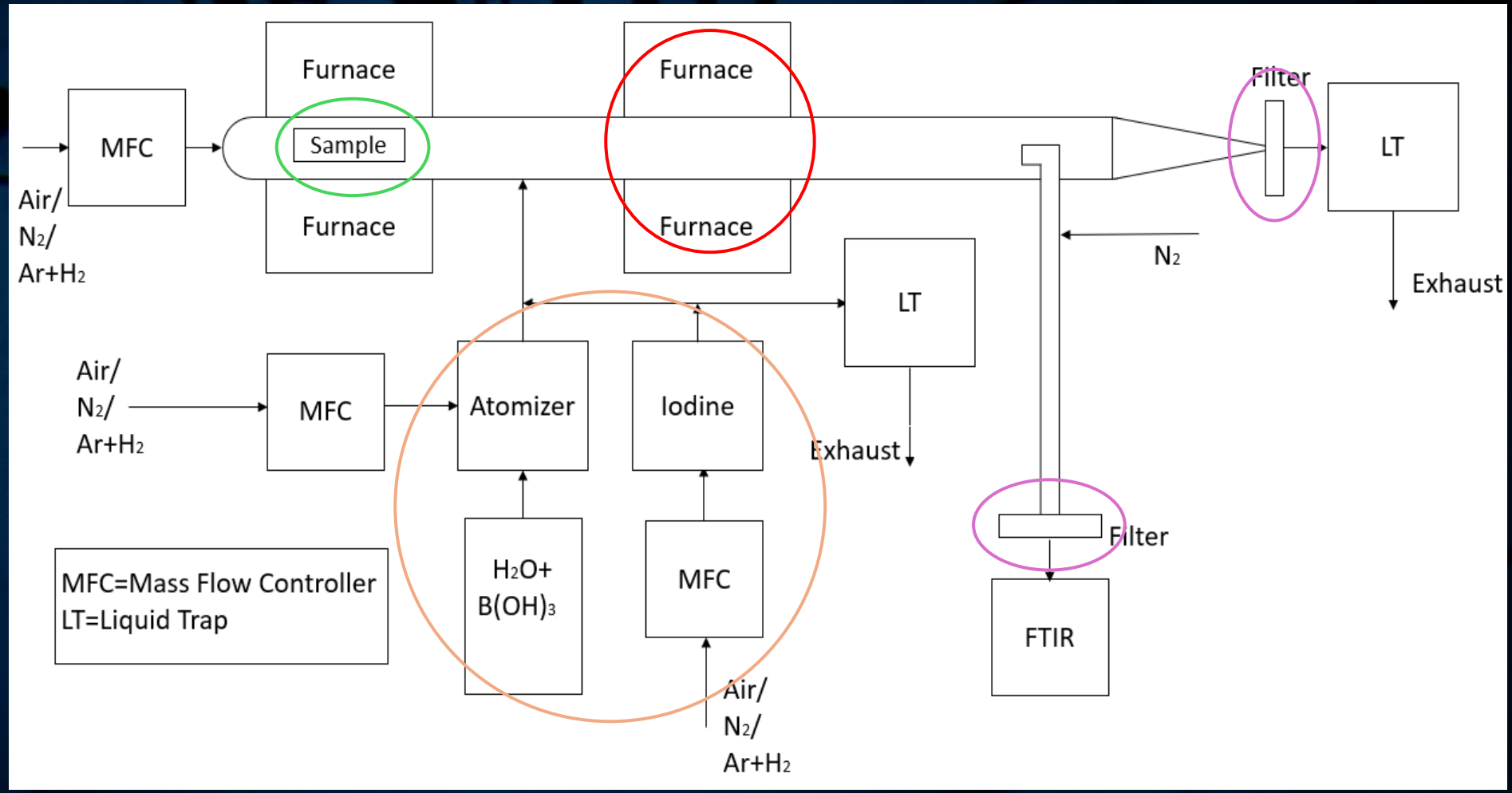

Experimental Setup

Precursor

Iodine+ dissolved species

Reaction Furnace (650°C)

Filter

Liquid Traps

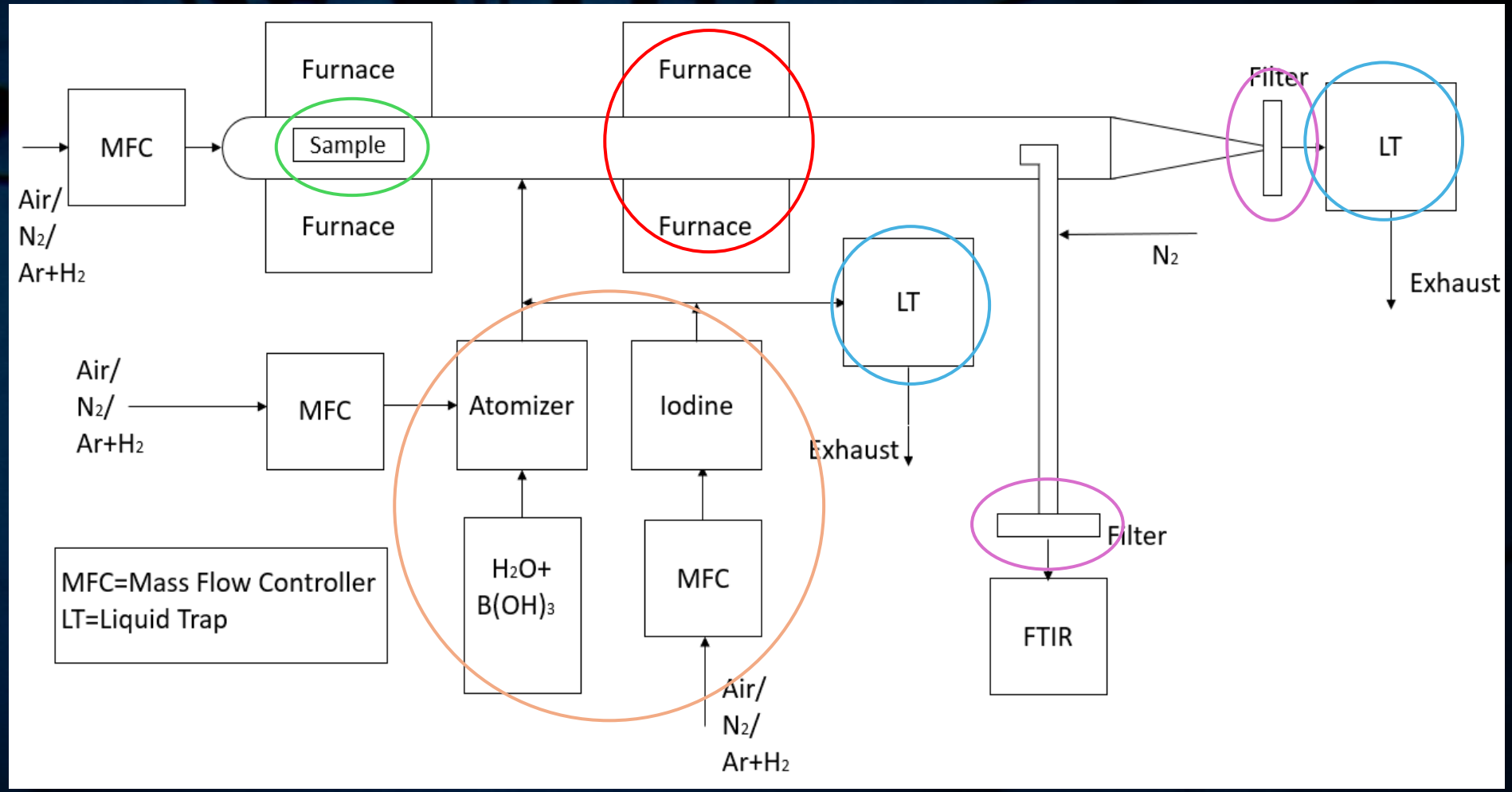

Experimental Matrix

Atmosphere	Fission Products	Injected through atomizer
Reducing (Ar/H_2)	Te	-
Reducing (Ar/H_2)	Te	H_2O, $B(OH)_3$
Reducing (Ar/H_2)	Te, I_2	-
Reducing (Ar/H_2)	Te, I_2	H_2O, $B(OH)_3$
Inert (N_2)	Te	-
Inert (N_2)	Te	H_2O, $B(OH)_3$
Inert (N_2)	Te, I_2	-
Inert (N_2)	Te, I_2	H_2O, $B(OH)_3$

Results- Liquid Trap Contents

Atmosphere	System [°C]	Tellurium [µM Te]	Boron [mM B]	Iodine [mM I]
N_2	Te	0,2	0,24	-
	Te, $B(OH)_3(aq)$	0,81	6,15	-
	Te, I_2	3,21	0,25	1,30
	Te, I_2, $B(OH)_3(aq)$	61,28	2,29	5,28
H_2/Ar	Te	41,74	1,11	-
	Te, $B(OH)_3(aq)$	6,75	3,27	-
	Te, I_2	0,04	0,53	4,18
	Te, I_2, $B(OH)_3(aq)$	117,12	1,36	5,00

Results- Liquid Trap Contents

Atmosphere	Temperature [°C]	Tellurium [µM Te]	Boron [mM B]	Iodine [mM I]
N_2	Te	0,2	0,24	-
	Te, $B(OH)_3$(aq)	0,81	6,15	-
	Te, I_2	3,21	0,25	1,30
	Te, I_2, $B(OH)_3$(aq)	61,28	2,29	5,28
H_2/Ar	Te	41,74	1,11	-
	Te, $B(OH)_3$(aq)	6,75	3,27	-
	Te, I_2	0,04	0,53	4,18
	Te, I_2, $B(OH)_3$(aq)	117,12	1,36	5,00

Results- Liquid Trap Contents

Atmosphere	Temperature [°C]	Tellurium [µM Te]	Boron [mM B]	Iodine [mM I]
N_2	Te	0,2	0,24	-
	Te, $B(OH)_3$(aq)	0,81	6,15	-
	Te, I_2	3,21	0,25	1,30
	Te, I_2, $B(OH)_3$(aq)	61,28	2,29	5,28
H_2/Ar	Te	41,74	1,11	-
	Te, $B(OH)_3$(aq)	6,75	3,27	-
	Te, I_2	0,04	0,53	4,18
	Te, I_2, $B(OH)_3$(aq)	117,12	1,36	5,00

Results- Reference Cases

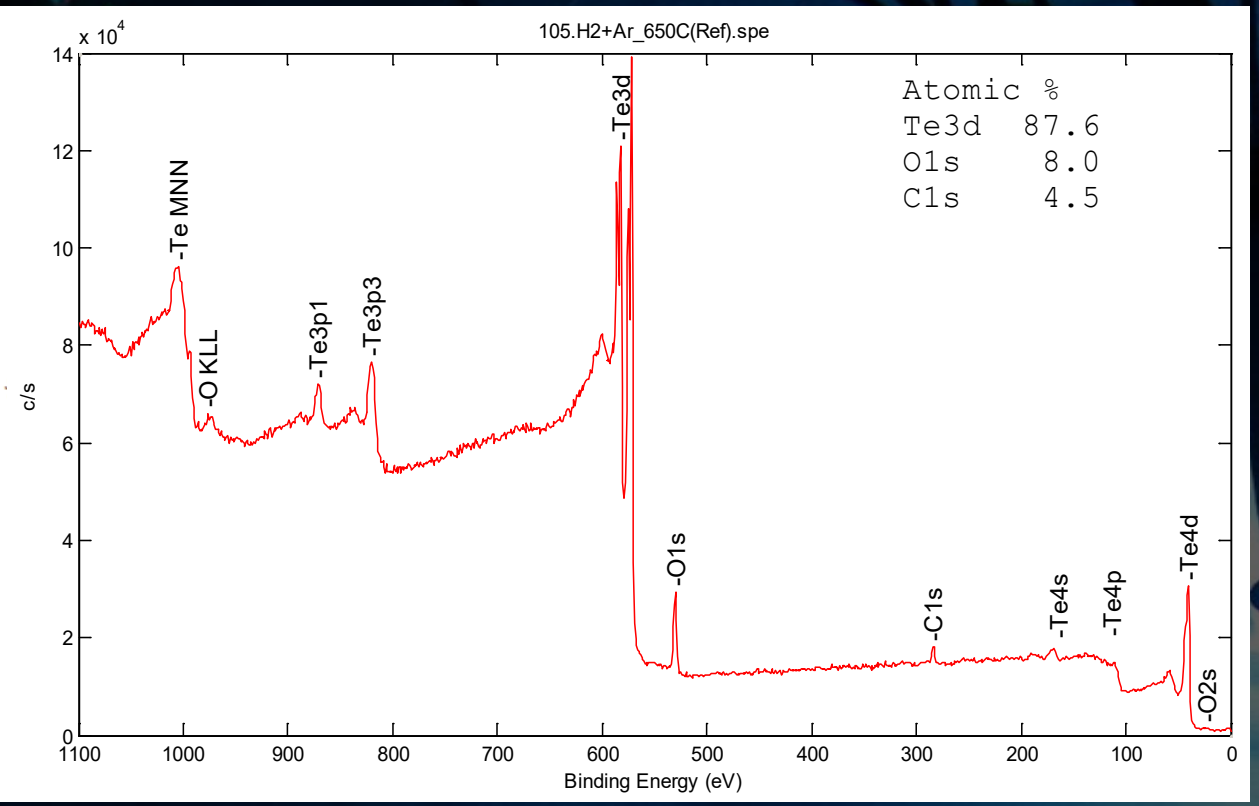

Reducing Conditions

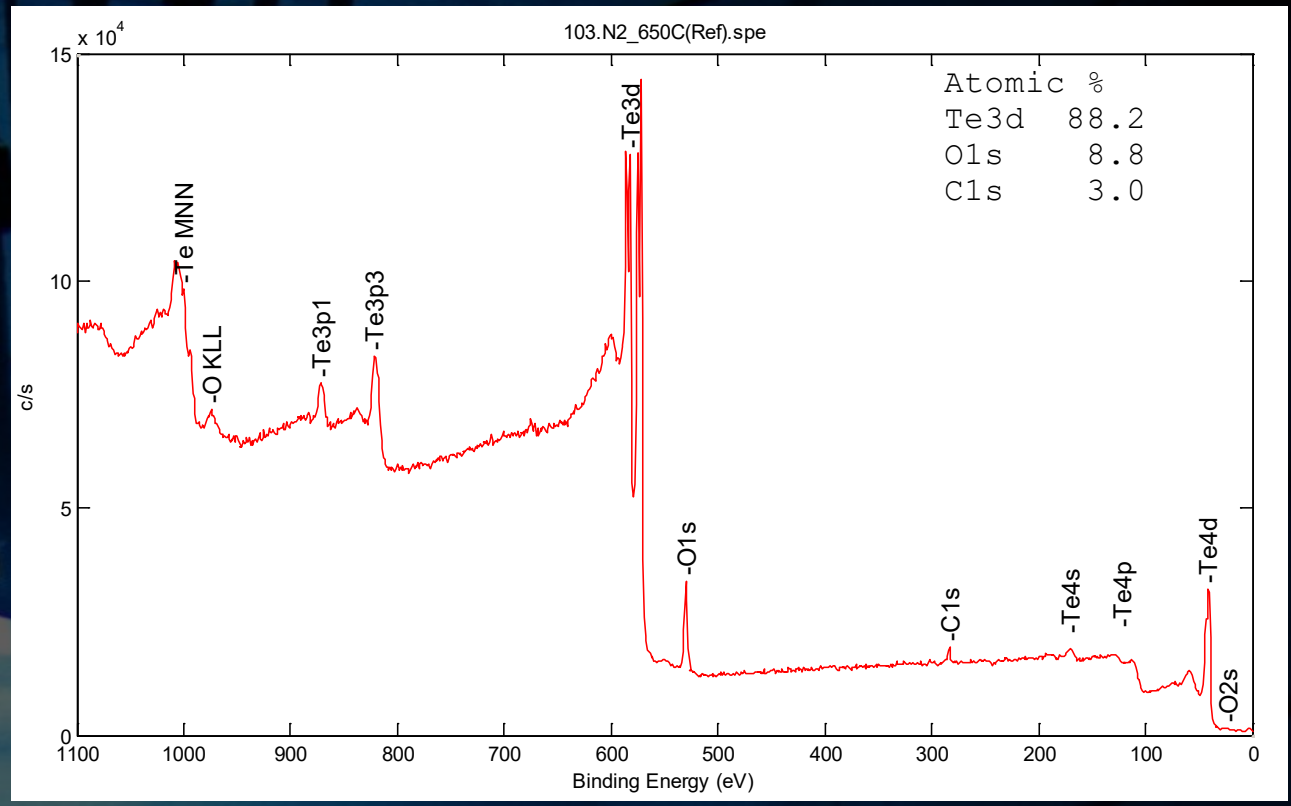

Inert Conditions

Results- Reference Cases

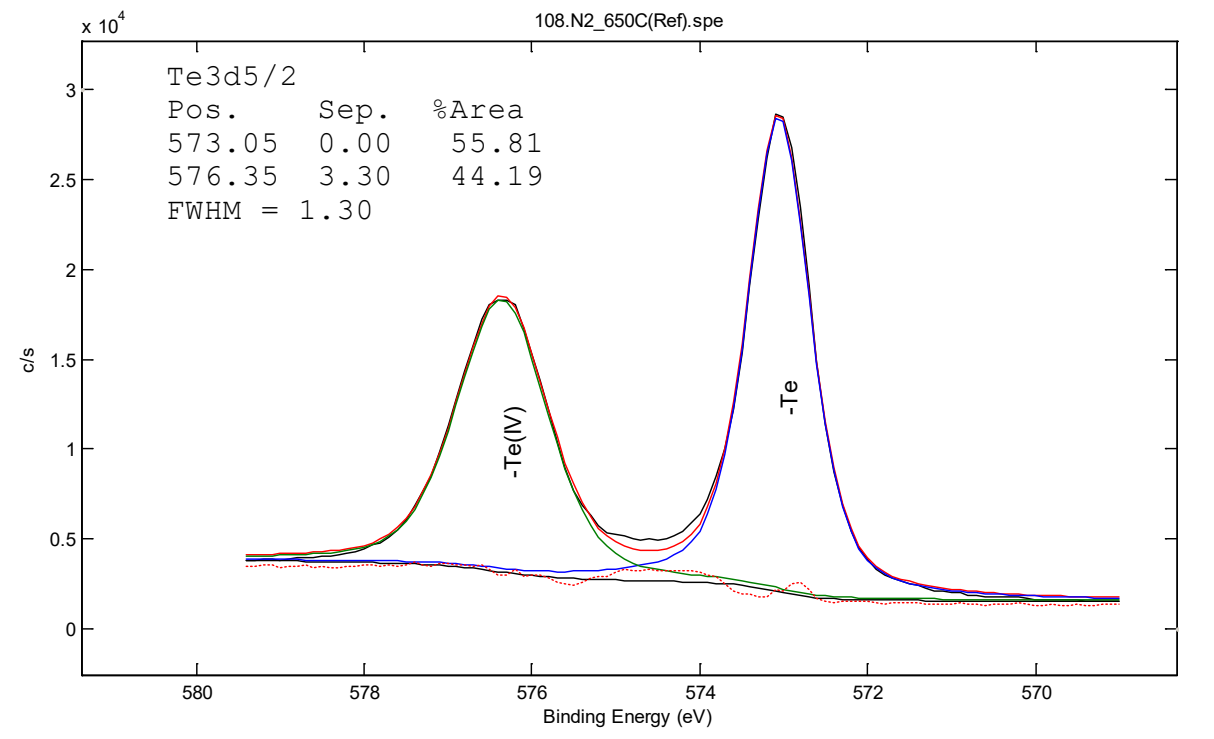

Tellurium speciation (similar in both atmospheres)
Mostly tellurium metal, but rather signigicant oxidation as well.

Results- Tellurium and Boric Acid

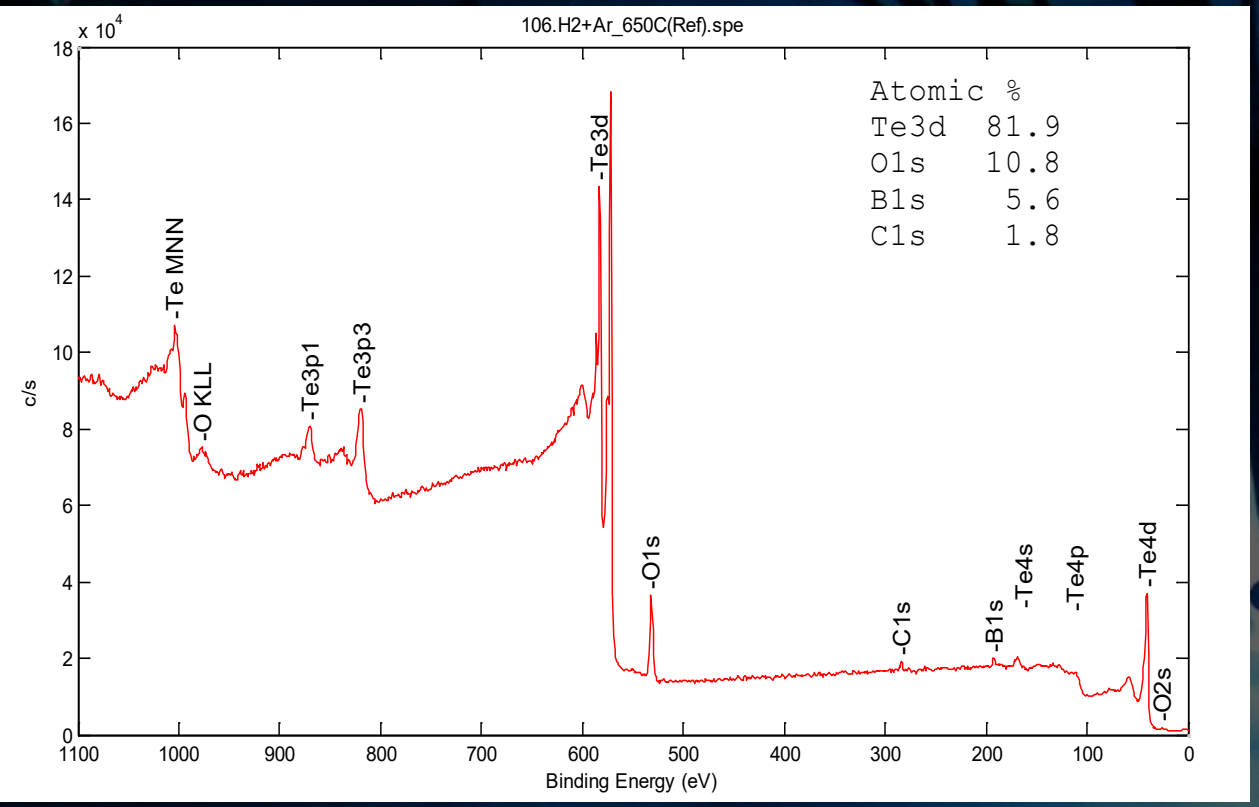

Reducing Conditions

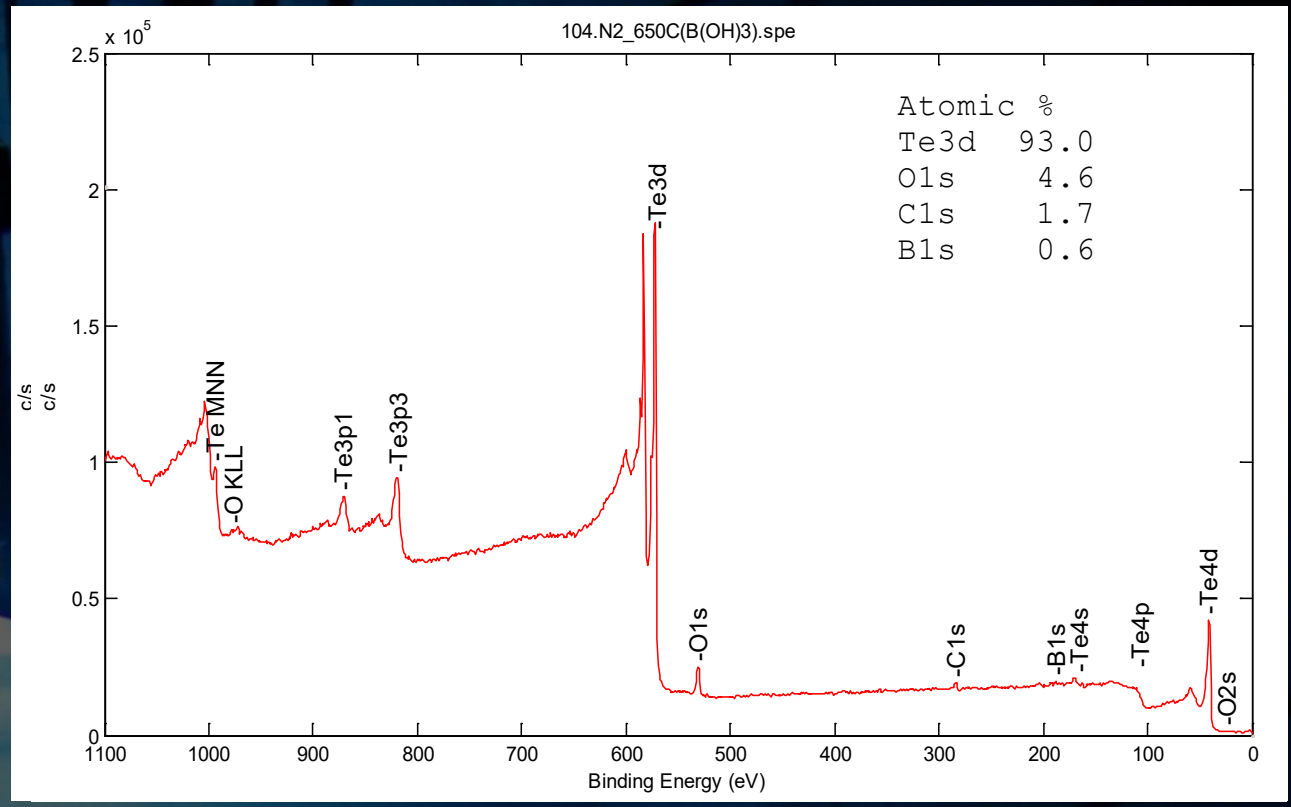

Inert Conditions

Results- Tellurium and Boric Acid

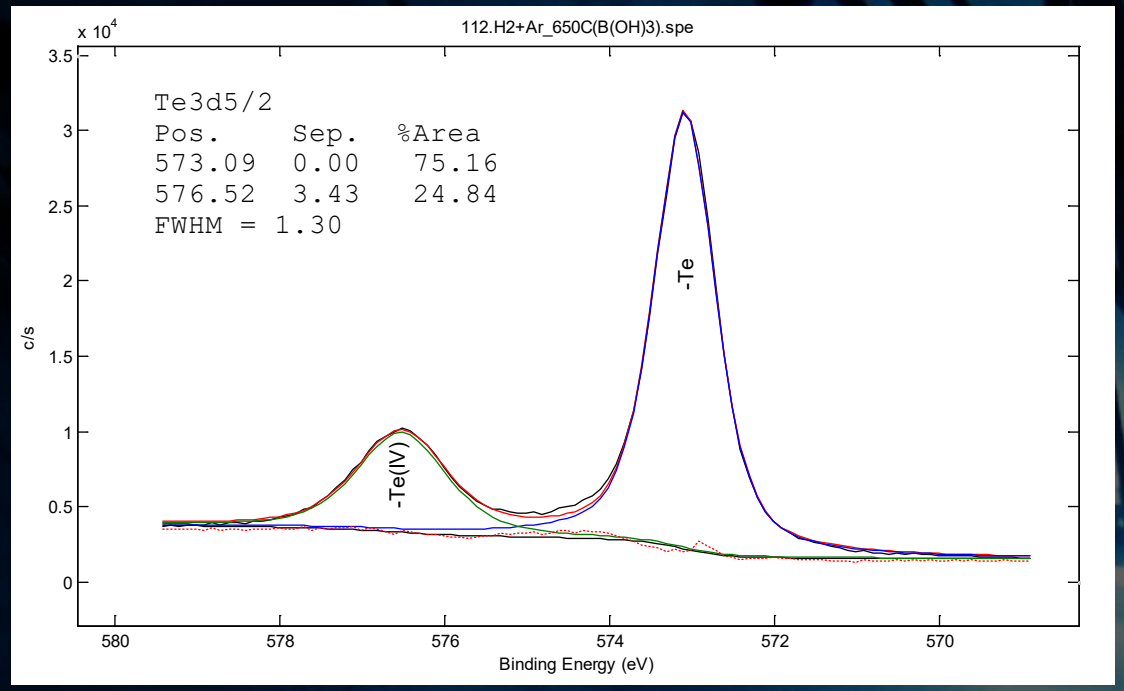

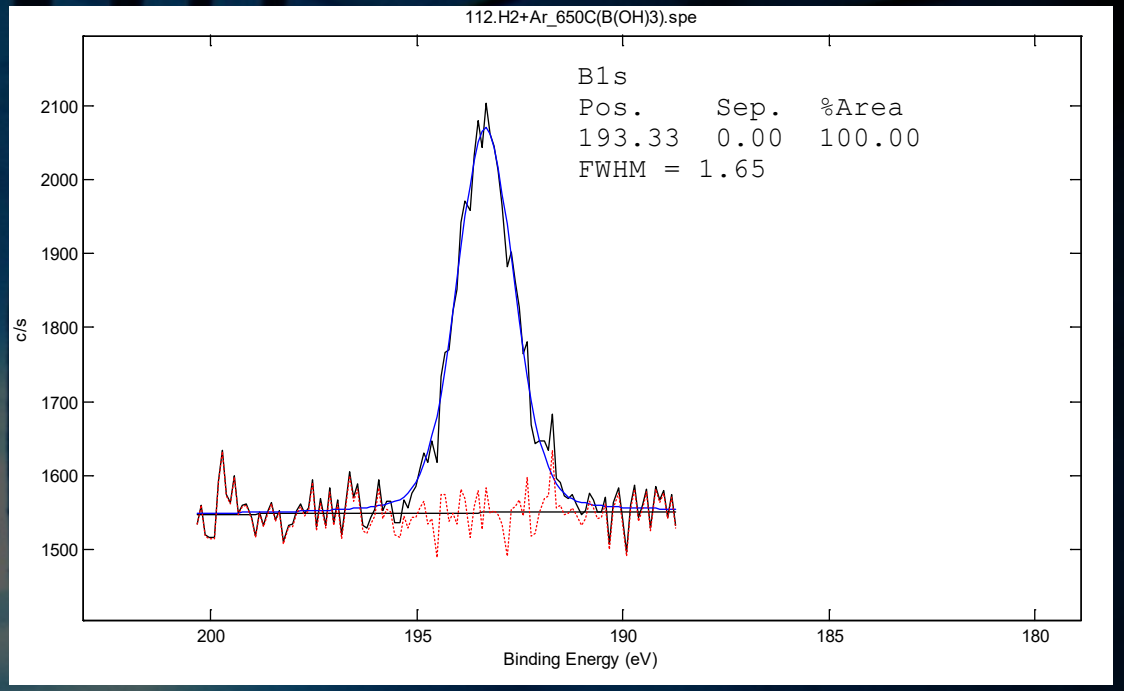

Tellurium speciation (similar in both atmospheres).
Less oxidation in this case, and no sign of direct interactionbetween boron and tellurium.

Boron speciation (again, the same species in both atmospheres).
Implies a B-O bond; either B_2O_3, or $B(OH)_3$.

Results- Tellurium, Iodine, and Boric Acid

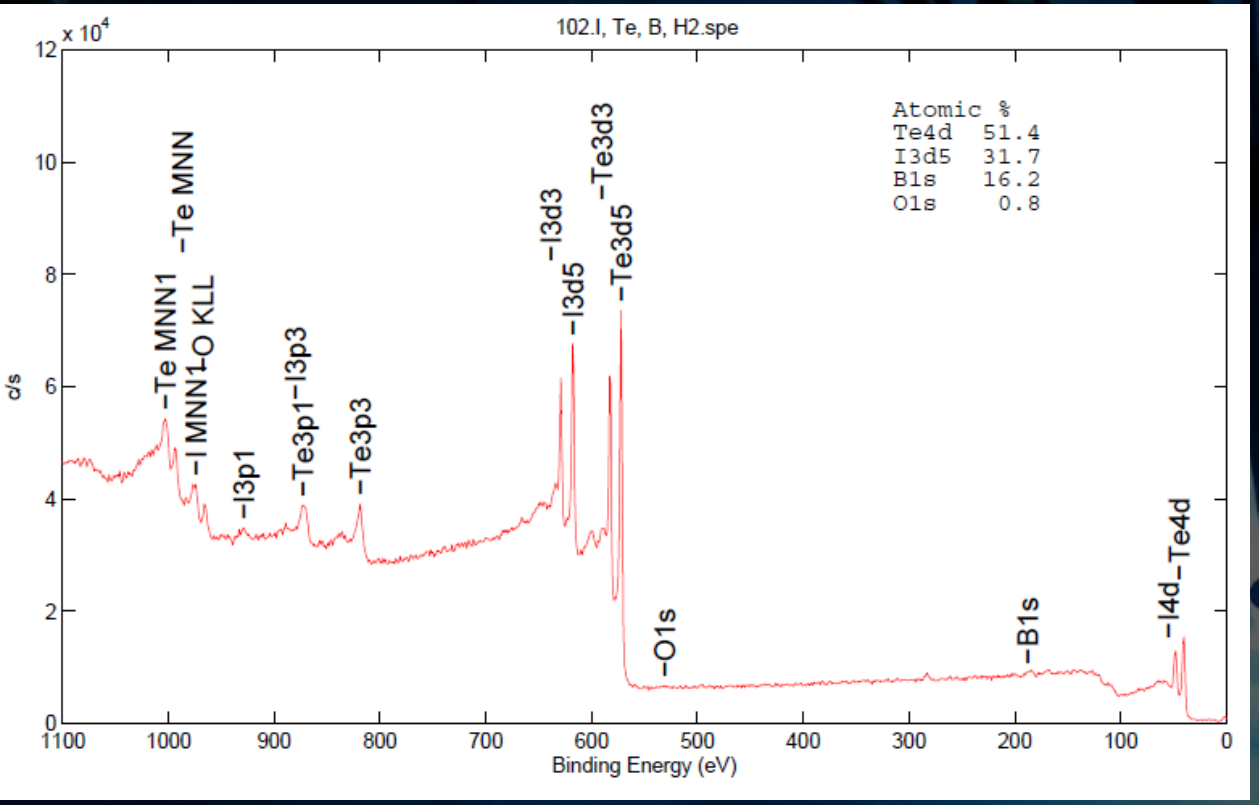

Reducing Conditions

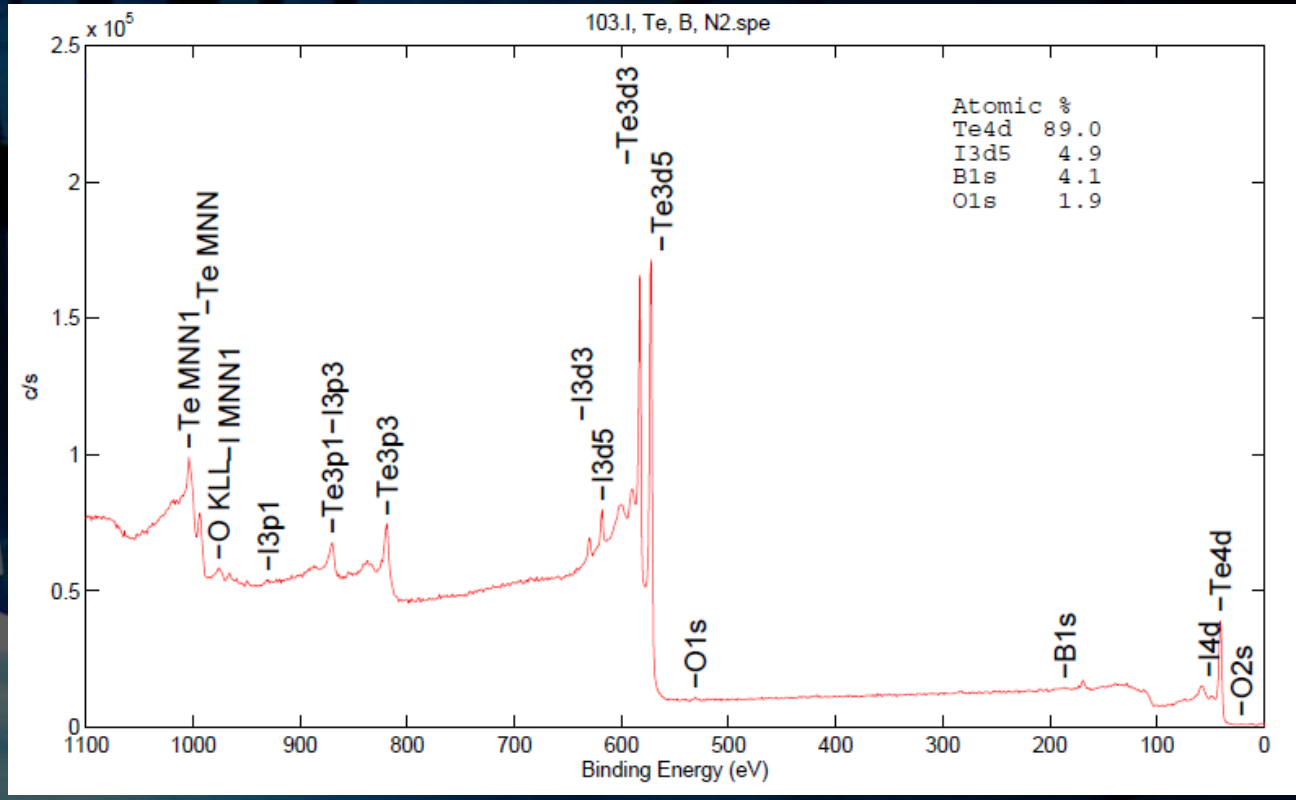

Inert Conditions

Results- Tellurium, Iodine, Boric Acid

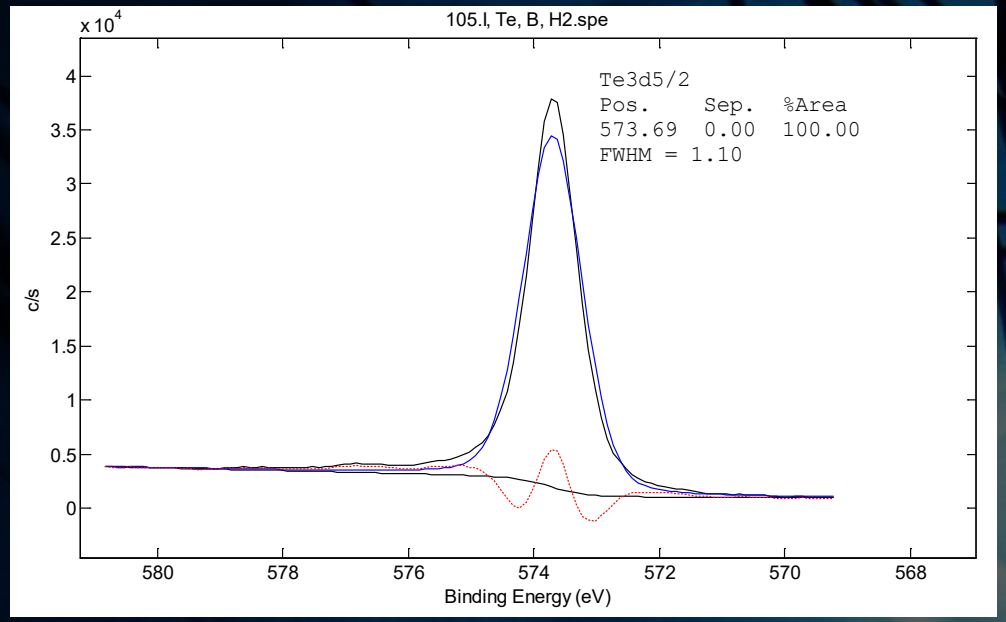

Tellurium speciation
Tellurium metal, or Tellurium Iodide
(similar for both atmospheres)

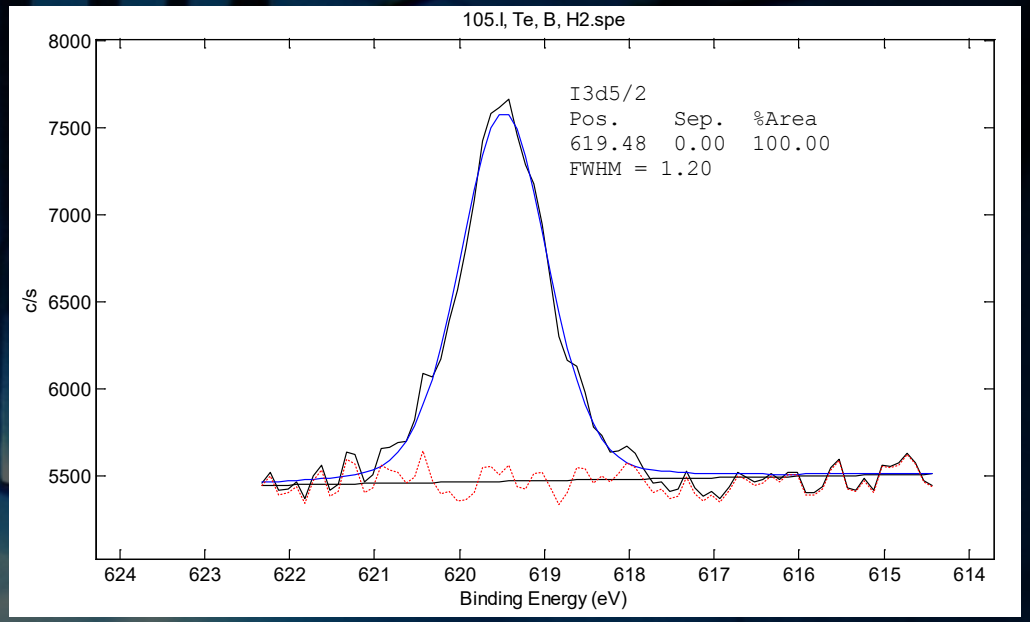

Iodine speciation
Possibly I2, but a bit too low. Matches well with Te-I
(practically identical for both atmospheres)

Results- Tellurium, Iodine, Boric Acid

The formation of Te-I appears likely, though it should decompose at 650°C.

This does not explain the increase in tellurium volatility, as Boric Acid is also necessary for that.

Atmosphere	Temperature [°C]	Tellurium [µM Te]	Boron [mM B]
N_2	Te	0,2	0,24
	Te, $B(OH)_3$(aq)	0,81	6,15
	Te, I_2	3,21	0,25
	Te, I_2, $B(OH)_3$(aq)	61,28	2,29
H_2/Ar	Te	41,74	1,11
	Te, $B(OH)_3$(aq)	6,75	3,27
	Te, I_2	0,04	0,53
	Te, I_2, $B(OH)_3$(aq)	117,12	1,36

Conclusive Remarks

What we can say for certain:

The combination of tellurium, iodine and boric acid, all together, increases the volatility of tellurium significantly.

The formation of Tellurium iodide is likely involved in the process.

XPS analysis does not indicate a Te-B bond being formed, but in principle a Te-O-B bond could be possible.

Conclusive Remarks

What we can speculate on:

The formation of Te-I may serve as a way to initially volatize the tellurium effectively, making it more available for further reaction.

The exact species responsible for the increased volatility have not been sucessfully identified.

Acknowledgements

-My co-authors Teemu Kärkelä and Anna-Elina Pasi

- My supervisor Christian Ekberg

- APRI (Accident Phenomena of Risk Importance in light water reactors) and NKS (Nordic Nuclear Safety Research)

- Eric Tam for teaching me to work with XPS

Interested in Accident Chemistry?



a Post-doc position at Chalmers

CHALMERS
UNIVERSITY OF TECHNOLOGY

CHALMERS
UNIVERSITY OF TECHNOLOGY

ERMSAR 2024-

Interactions between volatile fission products and Boric Acid

Fredrik Börjesson Sandén, Anna-Elina Pasi, Teemu Kärkelä, Christian Ekberg



Presented by: Fredrik Börjesson Sandén, Chalmers University of Technology

LOCAL MEASUREMENTS ON PARTICLE MASS TRANSFER IN GAS-LIQUID FLOWS

Alvaro Ramos Perez, Terttaliisa Lind, Victor Petrov, Annalisa Manera
Paul Scherrer Institute
Forschungstrasse 111, 5232 Villigen PSI, Switzerland
alvaro.ramos-perez@psi.ch; terttaliisa.lind@psi.ch; victor.petrov@psi.ch;
annalisa.manera@psi.ch

Annalisa Manera, Horst-Michael Prasser
ETH-Zürich
Rämistrasse 101, Zürich, Switzerland
annalisa.manera@ethz.ch; prasser@lke.mavt.ethz.ch

ABSTRACT

Particle mass transfer processes in multiphase flows are widely present in chemical engineering and energy conversion processes. During a severe accident event with core degradation in a nuclear power plant, aerosol pool scrubbing can be used to capture radioactive particles from the venting of a containment. Despite its fundamental nature and the significant effort made by numerous studies in characterizing such processes, accurately validated computational multiphase fluid dynamics predictions of the local particle mass transfer at the bubble scale are still unavailable.

In this study, we developed a new experimental technique based on high-speed tomographic conductivity measurements to visualize hydrodynamics and particle mass transfer in a particle-loaded gas-liquid bubbly flow in a vertical channel. The conductivity measurements are performed with a 1 mm resolution Wire-mesh sensor at 3200 Hz. The injected aerosols are NaCl micrometer diameter particles. The passage of the bubbles is characterized by a signal of lower relative conductivity than the liquid water. From the measured data, we can directly obtain the local value of the void fraction. The size and shape of every single bubble can be measured. Once the aerosol particles are transferred to the liquid phase, they dissolve, and the conductivity signal is proportional to the electrolyte concentration. The mass transfer is visualized in a concentration wake that follows downstream from the bubble. We performed experiments at different aerosol concentrations and particle sizes to assess the effects of the aerosol characteristics on the particle mass transfer.

We obtain first-of-its-kind data of cap ellipsoid bubbles and associated mass transfer wakes. These CFD-grade data results can be used to develop and validate high-fidelity aerosol pool scrubbing numerical codes. The resolution is such that the bubble's geometry can be characterized in detail. The geometry of the wake corresponds to the expected momentum wake behind a blunt body in the subcritical turbulent regime. The method is sensitive enough to capture the changes in the aerosol concentration for micrometer-size particles. Future work will extend the analysis and the measurements to obtain the particle mass transfer-related coefficients.

KEYWORDS
Aerosol, Mass transfer, Multiphase gas-liquid flow, Wire-mesh sensors, Local measurement

1. INTRODUCTION

During a severe accident in a nuclear power plant, radioactive particles can be released during containment venting [1] . Particle removal or retention by pool scrubbing in different liquid volumes is used to prevent the release to the atmosphere of potentially harmful aerosols. The so-called aerosol pool scrubbing [2] is a multiphase mass transfer process, i.e. a particle mass transfer in a gas-liquid flow, occurring at typical high gas velocities and heterogeneous two-phase flow conditions. The pioneer model of [3] started the study of the phenomena by looking at a single rising bubble where the flux F_{g-l} of particle mass from the bubble to the liquid is given by the following expression:

$$F_{g-l} = \alpha m_0 e^{-\alpha t} \quad (1)$$

where t is the rising time, m_0 is the initial particle mass inside the bubble, α is the aerosol deposition coefficient which depends on the added contribution of the inertial, sedimentation and diffusive deposition formulated in terms of the bubble and aerosol properties. From the simple mechanistic model of [3] to the current numerical codes on aerosol pool scrubbing [4], [5], there is still the need to further develop the models to capture more realistic conditions. However, the inherent physical complexity of the phenomenon imposes a great challenge in the experimental or computational study of the fundamental coupling between hydrodynamics and particle mass transfer.

Experimentally, the particle mass transfer in pool scrubbing has been frequently measured by the integral variation of the aerosol concentration between the inlet and outlet of the column [6], [7], [8], [9]. The measured retention is assessed in terms of operational relevant parameters such as the aerosol particle size, the steam content, the gas flow rate, the liquid height, or integral two-phase flow variables such as the void fraction or the bubble size distribution. The local information is critical to get in-depth knowledge of the aerosol retention, but up to now it could only be measured in 2D for ideal bubbles [10]. On the Computational Fluid Dynamics (CFD) side, current state-of-art multiphase flow simulations can capture the bubble dynamics with the Volume-of-Fluids method [11] and complex flow structures with the Euler-Euler method [12]. The lack of CFD-grade hydrodynamic experimental measurements in pool scrubbing providing individual bubble information imposes a further challenge in validating the two-phase computational codes. For the development and validation of future high-fidelity codes on aerosol retention, local experimental data both on the particle mass transfer and the hydrodynamics are required.

We aim to bring a more realistic and detailed picture of the aerosol retention under non-ideal conditions. To break this research gap, we need to develop and operate a measurement method capable of measuring simultaneously phase and mass at a high time and space resolution. This goal will be achieved via conductivity measurements using a Wire-mesh sensor (WMS). The WMS [13] is an electrode-mesh tomograph developed for the high-speed visualization and characterization of transient gas fractions in two-phase flows [14], [15].

If gas bubbles carry aerosols made of electrolytic content, the particle mass transfer F_{g-l} can be visualized in the water phase due to the increase in conductivity given by the dissolved aerosols, whereas the presence of the gas phase will be recorded as a decrease in conductivity. Thanks to a high-frequency data acquisition rate and a WMS with a high spatial resolution grid, near to gas-liquid bubble interface turbulent mass wake measurements can be performed.

This paper is organized as follows: the experimental facility, and processing methods for the WMS will be presented in Section 2. In Section 3, both the hydrodynamic and mass transfer results will be discussed. Finally, in Section 4, the main conclusions are outlined.

2. INSTRUMENTATION AND METHODS

2.1. Experimental set-up

2.1.1. ARAGO facility

The gas-liquid aerosol mass transfer experiments were performed in the **A**erosol **R**etention **A**nalysis in **G**as-liquid fl**O**ws (ARAGO) facility at the Paul Scherrer Institute. ARAGO is a flexible and modular set-up that allows aerosol retention experiments in stagnant and moving liquid conditions.

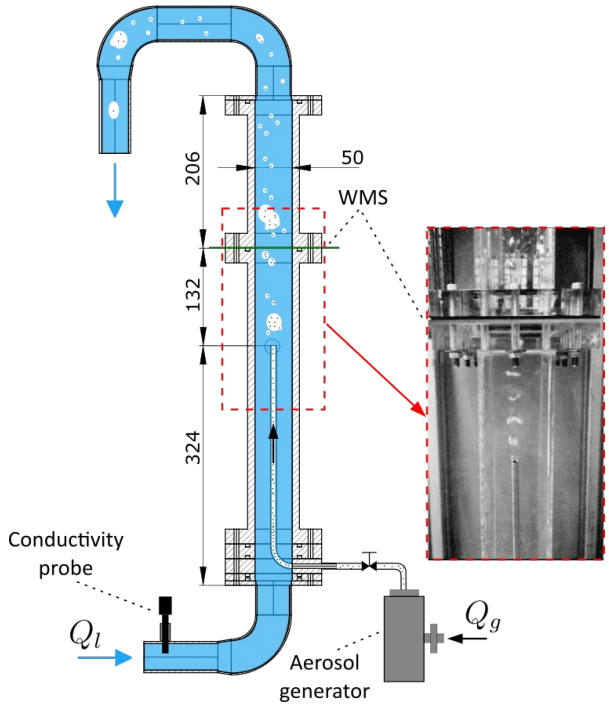

Figure 1. ARAGO facility, detail on the injection and WMS position. Spatial dimensions are in *(mm)*.

For these sets of experiments, the test column (**Figure 1**) was connected to a high-flow rate water pump, providing $Q_l = 8.25 \cdot 10^{-3}\ m^3/s$, coupled to a 0.8 m^3 water tank open to the atmosphere. The column test section consists of a set of methacrylate pieces with a total operational height of 600 mm and a 50 mm inner section of the square channel. The liquid flows upwards from the bottom to the top of the facility and transports the injected gas to the tank, where it is released into the atmosphere. The aerosols and air carrier gas are introduced in the column via a vertically oriented stainless-steel pipe of 6 mm inner diameter and 8 mm outer diameter. The sodium chloride (NaCl) aerosols are generated by an atomizer (TSI 3076) filled with an aqueous NaCl solution. The volumetric gas flow rate, i.e., aerosol gas flow rate, is $Q_g = 1.72 \cdot 10^{-5} m^3/s$ (flow rate measurements with DryCal DC-2 $\pm$ 1.0%).

The WMS is located 132 mm over the injection point. The liquid conductivity probe (GREISINGER GMH 34131 ± 2µS/cm with non-linear temperature compensation EN 27888) is installed in the piping upstream from the injector and pushed to the centre of the channel to measure the liquid bulk electrolytic concentration and to calibrate the WMS.

2.1.2. High-resolution WMS

Local recordings of a multiphase mass transfer process such as the aerosol pool scrubbing require a measurement system with high spatial and temporal resolution and high sensitivity to tracer concentration changes. The WMS is an electrode-mesh tomograph for high-speed visualization of multiphase flows. This sensor provides a matrix of the instantaneous local conductivities in the measuring plane at the intersection between the transmitter and receiver wires. The current measured on the receivers, due to the sequentially activated signal from the transmitter wires, is proportional to the fluid conductivity. Therefore, the result is a 3D matrix of conductivity values $u_{i,j,k}$ of two dimensions in space $[i, j]$ and one in time $[k]$. Whereas the time resolution of the measurements can be enhanced by changing only the acquisition frequency of the electronics, improving the spatial resolution requires modifying the wires grid, and this is typically limited due to constructive reasons to a $\Delta l = 1\ mm$ lateral pitch (distance between parallel wires).

The WMS is an intrusive measurement technique, and bubbles can be partially or completely damaged after passing the sensor. However, in the measurement plane, the bubble keeps its original shape. The bubble velocity is the most affected variable as compared to a flow without the WMS. The lower the lateral pitch, the higher the relative contribution to the bubble motion of the decelerating effect due to the surface tension at the contact of the liquid-gas interface with the solid wires [16]. A liquid flow velocity is required to enhance the inertial effects, which allow the bubble to travel through the sensor grid.

The installed WMS has a 48x48 measuring grid of $0.05\ mm$ diameter wires with a lateral (between wires) and axial (between transmitter and receiver plane) pitch of $\Delta l = 1\ mm$. The acquisition system is based on the WMS200 receivers, transmitter, and electronics box from TELETRONIC. The frequency of the data acquisition is set to $3200\ Hz$.

2.1.3. Aerosol characterization

The aerosol characteristics, particularly its dynamic properties, will govern, together with the hydrodynamic properties, the particle mass transfer. Therefore, we performed total mass concentration $C_{aerosol}$ and particle size measurements d_p for a series of different configurations of our aerosol generator (**Figure 2**). The aerosol characterization was performed with an Electrical Low-Pressure Impactor (ELPI) by diluting and heating the aerosol stream to obtain dried crystals. The relative humidity of the aerosols measured at the ELPI inlet is 11.0 ± 2.0 % (UFT75-AT MELTEC $\pm$ 2.0 %), which is below the efflorescence relative humidity[17]. The injected aerosols in the column have a relative humidity of 80.0 ± 2.0 %, which results in a growth factor $d_{p,total}/d_p = 1.8$ for NaCl aerosols, according to the model of [18]. Except otherwise indicated, we refer to d_p as the dried particle size. In the size distribution, the two upper stages were discarded (aerodynamic diameter $d_p > 3.7\ \mu m$) given the negligible particle number and the high signal-to-noise ratio at these stages.

At the constant operational flow rate, increasing the NaCl concentration of the base solution C_b increases the mass contained in each generated droplet, and thus, the size of the resulting aerosol particles and the total mass concentration (**Figure 2b**). The Aerodynamic Mass Median Diameter (AMMD) is close to one micrometre for all the different operation points. According to the model from [3], for these aerosol sizes, the relevant particle mass transfer will happen due to inertia, with diffusion and sedimentation being negligible. Error bars (**Figure 2a**) indicate variation of the mass concentration in time during the measurement. The size distribution stays stable in time and among different experiments. WMS measurements in the column are performed at steady-feed conditions.

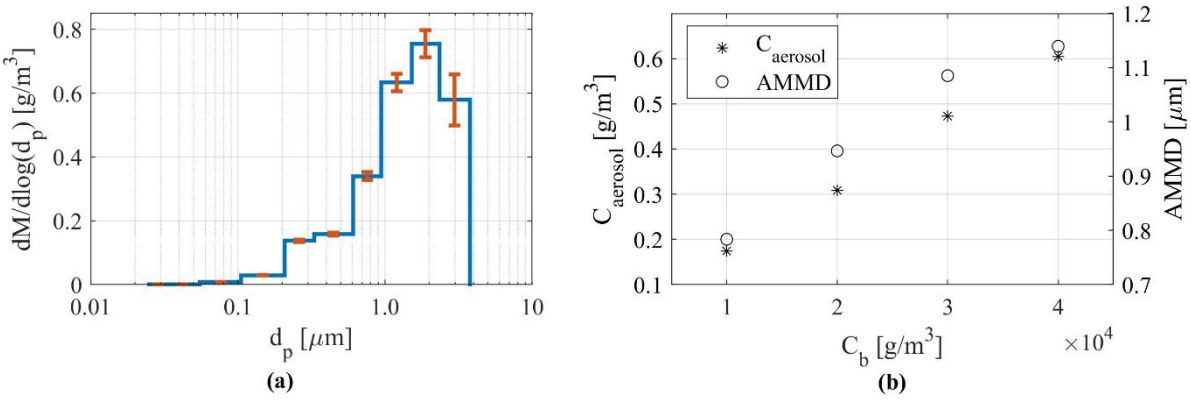

Figure 2. Measurements of dried aerosols with ELPI. Aerosol mass (M) size distribution at NaCl concentration of the base solution $C_b = 4.0 \cdot 10^{-4}\ g/m^3$ (a). Aerosol concentration ($C_{aerosol}$) and size ($AMMD$) as a function of the NaCl concentration of the base solution (C_b) in (b). The measurements for each operational point are repeated two times, and graphs show the average.

2.1.4. Test series

During the test series, the base solution in the aerosol generator is modified to get four different operational points: particle size and aerosol concentration, as shown in **Figure 2**. From $C_b = 1.0 - 4.0\ g/m^3$, we named these tests C1 to C4. We consider an additional point C0 where we operate with pure air so that no aerosols are present. Each experimental point of 30 s injection duration is repeated two times.

2.2. WMS data analysis models

2.2.1. Calibration

The two main physical quantities of interest in our study are the void fraction ε, which provides the gas-liquid phase information, and the concentration c_l, which indicates the mass transfer in the liquid phase.

From the WMS raw data, we get the measured conductivity $u_{i,j,k}$ at the node $[i,j]$ at the frame $[k]$. The conductivity $u_{i,j,k}$ can be made dimensionless by dividing by the bulk reference liquid conductivity $u_{i,j,base-liquid}$ to obtain the relative conductivity $g_{i,j,k}$ (**Figure 3a**):

$$g_{i,j,k} = \frac{u_{i,j,k}}{u_{i,j,base-liquid}} \tag{6}$$

The value $u_{i,j,base-liquid}$ is local but not instantaneous as it is obtained during the measurement series for a window of frames ($1\ s$ or 3200 frames) using the histogram of conductivities. Such calibration of the data is called dynamic calibration [19] and takes into account slow (compared to bubble dynamic timescale) variations of bulk liquid conductivity due to temperature variations or electrolyte concentration changes.

If the gas phase is present in the measuring cell, then the conductivity becomes $g_{i,j,k} < 1.0$ and the void fraction $\varepsilon_{i,j,k}$ (**Figure 3b1**) can be obtained by using the Maxwell-Hewitt expression:

$$\varepsilon_{i,j,k} = \frac{1 - g_{i,j,k}}{1 + \frac{g_{i,j,k}}{2}} \tag{7}$$

On the contrary, when a mass transfer wake is going through a crossing point, the conductivity increases $g_{i,j,k} > 1.0$, and the absolute variation of the concentration of the electrolyte in the liquid phase $c_{l,i,j,k}$ (**Figure 3b2**):

$$c_{l,i,j,k} = (g_{i,j,k} - 1)c_{ini} \tag{8}$$

where the calibration concentration $c_{ini} = \mu_{probe}/\lambda$. The value μ_{probe} is the measured bulk conductivity of the liquid stream by the conductivity probe, and λ is the characteristic constant which relates the electrolyte concentration with the electrolytic solution conductivity. According to Kohlbrauch's theory, at sufficiently low electrolytic concentrations, the conductivity of the solution is directly proportional to the concentration. The base solution conductivity during the experiments stays almost constant due to the large recirculating liquid volumes, typically $\mu_{probe} = 1.5 - 2.0\ \mu S/cm$. From dilution experiments for calibration of the conductivity probe, the characteristic constant is $\lambda = 2.16 \frac{g}{m^3} \frac{\mu S}{cm}$.

It is worth mentioning that the typical changes in conductivity due to the presence of a bubble are typically in the order of $g_{i,j,k} \in [0.0, 1.0]$, whereas for the wake $g_{i,j,k} \in [1.0, 1.1]$ for the base solution conductivity used during the experiments. Therefore, noise levels become much more critical in the concentration analysis than in the void fraction.

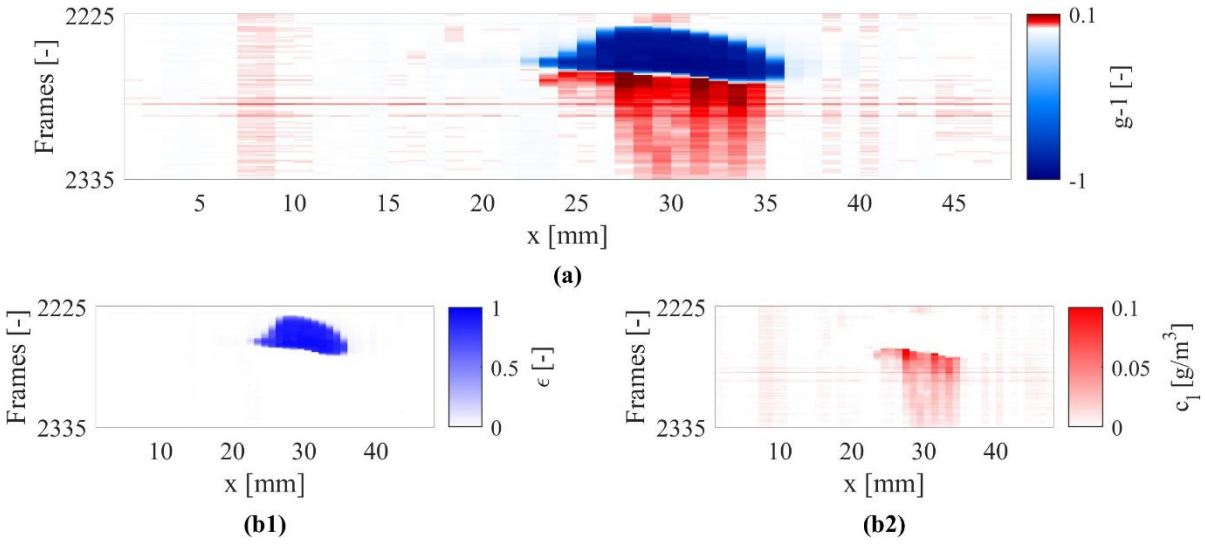

Figure 3. Relative conductivity (g) cut at $j = 24$ in (a), associated void fraction (ε) in (b1) and concentration (c_l) in (b2) cut.

2.2.2. Identification and reconstruction

Once the void fraction and the concentration are obtained, the data can be further post-processed in the so-called identification step. Here, we assign an ID number to all the cells that are part of a bubble, obtaining

a mask that allows us to study each bubble separately. The identification algorithm was developed by [15] using a recursive fill method. All interconnected cells with $\varepsilon_{i,j,k}$ above the noise level will be considered as being part of a bubble. The bubble void maximum is identified and compared to the surrounding maxima to check if a coexistent gas volume belongs to the same bubble.

Based on the $ID_{b,i,j,k}$ bubble matrix mask (**Figure 4b**), we get the $ID_{w,i,j,k}$ wake mask (**Figure 4c**) matrix using a 1D approach. Between the maxima of the integral in the measuring plane of the void fraction $\int \varepsilon dA$ of two subsequent bubbles (dotted points **Figure 4a**) we check for concentration values above a certain noise level $c_{l,i,j,k}$ (not necessarily interconnected) and associate them with the same ID. Our approach allows us to easily recognize the wakes as volumes of different salt concentrations following single bubbles, as happens for most bubbles. Coalescing or coexistent bubbles are neglected from this algorithm and not considered in subsequent analyses.

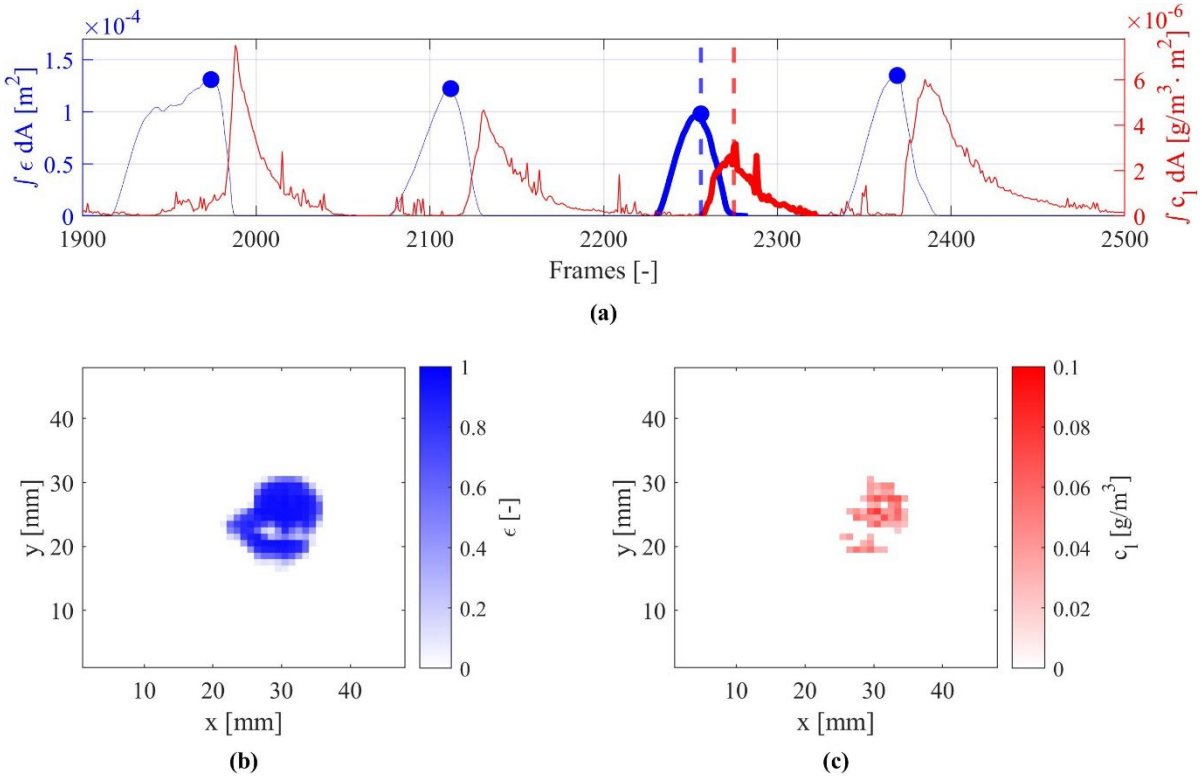

Figure 4. Plane integrals of the void fraction ($\int \varepsilon\, dA$) and concentration ($\int c_l\, dA$) in (a). Bubble mask at the void maxima (ε) in (b), and associated wake mask at the concentration (c_l) maxima in (c).

Under single-phase liquid flow conditions, the WMS shows noise values for the normalized standard deviation on the raw $u_{i,j,k}$ data $\sigma < 1.5$ %. We estimate the noise on the derived quantities based on (7) and (8). For the identification of the bubbles, we considered a cut-off threshold of $6\%(< 0.06)$ for the void fraction $\varepsilon_{i,j,k}$. For the identification of the wakes, we considered a cut-off threshold of $3\%(< 0.03 c_{ini})$ for the concentration $c_{l,i,j,k}$. In terms of the bubble volume or shape interface reconstruction, such threshold has negligible influence on the typically studied bubbles of 8 mm to 10 mm diameter for a pitch size of 1 mm. Regarding the concentration wakes, this imposes only the limit where the concentration contours cannot be

longer tracked. If we have enough cells with higher concentration, we can reconstruct a significant part of the wake close to the bubble interface.

3. RESULTS AND DISCUSSION

The hydrodynamic pattern or regime is crucial in multiphase mass transfer processes driven by inertia and impaction. Different small and large flow structures will be generated depending on the interaction between the individual bubbles in the bubble swarm and the swarm itself with the liquid bulk, affecting the gas's velocity field inside the bubble and the stability of the gas-liquid interface. Thanks to our high-resolution 3D measurements with the WMS (**Figure 5**), we can capture local information (up to $1\ mm$ resolution) of the bubbles. Such CFD-grade data can be directly used for development and validation of numerical codes aiming to solve bubble scale information.

The recorded hydrodynamics[1] is similar for the tests without (**Figure 5a**) and with (**Figure 5b**) aerosol injection. In terms of the time average void fraction in the measuring plane, $\bar{\varepsilon} = 0.033\ \pm 0.8\%$, with the uncertainty calculated from the standard deviation σ among all the tests. At the low gas superficial velocity ($j_g < 0.01\ m/s$) and the liquid circulation ($j_l > 0.1\ m/s$) used in the experiments, we obtain a bubbly flow [20] formed of single bubbles of similar size (distribution given by the injector diameter) rising at the center of the column. Some potentially leading and trailing coalescing bubbles are observed in the channel. However, most of the bubbles cross the WMS without interacting with their neighbors. The presence of the liquid flow around the injector prevents the bubble swarm from radial spreading, i.e the void fraction does not increase with height as typically for stagnant liquid conditions [21]. However, the bubble street is till subjected to swinging due to unstable lateral lift forces resulting from the deformation of the bubble interface while rising. The bubbles show an ellipsoid or spherical cap shape. The leading edge of the bubble is typically curved and prone to deformations, the trailing edge is flat. The transition between the leading and trailing edge is given by the major axis of the bubbles (between $10 - 15\ mm$) which corresponds also to the flow separation points for a blunt body.

Regarding the particle mass transfer measurements of aerosols from the gas to the liquid in which this work focuses, we are able to capture for the first time the mass transfer wake due to aerosol retention downstream from each rising bubble (**Figure 5b**). It is clear from the comparison with the pure air injection (**Figure 5a**) that the region with high concentration can only correspond to a mass transfer phenomenon.

[1] The projection-based visualizations from the 3D WMS data, as in **Figure 5b** from **Figure 5c**, are obtained by showing the maximum in the observation direction (y-axis in this case), i.e. as a viewer would see from one of the sides of the channel.

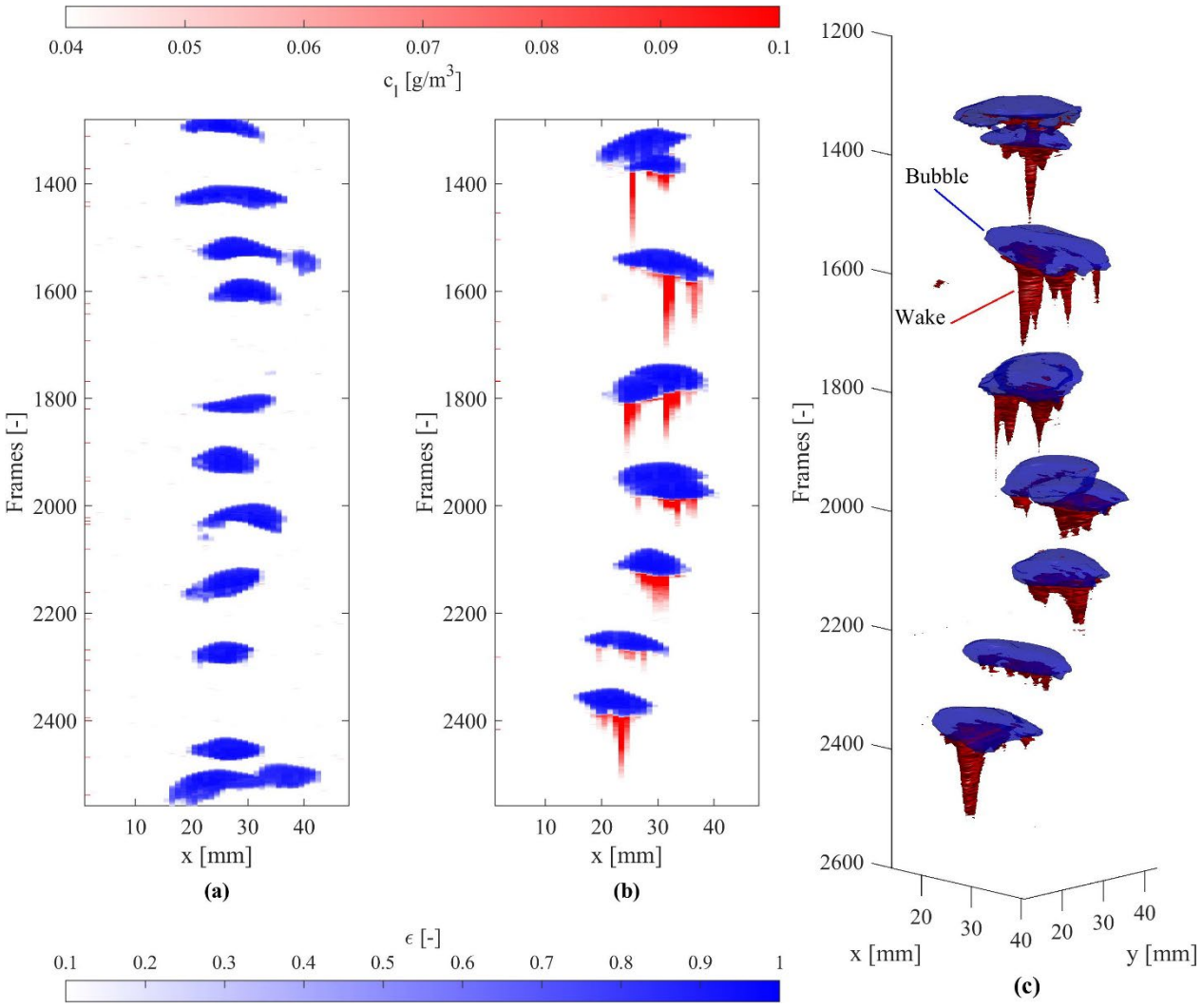

Figure 5. Instantaneous projection of the void fraction (ε) with threshold $\varepsilon > 0.1$ and the concentration (c_l) with threshold $c_l > 0.04\ g/m^3$ for test C0 in (a) and for test C4 in (b), and associated 3D view of isosurfaces $\varepsilon = 0.1$ and $c_l = 0.04\ g/m^3$ in (c) for test C4.

The hydrodynamics of the bubble defines the wake volume and corresponds in its dynamic sense to the region with strong recirculation and liquid mixing behind any blunt body moving in a fluid. The wake size is comparable to the bubble size in width, limited radially by the flow separation points. This structure or shape corresponds to the wakes in the turbulent subcritical regime. Close to the body or the phase interface, the turbulence is given by the interface oscillations and chaotic liquid flow recirculation, and leads to an intense turbulent mixing of the dissolved aerosols. Only relatively high concentrations will be detected downstream from the bubble, close to the interface. The contour between the measured mass wake and the liquid bulk is given by the transition from almost exclusively turbulent mixing to the additional contribution of the advection transport of the liquid fluid flow in the bulk. The axial spacing between the bubbles is similar to or larger than the typical maximum mixing height of the wake, and thus, each rising bubble could be studied independently.

For each experimental case with aerosol injection (with increasing aerosol concentration from C1 to C4), we isolate each bubble and associated wake with the methods described in **Section 2.2.2**. Bubbles are re-located in the middle of the channel according to their center of gravity. From averaging the ensemble (between 500-550 individual bubbles for each test), we get a representative first-of-its kind visualization (**Figure 6**) of the bubble and associated wake for the different aerosol properties.

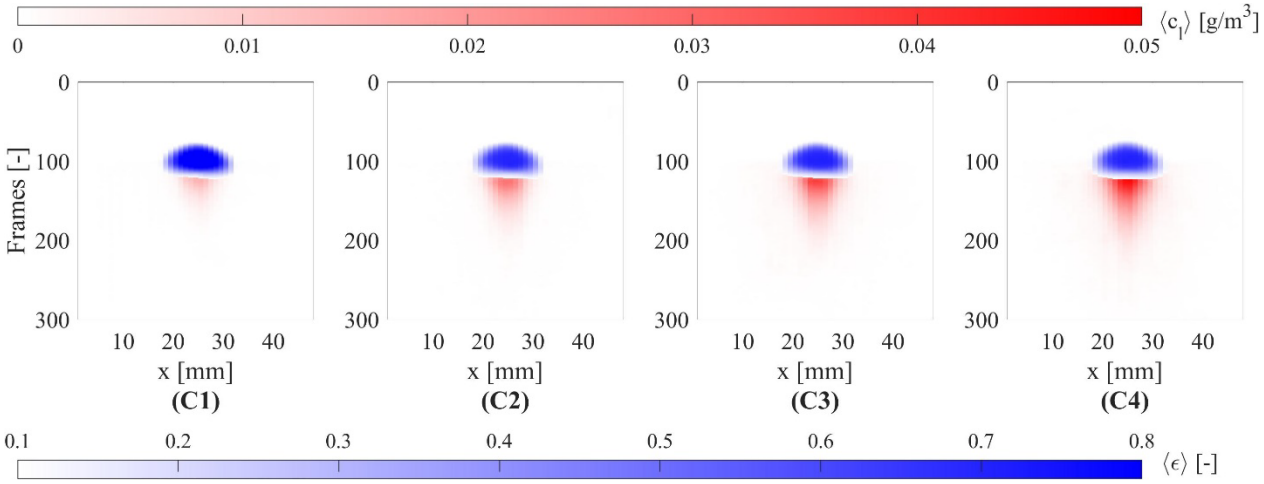

Figure 6. Projection of the ensemble average void fraction ($\langle\varepsilon\rangle$) with threshold $\langle\varepsilon\rangle > 0.1$ and the ensemble average concentration ($\langle c_l\rangle$) with threshold $\langle c_l\rangle > 0.0\ g/m^3$ for tests C1 to C4.

As we mentioned before, the hydrodynamics represented by the averaged bubble in **Figure 6,** is the same for all the tests given a sufficiently large ensemble of individual bubbles. The ellipsoidal or spherical cap is axisymmetric and so is also the wake. The value of the concentration in the observed wake is a result of the mass transfer. However, the size, understood as the covered area with the dissolved aerosols, is mostly given for low aerosol concentrations by the sensitivity of our measuring technique. Large areas with low concentration of dissolved aerosols are hidden as part of the liquid bulk. This consideration is particularly important when calculating advective mass transfer fluxes in the liquid phase. At higher aerosol concentrations (**Figure 6**, C4), the most external concentration contour shows the boundary between the turbulent diffusivity driven mass transfer (inside the wake) and the surroundings where the solute gets quickly advected into the bulk.

In these experiments the aerosol concentration C_{aero} is also coupled with the aerosol particle diameter d_p (**Figure 2**). Therefore, according to the reference model from [3] the mass transfer of aerosols from the bubble to the liquid will increase non-linearly with the aerosol. As expected, we observe in the measurements (**Figure 6**) an increase of the dissolved mass contained inside the wake with the aerosol concentration. However, it is worth to remember that the data reflects the mass transfer process in the liquid phase. It is non-trivial from the measurements to directly infer the mass transfer between the gas and the liquid. The transfer of aerosols to the liquid phase is non-steady process where the mass fluxes are coupled to the rate of decrease of particles inside the bubble and to the accumulation of dissolved aerosols inside the wake. We performed a great step in the visualization of the phenomena. In future work, we will develop the appropriate models to infer the key physical information this new data offers.

4. CONCLUSIONS

In this paper, we presented local data on the hydrodynamics and particle mass transfer for a non-ideal multiphase bubbly aerosol gas flow using a new experimental technique based on WMS measurements. We visualized and characterized the mass transfer for large individual ellipsoid cap bubbles in the bubble swarm at different aerosol conditions. Historically, such phenomena could only be modelled with analytical equations for ideal homogenous laminar conditions. Current CFD high-fidelity methods cannot effectively calculate particle mass transfer in non-ideal oscillating bubbles.

We performed the direct conductivity measurements with a high spatial ($1\ mm$) and temporal resolution ($3200\ Hz$) at liquid flow and low base conductivity conditions ($1.5 - 2.0\ \mu S/cm$). In the measuring section, the points with relative conductivity to water $g < 1.0$ are used to calculate the void fraction ε. When the local conductivity is higher than the reference $g > 1.0$, the dissolved electrolytic concentration in the liquid phase c_l is calculated. The void fraction (phase) and concentration fields (mass) are used to identify the individual bubbles and mass transfer wakes. The concentration field and shape of each wake can be obtained. The experimental results proved that the wakes are effectively captured in the measurements. The comparison with pure injected air showed that the increase of conductivity downstream from the bubbles is due to a mass transfer process and not to measuring artifacts such as the overshoots. The resolution of the experimental data is such that individual bubbles and associated wakes can be studied in detail and independently from its neighbors. We opened the possibility to obtain particle mass transfer coefficients for single non-ideal bubbles. The method can capture the effects of the variations on the aerosol properties.

Our high-resolution visualisation of local multiphase particle mass transfer for non-laminar flows provides CFD-grade data for the physics discovery and validation of high-fidelity codes. Further data analysis and experiments will be done to calculate particle mass transfer-related variables and coefficients. We also expect to extend our measurement technique to gas mass transfer in gas-liquid flows.

ACKNOWLEDGMENTS

The support of this work by Swiss National Science Foundation (SNSF) under Doctoral Grant 200021_200734 (03/2022-12/2026) for the project *Simultaneous measurement of aerosol mass transfer and hydrodynamics in gas-liquid two-phase flow systems* is gratefully acknowledged.

REFERENCES

[1] B. R. Sehgal, Ed., “Chapter 5 - Fission Product Release and Transport,” in *Nuclear Safety in Light Water Reactors*, Boston: Academic Press, 2012, pp. 425–517. doi: 10.1016/B978-0-12-388446-6.00005-8.
[2] J. Lopez-Jimenez *et al.*, “Pool scrubbing,” Spain, 1996.
[3] N. A. Fuchs, “The mechanics of aerosols,” Chemical warfare labs army chemical center MD, Jan. 1955. Accessed: Mar. 28, 2022. [Online]. Available: https://apps.dtic.mil/sti/citations/AD0227876
[4] S. A. Ramsdale, S. Guentay, and H. G. Friederichs, “BUSCA-JUN91 Reference manual for the calculation of radionuclide scrubbing in water pools,” Germany, 3-923875-66–5, 1995.
[5] P. C. Owczarski and K. W. Burk, “SPARC-90: A code for calculating fission product capture in suppression pools,” Nuclear Regulatory Commission, Washington, DC (United States). Div. of Regulatory Applications; Pacific Northwest Lab., Richland, WA (United States), NUREG/CR-5765; PNL-7723, Oct. 1991. doi: 10.2172/6120360.

[6] A. Charvet, N. Bardin-Monnier, and D. Thomas, "Can bubble columns be an alternative to fibrous filters for nanoparticles collection?," *J. Hazard. Mater.*, vol. 195, pp. 432–439, Nov. 2011, doi: 10.1016/j.jhazmat.2011.08.064.
[7] A. Dehbi, D. Suckow, and S. Guentay, "Aerosol retention in low-subcooling pools under realistic accident conditions," *Nucl. Eng. Des.*, vol. 203, no. 2, pp. 229–241, Jan. 2001, doi: 10.1016/S0029-5493(00)00343-5.
[8] T. Lind, A. Dehbi, and S. Güntay, "Aerosol retention in the flooded steam generator bundle during SGTR," *Nucl. Eng. Des.*, vol. 241, no. 1, pp. 357–365, Jan. 2011, doi: 10.1016/j.nucengdes.2010.10.025.
[9] S. Yuu, T. Jotaki, and K. Abe, "Investigation of the collection mechanism in absorption of aerosols by bubbling through water," *Powder Technol.*, vol. 17, no. 1, pp. 115–122, May 1977, doi: 10.1016/0032-5910(77)85050-X.
[10] K. Fujiwara *et al.*, "Experimental study of single-bubble behavior containing aerosol during pool scrubbing," *Nucl. Eng. Des.*, vol. 348, pp. 159–168, Jul. 2019, doi: 10.1016/j.nucengdes.2019.04.015.
[11] Y. Liao, J. Li, and D. Lucas, "Investigation on pool-scrubbing hydrodynamics with VOF interface-capturing method," *Nucl. Eng. Des.*, vol. 390, p. 111713, Apr. 2022, doi: 10.1016/j.nucengdes.2022.111713.
[12] E. Bicer, H. K. Cho, and H. S. Joon, "CFD Simulation of High Inlet Velocity Air Flow into a Large Tank at Pool Scrubbing Conditions," 2021.
[13] H.-M. Prasser, A. Böttger, and J. Zschau, "A new electrode-mesh tomograph for gas–liquid flows," *Flow Meas. Instrum.*, vol. 9, no. 2, pp. 111–119, Jun. 1998, doi: 10.1016/S0955-5986(98)00015-6.
[14] H.-M. Prasser, E. Krepper, and D. Lucas, "Evolution of the two-phase flow in a vertical tube—decomposition of gas fraction profiles according to bubble size classes using wire-mesh sensors," *Int. J. Therm. Sci.*, vol. 41, no. 1, pp. 17–28, Jan. 2002, doi: 10.1016/S1290-0729(01)01300-X.
[15] H.-M. Prasser, D. Scholz, and C. Zippe, "Bubble size measurement using wire-mesh sensors," *Flow Meas. Instrum.*, vol. 12, no. 4, pp. 299–312, Aug. 2001, doi: 10.1016/S0955-5986(00)00046-7.
[16] D. Ito, H.-M. Prasser, H. Kikura, and M. Aritomi, "Uncertainty and intrusiveness of three-layer wire-mesh sensor," *Flow Meas. Instrum.*, vol. 22, no. 4, pp. 249–256, Aug. 2011, doi: 10.1016/j.flowmeasinst.2011.03.002.
[17] C. Peng, L. Chen, and M. Tang, "A database for deliquescence and efflorescence relative humidities of compounds with atmospheric relevance," *Fundam. Res.*, vol. 2, no. 4, pp. 578–587, Jul. 2022, doi: 10.1016/j.fmre.2021.11.021.
[18] M. D. Petters and S. M. Kreidenweis, "A single parameter representation of hygroscopic growth and cloud condensation nucleus activity," *Atmospheric Chem. Phys.*, vol. 7, no. 8, pp. 1961–1971, Apr. 2007, doi: 10.5194/acp-7-1961-2007.
[19] T. T. Betschart, "Two-Phase Flow Investigations in Large Diameter Channels and Tube Bundles," Doctoral Thesis, ETH Zurich, 2015. doi: 10.3929/ethz-a-010656799.
[20] J. Weisman, "Two-phase flow patterns," *Handb. Fluids Motion*, pp. 409–425, 1983.
[21] R. F. Mudde, "Gravity-Driven Bubbly Flows," *Annu. Rev. Fluid Mech.*, vol. 37, no. 1, pp. 393–423, 2005, doi: 10.1146/annurev.fluid.37.061903.175803.

PAUL SCHERRER INSTITUT

PSI



A. Ramos, T. Lind, V. Petrov, A. Manera, H.M Prasser :: Paul Scherrer Institut :: ETHZ

Local measurements on particle mass transfer in gas-liquid flows

ERMSAR 2024, Stockholm

Introduction and motivation

During the event of an accident in the chemical or nuclear energy sector, **aerosol pool scrubbing** is an efficient way to collect harmful particle matter

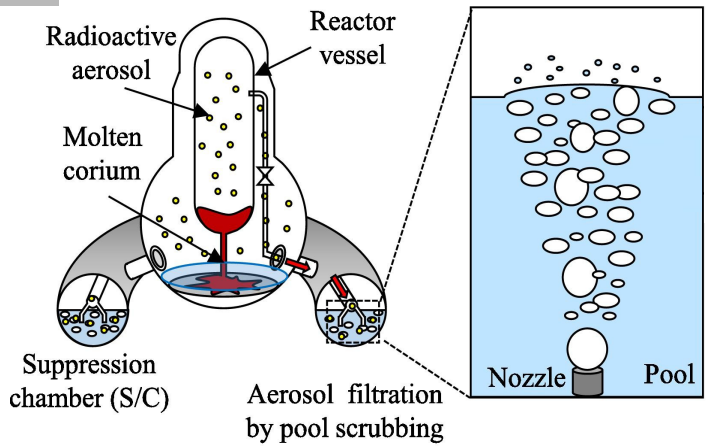

(Yoshida et .al, 2022)

Hydrodynamics → Mass transfer



Integral studies

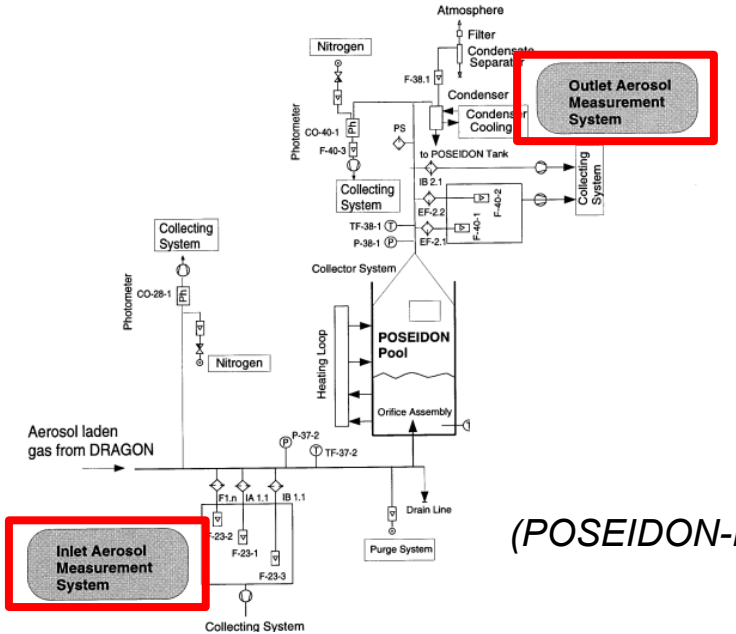

(POSEIDON-II, PSI)

Introduction and motivation

During the event of an accident in the chemical or nuclear energy sector, **aerosol pool scrubbing** is an efficient way to collect harmful particle matter

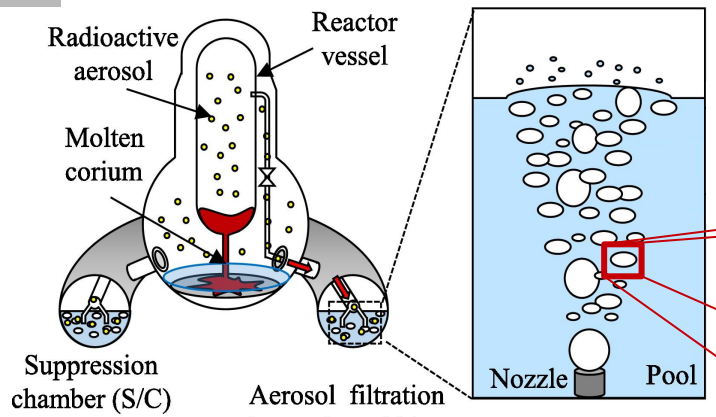

(Yoshida et .al, 2022)

Local studies

$J = \alpha N$ *from Fuchs (1955)*

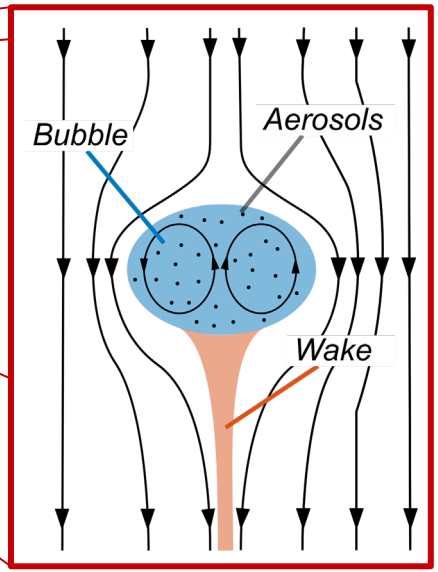

Hydrodynamics → Mass transfer



Introduction and motivation

Pool scrubbing fundamentals: solving computationally and experimentally aerosol retention for **non-ideal** bubbles

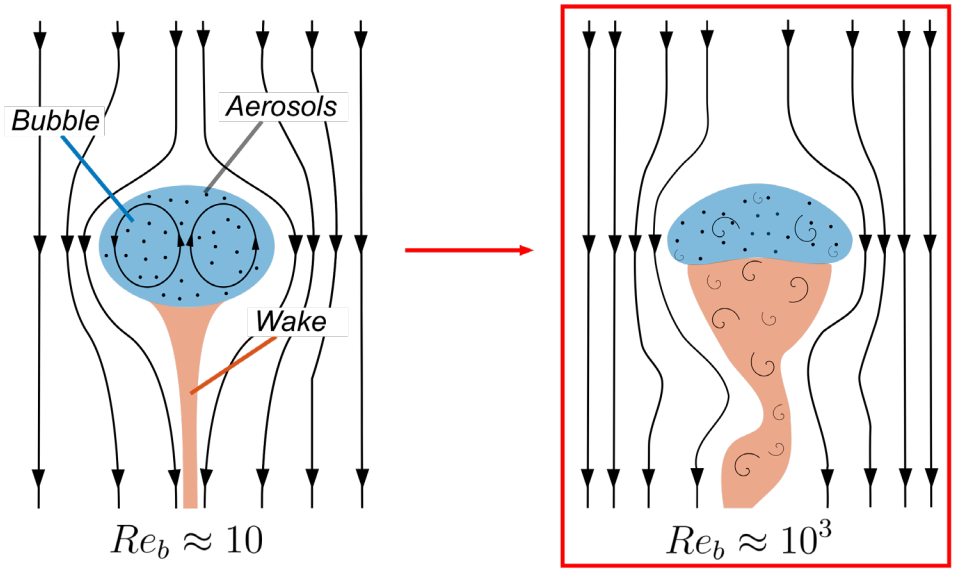

Ideal ellipsoid bubble

Non-ideal cap bubble

- ***Experimental method***
- ***WMS data analysis***
- ***Visualization***

Experimental method

Time and space high-resolution conductivity-based measurements with **Wire-mesh sensor**

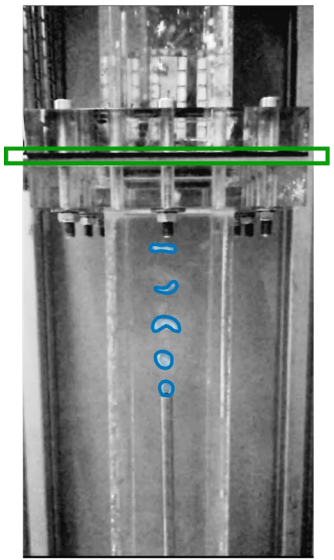

Experimental set-up

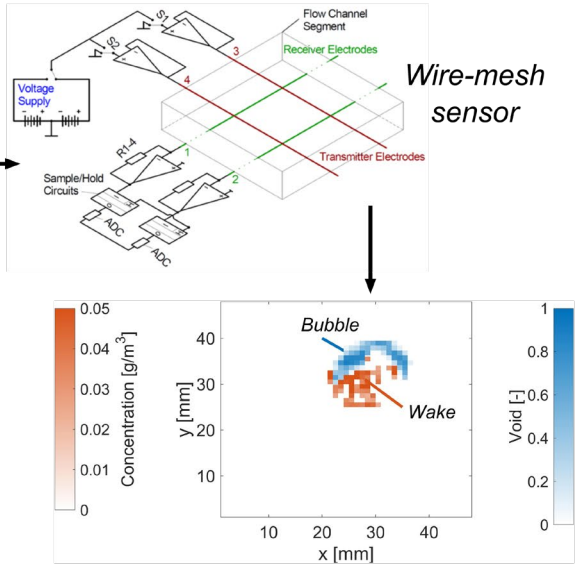

Calibrated measurements

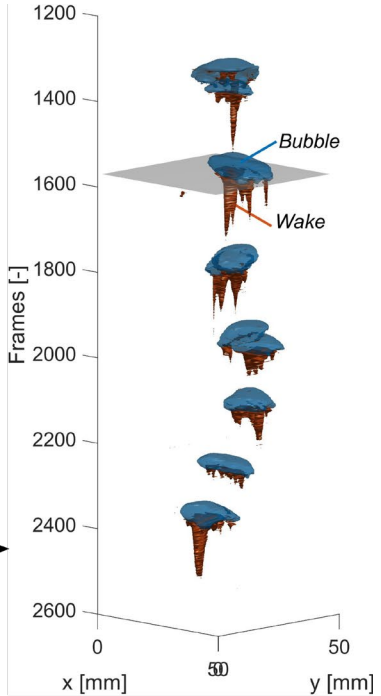

Bubble + wakes

WMS data analysis

WMS data calibration to obtain relevant physical quantities: **Void** fraction and local dissolved aerosol **Concentration**

$$g_{i,j,k} = \frac{u_{i,j,k}}{u_{i,j,base-liquid}}$$

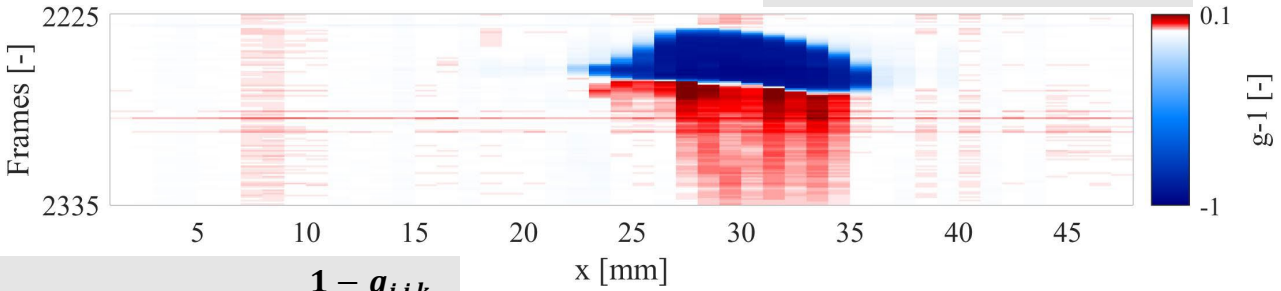

$$g_{i,j,k} < 1.0 \rightarrow \varepsilon_{i,j,k} = \frac{1 - g_{i,j,k}}{1 + \frac{g_{i,j,k}}{2}}$$

Relative conductivity

$$g_{i,j,k} > 1.0 \rightarrow c_{l,i,j,k} = (g_{i,j,k} - 1)\,\frac{\mu_{probe}}{\lambda}$$

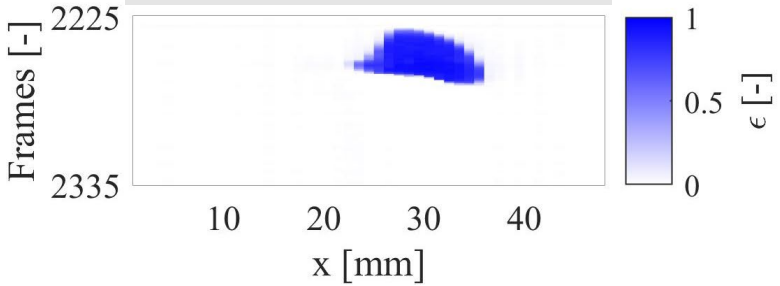

Void fraction

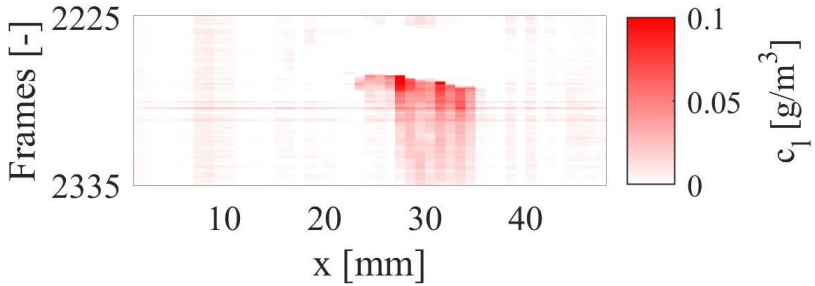

Dissolved aerosol Concentration

WMS data analysis

Bubble identification in 3D with 1D approach to recognize the wakes

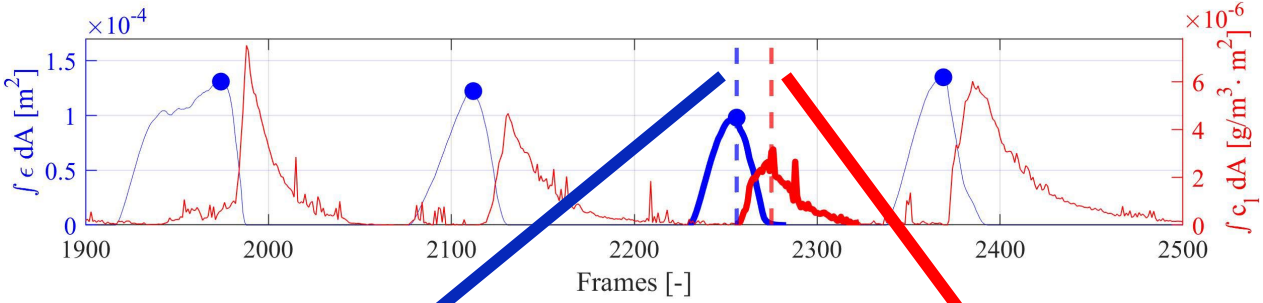

Void fraction maximum

Integral values

Concentration maximum

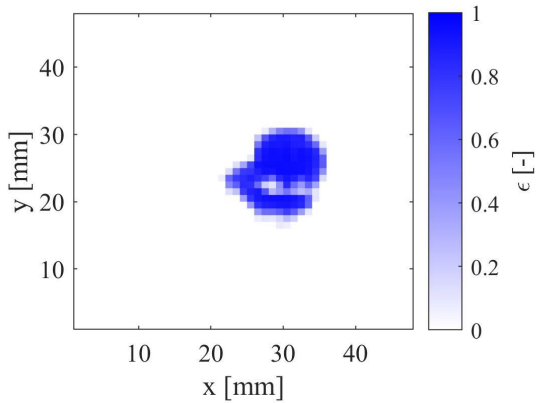

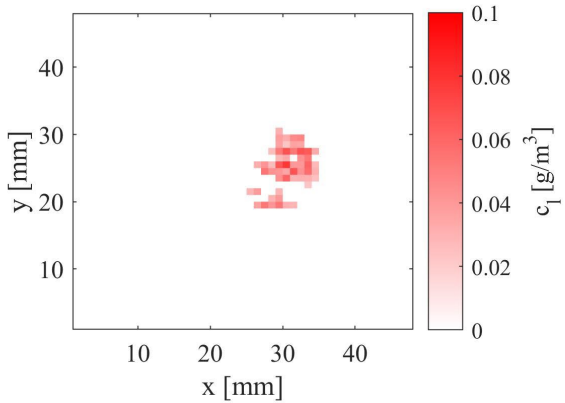

Visualization

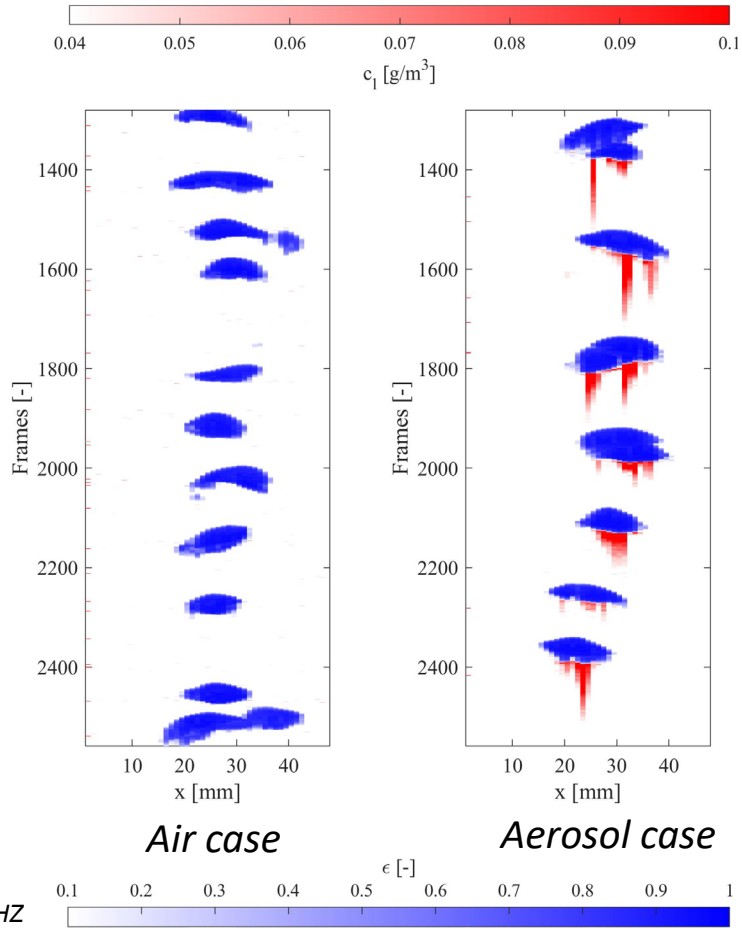

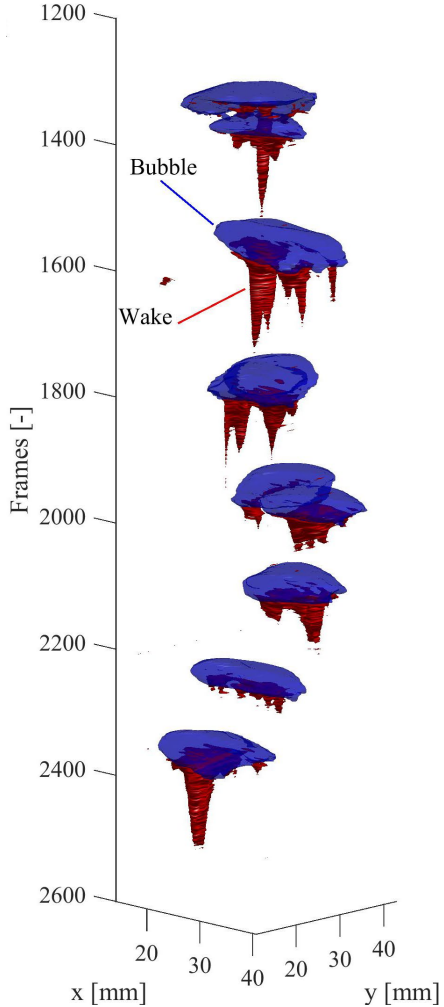

3D reconstruction

Visualization

Same bubble at **different** aerosol conditions

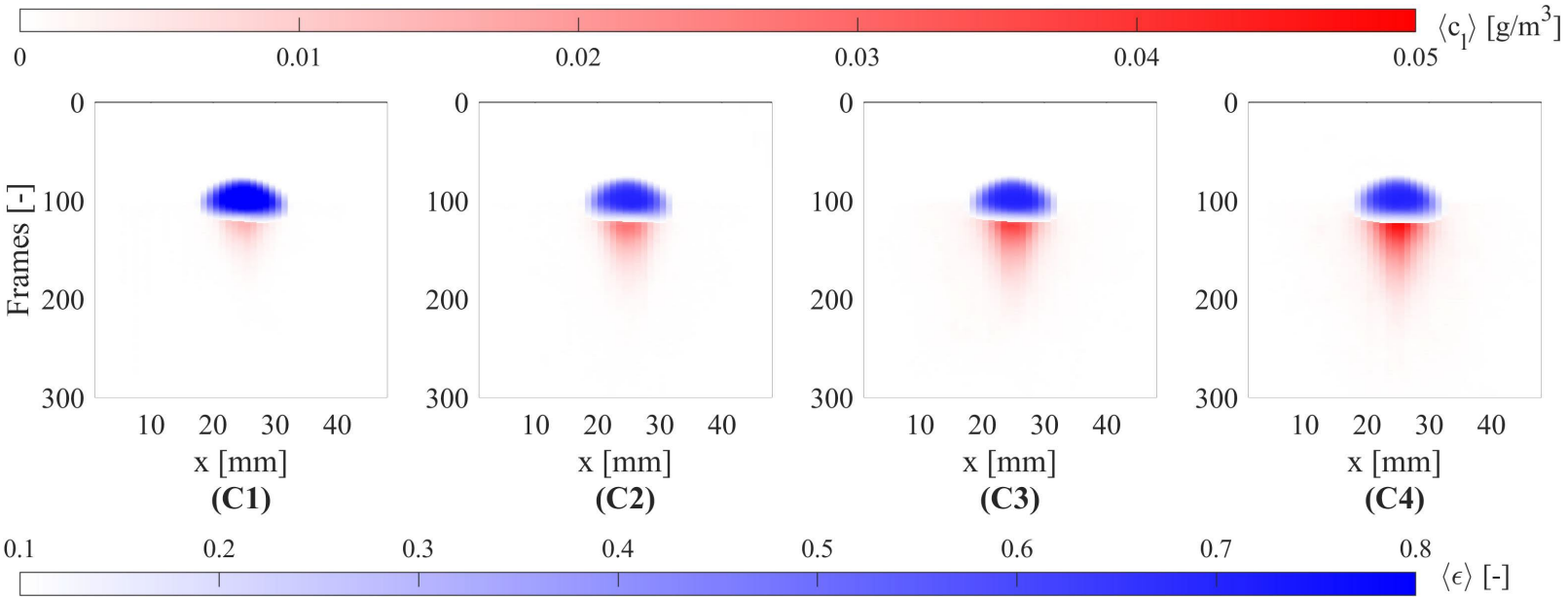

$0.17\ g/m^3(0.79\ \mu m)$ $0.31\ g/m^3(0.95\ \mu m)$ $0.47\ g/m^3(1.08\ \mu m)$ $0.60\ g/m^3(1.14\ \mu m)$

Increasing aerosol concentration

Conclusions

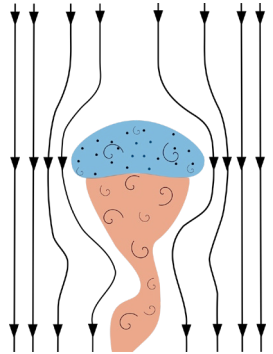

Local experimental **hydrodynamics** and particle **mass transfer** for **non-ideal bubbles**

Analysis of WMS data

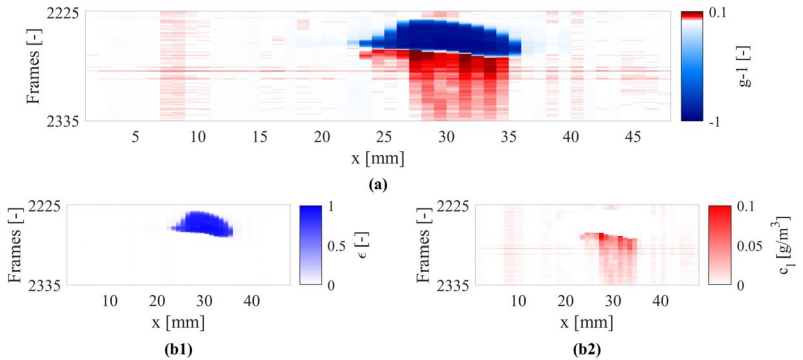

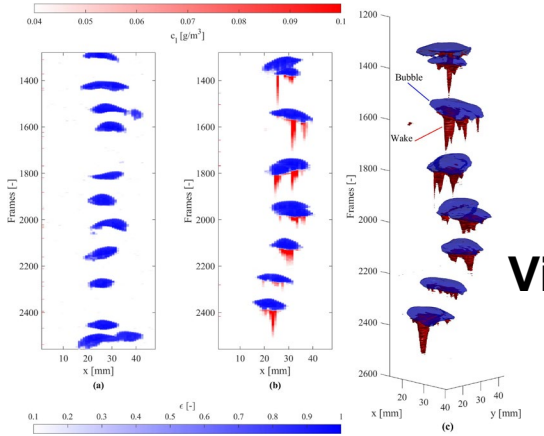

Visualization of multiphase mass transfer

Conclusions

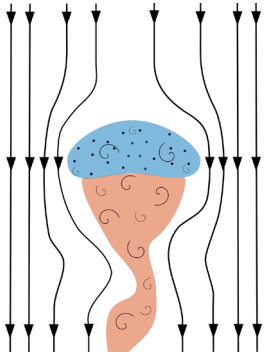

Local experimental **hydrodynamics** and particle **mass transfer** for **non-ideal bubbles**

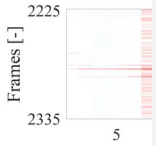

Analysis of WMS data

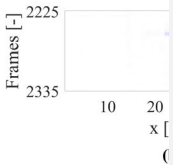

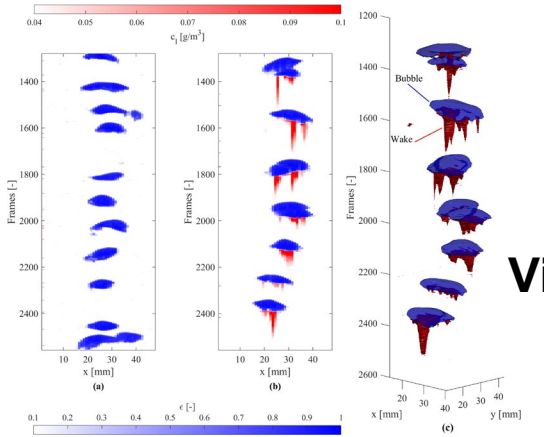

Visualization of multiphase mass

My thanks go to

Dr. Terttaliisa Lind

Prof. Annalisa Manera

Prof. Horst-Michael Prasser

Dr. Detlef Suckow

Dr. Victor Petrov

Francesco Pumilia

Dr. Petros Papadopoulos

…

NEW EXPERIMENTAL DEVICES FOR SEVERE ACCIDENT STUDY: A LASER BASED APPROACH

Y. Pontillon*, T. Doualle, C. Thevenot, C. Nonon, P. Bros
CEA.DES.IRESNE.DEC, Cadarache F 13108 St Paul Lez Durance, France
* yves.pontillon@cea.fr

L. Gallais
Aix Marseille Univ, CNRS, Centrale Med, Institut Fresnel, Marseille, France
laurent.gallais@fresnel.fr

ABSTRACT. Three complementary laser-based platforms, named CHAUCOLASE (French acronym for laser-controlled heating) for concepts validating, CHARTREUSE (French acronym for laser heating for experimental treatments on nuclear samples in extreme conditions) for qualification involving non irradiated nuclear fuel before implementation in hot-lab facilities and finally MALAGA for application on irradiated nuclear fuels are currently developed by the CEA-Cadarache (IRESNE/Fuel study department). This paper highlights how the use of laser technologies makes it possible to increase the experimental capacities of nuclear fuel studies for: (1) the quantification of thermophysical properties as a function of temperature, (2) applying complex temperature transients representative of the RIA and LOCA type accidents. In each case, recent results obtained thanks to the different methodologies developed in close collaboration between the CEA and the Fresnel Institute are presented as proof of concept.

KEYWORDS
Laser based platforms, thermophysical properties, RIA, LOCA

1. INTRODUCTION

Even though the overall severe accident phenomenology is relatively well known for both in and ex-vessel configurations, modelling of some physical phenomena needs to be enhanced to reduce uncertainties on severe accident calculations for reactor applications. International sensitive analyses studies have been devoted to identify the main sources of uncertainties in severe accident code calculation and nuclear safety assessment [1]. Among them, uncertainties both on corium thermophysical properties and fission product released have been assessed as being one of important source of uncertainty on simulation as it has been shown, for instance, in the OECD/NEA TCOFF-1 project [2].
To try to overcome these limitations, *COPS (COrium Properties for reactor Simulation and uncertainties)* project has been launched under the umbrella of OECD/NEA. The overall objective of this project is to enhance significantly the severe accident robustness simulation by developing methods to address key corium properties in modeling (density, surface tension, viscosity) thanks to an experimental program performed at CEA PLINIUS Severe Accident Platform (CEA-Cadarache) involving a limited number of well-designed experiences with prototypic corium –*i.e. with depleted uranium dioxide.*
In parallel with this approach and, in order to extend the domain covered by the COPS project, the CEA/DEC (Fuel study department) has launched, in collaboration with the Fresnel Institute and the Ecole Centrale Méditerranée, the development and qualification of experimental platforms based on laser technology. They rely on high-power Ytterbium fiber lasers, dedicated experimental chambers and sample holders. Optical systems to generate laser beams of variable shapes and intensity, and the associated instrumentation (pyrometers, high-speed and high-resolution infrared cameras) have also been implemented. These experimental means are systematically coupled with theoretical approaches regarding laser/material interactions thanks to multiphysics code modelling. Three complementary laser-based platforms are developed, named CHAUCOLASE (French acronym for laser-controlled heating) for concepts validating,

CHARTREUSE (French acronym for laser heating for experimental treatments on nuclear samples in extreme conditions) for qualification involving non irradiated nuclear fuel before implementation in hot-lab facilities and finally MALAGA for application on irradiated nuclear fuels.

This paper provides an overview of the two main R&D axes, in relation with future potential R&D needs for SA, that have been developed thanks to these very modular platforms, in order to access to many experimental configurations and studies. After describing the main characteristics of all the experimental laser platforms in operation, the methodology together with the major results obtained regarding the following R&D axis will be detailed:

- **The thermal properties of nuclear fuels and solidified corium**. Two techniques have been developed to evaluate thermal conductivity (by thermal diffusivity measurements) of nuclear fuel and its evolution as a function of temperature (up to 3100 K): (1) the laser flash method, which is a non-contact measurement of the thermal response of a studied sample at a scale of the mm, (2) the Infrared microscopy (IRM) technique.
- The **Nuclear fuel behavior under thermal loads.** The main goal here is to quantify the impact of thermal transients at extremely high temperatures and/or rates on the fuel thermomechanical response and fission products behavior/release.

We particularly focus on the application to irradiated fuels (and their evolution as a function of temperature). The perspectives associated with this work both in terms of results and the development of new experimental capacities are the subject of the last part of the article before the conclusions are drawn.

2. IRESNE's Laser platforms

To increase the experimental capabilities of IRESNE and answer scientific questions relating to the quantification of thermophysical properties as a function of temperature and the achievement of extreme conditions in terms of ramps and temperature levels accessible on irradiated nuclear fuels, a set of platforms, based on laser technologies, has been (or are currently being) developed at the fuel study department (IRESNE-Cadarache) and Institut Fresnel. This set is based on three platforms (CHAUCOLASE, CHARTREUSE and MALAGA) supplemented by an optical laboratory located in a "classical" building (Figure 1). The details of these three entities are given in the following section.

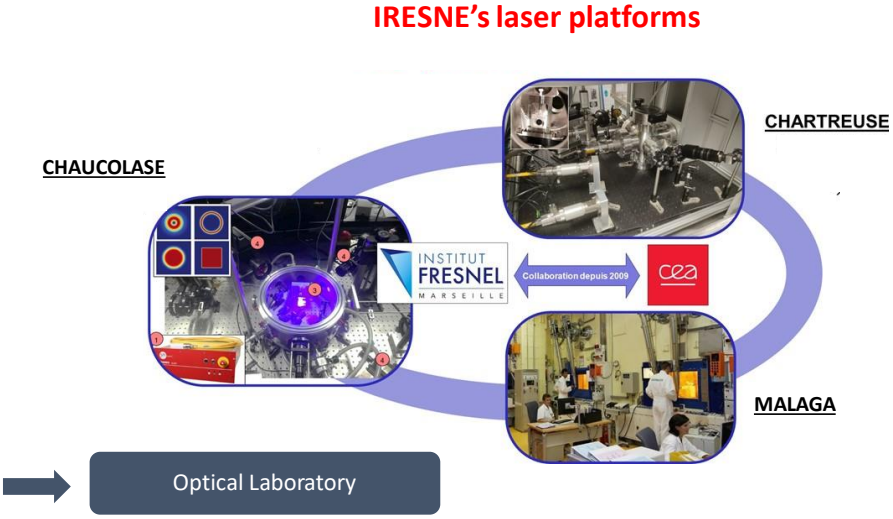

Figure 1. IRESNE's general scheme regarding Laser platforms

2.1. CHAUCOLASE

The experimental setup called ChauCoLaser (French acronym for laser controlled heating), available at the Fresnel Institute, is based on two high power CW ytterbium fiber lasers (SPI, laser Qube 1500 and Trumpf, TruFiber 2001 P) that can deliver 1500 W (monomode laser beam) and 2000 W (multimode laser beam) of maximum power. The beams are intrinsically non-polarized and have a central wavelength of 1080 nm with a bandwidth of < 4 nm. These lasers have a typical rising time of few microseconds that is suitable to generate well-controlled millisecond pulses and the beam diameters on the sample surface can be adjusted by using a collimator and lens combination. The laser is coupled in a dedicated experimental chamber equipped with laser windows and view-ports for optical monitoring, that can operate in vacuum (10^{-6} mbar) or controlled atmosphere (Argon). The sample of interest is placed at the center of the chamber on a sample holder made of high temperature insulating material (ZrO_2 support to hold the sample in a vertical position). Different optical instruments are deployed to observe the sample and to monitor its temperature through the different viewports of the experimental chambers. Other ports are available for thermocouple vacuum feedthroughs or pressure measurements. The temperature of the sample is monitored with several diagnostics, such as a thermocouples, infrared cameras, and several optical pyrometers operating in the near infrared spectral range. This modular platform allowed to develop and qualify laser heating techniques to study materials at high temperatures [3, 4, 5, 6, 7].

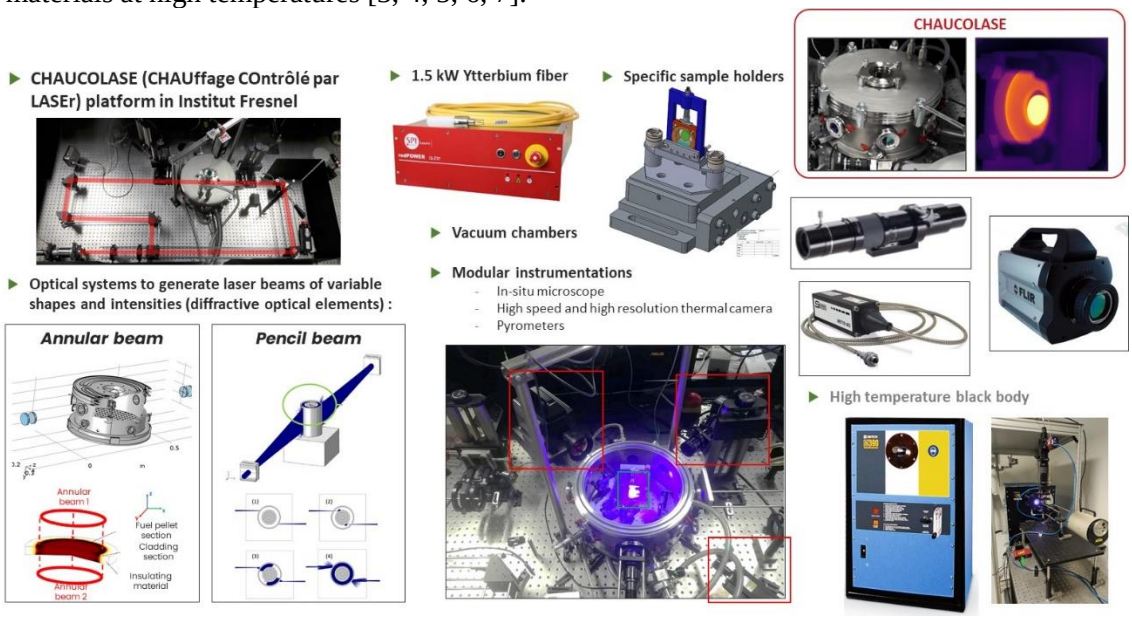

Figure 2. CHAUCOLASE platform

2.2. CHARTREUSE

Once the experiments and the methods are validated on the CHAUCOLASE platform, the laser techniques are transferred in nuclear environment in the CHARTREUSE (French acronym for laser heating for experimental treatments on nuclear samples in extreme conditions) platform at the CEA Cadarache. The main objective of CHARTREUSE is to qualify the possibility to implement high-power lasers in hot-lab facilities and confirm the feasibility of the different laser-based experiments in the future in very high activity environment.
The experimental loop CHARTREUSE carry on the CHAUCOLASE functions, namely it is very modular, comprises an experimental chamber, four high power lasers (2x500W and 2x300W) with beam guiding and shaping equipment and the associated instrumentations.

The specific feature of CHARTREUSE is that it comprises a set of interconnected glove boxes (Figure 3), designed to provide radiological shielding for experimentalists. This connecting glove box system contains different processes:

- an induction furnace (heating by magnetic field in the presence of a conductive material), named DURANCE, actually in operation in the laboratory [8],
- a sample preparation glove box, which can contain a micro-drilling system,the laser platform CHARTREUSE
- and a glove box serving as an exchange area between the different glove boxes.

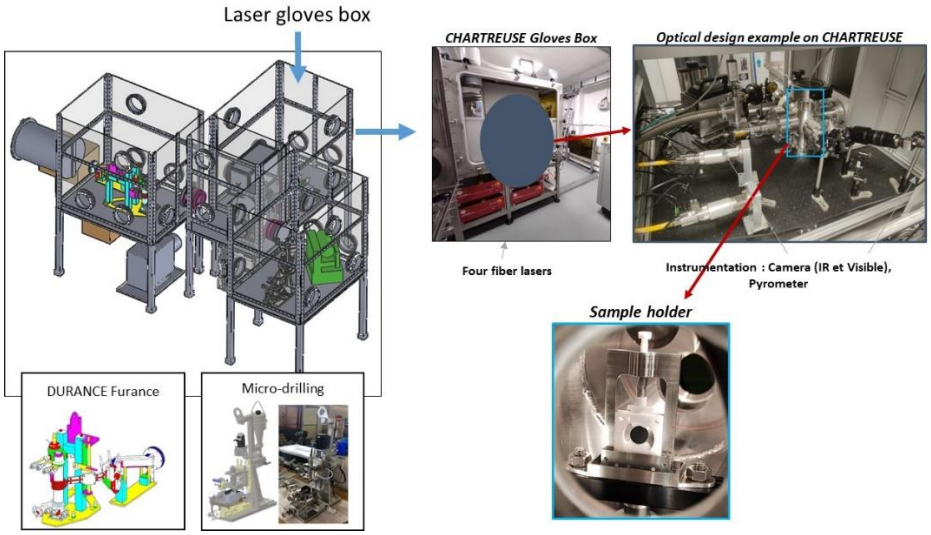

Figure 3. CHARTREUSE platform

2.3. MALAGA

The main objective, at the present time, of these new developments based on laser technology is to extend these experimental capabilities to the study of irradiated nuclear fuels. To do this, the CEA is committed to the nuclearization of the technologies deployed and qualified thanks to the two upstream platforms CHAUCOLASE and CHARTREUSE. The basic principles and methodologies will be redeployed in MALAGA to allow: (1) the quantification of thermophysical properties as a function of temperature (typically up to fuel melting), (2) the achievement of complex thermal transients (typically representative of RIA, LOCA, ..), (3) applying very high temperature tests (>3000°C according to controlled temperature ramps), or very high precision machining of nuclear ceramics (thanks to fs type laser). The first laser shots are planned for 2028, for an assembly deployed at the LECA hot laboratory.

3. THE THERMAL PROPERTIES OF NUCLEAR FUELS AND SOLIDIFIED CORIUM

The knowledge of the thermal conductivity of nuclear fuel and its evolution as a function of temperature and burn up is a major challenge in the context of the evaluation and understanding of irradiated fuel performances in current reactors. It is also the case for the development and qualification of fuel for future reactors. Indeed, numerical simulations of the fuel behaviour under various conditions require the accurate knowledge of thermal conductivity over a wide range of temperature (from ambient to melting point temperature) but also at the scale of few tens of micrometres to take into account the microstructural effects on the thermomechanical evolution of the fuel in normal or incidental irradiation conditions. Different methods, using laser matter interactions, can deduce the thermal conductivity from a thermal diffusivity measurement. We have investigated the potential of two techniques which present spatial resolution from

millimetre to few tens microns [9]: laser flash method and infrared microscopy. Hereafter, we present the methodology developed and the corresponding results for flash methods applied on UO_2 at high temperature.

First experiments (and associated simulations) were conducted on the CHAUCOLASE platform available at the Institut Fresnel. In a first time, experiments were carried out on graphite, that we consider as model materials. They allowed us to verify that a signal can be measured with the experimental devices envisaged, to validate the methodology and the potentiality for each techniques. The flash method was then apply on UO_2 at different temperatures (up to 500 °C)

3.1. Methodology

The laser flash (LF) method, gives a global thermal diffusivity value of a sample, as a function of temperature. This method has been successfully applied on irradiated sample in hot cell [9]. The driving force of this study is to appropriate this knowledge and then, on the one hand, apply it to very high temperatures (i.e. until the melting of the material studied) and on the other hand, develop an approach allowing to achieve spatial resolutions of the order of a hundred microns.
During a LF experiment, the sample is subject to a high-intensity, short pulse duration. The energy is absorbed on the front surface and the thermal diffusivity value is computed from the resulting temperature response on the back surface sample, typically measured by an infrared detector. The variation in back surface temperature is referred to as a ‘‘thermogram”. To determine the thermal diffusivity of sample as a function of temperature, our approach was to set up an experimental bench to carry out experiments and measure thermograms and develop a numerical model to calculate the thermal diffusivity value, through a parameter estimation method.
The schematic diagram of the experimental setup for the LF method bench developed is given in Figure 4a. Figure 4b displayed the corresponding experimental set up implemented at the Fresnel Institute. A laser diode operating at 880 nm, is used to heat the sample at different temperatures. The thermal perturbation, *i.e.* the flash, is created by an another laser: an 2KW Ytterbium fibre laser. The temporal evolution of the temperature of the back face is obtained by a two-colors pyrometer, which has a response time of 80 µs.

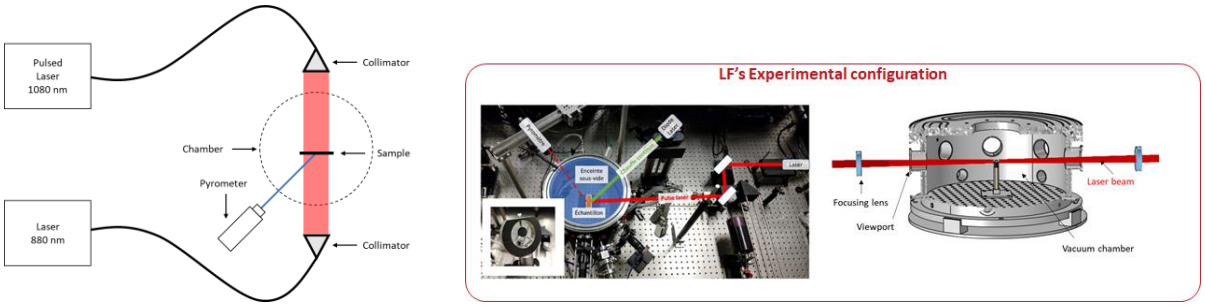

Figure 4. (a) Schematic of laser flash method setup, (b) Experimental configuration

The simulations are conducted with the commercial software COMSOL which is based on the Finite Element Method in axisymmetric configuration. The heat transfer model relies on several assumptions. First, the material is considered homogenous and isotropic. Second we take into account the heat transfers by conduction combined with thermal radiation to take into account losses at the surface (convection is neglected). Third, as the energy is absorbed on the surface, there is no heat source in the material but an incoming heat flux on the boundary. The corresponding non-linear heat transfer equation can be expressed as:

$$\rho(T)C_p(T)\frac{\partial T}{\partial t} + \nabla(-k(T)\nabla T) = 0, \qquad (1)$$

where ρ is the density, C_p is the specific heat capacity under constant pressure, T is the temperature, k is the thermal conductivity. The absorbed laser energy induces a heat flux F expressed as:

$$F(r,t) = A(T).I(r,t), \qquad (2)$$

where *A* is the temperature dependence absorption and *I* the laser intensity (the measured spatial laser profile is used).
This thermal model is associated to a parameter estimation study which enables to estimate the value of one or more parameters. In our case, we calculate the value of the specific heat capacity and the thermal conductivity, so that the computational results match the experimental reference data, i.e. the thermogram. A least-squares optimization, with a Levenberg-Marquardt method, is used. It defines an objective function representing the sum of squared differences between back surface sample temperature measurements stored in an experimental data file (and acquired through the pyrometer) and corresponding expressions evaluated in the thermal model: the specific heat capacity and the thermal conductivity.

3.2. Experiments and Results

Experiments have been carried out on EDM-3 graphite from POCO Graphite Inc. [10] and UO_2 samples fabricated at CEA. Graphite is a polycrystalline graphite produced by sintering and we use it as a model material to establish the methodology of the measurement techniques. The graphite and UO_2 samples have a disk morphology with a diameter of 8 mm and thicknesses of 1.66 mm and 1.44 mm respectively. They are placed in a sample holder in the dedicated experimental chamber operated in vacuum (10^{-2} mbar).
After reaching a steady state temperature, the laser pulse is delivered on the front surface of the sample. The pulse duration is about few milliseconds and the laser power of few tens of watts to few hundreds of watts, depending of sample thickness and in order to reach a temperature rise on the rear surface of few degrees.

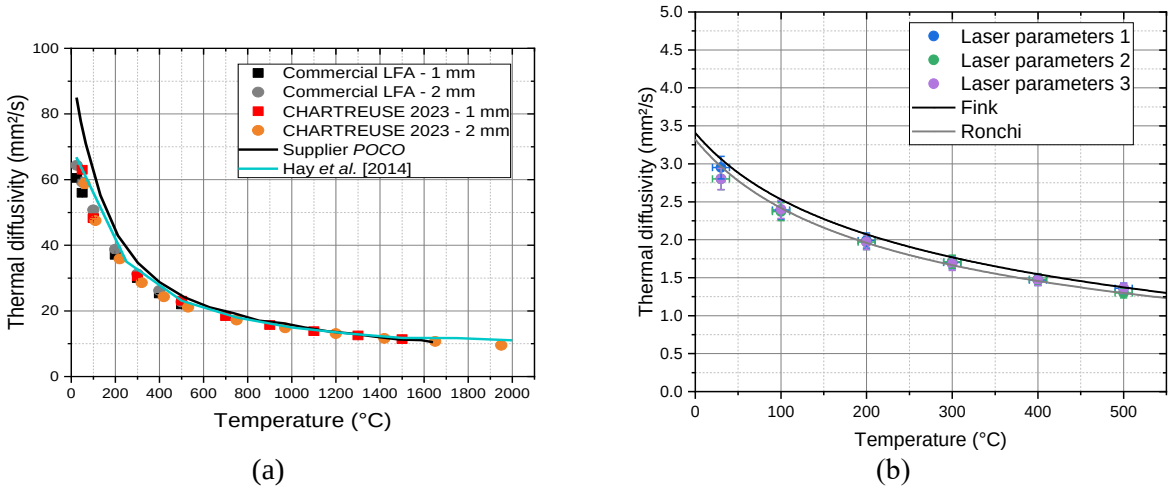

Figure 5. Thermal diffusivities as a function of temperature measured on CHARTREUSE platform by the laser-flash method on graphite (a) (red squares and orange dots). The black line is the reference measurements from supplier [10] and grey line results obtained with a similar-approach [11]. For UO_2 (b), the data-set acquired are represented by the colored dots and the black and grey lines are the thermal diffusivities results recommended in the literature [12][13]

The thermal diffusivity measurements of graphite are performed up to 2000 °C and are presented in the Figure 5a. We observe the temperature dependence of the thermal diffusivity: in the low temperature range up to about 500 °C, the thermal diffusivity strongly decreases, and for the temperature above the variation with the temperature is moderate. The diffusivity measurements obtained up to 500 °C show results in very good agreement with reference measurements obtained with a commercial diffusivity measurement system (LFA 467, Netzch). For the higher temperatures, we note a very good agreement with the recommended values from supplier [POCO] but also with the results obtained by *Hay et al*. [11] with a similar approach (laser-flash method).
The results of the experiments carried out on UO_2 are shown in Figure 5b and compared to reference results from the literature, obtained by Fink [12] and Ronchi et al. [13]. Overall, we notice that the measurements

of the thermal diffusivity as a function of temperature up to 500 °C on UO_2 are very consistent with reference data of the literature. Very good reproducibility is noted between the results obtained with the different sets of laser parameters. For the lowest temperatures (ambient and 50°C), we see that the values obtained on CHARTREUSE are slightly lower than the data from the literature. This discrepancy can be explained by the presence of impurities on the surfaces of the sample which involve a modification, on the one hand, of the laser deposition on the front surface and, on the other hand, of the temperature measurement on the rear surface.
Above 100°C, these impurities are probably cleaned and we note the very good agreement between our thermal diffusivity values and the literature data.

4. THE NUCLEAR FUEL BEHAVIOR UNDER THERMAL LOADS

The nuclear fuels behavior understanding in relation to the different thermal loads to which they could be subjected accidental conditions is of first importance in the nuclear field. By improving our knowledge, it is possible to upgrade nuclear reactor safety and to precisely define specific on-site emergency plans in the case of an extreme event. Predicting correctly fission product (FP, including Fission Gas (FG)) releases (i.e. the source term) and the corresponding fuel fragmentation from nuclear fuels at off-normal conditions, such as power transient, reactivity initiated accident (RIA) and loss of coolant accident (LOCA), is still a significant and important challenge.
In order to address these issues, several experimental devices, coupled with accurate modelling, have been developed throughout the world. However, in connection with the technologies involved in the design of these devices, certain limitations exist such as, for example, the capacity to apply extremely rapid temperature rise ramps, very localized power deposits to the fuel pellet, or still reach very high temperature levels (> 2700°C) while being able to view the sample and its morphology evolution in real time. To overcome these difficulties, a set of experimental platforms, based on laser technologies, was developed in close collaboration between the CEA and the Fresnel Institute. These make it possible to extend current capabilities for investigating the behavior of nuclear fuel during tests representative of accident situations. These developments and the associated results are described in the following sections respectively for RIA, LOCA type accidents.

4.1. Methodologies

RIA

In the specific case of the so-called RIA [14], a fast rise of nuclear power and of temperature occurs in the fuel. The power excursion may lead to failure of the nuclear fuel rods and release of radioactive material into the primary reactor coolant. In the most severe cases, the fuel rods may be shattered and a large amount of the fuel pellets can be dispersed into the primary coolant. To prevent those potential consequences, safety criteria are usually set up to limit the enthalpy rise of the fuel. During a RIA event, the temperature distribution in the cylindrical pellet is almost flat top with a maximum localized in an outer ring closed to the pellet periphery. Typical temperature increase above 2000°C occurs in a few tens of millisecond on the edges of the fuel as illustrated by the simulation results reported in a Figure 6a.
The capacity of laser-heating to reproduce RIA thermal transient at laboratory scale is based on the use of a high power Ytterbium fiber laser associated to diffractive optics. The samples are prepared from fuel pellets in the form of disks less than 1 mm thick. It is placed vertically in a sample holder made of zirconia with two optical sapphires that ensure optical access to the sample and retain any possible fragments in case of loss of integrity (Figure 6b). The sample is then heated at its periphery by one or two annular Gaussian beams of pre-selected dimensions (radius, waist). The corresponding laser configuration is given in Figure 6c together with schematic view of the laser/sample interaction. The optical instrumentation around the sample is a key-point to monitor and control the temperature, therefore optical diagnostics such as thermal

imaging and optical pyrometer can be implemented through the available viewports of the experimental chamber. While not being strictly representative of a RIA, these experiments lead nevertheless to high strain rates and temperature increase rates that are of the order of magnitude of those encountered during fast power transients [15].

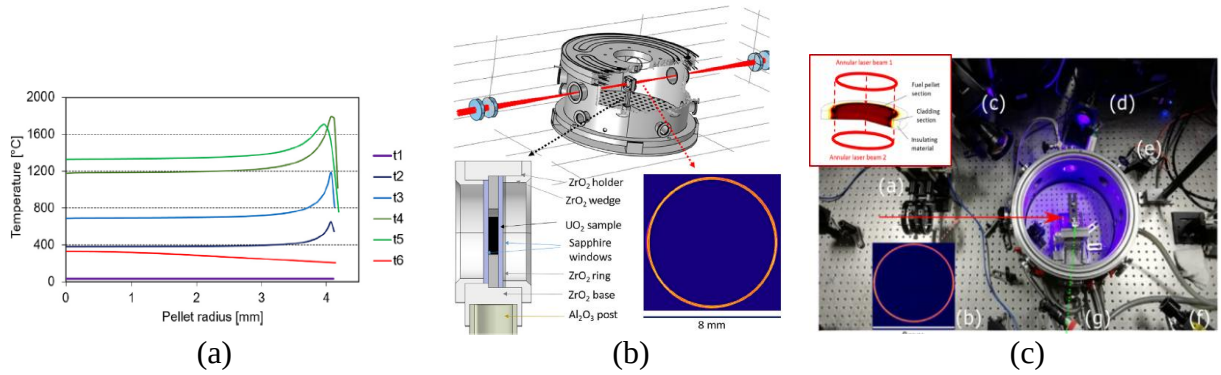

(a) (b) (c)

Figure 6. ***(a)*** *Simulations of a RIA event with ALCYONE [16], a fuel performance code co-developed by the CEA, EDF and FRAMATOME. Fuel pellet temperature radial profile evolution during a pulse irradiation is plotted before the beginning of the pulse (t1), during the power rise (t2), at peak power (t3), during the power descent (t4), at the end of the power descent after the pulse (t5), and just before return to cold state (t6). 0 corresponds to the centre of the sample ;* ***(b)*** *Sketch of the experimental chamber designed for the experiments. Bottom left: picture of the sample holder assembly at the centre of the vacuum chamber. A UO2 disk, 8 mm diameter and 1 mm thick is visible in the sample holder. Bottom right: image of the beam profile obtained in the sample place with a laser beam profiler ;* ***(c)*** *Experimental setup used to realize annular laser heating of one face of an UO_2 sample. The annular laser beam is depicted with the red arrow. (a) Diffractive optical element to transform an incoming Gaussian beam into an annular Gaussian beam. (b) False color image of the annular beam imaged at sample's plane. (c) High-speed infrared camera (heated face of the sample). (d) Illumination source. (e) Laser diode of a few watts to pre-heat the sample to a starting temperature. (f) Bi-chromatic pyrometer (rear face of the sample). (g) High-speed visible camera. Green insert: sketch and photo of the sample holder. (For interpretation of the references to colour in this figure legend, the reader is referred to the web version of this article.)*

LOCA

As explained above, predicting accurately the FP release from high burn up fuels at off-normal conditions is an important challenge. Classical approaches in this field require annealing tests in order to monitor both the absolute level and the time dependence of the released FP. In this context an annealing device, referred as MERARG (French acronym for Means of Study for Annealing and Gaseous Release Analysis) [17], has been developed to study the behavior of nuclear fuel under thermal transient representative of LOCA type scenario. It allows annealing at high temperature, usually between 1200 °C and 1600 °C but can reach peak of 2800 °C, on irradiated nuclear fuel pellets with slow (between 0.05 and 0.5 °C/s) and moderate (maximum 20–30 °C/s) temperature ramps thanks to an induction furnace.

In the context of the development of a laser-based platform as detailed above (RIA section) it was interesting to build on MERARG's concept by proposing an analogous experiment using lasers to reach similar performances and possibly to surpass current limitations. The perspective of this work is to propose a single laser platform able to investigate nuclear fuel behaviour under various conditions, by using the flexibility of the laser heating technique.

The heating should be as homogenous as possible within the sample, minimizing thermal gradients in order to avoid thermal stresses inside that can cause for instance fuel fragmentation. Illuminating directly a MERARG type crucible would ensure a homogeneous heating of the pellet by radiative and conductive heat exchanges. However, the crucibles typically used are made of either W, Pt or Mo, which have highly reflective surfaces. This would lead to important loss of laser power because an important amount of it being simply reflected instead of being absorbed. The retained concept [7] is depicted in Figure 7a. This configuration consists in confining the laser beam between the MERARG's metallic crucible and a second

metallic call “hood”. The beam is injected in this system through a small opening cut in this second wall. The beam is thus confined and absorbed through multiple reflections between the internal crucible and the hood, ensuring that almost all of the laser intensity is absorbed by the system (Figure 7b).

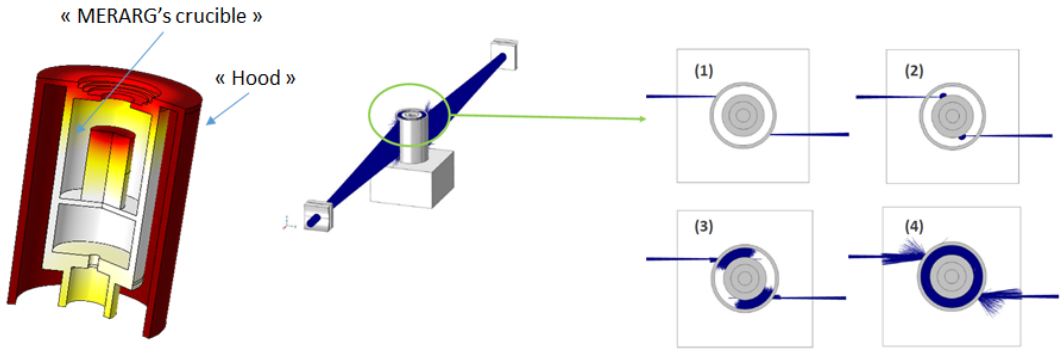

Figure 7. (a) Geometrical concept for LOCA type Laser based experiment; (b) two optical systems based on cylindrical lenses are used to shape the gaussian beam in a thin line at the entrance of the hood/crucible assembly. (1), (2), (3), (4) top view of hood/crucible assembly. After passing through the opening, the rays are absorbed and scattered on the tungsten surfaces

4.2. **Experiments and results**

RIA

In order to generate the annular beam for controlled energy deposition on the edges of the sample, a diffractive optical element has been used [4, 6]. A 8 mm beam diameter with a 150 µm width is obtained with a 13 mm incoming Gaussian beam (diameter at $1/e^2$). The image of the obtained ring in such conditions is shown in Figure 6b. A second Ytterbium fibre laser, could be used to heat the sample up to the initial conditions of interest. This second laser is controlled by a Proportional, Integral, Derivative (PID) feedback loop, based on the temperature monitoring of the sample with a pyrometer, in order to ensure stable temperature conditions.

First experiment (i.e. demonstration of the concept), UO_2 samples with 8 mm diameter and 0.7 mm thickness have been used. They were synthesized in the UO_2 laboratory (CEA Cadarache Centre) thank to standard process: the samples were synthesized with depleted UO_2 from a batch produced through wet process, followed by conventional pre-compaction (50 MPa), pressing (450 MPa) and sintering at 1650°C for 2h under flowing H_2.

In order to reach a controlled initial temperature, a first laser beam with a Gaussian profile was used to heat the sample at 100°C/s, with the PID regulation loop. The two laser beams with annular spatial profiles were then launched with the first laser beam still active, and the temperature profiles measured with a fast and high definition thermal camera operating in the mid infrared range (2-5µm). The temperature profiles corresponding to one experiment with a 20 ms pulse transient and a 1000 W incident power are displayed in Figure 8a together with temperature simulation [4, 6].

The temperature distribution during the transient has the expected radial symmetry, as illustrated by the good correspondence of the extracted temperature profiles on each side of the sample. A localized temperature up to 2000°C can be reached in few tens of milliseconds as requested by the RIA thermal conditions with spatial control, while keeping the sample integrity, which represent the initial goals of this study.

Thermo-mechanical model suitable for the interpretation of this type of laser heating experiments simulating the power increasing phase of a RIA transient on UO_2 samples has also been developed [6]. The application of this mechanical model to annular laser heating experiments led to a good estimation of the crushing and cracking location (near the sample periphery), of the crack orientation (circumferential) and of the beginning of cracking.

LOCA

The hood and crucible parts previously described have been produced in Tungsten (Figure 6). The slits have 3 mm width and 40 mm height. The surface has a rough finish with a surface roughness measured in the range 300-400 nm (root mean square height). Consequently, there is no specular reflection in the visible and near infrared.

A high power CW ytterbium fiber laser (1500 W of maximum power with a monomode laser beam and with a typical rising time of few microseconds) has been used. The main beam is splitted into two beamlets with a 50/50 beamsplitter and directed with high reflective mirrors. After passing through a set of cylindrical lenses, the beams are sent through laser windows in a vacuum chamber with a base pressure of 2×10^{-2} mbar. The crucible and hood assembly is placed at the center of the experimental chamber (as shown in Figure 6c), mounted on a ceramic sample holder. The chamber is equipped with lateral viewports that have been used for observation or temperature monitoring through different lines of sight (i.e. CMOS camera for the adjustment of the laser beam line, monochromatic pyrometer operating at 1.27 µm used to measure the surface temperature of the hood, thermal camera used to observe the thermal gradients on the hood surface). After calibration of the system [7], different temperature ramps and stabilized temperature plateaus have been applied on a UO_2 sample located inside the crucible as shown in Figure 8. The laser matter interaction model developed in support of these experiments and described in [7] (dashed lines in Figure 8) reproduces the experimental curves very well.

All of these results, as for the RIA, show the achievement of the initial objectives and the possibility of reproducing thermal transients typical of a LOCA with an experimental approach based on the use of laser heating.

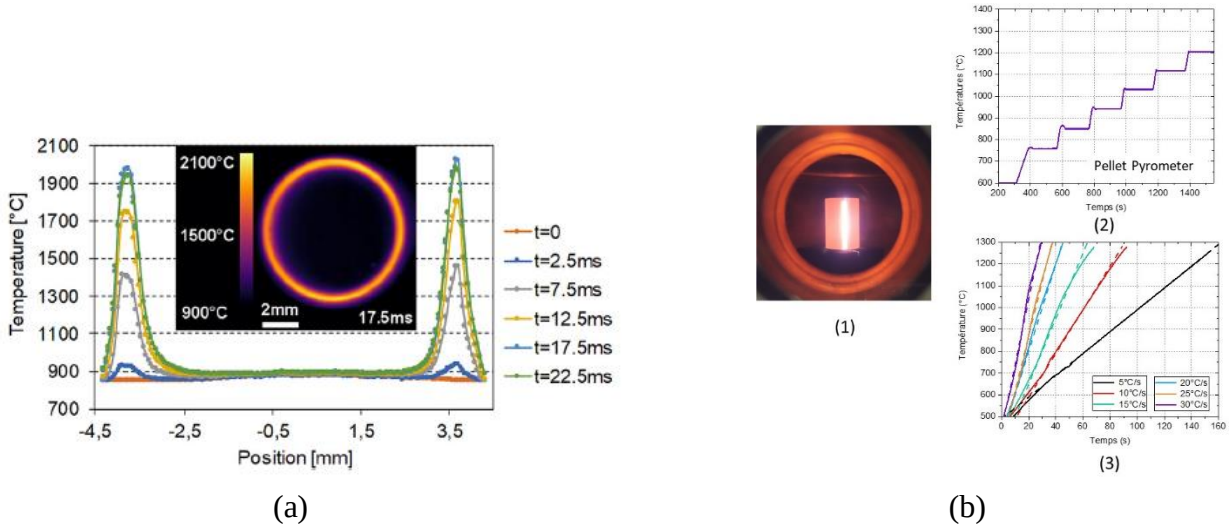

Figure 8. (a) Measured temperature at the surface of a UO_2 sample submitted to a 470 W annular beam irradiation during 20 ms on both sides. Image: thermal camera snapshot at the end of the laser pulse; Data plot: extraction of the temperature along vertical profile of the thermal images at different times ; (b) (1) photogrpahy of the crucible during heating, (2) Stabilized temperature plateaus from 450°C up to 1200°C obtained thanks to the described laser configuration for LOCA application; (3) Exemples of temperature rampes obtained thanks to the described laser configuration for LOCA applications together with simulation ones (dashed line)

5. CONCLUSION

We have presented different original methods, based on high power lasers to:

- quantified thermophysical properties of nuclear fuels as a function of temperature,
- applying dedicated thermal transient representatives of RIA or LOCA type conditions

In each case, the concept was tested and demonstrated first on model materials, then on natural UO_2 samples thanks to dedicated laser platforms (i.e. CHAUCOLASE and/or CHARTREUSE) developed in close collaboration between CEA and Fresnel Institute.
For thermophysical properties, the results obtained are very consistent with those available in the literature, or measured with commercial apparatus. As far as the RIA transient is concerned, transient localized temperatures up to 2000°C can be reached, with a spatial distribution on the edges on the sample that approaches the ones encountered in an RIA event. As an alternative to conventional furnace or induction annealing, we have introduced and demonstrated in this work a laser-heating device that can drive nuclear fuel pellets at high temperature in well-controlled conditions. The current system can be used to heat nuclear fuel pellets up to 1500°C at a maximum heating rate of 30°C/s with the use of kW lasers. The system is however easily scalable to higher heating rates or higher temperatures since few kW laser systems are now easily available.

6. PERSPECTIVES

We have demonstrated how the use of laser technologies makes it possible to significantly increase experimental capacities at the laboratory scale with regard to the measurement of the thermophysical properties of nuclear materials as a function of temperature and the application of specific thermal transients. Generally speaking, the chosen methodology is based firstly on the use of model materials to qualify the approaches adopted, then, secondly, on the use of non-irradiated UO_2 as a final proof of concept. The useful step being to develop these approaches on irradiated nuclear fuel. This is currently in progress with the development of the MALAGA platform which is planned to be operational in 2028. The final objective being to be able to achieve for each of the axes of study presented in this paper to bring the sample to very high temperature, and for the extreme conditions envisaged today up to the melting temperature. This last point, particularly ambitious, will make it possible to extend the field of study to situations and needs relating to the studies of severe accidents, particularly with regard to the properties of re-solidified post-accident corium.

ACKNOWLEDGMENTS

This work has been partly funded by EdF and Framatome under the CEA PERCO and PJIPG's program.

REFERENCES

1. Journeau et al., "SAFEST Roadmap for Corium Experimental Research in Europe," 24th International Conference on Nuclear Engineering, June 2016 : Piluso P. et al., "Status Report on Ex-Vessel Steam Explosion: EVSE", OECD/NEA/CSNI/R (2017) 15, 2017; F. Fichot et al., EU IVMR project, 2020
2. TCOFF-1, Thermodynamic Characterization of Fuel Debris and Fission Products Based on Scenario Analysis of Severe Accident Progression at Fukushima Daiichi Nuclear Power Station, NEA, 2021
3. Minissale, M., Durif, A., Hiret, P., Vidal, T., Faucheux, J., Lenci, M., Mondon, M., Kermouche, G., Pontillon, Y., Grisolia, C., Richou, M., and Gallais, L., "A high power laser facility to conduct annealing tests at high temperature," Rev. Sci. Instrum. 91, 035102 (2020).
4. Vidal, T., Gallais, L., Faucheux, J., Capdevila, H., Sercombe, J., and Pontillon, Y., "Simulation of reactivity initiated accident thermal transients on nuclear fuels with laser remote heating," J. Nucl. Mater. 530, 151944 (2020).
5. Gallais, L., Vidal, T., Lescoute, E., Pontillon, Y., and Rullier, J. L., "High power continuous wave laser heating of graphite in a high temperature range up to 3800 K," J. Appl. Phys. 129, 043102 (2021)
6. Reymond, M., Doualle, T., Sercombe, J., Rocca, M., Nasselahsen, M., Colin, C., Pontillon, Y. and Gallais L., "High power laser heating of nuclear ceramics for the generation of controlled spatiotemporal gradients", J. Appl. Phys. 134, 033101 (2023).

7. Cifuentes Quintal, C., Reymond, M., Fiorito, F., Martin, F., Pontillon, M., Richaud, J.C., Doualle, T., Pontillon, Y. and Gallais, L., "A laser-based system to heat nuclear fuel pellets at high temperature", Rev. Sci. Instrum. 94, 103905 (2023).
8. Fabert, M.; Gallais, L.; Pontillon, Y., On-line deformation measurements of nuclear fuel rod cladding using speckle interferometry, PROGRESS IN NUCLEAR ENERGY, 2014, 72
9. C. Ronchi, W. Heinz, M. Musella, R. Selfslag and M. Scheindlin, "A universal laser-pulse apparatus for thermophysical measurments in refractory materials at very high temperatures," International Journal of Thermophysics, vol 20, pp. 987-996, 1999, 10.1023/A:1022607924536 ; W. Parker, R. Jenkins, C. Butler and G. Abbot, "Flash method of determining thermal diffusivity, heat capacity and thermal conductivity," Journal of Applied Physics, vol 32, pp. 1679-1684, 1961, 10.1063/1.1728417 ; J. F. Bisson, "Realisation d'un diffusivimetre a haute resolution spaciale utilisant la thermographie infrarouge stimulee," M.S. thesis, Université Paris VI, 1999
10. Poco Graphite, Inc., in Properties and Characteristics of Graphite for the EDM Industry, edited by R. G. Sheppard, D. Morgan, D. M. Mathes, and D. J. Bray, 5th printing (POCO, 2002).
11. Hay, B., Anhalt, K., Chapman, L., Boboridis, K., Hameury J., Krenek, S., Vlahovic, L., Fleurence, N. and Beneš, O., "Traceability improvement of high temperature thermal property measurements of materials for new fission reactors", ANIMMA 2013.
12. Fink, J. K., "Thermophysical properties of uranium dioxide", J. Nucl. Mater. 102, 151944 (2000).
13. Ronchi, C., Scheindlin, M., Musella, M. and Hyland, G. J., "Thermal conductivity of uranium dioxide up to 2900 K from simultaneous measurement of the heat capacity and thermal diffusivity", J. Appl. Phys. 85, 776-789 (1999)
14. Nuclear Fuel Behaviour Under Reactivity-initiated Accident (RIA) Conditions - State-of-the-art ReportTechnical Report NEA/CSNI/R(2010)1, 2010
15. Reymond, Matthieu; Sercombe, Jerome; Gallais, Laurent; Doualle, Thomas; Pontillon, Yves ; Thermo-mechanical simulations of laser heating experiments on UO2, Journal of Nuclear Materials, 557, 153220, 2021

16. I. Guénot-Delahaie, J. Sercombe, T. Helfer, P. Goldbronn, Fédérici, T. Le Jolu, A. Parrot, C. Delafoy, C. Bernaudat, Simulation of reactivity-initiated accident transients on UO 2 -M5®fuel rods with ALCYONE V1.4 fuel performance code, Nucl. Eng. Technol. 50 (2) (2018) 268–279, doi: 10.1016/j.net.2017.12.006
17. Pontillon, Y., Desgranges, L., Poulesquen, A., ADAGIO technique: from UO2 fuels to MOX fuels. J. Nucl. Mater. 385, 137 (2009) ; Menegon, P., Desgranges, L., Pontillon, Y., Poulesquen, A., Evidence of two gas release kinetics during the oxidation of an irradiated PWR UO2 fuel. J. Nucl. Mater. 378, 1 (2008).

New experimental devices for (severe) accident study: A laser based approach

Y. Pontillon[1], T. Doualle[1], C. Thevenot[1], C. Nonon[1], P. Bros[1], L. Gallais[2]

[1] CEA.DES.IRESNE.DEC, Cadarache F 13108 St Paul Lez Durance, France

[2] Aix Marseille Université, CNRS, Ecole Centrale Marseille, Institut Fresnel, Marseille, France

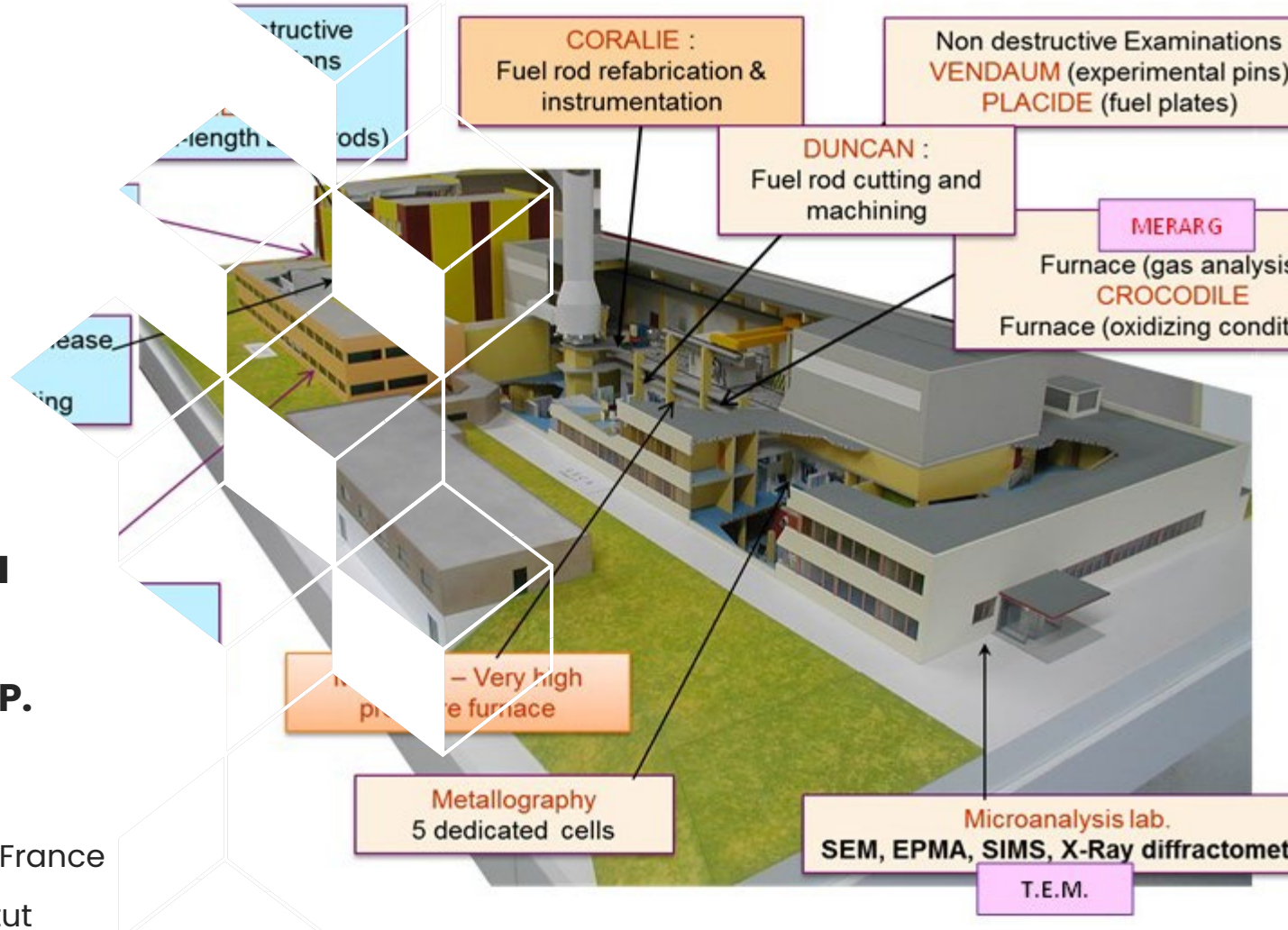

General context (CEA/Fuel study department)

- A long story based on accidental sequence simulation (at laboratory scale)
  - -> Complementary to integral tests
  - -> Create realistic data base for model validation implemented in fuel performance codes

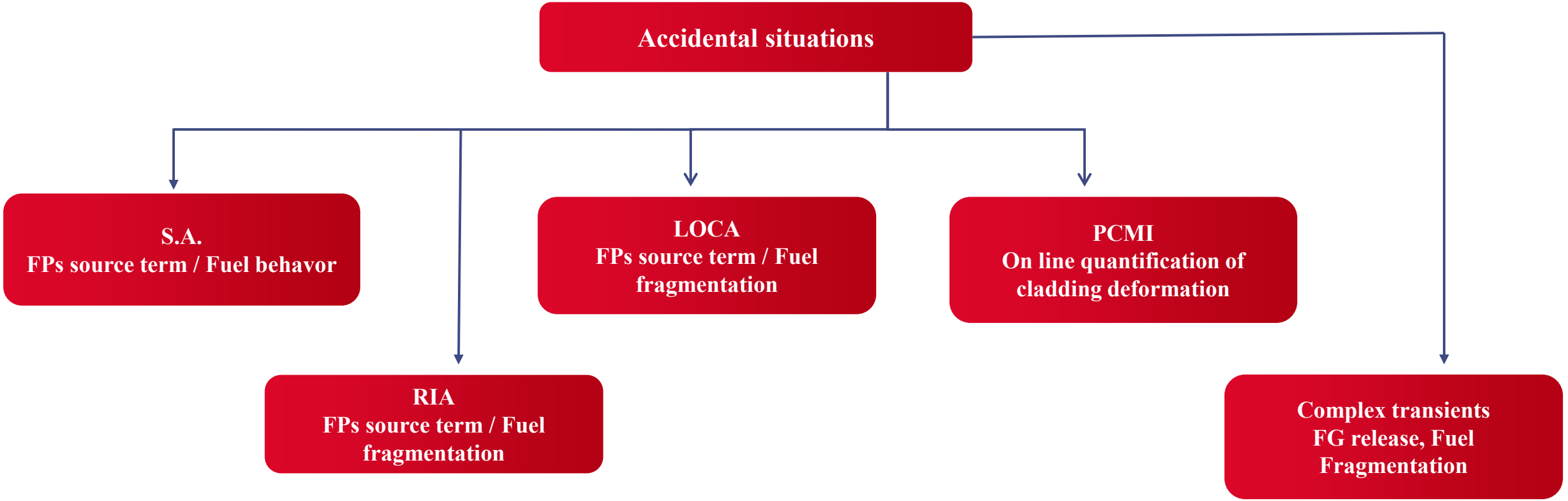

General context (CEA/Fuel study department)

- A long story based on accidental sequence simulation (at laboratory scale)
  - -> Complementary to integral tests
  - -> Create realistic data base for model validation implemented in fuel performance codes

A large number of experimental loops developped Based on HF or resistive furnace

VERDON

Pontillon, Yves; Ducros, Gerard; Malgouyres, P. P., NED, 2010, 240, 1843

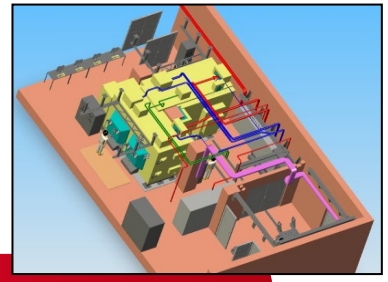

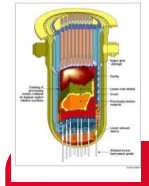

S.A.
FPs source term / Fuel behavor

MERARG

Menegon, P.; Desgranges, L.; Pontillon, Y.; Poulesquen, A., JNM, 2008, 378, 1





LOCA
FPs source term / Fuel fragmentation

DURANCE

Gallais, L; Burla, R; Martin, F; Richaud, JC; Volle, G; Pontillon, M; Capdevila, H; Pontillon, Yves ; RSI, 89, 1, 013110, 2018





PCMI
On line quantification of cladding deformation



RIA
FPs source term / Fuel fragmentation

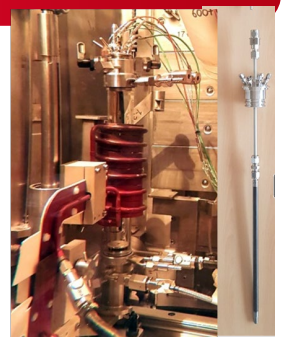

VINON



Complex transients FG release, Fuel Fragmentation

In short:

- ✓ A set of unique means of efficient, complementary heat treatment deployed on nuclear fuels (irradiated or not)
- ✓ However, a certain number of shortcomings (in terms of performance) identified and persisted:
  - ❑ Visualization within the crucible (evolution of fuel morphology as a function of temperature)
  - ❑ Direct measurement of sample temperature(Extremely)
  - ❑ Extremely rapid temperature ramps
  - ❑ Localized heating and/or complex evolution over time
  - ❑ Reaching very high temperatures (>2800-3000°C)
- ✓ Beyond the devices themselves:
  - ❑ Studies of thermophysical properties (depending on the nature of the sample and the temperature)
  - ❑ Precision machining (sample preparation)

→ **« Laser » as unique solution?**

Laser process:

- LASER heating: Many Different types of laser (solid, gas, diode laser, fiber) with a wide range of characteristics (wavelength, power/energy, temporality, beam shape, etc.)
- Laser source: power fiber laser, used for material processing (cutting, welding, heating, etc.)

Marquage



Découpe



Soudure



Perçage

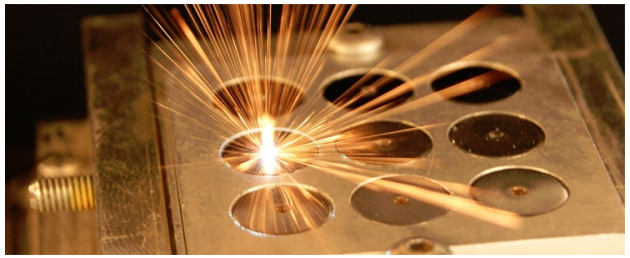

- Contactless → facility of instrumentation
  - Pyrometry, infrared thermography
  - Rapid camera



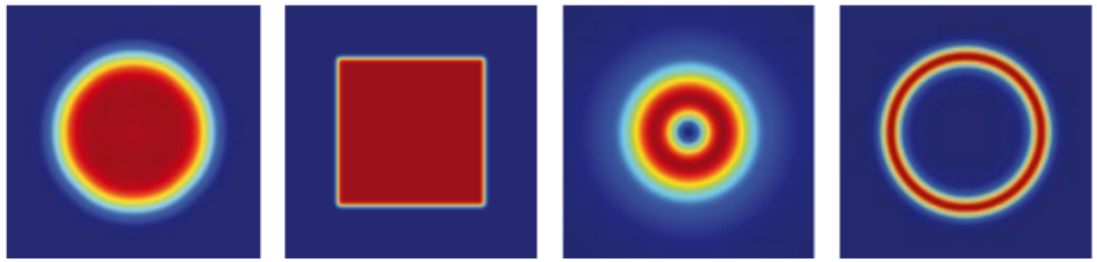

- Control of the localization of the energy deposition

- Significant power available almost instantly
  - For our purpose: 1500-2000 W in 50 µs
  - Easily handle.



CEA/Fuel Study Department's LASER platform: For what R&D objectives?

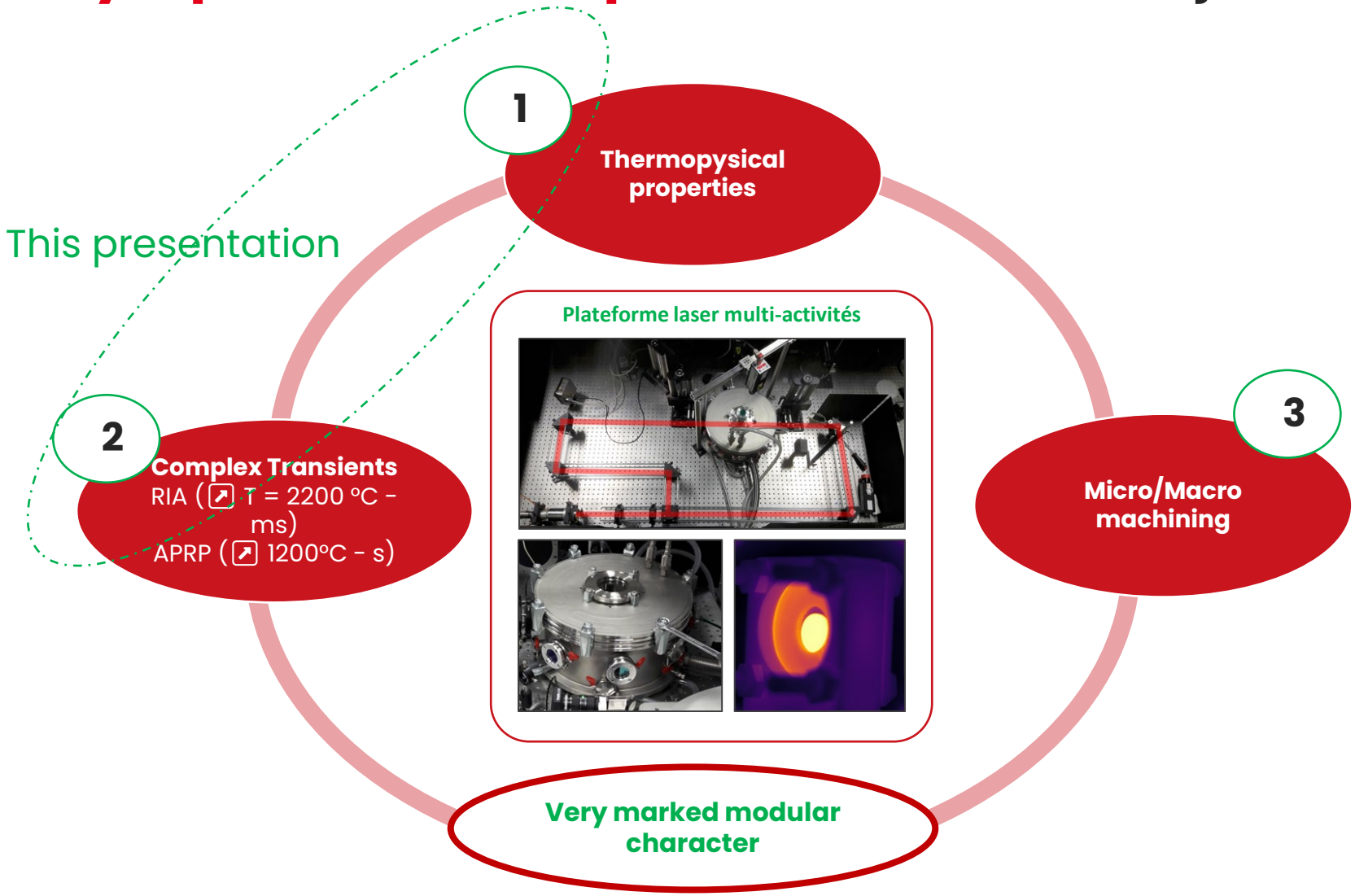

Laser technology for the study of nuclear fuels and materials

CEA/Fuel Study Department's LASER Platform:

CHAUCOLASE

Proof of concept, Methodology development
(Aix Marseille University, Fresnel Institut)

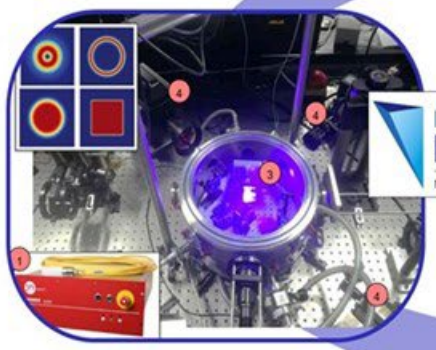

INSTITUT FRESNEL MARSEILLE

Collaboration depuis 2009

cea

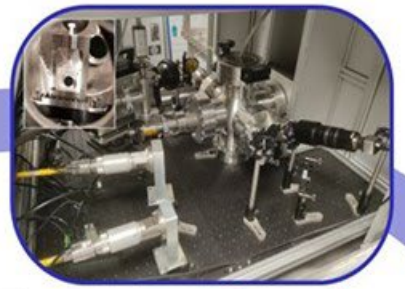

CHARTREUSE

Large amount of non irradiated UO_2, Technological development for nuclear fuel application
(UO_2 Laboratory, CEA/Cadarache)



MALAGA

Irradiated material study
(LECA-STAR Laboratory, CEA/Cadarache)

Optical Laboratory

Conventional Laboratory
(CEA/Cadarache)

CHAUCOLASE LASER platform:

- **CHAUCOLASE** (French acronym for laser controlled heating) **platform in Institut Fresnel**

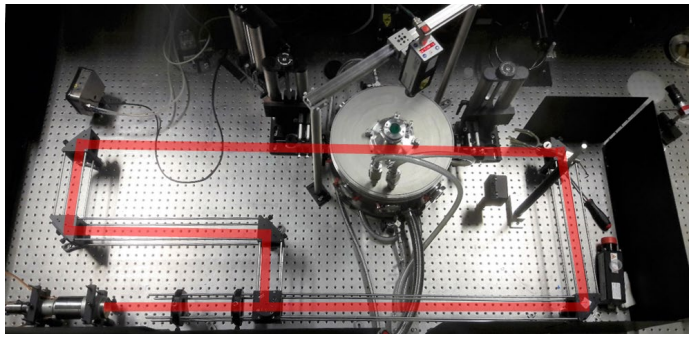

- **Optical systems to generate laser beams of variable shapes and intensities (diffractive optical elements) :**

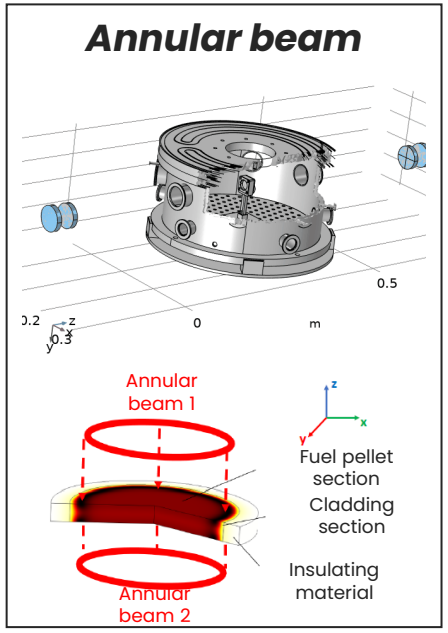

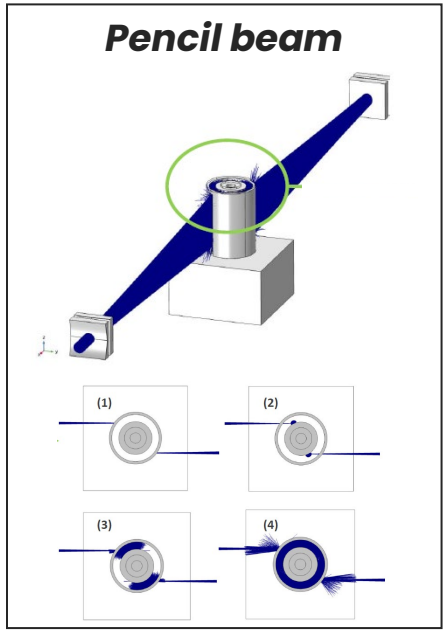

- **1.5 kW Ytterbium fiber**



- **Specific sample holders**

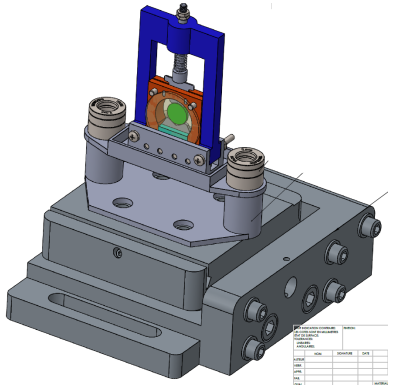

- **Vacuum chambers**

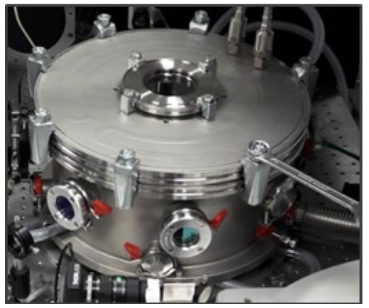



- **Modular instrumentations**
  - In-situ microscope
  - High speed and high resolution thermal camera
  - Pyrometers





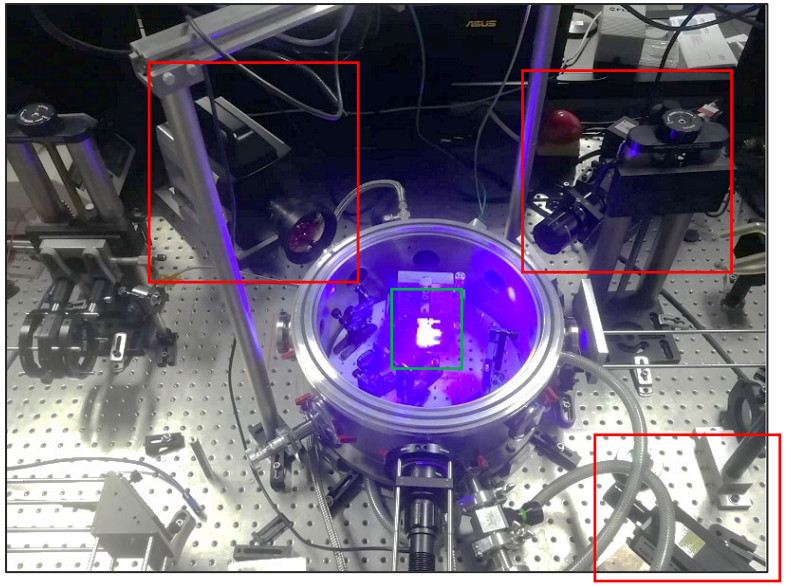

- **High temperature black body**



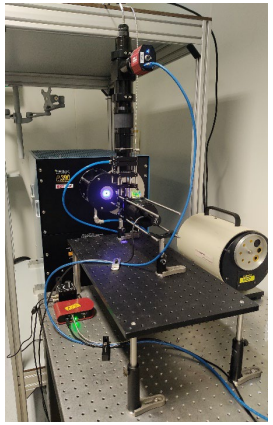

Vidal, T; Gallais, L; Faucheux, J; Capdevila, H; Sercombe, J; Pontillon, Yves ; JNM, 530, , 151944, 2020

CHARTREUSE LASER platform:

- **CHARTREUSE** (French acronym for laser heating for experimental treatments on nuclear samples in extreme conditions) **platform in CEA Cadarache**
- **Multi-objective glovebox, nuclearisation purposes**

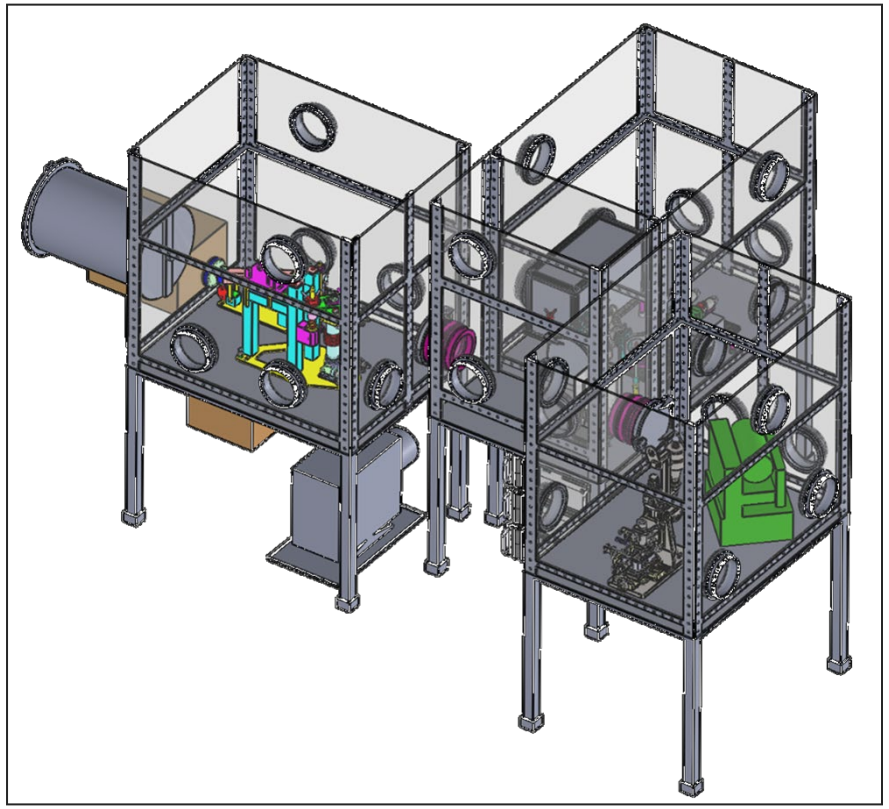

Induction furnace

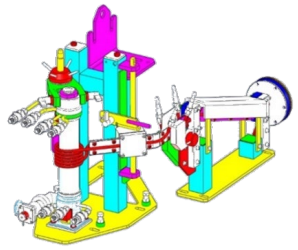

Core drill







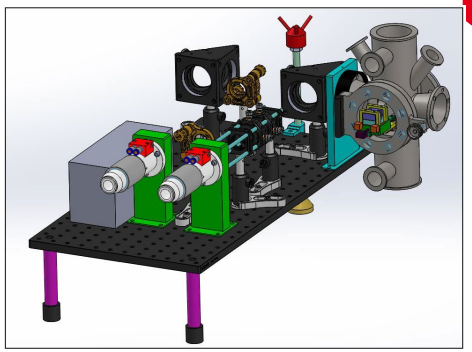



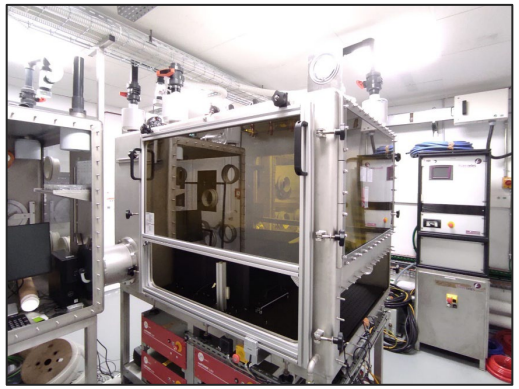

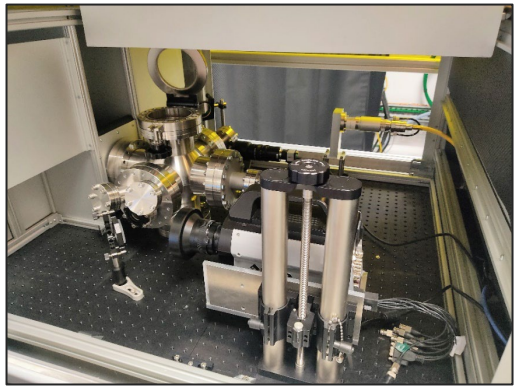

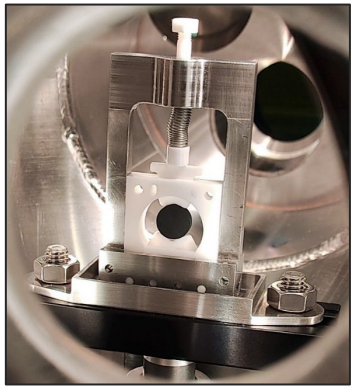

- **Integrates the different functions of CHAUCOLASE**

Thermal properties

T. Doualle, V. Le Guillous, V. Klosek, C. Onofri-Marroncle, M. Reymond, L. Gallais and Y. Pontillon, «Development of UO2 thermal diffusivity measurement with laser techniques », ANIMMA 2021

- **Context : evaluation and understanding of irradiated fuel performances in current reactors & development and qualification of fuel for future reactors**
  - Knowledge of the thermal conductivity of nuclear fuel and its evolution as a function of temperature and burn up
  - Over a wide range of temperature (ambient to melting point)
  - At the scale of few tens of micrometers

- **Different methods, using laser matter interactions, can deduce the thermal conductivity from a thermal diffusivity measurement**

1. Laser Flash

- **Parameter estimation thanks to a finite element numerical model developed in COMSOL**

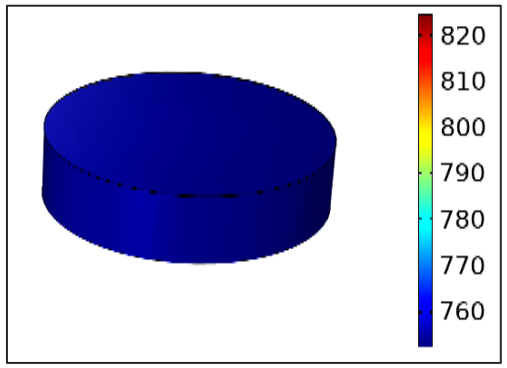

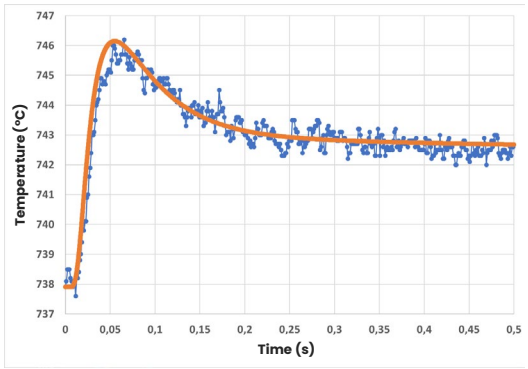

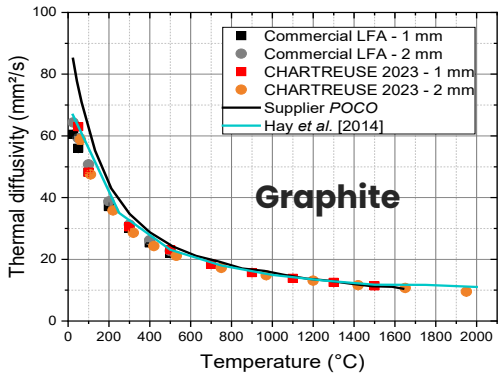

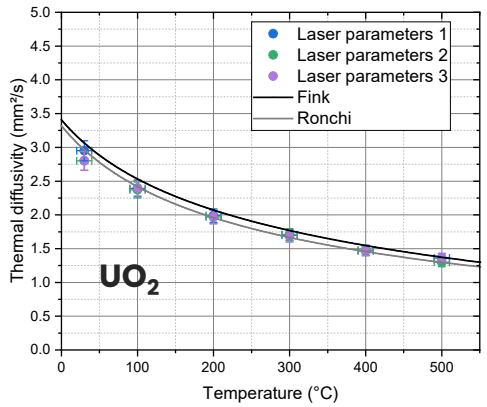

2. Infrared Microscopy

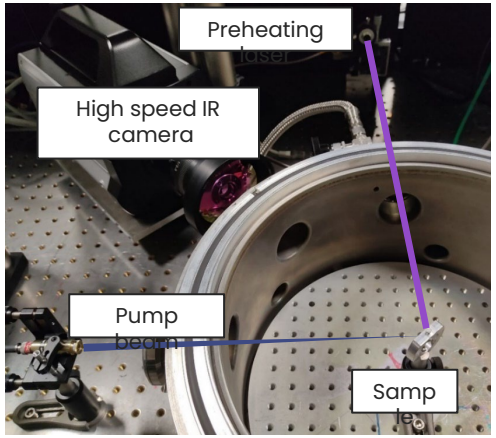

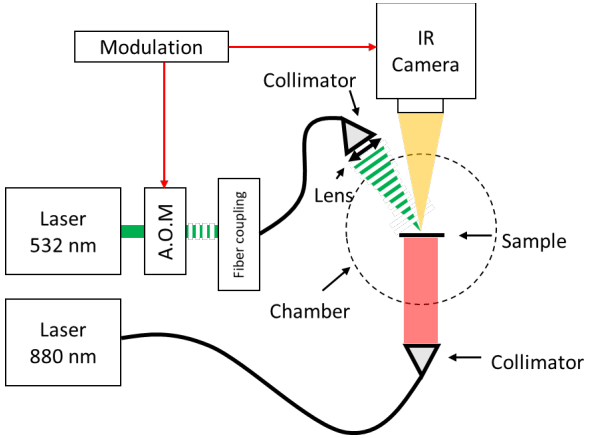

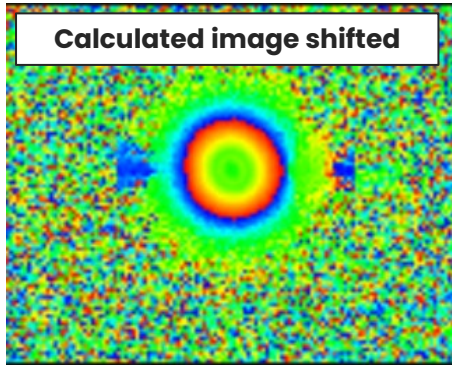

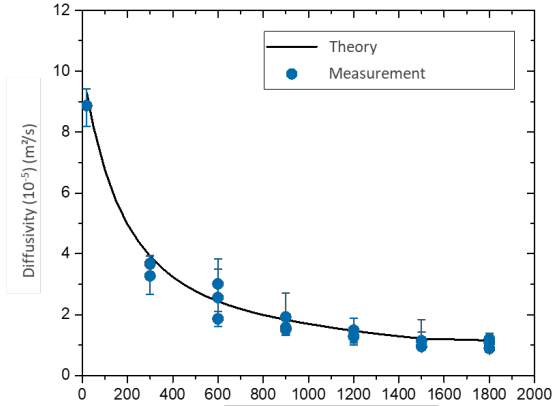

D. Rochais, « Microscopic thermal characterization of HTR particle layers », Nuclear Engineering and Design (2008)

Thermal transients (1/3)

M. Reymond, J.Sercombe, L. Gallais, T. Doualle and Y. Pontillon, «Thermo-mechanical simulations of laser heating experiments on UO_2 », Journal of Nuclear Materials 557 (2021)

- Studies are in line with a general continuous improvement of nuclear power reactors safety
- Thermal transients to understand the mechanisms and validate the fuel performances codes developed at CEA
- Various types of thermal transients can be reproduced

Experiments

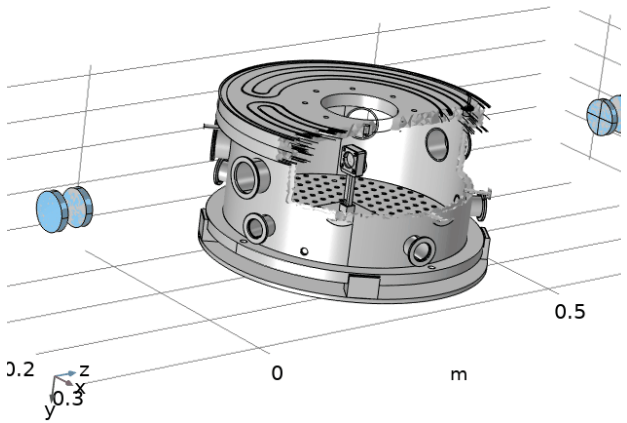

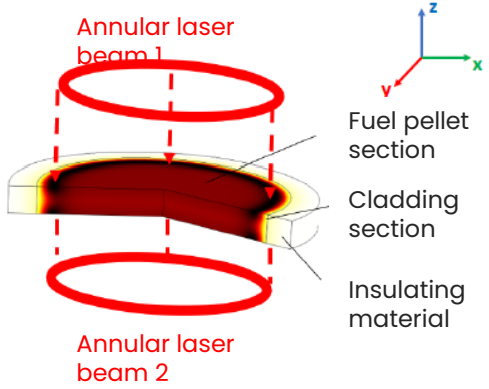



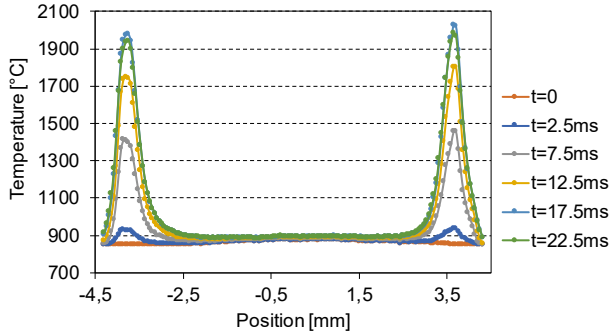

1. RIA | Reactivity-Initiated Accident

↗ Temperature = 2000 °C | Duration = ms | Scale = local (µm)

- Control rod ejection → fast rise of power and of temperature (several thousand °C/s) that occurs at the periphery of the pellet
- Integral experiments on fuel rods cannot be used to perform parametric studies on one phenomenon since they are complex and costly → Reproduce RIA transient thermal conditions at laboratory scale

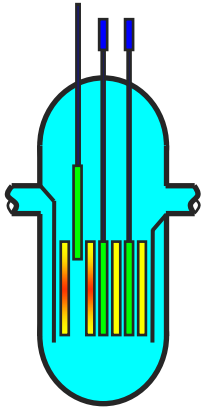

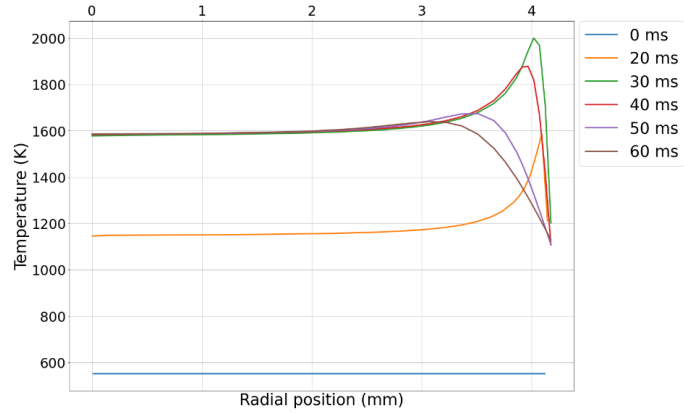

Modelling

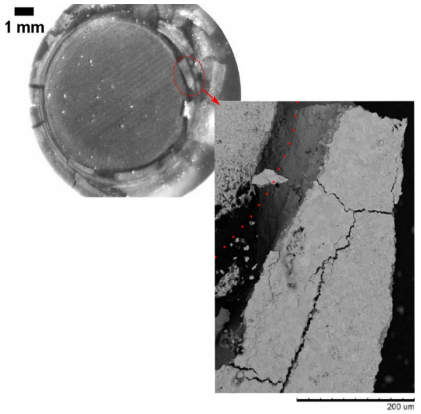

Fractured UO_2 sample after a 100 ms laser heating



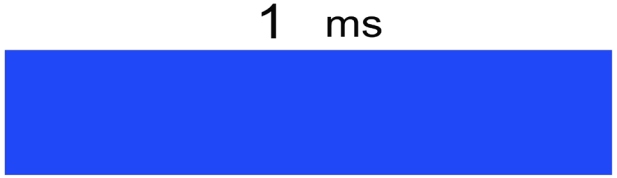

Simulation of the fracture and fragmentation (ie., grain boundary cracking) of an UO_2 sample submitted to laser heating

Thermal transients (2/3)

C. Cifuentes Quintal[1,2], M. Reymond[1,2], F. Fiorito[1], F. Martin[1], M. Pontillon[1], J.C. Richaud[1], T. Doualle[1], Y. Pontillon[1,*], L. Gallais[2], A laser-based system to heat nuclear fuel pellets at high temperature, *Rev. Sci. Instrum.* 94, 103905 (2023),

2. LOCA | Loss of Coolant Accident

↗ Temperature = 1200 °C | Duration = s | Scale = global (cm)

- It is caused by a break in one of the main primary circuit coolant pipes
  → Temperature of the reactor core continues to rise
- Dispersion of fission products and fuel

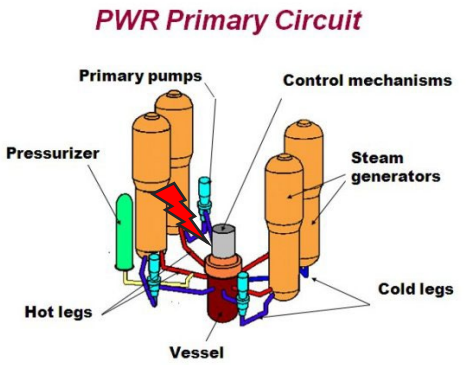



Induction furnace MERARG is used to conduct annealing at high temperature on irradiated fuel pellets



- Surpass current limitation → laser heating approach

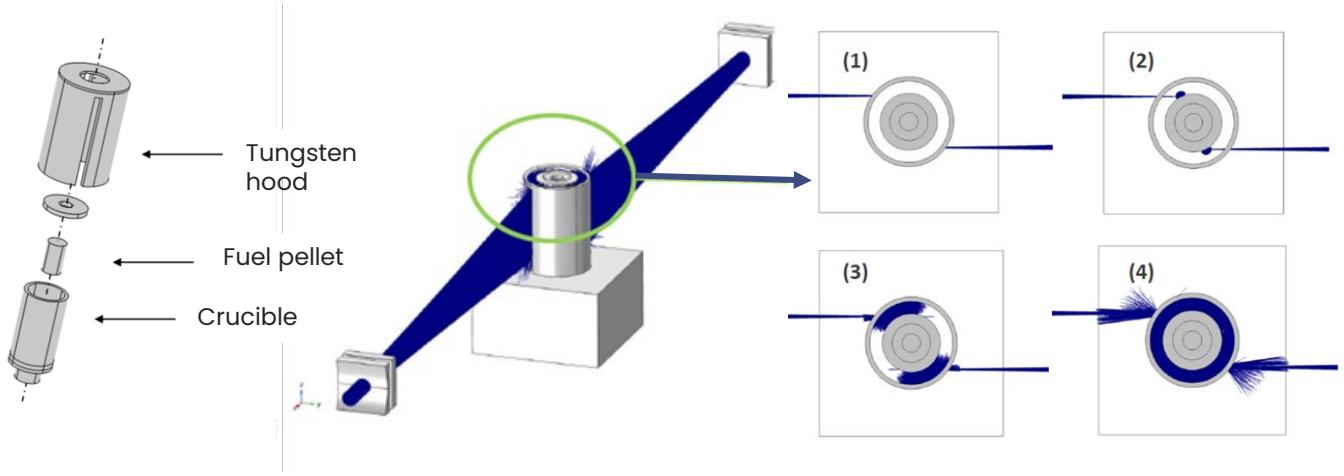

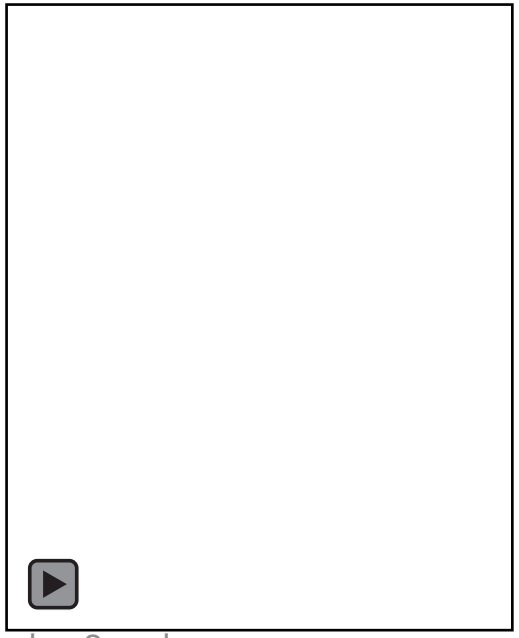

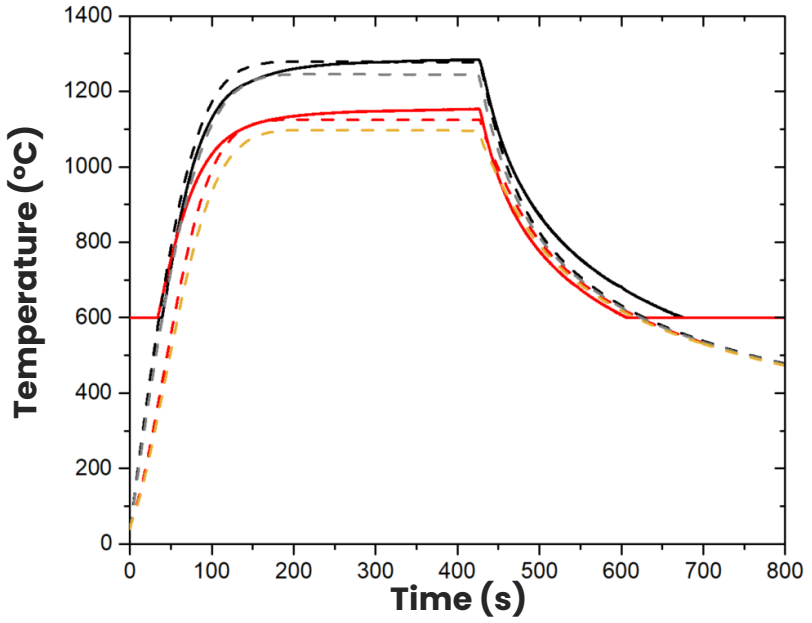

Thermal transients (3/3)

3. **Very high temperature process**
   ↗ Temperature > 3300 K

L. Gallais,[1,a] T. Vidal,[1] E. Lescoute,[2] Y. Pontillon,[3] and J. L. Rullier[4]
J. Appl. Phys. **129**, 043102 (2021); doi: 10.1063/5.0033530

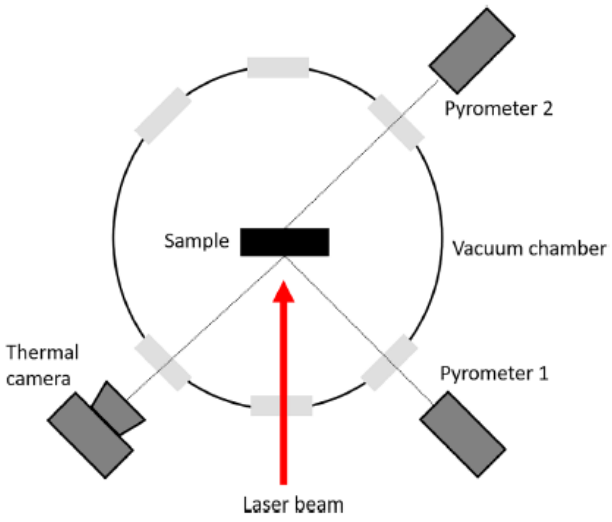

Experimental set up

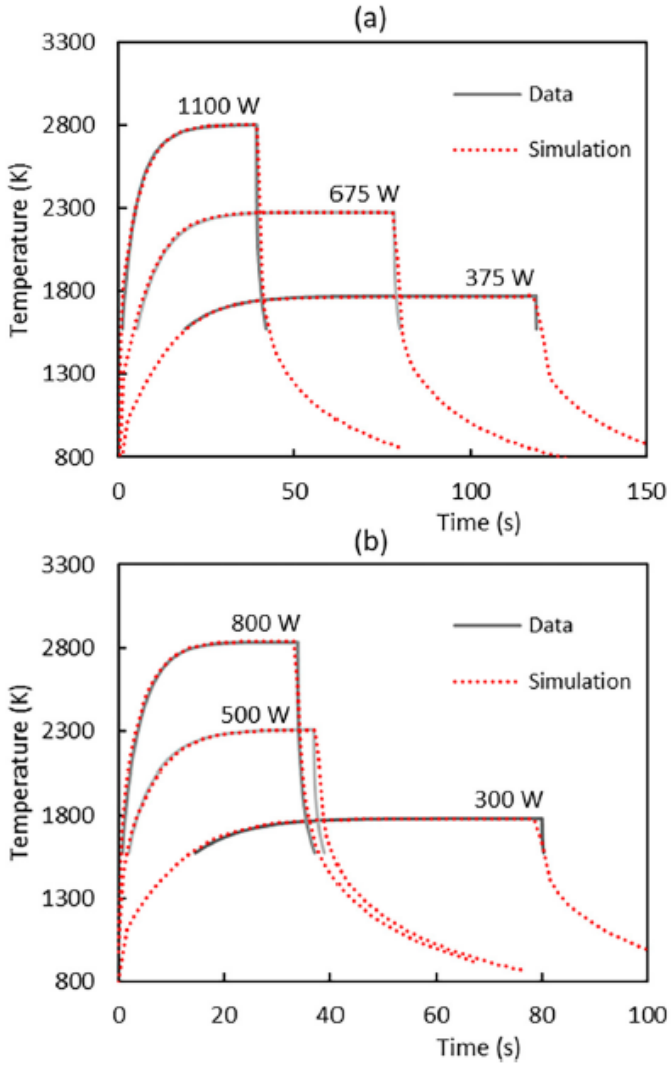

P Laser constant

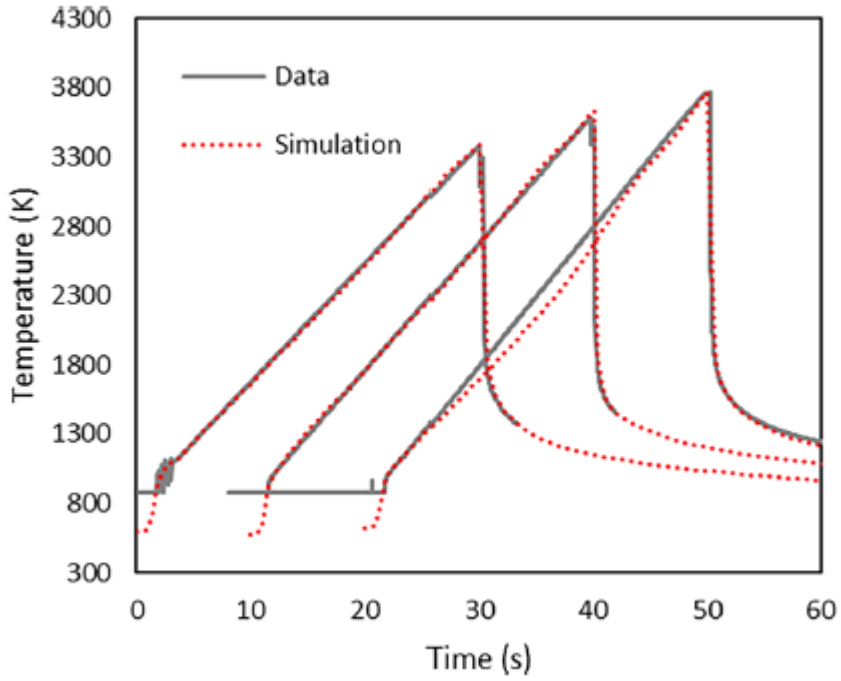

P Laser Regulated

Tmax : 3300 – 3800K

Conclusion and perspectives (1/3)

- Laser processing : very powerful technique to address various research topics in the field of nuclear fission research

Thermal properties

- Different techniques to measure thermal diffusivity and deduce the thermal conductivity
- Extend the temperature range on graphite. Transfer on UO_2

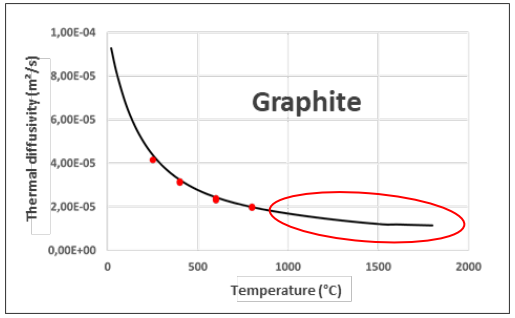

Thermal transients

- Quantify the impact of specific thermal transients at extremely high temperatures to validate the fuel performance codes
- Various types of thermal transients are accessible : temporal dynamics and spatial distributions

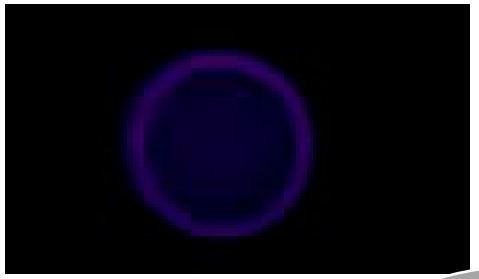

Laser micro/macro machining

- Laser micro-processing technique of graphite developed through experimental study with the support of a numerical model, to understand the laser ablation mechanisms processes
- First encouraging experiments on UO_2. To improve the quality of the processing and decrease the HAZ, experiments with dedicated picosecond laser will be performed



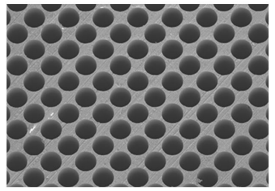

Thermal properties

CHAUCOLASE | Institut Fresnel

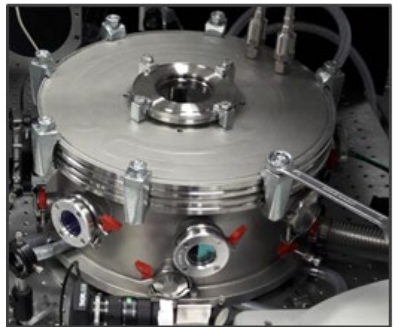

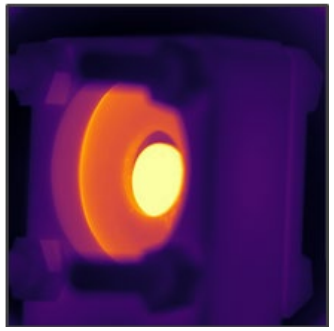

Micro/macro machining

CHARTREUSE | CEA



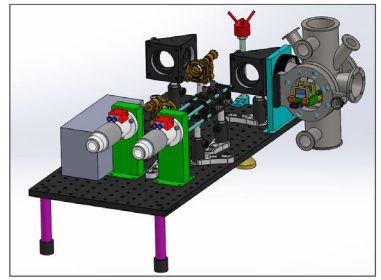

Thermal transients

Conclusion and perspectives (2/3) : MALAGA



End of experimental activities (Mid 2024)
MEXIICO furnace should be extracted from the cell
Hot cell should be refurbished

MEXIICO *



MERARG

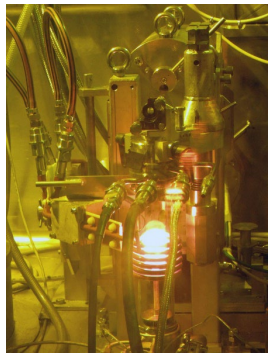

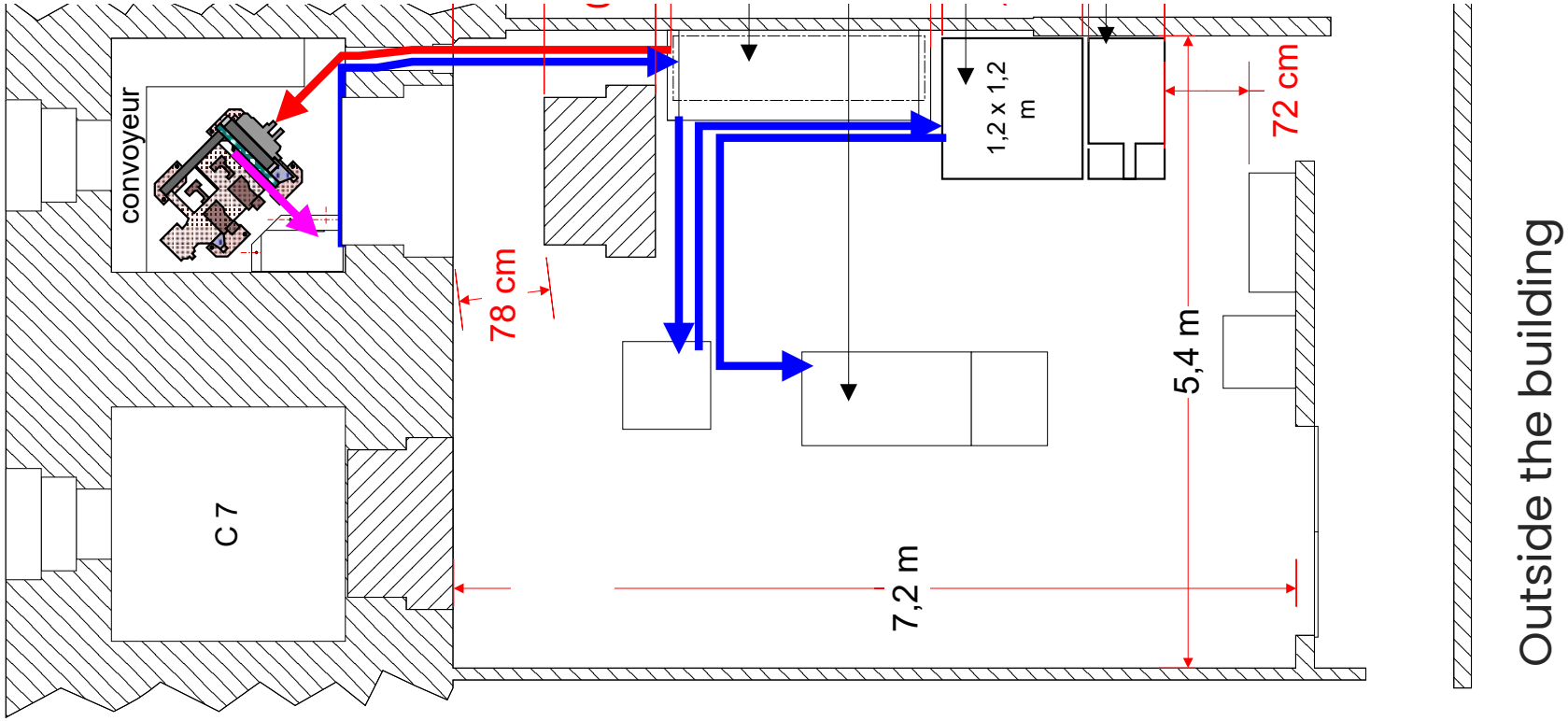

* - E. Hanus et al, "MEXIICO: a new equipment to study the pressure impact on the irradiated fuel behavior," Top Fuel Meeting 2016, Sep, Boise, 2016.

Conclusion and perspectives (2/3) : MALAGA



End of experimental activities (Mid 2024)
MEXIICO furnace should be extracted from the cell
Hot cell should be refurbished

MALAGA

MEXIICO 2

MERARG 1

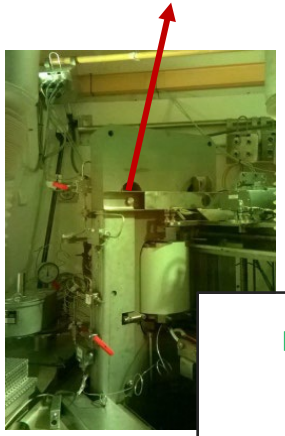

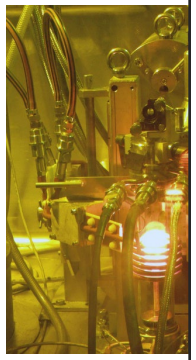

convoyeur

1,2 x 1,2 m

72 cm

5,4 m

7,2 m

Outside the building

Front Zone

Hot Cell

Back Zone

Laser dedicated area

Computer

Optical Instrumentation

Laser Chamber

γ Specrometry

Gloves box

Refrigeration unit

Electrical component

LASER x 5

Conclusion and perspectives (3/3): MALAGA for (Severe) Accident Study



- **Allows coriums (coming from irradiated nuclear fuels) to be:**
  - Produced (easily):
    - High temperature process / parametrical approach together with FP release study
  - Investigated (solid state):

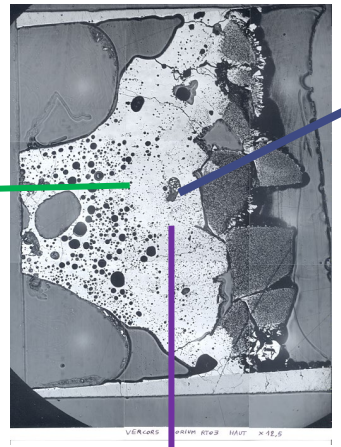

Thermal (and optical) properties:
- Diffusivity (local or average)
- Melting point
- Emissivity, …

Local FP (actinides) behaviour as function of T

µ-sampling:
- mechanical study
- Local FP (actinides) behaviour as function of T

Complementary to COPS (COrium Properties for reactor Simulation and uncertainties) (umbrella of OECD/NEA)

Thanks ☺

On the progress made in source terms evaluation and possible open issues relative to advanced technologies

L.Cantrel[(1)]*, L. Bosland[(1)], O. Coindreau[(1)], A.C. Grégoire[(1)], O. Leroy[(1)], D. Obada[(2)], M. Barrachin[(1)], S. Souvi[(1)], F. Kremer[(1)], J. Denis[(1)]

(*) laurent.cantrel@irsn.fr

1) **IRSN/PSN-RES – CEA Cadarache, F-13115 Saint Paul Lez Durance**

2) **IRSN/PSN-RES – 31 Av. de la Division Leclerc, F-92260 Fontenay-aux-Roses**

ABSTRACT

Since 2000's, many progresses have been made on the knowledge regarding the source term through different R&D programmes. The outside releases in severe accident (SA) conditions result from different phenomena: releases from degraded fuel, transport and chemistry in the RCS and aerosol physics and chemistry in the containment. Each phenomenon has been studied experimentally to provide the knowledge and data for developing and validating models.
The physical models gained were implemented, for IRSN side, in ASTEC software dedicated to SA scenario simulations for nuclear power plants providing an understanding of the main phenomena involved and finally a more accurate prediction of source term. The source term assessment contributes to enhance the prevention and mitigation of severe accident consequences by evaluating the effectiveness of mitigation systems and the Severe Accident Management Guidelines (SAMGs) effect. In addition, source term evaluations enable informed decision-making during crisis situations by helping to prepare emergency plans.
This paper gives an overview of the progress made over the last decade on ST issues, with new impacting phenomena, as well as a special focus on ongoing IRSN activities, mainly relative to chemical speciation of main fission products in the primary circuit under LOCA or Severe Accident conditions, and chemical reactivity of iodine in the containment.
Impact of new models dedicated to iodine behaviour in the containment coming from last R&D data, is presented using the results of ASTEC calculation of a LOCA scenario for French PWR 1300 MWe.
Finally, some possible open issues linked to new situations (LTO) and/or the development of a set of advanced technologies like Accident Tolerant Fuels (ATF) and Small Modular Reactors (SMR) will be discussed.

KEYWORDS
Source term; R&D, ASTEC, iodine, iodine aerosols

1. INTRODUCTION

The management of severe accident is a crucial to ensure the development of the nuclear energy and all the most, the source term issue which is used to estimate the radiological consequences and the post-management phase. In this paper, first a brief description of the R&D performed in this issue during the last decade is provided. Next, the approach and recent advances in term of modelling in the ASTEC code [1]

developed at IRSN are described. Third, some reactor applications will give some trends concerning these recent models and, finally the main R&D perspectives will be discussed.
IRSN's research approach enables us to acquire the knowledge we need to develop models, which are then capitalized on in simulation tools designed to assess as accurately as possible the dispersion of radioelements and the associated consequences. The importance of better assessment of FP behaviour in accident scenarios will be paramount in the future with projects for small-scale reactors (Small Modular Reactor), which meet industrial needs on devices that decentralize nuclear energy production close to the population.
The PHEBUS PF tests are the reference in the field of severe accidents and source term issues. The comparison of modelling results with PHEBUS tests enables us to identify gaps in knowledge. Assessing the potential release of radionuclides into the environment therefore requires to characterise the release of radionuclides from the fuel, their transport within the facility, the performance of static containment and radionuclide filtration/purification systems, and to study ways of mitigating the accident source term (trapping, filtration, etc.).
To be able to cover a broader spectrum of accident conditions (temperature, atmosphere, ambient irradiation, fuel type, etc.) which is a challenge, that has led us to adopt an ambitious two-level modeling approach detailed in section 3. The aim of this two-level approach is to increase the predictive power of phenomenological modelling, an important objective given the diversity of accident conditions. This diversity of conditions makes it difficult to cover them experimentally, and disqualifies an approach based exclusively on phenomenological modeling. In addition, it allows to improve the transferability of our models, which is a key point in the framework of the development of future projects for small-modular reactors or new concepts (Advanced Modular Reactor).
R&D activities support this strategy and declined results allow us to reassess the ST based on new knowledge.

2. R&D relative to the ST issue during this last decade

At the international scale several OECD experimental programs were performed to gain knowledge in fission products (FP) behavior.
Under severe accident conditions, the conditions prevailing in the containment are typically a steam-rich atmosphere, the presence of radiation and a high temperature (of the order of 100 to 140°C). Much of the R&D effort was focused on the behavior of iodine, which is likely to be present in gaseous form in the containment, and iodine-131 is critical to the countermeasures to be applied in the event of an accident.
We give some insights of the main programs.
With STEM2 (2016-2019) OECD program special focuses were paid on organic iodide formation (RI) from I_2-paint interactions (epoxy), the chemical/thermal stability of iodine oxides (I_xO_y) and the radiochemical stability of metallic iodide aerosols coming from the reactor coolant system (RCS). Experimental tests were performed, using ^{131}I labelled, in the EPICUR facility to simulate severe accident (SA) conditions. A typical profile of iodine species releases from the epoxy paint is observed [2]. RI and I_2 releases are correlated. These releases are fast during the first hours of the irradiation phase whereas the release kinetics for both species are significantly lower after this time. The RI release decreases as the relative humidity (R.H.) increases from 20% to 60%. The results show also that the pre-aging of the epoxy painted coupon has a significant influence on the release of iodine species, especially on the organic iodide release. The radiolytic pre-aging leads to a significant decrease of the gaseous organic iodide production. It has been clearly evidenced that iodine oxides aerosols, present in the containment atmosphere, are not stable in SA conditions and can be decomposed into I_2(g) [3]. Oxidation reactions could play a significant role in I_xO_y decomposition under radiation. In addition, the purely thermal decomposition leads to a significant release, which reveals that the thermal decomposition of iodine oxide aerosols is important particularly above 100°C. In STEM2, in Gas-IOx series, the possible impact of reducing gas (CO and H_2) was also investigated. Under the condition representative of a SA, the presence of 1% of CO or 1% of H_2 in the irradiation atmosphere (Air-50% R.H.) has no significant effect on the releases from I_xO_y aerosols irradiated at 80°C. In STEM project

(2011-2015), tests involving simple soluble metallic iodide aerosols were performed [4]. Seven dedicated tests have been carried out with CsI plus one with CdI_2, in EPICUR facility, in order to evaluate the influence of the nature of the coupon surface, of the relative humidity (R.H.), of the dose rate, of the aerosols concentration and of the temperature on the possible volatile iodine releases. In STEM2 project, effect of non-soluble iodide aerosol (AgI) and multi components aerosols were examined to extrapolate STEM results with better confidence. The global volatilization is almost total from CsI, CdI_2 and multi component aerosols deposited on quartz and stainless-steel surfaces. Tests highlight a high stability of AgI. A low humidity (RH =20%) promotes a higher CsI stability whereas higher RH (50%) promotes CsI decomposition. A decrease of the initial CsI concentration leads to a decrease of the inorganic gaseous iodine.

Concerning transport/reactivity of FP in the RCS, coming from the PHEBUS FP experimental data, it appeared that the widely accepted hypothesis that the iodine was transported entirely in the primary circuit in the form of CsI, to reach the containment in the form of an aerosol, was oversimplifying. The study of the iodine chemistry potentially out of thermodynamic equilibrium (influence of chemical kinetics) in the RCS was thus launched through the CHIP and CHIP+ programs [5] and extending to STEM/STEM2 OECD projects for oxidative conditions (air-ingress), which promote formation of gaseous ruthenium tetroxide [6]. Ruthenium isotopes contribute to potential high radiological impact in case of outside Ru releases [7].

ESTER program (2021-2025) is on-going and is currently studying 1) revolatilisation of PF deposits in the RCS in oxidative conditions 2) other sources of organic iodine in the main containment, like volatile organic compounds (VOC) or surface reactions with metallic surface or jacket insulation.

Several tests were performed in THAI facility within THAI-2 and THAI-3 programs [8], highlighting the possibility for gaseous I_2 to be quickly and efficiently trapped on silver aerosols (IOD-25 test, THAI-2) and in a slower manner on SnO_2 aerosols (IOD-26 test, THAI-2). An additional insight from THAI-3 was that organic iodides can be formed in a significant manner from a H_2 deflagration on Epoxy paints loaded with I_2 (IOD-34).

THEMIS program is on-going and is currently evaluating the effect the temperature on iodine oxides (IOx) stability at 140°C (IOD-37 test) and the effect of silver aerosol on IOx depletion in the gaseous phase (IOD-36 test, 80°C). Another phenomenon that is being quantified is the effect of passive autolytic recombiner (PAR) on I_xO_y thermal decomposition (HR-59 test) as PAR temperature is expected to increase up to several hundreds of °C when they are running.

To quantify outside releases, the efficiency of FCVS has to be known. Many works were developed to evaluate or develop the performance of current or advanced FVCS including pool-scrubbing topic as well as dedicated porous materials [9-12].

Table I. Main phenomena studied in the main OECD programs relative to ST.

	STEM-STEM2	ESTER	THAI-1-2-3	THEMIS
Org-I formation including paint, VOC and electric cable insulation interactions	yes	yes	yes	yes
Stability of iodide metallic aerosols	yes			
Reactivity and transport of Ru through the RCS	yes			
Stability of iodide metallic aerosols	yes			
Iodine oxides reactivity	yes		yes	
Chemical reactivity in the RCS (delayed releases)		yes		
Pool-scrubbing			yes	
Interactions gaseous iodine with aerosols (adsorption)			yes	

3. ASTEC model development for ST evaluation

Two types of models are usually developed at IRSN:

- phenomenological models for a direct description of the behavior of radioelements observed in semi-integral experiments. This modeling is intended to be promptly integrated into the system ASTEC software, which is the reference tool developed by IRSN for assessing releases to the environment (or source term) in accident situations;
- and more mechanistic models for a detailed description of underlying phenomena requiring detailed experiments and/or theoretical modeling techniques from the atomic scale to determine the thermodynamic and thermokinetic data needed to model the behavior of radioelements in accidental situations. The development of mechanistic models allows to check the transferability of the phenomenological models outside the conditions under which it was obtained. The development of such models requires the improvement of the databases, the upstream experiments dedicated to the identification of possible physical mechanisms and the collection of the data required for their development and/or validation.

The development of these models and tools requires the upstream development of experiments dedicated to the identification of possible physical mechanisms and the collection of the data required for their modeling and/or validation. On the other hand, this objective requires certain upstream research work, such as the improvement of databases, ultimately contributing to the modeling of these phenomena.
The aim of the tools validation process is to assess the ability of the models to describe one or more physico-chemical phenomena. It is essentially based on the comparison of simulations with two types of experiment: so-called analytical experiments, dedicated to the study of the smallest possible number of phenomena within a range of parameters representative of accident scenarios; and more global experiments, known as semi-integral or integral experiments, designed to simulate an accident situation to validate the simulation tools. Once the models have been developed or improved, comparisons with experimental data are carried out successively with data from analytical experiments to validate the models developed, and then with data from semi-integral and integral experiments to check that no important phenomena are missing.

- ***Release from fuel***

To assess the release of FP from fuel during an accident situation, IRSN has developed and validated the ASTEC and MFPR-F software packages. ASTEC is a "system" software package that covers the entire phenomenology of a severe accident - except for a steam explosion - from the initiating event to environmental release. It also takes into account the effect of the physical measures implemented to stop the progress of the accident and limit its consequences. The MFPR-F software is a mechanistic program that describes the detailed phenomenology of the release of FP from the fuel considering both chemistry and microstructure evolution, and therefore serves as a genuine reference for ASTEC. IRSN also develops and validates the NUCLEA and MEPHISTA thermodynamic databases for FPs in nuclear fuel (and also for corium).
With the objective to improve the ASTEC code, our recent work was focused on a better understanding of the mechanisms concerning the Cs and Mo releases and the improvement of the thermochemistry of SIC control rod elements (Ag-Cd-In), which are known to have a significant impact on iodine speciation in the primary circuit. To this purpose, a large number of semi-integral FP release experiments was performed (HEVA, VERCORS and VERDON) [13], in various conditions, in terms of temperature, atmosphere composition, fuel burn-up and nature (UO_2 and MO_X) which leads to have a very large experimental database covering all types of accidental situations. In parallel, more analytical experiments of implantation of Cs and Mo in fresh fuel and thermal annealing in different redox conditions were performed to get their diffusion coefficients which are now implemented in the MFPR-F code [14-15]. Finally, a large effort was devoted to the ruthenium thermochemistry [16-17] to get an assessed set of thermodynamic properties for

the gaseous species as well to the Ag-Cd-In chemistry [18] to be able to derive activity coefficients required to calculate the saturation pressures above the SIC melts.

- ***Transport/reactivity in the RCS***

During a nuclear reactor core meltdown accident, fission products contained in the fuel rods are released into the containment as particles (aerosols) or gases after transiting the reactor coolant system (RCS).
The understanding and modelling of the behavior of fission products in the reactor coolant system has been the subject of few experimental works in the past even if it is a crucial point for ST assessments.
The challenges involved in modeling the transport and reactivity of FPs in the RCS are as follows:

- to predict retention in the RCS, which determines the quantity of aerosols reaching the containment and the dose rate, as well as possible remobilization from deposits in the RCS, which may contribute to delayed releases, as recently demonstrated in the analysis of the Fukushima-Daichi accidents (in the OECD BASF 1 & 2 and ARC-F projects);
- to be able to predict the presence or absence of gaseous forms in the breach: how much and in what chemical form.

The CHIP/CHIP$^+$ experimental data were able to provide sufficient data for the development and validation of new models that were implemented in the ASTEC code.
Given that initial models considering thermodynamic equilibrium were not sufficient for describing FP behavior for certain situations [19], IRSN has recently extended a calculation method based on kinetic phenomena to deal with reactivity in the gaseous phase as well as gas/surface reactivity in ASTEC code. Naturally, this model tends towards thermodynamic equilibrium. This recent modelling work has consisted in investigating the phenomena related to surface effects, including the condensation/remobilisation of FP towards the gaseous phase. Surface chemistry has a direct impact on the speciation of PFs in the gas phase since species in the gas phase can react with the surfaces of the RCS and/or the previously deposited species. It also controls the so-called non-congruent condensation (non-condensable species containing a condensable fragment). Taking into account these surface effects (retention by adsorption, catalysis, ... and non-congruent condensation / remobilisation) requires a knowledge of the adsorption/desorption processes controlled by the chemical affinity between a gas and a given surface. For this, thermodynamic and thermo-kinetic parameters such as Gibbs energy of formation are needed for all phase (gas, sorbed, condensed). In a first approach, an approximation could be found but these data are fully accessible through ab-initio calculations [20-22].
This model has been integrated into ASTEC and allows to simulate satisfactorily the different ruthenium STEM tests. It can be transposed to all the species present in the RCS. This transposition is in course as well as the validation work. The next step is to use this model for the interpretation of the PHEBUS PF tests. From this comparison, it will be possible to identify the eventual additional thermodynamic and thermo-kinetic data to be acquired by ab initio calculation to complete the model.

- ***Containment***

Recently, the EPICUR tests performed within the OECD-STEM/STEM2 projects have led to the development of two phenomenological models in ASTEC to better model iodine behavior in the containment. The first concerns the radiolytic decomposition of iodine oxides aerosols [2] and the second is related to multicomponent aerosols (Iaer) [4]. Even if there are only few data, the influence of temperature, humidity and dose rate has been considered for I_xO_y decomposition whereas dose rate is the main parameter for Iaer decomposition. They complete the other models previously developed, i.e. the iodine-paint interaction [2], the iodine oxides aerosols formation [23-24] the gaseous radiolytic reaction leading to organic iodides (RI) formation from volatile organic compounds [25].
A more complete and global approach including uncertainty propagation calculations has recently been developed on PHEBUS FP tests. It has not only allowed us to identify the main kinetics parameters and reactions governing iodine volatility in the PHEBUS FP tests but also the evolution of their influence over

time. The gaseous reactions and the gaseous iodine coming from the PHEBUS reactor cooling system appear to be the main contributors to iodine volatility.
The phenomena that remain to be considered deal with the impact of a more representative steam mass fraction for I_xO_y behaviour and their chemical interactions with paint/steel, hydrogen recombiners and other aerosols. Another perspective is to find out, under irradiation, the fate of the iodine precipitates resulting from a dried out sump.

- ***Pool-scrubbing***

Pool scrubbing refers to a set of physical and chemical processes which lead to the FP retention, in the aerosol and gaseous forms, carried by a gas through a pool of water. The injection of the carrier gas leads to the formation of a jet or a bubble at the sparger outlet depending on the dynamic of the gas flow. Higher in the pool, a swarm of bubbles is established. During the bubbles' ascent, FP could reach the bubble surface leading thus to their trapping in the water. A recent review was made on this topic [26]. In consistency with that, currently a work is in progress at IRSN in order to develop a new pool scrubbing modelling in the ASTEC code. Three main steps have been identified to achieve this goal with the concern to separate the bubble hydrodynamics part and the retention part to set-up a flexible computer code. The first step has been dedicated to bubble hydrodynamics and thermalhydraulics modelling in the water pool based on an extended literature review performed to specify the models to be developed. These models allow describing the bubble formation and its size at the sparger outlet for different sparger configurations and the bubble plume behavior with the determination of the bubble plume velocity and the void fraction. The models have been implemented in ASTEC and validated with available data. It is planned to expand this validation with the recent data obtained at IRSN on the TYFON facility for the bubble size at the sparger [27]. The second step is in-progress and is devoted to the modelling of volatile iodine species retention mechanisms. It is based on the IRSN work which allows to describe the mass transfers and the chemical reactions in the gas phase and in the liquid phase for the species such as I_2, CH_3I and HOI. The implementation of this modelling in ASTEC is on-going. The validation will be notably performed with the decontamination factor data obtained from the tests carried out at on TYFON facility for I_2 and CH_3I. The last step concerns the modelling of the aerosol retention mechanisms. Firstly, the identification of the relevant deposition mechanisms and their modelling will be performed. It is thus planned to implement the modelling of each mechanism in ASTEC and to carry out the validation based on available data. The data obtained for CsI aerosols in TYFON facility will be used for this purpose [28].

4. Plant application: ST evaluation

This section presents the impact of the newly implemented iodine chemistry models on the source term to the environment in case of a severe accident scenario on a nuclear power plant. It is worth noting that the accident simulations detailed hereafter are not conservative evaluations and thus cannot be directly compared to safety assessment studies.
In order to quantify the impact of each new model, several computations were performed:

- A default computation, where all the iodine chemistry models are activated, except the metallic iodide aerosol decomposition;
- Sensitivity computations, by deactivating the studied chemical model, in order to measure its impact: iodine oxides chemistry and metallic iodides aerosols decomposition.

To perform the sensitivity study on iodine oxide modelling, ASTEC simulations of iodine behaviour in the containment have been carried out. Beforehand, the whole sequence was computed with ASTEC version 2.2_b. This provides the thermal-hydraulics and dose rate conditions in the containment as well as the amount of FP entering into the containment.

2.1. Plant description and scenario hypotheses

The computation was performed on a French 1300 MWe plant. The reactor building consists of a double containment and is equipped with a Filtered Containment Venting System (FCVS) containing a sand bed filter for trapping aerosols (DF=1000) and a metallic pre-filter with a limited capability for retaining gaseous molecular iodine (DF=10).
The chosen scenario is a Loss-of-Coolant Accident (LOCA), initiated by a 12-inch break in the hot leg of the primary circuit, with failure of the reactor Safety Injection System (SIS) and the Containment Spray System (CSS) at the start of the scenario (European FASTNET project scenario [29]). The pH of the liquid phase is set to 7, in order to simulate the borax baskets installed on the PWR 1300 MWe plants in France. Concerning the FP release into the containment, it is assumed that 5% of the amount of iodine entering into the containment is gaseous molecular iodine. Moreover, it is assumed that 10% of the silver initial inventory is released into the containment. The venting of the containment building through the FCVS is executed when the internal pressure reaches 5.2 bar.

2.2. Simulations

In this paragraph, the results of the simulations are detailed.

- ***Impact of iodine oxides modelling on iodine releases***

The SA scenario leads to a rapid transient. The cumulated iodine mass released into the containment at the break reaches 95.7% of the total iodine inventory of the core within 1.2h from the start of the scenario. As the break is located on the hot leg of the RCS, which is the outlet line of the reactor pressure vessel, the FP retention in the RCS is minimal with a high fraction reaching the containment. By assumption, the gaseous fraction of iodine entering the containment is set at 5% and the remaining part being under aerosol form (CsI and others).
With the loss of the Safety Injection Systems (SIS) and Containment Spray System (CSS), the pressure continues to rise in the containment, until it reaches the venting criterion at 5.2 bar, at which point the FCVS is activated, 29 h after the start of the scenario. Iodine is released in the environment through leaks (with and without filtration) and the FCVS.
The iodine mass distributions inside the containment are displayed on Figure 1.

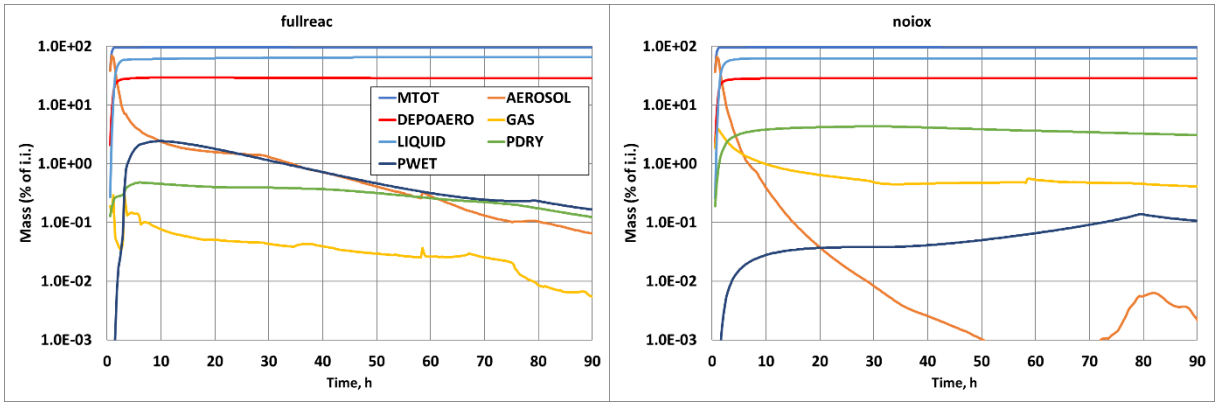

Figure 1. Evolution of iodine phase distribution in the containment (masses are related to the iodine element)**. Impact of I_xO_y formation.** *At the right without I_xO_y modelling to make a comparison*

Without iodine oxides modelling, metallic iodide aerosols (AEROSOL phase), coming from the RCS, are removed from the containment atmosphere by sedimentation into the sump and deposition onto the walls by phoretic phenomena., After about 1 day, the amount of metallic iodine aerosol (assimilated to CsI) in suspension in the containment atmosphere has decreased by almost 3 orders of magnitude.

With iodine oxides modelling, it is observed the persistence of aerosols results from iodine oxides formation. For both cases, after one day, iodine in the containment is mostly in the sump (LIQUID) and deposited onto the walls (DEPOAERO). The quantity of iodine in gaseous phase (GAS) and adsorbed on dry and wet paint (PDRY and PWET respectively) is very low.

In Figure 2, are displayed the airborne iodine species present in the containment atmosphere. In term of total mass, the amount is of the same order of magnitude for both computations but with a different repartition. Due to the rapid conversion of gaseous iodine (CH_3I) into iodine oxides, for fullreac, the dominant airborne iodine species is iodine oxides even if they are decomposed into I_2 whereas methyl iodide is dominant in noiox computations because this species is neither decomposed nor trapped, at least very weakly, on surfaces.

The iodine release to the environment by species is shown in Figure 3. The main released species in both cases is the organic iodide CH_3I, which is due to its non-retention by the FCVS filtering system. The release increases sharply 29 hours after the start of the scenario, which corresponds to moment when the containment building is vented through the FCVS. In presence of iodine oxides, the outside I_2 release is much higher. additionally, iodine oxides are also released to the environment. Even though the amount of iodine oxides in the containment atmosphere is higher than the amount of CH_3I, their release to the environment is lower. This is due to the fact that in the iodine oxides are assumed to be well filtered by the FCVS sand bed filter, as they behave as fine particles, while gaseous organic iodide is not filtered. Additionally, the thermal and radiolytic decomposition of iodine oxides in the sand bed, as described by [30] was not considered in this study. These mechanisms result in the production of volatile molecular iodine, which could lead to a significant increase in the iodine release to the environment.

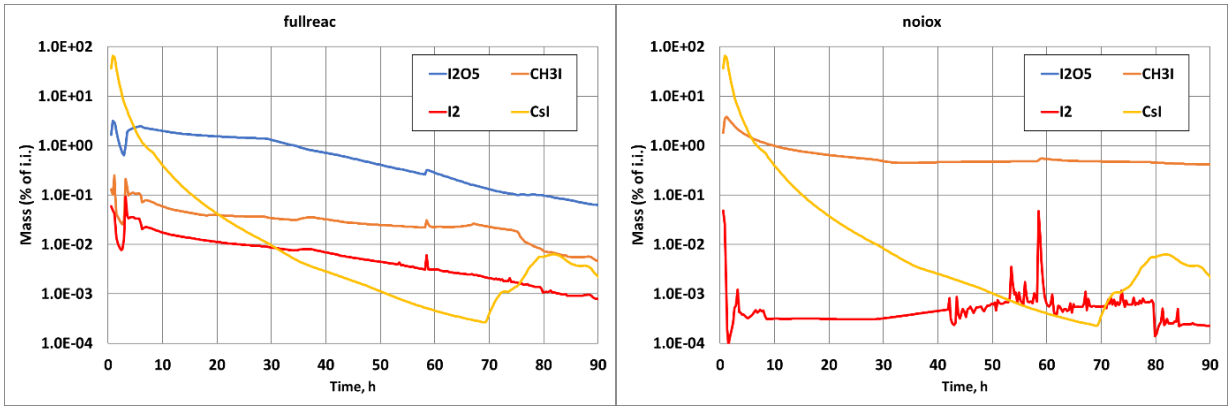

Figure 2. Evolution of airborne iodine species in the containment (masses are related to the iodine element). Impact of IxOy formation. *At the right without I_xO_y modelling to make a comparison.*

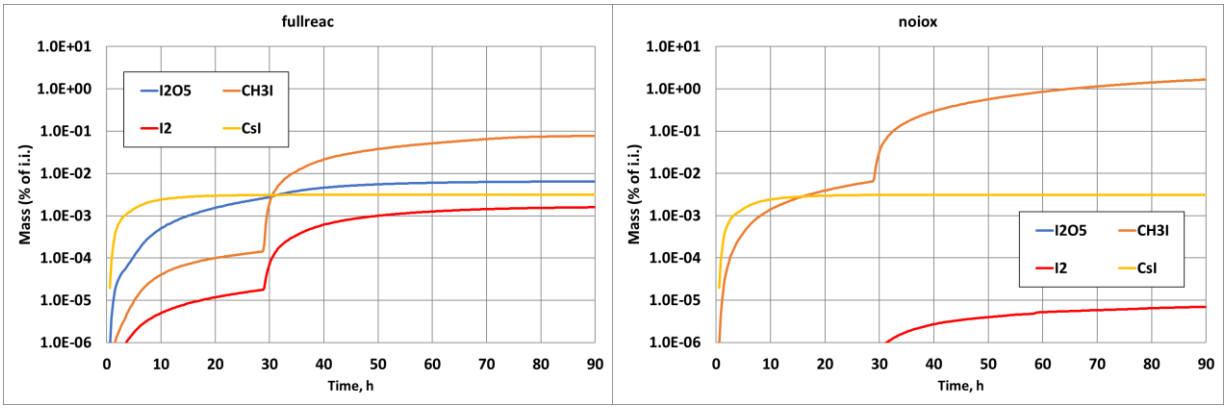

Figure 3. Evolution of iodine species released into the environment (masses are related to the iodine element)**. Impact of IxOy formation.** *At the right without I_xO_y modelling to make a comparison.*

Regarding the metallic iodide aerosols, represented by CsI, their main release to the environment occurs during the first 24 h after the start of the scenario, at which point most of them have settled down in the containment and are filtered by the FCVS as well.
When considering the total release to the environment, the absence of I_xO_y in the modelling produces a source term 25 times more important, that denotes an important influence of the iodine oxide modelling and could have an impact on accident mitigation actions.

- ***Impact of iodine metallic aerosol modelling on iodine releases***

The modelling of metallic iodide aerosol decomposition (decompo) computation leads to a decrease of iodine as deposited aerosols and an increase as aerosols in suspension and adsorbed on dry paint, as well as an increase of iodine mass in gaseous form in the medium and long term. In terms of iodine speciation, it is observed a decrease of CsI amount and an increase in the amount of I_xO_y, CH_3I and I_2 (more adsorption on paint in the atmosphere). At ~3 days, the amounts of aforementioned species in the containment atmosphere are roughly one order of magnitude higher in the "decompo" computation than in the standard configuration including I_xO_y modelling without metallic iodide aerosol decomposition, as shown in Figure 4. In the case of the "decompofast4" computation, which uses a much higher radiolytic decomposition constant, the I_xO_y, CH_3I and I_2 is much higher at the beginning of the simulation during the first 24 h, and by the end of the simulation it decreases to comparable values with the "fullreac" computation. This can be explained by the rapid decomposition of CsI aerosols in the first hours of the scenario, when the dose rate in the containment gas phase has the highest value: after few days the CsI amount is strongly reduced and its decomposition is no longer sufficient to maintain high amount of iodine in the gas phase.
For faster decomposition rates (two orders of magnitude higher due to uncertainties on the nature/compoistion of the aerosols), the I_2 formed by CsI decomposition has almost totally reacted (I_xO_y formation, paint trapping and in lesser extent CH_3I formation) in the first 24 h since the start of the scenario, before the venting of the containment happened. These competitive processes may, more or less, impact the outside releases depending on the leakages evolution as a function of time.
The dominant outside release is CH_3I with a large increase corresponding to the containment venting phase starting at 29 h.

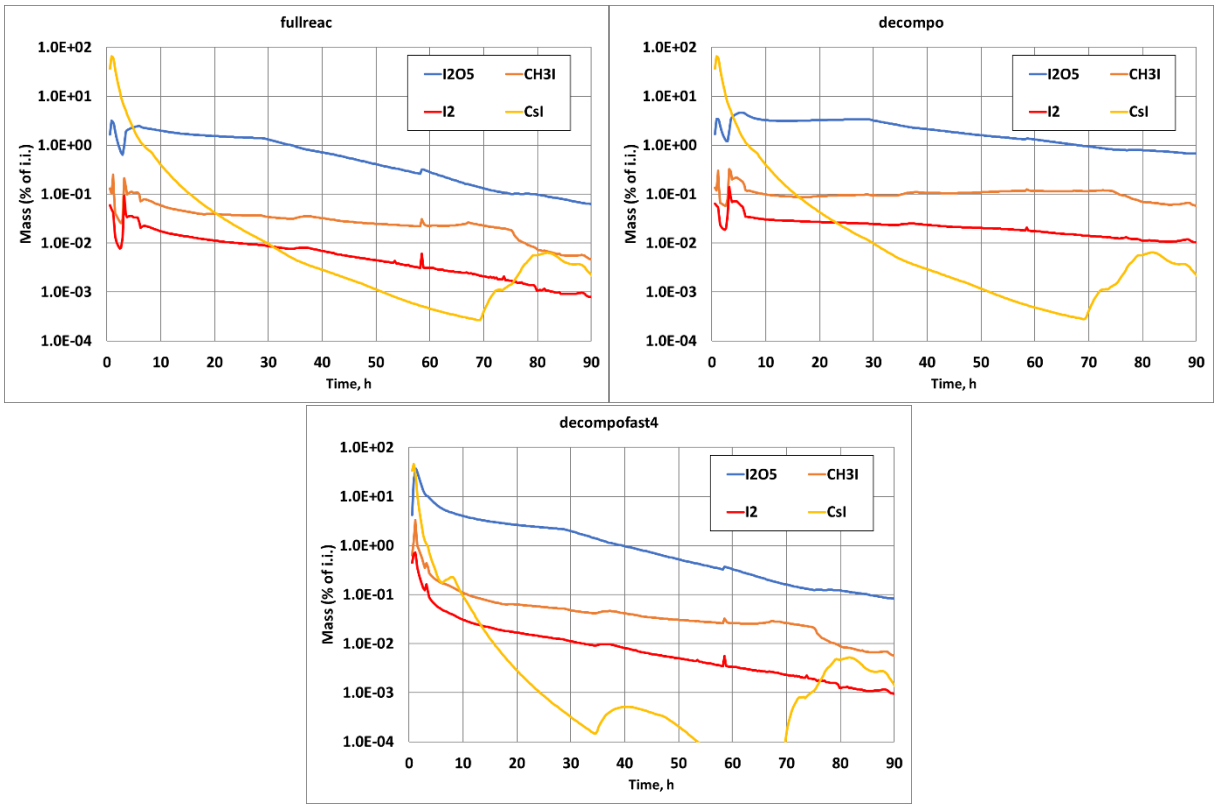

Figure 4. Evolution of airborne iodine species in the containment (masses are related to the iodine element)**. Impact of metallic iodide aerosol decomposition.** *Decompo includes metallic iodide oxidation.*

5. CONCLUSION/PERSPECTIVES

After Fukushima-Daichi (FD) accident, many efforts were performed to review safety assessments and SA scenarii leading to progress in capability of simulation tools, noticeably ASTEC, to cover a wide range of SA situations for PWR and also BWR. FD accident highlighted three main issues relative to ST: pool-scrubbing modelling, delayed released and management of contaminated water. For the two first, some R&D actions are still ongoing (IPRESCA and ESTER projects). For LTO management of contaminated water, it exists several uncertainties with a direct impact on; the two main points are, first, the chemical speciation of FP/actinides in the liquid phase after several days/weeks including possible debris interactions and second, the source of contamination coming from the leaching of FP deposits inside the NPP as well as lixiviation of corium inside or outside the reactor vessel. To deal with that, some R&D actions have been proposed.

Even if some uncertainties still exist on the kinetic of the phenomena for the involved iodine reactions due to limiting experimental data, it worth noting that all the main phenomena governing the iodine behavior should have been identified at the end of the ongoing projects.

Due to the quite rapid emergence of advanced/new technologies (SMR, AMR and e-ATF), the question arises if the current ST modelling is capable to cover these new boundary conditions with some specificities. After the end of OCDE ESTER project, IRSN would like to propose a program (FORESEEN project) oriented towards the ST relative to chromium E-ATF fuel covering fuel releases at high temperature, transport through the RCS and possible impact of FP chemistry in the containment (liquid and gas phases). For SMR, the European SASPAM (Safety Analysis of SMR with Passive Mitigation Strategies) project [31] deals with this topic with possible recommendations, based on SA scenarii for two designs of SMR, on R&D needs for ST evaluation.

ACKNOWLEDGMENTS

IRSN acknowledges all partners of the OECD programs for co-funding these R&D actions as well as IRSN staff which contribute to the ST activities.

REFERENCES

1. P. Chatelard; S. Belon and al., "Main modelling features of ASTEC V2.1 major version", Annals of Nuclear Energy **93**, pp. 83-93 (2016).
2. L. Bosland and J. Colombani, "Study of iodine releases from Epoxy and Polyurethane paints under irradiation and development of a new model of iodine-Epoxy paint interactions for PHEBUS and PWR severe accident applications" *J. Radio. Nucl. Chem.*, **314** (2), pp. 1121-114 (2017).
3. O. Leroy and L. Bosland, "Study of the stability of iodine oxides (IxOy) aerosols in severe accident conditions" *ANE*, **314** (2023).
4. L. Bosland and J. Colombani, "Study of the radiolytic decomposition of CsI and CdI_2 aerosols deposited on stainless steel, quartz and Epoxy painted surfaces" *ANE*, **141**, article number 107241 (2020).
5. L. Cantrel et al. "Research works on iodine and ruthenium behavior in severe accident conditions" *Journal of Nuclear Engineering and Radiation Science* **4(2)**, article number 020903 (2018).
6. M.N Ohnet, O. Leroy, L. Cantrel, T. Karkela, "Ruthenium behavior in the reactor cooling system in case of a PWR severe accident: study of oxidative conditions with stainless steel tube" *JNRC*, **333**, pp. 235-251 (2024).
7. F. Miradji, F. Cousin, S. Souvi, V. Vallet, J. Denis, V. Tanchoux,L. Cantrel, in The 7th European Review Meeting
8. S. Gupta M. Freitag, G. Poss. "THAI experimental research on hydrogen risk and source term related safety systems" *Frontiers in Energy*, **15**(4), pp. 887-915 (2021).
9. T Albiol et al. "Main results of the European PASSAM project on severe accident source term mitigation" *ANE*, **116**, pp. 42-56 (2018).
10. S. Gupta et al. "Integration of pool scrubbing research to enhance Source-Term calculations (IPRESCA) project – Overview and first results" *NED*, **404**, Article number 112189 (2023).
11. H. Jabraoui, E.P. Hessou, S. Chibani, L. Cantrel, S. Lebègue, M. Badawi. "Adsorption of volatile organic and iodine compounds over silver-exchanged mordenites: A comparative periodic DFT study for several silver loadings" *Applied Surface Science*, **485**, pp. 56-63 (2019).
12. A. Bentaib, R. Meignen, L. Cantrel, S. Morin, G. Repetto. "On the progress made in safety assessment and severe accident management as part of the French FUKUSHIMA post-accident research programme" *The 11th European Review Meeting on Severe Accident Research (ERMSAR 2024)*.
13. Y. Pontillon Y., E. Geiger, C. Le Gall, S. Bernard, A. Gallais-During, P.P. Malgouyres, E. Hanus, G. Ducros, "Fission products and nuclear fuel behaviour under severe accident conditions part 1: Main lessons learnt from the first VERDON test" *Journal of Nuclear Materials* **495**, pp. 363-384 (2017).
14. C. Panetier, Y. Pipon, C. Gaillard, R. Dubourg, R., Ducher, N. Moncoffre. "Cs diffusion mechanisms in UO_2 investigated by SIMS, TEM, and atomistic simulations" *Journal of Chemical Physics*, **156**(4), article number 044705 (2022).
15. C. Panetier, L. Sarrasin, C. Gaillard, R. Dubourg, R. Ducher, N. Moncoffre. "Effect of molybdenum on the behaviour of caesium in uranium dioxide at high temperature" *Journal of Nuclear Materials* **545**, article number 152602 (2021).
16. C. Chatillon, I. Nuta, F.Z Roki, E. Fischer. "Chemical thermodynamics of RuO_2(s)" *J. Nucl. Mater.* **509**, pp. 742-751 (2018).
17. I. Nuta, C. Chatillon, F.Z Roki, F.Z.; E. Fischer. "Gaseous phase above Ru–O system: A thermodynamic data assessment", *Calphad* **75**, article number 102239 (2021).
18. E. Fischer, K; Gajavalli, G. Mikaelian, P. Benigni, J; Rogez, A. Decreton, M. Barrachin, "Experimental study and thermodynamic modelling of the Ag-Cd-In system". *Calphad* **64**, pp. 292-305 (2019).
19. A-C Grégoire, Y. Délicat, C. Tornabene, F. Cousin, L. Gasnot, L. Lamoureux. "Study of the iodine kinetics in thermal conditions of a RCS in nuclear severe accident" *ANE*, **101**, pp. 69-82 (2017).
20. R. Vandeputte, D. Khiri, C. Lafont, L. Cantrel, F. Louis, Theoretical Investigation of Thermochemical Properties of Cesium Borates Species, *Journal of Nuclear Materials* **517**,pp. 63-70 (2019).

21. M. Saab, S. Souvi "Quantum Modelling of $AgHMoO_4$, $CsHMoO_4$ and $AgCsMoO_4$ Chemistry in the Field of Nuclear Power Plant Safety", *International Journal of Chemical and Molecular Engineering* **12**(5), pp. 244-248 (2018).
22. F. Miradji, S.M.O. Souvi, L. Cantrel, F, Louis, V. Vallet, "Reactivity of Ru oxides with air radiolysis products investigated by theoretical calculations", *Journal of Nuclear Materials* **558**, article number 153395 (2022).
23. L. Bosland; F. Funke, and al., "PARIS project: Radiolytic oxidation of molecular iodine in containment during a nuclear reactor severe accident. Part 1. Formation and destruction of air radiolysis products-Experimental results and modelling", *Nucl. Eng. Des*., **238**(12), pp. 3542-3550 (2008).
24. L. Bosland; F. Funke and al., "PARIS project: Radiolytic oxidation of molecular iodine in containment during a nuclear reactor severe accident: Part 2: Formation and destruction of iodine oxides compounds under irradiation – experimental results modelling", Nucl. Eng. Des., **241**(9), pp. 4026-4044 (2011).
25. L. Bosland and J. Colombani, "Review of the potential sources of organic iodides in a NPP containment during a severe accident and remaining uncertainties", T*he 9th European Review Meeting on Severe Accident Research (ERMSAR 2019)*, paper 099, Clarion Congress Hotel, Prague, Czech Republic, March 18-20, (2019).
26. S. Gupta, L.E. Herranz, L.S. Lebel, M. Sonnenkalb, M. Pellegrini, C. Marchetto, Y. Maruyama, A. Dehbi A., D. Suckow D., T. Kärkelä "Integration of pool scrubbing research to enhance Source-Term calculations (IPRESCA) project – Overview and first results" *Nuclear Engineering and Design* **404**, Article number 112189 (2023).
27. M. Farhat, M. Chinaud, P. Nerisson, and O. Vauquelin. "Characterization of bubbles dynamics in aperiodic formation". *International Journal of Heat and Mass Transfer*, 191, (2021).
28. M. Farhat, P. Nerisson, L. Cantrel, M. Chinaud, and O. Vauquelin. "Hydrodynamic aspects of aerosols pool scrubbing". *Chemical Engineering Research and Design* **180**, pp. 646-657 (2023).
29. Reviewed specifications and methodologies for accident database, FASTNET-DATA-D1.1, FAST Nuclear Emergency Tools project, January 2018.
30. L. Bosland; O. Leroy, and al., "Study of the stability of CsI and iodine oxides (IOx) aerosols and trapping efficiency of small aerosols on sand bed and metallic filters under irradiation", *Prog. Nucl. Energy* **142**, article number 104013 (2021).
31. European project. https://www.saspam-sa.eu/

RÉPUBLIQUE FRANÇAISE
Liberté
Égalité
Fraternité

SEAKNOT
ERMSAR 2024
11th Conference on
SEVERE ACCIDENTS RESEARCH
May 13-16, 2024 – Stockholm, Sweden

IRSN
INSTITUT DE RADIOPROTECTION
ET DE SÛRETÉ NUCLÉAIRE

ON THE PROGRESS MADE IN SOURCE TERMS EVALUATION AND POSSIBLE OPEN ISSUES RELATIVE TO ADVANCED TECHNOLOGIES

Authors : L. Cantrel(*), L. Bosland, O. Coindreau, A.C. Grégoire, O. Leroy, D. Obada, S. Souvi, F. Kremer , J. Denis

The 11th European Review Meeting on Severe Accident Research (ERMSAR2024)
KTH, Stockholm, Sweden, May 13-16, 2024 - Log Number: 033 – abstract id 08Y54Pvb

(*) laurent.cantrel@irsn.fr

[IRSN/FRM-296 ind. 07]

MEMBRE DE
ETSON

OUTLINES

1. Main R&D performed on the ST issues this last two decades and main achievements

2. Development of ASTEC software abilities for ST evaluation

3. Example of ST application for a French 1300 MWe PWR

4. Potential open issues for ST relative to new situations (LTO, SMR, eATF, AMR)

Main R&D performed on the ST issues this last two decades

→ Starting point: results of the integral PHEBUS FP TESTS in the 2000's

→ Results highlighting importance of reactions occurring in the gas phase with some interactions with surfaces

→ Several OECD programs lead by IRSN were launched to study gas phase reactions with also some thinkings coming from to FD accident in using **CHROMIA experimental** platform at IRSN Cadarache

(Other activities like those relative to PFs releases from fuel or FCVS efficiencies are not mentioned)

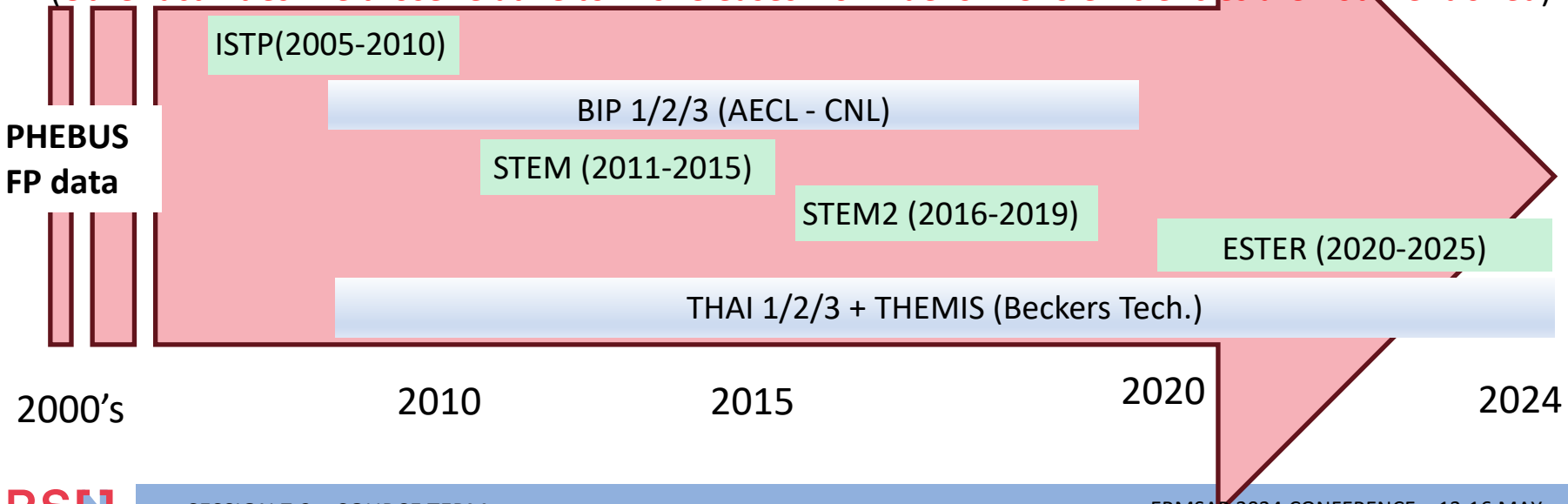

Presentation of the CHROMIA experimental platform devoted to ST studies

Radiochemistry of fission products

- γ EPICUR irradiator
- Temperature up to 140°C
- Variable atmosphere compositions (air, H_2O, H_2 …)
- Labelled iodine with gamma measurements
- Physico-chemistry of gases and aerosols in accident conditions



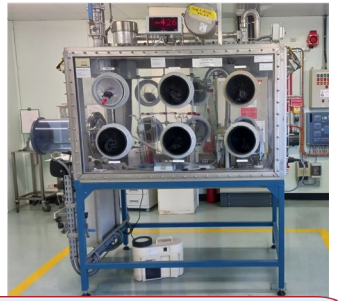





Research works focused on chemistry-transport coupling concerning fission products behaviour

- Chemistry-transport at high temperature (~1500°C)
- Interactions with surfaces
- Chemical reactivity
- Condensation/nucleation
- Aerosol physics
- CHIP and START experimental benches

Mitigation/trapping of contaminants in gaseous and liquid phases

- Benches for qualifying trapping performance at laboratory or semi-pilot scale (DOFIN exp. loop)
- Design of porous materials: zeolites and MOFs
- Epuration by pool-scrubbing
- Trapping on liquid filter: clogging issue







Main achievements

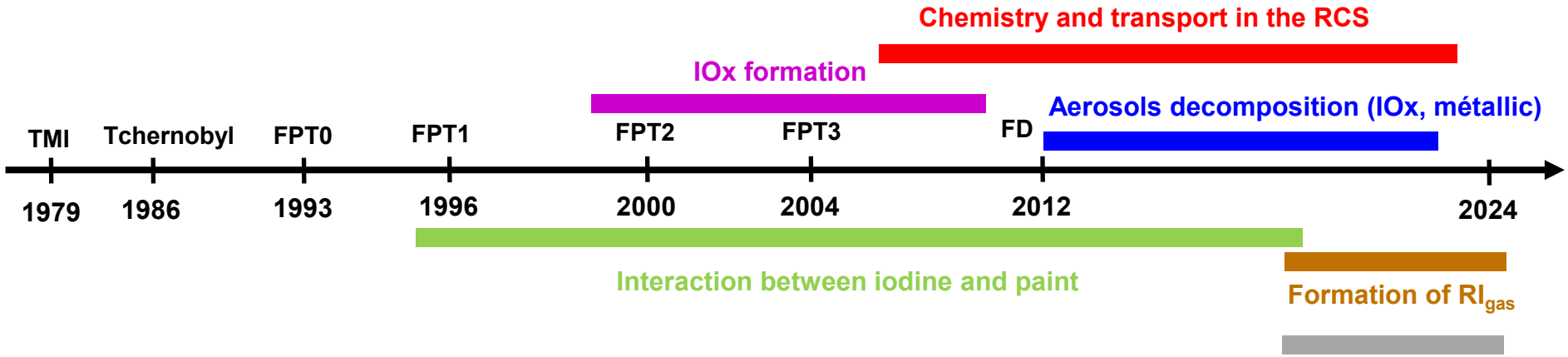

Phenomena involved in the RCS

1) Other form than CsI of iodide aerosol can be present in the RCS
2) Chemistry of molybdenum is of high importance to predict chemical speciation of Cs and I in the RCS
3) Impact of silver is less impacting than expected (moderate fraction of AgI is formed)
4) Depending on conditions prevailing in the RCS, fraction of volatile iodine (more or less significant) may be released at the break
5) In ESTER project, delayed releases of I and Cs in oxidative conditions are still ongoing

Main achievements

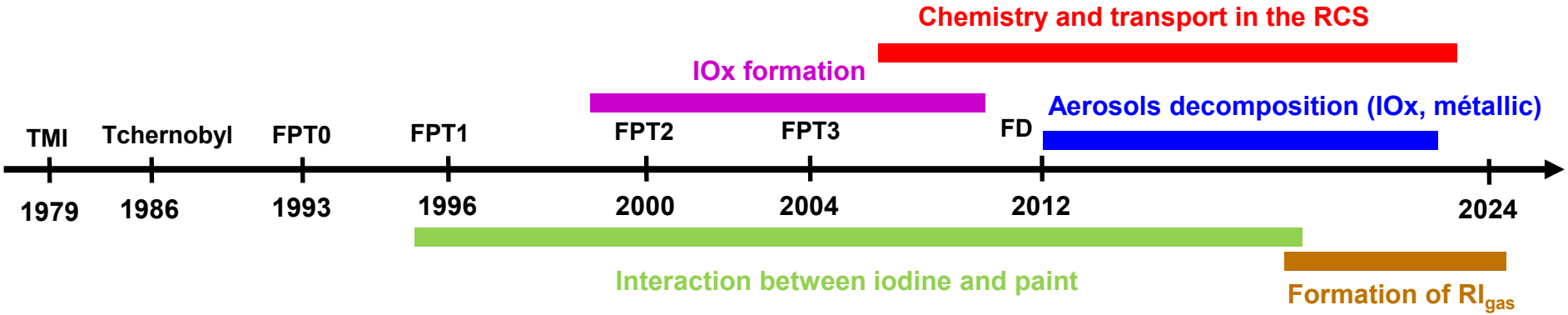

Phenomena involved in the containment

1) Main lessons learnt from the iodine-paint interaction (1995-2018): moderate rate of production of Org-I (much lower than expected) with a kinetic model has been developed
2) IOx formation: Rapid oxidation of volatile iodine (organic and molecular) to form fine particles under IO_x form (various species more or less stable)
3) IOx stability under thermal/radiation stresses: partial decomposition with significant influence of the T on their decomposition (T > 110°C, with/without γ) + humidity + dose rate
4) Metallic aerosol decomposition (CsI, CdI_2, AgI …): oxidation into $I_{2(g)}$ strongly dependant on aerosol solubility feature

Main conclusion for ST concerning current PWR/BWR reactors

1) Formation of Org-I in the gaseous phase: source coming from paint-interaction is not sufficient, quantification of other phenomena suspected to lead to significant Org-I formation (gas/steel interaction in the ESTER OECD program)

2) Iodine oxides have to be modelled to get a more accurate ST because they are involved in a formation-decomposition cycle with gaseous iodine (I_2, CH_3I)

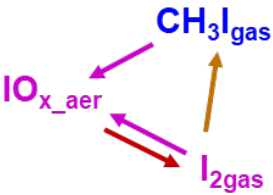

3) unwashed iodide aerosols contribute to iodine gaseous formation by decomposition

4) Possible delayed releases from deposited species (condensed on aerosol deposition) in the RCS are ongoing (ESTER project)

5) ST evaluations strongly depends on FCVS efficiencies and/or direct leakage rates

Large progresses have been performed on understanding and ST evaluations this last decade and some

Development of ASTEC software abilities for ST

Phenomenological models

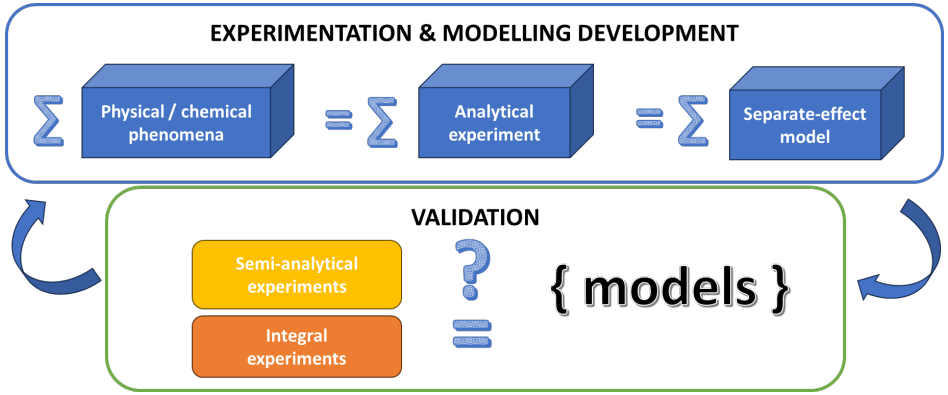

- ➔ + promptly implemented
- ➔ – questionable out of the validation range
- ➔ Useful for complex and coupled phenomena

Mechanistic models/ FPs in fuel and releases and in the RCS

Atomic scale up to

- **Parameters of interest**
- Physical process: diffusion coefficient, defect formation energy, etc.
- Chemical mechanisms: Gibbs energy, activity coefficient
- Tools: DFT, Molecular Dynamic, Knudsen cells, SIMS

Macroscopic scale

- Physical & chemical process: diffusion, reactivity mechanisms, adsorption isotherms
- Code: thermodynamic database (NUCLEA, MDB), TRANSURANUS/MFPR-F, ASTEC

Validation

- **Observable** and **measurable data**
- Released quantity, gas/particle partition, etc.

- ➔ + extensive, transferable
- ➔ – more time to develop
- ➔ Need of basic data
- ➔ To complement with experimental data

Development of ASTEC software abilities for ST: reactivity/transport in the RCS

EXTENDING AND IMPROVING DATABASES

Massive use of quantum-chemical methods to calculate missing thermo-kinetic data related to the solid and gaseous phases as well as to the interface

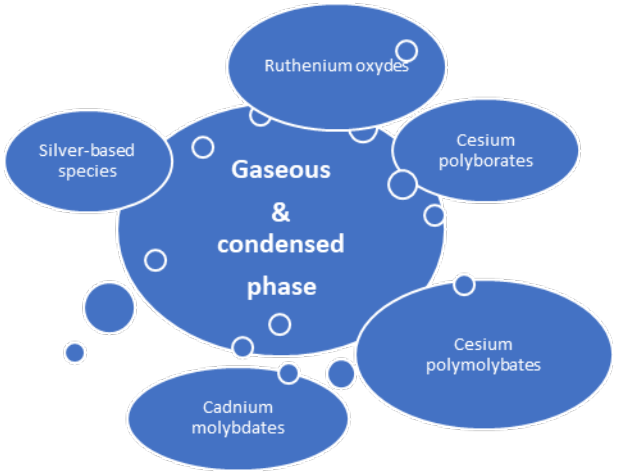

GENERALIZATION OF THE KINETIC APPROACH

3 limitations on reactivity :

- Physical: diffusion towards the surface
- Availability of reactive sites on the surface (heterogeneous phase)
- Chemical: energetic barriers (Arrhenius energy)

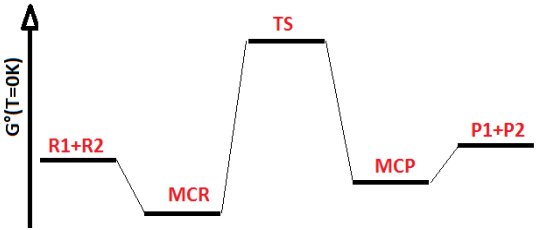

EXAMPLE: RUTHENIUM BEHAVIOR (STEM PRG)

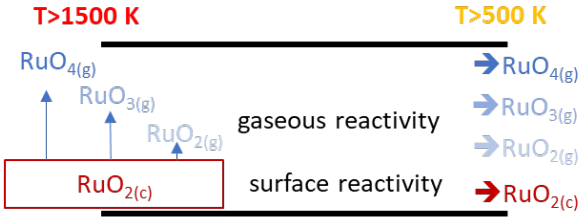

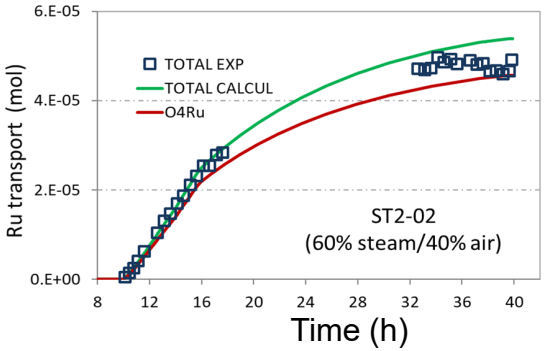

➔**ASTEC reproduces the experimental observations**

Development of ASTEC software abilities for ST: containment and FPs retention

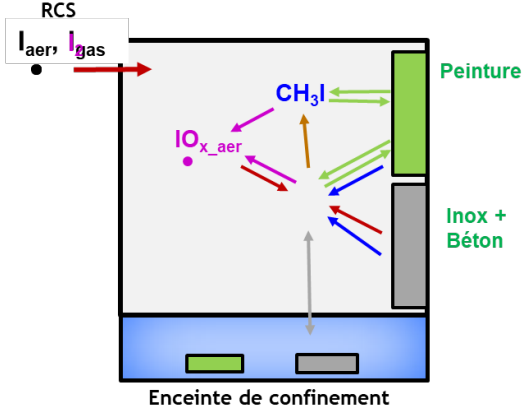

- ***Phenomena involved in the containment: models at the SOA by integrated all the data coming from R&D programmes***

- ***Pool scrubbing activities linked to trapping: Roadmap for a new pool scrubbing modelling in ASTEC***

  - **Bubble hydrodynamic modelling**
    - Extended literature review to specify the models in each zone (bubble size, shape, velocity, void fraction)
    - Implementation in ASTEC/SAF
    - Model validation and assessment: RSE tests (PASSAM project), THAI tests (Becker Technologies), EPRI tests, Lace Espana tests (CIEMAT) + **IRSN data (BULLET and TYFON facilities)**
  - **Volatile iodine (I2 and CH3I) retention modelling**
  - **Aerosol retention modelling**
  - **Heat transfers** (bubble/water interface)



Example of ST application for a French 1300 MWe PWR (1/3)

Methodology

- All-module ASTEC computation: thermal-hydraulic and dose rate boundary conditions
- SOPHAEROS stand-alone sensitivity studies:
  - At the break 5% of I_2 + 95% of metallic iodide aerosols
  - Default computation with all iodine chemistry models (except metallic iodide aerosol decomposition)
  - Sensitivity computation with iodine oxides models deactivated
  - Sensitivity computation with metallic iodide aerosol decomposition

Accident scenario

- French 1300 MWe PWR with double containment
- 12-inch LOCA in the hot leg
- Containment Spray System, Safety Injection System unavailable
- Containment venting through FCVS 29 hours after the initiating event

Leak ways and rates

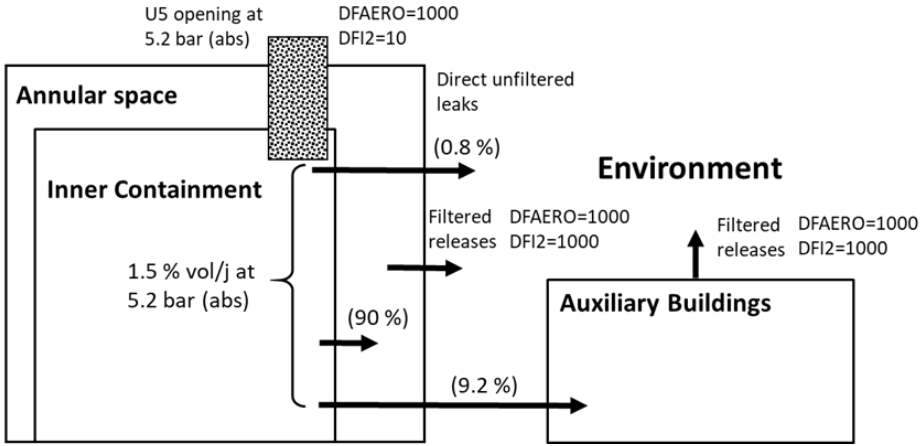

Example of ST application for a French 1300 MWe PWR (2/3)

With and without iodine oxides

- CsI releases dominant at short term (< 15 h) in both cases
- **No IOx** (dashed lines): Org-I is the main gaseous species (no decomposition, weak retention on surfaces)
- **With IOx** (solid lines): Org-I remains the main gaseous species but in lower amount (about one decade lower at 48 h)

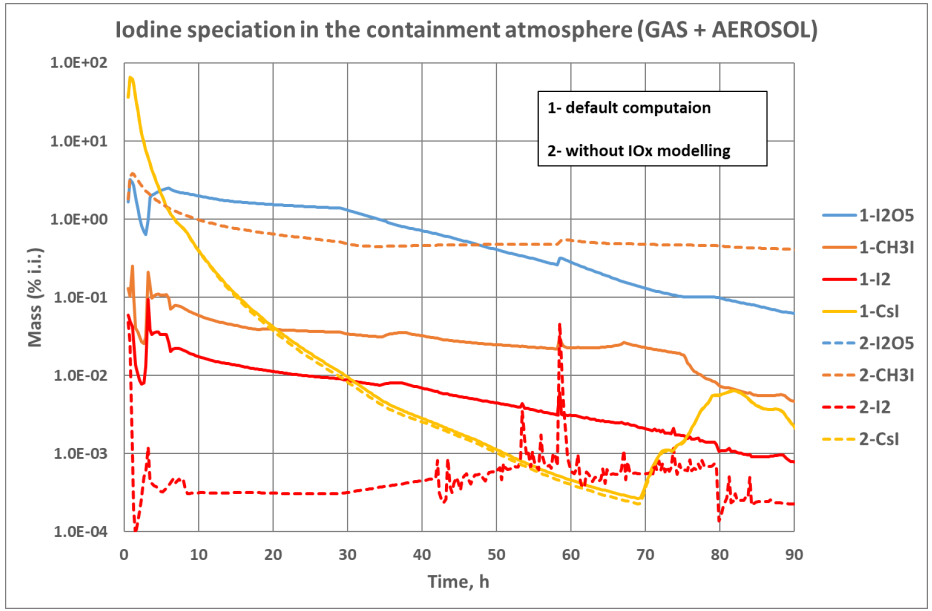

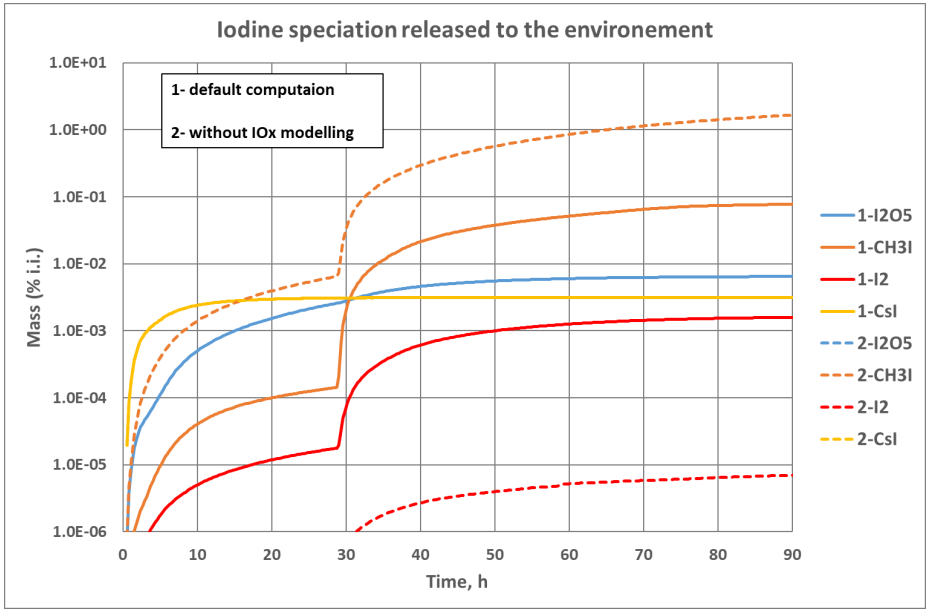

Example of ST application for a French 1300 MWe PWR (3/3)

With and without metallic iodide aerosol (CsI) oxidation

- **In both cases**: Org-I is the main gaseous species (no decomposition, weak retention on surfaces)
- **With metallic iodide aerosol decomposition** (dashed lines): Higher amounts of airbonne iodine (IOx, I_2 and Org-I) (dashed lines) released outside except for CsI (rapid deposition in the first 24 h of the accident)

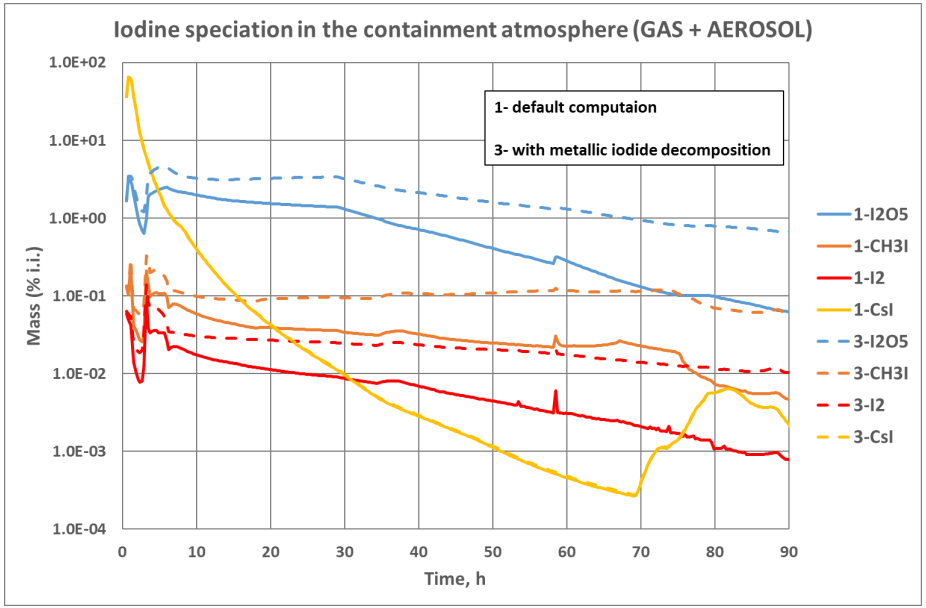

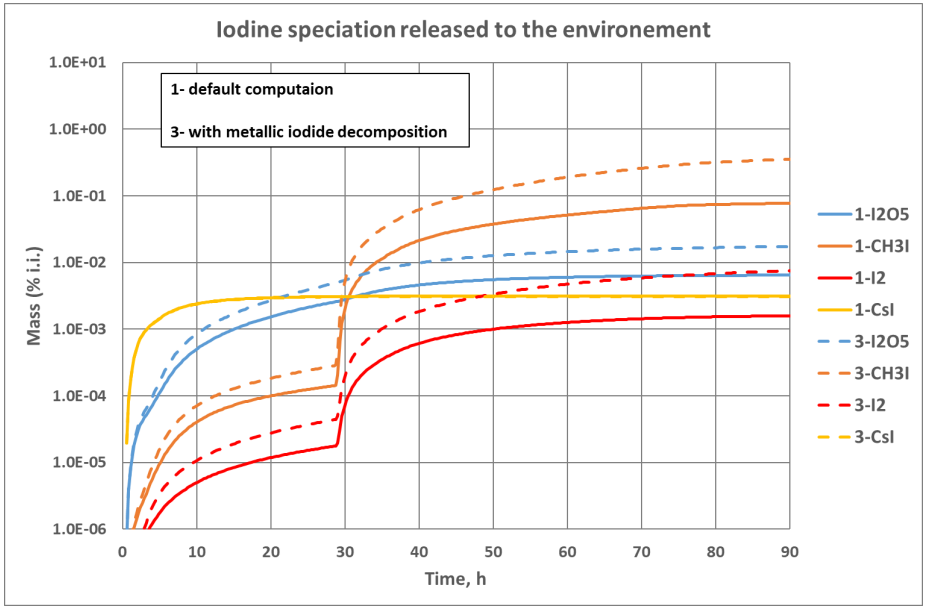

Potential open issues for ST relative to new situations (LTO, SMR, eATF, AMR)

For LTO topic

- Liquid source term is important to assess mainly for post-management accident
- **EUR SOCRATES project** (lead by VTT) will start in Oct. 2024 on this topic

For SMR

- **EUR SASPAM project** (lead by ENEA) is ongoing: The research priorities will be identified in terms of methodology, code development and experimental needs
- Current models are they directly applicable? Considering geometry and possible atmosphere? Aerosol and iodine models are still applicable?

For AMR

- **For molten salt reactor**: very few knowledge, research priorities have to be identified, trapping of gaseous fission products in the liquid/solid phases?

Possible open issues for ST relative to new situations (LTO, SMR, eATF, AMR)

For eATF

- Various designs
- UO_2 doped with Cr and/or Al elements → grain sizes increase a lot → may affect releases of FPs?
- Fuel cladding recovered with Cr_2O_3 → at high T, large release of chromium which may affect transport/reactivity of FPS (cesium in particular))

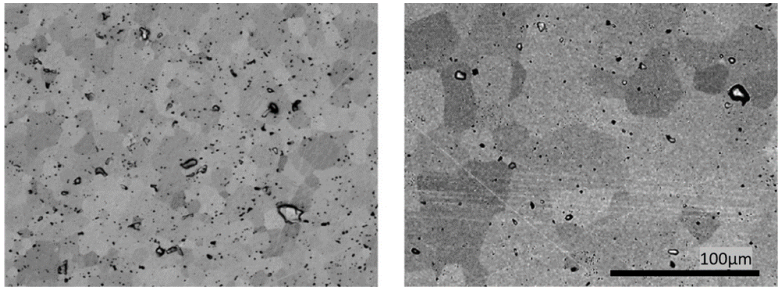

P. Kegler et al., Chromium Doped UO_2-Based Ceramics: Synthesis and Characterization of Model Materials for Modern Nuclear Fuels, Materials, vol. 14, no. 20, p. 6160, Oct. 2021

IRSN proposal for a FORESEEN OCDE project starting in 2025

- **Expert meeting planned in June 24 and 25, 2024**
  (OECD/NEA invitation for TEAMS Meeting)
- 3 phases covering the whole process: from fuel releases up to containment aerosol behavior in the containment

Fuel type Grain	size	^{85}Kr release after 30 min at 1700°C	release after 5 h
Large-grained UO_2	50 µm	13,4 %	28,9%
Large-grained $UO_{2.01}$	50 µm	2.0 %	2.8 %
$UO_{2.01}$	14 µm	13.1 %	38.8 %
UO_2 + 0.2 % Cr_2O_3	62 µm	5.6 %	9.7 %
UO_2 + 0.07 % Cr_2O_3	25 µm	10.1 %	14.6 %

Experimental data of **Valin at 1700°C on Kr release (AIEA TECDOC 1416, p181)**

Brief draft of the FORESEEN OECD/NEA joint project

FORESEEN = FissiOn pRoducts bEhavior under SeverE accidEnt with New fuel concepts

- **eATF targeted: in priority doped UO_2 with Cr and possible passive layer of Cr on the cladding fuel, possible fuel with Al**

- **Open issues:**
  - structure of the fuel (grain size enlargement) may impact fission products release for relatively high temperature?
  - Possible chemical speciation of Cs inside the fuel can be impacted?
  - In what extent chromium may be released? And transported through the RCS? May alter chemical speciation, size, solubility of the aerosol inside the containment, possibly under irradiation change of chemical behaviour of iodide aerosol (oxidation), formation of Cr(VI)?
  - Possible chemical interactions between Cr and Cs (or others) in the RCS

→ *Experiments should be performed at INL (US) to follow Cs release form fuel pellet with high BU*

→ *Experiments should be performed on CHROMIA experimental platform (IRSN) to study transport/reactivity in the RCS and also potential impact of FPs in the containment conditions (irradiation)*

- **After the expert meeting and considering remarks/comments, a technical proposal will be sent in September - Budget ~3.5 M€**

List of some publications relative to these works

- Miradji et al., *J. Phys. Chem. A* 119(20) (2015), DOI : 10.1021/acs.jpca.5b01645
- Bosland et Colombani, *Journal of Radioanalytical and Nuclear Chemistry* 314(2) (2017), DOI : 10.1007/s10967-017-5458-9
- Cantrel et al., *Journal of Nuclear Engineering and Radiation Science 4*(2) (2018), article n°020903, DOI : 10.1115/1.4038223
- Vandeputte et al., *Journal of Nuclear Materials* 517 (2019), DOI : 10.1016/j.jnucmat.2019.01.036
- Benigni et al., *Journal of Chemical and Engineering Data* 65(8) (2020), DOI : 10.1021/acs.jced.0c00210
- Bosland et Colombani, *ANE* 141 (2020), article n° 107241, DOI : 10.1016/j.anucene.2019.107241
- Bosland et al., *Progress in Nuclear Energy* 142 (2021), article n°104013, DOI : 10.1016/j.pnucene.2021.104013
- Obada et al., *Journal of Hazardous Materials* 4095 (2021), Article n°124519, DOI : 10.1016/j.jhazmat.2020.124519
- Grégoire et al., *ANE* 168 (2022), article n° 108900, DOI : 10.1016/j.anucene.2021.108900
- Leroy and Bosland, *ANE* 180 (2023), article n°109526, DOI : 10.1016/j.anucene.2022.109526
- Ohnet et al., *Journal of Radioanalytical and Nuclear Chemistry* 333(1) (2024), article n°109526, DOI : 10.1007/s10967-023-09230-7

Thank you for your attention!

The 11th European Review Meeting on Severe Accidents Research

May 13-16, 2024, Royal Institute of Technology, Stockholm, Sweden

TECHNICAL SESSION 6.2: HYDROGEN RISK AND CONTAINMENT BEHAVIOR

Chairs: I. Kljenak (IJS), S. Kelm (FZJ)

ID17	**Validation of REKO-DIREKT and ContainmentFOAM-9 Code Coupling Using THAI-HR Experiments** L. Serra Lopez (UPM)	**Paper** **Presentation**
ID11	**THAI Experiment on Iodine Absorption Capacity of Pre-Stressed Paint Coatings on Different Surfaces** K. Dieter (Becker Techn. GmbH)	**Paper** **Presentation**
ID37	**Validation of the PARUPM and GOTHIC 8.3 Code Coupling using THAI Hydrogen Recombination Tests** A. Domínguez-Bugarín (UPM)	**Paper** **Presentation**

VALIDATION OF REKO-DIREKT AND CONTAINMENTFOAM-9 CODE COUPLING USING THAI-HR EXPERIMENTS

Serra, L.*, Domínguez-Bugarín, A., Jiménez, G.
Universidad Politécnica de Madrid, ETSI Industriales
c/ José Abascal, 2, 28006 Madrid
luis.slopez@upm.es ; araceli.dominguez@upm.es; gonzalo.jimenez@upm.es

Kelm, S., Reinecke, E-A., Vázquez-Rodríguez, C.
Forschungszentrum Jülich (FZJ)
Wilhelm-Johnen-Straße, 52428 Jülich, Germany
s.kelm@fz-juelich.de; e.-a.reinecke@fz-juelich.de; c.vazquez-rodriguez@fz-juelich.de

Gupta, S.
Becker Technologies GmbH
Rahmannstraße 11, 65760 Eschborn, Germany
gupta@becker-technologies.com

ABSTRACT

During a severe accident in a pressurized water reactor, the release of combustible gases can lead to a potential combustion hazard and an associated pressure increase that may put the containment integrity at risk. To study the H_2/CO transport dynamics at reduced scales, experimental campaigns such as the OECD/NEA THAI or the THEMIS projects, have been conducted in the last decades. Specially, THAI-HR experiments explored the mitigation efficiency of several types of Passive Autocatalytic Recombiners (PARs). In the framework of AMHYCO project (Euratom 2019-2020), one of the modeling approaches to assess combustion risk management will make use of the tailored CFD package containmentFOAM, developed at Forschungszentrum Jülich GmbH (FZJ) and coupled with the detailed PAR model REKO-DIREKT. This work presents an iteration on the verification and validation methodology of that code coupling by simulating a selection of THAI-HR tests (between HR-3 and HR-12) in a simplified test-case environment. Thus, a representative range of severe accident conditions, namely vessel pressure, temperature, and gas concentrations, are evaluated from the inlet to the outlet computational domains of the PAR model. The objective is to prove the capability of REKO-DIREKT to reproduce the experimental measurements and to deliver the figures of merit of the recombination process to the containmentFOAM model, this being a preparatory step towards validating the simulations in a complete 3D THAI vessel model in containmentFOAM.

In general, the simulations catch the tendencies of the thermophysical properties of the vessel atmosphere and the general PAR performance characteristics. Nonetheless, the simulations show some deviations with respect to the measurement in the PAR flow rate when replicating the THAI conditions for low pressures and at oxygen starvation conditions. This occurs during the fast gas injection phases and affects the recombination rate and PAR temperatures. Finally, some refinements might be needed in the REKO-DIREKT modules to better capture the mass flow rates entering the PAR, thus replicating PAR efficiency more accurately.

KEYWORDS
AMHYCO, containmentFOAM, CFD, Passive Autocatalytic Recombiner, Severe Accident

1. INTRODUCTION

Over the years, a deeper understanding of several processes following a severe accident in a nuclear power plant has been achieved. In the case of the generation and risk of combustion of non-condensable gases, namely H_2 and CO resulting from core degradation and corium-concrete interaction, still some uncertainties arise regarding the destructive potential of deflagration flames and the performance of Passive Autocatalytic Recombiners (PARs) as mitigation measures [1]. Therefore, to assess the severity of the combustion hazard in representative accident scenarios, as well as optimize the distribution of mitigation equipment, state-of-the-art computational tools are increasingly being used to narrow the uncertainty gap surrounding the related phenomena. These codes need to be validated against experimental data at different scales before evaluating full accident sequences at containment scale. To that aim, some international collaborative experimental programs have focused on establishing a common database on the behavior of combustible gases within the containments of water-cooled reactors. One of those experimental campaigns is the OECD/NEA-THAI project, which started in 2007 with one of the objectives being the study of the spatial distribution of H_2 in the containment and its effective removal by PARs or slow H_2 combustion processes [2]. At the THAI facility, several hydrogen recombination (HR) tests investigated the onset of recombination, recombination rate, recombination efficiency and ignition potential under ambient/saturated/superheated steam atmospheres and ambient as well as elevated initial pressure and temperature conditions. Also, the consequences deriving from some phenomena appearing at the late phases of severe accidents, such as O_2 starvation (lack of sufficient O_2 for unimpaired recombination), were studied by performing tests with multiple H_2 injections and no further addition of O_2 to the vessel. Moreover, additional tests have been performed in subsequent upgrades of the THAI facility [3].

The data gathered from these THAI-HR experiments have supported the development and validation of several lumped parameter (LP) and computational fluid dynamics (CFD) codes and their modelling approaches regarding PAR operation. For instance, the codes ASTEC, COCOSYS and MELCOR were employed to simulate the performance of NIS and Framatome PARs [4]. In the 3D modelling field, the CFD code ANSYS Fluent was used to investigate the three-dimensional nature of secondary flows induced by PARs and to assess PAR efficiency with a correlation-based approach with both O_2 rich and poor conditions in the THAI vessel [5] [6]. Another example is the use of the GOTHIC code to model a scaled down AECL PAR unit by testing the performance of the code´s PAR built-in component [7]. Also, the PAR recombination model of GASFLOW-MPI was validated with THAI-HR tests and employed in a severe accident simulation in a small modular reactor 3D model [8]. Another tool for recombination phenomena simulation, which has been extensively validated using THAI-HR tests, is the mechanistic REKO-DIREKT code, which was developed at Forschungszentrum Jülich (FZJ). This code models PAR operation as the interaction of the recombiner chimney and the catalyst section [9] and was successfully coupled with the ANSYS-CFX code [10]. More recently, REKO-DIREKT was coupled with the tailored CFD package containmentFOAM, also developed at FZJ and used to analyze pressurization, H_2 transport, formation of combustible gas mixtures, and safety system performance [11]. This last code coupling will also play a role within the framework of the AMHYCO project (Euratom 2019-2020, GA-No-945057), which aims to improve simulation capabilities for the H_2/CO combustion risk management by simulating bounding severe accident sequences with LP and 3D/CFD codes [12].

In this work, a series of THAI-HR tests which employ a Framatome PAR unit are simulated with containmentFOAM-9 in a simplified test-case environment. The objective is to firstly validate the output of the embedded REKO-DIREKT PAR model (as the code was further developed in the last years) and secondly to verify that the variables are correctly exchanged between both codes. This would serve as a preliminary verification of the code coupling, and a step towards code validation by a 3D THAI model in future works. The basics of both codes will be explained in Section 2, whereas the THAI vessel configuration for HR experiments, together with the selected sequences tests (only tests with H_2 injection are considered, i.e., without CO) are explained in Section 3. Section 4 will discuss the results of the

simulation of four HR tests (two dry-atmosphere tests and two with presence of steam), highlighting the fitting of the main figures of merit between experimental database and model calculations. Finally, the article is closed by discussing future research in understanding the limitations of the codes towards the simulation of tests focused on PAR performance and H_2/CO dynamics.

2. REKO-DIREKT AND CONTAINMENTFOAM CODES

REKO-DIREKT is a 2D mechanistic PAR model based on Fortran-90 and developed based on the REKO separate effect test database. Its basic approach consists in simulating the whole PAR by a detailed representation of a sub-channel between two catalyst elements, thus modelling the heat and mass transfer phenomena inside the catalyst section, including conduction through the sheets and radiation between catalytic plates (see Figure 1) [10]. Also, the local reaction rates are calculated by means of a mechanistic diffusive mass transport approach instead of the usual Arrhenius-type approach for chemical surface reactions. This is combined with a chimney model to predict the buoyancy-driven flow through the recombiner unit, which is caused by the exothermic recombination reaction, as well as calculating the radiative and convective heat fluxes from the PAR to the gaseous flow and its environment. Besides the recombination rate, REKO-DIREKT provides the outlet gas composition, the catalyst sheet temperature profile, and the temperature of the metallic PAR housing.

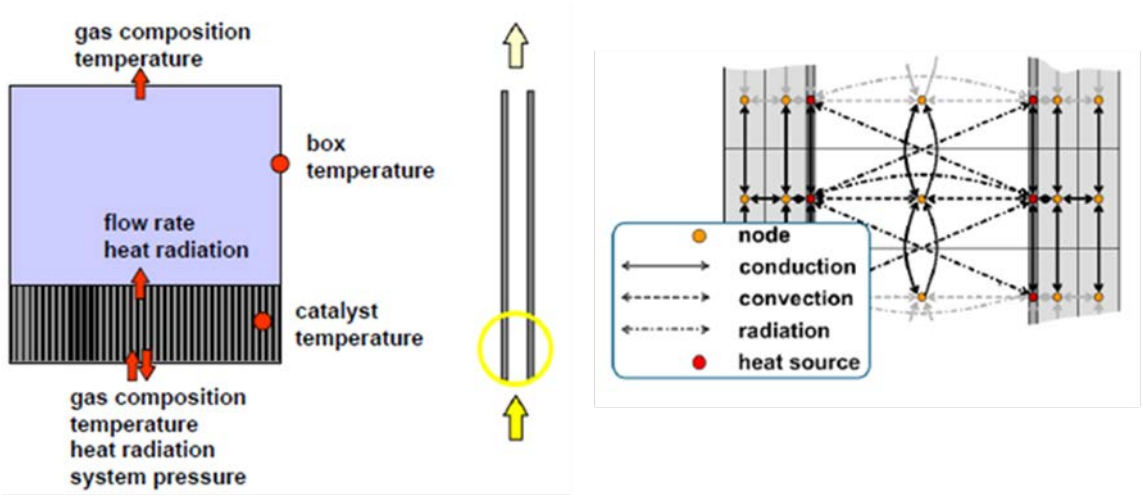

Figure 1. REKO-DIREKT´s General Modeling Approach (reproduced from [10]**).**

ContainmentFOAM is a CFD simulation package focused on nuclear reactor containment phenomena. The development of the package began in 2017 building on OpenFOAM® basic capabilities and available models. The basis of containmentFOAM was the 10-years' experience of FZJ using ANSYS-CFX for analyzing containment atmosphere transport processes and combustible gas mitigation [13]. In the following years, the package underwent validation campaigns against separate effect tests and application-oriented coupled and integral effect tests, such as the OECD/NEA-THAI or HYMERES projects [14]. The package consists of a tailored solver and model libraries. Its functionalities are developed to handle multi-species gas mixing and transport, thermal radiation and conjugate heat transfer, aerosol transport and steam condensation. Also, direct access to the source code and solver algorithm permits a flexible and stable implementation of all source terms, boundary conditions and material properties. Moreover, the model library serves recently as a basis for integrating multiphase phenomena [15]. Some code capabilities are the following: modelling of turbulent flow based on the k-ω SST model with specific source terms to account

for the effect of density gradients on the turbulent kinetic energy, the modelling of gas radiation (particularly relevant in humid atmospheres) by using a Monte Carlo transport solver, and the simulation of technical systems and components by means of specific code interfaces.

Regarding the implementation of PARs, containmentFOAM is coupled with REKO-DIREKT by means of a file-based coupling scheme and using a domain decomposition approach [11]. At containmentFOAM folder communicating with REKO-DIREKT´s executable, the user inputs the PAR geometry (effective chimney height, inlet width and depth, catalyst sheet number and thickness, unit weight), the start-up time point of recombination (which depends on the simulated transient) or alternatively, the minimum reactants concentration for which the PAR starts to recombine. At each time step of the containmentFOAM simulation, the gas composition, temperature, and pressure at the defined PAR inlet boundary cells is extracted and transferred to REKO-DIREKT, which then computes the PAR exhaust conditions. These are transferred to the outlet boundary cells at containmentFOAM (see Figure 2 center, where an excerpt of the code is depicted, showing the boundary domains definition and the communication between inlet and outlet). In this work, the PAR component is implemented in containmentFOAM at a small 2D arbitrary array of cells that serves as a test-case setup employed for user training and code verification (Figure 2 right). There, the user-defined PAR inlet, channel, housing, and outlet boundary condition domains are coupled with the fluid region, and the experimental data (mass fraction for the different gases involved, inlet temperature and pressure of the sequence) are set. Finally, the explicit transient coupling is realized by means of a Python wrapper which takes care of the data logistics and executes both codes serially (Figure 2 left).

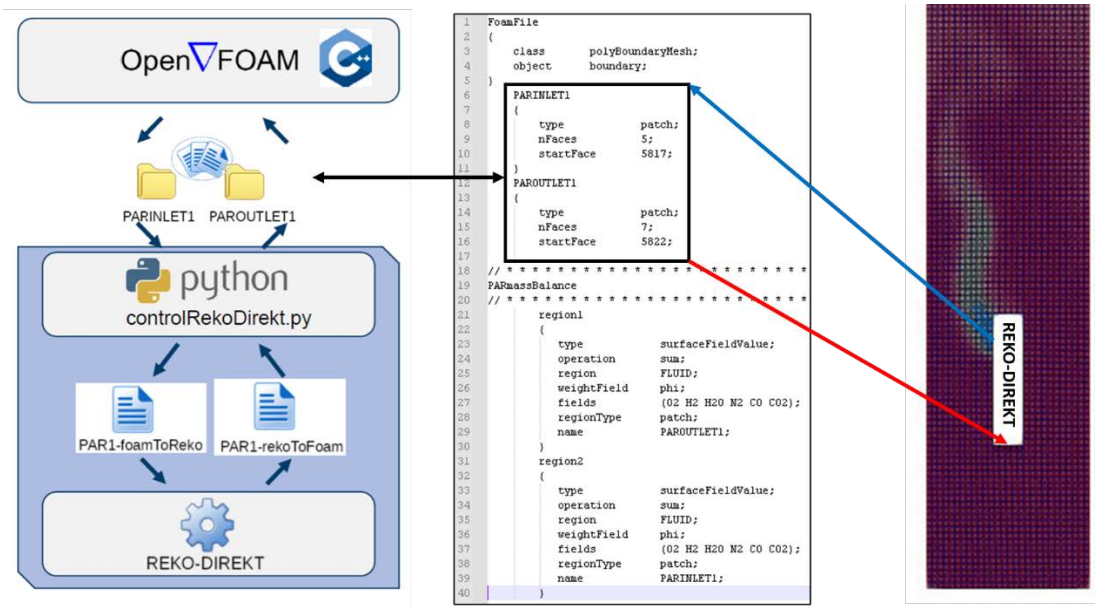
OpenFOAM
PARINLET1
PAROUTLET1
python
controlRekoDirekt.py
PAR1-foamToReko
PAR1-rekoToFoam
REKO-DIREKT
FoamFile
{
class polyBoundaryMesh;
object boundary;
}
PARINLET1
{
type patch;
nFaces 5;
startFace 5817;
}
PAROUTLET1
{
type patch;
nFaces 7;
startFace 5822;
}
// * * *

compressed air, and various gases, and with an oil cooling/heating jacket in the vessel walls used to establish the desired thermal-hydraulic conditions. Also, for the HR tests, an inner cylinder with a diameter of 1.4 m, is installed above the injection ring. The vessel is equipped with thermocouples to measure bulk and wall temperature at different positions, pressure transducers, a vane wheel to measure flow velocity at the PAR inlet, and at least 15 gas sampling lines. Figure 3-left depicts the inner vessel configuration in the HR tests. The PAR unit (half of a Framatome FR-380 model) and associated instrumentation were located 2.1 m above the vessel sump and mounted on the external wall of the inner cylindrical structure of the vessel [2]. For this work, only the thermocouples located at the outlet of the PAR are used, whereas the inlet temperature data is extracted from a thermocouple located at the opposite end of the vessel but at inlet elevation, as recommended in [16] to avoid the effect of thermal radiation coming from the catalyst section. It is important to note that only the catalytic section of the PAR, i.e., the heating source, was halved, whereas the whole PAR housing was installed. Therefore, it was considered that the full heat capacity of the PAR box should be taken into account in the calculations, as the thermal inertia of the metallic structure may have a significant effect in the test transient development [17].

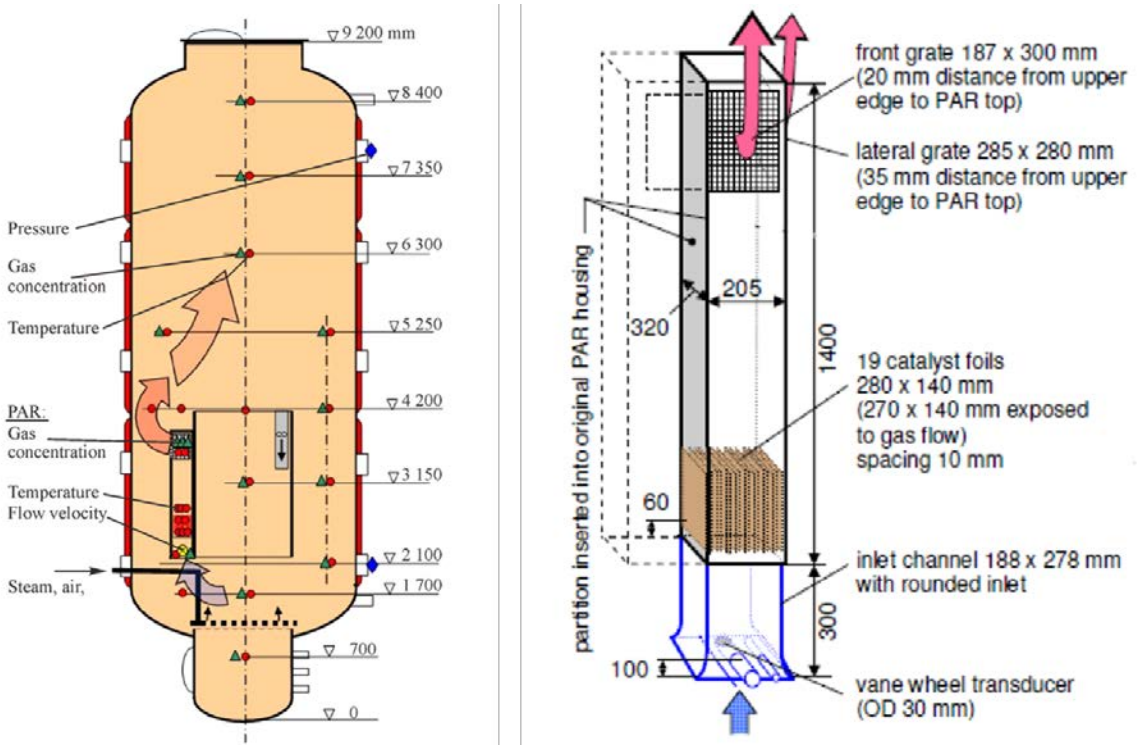

Figure 3. THAI-HR Vessel Configuration and Geometry of a 0.5Xframatome FR-380 PAR Unit (reproduced from Reference [2]**).**

3.2. THAI-HR Sequences for Validation

THAI-HR tests were characterized for having two or more series of fast injections of H_2 followed by depletion phases (with a lower recombination rate yield), while test parameters included initial pressures between 1 and 3 bar, gas temperatures up to 117°C, atmosphere steam volume fractions of 0–70%, and in some tests, induced ignition by high H_2 injection [18]. In this work, four transient sequences are selected with increasing complexity and accident typical test conditions: two of them in dry conditions varying the

pressure and another pair having an initial steam content and elevated temperature at higher pressure. Table I gathers the main parameters of the tests, namely initial pressure, temperature, and gas volume fractions. Figure 4 depicts the injection phases (I & III) and depletion phases (II & IV) of the tests in a temporal scheme [18], marking the H_2 release rates by intensity (yellow-mild injection, red-strong injection, blue-no injection). As can be seen, the selected sequences are quite similar in their injection profile, and initial pressure was resembling between HR-3&9, and HR-5&12, respectively. This is considered beneficial not only for validating the code coupling in representative accident conditions, but also for extracting coherent conclusions on the code´s strengths and weaknesses regarding the whole test sequence comparisons between simulated and experimental data.

Table I. HR Tests Used for Validation and their Main Parameters

Test	P [bar]	T [°C]	%vol H_2	%vol O_2	%vol H_2O	Ignition	O_2 starv.
HR-3	1.48	29.9	0.02	21.71	0.0	yes	no
HR-5	2.93	32.0	0.04	21.69	0.0	no	no
HR-9	1.44	89.7	2.19	11.30	48.15	no	slight
HR-12	2.92	115.0	0.00	7.35	61.12	no	yes



Figure 4. Selected THAI-HR Sequences and H_2 Injection Phases

Regarding the tests´ objectives, both dry tests (HR-3&5) studied the onset of recombination and recombination rate yield, although in HR-3, the ignition potential of the PAR was sought. At the end of HR-3´s second injection, a deflagration occurred in the upper vessel zone when H_2 volume fraction reached 6.7% and the temperature at the catalytic foils was 920ºC, with a pressure rise of 0.14 bar in the vessel (see yellow star mark at HR-3 time-bar on Figure 4). On the other hand, at HR-5 the onset of the PAR actuation occurred earlier, maybe because the test pressure was higher, and recombination is enhanced as pressure increases. This was also seen in the wet tests (HR-9&12) although the determination of the PAR onset is very dependent on the test initial conditions and difficult to forecast [4]. Nevertheless, HR-5 did not intend to reach ignition conditions and accordingly, H_2 injection was reduced to limit the catalyst temperature

excursion during Phase III when the temperature at the catalytic foils rose to 820ºC. For the cases HR-9&12, steam was injected from the beginning of the sequence (until 27 min and 9 min, respectively) to compensate for wall condensation, and the onset of recombination occurred at higher H_2 volume fractions than for the dry cases. Also, both tests had a late start of the velocity measurement device, which did not allow the determination of the mass flow entering the inlet in the first minutes of the sequences. Moreover, these tests studied not only the onset of recombination and recombination rate yield, but also the effect of low O_2 volume fractions in the late phases of the test (O_2 starvation). Interestingly, HR-9's original objective was to reach ignition (as HR-3) which was not possible as the test indeed reached slight O_2 starvation conditions which prevented the further increase in catalyst temperature due to reduction in H_2 recombination. On the other hand, HR-12 test included four more phases (one additional H_2 release sequence to confirm the O2-starvation condition), although the expected appearance of O_2 starvation was seen at phase III, when PAR performance was deemed strongly affected by the phenomenon (at the end of phase IV, gas composition included only a 0.9% volume fraction of O_2 in the vessel atmosphere).

4. RESULTS

As explained in Section 3.2, two tests were run with initial dry atmospheric conditions and another two with steam and O_2 starvation conditions reaching during test progress. The simulations start at the time zero as stated in the experimental database and finish approximately at the end of the second depletion phase (phase IV). For all sequences except HR-3, some limitations were found in the experimental values which could be leading to some discrepancies in the simulations (following previous database interpretations at reference [16]). Thus, small adaptations to the experimental database were undertaken to prepare the simulation input: HR-5 reported negative inlet H_2 values at the end of the first depletion which led to unphysical recombination rates, therefore its injection was interpolated around that time frame [5]; HR-9 measurement of velocity at the PAR inlet started 27 minutes after the first H_2 release and they are provided each 20 seconds, for what the PAR onset in the simulation was set at the first point in time with positive measurements; HR-12 O_2 gas fraction had to be corrected, as THAI sensors showed a miscalibration step at the beginning of the test.

Once the experimental data for comparison were collected, the numerical schemes and constant thermo-physical properties of the simulations were specified. containmentFOAM´s maximum Courant number was always below 10, and the corresponding time step below 0.1 s. After the simulation, the main figures of merit were post-processed, being the experimental recombination rate and recombination efficiency calculated as shown in equations 1 and 2 [19]. There, M_{H2} is hydrogen molar mass, $\Delta\left(x_{H2_{conc}}\right)$ is hydrogen volumetric fraction difference between inlet and outlet, v is gaseous inlet velocity, A is PAR inlet effective cross-section area, and R is the ideal gas constant. The recombination rate equation assumes that total molar mass is preserved.

$$\dot{m}_{H2}\ \left(\frac{g}{s}\right) = \frac{M_{H2}*\Delta\left(x_{H2_{conc}}\right)*p*v*A}{R*(273{,}15+T_{inlet})} \quad (1)$$

$$\eta\ (\%) = \frac{\Delta\left(x_{H2_{conc}}\right)}{x_{H2_{inlet}}} = \frac{\left(x_{H2_{inlet}} - x_{H2\_outlet}\right)}{x_{H2_{inlet}}} \quad (2)$$

Finally, as the conditions at the PAR inlet are user-defined, the dissimilarities in containmentFOAM´s outlet are to be understood as deviations between REKO-DIREKT calculations and the experimental data for specific instants throughout the tests. The following Figures (5-8) compare the predicted recombination rate, mass flow velocity at the inlet, outlet temperature, and the recombination efficiency of the PAR against the experimental data. As seen in Figure 5, the Recombination Rate (RR) is well captured for all transients. Furthermore, a check of the mass balance confirmed a correct coupling of the codes (e.g., no significant loss/production of N_2 in the interface between both codes). In the case of HR-3 the simulation is stopped

when ignition occurred in the experiment (see yellow mark), which cannot be reproduced in the model. In the case of HR-5, the second peak of the recombination rate is also underestimated. The latter may be explained by the low inlet concentration seen in the experiment and the correction applied to the input data. Nevertheless, looking into the integrated mass of recombined H_2, the relative error at the end of the transient is less than 1% for HR-3 and HR-12, while it is less than 7% and 10% for HR-5 and HR-9, respectively. Also, the agreement of simulation and experimental values is better the higher the test initial pressure. This holds true for both dry and wet cases and impacts the related variables. Also, it is noticeable that phase III at HR-12 reaches lower recombination rates than the first injection phase, which may be an effect of the strong O_2 starvation in the gas mixture towards PAR performance (marked at Figure 5).

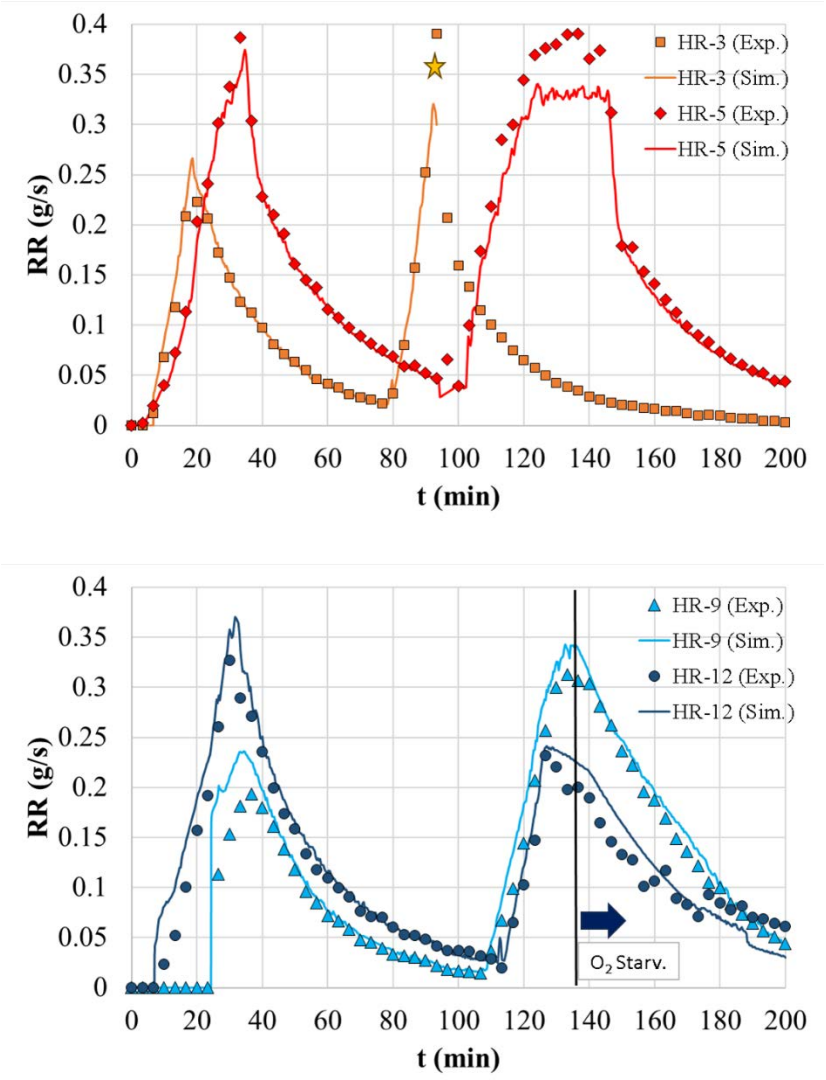

Figure 5. PAR Recombination Rate for Dry Tests (top) and Wet Tests (bottom)

The velocity of the mass flow is nearly systematically overestimated in the quick injection slopes of the tests, as can be seen in Figure 6. This is coherent with the overestimation of the recombination rate at the related time windows (higher RR induces higher catalytic temperature, promoting the mass flow through the PAR by differences between inlet/outlet gas density). One possible cause is that REKO-DIREKT ´s

chimney model correlations to calculate the pressure loss at the inlet or at the reaction zone are more accurate for higher flow Reynolds numbers, providing more realistic gas inflows. Another possibility is that the temperature of the PAR housing is better calculated at some tests, thus producing more realistic density gradients between the inlet and the outlet, and consequently a better flow velocity profile. However, the comparison of the PAR box temperature with the experimental data is not direct, although it would give interesting insight about the amount of heat transfer due to radiation from the metallic sheets. Besides, the gas temperature at the PAR outlet shows a good agreement between experiment and simulation, following the same trends as the RRs. Exceptions are the second peaks of HR-9 test, in which temperature is overestimated by 10%, and HR-5, having a better fit compared with its RR profile (see Figure 7). The recombination efficiency of the PAR is shown in Figure 8. REKO-DIREKT calculates it coherently with the experiment, especially in the first depletion phases. At the start of the simulation, the higher efficiency results from the overprediction of the recombination reactions (see Figure 5), although values quickly stabilize, and only significant dissimilarities arise near experimental data points with abrupt gradients. Also, the efficiency curves show some deviation at the end of the second depletion phase, which may be due to the inaccurate simulation of the flow velocity. Indeed, higher velocities imply a shorter residence time for the gases flowing through the catalyst section, thus reducing the reaction rate and thus efficiency of the recombination process. However, in the late phases the recombination rates are very low and small differences can have a significant impact on the efficiency calculation. O_2 starvation may as well influence the way the code calculates recombination, as can be seen at HR-12 efficiency values at phase IV of the transient (catalyst temperature was also underpredicted after the 9000 second mark).

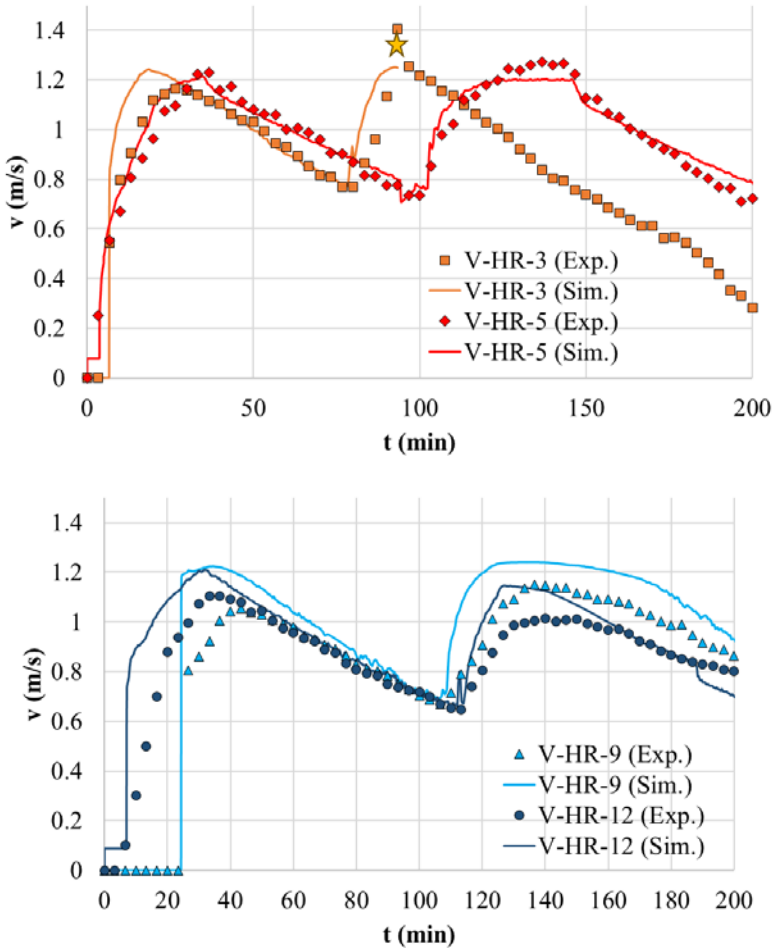

Figure 6. PAR Inlet Flow Velocity for Dry Tests (top) and Wet Tests (bottom)

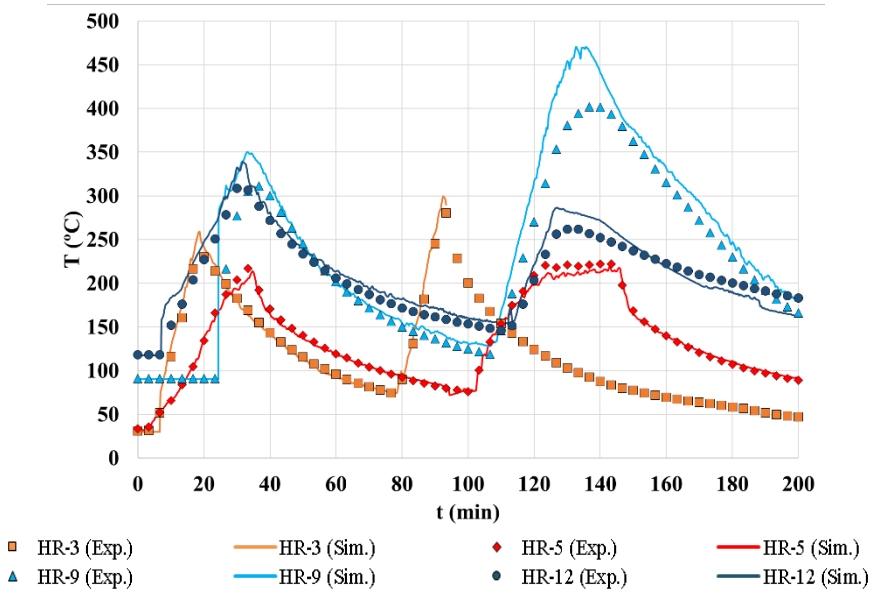

Figure 7. PAR Outlet Temperature

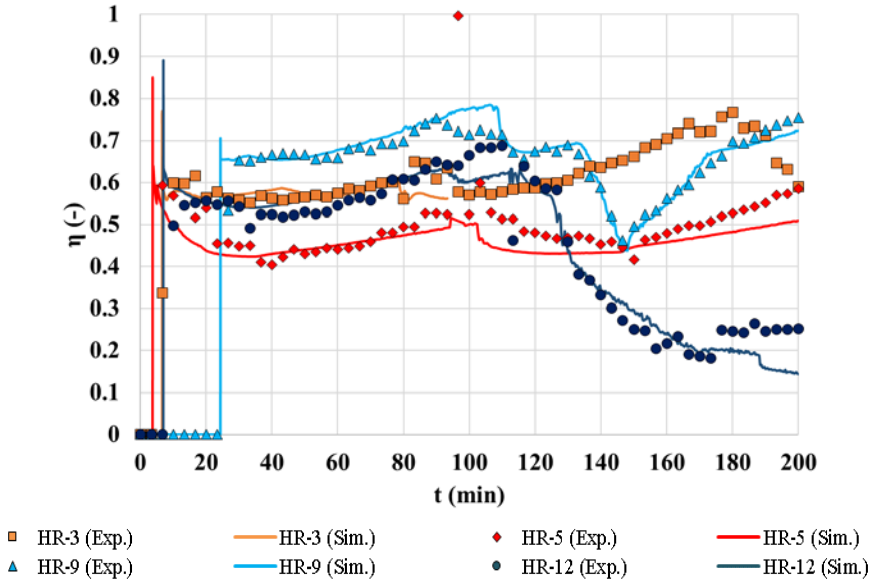

Figure 8. PAR Recombination Efficiency

The comparison of the calculated and experimental variables shows that the depletion phases are well captured, whereas the recombination rates during the fast injection phases are overestimated. Then, further development of the recombination modules is necessary to fit the curves since the beginning of the sequences, thus assuring that there are no accumulated errors impacting the efficiency calculations. Nevertheless, it is considered that the low values of the relative errors regarding the calculated integral recombined mass show that the code can reproduce the experimental values.

5. CONCLUSIONS AND FUTURE LINES

This work has focused on preliminarily validating the PAR model REKO-DIREKT and a verification of the coupling of REKO-DIREKT with the thermal-hydraulic CFD package containmentFOAM using four recombination tests from the THAI-HR experiment series. The calculated recombination rates and efficiencies have been compared to the experimental ones, and results indicate that the coupling of both codes successfully replicates the phases of the transients. However, further validation is needed to better understand the impact of the different test conditions on the code performance, and to refine the models used for calculating the behavior of the PAR unit. Future works will address the validation of tests with strong O_2 starvation conditions and with the presence of CO in the vessel atmosphere. Also, an integral THAI 3D model developed at FZJ, representing the free volume inside the vessel and its metallic walls, will be used to step up the validation process onto a scalable application. Modeling the THAI vessel, instead of just prescribing the operating conditions of the PAR by using experimental measurements, will help to investigate the vessel feedback on the PAR operation for the coupling scheme. That model will also be used to understand the inherent limitations of the recombination module, or even the available data of the experiments towards application-oriented analyses. Also, the validated 3D model would allow to implement and test other recombination modules such as PARUPM, which is developed at UPM and calculates recombination based on a physiochemical approach at the catalyst level.

ACKNOWLEDGMENTS

The lead author wishes to acknowledge the work and help of the team members and supervisors on both UPM and FZJ, as well as those involved in the AMHYCO project. The AMHYCO project has received funding from the Euratom research and training program 2019-2020 under Grant Agreement n°945057. The content of this paper reflects only the authors´ view. The European Commission is not responsible for any use that may be made of the information it contains. The assignment made at the FZJ has been possible thanks to the funding from the ENEN2plus mobility grant program. The THAI experiments presented in this paper have been conducted in the frame of OECD/NEA THAI project. The financial support by the countries that participated in the OECD/NEA THAI project is greatly acknowledged.



REFERENCES

[1] B. R. Sehgal, ‘Light Water Reactor Safety’, in *Nuclear Safety in Light Water Reactors*, Elsevier, 2012, pp. 1–88. doi: 10.1016/B978-0-12-388446-6.00001-0.

[2] T. Kanzleiter, S. Gupta, and K. Fischer, ‘Hydrogen and Fission Product Issues Relevant for Containment Safety Assessment under Severe Accident Conditions (Restricted Version)’, OECD/NEA, Becker Technologies GmbH, Eschborn, Germany, Reactor Safety Research Project 1501326, Jun. 2010.

[3] S. Gupta, M. Freitag, and G. Poss, ‘THAI experimental research on hydrogen risk and source term related safety systems’, *Front. Energy*, vol. 15, no. 4, Dec. 2021, doi: 10.1007/s11708-021-0789-1.

[4] S. Gupta, ‘Main outcomes and lessons learned from THAI Passive Autocatalytic Recombiner experimental research and related model development work’, presented at the The 17th International Topical Meeting on Nuclear Reactor Thermal Hydraulics (NURETH-17), Xi’an, Shaanxi, China, 2016.

[5] Y. Halouane and A. Dehbi, ‘CFD simulation of hydrogen mitigation by a passive autocatalytic recombiner’, *Nuclear Engineering and Design*, vol. 330, pp. 488–496, Apr. 2018, doi: 10.1016/j.nucengdes.2018.01.018.

[6] J.-S. Park, Y. Kim, and K. Lim, '3D simulation of hydrogen distributions affected by a passive auto-catalytic recombiner in an oxygen-starved condition', *International Journal of Hydrogen Energy*, vol. 47, no. 90, Nov. 2022, doi: 10.1016/j.ijhydene.2022.08.311.
[7] Z. Liang, 'GOTHIC Simulation of Passive Autocatalytic Recombiner Tests Performed in the OECD/THAI Project', presented at the NUTHOS-11: The 11th International Topical Meeting on Nuclear Reactor Thermal Hydraulics, Operation and Safety, Korea, 2016, p. 12.
[8] F. Wang *et al.*, 'Code validation and application of hydrogen mitigation by passive autocatalytic recombiner in small modular reactor', *Nuclear Engineering and Design*, vol. 396, Sep. 2022, doi: 10.1016/j.nucengdes.2022.111882.
[9] J. Böhm, 'Modelling of the processes in catalytic recombiners', Forschungszentrum Jülich (FZJ), Germany, 61, 2006.
[10] E.-A. Reinecke, S. Kelm, P.-M. Steffen, M. Klauck, and H.-J. Allelein, 'Validation and Application of the REKO-DIREKT Code for the Simulation of Passive Autocatalytic Recombiner Operational Behavior', *Nuclear Technology*, vol. 196, no. 2, Nov. 2016, doi: 10.13182/NT16-7.
[11] S. Kelm *et al.*, 'The Tailored CFD Package "containmentFOAM" for Analysis of Containment Atmosphere Mixing, H2/CO Mitigation and Aerosol Transport', *Fluids*, vol. 6, no. 3, Mar. 2021, doi: 10.3390/fluids6030100.
[12] G. Jiménez *et al.*, 'AMHYCO PROJECT – TOWARDS ADVANCED ACCIDENT GUIDELINES FOR HYDROGEN SAFETY IN NUCLEAR POWER PLANTS', presented at the International Conference on Hydrogen Safety (ICHS2021), Edinburgh, Scotland, Sep. 2021.
[13] S. Kelm *et al.*, 'Retrospect, Status and Perspective of the Development of containmentFOAM', presented at the IAEA Technical Meeting on the Development and Application of Open-Source Modelling and Simulation Tools for Nuclear Reactors, Politecnico di Milano, Italy, Jun. 2022.
[14] G. Vijaya Kumar, M. Kampili, S. Kelm, K. Arul Prakash, and H.-J. Allelein, 'CFD modelling of buoyancy driven flows in enclosures with relevance to nuclear reactor safety', *Nuclear Engineering and Design*, vol. 365, Aug. 2020, doi: 10.1016/j.nucengdes.2020.110682.
[15] A. George, S. Kelm, X. Cheng, and H.-J. Allelein, 'Efficient CFD modelling of bulk condensation, fog transport and re-evaporation for application to containment scale', *Nuclear Engineering and Design*, vol. 401, Jan. 2023, doi: 10.1016/j.nucengdes.2022.112067.
[16] E.-A. Reinecke, S. Kelm, B. Simon, M. Klauck, and H.-J. Allelein, 'Interpretation of the entire OECD/NEA-THAI HR test series including AREVA and AECL PARs using the code REKO-DIREKT', presented at the OECD/NEA THAI2, Final Seminar, Eschborn, Germany, 2014.
[17] S. Kelm, E.-A. Reinecke, and W. Jahn, 'Passive Auto-Catalytic Recombiner Operation-Validation of a CFD-Approach against OECD-THAI HR2 test', presented at the OECD/NEA CFD4NRS-4 workshop, Daejeon, Korea, 2012.
[18] T. Kanzleiter, 'Hydrogen Recombiner Tests HR-1 to HR-5, HR-27 and HR-28', Becker Technologies GmbH, Eschborn, Germany, Quick Look Report 150 1326–HR-QLR-1, 2009.
[19] E.-A. Reinecke, 'THAI-HR Experimental Data - Critical Assessment and Application to PAR Model Validation', presented at the AMHYCO WP3 Task 3.2 Meeting, FZJ, Jülich, Germany, 2021.

ERMSAR 2024

AMHYCO

Enhancing H_2 & CO Combustion Risk Management

VALIDATION OF REKO-DIREKT & CONTAINMENTFOAM CODE COUPLING USING THAI-HR EXPERIMENTS

Luis Serra López

Stephan Kelm

Gonzalo Jiménez Varas

Araceli Domínguez Bugarín

Carlos Vázquez Rodríguez

luis.slopez@upm.es

15/05/2024

This project has received funding from the Euratom research and training programme 2019-2020 under Grant Agreement n°945057.The content of this document reflects only the author's view. The European Commission is not responsible for any use that may be made of the information it contains.

Contents

1. Background:
   - H_2 generation & PARs
   - Experimental and simulation campaigns
   - The AMHYCO project
2. Objectives and previous works
3. REKO-DIREKT & containmentFOAM
4. THAI-HR series and selected sequences
5. Test-case model and code coupling
6. Result: test-case and 3D model
7. Conclusions and Future Lines

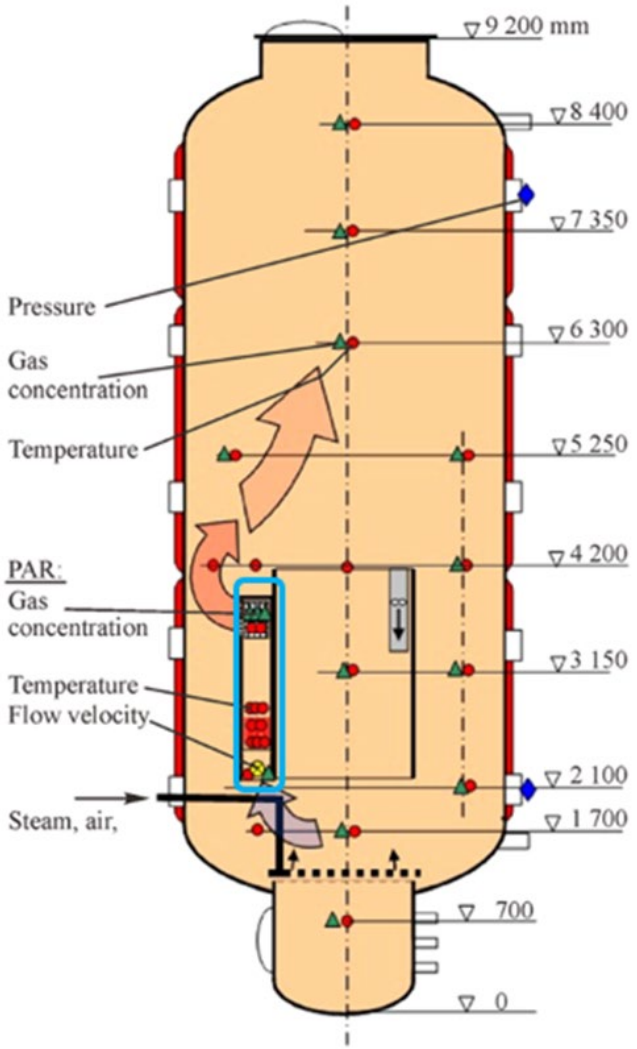

1. Background: H_2 generation

- **H_2 generation** depends on SA sequence, core configuration and evolution of metal T.
- Released H_2 will find several **paths to containment** compartments and dead-ends.
- Need to understand and foresee H_2 transport, **accumulation and stratification**.
- Containment conditions and atmosphere **flammability limits** vary along the phases of a SA.
- Effect of turbulent flows and **low O_2 concentrations**.

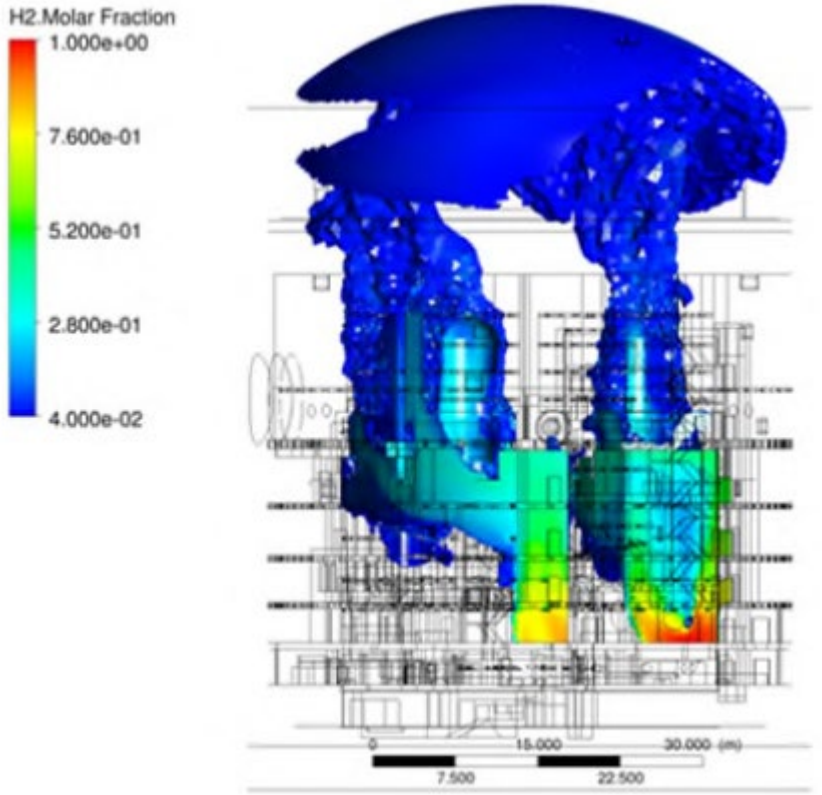

Cremer, I. (2022). "*Updated modelling and simulation of hydrogen recombination in full-scale containment analyses*". NURETH-19. Belgium.

1. Background: Passive Autocatalytic Recombiners

- Several designs with different **performance** and capacity.
- Strong interaction between **catalyst and chimney** sections.
- Importance of **flow resistance** and P losses regarding PAR recombination efficiency.
- **Uncertainties** in long-term SAs:
  - Catalytic poisoning
  - Oxygen starvation
  - Extreme P&T conditions
  - Cable fires and polluting species

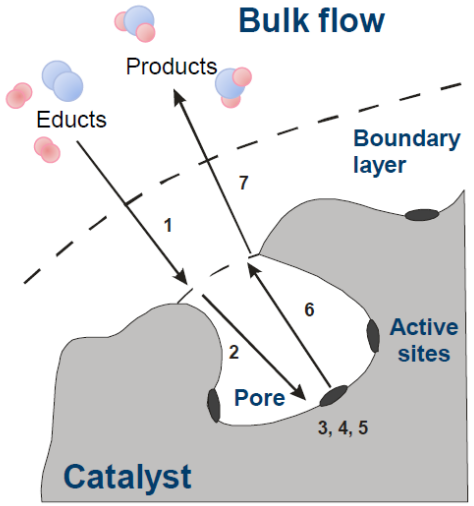

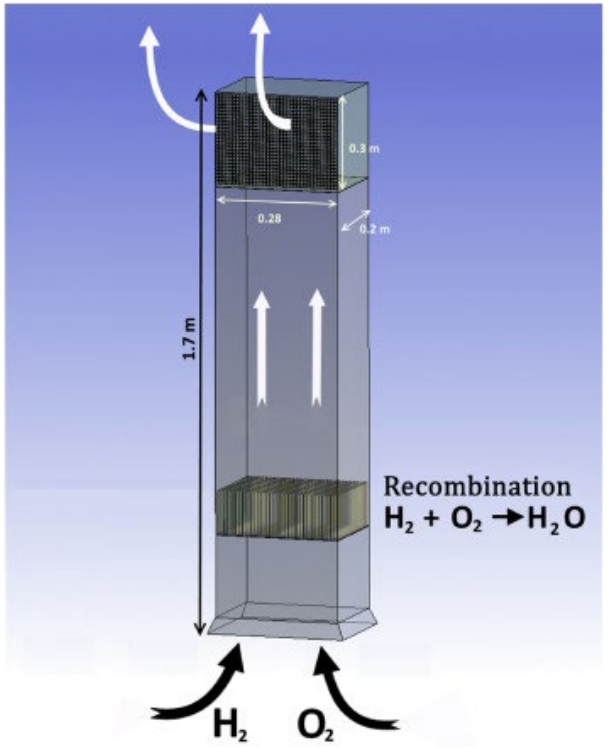

Reinecke, E. (2023). "*Hydrogen and carbon monoxide mitigation in light water reactors*". AMHYCO WORKSHOP, Orleans, France.

Halouane, Y. (2020). "*CFD prediction of hydrogen passive autocatalytic recombiner performance under counter-current flow conditions*". International Journal of Hydrogen Energy.

1. Background: Experimental campaigns

- **Feedback between containment conditions and PAR operation hampering?**
- Effect of increasing pressure and temperature
- Self-starting and shut-off thresholds.
- Ignition conditions at overheated catalytic plates.
- **PAR unit qualification campaigns.**

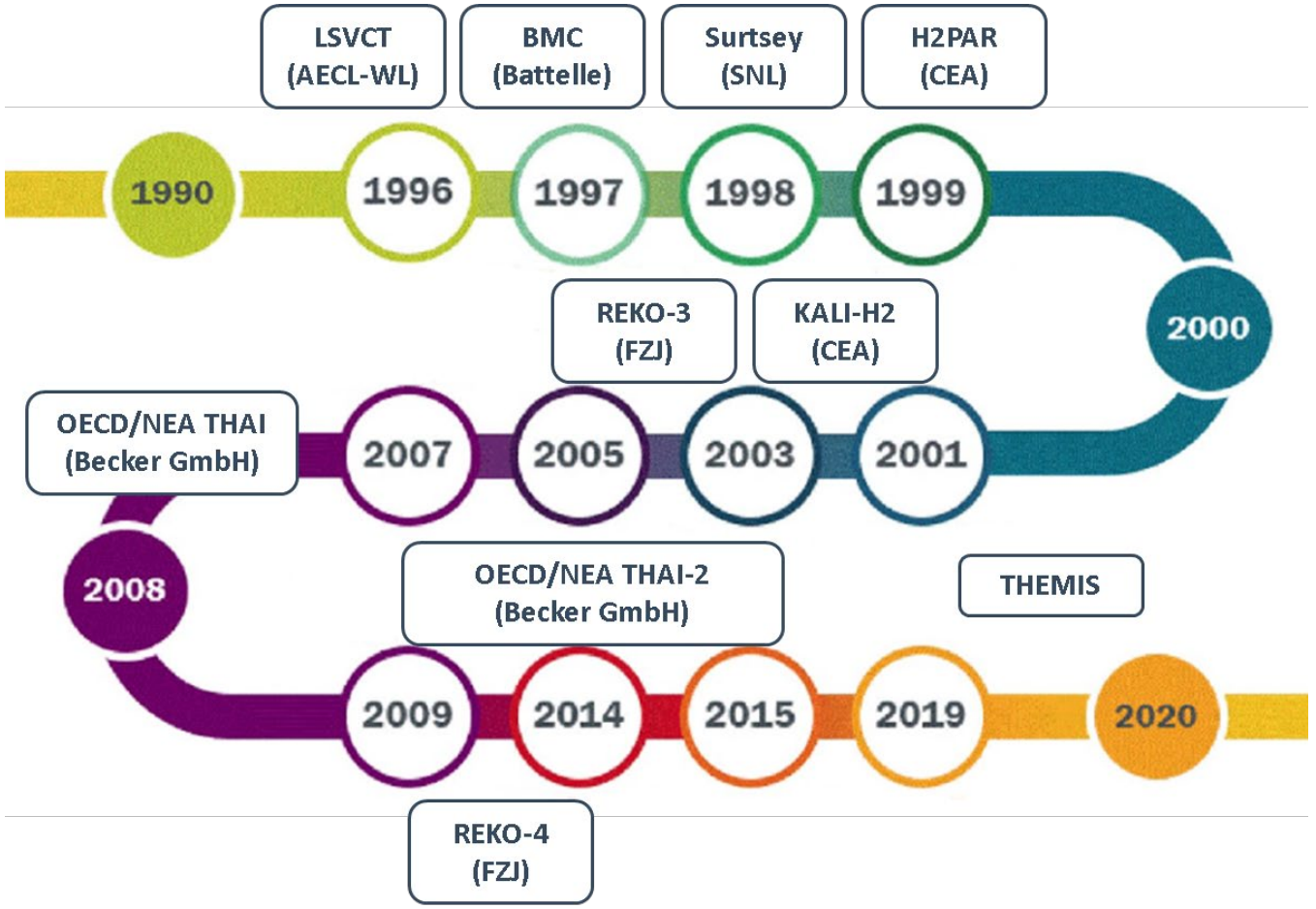

1. Background: PAR computational modelling

- Several approaches for PAR unit modelling:
  - **Black-box**: *calculation of efficiency using empirical manufacturer´s correlations by means of volumetric sinks/sources of energy & mass.*
  - **Mechanistic models**: *e.g., simulate the reaction kinetics with a mass diffusion approach.*
  - **Built-in** code tools: *e.g., MELCOR, GOTHIC*
  - Catalyst **physiochemical level**: *e.g., PARUPM, SPARK*

Objective: optimize correlations and PAR design and layout

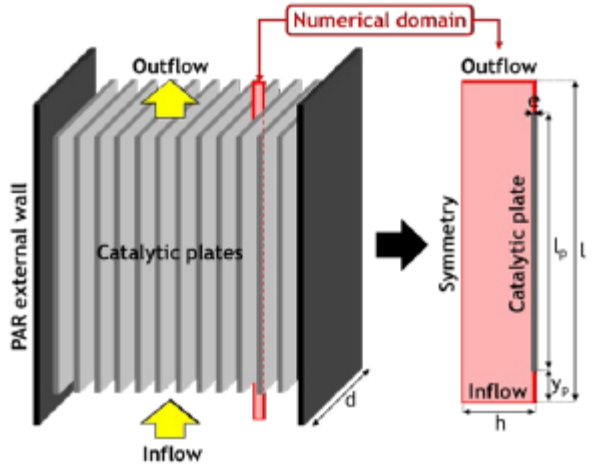

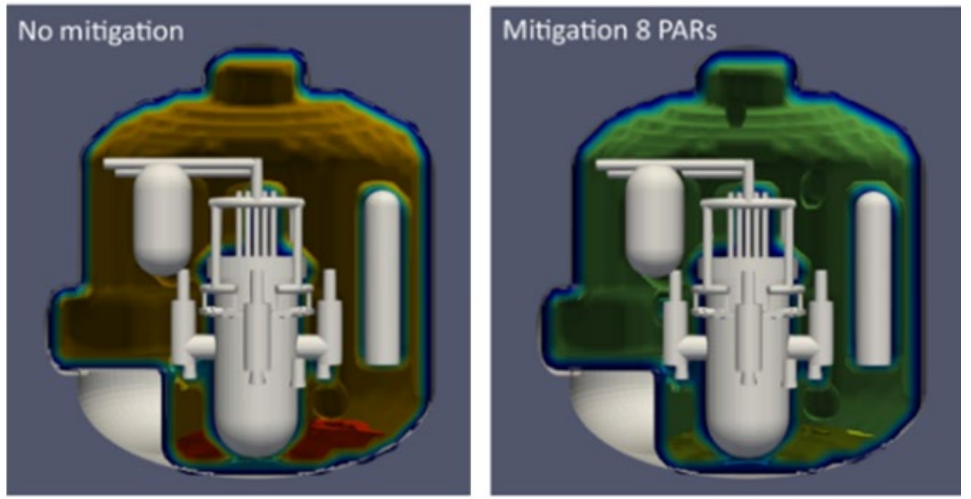

Chakraborty, A. (2017). "*Investigation of ignition characteristics of passive autocatalytic recombiners*". ICAPP 2017, Japan.

Wang, et. al. (2022). "*Code validation and application of hydrogen mitigation by passive autocatalytic recombiner in small modular reactor*". Nuclear Engineering and Design, 396.

1. Background: AMHYCO project (2020-2024)

WP1
- SAMG/EOP
- equipment survivability
- existing approaches



WP2
- GenCont database
- bounding accident sequences



WP3
- H2/CO combustion and recombination characteristics



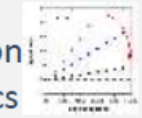

WP4

LP / System codes
(most penalizing scenarios from WP2)

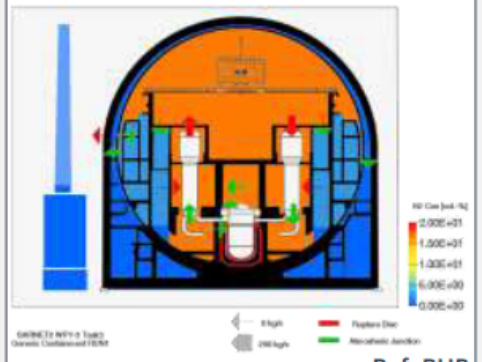

Ref: RUB

GOTHIC-3D
(Selected transients)



Ref: UPM

CFD
(Selected compartments)

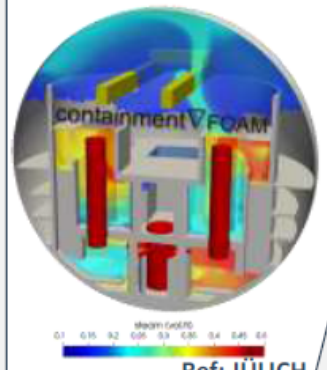

Ref: JÜLICH

- **Task 4.1:** Derive and implement extended correlations/parametric models
- **Task 4.2-3:**
  - 3 Containments: **PWR-KWU**, **PWR-W** and **PWR-VVER**
  - Consecutive analysis chain LP → 3D → CFD
- **Task 4.5:** Summarize Lessons Learned

WP5



- containment response and risk assessment

1. Background: AMHYCO project (2020-2024)

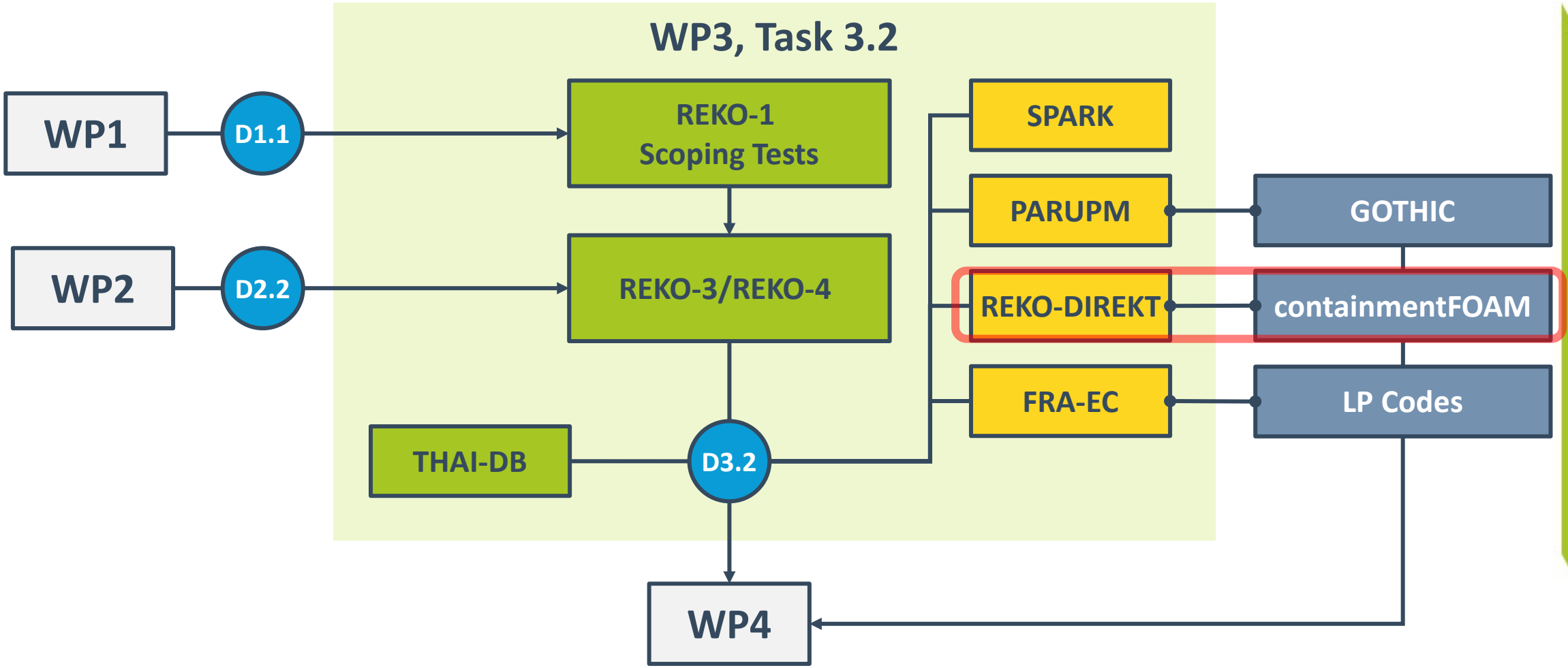

Reinecke, E. (2024). "*Outcomes of the Experimental and Numerical Work on the Operational Behavior of Passive Autocatalytic Recombiners in the Late Phase of a Severe Accident in the Framework of the AMHYCO Project*". ERMSAR 2024, Stockholm, Sweden.

2. Objectives

- Selection of THAI-HR sequences for REKO-DIREKT validation
- Verifying combined performance (coupling) of REKO-DIREKT & containmentFOAM with a test-case model
- Identification of code refinement needs and preliminary simulations with containmentFOAM 3D THAI model

2. Previous works

REKO-DIREKT: standalone & coupling to CFX

- 2016, first V&V w/ THAI-HR sequences

containmentFOAM & REKO-DIREKT

- 2021, coupling test & 3D THAI model (1 seq.)

containmentFOAM & REKO-DIREKT

- 2023, coupling test (8 seq.) & 3D preliminary simulations

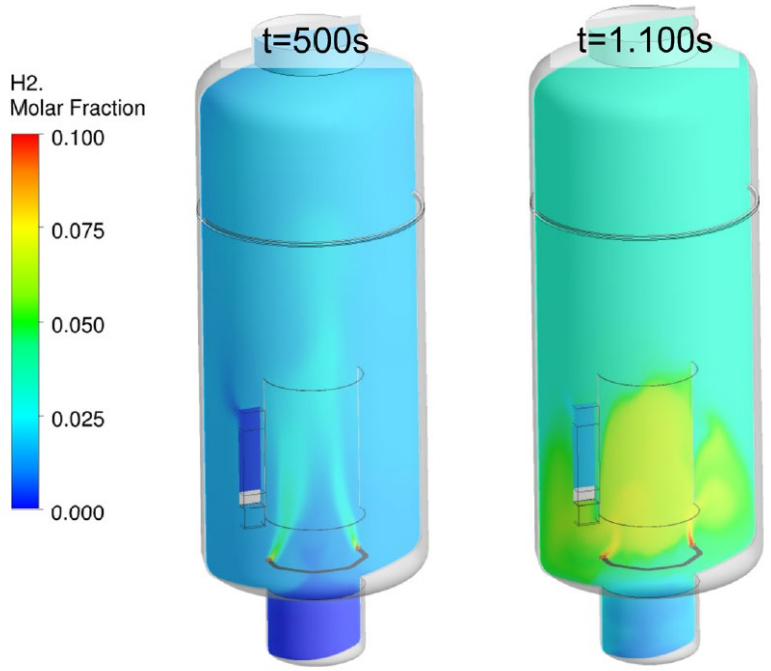

E., Reinecke (2016). *"Validation and Application of the REKO-DIREKT Code for the Simulation of Passive Autocatalytic Recombiner Operational Behavior".* Nuclear Technology, 196

S., Kelm (2021).*"The Tailored CFD Package 'containmentFOAM' for Analysis of Containment Atmosphere Mixing, H2/CO Mitigation and Aerosol Transport".* Fluids 2021, 6, 100

3. REKO-DIREKT recombination code

- **Catalyst** section and PAR **chimney** modules.
- **Input**: PAR geometry and inlet conditions (T, P, gas %´s).
- **Output**: outlet conditions and mass flow and velocity.
- Also calculates **catalytic** plate **temperatures**.
- Does not model ignition phenomena.
- Validated against **REKO-3 database**.

REKO-4 facility



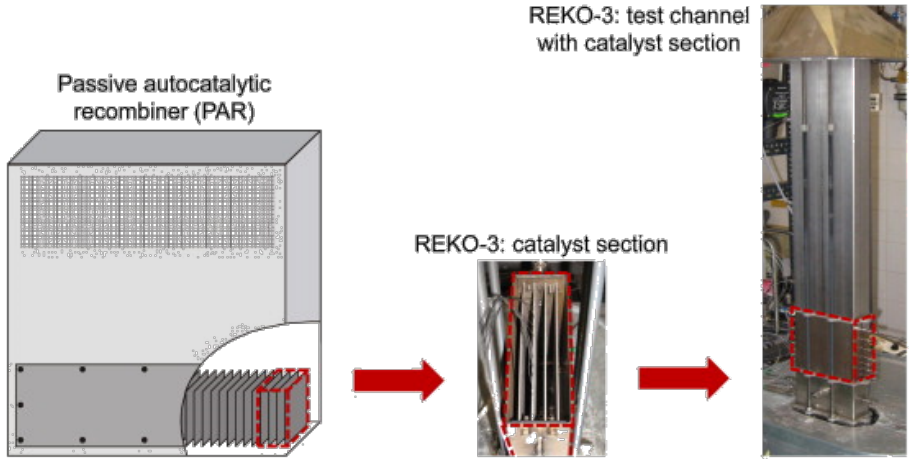

M., Klauck et.al. (2014). *"Passive auto-catalytic recombiners operation in the presence of hydrogen and carbon monoxide: Experimental study and model development"*. Nuclear Engineering and Design

3. REKO-DIREKT recombination code

- Catalytic reaction equations are based on a **mechanistic diffusive mass transport** approach.
- Modules validated against 32 THAI-HR tests (FRAMATOME and AECL PAR types).

$$\dot{m} = A \cdot \sqrt{\frac{g \cdot H \cdot (\rho_0 - \rho)}{\frac{1}{\rho} - \frac{1}{2 \cdot \rho_0} + \frac{\xi \cdot H}{2 \cdot d_h \cdot \rho}}}$$

Mass rate of gases flowing through the chimney of the PAR

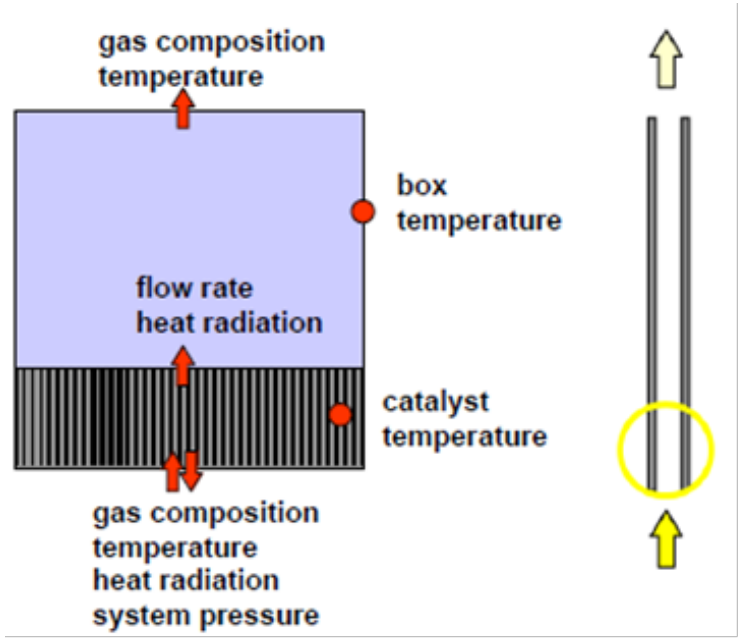

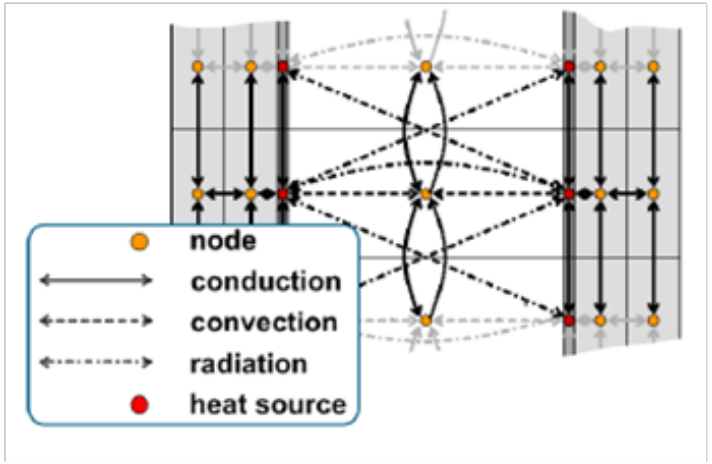

E., Reinecke (2016). *"Validation and Application of the REKO-DIREKT Code for the Simulation of Passive Autocatalytic Recombiner Operational Behavior"*. Nuclear Technology, 196

Simon, B. (2014). *"Enhancement and Validation of Models Describing the Operational Behavior of Passive Autocatalytic Recombiners in the Containments of Nuclear Power Plants"*. Faculty of Mechanical Engineering, Aachen

3. containmentFOAM

- **Multi-species** and **multi-physics** package based on OpenFOAM-9 (C++).
- ANSYS-CFX´s baseline models.
- Interfaces for **safety systems**, by a code coupling or following a porous media approach.
- Models for pressurization, heat and mass transfer in buoyant and turbulent flows, gas radiation heat transport, H_2 & CO mitigation, aerosol particle transport, etc.

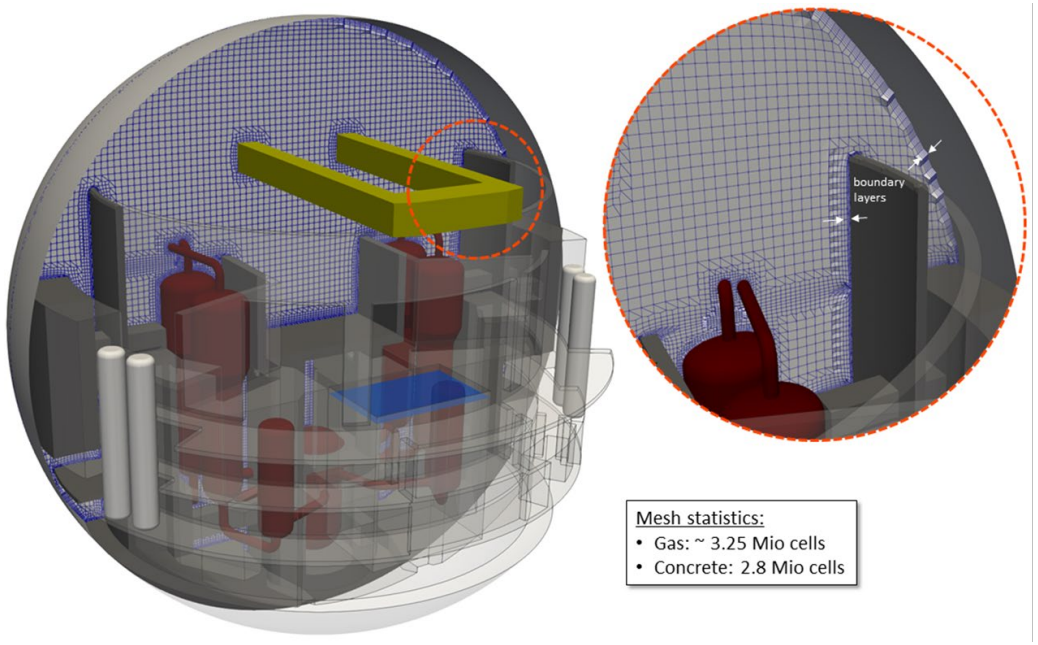

containmentFOAM

OpenFOAM®

Kelm, S. (2022). *Introduction to containmentFOAM - Theoretical Background*. IAEA Webinar Series

3. containmentFOAM

- Validated within the framework of OECD/NEA´s **SETH** and **HYMERES** projects.
- Simulation of **MISTRA** and **THAI** tests.
- Application-oriented validation. E.g., ISP-37 (**VANAM** M3) test.
- Containment studies (**AMHYCO**, **SASPAM-SA**).

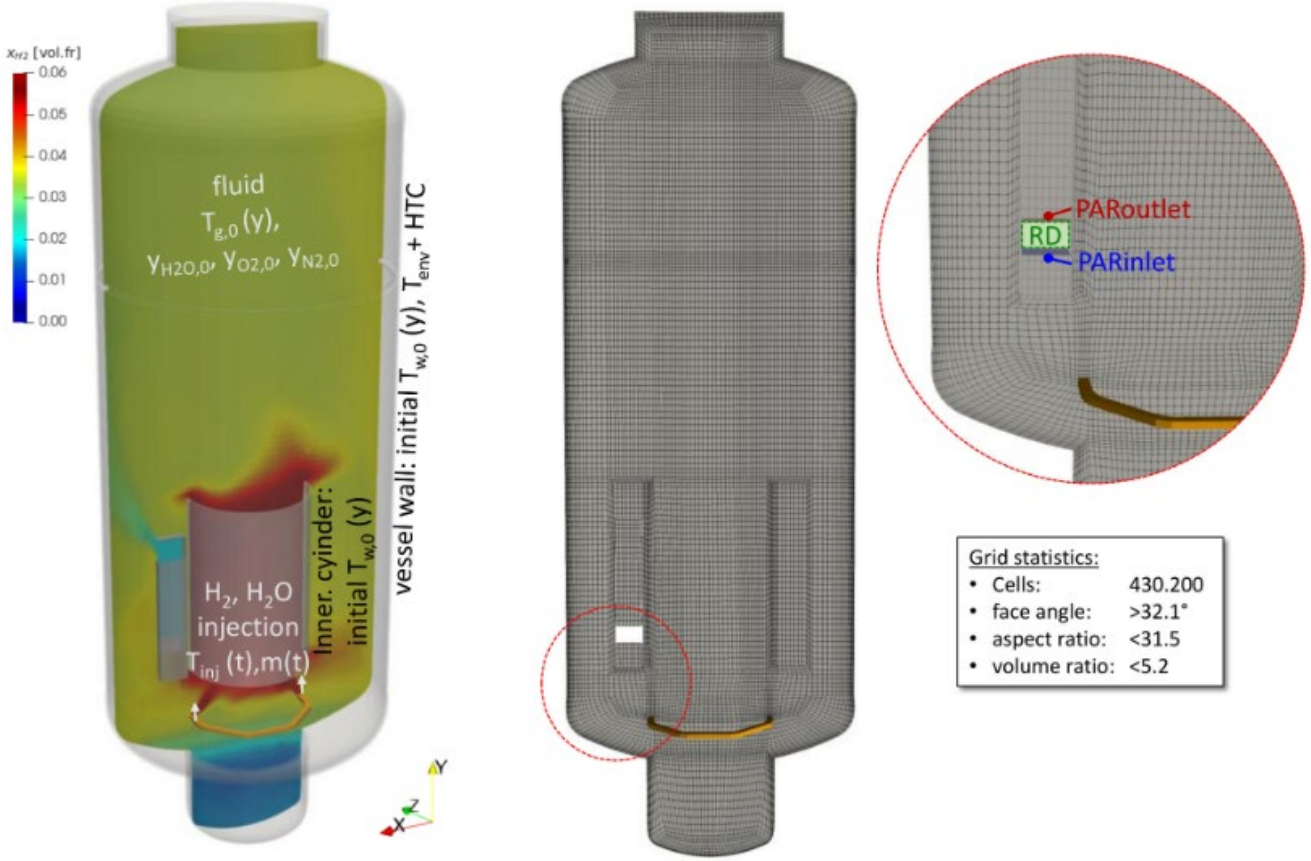

S., Kelm (2021). *"The Tailored CFD Package 'containmentFOAM' for Analysis of Containment Atmosphere Mixing, H2/CO Mitigation and Aerosol Transport"*. Fluids 2021, 6, 100

4. THAI-HR series

- **General objectives**
  - PAR start-up behavior
  - H_2 recombination rate & depletion efficiency
  - O_2 starvation effect
  - PAR induced ignition and resulting H_2 deflagration
  - PAR interaction with fission products
- Vessel conditions representative of SA scenarios

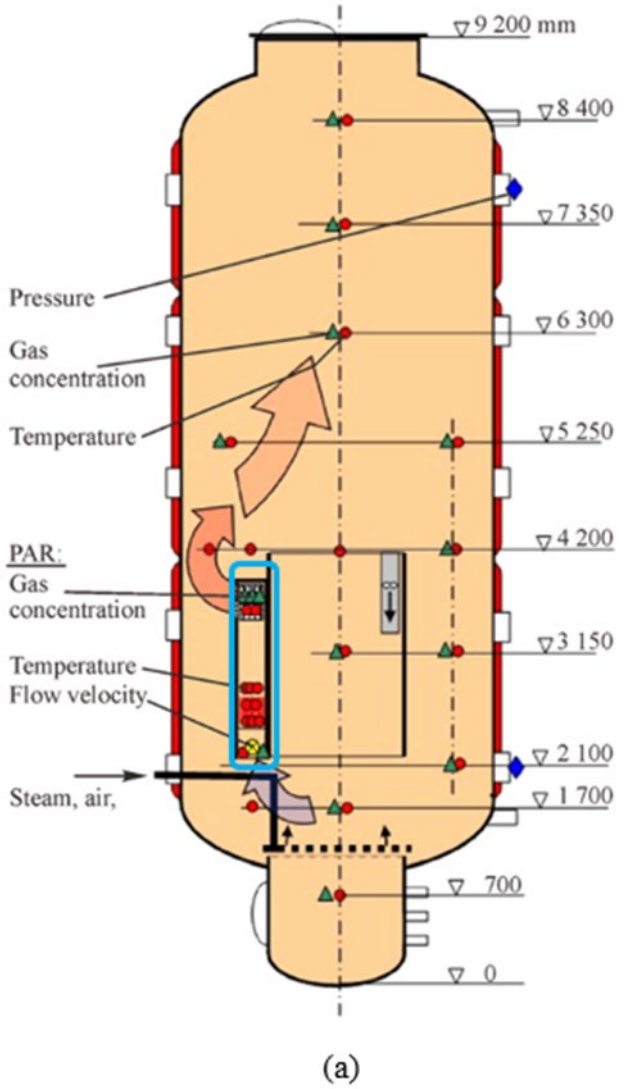

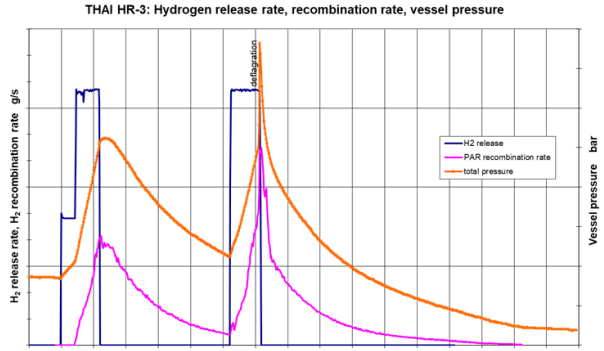

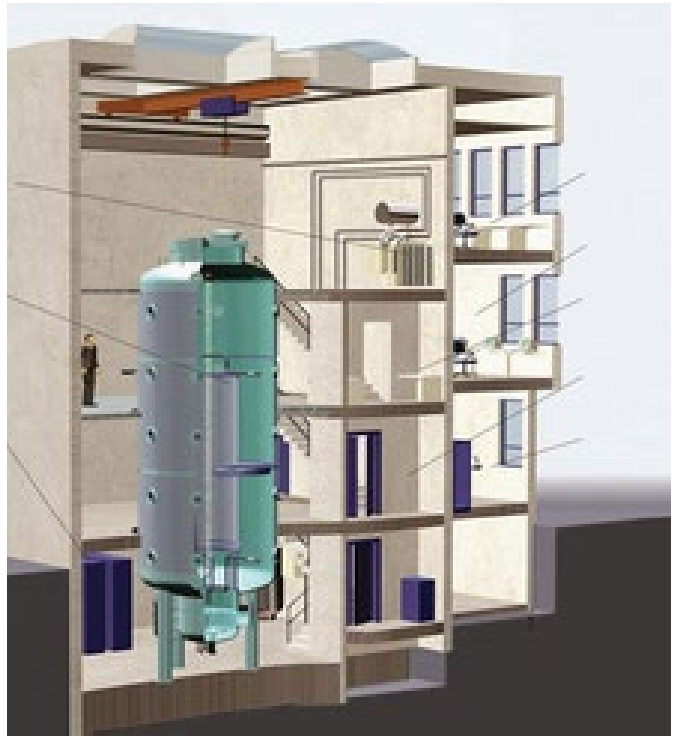

Gupta, S. (2015). "*THAI test facility for experimental research on hydrogen and fission product behaviour in light water reactor containments*" . Nuclear Engineering and Design, 294

4. THAI-HR series: Data points

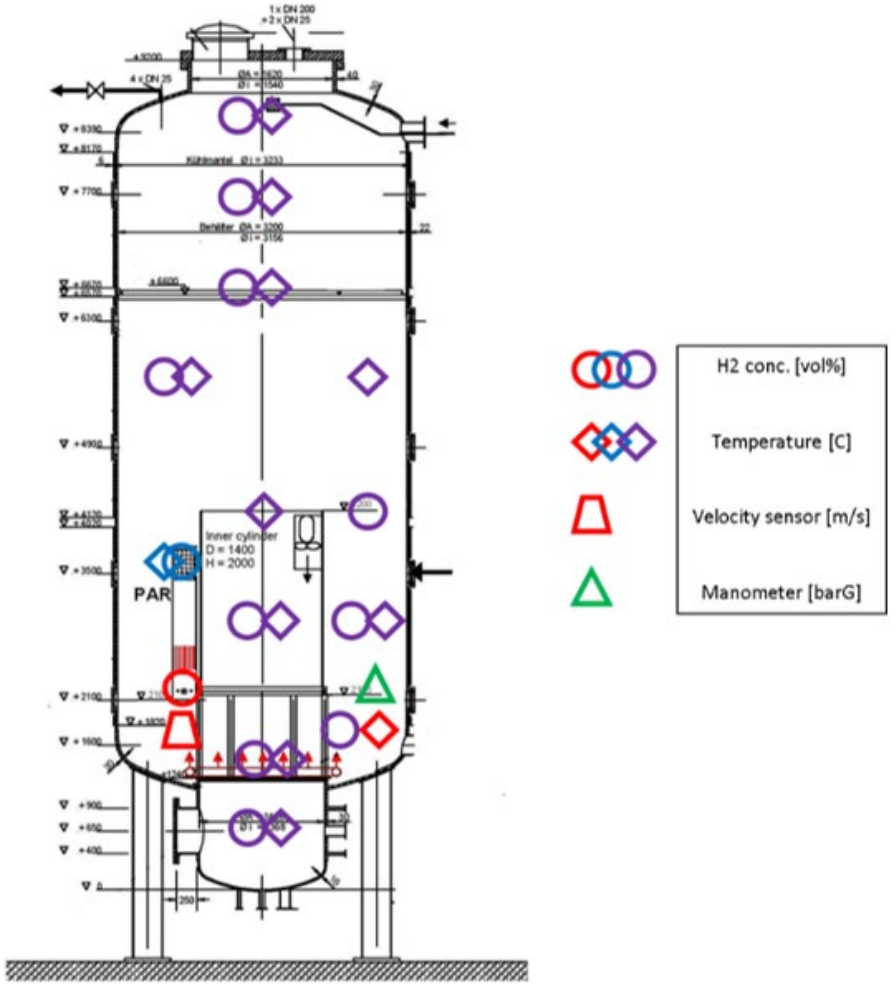

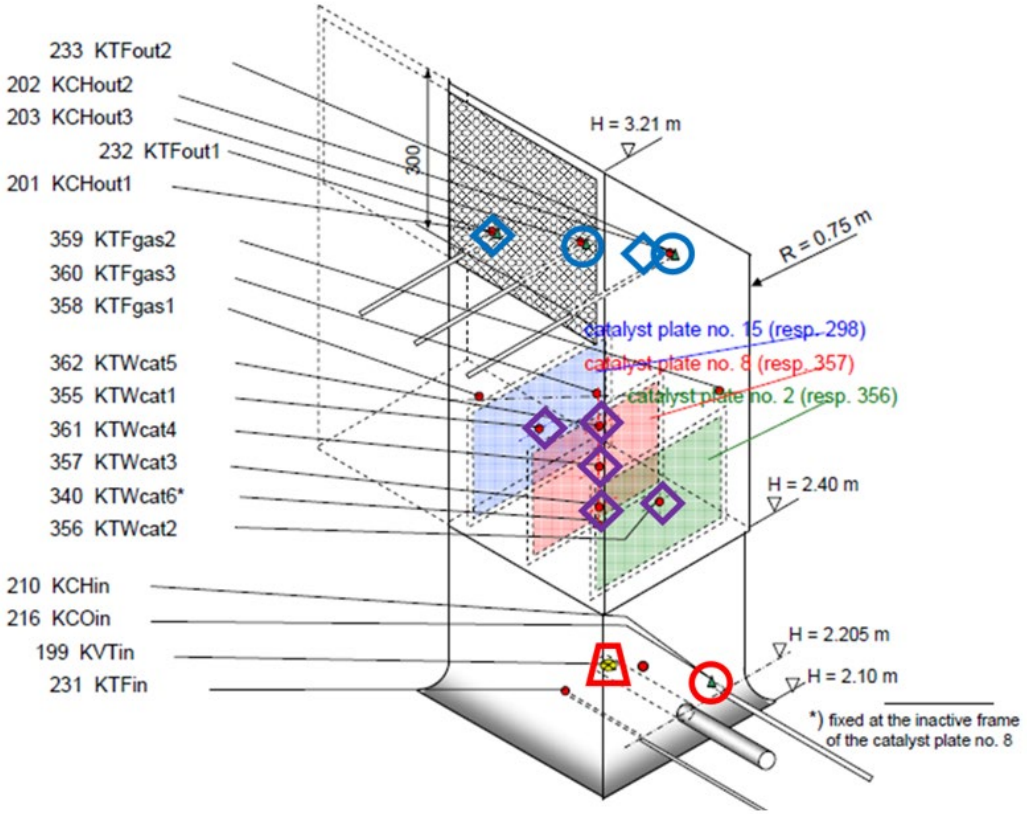

4. THAI-HR series: Selection of FOMs & sequences

$$\mathbf{M_{H2}}\ \left(\frac{g}{s}\right) = \frac{n_{H2} * 0{,}01 * \Delta(H2_{conc}) * p * v * A}{8{,}314 * (273{,}15 + T_{inlet})}$$

$$\eta\ (-) = \frac{(H_{2_{inlet}} - H_{2_{outlet}})}{H_{2_{inlet}}}$$

Test	P [bar]	T [°C]	%vol H_2	%vol O_2	%vol H_2O	Ignition	O_2 starv.
HR-2	1.00	27.90	0.00	21.00	0.00	yes	no
HR-3	1.48	29.90	0.02	21.71	0.00	yes	no
HR-5	2.93	32.00	0.04	21.69	0.00	no	no
HR-13	1.00	86.50	0.00	8.16	61.05	no	strong
HR-9	1.44	89.7	2.19	11.30	48.15	no	mild
HR-12	2.92	115.0	0.00	7.35	61.12	no	strong

4. THAI-HR series: Selection of sequences

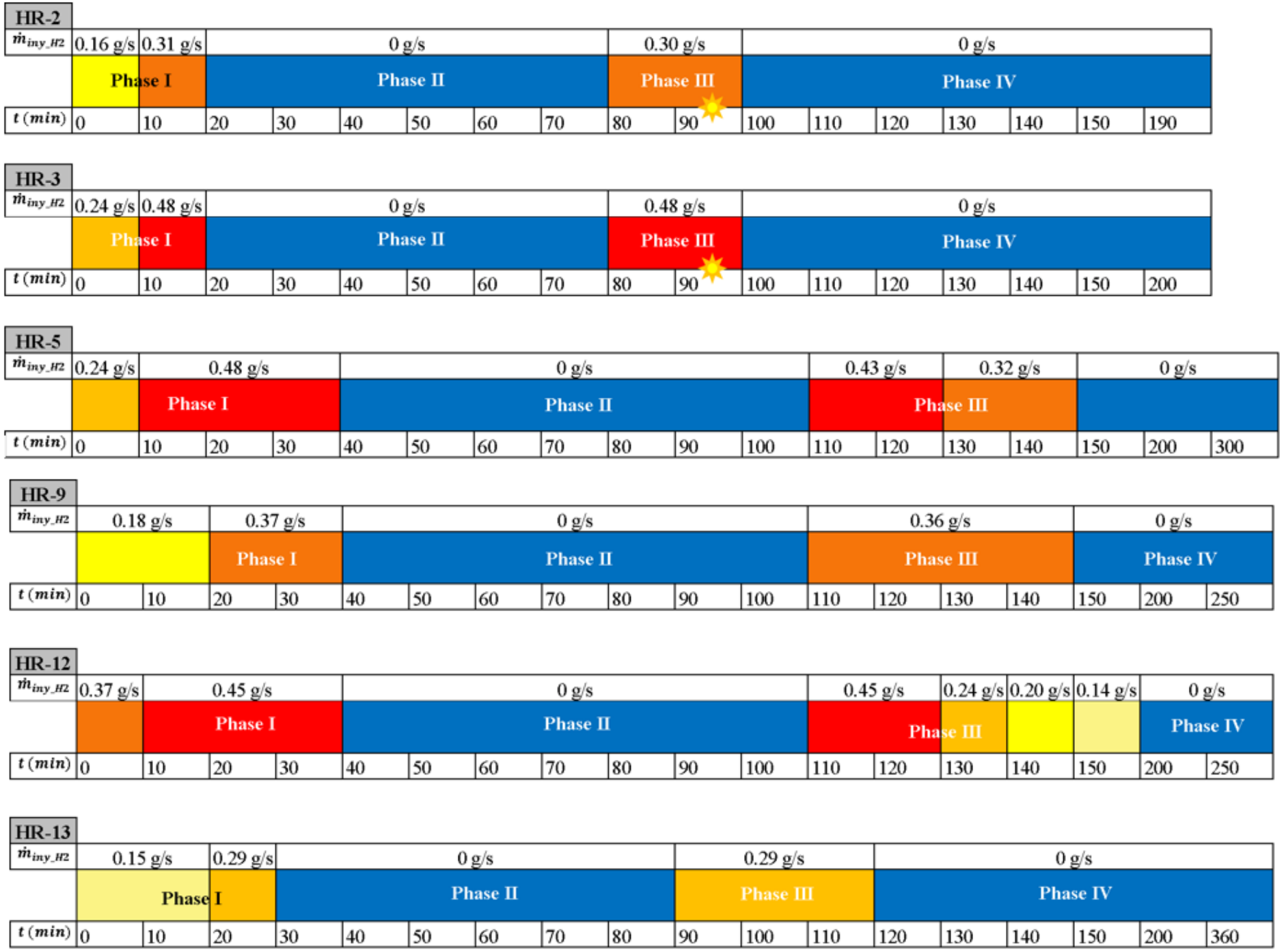

5. Test-case model and code coupling

- Coupling by means of a file-based scheme and using a domain decomposition approach.
- In the input interface, containmentFOAM evaluates and delivers the gases, P and T to REKO-DIREKT.
- REKO-DIREKT returns composition, flow and T of the exhaust gas.

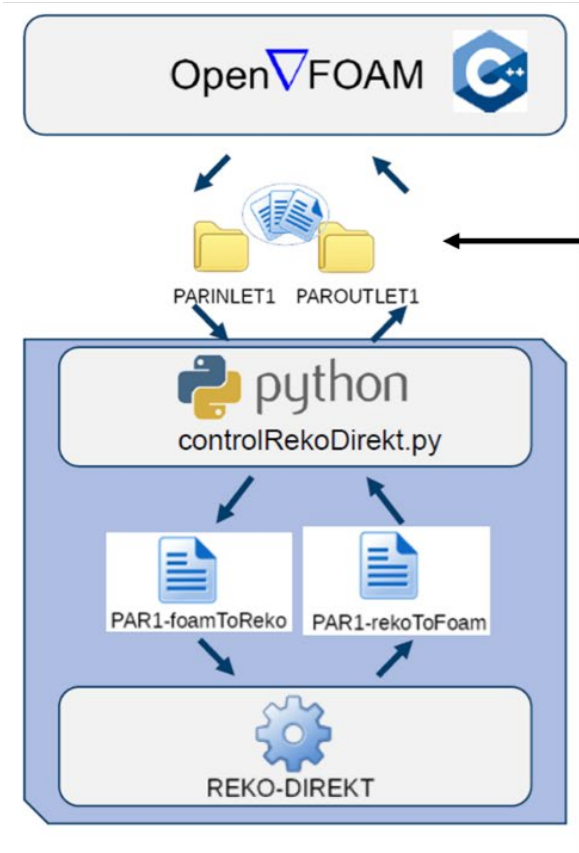


```
FoamFile
{
    class       polyBoundaryMesh;
    object      boundary;
}
    PARINLET1
    {
        type            patch;
        nFaces          5;
        startFace       5817;
    }
    PAROUTLET1
    {
        type            patch;
        nFaces          7;
        startFace       5822;
    }
// * * *
```

6. Results: Test-case validation

Recombination Rate [g/s]

- HR-2 & -3 simulated just until ignition point.
- Depletion phases better captured than injection ones.
- HR-5´s second recombination peak seemingly underestimated (low H_2 % seen in the experiment monitors).

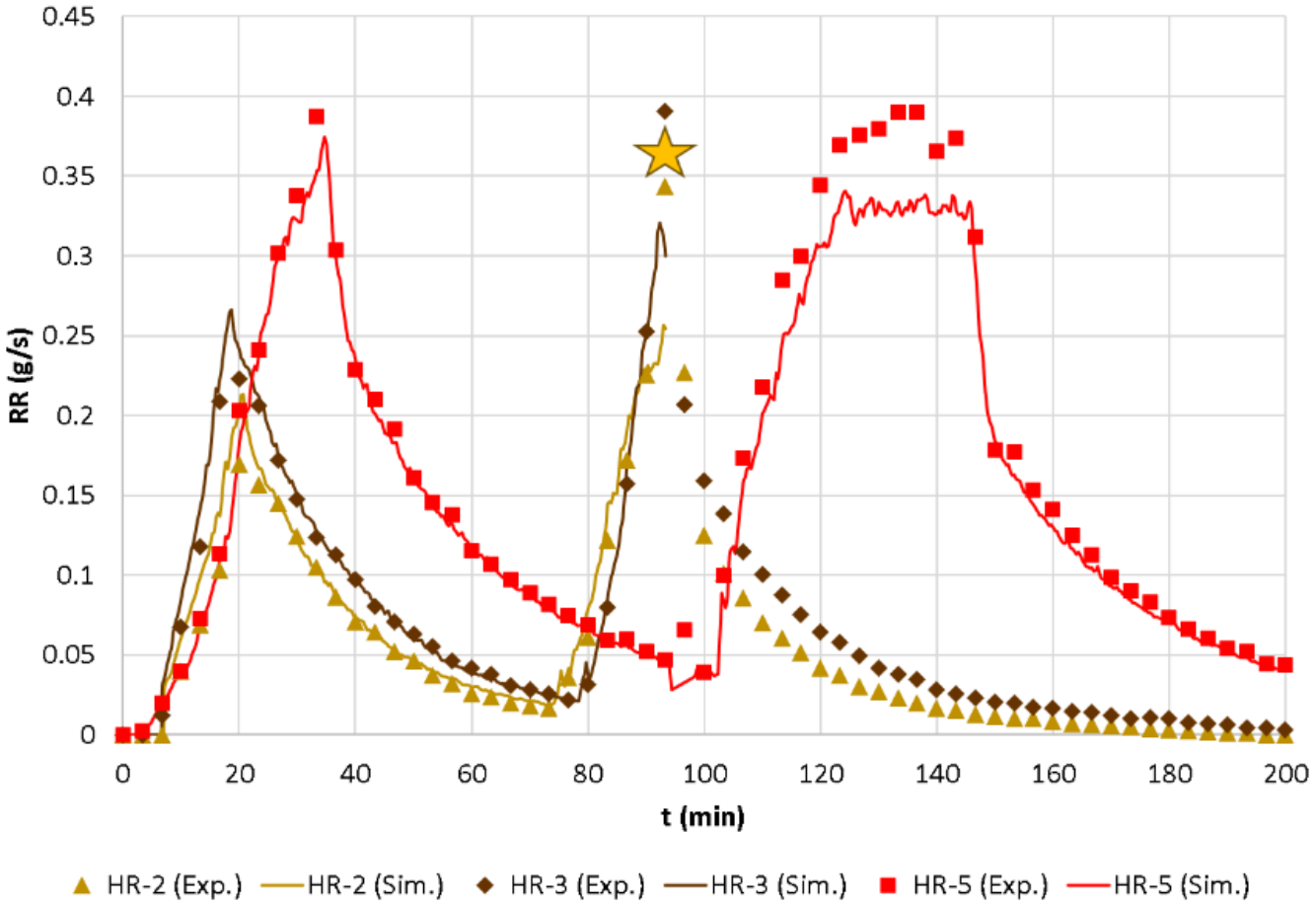

Test	P [bar]	T [°C]	%vol H_2	%vol O_2	%vol H_2O	Ignition	O_2 starv.
HR-2	1.00	27.90	0.00	21.00	0.00	yes	no
HR-3	1.48	29.90	0.02	21.71	0.00	yes	no
HR-5	2.93	32.00	0.04	21.69	0.00	no	no

6. Results: Test-case validation

Recombination Rate [g/s]

- Agreement btw. calculated and measured data seems to be higher the higher the test P (for dry and wet cases).
- Especially at Phases I & III.
- HR-12 & -13: effect of O_2-poor atm. (2nd recombination peaks lower than 1st ones).

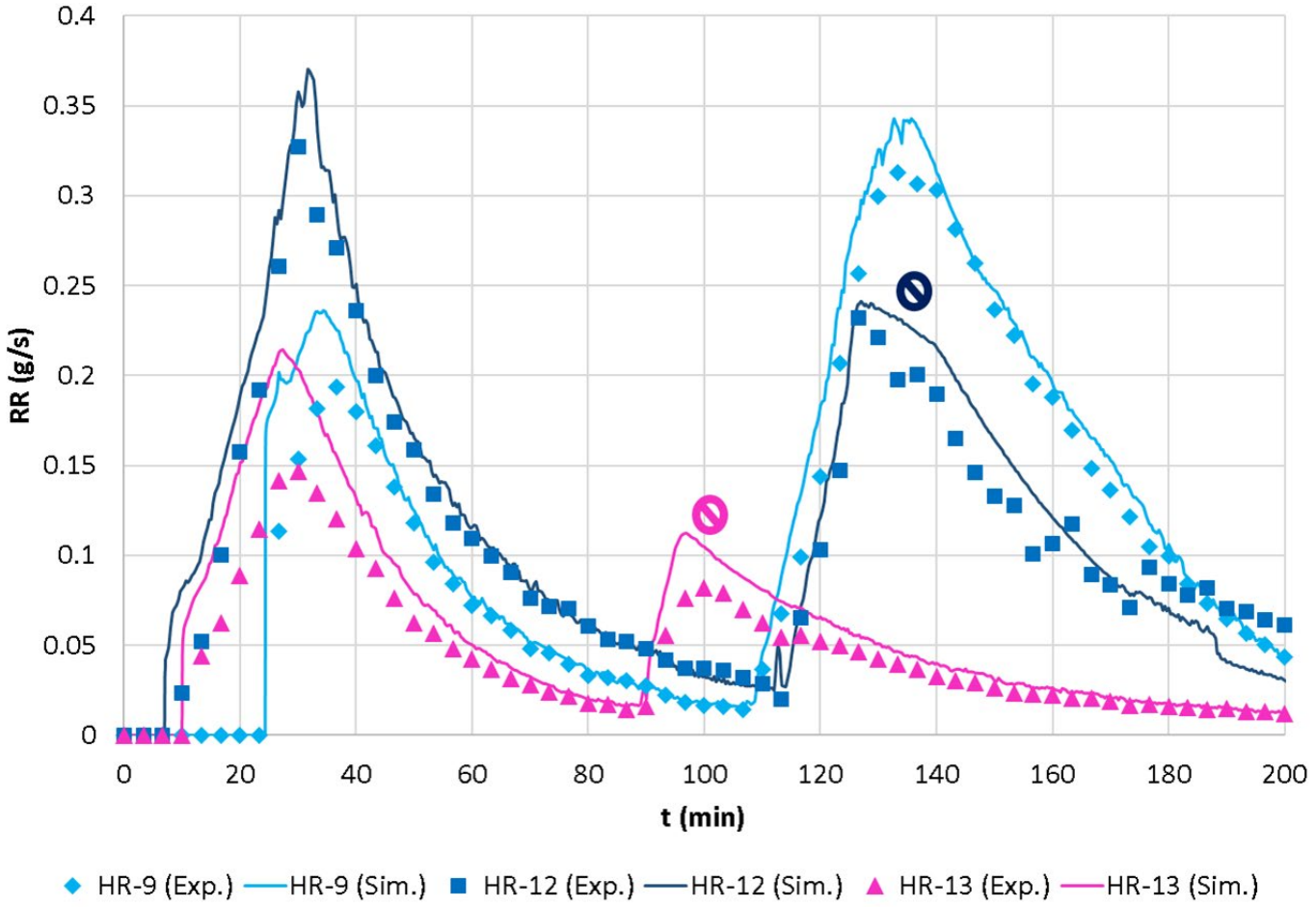

Test	P [bar]	T [°C]	%vol H_2	%vol O_2	%vol H_2O	Ignition	O_2 starv.
HR-13	1.00	86.50	0.00	8.16	61.05	no	strong
HR-9	1.44	89.7	2.19	11.30	48.15	no	mild
HR-12	2.92	115.0	0.00	7.35	61.12	no	strong

6. Results: Test-case validation

O_2 Surplus Ratio [-]

- As soon as Φ falls below 2, RR and catalyst T decrease drastically.
- HR-9 enters O_2 lean region after 130 min but doesn´t reach impairing 'sub-stoichiometric' conditions.

$$\Phi\,(-) = \frac{2 * x_{O_{2_{inlet}}}}{x_{H_{2_{inlet}}}}$$

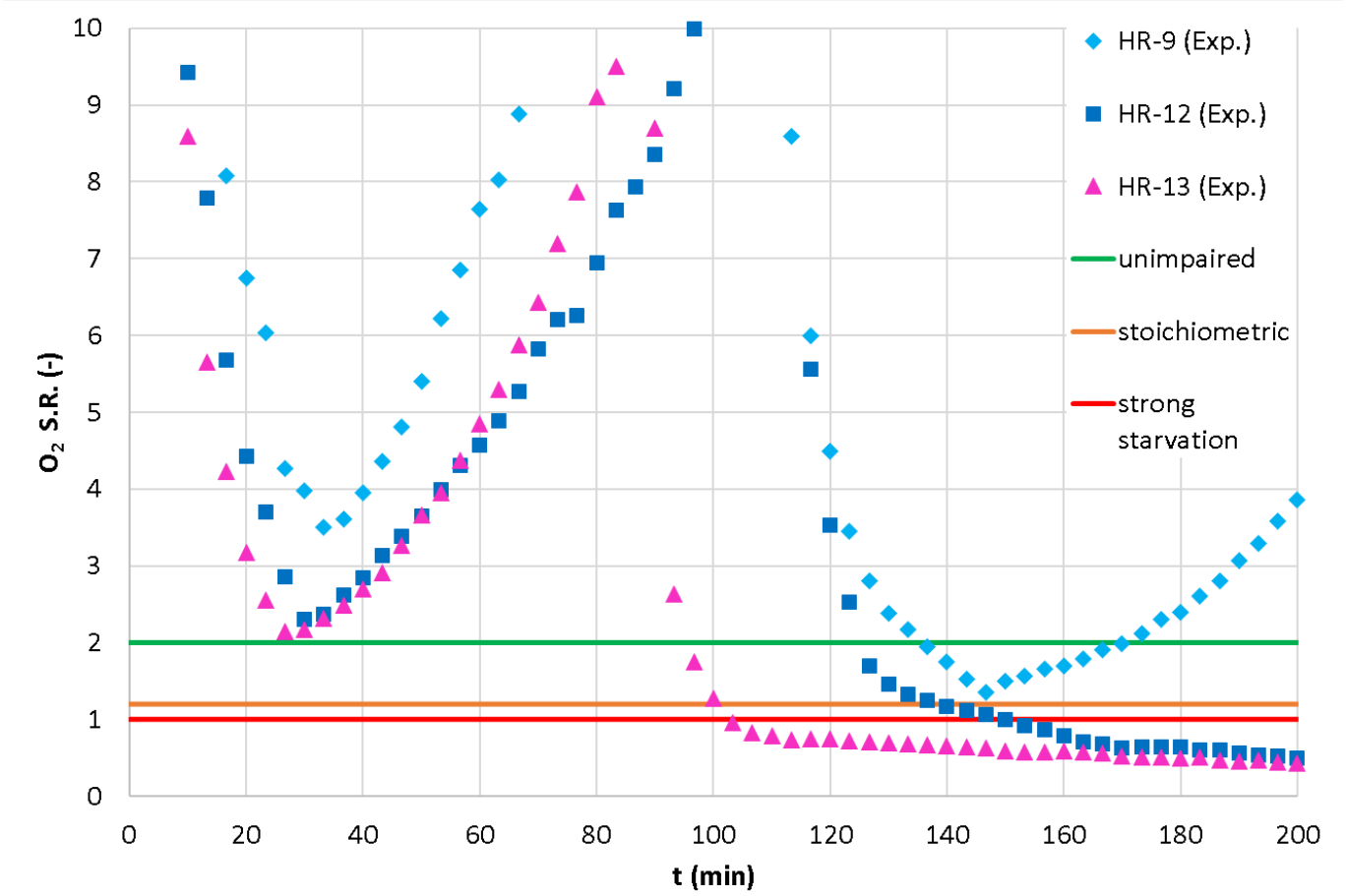

6. Results: Test-case validation

Inlet Flow Velocity [m/s]

- Overestimation at injection phases.
- Actual start-up is slower (as is the density gradient btw. i/o).
- Increased velocity might reduce recombination efficiency, as gas residency time between the plates is diminished too.

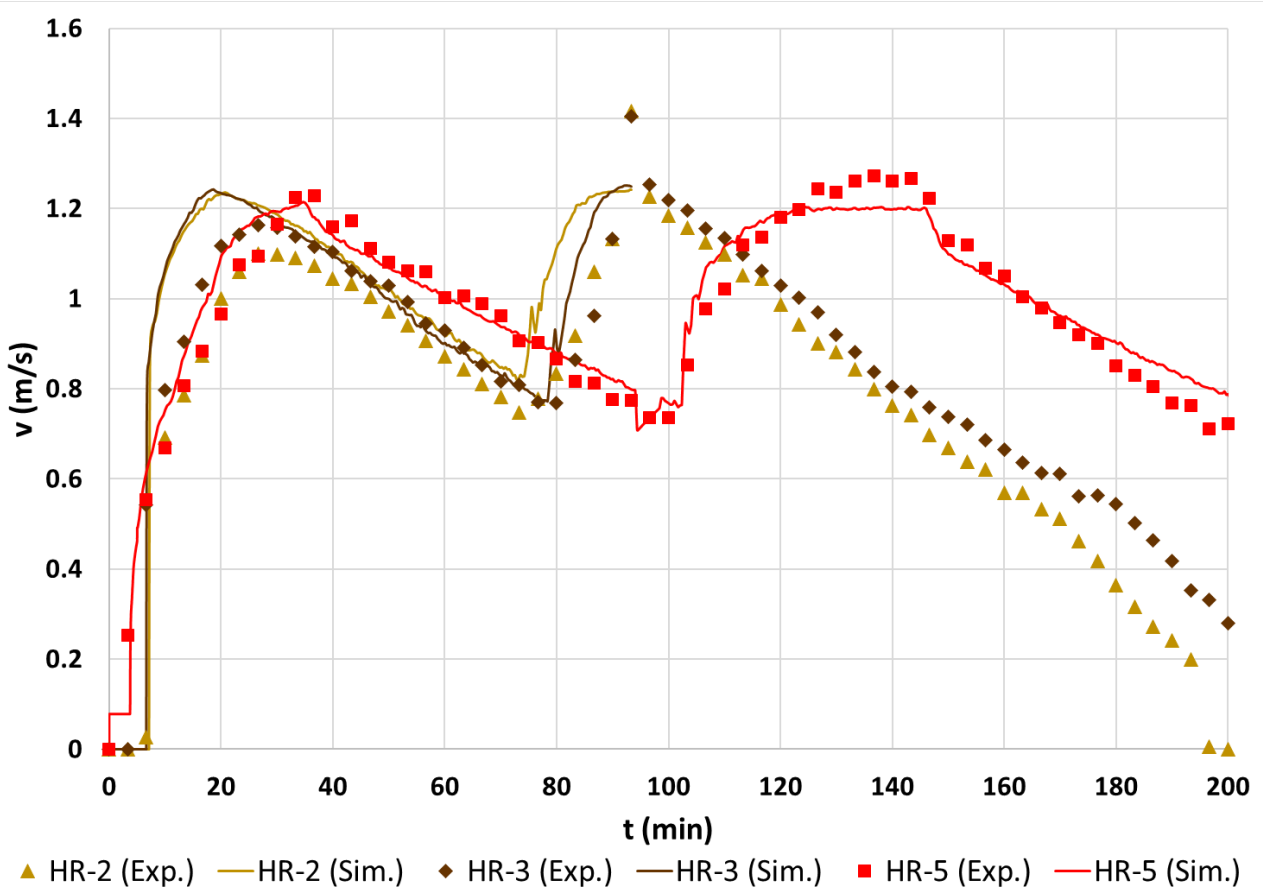

Test	P [bar]	T [°C]	%vol H_2	%vol O_2	%vol H_2O	Ignition	O_2 starv.
HR-2	1.00	27.90	0.00	21.00	0.00	yes	no
HR-3	1.48	29.90	0.02	21.71	0.00	yes	no
HR-5	2.93	32.00	0.04	21.69	0.00	no	no

6. Results: Test-case validation

Inlet Flow Velocity [m/s]

- Chimney model correlations are optimized for the 'full-operational' PAR.
- More accurate for higher flow Reynolds numbers, providing more realistic gas inflows.

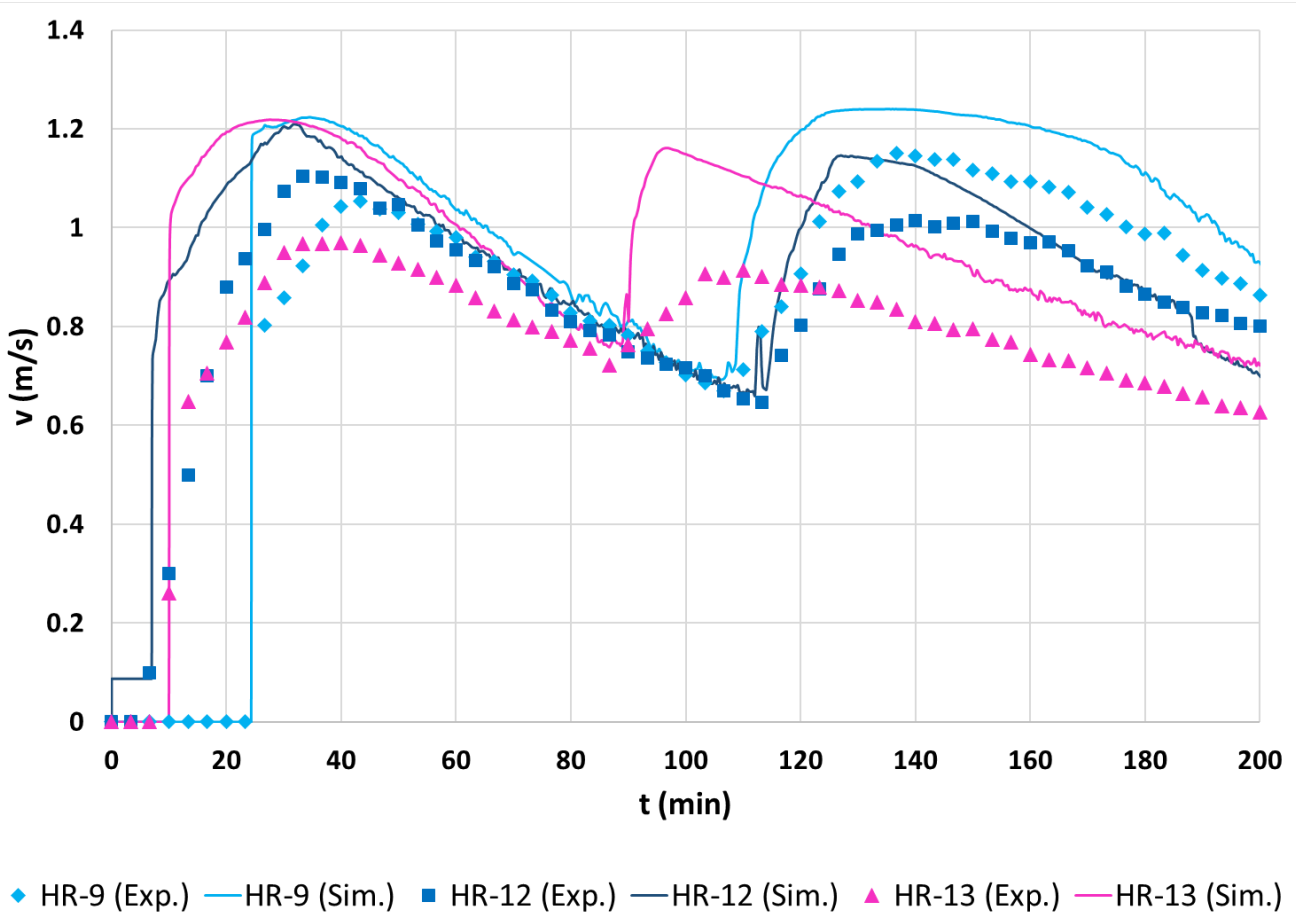

Test	P [bar]	T [°C]	%vol H_2	%vol O_2	%vol H_2O	Ignition	O_2 starv.
HR-13	1.00	86.50	0.00	8.16	61.05	no	strong
HR-9	1.44	89.7	2.19	11.30	48.15	no	mild
HR-12	2.92	115.0	0.00	7.35	61.12	no	strong

6. Results: Test-case validation

Outlet gas T [°C]

- Coherent trends.
- PAR box T does not have an experimental counterpart.
- How much heat is transferred from the PAR housing to the surroundings?

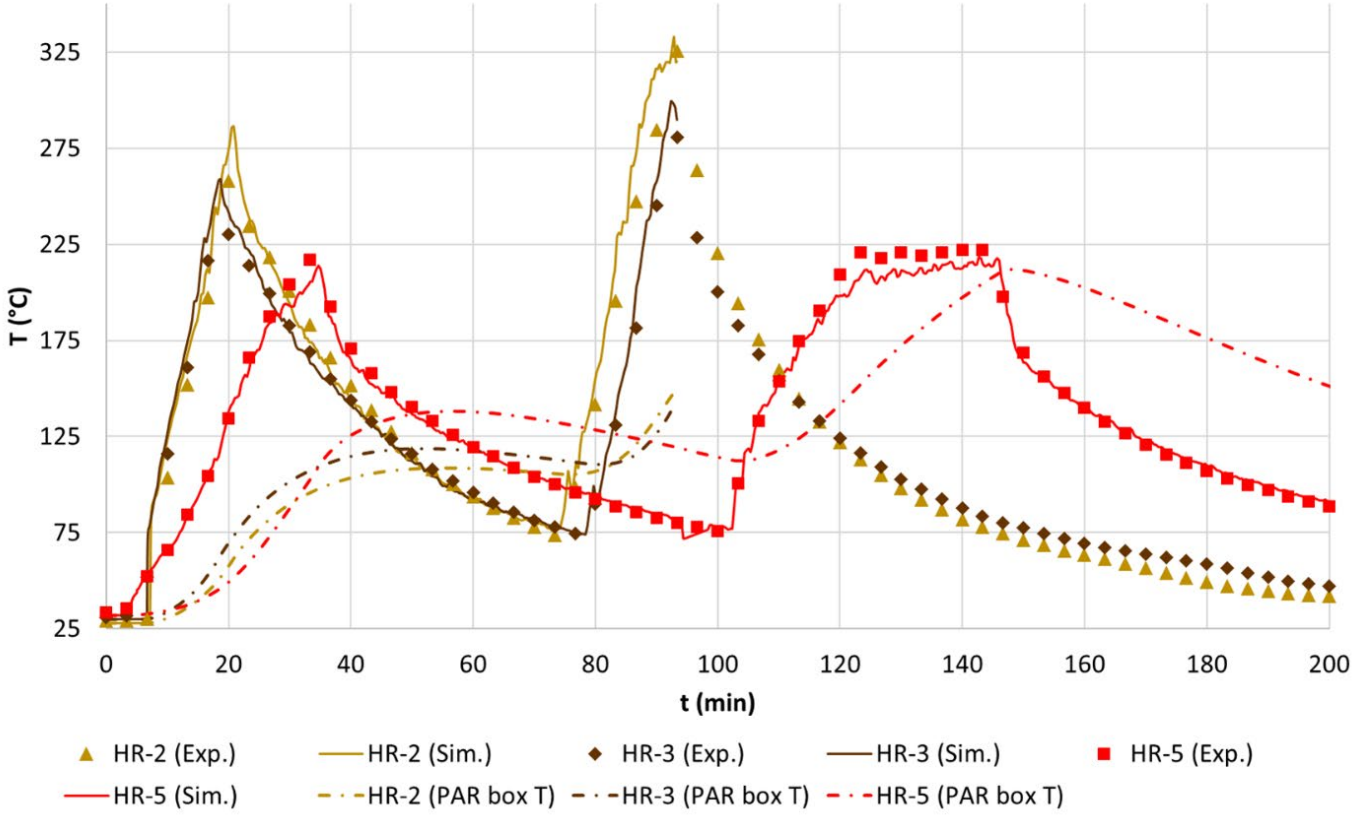

Test	P [bar]	T [°C]	%vol H_2	%vol O_2	%vol H_2O	Ignition	O_2 starv.
HR-2	1.00	27.90	0.00	21.00	0.00	yes	no
HR-3	1.48	29.90	0.02	21.71	0.00	yes	no
HR-5	2.93	32.00	0.04	21.69	0.00	no	no

6. Results: Test-case validation

Outlet gas T [°C]

- HR-12 shows better agreement:
  - Initial T is higher
  - Milder T gradients btw. i/o

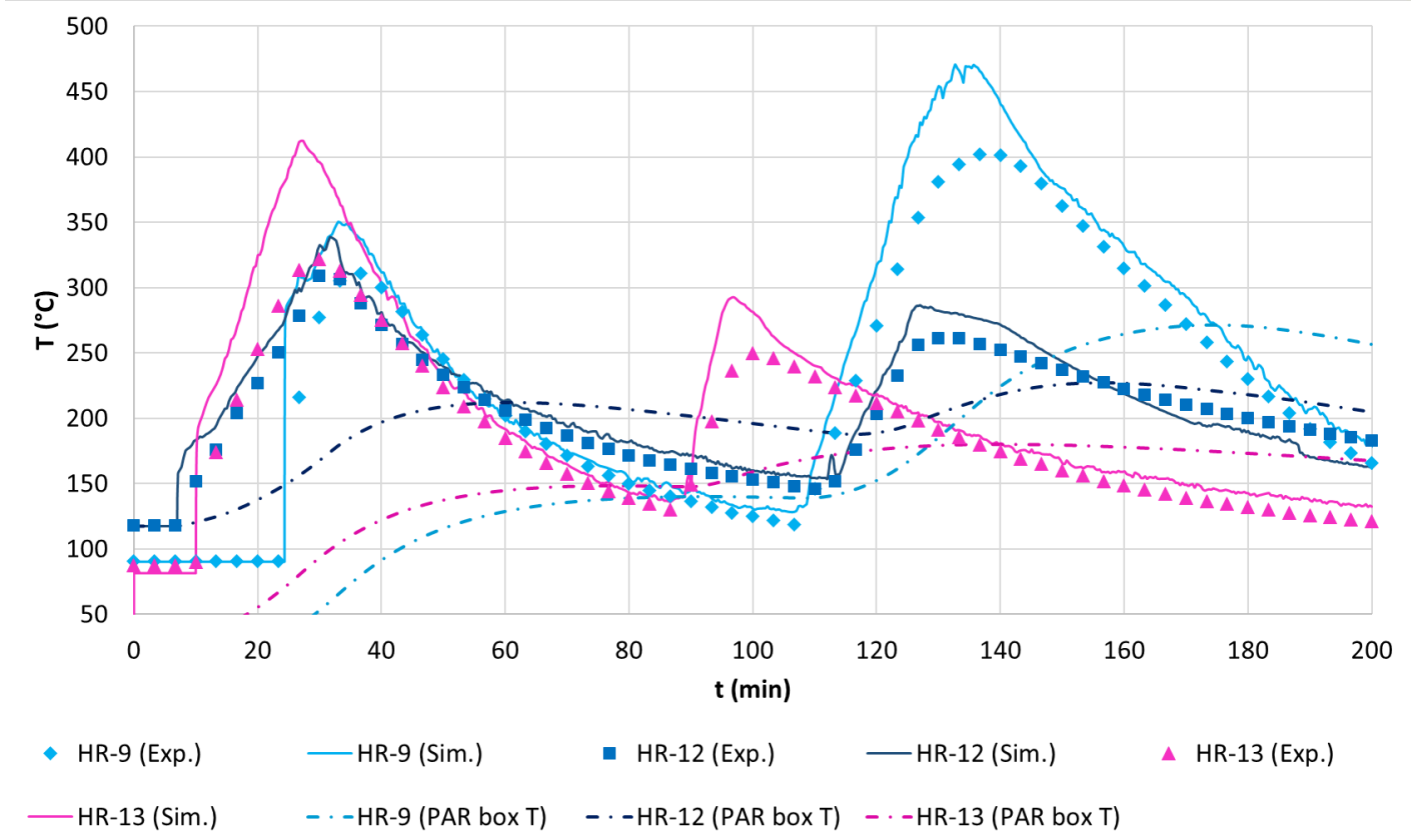

Test	P [bar]	T [°C]	%vol H_2	%vol O_2	%vol H_2O	Ignition	O_2 starv.
HR-13	1.00	86.50	0.00	8.16	61.05	no	strong
HR-9	1.44	89.7	2.19	11.30	48.15	no	mild
HR-12	2.92	115.0	0.00	7.35	61.12	no	strong

6. Results
Test-case validation

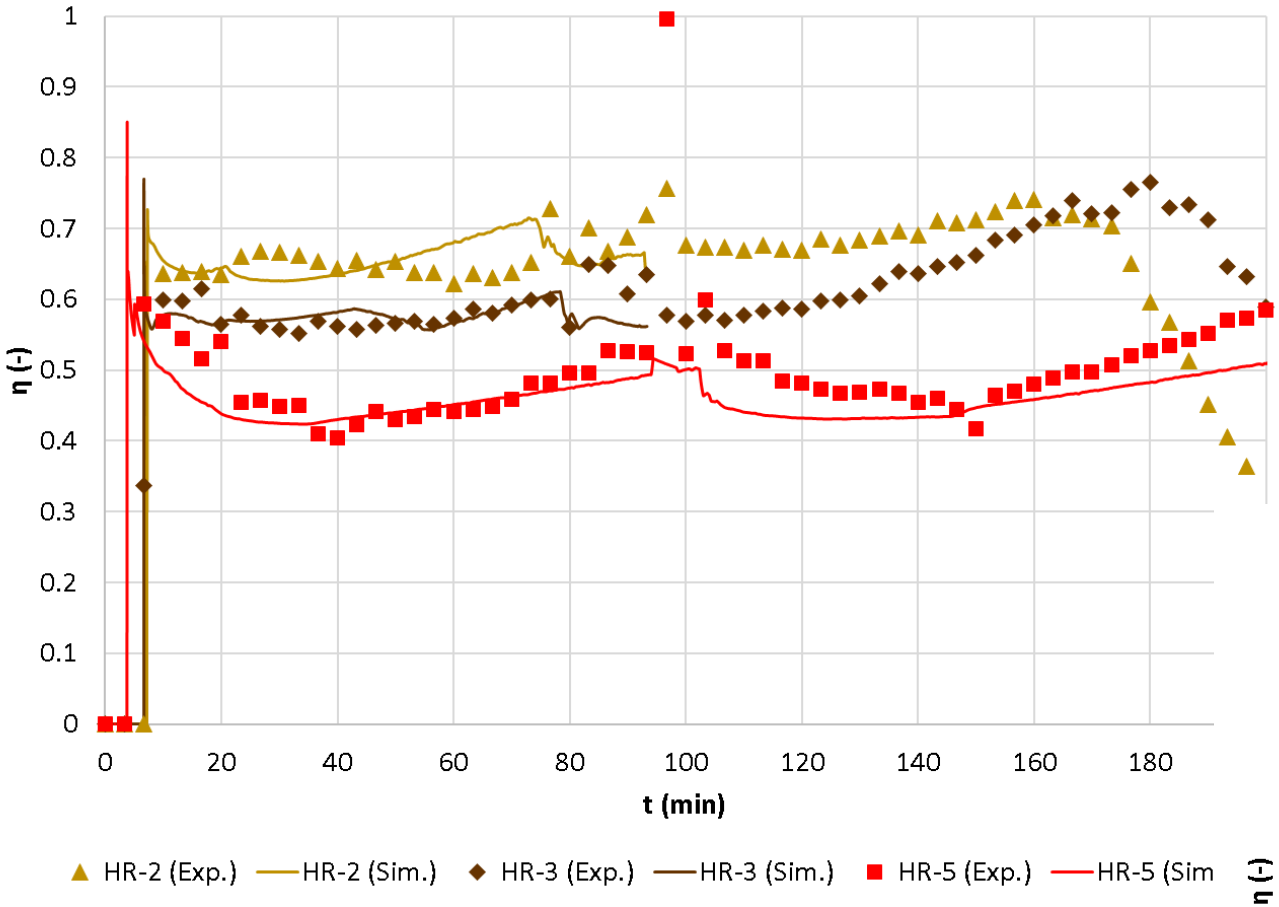

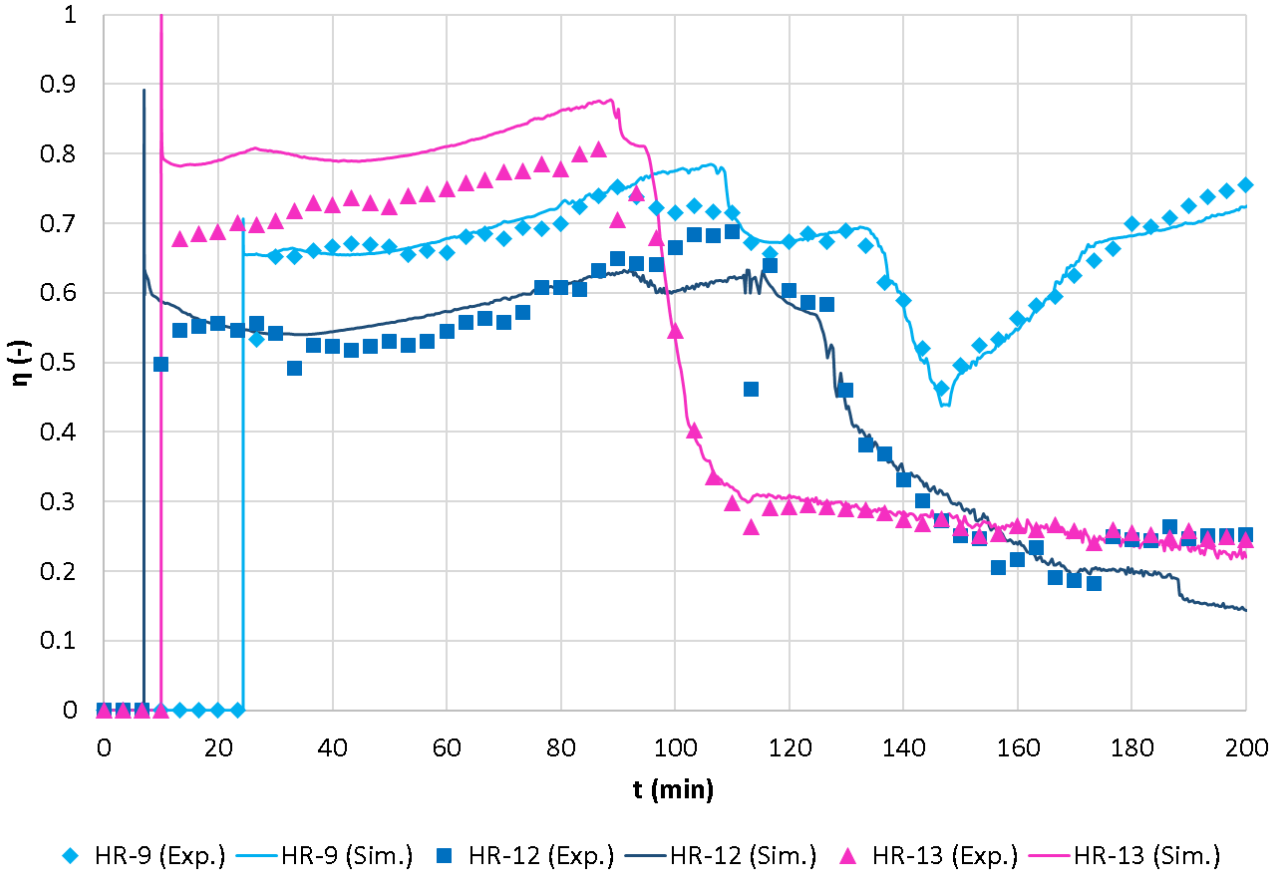

Recombination efficiency [-]

6. Results: Test-case validation

Integrated recombined mass

$$\int_i^{i+1} RR(t)dt \approx \frac{(t_{i+1} - t_i)(RR_i + RR_{i+1})}{2}$$

	IRM Phase II [g]	Rel. Err. Phase II [%]	IRM Phase IV [g]	Rel. Err. Phase IV [%]
HR-2	316	12.0	474	10.5
HR-3	412	4.9	545	1.9
HR-5	772	-4.4	1910	-7.1
HR-13	431	39.2	722	32.4
HR-9	459	18.4	1520	11.5
HR-12	810	12.2	1516	8.9

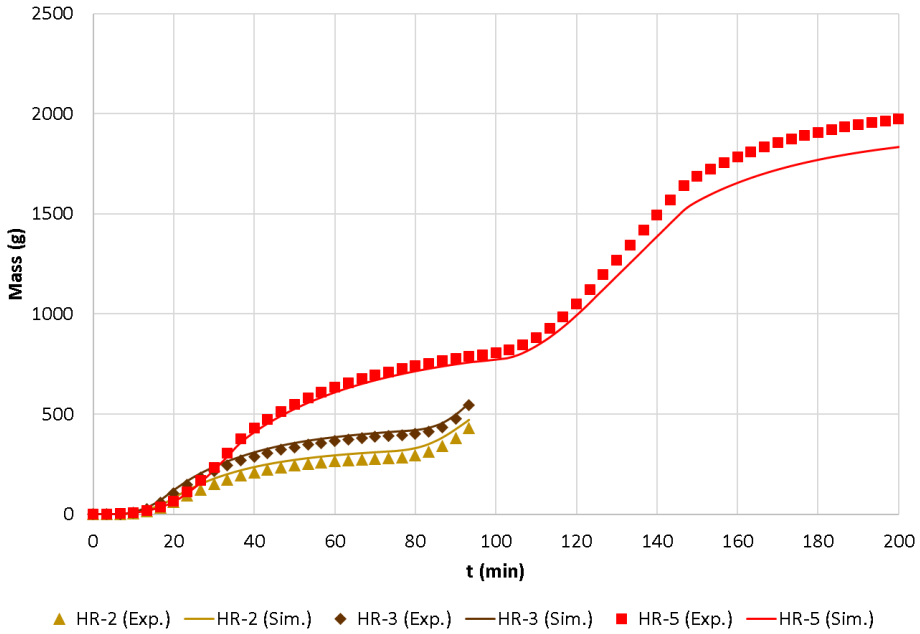

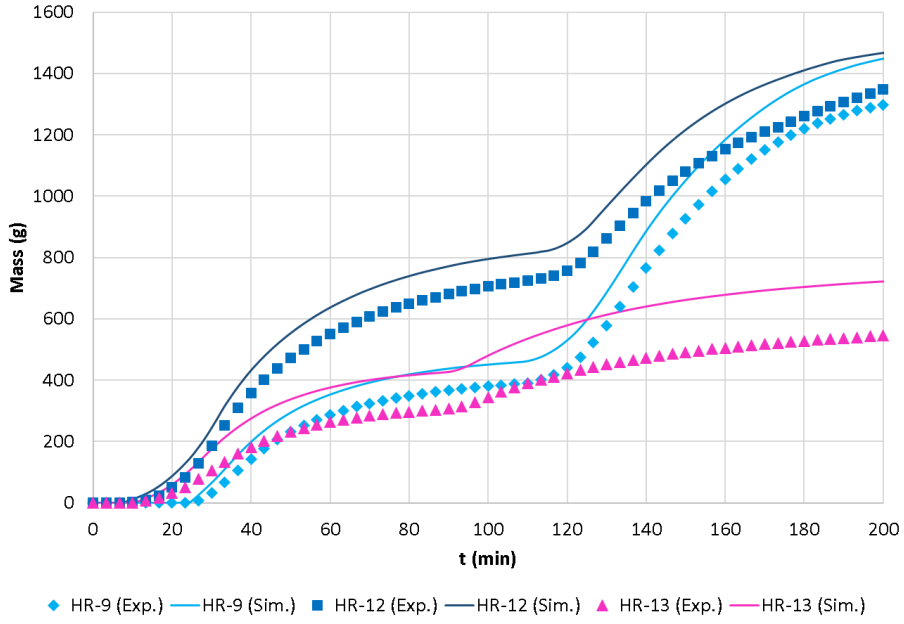

6. FZJ´s THAI 3D model

- Fully block-structured hexahedral mesh (375.000 cells, no symmetries).
- Grid refined close to the walls, injection zone and in the vicinity of the PAR.
- Gas ring-liked injection modeled in actual location (adiabatic inlet boundary patch, area equivalent of total nozzles).
- Atmospheric conditions initialized by averaged measured concentrations.

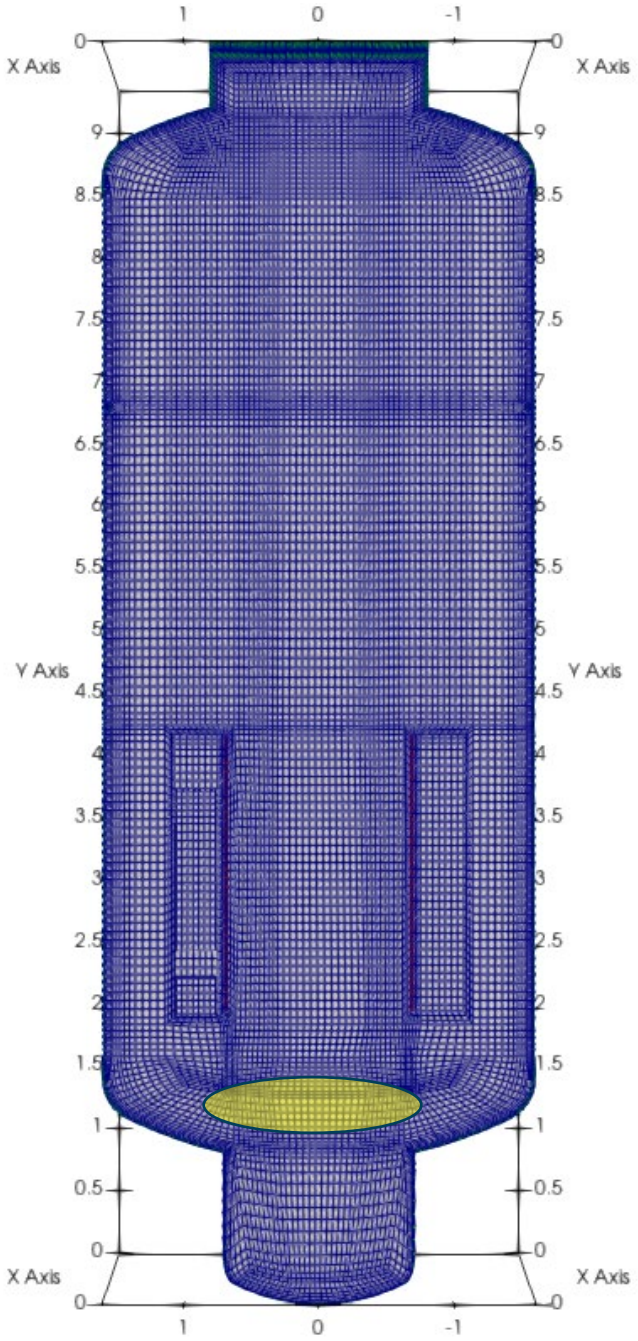

6. Results: 3D THAI model (HR-12)

		IRM Phase II [g]	Rel. Err. Phase II [%]	IRM Phase IV [g]	Rel. Err. Phase IV [%]
HR-12	Test-case	810	12.20	1516	8.90
	3D	808.70	11.60	1366	1.44

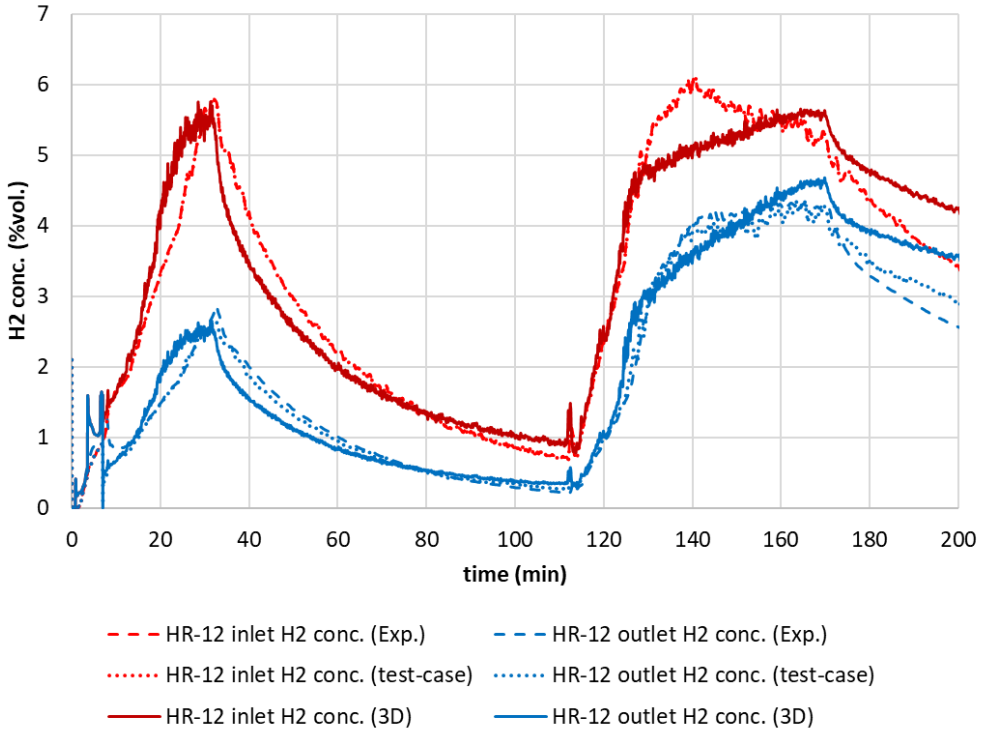

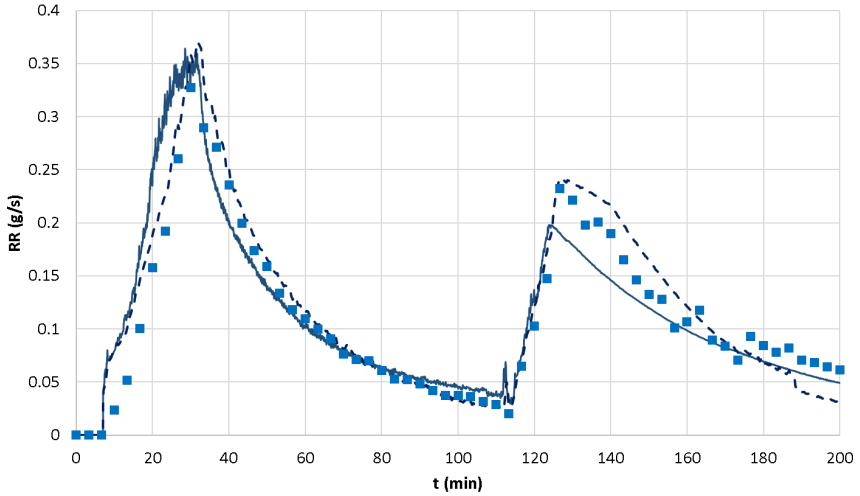

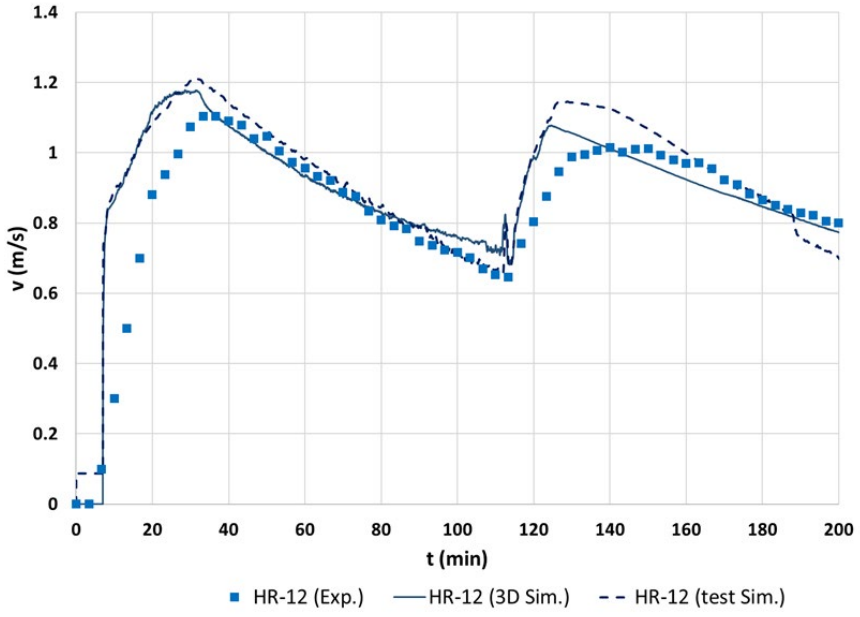

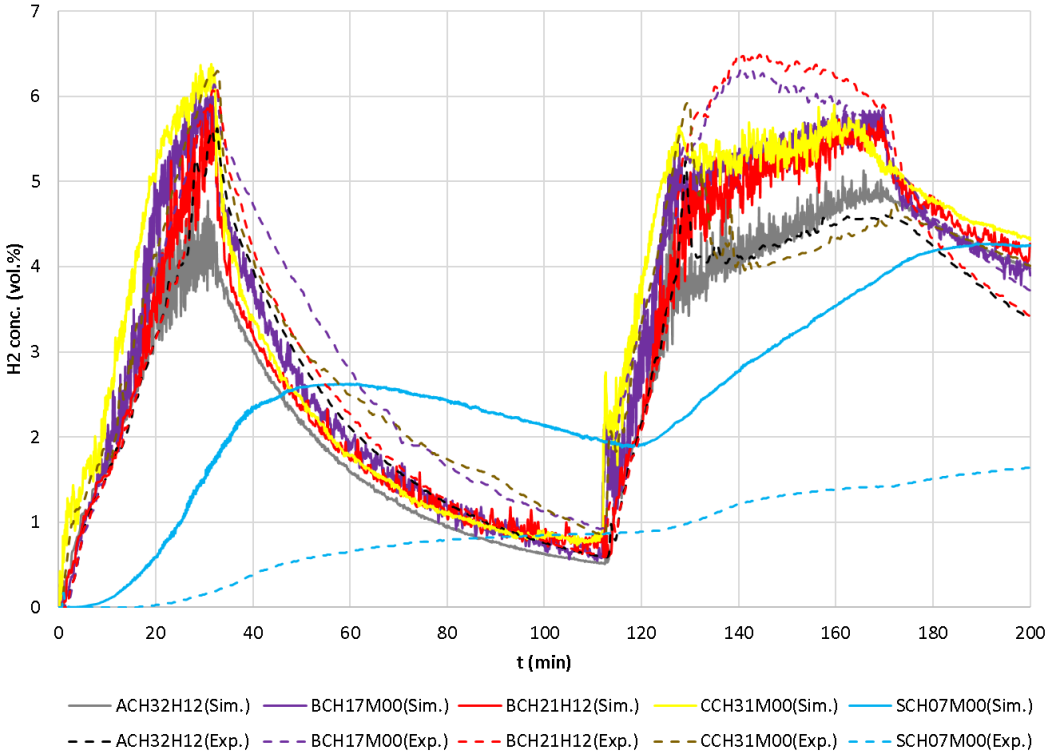

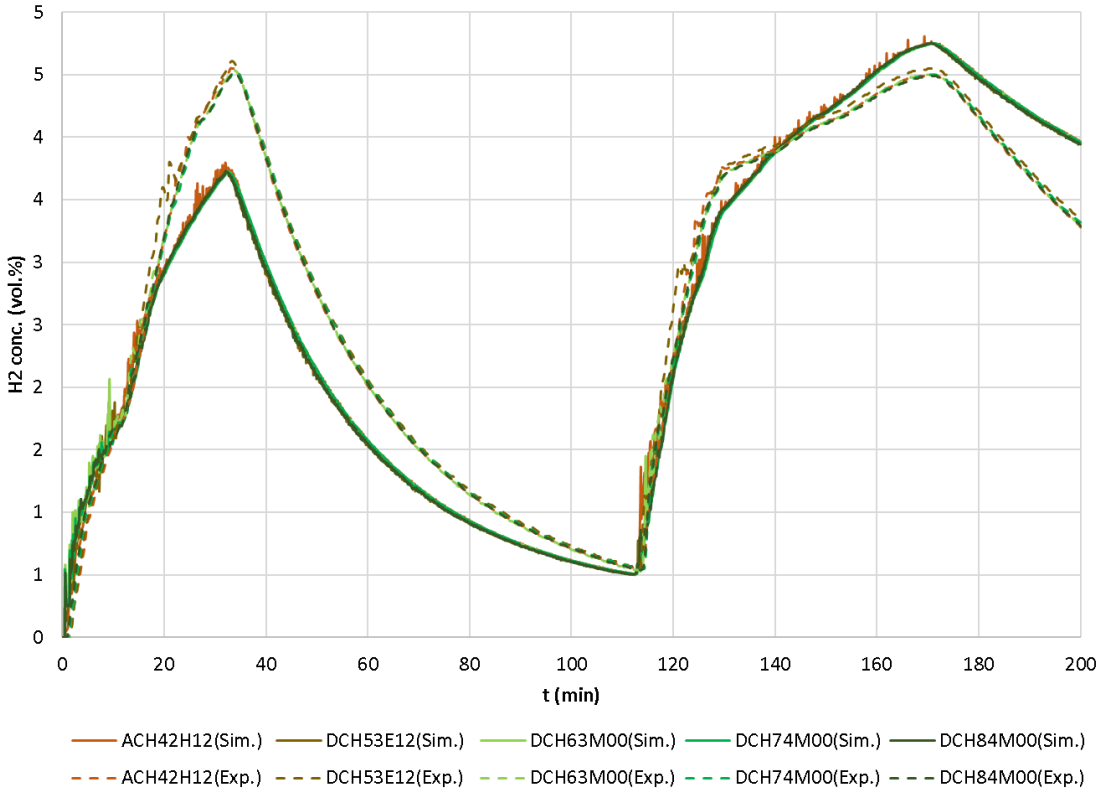

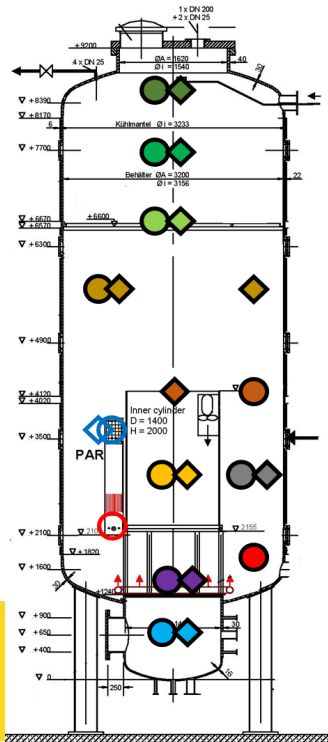

6. Results: 3D THAI model (HR-12)

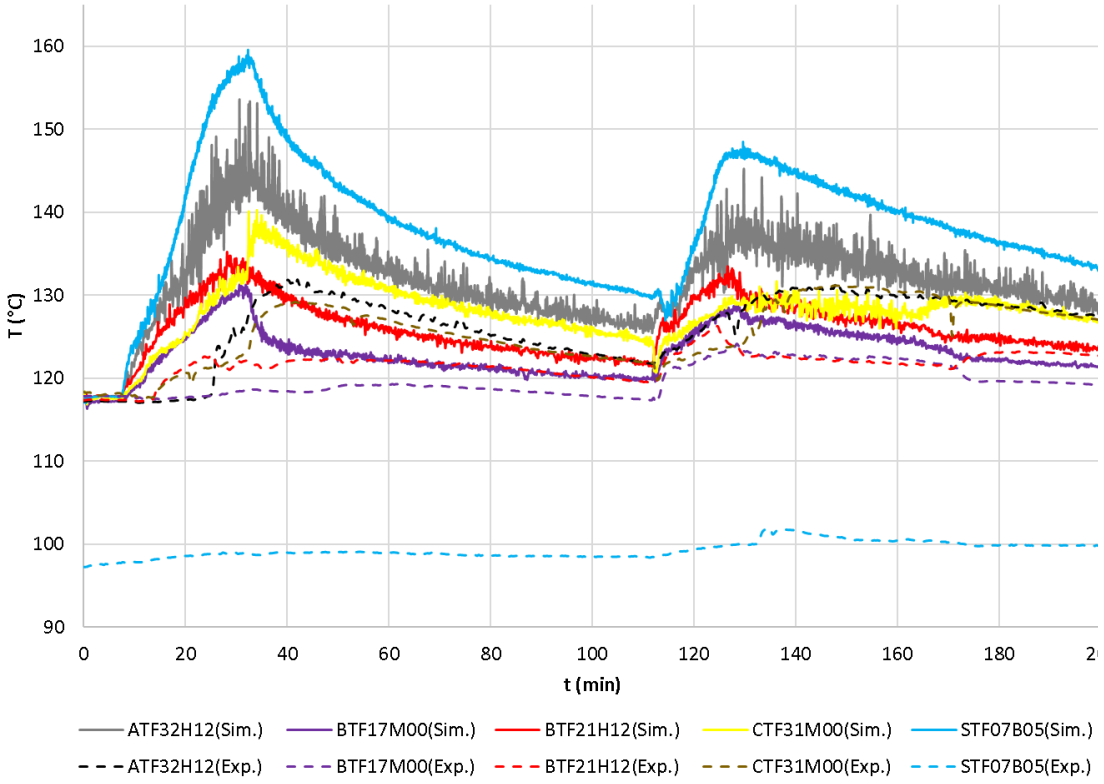

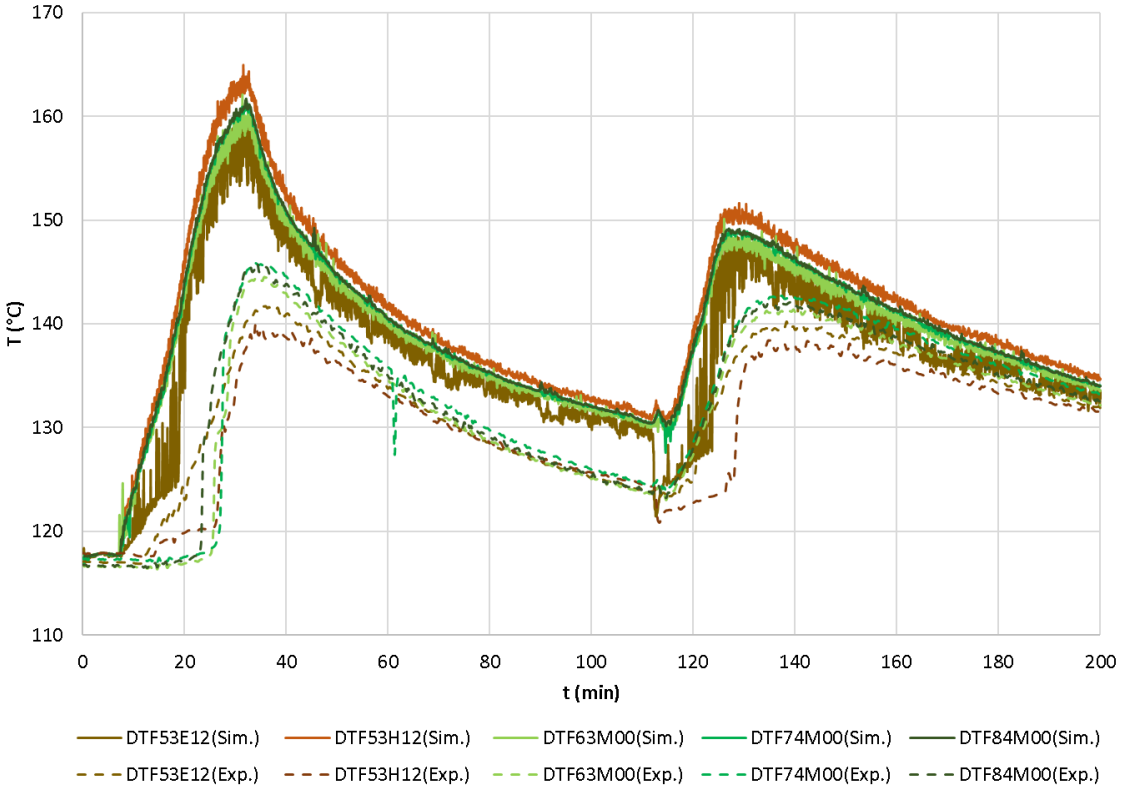

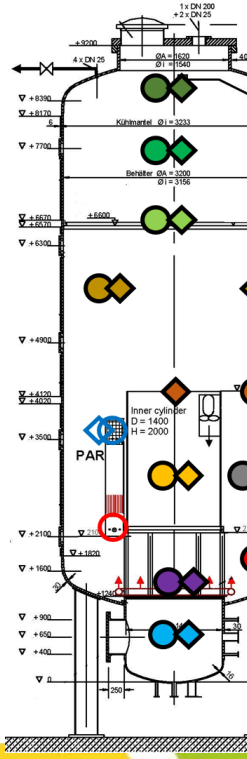

6. Results: 3D THAI model (HR-12)

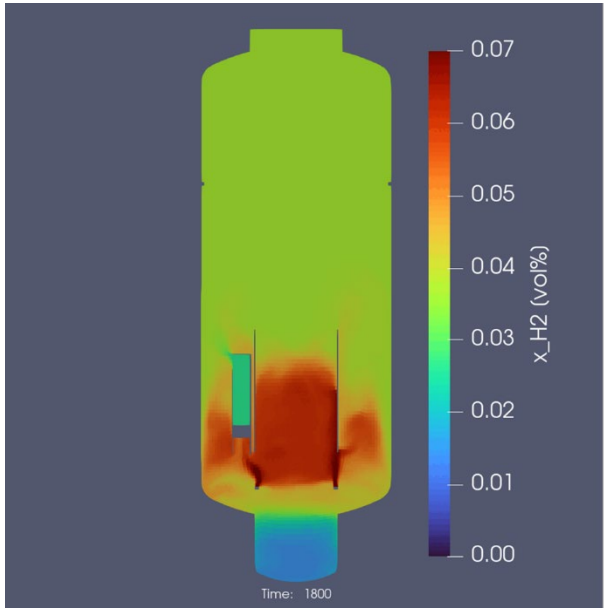

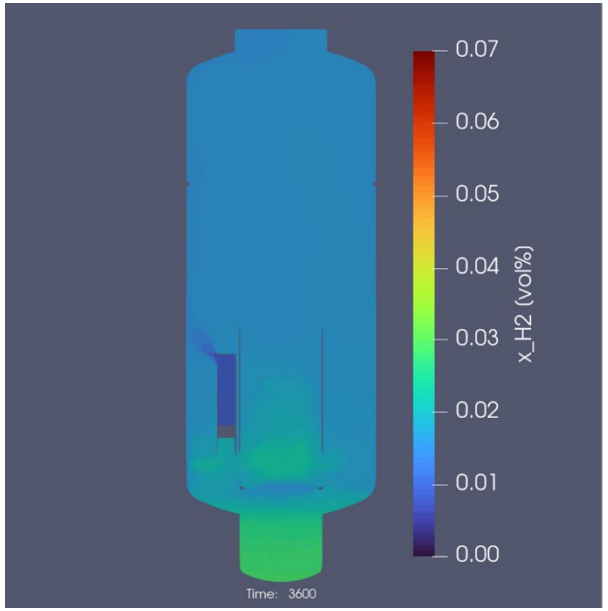

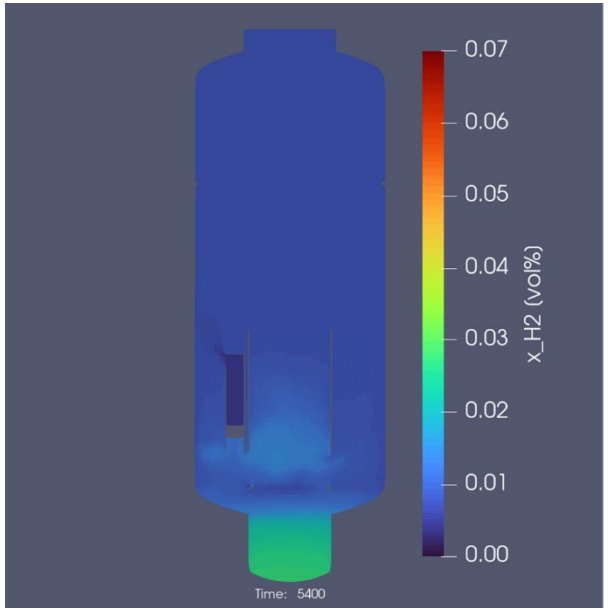

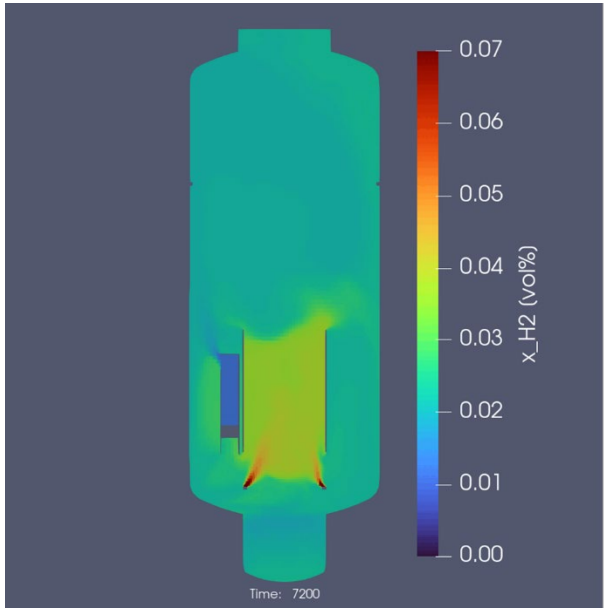

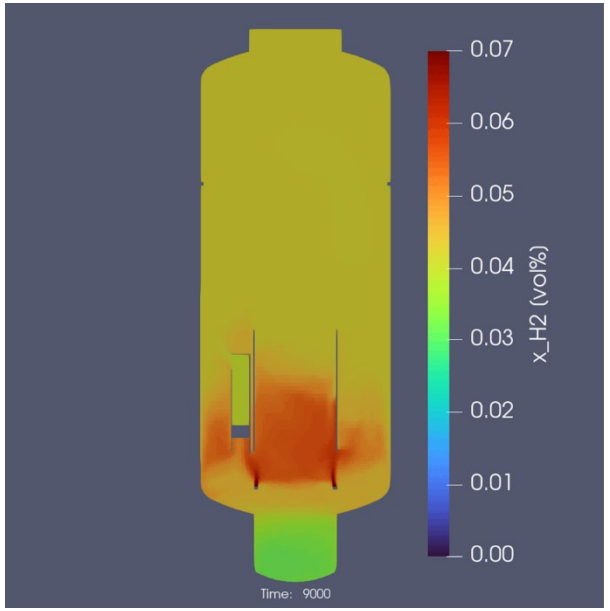

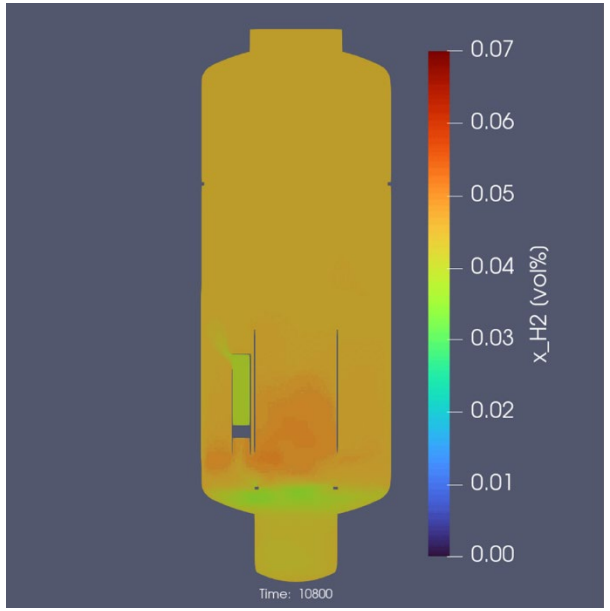

6. Results: 3D THAI model (HR-12)

H_2 concentration

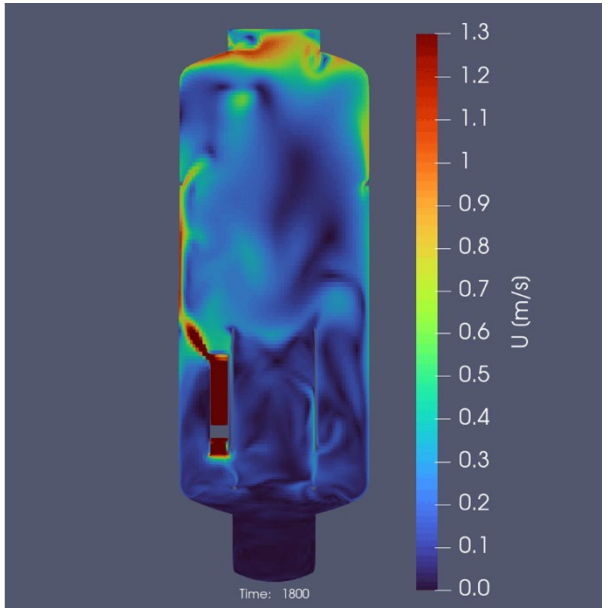

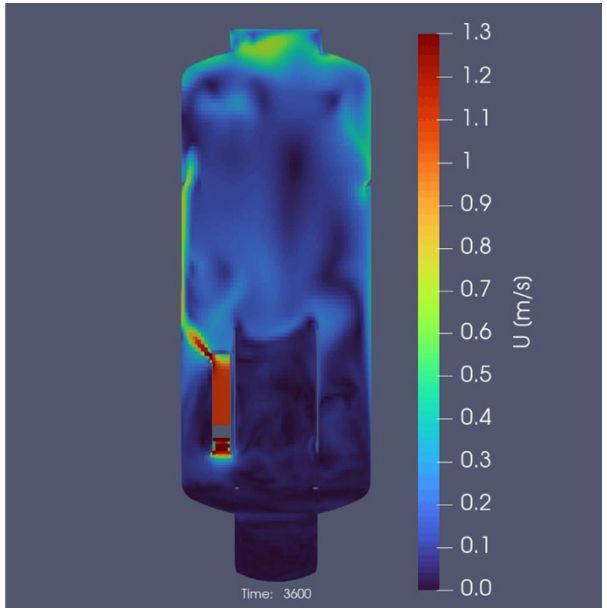

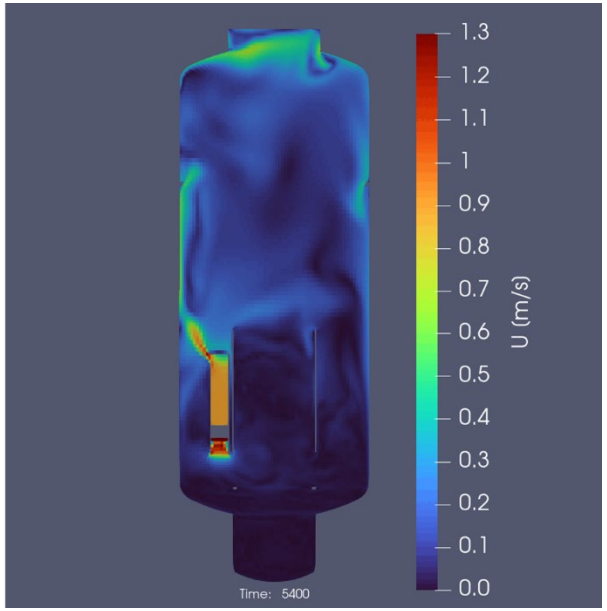

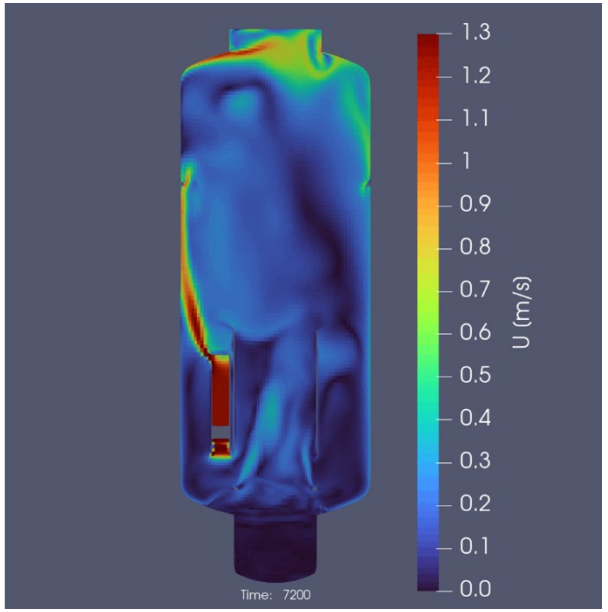

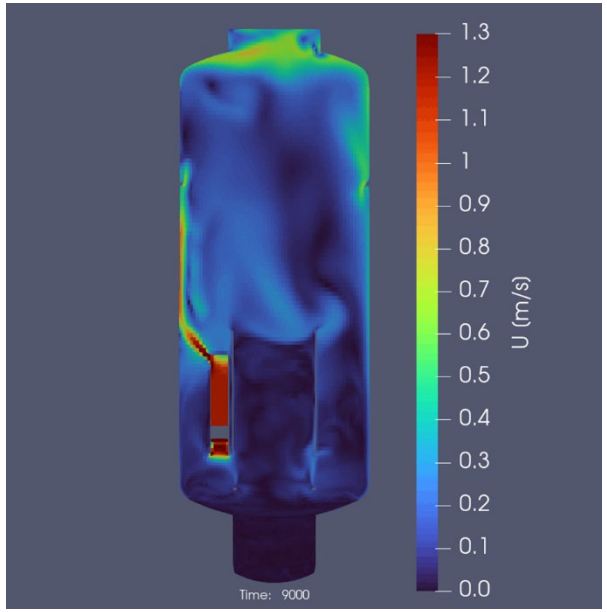

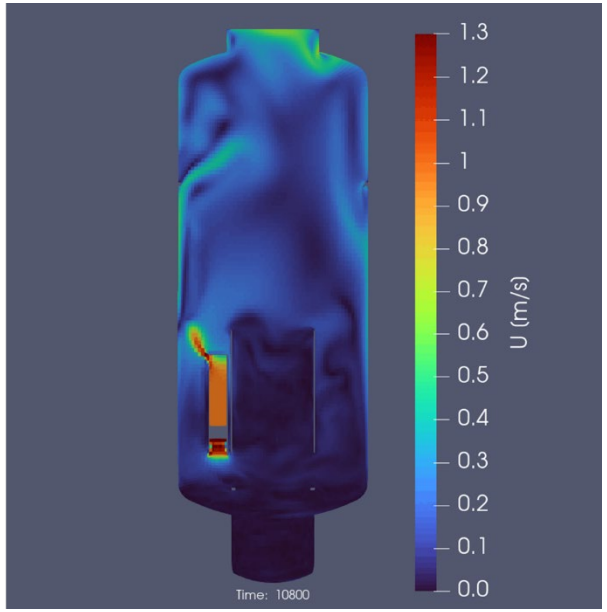

6. Results: 3D THAI model (HR-12)

Fluid velocity

6. Conclusions

Contribution to validation strategy with THAI-HR series

REKO-DIREKT <-> containmentFOAM coupling is stable

It is important to accurately capture PAR inlet fluid velocity

Checking chimney and heat transfer modules at REKO-DIREKT

6. Future lines of work

- Wider V&V simulation campaign in THAI 3D model after modifications to REKO-DIREKT (and prior testing).
- THAI-HR tests with CO
- Detailed simulation of THAI vessel wall.
- PARUPM-containmentFOAM coupling.

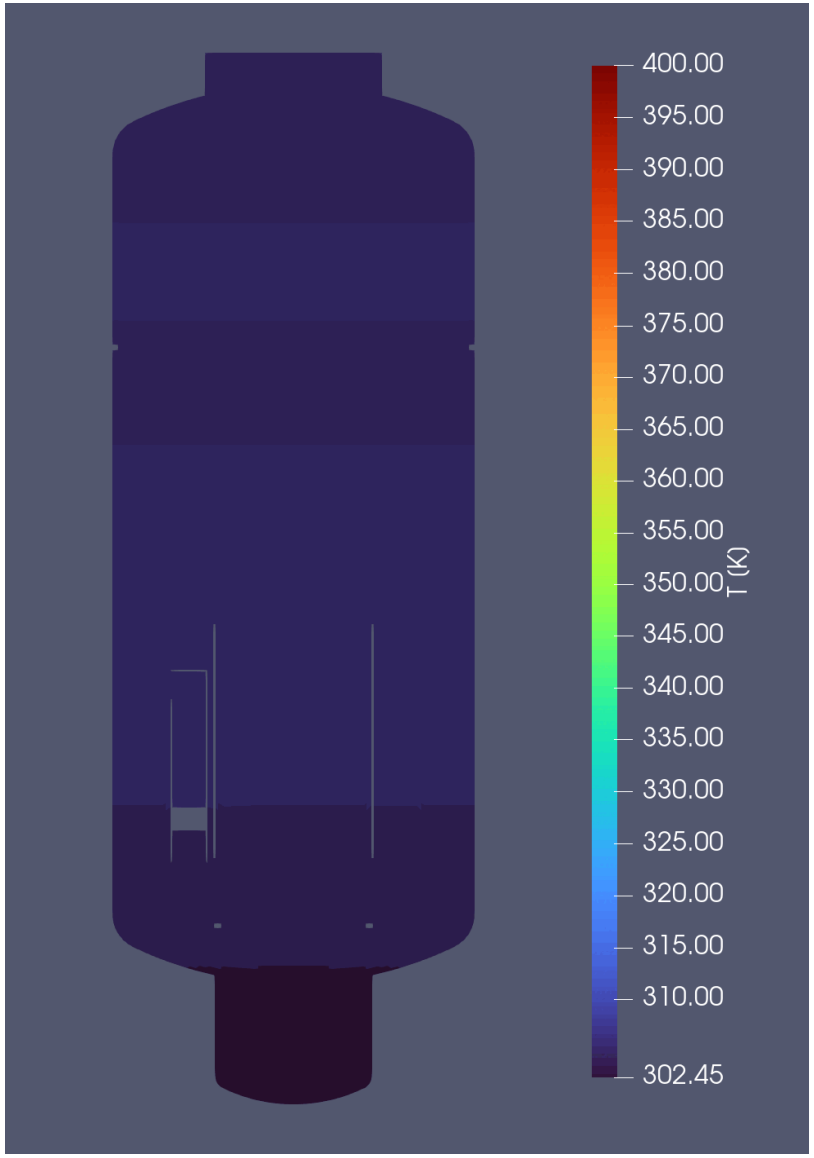

Acknowledgements

INDUSTRIALES
ETSII | UPM

JÜLICH
Forschungszentrum

BECKER
TECHNOLOGIES

AMHYCO
Enhancing H_2 & CO Combustion Risk Management

CSN
CONSEJO DE
SEGURIDAD NUCLEAR

Thank you

Connect with us for more information:

luis.slopez@upm.es

https://amhyco.eu/



4. THAI-HR series: PAR characteristics

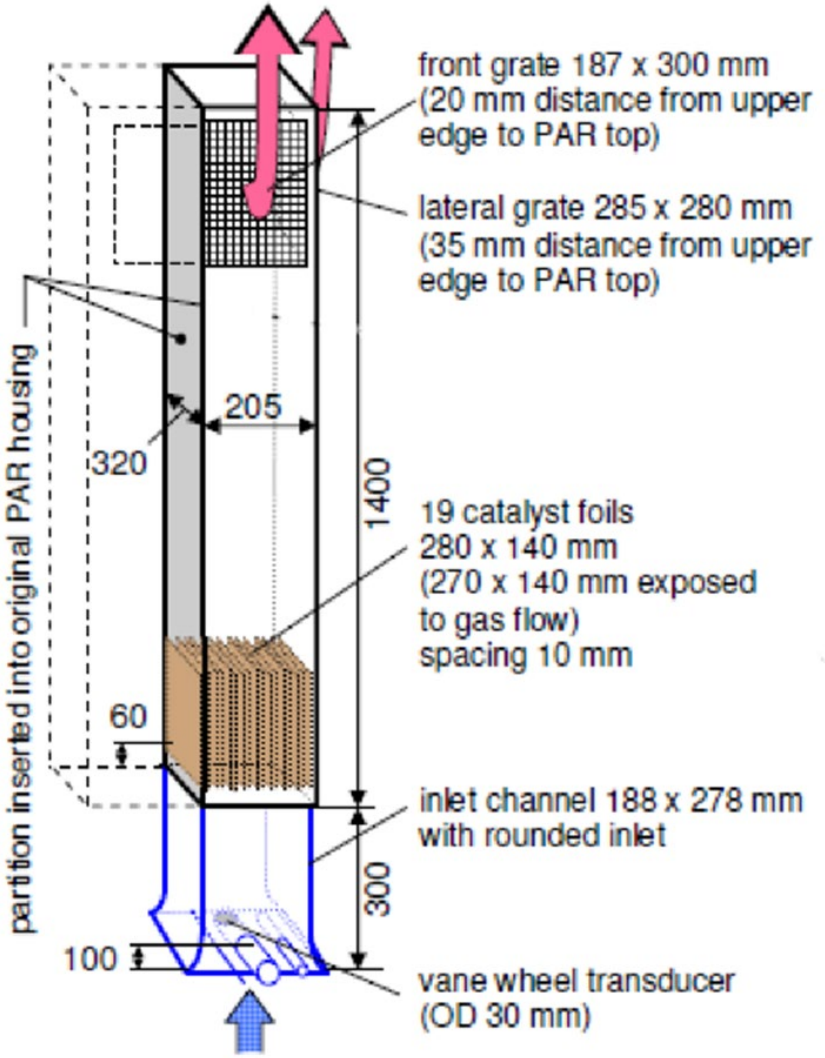

PAR characteristic	
Inlet opening area	0.0523 m2
Outlet opening area	0.1359 m2
PAR chimney height	1.4 m
PAR box metallic mass	60 kg
Number of catalytic sheets	19

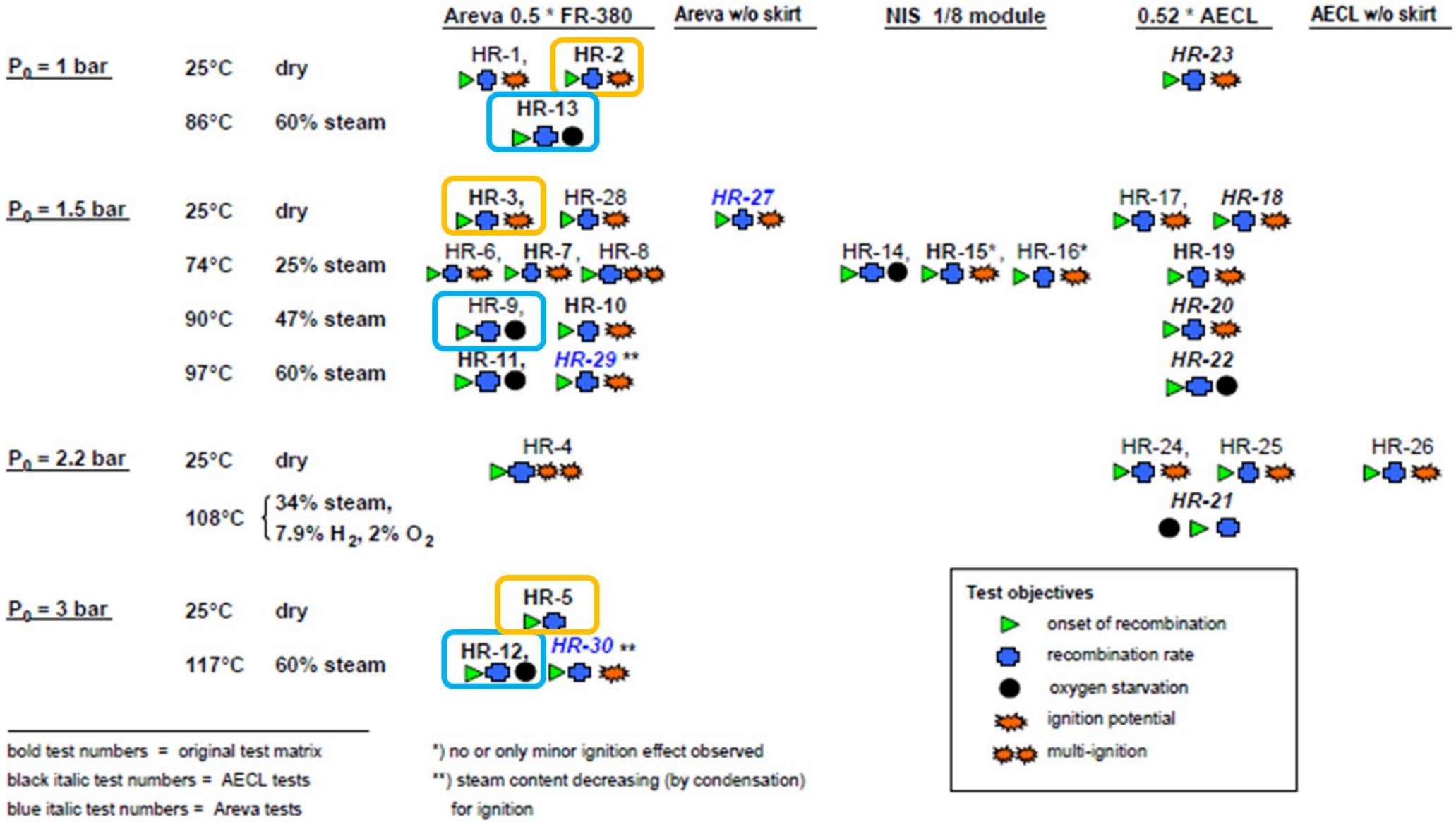
Areva 0.5 * FR-380
Areva w/o skirt
NIS 1/8 module
0.52 * AECL
AECL w/o skirt
P0 = 1 bar
25°C dry
HR-1, HR-2
86°C 60% steam
HR-13
HR-23
P0 = 1.5 bar
25°C dry
HR-3, HR-28
HR-27
HR-17, HR-18
74°C 25% steam
HR-6, HR-7, HR-8
HR-14, HR-15*, HR-16*
HR-19
90°C 47% steam
HR-9, HR-10
HR-20
97°C 60% steam
HR-11, HR-29 **
HR-22
P0 = 2.2 bar
25°C dry
HR-4
HR-24, HR-25
HR-26
108°C 34% steam, 7.9% H2, 2% O2
HR-21
P0 = 3 bar
25°C dry
HR-5
117°C 60% steam
HR-12, HR-30 **
Test objectives
onset of recombination
recombination rate
oxygen starvation
ignition potential
multi-ignition
bold test numbers = original test matrix
black italic test numbers = AECL tests
blue italic test numbers = Areva tests
*) no or only minor ignition effect observed
**) steam content decreasing (by condensation) for ignition

6. Results
Coupling verification

- Undertaken by checking the mass balance between REKO-DIREKT output and containmentFOAM outlet boundary cells.

- The confirmation of the coupling is made by looking at the loss/production of gases in the interface between codes, along with the H_2, O_2, and H_2O conversion rates.

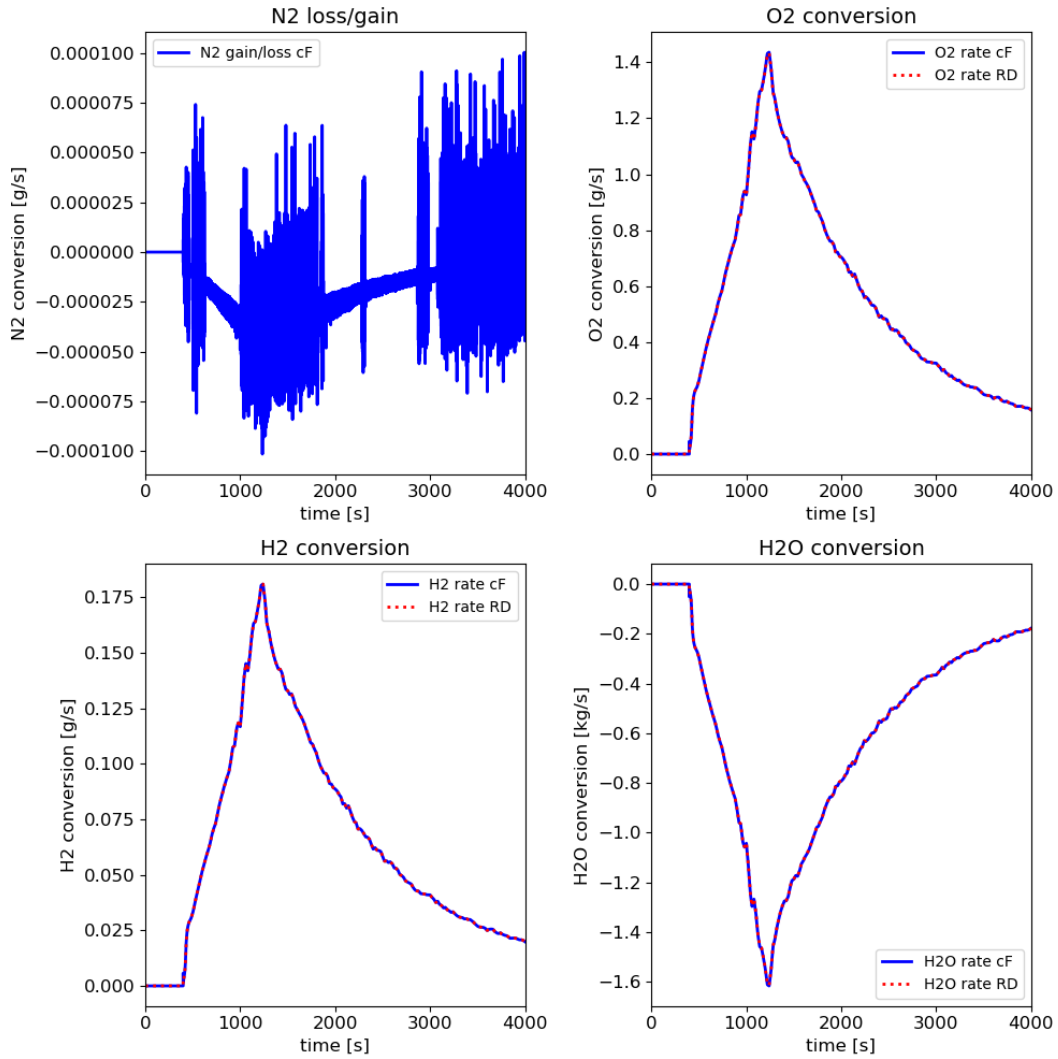

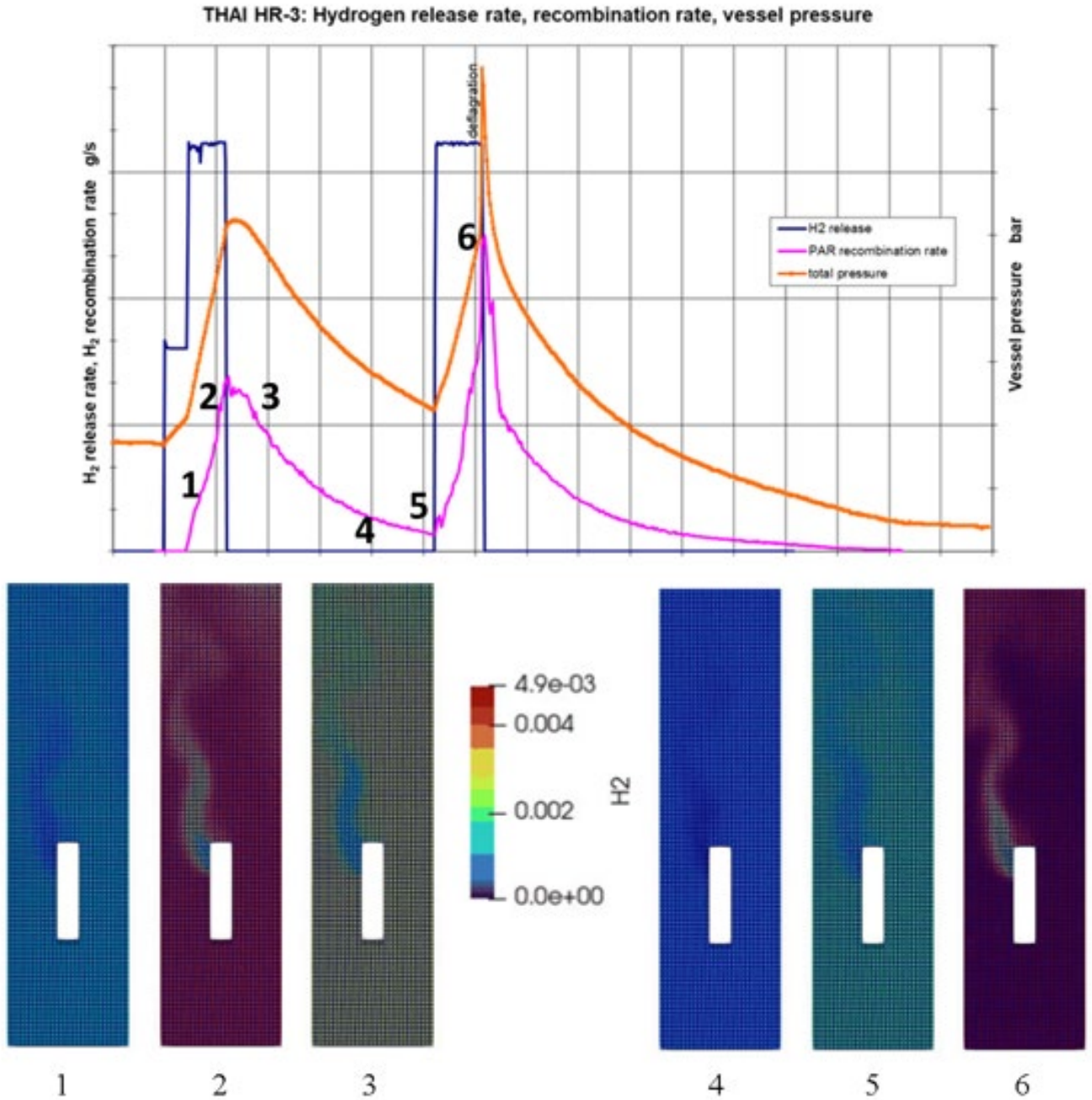
THAI HR-3: Hydrogen release rate, recombination rate, vessel pressure
H2 release rate, H2 recombination rate g/s
Vessel pressure bar
deflagration
H2 release
PAR recombination rate
total pressure
1
2
3
4
5
6
4.9e-03
0.004
0.002
0.0e+00
H2

6. Results: Test-case validation

Catalyst plate max. T [°C]

- On a first approach, it is evident that the heat transference from the plates to the gas is underestimated when the recombiner starts to cool down. This may be due to the way in which REKO-DIREKT transfers heat to the steam, which increases its concentration after the recombination peaks.

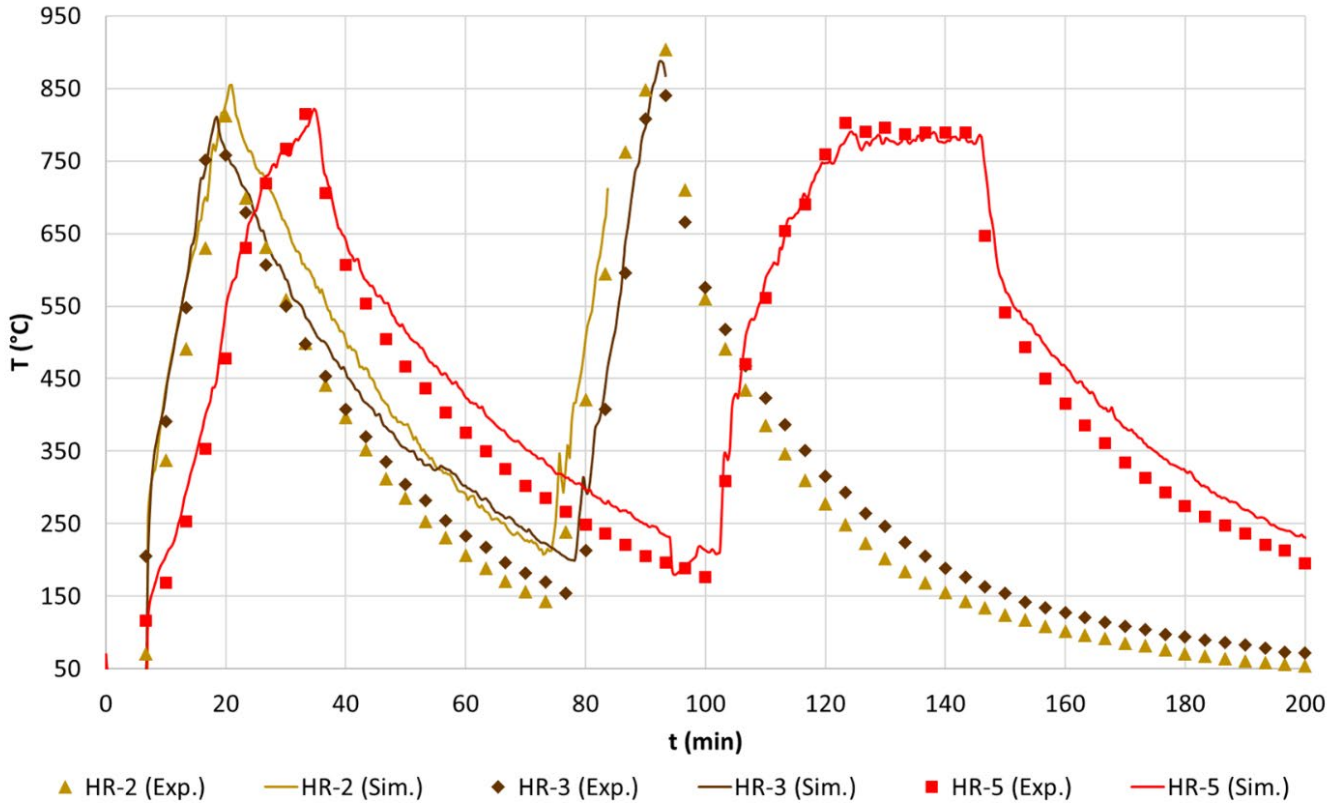

Test	P [bar]	T [°C]	%vol H_2	%vol O_2	%vol H_2O	Ignition	O_2 starv.
HR-2	1.00	27.90	0.00	21.00	0.00	yes	no
HR-3	1.48	29.90	0.02	21.71	0.00	yes	no
HR-5	2.93	32.00	0.04	21.69	0.00	no	no

6. Results: Test-case validation

Catalyst plate max. T [°C]

- Nevertheless, HR-9 shows a counter-intuitive behavior at Phases III and IV, as catalytic temperature is underestimated in the second injection to be overestimated afterwards.

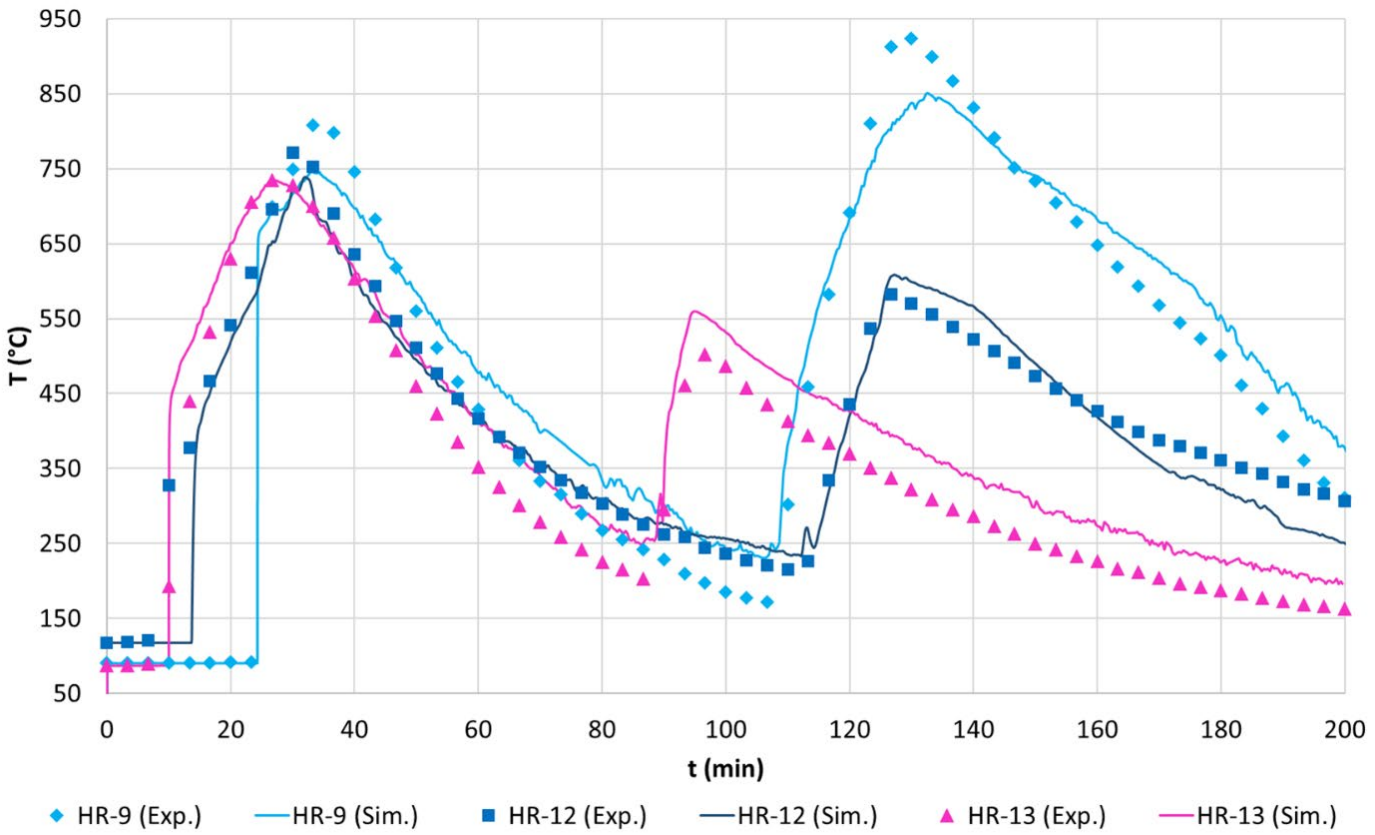

Test	P [bar]	T [°C]	%vol H_2	%vol O_2	%vol H_2O	Ignition	O_2 starv.
HR-13	1.00	86.50	0.00	8.16	61.05	no	strong
HR-9	1.44	89.7	2.19	11.30	48.15	no	mild
HR-12	2.92	115.0	0.00	7.35	61.12	no	strong

6. Results: 3D THAI model (HR-5 & HR-12)

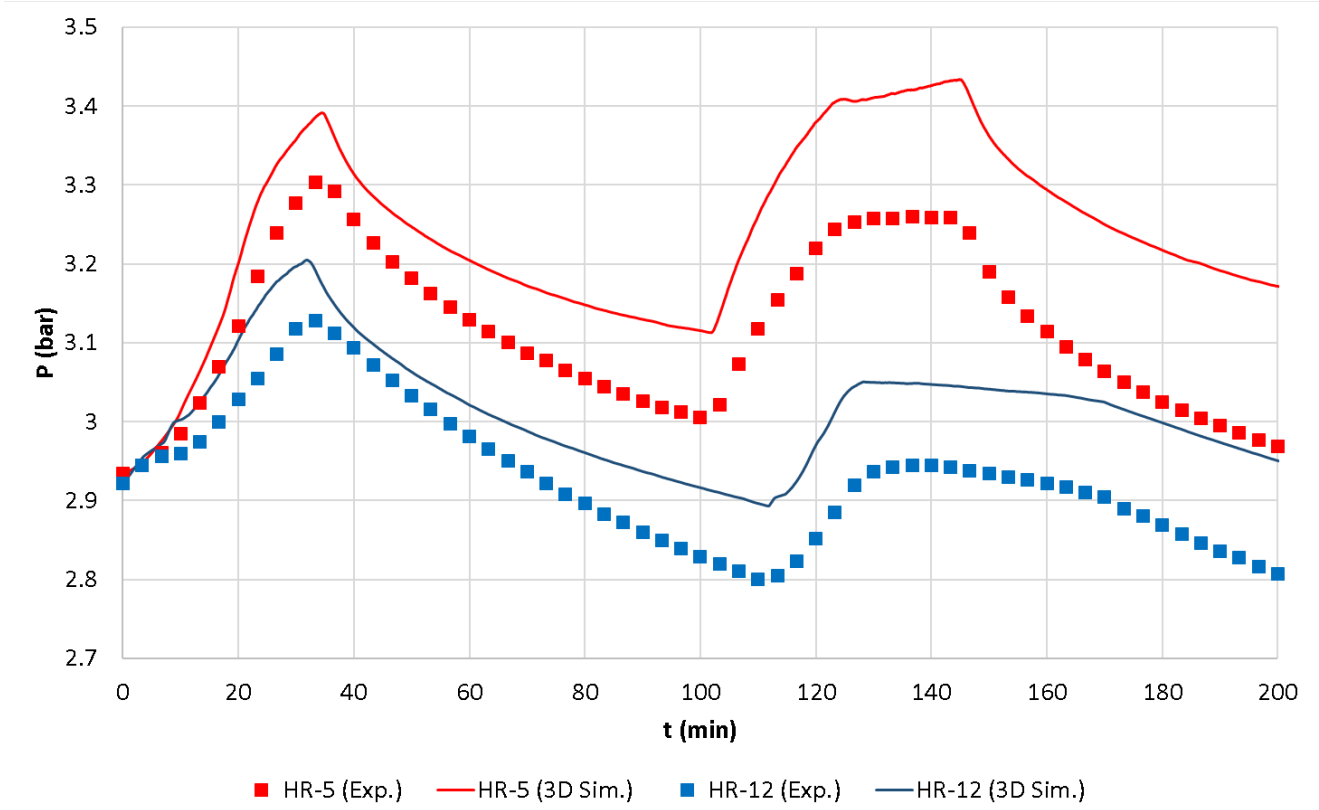

THAI EXPERIMENT ON THE IODINE ABSORPTION CAPACITY OF PRE-STRESSED PAINT COATINGS ON DIFFERENT SURFACES

K. Dieter, M. Freitag, B. von Laufenberg, and E. Schmidt
Becker Technologies GmbH
Rahmannstraße 11, 65760 Eschborn, Germany
dieter@becker-technologies.com; freitag@becker-technologies.com; von.laufenberg@becker-technologies.com; eike.schmidt@becker-technologies.com

G. Langrock and F. Funke
Framatome GmbH
Paul-Gossen-Straße 100, 91052 Erlangen, Germany
gert.langrock@framatome.com; friedhelm.funke@framatome.com

ABSTRACT

In the aftermath of severe nuclear accidents, the presence of fission products, particularly iodine, within the containment as gases or aerosols poses significant challenges to radiological safety. This has a strong influence on the radiological source term, including the dose rate distribution, corresponding decay heat, and formation of volatile compounds. This study investigates the impact of pre-stressed decontamination coatings on the efficiency of iodine depletion from the gas phase under extreme conditions. The experiment was conducted at the THAI facility in a closed and superheated containment configuration. Twenty stainless steel panels coated with GEHOPON epoxy-based decontamination paint were placed inside the THAI test vessel. Two cylindrical steel coupons were used for on-line monitoring of the iodine deposition process. One coupon was painted with Ripolin epoxy paint, while the other was unpainted. Additionally, a concrete block painted with GEHOPON was used.

The experiment involved short-term, high thermal loads on the paint surfaces, which were introduced by a hydrogen deflagration. Various measurement techniques were used to continuously monitor aerosol and iodine concentrations, including gas scrubbers, Maypacks, bulk filters, impactor measurements, and optical systems such as the light absorption system for iodine (LASI-SPEC) and laser extinction.

The hydrogen deflagration caused mechanical and thermal damage to the paint surfaces, resulting in the release of volatile organic compounds and aerosols. Airborne concentrations were closely monitored for 76 hours to measure the deposition behavior, including 25 hours of radiolabeled molecular iodine (I-123) deposition on painted surfaces and inner walls of the THAI test vessel. Surprisingly, the formation of aerosol-bound iodine was found to be significantly stronger than anticipated.

The results contribute to a deeper understanding of thermal-hydraulic conditions, damaged paint behavior, and airborne fission product concentrations in the late phase of an accident. These findings have implications for the fundamental understanding of severe accident scenarios, as the experimental data provide valuable insights for the development and validation of detailed reaction models in severe accident codes. The study underscores the importance of considering pre-stressed decontamination coatings in enhancing safety measures and mitigating the impact of fission products in the aftermath of severe nuclear accidents.

KEYWORDS
Severe Accident, Containment, Iodine, THAI, Decontamination Paint

1. INTRODUCTION

Severe nuclear accidents can result in the formation of iodine, which may be present in the containment as gas, as aerosol, in various water phases, or deposited on surfaces. To determine the iodine source term within the containment atmosphere, it is crucial to understand the transport behavior of such fission products for both safety measures and the validation of simulation codes. The interaction of iodine with decontamination paints applied to surfaces within the containment is of particular concern. This interaction could lead to iodine fixation on the organic substrate or partial conversion into organic iodides. The latter has the potential to increase the volatile iodine content in the containment atmosphere.

Extensive research has been conducted on the interaction between iodine and paint, including laboratory and large-scale experiments conducted under varying parameters such as temperature, humidity, irradiation, and different paint types [1–7]. Other research programs have also addressed questions related to the adsorption, chemisorption, and desorption of iodine species on containment surfaces, as well as the formation of organic iodides [8–10].

Despite these advancements, there are still open questions, particularly regarding the impact of short-term, high thermal stresses on paint surfaces. This includes stresses induced by a potential hydrogen deflagration. In the test ‘THAI Iod-34’, the paint surfaces experienced a hydrogen deflagration after being pre-loaded with iodine. As a result, the paint surfaces were visibly degraded, leading to an unexpected release of iodine-loaded aerosols and organic iodides into the containment atmosphere [11]. However, it was not possible to fully evaluate the performance of the degraded coatings in terms of adsorption and chemisorption of iodine species.

This paper reports on the objectives and outcomes of an experiment aimed at investigating the effect of pre-stressed decontamination coatings on iodine depletion efficiency. The coatings were applied to two different surfaces: stainless steel coupons with high thermal conductivity and concrete with lower thermal conductivity. Subsequently, the samples underwent a hydrogen deflagration before iodine injection into the THAI test vessel (TTV) [4,12]. The data evaluation aims to test the hypothesis that the applied stress varies depending on the surface type. This analysis provides valuable insights into the effectiveness of decontamination coatings in near-realistic accident scenarios. The results improve the understanding of the mechanisms of thermal heat release, the effects of coating degradation, and the behavior of volatile organic compounds during the later stages of severe nuclear accidents.

2. EXPERIMENTAL SETUP

2.1. Test Configuration

The experiment was conducted in the THAI (Thermal-hydraulics, Hydrogen, Aerosols and Iodine) containment test facility at technical sale. The TTV is a 60 m³ stainless steel vessel that is 9.2 m high and 3.2 m in diameter, designed to withstand a maximum overpressure of 1.4 MPa at 180 °C and can endure moderate hydrogen deflagrations. The facility is operated by Becker Technologies GmbH in Eschborn, Germany, in close cooperation with Gesellschaft für Anlagen- und Reaktorsicherheit (GRS) gGmbH (Cologne, Germany; Garching, Germany) and Framatome GmbH (Erlangen, Germany).

The facility is equipped with the necessary supply systems for steam, compressed air, nitrogen, oxygen, light gases (helium and hydrogen), aerosols, and gaseous iodine. The latter is radiolabeled with the isotope I-123 (half-life of about 13.5 hours). The vessel walls can be heated or cooled in sections to set the desired thermal hydraulic conditions, including both well-mixed and stratified gas atmospheres. The vessel walls are made of stainless steel (1.4571 = X6CrNiMoTi 17-12-2 ≈ AISI/SAE 316Ti) and are entirely enveloped by 120 mm of mineral wool for thermal insulation. The cylindrical vessel wall (inner diameter =

3156 mm) has four 150 mm nominal diameter block flanges and one 200 mm nominal diameter block flange integrated at five designated levels (H = 2.1 m, 3.5 m, 4.9 m, 6.3 m, and 7.7 m).

The experimental setup involved applying GEHOPON E24 primer and GEHOPON EW-10 surface finish to a total painted surface area of 10.65 m². The epoxy-type paint used was representative of German containments and met THAI standards. The painted area was distributed across 25 symmetrically arranged coupons within the TTV, which included 20 square stainless-steel sheets (1.5 mm thick, 500 mm edge length), as shown in Figure 1. Prior to the experiment, the surfaces coated with GEHOPON underwent artificial pre-aging by subjecting them to a 21.1-hour thermal treatment at 160 °C in an air atmosphere, following THAI standard procedures.

Two cylindrical steel coupons (30 mm thick, 360 mm diameter), one coated with Ripolin (PC63D-RI) and the other unpainted (pure stainless steel, SC63F), were positioned at a height of 6.3 m inside the TTV for online monitoring of iodine deposition. Additionally, a concrete coupon for online monitoring painted with GEHOPON (PC21D-GE) was installed at a height of 2.1 m. The concrete coupon had dimensions of 300 x 300 mm (height x width) with a thickness of 130 mm.

To initiate a hydrogen deflagration within the TTV, a remote arc igniter was placed in the sump compartment at a height of H = 0.5 m. The ignition process was initiated through a 1-second arc sequence using a VIESSMANN ignition unit DCZ 2/24. This ignition system initiates a controlled hydrogen deflagration to examine the effect of pre-stressed decontamination coatings on iodine depletion efficiency in the late phase of a severe accident scenario.

Gaseous and radiolabeled iodine was injected into the TTV at a level of 8.4 m. A flow of pre-heated nitrogen acted as carrier gas for the iodine, causing the gas mixture to impinge on a baffle plate in the center of the vessel.

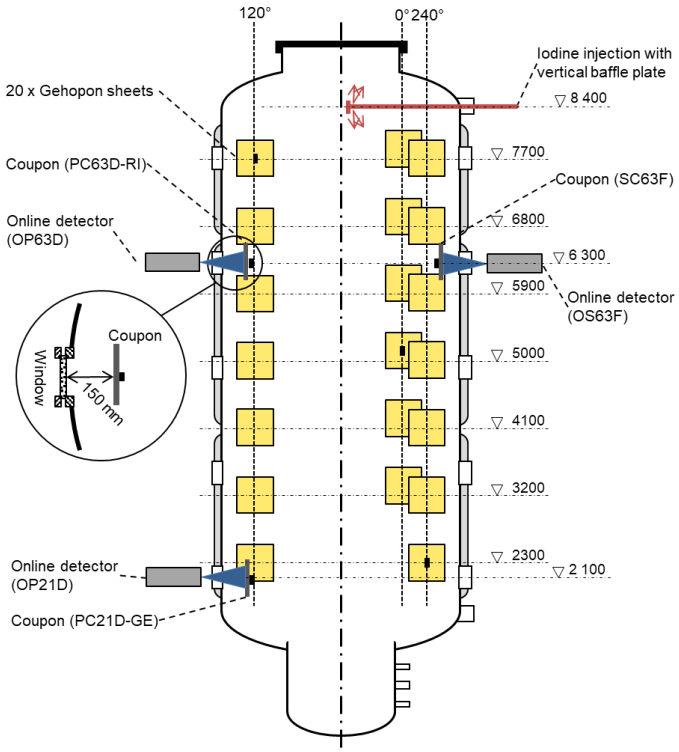

Figure 1: Scheme of the painted coupon placement and iodine injection within the TTV.

2.2. Instrumentation

The experimental setup included a wide range of measurement systems to ensure precise and synchronized data collection for evaluating iodine concentrations and associated thermal hydraulic parameters within the TTV at a high spatial and temporal resolution.

Six gas scrubbers (GS) were placed inside the TTV vessel to measure the concentration of I-123. An aqueous solution containing 0.4 wt.-% sodium hydroxide and 0.5 wt.-% sodium thiosulfate was used as an absorber liquid to effectively dissolve gaseous I_2 while maintaining a pH of 13. The GS also traps other forms of iodine in the gas phase, such as organic iodine or iodine in aerosol form. Unlike I_2, the absorption of organic iodide in the gas scrubber may be somewhat reduced quantitatively, which is a relevant aspect in tests with significant inventories of organic iodide.

Two Maypack filter stations were used for gas-phase iodine concentration measurements. Each Maypack consists of 5 cartridges to discriminate iodine in aerosol form, molecular iodine I_2 and volatile organic iodine. To prevent condensation and maintain optimal adsorption on the filters during sampling (typically 10 min at flow rates of 2 L/min), preheating procedures were employed to achieve overheating relative to the TTV.

An impactor station was positioned at a vessel height of H=3.5 m to measure the size distribution of aerosol particles by separating them into ten size classes. The mass of each particle size class collected during the sampling period was determined through gravimetric analysis (SARTORIUS CUBIS II MCE225P-"S00-A, resolution 0.01 mg). In an alternating order, aerosol mass concentrations were measured from inside the TTV using single bulk filter stations (47 mm borosilicate glass microfibers) at heights of H=3.5 m and H=7.7 m. The aerosol mass concentration was determined using gravimetric analysis. To ensure accurate measurements, preheating at 200°C, vacuum pump operation, and active heating (impactor only) measures were implemented. Vacuum pump protection measures, including an activated carbon filter and a condensate trap, were employed.

The specifically developed LASI-SPEC system (Light Absorption System for I_2 using spectroscopy) uses wide spectral light absorption spectroscopy to continuously measure the gas-borne iodine signal. The system consists of a White cell arrangement [13] and a spectrometer system (Tec5 SC-MCS UV-NIR 1M SB), with a data evaluation method based on the Beer-Lambert law. The online and non-intrusive measurement of the integral airborne iodine gas concentration at a reference wavelength of 530 nm was enabled by a spectral resolution of 3 nm with an accuracy of 0.3 nm. Furthermore, continuous aerosol concentration measurements were conducted using a photometer based on a line-of-sight laser light extinction method.

Three lead-shielded NaI scintillation detectors monitored the I-123 radiation inside the TTV. Placed at various heights and azimuthal angles, these detectors provided quasi-continuous measurements of the iodine activity on the deposition coupons (SC63F, PC63D-RI, PC21D-GE), see Figure 1.

Temperature, pressure, and humidity were measured at different locations inside the TTV. To measure the temperature, calibrated 1.5 mm thermocouples (type K, T_{63} = 130 ms) were placed throughout the vessel. The thermocouples were placed in the fluid and on the inner vessel walls, as well as at critical locations such as gas scrubbers, air and steam injections, sensor locations, and deposition coupons. This provided a comprehensive understanding of thermodynamics during the experiment. Thirteen thermocouples with an outer diameter of 0.5 mm were installed at different heights within the TTV to detect the flame propagation and temperature during the hydrogen combustion with a faster response time of T_{63} = 25 ms. The pressure was measured using piezoresistive pressure transducers (Keller PA-214/10 bar 81554.33),

which were cross-verified with a high-precision pressure gauge (accuracy ±10 mbar). Humidity sensors (Testo 6610 with control unit 6681) measured the relative humidity at two positions within the TTV.

In addition to the core measurement systems, several supplementary systems were used to enhance the overall understanding of the experiment. Three heat flux sensors (1x Thorlabs TD10XP and 2x Hukseflux GG01 sensors) were used to measure the convective and radiative parts of the heat flux during the hydrogen deflagration phase. In addition, a 15-channel gas concentration measurement system (GCMS) was employed, using gas sampling lines that were installed inside the TTV and connected to a gas concentration analyzer. Calibration gas injections were performed to reduce the measurement uncertainty to approximately ±0.25 vol.-% prior to the experiment.

2.3. Test Procedure

The experiment was designed to investigate several aspects. These included a preconditioning phase, a controlled injection of hydrogen followed by an initiated deflagration, an aerosol measurement and settling phase, and the injection of I_2 with its deposition on pre-stressed paint and steel surfaces during the main experiment phase.

The parameters for the initial and target experiment conditions included pressure, temperature, steam concentration, hydrogen concentration, and iodine quantity. Prior to the deflagration, specific thermal-hydraulic conditions were set, such as a vessel temperature of 88.8 °C at a pressure of 1.455 bar, 22.1 – 21.6 vol.-% steam concentration, and a hydrogen concentration of 10 vol.-%. Following the H_2 deflagration, 1.009±0.005 g of iodine with an activity of 1.104×10^9 GBq was injected. During the preconditioning and main test phases, various measurements were conducted, such as GCMS and humidity measurements, heat flux measurements, and filter and impactor sampling.

3. RESULTS

3.1. Thermal hydraulics and aerosols

Two steam injections were performed to achieve the specified steam concentrations, one during preconditioning and another before iodine injection (see Chapter 2.3). The injection of hydrogen began at t = −3120 min and ended at t = −3084.67 min. A small amount of air was injected to increase the vessel pressure by approximately 0.1 bar shortly before the sampling operations of the Maypacks and the gas scrubbers. Figure 2 shows the absolute pressure, the steam pressure, and the steam volume fraction within the TTV. It is important to note that the time on the x-axis in the following plots refers to the time of the iodine injection (t = 0). The deflagration event at t = −3060 min caused a sharp pressure increase, peaking at 4.539 bar, followed by a decrease to about 1.216 bar. Pressure fluctuations occurred due to subsequent injections of air and steam prior to the injection of iodine. Figure 3 shows the temperature with high temporal resolution during the deflagration event at the three coupons used for the online iodine measurements. The maximum temperature value and its cooling behavior differ significantly among the three materials. At a height of H=6.3 m, the peak temperature difference between the painted steel coupon (Ripolin, 236 DTW63D14) and the blank steel coupon (355 DTW63F14) reaches approximately 300 K. Due to its thermal resistance, the painted concrete coupon (GEHOPON, 061 BTW21D14) at a height of H=2.1 m exhibits a peak temperature similar to that of the painted steel coupon, but with a slower cooling rate.

Based on the temporal temperature values from various thermocouples distributed horizontally within the TTV during the deflagration event, the flame contour was calculated with a gradient-based assessment of the flame arrival at each thermocouple, as shown in Figure 4 (left). The observed upward flame

propagation pattern aligns with the typical behavior for bottom ignition under the specified initial conditions, that was conducted in previous studies [11,14].

The relative heat flux during the deflagration at a height of H=7.7 m is depicted in Figure 4 (right), as measured by three sensors described in Chapter 2.2. Note that the time $t_d = 0$ in this plots ordinate ($Time_d$) corresponds to the ignition event and not to the time of the iodine injection into the TTV. The sensor that was not equipped with a window simultaneously measures the radiative as well as the convective part. Therefore, the relative heat flux peaks at around 58700 W/m². The radiative part of the total heat flux is a factor of 4.2 smaller and peaks at around 13800 W/m², as measured by the second sensor. The third sensor measured an even lower peak radiative heat flux of around 9100 W/m² due to a greater thickness of its window (Vitron CVD Zinc Sulfide CLEAR grade, Ø 25.4±0.2 mm x 7.0±0.1 mm, bulk absorption coefficient at 10.6 µm < 0.2 cm^{-1}).

Figure 5 shows that the scaled values from the laser extinction measurement at a height of H=4.9 m lie between the bulk filter measurements at H=7.7 m and H=3.5 m. It is worth noting that at high aerosol concentrations, the bulk filter values exhibit a significant difference, which may be due to the filters being placed in the upper and lower section of the TTV. 1500 minutes after the hydrogen deflagration (t_d = 1500 min), the extinction measurement approaches its lower detection limit, introducing substantial uncertainty and precluding an accurate data evaluation. Regression curves were derived from the filter measurement values, excluding the pre-deflagration data. These curves assume stirred settling and do not account for particle agglomeration or size changes due to differential settling.

Figure 6 shows the normalized loading distribution of impactor stages for two measurements, indicating quasi-identical mass median diameters. The assumption of aerosol density is based on the density of the paint, as the overall minimal amount captured on impactor foils is insufficient for measuring the particle density.

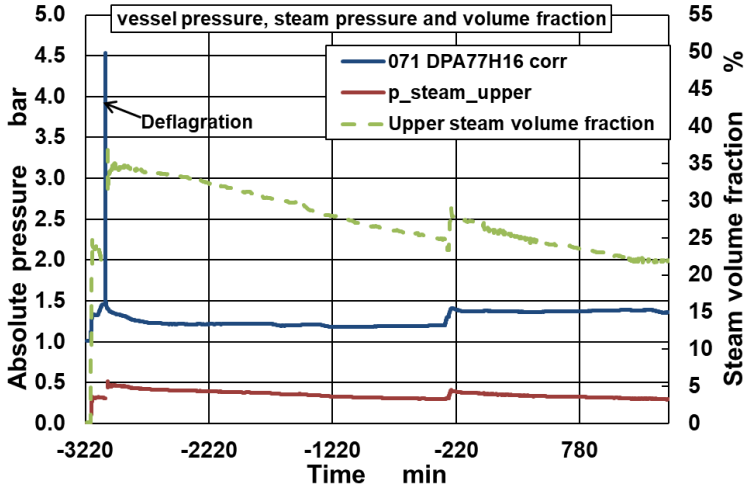

Figure 2: Absolute vessel pressure, steam pressure and volume fraction measured in the upper vessel section.

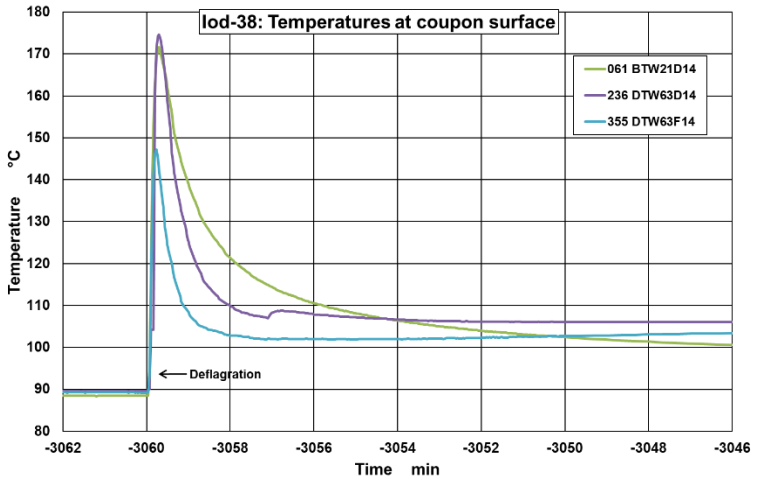

Figure 3: Temporal close-up of the surface temperatures of the coupons that were used for the online iodine measurement.

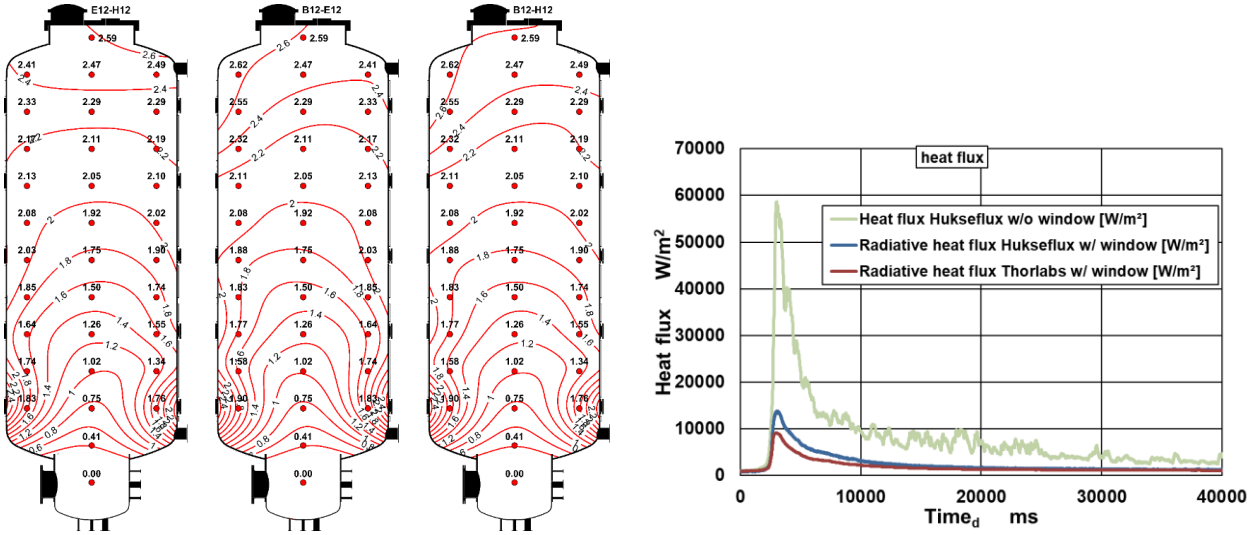

Figure 4: Left: schematic flame contour for three different section combinations. Right: measured heat flux values from three different sensors.

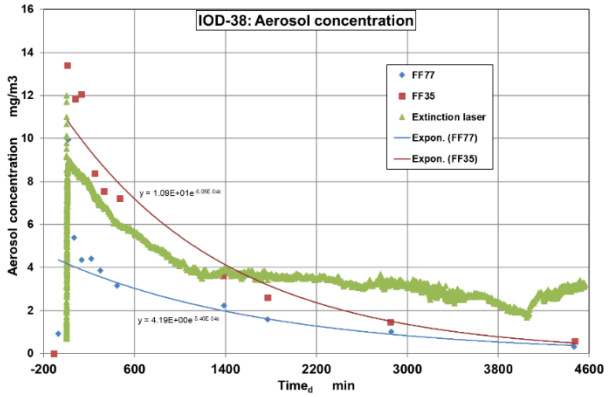

Figure 5: Aerosol concentration as measured by the bulk filters (heights 7.7 and 3.5 m) and the extinction laser measurement (height 4.9 m).

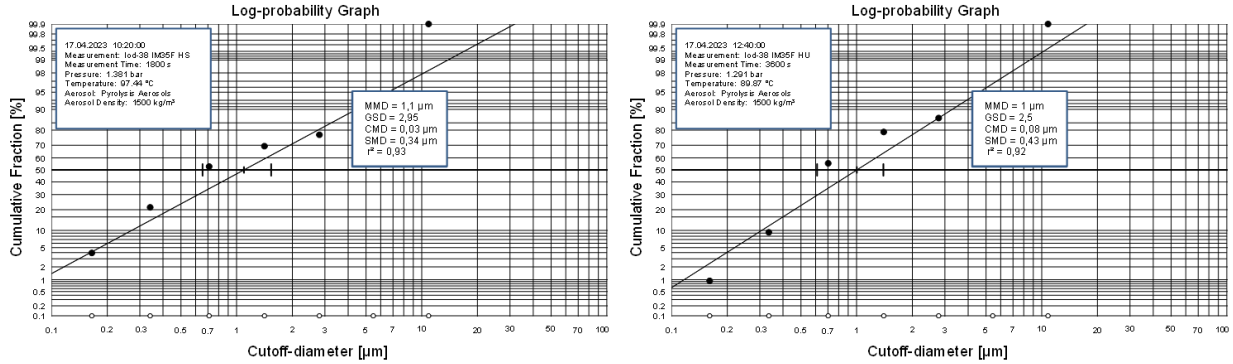

Figure 6: Aerosol particle size distribution from impactor measurements. Top: 50.42 h before the iodine injection (HS). Bottom: 47.83 h before the iodine injection (HU).

3.2. Iodine

To understand the subsequent discussion of the iodine results in terms of applying them for iodine simulation codes, the sensitivity of the iodine species measurements is summarized in Table I. The gas-borne iodine concentrations as measured by the GS are shown in Figure 7. Note that the volatile organic I_2 largely, but not completely, dissolved by the absorber liquid. The concentrations of gas-borne iodine decreased rapidly by two orders of magnitude within the first 4-5 hours due to I_2 deposition on paint and steel surfaces and the deposition of some iodine loaded aerosols. The decline in gas-borne iodine concentrations at the GS positioned at lower heights (H=18.2, 33.6, 43.6, 53.3 m) was similar to the trends observed in a previous experiment [11], indicating similar overall iodine deposition behavior. The data from these GS show minimal scatter, allowing a valid extrapolation to the theoretical initial I_2 concentration at t = 0. However, the concentrations measured at the GS at higher elevations (H=70.2, 83.5 m) appear to be too low. Although no clear reason for this discrepancy could be found, it suggests that the total iodine concentration at the higher positions of the uppermost GS was lower than in the lower parts of the TTV due to the deposition of iodine-containing aerosols. This confirms a well-mixed atmosphere, consistent with homogeneous gas temperatures. After approximately 4-5 hours, the concentration trend shifted to a slow decrease, indicating significant iodine deposition on steel and paint surfaces. After approximately 20 hours, the concentration of gas-borne iodine asymptotically approaches a value of approximately $1x10^{-7}$ g/L. From the comparison with the iodine speciation measurements of the Maypacks discussed below, the remaining gas-borne iodine consists primarily of I_2, with some iodine aerosols and organic iodine absorbed in the GS. It is worth noting that the GS absorber liquid emitted a distinct odor, similar to that observed in previous iodine-paint interaction experiments, indicating the ongoing release of organic matter into the atmosphere due to elevated temperatures.

Figure 8 compares the I_2 concentrations measured by the LASI-SPEC at a height of H=4.9 m with those measured by the Maypack filters at two heights (H=2.1, 7.7 m). Throughout the experiment, I_2 was the dominant species for gas-borne iodine. At the beginning of the experiment, the concentrations were approximately $3x10^{-6}$ g/L at the upper station (MP77) and $1.1x10^{-6}$ g/L at the lower station (MP21). At the end of the experiment, these concentrations decreased to approximately $5\text{-}6x10^{-8}$ g/L, which qualitatively confirms the results of the GS measurements. Additionally, the I_2 concentrations obtained from the Maypack measurements show a very good agreement with the LASI-SPEC signal until the optical system reaches its detection limit at approximately t = 6 h (refer to Figure 8).

A significant amount of iodine was detected on the Maypacks' aerosol filters, showing a gradual decrease from around $1x10^{-5}$ g/L after the injection of I_2 to about $2x10^{-8}$ g/L at the end of the experiment. However, this corresponds to an increasing total fraction of the airborne iodine (4-32 % of the total gas-borne iodine), as shown in Figure 9. This decrease is in line with the aerosol measurements, indicating the presence of fine aerosols. The aerosols released by the deflagration event may consist of a combination of inorganic (mineral) and organic paint components. These aerosols serve as a substrate for the reaction with gaseous iodine to form I-aerosol. Comparing the decrease in iodine aerosol concentrations to the decrease in gravimetric aerosol measurements, a factor of 3 in reduction can be observed. The Maypacks experienced a greater absolute decrease, with a factor of 6, indicating that the depletion of aerosol-borne iodine is not solely due to gravitational settling. Other mechanisms, such as evaporation from the aerosol surface or I_2 dissolved in the organic phase within the aerosol slowly evaporating, may also play a role. Activity measurements on the filters and steel parts showed that I_2 dominated with 95 % shortly after injection, decreasing to 65-70 % at a later time. Aerosol-bound iodine contributed up to 33 % of the total iodine inventory, highlighting its importance in the long-term accident transition. The fraction of organic iodide was smaller than expected based on previous studies [11], comprising only 5 to 10 % at the end of the experiment.

Figure 10 shows the local iodine loadings derived from online monitoring of the deposition coupons, with corrections applied for gas-borne iodine fractions between the coupons and the glass windows. The iodine loadings on the paint surfaces were within the expected ranges, consistent with observations from previous experiments [11]. Gehopon and Ripolin are fully matching, which is not unexpected as both are Epoxy-type paints.

Surprisingly, the steel coupon showed a high load of about half the paint load. The chemical reaction of gaseous iodine with reactive components such as cables [15] or degrading paints in this experiment is likely forming a complex product spectrum, which includes both inorganic and organic matter (refer to Figure 9). This might be a result of a significant deposition of I-aerosols generated after the hydrogen deflagration and the I_2 injection.

After the initial dynamic deposition of iodine on the paint surfaces, saturation is almost approached. However, a subtle linear increase persists, which can be interpreted as ongoing deposition of I_2 or I-aerosol on the paint surfaces. The source of the late I_2 deposition is probably the large steel surface area of the THAI vessel, which simultaneously releases physiosorbed I_2 and causes I_2 depletion by chemisorption on the paint. While the source of I-aerosols could be a very slow settling ultra-fine aerosols, a repartition of iodine has also been observed in previous THAI experiments [16].

Table I. Sensitivity of iodine species measurements.

Measurement device	Parameter	Iodine form
Gas scrubbers	total gas-borne iodine	I_2 + volatile OrgI + I-aerosol
Maypack	trapping in filter stages: I-aerosol / I_2 / volatile OrgI	Sum represents the total gas-borne iodine, I-aerosol is the sum of inorganic and organic forms
LASI-SPEC	I_2	
Online NaI scintillation detectors	deposited iodine	chemisorbed, physiosorbed or settled iodine forms
Impactor/iodine	I-aerosol	

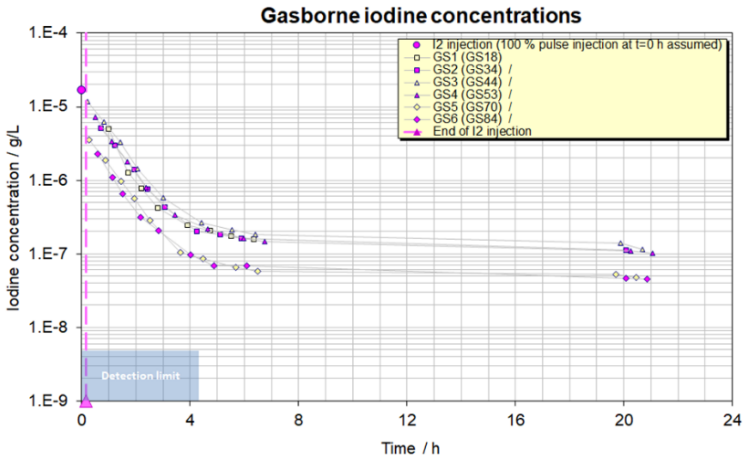

Figure 7: Gas-borne iodine concentrations from gas scrubbers.

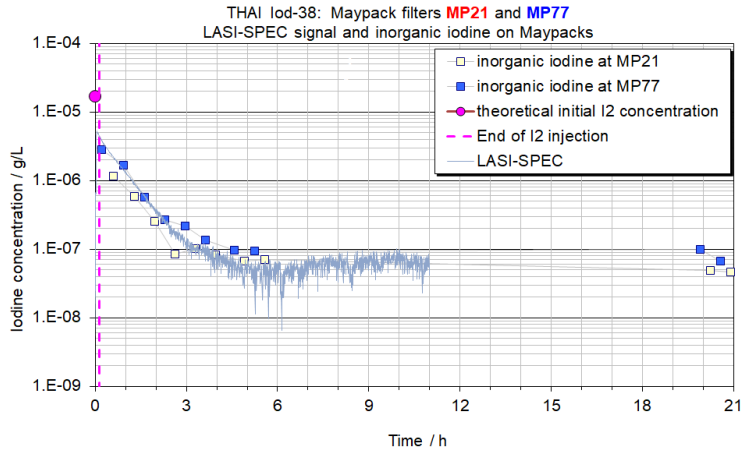

Figure 8: Comparison of inorganic iodine (I_2) concentrations between LASI-SPEC measurement (4.9 m) and Maypack filter measurements at two heights (H=2.1 m and H=7.7 m).

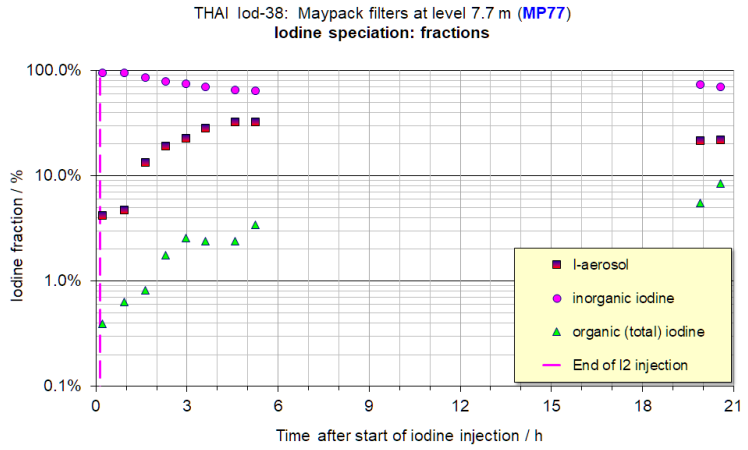

Figure 9: Different fractions of iodine speciation from Maypacks MP77.

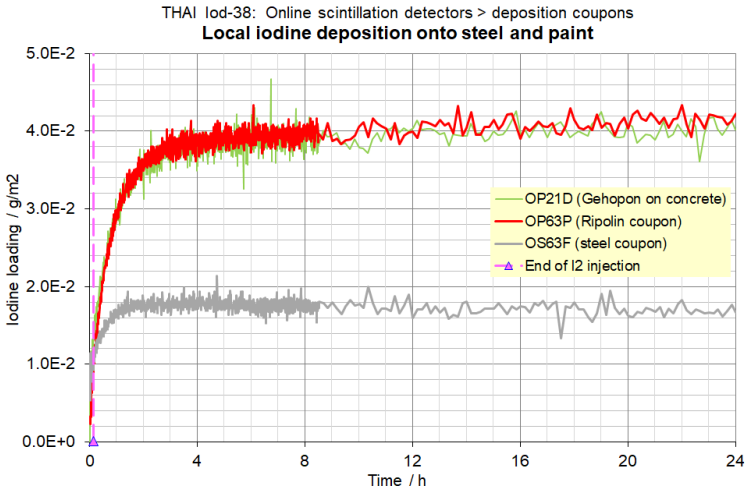

Figure 10: Local iodine loadings on deposition coupons, paint and steel surfaces.

4. SUMMARY AND CONCLUSION

This study investigated the effect of pre-stressed decontamination coatings on gas-phase iodine depletion under extreme conditions using the THAI facility in a closed and superheated containment configuration. For this experiment, twenty stainless steel panels coated with GEHOPON (an epoxy-based material) were subjected to short term, high thermal loads induced by a hydrogen deflagration. Two cylindrical steel coupons, one painted with Ripolin epoxy paint and the other unpainted, and a concrete block painted with GEHOPON were used for on-line monitoring of iodine deposition. The paint surfaces were mechanically and thermally damaged during hydrogen deflagration, releasing volatile organic compounds and aerosols. A variety of techniques were used to continuously monitor aerosol and iodine concentrations, including gas scrubbers, Maypacks, bulk filters, impactor measurements, and optical systems such as the LASI-SPEC and laser extinction.

The results revealed unexpected findings, with the steel coupon showing significantly higher iodine loading than anticipated at the end of the experiment. Comparative analysis of the epoxy coatings GEHOPON and Ripolin showed virtually identical trends in iodine deposition. The study contributes to a deeper understanding of thermal-hydraulic conditions, damaged paint behavior, and airborne fission product concentrations in the late phase of a severe nuclear accident. The results have implications for improving safety measures and mitigating the effects of fission products in such scenarios. Despite the progress in understanding iodine-paint interactions, open questions remain, particularly regarding the effects of short-term, high thermal stresses on paint surfaces, as demonstrated by the unexpected increase of iodine-laden aerosols. In conclusion, the experiment sheds light on the efficiency of pre-stressed decontamination coatings in iodine depletion under extreme conditions, providing valuable insights for the development and validation of detailed reaction models in severe accident codes. Finally, the work emphasizes the importance of considering such coatings in the late phases of severe nuclear accidents to improve radiological safety.

ACKNOWLEDGMENTS

Funding by the Federal Republic of Germany, represented by the Federal Ministry for the Environment, Nature Conservation, Nuclear Safety and Consumer Protection (BMUV) is greatly acknowledged. The experimental research program was funded under the project no. 150 1630. Responsible for the contents of this publication are the authors.

References

1. S. Gupta et al. "THAI Experiments on Volatility, Distribution and Transport Behaviour of Iodine and Fission Products in the Containment," *Proceedings of the International OECD-NEA/NUGENIA-SARNET Workshop on the Progress in Iodine Behaviour for NPP Accident Analysis and Management,* Marseille (France), March 30, April 1, 2015, NEA/CSNI/R(2016)5 (2016).
2. W. Klein-Heßling et al. "COCOSYS – New Modelling of Safety Relevant Phenomena and Components," GRS, Colone, (11 August 2010).
3. W. Klein-Heßling et al. "Specific validation of COCOSYS and ASTEC and implementation of application calculations: Report," (2016).
4. M. Sonnenkalb and G. Poss. "The International Test Programme in the THAI Facility and its Use for Code Validation," Brussels, (2 November 2009).
5. S. Gupta et al. "THAI experimental programme for containment safety assessment under severe accident conditions," *Kerntechnik*, **81,** *2*, 138 (2016).
6. NUCLEAR ENERGY AGENCY. "Improving Evaluations of Source Terms for Severe Accidents at Nuclear Installations: Final Report of the Source Term Evaluation and Mitigation Project (STEM)," NEA/CSNI/R(2018)5 (2018).
7. G. Weber et al. "Iodine and Silver Wash-Down Modelling in COCOSYS-AIM by Use of THAI Results," *Proceedings of the International OECD-NEA/NUGENIA-SARNET Workshop on the Progress in Iodine Behaviour for NPP Accident Analysis and Management,* Marseille (France), March 30, April 1, 2015, NEA/CSNI/R(2016)5 (2016).
8. NUCLEAR ENERGY AGENCY. "Behaviour of Iodine Project 3: Final Summary Report," NEA/CSNI/R(2020)14 (2023).
9. NUCLEAR ENERGY AGENCY. "OECD/NEA Behaviour of Iodine Project: Final Summary Report," NEA/CSNI/R(2011)11 (2012).
10. G. A. Glowa et al. "The main outcomes of the OECD Behaviour of Iodine (BIP) Project," *Annals of Nuclear Energy*, **61**, 179 (2013).
11. F. Funke et al. "Iodine Resuspension from Painted Surfaces by Hydrogen Deflagration - (Test Iod-34): Technical Report No. 1501516 – TR – Iod-34," Becker Technologies GmbH (2019).
12. S. Gupta et al. "THAI test facility for experimental research on hydrogen and fission product behaviour in light water reactor containments," *Nuclear Engineering and Design*, **294**, 183 (2015).
13. J. U. White. "Long Optical Paths of Large Aperture," *J. Opt. Soc. Am.*, **32,** *5*, 285 (1942).
14. T. Kanzleiter et al. "Hydrogen and fission product issues relevant for containment safety assessment under severe accident conditions: OECD-NEA THAI Project Final Report No. 150 1326–FR 1," Becker Technologies GmbH (2010).
15. G. Langrock and C. Penski. "Determination of decomposition products and decomposition rates in fire tests with typical NPP cables," Jahrestagung Kerntechnik, (2010).
16. M. Freitag et al. "THAI experiments on iodine behavior in a room chain representing flow conditions in large containments," *Annals of Nuclear Energy*, **184**, 109670 (2023).

THAI Experiment on the Iodine Absorption Capacity of Pre-Stressed Paint Coatings on Different Surfaces

K. Dieter, M. Freitag, B. von Laufenberg, and E. Schmidt
Becker Technologies GmbH, Germany
G. Langrock, F. Funke
Framatome GmbH

On behalf of:
Federal Ministry
for the Environment, Nature Conservation,
Nuclear Safety and Consumer Protection
of the Federal Republic of Germany

ERMSAR 2024

Introduction

Introduction

Motivation

- During a severe nuclear accident, iodine may be released into the containment as
  - gas
  - aerosol
  - in various water phases
  - deposited on surfaces
- Interaction between iodine and decontamination paints
  - fixation on the organic substrate
  - partial conversion into volatile, organic iodides


[1]

Objective

- Investigation of the effect of pre-stressed decontamination coatings on the iodine depletion efficiency
- Perform a hydrogen deflagration to introduce short-term, high thermal stresses to the paint surfaces before the interaction with iodine

[1] https://www.geholit-wiemer.de/en/industrial-coatings/industrial-coatings-by-industry

Experimental setup

Experimental setup

- THAI^{+}: Thermal-hydraulics, Hydrogen, Aerosols, Iodine, + Multi-compartment
- 2 vessel configuration
  - 14 bar at 180 °C max
  - 10 bar at 250 °C max
- System can be heated or cooled independently via three thermal oil mantles (accuracy +/- 1 °C)
- Access through flanges for (optical) measurement systems
- Approved for H_2, CO and radiolabeled I_2 in combination with deflagrations

Experimental setup

- THAI^{+}: Thermal-hydraulics, Hydrogen, Aerosols, Iodine, + Multi-compartment
- 2 vessel configuration
  - 14 bar at 180 °C max
  - 10 bar at 250 °C max
- System can be heated or cooled independently via three thermal oil mantles (accuracy +/- 1 °C)
- Access trough flanges for (optical) measurement systems
- Approved for H_2, CO and radiolabeled I_2 in combination with deflagrations

Experimental setup

- THAI$^+$: Thermal-hydraulics, Hydrogen, Aerosols, Iodine, + Multi-compartment
- 2 vessel configuration
  - 14 bar at 180 °C max
  - 10 bar at 250 °C max
- System can be heated or cooled independently via three thermal oil mantles (accuracy +/- 1 °C)
- Access trough flanges for (optical) measurement systems
- Approved for H_2, CO and radiolabeled I_2 in combination with deflagrations

Experimental setup

Aerosol and iodine

- 6 internal and 2 external gas scrubbers
- Maypacks
- Impactor
- Bulk filters
- LASI-SPEC & laser extinction
- Heat flux sensors
- 3x online detectors at coupons

Thermal hydraulics

- Temperature (fluid and surface)
- Pressure
- Humidity
- Gas concentrations of O_2, H_2, CO, CO_2

Experimental setup

- 25 painted coupons (corresponding to a surface area of 10.65 m²)
  - 23x *GEHOPON* square coupon, artificially pre-aged by a thermal treatment for 21.1 h at 160 °C
  - 1x *Ripolin* cylindrical coupon, artificially pre-aged by a thermal treatment for 96 h at 130 °C
  - 1x GEHOPON concrete block
  - 1x blank steel cylindrical coupon
- Activity is measured by online probes pointing at coupons
- A remote arc igniter was installed at the sump compartment

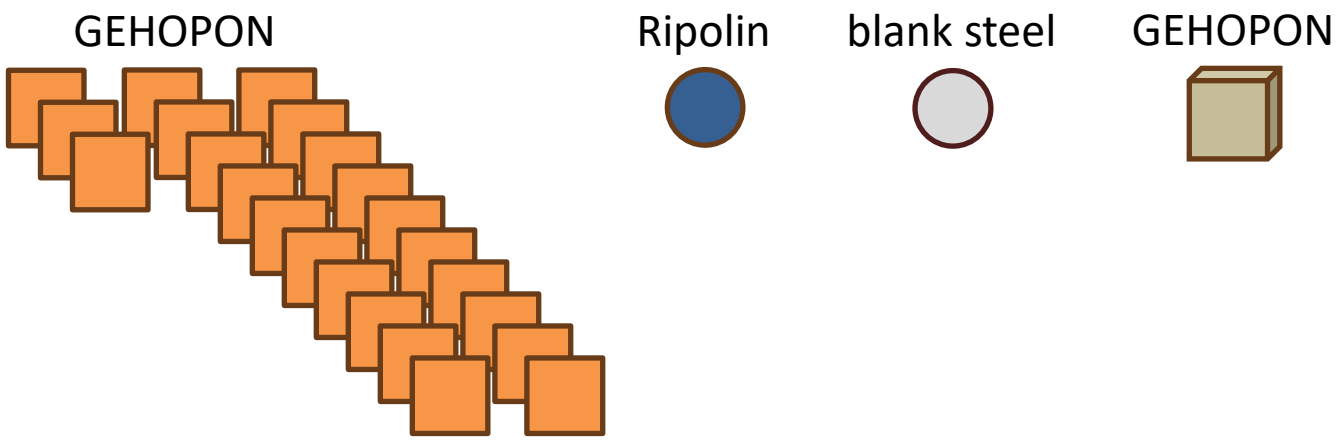

Test procedure

Test procedure

- Preconditioning phase 1
  - Temperature: 90 °C
  - 25 vol.-% of superheated steam
  - pressure: 1.36 bar
- Preconditioning phase 2
  - injection of 10 vol.-% hydrogen
  - ignition and deflagration
- Main phase
  - Injection of 1.009 g of radiolabeled iodine

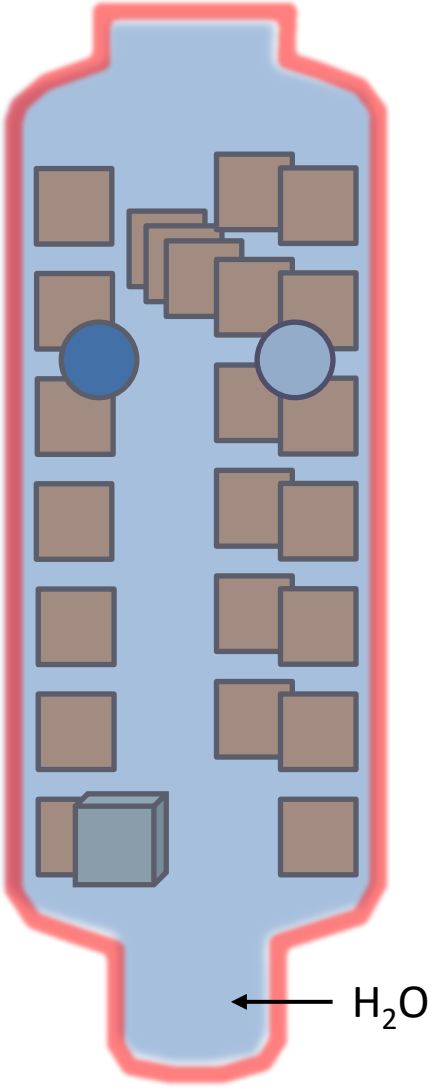

Test procedure

- Preconditioning phase 1
  - Temperature: 90 °C
  - 25 vol.-% of superheated steam
  - pressure: 1.36 bar
- Preconditioning phase 2
  - injection of 10 vol.-% hydrogen
  - ignition and deflagration
- Main phase
  - Injection of 1.009 g of radiolabeled iodine

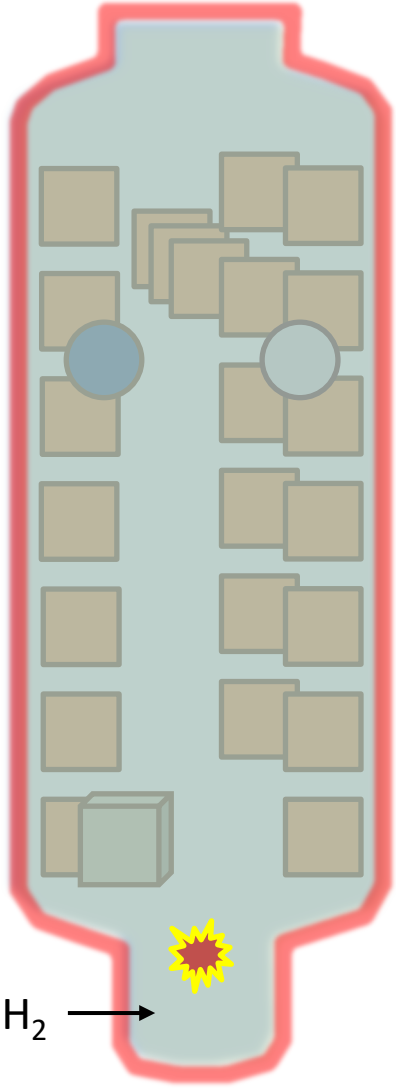

Test procedure

- Preconditioning phase 1
  - Temperature: 90 °C
  - 25 vol.-% of superheated steam
  - pressure: 1.36 bar
- Preconditioning phase 2
  - injection of 10 vol.-% hydrogen
  - ignition and deflagration
- Main phase
  - Injection of 1.009 g of radiolabeled iodine

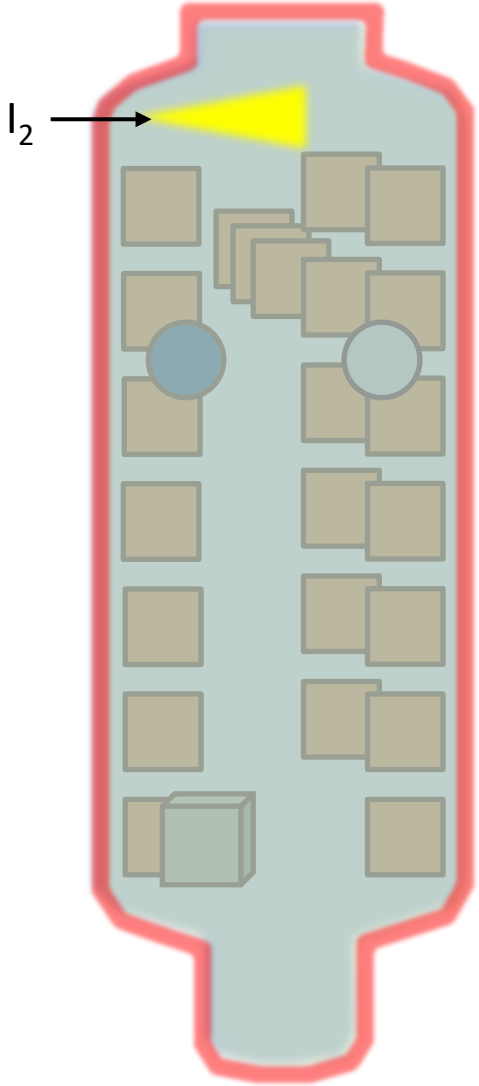

Results

Results

- Time t = 0 corresponds to iodine injection
- Sharp pressure increase to p = 4.539 bar due to hydrogen deflagration (t = -3060 min)
- Afterwards, decrease in steam volume fraction and steam pressure
- Second injection of steam/air prior to iodine injection at t = 0
- Slight decrease of steam partial pressure is caused by the GCMS operation and laser window purging

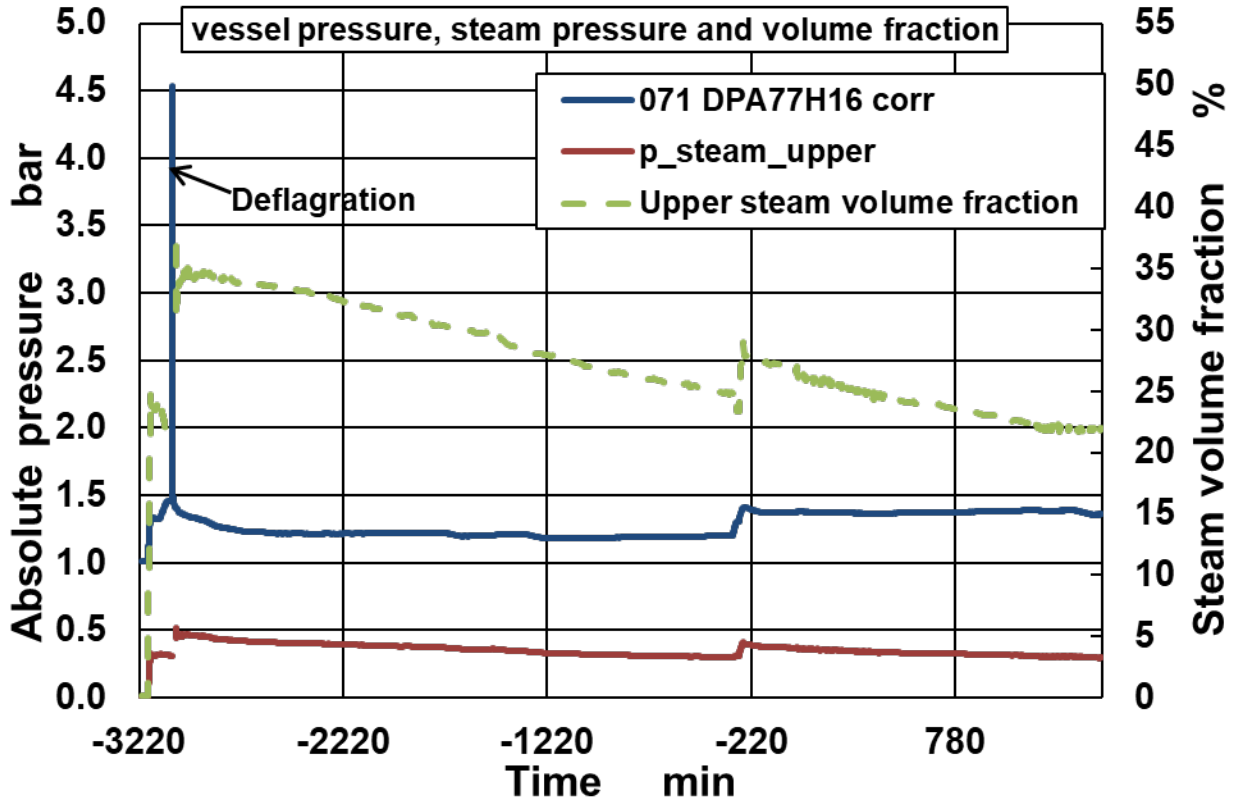

Results

- Time t_d = 0 corresponds to the ignition event
- Temperatures of the fast responding thermocouples at the centerline of the vessel
- Distributed horizontally
- Sequential sharp increase in temperature after ignition event

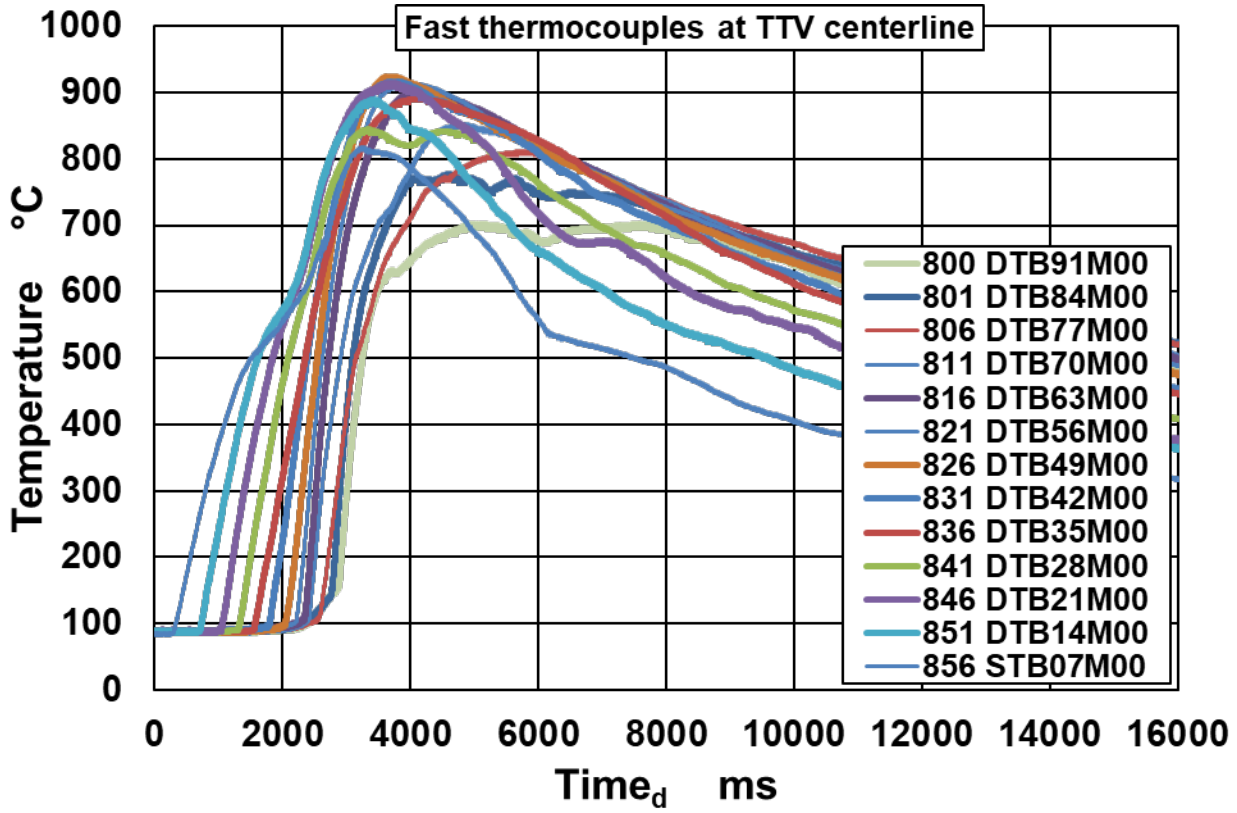

Results

- Gradient based evaluation of the flame arrival as measured by the fast thermocouples
- Schematic visualization of flame from at distinct times with isochrones
- Upward flame propagation pattern aligns with previous studied
- Homogeneous combustion without any hot pockets

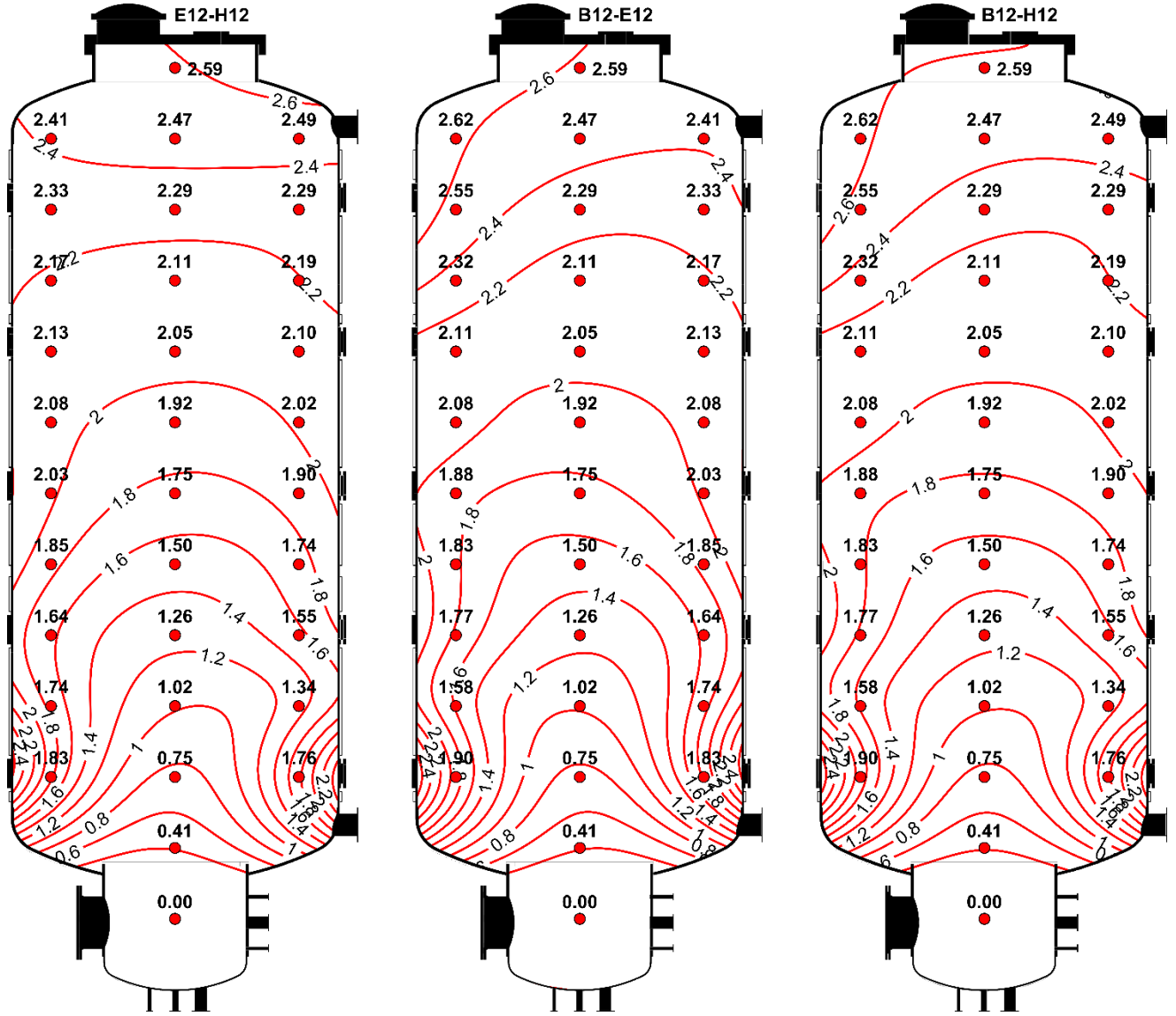

Results

- Temperature during the deflagration event at the three coupons that were used for the online iodine measurement
- Difference of approximately 300 K between steel coupon (Ripolin, 236 DTWD14) and blank steel coupon (355 DTW63F14) at a height of 6.3 m
- Similar peak temperature as of concrete block (GEHOPON, 061 BTW21D14) at a height of 2.1 m
  - higher thermal resistance of concrete material

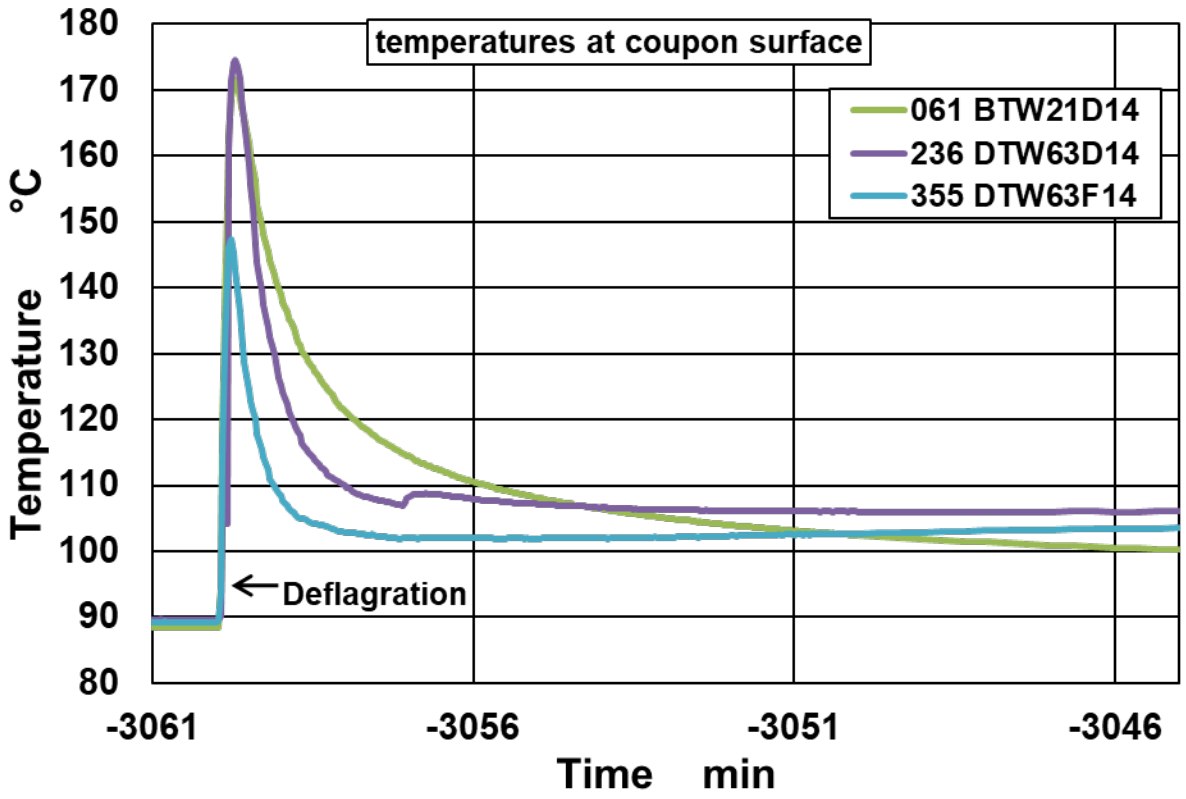

Results

- Time t_d = 0 corresponds to the ignition event
- Sensor w/o window simultaneously measured convective and radiative heat flux (relative)
  - peaks at approx. 58700 W/m²
- Sensor w/ window measured only the radiative heat flux
  - peaks at approx. 13800 W/m²
  - factor of 4.2 smaller
- Third sensor had a thicker window and a smaller field of view
  - peaks at approx. 9100 W/m²

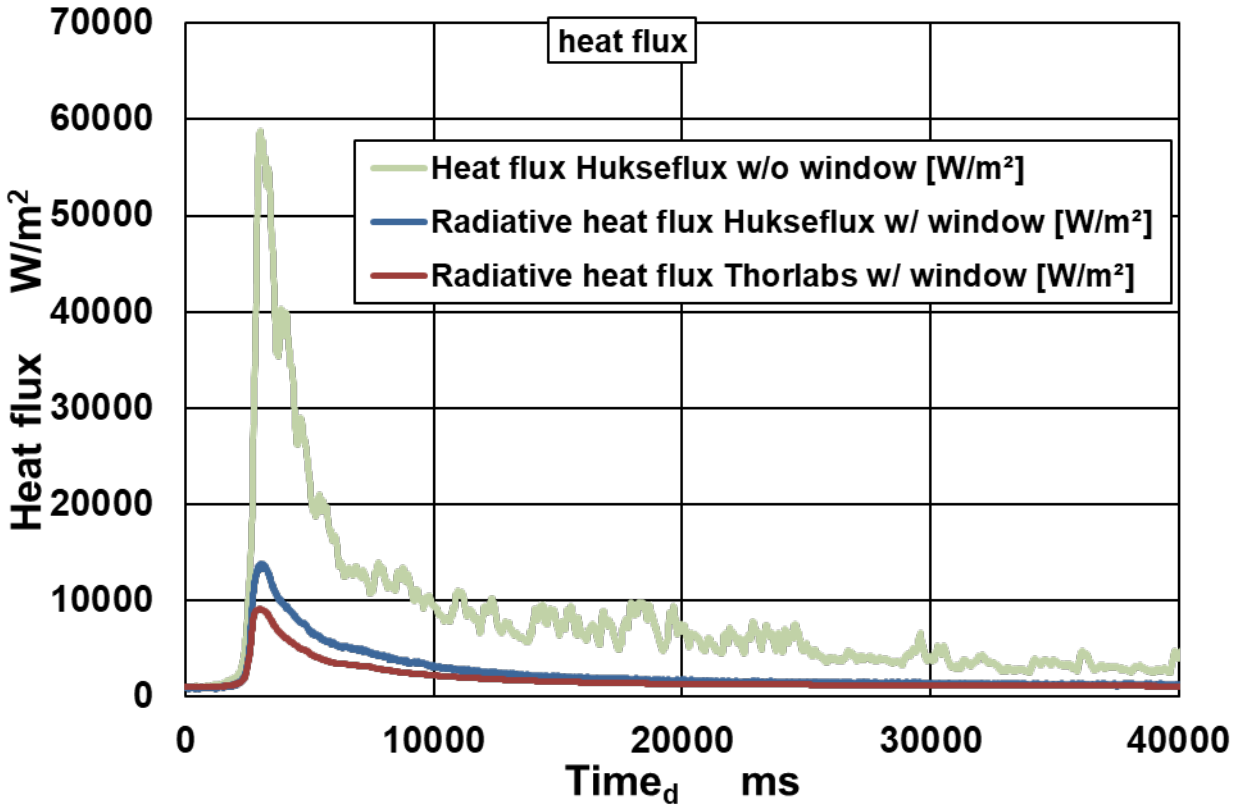

Results

- Thin steel coupons show significant visible damage
  - burns
  - blistering
  - peeling
- Paint applied to concrete block was visibly almost not affected



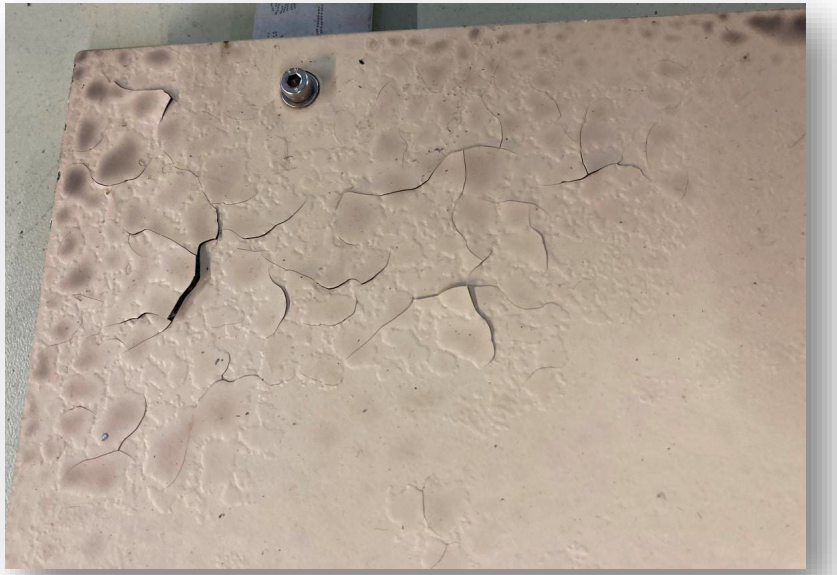

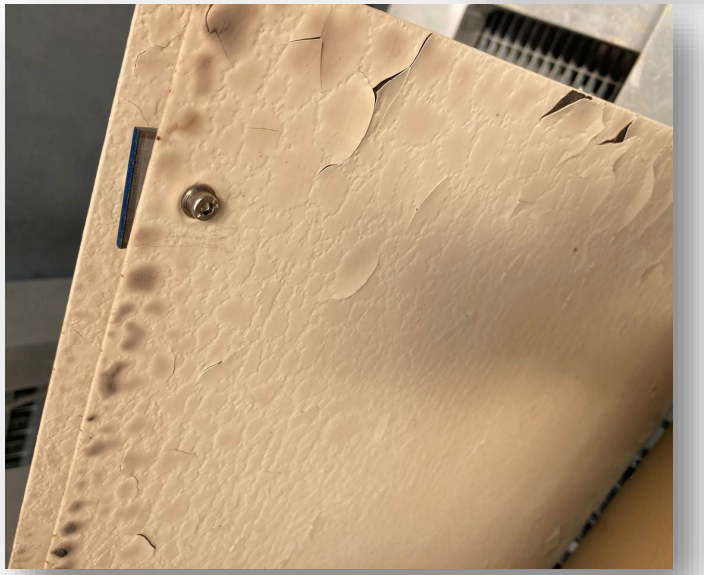

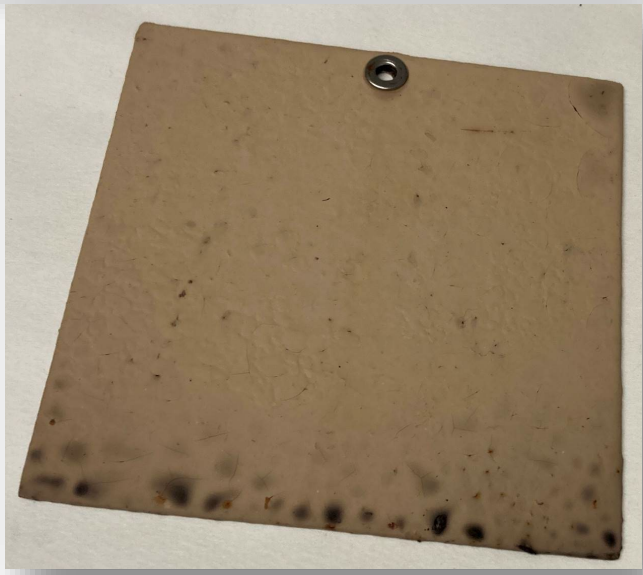

Results

- Time t_d = 0 corresponds to the ignition event
- Deflagration event produces significant amount of aerosol
- Difference between laser extinction and filter measurements is due to placement of measurement systems
- Exponential decay after the deflagration
  - assumed this is due to stirred settling

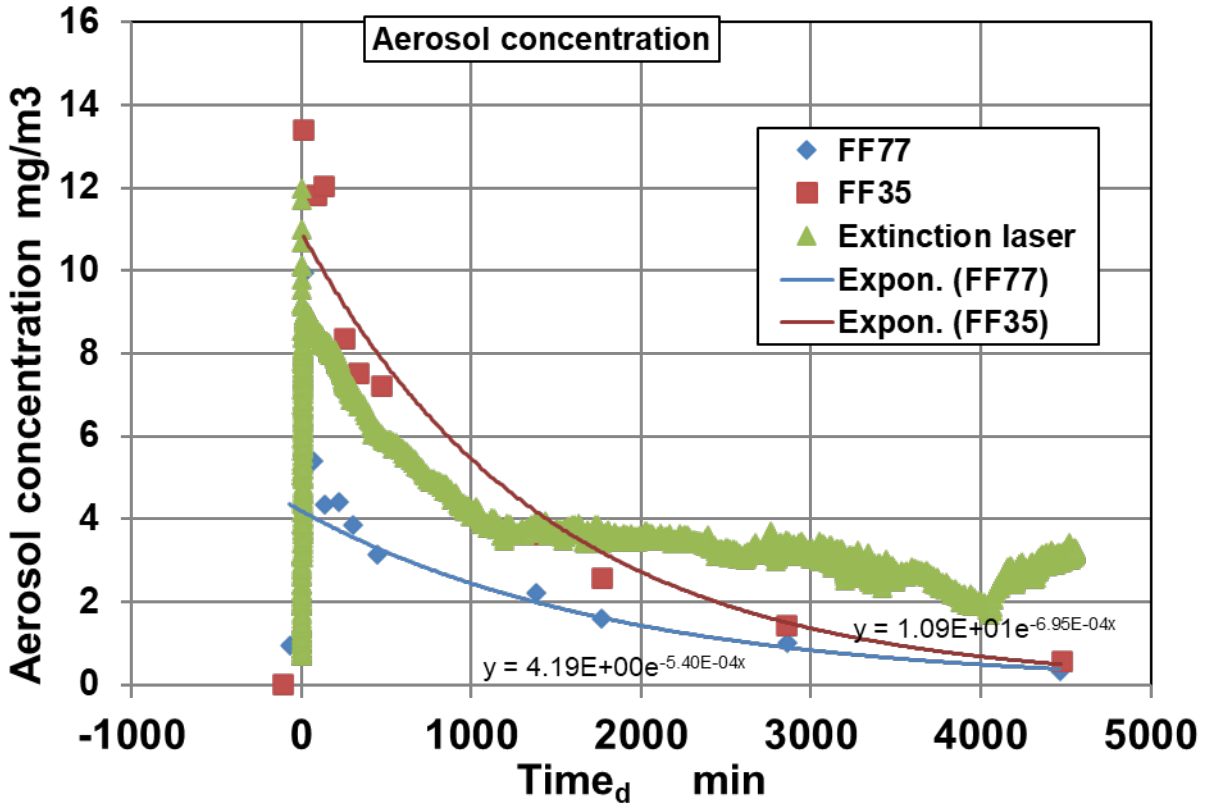

Results

- Gas-borne iodine concentration as measured by the gas scrubbers
- Sensitive for the following forms: molecular iodine, (partially) volatile organic iodine and iodine aerosol
- Well mixed atmosphere (small scatter)
- Rapid decrease within the first 4-5 hours
  - deposition on paint and steel surfaces
  - deposition of iodine loaded aerosols
- Extrapolation to theoretical initial I_2 concentration is valid
- Asymptotically reaches values of approx. $1x10^{-7}$ g/L
  - deposition on paint and steel surfaces

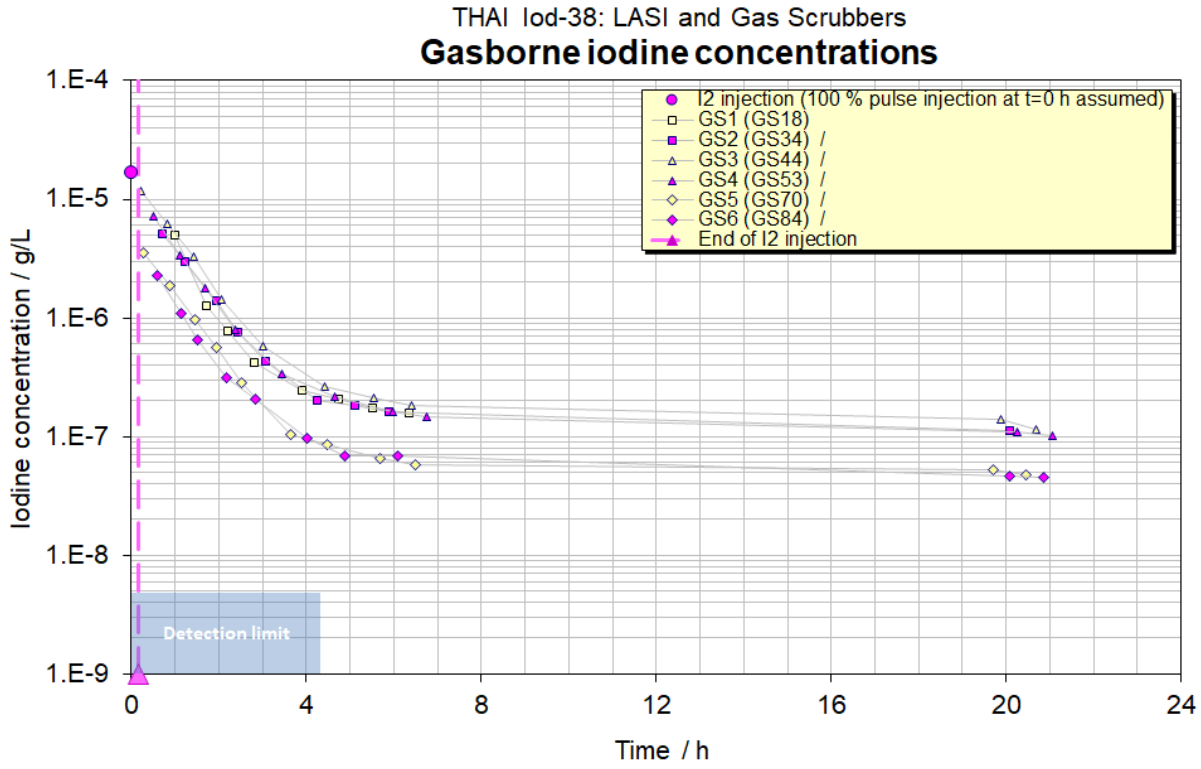

Results

- Inorganic iodine as measured by the Maypack filters
- Slightly higher values for the measurement at H = 7.7 m due to the proximity of the I_2 injection location
- Data correlate well with the LASI-SPEC signal and previously shown gas scrubber measurements
  - gas-borne iodine consists primarily of I_2

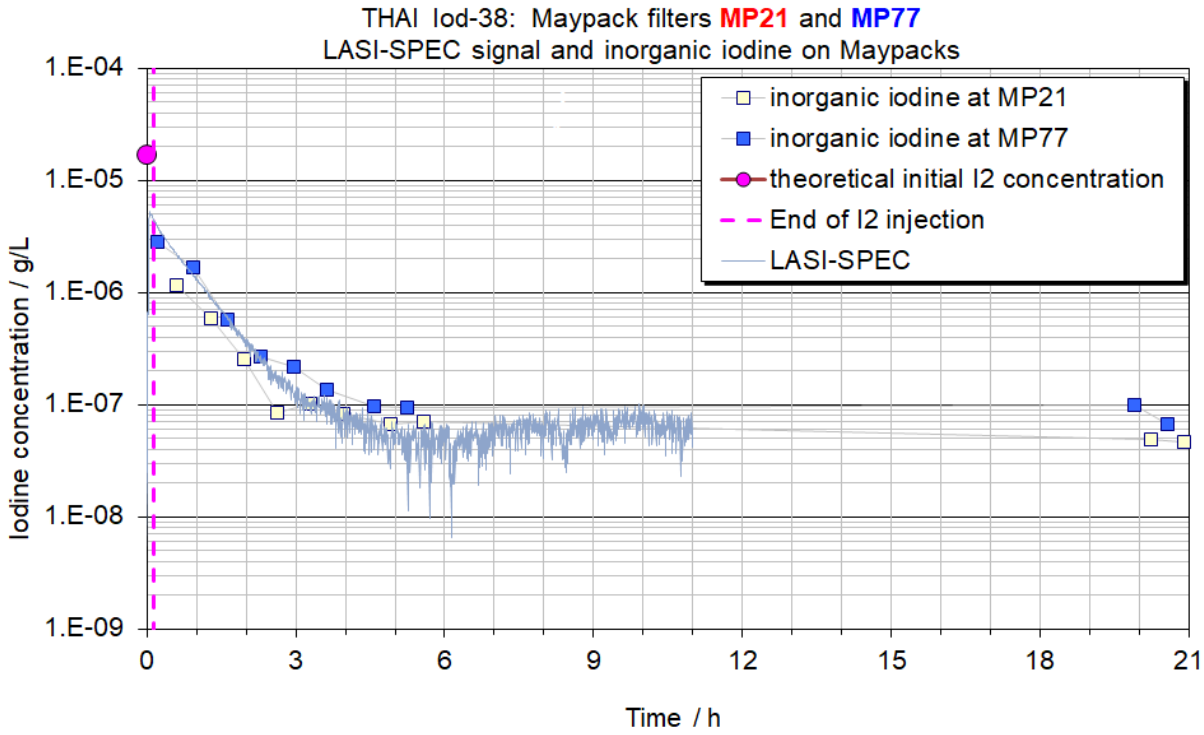

Results

- Iodine speciation as measured by the Maypack filter stages
- Significant decrease of iodine containing aerosol from $1x10^{-7}$ to $2x10^{-8}$ g/l
  - indicates fine aerosols
  - combination of inorganic and organic paint components served as substrate for the iodine

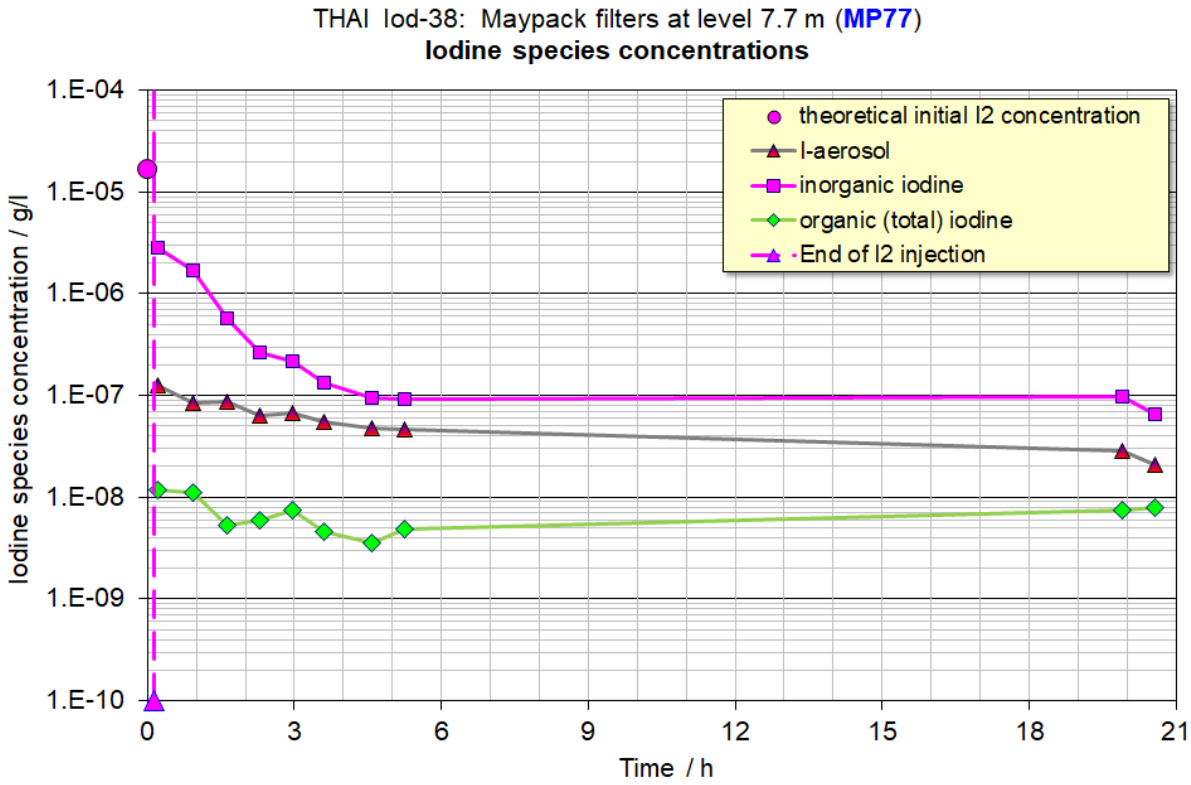

Results

- Iodine speciation as measured by the Maypack filter stages
- Significant decrease of iodine containing aerosol from $1x10^{-7}$ to $2x10^{-8}$ g/l
  - indicates fine aerosols
  - combination of inorganic and organic paint components served as substrate for the iodine
- Activity measurements on the filters and steel parts indicate that I_2 dominated with 95 % (shortly after injection) and 65-70 % (later)
- Aerosol bound iodine contributed up to 33 % of the total iodine inventory
  - important for long term accident transition
- Organic iodides contributed only up to 5 to 10 % at the end of the experiment

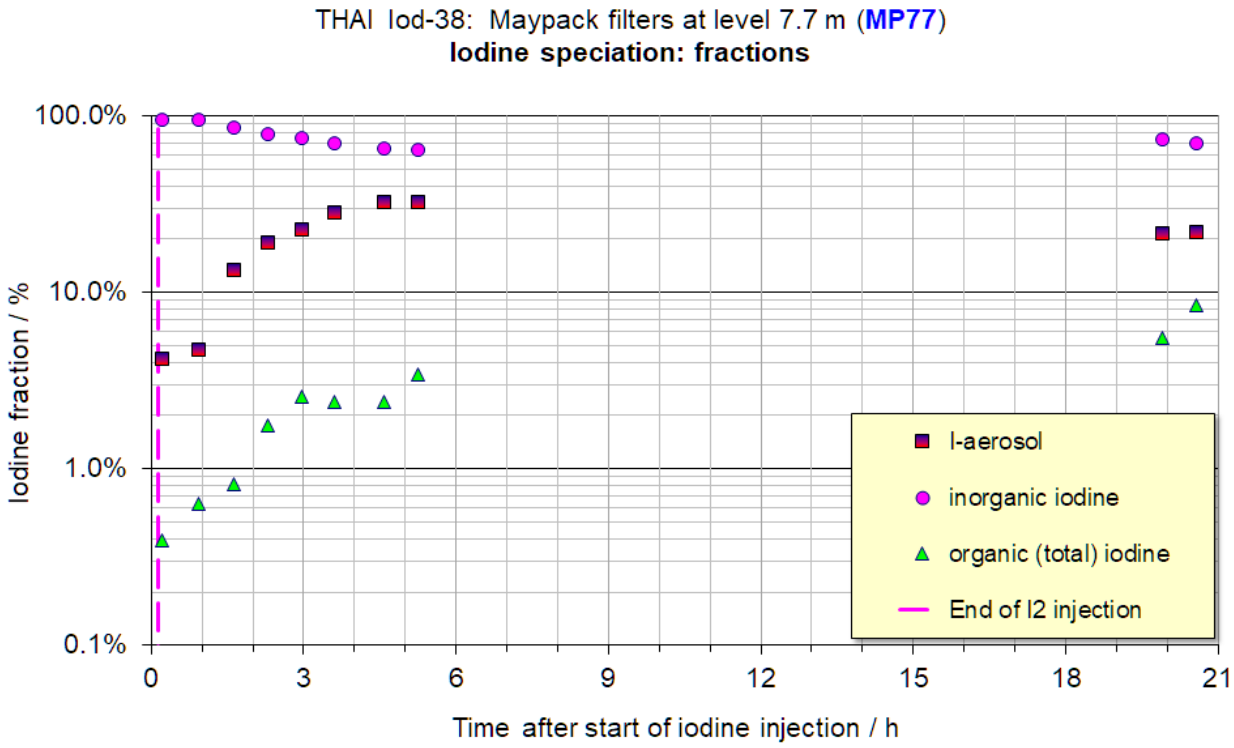

Results

- Local iodine loadings on painted and blank steel and concrete deposition coupons as measured by the online scintillation detectors
- GEHOPON and Ripolin painted coupons are almost identical with $4x10^{-2}$ g/m² iodine loading at almost saturated conditions (t > 20 h)
- Deposition at the blank steel coupon approx. half of the paint, but still surprisingly high
  - assumed that the deflagration produced reactive aerosols which later deposited on surfaces and provided additional reactivity to the gaseous iodine

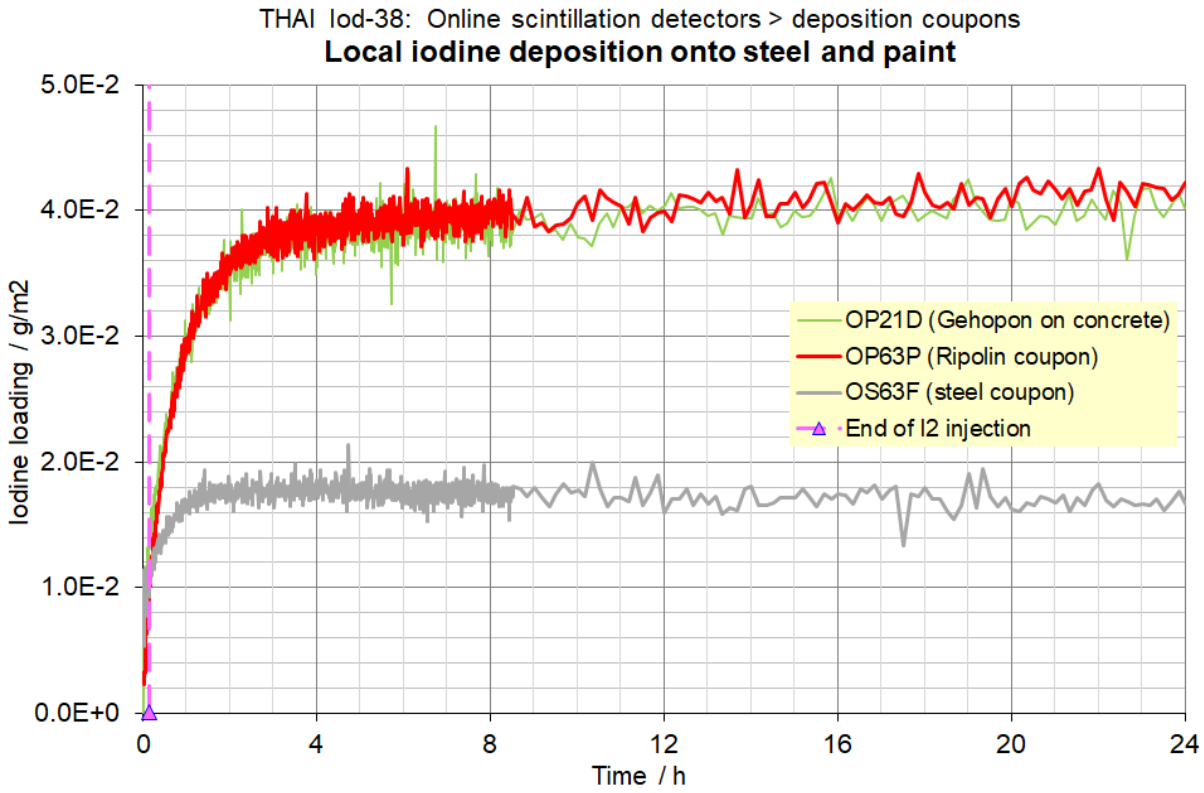

Summary and conclusions

Summary and conclusions

- Investigation of the effect of pre-stressed decontamination coatings on the gas-phase iodine depletion
- 25 painted coupons (23x GEHOPON, 1x Ripolin steel, 1x GEHOPON concrete) and one blank steel cylindrical coupon were subject to short term, high thermal loads induced by a hydrogen deflagration
- Release of volatile organic compounds and aerosols due to thermal damage of the paint

- A hydrogen deflagration event within the containment can thermally damage epoxy-based decontamination paints
  - Dependent on the material on which they're applied to (concrete or steel)
- Unexpected high amount of iodine-laden aerosols
- Unexpected iodine load on the blank steel coupon
- Provides data for the development and validation of detailed reaction models in severe accidents simulation codes

Acknowledgements

The THAI research program is carried out on behalf of the German Federal Ministry for the Environment, Nature Conservation, Nuclear Safety and Consumer Protection (BMUV) and is funded under the grant number 1501630.

On behalf of:

Federal Ministry
for the Environment, Nature Conservation,
Nuclear Safety and Consumer Protection

of the Federal Republic of Germany

Backup

Backup

- Both measurements indicate quasi-identical mass median diameters
- The density of the aerosols was assumed to be represented by the paint density
- The overall amount of captured aerosols on the impactor foils was considered too small for a particle density measurement, even by specialized laboratories

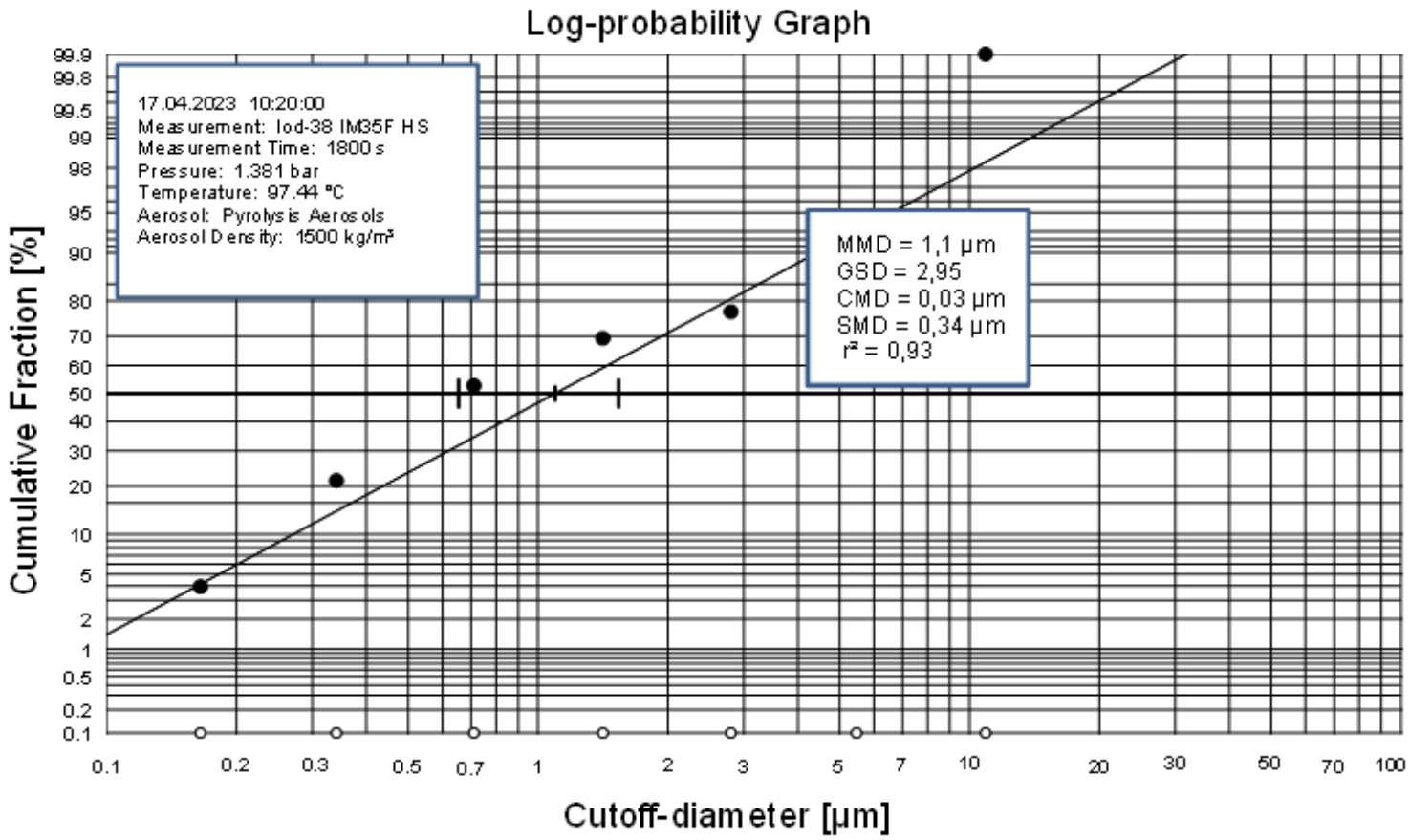

Backup

- Both measurements indicate quasi-identical mass median diameters
- The density of the aerosols was assumed to be represented by the paint density
- The overall amount of captured aerosols on the impactor foils was considered too small for a particle density measurement, even by specialized laboratories

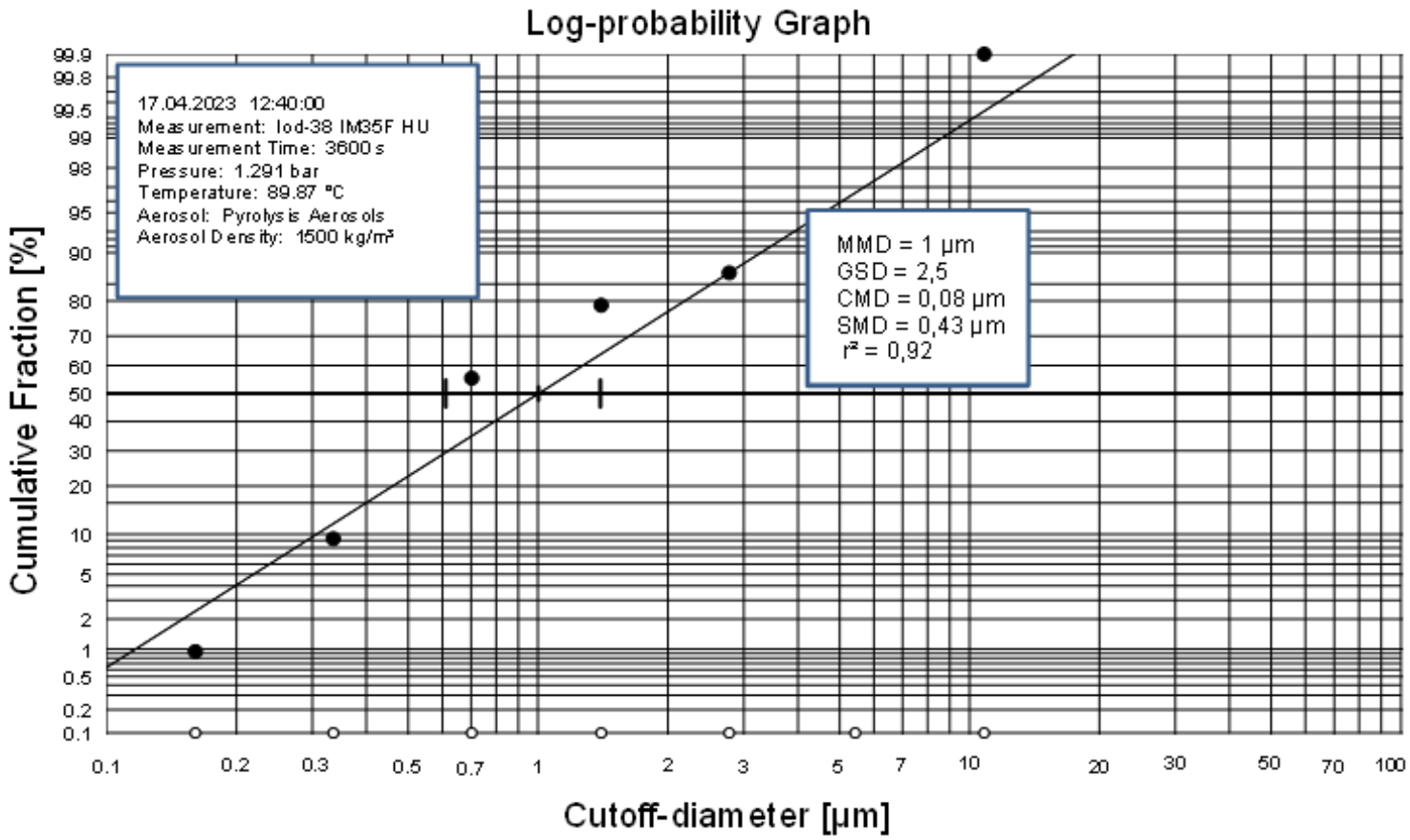

Backup

- Aerosol filter from a Maypack sample. The filter shows a brownish colour due to aero-sols dissolved in the fibreglass matrix.

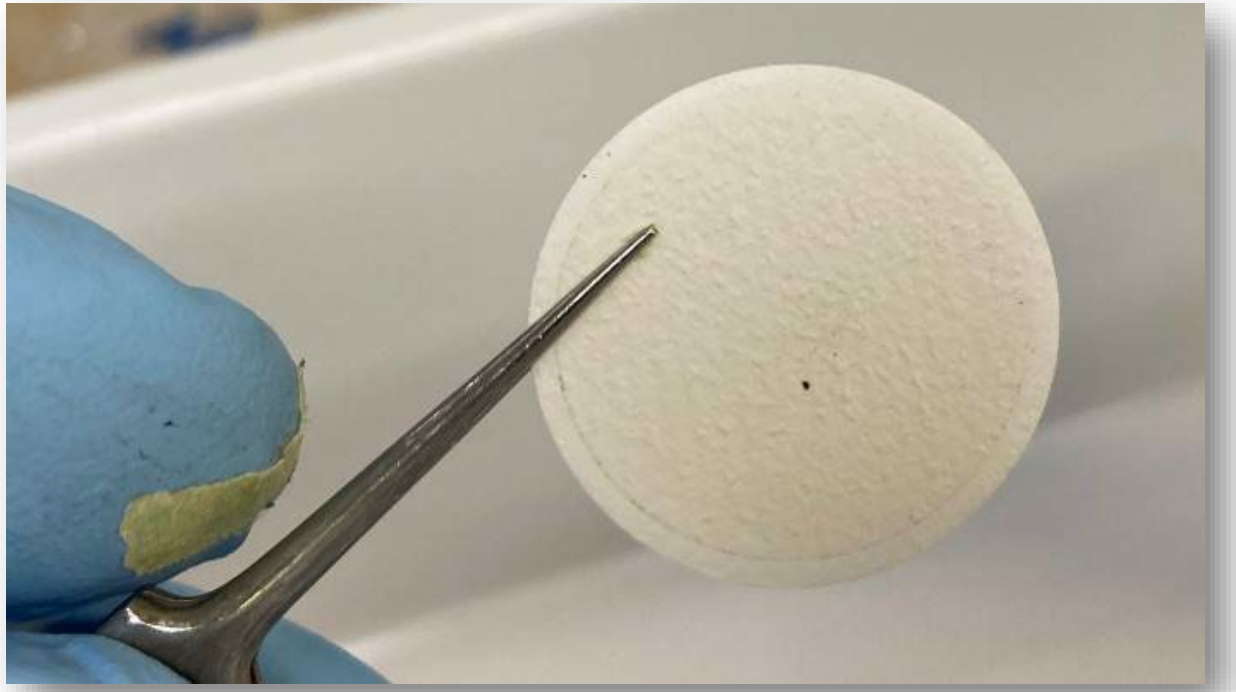

Backup

- Impactor foil after sampling. No small piles, but dried and brown splashes appeared after disassembling the impactors.

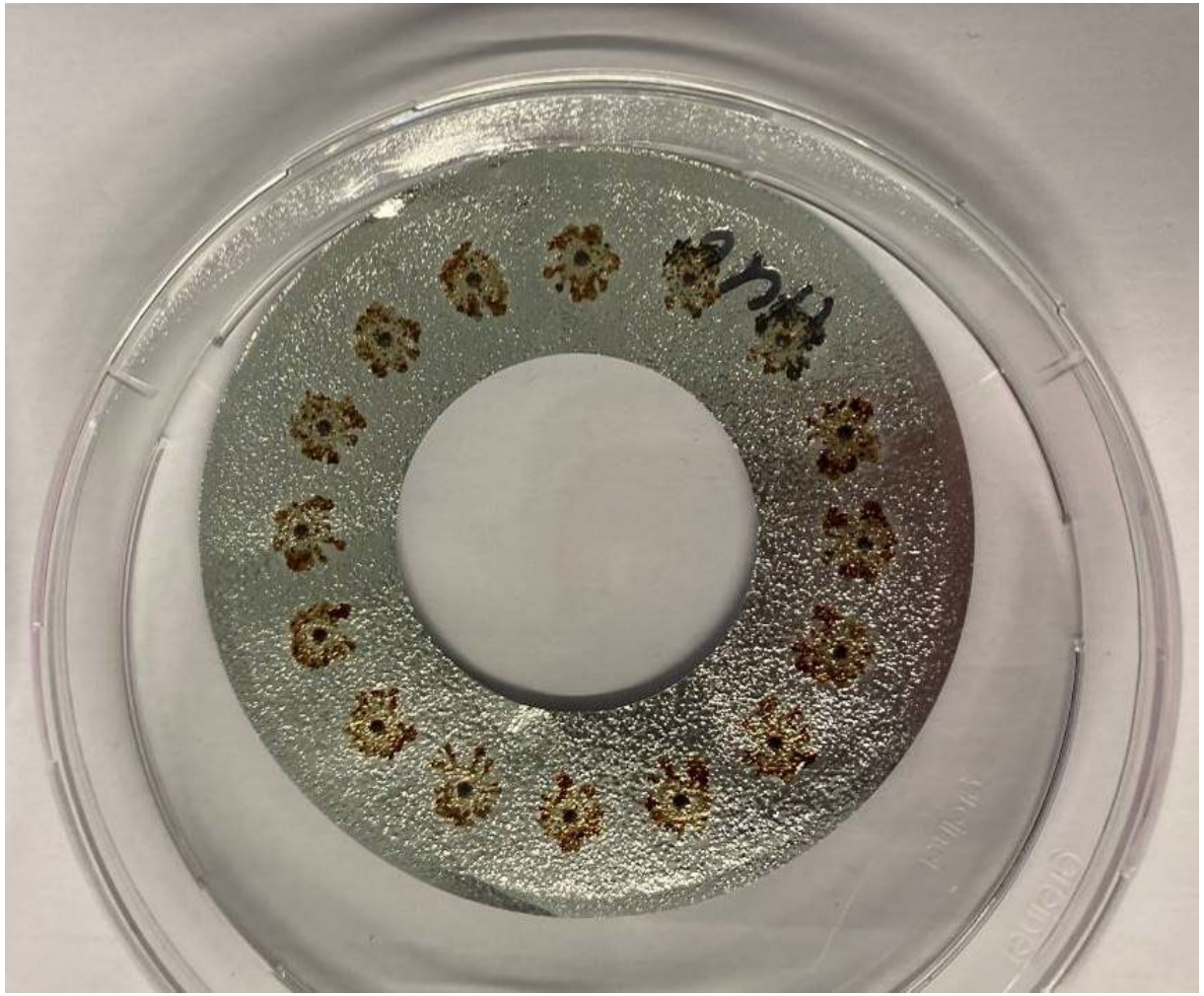

VALIDATION OF THE PARUPM AND GOTHIC 8.3 CODE COUPLING USING THAI HYDROGEN RECOMBINATION TESTS

Domínguez-Bugarín, A.*, Serra, L., Jiménez, G.
Universidad Politécnica de Madrid
C/ José Gutiérrez Abascal, 2, 28006 Madrid, Spain
araceli.dominguez@upm.es; luis.slopez@upm.es; gonzalo.jimenez@upm.es

Vázquez-Rodríguez, C., Reinecke, E.-A., Kelm, S.
Forschungszentrum Jülich GmbH
Wilhelm-Johnen-Straße, 52425 Jülich, Germany
c.vazquez-rodriguez@fz-juelich.de; e.-a.reinecke@fz-juelich.de; s.kelm@fz-juelich.de

Gupta, S.
Becker Technologies GmbH
Rahmannstraße 11, 65760 Eschborn, Germany
gupta@becker-technologies.com

Jiménez, M.-A.
Consejo de Seguridad Nuclear
C/ Pedro Justo Dorado Dellmans, 11, 28040 Madrid, Spain
miguelangel.jimenzg@upm.es

ABSTRACT

In case of a severe accident in a nuclear power plant (NPP), large amounts of H_2 and CO could be generated, potentially leading to uncontrolled combustion if concentrations within the flammability thresholds are reached. To mitigate this hazard, many NPPs equipped their containment buildings with passive autocatalytic recombiners (PARs). PARs are capable of recombining combustible gases such as H_2 or CO with oxygen, resulting in the production of steam and/or CO_2, even when gas concentrations fall below the flammability threshold.

The AMHYCO project (Euratom 2019-2020, GA Nº 945057) aims to advance experimental understanding and simulation capabilities for H_2/CO combustion risk management in severe accidents. Within the framework of this project, the computational model PARUPM, which uses a physicochemical approach to simulate PARs, has been validated as a standalone tool using experimental data obtained from both the REKO-3 flow channel at FZJ and the OECD/NEA THAI projects executed at Becker Technologies GmbH. In a next phase, PARUPM has been integrated as an add-on program within the thermohydraulic simulation code GOTHIC. This code coupling facilitates the evaluation of the interaction between the operation of PARs and the surrounding atmosphere in which they are located.

The present paper provides an overview of the capabilities of the joint simulation with PARUPM – GOTHIC 8.3. The coupling to GOTHIC has been validated based on a sequence of experiments on H_2 recombination by PARs performed at the THAI experimental facility. The relevant feedback from the THAI vessel to the recombiners performance involving gas stratification and change of boundary conditions is studied by a 3D model which reproduces the complex behaviour of gases inside the THAI vessel during the experiments.

KEYWORDS
AMHYCO, Passive Autocatalytic Recombiners, Hydrogen, GOTHIC, THAI, REKO, PARUPM

1. INTRODUCTION

Hydrogen is a potentially hazardous combustible gas produced during severe accidents in nuclear power plants, which poses a threat to containment integrity. To address this risk, passive auto-catalytic recombiners (PARs) have been widely installed within containment buildings, especially in Europe and Asia [1]. PARs are self-starting devices equipped with vertical catalyst sheets coated with materials like platinum or palladium (Fig. 1), which lower the activation energy and facilitate the conversion of hydrogen to steam. Moreover, PARs support the global convection and enhance the hydrogen mixing in the containment atmosphere, thereby reducing local peak hydrogen concentrations. Thus, recombiners are crucial in mitigating the hydrogen risk [2], [3]. This work focuses on the most widely adapted PAR geometry of vertical plate carriers for the catalytic materials.

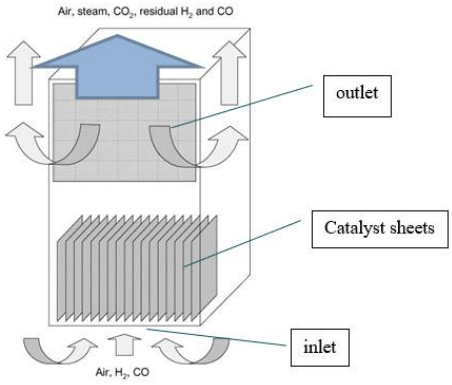

Figure 1. Passive Auto-Catalytic Recombiner (PAR)

To help in the development and validation of safety analyses codes, as well as in the general design and enhancement of passive mitigation systems, international projects have focused on reproducing the distribution, consequence, and mitigation of combustible gases in the containment of water-cooled reactors. Regarding PARs, these experiments were performed to establish a common database that allows developing advanced models that simulate the behaviour of a recombiner. One of those experimental campaigns is the OECD/NEA-THAI project, started in 2007 with one of the objectives of studying the spatial distribution of H_2 in the containment and its effective removal by PARs or slow H_2 combustion processes. This PAR performance database has been used for analytical research with numerous codes with different levels of complexity [4].

The AMHYCO project (Euratom 2019-2020, GA Nº 945057) [5] seeks to advance the simulation capabilities to support H_2/CO combustion risk management in severe accidents, based on knowledge from experimental investigations. In the context of this project, the physico-chemical code PARUPM has been selected for simulating PARs behaviour. The code considers surface chemistry on platinum-based catalytic surfaces as well as heat and mass transfer between the catalyst and gaseous mixtures of hydrogen, carbon monoxide, air, steam, and carbon dioxide [6].

This paper documents a validation effort of the PARUPM code. The first step in this validation process is a study of PARUPM as a standalone tool which was carried out using available data from the THAI facility. This process establishes the capability of the code to replicate the behaviour of real recombiners. As the second step of the validation effort, the integration of PARUPM as add-on program into the thermo-hydraulic analysis code GOTHIC [7] was studied. GOTHIC offers a good code platform for simulating the THAI test facility while integrating the PARUPM code as an external function. This part of the paper aims to study the capabilities and the accuracy of PARUPM for simulating the behaviour of PARs in full containments.

2. PARUPM SIMULATION MODEL AND GOTHIC CODE

Comprehensive computational codes for predictive safety analysis have traditionally relied on empirical expressions that correlate the recombination rate with parameters like gas concentrations and pressure [8]. The advantage of this approach lies in the low computational efforts. However, the applicability is limited to scenarios that lie within the parameter space on which the correlation was gauged. Thus, there is interest in creating a mechanistic model that can examine in greater detail the intricate processes that take place on the catalytic surface and enable dealing with a large variety of scenarios [9]. The involved physicochemical processes include species diffusion through the fluid boundary layer as well as chemical surface reactions. The heat produced by these reactions raises the catalytic surface temperature (heating phase), alters the reaction rates, warms the gas mixture between the plates, and increases the flow by inducing a self-sustaining natural flow. The operation of the PAR may be restricted or even prevented by the presence of chemical inhibitors, unfavourable density gradients, and pressure losses through the device [10].

PARUPM is a PAR simulation code developed at the ETSI Industriales School of the Universidad Politécnica de Madrid [6]. This code uses a physicochemical model based on surface chemistry to numerically simulate the operation of a PAR. The models implemented in PARUPM code accounts for the various phenomena that take place in the recombiner, which is conceptualised as a collection of vertical flow channels separated by vertical parallel catalyst sheets. Heat and mass transfer between the gas mixture and the catalytic surface is influenced by the vertical flow, which originates from density-driven convection. Heat generated on the catalyst surface depends on adsorption and desorption of species as well as the chemical reactions. Convective heat transfer between surface and gas phase as well as radiative heat exchange with the surroundings ensure heat distribution. These phenomena, which occur simultaneously, are numerically coupled. Hence, expressions of the mass and energy balance at the interface between the catalytic plate and the gaseous flow, which is continuously passing by, are used [11].

In particular, the code is adapted and developed for surface chemistry and heat and mass transfer between gaseous mixtures of H_2, CO, air, steam and CO_2 and platinum-coated parallel vertical surfaces in a recombiner. To describe the kinetics of the surface processes, a reaction scheme of the surface combustion of methane combustion reaction developed by Deutschmann [12] is used. The description of natural convection-induced heat transfer between parallel plates is based on the approach by Elenbaas [13]. Mass transfer is considered to be analogous to the occurring heat transfer. The proposed model can simulate the H_2 and CO recombination phenomena, characteristic of PARs with plane-parallel plates, by implementating a linear system of differential equations, which involves the simplified Deutschmann mechanism. The transient model can react to dynamic changes in the atmosphere surrounding the PAR, which involves both the heating phase and the cool-down phase.

A validation process of PARUPM was performed to study the accuracy and validity of the code [14]. The results for the physicochemical model (PARUPM stand-alone) have been compared to experimental data from THAI containment program tests [15]. From this validation process, we obtained a PARUPM code capable of replicating the operation of a real recombiner inside a containment. Next, the validated PARUPM code was implemented into GOTHIC to validate it further and optimise the model for its use as a coupled code for full containment analysis in GOTHIC.

GOTHIC [7] is an integrated, general-purpose thermal-hydraulics software package for design, licensing, safety and operating analysis of nuclear power plant containments, confinement buildings and system components. It solves the conservation equations for mass, momentum and energy for multi-component, multi-phase compressible flow in three fields: vapour, continuous liquid, and droplets. GOTHIC uses empirical correlations to calculate heat transfer between the fluid domain and 1D or 2D structures by

convection, condensation, and evaporation. It also uses 1D correlations for the fluid friction with solid structures.

The thermal-hydraulic calculations of GOTHIC are based on a single control volume (CV), or a network of volumes connected by flow paths or 3D connectors. A control volume can be subdivided into 2D or 3D Cartesian grids. Thus, GOTHIC can perform both lumped parameter and 3D containment analyses offering a balance between accuracy - due to its 3D capabilities - and computational cost. Furthermore, it uses empirical correlations, based on bulk properties, to define friction and heat transfer between the fluid and the solid structures, instead of attempting to model the boundary layers.

To include PAR operation in the analysis, GOTHIC provides a simple built-in component model which calculates the recombination rate based on a user-defined recombination efficiency and the H_2 mass flow rate that passes through the recombiner. PARUPM is implemented into GOTHIC as an external function to calculate the user-defined recombination efficiency depending on the pressure, temperature, and gas composition at the PAR entrance.

3. THAI EXPERIMENTS AND MODEL SETUP

3.1. Facility configuration

The test facility THAI (thermal-hydraulics, hydrogen, aerosol, and iodine) addresses open questions concerning gas distribution, behaviour of hydrogen, iodine, and aerosols in the containment of light water reactors during severe accidents. The main component of the facility is a 60 m^3 stainless steel vessel, 9.2 m high and 3.2 m in diameter, with exchangeable internals for multi-compartment investigations. The vessel structures are made of stainless steel and completely surrounded by Rockwool thermal insulation enveloped with aluminium cladding (Fig. 2 left). The cylindrical part of the vessel is double-walled, and the gap between the walls is filled with a thermal oil for heating or cooling [15].



Figure 2. THAI test facility [15] **and scheme of the vessel for the HR test**

In the context of the international OECD/NEA THAI projects [15], [16], [17], a series of experiments involving hydrogen recombination (HR) tests were conducted over the past decade. These tests systematically varied factors such as initial thermal hydraulic conditions to investigate the onset of recombination, recombination rate, recombination efficiency and ignition potential under ambient/saturated/superheated steam atmospheres and elevated initial pressure and temperature

conditions. The effect of O_2 starvation, a phenomenon expected during the ex-vessel phase of severe accidents, was also studied [4]. In the case of the HR tests, an inner cylinder is located in the centre of the THAI vessel. The recombiner is attached to the outer side of this cylinder (Fig. 2 right). Several of the recombiner experiments performed in THAI facility have been used for the validation exercise presented in this paper.

3.2. Description of test cases

The THAI-tests considered for the PARUPM validation were performed with an Framatome FR90/1-380T recombiner with a 50 % down-scaled inlet cross-section and number of catalyst sheets. All tests were run with an initial injection phase of hydrogen, a subsequent depletion phase, a second hydrogen injection phase, and a second and last depletion phase (Fig. 3) [18]. The tests considered for the validation presented in this paper are HR-2 and HR-12. The first one represents the base case with initial ambient temperature and pressure in dry atmosphere, while the conditions of the second one resemble closer a severe accident (higher pressures, temperatures, and steam concentration). These THAI-tests involve only hydrogen, not carbon monoxide. Thus, in this work, only the capability of PARUPM to simulate the hydrogen recombination was evaluated to better address the coupling and the THAI vessel feedback on the PAR performance.

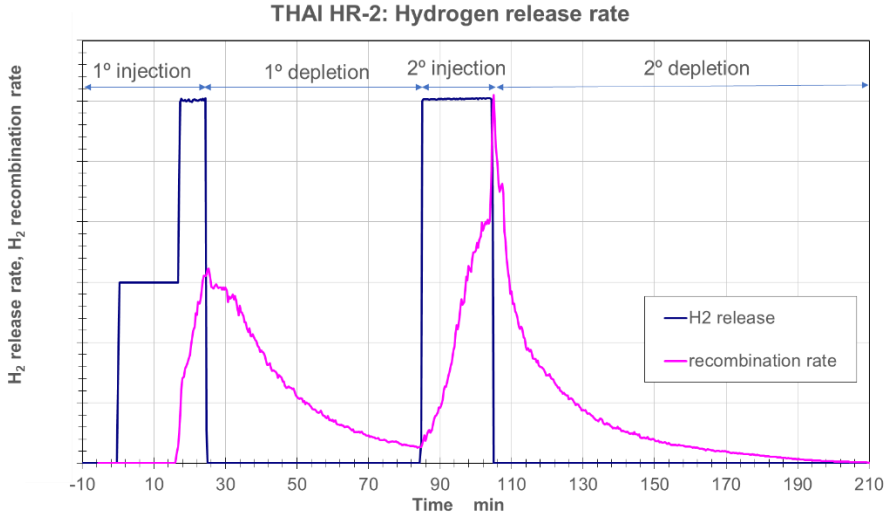

Figure 3. THAI HR-2 hydrogen release during the transient

Test HR-2 starts with a vessel atmosphere of dry air at an ambient temperature of 25 ºC. During the first test phase, H_2 is injected into the vessel. After 25 minutes, the injection stops and the first depletion (recombination only) phase starts, which lasts 60 minutes (Fig. 3). Then, the second hydrogen injection phase takes place for 20 minutes, followed by the second depletion phase, which runs until the recombination stops [19].

The initial conditions of test HR-12 include a mixture of air with 60 vol.% steam at a temperature of 86 ºC and a higher initial pressure of 3 bar. The test follows the same pattern of injection and depletion as HR-2. However, during the second injection and depletion, the recombination runs under oxygen starvation conditions, to clarify, the oxygen available on the surrounding environment is depleted, reducing the overall recombination and impacting the recombiner efficiency [20].

3.3. THAI model in GOTHIC 8.3

The THAI geometry was first modelled with CAD software (Fig. 4). This eases the identification and dimensionalisation of the different geometrical bodies to replicate the geometry in GOTHIC and to respect the original free volume of 60 m^3. The metallic inner cylinder placed inside the vessel, the injection ring, and the recombiner box were included in the CAD geometry. The mesh definition and optimisation, the extraction of relevant geometrical variables such as the wall surfaces, and the location of the injection boundary conditions are also performed in the more user-friendly CAD environment.

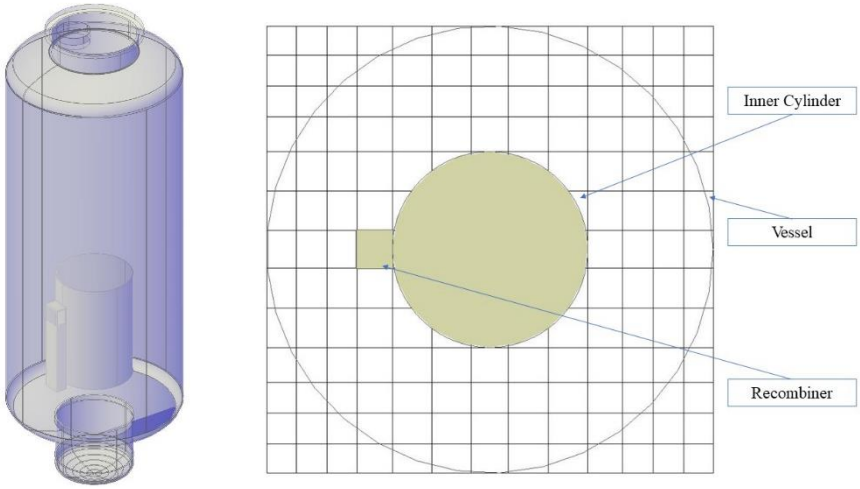

Figure 4. THAI vessel recreated in CAD and its mesh.

The geometrical information obtained with the CAD model is used to create the THAI vessel in the GOTHIC model (Fig. 5). The size of the PAR is the reference value for making the mesh implemented in the model. The model uses the coarsest mesh to represent the geometry of the PAR (entrance, chimney, and outlet) while keeping a cell centre in the vessel's central axis and maximising the smoothness of the mesh as much as possible. Thus, the total number of cells in the model is 5577 cells. The model is divided into two control volumes (CVs): one that represents the main vessel, and one for the inner cylinder (Fig. 5). 3D connectors connect both CVs to allow the flow between them. The recombiner is located in the main vessel CV (marked as yellow box in Fig. 5).

The inner space of the recombiner box is represented in the model. This enables the definition of all the main dimensions of the PAR, which cannot be captured by the commonly used approach of blocking the space occupied by the PAR box, representing it as a flow path. The catalytic plates are not explicitly included in the model geometry. Instead, the physics happening between the plates (recombination, temperature increase, flow resistance, etc.) are calculated by PARUPM. In GOTHIC nomenclature, the recombination process is calculated by a Flow Path and an H_2 Recombiner component at the location of the PAR catalytic plates.

Thermal conductors were used in the vessel CV to model heat transfer to internal structures and to model the heat transfer through the vessel walls to the environment. The full thickness of the wall, including a heating oil layer, was modelled with an external boundary condition with a 10 W/m^2 K heat transfer coefficient and a 20ºC ambient temperature. The heat transfer from the fluid to the walls is represented by engineering correlations adapted to the relatively coarse mesh used in this work. The condensation heat transfer uses a diffusion layer model with enhancement due to film roughening, heat transfer between the

wall and film and mist generation in the boundary layer (DLM-FM). The model also uses correlations for single-phase natural convection and radiation heat transfer is not considered.

The simulations used a finite second-order numerical upwind discretisation scheme and a biconjugate gradient solution method. The size of the time step is controlled by the solver but is limited to 10^{-9} s and 0.1 s. The standard $k-\varepsilon$ turbulence model was employed.

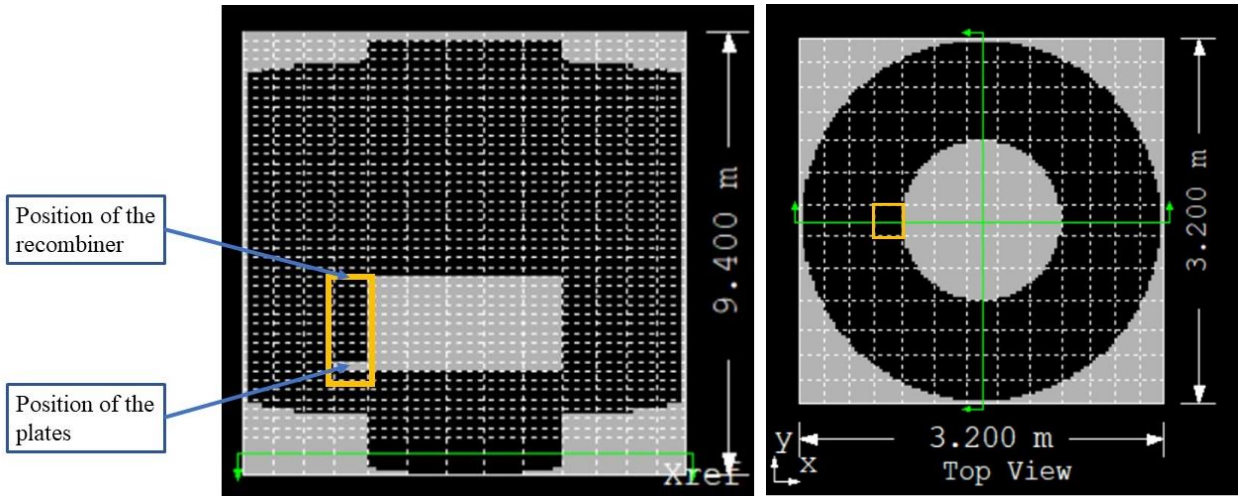

Figures 5. THAI vessel in GOTHIC.

4. SIMULATION RESULTS

4.1. PARUPM as a standalone tool

For the PARUPM stand-alone simulation, the code input parameters (gas concentration, pressure, temperature) were directly taken from the measurements at the PAR inlet in the THAI facility. Thus, the physical behaviour of the rest of the THAI vessel is not considered and does not impact the PARUPM simulation. As an example, this means that if PARUPM underpredicts the recombination for 1000 seconds, it will not have an excess of hydrogen available afterwards. PARUPM will always use the experimental recordings as input values.

Fig. 6 compares the experimental results for the PAR recombination rate and the average temperature of the catalyst plates for the experiment HR-2 with the values obtained with PARUPM. As shown in Fig. 6 there are not many discrepancies between the model and the experimental recombination rates. The only difference occurs at the end of the second injection phase, where the PARUPM recombination rate does not reach the experimental recombination peak. This peak is due to a PAR-induced ignition causing high hydrogen conversion rates during the combustion. Since, PARUPM does not contain an ignition module, the code does not capture this behaviour.

The average catalyst temperatures are higher than the experimental ones in both depletion phases. One possible explanation could be that the model does not consider heat transfer phenomena, such as the effect of radiative heat exchange between the PAR catalytic plates and the metallic structure of the recombiner, as well as between the PAR metallic walls and the vessel walls. Nevertheless, the comparison with the

experimental data confirms that the code produces reasonable results when simulating the behaviour of a realistic PAR.

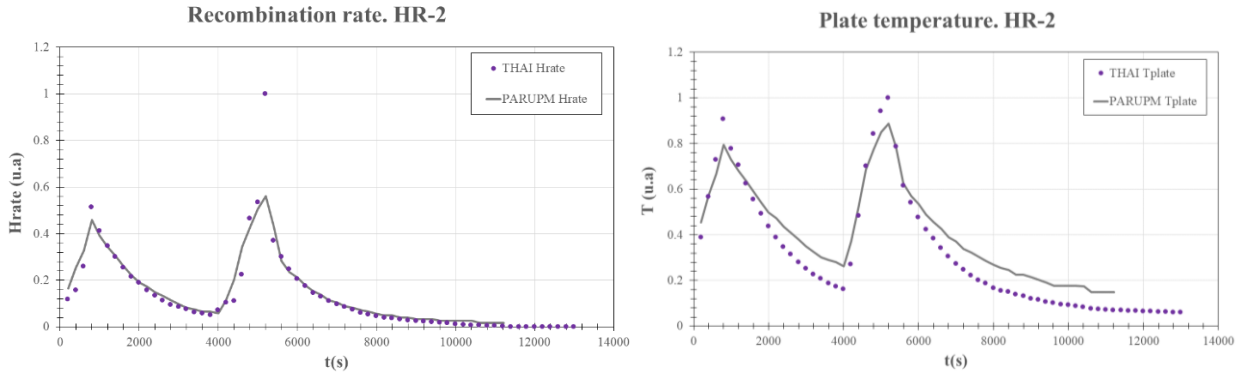

Figure 6. Recombination rate and catalyst temperature obtained with PARUPM (grey line) and measured on the vessel (purple dots) during the transient for HR-2.

Fig. 7 shows the recombination rate and average catalyst temperature obtained from the experiment HR-12 and the recombination rates and plate temperature calculated with PARUPM using the boundary conditions directly from the experiment. As before, the code reproduces well the behaviour of an actual PAR even at elevated pressure/temperature conditions and also during the second injection and depletion phase, when the recombiner is experiencing oxygen starvation. The same issue as discussed earlier for the HR-2 test appears with the catalyst temperature. Thus, the plate temperature of both depletion phases is higher than the experimental one. Nonetheless, this discrepancy is less pronounced during the second depletion, when the oxygen starvation conditions begin. A more detailed representation of the heat transfer processes affecting the catalyst plates may be needed to improve the catalyst temperature predictions.

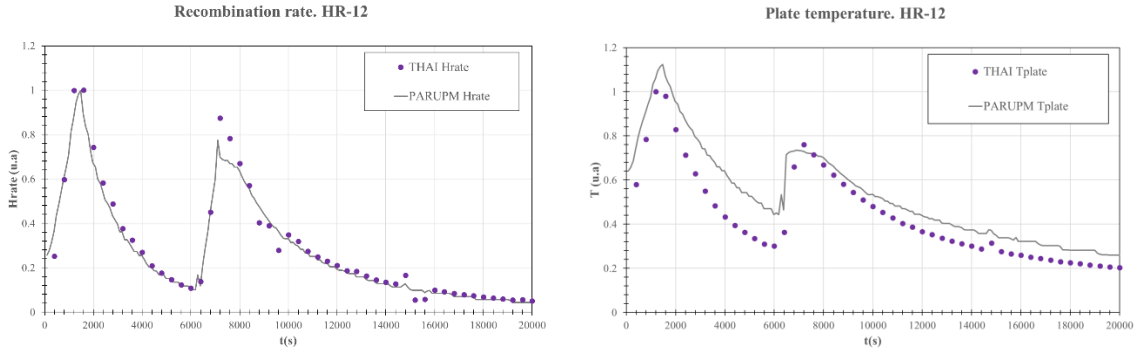

Figure 7. Recombination rate and catalyst temperature obtained with PARUPM (grey line) and measured (purple dots) during the transient for HR-12.

4.2. Full-scale analysis with GOTHIC

The next step in the validation process is to test the implementation of PARUPM into GOTHIC. This validation is performed by replicating test HR-2 by simulating the THAI vessel in the containment code GOTHIC and using PARUPM to simulate the recombiner, as described in section 3.3. Thus, in contrast to the stand-alone simulation described in section 4.1, the input parameters for PARUPM (pressure, temperature, and molar fractions of gases) are not taken from experimental measurements but are calculated by GOTHIC. Hence, there will be feedback between GOTHIC's and PARUPM's predictions.

PARUPM simulates the gas recombination, and the PAR exhaust gases are then returned into the GOTHIC code. The data exchange of PARUPM and GOTHIC occurs in each simulation time step.

Fig. 8 shows the recombination rate obtained with PARUPM, the vessel pressure for the simulated HR-2 test, and the flow velocity through the recombiner. Results obtained with the GOTHIC model are compared with the experimental results obtained in the THAI facility. The recombination rate is reproduced in the coupled simulation with an equivalent accuracy to the stand-alone calculation. Hence the vessel feedback calculated by GOTHIC does not worsen the accuracy of the simulations. Note that with the simulation of the vessel in GOTHIC, additional uncertainties are expected, compared to the approach in section 4.1. Nevertheless, the qualitative and quantitative agreements of the simulated hydrogen recombination rates with the experimentally obtained ones are maintained.

Furthermore, the GOTHIC simulation is able to represent the transport processes from the injection ring to the entrance of the PAR box. This is not a trivial observation since the multi-jet injection ring cannot be resolved in the relatively coarse mesh used in GOTHIC. Yet, the approach used proved its ability to replicate the initial expansion of the jet and the later suction effect induced by the PAR buoyancy.

During the first injection, the calculated recombination rate is higher than the experimental one due to the flow velocity calculated with GOTHIC. The code cannot estimate the gas flow rate through the PAR in early stages of the recombination as seen in Fig. 8 bottom. Thus, the H_2 concentration that reaches the recombiner during this first stage is higher than the experimental one, causing a higher recombination rate. The PAR-induced ignition is not calculated either since a combustion model was not added to the GOTHIC model. At later stages of the transient the recombination rate is better calculated, thus, once the recombiner reaches the stationary state the coupling PARUPM-GOTHIC is able to predict the experimental recombination rate and reproduce the phenomenology related to PARs inside a containment.

Pressure is slightly overpredicted during the whole transient, except during the first depletion phase, and the higher discrepancies are found at the peaks of the injection phases when the difference between the simulated and the experimental pressure is around 10 kPa. This pressure discrepancy indicates that the simulated vessel is not capturing all the relevant thermohydraulic phenomena of the actual vessel. Pressure is a very sensitive parameter to the heat transfer through the wall. Since the boundary conditions strongly affect the solid-fluid heat transfer, there is still ongoing work to enhance the pressure prediction. Nevertheless, the qualitative evaluation of the pressure results is consistent with the experimental recordings.

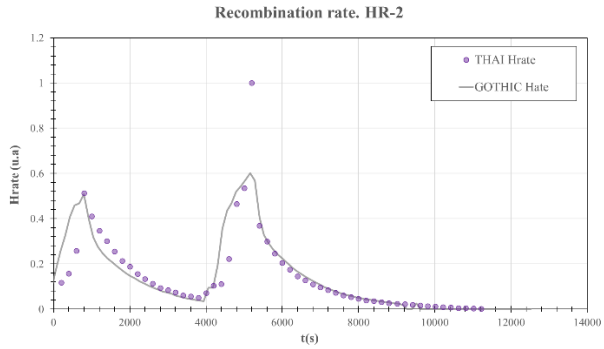

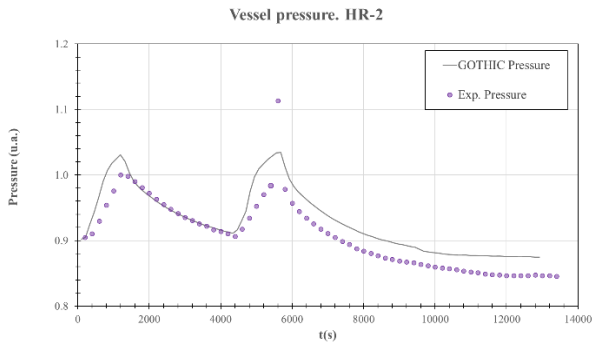

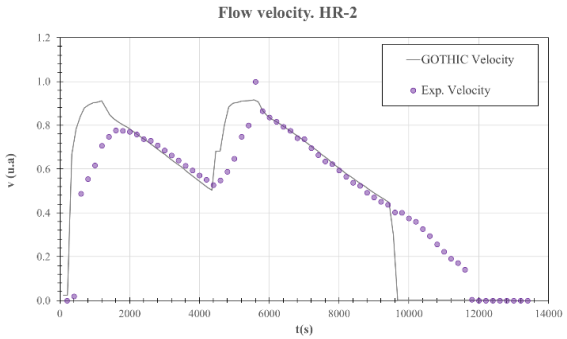

Figures 8. Recombination rate, vessel pressure and flow velocity through the PAR for the test HR-2 in GOTHIC using PARUPM as an external function to calculate the recombination rate.

Finally, the vessel temperatures at different heights have been compared between the model and the experiment. Fig. 9 left represents the gas temperatures on the top of the vessel and Fig. 9 right shows the temperatures at the vessel bottom. The gas temperatures reached on the vessel at different heights, represented with coloured lines in Fig. 9, follow the expected behaviour from experimental ones (coloured dots) during the depletion phases. Discrepancies are found during the injection phases, where the temperature is overestimated. Nevertheless, this deviation is consistent with what we obtained from the recombination rate and the vessel pressure. Thus, there is an overall overestimation during the injection phases probably due to the overprediction on the flow velocity through the PAR.

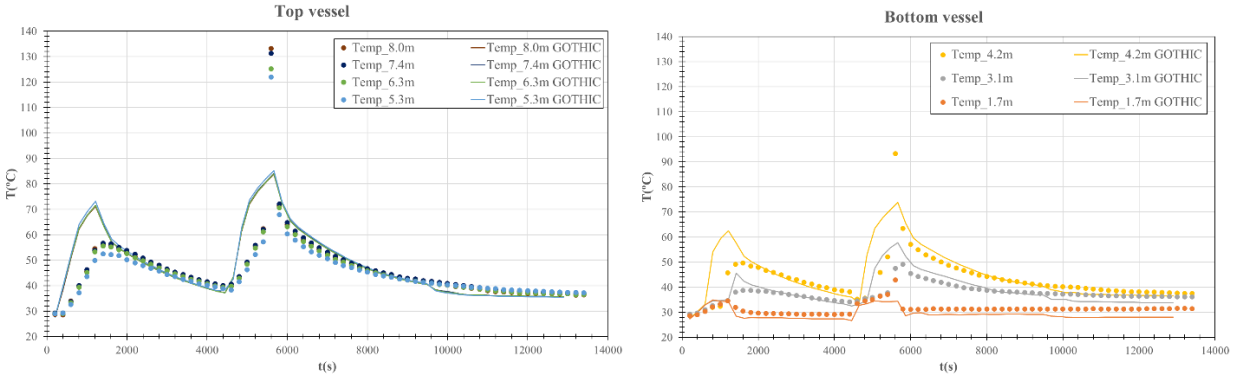

Figures 9. Vessel temperatures at different heights for the test HR-2 in GOTHIC using PARUPM as an external function to calculate the recombination rate.

5. CONCLUSIONS

This paper has detailed the development, validation, and application of the PARUPM code, first as a stand-alone tool and then coupled with the GOTHIC thermal-hydraulics software package.

Using the PARUPM code as a standalone tool, experiments HR-2 and HR-12 from the THAI facility were replicated. Thus, the code is capable of predicting the behaviour of real recombiners using the experimental recording as inlet conditions (pressure, temperature, and gases concentrations).

The simulation of test HR-2 with GOTHIC coupled with PARUPM shows adequate results for recombination rates, vessel pressure, and vessel gas temperatures during the transient compared to the experimental ones. Thus, the code simulates properly the behaviour of PARs in full containments, where the conditions of pressure, temperature, and gas concentrations are constantly changing.

In conclusion, the presented work establishes a foundation for using the coupled PARUPM-GOTHIC model as a valuable tool to predict PARs operation in nuclear power plant containments. The integration of the PARUPM code with the GOTHIC software as an add-on function highlights the potential of this code for comprehensive containment analysis.

In future works, a thorough refinement of the flow velocity calculated for the recombiner will be performed to better capture the phenomenology and the behaviour of a real PAR. Moreover, the validation of the PARUPM-GOTHIC coupling will be extended to cover a wider range of conditions (e.g. with the presence of carbon monoxide) for a comprehensive safety analysis of nuclear power plants.

ACKNOWLEDGMENTS

The THAI experiments presented in this paper have been conducted in the frame of OECD/NEA THAI project. The financial support by the countries participated in the OECD/NEA THAI project is greatly acknowledged. This project has received funding from the ENEN2plus mobility grant program. Furthermore, the AMHYCO project has received funding from the Euratom research and training programme 2019-2020 under Grant Agreement n°945057. GOTHIC™ incorporates technology developed for the electric power industry under the sponsorship of EPRI, the Electric Power Research Institute. This work used a GOTHIC license for educational purposes provided by Numerical Advisory Solutions, LLC.

Co-funded by the European Union

REFERENCES

[1] Z. Liang, M. Sonnenkalb, A. Bentaib, and M. Sangiorgi, ‘HYDROGEN MANAGEMENT STRATEGIES AND ANALYSIS CODES IMPLEMENTED BY THE OECD / NEA MEMBER COUNTRIES’, presented at the 16th International Topical Meeting on Nuclear Reactor Thermal Hydraulics (NURETH-16), Chicago, USA, 2015, pp. 711–723.

[2] A. Bentaib, N. Meynet, and A. Bleyer, ‘Overview on hydrogen risk research and development activities: Methodology and open issues’, *Nuclear Engineering and Technology*, vol. 47, no. 1, pp. 26–32, Feb. 2015, doi: 10.1016/j.net.2014.12.001.

[3] E. Bachellerie *et al.*, ‘Generic approach for designing and implementing a passive autocatalytic recombiner PAR-system in nuclear power plant containments’, *Nuclear Engineering and Design*, vol. 221, no. 1–3, Art. no. 1–3, Apr. 2003, doi: 10.1016/S0029-5493(02)00330-8.

[4] S. Gupta, M. Freitag, and Z. Liang, ‘Main Outcomes and Lessons Learned from Thai Passive Autocatalytic Recombiner Experimental Research And Related Model Development Work’, presented at the 17th International Topical Meeting on Nuclear Reactor Thermal Hydraulics (NURETH-17), Xi’an, Shaanxi, China, 2017.

[5] G. Jiménez *et al.*, ‘AMHYCO project– Towards advanced guidelines for hydrogen safety in nuclear power plants.’, Oct. 2020.

[6] M. Á. Jiménez, ‘Recombinación del hidrógeno en dispositivos autocatalíticos pasivos y sus implicaciones en la seguridad de las centrales nucleares’, Doctoral Dissertation, Universidad Politécnica de Madrid (UPM), Madrid, Spain, 2007. [Online]. Available: http://oa.upm.es/718/

[7] EPRI, ‘GOTHIC Thermal Hydraulic Analysis Package. Version 8.3(QA)’. EPRI, Palo Alto, CA, 2018.

[8] E.-A. Reinecke *et al.*, ‘PAR model development exercise in the framework of SAMHYCO-NET’, *Nuclear Engineering and Design*, vol. 399, p. 112035, 2022, doi: 10.1016/j.nucengdes.2022.112035.

[9] E.-A. Reinecke, A. Bentaib, S. Kelm, W. Jahn, N. Meynet, and C. Caroli, ‘Open issues in the applicability of recombiner experiments and modelling to reactor simulations’, *Progress in Nuclear Energy*, vol. 52, no. 1, Art. no. 1, 2010, doi: 10.1016/j.pnucene.2009.09.010.

[10] F. Arnould *et al.*, 'State of the art on hydrogen passive auto-catalytic recombiner (european union Parsoar project)', presented at the 9th international conference on nuclear engineering, France, 2001.
[11] M. A. Jiménez, J. M. Martín-Valdepeñas, F. Martín-Fuertes, and J. A. Fernández, 'A detailed chemistry model for transient hydrogen and carbon monoxide catalytic recombination on parallel flat Pt surfaces implemented in an integral code', *Nuclear Engineering and Design*, vol. 237, no. 5, pp. 460–472, Mar. 2007, doi: 10.1016/j.nucengdes.2006.08.002.
[12] O. Deutschmann, R. Schmidt, F. Behrendt, and J. Warnat, 'Numerical modeling of catalytic ignition', presented at the Symposium (International) on Combustion, Jan. 1996, pp. 1747–1754. doi: 10.1016/S0082-0784(96)80400-0.
[13] W. Elenbaas, 'Heat dissipation of parallel plates by free convection', *Physica*, vol. 9, no. 1, pp. 1–28, Enero 1942, doi: 10.1016/S0031-8914(42)90053-3.
[14] A. Domínguez-Bugarín, M. A. Jimenez, E.-A. Reinecke, and G. Jimenez, 'PARUPM: A simulation code for passive auto-catalytic recombiners', *EPJ Nuclear Science Technology*, vol. 8, no. 32, p. 6, Nov. 2022, doi: https://doi.org/10.1051/epjn/2022046.
[15] S. Gupta, G. Poss, and M. Sonnenkalb, 'OECD/NEA THAI program for containment safety research: main insights and perspectives', presented at the Eurosafe Forum 2016, Münich, Germany, Nov. 2016.
[16] NEA, 'OECD/NEA THAI Project Hydrogen and Fission Product Issues Relevant for Containment Safety Assessment under Severe Accident Conditions', NEA/CSNI/R(2010)3, 2010.
[17] NEA, 'Aerosol and Iodine Issues, and Hydrogen Mitigation under Accidental Conditions in Water-cooled Reactors: Thermal-hydraulics, Hydrogen, Aerosols and Iodine (THAI-2) Project – Final Report', Paris, France, Final Report NEA/CSNI/R(2016)8, 2017.
[18] NEA, 'International Standard Problem: ISP-47 on Containment Thermal Hydraulics – Final Report', OECD/NEA, Paris, France, Final Report NEA/CSNI/R(2007)10, 2007.
[19] T. Kanzleiter, 'Quick Look Report on Hydrogen Recombiner Tests HR-1 to HR-5, HR-27 and HR-28 (Tests without steam, using an Areva PAR)', Becker Technologies GmbH, Eschborn, Germany, 1501326-HR-QLR-1, 2009.
[20] T. Kanzleiter, 'Hydrogen Recombiner Tests HR-6 to HR-13, HR-29 and HR-30: Tests with steam, using an AREVA PAR', Becker Technologies GmbH, Eschborn, Germany, 1326-HR-QLR-2, 2009.

ERMSAR 2024

AMHYCO

Enhancing H_2 & CO Combustion Risk Management

Validation of the PARUPM and GOTHIC 8.3 code coupling using THAI hydrogen recombination tests

Araceli Domínguez-Bugarín. UPM

Luis Serra. UPM

Carlos Vázquez-Rodríguez. UPM, FZJ

Ernst-Arndt Reinecke. FZJ

Stephan Kelm. FZJ

Miguel Ángel Jiménez. UPM, CSN

Gonzalo Jiménez. UPM

Sanjeev Gupta. Becker Technologies

This project has received funding from the European Union's EURATOM Horizon 2020 research and innovation programme grant number: 945057. The content of this document reflects only the author's view. The European Commission is not responsible for any use that may be made of the information it contains.

Introduction

- **Hydrogen combustion risk**

  - During a Severe Accident large release of combustible gases.
  - Combustion risk increases.
  - Installation of Passive Autocatalytic Recombiners reduces this risk.

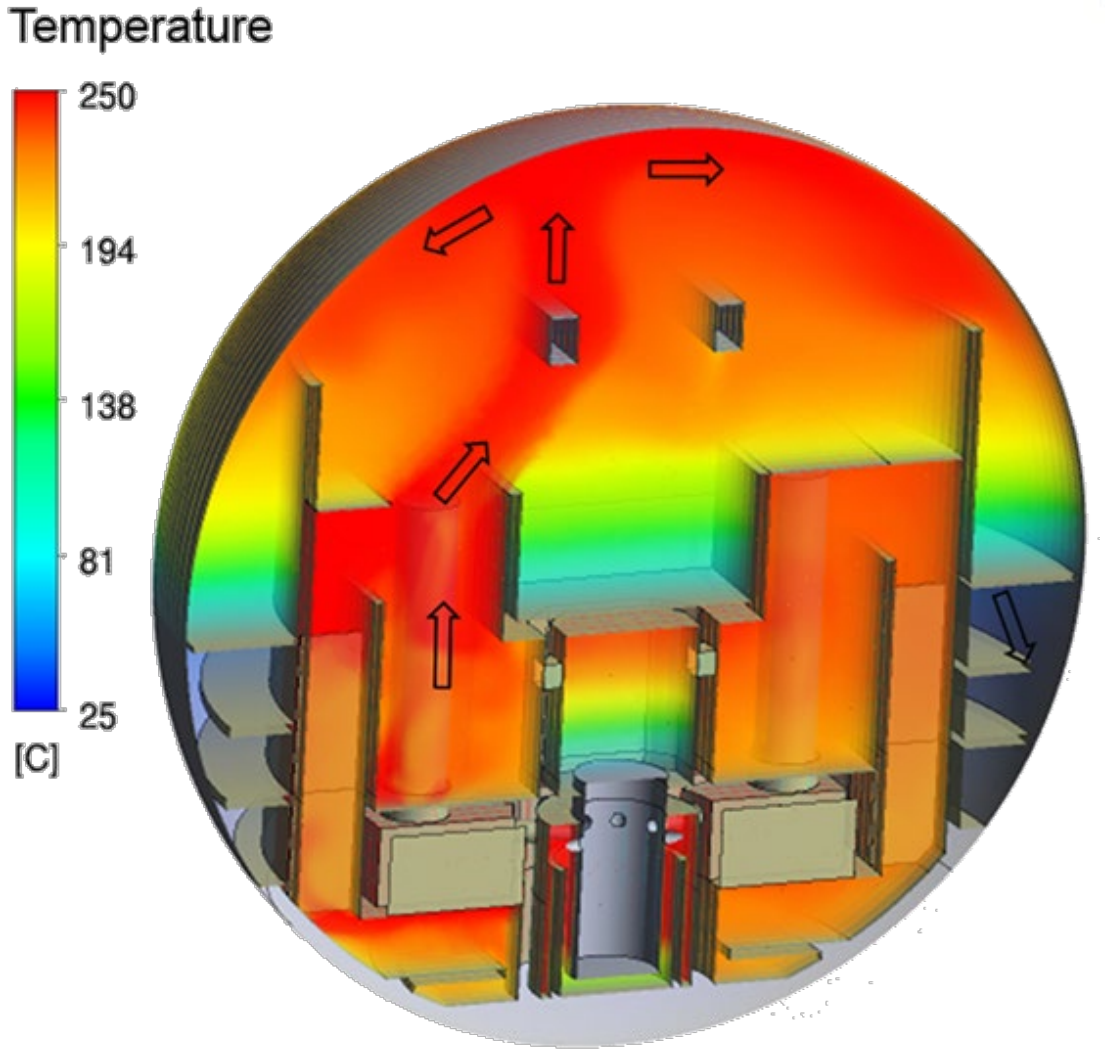

Reference: IKE, University of Stuttgart

Introduction

- **Hydrogen combustion risk**

  - During a Severe Accident large release of combustible gases.
  - Combustion risk increases.
  - Installation of Passive Autocatalytic Recombiners reduces this risk.



Framatome FR1-380T. Reference: Framatome, 2011

Introduction

PARs: H_2/CO recombination with O_2

$$H_2 + {}^1/_2\, O_2 \rightarrow H_2O + 242\ kJ/mol$$

$$CO + {}^1/_2\, O_2 \rightarrow CO_2 + 283\ kJ/mol$$

Natural convection

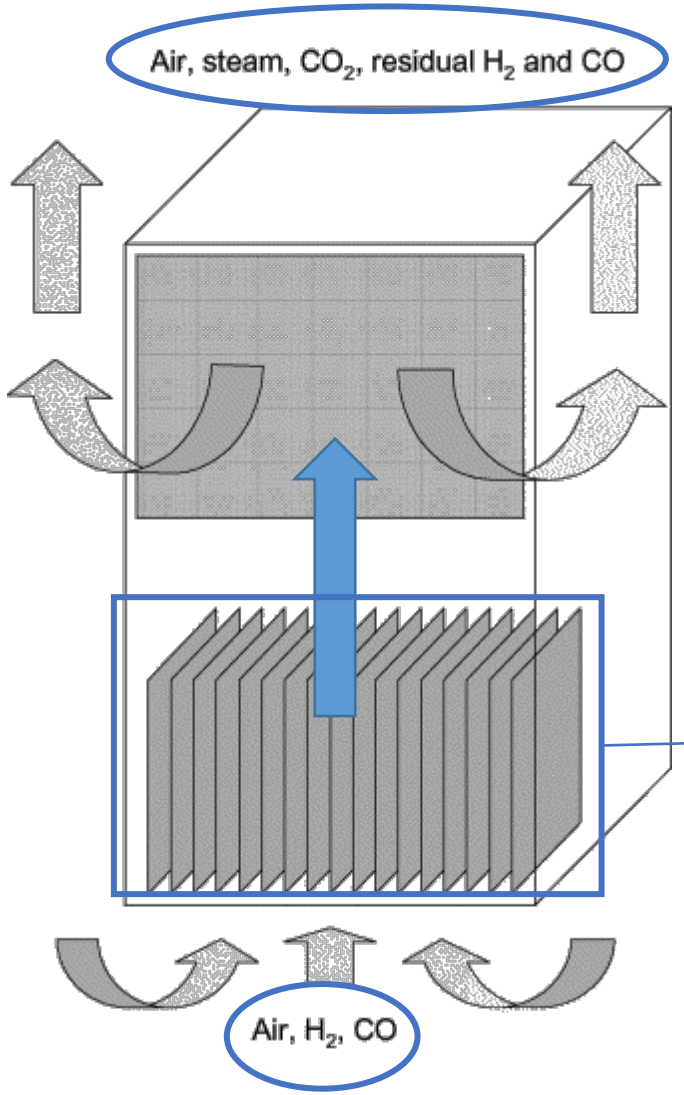

Stainless steel+ Pt

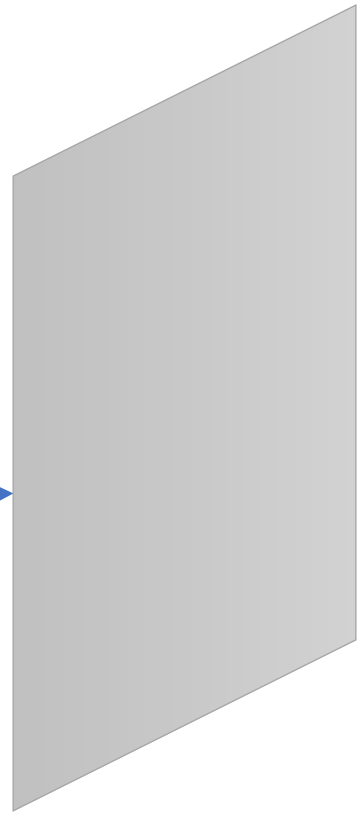

Introduction

PARUPM CODE

- Simulates the behaviour of a PAR device through a physical-chemical approach.
- Code accounts for the different phenomena intervening in the recombiner.
- Extended enhancement and validation process.
- Initially coupled with MELCOR (FORTRAN) -> standalone tool (FORTRAN) -> coupled with GOTHIC (C++)

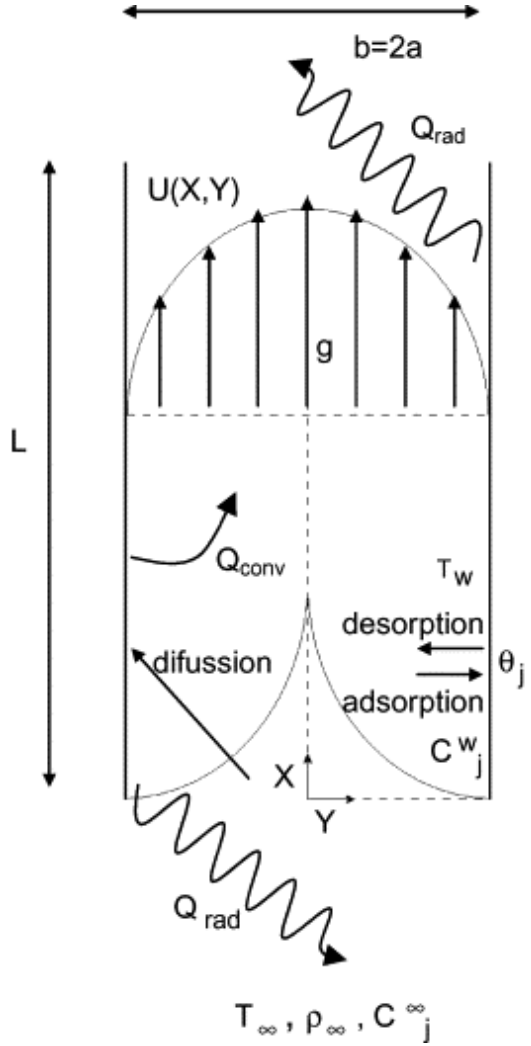

Introduction

PARUPM CODE VALIDATION

DECOUPLING AND DEVELOPMENT OF THE PARUPM CODE

↓

ENHANCEMENT USING REKO-3 AND THAI (STEADY-STATE)

↓

THAI TRANSIENT SIMULATIONS AS A STANDALONE TOOL

↓

COUPLING OF PARUPM INTO GOTHIC SIMULATING THAI FACILITY

↓

FULL CONTAINMENT SIMULATION USING PARUPM AND GOTHIC

PARUPM steady-state validation

PARUPM CODE VALIDATION

DECOUPLING AND DEVELOPMENT OF THE PARUPM CODE

↓

ENHANCEMENT USING REKO-3 AND THAI (STEADY-STATE)

↓

THAI TRANSIENT SIMULATIONS AS A STANDALONE TOOL

↓

COUPLING OF PARUPM INTO GOTHIC SIMULATING THAI FACILITY

↓

FULL CONTAINMENT SIMULATION USING PARUPM AND GOTHIC

PARUPM steady-state validation

- **Mass transfer model**:

$$Rate_{H_2,dif} = \frac{Sh_{H_2} D_{dif}}{D_h}\left(\frac{p_{H_2}}{RT}\right)$$

- **Study the effect of oxygen starvation** (i.e., low oxygen/nitrogen ratio).

- **Study the effect of CO** on the H2 recombination rate and the CO recombination capability of the code.

PARUPM validation: standalone tool

PARUPM CODE VALIDATION

DECOUPLING AND DEVELOPMENT OF THE PARUPM CODE

↓

ENHANCEMENT USING REKO-3 AND THAI (STEADY-STATE)

↓

THAI TRANSIENT SIMULATIONS AS A STANDALONE TOOL

↓

COUPLING OF PARUPM INTO GOTHIC SIMULATING THAI FACILITY

↓

FULL CONTAINMENT SIMULATION USING PARUPM AND GOTHIC

THAI vessel: facility configuration

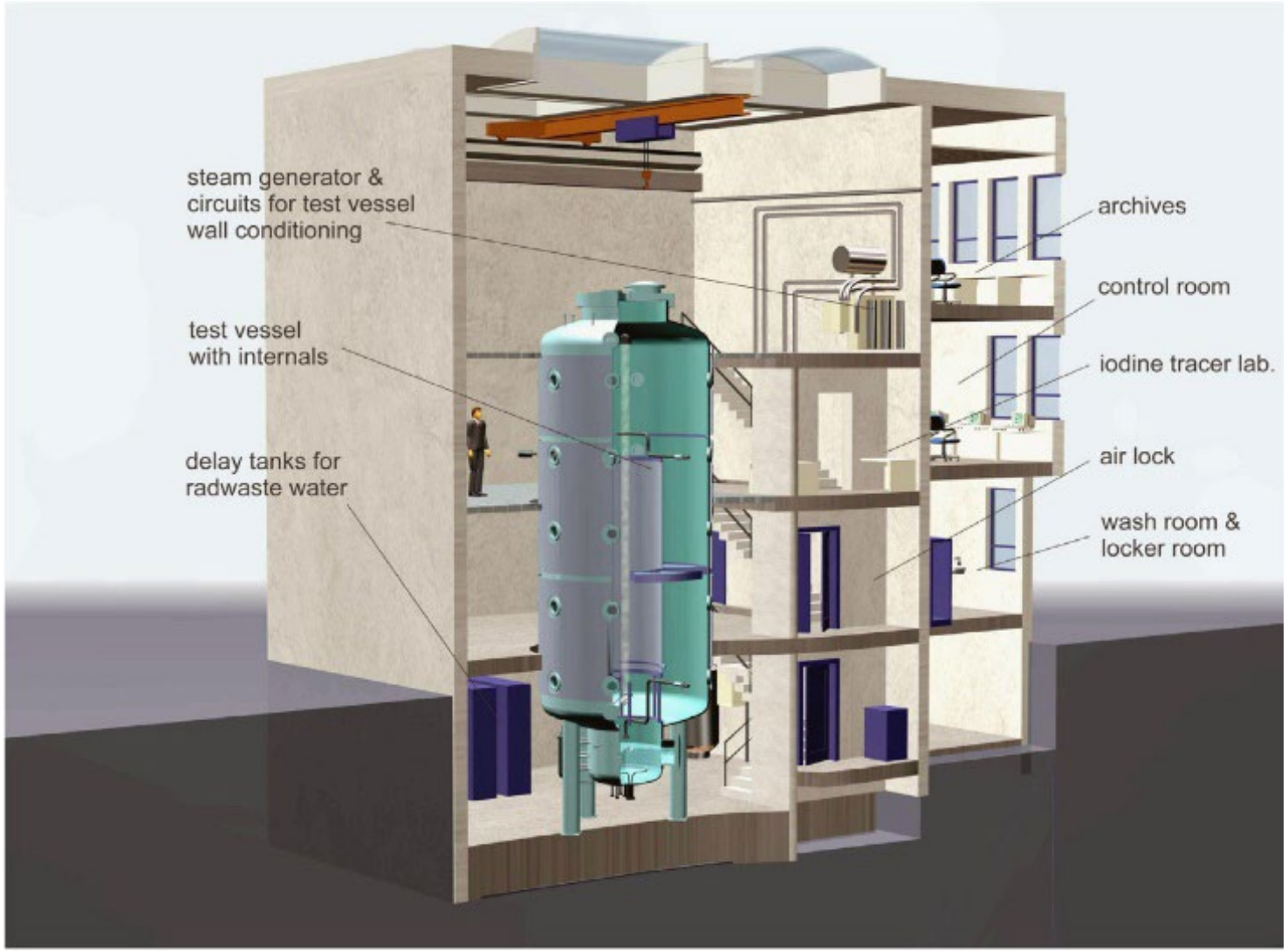



THAI vessel: test cases description

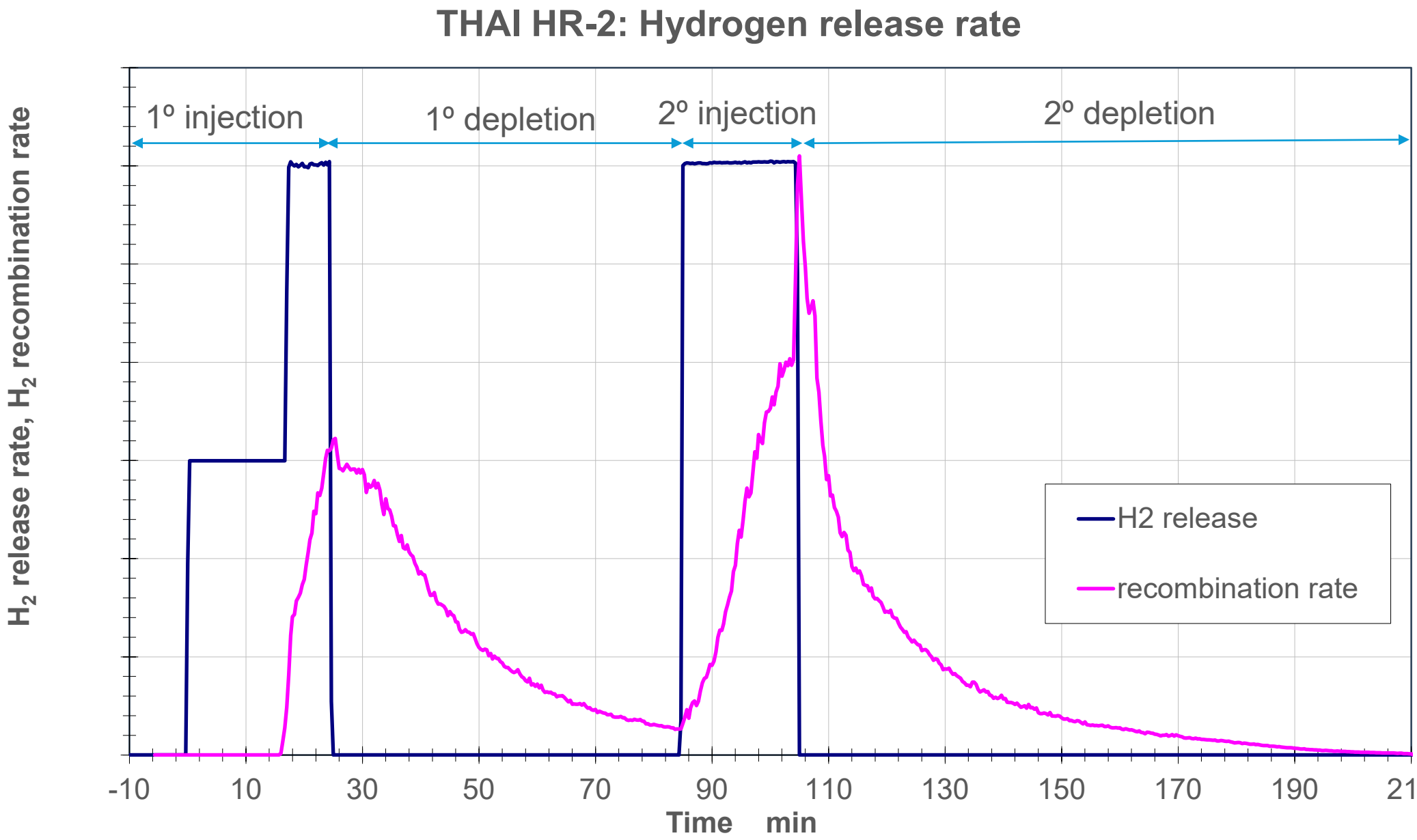

THAI vessel: test cases description

Pressure	Temperature	Steam	Experiment	Ignition	O2 starvation	H2/CO ratio
1 bar	25ºC	dry	HR-1, HR-2	X		
1 bar	86ºC	60 %	HR-13		X	
1.5 bar	25ºC	dry	HR-3, HR-28	X		
1.5 bar	74ºC	25 %	HR-7	X		
1.5 bar	90ºC	47 %	HR-9		X	
1.5 bar	97ºC	60 %	HR-11		X	
3 bar	25ºC	dry	HR-5			
3 bar	117ºC	60 %	HR-12		X	

THAI vessel: test cases description

Pressure	Temperature	Steam	Experiment	Ignition	O2 starvation	H2/CO ratio
1 bar	25ºC	dry	HR-2	X		
1 bar	86ºC	60 %	HR-13		X	
1.5 bar	25ºC	dry	HR-3, HR-28	X		
1.5 bar	74ºC	25 %	HR-7	X		
1.5 bar	90ºC	47 %	HR-9		X	
1.5 bar	97ºC	60 %	HR-11		X	
3 bar	25ºC	dry	HR-5			
3 bar	117ºC	60 %	HR-12		X	

PARUPM validation: standalone tool

- **Test HR-2: recombination rate**

  - Low pressure and temperature, and dry air
  - Self-ignition on the second injection
  - Initial conditions extracted from the inlet of the PAR.
  - Velocity is calculated with the chimney model

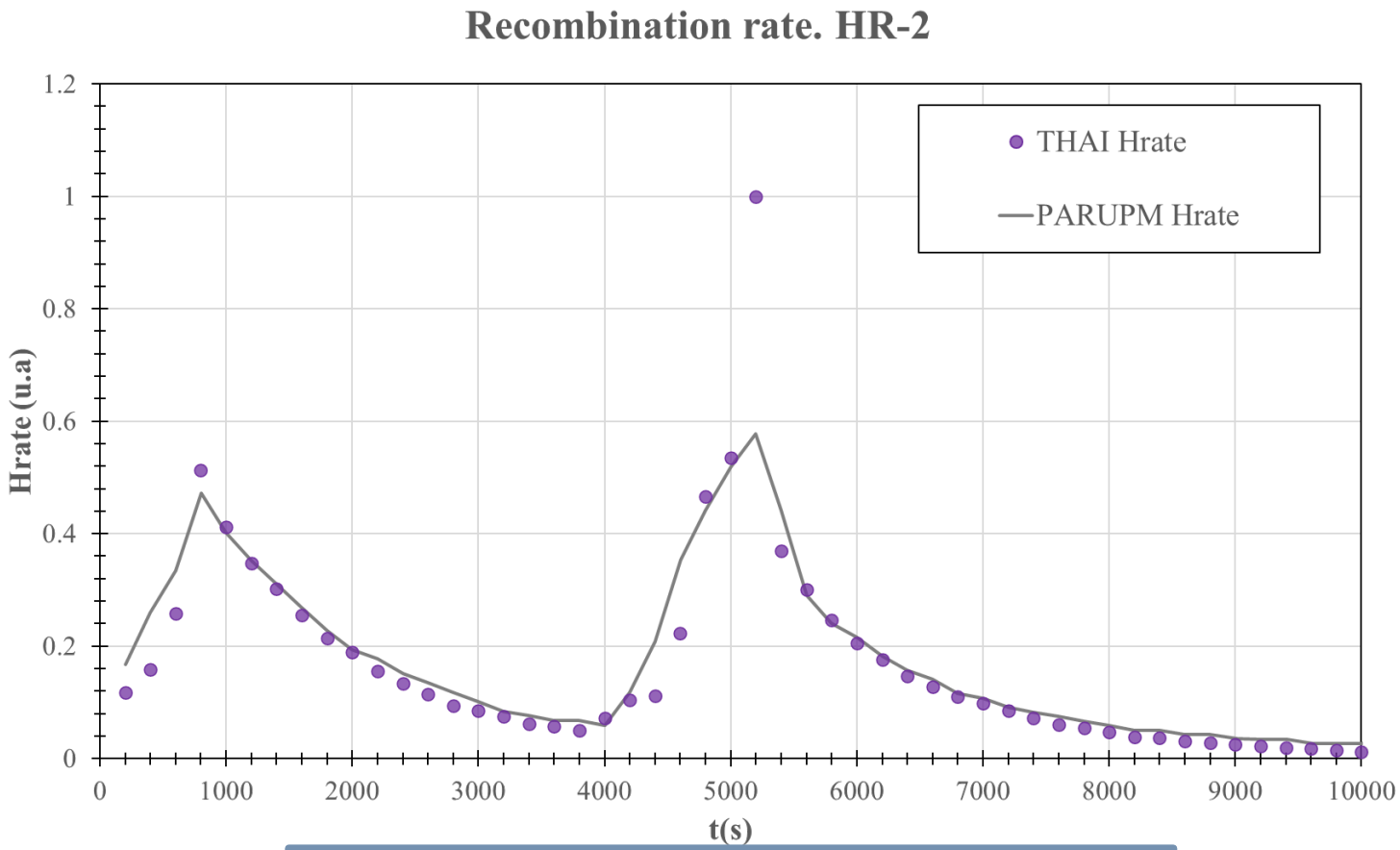

Good agreement of the recombination rate overall

PARUPM validation: standalone tool

- **Test HR-2: plate temperature**

  - Low pressure and temperature, and dry air
  - Self-ignition on the second injection
  - Initial conditions extracted from the inlet of the PAR.
  - Velocity is calculated with the chimney model

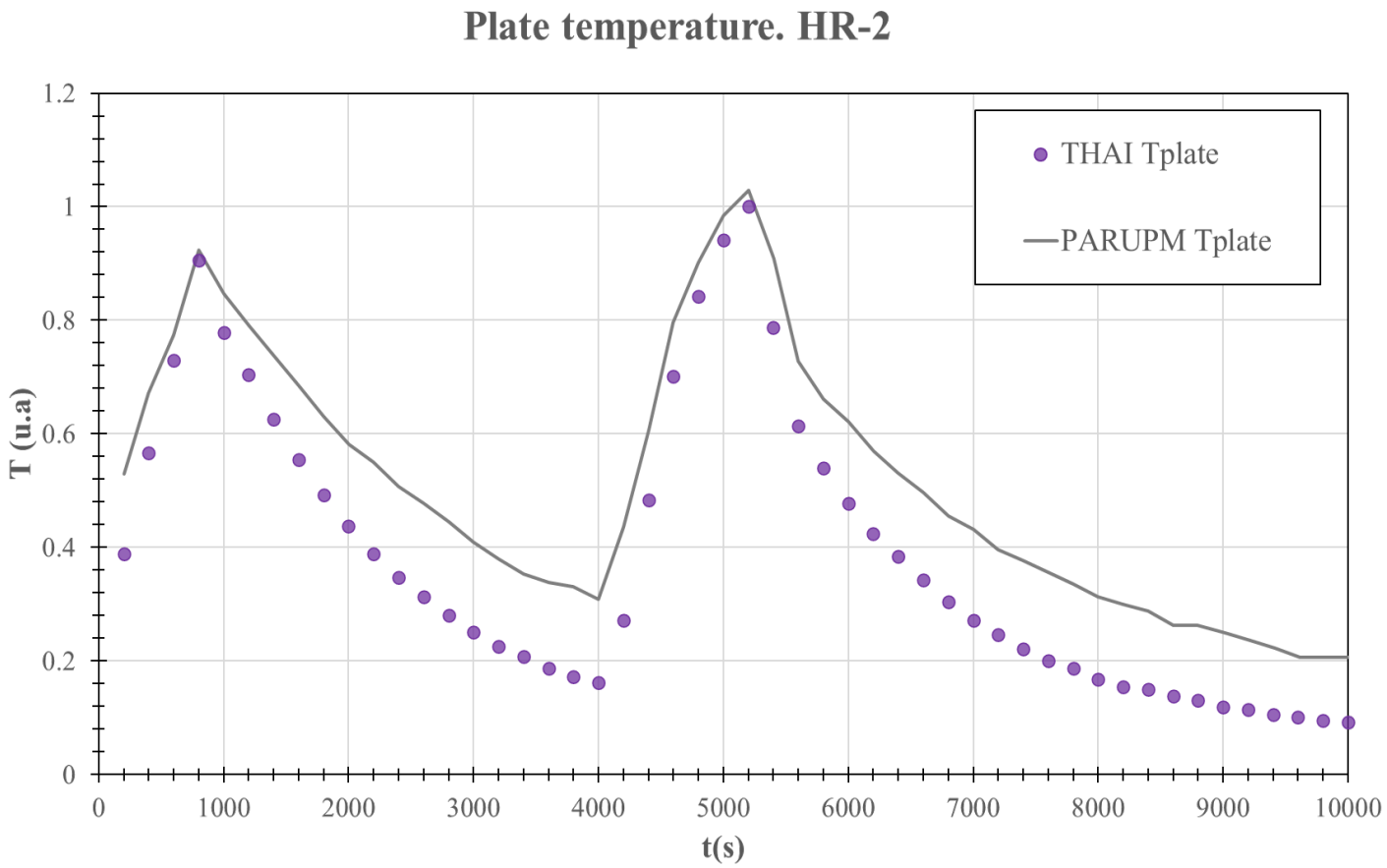

Slight overprediction on the depletion phases

PARUPM validation: standalone tool

- **Test HR-2: flow velocity**

  - Low pressure and temperature, and dry air
  - Self-ignition on the second injection
  - Initial conditions extracted from the inlet of the PAR.
  - Velocity is calculated with the chimney model

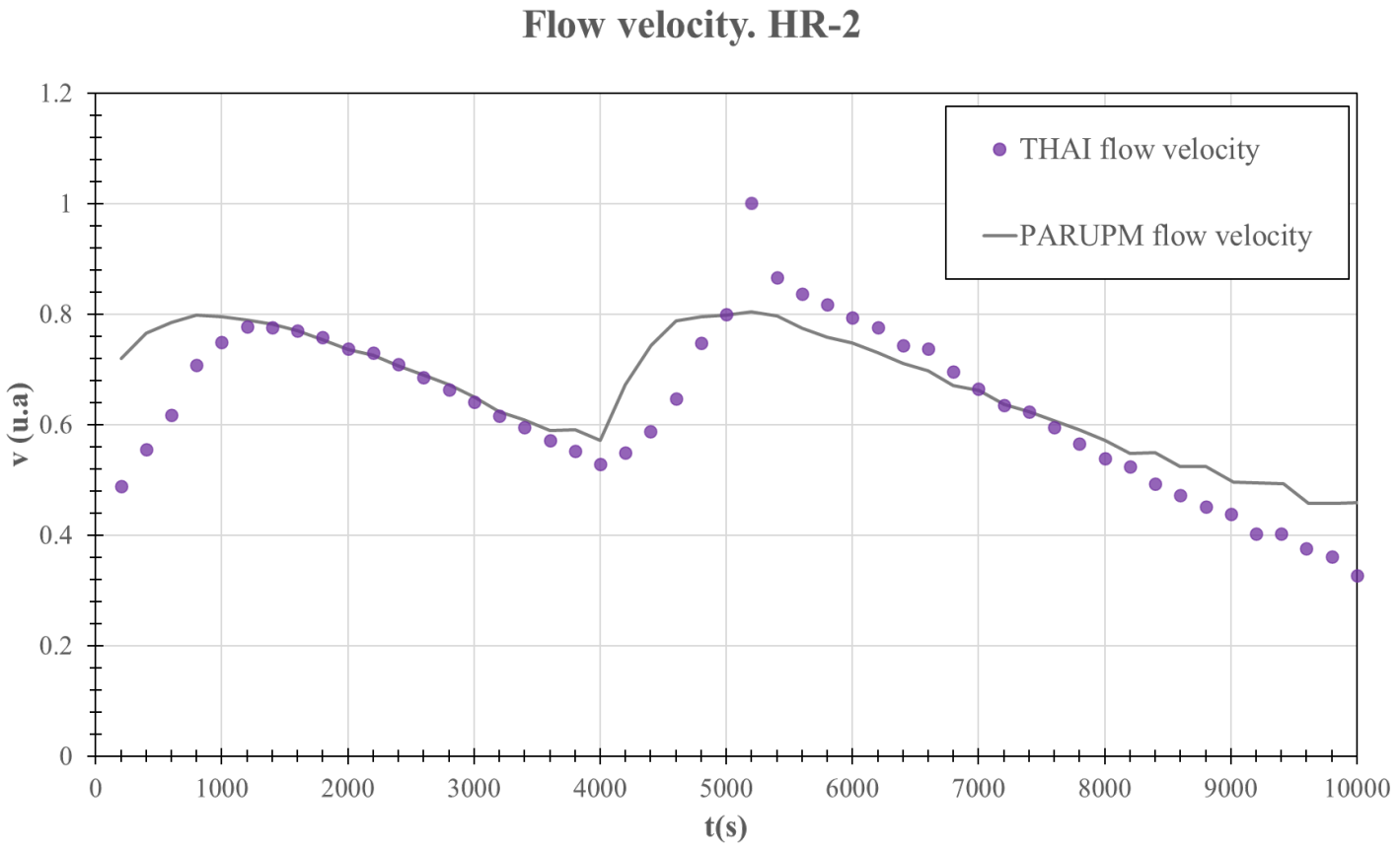

Slight overprediction on the depletion phases

PARUPM validation: standalone tool

- **Test HR-12: recombination rate**

  - High pressure and temperature, and high steam concentration
  - O_2 starvation during the second depletion
  - Initial conditions extracted from the intel of the PAR.
  - Velocity is calculated with the chimney model

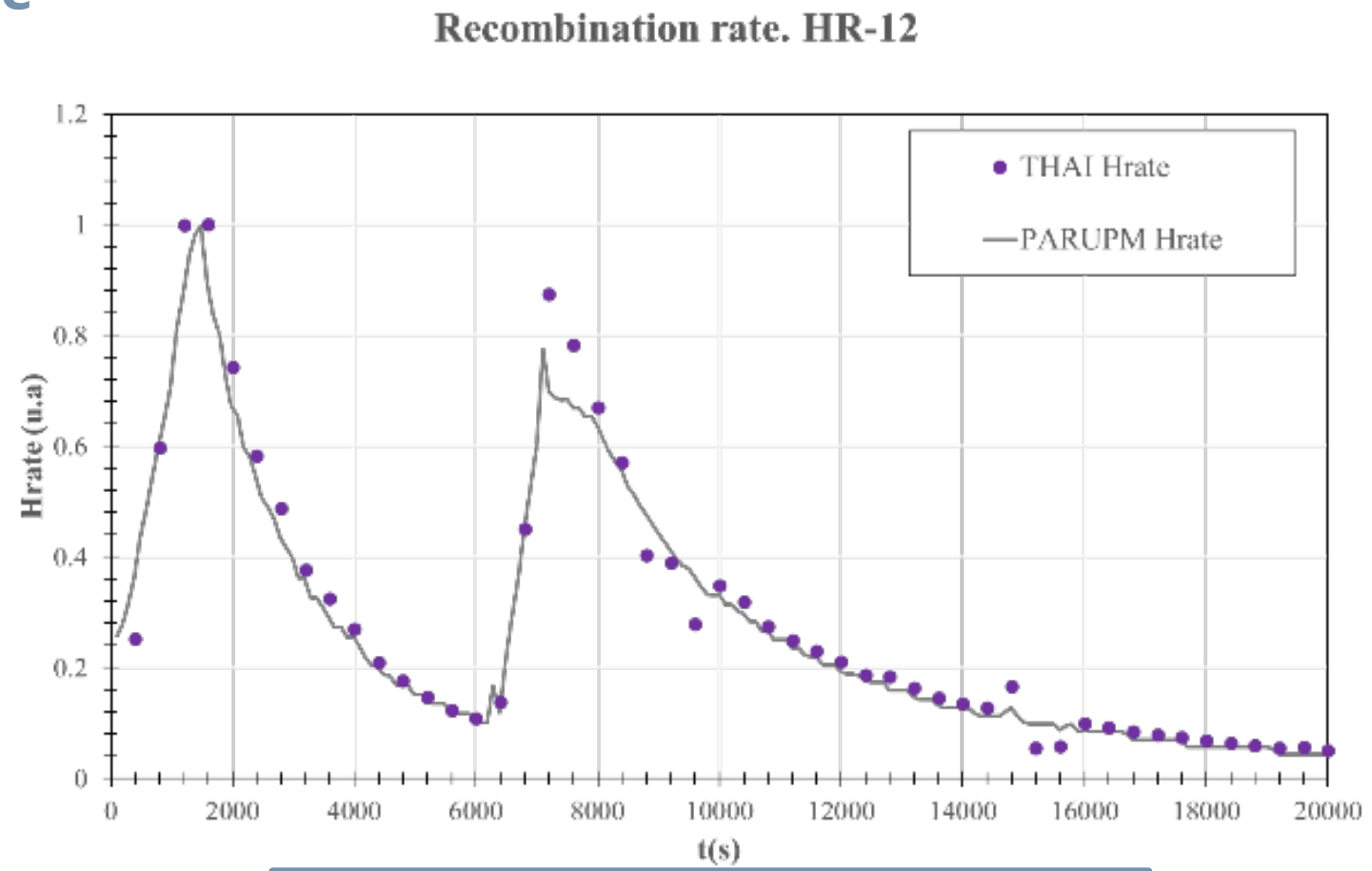

Good recombination rate prediction overall

PARUPM validation: standalone tool

AMHYCO

- **Test HR-12: plate temperature**

  - Low pressure and temperature, and dry air
  - Self-ignition on the second injection
  - Initial conditions extracted from the intel of the PAR.
  - Velocity is calculated with the chimney model

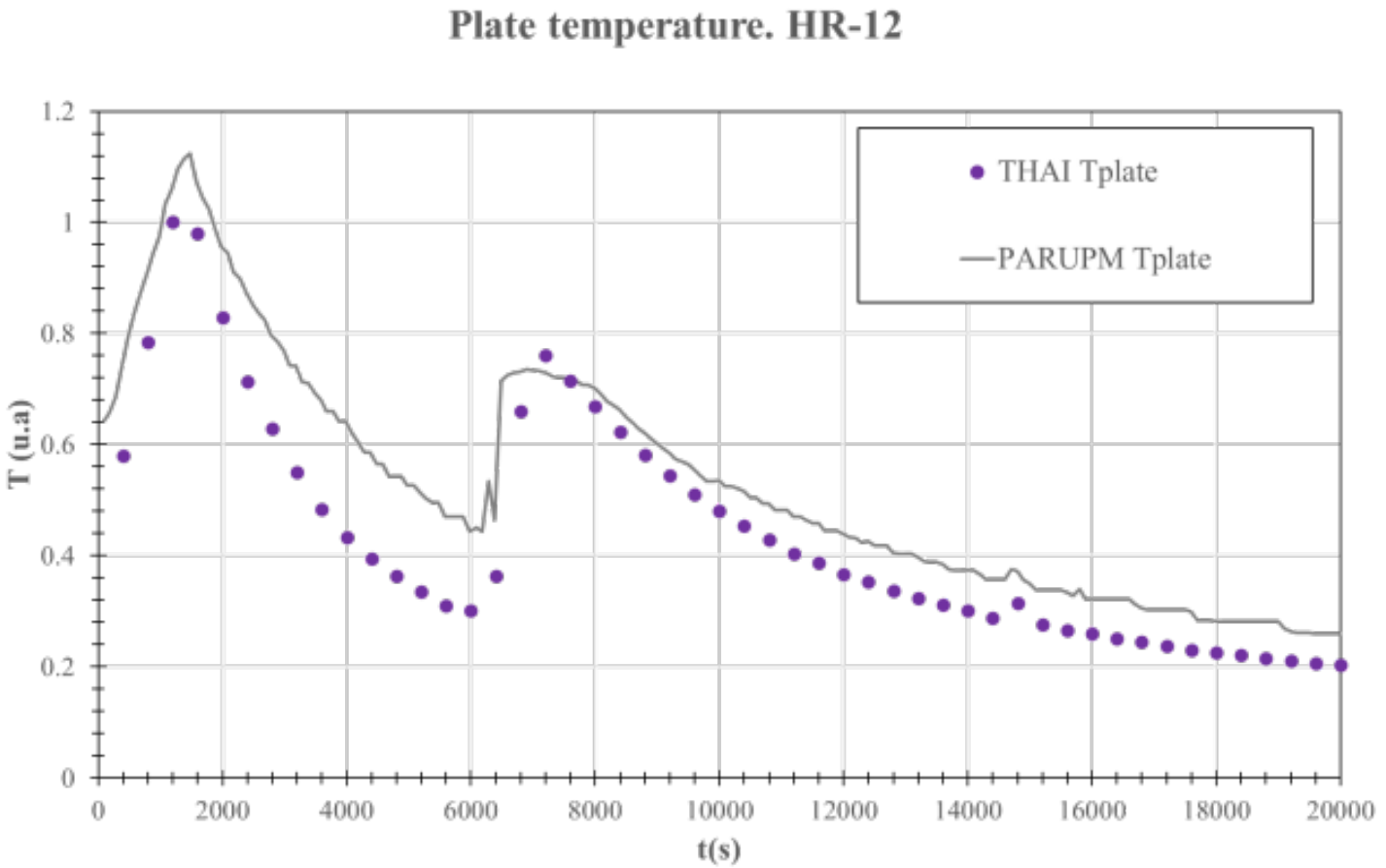

Slight overprediction on the depletion phases

PARUPM validation: standalone tool

- **Test HR-12: flow velocity**

  - Low pressure and temperature, and dry air
  - Self-ignition on the second injection
  - Initial conditions extracted from the intel of the PAR.
  - Velocity is calculated with the chimney model

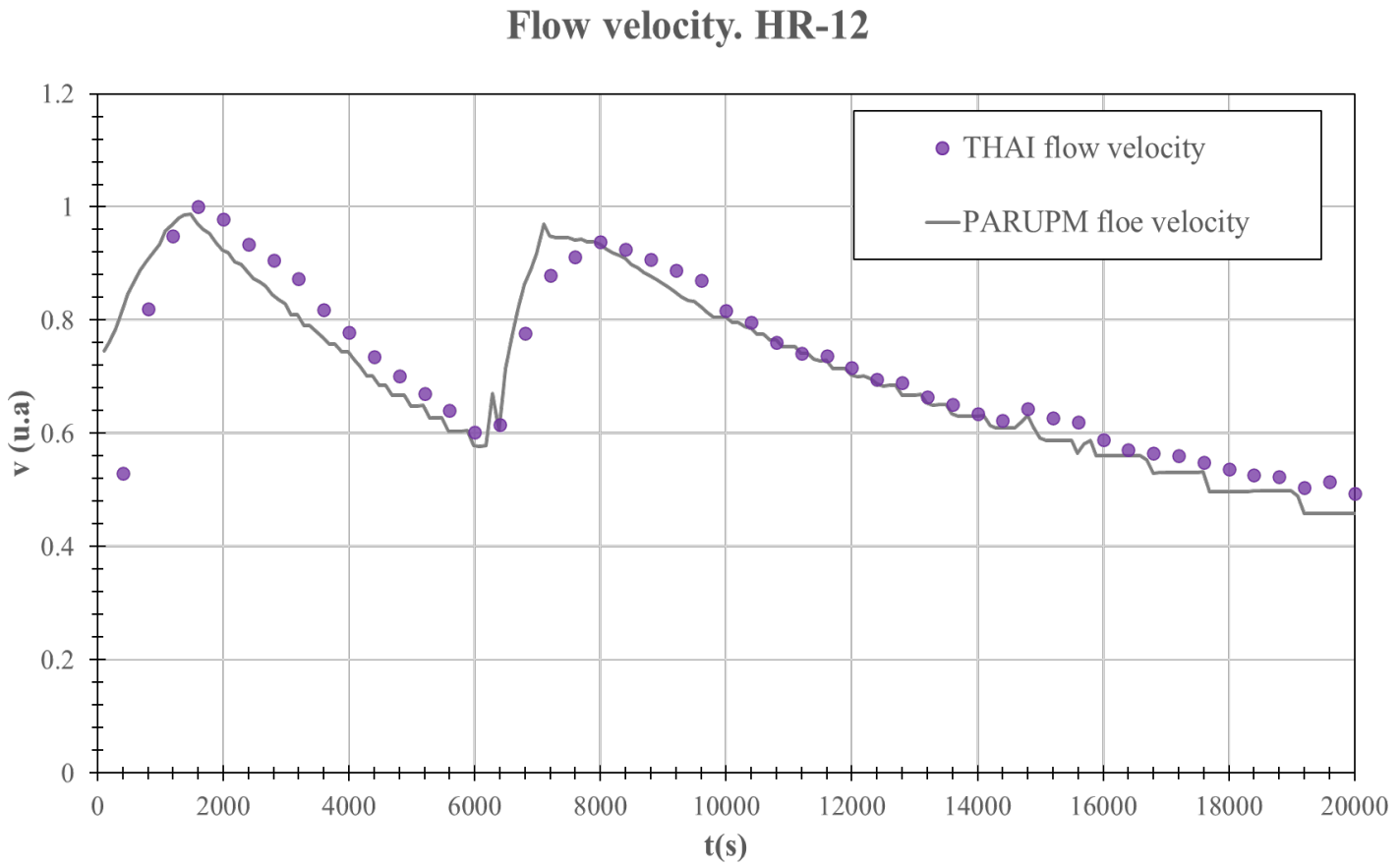

Good agreement of the flow velocity overall

Introduction

PARUPM CODE VALIDATION

DECOUPLING AND DEVELOPMENT OF THE PARUPM CODE

↓

ENHANCEMENT USING REKO-3 AND THAI (STEADY-STATE)

↓

THAI TRANSIENT SIMULATIONS AS A STANDALONE TOOL

↓

COUPLING OF PARUPM INTO GOTHIC SIMULATING THAI FACILITY

↓

FULL CONTAINMENT SIMULATION USING PARUPM AND GOTHIC

PARUPM-GOTHIC coupling

Stand-alone validation

- Input: experimental data base
- Vessel behaviour not captured
- Flow velocity is calculated with a chimney model module

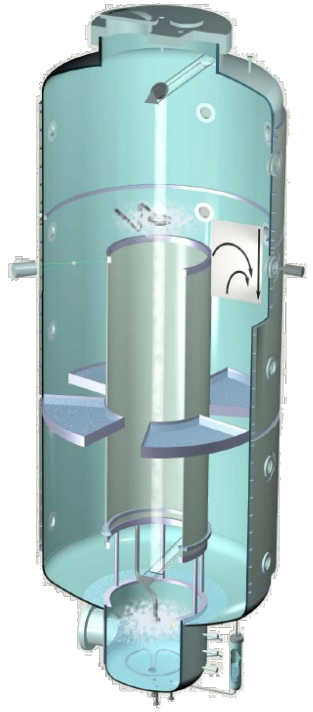

Coupled with GOTHIC

- Input: GOTHIC information
- Vessel behaviour captured
- Flow velocity is obtained from GOTHIC

GOTHIC 8.3: code description

- **GOTHIC description**

  - **Thermal-hydraulics software** package analysis of nuclear power plant containments.
  - GOTHIC can perform both **lumped parameter and 3D containment analyses**.
  - A control volume can be subdivided using **cartesian grids**.
  - Use **correlations and porous media** approximation for calculations
  - **Built-in PAR component** with add-on efficiency calculations

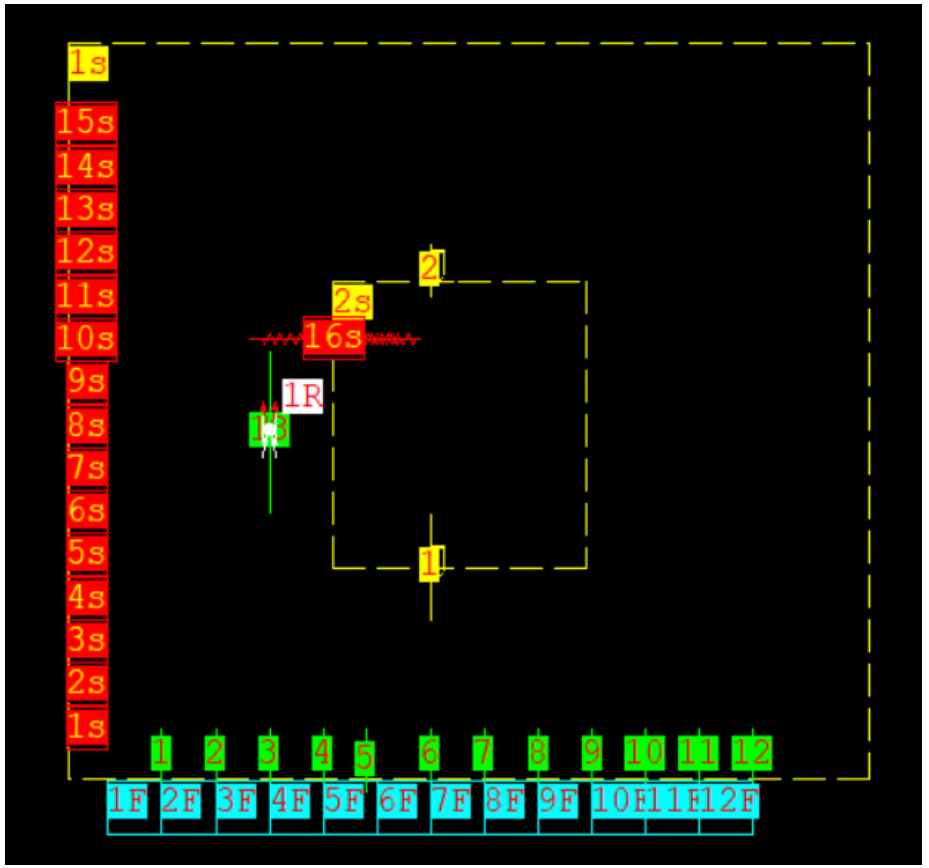

GOTHIC 8.3: THAI facility model

- **THAI vessel CAD model**

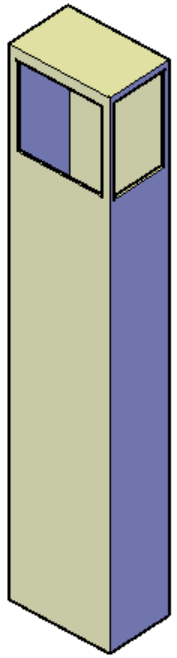

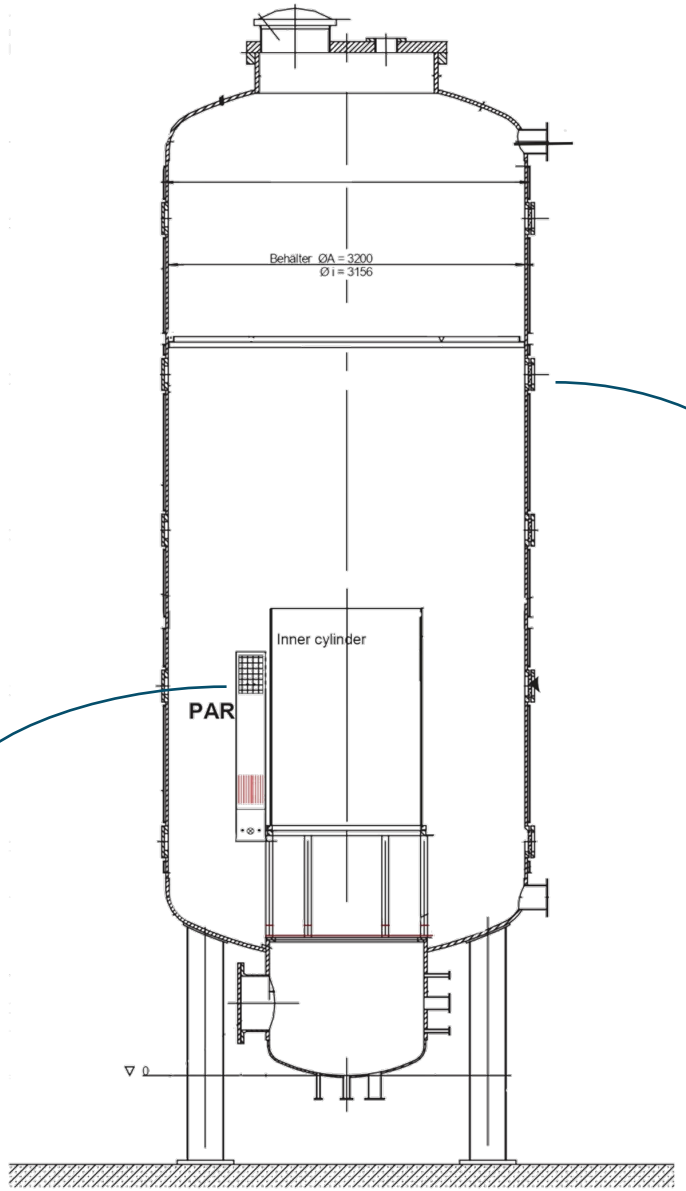

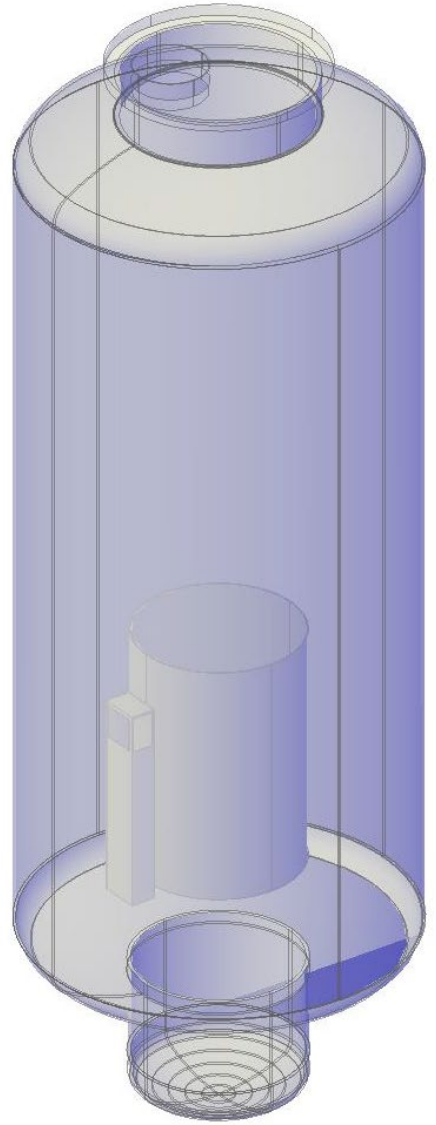

GOTHIC 8.3: THAI facility model

- **THAI vessel GOTHIC 8.3 model**

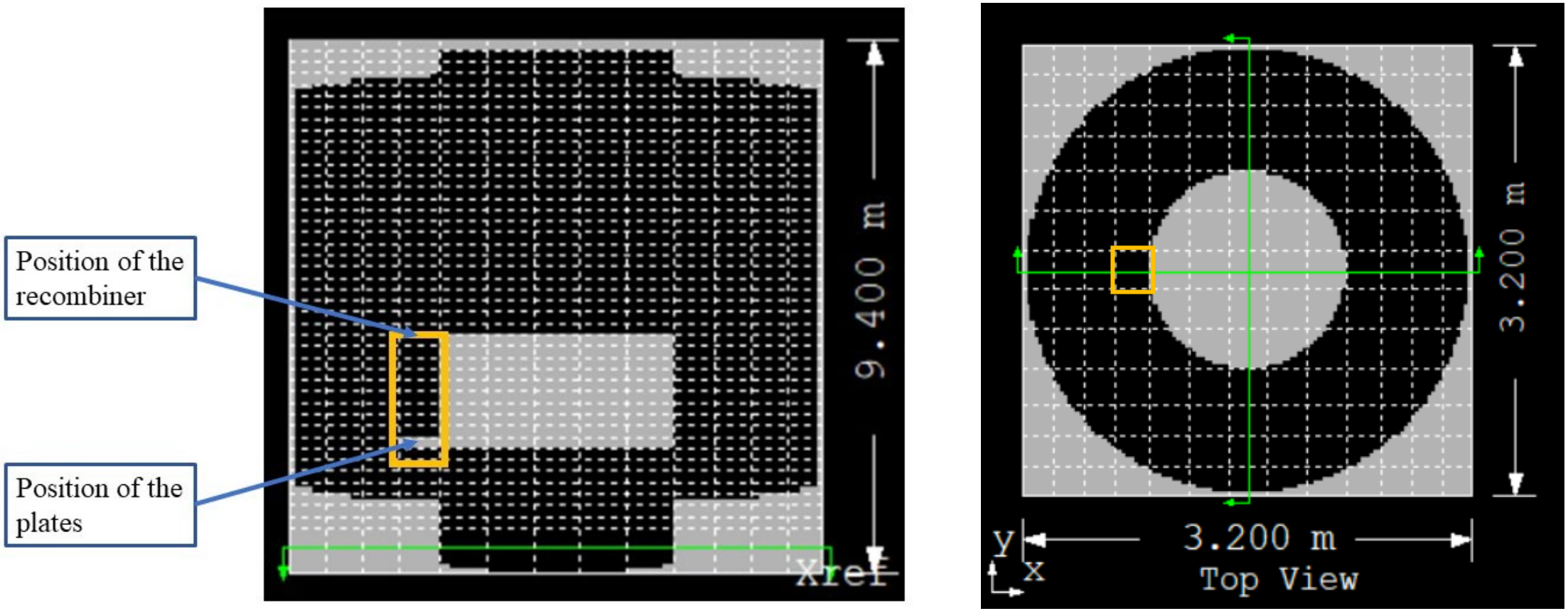

GOTHIC 8.3: THAI facility model

- **THAI vessel GOTHIC 8.3 model**

  - Vessel behaviour captured
  - Transport processes from the injection ring to the entrance of the PAR box is represented.
  - PAR positioning and size is replicated

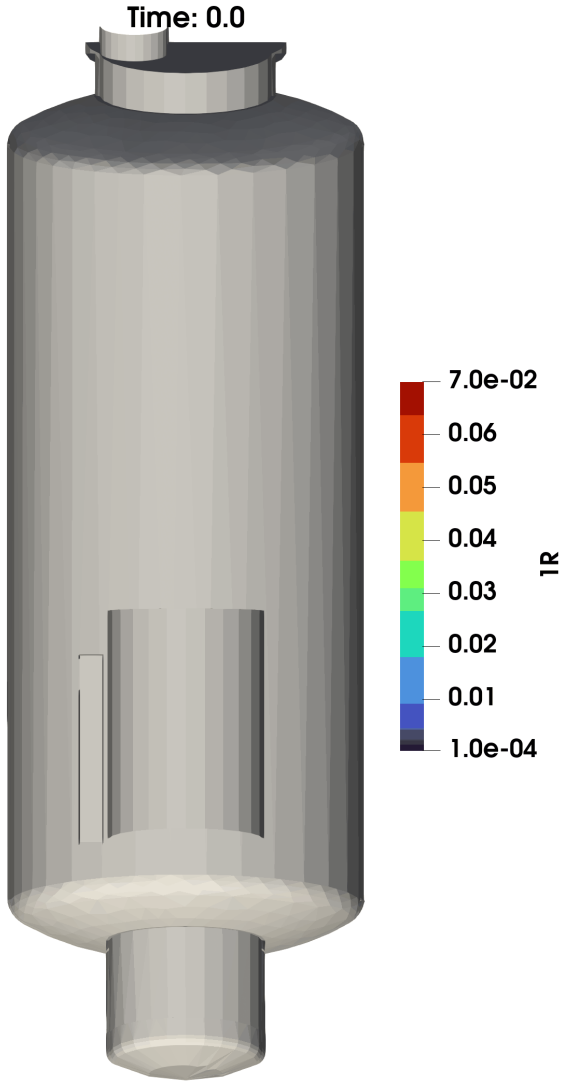

PARUPM-GOTHIC coupling

- **External functions implementation**

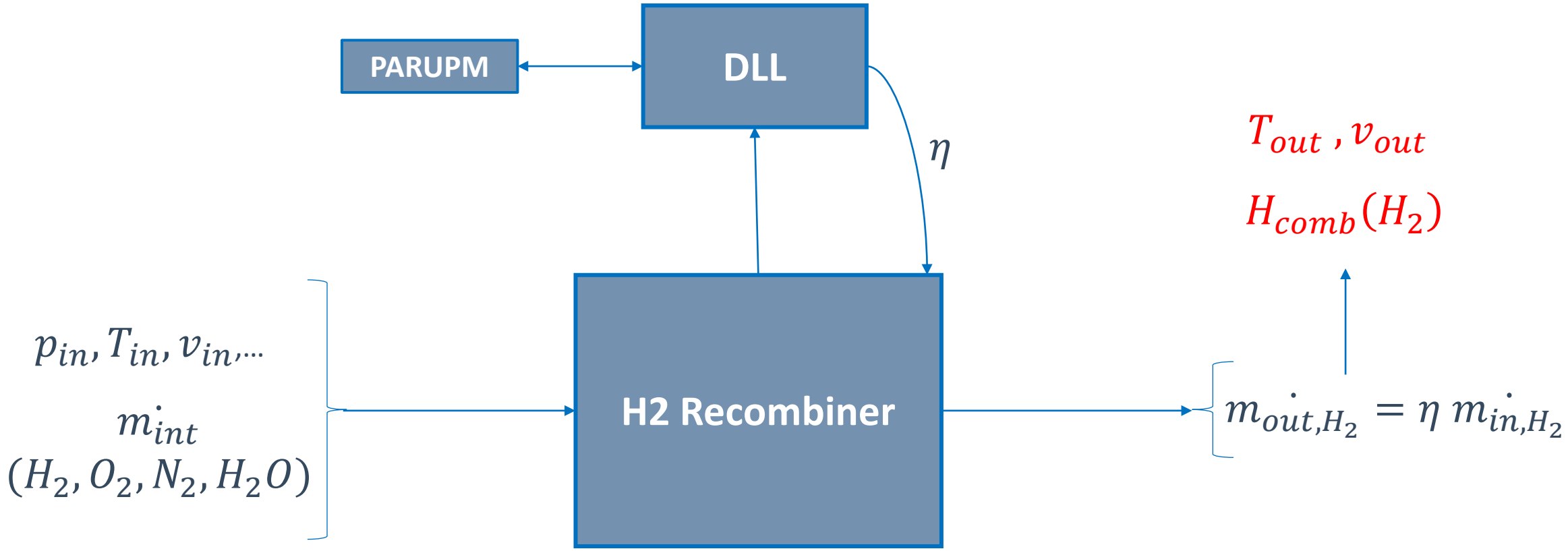

PARUPM-GOTHIC coupling. HR-2

- **Recombination rate**

  - Slight overprediction on the recombination rate on the first injection phase.
  - Self-ignition not captured.
  - Good agreement on both depletion phases
  - Total recombined H_2 mass agrees with the experimental value

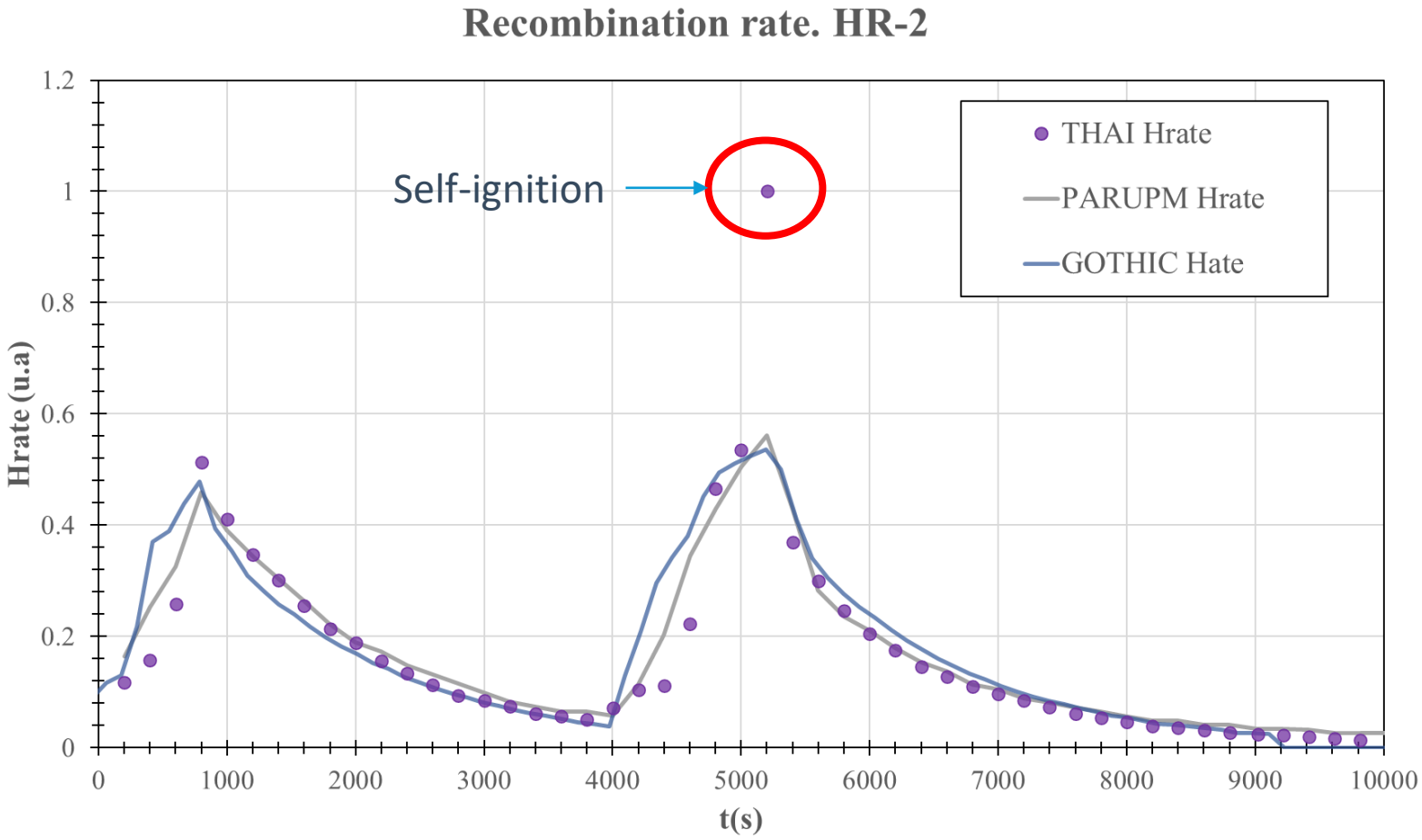

Recomb + burned H_2 mass (THAI): 635 g

Recombined H_2 mass (GOTHIC): 653 g
(Estimated difference: < 3%)

PARUPM-GOTHIC coupling. HR-2

- **Vessel pressure**

  - Slight overprediction on the vessel pressure on the injection phases.
  - Good agreement during the depletion.
  - Higher pressures during the second depletion due to the lack of the self-ignition phenomenon.
  - Overall, small deviation between the experimental pressure and the gothic one.

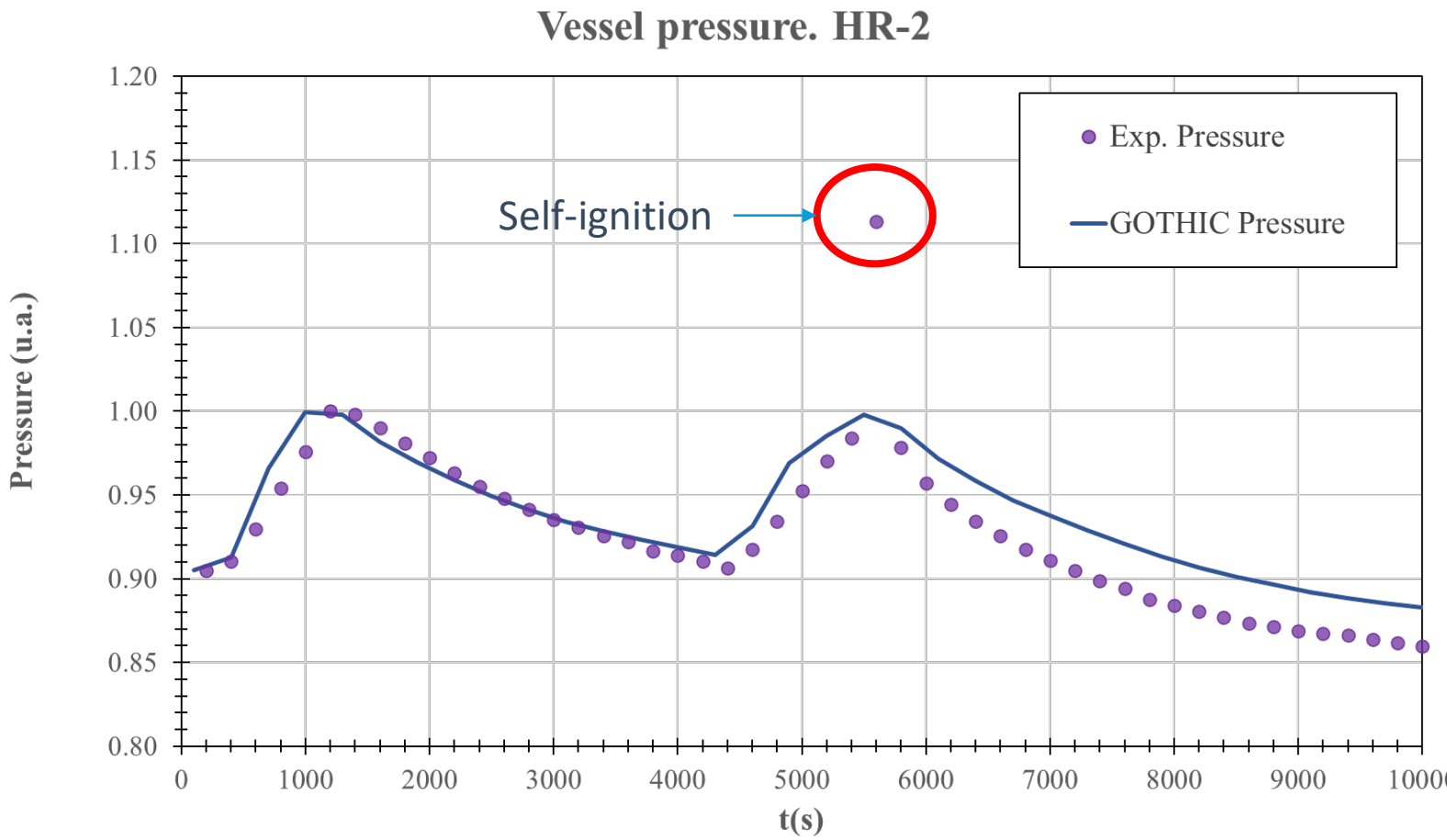

(Estimated difference: Δp< 3%)

PARUPM-GOTHIC coupling. HR-2

- **Flow velocity**

  - Flow velocity overprediction during injection phases.
  - Good agreement during the depletions.
  - Overall, the GOTHIC flow velocity works well for more steady-state conditions (depletions)

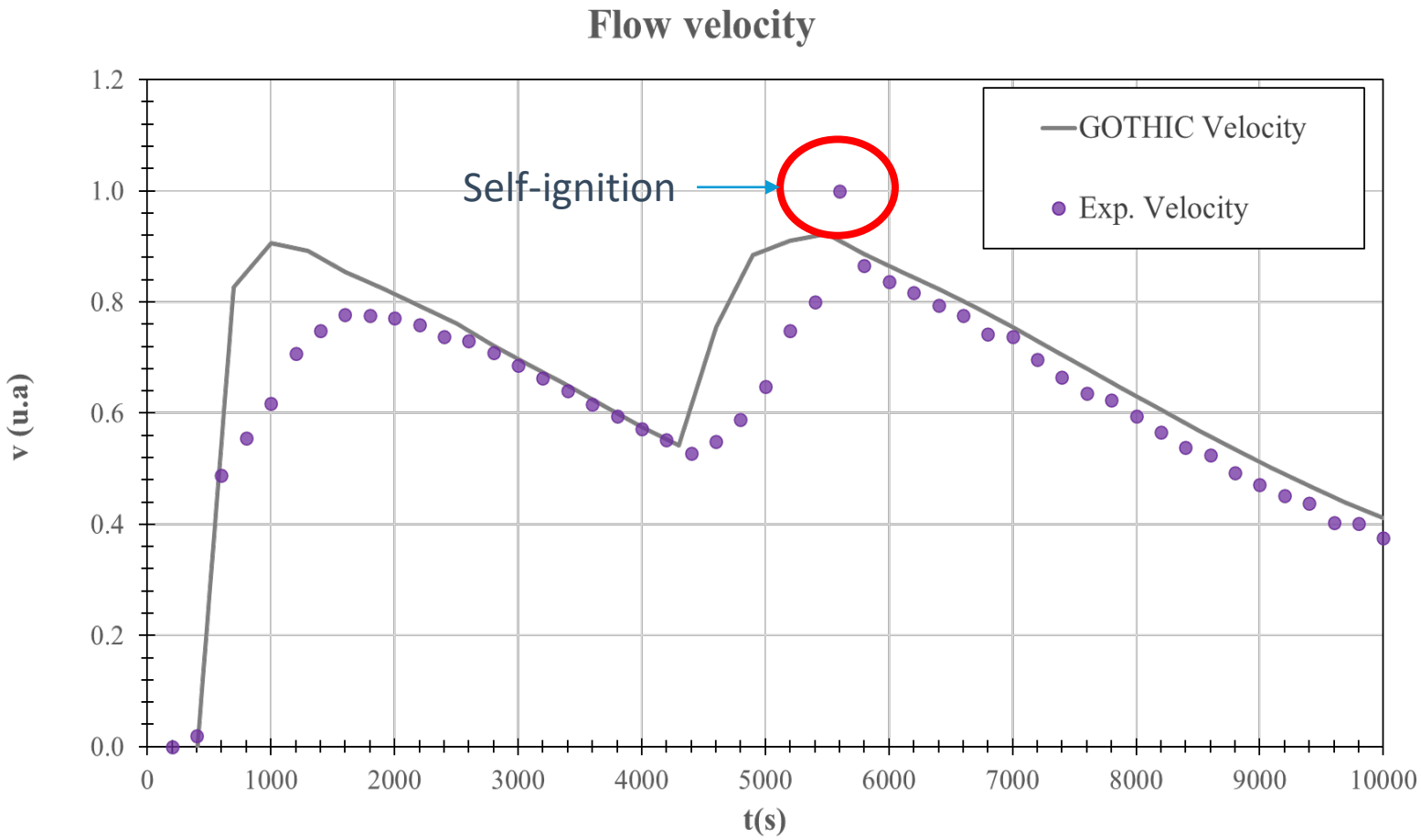

PARUPM-GOTHIC coupling. HR-2

- Gas temperature

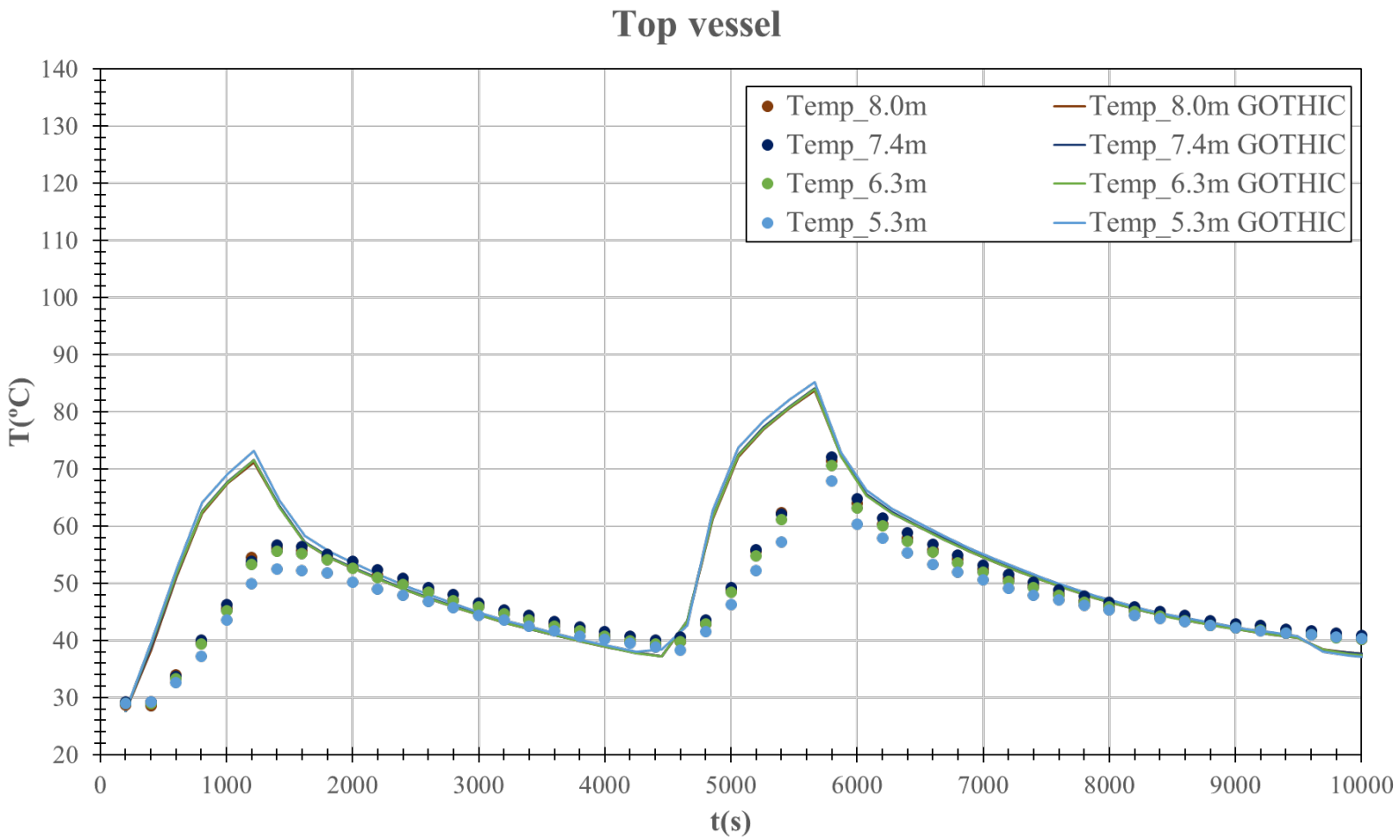

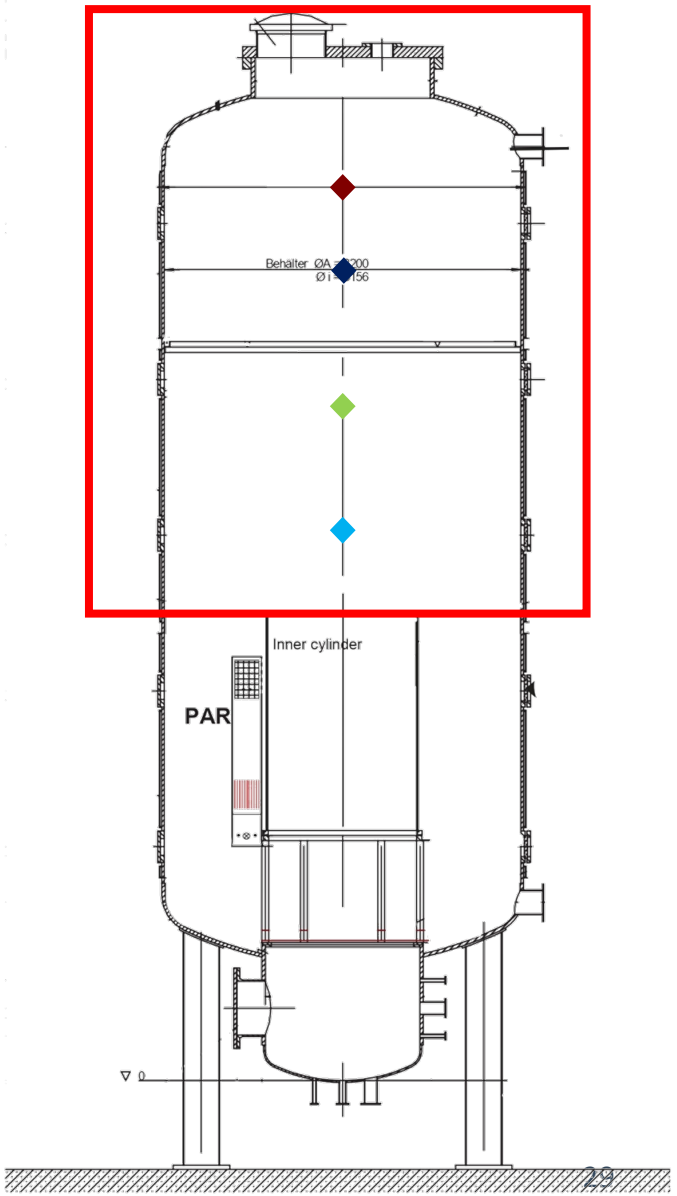

PARUPM-GOTHIC coupling. HR-2

- Gas temperature

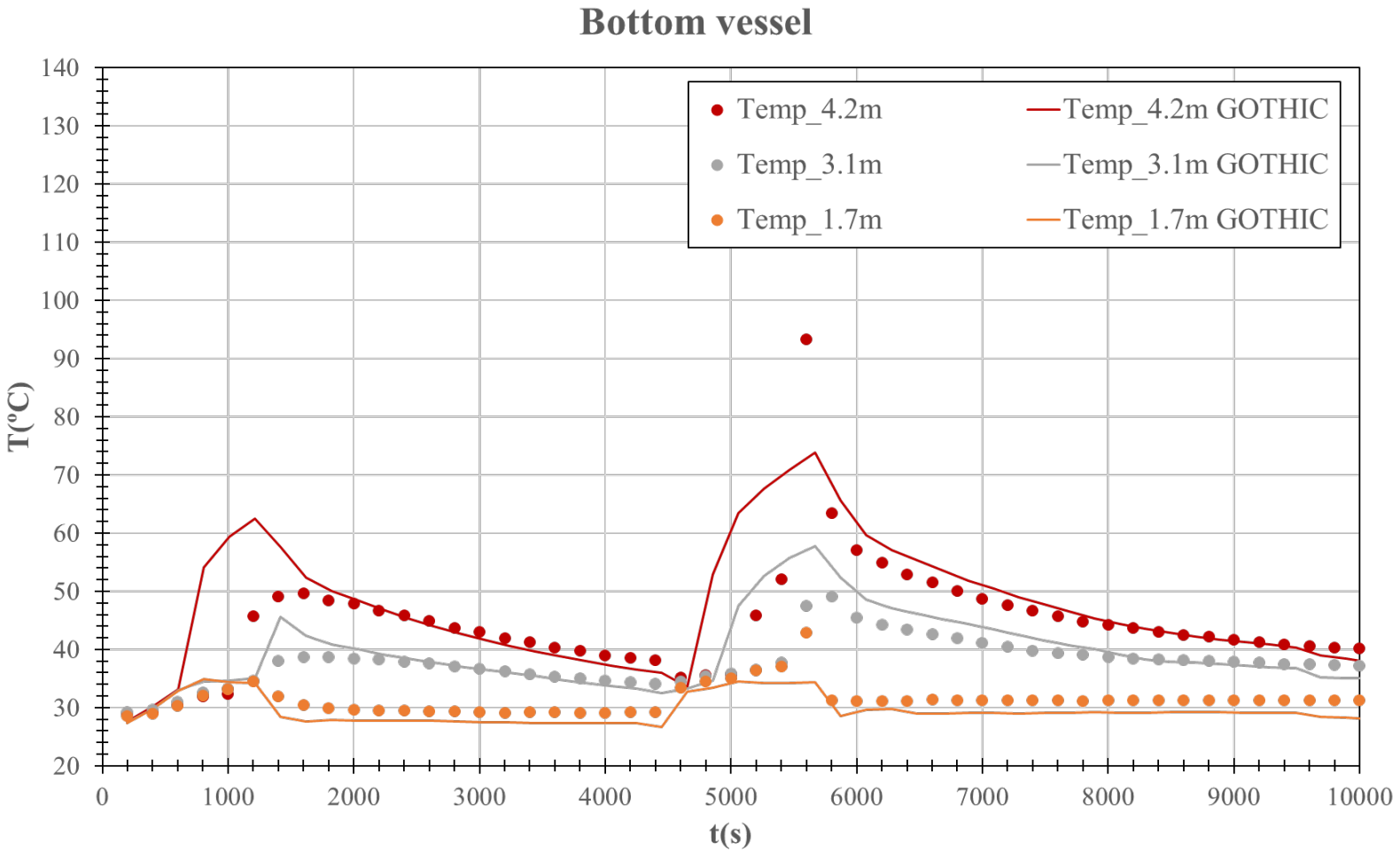

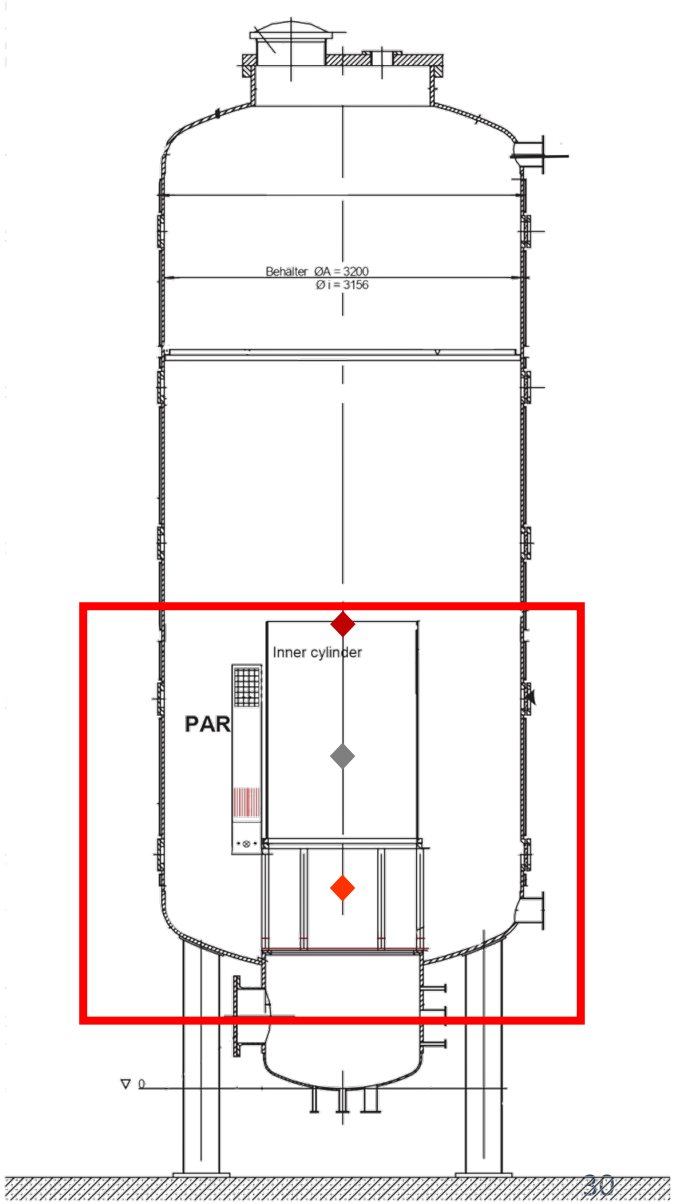

Conclusions

1. PARUPM is capable of predicting the behaviour of real recombiners using the experimental recording as inlet conditions.

2. The coupling GOTHIC 8.3 - PARUPM shows adequate results for recombination rates, vessel pressure, velocity, and vessel gas temperatures compared to the experimental ones.

3. The presented work establishes a foundation for using the coupled PARUPM-GOTHIC model as a valuable tool to predict PARs operation in nuclear power plant containments.

Future works

1. Further study the heat transfer from the PAR to the vessel to upgrade the plate temperature on the depletion phases.

2. Use the chimney model for calculating the flow velocity on the coupled

3. Run sensitivity cases for improve the PARUPM tool and reduce discrepancies.

Acknowledgements

JÜLICH Forschungszentrum
AMHYC
CSN CONSEJO DE SEGURIDAD NUCLEAR
BECKER TECHNOLOGIES
enen+

Thank you

Connect with us for more information:

araceli.dominguez@upm.es

http://amhyco.eu

@amhyco



The 11th European Review Meeting on Severe Accidents Research

May 13-16, 2024, Royal Institute of Technology, Stockholm, Sweden

TECHNICAL SESSION 7.3: SOURCE TERM

Chairs: T. Lind (PSI), F. Rocchi (ENEA)

ID35	**Gaseous and aerosol formations in the pseudo-binary CsI-MoO3 reaction system** M. Rizaal (JAEA)	**Paper** **Presentation**
ID69	**Experimental study on removal effect of radioactive materials in the course of the leakage through the equipment hatch** K. Nakamura (CRIEPI)	**Paper** **Presentation**

GASEOUS AND AEROSOL FORMATIONS IN THE PSEUDO-BINARY CsI-MoO_3 REACTION SYSTEM

Muhammad Rizaal[1,2], Kunihisa Nakajima[1,2], Eriko Suzuki[2], Shuhei Miwa[2]
[1] Nuclear Safety Research Center, Japan Atomic Energy Agency
[2] Nuclear Science and Engineering Center, Japan Atomic Energy Agency
Tokai-mura, Naka-gun, Ibaraki, Japan 319-1195
rizaal.muhammad@jaea.go.jp; nakajima.kunihisa@jaea.go.jp; suzuki.eriko@jaea.go.jp; miwa.shuhei@jaea.go.jp

ABSTRACT

The pseudo-binary CsI-MoO_3 reaction system during transportation in the reactor under severe accident conditions has been investigated by using the JAEA-TeRRa semi-integral test facility. An oxygen gas with approximately 10 mbar of partial pressure was given to argon-steam upstream gas flow during the reaction to study its effect on downstream chemistry between CsI and MoO_3 (Mo/Cs molar ratio of 2.13). The product of CsI-MoO_3 reactions both gas and aerosols were analyzed upon their condensation on type-304L stainless steel sampling coupons at respective temperatures (T= 1150-450 K). Post-test analyses revealed that at a low oxygen potential of -139 kJ/mol (i.e. reference case with argon-steam only), most of the CsI reached downstream (T < 400 K) without any reaction with MoO_3. On the other hand, when oxygen potential was increased to about -43 kJ/mol, the CsI vapor could react with MoO_3 to form cesium polymolybdates ($Cs_2Mo_3O_{10}$ and $Cs_2Mo_4O_{13}$) and gaseous iodine which predominated the aerosol and gas that reached the downstream region. Particle size at this location was found to be less than 2.7 μm in contrast to the former case having an irregularly large size. The gaseous iodine in the latter case, based on the thermodynamic analyses, was estimated to be hypoiodous acid (HIO) or molecular iodine (I_2). The results in this study indicated that speciation of both Cs and I with the Mo chemistry during a severe accident could be variedly formed depending on the prevailing oxygen potential.

KEYWORDS
Cesium molybdates, oxygen potential, gaseous reaction, aerosol attenuation

1. INTRODUCTION

The iodine chemistry during a nuclear severe accident has a great impact on the short-term radiological risk. It is a complex phenomenon to investigate because of the nature of contributing fission products such as cesium which has a high chemical affinity to iodine. The chemical stability of cesium iodide (CsI) was known to be affected by the presence of molybdenum as a semi-volatile fission product [1, 2]. Past research studies [1, 2] that focused on the behavior occurring in the gas phase have found that cesium iodide could react with molybdenum to form cesium molybdates and gaseous iodine regardless of steam-rich or steam-poor atmospheric conditions. Despite a better grasp of the molybdenum effect on iodine chemistry gained from those efforts, the underlying mechanism remained unclear. Moreover, the theoretical approaches used in the studies could not completely reproduce the formation of cesium molybdates, thus leaving a knowledge gap for real implications to nuclear safety research.

The research study presented here was aimed at identifying the proper mechanism for iodine chemistry affected by the presence of molybdenum in the gas phase. This was approached by scrutinizing the dependence on oxygen potential of the reaction system. Two independent reaction tests under a steam-

containing atmosphere were carried out and differed by adding one percent oxygen gas into one case. Formations of gaseous species were quantitatively determined from the gas trapping system, while the cesium molybdates were confirmed from material characterizations. The results were further elaborated using thermodynamic equilibrium calculations. A modified database of Scientific Group Thermodata Europe (SGTE) version 5 comprising other cesium molybdates (i.e. $Cs_2Mo_2O_7$, $Cs_2Mo_3O_{10}$, $Cs_2Mo_4O_{13}$, $Cs_2Mo_5O_{16}$, and $Cs_2Mo_7O_{22}$) was developed and used in the calculations based on the published works of Smith [3] for solidus phases and Stolyarova [4] for liquidus phases. Incorporation of these thermodynamic properties of cesium molybdates is important because they were overlooked despite past real tests showing the high possibility of encountering the formation. Therefore it was expected that a better overall understanding could be achieved from the present work.

2. EXPERIMENTAL AND CALCULATION METHOD

The reaction system of gaseous CsI and MoO_3 in the postulated accident condition was reproduced using test facility built in the Japan Atomic Energy Agency (JAEA) called Test-bench for FP release and transport (TeRRa). This facility is primarily designed to understand the chemical interaction of related simulant fission products during their transport in a severe accident where the resulting chemical and physical behaviors could be analyzed at specific temperatures. By combining the experimental data and the thermodynamic equilibrium calculation, elucidations of CsI-MoO_3 in the given reaction system could be obtained. The detailed analyses could provide a better understanding of the underlying mechanism such that demonstrated in the previous investigation on Cs, I, and B chemistry using TeRRa [5–7].

2.1. Experimental method

TeRRa facility consists of two horizontal interconnecting sections: An upstream section for the simulant fission products release and a downstream section for the transport behavior analyses. The setup of experiment including heating profiles on both sections follows our previous research studies [5–7], hence it will be briefly described. Fig. 1 shows the schematic view of the TeRRa facility where upstream and downstream sections are distinguished by the interconnection between the resistance furnace and thermal gradient tube (TGT). Two platinum crucibles filled with CsI (Wako Inc.) and MoO_3 (Mitsuwa Chemicals Co. Ltd) powders were inserted in the resistance furnace at the predetermined locations corresponding with these compounds' vaporization temperature. An alumina slab was placed axially in the furnace to separate the stream of vapor source from both crucibles thus preventing the reaction from occurring before the sampling locations.

Sampling tubes and coupons made of 304L-type stainless steel were located inside the TGT and partly in the resistance furnace to match the preset temperature of which reactions were likely to occur. The particles/aerosols in the gas flow were filtered at the end of TGT by using sintered 316-type stainless steel mesh and polyvinylidene fluoride (PVDF) membrane filters with the filtration accuracy of 0.8 and 0.3 μm respectively. After the tests, the formed deposits on coupons and filters were characterized by the scanning electron microscope equipped with an energy-dispersive X-ray spectrometer (SEM/EDS) for microstructure and micro-Raman spectrometer for chemical form identification. Further, the deposits formed in the sampling tubes of TGT and filters were dissolved in the solutions containing 0.04 M NaOH for 24 hours (room temperature), 3 M HNO_3 for 3 hours (room temperature), and 0.15 M HNO_3 + 0.25 M H_2SO_4 for 3 hours (343 K), sequentially. These solutions were firstly diluted to an appropriate concentration and then analyzed using the inductively coupled plasma-mass spectroscopy (ICP-MS). At the outlet of TGT, gas species would pass through the trapping system containing a mixed solution of 0.2 M NaOH and 0.02 M $Na_2S_2O_3$. Similarly, these solutions were diluted before the quantification of cesium, iodine, and molybdenum with ICP-MS.

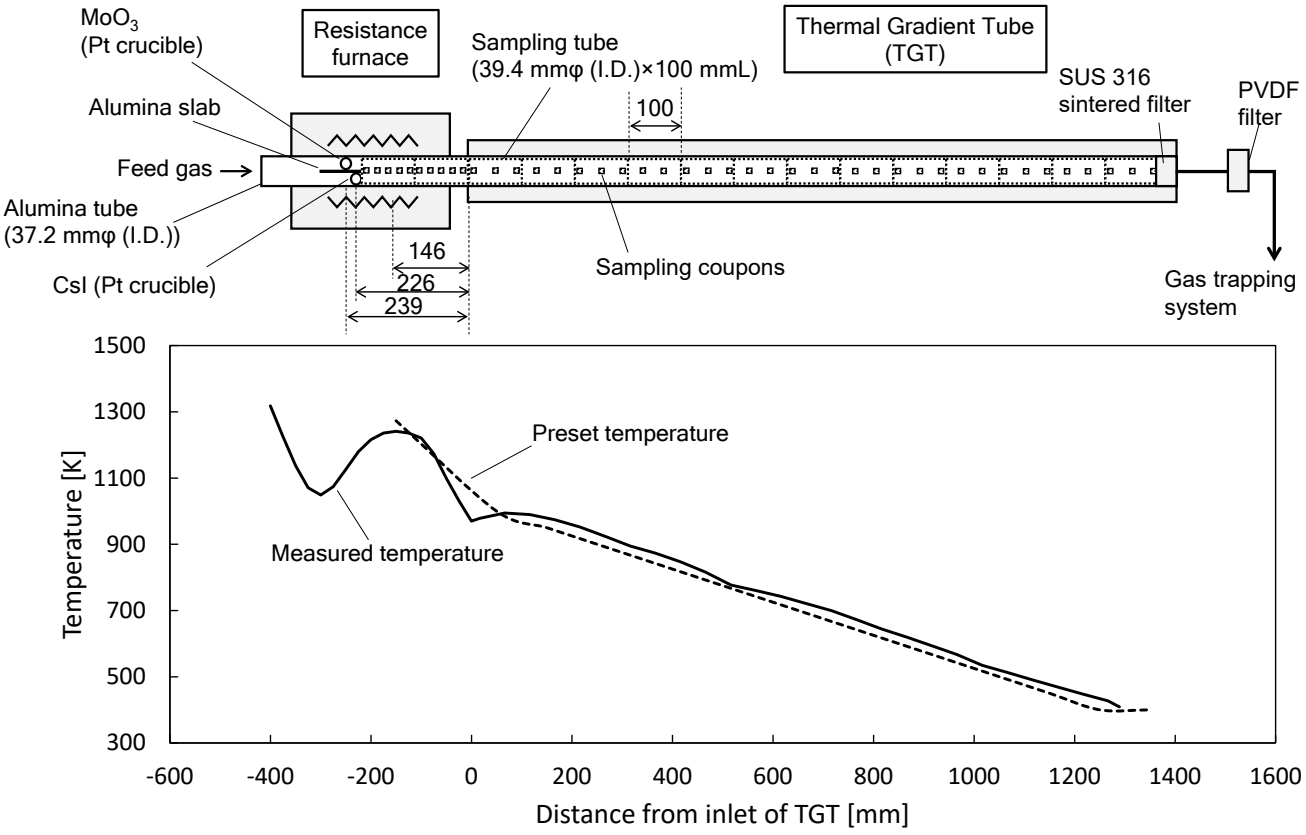

Figure 1. Experimental setup (top view) of CsI-MoO_3 gaseous reaction tests and temperature profile along the furnace and TGT of TeRRa

Table I. Summary of CsI-MoO_3 gaseous reaction tests

	TeRRa CsIMo-1	TeRRa CsIMo-2
Precursors (reagent-grade powder)	CsI / MoO_3	CsI / MoO_3
Initial amount (g)	1.3 / 1.3	1.3 / 1.3
Heating temperature (K)	1190 / 1160	1190 / 1160
Reaction time (min)	60	60
Evaporated amount (g)	0.178 / 0.177	0.192 / 0.226
Vaporization rate (mol/s)	1.907×10^{-7} / 3.420×10^{-7}	2.053×10^{-7} / 4.367×10^{-7}
Molar ratio of Mo/Cs [-]	1.79	2.13
Sampling temperature (K)	1250–450 K	1250–450 K
Feed gas composition	Ar-20%H_2O	Ar-20%H_2O-1%O_2
Flow rate (L/min)	2	2

In both tests (Table I), all parameters were almost identical except for the feed gas composition. One percent oxygen gas (approximately 10 mbar of partial pressure) was introduced to TeRRa CsIMo-2 to emphasize its significance (i.e. increase of the oxygen potential) toward the CsI-MoO_3 reaction system. It should be highlighted that molybdenum vaporization was higher than that of cesium regardless of the tests, to ensure a high chance of reaction as well as to anticipate the formation of cesium polymolybdates.

2.2. Calculation Method

Thermodynamic equilibrium calculations were carried out using Thermo-Calc software with SGTE database version 5 [8]. The Cs-I-Mo-O-H database was initially updated to include other cesium molybdates. This was done by incorporating the Gibbs energy function of the respective phases. For the solid phases, data from Smith [3] was straightforwardly used, whereas for the liquid phase, we calculated the Gibbs energy function from the chemical activity data reported by Stolyarova [4].

In the equilibrium calculations, each contributing species was approximated to represent the experimental conditions. Although the actual system may indeed differ from time to time during the experiment due to some inherent factors, we proceeded with the ideal calculation assuming that any changes occurred in minute effect toward the overall process. Upon combining the calculations and experimental observations, the mechanism taking place in the CsI-MoO_3 reaction system was derived.

The parameters used in the calculation are listed in Table II. As explained earlier, this calculation could aid in understanding the most stable phase of cesium molybdates and the speciation of gaseous iodine in a given condition. The amount of each element (Cs, I, Mo, O, H, and Ar) was derived from the CsI and MoO_3 vaporization in the crucibles and feed gas flow rate (ideal gas law), respectively. It should be emphasized that for the Ar-20%H_2O case, Mo was considered to have the form of MoO_2 rather than MoO_3 in an oxygen-deficient atmosphere, hence correcting the amount of both Mo and O. Such a consideration would be discussed further in subsection 3.1. The predominance diagram was obtained in the temperature range of 400 to 1100 K with a 10 K increment. The upper limit temperature of 1100 K was selected instead of 1250 K because material characterization was made until this temperature hence plausible comparison could be obtained.

Table II. Parameters used in the thermodynamic equilibrium calculation

	Ar-20%H_2O	Ar-20%H_2O-1%O_2
Cs amount (mol)	1.9074×10^{-7}	2.0528×10^{-7}
I amount (mol)	1.9074×10^{-7}	2.0528×10^{-7}
Mo amount (mol)	3.8474×10^{-7}	4.3673×10^{-7}
O amount (mol)	3.4138×10^{-4}	3.8073×10^{-4}
H amount (mol)	6.8123×10^{-4}	6.8985×10^{-4}
Ar amount (mol)	1.3625×10^{-3}	1.3625×10^{-3}
Temperature (K)	1100–400	1100–400
Pressure (MPa)	0.1	0.1

3. RESULTS AND DISCUSSION

3.1. Deposition profiles and characterizations

Temperature-dependent deposition profiles of cesium, iodine, and molybdenum after the reaction tests using TeRRa in the Ar-20%H_2O and Ar-20%H_2O-1%O_2 atmospheres are given in Fig. 2 a and b, respectively. The arrows attached to each figures are used to highlight the molar fractions of Mo/Cs or Cs/I in which either case suggests whether the reaction occurred or not. Because cesium iodide was used as the starting material, the congruent profile between Cs and I after the test indicates that the reaction with Mo did not occur in the given system hence the obtained profile is the deposition of CsI. On the other hand, once the reaction

proceeded, the low volatile Cs-Mo compounds could remain, so that they are indicated by a congruent profile between Cs and Mo.

In the Ar-20%H_2O atmosphere, it was found that from about 950 K to 450 K the deposition of both Cs and I were almost unity. As explained earlier, it is highly indicative that cesium iodide doesn't react with molybdenum oxide in the gas phase. This trend (i.e. deposition that began at 950 K) is similar to the previous studies of CsI that showed the deposition was a result of vapor condensation [7, 9, 10]. Since there were no reactions in the Ar-20%H_2O case, one could expect that the Mo profile in this temperature range was the deposition of molybdenum oxide. In the higher temperature, however, the Cs/I molar ratio was higher than unity, suggesting that some other Cs compounds might be formed at this location.

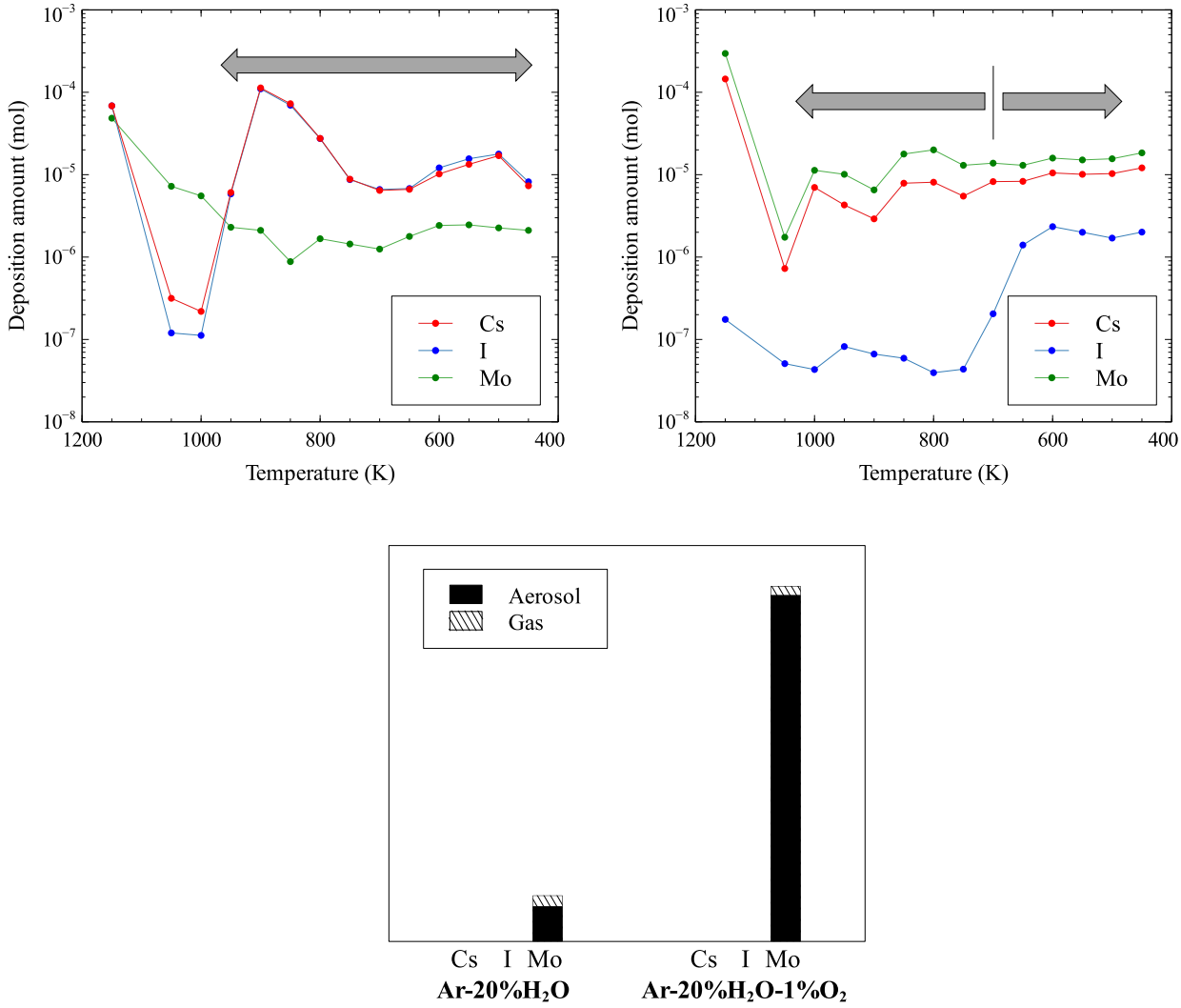

Figure 2. Temperature-dependent distribution of Cs, I, and Mo in Thermal Gradient Tube (TGT) under (a) Ar-20%H_2O and (b) Ar-20%H_2O-1%O_2 atmospheres, and (c) the corresponding generated aerosols and gas at the outlet of TGT

Unlike the Ar-20%H_2O case, the distribution of Cs and I (molar ratio of Cs/I) differed significantly by about an order when one percent oxygen was added to the upstream gas flow. Furthermore, a congruent deposition profile between Cs and Mo emerged, having Mo/Cs molar ratio of 2.2-2.4 in the temperature range of 1150–

700 K and 1.8 in the temperature less than 700 K. The Cs contribution in these ratios has been corrected using the iodine amount where cesium iodide could coexist. If the presumed reaction has prevailed, then the Mo/Cs ratio is the first information to predict the chemical compounds in the respective locations. In the pseudo-binary Cs_2MoO_4-MoO_3 system [11, 12], such molar ratios correspond to the compounds of $Cs_2Mo_3O_{10}$, $Cs_2Mo_4O_{13}$, and $Cs_2Mo_5O_{16}$. Therefore, the formation of these low volatile compounds would be confirmed through micro-Raman spectroscopy.

The distinction between the Ar-20%H_2O and Ar-20%H_2O-1%O_2 atmospheric conditions toward the reaction was also observed in the generated aerosols and gas collected at the TGT outlet (Fig. 2 c). In the former condition, most aerosols were likely formed as CsI (i.e. indicated by the Cs/I molar ratio of 1). At the same time, the latter showed a possibility of Cs-Mo compounds. Suppose that iodine (aerosol) exists as CsI like the former case, then one could correct the amount of Cs that led to a Mo/Cs ratio of 1.95. This value is consistent with the ratio obtained in the deposits inside TGT. Further, the most significant difference between the two cases is the generation of gaseous iodine. The transported gaseous iodine was considered as the non-condensation of monomer/dimer of CsI or the dissociation of CsI [6, 7] if there were no reactions with Mo. On the other hand, when the reaction with Mo occurred, the generation of gaseous iodine was closely related to the formation of low-volatile Cs-Mo compounds explained earlier. To this end, changes in the distribution patterns from Cs-I to Cs-Mo both in the TGT and aerosols/gas trapping system signify the key role of oxygen potential in the gas phase reaction of the CsI-MoO_3 system.

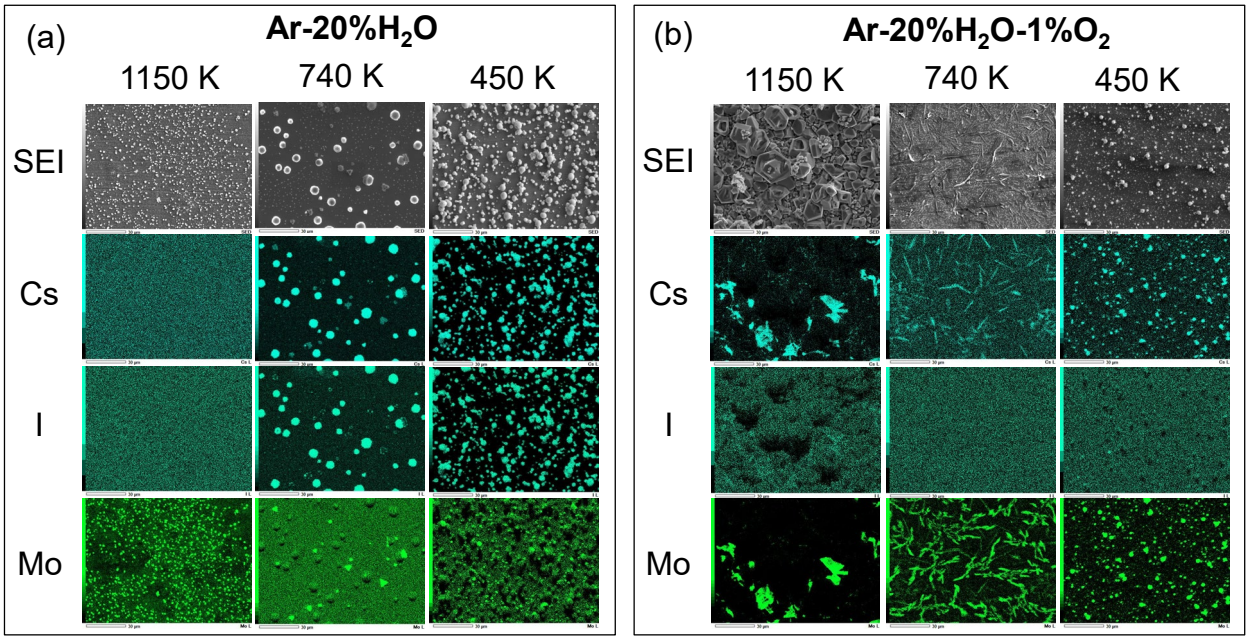

Figure 3. Microstructure of deposits formed on sampling coupons under (a) Ar-20%H_2O and (b) Ar-20%H_2O-1%O_2 atmospheres

The microstructure of deposits and the elemental mapping of Cs, I, and Mo on some selected sampling coupons that represent the temperatures during the heating test are provided in Fig. 3. In the Ar-20%H_2O case, it was observed that at 1150 K there were only Mo-containing deposits, while the Cs- and I-containing deposits formed at lower temperatures. This distinction supports the earlier data of ICP-MS that in the Ar-20%H_2O atmospheric case, the CsI-MoO_3 reaction could not proceed hence leading to vapor deposition of each starting material: MoO_3 (1068 K [13, 14]) and CsI (903 K [15]). Although Mo-containing deposits could be observed at temperatures lower than 1150 K, they have no similar distribution with Cs or I. In the

Ar-20%H_2O-1%O_2 case, the elemental distributions of cesium and molybdenum at all temperatures were found to be congruent, while the iodine distribution could only be observed at 450 K.

These elemental distribution characteristics have been indicated in the ICP-MS analysis (Fig. 2 b), particularly the iodine, where the increase was observed in locations having low axial temperature (T < 700 K). Concerning the Cs-Mo deposits, the form varied by temperature: irregular (1150 K), acicular (740 K), and spherical (450 K). At 1150 K, the irregularity was likely caused by the solidification of cesium molybdate compounds during the cooling process of TeRRa, as no solid phases could be expected in this temperature range from all cesium molybdates except Cs_2MoO_4 [11, 12]. Since the Mo/Cs molar ratio was about 2 at 1150 K, the Cs_2MoO_4 contributions were unlikely. The acicular deposits observed at 740 K were considered as the nucleation and crystal growth process of cesium molybdates while the spherical deposits at 450 K were the deposition of cesium molybdates aerosol. Between the two cases, aerosol in the Ar-20%H_2O-1%O_2 case was smaller than what was formed in the Ar-20%H_2O case, with the size of less than 2.7 μm. This specific size attenuation (Cs-containing particles) might result in a larger amount of aerosol transport to low-temperature regions (Fig. 2 c). Therefore, this issue must be addressed in future studies as the dynamics of aerosol in the event of a nuclear severe accident could influence the overall source term.

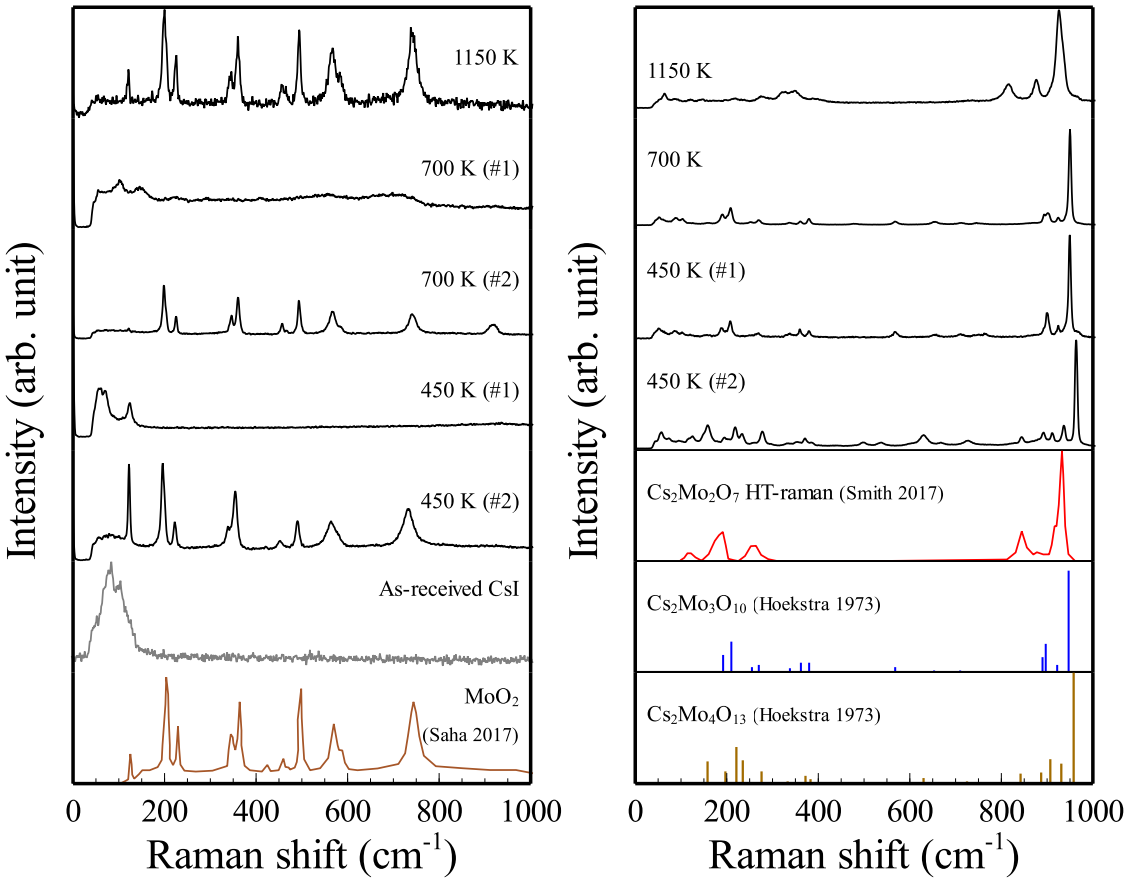

Figure 4. Raman spectra of deposits formed in the (a) Ar-20%H_2O and (b) Ar-20%H_2O-1%O_2 cases

The micro-Raman spectroscopy was carried out on the sampling coupons of both cases to identify the chemical compound of Mo- and Cs-containing deposits. In Fig. 4, the respective spectra were plotted together with the reference of cesium molybdates [11], molybdenum oxide [16], and the as-received CsI. In the case of Ar-20%H_2O atmosphere, the deposits were identified as MoO_2 (all temperature ranges) and CsI

(740 K and 450 K); without any trace of cesium molybdates. Under this experimental condition, i.e. lack of oxygen concentration, the vaporized MoO_3 (starting material) was decomposed into MoO_2, which might result in an unfavorable reaction with CsI. Such a decomposition, however, could be avoided by introducing sufficient oxygen in the atmosphere as reported by Wang and coworkers who demonstrated that air inclusion during high-temperature treatment of β-MoO_3 could lead to α-MoO_3 [17]. Upon the introduction of one percent oxygen in the upstream gas flow, we confirmed that the deposition of both CsI and MoO_3 or MoO_2 did not occur (Fig. 4 b). This means that interaction between the vapor species of starting materials was achieved during the reaction test.

There were two types of cesium molybdate could be well identified in the deposits: the dicesium trimolybdate ($Cs_2Mo_3O_{10}$), and dicesium tetramolybdate ($Cs_2Mo_4O_{13}$). Although the vibrational peak shifts and bandwidth changes on the deposits (700 and 450 K) appeared due to the anharmonic effects of temperature increment [18, 19], the identified compounds matched well with the reference ones. At 1150 K, the deposits could not be qualitatively determined even though some high-frequency vibrations seem to resemble the in-situ Raman data of $Cs_2Mo_2O_7$ at 713 K reported by Smith [20]. Such a discrepancy will be investigated in the future.

A coexistence of cesium trimolybdate and tetramolybdate that occurred at 450 K is consistent with the bulk molar ratio obtained by ICP-MS analysis (Fig. 2 b) having Mo/Cs of 1.8. It is worth noting that the variation of cesium polymolybdates highly depends on the abundance of molybdenum in the upstream regions as it could shift the phase formations into Mo-rich compounds. This is discussed in the thermodynamic evaluation in the following section. To this end, we have demonstrated that the oxygen potential in the CsI-MoO_3 system plays a key role in the reaction, evidenced by the formation of low-volatile cesium polymolybdates and volatile gaseous iodine.

3.2. Thermodynamic evaluations

In an Ar-20%H_2O atmosphere case, there is a possibility of cesium molybdates formation (i.e. $Cs_2Mo_2O_7$ and Cs_2MoO_4, Fig 5 c) in the temperature of 1100-850 K which is followed by an increase of gaseous hydrogen iodide (HI) (Fig. 5 a). This implies that, once thermodynamic equilibrium is satisfied, both cesium molybdates and HI would be the reaction products in the Cs-I-Mo-O-H system:

$$2\ CsI\ (g) + n\ MoO_3\ (g) + H_2O\ (g) = Cs_2Mo_nO_{3n+1}\ (s) + 2\ HI\ (g) \quad (1)$$

where n is a stoichiometric coefficient denoting the cesium molybdate species (n = 1–5, and 7). At lower temperatures (T < 850 K), within the given threshold (1×10^{-9} mol), CsI and MoO_2 were stably formed rather than cesium molybdates. Such a short temperature constraint suggests that obtaining equilibrium was unlikely in the actual experiment. Therefore this explains why most of the starting materials were the only condensed phase observed after the experiment (Fig. 4). In an Ar-20%H_2O-1%O_2 atmosphere, the formation of cesium molybdates (i.e. $Cs_2Mo_3O_{10}$, $Cs_2Mo_4O_{13}$ and $Cs_2Mo_5O_{16}$) occurs in all temperature ranges (Fig. 5 d) and, in contrast to the previous case, there are no CsI and MoO_2. Here, the addition of one percent oxygen increases the chemical potential to -43 kJ/mol (at the upstream location of 1100 K) as compared to the steam-only case (-139 kJ/mol). The increase of oxygen potential not only could generate the cesium molybdates but also gaseous iodine in the form of molecular iodine (I_2) and hypoiodous acid (HIO) (Fig. 5 b). Therefore, the following equilibria are considered

$$2\ CsI\ (g) + n\ MoO_3\ (g) + H_2O\ (g) + O_2\ (g) = Cs_2Mo_nO_{3n+1}\ (s) + 2\ HIO\ (g) \quad (2)$$

$$4\ CsI\ (g) + 2n\ MoO_3\ (g) + O_2\ (g) = 2\ Cs_2Mo_nO_{3n+1}\ (s) + 2\ I_2\ (g) \quad (3)$$

In the predominance diagram of the condensed phase (Fig. 5 d), some cesium molybdates are coexistent which could be a result of different prevailing equilibria described above. While it is evident from the experiment that the $Cs_2Mo_3O_{10}$ and $Cs_2Mo_4O_{13}$ were formed, the absence of a predicted $Cs_2Mo_5O_{16}$ indicates

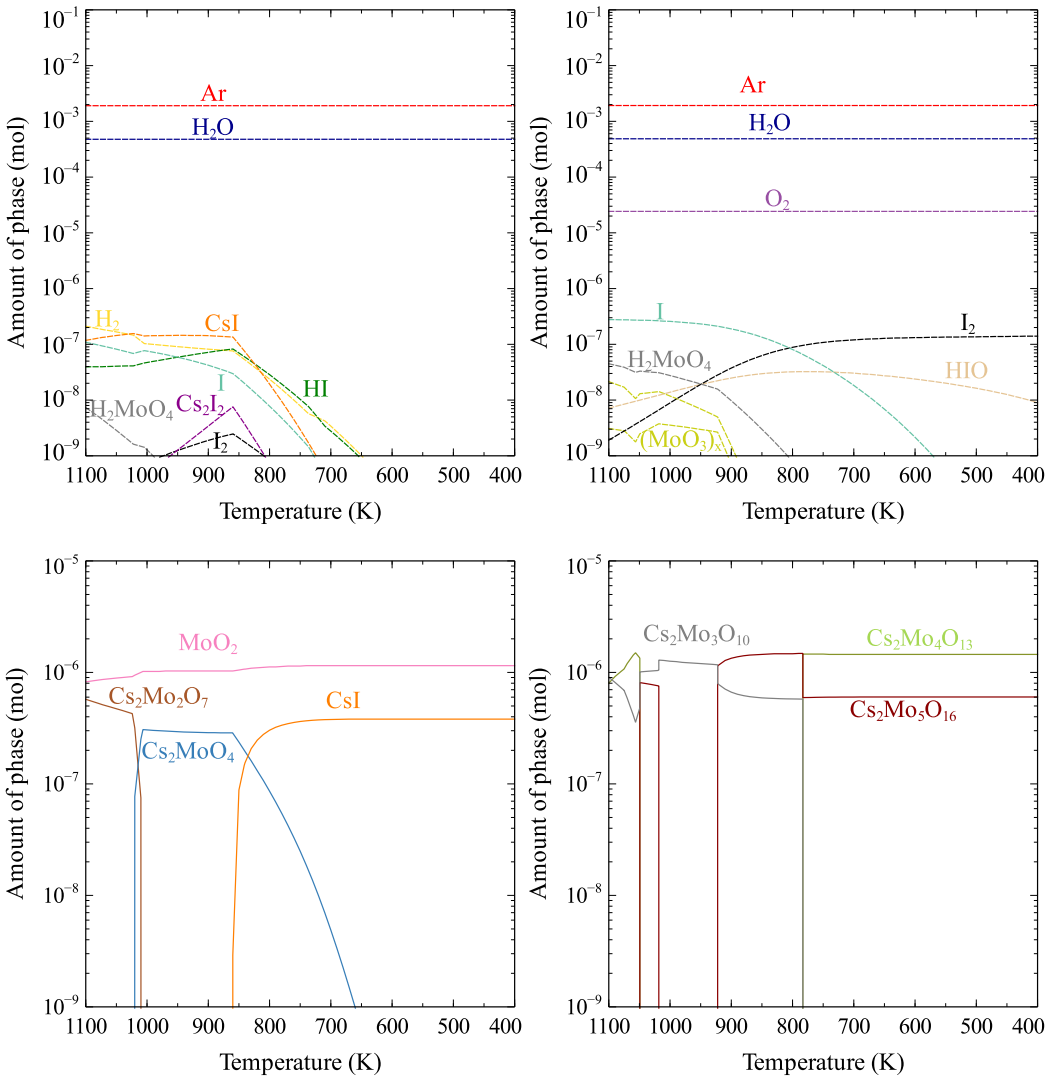

Figure 5. The estimated stable gaseous (a), (b) and condensed phases (c), (d) in the representative CsI-MoO_3 system by thermodynamic equilibrium calculations

the limitation of present equilibrium calculation. To resolve this, a non-ideal vaporization rate of each starting material (influences from the gas flow regime), for instance, could be sought to improve future thermodynamic evaluation.

4. CONCLUSIONS

Aiming at a better comprehension of the CsI-MoO_3 gaseous reaction system in the event of a nuclear severe accident, we have investigated the central role of oxygen potential and its implications for the reaction mechanism. In a steam-containing atmosphere, the reaction between CsI and MoO_3 gaseous species was hardly to occur experimentally due to the transformation of MoO_3 into MoO_2 in an oxygen-deficient

condition. The presence of MoO_2 hinders such a reaction in a temperature range that prevails during fission product transport in the reactor cooling system. To the least extent, however, for instance, in much higher temperatures and humid conditions, the reaction was predicted to proceed in the following reaction:

$$2\ CsI\ (g) + n\ MoO_3\ (g) + H_2O\ (g) = Cs_2Mo_nO_{3n+1}\ (s) + 2\ HI\ (g)$$

When the system has an increase in oxygen potential, the MoO_3 compound can be maintained in the gas phase, thus making the reaction achievable. We proved this by the addition of one percent oxygen to the steam-containing atmosphere and obtained that the cesium molybdates and gaseous iodine were generated. The following two reactions were considered as the underlying processes:

$$2\ CsI\ (g) + n\ MoO_3\ (g) + H_2O\ (g) + O_2\ (g) = Cs_2Mo_nO_{3n+1}\ (s) + 2\ HIO\ (g)$$

$$4\ CsI\ (g) + 2n\ MoO_3\ (g) + O_2\ (g) = 2\ Cs_2Mo_nO_{3n+1}\ (s) + 2\ I_2\ (g)$$

Besides the concern of gaseous iodine arising from these reactions that are likely to reach the containment vessel or even the reactor building during a severe accident, the cesium molybdates in the form of aerosols should also be accounted for. In our experiment, we found this aerosol was generated with a size of less than 2.7 μm and was able to reach low-temperature locations ($T < 400$ K). This is in contrast to the other cesium-containing aerosols such as CsI that is mostly trapped in higher temperatures [6, 7]. Therefore, the results obtained through this investigation in particular the elucidated mechanism should be further included in severe accident (SA) codes to obtain more reliable fission product transport behavior that affects the overall source term.

ACKNOWLEDGMENTS

This work was conducted under a research fund from the Nuclear Regulation Authority (NRA) in Japan. The authors would like to thank Mr. Juntaro Takada and Mr. Kunihiro Sumiya for their technical support on the experiments.

REFERENCES

1. A. C. Grégoire, J. Kalilainen, F. Cousin, H. Mutelle, L. Cantrel, A. Auvinen, T. Haste and S. Sobanska, “Studies on the Role of Molybdenum on Iodine Transport in the RCS in Nuclear Severe Accident Conditions,” *Annals of Nuclear Energy*, **78**, pp. 117–129 (2015).
2. M. Gouello, H. Mutelle, F. Cousin, S. Sobanska and E. Blanquet, “Analysis of the Iodine Gas Phase Produced by Interaction of CsI and MoO3 Vapours in Flowing Steam,” *Nuclear Engineering Design*, **263**, pp. 462–472 (2013).
3. A. L. Smith, T. N. Pham Thi, C. Guéneau, J. C. Dumas, E. Epifano, W. van Burik and N. Dupin, “Thermodynamic Modelling Assessment of the Ternary System Cs-Mo-O,” *Calphad*, **75**, 102350 (2021).
4. V. L. Stolyarova, V. A. Vorozhtcov, S. I. Lopatin, S. M. Shugurov, E. P. Simonenko, N. P. Simonenko, K. Masaki and D. Costa, “Vaporization and Thermodynamics of the Cs_2O–MoO_3 System Studied using High-temperature Mass Spectrometry,” *Rapid Communications in Mass Spectrometry*, **35**, e9097 (2021).
5. S. Miwa, G. Takase, J. Imoto, S. Nishioka, N. Miyahara and M. Osaka, “Boron Chemistry during Transportation in the High temperature Region of a Boiling Water Reactor under Severe Accident Conditions,” *Journal of Nuclear Science and Technology*, **57**(3), pp. 291–300 (2020).
6. N. Miyahara, S. Miwa, M. Gouëllo, J. Imoto, N. Horiguchi, I. Sato and M. Osaka, ”Experimental Study on Transport Behavior of Cesium Iodide in the Reactor Coolant System under LWR Severe Accident Conditions,” *Journal of Nuclear Science and Technology*, **57**(12), pp. 1287–1296 (2020).

7. M. Rizaal, S. Miwa, E. Suzuki, J. Imoto, M. Osaka and M. Gouëllo, "Revaporization Behavior of Cesium and Iodine Compounds from Their Deposits in the Steam–Boron Atmosphere," *ACS Omega*, **6**(48), pp. 32695–32708 (2021).
8. J. O. Andersson, T. Helander, L. Höglund, P. Shi and B. Sundman, "Thermo-Calc & DICTRA, Computational Tools for Materials Science," *Calphad*, **26**(2), pp. 273–312 (2002).
9. I. Sato, T. Onishi, K. Tanaka, M. Iwasaki and S. I. Koyama, " Influence of Boron Vapor on Transport Behavior of Deposited CsI during Heating Test simulating a BWR severe accident condition," *Journal of Nuclear Materials*, **461**, pp. 22–28 (2015).
10. A. Hidaka, M. Igarashi, K. Hashimoto, H. Sato, T. Yoshino and J. Sugimoto, "Experimental and Analytical Study on the Behavior of Cesium Iodide Aerosol/Vapor Deposition onto Inner Surface of Pipe Wall under Severe Accident Conditions," *Journal of Nuclear Science and Technology*, **32**(10), pp. 1047–1053 (1995).
11. H. R. Hoekstra," The Cs_2MoO_4-MoO_3 System," *Inorganic and Nuclear Chemistry Letters*, **9**(12), pp. 1291–1301 (1973).
12. A. L. Smith, J. Vlieland, M. C. Pignié, M. Abbink, G. Mikaelian and P. Benigni, "New Insights Into the Cs-Mo-O System: Experimental Studies of the Cs_2MoO_4-MoO_3 Pseudo-binary System," *Thermochimica Acta*, **696**, 178825 (2021).
13. L. Wang, Z. L. Xue, A. Huang and F. F. Wang, "Mechanism and Kinetic Study of Reducing MoO_3 to MoO_2 with CO-15 vol % CO_2 Mixed Gases," *ACS Omega*, **4**, pp. 20036–20047 (2019).
14. A. Chychko, L. Teng, and S. Seetharaman, "MoO_3 Evaporation Studies from Binary Systems towards Choice of Mo Precursors in EAF," *Steel Research International*, **81**, pp. 784−791 (2010).
15. E.H.P. Cordfunke and G. Prins, "The Thermochemical Properties of Caesium Iodide. I. Thermodynamic Functions of Solid CsI," *Thermochimica Acta*, **90**, pp. 169–176 (1985).
16. P. Saha, A. J. Anderson, T. Lee and M. Klemm, "The Solubility of Tugarinovite (MoO_2) in H_2O at Elevated Temperatures and Pressures," *Geofluids*, 5459639 (2017).
17. L. Wang, M. C. Li, G. H. Zhang and Z. L. Xue, "Morphology Evolution and Quantitative Analysis of β-MoO_3 and α-MoO_3," *High Temperature Materials and Processes*, **39**, pp. 620–626 (2020).
18. G. D. Saraiva, W. Paraguassu, M. Maczka, P. T. C. Freire, J. A. L. Jr., C. W. A. Paschoal, J. M. Filho and A. G. S. Filho, "Temperature-dependent Raman Scattering Studies of Na_2MoO_4," *Journal of Raman Spectroscopy*, **39**, pp. 937–941 (2008).
19. G. D. Saraiva, W. Paraguassu, M. Maczka, P. T. C. Freire, F. F. de Sousa, and J. M. Filho, "Temperature-dependent Raman Scattering Studies on $Na_2Mo_2O_7$ Disodium Dimolybdate," *Journal of Raman Spectroscopy*, **42**, pp. 1114-1119 (2011).
20. A. L. Smith, G. Kauric, L. van Eijck, K. Goubitz, G. Wallez, J. C. Griveau, E. Colineau, N. Clavier and R. J. M. Konings, "Structural and thermodynamics study of dicesium molibdate $Cs_2Mo_2O_7$: Implication for fast neutron reactor," *Journal of Solid State Chemistry*, **253**, pp. 89–102 (2017).

Gaseous and aerosol formations in the pseudo-binary CsI-MoO_3 reaction system

Muhammad Rizaal, Kunihisa Nakajima, Eriko Suzuki, Shuhei Miwa

Japan Atomic Energy Agency

The 11th European Review Meeting on Severe Accident Research (ERMSAR2024)

KTH, Stockholm, Sweden, May 13-16, 2024

Outlines

- Introduction
- CsI-MoO_3 gaseous reaction tests
- Results
- Thermodynamic analysis
- Conclusions

Introduction – Cs, I, Mo release during unmitigated LTSBO

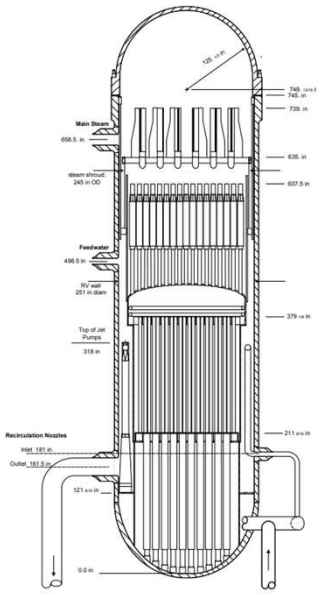

Peach Bottom Power Station*

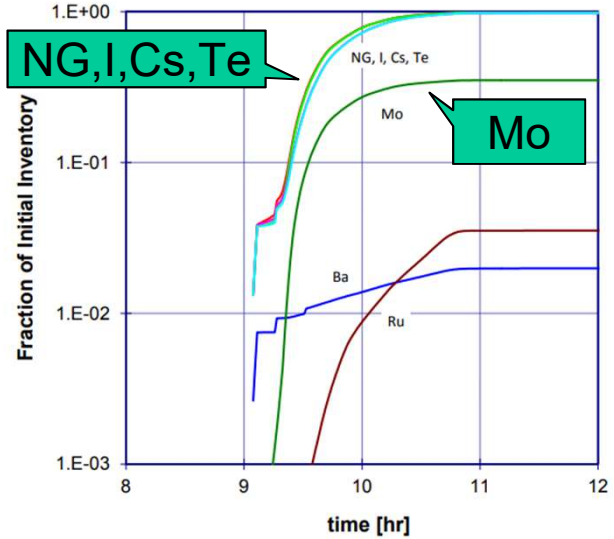

LTSBO In-vessel Fission Product Release from Fuel*

Present study

Primary objective

Mechanism identification of the impact of molybdenum in the gas phase on volatile iodine.

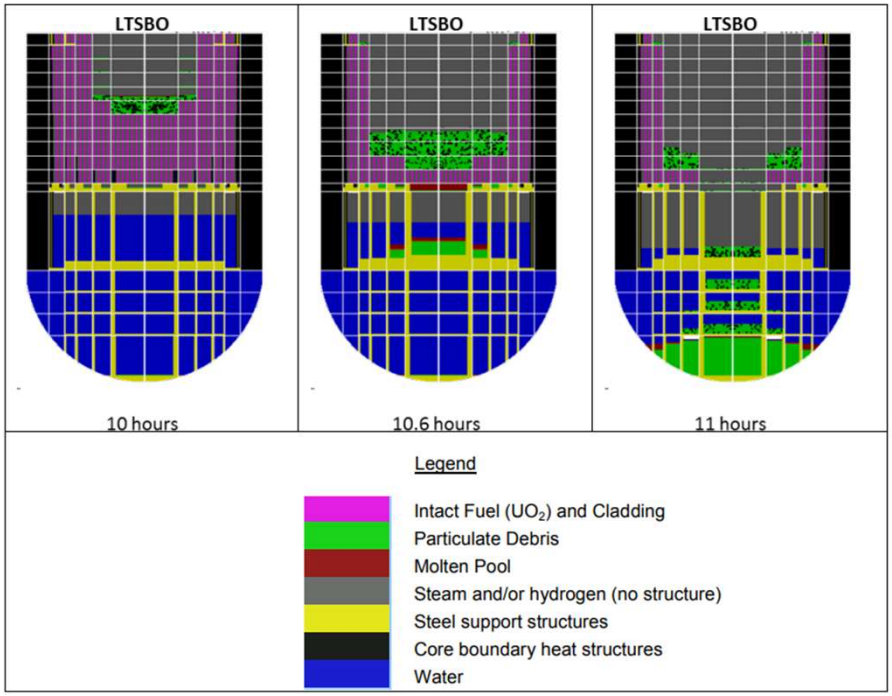

Schematic of accident progression during LTSBO*

Scope

Dependence of atmospheric oxygen potential into the gaseous phases interaction.

***NUREG/CR-7110 Vol. 1**

CsI-MoO_3 gaseous reaction tests (TeRRa JAEA)



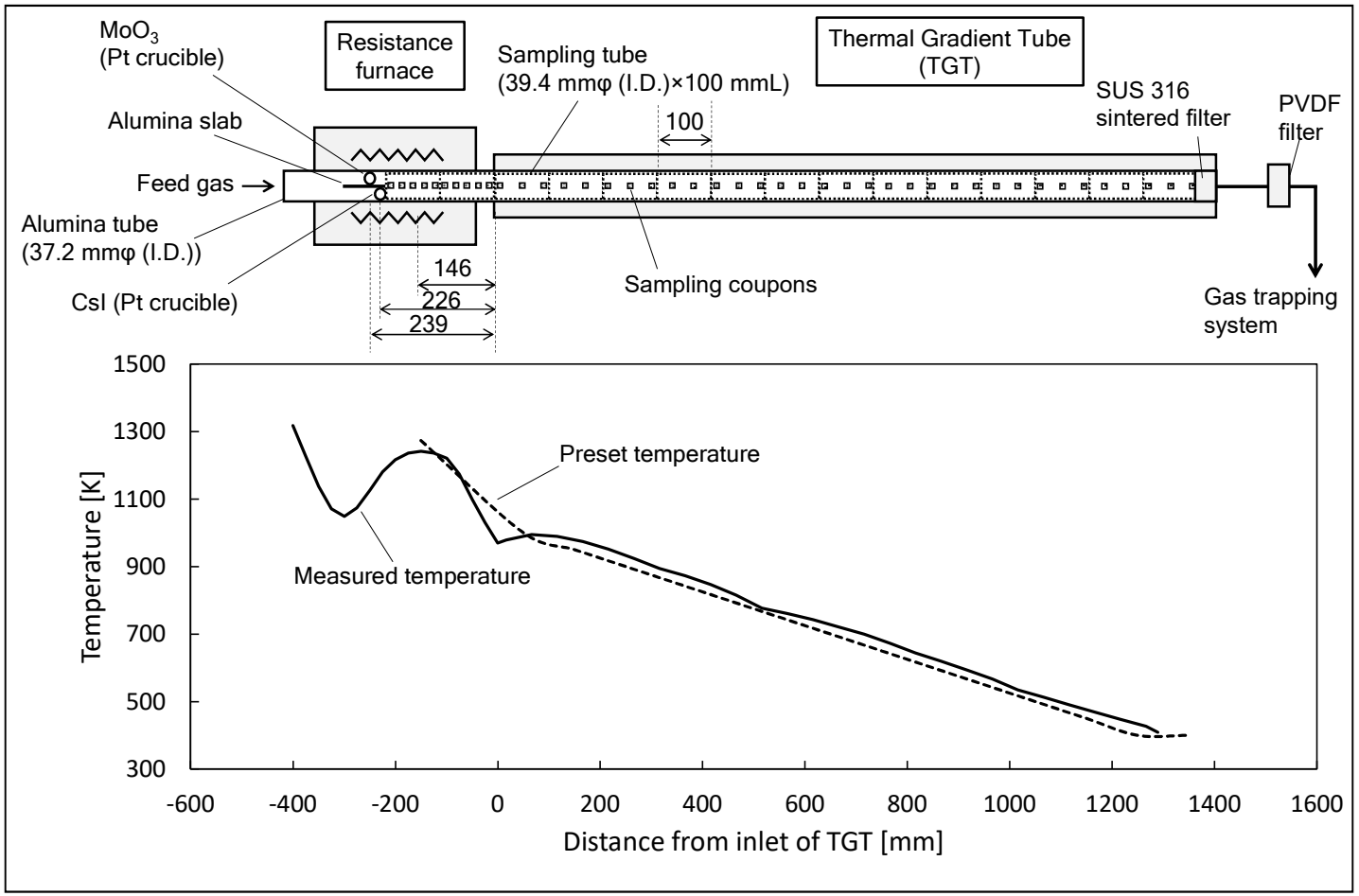

Crucible (top view)

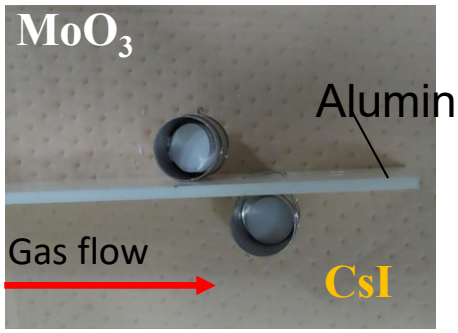

Cogeneration gaseous species → **Interaction** gaseous species → **Condensation** gaseous species

TGT inner tube


(top view)


(side view)

CsI-MoO_3 gaseous reaction tests (TeRRa JAEA)

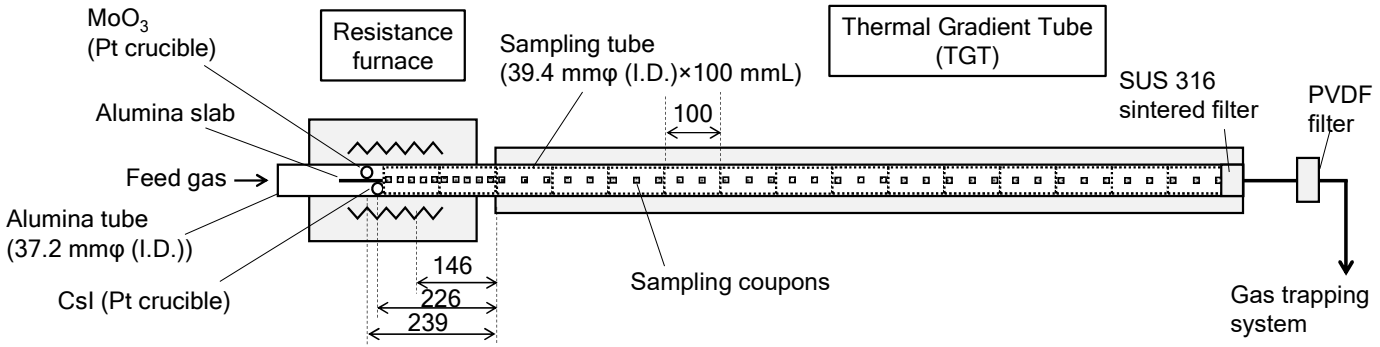

Experimental conditions	TeRRa CsIMo-1	TeRRa CsIMo-2
Materials	CsI & MoO_3	CsI & MoO_3
Initial amount (g)	1.3 both	1.3 both
Heating temperature (K)	1190, 1160	1190, 1160
TGT temperature (K)	1250–450	1250–450
Holding time (min)	60	60
TGT inner tubes	SUS304L	SUS304L
Gas composition	Ar-20%H_2O	Ar-20%H_2O-1%O_2
Flow rate (L/min)	2	2
SUS filter (µm)	0.8	0.8
PVDF filter (µm)	0.3	0.3

Focus on the oxygen potential:
Test CsIMo-1: -139 kJ/mol
Test CsIMo-2: -43 kJ/mol

Post-test analyses

Sampling tube → ICP-MS

Sampling coupons → SEM/EDS, µ-Raman spectroscopy

Results - Vapor sources after the tests

	Ar-20%H_2O	Ar-20%H_2O-1%O_2
Evaporated amount CsI (g)	0.178	0.192
Evaporated amount MoO_3 (g)	0.177	0.226
Vaporization rate CsI (mol/s)	1.91×10^{-7}	2.05×10^{-7}
Vaporization rate MoO_3 (mol/s)	3.42×10^{-7}	4.37×10^{-7}
Molar ratio Mo/Cs [-]	1.79	2.13

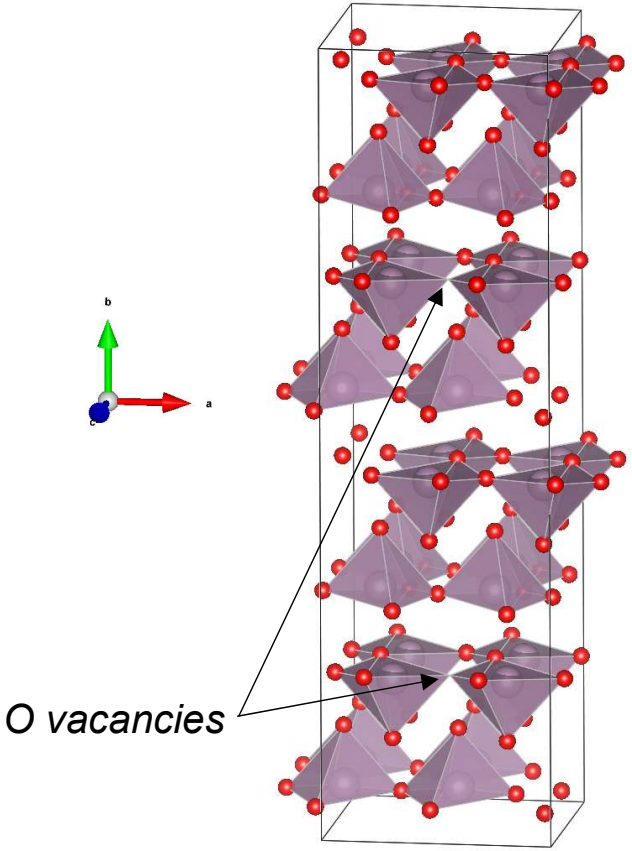

α-MoO_3



Molybdenum oxide complexes:
α-MoO_3, MoO_2, Mo_4O_{11}



Molybdenum oxide:
α-MoO_3

$$2MoO_3 \underset{\text{High } \mu_{O2}}{\overset{\text{Low } \mu_{O2}}{\rightleftharpoons}} 2MoO_{3-x} + xO_2$$

High atmospheric μ_{O2} to compensate O vacancies

Results – Deposition profile after the tests

TeRRa-JAEA

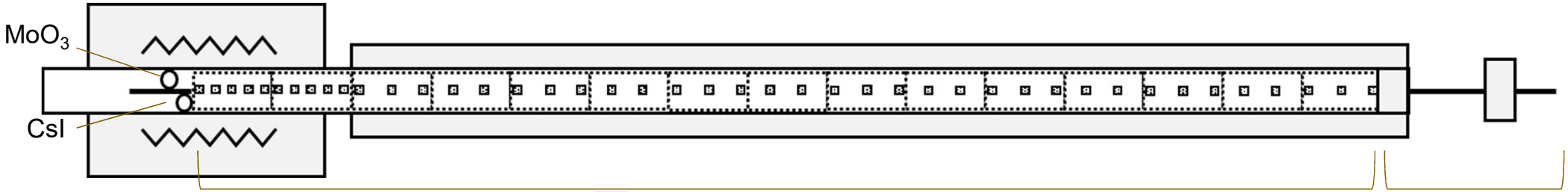

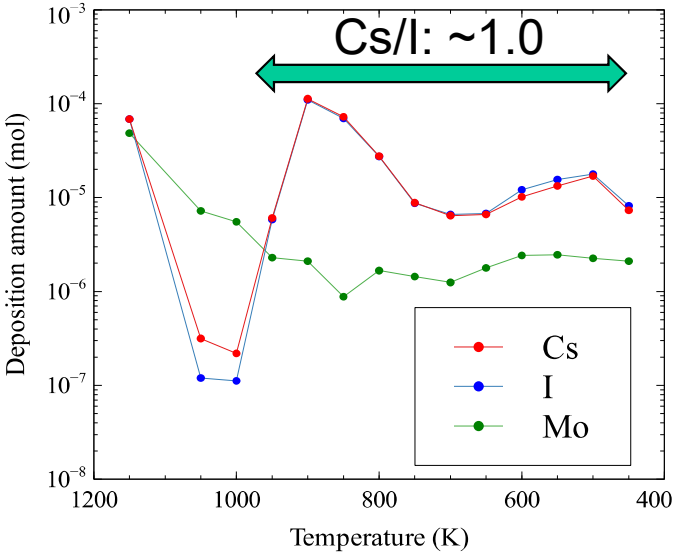

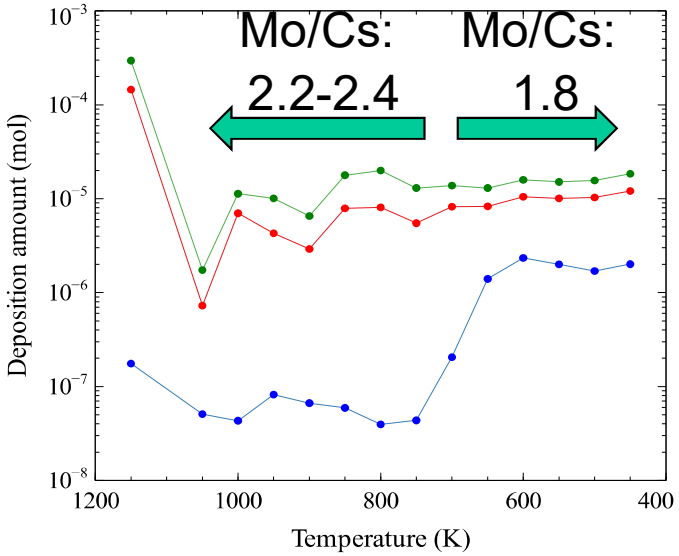

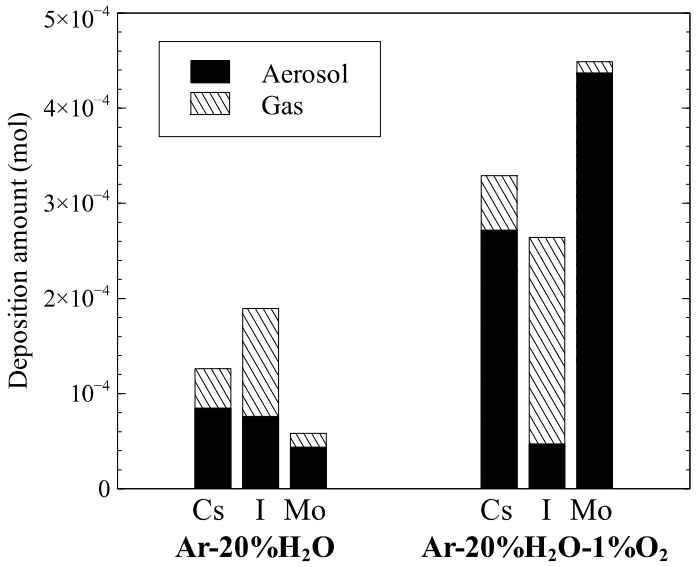

Ar-20%H_2O

- Congruent Cs-I distribution (< 950 K).
- Highly indicative of an unlikely reaction with Mo.

Ar-20%H_2O-1%O_2

- Cs-Mo congruently distributed.
- Reaction occurred with Mo.

upstream

downstream

More aerosol (Cs-Mo compd.) & gas (I compd.) generated

Results – Microstructure analysis on precipitates

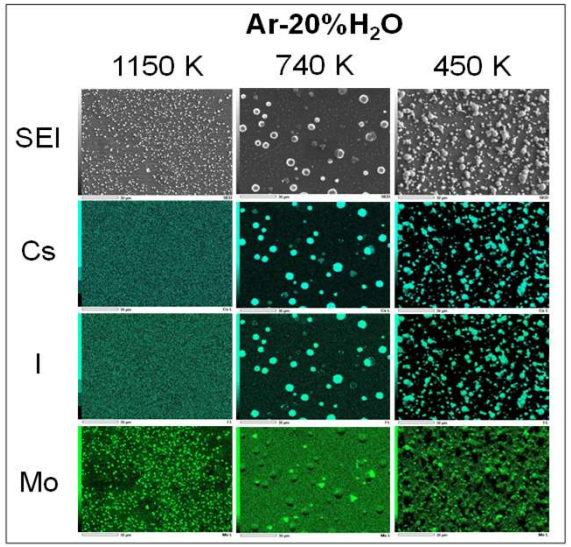

- Congruent distribution: Cs and I
- Mo compound:
  1150 K: Spherical
  740-450 K: Irregular

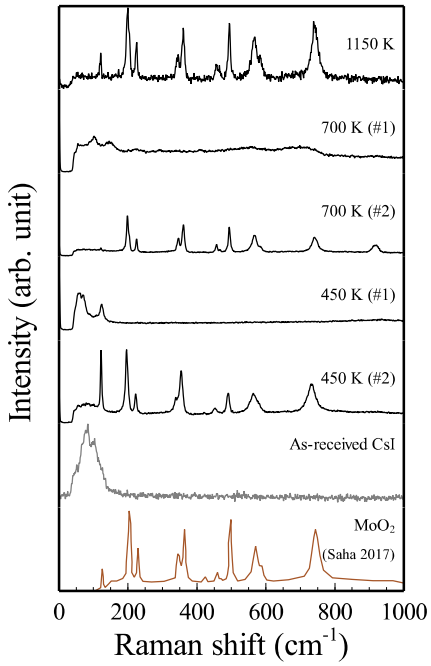

Main Chem. Compd.

Ar-20%H_2O

CsI and MoO_2

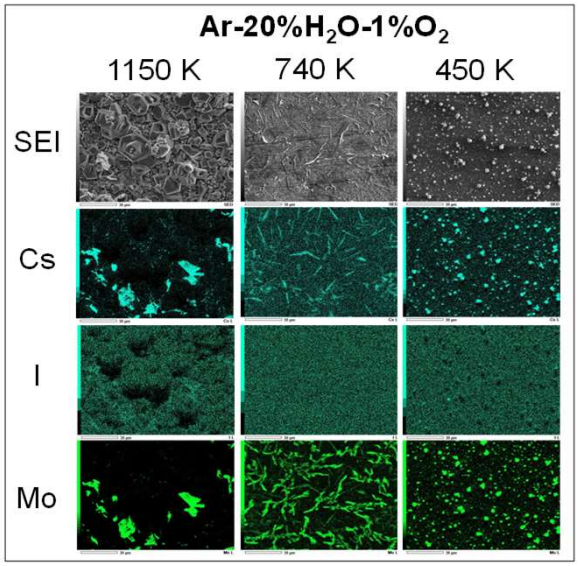

- Congruent distribution: Cs and Mo
- Cs-Mo compound:
  1150 K: Irregular;
  740 K: Acicular
  450 K: Spherical, (<2.77µm)

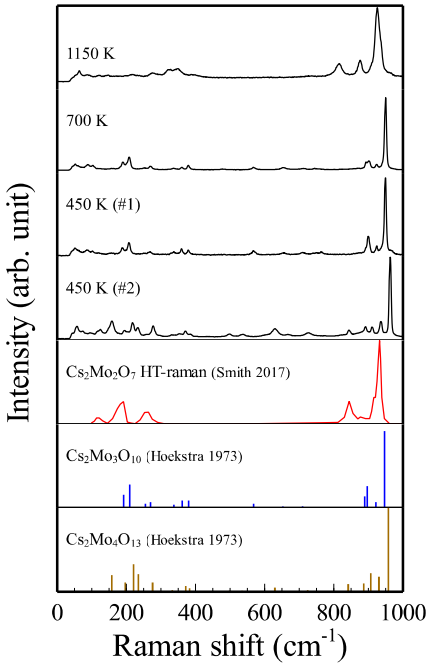

Main Chem. Compd.

Ar-20%H_2O-1%O_2

Cesium polymolybdates

Thermodynamics analysis (I /3)

Goal : To elucidate the Cs polymolybdates formation mechanism observed in the experiment

- Thermo-Calc 2021a; Database: modified-SGTE Substances version 5
- Cs-I-Mo-O-H-Ar system
- Added Cs-Mo-O compounds:
  $Cs_2Mo_2O_7$, $Cs_2Mo_3O_{10}$, $Cs_2Mo_4O_{13}$, $Cs_2Mo_5O_{16}$, $Cs_2Mo_7O_{22}$
  [based on thermodyn. data of Smith and Stolyarova]

(Smith et al., *Calphad* 2021, 75, 102350)
(Stolyarova et al., *Rapid Commun. Mass Spectrom.* 2021, 35, e9097)

Calculation: Chemical equilibrium calculation

	Ar-20%H_2O	**Ar-20%H_2O-1%O_2**
Cs amount (mol)	1.9074×10^{-7}	2.0528×10^{-7}
I amount (mol)	1.9074×10^{-7}	2.0528×10^{-7}
Mo amount (mol)	3.8474×10^{-7}	4.3673×10^{-7}
O amount (mol)	3.4138×10^{-4}	3.8073×10^{-4}
H amount (mol)	6.8123×10^{-4}	6.8985×10^{-4}
Ar amount (mol)	1.3625×10^{-3}	1.3625×10^{-3}
Temperature (K)	1100–400	1100–400
Pressure (MPa)	0.1	0.1

Thermodynamics analysis (2/3)

Gas phases

Condensed phases

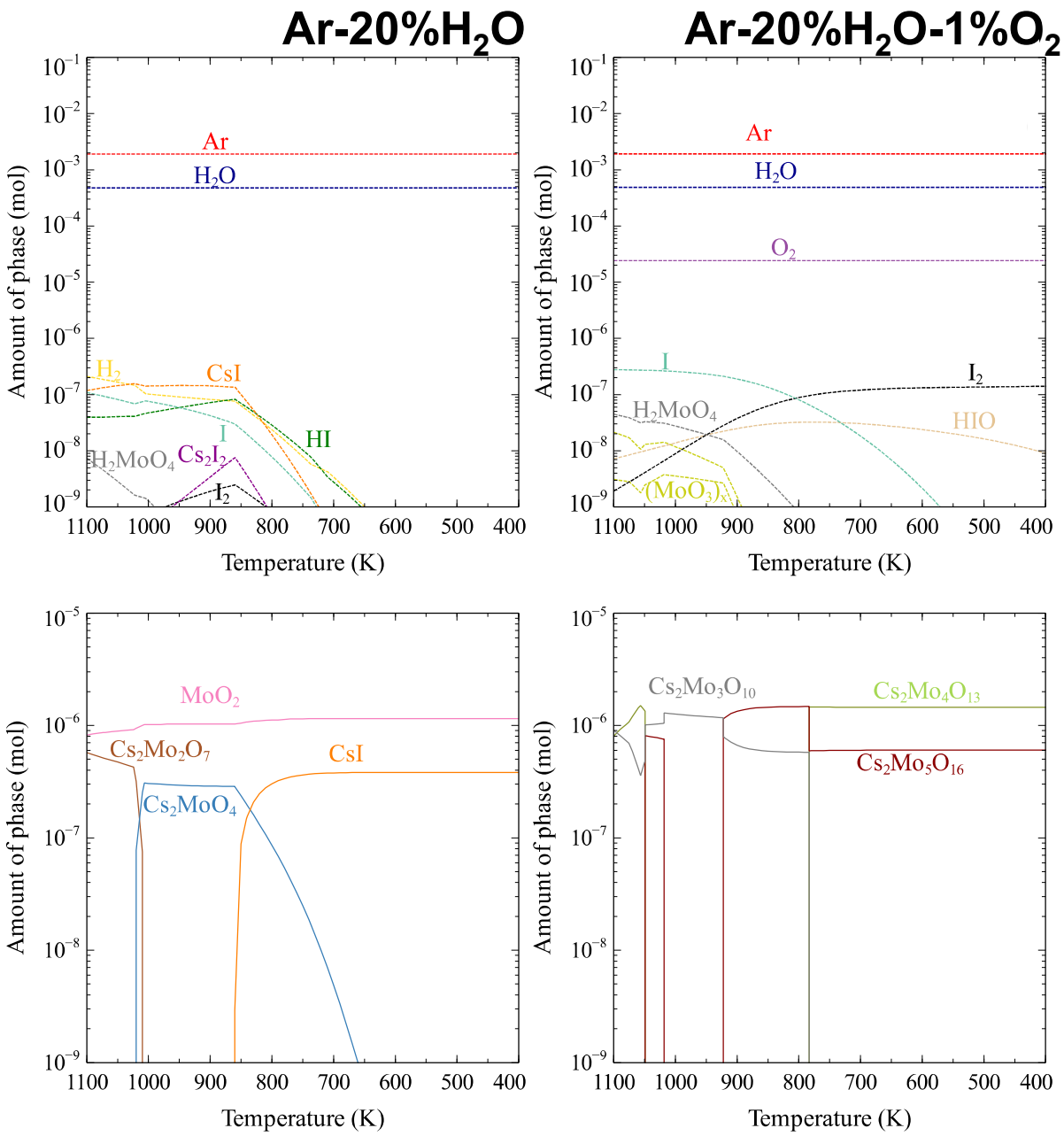

Ar-20%H_2O

-Thermodyn. equilib. cal-

- TGT Deposits:
  MoO_2, $Cs_2Mo_2O_7$, Cs_2MoO_4, CsI.

-Experiment-(Raman spec.)

- TGT Deposits:
  MoO_2 (1100-400K), CsI (900-400K)
- Aerosol filters:
  MoO_2 & CsI

Ar-20%H_2O-1%O_2

-Thermodyn. equilib. cal-

- TGT Deposits:
  $Cs_2Mo_3O_{10}$, $Cs_2Mo_5O_{16}$, $Cs_2Mo_4O_{13}$

-Experiment-(Raman spec.)

- TGT Deposits:
  $Cs_2Mo_3O_{10}$ (700-400 K),
  $Cs_2Mo_4O_{13}$ (400 K).
- Aerosol filters:
  $Cs_2Mo_3O_{10}$, $Cs_2Mo_4O_{13}$

Chem. Equi. Calc. with enhanced Cs-Mo-O database predict the interaction well

Thermodynamics analysis (3/3)

Gas phases

Condensed phases

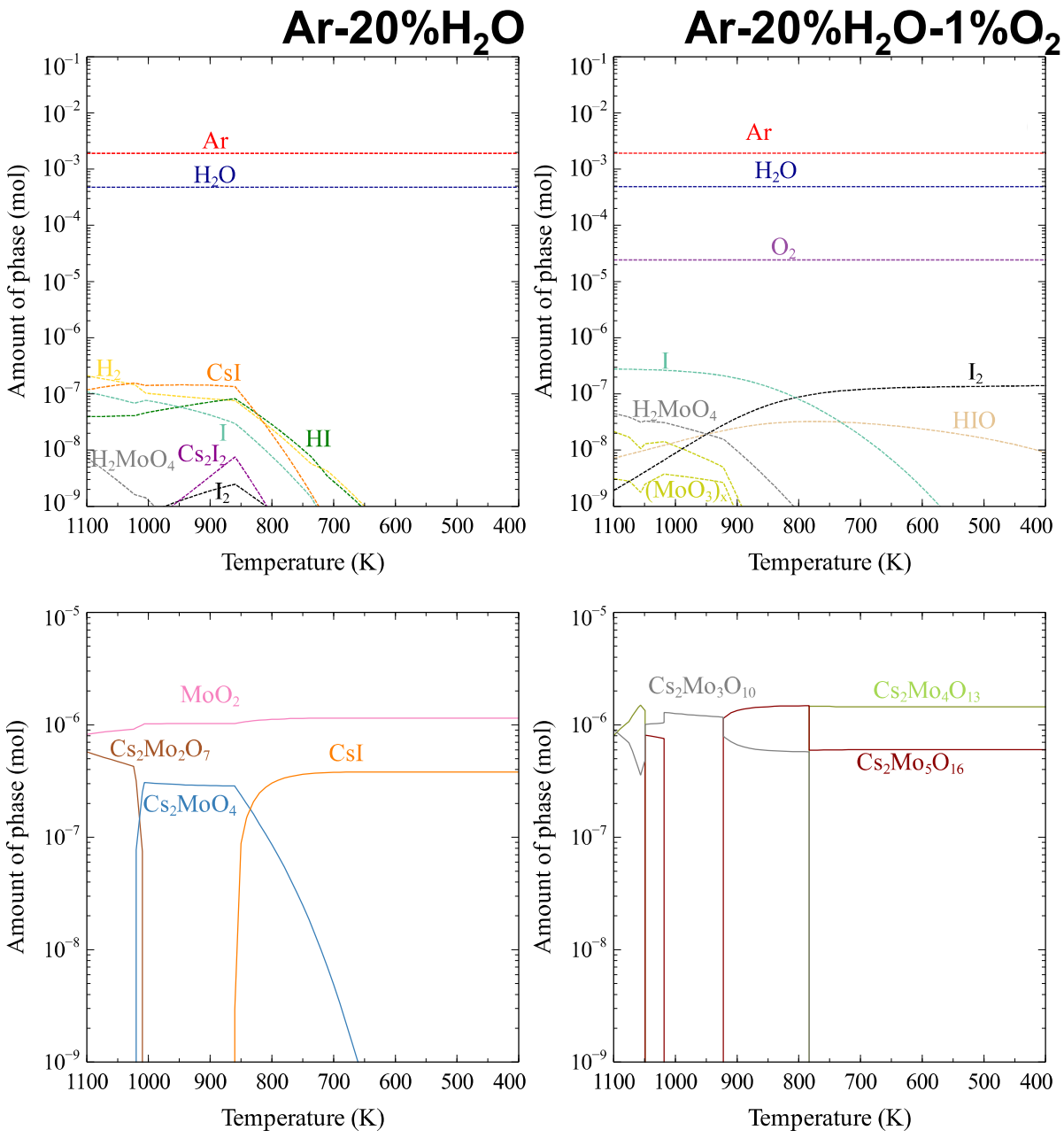

Ar-20%H_2O

2 CsI (g) + n MoO_3 (g) + H_2O (g)
= $Cs_2Mo_nO_{3n+1}$ (s) + 2 HI (g)

Ar-20%H_2O-1%O_2

Reaction 1

2 CsI (g) + n MoO_3 (g) + H_2O (g) + O_2 (g)
= $Cs_2Mo_nO_{3n+1}$ (s) + 2 HIO (g)

Reaction 2

4 CsI (g) + 2n MoO_3 (g) + O_2 (g)
= 2 $Cs_2Mo_nO_{3n+1}$ (s) + 2 I_2 (g)

Gaseous iodine speciation (HI, HIO, and I_2) was expected to occur

Conclusion

- Oxygen potential (μ_{O_2}) in the atmosphere was proved to be the influencing factor to yield the reaction.
- Depending on μ_{O_2}, gaseous iodine could be generated as:

Ar-20%H_2O (μ_{O_2} = -139 kJ/mol @1100 K)

$$2\ CsI\ (g) + n\ MoO_3\ (g) + H_2O\ (g) = Cs_2Mo_nO_{3n+1}\ (s) + 2\ HI\ (g)$$

Ar-20%H_2O-1%O_2 (μ_{O_2} = -43 kJ/mol @1100 K)

$$2\ CsI\ (g) + n\ MoO_3\ (g) + H_2O\ (g) + O_2\ (g) = Cs_2Mo_nO_{3n+1}\ (s) + 2\ HIO\ (g)$$

$$4\ CsI\ (g) + 2n\ MoO_3\ (g) + O_2\ (g) = 2\ Cs_2Mo_nO_{3n+1}\ (s) + 2\ I_2\ (g)$$

- In the latter case (when upstream Mo/Cs: 2.13), aerosol as $Cs_2Mo_3O_{10}$ and $Cs_2Mo_4O_{13}$.
- Under steam-rich atmosphere Ar-80%H_2O (μ_{O_2} = -130 kJ/mol) (IRSN study, *Nucl. Eng. Des*, 2013, **263**, 462-472), our reaction mechanism could elucidate the generation of gaseous iodine and Cs polymolybdates.

Table 2
Fractions of gaseous iodine in the sampling lines & condensed species on the filters and the quartz plates.

Test		Pure CsI	Mo-1	Mo-2	Mo-3	Mo-4
Average molar ratio in the HT zone	Mo/Cs	–	0.17	0.7	2.1	4.9
	Cs/I	0.92	0.81	0.89	0.97	0.95
I(g)/I(total HT)[a]		1–9%	6–14%	47–52%	60–76%	75–100%
I(g)/I(total sampled)[b]		3–14%	12–23%	43–48%	75–95%	80–97%
I_2(g)/I(g)		23–85%	56–94%	94–99%	76–97%	79–81%
Molecular species on the quartz plates[c]	Plate no. 1 (1100 °C > T > 850 °C)	–	$Cs_2Mo_2O_7$ $Cs_2Mo_3O_{10}$ $Cs_2Mo_4O_{13}$	$Cs_2Mo_2O_7$ $Cs_2Mo_3O_{10}$ $Cs_2Mo_3O_{10}$ $Cs_2Mo_4O_{13}$	$Cs_2Mo_3O_{10}$ $Cs_2Mo_4O_{13}$ $Cs_2Mo_5O_{16}$ $Cs_2Mo_7O_{22}$ MoO_3	$Cs_2Mo_3O_{10}$ $Cs_2Mo_4O_{13}$ $Cs_2Mo_5O_{16}$ $Cs_2Mo_7O_{22}$ MoO_3
	Plate no. 2 (800 °C > T > 550 °C)	–				
Measurements in the sampling lines	Mo/Cs	–	0.17	0.6	1.4	3.8
Cs/I[d]	0.86 (0.9)	0.89 (1.07)	0.91 (1.99)	0.79 (2.82)	0.85 (32.1)	
Molecular species[c]	–	$Cs_2Mo_3O_{10}$ $Cs_2Mo_4O_{13}$ $MoO_3 \cdot 3H_2O$	$Cs_2Mo_3O_{10}$ $Cs_2Mo_4O_{13}$	$Cs_2Mo_5O_{16}$ $Cs_2Mo_7O_{22}$ MoO_3	$Cs_2Mo_7O_{22}$ MoO_3	

Acknowledgment

This work was conducted under a research fund from the Nuclear Regulatory Agency (NRA) in Japan.

EXPERIMENTAL STUDY ON REMOVAL EFFECT OF RADIOACTIVE MATERIALS IN THE COURSE OF THE LEAKAGE THROUGH THE EQUIPMENT HATCH

Koichi Nakamura*, Masashi Himi, Satoshi Nishimura
Central Research Institute of Electric Power Industry (CRIEPI)
2-6-1, Nagasaka, Yokosuka-shi, Kanagawa, 240-0196, Japan
k-naka@criepi.denken.or.jp, yohimi@criepi.denken.or.jp, satoshi@criepi.denken.or.jp

1. ABSTRACT

The equipment hatch in the containment vessel of the nuclear power plant is a potential part from which fission products leak into the environment during a severe accident. If a gap height in the leak pathway is small, some fission products in the form of aerosol can be trapped inside the pathway during the leakage. The objective of this study is to clarify aerosols removal effects in the leak pathway of the equipment hatch quantitatively with an experimental approach. The study especially focuses on understanding the dependency of the removal effects on a gap height or a flow rate. The test section represents a partial arc length of the whole circumference of the equipment hatch. It enables to reproduce a leakage with a perpendicular flow to the gasket rings. Silica is used as an aerosol material of which particle diameter is equivalent with that observed in a severe accident. The decontamination factors, DF, which is defined as a ratio of aerosol concentration in the inlet to that in the outlet of the test section, was measured in each test. A wide range of flow rate is considered for experimental conditions not only to cover assumed leak conditions under actual accidents, but also to understand basis phenomenal mechanism. The results showed that DF decreases as flow rate increases. Massive aerosols deposition on the floor of the test section were observed after experiments with a low flow rate while little depositions on the ceiling were observed. The observation supports the consideration that sedimentation mainly contributes to higher DF under a lower flow rate. The results also showed the possibility that tests with a smaller gap height are linked with higher DF. It can be said that a smaller gap height causes a smaller falling distance of a sedimentation and a larger deposition. A series of experiments indicated that DF exceeds approximately several tens under the Reynolds number less than approximately 100 with any gap heights of 0.1 mm to 1 mm. It is noted that the condition of degraded gaskets in the accidents is unknown so far and hypothetical configuration of gasket is assumed in this study. The data obtained in the experiments can be useful to discuss basic mechanism of aerosol removal in the equipment hatch.

KEYWORDS
Severe accident, Fission product, Aerosol, Decontamination factor, Equipment hatch

2. INTRODUCTION

The containment vessel (CV) is an ultimate barrier against a leakage of fission products (FPs) during severe accidents (SA) in nuclear power plants. In a level 2 Probabilistic Risk Assessment (PRA), it is crucial to evaluate the sum of FPs leaked into the environment realistically. In a traditional way, it has been

conservatively assumed that most of FPs suspended in the CV immediately leak into the environment once the CV loses its integrity. However, the leak pathway in the CV penetration can configurate a complex geometry with a narrow gap. Thus, some FPs are expected to be trapped inside the leak pathway due to aerosol deposition mechanisms, such as an inertial impact. Many studies have been conducted regarding the effects so far. D A. Powers investigated related studies and presented his conclusions [1]. First, the report mentions about the possibility of plugging on a narrow leak pathway due to accumulated deposition and concluded that the criteria for the plugging condition with Stokes number and particle sedimentation velocity advocated by Davies [2], Agarwal and Liu [3] provide useful insights. The report also shows that a variety of useful databases regarding aerosol deposition in some flow channels have been developed. For example, Lewis [4], Mosely et al [5], Liu and Nazaroff [6][7] conducted experiments to investigate the penetration rate of aerosol transported through a slot flow channel. Considering the relationship between aerosol particle size and a penetration rate through their experiments, it is shown that the penetration rate of a slot increases as the particle size increases in a range of a small particle size. On the other hand, the penetration rate decreases as the particle size increases in a range of a large particle size. This is because, as a factor influencing the adsorption of particles to the wall surface, when the particle size is small, diffusion of the particles is dominant, and when the particle size is large, sedimentation due to gravity of the particles is dominant. Furthermore, the report mentions that a lot of experiments for examination of turbulent deposition were conducted. Parameters, dimensionless deposition velocity, V_d^+ and dimensionless relaxation time, τ^+ were introduced for the modeling of the turbulent deposition. Additionally, the report summarizes fluid dynamics in idealized flow channels, such as capillary or orifice, and findings from aerosol research on specific objects such as gaskets or cracks in concrete. The experimental database, correlation or qualitative consideration described in the report would totally help us consider experimental conditions and analyze experimental results based on the aerosol mechanics.

The Nuclear Power Engineering Corporation (NUPEC) conducted experiments on FPs aerosol removal effects at the penetration components where FPs may leak out from the CV of BWRs [8][9]. In a series of experiments, the conditions for leak initiation from the containment vessel were examined by heating up and pressurizing the penetrations components. Subsequently, the amount of FPs aerosol trapping effects along leakage pathway were examined using the same test pieces with decontamination factor (DF), which is a ratio of suspended FPs concentration at the inlet to that at the outlet of the test piece. The average DF for each penetration was evaluated to be approximately 600 for the low voltage module and approximately 16 for the flange gasket. It is noted that the NUPEC tests were the only full-scale experiment specialized in DFs of the actual penetration components under the equivalent condition with SA. On the other hand, the detailed dependency of related physical parameters (gap height, channel length, flow rate, etc.) on DFs were not necessarily clarified. It is guessed because they had difficulty to define these parameters in full-scale experiments using actual complex broken components. It is significant to understand the mechanics of the deposition and develop more detailed methods in order to apply the results to conditions not considered in the NUPEC test or to other components. Therefore, it makes a conclusion that further parametric experiments to complement the full-scale experiments are required.

In this study, DF experiments for the equipment hatch were conducted under a wide range of experimental conditions including accident conditions. In the NUPEC test, it is considered that the variations in a geometry of the leak path in each test piece caused by fracture mechanics uncertainty led to variations in DF results. The result might also have made it difficult to understand the detailed mechanism. In our experiments, the process of the fracture was excluded from experimental conditions, and a variety of potential geometries in the leak pathway were examined by setting gap height as changeable experimental parameter.

3. EXPERIMENTAL METHOD

3.1. Experimental apparatus

A series of experiments was conducted for a flange gasket (the type of tongue and groove flanges) applied to the Japanese 2 to 4 loops PWR's equipment hatches. The structure of the equipment hatch is shown in Figure 1. The component is one of potential parts that FPs can leak out during SA. Airtight condition can be achieved by a structure in which two raised rings (tongues) on the surface of the hatch lid are pushed into two circular gaskets rings made of silicone rubber installed in the grooves on the seat ground by bolting. If the CV pressure increases significantly, a gap can occur on the seal due to deformation of the hatch bodies. In addition, silicone rubber can degenerate due to high temperature and a leak pathway may also occur.
The form of leakage is assumed to be a central flow from an overall or a part of the circular gasket described by red arrows in the right sketch of Figure 1. The geometry of the test section is designed to agree with them of the equipment hatch in the leak flow direction, because it can strongly affect flow dynamic in the leak pathway. Figure 2 shows an overview of the test section simulating the equipment hatch. The major specifications are described below.

- The material of the hatch bodies: Stainless steel
- Gap height: Changeable (max. ~5 mm)
- Seal material: Silicon rubber
- Maximum pressure: 100 kPa gauge
- Maximum flow rate: 100 L/min

The experimental apparatus consists of the lower body and the upper body, which can be separated in assembly and disassembly processes. It enables to observe deposited aerosols on their surfaces after each test. Three inflow and outflow ports for gas including aerosols are installed to realize a uniform flow distribution in the test section. Furthermore, mixing parts are also set at the inlet and outlet part of the test section for the same purpose. The gap height defined as a distance between the surfaces of the upper body and the lower body is changeable between 0 to 5 mm.

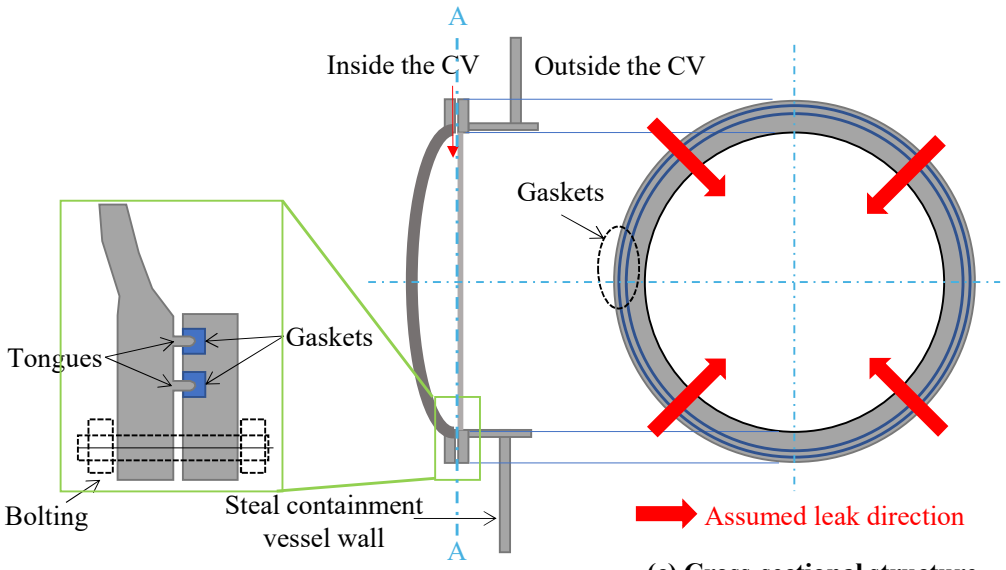

(a) Enlarged view of gasket **(b) Side-view of the equipment hatch** **(c) Cross-sectional structure (A-A cross section)**

Figure 1 Schematic diagram of PWR equipment hatch and gasket

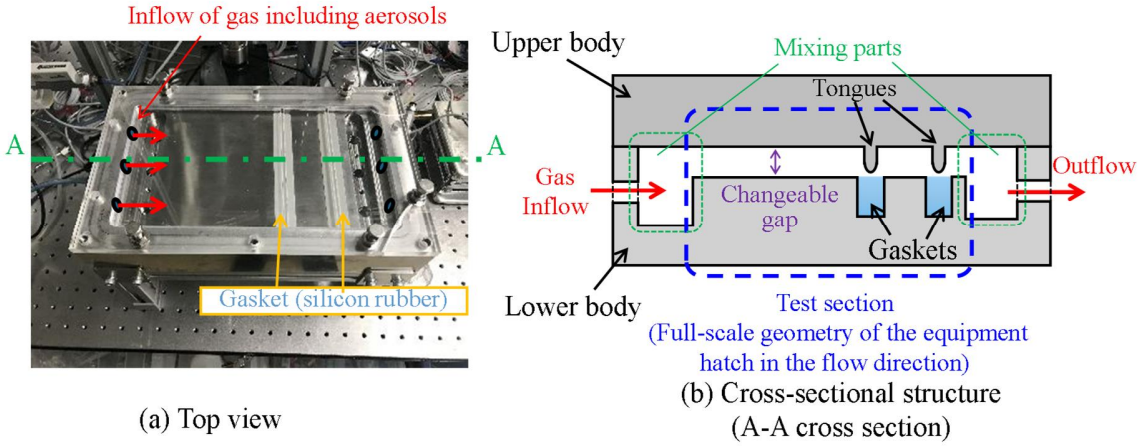

Figure 2 Overview of the test section simulating the equipment hatch of the PWR

3.2. Experimental conditions

For assuming SA conditions properly in the experiment, experimental conditions were carefully considered. The conditions are summarized in Table 1. Alternative values different from the SA conditions considering similarity of the aerosol behavior are applied for some conditions. Setting basis for major conditions is described below.

Table 1 Experimental conditions

Parameters	Range of values
Gap height	0.1 mm, 0.2 mm, 1 mm
Flow rate	0.1 - 70 L/min
Aerosol materials	- Nominal particle size:17.0 μm - Specific surface area：1.0 m^2/g - Circularity：0.97 - Composition：SiO_2（99.9 %）
Carrier Gas	- Composition: Ambient air - Temperature: 20-30 °C - Pressure: ~10 kPa - Humidity: 0.2-0.4

3.2.1. Gap height

The gap height between the hatch bodies can vary depending on the accident conditions. Under the normal operation, a gap height is almost 0mm and the tongues completely bite into the grooves. Our main scope is a small gap following a relatively small leak. The condition under which the tongues is pulled out largely from the grooves is out of scope because DF cannot be expected under the condition in the first place. Furthermore, the condition is also difficult to occur because the equipment hatch has a structure that hatches bodies are tightened for high pressure as described in 3.1. It is considered that a small leak can be formed due to shrinkage or crack of gaskets or small deformation of hatch bodies brought by high temperature or high pressure. In the experiments, gap height is considered from 0.1mm to 1mm to cover various accident conditions as possible in addition to understanding the basic mechanism of deposition.

3.2.2. Flow velocity/ flow rate

Inertial impact or turbulent deposition can be promoted under higher flow velocity. On the other hand, under lower flow velocity, retention time of suspended aerosols in the space of the gap becomes longer and sedimentation can be promoted. The design leakage is calculated the sum of minute leakages from all penetrations in the CV under design basis accidents in the design phase of nuclear power plants. As an assumption, the ratio of the leakage rate from the equipment hatch to the overall leakage rate was set at a median of 1 % (upper limit: 10 %, lower limit: 0.1 %). The Reynolds number (parallel plates flow) was eventually estimated to be less than 10 with an extremely small flow.
For a leak under the degraded CV, the leak condition tests conducted by the NUPEC for the drywell head of the BWR [10] were referred. The reference shows that equivalent area of the leak path is 10 mm^2 per 1m of a gasket length. Leaks can occur either uniformly around the entire circumference of the gasket or at partial lengths. As an assumption, the ratio of the gasket length at which leakage occurs to the entire circumference gasket length was considered as a median value of 100 % (upper limit: 100 %, lower limit: 10 %). The temperature and pressure in the containment vessel are assumed to be 200 to 400°C and 0.2 to 1 MPa, respectively, as the typical conditions under which containment loses its integrity during SA. The median values are assumed 345 °C and 0.8 MPa, respectively, applied to the NUPEC test. The calculations show that the gap height is 0.01 mm, and the Reynolds numbers regarded as a parallel plates flow of which characteristic length is 2 times gap height are 83 to 496, with a median value of 119. For the experiments, a wide range of a flow rate beyond these estimations was examined to understand basic mechanism of aerosol deposition.

3.2.3. Aerosol materials

Aerosols generated during SA are composite materials including various substances. Hygroscopic materials, such as cesium iodide or cesium hydroxide, are included in them. They have the potential to promote agglomerations and depositions on the wall. Depending on the accident conditions, the aerosol particle diameter ranges from 0.01 μm to several tens of micrometers[11]. For the experiments, silica is used as an aerosol material, considering equivalent particle diameters distribution and density with the accident conditions. Availability and ease of handling are also considered. Silica doesn't have hygroscopicity. Therefore, it is expected that DF will become less than the accident conditions and the results are more conservative.

3.2.4. Gas composition/ temperature /pressure

Under accident conditions, aerosols are carried into the penetration by gas inside the CV. The gas contains water vapor, air and non-condensable gas, such as hydrogen generated by the zircaloy-water reaction. It is considered that inertial impaction, turbulent deposition or sedimentation are dominant deposition mechanisms in narrow leak paths. Water vapor can promote diffusiophoresis. Furthermore, under supersaturation condition, condensation can trap massive particles. The high temperature of gas (sometimes, over 200°C) during SA can promote thermophoresis. The high pressure of gas can increase the flow velocity passing the penetrations. In the experiments, air with ambient temperature and pressure is used as a carrier gas to examine the deposition effects of inertial collision, turbulent deposition, or gravitational sedimentation. Contributions of other deposition mechanisms are excluded, and conservative DF can be obtained.

3.2.5. Gasket material/ shape

Silicone rubber was used for the gasket of the test section as same as the equipment hatch of an actual PWR plant. It is considered that shrink, deformation or crack of silicon rubber can cause leak initiation. The situation widely varies depending on the accident condition and it has a large uncertainty. For the experiments, hypothetical condition that gap height of 0 mm is equivalent to the condition under which tips of tongue contact slightly with the top surface of the silicon rubber is applied as shown in Figure 3(c). This is assumed based on the consideration that lower DFs would be conservatively obtained under more shrunken gaskets because of higher gap distance. Further studies to understand degradation of gaskets are desirable for more realistic experiments.

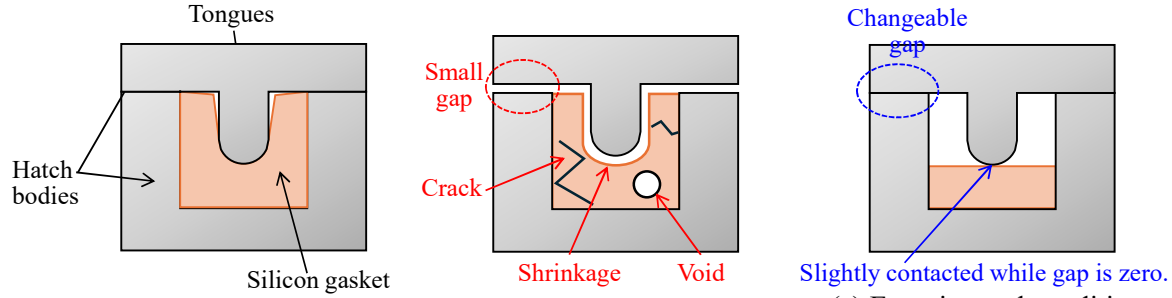

(a) Normal operation/ design leak condition

(b) Assumed leak

(c) Experimental conditions (hypothetical condition)

Figure 3 Configuration of the gasket in the equipment hatch and the test section

3.3. Experimental procedure

The setup of the experimental apparatus is shown in Figure 4. The aerosols generated in the aerosol generator carried by air are sufficiently dispersed in the mixing chamber. Some gas are released from the relief line to adjust a flow rate in the test section. The experiments were conducted in 2 steps. For the first step, a mixing chamber is directly connected with a sampling filter regarded as the inlet and aerosol concentration is measured. For the second step, the mixing chamber is connected with the test section and aerosol concentration at the outlet is measured by a sampling filter in the rear of the test section. Test duration in each step is set 15 minutes and 60 minutes, which were confirmed in advance to be long enough to measure DF stably.
The measurements are shown in Table 2. A flow rate and pressure are measured both in the front and in the rear of the test section. For the measurement related to aerosol, a particle size distribution is measured by an aerosol spectrometer. The concentrations of suspended aerosols are measured by multistage membrane filters. DF is calculated from the weights of aerosols collected by filters at the inlet and at the outlet of the test section using following equation.

$$DF = \frac{m_{in}}{m_{out}} \tag{1}$$

where, m_{in} is the amount of inflow aerosol and m_{out} is the amount of the outflow aerosol.
For the calculation of DF, the deposition in the tube connected in front of the test section, the deposition in the rear of the test section and the deposition in the mixing parts should be excluded. They were carefully quantified in each experiment by collecting them with clean paper.

Table 2 Measurement parameters

Parameters	Detail
Flow rate	- Flow rates in front of the aerosol generator and at the back of the test section (flowmeters)
Pressure	- Pressures at the inlet and the outlet of the test section (pressure gauges)
Aerosol	- Concentration of suspended aerosol at the inlet and outlet of the test section (multistage membrane filters with 99.9 % trapping efficiency) - Particle diameters at the inlet and the outlet of the test section (aerosol spectrometer)

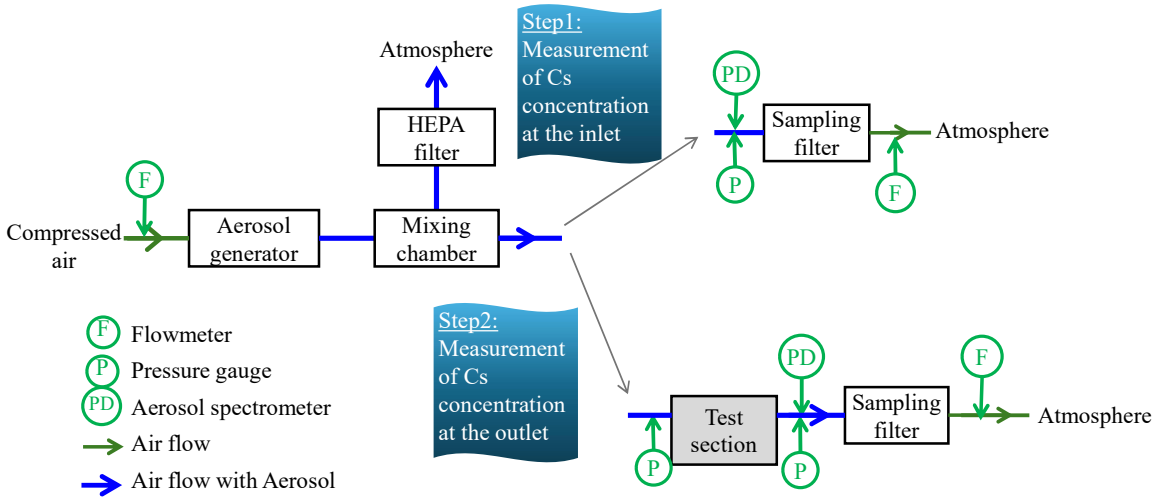

Figure 4 A setup of experimental system

4. EXPERIMENTAL RESULTS

4.1. Validation of the experimental method

Figure 5 shows one of the results of measuring the particle size distribution at the inlet of the test section. The count median diameter (CMD) was 1.0 μm and the mass median diameter (MMD) was 5.0 μm. The significant decrease of the diameter from the nominal particle size,17.0 μm, shown in Table 1 is caused by deposition of large particles inside the tube or other components before flowing into the test section. Since the aerosol particle size during SA is thought to be in the order of several micrometers, this result is almost acceptable. Note that considering stokes diameter or geometric standard deviation is significant in terms of discussion of aerodynamics, but our study hasn't achieved it yet.

The test section has a full-scale in the flow direction, but not in the lateral direction. There was concern that the interior side walls in the test section, which do not exist in the equipment hatch, may unacceptably affect flow behavior and deposition. Lateral deposition distribution after the test under typical experimental conditions was examined in advance in order to verify the concern. The hatch surface was divided into three zones in the lateral direction as shown in Figure 6(b). the deposits were collected by wiping or suction after the experiment. Their masses were measured. In addition to the test section, mixing parts, the upper body, and the tubes connected to the inlet of test section were targeted. The results are shown in Figure 6(a). The largely deposited parts are the inlet tube and the mixing area. It indicates that the heavy particles deposit before reaching the test section. For the test section, the deposits are distributed

almost equivalently in the three zones. It indicates that the experimental apparatus is appropriate geometry to simulate the FPs leak from the equipment hatch.
Major error factors introduced in the experiments caused by flow rate measurement and by aerosol concentration measurement. Each experiment was conducted at an intended constant flow rate. The average flow rates include an error of approximately 1-3 % occurs due to error specific to the measuring device and fluctuation errors during the experiments. The aerosol that flows out from the aerosol generator can be distributed in the following parts.

- Deposits on the test section
- Mass collected by sampling filters at the inlet and the outlet of the test section
- Deposits on each part, the inlet sampling filter to the test section, the test section to the outlet sampling filter

In several typical experiments, the mass balances were examined from a ratio of the above distributions. As a result, a mass loss of 5-10 % occurred in each experiment. This can be generated by the small differences of system states in 2 step experiments (described in 3.3) and by the deposition quantification. The errors are regarded as specific to this experiment.

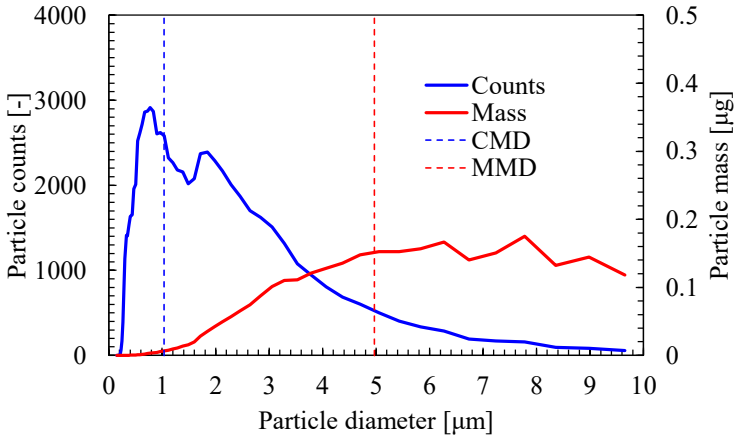

Figure 5 The distribution of particle diameters at the inlet of the test section

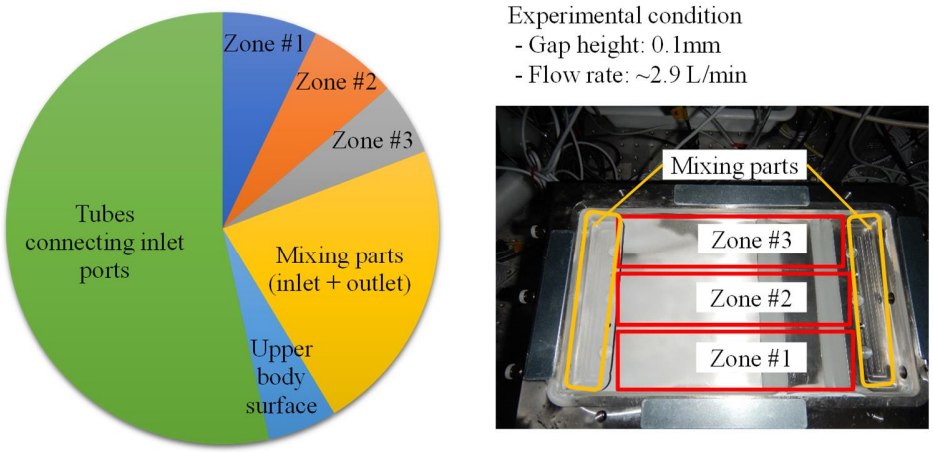

(a) Fraction of deposited aerosol mass (b) Zone division of the test section

Figure 6 The distribution of aerosol deposition in the test section

4.2. Measured DF

A series of experiments was conducted under the flow rates from 0.1 L/min to 70 L/min for the gap height 0.1 mm, 0.2 mm and 1.0 mm (Figure 7). The deposition in the parts except for the test section were excluded from the calculation of DF. An error in each result originated from a deviation of a mass balance is also considered here. For the low DF data, their errors might be too small to recognize them on the graph. At any gap height, DF tends to decrease as the flow rate increases. The highest DFs, 76 at the gap of 0.1 mm, 35 at the gap of 0.2 mm, and 53 at the gap of 1 mm were observed around the lowest flow rate. On the other hand, the lowest DFs, 2 to 5 were observed around the maximum flow rate at each gap height. Comparing the tendency according to the gap heights, the smaller the gap shows the tendency of larger DF, especially around lower flow rate.
In order to understand a principal aerosol removal mechanism, the states of aerosol deposition on the test section after the experiments were observed. Figure 8 shows the representative sample after the experiment under the low flow rate of 3.0 L/min at the gap height of 0.1 mm. The area on the test section more thickly covered with white particles indicates more deposited area. In particular, it can be observed that the plate part prior to the gasket of the lower body (hereinafter called "the prior plate") is mostly covered with aerosols. On the other hand, almost all smaller deposits can be observed on the gasket area. Almost no deposits were observed on the entire upper body as well. The observations suggest a conclusion that the sedimentation contributes to a larger DFs under lower flow velocities. This characteristic was observed at all the gap heights. Comparing the amount of the deposition on the prior plate in each gap, the smaller gap height brings the larger amount of the deposition. It can be said that the smaller height causes the smaller falling distance for the sedimentation and larger deposition.
Figure 9 shows the sample after the experiment under the representative condition of higher flow rate, 65.2 L/min at a gap height of 0.1 mm. Unlike the low flow rate, almost no deposition was observed on the prior plate of both the lower body and the upper body. On the other hand, a larger amount of deposits was observed around the two gaskets and the flat plate located between them on both the lower body and the upper body. These parts consist of complex flow channels where flow direction and gap height successively change. The observation suggests that inertial deposition and turbulent deposition make a large contribution under the condition with higher flow rate.
That is to say, the characteristic that the DF decreases down to a few values as the flow rate increases is brought about by the change of principal deposition mechanism from sedimentation to inertial collision and turbulent deposition. In the range of the flow rate examined in this experiment, higher flow rate showed lower DF. However, DF can shift to an increased tendency over a certain flow rate.
Measured DF toward Reynolds number is shown in Figure 10. An error in each result originated from a deviation of a mass balance is also considered here. For the low DF data, their errors might be too small to recognize them on the graph. For the calculation of the Reynolds number, a parallel-plate channel flow is assumed based on the consideration that a gap height is negligibly small compared to the lateral length of the test section. In this case, twice the gap height is applied to characteristic length for Reynolds number. The range of the Reynolds number were estimated 12 to 750 for 0.1 mm gap height, 58 to 750 for 0.2 mm gap height, and 35 to 470 for 1.0 mm gap, respectively. The values cover well the design leak condition (less than 10) and a large leak condition (83 to 496) discussed in 3.2.2. As same as the tendency of the flow rate, DF decreases as the Reynolds number increases. In the range of Reynolds numbers less than approximately 150, DFs at 1 mm gap are clearly lower than those of the other. A series of experiments indicated that DF exceeds approximately several tens under the Reynolds number less than approximately 100 with any gap heights. On the other hand, DF decrease to several values as Reynolds number increases. However, DF can shift to an increased tendency over a certain Reynolds number due to the promotion of turbulent deposition and inertial impact.

As discussed in 3.2, the experiments applied some different conditions from actual accidents. As for an aerosol material, silica, which has little hygroscopicity, is used. However, under accident conditions hygroscopic materials such as cesium included in aerosols can further promote deposition. As for the atmospheric conditions, water vapor can promote diffusiophoresis, but the effect was excluded. High temperature condition can also promote thermophoresis, but the effect was also excluded in the experiments. The condition of degraded gaskets in the accidents is unknown so far and hypothetical configuration of gasket is assumed in this study. Further realistic DF can be obtained by considering the accident condition in the experiment.

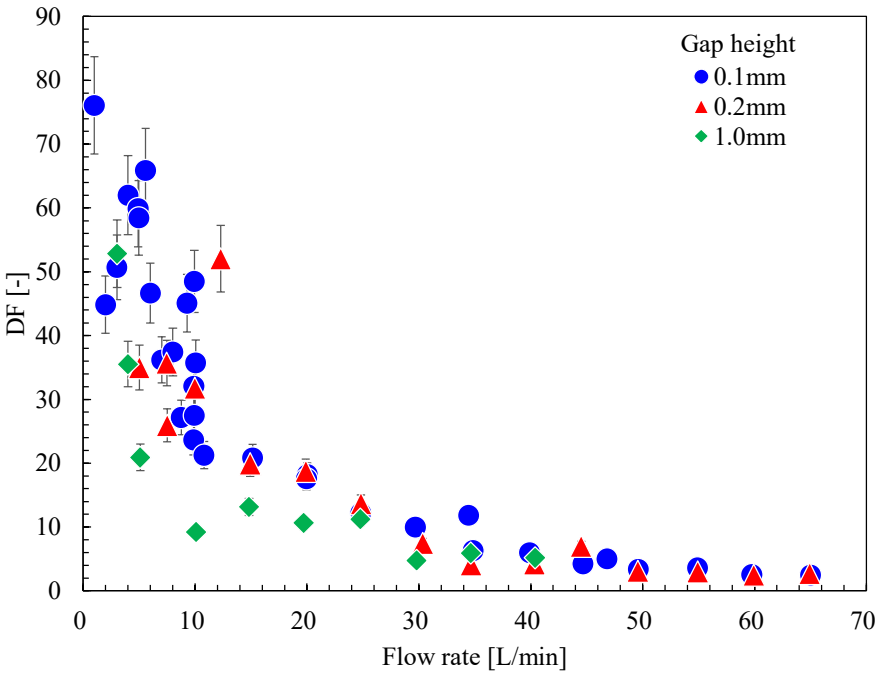

Figure 7 Measured DFs toward flow rate

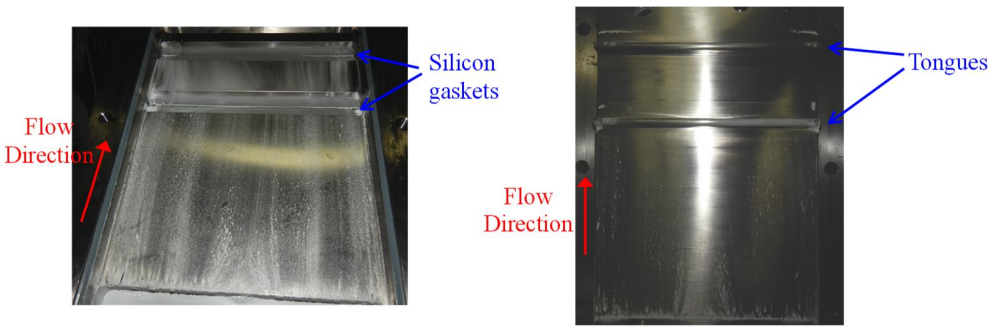

(a) The lower body (whole view from the inlet side) Massive aerosols deposit on the overall surface.

(b) The upper body (whole view from above) Little aerosols deposit.

Figure 8 Observation of aerosols deposition on the surface under a lower flow rate
(Gap height: 0.1 mm, Flow rate: 3.0 L/min, DF =21)

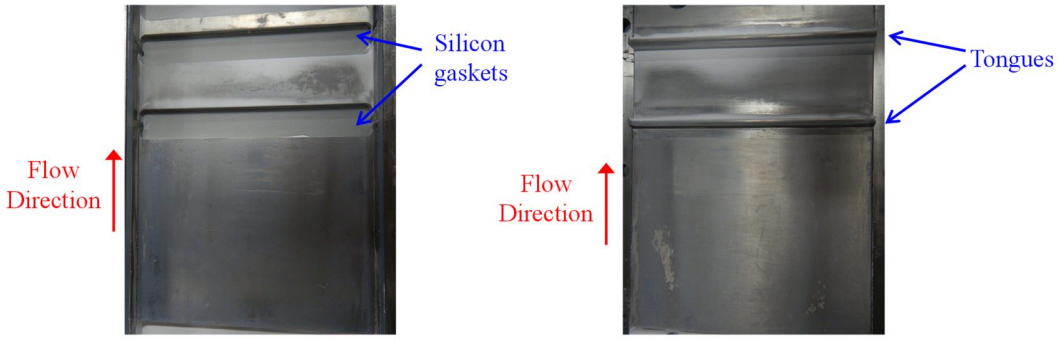

(a) Lower body (whole view from above)
Little deposition on the prior plate.
Massive deposition around gasket.

(b) Upper body (whole view from above)
Massive deposition around gasket
(same as the lower body).

Figure 9 Observation of aerosols deposition on the surface under a higher flow rate
(Gap height: 0.1 mm, Flow rate: 65.0 L/min, DF =3)

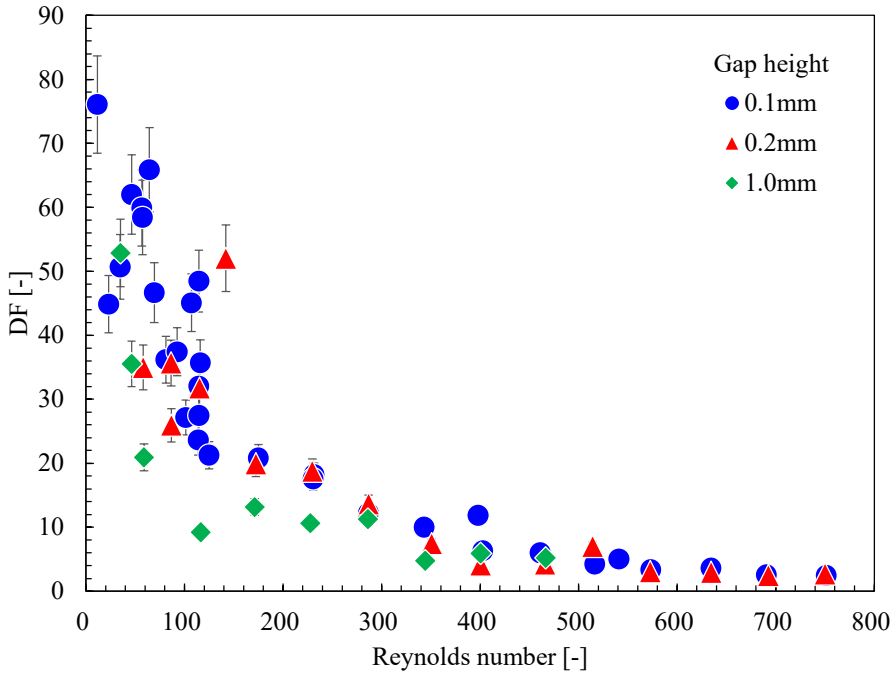

Figure 10 Measured DFs toward Reynolds number

5. CONCLUSION

- A series of experiments was conducted to evaluate the FPs removal effect at the equipment hatch under design leak conditions and under a large leak from the degraded CV during SA.
- From the following validations, it was confirmed that the experimental procedures were appropriate.
  - The diameter of aerosol particles flowing into the test section is almost consistent with that during a SA.
  - The lateral distribution of deposition on the test section was homogeneous. The observation supports the consideration that the interior side walls in the test section, which do not exist in the equipment hatch, cannot affect flow behavior and a deposition.

  - The error of a mass balance specific to the experiment was included. However, it was small enough to understand the tendency of DFs from the results.

- From measured DFs toward a flow rate, DF decreases as a flow rate increases. According to the observation of the deposition on the test section after the experiments, it was found that high DF at a low flow rate was caused by sedimentation, because massive depositions are observed only on the lower surface. On the other hand, in a high flow rate, the observation that massive aerosols deposit around gaskets, of which flow channel is complex, indicates that a certain degree of DF can be expected by the promotion of a turbulent deposition and an inertial impact.
- A series of experiments indicated that DF exceeds approximately several tens under the Reynolds number less than approximately 100 with any gap heights. On the other hand, DF decrease to several values as Reynolds number increases. However, DF can shift to an increased tendency over a certain Reynolds number due to the promotion of turbulent deposition and inertial impact. The data obtained in the experiments can be useful to understand basic mechanism of aerosol removal in the equipment hatch.
- In the experiment, some different conditions from the actual accident were adopted. They include aerosol material related to hygroscopicity, humidity related a diffusiophoresis, and temperature related to thermophoresis. The condition of degraded gaskets in the accidents is unknown so far and hypothetical configuration of gasket is assumed in this study. The effects can be clarified by further experiments under the condition consistent with the accident condition.

6. REFERENCES

1. D. A. Power, “Aerosol Penetration of Leak Pathways - An Examination of the Available Data and Models”, SAND2009-1701 (2009).
2. C.N. Davies, “The entry of aerosol into sampling tubes and heads”, *British J. Applied Physics, Journal of Physics D*, **1**, pp. 921-932 (1968).
3. J. K. Agarwal and B. Y. H. Liu, “A criterion for accurate sampling in calm air”, *American Industrial Hygiene Association Journal*, **41,** pp. 191-197 (1980).
4. S. Lewis, “Solid particle penetration into enclosures”, *J. Hazardous Materials*, **43**, pp. 195-216 (1995).
5. R.B. Mosely, D.J. Greenwell, L.E. Sparks, Z. Guo, W.G.Tucker, R.Fortmann, C. Whitfield, “Penetration of Ambient Fine Particles into the Indoor Environment”, *Aerosol Science and Technology*, **34**, pp. 127-136 (2001).
6. D-L. Liu and W.W. Nazaroff, “Modeling Pollutant Penetration Across Building Envelopes”, *Atmos. Environm.*, **35** pp. 4451-4462 (2001).
7. D-L. Liu and W.W. Nazaroff, “Particle Penetration Through Building Cracks”, *Aerosol Science and Technology*, **37** pp. 565-573 (2003).
8. A. Watanabe, K. Yamada, M. Ohsaki, “FP Aerosol Trapping Effect Along the Leakage Paths of Degraded Containment Penetrations During a Severe Accident (I)”, *J. Nucl. Sci. Technol.*, Vol. **8** (3), pp. 254-263 (2009).
9. A. Watanabe, K. Yamada, M. Ohsaki, “FP Aerosol Trapping Effect Along the Leakage Paths of Degraded Containment Penetrations During a Severe Accident (II)”, *J. Nucl. Sci. Technol.*, Vol. **8** (4), pp. 332-343 (2009).
10. NUPEC,” Summary report on safety assessment of important structures (reactor containment vessel reliability demonstration project)(in Japanese)” (2003)
11. H. Allelein et al., “State-of-the-art report on nuclear aerosols”, NEA/CSNI/R(2009)5, Nuclear Energy Agency/Committee on the safety of nuclear installations (2009).

Experimental study on removal effect of radioactive materials in the course of the leakage through the equipment hatch

Koichi Nakamura*, Masashi Himi,

Satoshi Nishimura

Central Research Institute of Electric Power Industry (CRIEPI)

The 11th European Review Meeting on Severe Accident Research (ERMSAR2024)

KTH, Stockholm, Sweden, May 13-16, 2024

© CRIEPI

CRIEPI Central Research Institute of Electric Power Industry

1. Background

- The containment vessel (CV) is an ultimate barrier against a leakage of fission products (FPs) during severe accidents (SA) in nuclear power plants.
- The equipment hatch (EH) in the containment vessel is a potential part from which FPs leak into the environment.
- the leak pathway created in the EH can be a complex geometry with a narrow gap. Thus, some FPs are expected to be trapped inside the leak pathway.
- It is crucial to evaluate source term including those effects.

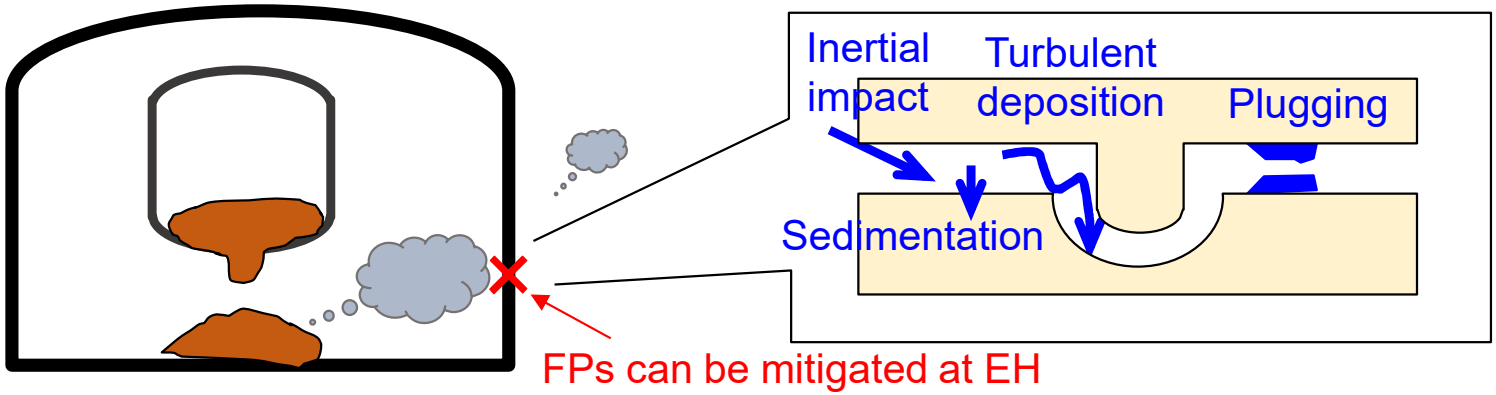

Related studies

Individual mechanism or application

D A. Powers reviewed various experimental or theoretical studies and created the data base [1].

It includes

- Plugging on a narrow leak pathway, penetration rate through various flow channel -> empirical or theoretical expressions
- Many studies database for turbulent deposition

Pilot study with full-scale tests

- NUPEC conducted experiments on FPs aerosol removal effects at the low voltage module and the flange gasket for BWR [2][3]
- Experiments includes leak condition test due to high temp. and press. and FP aerosol trapping tests using failed components.
- The average DF was evaluated to be ~ 600 for the low voltage module and ~16 for the flange gasket.
- Empirical expressions were given

[1] D. A. Power, SAND2009-1701 (2009). [2] A. Watanabe et al., *J. Nucl. Sci. Technol.*, Vol. **8** (3), pp. 254-263 (2009). [3] A. Watanabe et al., *J. Nucl. Sci. Technol.*, Vol. **8** (4), pp. 332-343 (2009).

2. Objective

- For FP trapping on containment penetration, many empirical or theoretical expressions were developed for individual mechanism.
- More robust and parametric correlation is required to apply various components or accident condition generally.

- The objective of this study is to clarify aerosols removal effects in the leak pathway of the EH quantitatively with an experimental approach and to develop a parametric correlation finally.

Experimental apparatus

A series of experiments was conducted for a flange gasket (the type of tongue and groove flanges) applied to the Japanese 2 to 4 loops PWR's equipment hatches.

Overview of the PWR EH and the gasket

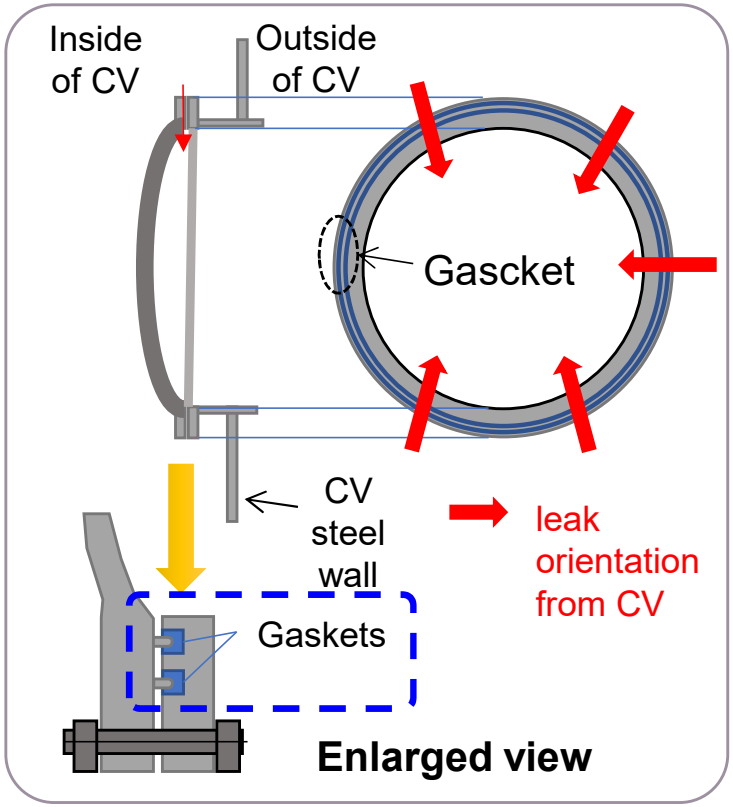

Test equipment

(a) Top view

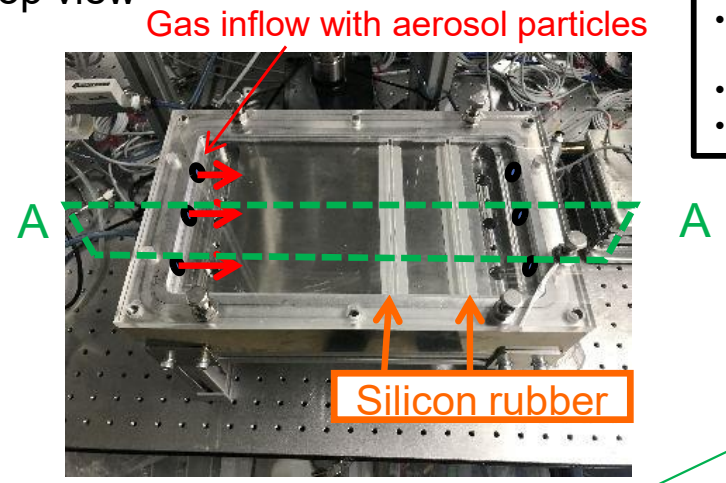

(b) Side view (A-A cross section)

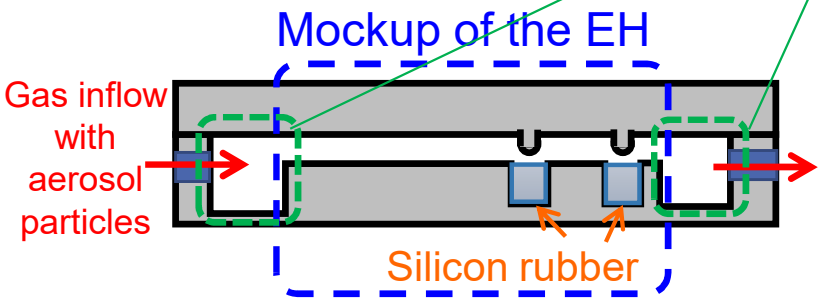

Specification
- Hatch material : SS
- Gap height: Changeable (max. ~5 mm)
- Seal material: Silicon rubber
- Max pressure: 100 kPa(g)
- Max flow rate: 100 L/min

※Decontamination factor（DF）

Performance indicator for aerosol removal at the subject

$$DF = \frac{C_{in}}{C_{out}}$$

$C_{in/out}$: Aerosol concentration at inlet / outlet

Experimental conditions

- Only small gap height and flow rate are targeted to expect practical DF for DBA (design leak condition) and SA.
- Some conservative conditions were applied to realize a lab-scale test.
  - ➢ Room temp. (not high temp.), low humid (not high humid), nonhygroscopic aerosol (not hygroscopic), seal condition (not degraded)

Parameters	Accident condition	Experimental condition
Gap height	DBA (~μm), SA (unknown)	0.1 mm, 0.2 mm, 1 mm
Flow rate	DBA (0.05～5L/min) and SA (40～260L/min)	0.1 - 70 L/min
Aerosol materials	- Mixed substance - Hygroscopic and no hygroscopic - Diameter: ~several μm	- Nominal particle size:17.0 μm - Specific surface area：1.0 m^2/g - Circularity：0.97 - Composition：SiO_2（99.9 %）
Carrier Gas	- Steam & air - High temp.	- Composition: Ambient air - Temperature: 20-30 ° C - Pressure: ~10 kPa - Humidity: 0.2-0.4

Gap and Seal condition

Normal operation and DBA: Fig (a)

- Gap height ~0mm (the tongues completely bite into the grooves(silicon rubber))

Leak condition: Fig (b)

- Shrinkage, Crack, Void in the groove due to overtemperature
- Small gap due to deformation of hatch bodies

Scope of the study: Fig (c)

- Small gap and shrinkage simulating the condition in
  - Rectangular groove
  - Parameters: gap height

Fig Configuration of the gasket in EH

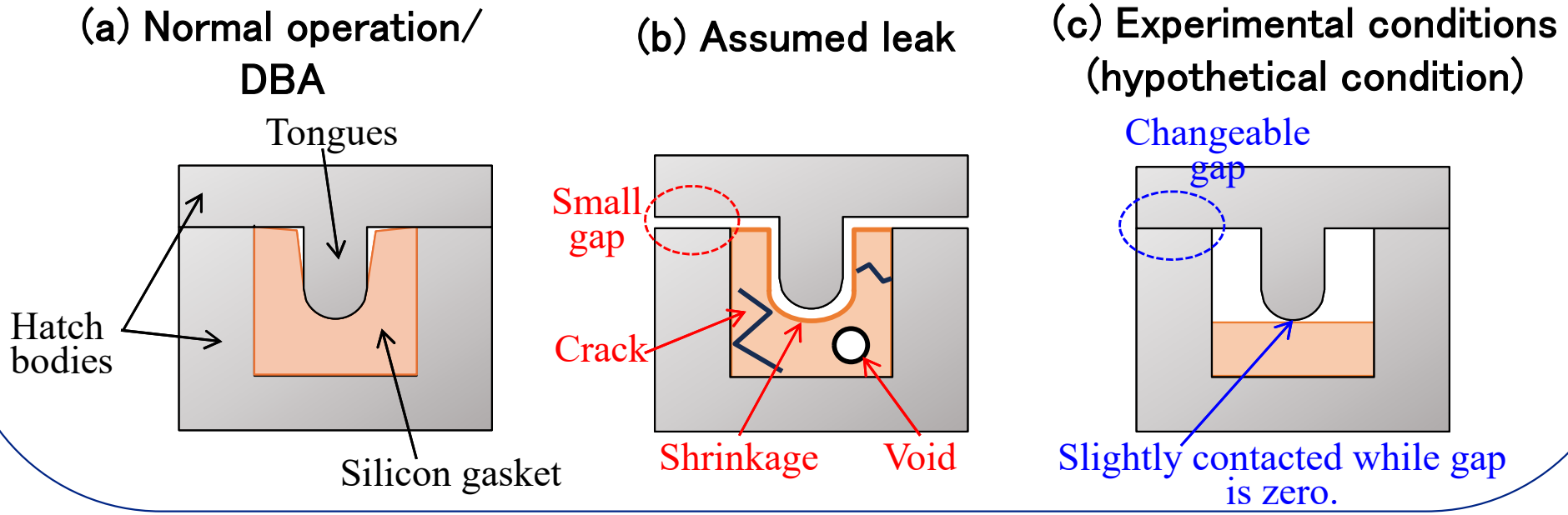

Estimation of leak flow rate and gap height

DBA condition

Assume: 0.1 %/day from CV

Design leak rate → Leak rate from EH (0.05～5L/min) → Gap height (2E-7～2E-4mm)

Ratio of leak rate from EH to overall CV leak rate
Assumption：0.1～10%

Radial flow between two disks (viscous laminar flow, compressible fluid)

$$m = \frac{\pi \varepsilon^3}{12 \ln(r_0/r_i)} \frac{M}{RT} \left({P_0}^2 - {P_i}^2 \right)$$

η	:	Viscosity coefficient
ρ	:	Specific gravity
P_o	:	Outside pressure (abs)
P_i	:	Internal pressure (abs)
M	:	Molar mass
R	:	Gas constant
T	:	Temperature
E	:	Distance between two planes
r_o	:	Gasket outer radius
r_i	:	Gasket inner radius
a	:	Radius of cylinder
L	:	Length of cylinder

Containment failure condition (SA)

10mm² (per 1m gasket) [4] → Equivalent leak area → Leak rate from EH (40～260L/min) → Gap height (<0.01mm)

Correlation between equivalent area and flow rate of compressed fluid

$$K \cdot C \cdot A_e = \frac{m \cdot \sqrt{R \cdot T_0}}{\sqrt{\frac{2 \cdot \gamma}{\gamma - 1} \left(\frac{P_b}{P_0} \right)^{2/\gamma} - \left(\frac{P_b}{P_0} \right)^{(\gamma+1)/\gamma}}}$$

Ratio of leakage flange length to total flange circumference
Assumption：10～100%

$K \cdot C \cdot A_e$	:	Leakage equivalent area
m	:	Mass flow rate
P_0	:	Primary pressure
P_b	:	Secondary pressure
γ	:	Specific heat ratio
T_0	:	Primary temperature
R	:	Gas constant

[4] NUPEC," Summary report on safety assessment of important structures (reactor containment vessel reliability demonstration project)(in Japanese)" (2003)

Experimental procedures

Single direction flow system was established

- Carrier gas brings aerosols to the test section and is finally exhausted through a filter.

2 steps procedures were conducted for each test

- Step1(without the test section) : Cs concentration at the inlet
- Step2(with test section): Cs concentration at the inlet

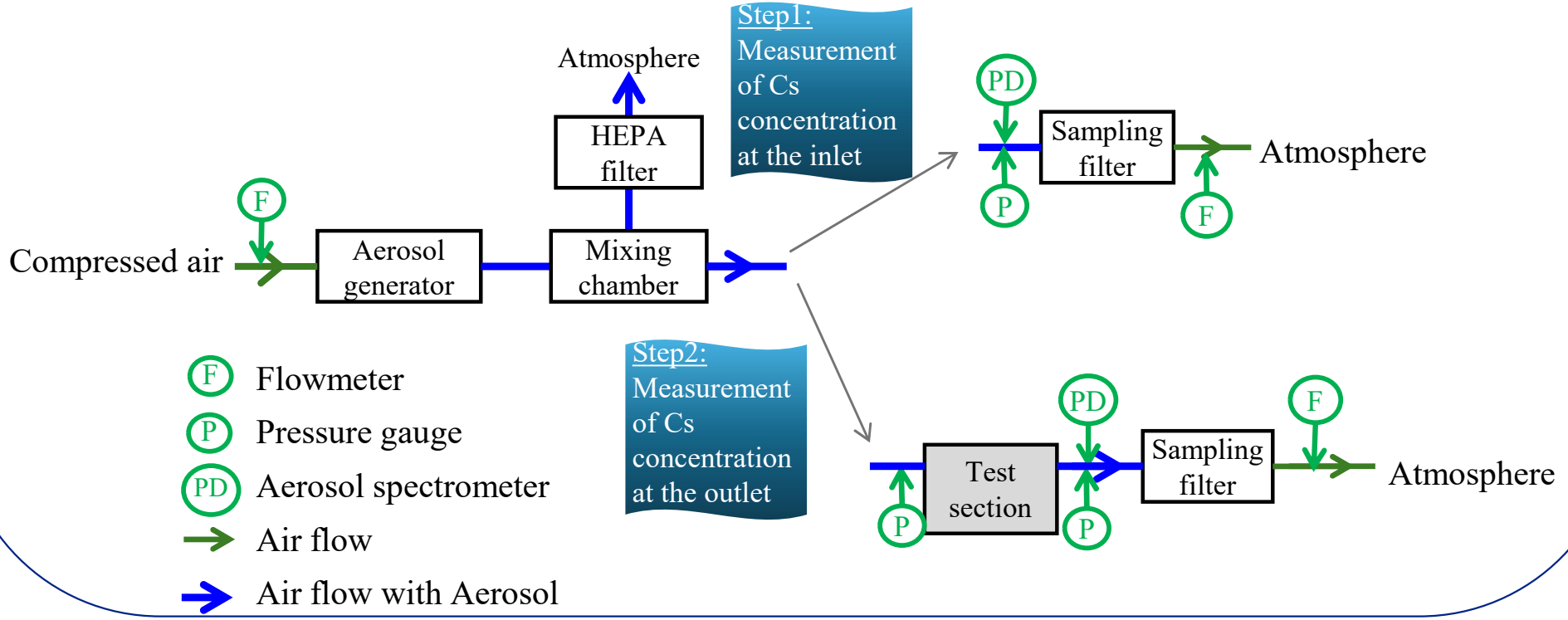

Validation of the procedure (1)

Particle diameter

- Measured by an aerosol spectrometer, which is a technique of wavelength analysis using white light, under the experimental conditions.
- The representative result shows that count median diameter (CMD) was 1.0 μm and the mass median diameter (MMD) was 5.0 μm.
  - ➡ Almost equivalent with SA condition.
- Note that stokes diameter and GSD are significant in terms of aerodynamics, but our study hasn't achieved them yet.

Fig The distribution of particle diameters at the inlet of the test section

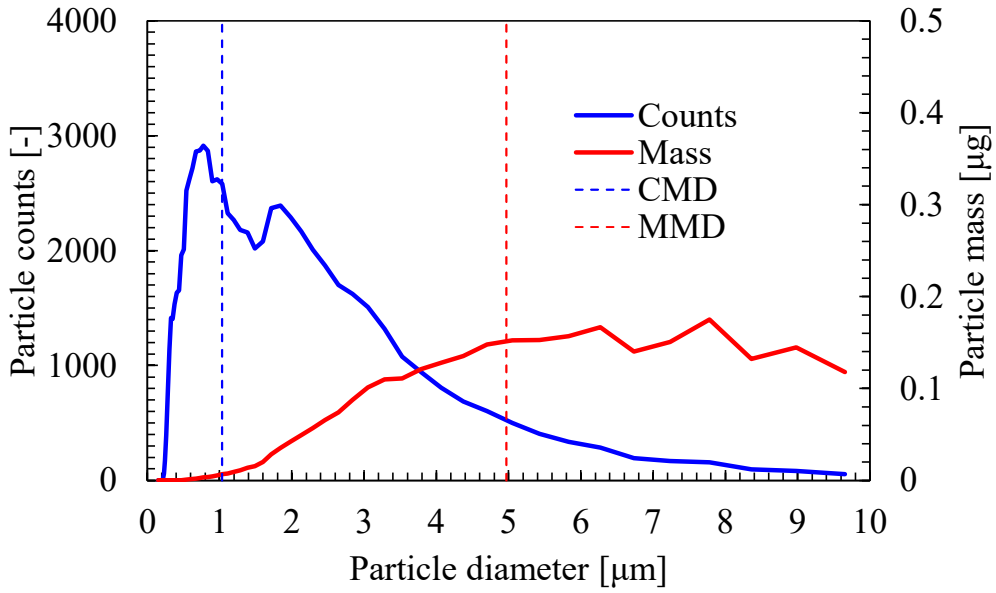

Validation of the procedure (2)

Flow distribution in lateral direction

- A series of experiments was intended to obtain DF per unit length of equipment hatch circumference
  - The effects of the interior side walls in the test section on flow and deposition distribution in lateral direction must be excluded.

Error factors

The major error factor is estimated mass balance error with 5-10 % caused by 2 step experiments. The values are small enough to identify the tendency of DF.

(a) Fraction of deposited aerosol mass

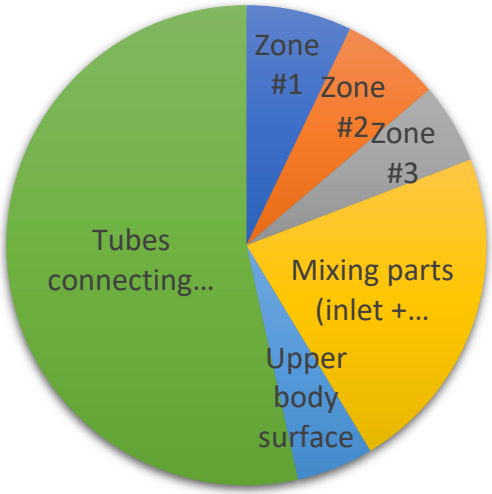

(b) Zone division of the test section

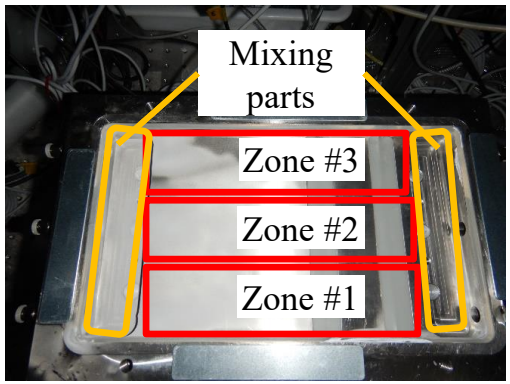

Experimental condition
- Gap height: 0.1mm
- Flow rate: ~2.9 L/min

Measured DF

- The results under the flow rates from 0.1 - 70 L/min for the gap height 0.1 mm, 0.2 mm and 1.0 mm
- DF tends to decrease as the flow rate increases.
  - ➢ Highest DFs: 76 (0.1 mm gap), 35 (0.2 mm gap), and 53 (1 mm gap)

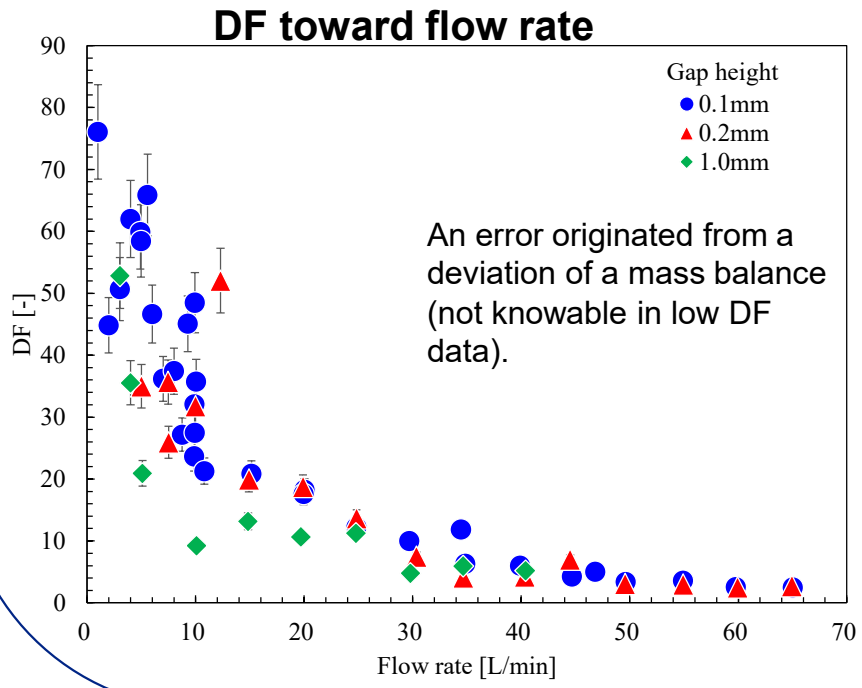

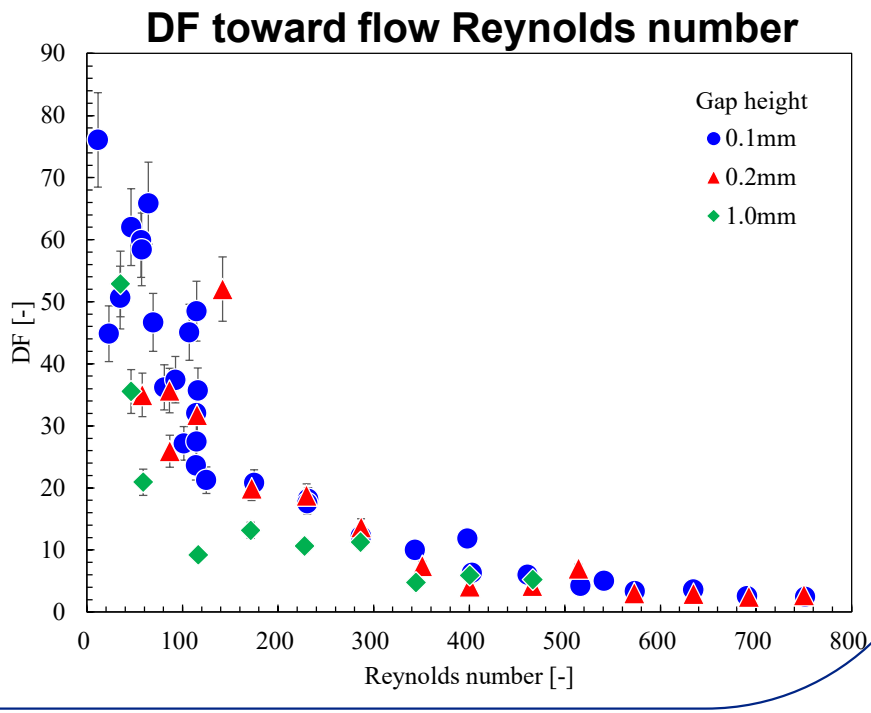

Deposition mechanism

Low flow rate (Gap: 0.1 mm, 3.0 L/min, DF =21)

Floor

Ceiling

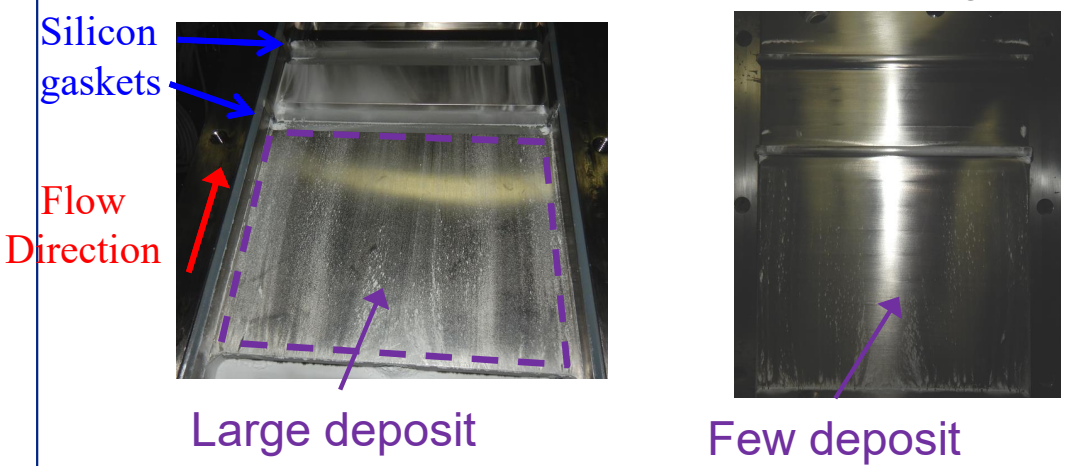

Floor: **large**
Tongue & silicon: **small**
Ceiling: **small**

Major mechanism: ***Sedimentation***

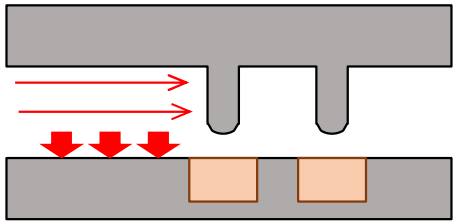

High flow rate (Gap: 0.1 mm, 65.0 L/min, DF =3)

Floor

Ceiling

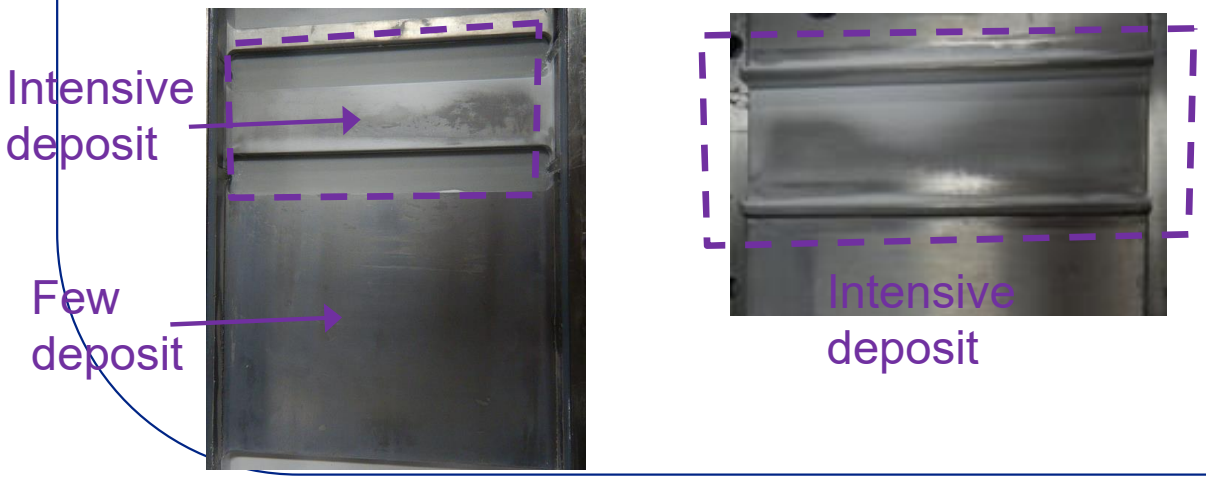

Floor: **small**
Tongue & silicon: **large**
Ceiling: **small**

Major mechanism: ***Turbulent deposition, inertial impact***

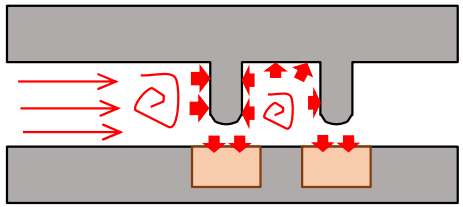

Conclusion

- A series of experiments was conducted to evaluate the FPs removal effect at the equipment hatch under DBA (design leak conditions) and under SA (degraded EH)
- The test procedure was validated from the particle diameter, uniform lateral distribution of deposition, the error of a mass balance
- DF decreases as a flow rate or Reynolds number increases. DF exceeds approximately several tens under the Reynolds number less than approximately 100 with any gap heights
- the observation of the deposition on the test section after the experiments shows
  - ➢ higher DF at a low flow rate was caused by high sedimentation
  - ➢ Lower DF at a high flow rate was caused by low sedimentation and some turbulent deposition and inertial impact.
- The data obtained in the experiments can be useful to understand basic mechanism and to develop the correlation.

© CRIEPI

The 11th European Review Meeting on Severe Accidents Research

May 13-16, 2024, Royal Institute of Technology, Stockholm, Sweden

TECHNICAL SESSION 6.3: HYDROGEN RISK AND CONTAINMENT BEHAVIOR

Chairs: I. Kljenak (IJS), S. Kelm (FZJ)

ID56	**Evaluation of hydrogen risk and its mitigation strategies adopted in isotope manufacturing building** C. Peng (Shanghai University)	**Paper** **Presentation**
ID85	**The Scaling of Turbulent Flame Acceleration and Detonation Transition for Hydrogen-Air mixtures in the RUT Facility** M. Kuznetsov (KIT)	**Paper**

EVALUATION OF HYDROGEN RISK AND ITS MITIGATION STRATEGIES ADOPTED IN ISOTOPE MANUFACTURING BUILDING

Cheng Peng[1*], Jian Deng[2], and Sheng Gao[1]
[1]Shanghai University of Electric Power; [2]Nuclear Power Institute of China
Corresponding Address: No.1851, Hucheng Ring Road, Pudong New District, Shanghai, China
diomio@shiep.edu.cn; dengjian_npic@163.com; 282997458@qq.com

ABSTRACT

Nuclear power plants produce isotopes as a support function for the growth of the nuclear technology field and to aid in industrial detection, such as the generation of ^{14}C and ^{60}Co. After the generation process, the rod bundles equipped with such isotopes should be put into a water pool to inhibit the radioactive release, lowering the dosage of the building where such isotopes were manufactured. However, the radioactive source of those isotopes can result in hydrogen produced by the irradiation of source product pool's cooling water, which could increase the risk of hydrogen combustion and explosion in a particular area of the building. The Spent Fuel Pool (SFP) may also have such hidden danger. The three-dimensional isotope manufacturing building and its primary internal structure (source product pool with hydrogen overflow channels, forklift room, venting pathways, etc.) were finely modeled in this study by using the Computational Fluid Dynamics (CFD) approach. By reviewing the progress of numerical research for hydrogen flow and distribution in severe accidents and hydrogen mitigation measures in other hydrogen energy industries all over the world, appropriate boundary conditions were selected to simulate the time-space distribution of hydrogen within the 3-D configuration, which shows hydrogen stratification in vertical direction and local gathering phenomena near the surface of the pool reflecting pronounced non-uniformity within the building. In order to quantify the effects of various hydrogen risk mitigation strategies, the introductions of the ventilation, air ingress, and emergency ventilation system were taken into consideration. It was discovered that while turning on the building's emergency venting system at the roof may greatly reduce the hydrogen risk, and the upper space of the water pool is a crucial place where hydrogen explosion may occur. Last but not least, the hydrogen risk inside the building can be reduced and alleviated by suitably adjusting the air permeability of the canvas that covers the pool, which could serve as a technical reference for the design of an isotope manufacturing building, and, moreover, for the development of new types of hydrogen mitigation strategies for SFPs and other industrial production.

KEYWORDS
Hydrogen distribution, source products pool, hydrogen risk, mitigation, isotope manufacturing building

1. INTRODUCTION

In order to produce the isotope of ^{60}Co which is much in demand in various industries, such as agriculture, medical treatment, industrial detection, bundles composed of cobalt-made rods are well-arranged and installed in the core of heavy water reactor in China. After unload the rod bundles from the reactor, they can be substantially cooled down in a finished source products pool locates in the isotope manufacturing building. Meanwhile, the high radioactivity may induce the water decomposition, generating hydrogen, which can also take place in the primary loop in which the neutrons and gamma ray largely contribute to the coolant irradiation [1]. A bunch of paramount work on hydrogen release and transport has been done in severe accident scenarios, where mixing gas of steam and hydrogen due to zirconium-water reaction distributes throughout the containment and possibly leads to hydrogen stratification with local hydrogen

concentrations up to the detonation limit. As a result, it may seriously influence the running conditions of equipment inside the containment, posing a huge threat to the integrity of the containment building, and thus give rise to the radioactive release to the environment.

Since 2011, the hydrogen explosion taken place in Fukushima nuclear power plants has drawn large number of researchers' attention, and likewise the safety regulatory authority of China. In the general technical requirements issued in the same year [2], it is asked to improve and amend the hydrogen control system adopted in Chinese nuclear power plants, and to conduct hydrogen safety analysis evaluating the effectiveness of the hydrogen control strategies. Therefore, in analogy, it is suggested to carry out hydrogen distribution and risk mitigation investigations for the isotope manufacturing building, in order to raise the safety level of the source term building, and to provide reliable accident emergency measures for the similar buildings, e.g. nuclear fuel storage building.

Currently, the lumped parameter (LP) code and the computational fluid dynamics (CFD) code are the two types of codes utilized globally for the simulation of hydrogen transport and its distribution. The LP code ignores spatial distribution of each specific variable within individual control volumes and describes the computational domain as a model with a number of controllers (each of order 10^1 to 10^2) connected by flow paths and a single variable (temperature, pressure, concentration, etc.). The control volume only contains information about mass and energy. To gain momentum information, one must solve one-dimensional momentum equations for various flow paths and interpret the turbulence by adjusting the flow loss coefficients in the momentum equations. In the recent decades, LP codes have gradually become the most crucial tools approaching thermal-hydraulic phenomena inside the containment [3-4]. The principal LP codes used to model the distribution of hydrogen are ASTEC [5-6], MAAP [7-8], and MELCOR [9-10], etc. However, the nature of LP approach dictates its limitations in accurately capturing the local behaviors within the containment during severe accident scenarios [11].

In contrast, three-dimensional transport equations are numerically solved by CFD approach with the discrete grid numbers up to order of 10^5 to 10^7, thus describing the gas mixing, flow and distribution characteristics in local region in detail. Up to now, CFX [12], Fluent [13], and STAR-CCM [14] have been commonly selected in analyzing hydrogen safety issues inside containment. Besides, numerical codes specifically designed to account for sub-grid phenomena with appropriate constitutive relations are introduced for coarse grids [15]. These kind of codes include models of containment-specific equipment and physical phenomena in containment under accident conditions in nuclear power plants, both validated by relevant experiments, e.g. GASFLOW [16], GOTHIC [17] etc.

Babic et al. [18] validated the predictive capability of CFX 4.4 against TH13 test to prove that it is feasible to use CFX to model the hydrogen distribution coupled with their user-defined condensation model, and moreover, it was shown that unmixing hydrogen cluster gathered in the upper dome of the container, in order to study the non-uniform distribution characteristics of temperature and gas concentration in THAI facility. Heitsch et al. [19] validated the CFX code against two series of hydrogen jet tests performed in BMC facility, which showed that the distribution of helium exhibited asymmetrical features in both vertical and radial directions during the end of the injection, due to the asymmetrically positioned compartments with respect to one another. In order to ascertain the hydrogen distribution in space, NRG [20] targeted a typical German spherical reactor containment and used the CFX code to simulate actual break sizes and leak directions. It is possible to deduce that there is a significant concentration build-up and stratification of hydrogen in the compartment No.6 close to the break in terms of the difference between the average and peak hydrogen concentrations. Developed by KIT in Germany, GASFLOW code is a computational fluid dynamics tool that uses numerous computational domains connected by one-dimensional flow channels to simulate complex geometries with multi-compartments in order to calculate gas distribution and mixing processes [21]. In order to simulate hydrogen distribution in containment of the M310-type nuclear power plant, Xiao et al. used different models from two numerical codes, GASFLOW and FLUENT [22]. By comparing the prediction results of both codes, the benefits and drawbacks of various calculation models

for hydrogen concentration simulation were addressed. By using STAR CCM+ code to numerically simulate the processes of steam condensation and gas transport outside a single tube, and to verify the results with experimental data, Liu et al. [23] were able to reveal the formation of a stable helium stratification of helium-air-vapor mixtures under the influence of vapor condensation.

According to the literature reviews, commercial CFD software has proved its ability to replicate the phenomena of hydrogen flow during injection in a way that is more consistent with experimental findings, which can be used to analyze hydrogen distribution issues at various scales in simple or complex spaces. In this article, we will use STAR CCM+ code to build the isotope manufacturing building and its internal main structure, studying the time-space distribution of hydrogen concentration under various typical boundary conditions, by using the hydrogen source term from theoretical analysis as the input condition. Finally, we will qualitatively and quantitatively propose solutions and suggestions for mitigating hydrogen risk.

2. PREPARATIONS FOR SIMULATIONS

2.1 Geometrical Modeling

The top view of the isotope manufacturing building can be found from Fig.1, in which a source products pool and a single compartment of garage locate in the position of +0m. The ceiling of the garage can reach up to +6.00m in height, and the roof of this whole building is in slope type with a linear transition from 12m to 13m in height. Overall, the effective free space can reach up to 3500 m^3. The detailed information of the water pool can be demonstrated in Fig.2, and hydrogen generates from the water pool may probably outflow through two channels: a porous coating-canvas and the overflow orifices on both sides. The overall geometry model of this building can be exhibited in Fig.3.

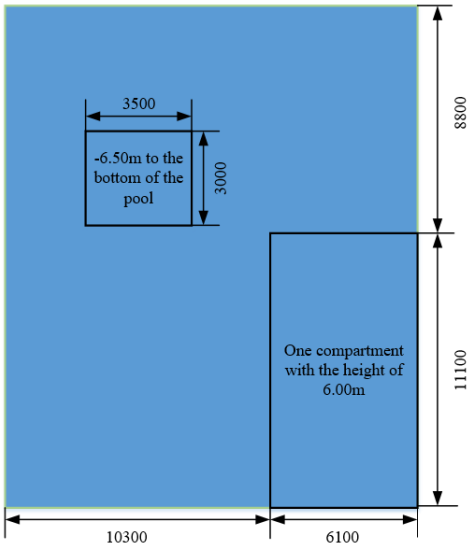

Figure 1. Top view of the isotope manufacturing building

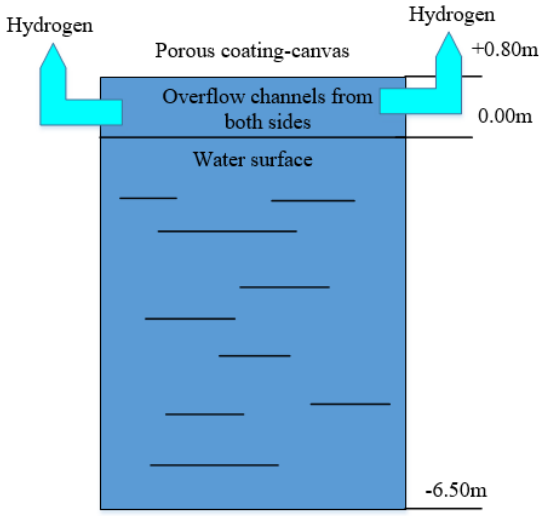

Figure 2. Detailed geometry of the water pool

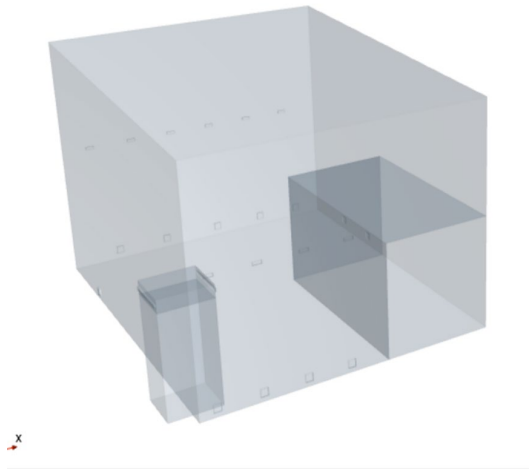

Figure 3. 3-D geometry model of the building and its inside structure

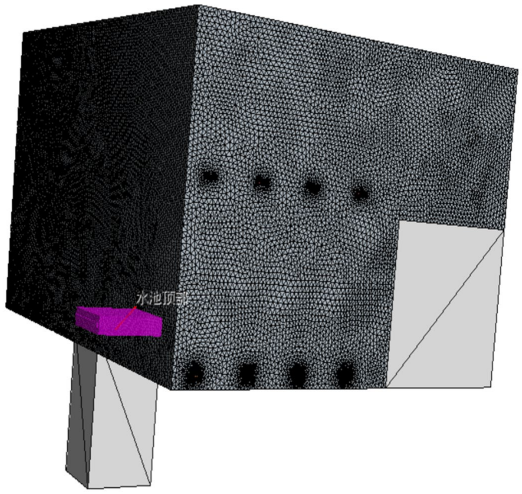

Figure 4. 3-D mesh model

2.2 Governing Equations and Cases Details

2.2.1. Mass and momentum equations

Assuming unsteady-state, three-dimensional conditions, the governing equations of mass, and momentum for the two species should be taken into account.

2.2.2. Estimation of hydrogen source

The water in the pool absorbs radiation energy of 100 eV, which can yield 0.45 mole of hydrogen molecules from Co-60 radioactive sources. Given that a single Co-60 source products pool has a design storage capacity of 10 million Ci and an average radiation energy of 1.25 MeV for Co-60 decays, it is possible to calculate that the water pool will produce 25 g/h of hydrogen under this given conditions.

2.2.3. Boundary conditions

Table 1 illustrates the four kinds of scenarios for which this study was conducted. In Case1, the canvas is impermeable, and hydrogen can only leak into the environment from the two opposite sides of the water pool by the overflow orifices, with an overflow area of 0.588 m^2 on each side. In order to further inert the combustible gases inside the building and drive the flow of light gases inside, in Case 2, 12 ventilation fans (with the outlets size of 400mm×400mm)and 10 air ingress channels (475mm×150mm) are turned on. In Cases 3 and 4, a new design is taken into consideration in order to lessen the risk of hydrogen, based on which, the use of high permeability fabric (enhancing the permeability of the canvas) enhances hydrogen's transport and diffusion above the water's surface. Besides, three emergency ventilation fans (with the outlets size of 500mm×500mm) installed at the top of the building are further applied to Case 3 and 4 in order to help mitigate the risk of hydrogen inside.

Table I. Test conditions

Case	Permeability of the canvas	Volume flow rate of normal ventilation	Air ingress flow rate	Volume flow rate of emergency ventilation

1	0	None	None	None
2	0	780m^3/h	1053 m^3/h	None
3	3m^3/(m^{2}min)	780m^3/h	1053 m^3/h	780m^3/h
4	8m^3/(m^{2}min)	780m^3/h	1053 m^3/h	780m^3/h

2.3 Mesh Models

The overall 3-D mesh model is displayed in Fig.4. To fully account for the boundary layer formation, local mesh refinement was performed for the area above the water's surface, close to the inclined roof, and near the ventilation channels, air ingress channels and the emergency ventilation channels. Fig.5 and Fig.6 illustrate the results of mesh refinements. The region where hydrogen may locally gather is above the water pool, which corresponds to an overall mesh number of 261927. For the calculation domain of the building, the mesh number is determined to be1465744 after mesh sensitivity analysis, and mesh quality is above 0.97, which satisfies calculation requirements.

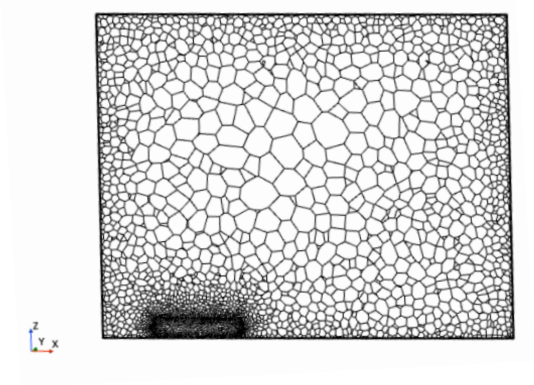

Figure 5. Mesh refinements above the water pool and close to the roof and sidewalls

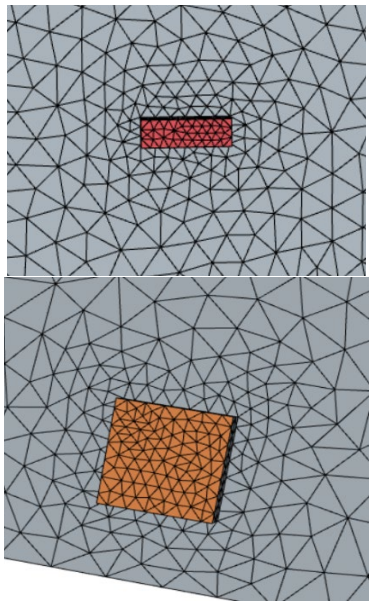

Figure 6. Mesh refinements near the air ingress channels (above) and ventilation channels (below)

3. RESULTS AND DISCUSSIONS

3.1 Hydrogen Distribution without Any Mitigation Measures

Fig. 7 depicts the hydrogen concentration distribution when hydrogen is released from the pool's surface. It should be noted that in this article, concentrations in % refers to volumetric %. As a result of the canvas's blockage, hydrogen can only leak through the overflow orifices on either side of the pool that are flush with the canvas. This leads to a rapid increase in the concentration of hydrogen, as seen in Fig. 8, and an average concentration of up to 40% can be found above the pool when the calculation time is 770s (12.83min). In addition, it is observed that a small amount of hydrogen enters the building space, as depicted in Fig.9, which also shows that this cluster of hydrogen is rapidly diluted after departure from the water pool, and that the concentration of hydrogen in the building area is still relatively low. However, a trace amount of hydrogen has transported to the building's roof.

With the continuous releasing of hydrogen, the hydrogen concentration above the pool and in the space of the building further increases, as shown in Fig. 10, when t=10800s (3h), without considering any mitigation measures, a certain hydrogen accumulation appears in the area adjacent to the pool, with the hydrogen concentration varied as high as 40%-50%, exhibiting a spatial asymmetry. However, no pronounced concentration build-up phenomenon occurs at the sloping roof, indicating that the potential hydrogen risk in the upper region of the plant is eliminated due to the sacrifice of the water pool.

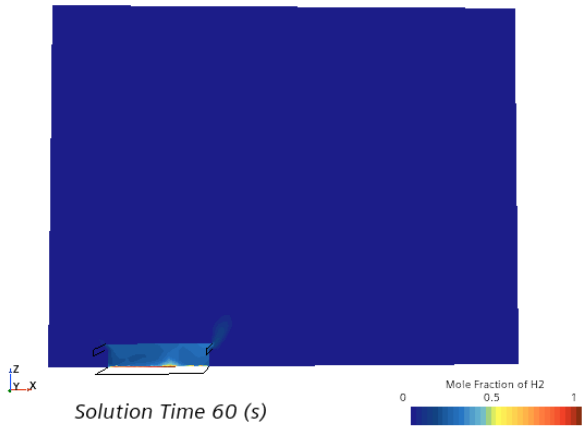

Figure 7. The hydrogen concentration distribution near the source products pool (t=60s)

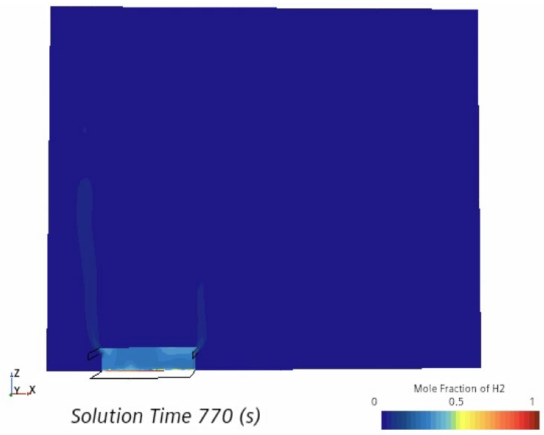

Figure 8. The hydrogen concentration distribution near the source products pool (t=770s)

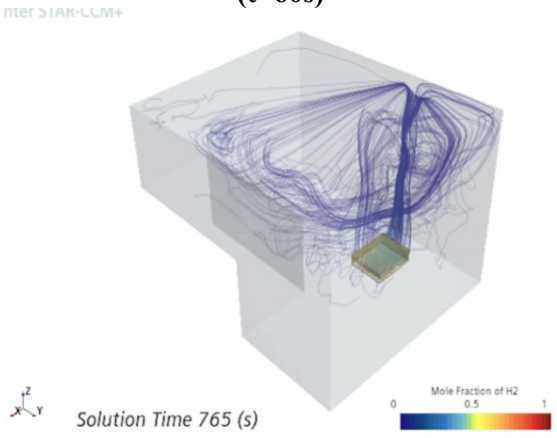

Figure 9. The streamline distribution of hydrogen within the building (t=765s)

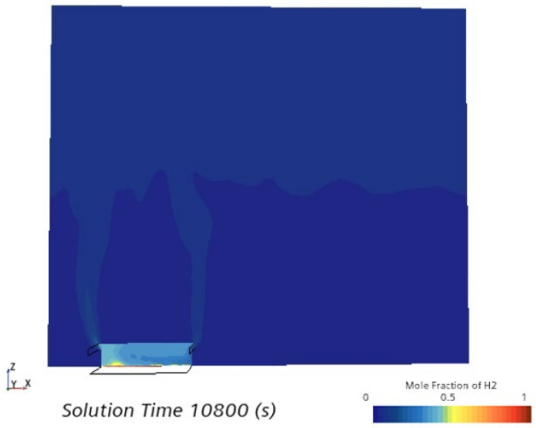

Figure 10. The hydrogen concentration distribution within the building (t=10800s)

3.2 Hydrogen Distribution with Normal Mitigation Measures

Fig. 11 shows the locations and the arrangements of the ventilation channels and air ingress channels. In the real normal operation, 10 ventilation channels are arranged specifically in the center area of the building's side wall, and 12 air ingress channels are arranged in the bottom area. These overall 22 channels work together to control the hydrogen risk inside the building.

It is evident that when the calculation time is around 10s, as in Fig.12, the building's flow field turns to be chaotic due to the ventilation effect in the middle part, intensifying the flow of hydrogen to the upper part of the building, in addition to the presence of the hydrogen flow region above the pool. This phenomenon can also be depicted in the following period of time, for example, hydrogen streamlines gradually distribute near the exit of the ventilation channels at the bottom. As a result, the hydrogen concentration in the

building's upper space progressively rises with time, and the area above the pool is where the hydrogen concentration firstly begins to rise. Subsequently, the hydrogen from the dome diffuses along the building's top and side walls, reaching the top of the forklift room and the lower portion of the building. The only area where the flow of hydrogen may be restricted with the lower concentration is on the left side of the forklift room.

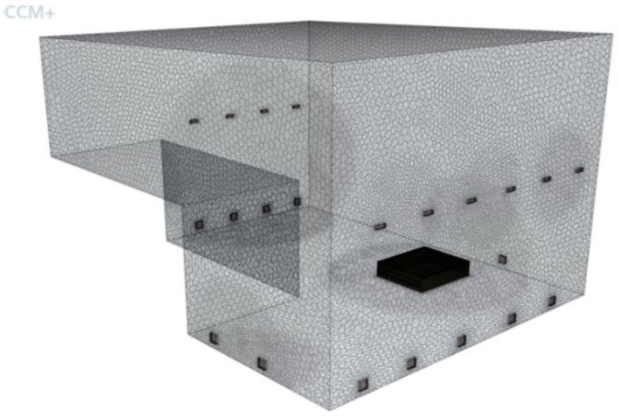

Figure 11. The streamline distribution of hydrogen within the building (t=765s)

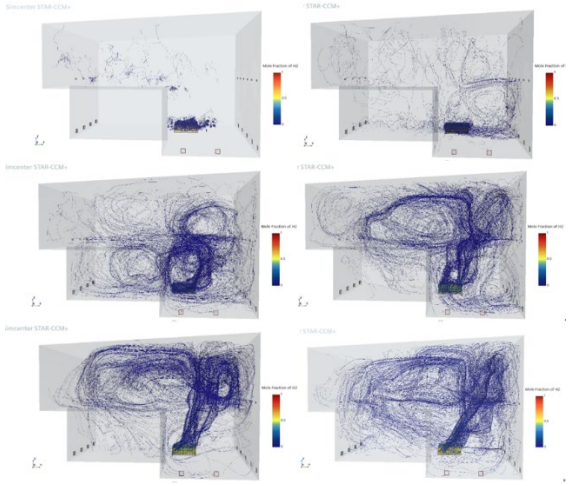

Figure 12. The streamline distribution of hydrogen within the bBuilding (t=10s, 521.7s, 1799.5s, 3599.5s, 7199.5s, and 10795s)

To gain a comprehensive understanding of the changes in hydrogen concentration in the building's local areas over the projected duration of three hours, a total of eighteen monitoring points are chosen within the building's space, which are well-arranged in Fig.13. The great majority of the points are placed throughout the building in various axial and lateral positions, with the exception of the monitoring point 1, which locates in the region between the water pool and the canvas. It is also noteworthy that, as shown in Fig.14, monitoring point 9 is situated close to one of the inlets of air ingress channels.

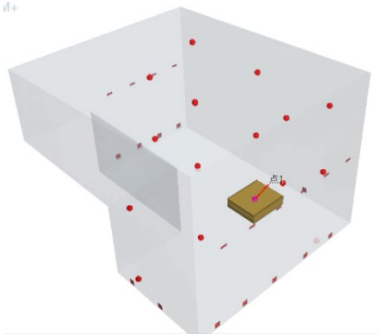

Figure 13. Arrangements of the monitoring points (point 1)

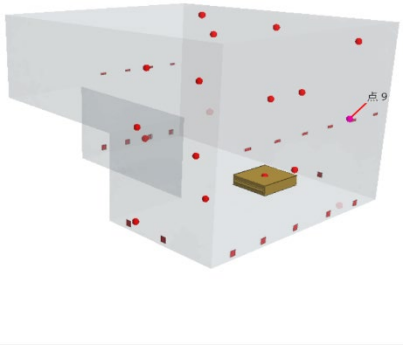

Figure 14. Arrangements of the monitoring points (point 9)

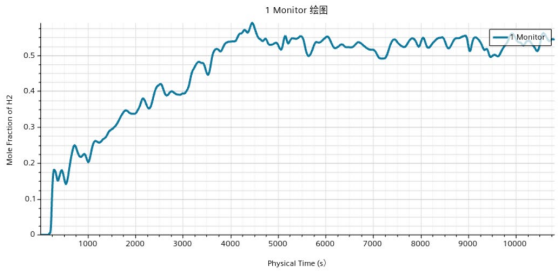

Figure 15. Mole faction of hydrogen (point 1)

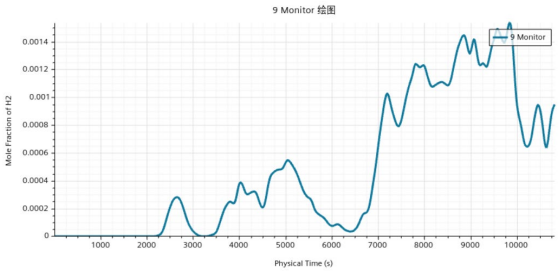

Figure 16. Mole faction of hydrogen (point 9)

Fig.15 and Fig.16 demonstrate the histories of hydrogen concentration at monitoring points 1 and 9. Compared to the point 9, which is situated at the air ingress entrance, where the hydrogen concentration in the early stages of the calculation (~2250s) remains 0, the hydrogen concentration above the water pool soars to 58% in 4400s and then drop to about 53%, which essentially no longer changes with time. The variations in hydrogen concentration for point 9 show an important inerting effect of the air ingress; however, the helium fraction of hydrogen gradually increased afterwards, but it is still lower than the restricted level of 0.4%.

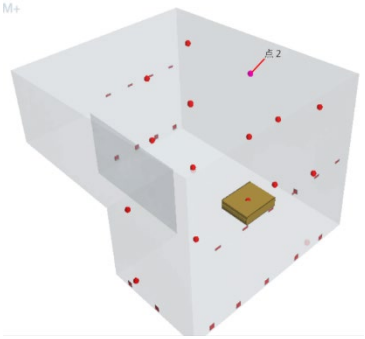

Figure 17. Arrangements of the monitoring points (point 2)

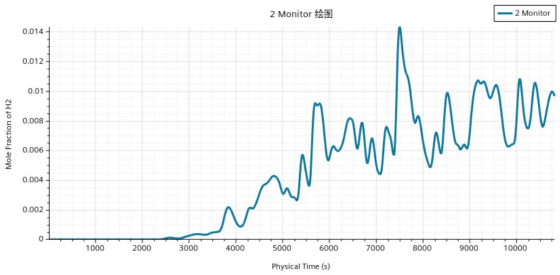

Figure 18. Mole faction of hydrogen (point 2)

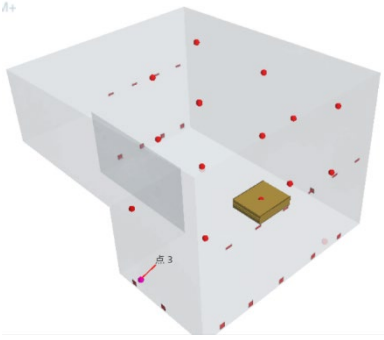

Figure 19. Arrangements of the monitoring points (point 3)

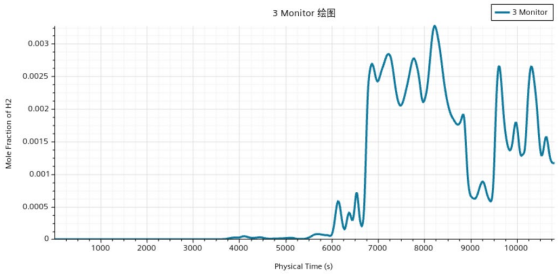

Figure 20. Mole faction of hydrogen (point 3)

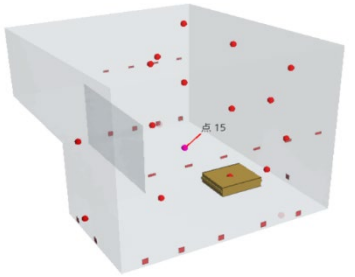

Figure 21. Arrangements of the monitoring points (point 15)

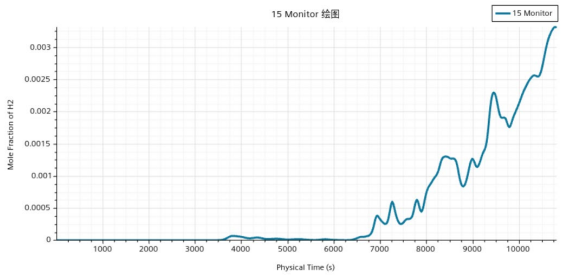

Figure 22. Mole faction of hydrogen (point 15)

Apart from these two unique points, the impact of hydrogen inerting within the building is additionally revealing by other monitoring points situated at varying axial levels. In Fig.17~Fig.22, it is possible to determine whether the region is in the middle, or near the ventilation channels (point 3), or the building's sloping dome (point 2), hydrogen stratification may still take place under normal mitigation measures. With concentrations of about 1%, the area beneath the building's sloping dome cannot genuinely be regarded as a non-explosive zone, even though localized concentrations are far below 4% for this three hours. This case illustrates how, with the exception of the pool area, regular ventilation combined with air ingress can reduce the building's hydrogen risk. The impact on the evolution of hydrogen concentrations is going to be taken into consideration after discussing canvas' permeability above the pools and giving additional thought to other ventilation methods.

3.3 Hydrogen Distribution with Combined Mitigation Measures

This "fake build-up of hydrogen concentration" above the pool in Case 1 &2 is caused by disregard for the air permeability of the canvas in such simulations. As a result, in Cases 3 & 4, the air permeability of the canvas will be changed independently to look into a potential mitigation plan for hydrogen build-up above the pool.

Fig.23 shows a comparison of hydrogen concentrations at the same monitoring points for Case3 and Case4 respectively, and it can be clearly noted that for the point 1 (locates above the pool), the hydrogen concentration has decreased significantly relative to Case2 (~55%), and in Case3 the value has decreased to within 7.0%, and moreover, as the air permeability is further enhanced, the value has further decreased to between 1%~6.5%. It is evident that the risk of hydrogen above the pool is much weakened by increasing the permeability of the canvas. Additionally, it should be noted that, for other representations in the space, the increased canvas permeability, adequate ventilation effects from the normal and emergency approaches, and air ingress all contribute to hydrogen concentrations' staying below 10% of the lower limit corresponding to hydrogen explosion, established in GB 50058-2014 (It is a criterion for hydrogen risk within any building documented and issued by Chinese authority) in China, not putting new hydrogen risk into effect. This may also be due to the fact that, even with enhanced permeability of the canvas, the hydrogen concentration distribution in the space rises somewhat, allowing it to be identified as a non-explosive dangerous zone.

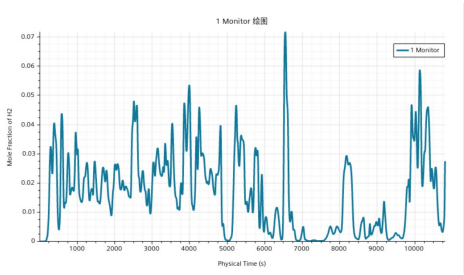

（a1）Point 1 (Case 3)

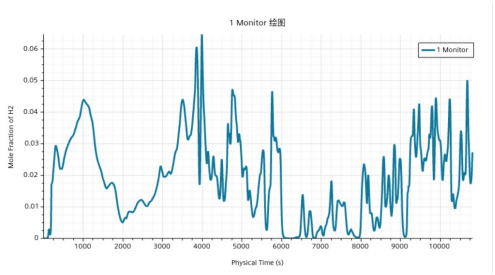

（a2）Point 1 (Case 4)

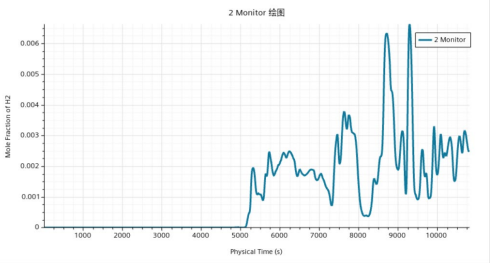

（b1）Point 2 (Case 3)

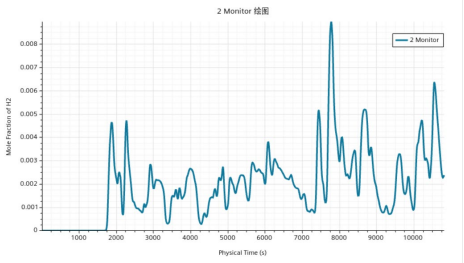

（b2）Point 2 (Case 4)

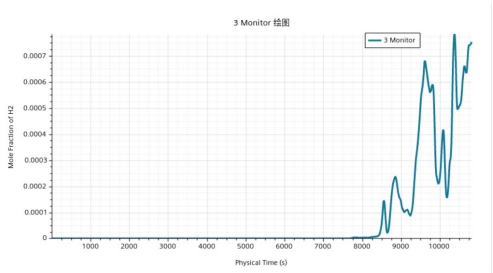

（c1）Point 3 (Case 3)

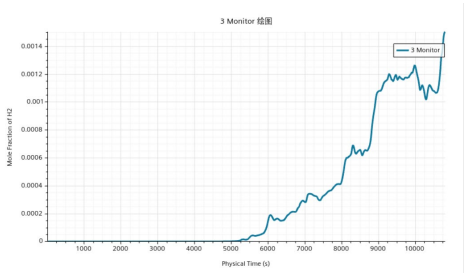

（c2）Point 3 (Case 4)

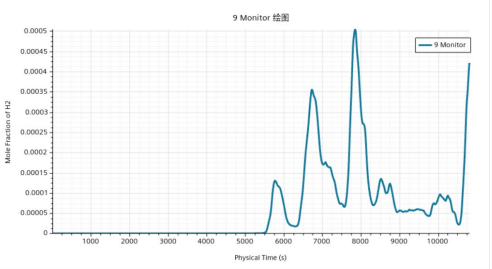

（d1）Point 9 (Case 3)

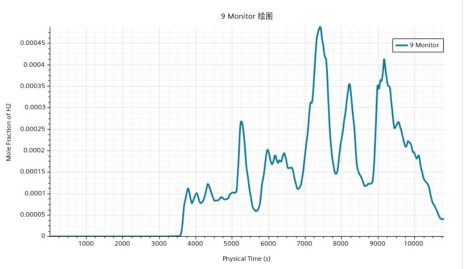

（d2）Point 9 (Case 4)

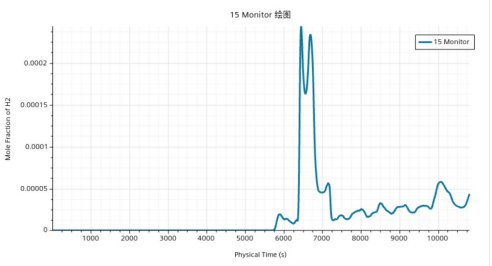

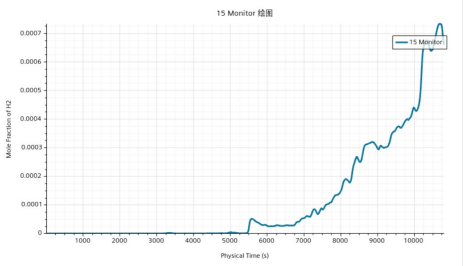

（e1）Point 15 (Case 3) （e2）Point 15 (Case 4)

Figure 23. Mole faction of hydrogen

4. CONCLUSIONS

Quantifying the concentration of hydrogen and the distribution of the streamlines in the isotope manufacturing building leads to the following conclusions based on the three-dimensional CFD modeling of the building, and the simulation analysis of the hydrogen flow and transport process following the irradiation of water:

(1) The hydrogen risk in most areas of the building can be significantly reduced, and the hydrogen concentration can be lowered to less than 1%, if normal ventilation and air ingress are all taken into account, with the exception of the area above the pool; however, not all of these areas can be categorized as non-explosive areas.

(2) The "fake build-up of hydrogen concentration" issue above the pool can be entirely eliminated by amending the air permeability of the canvas covering above the pool. The hydrogen concentration above the pool can quickly drop to 2%-7% when the air permeability is 3 $m^3/(m^2$ min); however, when the value is further raised to 8 $m^3/(m^2$ min), the hydrogen concentration above the pool may essentially be maintained below the lower limit of hydrogen explosion (4%).

ACKNOWLEDGMENTS

This work was supported by the National Natural Science Foundation of China (12105167) and Shanghai Sailing Program (21YF1414800).

REFERENCES

1. X.L. Huang, B. Yang, Y.B. Liu, “Water Radiolysis Processes, Dissociation Products and Impacts on Environment,” *Energy Investigation and Management*, **4**, pp. 32-35 (2013).
2. 国家核安全局, 《福岛核事故后核电厂改进行动通用技术要求（试行）》,国核安发 [2012] 98号 (2012).
3. J. Tills, A. Notafrancesco, J. Phillips, “Application of the MELCOR Code to Design Basis PWR Large Dry Containment Analysis,” Sandia National Laboratories Report, SAND2009-2858 (2009).
4. M. Wang, A. Manera, M.J. Memmott, et al, “Preliminary Design of the I2S-LWR Containment System,” *Annals of Nuclear Energy*, **3**, pp. 1835-1847 (2015).
5. H.J. Allelein, K. Neu, J.P.V. Dorsselaere, “European Validation of the Integral code ASTEC (EVITA),” *Nuclear Engineering and Design*, **235**, pp. 285-308 (2005).
6. C. Patrick and L. Laurent, “ASTEC V2.2 Code Validation: Illustrative Results and Main Outcomes,” *Nuclear Engineering and Design*, **413**, pp. 112547 (2023).
7. S.J. Lee, C.Y. Park, R.E. Henry, et al, “Benchmark of the Heiss Dampf Reactor E11.2 Containment Hydrogen-mixing Experiment Using the MAAP4 Code,” *Nuclear Technology*, **125**, pp. 182-196 (1999).
8. N. Sakai, H. Horie, H. Yanagisawa, et al, “Validation of MAAP Model Enhancement for Fukushima Daiichi Accident Analysis with Phenomena Identification and Ranking Table (PIRT),” *Journal of Nuclear Science and Technology*, **51**, pp. 951-963 (2014).
9. A. Flores y Flores and G. Mazzini, “Analyses of THAI 1 Hydrogen Deflagration Using MELCOR Code Version 2.1 and 2.2,” *Nuclear Engineering and Design*, **369**, pp. 110838 (2020).
10. S. Schwarz, K. Fischer, A. Bentaib, et al, “Benchmark on Hydrogen Distribution in a Containment Based on the OECD-NEA THAI HM-2 Experiment,” *Nuclear Technology*, **175**, pp. 594-603 (2011).

11. B.L. Smith, M. Andreani, U. Bieder, et al, "Assessment of CFD Codes for Nuclear Reactor Safety Problems – Revision 2," OECD/NEA Report, NEA/CSNI/R(2014)12, (2015).
12. C. Peng, L.L. Tong, X.W. Cao, "Numerical Analysis on Hydrogen Stratification and Post-inerting of Hydrogen Risk," *Annals of Nuclear Energy*, **94**, pp. 451-460 (2016).
13. D.C. Visser, E.M.J. Komen, M. Houkema, et al, "FLUENT Calculations of the Hydrogen Distribution in a Containment During the OECD-NEA THAI HM-2 Experiment," *Proceedings of 13th Int. Topl. Mtg. Nuclear Reactor Thermal Hydraulics (NURETH-13)*, Kanazawa, Japan, September 27–October, 2009 pp. N13P1159 (2009).
14. STAR-CD Version 3.20 Methodology Manual. CD-adapco, UK (2004).
15. B.R. Sehgal, *Nuclear Safety in Light Water Reactors - Severe Accident Phenomenology*. Amsterdam: Academic Press (2012).
16. J.R. Travis, P. Royl, R. Redlinger, et al, "GASFLOW-II: A Three-dimensional-finite-volume fluid-dynamics Code for Calculating the Transport, Mixing, and Combustion of Flammable Gases and Aerosols in Geometrically Complex Domains, Theory and Computational Model Vol. 1," Reports FZKA-5994, LA-13357-MS (1998).
17. H. Holzbauer and L. Wolf, "GOTHIC Verification on Behalf of the Heiss Dampf Reactor Hydrogen-mixing Experiments," *Nuclear Technology*, **125**, pp. 166-181 (1999).
18. M. Babic, I. Kljenak, B. Mavko, "Prediction of Light Gas Distribution in Experimental Containment Facilities Using the CFX4 Code," *Nuclear Engineering and Design,* **238**, pp. 538-550 (2008).
19. D. Luxat, "Severe Accident Management Guidance Technical Basis Report," Electric Power Research Institute Report, Report number: 1025295 (2012).
20. J.J. Xiao, and J.R. Travis, "How Critical Is Turbulence Modeling in Gas Distribution Simulations of Large-scale Complex Nuclear Reactor Containment?" *Annals of Nuclear Energy*, **56**, pp. 227–242 (2013).
21. K. Hiemenz, "Die Grenzschicht an Einem in den Gleichfaermigen Flfissigkeitsstrom Eingetauchten Geraden Kreiszylinder", *Dingl Polytech Journal*, **326**, pp. 321-410 (1911).
22. H. Wilkening, D. Baraldi, M. Heitsch, "CFD Simulations of Light Gas Release and Mixing in the Battelle Model-Containment with CFX," *Nuclear Engineering and Design*, **238**, pp. 618-626 (2008).
23. F. Liu, Z.N. Sun, M. Ding, et al, "Characteristics of Helium Stratification Driven by Steam Condensation in Containment," *Journal of Harbin Engineering University*, **4**2, pp. 1786-1791 (2021).

Proceedings of the 11th Conference on Severe Accidents Research
ERMSAR 2024
May 13-16, 2024, Stockholm, Sweden

Evaluation of hydrogen risk and its mitigation strategies adopted in isotope manufacturing building

Cheng Peng*, Jian Deng, Sheng Gao

E-mail: diomio@shiep.edu.cn

College of Energy and Mechanical Engineering

Shanghai University of Electric Power

2024-5-15

Outline

- Introduction
- Preparations for Simulations
  - Geometrical modeling
  - Case details
- Results and Discussions
  - Hydrogen distribution without any mitigation measures
  - Hydrogen distribution with normal mitigation measures
  - Hydrogen distribution with combined mitigation measures
- Concluding Remarks

Introduction

➢ Manufacturing Co-60



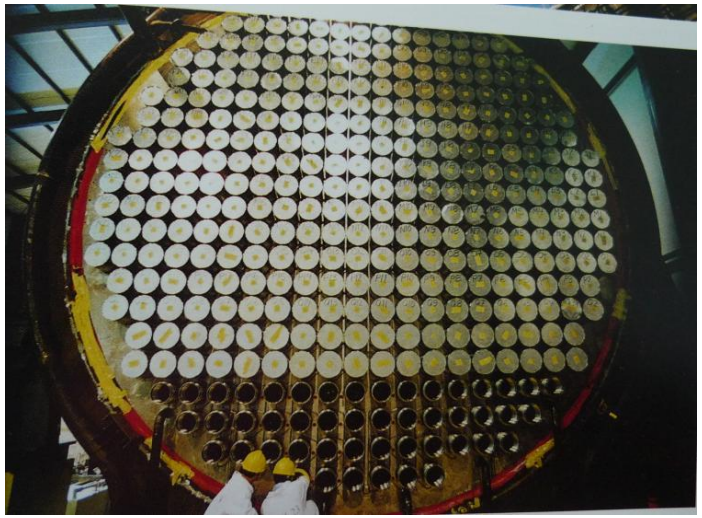

Isotope manufacturing building

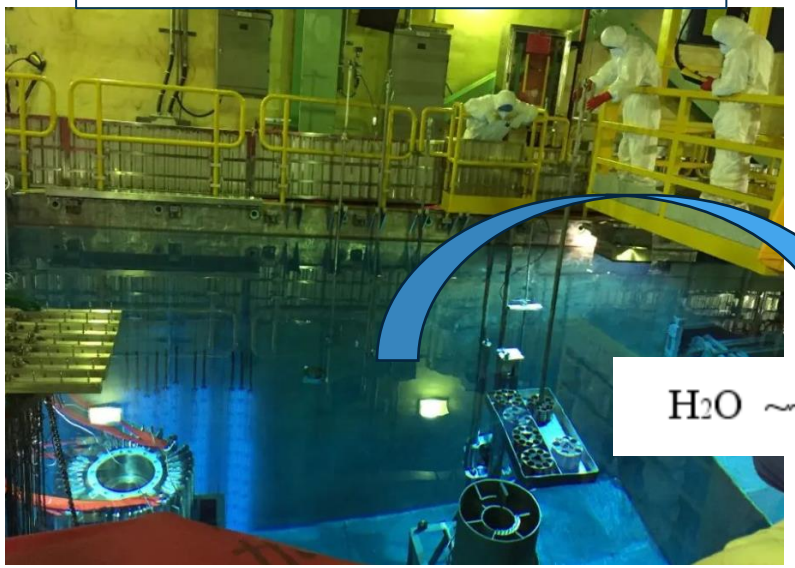

Coolant irradiation

n, γ ray…..

$$H_2O \rightsquigarrow H_2,\ H_2O_2,\ e^-_{aq},\ \bullet H,\ \bullet OH,\ H_3O^+,\ HO_2\bullet$$

Canvas

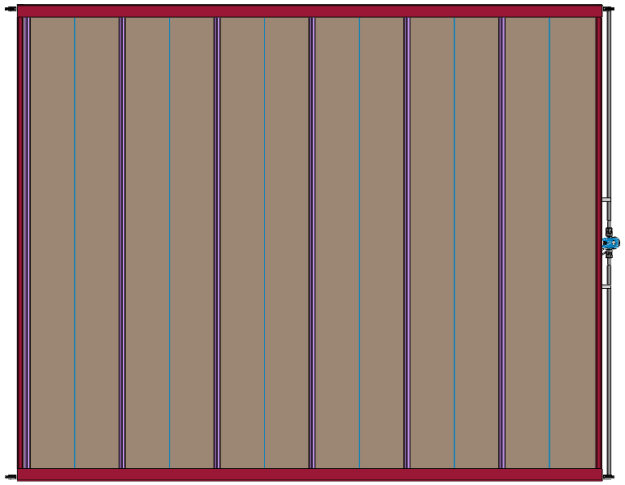

Co-60 rods-in

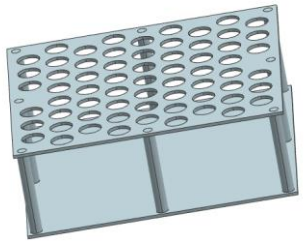

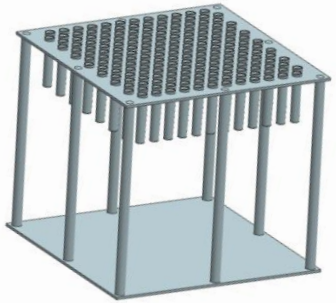

Spacer grid

Introduction

➢ China authority defends against hydrogen risk sort of issues


国家能源局
National Energy Administration

请输入关键字

首 页 信息公开 领导活动 新闻中心 能源要闻 在线办事

您当前位置：首页 > 正文

关于印发《福岛核事故后核电厂改进行动通用技术要求（试行）》的通知
国核安发[2012]98号

发布时间：2012-06-19 来源：环保部网站 大 中 小

国家核安全局文件
国核安发[2012]98号

关于印发《福岛核事故后核电厂改进行动通用技术要求（试行）》的通知

各有关单位：

根据《中华人民共和国民用核设施安全监督管理条例》（HAF001）及其实施细则的有关要求，为汲取日本福岛核事故的经验和教训，进一步提高我国核电厂的安全水平，我局编制了《福岛核事故后核电厂改进行动通用技术要求（试行）》，现予以发布，自发布之日起实施。

附件：福岛核事故后核电厂改进行动通用技术要求（试行）

二〇一二年六月十二日

主题词：环保 核安全 核电厂 通用技术要求 通知

‘General technical requirements for nuclear power plant improvements after the Fukushima nuclear accident’

- Improve and amend the hydrogen control system adopted in Chinese nuclear power plants
- Conduct hydrogen safety analysis evaluating the effectiveness of the hydrogen control strategies

In analogy



It is suggested to carry out hydrogen distribution and risk mitigation investigations for the isotope manufacturing building, in order to raise the safety level of the source term building, and to provide reliable accident emergency measures for the similar buildings, e.g. nuclear fuel storage building.

Introduction

➢ Hydrogen behaviors and its risk mitigation within an enclosure

10^2~10^3m^3

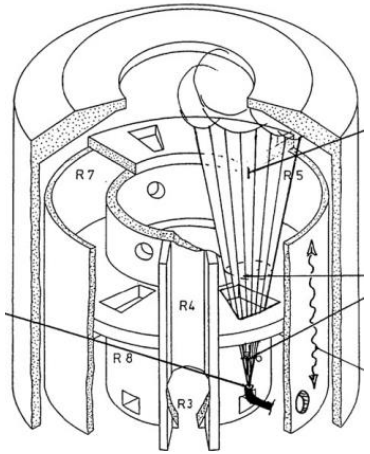

BMC-GRS in Germany

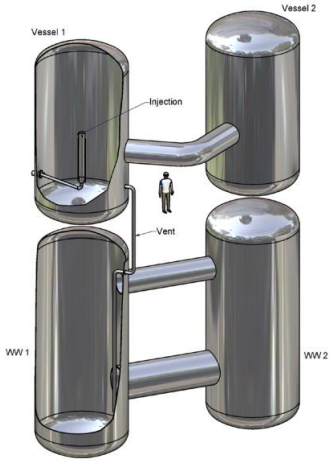

PANDA-PSI in Switzerland

➢PANDA facility: Scale-down ESBWR

➢In SETH，horizontal jet, plume along the wall and free plume on hydrogen and steam distribution

➢Erosion of hydrogen stratification and condensation effect are focused on.

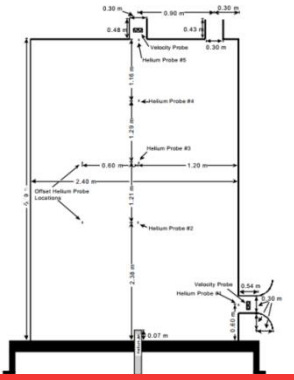

LSGMF-AECL in Canada

✓ Thermal stratification
✓ Natural circulation under small temperature difference
✓ Long-term condition

Steam distribution is more focused on.

➢Buoyancy, jet momentum, mixing driven by Fans effects on hydrogen mixing behaviors

Hydrogen stratification was not observed.

★The volume is as the same order of magnitude as the isotope manufacturing building.

★ Resulting from the severe accident conditions, steam may not be ignored, however, inerting effect of steam can help mitigate the hydrogen risk, which can not be applied to manufacturing building.

★ No local structure was arranged and installed in LSGMF, therefore, local hydrogen risk and its mitigation strategy can not be revealed from their investigation.

Introduction

➢ Hydrogen risk and mitigation measures: Numerical studies

The **lumped parameter (LP) code**-MAAP, MELCOR, ASTEC, etc.

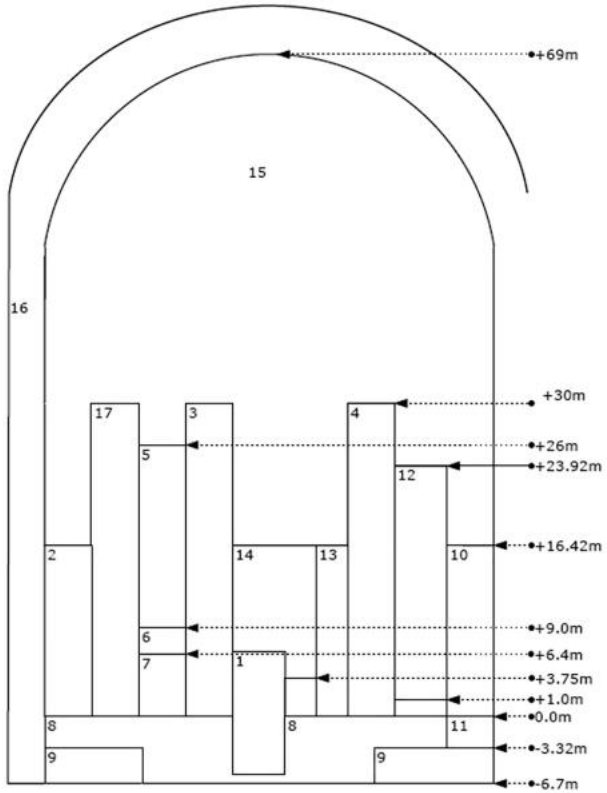

- ✓ There is a certain uncertainty in hydrogen risk assessment when using lumped parameter program method, which can be corrected by combining the gas distribution analysis results given by CFD software.

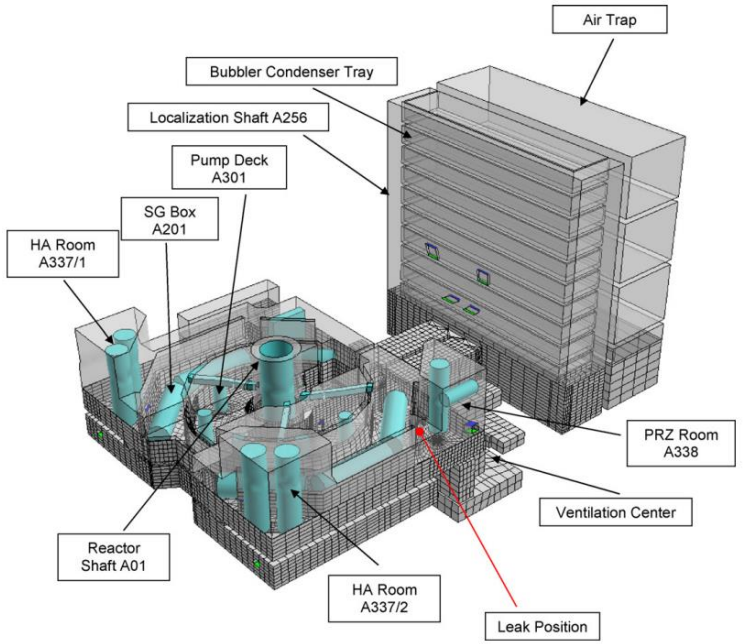

VVER-440/213 containment-Fluent/CFX/GASFLOW-Netherlands

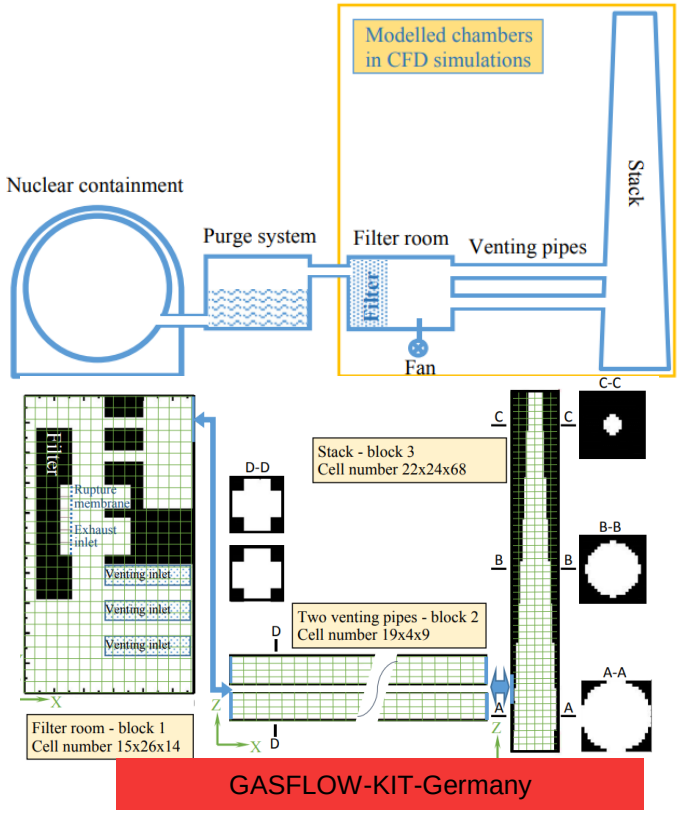

GASFLOW-KIT-Germany

- ✓ The results encourage the use of CFD in assessing the risk of losing containment integrity as a result of hydrogen deflagrations.
- ✓ The simulations give advice about the arrangements of recombiner units.

- ✓ A ventilation fan with sustained power supply can extinguish the hydrogen risk effectively.
- ✓ However, the hydrogen risk in local compartments is not recognized.

Introduction

➢ Hydrogen related issues in my research group

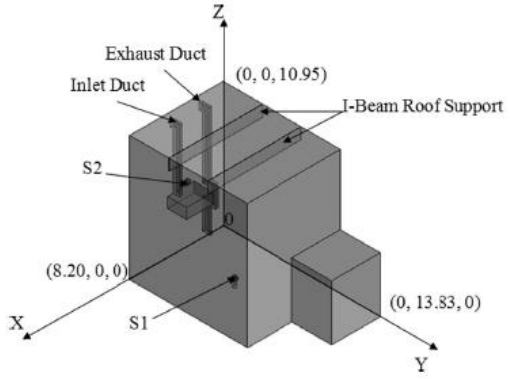

Fig. 1. The geometry model of LSGMF.

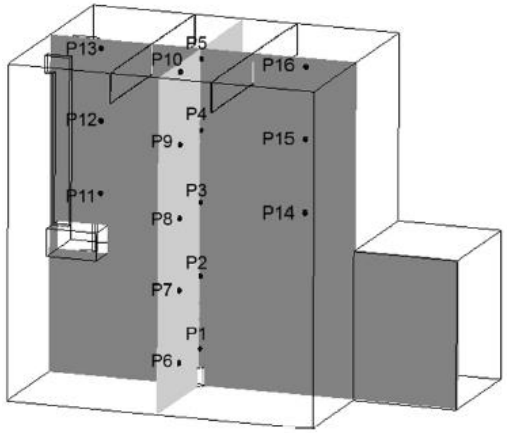

Fig. 2. Distribution of monitoring points.

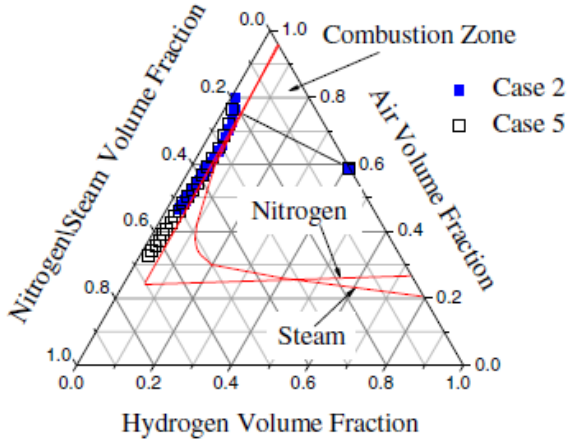

$$l'_s = \left(M_0^{3/4} \,/\, F_0^{1/2}\right) \cdot \mathrm{Re}_0^{0.11}$$

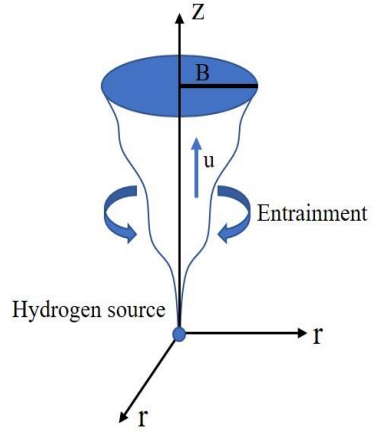

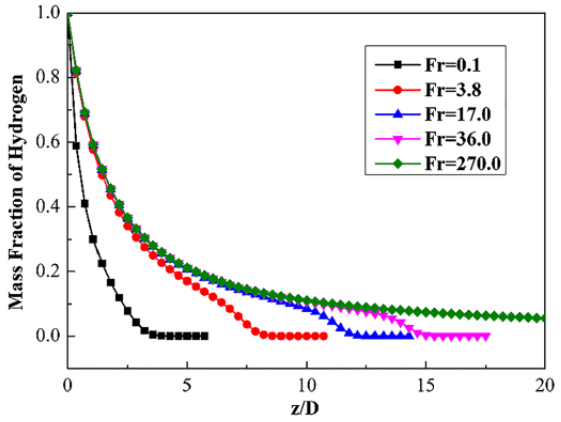

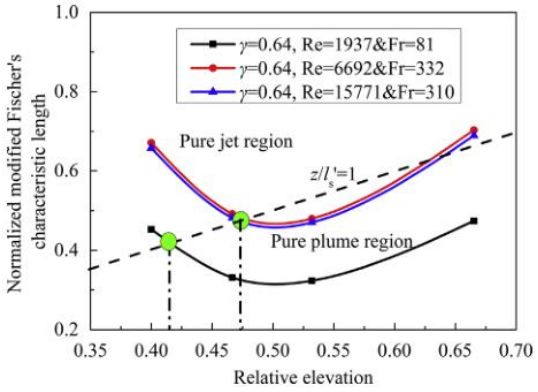

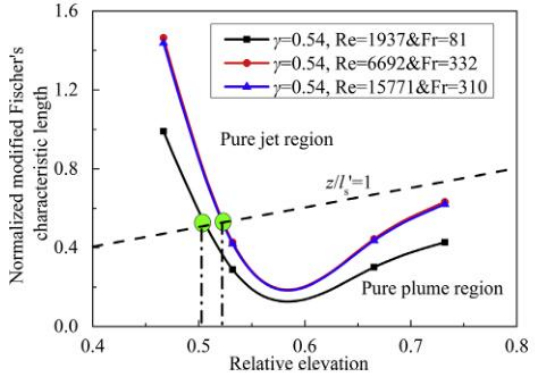

★ Cheng Peng, et al. **Numerical analysis on hydrogen stratification and post-inerting of hydrogen risk**. Annals of Nuclear Energy, 94(2016) 451-460.
★ Cheng Peng. **Build-up of hydrogen up-flow model in consideration of air resistance and entrainment**. International Journal of Energy Research, 43(2019) 7010-7020.
★ Cheng Peng. **Semi-empirical model of hydrogen distribution under presence of steam within a reactor building**. International Journal of Hydrogen Energy, 45 (2020) 22176-22188.

Preparations for Simulations

➢ Geometrical modeling

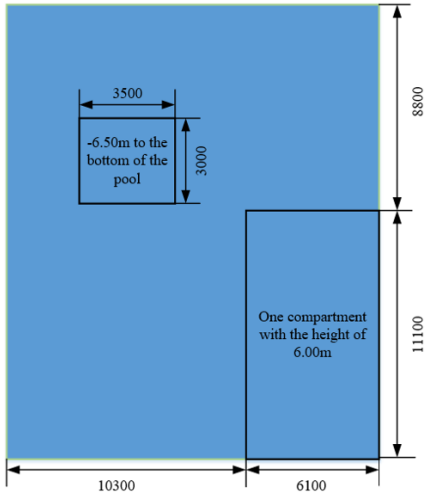

Figure 1. Top view of the isotope manufacturing building

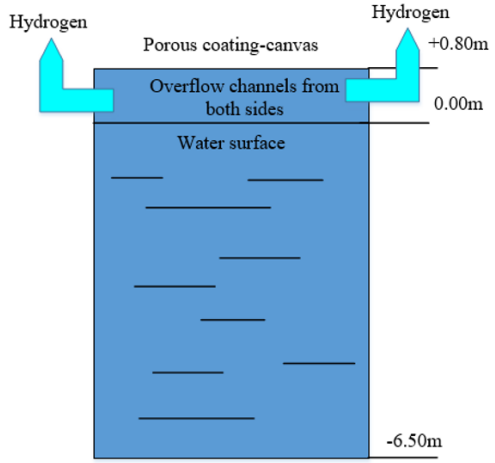

Figure 2. Detailed geometry of the water pool

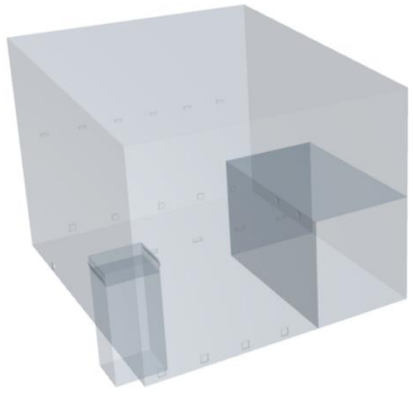

Figure 3. 3-D geometry model of the building and its inside structure

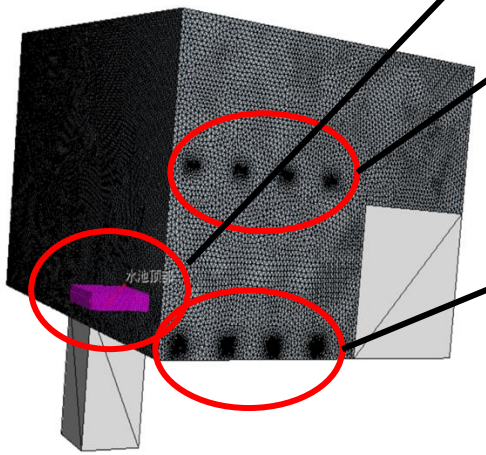

Figure 4. 3-D mesh model

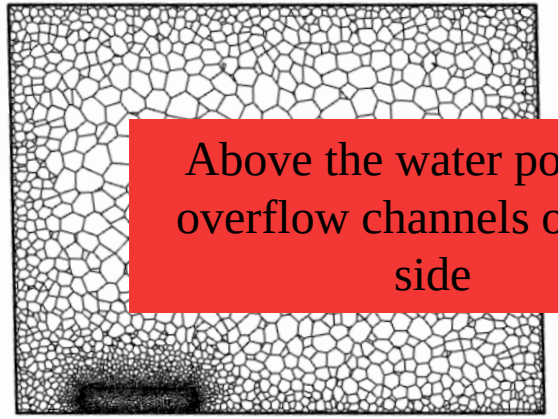

Above the water pool and overflow channels on each side

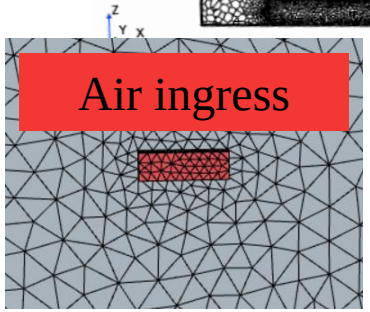

Air ingress

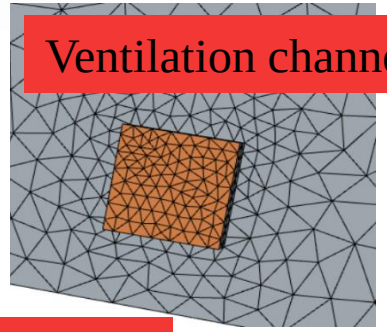

Ventilation channel

Grids refinement

The region where hydrogen may locally gather is above the water pool, which corresponds to an overall mesh number of 261927. For the calculation domain of the building, the mesh number is determined to be 1465744 after mesh sensitivity analysis, and mesh quality is above 0.97, which satisfies calculation requirements.

Preparations for Simulations

➢ Case details

Case	Permeability of the canvas	Volume flow rate of normal ventilation	Air ingress flow rate	Volume flow rate of emergency ventilation
1	0	None	None	None
2	0	780m^3/h	1053 m^3/h	None
3	3$m^3/(m^2min)$	780m^3/h	1053 m^3/h	780m^3/h
4	8$m^3/(m^2min)$	780m^3/h	1053 m^3/h	780m^3/h

In Case1, the canvas is **impermeable**, and hydrogen can only leak into the environment from the two opposite sides of the water pool by the overflow orifices, with an **overflow area of 0.588 m^2 on each side**. In order to further inert the combustible gases inside the building and drive the flow of light gases inside, in Case 2, **12 ventilation fans** (with the outlets size of 400mm×400mm)and **10 air ingress channels** (475mm×150mm) are turned on. In Cases 3 and 4, **a new design** is taken into consideration in order to lessen the risk of hydrogen, based on which, the use of **high permeability fabric** (enhancing the permeability of the canvas) enhances hydrogen's transport and diffusion above the water's surface. Besides, **three emergency ventilation fans** (with the outlets size of 500mm×500mm) installed at the top of the building are further applied to Case 3 and 4 in order to help mitigate the risk of hydrogen inside.

Results and Discussions

➢ Hydrogen distribution without any mitigation measures

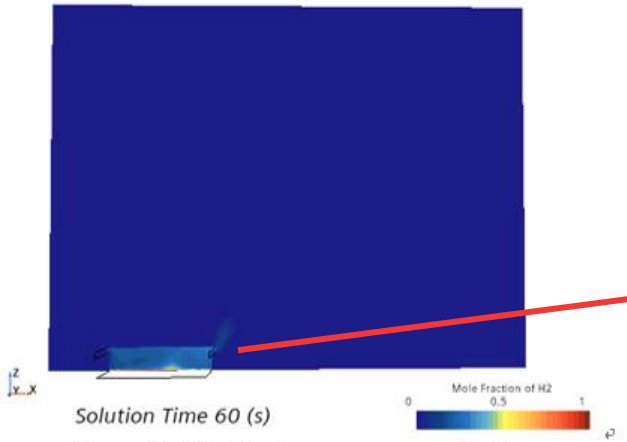

Figure 7. The hydrogen concentration distribution near the source products pool (t=60s)

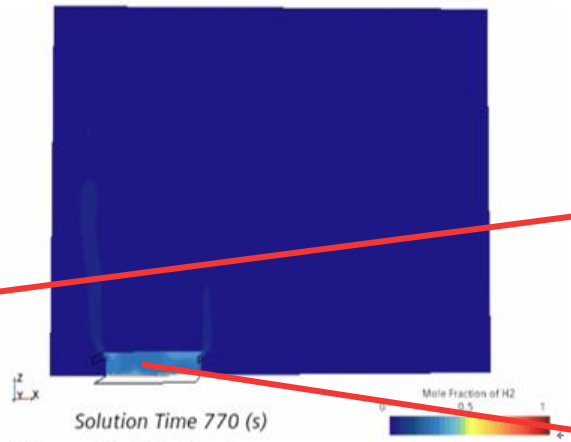

Figure 8. The hydrogen concentration distribution near the source products pool (t=770s)

As a result of the canvas's blockage, hydrogen can **only leak through the overflow orifices** on either side of the pool that are flush with the canvas.

An average volume concentration of up to **40%** can be found **above the pool**.

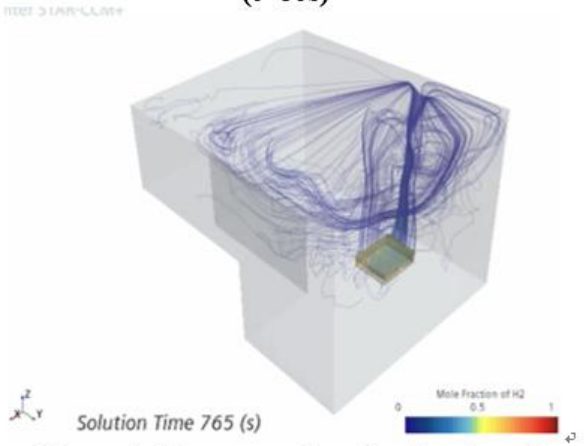

Figure 9. The streamline distribution of hydrogen within the building (t=765s)

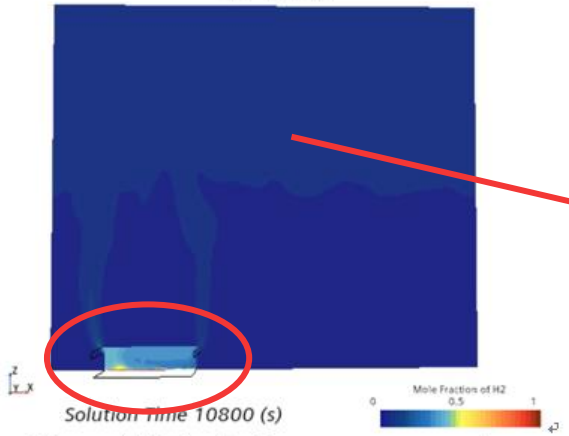

Figure 10. The hydrogen concentration distribution within the building (t=10800s)

No pronounced concentration build-up occurs at the sloping roof, indicating that the potential hydrogen risk in the upper region of the plant is eliminated due to the **sacrifice of the water pool**.

Results and Discussions

➢ Hydrogen distribution with normal mitigation measures

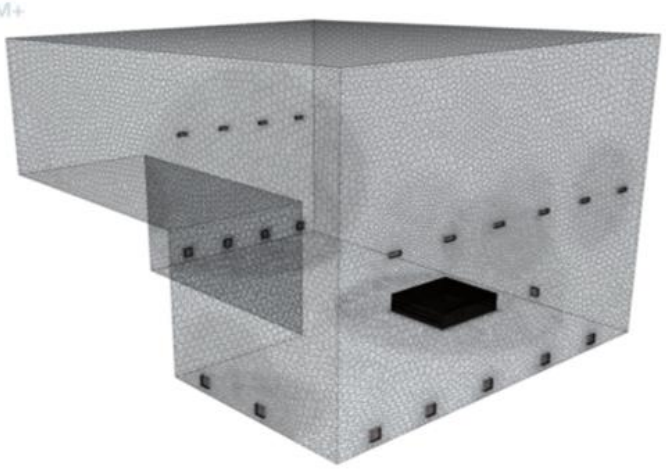

Figure 11. The streamline distribution of hydrogen within the building (t=765s)

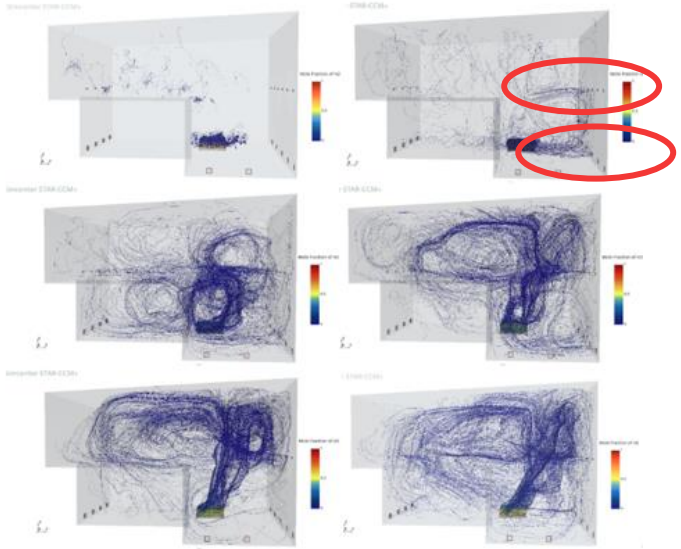

Figure 12. The streamline distribution of hydrogen within the building (t=10s, 521.7s, 1799.5s, 3599.5s, 7199.5s, and 10795s)

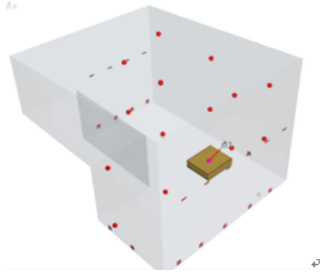

Figure 13. Arrangements of the monitoring points (point 1)

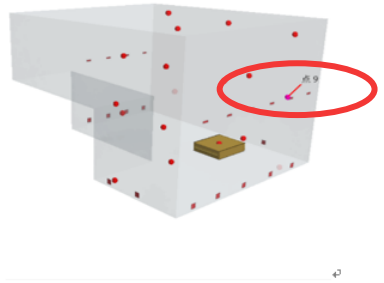

Figure 14. Arrangements of the monitoring points (point 9)

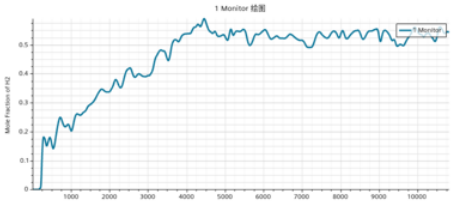

Figure 15. Mole faction of hydrogen (point 1)

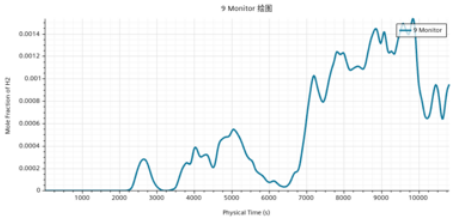

Figure 16. Mole faction of hydrogen (point 9)

These overall 22 channels work together to control the hydrogen risk inside the building.

1. The building's flow field turns to be chaotic due to the **air ingress in the middle part, and ventilation effect at the bottom**, intensifying the flow of hydrogen to the upper part of the building.
2. Clusters of hydrogen and air can be **tilted towards the right side** which is much closer to the air ingress channels.
3. The variations in hydrogen concentration for point 9 show an important **inerting effect of the air ingress**, and thus it is lower than the restriction limit of 0.4%.

Results and Discussions

➢ Hydrogen distribution with normal mitigation measures

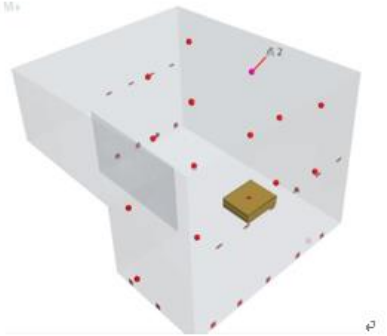

Figure 17. Arrangements of the monitoring points (point 2)

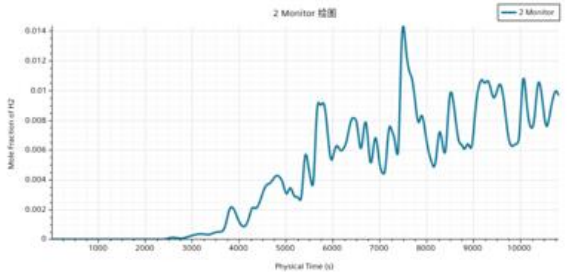

Figure 18. Mole faction of hydrogen (point 2)

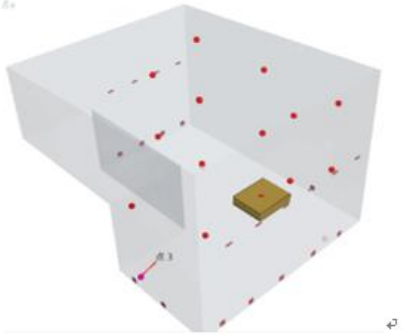

Figure 19. Arrangements of the monitoring points (point 3)

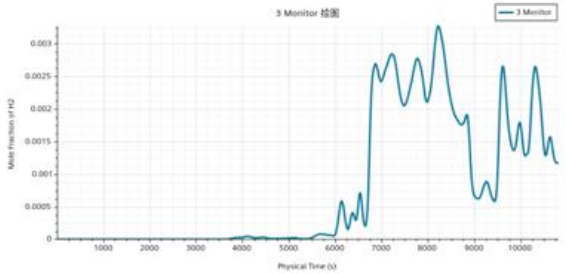

Figure 20. Mole faction of hydrogen (point 3)

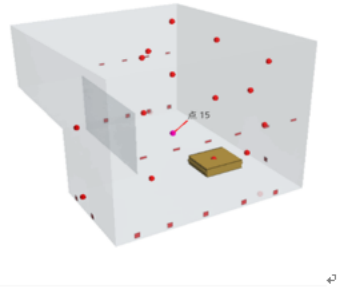

Figure 21. Arrangements of the monitoring points (point 15)

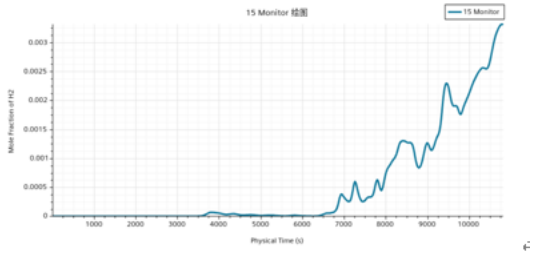

Figure 22. Mole faction of hydrogen (point 15)

1. It is possible to determine whether the region is in the middle, or near the ventilation channels (point 3), or the building's sloping dome (point 2), **hydrogen stratification** may still take place **under normal mitigation measures**.
2. With concentrations of about 1%, the area beneath the building's **sloping dome cannot genuinely be regarded as a non-explosive zone**, even though localized concentrations are far below 4% for this three hours.
3. Regular ventilation combined with air ingress can reduce the building's hydrogen risk, but needs to be strengthened.

Results and Discussions

➢ Hydrogen distribution with combined mitigation measures

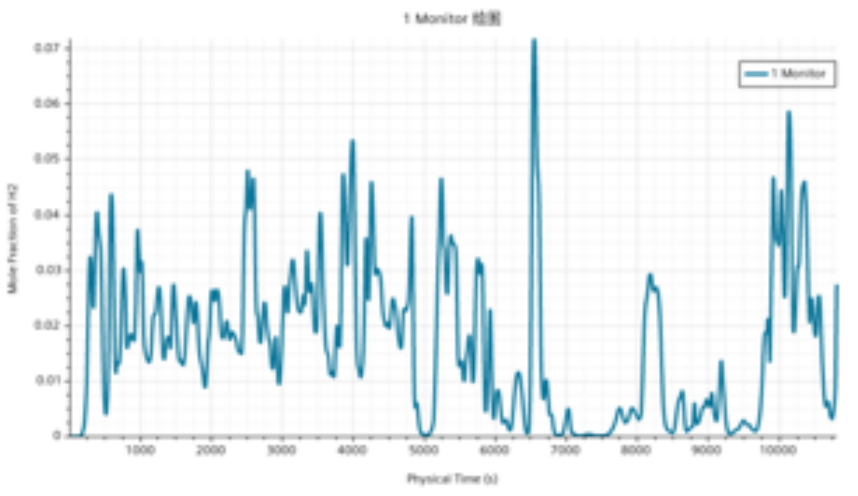

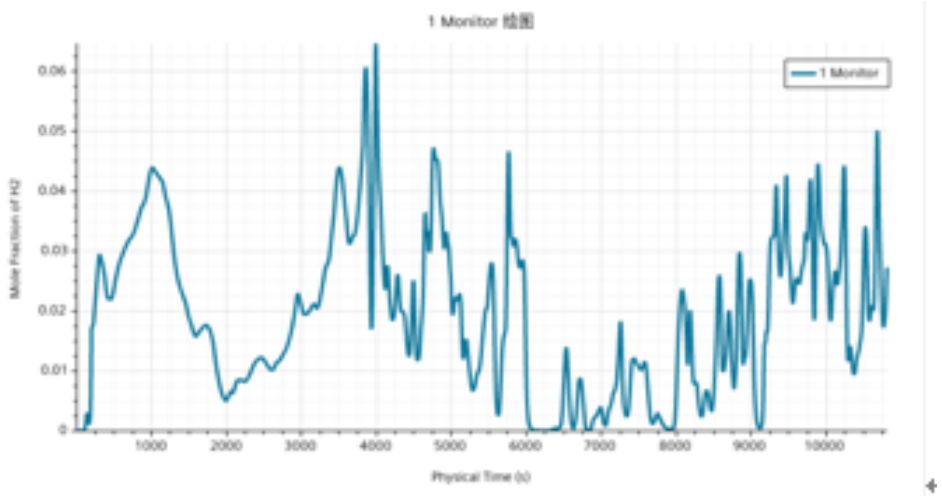

$3m^3/(m^2min)$

（a1）Point 1 (Case 3)

Above the pool

（a2）Point 1 (Case 4)

$8m^3/(m^2min)$

- The **air permeability of the canvas** will be changed independently to look into a potential mitigation plan for **hydrogen build-up above the pool**.

1. The hydrogen concentration has decreased significantly from **~55% (Case2), to within 7.0% (Case3),** and moreover, as the air permeability is further improved, the value has further decreased to **between 0%~6.5%.**
2. It is evident that the risk of hydrogen above the pool is **much weakened by increasing the permeability of the canvas**.

Results and Discussions

➢ Hydrogen distribution with combined mitigation measures

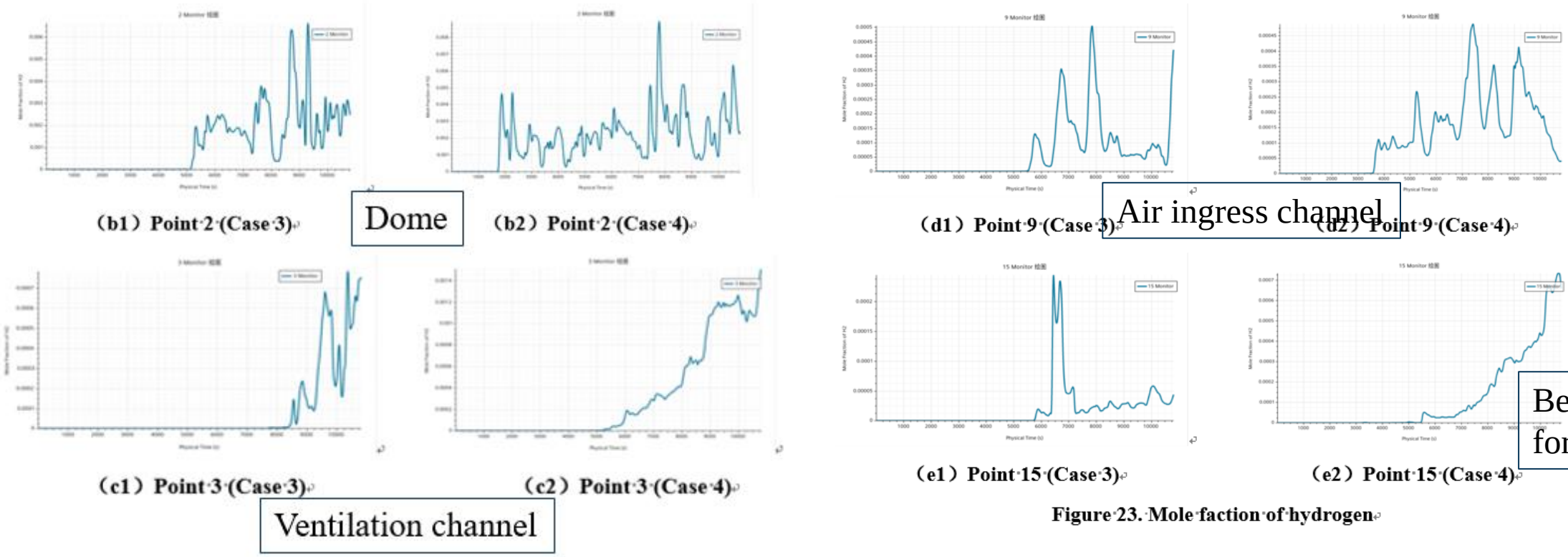

（b1）Point 2 (Case 3)　（b2）Point 2 (Case 4)　（d1）Point 9 (Case 3)　（d2）Point 9 (Case 4)

（c1）Point 3 (Case 3)　（c2）Point 3 (Case 4)　（e1）Point 15 (Case 3)　（e2）Point 15 (Case 4)

Figure 23. Mole faction of hydrogen

The increased canvas permeability, adequate ventilation effects from the normal and emergency approaches, and air ingress all contribute to hydrogen concentrations' staying below 10% of the lower limit corresponding to hydrogen explosion, established in GB 50058-2014 (It is a criterion for hydrogen risk within any building documented and issued by China authority) in China, not resulting in new hydrogen risk.

Concluding remarks

Quantifying the concentration of hydrogen and the distribution of the streamlines in the isotope manufacturing building leads to the following conclusions based on the three-dimensional CFD modeling of the building, and the simulation analysis of the hydrogen flow and transport process following the irradiation of water:

- The hydrogen risk in most areas of the building can be significantly reduced, and the hydrogen concentration can be lowered to less than 1%, if normal ventilation and air ingress are all taken into account, with the exception of the area above the pool; however, not all of these areas can be categorized as non-explosive areas.
- The "fake build-up of hydrogen concentration" issue above the pool can be entirely eliminated by amending the air permeability of the canvas covering above the pool. The hydrogen concentration above the pool can quickly drop to 2%-7% when the air permeability is 3 $m^3/(m^2$ min); however, when the value is further raised to 8 $m^3/(m^2$ min), the hydrogen concentration above the pool may essentially be maintained below the lower limit of hydrogen explosion (4%).

Thank you for listening!

Questions?

THE SCALING OF TURBULENT FLAME ACCELERATION AND DETONATION TRANSITION FOR HYDROGEN-AIR MIXTURES IN THE RUT FACILITY

Kuznetsov M*, Kotchourko A
Karlsruhe Institute of Technology
Kaiserstrasse 12, 76131 Karlsruhe, Germany
kuznetsov@kit.edu, alexei.kotchourko@kit.edu

Breitung W
Pro-Science GmbH
76275 Ettlingen, Germany
w.breitung@t-online.de

ABSTRACT

To model the Loss of Coolant Accident (LOCA) in the containment of a nuclear power plant (NPP) a series of large scale bench-mark experiments have been conducted in the RUT facility. Flame propagation regimes for very lean hydrogen-air mixtures from 10 to 14% H2 have been investigated in the RUT set-up. The facility consists of three parts: 34-m channel; 10.5-m canyon; 20-m second channel. The total volume of mixture was about 480 m^3. 30 and 60% of the channel cross-section was blocked by concrete blocks. Slow and sonic deflagrations in the channel have been established for hydrogen compositions up to 12.5%H2 as well as a detonation transition at 14% of hydrogen was registered. In a canyon of a bigger dimension, the detonation was observed even at 12.5%H2 due to shock reflection at the far corner of the canyon. Such detonable concentrations for channel and canyon geometries significantly extend the well-known conventional detonability limits of 18-59% H2 (NASA STD 8719.16 - Safety Standards) and demonstrate a very high danger of the detonation even for very lean hydrogen-air mixtures.
The scaling down of flame acceleration and detonation transition was investigated for similar geometry in a MINIRUT facility of 50 times smaller size (1:50) than the original RUT facility. The advantage of the small-scale facility was that it allows a high-speed video monitoring of flame acceleration and detonation transition. The detonation in the channel and in the canyon of 50 times smaller scale has occurred for hydrogen-air mixtures with a detonation cell size of 50-57 times smaller than for a real-scale RUT facility. The known criterion 7λ for detonation onset in an obstructed channel was experimentally confirmed. The video monitoring confirmed the shock reflection and shock-flame interaction mechanisms for deflagration to detonation transition (DDT). Beyond the detonation cases for leaner hydrogen-air mixtures, the flame can propagate as subsonic or sonic deflagration. The criterion for sonic deflagration will be the critical expansion ratio σ = 3.75 which corresponds to 10.5-11%H2. The experiments also confirmed that the flame dynamic for deflagration mode does not scale down as the DDT process.

KEYWORDS
Hydrogen, LOCA accident, Severe accident, Flame acceleration, Detonation transition

* Prof. Dr. Mike Kuznetsov e-mail: kuznetsov@kit.edu

1. INTRODUCTION

Hydrogen release through a leak due to the Loss of Coolant Accident (LOCA) or Molten Corium-Concrete Interaction (MCCI) accident results in the formation of a hydrogen-air cloud inside of the reactor building. Delayed ignition of such a cloud due to operating ignitors or catalytic recombiners may lead to hydrogen combustion in different regimes depending on geometry, scale, initial pressure and temperature, and hydrogen concentration. Under certain initial and boundary conditions, accelerated flames, fast turbulent deflagrations, and transition to detonation are principally possible. The DDT event and detonation propagation are able to produce the most severe loads to confining structures similar to the Fukushima-Daiichi accident in Unit 1 and Unit 3 [1-3].

Critical conditions for flame acceleration to the speed of sound and then to detonation onset in confined geometry have been experimentally defined [4-5]. Depending on the flame propagation regime and strength of the hydrogen explosion, different pressure loads can be expected. Global pressure loads affect the containment building. Generally, the level of global loads depends on the total amount of hydrogen burnt and flame propagation velocity. The local loads are more sensitive to details of the hydrogen distribution inside the containment, its geometry, venting areas and areas of connecting openings between subcompartments. It is possible that the global pressure rise remains below certain safety level limits for containment, but local loads could seriously damage specific containment components, internal walls and/or safety equipment.

The geometrical scale is one of the most important factors that affects the processes of turbulent flame propagation and DDT. For this reason, it is always important to have experimental data that explicitly show the effect of scale and can be used to verify corresponding models of these processes. For instance, a large scale methane explosion in obstructed channels of a coal mine was successfully numerically simulated in two scales using DNS [6-7]. The detonability limits for hydrogen-air mixtures from 18% to 59% (vol.) irrelevant to the scale have been included in the NASA standards [8] independent of the scale of the system. Using large scale experiments up to a 2.5 m cross-section the detonability limits were extended from 12.5% to 62% hydrogen [4-5].

A substantial data base relevant to hydrogen safety of nuclear power plants (NPP) has been accumulated on the behavior of turbulent flames and on DDT conditions in the RUT facility at a large scale. These data include a description of the turbulent flame propagation in the obstructed channel (2.5x2.3x34 m) with different configurations of obstacles, data on the evolution of turbulent flames propagating from the channel to the larger compartment (2.5x6x10.5 m), and data on limiting conditions for DDT in these compartments [9-11]. The data have been simulated with different CFD codes only for deflagrative combustion mode including turbulent flame acceleration until the sonic deflagration [12]. Some the numerical codes REACFLOW, TONUS 3D, and FLAME 3D demonstrated good agreement with experimental data.

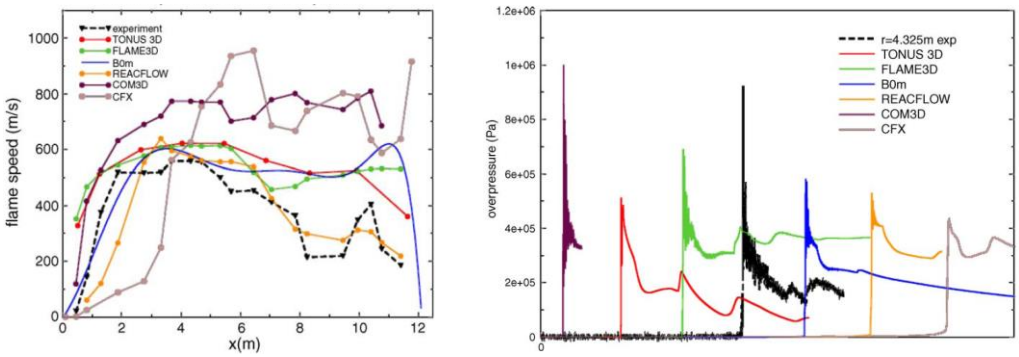

Figure 1. Comparison of different CFD-code simulations with RUT facility experiments: left – flame propagation velocity; right - pressure history.

The process of DDT is influenced by many physical factors. Among the most important ones is the effect of the scale. The difficulty for numerical simulations is that the typical geometrical size of a compartment can be ten orders of magnitude larger than the chemical scale to be used to numerically resolve the DDT process. In this situation, small scale laboratory studies on turbulent flame propagation and DDT must be supplemented by large-scale experiments. For numerical code validaton, the corresponding numerical and analytical models for flame acceleration, turbulent deflagration, and DDT should describe the effects of scale and should be validated against the large-scale experimental data. For the first time a 3D CFD code FOCUS-I with Adaptive mesh refinement (AMR) and detailed chemistry was successfully applied for numerical simulation of flame acceleration and DDT process in a large scale RUT facility [13].

The main goal of this work is to study the behavior of turbulent flames and DDT conditions at a scale of 50 times smaller than the original RUT facility. The small scale study using the MINIRUT apparatus gives an advantage to use a high-speed shadow photography to resolve the details of detonation onset which were not possible to resolve at the original scale experiments.

2. EXPERIMENTAL DETAILS

2.1. Large Scale Experiments

The scheme of the RUT facility is presented in Fig. 1. The facility consists of three parts. The first part is a long channel of 2.5x2.3 m cross-section and 34.6 m length. The second part is a large cavity called a "canyon" with a 6x2.5 m cross-section and 10.5 m length. The third part is a channel of 2.5x2.3m cross-section and 20 m length. The entrance of the facility, at the left end of the first channel, was closed by steel plates of 70-90 tons total mass. There were twelve concrete obstacles placed inside the facility along the first channel spaced by a 2.5 m distance. Seven fans were installed inside to mix the gas during mixture preparation. The mixture was ignited by an electric spark igniter placed at the beginning of the first channel (left end in Fig. 1). A series of tests with lean hydrogen-air mixtures under the normal initial temperature has been done. Hydrogen concentration was varied from 10 to 14 % vol. The blockage ratio was 0%, 30 % and 60%. A list of experiments is shown in Table 1.

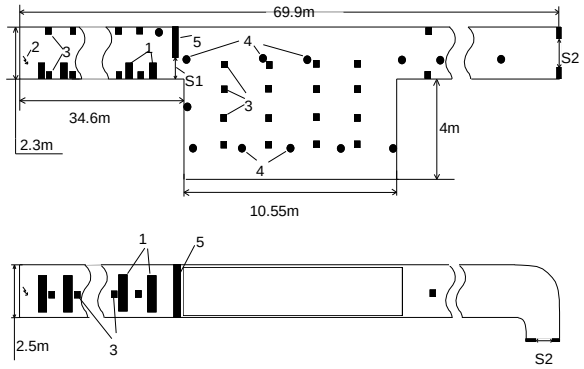

Figure 1. Scheme of the RUT facility. 1 - obstacles, 2 - ignition position; 3 - light flow transducers; 4 - pressure transducers; 5 - steel plate.

Table I. Initial conditions and main results

Test #	%H2	BR, %	S1, m^2	D_{CJ}, m/s	D_{exp}, m/s	P_{CJ}, bar	P_{exp}, bar	Regime
11	12.5	30	2	1405	830	9.1	9.6	DDT
13	11	30	2	1334	200-500	8.25	5.7	Deflagration
15	12.5	30	*2*	1405	1240-1690	9.1	12.6	DDT
16	12.5	30	5.6	1405	1360-1650	9.1	14.2	DDT

17	11	30	5.6	1334	250	8.25	3.5	Deflagration
18	9.8	0	1.4	1273	-	7.53	0.9	Deflagration
19	12.5	0	5.6	1405	30-40	9.1	1.06	Deflagration
20	14	0	5.6	1472	75-80	9.9	2.03	Deflagration
21	12.5	60	5.6	1405	350-600	9.1	8.4	Deflagration
22	14	60	5.6	1472	1000-1480	9.9	19.1	DDT
23	11.2	60	5.6	1344	560-620	8.37	3.8	Deflagration

2.2. Small Scale Experiments

Small-scale experiments have been carried out in the MINIRUT experimental apparatus. Its main dimensions are less than the RUT facility by a factor of 50. The apparatus consists of four sections (see Fig. 2). Sections #2 and #4 correspond to the channels of the RUT facility. Sections #2 and #3 are filled with a number of obstacles (blockage ratio - 0.3 (BR=30%), spacing is equal to transverse channel size). The length of each section (about 250 mm) was controlled by the light beam dimension of the shadow system windows. Section #1 corresponds to the canyon of the RUT facility and can also be equipped with a window. Canyon section dimensions are 211x125x50 mm. The windows have dimensions of 230x45 mm in the channel and 230x125 mm in the canyon. MINIRUT channel can be elongated by installing additional sections (0.2, 0.6 and 0.328 m) with or without obstacles.

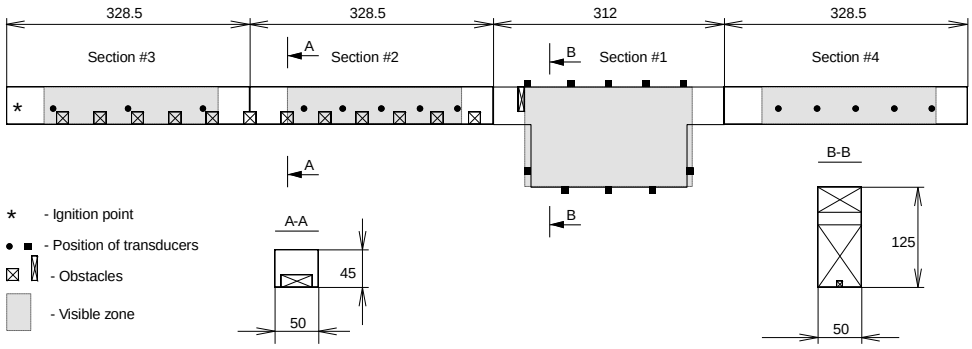

Figure 2. Schematic of MINIRUT apparatus.

Photodiodes and piezoelectric pressure transducers were used to record flame and shock front propagation. In small-scale experiments, photodiodes and pressure transducers can not provide detailed information on flame shape. Then, a schlieren technique was used to obtain detailed information on the development of turbulent flames and explosion processes. Experiments were made using a stroboscopic pulse generator with a frequency of about 5000 Hz and a high-speed drum camera SK-2.

Hydrogen-air mixtures with hydrogen concentration from 22 to 30% and stoichiometric hydrogen-oxygen mixtures diluted with nitrogen ($2H_2+O_2+\beta N_2$) were used in the tests. Mixtures were ignited using a high voltage spark plug located flush with the front cover of the channel. Tested mixtures are presented in Tables 2 and 3. The detonation cell sizes calculated using CELL_H2 code [14].

Table 2. N2-diluted stoichiometric H2-air mixtures

Mixture	β	%H2	%O2	%N2	λ, mm
1	3.76	29.59	14.79	55.62	12
2	3.6	30.30	15.15	54.55	11.4
3	3.5	30.77	15.38	53.85	11.1
4	3	33.33	16.67	50.	9.4
5	2	40.0	20	40.	6.2

Table 3. H2-air test mixtures

Mixture	β	%H2	%O2	%N2	λ, mm
1	3.76	29.59	14.79	55.62	12.0
6	3.76	28	15.13	56.87	14.1
7	3.76	27	15.34	57.66	15.1
8	3.76	26	15.55	58.45	16.5
9	3.76	25	15.76	59.24	18.3
10	3.76	24	15.97	60.03	20.8
11	3.76	23	16.18	60.82	24.7
12	3.76	22	16.39	61.61	30.9

3. EXPERIMENTAL RESULTS

3.1. Large Scale Experiments

From the observed combustion modes, four typical regimes can be distinguished. Slow subsonic turbulent deflagration was observed in tests 18-20 without obstacles (Table 1). Fast (sonic) deflagration was observed in tests 12,13,17,21,23. A regime with DDT in reflection was observed in tests 14-16. DDT in the first channel and further stable detonation propagation was observed in test 22. An example of an X-t (distance-time) diagram of the explosion regime with DDT due to reflection in a canyon based on photodiode signals and pressure sensors is shown in Fig. 4. Corresponding two-dimensional projection of flame shape, detonation and reflected wave evolution is shown in Fig. 3.

Results obtained in a series of large scale experiments have indicated that flame propagation, pressure build-up and transition to detonation depend on mixture composition, turbulence generation and geometrical scale. A significant peculiarity was that the compositions of 10-14 % H2 in air correspond to lean mixtures, which are not far from the flammability limit. Transition to detonation was observed at a minimum of 12.5% of hydrogen. Although unstable or deficit-velocity detonations may be expected in such mixtures and geometrical configurations, DDT events were clearly observed and reproduced. It was found that at critical conditions (12.5 % H2) the flame accelerates down the obstructed channel and reaches the quasi-stationary speed of about 600 m/s. This fast deflagration regime is analogous to the choking regime observed in laboratory experiments [14] when the velocity of combustion products with respect to the flame was about sonic. Shock and flame interactions with obstacles support this fast mode of combustion. However, they never resulted in the onset of detonation with 12.5 % H2, because the transverse dimensions of the obstructed channel were insufficient. Transition to detonation in the channel was observed at the distance x_D = 27-28 m for a more sensitive mixture with 14 % H2.

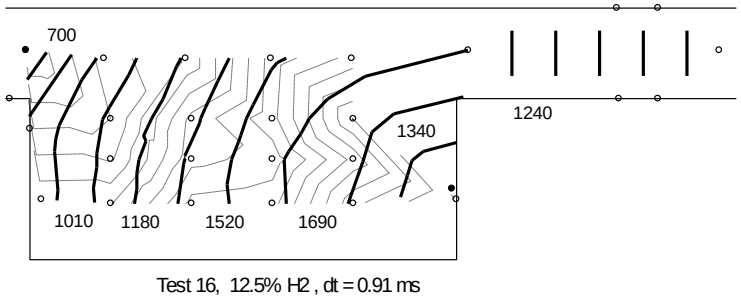

Figure 3. Flame shapes (dotted lines) and secondary explosion waves (solid lines) for DDT process in the canyon. Local velocities of explosion waves in m/s. (o) - locations of transducers, time step between iso-lines dt=0.91 ms.

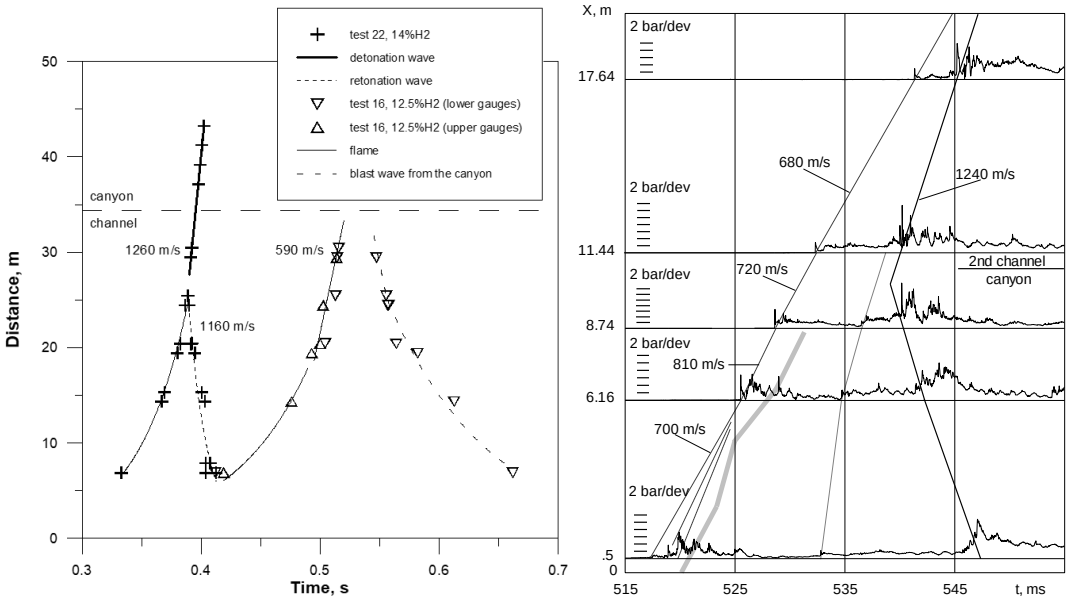

Figure 3. X-t diagrams of the DDT process in the channel and canyon based on photodiodes (left) and pressure sensors (right).

3.2. Small Scale Experiments

Flame accelerations in the channel with obstacles (BR=0.3) were investigated for H2-air mixtures containing 24-29.6% of H2 and for H2-O2 mixtures containing the N2 as diluent with b=2-3.76. The length of the channel was proportional to RUT's channel in a ratio of 1:50. A comparison of flame velocities versus hydrogen concentration is presented in Fig. 4 (left). Flame speed accelerates to the first obstacle to 25-40 m/s. Ratios of flame speed after the 1st, 3rd, 5th, and 7th obstacles to the first one were equal to 1 : (3-4.5) : (7.5-10) : (15-16). Flame speed achieved the sonic velocity to the end of the channel. So called "choking" regimes, typical for real RUT scale were established. However, the DDT processes were not observed in the channel for hydrogen-air mixtures. This means that the length of the channel L=0.7 m (1/50 of the RUT scale) is shorter than the run-up distance or mixture reactivity is too low for detonation onset. To obtain the detonation onset the channel length was increased in one section up tp L=1.03m.

To understand the effects of channel length on turbulent flame acceleration, burning velocities were measured for additional sections of different lengths L_a with obstacles or without ones. Measures were made for smooth sections of 0.2 and 0.6 m long and the section of L_a = 0.328 m with obstacles (BR=0.3). Experimental dependencies of flame velocity versus distance along the axis of set-up are presented in Fig. 4 (right). Additional sections allow to accelerate flame to the higher velocity at which DDT conditions in channel geometry are achieved. It should be noted, that smooth sections independent of the size lead to the same efficiency for a flame acceleration. The effect of obstacles on flame acceleration in the additional section is much greater. A series of experiments with additional sections of 0.2, 0.328 (BR=0.3) and 0.6 m long was made to determine critical conditions to DDT in the channel and canyon space. The mixtures considered in these experiments contained 22%-29.59% H_2 in air. The minimum hydrogen concentration in hydrogen-air mixtures at which DDT can be observed was equal to 27-28% for smooth additional sections of 0.2 or 0.6 m long. At the same time, the lower concentration limit of the DDT process in the channel and in the canyon with sections of 0.328 m long (BR=0.3) was defined experimentally as 24 and 25% hydrogen in air correspondingly.

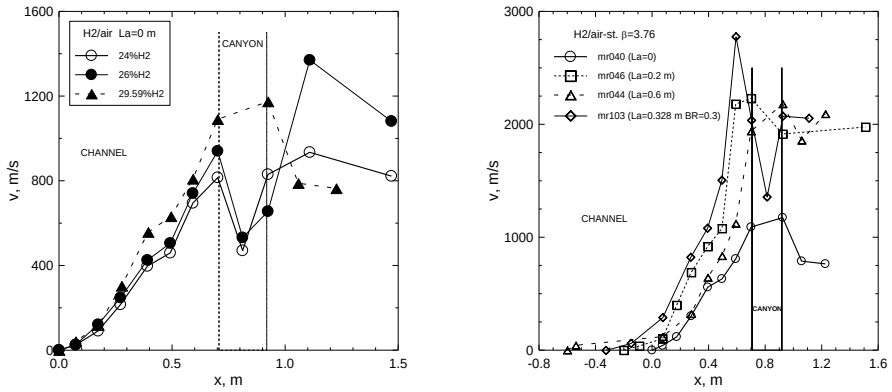

Figure 4. Evolution of flame speed along the axis:
Effect of mixture reactivity (left); effect of an additional section (right).

To demonstrate the effect of mixture reactivity on flame acceleration and detonation onset at the same scaling ratio (1:50), investigations of stoichiometric hydrogen-oxygen mixtures diluted by N_2 were undertaken with β=(2, 3, 3.5, 3.6 3.76). The evolution of the flame velocity for the nitrogen-diluted stoichiometric hydrogen-oxygen mixture is presented in Fig. 5 against a dilution coefficient β. Detonation transitions were observed for mixtures with $\beta \leq 3.5$ in a channel geometry. Other mixtures (β=3.6-3.76) have DDT in the canyon. Experimentally, it appeared that detonations were initiated in the canyon in 75% of cases for β=3.6 and in 25% of cases for β=3.76. Probably, the detonation occurred in the canyon by reflection more frequently for these mixtures, but the possibility of following detonation propagation depends on the flame speed at the channels exit and on the distance between the flame and shock front.

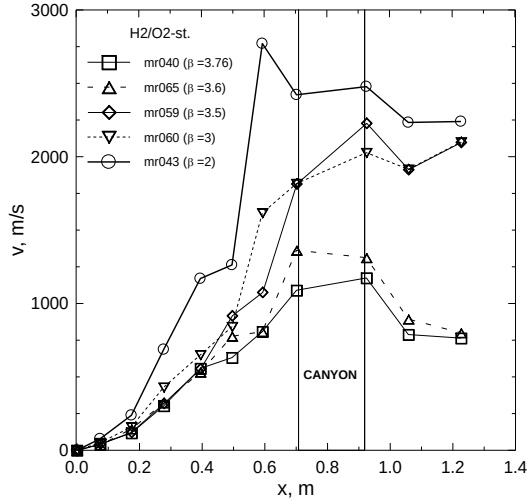

Figure 5. Effect of mixture reactivity on the evolution of flame speed along the axis.

The schlieren technique with high speed shooting and photodiode measurements was used for detailed investigation of turbulent flame propagation and interaction with obstacles and following DDT process. Fig. 6 presents shlieren photographs of the DDT process for a stoichiometric mixture with β_{N2}=3.76 (left, hydrogen in air) and β_{N2}=2 (center, more reactive). It should be noted a very specific shape of flame front for both those mixtures. Two regimes of turbulent flame propagation through obstacles were observed. In the first case (β_{N2}>3), the flame preferentially propagates at the top of the channel, avoiding the obstacles (Fig. 6, left). In the second case, typical to the "fast" mixtures (β_{N2}<=2) the flame propagates at the bottom through a gap between obstacles and a side wall (Fig. 6, center).

In both cases, an advancing shock wave follows ahead of the flame front at a distance of 15-20 cm. Then, a very intensive reflected shock wave is generated by the reflection of the leading shock wave from the obstacle interacting with flame and intensifying them. Due to such feedback, the complex shock-flame propagates for a long distance with a velocity close to the speed of sound in combustion products (about 1000 m/s). If the length of the channel is sufficient for flame acceleration then the detonation may occur in the channel, close to the exit to the canyon, at a distance of about 522 mm from the "zero" point. If the length is not enough, the complex shock-flame exits to the canyon and then it can detonate due to Mach reflection for the "fast" mixtures or due to reflected shock wave interaction at the far corner for hydrogen-air mixtures 24%-26%H2.

3-D numerical simulations of DDT in the channel in a real RUT scale [13] demonstrate very good agreement with small scale experiments (1:50). To be consistent for a larger scale, the mixture reactivity was reduced as for 14%H2-air mixture. Numerical simulations show a very high level of turbulence at the bottom of the channel, promoting preferential flame propagation at the bottom.

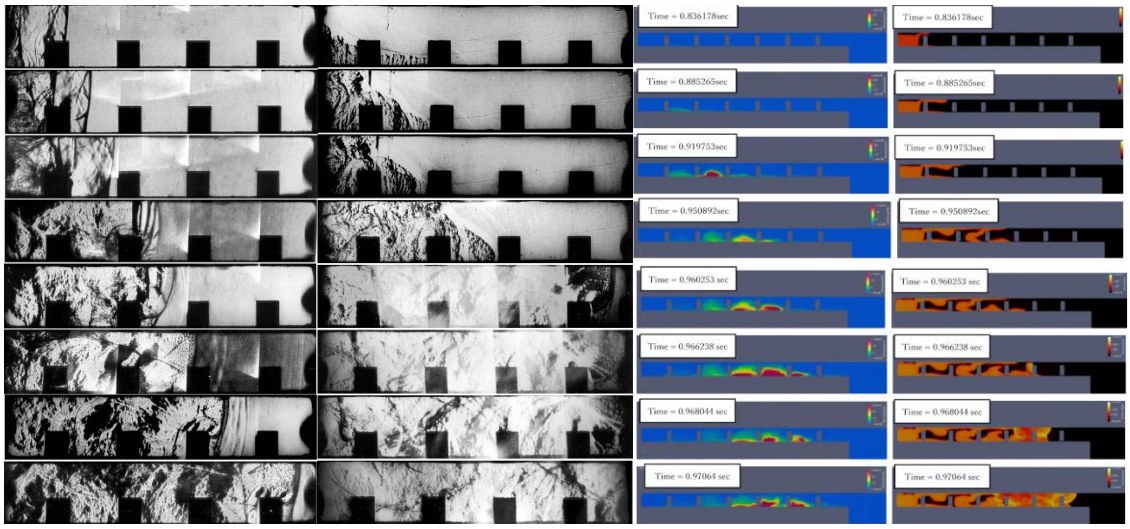

Figure 6. Shlieren images of flame propagation and DDT process in a channel: left, β_{N2}=3.76; center, β_{N2}=2, right, 14%H2-air mixture simulated [13].

A sequence of shadow photographs corresponding to the critical conditions for DDT in MINIRUT apparatus (24% H_2 in the air) is shown in Fig. 7 (left). As shown, the leading shock wave followed by the turbulent flame enters the canyon. The shock reflects at a later stage from the bottom of the canyon. No ignition is observed in this reflection. The first reflection of the lead shock from the end-wall also does not result in an immediate ignition. The only interaction of two reflected shock waves at the far bottom corner results in a strong local explosion. A strong detonation wave is formed in the unburned material between the flame and the leading shock. This wave propagates through the unburned part of the mixture. Then, the detonations propagated successfully into the second channel. The process shown in Fig. 7(left) is very similar to that observed under the critical conditions in the RUT facility (Fig. 3).

Another example of the DDT in the canyon is shown in Fig. 7 (right). This case corresponds to the stoichiometric hydrogen-air mixture. The exit of the first channel was partially blocked at the top part of the channel. A specific shape of the leading shock entering to the canyon is shown in the fist frame (Fig. 7, right). A Mach reflection of the lead shock from the ceiling results in a strong local explosion and in development of a detonation wave. The detonation wave propagates without decay through the unburned material. The processes of this type were not observed in the RUT tests, probably, due to the difference in the relative (to the scale) sensitivity of the mixtures.

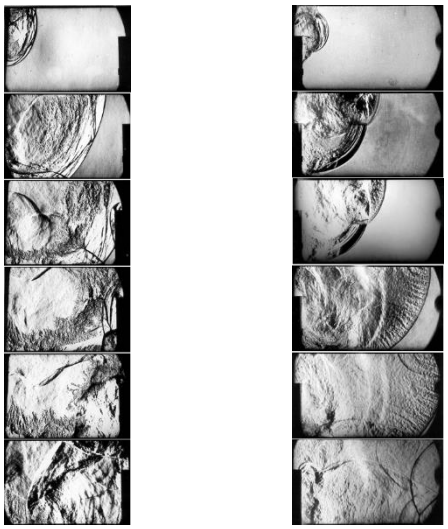

Figure 7. Schlieren images of the DDT process in a canyon: left, 24%H2-air, DDT at the far end reflection, right, stoichiometric hydrogen-air mixture, DDT due to Mach reflection.

4. DATA ANALYSIS

Application of experimental results to a wider range of initial conditions and geometrical sizes requires evaluation of theoretical models for DDT scaling because predictive computer tools describing all combustion regimes including DDT and detonations should still be developed and then validated to estimate the critical DDT conditions necessary for practical accident analyses. The critical conditions for DDT observed in current tests will be analyzed in terms of the detonation cell size λ as a measure of detonability. The possibility of detonation initiation in a given mixture of cell size λ is limited by a characteristic geometrical size. Experimental data for different fuel-air mixtures show a good agreement with the 7λ criterion over a wide range of compositions and scales [16, 17].

The scaling of DDT conditions in the RUT facility to a small-scale experimental apparatus gives an estimate for critical detonable mixture compositions using the 7λ criterion [16,17]. For instance, the critical mixture in which DDT in the RUT facility channel occurs has a cell width close to 1 m. This means that mixtures with λ close to 20 mm are expected to be critical for MINIRUT. Thus, mixtures close to stoichiometric hydrogen-air (β=3.76) can detonate. Similarly, the critical cell size for the case of DDT in the canyon could also be estimated using a CELL_H2 code [17]. Near-critical mixtures compositions estimated for small-scale experiments in $H_2/O_2/N_2$ mixtures are presented in Table 4.

Table 4. N2-diluted stoichiometric H2-air mixtures

Geometry	Characteristic size, L, mm	Critical cell size, λ, mm	Mixture composition, H2 vol. % (predicted)
Channel (section #2-#3):			
BR=0.3, spacing 1D	125	~18	24%H_2/air
BR=0.6, spacing 2D	75	~11	$(2H_2+O_2)+ \beta N_2$ (β=3.2)
Canyon (section #1):	165	~23	22%H_2/air

A comparison of experimental data on RUT and MINIRUT experiments with respect to the detonation size of critical mixtures to be detonated confirms the 7λ criterion very well (Table 4 and 5). It follows from exact geometrical scaling and detonation cell ratio $\lambda_{RUT}/\lambda_{MINIRUT}$. To keep the DDT scaling well it needs to increase

the length of the channel in 50% to successfully accelerate the flame to support the detonation onset (see Fig. 4, right). Keeping exact geometry scaling factor, without a channel elongation, it should be more reactive mixture (2H2+O2 diluted with N2, β_{N2}= 2-3.5) to provide a detonation onset in a channel (Fig. 5). Then, the ratio $\lambda_{RUT}/\lambda_{MINIRUT}$ = 80-90 or L/λ = 10-12.5 (much larger than L/λ = 7). It caused by a different scaling factors of detonation and deflagration processes.

Table 5. Critical cell widths for DDT

Geometry	RUT	MINIRUT (scale 1:50)	$\lambda_{RUT}/\lambda_{MINIRUT}$
	λ, mm		
Channel	900	18	50
Canyon	1200	21	57

Two main conditions of DDT have been formulated in [18,19]: (1) turbulent flame should accelerate to 500-1000 m/s (or to 1.5M) to create the conditions for DDT; (2) accelerating flame should be able to generate a shock wave with Mach number 2.25 or higher. Such conditions will be sufficient to ignite the mixture in reflections and generate a local explosion leading to detonation [19]. To satisfy such conditions, the run-up distance of the accelerating flame must be long enough. The length of this path depends on the level of turbulence produced by the flow ahead of the flame. Higher roughness or congestion of the channel leads to decreased run-up distance to detonation onset x_D. In a smooth channel the run-up distance x_D = 500λ [20]. The wall roughness and congestion of the channel may significantly reduce the run-up distance to detonation. A very rough estimation according to [21] gives the run-up distance x_D = 200λ for an obstructed channel with BR = 0.1; x_D = 160λ for BR = 0.3; x_D = 130λ for BR = 0.6. A comparison of real experimental data for RUT and MINIRUT facilities with rough estimation gives a 3-4 times shorter real run-up distance because the detonation cell size is not an appropriate scaling parameter for turbulent flame acceleration. The same problem was met during the numerical simulation of the pre-detonation part of the obstructed channel [13]. It was found that the flame acceleration in such geometry can be divided into two parts: quasi-laminar flame self-acceleration before obstructions due to hydrodynamic flame instability (Darrieus-Landau, Rayleigh-Taylor) leading to flame wrinkling and flame surface increase; turbulent flame acceleration in an obstructed part. Playing with a wrinkling factor, the authors of [13] adjust the calculated run-up distance to the experimental value of x_D = 27-28 m (Fig. 8). With a very small wrinkling factor the channel length can be to short to accelerate the flame to the speed of sound and promote the DDT in a channel.

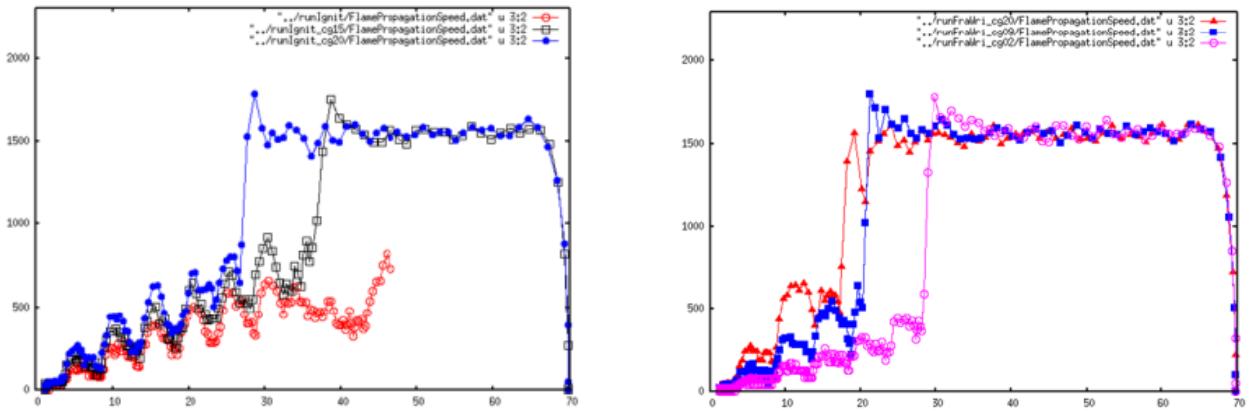

Figure 8. Numerical simulation of the DDT process in a channel with 14%H2-air.

As one can see, the scaling of the turbulent flame propagation cannot be made with the detonation cell size λ. For a laminar flame (small Reynolds number), other mixture properties, such as laminar burning velocity S_L, expansion ratio σ, etc., should be taken into account [22]. If the burning velocity and sound speeds in combustion products c_{sr} and reactants c_{sp} are chosen to give a range of the characteristic velocity scales, the corresponding range of the Reynolds number Re may be defined. Variations of these velocity scales for typical fuel-air and fuel-oxygen mixtures cannot compensate the difference in characteristic length scales (50 times) in order to provide similar range of the Reynolds number for turbulent flame propagation. Such an attempt was made using numerical simulations [13] by a wrinkling factor as a measure of hydrodynamic flame instability. However, a direct comparison of the behavior of turbulent flames in similar geometries and at different scales is important for the verification of turbulent combustion models.

5. SUMMARY AND CONCLUSIONS

Results of an experimental study on flame acceleration deflagration to detonation transition in RUT geometry (at a 1:50 scale) are presented. Flame acceleration in a channel with a number of obstacles (BR=0.3) and critical conditions for DDT both in the channel and in the canyon have been investigated.

The shadow photographs permitted to resolve in some details the processes of turbulent flame propagation and DDT in a complex geometry. Their comparison with the data from the RUT tests showed that not only the critical conditions but also the detailed picture of the processes of the onset of detonations are similar if geometry is scaled with λ. The scaling down in two orders of magnitude compared to the original RUT dimensions confirmed the validity of 7λ criterion for detonation onset in a channel and multi-room geometry. The cell sizes λ of these critical compositions were found to be exactly 50 times smaller than those for large-scale tests in the RUT facility.

The conventional detonability limit for hydrogen-air mixtures should be extended to 14%H2 for a channel and 12.5 for a canyon geometry compared to 18%H2 for NASA hydrogen safety guidelines. For the first time, a 3D CFD code FOCUS-I with Adaptive mesh refinement (AMR) and detailed chemistry was successfully applied for numerical simulation of flame acceleration and DDT process in a large scale RUT facility

The flame acceleration in the small scale tests was found to be less efficient compared to that in the RUT tests. With mixtures which were close to estimated critical compositions for DDT (λ about 20 mm), the flame acceleration did not result in the choked flames in the MINIRUT apparatus. In order to make a more accurate scaling of the critical conditions for the onset of detonation, special efforts were made to achieve the maximum possible speeds of turbulent flame propagation before DDT. As shown in numerical simulations, not only the turbulence plays a role in flame acceleration to the speed of sound but also hydrodynamic flame instability at the initial stage of combustion process.

REFERENCES

1. J. Yanez, M. Kuznetsov, A. Souto-Iglesias, “An analysis of the hydrogen explosion in the Fukushima-Daiichi accident”, *Int. J. Hydr. Energy*, **40** (25), pp. 8261-8280 (2015).
2. M. Kuznetsov, J. Yanez, J. Grune, A. Friedrich, T. Jorda,” Hydrogen Combustion in a Flat Semi-Confined Layer with Respect to the Fukushima Daiichi Accident”, *Nuclear Engineering and Design*, **286**, pp. 36-48 (2015).
3. J. Xiao, W. Breitung, M. Kuznetsov, H. Zhang, J. R. Travis, R. Redlinger, T. Jordan, “GASFLOW-MPI: A new 3-D parallel all-speed CFD code for turbulent dispersion and combustion simulations Part II: First analysis of the hydrogen explosion in Fukushima Daiichi Unit 1”, *International Journal of Hydrogen Energy*, **42** (12), pp. 8369-8381 (2017).

4. S.B. Dorofeev, Kuznetsov M.S., Alekseev V.I., Efimenko A.A., Breitung W. "Evaluation of limits for effective flame acceleration in hydrogen mixtures". *Journal of Loss Prevention in the Process Industries*, **14** (6), pp. 583-589 (2001).
5. M. Kuznetsov, Alekseev V., Matsukov I., Dorofeev S. "DDT in a Smooth Tube Filled with Hydrogen-Oxygen Mixtures". *Shock Waves*, **14** (3), pp 205 - 215 (2005).
6. V.N. Gamezo, C.L. Bachman, E.S. Oran, "Flame acceleration and DDT in large-scale obstructed channels filled with methane-air mixtures", *Proceedings of the Combustion Institute*, **38** (3), pp. 3521-3528 (2021).
7. D.A. Kessler, V.N. Gamezo, E.S. Oran, "Simulations of flame acceleration and deflagration-to-detonation transitions in methane-air systems", *Combustion and Flame*, **157** (11), pp. 2063-2077 (2010).
8. Safety standard for hydrogen and hydrogen systems, *National Aeronautics and Space Administration (NASA)*, NSS 1740.16, Office of Safety and Mission Assurance, Washington, DC 20546 (1997).
9. S.B. Dorofeev, V.P. Sidorov, A.E. Dvoinishnikov, W. Breitung, "Deflagration to detonation transition in large confined volume of lean hydrogen-air mixtures", *Combustion and Flame*, **104** (1–2), pp. 95-110 (1996).
10. S.B. Dorofeev, V. Sidorov, A. Dvoinishnikov, A. Denkevits, A. Efimenko, A. Lelyakin. "Large scale hydrogen-air-steam DDT experiments in the RUT facility. Test series 1995". RRC "Kurchatov Institute", Report RRC KI 80-05/60. July 1996.
11. S.B. Dorofeev, V. Sidorov, A. Dvoinishnikov, A. Denkevits, A. Efimenko, A. Lelyakin. "Large scale hydrogen-air-steam DDT experiments in the RUT facility. Test series 1996". RRC "Kurchatov Institute", Report RRC KI 80-05/16. March 1997.
12. W. Breitung, S. Dorofeev, A. Kotchourko, R. Redlinger, W. Scholtyssek, A. Bentaib, J.-P. L'Heriteau, P. Pailhories, J. Eyink, M. Movahed, K.-G. Petzold, M. Heitsch, V. Alekseev, A. Denkevits, M. Kuznetsov, A. Efimenko, M.V. Okun, T. Huld, D. Baraldi, "Integral large scale experiments on hydrogen combustion for severe accident code validation-HYCOM", *Nuclear Engineering and Design*, **235** (2–4), pp. 253-270 (2005).
13. K. Hayashi, I. Nakamori, T. Tomizuka, A. Takahashi, F. Onishi, M. Kuznetsov, T. Kodama, Y. Tamauchi, N. Sato, N. Tsuboi, "Numerical simulation of DDT with a flame front model in a real large scale channel". Submitted to *the 40th Combustion Symposium*, Milan, Italy (2024).
14. A.I. Gavrikov, A.A Efimenko, S.B Dorofeev, "A model for detonation cell size prediction from chemical kinetics", *Combustion and Flame*, **120** (1–2), pp. 19-33 (2000).
15. P. Peraldi, R. Knystautas, & J. H. S. Lee, "Criteria for transition to detonation in tubes". *Symposium (International) on Combustion,* **21**, pp. 1629-1637 (1988).
16. S.B. Dorofeev, Sidorov V. P., Dvoinishnikov A. E., Breitung W., "Deflagration to detonation transition in large confined volume of lean hydrogen-air mixtures", *Combustion and Flame*, **104**, pp. 95 - 110 (1996).
17. S. Dorofeev, Sidorov, V., Kuznetsov, M. *et al.* "Effect of scale on the onset of detonations". *Shock Waves* **10**, pp. 137 - 149 (2000).
18. I.O. Moen, M. Donato, R. Knystautas, and J.H. Lee. "Flame Acceleration Due to Turbulence Produced by Obstacles". *Combustion and Flame*, **39**, pp. 21-32 (1980).
19. C.K. Chan, Collision of a shock wave with obstacles in a combustion mixture. 25th International Symposium on Combustion. July 31-August 5, 1994, The University of California, Irvine. Abstracts of Symposium Papers. The Combustion Institute, Pittsburgh, pp. 50-51 (1994).
20. M. Kuznetsov, Alekseev V, Matsukov I, Dorofeev S. "DDT in a smooth tube filled with a hydrogen-oxygen mixture". *Shock Waves*;**14**, pp. 205-215 (2005).
21. M. Kuznetsov, A. Denkevits, A. Veser, A. Friedrich, "Flame propagation regimes and critical conditions for flame acceleration and detonation transition for hydrogen-air mixtures at cryogenic temperatures", *International Journal of Hydrogen Energy*, **47** (71), pp. 30743-30756 (2022).
22. M.S. Kuznetsov, I.D. Matsukov, V.I. Alekseev, S.B. Dorofeev. "Photographic study of unstable turbulent flames in obstructed channels". Proc. of the 17th ICDERS (Heidelberg, Germany, July 25-30, 1999), ISBN 3-932217-01-2, pp. 143.1-143.4 (1999).

The 11th European Review Meeting on Severe Accidents Research

May 13-16, 2024, Royal Institute of Technology, Stockholm, Sweden

TECHNICAL SESSION 9.1: SEVERE ACCIDENT SCENARIOS - ACCIDENT TOLERANT FUELS

Chairs: S. Gupta (Becker Tech. GmbH), M. E. Cazado (KIT)

ID74	**Overview of KIT activities on ATF cladding materials** M. Steinbrück (KIT)	**Paper** **Presentation**
ID118	**Application of AC²/ATHLET-CD and ASTEC for ATF Experiments in the Frame of OECD QUENCH-ATF and IAEA CRP ATF-TS** T. Hollands (GRS)	**Paper** **Presentation**
ID51	**The CODEX-ATF experiment** R. Farkas (EK-CER)	**Paper** **Presentation**

OVERVIEW OF KIT ACTIVITIES ON ATF CLADDING MATERIALS

M. Steinbrueck*, J. Stuckert, M. Grosse
Karlsruhe Institute of Technology, Institute for Applied Materials (IAM-AWP)
Hermann-von-Helmholtz-Platz 1, 76344 Eggenstein-Leopoldshafen, Germany
* martin.steinbrueck@kit.edu

ABSTRACT

Research on accident-tolerant fuel (ATF) cladding materials is being conducted worldwide to reduce the risk of hydrogen explosions and to extend the response time to severe nuclear accidents. This paper reviews experimental activities at KIT on the behavior of promising ATF cladding materials at high and very high temperatures. These are largely embedded in bilateral cooperations as well as international research projects under the umbrella of the European Commission (IL TROVATORE, SCORPION), IAEA (ATF-TS) and OECD-NEA (QUENCH-ATF).
First large-scale experiments with FeCrAl (QUENCH-19) and Cr-coated Opt. ZIRLO (QUENCH-ATF1) were performed at the QUENCH facility. The main results of these experiments are discussed to the extent permitted by the publication guidelines of the corresponding projects. The results of these experiments have been used for international benchmark tests, which are presented in a separate paper.
The bundle tests are accompanied by an extensive separate-effects test program that provides data on the oxidation kinetics and degradation mechanisms of ATF cladding materials up to very high temperatures. From these experiments, it is found that the maximum temperatures for protective cladding are 1300°C, 1400°C, and 1700°C for Cr-coated Zry, FeCrAl alloys, and SiC-based composites, respectively. Illustrative examples for the three ATF coating systems are shown.

KEYWORDS
ATF cladding, degradation, HT oxidation, bundle tests, separate-effects tests

1. INTRODUCTION

Nuclear fuel cladding envelops the fuel and is a major barrier against the release of fission products. Traditional fuel cladding materials, such as zirconium-based alloys, have served the nuclear industry well due to their excellent high-temperature properties and resistance to corrosion. However, under the extreme conditions of severe accidents, these materials can experience rapid oxidation connected with strong heat release and hydrogen generation, leading to potentially hazardous scenarios. Accident tolerant fuel cladding materials seek to address these concerns by providing enhanced performance and durability during normal operation and severe accident scenarios, thereby increasing the safety margins of nuclear power plants.

Following the Fukushima Daiichi accident in 2011, there has been a global surge in research and development efforts focused on accident tolerant fuel (ATF) cladding materials [1]. Governments, nuclear regulatory bodies, and industry stakeholders recognized the need to enhance the safety of nuclear reactors and mitigate potential severe accident scenarios. Numerous countries have launched dedicated research programs to explore and develop advanced ATF cladding solutions. The primary goal was to develop materials that exhibit superior corrosion resistance, could withstand higher temperatures, and reduce the risk of hydrogen generation compared to traditional zirconium-based alloys.

The main materials systems that emerged as promising candidates for accident tolerant cladding include chromium-coated zirconium alloys, iron-chromium-aluminum (FeCrAl) alloys, and silicon carbide (SiC) composites [2]. This paper will summarize the experimental activities at Karlsruhe Institute of Technology (KIT) on the high-temperature behavior of these most promising ATF cladding materials. The accident tolerance of all three materials relies on the formation of protective oxide scales during high-temperature oxidation in water steam atmosphere, namely chromia (Cr_2O_3) on chromium coating, alumina (Al_2O_3) on FeCrAl alloys, and silica (SiO_2) on silicon carbide. These three oxides are known by materials scientists as the only protective ones under the extreme conditions of severe nuclear accidents.

Most ATF related activities at KIT are embedded in international projects in the framework of the OECD-NEA, IAEA and the EURATOME program, which are first briefly introduced.

2. OECD-NEA JOINT UNDERTAKING QUENCH-ATF (CR-COATED ZR ALLOY CLADDING)

KIT is the Operating Agent of the OECD-NEA Joint Undertaking QUENCH ATF with 17 participating institutions from 9 countries that started in October 2021 and will run for four years. The main part of the project are three bundle experiments with ATF cladding in the QUENCH facility at KIT. This facility is a large-scale bundle facility with 24 electrically heated, >2 m long fuel rod simulators [3]. The bundle experiments are accompanied by supporting separate-effects tests and an extensive post-test examination campaign, as well as by benchmark exercises after each bundle experiment.

The first bundle test of this series the QUENCH-ATF1 was conducted in July 2022 with cold-spray (CS) Cr-coated Opt. ZIRLO cladding provided by Westinghouse Electric Company (WEC). The scenario was a slightly extended LB-LOCA similar to the QUENCH-LOCA-3HT experiment, with a heating phase (5 K/s) until maximum peak cladding temperatures of 1300°C, a 200 s lasting cool-down in steam and a final reflood phase by water. Beginning of 2024, all non-destructive post-test examinations were completed including determination of cladding strain, burst opening parameters and neutron radiography/tomography analysis of the hydrogen content and distribution. Destructive post-test examination, including mechanical testing and metallographic analyses, is carried out at KIT and IRSN in France, where four of the 24 cladding tubes were delivered.

The benchmark exercises on the first bundle test were coordinated by GRS, Germany, and contained a blind and an open phase simulation with almost all severe accident codes used in western countries. Overall, the simulations showed a qualitatively good accordance with the experimental results and a significant improvement in the open phase. However, code development for ATF fuel needs improvement and is going on worldwide.

The second bundle test, planed for the first half of 2024 will simulate a severe accident scenario with maximum temperatures of around 1600°C, i.e., significantly above the eutectic temperature in the Zr-Cr system (1332°C) and hence beyond the protective effect of the Cr coating. The QUENCH-15 bundle test with uncoated ZIRLO cladding is intended as reference test [4]. The cladding tubes with slightly modified CS Cr-coated Opt. ZIRLO are again provided by WEC. The third bundle experiment will be conducted with PVD Cr-coated cladding provided by the National Nuclear Laboratory (NNL, UK). The scenario will be decided after evaluation of the results of the first two tests.

3. IAEA CRP ATF-TS

The objectives of this Coordinated Research Project (CRP) with participants from 22 countries are 1) Conduction of experiments including single rod and bundle tests on the behavior of ATF materials under normal, Design Basis Accident (DBA) and Design Extension (DE) conditions, 2) Benchmarking of fuel

codes against new test data either obtained during this CRP or from existing data relevant to advanced fuel and cladding concepts, and 3) Development of LOCA evaluation methodology for ATF performance with a view for NPP applications.

KIT conducted high-temperature experiments on the oxidation of various Cr-coated cladding types. Chromium coatings with thicknesses of 7-8 µm were deposited on the substrate using PVD magnetron sputtering (on M5 and opt. ZIRLO substrates) and cathodic arc deposition (on E110 substrate). Cladding samples without pellets and sealed at both ends with welded Zr plugs were tested in induction heating (rapid heating, not adiabatic conditions) and tube furnaces (slow heating, adiabatic conditions). Three temperature conditions were studied: 1) design basis (DBA), 2) extended design conditions (DEC), both with rapid heating (5-8 K/s) to a maximum of 1250 °C or 1400 °C in steam, and 3) severe accident conditions (BDBA) with slow heating (0.25 K/s) up to target temperatures of 1350-1500°C in oxygen. The oxidation of samples with chromium coating tested under DBA conditions resulted in 15 times less hydrogen release compared to the reference samples without coating, **Figure 1**. During these DBA tests, a thin protective layer of Cr_2O_3 with a thickness of 1.5 to 2 µm formed on the surface of all coated samples. However, in experiments under DEC conditions, the chromium and chromium oxide layers lost the protective effect, and the maximum hydrogen release rate was comparable to the maximum hydrogen release rate of uncoated samples during DBA tests. For samples that were tested under severe accident conditions in an adiabatic tube furnace in oxygen atmosphere, after reaching the Zr-Cr eutectic temperature (approx. 1330 °C), a catastrophic temperature increase to 1600-1750°C occurred within a few seconds, followed by the destruction of the sample, **Figure 2**.

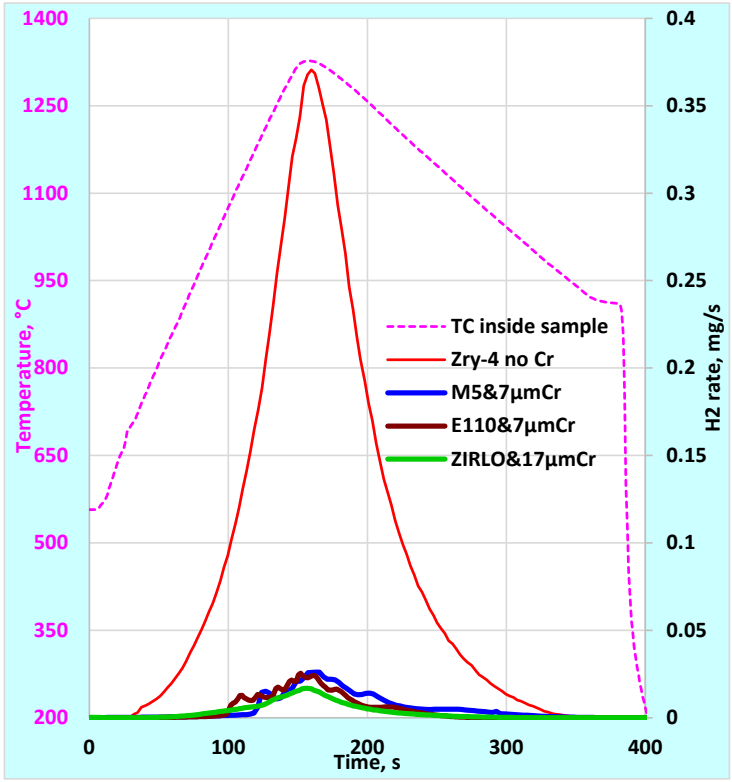

Figure 1. Hydrogen release under DBA conditions.



Figure 2. Catastrophic oxidation in oxygen under BDBA conditions.

Furthermore, KIT organized benchmarks on the pre- and post-test modelling of following bundle tests:

1) QUENCH-19 bundle test performed 2018 at KIT with FeCrAl claddings (see section 5),

2) DEGREE-B3 9-rods-bundle test performed in spring 2023 at CRIEPI/Japan with 280 mm long Zry-4 claddings provided by KIT and PVD-coated by CTU/Prague with 20 µm thick Cr layer,
3) CODEX-ATF 7-rod-bundle test performed in August 2023 at EK/Budapest with opt. ZIRLO claddings coated at CTU/Prague with 18 µm Cr layer.

To model the hydrogen release during the QUENCH-19 test, oxidation correlations were derived from single-effect tests performed at MIT [5] and KIT [6] with different adjustments for temperatures above the melting point of FeO. The cladding temperatures of the central rods of the bundle were noticeably overestimated by all codes, whereas there was wide scatter in the prediction of hydrogen release. DEGREE and CODEX-ATF benchmarks are underway and should be completed by the end of 2024.

4. EURATOM PROJECTS IL TROVATORE AND SCORPION

In the EU HORIZON 2020 project IL TROVATORE, 20 groups from the EU and 7 from the UK as well as associated groups from the USA and Japan are collaborating on the development of ATF cladding materials including modelling, processing, joining and testing [7]. The following material classes are included in the investigations:

- Oxidic claddings
- SiC ceramic matrix composites
- Chromium-coated Zircaloys with and without diffusion barrier
- MAX phases and
- FeCrAl alloy

The material tests comprise mechanical testing, corrosion tests under reactor operation conditions (temperature, pressure, water chemistry), oxidation tests at high and very high temperature simulating design basis and beyond design basis accident conditions as well as ion, proton and neutron irradiation. Most of the work has been completed. The irradiation tests and the post-irradiation examinations are still ongoing.

A highlight of the project is the development of a chromium coating at Zircaloy with a diffusion barrier withstanding even temperatures above 1500°C. Because this development shall be covered by patents, no further details can be given here. Further experiments were conducted with SiC and MAX-phase samples. **Figure 3** compares the transient high-temperature oxidation behavior in term of hydrogen release of several MAX phases and SiC_f/SiC up to 1600°C. The SiC sample show a very low hydrogen release and hence a very low reaction rate. The MAX phases behave differently. The lowest oxidation rate was observed for the (Ti0.85Nb0.15)2AlC alloy, the strongest oxidation was measured for Ti_2AlC without niobium. However, all oxidation rates are low compared to the ones for zirconium alloy.

The EU HORIZON project SCORPION is a kind of follow-up project to IL TROVATORE (in addition to the US/EURATOM project PERSEUS) concentrating on the improvement of SiC_f/SiC CMC for application as fuel cladding material by grain boundary engineering, porosity optimization and coating. The project started September 2022 with a duration of 4 years. 14 institutions from seven European countries, one from the USA and one from Japan are taking part in this joint project. Yttrium and ytterbium silicates are considered as promising coating materials for SiC. First oxidation tests at 1200 and 1600°C in steam show that bulk materials of these silicates resist these conditions and hence are promising coating candidates.

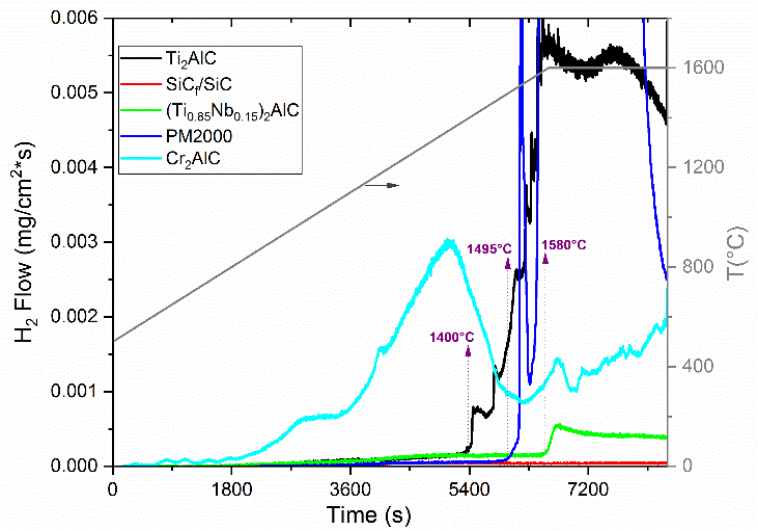

Figure 3. Comparison of the transient steam oxidation behavior of SiC, FeCrAl (PM2000) and the MAX phases Ti_2AlC, $(Ti_{0.85}Nb_{0.15})_2AlC$ and Cr_2AlC.

5. QUENCH-19 BUNDLE TEST WITH FeCrAl CLADDING

The first large-scale bundle test with ATF cladding material, namely with the FeCrAl alloy B136Y3 (Century Tubes Inc. /ORNL), was conducted in the QUENCH facility in cooperation with ORNL, USA, in August 2018 [8] [9]. QUENCH-19 was also run with a similar scenario as test QUENCH-15 with uncoated ZIRLO cladding with respect to bundle geometry and power input. The FeCrAl experiment was run 2000 s longer at the highest power input, until first local melting of the FeCrAl cladding was expected. Hence, the FeCrAl bundle was quenched 2000 s later than the ZIRLO bundle.

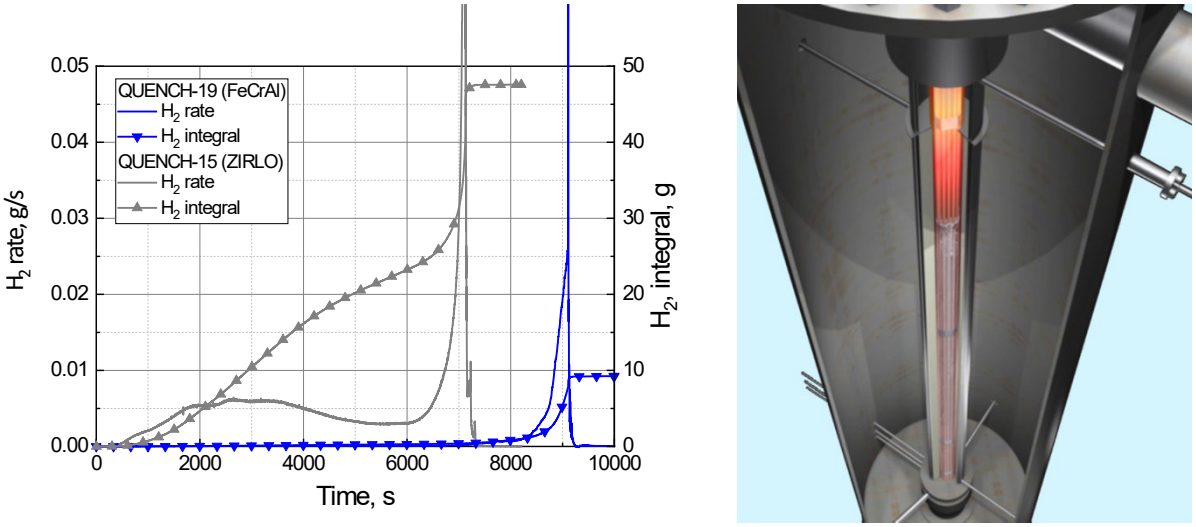

Figure 4. Left: Hydrogen release during experiment QUENCH-19 (FeCrAl) and reference test QUENCH-15 (ZIRLO); right: Scheme of the QUENCH facility during the reflood phase.

As expected, the hydrogen release was much less in the FeCrAl experiment: Until the time when the QUENCH-15 test was terminated by reflood, 100x less hydrogen was produced in the QUENCH-19 experiment compared to QUENCH-15 (0.4 g and 40 g, respectively), see **Figure 4**. Even at the end of the QUENCH-19 test after 2000 s longer heating time at the highest power level, only 9 g hydrogen were

measured compared to about 47 g in the shorter test with ZIRLO. Some melt formation was seen in the bundle after the test, which mainly came from stainless steel (SS 304) thermocouple sheaths. Rupture of some cladding tubes was observed most probably caused by strong shrinking during the quench phase due to the two times higher thermal expansion coefficient of FeCrAl compared to Zr alloys. Only low oxidation of the FeCrAl surfaces unaffected by SS melt attack was seen along the whole bundle.

Post-test calculations in the framework of the IAEA project ACTOF resulted in much too low values of the hydrogen release during the test [10]. A possible reason for this is that the codes used only one correlation for the oxidation of FeCrAl alloy resulting in a significant underestimation of the hydrogen release at temperatures below 1000 °C and above 1350°C, see section 6.2.

6. ILLUSTRATIVE SEPARATE-EFFECTS TEST RESULTS

Numerous experimental papers on the high-temperature oxidation and degradation behavior of ATF cladding materials have been published during the recent years. This section provides a summary of the main results of these studies together with selected results obtained at KIT for illustration.

6.1. Cr-coated zirconium alloy cladding

Cr-coated zirconium alloys are the near-term solution for ATF cladding materials, which should be associated with only moderate changes in technology and licensing procedures. They are developed worldwide according to different coating methods with typical Cr coating thicknesses of 5-30 µm. In general, well-produced Cr coatings provide very good performance under harsh operating conditions and result in a 1-2 orders of magnitude reduction in high-temperature oxidation kinetics compared to zirconium alloys. The first lead test assemblies (LTAs) are already being used in commercial reactors in the US and Europe. Recent reviews have been published, for example, by Bischoff [11], Brachet [12] [13], Maier [14], Yeom [15], Yang [16], and Li [17].

The oxidation behavior at high temperatures relevant for design-basis LOCA transients is strongly improved by the formation of a protective chromia (Cr_2O_3) layer at the surface and consequently, also the hydrogen uptake is reduced. The lack of oxygen (and hydrogen) diffusion in the substrate has a significant impact on the ductility since the α-Zr(O) phase formed by the solid solution of O in Zr in non-coated cladding is very brittle. As long as the Cr coating is protective, a four-layer structure is found in agreement by all research groups, consisting of bulk-Zry, $ZrCr_2$ interlayer, remaining Cr coating, and formed Cr_2O_3 layer. With increasing oxidation time and temperature, chromium diffuses into the Zry bulk forming $ZrCr_2$ precipitates during cooling. Investigations of the Cr coating degradation mechanisms resulting in transition to non-protective coating were made by various research groups [13] [18]. Depending on temperature and Cr coating thickness and morphology, they show the transition from protective to non-protective behavior at 1200°C after 30 min to 3 hours and at 1300°C after a few to tenths of minutes. In addition to Cr oxide formation and Cr diffusion into the Zry bulk, the main mechanism for this transition is the diffusion of zirconium along Cr grain boundaries towards the Cr/Cr_2O_3 interface and its oxidation by redox reaction with the Cr oxide. Finally, a through-going network of zirconia in the Cr layer is formed, which allows oxygen transport to the bulk Zry leading to the formation of oxygen-stabilized α-Zr(O) and, after its saturation, of ZrO_2. The ultimate limit for the protective effect of the Cr coating on Zircaloy is at around 1330°C, at which, according to the Zr-Cr phase diagram, the eutectic reaction between Cr and Zr results in the formation of a liquid phase.

In recent research at KIT, systematic transient oxidation experiments up to 1380°C (i.e., 50 K above eutectic temperature) in oxygen (as substitute for steam) have been conducted [19]. All samples showed increased oxidation rates after failure of the coating, being higher than the oxidation rates of the non-coated reference samples. Variation of the heating rate from 2 K/min to 50 K/min resulted in increasing reaction rate

overshooting with increasing ramp rate, **Figure 5**. During faster heatup, more metallic Cr is available for the eutectic reaction above 1330°C. Only at the slowest heating rate (2 K/min), the Cr coating failed before the eutectic temperature due to more time available for the oxidation and solid-state diffusion processes. It is estimated from the results of this study that the heat released temporarily by steam oxidation at high ramp rates may exceed the residual decay heat after reactor shutdown and hence significantly affect potential accident scenarios.

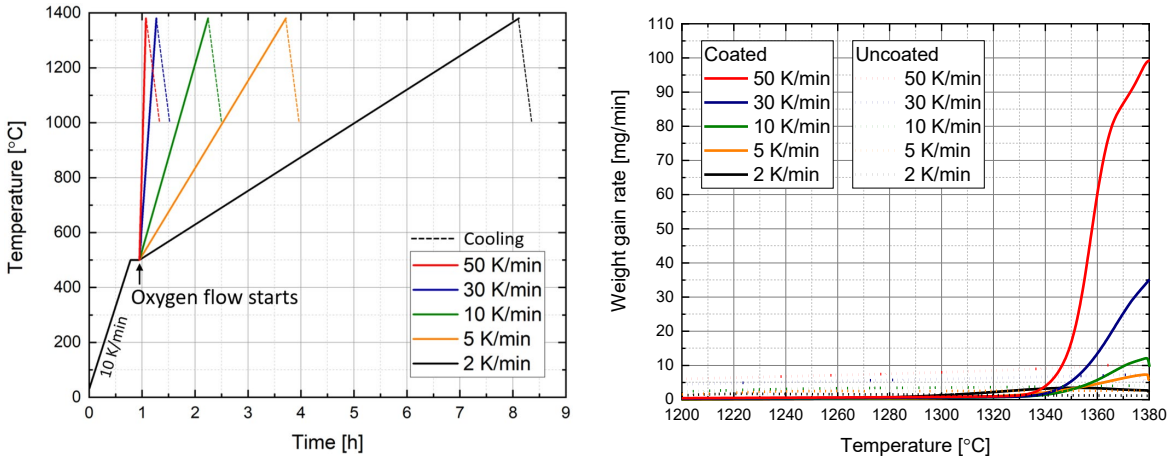

Figure 5. Left: Conduct of the transient test series. Right: Weight gain rates during high-temperature oxidation of Cr-coated samples in oxygen with varying heating rates. The dashed lines show the results of reference tests with non-coated Zircaloy-4 *[19]*.

6.2. FeCrAl cladding

FeCrAl alloys are ferritic body-centered cubic (bcc) iron-based alloys with 12-24 wt.% Cr and 3-6 wt.% Al contents. Nuclear grade FeCrAl alloys have comparably low Cr contents (12-13 wt.%) to avoid irradiation hardening. Beside the potential application to ATF cladding [20] [21] [22], FeCrAl alloys are primarily used for high-temperature applications such as for heating elements in industrial furnaces and for gas burners. The superior oxidation resistance of FeCrAl alloys at high temperature relies on the formation of a slowly growing and highly protective α-Al_2O_3 scale. A common understanding is that α-Al_2O_3 forms on FeCrAl alloys at temperatures exceeding 900-1000 °C.

Generally, all three elements of FeCrAl alloys can be oxidized by oxygen and steam resulting in the formation of the corresponding oxides. Al_2O_3 and Cr_2O_3 are the stable and protecting oxides in the corresponding binary metal-oxygen systems. The thermodynamic stability of the oxides is in the order Al_2O_3>Cr_2O_3>Fe_2O_3, i.e., alumina is by far the most stable oxide forming at the lowest oxygen partial pressure, which promotes the selective oxidation of aluminum at high temperatures. Other oxides may be formed under certain circumstances, especially due to kinetic limitations during the initial transient phase and in case of too low aluminum concentration in the alloy or due to Al depletion in the bulk alloy during oxidation. “Catastrophic” or “breakaway” oxidation at temperatures beyond 1300-1400°C was seen in various studies, i.e., an extreme acceleration of the oxidation rate due to the loss of protective effect of alumina at temperatures below the FeCrAl melting temperature.

At KIT, a comprehensive study on the high-temperature oxidation in steam was conducted with various FeCrAl alloys (including commercial Kanthal alloys and recent nuclear grade alloys) over a wide range of temperature between 600°C and 1500°C [6]. Three temperature regions were defined according to different oxidation mechanisms. The already discussed formation of a very protective α-Al_2O_3 layer was observed in the temperature range of approximately 1000-1350°C, see **Figure 6**. At lower temperatures, the oxidation

kinetics is determined by the formation of Al- and Fe-rich transient oxides, and it is therefore 2-3 orders of magnitude higher than the extrapolated correlation for α-alumina. However, this has only a limited effect on accident scenarios because of the generally low level of oxidation rates between 600°C and 900°C. Of greater relevance in this context is the tendency of lean-Cr nuclear-grade FeCrAl alloys to enter catastrophic oxidation at temperatures as low as 1300-1400°C, i.e., at lower temperatures than the commercial Kanthal alloys. As shown in **Figure 6**, the by five orders of magnitude higher oxidation rates under these conditions correlate with the kinetics of iron oxide formation, and this usually results in fast and complete oxidation of FeCrAl samples, as seen in the post-test images. The onset of catastrophic oxidation is dependent on alloy composition and heating rate with earlier transition for alloys with lower Cr and Al content and at higher heating rates [23].

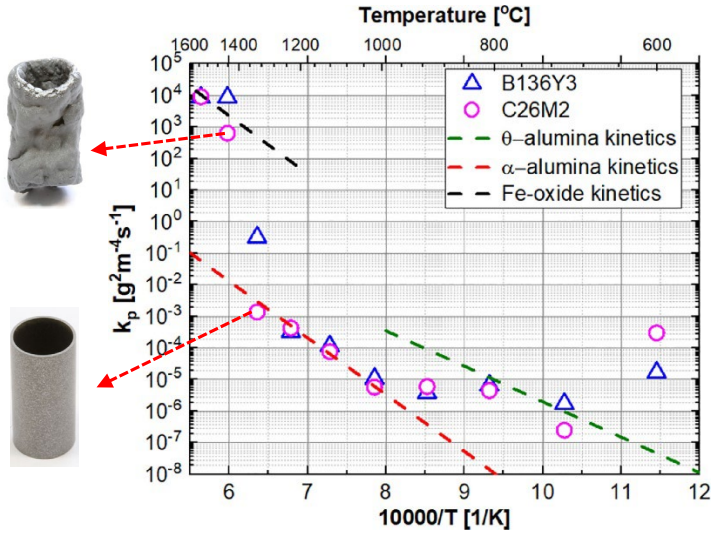

Figure 6. Parabolic rate constants of nuclear-grade alloys B136Y3 and C26M2 as a function of temperature with the parabolic correlations of Fe-oxide, α-alumina, and θ-alumina *[6]*. The images left shows the appearance of C26M samples after oxidation at 1300°C and 1400°C.

6.3. SiC_f/SiC cladding

Silicon carbide (SiC) ceramic composites have been intensively studied for application as heating elements and high-temperature structural materials e.g. for gas turbines, space travel, and in the nuclear industry. They offer excellent high-temperature mechanical properties, low density, high oxidation and irradiation resistance as well as very low interaction with thermal neutrons. Silicon carbide ceramic matrix composites (CMC) are considered the most promising long-term candidates for ATF cladding tubes in LWRs especially with regard to oxidation resistance at very high temperatures [24] [25]. A monolithic external SiC layer for corrosion/oxidation protection is needed to protect the fiber-matrix composite against high-temperature attack by steam. Even not further discussed here, it should be mentioned that the hydrothermal corrosion of SiC in water under operational conditions is one of the major issues for the applications in LWRs.

The high-temperature oxidation resistance of SiC relies on the formation of a protective silica (SiO_2) scale with a very slow parabolic oxidation kinetics. Hydrogen is released in addition to carbon-containing gases. CVD coated SiC CMC cladding survive 1200°C in steam atmosphere for days. Avincola et al. [26] conducted steam oxidation tests for 22 hours at 1600°C without severe degradation of the SiC_f/SiC cladding. SiC_f/SiC samples even survived transient testing up to 2000°C and water quenching with degradation of the CVD surface layer only. At these very high temperatures, the formation of volatile hydroxides or oxyhydroxides becomes significant. The linear volatilization rate is strongly dependent on system pressure, steam partial pressure, and gas flow velocity [27]. Formation and volatilization of a silica scale at the same

time finally lead to paralinear oxidation kinetics with the establishment of a constant SiO_2 thickness after a certain time. At very high temperatures above 1800°C, the interface reaction between SiC and SiO_2 resulting in the production of gaseous species SiO and CO may take place. SiO_2 bubble formation during steam oxidation at very high temperatures approaching or exceeding the silica melting temperature around 1730°C was observed by several authors [26] [27] [28] [29]. Such bubbles are formed due to the presence of a higher H_2 and CO gas pressure at the SiC/SiO_2 interface (where they are produced) compared to the ambient pressure.

At KIT, SiC_f/SiC cladding segments produced by CEA were oxidized at 1700°C for up to 3 hours and finally quenched by water [30] in the framework of the IL Trovatore project. All samples survived the harsh procedure and exhibited an only slight decrease of mechanical properties during tensile testing. A transient experiment was carried out until serious local degradation of the sample at maximum temperature of approximately 1845°C. The degradation was caused by local complete consumption of the outer CVD-SiC sealcoat resulting in steam access to the fiber-matrix composite with enhanced oxidation kinetics, **Figure 7**. Approaching these very high temperatures was accompanied by accelerated gas release mainly of H_2 and CO_2, as well as the formation of surface bubbles and white smoke indicating strong volatilization of Si-O-(H) species.

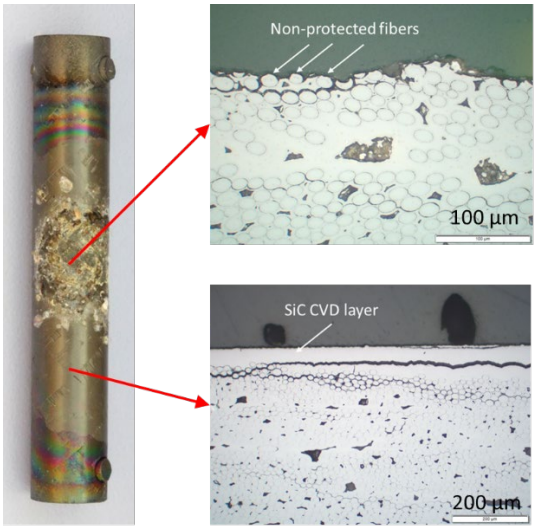

Figure 7. Post-test appearance of a SiC_f/SiC cladding sample after the transient test up to 1845 °C and optical micrographs from the failure region in the middle of the sample and from the non-failure region below *[30]*.

7. CONCLUSIONS

This paper provides an overview on the experimental activities on ATF cladding research at KIT, which is focused on the high-temperature oxidation behavior under prototypical conditions (except irradiation effects). Most of the work is embedded in international collaborations in the framework of the EC, IAEA and OECD-NEA, in which KIT plays an active and leading role.

All ATF claddings discussed in this paper offer improved high-temperature oxidation resistance compared to conventional zirconium alloys as long as they form stable protective oxide layers on the surface. They could contribute to reduce the risk of temperature escalation and hydrogen detonation in severe accidents and to increase the coping time for accident management measures at least for slower accident scenarios. The maximum survival temperatures for the ATF cladding materials are:

- 1200-1300°C for Cr-coated Zry
- around 1400°C for nuclear grade FeCrAl alloys
- >1700°C for SiC_f-SiC composites with monolithic external SiC layer

However, for all these materials, several issues need to be addressed for successful implementation in NPP fuel assemblies. These include hydrothermal corrosion under operating conditions for all ATF cladding types (depending on water chemistry), tritium permeation for FeCrAl alloys and leak tightness for SiC-based ceramic composites.

ACKNOWLEDGMENTS

The financial support by the international programs is greatly appreciated. The authors thank all contributors from KIT for the excellent technical support as well as all guest scientists for their valuable contribution.

REFERENCES

[1] NEA, "State-of-the-Art Report on Light Water Reactor Accident-Tolerant Fuels," Nuclear Science, OECD Publishing, Paris, 2018.

[2] R. Rebak, "Improved and Innovative Accident-Tolerant Nuclear Fuel Materials Considered for Retrofitting Light Water Reactors - A Review," *Corrosion and Materials Degradation,* vol. 4, pp. 466-487, 2023.

[3] M. Steinbrück, M. Große, L. Sepold and J. Stuckert, "Synopsis and outcome of the QUENCH experimental program," *Nuclear Engineering and Design,* vol. 240, pp. 1714-1727, 2010.

[4] J. Stuckert, J. Birchley, M. Große, B. Jaeckel and M. Steinbrück, "Experimental and calculation results of the integral reflood test QUENCH-15 with ZIRLO™ cladding tubes in comparison with results of previous QUENCH tests," *Nuclear Engineering and Design,* vol. 241, pp. 3224-3233, 2011.

[5] A. Gurgen and K. Shirvan, "Estimation of coping time in pressurized water reactors for near term accident tolerant fuel claddings," *Nuclear Engineering and Design,* vol. 337, pp. 38-50, 2018.

[6] C. Kim, C. Tang, M. Grosse, Y. Maeng, C. Jang and M. Steinbrueck, "Oxidation mechanism and kinetics of nuclear-grade FeCrAl alloys in the temperature range of 500–1500 °C in steam," *Journal of Nuclear Materials,* p. art. no. 153696, 2022.

[7] K. Lambrinou, "Innovative accident-tolerant fuel cladding materials: The H2020 IL TROVATORE perspective," in *Water Reactor Fuel Performanve Meeting WRFPM 2017*, Jeju Island, Korea, 2017.

[8] J. Stuckert, M. Grosse, M. Steinbrueck and K. Terrani, “Results of the bundle test QUENCH-19 with FeCrAl claddings,” in *GLOBAL 2019 - International Nuclear Fuel Cycle Conference and TOP FUEL 2019 - Light Water Reactor Fuel Performance Conference*, 2020.

[9] P. Doyle, J. Stuckert, M. Grosse, M. Steinbrück, A. Nelson, J. Harp and K. Terrani, "Analysis of Iron-Chromium-Aluminum Samples Exposed to Accident Conditions

Followed by Quench in the QUENCH-19 Experiment," *Journal of Nuclear Materials,* vol. 580, p. art. 154433, 2023.

[10] IAEA, "Final Report: Analysis of Options and Experimental Examination of Fuels for Water Cooled Reactors with Increased Accident Tolerance (ACTOF)," IAEA-TECDOC-1921, 2020.

[11] J. Bischoff, C. Delafoy, C. Vauglin, P. Barberis, C. Roubeyrie, D. Perche, D. Duthoo, F. Schuster, J.-C. Brachet, E. Schweitzer and K. Nimishakavi, "AREVA NP's enhanced accident-tolerant fuel developments: Focus on Cr-coated M5 cladding," *Nuclear Engineering and Technology,* vol. 50, pp. 223-228, 2018.

[12] J.-C. Brachet, I. Idarraga-Trujillo, M. Flem, M. Saux, V. Vandenberghe, S. Urvoy, E. Rouesne, T. Guilbert, C. Toffolon-Masclet, M. Tupin, C. Phalippou, F. Lomello, F. Schuster, A. Billard, G. Velisa, C. Ducros and F. Sanchette, "Early studies on Cr-Coated Zircaloy-4 as enhanced accident tolerant nuclear fuel claddings for light water reactors," *Journal of Nuclear Materials,* vol. 517, pp. 268-285, 2019.

[13] J.-C. Brachet, E. Rouesne, J. Ribis, T. Guilbert, S. Urvoy, G. Nony, C. Toffolon-Masclet, M. Le Saux, N. Chaabane, H. Palancher, A. David, J. Bischoff, J. Augereau and E. Pouillier, "High temperature steam oxidation of chromium-coated zirconium-based alloys: Kinetics and process," *Corrosion Science,* vol. 167, p. art. no. 108537, 2020.

[14] B. Maier, H. J. Yeom, G., T. Dabney, J. Walters, J. Romero, H. Shah, P. Xu and K. Sridharan, "Development of Cold Spray Coatings for Accident-Tolerant Fuel Cladding in Light Water Reactors," *JOM,* vol. 70, pp. 198-202, 2018.

[15] H. Yeom, B. Maier, G. Johnson, T. Dabney, M. Lenling and K. Sridharan, "High temperature oxidation and microstructural evolution of cold spray chromium coatings on Zircaloy-4 in steam environments," *Journal of Nuclear Materials,* vol. 526, p. art. no. 151737, 2019.

[16] J. Yang, M. Steinbrück, C. Tang, M. Große, J. Liu, J. Zhang, D. Yun and S. Wang, "Review on chromium coated zirconium alloy accident tolerant fuel cladding," *Journal of Alloys and Compounds,* vol. 895, p. art. no. 162450, 2022.

[17] Z. Li, X. Wang, H. Chen, R. Zhang, W. T., L. Yao and P. Wang, "Review on performance of chromium-coated zirconium and its failure mechanisms," *Frontiers in Nuclear Engineering,* vol. 2, p. 1212351, 2023.

[18] X. Han, C. Chen, Y. Tan, W. Feng, S. Peng and H. Zhang, "A systematic study of the oxidation behavior of Cr coatings on Zry4 substrates in high temperature steam environment," *Corrosion Science,* vol. 174, p. art. no. 108826, 2020.

[19] D. Kim, M. Steinbrück, M. Grosse, C. Tang and Y. Lee, "Eutectic reaction and oxidation behavior of Cr-coated Zircaloy-4 accident-tolerant fuel cladding under various heating rates," *Journal of Nuclear Materials,* vol. 583, p. art. no. 154538, 2023.

[20] S. Dryepondt, K. Unocic, D. Hoelzer, C. Massey and B. Pint, "Development of low-Cr ODS FeCrAl alloys for accident-tolerant fuel cladding," *Journal of Nuclear Materials,* vol. 501, pp. 59-71, 2018.

[21] K. Field, M. Snead, Y. Yamamoto and K. Terrani, "Handbook on the Materials Properties of FeCrAl Alloys for Nuclear Power Production Applications," ORNL/SPR-2018/905, 2018.

[22] K. Sakamoto, Y. Miura, S. Ukai, A. Kimura, A. Yamaji, K. Kusagaya, T. Kondo and S. Yamashati, "Progress on Japanese Development of Accident Tolerant FeCrAl-ODS Fuel Claddings for BWRs," in *Proceedings of the TOPFUEL 2018 Conference*, Prague, Czech Republic, 2018.

[23] C. Tang, A. Jianu, M. Steinbrueck, M. Grosse, A. Weisenburger and H. Seifert, "Influence of composition and heating schedules on compatibility of FeCrAl alloys with high-temperature steam," *Journal of Nuclear Materials,* vol. 511, pp. 496-507, 2018.

[24] L. Snead, T. Nozawa, Y. Katoh, T.-S. Byun, S. Kondo and D. Petti, "Handbook of SiC properties for fuel performance modeling," *Journal of Nuclear Materials,* vol. 371, pp. 329-377, 2007.

[25] J. Braun, C. Sauder, J. Lamon and F. Balbaud-Célérier, "Influence of an original manufacturing process on the properties and microstructure of SiC/SiC tubular composites," *Composites Part A: Applied Science and Manufacturing,* vol. 123, pp. 170-179, 2019.

[26] V. Angelici Avincola, M. Grosse, U. Stegmaier, M. Steinbrueck and H. Seifert, "Oxidation at high temperatures in steam atmosphere and quench of silicon carbide composites for nuclear application," *Nuclear Engineering and Design,* vol. 295, p. 468–478, 2015.

[27] K. Terrani, B. Pint, C. Parish, C. Silva, L. Snead and Y. Katoh, "Silicon carbide oxidation in steam up to 2 MPa," *Journal of the American Ceramic Society,* vol. 97, pp. 2331-2352, 2014.

[28] E. Opila, "Variation of the Oxidation Rate of Silicon Carbide with Water-Vapor Pressure," *Journal of the American Ceramic Society,* vol. 82, pp. 625-636, 1999.

[29] H. Pham, Y. Nagae, M. Kurata, D. Bottomley and K. Furumoto, "Oxidation kinetics of silicon carbide in steam at temperature range of 1400 to 1800 °C studied by laser heating," *Journal of Nuclear Materials,* vol. 529, p. art. no. 151939, 2020.

[30] M. Steinbrück, M. Große, U. Stegmaier, J. Braun and C. Lorrette, "Oxidation of silicon carbide composites for nuclear applications at very high temperatures in steam," *Coatings,* vol. 12, p. 875, 2022.

[31] M. Steinbrück, U. Stegmaier, M. Große, L. Czerniak, E. Lahoda, R. Daum and K. Yueh, "High-temperature oxidation and quenching of chromium-coated zirconium alloy ATF cladding tubes with and w/o pre-damage," *Journal of Nuclear Materials,* p. art. no. 153470, 2022.

Karlsruhe Institute of Technology

Overview of KIT activities on ATF cladding materials

M. Steinbrück, J. Stuckert, M. Große

11th European Review Meeting on Severe Accident Research (ERMSAR2024)

KTH, Stockholm, Sweden, May 13-16, 2024



Hydrogen detonation in Fukushima Daiichi NPPs



- 1979:
  TMI-2
- ➔ Severe accident research
- 2005:
  First ERMSAR
- 2011:
  Fukushima Daiichi
- ➔ ATF research

Karlsruhe Institute of Technology

Motivation for ATF cladding

- Prevent/reduce high-temperature steam oxidation of cladding materials
- Reduce release of hydrogen (and heat)
- Extent coping time for AMMs
- Most promising ATF cladding are Cr-coated Zircaloys, FeCrAl alloys, and SiC-based composites

- ATF = Accident Tolerant Fuel
- ➡ ATF = Advanced Technology Fuel

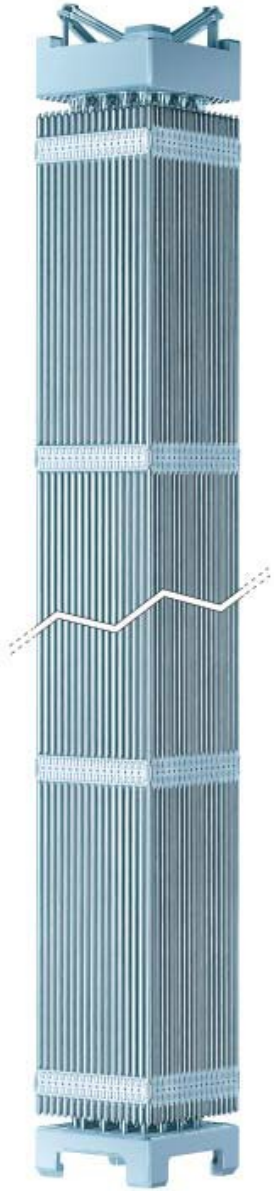

Karlsruhe Institute of Technology

Publications on ATF cladding*

* Based on a SCOPUS search for “ATF cladding”

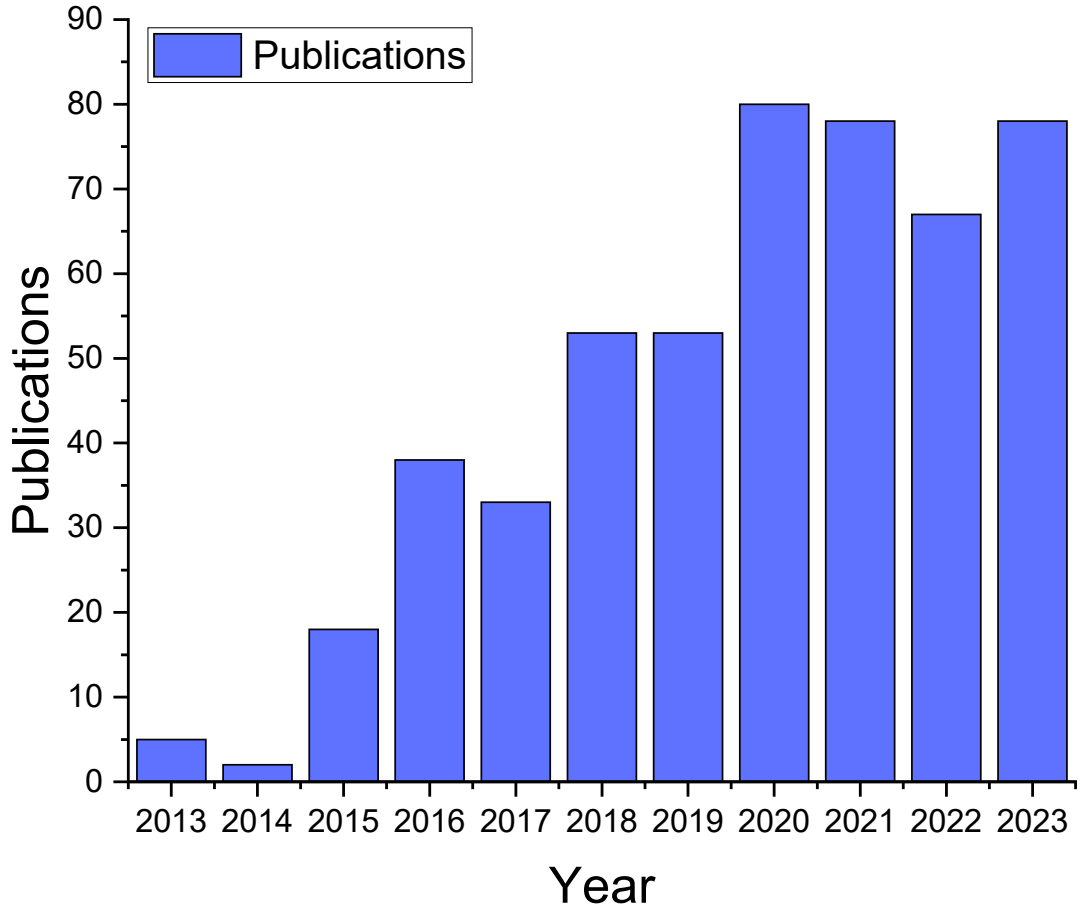

SCOPUS: >500 documents 2013-2023

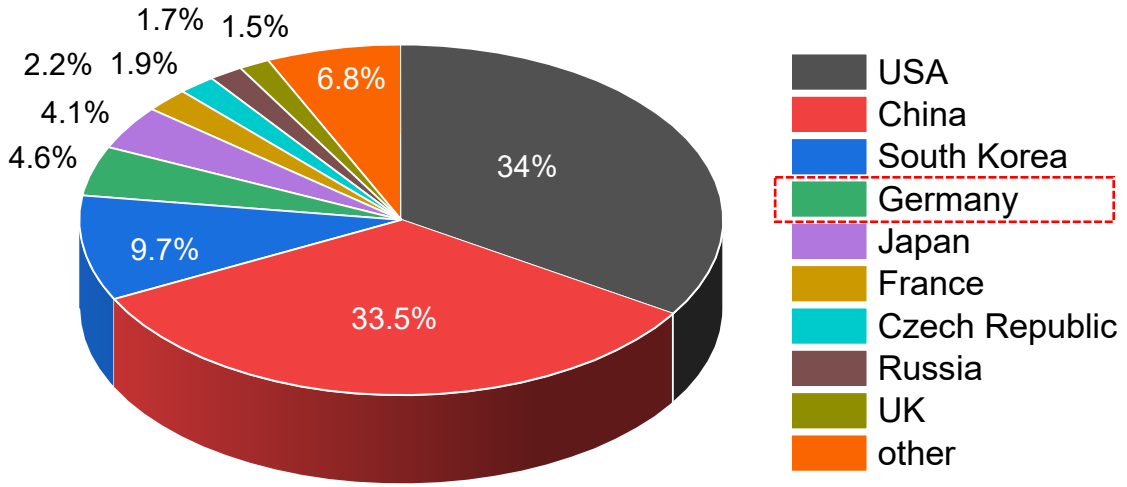

- 50% of German research is from KIT

Karlsruhe Institute of Technology

ATF cladding research at KIT

- Focused on HT behavior of promising cladding materials
- Separate-effects tests and bundle experiments
- Model development, code validation and code application
- Embedded in international cooperation programs
  - OECD-NEA
  - IAEA
  - EC Euratom
- and further international collaboration, e.g., with Westinghouse (USA) and SNU (South Korea)



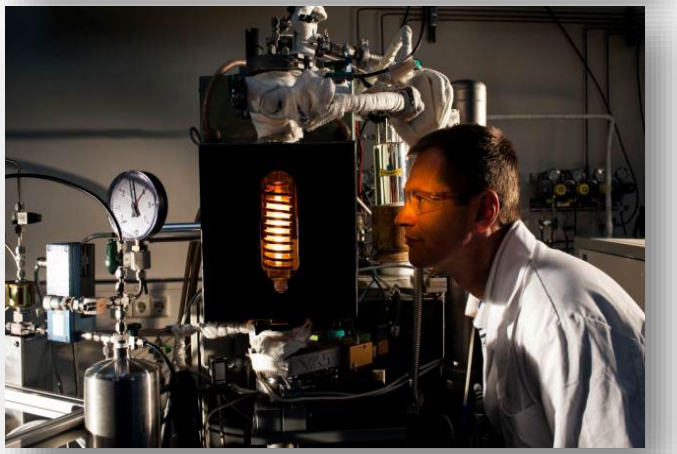



Outline

- International programs
  - OECD-NEA Joint Undertaking QUENCH-ATF
  - IAEA Coordinated Research Project ATF-TS
  - EC Programs IL TROVATORE and SCORPION
- Examples of KIT research
  - Cr-coated Zr alloys
  - FeCrAl alloys
  - SiC-based composites
- Conclusion

Karlsruhe Institute of Technology

International programs

Karlsruhe Institute of Technology

OECD-NEA Joint Undertaking QUENCH-ATF

- KIT is Operating Agent
- Three QUENCH bundle experiments with Cr-coated Zr alloy cladding tubes
  - First test with CS Cr/ZIRLO (Westinghouse) with slightly beyond DBA LOCA scenario (T_{max}=1300°C) - *completed*
  - Second test with CS Cr/ZIRLO (Westinghouse) with BDBA scenario (T_{max}=1600°C) - *July 2024*
  - Third test with PVD Cr/ZIRLO (WH/NNL) - scenario tbd.
- Benchmark exercises for each test (coordinated by GRS)
- Extensive post-test analyses (KIT, IRSN) and supporting SETs

Karlsruhe Institute of Technology

IAEA CRP ATF-TS

- KIT coordinates two work packages (Experiments, Benchmarks)
- Experiments in different scales
  - DEGREE: 9-rods bundle tests with PVD Cr/Zry cladding
  - CODEX: 7-rods bundle test with PVD Cr/ZIRLO cladding
  - QUENCH-19: 24-rods bundle test with FeCrAl cladding (ORNL)
  - Various separate-effects tests with Cr-coated cladding
- Code benchmarking on bundle tests (fuel codes, SA codes)
- LOCA evaluation methodology development for NPP applications including uncertainty and sensitivities studies

Karlsruhe Institute of Technology

EC programs IL TROVATORE & SCORPION

- KIT coordinates WPs (Fuel/clad/coolant interactions)

IL TROVATORE

- Development of ATF cladding materials including modelling, processing, joining and testing
  - Oxidic claddings
  - SiC ceramic matrix composites
  - Cr-coated Zircaloys with and without diffusion barrier
  - MAX phases
  - FeCrAl alloy

SCORPION

- Development of SiC/SiC_f CMC cladding with innovative design and corrosion resistant coating

Karlsruhe Institute of Technology

Cr-coated zirconium alloys

Karlsruhe Institute of Technology

Cr/Zry: Isothermal tests at 1100°C

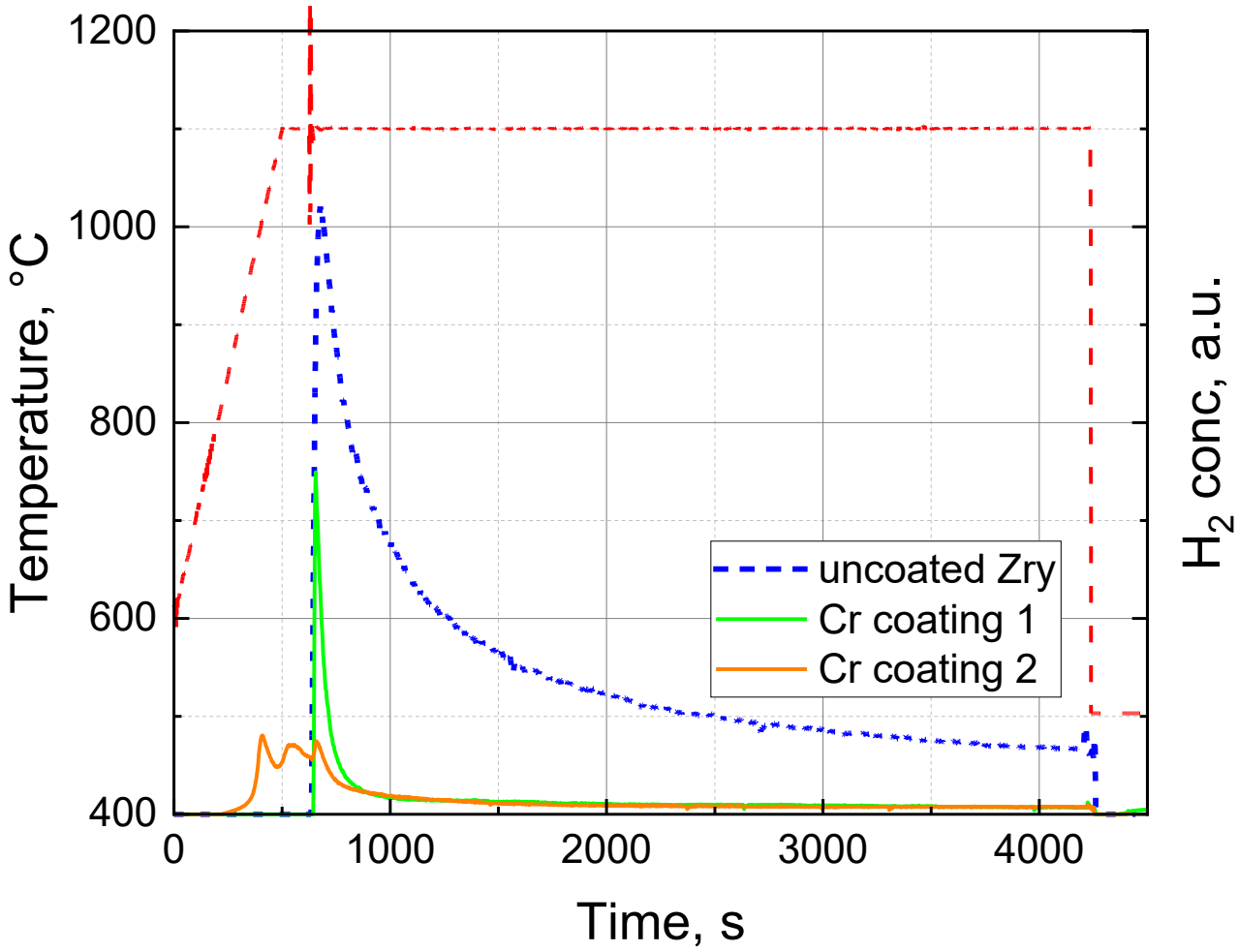

Temperature and hydrogen release during 1 hour oxidation at 1100°C in steam of coated and uncoated cladding

- Protective behavior of Cr until end of test
- About one order of magnitude less hydrogen released



Post-test appearance

Karlsruhe Institute of Technology

Cr/Zry: Isothermal tests at 1200°C

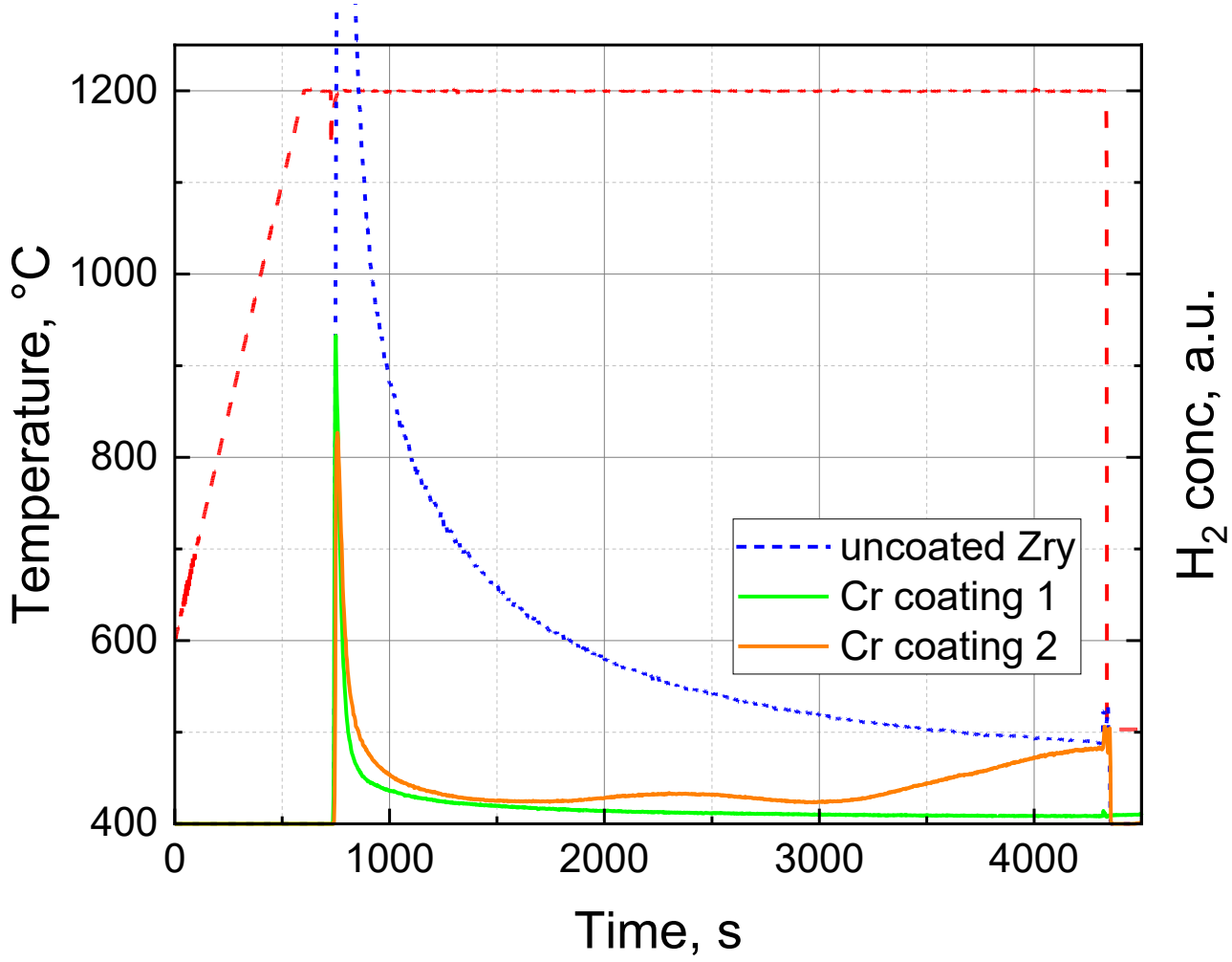

Temperature and hydrogen release during 1 hour oxidation at 1200°C in steam of coated and uncoated cladding

- Protective thicker Cr coating
- Degradation of protective effect of the thinner coating after ca. 1000 s
- Mechanical failure of the uncoated cladding during post-test handling
- Influence of coating thickness and structure



Post-test appearance

Karlsruhe Institute of Technology

Cr/Zry: Transient tests beyond eutectic temperature

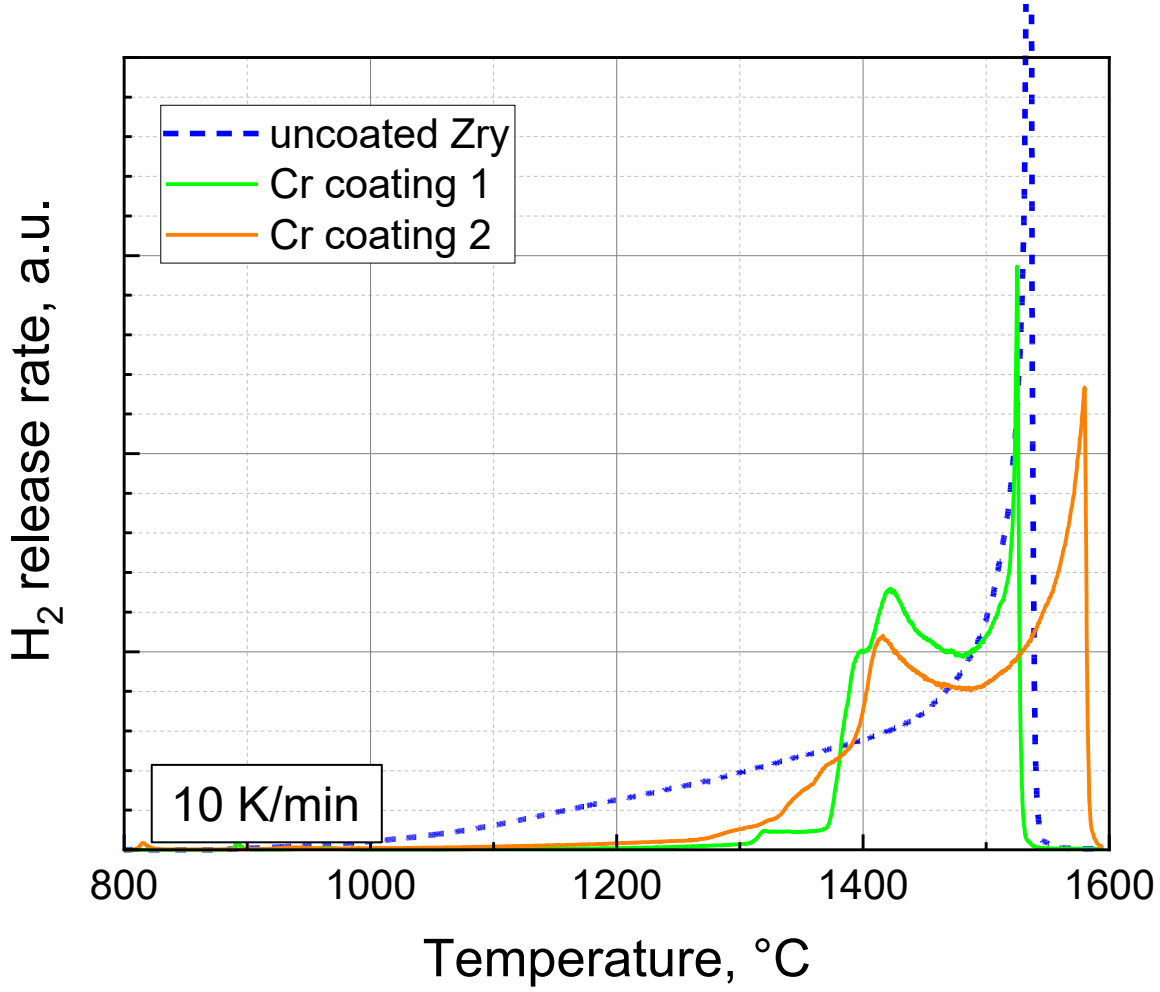

Hydrogen release during oxidation in steam of Cr-coated and non-coated Zr alloy

- Protective behavior of Cr coating up to ~1300°C
- Serious failure at ~1350°C
- Faster oxidation of coated samples after coating failure compared to Zry!



Post-test appearance

Karlsruhe Institute of Technology

FeCrAl alloys

Karlsruhe Institute of Technology

Oxidation kinetics of nuclear grade FeCrAl (600-1500°C)

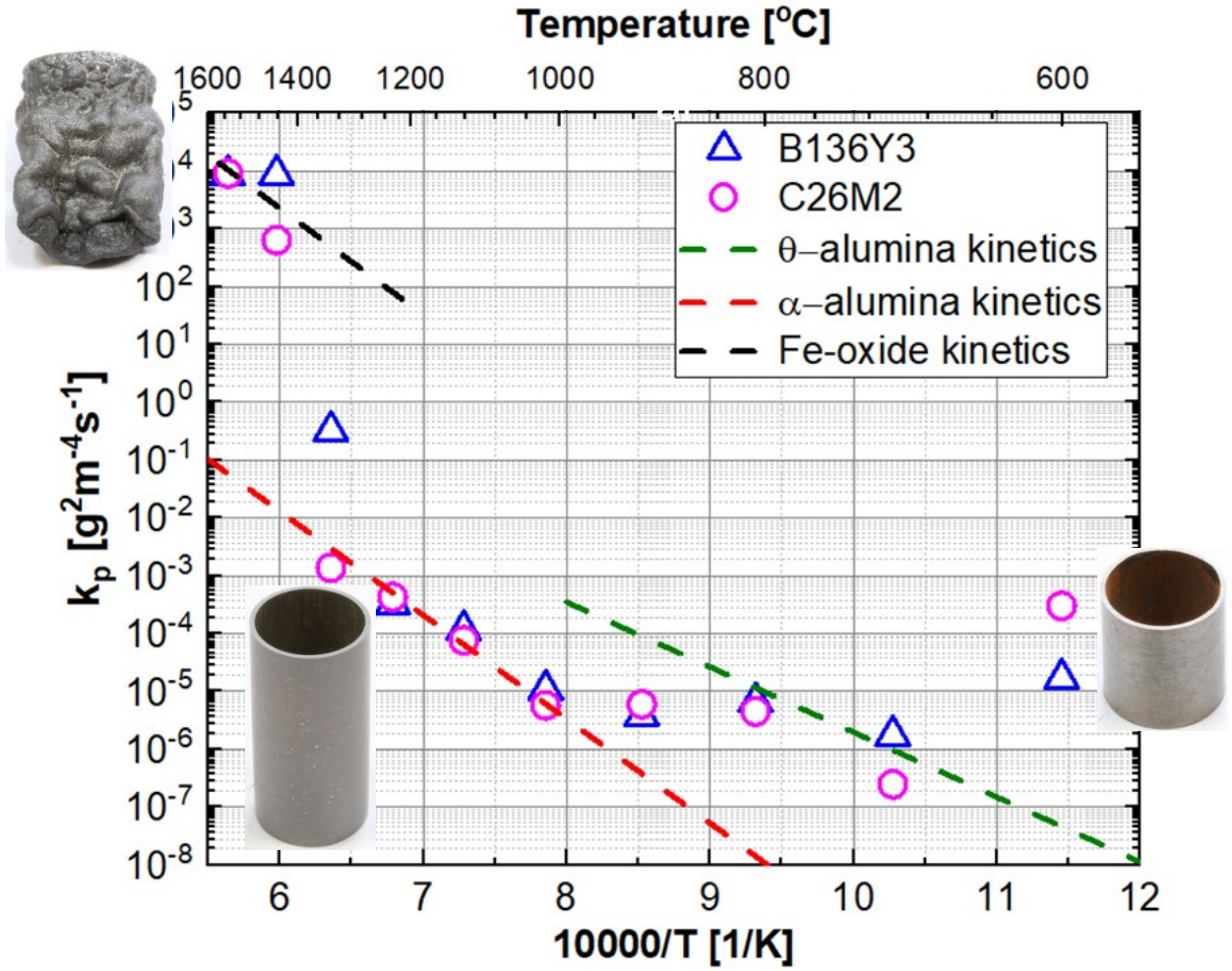

Steam oxidation kinetics of nuclear-grade FeCrAl alloys with kinetics of θ- and α-alumina and Fe-oxide

- 700°C < T < 900°C:
  Transient oxide kinetics
- 1000°C < T < 1350°C:
  α-alumina kinetics (2-3 orders of magnitude lower than of Zry oxidation)
- T ≥ 1400°C:
  Catastrophic oxidation with kinetics similar to Fe oxidation
- Transition temperature from protective α-alumina kinetics to catastrophic oxidation is dependent on composition, surface finish and heating rate, etc.
- Three different correlations needed for code simulation of SA scenarios with FeCrAl cladding

Karlsruhe Institute of Technology

Severe accident bundle test QUENCH-19 with FeCrAl

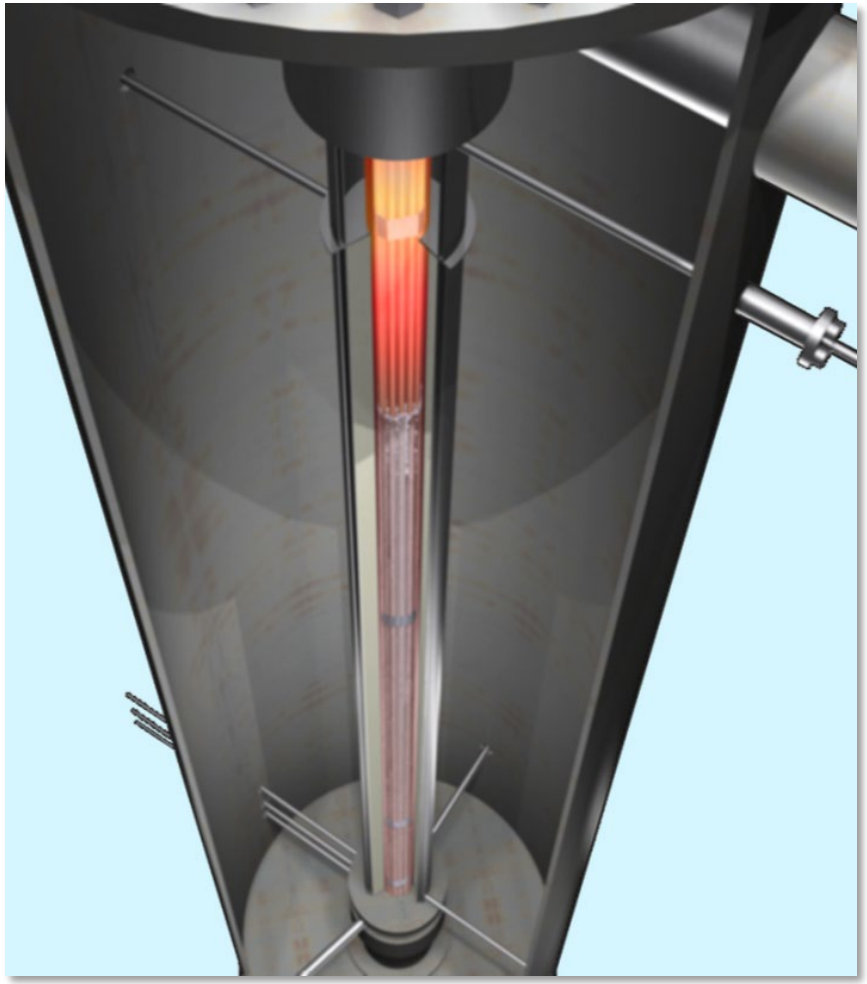

QUENCH facility at KIT

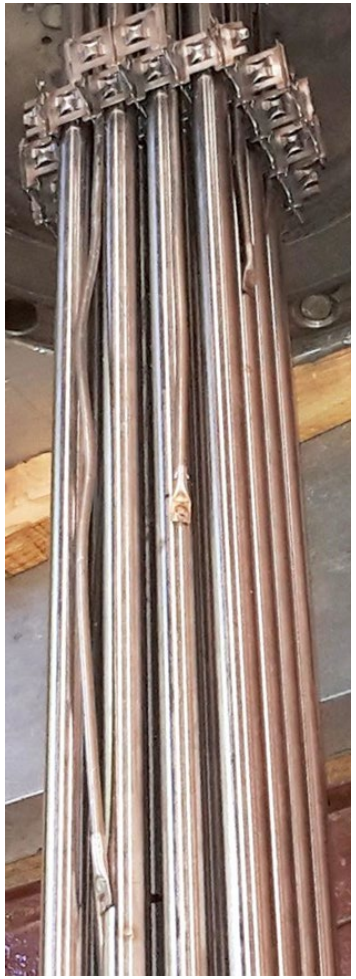

QUENCH-19 bundle with spacer and TCs

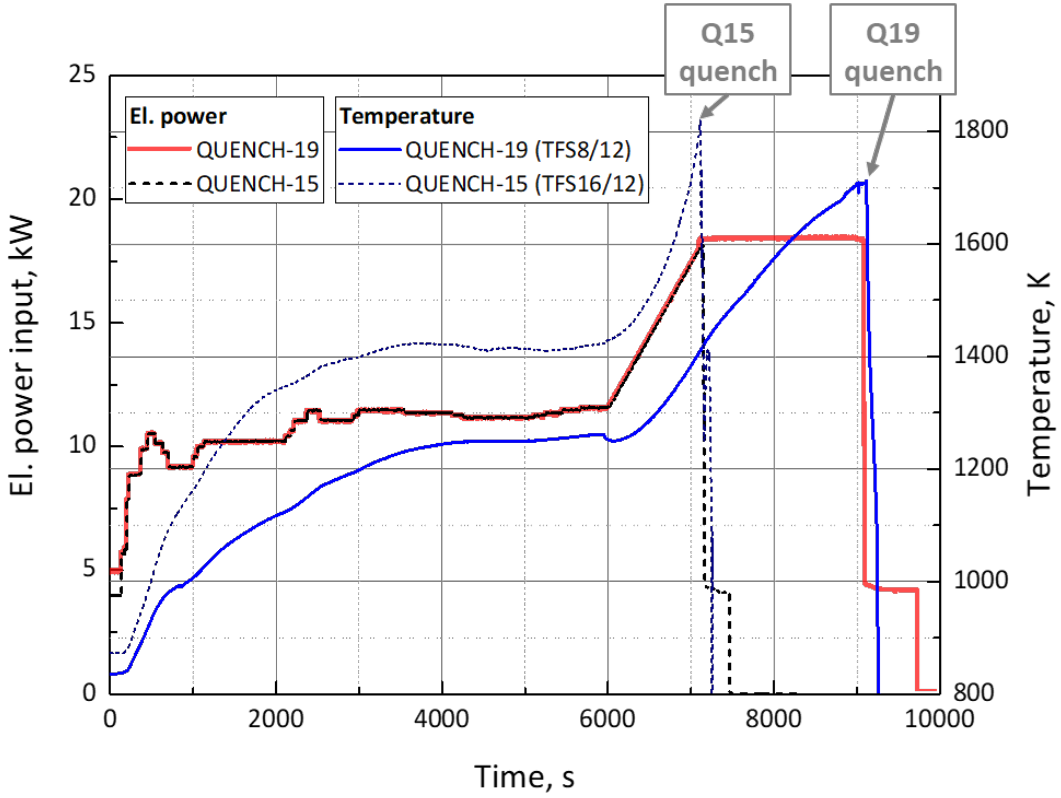

QUENCH-19 test conduct, QU-15 with ZIRLO cladding as reference

Karlsruhe Institute of Technology

QUENCH-19 results

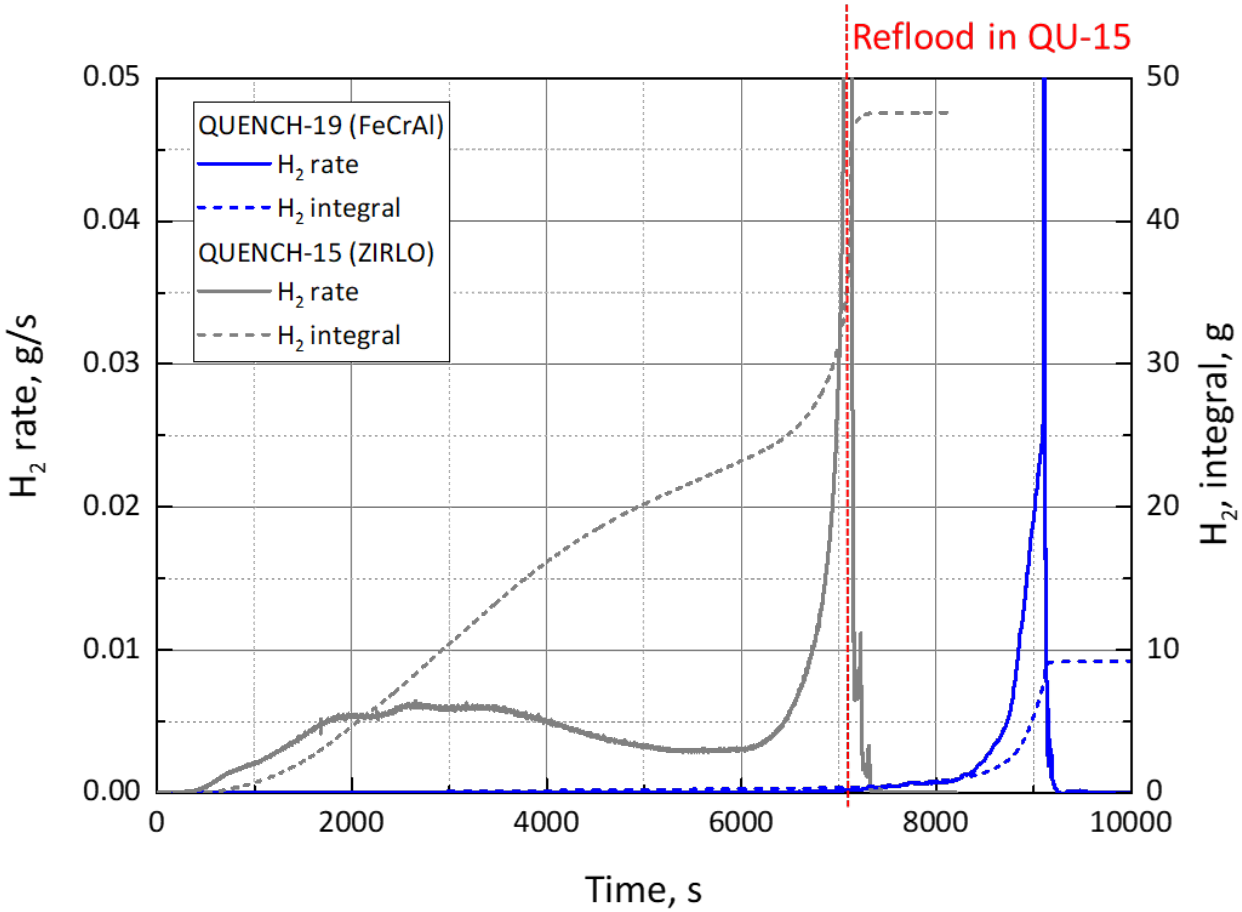

Hydrogen release during QU-19 with FeCrAl cladding compared to QU-15 with ZIRLO



Post-test bundle appearance

Karlsruhe Institute of Technology

SiC/SiC_f composites

Karlsruhe Institute of Technology

SiC: Isothermal oxidation at 1700°C

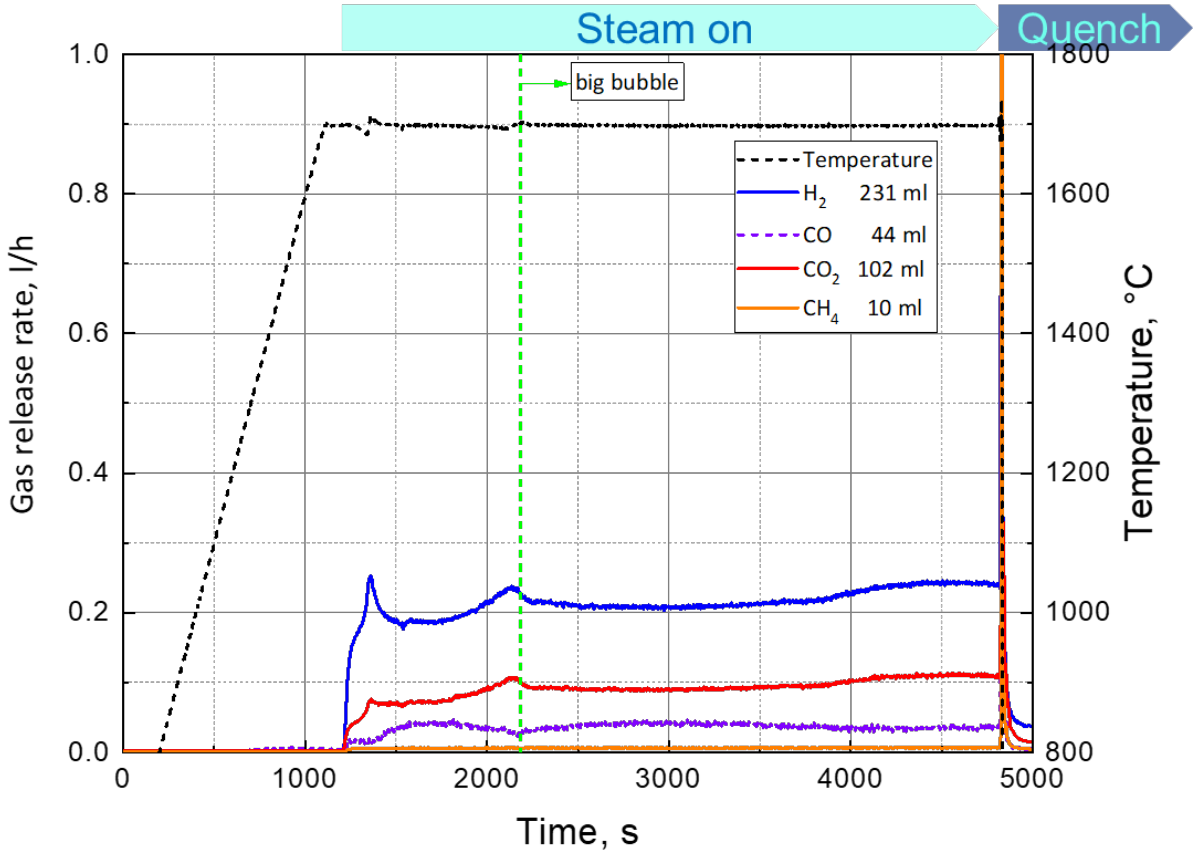

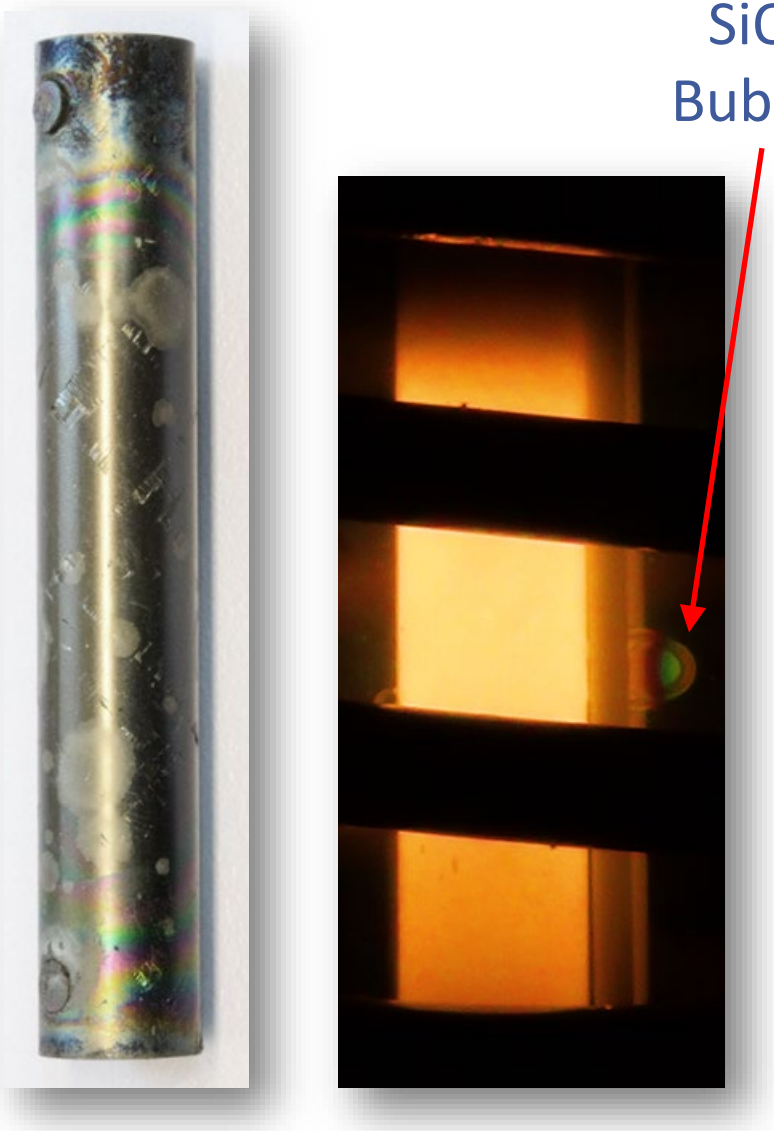

Post-test sample appearance and video snapshot after 30 min

- Very limited oxidation of the SiC_f/SiC cladding at 1700°C
- Recession rate 15-25 µm/h, but mechanical strength retained
- Strongly dependent on boundary conditions and impurities

Karlsruhe Institute of Technology

SiC: Transient test until failure of CVD layer

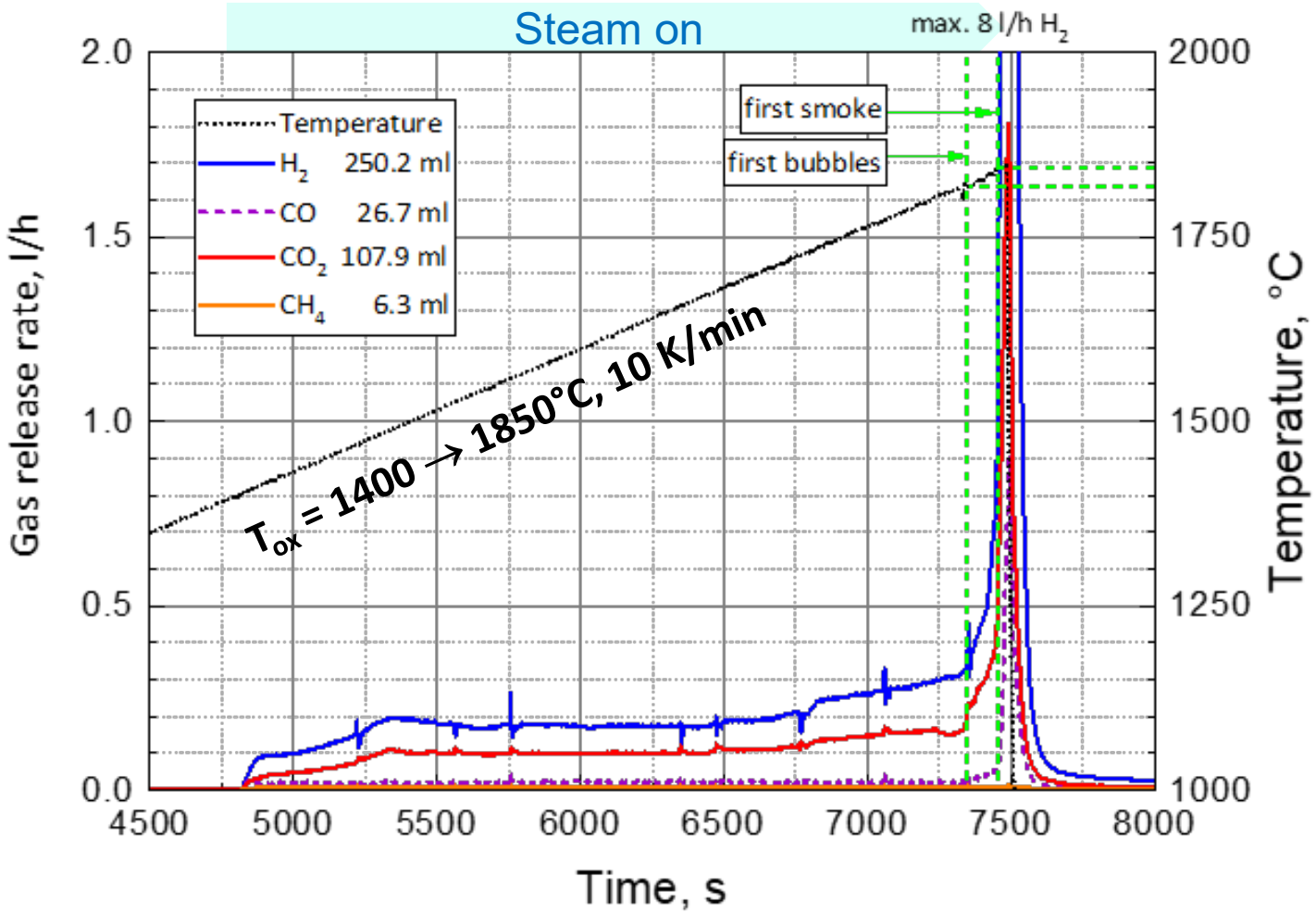



Video snapshot at 1845°C

- Low oxidation kinetics up to ca. 1750°C
- Bubble formation, strong gas release, SiO_x volatilization above ~1750°C

Karlsruhe Institute of Technology

SiC: Transient test until failure of CVD layer

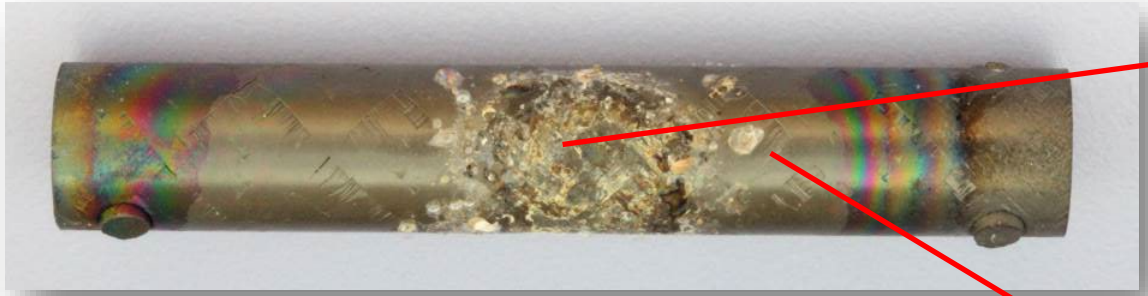

Sample after the transient test up to 1845°C

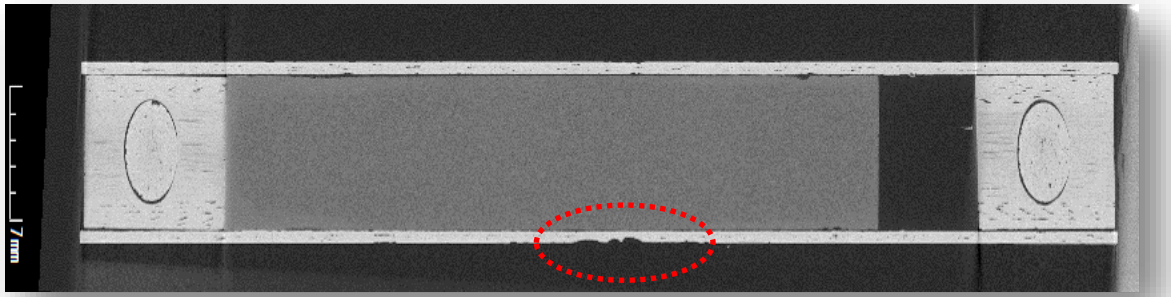

X-ray tomography, longitudinal cut

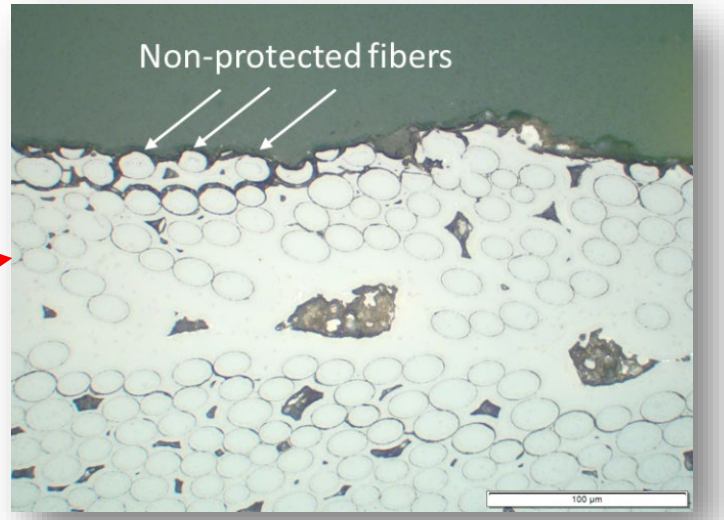

OM from the failure region

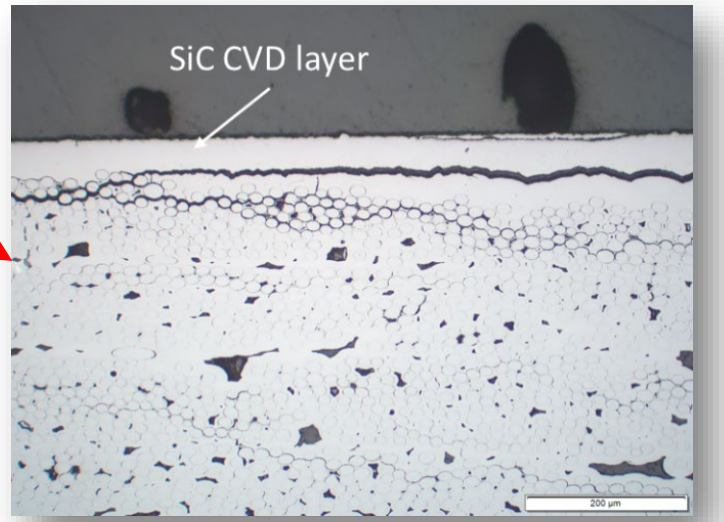

OM from the non-failure region

- Local failure of the monolithic CVI seal-coat above 1750°C and attack of SiC fibers

Karlsruhe Institute of Technology

Conclusion

- KIT significantly contributes to worldwide intensive research on ATF cladding with the focus on testing at (very) high temperatures
- Maximum temperatures:
  - Cr/Zry:1200°C
  - FeCrAl: 1300°C
  - SiC: 1700°C
- Coping times:
  - minutes to a few hours for Cr/Zry and FeCrAl
  - hours to days for SiC
- Issues remain with all potential cladding solutions, particularly with regard to integral behavior under irradiation, oxidation and mechanical loads

Karlsruhe Institute of Technology

Selected references

Steinbrueck, M., Grosse, M., Tang, C., Stuckert, J., Seifert, H.J.
An Overview of Mechanisms of the Degradation of Promising ATF Cladding Materials During Oxidation at High Temperatures
(2024) High Temperature Corrosion of Materials, .
DOI: 10.1007/s11085-024-10229-y

Kim, D., Steinbrück, M., Grosse, M., Tang, C., Lee, Y.
Eutectic reaction and oxidation behavior of Cr-coated Zircaloy-4 accident-tolerant fuel cladding under various heating rates
(2023) Journal of Nuclear Materials, 583, art. no. 154538, . Cited 5 times.
DOI: 10.1016/j.jnucmat.2023.154538

Doyle, P., Stuckert, J., Grosse, M., Steinbrück, M., Nelson, A.T., Harp, J., Terrani, K.
Analysis of iron-chromium-aluminum samples exposed to accident conditions followed by quench in the QUENCH-19 experiment
(2023) Journal of Nuclear Materials, 580, art. no. 154433, . Cited 2 times.
DOI: 10.1016/j.jnucmat.2023.154433

Liu, J., Meng, R., Steinbrück, M., Große, M., Stegmaier, U., Tang, C., Yang, J., Yun, D.
Microstructural evolution of pre-oxidized Cr-coated Zry-4 during annealing in argon
(2023) Journal of Nuclear Materials, 573, art. no. 154144, . Cited 8 times.
DOI: 10.1016/j.jnucmat.2022.154144

Steinbrueck, M., Grosse, M., Stegmaier, U., Braun, J., Lorrette, C.
Oxidation of Silicon Carbide Composites for Nuclear Applications at Very High Temperatures in Steam
(2022) Coatings, 12 (7), art. no. 875, . Cited 8 times.
OI: 10.3390/coatings12070875

Liu, J., Steinbrück, M., Große, M., Stegmaier, U., Tang, C., Yun, D., Yang, J., Cui, Y., Seifert, H.J.
Systematic investigations on the coating degradation mechanism during the steam oxidation of Cr-coated Zry-4 at 1200 °C
(2022) Corrosion Science, 202, art. no. 110310, . Cited 53 times.
DOI: 10.1016/j.corsci.2022.110310

Kim, C., Tang, C., Grosse, M., Maeng, Y., Jang, C., Steinbrueck, M.
Oxidation mechanism and kinetics of nuclear-grade FeCrAl alloys in the temperature range of 500–1500 °C in steam
(2022) Journal of Nuclear Materials, 564, art. no. 153696, . Cited 25 times.
DOI: 10.1016/j.jnucmat.2022.153696

Yang, J., Steinbrück, M., Tang, C., Große, M., Liu, J., Zhang, J., Yun, D., Wang, S.
Review on chromium coated zirconium alloy accident tolerant fuel cladding
(2022) Journal of Alloys and Compounds, 895, art. no. 162450, . Cited 122 times.
DOI: 10.1016/j.jallcom.2021.162450

Tang, C., Steinbrück, M., Grosse, M., Ulrich, S., Stüber, M.
The Effect of Annealing Temperature on the Microstructure and Properties of Cr–C–Al Coatings on Zircaloy-4 for Accident-Tolerant Fuel (ATF) Applications
(2022) Coatings, 12 (2), art. no. 167, . Cited 2 times.
DOI: 10.3390/coatings12020167

Steinbrück, M., Stegmaier, U., Große, M., Czerniak, L., Lahoda, E., Daum, R., Yueh, K.
High-temperature oxidation and quenching of chromium-coated zirconium alloy ATF cladding tubes with and w/o pre-damage
(2022) Journal of Nuclear Materials, 559, art. no. 153470, . Cited 41 times.
DOI: 10.1016/j.jnucmat.2021.153470

Liu, J., Tang, C., Steinbrück, M., Yang, J., Stegmaier, U., Große, M., Yun, D., Seifert, H.J.
Transient experiments on oxidation and degradation of Cr-coated Zircaloy in steam up to 1600 ℃
(2021) Corrosion Science, 192, art. no. 109805, . Cited 63 times.
DOI: 10.1016/j.corsci.2021.109805

Pham, H.V., Kurata, M., Steinbrueck, M.
Steam Oxidation of Silicon Carbide at High Temperatures for the Application as Accident Tolerant Fuel Cladding, an Overview
(2021) Thermo, 1 (2), pp. 151-167. Cited 13 times.
DOI: 10.3390/thermo1020011

Tang, C., Große, M., Ulrich, S., Klimenkov, M., Jäntsch, U., Seifert, H.J., Stüber, M., Steinbrück, M.
High-temperature oxidation and hydrothermal corrosion of textured Cr2AlC-based coatings on zirconium alloy fuel cladding
(2021) Surface and Coatings Technology, 419, art. no. 127263, . Cited 35 times.
DOI: 10.1016/j.surfcoat.2021.127263

Yang, J., Stegmaier, U., Tang, C., Steinbrück, M., Große, M., Wang, S., Seifert, H.J.
High temperature Cr-Zr interaction of two types of Cr-coated Zr alloys in inert gas environment
(2021) Journal of Nuclear Materials, 547, art. no. 152806, . Cited 81 times.
DOI: 10.1016/j.jnucmat.2021.152806

Tang, C., Stüber, M., Seifert, H.J., Steinbrück, M.
Metallic and Ceramic Coatings for Enhanced Accident Tolerant Fuel Cladding
(2020) Comprehensive Nuclear Materials: Second Edition, pp. 490-514. Cited 3 times.
DOI: 10.1016/B978-0-12-803581-8.11625-X

Grosse, M.M., van Loo, K., Frankberg, E.L., Tang, C., Lambrinou, K., Di Fonzo, F., Steinbrück, M.
Investigation of corrosion and high temperature oxidation of promising ATF cladding materials in the framework of the ll trovatore project
(2020) GLOBAL 2019 - International Nuclear Fuel Cycle Conference and TOP FUEL 2019 - Light Water Reactor Fuel Performance Conference, pp. 274-279. Cited 2 times.

Ševeček, M., Krejčí, J., Chalupová, A., Kabátová, J., Manoch, F., Kočí, J., Cvrček, L., Tang, C., Steinbrück, M., Grosse, M., Penttilä, S., Autio, J.-M., Lydman, J., Toivonen, A., Sartowska, B., Starosta, W., Waliś, L., Hózer, Z., Novotny, T., Perezné-Feró, E., Csordás, A.P., Horváth, M., Szabó, P., Giovedi, C., Xu, P.
Round robin exercise of the candidate ATF cladding materials within the IAEA ACTOF project
(2020) GLOBAL 2019 - International Nuclear Fuel Cycle Conference and TOP FUEL 2019 - Light Water Reactor Fuel Performance Conference, pp. 283-290. Cited 2 times.

Steinbrueck, M., Angelici Avincola, V., Markel, I.J., Stegmaier, U., Gerhards, U., Seifert, H.J.
Oxidation of SiC f -SiC CMC cladding tubes for GFR application in impure helium atmosphere and materials interactions with tantalum liner at high temperatures up to 1600°C
(2019) Journal of Nuclear Materials, 517, pp. 337-348. Cited 15 times.
DOI: 10.1016/j.jnucmat.2019.02.024

Tang, C., Jianu, A., Steinbrueck, M., Grosse, M., Weisenburger, A., Seifert, H.J.
Influence of composition and heating schedules on compatibility of FeCrAl alloys with high-temperature steam
(2018) Journal of Nuclear Materials, 511, pp. 496-507. Cited 54 times.
DOI: 10.1016/j.jnucmat.2018.09.026

Tang, C., Stueber, M., Seifert, H.J., Steinbrueck, M.
Protective coatings on zirconium-based alloys as accident-Tolerant fuel (ATF) claddings
(2017) Corrosion Reviews, 35 (3), pp. 141-165. Cited 317 times.
DOI: 10.1515/corrrev-2017-0010

APPLICATION OF AC²/ATHLET-CD AND ASTEC FOR ATF EXPERIMENTS IN THE FRAME OF ONGOING INTERNATIONAL PROJECTS

Thorsten Hollands
Gesellschaft fuer Anlagen- und Reaktorsicherheit (GRS) gGmbH
Boltzmannstrasse 14, 85748 Graching, Germany
thorsten.hollands@grs.de

Fabrizio Gabrielli, Mauricio Cazado, Zaira Balbuena
Karlsruhe Institute of Technology (KIT)
Hermann-von-Helmholtzplatz 1, 76344 Eggenstein-Leopoldshafen, Germany
fabrizio.gabrielli@kit.edu

Gregor T. Stahlberg
Ruhr-Universitaet Bochum (RUB), Plant Simulation and Safety (PSS)
Universitaetsstr. 150, 44801 Bochum, Germany
gregor.stahlberg@pss.rub.de

ABSTRACT

Zirconium based claddings have been widely used for decades due to their good mechanical properties, corrosion resistance and low neutron absorption at operational conditions. At elevated temperatures, these claddings have some negative characteristics such as the occurrence of exothermic oxidation reactions in steam or air environments. This has motivated research and development of Accident Tolerant Fuel (ATF) and Cladding (ATC) materials, which began prior to the Fukushima Daiichi nuclear power plant core melt events, though these events have highlighted the importance of developing such new materials. Potential ATF concepts should be more resistant to oxidation at least for design basis conditions (DBC), exhibiting significantly slower oxidation kinetics compared to the Zr-based alloys used in typical light water reactors (LWR). This should reduce the hydrogen generation along with the rate and magnitude of energy generation due to oxidation during and after uncovering of the reactor core. This can result in an increased time to introduce accident mitigation measures. Currently, two cladding concepts are under development with a relatively high technical readiness: FeCrAl claddings and Cr-coated Zr-based claddings. Both cladding concepts are topic of investigation in the frame of e.g. OECD QUENCH-ATF and IAEA CRP ATF-TS. In both projects bundle tests are performed or investigated on the one hand from material science point of view and on the other hand as evaluation tests for severe accident codes. In the frame of OECD QUENCH-ATF three experiments with Cr-coated claddings are foreseen, up to now one experiment under extended DBC were performed. In addition, three different bundle test facilities are considered in IAEA ATF-TS: QUENCH-19 with FeCrAl, CODEX with a mixed bundle considering Cr-coated and uncoatedZr-claddings as well as DEGREE tests with Cr-coated claddings. Selected experiments of these test series (pre- and post-test simulations) are calculated with the severe accident codes AC²/ATHLET-CD and ASTEC. Currently, both codes were extended for the prediction of FeCrAl and Cr-coated claddings by enhanced models or explicitly by input. The results of the simulations show that both codes are able to predict the physical behaviour of the experiments and different ATF concept correctly. The results of selected cases will be discussed in the paper in detail. Finally, the models will be evaluated possible model developments will be identified.

KEYWORDS
Accident Tolerant Fuel, core degradation, AC²/ATHLET-CD, ASTEC

1. INTRODUCTION

The investigation of ATFmaterials had already started before the accident at the Fukushima Daiichi plant in 2011, but after this event the development of new materials with significantly improved behaviour under accident conditions was considered an important issue for the safety of light water reactors. A main feature of the new ATF cladding materials is a significantly reduced kinetics of steam oxidation, which is accompanied by slower heating and therefore a longer time period before temperatures reach the melting point compared to zirconium-based cladding currently used in LWRs. One of the materials studied is FeCrAl: at 1200 °C, the oxidation rate of FeCrAl is about a factor of 1000 lower than for zirconium. A slower reaction of FeCrAl with steam therefore reduces the rate of hydrogen generation, slowing down the pressure build-up in the pressure vessel and delaying the onset of hydrogen release into the containment [1], [2]. Another option are coated claddings like Cr-coated optimised Zirlo, which have a much slower oxidation than uncoated claddings, but once the protective state of the Cr-coating is lost at app. 1330 °C the oxidation of pure Zr at high temperatures occurs, leading to a potential escalation [3].
Currently severe accident codes like AC² or ASTEC are qualified for both kind of ATF, but the status is different for the codes and ATF concepts. In the paper the status is shortly described and the results of the application on different experiments in different facilities is evaluated. The focus of the experiments calculated is mainly on the IAEA ATF-TS (Testing and Simulation for Advanced Technology and Accident Tolerant Fuels) [4] project. Additionally, the QUENCH-15 scenario will be applied on a Cr-coated bundle in the QUENCH facility and simulated with modified AC² and ASTEC. Complementary to the IAEA ATF-TS is the OECD QUENCH-ATF, which deals with Cr-coated claddings for DBA and DEC conditions [5], but is not focus of this paper.

2. CURRENT STATUS OF ATF MODELLING IN AC² AND ASTEC

The codes AC² and ASTEC are both able to predict the cladding behaviour of ATF namely FeCrAl and Cr-coating. While for AC² the oxidation model for FeCrAl and Cr-coatings are directly implemented in the code, in ASTEC there is the possibility to implement the data for oxidation and layer thickness growth directly in the input deck by the user. FeCrAl models are used for a longer time since the conduction of QUENCH-19 and permanently updated. For that, the dedicated correlations for the components used are considered. AC² allows the application of different correlations for different components, e.g Kanthal APM and B136Y like in QUENCH-19.
For Cr-coated claddings the phenomena are a bit more complex due to the additional Cr layer and related eutectics but the general model approach is the same like for Zr oxidation. In AC² a first model was implemented and applied by Ruhr-Universitaet Bochum which considers the Cr-coating oxidation until postulated failure at app. 1300 °C and standard Zr oxidation afterwards. This means that above this temperature nearly pure metallic Zr reacts with water or steam which could lead to stronger oxidation compared the pre-oxidised Zr like in classical claddings. The derived correlation from experimental data for Cr-coated claddings is shown in Figure 1 compared to the standard Zr oxidation correlation for Zr.

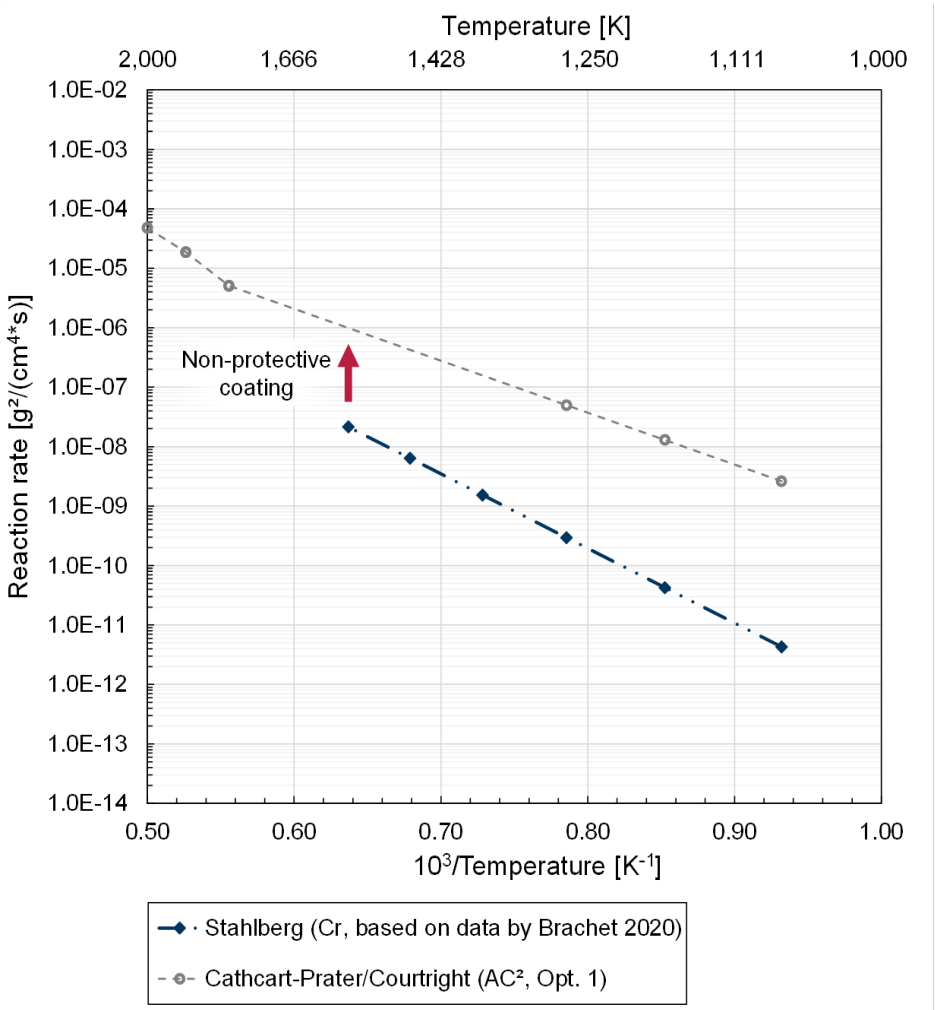

Figure 1. Derived reaction rates for Cr-coated claddings compared to standard Zr oxidation [3].

3. IAEA ATF-TS

The IAEA CRP ATF-TS is a follow-up project of IAEA CRP ACTOF and deals with experimental and modelling activities for Cr-coated claddings and FeCrAl under DBA and DEC conditions. Both single effect tests and bundle tests are considered which leads to a wide number of data and models for both ATF cladding concepts to enlarge the knowledge of their behaviour especially with regard to oxidation and ballooning/burst. As AC² and ASTEC are both able to calculate both ATF concepts they are applied for the bundle tests which are the objective within the CRP. Afterwards, the results for QUENCH-19 and its improved results since 2022 as well as pre-test simulations for a CODEX experiment with mixed Zr and Cr-coated claddings are given.

3.1. QUENCH-19

The experiment QUENCH-19 was the first QUENCH test dealing with ATF claddings, namely FeCrAl performed in 2019. For this, the QUENCH facility located at KIT was used with an electrically heated 24 rod bundle. A detailed description of the facility and implemented components are given in [6]. The scenario of the experiment QUENCH-15 with the same bundle geometry but optimised Zirlo claddings was

considered, which needed to be adjusted to achieve the test targets with a temperature below melting of FeCrAl at app. 1500 °C. QUENCH-19 was widely used for code validation and also presented at 10th ERMSAR in 2022 [7], which is used as basis to assess the improved capabilities of AC² and ASTEC.

3.1.1. Test conduct

Figure 2 shows the course of the QUENCH-19 experiment in comparison to the reference test QUENCH-15 [**Fehler! Verweisquelle konnte nicht gefunden werden.**]. The gradual increase in the electrical power output up to a maximum value of 18.12 kW is identical in both experiments. While in test QUENCH-15 a temperature excursion had already occurred when this power was reached, and the power was therefore switched off, Q-19 showed a temperature that was approx. 500 °C lower. Therefore, a power plateau was maintained at a constant value of 18.32 kW causing the maximum temperature to reach 1455 °C. Afterwards, the power was first reduced to 4.34 kW and finally switched off completely.
With regard to the feed-in mass flows of steam and argon, the comparison shows that the argon inflow rate of 3.5 g/s was identical for both tests, but the inflow rate for steam was slightly higher for QUENCH-19 than for QUENCH-15 (3.8 g/s and 3.2 - 3.4 g/s, respectively). The temperature of the inflowing steam and argon mixture is also about 80 °C lower for QUENCH-19 at 640 °C at the beginning of the test compared to the reference test. Thus, the comparison of these similar but not identical boundary conditions already provides a first indication of a possible reason for the difference of 200 °C occurring at the plateau of the maximum temperature already during the pre-oxidation phase, in which the different oxidation behaviour should not yet have a major influence.
After a maximum cladding tube temperature of 1455 °C was reached in Q-19, the water inflow was started at ~9100 s simultaneously with the reduction of the electrical power. While no temperature excursion was measured at the height of the maximum bundle temperature (950 mm), at the height of 1050 mm a brief increase can be recognized in the measured course before the start of the feed, which, however, did not reach the melting temperature of 1500 °C. The temperature excursion is also visible at the height of the maximum bundle temperature (850 mm). With the water injection of 46 g/s, the bundle is cooled down quickly.
The integral hydrogen production during the test was 9.2 g compared to 47.6 g for the QUENCH-15 test with a much shorter period of high electric power. While only a small fraction of 0.3 g was released during the pre-oxidation phase, there was a large increase after the maximum temperature had exceeded 1400 °C.

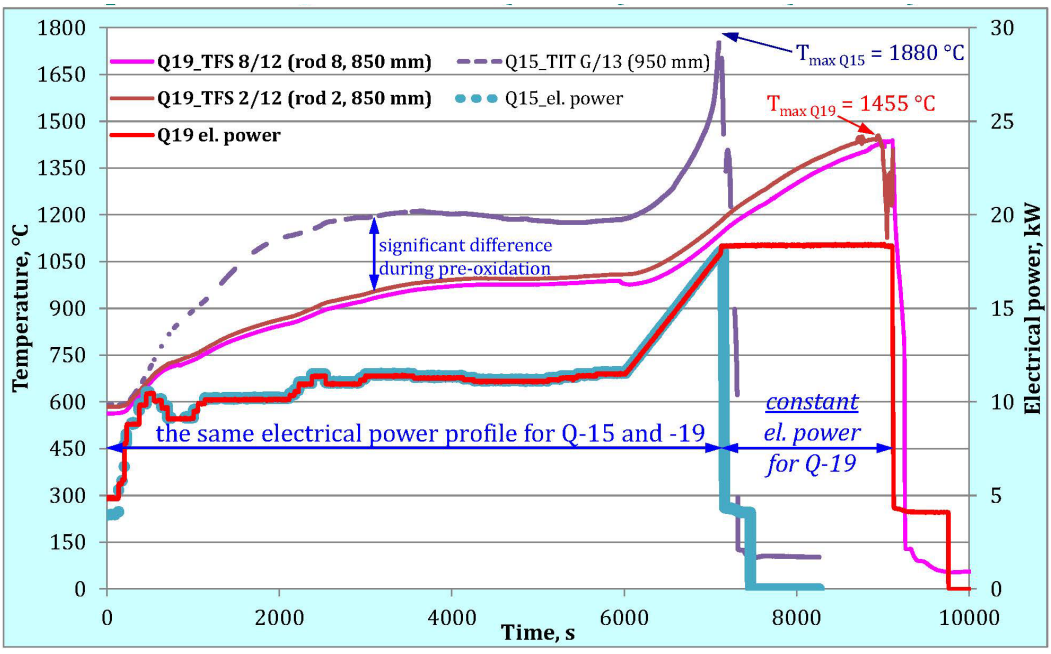

Figure 2. QUENCH-19 test conduct [Fehler! Verweisquelle konnte nicht gefunden werden.**].**

3.1.2. Simulation results

In Figure 3 and Figure 4 the simulation results achieved in 2022 [7] and 2024 with improved FeCrAl modelling in both codes are compared to measured data. The temperature evolution at 950 mm, which is the hottest elevation in the experiment, is overestimated in all simulations, but show a qualitatively correct behaviour for most of the transient. For AC² the melting temperature is never reached in both simulations which differs slightly to the experiment where melting is observed locally for a limited. Additionally, due to model improvements regarding the oxidation heat and masses it can be observed that at the time when the higher range of the correlation is active the temperature level increases. In contrast, ASTEC predicts an overestimation with escalation in the current calculations, which indicates that at that time and elevation also the hydrogen generation is overestimated. In general, the temperature evolution is improved for both codes except for the escalation in ASTEC (2024). For the hydrogen generation a significant qualitative and quantitative improvement can be observed in Figure 4 for both codes due to the enhanced FeCrAl oxidation modelling (e. g. [8]). In the current ASTEC (2024) simulation the measured value can be predicted while especially the oxidation in the pre-oxidation phase is calculated in better agreement to the experiment, but the change of the kinetics is noticeable in the calculated course. For AC² the B136Y correlation in 2022 was modelled via input and restarts and is now implemented directly in the code, which improves and smoothes the hydrogen generation. In general, both current simulations still predict the oxidation during the pre-oxidation phase in close agreement to the experiment, but subsequently show a too sharp increase afterwards, which could be potential for improvement, but needs to be evaluated with regard to the origin of the hydrogen in the experiments and its modelling in the codes.

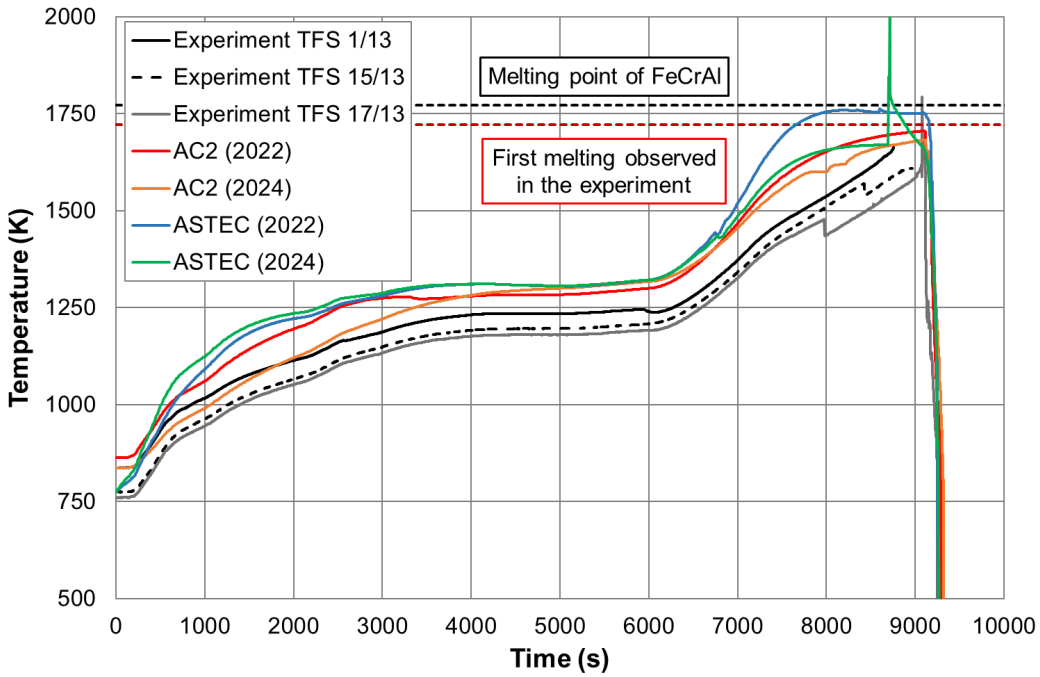

Figure 3. Measured and calculated temperatures at 950 mm.

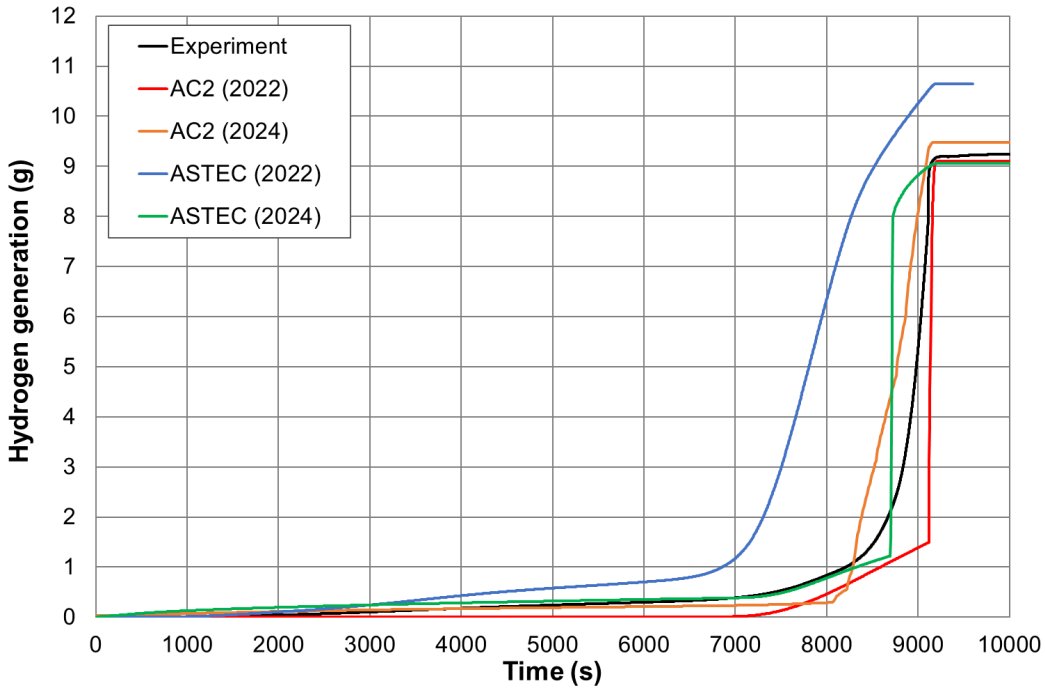

Figure 4. Measured and calculated hydrogen generation

3.1.3. Main findings

Both codes, AC² and ASTEC, are able to predict the transient evolution of QUENCH-19 correctly in most ranges regarding cladding temperature and hydrogen generation. Some deviations to the experimental behaviour can be observed but are reduced compared to previous simulations in 2022. That shows that the ongoing model development for FeCrAl oxidation and rod behaviour significantly improves the simulation results and the predictability of the codes. Nevertheless, the oxidation of individual FeCrAl compositions are different and currently only Kanthal APM and B136Y were considered in QUENCH-19 and validated for AC² and ASTEC.

3.2. CODEX-ATF1

In the frame of IAEA CRP ATF-TS the experiment CODEX-ATF1 was performed as the first ATF experiment in the CODEX facility which was frequently used for experiments with Zr based claddings under steam or/and air injection conditions.

3.2.1. Bundle Configuration and Proposed Test Conduct

The 7-rod test bundle of the CODEX facility is given in Figure 5. For the test CODEX-ATF1 two different types of claddings are implemented, four Cr-coated optimised Zirlo claddings and three uncoated optimized Zirlo claddings, which are located in the outer section with an angle of 120° [9]. The rods are electrically heated by an u-shape wire. The bundle is surrounded by a Zr2.5%Nb shroud which is insulated on the outer side.
The proposed scenario within this CRP should focus on the following phenomena [9]:

- Ballooning and burst,
- Oxidation of cladding external surface in high temperature steam,
- Oxidation of inner cladding surface and secondary hydriding after burst,
- Eutectic formation between Zr-Cr above 1300 °C.

For the specification of the test in order to fulfil the objectives above, some initial and boundary conditions for the length and power for the different phases prepatory, heat-up I and II as well as quenching by water were proposed as given in Table I.

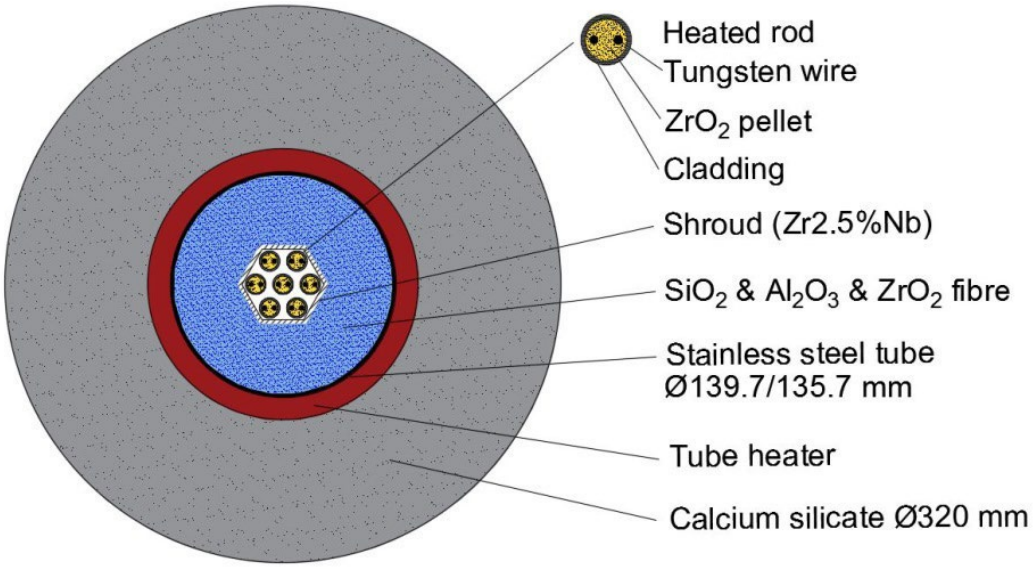

Figure 5. CODEX-ATF1 test bundle [9].

Table I. Scenarios investigated with AC²

Phase	Number of scenarios		Power (W)	Argon (g/s)	Steam/water (g/s)
	NUBIKI	Original			
Prepatory	0 - 1500	0 - 1500	600 (400, AC²)	0.2	0 - 0.2
Heat-up I	1500 - 2300	1500 - 2000	1000	0.2	0.2
Heat-up II	2300 - 2500	2000 - 3000	2000	0.2	0.2
Quench	2500 - 4000	3000 - 4000	0	0.0	10.0

3.2.2. Simulation Results

AC² simulations were performed for both scenarios also investigating the impact of Cr-coated claddings in addition to the three Optimised ZirloOptimised Optimised Zirlo rods. Additionally, for the Cr-coated claddings also two cases were considered: only Cr oxidation at any temperature and Zr oxidation after coating failure above 1300 °C as proposed in [3]. For the mixed core the different claddings need to be separated due to code specific limitations. Cr-coating rods are modelled as ECORE structure with the full capabilities of core degradation phenomena, while the three optimised Zirlo rods are modelled as HECU structure with limited capabilities during core degradation. This approach is valid as long as melting does not occur, which was one objective of the test. If melting temperatures are reached for HECU, failure is predicted, but in a simpler way than for ECORE objects. The matrix and names of each scenario is given in Table II.

Table II. Scenarios investigated with AC²

Name	Cr oxidation (ECORE)	Zr oxidation (HECU)
NUBIKI	Brachet (Cr only)	Cathcart Prater/Courtright
Original	Brachet (Cr only)	Cathcart Prater/Courtright
Escalation	Stahlberg with Cathcart Prater/Courtright above 1300 °C (Cr and Zr, cp. Figure 1)	Cathcart Prater/Courtright

In Figure 6 the predicted cladding temperatures at 550 mm, which is the highest and hottest elevation in CODEX, are given for all three scenarios separated into Cr-coated claddings and optimised Zirlo claddings. For the NUBIKI scenario, due to the shorter period of heat-up and power increase, both claddings show no temperature escalation above 1300 °C. That means for that case the protective character of the Cr-coating remains intact. The original scenarios lead to significantly higher temperatures with a maximum of app. 1500 °C for the Cr-coated claddings, while for optimised Zirlo rods temperatures up to 1750 °C are calculated, which is shortly below the melting temperature of optimised Zirlo.
The escalation case with optimised Zirlo oxidation after failure of Cr-coating leads to the highest cladding temperatures. For the coated claddings the temperature increases significantly above 1300 °C due to the oxidation of pure metal. By the generated heat also the temperature of the optimised Zirlo claddings rises which forces a more escalated oxidation of Zr. After some time, when the oxidation slows down also the temperatures of optimised Zirlo decrease again. This effect strongly shows the modelled interaction between the different components in AC², although the differences in cladding temperature are quite high and needs to be further investigated.

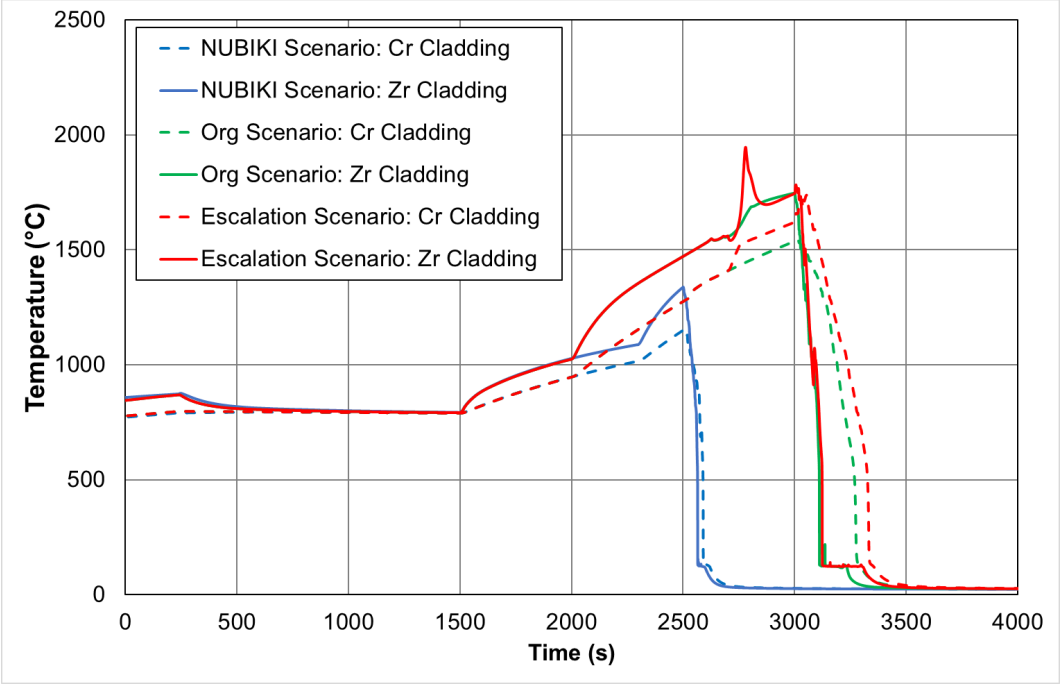

Figure 6. Calculated cladding temperatures at 550 mm

Corresponding to the temperature level of the different cases the hydrogen generation differs strongly between the NUBIKI scenario and the escalation scenario (Figure 7). For the NUBIKI case app. 1 g of H_2 is produced by optimised Zirlo only. AC² predicts app. 9.3 g H_2 including nearly 4 g from Cr oxidation. The highest mass of hydrogen is produced for the escalation scenario leading to app. 15 g. In this scenario the Cr oxidation with subsequent Zr oxidation above 1300 °C leads to 7 g H_2, which is nearly half of the total amount. The results show that Cr-coating reduces the mass of hydrogen as long as the layer is intact, but if

the transition is reached and temperatures go higher, the oxidation of metallic Zr leads to an escalation of the whole bundle.

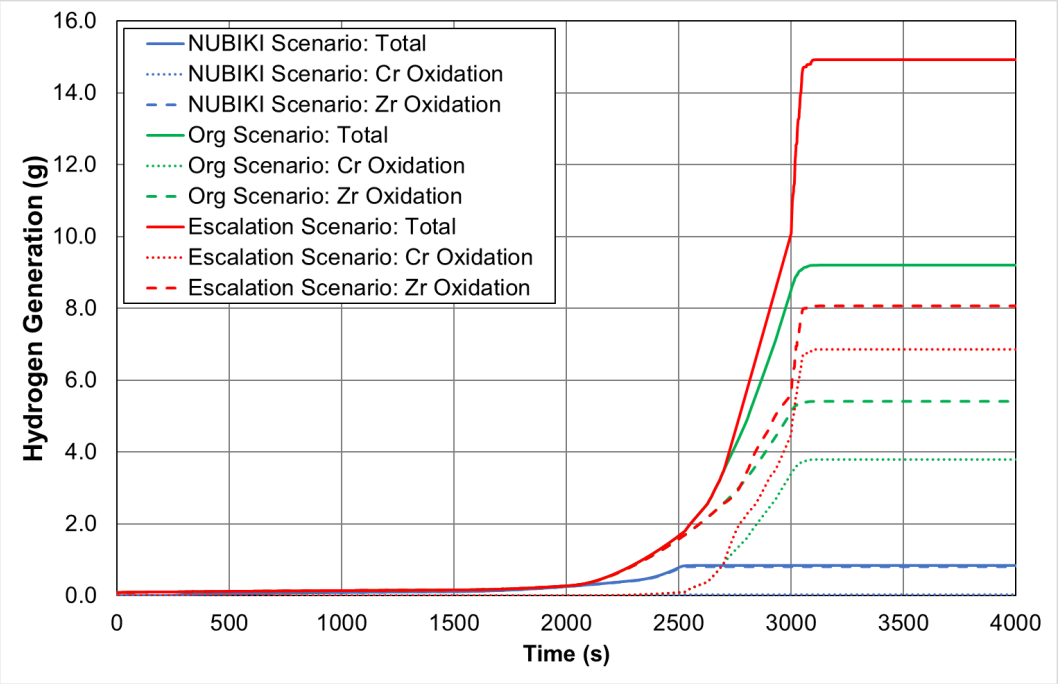

Figure 7. Calculated cladding temperatures at 550 mm

3.2.3. Main Findings

In general, AC² is able to predict the CODEX-ATF1 configurationm with mixed bundle claddings. Therefore, some assumptions are necessary. Especially, the separation of Cr-coated and Zr claddings into different structures due to code limitations. This requires further investigations about the thermal coupling of these structures.
The chosen scenarios show significantly different results of the specidication simultions:

- Due to shorter heat-up phases and power in the NUBIKI scenario the temperatures are predicted to be below 1150 °C for the Cr-coated cladding and 1350 °C for the Zr cladding.
- The total H_2 generation is below 1 g with less than 0.05 g from Cr oxidation.
- The original scenario leads to temperatures up to 2000 °C, if oxidation of pure Zr is considered above 1300 °C of Cr-coated claddings. Otherwise up to 1800 °C during quenching.
- In accordance to that, hydrogen generation is higher, up to 15 g.

Due to the assumptions and model limitations these results give only a first trend of the scenario evolution and was used a basis for the set-up of the CODEX-ATF1 experiment.

4. APPLICATION OF QUENCH-15 SCENARIO FOR CR-COATED CLADDING

To investigate the impact of Cr-coated cladding compared to optimised Zirlo, simulations were performed for the QUENCH-15 scenario applied on the 24 rod bundle used for that experiment. Therefore, simply the cladding material was changed in the AC² and ASTEC simulations, that means mainly material properties and oxidation correlation.

4.1. Test Scenario

The considered QUENCH-15 severe accident scenario and qualitative temperature evolution are given in Figure 8. After pre-oxidation with limited hydrogen generation, the power was increased in the transient phase leading together with oxidation by a constant steam flow to a maximum temperature of app. 2153 K at the beginning of subsequent reflooding of the bundle with water. Investigations revealed that the melting temperature of optimised Zirlo is reached for certain rods at the highest heated elevations. After a short temperature increase during quenching, the bundle was subsequently cooled down. The hydrogen generation significantly increased during the transient phase and the beginning of reflooding due to the strongly exothermal character of the Zr-steam reaction. The objective when considering Cr-coating is to compare the temperature and hydrogen generation to evaluate the effectiveness of Cr-coated claddings under severe accident conditions. [10]

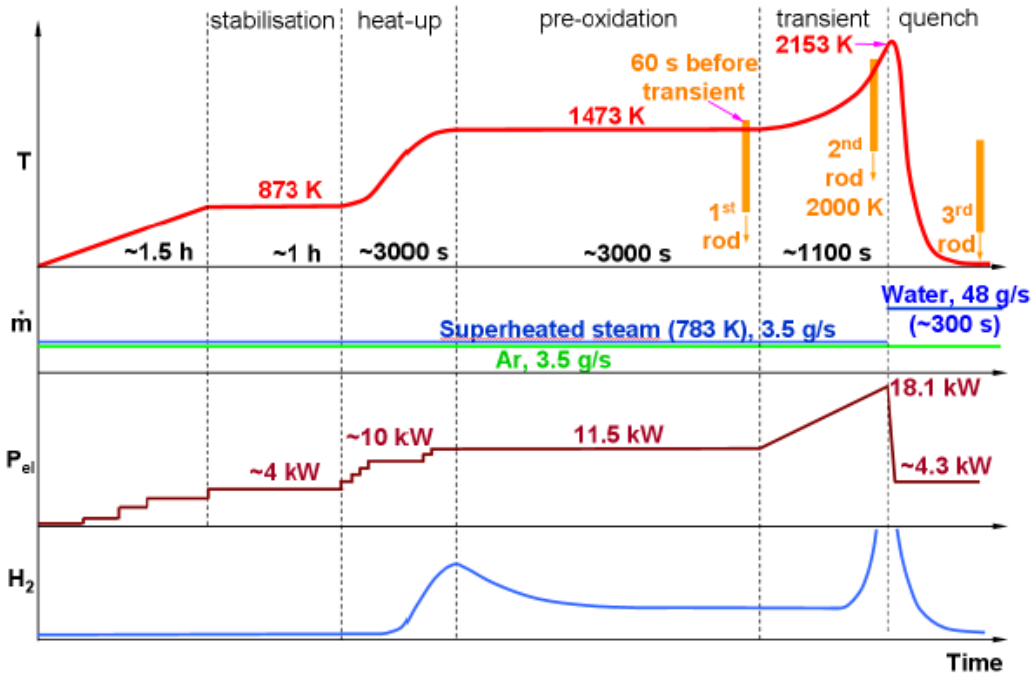

Figure 8. Original QUENCH-15 Scenario [10]]

4.2. Simulation with AC²/ATHLET-CD and ASTEC

4.2.1. Nodalisation

Figure 9 shows the nodalisation schemes for AC² (left) and ASTEC (right). Both models consist of three radial objects which reflects the 24-rod bundle geometry as used also for QUENCH-15, which is given in the middle of Figure 9. The axial separation into 10 nodes is also used in both approaches. The bundle is surrounded by the shroud and its insulation which is also considered for both nodalisations. The oxidation correlation in both simulations use a change from Cr-coating to Zr oxidation at 1300 °C with a transition ramp. Additionally, a second simulation is performed with AC² considering the transition at 1200 °C to investigate the impact of the uncertainty of the transition. For both codes the same standard correlation for Zr oxidation is applied. [11]

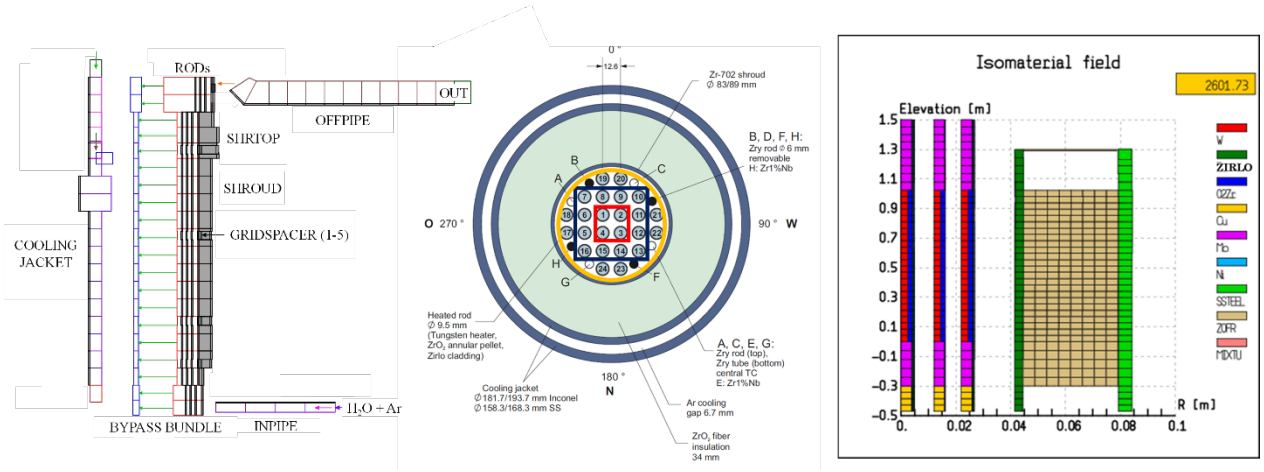

Figure 9. AC²/ATHLET-CD and ASTEC nodalisation with reference to QUENCH bundle

4.2.2. Simulation Results

First both codes were applied on the QUENCH-15 experiment to evaluate the quality of the input deck and chosen model options. The results show good agreement for both codes compared to the experimental data, but not given in the following due to clarity.

The results of the Cr-coating simulations show for both codes that during the pre-oxidation phase a higher temperature level is predicted compared to the measured QUENCH-15 data at 950 mm (Figure 10), but this is in agreement to the original QUENCH-15 results. In that phase the limited oxidation of Cr-coating has nearly no effect on the results because the related heat generation is low, although the specific one for Cr oxidation is higher than for Zr oxidation. When the transition temperature is reached and oxidation of pure Zr is considered, the temperatures rise in all simulations but does not reach melting temperature like it was observed in the QUENCH-15 experiment. A comparable behaviour but on lower level is predicted on the lower bundle elevations [11]. The results of the simulations imply that a temperature increase occurs due to the transition from Cr to Zr oxidation, but maybe not so severe as expected. For the hydrogen generation the effect of the transition can be observed much clearer as given in Figure 11. As long as Cr-coating is intact the hydrogen generation is much lower compared to optimised Zirlo in QUENCH-15, but afterwards the production is higher, which still leads to lower total masses than for optimised Zirlo. The predicted hydrogen production shows that Cr-coating is effective for temperatures below Cr-coating failure and as long as the Cr oxides are not dissolved in the metal phase which is not modelled in both codes. Therefore, the concept seems to offer some potential benefits that are worth considering in more detail. Ongoing research and development efforts should focus on addressing some current model limitations to ensure the predictive capabilities of the codes regarding the Cr-coating approach.

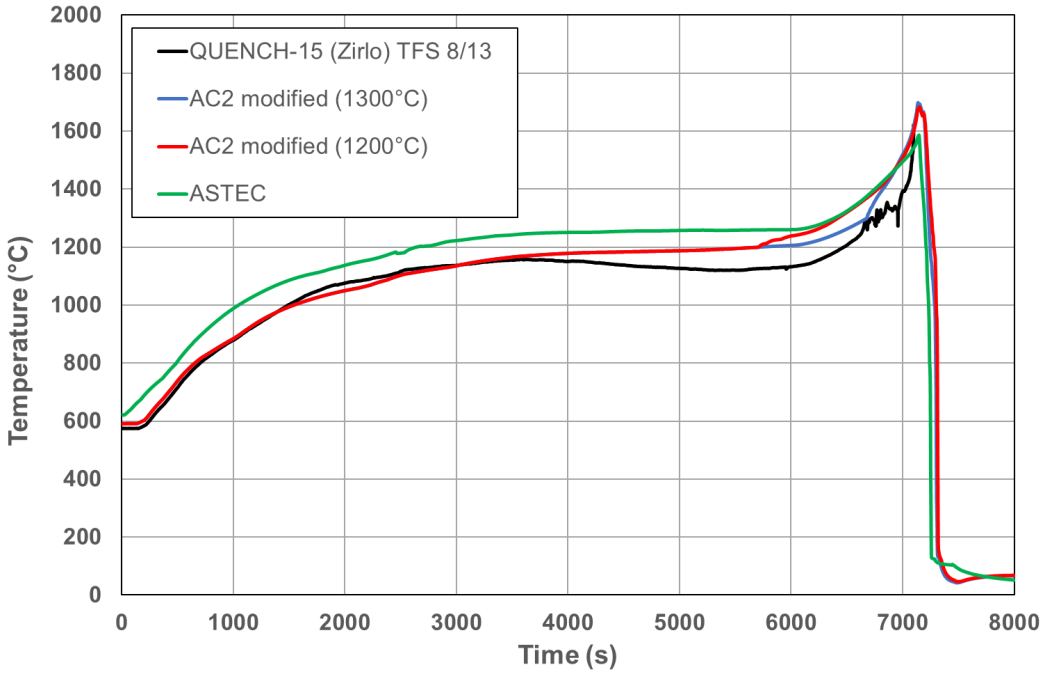

Figure 10. Calculated Cladding temperatures at 950 mm with reference to QUENCH-15

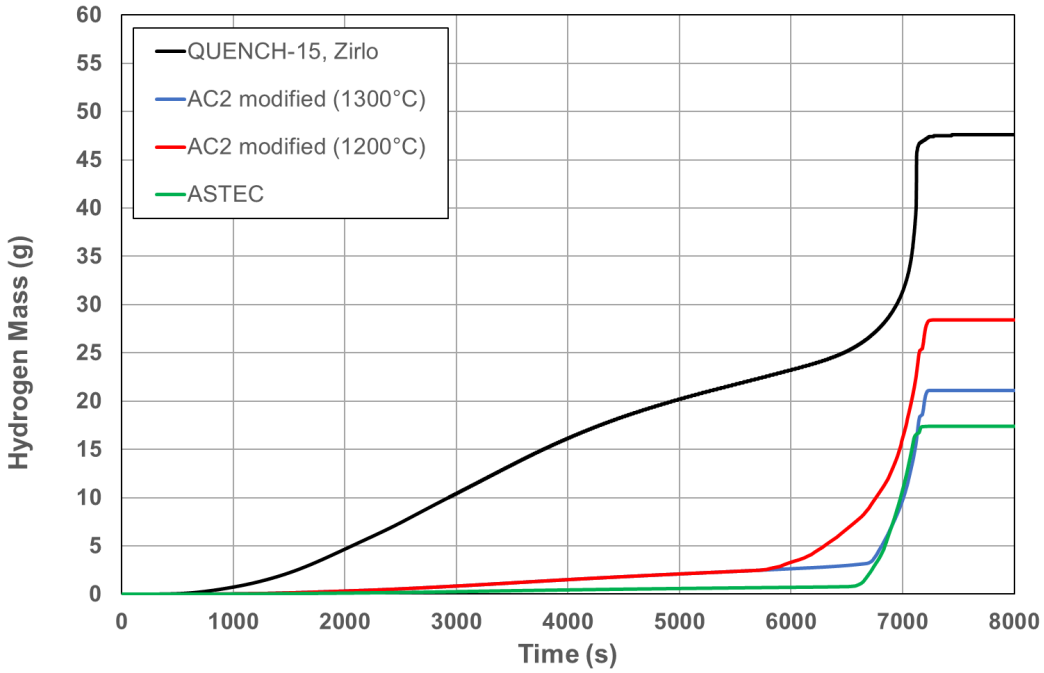

Figure 11. Calculated hydrogen generation with reference to QUENCH-15

4.3. Main Findings

AC² and ASTEC are able to predict scenarios with Cr-coated claddings applied on existing QUENCH test QUENCH-15. For the QUENCH-15 severe accident scenario nearly no influence on the temperature behaviour is predicted by the application of Cr-coated claddings, but the hydrogen generation is less for Cr-coated claddings due to the low hydrogen generation as long Cr acts as a protective layer. Afterwards, the

hydrogen generation is higher compared to the optimised Zirlo cladding oxidation, but no temperature escalation is predicted due to that. In total the hydrogen production is predicted lower for Cr-coated claddings compared to optimised Zirlo.

5. CONCLUSION

Currently investigated ATF concepts like FeCrAl and Cr-coating are topic of several international projects and activities. Beside the experiments on separate effect level also bundle experiments are carried out to estimate the impact of both concepts in comparison to classical Zr alloy claddings. Therefore, well known scenarios are applied for bundle configurations with FeCrAl or Cr-coated rods. For the analyses of these experiments and also for the application on reactor scale the two code packages to be applied for severe accident conditions AC² developed by GRS and ASTEC developed by IRSN and KIT were enhanced for ATF claddings and will be further improved.
The application of both codes on different bundle experiments dealing with FeCrAl and Cr-coatings show that both codes can predict the observed test behaviour regarding temperature evolution and hydrogen generation. The results obtained for QUENCH-19 with FeCrAl claddings show a significant improvement of the model basis in the last two years.
Additionally, the implemented model basis in AC² was used for specification simulations for CODEX-ATF1 which considers Cr-coated claddings and optimised Zirlo in a mixed bundle. The predictions show a significant impact of the Cr-coatings when the coating fails and pure metal can oxidise. The test was performed in 2023 and post-test analyses will be carried out to evaluate the predictions and investigate in detail the results of post-test simulations. Both codes were also applied on a QUENCH test, assuming a Cr-coating. The simulations show that compared to the reference scenario with optimised Zirlo the hydrogen generation is lower in total, but higher above 1300 °C when Cr coating fails. In that phase the temperatures rise but does not escalate as expected in the predictions. In general, the validation basis for ATF namely FeCrAl and Cr-coating is limited for bundle experiments and needs an enlargement to evaluate the model basis for ATF claddings in severe accident codes and to further improve the phenomenological understanding, also with respect to eutectics.

ACKNOWLEDGMENTS

The work of GRS is sponsored by the German Federal Ministry for the Environment, Nature Conservation, Nuclear Safety and Consumer Protection (BMUV).
The work of RUB PSS is funded by the German Federal Ministry for the Environment, Nature Conservation, Nuclear Safety and Consumer Protection (BMUV) under grant number 1501629 based on a decision by the German Bundestag.

Responsibility for the content lies with the authors.

The latest results were obtained using

- an in-house modified version of the GRS software package AC² 2021.0 at PSS and GRS (for Cr coating)
- AC² 2023 (for FeCrAl),
- ASTEC V3, developed by IRSN, at KIT.

REFERENCES

1. NEA, “State-of-the-Art Report on Light Water Reactor Accident-Tolerant Fuels”, NEA No. 7317, Nuclear Energy Agency, Organisation for Economic Co-Operation and Development, 2018.

2. IAEA, “Analysis of options and Experimental Examination of Fuels for Water Cooled Reactors with Increased Accident Tolerance (ACTOF)”, Final Report of a Coordinated Research Project, IAEA-TECDOC-1921, International Atomic Energy Agency, Vienna, 2020.
3. Stahlberg, G., Koch, M.K.: “Development of a model for Cr-coated Claddings for System Codes”, Proceedings of the 28th International QUENCH Workshop, 5-7 December 2023, Karlsruhe Institute of Technology, Karlsruhe, Germany, Editor: Martin Steinbrück, DOI: 10.5445/IR/1000165938
4. IAEA, “Testing and Simulation for Advanced Technology and Accident Tolerant Fuels (ATF-TS)”, International Atomic Energy Agency, Vienna, https://nucleus.iaea.org/sites/connect/NFEpublic/Pages/ATF-TS.aspx, last check: 19.04.2023.
5. NEA, “QUENCH-ATF project, Nuclear Energy Agency, Organisation for Economic Co-Operation and Development, https://www.oecd-nea.org/jcms/pl_36597/quench-atf-project, last check: 19.04.2023.
6. Stuckert, J., Grosse, M., Steinbrück, M.: “Results of the bundle test QUENCH-19 with FeCrAl claddings”, Wissenschaftliche Berichte NUSAFE 3574, Karlsruher Institut für Technologie, 2022, DOI : 10.5445/IR/1000148370.
7. Hollands, T. e “”, Proceedings of the 10th European Review Meeting on Severe Accidents Research (ERMSAR2022): Severe Accident Research Eleven Years after the Fukushima Accident, Karlsruhe, Deutschland, 16.05.2022 – 19.05.2022, Karlsruher Institut für Technologie (KIT), DOI: 10.5445/IR/1000151444.
8. Lovasz, L., Pandazis, P.: “Simulation of an SBO Accident in a PWR with AC2/ATHLET-CD with and without using ATF Cladding Material”, Proceedings of the 32nd International Conference Nuclear Energy for New Europe (NENE) 2023, Portoroz, Slovenien, September 11-14, 2023
9. Farkas, R. et al.: “The CODEX-ATF experiment”, Proceedings of the 28th International QUENCH Workshop, 5-7 December 2023, Karlsruhe Institute of Technology, Karlsruhe, Germany, Editor: Martin Steinbrück, DOI: 10.5445/IR/1000165938.
10. Stuckert, J. et al.: “Results of Severe Fuel Damage Experiment QUENCH-15 with ZIRLO cladding tubes”, KIT Scientific Reports KIT-SR7576, KIT Scientific Publishing, ISBN: 978-3-86644-670-0, 2011.
11. Hollands, T., Stahlberg, G., Gabrielli, F.: “Simulation of QUENCH-03 and -15 Scenarios with the Code AC² modified for Cr-coated Claddings compared with ASTEC”, Proceedings of the 28th International QUENCH Workshop, 5-7 December 2023, Karlsruhe Institute of Technology, Karlsruhe, Germany, Editor: Martin Steinbrück, DOI: 10.5445/IR/1000165938.

APPLICATION OF AC²/ATHLET-CD AND ASTEC FOR ATF EXPERIMENTS IN THE FRAME OF ONGOING INTERNATIONAL PROJECTS

Thorsten Hollands (GRS)
Fabrizio Gabrielli, Mauricio Cazado, Zaira Balbuena (KIT)
Gregor T. Stahlberg (RUB-PSS)

The 11th European Review Meeting on Severe Accident Research (ERMSAR2024)
KTH, Stockholm, Sweden
May 13-16, 2024

Outline

- Motivation and Objective
- Modelling Approach
  - Correlation
  - TFD-Model for AC² and ASTEC
- Experiment and Simulation Results
  - QUENCH-15 (AC² and ASTEC)
  - QUENCH-03 (AC²)
- Conclusions

Motivation and Background

- The investigation of ATF (Accident Tolerant Fuels) materials had already started before the accident at the Fukushima Daiichi plant in 2011.
- A main objective for new ATF cladding materials is a significantly reduced kinetics of steam oxidation, which is accompanied by slower heating and therefore a longer time period before temperatures reach the melting point compared to zirconium-based cladding currently used in LWRs.
- Two options are currently under investigation with a certain TRL:
  - FeCrAl: at 1200°C, based on the composition the oxidation rate of FeCrAl could about a factor of 1000 lower than for zirconium. A slower reaction of FeCrAl with steam therefore reduces the rate of hydrogen generation, slowing down the pressure build-up in the pressure vessel and delaying the onset of hydrogen release into the containment.
  - Cr-coated optimised Zirlo: much slower oxidation than uncoated claddings, but once the protective state of the Cr-coating is lost at app. 1330 °C the oxidation of pure Zr at high temperatures occurs, leading to a potential escalation.

➢ Experimental and analytical projects are performed in the frame of IAEA and OECD

➢ Additionally, the modelling capabilities of severe accident codes were extended to be able to consider ATF. These new models need to be validated.

Current international projects for ATF

- **OECD QUENCH-ATF**

  The OECD/NEA QUENCH-ATF project was launched in 2021 to investigate the bundle behavior under DBA/DBC or DEC/BDBA/SA in three tests at the QUENCH facility at KIT

  - Optimised Zirlo with Cr-coating: LOCA conditions,
  - Optimised Zirlo with Cr-coating: BDBA conditions,
  - Optimised Zirlo with Cr-coating or SiCf-SiC cladding tubes (to be decided)

- **IAEA CRP ATF-TS** (Testing and Simulation for Advanced Technology and Accident Tolerant Fuels)

  Experimental and modelling activities for Cr-coated claddings and FeCrAl under DBA and DEC conditions

  - Separate Effect Tests
  - Bundle Tests like
    - QUENCH-19
    - CODEX-ATF-1

Current international projects for ATF

- **OECD QUENCH-ATF**

  The OECD/NEA QUENCH-ATF project was launched in 2021 to investigate the bundle behavior under DBA/DBC or DEC/BDBA/SA in three tests at the QUENCH facility at KIT

  - Optimised Zirlo with Cr-coating: LOCA conditions,
  - Optimised Zirlo with Cr-coating: BDBA conditions,
  - Optimised Zirlo with Cr-coating or SiCf-SiC cladding tubes (to be decided)

- **IAEA CRP ATF-TS** (Testing and Simulation for Advanced Technology and Accident Tolerant Fuels)

  Experimental and modelling activities for Cr-coated claddings and FeCrAl under DBA and DEC conditions

  - Separate Effect Tests
  - Bundle Tests like
    - **QUENCH-19**
    - **CODEX-ATF-1**

Current Status of ATF Modelling in AC²/ATHLET-CD and ASTEC

- AC² and ASTEC are both able to predict the cladding behaviour of ATF namely FeCrAl and Cr-coating.
- In AC²/ATHLET-CD the oxidation models for FeCrAl and Cr-coatings are directly implemented in the code.
- In ASTEC there is the possibility to implement the data for oxidation and layer thickness growth directly in the input deck by the user.

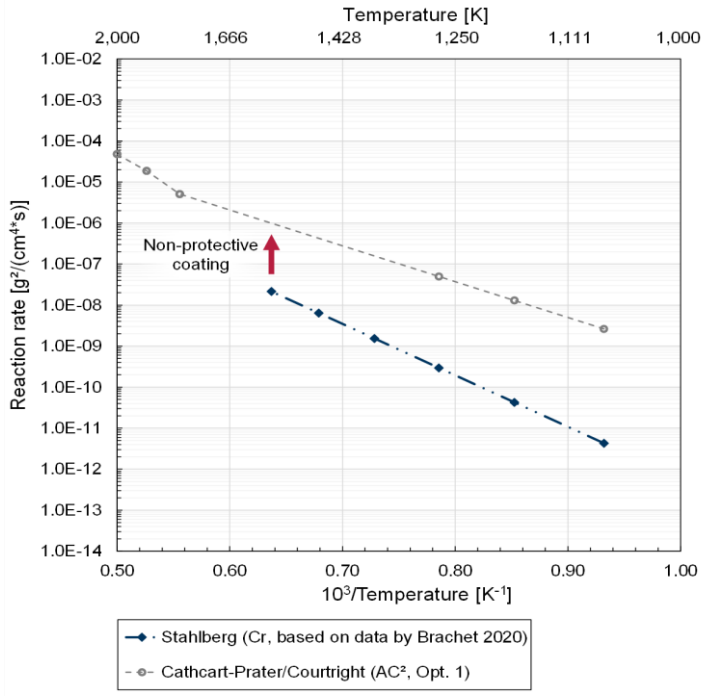

Cr-coating

B136Y

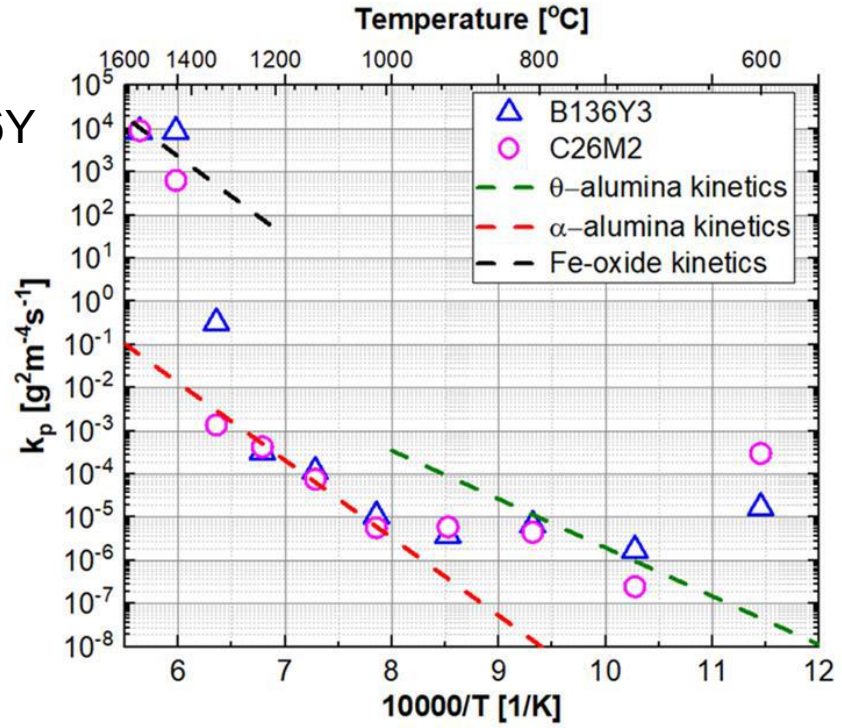

C. KIM et al.: OXIDATION KINETICS OF NUCLEAR GRADE FeCrAl ALLOYS IN STEAM IN THE TEMPERATURE RANGE 600-1500°C, TopFuel 2021

QUENCH-19

Bundle Configuration

- Performed at KIT 2018
- FeCrAl claddings to investigate the cladding material behavior under SA conditions
- Scenario: similar to QUENCH-15 with Zirlo cladding
  - same bundle geometry
  - same electrical power input
- Bundle configuration made of different FeCrAl alloys with slightly different compositions (see right):
  - 24 heated rods with tungsten heater and ZrO_2 pellet
  - 8 corner rods
  - 5 spacer grid
  - Shroud

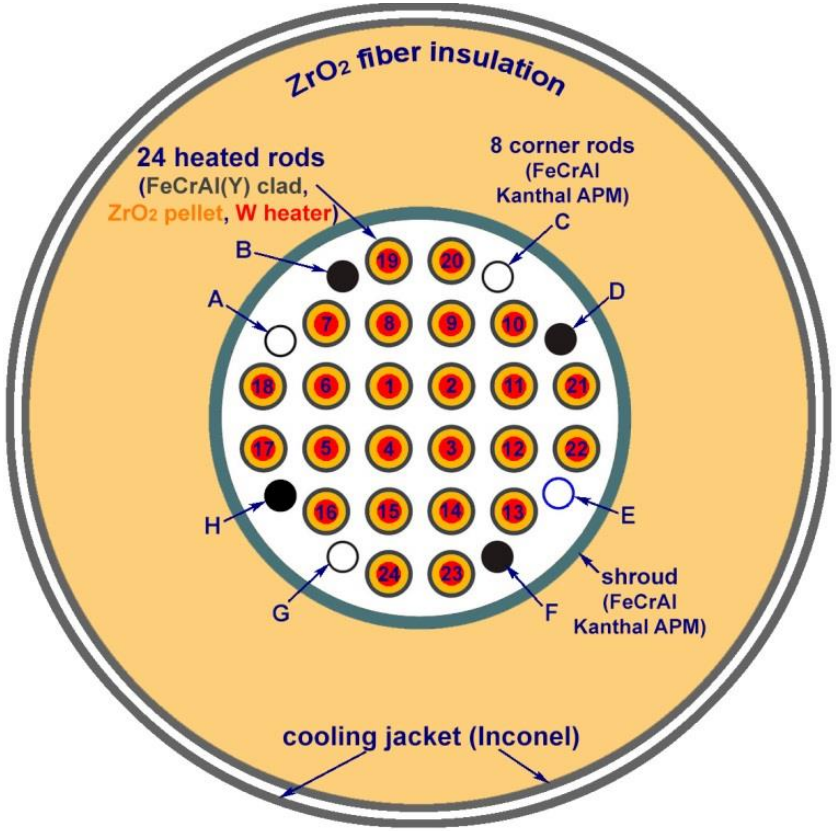

Source: KIT

Test Conduct

- Pre-Oxidation Phase 0 – 6020 s
- Transient Phase 6020 – 9106 s
- Quench Phase 9106 – 10000 s

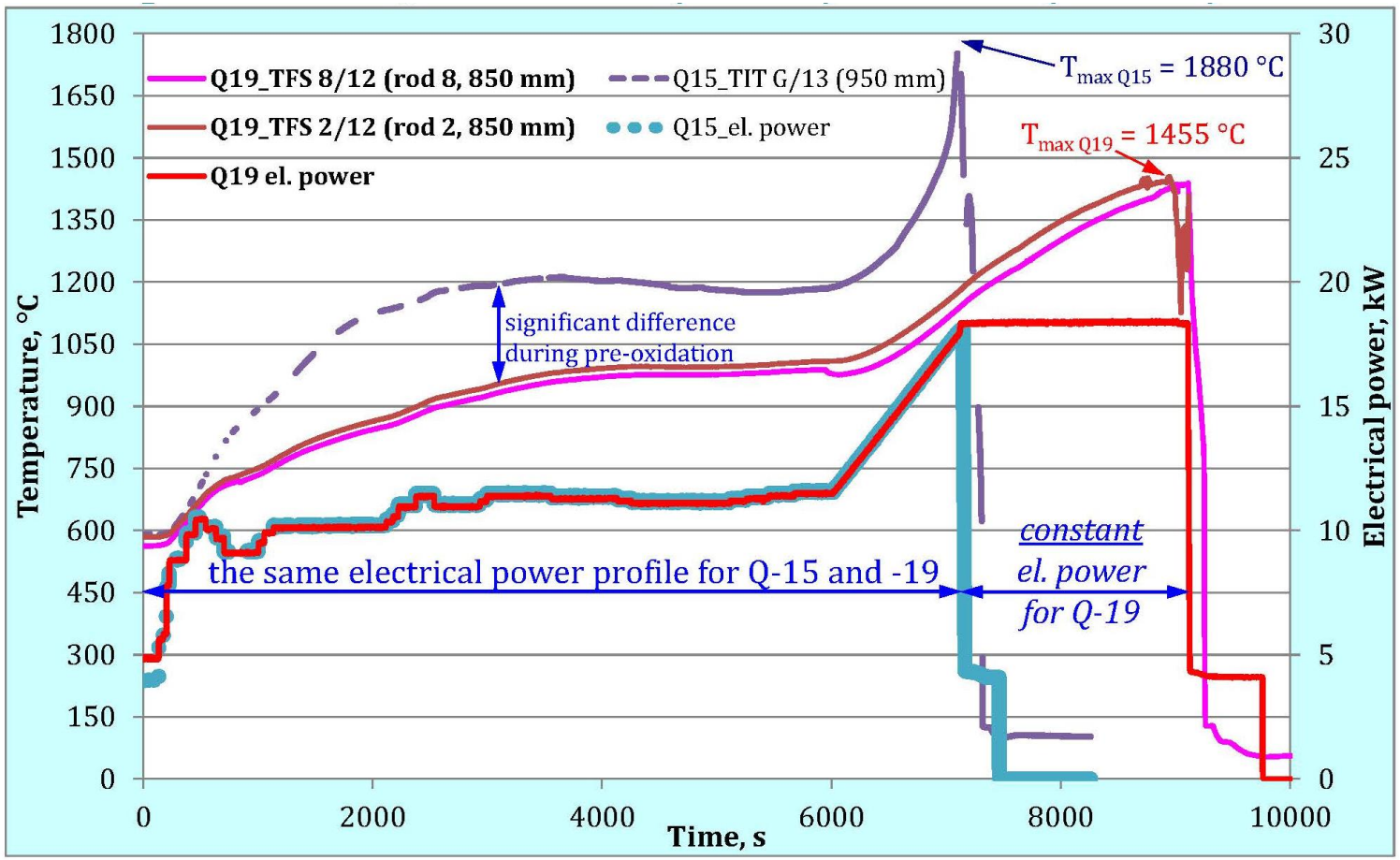

Source: KIT

Simulation Results – Cladding Temperatures at 950 mm

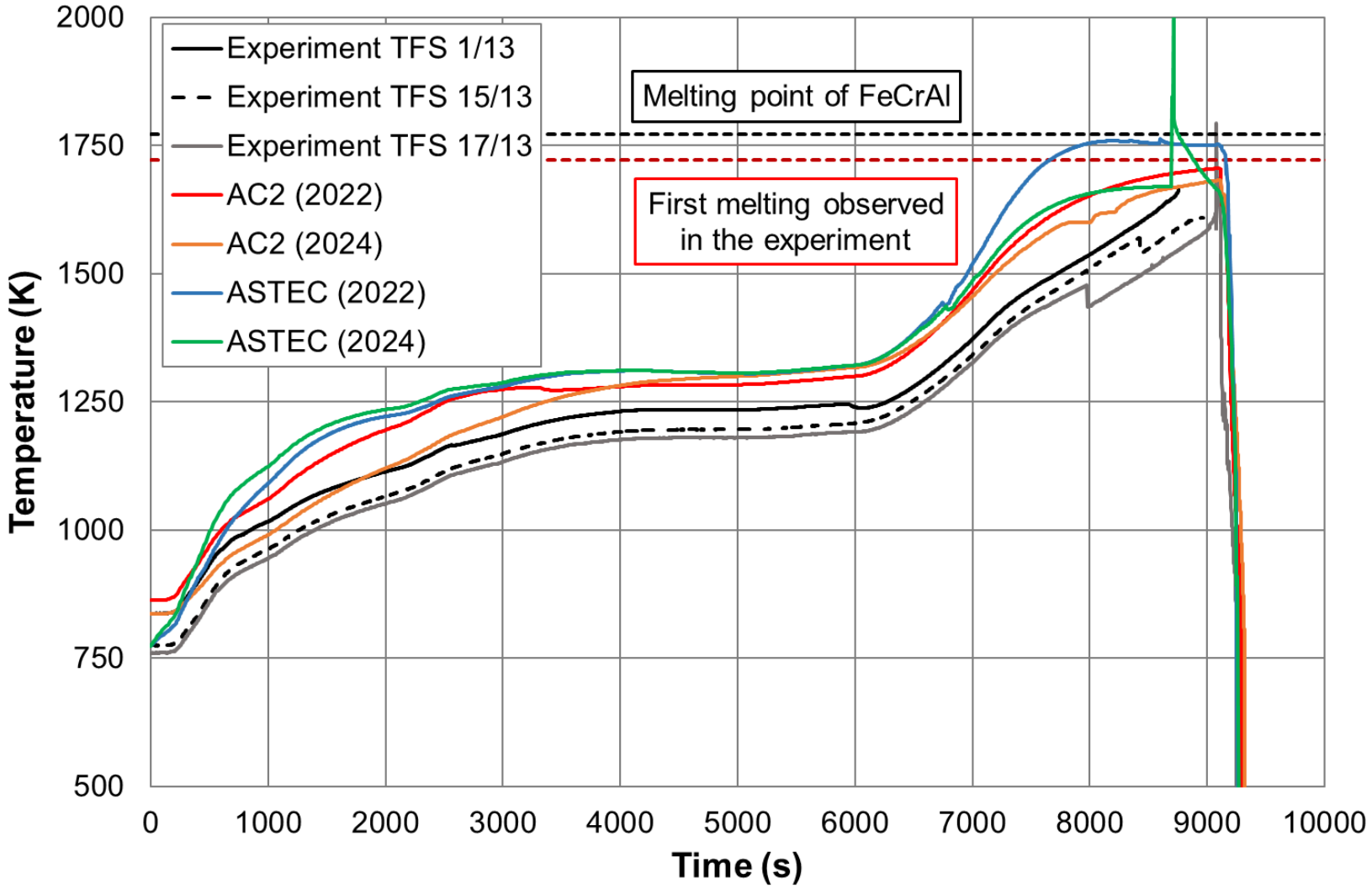

- The deviations to the measured cladding temperatures could be reduced due to model improvement.
- But there is still an overestimation at the highest heated elevation.
- A peak is predicted for ASTEC, while AC²/ATHLET-CD predicts no peak in contrast to the experiment.

Simulation Results – Hydrogen Generation

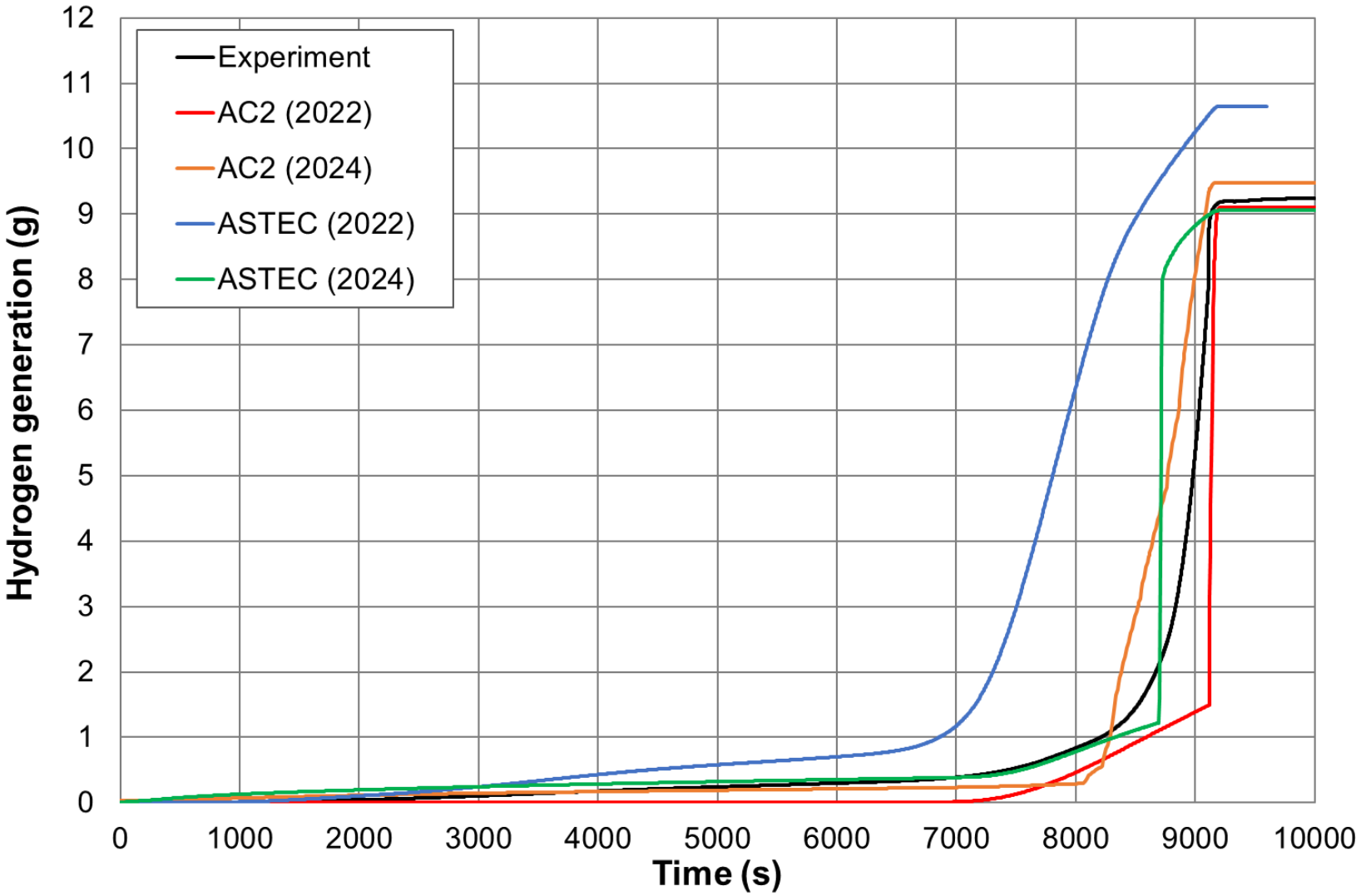

- The oxidation behaviour is in better agreement to the experiment due to the model improvement.
- For AC²/ATHLET-CD especially by implementing the model directly in the code which allows a nodewise prediction instead of a global as in 2022 simulations.

CODEX-ATF1

Bundle Configuration

- Performed at EK HUN 2023
- 7-rod test bundle
- For the test CODEX-ATF1 two different types of claddings are implemented:
  - four Cr-coated optimised Zirlo claddings and
  - three uncoated optimized Zirlo claddings, which are located in the outer section with an angle of 120°.
- The rods are electrically heated by an u-shape wire.
- Zr2.5%Nb shroud insulated on the outer side.

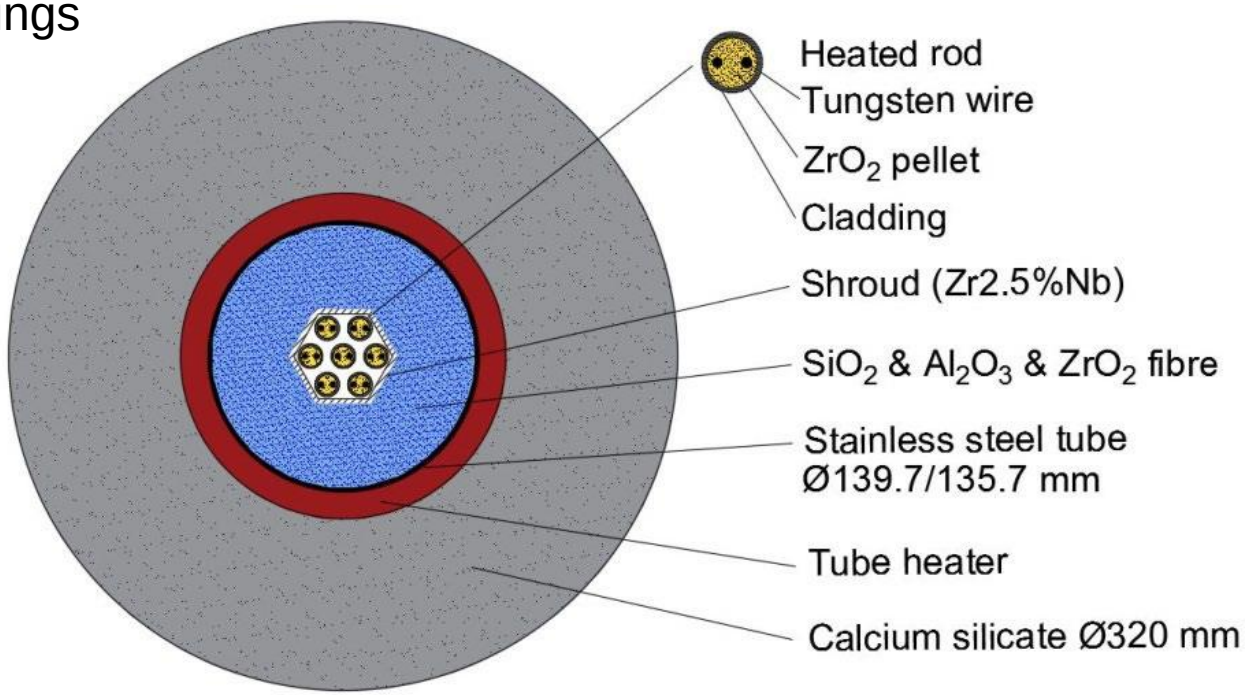

Source: EK HUN

Proposed Test Conduct

- The proposed scenario within CRP ATF-TS should focus on the following phenomena:
  - Ballooning and burst,
  - Oxidation of cladding external surface in high temperature steam,
  - Oxidation of inner cladding surface and secondary hydriding after burst,
  - Eutectic formation between Zr-Cr above 1300 °C.
- Scenario BIC

Phase	Number of scenarios		Power (W)	Argon (g/s)	Steam/water (g/s)
	NUBIKI	Original			
Prepatory	0 - 1500	0 - 1500	600 (400, AC^2)	0.2	0 - 0.2
Heat-up I	1500 - 2300	1500 - 2000	1000	0.2	0.2
Heat-up II	2300 - 2500	2000 - 3000	2000	0.2	0.2
Quench	2500 - 4000	3000 - 4000	0	0.0	10.0

- Oxidation options in simulations

Name	Cr oxidation (ECORE)	Zr oxidation (HECU)
NUBIKI	Brachet (Cr only)	Cathcart Prater/Courtright
Original	Brachet (Cr only)	Cathcart Prater/Courtright
Escalation	Stahlberg with Cathcart Prater/Courtright >1300°C	Cathcart Prater/Courtright

Simulation Results – Cladding Temperatures at 550 mm

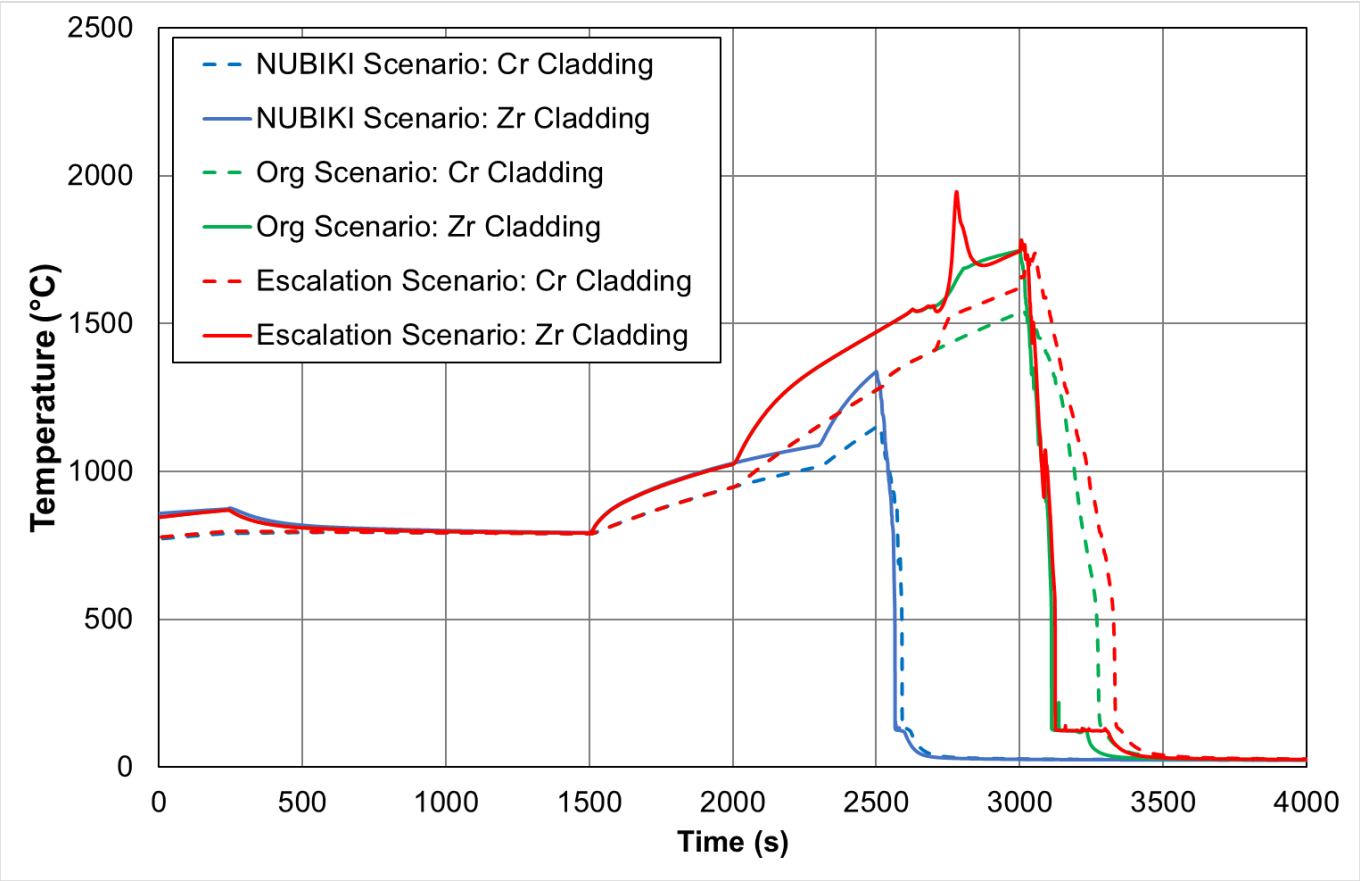

- For the NUBIKI scenario, due to the shorter period of heat-up and power increase, both claddings show no temperature > 1300 °C.
- The original scenarios lead to significantly higher temperatures with a maximum of app. 1500 °C (Cr) and 1750 °C (Zirlo).
- Esc. scenario: For the coated claddings the temperature increases significantly above 1300 °C due to the oxidation of pure metal. The optimised Zirlo claddings Temp. rises, forcing a strong oxidation of Zr. When oxidation slows down also the temperatures of both claddings do not escalate strongly.

Simulation Results – Hydrogen Generation

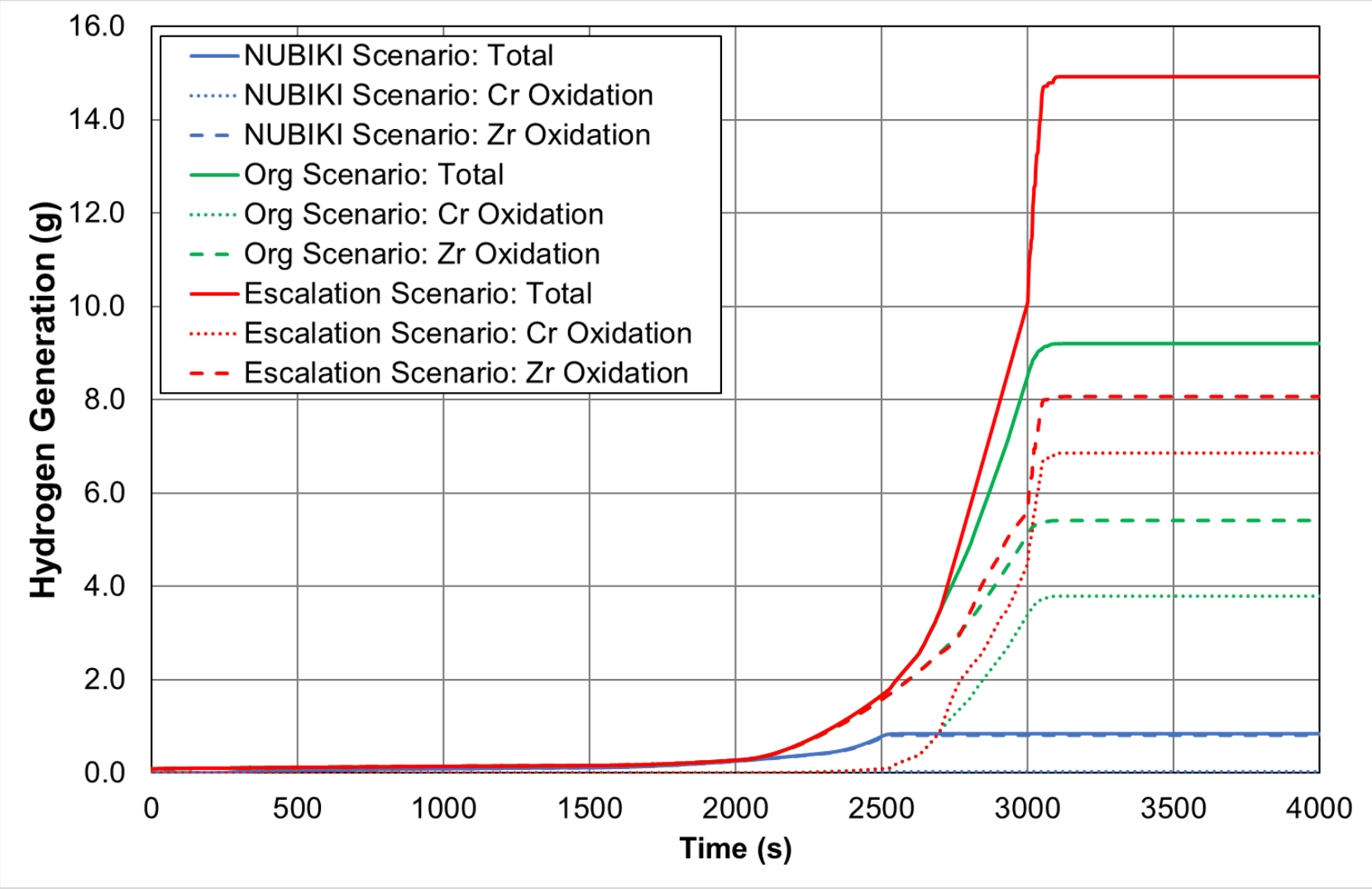

- NUBIKI scenario
  - Total 4.0 g
  - Cr + Zr 0.0 g
  - Zr 4.0 g
- Original scenario
  - Total 9.3 g
  - Cr + Zr 3.8 g
  - Zr 5.5 g
- Escalation scenario
  - Total 15.0 g
  - Cr + Zr 7.0 g
  - Zr 8.0 g

QUENCH-15

Test Bundle and Conduct

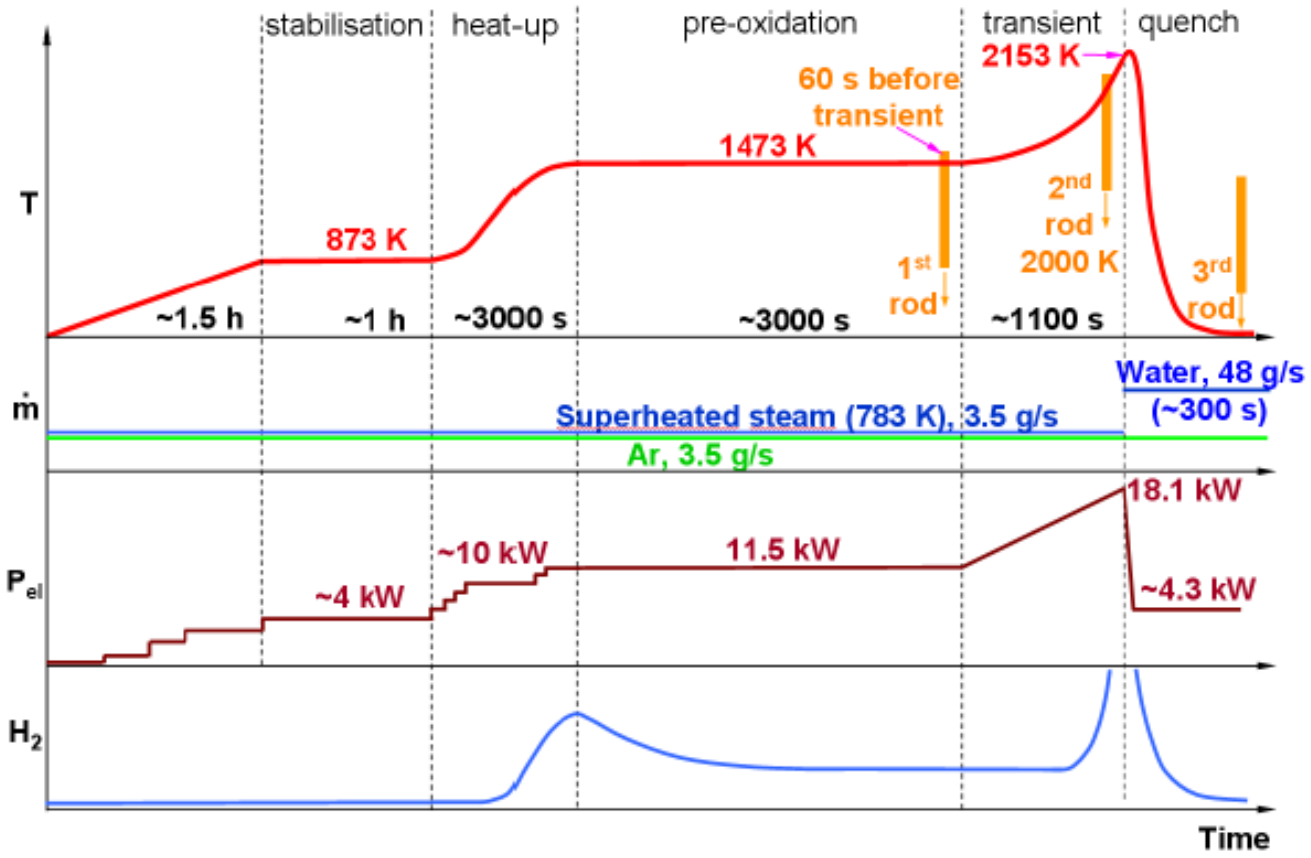

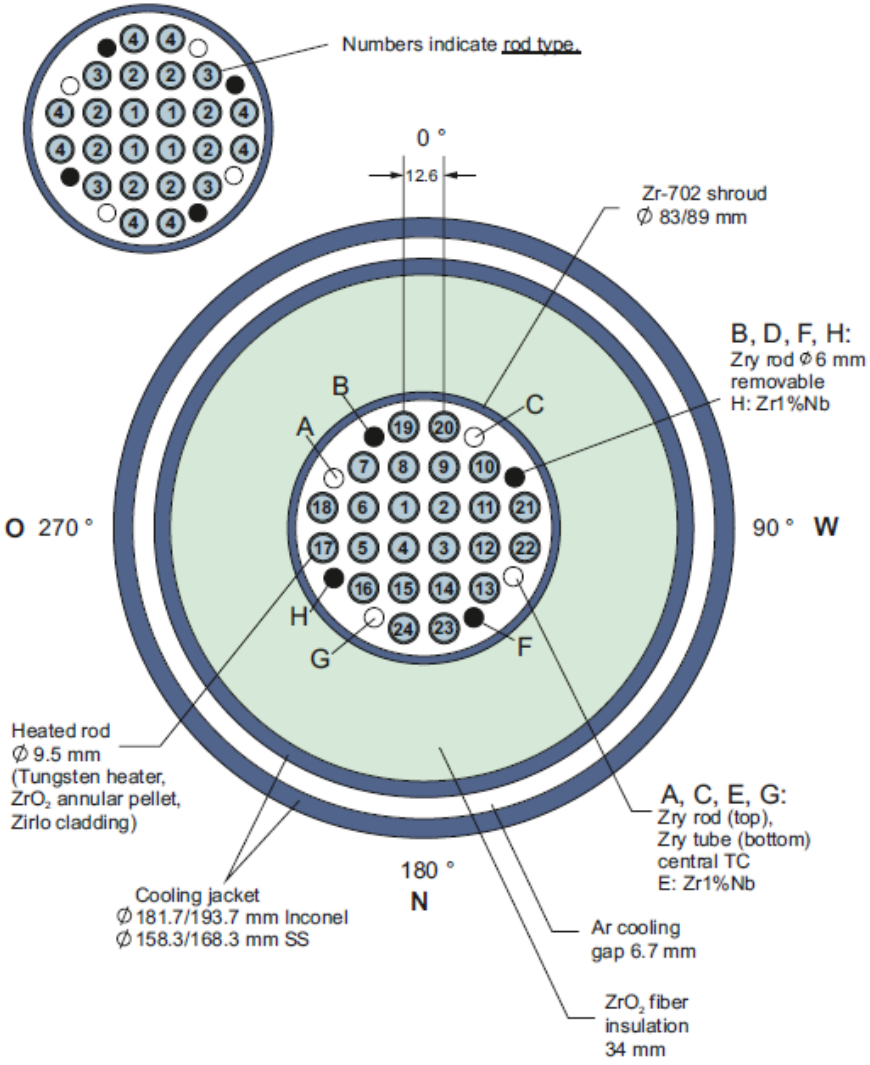

Source: KIT

Simulation Results – Cladding Temperatures at 950 mm

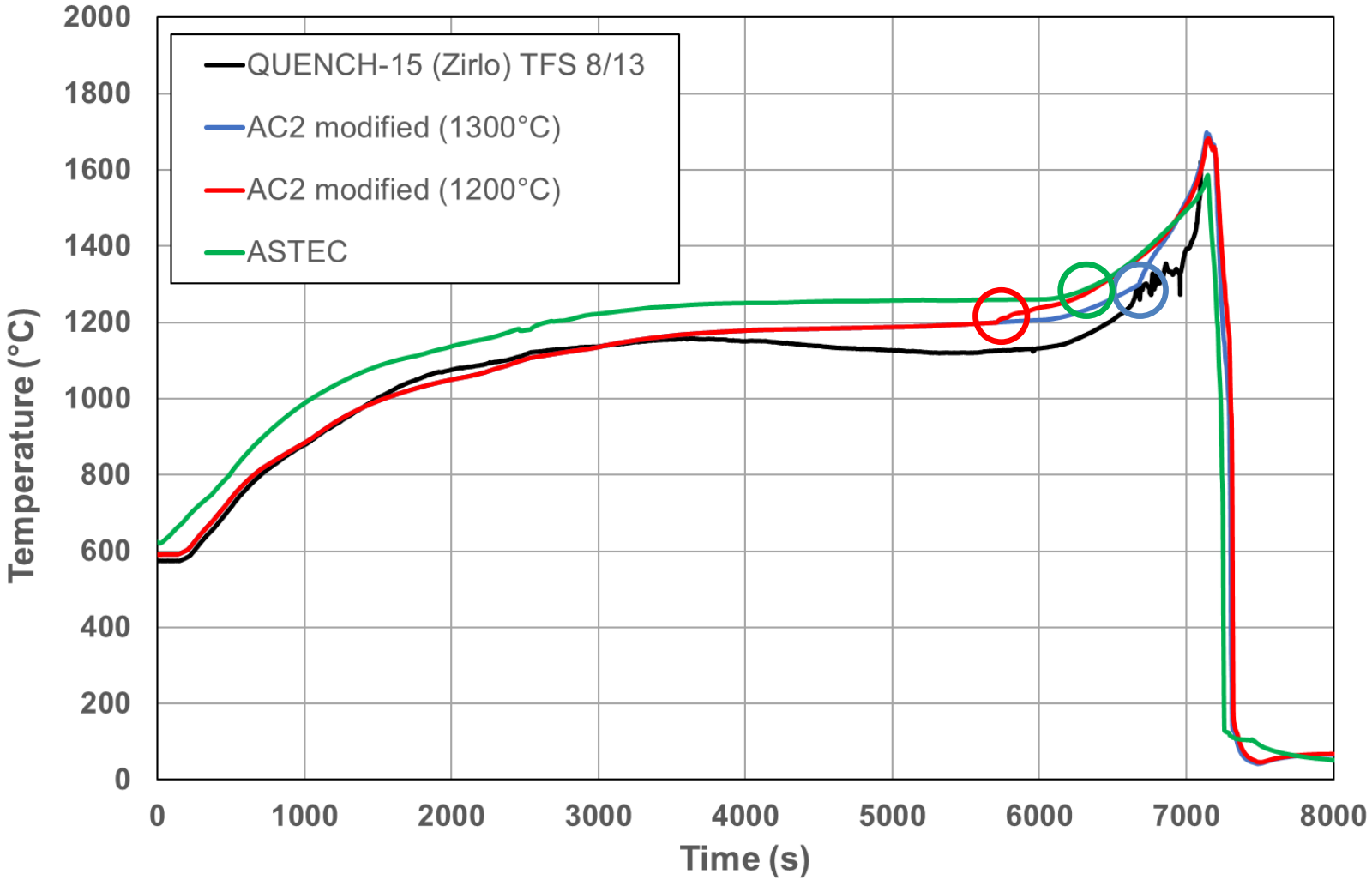

- All simulations reach the transition temperature to accelerated Zr oxidation
- The predicted temperatures for Cr-coating are comparable to original QUENCH-15 Zirlo behaviour

Simulation Results – Hydrogen Generation

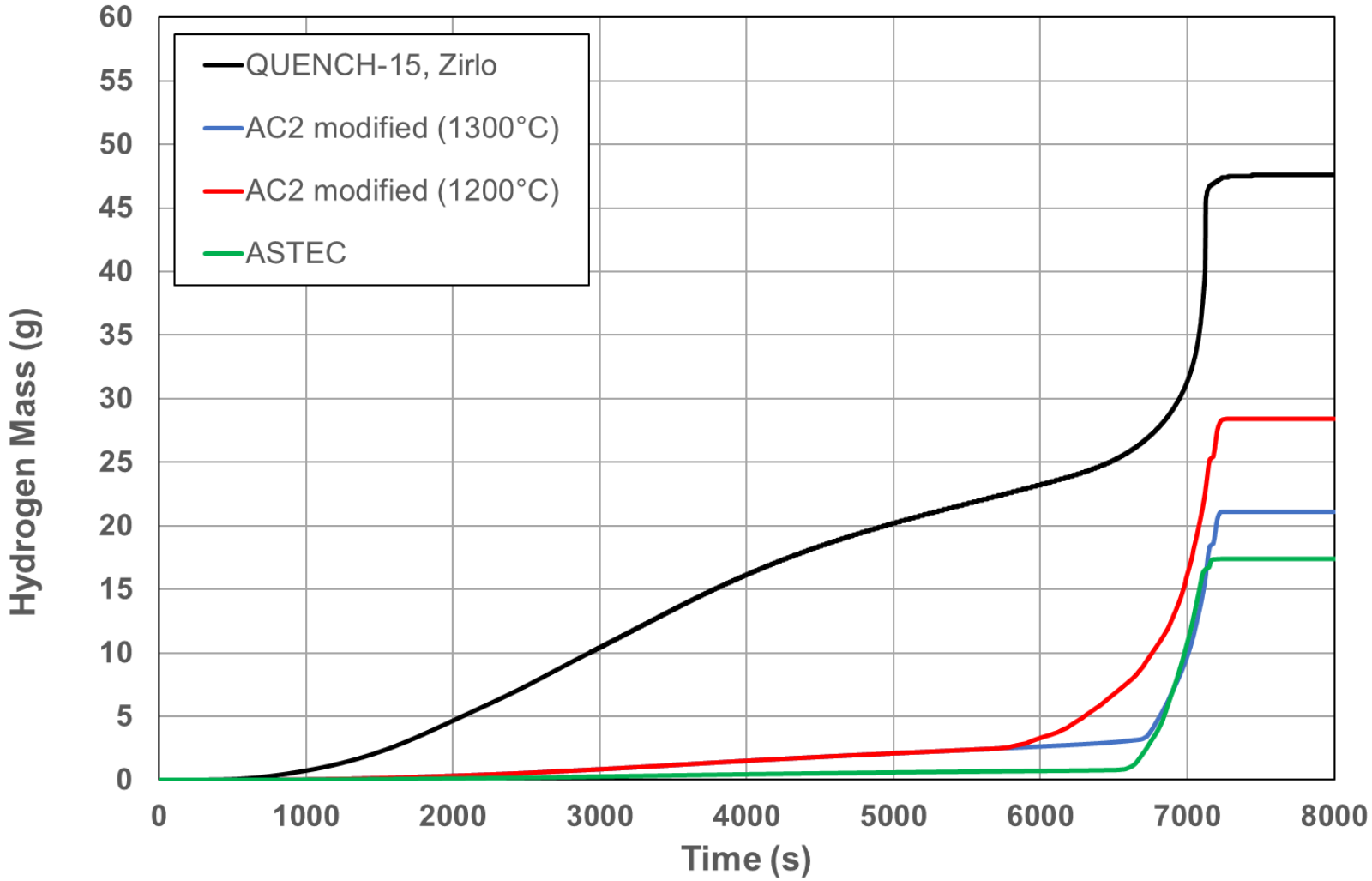

- Although the temperature evolution is comparable to QUENCH-15 with Zirlo claddings the mass of hydrogen is less than in QUENCH-15
- During pre-oxidation the hydrogen generation is significantly lower with Cr-coated components
- The increase of hydrogen is strongly connected to the transition temperature in each simulation
- When Zr oxidation occurs after failure of Cr-coating the hydrogen generation is higher than for Zirlo claddings with pre-oxidation

Conclusions

- Currently investigated ATF concepts like FeCrAl and Cr-coating are topic of several international projects and activities. Well known scenarios are applied for bundle configurations with FeCrAl or Cr-coated rods.
- AC²/ATHLET-CD and ASTEC were enhanced for FeCrAl and Cr-coated claddings.
- The application of both codes on different bundle experiments dealing with FeCrAl and Cr-coatings show that both codes can predict the observed test behaviour regarding temperature evolution and hydrogen generation. The results obtained for QUENCH-19 with FeCrAl claddings show a significant improvement of the model basis in the last two years.
- The predictions for CODEX-ATF1 with AC²/ATHLET-CD show a significant impact of the Cr-coatings when the coating fails and pure metal can oxidise.
- Both codes were also applied on a QUENCH test, assuming a Cr-coating. The simulations show that compared to the reference scenario with optimised Zirlo the hydrogen generation is lower in total, but higher above 1300 °C when Cr coating fails. In that phase the temperatures rise but do not escalate as expected in the predictions.
- In general, the validation basis for ATF namely FeCrAl and Cr-coating is limited for bundle experiments and needs an enlargement to evaluate the model basis for ATF claddings in severe accident codes and to further improve the phenomenological understanding, also with respect to eutectics.

Acknowledgement

The work of RUB PSS is funded by the German Federal Ministry for the Environment, Nature Conservation, Nuclear Safety and Consumer Protection (BMUV) under grant number 1501629 based on a decision by the German Bundestag.

The work of GRS is funded by the German Federal Ministry for the Environment, Nature Conservation, Nuclear Safety and Consumer Protection (BMUV).

Responsibility for the content lies with the authors.

The results were obtained using

- an in-house modified version of the GRS software package AC² 2021.0 at PSS and GRS,
- AC² 2023 at GRS,
- ASTEC V3, developed by IRSN, at KIT.

Supported by:

Federal Ministry
for the Environment, Nature Conservation,
Nuclear Safety and Consumer Protection

based on a decision of
the German Bundestag

THE CODEX-ATF TEST

Róbert Farkas, Nóra Vér, Berta Bürger, Péter Szabó, Zoltán Hózer
HUN-REN Centre for Energy Research
Corresponding Address
Robert.farkas@ek.hun-ren.hu

ABSTRACT

An integral bundle test was carried out in the framework of the IAEA Testing and Simulation for Advanced Technology and Accident Tolerant Fuels (ATF-TS) project in the CODEX (COre Degradation Experiment) facility. The test section included an electrically heated seven-rod bundle composed of 3 pieces uncoated and 4 pieces Cr coated optZIRLO cladding tubes. The main parameters of the scenario were selected on the basis of pre-test calculations.

Electrical heating with two tungsten heaters in each rod was applied. The heated length was 650 mm. The rods were pressurized during the test in order to reach ballooning and burst in the early phase of the experiment. The rods in the bundle were fixed by two spacer grids made of Zr1%Nb alloy. The bundle was placed into a hexagonal shroud. The shroud material was Zr2.5%Nb alloy, the total length of the shroud was 1000 mm. The bundle was heated by direct current power supply units. The steam generator provided hot steam to the test section. The water injection into the steam generator was performed with precision pump at constant flow rate. For heating up, argon gas was also injected into the steam generator.

In the preparatory phase the facility was heated up to 600 °C in 0.2 g/s steam and 0.2 g/s argon flow rates using both external heaters and fuel rod heaters. The heat-up phase continued with the same flow rates and with 1000 W heating power on the rods and 800 W power of external heaters. The rods were pressurised and cladding burst took place at ≈900 °C on most of the rods. The temperature increase was very smooth. At the initiation of water quench, the cladding temperature in the top of the bundle was above 1600 °C. In the upper part of the fuel rods 1400 °C was reached. It is expected that intense Zr-Cr eutectic formation took place at these temperatures. During the quench phase, room temperature water was injected to the bottom of the
test section. The total hydrogen production was about 3 g, which indicated significant oxidation of the Zr components.

KEYWORDS
Accident tolerant fuel, Zr-Cr interactions, station blackout event, ballooning, burst

1. INTRODUCTION

In order to investigate the high temperature behaviour of Cr coated Zr claddings an integral test was carried out in the CODEX facility at the HUN-REN Centre for Energy Research in the framework of the IAEA ATF-TS project.
Coated and uncoated optZIRLO™ tubes was used for the experiment with 9.1 mm external diameter. The main characteristics of the tests were agreed as follows:

• the bundle should include both coated and uncoated cladding tubes in order to allow direct comparison of their behaviour under accident conditions.
• the maximum local cladding temperature should be above 1300 °C for the observation of high temperature Zr-Cr interactions (eutectic formation).

2. THE TEST FACILITY

Hexagonal bundle was built in VVER geometry using VVER type spacer grids. The height of test section was 1000 mm, but the active part with the rods was only 580 mm, so the upper part of the shroud was used for thermocouples, without fuel rods.
The fuel rods were filled with zirconia pellets. The rods were pressurised by argon. Electrical heating with two tungsten heaters (0.049 Ω/m) in each rod was used. External heating was also applied to the test section.
The bottom of the test section was connected to the steam generator unit. The condenser cooled down the hot steam+gas flowing out from the top of the test section.
The bundle was covered by Zr shroud. The shroud had no perforations and it was surrounded by several thermal insulation layers, electrical heaters and a steel tube (Fig. 1). SiO2+Al2O3+ZrO2 fibre was used between the Zr shroud and the steel tube.

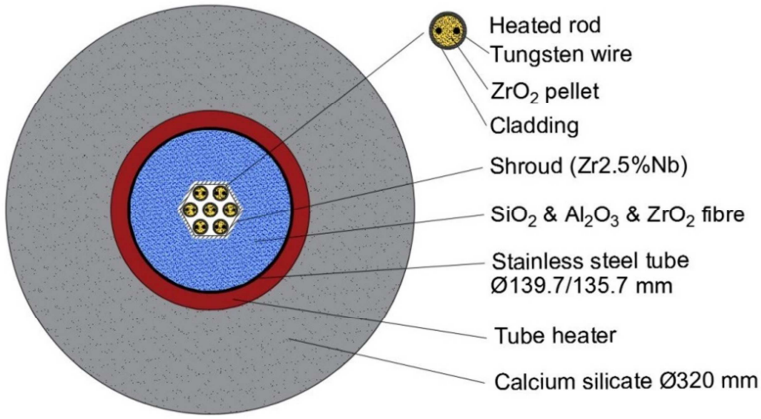

Figure 1. Horizontal cross section of the test section with thermal insulations

Steel vessel (diameter 139.7/135.7 mm) with external electrical heating housed the test section with fibre insulation. External heaters were applied on the surface of the stainless steel tube.
Calcium silicate covered the steel tube as external layer of thermal insulation with external diameter of 320 mm.

3. SCENARIO

It was intended to focus the simulated scenario on covering several phenomena of fuel behaviour during accidents.
• Ballooning and burst can place due to pressurisation of fuel rods (at ≈20-30 bars, between 800-900 °C).

- Oxidation of cladding external surface can be observed in high temperature steam, the degree of oxidation depends on the local temperatures.
- Oxidation of inner cladding surface and secondary hydriding may take place after cladding burst and penetration of steam into the fuel rods.
- Eutectic formation between Zr-Cr can be expected above 1300 °C.

There was no representative NPP scenario specified for the scenario, but the proposed sequences of events may be interpreted as a station blackout event with recovery of emergency water supply when the cladding temperature reaches 1400 °C.

The scenario consisted of the following phases (Fig. 2):

- Preparatory phase: technological heat-up of the facility, initiation of steam supply, moderate power and target temperature of 600 °C.
- Heat-up phase I: further heat-up with increased power, pressurisation of fuel rods to reach burst, target temperature of 1000 °C.
- Heat-up phase II: further heat-up with increased power, target temperature of 1400 °C.
- Quench: injection of water, switching off power and steam supply.

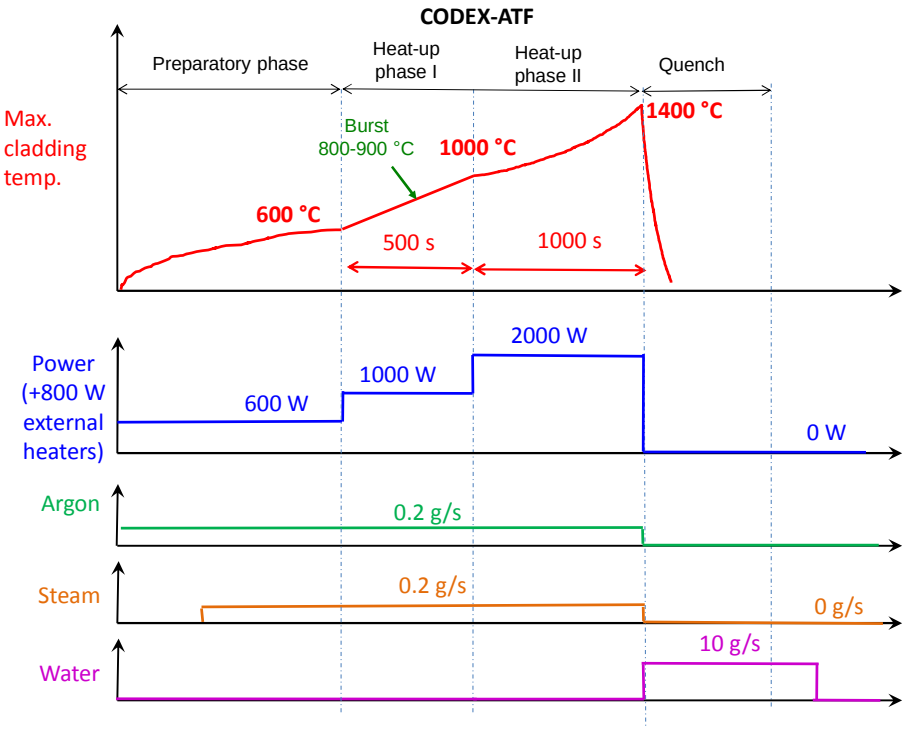

Figure 2. Main parameters of proposed CODEX-ATF scenario

4. COMISSIONING TEST

In order to check the operation of the components of the CODEX facility commissioning test was performed. The heating included the operation of both bundle heater and external heater systems. Stepwise power changes were performed with the fuel rod heaters in argon atmosphere (0.2 g/s). The maximum power was set to 500 W for the rods and 800 W for the external heaters.

The total duration of the heated period was about 1 hour. The maximum rod temperature was close to 650 °C at 500 mm elevation, while one of measured the shroud temperatures reached 550 °C at the same elevation.

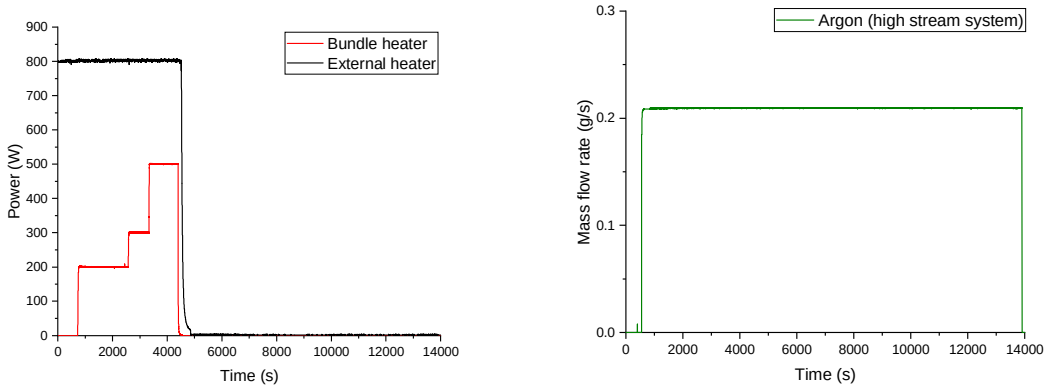

Figure 3. Power (left) and Ar flowrate (right) in the commissioning test

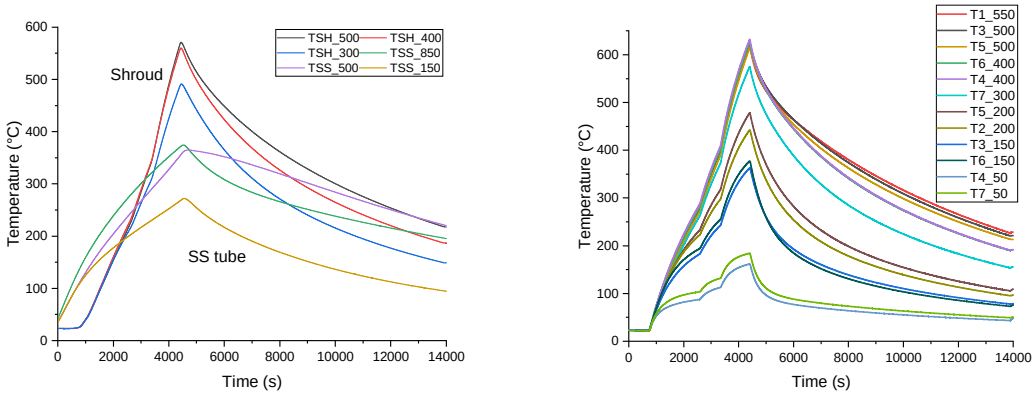

Figure 4. Temperatures of shroud, SS tube (left) and claddings (right) in the commissioning test

5. THE CODEX-ATF EXPERIMENT

The experiments included the following main phases:

I. Technological heat-up.

The experiment started with switching on the steam generator. The operation of external heaters started at 2259 s and 800 W power was reached at 2631 s (Fig. 5). The maximum temperature (428 °C) in this phase was measured in the stainless steel tube at 850 mm elevation, in the vicinity of external heaters. The maximum temperatures on the shroud and fuel rods remained below 230 °C and 220 °C.

The fuel rod internal pressure was set individually for each rod between 20-30 bars after 5112 s. Due to leakage of some rods, the pressure was not kept for long time and later additional pressurisation was taken.

Argon injection was performed with 0,2 g/s flowrate, the injection started after 6374 s.

Steam injection from steam generator was performed with 0.2 g/s flowrate.

II. Heat-up with 300-500 W bundle power.
The bundle power added at 8349 s and 500 W was reached at 8374 s. At 9559 s the power was decreased to 300 W to limit the heat-up rate. The next power level (400 W) was reached at 10179 s and it was decreased to 350 W at 10701 s. At the end of this phase (12165 s) the maximum temperature 679 °C was recorded on rod No. 1. at 550 mm elevation.

III. Heat-up with 1000 W bundle power.
The bundle power was increased to 1000 W at 12175 s and this power was kept until 14613 s. This power was provided continuous temperature increase on fuel rods. The maximum temperature was measured at 550 mm elevation on rod No. 1., its value was 1655 °C. The target 1400 °C was reached at 500 mm and 1300 °C was recorded at 400 mm elevations.
The cladding bursts took place mainly between 12500-12800 s. The rod No. 1. failed 25.0 bar pressure, while he maximum pressure in the fuel rod was 31.0 bar (probably before the ballooning started). The rod No. 2. failed at 15.1 bar and the maximum pressure was 23.2 bar. The rod No. 4. failed at 16.2 bar and the maximum pressure was 24.9 bar. The rod No. 5. failed at 17.8 bar and the maximum pressure was 33.3 bar. The rod No. 6. failed at 25.0 bar and the maximum pressure was 34.6 bar. The burst of rods No. 3 and No. 5. could not be detected clearly by the pressure data, probably the leakage prevented the ballooning process.

IV. Final cool-down by quench.
The final cool-down was initiated with water injection into the bottom of test section parallel with switching off bundle heating (14608 s) and external heating (14774 s). The response of the bundle was quick decrease of the temperatures and the bundle was cooled down to water temperature by 14750 s.

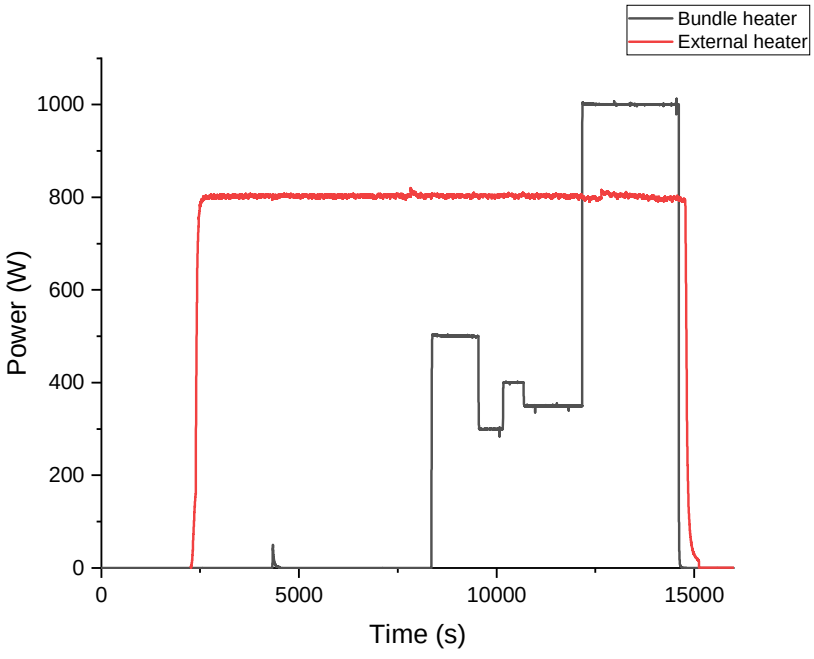

Figure 5. Power history of the CODEX-ATF test

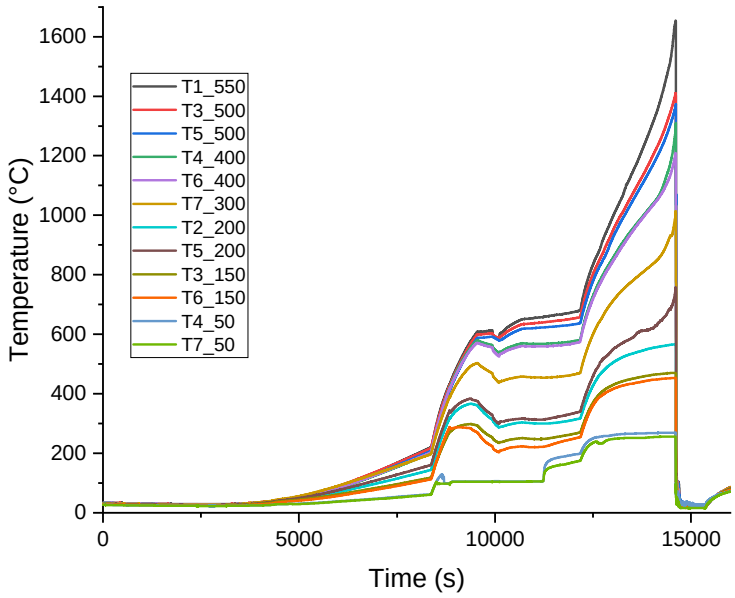

Figure 6. Cladding temperatures in the CODEX-ATF test

6. SUMMARY

The CODEX-ATF test was successfully performed on 23rd August, 2023 at the HUN-REN Centre for Energy Research, Budapest, Hungary in the framework of the IAEA Testing and Simulation for Advanced Technology and Accident Tolerant Fuels (ATF-TS) project. The test section included an electrically heated seven-rod bundle composed of 3 uncoated and 4 Cr coated optZIRLO^{TM} cladding tubes.

In the preparatory phase the facility was heated up to 600 °C in 0.2 g/s steam and 0.2 g/s argon flow rates using both external heaters and fuel rod heaters. The heat-up phase continued with the same flow rates and with 1000 W heating power on the rods and 800 W power of external heaters. The rods were pressurised and cladding burst took place at ≈900 °C on most of the rods. The temperature increase was very smooth and during the execution of the test it was decided to continue the heat-up beyond the original target temperature (1400 °C). At the initiation of water quench, the cladding temperature in the top of the bundle was above 1600 °C. In the upper part of the fuel rods 1400 °C was reached. It is expected that intense Zr-Cr eutectic formation took place at these temperatures. The total hydrogen production was about 3 g, which indicated significant oxidation of the Zr components.
The post-test examination of CODEX-ATF bundle will be completed in spring 2024.

ACKNOWLEDGMENTS

The CODEX-ATF experiment was carried out with the support of the IAEA Testing and Simulation for Advanced Technology and Accident Tolerant Fuels (ATF-TS) project.

HUN REN Centre for Energy Research

HUN-REN Hungarian Research Network

HUN-REN Centre for Energy Research

The CODEX-ATF experiment

Róbert Farkas, Nóra Vér, Berta Bürger, Péter Szabó, Zoltán Hózer

11th SARNET, KTH Stockholm, Sweden, May 13-16, 2024

Research. Innovation. Impact.

Introduction

- During the discussions with ATF-TS project (IAEA) partners, EK proposed to carry out an integral bundle test in the CODEX facility.
- Czech Technical University (CTU) offered to provide Cr-coated (18 µm) and uncoated optimised ZIRLO^{TM} tubes for the experiment with 650 mm length and 9.1 mm diameter.

The main characteristics of the tests were agreed as follows:

- The bundle should include both **coated** (4 pieces) and **uncoated** cladding (3 pieces) tubes in order to allow direct comparison of their behaviour under serious accident conditions.
- The maximum local cladding temperature should be above 1300 °C for the observation of high temperature Zr-Cr interactions (eutectic formation).

CODEX-ATF test section

Test section with seven-rod bundle

- Hexagonal 7-rod bundle in VVER geometry
- Length of heated rods 650 mm
- Tungsten heaters in the rods + external heating
- Zirconia and alumina pellets insulate the tungsten
- Rod pressurisation by argon
- Thermal insulation layers
- Zr2.5%Nb shroud

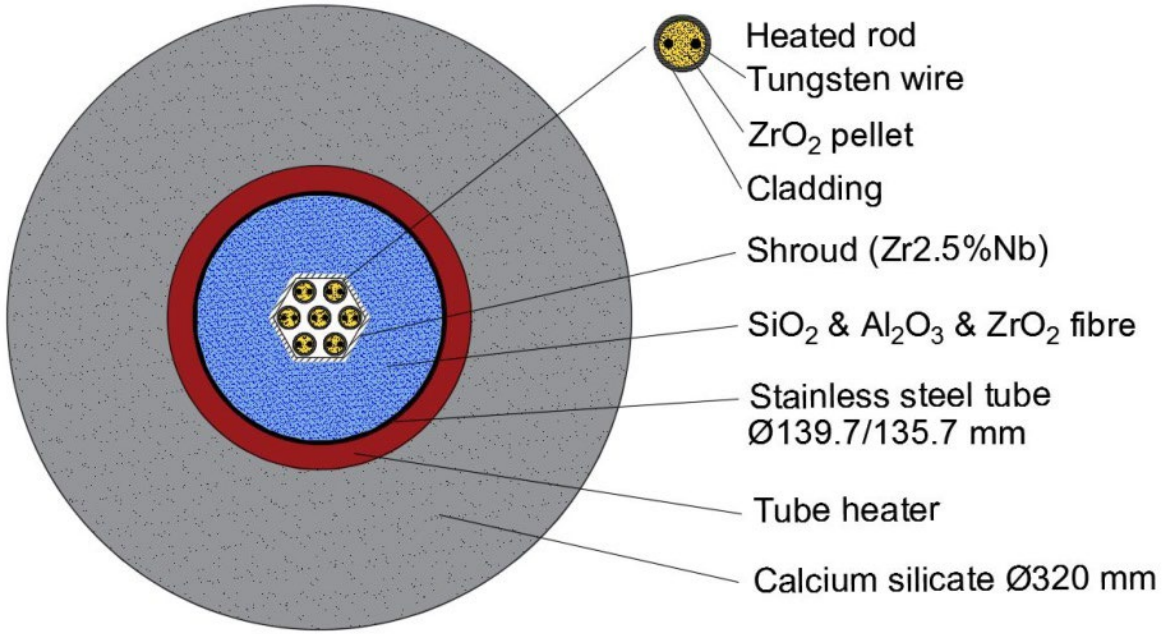

Heated fuel rod

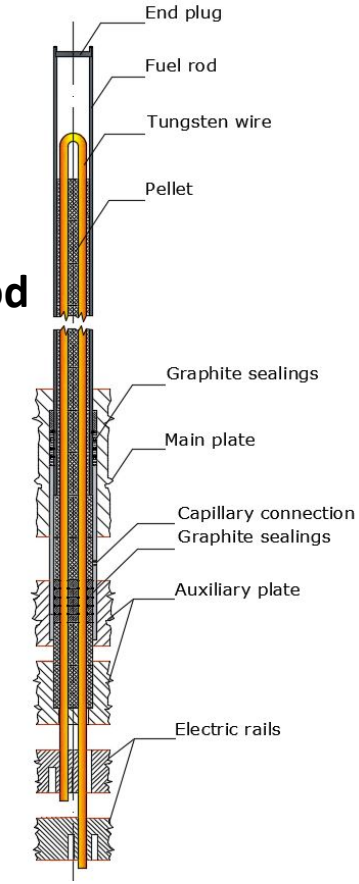

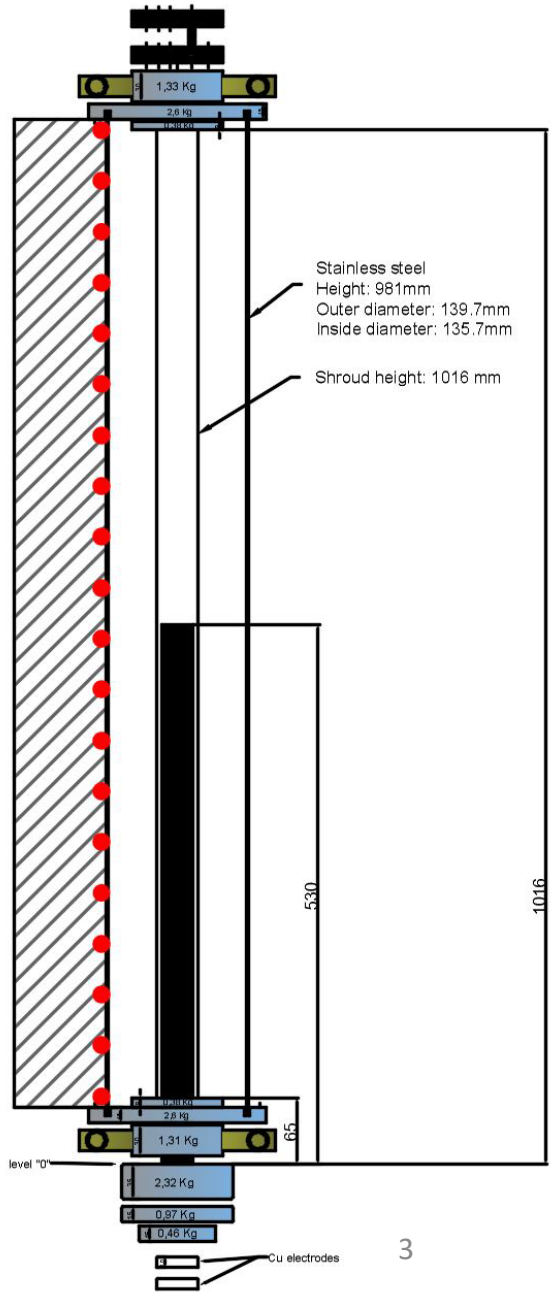

CODEX-ATF facility

Number of fuel rods	7
Cladding of fuel rods No. 2., 4. and 6.	optZIRLO™
Cladding of fuel rods No. 1. (central), 3., 5. and 7.	Cr-coated optZIRLO™
Length of fuel rods	650 mm
External diameter of fuel rods	9.1 mm
Cladding wall thickness	0.57 mm
Pellet material	ZrO_2
Pellet material in the bottom of the rods	Al_2O_3
Height of pellet	10 mm
Diameter of pellet	7.65 mm
Hole diameter in the pellet	2 mm
Spacer grid material	Zr1%Nb
Height of spacer grid	10 mm
Thickness of spacer grid	0.4 mm
Number of spacer grids	2
Shroud material	Zr2.5%Nb
Shroud thickness	2 mm
Length of shroud	1000 mm
Shroud key size	39 mm

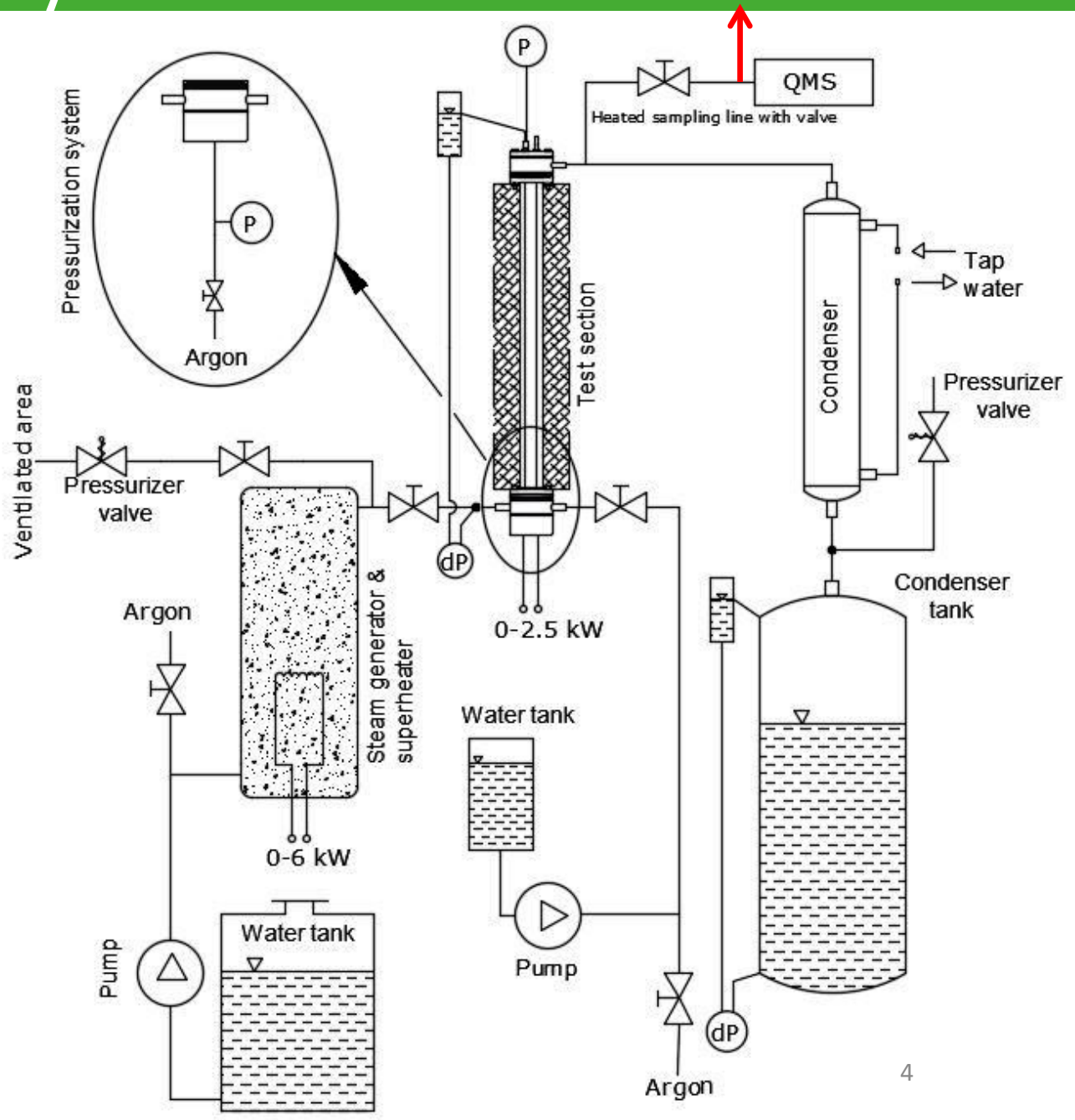

Thermocouple positions of the CODEX-ATF facility

High temperature thermocouples (6 pieces)

- ① W5Re/W26Re at elevation 550 mm with orientation of 180°
- ② W5Re/W26Re at elevation 500 mm with orientation of 300°
- ③ W5Re/W26Re at elevation 400 mm with orientation of 60°
- ④ W5Re/W26Re at elevation 200 mm with orientation of 60°
- ⑤ W5Re/W26Re at elevation 400 mm with orientation of 180°
- ⑥ W5Re/W26Re at elevation 300 mm with orientation of 180°

K-type thermocouples (33 pieces)

- ⑨ "K" type at elevation 50 mm with orientation of 0°
- ⑩ "K" type at elevation 50 mm with orientation of 180°
- ⑪ "K" type at elevation 150 mm with orientation of 300°
- ⑫ "K" type at elevation 150 mm with orientation of 120°
- ⑬ "K" type at elevation 500 mm with orientation of 240°
- ⑭ "K" type at elevation 200 mm with orientation of 240°
- ⑮ "K" type at elevation 300 mm
- ⑯ "K" type at elevation 400 mm
- ⑰ "K" type at elevation 500 mm

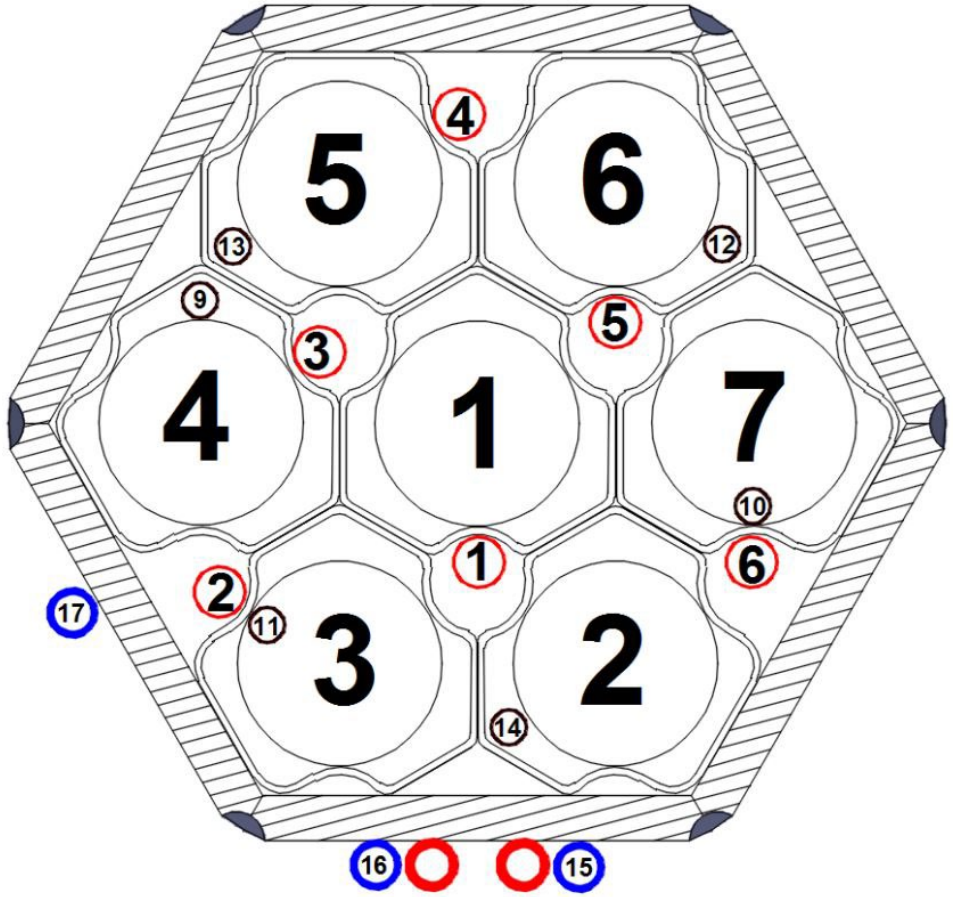

Proposed scenario

The proposed scenario will focus on covering several phenomena of fuel behaviour during accidents.

- **Ballooning and burst** will take place due to pressurisation of fuel rods (rod pressures between 1-3 MPa, all of them will burst between 800-1000 °C).

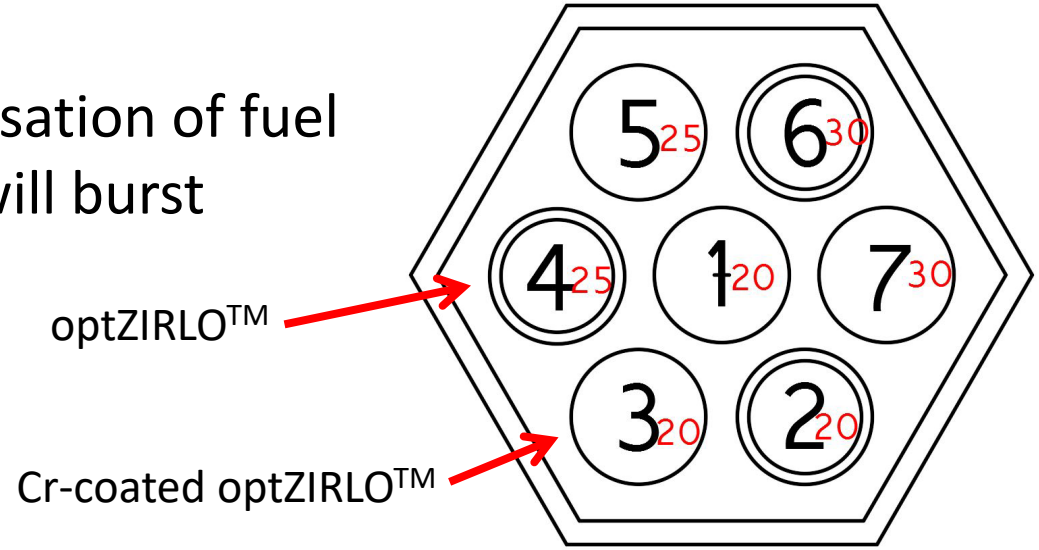

- **Oxidation of cladding external surface** will be observed in high temperature steam, the degree of oxidation will depend on the local temperatures.
- **Oxidation of inner cladding surface** and secondary hydriding may take place after cladding burst and penetration of steam into the fuel rods.
- **Eutectic formation** between Zr-Cr is expected above 1300 °C.

It is not intended to cover a representative NPP scenario in details, but the proposed sequence of events may be interpreted as a station blackout (SBO) event with combination of small break LOCA with recovery of emergency water supply when the cladding temperature reaches 1400 °C.

Proposed scenario for the CODEX-ATF test

technological heat-up of the facility, initiation of steam supply, moderate power and target temperature of 600 °C

further heat-up with increased power, pressurization of fuel rods to reach burst, target temperature of 1000 °C

further heat-up with increased power, target temperature of 1400 °C

injection of water, switching off power and steam supply

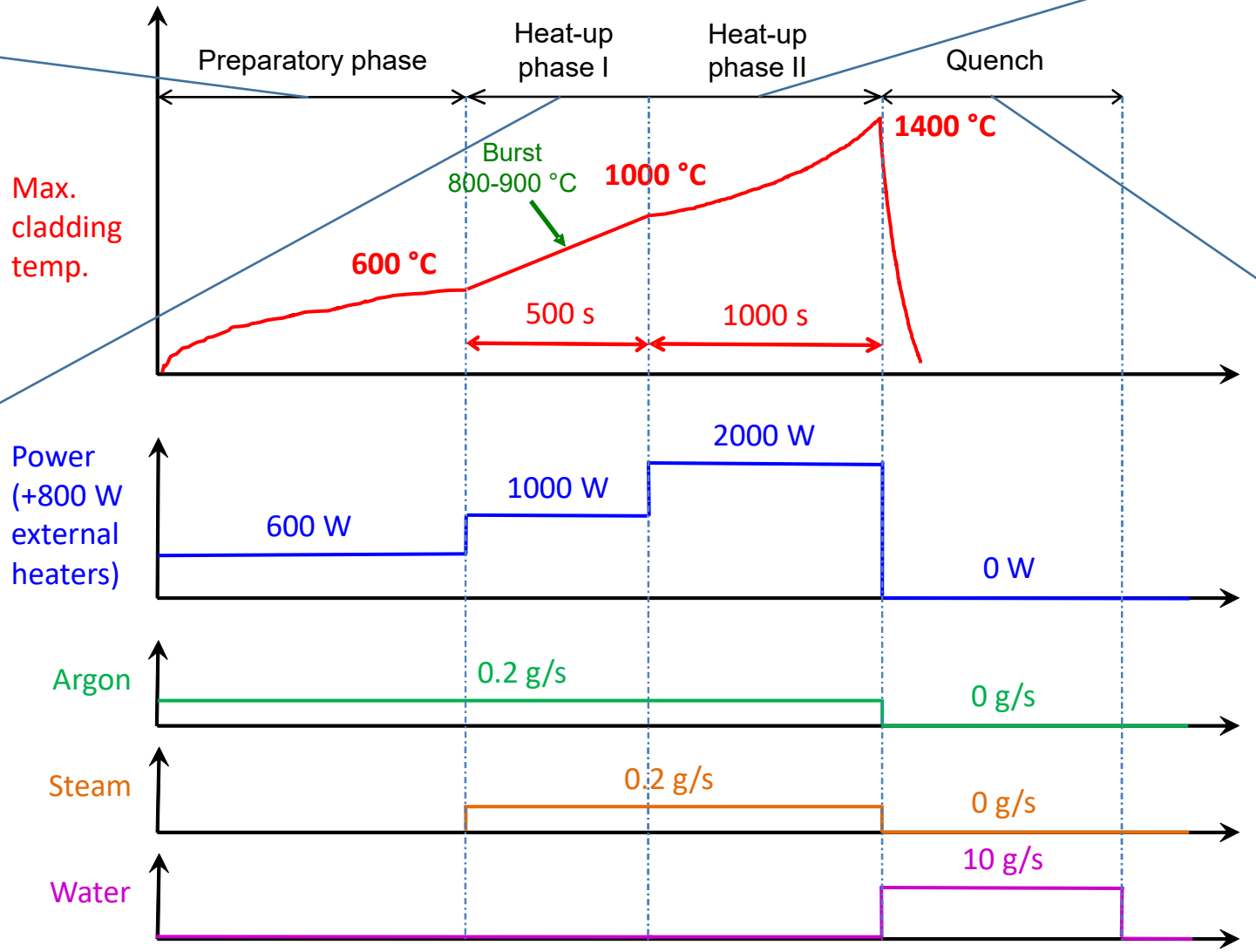

Measurement of parameters

During the tests there will be on-line measurements and data acquisition:

- temperatures,
- pressures,
- flowrates,
- power,
- outlet gas composition.

Parameter	Device	Placement
Temperature	K-type, W5% Re/W26% Re in Zr shield tube	Rod surfaces
	K-type	Others (coolant , off-gas, stainless steel tube, …)
Argon flowrate	Calibrated flowmeter	Gas supply system
Steam flowrate	Calibrated pump	Pump
Gas composition	Mass spectrometer	Gas outlet
Power	DC power units	Rail of electric connections
System pressure	P transducer, 6 bar/4-20 mA	Test section upper head
Fuel rod pressure	P transducer, 100 bar/4-20 mA	Pressurization system

Pre-test calculations by GRS, NUBIKI, IBRAE

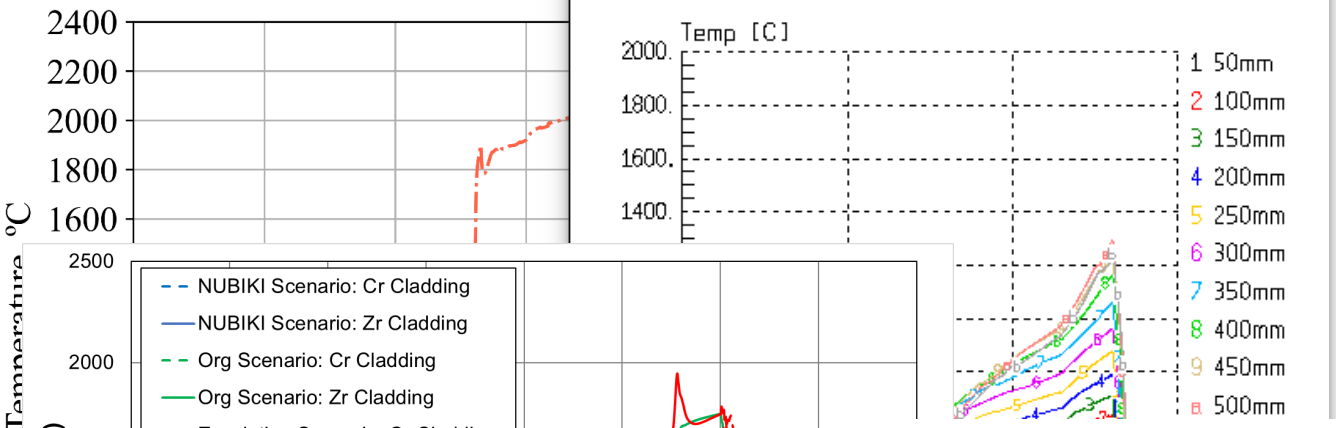

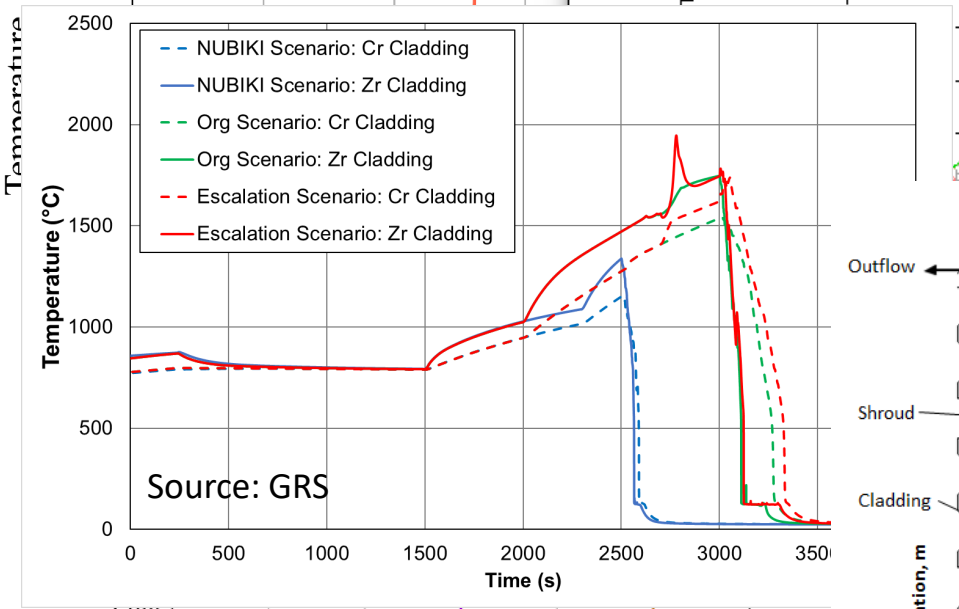

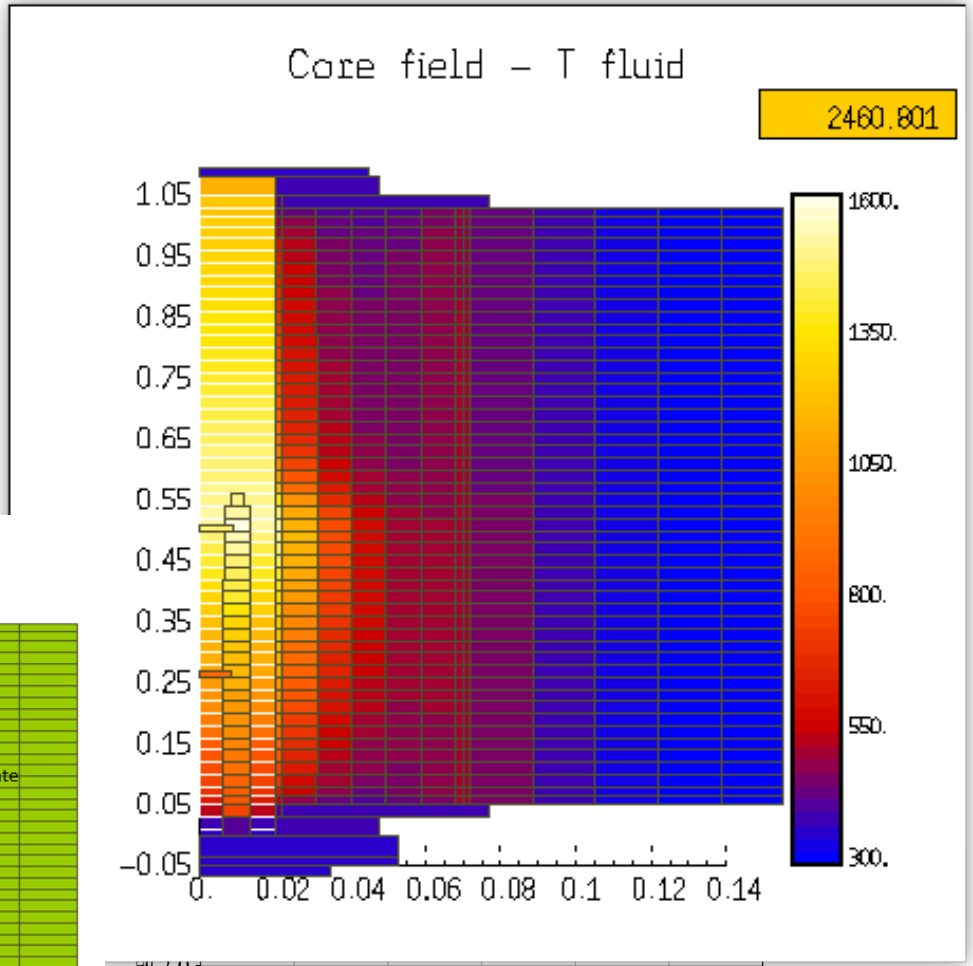

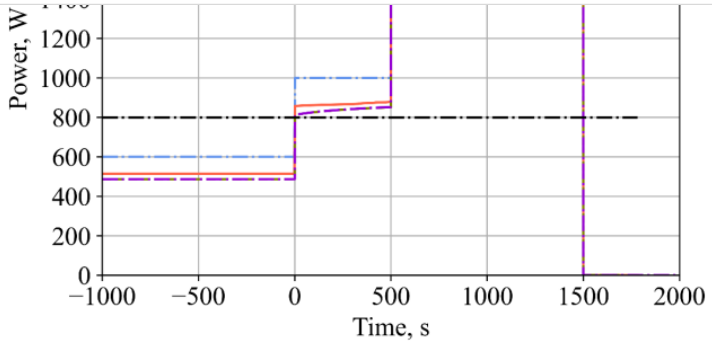

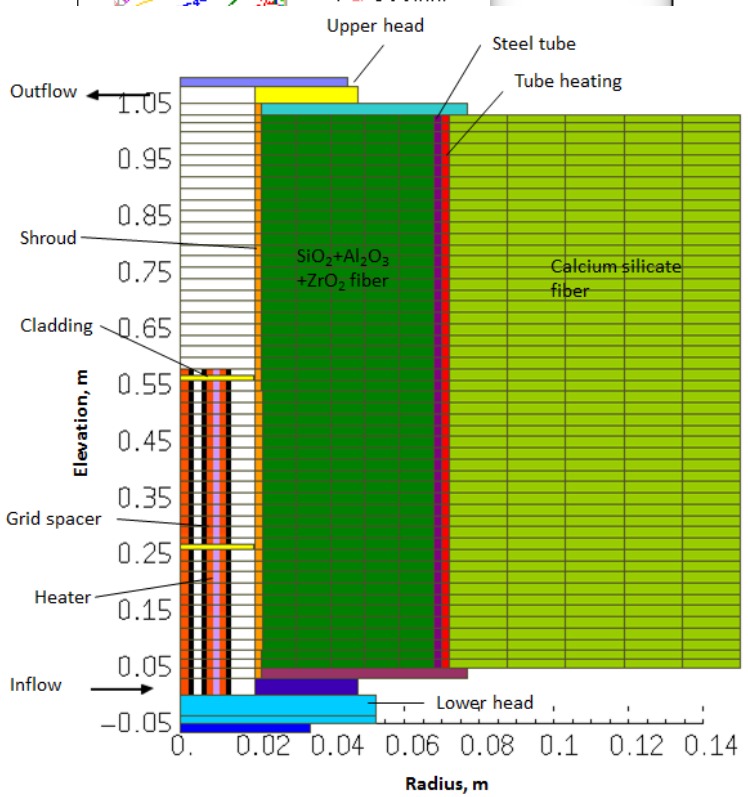

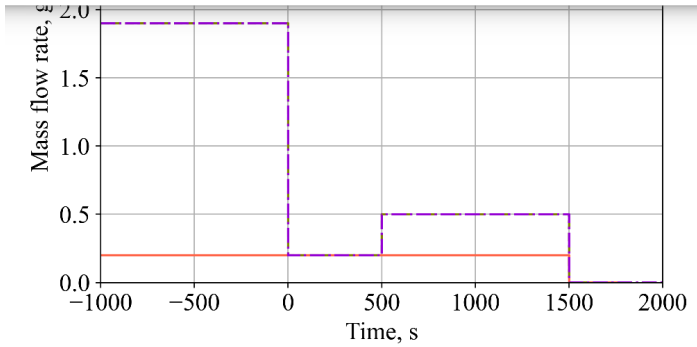

Assembly of the bundle





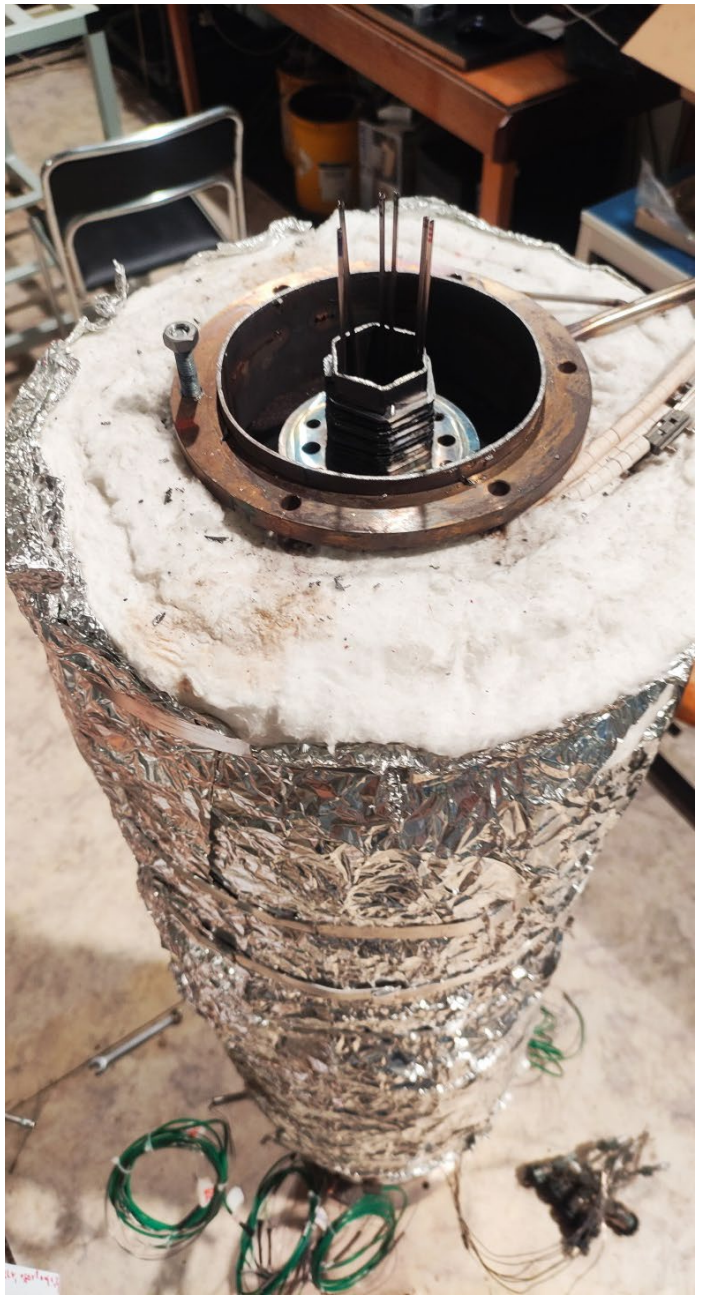



Comissioning test No. 1.

- The heating included the operation of both bundle heater and external heater systems. Stepwise power changes were performed with the fuel rod heaters in argon atmosphere (0.2 g/s). The maximum power was set to 500 W for the rods and 800 W for the external heaters.

- The total duration of the heated period was about 1 hour. The maximum rod temperature was close to 650 °C at 500 mm elevation, while one of measured the shroud temperatures reached 550 °C at the same elevation.

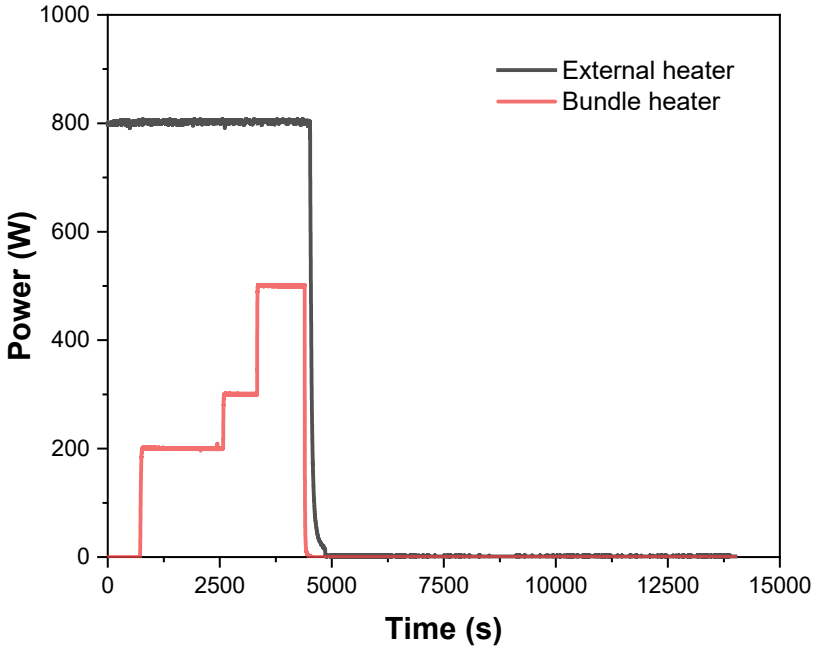

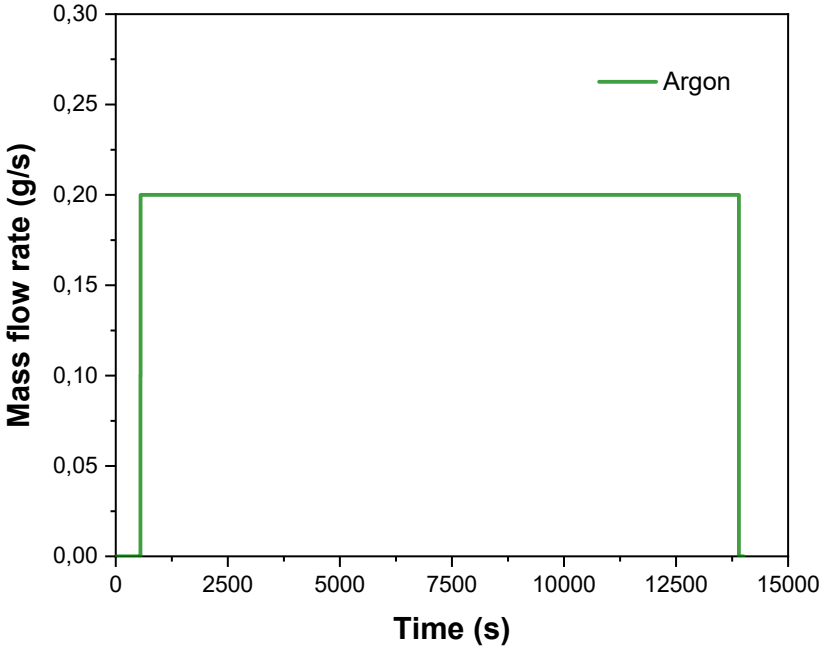

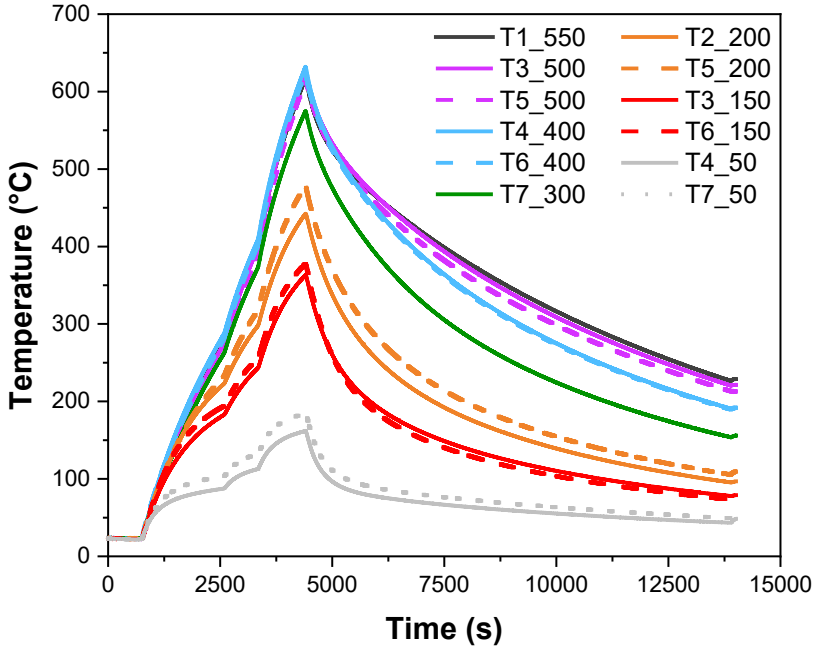

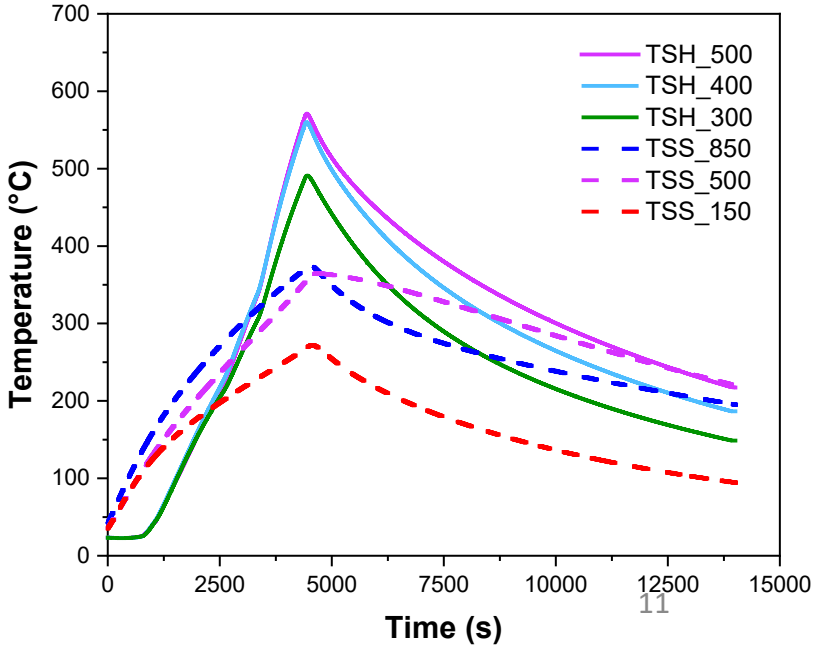

Comissioning test No. 2.

- The maximum power reached 1600 W for the rods (no external heater). The total duration of the heated period was 30 min. The maximum rod and shroud temperatures reached 650 °C and 450 °C at 500 mm elevation.
- The argon flow rates were varied.
- The pressurization of individual rods was tested several times during this commissioning test.
- The operation of steam generator was also tested.

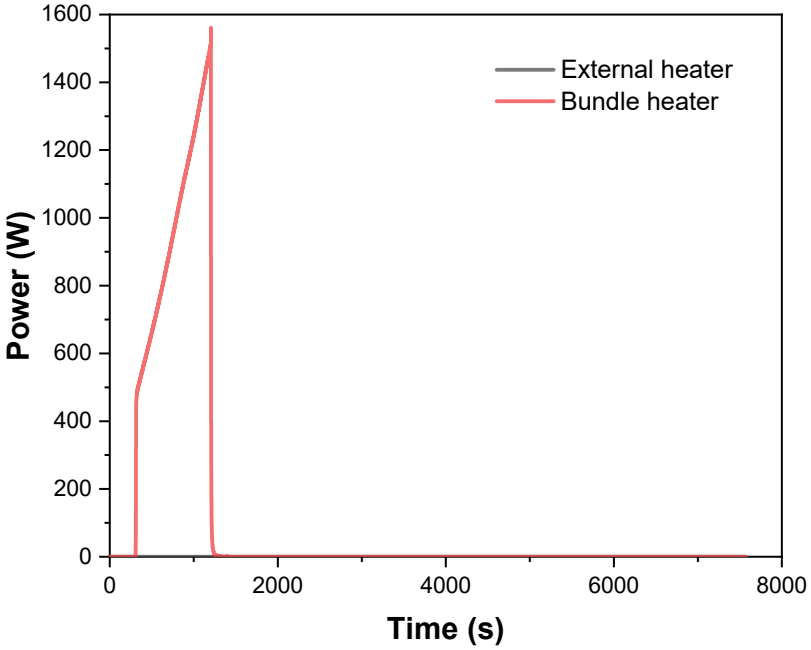

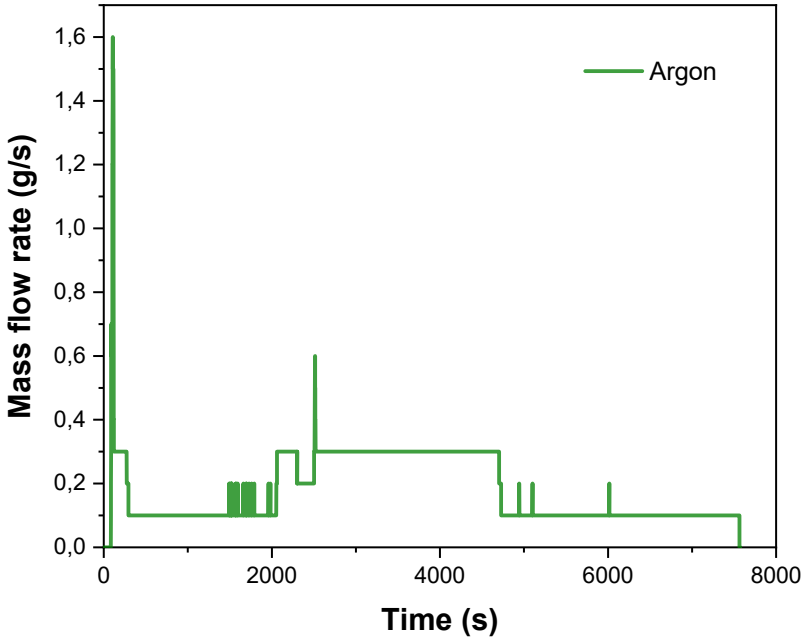

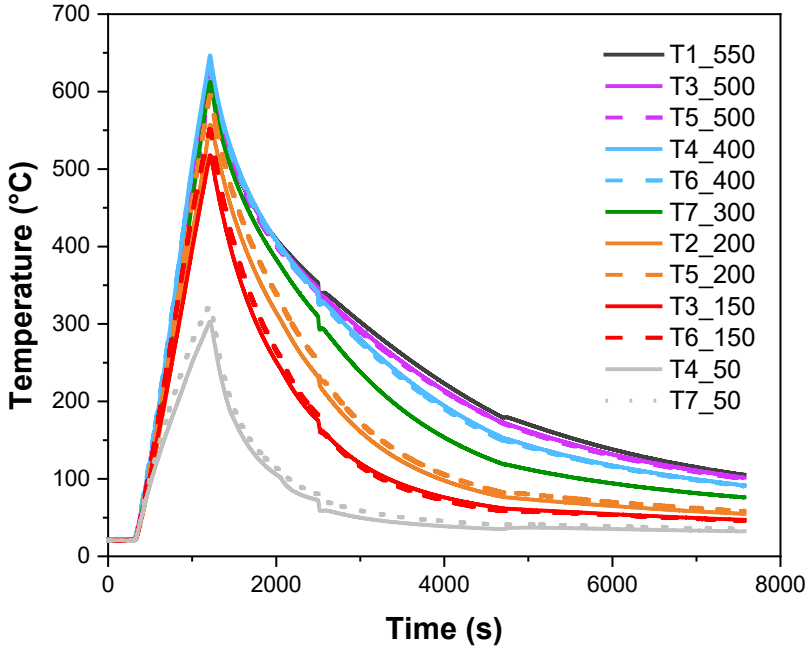

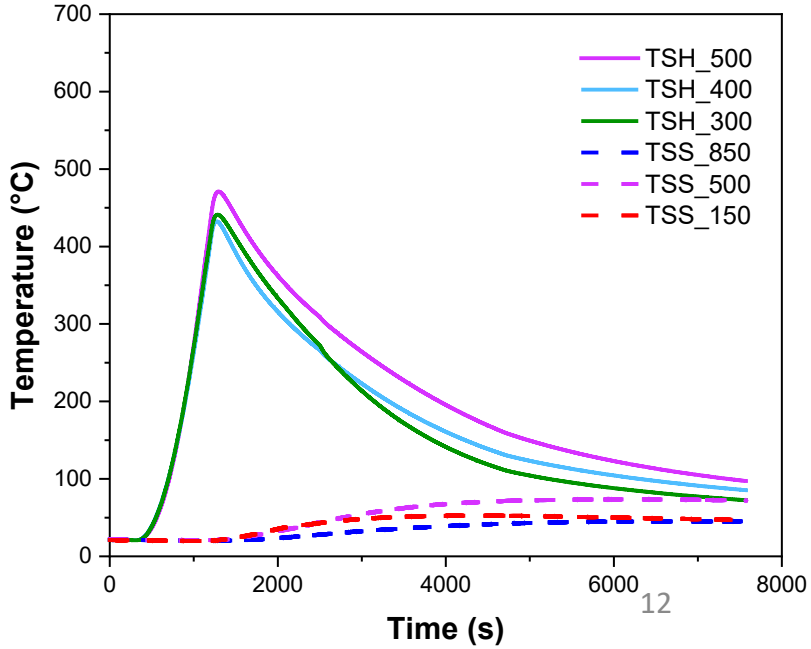

CODEX-ATF results

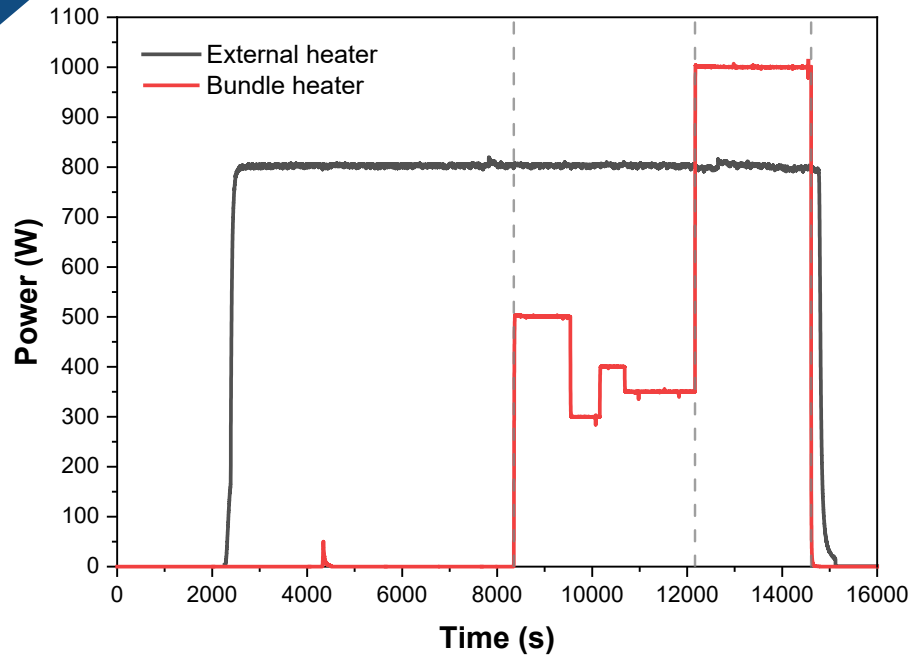

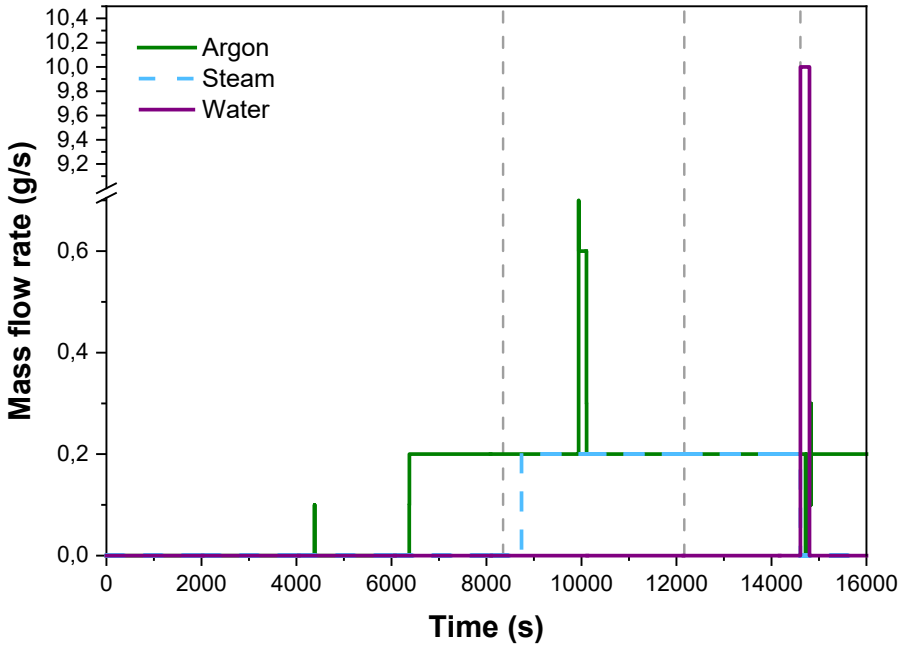

Maximum rod temperature T1_550mm, 1655 °C

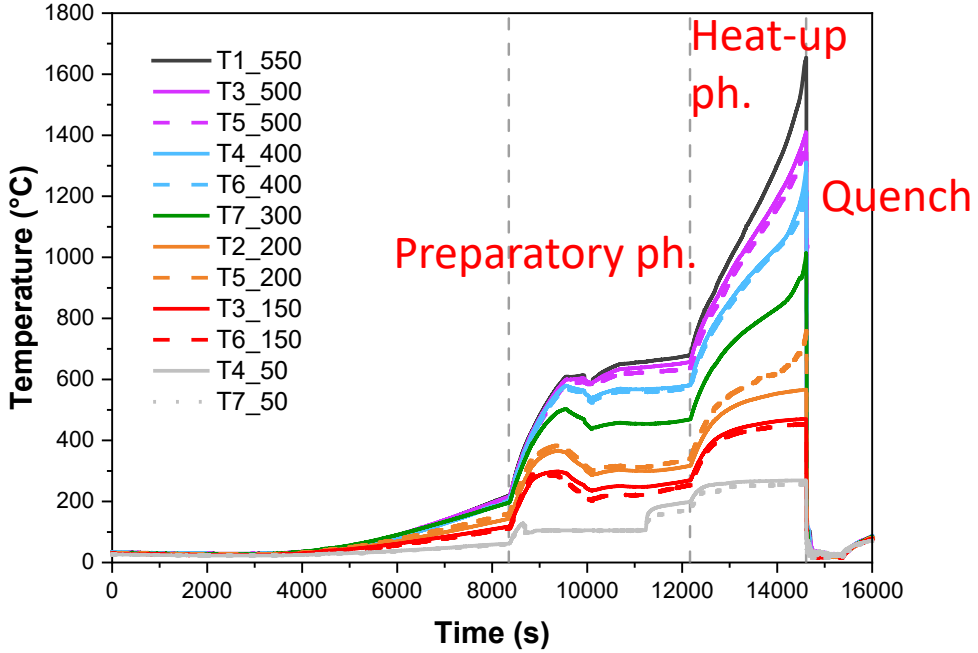

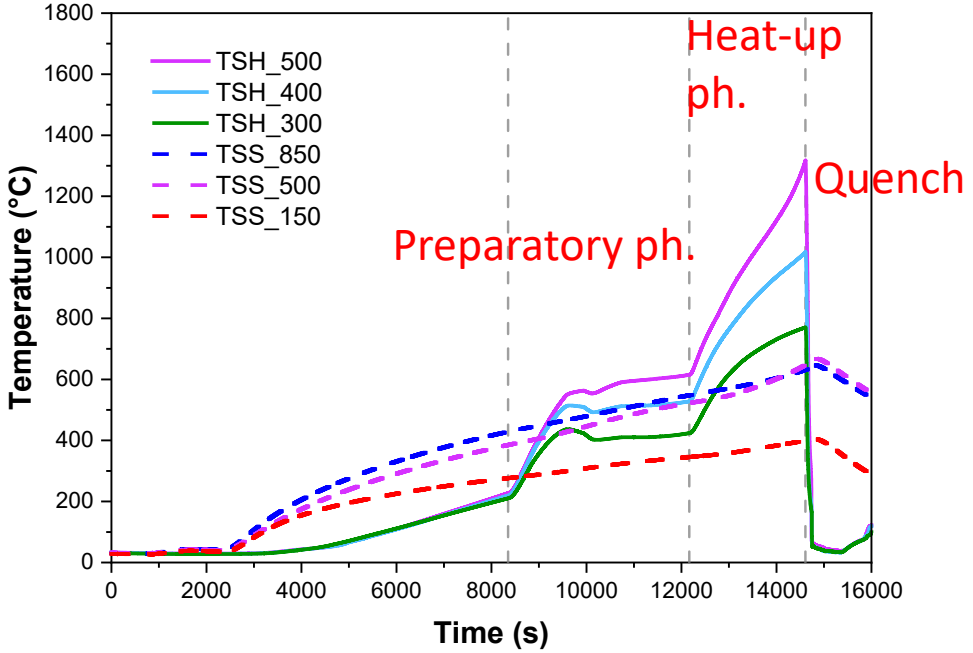

CODEX-ATF results

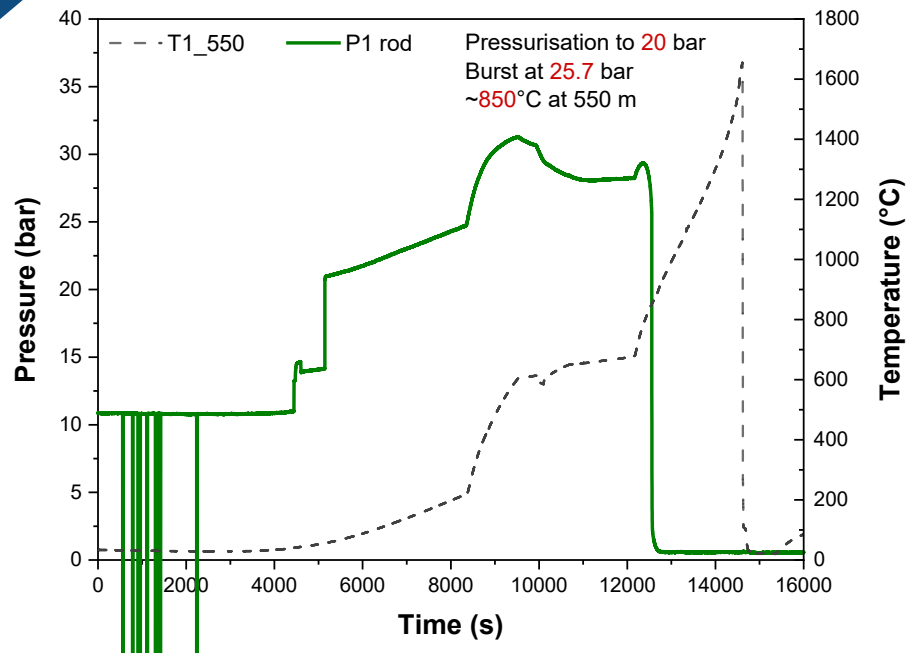

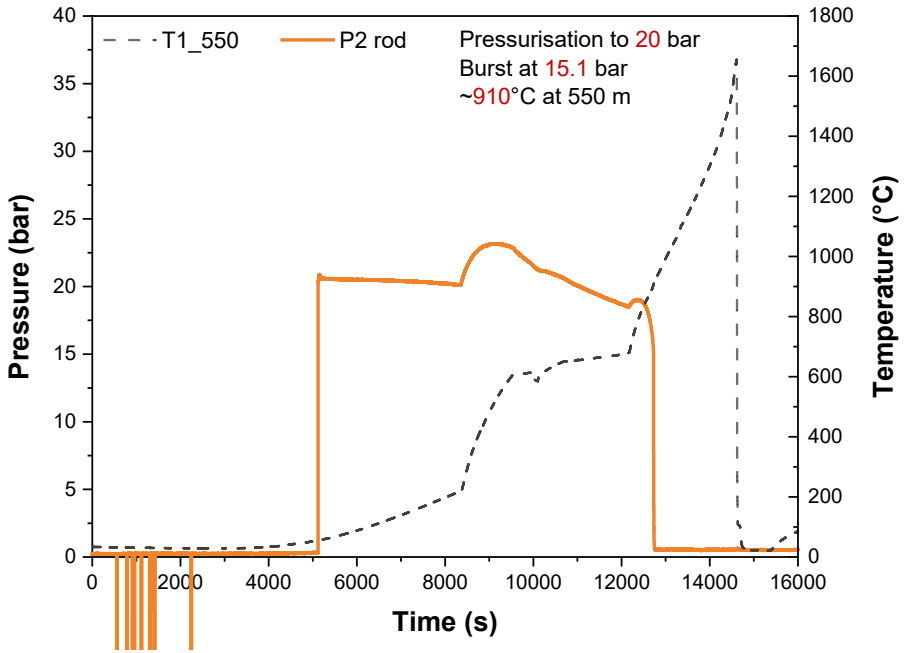

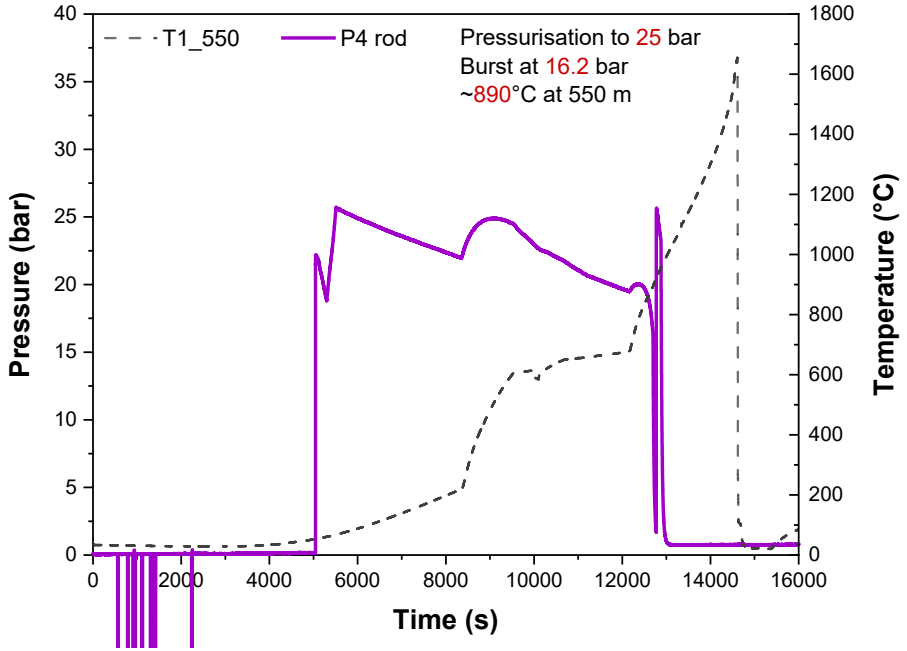

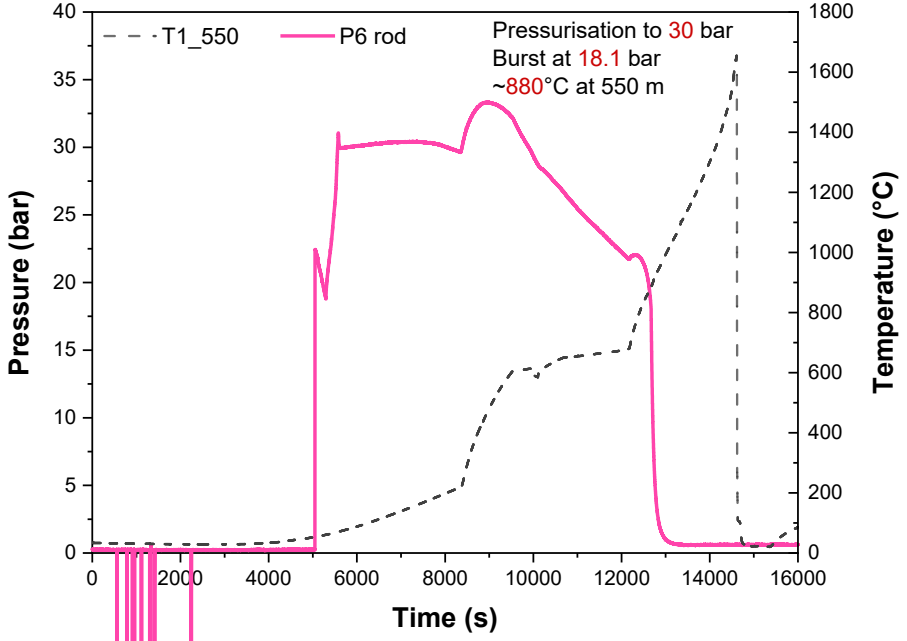

CODEX-ATF results

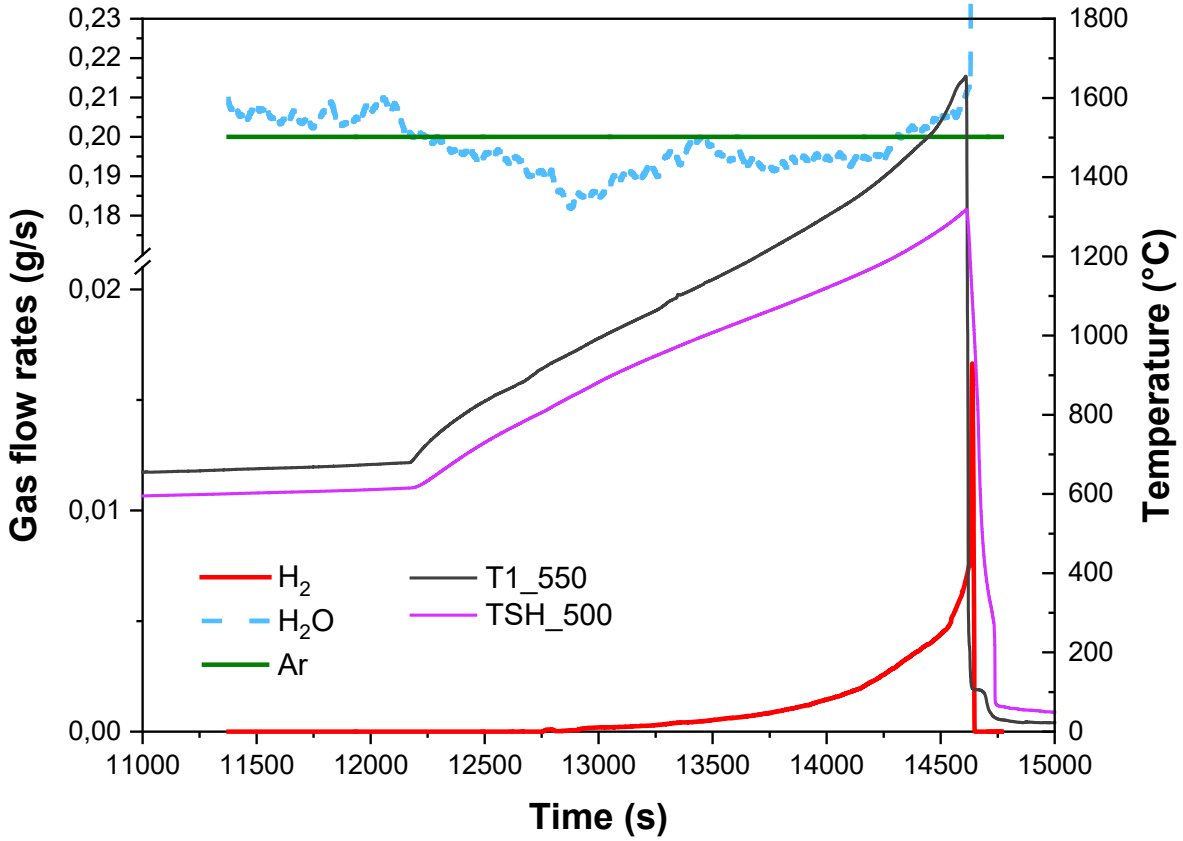

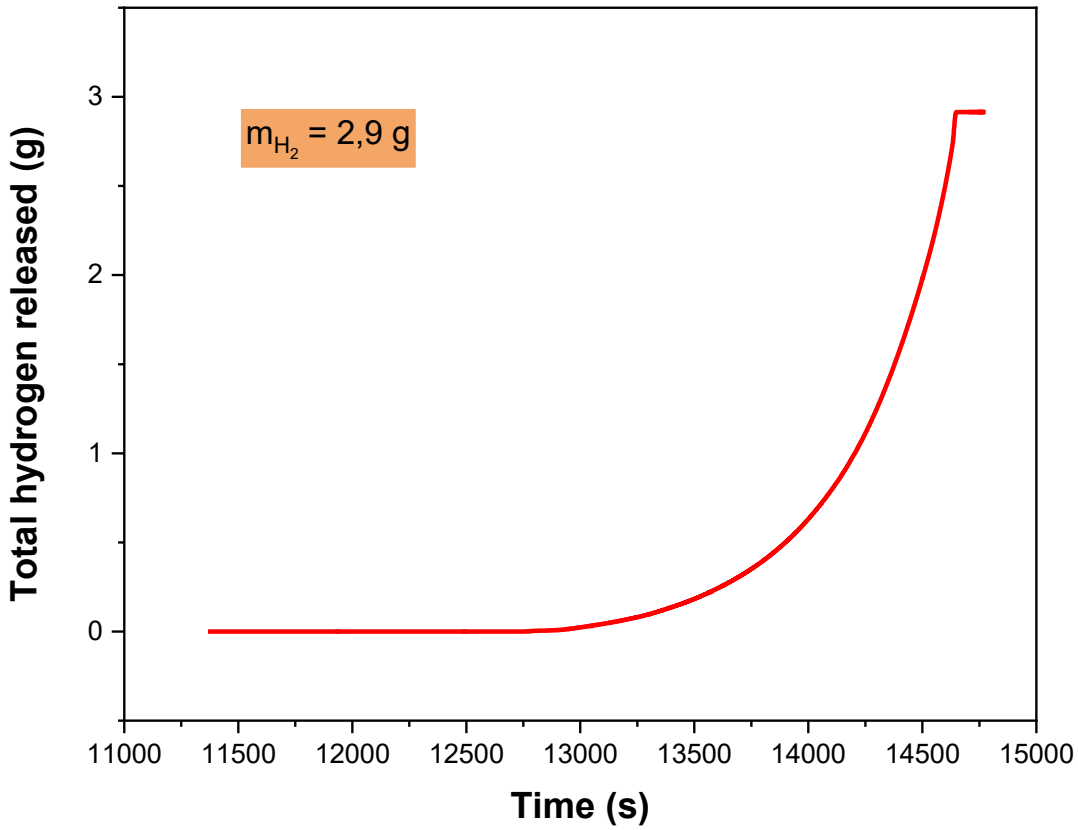

Total H_2 generation 2.9 g

Images of the bundle (endoscopic)



Top of the bundle







Removed parts of the CODEX-ATF bundle

≈590-630 mm, T_{max}>1350 °C

Rod No. 3 - Cr-coated optZIRLO™

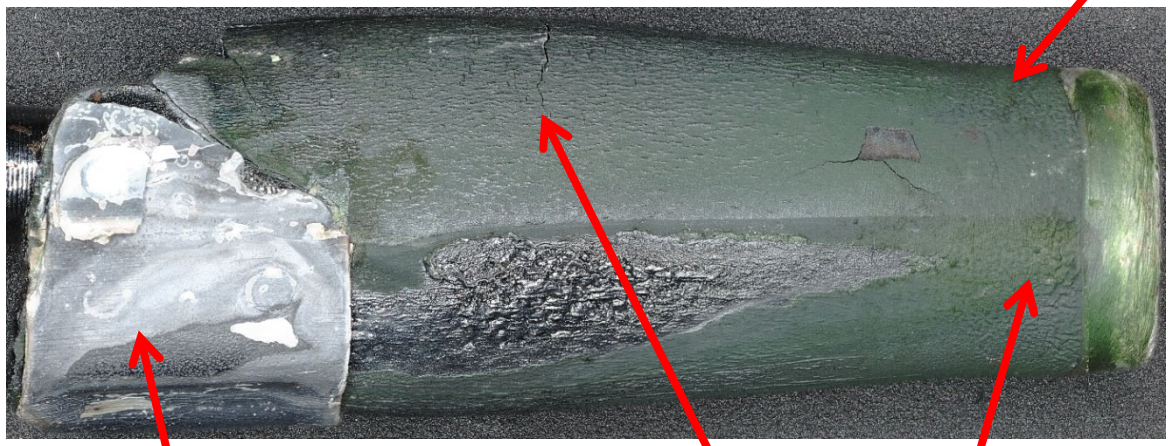

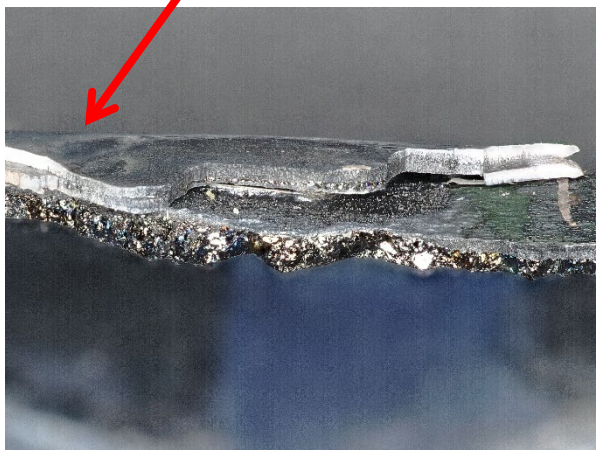

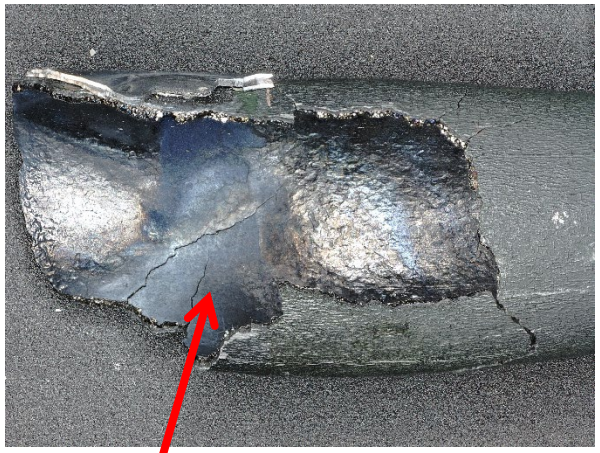

Rod No. 4 - optZIRLO™



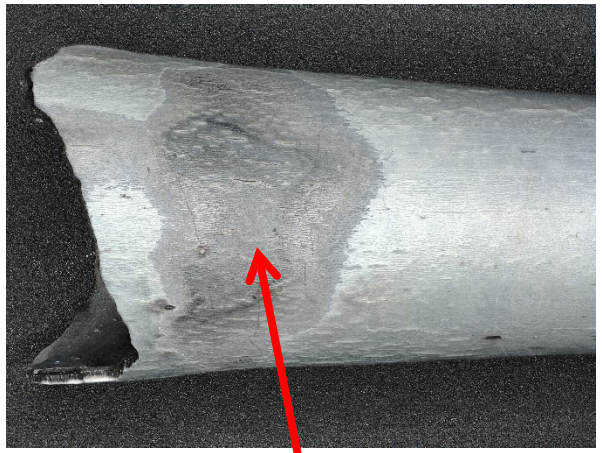

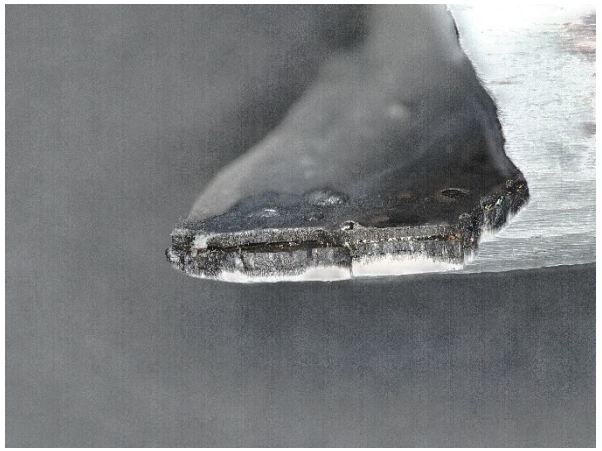

Cross sections of removed parts

Rod No. 3 - Cr-coated optZIRLO™

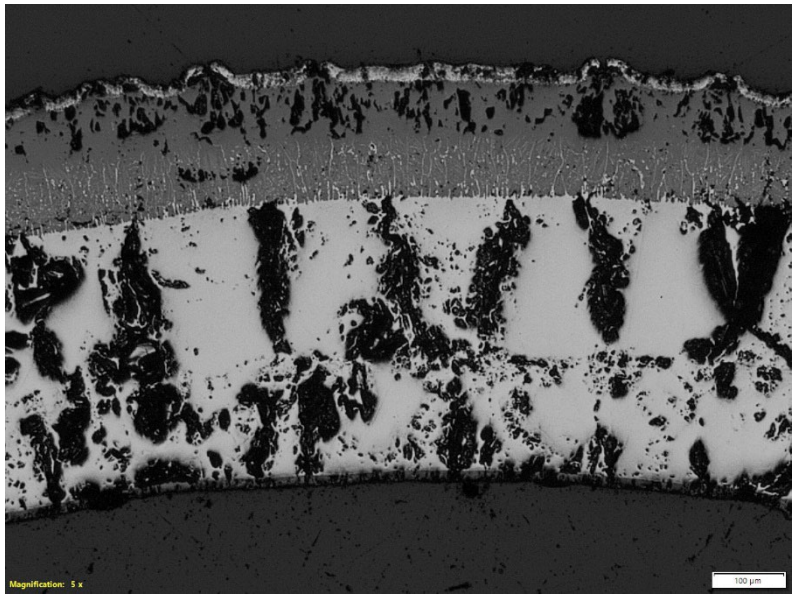

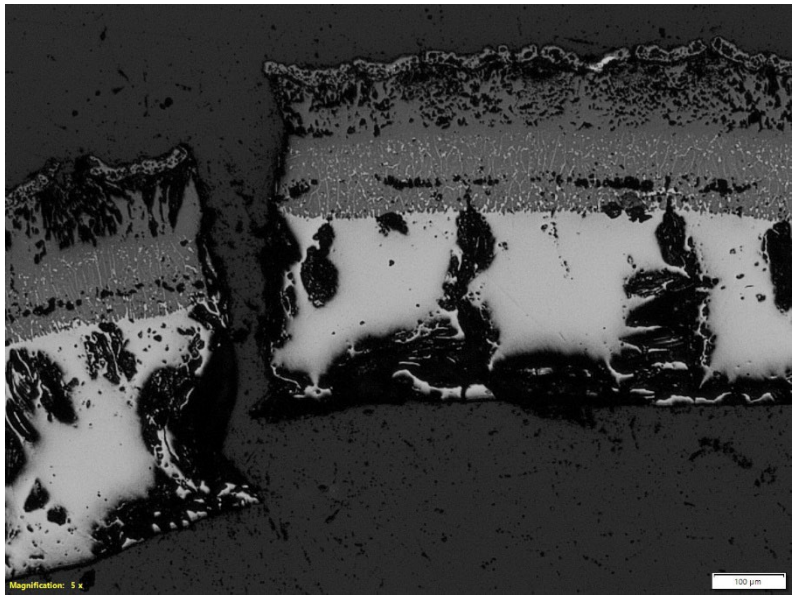

Cr_2O_3

Outside oxide layer

Inside oxide layer

≈620 mm, T_{max}>1350 °C

Metallography of the cross sections is ongoing

Rod No. 4 - optZIRLO™

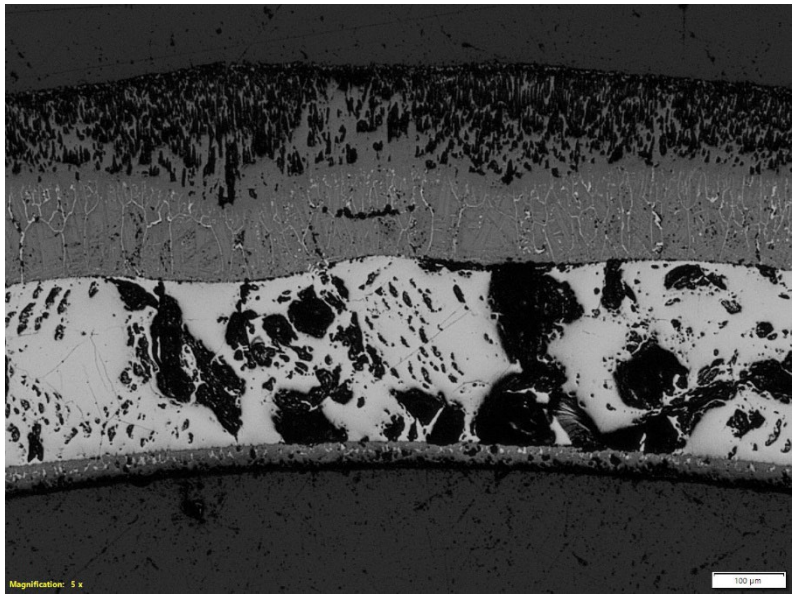

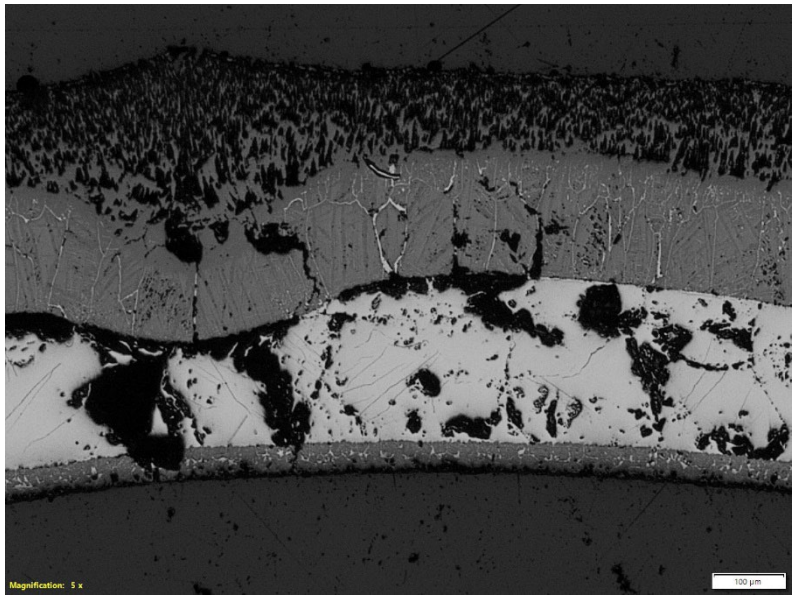

Summary

- The CODEX-ATF test was successfully performed on the 23th August 2023.
- Seven-rod electrically heated VVER type bundle with 650 mm heated length was used. Cr coated and uncoated optimised ZIRLO^{TM} cladding material was used.
- The experiment was carried out with temperature conditions which were close to the specified ones by pre-test calculations.
- The presence of steam in the atmosphere accelerated the oxidation of Zr components.
- In the first phase the maximum temperature reached 1000 °C. Cladding burst took place at the same temperature due to pressurization of the rods. Consequence of the opening the coolant entered to the rod and started chemical reactions on both sides of the claddings.
- In the second phase the maximum cladding temperature reached 1655 °C. Due to the high temperature eutectic formation between Zr-Cr took place.
- The composition of outlet gases was monitored with mass spectrometer. Total H_2 generation ≈ 2.9 g.
- Cool-down of the bundle was performed with water quench.
- The post-test examination was confirmed that oxide layers were formed and part of the bundle was suffered brittle failure.
- The metallography of the cross sections is ongoing.

HUN-REN Centre for Energy Research

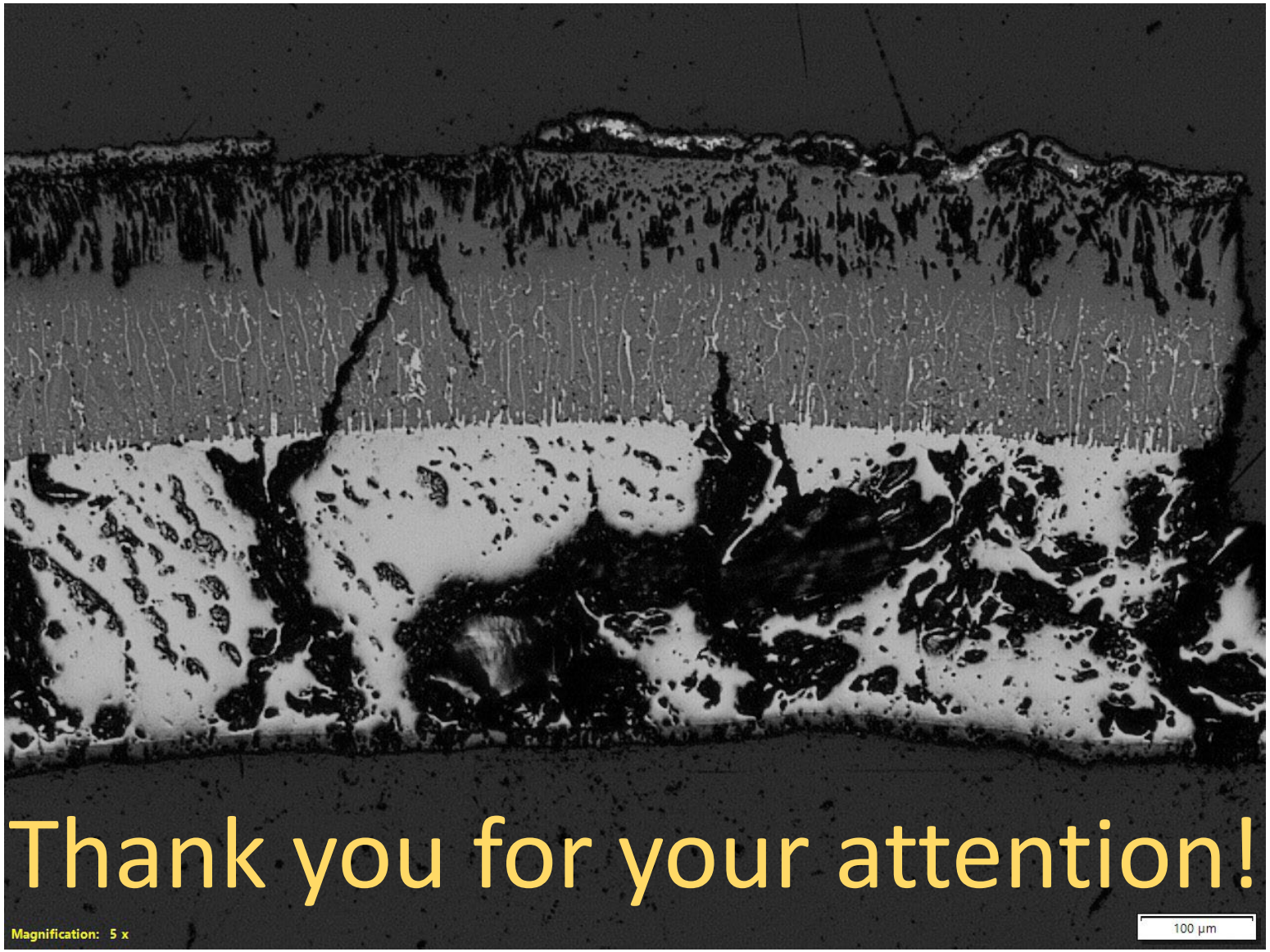

The 11th European Review Meeting on Severe Accidents Research

May 13-16, 2024, Royal Institute of Technology, Stockholm, Sweden

TECHNICAL SESSION 8.1: SEVERE ACCIDENT SCENARIOS - FAST REACTORS

Chairs: A. Stakhanova (KIT), F. Gabrielli (KIT)

ID13	**Preliminary Evaluation of Reactivity Insertion during BDBA-LOCA of Super Fast Reactor** K. Matsuoka (Waseda University)	**Paper Presentation**
ID54	**Development of severe accident simulation code for sodium-cooled fast reactors: SIMMER-V (1) Overview of the SIMMER-V code development** H. Tagami (JAEA)	**Paper Presentation**
ID08	**Experimentation & simulation of ablated surface by jet impingement for core-catcher safety issue** N. Seiler (CEA)	**Paper Presentation**

Preliminary Evaluation of Reactivity Insertion during BDBA-LOCA of Super Fast Reactor

Koki Matsuoka and Akifumi Yamaji
Waseda University
3-4-1 Ookubo, Shinjuku-ku, Tokyo, 169-8555, Japan
koki_kyoto@suou.waseda.jp; akifumi.yamaji@waseda.jp

ABSTRACT
The fast reactor core is not in its neutronically most reactive configuration, and the common challenge is to suppress the compaction reactivity to prevent excessive mechanical energy generation due to recriticality during the core degradation in an anticipated severe accident. The Super Fast Reactor (Super FR) is the fast reactor design concept of the Supercritical Light Water-cooled Reactor (SCWR) being developed at Waseda University. The core is loaded with enriched Pu MOX fuel and cooled by the supercritical water at 25 MPa during normal operation. The severe accident of the Super FR with the system depressurization leads to the core degradation together with the decrease of the coolant inventory, because of the low boiling point of the coolant. Consequently, positive reactivity insertion into the core is expected not only by the core compaction (due to degradation and melting) as expected for any other fast reactors, but also due to the water level decrease, because of the large neutron scattering and moderation characteristics of water. This study aims to reveal the combined effects of the core exposure and compaction on the reactivity insertion during anticipated severe accidents of the Super FR.

The 285 MWe (650 MWth) Small Modular Reactor (SMR) class Super FR with the active core height of 2000 mm and equivalent diameter of 1780 mm has been tentatively selected for the evaluations. A Beyond Design Basis Loss-Of-Coolant Accident (BDB-LOCA) without water injection is considered as an example of the severe accident scenario to give history of the water level decrease during the core degradation process. A 100% hot-leg break was considered as an initiating event. The neutron transport calculations based on the Monte Carlo method (MVP) were carried out with the JENDL-4.0 nuclear data library.

The reactivity changes from the normal operation condition to the core under the above assumptions were analyzed. The water level reduction was the dominant cause of the reactivity insertion until the water level decreased to about 2/3 of the active core. Then, the reactivity insertion due to the core compaction became non-negligible as the water level further decreased from about 2/3 to 1/3 of the active core. Eventually, as the compaction volume expanded, the additional reactivity insertion due to core compaction became less significant until the water level further decreased and the damaged core was fully uncovered.

KEYWORDS
Supercritical Water-Cooled Reactor (SCWR), Super FR, water cooled fast reactor, severe accident, re-criticality

1. INTRODUCTION
Supercritical Water-cooled Reactor (SCWR) is the only water-cooled reactor among the six Generation IV reactor concepts. It uses supercritical light water as the coolant. Above the critical point (22.1 MPa and 374 °C), water does not exhibit phase change (does not boil) and continuously changes from high-density liquid-like state to low-density gas-like state as temperature is increased. The combined nature of single-phase and large density change of supercritical water enables the unique plant system of “once-through direct cycle” as the entire core coolant is directly fed to the supercritical turbine, which has been

commercially utilized worldwide for coal-fired power plants since 1970s [1]. There needs to be no steam / water separation systems (e.g., steam generator, pressurizer, separators, dryers). It may be regarded as the simplest nuclear power reactor of all kinds and therefore the cheapest to build in principle.

The single-phase nature of supercritical water allows achieving high average core outlet coolant temperature, which typically ranges from about 500 to 625 ℃ at operating pressure of 25 MPa. The resulting plant thermal efficiency ranges from about 44 to 48% [2-5]. Furthermore, the large density change nature of the coolant enables designing of both thermal neutron spectrum reactors and fast neutron spectrum reactors with the same plant system by only modifying the core design [1][6].

Super FR is the fast reactor design concept of SCWR, which was originally developed at the University of Tokyo and currently being developed at Waseda University [1][6]. It utilizes enriched Pu in the form of MOX fuel. The hexagonal fuel assembly with tight fuel lattice is adopted to minimize neutron moderation by the coolant and each fuel assembly is equipped with a channel box, so that coolant flow rate can be assigned to each fuel assembly for efficient cooling and raising the outlet temperature. The core designs are also characterized by use of depleted U as blanket to attain negative coolant void reactivity [7]. In some designs, solid moderator (ZrH) was introduced to enhance resonance capture of neutron by ^{238}U under voided condition to further gain negative void characteristics [8]. Different core cooling schemes were designed in the past studies, such as downward flow cooling of blanket fuel assemblies [7] and multiple upward flow passes through different fuel assemblies [9] to achieve high average core outlet temperature. The current Japanese official reference Super FR design adopts the simple core cooling scheme as adopted in the current PWR cores [10].

One of the safety requirements of SCWR is to keep the peak fuel cladding temperature below limits of normal operation, abnormal transients and design basis accidents (DBAs) [11]. Under supercritical pressure, there is no water level in the core. Hence, the safety design principle of SCWR at supercritical pressure is to sustain sufficient core flow rate and depressurizing the system to induce core flow rate when the core flow rate cannot be sustained at supercritical pressure [12]. The earlier study on Super FR showed that all the safety criteria were satisfied including the Loss-Of-Coolant-Accident (LOCA) [13]. The key safety feature of all SCWRs is that rapid core depressurization always cools down the core [11-13].

However, for Beyond DBA (BDBA), the SCWR accident may extend to a severe accident with significant core degradation if water injection fails after depressurizing the system. Then, the unique issue of Super FR arises as the common issue for all kinds of water-cooled fast reactors. Namely, the total loss of coolant must be assumed, because of the low boiling temperature of the coolant at atmospheric pressure, and the reactivity insertion by core melting (compaction) must be assumed, because the fast reactor core is not in its neutronically most reactive configuration. The unique nature of the water-cooled fast reactor, including Super FR, is that these two issues must be addressed at the same time when the system is depressurized, which implies that criticality management is required with the assumption that the entire core melts-down [14].

One of the recent studies on severe accident management of Super FR showed that re-criticality of the fuel debris in the lower plenum of the Reactor Pressure Vessel (RPV) could be avoided by preparing some neutron absorbers in the lower plenum even if the entire core melts-down [15]. However, measures may also be necessary to avoid excess reactivity insertion during the core meltdown process. The purpose of this study is to clarify the reactivity change characteristics of Super FR during the severe accident, after the system has depressurized, with considerations of the followings:

- Lowering of the core water level may increase the neutron leakage to favor negative reactivity insertion but may also soften the neutron spectrum, which may favor positive reactivity insertion.
- Core compaction may favor positive reactivity insertion.

2. CORE AND PLANT DESIGN SPECIFICATIONS AND CHARACTERISTICS

The reference core and plant design specifications were tentatively determined by referring to the earlier design study of the small-modular class core design [16] and the earlier safety analysis [17] as summarized in Table 1. The core consists of the hexagonal fuel assemblies as shown in Fig. 1. The core is loaded with the 1st cycle to the 5th cycle fuel assemblies. The average fuel batch number is 4.2, which means that on average, each fuel assembly stays in the core for 4.2 cycles of operations before being discharged to the spent fuel pool. Each fuel assembly is equipped with a channel box so that different coolant flow rate can be assigned, depending on the loading positions by appropriate inlet orifice pressure loss design.

Table 1. The Reference core and plant design specifications and characteristics [16][17]

Parameters	Specifications, characteristics
Core thermal power (MWth)	650
Maximum / average linear heat rates (kW/m)	30.6 / 15.1
Average coolant inlet / outlet temperature (°C)	280 / 502
Number of fuel assemblies / average fuel batch number	127 / 4.2
Core equivalent diameter / active core height (m)	1.78 / 2.00
Average Pu enrichment (wt.%)	18.8
Fuel cladding and channel box material	Advanced stainless steel
Fuel rod diameter / pitch / cladding thickness (mm)	10.0 / 11.0 / 0.597
Fuel assembly size / pitch / channel box thickness (mm)	150.4 / 152.4/ 1.0
Operation cycle length(days)	720
Average fuel discharge burnup (GWd/t)	84.8
Void reactivity coefficient at BOEC / EOEC (10^{-4} dk/k/%void)	-0.009 / -0.099
Density reactivity coefficient at BOEC/EOEC (%dk/k/(g/cc))	6.20/6.20
Doppler reactivity coefficient at BOEC / EOEC (10^{-4}dk/k/°C)	-1.17 / -1.17

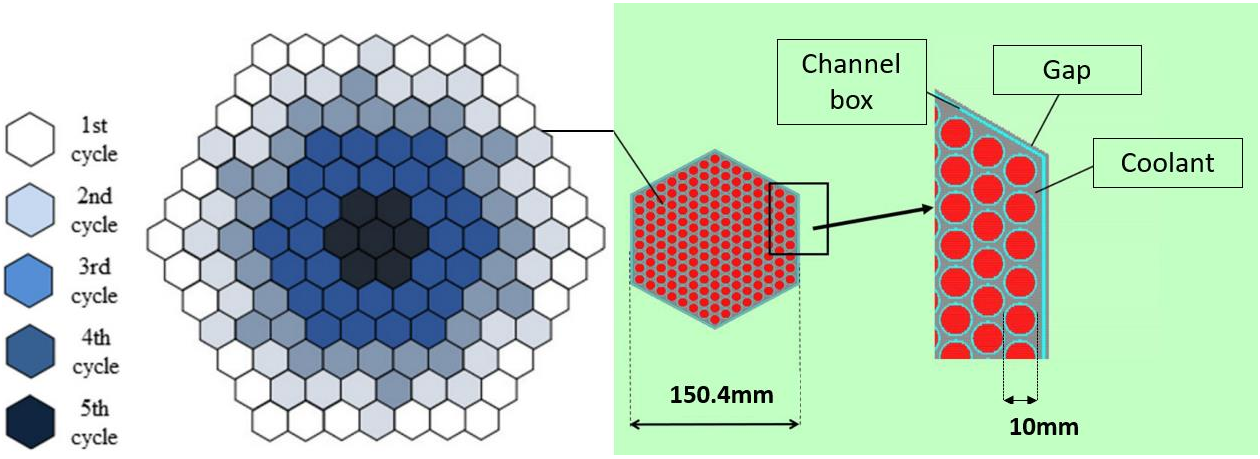

Figure 1. Core Configurations and the Fuel Assembly Design.

The basic plant control and safety systems of Super FR are the same as those of Super LWR (thermal reactor version) as described in the earlier study and shown in Fig. 2 [18]. The core power, pressure, and the main steam temperature are controlled by the control rods, the turbine control valves, and the feed water pump, respectively. The actuation conditions of the Automatic Depressurization System (ADS), Main Steam

Isolation Valve (MSIV) closure, and the Low-Pressure Core Injection (LPCI) system follow the same conditions as adopted in the preceding study [19]. Table 2 summarizes the logics, which are relevant for LOCA analyses.

Table 1. Actuation logics of the safety systems [19]

Actuation conditions		Safety system
Flow rate low level	1(90%)	Reactor scram
	2(20%)	Auxiliary Feedwater System(*)
	3(6%)	ADS/LPCI(*)
Pressure low level	1(24.0MPa)	Reactor scram
	2(23.5MPa)	ADS/LPCI(*)

(*) In this study, all water injections systems are assumed to fail as BDBA-LOCA.

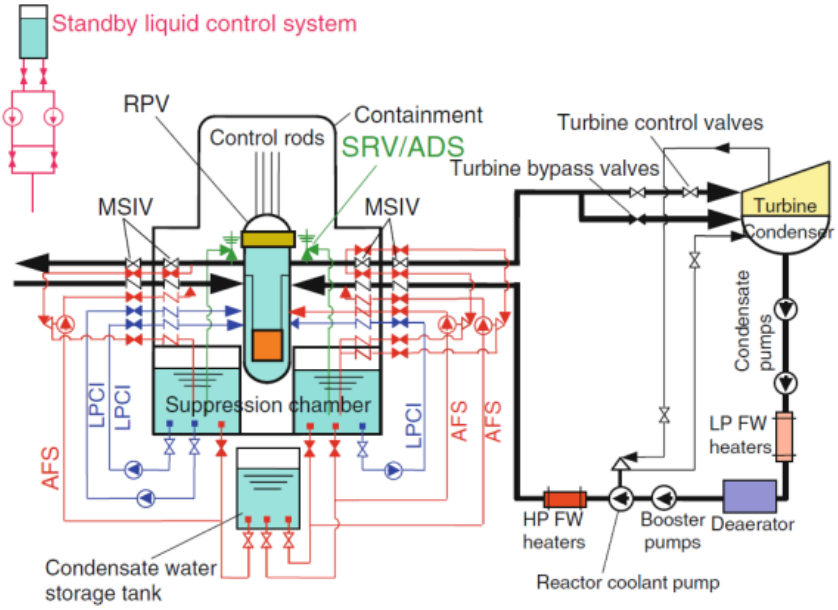

Figure 2. Plant System of Super FR (the same as that of Super LWR [19])

3. BEYOND DESIGN BASIS LOCA SCENARIO EVALUATION

3.1. Large Hot-Leg Break LOCA Blowdown and Core Heat-up Phase Analysis with ASYST code

To determine the core water level and compaction scenario for the criticality evaluation, a preliminary analysis of the blowdown and the subsequent core heat-up phase of the Super FR large hot-leg break LOCA was performed with ASYST code [20]. A 100% hot-leg break was considered as an initiating event, followed by the reactor scram and the system depressurization as defined in Table 2, but actuations of all water injection systems were assumed to fail to simulate BDBA-LOCA.

The ASYST code models the core with a point kinetics approximation and a single-channel thermal-hydraulics model while the plant system is modelled by the node and junctions as described in Figure 3. In this study, the core was modelled with the hot channel, the average channel, and the cold channel with relative power densities of 1.12,1.00, and 0.94, respectively. Each channel was axially divided into 20 calculation meshes.

For simulation of supercritical water cooling, the steam table has been extended to supercritical pressure, but the heat transfer is currently approximated with the widely used Dittus-Boelter's correlation for single-

phase heat transfer. It is expected that peak cladding temperature appears in the region, which is well above the critical or pseudo-critical points [21], where Reynolds and Prandtl numbers are are expected to be within the applicable range of the Dittus-Boelter equation (Re<1.0×104, 0.6≤Pr≤180) [22]. However, it should be noted various heat transfer correlations have been developed for supercritical water cooling, which can be applied over much wider regions including pseudo-critical points under various pressures [23][24]. For example, the Watts-Chou's correlation is used in the core design study of Super FR [25]. For consistency, it would be better to use the same correlation for the core design and safety analysis, if applicable and it would be considered for the future study. For the subcritical pressure heat transfer, different correlations have been applied depending on the boiling regime. Namely, the Chen's (nucleate boiling), Bromley's (nucleate boiling), and Dittus-Boelter's (superheated) [26].

The main steam line (hot-leg) was connected to the Steam Relief Valve (SRV), the Turbine Control Valve (TCV) and the Main Steam Isolation Valve (MSIV) while the cold-leg was connected to the MSIV. The wetwell (W/W) and drywell (D/W) of the PCV were modeled with sufficiently large dry control volumes. All water injection systems were deactivated to model Beyond Design Basis LOCA (BDBA-LOCA).

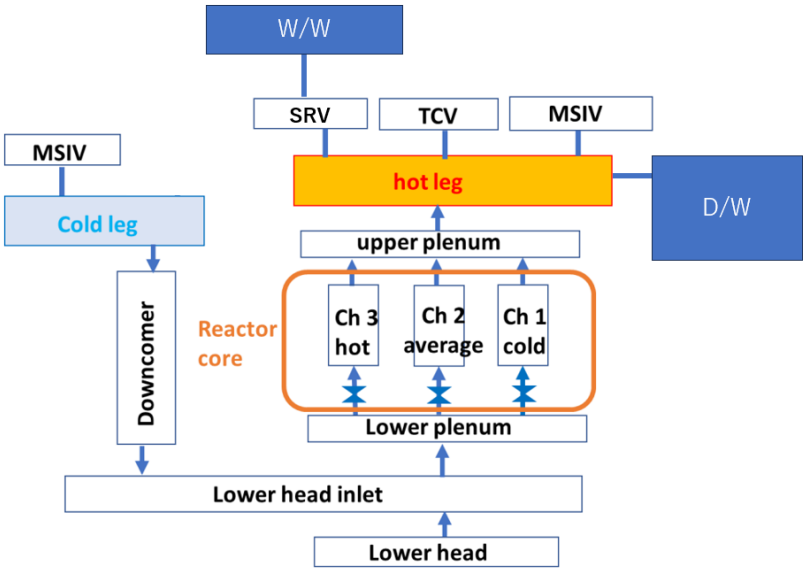

Figure 2.2 ASYST Node Junction Model of Super FR (BDBA-LOCA).

Fig. 3 shows the power, pressure, and the downcomer flow rate (as representative of the core flow rate) histories after the break. As the initiating event, large 100% hot-leg break (0.27 m^2) was assumed, which induced rapid depressurization and strong coolant flow through the core to the break. The reactor scram signal was released at 0.04 s (pressure < 24 MPa), followed by actuation of the Automatic Depressurization System (ADS), which opened all the SRVs (0.44 m^2) at 0.2s (pressure < 23.5 MPa) and further increased the coolant flow through the core. As the result, the core power was kept almost constant until the initiation of the reactor scram at about 0.70 s (0.55 s delayed after the scram signal). The reactor scram was completed, and the core power dropped to the decay power level (< 7% of the rated power) within a few seconds. In the meantime, the system pressure continued to decrease to subcritical pressure and dropped to about 6.2 MPa within about 1 s after the initial break. As the system pressure dropped, the discharge flow through the break and SRVs changed from supercritical water flow to subcritical saturated two-phase flow and the pressure reduction continued at much slower rate until the core was completely exposed above the water level at about 36 s.

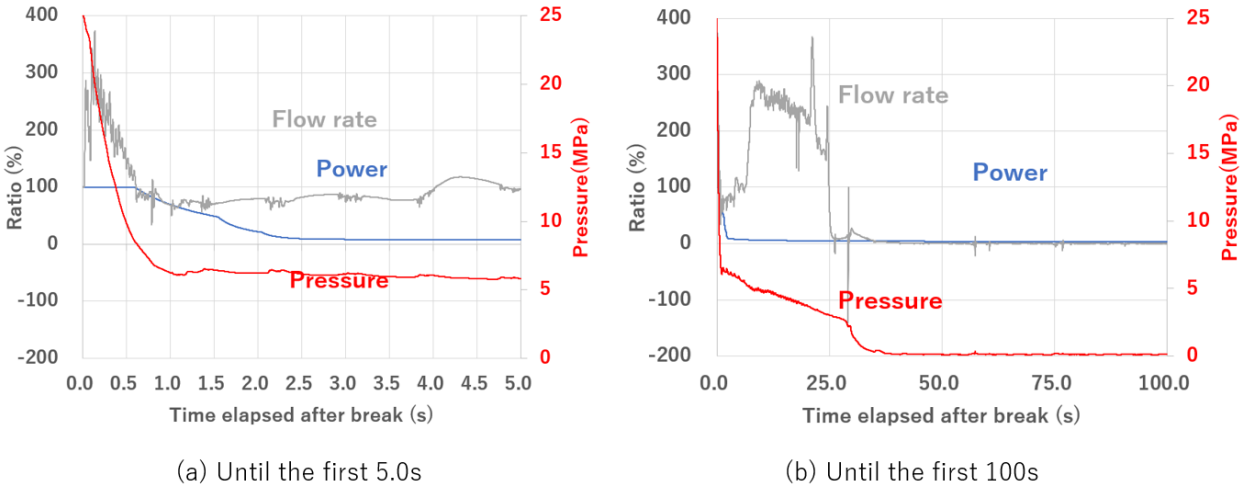

Figure 3. Core Power, Pressure, and Flow Rate Histories (Large Break Hot-Leg LOCA).

The Fig. 4 shows the fuel cladding temperature histories at different elevations from the bottom of the active core. Initially, there was large cladding temperature increase in the axial direction due to the axial coolant temperature increase towards the core outlet. Then, it rapidly decreased in the first 1 s, due to the strong coolant flow induced by the rapid depressurization, followed by relatively moderate cladding temperature decrease until about 30 s, by which time the axial cladding temperature distribution was uniform as the core was being cooled by saturated steam. As the water level decreased below the bottom of the active core, the core could no longer be cooled by steam. Then, the cladding temperatures at different elevations increased at different rates depending on the axial decay power distribution as shown in Fig. 4.

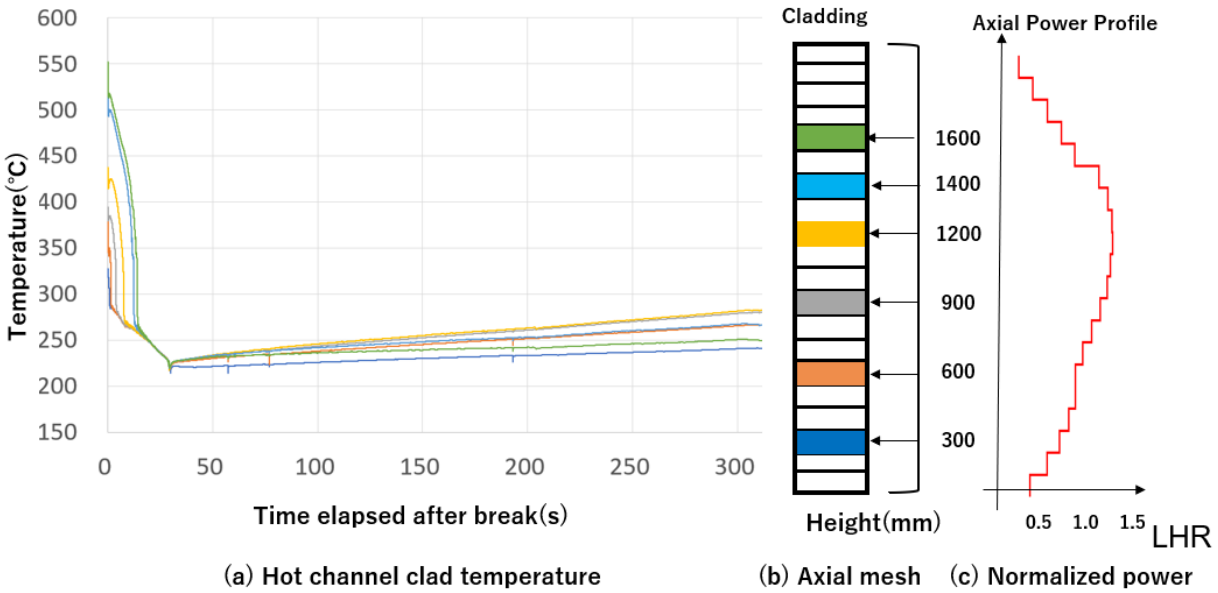

Figure 4. Cladding Surface Temperature Histories (Large Break Hot-Leg LOCA).

Thus, the ASYS analysis result of the large hot-leg break LOCA without water injection indicates the followings:

- The rapid core depressurization leads to core water level to decrease to below the active core within the first 30 - 40 s. However, there is large uncertainty regarding the post-blowdown in-vessel water level, depending on detailed in-vessel design, which has not been carried out.
- The entire core is rapidly cooled down to the saturation temperature followed by the reheating phase, in which the axial decay power distribution is reflected to the axial temperature distribution.

3.2. Water Level and Core Compaction Scenario and Criticality Evaluation with MVP

Following the results obtained by ASYST code, the water level and core compaction scenarios were tentatively determined as described in Fig. 5. According to the ASYST evaluation, the in-vessel water level quickly dropped to below the bottom of the active core during the blowdown phase. However, there is large uncertainty regarding the blowdown phase with regard to the water level. For example, the downcomer water may not boil-off depending on the downcomer volume design and heat transfer. Hence, in this study, the water level was assumed to remain in the core at the same level as the boundary of the molten core and the intact core.

Also, according to the ASYST code evaluation, the entire core once cooled down to the saturation water / temperature before reheating by decay heat. The reheating phase was governed by the axial decay heat power distribution and the temperature of the middle of the core region increased most rapidly. Hence, it is expected that the core region just above the water level melts first. When the core melting occurs, it may be sensible to assume that anything that is above the molten core region collapses and relocates down to mix with the molten core region. Hence, in this study, the core melting region was assumed to develop as the water level was assumed to decrease as shown in Fig. 5.

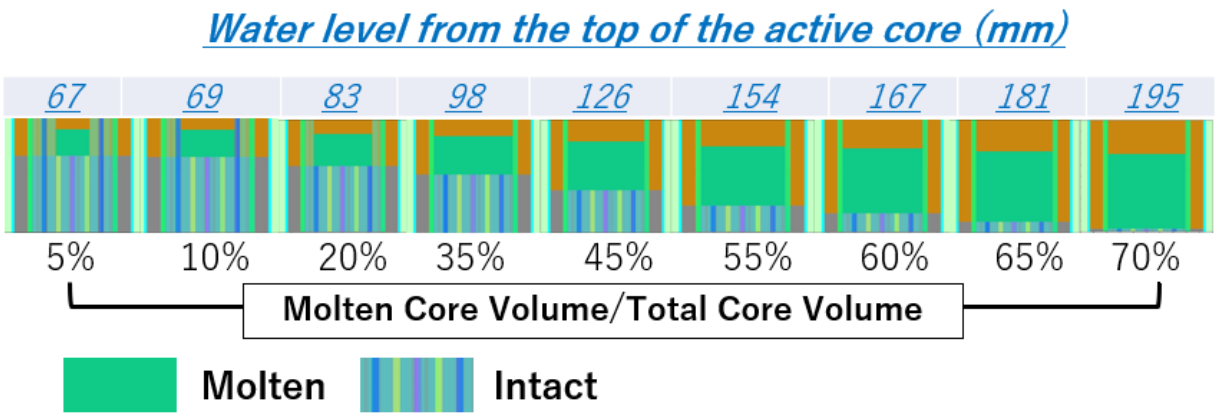

Figure 5. Water Level and Core Compaction Scenarios.

4. REACTIVITY INSERTION TO SUPER FR CORE DURING BDBA-LOCA

4.1 Core Models of MVP

In this study, the general purpose Monte Carlo code for neutron and photon transport calculations based on continuous energy and multigroup methods (MVP code) was used together with the JENDL-4.0 nuclear

data library [27] to analyze the reactivity insertion during BDB-LOCA of Super FR with considerations of the water level reduction and core compaction.

The MVP code estimates physical quantities when the specified event occurs within a certain range of space, time, and energy during the random walk of neutrons. The sample with statistical independence is the sum of the contributions to the physical quantity during the random walk of a source particle and the unit of samples is described as "history". A set of histories is defined as "batch" and the batch is used for the statistical estimation of the eigenvalue and corresponds to the generation of fission neutrons in eigenvalue problems. In this study, the parameter 10000 histories and 125 batches were used. 25 batches were skipped to make sure fission source converged sufficiently before calculating neutron fluxes, and the statistical error (3σ) was set to ±0.13%.

Fig. 6 shows an example of the MVP model for evaluating the criticality during BDBA-LOCA of Super FR. The fuel compositions of different fuel assemblies were determined from the reference core design [16]. In the reference core design, the fuel compositions were evaluated for each of the homogenized fuel assemblies at different elevations and different burnups in the 1/6 symmetric core geometry. Since it was demanding to prepare such detailed fuel compositions for different axial elevation levels for each of the 127 fuel assemblies through different burnup steps, the fuel compositions were averaged in this study. The representative fuel compositions were evaluated for the Beginning Of the Equilibrium Cycle (BOEC). Each fuel cycle assembly was represented with only one set of the fuel compositions, which were averaged for all the fuel assemblies of the same cycle and also averaged along the core axial direction.

For evaluation of the molten core region, it was assumed that all the constituting elements, such as the fuel pellets, the cladding, and the channel box, were molten and mixed homogeneously. The control rods were not considered for conservative evaluation of the reactivity insertion, and it was assumed that all the control rods were withdrawn from the core.

In the Super FR core, the coolant density greatly changes along the core axial direction during normal operation at supercritical pressure. In case of the reference core design the inlet coolant density is about 750 kg/m^3, while the average outlet coolant density is about 90 kg/m^3. Then, in BDBA-LOCA, the core pressure quickly dropped to subcritical pressure and the core was cooled by saturated water / steam with some voids. The effective water density (swollen water density) may be significantly below the saturated water density. For the criticality evaluation, the water density was not evaluated but assumed to be uniform and constant during normal operation at 360 kg/m^3. During BDBA-LOCA, the criticalities were evaluated with two cases: 360 kg/m^3 and 1000 kg/m^3.

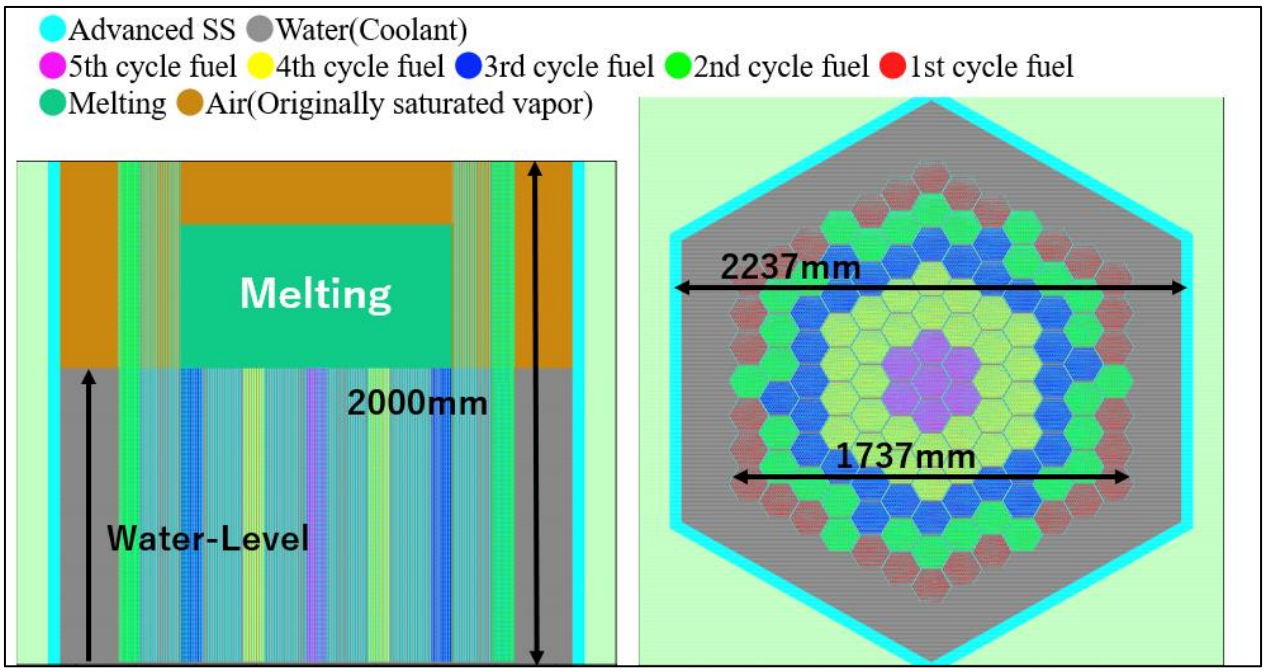

(a) Axial cross section (b) Horizontal cross section

Figure 6. MVP Core Model.

4.2 Reactivity Insertion to Super FR Core in BDBA-LOCA (Post-Blowdown Phase)

The reactivity changes (Δk_{eff}) from the normal operating condition were evaluated for the cases as shown in Fig. 5 after 5% of the core was melted. Two different cases were analyzed:

- Reactivity changes due to water level reduction with intact core
- Reactivity changes due to water level reduction and core compaction

The evaluated reactivity changes for the case when the water densities were assumed to be 360 kg/m^3 and 1000 kg/ m^3 are shown in Figs. 7 and 8, respectively. In both cases, the reactivities increased at the beginning due to the influence of the water level drop. When the water level dropped by about 1/3 of the active core, the effect of compaction by the molten core contributed to the reactivity. After that, the reactivity increased due to the effect of the lowering of the water level.

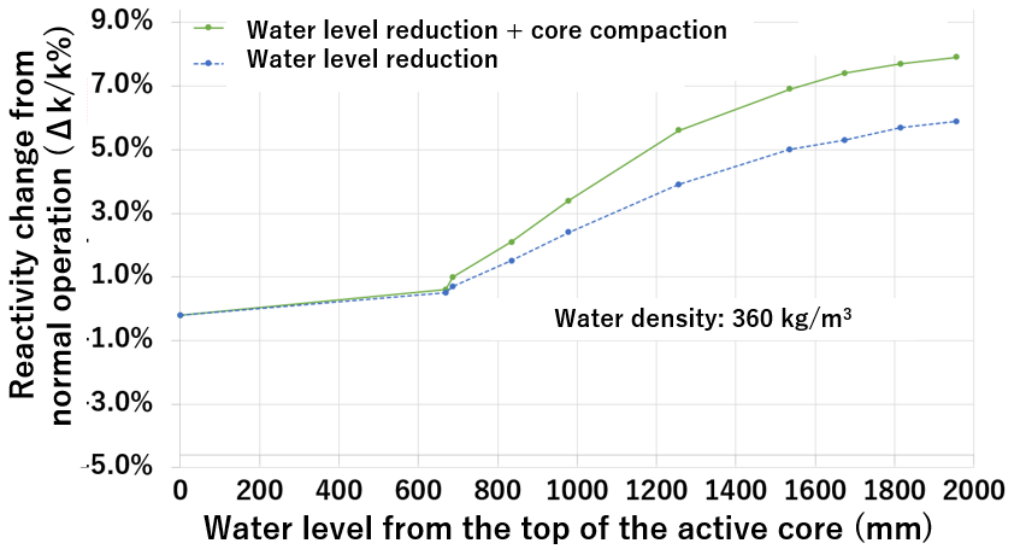

Figure 7. Reactivity Changes from Normal Operation in Post Blowdown Phase of BDBA-LOCA (360 kg/m³)

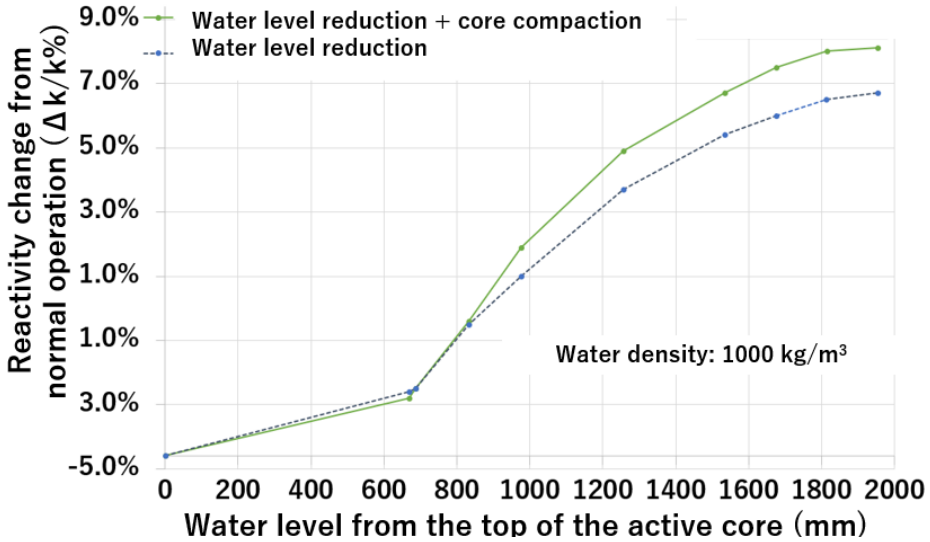

Figure 8. Reactivity Changes from Normal Operation in Post Blowdown Phase of BDBA-LOCA (1000 kg/m³)

5. CONCLUSIONS

Reactivity insertions to the Super FR core during post blowdown phase of BDBA-LOCA were analyzed as the core water level decreased while the core melting progressed above the water level. The water level reduction was the dominant cause of the reactivity insertion until the water level decreased to about 2/3 of the active core. Then, the reactivity insertion due to the core compaction became non-negligible as the water level further decreased from about 2/3 to 1/3 of the active core. Eventually, as the compaction volume expanded, the additional reactivity insertion due to core compaction became less significant until the water level further decreased, and the damaged core was fully uncovered.

ACKNOWLEDGMENTS

This work was partly supported by JSPS KAKENHI Grant Number 20H02669. A part of this study is the result of "Understanding Mechanisms of Severe Accidents and Improving Safety of Nuclear Reactors by Computer Science" of Waseda Research Institute for Science and Engineering and the authors acknowledge support of the Institute for Advanced Theoretical and Experimental Physics, Waseda University.

REFERENCES

1. Y. Oka, S. Koshizuka, Y. Ishiwatari, A. Yamaji, "Super Light Water Reactors and Super Fast Reactors", ISBN: 978-1-4419-6035-1. Springer (2010).
2. G. Edwards, L. Leung, "GIF Supercritical Water-cooled Reactor, Proliferation Resistance and Physical Protection White Paper", GIF/PRPPWG/2022/001 (2022).
3. T. Schulenberg, J. Starflinger, et al., "High Performance Light Water Reactor Design and Analyses. KIT Scientific Publishing", (2012).
4. J. Pencer, A. Colton, "Progression of the Physics Conceptual Design for the Canadian Supercritical Water Reactor", 34th annual CNS Conference. Canada, Toronto (2013).
5. IAEA, "Status Report - Chinese Supercritical Water-Cooled Reactor (CSR1000)", IAEA Advanced Reactors Information System (ARIS). Database (2015).
6. Y. Oka, H. Mori, et al., "Supercritical-Pressure Light Water Cooled Reactors", ISBN 978-4-431-55025-9. Springer (2014).
7. T. Mukohara, S. Koshizuka, Y. Oka, "Core Design of a High-temperature Fast Reactor Cooled by Supercritical Light Water", Annals of Nuclear Energy 26, pp 1423 – 1436 (1999).
8. Y. Oka, T. Jevremovic, "Negative void reactivity in large fast breeder reactors with hydrogeneous moderator layer", Ann. Nucl. Energy, 23(14), pp. 1105–1115 (1996).
9. Q. Liu and Y. Oka, "Improvements of Two-pass Core Design for Super Fast Reactor", Annals of Nuclear Energy 69, pp 108 – 115 (2014).
10. Liu, Q.; Oka, Y. Single pass core design for a Super Fast Reactor. Ann. Nucl. Energy 2015, 80, 451–459.
11. A. Yamaji, Y. Oka, Y. Ishiwatari, J. Liu, M. Suzuki, "Principle of Rationalizing the Criteria for Abnormal Transient of Super LWR with Fuel Rod Analyses", Annals of Nuclear Energy 33 pp. 984 – 993 (2006).
12. Y. Ishiwatari, Y. Oka, S. Koshizuka, A. Yamaji, J. Liu, "Safety of Super LWR, (I) Safety System Design", Journal of Nuclear Science and Technology, Vol. 42, No. 11, pp. 927 – 934 (2005).
13. Sutanto and Y. Oka, "Accidents and Transients Analyses of a Super Fast Reactor with Single Flow Pass Core", Nuclear Engineering and Design 273, pp. 165 – 174 (2014).
14. A. Yamaji, K. Matsuoka, K. Sumida, K. Funatsu, "Scope of Conceptual Development of Resilient Supercritical Light Water-cooled Reactor (SCWR-R)", Nuclear Engineering and Design 416 (2024) 112756.
15. R. Sasaki, A. Yamaji, K. Uchimura, "Design Study of Small Modular Reactor Class Super Fast Reactor Core for In-Vessel Retention", Journal of Nuclear Engineering and Radiation Science April 2023, Vol.9 021501 (2023).
16. K. Uchimura and A. Yamaji, "Preliminary Core Design Study of Small Supercritical Fast Reactor With Single-Pass Cooling", J. Nucl. Eng., 1(1), pp. 46–53 (2020).
17. S. Nakamoto, A. Yamaji, T. Okui., "LOCA analysis of super FR with RELAP/SCDAPSIM and FEMAXI-7", Proc. ISSCWR-10(2021).
18. T. Okui and A. Yamaji, "Preliminary Power Transient Analysis of the Super FR with Axially Heterogeneous Core" *Proc.* PHYSOR 2020, Cambridge, United Kingdom, March 29th-April 2nd, 2020.
19. S. Ikejiri, Y. Ishiwatari, Y. Oka, "Safety analysis of a supercritical-pressure water-cooled fast reactor under supercritical pressure", Nuclear Engineering and Design, 240, pp. 1218-1228 (2010).
20. ASYST THA VER 3 Manuals, Innovative Systems Software, April 2020.

21. International Atomic Energy Agency, Heat Transfer Behavior and Thermohydraulics Code Testing for Supercritical Water Cooled Reactors, Marketing and Sales Unit, Publishing Section International Atomic Energy Agency Vienna International Centre, Vienna, Austria (2014).
22. D. Taler, J. Taler, “Simple heat transfer correlations for turbulent tube flow”, E3S Web of Conferences 13, 0200 (2017).
23. Heat Transfer Behaviour and Thermohydraulics Code Testing for Supercritical Water Cooled Reactors (SCWRs), IAEA-TECDOC-1746, 2014.
24. Understanding and Prediction of Thermohydraulic Phenomena Relevant to Supercritical Water Cooled Reactors (SCWRs), IAEA-TECDOC-1900 (2020).
25. S. Noda, Sukarman, A. Yamaji, et al, “Core design study of Super FBR with multi-axial fuel shuffling and different coolant density”, Proceedings of 2018 26th International Conference on Nuclear Engineering ICONE26, Novotel London West, London, England, July 22–26, 2018 pp. 1-8 (2018).
26. Information Systems Laboratories, Inc., Idaho Falls- US," RELAP5/MOD3.3 CODE MANUAL VOLUME IV: MODELS AND CORRELATIONS, "2001.
27. K. Shibata, O. Iwamoto, T. Nakagawa, N. Iwamoto, A. Ichihara, S. Kunieda, S. Chiba, K. Furutaka, N. Otuka, T. Ohsawa, T. Murata, H. Matsunobu, A. Zukeran, S. Kamada, and J. Katakura, 2011, “JENDL-4.0: A New Library for Nuclear Science and Engineering,” J. Nucl. Sci. Technol., 48(1), pp. 1–30.

Preliminary Evaluation of Reactivity Insertion during BDBA-LOCA of Super Fast Reactor

Koki Matsuoka, Akifumi Yamaji
Waseda University

Outline

- Background: Super Fast Reactors and Severe Accident Issues
- CORE AND PLANT DESIGN SPECIFICATIONS
- BEYOND DESIGN BASIS LOCA SCENARIO EVALUATION
- Results (Analysis Result of large 100% hot-leg break)
- Water Level and Core Compaction Scenario and Criticality Evaluation
- Results (Reactivity Evaluation)
- Conclusion and Future Work

Outline

- Background: Super Fast Reactors and Severe Accident Issues
- CORE AND PLANT DESIGN SPECIFICATIONS
- BEYOND DESIGN BASIS LOCA SCENARIO EVALUATION
- Results (Analysis Result of large 100% hot-leg break)
- Water Level and Core Compaction Scenario and Criticality Evaluation
- Results (Reactivity Evaluation)
- Conclusion and Future Work

What is Super Fast Reactor?

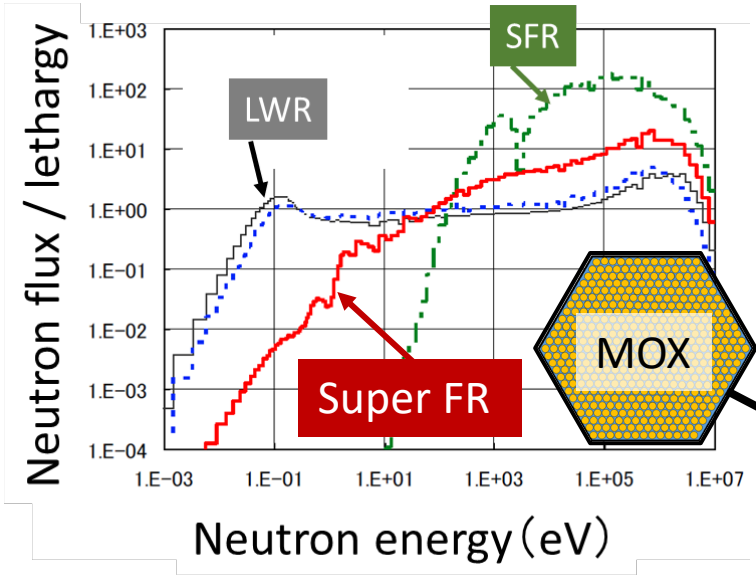

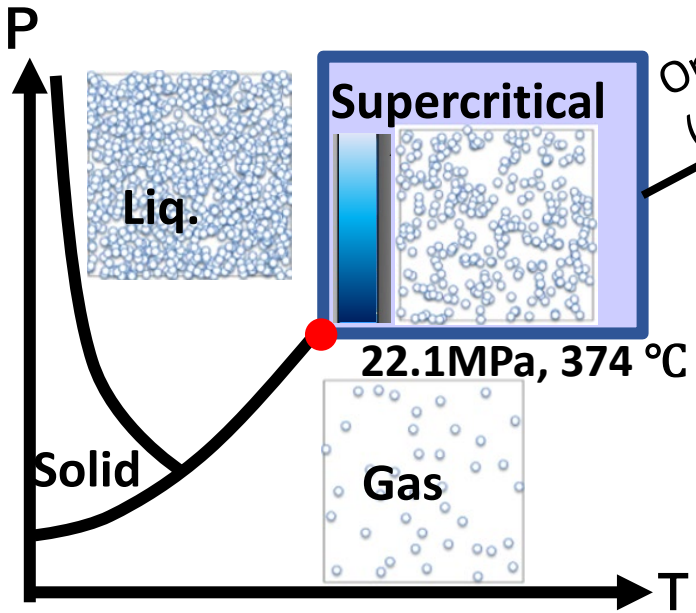

Operates at 25 MPa
(280 – 500 ℃)

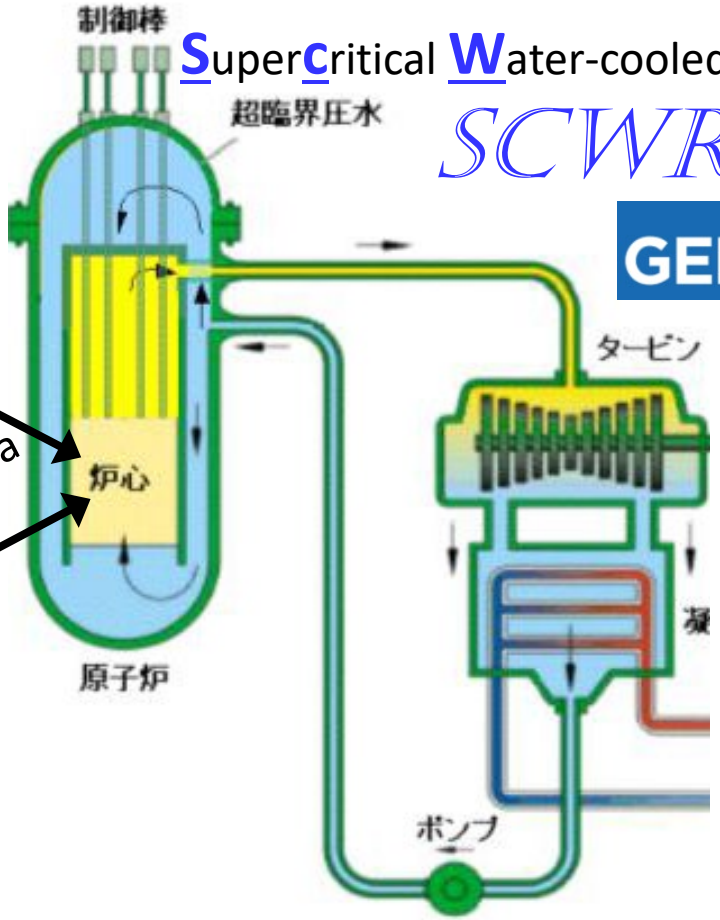

Super**c**ritical **W**ater-cooled **R**eactor

SCWR

GEN IV

Transients and Design Basis Accidents

Safety features

- **Negative reactivity** feedbacks
- **Depressurization** induces rapid (short-term) core cooling.
- **Water injections** ensures long-term core cooling.

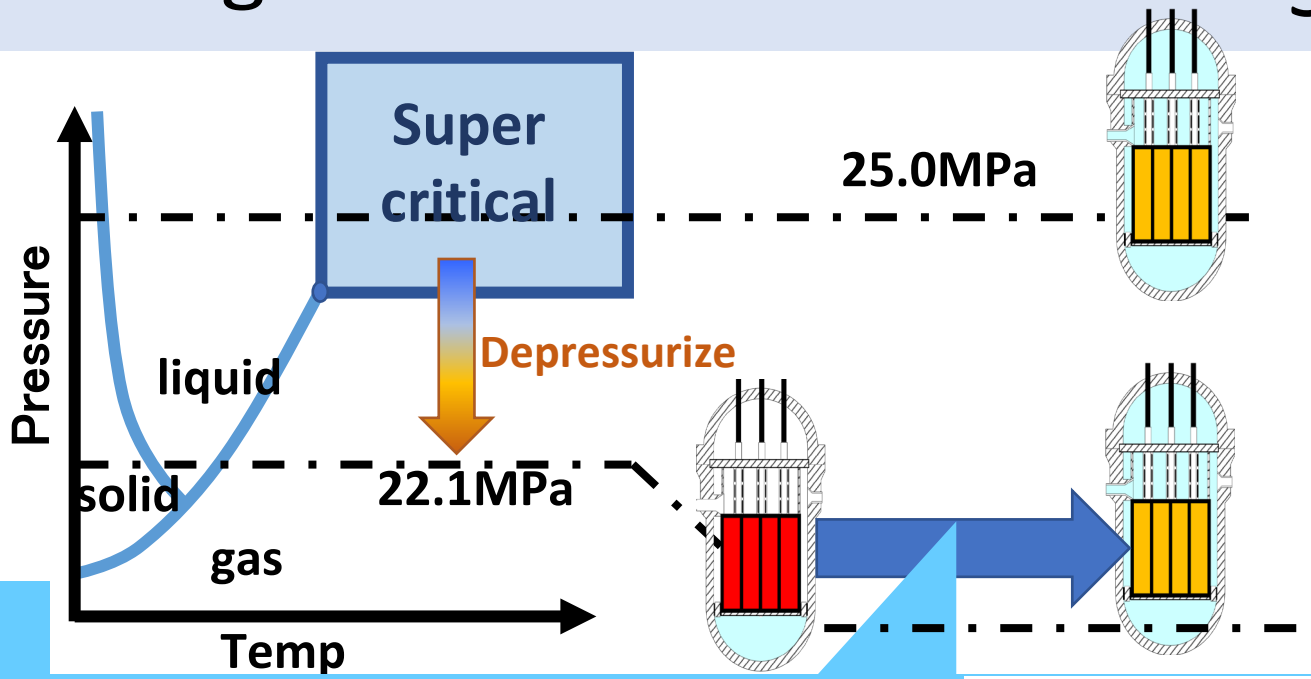

Well-established

Design of plant safety systems

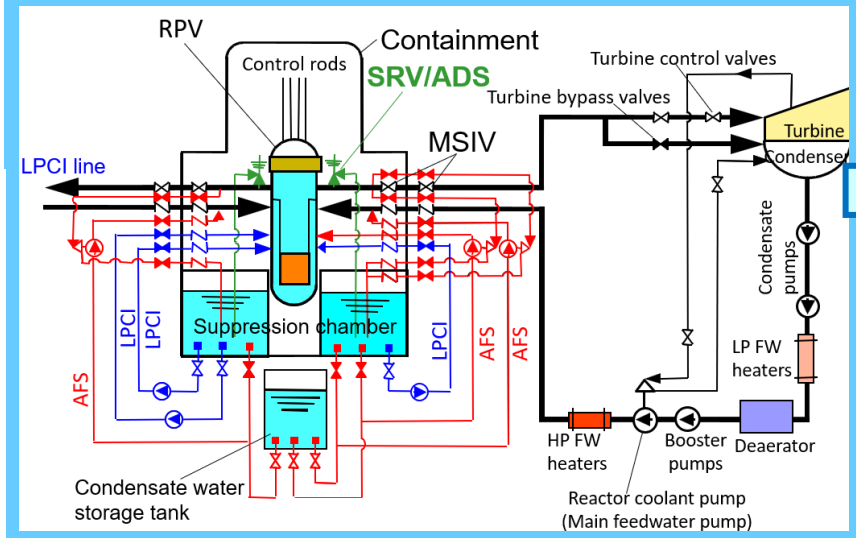

Design criteria

Accident analysis

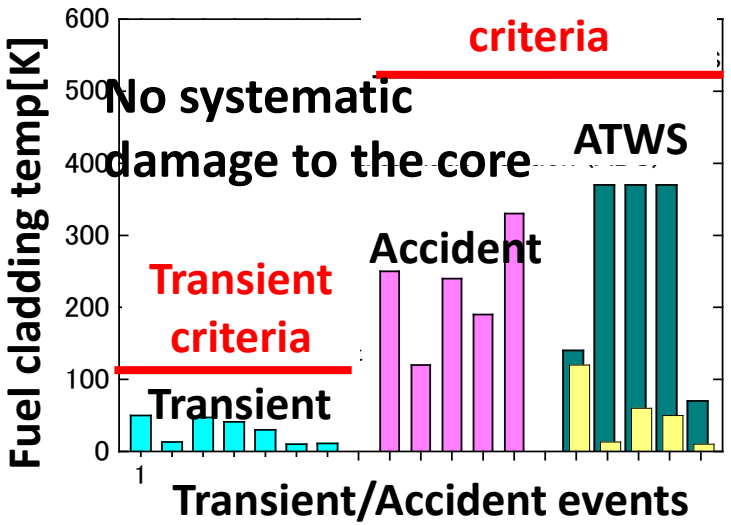

[1]Ishiwatari et al., Journal of NUCLEAR SCIENCE and TECHNOLOGY, Vol. 42, No. 11, p. 935–948 (2005)

Beyond Design Basis Accidents (BDBAs) to Severe Accidents (SAs)

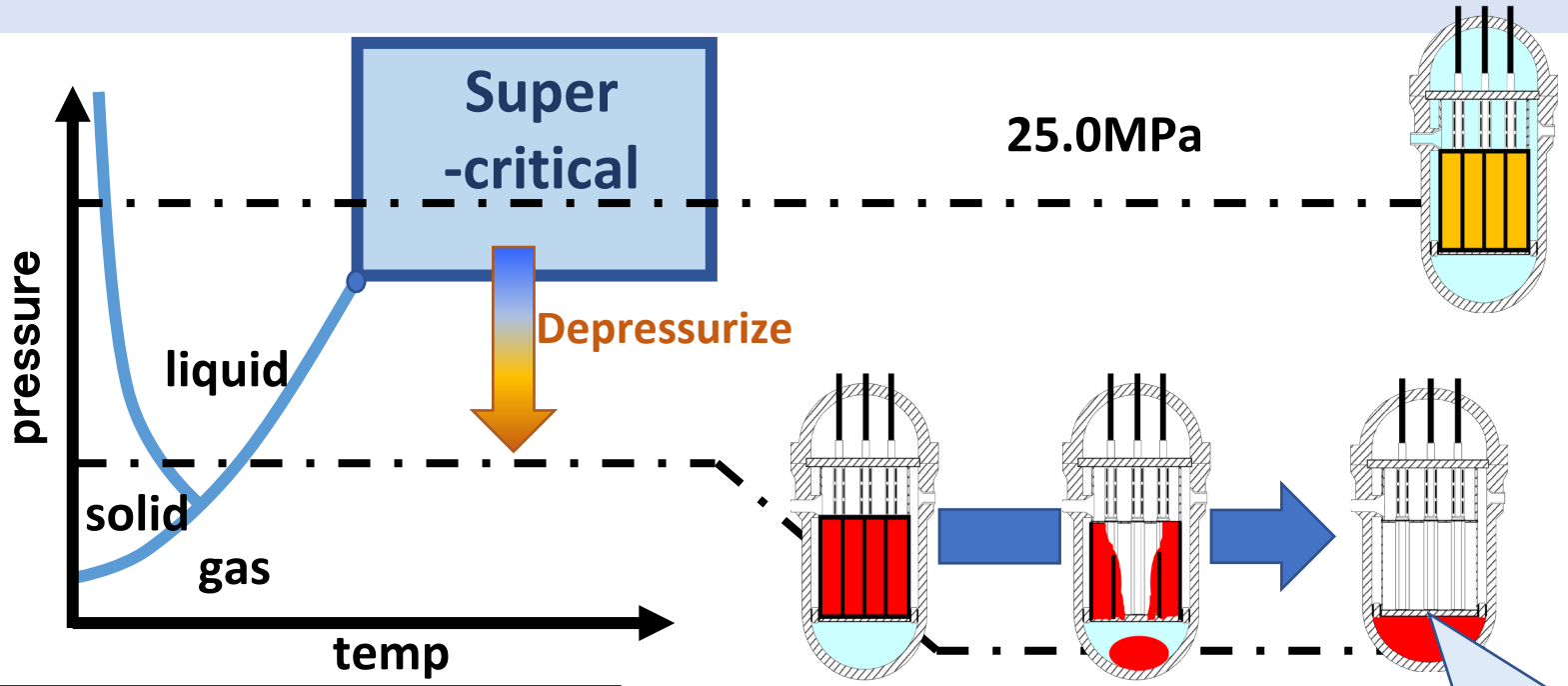

Similar but different studies

Sodium-cooled Fast Reactor (SFR)

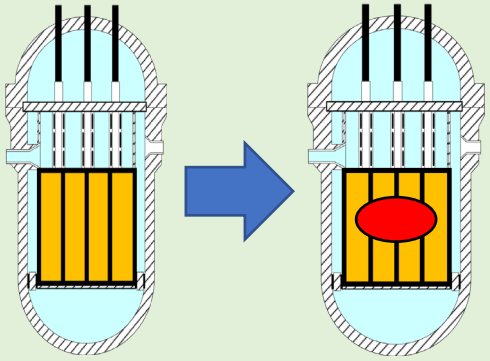

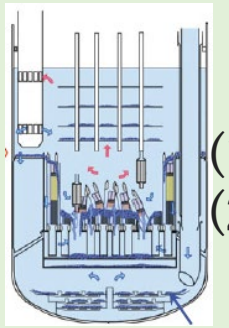

(1) No loss of coolant
(2) Fuel debris can be spatially dispersed for criticality control

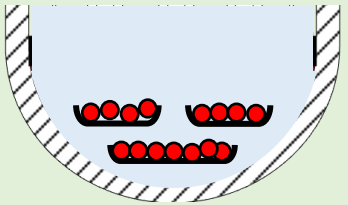

T. Suzuki et al., Journal of Nuclear Science and Technology Vol. 51, No. 4, 493–513 (2014)

Total Loss of Coolant
×
Core Melt Down

Focuses and the Purpose of this Study

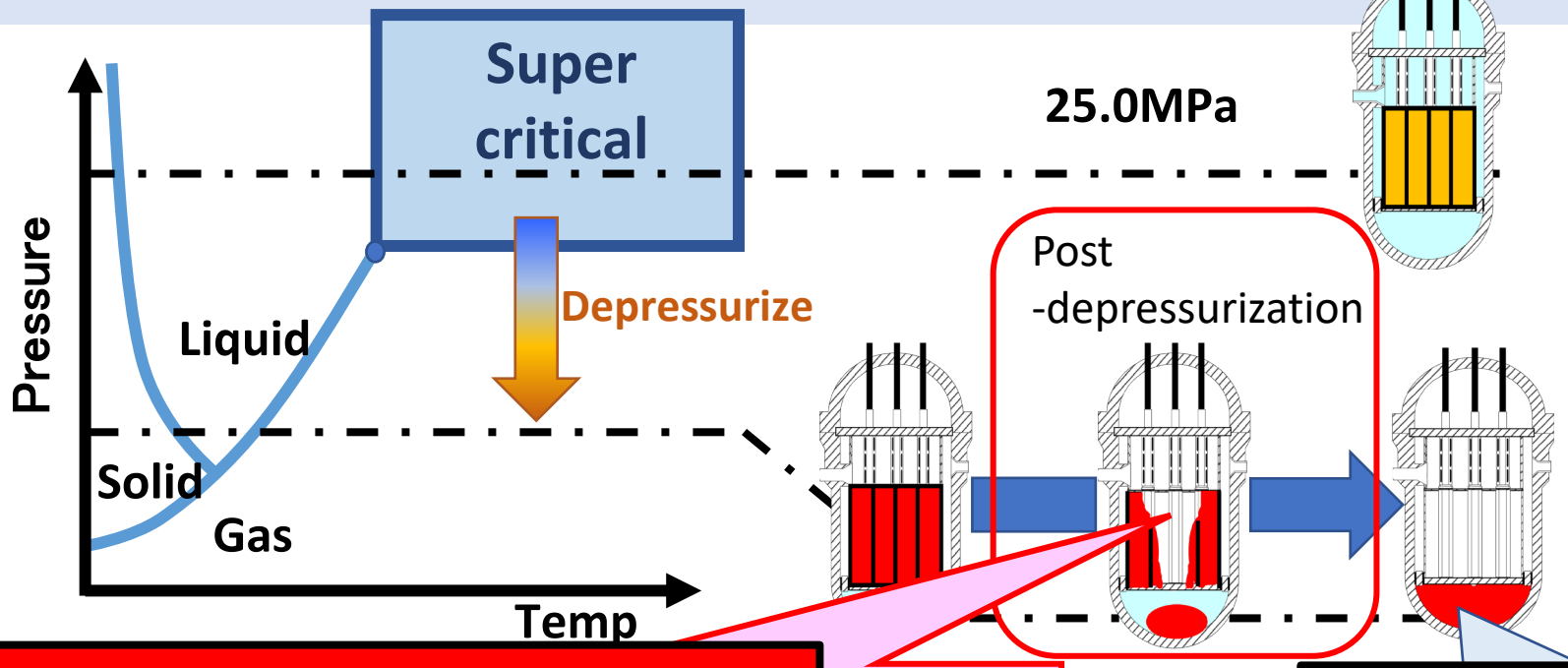

Focuses: Mid-state (this study)

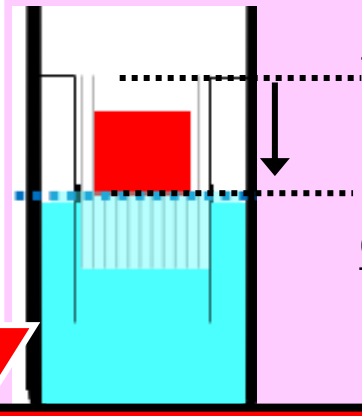

Reduction of the water level

- Promotes neutron leakage
- Hardens neutron spectrum

Core melting (compaction)

- Hardens neutron spectrum

Purpose: Evaluate the reactivity changes

End-state (preceding study)

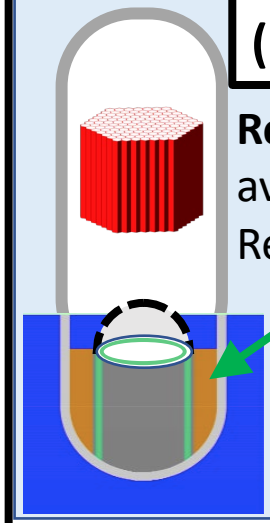

Re-criticality was avoided with In-Vessel Retention (IVR)

Neutron Absorber

R. Sasaki et al., Journal of Nuclear Engineering ans Radiation Science April 2023, Vol.9 021501

Outline

- Background: Super Fast Reactors and Severe Accident Issues
- CORE AND PLANT DESIGN SPECIFICATIONS
- BEYOND DESIGN BASIS LOCA SCENARIO EVALUATION
- Results (Analysis Result of large 100% hot-leg break)
- Water Level and Core Compaction Scenario and Criticality Evaluation
- Results (Reactivity Evaluation)
- Conclusion and Future Work

Design Specifications of the Core

Core System

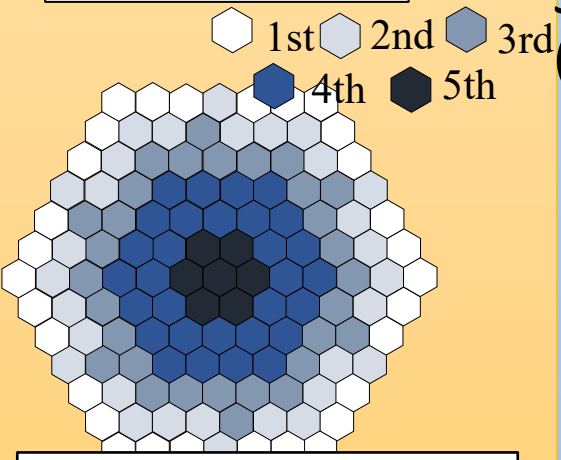

Equivalent diameter
1.78m

Thermal/Electrical Power[MW]
650/285

Void reactivity coefficient at BOEC / EOEC (10^{-3} dk/k/%void)	-6.4 / -4.3
Density reactivity coefficient at BOEC/EOEC (%dk/k/(g/cc))	6.20/6.20
Doppler reactivity coefficient at BOEC / EOEC (10^{-4}dk/k/℃)	-1.17 / -1.17

Fuel Rod

Structural materials
(channel boxes, cladding)

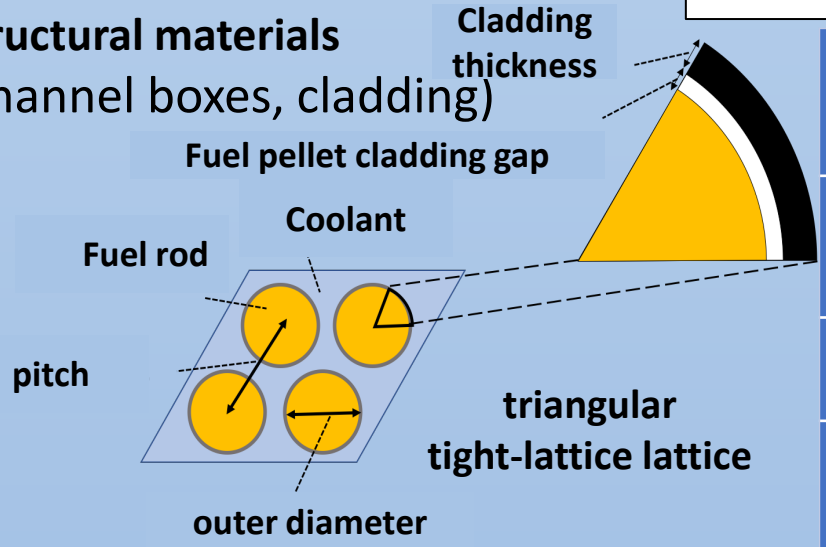

Fuel cladding and channel box material	Advanced stainless steel
Fuel rod diameter (mm)	10.0
Pitch(mm)	11.0
Cladding thickness (mm)	0.597

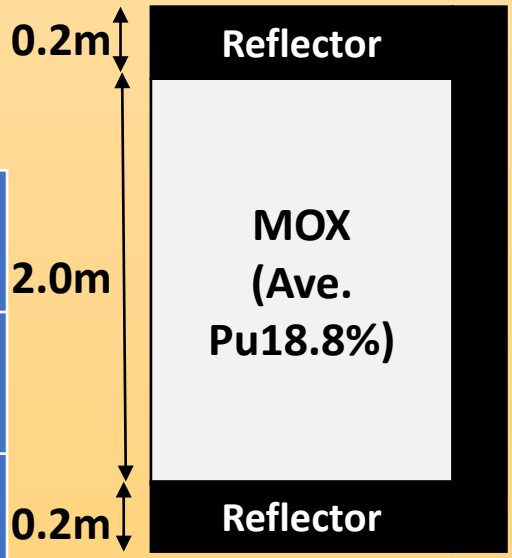

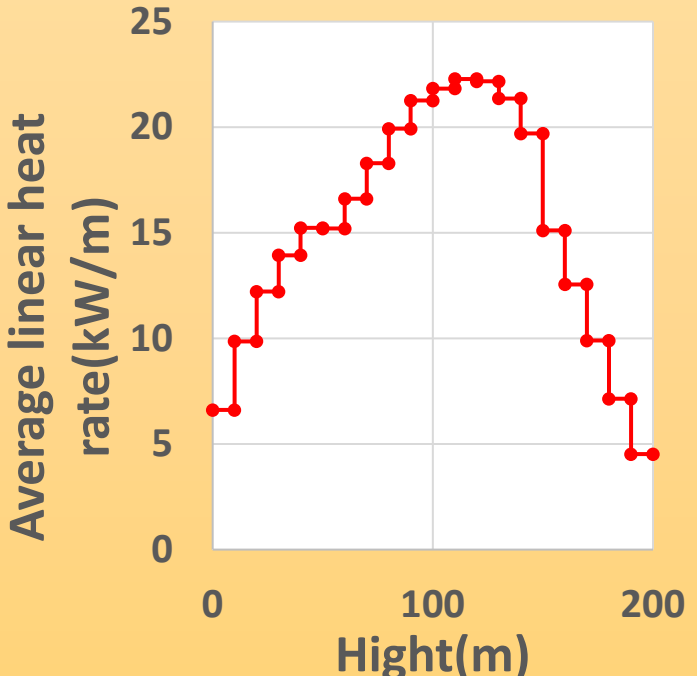

K. Uchimura and A. Yamaji, J. Nucl. Eng. 2020, 1, 46–53; doi:10.3390/jne1010004

Example of Plant Safety and Control

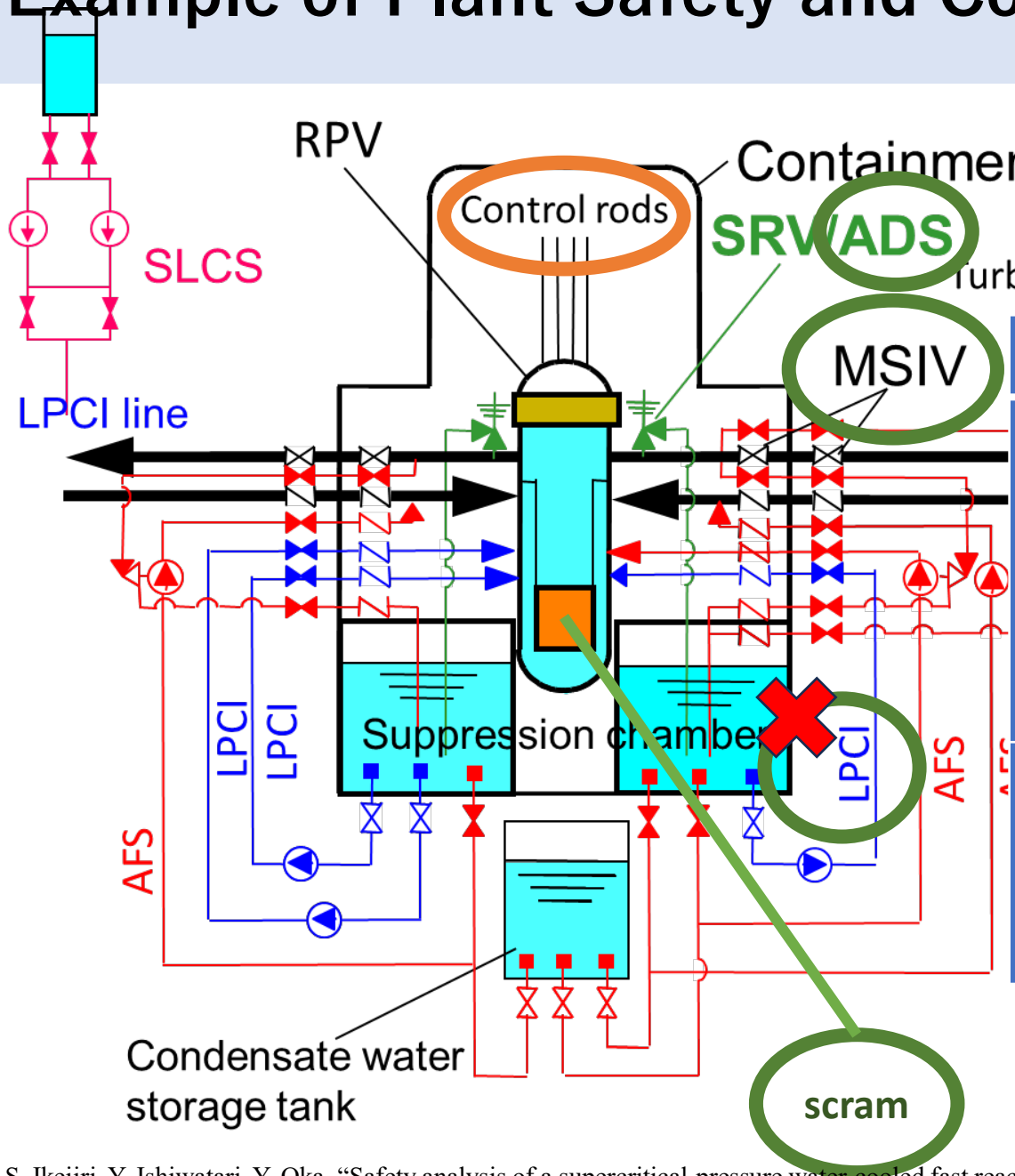

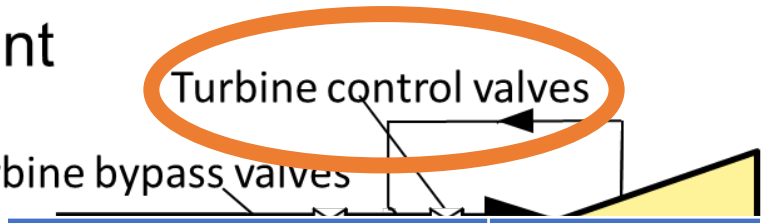

Actuation conditions		Safety system
Flow rate low level	1(90%)	Reactor scram
	2(20%)	Auxiliary Feedwater System(*)
	3(6%)	ADS/LPCI(*)
Pressure low level	1(24.0MPa)	Reactor scram
	2(23.5MPa)	ADS/LPCI(*)

heaters pumps

Reactor coolant pump

(Main feedwater pump)

S. Ikejiri, Y. Ishiwatari, Y. Oka, "Safety analysis of a supercritical-pressure water-cooled fast reactor under supercritical pressure", Nuclear Engineering and Design, 240, pp. 1218-1228 (2010).

Plant Modeling for BDBA-Loss-Of-Coolant Accident (LOCA)

1-D point reactor kinetics model

1-D thermal hydraulic model

Analysis code
ASYST

Heat transfer equation

Supercritical Pressure	Dittus-Boelter (single-phase flow)
Subcritical Pressure	Chen (nucleate boiling)
	Bromley (film boiling)
	Dittus-Boelter (superheated vapor)

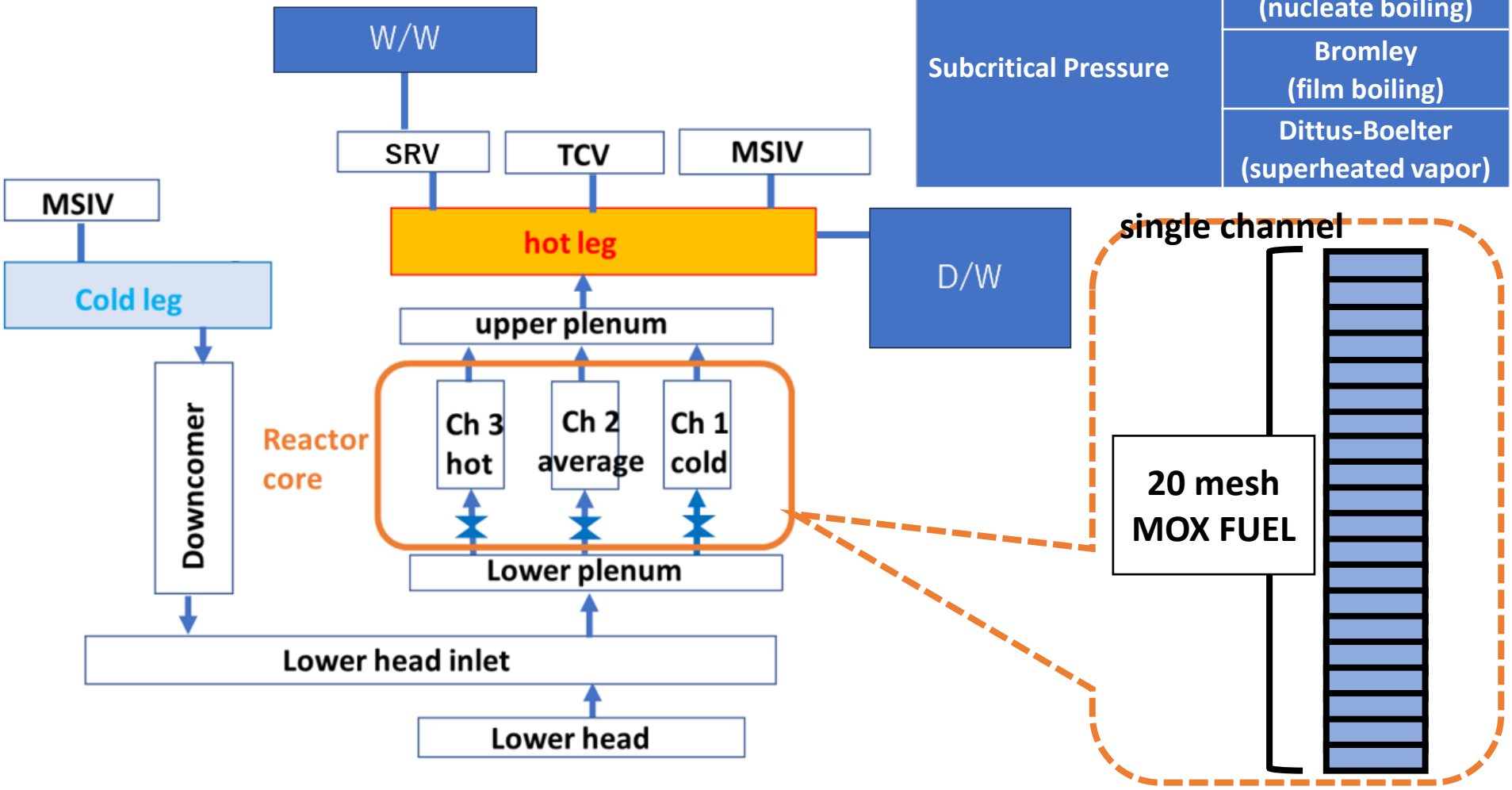

Outline

- Background: Super Fast Reactors and Severe Accident Issues
- CORE AND PLANT DESIGN SPECIFICATIONS
- BEYOND DESIGN BASIS LOCA SCENARIO EVALUATION
- Results (Analysis Result of large 100% hot-leg break)
- Water Level and Core Compaction Scenario and Criticality Evaluation
- Results (Reactivity Evaluation)
- Conclusion and Future Work

Analysis Result (Flow rate, Powe, Pressure)

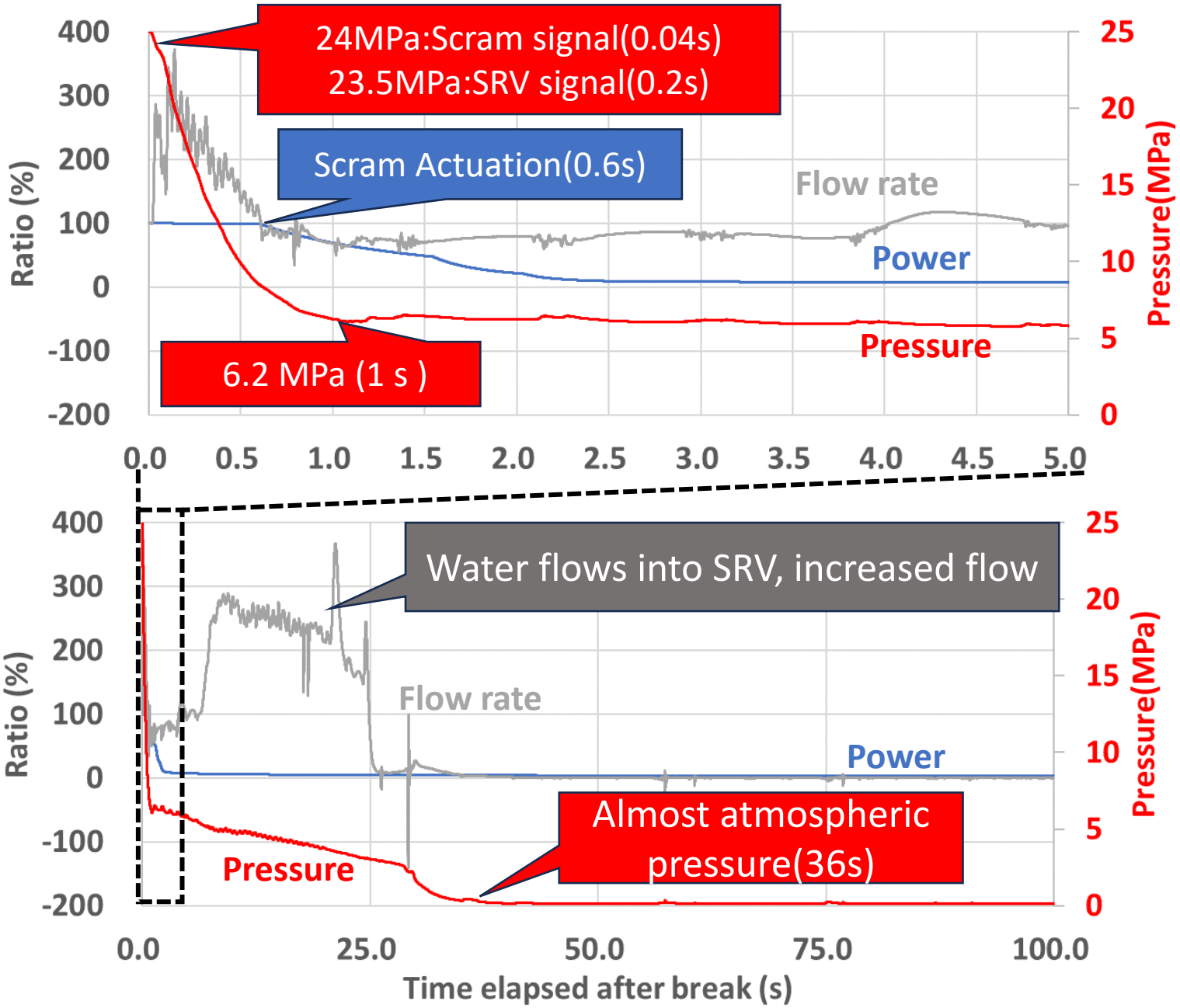

Analysis Result (Water Level, Water Density)

Water Level and Water Density

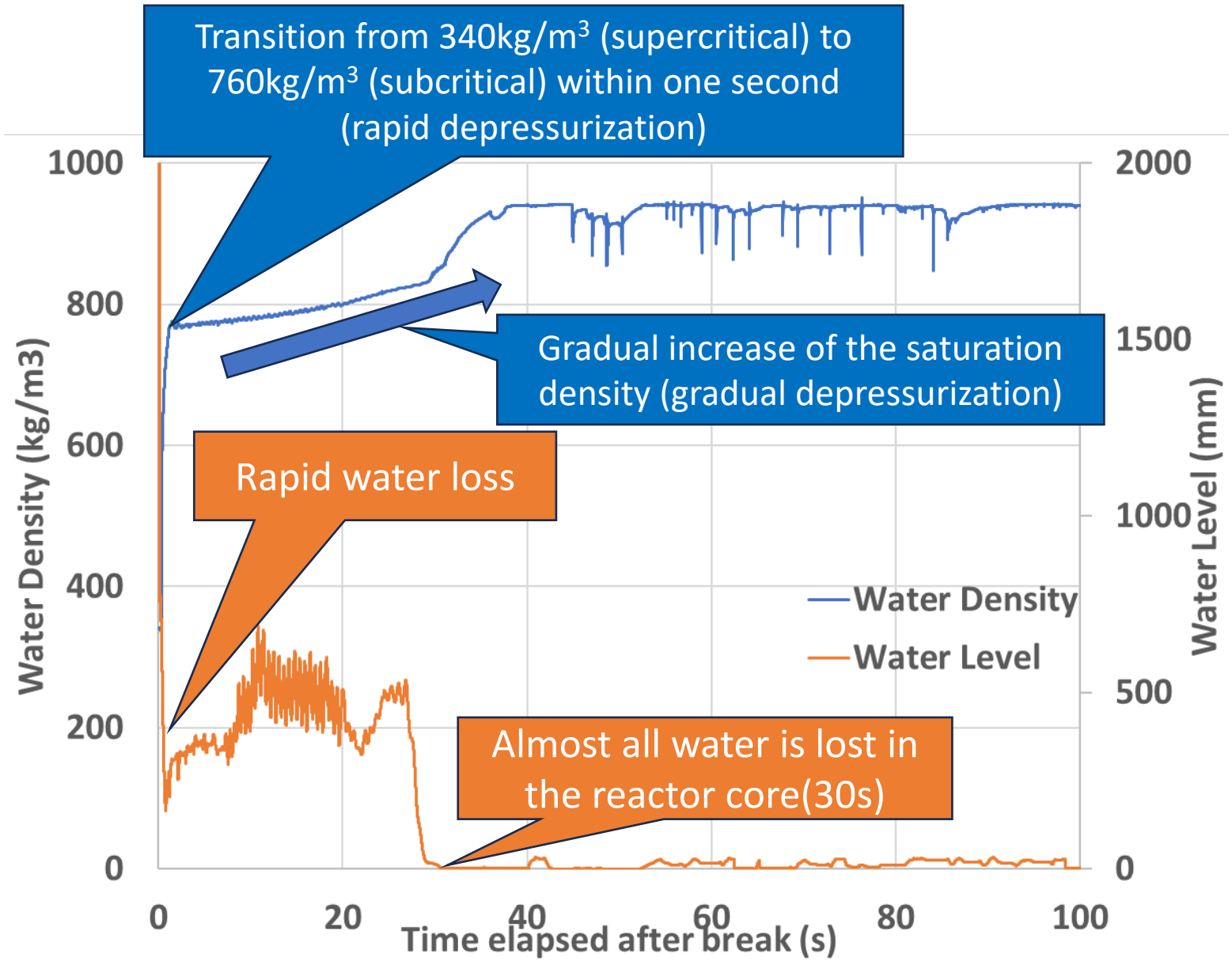

Water Level (collapsed)

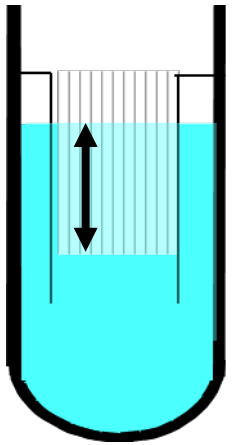

Core Meltdown Evaluation Scenarios and Focus Points

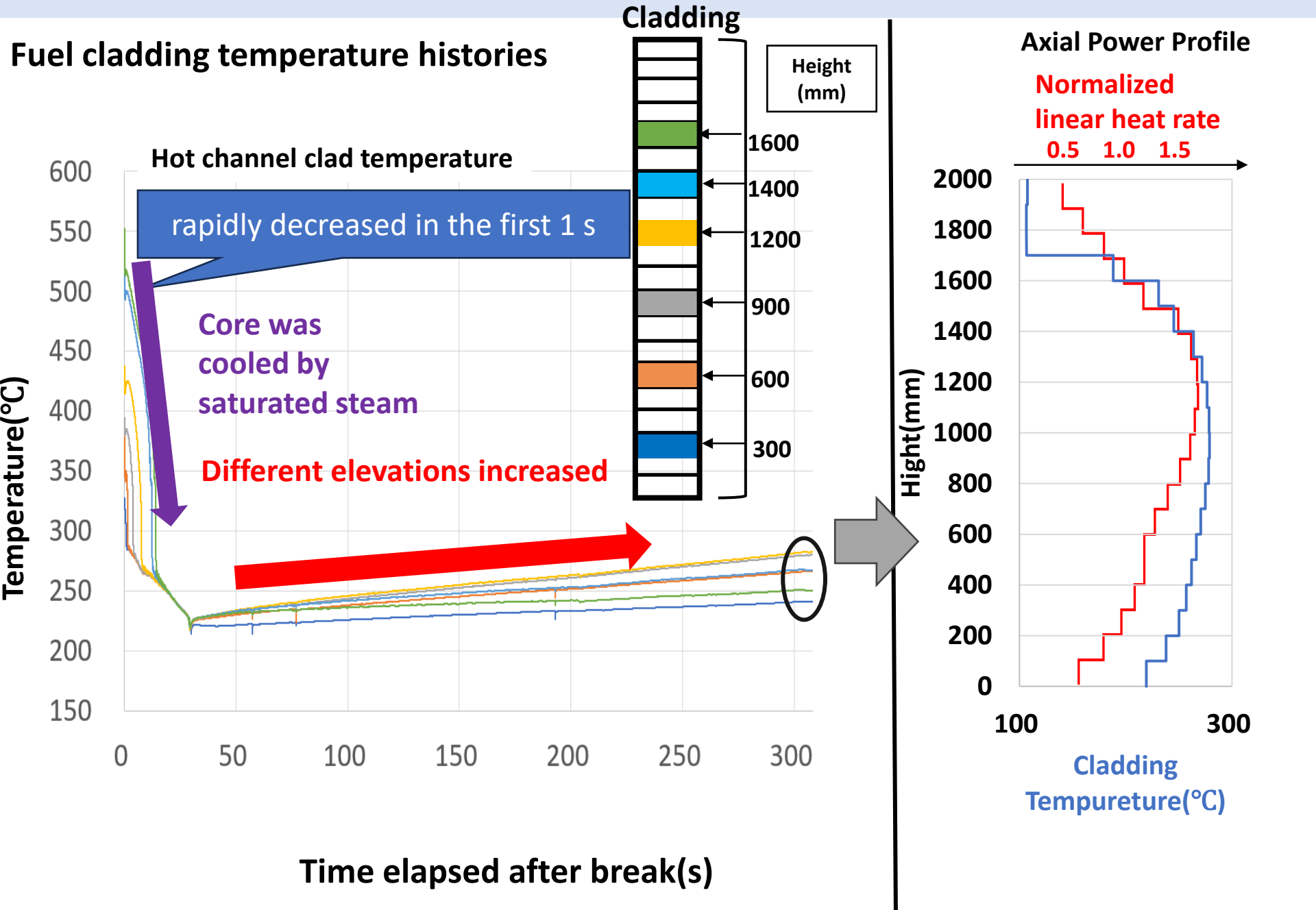

Outline

- Background: Super Fast Reactors and Severe Accident Issues
- CORE AND PLANT DESIGN SPECIFICATIONS
- BEYOND DESIGN BASIS LOCA SCENARIO EVALUATION
- Results (Analysis Result of large 100% hot-leg break)
- Water Level and Core Compaction Scenario and Criticality Evaluation
- Results (Reactivity Evaluation)
- Conclusion and Future Work

Two cases for reactivity evaluation

CASE1: 100% hot-leg LOCA

- **Blowdown phase (30 s)**: Rapid loss of core water level while the core is cooled down by the induced core flow rate.

- **Reheating phase**:
- Almost adiabatic core heat-up without water level.

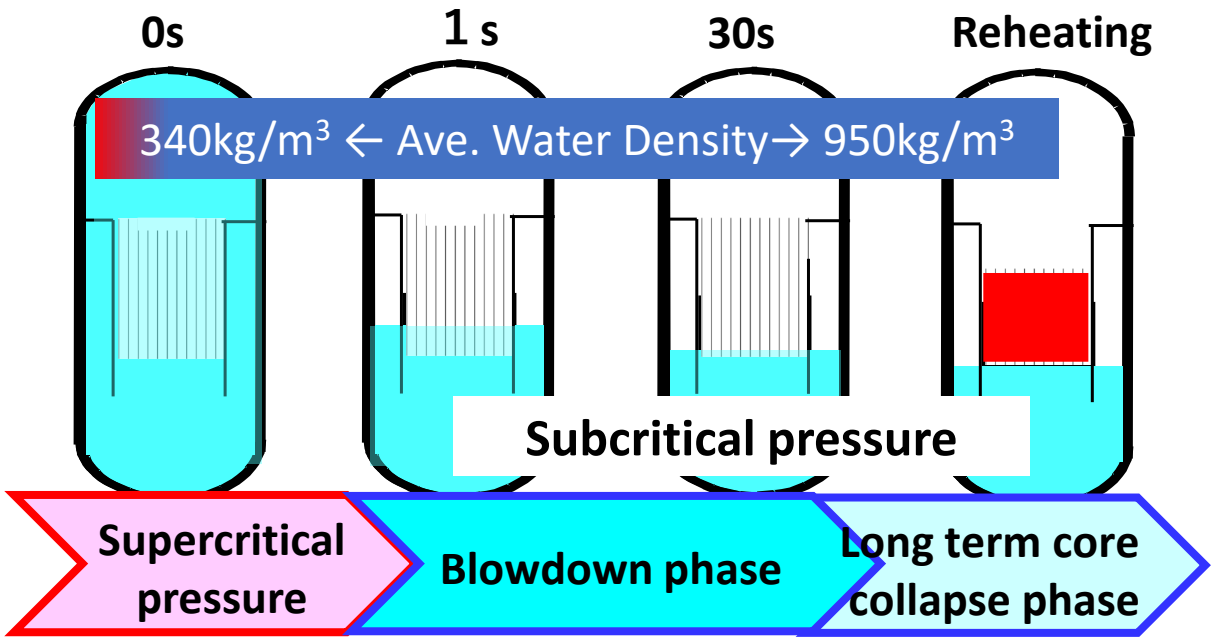

CASE2

Sensitivity analysis of the core melting process as the water level drops.

Subcritical water: 0% void

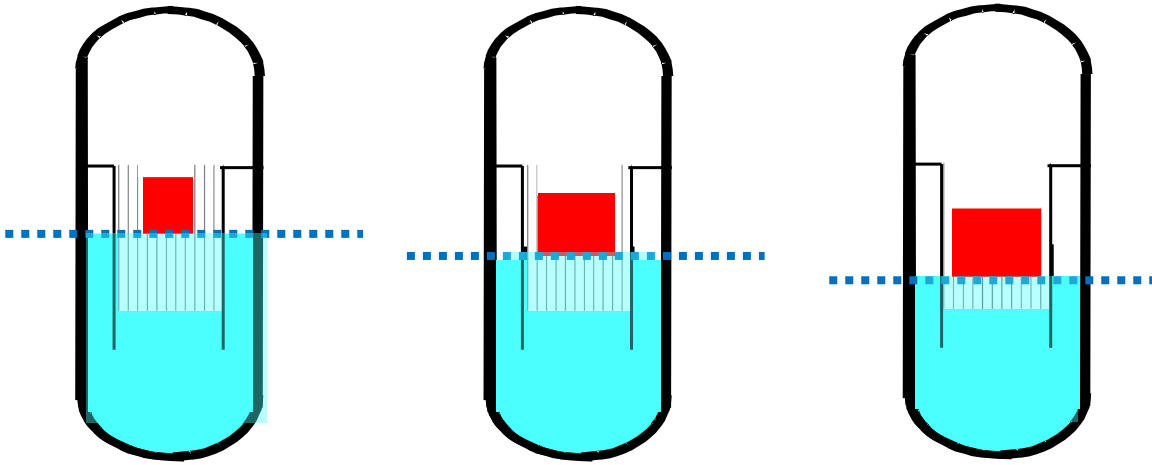

Evaluation Methods for Core Meltdown

Calculation Method

Neutron transport calculations based on Monte Carlo methods (MVP) ✚ 「JENDL-4.0 nuclear data library」

History:10000
Batch:125
Skip Batch:25

Statistical Error (3σ) ±0.13%

Calculation System

Mixing **Fuel pellets** and **Structural materials**

※ No consideration of control rods

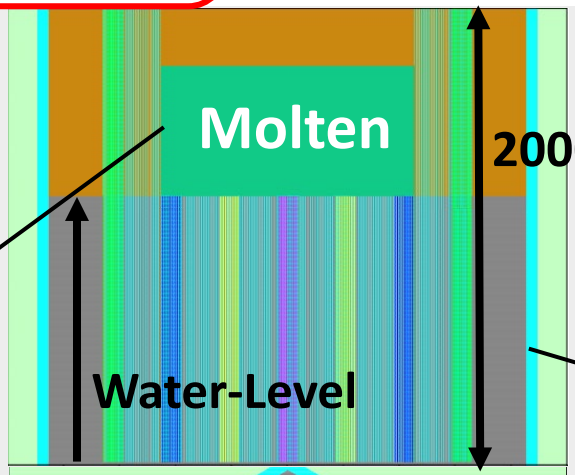

structural material
SUS316

Fuel composition at BOEC

Pu enrichment for each cycle

1st 2nd 3rd 4th 5th

High ⟷ Low

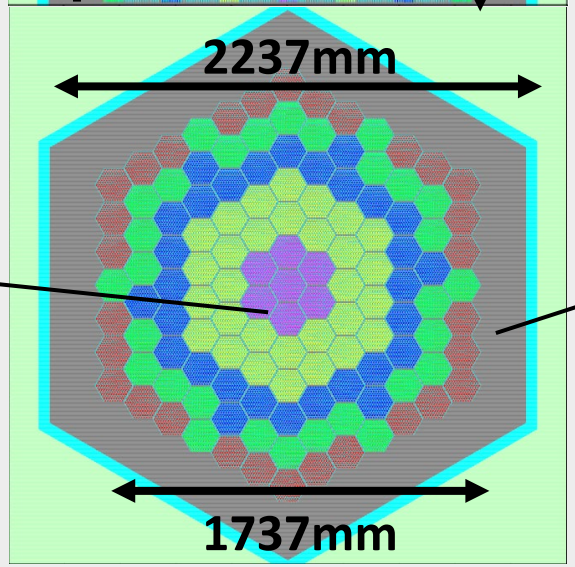

Water Reflector：
same density as the coolant

Outline

- Background: Super Fast Reactors and Severe Accident Issues
- CORE AND PLANT DESIGN SPECIFICATIONS
- BEYOND DESIGN BASIS LOCA SCENARIO EVALUATION
- Results (Analysis Result of large 100% hot-leg break)
- Water Level and Core Compaction Scenario and Criticality Evaluation
- Results (Reactivity Evaluation)
- Conclusion and Future Work

Result: 100% hot-leg LOCA Blowdown phase

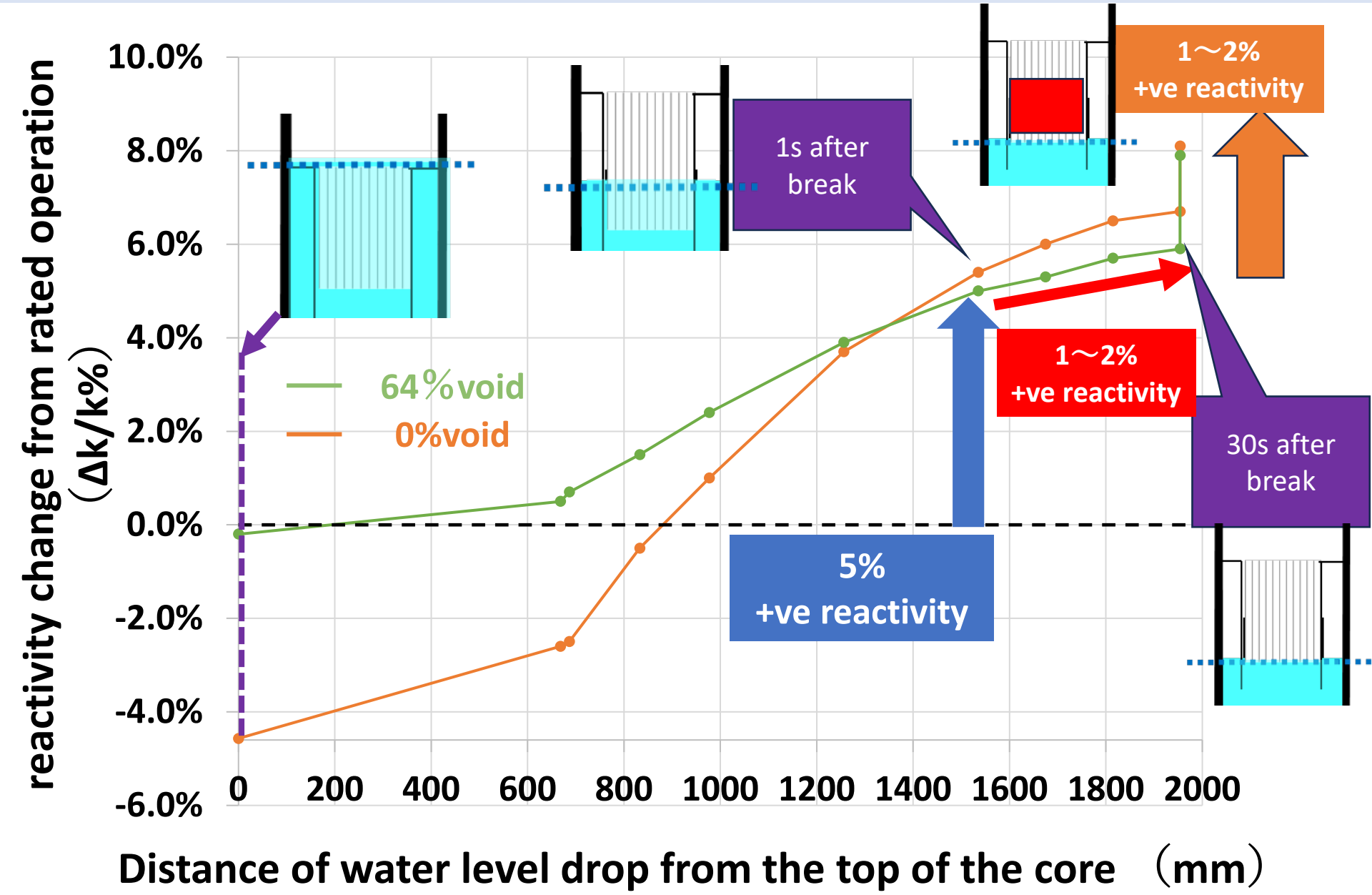

Result: Sensitivity analysis

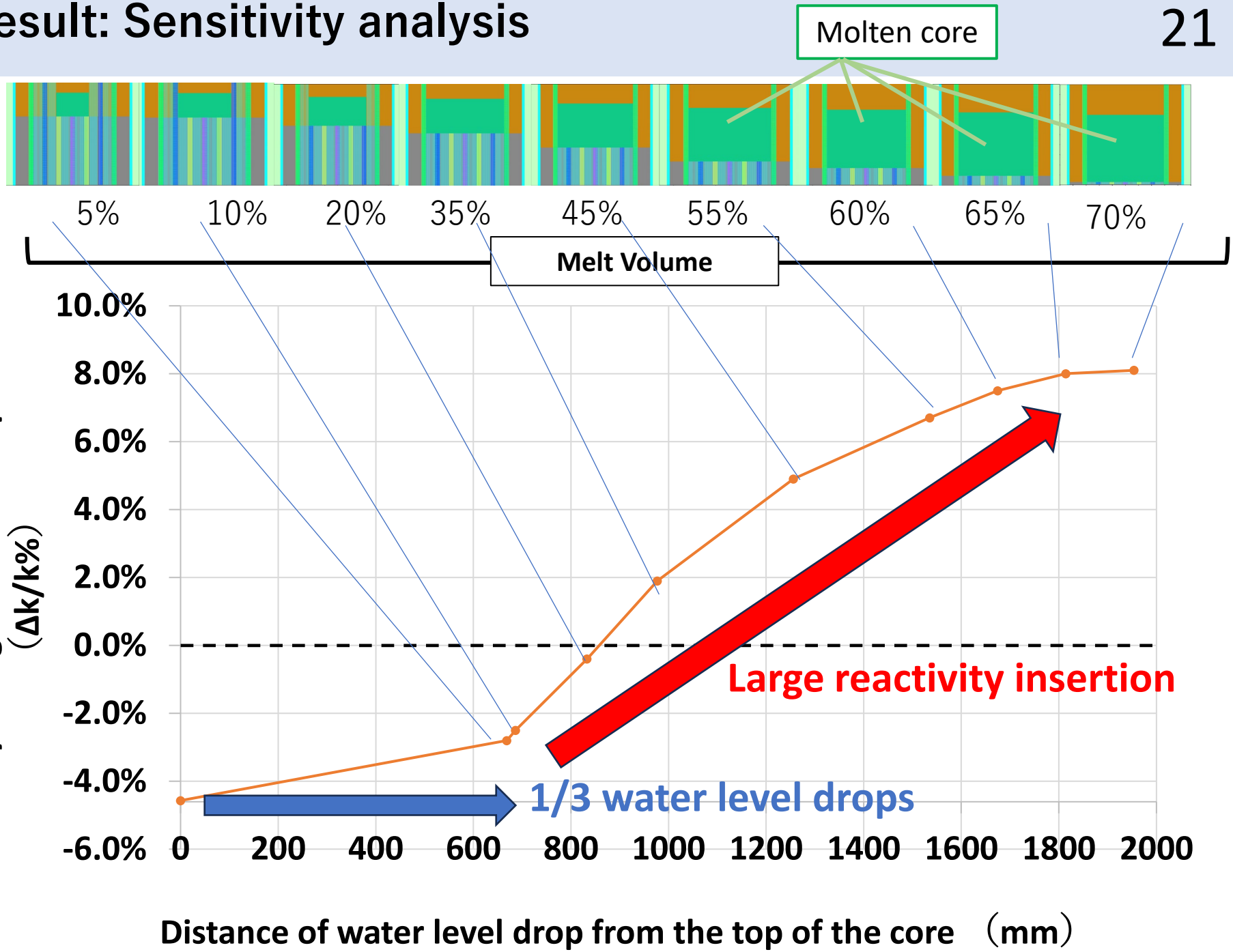

Outline

- Background: Super Fast Reactors and Severe Accident Issues
- CORE AND PLANT DESIGN SPECIFICATIONS
- BEYOND DESIGN BASIS LOCA SCENARIO EVALUATION
- Results (Analysis Result of large 100% hot-leg break)
- Water Level and Core Compaction Scenario and Criticality Evaluation
- Results (Reactivity Evaluation)
- Conclusion

Conclusion

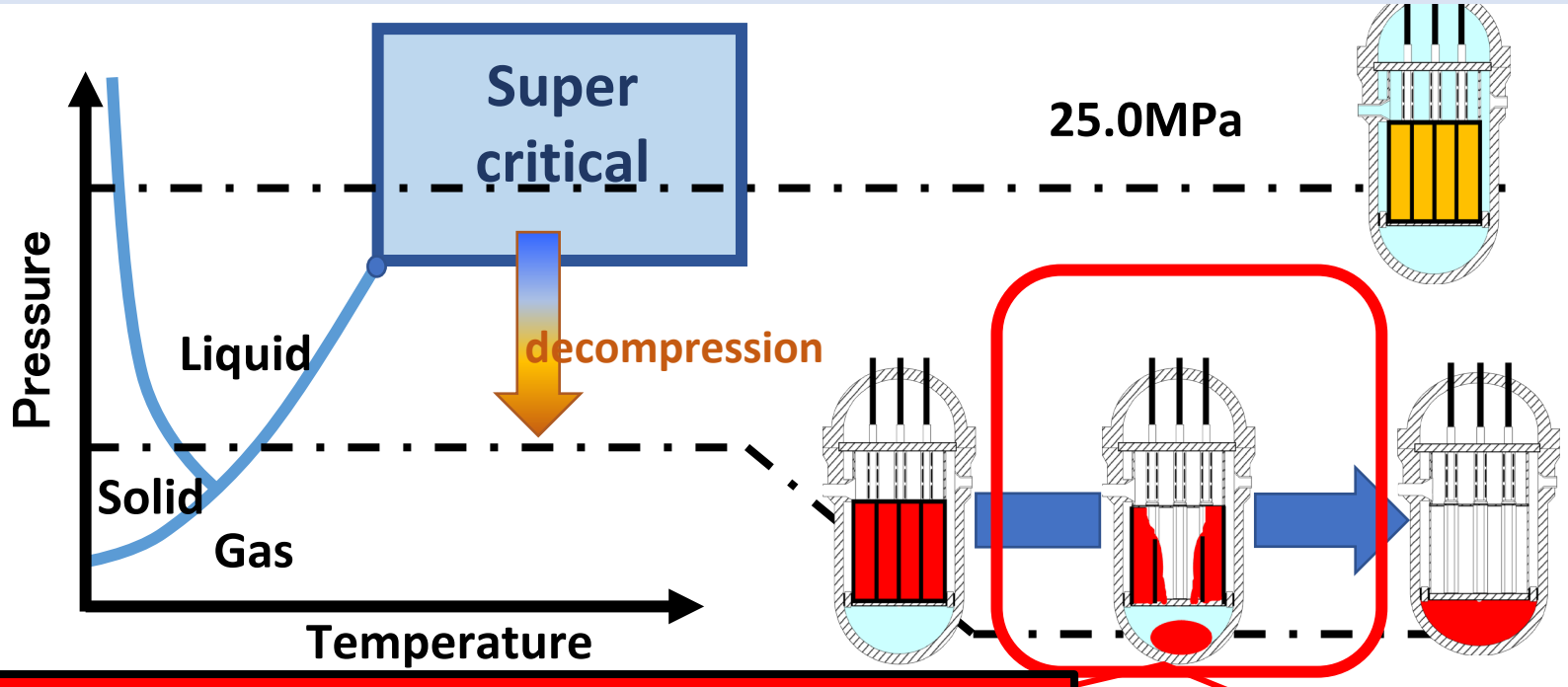

Conclusions (100% Large break LOCA)

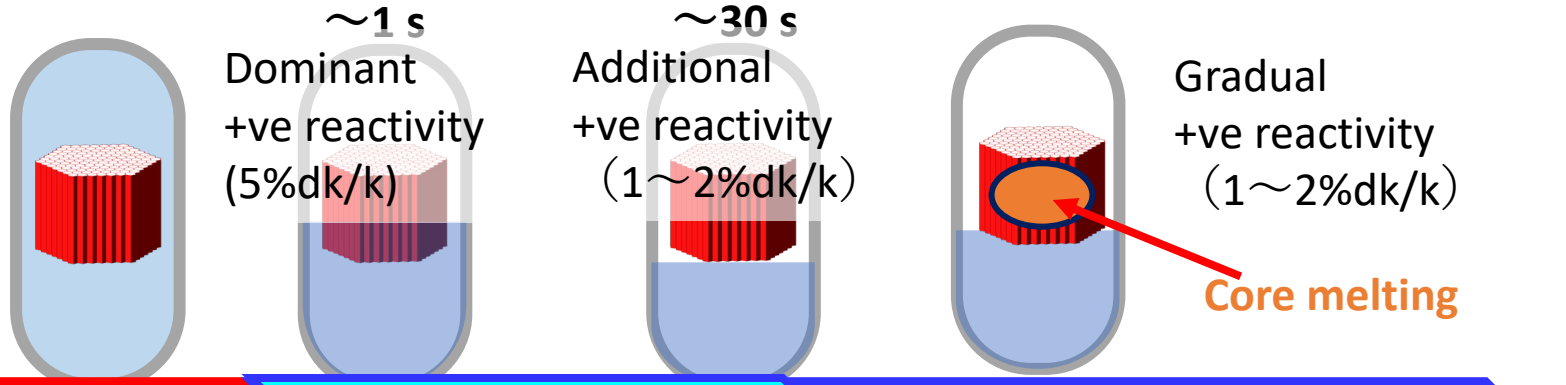

Development of severe accident simulation code for sodium-cooled fast reactors: SIMMER-V

(1) Overview of the SIMMER-V code development

Hirotaka TAGAMI, Shinya ISHIDA, Yasushi OKANO, Hidemasa YAMANO and Shigenobu KUBO
Japan Atomic Energy Agency
4002, Narita, Oarai, Ibaraki 311-1393, Japan
tagami.hirotaka@jaea.go.jp; ishida.shinya@jaea.go.jp; okano.yasushi@jaea.go.jp, yamano.hidemasa@jaea.go.jp, kubo.shigenobu@jaea.go.jp

Frederic PAYOT, Laurent SAAS, Laurent TROTIGNON, Pierre GUBERNATIS and Emmanuelle DUFOUR
Commissariat à l'énergie atomique et aux énergies alternatives
Cadarache F-13108 St Paul Lez Durance France
frederic.PAYOT@cea.fr, laurent.SAAS@cea.fr, laurent.trotignon@cea.fr, pierre.gubernatis@cea.fr, emmanuelle.dufour@cea.fr

Yoshiharu TOBITA
Japan Atomic Energy Agency (present affiliation: Karlsruhe Institute of Technology)
Hermann-von-Helmholtz-Platz 1, 76344 Eggenstein-Leopoldshafen, Germany
yoshiharu.tobita@kit.edu

ABSTRACT

JAEA has been developing the SIMMER-V code in collaboration with CEA to perform severe accident (SA) simulations of future sodium-cooled fast reactors (SFRs) including a unique core design with large-scale heterogeneous cores. An SA sequence in SFRs has been analyzed by: the SAS4A code for the Initiation Phase (IP), in which fuel pin disruption and vertical fuel dispersion occur in individual fuel subassemblies; and the two-dimensional SIMMER-III or three-dimensional SIMMER-IV code for the Transition Phase (TP), in which core disruption extends to the whole core. The joint development of SIMMER-V is of limited scope but aims at significantly expanding the code applicability by providing flexible interfaces to couple a SIMMER-V calculation with other computational domains or other codes, and by adding new advanced physical models such as a detailed fuel pin model and a model of flexible treatment of fuel isotopic composition. The former tasks are conducted by CEA the latter tasks by JAEA. In parallel to the code development, verification and validation of the new models and methods have been performed. This paper describes the objectives and overall framework of SIMMER-V code development program, representative new elements, and recent development progress.

KEYWORDS
Sodium cooled Fast Reactor, Severe accident, SIMMER, Code development

1. INTRODUCTION

Since an SFR core is not designed in its most reactive configuration, a potential recriticality energetics that results from a fuel compaction during postulated core disruptive sequence has been investigated as one of the major safety issues of SFR. If it is assumed that core damage prevention measures fail to work and a core is disrupted in anticipated transient without scram (ATWS) of SFR, an event may progresses as shown in Fig. 1. The event starts from an initiation phase (IP), in which fuel pin disruption and vertical fuel dispersion occur in individual fuel subassemblies, and progresses to a transition phase (TP), in which a core disruptive area extended to form a molten core pool. The molten core pool may result in a large-scale fuel motion having a significant reactivity effect. The SIMMER-series codes are designed to evaluate an event progression in TP and a mechanical energy generation due to a recriticality event. Japan Atomic Energy Agency (JAEA) has developed the SIMMER-III and SIMMER-IV codes [1]: initially to solve two-dimensional cylindrical systems with the goal of achieving more reliable analysis [2,3]; and later to enable three-dimensional simulations [4,5].

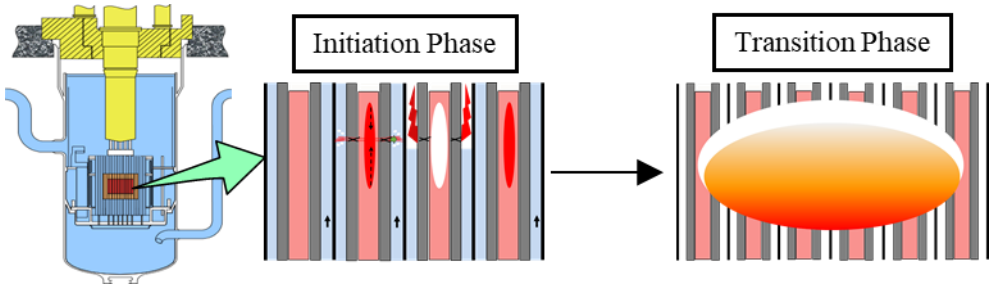

Figure 1. Image of disrupted core in initiation phase and transition phase.

The SIMMER-III and SIMMER-IV codes use physical models to calculate a thermal-hydraulics of disrupted core materials and a neutronic behavior in TP. The codes treat fuel, steel, sodium, control material and fission gas as reactor materials and classify them to core material components (e.g., wrapper tube, fuel pellet, cladding, etc.). The overall structure of the codes consists of three coupled modules, which are fluid dynamics, structure and neutronics. The fluid-dynamics module represents a horizontal cross section of subassembly by one mesh cell and calculates solid-liquid-gas multi-phase multi-component flow with phase changes. The neutronics module simulates a time- and space-dependent neutron flux, taking into account the changes in mass and temperature distributions of core materials. The structure module calculates heat and mass transfers involving fuel pin, cladding, fuel crust and subassembly wrapper tube, including their breakups. The necessary data are tightly exchanged among these modules. A TP analysis with SIMMER-III or SIMMER-IV has previously required the calculated results of the IP analysis code, e.g., SAS4A [6], as initial conditions.

For a future SFR design, a large horizontally heterogeneous core [7,8] with axially heterogeneous fuel pins including inner fertile zone [9] are proposed. For such a future SFR, the applicability of the current SIMMER-III and SIMMER-IV codes are limited, because of difficulty of representing complicated transient fuel material distribution. It was also desired that the previous practice of coupling IP and TP calculations should be improved.

Based on the above background, the development of SIMMER-V, introduced in the present paper, has been performed in collaboration with CEA and JAEA to enable a continuous (once-through) simulation from a fuel pin failure in IP to whole core disruption in TP. To attain this objective, JAEA develops a new detailed pin model for the axially heterogeneous fuel pin and adds a fuel isotope vector [10] for the large-scale and horizontally heterogenous core. CEA develops the SEASON (Severe Accident SimulatiON) platform [11]

for integrated evaluation of disrupted core and plans coupled analyses with SIMMER-V and other codes. CEA is now developing interface capabilities focusing on the integrated analysis. The present paper introduces a framework of the SIMMER-V development program, describes the contents of implementation items and newly developed physical models and interface capabilities, and explains a future schedule.

2. FRAMEWORK FOR DEVELOPMENT PROGRAM OF SIMMER-V

The collaboration with CEA and JAEA for SIMMER-V development started in 2014 and its first stage ended 2019. A prototype of the new detailed pin model was developed by JAEA in the first stage. In order to run large 3D reactor cases in acceptable CPU time, SIMMER-V was also equipped with a high-performance hybrid MPI-OpenMP parallelization scheme developed in modern Fortran standard by CEA in SIMMER-V. The second development stage started in 2020 and mainly focuses on model improvements and verification and validation (V&V) of the new detailed pin model for achievement of SIMMER-V development as an applicable code system to a future SFR analysis in 2024. The major tasks implemented in the second development stage are shown in Tab. I.

Table I. Major tasks in the SIMMER-V development collaboration from 2020 to 2024

	Title	Detail	Parties in charge
(1)	Verification of the new detailed pin model	Check of capabilities based on simple and idealized test cases comparing with other codes.	CEA/JAEA
(2)	Validation of the new detailed pin model	Model validation with in-pile experiment analysis.	JAEA
(3)	Upgrades of the new detailed pin model	Installation of important capabilities to calculate a future reactor.	JAEA
(4)	Applicability of fuel isotope vector model	Verification of capability and check an applicability of the fuel isotope vector model to a reactor simulation to express a heterogeneousness.	JAEA
(5)	SIMMER-V code applicability	Confirmation of capability of SIMMER-V including the new detailed pin model to calculate a future reactor.	CEA/JAEA
(6)	SIMMER-SIMMER boundary coupling	Development of a comprehensive time integration method that connects boundary conditions of SIMMER-V computational domains that have adjacent boundaries and are computed independently.	CEA
(7)	Update of SIMMER-V interface with SEASON	Installing interface for data transfer between SIMMER and other codes.	CEA

CEA and JAEA independently make own verification matrices and verify the new detailed pin model to enhance the model robustness in the task (1) in Tab I, which is ranked on an especially high importance in the SIMMER-V development program. The task (4) “Applicability of fuel isotope vector model” has been already finished by now. A prototype version of SIMMER-V for a future reactor analysis has been developed by the end of 2022. The final version of SIMMER-V is planned to be developed by the end of 2024 with reflecting results of tasks for a V&V of the new detailed pin model in (1), (2) and a check of applicability to a reactor study in (5).

The development of a new detailed pin model and the confirmation of applicability of the fuel isotope vector to reactor study developed made by JAEA (tasks (3) and (4) in Tab. I), and the new interface capabilities, which are a boundary coupling and an interoperability with other codes developed by CEA (task (6) in Tab. I), are introduced in Sections 3 and 4, respectively.

3. NEW PHYSICAL MODELS DEVELOPED BY JAEA

3.1. New Detailed Pin Model

One of the objectives of SIMMER-V development is for a continuous (or once-through) analysis from IP to TP in the future reactor. To achieve this objective, a new detailed pin model, which can represent important phenomena in IP in the axially heterogenous core, is required. The important phenomena to be modeled are: thermo-mechanical behavior of fuel pin, cladding failure, molten cavity formation in center of the fuel pin and thermal-hydraulics in the molten cavity. Especially, the formation of two cavities and the thermal-hydraulics in multi-cavity have to be calculated. The former SAS4A code is not applicable to the axially heterogeneous fuel pin design and SIMMER-III and SIMMER-IV do not have a detailed pin model to calculate IP in detail.

Figure 2 shows an outline of a new detailed pin model developed for SIMMER-V. The new detailed pin model calculates fuel-pin thermal calculation, mechanical loading to cladding and in-pin fuel motion in a two-dimensional cylindrical coordinate. The pin thermal calculation part includes heat transfer, thermal deformation and molten cavity formation as basic physical processes. The molten cavity is calculated in each axial calculation cell and the multiple cavities are automatically represented if the molten cavity cells are discontinuous in an axial direction. The thermo-mechanical part consists of fission gas release, fuel pellet swelling, stress calculation, pellet-cladding contact pressure, thermal stress and cavity pressure calculations and evaluates the mechanical failure of cladding. The in-pin fuel motion part calculates an axially one-dimensional thermal-hydraulics in the cavity and uses a simplified fluid-dynamics module of SIMMER-III. The in-pin fuel motion solves a vapor-liquid two-phase flow composed of liquid fuel, fuel vapor and fission gas with a semi-implicit method and calculates melting/freezing and vaporization/condensation. The solidified liquid fuel is treated as fuel crust in cavity.

The new detailed pin model is coupled to the SIMMER-V fluid-dynamics module. The thermal boundary condition at outside of cladding is given from the coolant temperature along the channel in the SIMMER-V fluid dynamics and the resultant heat flux at cladding surface evaluated by the pin thermal calculation is given to the SIMMER-V fluid-dynamics calculation. The mechanical loading obtains channel pressure as a boundary condition for the stress failure calculation of cladding. The in-pin fuel motion uses the channel pressure for molten fuel ejection upon cladding failure. The molten fuel and fission gas ejection amounts are calculated based on pressure equilibration between the cavity and the channel. Physical and thermo-physical properties are the same in the new detailed pin model and SIMMER-V to keep a consistency in a whole IP and TP calculation.

Figure 3 shows a geometry and a condition for a test calculation of the new detailed pin model. A subassembly, whose diameter and height are 16.4 and 2,000 mm, respectively, is expressed with 1 radial cell and 40 axial cells in the cylindrical coordinate. A fuel pin in the subassembly has its diameter and height are 7.6 and 1,200 mm, respectively. The fuel pin is expressed with 12 radial nodes for a fuel pellet part, 3 nodes for cladding and 1 node for the fuel/cladding gap. A gas plenum and a lower reflector are set below the fuel pellets and an upper reflector is set above the fuel pellet. Pressure boundary conditions, which generates 2 m/s upward sodium flow, are set at the bottom and top boundaries of the flow channel. A power distribution with two vertical peaks is given. The transient power history is provided such that the initially constant power is linearly increased up to 4 times between 30 and 35 s.

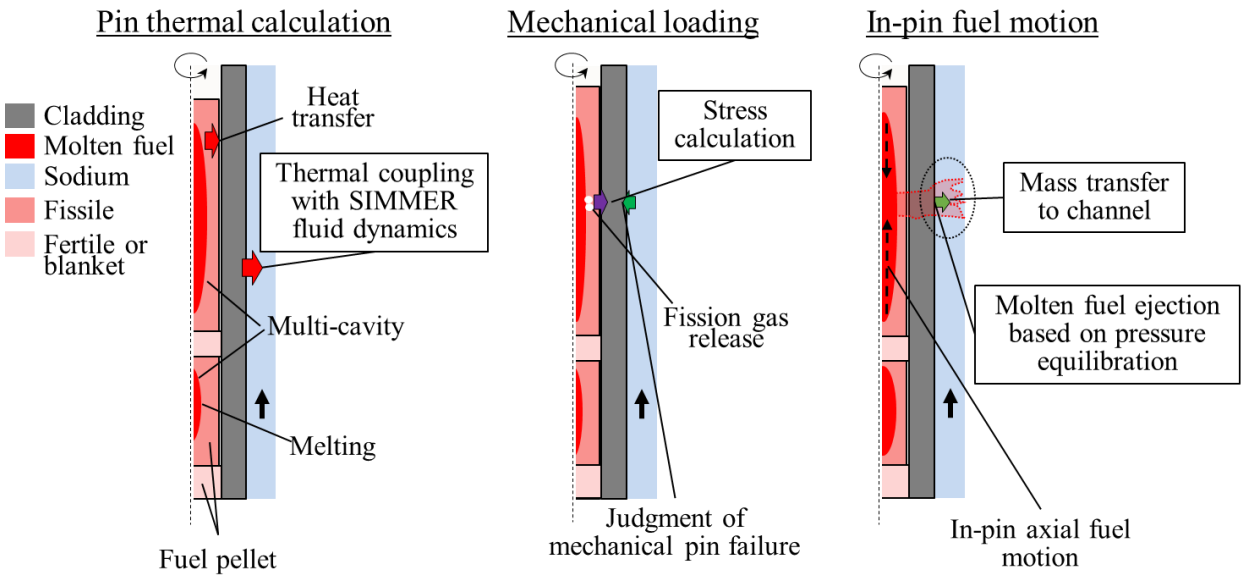

Figure 2. Model outline of the new detailed pin model.

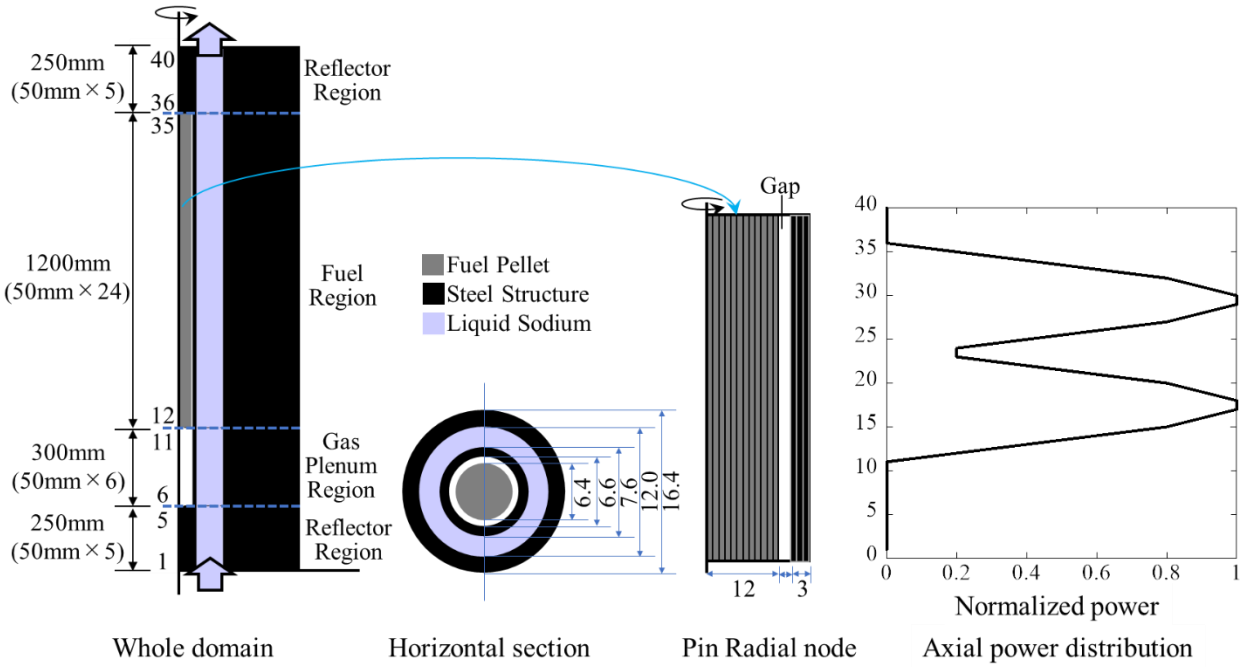

Figure 3. Test calculation setting for the new detailed pin model.

Figure 4 shows a calculation result. Two molten cavities are formed at 34.5 s and they are enlarged with time. The cladding failure occurs at 30th axial cell at 36.1 s when a contact pressure between cladding and fuel pellet exceeds an ultimate tensile strength of steel. Since a cavity pressure is higher than the channel pressure, the molten fuel and fission gas in cavity are ejected to the flow channel instantly upon cladding failure. The ejected fuel contacts with the sodium in channel and vaporizes it. A part of ejected fuel is forced out to upward by the sodium vapor pressure and the rest is solidified on the wrapper tube as fuel crust at

36.6 s. The cladding starts to melt around the first cladding failure location because of loss of heat removal due to sodium vaporization, and this leads to the fuel pin failure. The same process occurs at the lower molten cavity from 37.1 s. Almost all molten fuel mass in the cavity is ejected to the coolant channel and the fuel pin breaks with the melting of cladding. The test calculation result shows that the prospective phenomena in the ATWS of future reactor, which are pin thermal conduction, cladding mechanical failure, multi-cavity formation at the centerline of fuel pin and in-pin fuel motion, can be reasonably simulated by the new detailed pin model. It is also confirmed that the new detailed pin model is successfully coupled to the SIMMER-V fluid dynamics module.

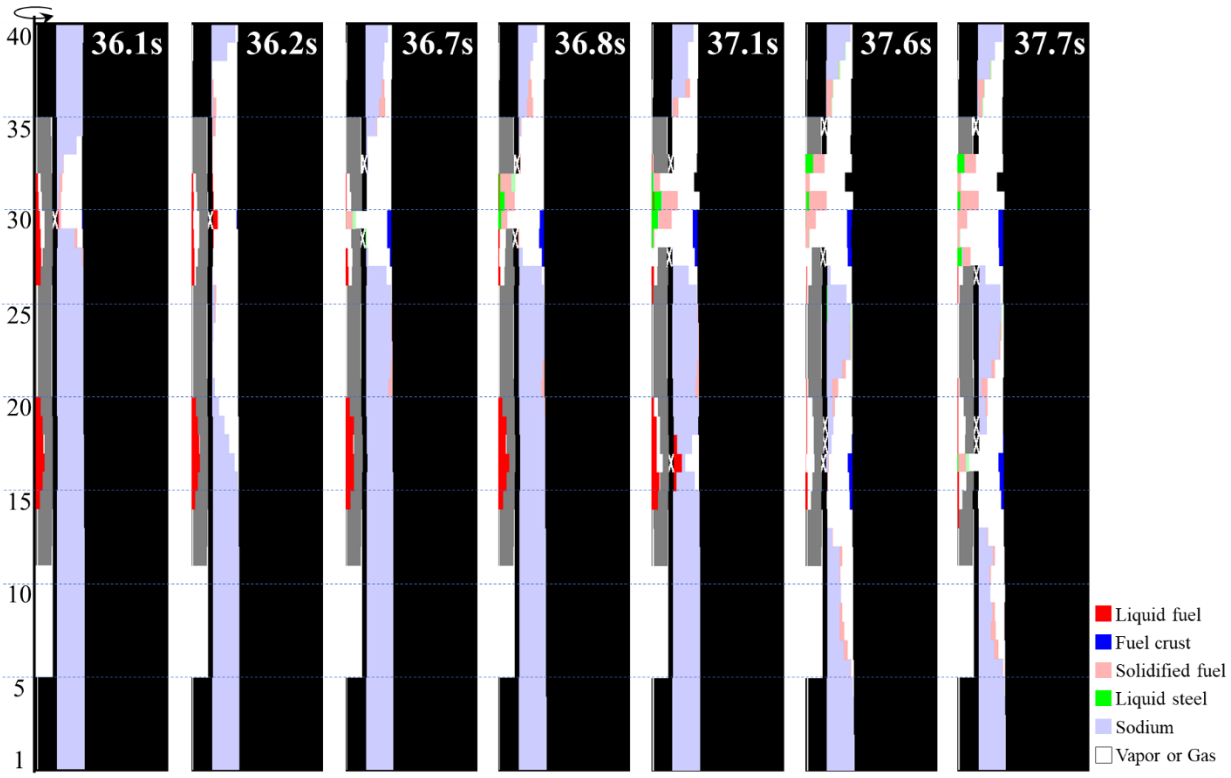

Figure 4. Test calculation result of the new detailed pin model. Each color shows only material volume fractions at each calculation cell, but not distribution.

The installation of new detailed pin model into SIMMER-V has brought three advantages. First, SIMMER-V becomes applicable to ATWS analysis of the future reactor with the axially heterogeneous fuel pin. Second, is a discontinuity problem between IP and TP analyses with using different codes is eliminated. Third, s accurate space-dependent neutron kinetics of the SIMMER neutronic module [12] can be used in the IP analysis as well. It is noted that, in previous IP analyses, only a simple point reactor kinetics model is used.

The present detailed pin model considers only fresh fuel and one of necessary development items is a reflecting of irradiation effects such as new thermal conductivity models. It will be attained in near future.

3.2. Fuel isotope vector

Material distribution, temperature and fuel isotope content are transferred to the neutronic module from the fluid-dynamics module. A fine fuel isotope distribution is desirable to obtain an accurate neutronic calculation result. This issue becomes serious for a large-scale heterogeneous reactor planned as a future

reactor, in particular when fuels with different enrichment are mixed during the degradation in TP. Although the most direct method to obtain the most accurate fuel isotope distribution in the fluid dynamics module is a solving mass, energy and momentum conservation equations for all fuel isotopes, this method is not preferable in view of computational cost.

The former SIMMER codes treated two densities, one energy and momentum field for a fuel component. Fuel isotopes were assigned to one of two fuel densities and they moved with a fuel component velocity. Fuel isotope ratios were always fixed with two fuel densities and a resultant fuel isotope distribution became obscure. Although the former method could give appropriate calculation results in case of small or middle scale reactors if the fuel isotopes were assigned with adequate considerations, it had issues on an analysis of large-scale heterogeneous core. Additionally, the adequate considerations took time and needed enough knowledge and experience for the neutronic calculation. Figure 5 shows an example of power distribution in middle-scale reactor. The real power distribution based on a design information shows a spatial inhomogeneity due to a fuel composition and loading position. The limitation by two fuel isotope components is too rough to express the spatial inhomogeneity in an actual core.

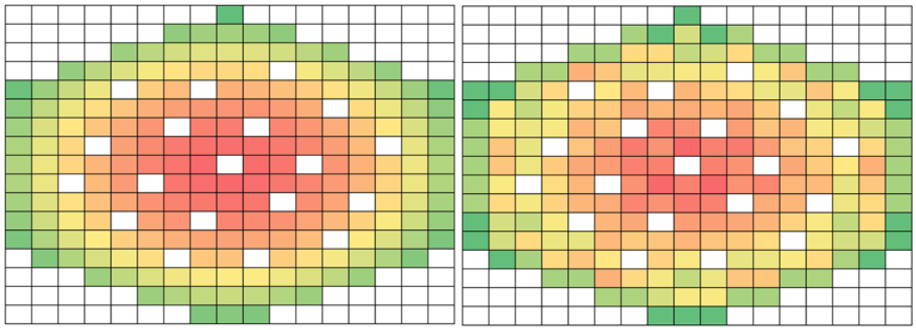

Figure 5. Example of power distributions in middle-scale reactor under real condition based on a design information and SIMMER without fuel isotope vector.

A fuel isotope vector is a method to refine a resolution of fuel isotope distribution in SIMMER without increasing computational load. A new physical variable, $f_{l,m}$, to represent the mass fraction of the mth fuel isotope in the lth component is introduced to calculate changes of fuel isotope composition due to local mass transfer and fluid convection. A macroscopic density of each fuel component $\bar{\rho}_l$ is expressed as

$$\bar{\rho}_{l,m} = f_{l,m} \sum_{m} \bar{\rho}_{l,m} , \tag{1}$$

where the component, l, includes pin fuel, crust fuel, liquid fuel, fuel particles, fuel chunks and fuel vapor. The following items are assumed to save the computational cost:

- Physical and thermo-physical properties are not so different for all fuel isotopes;
- Each fuel isotope moves at the speed of the velocity filed of the component to which it belongs; and
- The temperature of each fuel isotope is the same as the temperature of the component to which it belongs.

Energy equations and mass conservation equations for each fuel isotope need not to be solved and the pressure iteration procedure, which is the highest computational load in the fluid-dynamics module, is not

changed under these assumptions. Using the end-of-time-step velocities and fuel component masses, the fuel isotope mass fractions are updated as

$$f_{l,m}^{n+1} = \frac{\{\bar{\rho}_l^n f_{l,m}^n - \Delta t \nabla(\bar{\rho}_l^n f_{l,m}^n \boldsymbol{v}_l^{n+1})\}}{\bar{\rho}_l^{n+1}}, \tag{2}$$

from the convection of fuel components, and

$$f_{l_{c'},m}^{n+1} = \frac{\{\bar{\rho}_{l_{c'}}^n f_{l_{c'},m}^n + \Delta t \Gamma_{l_c,l_{c'}} f_{l_c,m}^n\}}{\bar{\rho}_{l_{c'},m}^{n+1}}, \tag{3}$$

for reflecting local mass transfers. Where,

$$\bar{\rho}_l = \sum_m \bar{\rho}_{l,m}, \tag{4}$$

In these equations, superscripts n and n+1 denote before and after updated values, Δt a time step size, $\boldsymbol{v}$ a velocity vector, $\Gamma_{l_c,l_{c'}}$ a mass transfer rate, subscripts c and c' before and after mass transfer.

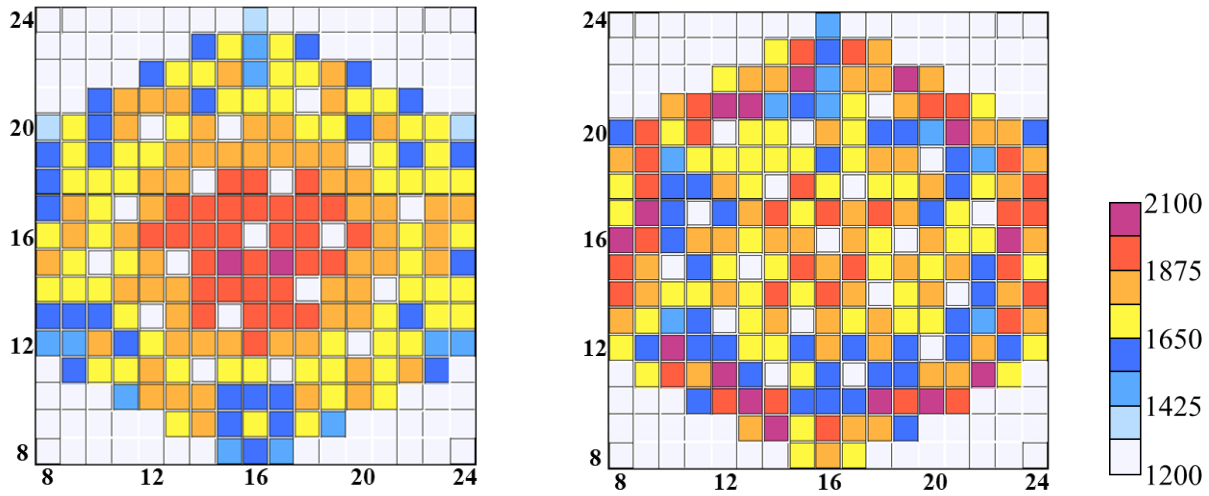

Two fuel density method Using fuel isotope vector

Figure 6. Fuel pellet temperature at mid-plane in medium-scale reactor at a rated operation from [10]**. Left shows a result of fuel isotope vector and right shows without fuel isotope vector.**

Figure 6 shows the fuel temperature distribution at mid-plane in a medium-scale reactor at rated operation using the fuel isotope vector method. The former two density method result shows a smooth fuel pellet temperature distribution with higher in the center and lower on the outer. The result with fuel isotope vector method expresses a heterogeneous fuel pellet distribution which depends on power/flow ratio, but does not depends on loading position. The fuel isotope vector method will improve a safety analysis accuracy with SIMMER-V for the continuous analysis from IP to TP in the large-scale heterogeneous core planned as the future reactor because an accurate expression of subassembly power distribution has a large impact on event sequence of ATWS.

4. NEW CAPABILITIES IN SIMMER-V DEVELOPED BY CEA

CEA develops the SEASON platform as an integrated analysis system to evaluate an event sequence of severe accidents in SFR [11]. It is planned that settings of data base for each subassembly, coupling with several necessary codes around SIMMER-V for severe accident analysis, calculation setting, execution of analysis etc. can be managed with graphical user interface environment on the SEASON platform. In this chapter, methods for several code coupling of the SEASON platform development are introduced.

4.1. Boundary coupling

The first capability is for a coupling method between SIMMER-V and SIMMER-V. As an example, consider a SIMMER-V analysis of large-scale pool-type SFR. A whole reactor is expressed as a single large calculation domain with a three-dimensional Cartesian coordinate and the domain will include unnecessary regions for the analysis. Because horizontal and vertical calculation cell size are fixed in vertical and horizontal directions, respectively, calculation cells in a relatively unimportant region increase and a calculation time increases. If the whole reactor is expressed with several SIMMER-V calculation domains and these domains are coupled maintaining continuity, the above issues will be solved. The boundary coupling is a method to enable two-way coupling of several calculation domains through each adjacent boundary as demonstrated by Kedzierska et al. [13,14] and sketched in Fig. 7.

The fluid-dynamics module of SIMMER-V includes: intra-cell calculations for surface area, heat transfer, phase change and momentum exchange functions; and convective calculations for energy, mass and momentum equations with pressure iteration calculation. The boundary coupling method receives and transfers only elements of pressure matrix at boundary cells between calculation jobs such as an MPI parallelized calculation in one calculation job to enable the two-way calculation. The data transfer between several calculation jobs is enabled with MEDCoupling (Data Exchange Model Coupling) for a geometry and field mapping library in SALOME platform developed by CEA and EdF (Electricité de France) [15]. The boundary coupling was in a first stage developed for conforming boundary meshes, it is now being extended to boundaries with non-conforming meshes. The boundary coupling will provide a great flexibility in terms of topology and meshing for a compounding system in addition to improved performance and memory saving.

4.2. Interoperability with other codes

SIMMER-V is a code for the thermal-hydraulics and neutronics of a reactor in an ATWS sequence. It will be necessary to be linked to other calculation codes which can calculate an irradiation, a plant dynamics analysis etc., in view of a whole plant comprehensive analysis in the SEASON platform. A capability of interoperability with other codes is a method to enable the comprehensive time integration with a data exchange between several different codes.

To achieve this, interfaces for the data exchange is installed into each code and the codes are compiled as dynamic libraries. These dynamic libraries are executed with ICoCo (Interface for Code Coupling) developed by CEA [16]. All dynamic libraries of codes are specified as Python or C++ script, called as application supervisor, in an order of execution as shown in Fig. 8. This application supervisor capability is enabled by ICoCo and calculation results is exchanged by MEDCoupling between codes. The interoperability with other codes makes it possible to automatically solve for ATWS event progression in a plant encompassing multiple severe accident analysis codes.

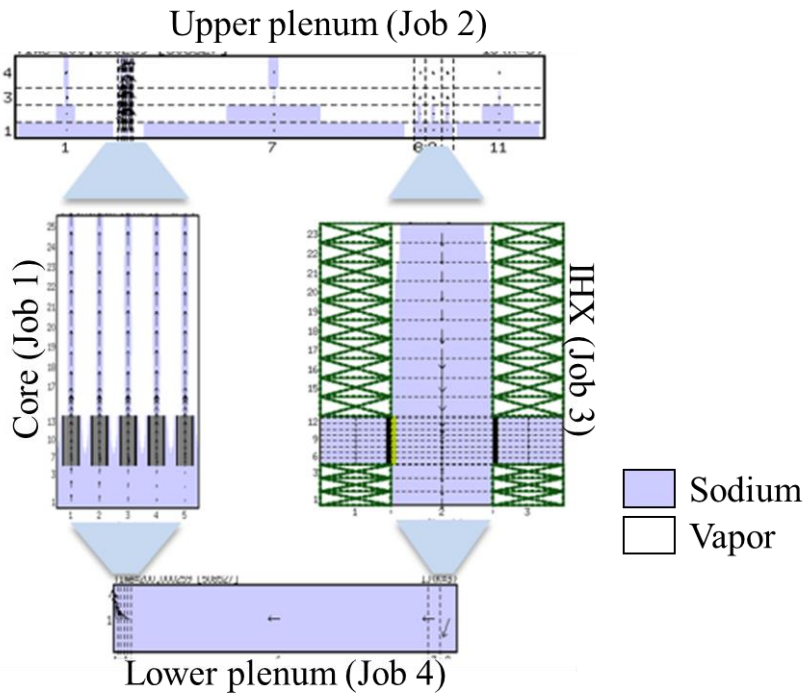

Figure 7. Example of boundary coupling. Each of four adjacent domains for imitations of core, upper plenum, IHX and lower plenum in a reactor is run as an independent calculation job, and their time integrals are solved simultaneously [13, 14].

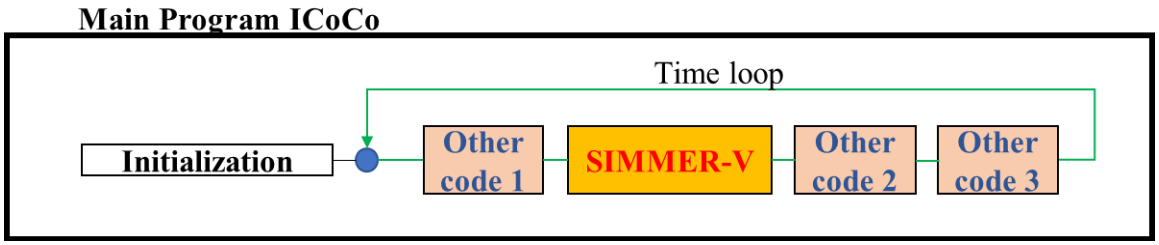

Figure 8. Tree diagram of interoperability with other codes using ICoCo. Green line shows a data transfer with MEDCoupling.

5. CONCLUSIONS AND FUTURE PLAN

SIMMER-V has been developed and improved through a series of tests and verifications based on a start-up version released in 2020. Development of a prototype version of SIMMER-V, which includes necessary physical models for a large-scale heterogeneous reactor analysis and high-performance computing capabilities, was finalized at the end of 2022.

A new detailed pin model and a fuel isotope vector model, which are necessary for an ATWS analysis of future SFR, are incorporated into SIMMER-V. The new detailed pin model can represent a mechanical fuel pin failure and is applicable to an axially heterogeneous fuel pin. The fuel isotope vector model calculates changes of the mass fractions of fuel isotopes due to fuel mass convection and local mass transfer. The updated fuel mass fractions are then used in the neutronics to calculate new reactivity and reactor power. These new developments in SIMMER-V will improve applicability and evaluation accuracy on an analysis

of the large-scale heterogeneous core planed as a future reactor. Newly introduced model and method will need to be verified and validated further. A verification and check of applicability have been completed for the fuel isotope vector by JAEA. For the new detailed pin model, CEA and JAEA have respectively created their own virtual test cases and verified its applicability and capability to important physical phenomena in a large range of situations. JAEA will install new thermal conductivity model as a capability for treating irradiation effects by the end of 2024.

CEA newly develops a boundary coupling and an interoperability with other codes in view of a development of SEASON platform. The boundary coupling enables two-way coupled calculation between adjacent regions computed by different calculation jobs through boundaries. It is now being extended to apply to boundaries with different mesh sizes. The interoperability with other codes enables a comprehensive whole plant ATWS analysis using several analysis codes with a data exchange by MEDCoupling and an application supervisor by ICoCo. Coupling applications between SIMMER-V and other codes will be verified in near future.

A version of SIMMER-V applicable to the future SFR will be released by the end of 2024. Validation of the new detailed pin model using in-pile experiments and a reactor analysis of virtual future reactor to verify the physical model behavior and applicability are now underway.

ABBREVIATION

ATWS	Anticipated Transient Without Scram
CEA	French Atomic Energy Commission
EdF	Electricité de France
ICoCo	Interface for Code Coupling
IP	Initiation Phase
JAEA	Japan Atomic Energy Agency
MED	Data Exchange Model
SA	Severe Accident
SEASON	Severe Accident SimulatiON
SFR	Sodium-cooled Fast Reactor
TP	Transition Phase
V&V	Verification and Validation

NOMENCLATURE

f	fuel isotope mass fraction
Δt	time step size
$\boldsymbol{v}$	velocity vector

Greek symbols

$\bar{\rho}$	macroscopic density
$\Gamma_{l_c,l_{c'}}$	mass-transfer rate from $l_{c'}$ to l_c

Subscripts

c, c'	before and after mass transfer
l	fuel component
m	fuel isotope
n, n+1	before and after updated value in the time step

ACKNOWLEDGMENTS

The Japan-side studies include the results of "Technical development program on fast reactor for demonstration" entrusted to the Japan Atomic Energy Agency (JAEA) by the Ministry of Economy, Trade and Industry (METI). The authors express their sincere gratitude to Mr. Masaaki Sugaya and Mr. Masahiro Mizuno of NESI Inc. for their enormous programming and computational supports.

REFERENCES

1. S. Kondo, et al., "SIMMER-III and SIMMER-IV: Computer Codes for LMFR Core Disruptive Accident Analysis," *Japan Atomic Energy Institute research report*, (to be published) (2024).
2. Y. Tobita, K. Morita, W. Maschek, P. Coste, T. Cadiou, "The development of SIMMER-III, an advanced computer program for LMFR safety analysis, and its application to sodium experiments," *Nucl. Tech.* **153**, pp. 245–255 (2006).
3. "Phase 1 Code Assessment of SIMMER-III; A Computer Program for LMFR Core Disruptive Accident Analysis," https://jopss.jaea.go.jp/pdfdata/JAEA-Research-2019-009.pdf (2019)
4. "SIMMER-IV: A Three-Dimensional Computer Program for LMFR Core Disruptive Accident Analysis," https://jopss.jaea.go.jp/pdfdata/JNC-TN9400-2003-070.pdf (2003)
5. H. Yamano, S. Fujita, Y. Tobita, et al. "Development of a three-dimensional CDA analysis code: SIMMER-IV and its first application to reactor case." *Nucl Eng Design*, **238**(1), pp. 66–73 (2008).
6. A.M. Tentner, D.P. Weber, G. Birgersson. "The SAS4A LMFBR whole core accident analysis code." *Proceedings on the International Topical Meeting on Fast Reactor Safety*, Knoxville, Tennessee, USA, April 21-24, (1985).
7. M. Hishida, S. Kubo, M. Konomura, et al. "Progress on the plant design concept of Sodium-cooled fast reactor," *J Nucl Sci Tech*, **44**(3), pp. 303–308 (2007).
8. Le Coz P, Sauvage J-F, Serpantie J-P. "Sodium-cooled fast reactors: the ASTRID plant project," *Proceedings of International Congress on Advances in Nuclear Power Plants (ICAPP)*, Nice, France, May 2–5, Paper 11249 (2011).
9. T. Beck, V. Blanc, J.M. Escleine, et al. "Conceptual design of ASTRID fuel sub-assemblies," *Nucl Eng Design*, **315**, pp. 51-60 (2017).
10. H. Tagami, S. Ishida, Y. Tobita, "Development of new treatment of fuel isotope vector in the core disru ptive accident analysis of fast reactors," *J. Nucl. Sci. Tech*, **60** (12), pp. 1548-1562, (2023)
11. E. Dufour, P. Gubernatis, L. Trotignon, "3D thermalhydraulics-neutronics simulation of SFR core degr adation with the SEASON French platform," *Technical Meeting on the Safety Approach for Liquid Me tal Cooled Fast Reactors and the Analysis and Modelling of Severe Accidents*, March 13-17,Vienna, A ustria, (2023).
12. S. Kondo, M. Ishikawa, "SIMMER-III code and space-energy dependent dynamics of fast reactors (in Japanese)," *7th Topical Meeting on Nuclear Code Development*, Ibaraki, Japan, October 30–31 pp. 129-151, (1991).
13. B. Kedzierska B., P. Gubernatis, M. Medale "Validation of SIMMER-V onto the GENEIS two phase e xperiments with the stability boundary evaluation" *The 19th Int.Topical Meeting on Nuclear Reactor T hermal Hydraulics (NURETH-19) Brussels, Belgium, March 6 - 11, 2022, Paper 35606.*
14. B. Kedzierska, P. Gubernatis, M. Medale, Implementation of MultiDomains in Simmer-V Thermohydraulic Code. Ann. Nucl. En., Vol. 178, article id. 109338, DOI 10.1016/j.anucene.2022.109338 (2022)
15. MedCoupling: https://docs.salome-platform.org/7/dev/MEDCoupling/index.html
16. ICoCo: Thermalhydraulic coupling using ICoCo: an interface for Code Coupling and SALOME, Fabie n Perdu. https://fr.slideshare.net/SalomePlatform/2011-11-15-jus-icoco

Development of SIMMER-V code system using new physical models

(1) Planning of SIMMER-V development and outline of code

Hirotaka TAGAMI[1], Shinya ISHIDA[1], Yoshiharu TOBITA[1*], Yasushi OKANO[1], Hidemasa YAMANO[1], Shigenobu KUBO[1]
Frederic PAYOT[2], Laurent SAAS[2], Laurent TROTIGNON[2], Pierre GUBERNATIS[2], Emmanuelle DUFOUR[2]

1: Japan Atomic Energy Agency, 2: Commissariat à l'énergie atomique et aux énergies alternatives
*Present affiliation: Karlsruhe Institute of Technology

What the SIMMER code is and what it can do

- The SIMMER-III (2-dimensional) and IV (3-dimensional) codes are the basis for the development of SIMMER-V and have been developed in JAEA to analyze a potential recriticality energetics, which is one of the safety issues of Sodium-cooled Fast Reactors (SFRs), in the disrupted core of Anticipated Transient Without Scram (ATWS).
- The animation is an example of SIMMER-IV calculation for medium-scale reactor.
- The SIMMER codes combine fluid dynamic, structure and neutronics modules.
- SIMMER can calculate core material distributions, temperature, phase changes, reactivity and reactor power in a disrupted core.

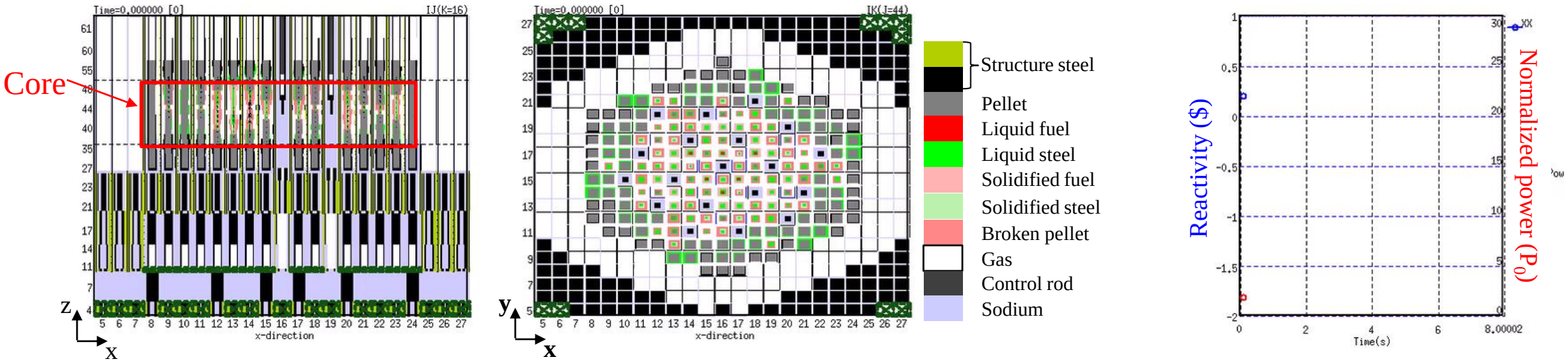

Example of ATWS and SIMMER-IV calculation

Former evaluation method and its issues on a future reactor

- In the evaluation with SIMMER-III and -IV:
  - Fuel pin disruption in initiating phase (IP) is evaluated by other codes, such as SAS4A.
  - The IP calculation result is used as an initial condition for SIMMER-III and IV.
  - Expansion of core disruption and molten core behavior in transition phase are evaluated by SIMMER-III and IV.
- SIMMER-III and -IV were used as a strategy for regulatory compliance of small and medium-scale SFRs in Japan, but has issue on the evaluation of a future SFR in a
  - Technical limitation to express fuel pin behaviors and a fuel isotope distribution in a future SFR (introduced in next slide).
- SIMMER-V code is developed to solve the issue.

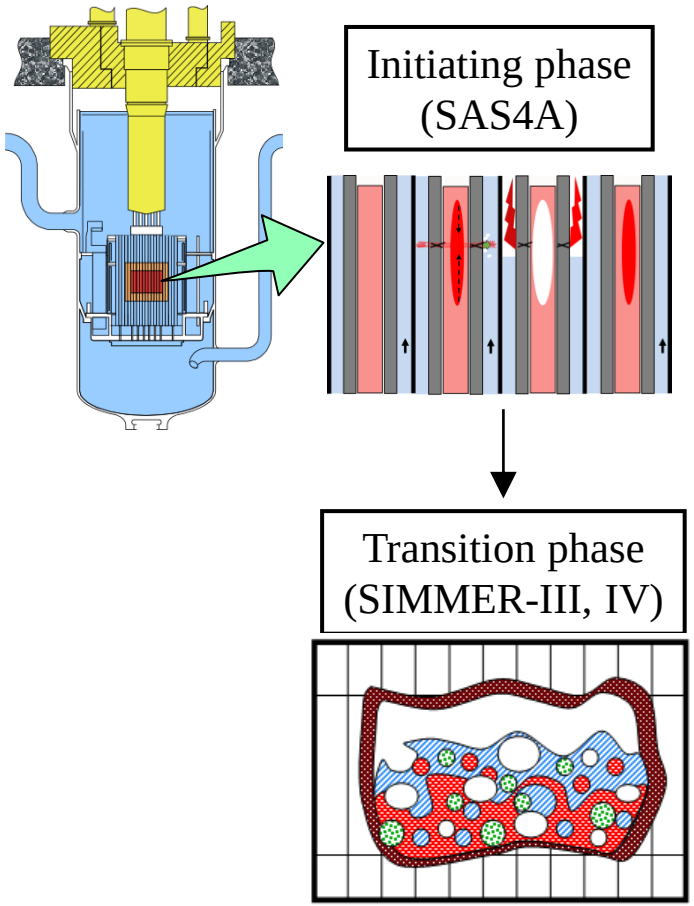

Image of event progress of ATWS and analysis codes in the former evaluation method

Objective of SIMMER-V development collaboration

- An objective of SIMMER-V code system development is to enable a comprehensive analysis from IP to TP in a future reactor with a large-scale heterogeneous core.
  - Fuel pins and their height are different between inner and outer core.
  - Inner core fuel pin has an inner fertile zone.
  - These features generate a three-dimensional heterogeneity.
- For the SIMMER-V development,
  - CEA equipped a hybrid MPI-OpenMP parallelization and the Fortran module capability for a calculation speed-up and a memory management for a future large-scale reactor calculation.
  - JAEA developed a new detailed pin model to calculate the axial heterogeneous fuel pin and a new method for refinement of fuel isotope distribution to calculate the 3D heterogeneous core.
- This presentation mainly introduces a framework of development collaboration and contents of implemented items.

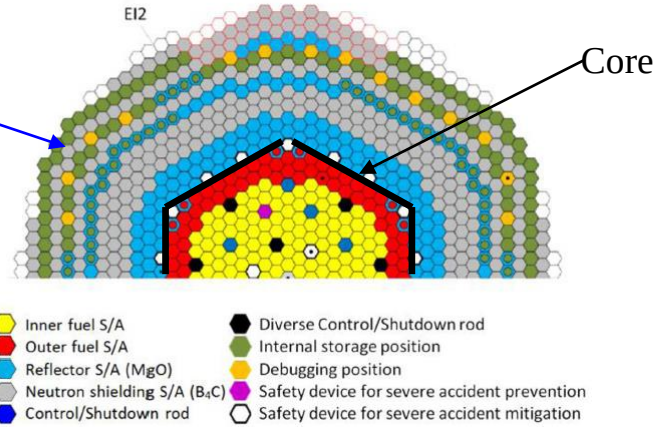

Layout of ASTRID core of CFV v4 from T. Beck et al. (2017)

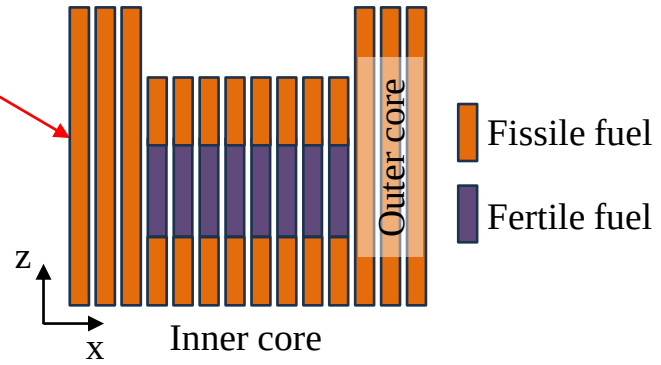

Image of inner and outer core fuel pin configuration

T. Beck et al, "Conceptual design of ASTRID fuel sub-assemblies", Nucl. Eng. Design, 2017; 315, 51-60,

Framework of collaboration

- In the framework for the code development, CEA and JAEA share and jointly perform 9 tasks.
- The main tasks are development and V&V*1 of new models, code management, and CEA platform development.

- Some high priority tasks in the collaboration are briefly introduced.
  - Development of a new detailed pin model by JAEA
  - Reactor applicability of the new method for refinement of fuel isotope distribution, called as “fuel isotope vector”, by JAEA
  - Development of new methods for coupling with several codes around SIMMER-V by CEA

*1: Ishida et al., Poster session

New detailed pin model by JAEA

JAEA works 1 (1/2) –Development of a new detailed pin model–

- A new detailed pin model includes necessary physical processes (heat transfer in pin, fission gas release in pin, thermal and mechanical stresses, cladding failure and in-pin fuel motion) to express a pin degradation.
- The new pin model enables a continuous analysis from initiating to transition phase with SIMMER-V.

	Pin thermal calculation	Mechanical loading	In-pin fuel motion
Old pin treatment	✓		
New pin model	✓	✓	✓

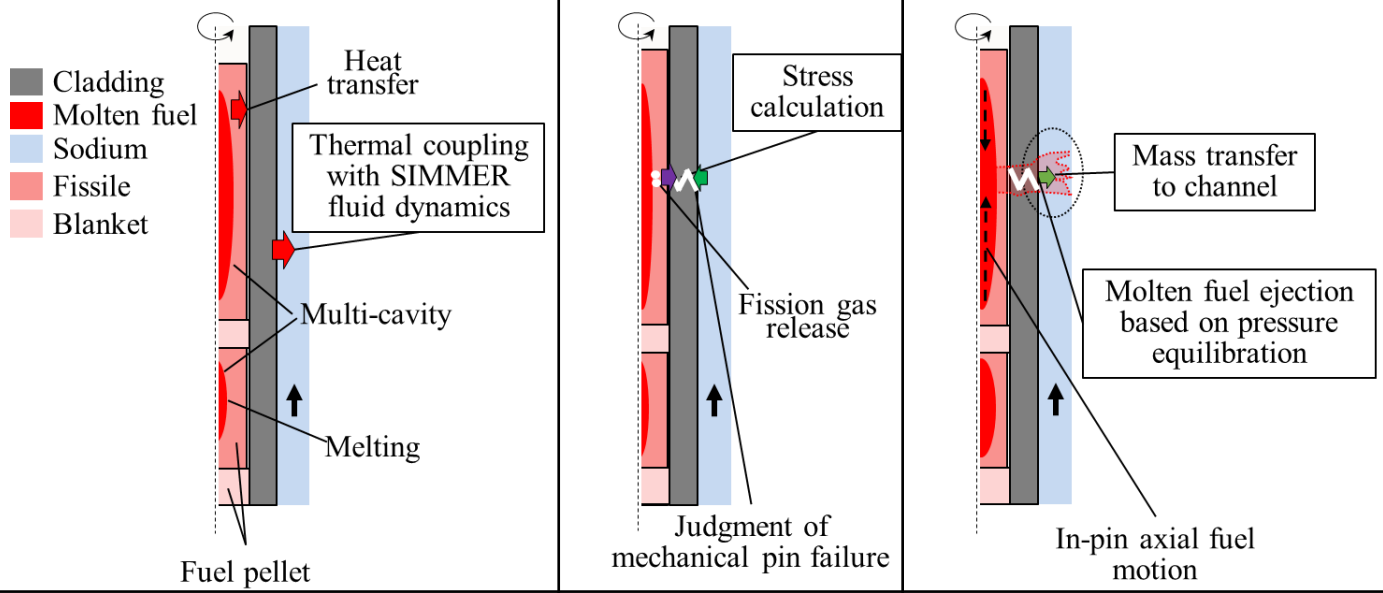

JAEA works 1 (2/2) –Development of a new detailed pin model–

- Test calculation result with following conditions.
  - Axial power profile has two peaks.
  - Power increases with time until 35 seconds as shown in right animation.
- Two molten cavities form in axial direction.
- Cladding failure by stress due to a contact of swelling pellet (shown with white "X" in animation).
- Molten fuel discharge through cladding mechanical failure from the molten cavity.
- Fuel pin is broken with melting of cladding.
- <u>The new pin model can reasonably simulate the prospective pin behaviors in the ATWS of the future reactor.</u>

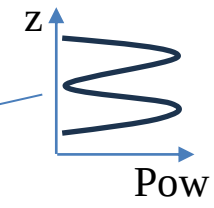

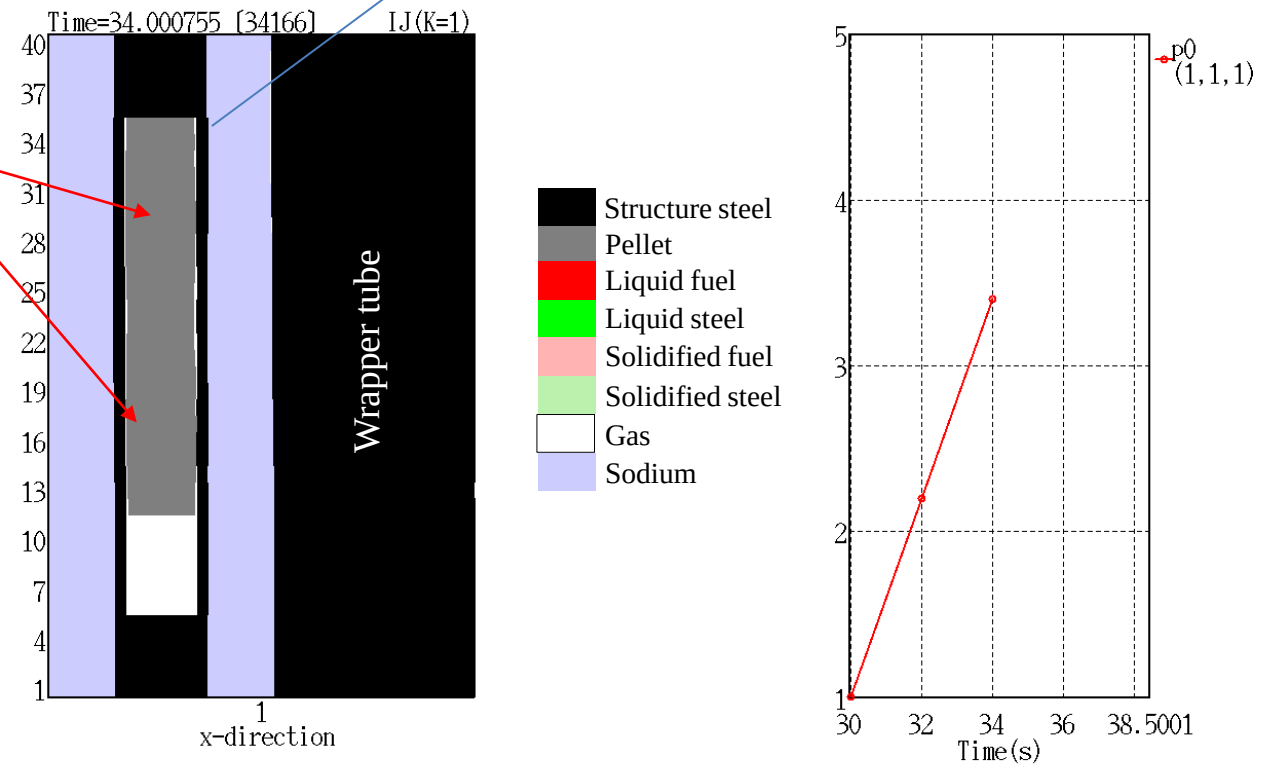

Material volume fractions of result

Normalized power

New method for refinement of fuel isotope distribution (fuel isotope vector) by JAEA

JAEA works 2 (1/2)–Study of applicability of fuel isotope vector–

- The fuel isotope vector method refines an isotope distribution in the fluid dynamic module.
- The refining of isotope distribution has been necessary for the heterogeneous core calculation.
- Image of fuel isotope treatments with an old method and a new method are shown in lower figures.
- Although the fuel isotope convection is roughly (only two components) treated in the old method, the fuel isotope vector treats them individually without increasing a large computational load under some assumptions.
- The method will improve an event progress between IP and TP, especially.

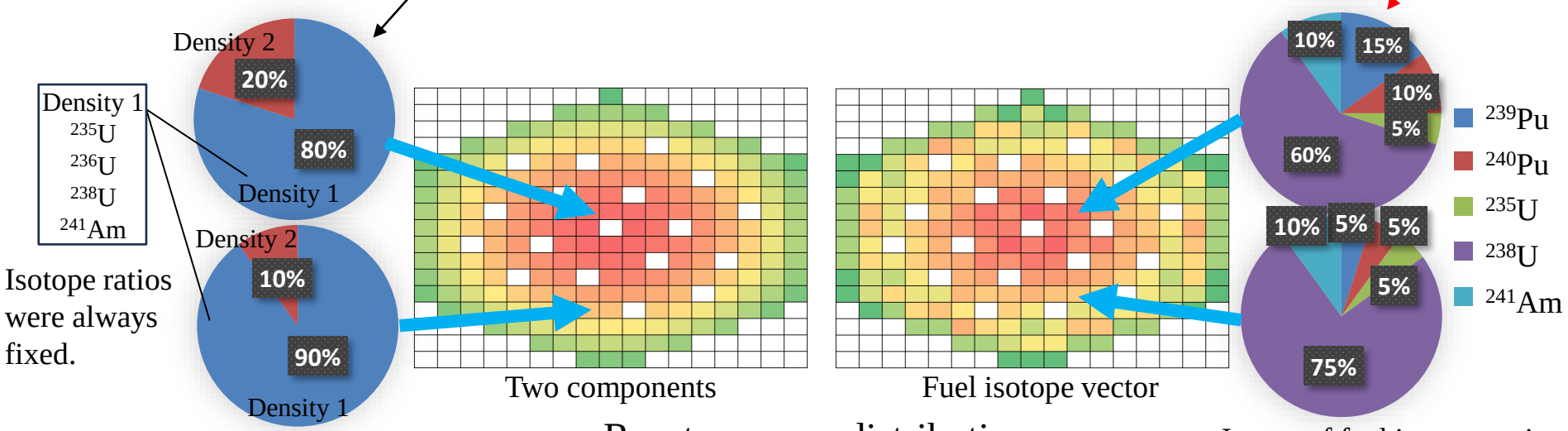

JAEA works 2 (2/2)–Study of applicability of fuel isotope vector–

- Test reactor simulation of fuel isotope vector
- ULOF in middle-scale reactor with positive void
- In case of the two components method, sodium vaporization and pin failures appear mainly at core center. As a result, a reactivity increase appears faster.
- In case of the fuel isotope vector, damaged sub-assemblies are dispersed. The distribution is realistic considering P/F distribution in the reactor.
- The method is expected to improve evaluations of the large-scale heterogeneous reactor as the future SFR.

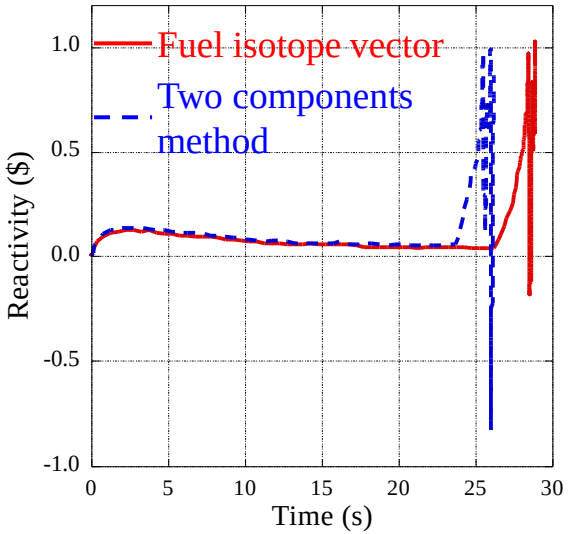

Reactivity

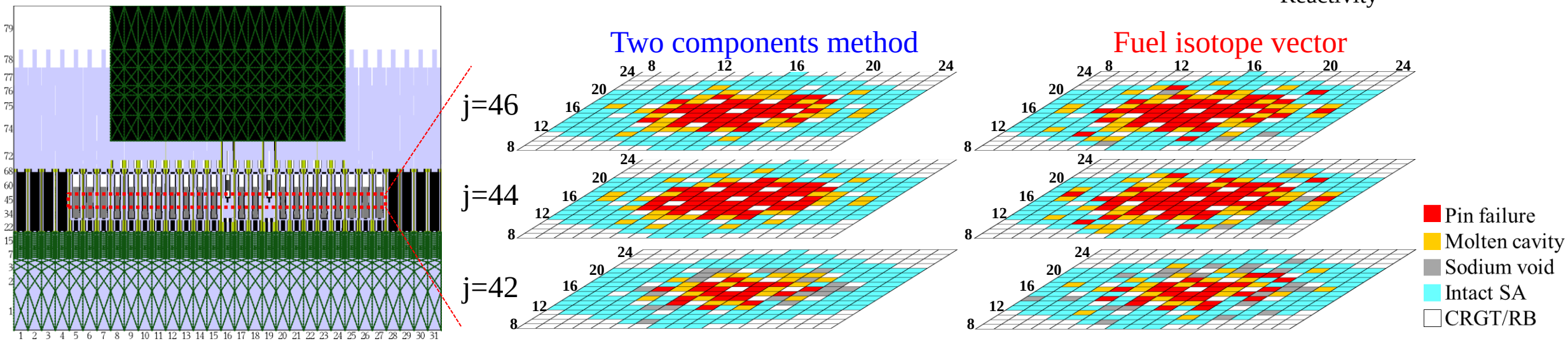

Distributions of core disrupted area just after the first reactivity peak in each calculation at core midplane (Tagami et al. 2023)

H. Tagami, S. Ishida and Y. Tobita, "Development of new treatment of fuel isotope vector in the core disruptive accident analysis of fast reactors", 2023, JNST,

New methods for coupling with several codes around SIMMER-V by CEA

SIMMER-V ⇔ SIMMER-V boundary coupling

- CEA plans to couple between SIMMER calculations and between SIMMER and other calculations in view of a whole plant comprehensive analysis in the CEA platform, called as SEASON.
- The boundary coupling is a method to enable two-way coupling of several SIMMER-V calculation domains through each adjacent boundary.
- The method receives and transfers elements of matrix for pressure iteration at boundary cells between several calculation jobs.
- This data transfer is enabled by MEDCoupling developed by CEA.

B. Kedzierska et al. "Implementation of MultiDomains in Simmer-V Thermohydraulic Code". Ann. Nucl. En., Vol. 178, (2022)

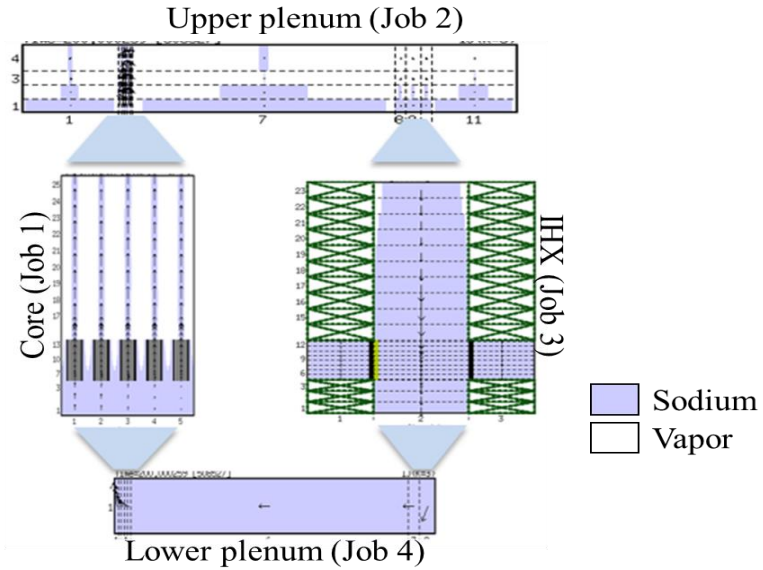

Example of boundary coupling Genesis loop (Kedzierska et al. 2022)

SIMMER-V interoperability with other codes

- This method enables one-way coupling between several different codes with a data exchange.
- An execution of several codes is enabled by Python or C++ script, called as application supervisor, as shown in the right figure.
- Calculation results are exchanged between each code by MEDCoupling.

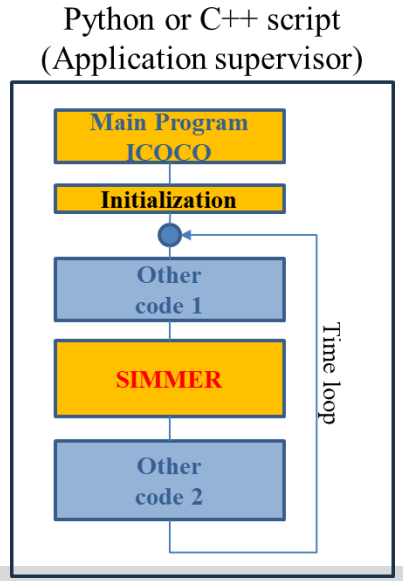

Document propriété du CEA – Reproduction et diffusion externes au CEA soumises à l'autorisation de l'émetteur

Conclusion –Present state and future plan-

- Development and improvement started based on a start-up version at year of 2020.
- Development of a prototype version for a large-scale heterogeneous reactor analysis was already finalized.
  - The version includes necessary physical models for the analysis.
- JAEA develops the new pin model and finished its verification. JAEA also finished a confirmation of the reactor applicability of fuel isotope vector.
  - They will improve an evaluation accuracy on analysis of a future large-scale heterogeneous SFR.
- CEA develops application capabilities for an integrated analysis system for severe accident in SFR with SEASON platform.
  - Coupling applications between SIMMER-V and other codes will be verified in near future.

- Remaining high priority tasks by the end of 2024:
  - Validation of the pin model using in-pile experiments
  - Confirmation of code applicability to safety analyses of the future reactor
- Development of an applicable version to the future SFR will be completed after these high priority tasks are finished.

Thank you for your attention

ACKNOWLEDGMENTS

The Japan-side studies include the results of "Technical development program on fast reactor for demonstration" entrusted to the Japan Atomic Energy Agency (JAEA) by the Ministry of Economy, Trade and Industry (METI). The authors express their sincere gratitude to Mr. Masaaki Sugaya and Mr. Masahiro Mizuno of NESI Inc. for their enormous programming and computational supports.

JAEA works 1 (2/2) –Development of a new detailed pin model (DPIN3)–

- Test calculation result with following conditions.
  - Axial power profile has two peaks.
  - Power increases with time until 35 seconds.
- Two molten cavities form in axial direction.
- Cladding failure by stress due to a contact of swelling pellet (at j=30 at 36.1s and j=17 at 37.1s).
- Molten fuel discharge through cladding failure from the molten cavity.
- Fuel pin is broken with melting of cladding.
- <u>The new pin model can reasonably simulate the prospective pin behavior in the ATWS of the future reactor.</u>

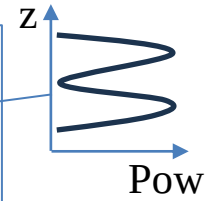

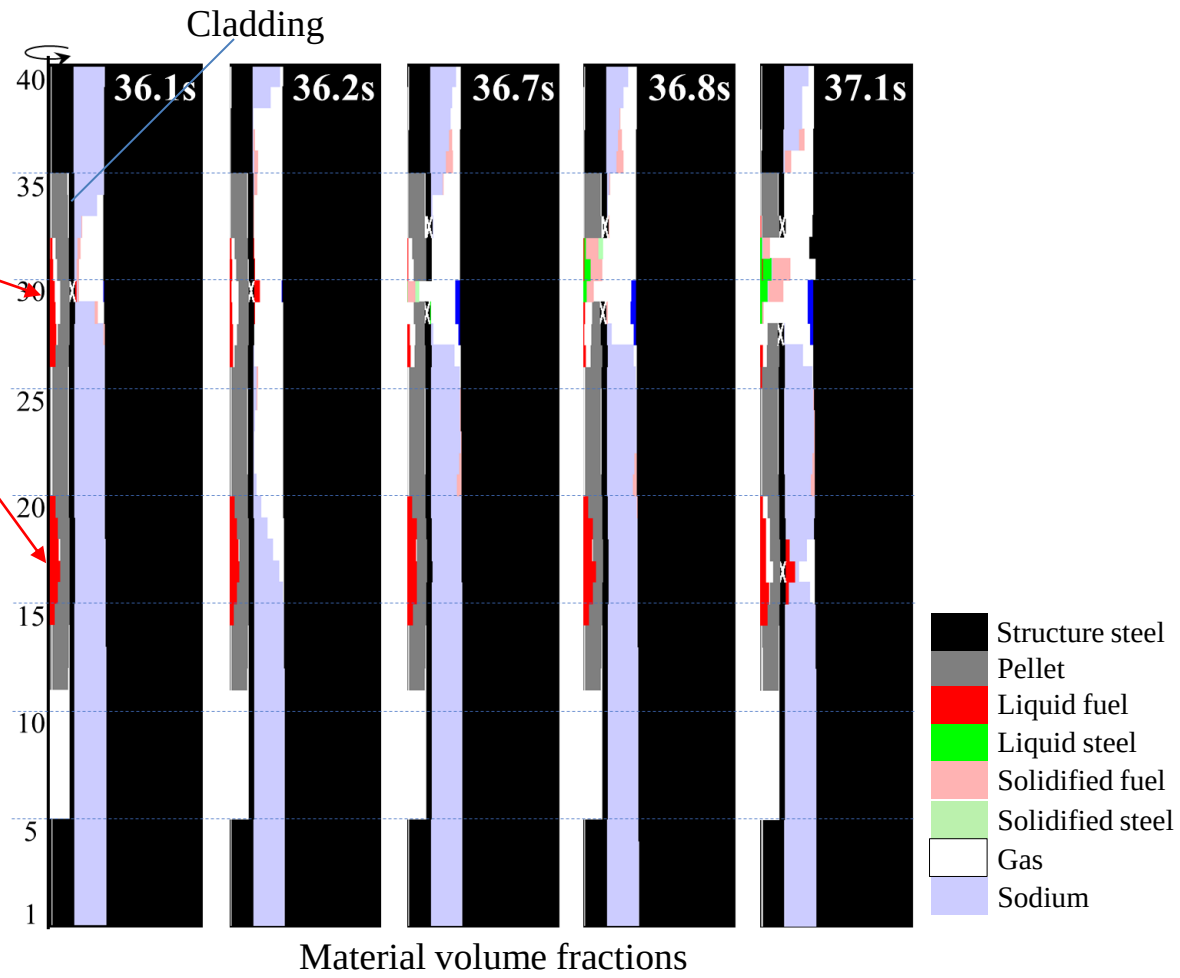

Material volume fractions

Methodology of fuel isotope vector

- An old treatment of fuel isotope in SIMMER had an issue on the large-scale heterogeneous core.
- JAEA developed a fuel isotope vector, which is a method to refine a resolution of fuel isotope distribution without increasing a large computational load, assuming the following items.
  - Physical and thermo-physical properties are not so different for all fuel isotopes.
  - Each fuel isotope moves with the velocity of fuel component to which it belongs.
  - The temperature of each fuel isotope is the same as the temperature of the fuel component to which it belongs.
- Only the fuel isotope mass fractions are updated by the convection and the phase change.
- The method improves the neutronic calculation results of the former treatment.

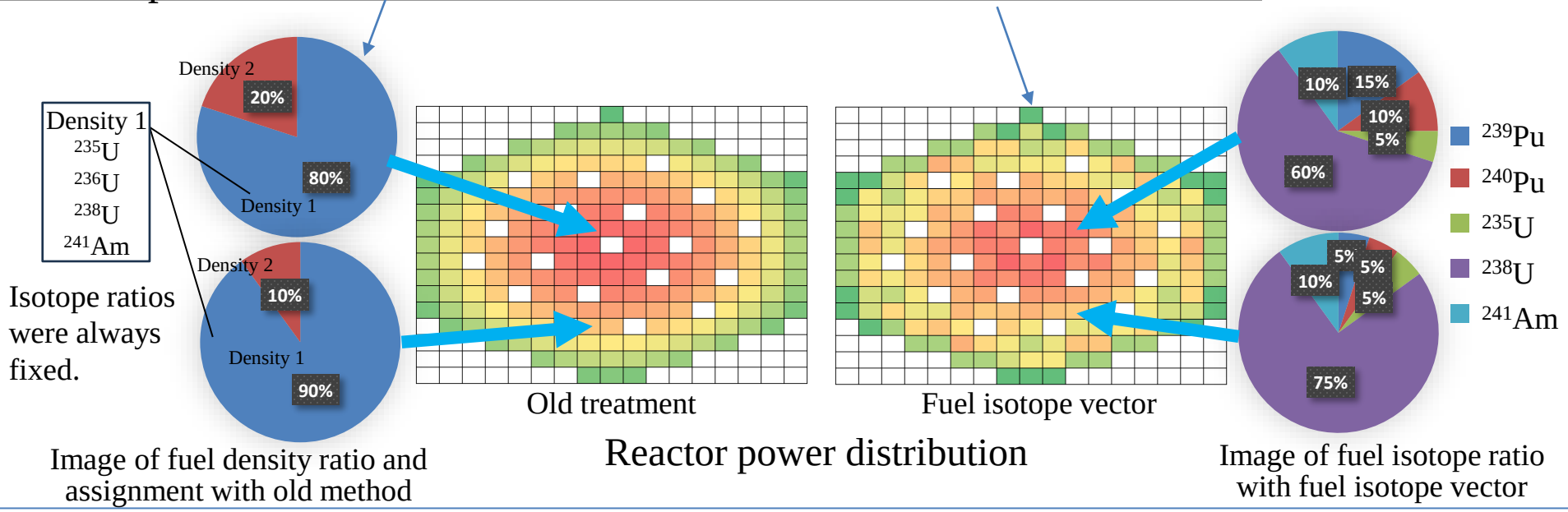

EXPERIMENTATION & SIMULATION OF SURFACE ABLATION BY A JET FOR CORE-CATCHER SAFETY ISSUE

Avrit A, Seiler N[1], Lecoanet A and Djermoune A
CEA, DES, IRESNE, DTN, SMTA
F-13108 Saint-Paul-Lez-Durance, France
nathalie.seiler@cea.f, alexandre.lecoanet@cea.fr, asma.djermoune@cea.fr

Rimbert N, Gradeck M
Université de Lorraine, CNRS, LEMTA
F-54000, Nancy, France
nicolas.rimbert@univ-lorraine.fr, michel.gradeck@univ-lorraine.fr

ABSTRACT

These coupled experimental and numerical studies support the safety demonstration of Sodium Fast Reactors SFR severe accident mitigation features. In order to limit potential power excursion in SFR core in the case of hypothetical severe accident, the implementation of the mitigation devices called transfer tubes was planned into the ASTRID core design. More specifically, they connect the core to the core-catcher and enable the early discharge of the corium towards the core-catcher. However, these devices, which effectively reduce the probability of reactivity excursions in the core, accentuate the issue of core-catcher resistance to corium inflow. Differing from past reactor core designs, the presence of these tubes could lead to coherent corium jets impinging on the core-catcher surface. In the past, numerous studies dedicated to thermal ablation of a solid by a jet have been carried out to characterize the maximum ablated depth. Although these experiments are very valuable at a macroscopic scale, they do not give information about the local physical phenomena governing heat transfer and melting. Keeping this final goal in mind, this study followed a R&D methodology based on an analytical situation using simulant materials enabling direct visualization. In this paper, the ablation of an ice block by an immersed water jet and a free surface jet are investigated in conditions shown to be close to the reactor case. Associated to the experimental part, CFD simulations of these tests are performed to validate the calculation methodology (mesh, turbulence models and interface melting…).
In this paper, the physical analysis of the heat transfer at jet impingement and in its vicinity is characterized for immersed jet conditions.

KEYWORDS
RNR Na, core-catcher, jet ablation, experiment, simulation, CFD

1. INTRODUCTION

As part of the ongoing drive to improve nuclear reactor safety, innovative concepts are being proposed for 4th generation nuclear reactors. Among these nuclear reactor concepts, those with a fast neutron spectrum are not in their maximum reactive neutron configuration, and may experience further reactivity insertion. To cope with this situation, in the event of a hypothetical severe accident (i.e. in the case of a core meltdown configuration), innovative mitigation designs have been developed. During the ASTRID project (Advanced

[1] Corresponding author

Sodium Technological Reactor for Industrial Demonstration), which was a liquid sodium-cooled fast reactor demonstrator, transfer tubes (or mitigation tubes - Figure 1) were installed inside the core to transfer molten fuel (and hence corium) outside the core to the lower plenum [1]. Corium accumulation and compaction in the core is thus prevented, but these devices entail other safety issues. Indeed, as can be seen from Figure 1, the mitigation tubes positioned in the core pass through diagrid with a small section restriction. In the case of a hypothetical severe accident, this new core design leads to the arrival of a coherent jet of very hot corium onto the core-catcher. This issue was not relevant for previous Sodium Fast Reactor (SFR) designs, for which the corium did not have a preferred path and all the more fragmented in contact with the sodium, leading to scattered debris bed as its arrival in the lower plenum was diverted.
This new design raises a new issue: the thermomechanical resistance of the core-catcher to the potential impact of this jet. To study this problem in the most penalizing case for safety, a coherent liquid steel jet is considered without fragmentation, which would be due to the boiling of sodium at its interface, and without the formation of a possible crust reducing thermal transfers.

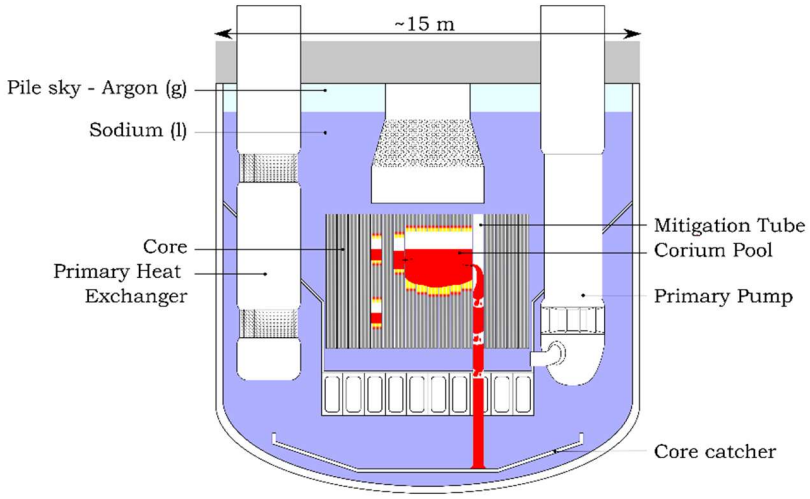

Figure 1: Accidental scenario and corium discharge through mitigation tubes

This issue was recently tackled in the framework of ESFR-SMART and ESFR-SIMPLE European projects [2][3]. Two prototypical experiments were conducted in KIT with the JIMEC facility [4][5] where a 1 ton metallic melt, produced by thermite reaction, impacted an instrumented cylindrical formed stainless steel block (thickness, 416 mm and diameter,425 mm). In these tests, the metallic melt had the same composition as the metallic test substrate. Indeed, as explained by Lecoanet [6], this configuration, which does not lead to the formation of a thermally protective solid crust at the interface (like it would have been the case with oxide fuel impacting a metal core-catcher), results in maximum ablation of metal core-catcher.
Under these macroscopic conditions, it is difficult to investigate in detail the local phenomenology of the interaction of the hot jet with the metal, which results in its thermal ablation. That's why, as part of these European projects, it was also decided to carry out small-scale laboratory experiments with simulating materials, with proven representativeness. In this context, instrumented experiments involving the impact of a free surface water jet on a block of ice were carried out [7][8]. The ranges of the dimensionless numbers characteristic of this problem are given in Table 1. For comparison, these numbers are also given for a hypothetical case of a severe accident on an SFR such as ASTRID.

	Experimental HAnSoLO set up	Severe Accident case
Reynolds : Re_j	1.2×10^4 - 1.5×10^5	$\sim 10^6$
Prandtl : Pr_j	2.5 – 5.5	~ 0.1- 0.6
Melting : B	0.3 – 0.9	~ 0.25- 0.95

Table 1: Dimensionless numbers

This table shows that the Reynolds range of the hot fluid impacting, defined as $Re_j = \frac{D_j V_j}{\nu_j}$ where ν_j is the cinematic viscosity of the jet, D_j its diameter and V_j its velocity evaluated at the nozzle exit, is one order of magnitude less than in severe accident circumstances but the fluid flow remains turbulent in both cases (i.e. the transition to turbulence for a jet is considered to be $Re_j > 4\,000$ [9]). Furthermore, the range of the melting number B is well covered. This number stands for the ratio between the energy supplied by the jet to the energy required to bring the solid to its melting temperature and melt it:

$$B = \frac{c_{p,j}\,(T_j - T_m)}{L + c_{p,s}\,(T_m - T_{s,ini})}$$

where j stands for jet, s for solid, m for melting and ini for initial. c_p and L are the specific and latent heat respectively. Scaling is discussed in detail in [6]. But, Table 1 raises the point that, using water/ice to simulate corium on a metal core-catcher, the main representativeness issue is about the range of fluid Prandtl number Pr_j which is more than unity for water and less for liquid metal /corium. This influences the thermal and dynamic boundary layer behaviors and will have some consequences on heat transfer between the jet and the solid. Li et al. [10][11] studied numerically the ablation by a free-surface jet with the reactor case material, using a particle method, showing an ablation dynamic quite different from what was observed for the water–ice case.

However, as the main advantage of water/ice experiments is that they allow visualization of the ablated interface evolution, this fluid was selected for tests aiming at better understanding the ablation phenomenology. The experimental water/ice set-up HAnSoLO is widely described in [7] for free surface jet. Interpretation of the results enabled us to distinguish two flow regimes, and hence heat transfers: the film regime, occurring when only a liquid film flows to the bottom of the cavity created by ablation, and the pool regime when this cavity is filled with water. Based on previous results [12-15], the phenomenology characteristic of both the regime change at jet impact (where heat transfer is maximal) and heat exchange along the wall (which determines the shape of the cavity) has been physically explained and correlated [4] [6-8]

As it is not possible to guarantee the representativeness of these heat exchanges for $Pr_j < 1$, a numerical approach was pursued. On the strength of the predictivity of CFD simulation tools whatever the Prandtl number, the validation of a CFD solver on a water/ice case is performed before using this solver for steel liquid jet on a metal core-catcher. To follow this methodology and to ensure the validity of the calculation results, the simulated configuration is of increasing complexity. Due to the very high complexity of simulating a turbulent jet impacting with ablation of the wall and its free surface with the surrounding air, the study began with an immersed jet. Furthermore, regarding safety issue, the case of an immersed jet is another limiting case, when liquid corium is already on the core-catcher or when the pool-effect is reached. To validate these initial simulations, the experimental set-up HAnSoLO has been adapted to immersed jets by [16] (Figure 2) in order to obtain an experimental database for validation. 20 immersed jet tests with a diameter of 6 mm and an initial jet/ice height of 10 mm were carried out with initial temperatures and speeds of: $V_j \in \{1.1, 2.5, 5.0, 7.5, 10.\}$ m/s & $T_j \in \{30, 50, 70\}$ °C

This experimental work led to local investigation (Figure 3), particularly at the stagnation point. We estimated the melt velocity, which led to the first establishment of a macroscopic heat transfer correlation at immersed jet impact in a form based on a literature review [16]. A macroscopic heat transfer correlation was proposed, where Nu is the Nusselt number:

$$Nu_0 = Nu(r=0) = Nu_0 = 0.054\,exp\left(-0.0775\,\frac{y_0}{D_j}\right) Re_j^{0.65}\,Pr_j^{0.73}\,\frac{\ln(1+B)}{B} \qquad (1)$$

with $y_0(t)$ the depth of the cavity at the stagnation point.

Heat transfer and ablation velocity (local velocity of the cavity surface) were characterized at the stagnation point by picture analysis (i.e. during cavity formation).

Moreover, the results of these experimental tests enabled to carry out local analysis of the ablation dynamics, investigating why the shape of the obtained cavity features a shoulder.
An empirical law giving the evolution of depth as a function of time has been derived from the previous law on Nu_0:

$$\frac{y_0(t)}{D_j} = \frac{1}{0.0775} \ln\left(\frac{4.18 \times 10^{-3}\, B\, \lambda_j Re_j^{0.65} Pr_j^{0.73}}{\rho_s D_j^2 c_{p,j}} \frac{\ln(1+B)}{B} t + 1\right) \quad (2)$$

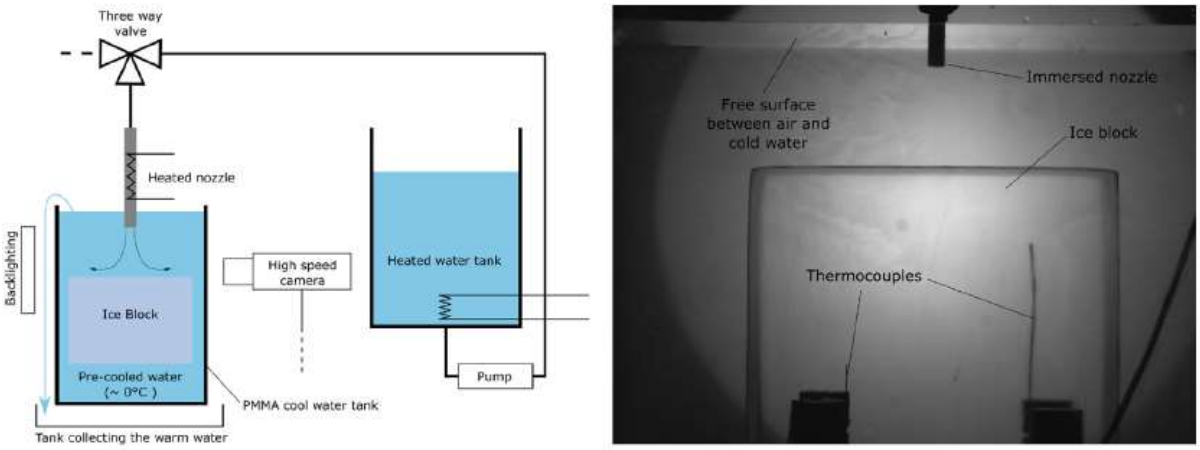

(a) *HAnSoLO* for immersed jets. (b) Picture from the high-speed camera.

Figure 2: (a) HAnSoLO set up for immersed jets and (b) high speed camera visualization at the initial time [16]

Finally, in this paper, we present the preliminary validation of the CFD code OpenFOAM® on the simulated ablation obtained in two experimental tests ($Re_j = 11.6\,10^3$ and $Re_j = 26.10^3$). Validation of the simulation methodology for a non-melting case is first presented, taking jet turbulence into account, followed by a discussion on the ablation results at jet impact.

2. PRELIMINARY RESULTS : IMMERSED JET WITHOUT MELTING

In the solver OpenFOAM® "buoyantPimpleFoam" [17], which is devoted to non-isothermal turbulent flow undergoing buoyancy, the LES approach has been selected to simulate ablation by an immersed jet. With reasonable calculation costs, it enables better resolution of near-wall turbulence and heat transfer. The LES approach also makes it possible to simulate fluctuating and unsteady flow. First, a study of the problem without melting is carried out with validation on literature results in order to ensure the validity of the methodology (turbulence resolution according to the initial jet turbulence model, which influences melting, mesh size and boundary conditions…).
The parameters for the considered case are a $Re_j = 11.6 \times 10^3$ (i.e. V_j = 1.1m.s^{-1}) and Pr = 3.55 (i.e. T_j = 50°C), corresponding to experiment with the lowest Re_j value in order to reduce the simulation time. At this Reynolds level, the flow is fully turbulent at the jet exit.

2.1 Initial jet turbulence

To generate a realistic fluctuating velocity field at the jet output, without performing a preliminary DNS for the establishment of flow in the tube, two methods are considered: Divergence-Free Synthetic Eddy Method (DFSEM) and Forward-Stepwise Method (FSM).
The Divergence-Free Synthetic Eddy Method [18] consists in generating velocity fluctuations, or eddies/turbulent structures, and superimpose them on the mean velocity on the inlet of the tube. This method considers as input parameter the mean velocity field, the Reynolds tensor and the local turbulent

characteristic scale (which is derived from the turbulent kinetic energy and the turbulent energy dissipation rate) on the inlet surface.

The concept of Forward-Stepwise Method [19] is to use a filter to obtain a velocity field from random signals with the desired turbulence statistics. Like the DFSEM, the FSM takes as input turbulent statistics, namely the mean velocity profile and the components of the Reynolds tensor. These data could be obtained from a RANS simulation of the jet established in the tube. RANS simulation of a velocity flow, similar to that imposed experimentally, is carried out in a 6mm tube, $40D_j$ long, with a no-slip wall condition to ensure fully developed turbulent flow [9].

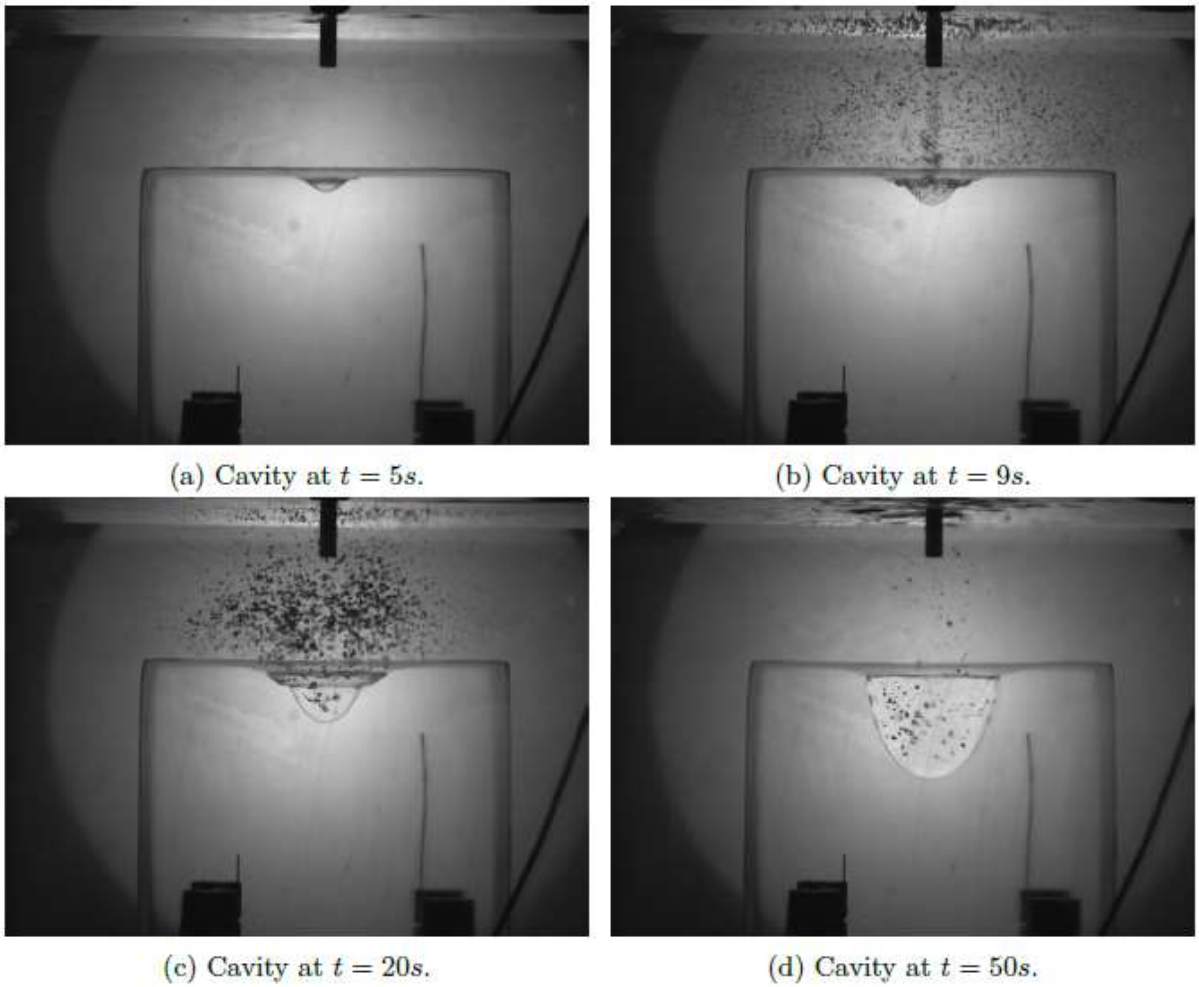

(a) Cavity at $t = 5s$. (b) Cavity at $t = 9s$.

(c) Cavity at $t = 20s$. (d) Cavity at $t = 50s$.

Figure 3 : Evolution of cavity shape from high-speed camera visualization (V_j = 5 m s−1 - $Re_j \sim 5.3 \times 10^4$ and T_j = 323 K – Pr_j = 3.55) [16]

Sensitivity studies on radial mesh refinement and the size of the first mesh cell at the wall as well as the turbulence model considered for the RANS calculation were carried out. The RANS calculation (models standard k- ε [20], realizable k-ε [21] and k-ε RNG [22] and their associated wall law) have been carried out with sensitivity studies to radial mesh refinement and the size of the first wall mesh and turbulence model. These results have been compared with DNS studies giving fluctuating radial velocity profiles at the nozzle outlet [23]. The influence of the turbulence model was less than that of the mesh, and a mesh such as $y^+ = 6.1$ (y^+ is the dimensionless size of the first mesh cell at the wall) provided initial data for the DFSEM and FSM. For the FSM, whose characteristic length is more complex to determine than that used in the DFSEM, a study concluded that the simulation considering an anisotropic reference length with $L_{u,x} = L_{u,y} = 10^{-3}$m and $L_{u,z} = 10^{-4}$m led to a Reynolds stresses tensor very close to the desired

tensor. This suggests that velocity fluctuations are correlated more with each other in the x-y plane than along the z axis.
Based on this data at the nozzle outlet, a simulation of a jet impinging a plate but without melting was carried out to validate the heat transfers.

2.2 Validation of heat transfer at jet impingement on a solid wall

A turbulent velocity field is imposed at the inlet of the domain either by the DFSEM or FSM method. The mesh used is three-dimensional (and not 2D axisymmetric, to catch 3D phenomena).
A half-cylinder is used for the domain to halve the calculation cost. The domain and boundary conditions considered for the impinging immersed jet are shown in Figure 4. The axis of the jet is placed at r = 0 and its height is 10 D_j.

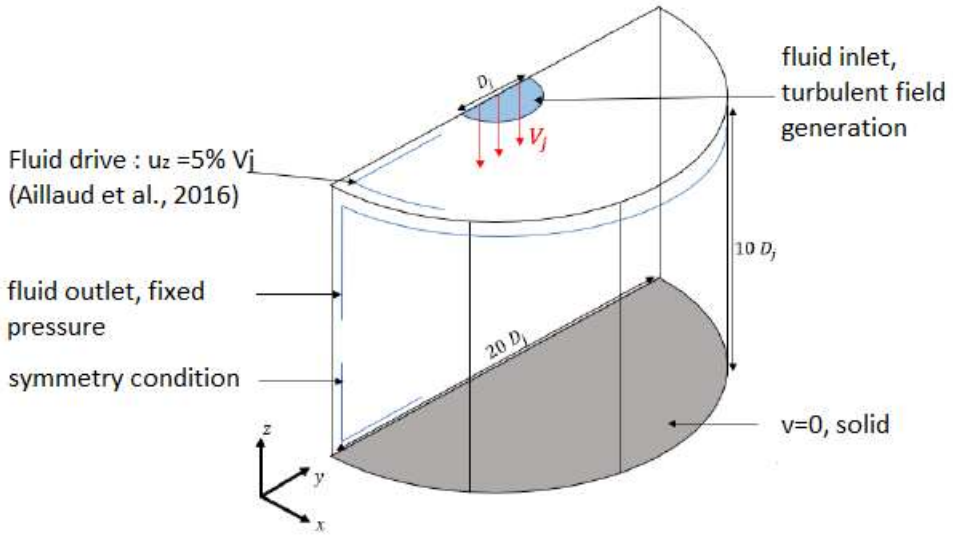

Figure 4: Domain and boundary conditions for immersed jet

In order to simply model fluid entrainment around the nozzle with negligible influence on jet dynamics, Aillaud et al. [24] suggest the use of a fixed velocity condition $u_z = 0.05V_j$. The pressure is fixed at the atmospheric pressure at the outlet surface, located far enough from the jet to reduced boundary influence. A constant heat flow condition is imposed on the bottom surface to derived Nusselt number. Simulations are performed using a LES (large Eddy Simulation) approach, with the WALE (Wall Adapting Local Eddy viscosity) model for turbulence [25]. This approach, which leads to a more realistic prediction of near-wall turbulent quantities, imposes mesh constraints. The characteristic cut-off length of the filter used in the LES approach corresponds to the mesh size, which must correspond to the turbulent Taylor scale length so that dissipative scales are filtered, and inertial scales are resolved. Estimates of turbulent scales have led to the definition of a progressive axial mesh of $N_z = 340$ cells and a wall cell size such that $z_1^+ = 0.001D_j$ (z_1^+being the dimensionless cell size, in the z direction). Sensitivity to mesh refinement confirmed these estimates, and results consistent with those of Lee and Lee [26], who obtained Nusselt profiles as a function of radial distance from the stagnation point for values of Re_j between 1.0×10^4 and 3.0×10^4, were obtained for $N_z \geq 500$ cells and $z_1^+ \leq 0.002D_j$. The mesh used for the simulations contains up to around 5×10^6 cells; a simulation requires around 10^5s using 192 processors.
Sensitivity to the methods of establishing turbulent fluctuations at the jet outlet has been carried out.
In order to characterize these fluctuations, the maximum of mag(Rij) defined as $mag(R_{ij}) = \sqrt{\sum_{i,j} {R_{ij}}^2}$ (magnitude of the Reynolds stresses tensor) is closer to the Lee & Lee experiments in the FSM simulation than in the DFSEM simulation (Figure 5). Mixing-induced turbulence reaches the

center of the jet at a shorter distance from the nozzle outlet in the FSM simulation (Figure 6 left). The literature review [27] indicates that the mixing-induced turbulence should reach the center of the jet at a distance from the nozzle of $\sim 5D_j - 6D_j$. The behavior observed for the DFSEM method is therefore consistent unlike the FSM method.

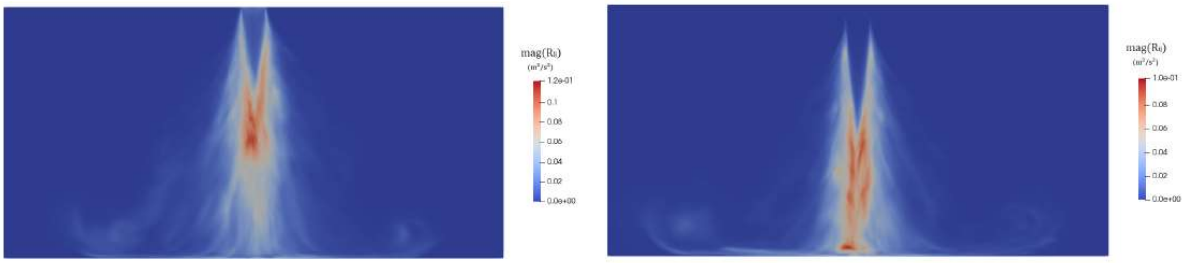

Figure 5: Mag(R_{ij}) obtained by FSM (left) and DFSEM (right) methods (related legend on the right)

Since the maximum fluctuations occur further from the wall in the FSM simulation, there is a decrease in transfer to the wall compared with the DFSEM simulation. This is confirmed by the evolution of the Nusselt numbers along the heated wall (obtained in our simulation for $Re_j = 11.6 \times 10^3$) with the results of Lee and Lee (obtained at $Re_j = 1.0 - 1.5 \times 10^4$) (Figure 6- right). The results presented in Figure 6 also show that results obtained without considering turbulent fluctuations (labelled "uniform") at the jet outlet lead to underestimate the potential core length and the heat flux extracted at the wall. Predictive simulation of the turbulence that develops in the jet, due to its stagnant fluid environment, is essential, but is not sufficient to correctly simulate wall heat transfer; the turbulence of the flow at the jet outlet must be simulated. It is demonstrated that the use of a uniform velocity field at the nozzle outlet produces results far from those found in the literature.

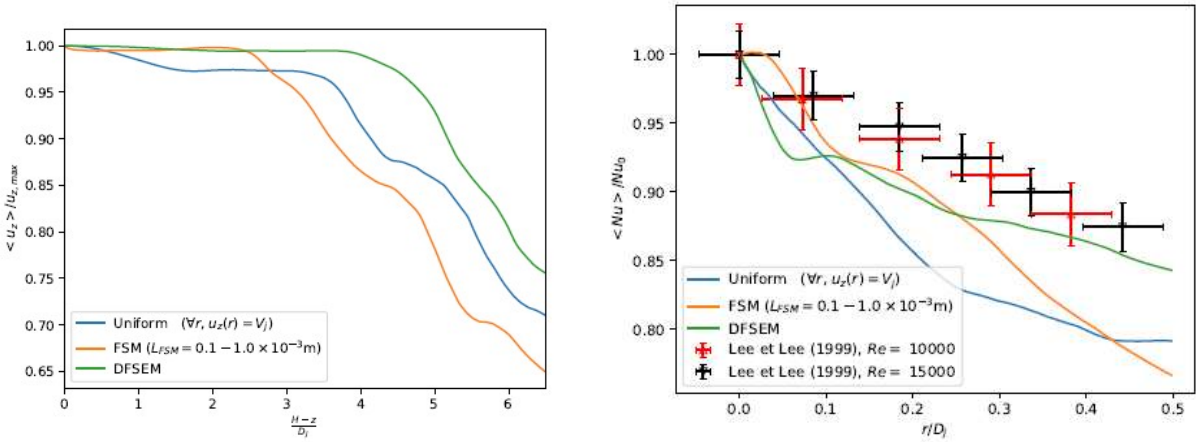

Figure 6 : $\frac{\langle u_z \rangle}{u_{z,max}}$ at the jet center along the height (left), $\frac{\langle Nu \rangle}{Nu_0}$ along the solid plate (right)

3. NUMERICAL RESULTS FOR IMMERSED JET ABLATION

The simulation parameters obtained in the previous preliminary study for the case without melting are applied to simulations with ablation. It requires much more numerical resources. The DFSEM method has been selected and the results are compared with the experimental results obtained on HAnSoLO.

3.1 Liquid/solid interface simulation method: enthalpy - porosity

To simulate the liquid/solid interface motion induced by thermal ablation, the enthalpy-porosity approach proposed by Voller and Prakash [28] is used. This method was developed to simulate the melting or

solidification of a non-pure material (typically an alloy) using a fixed mesh. It consists in describing the liquid-solid system with a presence volume fraction g_l such that g_l= 1 in the liquid and g_l = 0 in the solid. The principle is similar to the VOF method with the g_l fraction controlled by temperature. In this method, considering a single fluid with two phases characterized by the function g_l, the balance equations for momentum and enthalpy are solved with additional source terms, to consider the energy associated with the phase change for the enthalpy equation, and friction in a porous medium (according to Darcy's law) for the momentum equation. This term in the momentum equation is such that $S_m = -A\,v$ with v the velocity and A a coefficient, which derives from the Carman-Kozeny equation, and can be written in the following form:

$$A = C_{voller}\frac{1-g_l^2}{g_l^3+\varepsilon} \quad (3)$$

With C_{voller} representing the porous terms magnitude, which cancels out the velocity in the solid, and ε a numerical residue to avoid division by zero.

This method, adapted by Brent et al. [29] for a pure material in OpenFOAM, is used for these simulations. It is worth noting that this method does not consider the density jump at the liquid/solid interface. In a recent work, Faden et al. [30] obtained a formulation with the density jump, but this formulation is not yet available in OpenFOAM.

3.2 Simulation domain

The simulation domain is close to that the one considered for simulations without ablation, with an additional finely meshed solid domain (with respect to the turbulent scale of the fluid) to be sufficiently resolved when fluid enters this domain (Figure 7). As in the experiments described by Avrit et al. [16] (with evaluation of associated uncertainties), the initial temperature of the stagnant fluid is $277.15K$ ($T_{melting} + 4K$) and a linear temperature profile along z is initially applied to the ice between 271K and 273.15K.

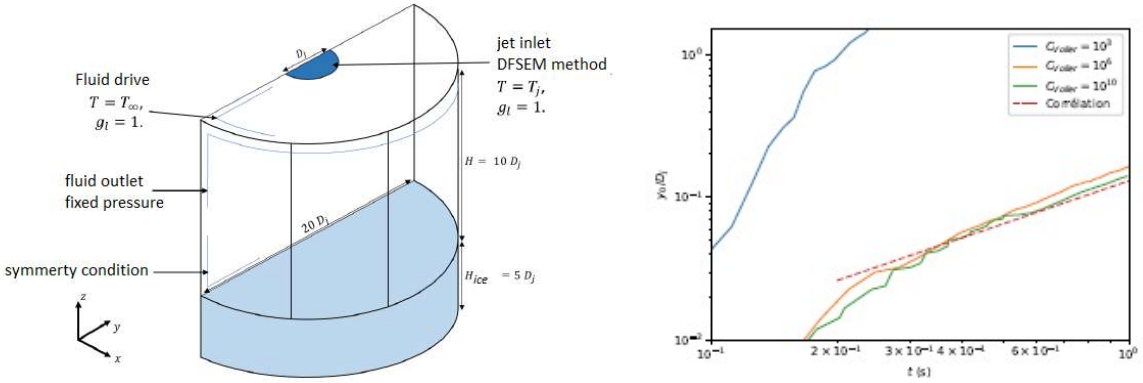

Figure 7 : Simulation domain (left), sensitivity to C_{voller} (right)

Voller and Prakash recommend $C_{voller} = 1600$ to simulate the solidification of an alloy presenting a mushy zone between its liquidus and solidus temperature. As water is a pure material, three different C_{voller} values were tested: 10^3; 10^6, 10^{10}. The ablated depth is extracted from the g_l field, assuming that the solid-liquid boundary is at g_l= 0.5. Figure 7 (right) shows the curves of the evolution of $\frac{y_0}{D_j}$, where y_0 is the localization of the interface solid/liquid at the stagnation point for the different C_{voller} values considered. The curve at $C_{voller} = 1000$ is extremely distant from the rest of the results which are converged. The correlation on $\frac{y_0(t)}{D_j}$ (eq. (2)), issued from the experimental work, is also plotted in Figure 7, and is the reference curve for low ablated depths, since the first experimental points are only obtained for t > 2s. The simulation results obtained for $C_{voller} > 10^6$ are consistent with the correlation. Based on these results, $C_{voller} = 10^{10}$ is used in the following simulations.

3.3 Results and Comparisons

Two experimental tests were simulated. For the first, the conditions remain unchanged: $Re_j = 11.6 \times 10^3$ (i.e. $V_j = 1.1\text{m.s}^{-1}$) and $Pr_j = 3.55$ (i.e. $T_j = 50°\text{C}$). For the second, the Reynolds number and thus the jet velocity is increased ($e_j = 26.0 \times 10^3$; $V_j = 2.5\text{m.s}^{-1}$). For this second case, the turbulent lengths were re-calculated to build the mesh accordingly.

First case: $Re_j = 11.6 \times 10^3$

The instantaneous temperature field T at different time are shown in Figure 8, to provide visualizations of the jet and ablation obtained by numerical simulation.

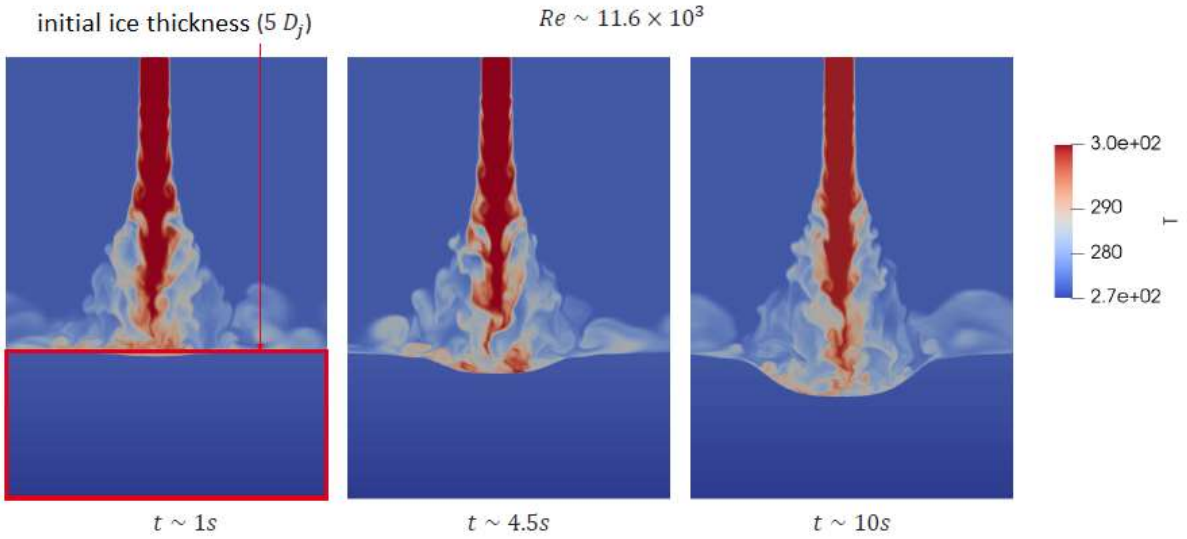

Figure 8: Temperature evolution in the simulation of the experimental test $Re_j = 11.6 \times 10^3$

The instantaneous temperature field enables instantaneous visualization of the jet, and observation of both mixing with the ambient fluid and the resulting temperature reduction as it moves away from the nozzle outlet. The solid-liquid boundary is well defined by the rapid temperature change in this region, particularly along the jet axis. The potential core can also be seen in Figure 8: the temperature remains constant at the center of the jet over a length consistent with literature ($\sim$ 5-6D_j) before mixing-induced turbulence reaches the center of the jet.

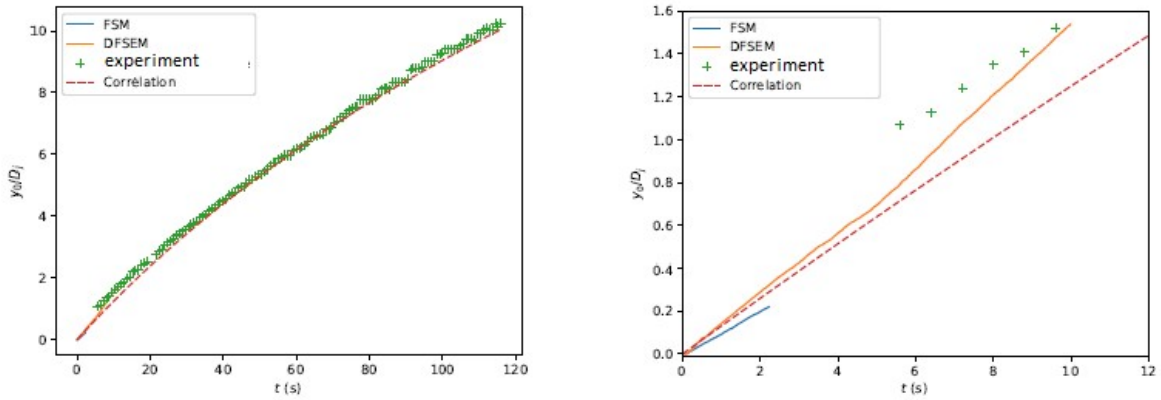

Figure 9 : Ablation depth at the stagnation point (zoom at low instant on the right) $Re_j = 11.6 \times 10^3$

The depth at the stagnation point is the most important data for the study of jet ablation, since it corresponds to the maximum ablation depth. Figure 9 shows the evolution of the cavity depth at the stagnation point and

compares the results of simulations (with DFSEM or FSM) with the experimental results and the correlation (eq. (2)), established from these results but allowing their domain to be extended to very low time (t < 6 s). As already observed, heat transfers are largely underestimated at the stagnation point using the FSM method. These calculations were not continued. In the case of simulation with the DFSEM method, we observe very good agreement of the ablation curve with the experimental points, and the correlation curve, even over the long term.

A good agreement is observed between the cavity shape obtained numerically and the experimental shape (**Figure 10**) at two different times. The same change in slope is observed around $\frac{r}{D_j} = 2.5$, which can be investigated by observing simulated local flows.

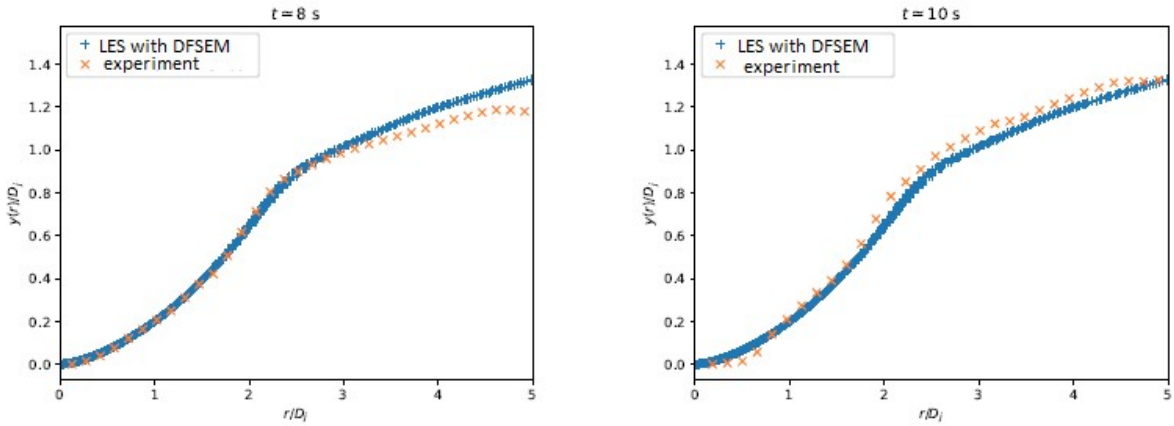

Figure 10: No dimensional localization of solid/liquid interface –Cavity profile -$Re_j = 11.6 \times 10^3$

Second case: $Re_j = 26.0 \times 10^3$

Because of the long computation time required for these high-Reynolds simulations ($\sim 10^6$ CPU hours), only 3s of transient were simulated.

The instantaneous temperature field and the cavity profile at 2.5 s are shown in **Figure 11** to visualize the jet and ablation obtained by numerical simulation.

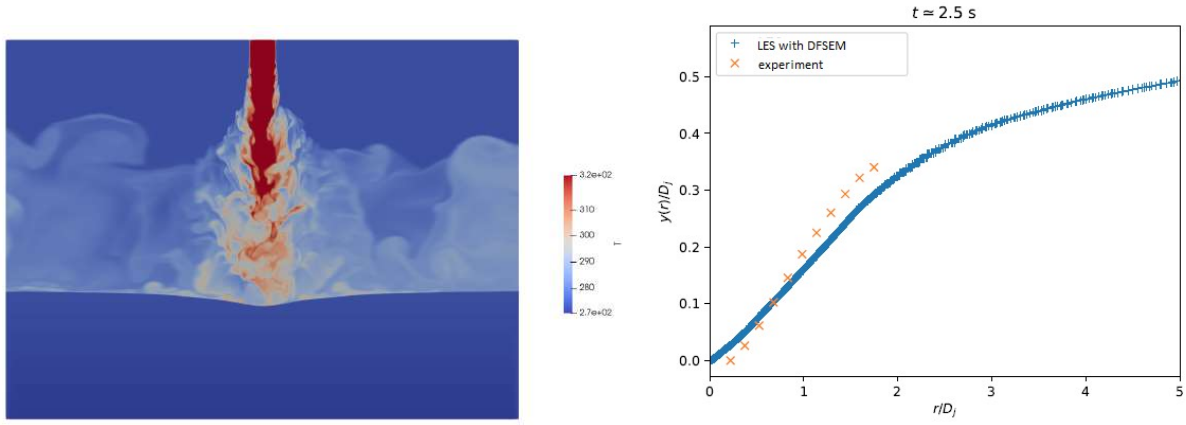

Figure 11 : Instantaneous temperature fields (left) and cavity profile (right) at t=2.5s $Re_j = 26.0 \times 10^3$

Once again, we can observe the jet and cavity formation, as well as the potential core region for which the temperature does not decrease at the center of the jet. Jet mixing is more intense than in the previous case at lower Reynolds. There is an acceptable agreement between the two cavity shapes shown. As the cavity shape detection algorithm (for the experimental shape) is less accurate at low ablated depths, only a low

number of points and a low radial extension are available for the experimental contour. However, there is still a cavity shape with an inflection point.
The ablation curve obtained by simulation, superimposed on the experimental points and the correlation (eq. (2)), is shown in the Figure 12 for the first instants. Once again, the curve obtained by simulation agrees very well with the results obtained from experiments.

4. CONCLUSIONS AND PERSPECTIVES

This experimental and numerical work are part of the design of mitigation devices defined in case of the hypothetical severe accidents in sodium fast reactor of ASTRID style. Indeed, the final aim of this work is to improve the safety of sodium-cooled fast reactors (RNR-Na). New devices are being studied for introduction into the core to mitigate potential reactivity insertions in the event of severe accidents with core meltdown.

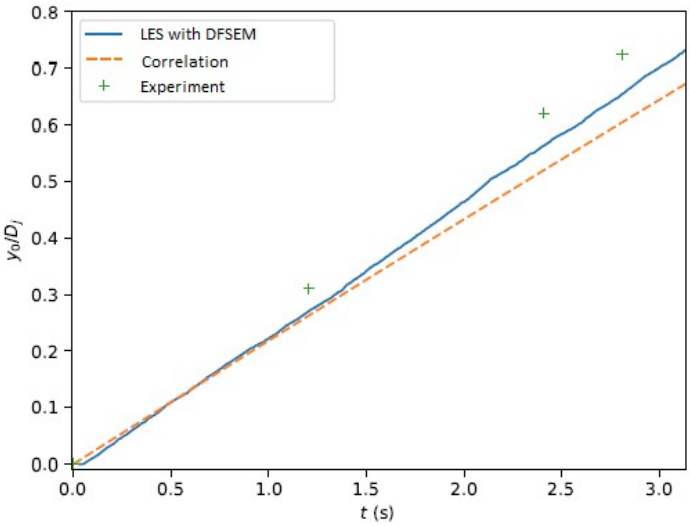

Figure 12 : Ablation depth at the stagnation point - $Re_j = 26.0 \times 10^3$

One of these devices uses transfer tubes to discharge corium (molten core and structural materials) directly onto the core-catcher, raising a new safety issue: the core-catcher's resistance to thermomechanical due to the ablation consecutive to the impact of a corium jet at ~2,000-3,000 K. In order to size this core-catcher accordingly, experiments were carried out with simulating materials (water/ice) under representative conditions on the HAnSoLO (Hot AblatioN of a Solid by a Liquid - Observations) facility. The new results have enabled to model ablation phenomenology on a local scale and derived a correlation of the evolution of the cavity depth at the stagnation point. Numerical simulations on a local scale (CFD) completed this study to take into account the representativeness bias due to the low Prandtl of the corium in relation to those of water. As part of a progressive approach, immersed jet experiments were carried out and simulated using OpenFOAM® code . A LES (Large Eddy Simulation) approach with the WALE (Wall Adapting Local Eddy viscosity) model was used to simulate turbulent jets. Studies were carried out to select the mesh consistent with the assumptions of this approach. The method DFSEM (Divergence-Free Synthetic Eddy Method) demonstrated its ability to deliver turbulent fluctuations at the nozzle outlet. Simulations of immersed jets impinging a solid without melting have been validated on experimental results. Based on these results, the ablation of the impacted wall was simulated using the enthalpy-porosity method. Simulation results are close to those observed experimentally for the two values of Re_j considered (Re_j = 11.6×10^3 and $Re_j = 26.0 \times 10^3$). The OpenFOAM® code has therefore been validated for the case of immersed jet ablation.
Subsequently, in order to extend this validation to the case of a liquid water jet in air, an interface tracking method will be selected to simulate the water/air interface. Free surface jet test simulations will be validated

on free surface jet experimental results obtained using HAnSoLO in a similar way to the work already carried out for immersed jet. Once these free surface jet simulations will have been validated, simulations of steel jets impinging a steel structure will be carried out at low jet Prandtl numbers. The enthalpy-porosity method will have to be revised to simulate the melting of this non-pure material.

ACKNOWLEDGMENTS

The ESFR-SIMPLE project is funded by the European Union under Grant Agreement 101059543. Views and opinions expressed are however those of the authors only and do not necessarily reflect those of the European Union. The European Union can't be held responsible for them.

REFERENCES

1. Bachrata, A., Bertrand, F., Marie, N., Edeline, A., Kubota, R., Kamiyama, K., Kubo, S., Severe accident studies on the efficiency of mitigation devices in a SFR core with SIMMER code. *Nucl. Eng. & Des*. **373**, 111037 (2021).
2. Mikityuk, K., Girardi, E., Enrico, Krepel J. et al., ESFR-SMART: new Horizon-2020 project on SFR safety, *Conference: FR17*, Yekaterinburg, Russian Federation, IAEA-CN-245-450 (2017).
3. Sciora, P., Mikityuk, K., Bonzom P.V., Fridman E., Bubelis E., et al.. ESFR-SIMPLE: new HORIZON-EURATOM project on SFR safety. *ICAPP 2023*, Gyeongju, South Korea. 1471 (2023).
4. Lecoanet, A., Gradeck, M., Gaus-Liu, X., Cron, T., Fluhrer, B., Payot, F., Journeau, C., Rimbert, N., Ablation of a solid material by high temperature liquid jet impingement: an application to corium jet impingement on a SFR core-catcher. ASME *J. Nuclear Radiat. Sci*. **8** (1), 011308 (2022).
5. Tromm, W., Gaus-Liu, X. KIT-JIMEC experiments to investigate jet impingement on the ablation of core catcher bottom. *In NENE30 Conference*, Bled, Slovenia (2021).
6. Lecoanet, A., Payot, F., Journeau, C., Rimbert, N., Gradeck, M., Study of the ablation consecutive to jet impingement on a meltable solid, Application to SFR core-catcher. *Nucl. Eng. Des*. **377**, 111147, (2021).
7. Lecoanet, A., Payot, F., Journeau, C., Rimbert, N., Gradeck, M. Classification of ablation mode during impact of hot liquid jet on a solid. *Int. J. Heat Mass Transfer* **181**, (2021)
8. Lecoanet, A., Gradeck, M., Payot, F., Journeau, C., Seiler, N., Rimbert, N., Nuclear Engineering and Design **414**, 112591 (2023).
9. Lienhard, J. H. V., Heat Tansfer by Impingement of Circular Free-Surface Liquid Jets, *18th National & 7th ISHMT-ASME Heat and mass transfer* conference IIT Guwahati, India (2006).
10. Li, G., Liu, M., Wang, J., Chong, D., Yan, J., Crust behavior and erosion rate prediction of EPR sacrificial material impinged by core melt jet. *Nucl. Eng. Des*., **314**, 44–55 (2017).
11. Li, G., Liu, M., Wang, J., Chong, D., Yan, J., Numerical study of thermal erosion behavior of RPV lower head wall impinged by molten corium jet with particle method. *Int. J. Heat Mass Transfer*, **104**, 1060–1068 (2017).
12. Tien, C., Yen, Y.-C., 1965. The effect of melting on forced convection heat transfer. *Journal of Applied Meteorology* **4** (4), 523–527 (1965).
13. Griffin, O.M., Heat, mass, and momentum transfer during the melting of glacial ice in sea water. *Journal of Heat Transfer* **95** (3), 317–323 (1973).

14. Saito, M., Sato, K., Furutani, A., Isozaki, M., Imahori, S., Hattori, Y.. Melting attack of solid plates by a high temperature liquid jet – effect of crust formation. *Nuclear Engineering and Design* **121** (1), 11–23 (1990).
15. Sato, K., Furutani, A., Saito, M., Isozaki, M., Suganuma, K., Imahori, S., 1991. Melting attack of solid plates by a high-temperature liquid jet –erosion behavior by a molten metal jet. *Nuclear Engineering and Design* **132** (2), 171–186.
16. Avrit A., Lecoanet, A., Seiler, N., Rimbert, N., Gradeck, M., Ablation of a solid by an immersed jet, *Nuclear Engineering and Design* **414**, 112590 (2023)
17. Greenshields C., OpenFOAM v10 User Guide, July 2022. Section : OpenFOAM v10
18. Poletto, R., Craft, T., Revell, A., A New Divergence Free Synthetic Eddy Method for the Reproduction of Inlet Flow Conditions for LES, Flow, *Turbulence and Combustion*, **91**, 519–539 (2013).
19. Kim, Y., Castro, I.P., Xie, Z.T.,Divergence-free turbulence inflow conditions for large-eddy simulations with incompressible flow solvers, *Computers & Fluids*, **84**, pp. 56–68 (2013).
20. Jones, W. P., Launder, B. E., The prediction of laminarization with a two equation model of turbulence, *International Journal of Heat and Mass Transfer*, **15**, 301–314 (1972)
21. Shih, T.H., Liou, W W., Shabbir, A., Yang, Z., Zhu, J., A new k-epsilon eddy viscosity model for high Reynolds number turbulent flows, *Computers & Fluids*, **24**, 227–238 (1995).
22. Yakhot, V., Orszag, S.A., Thangam, S., Gatski, T.B., C. G. Speziale, C.G., Development of turbulence models for shear flows by a double expansion technique, *Physics of Fluids A : Fluid Dynamics*, **4**, 1510–1520 (1992).
23. Pirozzoli, S., Romero, J., Fatica, M., Verzicco, R., Orlandi, P., One-point statistics for turbulent pipe flow up to Re tau = 6000, *Journal of Fluid Mechanics*, **926**, A28 (2021).
24. Aillaud, P., Duchaine, F., Gicquel, L.Y.M, and Didorally, S., Secondary peak in the Nusselt number distribution of impinging jet flows : A phenomenological analysis, *Physics of Fluids*, **28**, 095110, (2016).
25. Nicoud F., Ducros F., Subgrid-scale stress modelling based on the square of the velocity gradient tensor. Flow, *Turbulence and Combustion* (1999).
26. Lee, J. and Lee, S.J., Stagnation region heat transfer of a turbulent axisymmetric jet impingement, *Experimental Heat Transfer*, **12,** 137–156, (1999).
27. Viskanta, R., Heat transfer to impinging isothermal gas and flame jets, *Experimental Thermal and Fluid Science*, **6**, 111–134 (1993).
28. Voller, V. and Prakash, C., A fixed grid numerical modelling methodology for convection-diffusion mushy region phase-change problems, *International Journal of Heat and Mass Transfer*, **30**, 8, 1709 – 1719 (1987).
29. Brent, A. D., Voller, V. R. and Reid, K. J. Enthalpy-porosity technique for modeling convection-diffusion phase change : application to the melting of a pure metal, *Numerical Heat Transfer*, **13**, 297–318 (1988).
30. Faden, M., König-Haagen, A., and Brüggemann, D., An Optimum Enthalpy Approach for Melting and Solidification with Volume Change, *Energies*, **12**, 868 (2019).

EXPERIMENTATION & SIMULATION OF SURFACE ABLATION BY A JET FOR CORE-CATHER SAFETY ISSUE

Avrit A, **Seiler N**, Lecoanet A and Djermoune A, Rimbert N., Gradeck M.

The 11th European Review Meeting on Severe Accident Research (ERMSAR2024), KTH, Stockholm, Sweden, May 13-16, 2024

Outline

1. **Introduction and context**
2. **Preliminary results : immersed jet without melting**
3. **Results of immersed jet ablation**
4. **Conclusions and perspectives**

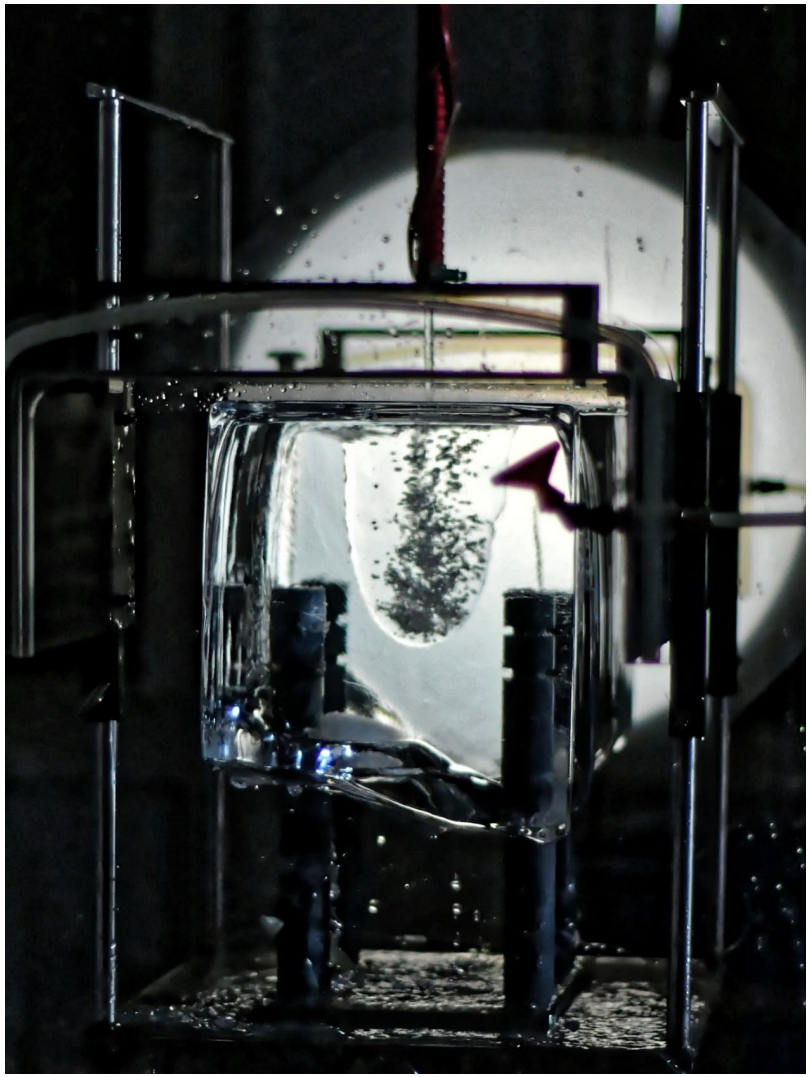

Photo credit : Simon Becker

Introduction and context (1/3)

Context: 4th Gen. Sodium Fast Nuclear Reactor safety.

Severe accident : Hypothetical case of core melting

Mitigation devices : transfer tubes in ASTRID

⇒ corium discharge (avoid recriticality)

⇒ **new safety issue** : corium jet on the core catcher

→ ablation

⇒ **core-catcher integrity : final objective of this study**

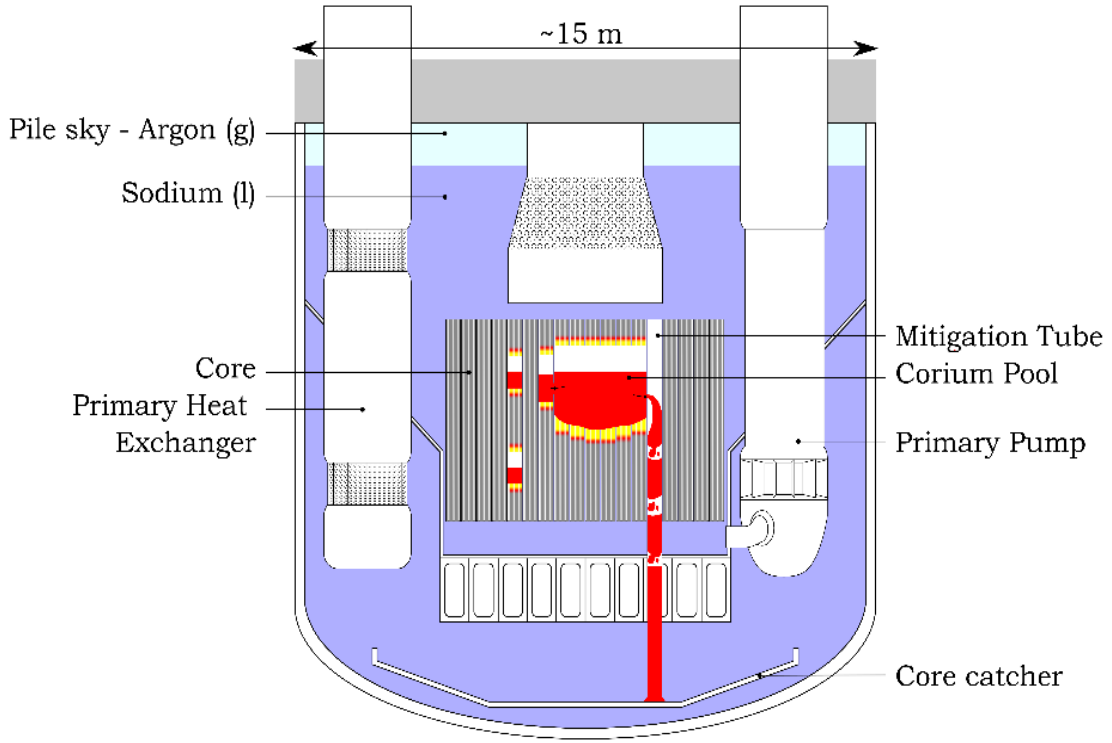

Several questions raised :

⇒ **Initial conditions** of jet and surrounding → the worst case for the safety :

assumption : coherent (not fragmented) metallic jet on a metallic core-catcher

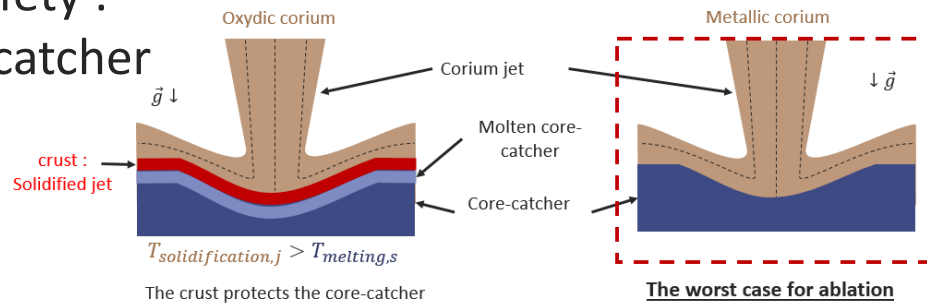

⇒ **Ablation : understanding of local phenomena, local measurements**

- **Reduced-size** mock-up with **simulating** fluid (**water** instead of steel)

→ Transposition issue to steel / reactor scale

NB: Macroscopic tests JIMEC at KIT (Tromm & Gaus-Lui, 2021)

Introduction and context (2/3)

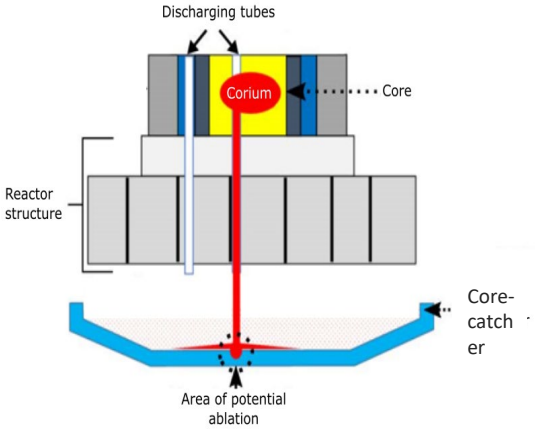

Transposition : HAnSoLO water-ice (transparent, easy to use, inexpensive).

No-dimensional numbers;

- Jet Reynolds number ***Re*** (inertia vs viscosity, Turbulence)
- Jet Prandtl ***Pr*** (diffusivity, thermal transfers)
- Melting number $\boldsymbol{B} = \frac{c_{p,j}(T_j - T_s)}{L + c_{p,s}(T_s - T_{s,init})}$ (jet energy / melting solid energy) – jet at ~3000K

	Reactor case	HAnSoLO water/ice (reduced-scale exp)	
$\boldsymbol{Re}$	$\sim 10^6$	$\sim 10^4 - 2\,10^5$	→ /10 to /100 smaller but **turbulent jets** ($Re > 4.10^3$)
$\boldsymbol{Pr}$	$\sim 0{,}1 - 0{,}6$	$2{,}5 - 6$	→ **No similarity in Pr**
$\boldsymbol{B}$	$\sim 0{,}25 - 0{,}95$	$0{,}25 - 0{,}95$	→ Similarity in B

R&D methodology :

- water-ice tests → dynamic representativity, phenomena understanding
- CFD simulations, validated on water-ice tests, in steel for themal deviation exploration

Introduction and context (3/3)

First HAnSoLO tests - free surface jet *(Lecoanet et al., 2021)*

Methodology of increasing complexity → first application on **immersed** jet (no free surface simulation)

$V_j \in \{1.5, 2.5, 5, 7.5, 10\}$ m/s
$T_i \in \{30, 50, 70\}$ °C ⇒ **15 experiments**.

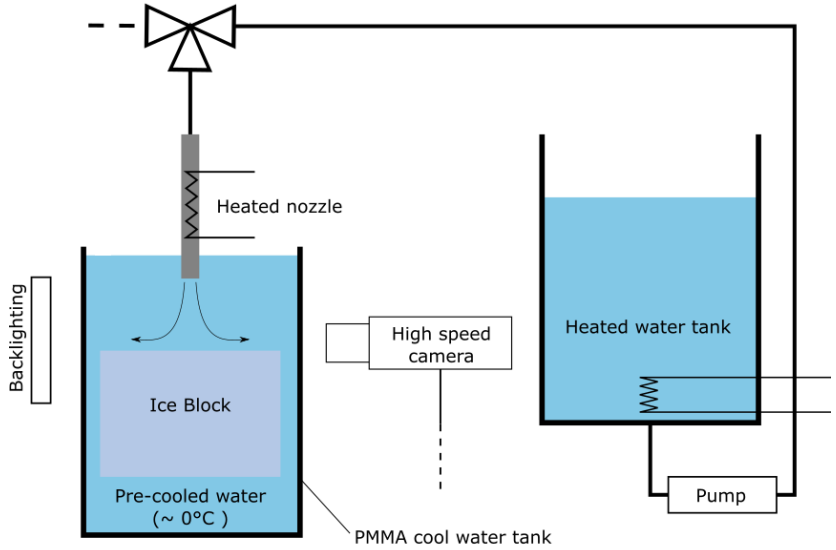

Cavity shape evolution over time with $T_j = 50\ °C$ and $V_j = 5\ m/s$

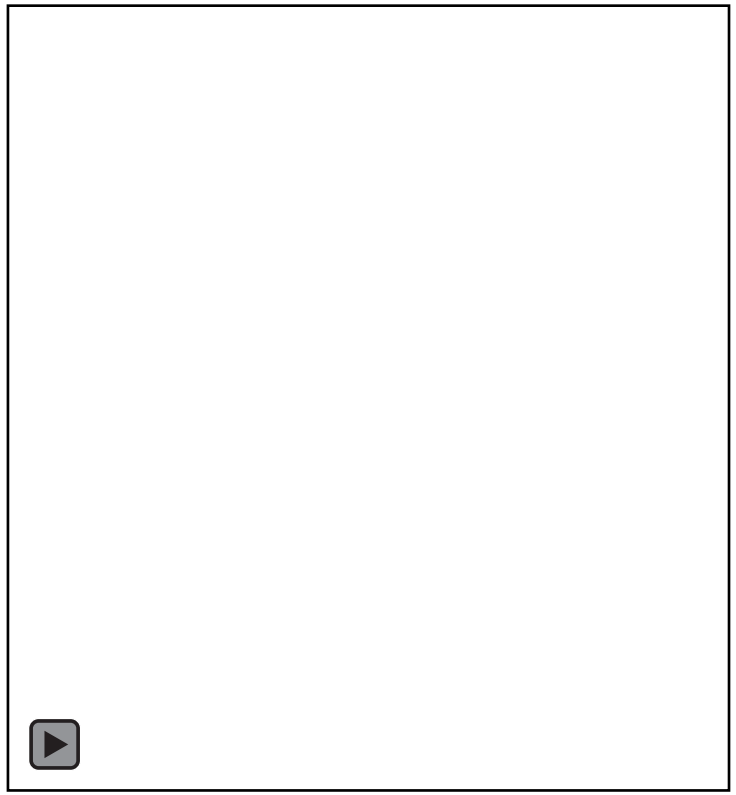

Image-treatment algorithm to rebuild the cavity shape.

Empirical law : ablation depth (y_0) at impingement & $Nu_0 \propto \frac{\partial y_0}{\partial t}$

$$\frac{y_0(t)}{D_j} = \frac{1}{0.0775} \ln\left(\frac{4.18 \times 10^{-3}\ B\ \lambda_j Re_j^{0.65} Pr_j^{0.73}}{\rho_s\ D_j^2\ c_{p,j}} \frac{\ln(1+B)}{B} t + 1\right)$$

<u>Aim of this presentation</u>: validation of CFD simulations of ablation of ice by immersed water jet (part of the methodology)

Preliminary results : immersed jet without melting (1/2)

Solver OpenFOAM® « bouyantPimpleFoam », non isothermal turbulent flow

Methodology of increasing complexity → first application on **immersed** jet (no free surface simulation)

Preliminary assessment : verification of jet thermal-hydrodynamics at impact

Turbulence traitement :

- **LES approch** (*Large Eddy Simulation*) : filtering of the equations, fine resolution of the heat transfer at the interface

→ Turbulence kinetics model: **WALE** (*Wall Adapting Local Eddy viscosity*) (Nicoud & Ducros, 1999) – near-wall precision

→ Energy Balance : **SGDH (**Standard Gradient Diffusion Hypothesis) (Mathur et al., 2023) : Pr_T=0.9

- Initialization of turbulence fluctuations at jet inlet:

→ Divergence-Free Synthetic Eddy Method **(DFSEM)** (Poletto *et al., 2013*).

Generate velocity fluctuations u_i' from turbulent stress tensor and turbulent integral scale, superimpose to $\langle u_i \rangle$

→Forward-Stepwise Method **(FSM)**(Klein *et al.*, 2003) :

Filter to obtain a velocity filed from random signal with the desired turbulence statistics.

Input data from RANS simulations (D=6mm, L=40D)

Fluctuating radial velocities profiles coherent with DNS numerical results of Pirozzoli et al, 2021

Preliminary results : immersed jet without melting (2/2)

Verification of the **heat transfer at impingement** according to the simulation of the turbulence at the inlet of the developed jet :

$Re \sim 11.6 \times 10^3$

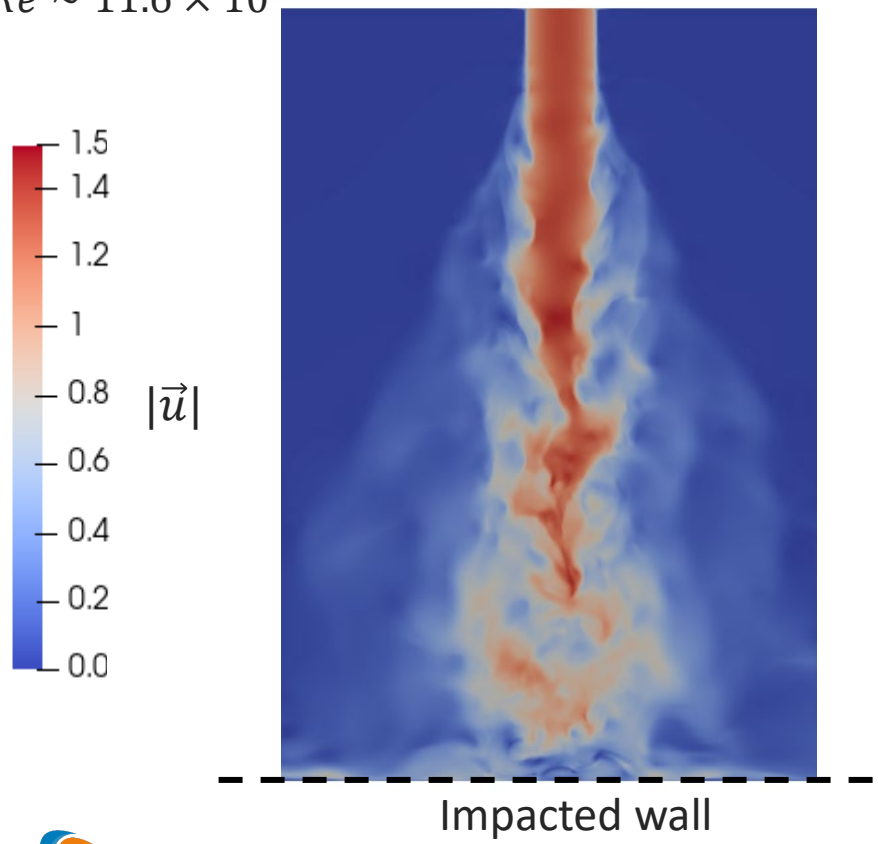

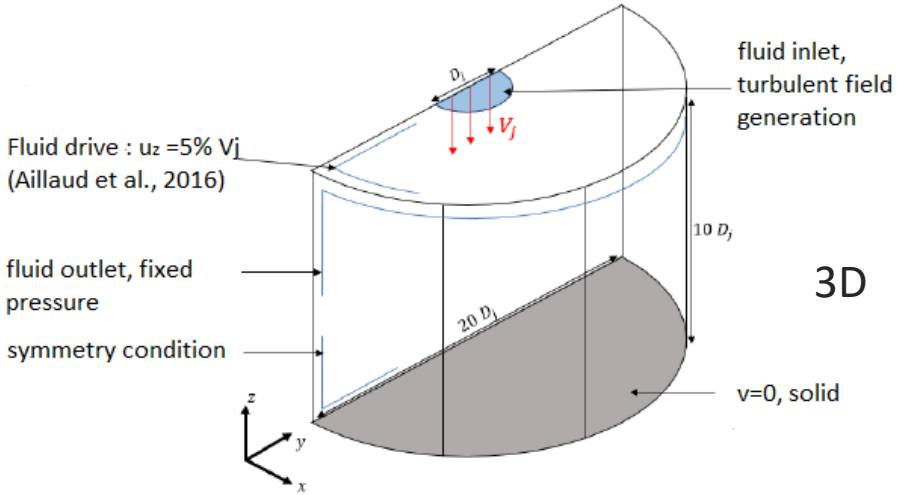

Simulation	Nu_0
Reference (Lee et Lee, 1999)	$143 - 173$
Without turbulence	132
FSM	127
DFSEM	162

⇒ Need to simulate turbulence at jet inlet;

⇒ Consistency of the **DFSEM** method → kept for the following

⇒ Size of cells ($z_1^+ \leq 0.002 D_j$ and $Nz \geq 500$)

Results of immersed jet ablation (1/6)

Numerical method for solid ablation

Enthalpy-porosity approach (Voller & Prakash, 1987)

- Solid modeled with volume fraction (g_l)
- In momentum balance: porosity source term (linear with C_{voller}) : in solid, $\vec{u} \to \vec{0}$
- In enthalpy balance: correction with latent heat

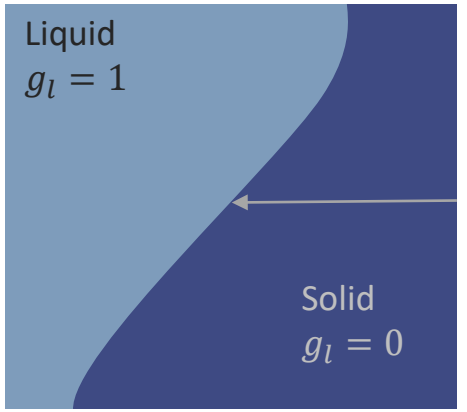

Simulation domain : ~5 10^6 cells

T_{fluid}= 277.15K= $T_{melting}$+ 4K

Sensibility to C_{voller} :

Water/ice : pur material

C_{voller} =10^{10} in the following

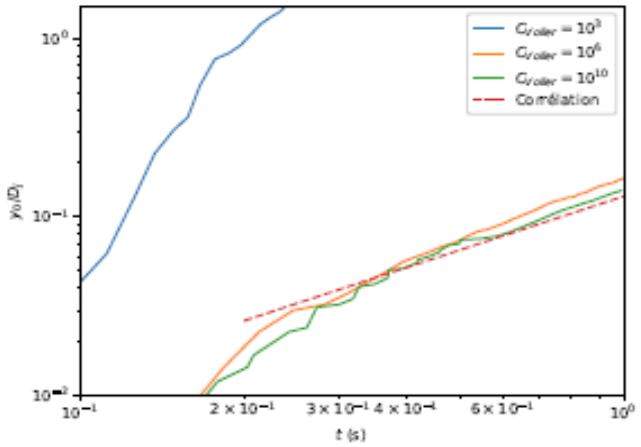

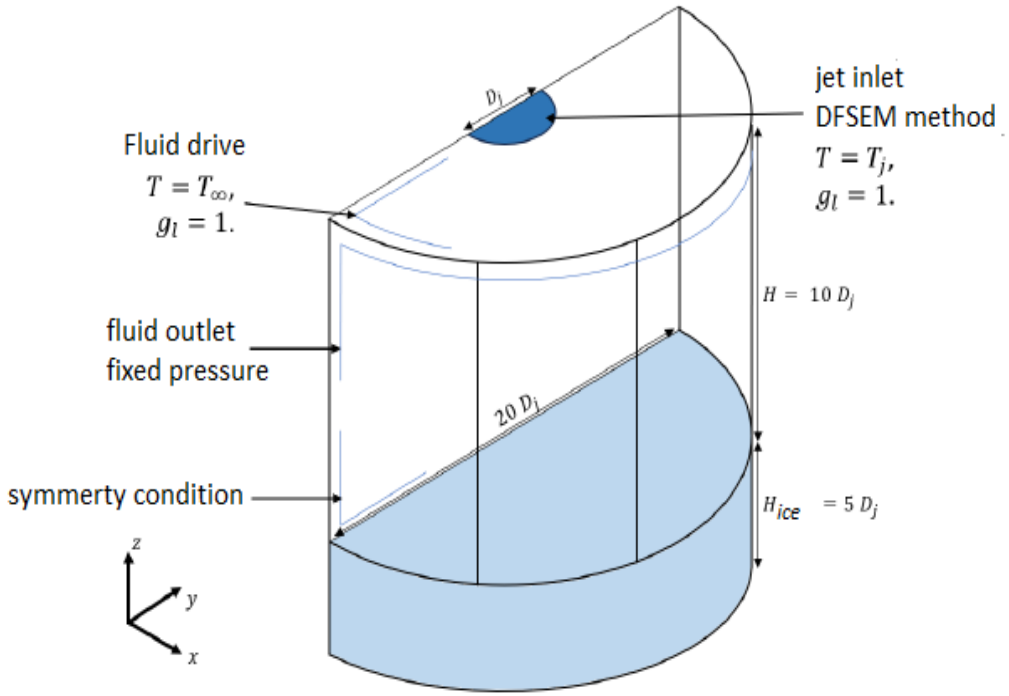

NB: 'correlation' = analytical law derived previously from experiment (Avrit et al., 2023)

Results of immersed jet ablation (2/6)

$\boldsymbol{Re \simeq 11600}$ **et** $\boldsymbol{Pr \simeq 3.6}$
$(V_j = 1.0\ \mathrm{m/s}, T_j = 50\ °\mathrm{C})$

D_i

$Re \sim 11$

T

Initial ice thickness

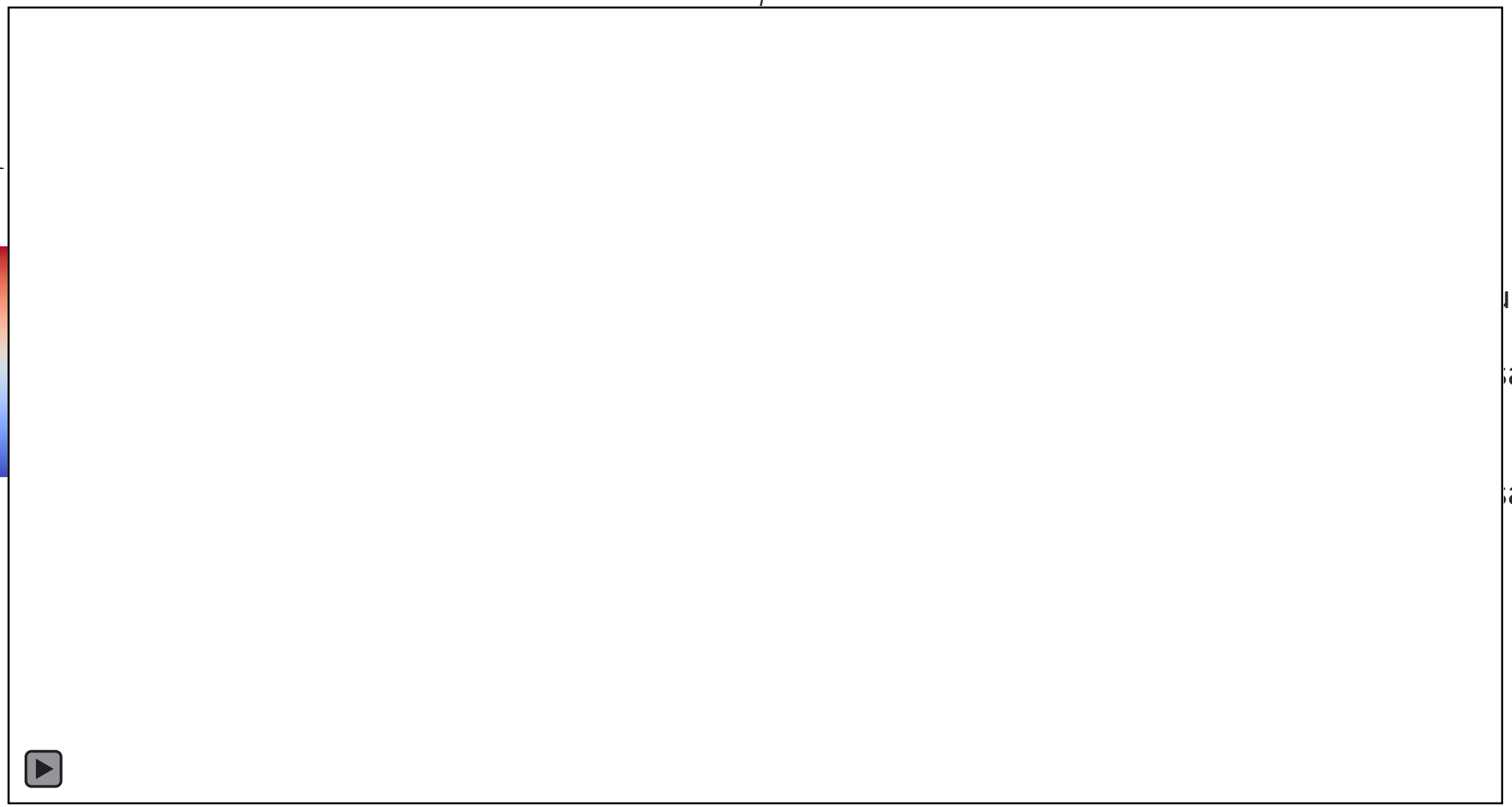

ure field:

sation of

sation of

Results of immersed jet ablation (3/6)

Simulation during 10^5s CPU time on 192 processors

Comparison of ablated depth curves at stagnation point

$\boldsymbol{Re \simeq 11600}$ **et** $\boldsymbol{Pr \simeq 3.6}$

$(V_j = 1.0\ \mathrm{m/s}, T_j = 50\ °\mathrm{C})$

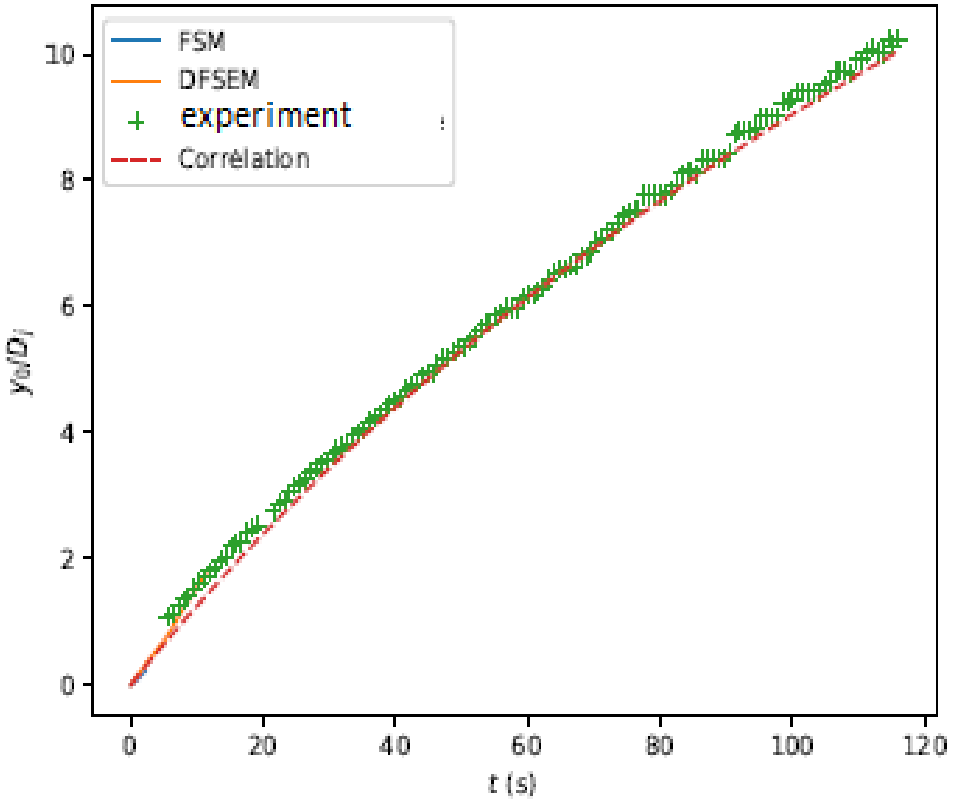

zoom

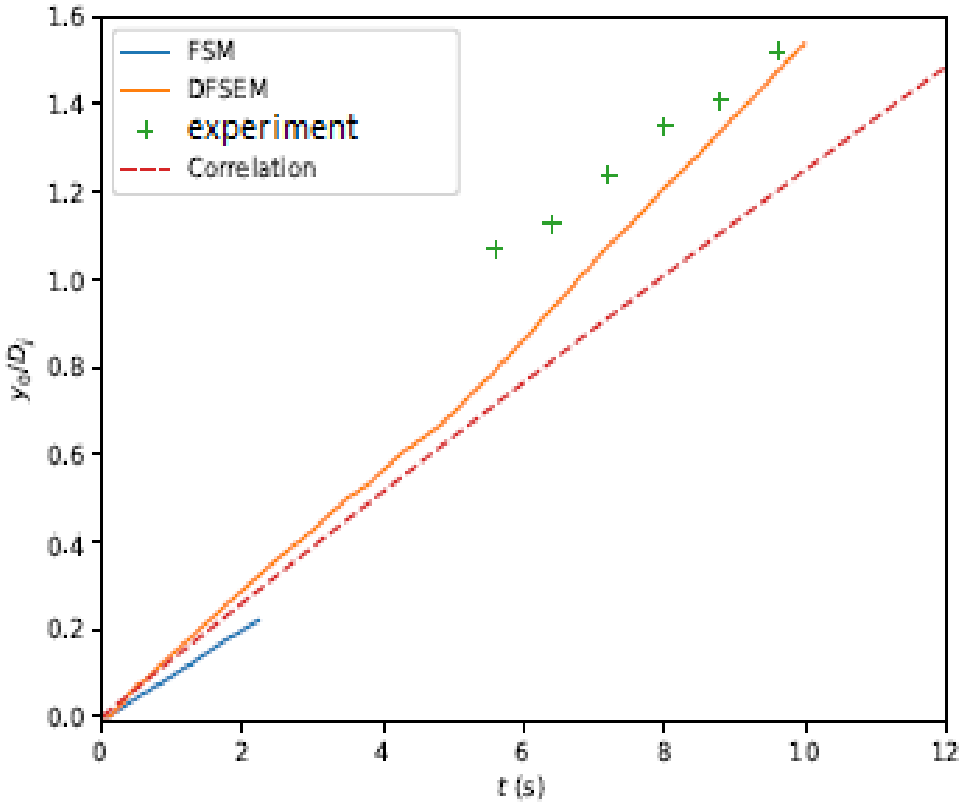

Correlation issued of experiment (Avrit et al., 2023)

$$\frac{y_0(t)}{D_j} = \frac{1}{0.0775} \ln\left(\frac{4.18 \times 10^{-3}\, B\, \lambda_j Re_j^{0.65} Pr_j^{0.73}}{\rho_s\, D_j^2\, c_{p,j}} \frac{\ln(1+B)}{B} t + 1\right)$$

⇒ Good agreement of simulation curve with correlation and experimental points.

Results of immersed jet ablation (4/6)

$\boldsymbol{Re \simeq 11600}$ **et** $\boldsymbol{Pr \simeq 3.6}$
$(V_j = 1.0\ \mathrm{m/s}, T_j = 50\ °\mathrm{C})$

Comparison of numerically obtained cavity with experimental shapes

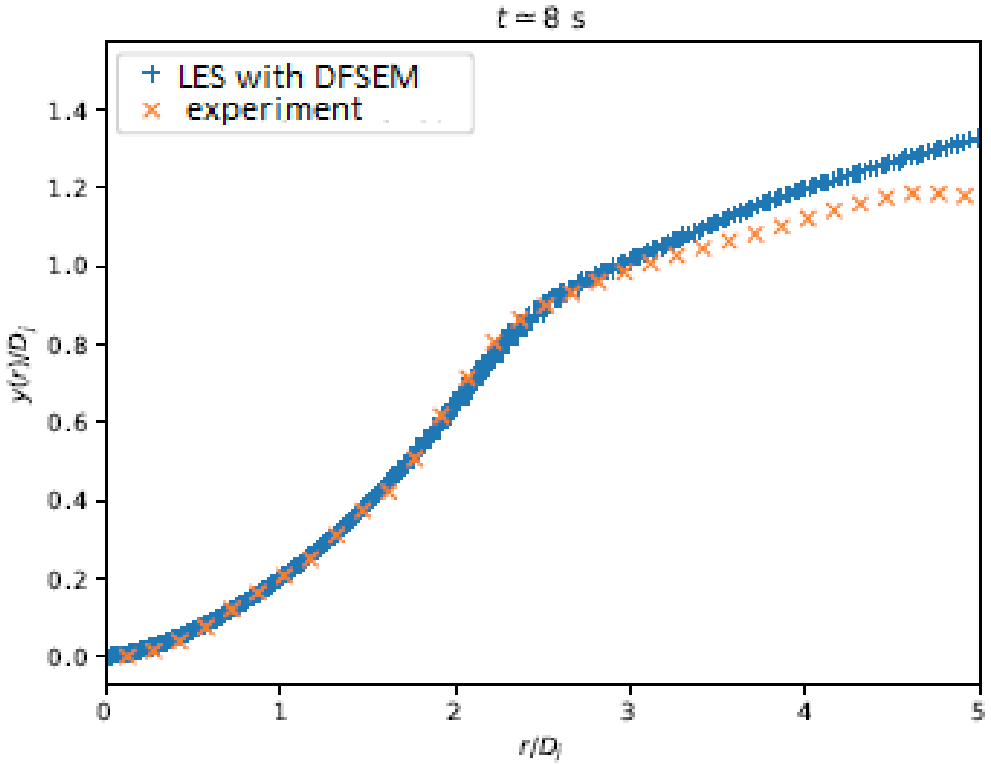

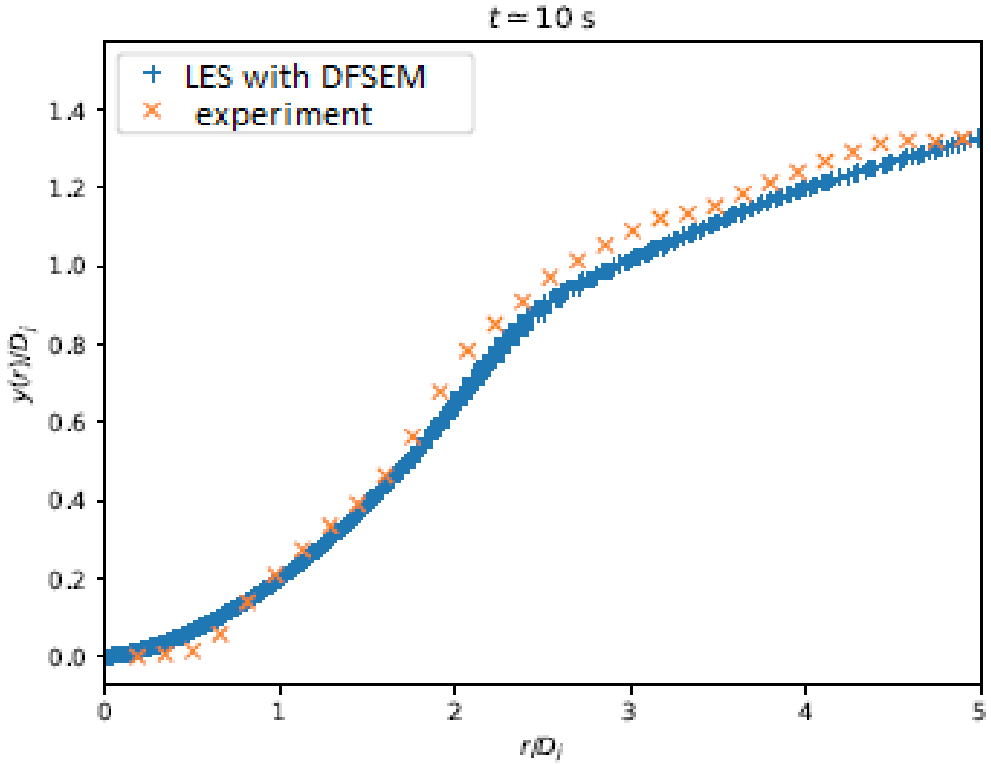

- Good agreement
- Same slope change around $\frac{r}{D_j} = 2.5$

→ Further investigation by observing simulated local flows → support to phenomena understanding

Results of immersed jet ablation (5/6)

$\boldsymbol{Re \simeq 26000}$ $\boldsymbol{Pr \simeq 3.6}$

Simulation during 2 months CPU time on 300 processors for 3s of physical times ($V_j = 2.5$ m/s, $T_j = 50$ °C)

Comparison of numerically obtained cavity with experimental shape

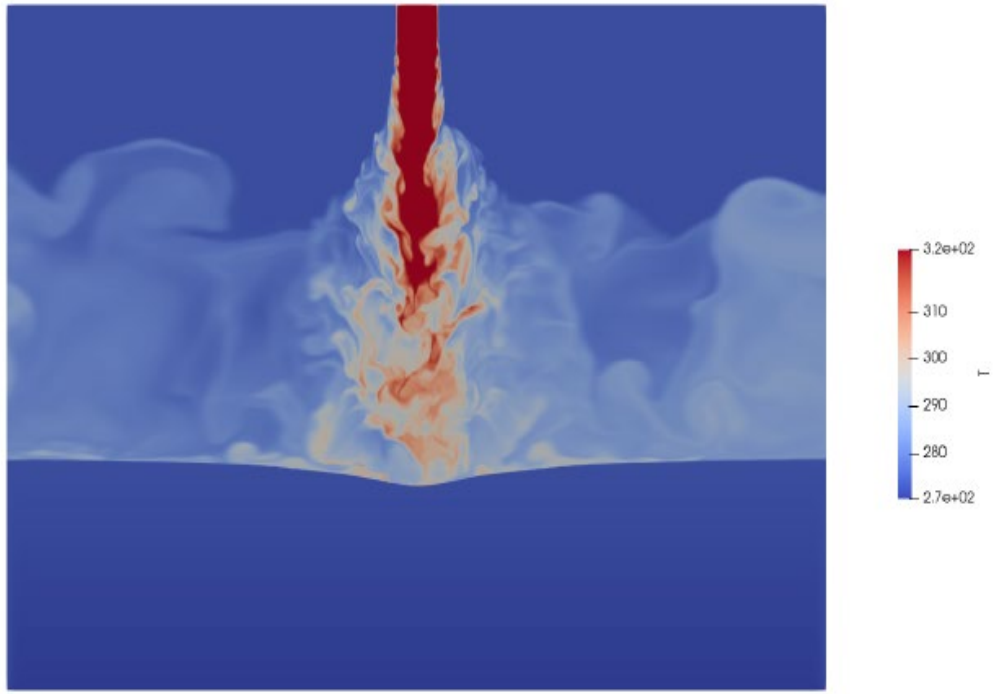

Instantaneous temperature fields at 2.5 s

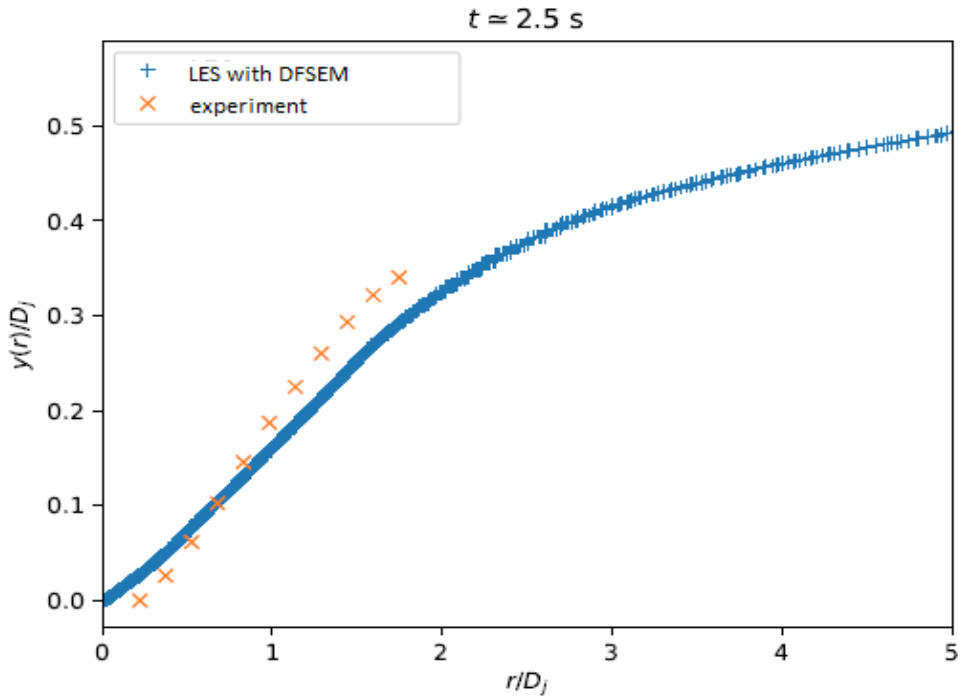

cavity profile at t=2.5s

Results of immersed jet ablation (6/6)

Comparison of ablated depth curves at stagnation point

$\boldsymbol{Re \simeq 26000} \quad \boldsymbol{Pr \simeq 3.6}$
$(V_j = 2.5\ \mathrm{m/s}, T_j = 50\ °\mathrm{C})$

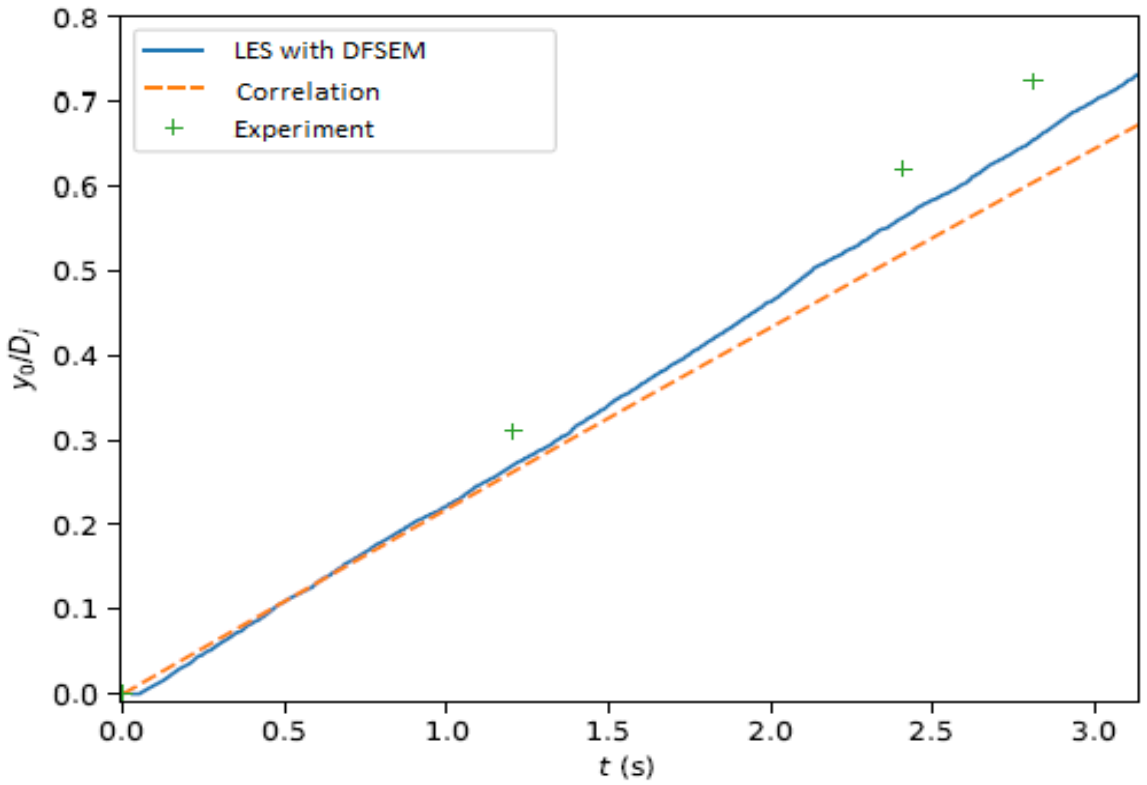

Good agreement of simulation curve with correlation and experimental points.

Conclusions and perspectives

- In Framework of mitigation studies on ASTRID SFR demonstrator, issue of core-catcher integrity due to corium jet impingement
- With conscience of similarity questions, **local well intrumented water/ice experimentation** : Nu_0 and cavity shape evolutions
- **For Pr transposition → CFD simulations with steel**

- **First step : validation** of CFD simulation for water/ice ablation by an immersed impinging jet
  - **OpenFOAM** solver with **LES** approach (**WALE**) and **enthalpy-porosity method** for melting simulation,
  - Special attention paid to inlet jet turbulence simulation → method Divergence-Free Synthetic Eddy Method **(DFSEM)** selected → mesh cell selection
    - 2 simulations of various Re: $11600 - 26000$;
    - Good agreement with experimental ablated depth and cavity
    - Expensive simulations for high Re values
- **Perspectives** :
  - simulation ablation by a **free-surface jet** (+ method to follow interface) → validation on experiments (Lecoanet et al., 2021)
  - Simulation of ablation by reduced-scale **steel** jet (immersed or not) → transposition deviation

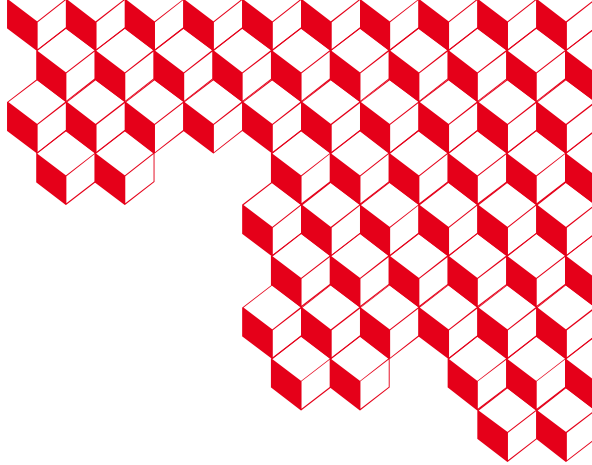

Laboratoire Énergies &
Mécanique Théorique et Appliquée

Thanks for your attention

The 11th European Review Meeting on Severe Accidents Research

May 13-16, 2024, Royal Institute of Technology, Stockholm, Sweden

PLENARY SESSION: CLOSING

Chairs: L.E. Herranz (CIEMAT), F. Gabrielli (KIT)

Summary and conclusions of the plenary sessions
L.E. Herranz (CIEMAT), Coordinator of the SEAKNOT project

Summary and conclusions of the technical sessions
NUGENIA TA2 Leaders

Concluding Remarks
L.E. Herranz (CIEMAT), Coordinator of the SEAKNOT project
F. Gabrielli (KIT)

Introduction of ERMSAR2026
L.E. Herranz (CIEMAT), Coordinator of the SEAKNOT project

SEAKNOT

NUGENIA TA2
Nuclear Generation II&III Alliance

SNETP
Sustainable Nuclear Energy Technology Platform

NEA
Nuclear Energy Agency

In cooperation with

IAEA
International Atomic Energy Agency
Atoms for Peace and Development

Insights from Plenary Sessions

Luis E. Herranz (CIEMAT)

Coordinator of the SEAKNOT project

Strål säkerhets myndigheten
Swedish Radiation Safety Authority

KTH Vetenskap och Konst

NPS Kärnkraftsäkerhet

Università di Pisa

KIT Karlsruher Institut für Technologie

SEAKNOT

NUGENIA TA2 Nuclear Generation II&III Alliance

SNETP Sustainable Nuclear Energy Technology Platform

NEA Nuclear Energy Agency

In cooperation with

IAEA International Atomic Energy Agency *Atoms for Peace and Development*

- **“Singular Careers in the Severe Accident Research”**
  R.O. Gauntt; J. Rempe; H. Nakamura
- **“Regulatory perspective and approaches for SA in SMRs”**
  J. Schaperow (NRC); S. Gyepi-Garbrath (CNSC); A. Tehrani (ONR); A.O. Mowitz (SSM)
- **“Looking ahead in Severe Accident research”**
  A. Iorizzo (EC); A. Miassoedov (IAEA); D. Jacquemain (OECD/NEA)

Strål säkerhets myndigheten Swedish Radiation Safety Authority

KTH Vetenskap och Konst

NPS Kärnkraftsäkerhet

Università di Pisa

KIT Karlsruher Institut für Technologie

SEAKNOT

NUGENIA TA2 Nuclear Generation II&III Alliance

SNETP Sustainable Nuclear Energy Technology Platform

NEA Nuclear Energy Agency

In cooperation with

IAEA International Atomic Energy Agency *Atoms for Peace and Development*

- **No room for complaciency in nuclear safety!**
  - Confidence should come with knowledge.
  - Knowledge is compatible with uncertainties & awareness of “unknowns”.
  - Uncertainty quantification, an essential perspective in SA analysis.
  - Big data & sound physical grounds promising “marriage” for future SA analysis.

- **“Imperfect knowledge” might be enough to enhance safety.**
  - Critical view of information, an essential “attitude” (no “blindfolded believers”).
  - Keep an “open mind” when controversial data show up.
  - Do not extrapolate: “Jumping into the void”, not a good strategy in nuclear safery.
  - When modeling: understand the scenario; start simple; be aware of uncertainties.
  - Never miss the chance ot testing your model, if reliable data becomes available.

Strål säkerhets myndigheten Swedish Radiation Safety Authority

KTH Vetenskap och Konst

NPS Kärnkraftsäkerhet

Università di Pisa

KIT Karlsruher Institut für Technologie

SEAKNOT

NUGENIA TA2
Nuclear Generation II&III Alliance

SNETP
Sustainable Nuclear Energy Technology Platform

NEA
Nuclear Energy Agency

In cooperation with

IAEA
International Atomic Energy Agency
Atoms for Peace and Development

- **Roadmaps: backbones for effective safety enhancements!**
  - Based on the “whole picture” with a view of the final goal.
  - International collaboration is an international ingredient for multiple reasons.
  - Scaling considerations should be ever present when assessing issues.
  - Research should “match demands” and “substantiate further knowledge needs”

Strål säkerhets myndigheten
Swedish Radiation Safety Authority

KTH Vetenskap och Konst

NPS Kärnkraftsäkerhet

Università di Pisa

KIT Karlsruher Institut für Technologie

SEAKNOT

NUGENIA TA2 Nuclear Generation II&III Alliance

SNETP Sustainable Nuclear Energy Technology Platform

NEA Nuclear Energy Agency

In cooperation with

IAEA International Atomic Energy Agency *Atoms for Peace and Development*

- **SMR licencing approaches and SA research**
  - Regulatory requirements are not size-dependent.
  - Regulatory frameworks being adapted and modernized.
  - Accident prevention, mitigation and lessons from FDNPP accidents, considered.
  - SA analysis and research outcomes, integrated in the licensing process.
  - SA analytical tools not to be extrapolated, but wisely extended and applied.
  - SMR “safe responses” to “challenging initiating and boundary conditions”, to be proved.
  - Capability building is a need and takes time and resources of multiple kinds.
  - Collaboration between regulators recognized as a measure to optimize reg. process.

Strål säkerhets myndigheten Swedish Radiation Safety Authority

KTH Vetenskap och Konst

NPS Kärnkraftsäkerhet

Università di Pisa

KIT Karlsruher Institut für Technologie

SEAKNOT

NUGENIA TA2 Nuclear Generation II&III Alliance

SNETP Sustainable Nuclear Energy Technology Platform

NEA Nuclear Energy Agency

In cooperation with

IAEA International Atomic Energy Agency *Atoms for Peace and Development*

- **EC, IAEA & OECD/NEA looking ahead SA research**
  - All three Agencies are “facilitators” (no “proposers”) and have instruments in place.
  - New instruments being shaped-up (SMR nuclear alliance; exptl. platforms; EG; …)
  - There is a need to optimize resources: they exist … but they are not on the rise.
  - SA research being fostered for upcoming SMRs, but also for LTOs.
  - Fuzzy definition of SA research needs in the “SMR jungle”, though.
  - Effective research need to prioritize according to designs and agenda.
  - SMR SA research, though, does not start from scratch. Do exist valuable knowledge!
  - SMR “safe responses” to “challenging initiating and boundary conditions”, to be proved.
  - Capability building is a need and takes time and resources of multiple kinds.
  - Availability of “capable resources” ever-present in running and future activities.

Strål säkerhets myndigheten Swedish Radiation Safety Authority

KTH Vetenskap och Konst

NPS Kärnkraftsäkerhet

Università di Pisa

KIT Karlsruher Institut für Technologie

SEAKNOT

NUGENIA TA2 Nuclear Generation II&III Alliance

SNETP Sustainable Nuclear Energy Technology Platform

In cooperation with

NEA Nuclear Energy Agency

IAEA International Atomic Energy Agency *Atoms for Peace and Development*

In-vessel Corium and debris coolability

#	Title and speaker
1	IVMR Modelling with Transient Effects during Molten Pool Formation and Stabilization – Outcomes from Models' Comparison Performed in the IAEA CRP J46002 L. Carénini (IRSN)
2	Numerical Analysis of Melt Penetration Behavior in the Control Rod Drive Housing of Fukushima Daiichi Nuclear Power Station Unit-2 X. Li (JAEA)
3	Reactor pressure vessel integrity during severe accident with core meltdown: characterization of material parameters, structure integrity assessment and thermal-hydraulic assessment P. Gal (UJV)
4	Improvement of thermochemical corium stratification accounting for uranium and zirconium composition difference in metallic and oxide phases A. Lecoanet (CEA)
5	Stainless Steel Oxidation at both Solid and Liquid State Under Ar-H_2O Gas Mixture in Severe Accident Conditions M. Nasselahsen (CEA)
6	A Thermodynamic Study of Molten Pool Stratification Morphology E. Chen (China Nuclear Power Eng. Co.)
7	In-Vessel Corium Thermochemistry Benchmark based on MASCA Experimental Data R. Le Tellier (CEA)
8	Coolability of a Corium Pool in a Debris Bed – Calculation of Critical Heat Flux (CHF) Tests with the ASTEC Code C. Sartoris (IRSN)

Strål säkerhets myndigheten Swedish Radiation Safety Authority

KTH Vetenskap och Konst

NPS Kärnkraftsäkerhet

Università di Pisa

KIT Karlsruher Institut für Technologie

SEAKNOT

NUGENIA TA2 Nuclear Generation II&III Alliance

SNETP Sustainable Nuclear Energy Technology Platform

NEA Nuclear Energy Agency

In cooperation with

IAEA International Atomic Energy Agency *Atoms for Peace and Development*

Messages, Innovative approaches and methodologies

- **IVMR modelling:** Use of more sophisticated benchmarks as one of the means for code validation in the absence of experiments
- **Continuous efforts to analyze the Fukushima events:** develpment and use of Moving Particle Semi-implicit model to evaluate the corium penetration in the CRDs
- **FEM analyses for safety demonstration of RPV** using BCs from integral codes → importance of improving the knowledge of material properties
- **New experimental results on steel oxidation** at solid and liquid state showing higher hydrogen production kinetics compared with previous studies
- **Code-to-experiment comparison of MASCA and CORDEB2 tests**
- **Need for further experimental investigations for kinetics evaluation of corium thermochemistry**
- **ASTEC validation for coolability of corium pools in a debris bed**

Strålsäkerhetsmyndigheten Swedish Radiation Safety Authority

UNIVERSITÀ DI PISA

SEAKNOT

NUGENIA TA2 Nuclear Generation II&III Alliance

SNETP Sustainable Nuclear Energy Technology Platform

NEA Nuclear Energy Agency

In cooperation with

IAEA International Atomic Energy Agency *Atoms for Peace and Development*

Key Highlights

- **Experiments on SS oxidation: New tests performed and updating the existing knowledge**

- **Corium thermochemistry:**
  - **codes‘ validation against relevant experiments performed**
  - **need for further experiments to evaluate the kinetics of the processes**

- **Heat exchange (CHF) between corium pool and its surrouding debris bed while reflooding**
  - **ASTEC application shows a good performance in pool-boiling configuration but a more adequate correlation for CHF in porous media configuration is needed**
  - **Parameters to be considered identified**

Strål säkerhets myndigheten Swedish Radiation Safety Authority

KTH Vetenskap och Konst

NPS Kärnkraftsäkerhet

Università di Pisa

KIT Karlsruher Institut für Technologie

11TH CONFERENCE ON
SEVERE ACCIDENTS RESEARCH
May 13-16, 2024 – Stockholm, Sweden
ERMSAR 2024

Sessions Summary
3-1 and 3-2 Ex-vessel Corium interactions and coolability

Pascal Piluso (CEA), Sevostian Bechta (KTH),
Laure Carénini (IRSN), Markus Hupp (Framatome GmbH)

Funded by the European Union
NEA NUCLEAR ENERGY AGENCY
SNETP Sustainable Nuclear Energy Technology Platform
NUGENIA NUclear GENeration II & III Association
Strål säkerhets myndigheten Swedish Radiation Safety Authority
KTH VETENSKAP OCH KONST

Sessions overview

- **Total number of presentations: 7**

- **Number of papers by subject:**
  - Experimental tests on MCCI and coolability: 2
  - Ex-vessel phenomena modelling: 4
  - Fukushima-Daiichi MCCI: 1+1

Sessions overview

The presentations aimed at providing new advancement in the ex-vessel–related issues

- New approach for modelling **stabilization of corium during MCCI by top flooding.**
- MCCI-Tests on **SSM-SICOPS** assessing the impact of zirconium on MCCI phenomena.
- Modelling of CCI-2 using innovative approach with **CFD methods.**
- Synthesis of prototypical corium including fission products representative of Fukushima Daiichi conditions on **PLINIUS platform**.
- Application of new method of prototypic corium melt generation based on combined (coupled) uranothermite reaction and induction heating on **PLINIUS platform**.
- A focus on (i) **MELTSPREAD** modeling of corium melt spreading to support ex-vessel corium stabilization concept of VVER-1000 reactor of Temelin NPP, (ii) pre-test simulation of melt spreading experiments (iii) **CFD modeling** of melt relocation from the ALEGRO reactor into the core catcher.
- MC3D computer code to analyse a series of debris re-flooding tests performed in the **FLOAT experimental facility**. The simulation and test results are in good qualitative agreement.

New advances and results

- Innovative method to simulate experimentally MCCI
- Modelling of the stabilization of corium by top cooling
- CFD development for ex-vessel phenomena
- New experimental efforts to simulate Severe Accidents Conditions- Fukushima Daiichi

SEAKNOT

NUGENIA TA2 Nuclear Generation II&III Alliance

SNETP Sustainable Nuclear Energy Technology Platform

NEA Nuclear Energy Agency

In cooperation with

IAEA International Atomic Energy Agency *Atoms for Peace and Development*

Severe Accident Scenarios: SMRs (4.1 – 4.2)

- **8 papers presented (increase, correlation with SASPAM-SA)**
- **SASPAM-SA: Assessment of the relevance and applicability of existing experimental databases to iPWR (PSI)**
- **Numerical Investigation of Natural Circulation onside a Scaled-down Prismatic Modular Reactor (Minia University)**
- **Development of a LW-SMR Dry Containment Model with containmentFOAM (FZJ)**
- **Comparison of a DBA sequence in a generic iPWR between MELCOR and ASTEC codes (ENEA)**

Strål säkerhets myndigheten Swedish Radiation Safety Authority

KTH Vetenskap och Konst

NPS Kärnkraftsäkerhet

Università di Pisa

KIT Karlsruher Institut für Technologie

SEAKNOT

NUGENIA TA2 Severe Accidents
Nuclear Generation II&III Alliance

SNETP
Sustainable Nuclear Energy Technology Platform

NEA
Nuclear Energy Agency

In cooperation with

IAEA
International Atomic Energy Agency
Atoms for Peace and Development

- **Analysis of Postulated Severe Accidents in Generic Integral PWR Small Modular Reactors in the frame of the Horizon Euratom SASPAM-SA Project (KIT)**
- **Update on Severe Accident Analysis Research at CNL for Small Modular and Advanced Reactor Designs (CNL)**
- **Application of the Probabilistic Method to Propagate Input Uncertainty on a DBA Sequence in a Generic iPWR (ENEA)**
- **Comparison between EDF MAAP5.04 and ASTECv3 codes on a hypothetical Severe Accident on the ELSMOR project NUWARD-Like SMR Design (EdF)**

+ Posters

Strål säkerhets myndigheten
Swedish Radiation Safety Authority

KTH Vetenskap och Konst

NPS Kärnkraftsäkerhet

Università di Pisa

KIT Karlsruher Institut für Technologie

SEAKNOT

NUGENIA TA2 Nuclear Generation II&III Alliance

SNETP Sustainable Nuclear Energy Technology Platform

NEA Nuclear Energy Agency

In cooperation with

IAEA International Atomic Energy Agency *Atoms for Peace and Development*

Key Highlights, Messages, Innovative Approaches and Methodologies

- **Focus on code applications (ASTEC, MELCOR, other codes)**
- **For now, attention mainly on DBA sequences, but need to beyond!**
- **Review of existing experimental data in view of their use for SMRs**
- **Importance of the topic, as evidenced in plenaries with Regulators and with Intl. Organizations**
- **Development of reference input-decks (ELSMOR E-SMR, SASPAM-SA D1 and D2), but absence of disclosed real designs**
- **Exploit also past designs (e.g., IRIS)!**

Strål säkerhets myndigheten Swedish Radiation Safety Authority

KTH Vetenskap och konst

NPS Kärnkraftsäkerhet

Università di Pisa

KIT Karlsruher Institut für Technologie

SEAKNOT

NUGENIA TA2
Nuclear Generation II&III Alliance

SNETP
Sustainable Nuclear Energy Technology Platform

NEA
Nuclear Energy Agency

In cooperation with

IAEA
International Atomic Energy Agency
Atoms for Peace and Development

Issues & Discussions

- **Discrepancies among some code results: need to be understood and, possibly, fixed**
- **Identification of remaining knowledge gaps in both modeling and experiments is crucial**
- **For next ERMSAR: more studies, possibly with a look also onto EP&R and EPZ issues!**

Strål säkerhets myndigheten
Swedish Radiation Safety Authority

KTH VETENSKAP OCH KONST

NPS Kärnkraftsäkerhet

Università di Pisa

KIT Karlsruher Institut für Technologie

In cooperation with

ERMSAR 2024 Conclusions

6. Hydrogen risk and containment behavior

Ivo Kljenak

Jozef Stefan Institute

SEAKNOT

NUGENIA TA2 Nuclear Generation II&III Alliance

SNETP Sustainable Nuclear Energy Technology Platform

In cooperation with

NEA Nuclear Energy Agency

IAEA International Atomic Energy Agency *Atoms for Peace and Development*

Hydrogen risk and containment behavior

- **Number of papers presented: 15**
  - oral: **9**
  - poster: **6**
- **Papers by topic:**
  - atmosphere mixing: **11**
  - hydrogen recombination: **1**
  - combustion: **1**
  - iodine absorption: **1**
  - general: **1**

Strål säkerhets myndigheten Swedish Radiation Safety Authority

KTH Vetenskap och Konst

NPS Kärnkraftsäkerhet

Università di Pisa

KIT Karlsruher Institut für Technologie

SEAKNOT

NUGENIA TA2 Severe Accidents
Nuclear Generation II&III Alliance

SNETP
Sustainable Nuclear Energy Technology Platform

NEA
Nuclear Energy Agency

In cooperation with

IAEA
International Atomic Energy Agency
Atoms for Peace and Development

Messages, innovative approaches and methodologies

- **Papers WITHOUT original approach or new experimental results or theoretical models: 9**
  - code application: **8** papers
  - project overview: **1** paper

- **Papers WITH original approach or new experimental results or theoretical models: 6**
  - code coupling: **2** papers
  - new results: **4** papers (PARs, atmosphere mixing, absorption, combustion)

Strål säkerhets myndigheten
Swedish Radiation Safety Authority

KTH Vetenskap och Konst

NPS Kärnkraftsäkerhet

Università di Pisa

KIT Karlsruher Institut für Technologie

SEAKNOT

NUGENIA TA2 Nuclear Generation II&III Alliance

SNETP Sustainable Nuclear Energy Technology Platform

NEA Nuclear Energy Agency

In cooperation with

IAEA International Atomic Energy Agency *Atoms for Peace and Development*

General impressions (1/2)

- **Not much original or novel results presented, but authors are not to blame.**
- **Possible reasons:**
  - many works not yet reached significant results
  - further research too complex or costly
  - not much to be "discovered" anymore

1. **Atmosphere mixing**
   - experiments: always welcome, but costly
   - theory: fluid mechanics with heat and mass transfer - difficult to "discover" anything new

Strål säkerhets myndigheten Swedish Radiation Safety Authority

KTH Vetenskap och Konst

NPS Kärnkraftsäkerhet

Università di Pisa

KIT Karlsruher Institut für Technologie

General impressions (2/2)

2. **Recombination, absorption:** research going on (both experimental and theoretical)

3. **Combustion in small volumes**
   - experiments: going on
   - theory: outside of nuclear field

4. **Combustion in large volumes**
   - experiments: much needed, but costly
   - theory:
     - modelling on local scale tedious because of long computation times
     - possible limitations to model local effects of combustion on continuum scale
     - attempts to scale combustion phenomena

SEAKNOT

NUGENIA TA2
Nuclear Generation II&III Alliance

SNETP
Sustainable Nuclear Energy Technology Platform

NEA
Nuclear Energy Agency

In cooperation with

IAEA
International Atomic Energy Agency
Atoms for Peace and Development

Issues & discussions

- PAR hydrogen recombining rate
- Code input models and results of atmosphere mixing simulation
- Comparative evaluation of LP code results when using same code and containment model

Highlight

- Experimental scaling of deflagration to detonation transition

Strål säkerhets myndigheten
Swedish Radiation Safety Authority

KTH VETENSKAP OCH KONST

NPS Kärnkraftsäkerhet

Università di Pisa

KIT Karlsruher Institut für Technologie

SEAKNOT

NUGENIA TA2 Nuclear Generation II&III Alliance

SNETP Sustainable Nuclear Energy Technology Platform

NEA Nuclear Energy Agency

In cooperation with

IAEA International Atomic Energy Agency *Atoms for Peace and Development*

Source Term

- **Number of papers presented: 10**
- The Reduction of Radiological Consequences of design basis and extension Accidents: re-assessment of calculation results and main outcomes of the R2CA project **N. Girault (IRSN)**
- Progress in understanding fission products remobilization behaviour and hydrogen risk in water cooled reactors under severe accident conditions: OECD/NEA THAI-3 project **S. Gupta (Becker Technologies GmbH)**
- Source Term Assessment for a VVER1000 Reactor Equipped with Filtered Venting: Sensitivity Study of the Impact of Different Forms of Iodine in the Containment **M. Kotouc (UJV)**
- Source Term Dispersion Analysis and Construction of the Risk Map around the Peach Bottom Unit-2 Plant Using the ASTEC and JRODOS codes **O. Murat (KIT)**

Strål säkerhets myndigheten Swedish Radiation Safety Authority

KTH Vetenskap och Konst

NPS Kärnkraftsäkerhet

Università di Pisa

KIT Karlsruher Institut für Technologie

SEAKNOT

NUGENIA TA2 Nuclear Generation II&III Alliance

SNETP Sustainable Nuclear Energy Technology Platform

NEA Nuclear Energy Agency

In cooperation with

IAEA International Atomic Energy Agency *Atoms for Peace and Development*

Source Term

- Effect of Boric Acid on Fission Product Tellurium and Iodine in Severe Accident-Like Conditions: Analysis with X-Ray Photoelectron Spectroscopy **F. Börjesson Sandén (Chalmers University of Technology)**
- Local measurements on particle mass transfer in gas-liquid flows **A. Ramos Perez (PSI)**
- New Experimental Devices for Severe Accident Study: a Laser Based Approach **Y. Pontillon (CEA)**
- On the progress made in source terms evaluation and possible open issues relative to advanced technologies **L. Cantrel (IRSN)**
- Gaseous and aerosol formations in the pseudo-binary CsI-MoO3 reaction system **M. Rizaal (JAEA)**
- Experimental study on removal effect of radioactive materials in the course of the leakage through the equipment hatch **K. Nakamura (CRIEPI)**

Strål säkerhets myndigheten Swedish Radiation Safety Authority

KTH Vetenskap och Konst

NPS Kärnkraftsäkerhet

Università di Pisa

KIT Karlsruher Institut für Technologie

SEAKNOT

NUGENIA TA2 Nuclear Generation II&III Alliance

SNETP Sustainable Nuclear Energy Technology Platform

NEA Nuclear Energy Agency

In cooperation with

IAEA International Atomic Energy Agency *Atoms for Peace and Development*

Messages, Innovative approaches and methodologies

- **Significant progress in source term knowledge** for DBA and SA conditions through R&D programs: EC/R2CA, OECD/THAI-3, OECD/ESTER, National programs
- **Continuous analysis/experimental efforts on source term related scenarios/phenomena including the effect of accident conditions,** e.g. fission product penetration in complex geometries with narrow gaps,
- **Enhanced understanding of hydrogen risks and fission product (speciation) behavior,** likeFPs speciation, impact of dynamic loads (H_2 combustion), FCVS operation effect
- **Importance of chemical speciation in safety analysis (**tellurium/boric acid interaction, study on CsI-MoO3 reactions)
- **Continuous work on development/application of measurement techniques to provide specific tests data:** E.g. Laser-based platforms for thermophysical property quantification, X-ray photoelectron spectroscopy for FPs interaction, Wire mesh sensor for particle mass transfer
- **Application of existent safety analysis tools:** Risk map construction, iodine speciation/FCVS manual operation

Strål säkerhets myndigheten Swedish Radiation Safety Authority

KTH Vetenskap och Konst

NPS Kärnkraftsäkerhet

Università di Pisa

KIT Karlsruher Institut für Technologie

SEAKNOT

NUGENIA TA2 Nuclear Generation II&III Alliance

SNETP Sustainable Nuclear Energy Technology Platform

NEA Nuclear Energy Agency

In cooperation with

IAEA International Atomic Energy Agency *Atoms for Peace and Development*

Issues & Discussions

- **Availability of experimental database** from projects conducted in different frameworks (EC, OECD/NEA, national,…) for code validation purpose – depends on specific project agreements
- **Extrapolation of experimental data towards reactor application** (ambient T/P, simplified geometries, test aerosol material, etc..)
- **Propagation of uncertainties** in case of couples codes analysis , e.g. for the purpose of source term dispersion in environment, assessing operation of mitigation actions w.r.t. FPs (e.g. FCVS operation)
- Need of continuous efforts to **enhance knowledge about source term scenarios/phenomena** and **coupling with dynamics events**, e.g. Organic iodine production by paint/H_2 deflagration interaction
- Perspectives **on applying the current ST knowledge to SMRs**, e.g. RC evaluation methodologies, experimental infrastructure, etc

Strål säkerhets myndigheten Swedish Radiation Safety Authority

KTH Vetenskap och Konst

NPS Kärnkraftsäkerhet

Università di Pisa

KIT Karlsruher Institut für Technologie

SEAKNOT

NUGENIA TA2
Nuclear Generation II&III Alliance

SNETP
Sustainable Nuclear Energy Technology Platform

NEA
Nuclear Energy Agency

In cooperation with

IAEA
International Atomic Energy Agency
Atoms for Peace and Development

Key Highlights

- **Continuous need for integration of experimental data with advanced simulation tools** to enhance the accuracy and reliability of source term predictions and emergency preparedness plans.
- **Importance of representative boundary conditions**, scaling towards extrapolation of experimental data to reactor scale
- **Development and utilization of novel experimental techniques** is a key to providing relevant data for nuclear safety analysis, thereby improving the understanding of severe accident phenomena.
- **Challenges in harmonizing safety analysis methodologies,** given that national regulations for radiological consequence evaluations differ from one country to another.
- **Re-orienting R&D Resources Towards SMRs, c**urrent and new R&D resources, both experimental and analytical, towards Small Modular Reactors (SMRs), assessment of different fuel types (e.g. ATF)
-

Strål säkerhets myndigheten
Swedish Radiation Safety Authority

KTH Vetenskap och Konst

NPS Kärnkraftsäkerhet

Università di Pisa

KIT Karlsruher Institut für Technologie

SEAKNOT

NUGENIA TA2 Severe Accidents
Nuclear Generation II&III Alliance

SNETP
Sustainable Nuclear Energy Technology Platform

NEA
Nuclear Energy Agency

In cooperation with

IAEA
International Atomic Energy Agency
Atoms for Peace and Development

Analysis, Management, and Consequences of Severe Accidents for Gen I/III reactors

Technical sessions 2.1, 2.2, 2.3, 2.4, 5.1, 5.2

23 Papers presented (about 1/3 of ERMSAR total)

2.1, 2.2 Severe Accident Scenarios **4, 4 papers**

2.3, 2.4 Severe Accident Scenarios: U&S analysis **4, 4 papers**

5.1, 5.2 Severe accident scenarios: Model development and validation **3, 4 papers**

Strål säkerhets myndigheten
Swedish Radiation Safety Authority

KTH Vetenskap och Konst

NPS Kärnkraftsäkerhet

Università di Pisa

KIT Karlsruher Institut für Technologie

SEAKNOT

NUGENIA TA2 Nuclear Generation II&III Alliance

SNETP Sustainable Nuclear Energy Technology Platform

NEA Nuclear Energy Agency

In cooperation with

IAEA International Atomic Energy Agency *Atoms for Peace and Development*

Innovative approaches, methodologies, and ideas

2.1 Severe Accident Scenarios

- SEAKNOT Project status – **PIRTSA** is identifying major SA issues worth new R&D activities; **SADD** review of exp data for SA codes D&V and creation of a database; **SAINET** Exp infrastructure network mapping status & capabilities of European facilities. C&D (ERMSAR) and K2T towards young generations (SAP courses, SASCamp) in **KNOS**
- ASTEC in support of PSA2 for French 1300 PWR – these simulations implement state-oriented Emergency Operating Procedures (EOPs) and SAMGs for **entire spectrum of events resulting from a Level 1 PSA**
- BWR analyses with MELCOR - importance of considering **leakages from PCV head flange** to RB and **PCV venting** in management of H2 risk
- Overview of IRSN research Projects – **main results** and applicability to innovative reactors

Strål säkerhets myndigheten Swedish Radiation Safety Authority

KTH Vetenskap och Konst

NPS Kärnkraftsäkerhet

Università di Pisa

KIT Karlsruher Institut für Technologie

SEAKNOT

NUGENIA TA2 Nuclear Generation II&III Alliance

SNETP Sustainable Nuclear Energy Technology Platform

NEA Nuclear Energy Agency

In cooperation with

IAEA International Atomic Energy Agency *Atoms for Peace and Development*

Innovative approaches, methodologies, and ideas

2.2 Severe Accident Scenarios

- ASSAS Project status –**First prototype of SA simulator based on AI**. Efficient programming will be applied to ASTEC with negligible impact on accuracy for shortening running time by different means (ML techniques).
- SBO surrogate model – (ASSAS) preliminary stage of development of a surrogate model for CESAR module (TH in primary and secondary circuits), focusing on **generation of training datasets necessary for machine learning** process, but further work foreseen.
- MELCOR analyses for Fukushima – **MELCOR 2.2 analysis applying plant data** from Units 1 to 3 (only the containment floor eroded and not the steel) to reproduce time of RPV failure and H2 explosion. Good agreement with measured data for FP release times.
- Long term SA management at Loviisa VVER 440 – identified strategy is to **use low pressure ECCS**, that will be taken in service after the early phase of the accident (water highly radioactive, equipment survivability is discussed)

Strål säkerhets myndigheten Swedish Radiation Safety Authority

KTH Vetenskap och Konst

NPS Kärnkraftsäkerhet

Università di Pisa

KIT Karlsruher Institut für Technologie

SEAKNOT

NUGENIA TA2 Severe Accidents
Nuclear Generation II&III Alliance

SNETP
Sustainable Nuclear Energy Technology Platform

In cooperation with

NEA
Nuclear Energy Agency

IAEA
International Atomic Energy Agency
Atoms for Peace and Development

2.3 Severe Accident Scenarios: U&S analysis

Innovative approaches, methodologies, and ideas

- Main achievements of MUSA project – **First systematic UaSA application for SAs**: UP database, methods & tools, reactor & scenarios UQ database, "first-of-a-kind" UQ for SFPs, "**needs to be addressed" before an effective UaSA implementation in SA domain**
- ST UA of FCV scenarios in Nordic BWR by MELCOR – **impact of uncertain MELCOR modeling parameters & code options** for a LBLOCA and a SBO, importance of various retention mechanisms
- UaSA for MBLOCA with CV activation in a generic KONVOI – (MUSA WP5) Application of KATUSA tool to ASTEC results. **Database of ~300 simulations**, solid basis for 1) understanding & identifying ASTEC modelling uncertainties 2) quantifying effects on ST
- UaSA for SBO in a PWR 1000 – (MUSA WP5) **BEPU in SA domain still requires further work concerning multiple aspects**: how to better set FOMs depending on BEPU final aim, how to choose uncertain parameters whose uncertainty should be propagated, how to optimize sensitivity analysis so that it is restricted to linear or monotonous correlation, and many others…

Strål säkerhets myndigheten
Swedish Radiation Safety Authority

KTH Vetenskap och Konst

NPS Kärnkraftsäkerhet

Università di Pisa

KIT Karlsruher Institut für Technologie

SEAKNOT

NUGENIA TA2 Nuclear Generation II&III Alliance

SNETP Sustainable Nuclear Energy Technology Platform

NEA Nuclear Energy Agency

In cooperation with

IAEA International Atomic Energy Agency *Atoms for Peace and Development*

Innovative approaches, methodologies, and ideas

2.4 Severe Accident Scenarios: U&S analysis

- ST UaSA for Loss of Cooling in a SFP with spray activation – (MUSA WP6) UQ helps in **identifying aspects of SA codes that need to be adapted to model SFP scenarios**. Clear influence of aerosol characteristics on he release fraction uncertainty band.
  SA codes generally not validated for spray cooling of FA, mandatory a validation work on TH.
- MELCOR UaSA for Loss of Cooling in a SFP – (MUSA WP6) UaSA for a SFP loss-of-cooling confirming modeling limitations in current SA codes.
  Discussion on FP "weighted" distribution in the different radial rings in MELCOR.
- UaSA using ACE model - The use of surrogate models based on ACE (Alternating Conditional Expectations) explored to foster the UaSA use in SAs. The approach shows some advantages, like make data analysis easier, but exacerbates sensitivity to outliers.
- SIRT for chemical thermodynamics of SAs – A System Identification and Ranking Table presented (TCOFF-2 project). Importance of expert judgment in the process pointed out. Discussion held on how to properly define the relevance of a chemical system.

Strål säkerhets myndigheten Swedish Radiation Safety Authority

KTH Vetenskap och Konst

NPS Kärnkraftsäkerhet

Università di Pisa

KIT Karlsruher Institut für Technologie

SEAKNOT

NUGENIA TA2 Nuclear Generation II&III Alliance

SNETP Sustainable Nuclear Energy Technology Platform

NEA Nuclear Energy Agency

In cooperation with

IAEA International Atomic Energy Agency *Atoms for Peace and Development*

Innovative approaches, methodologies, and ideas

5.1 Severe accident scenarios: Model development and validation

- Material property for calculation of RPV damage – for the interpretation of Fukushima data (RPV lower head rupture for creep), an update of material properties formulation as a function of temperature and **revision of MELCOR linear approach proposed**
- Aerosol retention in a pool - analytical methods and evaluation procedures utilized to determine a **correlation for dependence of retention efficiency on different boundary conditions**
- IVMR 0D model for iPWR – (SASPAM WP4) Python model developed for **0D modelling of IVMR steady-state analysis** for idealized cases in iPWRs

Strål säkerhets myndigheten Swedish Radiation Safety Authority

KTH Vetenskap och konst

NPS Kärnkraftsäkerhet

Università di Pisa

KIT Karlsruher Institut für Technologie

SEAKNOT

NUGENIA TA2 Nuclear Generation II&III Alliance

SNETP Sustainable Nuclear Energy Technology Platform

NEA Nuclear Energy Agency

In cooperation with

IAEA International Atomic Energy Agency *Atoms for Peace and Development*

Innovative approaches, methodologies, and ideas

5.2 Severe accident scenarios: Model development and validation

- PH of water pools using COCOSYS – assessment by **integrating distributions of pH relevant species** from primary circuit & corium, as B, Li, Cs, or created as HNO3 by radiolysis (it contributes to lower pH, becoming a major species influencing long-term pH).
- Oxidation resistance of ATFs using AC^2 – **extension of modelling** for FeCrAl alloy and Cr-coated ZR-alloy, application to QUECH-ATF project (KIT)
- ASTEC validation for SFP dewatering using DENOPI results – Simulations of tests with different heating patterns and power levels. **Different models of subcooled boiling tested, stressing their key role** for an accurate prediction of experimental flow.
- Correlations for modeling of SS oxidation in steam with MELCOR – MELCOR oxidation correlation is from 1966. A **new correlation by fitting Arrhenius equation** to 14 experiments from 4 facilities (can be entered into MELCOR by sensitivity coefficient 1002). In Fukushima calculation, 24% less steel oxidation and 6% less total in-vessel H2 generation than default correlation.

Strål säkerhets myndigheten Swedish Radiation Safety Authority

KTH Vetenskap och Konst

NPS Kärnkraftsäkerhet

Università di Pisa

KIT Karlsruher Institut für Technologie

SEAKNOT

NUGENIA TA2
Nuclear Generation II&III Alliance

SNETP
Sustainable Nuclear Energy Technology Platform

NEA
Nuclear Energy Agency

In cooperation with

IAEA
International Atomic Energy Agency
Atoms for Peace and Development

Highlights of the question time

- **PIRT methodology born in DBA domain: not-tailored to SAs**
- Problems in modelling **SFP scenarios**
- Importance of the determination of **realistic boundary conditions for SA analysis** as FPs weighted distribution in core radial rings, PCV leakages' position or fraction of dissolved species in a SFP
- ….

Strål säkerhets myndigheten
Swedish Radiation Safety Authority

KTH VETENSKAP OCH KONST

NPS Kärnkraftsäkerhet

Università di Pisa

KIT Karlsruher Institut für Technologie

Highlights on SA Scenarios

- Challenges for an **effective implementation of UaSA in the SA domain**: necessity to **consolidate a systematic methodology**
- Necessity to **addressing innovative nuclear technologies**, as ATFs and LR-SMRs BUT don't forget the existing Gen II NPPs (BWR, VVER, KONVOI, French NPPs)
- Increasing **attention towards AI** (surrogate models, machine learning…) as a "support" for existing SA codes
- SA codes need to be **adapted** to model **SFP scenarios** and **validated** (TH vs CFD, htc correlations, FA cooling by spray, …)
- Higher attention needed on **"knowledge" transfer and E&T** aspects, together the preservation of past and existing expertise in SA field (*it is not necessary to reinvent the wheel…*)

SEAKNOT

NUGENIA TA2 Nuclear Generation II&III Alliance

SNETP Sustainable Nuclear Energy Technology Platform

In cooperation with

NEA Nuclear Energy Agency

IAEA International Atomic Energy Agency *Atoms for Peace and Development*

Severe Accident scenarios: Fast Reactors

#	Title and speaker
1	Preliminary Evaluation of Reactivity Insertion during BDBA-LOCA of Super Fast Reactor K. Matsuoka (Waseda University)
2	Development of severe accident simulation code for sodium-cooled fast reactors: SIMMER-V (1) Overview of the SIMMER-V code development H. Tagami (JAEA)
3	Experimentation & simulation of ablated surface by jet impingement for core-catcher safety issue N. Seiler (CEA)

Strål säkerhets myndigheten Swedish Radiation Safety Authority

KTH Vetenskap och Konst

NPS Kärnkraftsäkerhet

Università di Pisa

KIT Karlsruher Institut für Technologie

SEAKNOT

NUGENIA TA2 Nuclear Generation II&III Alliance

SNETP Sustainable Nuclear Energy Technology Platform

NEA Nuclear Energy Agency

In cooperation with

IAEA International Atomic Energy Agency *Atoms for Peace and Development*

Messages, Innovative approaches and methodologies

- **Super Fast Water Cooled reactor concept presented → studies under way on SA**
- **SIMMER-V code development: new fuel pin model (multicavities) and fuel isotope vectror option → relevant for heterogeneous SFRs**
- **SIMMER-V on ICCOCO platform → possible coupling with other codes**
- **HAnSoLO: New experiments on core catcher behavior following jet impingement**
  - **CFD analyses for validation**

Strål säkerhets myndigheten Swedish Radiation Safety Authority

KTH Vetenskap och Konst

NPS Kärnkraftsäkerhet

Università di Pisa

KIT Karlsruher Institut für Technologie

SEAKNOT

NUGENIA TA2
Nuclear Generation II&III Alliance

SNETP
Sustainable Nuclear Energy Technology Platform

NEA
Nuclear Energy Agency

In cooperation with

IAEA
International Atomic Energy Agency
Atoms for Peace and Development

Key Highlights

- **SIMMER-V as mechanistic code for SA analyses in heterogeneous SFR cores**

- **Safety of the core catcher: new experiments on performed**

Strål säkerhets myndigheten
Swedish Radiation Safety Authority

KTH Vetenskap och Konst

NPS Kärnkraftsäkerhet

Università di Pisa

KIT Karlsruher Institut für Technologie

SEAKNOT

NUGENIA TA2
Nuclear Generation II&III Alliance

SNETP
Sustainable Nuclear Energy Technology Platform

NEA
Nuclear Energy Agency

In cooperation with

IAEA
International Atomic Energy Agency
Atoms for Peace and Development

Severe Accident Scenarios: Accident Tolerant Fuels

#	Title and speaker
1	Overview of KIT activities on ATF cladding materials M. Steinbrück (KIT)
2	Application of AC²/ATHLET-CD and ASTEC for ATF Experiments in the Frame of OECD QUENCH-ATF and IAEA CRP ATF-TS T. Hollands (GRS)
3	The CODEX-ATF experiment R. Farkas (EK-CER)

Strålsäkerhetsmyndigheten
Swedish Radiation Safety Authority

KTH Vetenskap och Konst

NPS Kärnkraftsäkerhet

Università di Pisa

KIT Karlsruher Institut für Technologie

SEAKNOT

NUGENIA TA2 Nuclear Generation II&III Alliance

SNETP Sustainable Nuclear Energy Technology Platform

NEA Nuclear Energy Agency

In cooperation with

IAEA International Atomic Energy Agency *Atoms for Peace and Development*

Messages, Innovative approaches and methodologies

- **New experimental integral campaigns on ATF cladding at QUENCH and CODEX facilities and (FeCrAl, Cr-coated, SiC based composite)**
- **OECD/NEA and IAEA ATF-TS projects running**
- **IL TROVATORE and SCORPION EURATOM projects**
- **AC2 and ASTEC integral codes applied to key ATF experiments in such framework → resulst show a general good agreement with exp. data**

Strål säkerhets myndigheten Swedish Radiation Safety Authority

KTH Vetenskap och Konst

NPS Kärnkraftsäkerhet

Università di Pisa

KIT Karlsruher Institut für Technologie

SEAKNOT

NUGENIA TA2
Nuclear Generation II&III Alliance

SNETP
Sustainable Nuclear Energy Technology Platform

In cooperation with

NEA
Nuclear Energy Agency

IAEA
International Atomic Energy Agency
Atoms for Peace and Development

Key Highlights

- **ATF experiments (also in DBA and BDBA) going on**

- **Integral codes look able to catch the main phenomena**

Strål säkerhets myndigheten
Swedish Radiation Safety Authority

KTH VETENSKAP OCH KONST

NPS Kärnkraftsäkerhet

Università di Pisa

KIT Karlsruher Institut für Technologie

SEAKNOT

NUGENIA TA2
Nuclear Generation II&III Alliance

SNETP
Sustainable Nuclear Energy Technology Platform

NEA
Nuclear Energy Agency

In cooperation with

IAEA
International Atomic Energy Agency
Atoms for Peace and Development

ERMSAR-2024 (SEAKNOT/WP4.2)
An Overview in numbers

F. Gabrielli, L. E. Herranz, S. Paci

Funded by
the European Union

Strål säkerhets myndigheten
Swedish Radiation Safety Authority

KTH VETENSKAP OCH KONST

NPS
Kärnkraftsäkerhet

Università di Pisa

KIT
Karlsruher Institut für Technologie

SEAKNOT

NUGENIA TA2
Nuclear Generation II&III Alliance

SNETP
Sustainable Nuclear Energy Technology Platform

NEA
Nuclear Energy Agency

In cooperation with

IAEA
International Atomic Energy Agency
Atoms for Peace and Development

Many thanks to KTH

Sean Roshan (KTH, Sweden)
Sevostian Bechta (KTH, Sweden)
Patrick Isaksson (SSM, Sweden)
Nils Sandberg (SSM, Sweden)
Marta Marko-Tisch (KTH, Sweden)

and all the team





Funded by the European Union

Strål säkerhets myndigheten
Swedish Radiation Safety Authority

KTH VETENSKAP OCH KONST

NPS Kärnkraftsäkerhet

UNIVERSITÀ DI PISA

KIT Karlsruher Institut für Technologie

SEAKNOT

NUGENIA TA2 Nuclear Generation II&III Alliance

SNETP Sustainable Nuclear Energy Technology Platform

NEA Nuclear Energy Agency

In cooperation with

IAEA International Atomic Energy Agency
Atoms for Peace and Development

Special thanks to L. E. Herranz and S. Paci

The Technical Scientific Committee

L. E. Herranz (CIEMAT, Spain)
S. Paci (University of Pisa, Italy)
F. Gabrielli (KIT, Germany)
P. Piluso (CEA, France)
S. Strola (LGI, France)
Ivo Kljenak (IJS, Slovenia)
S. Gupta (Becker Technologies, Germany)
F. Rocchi (ENEA, Italy)

A. Bentaib (IRSN, France)
T. Hollands (GRS, Germany)
P. Groudev (INRNE, Bulgaria)
M. Hupp (Framatome GmbH, Germany)
A. Miassoedov (IAEA, Austria)
S. Brumm (JRC, Netherlands)
M. Adorni (NEA, France)
D. Jacquemain (NEA, France)
V. H. Sanchez Espinoza (KIT, Germany)
W. Tromm (KIT, Germany)

The Chairpersons

T. Lind (PSI, Switzerland)
L. Carénini (IRSN, France)
O. Coindreau (IRSN, France)
M. Angelucci (University of Pisa, Italy)

A. Stakhanova (KIT, Germany)
S. Kelm (FZJ, Germany)
M. E. Cazado (KIT, Germany)

PS Swedish Radiation Safety Authority

Università di Pisa

KIT Karlsruher Institut für Technologie

SEAKNOT

NUGENIA TA2 Nuclear Generation II&III Alliance

SNETP Sustainable Nuclear Energy Technology Platform

NEA Nuclear Energy Agency

In cooperation with

IAEA International Atomic Energy Agency
Atoms for Peace and Development

Why joining ERMSAR?

A unique nuclear conference worldwide fully focused on severe accidents

- In-vessel corium and debris coolability
- Ex-vessel corium interactions and coolability
- Containment behavior including H2 explosion risk
- Source term issues
- Analysis, management, and consequences of Severe Accidents for Gen I/III reactors
- Severe Accidents in innovative reactor concepts
- Other applications (fusion reactors, interim SNF storage, ATF, etc.)

Continuous focus on the latest progress of international knowledge on severe accidents in NPPs

SEAKNOT

NUGENIA TA2 Nuclear Generation II&III Alliance

SNETP Sustainable Nuclear Energy Technology Platform

NEA Nuclear Energy Agency

In cooperation with

IAEA International Atomic Energy Agency
Atoms for Peace and Development

Why joining ERMSAR?

"Before I came here I was confused about this subject. Having listened to your lecture I am still confused. But on a higher level." (Enrico Fermi)

Preserving, Promoting, and Improving the knowledge by promoting the exchange among the participants

- Cheaper registration fees compared with other nuclear conferences
- **25' per lectures!**
- **Round tables on key topics**
- **Plenary sessions**

Funded by the European Union

Strål säkerhets myndigheten
Swedish Radiation Safety Authority

KTH Vetenskap och Konst

NPS Kärnkraftsäkerhet

Università di Pisa

KIT Karlsruher Institut für Technologie

SEAKNOT

NUGENIA TA2
Nuclear Generation II&III Alliance

SNETP
Sustainable Nuclear Energy Technology Platform

NEA
Nuclear Energy Agency

In cooperation with

IAEA
International Atomic Energy Agency
Atoms for Peace and Development

ERMSAR in Numbers

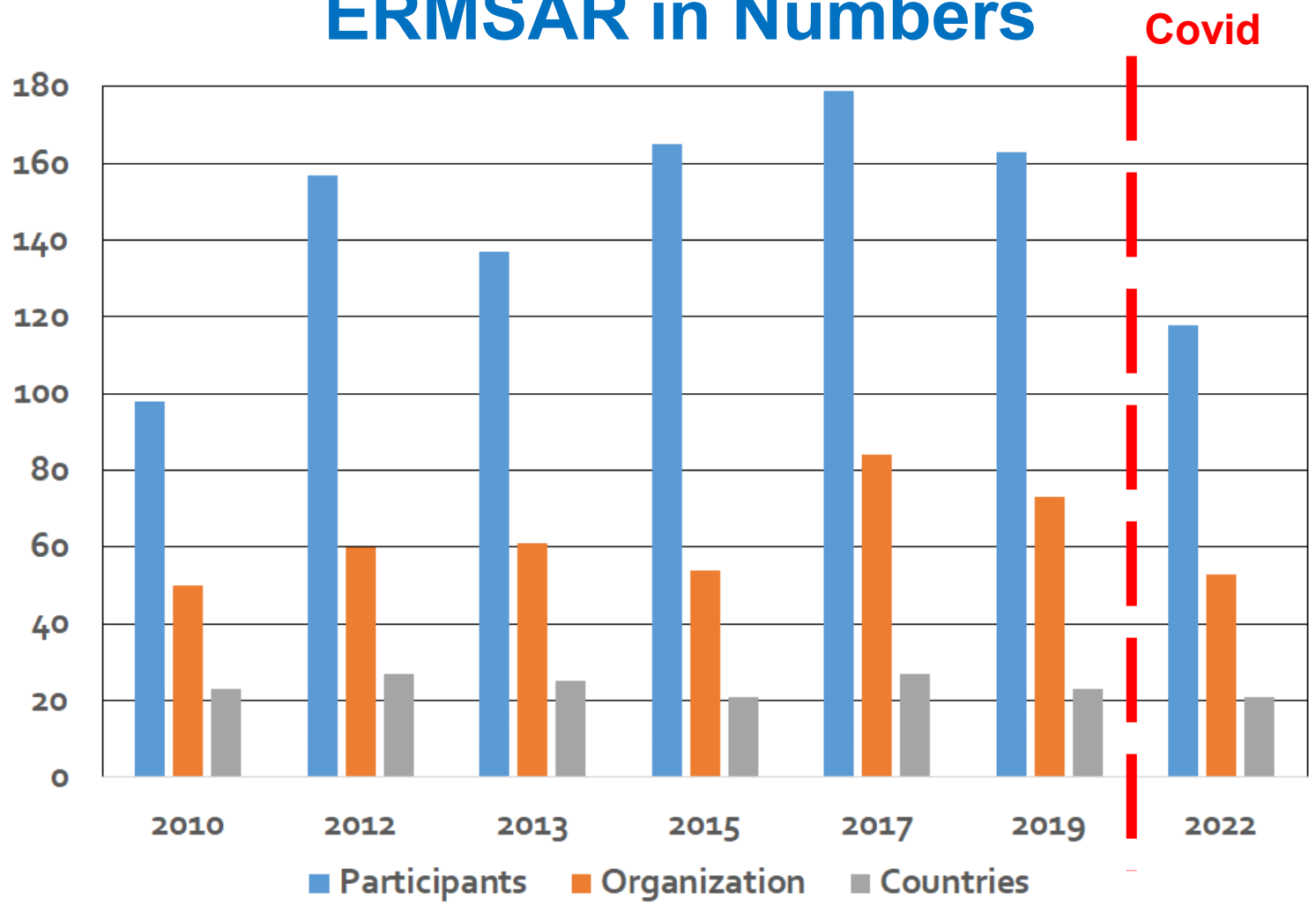

Funded by the European Union

myndigheten
Swedish Radiation Safety Authority

NPS Kärnkraftsäkerhet

Karlsruher Institut für Technologie

SEAKNOT

NUGENIA TA2
Nuclear Generation II&III Alliance

SNETP
Sustainable Nuclear Energy Technology Platform

NEA
Nuclear Energy Agency

In cooperation with

IAEA
International Atomic Energy Agency
Atoms for Peace and Development

ERMSAR2024 in Numbers

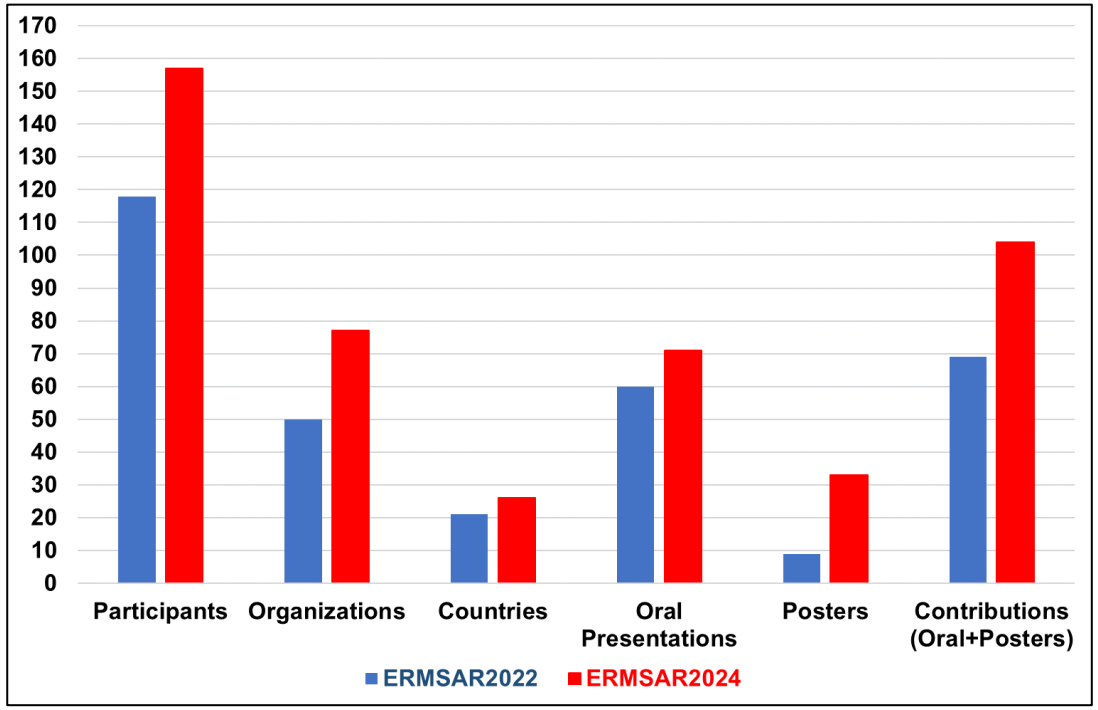

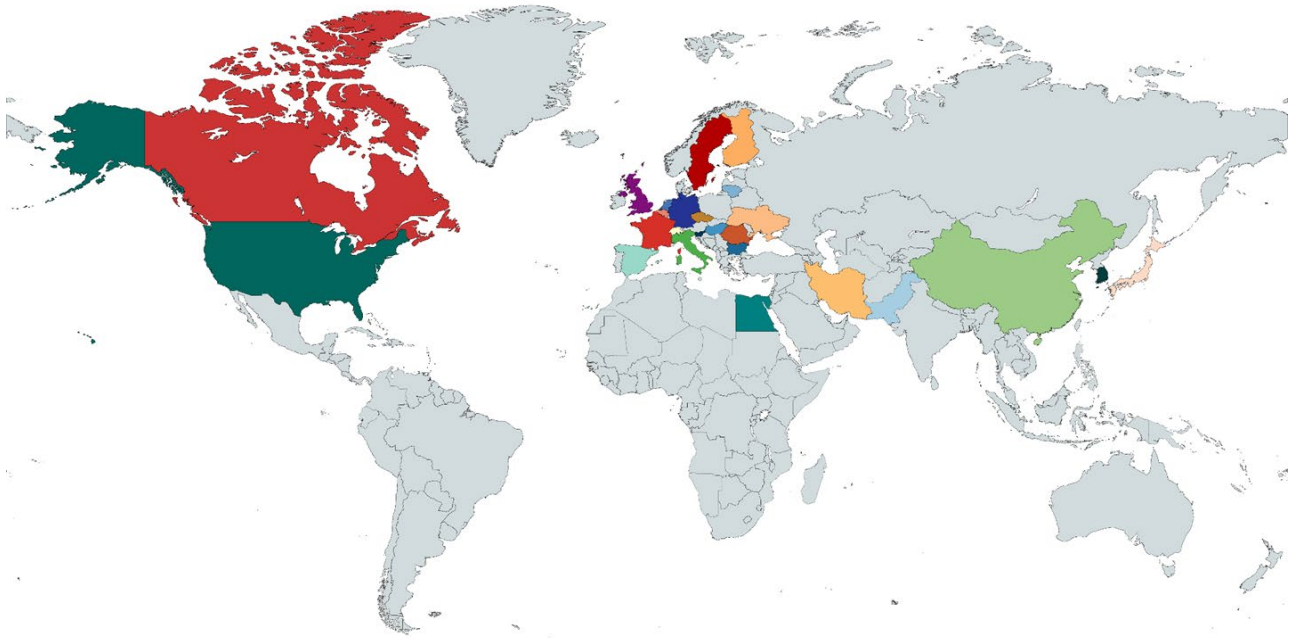

157 participants (21 students) from 21 countries
Contributions from 77 institutions from 26 countries

Funded by the European Union

Strål säkerhets myndigheten
Swedish Radiation Safety Authority

KTH Vetenskap och Konst

NPS Kärnkraftsäkerhet

Università di Pisa

KIT Karlsruher Institut für Technologie

SEAKNOT

NUGENIA TA2 Severe Accidents
Nuclear Generation II&III Alliance

SNETP
Sustainable Nuclear Energy Technology Platform

NEA
Nuclear Energy Agency

In cooperation with

IAEA
International Atomic Energy Agency
Atoms for Peace and Development

ERMSAR2024 in Numbers

Topic	Oral Presentations	Posters
In-vessel corium and debris coolability	10	3
Ex-vessel corium interactions and coolability	8	4
Containment behavior incl. Explosion risk	10	9
Source term	11	5
Analysis, Management, and Consequences of Severe Accidents for Gen I-III reactors	16	8
Severe accidents in innovative reactors such as Gen IV and SMRs	12	2
Other applications (fusion reactors, interim SNF storage, Accident Tolerant Fuels (ATFs), etc.	6	2
	73	33

Funded by the European Union

Strål säkerhets myndigheten
Swedish Radiation Safety Authority

KTH Vetenskap och Konst

NPS Kärnkraftsäkerhet

Università di Pisa

KIT Karlsruher Institut für Technologie

In cooperation with

Next steps: Dissemination of ERMSAR2024

Thanks to OECD/NEA and IAEA for co-organization and advertisement

1. **Book of the Proceedings**
   - will be edited and published in June as a book in the KITOpen library repository (with doi number)
   - will be uploaded on Zenodo
   - **Deadline for the final paper submission May 31st!**
2. Preparation of a summary report for CSNI
3. Selection of the papers for the Virtual Special Issue (VSI) in Annals of Nuclear Energy

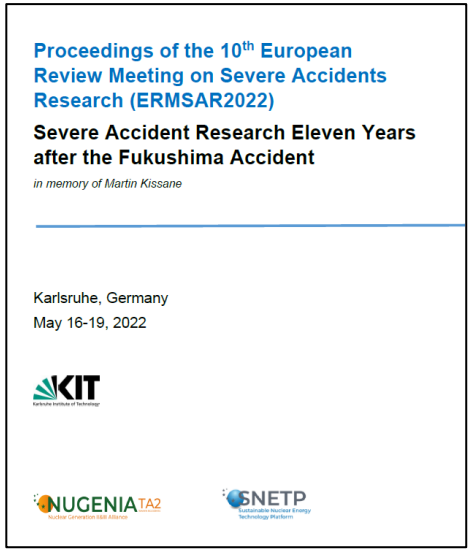

Funded by the European Union

SEAKNOT

NUGENIA TA2 Nuclear Generation II&III Alliance

SNETP Sustainable Nuclear Energy Technology Platform

NEA Nuclear Energy Agency

In cooperation with

IAEA International Atomic Energy Agency *Atoms for Peace and Development*

Lessons learned (from the technical scientific organization)

Respect the deadlines (on both sides ☺)



- **Speed-up the assessment and release of the technical program**
- **Facilitating the life of the authors (travel arrangements)**
- **Facilitate the life of the organizers (how many participants?)**

Changing the title of the papers on the way to be avoided

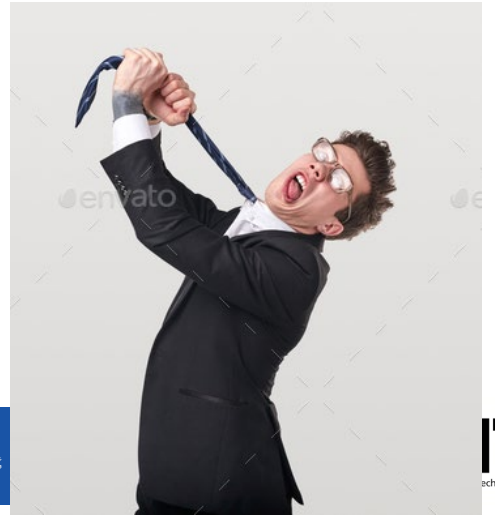

Funded by the European Union

Strål säkerhets myndigheten Swedish Radiation Safety Authority

KTH VETENSKAP OCH KONST

SEAKNOT

NUGENIA TA2
Nuclear Generation II&III Alliance

SNETP
Sustainable Nuclear Energy Technology Platform

NEA
Nuclear Energy Agency

In cooperation with

IAEA
International Atomic Energy Agency
Atoms for Peace and Development

Thanks to you all





'Knowledge is the antidote to fear.' (cit. Ralph Waldo Emerson)

…see you soon in 2026 (how you can resist to join?)

Funded by
the European Union

Strål säkerhets myndigheten
Swedish Radiation Safety Authority

KTH VETENSKAP OCH KONST

NPS Kärnkraftsäkerhet

Università di Pisa

KIT Karlsruher Institut für Technologie

GOBIERNO DE ESPAÑA
MINISTERIO DE CIENCIA, INNOVACIÓN Y UNIVERSIDADES

Ciemat
Centro de Investigaciones Energéticas, Medioambientales y Tecnológicas

Welcome

ERMSAR 2026



ERMSAR 2026 Venue



Madrid

Hosting Organization

https://www.ciemat.es/

GOBIERNO DE ESPAÑA
MINISTERIO DE CIENCIA, INNOVACIÓN Y UNIVERSIDADES

Ciemat
Centro de Investigaciones Energéticas, Medioambientales y Tecnológicas

CSN

JEN 1951

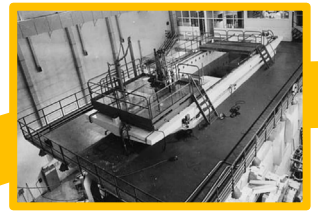

1980

CIEMAT 1986







Nuclear Safety Program



2023

Department of Nuclear Fission

- L & VL Wastes
- HLW & spent fuel
- Radionuclide migration
- Nuclear systems
- Nuclear safety research

2000

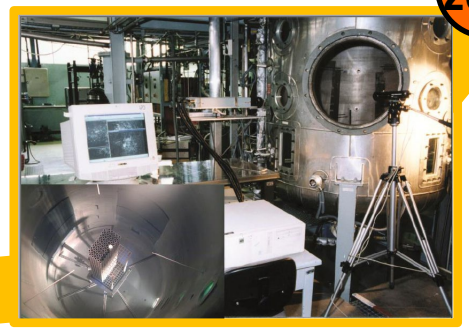



Unit of Nuclear Safety Research

Unit of Nuclear Safety Research

MATMEC (CSN)

ATF-TS (IAEA)

OCATS (ENRESA)

NUCLEAR

OperaHPC (UE)

EJP-EURAD (UE)

APIAS (CSN)

MUSA (UE)

SEAKNOT (UE)

FACE (OECD)

AMHYCO (UE)

THEMIS (OECD)

SAFETY

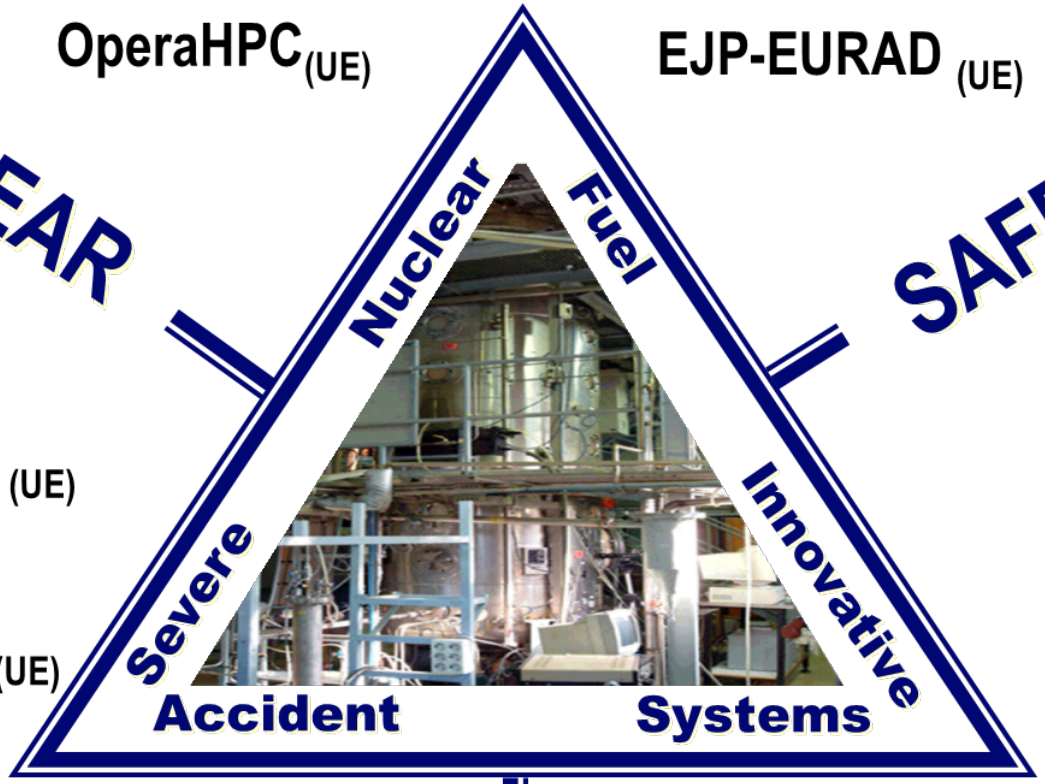

SASPAM-SA (UE)

ASSAS (UE)

R2CA (UE)

ESFR-SMART (UE)

GOBIERNO DE ESPAÑA
MINISTERIO DE CIENCIA, INNOVACIÓN Y UNIVERSIDADES
Ciemat
Centro de Investigaciones Energéticas, Medioambientales y Tecnológicas

CIEMAT Organization Team



Luis E. Herranz
Coordinator



Carlos Aguado
Webpage



Pau Aragon
Communication&Dissemination

We're on it!

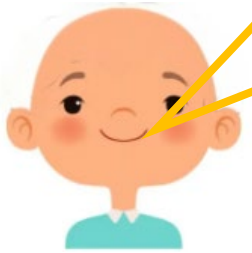

Joan Fontanet
Technical assistance



Monica Garcia
Logistics

Madrid is waiting for … you!

18-22 May, 2026





Welcome to Madrid, a lively, welcoming and cosmopolitan city, where no one feels anything other than at home. Its abundant artistic and natural heritage, its state-of-the-art transport network, the quality of its accommodation, its excellent gastronomy and the passion with which the people of Madrid enjoy both the day and the night make the capital of Spain one of the most attractive cities in the world.

https://www.esmadrid.com/en



ERMSAR 2026!!

(May 18-22)